Ibn Al-Haitham International Conference for Pure and Applied Sciences, University of Baghdad, Baghdad, Iraq (IHICPAS)

Ibn Al-Haitham International Conference for Pure and Applied Sciences, University of Baghdad, Baghdad, Iraq (IHICPAS).

Ahmed J. Obaid[1], Firas Abdulhameed Abdullatif [2], Moneer Hameed Tolephih[3], Hassan Ahmad Hasan [4], Salah Albermany[5], Hiba A. Ahmed[6]

[1, 5] Faculty of Computer Science and Mathematics, University of Kufa, Najaf, Iraq.
[2,3,4] Advanced Materials Science and Energy, CSIR Institute, RCED, India.
[6] Faculty of Science, University of Baghdad, Iraq.

E-Mails: [1]ahmedj.aljanaby@uokufa.edu.iq,

IHICPAS Conference Proceeding volume contain the novel contributions that were reviewed and presented through the Ibn Al-Haitham International Conference for Pure and Applied Sciences (IHICPAS) will be held in College of Education for Pure Science (Ibn al-Haitham), University of Baghdad on 20 and 21 December, 2020., where the conference covers 6 tracks which includes (Track1 Chemistry, Track 2: Mathematics, Track3: Computer Science, Track 4: Biology Sciences, Track 5: Physics, and Track 6: Remote Sensing and GIS). IHICPAS aims to gathering together all the new trends, projects, technologies, and recent research works in many fields in pure and Applied Sciences. The received papers which passed the double-blind reviews which successfully passed the reviewers comments and editorial board decisions comes from various authors around the world, where the authors are either working in academics centers, universities, research institutes, corporations, industries, and other agencies or postgraduate students where the presented works refers to their novelty in their research works.

IHICPAS Conference got very significant interesting from authors that comes from several countries like: UK, India, French, Morocco, Turkey, Nepal, Philippines, Indonesia, Australia, Egypt, Lebanon, Algeria, Iran, Pakistan, Malaysia, and Many other Countries where the authors are successfully presented their works and attend the sessions who managed by our scientific and organizing committee Members, and answered all the questions and dotes that directed by session chairs and attendances. We successfully held this conference within 2 days (20 and 21 December 2020), where in the first day we successfully listen to the keynote speakers' presentations then the session started from 10:00 AM based on Iraq Standard Time till 10:00PM. We would like to express our thanks and appreciation to all our session chairs for their hard work and attend our (12) sessions through two days and more than 10 hours per day to deliver the presented works in successful manner.

IHICPAS conference hosted 6 plenary sessions per day, where in the first day (20th December 2020) the Inauguration program started from (9:00 AM) till (10:00 AM). Then Sessions Started directly by dividing the authors into their certain session who managed by 4 Chairs (2 From Scientific Committee board, 1 from Organizing committee board and 1 from Conference Editors chairs board). The manuscripts which have presented and published in the IOP Conference Series: Journal of Physics under the peer-reviewed process. We love to express our gratitude for all of the participants, keynote speakers, organizing committee members, Scientific Committee members, and other Guest Chairs and Patrons for their supports and achievement, and we extend our thankful to all our reviewers (230+) reviewers, for their times and valuable notes. We extend our thanks to our international committee members for gaudiness of their participators and promote this conference in their regions, and successfully present very attractive presents. Also, we thank our authors for their effective contribution in our conference and participating with us in this conference proceeding. We also, acknowledge SICC Center at University of Kufa, Dijla Co. Pvt. Ltd., for their hospitality and sponsoring the conference. Furthermore, would like to thank SICC Center for supporting us to held this conference in successful manner.

Venue of the Conference

The conference has been organized Physically and virtually in College of Education for Pure Science (Ibn al-Haitham), University of Baghdad, in 20-21 December 2020. IHICPAS organizers aims through their scientific departments, and preparing a generation of students armed with knowledge and looking forward to building their country according to the new scientific developments. The university endeavors towards making use of them in an appropriate cultural means as well as building good and new scientific establishments for the sake of developing the present through scientific research.

The Reason(s) why IHICPAS Conference Held virtually:

Due Covid-19 Pandemic Situation in many countries around the world and the incredible increases cases through this Pandemic is very dangerous, and per day the number of cases in our peoples that infected by Covid-19 in the world and in Iraq, and due to the World Health Organization and Ministry of Health Recommendations, the conference organizers decided to conduct and held this conference Virtually to keep the life of participants and also due the challenges of lock down. Conduct IHICPAS virtually bring huge number of participants that non expected due many peoples are unable to attend conference physically, they able to attend our online Conference due to the friendly uses of Virtual Software without spending money for flight tickets or other matters to attend that type of conferences. However, we feel those peoples by attend our conference achieved our goal by inviting very attractive authors and participants who are interest to attending this conference, they will not able to attend it if it's held in non-virtually, However, The organizing committee have achieved these tasks and all sessions organized and managed successfully through Zoom Conference Meeting, where the team attend physically to use the University of Baghdad, College of Education for Pure Science (Ibn al-Haitham), infrastructure to achieve this conference Successfully.

Technology, Technical Difficulties and Drawbacks of Conference Virtually.

IHICPAS Conference Consider the ZOOM Meeting Software as the main software to conduct this conference, as the Main Software for delivering the Session discussions and Meeting information to all participants in Iraq and Other countries. The main advantages of this Technology is to reduce the time and space when someone would like to attend any scientific event and also broken the limitations for the peoples and authors who would like to attend this event from far away countries, in which the provide a facility to provide a platform that able to manage and control large number of participants is the main challenge of choosing the best software, we find Zoom meeting is the best software that fulfill our

requirements and provide amazing virtual platform to manage our authors and participants through our conference sessions.

The main technical difficulty in virtual software is the internet connection, due to covid-19 band, many peoples sitting at home and many jobs transformed from physical to virtual mode, However, internet connection and ISP infrastructure may affected due the large number of traffic devices that join to the network recently and may the ISP companies do not have good infrastructure to provide stable connection through the meeting or sessions. Hence, we conducted our sessions in the early morning time where the Babylon university, SICC, and Dijla Jewel Pvt. Ltd. Infrastructure used to achieve this task successfully. With Blessing of God, we held this conference successfully without any issue and we are looking to conduct this conference in future in physical manner after the world remedy from Covid-19 pandemic.

The Main Technical Difficulties of Virtual Meetings can be summarizing as follow:

Virtual Techniques and software that used to achieve these types of events and conferences in virtual mode, many software can be used, which can be offered by many companies either in free or paid own services. The main challenge to use online technique is to find the good software that able to manage large number of attendees with varied number of traffic data, we feel that the internet connections is the main source for any challenge in any online event. However, if the internet connection became slow, where many users are forced to exit and rejoin many times through the session. So many software's can used to achieve high quality meeting, need some certain limitations, like number of users, to keep the bandwidth little good, however not all interested peoples can attend meeting, difficulty of join and attend the meeting rooms, view and share the content, etc.

Drawbacks of virtual conference, we do not feel the virtual conference have much drawbacks than physical conferences, in which many peoples can avoid many fees payment for travels and hosting, registration fees, as well as flight tickets in which virtual conferences gives free offer for all the above issues. Another thing is, some famous figures and professors can easily join and attend without consider their fees in which they can attend and speak for hours when they sitting at home.

The main drawback we feel that if some authors would like to visit the conference venue for direct discussion and made good collaboration, so virtual meeting can also achieve this task easily, at the current time where all world suffer from Covid-19 pandemic.

Conference Chairs

- Prof. Dr. Firas Abdulhameed Abdullatif.
- Prof. Dr. Moneer Hameed Tolephih.

Conference Secretariat Chairs

- Prof. Dr. Salah Albermany
- Dr. Shubham Sharma
- A. Prof. Dr. **Ahmed J. Obaid.**

International Program Chairs

- Prof. Dr. Sandeep Kautish
- Prof. Dr Pradeep Kumar
- Prof. Dr. Macario G. Gayeta
- Prof. Dr. Tanusree Chatterjee
- Asst. Prof. Dr. Kamran Yeganegi

Scientific Committee

- Prof. Dr. Hasan Ahmed Hasan.
- Prof. Dr. Ghassan H. Abdulmajeed.
- Prof. Dr. Abdulkareem M. A. Alsammarraie.
- Prof. Dr.Nahla A.Al-Bakri.
- Prof. Dr. Alia A. Shehab.
- Prof. Dr. Mohamad J. Al-Jeboori.
- Prof. Dr. Ihsan Arfan Hussein.
- Prof. Dr. Ibrahim Mahdi Azooz Al-Salman.
- Prof. Dr. Luma N. Mohammed Tawfiq.
- Prof. Dr. Kareem Ali Jasim
- Prof. Dr. Dhafir T.A.Al-Heetimi
- Prof. Dr. Alaa A. Abdullatif
- Assist. Prof. Dr. Majeed Ahmed Weli
- Assist. Prof. Dr. Raied Mustafa Shakir
- Assist. Prof. Dr. Hanady Salim Abd Al-Sahib
- Assist. Prof. Dr. Wathiq Najah Abdullah
- Assist. Prof. Alaa Badr Hasan
- Assist.Prof. Dr. Rasha Naser Majeed
- Assist. Prof. Dr. Hussein Lefta Hussein
- Lect. Dr. Saba Naser Majeed

Organizing Committee

- Asst. Prof. Dr. Mohammed Mahdi Jawad
- Prof. Dr. Ahmed Waheed Nasir
- Prof. Dr. Tagreed Muslim Marush
- Prof. Dr. Bushra Hashim Hussein
- Asst. Prof Dr. Estabraq A. Mahmoud
- Asst. Prof. Dr. Salim Abdullah salman
- Asst.Prof.Dr. Ismaeel Yaseen Majeed
- Asst. Prof. Dr. Muazaz Azeez Hasan
- Asst. Prof. Dr. Auday Hattem Shaban
- Asst. Prof. Dr. Ahmed Mohammed Abbas
- Lec.Dr. Ali Adnan Nemah
- Lec.Dr. Sameer Sami Al-Obaidi
- Dr. Ahmed J. Obaid
- Lec.Dr. Ali Yahya Gheni
- Lec.Dr. Adel Rashed Abd Ali
- Lec.Dr. Mohammed Ali Ahmed
- Asst.Prof. Faisal Shallal Abbas
- Lec. Saad Ali Ahmed

- Asst. Lec. Harith Qasim Mahdi

Invited Speakers

- **Prof. Richard Winpenny,** Professor of Inorganic Chemistry, Materials Chemistry / Department of Chemistry Photon Science Institute / FSE Research Institutes Molecular Magnets Group.
- **Prof. Dr.Jure Ravnik**, Faculty of Mechanical, Slovenia Engineering, University of Maribor, Maribor, Slovenia.
- **Prof. Divya Maitreyi Chari,** Professor of Neural Tissue Engineering, University of Keele School of Medicine.
- **Prof. Dr. Sherein Salah el din Mohamed Ghaleb,** professor of forensic medicine and clinical toxicology, Cairo university, Egypt.
- **Ass.Prof. Ahmed saeed Alabed**, Ahmed Bin Mohammed Military college.

Organizing Institutions

- Ministry of Higher Education and Scientific Research
- University of Baghdad
- College of Education for Pure Science (Ibn al-Haitham).

Special Thanks to Conference Partners:

- **DIJLAH GOLDON JEWEL Company, Iraq, for their Supports and Sponsorship.**
- **SICC Center for Technical Supports.**

Conference Flyers and Posters:


ابن الهيثم
قاعة المرحوم الأستاذ الدكتور
فهد علي حسين الجبوري
رئيس
الجلسة

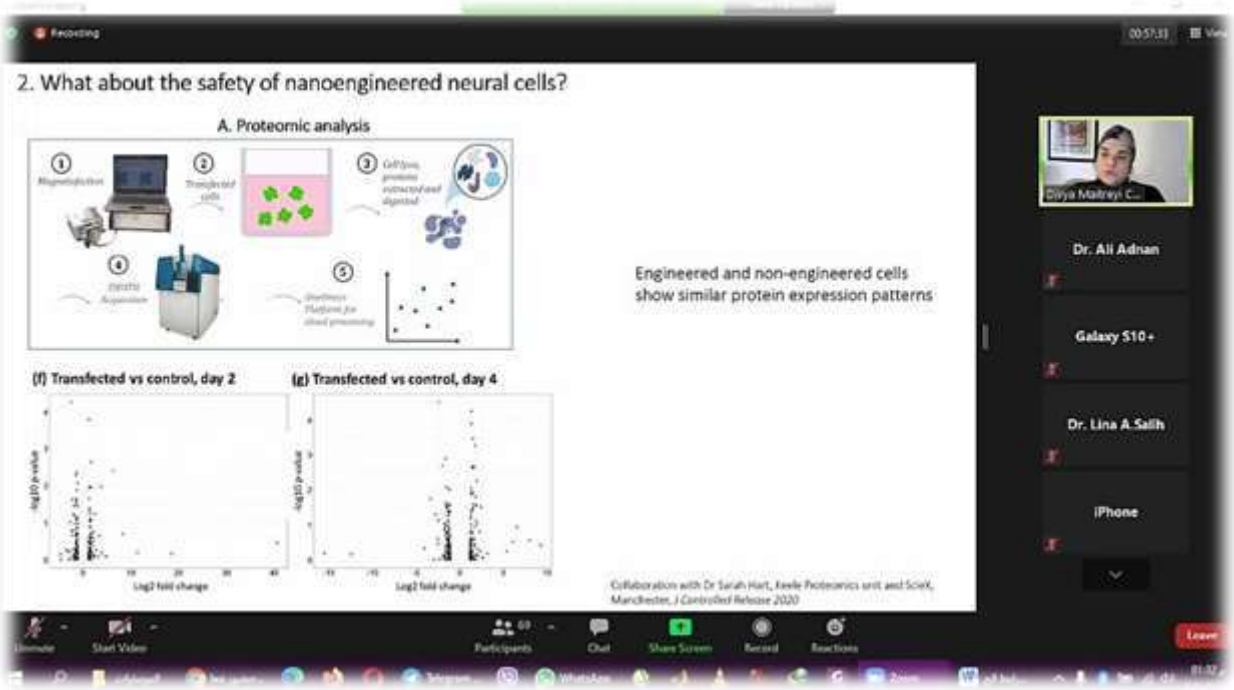
2. What about the safety of nanoengineered neural cells?
A. Proteomic analysis
Engineered and non-engineered cells show similar protein expression patterns
(f) Transfected vs control, day 2
(g) Transfected vs control, day 4
Log2 fold change
Collaboration with Dr Sarah Hart, Keele Proteomics unit and Sciet, Manchester, J Controlled Release 2020
Dr. Ali Adnan
Galaxy S10+
Dr. Lina A.Salih
iPhone


Dr. Ali Adnan
Dr. Lina A.Salih
Dr.Ahmed Moha...
proff.dr.satar ab...
Suhasahib
Sawsan Sorchee
Dr. Nahla Al-Bakri
Huda Ahmed H...
Galaxy A70
Esraa ahmed
Amel Ghanim
Proof.Dr.Bushra...
Farkad Hawas...
kareem
Shatha Moham...
Jacqueline Tickle
Tamadher Arif
Pro. Dr. Nadia H...
Baraa jafaar
Dr. Rawaa Salim...
Drshaimaa's Gal...
Abbas (Galaxy...
Dr.Maha Abduln...
Dr. Zahraa Huss...
Aisha Sulaiman...
Taqwa
Dr.shaimaa abe...
Dr.waheeda ras...
Dr .Huda Ali H...
Dr. Hanan Jame...
Wasan Abdulam...
Saba Naser
Baghdad1
dr.Zahraa Asim...
Hadeel Hadi Ja...
Galaxy A70
Noor Idan Jarad
atiaf ghanim

With our pleasure to attend our next conferences in Future

Dr. Ahmed J. Obaid, Conference Publication Chair

Peer review declaration

Peer review declaration

All papers published in this volume of Journal of Physics: Conference Series have been peer reviewed through processes administered by the Editors. Reviews were conducted by expert referees to the professional and scientific standards expected of a proceedings journal published by IOP Publishing.

- **Type of peer review: Single-blind / Double-blind / Triple-blind / Open / Other (please describe)**
  ICMAICT Conference follow Double-Blind Review where all received articles are checked for similarity through the official account of Turnitin All the Articles passed the similarity given to random authors for evaluation and given us their reports in certain forms, according to double review decision and Editors decision the paper either accepted, revised or rejected.

- **Conference submission management system:**
  At the beginning of Conference CFP has been received through Easy chair, then we are considering our own design system where the paper can be submitted, and tracked through this system, all papers has its own ID, for evaluation progress later.

- **Number of submissions received:**
  At the Beginning we received more than 525 submissions from all authors that comes from more than 8 countries, we consider only 290 papers for further progress, the conference organizers, scientific committee, guest Editors consider only the suitable submission (289) for further process.

- **Number of submissions sent for review:**
  Total Number sent for reviews was 420 and based on scientific committee decision and guest editor decision and alternative reviewers.

- **Number of submissions accepted:**
  Out of 525, papers we select 420 papers as initial Accepted Articles, we processed only 290 Articles due to the following reasons:
    - Some Corresponding authors do not complete the revision in well.
    - Some Papers do not complete the Copyright and Payments.
    - Some papers either published somewhere.
    - Some papers rejected based on editor's decision.

- **Acceptance Rate (Number of Submissions Accepted / Number of Submissions Received X 100):**

  Total Number of Received Papers = 525.

  Total Number of Accepted Papers = 290

Acceptance Rate = $\frac{Number\ of\ Submission\ Accepted}{Number\ of\ Submission\ Received} \times \% = \frac{290}{525}$ **= 55%**

- **Average number of reviews per paper:** 2 Reviewers for Each Paper
- **Total number of reviewers involved:** 188 Reviewers
- **Any additional info on review process:**
  - Each paper Assigned to 2 reviewers once passed the technical check.
  - Once Review Reports received the decision of Guest Editor will be as 3rd reviewer on each certain paper.
- **Contact person for queries:**

Main Guest Editors:

- **A. Prof. Dr. Ahmed J. Obaid, Bsc., M.Tech, PhD**
  Faculty of Computer Science and Mathematics, University of Kufa, Iraq
  ahmedj.aljanaby@uokufa.edu.iq
  Mobile (personal): (+964) 7802686683

- **Firas Ahmed Abdullatif,**
  Dean of College of Education for Pure Science (Ibn al-Haitham), Baghdad,
  dean@ihcoedu.uobaghdad.edu.iq

  Prof. Dr. Hassan Ahmad Hasan
  Head of Scientific Committee, Professor at Ibn alHaitham College, Baghdad,
  sci.assist.dean@ihcoedu.uobaghdad.edu.iq

- **Prof Dr. Salah Albermany,**
  Faculty of Computer Science and Mathematics, University of Kufa, Iraq
  salah.albermany@uokufa.edu.iq

- **Dr. Shubham Sharma,**
  Advanced Materials Science and Energy,
  CSIR-Central Leather Research Institute, RCED.
  shubhamsharmacsirclri@gmail.com

Table of contents

Volume 1879

2021

Previous issue Next issue

Ibn Al-Haitham International Conference for Pure and Applied Sciences (IHICPS) 9-10 December 2020, Baghdad, Iraq

Accepted papers received: 30 March 2021
Published online: 31 May 2021

Close all abstracts

Papers

This work was conducted to study the protective role of Moringa oliefera seeds extract (MSE) against the toxic effect of commercial lead nanoparticles (CPbNP) in rats. Twenty eight albino male rats were divided into four groups (seven animals in each one) as follow: (A) control group, (B) 160mg/kg body weight per day (b. wt./d.) of M. oliefera (MSE)seed extract, (C): 5mg CPbNP/kg b. wt./d. and (D): MSE + CPbNP. The experimental period was 45 days. Blood was drawn for protein and enzyme estimation at the end of the period of exposure. The rats were dissected and the liver, kidney, spleen and muscle were isolated for Pb estimation. Results showed that the levels of bioaccumulated lead, serum alanine aminotransferase, aspartate aminotransferase, alkaline phosphatase, malondialdehyde were significantly increased in exposed animals to CPbNP ($P < 0.05$). In contrast, there was a significant reduction of total proteins, albumin, glutathione, superoxide dismutase enzyme and catalase enzyme activities ($P <$

0. 05) in comparison to control. But the administration of the CPbNP with MSE, all the above biochemical changes were improved significantly. It is concluded that CPbNP has a significant toxic effect on rats, and that seed extract of M. Oleifera can reduce it.

https://doi.org/10.1088/1742-6596/1879/2/022001

OPEN ACCESS

022002

Biological control on plant pathogenic fungus, *Pythium* by using some plant extracts *in vivo* and *in vitro*

Rajaa Fadhil Hamdi, Farkad Hawas Musa and Sameer Sarhan Alrawi

The inhibitory activity of 5 plant extracts, *Allium sativum, Opuntia ficus-indica, Malva parviflora, Mentha spicata* and *Plantago lanceolata* with concentration 50 % and 100 % were assessed against the mycelial growth of *Pythium* fungus *in vivo* and *in vitro*. Results showed that all the concentrations of plant extracts give significant inhibition in the mycelial growth of *Pythium* fungus; the highest concentration (100 %) prevented large amounts of mycelial growth followed by lower concentration (50 %) of plant extracts. *Opuntia* extract at 100 % concentration gave great effective in inhibition of *Pythium*'s mycelial production, which gave 100 per cent inhibition ratio while 50 per cent concentration gave 77.28 % inhibition ratio followed by other plant extracts, *Mentha, Allium sativum, Plantago*, then *Malva* respectively. *In vivo* experiments, tomato seed infused in five plant extracts separately and then sown with soil contaminated with *Pythium* fungus and watered after that with these five plant extracts. After 30 days, the length of the stems and roots were measured in centimetres. While the tomato seeds which were soaked with distilled water and then sown in polluted soil with fungus *Pythium*, and watered with distilled water (control) did not show any growth.

https://doi.org/10.1088/1742-6596/1879/2/022002

OPEN ACCESS

022003

Anatomical study of *Solanum nigrum* L. from Solanaceae family growing in Iraq

Muazaz Azeez Al-Hadeethi, Ali T Al-Taie and A. Farman Al-Rawi

− Close abstract View article PDF

The most important features that we have reached through this study, are shown the cross-section of root were in the secondary growth stage and the epidermis of leaf were studded by stomata complex, the type of it was anomocytic that's mean no have subsidiary cells around the guard cells, the mesophyll bifacial also the midrib region of leaf like the pear and the vascular bundle located in the center crescent in shape. The cross-sections of petiole ovate shape with two ears in the lateral side and the vascular bundles crescent in shape. The cross-section of fruits circular component of three-layer the outer layer pericarp, mesocarp, and the endocarp, surrounding the ovary or the seeds.

https://doi.org/10.1088/1742-6596/1879/2/022003

OPEN ACCESS

022004

Morphological, histochemical and histological study of the ileum in the Iraqi Black Partridge (*Francolinus francolinus*)

Intidhar Mohammed Mnati, Ola Al-Bhadly and Nawar Rushdi Jaber

− Close abstract View article PDF

Objective: This project aimed to study the morphological description and histological structure of ileum in Iraqi black partridge (*Francolinus francolinus*). Methods: To conduct this investigation, 20 healthy Iraqi black partridge were collected from local suppliers. Birds were euthanized, dissected and then specimens were processed for histological and histochemical staining techniques. Results: A morphological study showed that the ileum appears as a short narrow tubular structure. It extends from the wide end of the jejunum and ends in the Ileo-caecal junction region. Histologically, the wall ileum consists of four tunica mucosa, submucosa, muscularis and serosa. The mucosa was lined by simple columnar epithelium with goblet cells. The muscularis mucosa is arranged in two thick layers of smooth muscle fibers, outer longitudinal and inner circular bundles. The tunica submucosa was a thin layer of fibrous connective tissue. Tunica serosa was loose connective tissue covered by mesothelium. The goblet cells gave a positive reaction with PAS stain. Conclusion: Goblet cells neutral

mucopolysaccharide secretions; in fact, the latter stain is an indicator mucin substance which are very important in digestion and absorption and subsequent body growth of the bird.

https://doi.org/10.1088/1742-6596/1879/2/022004

OPEN ACCESS

022005

The Correlation of Histopathological Findings with Ultrastructural Changes in Hepatocytes after Yangonin "Ya"-Intoxicated Rats Alone and In Combination with EtOH: Sub-Acute & Sub-Chronic Study

Mohammed A. Hasan

Yangonin "Ya" has been used for centuries as a herbal supplement, for its mood-altering properties. It has been used as a recreation agent, for relaxation, as well as for pain relief. However, hepatotoxicity is a widespread problem associated with medicines in general. Most herbal supplements are metabolized by the liver, and thus the liver represents the target organ. At present, Yangonin toxicity appears to be "idiosyncratic". Therefore, a study was designed in order to investigate the organelle-based changes in hepatocytes, after treatment with Yangonin alone and in combination with EtOH. Thirty rats were divided into five groups comprising of six animals each. The groups comprised of the control groups {(NCx) & (PCx)}, Yangonin (Ya) group, ethanol (EtOH) group, and the combination of (Ya) and ethanol (EtOH+Ya) group. The experiment was conducted over a period of 14 weeks, as a sub-chronic study. At the end of the 14 th week, mitochondria, peroxisome, rough and smooth endoplasmic reticulum, and nuclei of hepatocytes, were evaluated using a scoring system. The results were compared with histopathological findings, as well. Treatment with Ya significantly induced hepatotoxic scores as compared to the control groups. Organelle injury scores increased significantly with Ya treatment, while rats that received "EtOH+Ya" showed the severest lesions of liver scores such as, severe hepatocellular degeneration, necrosis, and hypertrophy. Ultrastructural and histopathological scores in both groups were in very strong correlation (r = 0.928 for EtOH, r = 0.921 for Ya alone and r = 0.903 for Ya plus EtOH group). In conclusion,

ethanol enhanced the sedative and hypnotic activity of Ya, and markedly increased toxicity. Findings based on TEM examination of organelles, supported the histological results as well as tissue lesions/injuries in hepatocytes, a result of hepatotoxin-induced hepatopathy.

https://doi.org/10.1088/1742-6596/1879/2/022005

OPEN ACCESS

022006

Evaluation of mycotoxins and heavy metals pollution in some types of noodles in local markets

Jameel Mohammed Mohammed, Marwa Ibrahem Abd and Saif Ali Khishan

− Close abstract View article PDF

This study was conducted to estimation mycotoxins and some heavy metals in some types of noodles in Salah Al-din governorate markets. In this study 6 species of Aspergillus were detected which were *A. flavus, A. parasiticus, A. fumigatus, A. terreus, A. ochraceus* and *A. niger* and 5 genus of fungi were *Fusarium verticillioides, Penicillium, Mucor, Alternaria* and *Rhizopus* isolated on the three types of media used. The results show presence of the three types of mycotoxins in all samples. The concentrations of the aflatoxin B1 ranged between 1.145 - 5.041 ppm. Concentrations of fumonisin between 8.498 - 19.496 ppm. Concentrations of ochratoxin A ranged between 3.960 - 52.543 ppm. The results also show that the concentration of copper and cadmium was at (0.50 - 1.23) (0.05 - 0.31) ppm respectively, while the concentration of lead was less than 0.1 ppm in all samples.

https://doi.org/10.1088/1742-6596/1879/2/022006

OPEN ACCESS

022007

Anatomical histological structure of the cerebellum in the Iraqi frog *Rana ridibunda ridibunda*

Nahla A. AL-Bakri and Jumana J. Al-Zuheri

− Close abstract View article PDF

The current study was designed to investigate the histological structure of the cerebellum in the Iraqi frog *Rana ridibunda ridibunda*. The cerebellum was removed surgically from 20 Iraqi frogs, *Rana ridibunda ridibunda*, and preserved in fixative of 10% formalin solution for a period of 72 hr, then the histological sections were prepared by the method of paraffin. The results of the study showed that the cerebellum of the adult Iraqi frog is one of the rhombencephalon regions, and consists of three layers, molecular layer, purkinje cells layer, and granular layer. The present histological findings suggest that the cerebellum of the Iraqi frog is very similar to that of other vertebrates, Therefore it represents the basic rule in understanding the histological formation of the cerebellum.

https://doi.org/10.1088/1742-6596/1879/2/022007

OPEN ACCESS

022008

First record of *Gyrodactylus hrabei* Ergens, 1957 (Monogenea: Gyrodactylidae) in Iraq from gills of mugilid fish *Planiliza abu* (Heckel, 1843)

Kefah Naser Abdul-Ameer

The A total of 118 specimens of the mugilid fish *Planiliza abu* (Heckel, 1843) were collected weekly from Al-Graiat region at the Tigris river in Baghdad city, during the period from July 2015-March 2016. In this study, investigated of fish gills of *Planiliza abu* and was noticed of Monogenean *Gyrodactylus hrabei*, Ergens, 1957 and registered for the first time in Iraq. The description and measurements of this parasite as well as its illustrations were given.

https://doi.org/10.1088/1742-6596/1879/2/022008

OPEN ACCESS

022009

A first record of seven species of terrestrial isopoda-crustacea in central Iraq

Maysaloon Lafta Al-Doori, Talal Aboud Hansh and Nibrass Lafta Al-Doori

This study is the first kind of it in Iraq. The samples were collected from April to Junuary 2018, we recorded seven species for the first time in Iraq (*Procellio laevis, P. cingendus, Lacasius pallidus, Armadillidium album, A. assimile, Orthodillo chiltoni, Cylisticus convexus*). These species belong to four famillies (Procellionidae, Armadillidae, Armadillidae, Cylistieidaeà). The samples were saved in the natural histroy museum in Baghdad-Iraq.

https://doi.org/10.1088/1742-6596/1879/2/022009

OPEN ACCESS

022010

Assessment of Health Awareness: Spreading and Prevention of Infection with SARS-CoV-2 Virus in the Anbar Governorate-Iraqi Community

Harith Abdulrahman Ahmed, Mustafa Nuhad Al-Darraji and Osama Abdulrahman Ahmed

SARS-COV-2 virus is one of the fastest spreading viruses targeting the respiratory and other system in the body. Therefore, it is necessary to emphasize the needs for preventive measures, particularly at the moment because the virus is spreading fast in various parts of the world, causing various levels of infections: medium to severe, and fatal. The study aimed at assessing health and environmental awareness apart from correcting some scientific healthy concepts related to COVID-19. Additionally, this study also attempted to spread awareness in a simple way that simulates all levels of society. The current study focused on Iraq, specifically Al-Anbar governorate, as it is free from COVID-19 infections according to the reports of the Iraqi Ministry of Health in cooperation with the WHO. In this study, a set of electronic questionnaire was selected to collect relevant data. The electronic questionnaire was chosen because of the quarantine order by the authority due to the COVID-19. The items were built based on a variety of health, preventive, and environmental scientific questions and it was electronically distributed to 2084 individuals in Governorate. The findings revealed that Ramadi city had the most participants responding to the questionnaire (47%). The participation rate for female was 52% while the rate for male is 48%. The biggest age group was 20-24 years old and the highest academic background was a bachelor's degree in education. The findings

indicated a good percentage of health awareness among the participants in the governorate emphasizing on health instructions and preventive measures taken by the Crisis Cell, which had an important role in being infectious-free during the period. It is summarized that the level of health awareness and the role of the Crisis Cell: worked together COVID-19 the infection. Additionally, this questionnaire had a great role in correcting some understanding of scientific concepts among the public.

https://doi.org/10.1088/1742-6596/1879/2/022010

OPEN ACCESS

022011

Detection of *Listeria monocytogenes* in frozen food using a specific *inlB* virulence gene

Aula M. Al-Ghanim and Basil A. Abbas

− Close abstract View article PDF

This study was undertaken to detect the presence of *Listeria monocytogenes* in frozen food. A total of 200 different food samples were collected from Basrah markets, southern Iraq, during September 2015 to March 2016. These samples included frozen fish, frozen burger, frozen chicken and worker's hands swabs, 50 each. The polymerase chain reaction technique was used to evaluate the presence of *Listeria monocytogenes* by using of *inlB* specific gene. The PCR results revealed that only four samples (7.27%) were contaminated by *Listeria monocytogenes*. In conclusion frozen food may carry a dangerous type of bacteria and lead to human illness.

https://doi.org/10.1088/1742-6596/1879/2/022011

OPEN ACCESS

022012

Role of toll like receptor-9 (*1237 T/C*) gene polymorphism in patients with type 2 diabetes and diabetic foot ulcer

Furqan Naeem Al-Karawi, Naji Al-Hasnawiand Abeer Thaher and Thekra Abd Jebur Al-Kashwan

− Close abstract View article PDF

This study aimed to evaluate whether (*1237 T/C*) polymorphism is related with diabetic foot ulcer in type-2 diabetes mellitus of Iraqi patients in Najaf city. Diabetic foot ulcer (DFU) is one of the most prevalent and serious diabetic complications. DFU accounts for about 15% of the diabetic population. It is commonly associated with the increased diabetic morbidities and mortalities. The type 2 diabetes is recognized by aberrations of glucose, lipid and protein metabolism. It is increasingly appreciated that wound healing defect seen in diabetic patients is attributed to the altered protein and lipid metabolism. This study involved (180) subjects, between them, 60 were patients as group one suffering from type 2 diabetes and 60 were patient suffering from type 2 diabetes and foot ulcer as group two. In addition, 60 healthy group three as control subjects. Polymerase chain analysis was used for detection of *TLR-9* genotypes followed by restriction analysis. We observed no significance differences in the distribution of the genotypes and alleles of (*1237 T/C*) polymorphism among the study groups.

https://doi.org/10.1088/1742-6596/1879/2/022012

OPEN ACCESS

022013

Biochemical study of alkaline phosphatase in *Escherichia coli*

Ibtihal Idrees Kanaan and Najwa Khaleel Ibrahim

The present research aimed to isolate and purify Alkaline phosphatase enzyme from crude protein extract (Lysate supernatant) of *Escherichia coli*, by using different biotechnologies. To proceed, the following steps were taken: Firstly, The verification of the existence of enzyme in bacteria, the bacteria were diagnosed by using the API 20 stripe that consists of (20) items. the enzyme was isolated to ensure its availability in bacteria within the logarithmic phase and this was done through proliferating them for 18 hours in a nutrient agar. It had been detected that the enzyme was intracellular because of the occurrence of enzyme activity in the lysate supernatant without occurring it in the cell free culture supernatant. Secondly, Enzyme purification, the enzyme had been purified through three stages: precipitation of protein by ammonium sulphate, dialysis and finally, the protein extract was passed through column chromatography by using Sephadex G-100

gel, the estimated enzyme activity after this step was 22.0 in comparison with its activity before the purification processes (crude protein extract). The approximate molecular weight of alkaline phosphatase was 81.000 Dalton estimated by using gel filtration technique.

https://doi.org/10.1088/1742-6596/1879/2/022013

OPEN ACCESS

022014

Using of RAPD-PCR markers to detect the genetic relationship of number of *Bellevalia Lapeyr* and *Ornithogalum* L. species developing in central and northern of Iraq

Najat Ameen Sa'eed, Akeel Hussein Ali Al-Assie and Naglaa Mustafa Al-Abide

This study evaluates eleven wild plant species belong to two genera of Asparagaceae family, naming of *Bellevalia lapeyr* and *Ornithogalum* L. and discuss the similarities and differences among all species by using eighteen random primers for the Random amplification polymorphic DNA (RAPD) markers were used to study the genetic relationship and genetic distance among these species. The study aimed to determination genetic relationships among all the eleven species by using RAPD markers and the method of extraction DNA from plants was CTAB with liquid nitrogen. The result show 16 primers success in giving 293 bands, of which 263 were polymorphic bands, 25 unique bands and 5 were absent. *B.chrisii* type also succeeded in showing two unique bands at OPG-08 primer without registering any other bands. The lowest genetic distance was 0.306 between *B. longipes* and *B.parva*, while the highest genetic distance was 0.943 between *B.chrisii* and *O.pyrenaicum*. It is concluded from our study based on the results of the RAPD test that the studied species were divided into two main groups, each group was divided into subgroups, the first group included three groups and the second main group included two main groups. The study found that the *O.pyrenaicum* type is distinguished by being far from the rest of the species.

https://doi.org/10.1088/1742-6596/1879/2/022014

OPEN ACCESS

022015

The isolation and identification of cadmium-resistant *Brevibacillus agri* C15

Nadia Jebril, Rich Boden and Charlotte Braungardt

Eight Cd-resistant bacteria were isolated from the soil. Based on the resistance and specific growth rate, one isolate from these was chosen. The 16S rRNA (rrs) gene sequence was used to assert this isolate belongs to the genus of *Brevibacillus* and closely related to *Brevibacillus agri* (*B.agri*) DSM 6348T (AB112716). The isolate was termed *B.agri* C15. The specific growth yields and the Cd-dependent fall in specific growth yield of *B.agri* C15 was determined under different concentrations of Cd. The current study provides a basis for isolation Cd resistant bacteria with maximum tolerable concentration (MTC) 15 mM Cd from a contaminated soil 490±50 μmolal Cd that could be suitable for a new Cd-bioremediation process; therefore, further studies are needed to investigate this possibility.

https://doi.org/10.1088/1742-6596/1879/2/022015

OPEN ACCESS

022016

Production of Cellulase and bioethanol by ethanol-tolerant coculture of *Bacillus cereus* and *Fusarium solani*

Mohammed Fadhil Abood, Haider Mousa Hamzah and Dhafer Fakri Al-Rawii

Cellulase is an enzyme produced by fungi and bacteria that hydrolyzes cellulose by breaking down the glycosidic bond, β-1,4 that binds sugar glucose units. Bioethanol and cellulase enzyme were produced by ethanol-tolerant of *Bacillus cereus* co-culture. So the production of filamentous solani were using the wastes of *Cynodon dactylon* L. The highest activity of enzyme was at 96 hour/30°C of incubation. The optimal pH value was 7.5, while the carbon concentration was 3%. On the other hand, the best inoculum ratio was 0.5/100 mL (52 × 10^8 cell/mL bacterial cells and 10^5 conidia/mL of the fungus). In order to test the efficiency of ethanol production by the co-culture by using different concentrations of pure ethanol was measured in the solid medium. Both *Bacillus* sp. and *B.cereus*

F. solani tolerated incubation with 5% ethanol. The best treatment when using 0.5% sulfuric acid which gave the best concentration of reduced sugars and the results showed a difference in the concentration of sugars produced by the fermentation process, it was 3.9 mg/mL in the first day, whereas it was 2.51 mg/mL after 120 hours of fermentation, the concentration of bioethanol produced after fermentation was 195 g/L. In conclusion *Cynodon dactylon* L. wastes were treated by sulfuric acid, cellulase digestion, and autoclave treatment to be a good source of reducing sugars.

https://doi.org/10.1088/1742-6596/1879/2/022016

OPEN ACCESS

022017

Investigation of fungal contamination in some types of chips in the market in Karbala

Ihsan Ali Al-Zamily

Different types of chips samples sell were collected from some markets in Karbala city, which its made in Jordan (Chipsico and Alsaada), Saudia (Liz, Gillts, Doritos), Iran (Bovac, G Toz and Macho) and Iraq (Hala, Dalia, Al-Aseel). The Iranian Chips were the most contaminated, where Iraqi and Jordanian Chips comes in the second. The results of isolating fungi study in chips types, showed diversity in numbers and kinds of fungi. The genus *Aspergillus* is a fungus predominate on all isolates and followed by *Penicillium*. Also different genera including *Fusarium, Alternaria, Curvularia* and *Rhizopus* have been isolated. It is mentioned that these fungi are dangerous because they produce myctoxins, especially aflatoxin and ochratoxin. It was noted that, the Saudi products are free from contamination. Ammonia test and Fluorescence was used to identify the aflatoxin-producing isolates and it appeared that isolates of *Aspergillus* had great potential to produce these toxins.

https://doi.org/10.1088/1742-6596/1879/2/022017

Biological control of *Azotobacter chroococcum* on *Fusarium solani* in tomato plant

Sraa Nsayef Muslim, Rawa Abdul Redha Aziz and Asmaa Mansour Al-Hakeem

this experiment aimed to study the effect of *Azotobacter chroococcum* in reducing infection of the tomato plant by *Fusarium solani* under the greenhouse condition. The results show that *Fusarium solani* isolates proved high pathogenicity and chosen isolate (Fs4) for being given a lower percentage of germination of cabbage seeds and the highest disease severity to tomato seedling. Also, the results were indicated that T6 (Biofertilizer at concentrations (25 ml\2Kg soil) with *F. solani* (F.s4) was the past this treatment reduced significantly the disease severity (73.10%) which also recorded a positive effect on the growth parameter of tomato plant compare to T1 (pathogen only).

https://doi.org/10.1088/1742-6596/1879/2/022018

OPEN ACCESS

022019

Evaluation activity of bacteria *Bacillus thurengensis* and different concentrations of plant extracts on adult of house fly *Musca domestica*

Raghad Khalaf Al-Joboory and Elaf Adnan

This research included evaluating the efficacy of plant aqueous extracts for myrtle *Myrtus communis, Nerium oleander, Eucalyptus* spp. and *Bacillus thuringiensis* on adults of the house fly *Musca domestica* L. under laboratory conditions at a temperature of 2 ± 28°C and with a humidity of 50-70 %. it was found that the highest rate of laying eggs was in the extract of eucalyptus leaves, where the number of eggs laid was 60 eggs on average and at a concentration of 5%, while in the concentration of 10% the average egg was 55 eggs then In the extract of the leaves of the oleander was at a concentration of 10% at a rate of 50 eggs and in control treatments the number of eggs reached 80 eggs and the results showed the highest death rate for adults before laying eggs was in the extract of the eucalyptus leaves at a concentration of 15% where the death of 6 adults and the lowest percentage of death by 5% was recorded One adult death and the highest rate priest for eggs; with a concentration of 10%, reached 94%, and the highest percentage of

larval mortality reached 68.12%, with a concentration of 10% in the transactions of extract of oleander leaves, and in it also the highest rate of exclusion is 31.93%. The third larval stage with a concentration of 5% with a ratio of 3.67 days and the highest incidence rate in the third larval stage with a concentration of 2.5% at a rate of 26.70% and the lowest incidence rate of 6.70% with a concentration of 2.5% and 5% and 7.5% in the first and second stages respectively and the lowest dawning rate was recorded in the larval phase the first with a concentration of 2.5% at 16.66% and the highest deformation rate in the third larval stage with a concentration of 7.5% at 66.66%. As for its effect on the number of eggs was a rate of zero% of all concentrations (2.5%, 5% and 7.5%) compared to 80 control egg either its effect on the longevity of the adult was the highest rate of longevity amounting to a concentration of 7.5% by 5.33 day..

https://doi.org/10.1088/1742-6596/1879/2/022019

OPEN ACCESS

022020

The effect of pH, calcium, phosphate and humic acid on cadmium availability and speciation in artificial groundwater

Nadia Jebril, Rich Boden and Charlotte Braungardt

− Close abstract View article PDF

The interface between the ions in groundwater affects the biogeochemical behaviour of metal, and metal bioremediate by bacteria. Therefore, this study was aimed to predict the influence of pH, calcium, phosphate and humic acid on cadmium availability in artificial groundwater (AGW). Speciation and the thermodynamic calculation (MINTEQ program) were used to predict this in AGW theoretically. In results, cadmium availability diminished with an increase in pH, increase of calcium concentration and the addition of phosphate and humic acid of AGW. According to MINTEQ program, cadmium binds to some cations leaving fewer free cadmium ions available in AGW such as $CdHCO_3^+$, $Cd(SO_4)_2^{2-}$, $CdCl^+$, $CdHPO_4$, HA1-Cd, FA1-Cd, FA2-Cd, and HA2-Cd. It is suggested though that pH in AGW is maintained at pH 4.00 for best availability of cadmium and bioremediate by bacteria.

https://doi.org/10.1088/1742-6596/1879/2/022020

OPEN ACCESS

022021

The effect of usage two methods of garlic extraction(foliar and ground application) on the growth of the tomatoes (*Solanum lycopersicum*) plant

Radhiyah Ali Hasan Ahmad

− Close abstract View article PDF

Garlic is rich in nutritional and medicinal value as it has been found that the water extract of garlic plant contains 31% carbohydrates and rich in elements calcium, phosphorus, magnesium, potassium, sodium, iron, zinc, manganese, vitamin C, thiamine, riboflavin, niacin and pyridoxine. The aim of this study was to investigate the effect of garlic extract (*Allium sativum* L.) on tomatoes (*Solanum lycopersicum* L.) plant. The trend is to use plant extracts in foliar and ground fertilization. Three levels of foliar application (4, 6, 8%), three levels of ground application (10, 20, 40%), one treatment 6% of foliar and 20% ground application together and the treatment of control (0) were used. The results showed that the usage of garlic extract led to a significant increase in the height of the plant 98.00 cm, chlorophyll content 46.33 spadm, increase the Carbohydrates 7.95%, the number of branches, the number of leaves, the foliar area, the dry weight of vegetative group, the number of flowers, the leaves content of nitrogen, protein and carbohydrates, fruit weight, fruit size, measurement T.S.S. and solidity of treated plant compared to control plants.

https://doi.org/10.1088/1742-6596/1879/2/022021

OPEN ACCESS

022022

Occurrence and composition of copepods abundance in Tigris river, southern Baghdad, and effects of Rasheed power plant effluents on its biodiversity

Muhanned R. Nashaat, Fatema S. Muftin, Enaam K. Abbas and Ali Eman H

− Close abstract View article PDF

The quantitative and qualitative structure of the Tigris River copepods communities, were identified to investigate the biological composition, especially near the outcome of Rasheed power plant (RPP), on its biodiversity at four sites those were chosen on the

Tigris River in south part of Baghdad Governorate during the period January to December 2012. The sites S2 was located near Rasheed Power Plant to represent the ecological features of the plant site, whereas other sites, S1 was located at the upstream of the RPP as a control site to investigate the ecological characters of the Tigris River. Moreover, the two other sites S3 and S4 were located down to the impact of RPP to reflect the possible effects of the plant on the copepoda fauna biodiversity by comparison with the control site. Thirty-nine taxonomic units of copepoda fauna were identified in the present study, Including 17 taxonomic units of Cyclpoida, 13 taxonomic units of Calanoida, six taxonomic units of Harpacyicoida and three taxonomic units of Parasitic Copepoda. This study found that the highest copepod density was recorded during the winter period on site below RPP. While at sites near RPP during the summer period, Copepoda showed the lowest density. The results also showed that the sites below RPP included the most constant species, while the lowest were included at site near RPP. The results of the biodiversity indexes generally showed the negative actual impact of RPP on the copepoda commu nity..

https://doi.org/10.1088/1742-6596/1879/2/022022

OPEN ACCESS

022023

Prospective gene therapy design against coronavirus COVID-19 by recruiting CRISPR Cas9 approach

Ayman Albanna and Arqam Alomari

A novel Coronavirus disease (COVID-19) has being originated from animals and causing to running outbreak of viral pneumonia in human all over the world. The World Health Organization (WHO) has considered COVID-19 infection as Epidemic disease in March 2020. The high percentages of death rate among people lead the researchers and scientists in different fields of medicine in order to find solution for this threating problem. In this regard, an editing gene technique was employed in this study, in order to deter the viability of coronavirus genetically. The main objective in this paper first has been determined and obtained the essential proteins of COVID-19 coronavirus proliferation by

using NCBI website which included *S, E, N, M, ORF3a, ORF6, ORF7a, ORF7b, ORF8, ORF10* proteins. The second objective is to use a very precise technique of editing gene called CRISPR-Cas9 to make changes to the virus's RNA, through designing single-guide RNA for the essential each protein of COVID-19, in order to inactivate an effective certain protein. These techniques will be provided for each patient and healthy person by injection of all genes components using the Gene-gun machine or spray aerosol to make ensure reach it to the target cell.

https://doi.org/10.1088/1742-6596/1879/2/022023

OPEN ACCESS

022024

Effect of amino acid proline on some growth characteristics of cowpea which exposed to drought stress

Maher Zaki Faisal Al-Shammari and Wael Shakir Hameed Al-Jboory

The study was conducted in Al-Youssoufia region which located in North West of Baghdad city during the growing season of 2018-2019. The experiment was aimed to demonstrate the optimum concentration of amino acid proline that reduce the effect of drought stress. By using three time for irrigation (4, 8, 12) day and four concentrations of proline (0, 20, 40, 60) mg. L-1 and their interaction on some growth characteristics: Root length, dry weight, nitrogen, phosphorous and potassium content, carbohydrate percentage and peroxidase activity in vegetative part. Data were statistically analysed to find out the least significant difference (LSD) between treatments at 0.05 level. The results indicated the increase of proline concentration from (0 to 60) mg.L-1 caused significant decrease in the average of growth characteristics and peroxidase activity unite.mg.proline-1 with increase in the average of irrigation periods under drought stress.

https://doi.org/10.1088/1742-6596/1879/2/022024

OPEN ACCESS

022025

Antioxidant, cytotoxicity and phytochemical analysis of *Laurus nacilatesF.* cocoon aqueous extract against lung cancer

Hanady S. Al-Shmgani, Zainab Thamer Alasady, Ehab M. Ali and Mohammad J. Al-Jassani

Cocoon of larva *Larinus maculates* F. from Curculionidae family (*Echinops* species), locally in Iraq known as Tihan, is one of traditional folk medicine used in the treatment of diversity respiratory system and fever. This study was carried out to assess the bioactive component and the antioxidant capability of aqueous beetle cocoon extract (*Larinus maculates* F.) along with its possible cytotoxic activity against A549 lung cancer cell line. For phytochemical analysis gas chromatography-mass spectrometry (GC-MS) was used, and to detected free scavenging activity 2, 2-diphenyl-1 picrylhydrazyl (DPPH) was used. To determine the cytotoxicity in the cancer cell line 3-(4,5-dimethylthiazol-z-yl)-2,5-diphenyltetrazolium (MTT) was used; peripheral blood monolayer cells (PBMCs) was used as a normal cell. GC-MS analysis identified the presence of 9 phytochemical components. DPPH results suggested a promising antioxidant activity in a dose-dependent, the best antioxidant potential was at 600 $\mu g.ml^{-1}$ concentration. Cytotoxic activity results showed that the increase in extract concentration decreases the cell viability, at 50 $\mu g.ml^{-1}$ concentration the percentage of viability was (86.76±0.87) where at 200 $\mu g.ml^{-1}$ the cell viability was (56.44±0.91) $\mu g.ml^{-1}$ Taken together, the results showed that larva cocoon of *Larinus maculates* F. extract has an important phyto-molecule with great potent antioxidant and cytotoxicity activity against lung cell line A549..

https://doi.org/10.1088/1742-6596/1879/2/022025

OPEN ACCESS

022026

Studying the levels of some Biochemical variables in blood serum for smoking of Tikrit University students

Saria Naji Muhsin, Shurooq hameed majeed Alnassiri and Sina Naji Muhsin

This study included (75) samples of the males students at the Tikrit University, The samples were divided into three groups; the first group: (25) blood samples pulled from healthy non-smoking students (males) as Control sample. The second group: (25 males)

samples of diabetic mellitus (smoker students). Third group: (25 males) samples of hypertension (smoking students). The results of the study indicated a significant increase in the concentration of the levels Cholesterol, Triglyceride, Malondialdehyde (MDA), Lactate dehydrogenase (LDH) at level (P <0.005) in the samples of smoker students when compared to the healthy group. And showed decrease in the concentration level of HDL, Glutathione Peroxidase (GPx) at level (P <0.005) when compared to the healthy group (non-smokers).

https://doi.org/10.1088/1742-6596/1879/2/022026

OPEN ACCESS

022027

New record of fresh water ciliates (Protozoa, Ciliophora) from Tigris river in Baghdad city, Iraq

Zahraa Y. Kadhim

Documenting the biodiversity and biogeography of ciliates will help expand the overall knowledge within the field, as well as, shed new light on the dispersal and survival potential for other microorganisms, such as protists. As organisms at the base of food webs, ciliates are an essential part of the microbial loop and the ecosystems that they support. This study deals with ciliates community in freshwater of Tigris river within Baghdad city. Four sites were chosen at Al-Grea`t & Al-Adhamiya area at the riverbank. Total of 44 ciliophora taxa were detected, 22 taxa of which were identified to the species level and 22 taxa to the genus level. Among them, 11 taxa were new recording for Tigris river in Baghdad city: *Cyrtolophosis* sp., *Monochilum frontatum, Orborhabdostyla bromelicola, Ophrydium sessile, Scyphidia* sp., *Vortecilla convallaria, Vortecilla octava, Zoothamnium Bory, Tokophrya lemnarum, Urostyla* sp. and *Stentor fluiginosus*.

https://doi.org/10.1088/1742-6596/1879/2/022027

OPEN ACCESS

022028

Histomorphological study of olfactory organ in rock dove, *Columba livia* Gmelin, 1789

Hussain A. M. Dauod, Ahmad A. Hussain and May F. Al-Habib

− Close abstract View article PDF

The present study aimed to investigate the morphological description and histological structure of olfactory organ in rock dove (*Columba* livia). Results of the present study revealed that the nasal cavity of the species under investigation is anteriorly located, starting with a pair of external nares which located at the dorsal side of the base of upper beak. The external nares lead to two short nasal cavities. Each nasal cavity consist of three conchae or turbinates represented by anterior or vestibular concha, middle or respiratory concha and posterior or olfactory concha. The nasal cavity ended by a pair of internal nares which opened at mouth cavity. Results related with the histological structure of olfactory organ revealed that the vestibular concha lined by stratified squamous epithelium, the respiratory concha lined by ciliated pseudostratified columnar epithelium, and olfactory concha lined by ciliated pseudostratified columnar epithelium. The last concha showed three types of differentiated cell represented by basal cells, supporting cells, and receptor cells.

https://doi.org/10.1088/1742-6596/1879/2/022028

OPEN ACCESS

022029

Phenotypic, anatomical and phytochemical investigation of Iraqi *Silybum marianum*

Rasha Eldalawy, Widad M K Al-Ani and Wasan Abdul Kareem

− Close abstract View article PDF

Asteraceae (Compositae) famous as the aster, daisy or sunflower family is the biggest flowering family divided into thirteen subfamily that involve approximately two thousand genus, an important member of this family is *Silybum marianum* (Milk thistle). Management of hepatic diseases is the main use of milk thistle in traditional medicine also it has anticancer activity against different type of cancer in addition to antiviral, antioxidant, antiinflammatory and anti-diabetic activity. This study was designed to investigate the pharmacognostical feature and the phytochemical ingredient of Iraqi *Silybum marianum*. The plant were examined macroscopically to investigate the

morphological characters of plant and microscopically to determine the type of stomata and trachoma then flowers, leaves, stems and seeds of the plant were extracted by ethanol in a soxhlet apparatus individually and subjected to standard methods for active constituents identification and that total flaononid, total phenolic and total tannins content were determined using aluminum chloride colorimetric, folin-ciocaltue and acidified vanillin methods respectively. The results shows that *Silybum marianum* leave have a thick cell wall, anomocytic stomata, annual vessel, and unicellular unbranched trichomas. Also an important active constituents have been detected that terpenes, steroid and flavonoids were present in all plant parts, saponin appear only in the leaves and stems while alkaloids and coumarins are not detected in any part. Also the study referred to the seeds as the richest part of the plant with flavonoid and phenolic compounds followed by the flowers, leaves and stems which contain the less amount, while the higher content of tannin were observed in the leaves and stems..

https://doi.org/10.1088/1742-6596/1879/2/022029

OPEN ACCESS

022030

Effect of Chloroquine on antioxidant enzymes and oxidative system on (*Vigna radiata*) plant tissues exposed to water stress

Hayder Nasser Hussain Al-Mentafji

The aim of the present study is to examine the effect of (Chloroquine CQ) on the oxidative stress under water stress effect Recently, this compound is used to treat COVID-19, Hydrogen peroxide H2O2 effect and Stimulate the enzymatic system through the exposure of the plant to water stress and interaction with Chloroquine, where the stress stimulate the production of these Oxidative Factors (Hydrogen Peroxide, Malondialdehyde(MDA), Protease increase the production of these oxidative factors increase activity through the effect of Chloroquine, This process was performed in the meristematic tissues of the cells of the permanent Mung bean (*Vigna radiata*) plants under experimental factors (water stress factor for 10 days with control period of 5 days) (Chloroquine factors and concentrations of 125 and 250 mg.L-1 with control treatment)

were designed using a Factorial Randomized Block Design (R.B.C.D) with three replicates and 18 experimental units The experimental unit area was 2 m. The results have shown the following; The water stress period of 10 days led to the production of toxic hydrogen peroxide and increased concentration by stress. The effect of water stress was Stimulate the Production of hydrogen peroxide in Meristematic tissues. The effect of Chloroquine CQ with increased concentrations had a role in inhibiting the production of enzymatic antioxidants (Superoxide dismutase(SOD) and Catalase (CAT). The interaction between water stress and increased Chloroquine CQ concentrations has been instrumental in stimulating the production of oxidative Factors.

https://doi.org/10.1088/1742-6596/1879/2/022030

OPEN ACCESS

022031

Histological structure of the Tongue in Mongoose (*Herpestes javanicus*)

Iman Sami Ahmed Al-Jumaily, Marwa Khalil Ibrahim and Wijdan Bashir Abid

The aim of the present study was to investigate the histological structure of the tongue in Mongoose (*Herpestes javanicus*) and its related to the feeding pattern. Five adult animals were used in this study. The tongues were dissected and fixed in 10% formalin, then prepared by following stages (dehydration, clearing, and embedding). The serial section(5μ) were stained with(H&E) and some special stains. The histological examination showed that the tongue consists of three tunicae (mucosa, submucosa and musclaris) and the lining epithelium of the filiform papillae is composed of keratinized stratified squamous epithelial tissue. The cylindrical papillae are covered with a highly keratinized stratified squamous epithelial tissue, whereas the keratinized stratified squamous epithelium tissue is weakly keratinized at fungiform papillae, whilst circumvallate papillae are non-keratinized. The medullary of the papillae consists of a loose connective tissue which is considered as the lamina propria of the tongue, while the tunica submucosa consists of dense connective tissue. The muscularis is composed of skeletal muscle fibres arranged in three direction longitudinal, transverse and obliquate.

The lingual glands(Von-Ebner and Weber) placed on both sides of the lingual root at the tunica submucosa and extend to the tunica muscularis. This study pointed out that the secretion of glands is mixed and the mucin is more neutral than acid.

https://doi.org/10.1088/1742-6596/1879/2/022031

OPEN ACCESS

022032

Quality study of the piped water of state company for drugs industry of Samarra and matching with the Iraqi and international drinking specification

Rafah Talal Ahmed Alsamaraay, Riadh Abbas Abdul Jabbar and Tawos Mohammed Alshawany

The research aimed to evaluate piped water that supply the general company for pharmaceutical industry of Samarra and its suitable for drinking through the comparison with Iraqi and international standard for drinking. The study started from May (2015) until January (2016). Moreover, know the physical, chemical and bacterial properties piped water. The results showed that the piped water was matching of the drinking water by WHO and Iraqi standard. Only calcium quantity was higher than determination. The values rate for: Air and water temperature (29.44, 21.33) C° respectively, EC (431.11) µs/cm. TDS (430) mg/L, the pH (7.7). DO (4.75) mg/L, while the BOD5 (1.25) mg/L, while Alkalinity hardness (157.77) mg/L, total hardness (155.55) mg/L, calcium and magnesium hardness (78.66, 72) mg/L Respectively. While chloride (68.22) mg/L, as for the phytonutrient, Nitrate concentration were (1.902) Mg/L, the phosphate concentration values rate (0.050) Mg/L, and silica concentration (1.981) Mg/L. The heavy metals, Cu (0.028) ppm, Iron (0.121) ppm, Zinc (0.203) ppm, Lead (Nil) ppm. And it was free from bacterial growth. Thus, quality of piped water, (completely purity).

https://doi.org/10.1088/1742-6596/1879/2/022032

OPEN ACCESS

022033

First record of *Myxobolus insignis* Eiras, Malta, Varella, Pavanelli, 2005 (Myxozoa: Myxobolidae) in Iraq from gills of the common carp *Cyprinus carpio*

Kefah Naser Abdul-Ameer and Rana Saheb Shalal

− Close abstract View article PDF

The Myxozoan parasite, *Myxobolus insignis* Eiras, Malta, Varella, Pavanelli, 2005 is recorded in the present study from gills of the common carp *Cyprinus carpio* for the first time in Iraq. The fishes were caught from the Al-Ataifiya location on the Tigris River at Baghdad city during the period from January to October 2020. The measurements and description of this external parasite in addition to its illustrations were given.

https://doi.org/10.1088/1742-6596/1879/2/022033

OPEN ACCESS

022034

Detection of *Bacillus cereus* genes responsible for diarrheal and emetic toxins

Ban M.S. Saeed, Basil A. Abbas and Shaker A.N. Al-Jadaan

− Close abstract View article PDF

Bacillus cereus isolated from different food sources. The diarrheal toxin genes such as *cytK*, hemolytic enterotoxin (*hblA, hblC* and *hblD*), non-hemolytic enterotoxin (*nheA, nheB* and *nheC), bceT* and *entFM* in addition to emetic toxin gene were detected by PCR. The *cyt K* gene was observed in 94.87 % of the isolates. *entFM* and emetic toxin gene were found very rare in all food samples at the percentage 2.56% and 7.69% respectively. Uncooked rice which has a highest number of bacterial isolation, also showed relatively high percentage of the *cytK* and *bceT* genes (90%). These two genes present in 100% of *Bacillus cereus* isolates in most food samples. Bacteria isolated from burger meat contain all investigated genes.

https://doi.org/10.1088/1742-6596/1879/2/022034

OPEN ACCESS

022035

Detection of antibiofilm formation by sliver nanoparticles created by tetracycline antibiotic

Alaa Z. Hameed and Nehia N. Hussein

− Close abstract View article PDF

Silver conjugated Tetracycline, was created and characterized by ultraviolet visible spectrophotometry (UV-vis), Fourier transform infrared (FT-IR), X-Ray Diffraction Patterns (XRD). Using antibacterial assays, the effects of tetracycline alone and drugs-conjugated with silver nanoparticles were tested against Gram-ve *Pseudomonas aeruginosa* isolates by well diffusion assay. The UV-vis spectra of silver-drug Nano conjugates showed a characteristic surface Plasmon resonance band in the range of 400–450 nm. FTIR analysis demonstrated the involvement of Hydroxyl groups in both drugs in the stabilization of silver nanoparticles. (XRD) showed that they cubic structure of silver and, antibacterial assays showed that biosynthesis silver nanoparticle conjugation enhanced antibacterial potential of Tetracycline compared with drug alone.

https://doi.org/10.1088/1742-6596/1879/2/022035

OPEN ACCESS

022036

Morphological characterization and its relation with yield traits of *Oryza sativa* L. genotypes in Iraq

Balqees Hadi Al-Musawi and Mohammed A. Al-Anbari

In the current study we reported for agronomic traits and yield of fifteen rice genotypes in season during 2018 and investigated at the field experimental of Al-Mashkab research station (AMRR), Najaf-Iraq. The experiment was conducted following Randomized Complete Block Design (RCBD) with having three replications. These data related days to 50% flowering and heading, plant height (cm), leaf area index (LAI), panicle length (cm), number of tiller per panicle, 1000 grain weight (g) and biological yield, harvest index and grain yield (kg ha-1) were evaluated. The results indicated that the rice genotypes differed in plant growth characteristics and yield and yield components. 1000 grain weight and grain yields both were highest in Gohar genotype. Shiroudi genotype required shorter days to maturity and Anber33 longest days to maturity. Some of the rice genotypes particularly (Gohar) showed high promise with grain yield. Recommended, intensification of introducing more genotypes to select the best rice genotype for Iraqi condition could maximize the benefits of genotype cultivation. Agronomic data collecte

in the current study would be significant to realize the suitability of an individual rice genotypes of the farmer field, also were found more appropriate of the agro climatic status of Iraq.

https://doi.org/10.1088/1742-6596/1879/2/022036

OPEN ACCESS

022037

Epidemiology of hydatid disease in Najaf province/Iraq

Raja Jawad Mohamed, Alyaa Neamah Najm Alsaedi and Jasim Hameed Taher

− Close abstract View article PDF

It was clinically and surgically proven that sixty-four patients were infected with a hydatid cyst. Follow up was done in Al-Sadder Medical City, Najaf/Iraq during the period between January and December 2018. The incidence of the prevalence of hydatidosis female was higher than that of males. The youngest patients infected was five years, and oldest was over than 70 years old. The age group 21-30 years old had the highest percentage of hydatidosis infections. The rate of infection in females 64 (61%) more than males 25 (39%). Compared to males, there was a substantial rise ($P < 0.05$) in females. The percentage of liver hydatidosis relative to other organs was higher (67.18%). There were many patients with big cyst size (>5cm) than those with small cyst sizes (<5cm).

https://doi.org/10.1088/1742-6596/1879/2/022037

OPEN ACCESS

022038

Effect of ginger alcoholic extract on the ovary tissue in quail

Mohammed Hayder Hamad, Nahla Al-Bakri and Abdul-Razak Labi

− Close abstract View article PDF

This research was carried out in quail in the laboratory of histopathology diseases during four months. The objectives of this study was to detecting the effects of the addition of the alcohol extract of ginger to ovary tissue of quail. The two groups of birds were in almost similar weights and were placed in cages. Each group consisted of 8 quails. The first group (control group) fed on regular feeding without adding alcoholic extract of

ginger. The second group (treated group) fed on the same normal food after adding the alcohol extract of ginger at a concentration of 300 mg / kg. The results indicated that ginger have positive effects on folliculogenesis.

https://doi.org/10.1088/1742-6596/1879/2/022038

OPEN ACCESS

022039

Physiological and histological protective role of *Astragalus spinosus* root alcoholic extract against oxidative stress induced by H_2O_2 in rabbits

Moafaq Mutlak Zeidan and Qussay Noori Raddam

This study amid to evaluate the role of plant's root (*Astragalus spinosus*), in biochemical parameters and histological sections effect in reduce the oxidative stress induced by hydrogen peroxide in rabbits *Oryctalagus cuniculus*, 7-9 months age and (1300-1500 g) of weight. Animals were distributed to three groups, every group were included five rabbits; group (1) control received water and diet. Group (2): animals treated with H2O2 (0.05) and drinking water. Group (3): animals treated with H2O2 and alcoholic extract of the plant root (5mg/kg body weight) for period one month. Study showed high significant increasing in Creatinine and ALP, LDH concentrations of animals treated with H2O2 alone (1.74±0.40) (9.900±1.058), (260.40±26.66) respectively, in compared with control (0.838±0.08) (8.420±1.132), (154.0±49.79) respectively while the concentration of Creatinine, ALP and LDH had been decreased with high significant (P≤ 0.05) in group treated with H2O2 and extract of the plant roots (0.79±0.09), (9.220±0.801) and (166.2±36.08) respectively in compared with H2O2 group. And the result of histological sections of liver, kidneys and heart, which showed an improvement of cells in group treated with the extract of the plant which had been induced by oxidative stress.

https://doi.org/10.1088/1742-6596/1879/2/022039

OPEN ACCESS

022040

Evaluation effect of different concentration of povidone Iodine on skin wound healing in rabbits

Falah Mahmood Hameed, Hayder Mohammed Mohsen Al-Tomah, Ali J. AL-Nuaimi and Ail Wasfi Sadeq

– Close abstract View article PDF

The goal of the current study was to assess the effects of povidone iodine 10% in comparison with 5% of povidone iodine on full-thickness cutaneous wounds healing in rabbits. This was on twenty-four healthy male rabbits, weighing from (1.5–1.8 kg). Under the effect of intramuscular administration of a mixture of xylazine hydrochloride 5mg / kg, ketamine hydrochloride 35mg / kg and diazepam 1 mg / kg. On each animal, in the dorsal back area, one square (2 × 2) cm full-thickness skin wounds were made. The animals were divided into two groups, group (A) as the treatment group was treated with 10% povidone iodine daily for 1 time for day 7 post operation. While, at the same time in group (B), the rabbits were treated with 5% povidone iodine. For clinical evaluation, each group was divided into four subgroups (two wounds/subgroup) on 3rd, 5th, 7th, 9th, 14th and 21th days post-wound induction and treatment. Clinically, the result showed that 10 % of iodine was more effective than 5 % of iodine, and the wound healing rate in group (A) was faster than group (B). This was followed by statistical analysis results showing the wound healing process ((20%, 40%), (70%, 85%) contraction) and ((10%, 20%), (50%, 70%) re-epithelization). Respectively, there were significantly more (P≤0.05) than the iodine 5% during the study period. Conclusion; Povidone-iodine solution 10% is more efficient than iodine 5% so that lead to acceleration and enhancement of full-thickness cutaneous wounds healing.

https://doi.org/10.1088/1742-6596/1879/2/022040

OPEN ACCESS

022041

In vitro study of the effect of zinc oxide nanoparticles on *Streptococcus mutans* isolated from human dental caries

Arshad Mahdi Hamad and Qanat Mahmood Atiyea

– Close abstract View article PDF

Dental caries is a public health concern worldwide for which *Streptococcus mutans* has been reported Known as the potential etiology of infection. In recent years, nanotechnology has applied to Creation of novel material properties. The research was studying the effects of Nanoparticles of Zinc Oxide on *Streptococcus mutans* isolate from dental caries. In this research, Different ZnO NPs concentrations were studied as its anti-bacterial effects on *Streptococcus mutans* was isolated from dental caries cases. 27 *Streptococcus mutans* isolates were obtained, which is equivalent to 20% of the total number of 135 isolates. This nanomaterial was chosen because it has a high affinity for human cells and does not cause harm compared to other nanoparticles. The nanoparticles are those very fine materials that can be produced so that their dimensions or the dimensions of their grains range from (1-100) nanometers, and because of the small size of the nanomaterials, which made them behave differently from large-sized materials whose size exceeds 100 nanometers, and because of the small size of the particles. Nanoparticles, which gave them electrical and magnetic properties that differ from large particles of the same compounds. The well diffusion method and the MIC experiment were conducted, and the results were good, as in the well diffusion method the efficacy increased with increasing the concentration of ZnO NPs. In the MIC experiment, it was observed that MIC in the sixth tube, meaning that the MIC of ZnO NPs towards *Streptococcus mutans* equals 0. 312 mg / ml.

https://doi.org/10.1088/1742-6596/1879/2/022041

OPEN ACCESS

022042

Response of model plant *Arabidopsis thaliana* to Plant growth promoting rhizobacteria & phosphate concentration

Sulaiman Abdulhusein Mashkoor and Mushtak F. Karomi Kisko

− Close abstract View article PDF

Several reports have shown that various rhizobia can interact with non-hosted plant species, enhancing mineral nutrition and promoting plant growth. To further investigate the effects of such non-host interactions on plant growth and phosphate nutrition, we inoculated *Arabidopsis thaliana* with the model rhizobacterium *Pseudomonas fluorescens*

at three phosphate concentrations in the nutrient medium. *In vitro*, we showed that root colonization by *Pseudomonas fluorescens* contributes to an increase in the amount of available phosphate that is important in plant growth, especially in the shoots, in all concentrations used in the study. In addition to improving plant growth as well as increasing plant biomass production.

https://doi.org/10.1088/1742-6596/1879/2/022042

OPEN ACCESS

022043

Use of ultraviolet-light mutagenesis to generate a mutant with elevated cadmium resistance, *B. agri* C15 Cd^R

Nadia Jebril, Rich Boden and Charlotte Braungardt

− Close abstract View article PDF

Cadmium (Cd) is toxic to living organisms; however, bacteria are adaptable to severe conditions, including Cd contamination. Bacteria can develop in the natural environment, as they generate resistant strains that can be used to remove Cd, but getting such adaptive strains usually takes a long time. In this study, ultraviolet (UV) light mutagenesis was used to accelerate the strain-resistant ability of *Brevibacillus agri* C15 to generate Cd^R mutant with high resistance to Cd. Its maximum tolerable concentration (MTC) to Cd was 15.00 mM. The UV light mutagenesis process resulted in the generation of the mutant *B. agri* C15 Cd^R (MTC: 20.00 mM Cd). Morphological and biochemical tests showed that there were no major differences between *B. agri* C15 Cd^R and *B. agri* C15. This study provides a basis for developing microbial Cd resistance and facilitating the application of Cd remediation.

https://doi.org/10.1088/1742-6596/1879/2/022043

OPEN ACCESS

022044

Morphological study of bronchial tree and lung in Iraqi weasel (*Herpestes javanicus*)

Baydaa H. Mutlak, Ahmed A. Al-Jawadi and Intidhar M. Mnati

− Close abstract View article PDF

The current study aimed to identify the morphological description and branches of the bronchial tree and lung for the weasel *Herpestes javanicus* as one of the Iraqi mammals inhabiting the Iraqi environment. In the current study, 10 samples with an mean weight of 288-564 g were used, trachea and lung were removed from the samples and confirmed using proven solutions and laboratory tests were conducted on 5 samples of the study to identify the branches of the bronchial tree using the technique of casting resin and then exposing the samples to erosion. Weasel has a pair of bright pink sponge lungs that occupy most of the thoracic cavity. The lungs look similar to the clover leaf have a top and three surfaces represented by the costal surface that is convex, and the middle surface, characterized by a narrow and diaphragm surface and is identical to the diaphragm. The right lung is larger than the left lung and the right lung consists of four lobes: apical, middle, caudal and an accessory lobe, while the left lung consists of three lobes: apical, middle, caudal lobes the top of the right lung appeared small and semi-sharp, while the left lung is round and blind. The right primary trachea branched into two branches, the upper branch enters into the apical lobe and branches in turn into two secondary branches, while the lower branched into three branches, the first of which enters into the middle lobe and the second to the middle lobe, the third branch into two branches enter the accessory lobes, while the primary left trachea branch into three secondary or lobe branches before entering the left lung branch, where the first branch enters into apical lobe when the second enters the middle lobe while the third section enters the caudal lobe.

https://doi.org/10.1088/1742-6596/1879/2/022044

OPEN ACCESS

022045

Study of chemical content in *Pimpinella armena* and *Pimpinella kotschyana*: tribe Pimpinelleae/Apiaceae

Zahra B. Muhammad and Talib O. Al-Khesraji

− Close abstract View article PDF

The flavonoid and alkaloid content in the alcoholic extract of the shoots and flowers were identified in two species of the tribe Pimpinelleae / Apiaceae: *Pimpinella armena* and *Pimpinella kotschyana*, and the flavonoids that were detected in this study are: (Apigenin, Coumarin, Kaempferol and Quercetin). The total alkaloids are estimated for these two species. It has been noticed that the species *Pimpinella armena* is a new record on the Iraqi flora, as it was identified through the genetic analysis of nucleotide sequences and registered in the National Center of Biotechnology (NCBI).

https://doi.org/10.1088/1742-6596/1879/2/022045

OPEN ACCESS

022046

Effect of application of Chitosan in skin grafting surgeries in rabbits

Hayder Mohammed Mohsen Al-Tomah, Falah Mahmood Hameed, Ali J. AL-Nuaimi and Ail Wasfi Sadeq

A study was done at the theatre of department of veterinary Surgery & obstetrics, College of Veterinary Medicine, University of Kerbala, Karbala, Iraq which performed to compare the effect of application of chitosan action as scaffold with collagen fibers. The histopathological findings in operation's sites showed the developments of skin graft's healing which was the guide to monitoring the healing. The results showed that the chitosan-treated grafts was healed more controllable with less scar tissue than non-treated grafts which indicates that the chitosan was coordinated the healing.

https://doi.org/10.1088/1742-6596/1879/2/022046

OPEN ACCESS

022047

Metal complexes of 1,6-bis(1-benzimidazolyl) hexane: synthesis, characterization and biological activity against some soil-borne fungi

Abbas Washeel Salman, Jawadayn Talib Alkooranee, Hayder Dawood Arkawazi, Haitham Kadhim Alsharifi and Michaele Hardie

Metal complexes Mn(II), Co(II), Cu(II), Zn(II) and Ag(I) of the ligand 1,6-bis(1-benzimidazolyl)hexane were synthesized by the reaction of the ligand and appropriate metal salts in l: 1 mole ratio. The ligand and its complexes were characterized using IR, Uv-Vis, 1H and 13C NMR, Mass spectroscopy, and elemental analysis CHN. Depending on the abovementioned techniques, a polymeric structure was proposed to the prepared complexes. Further, all the synthesized compounds were tested against some of the soil-borne fungi namely; *Rhizoctonia solani, Fusarium oxysporum, Fusarium solani* and *Pythium aphanidermatum*. The results showed that the tested compounds have an effect on the growth of pathogenic fungi. This leads to thinking that these compounds could be used one day as new chemical pesticides as an alternative to chemical compounds that have been shown to be resistant to pathogens.

https://doi.org/10.1088/1742-6596/1879/2/022047

OPEN ACCESS

022048

Laboratory evaluation of two isolates of *Meterhizium anisopliae* and *Beauvaria bassiana* to control infesting by *Trogoderma granarium* (Coleoptera: Dermestidae) larvae

Nawal S. Mehdi and Aymen W. Al-Fadili

Trogoderma granarium Everts (Khapra beetle) is a serious pest of stored barley and wheat worldwide. The current research evaluates the efficacy of local isolates of *Meterhizium anisopliae* and *Beauvaria bassiana* compared to an imported isolates when khapra larvae sprayed with concentration of later isolates under laboratory condition, mortalities were recorded for more than two weeks after treatment. Results demonstrated that the larvae were more susceptible to the local isolates of the two fungi than the imported isolates. Cumulative mortalities were 86.67 and 50 when larvae sprayed with 10^9 conidia/ml of local and imported isolates of *M. anisopliae* respectively, and 86.67 and 66.67 when larvae sprayed with 10^9 conidia/ml of laocal and imported isolates of *B. bassiana* respectively after two weeks. The findings of the current study clearly showed

that the local isolates caused higher mortalities than the imported one so they may be used as a good candidates for pragmas of integrated pest management of stored grain pests.

https://doi.org/10.1088/1742-6596/1879/2/022048

OPEN ACCESS

022049

Diversity of Mollusca in some sites of Euphrates River

Feryal Ameen Merza

This investigation of molluscs was carried out at some sites on the river of the Euphrates. Samples of molluscs were collected monthly from June 2019 to November 2019. Fourteen species were investigated which belonged to two Classes: Bivalvia (three species) and Gastropoda (eleven species). The species *Corbicula fluminalis, Pisidium dubium, Melanoides tuberculata, Physa acuta, Gyraulus convexiusculus*, and *Gyraulus intermixtus* seemed in all sites. According to the index of Shanon-Weiner, species diversity ranged from 0.5 to 2.5 bits/individual. Index of Jaccard's similarity showed that the highest similarity was recorded between site one and site two with 60 %.

https://doi.org/10.1088/1742-6596/1879/2/022049

OPEN ACCESS

022050

Diagnostic study to detect toxoplasmosis in some Iraqi sheep

Hiba Riyadh Al-abodi

Parasites are cause a lot of important and serious diseases which widespread to peoples and animals all over the world, vector for disease to humans by consumption of meat sheep fresh as liver or not cooked well meat, so in this way the toxoplasmosis in sheep considered one of the causes economic and social damage and important sources of transfer this infection human, for this fact we must value economic and social damage by investigate the incidence of this disease in sheep, and using accurate methods for

detection of this infection in blood fluids or tissue of sheep, so in this study we using immunological and molecular methods to detection of the parasite in sheep blood specimens in Al-Shamiya city/Al-Qadisiyah government/Iraq, the results explained presence that antibodies in 14 samples (14%) below level significant ($P \leq 0.05$) by using Rapid Test Cassette, while the results depending on (RT PCR) for detection of specific gene of parasite B1 gene in blood specimens showed to (9 of 100)(9%) positive infection results in examined sheep. from these results, we can give simple picture ensured rule the infected sheep in transmission the disease to human although a low percentage of positive infection, presence the disease in sheep indicator to role sheep to transfer the disease to the human an achieved the economic and social damage.

https://doi.org/10.1088/1742-6596/1879/2/022050

OPEN ACCESS

022051

Molecular study to detect *bla*$_{TEM}$ and *bla*$_{CTx-M}$ genes in ESpL *Escherichia coli* and their antimicrobial resistance profile

May Abdul Jaleal Raoof and Mohammed A. Fayidh

− Close abstract View article PDF

The common use of beta-lactam antibiotics resulted in the emergence of bacterial strains capable of spreading and extended-spectrum beta-lactamase (ESβL). Up to 70 of clinical samples, 30 of *Escherichia coli* (*E. coli*) were investigated as ESβL isolates. These isolates collected from inpatients and outpatients to some hospitals in Baghdad. The samples include urine, pus, stool, and blood from both genders, different age groups. The VITEK2 was used to check production of ESβL and for the automated diagnosis of rapid antimicrobial susceptibility experimentation and to the identification of the target bacteria. Technique of PCR was applied to detect the presence of *bla*$_{TEM}$ and *bla*$_{C}$*Tx-M* genes. The results demonstrated that 30(43%) isolates of the current study were ESβL producers. The gel electrophoresis of DNA for positive ESβL isolates gives differentiate results of both *bla*$_{TEM}$ and *bla*$_{CTX}$*-M* genes were observed in 15(50%) and 29(96%) isolates respectively. The antibiotic resistance pattern to 20 antibiotics were showed majority of isolates have the multi-drug resistant (MDR) phenotypes and susceptible to

carbapenems of antibiotic. Furthermore, the results of the genetic analysis, along with the pattern of isolates for antibiotic resistance, it may give an acceptable explanation for the higher presence of the $bla_{CTX\text{-}M}$ gene compared with the proportion of the bla_{TEM} gene in the same isolates.

https://doi.org/10.1088/1742-6596/1879/2/022051

OPEN ACCESS

022052

First record of *Thelohanellus wuhanensis* Xiao & Chen, 1993 (Myxozoa: Myxosporea) in Iraq on the gills of *Carassius auratus* (Linnaeus, 1758)

Kefah Naser Abdul-Ameer and Aisha Sulaiman Obaid

− Close abstract View article PDF

In the current study, the myxobolid, *Thelohanellus wuhanensis* Xiao & Chen, 1993 was recorded for the first time in Iraq from the gills of *Carassius auratus* (Linnaeus, 1758) that was caught from Tigris river near Al-Shawwaka location in Baghdad city during the period from May to October 2020. With this registration, *T. wuhanensis* become the fourth species of the genus *Thelohanellus* so far recorded from the Iraqi fish. The description and measurements of this external parasite as well as its illustrations are given.

https://doi.org/10.1088/1742-6596/1879/2/022052

OPEN ACCESS

022053

Arabidopsis thaliana L. Seeds are A novel source of somatic embryos

Rasha Fawzi Al-Jirjees, Shifa Mahdi Salih and Mozahim Kasim AL-Mallah

− Close abstract View article PDF

Somatic embryogenesis is a valuable tool for investigating the totipotency of plant cells. A simple and efficient protocol for inducing somatic embryogenesis from seeds of *Arabidopsis thaliana* were established. Surface sterilized seeds were placed on agar-solidified Murashige and Skoog (MS) medium free from growth regulators. Callus initiation began 7 days after seeds culture and became visible with the naked eye within

10-14 days. It was friable and yellowish white in color. Within 20 days, callus was transferred to Gamborg's B5 medium containing 1.0 mgL-1 2, 4-D (2, 4-dichlorophenoxyacetic acid) and 0.05 mgL^{-1} Kin for multiplication. The results indicated that somatic embryos had been recorded only in B5 medium supplemented with 0.4 mgL^{-1} TDZ (N-phenyl-N'-1,2, 3-thidiazol-5-ylurea) and it was the best one. Through our observation, different stages of somatic embryos have been found. The results revealed that the continuous transfer of small masses containing several embryos at different stages to the same induction medium subsequently formed a large cluster of shoots, which were rooted in MS medium free from growth regulators and MS hormone-free medium with 0.2activated charcoal. The percentages of rooting were 63% and 51% respectively. This study proved that Arabidopsis thaliana seeds are a novel source for somatic embryos.

https://doi.org/10.1088/1742-6596/1879/2/022053

OPEN ACCESS

022054

Antibacterial, antivirulence and antifungal activity of silver nanoparticles synthesized using alkhal mother shae

Esam J. Al-Kalifawi, Yasamine. J. Al-Azzawi and Mohammed A. Feaza

− Close abstract View article PDF

Silver nanoparticles were biosynthesized using alkhal mother shae. Nanoparticles were characterized using four methods. The results of the fourth methods proved that silver nanoparticles are spherical shape with a size ranging between 30-40 nm. AMS-AgNPs has antibacterial and antibiofilm activity against gram negative and gram positive tested bacteria, and it has antifungal and antivirulence activity against five types of fungi. Results declare the effect of AMS-AgNPs on the fungus, it can disrupt the integrity fungal cell wall, promoting the permeability and the leakage of the cell constituents, and eventually induce cell death, which is reached from the Congo red dye absorption test and the formation of swelling in the hyphae of the fungal. This study revealed that AMS-AgNPs can be used as an alternative medicin for pathogenic bacteria and fungi.

https://doi.org/10.1088/1742-6596/1879/2/022054

OPEN ACCESS

022055

Anatomical study of the *Carissa macrocarpa* (Apocynaceae family) in Iraq

Feryal K. Khalaf

This study was conducted to examine the anatomical aspects of *Carissa macrocarpa*, of stem, leaf and leaf venation. The results obtaind showed that the tissue of the studied parts have important anatomical characteristics in terms of the shape of the cross-sectional of stem and vertical-sectional of leaves. The stem section appeared in circular and the midrib was crescent shape and the stomata appeared on the upper surface of the leaf only, Tetracytic in type. Druses crystals and Aleurone granules appeared on both surfaces of leaves. The venation type was Brochidodromous in which the secondary veins do not end at the edge of the leaf, and each secondary race is connected with the higher race and linked together with a series of prominent arches.

https://doi.org/10.1088/1742-6596/1879/2/022055

OPEN ACCESS

022056

Design, Synthesis and Biological Screening of New Benzimidazole Derivatives

Ali Mohammed Sabur and Muayad Ahmed Rdaiaan

In this study, we synthesized a series of benzimidazole compounds containing. 1,3,4-thiadiazole ring from many reaction steps. The obtained benzimidazole series were characterized by melting point, Data from FT-IR and 1H-13C-NMR and In vitro screening of antibacterial activity against strains of selected pathogenic Gram-positive (*Staphylococcus aureus, Bacillus subtilis*) and Gram-negative (*Acinetobacter baumannii, Pseudomonas aeruginosa*) bacteria relative to (Amoxicillin) and (Ciprofloxacin) as standard antibacterial agents has shown high pharmacological activity.

https://doi.org/10.1088/1742-6596/1879/2/022056

OPEN ACCESS

022057

Purification and Determination of The Arginase Enzyme Activity from Kidney Patients

Nuha Ali Hadi Al-Samarrai and Nadia Ahmed Salih

− Close abstract View article PDF

The current study measuring the effectiveness and purification of the enzyme (arginase) in the serum of kidney diseases samples were collected from Samarra General Hospital from October to December 2019, 60 samples were collected from the infected and 25 samples from he healthy people control group of ages 30-55 years, the effectiveness of the control group was 6.87 ± 2.95, and the patient group was 25.71 ± 8.39., the purification process was carried out using Sephadex G-200 and EDEA cellulose - using a column of separation with dimensions (32 x 1.5nm), the molecular weight of the enzyme was 245 kDa. The study included measuring the level of urea 83.7 ± 23.4mg/dl, Creatinine 2.85 ± 1.19 mg/dl, Total protein 3.8 ± 0.6 mg/dl, Albumin 4.120 ± 0.02 mg/dl, Uric acid 5.19 ± 1.52 mg/dl and Globulin was 1.29 ± 0.01 mg/dl. at P≤0.01.

https://doi.org/10.1088/1742-6596/1879/2/022057

OPEN ACCESS

022058

Synthesis, Theoretical Treatment and Investigation of Adsorption of 4,4'-((1E,1'E)-(Methylenebis(4,1-phenylene))bis(diazene-2,1-diyl))bis(naphthalen-1-ol) on Olive Peel

Zainab J. Khudair, K. Jassim Khawla and Ameena N. Seewan

− Close abstract View article PDF

In this study, the compound 4,4'-((1E,1'E)-(methylenebis(4,1-phenylene))bis (diazene-2,1-diyl))bis (naphthalen-1-ol) synthesized by reaction of 4,4'-Diaminodiphenylmethane with Alpha-naphthol. This compound was identified by using an element C.H.N analyzer, Infra-Red spectrum, Ultraviolet and Visible spectrum, and GC-Mass spectrometry. We used olive peels to adsorb the synthesized dye from an ethanol solution. The results obtained showed that olive peel has a good adsorption on the bis-azo dye. Temperature

and pH effect were studied under multiple conditions. The result showed that the adsorption increased with temperature increasing, and adsorption efficiency according to pH as 7<4<9. Theoretical treatment was studied in gas phase for molecular mechanics and semi-empirical computations using the hyper chem8 program. Dipole moment, formation heat and binding energy were done via the methods (PM_3 and ZINDO/S) at 25°C. Electrostatic potential of active sites were also studied for the newly synthesized bis-azo dye. Vibrational values were evaluate using PM3 method, the theoretical frequencies obtained from the calculations were consistent with the experimental values. HOMO & LUMO (frontier orbitals) were studied by PM_3 method, electronic spectrum was also studied using ZINDO/S method and compared with experimental spectrums. The results obtained were closely related between the theoretical and experimental spectrum.

https://doi.org/10.1088/1742-6596/1879/2/022058

OPEN ACCESS

022059

Synthesis and DNA binding study of Co (II) and V(IV) complexes with O, N, O tridentate 3-methoxysalicylaldehyde-semicarbazide based ligand

Suher M. Dawoud

Cobalt and vanadium complexes with (E)-2-(2-hydroxy-3-methoxybenzylidene)hydrazine-1-carboxamide were synthesized. The ligand was structurally characterized by FTIR, ^{1}HNMR and ^{13}CNMR spectroscopy. The interaction activity of ligand and complexes was investigated with DNA by spectroscopical and physical methods. The results showed an intercalative binding between the synthesized compounds and DNA.

https://doi.org/10.1088/1742-6596/1879/2/022059

OPEN ACCESS

022060

Assessment The Suitable of The Groundwater for Civil uses in Kalhitta Village, Al-Ayadiyah S District, Iraq

Mohammed Hazim Sabry Al-Mashhadany

− Close abstract View article PDF

The current research describes the application of the water quality index (WQI) based on the collection of 50 samples of water sample for 10 wells for five months in the village of Kakhirta in Al-Ayadiyah subdistrict, northwest of Nineveh Governorate. The model was applied using 13 parameters (pH, TDS (total dissolved salts), DO (dissolved oxygen), T.A (Total Alkaline), Cl, Ca, Na, Mg, K, PO_4, SO_4, TPC (Total Plate Count), and F. Colif. (Faecal coliform) depending on the results obtained from the model. The groundwater quality ranged between (218 - 765), which indicates deterioration in water quality due to the high numbers of bacteria TPC and F. Colif., as well as the high total alkaline T.A and hypoxia in the water more the recommended limits for drinking water.

https://doi.org/10.1088/1742-6596/1879/2/022060

OPEN ACCESS

022061

Study of Corrosion Inhibition for Mild Steel in Hydrochloric Acid Solution by a new furan derivative

Israa M H Al-mousawi, Rana S Ahmed, Nafeesa J Kadhim and Ahlam M Farhan

− Close abstract View article PDF

The corrosion inhibition effect of a new furan derivative (furan-2-ylmethyl sulfanyl acetic acid furan-2-ylmethylenehydrazide) on mild steel in 1.0 M HCl was investigated using corrosion potential (ECORR) and potentiodynamic polarization. The obtained results indicated that the new furan derivative (furan-2-ylmethyl sulfanyl acetic acid furan-2-ylmethylenehydrazide) (FSFD) has a promising inhibitive effects on the corrosion of mild steel in 1.0 M HCl across all of the conditions examined. The density functional theory (DFT) study was performed on the new furan derivative (FSFD) at the B3LYP/6-311G (d, p) basis set level to explore the relation between their inhibition efficiency and molecular electronic structure. The final experimental results showed that FSFD act as a good corrosion inhibitor in the acidic solution for mild steel which is in agreement with the results of the theoretical study.

https://doi.org/10.1088/1742-6596/1879/2/022061

OPEN ACCESS

022062

Biochemical Aspect, Antimicrobial and Antioxidant Activities of *Melaleuca* and *Syzygium* Species (Myrtaceae) Grown in Egypt

Omar M. Khalaf, Mohamed S. Abdel-Aziz, Ali M. El-Hagrassi, Abeer F. Osman and Mosad A. Ghareeb

The objective of the present work was to establish the antimicrobial activity of four species of Melaleuca (i.e. Melaleuca leucandron, Melaleuca armillaris, Melaleuca linarifolia, & Melaleuca ericifolia) methanolic extracts and five species of Syzygium (i.e., Syzygium samaragense, Syzygium jambos, Syzygium gratum, Syzygium paniculatum & Syzygium malaccense). To research the chemical composition of the most promising extracts, as well. The antimicrobial activity was evaluated against four pathogenic microbial strains, namely Staphylococcus aureus, Escherichia coli, Candida albicans and Aspergillus niger, the antioxidant activity was evaluated by 2,2'-diphenyl-1-picrylhydrazyl radical (DPPH), while the chemical composition was calculated by gas chromatography coupled to a mass spectrometry method (GC/MS). For the genus of Melaleuca, S. After therapy, aureus pathogens were inhibited with their methanolic extracts with an 8.0-20.0 mm range of inhibition zones, E. Coli with a 0.0-21.0 mm inhibition zone size, C. Albicans with an inhibition zone size of 9.0-18.0 mm, and A. Niger with an inhibition zone scale of 0.0-15.0 mm. Whereas, for the genus Syzygium, S. After treatment with their methanolic extracts, aureus pathogens were inhibited with a 10.0-20.0 mm range of inhibition zones, E. Coli, with an inhibition zone size of 0.0-14.0 mm, C. Albicans with an inhibition zone size of 0.0-21.0 mm, and A. Niger with a range of inhibition zones of 0.0-9.0 mm. The IC50 values in the DPPH assay ranged from 34.60 to 60.97µg/ml for the species Melaleuca. The IC50 values for the Syzygium species ranged from 29.81 to 52.95µg/ml compared to 7.35µg/ml for the normal ascorbic acid. GC/MS research showed that Syzygium gratum's methanolic extract consists of 39 compounds comprising 99.08 percent, with Veridiflorol (7.16 percent) and 2-methyl, 3-

Hexanone being the main compounds (5.74 percent). While Melaleuca armillaris' methanolic extract consists of 30 compounds comprising 97.66%, with Veridiflorol (18.36%) and Globulolol compounds being the key compounds (12.57 percent).

https://doi.org/10.1088/1742-6596/1879/2/022062

OPEN ACCESS

022063

Adsorption Studies of Cobalt (II) Complex By Bentonite clay surface

Sahira S. Abd-Ulrazzaq, Farah A. Dawood and Ahmed T. Numan

− Close abstract View article PDF

This paper is summarized with one of the applications of adsorption behavior; A UV-Vis method has been applied to survey the isotherm of adsorption. Results for experimental showed the applicability of Langmuir equation. The effect of temperature on the adsorption of cobalt (II) Complex by bentonite surface was studied. The results shown that the amount of adsorption was formed to increase, such as the temperature increase (Endothermic process). Cobalt (II) Complex has adsorption studies by bentonite surface at different pH values (1.6-10); these studies displayed an increase in adsorption with increasing pH.

ΔG, ΔH, and ΔS thermodynamic functions of the cobalt (II) Complex for their adsorption have been calculated.

https://doi.org/10.1088/1742-6596/1879/2/022063

OPEN ACCESS

022064

Preparation of Mixed ligand Complexes of Heterocyclic Azo Quinoline Ligand and Imidazole Molecule with Some of Divalent Transition Ions and their Biological Activity Against Multi Drug Resistance Pathogenic Bacteria

Israa N. Witwit, Hawraa M. Farhan and Zahraa Y. Motaweq

− Close abstract View article PDF

Heterocyclic azo compound 2-(8-quinolyl azo)-4,6-dimethyl phenol as a primary ligand and imidazole molecule as a secondary ligand in the basic medium were prepared with novel mixed ligand complexes of Hg(II), Mn(II), Ni(II), Co(II) and Cu(II) ions, these compounds were characterized by Mass, 1HNMR, IR, UV-Vis, Magnetic susbtibility and Molar Conductivity, which suggested octahedral conductivity. Free ligands and five mixed ligand complexes of Hg(II), Mn(II), Ni(II), Co(II) and Cu(II) metal ions with a general formula of [M(L1)(L2)2C1] against eight pathogenic multidrug resistance bacteria, six G-ve bacteria (Pr. mirabilis, S. typhi, E. coli, P. aeroginosa, A. baumanii and K. pneumoniae) and two G+ve bacteria (E. faecalis and S. aureus) were capable of antimicrobial efficacy. The findings show that free ligands have had stronger antibacterial activity on S. Bacterial isolation of typhi and P. aeroginosa relative to other isolates. As for the effectiveness of metal complexes, compared to G+ve bacteria, they usually have a large antibacterial effect on G-ve bacteria, whereas the Hg(II) ion complex has a higher antibacterial effect on most bacterial isolates compared to other metal complexes. Compared with other metal complexes, Mn (II) ion complexes demonstrated poorer antibacterial activity..

https://doi.org/10.1088/1742-6596/1879/2/022064

OPEN ACCESS

022065

Preparation of Polystyrene/Polyacrylonitrile Blends by Electrospinning Technique

Ahmed H Oleiwi, Akram R Jabur and Qusay F Alsalhy

New blend material membranes as fibers produced by electrospinning technology and these membranes were characterized and evaluated their properties in this research. Polyacrynitrile polymer mixed physically with polystyrene to produce the blend membranes. FTIR confirm the occurrence of polymeric blends by establishing the absence of new chemical reactions occurs. The hydrophobicity of the membrane was reduced by increase the PAN percent in the blend. Field emission scanning electron microscopy used to study the morphologies of the membranes and illustrated the average

diameters of produced fibers which found about 1.68-0.73 μm. The average pore size found about 1.28 – 0.31 μm for blend membranes. The result showed an increasing in fibers diameter and pore size with increasing of the PAN percent while the membranes porosity still high percentage about 98%.

https://doi.org/10.1088/1742-6596/1879/2/022065

OPEN ACCESS

022066

Evaluation of Ceruloplasmin ferroxidase activity and lipid profiles in patients with Valvular heart diseases

H K Sacheat, S Z Husseinand and S S Al-Mudhaffar

One of the major health problems causing defects or damage to one or more of the four heart valves [aortic, mitral, pulmonary, and tricuspid] is valvular heart disease [VHD]; it occurs due to congenital abnormalities or acquired pathology. It is a defect that results in weak heart valves and is therefore unable to function as precise pathways of the blood. The aim of the current study was to evaluate the ferroxidase activity of ceruloplasmin (Cp) and the lipid profile of valvular heart disease patients in sera. Ninety subjects were included in this study and 60 patients with HDV were divided into two subgroups according to the affected valve: 33 patients with aortic valve disease (AV) and 27 patients with mitral valve disease (MV group). In addition, 30 healthy individuals were registered in all groups as control(C) group Serum copper (Cu), total protein (TP), activity and specific activity of ferroxidase Cp, and lipid profile were measured. The results showed that there was a highly significant increase in patient (AV & MV) groups compared to the C group in activity, specific Cp and Cu activity levels. In addition, compared to the C group, triglyceride (TG) and very low density lipoprotein (VLDL) levels showed a highly significant increase in the AV and MV groups. No significant differences were found between patients and control groups in TP, Total Cholesterol (TC), Low Density Lipoprotein Cholesterol (LDL-C) & High Density Lipoprotein Cholesterol (HDL-C)

levels. Likewise, for all parameters, there were no significant differences between the AV and MV groups. In conclusion, the high serum level of Cu and the activity of Cp ferroxidase may be considered to be a risk factor for VHD.

https://doi.org/10.1088/1742-6596/1879/2/022066

OPEN ACCESS

022067

Regeneration of Used Oils by Red Mud and DESs (Reline)

W M Saleh, R Z Al-Khayat, S h M Saied, A M SYassin and F fadil

– Close abstract View article PDF

To regeneration of oils which are used in cars engines to lubricate its moving parts, and to get rid of highly contaminants which must be separated to reuse the engine oils. In the column chromatography, the waste oil was treaded as mobile phase (eluent) with petroleum ether (40-60°C), while the red mud (alhuor) is a stationary phase for adsorbed the impurities. The effect of the new method using deepeutectic solvent (DESs Reline) as a kind of ionic liquids to help extract impurities by adsorption (choline chloride and urea). Moreover, some thermal and physicochemical properties like density, thermal and electrical conductivity, ash percentages, viscosity, specific gravity and pH values were determined. Values were determ.using TGA for blank oil for comparison and differential scanning calorimetric analyses (DSC).

https://doi.org/10.1088/1742-6596/1879/2/022067

OPEN ACCESS

022068

Conductometric Study of Proline-Mn (II) Complex in Some Solvents at Various Temperatures, with Computational Factors Calculation

Fanar M Al-Healy, Shayma H Abdulrahman and Anfal R Mahmoud

– Close abstract View article PDF

The equivalent conductivities of proline in water, methanol were studied in the temperature range of 288.15 to 313.15 K at 5 K intervals, in mixtures of methanol and water at percentages of 10 %, 20%, 30%, 40% and 50% of methanol at 37 °C. The

experimental data were treated by the Lee-Wheaton conductivity equation of unsymmetrical electrolytes (1:2) (1 molecule of metal with 2 molecules of ligand) derived to calculate the conductivity parameters, equivalent conductance at infinite dilution Λ_o, ionic conductivity, association constant Ka and the main distance between ions in solution(R) at best fit values of (6Λ). Thermodynamic quantities for the ion-association reaction ΔG°, Δ℧° and ΔS°) have been also measured. The results of the analysis showed that the ions of the complex can be separated by solvent molecules (SSIP). The values of Ka, Λ° and R were found to be different from one solvent to another depending on the interactions in the solution. Furthermore, the chemical structure of the Proline-Mn complex was optimized by using of Gaussian interface version 16.0 program of chem3D to optimiz the features of complex molecule. The suggested statistical model possesses only two parameters with excellent values of the square regression coefficient (r^2) and cross-validation (q^2) are equal to 0.999 and 0.994, respectively, which refers to the perfect relationship between Ka value and the physical properties of the solvent.

https://doi.org/10.1088/1742-6596/1879/2/022068

OPEN ACCESS

022069

Levels of Heavy Metal and Trace Element Among Children with Autism Spectrum Disorders

Furqan Moein Auda, Amar M Ali and Shaymaa Dhyaa

− Close abstract View article PDF

The aim of this study was estimation the concentration of heavy and trace element in blood samples for autism spectrum disorder *material and method*: sixty patients with autism participated in the present study, all of these patients are registered in an autism center in Basrah province(Iraq). At the same time, 30 healthy children contributed in the study as a control group. The heavy levels were estimated and trace elements (chromium, zinc, selenium, copper, lead, mercury and iron) in the patient and control groups by used energy dispersive X-ray spectroscopy (EDS). The basic principle should appear in the X-rays emitted by the different energies coming from the sample at the same time as a beam

of an electron is moving its factors. *Conclusion*: The results showed that there was no significant difference between patients and the control group in all trace elements except zinc. On the other hand, the study showed that there was no significant change between male and female in all levels of trace elements except selenium.

https://doi.org/10.1088/1742-6596/1879/2/022069

OPEN ACCESS

022070

Synthesis and Study Antibacterial Activity of Some New Polymers Containing Maleimide Group

Ruwaidah S. Saeed, Fatimah Ali Hussein, Sana Hitur Awad and Muna S. Al-rawi

By condensation of benzaldehyde with thiourea in absolute ethanol in the presence of glacial acetic acid as a catalyst, the Schiff base(1-benzylidenethiourea)[I] was synthesized by synthesis of 4-(3-benzylidenethioureido)-4-thioxobut-2-enoic acid compound[II] by reaction of maleic anhydride with schiff base [I] in DMF. When treating compound [II] with ammonium persulfate (NH4)2S2O8 (APS) as an ethanol initiator to obtain polymer [III], compound [III] reacted to polymer [IV] with SOCl2 in benzene. Sulfamethizole, celecoxib, salbutamol, 4-aminoantipyrine to yield polymers [V-VIII], compound [IV] reaction with different drugs. Spectral evidence established the structure of synthesized compounds: FTIR and 1HNMR, UV-Vis Spectroscopy and Elemental Analysis (C.H.N-S). These synthesized derivatives [V-VIII] were tested for their antibacterial activity against Bacillus subtilis (G+) and Escherichia coli (G-) by agar well diffusion process, and the results showed that all polymers had a greater diameter of the growth inhibition region. This may be relative to the presence of sulfamethizole medication, maleimide group and Schiff bases, Polymer[V] demonstrated excellent inhibition against Bacillus subtilisa and E.coli.

https://doi.org/10.1088/1742-6596/1879/2/022070

A Novel Coated Wire Electrode And Coated Graphite Electrode for Potentiometric Determination of Amitriptyline Hydrochloride in its pharmaceutical preparations, urine and blood plasma

Muthana Saeed Ali and Ali Ibraheem Khaleel

This paper uses the potentiometric method to evaluate (amitriptyline hydrochloride, AM) by creating selective electrodes for AM drugs with the active ingredient (Ammonium Reinackate, AR) using a plasticizer (Dibutyl phthalate, DBP). The results showed that for (Coated Wire Electrode (CWE)) and Coated Graphite Electrode (CGE) respectively, the Nernstian slope of the prepared Am-AR-DBP electrodes is (57.293, 58.803 mV / decade). With a pH range of (4-7) and a concentration range of 1 ?? 10 ?? Λ(-6)-1 ?? 10 ?? Λ(-1) M for both electrodes, the upper and lower limit of detection for the Am-AR-DBP CGE is 0.2042M, 4.8 ?? 10 ? Λ(-7) M, and the upper and lower limit of detection for the Am-AR-DBP CWE electrode is 0.2051M, 4.91 ?? 10Λ(-7) M, respectively. The response time ranges from 20-83 sec, 14-76 sec for CWE and CGE electrodes respectively. For the CWE electrode, the age of the electrodes is 26 days, and for the CGE electrode, 42 days. The research included calculating the selectivity with the presence of interferers of these electrodes where the K(i, j)Λpot values for all ions were less than 1. In the estimation of the drug Amitriptyline Hydrochloride in the pharmaceutical preparation (Amitriptyline tablets), the manufactured electrodes were used by following the direct process, the standard method of additions, the possible titration method and the homogeneity of the material sample, as well as the drug was estimated in urine and blood plasma with a recovery of not less than 100.57 for urine and 99.46 f for urine.

https://doi.org/10.1088/1742-6596/1879/2/022071

OPEN ACCESS

022072

Influence of ultrasonic pre-treatment on Pyrolysis and Combustion of Sewage Sludge by TG

Ruaa O. Taha and Farah Ali Mohammed

The combustion and pyrolysis processes of sewage sludge were studied in the current report. Two kinds of sewage sludge(SS) were used, SS the sewage sludge was not treated, while SS-U90KHz the ultrasonic bath pre-treated sewage sludge with a frequency of 90KHz was not treated. Wastewater treatment plants are the origins of waste sludge. Analyses were performed roughly and finally. Thermogravimetric research analyzed the thermal behaviour of the analysed sewage bucket (TGA). The samples were heated at a constant rate of 25 to 800 Celsius by air (combustion) and nitrogen flow (pyrolysis). For sludges which have been investigated. In the TG/DTG curves, comparable thermal profiles were available. All of the TG/curves DTG's were divided into three periods. At the same time, during the combustion stage, the sewage sludge decomposition occurred in the 180-580 0C range. The pyrolysis procedure took place at a lower rate, but less weight loss..

https://doi.org/10.1088/1742-6596/1879/2/022072

OPEN ACCESS

022073

Pretreated Fishbone as Low Cost-Adsorbent for Cationic Dye Adsorption from Aqueous Solutions: Equilibrium, Optimization, Kinetic and Thermodynamic Study

Muna Abd Ul Rasool Al-Kazragi and Dhafir T.A. Al-Heetimi

− Close abstract View article PDF

The present study investigated the use of pretreated fish bone (PTFB) as a new surface, natural waste and low-cost adsorbent for the adsorption of Methyl green (MG, as model toxic basic dye) from aqueous solutions. The functional groups and surface morphology of the untreated fish bone (FB) and pretreated fish bone were characterized using Fourier transform infrared (FTIR), scanning electron microscopy (SEM) and Energy dispersive X-ray spectroscopy (EDS), respectively. The effect of operating parameters including contact time, pH, adsorbent dose, temperature, and inorganic salt was evaluated. Langmuir, Freundlich and Temkin adsorption isotherm models were studied and the results showed that the adsorption of basic dye followed Freundlich isotherm. Kinetic modeling of the data at different temperatures confirmed pseudo-second-order(P-2-O) model, along with calculated thermodynamic parameters depicted that the adsorption

process is spontaneous and endothermic in nature. Diffusion studies suggested that intra-particle diffusion is not the singular rate-controlling factor. The results indicated that 92% of MG capable of being sequestered under optimum adsorption conditions: pH 10.64, adsorbent dose 0.1 g/L, and 60 min contact time. Finally, the results showed that the pretreated fish bone can be effectively used as a proper adsorbent for the adsorption of cationic dye from aqueous solutions.

https://doi.org/10.1088/1742-6596/1879/2/022073

OPEN ACCESS

022074

Metal Complexes of Multidentate N_2S_2 Heterocyclic Schiff-base Ligands;Formation, Structural Characterisation and Biological Activity

Baidaa K Al-Rubaye, Mohamad J. Al-Jeboori and Herman Potgieter

The synthesis of ligands with N_2S_2 donor sets that include imine, an amide, thioether, thiolate moieties and their metal complexes were achieved. The new Schiff-base ligands; N-(2-((2,4-diphenyl-3-azabicyclo[3.3.1]nonan-9-ylidene)amino)ethyl)-2-((2-mercaptoethyl)thio)-acetamide (H_2L^1) and N-(2-((2,4-di-p-tolyl-3-azabicyclo[3.3.1]nonan-9-ylidene)amino)ethyl)-2-((2-mercaptoethyl)thio) acetamide ($H2L^2$) were obtained from the reaction of amine precursors with 1,4-dithian-2-one in the presence of triethylamine as a base in the CHCl3 medium. Complexes of the general formula $K_2[M(Ln)Cl_2]$, (where: M = Mn (II), Co(II) and Ni(II)) and [M(Ln)], (where: M = Cu(II), Zn(II) and Cd(II); n =1-2, expect $[Cu(HL^2)Cl]$) were isolated. The entity of ligands and complexes including their purity were confirmed using elemental microanalysis (C.H.N.S), atomic absorption (A.A), chloride content, conductivity measurement's, melting point and thermal analysis technique. The molecular structures were elucidated with FT-IR, UV-Vis, magnetic susceptibility, ^{1}H-and ^{13}C-NMR and mass spectroscopy. The synthesised compounds were evaluated for their activity against bacterial strains (G+ and G-) and fungi species. The tested compounds indicated that; the ligands have not shown any antimicrobial activity against *Escherichia coli*. The Cd(II) complexes, for ligands $H2L^1$ and $H2L^2$, display the higher antimicrobial activity,

compared with the other complexes. The H_2L^1 and H_2L^2 have not shown any activity against *Candida albicans*. All complexes for ligands (H_2L^1 and H_2L^2) exhibited less activity against *Candida albicans*, compared with other types of fungi.

https://doi.org/10.1088/1742-6596/1879/2/022074

OPEN ACCESS

022075

Removal Congo Red Dye on Surface of Nano Charcoal Activated by Used Central Composite Chemometric Method

Aayad Ammar Sayhood, Noor Hassan Abdulrudhaand and Mohanad Hazim Halboos

In this paper; the modern method was used to remove the congo red dye (CR) from its aqueous solutions by chemometric separation. The nano charcoal activated (NCA) was used to remove the CR and the factors affecting the adsorption process were studied simultaneously to reduce the number of experiments followed and to rely on central composite design and the method of response surface by used statistica 12 program. This gives the relationship between all the variables simultaneously. It was found that the removal efficiency reached to 98.371%.

https://doi.org/10.1088/1742-6596/1879/2/022075

OPEN ACCESS

022076

Loading and Activating a Carbon Surface and Applied for Congo Red Adsorption, Kinetic Study

Russol Abdul Salam Faraj and Ahmed Mohammed Abbas

this paper contains preparation of Active carbon surface (AC) from pro so millet grain husks and Loading and activating by Iron oxide and hydrogen peroxide sequentially to obtain surface (ACIPE). The changes of previous processes on Active carbon surface were diagnosed by Fourier transform infrared spectroscopy (FTIR) and Scanning electron microscopy (SEM). These surfaces (AC and ACIPE) were using as adsorbent for

removing of congo red dye from aqueous solutions under certain conditions through batch system. More than one kinetic model was applied to congo red dye adsorption process and it was found that the most kinetic model applied to it is a model (pseudo second order model). In addition to the adsorption efficiency of the surface after activation and loading, it was much better than the main surface where the adsorption efficiency of the first and second surface was equal (27%, 85%) sequentially at higher temperatures.

https://doi.org/10.1088/1742-6596/1879/2/022076

OPEN ACCESS

022077

Audio source separation using supervised deep neural network

Riham J. Issa and Yusra F. Al-Irhaym

The speech signals inserted in the computer may be mixed as a result of interference with signals from other sources. These signals may be speech signals or noise. One of the most famous examples of this problem when a group of people speaking in the same time is the "Cocktail Party". This problem produces a mixture of different speech signals, called the mixed signal. To solve this problem, the audio signals that make up the mixed-signal must be restored to their sources. This task is called separating audio sources. In this paper, supervised Deep Recurrent Neural Networks with Bi-directional Long Short Term Memory (Supervised DRNN-BLSTM) were used. To achieve a monaural source separation, we build a model to separate audio signals from a monaural mixed signal. This mixed signal consists of two different audio signals (male-female). We predict two types of time-frequency masks (Ideal Ratio Mask (IRM), and Optimal Ratio Mask (ORM). They are used to achieve the separation of the target audio sources from the mixed signal. We test the model on a dataset with (500) mixed signals. Each mixed signal three seconds in length and consists of two speaker signals (Female-Male). They are recorded in a stereo format at 8192kHz, our approach achieves Signal-to-Distortion ratio

(SDR) (0.183.db), Source-to-interference Ratio (SIR) (0.198.db), and Source-to-Artifacts Ratio (SAR) (0.13.db) gain using (ORM) mask compared to the existing model using (IRM) mask.

https://doi.org/10.1088/1742-6596/1879/2/022077

OPEN ACCESS

022078

A Parallel Adaptive Genetic Algorithm for Job Shop Scheduling Problem

Wathiq N. Abdullah and Salwa A. Alagha

In order to enhance the production efficiency, scheduling problem of job-shop has used that thought of complex problem with complicated constraints and structure. This problem is characterized as NP-hard. In most cases, the excessive complexity of the problem makes it difficult to discover the best solution within affordable time. Hence, searching for estimated solutions in polynomial time rather than precise solutions at excessive cost is favored for challenging situations of the problem. In this paper, a parallel genetic algorithm with proposed adaptive genetic operators and migration operation is applied for job-shop scheduling problem. Through tests on numerous different experimental cases, the adaptive operator of genetic algorithm and the parallelism strategy are considerably improving the results effectively while decreasing the computation time. Also, the migration operation gives a greater effect on the performance of the algorithms.

https://doi.org/10.1088/1742-6596/1879/2/022078

OPEN ACCESS

022079

Human Activity Diagnosis System Based on the Internet of Things

Mohammed Khammas Jabar and Ali Kadhum M. Al-Qurabat

The Cognitive Internet of Things (CIoT) is the next step in enhancing the accuracy and reliability of the Internet of Things (IoT) technology used for Cognitive Computing, which plays a main role in health and disease diagnosis. The study was suggested a diagnosis method to sound sensitivity by developing a framework with IoT and cloud based on a facial expression recognition system. It was achieved through the creation of a cognitive IoT hardware-based environment and the elements of the programs that are implemented to test the behaviour of people suffering from sound sensitivity, this operation is done by using a camera and image processing and it used Convolutional Neural Network (CNN) as a facial recognition software to track human facial emotions through live video. The sentiment values were analysed that they were collected and stored in a cloud using Transmission Control Protocol (TCP) protocol. These emotions were categorized as abnormal or normal. Normal states represented by happy or natural feelings that give the impression that the environment is suitable for people's senses and that they do not suffer from discomfort towards this environment, therefore; the system operates on a mechanism to increase the volume in this environment by using an Arduino microcontroller. Although the device operates automatically in the event of hypersensitivity detection, it reduces this severity. The obtained results showed the efficiency of the proposed system in recognizing facial emotions with 80% accuracy.

https://doi.org/10.1088/1742-6596/1879/2/022079

OPEN ACCESS

022080

Personal identification system based on multi biometric depending on cuckoo search algorithm

Ansam Nazar Younis

In modern devices, many personal identification systems are used using various biometrics to confirm the identity of an individual and identify him for several purposes. Some of these essential biometrics are used in this paper to help identify a person while attaining social distance because of the widespread epidemics. The features of the face, eyes, nose, and finally, the features of the mouth are used in this article. The work begins

by detecting the parts of multibiometric from the input images using Viola-Jones face detection algorithm with a modification to it then segment them. After that, various initial treatment processes begin which helps clarify them to facilitate subsequent operations. Also, a Histogram of oriented gradient method(HOG) is used to extract the significant features of those image segments. The extracted features from these segments are entered into the developed cuckoo search algorithm(DCSA), the best image segment within the used dataset is searched for similar in terms of characteristics to the entered image segment. The work has also been developed so that the system is executed on two cores using parallel processing technology to utilize the processor as much as possible and reduce the time it takes to implement the system and identify the person concerned. A high identification rate has been reached, reaching 99.25%, and overall speed up 1.40323 sec relative to serial execution.

https://doi.org/10.1088/1742-6596/1879/2/022080

OPEN ACCESS

022081

Predictions of COVID-19 Spread by Using Supervised Data Mining Techniques

Wid Akeel Awadh, Ali Salah Alasady and Hadeel Ismail Mustafa

In the wake of the outbreak of the new coronavirus, the countries in the world have fought to combat the spread of infection and imposed preventive measures to compel the population to social distancing, which led to a global crisis. Important strategies must be studied and identified to prevent and control the spread of coronavirus COVID-19 disease 2019. In this paper, the effect of preventive strategies on COVID-19 spread was studied, a model based on supervised data mining algorithms was presented and the best algorithm was suggested on the basis of accuracy. In this model, three classifiers (Naive Bayes, Multilayer Perceptron and J48) depended on the questionnaires filled out by Basra City respondents. The questionnaires consisted of 25 questions that covered fields most related to and that affect the prevention of COVID-19 spread, including demographic, psychological, health management, cognitive, awareness and preventive factors. A total

of 1017 respondents were collected. This model was developed using Weka 3.8 tool. Results showed that quarantine played an important role in controlling the spread of the disease. By comparing the accuracy of the algorithms used, the best algorithm was found to be J48.

https://doi.org/10.1088/1742-6596/1879/2/022081

OPEN ACCESS

022082

Knowledge management model to enhance Enterprise Resource Planning system in Green software development process

Sarah M Yahya and Mustafa S Khalefa

The global economy is constantly evolving and corporate technology and business are an important factor in this development and because of the accompanying negative impact on the environment and society, the role of sustainability and sustainable development highlights. To further investigate the scope of the green software development process and its integration with information systems such as the Enterprise Resource Planning (ERP) system, we presented this study due to its importance in minimizing the negative effects of information technology on our natural environment. In this connection, there is a have to combine sustainability and information technology allow organizations to behave in a manner to going greener. Comprehending that the Enterprise Resource Planning (ERP) system is one of the very effective commercial enterprise solutions for organizations, it is necessary to align its use with sustainability factors through the utilization of green IT practices, the objective of this research study is to provide a design model to enhance ERP system in green software development process. So every company must look into the impact of the utilization of Information and communications technology (ICT) on our natural environment and take care to adopt methods to decrease the effects negative on its. Therefore, knowledge management (KM) can be used as the facilitation tool. This research paper presents the results of qualitative research, which

proposes a model that to the possibility of enhancing the implementation of the ERP system in the Green Software Development Process by using green IT practices and knowledge management as facilitation tools.

https://doi.org/10.1088/1742-6596/1879/2/022082

OPEN ACCESS

022083

The Prediction of COVID 19 Disease Using Feature Selection Techniques

Rasha H. Ali and Wisal Hashim Abdulsalam

COVID 19 has spread rapidly around the world due to the lack of a suitable vaccine; therefore the early prediction of those infected with this virus is extremely important attempting to control it by quarantining the infected people and giving them possible medical attention to limit its spread. This work suggests a model for predicting the COVID 19 virus using feature selection techniques. The proposed model consists of three stages which include the preprocessing stage, the features selection stage, and the classification stage. This work uses a data set consists of 8571 records, with forty features for patients from different countries. Two feature selection techniques are used in order to select the best features that affect the prediction of the proposed model. These are the Recursive Feature Elimination (RFE) as wrapper feature selection and the Extra Tree Classifier (ETC) as embedded feature selection. Two classification methods are applied for classifying the features vectors which include the Naïve Bayesian method and Restricted Boltzmann Machine (RBM) method. The results were 56.181%, 97.906% respectively when classifying all features and 66.329%, 99.924% respectively when classifying the best ten features using features selection techniques.

https://doi.org/10.1088/1742-6596/1879/2/022083

OPEN ACCESS

022084

The Classification of Fetus Gender Based on Fuzzy C-Mean Using a Hybrid Filter

Ahmed S Aljuboori, Firas A. Abdullatif and Duraid Y. Mahmmed

− Close abstract View article PDF

This paper proposes a new approach, of Clustering Ultrasound images using the Hybrid Filter (CUHF) to determine the gender of the fetus in the early stages. The possible advantage of CUHF, a better result can be achieved when fuzzy c-mean FCM returns incorrect clusters. The proposed approach is conducted in two steps. Firstly, a preprocessing step to decrease the noise presented in ultrasound images by applying the filters: Local Binary Pattern (LBP), median, median and discrete wavelet (DWT), (median, DWT & LBP) and (median & Laplacian) ML. Secondly, implementing Fuzzy C-Mean (FCM) for clustering the resulted images from the first step. Amongst those filters, Median & Laplace has recorded a better accuracy. Our experimental evaluation on real data from the Kadhimiya teaching hospital shows that the proposed CUHF is a better method when compared to the accuracy of the other integrated filters.

https://doi.org/10.1088/1742-6596/1879/2/022084

OPEN ACCESS

022085

Air Pollution Monitoring based Fuzzy Controller with Embedded System

Saja Sattar Hasanh, Abbas Hussein Miry and Tariq M. Salman

− Close abstract View article PDF

Air pollution has a wide and great influence on the concentration of constituents of the atmosphere, which leads to many effects such as acid rains and global warming. In order to avoid such unwanted adverse imbalances in the nature, designing an air pollution monitoring system (APMS) is very important. This paper discussed the development of an effective solution for monitoring the air pollution by making an Arduino-Based Air Pollution Monitoring System (APMS). Carbon monoxide and Carbon Dioxide concentration levels in air were measured and monitored using MQ4 and MQ7 gas sensors and Arduino atmega microcontroller. These sensors can detect many harmful gases and can be used for measuring their amount very accurately. The concentrations of CO and CO2 in particle per million (PPM) will be monitored and displayed on the LCD

very easily. Based on these measurements the pollution level could be monitored, determined, and displayed. The experiments were carried out using the developed wireless APMS under various physical conditions. The results showed that the designed system collects reliable and reasonable real time pollution data. Three hour sampling time was executed in each location. One of the logical functions that are widely used is fuzzy logic. A fuzzy logic artificial intelligence for gas sensors is used which clarifies the presence as well as the concentration of CO and CO2 efficiently. Fuzzy logic will gives the decision about whether the air is polluted or unpolluted. This logic function we can process some existing data into a form of output which can be in the form of a status or state of action that will be performed by a tool. This proposed system will contribute in the construction of an APMS in the outdoor or even in the indoor environment.

https://doi.org/10.1088/1742-6596/1879/2/022085

OPEN ACCESS

022086

An Automated Mammals Detection Based on SSD-Mobile Net

Elham Mohammed Thabit A. Alsaadi and Nidhal K. El Abbadi

Animal detection techniques are one of the researcher's interests and challenge. There are many difficulties faces by the researchers in this field that reduce the detection performance and efficiency, such as variation of image illumination, animal occlusion, the similarity of animal colors with background environment, etc.

Multi-label Image Detection and classification of Mammals animals is the goal of this paper which we proposed to achieve in this proposal by using Single Shot Multi-Box Detector (SSD) and MobileNet v1 coco_2017 model. Localizing and classifying multiple objects (animals) of the Mammal category in digital images is another goal. The suggested SSD is regarded as a more accurate, fast, and efficient way to detect objects of different sizes based on deep learning technology.

In this proposal, we used 2000 images in the network were collected from the standard dataset (such as Caltech 101) and the net. The SSD framework improves the detection and recognition processes of Convolution Neural Network (CNN). During the prediction time, the network introduces scores to the presence of every object class and bounded each object in the image with a box. Each box has a label that indicates the type of the object and the score represents the probability of the relationship of the object to that type. Boxes during the process are modified for getting the best matching to the object's shape. The experimental results of this work proved the efficiency of classifying and detecting animals even in the variation of illumination, pose, and occlusion. Detection and classification accuracy is up to 98.7 %. This suggestion is more reliable and accurate than other similar works and detects a wide range of Mammals animals, unlike other similar works.

https://doi.org/10.1088/1742-6596/1879/2/022086

OPEN ACCESS

022087

Image Steganography using Dynamic Threshold based on Discrete Cosine Transform

Namar A Taha, Amna Al Saffar, Alaa A Abdullatif and Firas A Abdullatif

The art of preventing the detection of hidden information messages is the way that steganography work. Several algorithms have been proposed for steganographic techniques. A major portion of these algorithms is specified for image steganography because the image has a high level of redundancy. This paper proposed an image steganography technique using a dynamic threshold produced by the discrete cosine coefficient. After dividing the green and blue channel of the cover image into 1*3-pixel blocks, check if any bits of green channel block less or equal to threshold then start to store the secret bits in blue channel block, and to increase the security not all bits in the chosen block used to store the secret bits. Firstly, store in the center of the block and then store another bit in the write or left bit depended on differences between them.

The proposed method was applied to many color images and many measurement terms used to show the efficiency of it. The experiment result showed good result that the PSNR = 53.76, MSE = 0.273, SSIM= 0.999, with embedding rates 0.55

https://doi.org/10.1088/1742-6596/1879/2/022087

OPEN ACCESS

022088

Impact of Feature Selection for Data Classification Using Naive Bayes Classifier

Eman Hato

In the field of data processing and analysis, the dataset may be a large set of features that restrict data usability and applicability, and thus the dimensions of data sets need to be reduced. Feature selection is the process of removing as much of the redundant and irrelevant features as possible from the original dataset to improve the mining process efficiency. This paper presented a study to evaluate and compare the effect of filter and wrapper methods as feature selection approaches in terms of classification accuracy and time complexity. The Naive Bayes Classifier and three classification datasets from the UCI repository are utilizing in the classification procedure. To investigate the effect of feature selection methods, they are applied to the different characteristics datasets to obtain the selected feature vectors which are then classified according to each dataset category. The datasets used in this paper are the Iris, Ionosphere, and Ovarian Cancer dataset. Experimental results indicate that the filter and wrapper methods provide approximately equal classification accuracy where the average accuracy value of the Ionosphere and Ovarian Cancer dataset is 0.78 and 0.91 for the same selected feature vectors respectively. For Iris dataset, the filter method outperforms the wrapper method by achieving the same accuracy value using only half number of selected features. The results also show that the filter method surpasses when considering the execution time.

https://doi.org/10.1088/1742-6596/1879/2/022088

OPEN ACCESS

022089

An Improved Data Hiding using Pixel Value Difference Method and Hyperchaotic System

Sameera Abbas Fadhel, Zeena N. Al-Kateeb and Muna Jaffer AL-Shamdeen

– Close abstract View article PDF

The present paper builds a security system to encrypt and hide important text data. The system utilized an AES method to conduct an encryption process, followed by hiding the encrypted data using an improved Pixel Value Difference (PVD) technique. The method works to builds a map to hide data in a non-sequential way by relying on a hyperchaotic system to increase the security level. The system methodology proposed that the data embedding process is in one of the three levels of the colour image (Red, Green, and Blue), where the embedding level will determined based on the coordinates of the PVD pair points that is increase the efficiency of performance. A set of measures was used to measure the quality of steganography where we used MSE, PSNR, SNR, and Corr, and the results are well and satisfactory. The proposed method records the least MSE value with 0.85348784908256, while the Corr values did not decrease about 0.994145776227782. The proposed method also proved successful and effective in retrieving and decoding data, where the BER scale was equal to zero for all retrieved text.

https://doi.org/10.1088/1742-6596/1879/2/022089

OPEN ACCESS

022090

Multi-Camera Collaborative Network Experimental Study Design of Video Surveillance System for Violated Vehicles Identification

Hasan Thabit Rashid and Israa Hadi Ali

– Close abstract View article PDF

In this paper, we propose an experimental study of multi-camera collaborative network for surveillance the highway traffic turn in real life scenario, the target of surveillance based offline video processing is capturing the violated vehicles that driving violated paths in many cases specified by user-defined rules. Best topology of the experiment zone is considered and covered by four pillars; each has two (fixed and motorized) cameras that casing the entire specific effective field of view. As to author knowledge, there is no

such available experiment, and hence, it could serve researchers that interested in. However, the experiment is done for around 180 recorded hours for 8 videos during 9 days, each video for one camera. It is designed based on the collaborative cameras principle for intelligent video surveillance systems and the outcomes show that the surveillance and the tracking of violated vehicles have been successes in most user-defined rules cases for more than 90 % cases.

https://doi.org/10.1088/1742-6596/1879/2/022090

OPEN ACCESS

022091

Higher Education's Certificates Model based on Blockchain Technology

Mustafa A. Ali and Wesam S. Bhaya

Blockchain technology has revolutionized economic transactions, and it is expected to spread and influence other fields. It can create innovative and destructive effects on the systems that need to be executed, store, verified, and continually update digital data among participating parties. Moreover, it provides security, privacy, trust, and transparency. In the education field, there is a shy presence of some blockchain applications, and the majority of them have a pilot character. Hence, a model based on blockchain is introduced in this study, which aims to provides easy to apply for certificates, as well as share and verify these certificates with a third party. Moreover, the mechanism of the proposed model proposes permanent distributed hashes records of students' certificates in Higher Education to reduce forgery. In conclusion, the study discussed the opportunities, benefits, features, and challenges are represented by deploying this model in the Higher Education field.

https://doi.org/10.1088/1742-6596/1879/2/022091

OPEN ACCESS

022092

Brain Computer Interface using EEG Based Sequential Minimal Optimization algorithms

Batool Abd Alhade, Israa Safaa Ahmed and Baidaa Zahid Kamil

− Close abstract View article PDF

The concept of interfacing brains with robots/machines has been capturing human interests for a long time. The technology of the Brain-computer interface (BCI) has been aimed at building an interface between the brain and any electronic/electrical device (such as, smart home appliance, a wheelchair, and robotics devices) with the use of the electroencephalogram (EEG) that can be defined as a non-invasive approach for the measurement of the electrical potentials from the electrodes that have been placed on the scalp, produced by the activity of the brain. Over the past years, pattern classification was a highly challenging research field. Presently, the tasks of the pattern classification. In this paper, we chose motor imagery with the use of the single trial EEG signal, the SOM has been utilized to classify the signal processing algorithm (FICA). In comparison to other algorithms of the EEG signal analyses. It has achieved a classification accuracy of up to 88.% in comparison with the other method where the reported accuracy has been 65%. The SOM classification algorithm has been fast, simple, efficient, and easy to use. It achieved satisfactory results at the BCI.

https://doi.org/10.1088/1742-6596/1879/2/022092

OPEN ACCESS

022093

Digital Modulation Classification Based On Chicken Swarm Optimization and J48 Algorithm

Zainab Kadhm Obeas, Shaimaa Safaa Ahmed Alwaisi and Nadie Kadom Abd

− Close abstract View article PDF

Automatic Modulation Recognition (AMR) has a significant impact in the military as well as civil applications. Recognizing the modulation of the received signal has been considered as an intermediate step between the detection and demodulation of the signal. Which is why, in many military and communication systems, the AMR is considered as part of the system. Presently, due to increasing digital modulations in military and civil applications. Digital modulation recognition is especially important. Usually for the AMR, a small number of the received signal features are obtained and utilized. The choice

of the suitable feature plays an important part in the increase of AMR efficiency. The presented paper indicates hybrid intelligent system for the recognitions of digital signal types, consisting of 3 major modules: classifier module, feature extraction module and J48 Classifier that was used for the first time in our research in the field of classification of modulated signals and optimization module by Chicken Swarm Optimization (CSO). To get better results of the system suggested optimization the features to discard weak or irrelevant features in the system and keep only strong relevant features Chicken Swarm Optimization. The results of simulation confirm the high accuracy of recognition that is related to the suggested system even at low SNR.

https://doi.org/10.1088/1742-6596/1879/2/022093

OPEN ACCESS

022094

TSCO: Trust-based secure and cooperative opportunistic resource utilization networks

Abduljaleel Al-Hasnawi

− Close abstract View article PDF

An opportunistic resource utilization network (denoted as Oppnet) is a type of network that enables its node to cooperate in an opportunistic and ad hoc manner. Cooperation in oppnet includes sharing node computational resources, rather than only opportunistic communication in the traditional opportunistic networks. The key idea of oppnet is its ability to grow from seed node (initiator) to expanded oppnet via joining more nodes until getting the desired resources in a timely manner. This expansion raises the security risk of joining malicious nodes and threatens the oppnet including nodes and data. Besides, uncontrolled oppnet expansion might allow joining nodes with low computational capabilities or limited resources that have delayed responses, and hence affect the performance of oppnet. This study aims to mitigate these two problems by proposing a new oppnet paradigm (an enhanced version of original oppnet) called Trust-based Secure Cooperative Oppnet (TSCO) that utilizing a trust as a foundation for security and cooperation. Trust foundation is the major aspect of TSCO, which relies mainly on establishing trust value for each oppnet node and updating these values based on

cooperation experience with those nodes. In TSCO, oppnet nodes have classified based on their trust values in which the highest trust value has the priority to join oppnet, if it exists within the specific range. Otherwise, the second-highest trust value takes priority, and so on. To test the feasibility of TSCO in realistic systems, a framework of using TSCO as an oppnet expansion control regarding security and cooperation is simulated. The experimental results show that TSCO has a better performance in terms of secure, success expansion, and cooperation. The success rate of TSCO is higher than the success rate of the original oppnet (our experimental baseline). In addition, regarding the time of satisfying oppnet tasks, TSCO shows less average latency than the baseline.

https://doi.org/10.1088/1742-6596/1879/2/022094

OPEN ACCESS

022095

Using Chebyshev Polynomials in Solving Diffusion Equations

Ghuson S Abed

In this work, we modified Chebyshev polynomials of the first kind to match the characteristics of a second order differential equation that is a result of a separation of the variable technique used to solve a partial differential diffusion equation. The resultant polynomials solution in one spatial dimension is found and the corresponding changing parameters for the first order differential equation in time are extracted accordingly. The method is tested for applicability, stability, and convergence.

https://doi.org/10.1088/1742-6596/1879/2/022095

OPEN ACCESS

022096

Three Weighted Residuals Methods for Solving the Nonlinear Thin Film Flow Problem

Areej Salah Mohammed and Majeed A Al-Jawary

In this paper, the methods of weighted residuals: Collocation Method (CM), Least Squares Method (LSM) and Galerkin Method (GM) are used to solve the thin film flow (TFF) equation. The weighted residual methods were implemented to get an approximate solution to the TFF equation. The accuracy of the obtained results is checked by calculating the maximum error remainder functions (MER). Moreover, the outcomes were examined in comparison with the 4^{th}-order Runge-Kutta method (RK4) and good agreements have been achieved. All the evaluations have been successfully implemented by using the computer system Mathematica®10.

https://doi.org/10.1088/1742-6596/1879/2/022096

OPEN ACCESS

022097

Improving Flower Pollination Algorithm for Solving 0–1 Knapsack Problem

Ghalya Tawfeeq Basheer and Zakariya Yahya Algamal

Binary knapsack problem has received considerable attention in combinational optimization. Various meta-heuristic algorithms are dedicated to solve this problem in the literature. Recently, a binary flower pollination algorithm (BFPA) was proposed, which has been successfully applied to solve 0-1 knapsack problem. In this paper, two new time-varying transfer functions are proposed to improve the exploration and exploitation capability of the BFPA with the best solution and short computing time. Based on small, medium, and high-dimensional scales of the knapsack problem, the computational results reveal that the proposed time-varying transfer functions not only to find the best possible solutions but also to have less computational time. Compared to the standard transfer functions, the efficiency of the proposed time-varying transfer functions is superior, especially in the high-dimensional scales.

https://doi.org/10.1088/1742-6596/1879/2/022097

OPEN ACCESS

022098

The Syriac Letters and e-Abacus Diagram II

Shukriyah S Ali, Mohammed K Ahmed, Hadil H Sami and Ammar S Mahmood

− Close abstract View article PDF

The Syriac language is one of the oldest languages in the world. So far, some people speak it, for example in Iraq, Syria, southeastern Turkey and other countries. In this work, the Syriac letters were coded according to what was adopted by Sami and Mahmood in 2017 using the e-abacus diagram. More than one method is used to encode the English letters or diagrams that follow the concepts of partition theory. Each of them was taking its own path and the vision was to start with what Mohommed et al looked like in 2015 through the orbit concept. Then make the comparisons to observe the most efficient, fastest and most accurate method that could be followed.

https://doi.org/10.1088/1742-6596/1879/2/022098

OPEN ACCESS

022099

Application of Fixed Point in Algebra Fuzzy Normed Spaces

Jehad R Kider

− Close abstract View article PDF

In the present paper first we recall the definition of algebra fuzzy metric space and some basic properties of algebra fuzzy metric space are introduced. Our goal is to prove the fixed point theorem in fuzzy complete algebra fuzzy metric space. Finally, the application to this theorem introduced.

https://doi.org/10.1088/1742-6596/1879/2/022099

OPEN ACCESS

022100

Some convergence results by using K — iteration process in $CAT(H)$spaces

Shahla Abd Al-Azeaz Kadhim

− Close abstract View article PDF

In this paper, we study the convergence and Δ —convergence results of K —iteration process for Lipschizian self-mapping with $L \geq 1$in $CAT(H)$ spaces, $H \geq 0$.

https://doi.org/10.1088/1742-6596/1879/2/022100

OPEN ACCESS

022101

Radiative peristaltic transport of Ree-Eyring fluid through porous medium in asymmetric channel subjected to combined effect of inclined MHD and convective conditions

Hayat A Ali

− Close abstract View article PDF

This study emphasizes the flow phenomenon of trapped bolus traveling along the interior walls of asymmetric inclined channels contains a non-Newtonian Ree-Eyring. The flow was exposed to influenced by inclined MHD field, thermal heat radiative, and porous media. Further, no slip and convective thermal conditions are considered. Mathematical expression for governing equations are reformulated and in accordance with lubrication approximations, nonlinear partial differential equations of the flow reduced into a system of ordinary differential equations associated with boundary conditions an approximate solution is deduced by implementing perturbation strategy for tiny A Ree-Eyring fluid parameter. Finally, a graphical description is presented to figure out the elevation behavior of flow quantities i.e. velocity profile, temperature distribution, pressure rise, and streamlines formulation due to variation of emerging involved parameters. The study analyzed that the velocity profile reveals mixed behavior via increment of Ree-Eyring parameters η, A as well as Hartman number H and Darcy number Da. whereas the thermal radiative parameter Rn accelerates the temperature distribution profile. The study calculations are made by the "Mathematica 11.3" package.

https://doi.org/10.1088/1742-6596/1879/2/022101

OPEN ACCESS

022102

A reduction of Dynamic Fault Tree to a Simple Form

Ali Salman Abdulkadhim

− Close abstract View article PDF

The dynamic fault tree expands fault tree by giving the design of complex system components' actions and crossings. Because DFT is high grade design and simple to use it is proving a rising not fail through reliability researchers. Unluckily, an issue of problems as yet stays when we using DFT These problems are (1) There are no formalities, (2) restriction in symbolic analysis and thus sensitiveness to increasing the trouble, and (3) there is a few of modular type-structure. Chain of Markov (I/O-IMC) input/output formularization are used to analyse DFT. I/O-IMC have accurate semantics and are expansion of uninterrupted-time Markov chains with output and input conducts.

https://doi.org/10.1088/1742-6596/1879/2/022102

OPEN ACCESS

022103

Paths and Cycles in Alpha Topological Spaces

Balqees K Mahmoud and Yousif Y Yousif

This paper presents the concepts of prepaths, paths, and cycles in α-topological spaces and studies them in orderable spaces. Also, many relationships are proved with their equivalences using some properties in topological spaces like compactness and locally connectedness.

https://doi.org/10.1088/1742-6596/1879/2/022103

OPEN ACCESS

022104

The Transmuted Topp Leone Flexible Weibull (TTLFW) distribution with applications to reliability and lifetime data

Mizal H Alobaidi, Pelumi E Oguntunde and Mundher A Khaleel

The Transmuted Topp Leone Flexible Weibull distribution was developed in this paper using the Transmuted Topp Leone family of distributions and its basic statistical properties were established. Estimation of model parameters was considered using the maximum likelihood estimation (MLE) method and three real life applications were

provided. The TTLFW distribution is a promising model as its performance relative to other compounds probability models like the Exponentiated Flexible Weibull, Weibull Flexible Weibull, Kumaraswamy Flexible Weibull, Beta Flexible Weibull, Gamma Flexible Weibull, and Exponentiated Generalized Flexible Weibull distributions is quite credible.

https://doi.org/10.1088/1742-6596/1879/2/022104

OPEN ACCESS

022105

Estimate the Parallel System Reliability in Stress-Strength Model Based on Exponentiated Inverted Weibull Distribution

Eman A Abdulateef, Abbas N Salman and Adil Abdulkadhim Hussein

In this paper, we employ the maximum likelihood estimator in addition to the shrinkage estimation procedure to estimate the system reliability (R_k) contain K^{th} parallel components in the stress-strength model, when the stress and strength are independent and non-identically random variables and they follow two parameters Exponentiated Inverted Weibull Distribution (EIWD). Comparisons among the proposed estimators were presented depend on simulation established on mean squared error (MSE) criteria.

https://doi.org/10.1088/1742-6596/1879/2/022105

OPEN ACCESS

022106

Some Properties of Regular and Normal Space on Topological Graph Space

Rasha A Isewid, Nabila I Aziz, Samer R Yaseen and Mahera Rabee Qasem

The goal of this article is to give the concepts of Regular space and Normal space in the topological graph space also generalize α and β that to Regular space and Normal space where the relationship between these concepts were given. Finally, some characteristics of these concepts were investigated.

https://doi.org/10.1088/1742-6596/1879/2/022106

OPEN ACCESS

022107

Separation Axioms with Grill-Topological Open Set

R B Esmaeel and M O Mustafa

– Close abstract View article PDF

The concepts G-g-closedness and G-g-openness were used to popularize presented modern classes of separation axioms in grill topological spaces. Many relationships between multiple kinds of these classes are summarized, too.

https://doi.org/10.1088/1742-6596/1879/2/022107

OPEN ACCESS

022108

Generalizations of Fuzzy k-ideals in a KU-algebra with Semigroup

Fatema F. Kareem and Majid Mohammed Abed

– Close abstract View article PDF

We present the notion of bipolar fuzzy k-ideals with thresholds (θ, λ) of a KU-algebra with semigroup and give some basic properties of this ideal. Also, we study some relations about a bipolar fuzzy k-ideal with thresholds (θ, λ) and a k-ideal of a KU-semigroup.

https://doi.org/10.1088/1742-6596/1879/2/022108

OPEN ACCESS

022109

Solution BBM-Burger Equation via Quartic Trigonometric B-spline Approach

Hamad Salih

– Close abstract View article PDF

In the present work, the new quartic trigonometric B-spline approach based on finite difference scheme is described to solve the one dimensional non-linear equation of (Benjamin – Bona-Mahony-Burger). Dirichlet boundary with the help of applying the von-Neumann stability analysis is also used in this description. While the time derivative

part is discretized by using the finite difference scheme. In the space dimension, the quartic trigonometric B-spline is also used as an interpolation function. The execution of this method which is used in the present work showed that the quartic trigonometric B-spline method is a more efficient and effective tool and gives better results according to the comparisons that are made with the precise solution for a different time and some other published numerical methods.

https://doi.org/10.1088/1742-6596/1879/2/022109

OPEN ACCESS

022110

On semi strongly (*E, F*)-convex functions and semi strongly (*E, F*)-convex optimization problems

S N Majeed and A A Enad

− Close abstract View article PDF

In this paper, a new class of non-convex functions called semi strongly (*E, F*)-convex functions are presented. This class represents a natural extension of semi strongly *E*-convex functions shown in the literature. Different properties of this class of functions are discussed. Optimality properties of constrained optimization problems in which the objective function or the inequality constraints functions are semi strongly (*E, F*)-convex are proved for this class.

https://doi.org/10.1088/1742-6596/1879/2/022110

OPEN ACCESS

022111

A New Type of Conjugate Gradient Technique for Solving Fuzzy Nonlinear Algebraic Equations

Hisham M. Khudhur and Khalil K. Abbo

− Close abstract View article PDF

In this paper, we suggest a new method for the numerical solution of fuzzy nonlinear equations in parametric form using a new Conjugate Gradient Technique. Table of the numerical solution is given to show the efficiency of the proposed method and which is

compared with classical algorithms such as (Fletcher and Reeves (FR), Polak and Ribiere (PRP), and Fletcher (CD)) techniques.

https://doi.org/10.1088/1742-6596/1879/2/022111

OPEN ACCESS

022112

A Geometric Construction of Surface Complete (k, r)-cap in PG (3, 7)

Ali Ahmed A. Abdulla and Nada Yassen Kasm Yahya

The aim of this paper is to a geometric construction of Surface Complete (k, r)-cap in PG(3,7). We found that the maximum complete (k, 2)-cap which is called an ovaloid, exists in PG (3, 7) when k = 23. Moreover the complete (k, 3)-caps, (k, 4)-caps and (k, 5)-caps,(k,6)-caps, (k,7)-caps, (k,8)-caps, and we obtain a new example for theorem(2.8).

https://doi.org/10.1088/1742-6596/1879/2/022112

OPEN ACCESS

022113

Stabilization study of a non-Linear self-regression model using Linear Approximation Technique

Kawther Abbood Neamah and Safa Abood Namah

In this paper, stability in a polynomial model called a polynomial self-regression model with trigonometric boundaries was studied. A linear approximation technique was used, and the Box-Genghis method was used in data analysis, and time series modeling of numbers of people with media. Data were obtained from AL-Yarmouk Hospital in Baghdad AL-Karkh for the period (2011-2016) shows the numbers of patients with the disease through the technique of Linear approximation. Then we found the single point and the stability of the final cycle, and we tried to apply the results that we obtained on the correct data for audit.

https://doi.org/10.1088/1742-6596/1879/2/022113

OPEN ACCESS

022114

Generalized Projectivity and *Generalized Projectivity

Mukdad Qaess Hussain and Ammar Saied Rasheed

Let R be a Ring with identity and let T be a unitary left Module over R. In this paper, we recall the concepts of generalized projectivity and *generalized projectivity. These types of projectivity are very useful for the study on direct sums of Modules to be semihollow-lifting.

https://doi.org/10.1088/1742-6596/1879/2/022114

OPEN ACCESS

022115

Equivalence of Some Iterations for Class of Quasi Contractive Mappings

Zena Hussein Maibed and Ali Qasem Thajil

In this article, we recalled different types of iterations as Mann, Ishikawa, Noor, CR-iteration and, Modified SP_iteration of quasi δ-contraction mappings, and we proved that all these iterations equivalent to approximate fixed points of δ-contraction mappings in Banach spaces.

https://doi.org/10.1088/1742-6596/1879/2/022115

OPEN ACCESS

022116

Some Properties of Fuzzy Compact Algebra Fuzzy Normed Spaces and Finite Dimensional Algebra Fuzzy Normed Spaces

Zainab A. Khudhair and Jehad R. Kider

Our goal in this article is to recall the notion of algebra fuzzy normed space and its basic properties to introduce the notion of fuzzy compact algebra fuzzy normed space. Then some properties of fuzzy compact algebra fuzzy normed spaces are proved. After that, we

study a finite dimensional algebra fuzzy normed space and we proved some properties that algebra fuzzy normed spaces do not admit it.

https://doi.org/10.1088/1742-6596/1879/2/022116

OPEN ACCESS

022117

QR and JCPI–Rings

Raida D. Mahmood and Roua S. Mohammed

In this paper, we continue studies of several other authors, on QR (quasi-regular) and JCPI (JCP-injective) rings. In particular, we investigate some characterizations of several basic properties of QR and JCPI rings. Also, we prove that, if R is a semisimple and quasi duo, then R is strongly regular if and only if every simple singular right R-modules are JCPI.

https://doi.org/10.1088/1742-6596/1879/2/022117

OPEN ACCESS

022118

The Analytic of Image Processing Smoothing Spaces Using Wavelet

Asma Abdulelah Abdulrahman, Mohammed Rasheed and Suha Shihab

Image analysis took wide areas in many fields, including medicine, physics, and other areas where you need a tool to deal with it smoothly and softly without losing the original image information. Using an image of a sample of a physical atom that was analyzed and highlighting the compression and raising the noise, histogram and statistics the image statistics where the best results were recorded when using a specific threshold i.e. when pressing the methods were used the first has the threshold methods is Balance sparsity-norm, Remove near 0 and Bal-sparsity-norm(sqrt). As for the methods of raising the noise are fixed form thresholding method with soft threshold, penalize high with hard threshold, penalize medium with hard threshold, penalize low with hard threshold, Bal sparsity norm (sqrt) with soft threshold, where image parameters were divided into

approximation coefficients and details coefficients. Through the analysis, a suitable threshold value was obtained, which helps to restore energy that leads to the fact that the compressed necessity did not lose much of its original information, which proves the new wavelets in the field of physical and medical imaging.

https://doi.org/10.1088/1742-6596/1879/2/022118

OPEN ACCESS

022119

The Homomorphism of a cubic set of a semigroup in a KU-algebra

Omniat Adnan Hasan and Fatema F. Kareem

− Close abstract View article PDF

The study of homomorphisms in cubic sets is considered one of the important concepts that transfer algebraic properties between different structures, so we study a homomorphism of a cubic set of a semigroup in a KU-algebra and defined the product of two cubic sets in this structure. Firstly, we define the image and the inverse image of a cubic set in a KU-semigroup and achieve some results in this notion. Secondly, the Cartesian product of cubic subsets in a KU-semigroup is discussed and some important characteristics are proved.

https://doi.org/10.1088/1742-6596/1879/2/022119

OPEN ACCESS

022120

A Novel Predictor-Corrector Hally Technique for Determining the Parameters for Nonlinear Solar Cell Equation

Suha Shihab, Mohammed Rasheed, Osama Alabdali and Asma Abdulelah Abdulrahman

− Close abstract View article PDF

This paper presents an iterative method Accelerated Predictor-Corrector Hally's Method (AHM) for finding the voltage of a single-diode model for a solar cell from the equivalent circuit. The purposes of the obtained results are to reduce the number of iterations. Two numerical methods are applied and compared; Newton's and Hally's methods. The results showed that the proposed is the most efficient compare with NRM. The purpose of the

present work is to acquire the results of photovoltaic parameters using two numerical models and the comparison between them. The acquired results presented the suggested technique (NRM) is a sufficient tool, powerful method to solve this model with the least iteration. All the calculations are achieved using Matlab program.

https://doi.org/10.1088/1742-6596/1879/2/022120

OPEN ACCESS

022121

Soft Convergence Via Soft-ĮĴ-Pre-Generalized-Open Sets

R B Esmaeel and A A Hammood

− Close abstract View article PDF

In this paper, the concept of soft open set is inserted by using soft ideal with soft *pre*-open sets, like: soft-ĮĴ-*pre-g*-open sets "*spĮg*-open" some of the characteristics of these sets are offered. New soft functions are given such as; sĮ*pg*-open functions, soft Į**pg*-open functions, soft Į** *pg*-open functions, soft Į*pg*-continuous *functions*, strongly soft Į*pg*-continuous functions and soft Į*pg*-irresolute-functions. New separation axioms and convergences are introduced by using soft-ĮĴ-*pre-g*-open sets like; *sĮpg*-$\mathcal{T}_0$-*space, sĮpg*-$\mathcal{T}_1$-*space, sĮpg*-$\mathcal{T}_2$-*space*. some figures and suggestions have been introduced the relationships with near soft functions as well some examples are explained.

https://doi.org/10.1088/1742-6596/1879/2/022121

OPEN ACCESS

022122

New Exact Operational Shifted Pell Matrices and Their Application in Astrophysics

Mohammed Abdulhadi Sarhan, Suha Shihab, Bushra E. Kashem and Mohammed Rasheed

− Close abstract View article PDF

In this work, the exact operational matrices for shifted Pell polynomials are achievable; so one can integrate and product the vector of basic functions s. The general form of the matrix of integration *P* is established, the dual matrix of integration *Q* is derived with general formulation, and the general form of the matrix derived from the product of two

shifted Pell polynomials has been given. This idea is implemented on shifted Pell basis vector. Using such exact matrices, then the resident function of the equation is reached which can be written as $R.P(x)$, where R is an algebraic equation vector and $P(x)$ is the shifted Pell basis vector. The presented matrices can be utilized to find the approximate solution of differential equations, integral equation and the calculus of variations problems. An investigation for the convergence and error analysis of the proposed shifted Pell expansion is performed. Numerical treatment for problems in physics are included in this work to demonstrate the accuracy, easy to implement as well as accurate and satisfactory results with a small number of shifted Pell basis. Using operational matrices and the spectral technique are used together for solving Lane-Emden equation.

https://doi.org/10.1088/1742-6596/1879/2/022122

OPEN ACCESS

022123

Two Embedded Pairs for Solve Directly Third-Order Ordinary Differential Equation by Using Runge-Kutta Type Method (RKTGD)

Firas A. Fawzi, Zeyad M. Abdullah and Nazar K. Hussein

In this paper, two pairs of embedded Runge-Kutta (RK) type techniques for straightforwardly tackling third-order ordinary differential equations (ODEs) of the form $v''' = f(x, v, v')$ signified as RKTGD strategies were proposed and explored. Relying on the order conditions, the primary pair with mathematical order 4 and 3 was called RKTGD4(3), while different has order 5 and 4, and was named RKTGD5(4). The new strategies were determined so that the higher-order techniques were exact and the lower order techniques would bring about the best error estimates. At that point, variables step-size codes were created to support the methods and utilized in solving a lot of third-order problems. Comparisons were made between mathematical results and existing embedded RK pairs within the scientific literature, that require the problems to be reduced into a system of first-order ODEs, and the effectiveness of the new RKTGD pairs have appeared.

https://doi.org/10.1088/1742-6596/1879/2/022123

OPEN ACCESS

022124

Estimation the Shape Parameter for Power Function Distribution

Alaa M. Hamad and Bareq B. Selman

In the paper estimate of the shape parameter for power function distribution was proposed. For different sample sizes (small, medium, and large). Using different methods, Maximum likelihood method, Moment method, Shrinkage methods, and Least square method. mean square error (MSE) was implemented as an indicator of performance and comparisons of performance have been carried out through data analysis and computer simulation between the estimation methods according to the applied indicator. It was observed from the results that the shrinkage method (constant weight factor (sh_2)) estimates for the shape parameter are the best in performance for each case.

https://doi.org/10.1088/1742-6596/1879/2/022124

OPEN ACCESS

022125

Parameters estimation of new mixed Weibull Rayleigh and Exponential distribution

Jassim N. Hussain and Ashraf Mohammed Shareef

A new idea of mixing was introduced in this paper. Mixing parameters; p_i where $0 \leq p_i \leq 1$ and $\sum_{i=1}^{n} p_i = 1$ are used to find a new distribution from mixing some distributions. Therefore, we can get many mixed distributions with several parameters. Three distributions Weibull, Rayleigh, and Exponential are mixed to get a new distribution which is more flexible than these distributions. The mixed distribution with a new parameter is representing the ratio of contribution of each of these distributions which are mixed. Several values of the mixing parameter were taken, and the properties of the mixed distribution were found. Two methods (MLE and OLS) of estimation are used to

estimate the parameters of the new distribution. Simulation studies are used to prove the properties of new distribution and to apply the estimation method to estimate the parameters of new distribution.

https://doi.org/10.1088/1742-6596/1879/2/022125

OPEN ACCESS

022126

Exact Method for Solving Single Machine Scheduling Problem Under Fuzzy Due Date to Minimize Multi-Objective Functions

Hanan A. Cheachan and Mustafa T. Kadhim

In this paper, the branch and bound technique used to solve a single machine scheduling problem, which is the problem of scheduling n-job on a single machine of multi-objective function with triangle fuzzy due date numbers which are formulated as $1\backslash \tilde{D}_j = TFN\backslash \sum_{j=1}^{n} C_j + L_{\max}$. The target of this paper is to obtained optimal sequence of our problem. The computational results are calculated by using Matlab program and compare the results with the complete enumeration method.

https://doi.org/10.1088/1742-6596/1879/2/022126

OPEN ACCESS

022127

Approximate Solution of Delay Integral Equations via Functions of two Variable

Abdul Khaleq O. Al-Jubory

In this work, we adopt B. spline function of two variables basis for solving linear multi-dimensional delay Volterra integral equations nonhomogeneous of the second type. We employ the two methods to approximate solution via B. spline function of two variables basis that yields linear system. Some examples are given, the results shown in tables and figures. These methods are very effective, convenient and overcome the difficulty of traditional methods. We solve this problem with the assistance of Matlab18.

https://doi.org/10.1088/1742-6596/1879/2/022127

OPEN ACCESS

022128

g-Closed Soft Sets in Soft Closure Spaces

R N Majeed and S T Ekram

− Close abstract View article PDF

The aim of the present work is to define a new class of closed soft sets in soft closure spaces, namely, generalized closed soft sets (*gc*-soft sets, for short) which are defined over an initial universe set with a fixed set of parameters. This new class is a generalization to the class of closed soft sets. A necessary condition for a *gc*-soft set to be a soft closed is also obtainable. Moreover, the union and intersection of two *gc*-soft sets are discussed. Besides, some properties of *gc*-soft sets in the product soft closure spaces are also studied. Also, as an application of *gc*-soft sets a new soft separation axiom, namely $T_{\frac{1}{2}}$-soft closure space is introduced and its basic properties are investigated.

https://doi.org/10.1088/1742-6596/1879/2/022128

OPEN ACCESS

022129

Face Detection for Color Image Based on MATLAB

Shahad laith abd al_galib, Asma Abdulelah Abdulrahman and Fouad Shaker Tahir Al-azawi

− Close abstract View article PDF

Amazing results in many works in the field of deep convolutional neural networks using them in many fields of machine learning such as image classification control of atrial play, and image annotation. Mathematical analysis of deep convolutional neural networks (CNN) has a broad role in many applications including image classification applications. Face recognition technology has occupied a wide field in research that is still continuing in this work. Face recognition technology is being developed depending on the MATLAB program to develop the subjecting of the color image to the neural convolution network and the work of a program to reduce the time the network deals with the image to reduce the number of layers to only two layers and access the algorithm Suggested in this work. Computer vision of a color image in a face detection study. In this work, the researcher

created a fast algorithm to reach the research goal based on new standards in the field of face detection. A new face detection program was designed using MATLAB, CascadeObjectDetector and trainCascadeObjectDetector the face detection devices were developed. In this work, a technique for panning and color image using the convolutional neural network for deep learning is proposed, the method used to reach the goal of this work.

https://doi.org/10.1088/1742-6596/1879/2/022129

OPEN ACCESS

022130

Univalence Criteria for Holomorphic Functions Involving Srivastava-Attiya Operator

Huda F. Hussian and Abdul Rahman S. Juma

The purpose of present paper is to introduce and investigate the univalence criteria of holomorphic functions by employ a basically general form of Srivastava-Attiya operator. In specific, we derive several sufficient conditions of univalence for the generalized Srivastava-Attiya operator. Furthermore, number of famous univalent conditions would follow across specializing the parameters involved. Relevant connections with other related previous works are also indicating.

https://doi.org/10.1088/1742-6596/1879/2/022130

OPEN ACCESS

022131

New Methods of Computing the Conjugate of Young Diagram

Fatmah Ahmed Basher and Ammar Seddiq Mahmood

Since the appearance of Young's diagram, it has played a fundamental and pivotal role in many fields of mathematics, perhaps the most prominent of which is algebra, graph theory, number theory...etc, and many closely related relationships, perhaps among them

The most prominent is called conjugation. Many people try to find a mathematical method to find the value of the hash value in its conjugated form. Here, we will propose two new methods for the same purpose.

https://doi.org/10.1088/1742-6596/1879/2/022131

Effects of *Moringa oleifera* seed extract on PbNP-Toxicity induced in rats

Effects of *Moringa oleifera* seed extract on PbNP- Toxicity induced in rats

Fiham Jassim Al-Obaidi[1], Asmiet Ramizy[2] and Abid A. Thaker[1*]

[1]Department of Biology, College of Science, University of Anbar, Iraq.
[2]Department of Physics, College of Science, University of Anbar, Iraq.

*E-mail: sc.thakerscianb@uoanbar.edu.iq

Abstract. This work was conducted to study the protective role of Moringa oliefera seeds extract (MSE) against the toxic effect of commercial lead nanoparticles (CPbNP) in rats. Twenty eight albino male rats were divided into four groups (seven animals in each one) as follow: (A) control group, (B) 160mg/kg body weight per day (b. wt./d.) of M. oliefera (MSE)seed extract, (C): 5mg CPbNP /kg b. wt./d. and (D): MSE + CPbNP . The experimental period was 45 days. Blood was drawn for protein and enzyme estimation at the end of the period of exposure. The rats were dissected and the liver, kidney, spleen and muscle were isolated for Pb estimation. Results showed that the levels of bioaccumulated lead, serum alanine aminotransferase, aspartate aminotransferase, alkaline phosphatase, malondialdehyde were significantly increased in exposed animals to CPbNP ($P < 0.05$). In contrast, there was a significant reduction of total proteins, albumin, glutathione, superoxide dismutase enzyme and catalase enzyme activities ($P < 0.05$) in comparison to control. But the administration of the CPbNP with MSE, all the above biochemical changes were improved significantly. It is concluded that CPbNP has a significant toxic effect on rats, and that seed extract of M. Oleifera can reduce it.

Keywords. *Moringa oliefera*, Toxicity, Lead Nanoparticles, Antioxidants, liver functions.

1.Introduction

Medical plants are traditionally used in treatments of different healthy cases because it has active biological materials. A significant number of researches have been done to using extracts from medicinal plants as preventive agents against specific pathogens or against xenobiotic toxicity [1, 2, 3, 4]. *Moringa* belongs to the Moringaceae family and spread in Africa, especially in Ethiopia, Kenya, and Sudan. It grows in tropical areas, originally in India, but known in Africa [5]. Each part of the Moringa has a lot of essential components. For example, the leaves contain minerals [6], vitamins [7, 8]. In addition to anti-cancer agents (such as glucosinolates, isothiocyanates), phytochemicals such as terpenoids, flavonoids, alkaloids and sugar reduction [9]. According to [10], *Moringa* leaves have significantly higher antioxidant contents. Other authors have reported the leaves' antioxidant potential [11, 12]. The study of [13] observed that folate's bioavailability from *Moringa* leaves using the rat model was 82%, suggesting that the *Moringa* leaves can be a potential dietary folate source. *Moringa* seeds are also found to have significant biological activity. Powder of seeds was investigated for its

antidiabetic activity in induced diabetic rats due to the presence of glucomoringin, phenols and flavonoids [14]. Ethanol extract of *Moringa* seed showed antifungal activity against *Trichophyton rubrum*, *Trichophyton mentagrophytes*, *Epidermophyton xoccosum* and *Microsporum canis* [15]; while the water extract of Moringa seed kernel possessed potent antioxidant activity [16].
Several studies were found that the seeds of *Moringa* have a protective effect against toxicants, prevented the elevation of triglycerides, glucose, and urea in rats exposed to arsenic [17], worked as a prevention against the toxic effect of mercury on rat testicular function [18], can act against liver damage caused by CCl4 and fibrosis in rats, hepatoprotective action against hepatocellular harm caused by DMBA in mice [19], alleviates (TiO2-NPs)-induced cerebral oxidative damage, and increases cerebral mitochondrial [20]. Lead is a toxic metal to the environment and organisms. Mining, smelting, refining, recycling, lead paint, and lead gasoline are significant sources. Children are sensitive to lead's poisonous effects and can suffer different health effects, particularly the brain and nervous system's development. Lead also causes harm in adults, including blood pressure, liver and kidney damage, miscarriage and stillbirth [21]. Lead nanoscale particles (PbO-NPS) may be released into the surrounding air and water during different activities, increasing the possibility of exposure to it. The high toxicity of nanoparticle raised concerns about particles impact with their nanoscale on human and animal health [22]. The study of [23] reported that in the exposed rats to lead sulfide nanoparticles caused changes in the fatty acid of lipids of the liver by increasing arachidonic fatty acid and reduction of the stearic fatty acid content. Long exposure of rats to lead sulfide nanoparticles had a harmful effect. They led to significant body and liver weight changes, total protein, albumin, glucose, lipids, triglycerides in blood serum, and dystrophic changes in the liver [24]. The exposure of mice to lead oxide nanoparticles (PbO-NPS) caused a formation of clusters inside the cytoplasmic vesicles in the lung. It was demonstrated that the liver, kidney, spleen, and brain were as tissue-specific subcellular processing [25]. This research was undertaken to determine the protective role of *Moringa oleifera* seed extract's against commercial lead nanoparticle toxicity in rats.

2.Materials and Methods

2.1. Plant material

Moringa oleifera seed was obtained from the Iraqi National herbarium (Baghdad) on 1-April-2019, after being picked from the trees, dried and crushed to be powder by using a Laboratory Grinder.

2.2. Moringa oliefera seed Extraction

Moringa seed was extracted by using the Soxhlet device in solvent acetone/ethanol (1:1). A 300 grams of the sample was used. The extraction process continued for 72 hours, and then the extract concentrated by using a vacuum rotary evaporator [26].

2.3. Commercial lead Nanoparticles

The nanoscale powder was obtained from NANOSHEL company and was less than 100 nm in diameter. Lead Oxide Nanopowder was dissolved in distilled deionized water using a sonicate device to prevent nanoparticles' aggregation [27].

2.4. Experimental animals

The adult white male Swiss Wistar Rats (*Rattus norvegicus*) were used in this experiment. It's were brought from the College of Veterinary Medicine, University of Tikrit, Iraq-with ages ranging between 12-14 weeks and with an average weight of 250 grams. The animals were reared under standard laboratory conditions (24 ± 1° C, 12h light and 12h dark, fed freely).

2.5. Design of the experiments

Article I. Four groups of animals were used with seven rats in each group. *Moringa* and commercial lead were given to the rats following [28] method. Group A or the control group was given distilled water. Group B was treated with 160 mg/kg body weight per day (b. wt./d.) *Moringa* seed extract (MSE) through the stomach (24Aleksiichuk et al., 2018). Group C was injected with 5 mg/kg commercial nanoscale lead (CPbNP.) via peritoneum [29]. Group D was administered with *Moringa* extract and commercial lead nanoparticles (CPbNP).

2.6. Animal dissection

After the end of the exposure period, the rats were left untreated for two days; on day 3, they were anesthetized with chloroform. Afterward, they were dissected, and their liver, kidneys, spleen and muscles were removed and digested for lead estimation. The blood was drawn from the animals by stabbing their hearts. The serum was separated by a centrifuge (3500 rpm) for 10 minutes to obtain blood serum, keeping in the freezer at -20° C until conducting chemical tests.

2.7. Determination of lead concentrations in tissues

The accumulated lead in rats' organs was determined using a Flameless Atomic Absorption spectrophotometer (Analytik Jena-Germany), following the method described by [30]. One gram was digested by 2.5 ml of HNO_3+0.5 ml $HCLO_4$ in a conical flask (100ml). The flasks were left for an hour at room temperature, then placed on Hotplate at 100° C until the appearance of red fumes, then the temperature was raised to 200 °C, until the formation of white vapor. The remaining yellow color liquid was dissolved in nitric acid and used for lead detection after suitable dilution.

2.8. Biochemical tests

Alkaline phosphatase (ALP), Alanine aminotransferase (ALT), Aspartate aminotransferase (AST) activities, total protein and albumin concentrations were determined by using the Spanish origin Biosystem A15 automated device. GSH was measured according to [31]. SOD and CAT activities were determined by Using the Elab science Analysis Kits. MDA was measured according to the method described by [32].

2.9. Statistical analysis

Statistical analysis of the results by using the statistical program SPSS (V.21), as the statistical analysis included calculating the mean and the standard error. The complete random design was used, and the mean of the coefficients was compared using a modified Least Significant Difference test at a 0.05 significant level.

3.Results

Rats were treated with 160 mg/kg b.wt./d. of seed extract of *M. oliefera* for 45 days. All rats in this group remain healthy. They did not show any significant changes in their behaviour or all studied parameters (accumulated lead, the activity of enzymes and concentration of proteins). The bioaccumulated lead was estimated in the liver, kidney, spleen and muscle of rats (Table 1). The lead concentrations in the control animals (group A) and animals, which given *Moringa* seed extract MSE (Group B) were between 5.1-8.4mg/kg in all tested organs. Its concentrations in animals exposed to commercial lead nanoparticles CPbNP (group C) in all tested organs were between 25.3 -30.8 mg/kg, which revealed a highly significant difference in comparing with groups A and B ($P \leq 0.05$). whereas in rats treated with MSE+CPbNP (group D) was 12.5 and 16.5 mg/kg, which differs significantly

(P≤0.05) in comparison with other groups. The liver's accumulated lead was the highest among other organs in different groups except for the animals' liver treated with *Moringa*.

Table 1. Lead bioaccumulation in the organs of rats. A (control), B, MSE (*Moringa* Seed Extract), C, CPbNP (commercial lead nanoparticles).

Organs / **Groups**	Liver (mg/kg)	Kidney (mg/kg)	Spleen (mg/kg)	Muscle (mg/kg)
A (Control)	8.4043±0.46570^{b}	6.8893±0.49005^{a}	6.3002±0.52075^{ab}	6.4960±0.55923^{ab}
B (MSE)	5.3960±0.36341^{a}	6.4565±0.37649^{a}	5.5837±0.10814^{a}	5.1599±0.18794^{a}
C (CPbNP)	30.8166±1.12046^{e}	25.3794±1.21682^{c}	25.7768±0.24178^{d}	25.8280±0.33186^{d}
D (CPbNP+MSE)	16.8850±0.89757^{c}	13.7378±0.76439^{b}	13.2402±0.45598^{c}	12.5153±0.24273^{c}

Data are represented as mean ±SE n=7, P≤0.05. Different letters refer to significant differences among the treatments.

Table (2) showed the concentrations of total serum proteins, albumin and the enzymes serum ALT, AST and ALP. By comparison, to control (group A), the CPbNP group (C) displayed significantly elevated levels of serum ALT, AST and ALP, (P≤0.05) but significantly reduced levels of total serum proteins and albumin (P≤0.05). There is an improvement in hepatic function parameters observed in the PbNP +MSE (group D).

Table 2. The result of commercial lead nanoparticles and seed extract of *Moringa* on serum markers of liver damage. A(control), B, MSE (*Moringa* seed extract), C,CPbNP (commercial lead nanoparticles), D, (MSE+CPbNP).

Parameters / **Groups**	AST (U/L)	ALT (U/L)	ALP (K.A.U./100ml)	Total protein (g/dl)	Albumin (g/dl)
A (Control)	47.2857±1.44279^{a}	50.7143±1.42619^{a}	563.0000±35.6517^{ab}	52.4286±2.31822^{c}	36.9286±2.65570^{c}
B (MSE)	50.0000±2.27826^{a}	48.2857±2.02031^{a}	497.2857±40.0896^{a}	49.8571±3.69960^{c}	32.7857±3.57547^{bc}
C (CPbNP)	64.5714±2.53412^{d}	61.3571±2.57902^{c}	690.1429±20.0674^{c}	38.5714±1.58651^{a}	21.6143±1.00058^{a}
D (CPbNP+MSE)	56.0714±1.32030^{bc}	52.2143±1.21429^{ab}	596.1429±5.70893^{b}	50.7143±2.17906^{c}	25.4286±1.14657^{ab}

Data are represented as mean ±SE n=7, P≤0.05. Various letters refer to significant differences among the treatments.

The levels of the antioxidants GSH, SOD, CAT and MDA were estimated (Figure 3). A significantly elevated level of MDA was found in the PbNP exposed animals (group C) in comparison with control animals (group A) (P≤0.05), but significantly reduced levels of GSH, SOD and catalase (P≤0.05). *Moringa* revealed improvement changes in oxidative stress markers in the MSE+PbNP (D group).

Table 3. The results of commercial lead nanoparticles and seed extract of *Moringa* on oxidants parameters. A(control), B, MSE (*Moringa* seed extract), C,CPbNP (commercial lead nanoparticles), D, (MSE+CPbNP).

Parameters / **Groups**	CAT (U/ml)	GSH (µmol/L)	SOD (U/ml)	MDA (µmol/L)
A (Control)	2.3583±0.16137^{a}	20.4239±1.19882^{c}	208.8857±23.1697^{b}	7.0765±0.33562^{cd}
B (MSE)	2.4417±0.20276^{a}	21.1656±0.47940^{c}	211.0000±4.54475^{b}	7.2921±0.30198^{d}
C (CPbNP)	6.2333±0.83479^{c}	11.7614±2.59223^{a}	90.7286±2.93474^{a}	6.1765±0.03419^{a}
D (CPbNP+MSE)	2.5166±0.33530^{a}	16.8125±2.61772^{bc}	142.7857±48.8149^{ab}	6.7312±0.04879^{bc}

Data are represented as mean ±SE n=7, P≤0.05. Different letters refer to significant differences among the treatments.

4.Discussion

This study aimed to investigate the protective role of *Moringa* seed extract (MSE) against the toxicity of commercial lead nanoparticles (CPbNP). The lead was found to be accumulated in different organs of rat [33]. The accumulation was mainly in the liver, led to toxic effects, enzymes inhibition, oxidative stress [34]. In this investigation, rats were treated with lead nanoparticles (CPbNP). The organs: liver, kidney, spleen and muscles accumulated significant concentrations of lead. The liver got a high concentration of lead (CPbNP group), but *Moringa* seed extract in combination with lead (CPBNP+MSE- group D) reduced accumulated metal to about a half. This reduction may be due to the *Moringa* ability to bind with toxic metal ions and form complex structures out of the body, as in chelating agents [35]. The present study revealed that exposed rats to CPbNP exhibited higher activities of serum ALT, AST and ALP and reduced levels in total serum proteins and serum albumin in comparison to control, which may indicate the cellular leakage and hepatic cell membranes functional disability. These results and conclusions were in agreement with those obtained by the effects of MSG [36, 37, 38], 4-tet-acetyphenol [39] and acetaminophen [40]. The ameliorative alterations observed in the accumulated lead, hepatic enzymes ALT, AST, ALP, total protein and albumin in rats treated with PbNP in combination with seed extract of *Moringa,* corroborating other studies' results [41, 42]. The cause for cellular toxicity may be due to lipid peroxidation in the presence of PbNP. This study reported that the PbNP group had significantly higher serum MDA levels ($P<0.05$) and considerably lower levels of GSH, SOD and catalase ($P< 0.05$). Thus, high levels of lipid peroxidation may be deduced to damage the hepatic tissue and inhibit the capacity of antioxidants to remove excess ROS output [43]. The obtained results were in agreement with [41], where that *M. oleifera* increased antioxidant enzymes' activity, improving the condition of liver antioxidants, while neutralizing the hepatotoxic effect triggered by paracetamol. Our study is also consistent with [44], who found that *Moringa* seed extract can neutralize acetaminophen's hepatotoxic effects. As a result, the current study presents evidence that the acetonic-alcoholic *Moringa oliefera* seeds extract provides effectively, protection against the changes caused by commercial lead nanoparticles in rats.

5.References

[1] Marwan M S, Suhaila W K and Thaker A A 2016 Gastroprotective Activity of *Eruca sativa* Leaf Extract on Ethanol-Induced Gastric Mucosal Injury in *Rattus norvegicus*. *Jord. J. Biol. Sci*. **9** 47.

[2] Bamola N, Verma P and Negi C 2018 A review on some traditional medicinal plants. *Int. J. Life-Sci. Scient. Res.* **4** 1550.

[3] Asraa A S, Thaker A A and Hussain A B 2019. Protective activity of *Capparis spinosa* against aflatoxin b1 poisons induced histopathological changes in mice. *Biochem. Cell. Arch*. **19** 717.

[4] Salmerón-Manzano E, Garrido-Cardenas J A and Manzano-Agugliaro F 2020 Worldwide Research Trends on Medicinal Plants. *Int. J. Environ. Res. Public Health* **17** 3376.

[5] Padayachee B and Baijnath H 2012 An overview of the medicinal importance of Moringaceae *J. Med. Plants Res.* **6** 5831.

[6] Kasolo J N, Bimenya G S, Ojok L, Ochieng J and Ogwal-Okeng J W 2010 Phytochemicals and uses of *Moringa oleifera* leaves in Ugandan rural communities. *J. Med. Plants Res.* **4** 753.

[7] Mbikay M 2012 Therapeutic potential of *Moringa oleifera* leaves in chronic hyperglycemia and dyslipidemia: a review *Front. Pharmacol*. **3** 24.

[8] Ameh S S and Alafi O F 2018 Effect of ethanol extract of *Moringa Oleifera* leaves in protecting anaemia induced in rats by aluminium chloride *IOSR J. Biotechnol. Biochem*. **4** 34.

[9] Berkovich L, Earon G, Ron I, Rimmon A, Vexler A and Lev-Ari S 2013 *Moringa Oleifera* aqueous leaf extract down-regulates nuclear factor-kappaB and increases cytotoxic effect of chemotherapy in pancreatic cancer cells. *BMC Complement. Altern. Med*. **13** 212.

[10] Yang R Y, Chang L C, Hsu J C, Weng B B, Palada M C, Chadha M L and Levasseur V 2006 *Nutritional and functional properties of Moringa leaves–From germplasm, to plant, to food, to health. Moringa leaves: Strategies, standards and markets for a better impact on nutrition in Africa*. *Moringanews*, CDE, CTA, GFU. Paris.
[11] Saini R K, Prashanth K H, Shetty N P and Giridhar P 2014 Elicitors, SA and MJ enhance carotenoids and tocopherol biosynthesis and expression of antioxidant related genes in *Moringa oleifera* Lam. leaves. *Acta Physiol. Plant.* **36** 2695.
[12] Saini R, Shetty N, Prakash M and Giridhar P 2014 Effect of dehydration methods on retention of carotenoids, tocopherols, ascorbic acid and antioxidant activity in *Moringa oleifera* leaves and preparation of a RTE product *J. Food Sci. Technol*. **51** 2176.
[13] Saini R K, Manoj P, Shetty N P, Srinivasan K and Giridhar P 2016 Relative bioavailability of folate from the traditional food plant *Moringa oleifera* L. as evaluated in a rat model *J. Food Sci. Technol.* **53** 511.
[14] Al-Malki A L and El Rabey H A 2015 The antidiabetic effect of low doses of *Moringa oleifera* Lam. seeds on streptozotocin induced diabetes and diabetic nephropathy in male rats *BioMed. Res. Int.* **2015**.
[15] Chuang P H, Lee C W, Chou J Y, Murugan M, Shieh B J and Chen H M 2007 Anti-fungal activity of crude extracts and essential oil of *Moringa oleifera* Lam *Bioresour. Technol*. **98** 232.
[16] Jahan I A, Hossain M H, Ahmed K S, Sultana Z, Biswas P K and Nada K 2018 Antioxidant activity of *Moringa oleifera* seed extracts. Orient. *Pharm. Exper. Med.* **18** 299.
[17] Sheikh A, Yeasmin F, Agarwal S, Rahman M, Islam K, Hossain E and Hossain K 2014 Protective effects of *Moringa oleifera* Lam. leaves against arsenic–induced toxicity in mice. *Asian Pac. J. Trop. Biomed*. **4** S353.
[18] Asomugha A L, Ezejindu D N and Nwabekee P O 2014 The protective effect of *Moringa oleifera* leaf extract on mercury induced testicular toxicity in adult wistar rats. *Unique Res. J. Med. Med. Sci*. **2** 43.
[19] Sharma V, Paliwal R, Janmeda P and Sharma S 2012 Chemopreventive efficacy of *Moringa oleifera* pods against 7, 12-dimethylbenz [a] anthracene induced hepatic carcinogenesis in mice. *Asian Pac. J. Cancer Prev*. **13** 2563.
[20] Kandeil MA, Mohammed E T and Hashem K S 2020 *Moringa* seed extract alleviates titanium oxide nanoparticles (TiO2-NPs)-induced cerebral oxidative damage, and increases cerebral mitochondrial viability. *Environ Sci Pollut Res* **27** 19169.
[21] WHO 2013 *International Lead Poisoning Prevention Week*. GENEVA.
[22] Amiri A, Mohammadi M and Shabani M 2016 Synthesis and toxicity evaluation of lead oxide (PbO) nanoparticles in rats. *Electron. J. Biol*. **12** 110.
[23] Omelchuk S T, Aleksijchuk V D, Sokurenko L M, Blagaia A and Prudchenko S 2016 Characteristics of rat liver exposed to nanoparticles of lead compounds *Georgian Med News* **261** 94.
[24] Aleksiichuk V, Omelchuk S, Sokurenko L, Kaminsky R, Kovalchuk O and Chaikovsky Y 2018 The influence of lead nanoparticles on the morpho-functional changes of rat liver during the postexposure period *Microsc. Res. Techn.* **81** 781.
[25] Dumková J, Smutná T, Vrlíková L, Le Coustumer P, Večeřa Z, Dočekal B, Mikuška P, Čapka L, Fictum P, Hampl A, Buchtová M 2017 Sub-chronic inhalation of lead oxide nanoparticles revealed their broad distribution and tissue-specific subcellular localization in target organs *Part Fibre Toxicol.* **14** 55.
[26] Suleiman K 2007 The inhibitory effect of onion plant extract and its active ingredients in a number of germs and synergies between active ingredients and antibiotics. *J. Edu. Sci.* **19** 14.
[27] Sárközi L, Horváth E, Kónya Z, Kiricsi I, Szalay B. Vezér T and Papp A 2009 Subacute intratracheal exposure of rats to manganese nanoparticles: behavioral, electrophysiological, and general toxicological effects. *Inhal. Toxicol.* **21** 83.

[28] Perret-Gentil M I 2010 *Rat Biomethodology. University Veterinarian & Director. Laboratory Animal Resources Center* The University of Texas at San Antonio 458.
[29] Oszlánczi G, Papp A, Szabó A, Nagymajtényi L, Sápi A, Kónya Z and Vezér T 2011 Nervous system effects in rats on subacute exposure by lead-containing nanoparticles via the airways *Inhalat. Toxicol.*, **23** 173.
[30] Josthna P, Geetharathan T, Sujatha P. and Deepika G. 2012. Accumulation of lead and cadmium in the organs and tissues of albino rat. *J. Pharm. Life Sci.* **3** 2186.
[31] Tipple T E and Rogers L K 2012 Methods for the determination of plasma or tissue glutathione levels. *Methods Molec. Biol.* (Clifton, N.J.), **889** 315.
[32] Alam MN, Bristi N J and Rafiquzzaman M 2013 Review on in vivo and in vitro methods evaluation of antioxidant activity *Saudi Pharmac. J*. **21** 143.
[33] Novikova M A 2013 Influence of chronic Pb intoxication on human organism *Siberian Med. J.* **117** 13.
[34] Assi M A, Hezmee M N M, Abd Wahid Haron M Y M and Sabri M A R 2016 The detrimental effects of lead on human and animal health. *Veterinary World* **9** 660.
[35] Flora S J and Pachauri V 2010 Chelation in metal intoxication *Int. J. Environ. Res. Public Health* **7** 2745.
[36] Ortiz G G, Bitzer-Quintero O K, Zárate C B, Rodríguez-Reynoso S, Larios-Arceo F, Velázquez-Brizuela I E and Rosales-Corral S A 2006 Monosodium glutamate-induced damage in liver and kidney: a morphological and biochemical approach *Biomed. Pharmacoth*. **60** 86.
[37] Onyema O O, Farombi E O, Emerole G O, Ukoha A I and Onyeze G O 2006 Effect of vitamin E on monosodium glutamate induced hepatotoxicity and oxidative stress in rats *Indian J Biochem Biophys* **43** 20.
[38] Albrahim T and Binobead MA 2018 Roles of *Moringa oleifera* Leaf Extract in Improving the Impact of High Dietary Intake of Monosodium Glutamate-Induced Liver Toxicity, Oxidative Stress, Genotoxicity, DNA Damage, and PCNA Alterations in Male Rats *Oxid. Med. Cell Longev*. **2018** 4501097.
[39] Saggu S, Sakeran M I, Zidan N, Tousson E, Mohan A and Rehman H 2014 Ameliorating effect of chicory (*Chichorium intybus* L.) fruit extract against 4-tert-octylphenol induced liver injury and oxidative stress in male rats *Food Chem. Toxicol.* **72** 138.
[40] Sakeran M I, Zidan N, Rehman H, Aziz A T and Saggu S 2014 Abrogation by *Trifolium alexandrinum* root extract on hepatotoxicity induced by acetaminophen in rats. *Redox Report* **19** 26.
[41] Uma N, Fakurazi S and Hairuszah, I 2010 *Moringa oleifera* enhances liver antioxidant status via elevation of antioxidant enzymes activity and counteracts paracetamol-induced hepatotoxicity. *Malays. J. Nut*. **16**.
[42] Santos A F, Argolo A C, Paiva P M and Coelho L C 2012 Antioxidant activity of *Moringa oleifera* tissue extracts. *Phytother. Res.* **26** 1366.
[43] Ranawat L, Bhatt J and Patel J 2010 Hepatoprotective activity of ethanolic extracts of bark of Zanthoxylum armatum DC in CCl4 induced hepatic damage in rats *J. Ethnopharmacol.* **127** 777.
[44] Sharifudin S A, Fakurazi S, Hidayat M T, Hairuszah I, Aris Mohd Moklas, M and Arulselvan P 2013 Therapeutic potential of *Moringa oleifera* extracts against acetaminophen-induced hepatotoxicity in rats. *Pharmaceut. Biol.* **51** 279.

Biological control on plant pathogenic fungus, *Pythium* by using some plant extracts *in vivo* and *in vitro*

Biological control on plant pathogenic fungus, *Pythium* by using some plant extracts *in vivo* and *in vitro*

Rajaa Fadhil Hamdi[1], Farkad Hawas Musa[2] and Sameer Sarhan Alrawi[2]

[1]Department of biology, College of Science, University of Anbar, Iraq.
[2]Department of biology, College of Education for Pure Science, University Of Anbar, Iraq.

*E-mail: Sc.moh_n2002@uoanbar.edu.iq

Abstract. The inhibitory activity of 5 plant extracts, *Allium sativum, Opuntia ficus-indica, Malva parviflora, Mentha spicata* and *Plantago lanceolata* with concentration 50 % and 100 % were assessed against the mycelial growth of *Pythium* fungus *in vivo* and *in vitro*. Results showed that all the concentrations of plant extracts give significant inhibition in the mycelial growth of *Pythium* fungus; the highest concentration (100 %) prevented large amounts of mycelial growth followed by lower concentration (50 %) of plant extracts. *Opuntia* extract at 100 % concentration gave great effective in inhibition of *Pythium*`s mycelial production, which gave 100 per cent inhibition ratio while 50 per cent concentration gave 77.28 % inhibition ratio followed by other plant extracts, *Mentha*, *Allium sativum*, *Plantago*, then *Malva* respectively. *In vivo* experiments, tomato seed infused in five plant extracts separately and then sown with soil contaminated with *Pythium* fungus and watered after that with these five plant extracts. After 30 days, the length of the stems and roots were measured in centimetres. While the tomato seeds which were soaked with distilled water and then sown in polluted soil with fungus *Pythium*, and watered with distilled water (control) did not show any growth. .

Keywords. *Pythium*, biological control, plant extracts, *Mentha*, *Allium*, *Opuntia*, *Malva*, *Plantago*, *in vivo*, *in vitro*.

1. Introduction

Fungiform diseases cause a significant loss of many economic crops worldwide. Fungi have the greatest impact on the reduction of crop productivity or post-harvest losses, leading to a massive loss for the human race [1]. It is estimated that crop losses from fungal infection are around 14 percent [2]. World annual crop losses as a result of diseases were estimated at US$ 25,000 million, a major part of which is due to seed-borne fungal pathogens [3]. Several pathogens, including *Alternaria* species are degrading the fruit quality, reducing and making market values unsuitable for human consumption [4]. Plants are the sources of natural pesticides that lead to the development of new pesticides [5]. The use of plants or plant products as fungicides is very critical and requires further attention [6]. The extracts and oils of plants in particular formed the basis of many applications, including raw and processed food preservation, pharmaceutical, alternative medicinal products and natural therapies [7]. Extracts from many plants have recently become popular and have become scientifically interested in their

antibacterial and antifungal function [8]. With a view to creating an eco-friendly antifungal control strategy, in the present study, different concentrations of five plant extracts including *Allium sativum, Opuntia ficus-indica, Malva parviflora, Mentha spicata* and *Plantago lanceolata* were assessed for their antifungal activity.

2. Materials and Methods

2.1. Plant extracts preparation

Cold, aqueous extracts of five plants' leaves: *Allium sativum, Opuntia ficus- indica, Malva parviflora, Mentha spicata* and *Plantago lanceolata* were obtained to prepare of 50 % and 100 % of plant extracts by using sterilized distilled water; 10 g of leaves of each plant were washed, then mortar and pestle were used to grind leaves with 100 ml distilled water. The plants material was homogenized for 10 min by homogenizer then filtered with two layered of gauze then with filter paper. The filtrate was centrifuged at 3000 rpm for 15 minute, those solutions were considered traditional (100 per cent) solutions. The other 50 per cent concentration was prepared by adding equivalent amounts of distilled water to the normal solution.

2.2. The experiment (in vitro)

The plant extracts were combined with the medium potato dextrose agar (2 ml of extract for 18 ml of PDA), then Sprinkled on Petri dishes, Petri dishes were inoculated after media solidification by placing 4 mm mycelial disks of *Pythium* fungus (from the active colony) in the center of each plate. The pure fungus was obtained from laboratory fungi, Department of Biology, University of Al-Anbar. Three replicates for each concentration were packed, then the plates were incubated at 28º C and recorded the results after 7 days of incubation. Petri dishes without plant extracts considered as control.

2.3. Inhibition factor calculation (Percent)

The percent inhibition for Various concentrations were computed as follows:

Inhibition of growth (percent)= [(Dc-Dt)/Dc]* 100 (percent) [9].

Dc= Fungal colony average diameter in control

Dt= fungal colony average diameter in treatment.

2.4. The experiment (in vivo)

2.4.1. Seeds preparation

Tomato seeds *Lycopersicon esculentum* was soaked with plant extracts (100 %) in petri dishes for 24 h. In the first dish, tomato seeds was soaked in sterile distilled water (control); the second dish, tomato seeds was soaked with *Allium sativum* extract ; the third dish, tomato seeds was soaked with *Opuntia* extract; and soaked with *Plantago* extract in the fourth dish, and soaked with *Malva* and *Mentha* in the fifth and sixth dish.

2.4.2. Soil and peatmoss sterilization and planting tomato seeds

In our research, we performed a pot culture experiment to test the efficacy of five plant extracts against damping-off and root rot of tomato, *Lycopersicon esculentum*. Disinfected tomato seeds in 2

per cent sodium hypochlorite for 1 minute, rinsed in distilled sterile water and dried overnight [10]. Tomato seeds were grown at four seeds per pot. mixed soil and peat moss with ratio 1 : 2 and sterilized by autoclave for 30 min then left for 7 days, and putting in the pots. The soil polluted with *Pythium* fungus (three day-old actively growing mycelial discs) five discs, 4.5 mm for each pots then the seeds (soaking seeds) were planted in the pots and watered with the five extracts (each one alone) the control watered with distilled water every two days then left for growth (in greenhouse) until reach to 30 days in age. For each treatment three replicates were preserved . The shoot length and root length (cm) were recorded at 30 days after planting.

3. Results and Discussion

3.1. In vitro

The results of the study referred, That the inhibitory function of all plant extracts showed major variations against mycelial growth of the *pythium* fungus.

3.2. Impact of 5 plant extracts on in vitro growth of Pythium fungus.

The results showed (Table 1, Figure 1, 2, 3, 4, 5, 6) that five plant extracts triggered a significant inhibition of the growth of *Pythium* fungus. The 50 per cent concentration of *Opuntia* extract was the most effective against *Pythium* and caused the highest inhibition of mycelia production (77.28 %) followed by *Allium sativum* (60.60 %), *Mentha spicata* (53.30 %), *Plantago lanceolata* (26.65 %), *Malva parviflora* (15.06 %). The results also showed, *Opuntia* with concentration 100 % was the most effective against *Pythium* and gave great inhibition of mycelia growth (100 %) followed by *Mentha spicata* (69.85 %), *Allium sativum* (60.78 %), *Plantago lanceolata* (38.72 %) and *Malva parviflora* (38.35%). [11] Zena *et al*. (2013) mentioned that *Mentha* extract contain tannins, alkaloids, phenols, flavones, resins and saponins which have very important role in inhibition of many pathogenic organisms. Also [12] mentioned that the alkaloids compound has direct contact with plasma membrane of microorganisms which has proteins and lipids, or it interferes with a series of metabolic reactions of the microscopic organism which is very necessary for the growth and production of spores.

Table 1. Impact of 5 plant extracts on in vitro growth of *Pythium*.

Plant extracts	Growth inhibition (%)	
	Mean. 50 conc.	Mean. 100 conc.
Allium sativum	60.60	60.78
Opuntia ficus-indica	77.28	100
Malva parviflora	15.06	38.35
Mentha spicata	53.30	69.85
Plantago lanceolata	26.65	38.72
Control (PDA without extract)	0	0

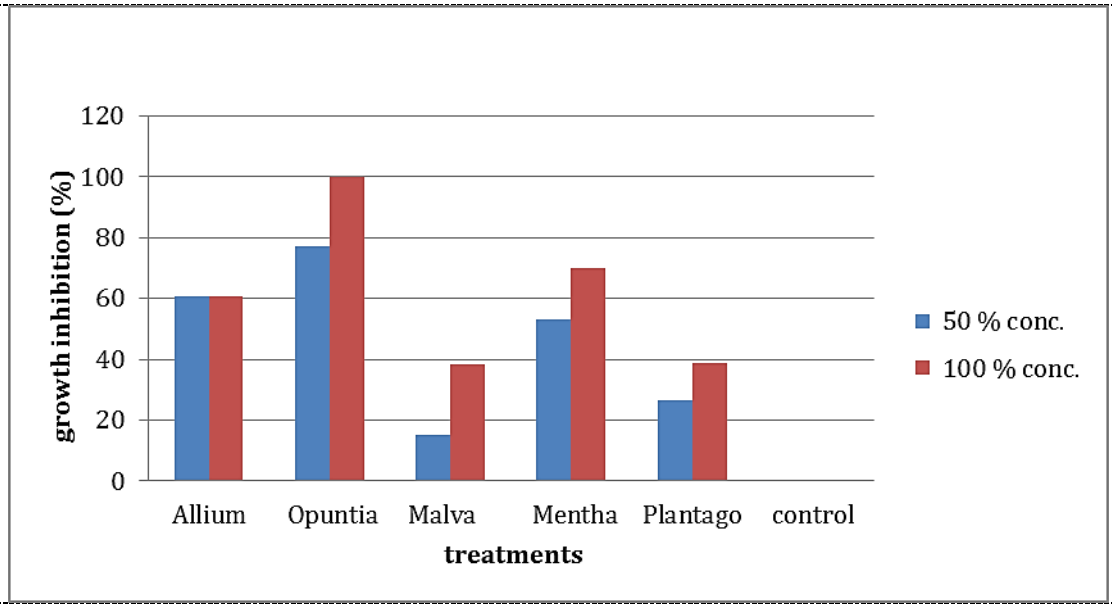

Figure 1. Impact of 5 plant extracts on in vitro growth of *Pythium*.

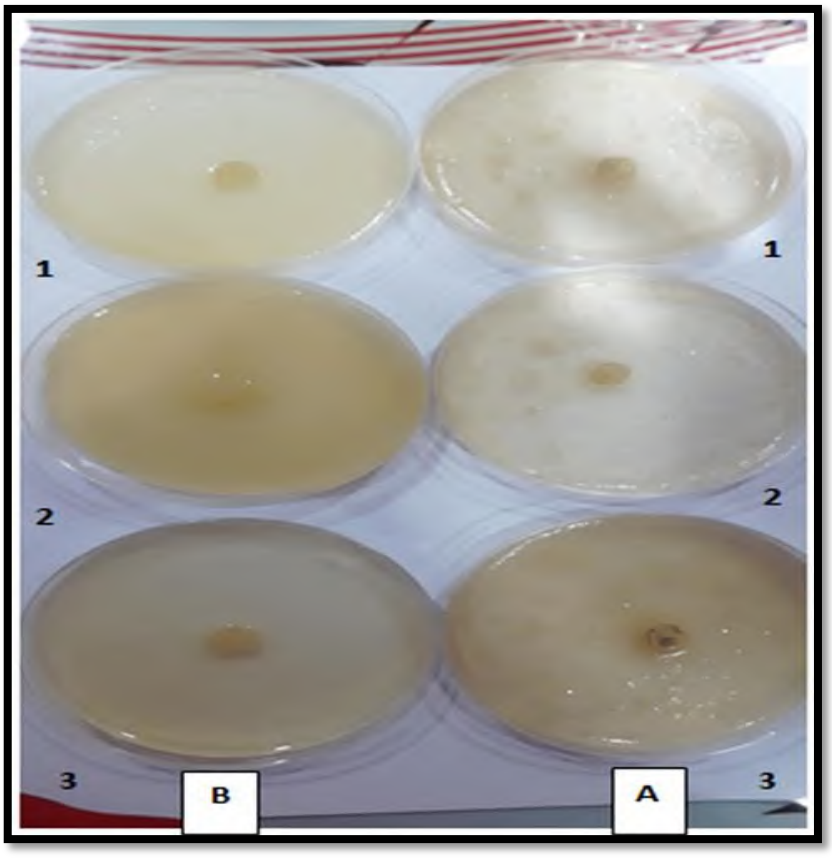

Figure 2. A (replicate; 1,2,3) PDA with 50% Opuntia extract and cultured with Pythium fungus.
B (replicate; 1,2,3) PDA with 100% Opuntia extract and cultured with Pythium fungus.

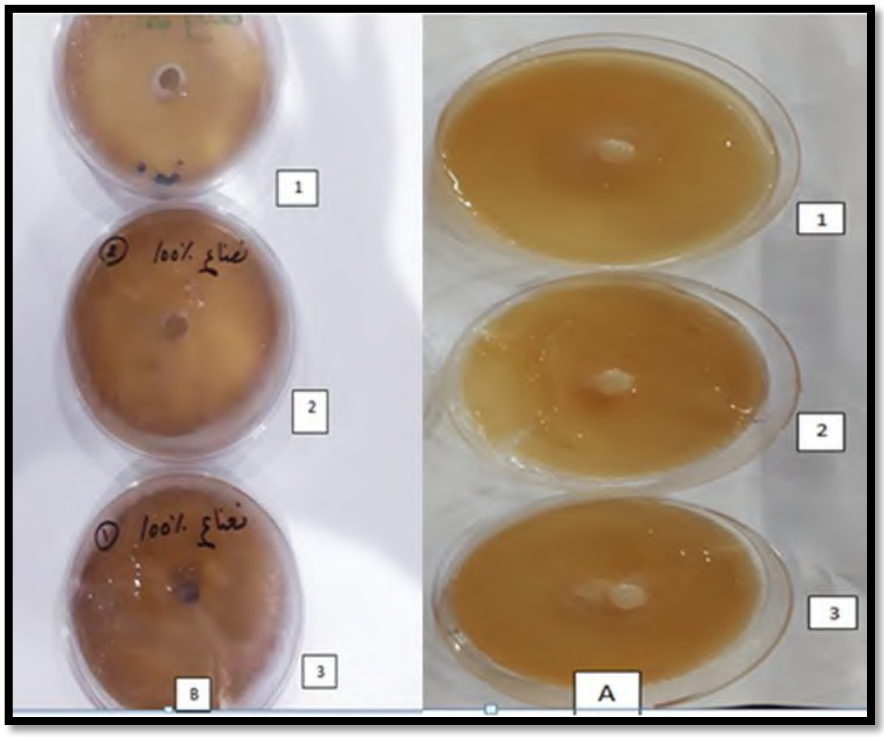

Figure 3. A (replicate; 1, 2, 3) PDA with 50% Mentha extract and cultured with *Pythium* fungus
B (replicate; 1,2,3) PDA with 100% *Mentha* extract and cultured with *Pythium* fungus.

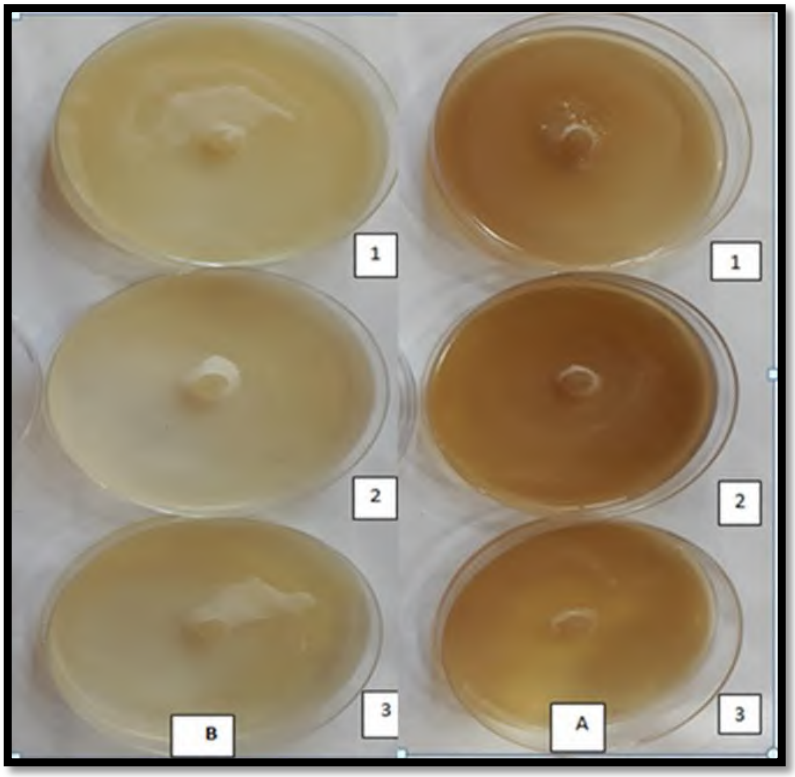

Figure 4. A (replicate; 1, 2, 3) PDA with 50% *Plantago* extract and cultured with *Pythium* fungus.
B (replicate; 1, 2, 3) PDA with 100% *Plantago* extract and cultured with *Pythium* fungus.

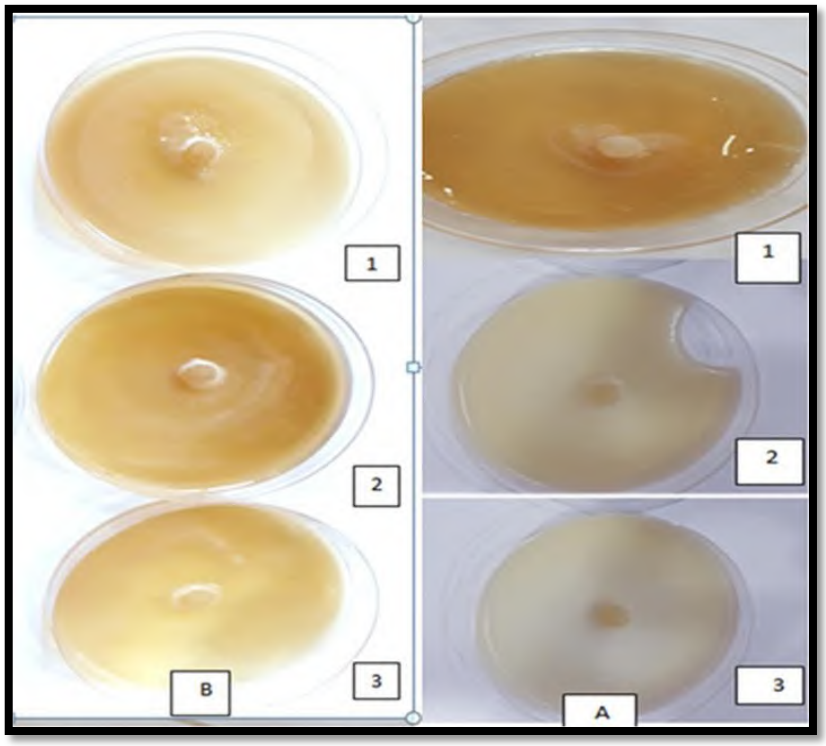

Figure 5. A (replicate; 1, 2, 3) PDA with 100% *Allium sativum* extract and cultured with *Pythium* fungus.
B (replicate; 1, 2, 3) PDA with 50% *Allium sativum* extract and cultured with *Pythium* fungus.

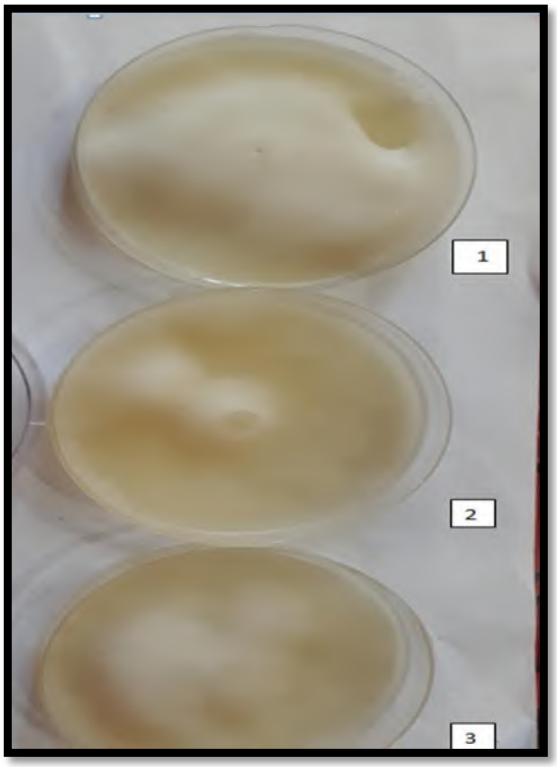

Figure 6. Control (Replicate; 1, 2, 3) PDA without plant extract and cultured with *pythium* fungus.

Table 2. Effect of five plant water extracts on shoot length.

Shoot length(cm)			
Plant extracts	mean		Std. Deviation
Allium	13.966	cd	1.436
Opuntia	15.066	e	1.563
Malva	11.433	b	0.611
Plantago	12.666	bc	0.568
Mentha	14.566	de	0.650
control	0.000	a	0.000

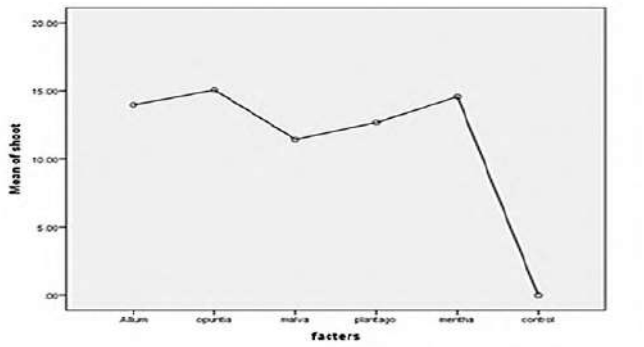

Numbers with similar letters are not significantly different from each other.

Table 3. Effect of five plant water extracts on root length.

Root length (cm)			
Plant extract	mean		Std. Deviation
Allium	3.733	bc	0.568
Opuntia	4.800	d	0.458
Malva	3.700	b	0.435
Plantago	3.433	b	0.503
Mentha	4.500	cd	0.871
control	0.00	a	0.00

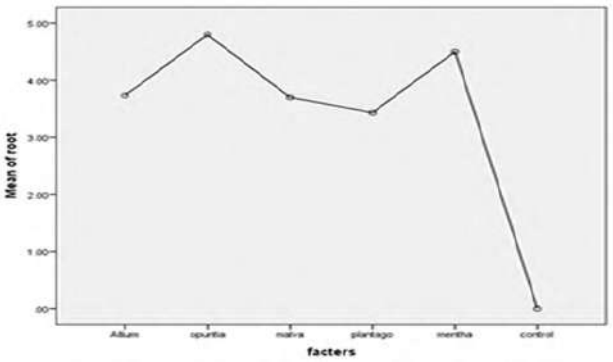

Numbers with similar letters are not significantly different from each other.

4. References

[1] Tapwal A, Nisha, SG, Guatam N and Kumar R 2011 *In vitro* antifungal potency of plant extracts against five phytopathogens Braz. Arch. Biol. Technol. **54** 1093.
[2] Agrios GM 2005 *Plant pathology* 5th edition. AP, New York, NY 922.
[3] Chandler J 2005 Cost reduction in SIT programs using exosect auto – dissemination as part of area wide integrated pest management *Int. J. Pest Control* **47** 257.
[4] Spots RA and Cervantes LA 1986 Population, pathogenicity and benomoyl resistance of *Botrytis* spp., *Penicillium* spp. and *Mucor pyriformis* in packing houses *Plant Dis.* **70** 106.
[5] Jagadish L, Anand Kumar VK and Kaviyarasan V 2009 Effect of *Triphala* on dental bio-film *Indian J. Sci. Techno*l. **2** 30.
[6] Bodde T 1982 Entomologists probe chemical defenses and natural enemies. *Bioscience* **32** 308.
[7] Baytop T 1984 Health treatment in turkey using plant extracts *Clin. Microbiol. Rev*. **12** 564.
[8] Santas J, Almajano MP and Carbo R 2010 Antimicrobial and antioxidant activity of crude onion (*Allium cepa*) extracts. *Int. J. Food sci. Technol*. **45** 403.
[9] Shazia P, Wani AH, Ganie, AA, Pala SA and Mir RA 2014 Antifungal activity of some plant extracts on some pathogenic fungi Arch. Phytopathol. Plant Protect. **47** 279.
[10] Latha P, Anand T, Ragupathi V, Prakasam R and Samiyappan R 2009 Antimicrobial activity of plant extracts and induction of systemic resistance in tomato plants by mixtures of PGPR strains and *Zimmu* leaf extract against *Alternaria solani Biol. Control* **50** 85.

[11] Zena HA, Mahmood N and Muzher A. 2013 Effect of aqueous extract of *Punica granatum* and *Mentha spicata* on the effectiveness and growth of the fungus, *Alternaria alternata* (in Arabic).
[12] Nor Azha MA, Mastura M, Mawardi R, Abdul Munaf A and Khoziran S 2002 The essential oil and antimicrobial properties of some *Ginnamomum* species.

Anatomical study of *Solanum nigrum* L. from Solanaceae family growing in Iraq

Anatomical study of *Solanum nigrum* L. from Solanaceae family growing in Iraq

Muazaz Azeez Al-Hadeethi[1*], Ali T Al-Taie[2] and Areej A. Farman Al-Rawi[1]

[1]Department of Biology, College of Education of pure Sciences (Ibn Al-Haitham), University of Baghdad, Baghdad, Iraq.
[2]Continuous Learning Center, Mustansiriyah University, Iraq

*E-mail: muazaz.a.h@ihcoedu.uobaghdad.edu.iq

Abstract. The most important features that we have reached through this study, are shown the cross-section of root were in the secondary growth stage and the epidermis of leaf were studded by stomata complex, the type of it was anomocytic that's mean no have subsidiary cells around the guard cells, the mesophyll bifacial also the midrib region of leaf like the pear and the vascular bundle located in the center crescent in shape. The cross-sections of petiole ovate shape with two ears in the lateral side and the vascular bundles crescent in shape. The cross-section of fruits circular component of three-layer the outer layer pericarp, mesocarp, and the endocarp, surrounding the ovary or the seeds.

Keywords. *Solanum nigrum*, Solanaceae, Anatomy, Iraq.

1. Introduction

Solanum nigrum, the common name wolf grape, black nightshade or blackberry nightshade, also refer that it is an annual herbaceous plant belonging to the Solanaceae family, it is a widespread species that contain alkaloids and is considered toxic [1]. The species may reach a meter height, leaves are Flat with white-colored flowers appear in numbers from four to ten, the fruits of the plant are green in the first place, and then they become black or blue, juicy, sweet when ripe, and contain many small kidney-shaped seeds, and are collected in the autumn, the plant distribute in fields, orchards, gardens, canal banks, deserted places, and spreads all over the world [2]. The whole plant contains Solanine, Asparagine, Lutein, Tannin, linoleic acid, and Palmitic acid, the plant is used medicinally as a sedative and skin softening agent. This plant began to be used since its anesthetic and paralytic effect on nerve endings was known. Fruit juice has a pain-relieving effect by letting a drop of the juice evaporate over the sore tooth [3]. [4] refers that the fruits of the plant cause poisoning in children when they are eaten, especially if the fruits are not fully ripe and their color is between red and purple, and too much eating the loss of the latter cause of memory and consciousness and often leads to poisoning and then death because they contain steroidal alkaloids. The foliage also harms livestock when grazing on them. This is not recommended to use the plant internally due to its toxic effects, but it can be used externally to relieve some pain such as joint pain [5]. There are a few studies and data concerning the anatomy of *S. nigrum* in describing some species of the family Solanaceae only original anatomical characteristics

have been given by [6]. [7] also studied the morphological and anatomical characteristics of vegetative parts of some species belonging to Solanaceae family like S. *nigrum, S. americanum, S. sarrachoides*, and *S. ptycanthum*. They noticed that they varied in relation to environmental conditions. As well as [8] refers to the Anatomical and Comparative study of selected wild species from the family Solanaceae in Iraq included *S. nigrum*.
The aim of this study is to investigate the important anatomical features for the parts of the species *S. nigrum*, to recognize the tissues and cells, and to be able to distinguish between the other species in the same genus.

2. Materials and Methods

The species collected from the herbal garden at AL- Rashidiya city north of Baghdad (Latitude of Rashidiya: 33, 5528 (3333'10.080"N), Longitude of Rashidiya: 44, 3725 (4422'21.000"E)) at April 2019. The plant material was identified and authenticated by Flora of Turkey [9] and flora of Nouvelle Flore du Liban et de la Syrie [10]. Firstly the parts of plant like as root, stem, leaves and fruits were kept in formalin acetic acid alcohol (FAA) for 48 hours, which was prepared according to [11] as follow: 50 ml of Ethyl alcohol, 5 ml of Glacial acetic acid, 10 ml of Formaldehyde 37 to 40% concentration and 35 ml Distilled water, then the samples were washed by distilled water and were kept in 70% Ethyle alcohol. The epidermis of leaves was prepared according to[12] were peeling by a razor blade and washing with distilled water then put in 5% sodium hypochlorite for 5 mins to remove the chlorophyll pigment. The sectioning parts of root, stem, leaf, petiole, and fruit were done by hand section, the procedure was performed according to [13], the fresh material sectioned by a razor blade into thin and small pieces then put in 0.5% sodium hypochlorite for 5 mins to clear the tissue and remove the chlorophyll pigment. Finally all the samples are put on the slide and mounted by cover slides and fixed by Olympus KRÜSS light microscope then photographed using AmScope camera.

3. Results and Discussion

3.1. Cross section of root

The shape of the outline root is circular, and in the secondary growth stage, that's mean that this stage consists of the first annual ring in the plant. The root covered by the periderm, the thickness of it reached to 16.2 µm followed by several rows of parenchyma tissues longitudinal and ovate cells known the cortex and they are interspersed the cells of the cortex the ordinary schizogenous intercellular spaces and the thickness of it 25.4 µm. The vascular cylinder is consist of xylem and phloem, the thickness of it 266.7 µm, the pith located in the center of the stem filled with parenchyma cells and the thickness of it reached to 75.8 µm (Figures 1).

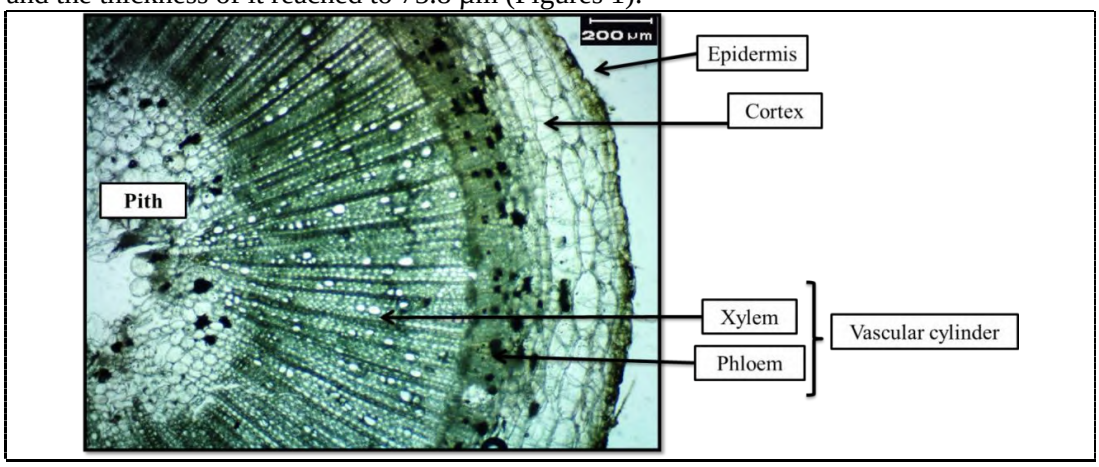

Figure 1. Root cross section of *Solanum nigrum.*

3.2. Cross section of stem

The shape of the outline stem is tetragonal, the cross section of the stem consists of a uniseriate epidermis covered by cuticle, the cuticle thickness 3.4 µm and the epidermis thickness 18.9 µm, and the cortex consists of 2 layers, the first one is located under the epidermis and consist of the collenchyma tissue and after it comes the second layer of parenchyma tissues, the thickness of cortex 34.7 µm. The vascular bundles are collateral and open and take the shape of a stem, consist of xylem and phloem, the vascular thickness is 107.9 µm, the pith located in the center of the stem filled with parenchyma cells and the cells circular and the ordinary schizogenous intercellular space among it (Figures 2), the result agrees with [6].

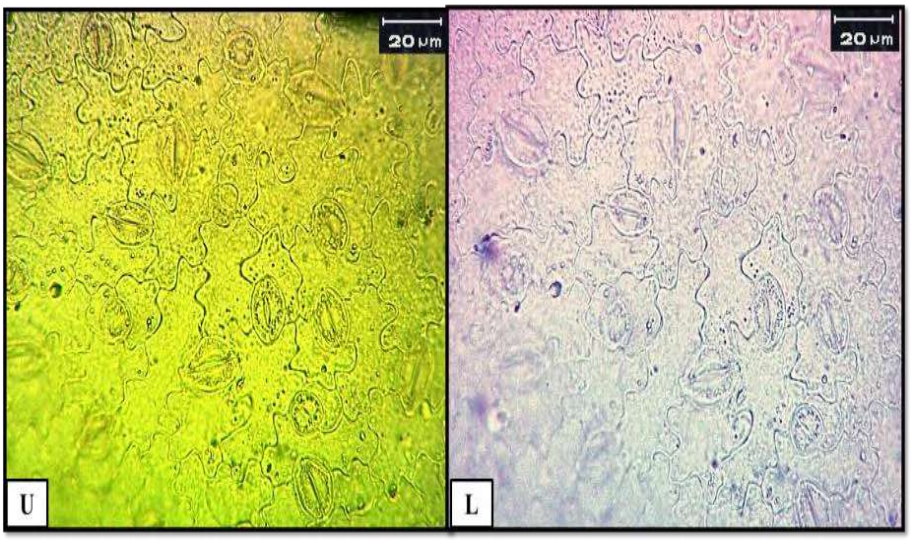

Figure 2. Stem cross section of *Solanum nigrum*.

3.3. Study of leaves

The epidermis of the leaf shows the stomata complex, the type of stomata was anomocytic that's mean it has no subsidiary cells around the guard cells, the guard cells are kidney shaped and the anticlinal walls of epidermal cells are wavy, (Figures 3), this agrees with [7] who refer that the stomata of these species are anomocytic to anisocytic, somewhat larger in *S. nigrum*, which can be explained by its polyploidy. The transfer section of the leaf consists of the upper and lower uniseriate epidermis, the upper epidermis is covered by cuticle with the thickness ranging from 2.1µm, also the cells of upper epidermis ovule shape and the thickness of it is 35.5 µm, while the thickness of the lower epidermis is 20.4 µm. The leaf described as the bifacial mesophyll consists of palisade layers and spongy layers, the thickness of palisade layers was 95.5 µm and the thickness of spongy layers was 153.7 µm (Figures 4). The midrib region of the leaf have a pear-like shape, the epidermis is covered with the eglandular uniseriate and multicellular trichomes followed by the cortex and the vascular bundle located in the center have crescent in shape ranged to 195.5 µm include xylem and phloem (Figures 5), the results agree with [14].

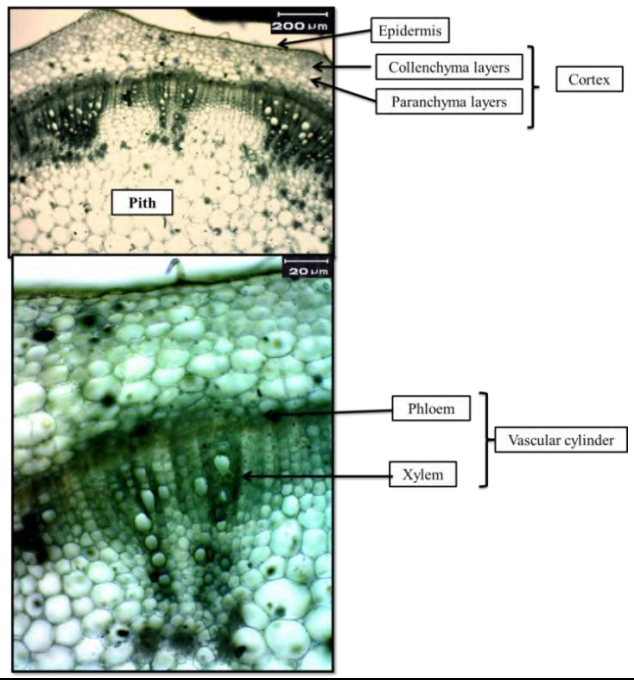

Figure 3. Surface view of epidermis in the species *Solanum nigrum*.

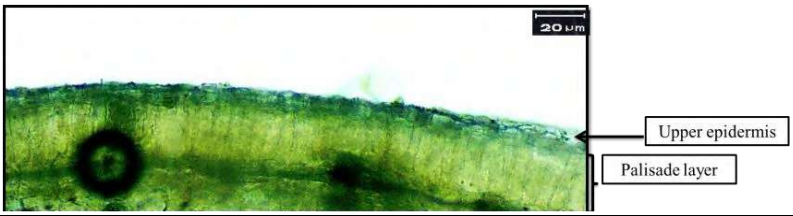

Figure 4. Leaf blade cross section of *Solanum nigrum*.

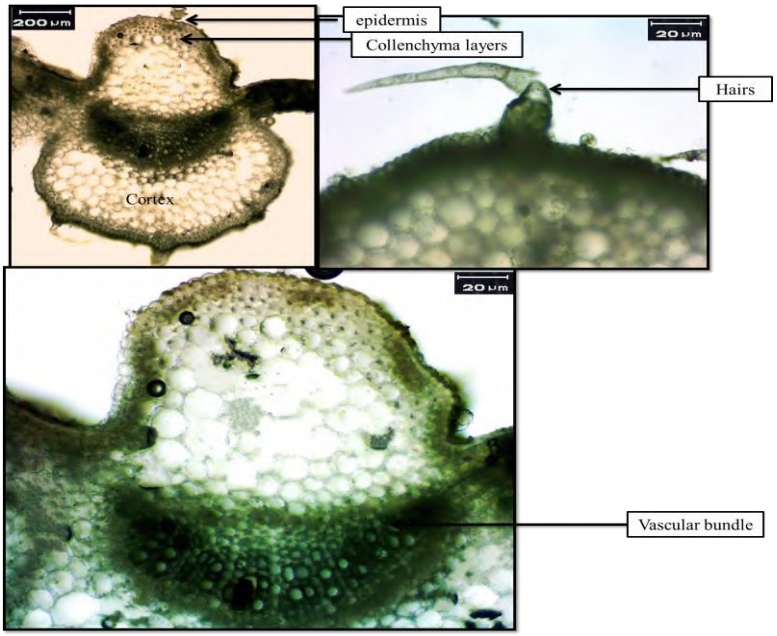

Figure 5. Cross section of leaf midrib of *Solanum nigrum*.

3.3.1. Petiole cross section:

The cross sections of petiole ovate shape with two ears in the lateral side, the epidermis was uniseriate covered with a cuticle, the average thickness of it 1.5 µm and many unicellular and uniseriate trichomes diffuse on it, the average thickness of the petiole epidermis reached to 16.5 µm. And below the epidermis, the cortex is located, the average thickness of the cortex ranged from 38.2 µm. Whilst the vascular bundles are crescent in shape and are found in the center of the pith which consists of xylem and phloem (Figures 6), the results agrees with [8].

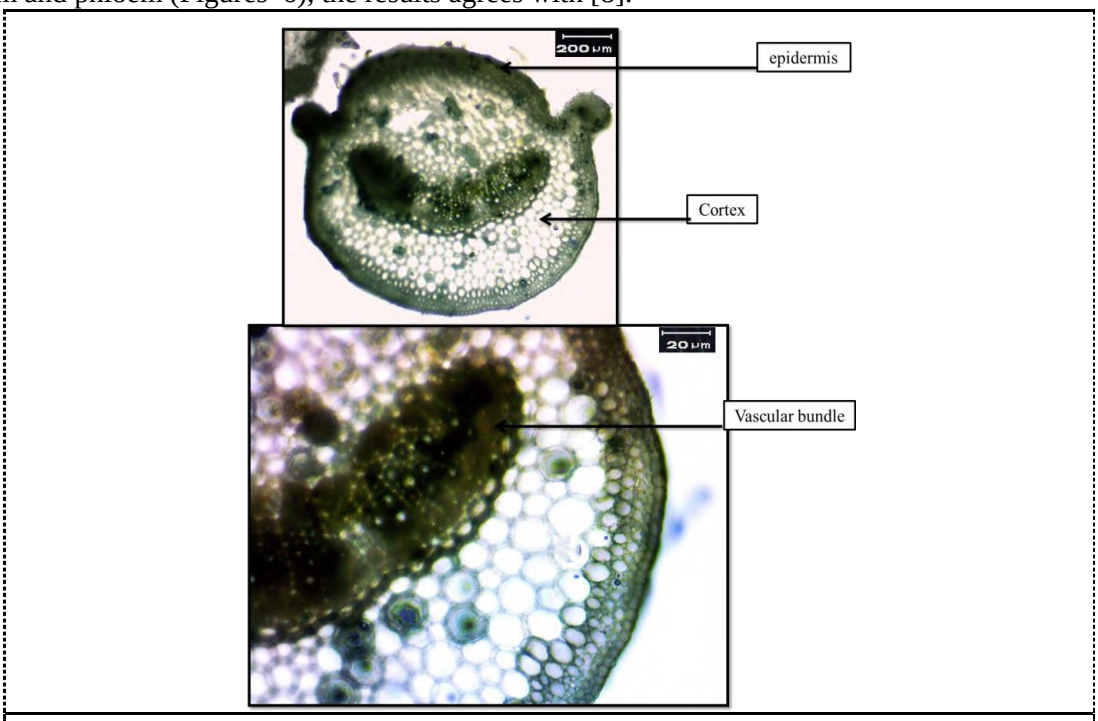

Figure 6. Petiole cross section of *Solanum nigrum*.

3.4. Cross ***section of fruits and seeds:***

The cross section of the fruits have circular component of three layers; the outer layer is known as the pericarp, followed by the mesocarp, and the endocarp, which (the endocarp) is the inner layer surrounding the ovary or the seeds (Figures 7).

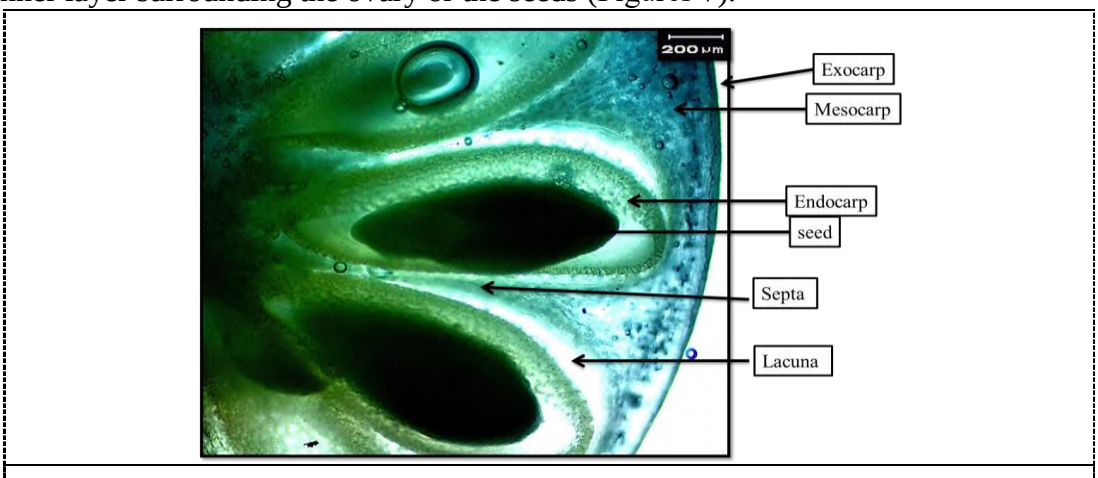

Figure 7. Fruit cross section of *Solanum nigrum*.

4. References

[1] Grubb A and Raser-Rowland A 2012 *The Weed Forager's Handbook* Australia Hyland House Publishing Pty Ltd. p 35. ISBN 9781864471212.
[2] Ogg A G, Rouger B S and Schiling E E 1981 Characterization of Black Nightshade (*Solanum nigrum*) and Related Species in the United States. *Weed Sci*. **29** 27.
[3] Mohyuddint A, Khan Z, Ahmad M and Kashmiri M A 2010 Chemotaxonomic value of alkaloids in *Solanum nigrum* complex *Pak. J. Bot.* **42** 653.
[4] North P 1977 *Poisonous Plants and Fungi in Colour*. Blandford Press 140.
[5] Schep L J, Slaughter R J and Temple W A 2017 Contaminant berries in frozen vegetables *New Zealand Med. J.* **122** 95.
[6] Metcalfe C R and Chalk L 1957 *Anatomy of the Dicotyledons* Vol. 2, Clarendon Press, Oxford.
[7] Rogers B S and Ogg, A G 1981 *Biology of weeds of the Solanum nigrum complex (Solanum section Solanum) in North America* U.S. Department of Agriculture, Science and Educational Administration Agricultural Reviews and Manuals 69.
[8] Al-Allalq S A, Al-Musawi A H E and Al-Mousawi A H 2011 Anatomical and Comparative study of selected wild species from the family solanaceae in Iraq *J. Baghdad Sci.* **8** 197.
[9] Davis P H 1975 *Flora of Turkey & the East Aegean Island* Edinburg, Univ. Press **5** 788.
[10] Paul M S J 1986 *Nouvelle flore de liban et de syrie* Dar El-Machreo sarl B. P. 946 Beyrouth liban librairie orintale. Part III.
[11] Johanson A D 1940 *Plant Microtechnique* .1st ed Mc Graw-Hill Book Company, New York and London 523 PP.
[12] Al-Hadeethi M A 2016 Anatomical and palynological study of *Myrtus communis* L. *Diyala J. Pure Sci*. **12** 1.
[13] Thammathaworn A 1996 *Handbook by paraffin method. Department of biology*, Faculty of science, Khon Kaen Universality, Thailand.
[14] Seithe A and Anderson G J 1982 Hair morphology and the relationships of species in *Solanum* sect. Basarthrum *Plant System Evol.* **139** 229.

Morphological, histochemical and histological study of the ileum in the Iraqi Black Partridge (*Francolinus francolinus*)

Morphological, histochemical and histological study of the ileum in the Iraqi Black Partridge (*Francolinus francolinus*)

Intidhar Mohammed Mnati[1*], Ola Al-Bhadly[2] and Nawar Rushdi Jaber[2]

[1]Department of Biology, Collage of Education for Pure Science (Ibn Al- Haitham), University of Baghdad, Baghdad, Iraq.
[2] Department of medical analysis techniques, Dijlah University College, Iraq

*E-mail: entidhar.m73@gmail.com

Abstract. Objective: This project aimed to study the morphological description and histological structure of ileum in Iraqi black partridge (*Francolinus francolinus*). Methods: To conduct this investigation, 20 healthy Iraqi black partridge were collected from local suppliers. Birds were euthanized, dissected and then specimens were processed for histological and histochemical staining techniques. Results: A morphological study showed that the ileum appears as a short narrow tubular structure. It extends from the wide end of the jejunum and ends in the Ileo-caecal junction region. Histologically, the wall ileum consists of four tunica mucosa, submucosa, muscularis and serosa. The mucosa was lined by simple columnar epithelium with goblet cells. The muscularis mucosa is arranged in two thick layers of smooth muscle fibers, outer longitudinal and inner circular bundles. The tunica submucosa was a thin layer of fibrous connective tissue. Tunica serosa was loose connective tissue covered by mesothelium. The goblet cells gave a positive reaction with PAS stain. Conclusion: Goblet cells neutral mucopolysaccharide secretions; in fact, the latter stain is an indicator mucin substance which are very important in digestion and absorption and subsequent body growth of the bird.

Keywords. Histomorphological study, Ileum, Iraqi Black Partridge.

1. Introduction

The food mechanism is an important determinant of the success of the adaptation of birds in their environment, also the nature of nutrition and the way it is obtained is considered as an effective factor on the morphological and histological composition of the digestive tracts parts [1, 2]. The digestive system in birds is necessary to convert the food intake by the bird into simple materials used by the body to carry out its daily activities. Food is then transformed into crude materials that synthesis, nutrition and restore the cells of the body through the destruction of food molecules, absorption and transmission through the bloodstream and the body disposes of its remains. The small intestine is the first site concerned with the breakdown of enzymes, in addition to absorption of carbohydrates, fatty acids, and amino acids [3]. The small intestine in birds is characterized by its length and frequent wrap, the small intestine begins from the back end of the stomach and ends with the ileo-caecal junction and divides into three parts: duodenum (part one), jejunum (middle part) and ileum (last part)

[4, 5]. Iraqi black partridge (*Francolinus francolinus*) returns to Phasianidae family of Galliformes order, and all of this family's birds are wild and are called the same name to the male and female as well as they rely on the grains as food (Graniivorous) [6]. The aim of study is designated to determine the Morphological description and histological structure of ileum in Iraqi black partridge (*Francolinus francolinus*).

2. Materials and Methods

2.1. Birds Collection

Twenty of Iraqi black partridge (*Francolinus francolinus*) collected from local suppliers in Baghdad Province.

2.2. Morphological Study

Gross morphology, topographical relationship in situ and other anatomical observations were studied. The ileum was identified and photographed in situ using a Digital Sony camera.

2.3. Histological and Histochemical Preparation

For histological study, the specimens were fixed in neutral buffered formalin of 10% concentration for 48 hours. After well fixation, the specimens were dehydrated by passing them through a series of ascending ethanol concentrations (70, 80, 90 and 100 %) and then the specimens were cleared by xylene. After that, they were embedded in paraffin wax, then the blocks were sectioned at 3-5 μm thickness and stained with the following stains: Hematoxylin and eosin routine stain for general features identification. The histological examination was done by using light microscope (Kruss) and photographed using (14.1) mega pixels power digital Sony camera. In the histochemical study, sections were stained with Periodic Acid Schiff (PAS) and was used for the illustration of the goblet cells and the basement membranes of the epithelial lining of the ileum [7].

3. Results and Discussion

3.1. Morphological Study

The results of the gross examination showed that the ileum appears in the form of a short tubular composition of a thin diameter, the jejunum is associated with ileum by a fold of mesenteric membrane to form together a group of coils or irregularly shaped open twists. The ileum begins at the wide end of the jejunum and ends with the ileo-caecal junction. The caeca appear conjoined along the sides of the ileum, as the ileum appears less diameter at the bottom near the area of contact with the caecum (Figure 1). Because of the absence of vitlline diverticulum or what is known as Meckel's diverticulum, there is no separation border between the jejunum and the ileum but there is a clear difference in diameter (Figure 2). The results of the current study are consistent with those of [8] in *Coturinx coturinx* and are contrary to the results of [9] in *Anas platyrhynchos*, which stated that the jejunum and the ileum were arranged in large parallel rings taking the letter U overlapping with each other.

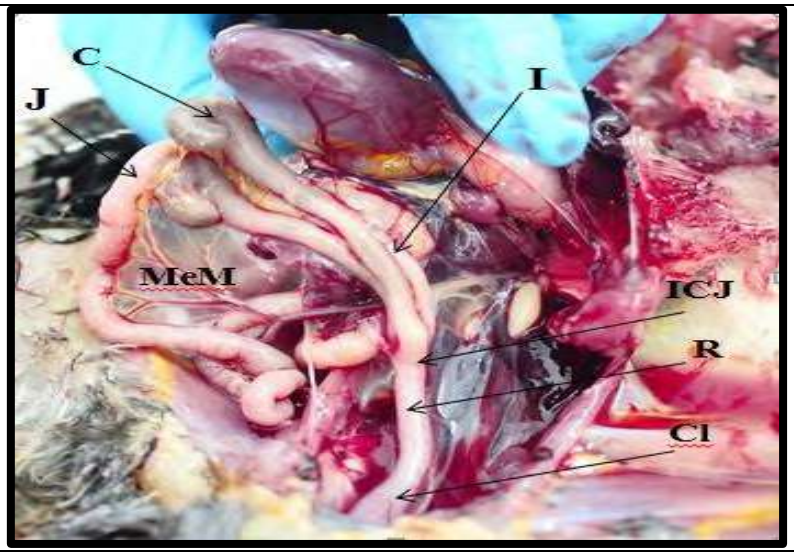

Figure 1. The position of jejunum and ileum is illustrated within the body of Iraqi black partridge, jejunum (J), ileum (I), ileo-caecal junction (ICJ), mesenteric membranes (MeM), the rectum (R), the cloaca (CI).

Figure 2. difference between jejunum (J), ileum (I), caecum (C), duodenum (D), pancreas (Pa), mesenteric membranes (MeM) in the Iraqi black partridge.

3.2. Light microscopic observation

The ileum wall consists of four main tunicae represented by the tunica mucosa, the tunica submucosa, tunica muscularis, and tunica serosa (Figure 3), which is consistent with the results of [10] study. However, it contradicts the results of [11] when the researcher studies the Japanese Quail (*Coturnix Coturnix Japonica*) study which showed that the ileum consists of three tunicae represented by mucosa, muscularis and serosa. This variation in compatibility seems to have something to do with the structural composition based on functional need as well as the specificity of the bird in this study.

3.2.1. Tunica Mucosa

Tunica mucosa consists of three secondary layers represented by the lining epithelium, lamina propria and muscularis mucosa (Figure 4) this result in agreement with [12] when the researcher studies the guinea fowl, while differ from those of *Corvus albus* study [13], which showed the absence of muscularis mucosa layer in the tunica mucosa.

3.2.1.1. Lining epithelium

The tunica mucosa consists of villi coated by simple columnar epithelium tissue, in which the main columnar cells have a pale cytoplasm, and the nucleus is spherical clearly pigmented, located in the last third of the cell, and based on a membrane basement membrane. The apical surface of the cell is characterized by the presence of a striated border and spread between the columnar cells. Many of the goblet cells possess a swollen apical surface (Figure 5) and this result was identical to the results of [12]. Epithelial cells absorb sugars, amino acids, fatty acids, water and other useful substances [14]. The results of histochemical study showed a positive reaction with periodic acid Schiff (PAS) stain (Figure 5) and used this reagent to confirm the presence of glycoprotein and polymucosaccharides in the goblet cells, basal membrane and striated border. Therefore, the mucin substances stained by purple color and this result came with similar of [15] study. The villi in ileum is characterized by different lengths and some of them take a finger shape (Figure 6) while a few of them show a leaf shape containing some meanders (Figure 7). This result was in full compliance with the results of *Tyto alba* and *Columba palumbus* [16] and *Anas platyrhynchos* [17]. The presence of meanders in leaf shape villi may be due to the fact that nutrient absorption is more efficient when the villi are arranged in this way than if they were parallel; as well as the passage of nutrition will take less time than if the surface was plane. Moreover, the connection between the nutrients and the surface of the cells would be better [18]. The results of the current study differ from those of the Japanese quail *Coturnix coturnix japonica* study [11], where the villi appeared in the spatula shape. The goblet cells produce a mixture of glycoproteins called mucinogen that acts to lubrication of the intestinal tract as well as protecting them from infection with pathogens, viruses and stomach acidity [19].

3.2.1.2. Lamina propria

The lamina propria is composed of loose connective tissue in which blood vessels, lacteal lymphatic vessels, smooth muscle fibers and nuclei of connective tissue cells are spread as well as positioned intestinal glands (Figure 4). This finding is consistent with the results of *Ara ararauna* [20], while contrary to [11] study in the Japanese quail *Coturnix coturnix japonica*, as it was shown that the lamina propria is composed of irregular dense connective tissue contain on reticular fiber, smooth muscle fiber and many blood vessels. This variation in tissue type may be due to the tissue structure associated with the functional specificity performed by the small intestine. The connective tissue that is the component of the lamina propria in partridge at the current study is composed of most connective tissue cells whose main function is support as well as the collagenous and elastic fibers that gain strength and flexibility. Intestinal glands, or Crypts of Lieberkuhn, open in the base of the villi which are simple tubular gland and their wall consists of low columnar cells with pale cytoplasm and spherical nuclei located near the base of the cell. The presence of goblet cells with mucin secretion and basal cells (Stem cells) these cells are based on a basement membrane and surround these cells with a small cavity (Figure 8) and this result corresponds to [12, 21]. These glandular units produce a large number of digestive enzymes whose role lies in facilitating the digestion and absorption of food such as peptidase enzymes and disaccharides that digest dietary bonds [22]. Enteroendocrine cells that appear within the cells lining the intestinal glands are few in number, and are characterized by their pyramidal shape and nucleus spherical shape and occupy a base position of the cell. These cells are characterized by the presence of secretion granules near the bottom of the nucleus present mainly in

the crypts and occasionally on the villi, these Enteroendocrine cells are of different types. (Figure 8). The histological examination also showed the presence of a limited number from Paneth cells in the bases of the intestinal glands. Paneth cells are characterized as pyramidal cells with cytoplasm containing secretory granules receptive to acidic stains (Figure 9). The importance of enteroendocrine cells is that they are responsible for the secretion of hormones that control the movement of the intestine are organized. Paneth cells are responsible for the production of lysozyme enzymes, which play an important role in the elimination of pathological bacteria [22].

3.2.1.3. Muscularis mucosa

This layer consists of two layers of smooth muscle fibers, longitudinal and circular. The longitudinal muscle fibers lie out wards in the form of bundles thicker than circular muscle fibers. Circular muscle fibers located inward the layers of muscle are separated with auerbrach's plexus of nerves (Figure 10). The results of the current study are similar to the results of *Anas platyrhynchos* [17] and are contrary to the results of *Otus scor brucie* study because of this layer is missing [23]. The importance of this secondary layer lies in the mixing process and the movement of nutrients through contraction within the gut, particularly in the small intestine [24].

3.2.2. Tunica Submucosa

It consists of areolar connective tissue which contains blood capillaries, lymphatic and nerves in the ileum (Figure 10) and this result is consistent with the results of the Guinea fowl study [12].

3.2.3. Tunica Muscularis

This tunica consists of two smooth muscle fiber layers, where the inner smooth muscle fiber sits in a circular order and thicker. While the second layer appears with a longitudinal order and a lower thickness located outward, as interspersed between these two secondary layers are thin tapes of fibrous connective interspersed with blood and lymphatic vessels and nerves (Auerbach's plexus) as well as collagenous and elastic fibers (Figure 10 and 11). This result is consistent with the result of *Tyto alba* [16] and a contrast with Japanese quail *Coturnix coturinx japonica* study, as the tunica muscularis consists of three secondary layers interior and external longitudinal arrangement, while the middle is circular in order [11]. Circular muscles contribute to the expansion of the small intestine diameter while the longitudinal muscles work in the mechanism of pushing food towards the large intestine, and therefore we find that both layers come together to complement the other to complete digestion.

3.2.4. Tunica Serosa

This layer is represented by loose connective tissue. The areolar connective tissue is covered by simple squamous mesothelium interspersed with blood vessels, nerves and adipose tissue and bordered from the outside by a row of mesothelium cells (Figure 11). This result was consistent with the results of [18], in the brown falcon *Falco berigora*.

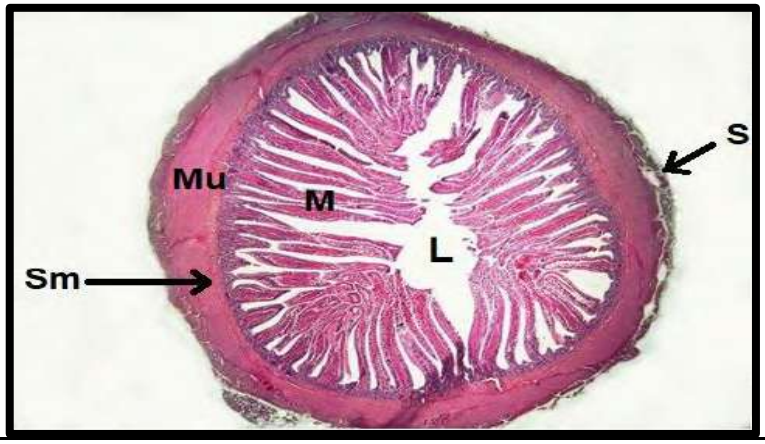

Figure 3. Cross section in the ileum wall for the Iraqi black partridge showing the four tunicae: mucosa (M), submucosa (Sm), muscularis (Mu), serosa (S), lumen (L) (H&E x4).

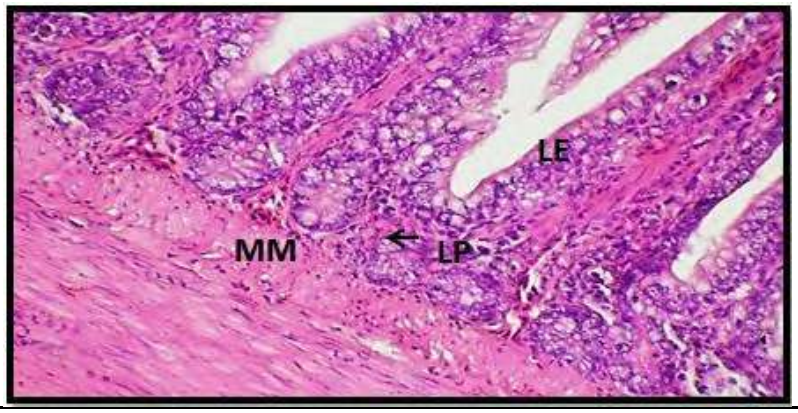

Figure 4. Transverse section in the ileum wall for the Iraqi black partridge showing the three secondary layers of mucosa tunica: lining epithelium (LE), lamina propria (LP), muscularis mucosa (MM) (H&E x 40).

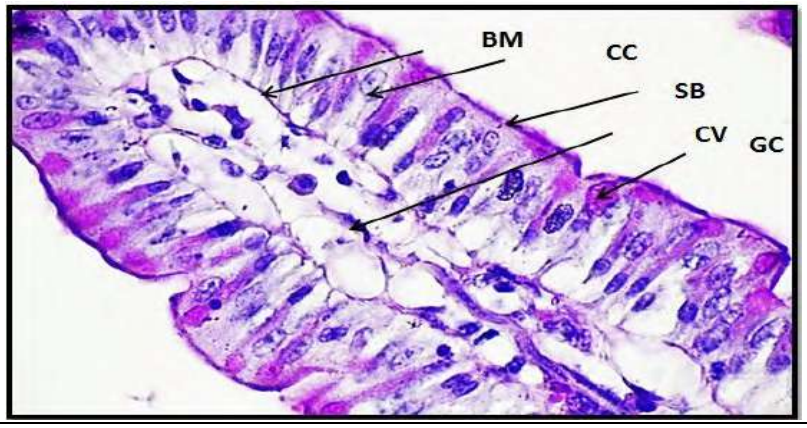

Figure 5. Cross section in the ileum wall for the Iraqi black partridge showing the components of the lining epithelium and the medullary of the villi (CV), columnar cell (CC), goblet cell (GC), a striated border (SB), base membrane (BM) (PAS x100).

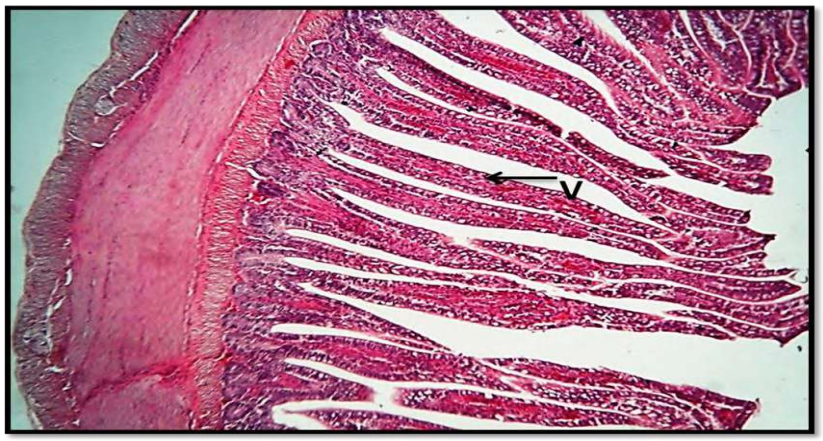

Figure 6. Cross section in the wall of the ileum for the Iraqi black partridge showing the finger shape of the villi (V) (H&E x10).

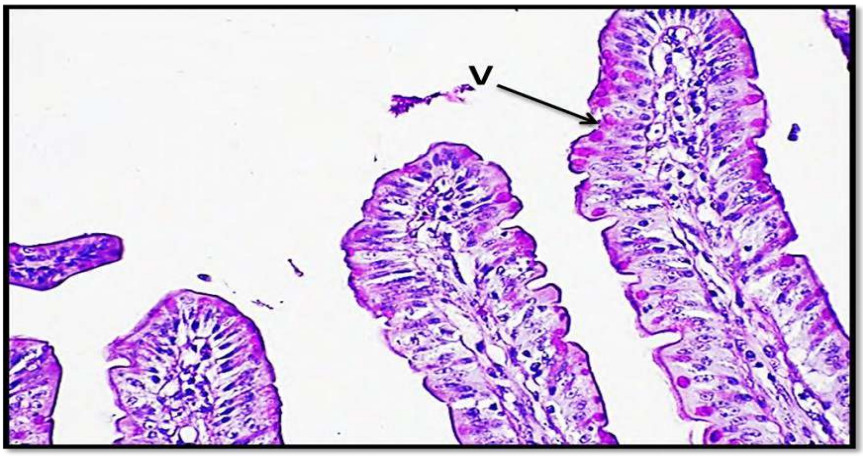

Figure 7. Cross section in the wall of the ileum for the Iraqi black partridge showing the leaf shape of the villi (V) (PAS x40).

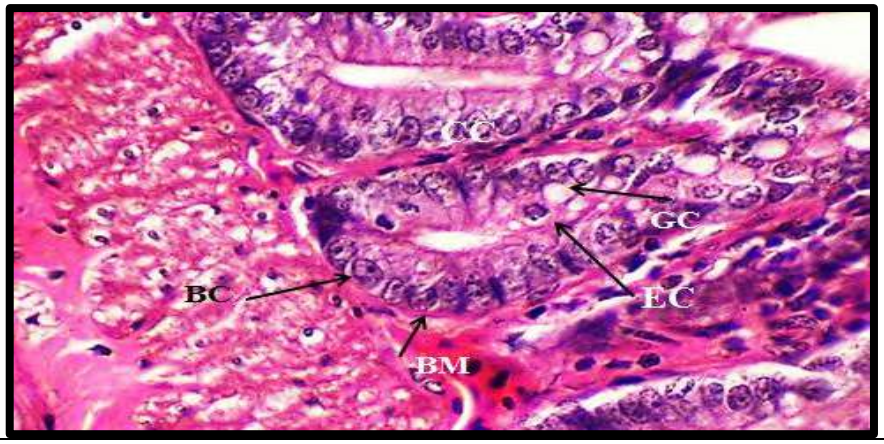

Figure 8. Transverse section in the ileum wall for the Iraqi black partridge showing the cells that formed the intestinal glands and the enteroendocrine cell (EC), columnar cell (CC), goblet cell (GC), base cell (BC), basement membrane (BM) (H&E x100).

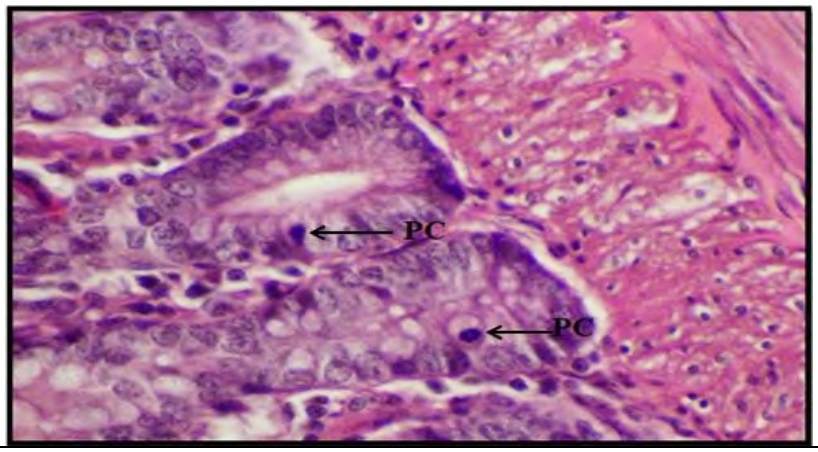

Figure 9. Cross section in the intestinal gland bases of the ileum wall for the Iraqi black partridge showing Panith cell (PC) (H&E x100).

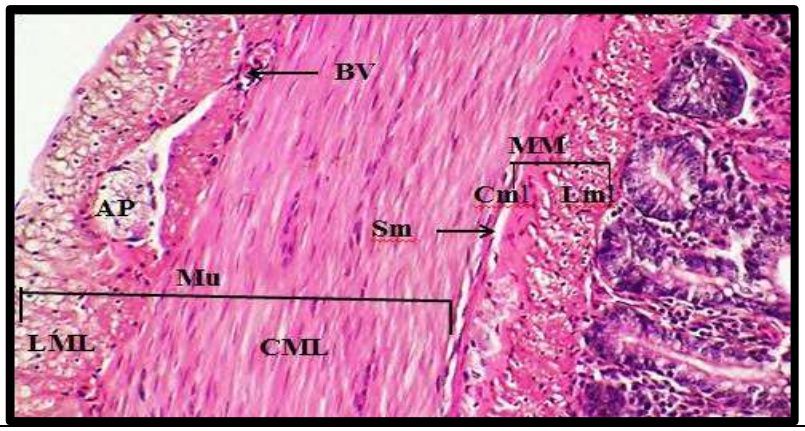

Figure 10. Transverse section in the ileum wall for the Iraqi black partridge showing the muscularis mucosa layer (MM) with its longitudinal muscular layer (Lml) and circular muscle layer (Cml), as illustrated by tunica submucosa (Sm) and tunica muscularis (Mu) by its longitudinal muscular layer (LML) and circular muscular layer (CML), blood vessel (BV), Auerbach's plexus (AP) (H&E x40).

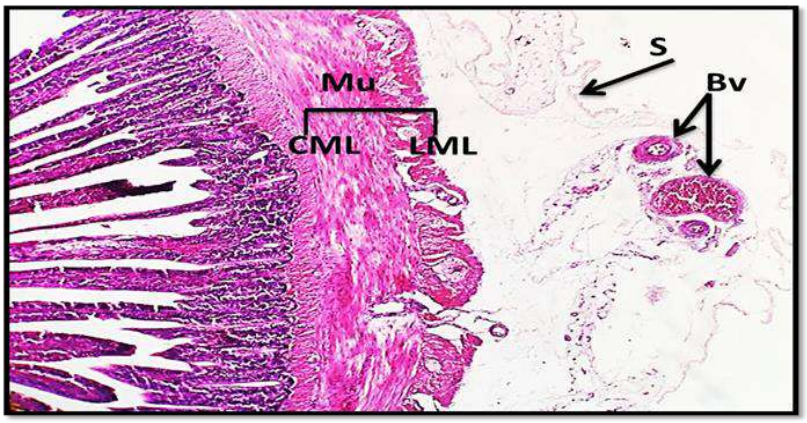

Figure 11. Cross section in the ileum wall for the Iraqi black partridge showing tunica mucosa (Mu), circular muscular layer (CML), longitudinal muscular layer (LML), tunica serosa (S), blood vessels (Bv) (H&E x10).

4. References

[1] Marshal PT and Hughes GM 1980 *Physiology of mammals and other vertebrates* 2nd ed. Cambridge University Press 64.
[2] Iwasaki S 2002 Evolution of the structure and function of the vertebrate tongue *J. Anat*. **201** 1.
[3] Jacob J, Pescatore T 2013 *Avian digestive system* University of Kentucky Collage of Agriculture Family and Consumer Sciences Food and Environment Lexington KY 40546.
[4] Mahmud MA, Shaba P, Shehu SA, Danmaigoro A, James Gana J and Abdussalam W 2015 Gross Morphological and Morphometric Studies on Digestive Tracts of Three Nigerian Indigenous Genotypes of Chicken with Special Reference to Sexual Dimorphism. *J. World's Poult. Res*. **5** 32.
[5] Al-Bhadly O and Mnati I 2018 Histomorphological Study and Scanning Electron Microscopy of the Duodenum in the Iraqi Black Partridge (*Francolinus francolinus*). *JGPT*. **11** 549.
[6] Mahdi N and George PV 1969 Systematic list of Iraqi vertebrates - Aves *Iraq Nat. History Museum Public*. **26** 34.
[7] Bancroft J D and Stevens A 2010 *Theory and practice of histological techniques* 4th ed. Churchill Livingston London 726.
[8] Zaher M, EL-Ghareeb AW, Hamdi H and Abu Amod F 2012 Anatomical, histological and histochemical adaptations of the avian alimentary canal to their food habits I-*Coturinx coturinx Life Sci. J*. **9** 253.
[9] Dawood GA 2013 *Anatomical and histological study of the small intestine between male and female indigenous ducks* MSc. thesis. Anatomy and Histology department College of veterinary medicine University of Baghdad.
[10] Taşçi SK, Deprem T, Bìngöl SA and Akbulut Y 2018 The Anatomical and Histological Structures of Buzzard's (*Buteo buteo*) Small Intestine and Liver, and Immunohistochemical Localization of Catalase *Kafkas Univ. Vet. Fak Derg*. **24** 69.
[11] Ahmad JM, Mamde CS, Patil VS and Dehaker NM 2012 Histomorphological Studies on the Small Intestine of Japanese Quail (*Coturnix coturnix japonica*). *IJVA*. **24** 103.
[12] Singh SP, Katiyar RS, Farooqui MM, Kumar P and Prakash A 2017 Histogenesis of guinea fowl duodenum *IJPS*. **52** 193.
[13] Igwebuike UM and Eze UU 2010 Morphological characteristics of the small intestine of the African pied crow (*Corvus albus*) *A.R.I*. **7** 1116.
[14] Gartner LP and Hiatt JL 2006 *Color textbook of histology* 3rd ed Sanuders company Aharcourt Health science co. Philadelphia Toronto 1.
[15] Rana J, Dhote BS, Ambwani TK and Patel SK 2016 Histochemical studies on small intestine of Uttara fowl *IJEST*. **5** 1181.
[16] Al-Juboury RW 2016 *Comparative anatomical and histological study on the digestive tract in two Iraqi birds, common wood pigeon Columba palumbus (L.) and barn owl Tyto alba (Scopoli)* PhD thesis College of Science Babylon University.
[17] Al-Samawy ERM, Al-Saffar FJ, Naji WA and Jarad AS 2017 Histomorphological and histochemical study of the small intestine of the mallard (*Anas platyrhynchos*) in south Iraq *I.J.S.N*. **8** 757.
[18] Al-Taee AA 2017 Macroscopic and Microscopic Study of Digestive Tract of Brown Falcon Falco berigora in Iraq *JUBPAS.* **25** 915.
[19] Vandijk J, Huisman J and Koninkx JFJG 2002 *Structural and functional aspects of a healthy gastrointestinal tract* In: Blok MC, Vahl HA, Lange LD, Vandebraak AEG, Hemke G and Hessing M (eds) Nutrition and health of the gastrointestinal tract Wageningen Academic Publishers Wageningen Netherlands 71.
[20] Rodrigues MN, Abreu JAP, Tivane C, Wagner PG, Campos DB, Guerra RR, Rici RE and Miglion MA 2012 Microscopical study of the digestive tract of blue and yellow macaws *Curr. Micr. Cont. Adv. Sci. Technol*. 414.

[21] Al-Aaraji AS and Al-Kafagy S M 2016 A comparative anatomical, histological and histochemical study of small intestine in Kestrel (*Falco tunniculus*) and white eared bulbul (*Picnonotic leucotis*) according to their food type *Iraqi J. Vet. Sci*. **40** 36.
[22] Southgate DAT 1995 Digestion and metabolism of sugar *AJCN.* **62** 2035.
[23] Al-Saffar FJ and Al-Samawy ERM 2016 Histomorphological and Histochemical Study of the Small Intestine of the Striated Scope Owls (*Otus scors brucei*). *Singapore J. Chem. Biol*. **5** 1.
[24] Lesson TS, Leson AA and Papro M 1988 *Text and atlas of histology* W. B. Saunders Co. Philadelphia 434.

The Correlation of Histopathological Findings with Ultrastructural Changes in Hepatocytes after Yangonin “Ya”-Intoxicated Rats Alone and In Combination with EtOH: Sub-Acute & Sub-Chronic Study

The Correlation of Histopathological Findings with Ultrastructural Changes in Hepatocytes after Yangonin "Ya"-Intoxicated Rats Alone and In Combination with EtOH: Sub-Acute & Sub-Chronic Study

Mohammed A. Hasan[1*]

[1]Biology Science Department, College of Education for Girls / Thi-Qar University, Iraq.

E-mail: mohammedn10@utq.edu.iq

Abstract. Yangonin "Ya" has been used for centuries as a herbal supplement, for its mood-altering properties. It has been used as a recreation agent, for relaxation, as well as for pain relief. However, hepatotoxicity is a widespread problem associated with medicines in general. Most herbal supplements are metabolized by the liver, and thus the liver represents the target organ. At present, Yangonin toxicity appears to be "idiosyncratic". Therefore, a study was designed in order to investigate the organelle-based changes in hepatocytes, after treatment with Yangonin alone and in combination with EtOH. Thirty rats were divided into five groups comprising of six animals each. The groups comprised of the control groups {(NCx) & (PCx)}, Yangonin (Ya) group, ethanol (EtOH) group, and the combination of (Ya) and ethanol (EtOH+Ya) group. The experiment was conducted over a period of 14 weeks, as a sub-chronic study. At the end of the 14th week, mitochondria, peroxisome, rough and smooth endoplasmic reticulum, and nuclei of hepatocytes, were evaluated using a scoring system. The results were compared with histopathological findings, as well. Treatment with Ya significantly induced hepatotoxic scores as compared to the control groups. Organelle injury scores increased significantly with Ya treatment, while rats that received "EtOH+Ya" showed the severest lesions of liver scores such as, severe hepatocellular degeneration, necrosis, and hypertrophy. Ultrastructural and histopathological scores in both groups were in very strong correlation (r = 0.928 for EtOH, r = 0.921 for Ya alone and r = 0.903 for Ya plus EtOH group). In conclusion, ethanol enhanced the sedative and hypnotic activity of Ya, and markedly increased toxicity. Findings based on TEM examination of organelles, supported the histological results as well as tissue lesions/injuries in hepatocytes, a result of hepatotoxin-induced hepatopathy.

Keywords. Hepatopathy, Yangonin, alcohol, ultrastructure, sER, mitochondria.

1. Introduction

Drug-induced hepatotoxicity has been cited as the most common reason for the withdrawal of approved drugs from the market. In addition, 50% of acute liver failure cases in the United States, have been attributed to drug-induced hepatic injury. The actual incidence of drug-induced hepatic

injury is difficult to estimate, as most cases are under-reported, or sourced from retrospective studies. Another problem associated with determining prevalence, is the lack of information or data pertaining to self-medication and use of herbal products that could interact adversely with prescription and non-prescription drugs [1, 2, 3]. Though the incidence of drug-induced hepatic injury appears to be quite low, data from the Centers for Disease Control and Prevention (CDC) in the U.S., has reported that, about 1600 new acute cases of liver failure are reported annually, of which 41% are due to paracetamol hepatotoxicity [4].The cases of adverse drug reactions and fatalities related to drugs, has more than doubled, during the period between 1995 and 2005 [5]. A lot of the cases of drug-induced liver injury are idiosyncratic, which means that the drug reactions cannot be predicted based on the known pharmacological properties of the substance, and therefore are often missed during pre-clinical stages of development. Regardless of their etiology, drug-induced hepatotoxicity is of major concern to the pharmaceutical industry, during the development of drugs, not only due to the increased risk for patients undergoing clinical trials but also to patients, after the launch of a new drug into the market. It could also result in increased costs and losses for pharmaceutical industries, due to the recalling of a drug at the later stages of development, or after it has been launched [6]. *Piper methysticum* Forster, is an ancient crop originating from Oceania (Polynesia, Melanesia and Micronesia [7]. *Piper methysticum* is cultivated for its rootstock which has been traditionally used to produce a drink. *Piper methysticum* extracts (both fresh and dried rhizome and roots) were prepared by grinding it into an aqueous suspension with water or coconut milk, and then strained and directly consumed [8, 9]. The effects of Yangonin (is found in *Piper methysticum* root as the main component) are considered to be mild, and less drastically mind-altering than most common drugs like alcohol, and when consumed in moderate amounts, there are no aftereffects such as "hangovers". *Piper methysticum* drinks when consumed, gives a sense of well-being, which is associated with its anxiolytic, sedative, muscle relaxant, and diuretic properties, among others [8].8 Commonly observed side effects related to *Piper methysticum* consumption include allergic reactions, red eyes, yellowing of the skin, gastrointestinal complaints and lethargy, which affects the individual's appetite and ability to sufficiently eat [8, 10, 11]. In addition, due to confounding factors that may have contributed to the toxicity, it is difficult to confirm whether there is a direct association between *Piper methysticum* and severe liver toxicity. Therefore, we hypothesize that, a synergistic interaction between alcohol and Yangonin contributes to marked increasing in cell toxicity, particularly hepatocytes. The main aim of this study was to determine whether Yangonin (with or without alcohol) may predispose oxidative stress and free radicals and then cytotoxicity, by affecting levels of availability of hepatic glutathione. Also, to search the organelle-based changes in hepatocytes after Yangonin treatment (alone and in combination with EtOH) in experimental rats. As well as, to determine the correlation of histopathological changes with ultrastructural findings..

2. Materials and Methods

2.1. Reagents

Yangonin is one of the six major kavalactones found in the kava plant. Commercially available Yangonin extract, a medium yellow powder was used (70% Yangonin HPLC Piper Methysticin Root extract) was obtained from Shaanxi Herb Sky Biotech Co., Ltd (Fiji) in one lot, which was received in batch (JT160314). The powdered extract was gavaged to each animal after being dissolved in distilled water (800 mg/kg. body weight/day). Below the chemical structure of “Yangonine” 4-Methoxy-6-[(E)-2-(4-methoxyphenyl) ethenyl] pyran-2-one (Figure 1).

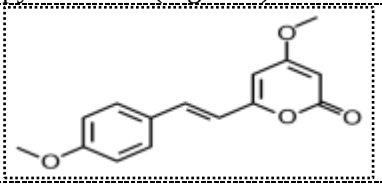

Figure 1. Chemical structure of Yangonine.

2.2. Animals and Exposure

The study was conducted in the Pathology Lab (Vet. Med/UPM). The protocol of the study was approved by Animal Care and Use Committee (ACUC), Faculty of Veterinary Medicine, University Putra Malaysia (UPM) with UPM/IACUC/AUP-R082/2015, the reference number for notice of approval. Thirty, nine-weeks-old Sprague-Dawley rats, weighing about 200±25gm were supplied with LAR Unit. They were housed in animal cages under standard conditions with a period of 12 h light/dark at 22 to 28°C and 70 to 80% relative humidity in the animal house, UPM. The animals were allowed to acclimatize for seven days before the start of the experiments. The animals were dosed with a standard rat chow pellet and allowed to drink water *ad libitum.*

2.3. Experimental Design

Animals were equally divided into five groups of approximately equal initial body weight, which are considered as negative control (NCx), positive control (PCx) and treated groups (EtOH, Ya and EtOH+Ya). The rats were examined for changes in body weight, feed and water intake, biochemical, liver parameters, macroscopically, microscopically histological changes and ultrastructural changes. At the end of the investigational period and under appropriate anesthesia by 87 mg ketamine/kg (b.w) mixed with 13 mg xylazine /kg (b.w), the animals were subjected to cardiac puncture to collect blood samples into sterile heparinized and non-heparinized test tubes for clinical chemistry study; the animals were then sacrificed by cervical dislocation, and finally, liver was dissected and weighted after being washed and blotted dry to somatic index determination. The absolute and the relative weights [(Liver W./ body W.) × 100)] were recorded [12].

2.4. Histological examination

At sacrifice, whole necropsies were performed on all rats utilizing standardized methodology. Liver weight, size and color were determined from all animals. Tissues including macroscopic abnormalities were removed, fixed, and preserved in 10% neutral buffered formalin for microscopic evaluation. Four to five micrometers (µm) thick sections were cut and mounted onto glass slides, stained with hematoxylin and eosin (H & E), while for Transmission Electron Microscopy, small pieces of liver (1mm3 slices) were immediately fixed in 4% glutaraldehyde buffer. Ultra-thin sections were collected on copper grids, double-contrast staining was applied with uranyl acetate (100 mL methanol and 5 g uranyl acetate) and Reynold's lead nitrate solution (1.76 g sodium citrate, 1.33 g lead nitrate, 50 mL distilled water and 8 mL 1N NaOH). Thin sections were examined under a transmission electron microscope (Hitachi H7100 TEM, Japan) [13]. Twenty-Five cells from each specimen were examined. Mitochondria, peroxisome, nuclei and smooth endoplasmic reticulum (sER) of hepatocytes were evaluated by using a previously described scoring system (Table 1). Twenty-Five nuclei, 60 mitochondria and 20 sER were examined for each animal.

2.5. Statistical analysis for histopathologic scores

The data was presented as mean ± SEM. In order to determine significant differences between groups, the Mann-Whitney U test was used for histopathologic scores, and for ultrastructure scores the Student's t-test was employed. The Pearson correlation procedure was used to evaluate the correlation of histopathological and ultrastructural scores. Values of $P < 0.05$, were considered statistically significant.

Table 1. Criteria for histopathological scoring system (light and transmission electron) microscope.

Light microscopy (H&E)		
Severity of Hepatopathy	Grade	Description
Minimal	1	0% of organ affected (normal histological appearance of hepatocytes).
Mild	2	1–39% of organ affected (congestion with slight sinusoidal space and central vein dilatation).
Moderate	3	40–79% of organ affected (cystic and fatty degeneration, hepatocellular hypertrophy and necrosis), and dilatation with congestion of sinusoids and central vein.
Marked (severe)	4	80%–100% of organ affected. Greater severity of changes noted in grade 3 with Kupffer cells hyperplasia and hypertrophy and possible pathological evidence of liver damage/fibrosis and cirrhosis.
Transmission Electron Microscopy/TEM		
Ultrastructure changes	Grade	Description
Nucleus affected	0	Normal
	1	Irregular chromatin distribution (margination, clumping)
	2	Increased and aggregation of heterochromatin with fragmented irregular envelope
	3	Degenerated and necrotic nucleus
sER and peroxisome proliferation	0	Normal
	1	Slight dilatation
	2	High proliferation and dilatation
	3	Presence of large degenerated area and highly vacuolization of sER and highly proliferation of peroxisome
Cytoplasmic vacuoles and lipid droplets accumulation	0	Normal
	1	Slight vacuolation of cytoplasm
	2	Moderate number of lipid droplets with cytoplasmic vacuoles
	3	Severe accumulation of lipid droplets in cytoplasm

3. Results

Throughout the course of the sub-acute experimental study, mortality was not observed in either of the "Ya" alone groups, Ya in combination with EtOH group, nor any of the other treatment groups. The most notable clinical abnormalities were observed in rats that were administered Ya, mainly those given Ya in combination with EtOH. The abnormalities were observed from the first week of the trial and increased gradually with time; this persisted for the duration of the experimental study. Clinical findings included, abnormal breathing, ataxia, dehydration due to loss of appetite, indigestion, lethargy, and loss of coordination. On the other hand, the withdrawal of 800mg/kg per day of Ya ingestion (alone and in combination with alcohol), after the third week induced a detectable change in behavioral patterns such as, increased sleeping time which subsequently lead to a decrease in the amount of feed intake and water consumption. While, at the end of the experimental period, most of clinical signs were as arching of the back, twitching as well as seizures, cutaneous lesions, characterized by flaky, dry skin with at times yellowish discoloration, which caused peripheral scaly

eruptions followed by hair loss (alopecia) beneath the lower jaw, known as Kani Kani lesions (Figure 2).

Figure 2. Photographs demonstrating the clinical observation throughout the sub-chronic trial. Ya group: abnormal red, congested eyes of rats, ruffled coat with alopecia area (dermopathy lesion/ Kani Kani lesion) beneath the lower jaw and under two eyes. Et+Ya group: severe eyes and lids congestion with more severe Kani Kani lesion approximately for whole head especially under eyes with severe weight loss, hunched posture, ruffled coat, head tilt.

3.1. Macroscopic investigation

Gross examination of the liver revealed various gross pathological changes among animals in the Ya and EtOH+Ya groups. Multiple necrotic foci around 2-3 mm in diameter were seen in the liver of rats belonging to both the Ya and Ya+EtOH groups, at 14 weeks. Significant lesions were observed in the enlarged oily heavy liver of the Ya-intoxicated group, and similar gross changes in the liver were also seen in the EtOH+Ya supplemented group, but much more severe. Also, the liver of rats from the EtOH+Ya group, were mottled with a yellowish or pale appearance, sometimes darkened color, with hepatic granuloma, as compared to the NCx group. The liver of EtOH intoxicated group, were mostly pale, oily and enlarged.

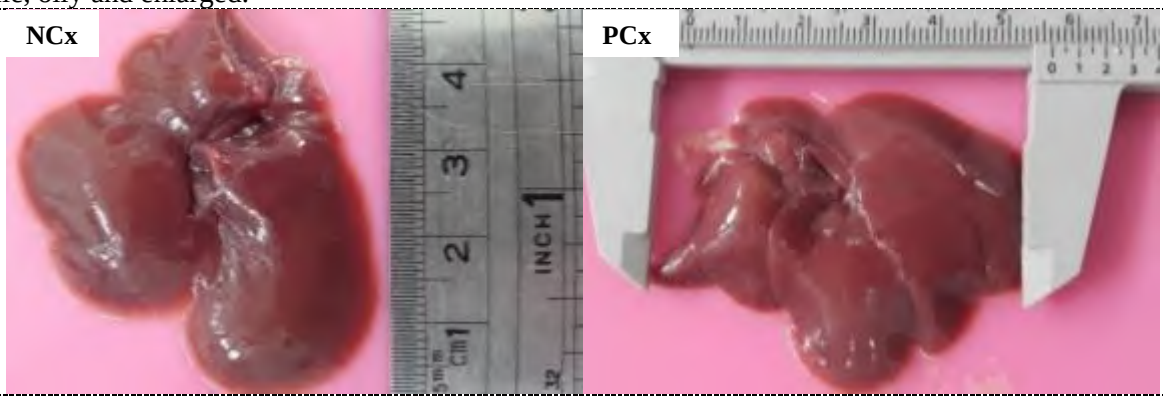

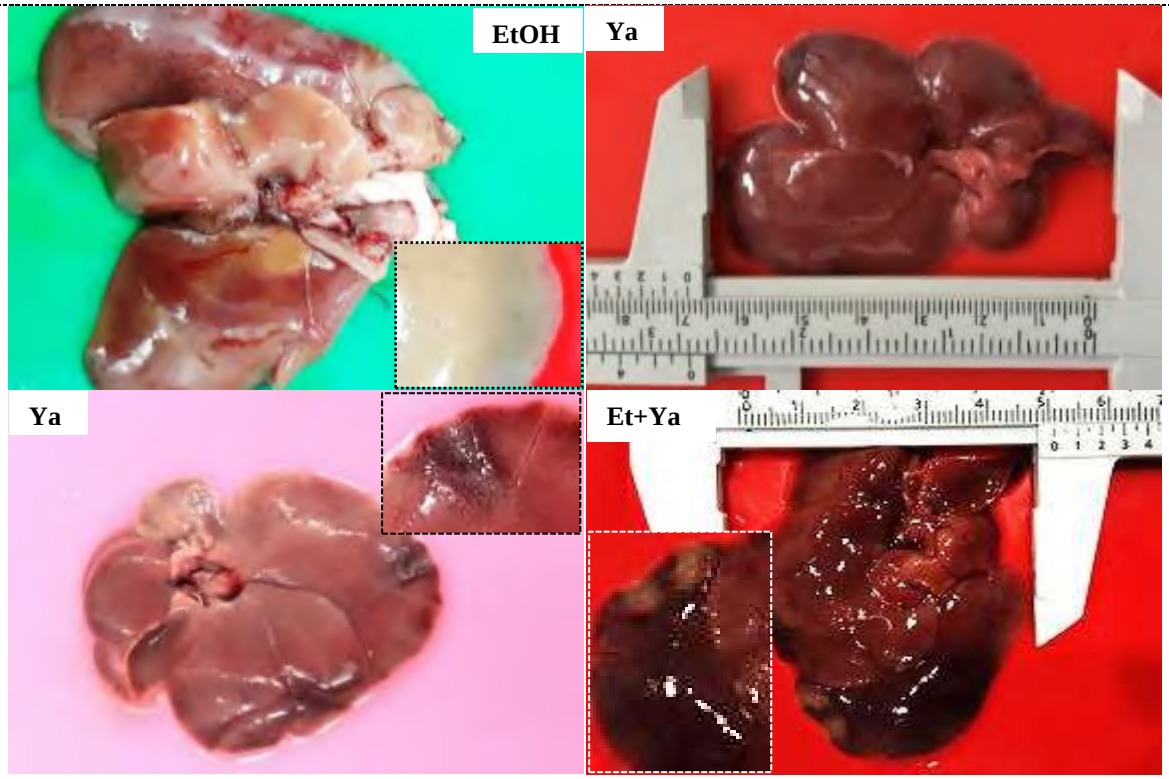

Figure 3. Photograph illustrating the gross morphological changes of liver. At necropsy, control (Cx) showing a normal structure, color, size and weight for all rats. Moderate to severe fatty changes is observed in liver of rats from EtOH group and Ya group with necrotic dark area demarcated from unaffected region and rounded edges showing in Ya group. Et+Ya group showing congested, severe dark red colored liver, necrotic black area with rounded edges and increase size and weight compare to Cx group.

3.2. Light Microscopic evaluations

Through H&E microscopic examination, the liver of the control (Cx) group, appeared a normal architecture of hepatic tissue while, Ya-intoxicated rats revealed different histopathological changes, which observed primarily (initial 3 weeks) in the centrilobular zone and the two zones were significantly less affected. Later, at week 14th most of hepatic lesions were seen in the outer/periportal zone. Angiectasis, vacuolization and dilatation of hepatic sinusoids with hyperplastic of the endothelial layer of the central vein. Clear hepatocellular necrosis and hypertrophic (3-4 times larger than normal hepatocytes), other hepatocytes showed cystic and fatty degeneration (macrovesicular and microvesicular steatosis). The lesions observed in the sections of Ya-intoxicated rats, were also seen in the EtOH+Ya group, but with more severity and more diffuse, especially in the periportal zone and the hypertrophic cells appeared to be six times larger than normal hepatocytes.

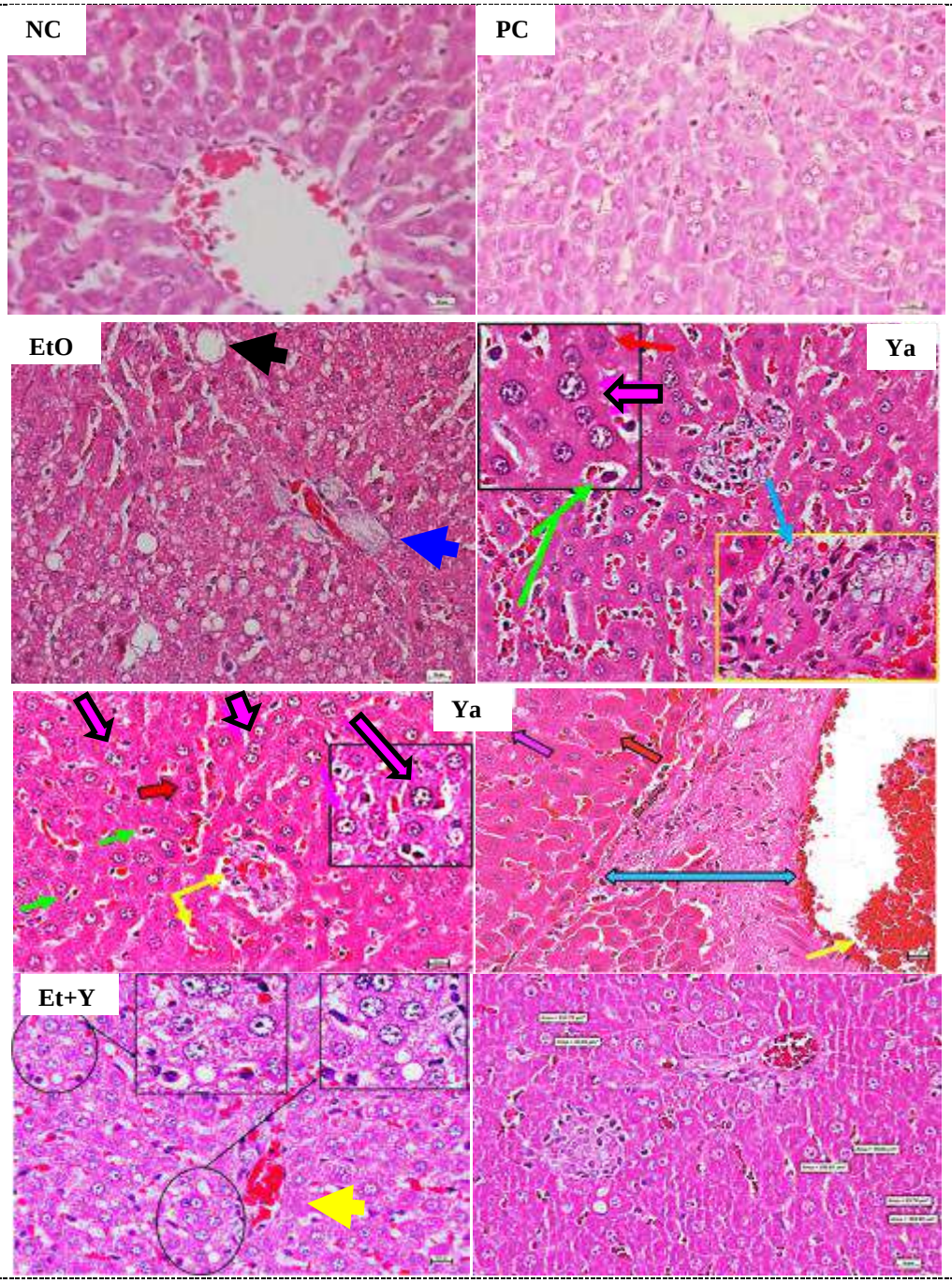

Figure 4. Figure 3: Photomicrograph of liver from, Control groups showing normal limit, represented by normally arranged hepatocytes around the central vein together with normal sinusoidal capillaries. Fatty change (steatosis) was observed in diffuse manner all over the hepatocytes (black arrow) with severe dilatation and congestion of central vein and sinusoidal space, moderate centrilobular necrosis, hypertrophic of some Kupffer cells, with slight periductal fibrosis surrounding the bile ducts (blue arrow) in Ya treated group. Et+Ya group showing clear centrilobular necrosis (red arrow) and centrilobular cystic degeneration (black arrow), hepatocellular hypertrophy in central zone (purple arrow), Kupffer cells hypertrophy and hyperplasia (shiny green arrow), dilation and multifocal angiectasis of sinusoids (yellow arrow), proliferation endothelial layer if central vein (light blue arrow) (H&E 40X).

3.3. Electron Microscopic evaluations

TEM displayed numerous vacuoles and fat droplets in the cytoplasm of hypertrophic hepatocyte, severe degeneration and necrosis of hepatocytes organelles, an irregular nucleus with highly irregular chromatin distribution and dense electron membrane-bound granules in cytoplasmic affected cells of Ya and EtOH+Ya groups. Many of nuclei displayed an indistinct membrane, and dark staining revealed a dense amorphous mass of clumped nucleoplasm, and most of the nucleus of the hepatocellular necrotic cells were in pyknosis and sometimes in karyolysis. Large activated Kupffer cells with hypertrophic stellate cells in dilated blood sinusoids, were also seen. The higher magnifications revealed, many lysosomes in KCs, filled with electron-dense nanoparticles and extensive swollen mitochondria. Massive dilated/expanded sER with well-developed cisternae of rER and high proliferation of peroxisomes were also observed.

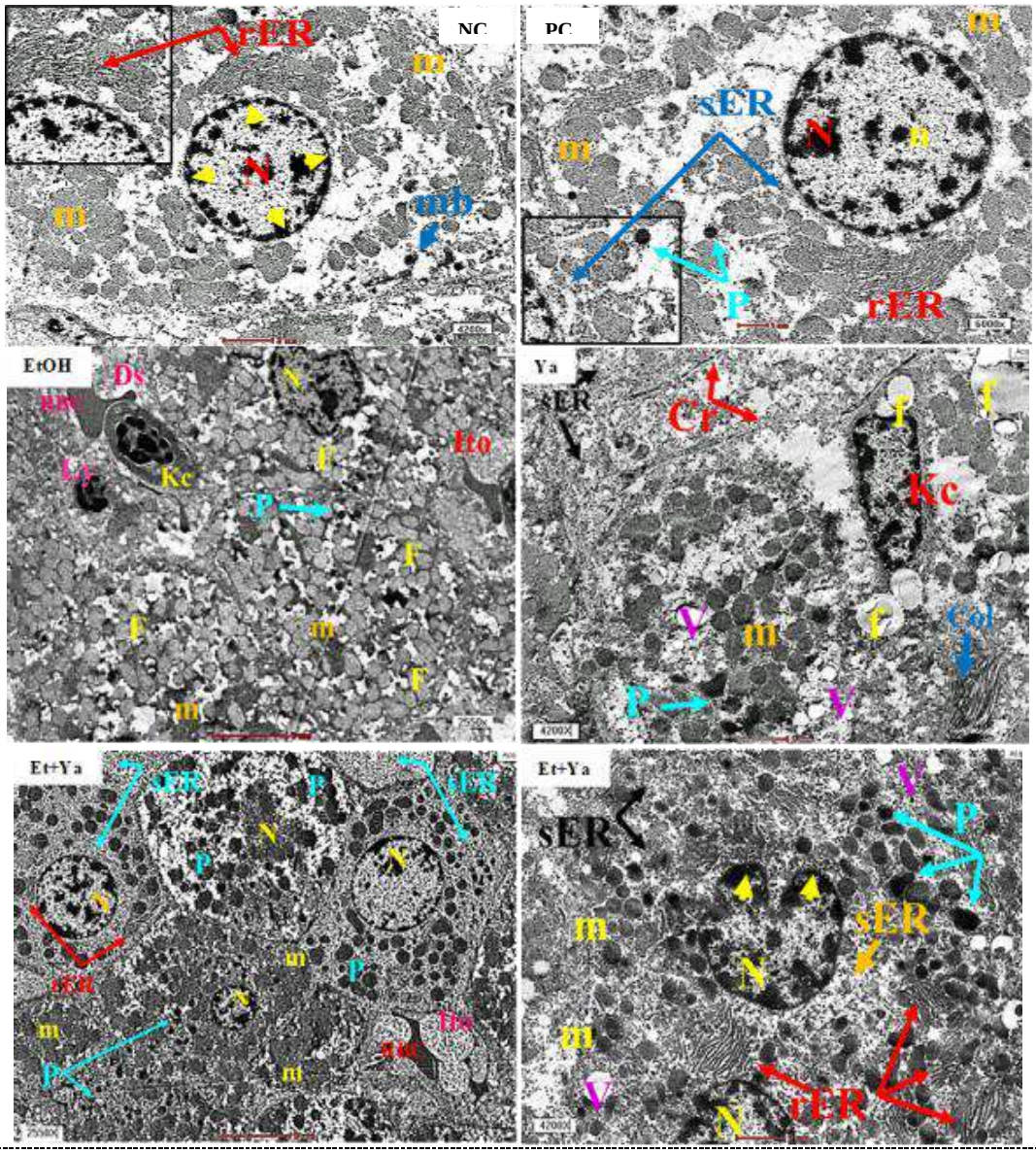

Figure 5. Transmission Electron micrographs from untreated (Cx) normal manifestation of hepatocyte with a euchromatic nucleus (N) as well as developed a nuclear membrane (yellow head arrow), and the cytoplasm contains normal mitochondria (m), an array of rough endoplasmic reticulum (rER) and smooth endoplasmic reticulum (sER), normal peroxisome (P). EtOH-treated rat showing hepatocytes

with intracytoplasmic vacuolization (V), clumping of its organelles, extensive lipid droplets "steatosis liver" (f), swollen mitochondria (m), and large stellate "Ito" cells in the space of Disse, dilatated blood sinusoids (S) with hypertrophic Kupffer cells (KC) and degenerative hepatic nuclei (N) surrounded by a fragmented irregular nuclear envelope, while the hepatocytes of Ya-treated rats (alone and in combination with EtOH) showing intracytoplasmic vacuolization (V), swollen mitochondria (m), dilatated blood sinusoids (S) with severe hypertrophic Kupffer cells (KC), severe dilated smooth endoplasmic reticulum (sER) and highly proliferation of peroxisome (P), electro-dense bodies (mb) and debris of necrotic nuclei, a lot of lysosomes (Ly) and collagen fibers adjacent to Kupffer cells.

Table 2. Lesion scoring for liver tissue obtained at 14th weeks sub-chronic trial.

Groups	NCx & PCx	EtOH	Ya	EtOH+Ya
Histopathological scoring (Mean ± SE)				
Hepatocellular necrosis	0.00	0.86±0.04	1.78±0.14	2.18±0.10
Hepatocellular hypertrophy	0.00	0.74±0.02	1.76±0.14	2.03±0.13
Cystic and fatty degeneration	0.00	1.67±0.07	1.26±0.06	1.72±0.12
Total lesions score	0.00	3.27±0.29	4.80±0.17	5.93±0.14
Organelle injury scores (Mean ± SE)				
Nucleus affecting	0.00	0.42± 0.03	0.63± 0.02	0.93± 0.02
sER & Peroxisome Proliferation	0.00	0.55± 0.06	1.02± 0.04	1.19± 0.03
cytoplasmic vacuoles and lipid droplets accumulation	0.00	0.83±0.04	1.03±0.05	1.24±0.03
Total lesions score	0.00	1.80±0.12	2.68±0.13	3.36±0.1

The histopathologic lesions scores of light microscopes in EtOH, Ya and EtOH+Ya groups are a very strong correlation with Ultrastructural changes scores in that groups (r = 0.928 for EtOH Group, r = 0.921 for Ya group and r =0.903 for EtOH+Ya group) (Figure 5). While the table (3) represent the correlation between lesions under light and transmission electron microscope.

Table 3. The correlation between lesions of light and transmission electron microscope.

TEM lesions	Light microscope lesions (H&E)		
	Hepatocellular necrosis	Hepatocellular hypertrophy	Cystic and fatty degeneration
Nucleus affecting	.988**	.978**	.893*
sER & Peroxisome Proliferation	998**	.995**	.873*
Cytoplasmic vacuoles and lipid droplets accumulation	.966**	.955**	.954**

** Correlation is high significant at the level 0.01, *Correlation is significant at the 0.05.

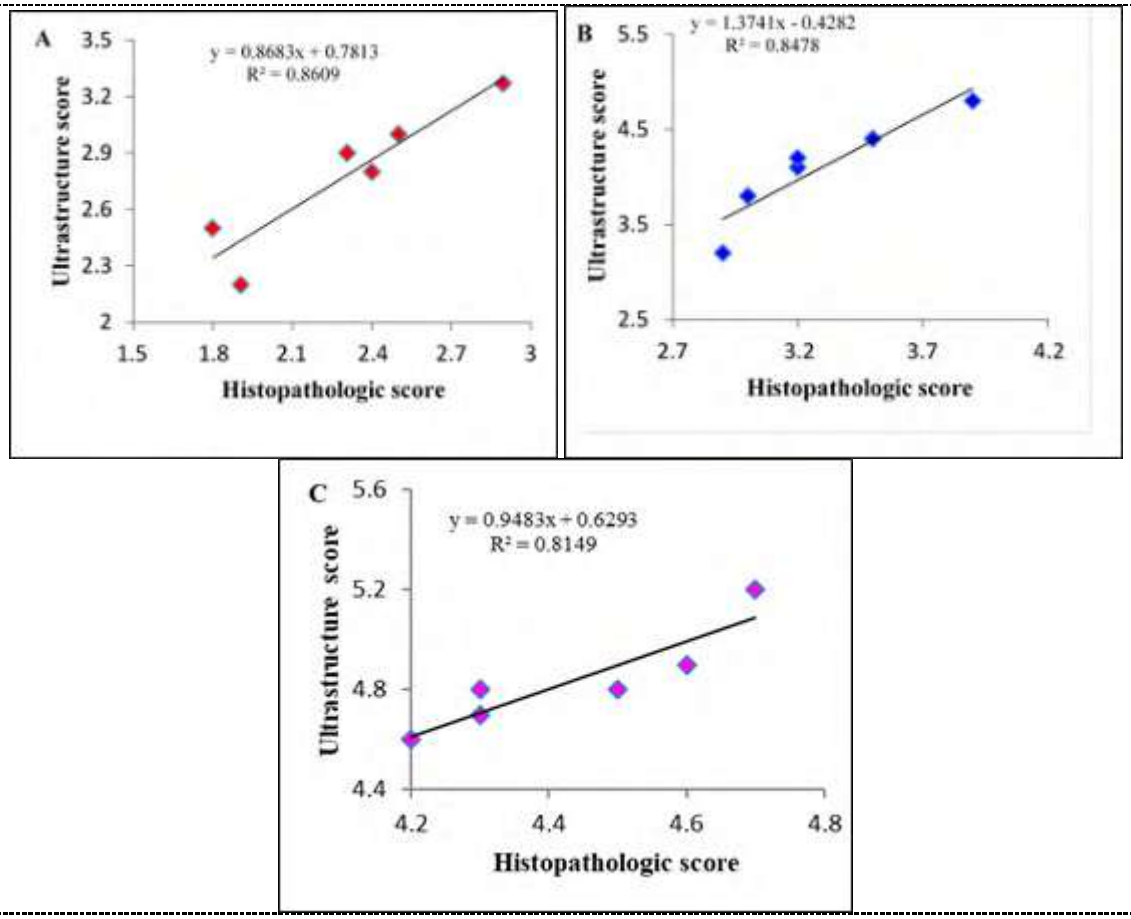

Figure 6. Correlation of histopathologic and ultrastructure scores in A: EtOH treated group (r = 0.928); B: Ya treated group (r = 0.921) and C: EtOH+Ya treated group (r = 0.903).

4. Discussion

The current study investigated the histopathological findings and their correlation with ultrastructural results in hepatocytes, after EOH treatment in “Ya" induced experimental liver toxicity. As described previously in a few studies, *Piper methysticum* 'awa' feeding induced histopathological changes in the liver of experimental animals [12, 14]. Examination of the H & E-stained liver sections from Ya-gavaged rats under the light microscope, revealed different histological changes in hepatic architectures, such as clear cytoplasmic vacuolation and lipid droplets accumulation, other hepatocytes showed degeneration and necrosis with deep acidophilia and pyknotic nuclei; sometimes extensive karyorrhexis or fragmented nuclei were indicative of acute hepatocellular necrosis. Therefore, TEM examination revealed that, Ya induced alterations in chromatin distribution in the nuclei of hepatocytes. Furthermore, abundant heterochromatin was detected, disorganization of nuclear content as margination and clumping of chromatin, in Ya treated animals could be morphological evidence of injury in the nucleus. In addition, severely degenerated nuclei were detected, and most of the nuclear content was abnormal in appearance such as, fragmented irregular nuclear envelope and disturbed heterochromatine among the Ya group, which has been previously reported to induce DNA damage [14, 15]. These results support the well-known fact that, nucleoplasmic constituents represent the structural counterpart of transcription and processing of messenger and ribosomal RNAs and are therefore highly sensitive indicators of cellular activity [16]. Such a scoring system may be potentially useful for the researchers, in monitoring the changes in the ultrastructure of hepatocytes under pathogenic stress, or medications. The most significant ultrastructural changes with Ya treatment,

occurred in the mitochondria, sER and peroxisomes. The molecules in the electron transport chain, which play the central role in ATP synthesis, are found in the cristae mitochondria. It is also well known that mitochondria are a major source of endogenous production of ROS [17]. The major mitochondrial pathology observed in this study was, edema, the major ultrastructural sign of cellular injury, extensively invading the matrix resulting in swelling of the organelle and structural damage to cristae. Though edema was seen in both groups, it was much more pronounced in EtOH+Ya treated animals. In addition, there was marked disruption in cristae with EtOH+Ya treatment, and cristae integrity was highly affected. Swelling and a loss of regular cristae structure with a ruptured outer membrane, characteristics of deteriorated function of mitochondria [18, 19, 20], were observed among the rats of the EtOH+Ya group. In rats receiving "EtOH+Ya", an increase in liver weight was consistent with an increase in the incidence of hepatocellular hypertrophy, as observed under the light microscope. Hepatocellular hypertrophy was recognized as, an irregular, diffuse increase in cell size associated with ground-glass cytoplasmic eosinophilia and cytoplasmic glycogen content and enlarged nuclei, primarily located in the centrilobular regions. Severely dilated ERs are indicative of severely damaged hepatocytes [21]. When the ER of rats treated with Ya were examined under TEM, serious damage was observed in the form of irregular lamellar organization, large dilatations and focal breaks in rER, vacuolisations, myelin figures and high proliferation in sER in various regions. However, more severe changes (focal and dilatations) were observed in rER and sER of EtOH+Ya treated animals. Besides the absence of a normal or intact appearance, that is known to be irreversible in the toxic state, as a result of the synergistic action of more than one toxic compound [22], sacs forming lamely-like shapes (disorganization) and vacuolization with high dilatation, contribute to the abnormal functioning of the ERs. The possible mechanisms that could explain the hepatocellular hypertrophy observed in Ya-intoxicated rats, suggest that the induction of drug-metabolizing enzymes by administration of *Piper methysticum* extract could cause the intrahepatic accumulation of proteins and lipids. It is a result of a slowdown in protein catabolism and particularly those intracellular proteins degraded in lysosomes by autophagy, after the intake of awa in combination with EtOH [12, 23, 24, 25, 26] Another possible mechanism suggests that, hepatomegaly occurs because the awa extract causes a significant induction and modulation of drug metabolizing enzymes particularly CYP isozymes [27, 28]. It is associated with a concomitant increase in peroxisome proliferation in hepatocytes and proliferation of the smooth endoplasmic reticulum (sER). Furthermore, the expansion and proliferation caused significant hepatomegaly, and these findings are in full agreement with previous results of [29] and [30] who reported that hepatocellular hypertrophy is indicative of enzyme induction, protein synthesis enhancement, and increased hepatocyte size could be a result of the proliferation of subcellular cytoplasmic organelles (typically sER and/or peroxisomes) or formed due to the accumulation of glycogen, lipid and water (hydropic degeneration). In addition, the results of the current study corroborated with the findings of previous studies, in respect to hypertrophic hepatocytes that could be caused by acetaldehyde, after the induction of CYP during alcohol consumption [31]. Through the process of binding the tubulin of microtubules, acetaldehyde blocks the secretion of proteins, which leads to increased levels of protein, lipid, water and electrolytes, causing hepatocytes to enlarge, a hallmark of alcoholic liver disease [32]. The excessive generation of free radicals following Ya supplementation, significantly increased MDA levels and was more pronounced in combination with EtOH, which adversely affected cellular membrane integrity and mitochondrial function, as demonstrated by the TEM results. This could be responsible for the enlargement of hepatocytes, via a decreased activity and/or levels of the Na-K ATPase pump (located in the plasma membrane), due to decreased levels of ATP following mitochondrial change, or through direct membrane damage caused by ROS, generated after Ya consumption, resulting in the influx of sodium (accompanied by water) causing cellular swelling/enlargement. These findings were in accordance with a previous study, which reported that, awa root extract induced mitochondrial dysfunction, and a 35% to 40% decrease in total cellular ATP after 3 to 4 hrs of treatment, respectively [33]. However, the highest increase in lesion scores particularly hepatomegaly, observed in the EtOH+Ya combination group, could be a result of a synergistic action or herbal-drug interaction, of ethanol with *Piper*

methysticum, which produced more severe adverse effects. To date, electron microscope findings in hepatocytes as a result of hepatotoxins, have not been defined systematically. Moreover, it was unclear whether the changes observed in various organelles wee reversible or not. However, the present study was not only able to identify the specific changes observed in different organelles, but also provided a better assessment and measurement of ultrastructural injury. Furthermore, this study is the first of its kind, a preliminary investigation of the histopathological lesion scores under a light microscope, following treatment with Ya and in combination with EtOH.

5. Conclusion

In conclusion, this study elucidated changes in morphology of hepatocyte organelles, following the induction of a certain hepatotoxin. Ya was shown to change or alter the morphology of major organelles of hepatocytes and hastened the development of hepatopathy, particularly in combination with EtOH. The structural adverse changes observed in hepatocyte organelles in this study, are likely the cause of significant histological injuries. Since the transmission electron microscope is the highest magnification tool at present, modeling new ultrastructural scoring systems including more organelles and parameters can be useful in estimating the degree of injury and outcome of alternative treatment strategies in management of chronic liver diseases.

References

[1] Almdal TP and Sørensen TIA 1991 Incidence of parenchymal liver diseases in Denmark, 1981 to 1985: analysis of hospitalization registry data *Hepatology* **13** 650.
[2] Rodriguez LAG, Ruigómez A and Jick H 1997 A Review of Epidemiologic Research on Drug-Induced Acute Liver Injury Using the General Practice Research Data Base in the United Kingdom *Pharmacother. J. Hum. Pharmacol. Drug Ther*. **17** 721.
[3] De Abajo FJ, Montero D, Madurga M and Rodr'iguez LAG 2004 Acute and clinically relevant drug-induced liver injury: a population based case-control study. *Br. J. Clin. Pharmacol.* **58** 71.
[4] Norris W, Paredes AH and Lewis JH 2008 Drug-induced liver injury in 2007 *Curr. Opin. Gastroenterol.* 24 287.
[5] Moore TJ, Cohen MR and Furberg CD 2007 Serious adverse drug events reported to the Food and Drug Administration, 1998-2005 *Arch. Int. Med*. **167** 1752.
[6] Butura A 2008 *Drug and alcohol induced hepatotoxicity*. MSc. Thesis Institutionen för fysiologi och farmakologi / Department of Physiology and Pharmacology. Karolinska Institutet, Sweden,. Stockholm.
[7] Lüde S 2005 *Hepatotoxicity of the phytomedicines Kava kava and Cimicifuga racemosa* University of Basel .
[8] Lebot V, Merlin M and Lindstrom L 1997 *Kava: The Pacific elixir: The definitive guide to its ethnobotany, history, and chemistry*. Inner Traditions/Bear & Co.
[9] Johnson T 1998 *CRC ethnobotany desk reference* CRC Press.
[10] Singh YN 1992 Kava: an overview *J Ethnopharmacol*. 37 13.
[11] Baynes J and Dominiczak MH 2014 *Medical biochemistry*. Elsevier Health Sciences.
[12] Clayton NP, Yoshizawa K, Kissling GE, Burka LT, Chan PC and Nyska A 2007 Immunohistochemical analysis of expressions of hepatic cytochrome P450 in F344 rats following oral treatment with kava extract *Exp Toxicol Pathol*. **58** 223.
[13] Hayat MA and Giaquinta R 1970 Rapid fixation and embedding for electron microscopy *Tissue Cell* **2** 191.
[14] El-Kholy SMS and El-Salam SA 2011 Kava extract drug: what is the actual risk of hepatotoxicity in adult male albino rats? *Egypt J. Histol.* **34** 697.

[15] Fu PP, Xia Q, Guo L, Yu H and Chan PC 2008 Toxicity of kava kava *J. Environ. Sci. Heal.Part C.* **26** 89.
[16] Tasci I, Mas N, Mas MR, Tuncer M and Comert B 2008 Ultrastructural changes in hepatocytes after taurine treatment in CCl4 induced liver injury *World J. Gastroenterol*. **14** 4897.
[17] Balaban RS, Nemoto S and Finkel T 2005 Mitochondria, oxidants, and aging *Cell* **120** 483.
[18] Ernster L and Schatz G 1981 Mitochondria: a historical review *J. Cell Biol*. **91** 227s.
[19] Vanhorebeek I, De Vos R, Mesotten D, Wouters PJ, De Wolf-Peeters C and Van den Berghe G 2005 Protection of hepatocyte mitochondrial ultrastructure and function by strict blood glucose control with insulin in critically ill patients *Lancet* **365** 53.
[20] Szeto HH 2006 Mitochondria-targeted peptide antioxidants: novel neuroprotective agents *AAPS J*. **8** E521.
[21] Gartner LP and Hiatt JL 2001 *Cytoplasm. Color Textb Histology* 2nd Ed WB Saunders Co. 11.
[22] Kumar V, Abbas AK and Fausto N 2005 *Cellular adaptations, cell injury, and cell death*. Kumar V, Abbas AK and Fausto N Robbins Cotran Pathol. Basis. Dis. 7th ed Philadelphia Elsevier 3.
[23] Baraona E, Leo MA, Borowsky SA and Lieber CS 1977 Pathogenesis of alcohol-induced accumulation of protein in the liver *J Clin Invest*. **60** 546.
[24] Donohue TM, Zetterrnan RK and Turna DJ 1989 Effect of chronic ethanol administration on protein catabolism in rat liver *Alcohol Clin. Exp. Res.* **13** 49.
[25] Vandenberghe J 1996 *Hepatotoxicology: Mechanisms of liver toxicity and methodological aspect* In: Raymond JM. Toxicalogy, Princ Appl Florida, USA CRC Press 703.
[26] Singh R, Kaushik S, Wang Y, Xiang Y, Novak I, Komatsu M 2009 Autophagy regulates lipid metabolism *Nature* **458** 1131.
[27] Clouatre DL 2004 Kava kava: examining new reports of toxicity *Toxicol Lett*. **150** 85.
[28] Guo L, Li Q, Xia Q, Dial S, Chan P-C and Fu P 2009 Analysis of gene expression changes of drug metabolizing enzymes in the livers of F344 rats following oral treatment with kava extract *Food Chem Toxicol*. **47** 433.
[29] Lock EA, Mitchell AM and Elcombe CR 1989 Biochemical mechanisms of induction of hepatic peroxisome proliferation *Ann. Rev. Pharmacol. Toxicol*. **29** 145.
[30] Maronpot RR, Yoshizawa K, Nyska A, Harada T, Flake G and Mueller G 2010 Hepatic enzyme induction: histopathology *Toxicol Pathol*. **38** 776.
[31] Lieber CS 1994 The discovery of the microsomal ethanol oxidizing system and its physiologic and pathologic role *Drug Metab. Rev*. **36** 511.
[32] Wondergem R and Davis J 1994 Ethanol increases hepatocyte water volume *Alcohol Clin. Exp. Res*. **18** 1230.
[33] Lim STS, Dragull K, Tang C-S, Bittenbender HC, Efird JT and Nerurkar P V 2007 Effects of kava alkaloid, pipermethystine, and kavalactones on oxidative stress and cytochrome P450 in F-344 rats *Toxicol Sci.* **97** 214.

Evaluation of mycotoxins and heavy metals pollution in some types of noodles in local markets

Evaluation of mycotoxins and heavy metals pollution in some types of noodles in local markets

Mohammed Jameel Mohammed[1*], Marwa Ibrahem Abd[1] and Saif Ali Khishan[2]

[1]Department of Food science ,College of Agriculture, University of Tikrit, Tikrit, Iraq.
[2]Agriculture directorate of Anbar, Iraq.

*E-mail: m_jamel68@yahoo.com

Abstract. This study was conducted to estimation mycotoxins and some heavy metals in some types of noodles in Salah Al-din governorate markets. In this study 6 species of Aspergillus were detected which were *A. flavus*, *A. parasiticus*, *A. fumigatus*, *A. terreus*, *A. ochraceus* and *A. niger* and 5 genus of fungi were *Fusarium verticillioides*, *Penicillium*, *Mucor*, *Alternaria* and *Rhizopus* isolated on the three types of media used.The results show presence of the three types of mycotoxins in all samples. The concentrations of the aflatoxin B1 ranged between 1.145 - 5.041 ppm. Concentrations of fumonisin between 8.498 - 19.496 ppm. Concentrations of ochratoxin A ranged between 3.960 - 52.543 ppm. The results also show that the concentration of copper and cadmium was at (0.50 - 1.23) (0.05 - 0.31) ppm respectively, while the concentration of lead was less than 0.1 ppm in all samples.

Keywords. Noodles, Aflatoxin, Ochratoxin, Fumonisin, Fungi, Heavy metals.

1. Introduction

Instant noodles is one of breakfast and staple food item of East Asian countries, whose consumption is gradually increasing day by day worldwide. Noodles, being a poor source of proteins due to use of refined flour in its production [1]. Worldwide, China ranks first in the consumption of noodles followed by Indonesia, Japan, and Vietnam [2]. [3] listed the ingredients of Instant Noodles (product) Neoguri Udon (Seafood & Spicy) consist of, noodles, potato starch, wheat flour, palm oil and salt, Dried solids packet, Mussel, green onion, carrot. Powder soup packet, salt, monosodium glutamate, glucose sugar, Soy sauce powder, Spices, corn flour, caramel color. Mycotoxins can be produced at the growth and storage of crops [4]. Aflatoxins considered toxic secondary metabolites of fungal origin contaminate agricultural crops before, during and after harvest [5]. Aflatoxins are a poisonous, carcinogenic of mycotoxins that are produced by the fungi *Aspergillus flavus* and *Aspergillus parasiticus*, there are 20 different types of aflatoxins identified until now, four groups of aflatoxins B1, B2, G1 and G2 [6]. Aflatoxins are toxic products by fungal metabolism, associated with serious health consequences and substantial economic losses for agriculture, livestock and poultry sectors in the developing countries [7]. One hundred wheat product samples (50 instant noodle and 50 bread samples) were collected from supermarkets in Bangkok, Thailand aflatoxin B1 contamination in these products 1 ng / g [8]. In another study no contamination with Afla B1 was detected in wheat flour in

Italy [9]. A broad spectrum of *Fusarium* species causes diseases in plants and produces important mycotoxins like trichothecenes, zearalenone and fumonisins, which are the major threats to animals and humans [10]. Fumonisin B1 (FB1) is a mycotoxin produced in some grains (mainly corn) by *Fusarium* species such as *Fusarium verticillioides* and *Fusarium proliferatum* [11]. Fumonisin B1 include many types FB1, FB2, and FB3, occured with the highest frequency, whereas FB1 found at the highest concentrations [12]. Fumonisins cause health effects in the liver and kidney, the health effects of fumonisins in humans was limited [13]. Fumonisins contamination most commonly in the cereals (rice, barley, wheat, maize, oat, rye and millet) [14, 15]. Ochratoxin (OTA) has been to be nephrotoxic, hepatotoxic, and immunotoxic in various animals and was classified by the International Agency for Research on Cancer as possibly carcinogenic to humans [16]. The mode of action is not clear discussed [17, 18]. *Aspergillus ochraceus* known to produce OTA and OTB, is a contaminant in many foods including wheat (grains and berries) and cereals [19]. Ochratoxin A content in the corn and wheat samples ranging 0-25.90 ng /g [20]. Concentration of OTA in raw wheat grain including (durum wheat, spelt, and emmer) should contain at maximum 5 μg/kg [21]. Heavy metals on the earth's crust are significantly contaminated to environment by mining and processing metal, Human activity such as pesticide and herbicide also occured heavy metals in environment [22]. Studies on heavy metals considerd important from public point, where the attention has drawn to necessity of measuring the accumulation of heavy metals, those metals which serious hazards to human [23]. The study aimed to detect the presence of fungi, mycotoxins and the levels of Cd, Pb and Cu in instant noodle types (packets) that manufactured in some different countries which may effect on human consumption.

2. Materials and Methods

2.1 Collection of samples

Ten types of noodles samples (curry with vegetables, spring vegetables, cream of mushrooms, chicken cream, maggi mushroom cream, bechamel mix, chicken with noodles, creamy vegetables, pasta flavored chicken, lentil soup) were collected from Salah al-din Governorate markets with three replicates and it was saved until the estimate.

2.2 Isolate and identification of fungi

The fungal isolates were depending on classification key ([24, 25, 26] by observing growing on (CYA) Czapek Yeast Capek extract Agar, and Rose Bengal agar and PDA media, and the physical characteristics of the mycelia such as features (shape, size, color, and hyphae) by the compound microscope contain a digital camera and using a lactophenol cotton blue stained on slide mounted with small parts of mycelium.

2.3 Quantification of aflatoxin B1, fumonisin B1 and ochra A by ELISA

The mentioned method was followed by a company Shenzhen Lvshiyuan Biotechnology Co. Ltd. China prepared for the materials and solutions used in extraction and determining the aflatoxin B1, fumonisin B1 and ochratoxin A using the ELISA method [27]. This method depends on mixing a specific amount of the complex of each poison-enzyme with a specific amount of the sample to be examined and mixed well and added to the titration plate covered with antibody surface. After incubation for a period of 15 minutes at room temperature, competition is between the toxin in the sample and the toxin associated with the enzyme with these bodies. Then the substance subject to the enzyme is added to the reaction solution and the reaction is stopped when the blue turns yellow. The optical intensity of the color of each slide was read using the spectrometer of the ELISA plates Bio_Tek Korean origin at a wave length 450 nm, in the central laboratory of Tikrit University.

2.4 Determination of heavy metals

Determination of heavy metal in 10 duplicate Noodles samples are analysis by the Atomic Absorption type ELCO [28]. A known volume of noodles samples was transferred to electric oven for drying and Muffle Furnace USA at 600 ^{0}C to weight stable. Ashed taken up in 5 ml of 5 % HNO_3 and filtration by Whatman No. 1. The contents of Cd, Cu and Pb were direct determined by Atomic Absorption Spectrophotometer type Shimadzo-6200 (Japan) for each heavy metals copper, cadmium and lead to be determined and measured by placing the sample in a transparent liquid form.

3. Results and Discussion

3.1 Occurrence of fungi in noodles

In this study 6 species variety of *Aspergillus* were detected such as *A. flavus*, *A. parasiticus*, *A. fumigatus*, *A. terreus*, *A. ochraceus* and *A. niger* and 5 genus of fungi were isolated on the three types of media used, other genus *Mucor* spp., *Fusarium verticillioides*, *Penicillium* spp., *Rhizopus* spp. and *Alternaria* spp. (Table 1). *A. flavus*, *A. parasiticus*, *A. ochraceus* and *Fusarium verticillioides* found in all samples, other genus were isolate from some samples. Numerous studies have shown that fungi generating toxins, especially *Aspergillus considerd* one of the main pollutants in foods and fungi *A. flavus* and *A. niger* are the most isolated species [29].

Table 1. Number of Fungi isolates in some types of noodles.

No.	Fungi	Isolates No.
1	*A. flavus*	15
2	*A. parasiticus*	12
3	*A. fumigatus*	5
4	*A. terreus*	4
5	*A. ochraceus*	11
6	*A. niger*	8
7	*Mucor spp.*	3
8	*Fusarium verticillioides*	15
9	*Penicillium spp.*	6
10	*Rhizopus spp.*	3
11	*Alternaria spp.*	2

The current results coincided with [30] isolate and identify fungi from food resources (Indian rice, rice, popcorn, pasta, pistachios and noodles), showed to 577 isolates of fungal genera and species, *A. flavus*, *A. niger*, *Altrenaria*, *Penicillium*, *Aspergillus terreus*, *Rhizopus* and *Aspergillus prasiticus* are 249, 149, 91, 43, 28, 10, and 7 isolates, respectively. One of the most common types is found in food sources *A. niger*, *A. ochraceus*, *A. terreus*, *A. flavus*, *A. fumigatus*, *A. parasiticus* and *A. versicolor* [31]. The reason for the emergence of fungal in foodstuffs is that the species possesses the ability to secrete a large number of enzymes that analyze foodstuffs that are used in nutrition and growth as well as increasing its spreading capacity, especially since some of its types can grow in a low moisture content as well as the relative density of the boards that produce them [32].

3.2 Concentrations of mycotoxins in noodles samples

Figures 1, 2 and 3 show the concentrations of the toxins of aflatoxin B1, fumonisin B1, and ochra A in some types of noodles in Salah El-Din Governorate markets. The results show the presence of the three types of mycotoxins in all samples. The concentrations of the aflatoxin B1, fumonisin B1and ochratoxin A between (1.145 - 5.041) (8.498 - 19.496) (3.960 - 52.543) ppm respectively. This may

be due to infection with molds that produce toxins in the field or during storage, and provide the appropriate conditions for the production of these types of mycotoxins [33].

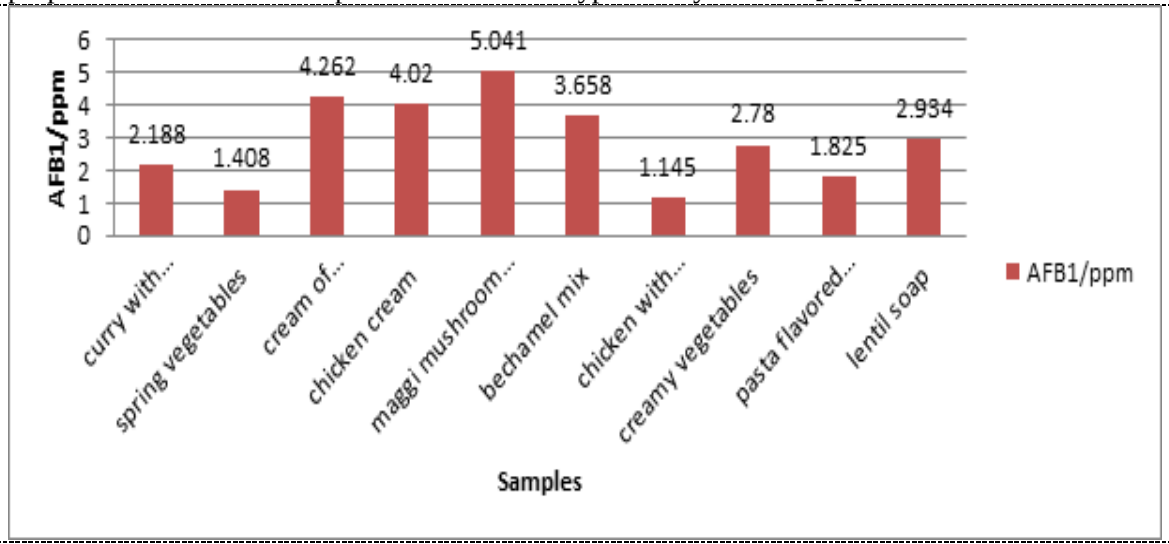

Figure 1. Concentration of aflatoxin B1 in some types of noodles

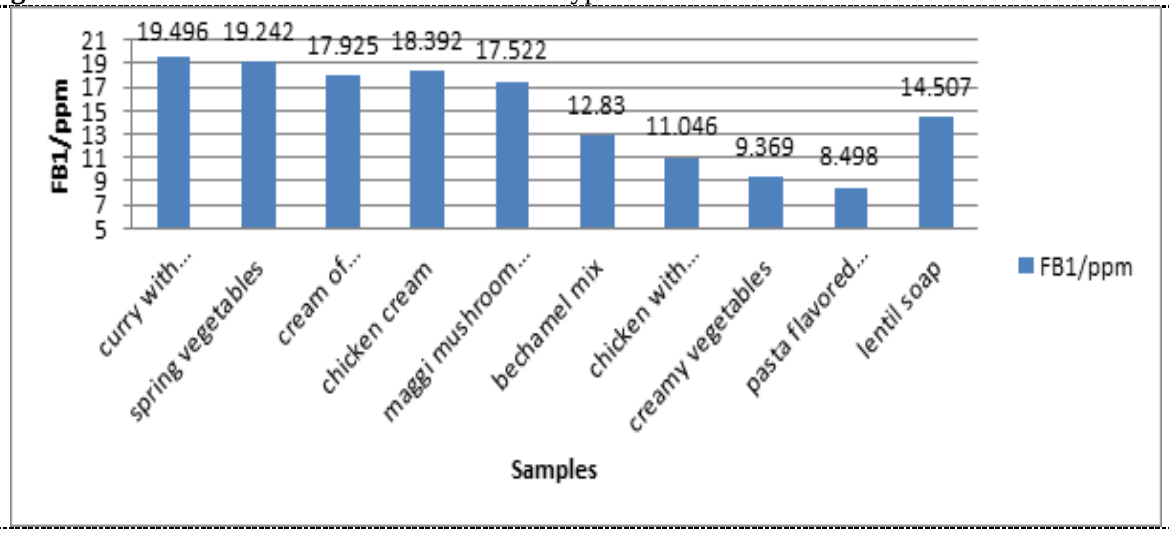

Figure 2. Concentration of fumonisin B1 in some types of noodles.

The highest of aflatoxin concentrations of Afla B1, Afla B2, Afla G1 are 65.77, 19.27, 1.02 µg/kg respectively. For the cereal food category, CBS11 recorded the quantities of Afla B1, Afla B2, Afla G1 and Afla G2 at 35.46, 4.92, 3.39 and 0.32 µg/kg respectively, the pasta category, PS1 recorded the highest quantities of 0.94 and 0.85 µg/kg for Afla B1 and Afla B2 respectively [5]. The highest fumonisin B1 value 1.46 and 0.46 mg/kg was measured in 64 maize flour and corn flakes samples respectively [34]. [35] showed positive OTA levels ranging from 0.6–3.4 in wheat flour samples µg/kg. OTA was detected in forty samples contain corn flour, corn flakes, wheat flour, bread and biscuits samples was 0 - 25.90 ng /g, the greatest level was measured at 360 ng /g of ochratoxin A in biscuit sample [20]. And that these results obtained were higher than the allowable limit by the European Union, which is 2 µg / kg of aflatoxins, also the concentrations of fumonisin B1, the permissible limit ranges between 200 - 800 ppb, according to the standard specifications set by the Codex Committee [36].

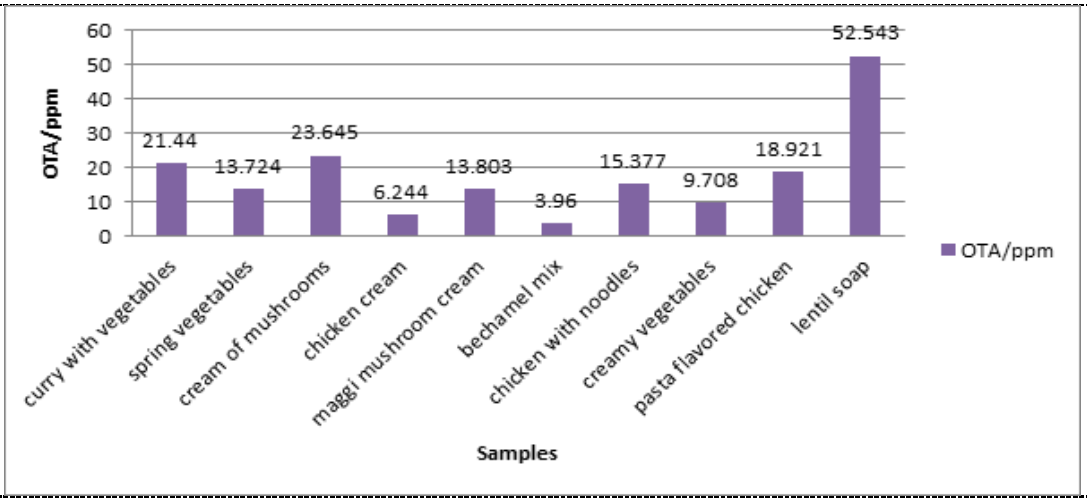

Figure 3. Concentration of ochratoxin A in some types of noodles.

FB1 toxicity affects mainly the liver organ, which is characterized by apoptotic, necrosis, and regeneration [37]. A recent study has found that FB1 can cause changes in the tissues of liver, lung, and kidney such as apoptosis and necrosis, leading to infiltration of inflammatory cells which were observed in these organs [38] .As well as for other agricultural crops, such as wheat, rice, field pistachios, and soybeans, where many studies have recorded high rates of pollution of these crops from aflatoxins [39]. The JECFA (FAO)/ (WHO) has set the provisional acceptable weekly intake of OTA at the rate of 100 ng / kg and 14 ng / kg of body weight per day [40].

3.3 Concentration of heavy metals in noodles samples

Figure 4, 5 and 6 showed that the concentration of heavy metal in some types of noodles. The results indicate to the concentration of Copper and Cadimium at (0.50 - 1.23) (0.05 - 0.31) ppm respectively. While the concentration of Lead less than 0.1 ppm in all samples. These results was accepted with [41] reported the concentrations of Cd, Pb and Cu in Iranian noodles at 0.469, 2.797 and 1.563 mg/kg and in imported noodles 0.62, 3.07 and 11.866 mg/kg respectively. Also accepted with [42] found the magnitude of heavy metals as Pb Ca Ni and Ar (1.17-1.67), (0.53-0.82), (0.27-0.43), (0.17-0.41) mg/kg respectively contamination in noodles samples. The concentration levels of heavy metals Tin, Cadimium, Zinc, Manganise, Iron, and Cobalt in six type of noodles, i.e., Maggi, Knorr, Shan shoop, Shinramayun, Indomie, and Mama observed at (3.3–9.7), (0.066–0.59), (6.2–11.4), (2.4–6.3), (4.8–17.5), and (0.39–0.74) mg / kg respectively [43].

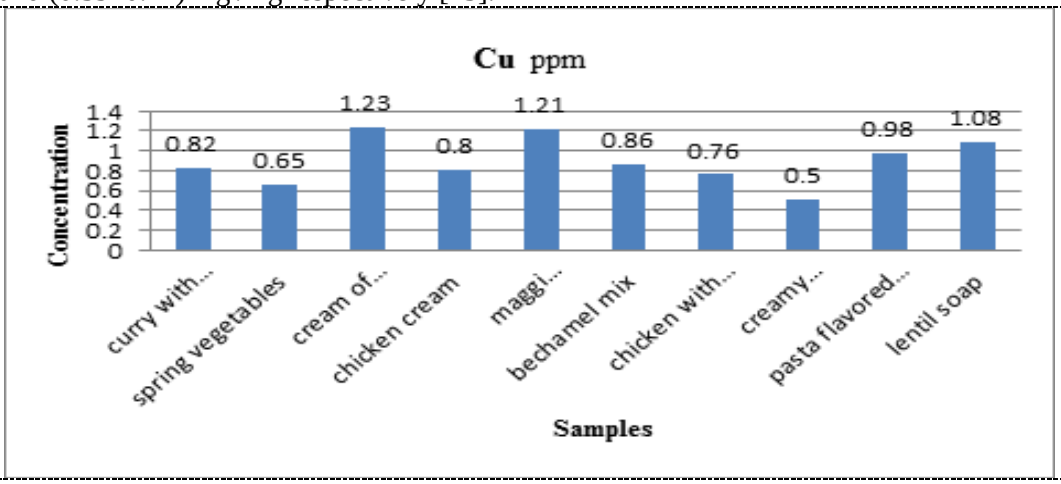

Figure 4. Concentration of Copper in some types of noodles.

The concentration of lead, Cr, cadimium and alominium in Iranian instant noodle at 1.21, 0.08, 0.03 and 9.15 mg/kg and in imported instant noodle at 1.00, 0.07, 0.04 and 15.90 mg/kg, respectively [44]. [45] reported that cadmium concentration determined in some foods and beverages in Japan follows cereals, seasoning and canned in syrup at (0.004 - 0.380) (0.01 - 0.06) (0.01) ug/ g respectively. [46] reported that the conventional agriculture was contaminated by lead, the possible sources of Pb in wheat include irrigation with contaminated water, metal based pesticides, industrial emissions, transportation and method of harvesting and storage. According to [47, 48] weekly intake of metals from sources not exceed 0.05 and 0.075 mg/kg body weight for Pb and Cd respectively, it accumulation in the skeleton and cause renal tubular damage and may give rise to kidney damage, Cd is among the most heavy metals and is particularly toxic. [49] Showed that changes were recorded in various parameters of oxidative damage, while the accumulation of metals in tissues with disturbances of hematological and biochemical parameters, it was observed levels of heavy metals in tissues had different pattern after mixture and single exposure.

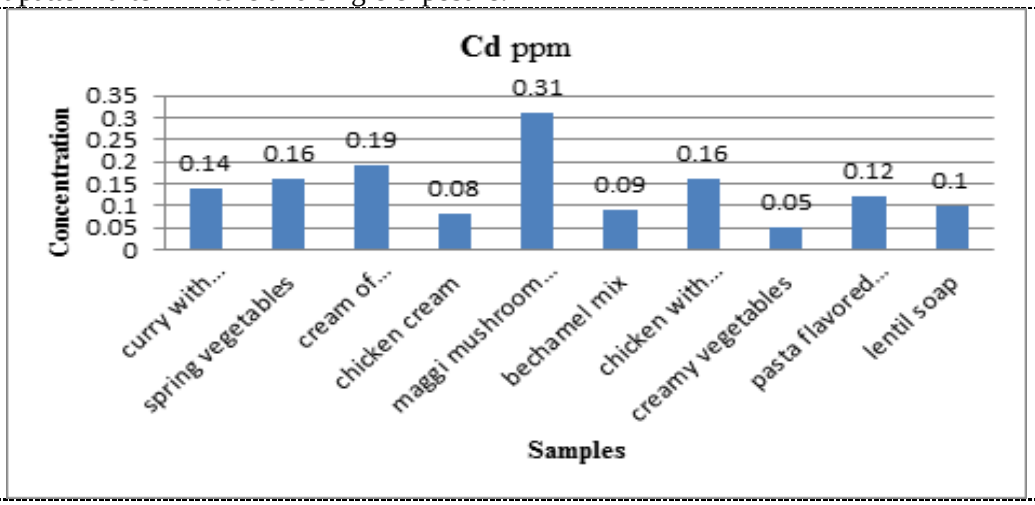

Figure 5. Concentration of Cdimium in some types of noodles.

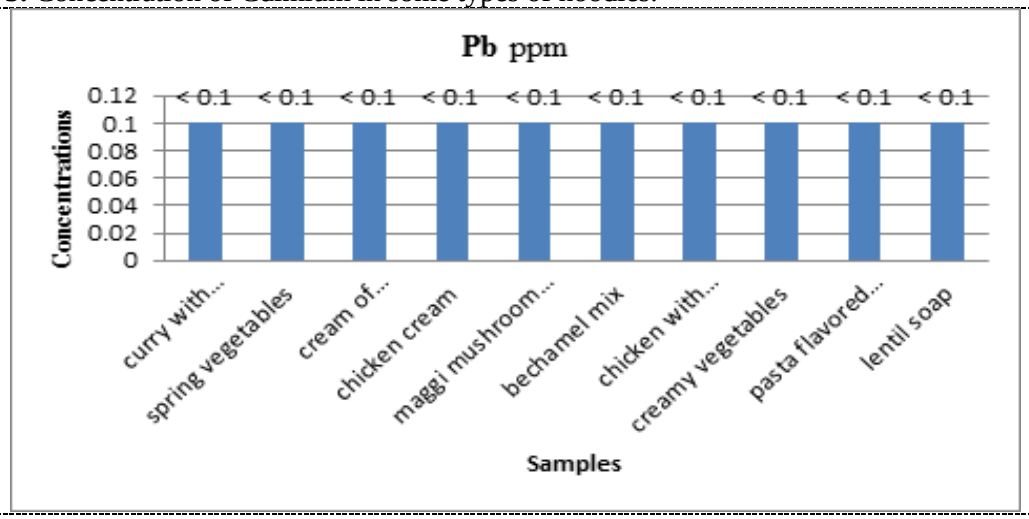

Figure 6. Concentration of lead in some types of noodles.

4. Conclusion

The current study represents for detecting mycotoxins AFB1, OTA, FB1 by ELISA. Isolate and identify fungi and determination of heavy metals in some noodles samples. The results show to the all samples of noodles were contamination with aflatoxin B1, ochratoxin A and fumonisin. Fungi *A.*

flavus, *A. parasiticus*, *A. fumigatus*, *A. terreus*, *A. ochraceus* and *A. niger*, other genus *Mucor*, *Fusarium verticillioides*, *Penicillium*, *Rhizopus* and *Alternaria*. Heavy metals copper, cadmium and lead.

5. References

[1] Pakhare KN, Dagadkhair AC and Udachan IS 2018 Enhancement of Nutritional and Functional Characteristics of Noodles by Fortification with Protein and Fiber: A Review *J. Pharmacogn. Phytochem*. **7** 351.
[2] Anonymous B 2016 WINA (*World instant noodle association*) *Expanding market* http:// instantnoodles.org/ noodles /expanding-market html.
[3] Nong SC 2005 *Neoguri Udon (Seafood &Spicy)* Product of Korea, Instant Noodles Review. Word Press.
[4] Anfossi L, Cristina G and Claudio B 2016 Mycotoxin detection *Curr. Opin. Biotechnol.* **37** 120.
[5] Kortei NK, Agyekum AA, Akuamoa F, Baffour VK and Alidu HW 2019 Risk assessment and exposure to levels of naturally occurring aflatoxins insome packaged cereals and cereal based foods consumed in Accra, Ghana *Toxicol. Rep.* **6** 34.
[6] Xie L, Chen M and Ying Y 2016 Development of Methods for Determination of Aflatoxins. Critical Reviews *Food Sci. Nutr.* **56** 2642.
[7] Iqbal M, Abbas M, Muhammad AM., Nazir A and Ahmad I 2019 Aflatoxins biosynthesis, toxicity and intervention strategies: A review *Chem. Int.* **5** 168.
[8] Pralatnet S, Poapolathep S, Giorgim M, Imsilp K, Kumagai S and Poapolathep A 2016 Survey of Deoxynivalenol and Aflatoxin B1 in Instant Noodles and Bread Consumed in Thailand by Using Liquid Chromatography–Tandem Mass Spectrometry *J. Food Protect*. **79** 1269.
[9] Armorini S, Altafini A, Zaghini A and Roncada P 2015 Occurrence of aflatoxin B1 in conventional and organic flour in Italy and the role of sampling *Food Control* **50** 858.
[10] Shi W, Tan Y, Wang S, Gardiner DM, De Saeger S, Liao Y, et al. 2017 Mycotoxigenic potentials of Fusarium species in various culture matrices revealed by mycotoxin profiling *Toxins* (Basel) **9** 401.
[11] Mohammed SW, Khashman BM, Khalaf NF, Ismeeal MC and Al-Malkey MK 2020 Immunohistochemical Expression of P16 Protein and TGF β1 in Mice Liver Exposed to Fumonisin B1 *Baghdad Sci. J.* **17** 401.
[12] Alberts JF, van ZWH and Gelderblom WCA 2016 Biologically based methods for control of fumonisin-producing *Fusarium* species and reduction of the fumonisins *Front. Microbiol*. **7** 00548.
[13] Joint Food and Agriculture Organization 2018 *World Health Organization Expert Committee on Food Additives (JECFA)* Co-Exposure of Fumonisins with Aflatoxins; Food Safety Digest; World Health Organization: Geneva, Switzerland,; pp. 1–4.
[14] Kamle M, Dipendra KM, Sheetal D, Kyung EL, Sang GK and Pradeep K 2019 Fumonisins: Impact on Agriculture, Food, and Human Health and their Management Strategies *Toxins* **11** 1.
[15] Li L, ChenW, Li H, Iqbal J, Zhu Y, Wu T and Du Y 2020 Rapid determination of fumonisin (FB1) by syringe SPE coupled with solid-phase fluorescence spectrometry Spectrochim *Acta Part A Mol. Biomol. Spectrosc.* **226** 117549.
[16] Malir F, Ostry V, Pfohl-Leszkowicz A, Malir J and Toman J 2016 Ochratoxin A: 50 years of research *Toxins* **8** 191.
[17] Ostry V, Malir F, Toman J and Grosse Y 2017 Mycotoxins as human carcinogens—the IARC Monographs classification *Mycotoxin Res*. **33** 65.
[18] Rottkord U, Röhl C, Ferse I, Schulz MC, Rückschloss U, Gekle M, Schwerdt G and Humpf HU 2017 Structure–activity relationship of ochratoxin A and synthesized derivatives: Importance of amino acid and halogen moiety for cytotoxicity *Arch. Toxicol*. **91** 1461.

[19] Leonard KJ and Bushnell WR 2003 *Fusarium Head Blight of Wheat and Barley*; Eds. American Phytopathological Society (APS Press): St. Paul, MN, USA, ISBN 089054302X.
[20] Majeed M, Khaneghah AM., Kadmi Y, Muhammad UK, and MU and Shariati MA 2017 Assessment of Ochratoxin A in Commercial Corn and Wheat Products *Curr. Nutr. Food Sci.* **13** 1.
[21] CAC 2017 *General standard for contaminants and toxins in food and feed* (CODEX STAN 193–1995, revised and amended).
[22] Onakpa MM, Njan AA and Kalu OC 2018 A review of heavy metal contamination of food crops in Nigeria *Ann. Glob. Health* **84** 488.
[23] Olayiwola O, Abidemi S, Abdulsalam S and Adebayo RO 2012 Evaluation of Heavy Metals in Three Common Nigerian Cowpea (*Vigna unguiculata*) Paste End Product (''Moinmoin'') using Different Packaging Materials *Int. J. Environ. Sci.* **3** 833.
[24] Pitt JI and Hocking AD 2009 *Fungi and Food Spoilage* Springer-Verlag, USA, ISBN 978-0-387-92207-2.
[25] Samson RA, Houbraken J, Thrane U, Frisvad JC and Andersen B 2010 *Food and Indoor Fungi* CBS Laboratory Manual Series 2. Centraalbureau voor Schimmelcultures, Utrecht. The Netherlands.
[26] Gaddeyya G, Niharika PS, Bharathi P and Kumar PKR 2012 Isolation and identification of soil mycoflora in different crop fields at Salur Mandal *Adv. Appl. Sci. Res*. **3** 2020.
[27] Leszczynska J, Maslowska J, Owczarek A and Kucharska U 2018 Determination of aflatoxinsin food products by the ELISA method *Czech J. Food Sci*. **19** 8.
[28] A.O.A.C. 2004 *Association of Official Chemists*, 12th ed., Washington, D.C.
[29] Benlioglu S, Yildiz A and Baspinar N 2008 Aydin ili'nden ihraç edilen kuru incirlerde fungal bulasiklik. *Adnan Menderes Üniversitesi Ziraat Fakültesi Dergisi* 5 3.
[30] Al-Aboody SAM, Al-Hussainy EMA and Abeed HJ 2015 Isolation and diagnosis of fungi producing aflatoxin B1from some local food in the markets of Babylon Governorate *Babylon Univ. J. Pure Appl. Sci.* **23** 925.
[31] Shaker RJ, Thalij KM and Bdeewi AS 2015 Isolation and diagnosis of mold-producing mycotoxins from the most consumed foods in the Iraqi market *Tikrit Univ. J. Pure Sci.*, **13** 39.
[32] Bouakline A, Claire L, Nicole R, Jean PG and Francis D 2000 Fungal Contamination of Food in Hematology Units *J. Clin. Microbiol.* **38** 4272.
[33] Al-Nazal AI 2004 *Degradation methods of ochratoxin A in maiz and its effect on broiler meat* Thesis. Baghdad University.
[34] Zentai A, Szeitzné-Szabó M, Mihucz G, Szeli N, Szabó A and Kovács M 2019 Occurrence and Risk Assessment of Fumonisin B1 and B2 Mycotoxins in Maize-Based Food Products in Hungary *Toxins* **11** 1.
[35] Elaridi J, Yamani O, Al Matari A, Dakroub S and Attieh Z 2019 Determination of Ochratoxin A (OTA), Ochratoxin B (OTB), T-2, and HT-2 Toxins in Wheat Grains, Wheat Flour, and Bread in Lebanon by LC-MS/MS *Toxins* **11** 1.
[36] Mwalwayo DS and Thole B 2016 Prevalence of aflatoxin and fumonisins (B1+ B2) in maize consumed inrural Malawi *Toxicol. Rep.* **3** 173.
[37] Szabó A, Szabó-Fodor J, Kachlek M, Mézes M, Balogh K and Glávits R 2018 Dose and Exposure Time-Dependent Renal and Hepatic Effects of Intraperitoneally Administered Fumonisin B1 in Rats *Toxins* (Basel), **10**.
[38] Mohammed SW, Habib KA, Al-Obaidie SR, Nayyef HJ and Khalaf N 2017 Determination of the Toxicity of Fumonisin B1 on Male Albino Mice *Iraqi J. Sci.* **58** 4.
[39] Sangare-Tigori B, Moukha S and Kouadio HJ 2006 Co-occurrence of aflayoxin B1, fumonisin B1, ochartoxin A and zearalenone in cereals and peanuts from dIvoire *Food Addit. Contam*. **23** 1000.

[40] JECFA (Joint FAO/WHO Expert Committee on Food Additives) 2001 *Fifty-sixth Meeting of the Joint FAO/WHO expert committee on food additives* Safety evaluation of certain mycotoxins in food. WHO food additives series (Vol. 47) FAO food and nutrition paper 74. Geneva: WHO.
[41] Divanian S, Akbari-adergani B and Ziarati P 2016 Study on Chemical Contamination Problem in Macaroni and Pasta Production Technology *J. Pharmac. Health Sci.* **4** 227.
[42] Jothi JS and Uddin MB 2014 Detection of Heavy Metals in Some Commercial Brands of Noodles *Europ. Acad. Res.* **2** 10667.
[43] Idrees M 2020 Analysis and Human Health Risk from Selected Heavy Metals in Common Instant Noodles *Biol. Trace Element Res.* 1.
[44] Tajdar-Oranj B, Shariatifar N, Alimohammadi M and Roudsari LP 2018 The concentration of heavy metals in instant noodle samples from Iran's market: probabilistic health risk assessment *Environ. Sci. Pollut. Res*. **25** 712.
[45] Kikuchi Y, Nomiyama T, Kumagai N, Uemura T and Omae K 2002 Cadmium concentration in current Japanese Foods and Beverages *J. Occupat. Health* **44** 240.
[46] Maleki A and Zarasvand M 2008 Heavy Metals in Selected Edible Vegetables and Estimation of Their Daily Intake in Sanandaj *Southeast Asian J. Trop. Med. Public Health* **39** 335.
[47] WHO 1995 *Lead. Environmental Health Criteria*. 165, Geneva.
[48] WHO 1992 *Cadmium. Environmental Health Criteria*. 134, Geneva.
[49] Andjelkovic M, Djordjevic AB, Antonijevic E, Antonijevic B, Stanic M, Kotur-Stevuljevic J, Spasojevic-Kalimanovska V, Jovanovic M, Boricic N, Wallace D and Bulat Z 2019 Toxic Effect of Acute Cadmium and Lead Exposure in Rat Blood, Liver, and Kidney *Int. J. Environ. Res. Public Health* **16** 1.

Journal of Physics: Conference Series

PAPER • **OPEN ACCESS**

Anatomical histological structure of the cerebellum in the Iraqi frog *Rana ridibunda ridibunda*

To cite this article: Nahla A. AL-Bakri and Jumana J. Al-Zuheri 2021 *J. Phys.: Conf. Ser.* **1879** 022007

Anatomical histological structure of the cerebellum in the Iraqi frog *Rana ridibunda ridibunda*

Nahla A. AL-Bakri[1] and Jumana J. Al-Zuheri[1*]

[1]Department of Biology, College of Education for Pure Sciences Ibn-AL-Haitham, University of Baghdad, Baghdad, Iraq.

*E-mail: juomanajabar@gmail.com

Abstract. The current study was designed to investigate the histological structure of the cerebellum in the Iraqi frog *Rana ridibunda ridibunda*. The cerebellum was removed surgically from 20 Iraqi frogs, *Rana ridibunda ridibunda*, and preserved in fixative of 10% formalin solution for a period of 72 hr, then the histological sections were prepared by the method of paraffin. The results of the study showed that the cerebellum of the adult Iraqi frog is one of the rhombencephalon regions, and consists of three layers, molecular layer, purkinje cells layer, and granular layer. The present histological findings suggest that the cerebellum of the Iraqi frog is very similar to that of other vertebrates, Therefore it represents the basic rule in understanding the histological formation of the cerebellum. .

Keywords. Cerebellum, Brain tissue, *Rana ridibunda*, Iraqi Frog.

1. Introduction

Cerebellum is the part of brain responsible for balance and movement, it is incomplete developed in amphibian, while it is well developed in other advanced vertebrates, all the sensory neurons pass through cerebellum with the exception those responsible for vision and olfaction, the reflex induces of hearing, respiration and engulfing [1]. The cerebellum is responsible the metencephalon and is histologically formed in amphibians from the corpus cerebelli and the auricular lobes [2, 3]. The corpus cerebellum presents the center of the cerebellum and consists of a transverse plate consisting of three layers: the molecular layer consisting mainly of fibers and a few neurons, purkinje cells layer which is characterized by containing large-sized purkinje cells, and granular cells layer that contains dense granular cells, auricular lobes are less developed [4].

2. Materials and Methods

A total of twenty adult Iraqi frog (*Rana ridibunda*) samples were obtained from some gardeners at Baghdad governorate during the period of 2018 to 2019. The samples were anesthetized by Chloroform. The isolation of frog brain as followed method by[5], the frog was attached at the dissection board and its back facing up, then cutting the skin crosswise behind the head and pulling forward to remove it from above the head area using the scalpel, and the edge of the scalpel was

placed above the dorsal midline of the skull, and moving the scalpel forward and backward several times with slight pressure until the cranium is opened to raise the roof cranium bones with the edge of the scalpel and cut it to reveal the brain. After the brains have been removed from the skulls, fixed in 10% formalin solution for 72 hr [6]. later, the samples washed by tap water and kept in 70% ethanol, after that the fixed tissues were processed by successive in a series of ethanol treatments, then cleared by xylene, two times was treated half an hour each, infiltrated and embedded into two changes of soft paraffin, one hour each at oven 58° C, Then paraffin blocks were obtained, serial sections of (7) µm thickness were cut and stained with the following histological stains [7, 8]. Stained with haematoxylin-van gieson stain and methylene blue stain and crystal fast violet stain for histological study [9, 10]. The sections were observed with an Olympus light microscope and were photographed with a digital camera Canon mounted on the microscope.

3. Results and Discussion

The sections view of cerebellum in adult Iraqi frog (*Rana ridibunda*) showed that its consists of three layers, which are from top to bottom the molecular layer, purkinje cells layer, and granular layer (Figure 1 and 2).

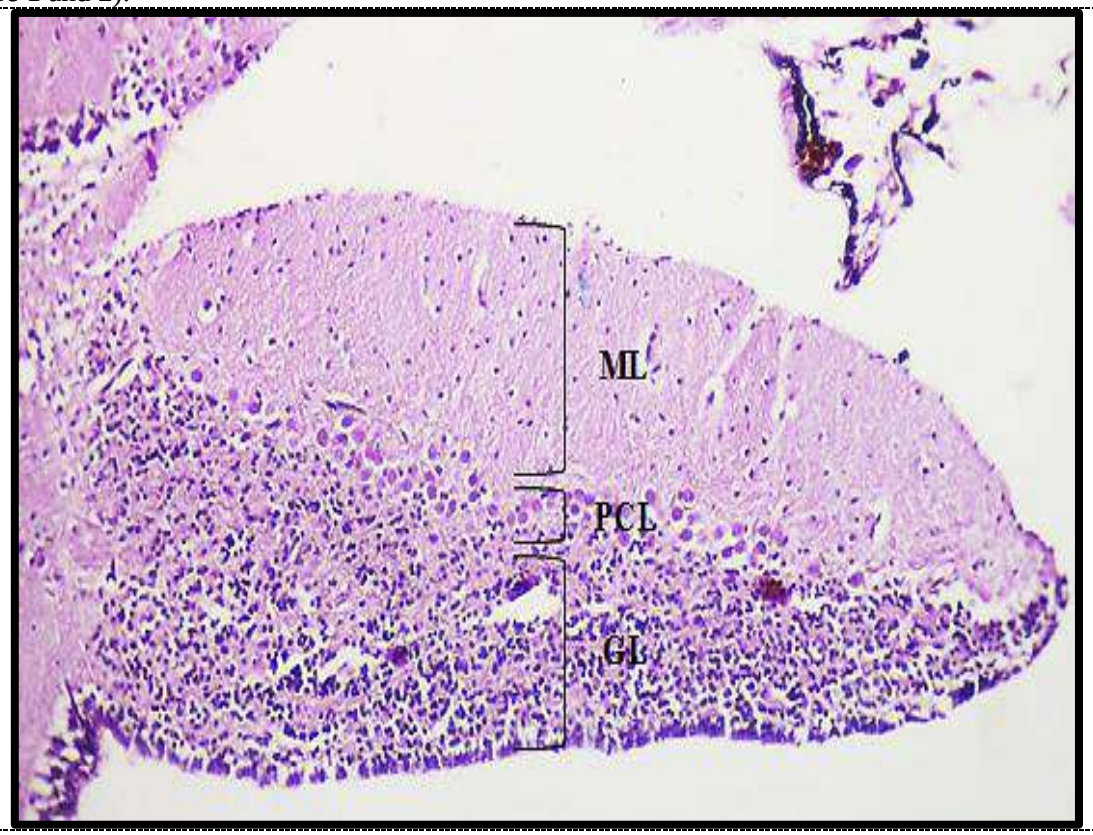

Figure 1. Sagittal section of the Iraqi frog's brain passing through the cerebellum, note: molecular layer (ML), purkinje cell layer (PCL), granular layer (GL), (Haematoxylin- Van Gieson stain, 10X) .

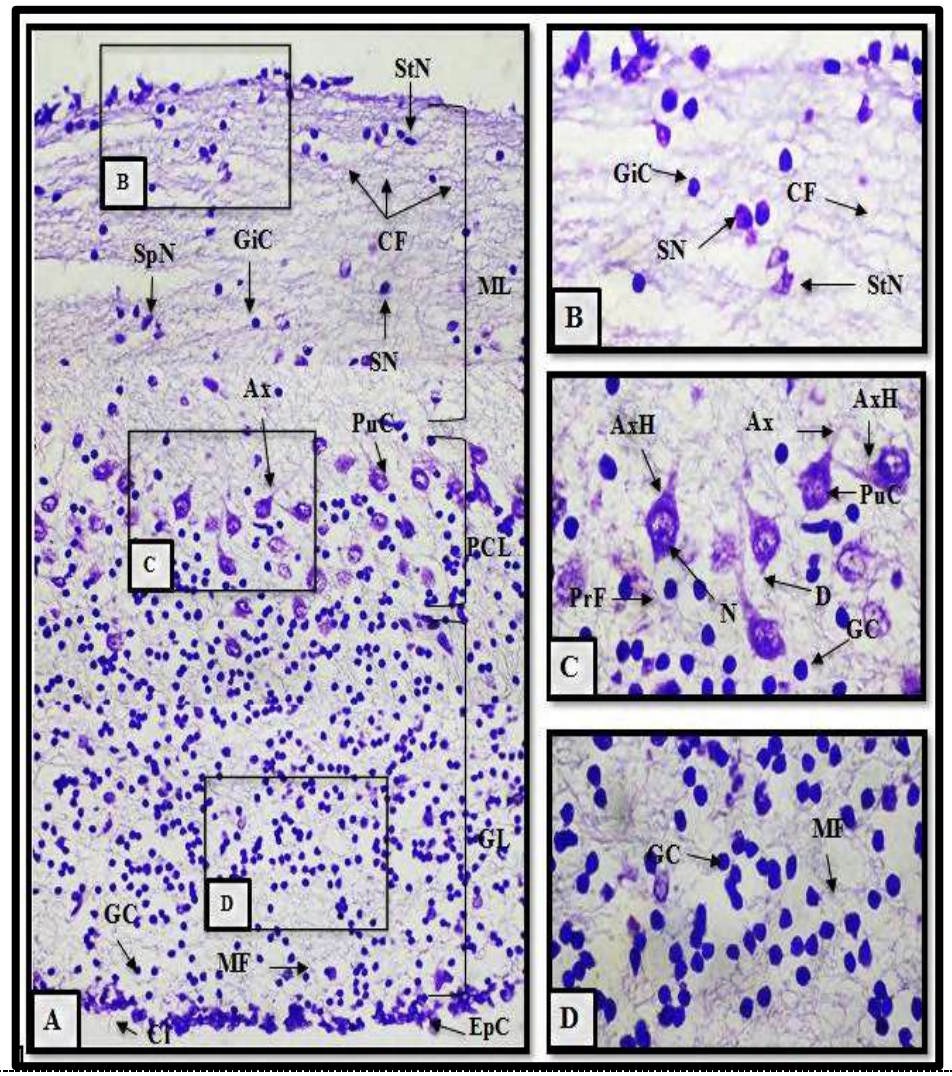

Figure 2. Sagittal section passing through the cerebellum of the brain Iraqi frog, note: molecular layer (ML), purkinje cell layer (PCL), granular layer (GL), ependymal cell (EpC), purkinje cell (PuC), spherical neuron (SN), satellite neuron (StN), spindle neuron (SpN), granular cell (GC), parallel fiber (PrF), climbing fiber (CF), mossy fibers (MF), axon hellock (AxH), dendrite (D), axon (Ax), glial cell (GiC), cilia (Ci) , (Crysel fast violet stain), A- cerebellum layers (10X), B- molecular layer (100X), C- purkinje cell layer (100X), D- granular layer (100X).

3.1. Molecular later

In the outer surface layer, It was observed when using the (crysel fast violet stain), the presence of irregularly distributed neurons such as spherical neurons with an average diameter of 6 micrometers, and satellite neurons with an average diameter of 4 micrometers , and spindle neurons with an average diameter of 3 micrometers (Figure 2 B). All of these cells have dendrites and axons that extend towards the layer of purkinje cells and intertwine with their dendrites, in addition to the presence of diffuse glial cells, and it was also observed when using (methylene blue stain) that the molecular layer contains neurofibers that extend vertically called climbing fibers formed from the extensions of the

dendrites of purkinje cells through the surface layer and the dendrites of the cells of the molecular layer. These fibers represent the main component of the molecular layer (Figure 3). .

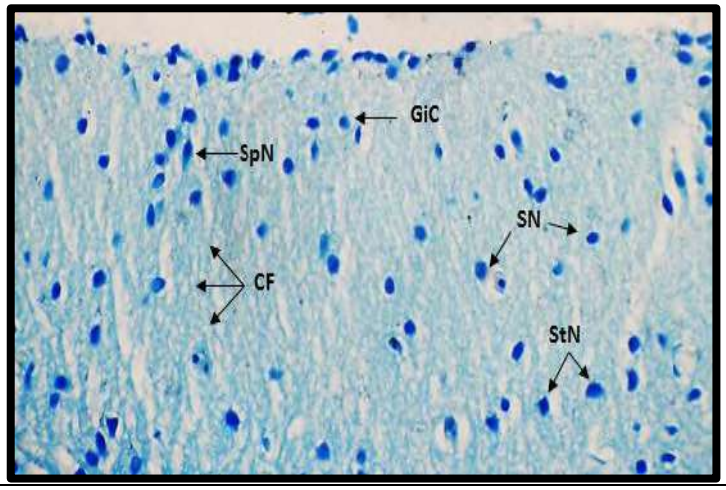

Figure 3. A sagittal section through the molecular layer in the cerebellum of the brain Iraqi frog, note: the spindle neuron (SpN), the spherical neuron (SN), satellite neuron (StN), Climbing fibers (CF), (Methylene blue stain 40X).

3.2. Purkinje Cells Layer

In the middle layer of the cerebellum, which is a narrow region located between molecular layer and granular layer, A sagittal section showed that its consists of two to three rows of purkinje cells, which are characterized by large cells with an average diameter of 11 micrometers, characterized by their elliptical or spherical shape It is characterized by its elliptical or spherical shape, containing large nuclei of central location, as well as containing the Nissl's granules, and the axon hellock is evident, which is devoid of Nissl's granules, and attached to the axon which is long and extends towards the outer molecular layer (Figure 2C). Purkinje cells are also distinguished by their dendrites that intertwine with the parallel fibers and with the dendrites of the cells of the molecular layer as well (Figure 4).

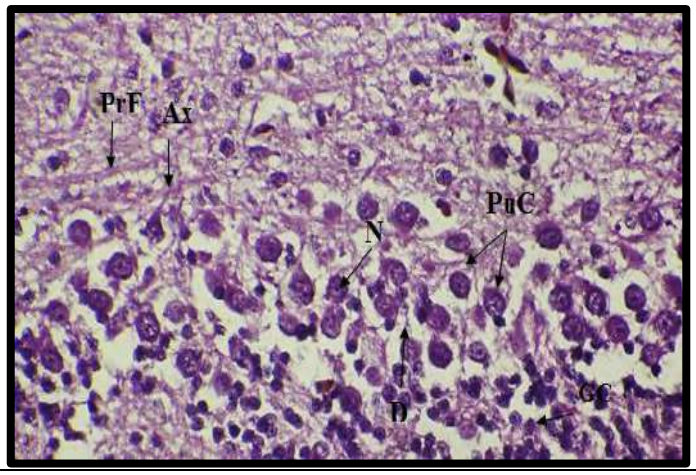

Figure 4. A sagittal section passing through the cerebellum of the brain Iraqi frog, note: purkinje cell (PuC), parallel fiber (PrF), granular cell (GC), nuclei (N), axon (Ax), dendrite (D), (Haematoxylin- Van Gieson stain, 40X).

3.3. Granular Layer

The inner layer of the cerebellum, which is a thick layer, is made up of granular neurons smaller than purkinje cells. They are dense in number, spread in a converging way and have a spherical shape with an average diameter of 5 micrometers. They have dense dendrites, its axons extend up towards the molecular layer and then branch into two branches, each opposite in direction to the other if it extends in a direction parallel to the outer surface of the cerebellum in the shape of a (T), forming a bundle of parallel fibers (Figure 2D and 4). It has been observed, by using the methylene blue stain, the presence of filamentous nerve fibers located between granular cells called mossy fibers, which are intertwined with granular cells, below the granular layer lies ependymal cells that lining of the cerebellum, which is made up of a single row of columnar cells ciliated towards the 4th ventricle (Figure 5).

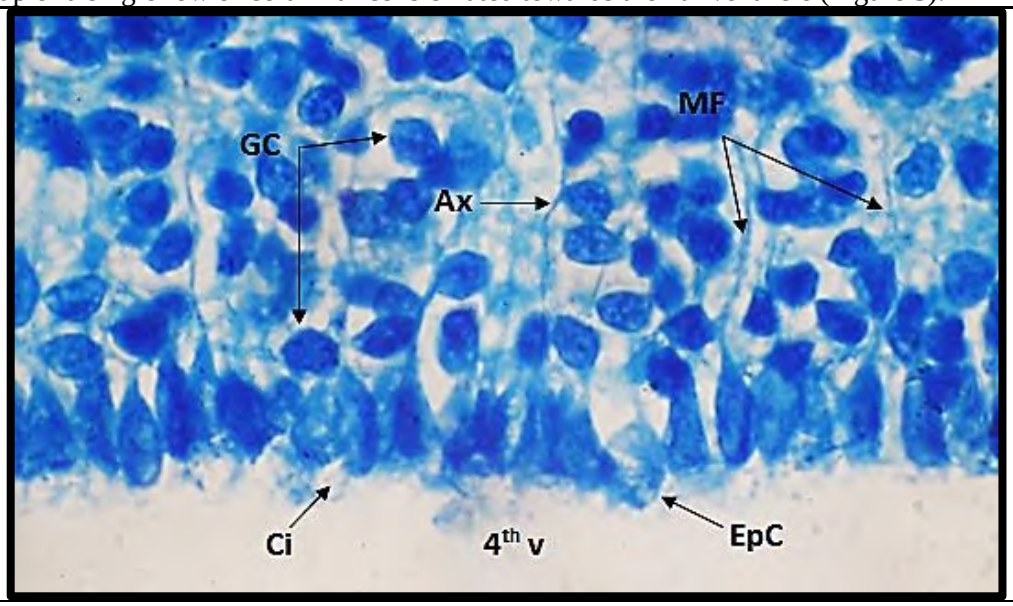

Figure 5. Sagittal section of Iraqi frog's brain passing through the granular layer in the cerebellum. Ependymal cell (EpC), granular cell (GC), mossy fibers (MF), axon (Ax), cilia (Ci),fourth ventricle (4th v), (methylene blue stain 100X).

4. Discussion

In the present result, the cerebellar wall appeared that consisting of three layers, which are from top to bottom: the Molecular layer, the Purkinje cells layer and the Granular layer and this is in agreement with what [3, 4]. In their study of different amphibians as well as similar to what was found in other vertebrates as in the study of [11] in their study on the bird *Coturnix coturnix*. The current result also showed that, the molecular layer represents the outer layer of the cerebellum, and it consists of irregularly scattered neurons such as spherical neurons with an average diameter of (6) µm, and satellite neurons with an average diameter of (4) µm, and spindle neurons with an average diameter of (3) µm .These cells have dendrites and axons that extend towards the purkinje cell layer and intertwine with the dendrites of purkinje cells, and this is consistent with [12] in his study of *Rana esculenta* frog as he indicated that the molecular layer is composed of spherical and pyramidal cells, and astrocytic cells reached (7-13) µm. The molecular layer also contains nerve fibers (climbing fibers), it extends vertically and consists of the extension dendrites of purkinje cells to the surface layer and cell dendrites in the molecular layer, this is consistent with the study of [12] on a group of frogs, *Rana cateshiana*, *Rana pipiens* and *Hyla regilla*. On the other hand, the current result showed that the layer of purkinje cells represents the middle layer of the cerebellum, which is a narrow region located between the outer molecular layer and the inner granular layer, consisting of rows of purkinje cells, characterized by being large cells with an average diameter of (11) µm, characterized by their elliptical

shape. Spherical, containing large nuclei in central location, and this corresponds to[13] as he indicated that purkinje cells are distinguished by their elliptical or pear-shaped shape and have an average diameter of (16) µm in his study on the cerebellum of the frog *Rana esculenta*. The granular layer, it represents the inner layer of the cerebellum, and it consists of dense granular neurons close to each other, small in size, smaller than purkinje cells of a spherical shape with an average diameter of (5) µm and have dense dendritic dendrites that extend their axons towards the molecular layer to the top and then branch to two branches, each opposite in direction to the other, if it extends parallel to the outer surface of the cerebellum forming parallel fibers a bundle of T-shaped. This is consistent with the study of [14] in their study of amphibians that the granular layer consists of small-sized granular cells with a spherical shape with an average diameter of (5-9) µm, and their dendrites and axons extend towards the molecular layer and then branch into two branches each they are opposite to each other, forming a bundle of parallel fibers T-shaped, [15] also indicates the presence of filamentous nerve fibers located between granular cells called mossy fibers, which are intertwined with the granular cells, and this is evident in the present result as well, as the mossy fibers were found intertwined with the granule cells in the form of anastomosis. The function of the moss fiber is that it is one of the incoming fibers that communicate information to the cerebellum [16]. The ependymal cells layer which lies below the granular layer, consists of a single row of ciliated columnar ependymal cells, and this is consistent with what was reported by [17] in their study of the cerebellum in the different species of frogs.

5. References

[1] Hickman J R, Roberts C P 1994 *Biology of animal* 6th ed. Wm.c. Browon publishers: ix + 764 pp.
[2] Nieuwenhuys R, Hans J, Nicholso C 1998 *The central nervous system of vertebrates* Springer , Berlin Heidelberg, vi+2219 pp.
[3] Butle A B, Hodos W 2005 *Comparative vertebrate neuroanatomy* 2nd ed . Wiley Int., USA, vii+ 715 pp.
[4] Roth G, Walkowiak W 2015 The influence of genome and cell size on brain morphology in amphibians *Cold Spring Harbor Boil.* **7** 1.
[5] Al-Hussaini A H, Demain E S 1977 *Practical tactical animal biology* 10th ed., Dar Al-Maaref, 300 pp.
[6] Abid A B, Al-Bakri N A 2012 Histological structure of the optic tectum in the fresh water turtle in the *Clemmys caspica caspica* (Gmelin, 1774) *Iraqi J. Vet. Med*. **36** 123.
[7] Hussien A R, Al-Bakri N A 2010 Histological study on optic tectum in Iraqi water snake *Tessela tatesselata Baghdad Sci. J*. **7** 300.
[8] Al-Bakri N A, Al-Hamawandy D H 2020 Morphological description and histological structure of Gallbladder in local adult chicken *Gallus gallus domesticus AAJPS* **1** 6.
[9] Suvarna S K, Layton L, Bancroft J D 2019 *Bancroft's theory and practice of histological techniques*, 7th ed. Churchill Livingstone Elsevier Ltd., Shanghai, China , 609 pp.
[10] Al-Bakri N A, Al-Zuheri J J 2020 Histological structure of the spinal cord in the Iraqi Frog *Rana ridibunda ridibunda* AAJPS **1** 27.
[11] Abid, A B, Al-Bakri, N A 2017 Histological study of the cerebellum in adult Q*uail Coturnix coturnix* (Linnaeus, 1858) *Ibn AL-Haitham J. Pure. App. Sci*. **29** 351.
[12] Larsall O 1923 The cerebellum of the frog *J. Comp. Neurol*. **36** 89.
[13] Hillman D E 1969 Light and electron microscopical study of the relationships between the cerebellum and the vestibular organ of the frog . Exper. Brain Res. **9** 1.
[14] Llinas R, Precht W 1976 *Frog neurobiology hand book* Springer Verlag , New York, Vii+1046 pp.
[15] Pellionisz A, Llinas, R, Perkel, D H 1977 A computer model of the cerebellar cortex of the frog *Neuroscience* **2** 19.

[16] Albus J S 1971A theory of cerebellar function *Math. Bio*. **10** 25.
[17] Manzano A S, Herrel A, Fabre A C, Abdala V 2017 Variation in brain anatomy in frogs and its possible bearing on their locomotor *Ecol. J. Anat*. **231** 38.

First record of *Gyrodactylus hrabei* Ergens, 1957 (Monogenea: Gyrodactylidae) in Iraq from gills of mugilid fish *Planiliza abu* (Heckel, 1843)

First record of *Gyrodactylus hrabei* Ergens, 1957 (Monogenea: Gyrodactylidae) in Iraq from gills of mugilid fish *Planiliza abu* (Heckel, 1843)

Kefah Naser Abdul-Ameer[1*]

[1]Department of Biology, College of Education for Pure Science, University of Baghdad, Baghdad, Iraq.

*E-mail: kefahnaser59@yahoo.com

Abstract. The A total of 118 specimens of the mugilid fish *Planiliza abu* (Heckel, 1843) were collected weekly from Al-Graiat region at the Tigris river in Baghdad city, during the period from July 2015-March 2016. In this study, investigated of fish gills of *Planiliza abu* and was noticed of Monogenean *Gyrodactylus hrabei*, Ergens, 1957 and registered for the first time in Iraq. The description and measurements of this parasite as well as its illustrations were given.

Keywords. *Gyrodactylus hrabei, Planiliza abu,* Gyrodactylidae, Tigris river, Iraq.

1. Introduction

The genus *Gyrodactylus nordmann*, 1832 belongs to the family Gyrodactylidae, class Monogenea, of the phylum Platyhelminthes [1]. This genus is one of 23 genera of the family Gyrodactylidae, with 19 viviparous genera and four oviparous genera [2]. Species of this genus have a direct life cycle and the young newborn has several generations of embryos within its uterus in consecutive stages of development. This "Russian-Doll" mode of reproduction, termed hyperviviparity, joined with a fast generation time (< 24hrs at 25°C for the 1st born daughter in some species), can lead to quickened parasite population outgrowth on a single host [3]. This directly transmitted viviparous gyrodactylids have high species richness but low morphological and biodiversity, this group has the broadest host range of any monogenean family, as it is found on 19 orders of bony fishes [4]. The 409 valid *Gyrodactylus* species are reported from about 400 host species from a wide diversity of fish groups [5]. Species of this genus are common ectoparasites of fishes, living on the gills, skin and fins of many of teleost fishes and place in freshwater and brackish and marine environments [6]. In Iraq, the first species of Gyrodactylidae, includes of *G. elegans* was described from gills of both *Cyprinus carpio* and *Planiliza abu* (which was reported as *Liza abu*) [7], Later on, many studies on fish parasites revealed the record of 56 Gyrodactylidae species from different water bodies of Iraq [8]. For this, more studies on parasites of fishes are in need to record further species and to increasing knowledge on the fish parasites of Iraqi freshwater. This paper documents the first record of *Gyrodactylus hrabei*, Ergens, 1957 in Iraq from gills *Planiliza abu* (Heckel, 1843) from the Tigris river at Al-Graiat region in Baghdad city.

2. Materials and Methods

During the period from July-December 2015, a total of 118 specimens of *Planiliza abu* (Heckel, 1843) were collected weekly from Al-Graiat region river at the Tigris in Baghdad city (33° 24' 18' N, 44° 20' 53' E). The fishes were transported alive to the laboratory and were identified according to an account on freshwater fishes of Iraq [9], then freshly examined for ectoparasites. Skin and gill smears prepared and microscopically examined. Care was taken to isolate and flatten the parasite specimens, which were then stained with aqueous neutral red. Permanent smears were prepared with glycerin. Drawings of the sclerotized pieces of the haptor were done by using a Camera Lucida. Parasite identification was performed in accordance [10]. In the current study, all the measurements used in the description of the parasite were mentioned as follows: minimum-maximum (mean) values. Updating the scientific name of fishes based on widely used electronic sites [11]. All recordings of Gyrodactylidae species in fishes of Iraq were reviewed with the index-catalogue of parasites and disease agents of fishes of Iraq [8].

3. Results and Discussion

3.1. Gyrodactylus hrabei Ergens, 1957

This parasite was found in the gills and fins of three out of 118 specimens of the *Planiliza abu* with a percentage of 2.5% and a density of 2.7. In the follows is a concise description and measurements of this parasite (in mm established on four specimens of parasites) as shown in Figure 1.

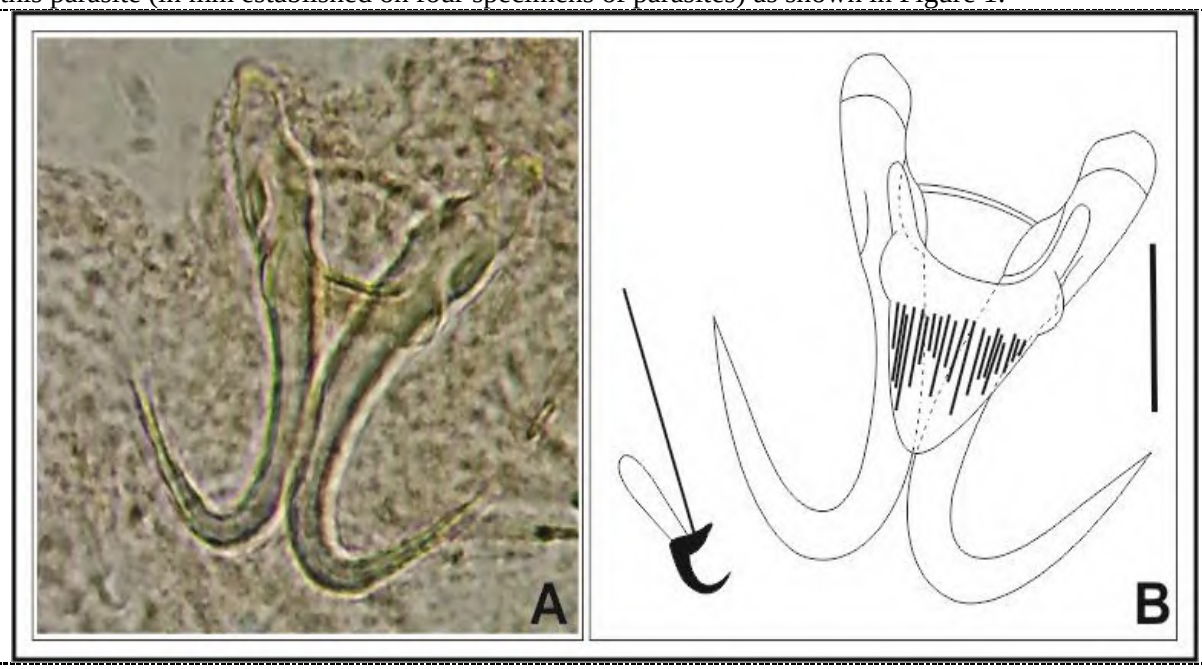

Figure 1. *Gyrodactylus hrabei.*
A- Photomicrograph of the haptor (400x), B- Camera Lucida drawing of the haptor (Scale bar = 0.02 mm)

Body length 0.57-0.61 (0.59). Total length of marginal hooks 0.037-0.04 (0.038), hooklet 0.008. Total length of anchor 0.062-0.068 (0.065), main part 0.044-0.048 (0.046), point 0.031-0.035 (0.033); inner root 0.018-0.022 (0.02). Size of ventral bar 0.008-0.009 (0.0085) x 0.025-0.027 (0.026), membrane 0.018-0.02 (0.019); size of dorsal bar 0.002 x 0.019-0.023 (0.021).
The description and measurements of the present *G. hrabei* are in agree with those reported by [10] from gills of *Cottus gobio* and *C. poecitopus*.

According to the index-catalogue of parasites and disease agents of fishes of Iraq [8], the present record of *G. hrabei* considers the first time in Iraq, as no previous report was given for this parasite in Iraqi fishes. Many species belonging to the genus *Gyrodactylus* were so far recorded from freshwater fishes in Iraq, among which some were reported from *Planiliza abu*. The following report, is the alphabetical arrangement list with the show of only the first registration from *Planiliza abu* for each *Gyrodactylus* species in order to economize space and references: *G. baicalensis* from Tigris river at Al-Rashidia, north of Baghdad [12], *G. cotti* fromTigris River in Baghdad city [13], *G. elegans*: from ponds and in Tigris- Al-Tharthar canal region [7], *G. jalalii* and *G. varicorhini* from Tigris river at Baghdad city [14], *G. markevitschi* and *G. masu* from Tigris river in Al-Kamirah region at north of Baghdad province [15], *G. menschikowi* from Hilla River [16], *G. sprostonae* from Tigris river at Baghdad city [17], *G. tincae* and *G. umbrae* from Euphrates river at Al-Qaim city Al-Anbar Governorate [18], and *G. vicinus* in a man-made lake at Baghdad area [19]. With the current record of *G. hrabei*, the number of *Gyrodactylus* species from Iraqi fishes has so far become 57 species [8] in comparison with 25 *Gyrodactylus* species which were known from fishes of Iraq till 2013 according to [20].

4. Conclusion

The present study revealed the monogenean *Gyrodactylus hrabei*, Ergens, 1957 from gills of mugilid fish *Planiliza abu* (Heckel, 1843) for the first time in Iraq.

5. Acknowledgement

Thanks to Prof. Dr. Furhan T. Mhaisen for his permission to use his index- catalogue of parasites and disease agents of fishes of Iraq to provide us with the information on the previous account records of parasites in Iraq, as well as the data of *Gyrodactylus* species registrations in the fishes at the different parts of Iraq.

6. References

[1] WoRMS 2020 World Register of Marine Species at http://www. marinespecies.org (Accessed 10 Sept. 2020).
[2] Bakke TA, Cable J and Harris PD 2007 The biology of gyrodactylid monogeneans: the ‘‘Russian-doll killers’’ *Adv. Parasitol*. **64** 161.
[3] Cable J and Harris PD 2002 Gyrodactylid developmental biology: historical review, current status and future trends *Int. J. Parasitol*. **32** 255.
[4] Bakke TA Harris PD and Cable J 2002 Host specificity dynamics: Observations on gyrodactylid monogeneans *Int. J. Parasitol*. **32** 281.
[5] Harris PD, Shinn AP, Cable J and Bakke TA 2004 Nominal species of the genus *Gyrodactylus* v. Nordmann 1832 (Monogenea: Gyrodactylidae) with a list of principal host species *Syst. Parasitol*. **59** 1.
[6] Buchmann K and Bresciani J 2006 *Monogenea (Phylum: Platyhelminthes)* In: Woo PTK (ed.) Fish diseases and disorders, Vol. 1: Protozoan and metazoan infections 2nd Edition, CAB International, Wallingford 297.
[7] Ali MD and Shaaban F 1984 Some species of parasites of freshwater fish raised in ponds and in Tigris- Al-Tharthar canal region. Seventh Sci. Conf. *Iraqi Vet. Med. Assoc., Mosul* **23** 44. (Abstract).
[8] Mhaisen FT 2020 Index-catalogue of parasites and disease agents of fishes of Iraq (Unpublished: mhaisenft@yahoo.co.uk).
[9] Coad BW 2010 *Freshwater fishes of Iraq* Pensoft Publ., Sofia: 274 pp. + 16 pls. www.briancoad.com.

[10] Pugachev ON, Gerasev PI, Gussev AV, Ergens R and Khotenowsky I (eds) 2009 *Guide to Monogenoidea of freshwater fish of Palaearctic and Amur regions* Ledizioni-Ledi Publishing, Milano 567.
[11] Froese R and Pauly D (Eds.) 2020 *Fish Base* World Wide Web electronic publication. www.fishbase.org, version (9/2020).
[12] Mhaisen FT, Al-Yamour KY and Allouse SB 1995 New records of three monogenetic trematodes on some freshwater fishes from Diyala River Iraq *J. Biol. Scs. Res*. **17** 253.
[13] Rasheed RAR 2016 *Parasites of some fishes of Tigris river in Al-Shawwaka region, Baghdad city-Iraq* MSc. Thesis, Coll. Educ. Ibn Al-Haitham, Univ. Baghdad 106 (In Arabic).
[14] Hammood NW 2017 *Investigation of some parasitic and bacterial infections in some fish species of Tigris river at Baghdad city*. MSc. Thesis Coll. Sci. Univ. Tikrit 141 (In Arabic).
[15] Hameed RS 2019 *Parasites of some fish species from Tigris river in Al-Kamirah region at north of Baghdad province, Iraq*. MSc. Thesis Coll. Educ. Pure Sci. Ibn Al-Haitham, Univ. Baghdad 132 (In Arabic).
[16] Al-Zubaidy AB 2007 A study for some protozoan fauna of freshwater fishes from Hilla River, Babylon province, Iraq *Afr. J. Biol. Sci.* **2** 97.
[17] Atwan FK 2016 *Parasitic infections in some fishes from Tigris river, Al-Graiat location in Baghdad province, Iraq* MSc. Thesis Coll. Educ. Pure Sci. (Ibn Al-Haitham), Univ. Baghdad 136 (In Arabic).
[18] Al-Salmany SOK 2015 *Parasitic infections of some fish species from Euphrates river at Al-Qaim city, Anbar province*. MSc. Thesis, Coll. Sci., Univ. Tikrit 193 (In Arabic).
[19] Al-Nasiri FS 2000 *Parasitic infections of fishes in a man-made lake at Al-Amiriya region, Baghdad*. MSc. Thesis, Coll. Educ. (Ibn Al-Haitham), Univ. Baghdad 133 (In Arabic).
[20] Mhaisen FT and Abdul-Ameer KN 2013 Checklists of *Gyrodactylus* species (Monogenea) from fishes of Iraq *Basrah J. Agric. Sci*. **26** 8.

A first record of seven species of terrestrial isopoda-crustacea in central Iraq

A first record of seven species of terrestrial isopoda-crustacea in central Iraq

Maysaloon Lafta Al-Doori[1*], Talal Aboud Hansh[1] and Nibrass Lafta Al-Doori[1]

[1]Department of Biology, College of Education for Pure Science (Ibn Al-Haitham), University of Baghdad, Baghdad, Iraq.

*E-mail: maysaloon.l@ihcoedu.uobaghdad.edu.iq

Abstract. This study is the first kind of it in Iraq. The samples were collected from April to Junuary 2018, we recorded seven species for the first time in Iraq (*Procellio laevis*, *P. cingendus*, *Lacasius pallidus*, *Armadillidium album*, *A. assimile*, *Orthodillo chiltoni*, *Cylisticus convexus*). These species belong to four famillies (Procellionidae, Armadillidae, Armadillidae, Cylistieidaeà). The samples were saved in the natural histroy museum in Baghdad-Iraq.

Keywords. Isopoda, Porcellionidae, Armadillidae, Armadillidae, Cytisticidae.

1. Introduction

There are about 3000 species recorded of terrestrial isopoda belong to 18 families in the world [1]. The isopoda vary in size, it ranges from 0.3-50 cm [2], at the end of its body there is a telson which varies in size and form between species. In addition there are the uropods which used to distinguish between types, and an essential characteristics of classification of them are long and concile such *Porcellides*, other are short, truncated or similar of hounglass like *Armadillidium* [3]. The color of the isopoda varies from white to grey [4], some are red, green or brown, depending on the type of feeding [5]. It's study is important because of its role in the food chain in stimulating the soil [6].

2. Materials and Methods

Central Iraq has been identified for this study, it included specific areas that were distinguished by their geographical nature, as they varied between agricultural, gardens and residential areas (Figure 1). 560 samples were collected for the period (April to Junuary 2018) from various places on the surface of the soil and under it to a depth of 6 cm and between trees, weeds, dead decomposing plants, fresh fruits and cracks of buildings randomly. The samples were collected manually, then isolated and then stored in 70% ethanol [7] in the laboratory. The samples were identified by using a dissecting microscope 1x and 2x . A phone camera Galaxy note 5 was using to photographed., Identification of isopods species were done on the basis of their morphological characters by using taxonomic keys available in the local and regional publications [8, 9, 10, 11, 12, 13].

Figure 1. A map showing the study areas in Iraq.

3. Results and Discussion

This Samples were diagnosed using some distinct parts of the isopods body, included the difference in the thoracic region and distribution of the ocelli, the frontal lobes of the head, the shape of the endo and exopod and the difference of the telson. The recorded species were distinguished in lengths from 4 to 17 mm. Seven species of four families were diagnosed which were:

3.1. Family: Procellionidae (Brandl, 1831)

The outline of its body in cross section not strongly arched, then the flagella of antennae two sections, we found three species as first record in Iraq which were:

3.1.1. Procellio laevis (Latreille, 1804).

Its mean length was 17 mm and dark grey with brown spots in color (Figure 2-a), cephalothorax with three lobs, black eyes with 18 ocelli. The dorsal surface is smooth and the posterior edge of the pereonite is convex (Figure 2-b). The edge of pereon straight with poleon, the exopod was spear-shaped (Figure 2-c (A, B)), this compatible with [14, 15].

3.1.2. Procellionides cingendus (Kinahan, 1857).

Its mean length was 7 mm, reddish brown with yellow spots in color (Figure 3-a), cephalothorax was small and not convex, large eyes with 32 ocelli and without lobes (Figure 3-b). The edge of peleon narrower than edge of pereon, exopod is long and thin and the uropod was small not tapered (Plat2-c). it was observed that this diagnosis is appropriate with [16].

3.1.3. Lucasius pallidus(Budde-Lund, 1885).

Its mean length was 8 mm, it's color is bright orange with white short tentacle (Figure 4-a). The cephalothorax is small in size without lobes and triangular, small black eyes (Figure 4-b). The endopod and exopod are small white the telson was distinguished by its wide and triangular basal (Figure 4-c (A, B)). The results of this study were consistent with the diagnostic samples in Australia [17].

a

b

c-A

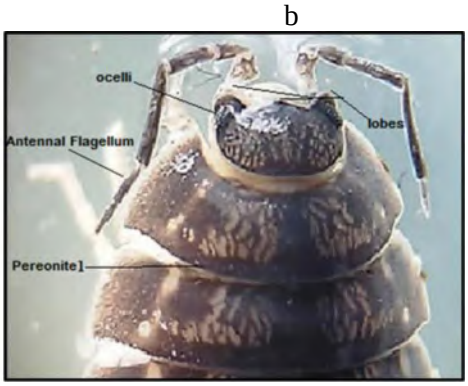

c-B

Figure 2. *Procellio laevis* (a-The mean length, b-The cephalothorax, c-A-Dorsal view of the uropod and telson, c-B-Ventral view of uropod and telson).

a

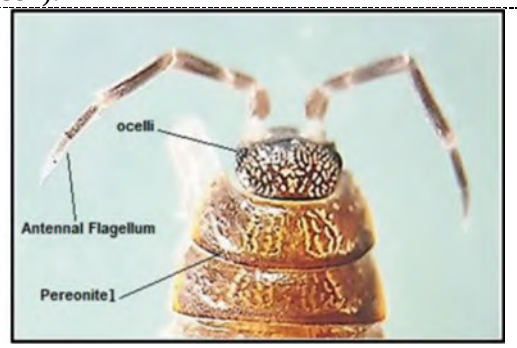

b

c

Figure 3. *Procellionides cingendus* (a-The mean length (mm), b-The cephalothorax, c-The pelean and pereon not straited, the uropod and telson).

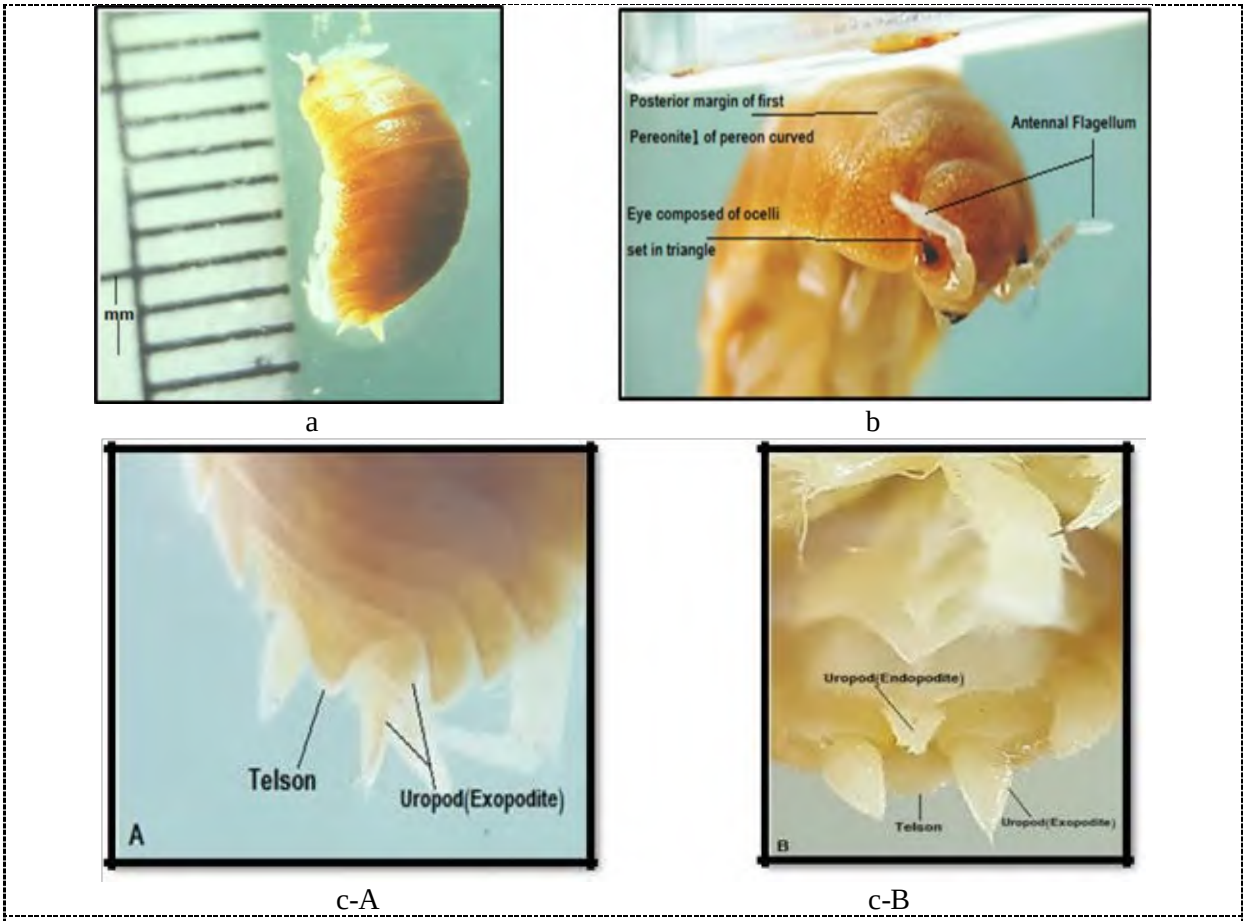

Figure 4. *Lucusius pallidus* (a-The mean length (mm), b-The cephalothorax, c-A-A dorsal veiw of the uropod and telson, c-B- A ventral veiw of uropod and telson).

3.2. Family: Armadillididae (Brandt, 1833).

It control itself into a ball, we found two species as a new record in Iraq it was:

3.2.1. Aramadillidium album (Dollfus, 1887).

It is pale sand with yellow spots in color, the mean length was 4 mm, with small spines on the dorsal surface and it roll into a not completely ball (Plate 5-a (A, B)). The cephalothorax was small not lobeded with small eyes consisting 9 ocilli (Plate 5-b). The exopod was truncated and the endopod was very small than telson is flat and curved (Plate 5-c (A, B)). So [18] has demonstrated the same characteristics to the species.

3.2.2. Aramadillidium assimile (Budde-Lund, 1885).

It's mean length 6 mm, brown in color with yellow anterior region (Plate 6-a). small oval cephalothorax with small eyes consisting 12 ocilli (Plate 6-b) its fifth peleon with keel, and the edge peleon narrower than pereon (Plate 6-c). The exopod was wide, the endopod was small narrow and the telson was wide triangular (Plate 6-d). It was noted that this study was similar to other studies in U.K [19].

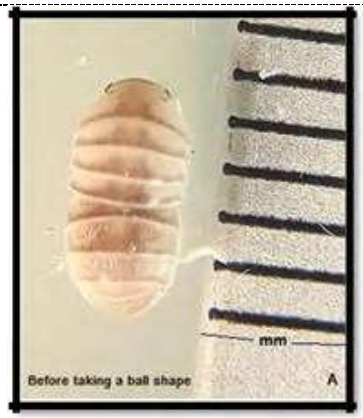

a-A

b-B

b

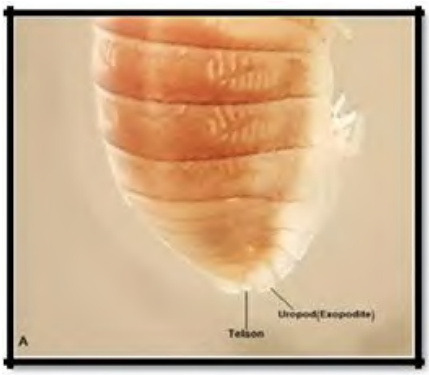

c-A

c-B

Figure 5. *Armadillidium album* (a-A, B- The total length, b- The cephalothorax, c-A, B- the dorsal and ventral veiw of uropod and telson).

a

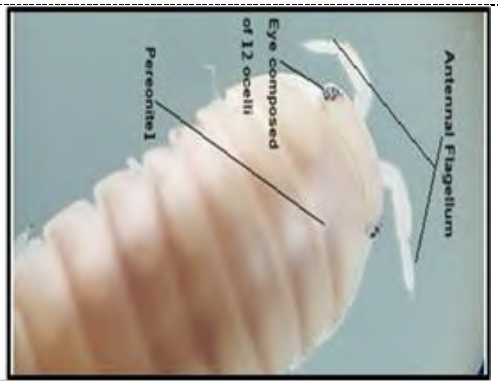

b

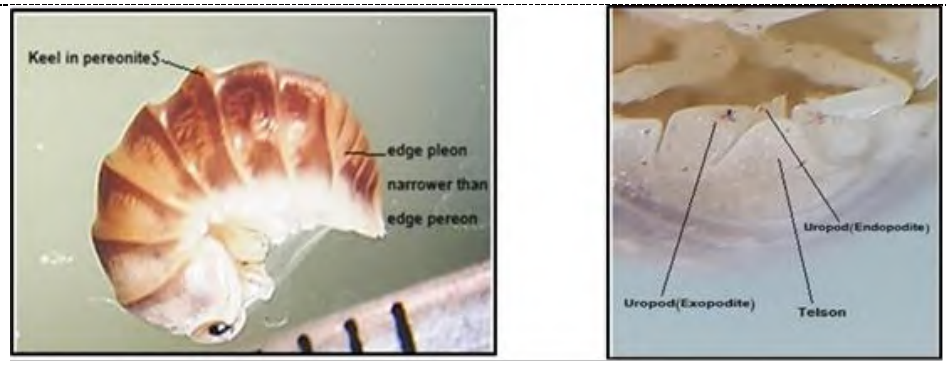

c d

Figure 6. Armadillidium assimile (a-the mean length, b-The cephalothorax, c: lateral view showing the keel, d-the uropod and telson).

3.3. Family: Armadillidae (Brandt, 1831).

This family is distinguished by its rough surface, the uropods was small and the telson hour-glass shaped [20], there was one species as a first record in Iraq which was:

3.3.1. Orthdillo chiltoni (Vandel, 1973).

It's mean length was 15 mm, dark grey in color (Plate 7-a), the cephalothorax was small with black eyes consisting 10 ocilli (Plate 7-b), the exopod was square shape and the endopod was small and cylindrical than the telson quad-angle and it's holy edge was hour-glass shaped (Plate 7-c (A, B)). This results came compatible with the results of [21].

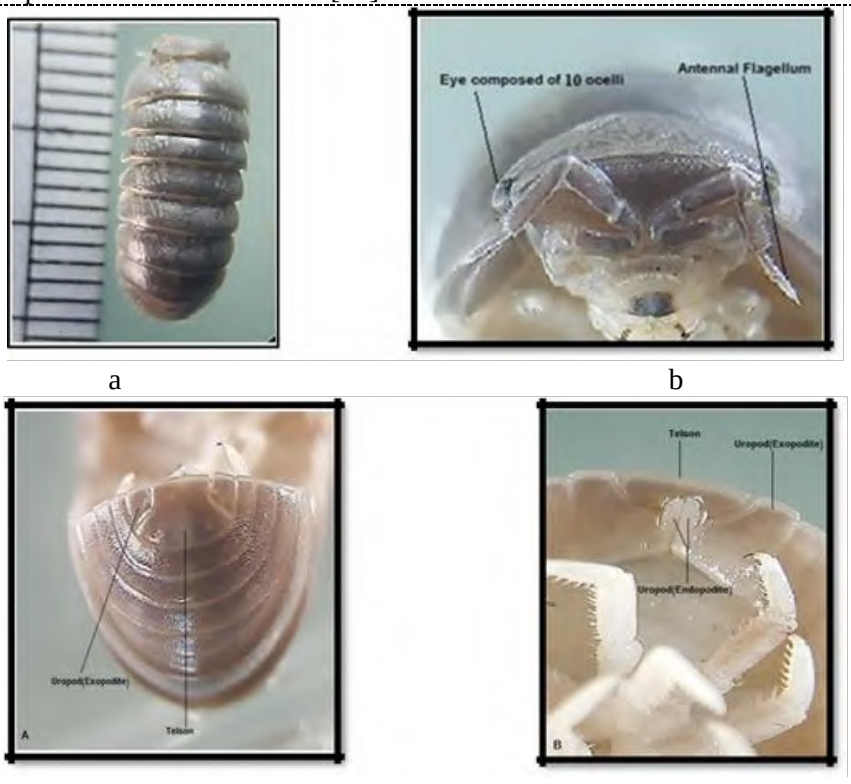

a b

c-A c-B

Figure 7. *Orthodillo chiltoni* (a-The mean length, b-The cephalothorax, c-A, B: The dorsal and ventral veiw of uropod and telson).

3.4. Family: Cylisticidae (Verthaff, 1949).

This family has distinguished by its curry surface, we found one species as a first record in Iraq which was:

3.4.1. Cylisticus convexus (DeGeer, 1778).

It's mean length was 17 mm, and dark brown in color (Plate 8-a), the cephalothorax with three lobs, dark grey eyes with 22 ocilli a,d long antenna (Plate 8-b). The edge of peleon very narrower than the edge of pereon (Plate 8-c). The exopod was large and long while the endopod was small and the telson was square in shape (Plate 8-d).This study is the similar with [22].

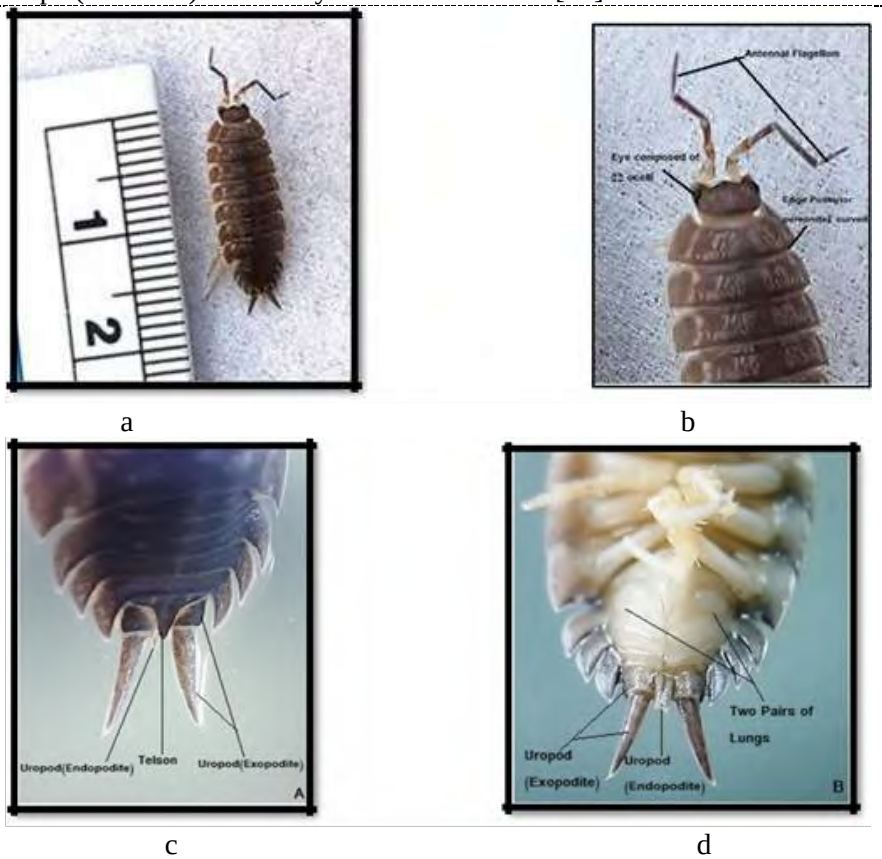

a b

c d

Figure 8. *Cylisticus convexus* (a-The mean length, b-The cephalothorax, c-The pereon and pelein, d-Dorsal veiw of uropod and telson).

4. References

[1] Rodcharoen E, Bruce NL and Pholpunthin P 2017 *Cirolana phuketensis*, a new species of marine isopod (Crustacea, Isopoda, Cirolanidae) from the Andaman Sea coast of Thailand, ZooKeys. *Pensoft Publ.* **695** 1 .

[2] Hegna TA, Vega FJ and González-Rodríguez KA 2014 First Mesozoic Thylacocephalans (Arthropoda, Crustacea; Cretaceous) in the Western Hemisphere: New Discoveries from the Muhi Quarry Lagerstätte *J. Paleontol.* **88** 606.

[3] Browne CL and Paszkowski CA 2014 The influence of habitat composition, season and gender on habitat selection by western toads (*Anaxyrus boreas*) *Herpetol. Conserv. Biol.* **9** 417.

[4] Piégu B 2014 Genome sequence of a crustacean iridovirus, IIV31, isolated from the pill bug, Armadillidium vulgare, Journal of General Virology *Microbiol. Soc.* **95** 1585.

[5] Ziegler A 2017 Mineral in skeletal elements of the terrestrial crustacean Porcellio scaber: SRμCT of function related distribution and changes during the moult cycle *Arthropod Struct. Develop.* **46** 63.
[6] Culliney T 2013 Role of arthropods in maintaining soil fertility, Agriculture *Multidiscipl. Digital Publish. Instit.* **3** 629.
[7] Ortiz M, Winfield I and Cházaro-Olvera S 2012 *Una especie nueva* de isópodo (Isopoda: Flabellifera: Sphaeromatidae) de Cuba, con una clave de identificación para las especies de Paraimene *Revista Mexicana de Biodiversidad* **83** 976.
[8] Farkas S, Vilisics F 2013 A key to the terrestrial isopods of Hungaary *Nat. Somogyiensis* **23** 89. [In Hungarian].
[9] Taiti S and Rossano C 2015 Terrestrial isopods from the Oued Laou basin, north-eastern Morocco (Crustacea: Oniscidea), with descriptions of two new genera and seven new species *J. Nat. Hist.* **49** 2067.
[10] Rife GS 2000 *Key to the isopodaof Ohio-after "AAW 1964"* The entomology Greenhouse, Ohio state university.
[11] Minor M, Meyer V, Robertson A and Taiti S 2016 *Illustrated key to terrestrialIsopoda of New Zealand* Working paper update, http//nzslaters.massey.ac.nz.
[12] Judd S and Perina G 2013 An Illustrated key to the morphospecies of terrestrial isopods(Crustacea: Oniscides) of Barrow Island, Western Australia . *Rec. Westr. Austuralia Museum* **83** 185.
[13] Hopkin S 2012 *A key to the woodlice of Britain and Ireland. First edition 1991*. Reprinted 2012. FSC 2012 52.
[14] Kashani GM, Waegele JW and Schmalfuss H 2011 Redescription of *Porcellio brevicaudatus* Brandt, 1833 (Isopoda: Oniscidea); with some notes on other synonyms of *Hemilepistus reaumurii* (Milne-Edwards, 1840) *Zootaxa*, **2924** 63.
[15] Taiti S and Gruber GA2008 Cave-dwelling terrestrial isopods from Southern China (Crustacea, Isopoda, Oniscidea), with descriptions of four new species, Research in South China karsts. Memorie del Museo Civico di Storia Naturale di Verona, *Monografie Naturalistiche* **3** 101.
[16] Reboleira ASPS 2015 The cavernicolous Oniscidea (Crustacea: Isopoda) of Portugal *Europ. J. Taxon.* **161** 1.
[17] Taiti S and Rossano C 2015 Terrestrial isopods from the Oued Laou basin, north-eastern Morocco (Crustacea: Oniscidea), with descriptions of two new genera and seven new species *J. Nat. Hist.* **49** 2067.
[18] Waller A and Verdi A 2016 Reproductive patterns of terrestrial isopods (Crustacea, Isopoda, Oniscidea) from Uruguay *Int. J. Biol.* **8** 12.
[19] Gregory S 2014 Woodlice (Isopoda: Oniscidea) from the Eden Project, Cornwall, with descriptions of species new to Britain and poorly known British species *Bull. Br. Myriapod Isopod Group*, **27** 3.
[20] Vilisics F and Terhivuo J 2009 Inspection on materials contributing to the knowledge of terrestrial Isopoda (Crustacea, Oniscidea) in Finland *Memoranda Societatis pro Fauna et Flora Fennica* **85** 9.
[21] Bradford TM 2010 *Modes of speciation in subterranean diving beetles from a single calcrete aquifer in Central Western Australia* PhD. thesis, University of Adelaide.
[22] Tabacaru I and Giurginca A 2014 Identification key to the cavernicolous oniscidea of Romania, *Travaux de l'Institute Speologie Émile Racovitza* **53** 41.

Assessment of Health Awareness: Spreading and Prevention of Infection with SARS-CoV-2 Virus in the Anbar Governorate-Iraqi Community

Assessment of Health Awareness: Spreading and Prevention of Infection with SARS-CoV-2 Virus in the Anbar Governorate-Iraqi Community

Harith Abdulrahman Ahmed [1*], Mustafa Nuhad Al-Darraji[2] and Osama Abdulrahman Ahmed[3]

[1]Iraqi Ministry of Education, Iraq.
[2]Department Biology, College of Science, University of Al-Anbar, Iraq.
[3]Public health, Iraqi Ministry of health and Environmental, Iraq.

*E-mail: sc.mustafa_79nt@uoanbar.edu.iq

Abstract. SARS-COV-2 virus is one of the fastest spreading viruses targeting the respiratory and other system in the body. Therefore, it is necessary to emphasize the needs for preventive measures, particularly at the moment because the virus is spreading fast in various parts of the world, causing various levels of infections: medium to severe, and fatal. The study aimed at assessing health and environmental awareness apart from correcting some scientific healthy concepts related to COVID-19. Additionally, this study also attempted to spread awareness in a simple way that simulates all levels of society. The current study focused on Iraq, specifically Al-Anbar governorate, as it is free from COVID-19 infections according to the reports of the Iraqi Ministry of Health in cooperation with the WHO. In this study, a set of electronic questionnaire was selected to collect relevant data. The electronic questionnaire was chosen because of the quarantine order by the authority due to the COVID-19. The items were built based on a variety of health, preventive, and environmental scientific questions and it was electronically distributed to 2084 individuals in Governorate. The findings revealed that Ramadi city had the most participants responding to the questionnaire (47%). The participation rate for female was 52% while the rate for male is 48%. The biggest age group was 20-24 years old and the highest academic background was a bachelor's degree in education. The findings indicated a good percentage of health awareness among the participants in the governorate emphasizing on health instructions and preventive measures taken by the Crisis Cell, which had an important role in being infectious-free during the period. It is summarized that the level of health awareness and the role of the Crisis Cell: worked together COVID-19 the infection. Additionally, this questionnaire had a great role in correcting some understanding of scientific concepts among the public. .

Keywords. Awareness, COVID-19, Crisis Cell, Health, Prevention.

1. Introduction

Coronavirus (CoVs) is a form of single-stranded RNA viruses that can infect peoples and animals, causing respiratory, other diseases of which gastrointestinal, hepatic, and neurologic diseases. [1]. As

large family known RNA viruses, coronavirus are further divided into genera: alpha-coronavirus, beta coronavirus, gamma-coronavirus, and delta coronavirus [2]. As well, (CoVs) are the largest of respiratory viruses that can cause mild to moderate diseases, ranging from the common cold to severe respiratory syndromes [3]. COVID-19 disease is an infectious disease caused by the newly discovered coronavirus. The most common symptoms of COVID-19 disease are fever, fatigue, and dry cough. Some patients may experience pain and aches, nasal congestion, cold, sore throat, or diarrhea. These symptoms are usually mild and begin gradually. Some people become infected without showing any symptoms and without feeling ill. Most people (about 80%) recover from the disease without the needs for special treatment [4]. Also, the severity of the disease intensifies in approximately one person out of every six people who develop COVID-19 infection, who suffer from difficulty breathing. The risk of the elderly and people with underlying medical problems such as high blood pressure, heart disease, or diabetes are severe. About 2% of people who have contracted the disease have died. People with fever, cough, and breathing difficulty should seek medical care. The disease can be transmitted from a person to a person through small droplets scattered from a nose or mouth when a person with COVID-19 disease coughs or sneezes. These droplets fall on the objects and surfaces surrounding the person. Other people can then develop COVID-19 disease when they are exposed to these objects or surfaces and then touch their eyes, nose, or mouth. People can also get COVID-19 disease if they breathe droplets that come out of the person with the disease with a cough or exhale. Therefore, it is important to stay away from a sick person more than one meter (3 feet) [4]. In December 2019, an outbreak of pneumonia due to unknown cause occurred in Wuhan, China and rapidly spread throughout the country within 1 month. Coronavirus disease 2019 (COVID-19) is an announced universal pandemic, by a WHO on 30 January 2020 [5]. It then resulted in a challenging outbreaks in many regions in China and expanding globally [6]. Serious pandemic continues to progress until most invaded the world, reaching Iraq, recorded the first case with COVID-19 in late February in Baghdad [7]. The incidence started to increase, reaching 1,400 COVID-19 cases by mid-April according to Iraqi Ministry of Health. The highest incidences were in the southern governorates of Iraq, for example, Basra, Najaf, and Karbala, as well as the northern governorates such as Erbil and Sulaymaniyah. The number of incidence in the middle governorates was very few, such as Anbar, Nineveh, and Salah Uddin, compared to other governorates according to the Iraqi Ministry of Health. Al-Anbar Governorate is the largest governorate of Iraq, with an area equivalent to a third of the country's area, with an area of 138,500 square kilometers, and a total population of 1,818,318 people (2019 census) according to the yearly report of the Planning Directorate in Anbar Governorate. It is a border to the north by Salah al-Din and Nineveh governorates, to the northwest by Syria, to the west by Jordan, to the east by the Baghdad governorate, to the south by Saudi Arabia, and the southeast by governorates of Karbala and Najaf. It is worth mentioning that the Anbar Governorate did not record COVID-19 incidence except for two cases according to the Iraqi Ministry of Health. This study aimed to assess health awareness and investigate the extent to which citizens in Anbar Governorate have absorbed this serious pandemic, invading most of the countries in the world and claimed the lives of many people in various regions in very short periods. However, the issue cannot be compared to a similar pandemic in previous periods. It is stressed that this study did not have the intention to spread fear among people and curb their hopes for recovery, but rather to show the reality of seriousness and ways to survive from this pandemic. The effective role of the Crisis Cell (Al-Anbar Governorate) was also highlighted to face this disease, especially referring to the decisions taken by the Iraqi Government generally and Al-Anbar Governorate particularly as a distinct role in the non-expansion for the disease among the citizen. Besides, it aimed to investigate the requirements that must be provided to citizens by the Crisis Cell in terms of health and services during this period, which contributed to overcoming this dangerous stage.

2. Materials and Methods

The responses from the questionnaire were received from April 8 to April 20, 2020 during the quarantine period in the Al-Anbar Governorate. This period was chosen because it is considered the most appropriate time for people to sit at homes, thus, this condition resulted in a large number of participants. A large number of participants are an advantage for this study to build their health awareness and to correct misconceptions of some people about COVID-19. The research team decided to collect the data online: the questions was developed through a Google Form and sent to a large number of residents in cities of Al-Anbar through the social media such as WhatsApp, Viber, Messenger, and others [8]. The questionnaire was followed by an explanation on objectives of the questionnaire and also an instruction on responding to the items based on their beliefs which they feel appropriate. The participants were residents of Al-Anbar province aged 20 years and above who agreed to participate and were instructed to complete the questionnaire by clicking the provided link. The approval in distributing the questionnaire was obtained from the President of the Crisis in Al-Anbar Governorate. The questionnaire was designed to investigate the demographic details and evaluation of health awareness among the participants. The questionnaire consisted of several parts. The first part includes demographic details: place of current residence, gender, age, education [9] as illustrated in Table 1.

Table 1. Demographic details of the participants

No.	Demographic details	Options		
1	**Place of residence**	Ramadi	Fallujah	Haditha
		Khalidiya	Aana	Rawah
		Heet	Ratba	Qaam
2	**Gender**	Male		Female
3	**Select your age group**	20-24	25-29	30-34
		35-39	40-44	45-49
		50-54	55-59	+60
4	**Education**	Master’s degree and above		
		Bachelor's degree		
		Diploma degree		
		Middle school and below		
		I did not get a degree but read and write		

The second part consisted of seven questions about the coronavirus: its existence, origin, methods of spreading, assessing health awareness, and the role of environmental pollution in addition to other questions related to the virus SARS-CoV-2. The third part investigated the participants’ views on assessing health awareness and ways to prevent COVID-19 and the role of the Crisis Cell in the province in controlling the disease in addition to health and services provided to the citizens. The last part consisted of an assessment of health awareness about how to curb COVID-19 in the society, as well as how those who had recovered from COVID-19 joined into the society again. More than one correct answer was discovered from the responses; however, there was more correct answer, as well as incorrect answers. Rates were used to present the correct answers and various practices. The results from the questionnaire were presented through percentages in terms of knowledge scores, attitudes and practices of the participants according to the level of health awareness among them. In addition, the demographic details were independent variables and knowledge score as the outcome variable. These were conducted to identify factors associated with knowledge.

3. Results and Discussion

There were 2084 participants in this study who came from different cities in the Governorate of Anbar and were divided according to their approximate ratio from high to low. Where Ramadi was the largest number of respondents participating in the questionnaire with 47%, and then followed by the

city of Fallujah (21.1%), Haditha (11.9%), Khalidiyah (7%), Heet (6.8%), Al Qaam (1.9%), while the rest of the cities was 1% and less. The female participation rate was 52%, while the male participation was 48%.The percentages of age groups were 38.6%, 16.7%, 14.7%, 9.3%, 9.0%, 4.8%, 3.8%, 1.3% and 1.7 for age groups of 20-24, 25-29, 30-34, 35-39, 40-44, 45-49, 50-54, 55-59 and 60 above respectively. As for the level of education, the percentages were 17.6%, 54.8%, 21.6%, 5.3% and 0.7% master's degree and above, Bachelor's degree, diploma degree, Middle school and below, and I did not get a degree but read and write, respectively. All the demographic details are illustrated in Table 2.

Table 2. Demographic details of the questionnaire.

No.	Demographic details	Options	Number of participants	Percentage %
1	**Place of living**	Ramadi	985	47.3
		Fallujah	440	21.1
		Khalidiya	145	7
		Heet	142	6.8
		Haditha	249	11.9
		Aana	33	1.6
		Rawah	24	1.2
		Qaam	41	1.9
		Ratba	25	1.2
2	**Gender**	Male	1006	48.3
		Female	1078	51.7
3	**Age group**	20-24	804	38.6
		25-29	348	16.7
		30-34	307	14.7
		35-39	194	9.3
		40-44	188	9
		45-49	100	4.8
		50-54	80	3.8
		55-59	27	1.3
		60+	36	1.7
4	**Education**	Master's degree and above	367	17.6
		Bachelor's degree	1141	54.8
		Diploma degree	450	21.6
		Middle school and below	111	5.3
		I did not get a degree but read and write	15	0.7

In this part, the results of the questionnaire on evaluating health and environmental awareness of the community in Anbar Governorate were presented based on the responses to each item in the questionnaire.

3.1. Item 1: Do you think there is a disease called COVID-19 (or locally called the Corona) caused by a type of corona virus?

Based on the analysis, 68% of the respondents chose (A) Yes, there is a reasoned virus COVID-19 according to reports by WHO, which confirms this [10]. This is the most correct answer if compared

to answers to others. While 10% of the respondents chose (B) I think it is a way to control and fabricate the global economic crises, followed by 6% who chose (C) Do not think a virus but the sarin gas according to what is circulating in social media [11]. Next, is followed by 7% who chose (D) I think it is simpler than that because its symptoms are somewhat similar to flu, I do not think it is so scary [12]. While the last choice indicated 9% who chose (E) I do not know. These findings are illustrated in Figure 1.

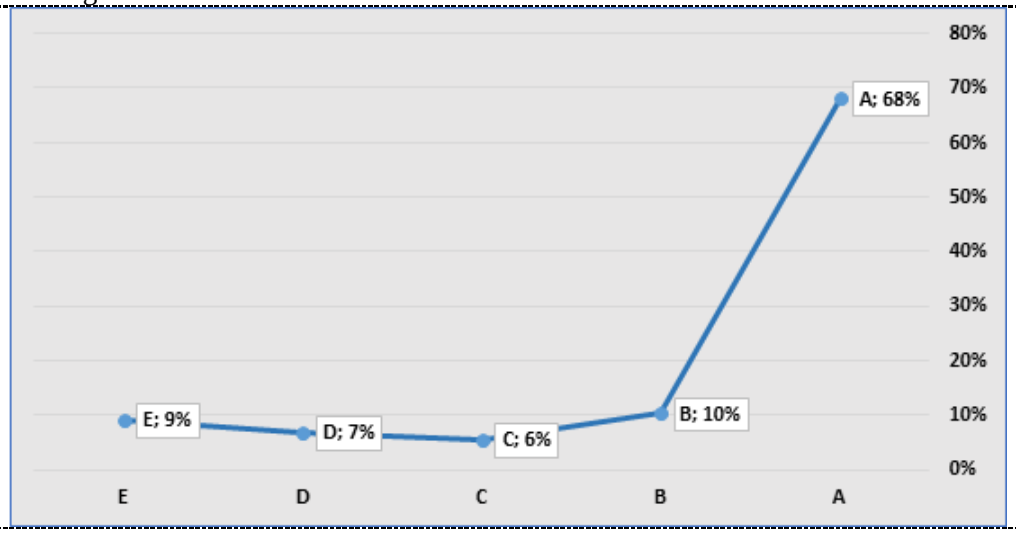

Figure 1. Findings for Item 1: Do you think there is a disease called COVID-19 (or locally called the Corona) caused by a type of corona virus?

3.2. Item 2: How do you rate your knowledge about viruses in terms of infection and prevention methods and others?

There are four options of answers the participants can choose for their respond. Based on the findings, it revealed that 30% of the respondents chose (A) excellent through published scientific research and reports WHO while 30% chose (B) very well through the instructions posted by the Crisis Cell on governorate. In addition 25% of the respondents chose (C) good through reports on social media and finally 10% of the respondents chose (D) I have no interest in the subject. This findings indicated a danger to the society because they are lack of interest in personal protective methods against COVID-19.

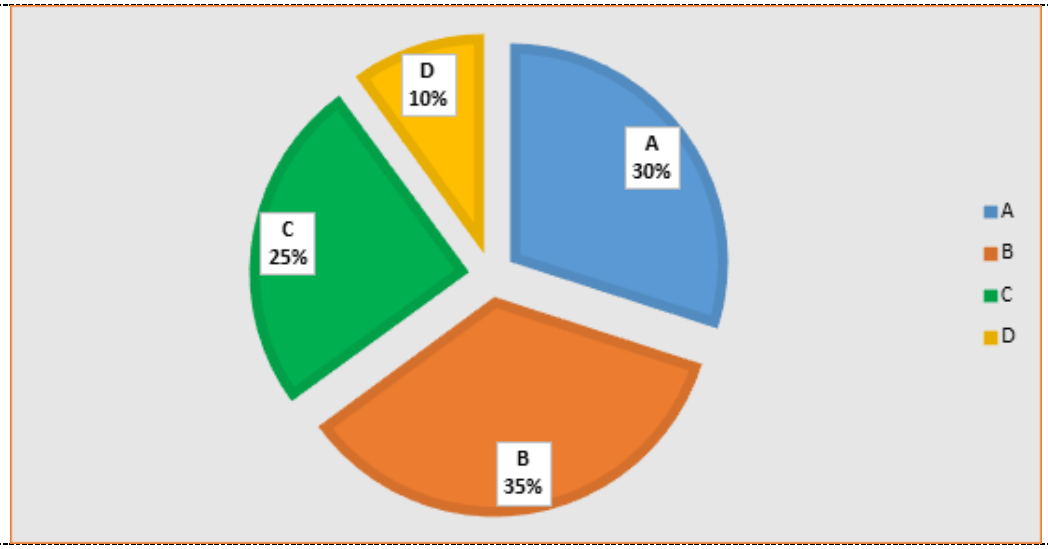

Figure 2. Findings for Item 2: How do you rate your knowledge about viruses in terms of infection and prevention methods and others?

3.3. Item 3: What distinguishes the SARS-CoV-2 causing COVID-19 from other viruses?

According to the findings, 59% of the respondents chose (A) Rapid spread in societies, this answer was considered correct because since the outbreak of the disease in late December 2019 till the present time, according to the reports of the World Health Organization, the infection has reach 3 million worldwide [13]. While 10% chose (B) Style of infection through the respiratory tract. This answer is considered correct as it indicates that the virus is characterized by a respiratory infection. However, a new study showed that the virus infects blood hemoglobin and reduces its efficiency in carrying oxygen and carbon dioxide [14]. This is followed by options (C), (D), and (F) which obtained 6% respectively. The choice of (C) Multiple strains and mutations of the virus is considered correct because the statement is proven by studies on the virus [12]. However, it is not considered a characteristic because most viruses have this characteristic. This is followed by choice (D) The number of deaths caused by the virus, which this is also not a distinctive characteristic due to the fact that the number of deaths does not exceed 3%, according to the statistics of the WHO [13]. As for option (F) I did not know what distinguishes this virus, 6% of the respondents had chosen this option. Finally, as for option (E) few studies are available on the virus, 12% of the respondents chose this option, thus this answer is considered an incorrect answer because there are thousands of studies on this pandemic. The findings are illustrated in Figure 3..

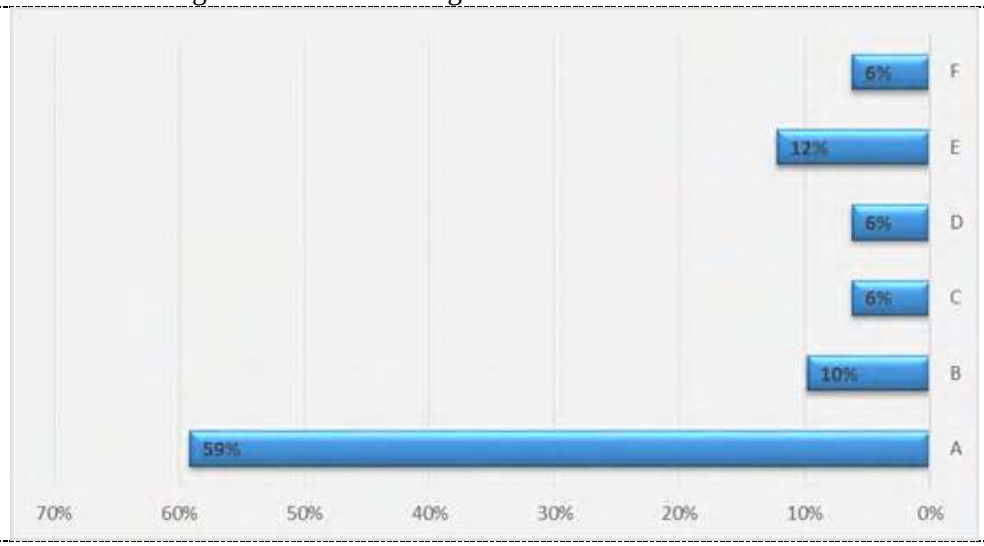

Figure 3. Findings for Item 3: What distinguishes the SARS-CoV-2 causing COVID-19 from other viruses?

3.4. Item 4: So far, no treatment or vaccine has been found against the disease. What do you think are the methods that increase your body's immunity against COVID-19 disease?

Based on the analysis of the questionnaire data, foods rich in vitamins A, C, E, B6 and B12, zinc, and iron such as citrus fruits, dark green leafy vegetables, nuts, and dairy products were some of the responses given by the participants [15]. From the findings, evidence showed that there is a 12% overall protective effect of vitamin D supplements against bacterial and viral acute respiratory tract infection. In addition, vitamin C (L-ascorbic acid) has a pleiotropic physiological role, and there is evidence supporting the protective effect of high dose intravenous vitamin C against COVID-19 [16]. Maintain a healthy lifestyle by exercising (home-exercises), regular sleep and meditation and avoid

smoking, alcohol, and drugs [15] but high-intensity exercises probably due to the production of oxidants and suppression of the immune system may be dangerous, however, it helps to exacerbate the COVID-19 virus. It means that moderate-intensity exercise should be recommended as a non-pharmacological, inexpensive, and viable way to cope with the COVID-19 virus [17]. This COVID-19 epidemic has aroused an increasing attention worldwide. Patients, health professionals, and the public are under insurmountable psychological pressure, which may lead to various psychological problems, such as anxiety, fear, depression, and insomnia. Psychological crisis intervention plays a pivotal role in the overall deployment of the disease control. In addition, awareness regarding the devastating consequences of hoarding and panic buy should be spread in the community [18]. The item consists of two correct options (A) Through exercise sport, healthy nutrition, and mental health and (B) may be by using some vitamins that increase my immunity. This is followed by the third options (C) that contains the previous two options which obtained 90% compared to the other first two options. Finally, option (D) I have obstacles that prevent me from changing my lifestyle, and so I do not think as affecting which is the wrong answer, and therefore resulted in only 10% of the overall percentage. These findings are shown in Figure 4.

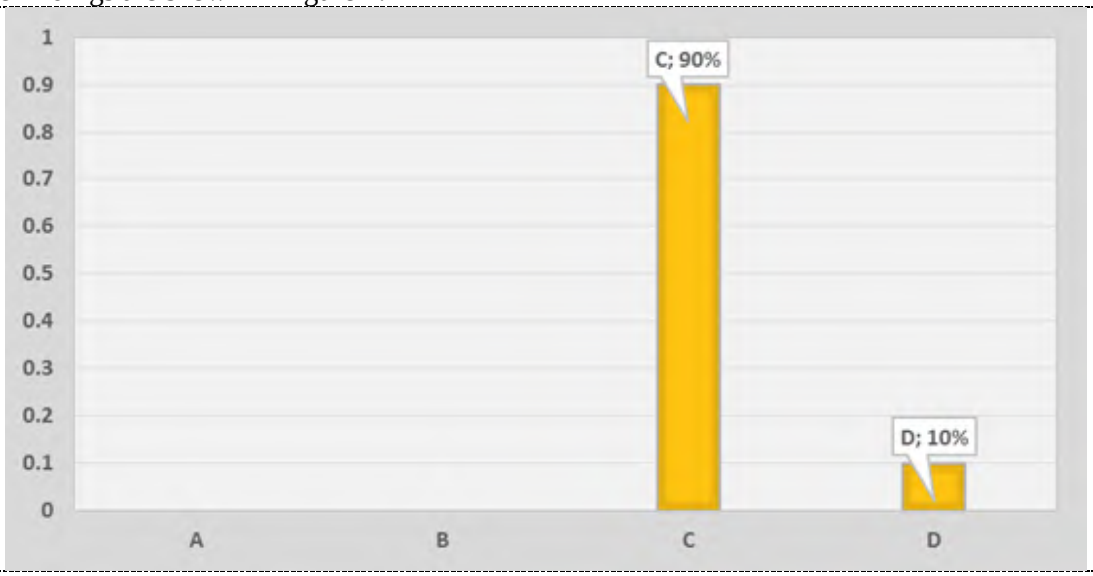

Figure 4. Findings for Item 4: So far, no treatment or vaccine has been found against the disease. What do you think are the methods that increase your body's immunity against COVID-19 disease?

3.5. Item 5: In light of the advanced scientific capabilities, why have not been reached so far as a treatment or vaccine for COVID-19 disease?

The first three options for Item 5 were considered wrong or not yet proven. From the options provided, option (A) Difficulty dealing with this type of virus due to its dangers obtained 22% from the overall response. As for option (B) This is a virus genetically modified and has many mutations, the findings indicated 20% of the response rate by the respondents. This is followed by option (C) Failure to unify efforts and consider the matter materially which obtained 7%. The current COVID-19 pandemic is an international public health problem. There have been rapid advances in what we know about the pathogen, how it infects cells and causes disease and clinical characteristics of the disease due to the rapid transmission around the world [19].As for option (D) the rapid spread led to the dispersion of efforts between researches and redress health reality, the findings indicated that this option obtained 26% of response rate. Currently, there is not sufficient evidence that any existing antiviral drugs can efficiently treat COVID-19 pneumonia. In addition, the vaccines and therapeutic antibodies aimed to specifically target SARS-CoV-2 are also being tested; this solution is more long-term, as they require

thorough testing of their safety [20]. This is similar to option (E) the topic needs time to ensure the safety and security of the treatment or vaccine which obtained 25% of the response rate. These findings are shown in Figure 5.

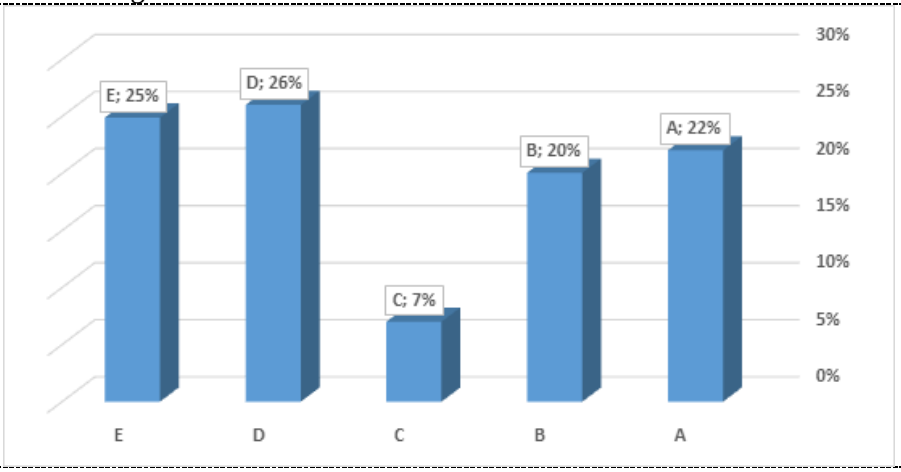

Figure 5. Findings for Item 5: In light of the advanced scientific capabilities, why have not been reached so far as a treatment or vaccine for COVID-19 disease?

3.6. Item 6: One of the theories of the emergence of viruses due to environmental pollution. Do you think that environmental pollution has a role in the emergence of viruses?

One theory hypothesizes that viruses arose from circular DNA (also called a plasmid) that can replicate independently and move between cells, transferring genetic information from one organism to another. For example, some plasmids carry the genes responsible for antibiotic drug resistance. According to this theory, the plasmid escapes from cells and evolves in a way that allows it to enter another cell to produce viruses. Another theory suggests that viruses could have evolved from more complex free-living organisms, such as bacteria or cells. A recent study showed that a protein called ARC that is important for memory in humans could form virus-like particles and transfer RNA between cells. In all cases, environmental pollution contributes significantly to the emergence of viruses [21]. This is somewhat similar to option (A) Yes, a belief that it contributes significantly to the emergence of viruses, which received 36% of the response rate. This is followed by option (B) I do not think that environmental pollution cause it with 20% response rate, option (C) I think this virus is laboratory-produced which suggests the conspiracy theory circulated in various media outlets and obtained 35% response rate, and the final option (D) I do not know obtained 9% response rate. These findings are shown in Figure 6.

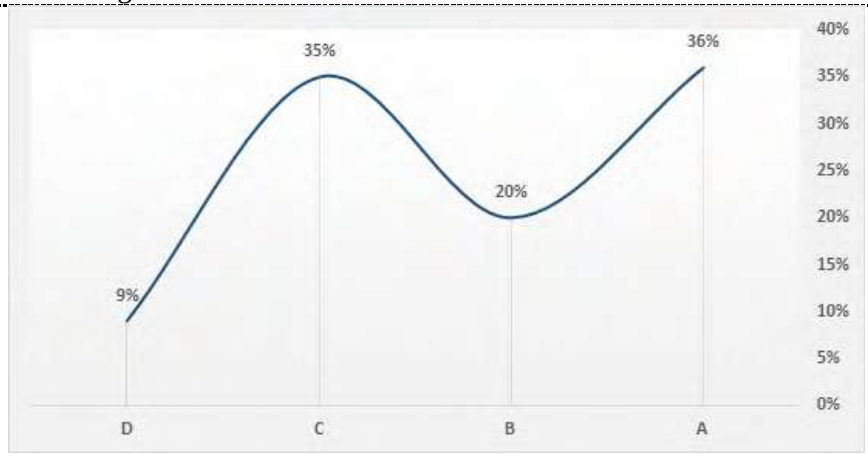

Figure 6. Findings for Item 6: One of the theories of the emergence of viruses due to environmental pollution. Do you think that environmental pollution has a role in the emergence of viruses?

3.7. Item 7: In your opinion, what are the most important ways to spread the virus in societies?

According to WHO Guidance, it is suggested to maintain at least 1-meter distance between two people. When someone coughs, sneezes, or speaks he or she sprays small liquid droplets from their nose or mouth which may contain viruses. If a person is too close to someone else, he or she can breathe in the droplets, including the COVID-19 virus if the person has the disease because it is considered the primary method of virus infection. From the analysis of Item 7, option (A) Through flying drizzle from coughing and sneezing of a person with COVID-19 obtained 55% response rate [4]. Likewise, WHO considers option (B) touching surfaces, food, or commercial goods contaminated with the virus to be correct and obtained 20% response rate. It can be considered as a correct answer if it is assumed that a person sneezes or coughs on certain surfaces that may be touched by a healthy person and then places his hand on his mouth, nose, or eye [4]. As for option (C) studies are indicating that animals a role has been of Virus transport, the findings indicated that this option obtained 7% response rate where bats harbor viruses including sars-COV-2. In some circumstances, facilitating spillover happens which includes direct contact with bats (bites, scratches, consumption of bats), contact with materials contaminated by bat saliva, feces or urine, and amplification via intermediate hosts such as domestic animals or other wildlife species. Due to this reasons, a person must stay away from bats to reduce the transmission risk of viruses from bats to humans and livestock [22, 23]. The last option (D) overpopulation, received 18% response rate. This indicated that a person must avoid going to crowded and overpopulation places because when people are together in crowds, they are more likely to come into close contact with someone who has COVID-19 and it is more difficult to maintain a physical distance of 1 meter, thus, this has been confirmed by the World Health Organization [4]. The findings for Item 7 is illustrated in Figure 7.

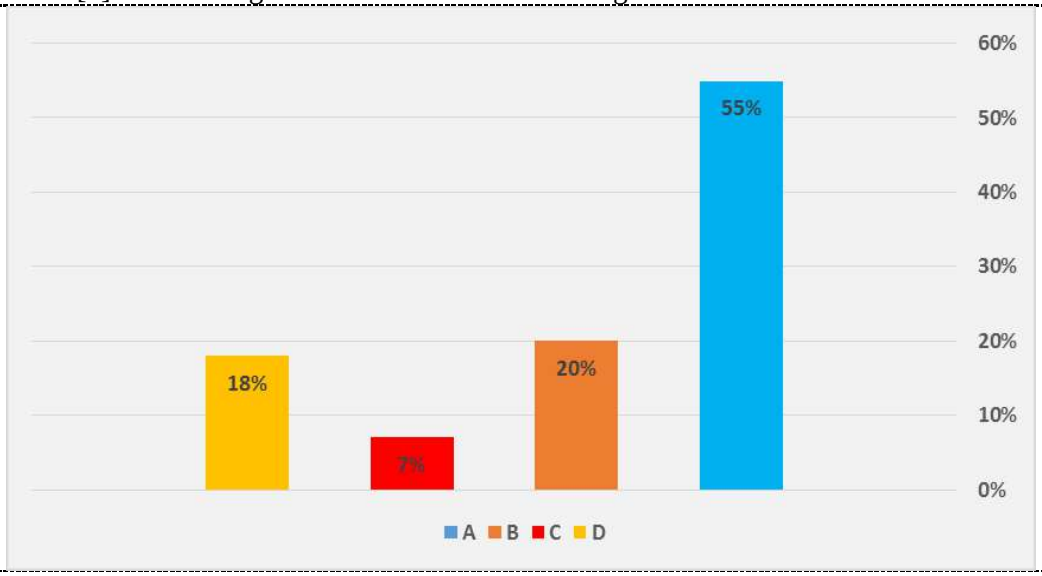

Figure 7. Findings for Item 7: In your opinion, what are the most important ways to spread the virus in societies?

3.8. Item 8: WHO urges to stay at home, not go out except when necessary, follow good hygiene practices, practice social spacing, and take preventive measures such as wearing masks and gloves to reduce the spread of COVID-19, do you follow these procedures?

Findings for Item 8 revealed that 67% of the respondents chose option (A) I apply it at all times to protect the community and myself, and this is evident as what was observed in the cities of Al-Anbar Governorate who applied the procedures of the home quarantine approved by the Crisis Cell in the Governorate. Nevertheless, option (B) I am committed to staying at home, but sometimes when I leave the house cannot apply precautions obtained 21% response rate. This is considered an incorrect answer because it is a failure not to apply preventive measures that are not available continuously during this period and their prices are high. In addition, option (C) I Apply it well but I cannot stay home is considered valid because this is the same for some categories of employees if he applies the preventive measures recommended by the WHO [24] and this option obtained 8% response rate. As for the final option (D) I do not expect these measures to work, this option is considered a wrong choice and obtained only 4% due to community fear of COVID-19 infections. The findings are shown in Figure 8.

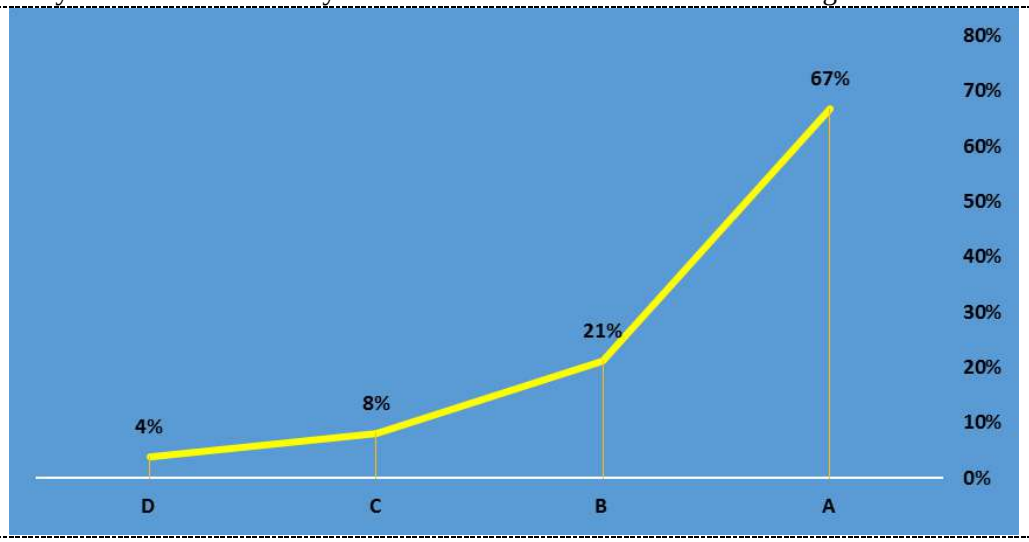

Figure 8. Findings for Item 8: WHO urges to stay at home, not go out except when necessary, follow good hygiene practices, practice social spacing, and take preventive measures such as wearing masks and gloves to reduce the spread of COVID-19, do you follow these procedures?

3.9. Item 9: At this difficult time, Iraq is going through in general and Anbar Governorate in particular because of the spread of COVID-19. What aspects do you think need to be strengthened during this period in the al Anbar governorate inside the health aspect?

In this period, some of the options which can be done in combating COVID-19 are increase sterilization, spread health awareness in the community about methods of prevention from COVID-19, as well as establish quarantine places and examine samples. As for the options for Item 9, option (A) By increasing the sterilization and fumigation processes for institutions health, streets, and methods of basic preventive e obtained 42% response rate. In addition, option (B) By spreading community health awareness around methods infection, disease prevention, and others obtained 26% of response rate, followed by option (C) Create more places of quarantine and examine the samples inside the governorate which obtained 4% of the response rate. Based on the correct options mentioned, the total response rate was 72%. As far as the incorrect options are concerned, option (D) Perform a field examination of all the regions of the governorate to ensure that they are free from the incidence of COVID-19 obtained 20% of the response rate because there is no record of cases in the governorate. This is followed by option (E) Providing mobile ambulances in the governorate areas for helping citizens who are unable to reach hospitals which obtained 8% because of our needs to have all health personal and medical equipment to fight COVID-19. The findings are shown in Figure 9.

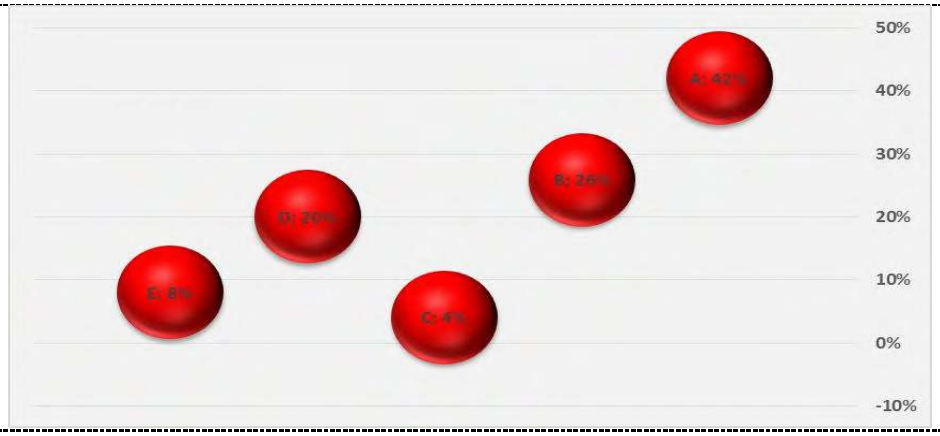

Figure 9. Findings for Item 9: At this difficult time, Iraq is going through in general and Anbar Governorate in particular because of the spread of COVID-19. What aspects do you think need to be strengthened during this period in the al Anbar governorate inside the health aspect?

3.10. Item 10: What do you think of the Crisis Cell in the Al Anbar governorate in terms of security and service, and what aspects need to be strengthened during this period?

From the analysis, 76% of the participants chose option (A) Preventing the entry of expatriates to the governorate except after making sure of their safety from an incidence of COVID-19 no matter how important. This option obtained the highest percentage because all the recorded cases in the governorate were imported cases which may cause an epidemic in the governorate. Therefore, all expatriates must be ensured to be free from the disease in order to make sure of their safety from COVID-19. As for option (B) Sterilization and fumigation of all goods and foodstuffs entering into governorate, it obtained 5%. This option is correct, however, it is less important than option (A). Based on this findings, the correct choices for Item 9 obtained a total of 81% response rate. Referring to the wrong choices, the total percentage is 19%. This findings included option (C) Providing the necessary services that the citizen needs, for example, electricity, the Internet, and others which obtained 2%; having services is one of the essential things in life, not just in times of crisis. This is followed by option (D) Open the ban is partially for helping the citizen to fetch his needs, especially after the end of the official working hours with 7% response rate; this option is unnecessary because the crisis cell allowed the opening of food stores and pharmacies to provide people with their basic needs. Finally was option (E) Providing the necessary foodstuffs to the low-income individuals during this period which obtained 10% response rate. The findings for Item 9 are illustrated in Figure 10.

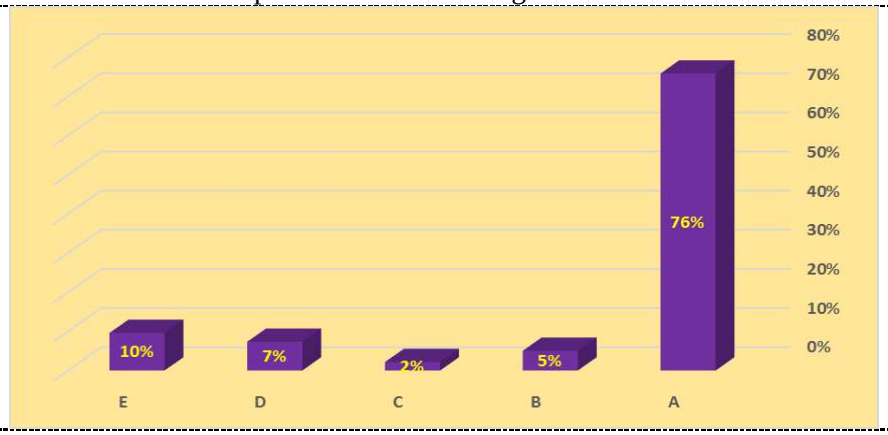

Figure 10. Findings for Item 10: What do you think of the crisis cell in the Al Anbar governorate in terms of security and service, and what aspects need to be strengthened during this period?

3.11. Item 11: Will the Crisis Cell in Anbar Governorate succeed in overcoming the COVID-19 crisis by keeping the province free of casualties?

Based on the analysis, 80% of the respondents in the cities of Al-Anbar province trust the work of the Crisis Cell by applying the preventive measures recommended by the WHO [4] by selecting option (A) yes, by implementing preventive measures for the Crisis Cell in Al-Anbar Governorate and thus constitutes a kind of healthy cultural awareness to overcome the COVID-19 crisis. While option (B) Perhaps there will be no the infection of COVID-19 in the governorate, but I am not sure about the work of the Crisis Cell obtained 13% response rate, and the reason is due to unavailability of some preventive and hygienic supplies in the world in general [25]. While option (C) I do not expect its success and often infection of COVID-19 will occur in the future obtained 5% response rate due to the two new cases; it was found that the person had COVID-19 and the Crisis Cell sent the person to their governorate for further action. As for the last option (D) thinks they do not care about the success or failure of the Crisis Cell the findings indicated 2% response rate. It is considered as a negative view and lack of awareness. The findings are shown in Figure 11.

Figure 11. Findings for Item 11: Will the crisis cell in Anbar Governorate succeed in overcoming the COVID-19 crisis by keeping the province free of casualties?

3.12. Item 12: When reading health reports about COVID-19, how would you rate the health status of any community?

From the analysis of Item 12, option (A) according to the number of registered epidemic infections obtained 60% response rate, this referred to the WHO recorded cases according to its latest report on April 30, 2020, in which the number of infections reached more than 3 million [26]. This is the correct option in which the health situation in the world is assessed, and for Al-Anbar Governorate, the number of infections in Al-Anbar did not exceed five cases since the first infection recorded in Iraq. As for the remaining options, they were considered wrong because the WHO has yet to find an approved treatment from this pandemic and always the right choice. The society can be protected by not recording through cases of the disease [4]. As for the remaining options, option (B) according to the number of deaths recorded obtained 10%; through it the quality of health care can be assessed and the only case remained in the isolation hospital in the governorate was cured. As for option (C) according to cases of recovery from illness, it obtained 21% response rate. In addition, option (D) I don't know obtained 9% response rate. Therefore, the society needs to be educated more about protecting themselves from the COVID-19 pandemic. The analysis of the findings is shown in Figure 12.

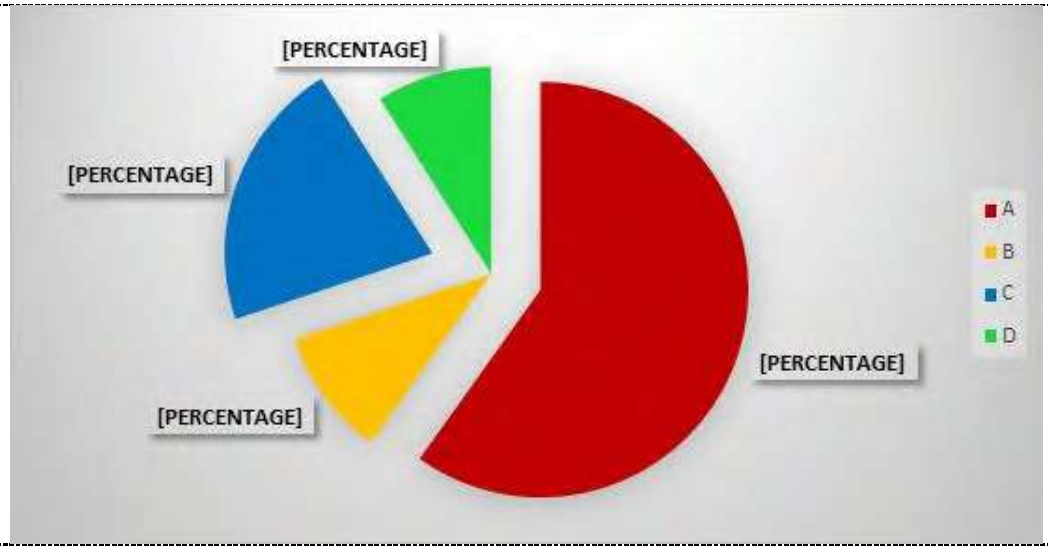

Figure 12. Findings for Item 12: When reading health reports about COVID-19, how would you rate the health status of any community?

3.13. Item 13: If one day, if you notice symptoms of COVID-19 what will you do?

According to the data anlaysed for Item 13, option (A) I call the Crisis Cell or go to the hospital, and check for infection with COVID-19 obtained 60% response rate. A high percentage indicated that the respondents are aware of their health and environment towards this epidemic in order not to spread the epidemic in the governorate. As for option (B) I will quarantine myself at home until you confirm I hit of COVID-19 and I will not approach anyone obtained 37% response rate. This answer is also considered correct despite fears in the case of infection, the disease may be transmitted to one of the family members, but the WHO confirms this until symptoms appear and then the patient is transferred to the special quarantine hospitals of COVID-19 [4]. As for the last two options which were considered incorrect answers, they only obtained 3% response rate: option (C) I do not care about the topic and go to work because I do not think I am infected COVID-19, but I will not come close to my family and option (D) Even if I have infected COVID-19 I will go to work, but I take care of preventive measures. These are illustrated in Figure 13.

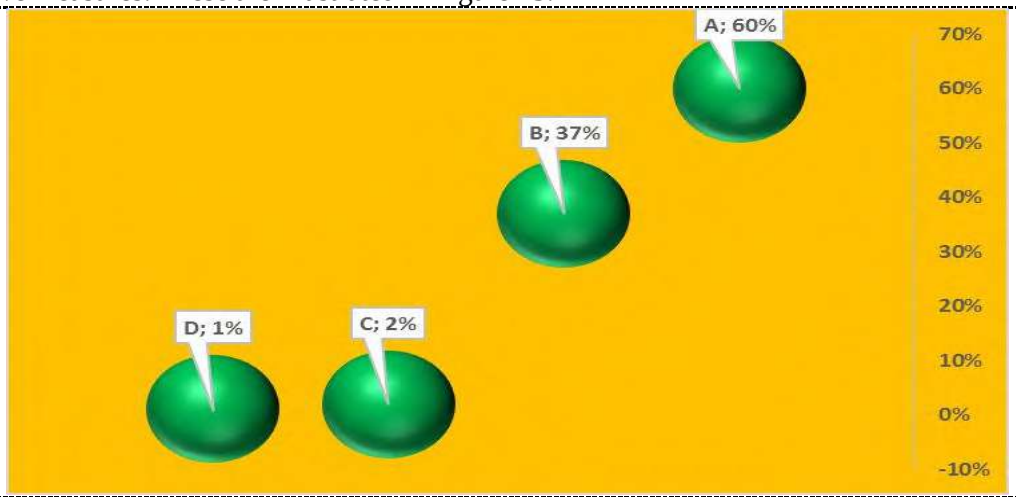

Figure 13. Findings for Item 13: If one day, if you notice symptoms of COVID-19 what will you do?

3.14. Item 14: What is your personal opinion is it possible for people who have recovered from COVID-19 to integrate into society and practice their lives as they were before the infected occurred?

The data analysis for Item 14 revealed that option (A) Yes, after ensuring complete recovery obtained 72% response rate and it is considered as the wrong option because many cases in the world which were recovered from COVID-19 were infected again as a result of the virus developed again and infectious. Patients who recovered from the disease need health care so that the infection will not repeat [27]. This is similar to option (B) Maybe, but it may adversely affect the health of the recovered in the future which obtained 14% followed by option (C) Often appear to have future health problems which obtained 6% response rate. While the last incorrect option (D) I don't know obtained 8% response rate, therefore, the total percentage of response rate for incorrect options for Item 14 is 80%. This findings indicated that the Crisis Cell must educate people about this pandemic despite their recovery from COVID-19 because the possibility of them being infected again is very high. In addition, it is also observed that those who discovered from COVID-19 were then infected by other diseases such as cirrhosis of the lungs, testicular atrophy in males [27]. Therefore, good awareness among the society is crucial and required in the aspect mentioned before. The findings are illustrated in Figure 14.

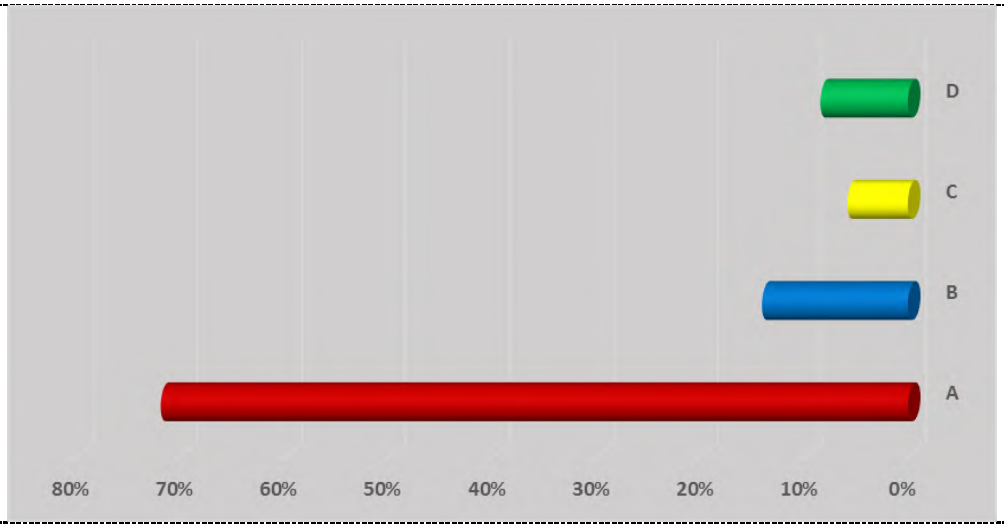

Figure 14. Findings for Item 14: What is your personal opinion is it possible for people who have recovered from COVID-19 to integrate into society and practice their lives as they were before the infected occurred?

4.Conclusion

From the results of the questionnaire on the evaluation of health and environmental awareness of citizens in Al-Anbar Governorate, it revealed a very good level of awareness about the virus, its causes, and methods of prevention. This is demonstrated through the commitment of citizens in obeying the quarantine procedures by the governorate very well. However, some aspects about health and environmental culture about COVID-19 need to be delivered to the society including how to deal with the recovering patients from COVID-19. In addition, environmental pollutants need to be avoided because it is harmful to human health and one of the etiologies of viruses. It is a need to pay a tribute to the main roles of the Crisis Cell in Al-Anbar Governorate in the process of fighting this pandemic by following procedures, as well as through the awareness methods used in addition to all the possibilities that were harnessed to serve the citizens in Al-Anbar.

5. Acknowledgments

Thank you to Dr. Ali Farhan Khalaf, head of the Crisis Cell in the governorate and the Governor of Al-Anbar for the assistance provided in particular moral support in completing this research and spread health and environmental awareness to the residents of the province in order to control the Corona epidemic.

6. References

[1] Wu D, Wu T, Liu Q and Yang Z 2020 The SARS-CoV-2 outbreak: what we know *Int. J. Infect. Dis.* **94** 44.
[2] Yang D and Leibowitz JL 2015 The structure and functions of coronavirus genomic 3′ and 5′ ends *Virus Res.* **206** 120.
[3] Chen N, Zhou M, Dong X, Qu J, Gong F, Han Y, Qiu Y, Wang J, Liu Y, Wei Y and Yu T 2020 Epidemiological and clinical characteristics of 99 cases of 2019 novel coronavirus pneumonia in Wuhan, China: a descriptive study *Lancet*. **395** 507.
[4] World Health Organization (WHO) 2020 *Q&As on COVID-19 and related health topics*.
[5] Lai CC, Liu YH, Wang CY, Wang YH, Hsueh SC, Yen MY, Ko WC and Hsueh PR 2020 Asymptomatic carrier state, acute respiratory disease, and pneumonia due to severe acute respiratory syndrome coronavirus 2 (SARSCoV-2): Facts and myths *J. Microbiol. Immunol. Infect*. **53** 404.
[6] Meo SA, Al-Khlaiwi T, Usmani AM, Meo AS, Klonoff DC and Hoang TD 2020 Biological and Epidemiological Trends in the Prevalence and Mortality due to Outbreaks of Novel Coronavirus COVID-19 *J. King Saud Univ. Sci*. **18** 100.
[7] World Health Organization 2019 *Coronavirus disease 2019 (COVID-19):* situation report, 36.
[8] Zhong BL, Luo W, Li HM, Zhang QQ, Liu XG, Li WT and Li Y 2020 Knowledge, attitudes, and practices towards COVID-19 among Chinese residents during the rapid rise period of the COVID-19 outbreak: a quick online cross-sectional survey *Int. J. Biol. Sci*. **16** 1745.
[9] Oraby T, Tyshenko MG, Balkhy HH, Tasnif Y, Quiroz-Gaspar A, Mohamed Z and Arabi YM 2020 Analysis of the Healthcare MERS-CoV Outbreak in King Abdulaziz Medical Center, Riyadh, Saudi Arabia, June–August 2015 Using a SEIR Ward Transmission Model *Int. J. Environ. Res. Public Health* **17** 2936.
[10] Lai CC, Shih TP, Ko WC, Tang HJ and Hsueh PR 2020 Severe acute respiratory syndrome coronavirus 2 (SARS-CoV-2) and corona virus disease-2019 (COVID-19): the epidemic and the challenges *Int. J. Antimicrob. Agents* **55** 105924.
[11] Reis J and Mizusawa H 2019 Environmental challenges for the nervous system and the brain in Japan *Revue Neurologique* **175** 693.
[12] Cao Y, Li L, Feng Z, Wan S, Huang P, Sun X and Wang W 2020. Comparative genetic analysis of the novel coronavirus (2019-nCoV/SARS-CoV-2) receptor ACE2 in different populations *Cell Discov*. **6** 1.
[13] World Health Organization 2020 *Coronavirus disease 2019 (COVID-19)*: situation report, 97.
[14] Liu W and Li H 2020 COVID-19: attacks the 1-beta chain of hemoglobin and captures the porphyrin to inhibit human heme metabolism. *ChemRxiv*. **10**.
[15] Naja F and Hamadeh R 2020 Nutrition amid the COVID-19 pandemic: a multi-level framework for action *Europ. J. Clin. Nutr*. **74** 1117.
[16] Kakodkar P, Kaka N and Baig MN 2020 A comprehensive literature review on the clinical presentation, and management of the pandemic coronavirus disease 2019 (COVID-19) *Cureus* **12** e7560.
[17] Rahmati-Ahmadabad S and Hosseini F 2020 Exercise against SARS-CoV-2 (COVID-19): Does workout intensity matter?(A mini review of some indirect evidence related to obesity) *Obes. Med*. **19** 100245.

[18] Li W, Yang Y, Liu ZH, Zhao Y J, Zhang Q, Zhang L and Xiang YT 2020 Progression of mental health services during the COVID-19 outbreak in China. *Int. J. Biol. Sci*.**16** 1732.
[19] Harapan H, Itoh N, Yufika A, Winardi W, Keam S, Te H and Mudatsir M 2020 Coronavirus disease 2019 (COVID-19) A literature review *J. Infect. Public Health* **13** 667.
[20] Tu YF, Chien CS, Yarmishyn AA, Lin YY, Luo YH, Lin YT and Wang ML 2020 A review of SARS-CoV-2 and the ongoing clinical trials *Int. J. Molec. Sci.* **21** 2657.
[21] Wec AZ, Wrapp D, Herbert AS, Maurer DP, Haslwanter D, Sakharkar M and Longping VT 2020 Broad neutralization of SARS-related viruses by human monoclonal antibodies *Science* **369** 731.
[22] Ye ZW, Yuan S, Yuen KS, Fung SY, Chan CP and Jin DY 2020 Zoonotic origins of human coronaviruses *Int. J. Biol. Sci.* **16** 1686..
[23] Bai Z, Gong Y, Tian X, Cao Y, Liu W and Li J 2020 The Rapid Assessment and Early Warning Models for COVID-19 *Virol. Sin.* **35** 272.
[24] De Jonge S, Boldingh Q, Solomkin J, Dellinger P, Egger M, Salanti G and Boermeester M 2019 Conference on Prevention & Infection Control (ICPIC 2019) *Antimicrob. Resist. Infect. Control* **8** 148.
[25] World Health Organization 2020 *Coronavirus disease 2019 (COVID-19):* situation report, 101.
[26] Hoang VT, Dao TL and Gautret P 2020 Recurrence of positive SARS-CoV-2 in patients recovered from COVID-19 *J. Med. Virol*. **92** 2366.
[27] Chen D, Xu W, Lei Z, Huang Z, Liu J, Gao Z and Peng L 2020 Recurrence of positive SARS-CoV-2 RNA in COVID-19: A case report *Int. J. Infect. Dis*. **93** 297.

Journal of Physics: Conference Series

PAPER • **OPEN ACCESS**

Detection of *Listeria monocytogenes* in frozen food using a specific *inlB* virulence gene

Detection of *Listeria monocytogenes* in frozen food using a specific *inlB* virulence gene

Aula M. Al-Ghanim[1] and Basil A. Abbas[1*]

[1]Department of Microbiology, College of Veterinary Medicine, University of Basrah, Iraq.

*E-mail: basilabbas63@yahoo.com

Abstract. This study was undertaken to detect the presence of *Listeria monocytogenes* in frozen food. A total of 200 different food samples were collected from Basrah markets, southern Iraq, during September 2015 to March 2016. These samples included frozen fish, frozen burger, frozen chicken and worker's hands swabs, 50 each. The polymerase chain reaction technique was used to evaluate the presence of *Listeria monocytogenes* by using of *inlB* specific gene. The PCR results revealed that only four samples (7.27%) were contaminated by *Listeria monocytogenes*. In conclusion frozen food may carry a dangerous type of bacteria and lead to human illness.

Keywords. *Listeria monocytogenes*, meat, burger, chicken, *inlB*, Basrah.

1. Introduction

Contamination of raw meat is one of the main sources of food-borne diseases [1, 2]. The presence of microbes in meat products cannot be detected visually [3]. This increases the risks of food borne microbes and the incidence of human illnesses [4]. Food associated bacteria are on two types; pathogenic bacteria which cause a disease and spoilage bacteria which may cause loss of quality of food and developing a bad smell or texture. Pathogenic bacteria that cause food-borne disease and cannot be detected during food consumption such as *Salmonella*, *Escherichia coli* O157:H7, *Campylobacter jejuni*, *Listeria monocytogenes*, *Staphylococcus aureus*, etc.[5]. *Listeria* causes a food-borne disease called Listeriosis that has become a major problem for the public health in developed countries in addition to food industry [6, 7]. The disease also affects humans, and rised during the 1980s. There was rising in the numbers of human cases in several countries together with evidence for food-borne transmission of this disease [8]. The uterus of pregnant and the central nervous system or the blood stream are mostly affected by listeriosis. In non-pregnant women or in the immunocompromised or elderly people, listeriosis usually presents as meningitis or septicemia [9]. At the studied area less attention has been made for studying listeriosis or isolation of *Listeria* from imported meat and meat products. Milk was extensively studied previously including isolation of *Listeria* [10] and other types of bacteria [11, 12, 13, 14, 15, 16]. The aim of this study was to evaluate the microbial quality of imported frozen meat regarding Listerial contamination, which cause severe health problems.

2. Materials and Methods

2.1. Samples collection

Imported frozen food samples were collected from different local markets and workers in Basrah city for bacterial investigation of *Listeria monocytogenes*. A total of 200 samples were collected during the period from September 2015 to March 2016,including 50 samples of each frozen burger, frozen chicken, frozen fish and swabs from worker's hands.Twenty-five grams of the samples were collected in a sterile containers and immediately transported inside ice box to the laboratory for bacteriological analysis.

2.2. Culturing the samples

Cold enrichment procedure was applied by adding 10gm of each sample to 90 ml of TSB broth (Himedia, India) which was kept at 4ºC for 4 weeks [17]. The samples were streaked on TSB agar containing nalidixic acid (40µg/ml) and lithium chloride 0.5gm /L and incubated for 48 h at 37°C [18].

2.3. Detection of Listeria monocytogenes

Fifty-five samples showing bacterial growth including 15 frozen fish,15 frozen burgers,15 frozen chicken and 10 swaps of worker's hand were selected. These samples were subjected to detection of *Listeria monocytogenes* by detecting the presence of the *inlB* specific gene by PCR technique.

2.4. Extraction of bacterial DNA

This procedure was done by using commercially available DNA extraction and purification kits (Geneaid, Korea). Five hundred microlitres of the culture, containing approximately 1 x 109 cells, were transferred to a 1.5 ml microcentrifuge tube. The tubes were centrifuged for 1 minute at 14,000-16,000 xg to pellet the cells and the supernatant was then carefully discarded by pipetting or pouring . One hundred and eighty microlitres of GT buffer were added to the tubes, and mixed by pipetting, and then followed by adding 20 µl of proteinase K. The samples were then incubated at 60°C for at least 10 minutes. During incubation, tubes were inverted every 3 minutes.

2.5. Primers

Oligonucleotide primers of inlB gene with a length of 343bp were used in this study [19]. Sequences of primers were;

F: CTGGAAAGTTTGTATTTGGGAAA

R:TTTCATAATCGCCATCATCACT

The electrophoresis of amplified product was carried out in 1.5% agarose gel (Promega, USA) using7µl DNA ladder as molecular weight marker and 7µl of PCR reactions at 70V for 30 min,and then at 80V for 20 min. The gel was visualized by UV transilluminator (Verlber Louemal, EEC), and then photographed

3. Results

3.1. Enrichment procedure

Out of 200 samples only 55 samples showed bacterial growth after cold enrichment. These samples were 15 from frozen fish,15 from frozen burgers, 15from frozen chicken and 10 from worker's hand (Table 1).

Table 1. Number and percentage of positive bacterial culture isolated from frozen food and worker's hand.

Sample source	No. of samples	No. of culture positive samples	% culture Positive
Frozen fish	50	15	30
Frozen burger	50	15	30
Frozen chicken	50	15	30
Worker's hand	50	10	20
Total	200	55	27.5

3.2. PCR results for inlB gene in Listeria monocytogens

PCR amplification of 343bp of inlB gene was applied on the extracted DNA from all the culture positive samples (Figure 1). According to PCR results out of 55 examined samples, the positive PCR results were observed in 4 samples only at the rate of 7.27% (Table 2).

Table 2. Molecular identification of *Listeria monocytogenesin* studied samples according to PCR assay using *inlB* gene.

Sample	No. of culture positive samples	No. of *inlB* positive samples	% PCR Positive
Frozen fish	15	2	13.3
Frozen burger	15	1	6.6
Frozen chicken	15	1	6.6
Worker's hand	10	0	0
Total	55	4	7.27

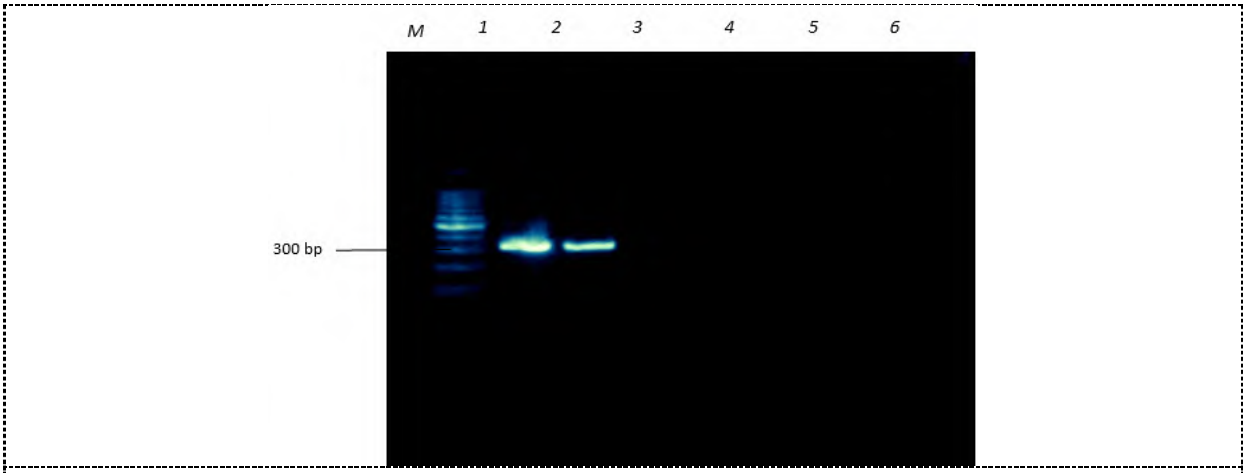

Figure 1. PCR amplification of *Listeria monocytogenes inlB* gene (343 bp) on 1.5% agarose gel and stained with ethidium bromide. Lane: M, Marker; Lane 1 and 2 *Listeria monocytogenes inlB* gene positive; Lane 3-6 negative results.

4. Discussion

Listeria monocytogenes considered as a cause of listeriosis disease in humans and animals [20,21]. Many deal with *Listeria* spp show that these bacteria can be found in a different food sources such as dairy products [22], meat and poultry [23], and in vegetables [24]. Different listeriosis outbreaks were found to be associated with milk consumption. This case is causing high concern in the industry of dairy due to the number of cases and increasing in the rate of mortality in these outbreaks to 30% [25]. Special groups of risk also observe in listeriosis outbreaks which include pregnant women, new born, immunecompromized patients and the old persons [26]. Polymerase chain reaction technique is a highly sensitive and more accurate than culture-based methods for detecting the pathogenmicroorganismsin the contaminated food. Many samples gave a positive result in their tests for *L. monocytogenes* by using the method of PCR while it gave a negative result by cultural methods. The attribute authors the sensitivity of PCR detection method increase over culturing methods to the truth that the former does not have selection initial step. Polymerase chain reaction detectionmethod solved the problem of some cells that cannot grow in the selective media when there is a small number present only. The false–negatives of some reported for the cultural detection methods are sometime these methods depended on using color changes for differentiate between species. These methods are influenced by the observer ability [27,28]. The target gene of *L. monocytogenes* is the primer pair,inlB-F and inlB -R of the inlBgene which detected by PCR [19;29; 30; 31] will amplify and produce a double-stranded fragment of 343bp. At this study, the rate of isolation *Listeria monocytogenes* was 4/55 isolates (7.27%) by inlB gene. this result is in agreement with [32] who found (6.2%) of *Listeria monocytogenes* by inlB gene.

5. Conclusion

From the above results, it can be concluded that the imported frozen food are not safe from a pathogenic bacteria such as *Listeria monocytogenes*. Culture method without more investigation is not sufficient for bacteria identification and PCR techniques is a rapid sensitive method for this purpose.

6. References

[1] Acuff GC 2005 *Chemical decontamination strategies for meat* Wood head Publishing Ltd and CRC Press LLC, Wood head Publishing Ltd. 780.
[2] Podpecan B, Pengov A and Vadnjal S 2007 The source of contamination of ground meat for production of meat products with bacteria *Staphylococccus aureus Slov. Vet. Res*. **44** 24.
[3] Movassagh MH, Shakoori M and Zolfaghari J 2010 The prevalence of Salmonella spp. In Bovine carcass at Tabriz slaughterhouse, Iran *Glob. Vet.* **5** 146.
[4] Ateba C and Mochaiwa B 2014 Use of *invA* gene specific PCR analysis for the detection of virulent Salmonella species in beef products in the north west province, South Africa *J. Food Nutr. Res.* **6** 294.
[5] International Commission on Microbiological Specifications for Foods 1996 *Microorganisms in foods* 5. Characteristics of microbial pathogens. ICMSF, International Union of Biological Societies. Blackie Academic & Professional London, England 513.
[6] Farber JM, Ross WH and Harwig J1996 Health risk assessment of *Listeria monocytogenes* in Canad. *Int. J. Food Microbiol*. **30** 145.
[7] Shank FR, Elliot EL, Wachsmuth IK and Losikoff ME 1996 US position on *Listeria monocytogenes* in foods *Food Control* **7** 229.
[8] McLauchlin J 1993 Listeriosis and *Listeria monocytogenes* Environ. Policy Pract, **3** 201.
[9] Hoffman AD and Weidmann M 2001 Comparative evaluation of culture and BAX polymerase chain reaction-based detection methods for *Listeria* spp. and *Listeria monocytogenes* in environmental and raw fish samples *J. Food Prot*. **64** 1521.

[10] Abbas BA and Jaber GM 2012 Occurrence of Listeria monocytogenes in raw milk of ruminants in Basrah province *Iraqi J. Vet. Sci.* **26** 47.
[11] Abbas BA,A. B. Aldeewan, 2009.Occurrence and epidemiology of Brucella Spp. in raw milk samples at Basrah Province, Iraq. Bulgarian Journal of Veterinary Medicine, 12(2) : 136−142.
[12] Abbas BA and Talei AB 2010 Isolation, Identification and Biotyping of *Brucella* spp. from Milk Product at Basrah Province *Bas. J. Vet. Res.* **9** 152.
[13] Khudor MH and Abbas BA and Saeed BMS 2012 Molecular Detection Of Enterotoxin (CytK) Gene And Antimicrobial Susceptibility of Bacillus cereus Isolates From Milk And Milk Products *Bas. J. Vet. Res*. **11** 164.
[14] Abbas BA 2013 Detection of Virulence and Adherence gene In Escherichia Coli O157:H7 isolated from animal products *Bas. J. Vet. Res*. **12** 59.
[15] Abbas BA, Ghadban MK and Alghanim AM 2017 Microbial Evaluation of Milk and Milk Products during a Past Two Decades, in Basrah Southern Iraq: A Review *Ann. Res. Rev. Biol.* **14** 1.
[16] Abbas BA, Khudaier BY and Khudaier AM 2017 Studies on mecA gene in methicillin resistant Staphylococcus aureus isolates *Jokull* **67** 58.
[17] Doyle MP and Schouel JL 1987 Comparison of procedure for isolating *Listeria monocytogenes* in soft surface ripened cheese *J. Food Prot*. **48** 4.
[18] Lovett J, Fracis DW and Hunt JM 1987 *Listeria monocytogenes* in raw milk: detection, Incidence and pathogenicity *J. Food Prot*. **50** 188.
[19] Pangallo D, Kaclkov E, Kuchta T and Drahovsk H 2001 Detection of *Listeria monocytogenes* by polymerase chain reaction oriented to *inlB* gene *New Microbiol*. **24** 333.
[20] Bille J 1990 *Epidemiology of human listeriosis in Europe, with special reference to the Swiss outbreak* In: Miller AJ, Smith JL and Somkuti GA (Eds.) Foodborne Listeriosis. Elsevier, New York 71.
[21] Broome CV, Gellin B and Schwartz B 1990 *Epidemiology of listeriosis in the United States* In Miller AJ, Smith JL and Somkuti GA (ed.), Foodborne listeriosis. Society for Industrial Microbiology. Elsevier Science Publishing, Inc., New York. p. 61-65.
[22] Marth, E. H and Ryser ET 1990 *Occurrence of Listeria in foods: milk and dairy foods* In: Miller AL, Smith JL, Somkuti GA, editors. Foodborne listeriosis. Elsevier Science Publishers B. V. (Biomedical Division); Amsterdam 151.
[23] Carosella JM 1990 *Occurrence of Listeria monocytogenes in meat and poultry*. In: Miller AL, Smith JL and Somkuti GA, editors. Foodborne listeriosis. Elsevier Science Publishers B. V. (Biomedical Division); Amsterdam 165.
[24] Beuchat LR, Berang ME and Brackett RE 1990 *Presence and public health implications of Listeria monocytogenes on vegeta*ble. In: Miller AL, Smith JL and Somkuti GA, editors. Foodborne listeriosis. Elsevier Science Publishers B. V. (Biomedical Division). Amsterdam 175.
[25] Griffiths MW 1989 *Listeria monocytogenes* its importance in the dairy industry *J. Sci. Food Agric.* **47** 133.
[26] Schuchat A, Swaminathan B and Broome CV 1991 Epidemiology of human listeriosis *J. Clinic. Microbiol*. **4** 169.
[27] Aznar R and Alarco´n B 2002 On the specificity of PCR detection of *Listeria monocytogenes* in food: a comparison of published primers. *Syst. Appl. Microbiol*. **25** 109.
[28] Shearer AE.H, Strapp CM and Joerger RD 2001 Evaluation of a polymerase chain reaction-based system for detection of *Salmonella enteritidis*, *Escherichia coli* O157:H7, *Listeria* spp. and *Listeria monocytogenes* on fresh fruits and vegetables *J. Food Prot*. **64** 788.
[29] Ingianni A, Floris M, Palomba P, Madeddu MA, Quartuccio M and Pompei R 2001 Rapid detection of *Listeria monocytogenes* in foods, by a combination of PCR and DNA probe *Mol. Cell. Probes*.**15** 275.

[30] Jung YS, Frank JF, Brackett RE and Chen J 2003 Polymerase chain reaction detection of Listeria monocytogenes in frankfurters using oligonucleotide primers targeting the genes encoding internalin AB *J. Food Prot*. **66** 237.
[31] Lunge VR, Miller BJ, Livak KJ and CBatt CA 2002 Factors affecting the performance of 5' nuclease PCR assays for Listeria monocytogenes detection *J. Micriobiol. Methods* **51** 361.
[32] Zhao HK, Wang WJ, Zhao P, Zhang HB, Kong N, Zhou MD and Zhang H 2014 Simultaneous Detection of *Salmonella*, *Listeria monocytogenes* and *Shigella* in Poultry Samples by Triplex PCR *J. Bacteriol. Mycol*. **1** 5.

Role of toll like receptor-9 (*1237 T/C*) gene polymorphism in patients with type 2 diabetes and diabetic foot ulcer

Role of toll like receptor -9 *(1237 T/C)* gene polymorphism in patients with type 2 diabetes and diabetic foot ulcer

Furqan Naeem Al-Karawi[1], Abeer Thaher Naji Al-Hasnawi[1*] and Thekra Abd Jebur Al-Kashwan[2]

[1]Medical Microbiology Department, College of Medicine, Kerbala University, Kerbala, Iraq.
Medical Microbiology Department, College of Medicine, Kufa University, Najaf, Iraq.

*E-mail: abeer.zahir@uokerbala.edu.iq

Abstract. This study aimed to evaluate whether *(1237 T/C)* polymorphism is related with diabetic foot ulcer in type-2 diabetes mellitus of Iraqi patients in Najaf city. Diabetic foot ulcer (DFU) is one of the most prevalent and serious diabetic complications. DFU accounts for about 15% of the diabetic population. It is commonly associated with the increased diabetic morbidities and mortalities. The type 2 diabetes is recognized by aberrations of glucose, lipid and protein metabolism. It is increasingly appreciated that wound healing defect seen in diabetic patients is attributed to the altered protein and lipid metabolism. This study involved (180) subjects, between them, 60 were patients as group one suffering from type 2 diabetes and 60 were patient suffering from type 2 diabetes and foot ulcer as group two. In addition, 60 healthy group three as control subjects. Polymerase chain analysis was used for detection of *TLR-9* genotypes followed by restriction analysis. We observed no significance differences in the distribution of the genotypes and alleles of *(1237 T/C)* polymorphism among the study groups.

Keywords. Type-2 diabetes mellitus, Diabetic foot ulcer, Toll Like Receptor-9 gene polymorphism, RFLP-PCR.

1. Introduction

Type 2 diabetes is considered the most prevalent metabolic aberration, and its consequences constituted the leading cause of morbidity and mortality. It comprises the majority of diabetic cases (85%) [1]. The macro- and micro-vascular complications, such as diabetic retinopathy, nephropathy and neuropathy are strongly associated with metabolic aberrations. The risk of hypertension, atherosclerosis and coronary artery diseases are also increasing. The underlying mechanisms, explaining the metabolic aberrations and its consequences are not fully clear [2]. It is increasingly demonstrated that most subjects diagnosed as overt type-2 diabetics showed relative diminution in insulin secretion and dysfunction of the β-cells of the pancreas. It probably preceded by compensative hyper-secretion of β-cells and peripheral resistance of insulin. Nevertheless, it is increasingly considered that the peripheral resistance and insulin hyper-secretion are just initiating events, whilst β-

cells dysfunction and insulin defects are considered the critical main event for development of overt type-2 diabetes [3]. Moreover, type-2 diabetes is multi-factorial. Environmental factors combined with the genetic component to explain the dramatic increase in the prevalence of type 2 diabetes. TLR4 and TLR9 genes as a molecular risk factors forT2DM and its complications such as foot ulcer in the discrete diabetic population [4]. Wound healing refers to the natural dynamic process which is responsible for removal and replacement of the devitalized skin structures in response to tissue injury to restore the normal skin integrity. It is characterized by a stepwise pattern of 4 consecutive phases. The first and second phase are inflammation and hemostasis. The ultimate goal of this phase is limitation of the tissue damage and conditioning of the field for reconstruction. The third phase comprises activation and proliferation of fibroblasts to form granulation tissue. The final step concerned about maturation of the granulation tissue to restore the tensile surface of the skin. Importantly, wound healing requires harmony between multiple factors to obtain its maximal benefits. Nevertheless, certain pathological, nutritional and metabolic aberrations may interfere with the process of wound healing [5]. Diabetes is one of the most common metabolic aberrations that interfere with wound healing. It has been reported that diabetic subjects show prolonged inflammatory and proliferative phases of wound healing. In addition, diabetic foot ulcer (DFU) occurs in 15% of the diabetic population, and responsible for 85% of the associated lower extremity amputations [6]. In both innate and adaptive immunity, the toll like receptor (TLR) have essential role. The different infectious diseases are related with genetic diversity in the toll like receptor genes. Different autoimmune disease is associated with toll like receptor 9, because it is contributes in the maturation of dendritic cells and proinflammatory cytokines production [7]. In European Americans, the high risk of asthma disease is associated with the genetic variation at position -1237 [8]. Further studies needed to confirmed the relationship between the very low frequency of these toll like receptor variants and the lower incidence of different diseases like diabetes.

2. Materials and Methods

2.1. Subjects

This study included 180 Iraqi subjects. Group 1 including 60 patients with T2DM and DF, their age mean, disease duration, and body mass index were 56.9±9.2year, 10.7 ±4.8year,and 27.1± 3.8kg/m2, respectively. Group 2 including 60 patients with T2DM and without DFU, their mean of age, duration of disease and body max index were 47.9± year 8.6, 2.9±year 3.0, 30.1± 4.1kg/m2, respectively. Group3 including 60 the healthy control their age mean and BMI were 45.0±8.9, 45.0±8.9 respectively. Also, the gender and smoking history were performed for three groups. The patients were recruited to Al-Sader hospital in Najaf city and the study protocol was approved by Kufa University ethical committee. The medical history, clinical examination, and assessment of BMI are taken from all participants. The parameters like fasting and glycated hemoglobin, Urea and creatinine , total cholesterol, and triglycerides data as shown in (Table1). Polymerase Chain Reaction-Restriction Fragment Length Polymorphism analysis was used for detection the genotypes of *TLR-9(1237 T/C)* polymorphism.

2.2. Genotyping of TLR-9 (1237 T/C)

From peripheral blood leukocytes, the genomic DNA extracted by using Flexi Gene DNA kit (Qiagen), Restriction fragment length polymorphism technique used for detection the genotypes of *TLR-9* polymorphism. The total volume of PCR reactions consist of 25mL includes 2 µl of DNA, 12.5X of Master Mix, 0.3 µl of each forward and reverse primers for detection of *TLR-9(1237 T/C)* polymorphism. The set of primer used was included the forward primer: 5'ATGGGAGCAGACATAATGGA-3' and reverse primer: 5'CTGCTTGCAGTTGACTGTGT-3' [4].

3% agarose gel electrophoresis was performed and run at 60 volt for 3hrs for visualized the PCR products under UV light by using ethidium bromide dye.

2.3. The cycling conditions

The conditions includes 5 minutes of initial denaturation at 95°C followed by 40 second of 35 cycles of denaturation at 95°C, in addition to 40 seconds of annealing at 62°C and 1 minute of extension at 72°C with a final extension step at 72°C for 10 minutes. The created is about 135 bp fragments. The PCR product was then restricted with BstNI enzyme. The T allele represent the wild type consist of 108 and 27 bp fragments while the C allele represent the mutant type and composed of 60, 48 and 27 bp fragments.

2.4. Statistical Analysis:

ANOVA test, and student t test was used to test the level of significance (p-value) for all parameters between the study groups. Chi-square test, Odds ratios (ORs) and 95% confidence intervals was used also to determine the significant level of the categorical variables. The Statistical Package of Social Science software (Version 22, SPSS Inc., Chicago, IL, USA) was used to performed for all data statistical analysis [9].

3. Results and Discussion

There were no significant differences between study groups regarding gender, as shown in Figure 1. About smoking patients, there was highly associated between diabetic foot ulcer group (P<0.001) comparing with diabetic patients and control, as shown in Figure 2. The mean-fasting blood glucose, glycated hemoglobin, urea and creatinine were highly significant in group I, as in Table 1. There was a non-significant association in the allocation of the polymorphic *TLR-9* genotypes or allele frequency between different study groups, as shown in Table 2. The *TLR-9* gene polymorphism was done by using the *BstNI* restriction enzyme. The (TT) homozygous allele, (CT) heterozygous and (CC) homozygous mutant alleles were result from digestion by restriction enzyme, as shown in Figure 3.

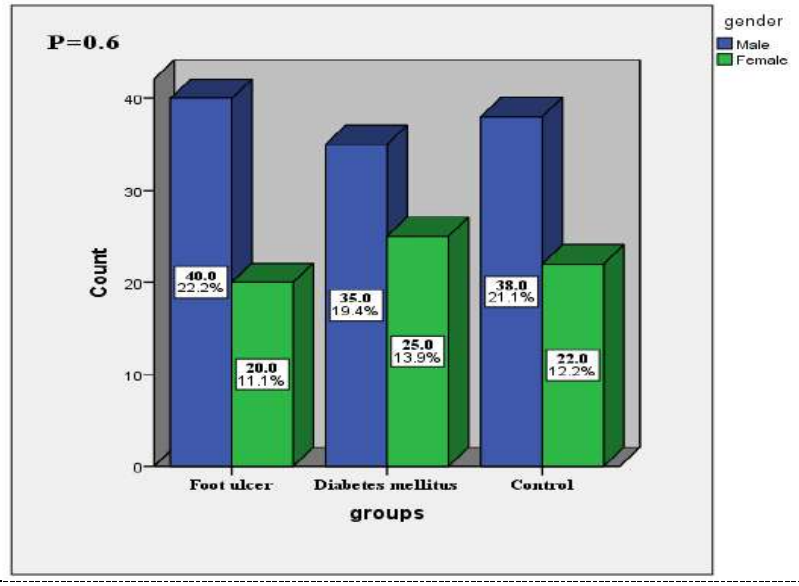

Figure 1. Distribution of study groups according to gender.

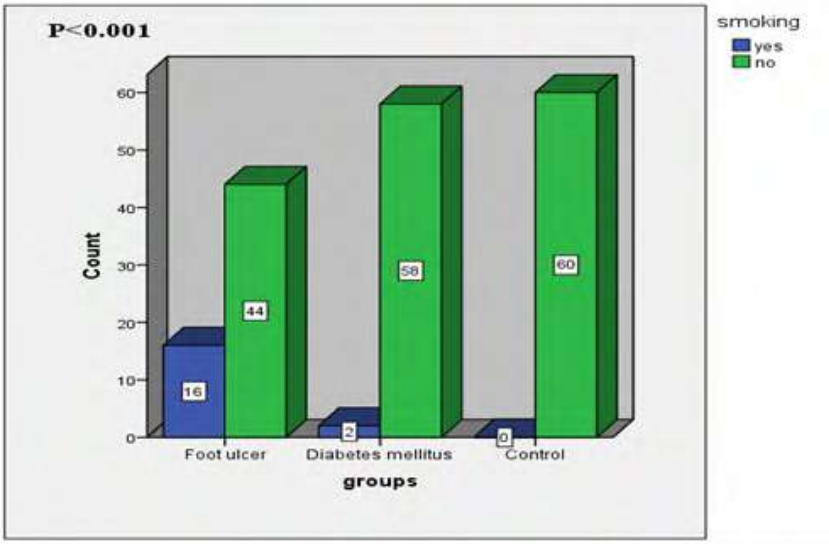

Figure 2. Distribution of study groups according to smoking history.

Table 1. Mean differences of age, duration, clinical and biochemical parameters according to study groups.

Parameter (mean ±SD)	Group 1	Group 2	Group 3	*P-value*
Age (years)	56.9±9.2#	47.9±8.6	45.0±8.9	<0.001*
Duration (years)	10.7 ±4.8	2.9± 3.0	_	<0.001*
Body Mass Index (kg/cm2)	27.1± 3.8	30.1± 4.1#	27.8±3.3	<0.001*
Fasting Blood Sugar (mg/dl)	223.6 ± 83.1#	212.2± 69.7#	101.9± 17.5	<0.001*
HbA1c (%)	9.0 ± 2.8#	8.0 ± 1.9	5.3± 0.5	<0.001*
Total cholesterol(mg/dl)	210.7±65.1	214.5±51.6	201.9±58.1	0.48
HDL(mg/dl)	42.8±12.1	42.8±9.3	40.1±10.9	0.30
LDL(mg/dl)	123.2±50.2	135.5±36.5	125.3±44.3	0.44
Triglycerides(mg/dl)	170.7±96.7	181.9±87.0	157.8±80.6	0.33
Blood urea(mg/dl)	42.7±21.7#	32.2±11.0	29.1±7.1	<0.001*
Serum creatinine (mg/dl)	6.5±2.8#	4.5±3.2	0.6±0.15	<0.001*

*P value is of statistical significant, # significant group by post hoc tests for one- way ANOVA, Group1=diabetic patient with foot ulcer, Group2=diabetic patient without foot ulcer, Group 3= healthy control, Hb= hemoglobin, SD= standard deviation, HDL= high density lipoprotein, LDL= low density lipoprotein.

Table 2. *TLR-9* gene polymorphism and their allele frequencies in the studied groups.

***TLR-9* gene polymorphism results**	Group1(G1) N= 59 N%	Group2(G2) N= 60 N%	Group3(G3) N= 59 N%	All groups P	G1 with G2 P OR(95%CI)	G1 with G3 P OR(95%CI)	G2 with G3 P OR(95%CI)
***TLR-9* genotypes**							
TT	45 (76.3)	38 (63.3)	45 (76.3)				
TC	13 (22.0)	21 (35.0)	14 (23.7)	0.4	0.1	1.0	0.1
CC	1 (1.7)	1 (1.7)	0 (0.0)		1.9 (0.8-4.1)	1.0 (0.4-2.3)	0.5 (0.2-1.2)
***TLR-9* allele**							
C allele	15 (12.7)	23 (19.2)	14 (11.9)	0.2	0.2	0.8	0.1
T allele	103 (87.3)	97 (80.8)	104 (88.1)		1.6 (0.8-3.3)	0.9 (0.4-2.0)	0.6 (0.3-1.2)

Group1= diabetic patients with foot ulcer, Group2= diabetic patients without foot ulcer, Group 3= healthy control, CI= confidence interval, OR= odd ratio, TLR= toll-like receptor.

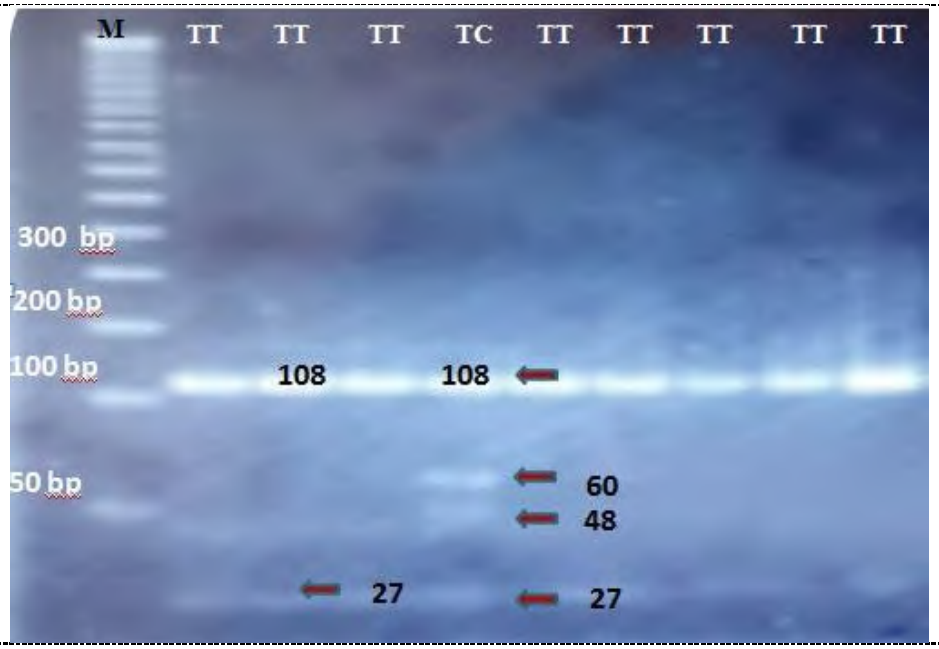

Figure 3. Gel electrophoresis of RFLP- PCR product of *TLR-9* (1237 T/C) gene polymorphism digested with *BstNI* restriction enzyme were separated by using 3% agarose gel at 60 volt for 3hrs. Homozygous TT genotype and Heterozygous TC genotype results. M: DNA molecular marker 50bp size by ethidium bromide stained bands in the gel.

4. Discussion

The Current study showed a considerable difference (P<0.001) of age on the development of DFU. A similar observation was reported in the studies of [10, 11, 12], whose found that the prevalence of DFU increases with rising age. This is reasonable because the old age patients have higher risk for development of DFU. According the gender, our study revealed to a non statistical association (P=0.6). This result was related with study by [13, 14], whose found a non statistical association in pervasiveness of DFU in patients gender. In contrast to [9, 15], show that male sex has been recognized as a riskiness factor to the development of diabetic foot ulcer. This may be due to a small female population in the study. Additionally, this study refers to enormous difference about smoking on the prevalence of DFU and these results was compatible with the results of [16, 17] whose proved a connection of cigarette smoking with the development of DFU. In the present study, the finding that the mean duration of diabetes in patients with DFU was highly significant (P < 0.001) compared with non-DFU patients. The present study in agreement with a study conducted by [18, 19, 20, 21] whose found that the long duration of diabetes was the main factor causing DFUs. About BMI (P<0.001) and these results were in agreement with a number of studies conducted by [22, 23], significant difference between BMI and development of DFU in T2DM. Previous studies have also shown that HbA1c was a contributory factor for DFU [13, 24]. But the current study differ from other studies conducted by [15, 25], whose demonstrated that poor glycemic control is an independent risk factor for the development of ulcers. This may be due to the method of assessing ,sample collection and patients number . There was no significant association between DFU group and metabolic factors that includes, cholesterol, triglyceride, HDL and LDL, this consequence was correlated with a study accomplished by (25). In regard to serum urea and creatinine there was high significant differences in DFU (P<0.001) compared with other studied groups. The result of this study agrees with other studies conducted by [15, 26], whose demonstrated that the possibility of kidney dysfunction associated with the diabetic foot disease. According to the several studies, the development and complications of type 2 diabetes are associated with different types of toll like receptors [27, 28]. Genetically susceptibility

to diabetic complication such as a foot ulcer involving several factors that are associated with the stimulation of immune response. *TLR-9* is a necessary endosomal member of the TLRs family [4] reported that *TLR-9* was associated with severity of diabetic injury. Unfortunately, in Iraq there are no studies involved the effect of TLR9-1237T/C polymorphism on development of DFU and T2DM. Our study demonstrated a non correlation among all groups of *TLR-9 (1237T/C)* genotype frequencies (P= 0.5). Also, allele frequencies showed non significant difference among all groups for *TLR-9 (1237T/C)* gene polymorphism (P= 0.5) and these results were close to the results of [8], who found that the recurrence of *TLRs- 2, 4* and 9 gene polymorphism don't detected in T2DM as well as coronary artery disease (CAD), otherwise, it is still not full clarified correlation of the very relatively low-frequencies of these variants of TLRs with the incidence of T2DM and CAD in the or population. Furthermore, the present study results were disagreement with the studies conducted by [4, 29], whose reported that the (TC and CC) polymorphic genotypes frequencies have high significant among DFU and T2DM groups compared with healthy individuals. Ethnic diversity may be linked with the variation of above results.

5. Conclusion

Current study have shown that the TLR-9 gene polymorphism may not have a role in diabetic foot ulcer disease. There is no significant association between this polymorphism gene and development of diabetic foot ulcer disease in T2DM.

6. References

[1] Forouhi NG and Wareham NJ 2014 Epidemiology of diabetes *Medicine (Abingdon)* **42** 698.
[2] Kaul K, Tarr JM, Ahmad SI, Kohner EM, Chibber R 2012 Introdction To Diabetes Mellitus Kirti *Adv. Exper. Med. Biol.* **771** 1.
[3] Steyn NP, Lambert EV and Tabana H 2009 Conference on & quot; Multidisciplinary approaches to nutritional problems & quot;. Symposium on & quot; Diabetes and health & quot; Nutrition interventions for the prevention of type 2 diabetes *Proc. Nutr. Soc*. **68** 55.
[4] Wifi MNA, Assem M, Elsherif RH, El-Azab HAF and Saif A 2017 Toll-like receptors-2 and-9 (TLR2 and TLR9) gene polymorphism in patients with type 2 diabetes and diabetic foot *Medicine* **96** 17.
[5] Pendsey SP 2010 Understanding diabetic foot *Diabetis Dev. Ctries*. **30** 75.
[6] Hunt DL 2010 Diabetes : foot ulcers and amputations Search *Clin. Evid.* **2010** 1.
[7] Hur JW, Shin HD, Park BL, Kim LH, Kim SY and Bae SC 2005 Association study of Toll-Like receptor 9 gene polymorphism in Korean patients with systemic lupus erythematous *Tissue Antigens* **65** 266.
[8] Liu F, Lu W, Qian Q, Qi W, Hu J and Feng B 2012 Frequency of TLR 2, 4, and 9 gene polymorphisms in Chinese population and their susceptibility to type 2 diabetes and coronary artery disease *BioMed. Res. Int.* **2012**.
[9] Daniel W W 2009 *BIOSTATISTICS: A Foundation for Analysis in the Health Sciences* Ninth Edition. ISBN 978-0-470-10582-5.
[10] Manda V, Sreedharan J, Muttappallymyalil J, Das R and Hisamatsu E 2012 Foot ulcers and risk factors among diabetic patients visiting Surgery Department in a University Teaching Hospital in Ajman, UAE *Int. J. Med. Publ. Health* **2** 3
[11] Al-Rubeaan K, Al Derwish M, Ouizi S, Youssef AM, Subhani SN, Ibrahim HM and Alamri BN 2015 Diabetic foot complications and their risk factors from a large retrospective cohort study *PloS one* **10** e0124446.
[12] Navarro-Peternella FM, Lopes APAT, de Arruda GO, Teston EF and Marcon SS 2016 Differences between genders in relation to factors associated with risk of diabetic foot in elderly persons: A cross-sectional trial *J Clin. Transl. Endocrinol.* **6** 30.

[13] Shahbazian H, Yazdanpanah L and Latifi SM 2013 Risk assessment of patients with diabetes for foot ulcers according to risk classification consensus of International Working Group on Diabetic Foot (IWGDF) *Pakistan J. Med. Sci*. **29** 730.
[14] Saleem S, Hayat N, Ahmad I, Ahmed T and Rehan A 2017 Risk factors associated with poor outcome in diabetic foot ulcer patients *Turk. J. Med. Sci.* **47** 826.
[15] Alam M, Butt SJ, Hayyat K, Arshad A and Mubarak S 2017 Study of Risk Factor Cotributary in the Development of Diabetic Foot Ulceration *Pakistan J. Med. Health Sci*. **11** 1282.
[16] McDaniel JC and Browning KK 2014 Smoking, chronic wound healing, and implications for evidence-based practice *J. Wound Ostomy Contin. Nurs.* **41** 415.
[17] Syafril S 2018 Pathophysiology diabetic foot ulcer. In *IOP Confer. Series: Earth Environ. Sci.* **125** 012161
[18] Syafril S 2018 Pathophysiology diabetic foot ulcer. In *IOP Confer. Series: Earth and Environ. Sci.* **125** 012161.
[19] Brownrigg JRW, Davey J, Holt PJ, Davis WA, Thompson MM, Ray KK and Hinchliffe RJ 2012 The association of ulceration of the foot with cardiovascular and all-cause mortality in patients with diabetes: a meta-analysis *Diabetologia* **55** 2906.
[20] Shahi SK, Kumar A, Kumar S, Singh SK, Gupta SK and Singh TB 2012 Prevalence of diabetic foot ulcer and associated risk factors in diabetic patients from North India *J. Diabetic Foot Compl.* **4** 83.
[21] Bajaj S, Mahajan A, Grover S, Mahajan V, Goyal P and Gupta VK 2017 Peripheral vascular disease in patients with diabetic foot ulcers-an emerging trend: a prospective study from north India *J. Assoc. Physicians India* **65** 14.
[22] Sohn MW, Budiman-Mak E, Lee TA, Oh E and Stuck RM 2011 Significant J-shaped association between body mass index (BMI) and diabetic foot ulcers *Diabetes Metab. Res. Rev.* **27** 402.
[23] AlGoblan AS, Alrasheedi IM, Basheir OH and Haider KH 2016 Prediction of diabetic foot ulcer healing in type 2 diabetic subjects using routine clinical and laboratory parameters *Res. Rep. Endocr. Disorder* **6** 11.
[24] Christman AL, Selvin E, Margolis DJ, Lazarus GS and Garza LA 2011 Hemoglobin A1c predicts healing rate in diabetic wounds *J. Investig. Dermatol.* **131** 2121.
[25] Almobarak AO, Awadalla H, Osman M and Ahmed MH 2017 Prevalence of diabetic foot ulceration and associated risk factors: an old and still major public health problem in Khartoum, Sudan? *Ann. Transl. Med.* **5** 17.
[26] Akha O, Kashi Z and Makhlough A 2010 Correlation Between Amputation of Diabetic Foot and Nephropathy *Iranian J. Kidney Dis.* **4** 1.
[27] Xu Y, Zhou Y, Lin H, Hu H, Wang Y and Xu G 2013 Toll-like receptor 2 in promoting angiogenesis after acute ischemic injury *Int. J. Molec. Med.* **31** 555.
[28] Dasu MR and Martin SJ 2014 Toll-like receptor expression and signaling in human diabetic wounds *World J. Diabetes* **5** 219.
[29] Junjie X, Songyao J, Minmin S, Yanyan S, Baiyong S, Xiaxing D, Jiabin J, Xi Z and Hao C 2012 The association between Toll-like receptor 2 single-nucleotide polymorphisms and hepatocellular carcinoma susceptibility *BMC Cancer* **12** 57.

Biochemical study of alkaline phosphatase in *Escherichia coli*

Biochemical study of alkaline phosphatase in *Escherichia coli*

Ibtihal Idrees Kanaan[1*] and Najwa Khaleel Ibrahim[2]

[1]College of Environmental Sciences and Technology, Al-Mosul University, Iraq.
[2]Department of Biology, College of Education for Pure Sciences, Al-Mosul University, Iraq.

*E-mail: kanaan84@uomosul.edu.iq

Abstract. The present research aimed to isolate and purify Alkaline phosphatase enzyme from crude protein extract (Lysate supernatant) of *Escherichia coli*, by using different biotechnologies. To proceed, the following steps were taken: Firstly, The verification of the existence of enzyme in bacteria, the bacteria were diagnosed by using the API 20 stripe that consists of (20) items. the enzyme was isolated to ensure its availability in bacteria within the logarithmic phase and this was done through proliferating them for 18 hours in a nutrient agar. It had been detected that the enzyme was intracellular because of the occurrence of enzyme activity in the lysate supernatant without occurring it in the cell free culture supernatant. Secondly, Enzyme purification, the enzyme had been purified through three stages: precipitation of protein by ammonium sulphate, dialysis and finally, the protein extract was passed through column chromatography by using Sephadex G-100 gel, the estimated enzyme activity after this step was 22.0 in comparison with its activity before the purification processes (crude protein extract). The approximate molecular weight of alkaline phosphatase was 81.000 Dalton estimated by using gel filtration technique.

-Keywords. Alkaline phosphatase, *Escherichia coli*, Molecular weight.

1. Introduction

Escherichia coli is a bacillus bacterium negative for a gram stain, located within the family of Enterobacteriaceae, negative for oxidase, facultative anaerobic, animated by peripheral flagella, capable of fermentation for various carbohydrates with gas and acid production [1] (Colonies of bacteria are circles, small, slightly convex, pale, and on the MacConkey agar appear to be pink because of its fermentation of lactose sugar. *E. coli* bacteria widespread in nature and in the intestines of humans and animals. It has the potential to cause many opportunistic infection such as Urinary infection, Cystitis and Pyelonephritis pelvic inflammatory [2]. Alkaline phosphatase enzyme is referred to as ALP (EC 3.1.3.1), [3, 4, 5], which was approved by the International Association of Enzymes. The Alkaline phosphatase enzyme is also called Orthophosphate monoester-phosphohydrolases [6, 7], a hydrolases enzyme [8], and metalloenzyme [9], to contain its active positions on four zinc ions Zn^{+2} and ioni magnesium Mg^{+2} [10, 11,12], as many researchers pointed out that the wide-ranging peculiarity of the enzyme of the foundation material [12] led to the study of its role in the processes of: analysis of both phosphoester phosphate compounds [5], and phosphate

endings of DNA and in the transfer of phosphates to their receptors Trans phosphorylation, especially when there are high concentrations of phosphate receptors such as Tris-buffer and Ethanol amine. The Alkaline phosphatase enzyme is positioned in bacteria within the periplasmic space [13]. While it is associated with the plasma membrane in the leubes [7, 14]. This explains his role in the latter with cellular transport mechanics [5]. The synthesis of the enzyme begins during the logarithmation and under the conditions of phosphate limitation [15] in the bacterial cell cytoplasm. It is characterized by a molecular weight of (110,000-67,000) Dalton [4] and its lack of both carbohydrates and fatty acids within its composition. As well as its stability towards temperatures up to (80) °C [16], it has optimum pH at 8 [17]. The alkaline phosphatase enzyme in the mamliam is characterized as sugar and protein [18] contains between 12 [19] to 15% [20] carbohydrates from the total weight of protein. There is no evidence of the participation of carbohydrate units in stimulation [21]. The enzyme is associated with the plasma membrane in most animal cells [4, 22], which releases from the membrane to the bloodstream in the case of inflammation and when regeneration, redivision of cells [23], and in body fluids, cancer cells. Therefore it is used to track the development of malignant diseases [24]. The enzyme has a molecular weight of (130,000-170,000) Dalton [25], and plays a defensive role in its removal of phosphate from the exocellular ATP molecule, which is considered as Pro-inflammatory. It has a role during acute inflammatory response by removing endogenous dephosphorylating when it is in great need [9].

2. Materials and Methods

2.1. Bacteria used and sources of access

Escherichia coli bacteria, obtained from microbiology laboratories / Al-Salam Hospital in, Mosul, which was diagnosed using the tape (API 20) (Analytical profile Insera, Biomeriuex France).

2.2. Isolation of the alkaline phosphatase enzyme

2.2.1. Detection the logarethmetic phase of bacteria

This phase was determined by the measurement of the bacterial turbidity in the nutrient broth after every two hours of incubation in a rocking incubator of the type (Wink Hamp, England) at a temperature (37) °C in succession for 24hours, using spectrophotometer (Sartorius BL 210S, Labomed, Inc. sepec setrosc), at (600) nanometer [26].

2.2.2. Preparation bacterial suspension

Prepare the nutrient broth media in a glass sized (1000 cm3) and sterilized by autoclave under temperature (121) °C and pressure (1) atmosphere for (20) minutes. Then leave to cool to a (45-50) °C and culture with *E.coli* for (18) hours at temperature (37) °C in a vibrator incubator (180 cycles / minutes).

2.2.3. Isolation of alkaline phosphatase

Measured the bacterial growth at the wavelength (600) nm, the bacterial cells precipitated using a centrifuge Cooling ultracentrifuge (Heraeus chrest Gm bH, Cryofuge 6-4) at speed (19470xg), temperature (4) °C for 30 minutes, cell-free broth preservation at (4) °C, washed sedimentary cells (3) times using Tris - HCL buffer 8.0 mM [16] (Kumar et al., 2008). The walls of bacterial cells were destroyed using the Ultrasonic MSE, SEP. No PG 1545) by exposing it to (20,000) pulse / seconds, for (30) seconds and repeated the process (3) times with stops of (30) seconds at a temperature (4) °C. Separate the sediment from the precipitated cells using a refrigerated centrifuge, at the same

conditions mentioned above, preservation of broken cells supernatant (lysate supernatant) at a temperature (4) °C [27].

2.3. Purification of alkaline phosphatase

2.3.1. Precipitation of protein by ammonium sulphate

Ammonium sulfate has been added in its solid state to the lysate supernatant and with full saturation to (75%). Then separate the mixture with the cooled centrifuge for (30) minutes (19470Xg), and quickly after which it was obtained on the deposit and melted in the 100 mMTris HCL buffer pH 9.8 [16, 27].

2.3.2. Dialysis

It was carried out by placing the protein solution in the plastic tying cellophane bags. Then plunged into a volume container containing the 100 mM Tris HCL buffer 9.8 [16]. The screening process was conducted at a temperature of (4) °C with movement using the magnetic motor)

2.3.3. Gel Filtration Chromatography

2.3.3.1. Gel preparation

Use Sephadex-G100 gel [28, 29], which separates protein compounds with molecular weights that fall within range (150,000-4000) Dalton [30]. Swelling of the gel and then degassing gas exhalation was performed under a sieve using the Aspirator A-2S Eyela of Japanese origin [27].

2.3.3.2. Packing of the Column

Use the column with the (1.7×75) cm dimenostraion to separate the enzyme that was filled with gel quickly on the walls of the column [27].

2.3.3.3. Add standard materials

Recovery volumes were estimated for five standard proteins known as molecular weight (blue dextran, cow serum albums, egg albums, a pepsin enzyme, insulin).

2.3.3.4. Add the sample

(2.5) cm^3 of protein solution resulting from dialysis and standard materials were injected circularly on the walls of the column. By the addition of (2,5) cm^3 of distilled water, which was used as an Elution solution for the purpose of pushing the model inside the column. Then the protein material was recovered manually and followed up with its protein content by reading the absorption at 280 nm using a UV-Visible spectrophotometer from APEL company. In addition, the effectiveness of the alkaline phosphatase enzyme was followed up in each of the separated parts. When the unknown protein solution was injected into the separation column for the purpose of follow-up the enzyme during the separation process, that's the combination of protein parts that are in enzyme-effective. A linear relationship was then drawn between standard protein recovery volumes. It is known as molecular weights for use in estimating the approximate molecular weight of the Alkaline phosphatase enzyme [27].

2.4. Cooling Drying Technology (Lyophilization)

Lyophilization of the protein pack produced by the gel filtration technique was dried using a lyophilization device after freezing at a temperature (-20) °C to obtain a concentrated protein solution (Crude protein).

2.5. Estimation of alkaline phosphatase activity

The activity of the enzyme was estimated in both lysate supernatant and cell-free broth. After each step of purification by rapid detection of the phenol liberated from the reaction using the 4-amino antipyrine reagent and Potassium ferric amide. The reaction was stopped by adding Sodium arsenate using Ready packaging) alkaline phosphatase –kite (manufactured by Biomerieu xsa).

2.6. Estimation of total protein

The amount of protein was estimated in both lysate supernatant and cell-free broth. After each step of purification using the Folin-Lowry method [31] and modified by researchers [32]. Bovine Serum Albumin (BSA) was used as a standard solution to prepare the standard protein curve with optical absorption coefficient (Extinction coefficient) equal to 0.67 [33]. Figure 1 shows the typical standard curve of protein.

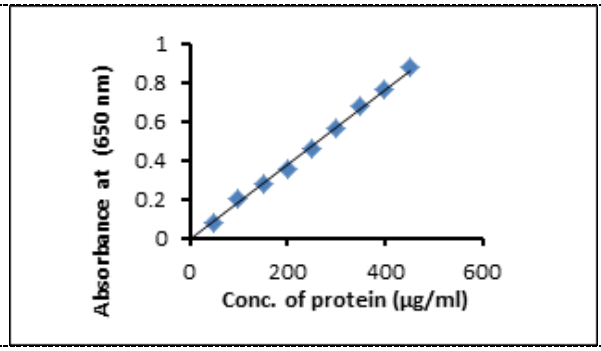

Figure 1. Illustrates a typical standard curve for a protein.

3. Results

3.1. Diagnosis of Escherichia coli bacteria

This Based on the biochemical tests and tests found in the API20 strip, *E.coli* bacteria are diagnosed in Figure 2.

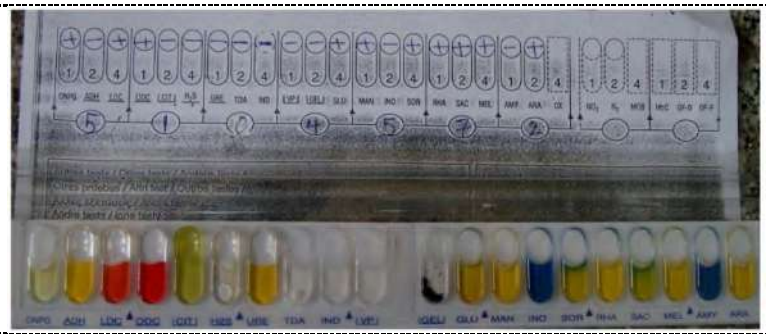

Figure 2. Results of the API20E diagnostic System.

3.2. Alkaline phosphatase enzyme

3.2.1. Determine the Logarithmic growth phase

The logarithmic growth phase of *E. coli* bacteria was determined, and due to the fact that the bacteria in this phase are almost all of their cells are alive and the speed of growth is constant. So the Spectrophotometer was used to calculate the bacterial growth in the nutrient broth media used under the study, after every two hours of incubation for a period of 24 hour (Figure 3). It was found that this phase starts approximately from the hour (4) to the hour (20) (Figure 3), and accordingly, the bacteria were adopted at an age of (18) hours, which is the logarithmic growth phase, for use in subsequent experiments.

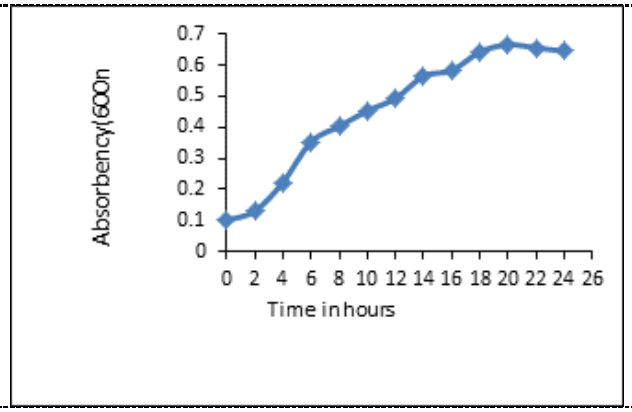

Figure 3. Growth curve and logarithmic phase determination of *Escherichia coli*.

3.2.2. Growth curve and logarithmic phase determination of Escherichia coli

The location of the alkaline phosphatase enzyme was determined by measuring its effectiveness according to paragraph (Isolation of alkaline phosphatase) described in the materials and methods of work. After the growing of bacteria in the nutrient broth for 18 hours, and after depositing their cells using a refrigerated centrifuge. The results showed lack of effectiveness of the enzyme in the cell-free filtrate and its presence in the layers of broken cells by the ultrasound device. The total activity reached (1.52) units (Table 1), and the total protein amount (47.48) mg (Figure 4). This confirms that the alkaline phosphatase enzyme is an internal enzyme. It is located inside the cells and not outside it. Therefore, the suspension of broken cells was approved as a raw extract of the enzyme in experiments related to its purification.

3.3. Purification of the alkaline phosphatase enzyme

Use lysate supernatant as a pure extract of the alkaline phosphatase enzyme, which has been purified and according to the following sequential steps:

3.3.1. Protein precipitation using ammonium sulphate

Proteins found in the raw extract were deposited by adding ammonium sulfate gradually and saturation (75%). And after obtaining the protein deposit dissolved in the 100 ml mollur tris-HCl pH9.8. Then estimated the enzymatic activity, where the specific activity of each protein extract was observed to increase by (2.0). Once compared to the raw extract as shown in Table (1), the amount of protein in it (according to the Lowry modified method) where a decrease in the amount of the total protein is about in the raw extract and as shown in Figure (4).

3.3.2. Dialysis

The results showed an increase in the specific activity of the alkaline phosphatase enzyme , which amounted to (0.10) Unit /amalgam Table (1), with low protein content compared to raw protein extract as shown in Figure (4).

3.3.3. Gel filtration chromatography

After the treatment of the lysate supernatant (crude protein) by ammonium sulfate and dialysis was separated the protein compounds by passing the separation column (containing the gel Sephadex G-100). It gave two protein packs (A and B), and by measuring the effectiveness of the alkaline phosphatase enzyme in all parts collected separately, it was found that the effectiveness is concentrated in the protein pack (B), as shown in Figure (5). A percentage increase in specific activity of (22.0) times was observed compared to its effectiveness in the crude protein, as shown in Tables (1) which confirms the purification of the enzyme by this technique. As well as a decrease in the total protein intake during the purification stages of the enzyme as shown in the Figure (4).

Table 1. Steps of purification alkaline phosphatase from *Escherichia coli*.

Steps of purification	volume (cm^3)	Total enzymatic activity unit (U)	Specific activity** Unit/mg	Percentage increase in specific activity%	Percentage of restoration %
Crude extract	20	1.52	0.03	1.0	100.0
Precipitate solution of ammonium sulfate	4	1.37	0.06	2.0	90.0
dialysis	7	1.32	0.10	3.3	86.8
Gill filteration by Sephadex G-100 Peak (B)	75.5	1.15	0.66	22.0	75.7

**Specific activity: the number of enzyme units [the enzyme unit measured in (Kind and King U / dl)] / mg protein. Kind and King: It expresses the amount of enzyme needed to release (1) mg of phenol in 15 minutes at a temperature of (37)° C.

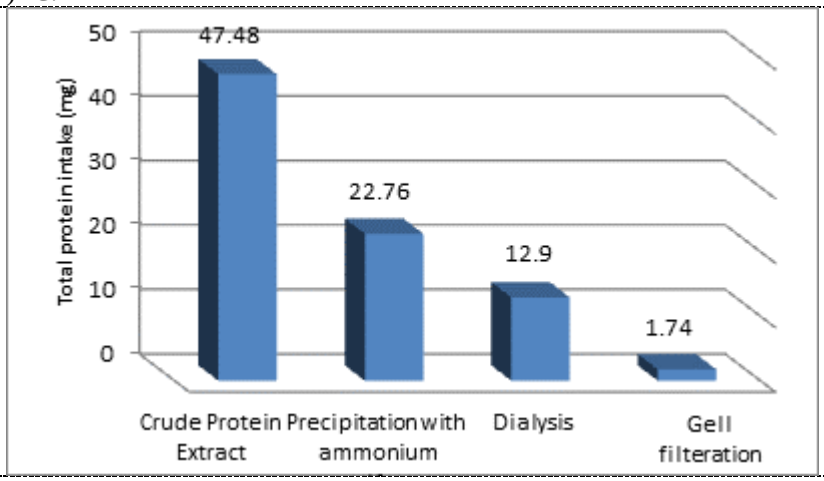

Figure 4. Total protein intake during the purification phases of alkalinel phosphatase for *Escherichia coli*.

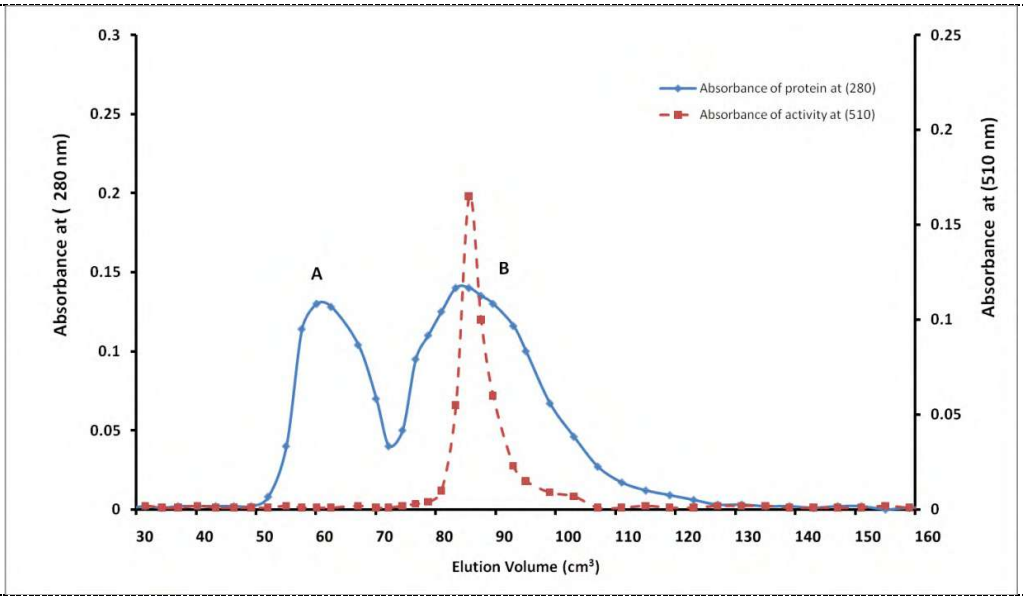

Figure 5. Profile of *Escherichia coli* proteolytic extract profile using gel filtration technique by using a separation column with dimensions (1.7 × 75 cm^3) containing the gel material (Sephadex G-100) at a height of 70 cm) at a flow velocity of 36 cm 3 / hour, volume Each segment is (3) cm^3**.**

3.4. Estimating the molecular weight of the alkaline phosphatase enzyme using the technique gel filtration

The approximate molecular weight of the protein pack (B) was estimated for *E. coli* bacteria containing the alkaline phosphatase enzyme by the researcher method (Andrews, 1965) using the gel filtration technique. The number of compounds known as molecular weight were passed by its molecular weights range from (2,000,000-204) Dalton on the separation column for the purpose of setting the characteristics of the column in terms of internal size (Vi). As well as the empty size of granules (Vo). The standard curve was then drawn Figure (6), based on the size of the organ for each substance versus the molecular weight of the lugarium. The approximate molecular weight (81,000) Dalton was determined based on the sizes of the Proteins bundle (83.3) cm^3.

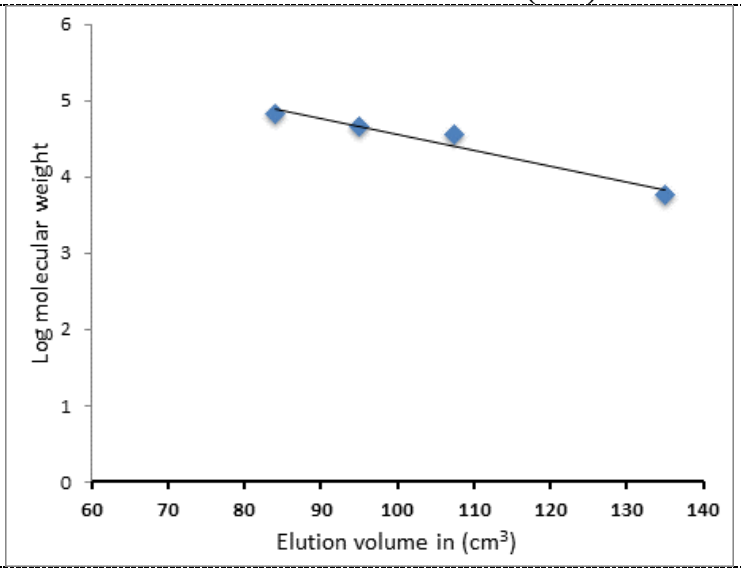

Figure 6. Standard curve for determination of molecular weight by gel filtration technology using sephadex G-100.

4. Discussion

The current study was based on the isolation and purification of the alkaline phospatase enzyme (EC 3.1.3.1) from the pathogenic bacteria *Escherichia coli*. It is based for its diagnosis on the shape of its cells after staining it with a gram stain and on the biochemical tests in the API20 strip. It is one of the rapid diagnostic methods used worldwide as well as the easy and accuracy of diagnosis. The logarithmic phase is one of the most important phases that bacteria go through during their growth, because the cells in it are highly metabolically effective [34] and have distinct physiological and chemical properties. Therefore, bacteria at this stage are suitable for use in physiological and biochemical studies [35]. Because the formation and production of the alkaline phosphatase enzyme begins during this phase in the cytoplasm. Then it is exported through the plasma membrane to the area surrounding the plasma [15]. The effectiveness of the enzyme increases only after folding, which occurs only after it is transferred to the space around the plasma. Then the formation of the dimethyl sulfur [16, 36] which is considered the important part of in bacteria because they contain most of the enzymes necessary to obtain phosphate and carbon sources [37]. So this phase of bacteria under study has been identified and is approximately 20-4 hours long. Previous studies have identified this phase within the time period (15-6) hours [38], and within the period (16-6) hours in bacteria *E. coli* [39]. The relative disparity observed with the results of this study, may be due to the size of the inoculum and the type of nutrient media, noting that increasing the size of the inoculum and adding a new nutritional medium shortens the printing period to a few hours. As well as the source of bacteria isolation and the extent of their virulence, play an important role in determining the period of the phases of the bacterial growth curve [40]. The alkaline phosphatase enzyme was isolated from the bacteria under study after it was grown in the appropriate nutrient medium incubated for about 18 hours. The study revealed that the alkaline phosphatase enzyme is one of the endogenous enzymes [41]. In terms of the absence of any activity of enzyme in the cell free culture supernatant. Its specific activity was recorded in the extract of broken cells (Lysate supernatant) (0.03) because the outer membrane of the gram-negative bacteria acts as a barrier that prevents the enzyme from escaping into the medium surrounding the bacteria [42]. The phospholipid layer present within the plasma membrane in the Gram-negative bacteria also acts to prevent the secretion of the enzyme externally. The enzyme is located within the space surrounding the plasma and it is one of the proteins that are never secreted outside the bacterial cells into the growing culture medium in it. [43] So the total enzyme units were obtained from the extract of broken cells and not from the full and Intact cells [41]. As the researcher [44, 45] pointed out the presence of the enzyme is also present in the expanse surrounding the plasma of a bacterium *Pseudomonas aerogenosa*. The enzyme was purified after obtaining the crude protein from the broken cell of the ultrasonic frequency device through the following steps; First: Protein percipitation with ammonium sulfate. This step is one of the first stages of purification during which proteins found in the crude extract are deposited depending on the degree of saturation of Ammonium sulfate [27]. By gradually adding it to the protein extract, because it is a salt that is characterized by its ability to dissolve at high speed, and its non-effect on enzymes, and depending on the type of competition between ammonium sulfate and proteins to dissolve and combine with water molecules, protein molecules tend to combine aggregation with each other in high concentrations of salt which is due to strong protein-protein interferences that overcome protein-solvent overlaps [46]. So they were used in the current study of alkaline phosphatase enzyme deposition and saturation (75%). It was shown that the results compared to the raw protein extract increase dissertated in quality efficacy and correspond to the results obtained by many researchers who used ammonium sulfate at different saturation rates [47, 48]. Second: dialysis, which is one of the methods widely used during the purification stages to get rid of salts and materials with low molecular weights in enzymatic solutions. [27] such as proteins with molecular weights that are smaller than 14,000 Dalton and some carbohydrates. Although from the reduction of the extract as a result of this process, an increase in qualitative effectiveness was observed about three times that of the raw extract and in comparison to the increase referred to by [16]. Third: The technique of gel filtration

chromatography. This technique is one of the methods used globally to separate compounds depending on the difference in the size of the rogane Elution volume. Large particles pass through a column separation of gel granules while small particles take longer due to their entry into their granules. Therefore, this technique has been used to separate protein compounds that were made and obtained from sedimentation with ammonium sulfate (after the process of dialysis and reduction of its volume by lyophilization method) using Sephadex G-100 gel. This is because it separates protein compounds with weights of molecular that falls within range (150,000-4,000) Dalton[29]. A protein pack (B) was obtained and as shown in Figure (5) and when measuring the enzymatic effectiveness of the package, it was found that the protein pack (B) is highly enzymatic. This confirms the presence of one type of alkaline phosphatase enzyme in *E. coli* bacteria [49]. The results also showed an increase in the specific effectiveness of the enzyme by about 22.0 times it in the raw protein extract, which confirms that the enzyme purification using this technique [50]. Also, the decrease in the total protein amount along the purification stages indicates that the enzyme has been purified. This is consistent with the results of many researchers in studies related to this aspect [41, 47, 48, 50]. Also, using gel filtration technology, the approximate molecular weight of the molecularly purified alkaline phosphatase enzyme was determined, as it was found that its molecular weight in *E. coli* (81,000) Dalton was similar to what was found by [5]. [5] indicated that the molecular weight of the enzyme in these bacteria is located within the run (90,000-85,000) Dalton.

5. References

[1] Gillespie SH and Hawkey PM 2006 *Principles and Practice of Bacteriology* 2nd ed. John Wiley & Sons, Ltd.
[2] Johuson JR, Stapleton AE, Russo TA, Scheutz F, Browen JJ and Maslow JN 1997 Cheracteristics and prevclene withen sero qroup O4 *E. coli* O4 :H15 containing the glass I and glass III alleles of pap G. *Infect. Immun*. **65** 2153.
[3] Posen S 1967 Alkaline phosphatase *Ann. Int. Med*. **67** 183.
[4] Reid T and Wilson I 1971 *E. coli phosphatase* (Ed., Boyer PD) The Enzymes Academic Press, Inc. New York, 373.
[5] McComb R, Bowers G and Posen S 1979 *Alkaline phosphatase* Plenum Press New York, 189.
[6] Whittaker J 1990 Determination of alkaline phosphatase expression in endodermal cell lineages of an ascidian embryo *Biol. Bull*. **178** 222.
[7] Trowsdale J, Martin D, Bicknell D and Campbell I 1990 Alkaline phosphatases *Biochem. Soc. Trans*. **18** 178.
[8] Spiro T 1973 *Inorganic Biochemistry* Eichorn GL Elsevier Amsterdam, 1: 549.
[9] Le Du MH, Stigbrand T, Taussig MJ, Ménez A and Stura EA 2001 Crystal structure of alkaline phosphatase from human placenta at 1.8 Å resolution implication for a substrate specificity *J. Biol. Chem.* **276** 9158.
[10] Anderson R, Bosron W, Kennedy F and Vallee B 1975 The role of magnesium in *Escherichia coli* alkaline phosphatase *Proc. Nut. Acad. Sci. USA*. **72** 2989.
[11] Anderson R, Kennedy F and Vallee B 1976 The effect of Mg (I1) on the spectral properties of Co(ll) alkaline phosphatase *Biochemistry* **15** 3710.
[12] Coleman JE, Nakamura I and Chlebowski JF 1983 65ZnII, 115mCdII, 60CoII, and MgII binding to alkaline phosphatase of *Escherichia coli*. Structural and functional effects *J. Biol. Chem*. **258** 386.
[13] Wyckoff H. 1987 *Phosphote metabolism and cellular regulation in microorganism* (Ed. Torriani-Gorini A, Rothman FG, Silver S, Wright A and Yagil E.) American Society of Microbiology Press, Washington, D. C. 118.
[14] Noda M, Yoon K, Rodan G and Koppel D 1987 High lateral mobility of endogenous and transfected alkaline phosphatase: a phosphatidylinositol-anchored membrane protein *J. Cell Biol.* **105** 1671.

[15] Wang J, Stieglitz KA and Kantrowitz ER 2005 Metal specificity is correlated with two crucial active site residues in *Escherichia coli* alkaline phosphatase *Biochemistry* **44** 8378.
[16] Kumar, M.; Kaur, P. P., and Ganjewala, D. (2008). Isolation of periplasmic alkaline phosphatase from Rhizobium bacteria *Res. J. Microbiol*. **3** 157.
[17] Garen A and Levintal C 1960 A fine-structuer genetic and chemical study of the enzyme alkaline phosphatase of *E. coli* purification and characterization of alkaline phosphatase *Biochim. Biophys. Acta*. **38** 470
[18] OMoss DW, Eaton RH, Smith JK and Whitby L 1966 Alteration in the electrophoretic mobility of alkaline phosphatases after treatment with neuraminidase *Biochem. J.* **98** 32.
[19] Fosset M, Chappelet-Tordo D and Lazdunski M 1974 Intestinal alkaline phosphatase physical properties and quaternary structure *Biochemistry* **13** 1783.
[20] Cathala G and Brunel C 1975 Bovine kidney alkaline phosphatase : Purification, Subunit structure, and metalloenzyme properties *J. Biol. Chem.* **250** 6040.
[21] Berenson G, Radhakrishnamurthy B, Fishkin A, Dessauer H and Arquembourg P 1966 Individuality of glycoproteins in human aorta *J. Atheroscker. Res*. **6** 214.
[22] Bortolato M, Besson F and Roux B 1999 Role of metal ions on the secondary and quaternary structure of alkaline phosphatase from bovine intestinal mucosa *Proteins* 37 310.
[23] Abe T, Abe YA, Hara Y and Maeda K 2001 Extracellular matrix regulates induction of alkaline phosphatase expression by ascorbic acid in human fibroblasts *J. Cell. Physiol.* **189** 144.
[24] Hofmann M and Milla´n J 1993 Developmental expression of alkaline phosphatase genes; reexpression in germ cell tumours and in vitro immortalized germ cells *Eur. Urol.* **23** 38e45.
[25] Malik A 1986 Conversation of human placental alkaline phosphatase from a high Mr form to a low Mr form during butanol extraction *Biochem. J.* **240** 519.
[26] Harris LG, Foster SJ and Richards RG 2002 An introduction to *Staphylococcus aureus*, and Techniques for identifying and quantifying *S. aureus* adhesions in relation to adhesion to biomaterials Review *Eur. Cell Mater*., **31** 39.
[27] Hostacka A., Maytan V and Majtanova L 1993 Profile of toxic and biological activities of Salmonella typhimurium strains *Biolgia. Bratislava* **48** 677.
[28] Robyt FJ and White JB 1987 *Biochemical Techniques Theory and Practice* Books Cole Publishing Com U S A.
[29] Yoo SH 1985 Evidence for alkaline phosphatase involvement in tRNA-stimulated amino acid transport system *Korean Biochem. J*.**18** 63.
[30] Husson MO, Mielcarek C, Gavini F, Caron C, Izard D and Leclerc H 1989 Isolation and characterization of monoclonal antibodies against alkaline phosphatase of *Pseudomonas aeruginosa J. Clin. Microbiol*. 1115.
[31] Al-Muzaffar S 1999 *Basics of Biochemistry* first edition, Dar Al Masirah for publishing, distribution and printing, Amman (In Arabic)
[32] Lowry OH, Rosebrough NJ, Farr AL and Randall RJ 1951 Protein measurement with folin-phenol reagent. J. Biol. Chem., 193: 265-275.
[33] Schacterle GR and Pollack RL 1973 A simplified method for the quantitative assay of small amount of protein in biological material *Anal. Biochem*. **51** 654.
[34] Holme DJ and Peck H 1988 *Analytical Biochemistry* John Wiley & Sons. Inc., New York, p: 86.
[35] Al-Zaidi HM 1988 *Microbiology* Dar Al-Kutub for Printing and Publishing, University of Mosul (In arabic).
[36] Prescott LM, Harely TP and Klein DA 2005 *Micobiology* 4th ed. McGraw-Hill Companies, Inc., USA.
[37] Sone M Kishigami S Yoshihisa T and Ito K 1997 Roles of disulfide bonds in bacterial alkaline phosphatase *J. Biol. Chem*. **272** 6174-6178.
[38] Nugent KM, Huffe E, Cole RM and Theodore TS 1974 Cellular location of degradative enzymes in *Staphylococcus aureus J. Bacteriol*. **120** 1012.

[39] Alias BAA 1996 *Numerical classification by cluster analysis of coliform bacteria* PhD thesis Faculty of Science University of Mosul (In arabic).
[40] Al-Nu'man, YSH 1998 *Partial effect of some plant extracts on the growth and metabolism of a number of bacteria positive and negative for the cram stain* PhD thesis Faculty of Science, University of Mosul (In arabic).
[41] Koneman EW, Allen SD, Janada WM, Schreckenberg PC and Winn WC 1997 *Color Atlas & Textbook of Diagnostic Microbiology* 5th ed., J.B. Lippincott Com, Philadelphia, New York.
[42] Csopak H, Garellick C and Hallberg B 1972 Purification of *Escherichia coli* alkaline phosphatase *Acta .Chem. Scand* **26** 2401.
[43] Manoil C, Mekalanos J and Beckwith J 1990 Alkaline phosphatase fusions: sensors of subcellular location *J. Bacteriol*. **172** 515.
[44] Beacham IR, Taylor NS and Youell M 1976 Enzyme secretion in *Escherichia coli*: Synthesis of alkaline phosphatase and acid hexose phosphatase in the absence of PhQspholipid synthesis *J. Bacteriol*.**128** 522.
[45] Cheng K, Ingram J and Costerton J 1970 Alkaline phosphatase localization and spheroplast formation of *Pseudomonas aeruginosa Can. J. Microbiol*. **16** 1319.
[46] Cheng K, Ingram J and Costerton J 1971 Interactions of alkaline phosphatase and the cell wall of *Pseudomonas aeruginosa J. Bacteriol*. **107** 325.
[47] Zubay, G. L. (1998).Biochemistry .4th ed., McGraw-Hill Comp. Inc., USA. , pp. 964 , 1962.
[48] Brenna O, Perrella M, Pace M and Pietta PG 1975 Affinity-chromatography purification of alkaline phosphatase from calf intestine *Biochem. J.* **151** 291.
[49] Yamashita Y, Toyoshima K, Yamazaki M, Hanada N and Takehara T 1990 Purification and Characterization of Alkaline Phosphatase of *Bacteroides gingivalis* 381 *Infect. Immun.* **58** 2882.
[50] Zhang L, Buchet R and Azzar G 2005 Distinct structure and activity recoveries reveal differences in metal binding between mammalian and *Escherichia coli* alkaline phosphatases *Biochem. J.* **392** 407.
[51] Woolkalis M J and Baumann P 1981 Evolution of alkaline phosphatase in marine species of Vibrio *J. Bacteriol*. **147** 36.

Using of RAPD-PCR markers to detect the genetic relationship of number of *Bellevalia Lapeyr* and *Ornithogalum* L. species developing in central and northern of Iraq

Using of RAPD-PCR markers to detect the genetic relationship of number of *Bellevalia Lapeyr* and *Ornithogalum* L. species developing in central and northern of Iraq

Najat Ameen Sa'eed[1*], Akeel Hussein Ali Al-Assie[2] and Naglaa Mustafa Al-Abide[1]

[1]Department of Biology, College of Education for Pure Sciences, University of Tikrit, Iraq.
[2]Department of Biology, College of Sciences, University of Tikrit, Iraq.

*E-mail: najatameenbio@gmail.com

Abstract. This study evaluates eleven wild plant species belong to two genera of Asparagaceae family, naming of *Bellevalia lapeyr* and *Ornithogalum* L. and discuss the similarities and differences among all species by using eighteen random primers for the Random amplification polymorphic DNA (RAPD) markers were used to study the genetic relationship and genetic distance among these species. The study aimed to determination genetic relationships among all the eleven species by using RAPD markers and the method of extraction DNA from plants was CTAB with liquid nitrogen. The result show 16 primers success in giving 293 bands, of which 263 were polymorphic bands, 25 unique bands and 5 were absent. *B.chrisii* type also succeeded in showing two unique bands at OPG-08 primer without registering any other bands. The lowest genetic distance was 0.306 between *B. longipes* and *B.parva*, while the highest genetic distance was 0.943 between *B.chrisii* and *O.pyrenaicum*. It is concluded from our study based on the results of the RAPD test that the studied species were divided into two main groups, each group was divided into subgroups, the first group included three groups and the second main group included two main groups. The study found that the *O.pyrenaicum* type is distinguished by being far from the rest of the species. .

Keywords. Asparagaceae, Genetic relationship, *Bellevalia*, *Ornithogalum*, RAPD.

1. Introduction

Asparagaceae family of plants belong to monocots plants, and it is a widely spread family in the temperate zones, tropical and subtropical zones. It includes around 114-143 genera and 3632 [1] species, and they were mentioned, for the first time, by the scientist Jussieu [2] and considered part of the lily family. Asparagaceae family is characterized by a perineal herbal nature or seasonal. The species of this family are characterized by their economic importance as they are used for ornamental purposes of as fodder or livestock [3]. According to the scientific researches, the two genera *Bellevalia lapeyr* and *Ornithogalum* L. belong to the Asparagus family [4], but they were considered for a long time that they belong to Liliaceae family. In the Turkish flora, [5, 6, 7] mentioned that *Bellevalia*

belongs to the Asparagus family. [8classified it within the same family in the Iranian Flora and [9] mentioned *Bellevalia* in Asparagus family in his study to the Italian Flora. Moreover, the study of [10] categorized both of the genera within the liliaceous family in the Iraqi Flora. The molecular markers are regarded as markers of the stable genetic material, which have specific locations on the genome, through which we can identify the specific genetic differences and the type of mechanisms responsible for a certain characteristic and also the inhibitory genes. Amongst the molecular markers is the DAN Markers, through which we can detect the genetic variations in any piece of the genetic material whether it was DNA or RNA or cytoplasmic DNA or cpDNA (mtDNA), whose sizes range from one pair of nitrogen base to a couple of thousands [11]. Researchers and authors endeavored to use techniques that depend on the plant genetic material to identify the kinship relations amongst the plant species and genetic distance between them [12]. One of these techniques is the Polymerase Chain Reaction (PCR), and one of the markers that depend on the PCR technique is the Random Amplified Polymorphic DNA. The number of the amplified pieces is dependent upon the primer length, the genome size, and its sequence sample, rapid and needs small quantities of DNA (20-25) nanograms [13]. The purpose behind using these techniques, which rely on the genetic material is to solve several problems related to the classification of plants, identifying the genetic print and variation as well as using the results of these techniques in asserting the deduction of new dynasties and the selection of high quality and specifications species that contribute to enhancing the agricultural production [14]. Therefore, The current study aims to identifying the genetic relation among eleven wild species, which belong to *Bellevalia lapeyr* and *Ornithogalum* L.

2. Materials and Methods

2.1. Samples collection and identification

A total Plant samples were collected during one season from March to May 2019 from many areas in the middle and north of Iraq, which included four governorates: Salahaldeen (Sherqat, Haweejah, AlAlam, AlAbbasi, Balad and Amerli), Nineveh (Rabee'a, Zummar and Qayyarah), AlTa'meem governorate (Kirkuk center, Haweejah and Lower Zab, Erbil governorate (Koysanjaq) and the information related to each species were registered. The information about specimens was recorded; and they identified by the second author. Also assured by comparing them with the specimens available at the National herbarium of Iraq.

2.2. Genomic DNA extraction

The DNA was isolated from the fresh leaves of the plants and 2 grams were taken from the leaves, using the (CTAP) in accordance with the method mentioned by [15, 16] and which is used by [17]. The DNA was extracted from the fresh leaves, purified and then its concentration and pureness were measured by the Nanodrop.

2.3. RAPD – PCR reactions [18]

According to the method mentioned by [19], the reactions of RAPD for the DNA samples of the plant species *Bellevalia* and *Ornithogalum* L. The number of primers used were provided by Promega company they were 18 random primerֹ and their sequence is shown in table (1). The reaction solution was prepared.

Table 1. Shows the random primers used in the study of RAPD – PCR.

No.	Primer code	Nucleotide sequence 5 to3
1	OPA-01	CAGGCCCTTC
2	OPA-06	GGTCCCTGAC
3	OPB-14	TCCGCTCTGG
4	OPB-20	GGACCCTTAC
5	OPC-08	TGGACCGGTG
6	OPC-16	CACACTCCAG
7	OPD-03	GTGGCCGTCA
8	OPD-18	GAGAGCCAAC
9	OPE-03	CCAGATGCAC
10	OPE-11	GAGTCTCAGG
11	OPF-05	CCGAATTCCC
12	OPF-20	GGTCTAGAGG
13	OPG-08	TCACGTCCAC
14	OPG-14	GGATGAGACC
15	OPH-08	GAAACACCCC
16	OPH-16	TCTCAGCTGG
17	OPI-02	GGAGGAGAGG
18	OPI-19	AATGGGGGAG

Tubes with capacity of 0.2 ml contained the reaction mixture were prepared as shown in table (2), put in the ice to complete the required additions and then the mixture was cast away for 2-5 seconds by the Microfuge to make reaction components mix well. After that the tubes were put in the Thermo cycler according to the program shown in table (3).

Table 2. Materials used in the main reaction mixture of PCR.

No.	Components	Final concentration	Final volume of each sample/µL
1	Premix	**-**	2
2	Nuclease free water	**-**	15
3	Primer	10 pmol	1
4	DNA template	50 ng/µg	2

Table 3. The steps of the PCR reaction program.

Stage	Temperature	Time	No. of cycles
initiation denaturation	94	7 min.	1
denaturation	93	45 sec.	
annealing	36	45sec.	40
extension	72	90 sec.	
Final extension	72	7 min	1

When time of reaction was ended, the mixture was kept in the fridge. An amount of 5 microliter was withdrawn from each tube to be borne in the Holes of Agarose gel which was prepared previously in a concentration of 1.5% and the marker was put. Samples electrophoresis gel was conducted for 60 minutes in 70 volt, after that the gel was subjected to ultraviolet ray in UV-Transilluminator and photographed with a high resolution camera.

2.4. Estimation of the genetic distance using RAPD markers

In depending on the RAPD reactions results, the genetic distance for the plants species in question was estimated by means of the Genetic statistical package (2.02i NTSYS-PC.Version), which relies on the bands shared between the genetic structures according to the equation mentioned by [20]. A tree diagram that elucidates the genetic relation between the species was drawn by using SAS program.

3. Results and Discussion

Results of the current study revealed that there are two types of primers; the productive primers and the non-productive primers, which are two OPB-14 and OPD-03, that showed no bands on the Agarose gel. All the productive primers, which are 16 random primer, produced Polymorphic loci. The sizes of the molecular bands ranged between (100-1500 bp). Using of many number of primers is regarded as an marker of the increase of the genetic distance accuracy [14], and eventually results in more accurate results which can identify the genetic relation amongst the species as 293 bands appeared, 263 of them are polymorphic band, 25 are Unique bands and 5 are Absent bands. The unique bands appeared in several primers such as OPA-01, OPE-11, OPG-14 and OPA-06 and their appearance varied on the molecular volumes 400, 800, 1000 and 1250 bp. Both the species *B.flexuosa* and *B.parva* were distinguished in a number of the productive unique bands when using the primers OPC-08, OPD-18, OPF-20 and OPH-16. The species *O.brachystachys* recorded three unique bands at the primers which are: OPA-06, OPE-03 and OPI-19, while the species *B.saviczii* produced two unique bands at the two primers OPA-01 and OPA-06 in two different locations and the same was for *B.kurdistanica* which recorded two unique bands at the primers OPD-18 and OPF-05 at two different locations and we notice the superiority of the primer OPC-08 in terms of the number of the bands, followed by OPF-20. So, we concluded that all the primers shared the feature of showing unique bands for different species except for the primers OPB-20 and OPC-16 which did not produce unique bands. This emergence demonstrates Genomic DNA sequence of that species per se and it can be considered as a diagnostic feature to discriminate between the species. The second type of the distinguished bands was represented by the absent bands, which emerged at the primers OPC-16, OPE-03, OPF-05, OPG-14 and OPI-02. The appearance of the absent bands is regarded as a type of mutations that took place at the location of the primer identification of one genetic structure that led to abolishing the identification location and eventually that band did not emerge [14]. In table (4), we observed the primers varied in their proficiency values, which result from their capability to show that variance among the genetic structures of plants species in question. The primer OPG-08 was less proficient and with less distinguishing capability (0.6) and (0.7) respectively, while the primer OPI-19 was characterized with the highest proficiency and distinguishing capacity amongst the primers (8.8) and (8.9) respectively in terms of producing 26 different bands. From the other hand, the proficiency and the distinguishing capability of the two primers OPE-11 and OPF-05 were similar. Therefore, it is concluded that more bands are more proficiency the primer has. At the same time, the increase of the primers used in RAPD markers results in increasing the accuracy of identifying the genetic distance and the increasing the possibility of detecting larger area for the genome [21]

Table 4. Represents the results of the random primers used in RAPD.

No	Primer-name	No. of loci	Polymorphic bands	Total bands	unique bands	absent bands	primer's efficiency	Discrimination power
1	OPA-01	6	6	20	1	-	6.8	7.6
2	OPA-06	4	4	13	2	-	4.4	4.9
3	OPB-20	5	5	22	-	-	7.5	8.3
4	OPC-08	9	9	22	4	-	7.5	8.3
5	OPC-16	3	3	16	-	1	5.4	6.0
6	OPD-18	8	8	24	2	-	8.1	9.1
7	OPE-03	6	6	25	2	1	8.5	9.5

8	OPE-11	6	6	18	1	-	6.1	6.8
9	OPF-05	6	6	18	2	1	6.1	6.8
10	OPF-20	6	6	17	3	-	5.8	6.4
11	OPG-08	2	2	2	2	-	0.6	0.7
12	OPG-14	5	5	23	1	1	7.8	8.7
13	OPH-08	8	8	21	1	-	7.1	7.9
14	OPH-16	4	4	12	1	-	4.0	4.5
15	OPI-02	3	3	14	1	1	4.7	5.3
16	OPI-19	8	8	26	2	-	8.8	9.8
	Total	89	89	293	25	5		

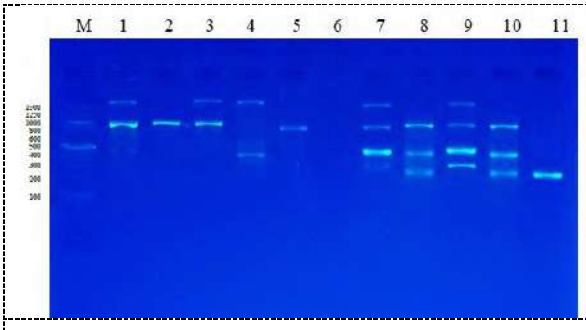

Figure 1. Reaction resluts for primer OPB-20 for plants under study in agarose gel electrophoresis with concentration 1.5 and Marker.

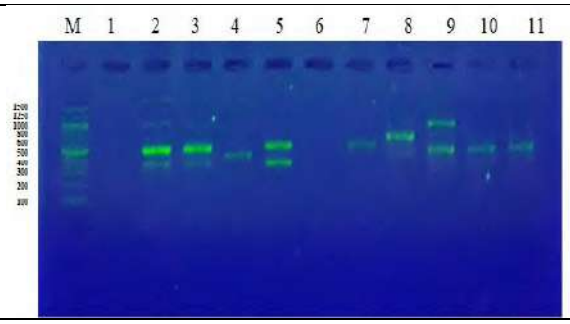

Figure 2. Reaction resluts for primer OPA-06 for plants under study in agarose gel electrophoresis with concentration 1.5 and Marker.

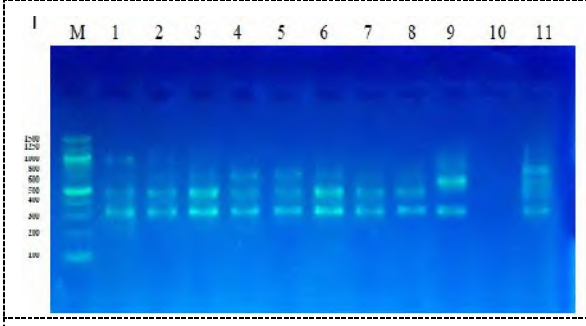

Figure 3. Reaction resluts for primer OPE-03 for plants under study in agarose gel electrophoresis with concentration 1.5 and Marker

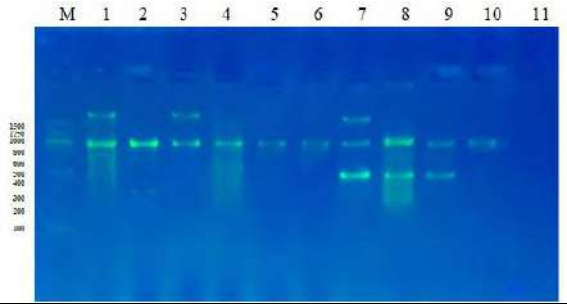

Figure 4. Reaction results for primer OPC-16 for plants under study in agarose gel electrophoresis with concentration 1.5 and Marker

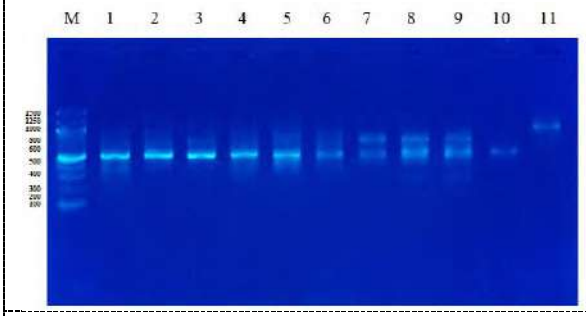

Figure 5. Reaction results for primer OPI-02

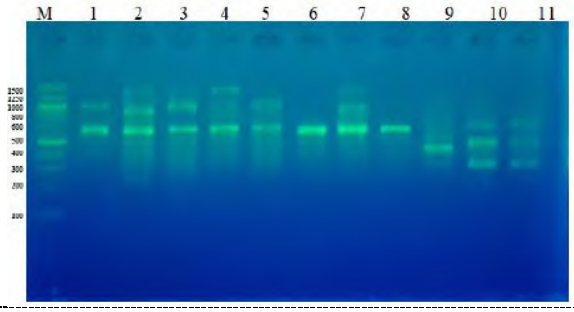

Figure 6. Reaction results for primer OPG-14

for plants under study in agarose gel electrophoresis with concentration 1.5 and Marker	for plants under study in agarose gel electrophoresis with concentration 1.5 and Marker

From table (5), we find that the values of the genetic distance ranged between (0.306 - 0.943). the least genetic distance was 0.306 between the species *B.longipes* and *B. parva*, and thus they are the most similar among the species because they belong to the same genus and in spite of the difference between them in some morphological characteristics, but the a proximity in the genetic distance value demonstrates the similarity in the genetic material. From the other hand, the highest genetic distance was 0.943 between *B.chrisii* and *O.pyrenaicum* they were least similar to those which belong to two different genera; *B.chrisii* belongs to the genus *Bellevalia* and *O.pyrenaicum* belong to the genus *Ornithogalum* and this lead to why they are genetically distant.

Table 5. The genetic distance amongst the species in this study.

S1	S2	S3	S4	S5	S6	S7	S8	S9	S10	S11
0.000										
0.446	**0.000**									
0.446	**0.433**	**0.000**								
0.720	**0.506**	**0.464**	**0.000**							
0.629	**0.315**	**0.433**	**0.378**	**0.000**						
0.718	**0.543**	**0.606**	**0.306**	**0.403**	**0.000**					
0.460	**0.489**	**0.446**	**0.352**	**0.446**	**0.461**	**0.000**				
0.642	**0.734**	**0.692**	**0.520**	**0.533**	**0.461**	**0.460**	**0.000**			
0.777	**0.889**	**0.665**	**0.750**	**0.825**	**0.752**	**0.666**	**0.432**	**0.000**		
0.718	**0.830**	**0.663**	**0.886**	**0.766**	**0.901**	**0.718**	**0.607**	**0.389**	**0.000**	
0.943	**0.850**	**0.734**	**0.629**	**0.707**	**0.703**	**0.720**	**0.720**	**0.693**	**0.509**	**0.000**

S1: *B.chrisii,* **S2:** *B.flexuosa,* **S3:***B.kudistanica,* **S4:** *B.longipes,* **S5:** *B.macrobotrys,* **S6:** *B.parva* **S7:** *B.pycnantha* **S8:***B.saviczii,* **S9:***O.brachystachys,* **S10:***O.neurostegium* **S11:***O.pyrenaicum*.

In depending on the values of the genetic distance shown in table (5), the tree diagram was drawn, according to which the plants species were divided into two main groups, as follows:

3.1. The first main group:

It included seven species, included : *B.chrisii*, *B.flexuosa*, *B.kudistanica*, *B.longipes*, *B.macrobotrys*, *B.parva* and *B.pycnantha*.

3.1.1. The first secondary group:

It involves the species *B.chrisii*, this species is alone in a genetic group indicated in the dissimilarity of its genetic material with other species and it has a genetic distance of 0.446.

3.1.2. The second secondary group: It contains three species:

The genetic distance of *B.flexuosa* and *B.macrobotrys* was 0.315, while it was 0.433 between *B.macrobotrys* and *B.kurdistanica* and the same genetic distance is between *B.flexuosa* and *B.kurdistanica*. This indicates that the three species belong to one common origin and approved by the morphological classification results as they belong to the same genus.

3.1.3. The third secondary group:

It involves *B.longipes*, *B.parva* and *B.pycnantha* with genetic distance of 0.306 between the two species *B.longipes* and *B.parva*; and 0.461 between *B.parva* and *B.pycnantha*. From the other hand, the genetic distance between *B.longipes* and *B.pycnantha* was 0.352 and the genetic convergence of these species is in accordance with their similarity in several morphological features.

3.2. The second main group:

It includes *B.saviczii*, *O.brachystachys*, *O.neurostegium* and *O.pyrenaicum*. They are divided into two secondary groups involve:

3.2.1. The first secondary group:

It included three species,: *B.saviczii*, *O.brachystachys* and *O.neurostegium*. The genetic distance between *B.saviczii* and *O.brachystachys* was 0.432 and between the species *O.brachystachys* and *O.neurostegium* was 0.389. The presence of these species in one group indicates that they share the same origin, despite the fact that the species *B.saviczii* belongs to the *Bellevalia* genus and the other two species belong to the *Ornithogalum* genus according to the morphological classification.

3.2.2. The second secondary group:

It included one species, which is *O.pyrenaicum* and its presence in an independent genetic group confirms that its genetic material is different from the rest of the species according to the results of RAPD – PCR, this species showed no band at the primers OPC – 08, OPF – 20 and OPI – 19. From the other hand, the species *O.pyrenaicum* was characterized with four unique bands at the primers OPA – 01, OPD – 18, OPH – 08 and OPI – 02 at the molecular size (300, 1500, 1500 and 1250) respectively, with three absent bands when using the primers OPC – 16, OPF – 05 and OPI – 02.

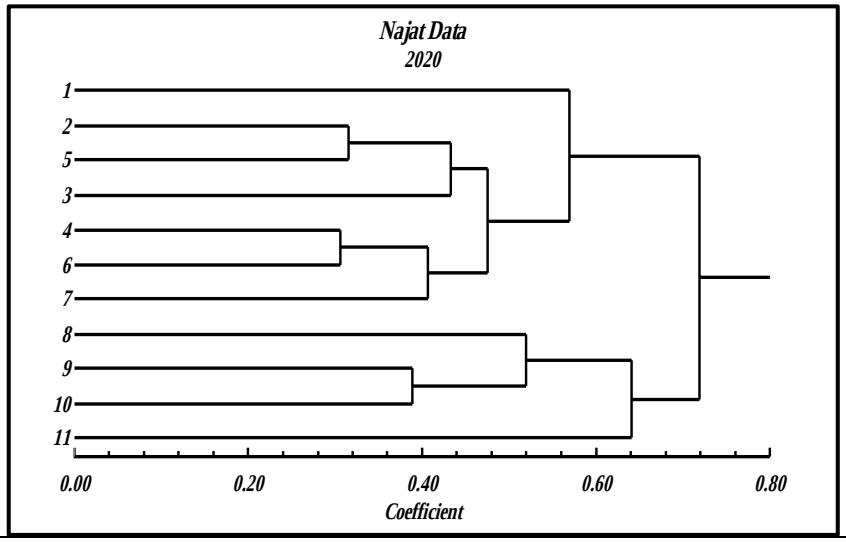

Figure 7. The genetic relationship between the plants species according to the Genetic distance values of RAPD markers.

The use of plenty molecular markers indicates its efficiency and accuracy in giving the results besides being inexpensive. Regarding the molecular studies of plants species which they are not available except for the study of [22] for three species belong to the genus *Ornithogalum*, they are: *O.brevipedicellatum*, *O.oligophyllum*, and *O.pamphylicum*. Study used the PCR technology using two

specific genera, trnL and rbcL. The study of [23] was a cellular study of the number, size and shape of the chromosomes of three species that belong to *Bellavalia* genus, whereas [24] studying the shape and number of chromosomes for the species *O.alpigenum*, which belong to -*Ornithogalum* genus. The results show the primer OPC-08 was unique to the appearance of 4 unique bands, 3 unique bands recorded by type *B.parva*, two with molecular size ranging from (1250 to1500), the third band of the same species with a molecular size (300bp), and the fourth unique bands of the primer OPC-08 recorded by *B.flexuosa* at molecular size (250bp) thus being the most unique prime in the number of unique bands. Whereas, the primers OPB-20 and OPC-16 did not produce any unique bands. The two species *B.parva* and *B. flexuosa* similar to each other in having 4- unique bands, this meaning they are similar in many morphological characters like color of flowers are violet and the long leaves so they are related to each other, while the species *O.pyrenaicum* have shown no bands in many primers, this mean that the species is genetically divergent from the rest of the species.

4. Conclusion

The Results showed that there was a high genetic variance amongst the plant species, they were characterized with the emergence of different bands and distinguished bands (unique and absent). Also, the results showed the efficiency of using RAPD-PCR markers in defining the genetic relation between these species and the genetic print.

5. Acknowledgment

The author would like to thank the Department of Biology, and the Central laboratory, University of Tikrit, Iraq for providing the facilitating to the research work. I also would like to thank my Supervise, Dr. Akeel H. Al- Assie, and Dr. Naglaa M. Al-abide for their supporting in my studies and providing me with information.

6. References

[1] APGIII (Angiosperm Phylogeny Group) 2009 An update of the angiosperm phylogeny group classification for the orders and families of flowering plants APG III. *Bot. J. Linnaean Soc.* **161**(N) 105.
[2] Jussieu AL 1789 "*Lilia*". Gener a plantarum, secondum ordines naturales dispositajuxta methodum in Horto Regio Parisiensiexaratam. Paris 48.
[3] Li P 2017 Comparative genomics and phylogenomics of East Asian tulips (Amana,Liliaceae). Front *Plant Sci.* **451** 1.
[4] Chase MW, Reveal JL and Fay MF 2009 A sub-family classification for the expanded as-paragalean families Amaryllidaceae, Aspara gaceae and Xanthorrhoeaceae. *Bot. J. Linnaean Soc.* **161** 132.
[5] Firat M 2014 *Three new species of Bellevalia lapeyr. (Asparagaceae) from East Anatolia/ (Asparagaceae)* Li Kurdistana Bakur SêCureyên Nû Yên Bellevalia Lapeyr. Türü, Sitavyayınevi, Van, 200. ISBN: 978-605-5081-18-8.
[6] Yildirim H, Altioğlu Y, Şahin B and Aslan S 2014 *Bellevalia chrisii* sp. nov. (Asparagaceae) from eastern Anatolia, Turkey *Nordic J. Bot.* **33** 45.
[7] Fidan M 2019 *Bellevalia sasonii* (Asparagaceae): a new species from Turkey *Phytotaxa* **394** 126.
[8] Jafari A, Forghanifard M, Farsi M and Behroozian M 2016 Comparative morphological and anatomical study on Bellevalia lapeyr. Sect. Conica and Nutans in Iran. *Int. J. Biol. Pharm. Allied Sci.* **5** 206.

[9] Astuti G, Brullo S, Domina G, El Mokni R, Giordani T and Peruzzi L 2017 Phylogenetic rela¬tionships among tetraploid species of Bellevalia (Asparagaceae) endemic to south central Mediterranean. *Plant Biosyst.* **151** 1120.
[10] Abdul–Raheem IA and Al-Bayaty AJ 2018 Morphoanatomical study of some species from Liliaceae Juss. Family in Ghurfa-Adhaim district. *Tikrit J. Pure Sci.* **23** 1813.
[11] Batley J 2015 *Plant Genotyping Methods And Protocols* Springer New York Heidelberg Dordrecht London **6** 4939.
[12] Al-Assie AA 2002 *Using AND marker in analysis genetic diversity for Hordeum (Hordeum vulgare L.) Cultivated in Iraq* Doctorate of Philosophy. College of Education, Ibn Al-Haitham, University of Baghdad, Iraq.
[13] Al-Jubouri HMH 2014 *The effect of distances between the mellow on the yield and its components for some broadbeans species (faba vicia L.)* A master thesis, College of Agriculture, Kirkuk University.
[14] Al-Sugmiany R, Al-Assie A and Al-Juburyi JM 2018 Determination Fingerprinting DNA and genetic distance to number of genetic structure of (*Vicia faba* L.) by using RAPD-PCR marker. In: Proceedings of the first and third international scientific conference of the Faculty of Science / University of Tikrit, **3** 81.
[15] Huang QX, Wang XC, Kong H, Guo YL and Guo AP 2013 An efficient DNA isolation method for tropical plants. *Afr. J. Bio.* **12** 2727.
[16] Weigand F, Baum M and Udupa S 1993 *DNA molecular marker techniques, technical manual*. No.20. International Center for Agricultural Research in the Dry Area(ICARDA). Aleppo, Syria.
[17] Al-Assie AH, Jaladit MSJ and Tahreer RA 2003 Using RAPD markers to identify the genetic print of some barley species (*Hordeum vulgare* L.) planted in Iraq *Tikrit J. Pure Sci.* **9**.
[18] Al-Sugmiany RZM 2017 *The use of morphological ad molecular markers to assess the genetic performance for a number of genotypes of (Vicia faba L.) and their di alleles crossing* Ph.D. Degree College of Pure Education, Department of Biology Tikrit University Iraq.
[19] Williams JGK, Kubelik AR, Livak KJ, Rafalski JA and Tingey SV 1990 DNA polymorphisms amplified by arbitrary primers are useful as genetic markers. *Nucl. Acids Res.* **18** 6531.
[20] Nei M and Li WH 1979 *Mathematical model for studying genetic variation in terms of restriction endonucleases.* Proceeding of the National Academy of Science, USA. 74, 5269-5273. C. F. by Henry, R.J. (1997).
[21] Al-Qaisi EKK 2013 *The estimation of the genetic action in some field qualities of Zea maize*. Ph. D. Thesis, College of Agriculture and Forestry, Mosul University.
[22] Aykurt C, Deniz İG, Sarı D, Vural M and Sümbül H 2016 Resurrection of *Ornithogalum brevipedicellatum* (Asparagaceae) with morphological and molecular data *Acta Bot. Croat.* **75** 60.
[23] Kayiran SD and Özhatay N 2017 Karyomorphological contribution to the genus *Bellevalia* (Asparagaceae) in Turkey. *Pak. J. Bot.* **49** 1345.
[24] Yetişen K and Özdemir C 2015 A morphological, anatomical and Caryological study on endemic *Ornithogalum alpigenum* Stapf (Hyacinthaceae). *Pak. J. Bot.* **47** 2289.

The isolation and identification of cadmium-resistant *Brevibacillus agri* C15

The isolation and identification of cadmium-resistant *Brevibacillus agri* C15

Nadia Jebril[1,2*], Rich Boden[2]and Charlotte Braungardt[3]

[1]Department of Biology, College of Sciences for Women, University of Babylon, Iraq.
[2]School of Biological and Marine Sciences, University of Plymouth, Drake's Circus, Plymouth PL4 8AA, United Kingdom.
[3]School of Geography, Earth and Environmental Sciences and Plymouth University, Drake Circus, Plymouth, PL4 8AA, United Kingdom.

*E-mail: nadia.tawfiq@uobabylon.edu.iq

Abstract. Eight Cd-resistant bacteria were isolated from the soil. Based on the resistance and specific growth rate, one isolate from these was chosen. The 16S rRNA (rrs) gene sequence was used to assert this isolate belongs to the genus of *Brevibacillus* and closely related to *Brevibacillus agri* (*B.agri*) DSM 6348T (AB112716). The isolate was termed *B.agri* C15. The specific growth yields and the Cd-dependent fall in specific growth yield of *B.agri* C15 was determined under different concentrations of Cd. The current study provides a basis for isolation Cd resistant bacteria with maximum tolerable concentration (MTC) 15 mM Cd from a contaminated soil 490±50 µmolal Cd that could be suitable for a new Cd-bioremediation process; therefore, further studies are needed to investigate this possibility.

Keywords. *Brevibacillus agri*, cadmium, growth rate, isolation, soil.

1. Introduction

The contamination of environments with metals has become a global challenge in the relation to human health. Cadmium is a non-essential element for life, and it is toxic to Homo Sapiens. The United States Environmental Protection Agency (US EPA) and the International Agency for Research on Cancer (IARC) classified some elements, including Cd, As, Hg, and Pb, as human carcinogens [1]. Furthermore, chronic exposure to low levels of Cd is associated with several diseases, such as deranged blood pressure regulation, osteoporosis, early onset of diabetic renal complications, and end-stage renal failure. The Cd contamination, exceeding the US EPA limit of 3 µg/L, has become a major concern, especially in the relation to increasing groundwater withdrawals for human use and agricultural irrigation. This contamination may be subject to regulatory requirements for treatment, and more effective methods for removing Cd are required. Techniques, such as physiochemical methods (precipitation, adsorption and ion exchange) biological methods (bioremediation) are used to remove Cd from groundwater [2]. Bioremediation is the process of transfer, forming contaminants to less harmful substances, and depending on the type of pollutant, different approaches can be employed. One approach is the isolation of bacterial resistance to the pollutant with the aim of

enhancing remediation efficiency. The first use of bacteria for Cd removal was investigated in species of Citrobacter in the batch experiment [3, 4]. Following these studies, this Citrobacter was also studied for cadmium removal in reactor experiments [5, 6]. And later, more modification methods were applied for using Citrobacter sp. in cadmium removal such as in solutions supplemented with phosphatase substrate [7, 8]. Also, *Citrobacter* MCM B-181 was used for removal of cadmium by [9]. The main aim of the present study was to isolate Cd-resistant bacteria from well-known contaminated soil, identify the strain, optimise its growth, and determine its tolerance to Cd.

2. Materials and Methods

2.1. Soil sampling from the contaminated site and isolation of bacteria to resistant cadmium

2.1.1. Soil sampling

In the current study, for the isolation of Cd-resistant bacteria, HayTor quarry, Dartmoor, England was chosen as a source for the isolation of the strains, as this soil has been contaminated with cadmium copper, tin, silver, and lead due to historic mining activities [10]. The global positioning system (GPS) coordinates of HayTor are 50-577054" N latitude and 3.75549" W longitude. One kg of clayey soil from the surface was collected in a sterilised plastic box, and transferred to the laboratory, then stored in a refrigerator at 4 ºC until required at 24 hrs.

2.1.2. Soil analysis

For elemental analysis, a sub-sample of the soil was dried at 50ºC–60ºC for 72 hrs., then disaggregated and ground using a mortar and sieved by 180-micrometer particle sizes. Cadmium was extracted from the soil via aqua regia digestion [11], and the concentrations in the extract were determined using inductively coupled plasma mass spectrometry (ICP-MS). The ICP-MS analysis was conducted according to work carried out by [12]. Briefly, 1.0 g of sieved soil (n = 3 samples) was processed following aqua regia digestion using a Tecator digestion at 60ºC for 2hrs. After digestion, the solution was cooled, filtered (Whatman 541) into a clean volumetric flask, and the volume was completed with 2% HNO_3. The limit of detection (LOD) for the ICP-MS analysis for Cd (0.02 µM) was established from the five standard deviations (SDs) of measuring the lowest standard (n = 10). As no certified reference material (CRM) containing appropriately high Cd concentrations was available and hence, an in-house reference material, contaminated soil SS-2, was used to indicate recovery. The percentage recovery of ICP-MS via the use of contaminated soil- SS-2 was Cd (50%), which was calculated from the recorded (4.0±0.3 µmolal Cd) and certified (8.0±0.06 µmolal Cd) values of the reference material. However, the procedural blank (n = 3 samples) was of a similar magnitude (3.0±0.03 µmolal Cd) as this reference material, explaining the poor recovery obtained.

2.1.3. Isolation of Cd resistant bacteria

For the enrichment of bacteria, 0.5 g of the soil sample was transferred into 250 mL of Erlenmeyer flask containing 50 mL of E-Basal salts media (EBS) supplemented with D-fructose (10 mM) as a carbon source [13]. The flask was incubated at 37°C for five days, and the turbidity was monitored regularly. After incubation, 5 mL of enriched bacterial culture was transferred to 45 mL of EBS/D-fructose. The serial subculture was repeated for four-time cycles until an enriched bacterial growth was obtained, at which point isolation was attempted. The isolation was preliminarily done in terms of MTC to Cd [14]. Five mL of the bacterial culture was inoculated into 45 mL of EBS/D-fructose in Erlenmeyer-flasks (250 mL) in triplicate, amended with Cd and incubated at 37°C for 48 h. The nominal concentration of Cd (supplied as Cd $(NO_3)_2 \oplus 4H_2O$) started at 1 µM and increased by 2 µM at each transference of the screening process. A control without Cd was used to determine whether there

was growth at each step. The concentration at that below no growth occurred, and was accepted as the MTC. After the determination of MTC values, three cultures were grown with Cd at their MTC values, which is 10 mM for two cultures and 15 mM for the third. To obtain single colonies from each bacterial culture (the MTCs of 10 mM and 15 mM), 100 ♣L of the culture was spread onto EBS/ D-fructose agar plates supplemented with Cd (in triplicate). The nominal concentrations of Cd (mM) were below and above MTC values of the bacterial culture. The plates were incubated at 37°C until the colonies were visible. After growing the colonies, each one was purified, and considered as a Cd-resistant isolate.

2.2. Optimising growth conditions and the selection of isolates

Different bacterial growth conditions, including temperature, carbon, and nitrogen sources, were studied in 50 mL of EBS in the Erlenmeyer-flasks (250 mL) in triplicate, and the amount of biomass was determined. The optimum temperature for the isolate was first studied by growing of the culture in EBS/D-fructose and incubation at different temperatures of 4°C, 18°C, 25°C, 30°C, 37°C, 42°C, 44°C, 50°C, and 60°C for 4 days. The most suitable carbon source for the growth of isolates was studied using glucose and fructose (10 mM concentration), acetate, pyruvate, and sucrose (20 mM concentration), separately. The experiments were carried out at an optimised temperature of 37°C for seven days and incubated at a shaking speed of 100 rpm. Finally, the suitable nitrogen source for the growth was studied by the addition of ammonia, urea, thiocyanate, cyanate, nitrate, or glycine (3 mM concentration), in addition to the dinitrogen in the air. The experiments were performed at 37°C, and the carbon sources were either fructose for some isolates or pyruvate for other isolates. Based on their Cd MTC value, four out of eight Cd-resistant isolates with the highest MTC ability (C15-1, C15-2, C15-3 and C15-4), were chosen for further study.

2.3. Estimation of the specific growth rate and selection of one isolate

The specific growth rate was determined for isolates C15-1, C15-2, C15-3, and C15-4 under their respective optimised conditions. One mL of the growing culture of each isolate was inoculated into 50 mL of EBS/ pyruvate (20 mM), or D-fructose (10 mM) for isolate C15-4. During the incubation at 37°C, samples were collected at regular time intervals, and the amount of biomass was determined. The growth of cells in the EBS was determined in terms of dry biomass. From the batch cultures, samples were collected at regular times, and the dry biomass was determined. The growth of bacterial strains was determined by measuring the optical density (*OD*) at 440 nm using a UV visible spectrophotometer against a cell-free EBS medium as a blank. The *OD* should be within the range of 0.2 to 0.9. It was assumed that 0.1 of *OD* was equivalent to 23 mg/L of dry cell biomass of strains. After determining the dry biomass of the growth culture at regular times, the logarithmic dry biomass against the times was plotted to obtain the bacterial growth curve as a semi-logarithmic graph. The curve was fitted with the nonlinear regression of the biomass mean data using the SigmaPlot (version 13). The growth curve was used to measure the specific growth rate by plotting one point of the exponential phase of the amount of biomass of bacterial growth (axis y) and its double point against time (axis x). Monod`s equation (1949) was used to calculate the growth rate. Based on the specific growth rates of four isolates, the isolate with the highest growth (re-coded as 'C15'), was chosen to achieve the objectives of the present study.

2.4. Characterisation of B.agri C15

The morphology isolate of *B.agri* C15 was observed after being stained with Gram stain and observed under a light microscope, according to the work of [15]. Biochemical tests, including indole, methyl red, Voges-Proskauer, and citrate tests (IMVIC) were performed in triplicate, with control. The genomic DNA (gDNA) isolate of *B.agri* C15 was extracted according to the JGI (Doe Joint Genome

Institute) method [16]. Quality and quantity of gDNA, agarose gel electrophoresis, gDNA quantification using Nanodrop spectrophotometer, gDNA quantification using the Qubit 2.0 Fluorometer were used. The electrophoresis was run at 60 V for 60 mins and then the gel was illuminated with a UV transilluminator to be photographed using the gel-imaging system. The quantity of pure gDNA was determined using a NanodropTM 1000 spectrophotometer (Thermo Scientific Ltd., DE, USA) at 260 nm based on the measurement ratios of A260/A230 and A260/A280. A260/A230 ratio indicates residual phenol and protein contaminations, whereas the A260/A280 ratio indicates isopropanol or phenol contaminations. The accurate method for the quantity of pure gDNA was determined using the dsDNA BR Assay Kit (catalogue number Q32850, Q32853, Life Technologies) and the Qubit 2.0 Fluorometer (Life Technologies). The Qubit 2.0 fluorimeter was turned on for three h, before starting the measurements, to stable its signal. Two µL of the gDNA sample was diluted with 199 µL of Qubit dsDNA BR buffer and with 1 µL of Qubit dsDNA BR reagent (200X concentrate in DMSO) in an Eppendorf tube. A calibration curve, zero ng/µL DNA (Qubit® dsDNA BR standard #1) and 100 ng/µL DNA (Qubit dsDNA BR standard #2) were diluted with 190 µL of Qubit dsDNA BR buffer and with 1 µL of Qubit dsDNA BR reagent (200 concentrates in DMSO) in an Eppendorf tube. All samples were incubated for 2 mins, and the concentrations of gDNA were measured using the fluorimeter by sequentially putting in 2 µL from each sample and recording the gDNA concentrations. The acceptable gDNA samples for sequencing required a concentration of 10 – 30 ng gDNA /µLTris-HCl. The gDNA was subjected to 16S rRNA (rrs) gene sequence. MUSCLE (Multiple Sequence Comparison by Log-Expectation) was used to make the multiple sequence alignment to be tested for the best fit of models, based on the Bayesian Information Coefficient (BIC). The Phylogenetic analysis was done using MEGA software (Version7.0.26); the trees were reconstructed accordingly (with a percentage of 5,000 bootstrap replications) with a discrete gamma distribution to model rate differences across the sites (5 categories and gamma parameter 0.1466) allowance for some (40.39 %) evolutionarily invariant sites.

3. Results

3.1. Isolation of bacteria resistant to cadmium

The isolation was carried out from the soil of HayTor quarry. For the soil, a concentration of 490±50 µmolal Cd was determined after aqua regia acid extraction and analysis by ICP-MS. Although the reference material used for quality control showed poor recovery (50%), this concentration is two orders of magnitude higher than Cd in the reference material. Therefore, the Cd concentration in the soil clan is seen as a reasonable, probably low estimate. Compared to soil contamination assessment criteria in the UK (EA, 2015; CLEA: e.g., for residential lifetime exposure: 98 µmolal Cd or allotment soil: 9.38 µmolal Cd, both at pH 7) and the US EPA [17] guidelines for soil (recommendation: Cd < 44 ♣ molal). This soil is considered as contaminated with Cd concentrations greater than one order of magnitude higher than the guidelines levels. Based on the MTC values of bacterial cultures, eight Cd-resistant bacteria were isolated from three different Cd-tolerant bacterial cultures. These isolates were named depending on their MTC abilities as C10-1, C10-2, C10-3, C10-4, C15-1, C15-2, C15-3, and C15-4 (Table 1). The isolates C15-1, C15-2, C15-3, and C15-4 showed the highest MTC (15 mM Cd), followed by the isolates C10-1, C10-2, C10-3, and C10-4 (10 mM Cd).

Table 1. MTC values of Cd-resistant bacterial isolates. The isolate names were coded depending on the MTC values; 10: Means the isolate resist to 10 Cd mM, 15: Means the isolate resist to 15 Cd mM, and 1, 2, 3, and 4: Mean the number of the isolate from each resistant culture.

Isolate	MTC (mM Cd)
C10-1	10
C10-2	10
C10-3	10
C10-4	10
C15-1	15
C15-2	15
C15-3	15
C15-4	15

3.2. Optimising growth conditions and selection of isolates

The growth conditions were optimised. The amount of the biomass of eight Cd-resistant isolates at different temperatures (4 °C, 18 °C, 25 °C, 30 °C, 37 °C, 42 °C, 44 °C, 50 °C, and 60 °C), as summarised in Figure 1. The optimum temperature for the growth of these isolates was 37°C, which showed the significant highest dry biomass (Figure 1, $^{a}P<0.05$). At 37°C, the lowest growth was demonstrated by the isolates C10-1 and C10-2, compared to isolates C10-3 and C10-4, respectively. Similarly, the isolates C15-1, C15-2, C15-3, and C15-4 demonstrated the highest dry biomass at 37°C, and there were no differences observed among them (Figure 8,$^{a}P<0.05$). Eight isolates showed no growth at temperatures, 4°C, 18°C, 50°C, and 60°C compared to other temperatures. With the temperature increase to 25°C and 30°C, all the isolates displayed a significant increase in biomass amounts compared to lower temperatures. However, the increase in the temperatures to 42°C and 44°C significantly decreased the biomass amounts.

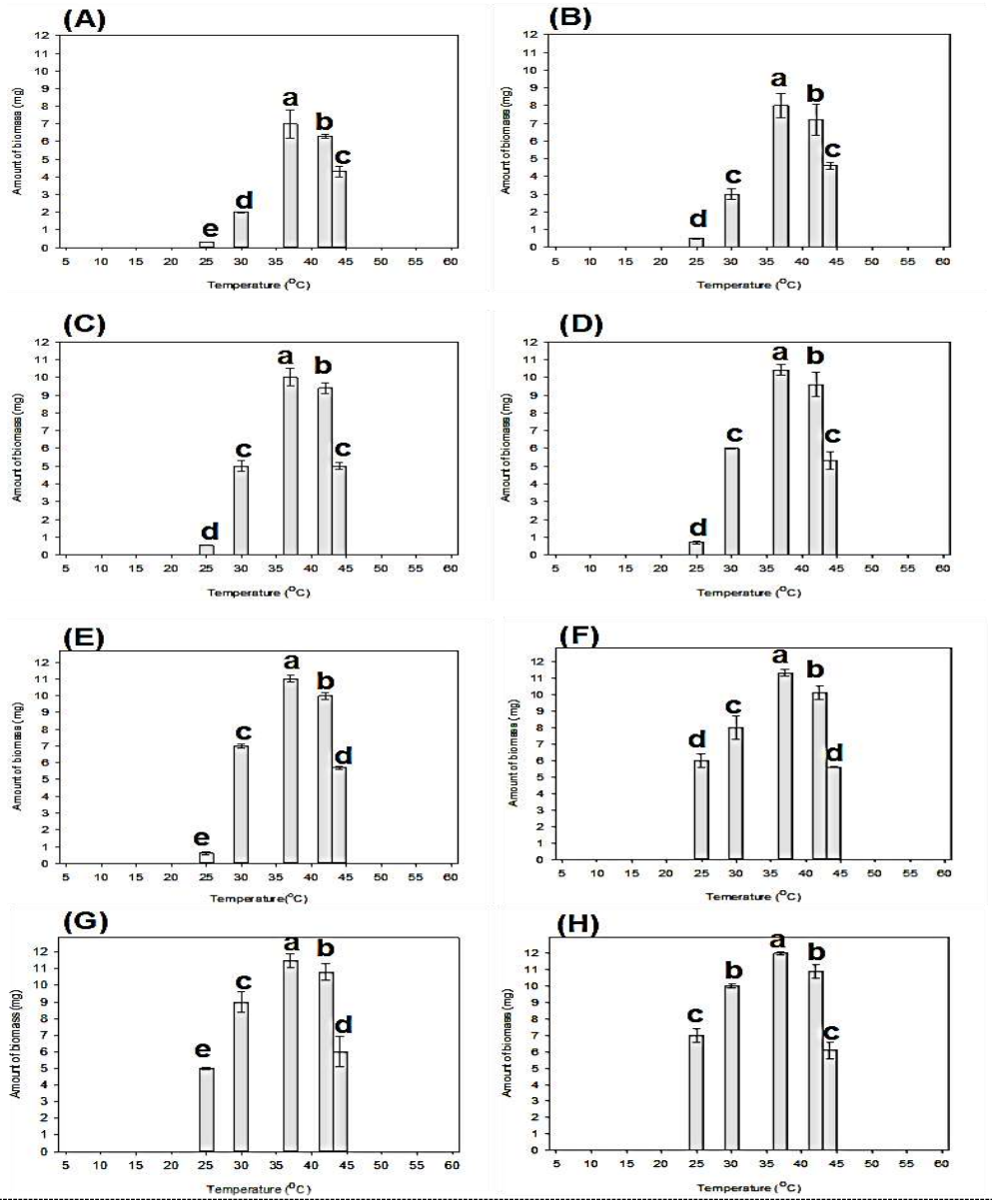

Figure 1. Determination of suitable temperature for the growth of eight Cd-resistant isolates. (A) Isolate C10-1, (B) isolate C10-2, (C) isolate C10-3, (D) isolate C10-4, (E) isolate C15-1, (F) isolate C15-2, (G) isolate C15-3, and (H) isolate C10-4. These isolates were grown in the EBS/D-fructose, incubated for 48 h at 37 °C and shaken at 100 rpm. The error bars represent the standard errors of the mean (n = 3, batch experiments) and a different letter on the bars indicates a significant difference among temperatures within isolates.

The determination of a suitable carbon source was identified by measuring the growth of each isolate in batch cultures, supplemented with glucose or fructose (10 mM), acetate, sucrose, or pyruvate (20 mM). The suitable carbon source for the growth of eight isolates demonstrated that the isolates C10-1, C10-2, C10-3, C10-4, and C15-4 had the highest biomass when growing with 10 mM of fructose (Figure 2, A, B, C, D and H, $^{a}P<0.05$) compared to other isolates, C15-1 (Figure 2, E $^{c}P<0.05$), C15-2 (Figure 9, F $^{b}P<0.05$) and C15-3 (Figure 2, G $^{c}P<0.05$). At the same time, the isolates; C15-1, C15-2, and C15-3, as outlined in the Figures 2E 2F 2G, respectively. Figure (2) showed the highest biomass ($^{a}P<0.05$) in growing within 20 mM pyruvate compared to their growth within other carbon sources.

The suitable nitrogen sources for growing the eight isolates were optimised under different nitrogen sources at an optimised temperature (37°C), and carbon sources, either with fructose (10 mM) for isolates C10-1, C10-2, C10-3, C10-4, and C15-4 or pyruvate (20 mM) for isolates C15-1, C15-2, and C15-3. All isolates illustrated the highest growth when grown with ammonia (Figure 3, $^{a}P<0.05$) that was initially used in the composition of EBS medium, compared to other nitrogen sources. Based on the MTC abilities of the eight Cd-resistant isolates, four isolates i.e. C15-1, C15-2, C15-3, and C15-4 demonstrated the highest MTC abilities, and were then chosen for further study.

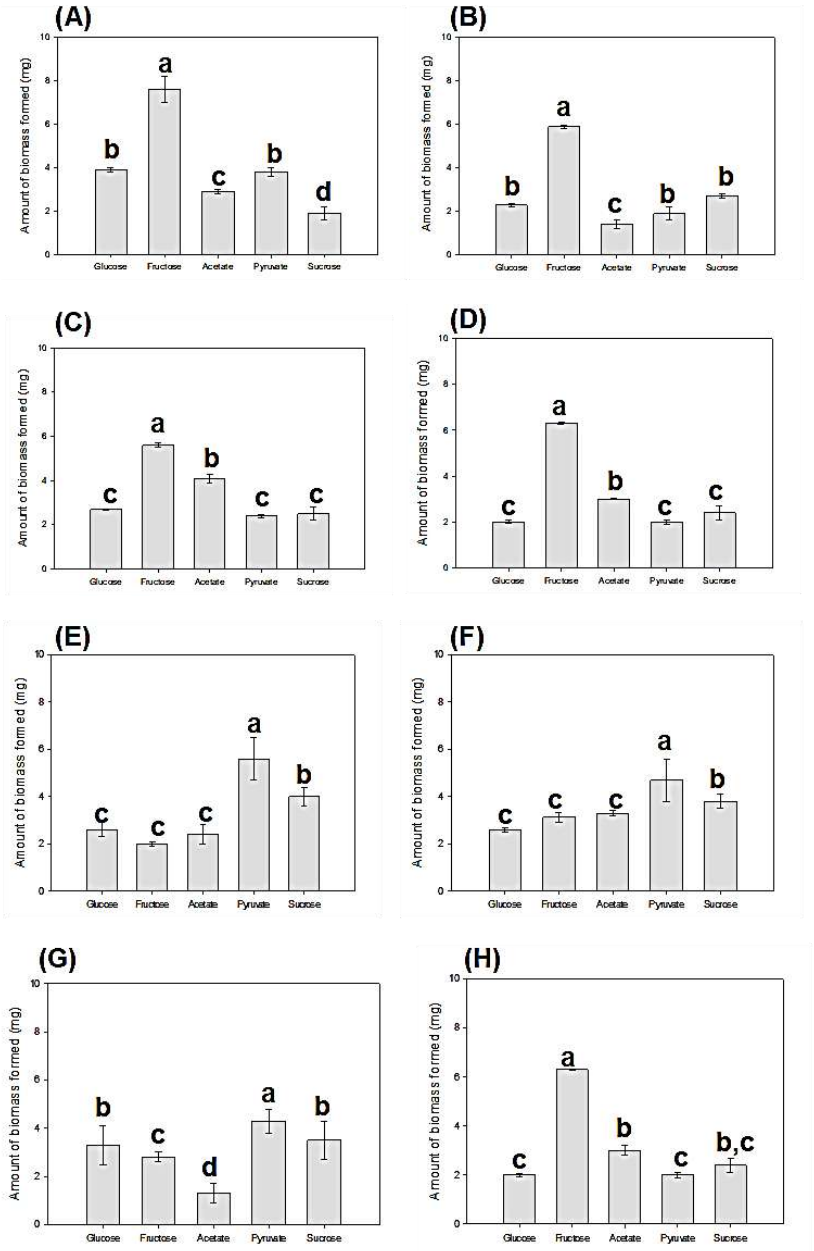

Figure 2. Determination of suitable carbon sources for the growth of eight Cd-resistant isolates. (A) Isolate C10-1, (B) isolate C10-2, (C) isolate C10-3, (D) isolate C10-4, (E) isolate C15-1, (F) isolate C15-2, (G) isolate C15-3, and (H) isolate C10-4. The isolates were grown in EBS supplemented with different carbon sources, incubated for seven days at 37°C and shaken at 100 rpm. The error bars represent the standard errors of the mean (n = 3, batch experiments) and a different letter on the bars indicates a significant difference among carbon sources within isolates.

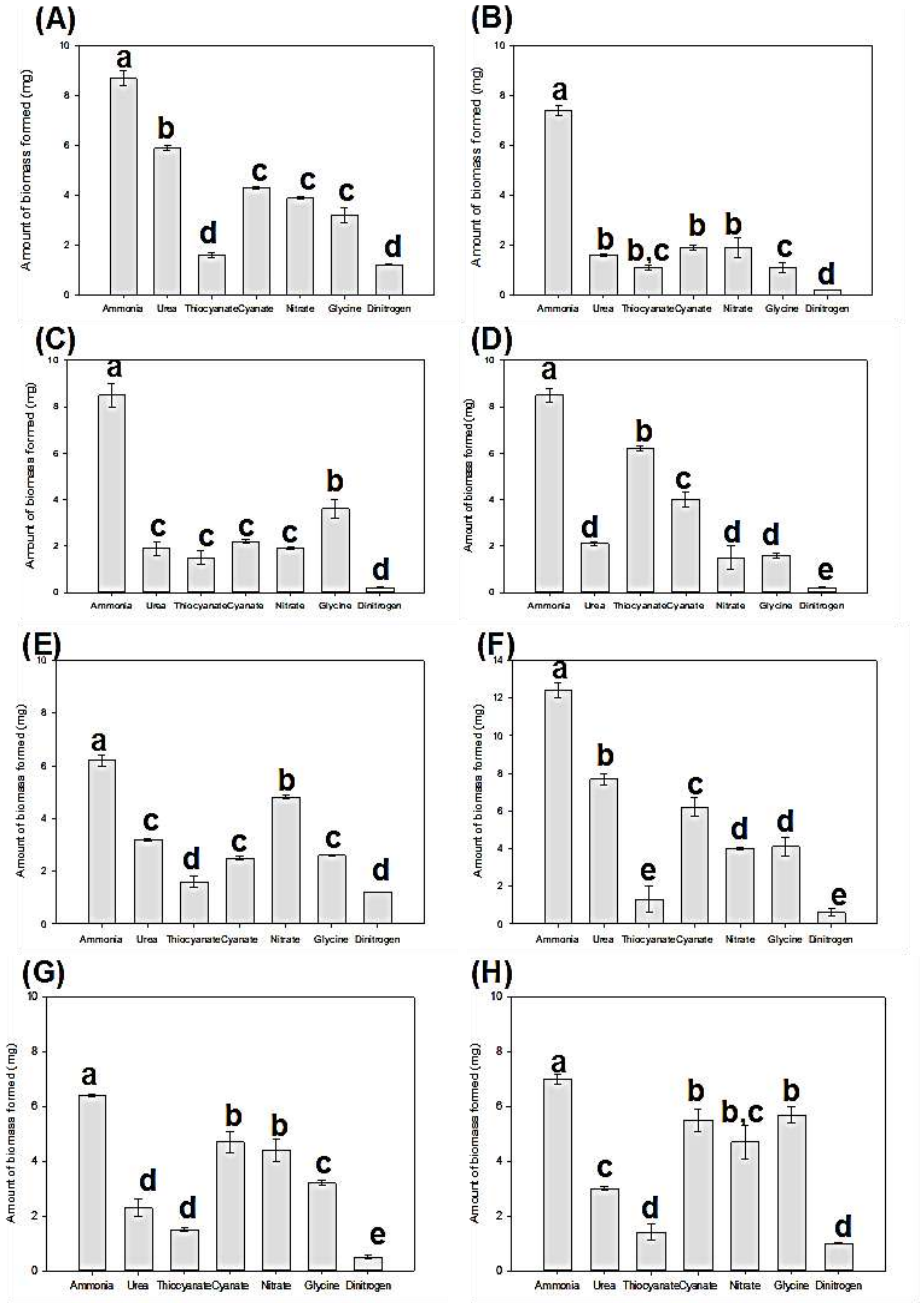

Figure 3. Determination of nitrogen sources for the growth of eight Cd-resistant isolates. (A) Isolate C10-1, (B) isolate C10-2, (C) isolate C10-3, (D) isolate C10-4; (E) isolate C15-1, (F) isolate C15-2, (G) isolate C15-3, and (H) isolate C10-4. The isolates were grown in EBS supplemented with fructose (10 mM) for isolates C10-1, C10-2, C10-3, C10-4, and C15-4 or with pyruvate (20 mM) for isolates C15-1, C15-2, and C15-3, incubated for seven days at 37°C and shaken at 100 rpm. The error bars represent the standard errors of the mean (n = 3, batch experiments) and a different letter on the bars indicates a significant difference among nitrogen sources within isolates.

3.3. Estimation of the specific growth rate and selection of one isolate

The selection of the potential isolate was based on its specific growth rate in addition to its MTC ability. The dry biomass of isolates C15-1, C15-2, C15-3, and C15-4 were determined, and their growth curves were plotted to identify a specific growth rate (Figure 4). The values of the specific growth rate ranged from 0.09 to 0.12 h^{-1}. Among the four isolates, C15-1 and C15-2 significantly showed (Figure 4A, B, $^{c}P<0.05$) the lowest specific growth rate (0.09 ± 0.004 h^{-1} and 0.09 ± 0.005 h^{-1}, respectively). The isolate C15-3 displayed the highest specific growth rate (0.12 ± 0.007 h^{-1}) , as summarised in the Figure 4C, $^{a}P<0.05$, followed by the isolate C15-4 (0.11 ± 0.02 h^{-1}), as outlined in the Figure 4D, $^{b}P<0.05$. Therefore, the isolate C15-3 was re-coded as 'C15' and chosen for further experiments.

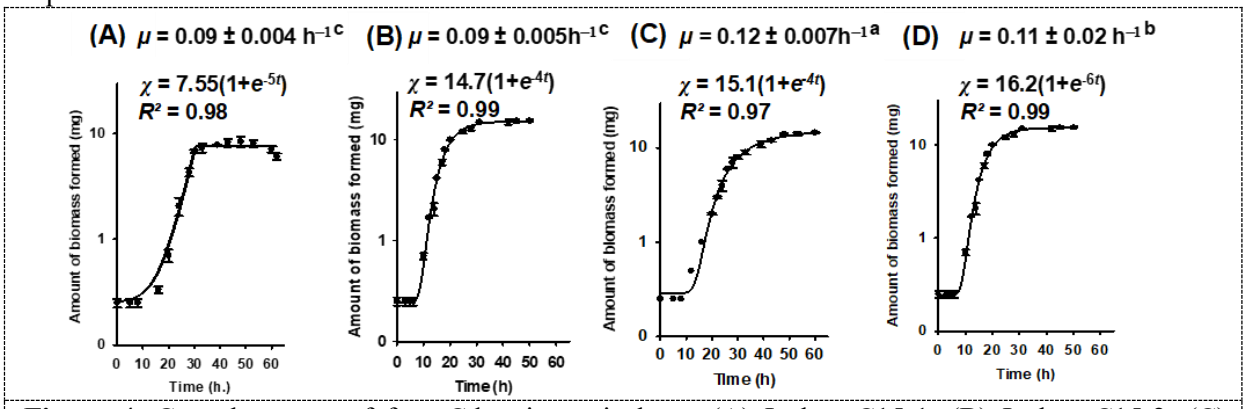

Figure 4. Growth curves of four Cd-resistant isolates. (A) Isolate C15-1, (B) Isolate C15-2, (C) Isolate C15-3, and (D) Isolate C15-4. The isolates were grown in EBS supplemented with D-fructose (10 mM) for isolate C15-4 or with pyruvate (20 mM) for isolates C15-1, C15-2, and C15-3, incubated at 37°C and shaken at 100 rpm for 72 h. The error bars represent the standard errors of the mean (n = 3, batch experiments). The specific growth rate (♣) is shown and a different letter on the ♣ indicates a significant difference among isolates.

3.4. Morphological, biochemical, and 16S rRNA sequence analysis

Morphological observation of isolate C15 showed Gram-stain-positive bacilli (Figure 5A). The biochemical characterisation (IMVIC test) of the isolate C15 was performed. The isolate was negative and did not produce indole from tryptophan; the acid formed from glucose but produced acetone from the glucose and did not use the citrate as a carbon source. The 16S rRNA (rrs) gene sequence of the isolate C15 identified that the isolate belongs to the genus of *Brevibacillus*, closely related to *B. agri* DSM 6348T (AB112716) with 100% identification. The isolate C15 was named *B.agri* C15, as outlined in the Figure 5E.

3.5. Assessment of the inhibition effects of cadmium on B. agri C15

The inhibition effects of Cd on *B. agri* C15 under 2.5, 5, 10, and 15 mM Cd were studied. An increase in the Cd concentration led to an increase in the amounts of unconsumed pyruvate. The exposure to 2.5 mM Cd decreased the utilised pyruvate (mM) from 14.1 (Figure 6A) to 12.3 (Figure 6B). The amounts of unconsumed pyruvate were inhibited with the nominal concentrations of 5 mM Cd (Figure 6C) and 10 mM Cd (Figure 6D). In contrast, the amount of unconsumed pyruvate under 15 mM Cd was reduced to 9.76 mM (Figure 6E). Nevertheless, the amounts of the biomass under the inhibited effect of Cd were recorded as small differences, and the specific growth rates under these toxic concentrations were significantly inhibited at the nominal concentration of 15 mM Cd (Figure 6E, $^{a}P<0.05$). All of these results indicated that the toxic effect of Cd controlled the consumed amounts of pyruvate.

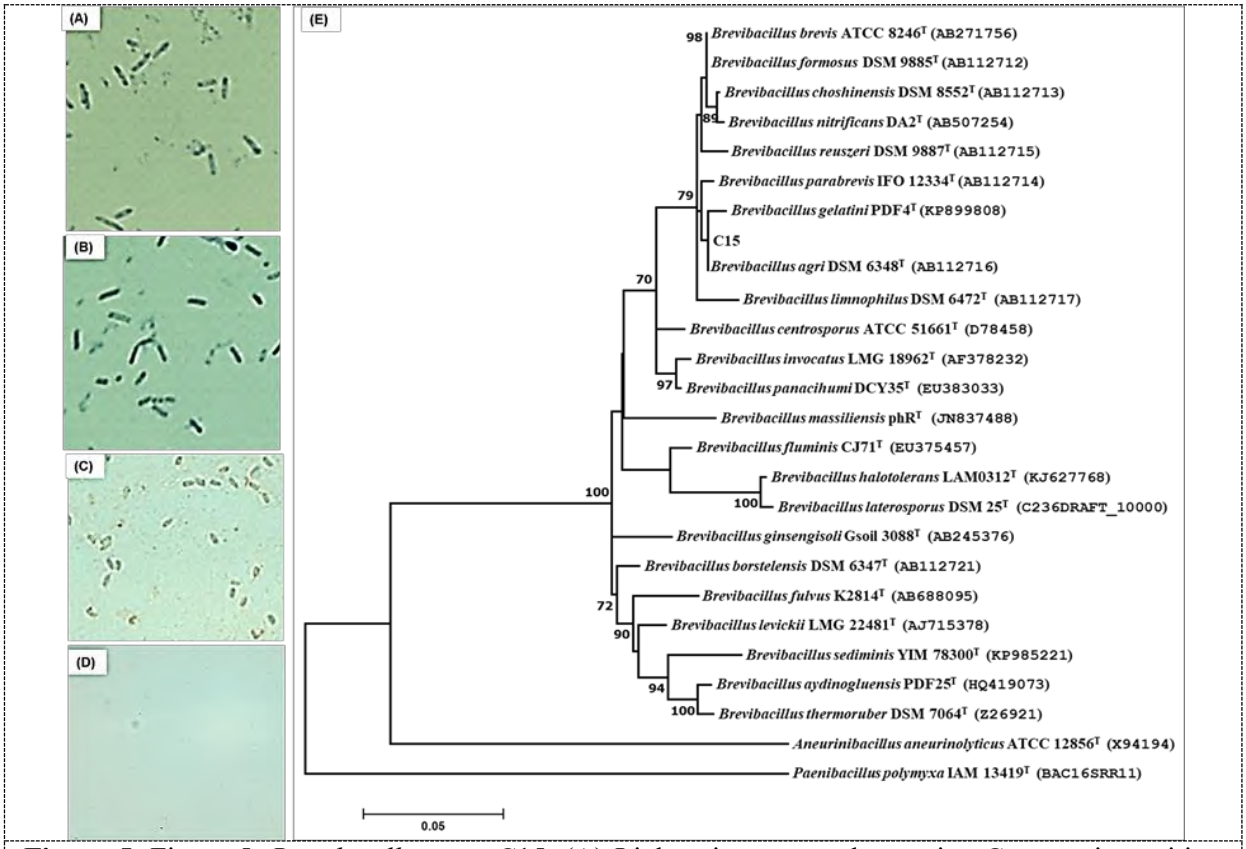

Figure 5. Figure 5. *Brevibacillus agri* C15. (A) Light microscopy observation Gram-stain-positive. The stains were analysed simultaneously in triplicates of three separately grown on nutrient agar plates. Control strains (B) *Bacillus subtilis*, showing Gram-stain-positive, (C) *Cupriavidus metallidurans* DSM 2839T, showing Gram-stain-negative and (D) uninoculated slides. (E) Phylogenetic analysis. The maximum likelihood tree produced based on the 16S rRNA (rrs) gene showing the positions of isolates C15 versus *Brevibacillus* species with validly published names. The tree shown is the optimal tree with the lowest log-likelihood (-4773.56), with numbers at nodes indicating the percentage of 5,000 bootstrap replications in which the topology was preserved (values <70 % omitted for clarity). All of the positions at which there was less than 95 % coverage were omitted from the final analysis, in which 1,342 nucleotides were used. The branch lengths are to scale, and they indicate the number of substitutions per site, and the bar represents 0.05 substitutions per site. The outgroup is the same gene from *Paenibacillus polymyxa* IAM 13419T, type genus of the Paenibacillaceae, in which all members of the in-group are circumscribed. The accession numbers are given in parentheses and refer to the GenBank or Integrated Microbial Genomes (IMG) databases (the latter contain an underscore " _").

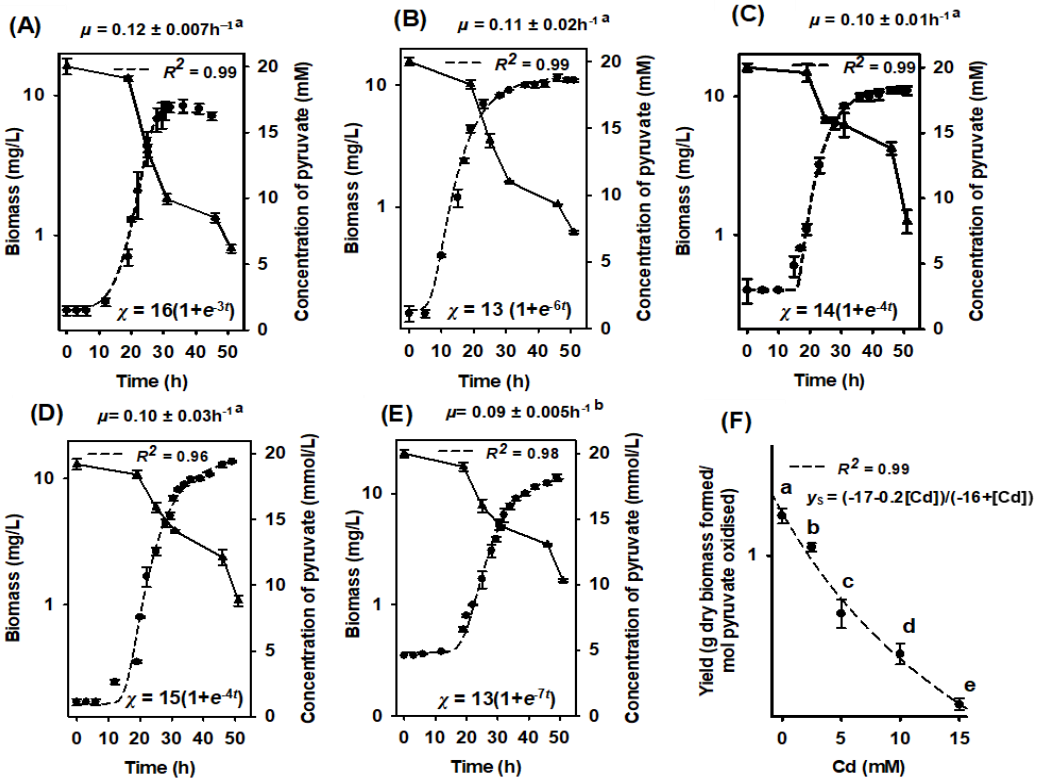

Figure 6. The effects of Cd on the concentration of biomass (●) and pyruvate utilisation (▼) of *B. agri* C15. The strain was grown in EBS/ pyruvate, (A) control and with nominal concentrations of Cd (B) 2.5 mM, (C) 5 mM, (D) 10 mM, and (E) 15 mM. The specific growth rate ( ) is shown. Inhibition effects of Cd on (F) their respective values of the Y_S formed. The error bars represent the standard errors of the mean of three independent cultures at each Cd concentration. b, c, d, and e are significantly different compared to the value of control without Cd.

The results observed that the specific growth produces were intensely inhibited under the Cd concentrations (Figure 6F); the highest yield was obtained in grown without Cd; this showed statistical differences (Figure 6F, $^{a}p\leq0.05$) compared to growth under other Cd exposures (2.5 mM, $^{b}p\leq0.05$), (5 mM, $^{c}p\leq0.05$), (10 mM, $^{d}p\leq0.05$), and (15 mM, $^{e}p\leq0.05$).

4.Discussion

In the current study, soil from Hay Tor quarry was chosen for the isolation of Cd-resistant bacteria, due to its history of mining, where metal ores have been observed in the soil. This soil is known to be contaminated with Cd (this study), and with other metals [10]. Therefore, it was assumed that it could be possible to isolate Cd-resistant bacteria from it. The isolation of Cd-resistant bacteria was screened sequentially by increasing the Cd concentration in the cultures. Moreover, the isolates were obtained from the highest concentrations that permitted culture survival. [18] reported that increases in Cd concentrations affect the properties of bacterial cells, such as protein activity and DNA stability, leading to evolutionary adaptations in phenotype (adaptation) and acclimatisation (changes in gene expression). Also, eight Cd-resistant isolates observed Cd-tolerant abilities, and their growth was optimised under different conditions. The best incubation temperature was established at 37°C. It is common to assume that different bacteria will prefer different carbon sources for the enrichment and that structurally similar carbon sources, which are metabolised by relevant biochemical pathways, are selected by the same microbial strains. About 55% of the carbon taken by the bacteria serve as

substrates of the metabolic network after being broken down to supply pools of amino acids and other components of a cell [19]. The isolated bacteria in the present study were enriched in EBS medium on five different carbon sources. The biomass of the isolates generated from enrichment cultures containing different carbon sources showed that pyruvate or fructose were the preferred sources of different strains. Fructose was added as the carbon source in the first steps of the enrichment culture of the soil sample; therefore, some isolates choose this source. Other strains preferred pyruvate as a carbon source. This could be as a result of using more than one carbon source for the enriched isolates and the changes in the composition of the growth medium over time will be reflected by changes in the behaviour of the isolates[20]. As well as, [21] observed that bacteria chose fructose as the sole carbon source and did not use glucose at all. Ammonia, which was used in the original EBS medium, was preferred among the nitrogen sources added. The specific growth rate of the selected four isolates (C15-1, C15-2, C15-3 and C15-4) from the eight isolates showed that isolate C15-3 grew faster than other isolates. So it was chosen for further experiments and re-coded as 'C15'. Isolate C15 was tolerant to 15 mM of Cd (supplied as Cd $(NO_3)_2 \oplus 4H_2O$); it was considered as a potential isolate. Isolate C15 was identified as *Brevibacillus* agri C15 that used pyruvate as a carbon source, showing a new characteristic compared to other *Brevibacillus* species, which was reported by [15]. It has been published in a recent study that several species of *Brevibacillus* have been isolated from diverse habitats and geographical locations. *Brevibacillus* sp. has been previously demonstrated to have the ability to grow in the presence of Cd (85 mg/kg or ~760 μmolal) [22]. The mechanisms of resistant bacteria to resist Cd have been described and involve an efflux pump, adsorption, precipitation, and intracellular accumulation processes [23]. The bioaccumulation process consists of the accumulation and localisation of Cd in specific organelles; Cd-resistant bacteria can resist Cd through other mechanisms as well. The proposed Cd resistance of *B. agri* C15 may be due to a mechanism as mentioned above. The isolate *B. agri* C15, which had a natural resistance in Cd-contaminated soil, may harbour one or several ATP, RND, or CDF transporter responsible for the efflux system [24]. In addition, [25] mentioned that a PIB-type ATPase gene in a uranium-resistant bacterium isolated from uranium-contaminated soil. Similar efflux systems were reported with Cd resistance in *Acidithiobacillus ferrooxidans* [26]. Another mechanism of effective resistance is the precipitation or the adsorption of Cd on the cell surface. The extracellular polymeric substance (EPS) produced by *B. agri* C15 could allow the binding of Cd to anionic carboxyl groups (COO-) on the EPS. When exposed to Cd, the growth of *B. agri* C15 was adversely affected. The efflux of Cd outside the cells was likely responsible for the higher concentrations of Cd in the growth medium that changed the efflux process, increasing the intracellular uptake of Cd. [27] reported that Cd might cause damage to the cells through the accumulation of reactive oxygen species (ROS). The cell numbers of *Acidithiobacillus ferrooxidans* were reduced when exposed to CdSO4 [26]. It has also been reported that the growth of *Pseudomonas fluorescens* H_2 was affected by Cd exposure [28]. The results in the current study agreed with results as found [29], and [30], and reporting that Cd damages bacteria and leads to growth inhibition. The inhibition effect of Cd on the specific growth yield of *B. agri* C15 could also be due to the presence of other cations in the EBS growth medium. [28] found that Cd toxicity in cells decreased with the presence of Zn in the medium, a result of the inhibition of Cd uptake due to competing effects. In the present study, the EBS growth medium was used, and the possible competing effects were EDTA and Zn, both with lower concentrations compared to the Cd concentrations used in the exposure test. The high concentration of Cd suggests that the Cd were the cause of inhibited bacterial growth.

5. Conclusion

The *B. agri* C15 was isolated from a contaminated soil based on the MTC, and this strain showed tolerance to Cd and had a MTC value of 15 mM to Cd, which is considered as Cd-resistant bacteria. Thus, it is concluded that this strain could be suitable for a new Cd-bioremediation process; therefore, further studies are needed to investigate this possibility..

6. References

[1] Agency for Toxic Substances and Disease Registry (ATSDR) 2012 *Toxicological profile for Cadmium*. Atlanta, GA: U.S. Department of Health and Human Services, Public Health Service.
[2] Hashim MA, Mukhopadhyay S, Sahu JN and Sengupta B 2011 Remediation technologies for heavy metal contaminated groundwater *J. Environ. Manag.* **92** 2355.
[3] Macaskie LE and Dean A 1984 Cadmium accumulation by a *Citrobacter* sp. *Microbiology* **130** 53.
[4] Macaskie LE and Dean A 1984 Cadmium accumulation by immobilized cells of a *Citrobacter* sp *Environ. Technol*. **5** 177.
[5] Macaskie LE and Dean A 1984 Heavy metal accumulation by immobilized cells of a *Citrobacter* sp *Biotechnol. Lett*. **6** 71.
[6] Macaskie L, Wates J and Dean A 1987 Cadmium accumulation by a *Citrobacter* sp. immobilized on gel and solid supports: applicability to the treatment of liquid wastes containing heavy metal cations *Biotechnol. Bioeng*. **30** 66.
[7] Michel L, Macaskie L and Dean A 1986 Cadmium accumulation by immobilized cells of a Citrobacter sp. using various phosphate donors *Biotechnol. Bioeng*. **28** 1358.
[8] Macaskie L, Bonthrone K and Rouch D 1994 Phosphatase-mediated heavy metal accumulation by a Citrobacter sp. and related enterobacteria *FEMS Microbial. Lett.* **121** 141.
[9] Puranik P and Paknikar K 1999 Biosorption of lead, cadmium, and zinc by Citrobacter strain MCM B-181: Characterization Studies *Biotechnol. Prog*. **15** 228.
[10] Howard AJ, Kincey M and Carey C 2015 Preserving the legacy of historic metal-mining industries in light of the water framework directive and future environmental change in Mainland Britain: challenges for the heritage community *Historic Environ. Policy Pract*. **6** 3.
[11] Jebril NMT 2020 Novel use of XRF in the adsorption processes for the direct analysis of cadmium and silver in absorbent Na- alginate beads *Baghdad Sci. J*. **17** 1139.
[12] McBride MB and Spiers G 2001 Trace element content of selected fertilizers and dairy manures as determined by icp–ms *Comm. Soil Sci. Plant Anal*. **32** 139.
[13] Boden R and Hutt LP 2018 *Determination of Kinetic Parameters and Metabolic Modes Using the Chemostat* In: Steffan R (ed.) Consequences of Microbial Interactions with Hydrocarbons, Oils, and Lipids: Biodegradation and Bioremediation. Handbook of Hydrocarbon and Lipid Microbiology Springer, Cham 1.
[14] Schmidt T and Schlegel HG 1994 Combined nickel-cobalt-cadmium resistance encoded by the ncc locus of *Alcaligenes xylosoxidans* 31A. *JB* **176** 7045.
[15] Vos P, Garrity G, Jones D, Krieg NR, Ludwig W, Rainey FA, Schleifer KH and Whitman WB 2011 *Bergey's Manual of Systematic Bacteriology*: Volume 3: The Firmicutes. vol. 3. Springer Science and Business Media.
[16] William S, Feil H and Copeland A 2012 Bacterial genomic DNA isolation using CTAB *Sigma* **50** 6876.
[17] United States Environmental Protection Agency (US EPA) 2011 *Edition of the drinking water standards and health advisories.* Washington, DC: U.S. Environmental Protection Agency, Office of Water. EPA822R06013. PB2007101258.
[18] Podrabsky JE and Somero GN 2004 Changes in gene expression associated with acclimation to constant temperatures and fluctuating daily temperatures in an annual killifish *Austrofundulus limnaeus J. Exp. Biol*. **207** 2237.
[19] Lehninger AL, Nelson DL and Cox MM 2008 *Lehninger principles of biochemistry* W.H. Freeman, New York, 5th Ed.
[20] Wawrik B, Kerkhof L, Kukor J and Zylstra G 2005 Effect of different carbon sources on community composition of bacterial enrichments from soil. *Appl. Environ. Microbiol*. **71** 6776.

[21] Costa E, Teixido N, Usall J, Atares E and Vinas I 2002 The effect of nitrogen and carbon sources on growth of the biocontrol agent Pantoea agglomerans strain CPA-2 *Lett. Appl. Microbiol.* **35** 117.
[22] Ruiz-Lozano JM and Azcón R 2011 *Brevibacillus, arbuscular mycorrhizae and remediation of metal toxicity in agricultural soils Endospore-forming Soil Bacteria* Springer: 235-258.
[23] Bruins MR, Kapil S, and Oehme FW 2000 Microbial resistance to metals in the environment *Ecotoxicol. Environ. Safe* **45** 198.
[24] Leedjärv A, Ivask A and Virta M 2008 Interplay of different transporters in the mediation of divalent heavy metal resistance in *Pseudomonas putida* KT2440 *JB* **190** 2680.
[25] Nongkhlaw M, Kumar R, Acharya C and Joshi SR 2012 Occurrence of horizontal gene transfer of PIB-type ATPase genes among bacteria isolated from the uranium rich deposit of Domiasiat in North East India *PloSone* **7**: e48199.
[26] Ramos-Zúñiga J, Gallardo S, Martínez-Bussenius C, Norambuena R, Navarro CA, Paradela A, and Jerez CA 2019 Response of the biomining *Acidithiobacillus ferrooxidans* to high cadmium concentrations *J. Proteom*. **198** 132.
[27] Stohs SJ and Bagchi D 1995 Oxidative mechanisms in the toxicity of metal ions *Free Radic. Biol. Med*. **18** 321.
[28] McEldowney S 2000 The impact of surface attachment on cadmium accumulation by Pseudomonas fluorescens H_2 *FEMS Microbiol. Ecol*. **33** 121.
[29] Peptides P 2009 A Common Highly Conserved Cadmium Detoxification Mechanism from Bacteria to Humans *J. Biol. Chem*. **284** 4936.
[30] Chudobova, D, Dostalova S, Ruttkay-Nedecky B, Guran R, Rodrigo MAM and Tmejova K 2015 The effect of metal ions on *Staphylococcus aureus* revealed by biochemical and mass spectrometric analyses *Microbiol. Res*. **170** 147.

Production of Cellulase and bioethanol by ethanol-tolerant coculture of *Bacillus cereus* and *Fusarium solani*

Production of Cellulase and bioethanol by ethanol-tolerant co-culture of *Bacillus cereus* and *Fusarium solani*

Mohammed Fadhil Abood[1*], Haider Mousa Hamzah[2]and Dhafer Fakri Al-Rawii[1]

[1]College of Education for Pure Sciences, Anbar University, Iraq.
[2]Department of Biology, College of Science, University of Sulaimani, Iraq

*E-mail: eps.mohammed.fadhel@uoanbar.edu.iq

Abstract. Cellulase is an enzyme produced by fungi and bacteria that hydrolyzes cellulose by breaking down the glycosidic bond, β-1,4 that binds sugar glucose units. Bioethanol and cellulase enzyme were produced by ethanol-tolerant of *Bacillus cereus* co-culture. So the production of filamentous solani were using the wastes of *Cynodon dactylon* L. The highest activity of enzyme was at 96 hour/30°C of incubation. The optimal pH value was 7.5, while the carbon concentration was 3%. On the other hand, the best inoculum ratio was 0.5/100 mL (52 × 10^8 cell/mL bacterial cells and 10^5 conidia/mL of the fungus). In order to test the efficiency of ethanol production by the co-culture by using different concentrations of pure ethanol was measured in the solid medium. Both *Bacillus* sp. and *F. solani* tolerated incubation with 5% ethanol. The best treatment when using 0.5% sulfuric acid which gave the best concentration of reduced sugars and the results showed a difference in the concentration of sugars produced by the fermentation process, it was 3.9 mg/mL in the first day, whereas it was 2.51 mg/mL after 120 hours of fermentation, the concentration of bioethanol produced after fermentation was 195 g/L. In conclusion *Cynodon dactylon* L. wastes were treated by sulfuric acid, cellulase digestion, and autoclave treatment to be a good source of reducing sugars.

Keywords. Ethanol, Cellulase enzyme, *Fusarium*, *Bacillus*.

1. Introduction

Cellulose is the main component of the plant cell wall, while the massive of cellulosic sources containing raw materials that not exploited or can be used more efficiently [1]. Lignocellulosic biomass in plants consists of about 10-25% lignin, 20- 30% hemicellulose and 40-50% cellulose [2]. Cellulase is an enzyme produced by fungi and bacteria that hydrolyzes cellulose by breaking down the glycosidic bond, β-1,4 that binds sugar glucose units. This enzyme has the ability to hydrolyze cellulose into its essential components, glucose-β or oligosaccharides [3]. Cellulose biomass is an important source of energy. Through this mass, carbon is recycled by microorganisms that secrete the cellulase enzyme, which catalyzes the process of cellulose hydrolysis into cellobiose and then converts it into glucose that can be converted to biofuel such as ethanol [4]. The world faces major economic and environmental problems due to higher fuel prices and increased gas emissions, contributing to global warming. As the sources of these conventional fuels have been depleted, it becomes imperative that alternative energy sources such as bio-ethanol, which has been widely produced in the world by

fermentation processes be explored [5]. Ethanol is the most important alternative source of fuel. Its production has increased in recent years, and its production reached about 11% of the fuel used due to the rapid depletion of the global extra oil until global production reached 100 billion liters in 2015 [6]. The present study is aimed to produce the cellulase enzyme and ethanol by using of the co-culture of local isolates of *Bacillus cereus* and *F. solani* by culturing of the *Cynodon dactylon* plant as a production medium. The study also identified the optimum conditions for the production of the enzyme and ethanol using the liquid state fermentation.

2. Materials and Methods

2.1. Preparation of Cynodon dactylon wastes

Cynodon dactylon L. was collected from the gardens of the University of Sulaimani and was washed, cut into pieces and then dried using an electric oven at 65 °C for 24 hours. The wastes were then grinded using an electric mill and passed through a 2 mm sieve and stored in sterile polyethylene bags until use.

2.2. Cellulase production

The media for the enzyme production was prepared by dissolving 2 g ($(NH_4)2NO_3$, 2 g (KH_2PO_4), 5 g ($MgSO_4.7H_2O$), 0.2 g ($CaCl_3.H_2O$), 0.2 g ($MnSO_4.7H_2O$), 0.2 g ($FeSO_4.7H_2O$), 0.2 g (Yeast extract), 0.2 g (Peptone), 40 g (*Cynodon dactylon* wastes) in one liter of distilled water, and adjusting the pH to 7.5. The 1 liter of media was prepared in a 2000 mL flask and sterilized using the autoclave. The media was then allowed to cool, after which it was used to inoculate the selected isolates *F. solani* and *Bacillus* sp. 0.5 ml / 100 ml of media was used to inoculate the bacteria and fungi and incubated in shaking incubator at 30°C with 150 cycle/min for 96 hours [7]. The raw enzyme was extracted by separating the supernatant from the residual media by using the centrifuge at 5000 rpm for 30 min at 4°C and enzyme activity in supernatant estimated according to the protocol by Miller [8], using a microtiter plate reader with wavelength of 450 nanometres.

2.3. Determination of the cellulase activity in the liquid media and the use of carboxymethyl cellulose (CMC)

The enzyme activity was estimated in the liquid media based on the standard glucose curve prepared according to the method described in [8].

2.4. Determination of optimal conditions for the production of cellulase enzyme in the liquid cellulose media

Different standards were used to determine the optimal conditions of the production of the enzyme, including the volume of the inoculum, specifically, 0.5, 1.0, 1.5, 2.0, and 2.5 ml / 100 ml media. Each aliquot of the fungi and bacteria isolate was used to inoculate the liquid media in order to detect the effect of amount of inoculum on enzyme activity and production while the pH of the growth media was adjusted to 5.5, 6.5, 7.5, 8.5 to determine the optimal pH for the production of the enzyme in the liquid media. Several concentrations (1%, 2%, 3%, 4%) of the carbon source were used to determine the best concentration of carbon source for the production of enzyme cellulose. The fungal and bacterial isolates tested on liquid media contain ground *Cynodon dactylon* as sole carbon source at different incubation periods (48, 96, 144, and 192 hours). The media was inoculated with both isolates and the activity of enzyme was estimated at each incubation period.

2.5. Pre - treatment for biomass of Cynodon dactylon wastes plant

The process of production of ethanol using the wastes of *Cynodon dactylon*, which was the first pretreatment done for the purpose of increasing the efficiency of both bacteria and fungi for digestion and consumption of cellulose, were done by adding 0.5% diluted sulfuric acid to the crude enzyme and autoclaving.

2.6. Determination of the capacity of isolates to Ethanol Stress Tolerance

F. solani and *B. cereus* were tested for different concentrations of ethanol (2.5%, 5%, 7.5% and 10%) and for different incubation periods (24, 48, 72 hours). After inoculation of the PDA media, pure ethanol, with concentrations suggested by the method of spot assay, was added in order to give an idea of the tolerance of these isolates in the production experiment. The fungal inoculum was prepared and the number of conidia was 10^4 conidia / ml, and the density of bacteria being 52 × 108 cells / ml. The samples were diluted ten to ten thousand folds after which 5 µl of each dilution was taken and cultured on the surface of the petri dish containing the culture media with ethanol [7].

2.7. Production of ethanol

The wastes of the *Cynodon dactylon* plant treated with fungus *F. solani* (0.5 ml inoculums), as mentioned above, and containing 104 conidia /ml and 0.5 ml of bacteria (52 × 108 cells / mL) were placed in a shaking incubator at a speed of 100 rpm at 30 °C and at different incubation periods (24, 48,72, 96 hours). Glucose concentration was measured after each incubation period in the supernatant after removal of liquid media by using centrifuge at 5000 rpm for 15 minutes at 5°C and separating the supernatant from the precipitate. The reduced sugars present in the supernatant were estimated by taking 0.5 ml of supernatant in each test tube followed by the addition of 1 ml 3,5 DNS reagent to each tube. The tubes were then placed in water bath at 100 °C for 5 minutes, after which then the tubes were cooled down to RT. 10 ml of distilled water was added to each tube and mixed well. Absorbance measurements were taken at a wavelength of 540 nm using a Microtiter plate reader. The concentration of the reduced sugars were determined by extrapolating the corresponding absorbance measurements from the standard curve of glucose as described by [8].

2.8. Determination of Ethanol

The process of bioethanol production involved addition of the *Cynodon dactylon* plant waste treated with sulfuric acid into the conical flasks containing fungus and bacteria, and inoculating with the fungus inoculum (10^4 conidium /ml) and bacteria (52 × 10^8 cell / ml). Samples were placed on the shaking incubator, then the amount of glucose were measured by using a microtiter-plate reader, before and during the fermentation process. After the 120 hours fermentation process, the supernatant was separated from the precipitate, distilled at 80°C and the ethanol collected from the distillation process. The ethanol concentration was estimated using gas chromatography (GC).

3. Results and Discussion

The co-culture system has been used in many food biotechnologies, but it is important that the mixed isolates be commensals with each other and not to compete or antagonize with each other [9]. Figure 1 illustrates that there is a synergistic relationship between the two isolates with their growth on the same media and close to each other. This indicates that there is no antagonism between the two

isolates and thus the possibility of using the two isolates together to enhance the production capacity and thereby increase the production of the enzyme and bioethanol

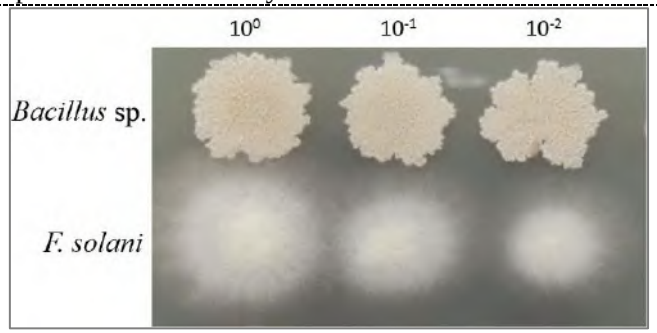

Figure 1. The relationship between *Bacillus* sp. and *F. Solani* (F7), cultured on Luria-Bertani media using the Spot dilution plate assay at 30 ° C for 96 hours; number of fungi / ml (10^5conidium/ ml), number of bacteria / ml (52 x 10^8 cell /ml).

3.1. Determination of Ethanol

The process of bioethanol production involved addition of the *Cynodon dactylon* plant waste treated with sulfuric acid into the conical flasks containing fungus and bacteria, and inoculating with the fungus inoculum (10^4 conidium / ml) and bacteria (52 × 10^8 cell / ml). The samples were then placed in the shaking incubator, and the amount of glucose measured, using a microtiter-plate reader, before and during the fermentation process. After the 120 hours fermentation process, the supernatant was separated from the precipitate, distilled at 80°C and the ethanol collected from the distillation process. The ethanol concentration was estimated using gas chromatography (GC).

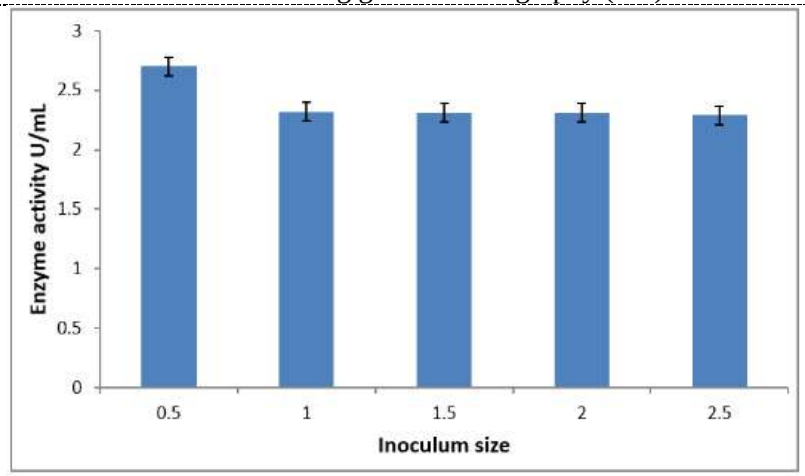

Figure 2. Effect of inoculum size on the activity of the enzyme.

The decrease in enzymatic activity when using an inoculum size greater than 0.5 ml / 100 ml was due to competition between bacteria and fungi for nutrient utilization in the culture media [10]. The statistical analysis showed no significant difference between the inoculum sizes used in this study except the size of the inoculum (0.5 and 1 ml) and at a significant level $P < 0.05$. The effect of the change in pH of liquid media on the production of the cellulase enzyme were also studied. Figure 3 shows that the best enzyme activity was at pH 7.5 with mean value of 2.70 unit / ml.

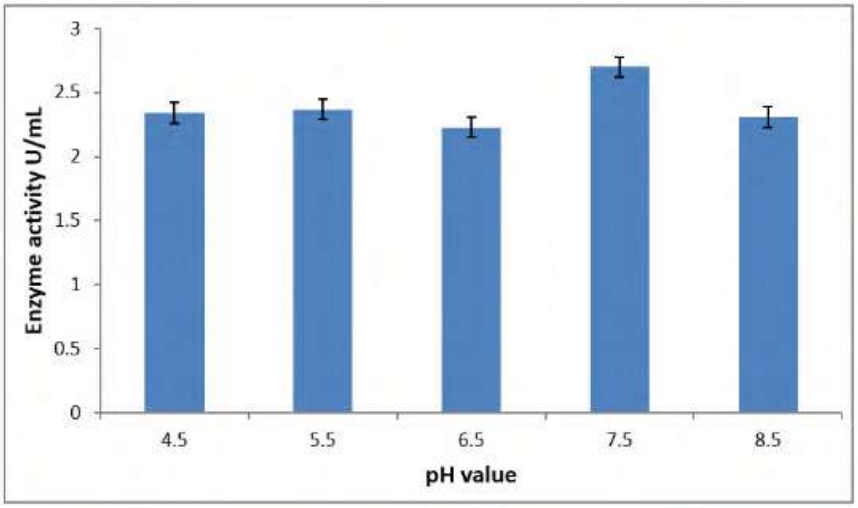

Figure 3. Effect of pH on the activity of cellulase enzyme.

These results were agreement with a previous study [11], which found that the best enzyme activity was at pH 7.5, and to some extent with the findings of [12], which found that pH 7.0 is the best in the production of cellulase enzyme and using *Bacillus* sp. isolate. The presence of more than one or more enzymatic profiles of the enzyme complexes produced by microorganisms may cause fluctuation in pH values, which may lead to reduced enzyme production during fermentation. It has also been reported that the optimal pH for the production of the cellulase enzyme may vary depending on the type of micro-organism used in the production [13]. The statistical analysis showed a significant difference in the values obtain at pH between 6.5 and 7.5 as well as 7.5 and 8.5. There was no significant difference, however, for values obtained at pH between 4.5 and 5.5; 5.5 and 6.5 at $P < 0.05$. Figure 4 shows the effect of the concentration of carbon source on the production of the cellulase enzyme, and from the observation of the results, the best concentration of the carbon source in which the best production of the enzyme was found is 3%, with enzyme activity of 2.75 unit / ml. Next was the concentration of 4% , showing enzyme activity of 2.73 unit / ml while the enzyme activity at 1% and 2%, concentrations were 2.70 and 2.49 respectively.

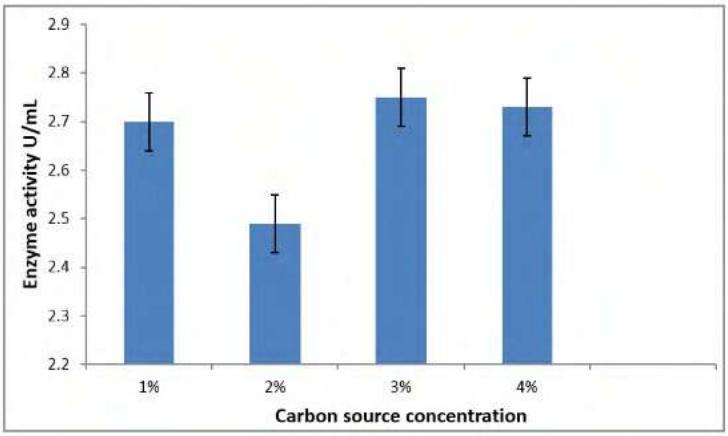

Figure 4. Effect of carbon source on the production of the cellulase enzyme.

These results differed from those obtained previously [14], in which the highest enzymatic activity was obtained at a concentration of 1% carbon source by the culture of *Bacillus* on corn husks and using liquid state ferments. The statistical analysis confirmed a significant difference in the enzymatic activity of the cellulase enzyme among all concentrations of carbon source and at the probability level $P < 0.05$.

Figure (5) shows the effect of incubation period on the production of the cellulase enzyme using the fungus *F. solani* and *Bacillus*. It was observed that the best enzyme activity was after 4 days of incubation at 30 °C, which yielded an enzyme activity of 2.83 unit / ml. The enzymatic activity decreased to 2.7 unit / ml after a 6-day incubation period and continued to decline to 2.59 unit / ml after 8 days of incubation.

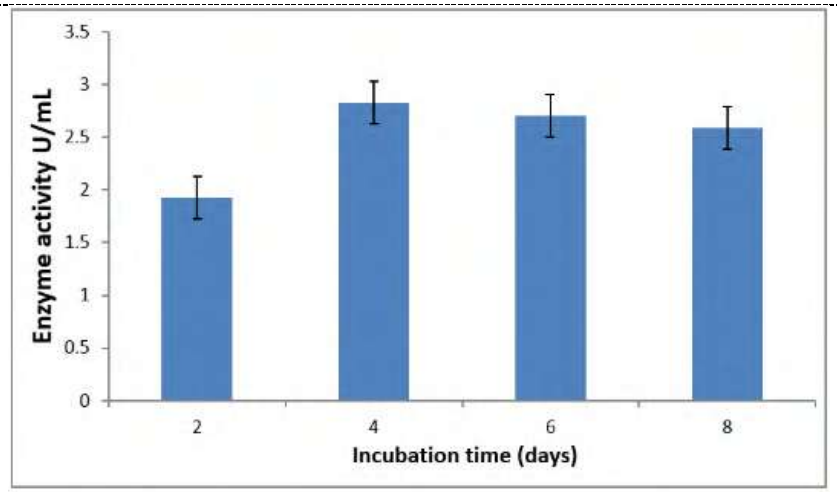

Figure 5. Effect of incubation period on the production of the cellulase enzyme.

The decrease in enzyme activity with increased incubation duration may be attributed to cell autolysis, release of metabolic substances affecting enzyme productivity, and the possibility of altering the structural composition of the enzyme over time, as well as environmental changes in the production media [15]. [16] reported that most isolates of *Bacillus* sp. begins the production of cellulase enzyme after 3-12 hours of growth. The difference in production depends on the quality of the nutrients in the media and the stage in which the microorganism passes. The results obtained in this study agreed with previous work [17], which showed that the best production of the cellulase enzyme is achieved after 96 hours. The results of the statistical analysis showed a significant difference at $P < 0.05$ between the incubation period of 2 days and 4 days, while there were no significant differences between the other incubation periods.

3.2. Ethanol Production

Figure (6) shows the ability of the isolates *F. solani* and *Bacillus* sp. to tolerate different concentrations of ethanol (2.5, 5, 7.5, 10%). It is observed that the isolates have a strong ability to tolerate 5% of the ethanol, while there is no growth of the two isolates at the concentrations higher than 5%. These results are consistent with those of [18], who concluded that *B. cereus* is excellent for bioethanol production due to its ability to tolerate ethanol concentration at 6%. [19] reported that *F. oxysporum* had the ability to produce bioethanol from the fermentation of hexoses and pentoses, but there was no growth at 3.5% ethanol level. The increase in concentrations of ethanol and the inability of cells to tolerate high concentrations affect the formation of mycelium and the permeability of the wall of fungi and low net weight of the biomass. The presence of ethanol of about 0.5 - 2% inhibits the secretion of the cellulase enzyme by the fungus *Trichoderma reesei* [20]. Aldehyde Dehydrogenases enzyme is reported to play an important role in the tolerance of ethanol by fungus [21].

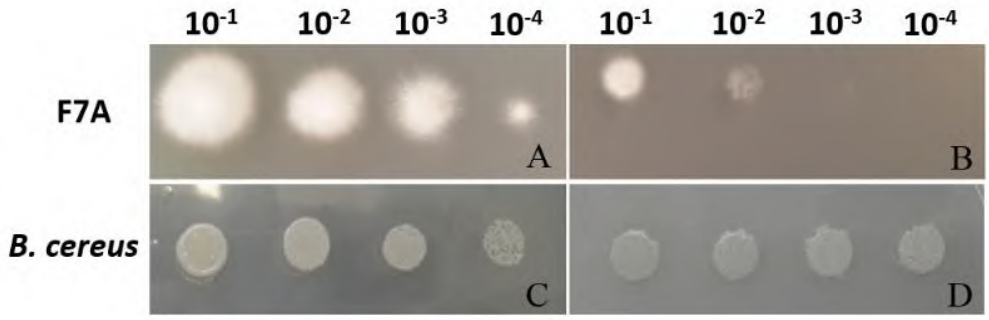

Figure 6. Ethanol tolerance using the Spot dilution plate assay: (A) Isolation (F7A) *F. solani* without ethanol. (B) The fungus sample treated with 5% ethanol. (C) *Bacillus* isolate without ethanol. (D) Sample of bacteria treated with 5% ethanol..

3.3. Bioethanol production

The results of the treatments for the *Cynodon dactylon* wastes shown in Figure 7, based on the concentration of sugars produced after treatment, were higher than the 0.5% H_2SO_4 treatment on the rest of the treatments. The concentration of reduced sugars was 3.5 mg / ml while the concentration of sugars of the *Cynodon dactylon* waste treated cellulase enzyme was 2.51 mg / ml. The *Cynodon dactylon* waste treated with distilled water and autoclave recorded the lowest concentration of produced sugars at 2.0 mg / ml. Pre-treatment is essential for obtaining the best degradation of plant wastes by the use of thermal chemical reactions involving the breakdown of solids from the mass of lignocellulose. These factors increase the readiness of the substrate and the redistribution of the lignin so that it can achieve the minimum energy consumption and obtain high percentages of sugars [22, 23]. The results of this study were in agreement with the results obtained by [24] in which H_2SO_4 was used for pre-treatment and high percentage of reducing sugars obtained. Removal of more than 65% of the lignin were observed when *Saccharum* plant was used. The results of the statistical analysis showed a significant difference between all the treatments used in this study at probability level $P < 0.05$.

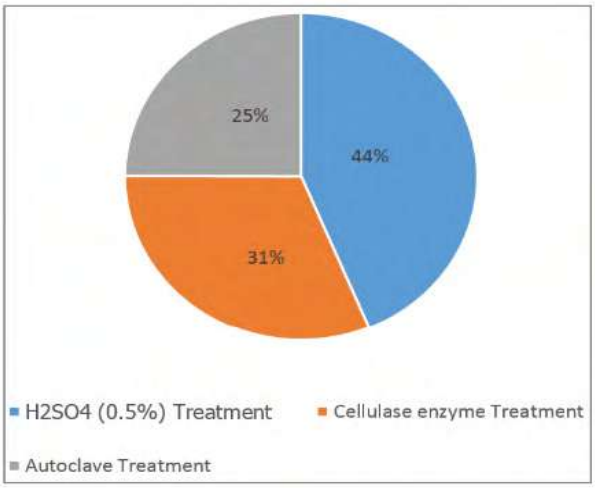

Figure 7. Concentration of glucose sugar after pre-treatment of *Cynodon dactylon* wastes.

Figure (8) shows the concentration of glucose produced by the treatment of *Cynodon dactylon* wastes with 0.5% sulfuric acid, on which the *F. solani* and *Bacillus* were cultured. , The daily glucose concentration were then calculated for the 5 days of incubation. The figure clearly suggests that there is a decrease in the concentration of sugars with an increase in fermentation time. Concentration of

glucose after 24 hours of fermentation time was 3.9 mg / ml and then the concentration decreased after 48 hours to 2.62 mg/ ml with a decrease in pH from 6.8 to 6.3. We noticed increments in sugar concentration after 72 hours of fermentation. The concentration reached 3.2 mg/ ml while the pH dropped to 6.1. The increase in glucose concentration after 72 hours of fermentation time may be due to fungal activity, which increased on the third day. Concentration of glucose started to decrease to 2.89 and 2.51 mg/ ml respectively, after 96 and 120 hours of fermentation time, while glucose concentration for control sample was 3.14 mg / ml, and there was an increase in pH value to 7.7 after 120 hours fermentation.

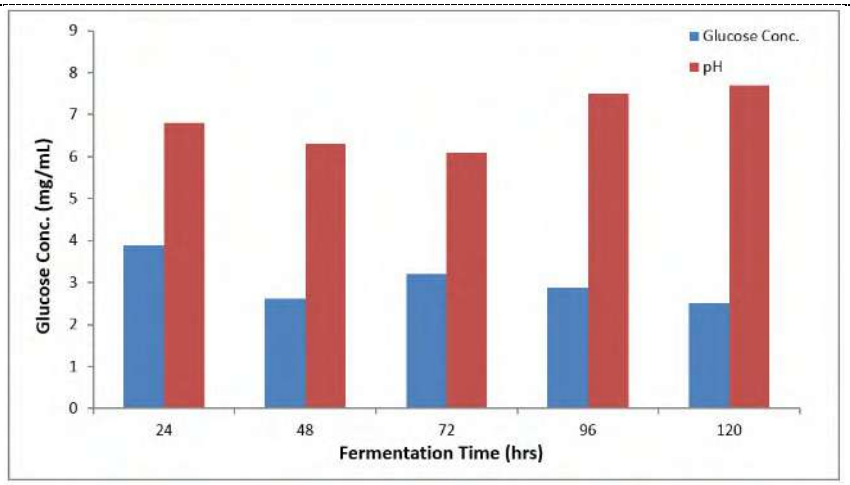

Figure 8. Concentration of glucose resulting from the fermentation process using a mixed fungal *F. solani* culture and *Bacillus*.

The growth of isolates in cellulose-containing culture media has been shown to be characterized by the length of the lag phase [25]. Growth depends on the adhesion of microorganisms to the cellulosic fibers found in the culture media and stimulates the secretion of cellulolytic enzymes, in contrast to the culture media containing dissolved substances as the lag phase is short in length. The concentration of reduced sugars in the culture media depends on the enzyme activity in the growth media and on the type of cellulosic material and its capacity of enzymatic degradation, and also depends on the growth phase of the bacteria. The passage of the bacteria in the stationary phase indicates that more sugars are consumed by the bacteria to sustain their activity. This study was conducted to produce bioethanol from the wastes of *Cynodon dactylon* with *Bacillus* isolate and *F. solani*. The important factor in making ethanol production more economical is the use of large quantities of cellulose available in the environment and containing large amounts of cellulose that can be converted into ethanol [26]. Table (1) and Figures (9) and (10) show the concentration of bioethanol produced from the fermentation process after 120 hours of fermentation and saccharification using co-cultures, as well as the results of the analysis of the correlation curve for the produced ethanol and standard ethanol. Table (1) shows that the ethanol concentration was 195 g/liter. This concentration increases with the availability of extra fermented sugars in the media so it is necessary to increase the concentration of sugars in the media to produce ethanol in large quantities and the efficiency of fermentation depends on the speed of sugar consumption by the cell [27]. The concentration of ethanol produced in this study was higher than those obtained by several other researchers who used single isolates. For example, [28], produced bio-ethanol from *Saccharum* plant and cassava husks using *B. cereus* bacteria and obtained a concentration of 18.4 g / L of Saccharum wastes sugar and 17.80 g / l of cassava husks Our results also show significant improvement over the works of [29], who reported concentration of bio-ethanol obtained to be 8.3 g / L using *B. subtilis* and potato wastes. Our work remains supreme when we further compare our results to that of [30] who used rice bran with *B. cereus* and obtained bio-ethanol concentration of 10.2% at 37 °C and pH 5, after 120 hours of fermentation.

Table 1. Ethanol concentration (g / L) resulting from the fermentation process Using a co-culture of fungus *F. solani* and *Bacillus* species.

Concentration of Ethanol g/l	Area	R. Time	No. Peak
195	179108	3.566	6

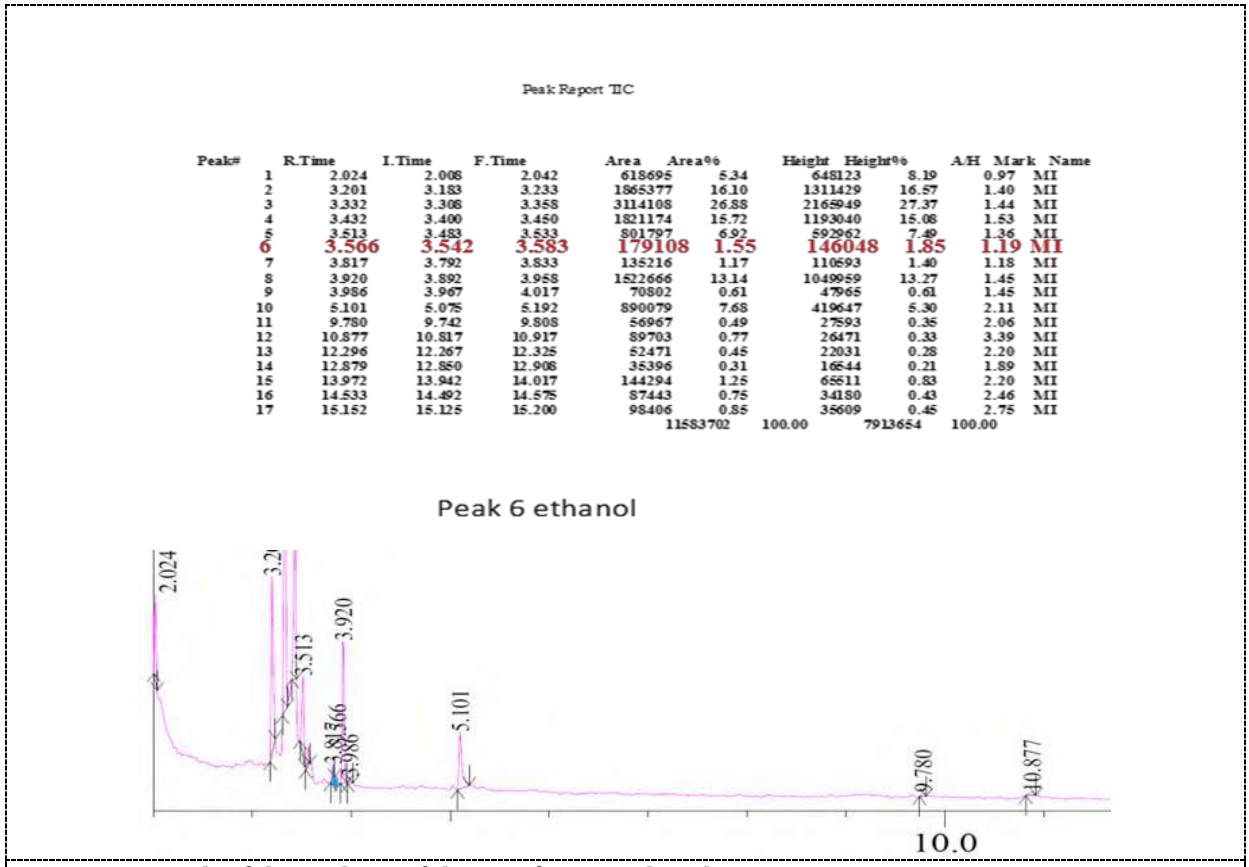

Figure 9. Result of the analysis of the interference ethanol curve.

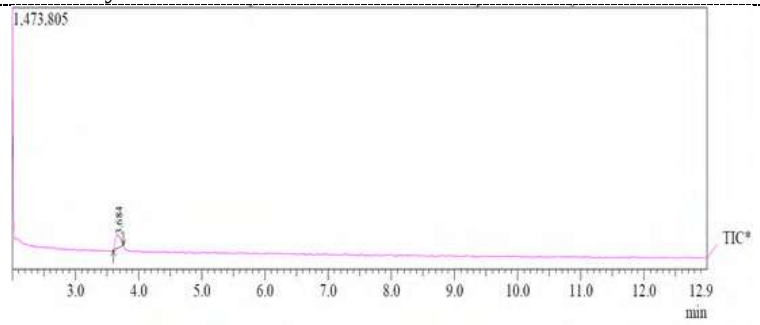

Figure 10. Result of the analysis of the standard correlation coefficient of ethanol.

4. References

[1] Phitsuwan P, Laohakunjit N, Kerdchoechuen O, Kyu KL and Ratanakhanokchai K 2013 Present and potential applications of cellulases in agriculture, biotechnology, and bioenergy *Folia Microbiol*. **58** 163.

[2] Iqbal HMN, Kyazze G and Keshavarz T 2013 Advances in the valorization of lignocellulosic materials by biotechnology: an overview. *BioResources* **8** 3157.
[3] Zou N and Plank J 2015 Intercalation of cellulase enzyme into a hydrotalcite layer structure *J. Phys. Chem. Solids* **76** 34.
[4] Park EY, Naruse K and Kato T 201 One-pot bioethanol production from cellulose by co-culture of *Acremonium cellulolyticus* and *Saccharomyces cerevisiae Biotechnol. Biofuels* **5** 64.
[5] Franco CJ, Zapata S and Dyner I 2015 Simulation for assessing the liberalization of biofuels *Renew. Sustain. Energy Rev*. **41** 298.
[6] Hernández D, Riaño B, Coca M and García-González MC 2015 Saccharification of carbohydrates in microalgal biomass by physical, chemical and enzymatic pre-treatments as a previous step for bioethanol production *Chem. Engineer. J.* **262** 939.
[7] Abood MF, Al-Rawii DF and Hamzah HM 2017 Production of single cell protein from the wastes of *Cynodon dactylon* L. using mixed culture of *Bacillus cereus* and *Fusarium solani J. Biotechnol. Res. Center*. (in Arabic). In press.
[8] Miller G L 1959 Modified DNS method for reducing sugars *Anal. Chem*. **31** 426.
[9] Immanuel G, Dhanusha R, Prema P and Palavesam A 2006 Effect of different growth parameters on endoglucanase enzyme activity by bacteria isolated from coir retting effluents of estuarine environment *Int. J. Environ. Sci. Technol.* **3** 25.
[10] Robinson PK 2015 Enzymes: principles and biotechnological applications *Essays Biochem.* **59** 1.
[11] Irfan M, Safdar A, Syed Q and Nadeem M 2012 Isolation and screening of cellulolytic bacteria from soil and optimization of cellulase production and activity *Turkish J. Biochem*. **37** 287.
[12] Khianngam S, Pootaeng-on Y, Techakriengkrai T and Tanasupawat S 2014 Screening and identification of cellulase producing bacteria isolated from oil palm meal *J. Appl. Pharmac. Sci.* **4** 90.
[13] Melo IR, Pimentel MF, Lopes CE and Calazans GMT 2007 Application of fractional factorial design to levan production by *Zymomonas mobilis Braz. J. Microbiol*. **38** 45.
[14] Rahmat H, Hodge RA, Manderson GJ and Yu PL 1995 Solid-substrate fermentation of *Kloeckera apiculata* and *Candida utilis* on apple pomace to produce an improved stock-feed *World J. Microbiol. Biotechnol.* **11** 168.
[15] de Cassia Pereira J, Paganini Marques N, Rodrigues A, Brito de Oliveira T, Boscolo M, da Silva R, Gomes E, Bocchini Martins DA 2015 Thermophilic fungi as new sources for production of cellulases and xylanases with potential use in sugarcane bagasse saccharification *J. Appl. Microbiol*. **118** 928.
[16] Duenas R, Tengerdy RP and Gutierrez-Correa M 1995 Cellulase production by mixed fungi in solid-substrate fermentation of bagasse *World J. Microbiol. Biotechnol.* **11** 333.
[17] Nema N, Alamir L and Mohammad M 2015 Production of cellulase from *Bacillus cereus* by submerged fermentation using corn husks as substrates. *Int. Food Res. J.* **22** 1831.
[18] Tawfiq AA 2000 *Isolation and identification of Cellulolytic Streptomyces species from the local soil* A thesis submitted to the College of Science of Al-Nahrain University.
[19] Yang VW, Zhuang Z, Elegir G and Jeffries, TW 1995 Alkaline-active xylanase produced by an alkaliphilic *Bacillus* sp isolated from kraft pulp *J. Industr. Microbiol. Biotechnol.* **15** 434.
[20] Olajuyigbe FM, Nlekerem CM and Ogunyewo OA 2016 Production and characterization of highly thermostable β-glucosidase during the biodegradation of methyl cellulose by *Fusarium oxysporum Biochem. Res. Int*. **2016**.
[21] van Maris AJ, Abbott DA, Bellissimi E, van den Brink J, Kuyper M, Luttik MAH, Wisselink H W, Scheffers WA, Van Dijken E and Pronk JT 2006 Alcoholic fermentation of carbon sources in biomass hydrolysates by *Saccharomyces cerevisiae*: current status. *Antonie Van Leeuwenhoek* **90** 391.
[22] Ibeto CN, Okoye COB and Ofoefule AU 2014 Bio-ethanol Production from Thermally Pre-treated Corn Chaff and Cassava Waste Water. *Int. Res. J. Pure Appl. Chem*. **4** 227.

[23] Paschos T, Xiros C and Christakopoulos P 2015 Simultaneous saccharification and fermentation by co-cultures of *Fusarium oxysporum* and *Saccharomyces cerevisiae* enhances ethanol production from liquefied wheat straw at high solid content. *Industr. Crops Prod.* **76** 793.
[24] Haab D, Hagspiel K, Szakmary K and Kubicek CP 1990 Formation of the extracellular proteases from *Trichoderma reesei* QM 9414 involved in cellulase degradation *J. Biotechnol.* **16** 187.
[25] Tesfaw A and Assefa F 2014 Co-culture: A great promising method in single cell protein production *Biotechnol. Molec. Biol. Rev.* **9** 12.
[26] Dinita BJMRB, Malla SJJR and Sreerama L 2011 Lignocellulosic ethanol production: current practices and recent developments *Biotechnol. Molec. Biol. Rev.* **6** 172.
[27] Yang B and Wyman CE 2008 Pretreatment: the key to unlocking low-cost cellulosic ethanol. *Biofuels, Bioprod. Biorefin.* **2** 26.
[28] Zheng Y, Pan Z and Zhang R 2009 Overview of biomass pretreatment for cellulosic ethanol production *Int. J. Agric. Biol. Engineer*. **2** 51.
[29] Ali SS, Nugent B, Mullins E, and Doohan FM 2016 Fungal-mediated consolidated bioprocessing: the potential of *Fusarium oxysporum* for the lignocellulosic ethanol industry *AMB Express* **6** 1.
[30] Kongkiattikajorn J and Yoonan K 2006 *Conversion of cassava industry waste to fermentable sugar* In The 2nd Joint International Conference on Sustainable Energy and Environment (SEE 2006) (p. 21-23).
[31] Xiros C, Katapodis P and Christakopoulos P 2009 Evaluation of *Fusarium oxysporum* cellulolytic system for an efficient hydrolysis of hydrothermally treated wheat straw *Bioresour. Technol.* **100** 5362.
[32] Gupta P, Samant K and Sahu A 2012 Isolation of Cellulose-Degrading Bacteria and Determination of Their Cellulolytic Potential *Int. J. Microbiol.* Article ID 578925, 5.
[33] Alves-Araújo C, Pacheco A, Almeida MJ, Spencer-Martins I, Leão C and Sousa MJ 2007 Sugar utilization patterns and respiro-fermentative metabolism in the baker's yeast *Torulasporadel brueckii Microbiology* **153** 898.
[34] Ezebuiro V, Ogugbue CJ, Oruwari B and Ire FS 2015 Bioethanol production by an ethanol-tolerant *Bacillus cereus* strain GBPS9 using sugarcane bagasse and cassava peels as feedstocks *J. Biotechnol. Biomater.* **5** 1.
[35] Elsayed B, Belal MA, Farid and Abo-Shosha AA 2015 Production of Bioethanol Via Microbial and Enzymatic Hydrolysis of Potato Wastes Under Solid State Fermentation *International J. Curr. Microbiol. Appl. Sci.* **4** 511.
[36] Tiwari S, Jadhav SK and Tiwari KL 2015 Bioethanol production from rice bran with optimization of parameters by *Bacillus cereus* strain McR-3. *Int. J. Environ. Sci. Technol*. **12** 3819.
[37] Gomaa EZ 2013 Bioconversion of orange peels for ethanol production using *Bacillus subtilis* and *Pseudomonas aeruginosa*. *African J. Microbiol. Res.* **7** 1266.
[38] Xiros C and Christakopoulos P 2009 Enhanced ethanol production from brewer's spent grain by a *Fusarium oxysporum* consolidated system *Biotechnol. Biofuels* **2** 4.

Investigation of fungal contamination in some types of chips in the market in Karbala

Investigation of fungal contamination in some types of chips in the market in Karbala

Ihsan Ali Al-Zamily[1*]

[1]General Directorate of Education in Karbala.

*E-mail: ihsanalzamily@gmail.com

Abstract. Different types of chips samples sell were collected from some markets in Karbala city, which its made in Jordan (Chipsico and Alsaada), Saudia (Liz, Gillts, Doritos), Iran (Bovac, G Toz and Macho) and Iraq (Hala, Dalia, Al-Aseel). The Iranian Chips were the most contaminated, where Iraqi and Jordanian Chips comes in the second. The results of isolating fungi study in chips types, showed diversity in numbers and kinds of fungi .The genus *Aspergillus* is a fungus predominate on all isolates and followed by *Penicillium*. Also different genera including *Fusarium, Alternaria, Curvularia* and *Rhizopus* have been isolated. It is mentioned that these fungi are dangerous because they produce myctoxins, especially aflatoxin and ochratoxin. It was noted that, the Saudi products are free from contamination. Ammonia test and Fluorescence was used to identify the aflatoxin-producing isolates and it appeared that isolates of *Aspergillus* had great potential to produce these toxins.

Keywords. Chips, *aflatoxin, Aspergillus*, *Penicillium*.

1. Introduction

Fungi are eukaryotic organisms that present in all parts of the earth and are characterized by their great variability in terms of color, size and shape. Fungi it's very important in our daily life as they are a source of food, antibiotics and some important compounds such as proteins, vitamins, organic acids and others [1].But it may be harmful, as it spoilage foodstuffs, especially those stored and contaminates them with their lethal toxins. Mycotoxins are among the most dangerous known contaminants at the present time, especially aflatoxins, ochratoxin, ergot, and others [2]. Fungi can reach to foodstuffs in a variety of ways. For example, the foodstuff from which these products are made may be originally contaminated and contamination is transmitted to the manufacturing factory. It has not been sterilized, or contamination comes from the environment. Polluted air and water are an important source of contamination, or it may come from hands workers in these factories, especially if they did not observe the health conditions, such as wearing special clothes , wearing gloves and masks, or the pollution may arise from the materials used in the packaging [4]. What exacerbates and increases the problem is the incorrect storage and transportation conditions. Storage for a long time with suitable humidity helps the growth and prosperity of fungi. These fungi begin to secrete their toxins on the food. among the fungi and yeasts known to be a cause of food spoilage, such as *Aspergillus* and *Penicillium*, which were considered the source of toxins and organic acids. *Rhizopus*

is considered a widespread fungus and is a likely pollutant of foodstuffs, whether it open or packed, as it is characterized by fast growth and resistance to difficult conditions. One of the contaminated yeasts of foodstuffs is *Candida albicans*, a widespread yeast that has been isolated from various sources such as milk, fruits, vegetables and others. Food products are considered very suitable medium for growth of fungi because they contain sugars, proteins and salts supporting the requirements of growth, they are either made from grains such as wheat and barley grains as in nestles or from agricultural crops such as potatoes, peppers and strawberries as in chips, ice cream add to it other additives, flavors, preservatives, salts , spices and other substances that add desired taste to the food product [5]. Chips are among the most famous and most popular food demand for it by children and even adults as they are a fast and light meal and do not need preparation and cheap price and there are different forms, types and flavors, some of which are made from potatoes, grains , crops and fruits, and there is no house is almost empty without this food product. Therefore, it is necessary to avoid contaminated types and not consume them, as they may be the cause of many health problems, including toxins, fungal spores, yeast cells and bacteria [6]. The local markets in Karbala city are filled with various local and imported food products and the demand for which has increased recently, these include canned food, chips, juices and other. There has been a great openness in the field of manufacturing and importing these foodstuffs and in some cases the absence of control and follow-up on these products which causes their entry into the markets causing contaminated it with fungi [3]. The aim of the study was to investigate the fungi transmitted by chips and to know which companies and brands are best regarding fungi contamination and comparing local origin with imported ones.

2. Materials and Methods

2.1. Sample collection

The current study included the collection of different samples of chips that existing in the markets of Karbala city randomly, which included all the prevailing brands in the markets from local and imported origins, which are Jordanian (Chipsico and Alsaada), Saudian (Liz, Gillts, Doritos), Iranian (Bovac, G Toz and Macho) and Iraqi (Hala, Dalia, Al-Aseel), samples were transported as quickly as possible to the laboratory for cultivation on the prepared culture medium.

2.2. Culture media

Three culture media were used as the following:

2.2.1. Potato Dextrose Agar (PDA)

Use for growth of sample in food and dairy samples [7].

2.2.2. Cocconut Extract Agar (CEA)

Use the medium for Detection of aflatoxins [8].

2.2.3. Yeast Extract Agar

It is highly nutritive medium recommended for plate count of microorganisms [9].

2.3. Fungi isolation

Small pieces of each brand of sample were taken with forceps and placed in Petri dishes, and with three replicates per sample, the dishes were transferred to the incubator at 28 degrees while group of

control, and all dishes were incubated for 7 days with daily examination until appearance of growth [9].

2.4. Purification and Diagnosis

The growing cultures were purified by re-cultivation them on (PDA) medium until obtaining pure cultures. The cultures were examined for the purpose of diagnosis. The diagnosis was according to the shapes, color, nature of the cultures growth, edges and height, as well as examining the cultures under a microscope to observe the hyphae and the structural and reproductive structures of the fungi under study and were compared with the classification keys of fungi to determine fungal species [9].

2.5. Detection of aflatoxins

To detect the ability of isolated fungi to produce mycotoxins, the following two methods were used:

2.5.1. Ammonia solution

For this method a single colony is grown in the middle of a petri dish containing a medium like PDA. Turn over the plate and one or two drop of concentrated ammonium hydroxide solution is placed inside lid. The undersides colonies that produce aflatoxin quickly turn plum to red after the bottom of the Petri dish are inverted over the lid containing ammonium -hydroxide. Basically, if there is no change in color of colonies that's means do not produce of aflatoxin. note the greatest color change in the colonies grown on the yeast extract - sucrose and coconut media, a less intense color change in PDA , and the slightest change in color in the media of glucose salts - minerals, all of which prefer the production of aflatoxin [10].

2.5.2. Fluorescence

The isolates of fungi were grown on PDA medium by placing 3(replicates) for each fungal isolate after which it was incubated at a temperature of 25 °C ± 2 °C for a period a week later, a dish was selected for each isolation, and the cultured medium was cut on it by isolating the fungus with a sterile knife in the form of small pieces. Then the pieces were transferred with a sterile needle to an electric mixer containing 50 ml of chloroform and the mixture was mixed for 3 minutes and the mixture was filtered by filter paper. The filtrate sample was taken and put in a clean and sterile beaker and placed in an electric oven at a temperature of 60 ° C, where the amount was concentrated to approximately (1) ml only. The presence of aflatoxin B1 was detected, then it was examined under ultraviolet rays with a wavelength of 360 nanometers. The presence of aflatoxin B1 was detected by matching transfer coefficient (Rf) and fluorescence color of the extracts content of aflatoxins with Standard Substance Dorner and AFB1 [11].

3. Results and Discussion

The results of isolations in Table (1) existence variations in the numbers and genera of isolated fungi. The isolated fungi predominate the fungus *Aspergillus*, followed by *Penicillium* fungus. Also *Fusarium*, *Alternaria*, *Curvularia* and *Monillia* fungi have been isolated. It is mentioned that these fungi are dangerous because they are producing toxins, especially the Aflatoxins and ochratoxins [12]. *Aspergillus* is one of the moulds found all over the world. Its ability to contaminate food and animal feed is widespread under favourable environmental conditions. It is a large proportion of all molds found in industrial foods. It has a special importance as spoilage organisms of food. The changes due to spoilage caused by the *Aspergillus* species can be sensorial, nutritional and qualitative nature such as discolouration, pigmentation and moldy development of odors and destinations. Many species grow in very low water activity and are found attacking different foods and producing mycotoxins

[13]. *Aspergillus niger* is distributed worldwide on a large variety of substrates, which are the most common types of *Aspergillus* responsible for post-harvest decay [14]. *Penicillium* is another group of molds with a high appearance. The occurrence of *Penicillium* in some samples during this investigation is consistent with the. He reported that there is a high percentage of *Penicillium* types of fodder obtained from the farm with the *Penicillium citrinum* with the highest incidence. Many types of *Penicillium* can also produce a wide range of toxic compounds such as Citrine and Citroveridin [15]. [16] noted that the presence in food products of some of these molds, especially *Aspergillus flavus* and *Aspergillus niger*, is highly undesirable. Some of it reported to have public health significance because of the production of mycotoxins, which have implication on consumers' health and food shelf-life decreasing. This is especially prevalent in developing countries, *Aspergillus flavus* and *Aspergillus parasiticus* are mainly responsible for mycotoxin production [17].

Table 1. Isolated fungi from Some type of chips.

Origin	brand	fungi	percentage of appearance	Total
Iranian	Bovac	*Penicillium digitatum*	9	17
		Aspergillus flavus	7	
		Curvularia platzii	1	
	G Toze	*Rhizopus stolonifer*	1	1
	Masho	*Aspergillus flavus*	6	12
		Penicillium digitatum	3	
		Fusarium sp.	1	
		Alternaria alternata	2	
Jordanian	Chipsico	*Asprgillus niger*	3	4
	Alsaada	*Penicillium digitatum*	1	
Saudian	Liz	-	0	0
	Gillts	-	0	
	Doritos	-	0	
Iraqian	Hala	*Aspergillus flavus*	2	12
		Penicillium sp.	1	
	Dalia	*Fusarium sp.*	1	
		Penicillium sp.	2	
	Al-Aseel	*Aspergillus niger*	6	

The Iranian chips types were find the most contaminated samples and Iraqian chips types came second followed by Jordanian chips and finally Saudian chips without any fungal contamination. This may be due to the fact that the Iranian chips remain in the stores for long periods, not to mention the time needed to reach Iraq, as well as the machines used in production from the old generations due to the blockade imposed on the Islamic Republic, while notes that Saudi products are free from contamination. The reason for this may be due to adopting modern methods of production and marketing and benefiting from foreign expertise.

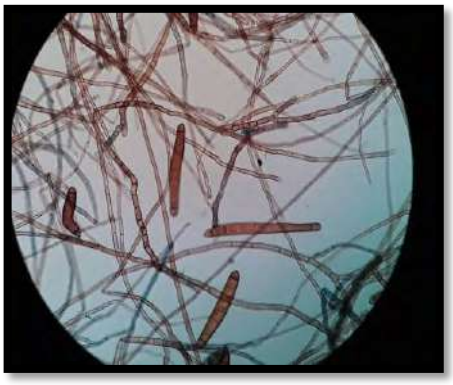

Figure 1. *Curvularia platzii*.

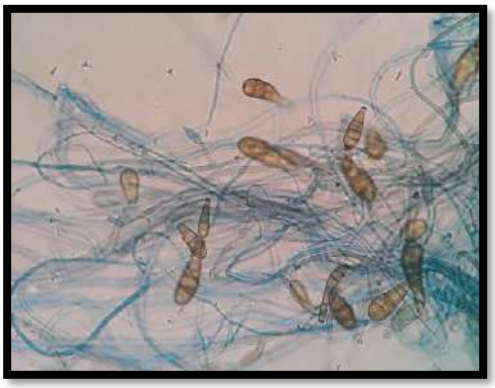

Figure 2. *Alternaria* sp.

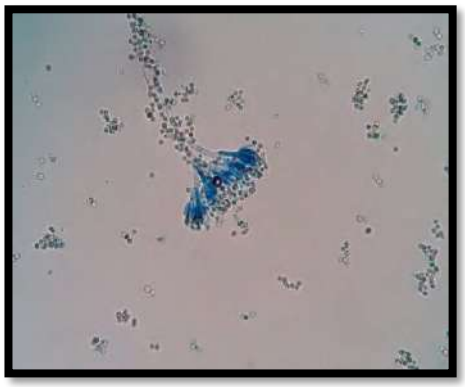

Figure 3. *Penicillium*

Figure 4. *Aspergillus*.

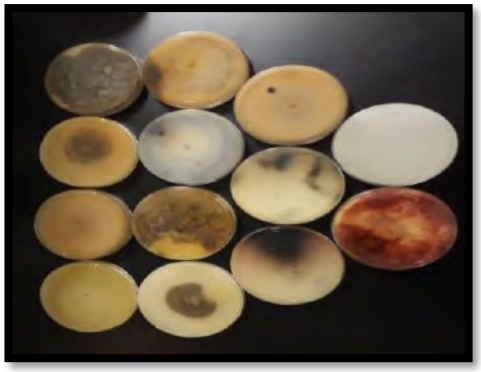

Figure 5. Aflatoxin production on (CEA).

Figure 6. Aflatoxin production on (CEA).

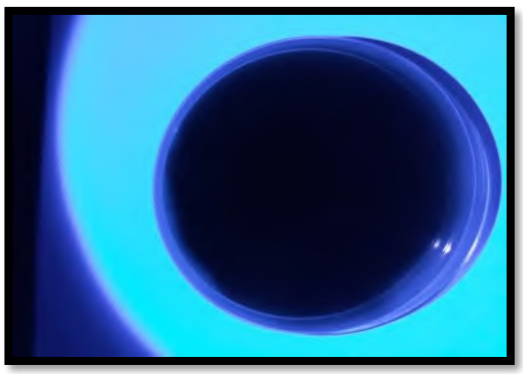

Figure 7. Aflatoxin detection under (UV).

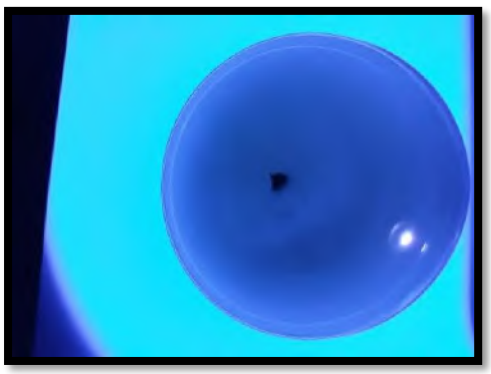

Figure 8. Aflatoxin detection under (UV).

Table 2. Aflatoxin production by fungal isolates on different media.

Chips samples	Fungal isolates	Fungal toxins secreted on three media		
		PDA	CEA	Yeast
Bovac	*Penicillium digitatum*	-	++	++
	Aspergillus flavus	+	++	++
	Curvularia lunata	+++	+	+++
G Toze	*Rhizopus stolonifer*	++	+	+
Masho	*Aspergillus flavus*	++	+++	+++
	Penicillium digitatum	-	++	++
	Fusarium sp.	+	+	-
	Alternaria alternata	+	+++	++
Chipsico	*Asprgillus niger*	-	+++	+++
Alsaada	*Penicillium digitatum*	-	+	+
Hala	*Aspergillus flavus*	+	+++	+++
	Penicillium sp.	-	++	+
Dalia	*Fusarium sp* .	+	+	++
	Penicillium sp.	-	+	++
Al-Aseel	*Aspergillus niger*	-	++	+++

+++ fungal production of aftoxin (very sparkling)
++ fungal production of aftoxin (medium sparkling)
+ fungal production of aftoxin (weak sparkling)
- Non-toxic

The Table (3) showed the ability of fungal isolates to produce toxins on three different media (PDA,CEA and Yeast) as the results showed great susceptibility of both *Aspergillus* and *Penicillium* to produce aflatoxin followed by other fungal species, the culture medium yeast was the suitable medium that stimulate fungi to produce toxins followed by CEA medium and finally PDA medium.

4. Conclusion

According to this study we conclude that these different types of chips are the same as the foodstuffs be exposed to contamination with various contaminants and therefore have a great impact on the health of human who deals with these foods tuffs, and the possibility of producing various types of toxins, therefore we recommend the need to use modern technologies in the production of foodstuffs such as chips and not to import them from poor and cheap sources.

5. References

[1] Al-Khalaf SS 2011 *Study of the toxicological effects of aflatoxin B1 and B2 in some pathological, biochemical and histological parameters of male white rat and ways to reduce their effects* Master Thesis, College of Science, University of Kufa.
[2] Al-Fatlawi IA-W A-R 2014 *A molecular study of some fungi producing aflatoxins isolated from some types of nuts* Master Thesis, College of Science for Girls, University of Babylon.
[3] Qahtan F and Abdullah A 2002 *Detection of Avala B1, B2 toxins, orca A in yellow corn and some of its products* Master Thesis, College of Agriculture, University of Baghdad.

[4] Pitt JI and Hocking AD 2009 *Fungi and food spoilage* 3rd Edition Springer Science and Business Media, London, New York.
[5] Aziz NH and Moussa LAA 2002 Influence gamma radiation on mycotoxin producing molds and mycotoxins in fruits *Food Control* **13** 281.
[6] Shaker R J, Thalaj MM and Bedewi AS 2012 Isolation and diagnosis of molds producing mycotoxins from the most consumed foods in Iraqi markets *Tikrit Univ. J.* **13** 44
[7] Majid K A and Ihsan AA 2019 Survey of fungi found in books on the shelves of the libraries of the University of Qadisiyah - Iraq. *IOP Conf. Series: Materials Science and Engineering* **571** 012042.
[8] Saito M and Machida S 1999 Arapid identification method for aflatoxin producing strains *A. flavus* and *A. parasiticus* by ammonia vapor. *Mycoscience* **40** 205.
[9] Watanabe T 2002 *Pictorial atlas of soil and seed fungi morphologies of cultured fungi and key to species* 2nd edition. CRC press Washington.
[10] Akbas M and Ozdemir M 2006 Effect of different ozone treatments on aflatoxin degradation and hysicochemical properties of pistachios *J. Sci. Food Agric.* **86** 2099.
[11] Sobolev VS and Dorner JW 2002 Clean up procedure for determination of aflatoxins in major agricultural commodities by liquid chromatography *J. Assoc. Offic. Analyt. Chem. Int*. **85** 642.
[12] Hong LS, Yusof, NIM and Ling H 2010 Determination of aflatoxins B1 and B2 in peanuts and corn based products *Sains Malaysiana* **39** 731.
[13] Adejumo TO and Adejoro DO 2014 Incidence of aflatoxins, fumonisins, trichothecenes and ochratoxins in Nigerian foods and possible intervention strategies *Food Sci. Qual. Manag.* **31** 127.
[14] Ashiq S 2015 Natural occurrence of mycotoxins in food and feed: Pakistan perspective. *Comprehen. Rev. Food Sci. Food Safety* **14** 159.
[15] Barbosa TS, Pereyra CM, Soleiro CA, Dias EO, Oliveira AA, Keller KM and Rosa CAR 2013 Mycobiota and mycotoxins present in fnished fsh feeds from farms in the Rio de Janeiro State. *Brazil. Int. Aquat. Res.* **5** 1.
[16] Adegoke GO 2004 *Understanding Food Microbiology* 2nd ed.; Shalom Press: Ibadan, Nigeria.
[17] Bankole S, Shollenberg M and Drochner W 2006 Mycotoxins in food systems in Sub Saharan Africa: A review *Mycotoxin Res*. **22** 163.

Biological control of *Azotobacter chroococcum* on *Fusarium solani* in tomato plant

Biological control of *Azotobacter chroococcum* on *Fusarium solani* in tomato plant

Sraa Nsayef Muslim[1], Rawa Abdul Redha Aziz[1] and Asmaa Mansour Al-Hakeem[1*]

[1]Department of Microbiology, College of Science, Al-Karkh University of Science, Baghdad, Iraq.

*E-mail: asmaa.mansoor@kus.edu.iq

Abstract. this experiment aimed to study the effect of *Azotobacter chroococcum* in reducing infection of the tomato plant by *Fusarium solani* under the greenhouse condition. The results show that *Fusarium solani* isolates proved high pathogenicity and chosen isolate (Fs4) for being given a lower percentage of germination of cabbage seeds and the highest disease severity to tomato seedling. Also, the results were indicated that T6 (Biofertilizer at concentrations (25 ml\2Kg soil) with *F. solani* (F.s4) was the past this treatment reduced significantly the disease severity (73.10%) which also recorded a positive effect on the growth parameter of tomato plant compare to T1 (pathogen only).

Keywords. Biocontrol, Tomato, Root rot, *Azotobacter*, *Fusarium*.

1. Introduction

Lycopersicon esculentum is one of the important vegetable crops in most agricultural areas in Iraq and used for food and industrial purpose [1]. Tomato plants are infected by several fungal pathogens such as Fusarium spp., which cause several diseases as wilt and root rots and finally reduced crop yield [2, 3]. Several strategies are used to control and reduce the risk of diseases; especially fungicides [4, 5]. However, increase the application of fungicides would affect the environment and human health negativly but is not always satisfactory, as well as the emergence of resistant strains of fungi towards these pesticides [6] (Cooper and Dobson,2007). Therefore, studies have tended to find alternatives methods to control plant diseases by using biological control agents [7] (Lee, et al., 2008). The success of some biological resistance factors has been a major role in pushing some researchers to find other organisms such as bacteria and fungi that can be hosted as successful biological resistance agents in showing the best performance to combat pathogens and to enhance plant growth. *Azotobacter chroococcum* is one of the organisms that were used in the biocontrol and also plays a large role against many pathogens, as it works directly or indirectly as a biological resistance agent for a visit to plant growth and the prevention of harmful effects of pathogens as well as play another important role, such as producing inhibitory antibiotics that stop fungi growth, including Agrocin 84, Agrocin434, 2-4-diacetyl phorogluinol, Herbicolin, Phenazin, Phenazin, Oomycin, Pyoluteorin, as these antibiotics act as inhibitors of pathogenic fungi, including *Fusarium* [8, 9]. In our research, the biofertilizers and

biological control with Azotobacter chroococcum will be studied in terms of controlling root rot disease which is usually caused by the fungus (*Fusarium solani*). Also, its effect on the growth parameter of the tomato plant and the resistance of the *Fusarium solani* under greenhouse condition.

2. Materials and Methods

2.1. Isolation and diagnosis of Fusarium from tomato plants

2.1.1. Sample collection

Samples were collected from the roots of tomato plants grown in greenhouses from some farms in Baghdad city, which showed symptoms of infection. The samples were placed in polyethylene bags, transferred to the laboratory, and then kept in the refrigerator until the isolation process was performed.

2.1.2. Isolation from infected tomato plants

The roots of tomato plants were rinsed under tap water for 30 minutes to remove the suspended soil, chopped the roots into small pieces, and disinfected with sodium hypochlorite solution (1%) for 3 minutes and rinsed with sterile distilled water for 2-3 minutes and then dried using sterile filter papers. The pieces were placed on Potato Dextrose Agar (PDA) plates. The plates were then incubated at (25± 2 °C)/ 5 days. Microscope examinations were then carried out of the growing fungi colonies. The colonies of the *Fusarium* appeared which were transferred to fresh PDA medium.

2.1.3. Diagnosis of Fusarium

Fusarium solani has been diagnosed based on certified classification keys [10, 11].

2.2. Pathogenicity test

Four isolates of *F. solani* were taken from roots of tomato plants and tested based on [12] process. PDA disk of 0.5 cm/ 7days old Fungus colonies were put in the center of water agar medium petri dishes. Other petri dishes used as a control treatment, and containing the same medium but not inoculated with fungus. All petri dishes (inoculated and non-inoculated) were incubated at 25±2°C for 72 hours. After that, the local cabbage seeds were sterilized using 1% solution sodium hypochlorite for 2 min and then washed with distilled water 3 times and then twenty five seeds were cultured circularly edge of inoculated and non-inoculated petri dishes. This culture was done twice so end up with 3 treatments for each. Then they were incubated at 25 ± 2°C. Seven days later, the percentage of seed germination calculated using:

$$\text{The Percentage of germination} = \frac{The\ number\ of\ seeds\ \ germinated}{The\ total\ number\ of\ seeds} \times 100$$

2.3. The pathogenicity of Fusarium solani on tomato plants under greenhouse conditions

This experiment was conducted in greenhouse of Agriculture College / Baghdad University in 20/12/2019 and it was done in three randomizelly replicate. This experiment was included in fungal treatment and control treatment without fungal inoculum. The plastic pots were filled with sterile soil, tomato seedlings were transplanted in each pot at 35 days after sowing. Previously, the fungal inoculum was prepared according to the [13], the inoculum was added after 3 days from seedling transplant to pots. The percentage of disease severity was calculated after 30 days based on [14] equation by the following.

$$\text{Disease severity}(\%)=\frac{(\sum scale \times number\ of\ plants\ infected) \times 100}{Highest\ scale \times total\ number\ of\ plant}$$

0 refers to healthy plants

1 = 1- less than 25% of the plant root are slightly brown color.

2 = 25- less than 50% of plant roots are a dark brown color.

3 = 50- less than 75% of plant roots are a dark brown color.

4 = 75- less than 100% of plant roots are a dark brown color.

2.4 Isolate and diagnose of Azotobacter chroococcum

Soil samples were collected from rhizospheric soil from the rhizosphere of the different crops (tomato, wheat, cotton). About 10 g of dry soil sample was put in 90 ml of D.W in a conical flask. Basic dilution was prepared to 10-6. Bacterial isolation was performed based on [15] manner. *Azotobacter chroococcum* were identified phenotypically based on their appearance under the microscope and biochemical test. Later on, *Azotobacter chroococcum* strain (A.ch1) was used in a greenhouse experiment due to its high ability against the pathogenic fungal.

2.5. Antagonistic effect of A. chroococcum against F. solani (F.s4)

For studying the antagonistic effect of *A. chroococcum* bacteria against *F. solani* (F.s4)., PDF plates were inoculated with two days old bacterial colony by streaking with needle on opposite sides of periphery plates. Each plates then were inoculated in the center with *F. solani* (F.s4) disk as control and incubated at (28)°C. Antagonistic effect of pathogen fungal growth on control petri dishes surface was calculated by [16].

$$\text{Inhibition percentage } \% =\frac{A_1 - A_2}{A_1} \times 100$$

Where the A_1 refers to the fungus growth area on the control surface.

A_2= refers to the fungus area in the dual culture.

2.6. The effect of A. chroococcum on rot disease under greenhouse condition

The experiment was carried at greenhouse during 2019 following a completely randomized design. There were 3 replication for each treatment. Antagonistic bacteria isolates was cultured on Nutrient agar plates (28°C/45 hours). Then, bacterial suspension of (108CFU/ ml) was prepared by using distil water and O.D of 0.1(600nm) [spectrophotometer model 6405UV/ VIS].The plastic pots (2 Kg capacity) were filled with a mixture of sterile soil and peat-moss 2:1,afterthat seedlings were transplanted to pots (30 days after sowing). The experiment was included in the following treatments (Table 1).

Table 1. Treatments of experiment.

Symbol treatment	Treatment
T1	*F. solani* (F.s4) only (pathogen only)
T2	Biofertilizer at concentrations (5ml\2Kg soil) with *F. solani* (F.s4).
T3	Biofertilizer at concentrations (10 ml\2Kg soil) with *F. solani* (F.s4).
T4	Biofertilizer at concentrations (15ml\2Kg soil) with *F. solani* (F.s4).
T5	Biofertilizer at concentrations (20ml\2Kg soil) with *F. solani* (F.s4).
T6	Biofertilizer at concentrations (25 ml\2Kg soil) with *F. solani* (F.s4).
T7	Chemical fertilizer only (Beltanol 1ml\L) with *F. solani* (F.s4).

The some pots were inoculated with the *A. chroococcum* (A.ch1) at concentrations (5, 10,15,20,25 ml\2Kg soil). It was applied 7 days before fungal inoculation millet seeds which contain on *F. solani* (F.s4) isolate. Some pots were treated with a chemical fungicide. The fungicide was applied one day before fungi inoculation. The plants were harvested and calculated the following:

- Disease severity.

- Height and weight of shoot (dry and fresh).

- Number of leaf and flower.

- Weight of one fruit per plant.

- Number of fruit per plant .

- Yield fruit.

2.7. Data analysis

ANOVA variance analyzer with the aid of GENSTAT computer software package were used to analyze the data and the means different between treatments were compared by using 0.05 probability level.

3. Results and Discussion

3.1. Isolation and diagnosis of Fusarium spp. from tomato plants

The colonies of 4 *Fusarium solani* isolates showed creamy pigmentations. The thin microconidia were oval to ellipsoid shaped. The macroconidia were subcylindrical, usually predominantly with three septate. The chlamydospores were single, in pairs, chains or clusters, arranging terminal or intercalary.

3.2. Pathogenicity tests

Table (2) showed that all isolates *Fusarium solani* were caused a significant reduction in the percentage of seed germination compared to control treatment. The results revealed that isolate *Fusarium solani* (F.s4) was more virulent than other isolates. These results may be attributed to that *Fusarium solani* are secreted many toxins such as (Fusarubin, Javanicin, Polypetide, Anhydrofusarubin, and Protenoneons) that is important in pathogenicity [17].

Table 2. Pathogenicity tests of *Fusarium solani* (F.s4) on cabbage seeds.

Isolates	Percentage of germination
***F. solani* (F.s1)**	11
***F. solani* (F.s2)**	9
***F. solani* (F.s3)**	14
***F. solani* (F.s4)**	7
Control	95
LSD=0.05	1.97

3.3. The pathogenicity of Fusarium solani on tomato plants under greenhouse conditions.

Disease severity was recorded after 30 days of transplantation. Disease severity of root tomato was found within the range of 48.10-73.10 %. The isolate *Fusarium solani* (F.s4) has maximum disease severity was further used in the experiment. As well as, three isolates (F.s1, F.s2, F.s3) were the least aggressive disease severity compared with isolate (F.s4) Table (3). [18] found that isolates have different abilities to the secretion of analyzing enzymes that play role in penetrating the plant roots.

Table 3. The pathogenicity of *Fusarium solani* on tomato plants under greenhouse conditions.

Isolates	Disease severity%
***F. solani* (F.s1)**	52
***F. solani* (F.s2)**	55.10
***F. solani* (F.s3)**	48.10
***F. solani* (F.s4)**	73.10
control	0
LSD=0.05	1.85

3.4. Isolate and digamous of the Azotobacter chroococcum and inoculum prepare.

Tables (4, 5, 6) shows the morphological, microscopic characteristics, and physiological test of bacterial isolates of rhizosphere of tomato, wheat, cotton crops. Colonies of bacteria exhibit viscous, brown-color, on pairs resampling *Azotobacter chroococcum* in its characteristics. Bacteria were gram-negative with rounded ends. These results were similar to as described by Bergey's manual of Determinative Bacteriology [19]. Table (7) reports the biochemical patterns of bacteria tested in this study. Three *A. chroococcum* isolates were positive in each test. Also, these bacterial shows cannot able to grow on Burk's medium and the same was used inoculation.

Table 4. Colonies morphology characteristics of *Azotobacter chroococcum*.

Morphological characters	*A. chroococcum* (A.ch1)	*A. chroococcum* (A.ch2)	*A. chroococcum* (A.ch3)
Plant type	tomato	wheat	cotton
Growth of colonies	+++	++	++
Consistency	Very viscous	viscous	viscous
color	Light brown	Dark brown	Dark brown
Surface	smooth	smooth	smooth

Table 5. Microscopic characteristics of *Azotobacter chroococcum* (G^{-ve}).

Microscopic characters	*A. chroococcum* (A.ch1)	*A. chroococcum* (A.ch2)	*A. chroococcum* (A.ch3)
Aggregation	pairs	pairs	pairs
Cell shape	Rod	Rod	Rod
Cyst formation	+	+	+

Table 6. Physiological test of *Azotobacter chroococcum*.

Physiological test	*A. chroococcum* (A.ch1)	*A. chroococcum* (A.ch2)	*A. chroococcum* (A.ch3)
Growth at NaCl (1%)	+	+	+
Growth at temperature 37°C	+	+	+
Motility	+	+	+
N_2 fixed ($mg.l^{-1}$)	+	+	+

Table 7. Biochemical test of *Azotobacter chroococcum.*

Biochemical test		*Azotobacter chroococcum* (A.ch1)	*Azotobacter chroococcum* (A.ch2)	*Azotobacter chroococcum* (A.ch3)
Burk's medium		-	-	-
Carbon source utilized	**Starch**	+	+	+
	Manitol	+	+	+
	Rhaminose	-	-	-
	Sucrose	+	+	+
	Fructose	+	+	+
	Glucose	+	+	+
Nitrate reduction		+	+	+
Catalase test		+	+	+
Gelatine hydrolysis		+	+	+
Utilize citrate		+	+	+

3.5. Antagonistic effect of A. chroococcum against F. solani (F.s4).

Table (8) showed higher reduction in mycelia linear growth of the *F. solani* (F.s4) isolate by *A. chroococcum* (A.ch1).

Table 8. Antagonistic effect of *A. chroococcum* against *F. solani* (F.s4) isolate.

Bacterial isolates	Radial growth (cm)	Inhibition percentage (%)
***A. chroococcum* (A.ch1)**	2.45	69.37
***A. chroococcum* (A.ch2)**	2.63	67.13
***A. chroococcum* (A.ch3)**	2.89	63.87
control	8.00	0.0

3.6. Evaluation of A. chroococcum against root rot disease some growth parameter of tomato plants in greenhouse environmental condition

Table 8 reported *A. chroococcum* and Beltanol treatments with pathogens were led to the lowest disease severity compared with pathogen treatment only. Also, *A. chroococcum* (25 ml/2Kg soil) with pathogen treatment was recorded highest disease severity (0.0%) compared with other treatments treated with the pathogen. Plant height records of growth parameters have been noticed in tomato inoculation with *A. chroococcum* (25ml/ 2Kg soil) with *F. solani* (F.s4). All treatment inoculation with *A. chroococcum* gave higher records of growth parameters in combination with control. Inoculation of *A. chroococcum* can increase plant growth through the ability of bacteria to synthesis IAA, fix nitrogen, provide P nutrients, and other elements [20]. The production of plant growth regulates by bacteria in the rhizosphere around roots was increased by the fixation of nitrogen [21]. The weight of one fruit recorded increase due to the application of *A. chroococcum* in combination with T1 (treated with pathogen only) (Table 9). The maximum weight of one fruit was recorded from the untreated plants. The fungicide application significantly increased the weight of one fruit. These results are in

agreement with [22] who found that inoculation with *A. chroococcum*, Alipoferum+ NPK resulted in earlier flowering, increasing fruits, and increased yields. *A. chroococcum* has many benefits like N2 fixing, antibacterial and antifungal production growth regulators, and siderophores. It is reported that the application biofertilizer such as *Azospirillum*, *Azobacter* and *Bacillus* sp. significantly increased tomato fruits and total yield/fed compared with control [23].

Table 9. Evaluation of *A. chroococcum* against root rot disease some growth parameter of tomato plants under greenhouse condition.

Treatments	Disease severity	Height plant (cm)	fresh weight of shoot	dry weight of shoot	No. of leaves	No. of flowers
T1	73.00	30.33	12.67	3.33	16.33	8.33
T2	21.67	37.67	20.33	5.67	25.33	12.33
T3	11.00	38.67	24.67	6.33	28.00	13.00
T4	12.00	43.33	27.33	6.67	30.33	13.00
T5	5.67	44.67	30.33	7.33	35.67	13.33
T6	0.00	50.33	32.00	7.67	40.00	15.67
T7	6.67	47.33	25.33	5.67	29.33	12.00
LSD	1.26	1.50	1.22	1.03	1.57	1.06

Table 10. Evaluation of *A. chroococcum* against root rot disease some growth parameter of tomato plants under greenhouse condition.

Treatments	Weight of one fruit per plant	Number of fruit per plant	Yield fruit
T1	7.33	3.67	0.2733
T2	18.33	5.33	0.3233
T3	31.33	6.67	0.5467
T4	46.67	9.33	0.7200
T5	56.00	10.67	0.9267
T6	65.00	12.33	1.0400
T7	46.67	10.67	0.9200
LSD	1.700	0.868	0.04580

References

[1] Sekhar L; Salimath PM, Sridevi O and Patil AA 2008 Genetic Diversity among some productive hybrids of tomato *Karnataka J. Agric. Sci*. **21** 264.
[2] Jones JB, Jones JP, Stall RE and Zitter TA 1991 *Compendium of tomato diseases* Am. Phytopathological Society, St. Paul, MN 75.
[3] Dodson M, Bachmann J and Williams P 2002 *Organic greenhouse tomato production, Horticulture Production GuideAppropriate Technology Transfer for Rural Areas* (ATTRA), the University of Arkansas in Fayetteville, AR.
[4] Ozgnen H, Mchemt BI and Ali E 2001 The Effect of salicylic acid and Endomoycorrhizal fungus Glomus etunicatum on plant Development of Tomatoes and *Fusarium oxysporum* f. sp. *lycopersici Turk. J. Agric*. **25** 25.
[5] Malfanova NV 2013 *Endophytic bacteria with plant growth-promoting and biocontrol abilities* Chapter 4 Microbial control of plant diseases Leiden University 92 pp.
[6] Cooper J and Dobson H 2007 The benefits of pesticides to mankind and the environment *Crop Prot*. **26** 1337.
[7] Lee KJ, Kamala-Kannan S, Sub HS, Seong CK and Lee GW 2008 Biological control of phytophthora blight in red pepper (*Capsicum annuum* L.) using *Bacillus subtilis*. *World J. Microbiol. Biotechnol*. **24** 1139.

[8] Verma S, Kumar V, Narula N and Merbach W 2001 Studies on in vitro production of antimicrobial substances by Azotobacter chroococcum isolates\mutants *J. Plant Dis. Prot.* **108** 1152.
[9] Deniel P, Rey M, Cherif AG and Tirilly Y 2004 Indige-nous bacteria with antagonistic and plant growth promoting activities improve slow –filtration efficiency in soilless cultivation *Can. J. Microbial*. **50** 499.
[10] Booth C 1977 *Fusarium Laboratory Guide to the Identification of the major species Commonwealth Mycological Institute,* Kew, surrey, England 58.
[11] Leslie JF and Summerel BA 2006 *The Fusarium Laboratory manual* 388.
[12] Bolkan HH and Butler EE 1974 Studies on Heterokaryosis Virulence of *Rhizoctonia solani Phytopathology* **64** 513.
[13] Dewan MM 1989 *Identity and frequency occurrence of fungi in roots of wheat and rye grass and their effect on take-all and host growth*. Ph.D. thesis Univ. of Western Australia 201.
[14] Mckinney HH 1923 Influence of soil temperature and moisture on infection of wheat seedling by *Helminthosporum sativum J. Agric. Res.* **26** 195.
[15] Becking JH 1981 *The family Azotobacteraceae* . In: Starr, M.P.(Ed): Theprokaryotes Vol 1 . Springer-Verlag. Berlin. Heidelberg. New York 795.
[16] Dennis C and Webster J 1971 Antagonistic Properties of Species-Groups of *Trichoderma*: II. Production of Volatile Antibiotics *Transac. Br. Mycol. Soc*. **57** 363.
[17] Manici LM, Kelderer M, Eschbaume G. Capato F, Babini V and Casera C 2000 Replant problems in south Tyrol: role of fungal pathogens and microbial population in conventional and organic apple orchards. Research institute for industrial crops *Viad corticella* **133** 218.
[18] Lozovaya VV, Lygin AV, Zernova OV, Li S, Hartman GL and Widholm JM 2006 Lignin degradation by *Fusarium solani* f. sp. *glycines Plant Dis*. 90 77.
[19] Brenner DJ, Noel RK and Staley JT 2005 *The Proteobacteria*. Part B The Gammaproteobacteria In: Garrity G.M (ed.) Bergey's Manual of Systematic Bacteriology Second Ed Springer Science and Business Media, Inc., New York.
[20] Rahni NM 2012 Efek Fitohormon PGPR Terhadap Pertumbuhan Tanaman Jagung (*Zea mays*) *CEFARS J. Agribisnis dan Pengembangan Wilayah* **3** 27.
[21] Baba ZA, Tahir S, Wani FS, Hamid H, Nazir M and Hamid B 2018 Impact of Azotobacter and Inorganic Fertilizers on Yield Attributes of Tomato *Int. J. Curr. Microbiol. App. Sci*. **7** 3803.
[22] Martinez VR, Dibut BV, Gonzalez RP and Acosta CMR 1994 Effect of the application of bioprepartions based on Azotobacter chroococcum on tomato and onion crops in red ferrallitic soils. 90 anons dr la Estaction Experimental *Agronomica de Santiago de Las Vegas*, 167-184.
[23] Kennedy IR, Choudhury ATMA and Kecskes ML 2004 Non symbiotic bacterial diazotrophs in crop farming systems. Their potential for plant growth promotion be better exploited *Soil Biol. Biochem*. **36** 1229.

Evaluation activity of bacteria *Bacillus thurengensis* and different concentrations of plant extracts on adult of house fly *Musca domestica*

Evaluation activity of bacteria *Bacillus thurengensis* and different concentrations of plant extracts on adult of house fly *Musca domestica*

Raghad Khalaf Al-Joboory [1*] and Elaf Adnan[1]

[1]Department of Biology, Education College, Iraqia University, Baghdad, Iraq.

*E-mail: raghadaljoboory@yahoo.com

Abstract. This research included evaluating the efficacy of plant aqueous extracts for myrtle *Myrtus communis*, *Nerium oleander*, *Eucalyptus* spp. and *Bacillus thuringiensis* on adults of the house fly *Musca domestica* L. under laboratory conditions at a temperature of 2 ± 28 ° C and with a humidity of 50-70 %. it was found that the highest rate of laying eggs was in the extract of eucalyptus leaves, where the number of eggs laid was 60 eggs on average and at a concentration of 5%, while in the concentration of 10% the average egg was 55 eggs then In the extract of the leaves of the oleander was at a concentration of 10% at a rate of 50 eggs and in control treatments the number of eggs reached 80 eggs and the results showed the highest death rate for adults before laying eggs was in the extract of the eucalyptus leaves at a concentration of 15% where the death of 6 adults and the lowest percentage of death by 5% was recorded One adult death and the highest rate priest for eggs, with a concentration of 10%, reached 94%, and the highest percentage of larval mortality reached 68.12%, with a concentration of 10% in the transactions of extract of oleander leaves, and in it also the highest rate of exclusion is 31.93%. The third larval stage with a concentration of 5% with a ratio of 3.67 days and the highest incidence rate in the third larval stage with a concentration of 2.5% at a rate of 26.70% and the lowest incidence rate of 6.70% with a concentration of 2.5% and 5% and 7.5% in the first and second stages respectively and the lowest dawning rate was recorded in the larval phase the first with a concentration of 2.5% at 16.66% and the highest deformation rate in the third larval stage with a concentration of 7.5% at 66.66%. As for its effect on the number of eggs was a rate of zero% of all concentrations (2.5%, 5% and 7.5%) compared to 80 control egg either its effect on the longevity of the adult was the highest rate of longevity amounting to a concentration of 7.5% by 5.33 day..

Keywords. House fly, *Musca domestica*, Myrtle, Oleander, Eucalyptus, *Bacillus thuringiensis*.

1. Introduction

The The house fly (*Musca domestica*) is considered the most common among all other types of flies, accounting for 90% of all types of flies in human housing all over the world, as it is one of the most important insects spread widely around the world, especially in warm regions [1]. Where it lives in association with humans and poses a major threat to public health due to its ability to transmit intestinal parasites and other pathogenic microorganisms [2]. Adults can emergence from pupa in as

little as three and a half days at 35º C and five days under normal conditions, while there may be a need for several weeks under adverse conditions [3]. Despite the effectiveness of chemical control methods for flies, they have become resistant to many chemical groups, which prompted researchers to turn to modern control methods, like the use of microbes and plants control [4, 5]. The bacteria *Bacillus thuringiensis* is a widely used biocide against biological microbes in controlling harmful insects [6]. As it is natural, degradable and safe for pest control based on the insecticide activity of *Bacillus thuringiensis*, commercial biopesticides have been developed to control larvae of Diptera, Lepidoptera, and Coleoptera [7]. Several compounds and plant extracts were evaluated for their toxicity and effect and for reducing the density of different species of double winged flies, especially house flies, including petroleum-ether extracts of *Griffonia simplicifolia* and *Zanthoxylum xanthoxyloides* were evaluated as toxic to house flies [8] . The secondary metabolites in plants work with different mechanisms to affect the life of the insect. They may be contraindicated to nutrition, some of which affect the effectiveness of digestion, reduce the metabolism, or have a repellent effect for the feeding stages of the insect, or be toxic to the insect's tissues, or they may affect the biosynthesis process of chitin thus preventing the phases shedding. The larva and its development, or the nymph, and finally it may affect the productivity of the adult insect, such as preventing egg laying, leading to sterility of adults, or preventing the meeting of the sexes for the same species [9]. The study was conducted with the aim of determining the biological effect between plant extracts and bacteria on house flies *Musca domestica*.

2. Materials and Methods

2.1. Insects breeding

The larvae of house flies were collected from north of Baghdad city were transferred to the insect laboratory . They were divided and placed in 500 gm plastic containers containing larvae feeding and colony maintenance media consisting of 100 gm of floating fish meal consisting of phosphories 1.8%, Ash 10-15%, Crude Fiber 6-8%, Crude fat 8-10%, Crude protein 30 ± 2%) produced by company from Iran and obtained from the local market after being milled and sterilized with an Autoclave at a temperature of 121 degrees 1 centigrade and pressure 1 atmosphere for 25 minutes, 200 ml sterile distilled water and 10 g of dry yeast were added to it, and the center of the feeding was divided on plastic pots, which were transferred to wooden crates with dimensions (30*30*30 cm) made of wood and covered with muslin cloth (with Small porces prevent the exit of the insect.) After the larvae reached the third stage, sawdust were placed on the edges of the pots in order for the larva to dwell and transformed into a pupa, and after 6-7 days of excuses, the virgins began to emerge, and in order to feed the budding adolescents and maintain the group. A clove of a container containing 50 grams of sugar powder and powdered milk (1: 1) (weight: weight) to feed the whole grains and a bottle filled with water and the nozzle of it covered with cotton 12 light: 12 dark hours.

2.2. Preparing plant extracts

Collected plant leaves (myrtle, oleander, eucalyptus) the leaves were washed in running water well several times and left to dry completely in a dark place , at room temperature, taking into account constant stirring to prevent rotting, then these dried leaves were ground using an electric grinder sterilized using sterile alcohol, and after grinding them well, they were placed in sterile cans . The plant extracts were prepared according to the method of [10], where 25 g of each dried plant was weighed and dissolved with 250 ml of distilled water and placed in a Soxhlet extractor for 7 hours at a temperature of 45 ° C and then filtered. Using filter paper, then dry the raw extract produced by a Rotary Evaporator until it becomes in a powder form, and is well preserved until use in the transactions.

2.3. Study of the effect of plant extract concentrations on whole house flies

Prepared 12 wooden crates (30*30*30) cm , in each box, a plate containing 30 grams of whole milk, consisting of (15 grams of milk powder + 15 grams of sugar) was placed and added to it The three concentrations of each extract (myrtle, oleander, eucalyptus) (5,10,15%) for each one of them plus the comparison treatment In another vessel, water was placed for her to drink, where the mouth of the vessel was covered with cotton , a pair of camels, a male and a female, were entered into each cage, and the observation and examination were carried out, and for each repeat a pair of whole house flies (1 male: 1 female) was entered at the age of two days, and the daily monitoring and recording of the effect of the extract on the pair of adults and their survival time and its effect on the laying of eggs and hatched larvae and their duration of survival and the resulting distortions.

2.4. Study of the effect of bacteria on adults house flies

In the first group, three previously described wooden crates (representing 3 replicates) were prepared. In each duplicate, a plate consisting of 30 gm of adult food was placed (15g milk powder + 15g sugar) and 0.075g of the biocide *B.t.k.* was added to it. (It represents a concentration of 2.5%), the materials were mixed well for a minute with each other and in another container put drinking water and the mouth of the vessel was covered with cotton The second group included three cages representing three replicates, each one containing a food dish with 0.15 gm (5% concentration) added to a bacterial pesticide in addition to a bowl of water, while the third group included the same previous details with the addition of the bacterial pesticide at a concentration of 7.5% at 0.21 g per dish in addition to cages the comparison, which contained only food and water, included in each repeat a pair of whole house flies (1 male: 1 female) at the age of two days, and daily monitoring and recording of the effect of the biocide on the pair of adult and their survival time and its effect on laying eggs and hatched larvae and their duration of survival and deformities were carried out.

2.5. Statistical analysis

Completely Randomize Design (CRD) was followed in the implementation of the experiments, and the percentages of larval decay were corrected based on the [11] equation which states:

$$\text{Loss\%} = \frac{Perishing\ in\ comparison - Perishing\ in\ the\ treatment}{100 - Perdition\ in\ comparison} \times 100$$

3. Results and Discussion

3.1. Study of some biological aspects of the house fly by adding different concentrations of plant extracts to the diet of adults

It is evident from the results of the table(1) that the highest rate of egg laying was in the eucalyptus leaf extract, where the average number of eggs laid was 60 eggs at a concentration of 5%, where at a concentration of 10%, the rate of eggs laid was 55 eggs, where in the extract of the leaves of the oleander it was at a concentration of 10 An average of 50 eggs, and in the control factors, the number of eggs was 80 eggs , the results of the statistical analysis showed that there are high significant differences between plant extracts and the reason for the low female productivity is that the chemical compounds contained in the plant extracts inhibit the insect's nutrition while it is in the larval stage, which led to the inhibition of egg formation later because this process depends on the active substances that were stored during Larval feeding , whereas the toxic effect of myrtle plant is due to monoterpens. He confirmed that these compounds affect the female reproductive system of insects and

reduce the number of eggs produced from each ovary [12]. The results of the statistical analysis showed that there were significant differences between the death rates of adult females before laying eggs, as some of the adults did not lay eggs because of their infertility, no eggs were laid, and some adult deaths were recorded before laying eggs in eucalyptus extract at a concentration of 5%, and some adult deaths were recorded before laying eggs in eucalyptus and oleander extract at a concentration of 10%. In the control treatments, the adult mortality rate was 0% in the myrtle and babble treatments, the reason for the superiority of myrtle leaf extract over eucalyptus in reducing the life expectancy of male and female adults is due to the fact that myrtle leaf extract contains compounds that are more toxic than the compounds in eucalyptus leaf extract, which led to the death of adult females in a faster time compared to eucalyptus extract, whose effects were slow and not. Shows clear adult toxicity when food is treated.

Table 1. The biological aspects of the *Musca domestica* house fly by adding different concentrations of plant extracts to the adult death.

CON. / Extract	Number of eggs				Mortality				Longevity of females				Longevity of males			
	5%	10%	15%	control	5%	10%	15%	control	5%	10%	15%	control	5%	10%	15%	control
Myrtle	0	0	0	80	6	6	6	0	2.67	4	2.67	3.67	3.33	4	3.33	4.33
	±	±	±	±	±	±	±	±	±	±	±	±	±	±	±	±
	0	0	0	0.577	0	0	0	0	0.33	0.58	0.33	0.33	0.33	0.58	0.33	0.33
Oleander	0	50	0	80	6	2	6	0	3.33	3.33	3.67	3.33	4	3	5	4.67
	±	±	±	±	±	±	±	±	±	±	±	±	±	±	±	±
	0	0.577	0	0.577	0	0	0	0	0.33	0.33	0.33	0.33	0.58	0	0.58	0.33
Eucalyptus	60	55	0	80	1	2	6	2	4	3	4	3.33	4.67	3.33	5.33	4
	±	±	±	±	±	±	±	±	±	±	±	±	±	±	±	±
	0.577	0.577	0	0.577	0	0	0	0	0.58	0.33	0	0.33	0.33	0	0.33	0.58
LSD	*0.69				*				N.S				N.S			

NS means that there are no significant differences, and * means that there are significant differences between some treatments between the probability level ($0.05 \leq p$) according to the LSD test.

It is agreed with [13] that the extract of crude terpenes for leaves and fruits of *C.spinosa* had a significant effect on some life performance parameters of the house fly, as the productivity of females treated with leaf and fruit extract decreased from 1147 eggs / female in control factors to 498 and 555. Egg / female, respectively, at a concentration of 20 mg / ml.

3.2. Study the biological aspects of the house fly by adding different concentrations of plant extracts in the death of adults to the laid eggs

The results of Table (2) showed that the highest rate of laying eggs was in eucalyptus extract, where the number of eggs laid was 60 eggs on average with a concentration of 5%, but at a concentration of 10%, the rate of eggs laid was 55 eggs, and then in the extract of leaves of oleander, it was at a concentration of 10% at a rate of 50 eggs compared to the treatments. Control where the number of eggs reached 80 eggs. The reason for the difference in the rate may be due to the different nature of the active substances present in the plants used with food and their effect on the performance of the reproductive system. It has been found that limonene, which is one of the volatile compounds found in plant extracts, which inhibits growth and reproduction and has a toxic effect on the nervous system of insects in several types of insects. a number of researchers have confirmed its presence in the eucalyptus and myrtle plants. The results of the statistical analysis showed that there were significant differences between the rates of egg hatching, where the highest percentage of eggs hatching was recorded in the oleander leaf extract at a concentration of 10%, reaching 94%, followed by the

eucalyptus extract at a concentration of 5%, at 86.67%, compared with the control treatment for eucalyptus 93.75% and the guava 96.25%, respectively. The cause of egg decay may be attributed to the effect of toxic substances in the extracts on the biological systems of the embryo, or to impede the gas exchange inside the egg, which leads to its destruction. The failure to hatch eggs in general may be due to the fact that the secondary compounds present in myrtle and eucalyptus were Toxic to the embryos and led to failure of hatching eggs [14], the results showed that there were high significant differences between the mortality rates of larvae after hatching, as the highest percentage of mortality was 100% in eucalyptus leaf extract, followed by the oleander leaf extract at a concentration of 10%, reaching 68.12% compared to the control factor, where it reached 0%. and there were no significant differences between the exclusion ratios for the larvae, as the highest percentage of exclusion was reached in the extract of oleander, at 31.93%. The results showed significant differences between the rates of eruption failure, as the highest rate of eruption failure was 100% in all concentrations of ace and eucalyptus and in oleander at a concentration of 5% and 15%, and the lowest rate of emergence in oleander extract at a concentration of 10% at a concentration of 33.30% compared to control, where it was 0%. The results of the statistical analysis showed significant differences between the deformation rates of the buds, as the lowest deformation percentage reached 0% in all concentrations of myrtle and eucalyptus, respectively, and the highest deformation percentage in the oleander extract at a concentration of 10% by 30%. Organic extracts produce pupae with deformed shapes, and adults who have successfully exited often suffer from wing reduction.

Table 2. The biological aspects of the house fly by adding different concentrations of plant extracts in the adult death to the laid eggs.

Con. / Extract	The percentage of hatchability				The percentage of larvae mortality after hatching				Percentage pupa				Emerges failure				Distortion ratio			
	5%	10%	15%	control	5%	10%	15%	control	5%	10%	15%	control	5%	10%	15%	control	5%	10%	15%	control
Myrtle	0±0	00	0±0	96.2±0.72	0±0	0±0	0±0	0±0	0±0	0±0	0±0	100±0	100±0	100±0	100±0	0±0	0±0	0±0	0±0	0±0
Oleander	0±0	9±1.15	0±0	96.2±0.72	0±0	68.12±1.82	0±0	0±0	0±0	31.93±0	0±0	100±0	100±0	33.3±0	100±0	0±0	0±0	30±0	0±0	0±0
Eucalyptus	86.67±0.96	0±0	0±0	93.7±0.72	100±0	0±0	0±0	0±0	0±0	0±0	0±0	100±0	100±0	100±0	100±0	0±0	0±0	0±0	0±0	0±0
L S D	* 0.95				*0.89				N.S				*				*			

3.3. Study of the effect of adding concentrations of Bacillus thuringiensis to the whole food of house fly

The results of table (3) proved that no eggs were laid for adult domestic flies in all concentrations compared to the control factor, where the number of eggs was 80 eggs, as well as the results showed that there were no significant differences between the longevity of adult females, where the longest life span for adults was 5.33 days with a concentration of 7.5% and the lowest age for adults was 4.33 A day compared to the control was 5 days.

Table 3. Effect of addition of *Bacillus thuringiensis* bacteria to the death of *Musca domestica* whole flies.

Bacterial concentration	The number of eggs for the adult	Adult longevity
2.5%	0.00 b©	4.33 a
%5	0.00 b	4.67 a
%7.5	0.00 b	5.33 a
Control	80.00 a	5.00 a
LSD	-	N.S

Multiple comparisons cannot be calculated as its standard errors are zero

The cause of death of adult adults is that the microscopic crystals that they eat with food turn into toxic protein particles that destroy the stomach walls, so the insect stops feeding within hours after exposure to the bacteria and dies within 2 to 5 days [15]. This is in agreement with [16], who proved that females treated with *B.t.k* bacteria lay the lowest rate of eggs, ranging between 24 - 42 eggs as a maximum, compared to normal treatments that lay eggs at a rate of 33-59 eggs.

References

[1] Deakpe TE, Manyi MM and Utume LN 2018 Pathogenic parasites and bacteria associated with the housefly (*Musca domestica*) in Makurdi; a fly-infested area in central Nigeria *Nigerian J. Parasitol.* **39** 111.
[2] Onyenwe E, Okore OO, Ubiaru PC and Abel C 2016 Housefly-borne helminth parasites of Mouau and its public health implication for the university community *Anim. Res. Int*. **13** 2352.
[3] Tian Y 2017 *Toxicity and repellency of essential oils to the house fly (Musca domestica)* Thesis Auburn University 1.
[4] Khan HA A, Shad SA and Akram W 2013 Resistance to new chemical insecticides in the house fly, Musca domestica L., from dairies in Punjab, Pakistan *Parasitol. Res.* **112** 2049.
[5] Gronvold J, Henriksen SA, Larsen M, Nansen P and Wolstrup J 1996 Biological control aspects of biological control with special reference to arthropods, protozoans and helminths of domesticated animals *Vet. Parasitol.* **64** 47.
[6] Brar SK, Verma M, Tyagi RD and Valéro JR 2006 Recent advances in downstream processing and formulations of *Bacillus thuringiensis* based biopesticides *Process Biochem.* **41** 323.
[7] Glare TR and O'Callaghan M 2000 Bacillus thuringiensis biology, ecology and safety Wiley, Chichester ; New York, No:632.
[8] Ogbalu OK, Umeozor OC and Ebere N 2005 Oviposition deterrent effect of extracts of neem against *Atherigona orientalis* (Schiner) on pepper (*Capsicum annum*) and tomato (*Lycopersicon esculentum*) fruits in Nigeria *Indian J. Agric. Res.* **39** 18.
[9] Kelany IM 2001 *Plant extracts and utilization of their products for safe agricultural protection and for reducing environmental pollution. proceeding of the workshop on practice oriented result on use of plant extract and pheromones in integrated biological pest control Plant protection* Dept , Faculty of Agriculture Zagazig University Egypt,10.
[10] Rios JL, Recio MC and Villar A 1987 Antimicrobial activity of selected plants employed in the Spanish Mediterranean area *J. Ethnopharmacol.* **21** 139.
[11] Schneider-Orelli O 1947 *Entomologisches praktikum verlag sauerlander* Aarau: 237.
[12] Zayzafoon G, Odeh A and Allaf WA 2011 The use of photo chemiluminescenc eassay for the measurement of integral antioxidant capacity in Syrian *Myrtus communis* L. Leaves *Herba Polonica* In press.

[13] Al-Zubaidi FS, Al-Rubaie HMA and Al-Okaily L 2005 Terpenoids crude extract of Caparis spinosa affecting some biological aspects of house fly, *Musca domestica* L.(Diptera: Muscidae) *J. Al-Nahrain Univ*. **8** 28.
[14] Don-Pedro KN 1989 Mode of action of fixed oils against eggs of *Callosobruchus maculatus* (F.) *Pestic. Sci.* **26** 107.
[15] Sante Canada 2013 *Fiche technique sur le Bti–Bacillus thuringiensis variété israelensis* Canada, 6 http://www.hc-sc.gc.ca/cpsspc/pubs/pest/_factfiche/bti/index-fra.php.
[16] Saliha B, Wafa H and Laid OM 2017 Effect of Bacillus thuringiensis var krustaki on the mortality and development of Culex pipiens (Diptera; Cullicidae) *Int. J. Mosquito Res*. **4** 20.

The effect of pH, calcium, phosphate and humic acid on cadmium availability and speciation in artificial groundwater

The effect of pH, calcium, phosphate and humic acid on cadmium availability and speciation in artificial groundwater

Nadia Jebril[1,2], Rich Boden[2] and Charlotte Braungardt[3]

[1]Department of Biology, College of Sciences for Women, University of Babylon, Iraq.
[2]School of Biological and Marine Sciences, University of Plymouth, Drake's Circus, Plymouth PL4 8AA, United Kingdom.
[3]School of Geography, Earth and Environmental Sciences and Plymouth University, Drake Circus, Plymouth, PL4 8AA, United Kingdom.

*E-mail: nadia.tawfiq@uobabylon.edu.iq

Abstract. The interface between the ions in groundwater affects the biogeochemical behaviour of metal, and metal bioremediate by bacteria. Therefore, this study was aimed to predict the influence of pH, calcium, phosphate and humic acid on cadmium availability in artificial groundwater (AGW). Speciation and the thermodynamic calculation (MINTEQ program) were used to predict this in AGW theoretically. In results, cadmium availability diminished with an increase in pH, increase of calcium concentration and the addition of phosphate and humic acid of AGW. According to MINTEQ program, cadmium binds to some cations leaving fewer free cadmium ions available in AGW such as $CdHCO_3^+$, $Cd(SO_4)_2^{2-}$, $CdCl^+$, $CdHPO_4$, HA1-Cd, FA1-Cd, FA2-Cd, and HA2-Cd. It is suggested though that pH in AGW is maintained at pH 4.00 for best availability of cadmium and bioremediate by bacteria.

Keywords. Availability, cadmium, calcium, groundwater, humic acid, pH, phosphate, speciation.

1. Introduction

The Metals speciation and availability in environments and their biogeochemical activities are the main area of research for biochemistry and ecotoxicology of metals [1]. This is important since chemical or mineral speciation is a crucial factor inducing; the solubility, mobility, bioavailability, bioaccumulation, biodegradability, persistence and toxicity [2]. Metals can occur in environments as free metal ions and/or complexed with inorganic components or organic ligands. Is typically, the dissolved and transferrable forms of metals are well-known as bioavailable. Comparably, the fraction of a metal that forms as a portion of the solid-phase minerals may not be bioavailable [3]. Therefore, it is impossible to measure the total metal concentration as its concentration is often insufficient to clarify its ions. Expecting metal speciation has increasingly gained inclusive application as an active constituent of environmental chemistry in enhancing our knowledge of studies such as agriculture, pollution risk assessment or remediation. Cadmium is considered as a serious environmental issue because of its toxicity, non-biodegradability and bioaccumulation [4]. The contamination of

groundwater with cadmium has become a global challenge, and more effective methods for removing cadmium are required. The bioavailability and toxicity of cadmium in water are strongly affected by the cadmium forms. Predication of metal speciation aids our understand of metal performance in water and few analytical techniques are used to estimate metal speciation in water such as sorption onto C18 columns, anodic stripping voltammetry, ion-selective electrodes and competitive ligand equilibration/adsorptive stripping cathodic voltammetry [5]. Nevertheless, these methods are acknowledged as very time consuming in sample preparation. Alternatively, the use of geochemical speciation software programs offers a rapid method to establish metal speciation such as Visual PHREEQC, CHEAQS, ORCHESTRA, ECOSAT, CHESS and MINTEQ. These geochemical speciation software programs can predict metal speciation theoretically. This study, aimed to predict the cadmium speciation in typical groundwater without any contamination; AGW was prepared in the laboratory, and cadmium speciation was then predicated under the contamination of a change in pH, an increase of calcium concentration and the addition of phosphate and humic acid.

2. Materials and Methods

2.1. Cadmium precipitation and speciation

2.1.1. Uncontaminated AGW

The component of AGW is specified in Table 1 (first column, Cd-AGW), according to [6]. To theoretically assess the experimental conditions of Cd-AGW, the inorganic chemical speciation at 22°C was calculated using the geochemical speciation software Visual MINTEQ, version 3.1 [7]. The input file contained the components and concentrations of AGW, with a nominated concentration of 10 µM Cd at pH 7.00; (Table 1), oversaturated solids were allowed to precipitate, ionic strength was calculated, and activity corrections were performed after Davies. Redox calculations were not performed.

2.1.2. Contaminated AGW: Chang the pH, increase of calcium concentration and the addition of phosphate and humic acid

The inorganic Cd speciation at different pH values (fixed at pH 4.00, 7.00, 7.50, and 8.50, respectively) was calculated. At pH 8.50, calcium carbonate species (e.g., calcite) and Cd carbonate (otavite) were predicted to precipitate, and the proportion remaining in the AGW was 84.9% of Ca2+, 4.8% of Cd2+, and 76.5% of CO32-. The otavite precipitation predicts that only 0.48 µM remained in AGW as Cd2+. Consequently, the experiment was not run at pH 8.50. The concentration of calcium in AGW was increased from 1.75 to 17.5 mM, applied as CaCl2. Similarly, the effects of the higher concentration of the anion on the cadmium speciation were studied by adding phosphate (10 mM), which does not consist of AGW. Phosphate (10 mM) consisted of two components of 6.15 mL of K2HPO4 (1 M) and 3.85 mL of KH2PO4 (1 M) in a litre. Humic acid constitutes the significant fractions of OM in natural water, which consists of 90% of the total dissolved organic carbon (DOC) [8]. Thus, humic acid (Sigma-Aldrich) was added at the concentration of 10 mg/L to Cd-AGW. This concentration of humic acid was chosen as the average concentration is presented in natural water [9]. With the addition of humic acid (10 mg/L), the NICA-Donnan model in Visual MINTEQ was used. It was found that the parameters and constants for a ‘generic’ fulvic acid were assumed to be 82.5% of the input; dissolved organic carbon (DOC) consists of fulvic acid with a carbon content of 50% (the portion designated ‘active’ concerning metal complexation because humic acid is assumed not to be dissolved in solution), as described by [10]. Fifty percent was in a DOC: DOC ratio of 1.65, which is an average based on stream and lake sediments from the Swedish environmental monitoring network. However, default parameters were used for VMINTEQ for humic acid: 1.4. The total molar

concentration of DOC was10 mg/L (gave 551% C in HA), which is equal to 459 µM. Therefore, the input parameter for humic acid is 459 µM (Table 1).

Table 1. The input file of software Visual MINTEQ contained the components and their concentrations in AGW with a concentration of 10 µM Cd at pH 7.00 under the increase of calcium concentration (17.5 mM) and the addition of a phosphate (10 mM) and humic acid (10 mg/L).

Component	Concentration (µM)			
	Cd-AGW	Increase of $CaCl_2$	Addition of phosphate	Addition of humic acid
Ca^{2+}	1750	17500	1750	1750
Cd^{2+}	10	10	10	10
Cl^-	1750	17500	1750	1750
CO_3^{2-}	1162	1162	1162	1162
K^+	103	103	103	103
Mg^{2+}	448	448	448	448
Na^+	1144	1144	1144	1144
NO_3^-	44	44	44	44
PO_4^{3-}	*	*	10000	*
SO_4^{2-}	448	448	448	448
Humic acid	*	*	*	459

*No component added.

2.2. Statistical analysis

ANOVA followed by Tukey post hoc was performed on the data of Cd species distribution of AGW with a concentration of 10 µM Cd, which predicted using Visual MINTEQ to find the differences under the effect of different factors on the percentages of Cd species.

3. Results and Discussion

3.1. Cadmium precipitation

At pH 7.50, the calculations revealed the precipitation of otavite (80% of the added Cd concentration), as shown in Table 2, leaving a dissolved concentration of 2 µM in AGW. At pH 7.00, the calculations indicated that the precipitation of otavite (57.7% of the added Cd concentration), leaving a dissolved concentration of 4.22 µM in AGW. It has been recently reported by [11] that cadmium could be precipitated at alkaline pH (>8.00). The calculations revealed the potential loss of Cd from the solution, as the initial concentration in the AGW was 10 µM Cd. At pH 4.00, the calculated saturation index for all species was negative, and Cd was not predicted to precipitate.

Table 2. Effect of pH on the percentages of dissolved and precipitated components in AGW with a concentration of 10 µM Cd. The percentages of values were predicted using Visual MINTEQ.

Component	pH 4.00		pH 7.00		pH 7.50	
	Dissolved (%)	Precipitated (%)	Dissolved (%)	Precipitated (%)	Dissolved (%)	Precipitated (%)
Ca^{2+}	100	0.00	100	0.00	100	0.00
Cd^{2+}	100	0.00	42	57.7	19.5	80
Cl^-	100	0.00	100	0.00	100	0.00
CO_3^{2-}	100	0.00	99	0.40	99	0.40
K^+	100	0.00	100	0.00	100	0.00
Mg^{2+}	100	0.00	100	0.00	100	0.00

Na^+	100	0.00	100	0.00	100	0.00
NO_3^-	100	0.00	100	0.00	100	0.00
SO_4^{2-}	100	0.00	100	0.00	100	0.00

However, when CaCl2 was increased from 1.75 mM to 17.5 mM (for the removal process under cation competition), the calculated saturation index for all species was negative, and no precipitation was predicted (Table 3). The dissolved Cd concentration at the beginning of the experiment can be assumed as 10 µM, and the initial measured concentration was approximately 10 µM. Also, the addition of a phosphate (10 mM) showed no potential precipitation of Cd in AGW (Table 3). The NICA-Donnan model indicated that there was no Cd precipitated (Table 3), leaving a dissolved concentration of 10 µM in the test AGW. The measured and predicted dissolved Cd concentrations were the same, due to the low concentration of humic acid, which explains the lack of Cd complexation with the humic acid. [12] used 200 mg/L of humic acid, which is higher than the concentration in this study, and they found that the log activities of binding of $Cd(OH)_2$ and $CdOH^+$ with humic acid were -9.5 and -8.4 mol/L, respectively. While, in this study, the log activities for the same species of Cd were low -11.5 and -8.5 mol/L, respectively.

Table 3. Effect of increased calcium (17.5 mM), additional phosphate (10 mM), and humic acid (10 mg/L) on the percentages of dissolved and precipitated components in AGW with a concentration of 10 µM Cd. The percentages were predicted using Visual MINTEQ.

Component	Calcium (17.5 mM)		Phosphate (10 mM)		Humic acid (10 mg/L)	
	Dissolved (%)	Precipitated (%)	Dissolved (%)	Precipitated (%)	Dissolved (%)	Precipitated (%)
Ca^{2+}	100	0.00	0.59	99.4	100	0.00
Cd^{2+}	100	0.00	100	0.00	100	0.00
Cl^{1-}	100	0.00	100	0.00	100	0.00
CO_3^{2-}	100	0.00	100	0.00	100	0.00
K^{1+}	100	0.00	100	0.00	100	0.00
Mg^{2+}	100	0.00	100	0.00	100	0.00
Na^{1+}	100	0.00	100	0.00	100	0.00
NO_3	100	0.00	100	0.00	100	0.00
PO_4^{3-}	*	*	94.7	5.21	*	*
SO_4^{2-}	100	0.00	100	0.00	100	0.00
FA1	*	*	*	*	100	0.00
FA2					100	0.00
HA1					100	0.00
HA2					100	0.00

* No component added.

3.2. Cadmium speciation

Predicting Cd speciation in AGW versus pH showed that Cd^{2+} was the dominant type in AGW with a concentration of 10 µM Cd at a different pH (**Error! Reference source not found.**A, $^a p<0.05$), compared to other dissolved Cd species. Similarly, $CdCl^+$ recorded no differences at different pH values (**Error! Reference source not found.**A). The appearance of $Cd(SO_4)_2^{2-}$ at pH 4.00 and 7.00, which disappeared at pH 7.50, showed no significant differences between pH 4.00 and 7.00. The occurrence of $CdHCO_3^+$ was the unique species predicted at pH 7.00 and 7.50 (**Error! Reference source not found.**A, $^c p<0.05$). The effect of increased Ca concentration (17.5 mM) of Cd speciation in AGW at pH 7.00 showed Cd^{2+} was lower than the value recorded at a natural concentration of Ca (1.75 mM). However, Cd^{2+} was the dominant species and showed significant differences (**Error!**

Reference source not found.B, [a]p<0.05) compared to other Cd species. However, $CaCl^+$ was predicted to be 41%, which was higher than the percentage recorded at the initial concentration of $CaCl_2$ (1.75 mM). Moreover, both species of $CdHCO_3^+$ and $Cd(SO_4)_2^{2-}$ were predicated at an increase of Ca as a natural concentration of Ca (1.75 mM), without any differences between them (**Error! Reference source not found.**B, [c]p<0.05). While the addition of a phosphate (10 mM) showed that the domain of Cd species was $CdHPO_4$ (89%), the presence of other Cd-species was rare. Fraction Cd^{2+} was the highest predicted percentages (9.2%) among $CdCl^+$, $Cd(SO_4)_2^{2-}$, $CdHCO_3^+$, and $CdCO_3^+$ (**Error! Reference source not found.**C). Similarly, as Cd^{2+} was the dominant species in AGW at pH 7.00, with the addition of humic acid (10 mg/L) into the AGW, Cd^{2+} was the dominant species (84%), followed by $CdCl^+$ (10%, Figure 1D).

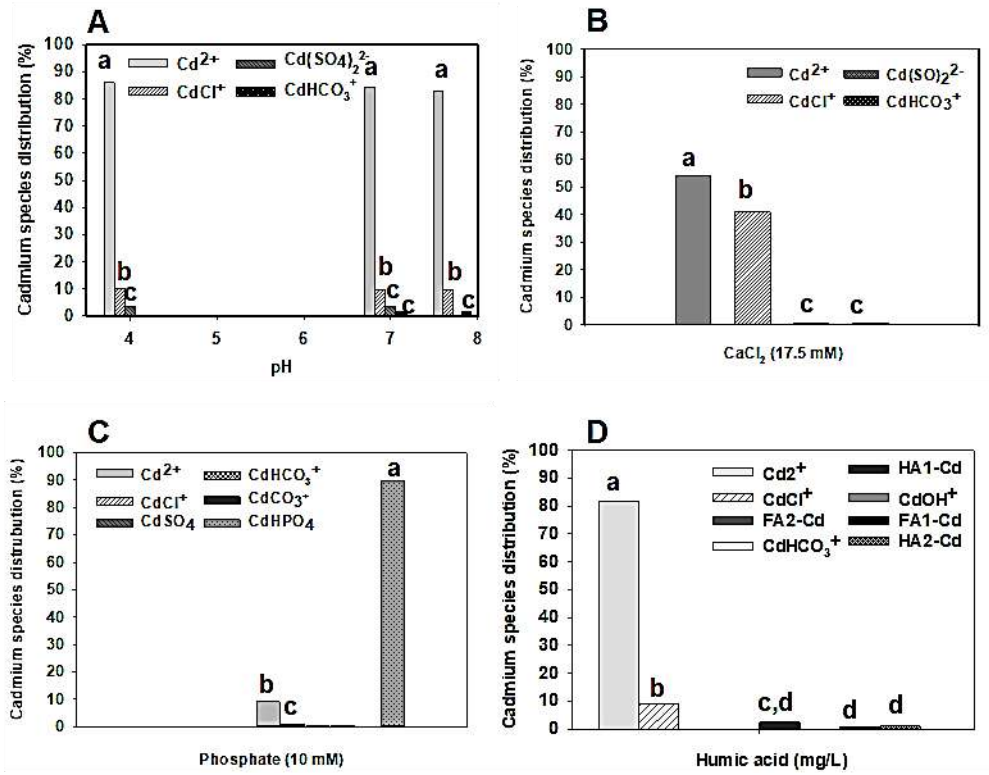

Figure 1. The effect of different factors on the percentages of Cd species distribution of AGW with a concentration of 10 µM Cd, predicted using Visual MINTEQ. (A) At pH 4.00, 7.00, and 7.50, (B) increase of calcium (17.5 mM), additions, (C) phosphate (10 mM), and (D) humic acid (10 mg/L) on Cd speciation in AGW. The Cd species were subjected to two-way ANOVA, Tukey *post hoc* test, and a different letter indicates a significant difference between Cd species under different factors.

With the use of two types of Cd-binding with fulvic and humic acids in the NICA-Donnan model, complex HA1-Cd occurred in addition to other complexes in rare percentages (FA1-Cd, FA2-Cd, and HA2-Cd) as well as the occurrence of fractions $CdHCO_3^+$ and $CdOH^+$. The complexation of Cd with humic acid (Cd-HA) was predicted as this complex is the most formed complex with Cd [13].

4. Conclusion

The ions of cadmium diminished with increase in pH of AGW, in which cadmium binds to cations present in water, leaving less availability of cadmium ions. Increase of calcium concentration and the addition of phosphate and humic acid formed of insoluble cadmium species that appeared in the water. It is recommended though that free cadmium ions were available at a pH of 4.00, which would make cadmium soluble, available and toxic.

5. References

[1] Fayiga AO, Saha U and Ma LQ 2011 Chemical and physical characterization of lead in three shooting range soils in Florida *Chem. Spec. Bioavailab*. **23** 163.
[2] Dumat C, Quenea K, Bermond A, Toinen S and Benedetti MF 2006 Study of the trace metal ion influence on the turnover of soil organic matter in cultivated contaminated soils *Environ. Pollut*. **142** 521.
[3] Cecchi M, Dumat C, Alric A, Felix-Faure B, Pradère P and Guiresse M 2008 Multi-metal contamination of a calcic cambisol by fallout from a lead-recycling plant *Geoderma* **144** 287.
[4] Shahryari T, Mostafavi A, Afzali D and Rahmati M 2019 Enhancing cadmium removal by low-cost nanocomposite adsorbents from aqueous solutions; a continuous system, Compos *Part B Eng*. **173** 106963.
[5] Cobelo-Garcıa A and Prego R 2004 Chemical speciation of dissolved copper, lead and zinc in a ria coastal system: the role of resuspended sediments *Anal. Chimica acta* **524** 109.
[6] Knobel L, Bartholomay R, Cecil L, Tucker B and Wegner S 1992 *Chemical constituents in the dissolved and suspended fractions of groundwater from selected sites, Idaho National Engineering Laboratory and vicinity, Idaho, 1989*. Geological Survey, Idaho Falls, ID (United States). Available at: https://pubs.usgs.gov/of/1992/0051/report.pdf.
[7] Gustafsson J 2011 *Visual MINTEQ Version 3.1*: A Windows version of MINTEQA2.
[8] Croué JP 2004 Isolation of humic and non-humic NOM fractions: structural characterization *Environ. Monit. Assess*, **92** 193.
[9] Hudson N, Baker A and Reynolds D 2007 Fluorescence analysis of dissolved organic matter in natural, waste and polluted waters-a review *River. Res. Appl*. **23** 631.
[10] Pearson HB, Comber SD, Braungardt CB, Worsfold P, Stockdale A and Lofts S 2018 Determination and prediction of zinc speciation in estuaries *Enveron. Sci. Tech.* **52** 14245.
[11] Siswoyo E, Qoniah I, Lestari P, Fajri JA, Sani RA, Sari DG and Boving T 2019 Development of a floating adsorbent for cadmium derived from modified drinking water treatment plant sludge *Enveron. Tech. Inno*. **12** 34.
[12] Gondar D, López R, Fiol S and Antelo Arce, F 2006 Cadmium, lead, and copper binding to humic acid and fulvic acid extracted from an ombrotrophic peat bog *Geoderma* **135** 196.
[13] Datta A, Sanyal S and Saha S 2001 A study on natural and synthetic humic acids and their complexing ability towards cadmium *Plan. Soi*. **235** 115.

The effect of usage two methods of garlic extraction(foliar and ground application) on the growth of the tomatoes (*Solanum lycopersicum*) plant

The effect of usage two methods of garlic extraction(foliar and ground application) on the growth of the tomatoes (*Solanum lycopersicum*) plant

Radhiyah Ali Hasan Ahmad[1*]

[1]Department of Biology, College of Education for Pure Science (Ibn Al-Haitham), University of Baghdad, Baghdad, Iraq.

*E-mail: radia.a.h@ihcoedu.uobaghdad.edu.iq

Abstract. Garlic is rich in nutritional and medicinal value as it has been found that the water extract of garlic plant contains 31% carbohydrates and rich in elements calcium, phosphorus, magnesium, potassium, sodium, iron, zinc, manganese, vitamin C, thiamine, riboflavin, niacin and pyridoxine. The aim of this study was to investigate the effect of garlic extract (*Allium sativum* L.) on tomatoes (*Solanum lycopersicum* L.) plant. The trend is to use plant extracts in foliar and ground fertilization. Three levels of foliar application (4, 6, 8%), three levels of ground application (10, 20, 40%), one treatment 6% of foliar and 20% ground application together and the treatment of control (0) were used. The results showed that the usage of garlic extract led to a significant increase in the height of the plant 98.00 cm, chlorophyll content 46.33 spadm, increase the Carbohydrates 7.95%, the number of branches, the number of leaves, the foliar area, the dry weight of vegetative group, the number of flowers, the leaves content of nitrogen, protein and carbohydrates, fruit weight, fruit size, measurement T.S.S. and solidity of treated plant compared to control plants.

Keywords. Fruit quality, Garlic, Plant extracts, Tomato.

1. Introduction

Tomatoes esculentum belonged to Solanaceae family, its native habitat is South America and is one of the most consumed vegetables in the world with more than 120 million metric tons of global production [1], and is the second most important vegetable after potatoes in many countries of the world [2]. In Iraq, according to Food and Agriculture Organization (FAO) statistics for 2011 reported, the area under cultivation was 61,042 hectares and the production rate was 17.36 tonne. h-1. It is represent an important source of minerals, vitamins and antioxidants [3], so is grown either in open field or in covered farming systems. Statistics indicate high annual consumption rates, due to the high nutritional value, as its fruits contain ascorbic, citric and malic acid, some minerals, vitamins and pigments such as carotene and lycopene, which are a major source of antioxidants [4]. The researchers adopted the foliar application method of nutrients in supplying plants with the necessary elements to sustain their continued improvement in their growth and to achieve qualitative and quantitative improvement in the outcome [5]. Plant extracts are the products of the newly used substances to

stimulate and encourage the vegetative and flowering growth. While, the yield are consider as a source of nutrients and natural growth regulations as well as they are easy to absorb and contain effective and effective substances and natural chemical compounds that vary by different species and plant parts and may be stimulating or inhibitory to growth [6]. *Allium sativum* L. was known by many civilizations it is mentioned in many Egyptian, Greek, Indian and Chinese authors. It is a vegetable annually herbaceous crop belong to Liliaceae family [7] regenerated annually and reproductive with bulb and seeds characterized by a special scent containing active substances as: Allicin and Alliin, an effective antibiotic that contains yeasts and vitamins [8, 9]. Garlic is rich in nutritional and medicinal value as it has been found that the water extract of garlic plant contains 31% carbohydrates and rich in elements calcium, phosphorus, magnesium, potassium, sodium, iron, zinc, manganese, vitamin C, thiamine, riboflavin, niacin and pyridoxine [10]. The study aim to investigate the effect of using garlic extract in the methods of foliar and ground application growth, yield and fruit quality of tomatoes.

2. Materials and Methods

The experiment was conducted using Plastic pots 5 kg soil and 30 cm diameter in the botanical garden of Biology Department in College of Education for Pure Sciences (Ibn Al-Haitham) for the growth season 2017-2018. The seeds of the hybrid tomatoes called Jinan were obtained from agricultural equipment in the local markets planted seeds in the pots by 10 seeds in each pots on 15 January 2018, took 10 gm. of fresh garlic cloves and added 100 ml of distilled water and was mashed in an electric mixer and filtered with a soft cloth and considered the stock solution according to [11], method and the concentrations used in the experiment was prepared as follow:

Treatment (0) without treatment (control)

Treatment (1) foliar application at a concentration of 4%

Treatment (2) foliar application at a concentration of 6%

Treatment (3) foliar application at a concentration of 8%

Treatment (4) ground application at a concentration of 10%

Treatment (5) ground application at a concentration of 20%

Treatment (6) ground application at a concentration of 40%

Treatment (7) foliar application at a concentration of 6% and ground application at a concentration of 20% together.

The plants were sprayed in the early morning until the total wetness when the plant became phase 4-5 real leaves on two periods. The first date is 20/3/2018 and the second date is 20/4/2018 then took measurements on 20/5/2018. The following parameters were studied:

2.1. Vegetative growth parameters

2.1.1. Measuring chlorophyll content in leaf by Spad

Spad it's calculated with a device Chlorophyll meter equipped by a Minolta company by taking mean of three readings of three plants randomly selected from each treatment. This was done by placing the most exposed part of the leaf under the arm of the device and pressing it then taking the reading.

2.1.2. The height of the plant (cm)

Measured by a measuring tape from the area of contact the plant with the soil to the highest point in the main branch of the stem at the end of the growth season.

2.1.3. Number of total branches per plant at the end of the growing season.

2.1.4. Number of leaves (leaf.plant^{-1}) end of growing season.

2.1.5. Leaf area (dcm^2.plant^{-1})

The leaf area was designed on the basis of dry weight as it took 30 foliar disks known area and dried until the weight in an electric oven stabilized at a temperature of 70 °C and from the total dry weight of the plants leaves calculated the foliar area in the following equation: Foliar area (dcm^2)= foliar area of discs × total dry weight of plant leaves / dry weight of discs [12].

2.1.6. Dry weight (gm) for the vegetative total

It was taken at the end of the season.

2.2. Specific qualities

Estimate the percentage of nitrogen in the leaves according to their component content based on dry weight using a Microkjeldahal device [13]. Calculating the percentage of protein in the leaves according to the following equation: Protein ratio = nitrogen × 6.25% [14] Estimating the percentage of carbohydrates in the leaves was done using a Spectrophotometer device [15].

2.3. Flowering parameters

Number of flowers in inflorescence (flowering. inflorescence^{-1}).

2.4. Fruit parameters

2.4.1. Number of fruits (fruit.plant^{-1})

2.4.2. Weight of fruit (gm.fruit^{-1})

2.4.3. The size of the fruit (cm^3)

The size of the fruit were measured by a method of the graduated cylinder and displaced distilled water. A known volume of water was placed in the graduated cylinder and the fruits were flooded at the rate of six fruits of regular growth inside the cylinder and the size was measured by finding the difference between the water level in the two cases then extracting the rate of the fruit size by dividing the difference of size by dividing the difference of size by the number of fruits and calculated in a unit of cm^3.

2.5. Fruit quality parameters

2.5.1. The proportion of total soluble solids in the fruits

It was estimated by Hand Refractometer and the reading was corrected by laboratory temperature at the measurement [16] (Ibrahim, 2010).

2.5.2. Measuring fruit hardness (kg.cm^{-2})

Hardness measured by a Pentrometer device [17].

2.6. Statistical analysis

The statistical analysis was carried out according to Randomized Complete Block Design (RCBD) by triplicates sample per treatments, examined the results according to the analysis of variance then compared the means using the test of the least significant difference (LSD) at the probability level of 5% [18].

3. Results and Discussion

The results indicated that the foliar ground application with fresh garlic extract have a significant effect on the content of the chlorophyll in the leaves of Table (1). while it is noted that the treatment of 6 and 7 gave the highest content of chlorophyll in the leaves which was 45.33 and 46.33 respectively. While the comparison treatment (0) gave the lowest chlorophyll content in the leaves was 31.06. As for the height of the plant, it was a clear significant increase between treatments where the treatment 7 outperformed all treatments by giving the highest rate of height of the plant length reached 98.00 cm and did not differ significantly the treatments 3 and 5 from each other and gave 88.19 and 88.95 cm respectively while the treatment 0 gave the lowest rate of height of the plant length reached 54.45 cm. The treatments 6 and 7 did not differ from each other significantly in the number of plant branches and gave the highest rate of the number of plant branches reached 12.55 branches for both treatments and outperformed the rest of the treatments while the comparison treatment gave the lowest rate on the number of plant branches by giving it 5.55 branches, while the number of leaves did not recorded a significant differences between treatments 5, 6 and 7, where they gave the highest rate on the leaves number reached 12.88, 12.77 and 12.88 leaves respectively, while the treatment 0 gave the lowest rate on the leaf number reached 10.33 leaves, which did not differ significantly from treatment 1 which gave 10.55 leaves. As for the foliar area of the table results, it is clear that the treatments gave a clear significant difference where the treatment of application 7 outperformed by giving it the highest value reached 153.58 dcm2.plant-1, which did not differ significantly from the treatment 6 which gave 152.67 dcm2 compared to the measurement treatment that gave the lowest value with a foliar area of 120.29 dcm2.plant-1 and did not differ significantly from treatments 1 and 2, which gave 121.77 and 121.99 dcm2.plant-1 respectively.

Table 1. The effect of foliar and ground application with garlic extract on the content of the chlorophyll in the leaves, plant height, number of branches and leaves and foliar area of the tomatoes plant.

Treatments	Chlorophyll content in the leaf SPAD	Plant height (cm)	Number of branches. plant^{-1}	Number of leaves. plant^{-1}	Leaf area (dcm^2. Plant^{-1})
0	31.06	54.45	5.55	10.33	120.29
1	32.60	58.06	7.00	10.55	121.77
2	42.30	64.85	8.11	11.11	121.99
3	43.71	88.19	9.55	11.88	126.07
4	44.15	91.34	10.89	12.11	137.44
5	44.81	88.59	11.00	12.88	144.36
6	45.33	94.63	12.55	12.77	152.67
7	46.33	98.00	12.55	12.88	153.58

LSD5%	1.322	1.269	0.961	0.741	5.660

Table 2 shows the effect of foliar and ground application with garlic extract on the measured parameters where the treatment of application 7 exceeded significantly in giving the highest level of nitrogen in the leaves of the plant reached 2.843%, which did not differ significantly from treatment 6, which gave a ratio of 2.733 compared to the treatment of comparison 0 which gave the lowest nitrogen ratio of 1.430, which leads us to exceed the treatments 6 and 7 with the content of the protein in the leaves reached 17.08 and 17.77, which did not differ between them significantly compared to the measurement treatment which gave the lowest value 8.94. As for the percentage of carbohydrates in the leaves, the table showed that the treatment of application 6 and 7 gave a significant differences to the rest of the treatments by giving them the highest percentage of carbohydrates in leaves and reached 6.96 and 7.95 respectively while they did not differ significantly while the treatment of application 0 gave the lowest percentage of leaf carbohydrates, which reached 1.88, that did not differ significantly from the comparison treatment of 1.96, and the treatment of application 7 had a significant superiority over the rest of the treatments by giving it the highest rate of plant flowers where it reached 22.56 flowers, while the treatment compared with control gave the lowest rate of the number of flowers reached 11.56 flowers, which did not differ significantly from the treatment 1 which gave 12.11 flowers.

Table 2. The effect of foliar and ground application with garlic extract on the percentage of protein, nitrogen, carbohydrates in the leaves, number of flowers and dry weight of the tomatoes plant.

Treatment	N%	Percentage of protein in the leaves	Percentage of carbohydrates in the leaves	Number of flowers. Plant^{-1}	Dry weight of plant
0	1.430	8.94	1.96	11.56	55.81
1	1.623	10.15	1.88	12.11	66.74
2	1.653	10.33	3.58	13.22	75.47
3	1.767	11.04	4.05	15.11	77.70
4	2.180	13.62	4.74	17.62	80.44
5	2.597	16.23	6.11	19.26	88.92
6	2.733	17.08	6.96	21.11	90.38
7	2.843	17.77	7.95	22.56	93.97
LSD5%	0.172	1.076	1.649	1.456	4.601

As for the dry weight, the treatments 6 and 7 outperformed the rest of the treatments and gave the highest dry weight rate reached 90.38 and 93.97 gm respectively and did not differ significantly between them, while the lowest dry weight at the treatment 0 was 55.81 gm. and did not differ significantly at the treatment of application 1, which gave a dry weight rate of 66.74gm from the results of Table 3, which shows the effect of foliar and ground application with garlic extract on the number, weight and size of fruits and measurement of the Total Soluble Solids (TSS) and hardness of tomatoes fruits. The results showed the presence of a significant effect of application with garlic extract on the number of fruits where the treatment 7 gave the highest rate of fruit numbers and reached 11.62 fruits while the lowest rate of fruits when the measurement treatment 0 and reached 4.96. As for the weight of the fruit, the treatments 6 and 7 did not differ significantly from each other by giving them 78.10 and 84.07 gm respectively superior to the rest of the treatment while the treatment 0 gave the lowest weight of the fruits and reached 43.37 gm., which did not differ significantly from the treatment 1, which gave a weight rate of 45.32 gm. As shown by the table the effect of application on the size of the fruits where the treatments 6 and 7 showed significant superiority over the rest of the treatments and gave the highest rate of the fruit size reached 98.22 and 98.72 cm3 respectively, while they did not differ significantly, compared with the lowest rate of the fruit size reached 371.92 in the compared with control. As for the measurement of Total Soluble

Solids (TSS), the treatment of application 7 exceeded the rest of the treatments by giving the highest measure and reached 9.070 while the treatments 5 and 6 did not differ significantly, which gave 8.577 and 8.477 respectively, while the measurement treatment gave the lowest percentage measurement of Total Soluble Solids (TSS) reached 6.653. As evidenced by the results of the table the effect of the garlic extract application on the hardness of the fruits, where the measurement treatment gave the highest rate of solidity of the fruits reached 16.99 $kg.cm^{-2}$, while the treatment 7 gave the lowest rate of hardness reached 12.74kg.cm-2 which did not differ significantly with treatment 6 which gave a hardness rate of 12.96 kg.cm-2. The processes of application with garlic extract in both types of foliar and ground application treatments to improve the physiological, morphological and quality characteristics in the tomatoes plant where it gave clear significant differences compared to the control treatment of garlic effective role in it, that the garlic plant contain vitamins, mineral salts and elements such as sulfur, phosphorus, calcium, potassium and iron as well as 31% carbohydrates and organic acids such as citric, malic and amino acids such as valine, leucine and glutamine [10]. All these compounds contribute to the process of photosynthesis and increase the products of photosynthesis and the cycle of Krebs and all of this contribute to the construction of the main compounds in the plant and improve its physiological characteristics. Garlic extract contains an effective compound and has all the properties of garlic and turns into many compounds such as Allicin, Allylsufid included allyl methyltrisulfide and diallyl disulfides which a volatile substances and have many effects [19]. In a study on the cucumber plant, noted [20] that the foliar application with garlic extract by a concentration of 2.5 $ml.L^{-1}$ led to a significant increase in the length of the plant, the number of leaves and foliar area and the content of total chlorophyll in the leaves, the proportion of the nodes and Total Soluble Solids (TSS), which is due to the fact that the water extract of the garlic plant contains 30% carbohydrates and is rich in the elements of potassium, iron, magnesium, phosphorus, thiamine, riboflavin, niacin and ascorbic acid in addition to volatile oils. [21] stated that the inclusion of garlic extract on amino acids such as Cysteine and Methionin, which have an important role in the biological processes of the plant and led to a significant increase in the vegetable growth characteristics, the number of fruits, the yield of the one plant when application the tomatoes plant with garlic extract at a concentration of 40 $ml.L^{-1}$. [22] pointed that the use of foliar application with a 30% concentration on chickpeas led to a significant increase in the content of chlorophyll in the leaves and the proportion of carbohydrates and protein in the seeds. [23] confirmed that the application of cherry tomatoes with Agrosol at a concentration of 6 $gm.L^{-1}$. [24] pointed that the ground application of *Schefflera araboricola* plant by garlic extract at a concentration of 250 $ml.L^{-1}$ led to a significant increase in the number of leaves, foliar area, leaf content of chlorophyll, dry weight of the vegetative total and the percentage of carbohydrates in the leaves compared to the treatment of foliar application of the plant led to improve the most of the vegetative parameters, root and flower growth in open and covered agriculture. In a study on *Beta vulgaris* var. *cicla* plant stated [25] the use of peppermint leaf powder and celery at 5 and 10 gm per kg of soil alone or together work to improve the morphological and physiological characteristics of the plant through an increase in the height of the plant, the number of leaves, dry weight and the content of chlorophyll in the leaves, nitrogen, phosphorus and potassium compared to the treatment of control. The content of garlic extract from the elements of phosphorus, potassium, nitrogen and iron, which worked to increase the height of the plant, the number of leaves, their content of chlorophyll and dry weight helped to synthesize biological components such as proteins and carbohydrates, which worked to improve the physiological characteristics of the plant where these elements enter in the synthesis of cellular membranes and work to increase the number of cells and cellular divisions as well as being involved in the synthesis of chlorophyll such as nitrogen and iron, potassium acts to regulate the opening and closing of the stomata as well as the regulator of biological processes in the plant. The presence of elements a lot provide the requirements for the synthesis of biological ingredients in the plant as well as transmitted with water through the roots, which makes the cells in the plant in a state of fullness and therefore perform their normal functions better [26, 27].

Table 3. The effect of foliar and ground application with garlic extract on the number, weight, size of fruits, and measurement of TSS and hardness of fruits for the tomatoes plant.

Treatment	Number of fruits. plant^{-1}	Weight of fruits (gm)	Size of fruits (cm^3)	TSS (%)	Hardness of fruits kg.cm^{-1}
0	4.96	43.37	71.92	6.653	16.99
1	5.80	45.32	76.20	7.147	14.74
2	6.44	59.38	81.95	7.947	14.70
3	7.10	63.04	86.64	7.777	15.04
4	7.81	56.87	90.84	8.147	13.54
5	7.85	67.75	93.59	8.577	13.75
6	8.96	78.10	98.22	8.477	12.96
7	11.62	84.07	98.74	9.070	12.74
LSD5%	0.874	7.155	2.951	0.440	1.241

4. Conclusion

To conclude that, the usage of garlic extract in two methods of foliar and ground application, were led to a significant differences in the parameters of growth in the characteristics studied for all treatments. Moreover, the higher effect was a significantly usage of both methods and the concentration of 6% foliar application+ 20% ground application in all the characteristics studied for the tomatoes plant.

5. References

[1] FAO 2011 *Production Year Book*. Rome, Italy.
[2] Heuvelink E 2005 *Tomatoes, Crop Production Science* In Horticulture Series Cromwell Press, Trowbridge. UK 352.
[3] Grieson D and Kader AA 1986 *Fruit ripening and quality* The tomato crop. Chapman and Hall, London 240.
[4] Gerszberg A, Hnatuszko-Konka K, Kowalczyk T and Kononowicz AK 2015 Tomato (*Solanum lycopersicum* L.) in the service of biotechnology *Plant Cell Tiss Organ Cult*. **120** 881.
[5] Kathiroson GAD 2000 Fluency In of untried levels on séance in different seasons sesame and safflower *News Lett*. **15** 42.
[6] Ric EL 1984 *Allepathy* 2nd ed. Academic Press. New York.
[7] Al-Kateb YM 1988 *Classification of seed plants* University of Baghdad. Ministry of Higher Education and Scientific Research 342.
[8] Qanbes AJ 2007 *Human adviser in food and drugs. Herbal Medicine and Nutrition Dictionary* Dar Al-Bashair for Printing, Publishing and Distribution. Damascus, Syria:. 95-111.
[9] Talass M 2008 *Herbal medical Dictionary*. Dar Talass Library, Damascus, Syria 557.
[10] Moursi, HAS, Al-Khatib MH and Alshabibi MMA 1981 Determination of same active component of *Allium cepa* and *Allium sativum*. Abstract presented to the first Arab determinations Amman Jordon,7.
[11] Harbone JB 1984 *Phytochemical methods*. A guide to modern techniques of plant analysis (2nd ed) chapman and Hall, London: 282.
[12] Watson DJ and Watson MA 1953 Comparative physiological studies on the growth of yield crops III-Effect of infection with beet yellow *Ann. Appl. Biol*. **40** 1.
[13] Jackson ML 1958 Soil *Chemical Analysis* Prentice Hall, Inc. Englewood Cliff, N.J. USA. 276.

[14] Dalaly BK and Al-Hakim S H 1987 *Food Analysis* Directorate of the House of Books for Printing and Publishing University of Al-Mosul, Iraq.
[15] Herbert D, Philips PJ and Strage RE 1971 *Methods in microbiology*. Acad. Press. London.
[16] Ibrahim HIM 2010 *Plant samples collected and analyzed* First edition. Dar Al-Fajr for Publishing and Distribution, Egypt.
[17] Abbas MF and Muhsin JA 1992 *Care and storage of fruits and vegetables practical. Ministry of Higher Education and Scientific Research* University of Basra. Dar Al Hekma Press. Iraq.
[18] Al-Rawi KM and Khalafallah AAM 2000 *Design and analysis of agricultural experiments* Ministry of Higher Education and Scientific Research, Iraq.
[19] Staba E, Lash JL and Staba E J 2001 A Commentary on the effects of Garlic Extraction and formulation on product composition *J. Nutr.* **131** 11185.
[20] Hussain WA 2002 *Effect of spraying garlic extract, licorice and urea in the characteristics of flowering growth of Cucumis sativus L. and the yield of cucumber plant* MSc. Thesis. College of Agriculture, University of Baghdad.
[21] Saadoun AHS, Merzah TK and Rahman RK 2004 The effect of spraying garlic extract and licorice roots with a mixture of zinc and iron on the growth and yield of two varieties of tomatoes *J. Coll. Iraqi Agric. Sci.* **55** 35.
[22] Al-Kaisy WA, Mahmood RW and Al-Hayani EH 2013 Effect of Garlic (*Allium sativum*) extract and root extract of Ginger (*Zingiber officinale*) on growth and yield of Chick plant (*Cicer arietinum*) *Baghdad Sci. J.* **10** 1120.
[23] Salman AD 2014 *Growth variants and quantitative and qualitative yield of Cherry tomatoes by Agrosol and Enraizal application under open cultivation conditions and greenhouse* MSc Thesis College of Agriculture University of Baghdad.
[24] Jumaa RMA 2015 *The effect of some natural extracts on the growth and chemical components of Schefflera araboricola plant* MSc. Thesis, College of Agriculture. Cairo University.
[25] Al-Kaisy WA, Al-Hallaq, AM, Hassan RA and Al-Adhami LQA 2019 The effect of Mentha viridis and Apium graveolens leaves on growth of *Beta vulgaris* var. *cilica J. Coll. Basic Educ.* **25** 545.
[26] Devlin RM and Witham FH 1982 *Plant Physiology* 4th ed Willard Grant press. Boston 113.
[27] Verma SK and Verma M 2008 *A textbook of Plant Physiology, Biochemistry and Biotechnology* Chand S and Company, LTD. Ram Nager, New Delhi.

Occurrence and composition of copepods abundance in Tigris river, southern Baghdad, and effects of Rasheed power plant effluents on its biodiversity

Occurrence and composition of copepods abundance in Tigris river, southern Baghdad, and effects of Rasheed power plant effluents on its biodiversity

Muhanned R. Nashaat[1*], Fatema S. Muftin[1], Enaam K. Abbas[1]and Eman H. Ali[1]

[1]Agricultural Research Directorate, Ministry of Science & Technology, Baghdad, Iraq.

*E-mail: muhanned_nashaat@yahoo.com

Abstract. The quantitative and qualitative structure of the Tigris River copepods communities, were identified to investigate the biological composition, especially near the outcome of Rasheed power plant (RPP). on its biodiversity at four sites those were chosen on the Tigris River in south part of Baghdad Governorate during the period January to December 2012. The sites S2 was located near Rasheed Power Plant to represent the ecological features of the plant site, whereas other sites, S1 was located at the upstream of the RPP as a control site to investigate the ecological characters of the Tigris River. Moreover, the two other sites S3 and S4 were located down to the impact of RPP to reflect the possible effects of the plant on the copepoda fauna biodiversity by comparison with the control site. Thirty-nine taxonomic units of copepoda fauna were identified in the present study, Including 17 taxonomic units of Cyclpoida, 13 taxonomic units of Calanoida, six taxonomic units of Harpacyicoida and three taxonomic units of Parasitic Copepoda. This study found that the highest copepod density was recorded during the winter period on site below RPP. While at sites near RPP during the summer period, Copepoda showed the lowest density. The results also showed that the sites below RPP included the most constant species, while the lowest were included at site near RPP. The results of the biodiversity indexes generally showed the negative actual impact of RPP on the copepoda commu nity..

Keywords. Biodiversity, Copepoda, Tigris River, Power plant.

1. Introduction

The Power plants drain hundreds of millions or billions of gallons of water each day from rivers , lakes or oceans [1]. According to the United States Geological Survey (USGS) [2]. Water use survey data, 346 billion gallons of freshwater per day (BGD) was used in the United States in 2000, Each kWh of thermoelectric generation requires approximately 25 gallons of water, primarily used for cooling purposes a 500MW power plant would use approximately 300 million gallons of water per day [3]. Power plants and all other cooling water users harm and kill large quantities of fish and other aquatic biota [1]. Through more processes: entrainment (passage through the cooling system of smaller, typically planktonic organisms with cooling-water flow) and impingement (trapping of larger aquatic organisms against intake screens). Both of these processes can cause organism mortality [4].

Rasheed power plant (RPP) in Al-Zafaraniya Region, south of Baghdad, polluted Tigris River water as a result of hot water effluents containing organic compounds, disposed of 430 $m3*h^{-1}$ per high water temperature unit that caused damage to aquatic species in the river environment. Black oil and hot water were used to operate the power plant also it prepared the main sources of air and water pollution in this area. While there are industrial water treatment units, such as acidic acid equation basins and good mixing. As well as the presence of control units for the purification of air from pollutants which resulting from the combustion of fuel to do it within the limits allowed by the environment. The impact on aquatic life of the Iraqi power plant is limited including: [5] led a study to demonstrate the impact of Al–Durah power plant effluents on physical, chemical and invertebrate biodiversity in the Tigris River, southern Baghdad. However, many researchers evaluate series professional studies that included the impact of RPP effluents on the food chain assemblage biodiversity, such as Rotifer [6]; Cladocera [7]; Benthos fauna [8] and Phytoplankton [9]. In addition, [10] and [11] reported the effect of the same power plant on Tigris River ecological characteristics, and water quality using the Canadian Water Quality Index (CCME WQI); respectively. Furthermore, [12, 13] assessment the ecological risk of ash toxicity from Doura power plant in the freshwater Crustacean Simocephalus vetulus Schϕdler; and the Induced of Ash Toxicity Effects from Doura power plant on the hematological and biochemical changes of *Cyprinus carpio* L. 1785. From the literature cited above, It's appear limited work were done on the effects of the power plant (heat waste effluent) discharged into this important groups of zooplankton, Thus, to see the impact of this power plant on its biodiversity, it is necessary to study the biological composition, especially copepoda fauna of the Tigris River near RPP. A current study was the first study after the 2003 war, thus the current study was designed to determine the effect of the RPP on the copepoda community's quantity and biodiversity.

2. Materials and Methods

2.1 Description of the Study Area

Rasheed power plant is designed on the principle of steam generation as a running design and consists of six units and a design capacity for each units 25 MW and the fourth unit 45 MW, it was built in 1963 on the eastern side of the Tigris River, which is considered a source of water for operation and cooling, and near the Al-Dora refinery for the purpose of obtaining crude oil fuel. RPP had withdrawn $500m3*hour^{-1}$ from the Tigris River for each unit. It is tested daily to be treated for relieving them from dissolved and suspended salts according to the permissible limits. So its use of generation steam which it used in the operation of the turbines for the production of electricity [14].

2.2 The Samples Collection

During the period from January to December 2012, the quantitative and qualitative composition of copepoda communities was studied at four sites selected at Baghdad Governorate on the Tigris River. One of the sites was S2 which located near RPP to represent the ecological features of the plant site, whereas other sites, S1 was located upstream RPP as a control site to investigate the ecological characters of the Tigris River. Moreover, the two other sites S3 and S4 were located down to the impact of RPP to reflect the possible effects of the plant on the copepoda fauna biodiversity by comparison with the control sites (Figure 1).

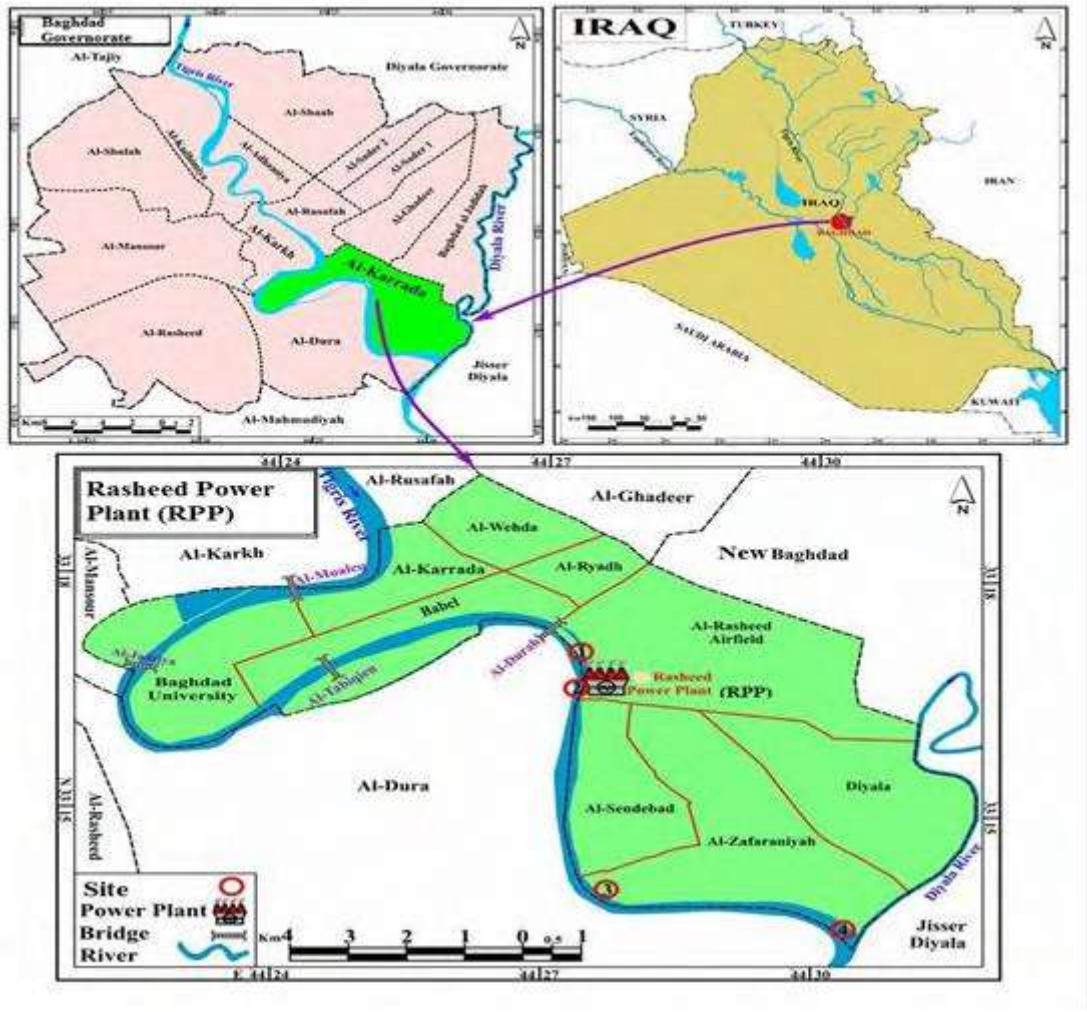

Figure 1. Map represents the study sites.

Monthly sampling was started from January until December 2012 from the four sites under from a depth of 0.5 to 1 m below the water surface, then 45 litre was passing through the zooplankton net with mesh size 55 microns and preserved samples by adding formalin 4%. The samples were examined under a compound microscope and the species was identified according to the diagnostic keys below [15, 16]. The results expressed for individual*m^{-3}. The following Ecological Indices were account:

Relative Abundance Index (Ra): The calculated by (Ra) was depending on the formula contained in [17]. Constancy Index (S): By the presence and frequency of each species, calculated according to the formula contained in [18]. The Species Richness Index (D): This indicator is calculated monthly according to the formula contained in [19]. Shannon - Weiner Diversity Index (H): Values of this indicator were calculated monthly for all groups of invertebrates by using the equation of Shannon and Weiner according in [20]. And the result expressed as the unit bit/Ind. as a bit equal one piece of information. Values < 1 bit * Ind^{-1}. is a little diverse while the values seem more than 3bit *$Ind.^{-1}$ is very diversified [21]. The Species Uniformity Index (E): The species uniformity index measured by the formula referenced in [22]. Values greater than 0.5 in appearance were considered equal or uniform.

3. Results and Discussion

The density of copepoda in the present study varied between great value reached 15577 Ind.* m^{-3} during of January at site 4 and does not appear in the site 2 during January (Figure 2).

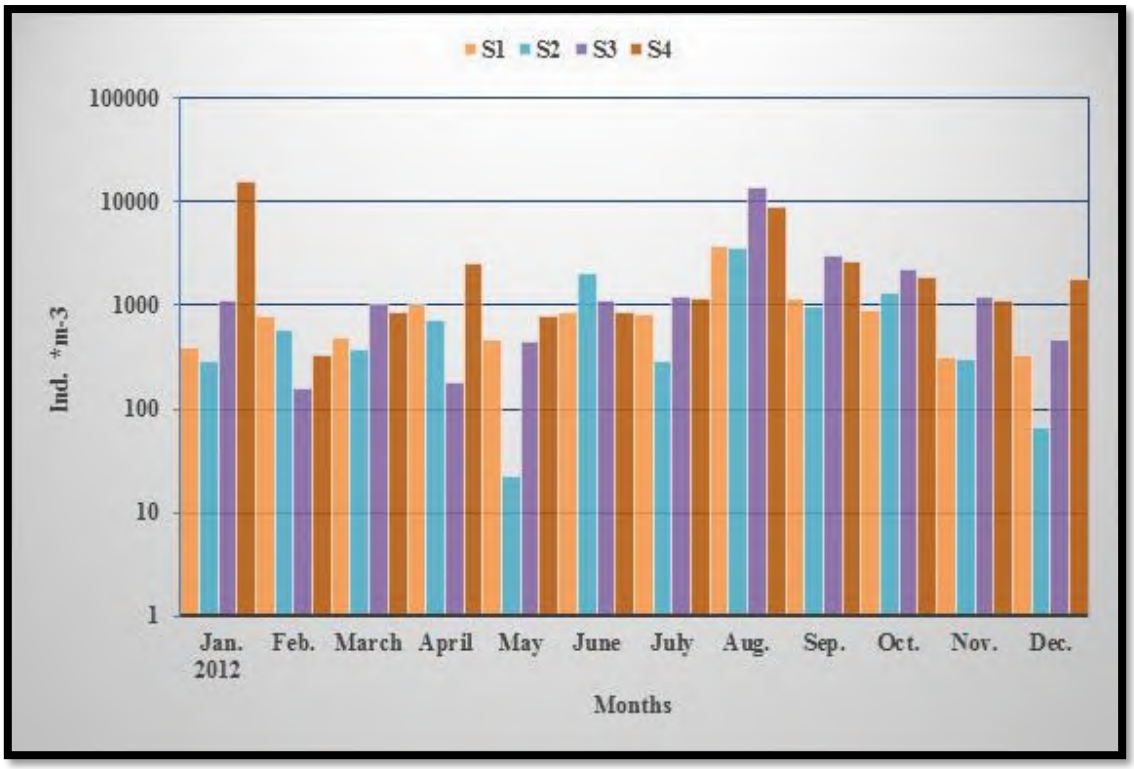

Figure 2. Monthly variations of the copepoda total density Ind.* m^{-3} during the period study.

At site 1 before RPP the density varied between great value reached to 3777 Ind.* m^{-3} during August and minimum 311 Ind.* m^{-3} in November, Whereas great value at site 2 near RPP was recorded 3577 Ind.* m^{-3} in August and minimum 22 Ind.* m-3 in May, while as great value at sites down of RPP reached to 15577 Ind.* m^{-3} in January at site 4 and the minimum value was 155 Ind.* m^{-3} in February at site 3. Throughout the winter season, 15577 Ind. * m^{-3} was observed at site 4 at the maximum copepod density at the site below RPP.. While, sites 2 showed the lowest zooplankton density with 22 Ind.*m^{-3} during summer season. Which may be due to affecting copepoda distribution with two stresses, summer season, and RPP thermal effluents that increase the temperature of the water. What's more, other considerations such as oil spill and sewage effluents that disposal from RPP itself, the same result was obtained by [5] on Al-Duara power plant. [6, 7, 8, 9, 23, 24] a decrease in aquatic group density was also recorded when the impact of other power plants on various groups of invertebrates and phytoplankton at the Euphrates River and Tigris River was studied. With regard to relative abundance index (Table 1, Figure 3), nuuplii recorded the highest percentage relative in compared with a total density of other species which it reached to 77%, 34%, 65% and 80% of sites 1, 2, 3 and 4, respectively. While other species such as immature Calanoid, *Halicyclops* sp., *Paracyclops fimbriatus* appeared in different percentages (Figure 3).

Table 1. Aquatic copepods distribution, relative abundance and constancy index frequencies in study area.

Sites / Taxa	Ra 1	Ra 2	Ra 3	Ra 4	S 1	S 2	S 3	S 4
CYCLOPOIDA								
Cyclop sp.	R	R	R	R	Ac	A	A	Ac
Cyclop (♂)	R	R	R	R	A	A	C	C
C.insignist			R				Ac	
C. magnus				R				A
C. navus	R				A			
C.viridis				R				A
Ectocyclop sp.	R	R		R	A	A		Ac
Eusyclop agilis	R	R	R	R	A	A	Ac	Ac
Haicyclops sp.	R	R	La	R	C	C	C	C
Immature Cyclop	R		R	R	A		A	C
Macrocyclop ater			R	R			A	Ac
Mesocyclop hyalinus	R	R	R	R	A	A	Ac	A
Mesocyclop oithonoides				R				A
Paracyclop fimbritus	R	La	La	R	C	C	C	C
P.affinus	R	R	R	R	A	A	A	A
Tropocyclops prasinus				R				A
Nauplii of Copepoda	D	La	A	D	C	C	C	C
CALANOIDA								
Diaptomus sp.	R	R		R	A	Ac		A
Diptomus arapahoensis	R		R		A		A	
Diaptomus amatitlanensis		R				A		
Diabtomus fimbriatus				R				A
Diptomus lech	R	R	R		A	A	A	
D.minutus			R	R			A	A
Diptomus nudus	R				A			
D. sarsiol		R				A		
D.sens			R				A	
Leptodiaptomus minutus				R				A
0nychooleaptomus sanguineus				R				A
Other Calanoid		R	R			A	Ac	
Immature Calanoida	R	La	R	R	Ac	C	A	A
HARPACTECOIDA								
Harpactecoida sp.		R	R	R		A	A	A
Acroperus harpae				R				A
Nitocra sp.	R	R		R	C	Ac		C
Nitocra lacucetrus			R				C	
Pseudonychocamptus proximus		R	R	R		A	A	A
Immature Harbectecoida				R				A
PARASITIC COPEPODA								
Ergasilus sp.	R	R	R	R	A	Ac	Ac	A
Ergasilus versicolor		R				A		
Lernia			R	R			A	A

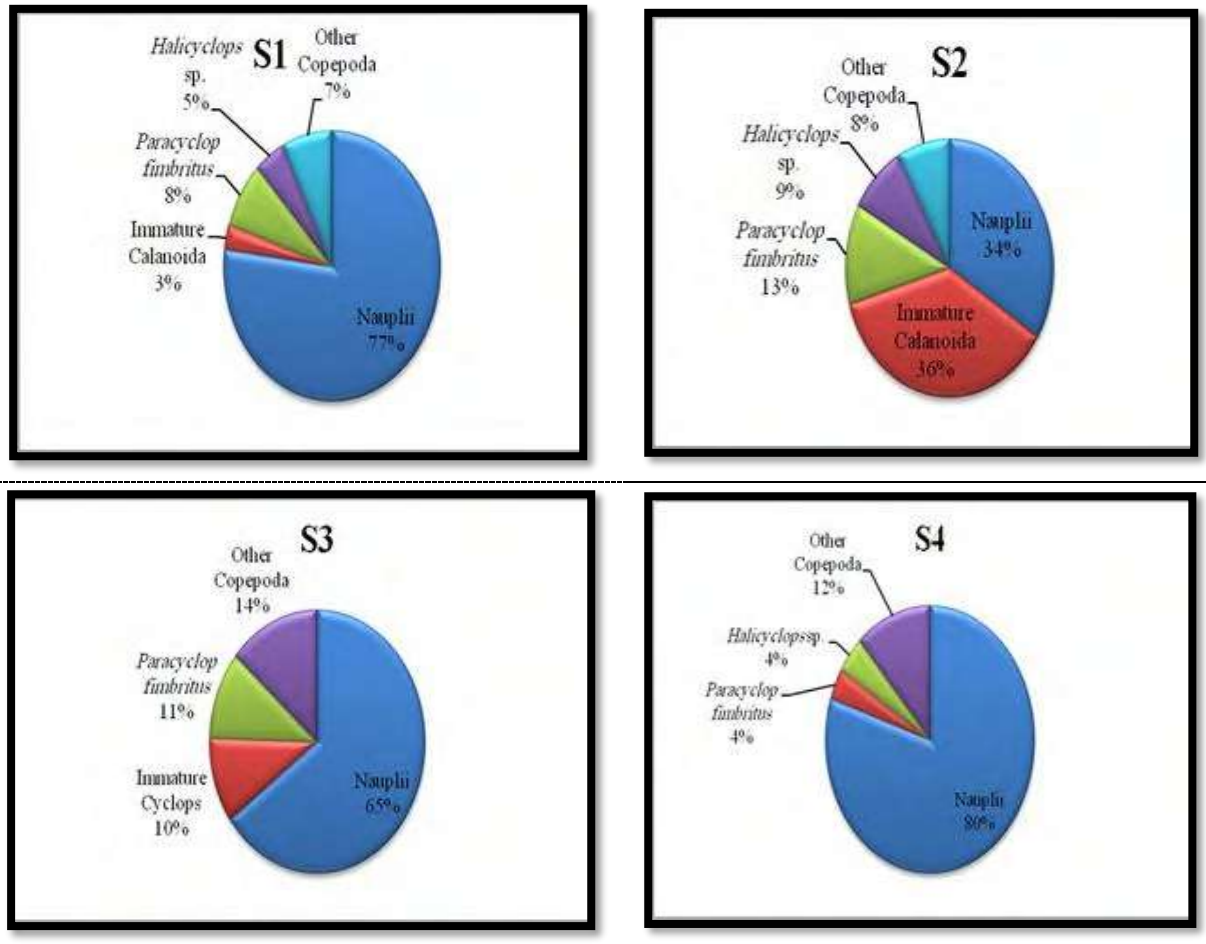

Figure 3. The relative abundance of dominating Copepoda species.

The difference in increased copepoda density may be associated with the nutrients appropriate and their individual is affected by concentrations of salts and organic matter in water [25]. In addition, they are affected by selective vertebrate and aquatic organisms that may be predation of certain sizes, also cyclopoida is the most susceptible to predation by fish larvae [26]. In population of copepoda the numerical predominance of young forms, especially nauplii is the most common pattern, as observed by [22, 27, 28] in different freshwater habitats and as also found in the present study. [29] refer that the dominant group among copepods on lake Lichenskie (with two power plants) were juvenile and harpacticoida found among aquatic plants, and were the most common, constituting nearly 60-80% of zooplankton communities. The low density of the Calanoid group compared to the other suborder may be due to the fact that most species are planktonic, rarely lateral and bloom in lakes and ponds which appropriate in a lentic available environment (Figure 4).

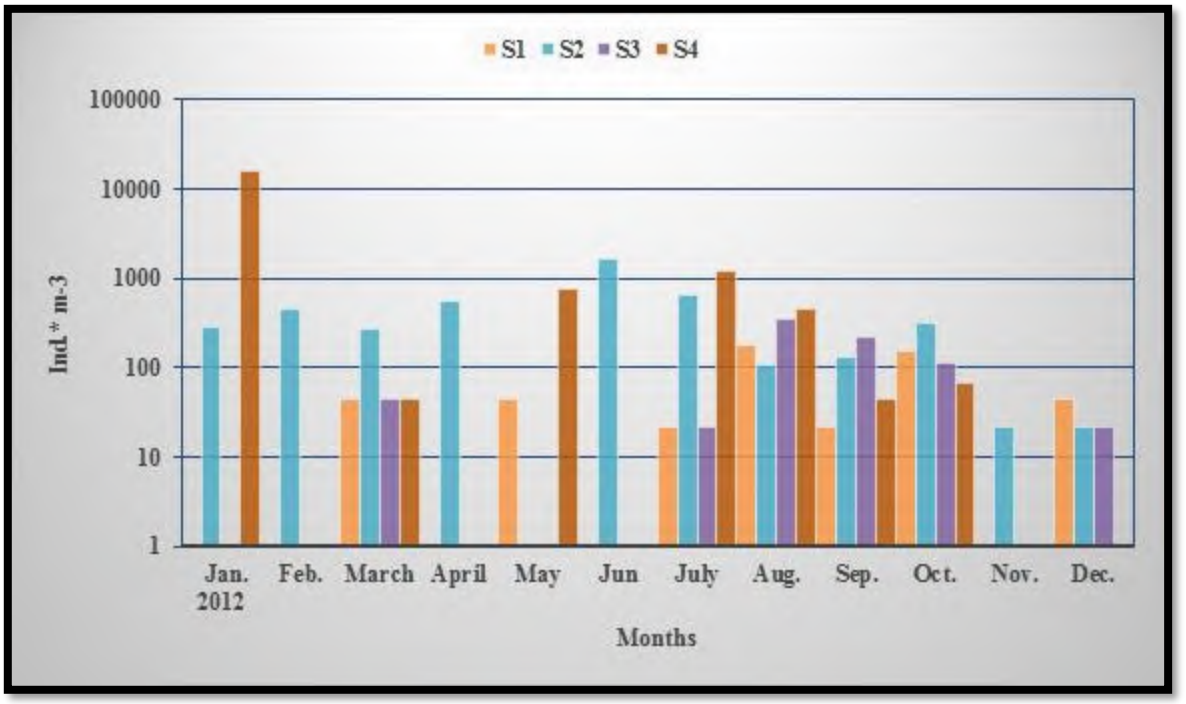

Figure 4. Monthly variations of the Calanoid group density Ind.* m^{-3}.

As for the other two suborders, Cyclopoida and Harpacticoida, they prefer the coasts of the water bodies, especially when there is a covered with vegetation [30] (Figures 5, 6).

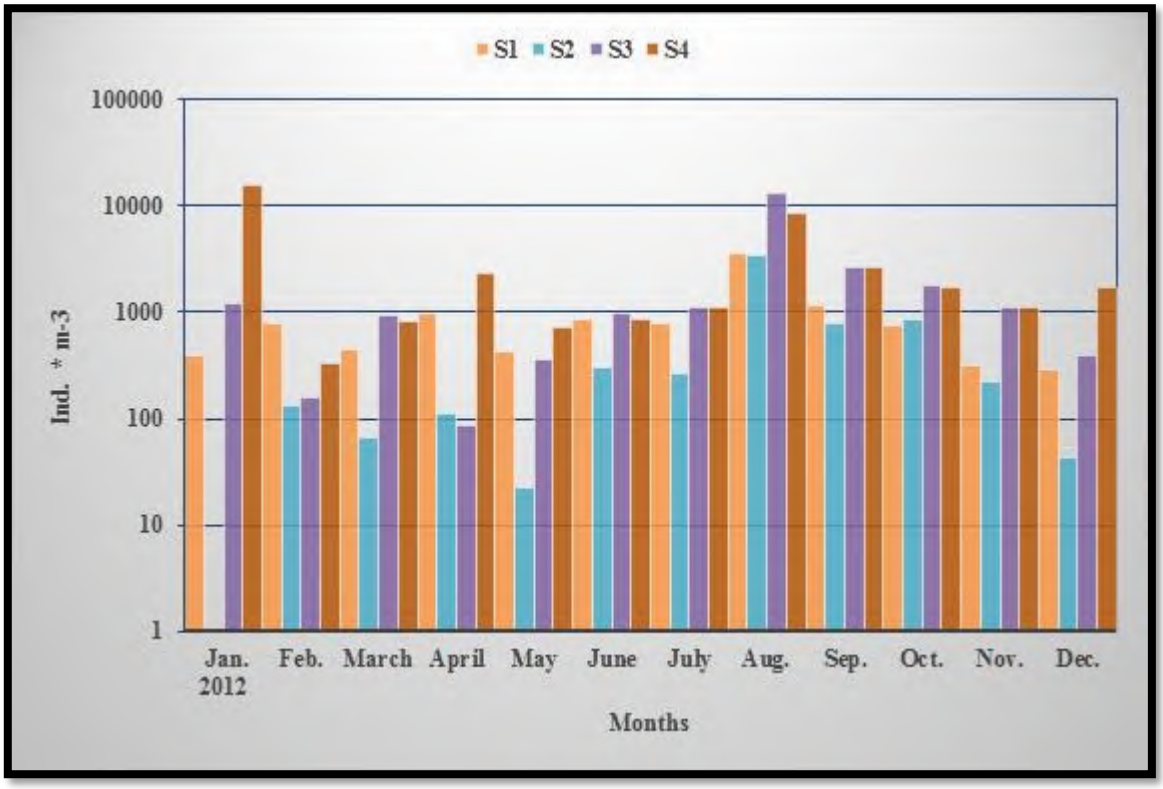

Figure 5. Monthly variations of the Cyclopoida group density Ind.* m^{-3}.

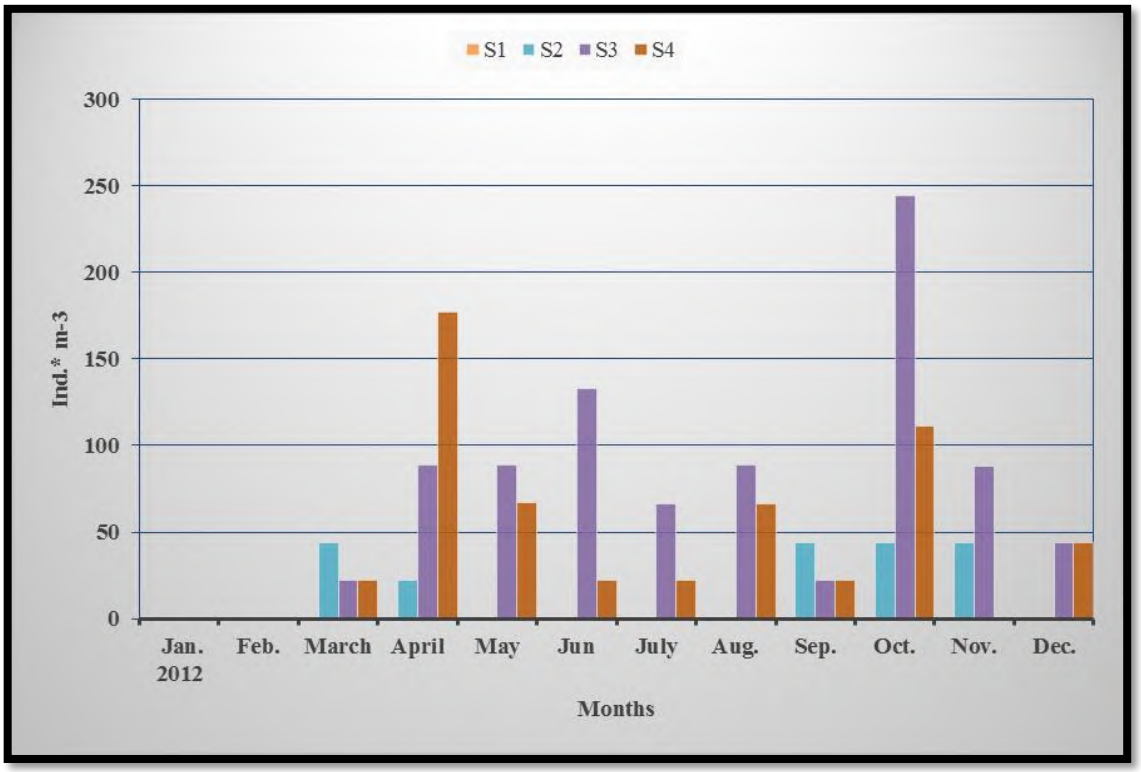

Figure 6. Monthly variations of the Harpacticoida group density Ind.* m^{-3}.

The high density of the copepoda group may be due to the increase of the nauplii, as this group has the ability to withstand the environmental conditions of the RPP more than the rest of the group may be of its small size with few appendixes and the hardness of the outer wall This case was recorded by other researchers [5, 28] (Figure 7).

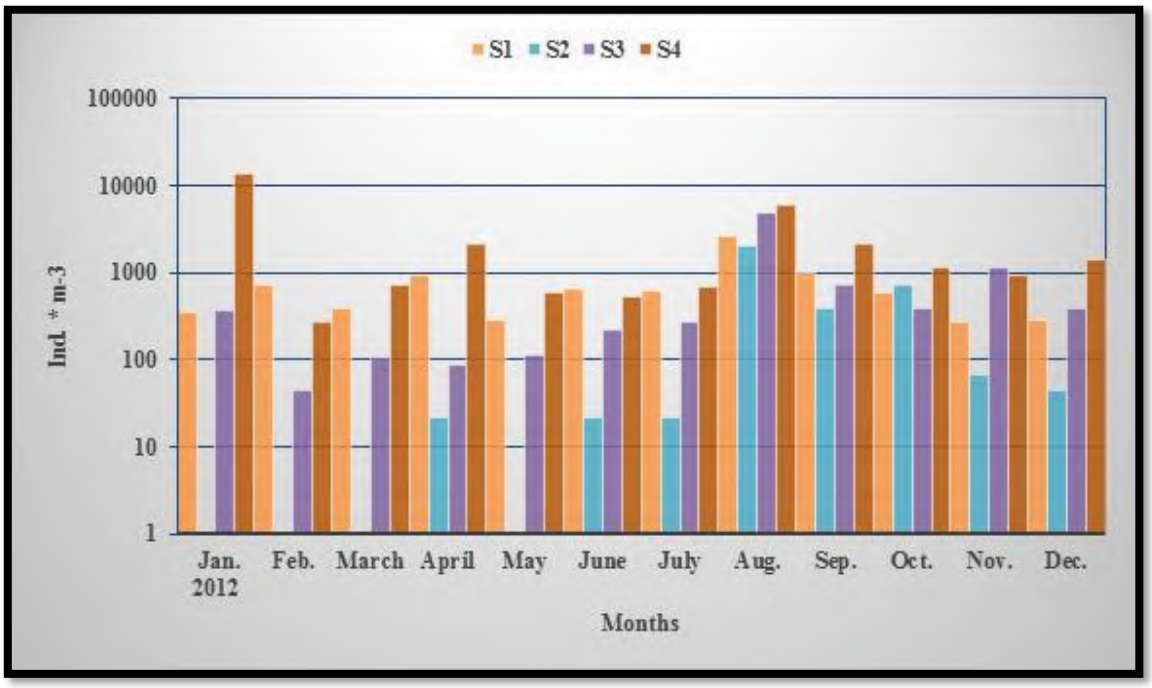

Figure 7. Monthly variations of the nuplii density Ind.* m^{-3}.

As for constancy index(S) Table (1) shows that species:- Cyclops♂, *Haicyclops* sp., Immature *Cyclop*, *Paracyclops fimbriatus*, *Nauplii*, Immature Calanoid, *Nitocra* sp., *Nitocra lacucetrus* were the most appeared and frequent. Therefore they are constancy species in the environment of the Tigris River, according to the constancy index, due to it was found in more than 50% of the total samples that taken in the current study. The results showed that sites 3 and 4 were included the most constancy species, while site 2 was included the lowest. However, the location of both sites 3 and 4 were below RPP and with more environmentally stable than other sites [28]. The presence of species belonging to zooplankton were under to a number of factors to be settled to the aquatic environment, including temperature, salinity, light, turbidity, and the presence or absence of predators, so the constant species in the environment is not an absolute issue, As it may turn out the taxonomic units from Accessory to constant species when conditions are favourable [30] especially after removals the effect of RPP effluents. The different in appearance frequency of taxonomic units was varying during the current study or along study sites in both up and below RPP, so some of which were wide-ranging and abundance species, may be due of the widespread tolerance to environmental variability, especially the presence of RPP effluents, Including the temperature, the presence of more than one generation, the suitable environmental conditions and location of the presence and reproduction of some species, and the ability of some species to continuation along the river [31], such as *Cyclops* sp. and nauplii which appeared seasonally and locally in high density, this may be due to the fact that each of them contained more than one undiagnosed species so these taxonomic units formed for a high percentage or may be due to contains it a various strategies that it ability to resist the unsuitable conditions that imposed on it by the RPP, so some of its individuals enter the diapuse stage, horizontal migration, change their location or change the source of depends food as a result of changing environmental conditions [32]. On the other hand, it was found a clear presence of limited species at a specific location at sites 3 and 4 below the RPP this may be due to the adaptation of some species to situational conditions or to the narrow tolerance of some species to the environmental conditions or as a result of the process of predation and competition, or due to the drift of some species to the sites 3 and 4 and from surrounding areas and their inability to continuation for further distances. Few species exceeded 50% of occurrence frequency were noticed, and the result agreed with [5, 6, 7, 29]. In the current study, the presence of few high frequency species was incompatible with [21] description of clean environment; that this environment with many species and high frequency species especially those didn't tolerate pollution. As for Species Richness Index, Thirty-nine copepoda taxonomic units have been identified, 17 of which belong to Cyclopoda, 13 to Calanoid, 6 to Harpactecoida and 3 to Parasitic Copepoda (Table 1). To compare the species composition of this study with the investigated copepoda fauna near Al-Mussaib power site at the Euphrates River by [24] they identified 27 copepod taxa. While as at Al-Durah power plant on Tigris River [5] identified 44 taxa of copepod. On the other hand, [29] identified 18 taxa of copepod in the Lake Lichenskie with two power plants in Poland, Sometimes these differences can be related to the level of classification in the study and to the quantity of power plant discharge. The species richness index ranged from lowest value reached in 0 at site 2 in May and highest value reached to 5.1 at site 4 in August (Figure 8).

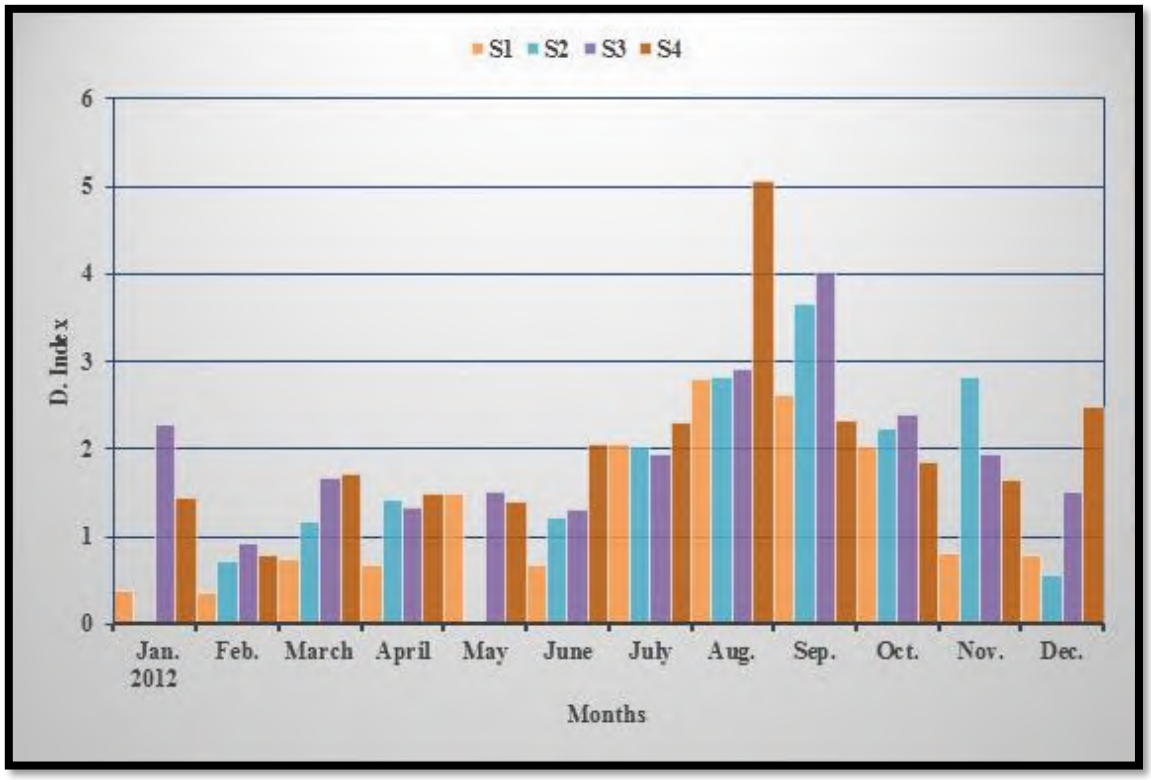

Figure 8. Monthly variation of the copepoda species richness index in the Tigris River during the period study.

The species richness index values varied in the site 1 from 0.34 – 2.79 was recorded in the February to August respectively, either at sites that located after RPP the values of this index was decreased, so at site 3 the value ranged from 0.91-4.02 in February to September respectively, finally at site 4 the ranged value of this index has increased from 0.79-5.06 in February to August respectively. On the other hand, at site 2 the values of this index show a decline in values throughout the period of the current study, which had an impact clearly on the sites that located close to the RPP. [29] showed that species richness varied significantly in particular months, and was the lowest in June and highest in September at Lake Lichenskie with two power sites in Poland. Our result agrees with [5, 6, 7] when they recorded the greatest species richness index at the site below Al-Durah and Rasheed power plant on the Tigris River. The results of the present study showed that the high values of the species richness index were recorded at the end of the summer and at the beginning of the autumn season, and this may be due to higher primary productivity through these seasons [33]. It was found in the current study some of the species showed with the highest number of species such as: *Cyclops* appeared in 6 species, *Diaptomus* with 9 species, one species for *Macrocyclops* and two species for each of *Mesocyclops* and *Paracyclops*. The genus *Diaptomus* belongs to the Calanoid group and is characterized by its large size compared with other groups. Several studies have confirmed it's as dominated species in the Iraqi water bodies [34; 35]. The Shannon-Weiner diversity index is one of the most widely indicators used for biodiversity. This indicator has a value from 0-5 and where the value of this indicator is exceeds 3 it indicates that the stricter of the ecological habitat is stable. When this indicator has a value of less than 1 it indicates that there is ecosystem defect caused by pollution [36]. The Shannon-Weiner indice values for the copepoda groups ranged from the lowest value of 0 bit.*Ind.$^{-1}$ was recorded at sites 2 in January and May, whereas the highest value 3.855 bit.*Ind.$^{-1}$ was recorded at site 2 in April (Figure 9).

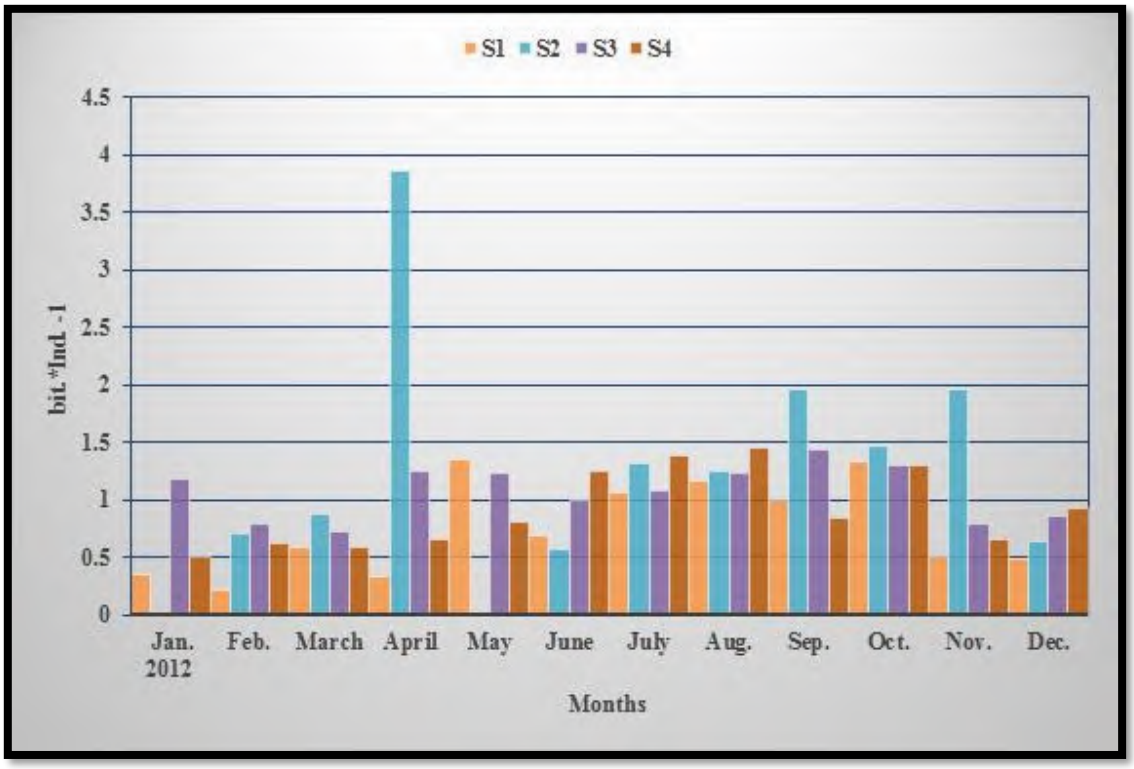

Figure 9. Monthly variation of the copepoda species Shannon-Weiner Index (H) in the Tigris River during the period study.

With regard to the copepoda species uniformity index, the lowest value ranged from 0 was recorded at site 2 in January and May to 2.39 was recorded at site 2 in April (Figure 10).

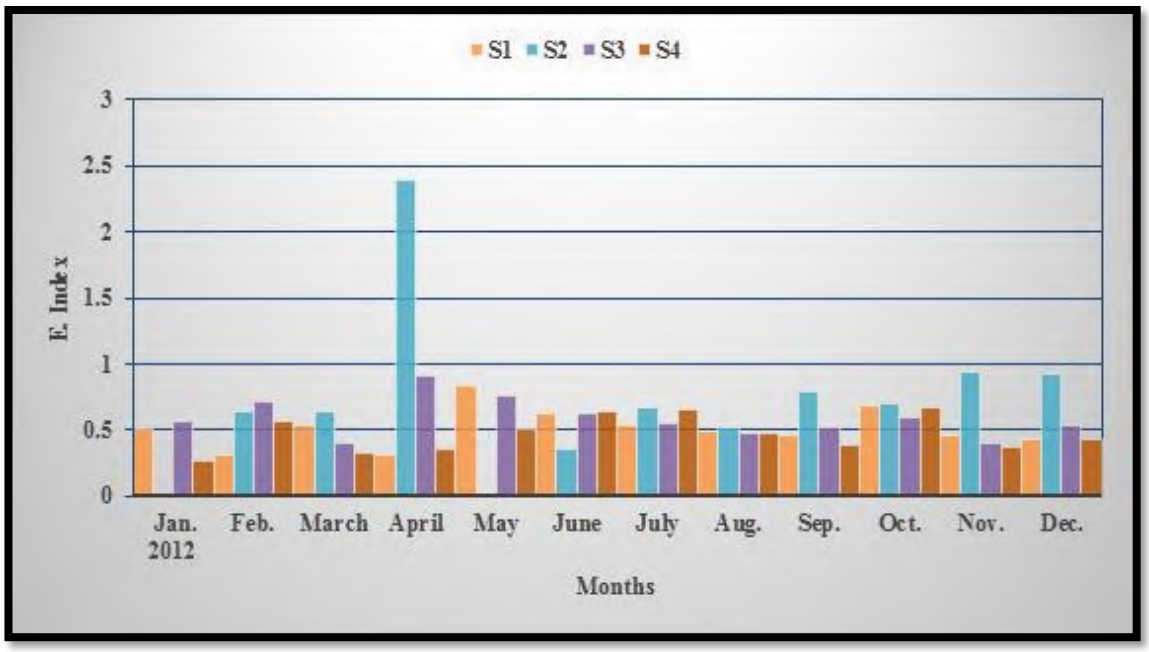

Figure 10. Monthly variation of the copepoda species uniformity index (E) in the Tigris River during the period study.

It was clear as for copepoda Shannon Weiner index at site 1 values did not lower than 0.21 bit *Ind^{-1}. during the period of study, whereas the values of this index decreased at all sites below RPP, especially at site 3 which as ranged from 0.7-1.43 bit * Ind.-1 Either at sites 2, it was a clear decline due to the effect of RPP effluents on the values of this index which reached to the highest value 1.97% in October except on April which it reached to 3.85 bit * $Ind.^{-1}$ that may be related with increased primary productivity in this season from phytoplankton bloom, because zooplankton is determined by the density and structure of phytoplankton [37] (Figure 6). According to [22] the environments in rich with organic matter characterized by having low diversity with a few dominated species. Our study agrees with [23] when they recorded the average values for the Shannon-Weiner index of the cladocera group of ranged from 1.5-2.9 bit /Ind. on in the Euphrates River near the Al-Musayib power plant and found that the hot effluents had a negative impact on the presence of individuals of different cladocera species. Our result also agrees with [5, 6, 7] when they recorded the greatest Shannon Weiner index at the site below Al-Durah and RPP on the Tigris River Presence of Aquatic Plant abundance leads to the formation of environmentally heterogeneous habitats that are stimulated to present different zooplankton communities [38]. Whereas low Shannon-Weiner index values were recorded at site 2, may be due to the impact of the direct effluents of RPP to the river as well as other human interventions [39]. Or may be the reason for the lower values of the Shannon-Weiner index at site 2 related with the increased turbidity and total suspended solids at this site which resulting from the RPP discharge effluent, where turbidity is the reason for the lack of biodiversity, [20] also showed that increased turbidity leads to an increase in the diversity of zooplankton. Regarding to species uniformity index, It was found that the highest value of copepoda uniformity index at site 1 was 0.8 in May, while these values decreased at the sites after RPP which reached to the minimum value of 0.67 in October at site 4, whereas repeated non-appearance of this value of for several time appeared at site 2 near RPP (Figure 9). Higher values of this index in the study sites indicate that the species was uniformity in appearance because of the absence of any environmental stress, which provides a favourable environment for the stability of the zooplankton community and allow to dominate of the larger species, and this is what happened at the site 1 where they exceeded the values of 0.5 throughout the study period, thus considered uniformity species in appearance. While indicating low values of this index to the dominated by a few species with a high density of it, which is a indicate of the presence of environmental stress, and this agrees with [28] when they referred that the decline in the value of uniformity species index indicates the presence of stress prevents the appearance of the dominated many species, which is what happened at the site 2, where that the decline the value of uniformity index of the species due to increasing organic matter, low of dissolved oxygen concentrations, high nutrient requirement of life and values to the degree of food abundance that allowed to dominated of few species with high densities of it. Our result was conflicted with the study of [5] when he recorded a value of the species uniformity index, ranged from 0.364 to 1.06 at sites up to Al-Duarah power plant while at sites below Al-Duarah power plant a values were ranged from 0.31- 1.05. But the results of the current study agree with [6, 7] when they studied the effect of RPP on rotifer and cladocera of this index was not affected by the effluents of RPP.

4. Conclusion

From a current study we can concluded that copepod assemblage especially near RPP affected on it density and constancy species index by it. Also the other biodiversity Indicators showed the negative RPP effect on the copepoda community.

5. Acknowledgement

The authors appreciated to thank staff of Fish Environment and Diseases Laboratory, Department of Fisheries, Agricultural Research Directorate, Ministry of Science &

Technology, to accomplish this series of research on the impact of RPP on the food chain organisms

References

[1] Supper R W and Gordon D K 2005 *Minimizing adverse environmental impact: How murky the waters* 213 In: Dixon DA, Veil JA and Wisniewski J (Eds.).Defining and assessing adverse, environmental impact from power plant impingement and entrainment of aquatic organisms. A.A. Balkema Publishers, Tokyo 291.

[2] USGS, United State Geological Survey 2004 *Estimated Use of water in the United States in 2000; USGS Circular 1268*; March 2004. https://pubs.usgs.gov/circ/2004/circ1268/.

[3] Feeley TJ, Pletcher SO, Carney B and McNemar AT 2006 *Department of energy/national energy technology laboratory's power plant-water R&D Program*.Power-Gen International Conference, November 28-30, Orlando, Florida 1.

[4] Dey W *2005 Use of Equivalent loss Models Under section 316 (b) of the clean water Act*. 247 In: Dixon DA Veil JA and Wisniewski J (Eds.) Defining and assessing adverse environ mental impact from power plant impingement and entrainment of aquatic organisms. A.A. Balkma Publishers, Tokyo 291.

[5] Nashaat M R 2010 *Impact of Al–Durah Power Plant effluents on physical, chemical and invertebrates biodiversity in Tigris River, Southern Baghdad* Ph. D. Thesis, Coll. Sci., Univ. Bagh., Iraq. 183.

[6] Nashaat MR, Ali EH, Abbas EK and Moftin FS 2013 Impact of Al-Rasheed power plant effluents on rotifera biodiversity at Tigris River, Southern Baghdad Proceedings of 6th *Nat. Conf. Environ. Nat. Res*. October 29-31 Environment Dep. Coll. Sciences, Univ. Basrah, 122 (In Arabic).

[7] Nashaat MR, Abbas EK, Ali EH and Moftin F S 2015 Impact of Al-Rasheed power plant effluents on cladocera fauna biodiversity in Tigris River, Southern Baghdad *Iraqi J. Biotechnol*. **14** 243. (In Arabic).

[8] Nashaat MR, Radhi AG, Mohammad AA and Reassn KH 2017 Impact of Al-Rasheed power plant effluents on biodiversity of benthic fauna in Tigris River, Southern Baghdad *Ibn Al-Haitham J. Pure Appl. Sci*. **30** 315. (In Arabic).

[9] Nashaat MR, Merhoon KA, Salman SK, Abbas EK and Ali EH 2019 Impact of Al-Rasheed Power Plant Effluents on Phytoplankton-Biodiversity in Tigris River, Southern Baghdad. 1st Int. Sci. Conf. Pure Science, IOP Conf. Series: *J. Physics: Conf. Series*, 1234(2019)012064.Doi:10.1088/1742-6596/1234/1/012064.

[10] Muftin FS, Nashaat MR, Rasheed RS and Racine KH 2018 Impact of Al-Rasheed power plant effluents on some ecological characteristics of Tigris River, Southern Baghdad City *J. of Madenat Alelem Univ. Coll*. *11* 114 (In Arabic).

[11] Al-Azawii LHA, Nashaat MR and Muftin FS 2018 Assessing the effects of Al- Rasheed electrical power plant on the quality of Tigris River, Southern of Baghdad by Canadian Water Quality Index (CCME WQI) *Iraqi J. Sci.* **59** 1162.

[12] Al-Naymi NAS, Mohammed AJ and Nashaat MR 2019 The Ecological risk assessment of ash toxicity in the freshwater crustacean *Simocephalus vetulus* Schϕdler 1858 *Iraqi J. Sci*. **60** 972.

[13] Al-Naymi NAS, Nashaat MR and Mohammed AJ 2019 The induced of ash toxicity effects on the hematological and biochemical changes of Cyprinus carpio L. 1785. *Biochem. Cell. Arch.* **19** 2983.

[14] Waheed A 2007 Environmental requirements for electrical power plants in Iraq, seminar on environmental problems in the electricity sector *Environ. Maga*. 25 (In Arabic).

[15] Edmondson WT 1959 *Freshwater Biology* 2nd ed. Wiley and Sons-Inc., New York. 1248 .

[16] Smith D G 2001 *Pennaks Freshwater Invertebrates of the United States* 4th ed. John Wiley and Sons. Inc. 538.
[17] Omori M and Ikeda T 1984 *Methods in marine zooplankton ecology* Wiley and Sons, New York on plankton population. Report, MN7B, National Grants Competition.
[18] Serafim Jr M, Lansac-Toha FA, Paggi JC, Velho L FM and Robertson B 2003 Cladocera fauna composition in a river-lagoon system of the upper Parana River Floodplain, with a new record for Brazil *J. Biol*. **63** 34.
[19] Sklar F H 1985 Seasonality and community structure of the Back swamp invertebrates in *Alonisiana tupelo* wetlands. *Wetlands J*. **5** 69.
[20] Floder S and Sommer U 1999 Diversity in planktonic communities: An Experimental test of the intermediate disturbance hypothesis *Limnol. Oceanogr*. **44** 1114.
[21] Proto-Neto VF 2003 *Zooplankton as bioindicator of environmental quality in the Tamandane Reff system (Pernambuco-Brazil): Anthropogenic influences and interaction with mangroves* Ph. D. Thesis, Univ. Bremen, Brazil. https://pdfs.semanticscholar.org/bd17/b743d7743d0d6fbc85f45d05fe62eeb0f0f0.pdf
[22] Neves IF, Rocha O, Roche KF and Pinto AA 2003 Zooplankton community structure of two marginal lakes of the river Cuibá (Mato Grosso, Brazil) with analysis of Rotifera and Cladocera diversity *Braz. J. Biol*. **63** 329.
[23] Radi AG, Al-Lami AA, Al-Rudainy AA and Nashaat MR 2005 Distribution and composition of zooplankton in Euphrates River near Al-Musaib power station *Iraq J. Aqua*. **2** 143-154. (In Arabic).
[24] Radhi AG and Abbas LM 2009 The impact of thermal effluents of Al- Mussaib power station on zooplankton community and biodiversity in Euphrates River, Middle of Iraq. *The 6th Sci. Conf. Fish. Res*. 3-4 March. (**2009**), Basrah, Iraq. (Abst.).
[25] Claps MC, Gabellone NA and Benitez HH 2004 Zooplankton biomass in an eutrophic shallow lake (Buenos Aires, Argentiua): Spatio- temporal variations *Ann Limnol. Int. J. Lim*. **4** 201.
[26] Shiel RJ, Costelloe JF, Reid JRW, Hudson P and Powling J 2006 Zooplankton diversity and assemblages in arid zone rivers of the lake Erye basin, Australia *Mar. Freshwater Res*. **57** 49.
[27] Sampaio EV and Lopez CM 2000 Zooplankton community composition and some limnological aspects of an Oxbow lake of Paraopeda River, Francisco River basin, Brazil *Arch. Biol. Technol*. **43** 285.
[28] Abbas EK, Nashaat MR, Moftin FS and Ali EH 2017 Distribution and occurrence of copepoda in Tigris River, and effect of Diyala River on its biodiversity *Europ. Academic Res*. **4** 8561.
[29] Paturej E, Bogacka E and Kapusta A 2007 Abundance and diversity of zooplankton in the littoral zone of lake Lichenskie *Arch. Pol. Fish*. **15** 353.
[30] Hofmann W 1987 Population dynamics of hypolimentic rotifers in the Pluss Sea (North Germany). *Hydrobiologia*, **147** 197.
[31] Telesh IV 2001 Zooplankton studies in the Neva Estuary (Baltic sea) *Proc. Estonian Acad. Sci. Biol. Ecol*. **50** 200.
[32] Papinska K 1984 The life cycle and the zones of occurrence of *Mesocyclops leuckarti* Clans (Cyclopoida, Copepod) *Ekol . Pol*. **32** 493.
[33] van Dijk GM and van Zanten B 1995 Seasonal changes in zooplankton abundance in the lower Rhine during 1987-1991. *Hydrobiologia*, **304** 29.
[34] Al-Lami AA, Bassat SF and Nashaat MR 2004 Comparative Ecological Study of Zooplankton in Different Salinity Aquatic Ecosystems Mid of Iraq *Ibn Al-Hitham J. Pure Appl. Sci*. **17** 1.
[35] Leland HV and Berkas WR 1998 Temporal variation in plankton assemblages and physicochemistry of Devils Lake, North Dakota *Hydrobiologica*, **377** 57.

[36] Turkmen G and Kazanci AN 2010 Applications of various biodiversity indices to benthic macroinvertebrate assemblages in Streams of a National Park in Turkey *Rev. Hydrobiol*. **3** 111.
[37] Tumas R 2003 Lithuanian Kart Region Rivers water ecology, hydrochemical and hydrobiological evaluation *Nordic Hydrol*. **35** 61.
[38] Kuczynska- Kippen N and Nagengast B 2003 The impact of the spatial structure of hydromacrophytes on the similarity of rotifer communities (Budzynskie Lake, Poland) *Hydrobiolgica*. **333** 506.
[39] Abed I F and Nashaat MR 2018 Species composition, abundance, biodiversity and temporal variations of rotifera in the Dejiala River, Southern Iraq *Biochem. Cell. Arch*. **18** 1877.

Prospective gene therapy design against coronavirus COVID-19 by recruiting CRISPR Cas9 approach

Prospective gene therapy design against coronavirus COVID-19 by recruiting CRISPR Cas9 approach

Ayman Albanna[1*] and Arqam Alomari[2]

[1]College of Environmental Science and Technology, University of Mosul, Mosul City, 41002, Iraq.
[2]College of Agriculture and Forestry, Department of Basic Sciences, University of Mosul, Mosul, 41002, Iraq.

*E-mail: aymanalbanna@uomosul.edu.iq

Abstract. A novel Coronavirus disease (COVID-19) has being originated from animals and causing to running outbreak of viral pneumonia in human all over the world. The World Health Organization (WHO) has considered COVID-19 infection as Epidemic disease in March 2020. The high percentages of death rate among people lead the researchers and scientists in different fields of medicine in order to find solution for this threating problem. In this regard, an editing gene technique was employed in this study, in order to deter the viability of coronavirus genetically. The main objective in this paper first has been determined and obtained the essential proteins of COVID-19 coronavirus proliferation by using NCBI website which included *S, E, N, M, ORF3a, ORF6, ORF7a, ORF7b, ORF8, ORF10* proteins. The second objective is to use a very precise technique of editing gene called CRISPR-Cas9 to make changes to the virus's RNA, through designing single-guide RNA for the essential each protein of COVID-19, in order to inactivate an effective certain protein. These techniques will be provided for each patient and healthy person by injection of all genes components using the Gene-gun machine or spray aerosol to make ensure reach it to the target cell.

Keywords. CRIPR Cas9, Coronavirus, Gene Therapy, WHO.

1. Introduction

The A novel Coronavirus disease (COVID-19) has being originated from animals and causing to running outbreak of viral pneumonia in human all over the world [1, 2, 3]. Coronavirus (Covid-19) is a considerable aggressive comprehensive public health threat. It is a large family of enveloped RNA viruses [4]. There are four groups of coronaviruses, which originated from animals. Alpha and beta presence at bats, while Gamma and Delta are avian species reservoir. Coronaviruses are responsible for wide range diseases in many animals including the human. In human they cause mild self-limiting respiratory infections. Different kinds of animals had been recorded previously historically infected with coronavirus, like Avian, Murine, Ferret, Swine, Rat, Rabbit, Whale, Camel, Bat and Human [5]. All of these types of creatures have big issues problem for us and the possibility of the virus developing inside their cells and transmission it to each other easily. For instance, in terms of SARS-

CoV strain was conveyed from civet cat to human, while the MERS-CoV strain has been transmitted from camel to human. Usually, the virus access to the human body into the respiratory system reach lung cells through attachment by S proteins that covered the outside viral surface with the human receptor and then, an inject the ssRNA inside the intact human cell and start to replicate through many process [6]. In this study, ten important proteins have been virtualized by the stated NCBI website and then tag each protein from a precise RNA site by guide RNA in order to inactivation of protein using technique called CRISPR-Cas9, that prospective will aid for stop proliferation against specified coronavirus COVID-19 . These techniques will be provided for each patient and healthy person by injectable by gene gun machine or spray aerosol to make ensure reach it the target cell. In general, CRISPR-Cas9 is very accurate technique of editing gene, which allows the scientist to manipulate the DNA for repairing and cure the gene disorder. CRISPR-Cas9 system has only two compounds, a Cas9 endonuclease and a single-strand guide RNA (sgRNA) [7, 8]. It is adopted immunity system in the bacteria to detect and match virus's DNA or RNA and stop action. CRISPR-Cas9 is having a major effect on practical genomic carried out in experimental systems [9]. The scientific term of CRISPR is derived from Clustered Regularly Interspaced Short Palindromic Repeats that tied inside the genome of the bacteria with their associated nuclease enzyme called Cas9. This specific sequencing of gene allowed the bacteria to record over the time the virus's DNA that injected to the bacteria and protect itself. CRISPR-Cas9 considered as a genetic vaccination card in the bacteria that offer an opportunity to manipulate with the gene to edit or delete any desired gene. Overall, this complex is programmable, which is meaning we can program any specific fragment of the gene within the genome and cure it [10].

2. Materials and Methods

CRIPR-Cas9 system has designed to allow inducing cleave at target 10 gene sites for essential proteins for invasion and proliferation for Coronavirus. All ten genes sequences were obtained from the NCBI database, in order to complete the coding sequence of the open reading frame (*s, e, n, m, orf3a, orf6, orf7a, orf7b, orf8, orf10*) genes. The gene code (Gene ID) for all these proteins in NCBI website were as follow: Spike protein (S) is NC_030886.1, the Envelop protein (E) is 43740570, The Nuleocapsid phosphoprotein (N) is 43740575, the Membrane glycoprotein (M) is 43740571, the ORF3a protein is 43740569, the ORF6 protein is 43740572, the ORF7a and b proteins are 43740573, the ORF8 protein is 43740577 and the ORF10 is 43740576. This study, we have designed guide RNA for only S protein which is considered the most important part of the virus to cause infection (AGGGTCCACCAAACGTAATGCGG). Then, the interference leads to synthesis dsRNA, which will be formed of the guide RNA (sgRNA), thereby the sequence of each gene to be used accurately by the CRISPR-Cas9 technique inside the infected cell. The sgRNA directs the Cas9 endonuclease to cleave both DNA strands in a specific sequencing (Table 1 and 2). DNA cleavage happens at a sequence 3 base pairs upstream of an “NGG” proto-spacer adjacent motif (PAM). The CRISPR/Cas9 requires the co-expression of a Cas9 protein with a single guide RNA vector that will be expressed by the promoter [11]. Figure 1 refers to prospective cycle treatment of COVID-19 infection by using CRISPR-Cas9 technique as a novel treatment.

Table 1. Step by step for the experiment for Crispr primers design.

Step A: Design guide-RNA criRNA.

Name	Primer Sequence
S protein_guideRNA39rvGeneArtFw	TACGACTCACTATAG**AGGGTCCACCAAACGTAATG**
S protein_guideRNA39rvGeneArtRev	TTCTAGCTCTAAAAC**CATTACGTTTGGTGGACCCT**

Step B: Lentiviral vectors: cloning with Gibson assembly.

Name	Oligonucleotide Sequence
batchOligo39rv	*GGAAAGGACGAAACACCG*AGGGTCCACCAAACGTAATG*GTTTTAGAGC TAGAAATAGCAAGTTAAAATAAGGC*

Step C: PCR to amplify the on-target site (S-protein).

Name of Primers genomic fragments	Sequences	Annealing Temperature
S_protein__OntargetGuideRna39rvLeft	GAATTGTGCGTGGATGAGGC	Tm 59.901
S_protein__OntargetGuideRna39rvRight	TGAGAGCGGTGAACCAAGAC	Tm 59.966

Table 2. Restriction map of Crispr _S protein sequence sites for Covid-19 by using Serial-cloner-V2.5, showing the green color codes regions for restriction enzymes that inactivation protein action.

TfiI
PfeI
<59rev: Spec 100, Eff 57/30_misc_feature
<58rev: Spec 100, Eff 60/48_misc_feature
>54forw: Spec 100, Eff 50/36_misc_feature
>51forw: Spec 100, Eff 45/51_misc_feature
<39rev: Spec 100, Eff 52/50_misc_feature
<38rev: Spec 100, Eff 50/31_misc_feature
<37rev: Spec 100, Eff 68/44_misc_feature >99forw: Spec 100, Eff 66/36
_misc_feature
<18rev: Spec 100, Eff 18/57_misc_feature >87forw: Spec 100, Eff 66/56_misc_feature
<17rev: Spec 100, Eff 19/42_misc_feature <81rev: Spec 100, Eff 24/37_misc_feature
<16rev: Spec 100, Eff 53/36_misc_feature >72forw: Spec 100, Eff 50/39_misc_feature
||| ||| | | || | | | | |
ATGTCTGATAATGGACCCCAAAATCAGCGAAATGCACCCCGCATTACGTTTGGTGGACCCTCAGATTCAACTGGCAGTAACCAGAATGGAGAACGCAGTG < 100
M S D N G P Q N Q R N A P R I T F G G P S D S T G S N Q N G E R S G
C L I M D P K I S E M H P A L R L V D P Q I Q L A V T R M E N A V
V * * W T P K S A K C T P H Y V W W T L R F N W Q * P E W R T Q W
TACAGACTATTACCTGGGGTTTTAGTCGCTTTACGTGGGGCGTAATGCAAACCACCTGGGAGTCTAAGTTGACCGTCATTGGTCTTACCTCTTGCGTCAC
10 20 30 40 50 60 70 80 90
Eco88I
Ama87I
BsiHKCI
Sfr274I
XhoI
SciI
AvaI
StrI
<199rev: Spec 100, Eff 61/19
_misc_feature
Nli3877I
<161rev: Spec 100, Eff 65/55_misc_feature
>AccBSI >BpuAI BmeT110I
>MbiI >BpiI SlaI
<137rev: Spec 100, Eff 27/16_misc_feature PaeR7I
<136rev: Spec 100, Eff 25/37_misc_feature <189rev: Spec 100, Eff 16/43
_misc_feature
>129forw: Spec 100, Eff 63/41_misc_feature >Bbr7I BsoBI
<126rev: Spec 100, Eff 53/30_misc_feature >BbsI PspXI
<124rev: Spec 100, Eff 67/33_misc_feature >BstV2I <198rev: Spec 100, Eff 58/85
_misc_feature
>121forw: Spec 100, Eff 76/41_misc_feature >BbvII AbsI
Hpy99I <125rev: Spec 100, Eff 39/51_misc_feature >182forw: Spec 100, Eff 54/21_misc_feature
>101forw: Spec 100, Eff 70/49_misc_feature >BsrBI >177forw: Spec 100, Eff 61/25_misc_feature
>100forw: Spec 100, Eff 61/56_misc_feature >154forw: Spec 100, Eff 54/28_misc_feature
|| | | ||| | || | || | | ||
GGGCGCGATCAAAACAACGTCGGCCCCAAGGTTTACCCAATAATACTGCGTCTTGGTTCACCGCTCTCACTCAACATGGCAAGGAAGACCTTAAATTCCC < 200
A R S K Q R R P Q G L P N N T A S W F T A L T Q H G K E D L K F P
G R D Q N N V G P K V Y P I I L R L G S P L S L N M A R K T L N S L
G A I K T T S A P R F T Q * Y C V L V H R S H S T W Q G R P * I P
CCCGCGCTAGTTTTGTTGCAGCCGGGGTTCCAAATGGGTTATTATGACGCAGAACCAAGTGGCGAGAGTGAGTTGTACCGTTCCTTCTGGAATTTAAGGG
110 120 130 140 150 160 170 180 190
<PciSI
<SapI
>252forw: Spec 100, Eff 48/68_misc_feature
<246rev: Spec 100, Eff 32/57_misc_feature
>RdeGBIII <LguI
>204forw: Spec 100, Eff 69/33_misc_feature <261rev: Spec 100, Eff 50/45_misc_feature
<AloI <227rev: Spec 100, Eff 44/51_misc_feature >288forw: Spec 100, Eff 71/23
_misc_feature
>RpaB5I <Bsp24I <238rev: Spec 100, Eff 37/27_misc_feature >294forw: Spec 100, Eff 62/49
_misc_feature
TaqI <217rev: Spec 100, Eff 29/36_misc_feature EcoRI >285forw: Spec 100, Eff 60/36_misc_feature
EsaBC3I >210forw: Spec 100, Eff 55/28_misc_feature <BspQI <272rev: Spec 100, Eff 52/22_misc_feature
|| | | | | | | | | | | | | | | | |
TCGAGGACAAGGCGTTCCAATTAACACCAATAGCAGTCCAGATGACCAAATTGGCTACTACCGAAGAGCTACCAGACGAATTCGTGGTGGTGACGGTAAA < 300

R G Q G V P I N T N S S P D D Q I G Y Y R R A T R R I R G G D G K
E D K A F Q L T P I A V Q M T K L A T T E E L P D E F V V V T V K
S R T R R S N * H Q * Q S R * P N W L L P K S Y Q T N S W W * R * N
AGCTCCTGTTCCGCAAGGTTAATTGTGGTTATCGTCAGGTCTACTGGTTTAACCGATGATGGCTTCTCGATGGTCTGCTTAAGCACCACCACTGCCATTT
210 220 230 240 250 260 270 280 290
>FalI
<349rev: Spec 100, Eff 49/35_misc_feature
AccB7I
BsiYI
Bsc4I
BslI
BseLI
BasI
Van91I FauNDI
AfiI >384forw: Spec 100, Eff 52/60_misc_feature
PflMI >BceAI
>346forw: Spec 100, Eff 65/39_misc_feature
>339forw: Spec 100, Eff 54/32_misc_feature
<336rev: Spec 100, Eff 41/53_misc_feature NdeI >395forw: Spec 100, Eff 52/41
_misc_feature
XmaJI >BmrI AlwNI <365rev: Spec 100, Eff 47/62_misc_feature
AspA2I >345forw: Spec 100, Eff 42/18_misc_feature
AvrII >BfiI PstNI <364rev: Spec 100, Eff 50/44_misc_feature
BlnI >BmuI CaiI >357forw: Spec 100, Eff 41/41_misc_feature
>322forw: Spec 100, Eff 61/30_misc_feature >BcefI >394forw: Spec 100, Eff 39/34
_misc_feature
BglII <316rev: Spec 100, Eff 48/35_misc_feature >369forw: Spec 100, Eff 52/57_misc_feature
| | | || | | || || | | | | | ||
ATGAAAGATCTCAGTCCAAGATGGTATTTCTACTACCTAGGAACTGGGCCAGAAGCTGGACTTCCCTATGGTGCTAACAAAGACGGCATCATATGGGTTG < 400
M K D L S P R W Y F Y Y L G T G P E A G L P Y G A N K D G I I W V A
* K I S V Q D G I S T T * E L G Q K L D F P M V L T K T A S Y G L
E R S Q S K M V F L L P R N W A R S W T S L W C * Q R R H H M G C
TACTTTCTAGAGTCAGGTTCTACCATAAAGATGATGGATCCTTGACCCGGTCTTCGACCTGAAGGGATACCACGATTGTTTCTGCCGTAGTATACCCAAC
310 320 330 340 350 360 370 380 390
<444rev: Spec 100, Eff 54/69_misc_feature
<443rev: Spec 100, Eff 44/34_misc_feature
>TstI <451rev: Spec 100, Eff 50/30_misc_feature
>438forw: Spec 100, Eff 68/34_misc_feature
<424rev: Spec 100, Eff 45/55_misc_feature
<413rev: Spec 100, Eff 32/16_misc_feature
>408forw: Spec 100, Eff 58/51_misc_feature <484rev: Spec 100, Eff 57/54_misc_feature
>407forw: Spec 100, Eff 53/38_misc_feature <AquIV >489forw: Spec 100, Eff 63/21
_misc_feature
|| | | | | || | | |
CAACTGAGGGAGCCTTGAATACACCAAAAGATCACATTGGCACCCGCAATCCTGCTAACAATGCTGCAATCGTGCTACAACTTCCTCAAGGAACAACATT < 500
T E G A L N T P K D H I G T R N P A N N A A I V L Q L P Q G T T L
Q L R E P * I H Q K I T L A P A I L L T M L Q S C Y N F L K E Q H C
N * G S L E Y T K R S H W H P Q S C * Q C C N R A T T S S R N N I
GTTGACTCCCTCGGAACTTATGTGGTTTTCTAGTGTAACCGTGGGCGTTAGGACGATTGTTACGACGTTAGCACGATGTTGAAGGAGTTCCTTGTTGTAA
410 420 430 440 450 460 470 480 490
BstBAI
BsaAI
<545rev: Spec 100, Eff 53/35_misc_feature
>534forw: Spec 100, Eff 55/81_misc_feature
>531forw: Spec 100, Eff 60/45_misc_feature >597forw: Spec 100, Eff 52/14
_misc_feature
>523forw: Spec 100, Eff 59/46_misc_feature <595rev: Spec 100, Eff 49/25
_misc_feature
>522forw: Spec 100, Eff 52/45_misc_feature <BpmI
>507forw: Spec 100, Eff 57/40_misc_feature Ppu21I <GsuI
<502rev: Spec 100, Eff 26/39_misc_feature <557rev: Spec 100, Eff 69/42_misc_feature
| | || | | | | | | | |
GCCAAAAGGCTTCTACGCAGAAGGGAGCAGAGGCGGCAGTCAAGCCTCTTCTCGTTCCTCATCACGTAGTCGCAACAGTTCAAGAAATTCAACTCCAGGC < 600
P K G F Y A E G S R G G S Q A S S R S S S R S R N S S R N S T P G
Q K A S T Q K G A E A A V K P L L V P H H V V A T V Q E I Q L Q A
A K R L L R R R E Q R R Q S S L F S F L I T * S Q Q F K K F N S R Q
CGGTTTTCCGAAGATGCGTCTTCCCTCGTCTCCGCCGTCAGTTCGGAGAAGAGCAAGGAGTAGTGCATCAGCGTTGTCAAGTTCTTTAAGTTGAGGTCCG
510 520 530 540 550 560 570 580 590
>633forw: Spec 100, Eff 47/32_misc_feature
BstC8I >642forw: Spec 100, Eff 65/76_misc_feature
Cac8I >639forw: Spec 100, Eff 51/50_misc_feature
>629forw: Spec 100, Eff 40/46_misc_feature
>609forw: Spec 100, Eff 53/54_misc_feature
>608forw: Spec 100, Eff 49/36_misc_feature
>607forw: Spec 100, Eff 51/38_misc_feature
<BarI <619rev: Spec 100, Eff 53/22_misc_feature <684rev: Spec 100, Eff 50/15_misc_feature
| ||| | | | | | |
AGCAGTAGGGGAACTTCTCCTGCTAGAATGGCTGGCAATGGCGGTGATGCTGCTCTTGCTTTGCTGCTGCTTGACAGATTGAACCAGCTTGAGAGCAAAA < 700
S S R G T S P A R M A G N G G D A A L A L L L L D R L N Q L E S K M
A V G E L L L L E W L A M A V M L L L L C C C L T D * T S L R A K
Q * G N F S C * N G W Q W R * C C S C F A A A * Q I E P A * E Q N
TCGTCATCCCCTTGAAGAGGACGATCTTACCGACCGTTACCGCCACTACGACGAGAACGAAACGACGACGAACTGTCTAACTTGGTCGAACTCTCGTTTT
610 620 630 640 650 660 670 680 690
CviQI
AfaI
<Bpu10I >775forw: Spec 99, Eff 61/62_misc_feature
<BbvCI PcsI RsaI
<729rev: Spec 100, Eff 43/51_misc_feature PabI
>726forw: Spec 100, Eff 69/29_misc_feature RsaNI
<714rev: Spec 100, Eff 31/54_misc_feature <772rev: Spec 100, Eff 56/28_misc_feature
>711forw: Spec 100, Eff 54/60_misc_feature <NmeAIII Csp6I <791rev: Spec 100, Eff 38/43
_misc_feature
>705forw: Spec 100, Eff 55/46_misc_feature >758forw: Spec 100, Eff 59/41_misc_feature
| | | | | | | || | | |

TGTCTGGTAAAGGCCAACAACAACAAGGCCAAACTGTCACTAAGAAATCTGCTGCTGAGGCTTCTAAGAAGCCTCGGCAAAAACGTACTGCCACTAAAGC < 800
S G K G Q Q Q Q G Q T V T K K S A A E A S K K P R Q K R T A T K A
C L V K A N N N K A K L S L R N L L L R L L R S L G K N V L P L K H
V W * R P T T T R P N C H * E I C C * G F * E A S A K T Y C H * S
ACAGACCATTTCCGGTTGTTGTTGTTCCGGTTTGACAGTGATTCTTTAGACGACGACTCCGAAGATTCTTCGGAGCCGTTTTTGCATGACGGTGATTTCG
710 720 730 740 750 760 770 780 790
<864rev: Spec 100, Eff 27/23_misc_feature
>860forw: Spec 100, Eff 54/25_misc_feature
>859forw: Spec 100, Eff 28/25_misc_feature
>BsmFI
>831forw: Spec 100, Eff 63/39_misc_feature
<AjiI >BslFI
<BmgBI >FaqI >866forw: Spec 100, Eff 43/39_misc_feature
<BtrI >849forw: Spec 100, Eff 69/50_misc_feature
PsyI <846rev: Spec 100, Eff 35/15_misc_feature
AspI XcmI >858forw: Spec 100, Eff 22/19_misc_feature
PflFI <845rev: Spec 100, Eff 39/46_misc_feature
HindIII Tth111I <835rev: Spec 100, Eff 29/22_misc_feature
>WviI >822forw: Spec 100, Eff 43/40_misc_feature >882forw: Spec 100, Eff 68/20_misc_feature
| | | | | | | | |||| | | |
ATACAATGTAACACAAGCTTTCGGCAGACGTGGTCCAGAACAAACCCAAGGAAATTTTGGGGACCAGGAACTAATCAGACAAGGAACTGATTACAAACAT < 900
Y N V T Q A F G R R G P E Q T Q G N F G D Q E L I R Q G T D Y K H
T M * H K L S A D V V Q N K P K E I L G T R N * S D K E L I T N I
I Q C N T S F R Q T W S R T N P R K F W G P G T N Q T R N * L Q T L
TATGTTACATTGTGTTCGAAAGCCGTCTGCACCAGGTCTTGTTTGGGTTCCTTTAAAACCCCTGGTCCTTGATTAGTCTGTTCCTTGACTAATGTTTGTA
810 820 830 840 850 860 870 880 890
<AcuI
BfoI
BstH2I
AfeI
Eco47III
Aor51HI
LpnI <995rev: Spec 100, Eff 54/42
_misc_feature
HaeII MslI HindII
<926rev: Spec 100, Eff 40/27_misc_feature HincII
<925rev: Spec 100, Eff 47/58_misc_feature >988forw: Spec 100, Eff 61/61
_misc_feature
<904rev: Spec 100, Eff 54/55_misc_feature >960forw: Spec 100, Eff 50/57_misc_feature
>901forw: Spec 100, Eff 57/70_misc_feature RseI >981forw: Spec 100, Eff 41/37_misc_feature
EaeI <924rev: Spec 100, Eff 59/47_misc_feature >980forw: Spec 100, Eff 49/74_misc_feature
CfrI >BseYI SmiMI >965forw: Spec 100, Eff 53/44_misc_feature
AcoI BstAPI >GsaI <Eco57I >945forw: Spec 100, Eff 40/47_misc_feature
<GdiII ApaBI <923rev: Spec 100, Eff 62/63_misc_feature <976rev: Spec 100, Eff 63/60_misc_feature
|| | | |||||| | | | | | | | | || | |
TGGCCGCAAATTGCACAATTTGCCCCCAGCGCTTCAGCGTTCTTCGGAATGTCGCGCATTGGCATGGAAGTCACACCTTCGGGAACGTGGTTGACCTACA < 1000
W P Q I A Q F A P S A S A F F G M S R I G M E V T P S G T W L T Y T
G R K L H N L P P A L Q R S S E C R A L A W K S H L R E R G * P T
A A N C T I C P Q R F S V L R N V A H W H G S H T F G N V V D L H
ACCGGCGTTTAACGTGTTAAACGGGGGTCGCGAAGTCGCAAGAAGCCTTACAGCGCGTAACCGTACCTTCAGTGTGGAAGCCCTTGCACCAACTGGATGT
910 920 930 940 950 960 970 980 990
<1030rev: Spec 100, Eff 31/26_misc_feature
<AlwI
<AclWI
<BspPI
<BinI <ArsI
<1007rev: Spec 100, Eff 31/27_misc_feature <1093rev: Spec 100, Eff 45/39
_misc_feature
BstXI >1016forw: Spec 100, Eff 38/40_misc_feature <1090rev: Spec 100, Eff 40/31
_misc_feature
>1002forw: Spec 100, Eff 63/54_misc_feature <1089rev: Spec 100, Eff 45/40
_misc_feature
| || | | | | | | |
CAGGTGCCATCAAATTGGATGACAAAGATCCAAATTTCAAAGATCAAGTCATTTTGCTGAATAAGCATATTGACGCATACAAAACATTCCCACCAACAGA < 1100
G A I K L D D K D P N F K D Q V I L L N K H I D A Y K T F P P T E
Q V P S N W M T K I Q I S K I K S F C * I S I L T H T K H S H Q Q S
R C H Q I G * Q R S K F Q R S S H F A E * A Y * R I Q N I P T N R
GTCCACGGTAGTTTAACCTACTGTTTCTAGGTTTAAAGTTTCTAGTTCAGTAAAACGACTTATTCGTATAACTGCGTATGTTTTGTAAGGGTGGTTGTCT
1010 1020 1030 1040 1050 1060 1070 1080 1090
<BstMAI
<BcoDI BfmI
<Alw26I SfcI
<BsmAI BstSFI
<1147rev: Spec 100, Eff 61/39_misc_feature
<PlaDI <1142rev: Spec 100, Eff 49/49_misc_feature
>1124forw: Spec 100, Eff 58/34_misc_feature SfeI
>1109forw: Spec 100, Eff 31/30_misc_feature PstI >1199forw: Spec 100, Eff
24/45_misc_feature
<1102rev: Spec 100, Eff 11/18_misc_feature <1186rev: Spec 100, Eff 52/21_misc_feature
| | | | | | | | | | |
GCCTAAAAAGGACAAAAAGAAGAAGGCTGATGAAACTCAAGCCTTACCGCAGAGACAGAAGAAACAGCAAACTGTGACTCTTCTTCCTGCTGCAGATTTG < 1200
P K K D K K K K A D E T Q A L P Q R Q K K Q Q T V T L L P A A D L
L K R T K R R R L M K L K P Y R R D R R N S K L * L F F L L Q I W
A * K G Q K E E G * * N S S L T A E T E E T A N C D S S S C C R F G
CGGATTTTTCCTGTTTTTCTTCTTCCGACTACTTTGAGTTCGGAATGGCGTCTCTGTCTTCTTTGTCGTTTGACACTGAGAAGAAGGACGACGTCTAAAC
1110 1120 1130 1140 1150 1160 1170 1180 1190
>1253forw: Spec 100, Eff 55/54_misc_feature
PceI
Eco147I
StuI
MunI SseBI
MfeI <1229rev: Spec 100, Eff 54/23_misc_feature
>Hin4I <1211rev: Spec 100, Eff 35/45_misc_feature
| | | | ||

GATGATTTCTCCAAACAATTGCAACAATCCATGAGCAGTGCTGACTCAACTCAGGCCTAA < 1260
D D F S K Q L Q Q S M S S A D S T Q A *
M I S P N N C N N P * A V L T Q L R P X
* F L Q T I A T I H E Q C * L N S G L X
CTACTAAAGAGGTTTGTTAACGTTGTTAGGTACTCGTCACGACTGAGTTGAGTCCGGATT
1210 1220 1230 1240 1250

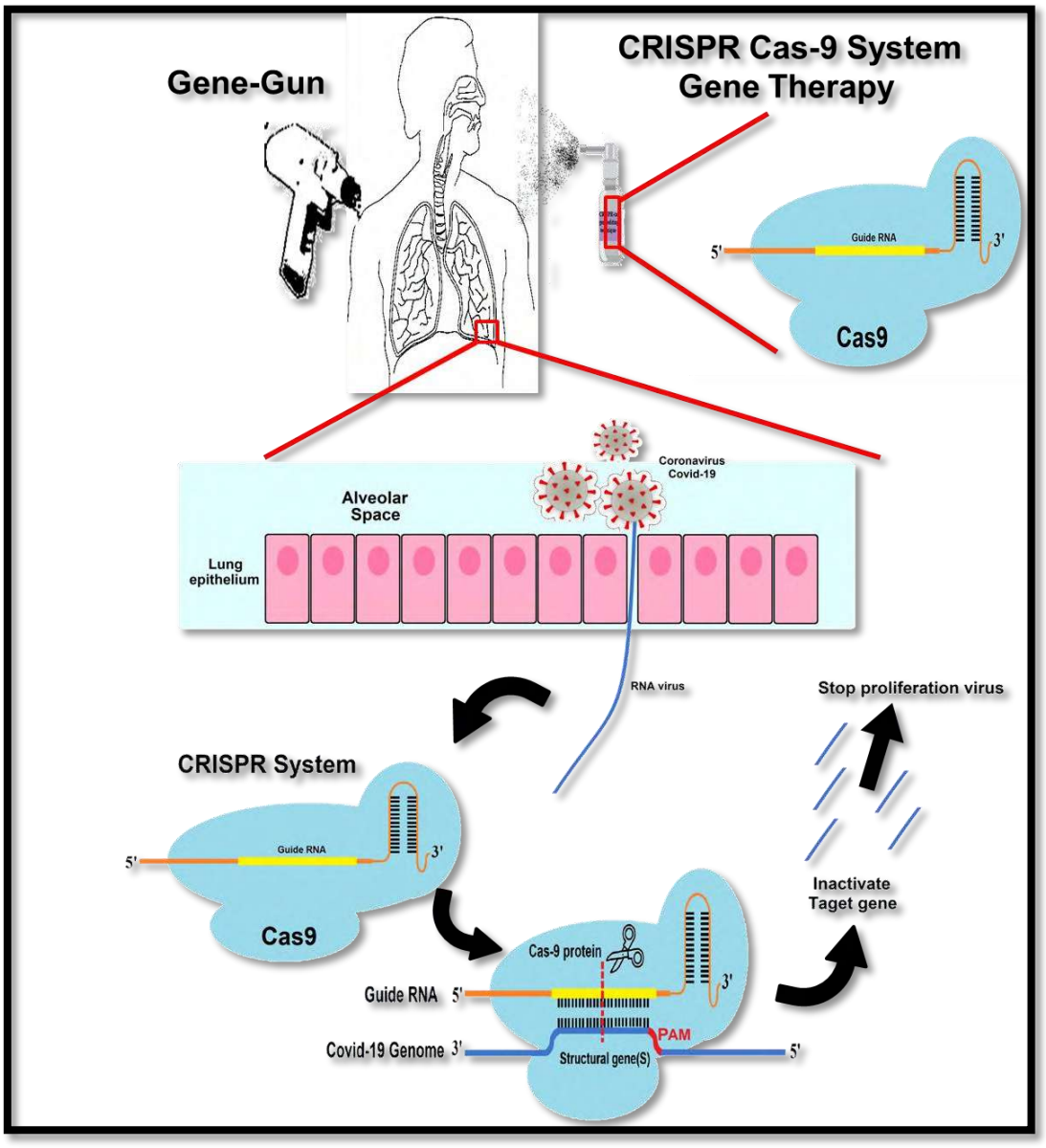

Figure 1. Overview of the stages for how to delivering gene therapy via CRISPR/Cas9 system with a specific guide-RNA for fighting Coronavirus Covid-19 by using a Gun-gene machine or spray aerosol. Also, how the CRISPR/Cas9 binds to the target gene site within sgRNA virus.

2. Results and Discussion

This Even though most of the researchers are considering finding a safe vaccine against Covid-19. However, in this study has suggested that CRISPR/Cas9 systems can accurately link certain gene with specific single guide-RNA in many essential sites into the Coronavirus genome (*s, e, n, m, orf3a, orf6, orf7a, orf7b, orf8, orf10*). Our study proposes to complete inactivation for each protein target, which has ability caused the infection by using bioinformatics analysis to do cleavage each gene through

binding with guide-RNA and stop expression. In addition, it has believed that the using design guidelines will induce decrease potential effects of proliferation coronavirus inside human cells and gives our body at least an initiate immunity. In this study, we just focus an example of one important protein (Spike -protein) out of ten proteins persist into the virus, which have capability inhibited for invasion and proliferation action inside the host cell. The idea has been developed throughout designed guide-RNA for S-gene sequences, in order to inactivate and impeding gene expression into the S-gene and ceases their action. Conservatively determining target gene sequences in order to avoid interfering with human genes contents, thereby make ensure to destroy the only target virus away from others. The limitation of facility and to save the time, the overall aim of our research is to bring together a serious detecting of genes and proteins sequencing of the essential proteins of COVID-19 coronavirus to make them as a target to inactivate the infection of virus by using CRISPR-Cas9 technique. The editing gene- CRISPR/Cas9- permits for precise genome destruction and replacement in a flexible way resulting in high activity and low cellular toxicity [10]. This will be a building block towards these potential proteins in the future studies that could then explore and exploit very applied method clinically to destroy this disease genetically and radically.

3. Acknowledgement

The authors are very grateful to the University of Mosul / College of Environmental science and Technologies for their provided facilities, which helped to improve the quality of this work.

References

[1] Paules CI, Marston HD and Fauci AS 2020 Coronavirus infections—more than just the common cold *JAMA.* Published online January 23, 2020.
[2] Li Q, Guan X and Wu P 2020 Early transmission dynamics in Wuhan, China, of novel coronavirus-infected pneumonia *N Engl. J. Med*. Published online January 29, 2020.
[3] Wang D, Hu B and Hu C 2020 Clinical characteristics of 138 hospitalized patients with 2019 novel coronavirus–infected pneumonia in Wuhan, China. *JAMA*. Published online February 7, 2020.
[4] Acheson NH 2011 *Fundamentals of molecular virology* (No. Ed. 2). John Wiley & Sons, Inc.
[5] Malik YS, Sircar S, Bhat S, Vinodhkumar OR, Tiwari R, Sah R, Rabaan AA, Rodriguez-Morales AJ and Dhama K 2020 Emerging Coronavirus Disease (COVID-19), a pandemic public health emergency with animal linkages: Current status update. Preprint.
[6] Xu Z, Shi L, Wang Y, Zhang J, Huang L, Zhang C, Liu S, Zhao P, Liu H, Zhu L and Tai Y 2020 Pathological findings of COVID-19 associated with acute respiratory distress syndrome. *The Lancet respiratory medicine*.
[7] Cong L, Ran FA, Cox D, Lin S, Barretto R, Habib N, Hsu PD and Wu Z 2013 Multiplex genome engineering using CRISPR/Cas systems *Science* **339** 819.
[8] Mali, P. Mali P, Yang L, Esvelt KM, Aach J, Guell M, DiCarlo JE, Norville JE and Church GM 2013 RNA-guided human genome engineering via Cas9 *Science* **339** 823.
[9] Tian X, Gu T, Patel S, Bode AM, Lee MH and Dong Z 2019 CRISPR/Cas9–An evolving biological tool kit for cancer biology and oncology *NPJ Prec. Oncol.* **3** 1.
[10] Doudna JA and Emmanuelle C 2014 The new frontier of genome engineering with CRISPR-Cas9 *Science* **346** 1258096.
[11] Jinek M, Chylinsk K, Fonfara I, Hauer M, Doudna JA and Charpent E 2012 A programmable dual-RNA-guided DNA endonuclease in adaptive bacterial immunity *Science* **337** 816.

Effect of amino acid proline on some growth characteristics of cowpea which exposed to drought stress

Effect of amino acid proline on some growth characteristics of cowpea which exposed to drought stress

Maher Zaki Faisal Al-Shammari[1*] and Wael Shakir Hameed Al-Jboory[2]

[1]Department of Biology, College of Education for Pure Science (Ibn Al-Haitham), University of Baghdad, Baghdad, Iraq.
[2]Al-Karkh II / General Directorate of Education of Baghdad / Ministry of Education, Baghdad, Iraq.

*E-mail: zakimaher164@gmail.com

Abstract. The study was conducted in Al-Youssoufia region which located in North West of Baghdad city during the growing season of 2018-2019. The experiment was aimed to demonstrate the optimum concentration of amino acid proline that reduce the effect of drought stress. By using three time for irrigation (4, 8, 12) day and four concentrations of proline (0, 20, 40, 60) mg. L-1 and their interaction on some growth characteristics: Root length, dry weight, nitrogen, phosphorous and potassium content , carbohydrate percentage and peroxidase activity in vegetative part. Data were statistically analysed to find out the least significant difference (LSD) between treatments at 0.05 level. The results indicated the increase of proline concentration from (0 to 60) mg.L-1 caused significant decrease in the average of growth characteristics and peroxidase activity unite.mg.proline-1 with increase in the average of irrigation periods under drought stress.

Keywords. Proline, Cowpea, drought stress.

1. Introduction

The Cowpea (*Vigna unguiculata* L.) is a specific type of small oval bean with black dot on it, and have different colors such as; red white, black and brown and although it is very popular for its flavor and delicious taste [1]. The cowpea contains all the essential vitamins and minerals including vitamins A, B and C, folic acid, iron, potassium, magnesium, calcium, selenium, sodium, zinc, copper and phosphorus [2]. People with diabetes can depend cowpea on their diet because it have magnesium in high levels which improve bone health and play a key role in carbohydrate metabolism [3], and can help the body to maintain balanced levels of blood sugar, and it essential for people with colitis because of its rich source of fiber and it can also improve the efficiency of digestion and help in eliminating urination problems [4] it used as a treatment for anemia and iron deficiency, and it is rich with antioxidants vitamin A and C which are benefit for the skin, and for hair, its solution prevent hair loss, and is very rich in vitamin B1 (Thiamine) there for play a role in preventing heart failure and controling ventricles of the heart [5]. The treatment with amino acid proline it play positive role correlation between proline accumulation and plant stress, it plays three major roles during stress like

as metal chelator, antioxidative defense molecule and a signaling molecule. Review of the literature indicates that a stressful environment results in an overproduction of proline in plants which in turn enhance stress tolerance by maintaining cell turgor or osmotic balance and stabilizing membranes, and minimize concentrations of reactive oxygen species (ROS) within normal ranges, thus preventing oxidative burst in plant [6]. Proline can enhanced stress tolerance when supplied exogenously at low concentration, but have a toxic effects when supplied exogenously at higher concentration. Plants are subjected to various types of environmental stresses, which include salinity, water deficit, temperature extremes, toxic metal ion concentration and UV radiation. The exogenous applied proline at seedling stage or at vegetative stage of *Zea mays* resulted in enhanced growth under water deficient environment [7]. The present study aimed to study the effect of increasing concentration of proline and irrigation times and their interaction on growth of cowpea plant and to determine the suitable concentration of proline acid that can avoid the decrease in water content in the plants.

2. Materials and Methods

The experiment was conducted in growth season at 2018-2019 in the Al-Youssoufia region which located in northwest of Baghdad city. The experiment designed at four levels of proline and three time of irrigation, (3x4x3) by using 30 plants in each treatment unit which was designed according to the Randomized Complete Block Design (R.C.B.D) with three replication.

2.1. Soil analysis

Top soil samples were taken from the (0-30) cm layers. Samples were air dried and sieved to a particle size (2 mm) for soil chemical analysis [8] the result of the chemical and physical properties of the soil used in the experiment.

Table 1. Some of the chemical and physical properties of the soil used in the experiment.

pH	EC $ds.m^{-1}$	N $mg.kg^{-1}$	P $mg.kg^{-1}$	Soil texture		
				Sand $g.Kg^{-1}$	Silt $g.Kg^{-1}$	Clay $g.Kg^{-1}$
7.08	2.6	0.132	23.10	200	240	390

2.2. Studied characteristics

2.2.1. Dry weight (g)

Shoot dry weight were calculaed by using sensitive balance after drying in an oven at temperature (60±0.2) C° until weight constant.

2.2.2. Root length

Root measurements were taken from the area associated with the stems to the furthest penetration from the soil and left in the water until the disposal of all clay.

2.2.3. Determination of the Nitrogen concentration (%)

To determine the nitrogen, known weight of plant samples, digested according to [9] method. Nitrogen was determined in the shoot by micro-Kjeldahl using the following equation:

$$\%N=\frac{V_1\times V_2\times N_1\times 14\times 100}{A\times B\times 1000}$$

In which:

V1= HCl volume from the burette.

V2= Total volume of digested plant sample in (50) ml.

N1= Used HCl normality (0.005 N).

14= Nitrogen atomic weight.

100= Conversion to the percentage rate.

A= Digested plant sample solution in the distillation unit.

B= The weight of the dried plant digested sample.

1000= To convert mg. to g. unit.

2.2.4. Determination of soluble carbohydrate percentage

The stock solution of glucose and fructose is prepared by solute (50) gm of glucose and (50) gm of fructose in one litter distiled water, then prepared many concentration of them like (0.0, 0.2, 0.4, 0.6, 0.8, and 1.0) $mg.L^{-1}$, (1) ml of each concentration and (1) ml of phenol indicator (5%) is added to each concentration, mixture is read by spectrophotometer at (488) mm wave length. From the relationship between the concentration curve is drawn [10].

2.2.5. Determination of total phosphorus content ($mg.plant^{-1}$)

Estimate phosphorus concentration in spectrophotometer digested samples and at length 882 nm according to [11], the concentration was multiplied by plant dry weight to estimate the total phosphorus content.

2.2.6. Determination of total potassium content ($mg.plant^{-1}$)

Potassium concentration in digested samples was first determined by the flame spectrophotometer according to [8] it was calculated by multiplying the potassium concentration by dry weight of plant to estimate total potassium content.

2.2.7. Determination of antioxidant enzyme (Super oxide dismutase) (SOD) $U.ml^{-1}$

Estimated by method [12] by used reagents:

- Nitro blue tetrazolioum.

- Ribovlavin

2.2.8. Prepare solution volume

Table 2. Preparation of solution.

Solution	2	2	3	4	Total volume
Component	Potassium phosphate buffer 82.4 ml.mol	Amino acid L. methionine 14 ml.mol.	Tritron-X 1%	14.4 ml.mol + 10 ml d.w	-

Volume ml	18.35	1.5	0.75	1	21.60

Prepare riboflavin in solution 47.7 micromole by dissolving 0.0018 gram with, distilled water and complete volume to 100 ml of distilled water

2.2.9. Method of work

Crush 1 gm of soft vegitative tissue from 90-day-old sample with 10 ml potassium phosphate buffer (0.1) molar and kept under the temperature of 3°C refrigeration for 24 hours and put it on centrifuge at 1000 rpm for quart of an hour, 1.5 ml from total volume above in the tubes and add 40 microliter of the solution filtration the transferred to spectrophotometer for absorbance reading at 560 wavelength and comparison with blank sample which did not contain plant tissue were added to then just distilled water, samples were then brought to light using two lamps (20 watt) in box for ten minutes then read the absorbance below the same wavelength the standard was drawn and the inhibitor ratio was calculated from the follow equation:

Enzyme activity=$\frac{\text{Sample inhibition ratio}}{\text{Highest inhibition ratio}} \times \frac{\text{Dilution coefficient(D.F)}}{\text{Volume of samples}} = \frac{60}{40}$

3. Results and Discussion

Effect of proline on some growth characteristics of cowpea plant exposed to water stress:

3.1. Dry weight

In Table (3) showed that there was significant increasing at (P= 0.05) in the dry weight with the increasing proline concentration without irrigation time and irrigation time without proline, the dry weight means increased with increasing in the proline levels from (0 to 40) gm.plant-1 this resulted significant in the average dry weight, an increase of (38.397%). The results also indicated a significant increase in the rate dry weight with increases the irrigation time from (4 to 8) day an increase of (7.710%). The effect of bilateral overlap of the study workers showed results, there was significant increase in this characteristic. The highest value for dry weight was at concentration 40 $mg.L^{-1}$ proline acid and (8) day irrigation time, where it reached (2.704 $gm.plant^{-1}$) compared with (0) $mg.L^{-1}$ proline and (4 day) where it reached to (1.995 $gm.plant^{-1}$) an increase of (35.538%). We conclude that the spacing of irrigation time affects dry weight as it leads to a decrease in photosynthesis rate as well as few absorption of important nutrient and consequently in metabolism, it is related reduced dry weight by low plant elongation rate and low leaf area rate, where dry matter is the net production of photosynthesis and depends on the balance between two processes photosynthesis and respiration, therefore spraying with proline acid increased that plant ability to build photosynthesis by controlling the opening and closing of stomata the ability of plant to build chlorophyll pigments and prevent them from decomposing and thus helped to balance taking CO_2 and water loss during transpiration [16]. It is believed that the effects of saturation mater deficit and the accumulation of ABA and pick up the leaves, close the stomata, decrease the CO_2 gas representation and increase the concentration of IAA-oxidase enzyme which oxidation of natural oxygen in the area of separation of the abscission zone which caused accumulation of ethylene hormone that causes the distraction of chlorophyll [17]. It is believed that the lack of water leads to an increase accumulation of hydrogen peroxide (H_2O_2) and inhibition of energy production by enzyme NADPH oxidase [18].

Table 3. Effect of different levels of amino acid proline on length of root (cm) of cowpea plant which exposure to drought stress.

Irrigation time	Concentrations of spraying proline ($mg.L^{-1}$)				Mean
	0	20	40	60	
Every 4 days	4.50	5.53	6.40	4.13	5.14
Every 8 days	4.30	5.03	6.17	6.07	5.39
Every 12 days	3.20	4.25	5.23	5.07	4.95
LSD (0.05)		1.25			0.62
Mean	3.00	4.94	5.93	5.29	
LSD (0.05)		0.72			

3.2. Root length

In Table (4) it can be observed that there was significant increasing in the root length with increasing in the proline without irrigation time in (40) mg.L-1 concentration which were (5.93) cm root length. In the irrigation time without proline we observed that there was significant increasing in the root length with increasing in the irrigation time at (8) day compared with other irrigation time which recorded (5.93) cm root length compared with other periods. The proline with irrigation time interaction showed that the increasing in the proline and irrigation time levels from (40 mg.L-1 and 8 day) led to significant increasing in the levels root length values at rat of (6.17) cm compared with another means. This may be due to increased dehydration causes to dysfunction of the internal hormonal system so down the gibberellic acid hormone, this leads accumulation of abscisic acid in the plant which reduces the division and size of cells in the apical areas [13]. The water stress is thought to be leads to increase the activity of free radicals of the effective oxygen and nitrogen group and inability for that the plant is inhibited and scavenged in chloroplasts and mitochondria stops the process CO2 stabilization and accumulation of dry matter [14], for that inhibits root growth, and water stress is thought to decrease in the oxygen content due to the activity of the IAA oxidase enzyme which prevents the descent oxygen and the factor of the leaves which causes weakness in growth of root [15].

Table 4. Effect of different levels of amino acid proline on dry weight (g) of cowpea plant which exposure to drought stress.

Irrigation time	Concentrations of spraying proline ($mg.L^{-1}$)				Mean
	0	20	40	60	
Every 4 days	1.995	2.317	2.571	1.780	2.166
Every 8 days	1.850	2.317	2.704	2.616	2.333
Every 12 days	1.545	1.805	2.186	2.432	1.992
LSD (0.05)		0.396			0.198
Mean	1.797	2.094	2.487	2.276	
LSD (0.05)		0.229			

3.3. Effect of different levels of amino acid proline on content of macro elements (NPK) of cowpea plant which exposure to drought stress

In Tables (5, 6, 7) showed that there was significant decrease in the means of nitrogen phosphor and potassium which affect by drought stress when irrigation intervals diverged from 4 days to 12 days the means decreased specials at 12 days an decreased of (8.070, 8.994, 20.717) % for N, P and K sequentially compared to 4 day treatment. The proline without irrigation time we observe through same Tables there was increased (NPK) means in concentration of proline at (40) mg.L-1 an increase of (38.372, 50.000, 57.418)% sequentially compared to control treatment without spraying proline (0) mg.L-1. The interaction between treatment was significant, an increase at (40 mg.L-1 and 8 day) for N

and P and (20 mg.L-1 and 4 day) for K (35.523, 51.445, 74.944) % compared with (0) proline and (4) day irrigation time. Metabolism disorder of nucleic acid, amine acid and protein where it is believed to affect straining dehydration in polyribosomes and low content in polyribosomes ATP levels and nitrogen content and effect on metabolism disorder due to the increase in effective oxygen compounds, this leads to an increase in the activity of nitrat-redutase and hydrolysis of nucleic acid that effect the absorption of mineral [19]. It is also believed that the cause of low protein content is an increase in activity enzymes such as lipoxygenase, protease and RNase are caused by drought stress and they act on reducing nucleic acid metabolism, as well the glutathione concentration to be increasing at extreme stress to release the accumulation of glutamate resulting from the decomposition of organelles and cell membranes [20], polyamines like glutathione and some amino acids such as proline ammonia modification to maintains the cell's osmotic pressures resulting from the effect of cell water loss due to dehydration which ultimately leads to increase cell osmosis and water absorption [21].

Table 5. Effect of different levels of amino acid proline on nitrogen percentage (%) in vegetative total of cowpea plant which exposure to drought stress.

Irrigation time	Concentrations of spraying proline ($mg.L^{-1}$)				Mean
	0	20	40	60	
Every 4 days	1.050	1.220	1.353	0.937	1.140
Every 8 days	0.973	1.137	1.423	1.377	1.228
Every 12 days	0.813	0.950	1.150	1.280	1.048
LSD (0.05)		0.209			0.104
Mean	0.946	1.102	1.309	1.198	
LSD (0.05)		0.121			

Table 6. Effect of different levels of amino acid proline on phosphorus percentage (%) in vegetative total of cowpea plant which exposure to drought stress.

Irrigation time	Concentrations of spraying proline ($mg.L^{-1}$)				Mean
	0	20	40	60	
Every 4 days	0.173	0.204	0.246	0.136	0.189
Every 8 days	0.162	0.189	0.262	0.229	0.210
Every 12 days	0.126	0.158	0.183	0.219	0.172
LSD (0.05)		0.049			0.024
Mean	0.154	0.184	0.231	0.192	
LSD (0.05)		0.028			

Table 7. Effect of different levels of amino acid proline on potassium percentage (%) in vegetative total of cowpea plant which exposure to drought stress.

Irrigation time	Concentrations of spraying proline ($mg.L^{-1}$)				Mean
	0	20	40	60	
Every 4 days	1.353	2.367	2.210	1.987	1.979
Every 8 days	1.270	1.640	2.113	1.763	1.696
Every 12 days	1.260	1.630	1.787	1.600	1.569
LSD (0.05)		0.282			0.141
Mean	1.294	1.879	2.037	1.783	
LSD (0.05)		0.163			

3.4. Carbohydrate concentration

In Table (8) showed that there was significant decrease in the means of carbohydrate under effect of irrigation time from (4 to 12) day the means decreased carbohydrate and decreased of (26.23%)

compared with (4) day. As for the effect of proline without irrigation periods, the effect was significant in increasing the percentage of carbohydrates at concentration (20 mg.L^{-1}) an increase rate estimated at (58.87%) compared with zero concentration. The interaction between proline and irrigation time was significant at (40 mg.L^{-1}) and (4 day) an estimated increase at (74.9%) carbohydrate compared with (0) proline and (4 day) irrigation time. The reduction of carbohydrates are due to the dehydration which effect in photosynthesis as the effect of water tension begins to close the stomata first accompanied by a shortage of the amount of carbon dioxide entering and installed in the leaves results in a significant drop in photosynthesis and this affects the amount of nutrients finally in the overall growth of plant [22].The increase in the percentage of carbohydrates due to effect of proline in increasing leaf area and number of leaves, as well as increasing leaf content of chlorophyll this will increase the efficiency of photosynthesis and then produce carbohydrates [23].

Table 8. Effect of different levels of amino acid proline on carbohydrate percentage (%) in vegetative total of cowpea plant which exposure to drought stress.

Irrigation time	Concentrations of sprying proline (mg.L^{-1})				Mean
	0	20	40	60	
Every 4 days	15.15	24.66	26.42	22.19	22.11
Every 8 days	14.09	23.61	18.32	19.73	18.94
Every 12 days	12.86	18.60	17.23	16.56	16.31
LSD (0.05)			2.78		1.39
Mean	14.03	22.29	20.66	19.49	
LSD (0.05)			1.60		

3.5. Peroxidase enzyme

In Table (9) showed that there was significant at all treatment, the means of peroxidase enzyme under effect of irrigation time increased by increasing the irrigation time, and the time of (12 day) highest value of the enzyme an increase of (88.46 unit. mg.$plant^{-1}$) compared with (4 day) irrigation treatment. As for the addition of increased concentration of proline we note decrease in the content of the peroxidase enzyme especially at concentration 60 unit.mg.plant-1 and a decreased as (36.36 unit.mg.$plant^{-1}$). The interaction between increased proline spraying and (8 day) irrigation time inhibited the activity content of peroxidase enzyme and decreased as (46.67%) compared with (0) proline unit (4) day irrigation time. Irrigation spacing led to an increase in the activity of the enzymatic oxidation system, which includes super enzymes SOD and peroxide resulting from the activity of oxidized enzymes and free radicals be mater stress and reduced scavenging [24]. Increasing the activity of the enzyme peroxidase by increasing the production of hydroxyl radical and single oxygen with water stress effect is also believed to increase concentration the activity of malonedihyde is vital guide for the plant to provoke antioxidant production [25].

Table 9. Effect of different levels of amino acid proline on plant content of peroxidase enzyme (Unit. mg $protein^{-1}$) in vegetative total of cowpea plant which exposure to drought stress.

Irrigation time	Concentrations of sprying proline (mg.L^{-1})				Mean
	0	20	40	60	
Every 4 days	0.03	0.028	0.022	0.026	0.026
Every 8 days	0.039	0.032	0.024	0.016	0.029
Every 12 days	0.059	0.050	0.048	0.042	0.049
LSD (0.05)			0.008		0.004
Mean	0.044	0.036	0.031	0.028	
LSD (0.05)			1.60		

4. References

[1] Gonçalves A, Goufo P, Barros A, Domínguez-Perles R, Trindade H, Rosa EAS, Ferreira L and Rodrigues M 2016 Cowpea (*Vigna unguiculata* L. Walp), a renewed multipurpose crop for a more sustainable agri-food system: nutritional advantages and constraints *J. Sci. Food Agric*. **96** 2941.
[2] Olusanya AO, Gidon OO, Emmanuel TK, Akinhide MA, Aash T and Ademayowa AO 2016 Yield and growth characteristics of cowpea (*Vigna unguiculata*) as effected by prior heat stress and nutrient addition *African J. Agric. Res*. **11** 2269.
[3] Silveira JAG, Costa RCL, Viegas RA, Oliveira JTA and Figueiredo MVB 2003 N-compound accumulation and carbohydrate shortage on N2 fixation in drought-stressed and rewarded cowpea plants.
[4] Francar FP 1999 Alteration of water stress effects in cowpea by Bradyrhizobium spp. Inoculation *Plant Soil* **207** 67.
[5] Carvalho M, Lino-Neto T, Rosa E and Carnide V 2017 Cowpea a legume crop for a challenging environment *J. Sci. Agric*. **97** 4273.
[6] Cvikrová M, Gemperlová L, Martincová O and Vanková R 2013 Effect drought and combined dough and heat stress on polyamine metabolism in proline over producing tobacco plants *Plant Physiol Biochem*. **73** 7.
[7] Ali O, Ashraf M and Athor HU 2007 Exogenously applied proline at different growth stages enhances growth of two maize cultivars grown under water deficit conditions *Pak. J. Bot*. **39** 1133.
[8] Page AL, Miller RH and Kenney DR 1982 *Method of soil analysis*, 2nd (ed) Argon. 9, publisher, Madiasen, Wiconsin.
[9] Gresser MS and Parson JW 1979 Sulpheric perchloric acid digestion of plant material for the determination of nitrogen, phosphorus, calcium and magnesium *Anal. Chem. Acat*. **109** 431.
[10] Herbert D, Philips PJ and Strange RE 1991 *Methods in microbiology* Academic Press. London.
[11] Matt KJ 1970 Colorimetric determination of phosphorus in soil and plant materials with ascorbic acid *Soil. Sci.* **109** 214.
[12] Beyer FW and Fridowich I 1987 Assaying for superoxide dismutase activity. Some large consequences of minor changes in conditions *Anal. Biochem*. **161** 559.
[13] Jain VK 2010 *Fundamentals of plant physiology* S. Chand & Company Ltd.
[14] Nobel PS 2009 *Physicochemical and environmental plant physiology* 4th ed. Elsevier lac. Oxford. UK. 635.
[15] Shahiid AA 2013 *Physiology of reconstruction in sub-plants installed and under proof and proposed* Baghdad, Iraq 228.
[16] Raven JA 2002 Selection pressures on stomatal evolution *New Phytol*. **153** 371.
[17] Rao, KVM, Raghavendra AS and Redoly KJ 2006 *Physiology and molecular biology of stress tolerance in plants* Springer. Dordrecht. Netherlands 345.
[18] Chesseman IM 2007 Hydrogen peroxide and plant stress, a challenging relationship *Plant Stress* **1** 4.
[19] Igor CA, Gonzales EM, Morino D, Ladera R, Larranazar E and Quintana E 2011 Physiological response of legume nodule to drought *Plant Stress. Sci*. 24.
[20] Rao, NKS, Shivashnakara KS and Laxman RH 2016 *Abiotic stress physiology of horticultural crops* Springer. India: 368.
[21] Dawood MG 2016 Influence of osmoregulators on plant tolerance to water stress *Sci. Agri*. **13** 42.
[22] Singh BB, Mai-odomi Y and Terao T 1999 A simple screening method for drought tolerance in cowpea *Indian J. Genet*. 59: 211-220.
[23] Bradford KJ and Hsiao TC 1982 *Physiological responses to moderate water stress* 263.

[24] Ahari AK 2006 *A study of superoxide dismutase activity and superoxide production in kiwi fruit* MSc. Thesis. University of Canterbury
[25] Shankers AK and Ventateswarlu B 2011 *Abiotic stress response in plant-physiological biochemical and genetic perspectives*. INTECH. Pup. Rijeka. Croatia 440 .

Antioxidant, cytotoxicity and phytochemical analysis of *Larinus maculates* F. cocoon aqueous extract against lung cancer

Antioxidant, cytotoxicity and phytochemical analysis of *Larinus maculates* F. cocoon aqueous extract against lung cancer

Hanady S. Al-Shmgani[1*], Zainab Thamer Alasady[2] , Ehab M. Ali[3] and Mohammad J. Al-Jassani [2]

[1]Department of Biology, College of Education for Pure Science, University of Baghdad, Baghdad, Iraq.
[2]Microbiology Department, College of Science, Al-Karkh University for Science, Iraq.
[3]Chemistry Department, College of Applied Sciences, University of Fallujah, Iraq.

*E-mail: hanadysalim@yahoo.com

Abstract. Cocoon of larva *Larinus maculates* F. from Curculionidae family (*Echinops* species), locally in Iraq known as Tihan, is one of traditional folk medicine used in the treatment of diversity respiratory system and fever. This study was carried out to assess the bioactive component and the antioxidant capability of aqueous beetle cocoon extract (*Larinus maculates* F.) along with its possible cytotoxic activity against A549 lung cancer cell line. For phytochemical analysis gas chromatography-mass spectrometry (GC-MS) was used, and to detected free scavenging activity 2, 2-diphenyl-1 picrylhydrazyl (DPPH) was used. To determine the cytotoxicity in the cancer cell line 3-(4,5-dimethylthiazol-z-yl)-2,5-diphenyltetrazolium (MTT) was used; peripheral blood monolayer cells (PBMCs) was used as a normal cell. GC-MS analysis identified the presence of 9 phytochemical components. DPPH results suggested a promising antioxidant activity in a dose-dependent, the best antioxidant potential was at 600 µg.ml^{-1} concentration. Cytotoxic activity results showed that the increase in extract concentration decreases the cell viability, at 50 µg.ml^{-1} concentration the percentage of viability was (86.76±0.87) where at 200 µg.ml^{-1} the cell viability was (56.44±0.91) µg.ml^{-1}. Taken together, the results showed that larva cocoon of *Larinus maculates* F. extract has an important phyto-molecule with great potent antioxidant and cytotoxicity activity against lung cell line A549..

Keywords. *Larinus maculates* cocoon shell, GC-MS analysis, DPPH, A549 cell line.

1. Introduction

In many cultures, traditional medicine as an alternative medication is still important therapeutic source due to its adequate properties, heritage and popular belief along with the low cost [1]. Therefore, there is growing interest in the study of medicinal therapy in the field of biomedical research. Natural products such as plants, animals and marine organisms contain a large number of active compounds that reflect the potential treatment activity of these organism [2]. It has been suggested that some

alternative drugs might have a greater remedial capacity than those that are owned by manufactured drugs in the treatment of certain diseases with less side effects that accompany the use of chemical drugs [3]. One of the interested folk remedy use in Iraq is the cocoon shell produced by salivary glands of beetle larva of *Larinus maculates* F. from *Curculionidae* family commonly known as (Tihan). Also known in neighboring countries (Iran and Syria) *Trehala manna* (Shekar tighal). Commonly used in treatment from various diseases including respiratory system diseases, viral or bacterial infection, antitussive, anti-asthmatic and febrifuge [4]. In our *in vivo* previous study [5]. Tihan exhibited potential role in activated immune system where orally treated mice showed a significant increase in mitotic index and phagocytosis. Other study by [6] reported *in vitro* immunostimulatory effects on splenocytes and macrophages by increased PHA- and LPS-stimulated splenocytes proliferation and IFN-γ production. Additionally, Iranian researcher reported contains analysis of *Trehala manna* such as water-soluble polysaccharides (e.g. cellulose and trehalose), tannin, albuminoid matter, lipid, and mucilage [7, 8, 9]. As attributable the important role and their biological activities of *Trehala manna* due to its polysaccharides molecular weights [8]. It is well known that the unnecessary generation of reactive oxygen species (ROS) causing imbalance in oxidant/antioxidant status and leading to oxidative stress and consequently oxidative damage induced cell injured. The implication of ROS as one of the molecular mechanisms involved in carcinogenesis has been reported [10)] Therefore, antioxidants are proposed as possible applicant for prevention or/and treatment of cancer. Antioxidants play important role in determining the therapeutic effect of plants and other traditional agent and to make them a good remedy against acute and chronic diseases. These antioxidants usually found and taken in our dietary from the natural compounds. The current study aims to investigate the active compounds in comestible Iraqi aquatic cocoon shell of beetle larva of *Larinus maculates* and their anti-oxidant and cytotoxicity effects on A549 lung cell line. For our knowledge, this is the first study in this aspect in Iraq.

2. Materials and Methods

2.1. Chemical and reagent

Cell culture media and reagents were obtained from GIBCO (Rockville, MD, USA), all other chemicals and reagents were obtained from Sigma Aldrich (Louis, USA).

2.2. Beetle cocoon collection and extract preparation

Tihan cocoon shells were obtained from local shelf market (Iraq/Baghdad), identified by expert in Iraqi Natural History Museum Figure (1). Cocoons aquatic extract were prepared as the following (5) firstly emptied from inside insect, grounded using a laboratory electric grinder. 10 g from the powder dissolved in 100 ml of distal water using heating stirrer for two hour. Followed by centrifuging at 4000 rpm for 30 min and then the filtered supernatant dried using a rotary evaporator under reduced pressure and kept at 4°C until uses in the experiment.

Figure 1. Tihan cocoon shells produced by of *Larinus maculates* F from Curculionidae family.

2.3. Gas chromatography-mass spectrometry (GC-MS) analysis and identification of phytochemical components

The GC-MS analysis for aqueous beetle cocoon extract was performed as descripted previously [11] using a Clarus 500/580 Perkin Elmer GC (Connecticut, USA). The unknown components mass spectrum of the unknown components was compared with the spectrum of the components stored in the NIST library [12].

2.4. Anti-oxidant activity measurement

The antioxidant activity was determined according to [13] using 2, 2-diphenyl-1-picrylhydrazyl (DPPH). Briefly, 1 ml of the samples (different concentration 100, 200, 400 and 600 µg.ml^{-1} was mixed 1:1 with DPPH solution (60 ⌈M, 1 ml). After incubation in darkness at 37°C for 30 min, the absorbance was read at 517 nm spectrophoto-metrically (Perkin-Elmer Lambda 25, Germany). Vitamin C considers as a positive control, and measurements were carried out in triplicate. The IC50 value was calculated according to the absorbance and the inhibition percentage of was calculated using the following equation:

Scavenging activity(%) by DPPH = (Ac – As) / Ac * 100

Where, Ac = absorbance of control and As= absorbance of samples

2.5. A549 Cell line culture

The lung cell line A549 was provided by Center of Biotechnology at AL-Nahrain University. A549 cell line is usually used as a representative of type two alveolar pulmonary epithelial cell derived from pulmonary adenocarcinoma of 58-years old man [14] Dulbecco's Minimal Essential Medium (DMEM) was used for cell culture and maintenance and provided with 10% fetal bovine serum (FBS) and antibiotic penicillin & streptomycin (1%). Cells were incubated at 37°C in humidified 5% CO_2 and cultured at 2 ×10^5 cells ml^{-1} concentration.

2.6. Human Peripheral blood isolation and culture

In order to evaluate Tihan extraction effect on normal cells Human peripheral blood samples, blood samples were collected from healthy volunteers in heparinized tubes after taken their permission to participate. The peripheral blood mononuclear cells were isolated by using Ficoll-Paque after centrifuged in a falcon tube for 30 min at 3000 rpm. Cells were cultured in 96-well plates in RPMI medium and incubated for 4 h in 5% CO_2 at 37 °C. Concentration of 50, 100, 150 and 200 µg.ml^{-1}, the same concentration used with A549 cell, was add, lymphocytes in culture media without extract was considered as control and the cell viability calculated using MTT assay after 24 h incubation. Cisplatin was used a positive control (stock solution 1000µg/ml).

2.7. Measurement of cell viability

The 3-(4,5-dimethylthiazol-z-yl)-2,5-diphenyltetrazolium (MTT) assay was used as described by [15] for cell viability detection. Extract concentrations of 50, 100, 150 and 200 µg ml^{-1} was used. Cells were seeded at a concentration of 1 × 10^5 cell ml^{-1} and 100 µl of extracts was. After the incubation period, 10 µl of (5 mg ml^{-1}) MTT solution was added to each well and incubated 4 h at 37°C. Then 50 µl of dimethyl sulfoxide (DMSO) was added and left for 10 min. A549 cells without aqueous beetle cocoon extract represent control group. The absorbance was read at 570 nm using spectrophotometer

reader (VersaMaxTM, Molecular Devices, Sunnyvale, CA). Based on the inhibition concentration the IC_{50} value calculated using GraphPad Prism 6 software.

2.8. Statistical analysis

SPSS software version 16.0 was used for Statistical analysis. The results are accessible as means ± standard error. Analysis of variance (ANOVA) was used and Fisher Least Significant Difference (LSD) test.

3. Results and Discussion

3.1. GC-MS analysis

The GC-MS analysis of the cocoon extract showed the presence of 9 compounds (Table1). The major components were identified are benzoic acid, (19.89%); 2-butanol, (17.86%); followed by hexamethy l-3 (16.41%) and purin-6-1 (15.68%) as the major constituents cocoon extract. These elements have been reported for their biological and therapeutic properties including the antioxidant for example, Hydroxy benzoic acids and its derivatives showed antioxidant and anti-inflammatory properties against free radicals especially superoxide radical [16, 15, 17] where it decrease overproduction of reactive species. Also, it has been reported that antioxidant activity of butanol fraction was higher than α-tocopherol and butyrated hydroxyl toluene (BHT) [18].

Table 1. Phytochemical analysis of *Larinus maculates* F. cocoon extract by GC-MS.

NO.	RT	Phytochemical compound	Peak area %	CAS NO.
1	4.316	Performic acid, trimethysilyl derivative	7.92	1000368-52-2-25
2	4.536	Glyceraldehyde	2.93	000056-82-6
3	4.961	Cyclotrisiloxane, hexamethyl-	2.19	000541-05-9
4	5.136	Tricyclo [4, 3, 1, 1 (3, 8)] undecane-3-carboxylic acid, methyl ester	6.06	031061-61-7
5	5.477	Acetophenone, 4'-methoxy-, oxime	11.06	002475-92-5
6	5.675	6H-Purin-6-one, 2-amino-1, 7-dihydro-1-methyl-	15.675	000938-85-2
7	6.069	2-Butanol, 3-methyl-	17.86	000598-75-4
8	7.268	Benzoic acid, 3-methyl-2-trimethyl silyloxy-, trimethylsilyl ester	19.89	1000153-57-1
9	8.088	7, 7, 9, 9, 11, 11- Hexamethyl-3, 6, 8, 10, 12, 15-hexaoxa-7, 9, 11-trisilaheptadecane	16.41	1000375-89-1

3.2. Antioxidant activity

The aqueous extract was tested for its antioxidant activity with DPPH at 100,200, 400, and 600 $\mu g.ml^{-1}$ concentration. The results showed a significant higher radical scavenging activity as compared with the positive control (L-ascorbic acid) in a concentration-dependent inhibition. Higher activity ($P \leq 0.01$) was shown at 600 $\mu g.ml^{-1}$ concentration, while the lower one was with 100 $\mu g.ml^{-1}$ concentration ($P \leq 0.05$) compare with ascorbic acid control (Figure2). Many different compounds found in the extract of the present study can be contribute to free radical scavenging activity, such as the phenolic

compounds with its multiple hydroxyl groups showed higher ability to quench DPPH [19]. Moreover, [20] reported that the number of hydroxyl groups attached to the aromatic ring is associated with the phenolic acids anti-radical activity, though some other compounds may also be involved. Present study finding support this suggestion by which Butanoic acid, Oleic acid, Pimaric acid, Phenol and Benzoic acid found in the extracts might be responsible to the antioxidant activity. As a little-known of functional food sources of the cocoon extract, therefore, the isolation and purification of these phyto-compounds may be useful in the research of new treatment drug. The antioxidant activity performance in two levels, the first one at the cellular membrane level by breaking peroxyl radical chain reactions followed by the second level by reacting with intracellular ROS [21].

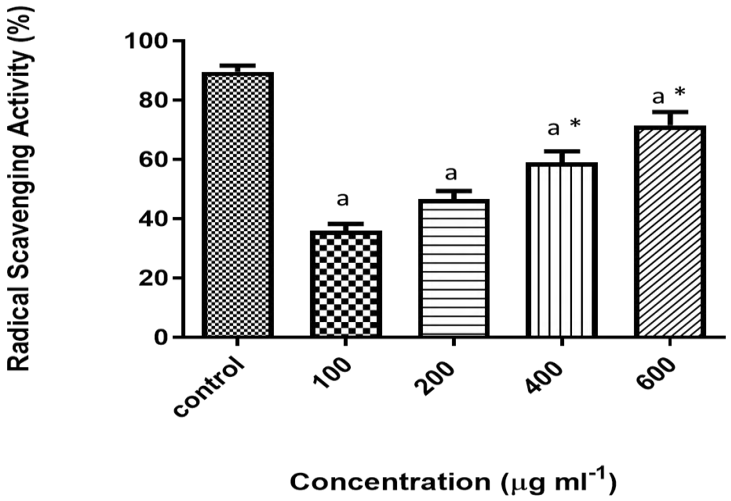

Figure 2. DPPH free radical scavenging activity. The inhibition percentage of different concentrations of extract observed at 517 nm. Data are means ± SE (n = 3). a significantly different at P≤ 0.05 as compared to L-ascorbic acid (positive control). * significantly different at P≤ 0.05 as compared to 100 μg.ml^{-1}.

3.3. Cell cytotoxicity

The cytotoxicity effect of different concentrations of the aqueous Tihan extract was evaluated using two Human cell line, A549 lung cancer cell line and PBMCs as a normal cell. The results showed significant cytotoxic effect in a dose dependent manner. The treatment of A549 cells with concentrations of (50, 100, 150 and 200 μg.ml^{-1} decreased significantly the % viability. Where the highest inhibition was at higher doses, however, a moderated inhibition (not significant) was found at the lower doses (Table 2). However, there was no potent cytotoxic effect on normal PBMCs cell (Table 2). Cisplatin effect on the percentage viability of PBMC cell was dose dependent by which the viability decreased significantly as the dose 8 and 12 μg.ml^{-1} compared to the control. However, at the dose 2 and 4 μg.ml^{-1} there was no significant difference.

Table 2. Cell percentage of viability on A549 and PBMCs cell line using MTT assay and treated with different concentrations of cocoon extract for 24 h. Data are means ± SE in triplicate. A significant at p≤0.05.

Cell Viability (%)	Concentration (μg. ml^{-1})				IC50
	50	100	150	200	
A549 cell line	86.76±0.87	71.52±0.79	63.14±0.64[a]	56.44±0.91[a]	139.01
PBMCs	96.34±0.56	100.30±0.89	118.59±0.72	126.73±0.88	43.7
CisP	2	4	8	12	
	89.96±2.24	74.08±2.48	66.14±1.56[a]	53.08±2.34[a]	0.27

This is because the cocoon extract of Tihan contains polysaccharide [22] and when the concentration of the extract is increased the ratio of polysaccharide increased that stimulate the production of IL-2, which plays a role in the activation of NK cells [23] as well as its role in T cell division. This demonstrates the role of polysaccharide in the development of immunity and its potential for use in therapeutic applications such as bacterial infections and cancer [24]. Study by [5] have indicated the role of these polysaccharide in increasing phagocytic index(PI). The reason for this increase is the effect of the active ingredient in the extract in stimulating phagocytosis by stimulating the release of certain cellular attractions specifically TNF And IL^{-1}, which stimulates macrophage cells, including neutrophils to leave the blood stream to the peritoneal cavity [25]. But the inhibition was decreased with reducing the concentration at 100 $\mu g.ml^{-1}$ concentration. The suppression of proliferation was concentration-dependant. Additionally, elevated ROS level has been associated with cancer, one of the causes is the abnormal mitochondrial oxidative metabolism which is responsible for the initiation and progression of cancer.

4. Conclusion

In conclusion, the finding of the present study identified that *Larinus maculates* F. cocoon aqueous extract has several phyto-molecule possessing anti-cytotoxicity and anti-oxidant therapeutic activities. The results of antioxidant activity suggested that ROS may be a potential mechanism involved in cancer cell death and the antioxidant capacity of the extract can decrease cell proliferation. For our knowledge this is the first study that recorded the *in vitro* toxicity for the cocoon extract. However, further research on cyto-toxicology still needed in order to insure the safety especially *in vivo*.

5. References

[1] Yuan H, Ma Q, Yeb L and Piao G 2016 The traditional medicine and modern Medicine from natural products *Molecules* **21** 1.
[2] Cragg GM and Newman DJ 2013 Natural products: a continuing source of novel drug leads *Biochimica et biophysica acta* **1830** 36703695.
[3] Sofowora A, Ogunbodede E and Onayade A 2013 The role and place of medicinal plants in the strategies for disease prevention *Afr. J. Trad. Compl. Altern. Med.* **10** 210.
[4] Mohammadi M and Dini M 2003 Identification of manna sources production mechanism and utilization in Iran *Iran J. Med. Arom. Plants* **17** 75.
[5] Alasady ZT, Abd-Alsaheb HS and Jwad MSM 2017 The effect of *Larinus maculates* F. cocoon aqueous extract in some Immunological Aspects of male albino mice. *J. Pure Appl. Sci.* 153.
[6] Ahmadabad HN, Firizi MN and Behnamfar M 2016 Immunostimulatory effects of Trehala mana ethanolic extract on splenocytes and peritoneal macrophages *in vitro*. *J. Med. Plants Nat. Prod.* **1** 23-32.
[7] Karami A H 2012 Structure elucidation of water-soluble polysaccharides of *Trehala manna*. *Res. Pharmac. Sci.* **7** S731.
[8] Hamedi A, Farjadian S and 2015Karami M R 2015 Immunomodulatory properties of *Trehala manna* decoction and its isolated carbohydrate macromolecules *J. Ethnopharmacol.* **162** 121.
[9] Mohammadi M and Dini M 2003 Identification of manna sources production mechanism and utilization in Iran *Iran J. Med. Arom. Plants* **17** 75.
[10] Liou GY and Storz P 2010 Reactive oxygen species in cancer *Free Radic. Res.* **44** 479-96.
[11] Al-Shmgani HAS, Kadri ZHM, Al-Halbosiy MMF and Dewir YH 2019 Phytochemical analysis, cytotoxicity and antioxidant activity of cuckoo pint (*Arum maculatum*) leaf extract *Acta Biologica Szegediensis; Szeged* **63** 119.
[12] Sathyaprabha G, Kumaravel S and Panneerselvam A 2011 Bioactive Compounds Identification of Pleurotus platypus and Pleurotuseous by GC-MS. *Adv. Appl. Sci. Res.* **2** 51.

[13] Al-Kubaisi ZA, Al-Shmgani H S and Salman MJ 2020 Evaluation of In vivo and In vitro protective effects of quercetin on Lipopolysaccharide -Induced Inflammation cytotoxicology *Res. J. Pharm. Tech*. **13** 3897.
[14] Foster KA, Oster CG, Mayer MM, Avery ML and Audus KL 1998 Characterization of the A549 cell line as a type II pulmonary epithelial cell model for drug metabolism. *Exper. Cell Res*. **243** 359.
[15] Al-Rikabi R, Al-Shmgani H, Dewir YH and El-Hendawy S 2020 *In vivo* and *in vitro* Evaluation of the Protective Effects of Hesperidin in Lipopolysaccharide-Induced Inflammation and Cytotoxicity of Cell. *Molecules* **25** 478.
[16] Velika B and Kron I 2012 Antioxidant properties of benzoic acid derivatives against superoxide radical *Free Radic. Antioxid*. **2** 62.
[17] Thierry F, Ange M M, Thierry R, Gianangelo G, Philippe N and Didier S 2012 Antioxidant and anti-inflammatory like properties of benzoic acid analogs on the oxidant response of neutrophils: structure/redox potential relationship study *Free Radic. Biol. Med*. **53**.
[18] Surh J and Yun J M 2012 Antioxidant and Anti-inflammatory Activities of Butanol Extract of *Melaleucaleus cadendron* L. *Preven. Nut. Food Sci.* **17** 22.
[19] Mathew S, Abraham TE and Zakaria ZA 2015 Reactivity of phenolic compounds towards free radicals under in vitro conditions *J. Food Sci. Technol.* **52** 5790.
[20] Sroka Z and Cisowski W 2003 Hydrogen peroxide scavenging antioxidant and anti-radical activity of some phenolic acids *Food Chem. Toxicol*. **41** 753.
[21] Gulcin İ 2020 Antioxidants and antioxidant methods: an updated overview *Arch Toxicol*. **94** 651.
[22] Yang F, Shi Y, Sheng J and Hu Q 2006 *In vivo* activity of polysaccharides derived from *Chlorella pyrenoidosa Eur. Food Res. Techol*. **224** 225.
[23] Chen J, Zhu X, Yang L, Luo Y, Wang M and Liu X 2016 Effect of *Glycyrrhiza uralensis* Fisch polysaccharide on growth performance and immunological function in mice in Ural city Xinjinang *Asian Pac. J. Top. Med*. **9** 1078.
[24] Mutlag S H, Hamad M N, Abbas I S and Ismael S H 2017 The evaluation of Ethyl acetate fraction of *Crerra cretica* effect on mitotic index and micronucleus frequency in mice *Int. J. Pharm. Sci. Rev. Res*. **45** 147.
[25] Matsukawa A, Yoshimura T, Maeda T, Takahashi T, Ohkawara S and Yoshinaga M 1998 Analysis of the cytokine network among tumor necrosis factor. Interleukin-1, interleukin-8, and Interleukin-1 receptor antagonist in monosodium urate crystal-induced rabbit arthritis *Lab. Invest*. **78** 559.

Studying the levels of some Biochemical variables in blood serum for smoking of Tikrit University students

Studying the levels of some Biochemical variables in blood serum for smoking of Tikrit University students

Saria Naji Muhsin[1*], Shurooq hameed majeedAlnassiri[2] and Sina Naji Muhsin[3]

[1]Department of Biology, College of Science, Tikrit University, Iraq.
[2]Department of Biology, College of Education for girls, Tikrit University, Iraq.
[3]College of Dentistry, Tikrit University, Iraq.

*E-mail: saria7052@gmail.com

Abstract. This study included (75) samples of the males students at the Tikrit University, The samples were divided into three groups; the first group: (25) blood samples pulled from healthy no smoking students (males) as Control sample. The second group: (25 males) samples of diabetic mellitus (smoker students). Third group: (25 males) samples of hypertension (smoking students). The results of the study indicated a significant increase in the concentration of the levels Cholesterol, Triglyceride, Malondialdehyde (MDA), Lactate dehydrogenase (LDH) at level ($P < 0.005$) in the samples of smoker students when compared to the healthy group. And showed decrease in the concentration level of HDL, Glutathione Peroxidase (GPx) at level ($P < 0.005$) when compared to the healthy group (non-smokers).

Keywords. Biochemical variables, Blood serum, Smoking.

1. Introduction

The Antioxidants are a class of chemical substances naturally found in our food which can prevent or reduce the oxidative stress of the physiological system. The body is constantly producing free radicals due to regular use of oxygen. These free radicals are responsible for the cell damage in the body and contribute to various kinds of health problems, such as heart disease, diabetes, macular degeneration, and cancer. Antioxidants being fantastic free radical scavengers help in preventing and repairing the cell damage caused by these radicals [1] .Plants and animals are the abundant source of naturally producing antioxidants. Alternately, antioxidants can also be synthesized by chemical process as well as from the different kinds of agro-related wastes using biological process. Based on their solubility, antioxidants are broadly categorized into two groups: water soluble and lipid soluble. [2]In general, water-soluble antioxidants, such as ascorbic acid, glutathione, and uric acid, have functions in the cell cytosol and the blood plasma. Ascorbic acid is a redox catalyst which reduces and neutralizes the reactive oxygen species (ROS), glutathione has antioxidant properties as reducing agent and can be reversibly oxidized and reduced, while α-tocopherol, carotenoid, and ubiquinol are the examples of lipid-soluble antioxidants and protect the cell membranes from lipid peroxidation [3]. Enzymes are types of antioxidants that come from the protein and minerals we eat as part of our daily diets. These enzymes are synthesized in the human body, and include superoxide dismutase (SOD), glutathione

peroxidase, glutathione reductase, and catalases. The human body does not produce antioxidant vitamins naturally, so it is essential to include dietary sources of them in our daily intake of food, be it through foods or supplements. Common antioxidant vitamins include vitamins A, C, E, folic acid, and beta-carotene [4]. Free radicals are highly reactive and unstable molecules, usually oxygen molecules, but not always. Their unstable nature is caused by having an unpaired electron. As a result of this unpaired electron, free radicals seek out and take electrons from other molecules, which oftentimes causes damage to the second molecule. When a free radical molecule does this, it is called "oxidation." A molecule that has had its electron "stolen" from a free radical has been "oxidized." Molecules that have been oxidized are now transformed into free radicals themselves and will seek to interact with another healthy molecule, thereby creating a vicious chain reaction of electron stealing in the body. When the body has undergone excessive oxidation, or more oxidation than can be combatted, it is said be undergoing "oxidative stress."[5]. Like many things that occur in nature, free radicals are not only impossible to avoid, but necessary for life. Free radicals help us fight infection, begin the inflammation process that helps repair tissue injury, and short-term oxidative stress may inhibit aging. At the same time, excessive amounts are harmful to humans[6]. Free radicals can form in the body in a number of ways; Environmental exposure, Carcinogens like radiation from the sun, cigarette smoke, air and water pollution, pesticides and herbicides in the food we eat, asbestos and other nasties can cause free radical formation in our bodies. Exercise, while consistent moderate exercise has many positive benefits and can reduce the risk of breast cancer, excessive exercise or inconsistent but vigorous exercise uses a high amount of the body's oxygen store and as a result, generates excessive free radicals. Stress, the chemicals cortisone and catecholamines created by mental stress can create free radicals. Our bodies, Free radical molecules are a natural byproduct of cell metabolism. Alcohol, consumption of alcohol of any kind of any amount produces free radicals in the body. Fat polyunsaturated fat like that found in vegetables oils is easily oxidized in the body and can create free radicals. Substitute polyunsaturated fats with monounsaturated fat [7]. Some conditions caused by free radicals include; deterioration of the eye lens, which contributes to vision loss, inflammation of the joints (arthritis), damage to nerve cells in the brain, which contributes to conditions (such as Parkinson's or Alzheimer's disease), acceleration of the ageing process, increased risk of coronary heart disease, since free radicals encourage low-density lipoprotein (LDL) cholesterol to stick to artery walls, certain cancers triggered by damaged cell DNA [8]. Smoking considers being wide public health problem, which reached today to the level of global epidemical. It is a risk factor for variety of disease (cardiovascular disease, stroke, chronic pulmonary disease, Alzheimer's disease, Parkinson's disease) [9]. About more than 5 million people die from smoking related illnesses, as the report of World Health Organization [10], this number will be doubled by 2025. The main addictive component of smoke are Nicotine, Hydrogen cyanide, Methanol, Butan and about more than 400 other chemicals. These chemicals induced the rate of Reactive Oxygen Species (ROS), which is a part of free radicals. Free radicals are highly unstable and capable of undergoing complex interaction in biological system, make oxidative stress, which occur when there are not enough antioxidant molecules to counteract their side effects [11]. Antioxidant are natural molecules in the biological system that scavenging free radicals or protecting from its effects. They can be synthesized endogenously in the body or determined by food intake [12].Smoking is a rich source of oxidants. It has been considering the main cause of increase production of (ROS) which may exceed the capacity of antioxidants defense system [13].

2. Materials and Methods

This study has carried out in College of Science (November 2019) to (February2020) at Tikrit University. The study included (50) samples of the smoker students their ages (21-23) years old. As well as choosing randomly group included (30) sample of (non- smoker students) of age (21-23) years old.

2.1. The samples divided into three groups

First Group, included (25) non-smoker students. Second Group, included (25) diabetic mellitus (smoker students). Third Group, included (25) hypertension (smoker students).

2.2. Method Of Collection The Sample

The blood sample was collected from (75) samples of the students healthy (non-smoker) as well as smoker students of age (21-23) years old. The blood samples were taken from the vein.10 mL from each student, the blood was put in disposable test tubes. The tubes are empty of (EDTA) in order make Biochemical tests. After that, The blood was left at room temperature for 20 minutes, The blood was separated by using a centrifuge at speed of (3000) rpm for 10 minutes. The serum was extracted using Micropipette, in order to make Biochemical tests which included (Cholesterol, Malondialdehyde, Lactate dehydrogenase, HDL-Cholesterol, Alanine aminotransferase (ALT), Aspartate aminotransferase (AST), Glutathione Peroxidase, Triglyceride, Uric acid, Creatinine.

2.2.1. Measurement of Cholesterol concentration

To evaluate and estimate the Cholesterol in the blood serum, was dependent and using the (Kit) which its equipped (Biolabo) Company made in France with reference number 02160 [14].

2.2.2. Measurement of Triglycerides concentration

It have been used the (Kit) of Triglycerides equipped by (Biomaghreb) Company made in France with number 20133[15] to estimate and evaluate the Triglycerides enzyme in the blood serum.

2.2.3. Measurement of HDL-Cholesterol concentration

It have been used the (Kit) of HDL-Ch., equipped by (Biolabo) Company mad in France with number 02160 [14] to evaluate and estimate the HDL-Ch in the blood serum

2.2.4. Measurement of Lactate dehydrogenase

It have been measured (LDH) in the blood serum by the following the steps of attached with inspection (Kit) provided by(Biolabo) Company mad in France [16].

2.2.5. Measurement of Glutathione Peroxidase

It have been measured (GPx) in the blood serum by the following the steps of attached with inspection (Kit) provided by(Biolabo) Company mad in France [17].

2.2.6. Measurement of Malondialdehyde

It have been measured (MDA) in the blood serum by the following steps of attached with inspection (Kit) provided by(Biolabo) Company mad in France [18].

2.3. Statistical analysis

The data of the samples study were collected and analysed statistically by using program (SAOOS) of windows. Including (Mean ±S.D). The significant differences at level ($P < 0.005$)[19].

3. Results and Discussion

The results in (Figure 1) Showed significant increase in the Cholesterol concentration under levels of (P <0.005) in the smoker students as compared with in other groups, and this agree with results study of [20]. This increase of the Cholesterol concentration might be because high activity Cholesterol transferase responsible about Cholesterol absorption intestine and then induce as a result of oxidative stress which infect B-cell in pancreatic by the effect of reactive oxygen species [21]. On the hand, this results was revealed to the change in the concentration of the cholesterol is caused by the smoking which increase Cholesterol levels in the blood serum. The Smoking increases inflammation in the body when occurs chemicals in cigarette smoke injure cells, causing swelling and interfering with proper cell function. Also, the Smoking causes oxidative stress, a condition that occurs as chemicals from cigarette smoke combine with oxygen in the body [22] and all these reasons causes ledes to damage of cells. Evidence strongly suggests that both inflammation and oxidative stress may be related to an increased risk of diabetes. The Smoking causes rise both of Hypertension and glucose level in the body, so the Smoker people are less response for the insulin and subsequently the glucose rises in their blood causing Hypertension [23].

Table 1. Arithmetic average for studied croups according to the Disease kind and smoking kind (Heavy smokers).

The samples	NO.	Cholesterol mmol /L	Triglyceride mmol /L	HDL mmol /L
Control Group	25	4.2±2.3	1.7±0.3	1.51±0.01
group (diabetic mellitus)	25	6.8±3.5	5.6±3.2	1.02±0.03
group Hypertension	25	7.4±4.6	6.2±4.1	1.03±0.02

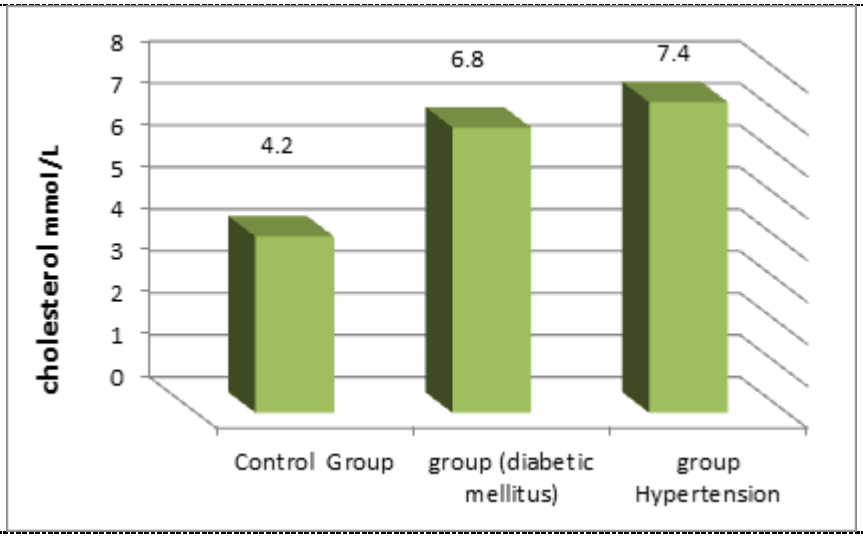

Figure 1. Illustrated the concentration of the cholesterol in the smoker students and compare with in other groups.

The results in (Figure 2) showed significant increase in the triglyceride concentration levels (P <0.005) in the smoker students as compared with in other groups, and this agree with results study of [24]. [25] , during his study on the association between the lipid profile and chronic smoking. Both research above also finded very low levels of HDL, with an increase in the levels of TC, in smokers and these

resulets were an agreement with the finding of our study. Previous studies have reported that smokers have higher serum triglyceride (TG) and blood glucose concentrations and lower high-density lipoprotein cholesterol (HDL-C) concentrations than non-smokers [26]

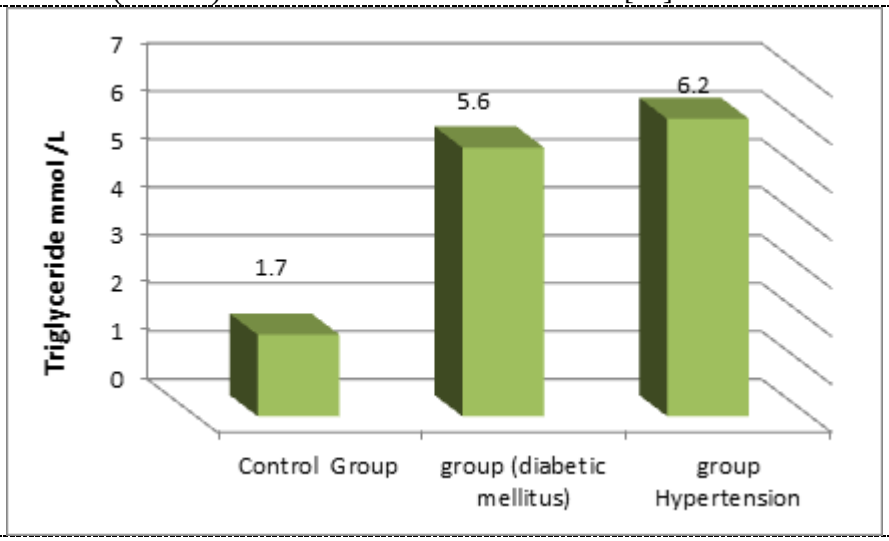

Figure 2. Illustrated the concentration of the triglycerides in the smoking students and compare with in other groups.

The results in (Figure 3) Showed significant decrease in the HDL-Cholesterol concentration levels (P <0.005) in the smoking students as compared with in other groups, smoking is associated with reduced HDL cholesterol levels. Cigarette smoking can alter the critical enzymes of lipid transport, lowering lecithin: cholesterol acyltransferase (LCAT) activity and altering cholesterol ester transfer protein (CETP) and hepatic lipase activity, which attributes to its impact on HDL metabolism and HDL subfractions distribution. In addition, HDL is susceptible to oxidative modifications by cigarette smoking, which makes HDL become dysfunctional and lose its anther protective properties in smokers. Therefore, cigarette smoking has a negative impact on both HDL quantity and function, which can explain, in part, the increased risk of cardiovascular disease in smokers [27, 28].

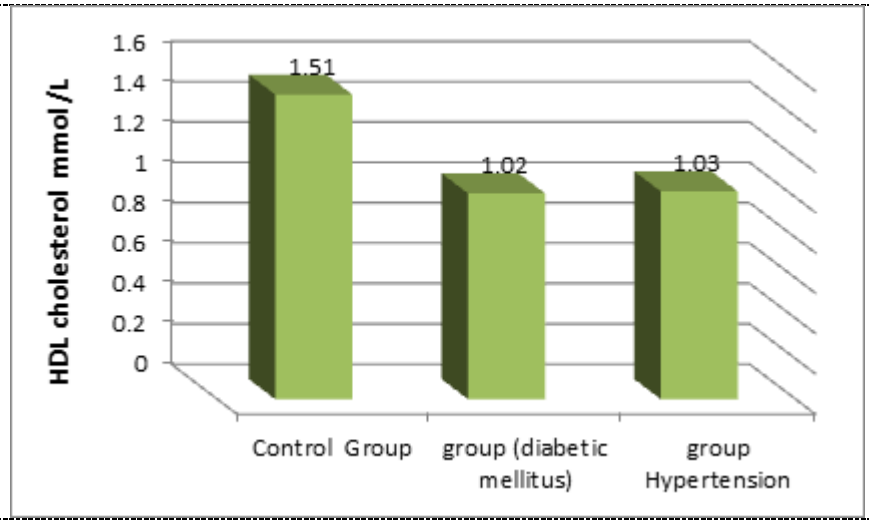

Figure 3. Illustrated the Concentration of the HDL-cholesterol in the smoker students and compare with in other groups.

Table 2. Arithmetic average for studied croups according to the disease kind and smoking kind (Heavy smokers).

The samples	NO.	Malondialdehyde (MDA) ug/l	Lactate dehydrogenase (LDH) u/l	Glutathione Peroxidase (GPx) u/l
Control Group	25	2.65±1.33	181.8±1.02	1.53±0.24
group (diabetic mellitus)	25	5.67±3.2	277.8±133.1	0.191±0.180
group Hypertension	25	6.4±4.1	302±214.2	0.195±0.183

The results in (Figure 4) In this study MDA levels were found to be significantly ($p<0.005$) raised in smokers. High serum levels of MDA in smokers could have amplified production of reactive oxygen species (ROS) which in turn might have accelerated lipid peroxidation manifested by increased levels of MDA, as well as the role of oxidative stress on glucose metabolism in a high-risk of diabetes. ROS can activate specific pathways whose products interfere with insulin signalling, the activation of the redox-sensitive nuclear factor-kappa beta (NF-kB) leads to the expression of cytokines such as temporal necrosis factor α (TNF-α), and interleukins (ILs) such as IL-1α and IL-6 and all these products have a quenching effect on insulin signalling [29, 30, 31].

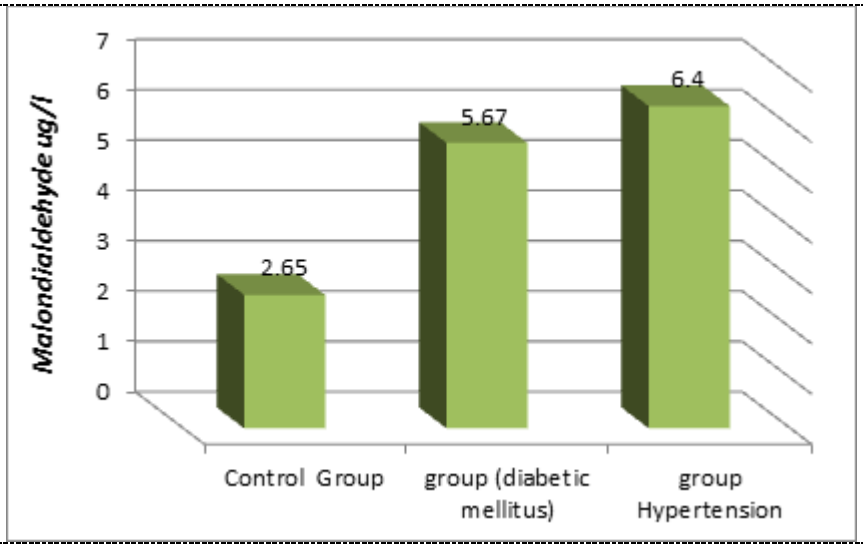

Figure 4. Illustrated the Concentration of the malondialdehyde in the smoker students and compare with in other groups.

While in the (Figure 5) findings showed significantly increasing in LDH level of smoker's group. Lactate dehydrogenase enzyme is found in almost every tissue in the body and its level increase in blood in many tissues damage pathological disorders. We think that the reasons for elevated of LDH significantly due to the smoke chemicals compounds may affect the respiratory tract as well as all of the cells in respiratory system [32]. The increased of LDH considered as indicator of cell necrosis or tissues damage or may be attributed on the smoking induced cell damage anywhere in the body, which may leak cellular contents along with LDH into serum [33]. Elevated of LDH levels is usually considered to reflect cell damage, and this is agree with the bad effect of smoking in generated free radicals and oxidative stress in cell which lead to release more of LDH to the blood stream by cell injury [34].

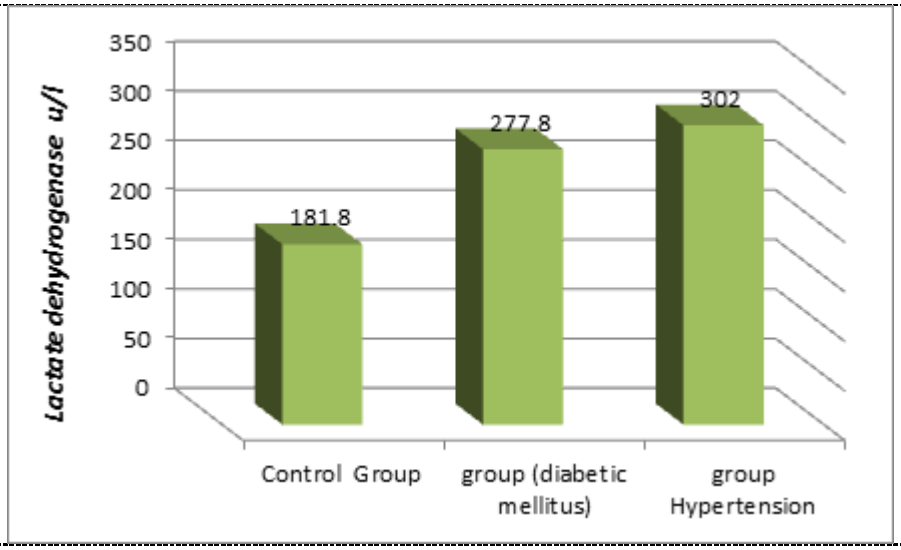

Figure 5. Illustrated the concentration of the lactate dehydrogenase in the smoker students and compare with in other groups.

The results in (Figure 6) showed Glutathione Peroxidase levels were found to be significantly ($p<0.005$) lowered in smokers than in non-smokers. The significantly differences of oxidative enzymes levels GPx may be due to nicotine increased generation of superoxide anion and hydrogen peroxide, which in turn results in generation of hydroxyl free radicals. Generation of these free radicals have been shown to participate in many toxic reaction and increased production of superoxide and hydrogen peroxide may cause deleterious injury to alveolar macrophages by causing release of proteolytic enzymes [35].

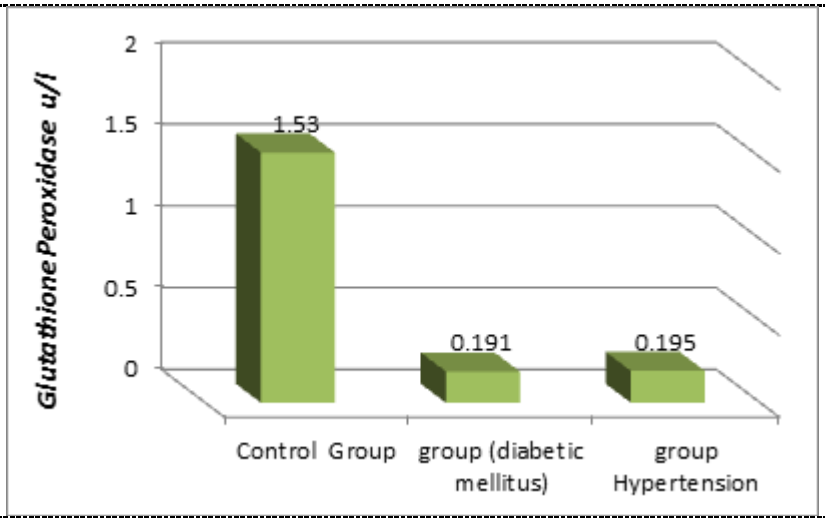

Figure 6. Illustrated the concentration of the glutathione peroxidase in the smoker students and compare with in other groups.

Table 3. Body Mass Index (Kg/m^2) sample of the study.

(BMI)	mean±S.D
Control Group	23.62± 0.52
smoking students	26.23±0.83

Figure (7) shows the relationship of Body Mass Index (BMI) among the studied samples, as there was a statistically significant ($p < 0.05$). The results rates increase between the BMI of smokers' students compared with the control group. Smoking and obesity are major public health challenges and the prevalence of both is increasing globally. Smoking increases the risk of cancer, respiratory and cardiovascular diseases, and is the leading preventable cause of death in developed countries [36]. Obesity is the fifth leading cause of death, globally, and accounts for 44% of cases of diabetes and 23% of ischaemic heart disease [37].

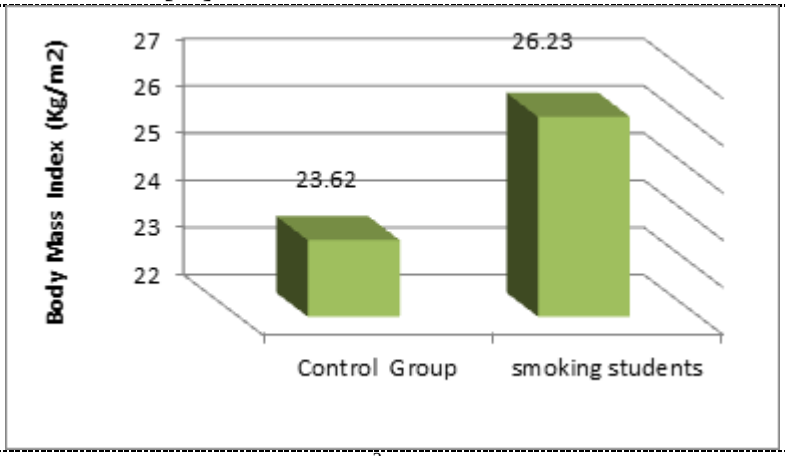

Figure 7. Illustrated the Body Mass Index (Kg/m^2) sample of the study.

4. Conclusion

The smoking effects on the levels of the Cholesterol, Triglyceride, Malondialdehyde (MDA), Lactate dehydrogenase (LDH) (increase) and decrease in the concentration level of (HDL-Cholesterol, Glutathione Peroxidase (GPx) in the smoker students, and smoking effect on the diabetic mellitus, hypertension and Body Mass Index.

5. References

[1] Huang G, Mei X and Hu J 2017 The Antioxidant Activities of Natural Polysaccharides *Curr Drug Targets* **18** 1296.
[2] Elias RJ, Kellerby SS and Decker EA 2008 Antioxidant activity of proteins and peptides *Crit Rev Food Sci. Nutr.* 48 430.
[3] Huang D, Ou B and Prior RLJ 2005 The chemistry behind antioxidant capacity assays *Agric Food Chem.* **53** 1841.
[4] Neha K, Haider MDR, Pathak A and Yar MS 2019 Medicinal prospects of antioxidants: A review *Eur. J. Med. Chem*. **178** 687.
[5] Herzberg G 1971 *The spectra and structures of simple free radicals* ISBN 0-486-65821-X..
[6] Halliwell B 1994 Antioxidants, and Human Disease: Curiosity, Cause, or Consequence *Lancet* **344** 721.
[7] Halliwell B 2012 Free radicals and antioxidants: updating a personal view *Nutr. Rev.* **70** 257.
[8] Halliwell B 2007 *Free Radicals in Biology and Medicine* 4th ed. Oxford, UK: Oxford University Press.
[9] Gboyega EA, Adesegun JK and Chikezie UE 2013 Tobacco smoking and awareness of smoking cessation products in a University community *J. Public Health Epidemiol*. **5** 351.
[10] World Health Organization (WHO) (2002) *The World Health Organization Report reducing risks, promoting health life*. Geneva, Switzerland..
[11] Gandhi KK, Foalds J and Steinberg MB 2009 Lower Quit rates among African American and Latino menthol cigarette smokers at a tobacco treatment clinic *Int. J. Clin. Pract.* **63** 360.

[12] Akpotuzor JO, Udoh AE and Etukudo H 2012 Total antioxidant status and other antioxidant agent levels in children with *P. falciparum* infection in Calabar, Nigeria *Int. J. Biomed. Lab. Sci*.**1** 35.
[13] Chundru VN and Ram MM 2013 Study of oxidant enzymes superoxide dismutase and glutathione peroxidase levels in tobacco chewers and smokers A pilot study. *J Cancer Res Ther* **9** 210.
[14] Tietz NW 1999 *Textbook of clinical Chemistry* 3rd Ed. Buetis, CA, Ashwood ER and Saundersp WB 809.
[15] Fossati P and Prencipe L 1982 Serum Triglycerides Determined Colorimetrically with an Enzyme that Produces Hydrogen Peroxide *Clin. Chem*. **28** 2077.
[16] Tietz NW and Berger S 1970 *Fundamentals of clinical chemistry* Philadelphia Saunders 446.
[17] Cunningham-Rundles S 1991 Zinc modulation of immune function: specificity and mechanism of interaction *J. Lab. Clin. Med*. **128** 9.
[18] Guidet B and Shah SV 1989 England in vivo H_2O_2 generation by rat kidney in glycerol-induced renal failure *Am. J. Physiol*. **257** 440.
[19] Kirkwood BR 1988 *Medical statistical* Black well scientific publications Oxford 1st ed. 39.
[20] Ledingham J and Warell D 2000 *Concise oxford text book of medicine oxford university press* Oxford London 718.
[21] Grimm MOW, Regner L, Mett J, Stahlmann CP, Schorr P, Nelke C, Streidenberger O, Stoetzel H, Winkler J, Zaidan SR, Thiel A, Endres K, Grimm HS, Volmer DA and Hartmann T 2016 Tocotrienol Affects Oxidative Stress, Cholesterol Homeostasis and the Amyloidogenic Pathway in Neuroblastoma Cells: Consequences for Alzheimer's Disease *Int. J. Mol. Sci*. **17** 1809.
[22] Chung KF 2005 Inflammatory mediators in chronic obstructive pulmonary disease *Curr. Drug Targets Inflamm. Allergy* **4** 619.
[23] Kawakami N, Takatsuka N, Shimizu H and Ishibashi H 1997 Effects of smoking on the incidence of non-insulin-dependent diabetes mellitus". Replication and extensions in a Japanese cohort of male employees *Am J Epidemiol*. **145** 103.
[24] Håglin LM, Törnkvist B and Bäckman LO 2014 High serum phosphate and triglyceride levels in smoking women and men with CVD risk and type 2 diabetes *Diabetol Metab Syndr*. **6** 39.
[25] Neki NS 2002 Lipid profile in chronic smokers *JIACM*. **3** 51.
[26] Craig WY, Palomaki GE and Haddow JE. 1989 Cigarette smoking and serum lipid and lipoprotein concentrations": an analysis of published data *BMJ*. **298** 784.
[27] Soran H, Hama S, Yadav R and Durrington PN 2012 HDL functionality *Curr. Opin. Lipidol.* **23** 353.
[28] Ambrose JA and Barua RS 2004 The pathophysiology of cigarette smoking and cardiovascular disease: An update *J. Am. Coll. Cardiol*. **43** 1731.
[29] Chaitanya KV, Pathan AAK, Mazumdar SS, Chakravarthi GP, Parine N and Bobbarala V 2010 Role of oxidative stress in human health: An overview *J Pharm Res*. **3** 1330.
[30] Kashinakunti SV, Kollur P, Kallaganada GS, Rangappa M and Ingin JB 2011 Comparative study of serum MDA and vitamin C levels in non-smokers, chronic smokers and chronic smokers with acute myocardial infarction in men *J. Res. Med. Sci.* **16** 993.
[31] Rahman T, Hosen I, Islam MMT and Shekhar HU 2012 Oxidative stress and human health *Adv. Biosci. Biotechnol.* **3** 997.
[32] Madole MB, Dilip B, Mamatha MT and Ankur P 2016 Study of serum lactate dehydrogenase and lipid profile in patients with chronic cough *Int. J. Clin. Biochem. Res*. **3** 409.
[33] Pannuru P, Vaddi DR and Nallanchakravarthula V 2009 Influence of chronic cigarette smoking on serum biochemical profile in male human volunteers *J. Health Sci*. **55** 265.
[34] Robert L, Smith MD, Carolyn SR and Milena LL 1988 Elevated Lactate dehydrogenase values in patients with pneumocystis *Carinii pneumonia Chest* **95** 987.
[35] Yildiz D 2004 Nicotine, its metabolism and overview of its biological effects *Toxicon* **43** 619.

[36] Doll R, Peto R, Boreham J and Sutherland I 2004 Mortality in relation to smoking 50 years' observations on male British doctors *BMJ* **328** 1519.
[37] Dvorak RD, Del Gaizo AL, Engdahl RM and Eliason CJ 2009 Tobacco use and body mass index: mediated effects through physical inactivity *J. Health Psychol*. **14** 919.

New record of fresh water ciliates (Protozoa, Ciliophora) from Tigris river in Baghdad city, Iraq

New record of fresh water ciliates (Protozoa, Ciliophora) from Tigris river in Baghdad city, Iraq

Zahraa Y. Kadhim[1*]

[1]Department of Research & Development, Ministry of Higher Education & Scientific Research, Baghdad, Iraq.

*E-mail: zahraa.yahia76@gmail.com

Abstract. Documenting the biodiversity and biogeography of ciliates will help expand the overall knowledge within the field, as well as, shed new light on the dispersal and survival potential for other microorganisms, such as protists. As organisms at the base of food webs, ciliates are an essential part of the microbial loop and the ecosystems that they support. This study deals with ciliates community in freshwater of Tigris river within Baghdad city. Four sites were chosen at Al-Grea`t & Al-Adhamiya area at the riverbank. Total of 44 ciliophora taxa were detected, 22 taxa of which were identified to the species level and 22 taxa to the genus level. Among them, 11 taxa were new recording for Tigris river in Baghdad city: *Cyrtolophosis* sp., *Monochilum frontatum*, *Orborhabdostyla bromelicola*, *Ophrydium sessile*, *Scyphidia* sp., *Vortecilla convallaria*, *Vortecilla octava*, *Zoothamnium Bory*, *Tokophrya lemnarum*, *Urostyla* sp. and *Stentor fluiginosus*.

Keywords. Protists, Ciliates community, Tigris river, Ciliophora taxa.

1. Introduction

The Ciliates are unicellular microscopic eukaryotes moving with hair-like projections called cilia [1]; they have appropriate characteristics that being a large group found in all aquatic environments [2]; the short duration of their life cycle with high average of reproduction and authorized detection of environmental impacts in a short period [3]. Ciliates are the most prominent and major group of eukaryotic [4] which occur in alternative kind of environments, wherever there are moisture, sufficient nutrients and suitable microhabitats [5]. These organisms are found from the poles to the equator, in hot springs and in sea ice, in tropical forest litter and desert soils, in major oceans to the small temporary ponds and flooded regions of the inland waters [6, 7, 8, 9, 10, 11, 12, 13, 14]. Many studies showed that obviously ciliated protozoa are components of many microhabitats [15, 16]. The phylum Ciliophora is an ancient group, present on the earth for hundreds of millions of years [17]. Ciliates have an importance in total ecosystem function in some environments because they are the top predators in the microbial food webs [18, 19, 20], and they have a role in microbial loop [1, 9, 41]. Furthermore, ciliates are effective bioindicators of freshwater environments and they can be used in biomonitoring of streams, reservoirs and lakes under different scales of anthropogenic impact [21, 22, 23]. In addition, they are reducing conditions or indicative of oxidizing in the decomposition of

organic matter, share in phosphorus and nitrogen cycling, sensitive to different concentrations of pollutants and have high taxonomic density, providing responses to different levels of contamination [24]. In spite of their broad functionality, taxonomic diversity, and ability to gain large population densities in a short period of time [25], the structure and geographical distribution of ciliate communities is still uninvestigated in many regions of the world [26, 27] and poses an obstruction for studies of ciliate biogeography. Research into ciliates are differential biased to institutions of the researchers and their sampling areas mostly in Northern Europe [28]. There are over 1,100 ciliates genera and over 8,000 species included in these genera [29]; in spite of some argue that this diversity might represent only 10% of the actual diversity of species [28]. The mainly aim of this study was to document and record ciliates species which could be new recording in Tigris river at Baghdad city.

2. Materials and Methods

2.1. The study area and Methodology

This study deals with ciliates community in freshwater of Tigris river within Baghdad city that is located in the Mesopotamia alluvial plain between latitudes 33°14°- 33° 25° N and longitudes 44° 31°- 44° 17° E. Four sites were chosen at Al-Grea`t and Al-Adhamiya area at the riverbank (Figure 1). These sites are located close to the residential, agricultural and restaurants area within Baghdad city, thus, there is a lot of water utilization such as transportation purposes, household usage, agricultural usage and restaurant waste. Variable species of vegetation (reeds and wild grasses) were observed to grow at S4, while the remaining three sites was paved at the edges of the river. Monthly intervals, three samples were collected from each site of the riverbank over a period from June to September 2020, and each sample was 60 liters of water which was horizontally taken from the water surface with the aid of plankton net. This net made of bolting cloth with a fine mesh size (40 µm), with a small bottle container of 30 ml capacity attached to its narrow end [30].

2.2. Water samples

During the period of study (48), the fresh water samples were examined. One milliliter from each collecting water sample was investigated within 5-48 hours [31, 32, 33] by direct observation. All samples were examined alive [33] with the aid of compound microscope (Olympus, Japan) at a magnification of (X10- X40), and identification guides by [31, 34, 35, 36]. The classification of ciliates were followed [29]. Each species was photographed using camera (Casio). All of the photographs presented here are digitally processed (cropped, resized, contrast enhanced, white balance corrected, and background removed).

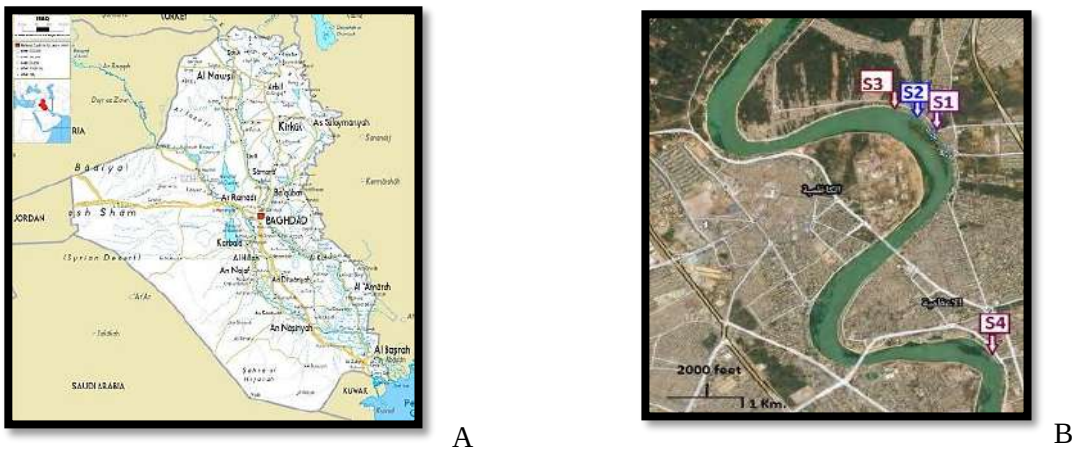

A B

Figure 1. The map of Iraq shows the sampling area at A. Ocular micrometer was used for specimens

measuring, B. Tigris river within Baghdad city.

3. Results and Discussion

Total of 44 ciliophora taxa were detected; 22 taxa of which were identified to the species level and 22 taxa to the genus level (table 1). Among them 11 taxa were new recording for Tigris river in Baghdad city, while the remaining previously recorded by [37]. Number of recording species in the present study was lower than [38], who recorded 208 ciliates species in Argentina; [39] recorded 84 cilites species from Southern Brazil and [40] recorded 63 cilites species from Tigris river in Baghdad city, while it was higher than [41] who recorded 7 ciliates species from Salim Ali Lake in Aurangabad. The lower number of ciliates were recorded in the present study could be refer to both limited of investigated area and limited duration of this work. Some taxa are rare in one environment could be abundant in others and the species which are rare under certain environment conditions could become abundant when the chemical, physical and biological inconsistent of their habitat are change. Despite it's not known if there are some species which are always rare in every suitable environment [42]. The new recording ciliophora taxa in Tigris river within Baghdad city are: *Cyrtolophosis* sp., *Monochilum frontatum*, *Orborhabdostyla bromelicola*, *Ophrydium sessile*, *Scyphidia* sp., *Vortecilla convallaria*, *Vortecilla octava*, *Zoothamnium bory*, *Tokophrya lemnarum*, *Urostyla* sp. and *Stentor fluiginosus*.

Table 1. The taxonomy of the species in phylum ciliophora (Doflein, 1901) were recorded from freshwater of Tigris river at four investigated sites during the study period from June to September 2020.

No.	Protozoa taxa	Class	Order	Family
1.	**Cyrtolophosis* sp. Stokes,1885	Colpodea	Cyrtolophosidida	Cyrtolophosididae
2.	*Lacrymaria olar* Müller,1786	Litostomatea	Haptorida	Lacrymariidae
3.	*Litonotus* sp. Wrzesniowski,1870		Pleurostomatida	Litonotidae
4.	*Pseudomicrothorax* sp. Mermod,1914	Nassophorea	Microthoracida	Pseudomicrothoracidae
5.	**Monochilum frontatum* Schewiakoff,1893	Oligohymenophorea	Tetrahymenida	Glaucomidae
6.	*Frontonia* sp. Ehrenberg, 1838		Peniculida	Frontoniidae
7.	*Paramecium aurelia* Müller, 1773			Parameciidae
8.	*Paramecium caudatum* Ehrenberg,1833			
9.	*Paramecium multimicronucleatum* Powers& Mitchell,1910			
10.	*Epistylis* sp. Ehrenberg,1830		Sessilida	Epistylididae
11.	* *Orborhabdostyla bromelicola* nov. Spec.			Operculariidae
12.	**Ophrydium sessile* Ehrenberg,1830			Ophrydiidae
13.	**Scyphidia* sp. Dujardin,1841			Scyphidiidae
14.	*Cothurnia* sp. Ehrenberg,1831			Vaginicolidae
15.	*Pyxicola affinis* Kent, 1881			
16.	*Thuricola* sp. Kent, 1881			
17.	*Vaginicola* sp. Lamarck,1816			
18.	*Carchesium* sp. Ehrenberg,1831			Vorticellidae
19.	*Vortecilla* sp. Linnaeus,1767			
20.	*Vortecilla campanula* Ehrenberg,1831			
21.	**Vortecilla convallaria* Linnaeus,1758			
22.	*Vortecilla microstoma* Ehrenberg,1830			
23.	**Vortecilla octava* Stokes,1885			

No.	Protozoa taxa	Class	Order	Family
	(*V. striata* Dujardin,1841)			
24.	*Vortecilla picta* Ehrenberg,1831			
25.	**Zoothamnium* Bory de St. Vincent,1824			Zoothamniidae
26.	*Cinetochilum* sp. Perty,1849		Philasterida	Cinetochilidae
27.	*Cyclidium* sp. Müller, 1773		Pleuronematida	Cyclidiidae
28.	*Chilodonella* sp. Strand,1928	Phyllopharyngea	Chlamydodontida	Chilodonellidae
29.	*Acineta* sp. Ehrenberg,1834		Endogenida	Acinetidae
30.	**Tokophrya lemnarum* Stein,1859			Tokophryidae
31.	*Sphaerophrya sp.* Claperède & Lachmann 1859		Exogenida	Podophryidae
32.	*Coleps hirtus* Müller,1786	Prostomataea	Prorodontida	Colepidae
33.	*Prorodon* sp. Ehrenberg,1834			Prorodontidae
34.	*Euplotes* sp. Ehrenberg,1831	Spirotrichea	Euplotida	Euplotidae
35.	*Strombidium* sp. Claperède & Lachmann 1859		Strombidiida	Strombidiidae
36.	*Halteria* sp. Dujardin,1841		Sporadotrichida	Halteriidae
37.	**Urostyla* sp. Ehrenberg,1830		Urostylida	Urostylidae
38.	*Spirostomum ambiguum* Ehrenberg, 1834	Heterotrichea	Heterotrichida	Spirostomidae
39.	*Spirostomum minus* Roux, 1901			
40.	**Stentor* sp. Oken			Stentoridae
41.	**Stentor fluiginosus* Forbes,1891			
42.	*Stentor niger* Müller, 1773			
43.	*Stentor polymorphus* Müller, 1773			
44.	*Loxodes magnus* Stokes, 1887	Karyorelictea	Loxodida	Loxodidae

Note:* new recording species

3.1. Description and Photographs of the new recording species obtained during the study period (from June to September 2020)

3.1.1. Cyrtolophosis sp. Stokes, 1885

Small species, ovoid to pyriform in shape. Somatic ciliation uniform in longitudinal rows curving a little down the body and there is an anterior tuft of cilia in some species. The oral aperture within a shallow groove in the anterior third of the cell, and some species produce gelatinous tubes. Spherical macronucleus located centrally, and the contractile vacuole is in posterior third of body. Feeds on bacteria; Length of cell less than 40 μm as shown in Figure 2.

3.1.2. Monochilum frontatum Schewiakoff, 1892

Medium to large species (60-200 μm long), ellipsoid to elongate ovoid in shape. Oral aperture occurs in the anterior body half usually about a quarter of the cell length from the apical end, oval in outline and leads to a conical buccal cavity. There is an undulating membrane on the right and a prominent membranelle on its left of the oral aperture. In the posterior body half there is a contractile vacuole, usually near the equator. Ovoid macronucleus is locate centrally. Anterior end is broader, ventrally flattened, dorsally slightly convex, macronucleus is ellipsoid, feeds on algae. As shown in Figure 3.

3.1.3. Orborhabdostyla bromelicola nov. Spec

Narrowly conical, more or less asymmetrical. Size about (50–75 × 13–18) μm in vivo, with stalk-like narrowed usually less than 10 μm long and 2 μm wide. Cytoproct and Contractile vacuole on dorsal

wall of vestibulum slightly posterior of oral bulge. Peniculus 2 shortened posteriorly. Highly contractile. Fresh water cell. As shown in Figure-4.

3.1.4. Ophrydium sessile Ehrenberg, 1830

Cell body is long and contractile, in gelatinous matrix and posterior end rounded or pointed. As shown in Figure 5.

3.1.5. Scyphidia sp. Dujardin, 1841

Body drawn out, some species seem stalklike at rear, peristomal disc not stalked. There is no trochal band when mature, macronucleus often C-shaped and long. Cell body length about 60 μm. As shown in Figure 6.

3.1.6. Vortecilla convallaria Linnaeus

Body with bell-shaped; length (30-120) μm, width (35-70) μm, peristome width is (55-75) μm and stalk length is (100-500) μm. The animal never looks dark, but it is often yellow-tinted because there are (no) or (a few) darkishlooking refractile granules; the peristomal area is narrower than in V. campanula; the pellicle annulation is easily visible; contractile vacuole is one nearby the buccal cavity, food vacuole within oval contour as shown in Figure 7.

3.1.7. Vortecilla octava Stokes (V. striata Dujardin, 1841)

Vase-like shape, body length is 20-60 μm, width is 15-40 μm, peristome width is 13-40 μm and stalk length 20-300 μm. Vortecilla octava is similar to V. microstoma but smaller than it. The macronucleus lies transversal to the longitudinal axis, the peristome border shows much variation and it is thicker than in *V. microstoma*. Cytoplasm translucent or a little misty white, pellicle annulations pretty distinct, about 25-40 striae, surface of body a little ribbed, macronucleus sausage-like and thick, contractile vacuole is one nearby the buccal cavity as shown in Figure 8.

3.1.8. Zoothamnium Bory de St. Vincent, 1826

Resemble to *Carchesium*, but myonemes of all stalks of a colony are continuous together, so that the entire colony contracts or expands with each other, fresh or salt water, colonies some millimeters high. As shown in Figure 9.

3.1.9. Tokophrya lemnarum Bütschli

Pyramidal or pyriform, with no lorica, tentacles order in 1-4 fascicles on anterior surface, stalk not tough, endogenous budding is simple, fresh water. Tentacles emerge from distal, bullbous processes, about (70-260) μm as shown in Figure10.

3.1.10. Urostyla sp. Ehrenberg, 1830

Ellipsoid with 2 or more right marginal cirri (files). Pliable, posterior rounded, ventral surface is flatten with (4-10) rows of cirri, 2 marginal rows, (5-12) anals and 3 or more frontals as shown in Figure 11.

3.1.11. Stentor fluiginosus Forbes, 1891

Cylindrical or trumpet-shaped (when extended), contractile vacuole anterior-left; highly contractile; some with mucilaginous lorica; conspicuous peristomal field frontal, several micronuclei and a single macronucleus; cortical and cytoplasmic granules coloured with yellow-brown or red-orange. Body length is (200-300) μm when fully extended; freshwater cell as shown in Figure 12.

Figure 2. *Cyrtolophosis* sp.

Figure 3. *Monochilum frontatum.*

Figure 4. *Orborhabdostyla bromelicola*.

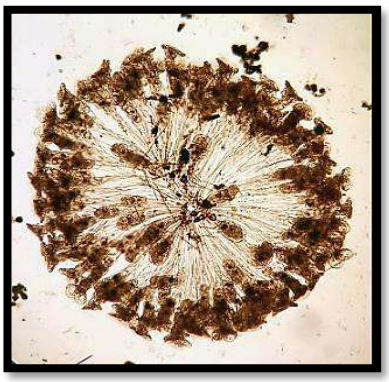

Figure 5. *Ophrydium sessile.*

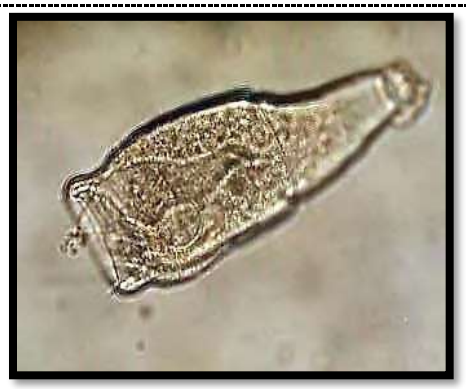

Figure 6. *Scyphidia* sp.

Figure 7. *Vortecilla convallaria*.

Figure 8. *Vortecilla octava*.

Figure 9. *Zoothamnium bory*.

Figure 10. *Tokophrya lemnarum*

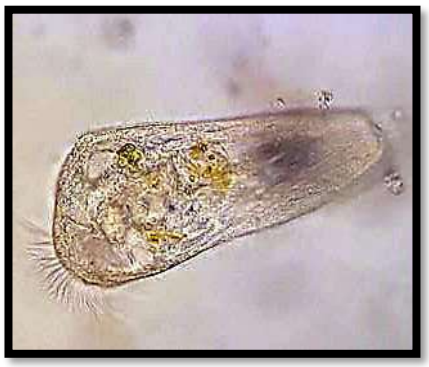

Figure 11. *Urostyla* sp.

Figure 12. *Stentor fluiginosus*.

4. Conclusion

A total of 44 ciliophora taxa were detected; 22 taxa of which were identified to the species level and 22 taxa to the genus level. Among them 11 taxa were new recording for Tigris river in Baghdad city: *Cyrtolophosis* sp., *Monochilum frontatum*, *Orborhabdostyla bromelicola*, *Ophrydium sessile*, *Scyphidia* sp., *Vortecilla convallaria*, *Vortecilla octava*, *Zoothamnium bory*, *Tokophrya lemnarum*, *Urostyla* sp. and *Stentor fluiginosus*.

5. References

[1] Lynn D 2008 *The ciliated protozoa: characterization, classification, and guide to the Literature* (3rd edition). New York. Springer Science &Business Media.
[2] Zingel P 2005 Vertical and seasonal dynamics of planktonic ciliates in a strongly stratified hypertrophic lake. *Hydrobiologia* **547** 163.
[3] Grolière CA, Chakli R, Sparagano O and Pepin D 1990 Application de la colonization d'un substrat artificial par les ciliés à l'étude de la qualité des eaux d'une rivière *Europ. J. Protistol*. **25** 381.
[4] Buitkamp U 1979 Vergleichende Unter suchungen zur Temperaturadaptation von Bodenciliaten aus klimatisch verschiedenen Regionen *Pedobiologia* **19** 221.
[5] Hattori T 1994 *Soil microenvironment* Soil Protozoa, (eds) Darbshire, J CAB International, UK, 43.
[6] Foissner W 1995 Tropical protozoan diversity: 80 ciliate species (Protozoa: Ciliophora) in a soil sample from a trophical dry forest of Costa Rica, with descriptions of four new genera and seven new species *Arch. Protistenk* **145** 37.
[7] Foissner W 1997 Soil ciliates (Protozoa: Ciliophora) from evergreen rain forest of Australia, South America and Costa Rica: diversity and description of new species *Biol. Fertil. Soils* **25** 317.
[8] Foissner W 1997 Faunistic and taxonomic studies on ciliates (Protozoa, Ciliophora) from clean rivers of Bavaria (Germany), with descriptions of new species and ecological notes, *Limnologica* **27** 179.
[9] Esteban G and Finlay B 2015 *Thorp & Covich's Freshwater Invertebrates*, (4th) edition, Volume I.: Ecology and General Biology San Diego, CA. Academic Press, Elsevier.
[10] Foissner W 1999.Notes on the soil ciliate biota (Protozoa, Ciliophora) from the Shimba Hills in Kenya (Africa): diversity and description of three new genera and ten new species *Biodivers. Conserv*. **8** 319.
[11] Foissner W 2000 A compilation of soil and moss ciliates (Protozoa: Ciliophora) from Germany, with new records and descriptions of new and insufficiently known species *Europ. J. Protistol*. **36** 53.
[12] Foissner, W, Agatha S and Berger H 2002 Soil ciliates (Protozoa, Ciliophora) from Namibia (Southwest Africa) with emphasis on two contrasting environments, the Etosha region and the Namib Desert *Biologiezentrum der Oberösterreichischen Landesmuseums Denisia* **5** 1459.
[13] Foissner W 2004 Some new ciliates (Protozoa, Ciliophora) from an Austrian floodplain soil, including a giant, red "flagship", *Cyrtohymena* (Cyrtohymenides) *aspoecki* nov. subgen, nov. spec *Denisia* **13** 369.
[14] Laybourn-Parry J.1992 *Protozoan planktonecology* Chapman and Halm, 2-6 Boundary Row, London.
[15] Fenchel T 1987 *Ecology of Protozoa: the Biology of free-living phagotrophic protists* Madi-son: Science Tech. Publishers..
[16] Laybourn-Parry J 1984 *A functional biology of free-living protozoa* University of California Press, Berkeley.
[17] Bomfleur B, Kerp H, Taylor N, Moestrup Ø and Taylor E 2012 Triassic leech Cocoon from Antarctica contains fossil bell animal *Proc. Nat. Acad. Sci.* **109** 20971.
[18] Finlay B and Esteban G 1998 Freshwater protozoa: biodiversity and ecological function. *Biodivers. Conserv.* 7 1163.
[19] Xu Y, Vick-Majors T, Morgan-Kiss R, Priscu J and Amaral-Zettler L 2014 Ciliate diversity, community structure, and novel taxa in lakes of the McMurdo Dry Valleys, Antarctica *Biol. Bull.* **227** 175.
[20] Schmid-Araya J, Schmidt P, Tod S and Esteban G 2016 Trophic positioning of meiofauna revealed by stable isotopes and food-web analyses *Ecology* **97** 3099.

[21] Paiva TS and Silva-Neto ID 2004 Ciliate protists from Cabiúnas lagoon (restinga de Jurubatiba, Macaé, Rio de Janeiro) with emphas is on water quality indicator species and description of Oxytricha marcili sp. n. *Braz. J Biol. Revista Brasileira de Biol.* **64** 465.
[22] Madoni P 2005 Ciliated protozoan communities and saprobic evaluation of water quality in the hilly zone of some tributaries of the Po River (northern Italy) *Hydrobiologia* **541** 55.
[23] Dias RJP, Wieloch AH and D'agosto M 2008 The influence of environmental characteristics on the distribution of ciliates (Protozoa, Ciliophora) in an urban stream of southeast Brazil. *Braz. J Biol. Revista Brasileira de Biol.*, **68** 287.
[24] Paerl HW, Dyble J, Moisander PH, Noble RT, Piehler MF, Pinckney JL, Steppe TF, Twomey L and Valdes LM 2003 Microbial indicators of aquatic ecosystem change: current applications to eutrophication studies. *Microb. Ecol.* **46** 233.
[25] Finlay B and Fenchel T 1986 *Physiological ecology of the ciliated protozoon Loxodes* Aquatic Commons,73-96
[26] Foissner W 1987 Soil protozoa: fundamental problems, ecological significance, adaptations in ciliates and testaceans, bioindicators, and guide to the literature. *Progr. Protistol* **2** 69.
[27] Clamp J and Lynn D 2017 Investigating the biodiversity of ciliates in the 'Age of Integration *Europ. J. Protistol.* **61** 314.
[28] Foissner W, Chao A and Katz L 2008 Diversity and geographic distributions of ciliates (Protista: Ciliophora). *Biodivers. Conserv.* **17** 345
[29] Azam F, Fenchel T, Field J, Gray J, Meyerreil L and Thingstad F 1983 The ecological role of water-column microbes in the sea. Marine ecology progress series *Oldendorf* **10** 257.
[30] Ibrahim S and Abdullah BA 2008 Effect of lead on zooplankton dynamics in Challawa river, Kano state, Nigeria. *Bajops* **1** 88.
[31] Corliss JO 1979 *The Ciliated Protozoa: Characterization, Classification, and Guide to the Literature* (2nd ed). Pergamon Press, Oxford and New York.
[32] Foissner W 1987 Soil protozoa: fundamental problems, ecological significance, adaptations in ciliates and testaceans, bioindicators, and guide to the literature *Progr. Protistol* **2** 69.
[33] Senler,NG and Yildiz I 2004 Faunistic and morphological studies on ciliates (Protozoa, Ciliophora) from a small pond, with responses of ciliate populations to changing environmental conditions *Turk J. Zool*. **28** 245.
[34] Kudo RR 1966 *Protozology* 5th ed. Spring- field III Thomas..
[35] Bick H1972 *Ciliated Protozoa*. World Health Organization. Geneva.
[36] Foissner WN Blake K, Wolf HW, Breiner and Stoeck T 2010 Morphological and Molecular Characterization of Some Peritrichs (Ciliophora: Peritrichida) from Tank Bromeliads, Including Two New Genera: Orborhabdostyla and Vorticellides *Acta Protozool*. **48** 291.
[37] Kadhim ZY and Mahmood SH 2013 *Ecological and taxonomic study of protozoa community in the east bank of river Tigris within Baghdad city* MSc. thesis, collage of Science, University of Baghdad, Iraq.
[38] Küppers, GC and Claps MC 2012 *Freshwater ciliates (Protozoa, Ciliophora) from Argentina: an annotated and updated compilation* 61–100 In: Thangadurai D, Busso, CA, Abarca Arenas LG and Jayabalan S (Eds.) Frontiers in Biodiversity Studies. New Delhi, India, IK International Publishing..
[39] Debastiani C, Meira BR, Lansac-Tôha FM, Velhoand LFM and Lansac-Tôha FA 2016 Protozoa ciliates community structure in urban streams and their environmental use as indicators *Braz. J. Biol.* **76**.
[40] Shaikh JD, Shaikh TT, Kamble UP, Jadhav TJ and Kazim M 2012 Studies on some free living protozoan from Salim Ali lake.Aurangabad. *Int. Multidiscipl. Res. J.* **2** 27.
[41] Weisse T 2014 Ciliates and the rare biosphere- community ecology and population dynamics *J. Eukaryot. Microbiol.* **61** 419-433.
[42] Weisse T 2017 Functional diversity of aquatic ciliates *Europ. J. Protistol.* **61** 331.

Histomorphological study of olfactory organ in rock dove, *Columba livia* Gmelin, 1789

Histomorphological study of olfactory organ in rock dove, *Columba livia* Gmelin, 1789

Hussain A. M. Dauod[1*], Ahmad A. Hussain[2] and May F. Al- Habib[3]

[1]Al-Rasheed University College, Baghdad, Iraq.
[2]Al-Qasim Green University, Iraq.
[3]Al-Nahrain University, Iraq.

*E-mail: dr.hussain355@gmail.com

Abstract. The present study aimed to investigate the morphological description and histological structure of olfactory organ in rock dove (*Columba livia*).Results of the present study revealed that the nasal cavity of the species under investigation is anteriorly located, starting with a pair of external nares which located at the dorsal side of the base of upper beak . The external nares lead to two short nasal cavities. Each nasal cavity consist of three conchae or turbinates represented by anterior or vestibular concha, middle or respiratory concha and posterior or olfactory concha. The nasal cavity ended by a pair of internal nares which opened at mouth cavity. Results related with the histological structure of olfactory organ revealed that the vestibular concha lined by stratified squamous epithelium, the respiratory concha lined by ciliated pseudostratified columnar epithelium, and olfactory concha lined by ciliated pseudostratified columnar epithelium. The last concha showed three types of differentiated cell represented by basal cells, supporting cells, and receptor cells.

Keywords. Olfactory organ, Rock Dove, Morphology, Histology.

1. Introduction

The olfactory organs of vertebrates play an important role for feeding, reproduction, behavior and migration [1, 2, 3]. All vertebrates have olfactory regions which are represented by an internal invagination of the ectoderm to form the olfactory sacs in fish and the lining of nasal passages in tetrapoda [1, 2]. The avian olfactory organs are differ in different species of birds according to the differences of their position at the beak, feeding and behavior [4]. Generally the olfactory organs are located at the base of the beak or in some species of birds at the anterior end of beak [5], they are opened to outside via the external nares which leads to the nasal cavity, while they are opened in the mouth or oral cavity via the internal nares [1, 2, 5]. The ability of olfaction in birds is differ according to the structure of olfactory organs and the environment in which birds live [4, 7]. Review of the literature revealed that there are almost lack information related with olfactory organs of Iraqi birds with the exception of [7] on the morphology and histology of olfactory organ in local chicken, and the study of [8] who studied the cellular differentiation in the olfactory epithelium in chick embryo .This situation support our suggestion to investigate the olfactory organ in rock dove (*Columba livia*). This

study is a part of an extensive study conducted to investigate the olfactory organs in several Iraqi vertebrates in addition to the current study [7, 9, 10].

2. Materials and Methods

A total of 16 birds were collected from Al-Madhatia region /Babylon province. The olfactory organs removed after dissection the head of animals [11]. Paraffin wax methods were used for histological study according to the methods of [12].

3. Results and Discussion

3.1. Morphological description

Results of the present study revealed that the olfactory organ in bird under investigation started with two external nares which located at the dorsal surface of the upper beak base. The opening of external nares appear as a longitudinal slits with about (6 mm) length, they are covered by a keratinized flaps and the distance between them was (2.5-3.0 mm) (Figure 1 and 2).Each external naris lead to the nasal cavity. The nasal cavity was cone-like, with confined anterior part and wide posterior part, separated into left and right halves by incomplete cartilaginous septum. Each nasal cavity in the bird under investigation consist of three conchae or turbinates, which were respectively situated in the anterior, middle, and posterior parts of nasal cavity, their internal surface being covered with mucosa. The anterior concha represented the vestibular region of the nasal cavity, the middle concha represented the respiratory region of nasal cavity, and the posterior concha represented the olfactory region of the nasal cavity (Figure 3). The nasal cavity ended by a pair of internal nares, which are (5-6mm) in length and located in a V-shaped slit situated at the roof of the mouth cavity (Figure 4). The olfactory region attached to the olfactory bulb via the first cranial nerve (I-Olfactory nerve) (Figure 5). The olfactory bulb is triangular- shaped and situated at the anterior end of brain at eye level, which mean that the olfactory bulb of the studied bird is pedunculated bulb.

Figure 1. Dorsal view of the head showing the position of external nares (→).

Figure 2. Lateral view of head showing the external naris and flap, (B) beak,(F) flap.

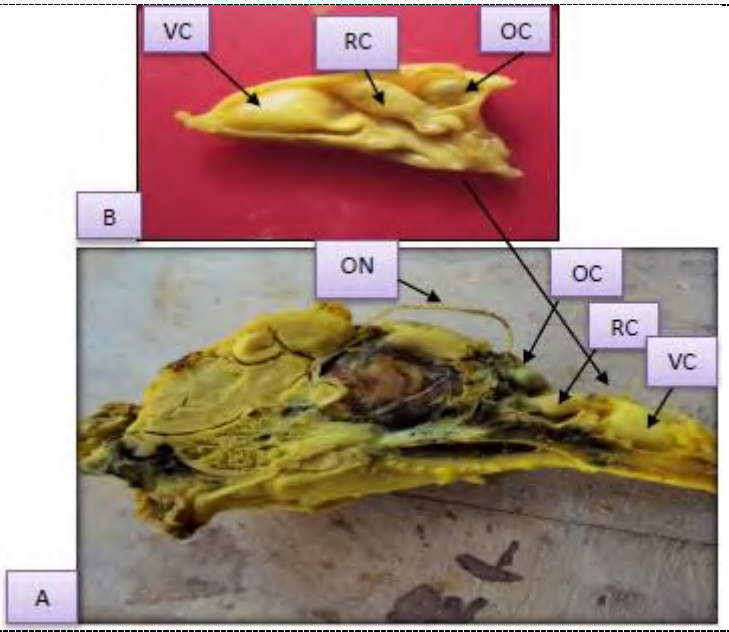

Figure 3. (A) Mid-section in bird head showing the conchae and olfactory nerve.(B) nasal cavity, [VC] Vestibular concha, [RC] Respiratory concha, [OC] Olfactory concha, [ON] Olfactory nerve.

Figure 4. Ventral view of head showing the position of internal Nares [IN].

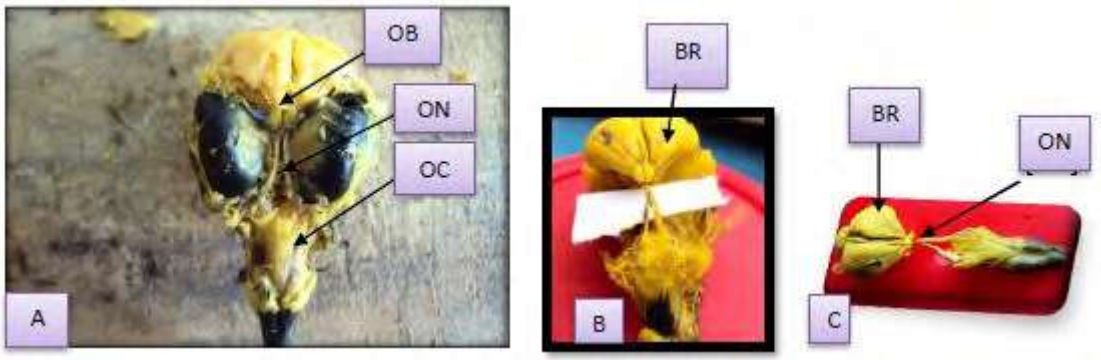

Figure 5. (A) Dorsal view of head showing, the olfactory bulb[OB], olfactory nerve [ON], Olfactory concha [OC],(B) Olfactory nerve, [BR] brain, (C) The connection of olfactory nerve with the olfactory concha [BR] brain, [ON] olfactory nerve.

3.2. Histological Structure

Results of the present study revealed that the histological structure of the integument (the flap) that surrounded the external nares is keratinized stratified squamous epithelium (Figure 6). The vestibular

concha is lined by stratified squamous epithelium, which called vestibular epithelium (Figure 7), the respiratory concha lined by ciliated pseudostratified columnar epithelium rich with goblet cells that secret mucin to protect the epithelial surface (Figure 8), and the olfactory concha lined by ciliated pseudostratified columnar epithelium which consist of three types of cells represented by basal cells, supporting or sustentacular cells, and receptor cells (Figure 9 and 10). Results revealed that Bowman's glands are located beneath basement membrane in the lamina propria and the ducts of the glands pass through the basement membrane and the olfactory epithelium, their mucous secretion reach to the epithelial surface to protect it from drying (Figure 11).

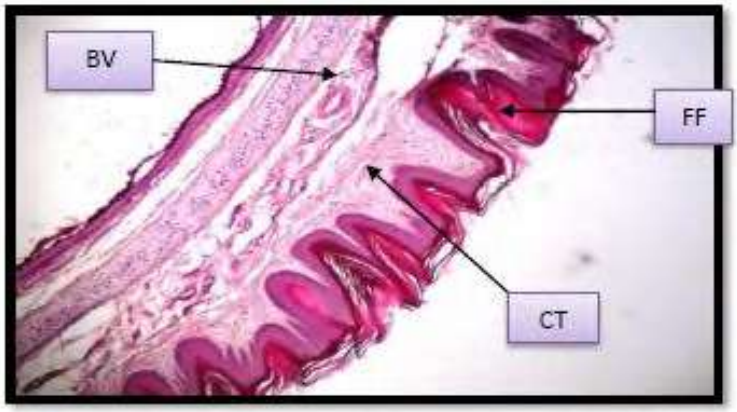

Figure 6. Cross section through the fleshy flap of external naris,[BV] blood vessel, [CT] connective tissue, [FF] feather follicle, (H&E stain), (10x).

Figure 7. Cross section through the vestibular concha of rock dove, [CT] connective tissue, [KL] keratinized layer, [SE] squamous epithelium, (H&E), (10x).

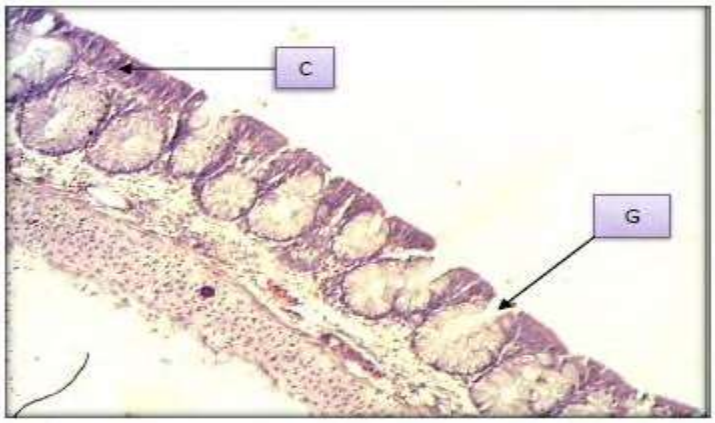

Figure 8. Cross section through the respiratory epithelium, [C] cilia, [G] gland, (H&E), (10x).

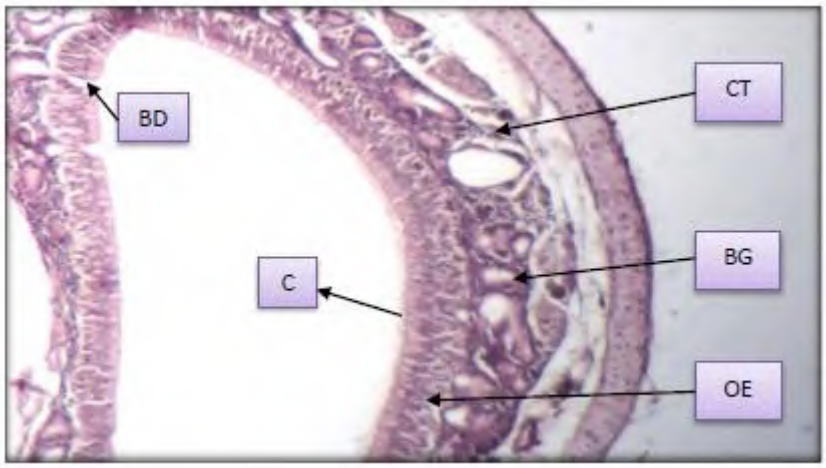

Figure (9). Cross section through olfactory epithelium of rock dove [BD] duct of Bowman's gland, [BG] Bowman's gland, [C] cilia, [CT] connective tissue, [OE] olfactory epithelium, (H&E), (10x).

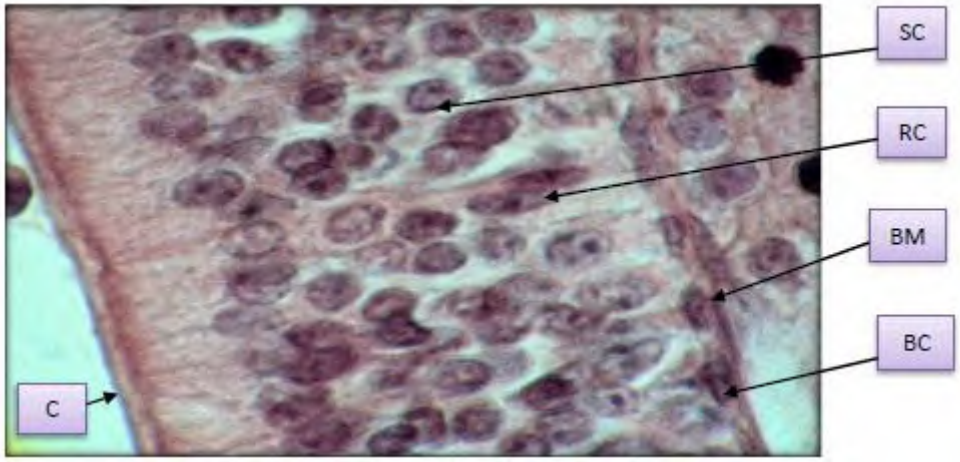

Figure 10. Cross section through olfactory epithelium showing the different type of cells ,[BC]basal cell , [BM] basement membrane, [C] cilia, [RC] receptor cell, [SC] supporting cell (H&E) (40x).

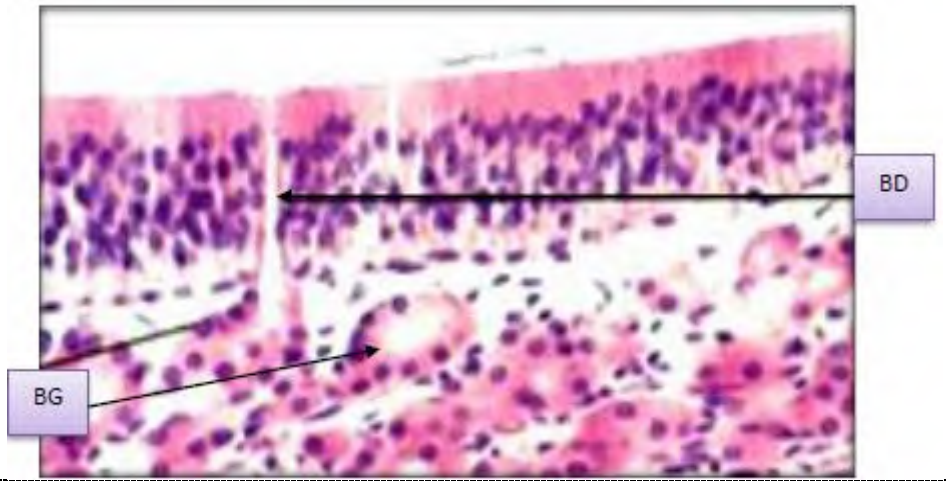

Figure 11. Cross section through the olfactory epithelium showing the Bowman's gland, [BD] Bowman's gland duct, [BG] Bowman's gland, (H&E), (20x).

4. Discussion

The external nares of vertebrates located at different sites of head region but mostly at the dorsal surface of anterior region of head [1, 2, 7]. In birds external nares located at different sites of head according to the type of food and feeding behaviour [13,14]. In penguin external nares located at the middle of beak [14], in kiwi the external nares located at the tip of the beak [16]. The external nares opening appear oval, elliptical, tubular and even spiral in different species of birds [13, 19]. In the species under investigation the external nares are slits-like located at the base of upper beak, which revealed poor olfaction due to this position [8]. The external nares in some species are protected by a keratinized flap [7, 17, 18]. Results of the present study revealed that the external nares in rock dove are covered by keratinized membranous layer. This results agree with [18, 20] foundation. The nasal septum showed clear variation in different species of birds, as it is appeared a complete septum and called naris impervia in ostrich [13], or the nasal cavities are fused and have a long narrow opening in the nasal septum, which is called naris pervia [20], in species under investigation the nasal cavities similar to Demirkan foundation[20] .The nasal cavity in rock dove located anteriorly started with the external nares which extend longitudinally at the upper part of the beak base, which is suitable with the shape of bird and the feeding habit [21]. Birds have in their nasal cavities three conchae or turbinates vary in their shapes in different species. They are represented by vestibular, respiratory, and olfactory conchae respectively [17, 21]. In sulida birds the vestibular concha is lost, while in palacoracida birds the middle concha is lost, and in collacoilia and jungle crow olfactory concha is lost [22, 23, 24]. Results of the present study revealed that in species of bird under investigation, there are three conchae which confirm the results reported by [17, 19]. The intensity of olfaction can determined through the correlation of the diameter of the olfactory bulb and the brain diameter of each species [25]. Generally the birds with large olfactory bulbs have high intensity of olfaction and vice versa [25, 26]. Results of the present study revealed that the olfactory bulb of the species under investigation is small and connected with the olfactory epithelium via relatively long olfactory nerve. These results agree with Allison [27]. Results of the present study showed that the tissue surrounded the external nares represented by keratinized stratified squamous epithelium, which agree with foundation of [28]. The wavy surface of the squamous epithelium in rock dove is agree with [2, 28, 29]. The degree of keratinization is high in the species under investigation perhaps due to the location of the external nares. The histological structure of respiratory epithelium is formed from ciliated pseudostratified columnar epithelium rich with goblet cells to prevent drying and give a chance to perform the function [29, 30]. Results of the present study agree with the above foundation due to the function need. The olfactory epithelium in vertebrates including birds is ciliated pseudostratified columnar epithelium with three types of cells represented by basal cells, supporting cells, and sensory receptor cells [28, 29].This result agree and confirm the present study results and the agreement probably related with the function need.

5. References

[1] Gali MA and Dauod HAM 2014 *Comparative anatomy of chordates*. Dar Al-Doctor Press, Baghdad-Iraq.(In Arabic).
[2] Kotpal PL 1996 *Modern textbook of zoology*,(2nd ed.). Raker Kuker Rastogi Publication, Gangotri, India : XVI + 632pp..
[3] Valetincic T, Wegerts S and Capiro J 1994 Learned olfactory discrimination versus innate taste responses to amino acid in channel catfish *Ictalurus punctatus*. *Physiol. Behav*. **55** 586.
[4] Grubb TC 1974 Olfactory navigation to the nesting burrow in Leach Petrel *Anim. Behav*. **22** 192.
[5] Kent GC and Carr RK 2001 *Comparative anatomy of the vertebrates* (9th ed.). McGraw-Hill, New York.

[6] Shumak SA, Smith JC and Tucker D 1996 Olfactory intensity difference thresholds in the pigeon *J. Comp. Physiol*. **67** 64.
[7] Hussain AA 2012 *Comparative study of morphological description and histological structure of olfactory organs in local chicken (Gallus domesticus) and domestic rabbit (Oryctolagus cuniculus)*. MSc. Thesis, College of Education for Pure Science (Ibn-Al-Haitham), University of Baghdad, 113.
[8] Zako SJ 1980 *Cellular differentiation of the olfactory epithelium in the chick embryo* MSc. Thesis, College of Medicine., Baghdad University: 209pp.
[9] Hussain AA and Dauod Hussain AM 2012 Morphological description and histological structure in rabbit (*Oryctolagus cuniculus*) *JMAC* **4** 5.
[10] Hussain AO, Dauod HAM and Al-Habib MF 2020 Mophological description and histological structure of olfactory organ in long ear hedgehog (*Hemiechinus auritus*).*AAJPS* **1** 24.
[11] Abid AB and Al-Bakri NA 2016 Morphological and histological study of the fore brain (Cerebrum) in quail, *Coturnix coturnix* (Linnaeus, 1758) *Ibn Al-Haitham J. Pure Appl. Sci*. **29** 25.
[12] Bancroft JD and Stevens A 1982 *Theory and practice of histochemical technique* (2nd ed.). Churchill Livingston, London.
[13] Jin EH, Peng KM, Wang JX, Du AN, Tang L, Wel L, Wang Y, Li SH and Song H 2008 Study of the olfactory organ of African ostrich chick *Anat. Histol. Embryol J.* **37** 161.
[14] Negus V 1958 *The comparative anatomy and physiology of the nose and paranasal sinuses*. Churchill Livingstone, London.
[15] Frank BG 2006 Characteristics of the nostrils in birds *J. Biol. Ornithol*. **9** 354.
[16] Cunningham S, Castro I and Alley M 2007 A new prey-detection mechanism for kiwi (*Apteryx* spp.) suggests convergent evolution between paleognathous and neognathous birds *J. Anat.* **211** 493.
[17] McLelland J 1990 *A colour atlas of avian anatomy* published by Wolfe Publishing Ltd. England.
[18] Thomas NT, Martin PC, Lawton GM and Dorrestein M 2000 *Avian medicine* People Eku edu.-Ritchisong-Bird nostril. htm.
[19] Hussain AO 2012 *Comparative study of morphological description ,histological structure and ultrastructure of nasal cavity in two Iraqi vertebrate species (Rock dove, Columba livia and long eared hedgehog Hemiechinus auritus)* PhD. Thesis, College of Education for Pure Science, Baghdad University, (In Arabic)..
[20] Demirkan AC, Kurtul I and Haziro glu RM 2007 Gross morphological features of the nasal cavity in Japanese quail *Vet. Fak. Derg*. **54** 1.
[21] Baumel JJ, King AS, Breazile JE, Evans HE and Vanden JC 1993 *Nomina anatomica avium*. Published by the Nuttall Ornithological Club., Cambridge, Massachusetus.
[22] Wenzel BM 1971 *Olfaction in birds* In hand book of sensory physiology, Vi.4, L.M. Beidler, Ed., 432-438.
[23] Yokosuka M, Hagiwara A, Sation TR, Tsukahara N, Aoyama M, Wakaba yashi Y, Sugita S and Ichikawa M 2009 Histological properties of the nasal cavity and olfactory bulb of the Japanese jungle crow *Chem. Senses* **34** 581.
[24] Bang BG 1971 Functional anatomy of the olfactory system in 23 orders of birds. *Acta. Anat*. **79** 1.
[25] Ropper T 1999 *Olfaction in birds*. In Advances in the study of behavior Slater P, Rosenblatt J and Snowden C Editors. Academic Press, New York.
[26] Kardong K 2006 *Vertebrate comparative anatomy of the vertebrates* 4th ed. McGraw-Hill Co., New York.
[27] Allison AC 1953 The morphology of the olfactory organ in the vertebrates *Biol. Rev.* **28** 195.
[28] King AS and Mclelland J 1984 *Birds :Structure and function* (2nd ed. Bailhere Tindall, London..

[29] Ross M and Pawlina W 2006 *Histology A text & Atlas, with correlated cell and molecular biology* 5th ed. Lippocott William & Wikins, USA.
[30] Watelet JB and Cauweberge V 1999 Applied anatomy and physiology of the nose and paranasal sinuses *J. Allergy Clin. Immunol*. **54** 14.

Phenotypic, anatomical and phytochemical investigation of Iraqi *Silybum marianum*

Phenotypic, anatomical and phytochemical investigation of Iraqi *Silybum marianum*

Rasha Eldalawy[1], Widad M K Al-Ani[2] and Wasan Abdul Kareem[3]

[1]Pharmacognosy and Medicinal Plants Department, College of Pharmacy, Mustansiriyah University, Baghdad- Iraq.
[2]Ashur University College, Baghdad, Iraq.
[3]Clinical Laboratory Science department, College of Pharmacy, Mustansiriyah University, Baghdad, Iraq.

*E-mail: rashaeldalawy@uomustansiriyah.edu.iq

Abstract. Asteraceae (Compositae) famous as the aster, daisy or sunflower family is the biggest flowering family divided into thirteen subfamily that involve approximately two thousand genus, an important member of this family is *Silybum marianum* (Milk thistle). Management of hepatic diseases is the main use of milk thistle in traditional medicine also it has anticancer activity against different type of cancer in addition to antiviral, antioxidant, anti-inflammatory and anti-diabetic activity. This study was designed to investigate the pharmacognostical feature and the phytochemical ingredient of Iraqi *Silybum marianum*. The plant were examined macroscopically to investigate the morphological characters of plant and microscopically to determine the type of stomata and trachoma then flowers, leaves, stems and seeds of the plant were extracted by ethanol in a soxhlet apparatus individually and subjected to standard methods for active constituents identification and that total flaononid, total phenolic and total tannins content were determined using aluminum chloride colorimetric, folin-ciocaltue and acidified vanillin methods respectively. The results shows that *Silybum marianum* leave have a thick cell wall, anomocytic stomata, annual vessel, and unicellular unbranched trichomas. Also an important active constituents have been detected that terpenes, steroid and flavonoids were present in all plant parts, saponin appear only in the leaves and stems while alkaloids and coumarins are not detected in any part. Also the study referred to the seeds as the richest part of the plant with flavonoid and phenolic compounds followed by the flowers, leaves and stems which contain the less amount, while the higher content of tannin were observed in the leaves and stems..

Keywords. *Silybum marianum*, Milk thistle, Stomata, Trachoma, Flavonoid, Phenolic and tannin.

1. Introduction

The Asteraceae (Compositae) is famous as the aster, daisy or sunflower family; this biggest flowering family is divided into thirteen subfamily that involve approximately two thousand genus, *Silybum marianum* is an important member of this family [1]. The famous widespread name for S. marianum is

milk thistle, various other names are also used such as Pig leaves, Royal thistle, Marian thistle, Lady's thistle, Christ's crown, Snake milk,Venus thistle, Heal thistle, Variegated thistle , Sow thistle and Wild artichoke [2]. The plant is high biennial herb of about 5-10 feet, stiff, have a greenish shine leaves with barbed margins and a whitish lines along the veins. The flower is purple containing a small seed inside [3]. Its fruits have stiff skin achenes of about six to eight mm long; have a brown color with a white silk at the top which is collected after flowering in May [4]. Management of hepatic disease was the main use of milk thistle in traditional medicine that at early 19^{th} century it was advised and administered for the management of blood and liver problems as well as for intestinal cleansing [5], also it have anticancer activity against different type of cancer in addition to antiviral, antioxidant, anti-inflammatory and anti-diabetic activity [6]. This study was designed to investigate the phenotypic, anatomical and the phytochemical ingredients of Iraqi *Silybum marianum*, with the determination of the total flavonoid, tannin and phenolic content in the seeds, flowers, leaves and stems of the plant.

2. Materials and Methods

2.1. During Plant materials

All the parts of the plants were collected from the College of Pharmacy/ Al-Mustansiriyah University. The plant was authenticated by Dr. Sukaina Abbas/ College of Science/ Baghdad University/ Baghdad/ Iraq, and then it was identified microscopically in College of Pharmacy / Al-Mustansiriyah University. Leaves, flowers, stems and seeds of the plant were washed thoroughly by tap water, dried in shade, at room temperature from 2 weeks for flowers and seeds up to 1 month for leave and stems, then grinded to a powder and weight for further investigations.

2.2. Pharmacognostical (phenotypic and anatomical) study

2.2.1. Macroscopic examination

Fresh specimens of S. marianum were used to investigate the morphological characters of plant, such as shape, color, size, and margins of leaves, flowers, stems and seeds.

2.2.2. Microscopic examinations

Fresh and dried leaves powder is used for the microscopic examination, The type of stomata and trachoma were observed by taken the outer epidermal layer of fresh leaf on a slide and added few drops of chloral hydrate solution to obtain a clear section and observed under a microscope. Then the powder of the dried leaves were placed on slide and 2 drops of chloral hydrate were added and discarded (2 to 3 times) to bleach the color and clarify the picture then heated at a heater, finally examined under microscope after covering the slide [7], The photographers were obtained by using digital camera and diagnosis the different cell components.

2.3. Extraction method

Each part of the plant was put in a thimble and extracted by absolute ethanol using Soxhlet apparatus for 3 days and then the extract were completely evaporated by a rotary evaporator, the total dried extract of each part was weight to subsequently determine the amount of the contents in the dry weight and then labeled for further investigation [8].

2.4. Phytochemical study

2.4.1. Preliminary phytochemical screening

The plant extract was phytochemically screened for the qualitative investigation of major classes of secondary metabolites.

2.4.1.1. Flavonoids

A positive result is recorded when a yellow color is observed after the addition of 2ml ethanolic KOH to 1ml alcoholic extract of plant [9].

2.4.1.2. Tannins

Few drops of alcoholic extract were diluted to 10 times its volume, filtered and mixed with 1% aqueous ferric chloride, formation of dark green-blue color ensure tannin presence [10].

2.4.1.3. Saponin

Froth assay is used for saponin identification that by shaking distilled water vigorously with few ml of plant extract for fifteen minute. A persistent froth is an indication for saponins presence [11].

2.4.1.4. Terpenoids

4ml of the plant extract was treated with 1ml of equal quantity of acetic anhydride and chloroform. Then concerted solution of sulphuric acid was added gradually and red violet color was seen for terpenoids [12].

2.4.1.5. Sterols and steroids

Liebermann reaction was used to indicate the presence of steroids. Dried ethanolic extract was diluted with 0.5ml of hot acetic anhydride and filtered, then treated with *Libermann burrchardt*. The appearance of a blue-green ring at the interphase indicated sterol nucleus presence [13].

2.4.1.6. Coumarins

A few spot from a mixture of 0.5ml 10% NH4OH and 5ml of ethanolic extract was added on a filter paper and examined under U.V light. Coumarins give intense fluorescence under UV [14].

2.4.1.7. Alkaloids

Extracts were dissolved individually in 8ml of 1% hydrochloric acid and filtered. The filtrate was divided into two parts; the first one was reacted with Mayer's reagent, a positive result is indicated by white precipitate. The second part was reacted with Dragendroff's reagent. A red precipitate refers to alkaloid existence [15].

2.4.2. Estimation of total phenolic content

Total phenolic content was measured by adding 1ml of deionized water and 1ml of folin-ciocalteu reagent to 1ml of probably diluted extract sample, 5 minute later 1ml of 10% $NaCO_3$ was added and

the mixture was kept at room temperature for at least 90 min, the absorbance was measured at 760nm by UV spectrophotometer, the process was repeated three times for each sample and the average was recorded [16]. Calibration curve was done by measuring different concentration of gallic acid by the same procedure, and the result was expressed as mg gallic acid equivalent/g of dry plant material.

2.4.3. Estimation of total tannins content

0.05 ml of diluted alcoholic extract were reacted with 3ml of 4% methanolic vanillin solution and 1.5ml H2SO4, that condensed tannin will react with vanillin solution and form anthocyanidols in the presence of concentrated sulphuric acid, the absorbance was measured at 500nm after fifteen minute for three replicate of each sample, the result was expressed in mg equivalent of gallic acid/ g of dry plant material [17].

2.4.5. Estimation of total flavonoid content

0.5 ml of diluted extract was mixed with 0.15 ml of 7% $NaNO_2$ solution, after 7 minute 0.3 ml of 10% AlCl3 solution was added, later after 6 minute 1 ml of NaOH was added to the mixture and the volume was completed to5 ml by distilled water, the absorbance was measured at 510 nm and the result was recorded as mg quercetin equivalent /g of dry weight [18].

3. Results and Discussion

3.1. Macroscopic identification

Silybum marianum range from 25 cm to 2 m in height and from 5 cm to 1.5 m base diameter, the stem is green, grooved, branched, rigid and contain multiple leaves, large stem have a hollow in the middle. The leaves are lanceolate, lobate, and pinnate with spinny margin, they are hairless, greenish with milk-white veins, growing only on the base of the plants; they are small at December when they start growing and reach their maximum size at the end of March and April. Flowers are 4 to 13 cm long and wide, pale yellow to white at summer and purple at the end of winter and during spring; they are round, solitary at the apex of the stem or its branches, surrounded by needle like bracts, The seeds (fruits) are about 1 cm long, smooth, shiny with a simple long very fine pappus, surrounded by a yellow basal ring, it have a white color surrounded by a hard brownish to black achenes. Figure1. These morphologicl characteristic are identical to the plant characteristic prescribed at world health organization monograph [19], a guide of medicinal plants in Africa [20] and many papers around the worlds [21, 22, 23, 24].

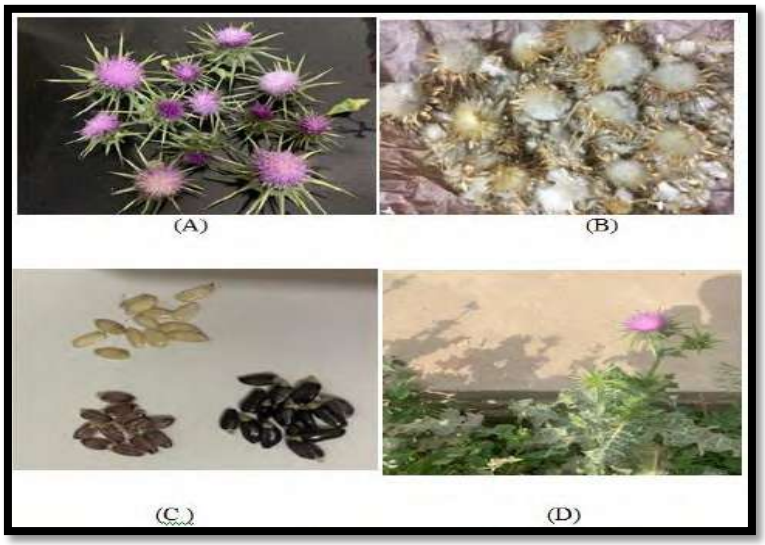

Figure 1. *Silybumm arianum* picture. A- purple flower, B- white flower, C- seed, D- whole plant.

3.2. Microscopic examination

Powdered leaves of *Silybum* were diagnosed under microscope by a thick cell wall, anomocytic stomata, annual vessel, and unicellular unbranched trichomes as shown in Figure 2.

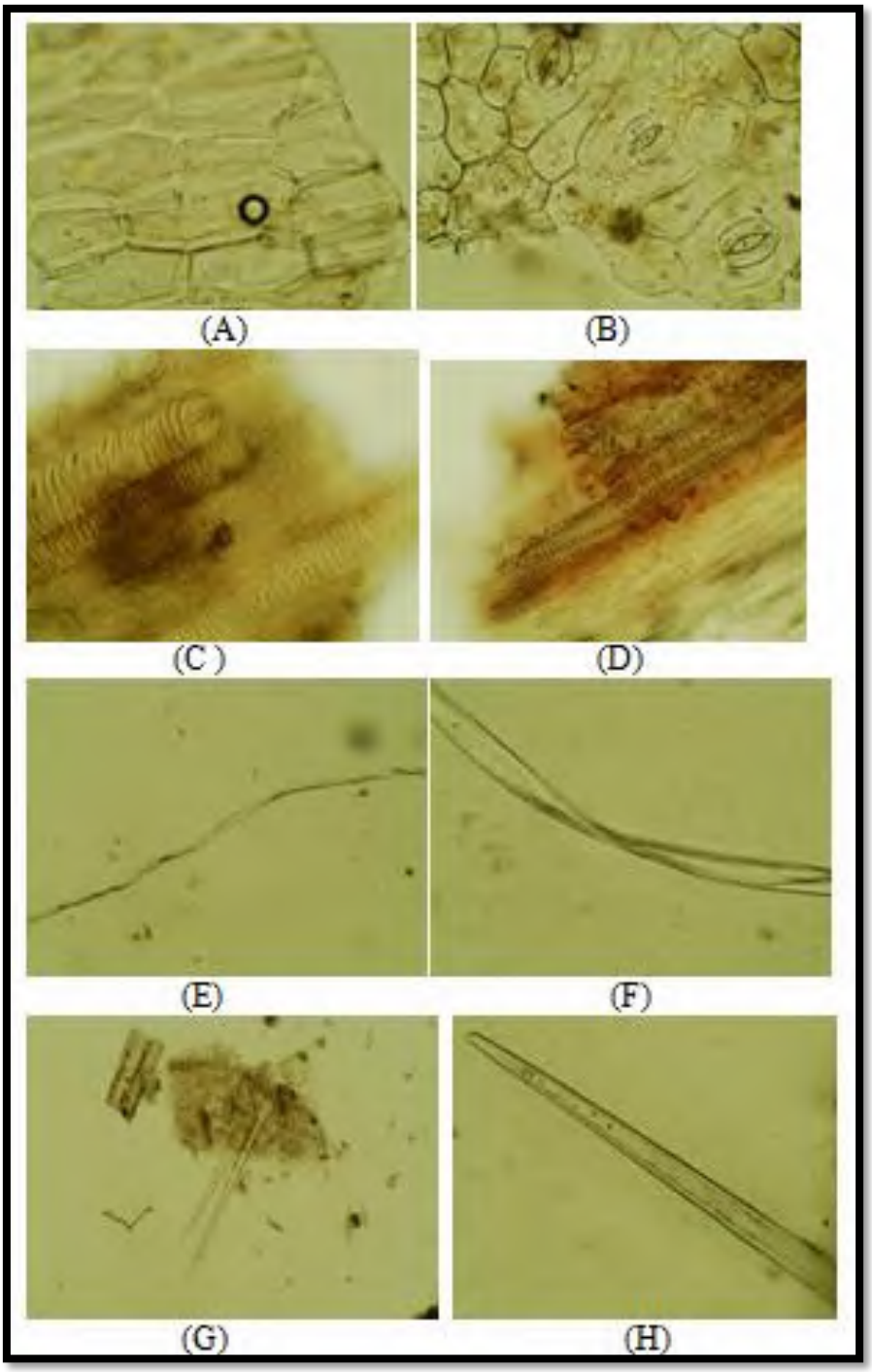

Figure 2. A-Thick cell wall, B- Anomocytic stomata, C- Annual vessle, D- Annual vessle 40X. E- fiber 10X, F- fiber 40X. G- Unicellular unbranched trichomas, H- Unicellular unbranched trichomas 40X.

3.3. Phytochemical results

3.3.1. Qualitative identification of Silybum marianum

Various qualitative phytochemical screening tests were done to establish the chemical composition of each extract; these tests provide important information regarding the type of secondary metabolites present in plant to establish a suitable procedure for isolation of these metabolites from different extracts. Primary chemical experiments for the extract of flowers, leaves, seeds and stems revealed the presence of terpenes, steroid and flavonoids while saponin appear only in the leaves and stems and the extract of flowers and seeds give a negative result, Alkaloids and coumarins are not detected in any part as shown in Table 1.

Table 1. Qualitative profile for phytochemicals found in S. marianum.

Part of the plant	Type of secondary metabolite					
	Alkaloid	Terpenoid	Steroid	Flavonoid	Saponin	Coumarin
Leave	-ve	+ve	+ve	+ve	+ve	-ve
Flower	-ve	+ve	+ve	+ve	-ve	-ve
Seed	-ve	+ve	+ve	+ve	-ve	-ve
Stem	-ve	+ve	+ve	+ve	+ve	-ve

3.4. Quantitative assessment of S. marianum

Different concentration of gallic acid, tannic acid and quercetin was used for calibration curve calculation of phenolic, tannins, and flavonoids respectively as shown in Figure 3, 4 and 5. different phytochemical ingredients vary considerably among different parts of the plant and affected by different biological stress and environmental conditions [25], therefore flavonoid, phenolic, and tannin content were determined in different parts of the plant and each measurement were repeated three times to reduce error and the results are documented in table 2.

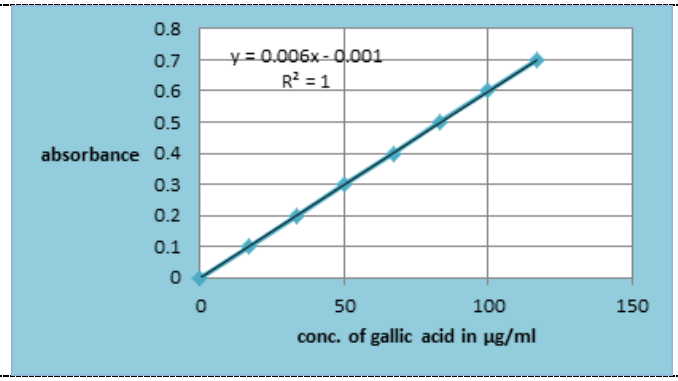

Figure 3. Standard curve for the determination of total phenolic content.

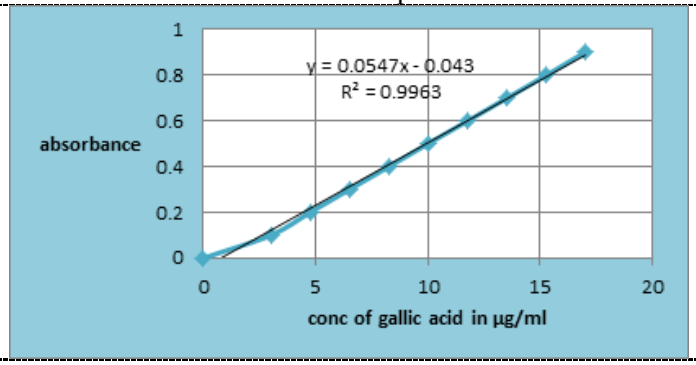

Figure 4. Standard curve for the determination of total tannin content.

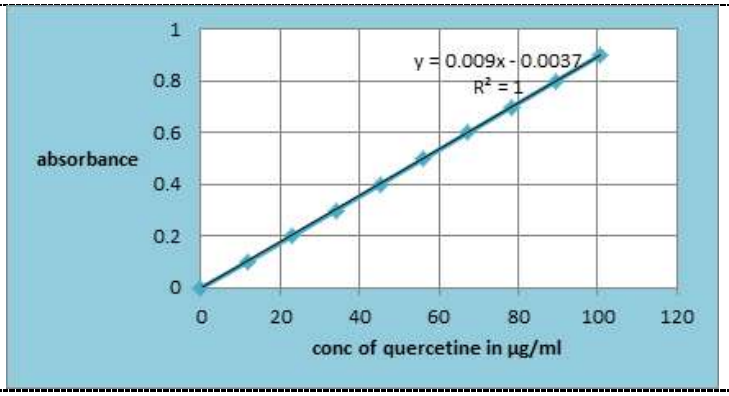

Figure 5. Standard curve for the determination of total flavonoid content.

Table 2. Total phenolic, flavonoid and tannin content in different parts of Iraqi *Silybum marianum*.

Part of the plant	Total phenolic content as µg gallic acid /mg dry plant	Total flavonoid content as µg quercetin /mg dry plant	Total tannin content as µg tannic acid /mg dry plant
Flowers	22.64±0.07	9.08±0.3	17.7±0.05
Seeds	67.03±0.56	12.32±0.45	15.6± 0.43
Leaves	12.6±0.5	10.02±0.09	74±0.63
Stems	11.03±0.45	7.5±0.2	66.34±0.35

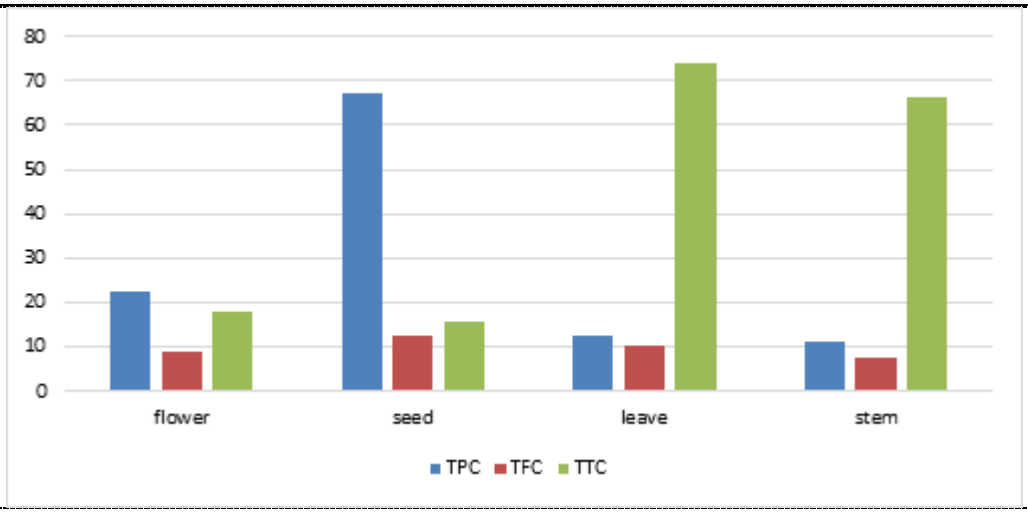

Figure 6. A comparison of total phenolic, flavonoid and tannin content in different parts of Iraqi *Silybum marianum*. TPC: total phenolic content, TFC: totat flavonoid content, TTC: total tannin content.

From the information above its obvious that the seeds are the richest part of the plant with flavonoid and phenolic compounds followed by the flowers then the leaves, the stems contain the less amount, while the higher content of tannin were observed in the leaves and stems.

4. Conclusion

Silybum marianum which is distributed widely in Iraq is an important medicinal plant and contain highly valuable active constituents in all the plant parts such as terpens, flavonoids, steroids and saponins, and this is the first study that describes the microscopic feature of Iraqi *Silybum* and

compare between the phytochemical components of the plants parts, further fractionation and isolation of this constituents are required.

5. Acknowledgement

The authors would like to thank Mustansiriyah University (www.uomustansiriyah.edu.iq) Baghdad-Iraq for its support in the present work.

6. References

[1] Samah NA, Hend MF and Azza MS 2019 Comparative botanical studies two varieties of *Silybum marianum* (L.) Gaertn. (Asteraceae) in Egypt *Int. J. Adv. Res. Biol. Sci.* **6** 154.
[2] Silybin MB 2017 a major bioactive component of milk thistle (*Silybun marianum* L. Gaernt.). *Chem. Bioavail. Metabol. Molec.* **22** 1942.
[3] Ajit KK, Wahi AK, Brijesh K, Anil B and Neelkant P 2011 Milk thistle (*Sylibum marianum*): A review *Int. J. Pharma Res. Develop.* **3** 974.
[4] *A Guide to Medicinal Plants in North Africa* 2005 2-8317-0893.
[5] Fei X and Yong-Song G 2017 Cautiously using natural medicine to treat liver problems *World J. Gastroenterol.* **23** 3388–3395.
[6] Al-Ezzi MI and Jasim GA 2020 Pharmacological and pharmacognostical activity of Silybum marianum (A review article). *Almustansiriyah J. Pharmacy. Sci.* **20** 72.
[7] Jasim TM, Nasser NM, Baderden SQ and Hasan H A 2019 Pharmacognostical and phytochemical studies of Iraqi *Hibiscus-rosa sinensis The 7th international conference on applied science and technology, AIP Conference proceedings* **2144**, 040002-1-040002-6.
[8] Mehdi A, Al-ani WMK and Raoof A 2018 Isolation of *Astragalin* from Iraqi *Chenopodium album*. *Asian J. Pharmacy. Clin. Res.* **11** 530.
[9] Zahraa AA, Huda KA, Fatima MS and Shahad QI 2019 GC-Mass and phytochemical investigation of *Cymbopogon citrates Res. J. Pharm. Technol.* **12** 67.
[10] Gul R, Jan SU, Faridullah S, Sherani S and Jahan N 2017 Preliminary phytochemical screening, quantitative analysis of alkaloids and antioxidant activity of crude plant extracts from *Ephedra intermedia* indigenous to Balochistan *Sci. World Res.* **2017** 5873648.
[11] Auwal MS, Saka S, Mairiga IA, Sanda KA, Shuaibu A and Ibrahim A 2014 Preliminary phytochemical and elemental analysis of aqueous and fractionated pod extracts of Acacia nilotica (*Thorn mimosa*). *Vetern. Res. Forum* **5** 95.
[12] Doss A 2009 Preliminary phytochemical screening of some Indian medicinal plants *Ancient Sci. Life* **29** 12.
[13] Rasha E, Noor MN and Zahraa AA 2020 Antimicrobial and antioxidant activity of Iraqi *Cupressuss emperverines* cones *AIP Conference* **2213**, 020006-1-020006-5.
[14] Yadav M, Chatterji S, Gupta SK and Watal G 2014 Preliminary phytochemical screening of six medicinal plants used in traditional medicine *Int. J. Pharm. Pharmacy. Sci.* **6** 539.
[15] Ingle KP, Padole DA and Khelurkar VC 2017 Preliminary phytochemical screening of methanolic extract from different parts of *Jatropha curcas* (L.). An international refereed, per reviewed and indexed *Quart. J. Science,Agric. Eng.* **6** 111.
[16] Jing S, Xinhua L and Xiaolei Y. 2016 Antioxidant activities, total flavonoids and phenolics content in different parts of *Silybum marianum* L plants *Chem. Eng. Transact.* **55** 37.
[17] Baya M, Feten A, Abderrazak S, Chedly A, and Brahim M 2016 Fatty acids, essential oil and phenolics composition of *Silybum marianum* seeds and their antioxidant activities *Pak. J. Pharm. Sci.* **29** 951.
[18] Eldalawy R 2017 Quantitative estimation of rutin in Rue (*Ruta graveolens* L.) cultivated in Iraq wuth the evaluation of its antioxidant activity. *Asian J. Pharmac. Clin. Res.* **10** 353.
[19] Who 2012 *Monograph on selected medicinal plants*- volume 2, who health system library.

[20] Pedro M 2005 A guide to medicinal plants in North Africa. *Int. Union Convers. Nat. Nat. Sour.***1**: 255.
[21] Veronica V, Hana D, Jana B and Miroslav H 2020 Milk thistle (*Silybum marianum*): A valuable medicinal plant with several therapeutic purposes *J. Microbiol. Biotechnol. Food Sci.* **9** 836.
[22] None 1999 Monograph *Silybum marianum* (Milk thistle). *Altern. Med. Rev.* **4** 272.
[23] Farhat AK, Muhammad Z, Nassem U, Shazeb K, Muhammad K, Sartaj K and Javid A 2014 A general introduction to medicinal plants and *Silybum marianum Life Sci. J.* **11** 471.
[24] Nassrin Q, Hassanali NB, Mohammad RL and Ali M 2013 A review on pharmacological, cultivation and biotechnology aspect of milk thistle (*Silybum marianum*) L. Gaertn *J. Med. Plants* **12** 19.
[25] Liu W, Yin D, Li N, Hou X, Wang D, Li D and Liu J 2016 Influence of environmental factors on the active substance production and antioxidant activity in *Potentilla fruticosa* L. and its quality assessment *Science reports* **6** 28591.

Effect of Chloroquine on antioxidant enzymes and oxidative system on (*Vigna radiata*) plant tissues exposed to water stress

Effect of Chloroquine on antioxidant enzymes and oxidative system on (*Vigna radiata*) plant tissues exposed to water stress

Hayder Nasser Hussain Al-Mentafji[1*]

[1]Ministry of Education, Baghdad, Iraq.

*E-mail: hayderalmentafji@gmail.com

Abstract. The aim of the present study is to examine the effect of (Chloroquine CQ) on the oxidative stress under water stress effect Recently , this compound is used to treat COVID-19 , Hydrogen peroxide H2O2 effect and Stimulate the enzymatic system through the exposure of the plant to water stress and interaction with Chloroquine , where the stress stimulate the production of these Oxidative Factors (Hydrogen Peroxide, Malondialdehyde(MDA), Protease increase the production of these oxidative factors increase activity through the effect of Chloroquine, This process was performed in the meristematic tissues of the cells of the permanent Mung bean (*Vigna radiata*) plants under experimental factors (water stress factor for 10 days with control period of 5 days) (Chloroquine factors and concentrations of 125 and 250 mg.L-1 with control treatment) were designed using a Factorial Randomized Block Design (R.B.C.D) with three replicates and 18 experimental units The experimental unit area was 2 m. The results have shown the following; The water stress period of 10 days led to the production of toxic hydrogen peroxide and increased concentration by stress. The effect of water stress was Stimulate the Production of hydrogen peroxide in Meristematic tissues. The effect of Chloroquine CQ with increased concentrations had a role in inhibiting the production of enzymatic antioxidants (Superoxide dismutase(SOD) and Catalase (CAT). The interaction between water stress and increased Chloroquine CQ concentrations has been instrumental in stimulating the production of oxidative Factors.

Keywords. Chloroquine (CQ), Antioxidants, Meristematic tissue, *Vigna radiata*, Water stress.

1. Introduction

Chloroquine (CQ) has been used extensively as an antimalarial agent with immunomodulatory effects. A derivative of CQ, Hydroxychloroquine sulfate (HCQ) was synthesized firstly in 1946 by addition of a hydroxyl group to CQ and is much is less toxic than CQ in animal studies [1, 2, 3]. CQ has been used in Severe acute respiratory syndrome (SARS) Coronavirus infection due to its antiviral properties. Recently CQ has also been found to have Anti-COVID-19 activity in vitro [4]. For these reasons, CQ and HCQ could be the potential drug for treating COVID-19 infection. To date, there is no clinical evidence to support the use of CQ or HCQ for treating SARS-CoV-2 infection though many clinical trials with these drugs are already underway [5]. This study aims to systematically review the available literature for the use of CQ or HCQ in treating COVID-19 infection [6]. Oxidative stress is produced by increasing the number of reactive oxygen species or free radicals,

which results in early aging, increased permeability, ions leakage from the cell membranes, and reduced photosynthesis in plants [7]. Free radicals result in cellular damage through lipid peroxidation (mainly cell membranes) and the blocking of natural antioxidants. By measuring the malondialdehyde (MDA), which is the result of lipid peroxidation, the level of oxidative stress in plant cells can be estimated [8]. Under oxidative stress conditions, by producing oxygen intermediates, which are relatively reduced or energy-intensive forms of atmospheric oxygen (O_2), the plant finds itself under stress conditions and activates a variety of defense systems such as antioxidants to protect against stress [9]. The goal for measuring the amount of stress created in the plant generally, is the measurement of the activity of the peroxidase enzymes, such as hydrogen peroxide (H_2O_2). In the case of the excessive accumulation of these activated oxygen's, a variety of cell damage such as DNA damage, membrane lipid peroxidation, RNA damage, protein oxidation, and enzymatic inhibition, occurs in the cell [10]. Free oxygen radicals or lipid peroxidation reactions in the plant membrane will selectively break up unsaturated fatty acids and accumulate hydrocarbons, aldehydes, and the like [11]. Therefore, frequently to determine the effect of environmental stresses on the membrane of plant cells, the amount of lipid peroxidation products, such as malondialdehyde (MDA) or hydrogen peroxide (H_2O_2), must be measured and their results suggest the involvement of free oxygen radicals in response to stress [12]. The antioxidant system stimulates, activates Enzymes activities or a group of antioxidants resulting from the oxidative stress effect. The mung bean (*Vigna radiata*) has been consumed as a common food in China for more than 2,000 years. It is well known for its detoxification activities and is used to refresh mentality, alleviate heat stroke, and reduce swelling in the summer it's contain balanced nutrients, including protein and dietary fiber, and significant amounts of bioactive phytochemicals. High levels of polyphenols ,antioxidant, antimicrobial, anti-inflammatory, and antitumor activities [13, 14].

2. Materials and Methods

The experiment was carried out in the gardens and laboratories of Al-Farahidi University for the 2018 season located at latitude 33.4o and longitude 44.4o and 23 meters above sea level. The experiment was designed according to Randomize Complete Blocks Design (3*3*2) and three replicates. The land was divided into 18 experimental units (2*1) m. The mung bean (*Vigna radiata*) seeds were planted on 1/7/2020 after sifting and testing the proportion of germination with the plant distance between another in field 25 cm and were taken samples on 1/8/2020 and frozen and stored in the (Deep Freezer) for the analysis and extraction of antioxidants.

2.1. Experimental factors

2.1.1. Irrigation and stress factors

The plants were irrigated every 5 days and treated with control. The stress factors were irrigated every 10 days. The water quantity (100%) of the field capacity (F.C) of the soil was controlled by the Soil Moisture Meter.

2.1.2. Chloroquine dose CQ concentrations

(125 and 250 $mg.L^{-1}$ and control treatment) Preparation of chloroquine doses(CQ) concentration: Standard chloroquine Phosphate (Bayshore Brand) solution was prepared with water by dissolving 125 mg in a liter of distilled water and then concentrated to 250 mg. Plants were sprayed with Chloroquine CQ concentrations before sunrise by manual sprayer after four plant leaf stage. The control treatment was sprayed with distilled water. The apical meristems (20-day age) were cut by Medical scalpel from the developing apex to the first leaf under the developing and were placed directly with Petri dishes and frozen at $-10^{o}C$.

2.2. Estimation of free radicals and oxidative factors

It was performed on the basis of:; Hydrogen peroxide level (µmol.gm^{-1}) according to the method of [15] was determined. Protease enzyme level (µmol.gm-1) Was determined according to the method of [16]. Free Radicals scavenging activity of antioxidants was evaluated from method of DPPH (2,2-diphenyl-1-picryl-hydrazyl-hydrate) assay [17].

- Lipid peroxidation indicator of Cell membrane Malondialdehyde (MDA) according to [18].

2.3. Antioxidants enzymes activities

They were performed on the basis of; Concentration of Catalase enzyme (CAT): (µmol.ml^{-1}): Estimated according to the method of [19]. Superoxide Dismutase enzyme (SOD) (µmol.ml-1). was estimated according to [20].

2.4. Statistical analysis

Results of the present study were statistically analyzed according to the statistical program (SAS) according to a global experience (3 × 2) with the design of the complete random sectors (RBCD) and the use of the least difference (LSD) to compare the arithmetic averages of the studied transactions at the probability level [0.05] [21].

3. Results

Regarding Hydrogen peroxide concentrations under concentrations of chloroquine CQ for the Vigna radiata Meristematic tissue affected by water stress (µg.g^{-1}) Table1 have shown that water stress had a significant increase in the hydrogen peroxide level at 10 days of water stress, with the increase in hydrogen peroxide level from 2.50 to 3.58 µg.g^{-1} with an increase of 72.00%, besides, spraying with Chloroquine CQ significantly increased the average hydrogen peroxide concentration and increased CQ concentration. At 125 mg.L^{-1} concentration of CQ , the average hydrogen peroxide level increased to 3.00 µg.g^{-1} when spraying at 125 mg.L^{-1} concentration and increased hydrogen peroxide level with CQ concentration of 4.50 µg.g^{-1} concentration at 250 mg.L^{-1} compared with the control treatment, which had a concentration rate of 1.63 mg.L^{-1} results of the interaction between the levels of water stress and spraying of Chloroquine CQ have shown significant in Hydrogen peroxide levels, where the highest level of hydrogen peroxide it was 5.08 µg.g^{-1} comparing with1.30 µg.g^{-1} under control level .

Table 1. Hydrogen peroxide level under different concentrations of Chloroquine CQ for the *Vigna radiata* meristematic tissue affected by water stress (µg.g^{-1}).

Stress levels	Chloroquine(CQ) con. (mg)			Stress level mean
	0	125	250	
days 5 (control)	1.30	2.30	3.91	2.50
days 10	1.95	3.71	5.08	3.58
Chloroquine(CQ) (mean)	1.08	3.00	4.50	.....
Stress levels (LSD)				0.08 at (0.05)
Chloroquine(CQ) con. LSD				0.07 at (0.05)
interaction LSD				0.18 at (0.05)

Activities of Protease Enzyme under different concentrations of chloroquine CQ for the Vigna radiata meristematic tissue affected by water stress. The results in Table (2) have shown a significant increase in the activities of protease when the stress increased to 10 days, with the enzyme Activity

increasing to 27.49 µmol.ml^{-1} compared with the control treatment in which the Activity of the enzyme was 11.29 µmol.ml^{-1} and with the same effect, CQ effect increased the mean Activity of Protease with a concentration of 125 mg.L^{-1} The Activity of protease increased to 19.68 ìmol.ml^{-1}when spraying with a concentration of 125 mg.L^{-1} and the Activity of the enzyme increased by increasing CQ concentration, where it reached 27.06 µ.mol.ml^{-1} at 250 mg concentration compared with the control treatment, which was 11.43 mol.ml^{-1}. The results of the double interaction between the effect of stress and concentrations of CQ showed a significant increase, with the highest value of the increase in the activity of enzyme at the interaction between the 10 day stress period and the concentration of 250 mg.L^{-1} which reached 11.43 µmol.ml^{-1} compared to the lowest Activity of 5.77 µmol.ml^{-1} at the concentration of nill concentration of CQ and the absence of stress and an increase of 72.84%.

Table 2. Activities of Protease Enzyme under diffrent concentrations of chloroquine CQ for the *Vigna radiata* meristematic tissue affected by water stress(µmol.ml^{-1}).

Stress levels	Chloroquine(CQ) con. (mg)			Stress level mean
	0	125	250	
days 5 (control)	5.77	10.96	17.15	11.29
days 10	17.09	28.41	36.98	27.49
Chloroquine(CQ) (mean)	11.43	19.68	27.06	.....
Stress levels (LSD)				0.15 at (0.05)
Chloroquine(CQ) con. LSD				0.16 at (0.05)
interaction LSD				0.40 at (0.05)

Percentage of Free Radicals scavenging activity under concentrations of chloroquine CQ for the *Vigna radiata* meristematic tissue affected by water stress. The results of Table (3) Have shown a significant decrease in the concentration of Free Radicals scavenging activity during the 10-day stress period, with the Free Radicals scavenging activity decreasing to 72.35 (%) compared with the control treatment of which the Free Radicals scavenging activity was 21.65 (%) also and CQ doses decreased the average of the Free Radicals scavenging activity at 125 mg.L^{-1} reached to 76.01 (%) compared with 76.25 (%) under control dose. The mean of the Free Radicals scavenging activity a significant decreased by CQ concentration to 73.94 (%) at a concentration of 250 mg.L^{-1} compared with the control treatment of which the concentration of CQ was 76.25(%),The results showed a significant decrease in the Free Radicals scavenging activity, with the lowest value of Free Radicals scavenging activity at the interaction between the 10-day stress period and the concentration of 250 mg.L^{-1} reached to 71.88 (%) compared to the highest percentage of Free Radicals scavenging activity was 80.05 (%) at a concentration of 0 mg concentration of CQ and lack of stress.

Table 3. Percentage of Free Radicals scavenging activity under different concentrations of chloroquine CQ for the *Vigna radiata* meristematic tissue affected by water stress(%).

Stress levels	Chloroquine(CQ) con. (mg)			Stress level mean
	0	125	250	
days 5 (control)	80.05	77.30	75.00	77.45
days 10	72.45	72.73	71.88	72.35
Chloroquine(CQ) (mean)	76.25	75.01	73.44	.....
Stress levels (LSD)				0.10 at (0.05)
Chloroquine(CQ) LSD				0.12 at (0.05)
interaction LSD				0.20 at (0.05)

MDA levels under concentrations of chloroquine CQ for the Vigna radiata meristematic tissue affected by water stress (µg.g^{-1}) Table 4 showed that water stress had a significant increase in the MDA level at 10 days of water stress, MDA level increasing from 1.50 to 2.58 µg.g^{-1}, spraying with chloroquine CQ significantly increased the average MDA concentration and increased CQ

concentration. at 125 mg.L^{-1} of CQ concentration, the MDA level increased to 2.00 µg.g^{-1} when spraying at 125 mg.L^{-1} concentration and increased MDA levels with CQ concentration of 3.49 µg.g^{-1} concentration at 250 mg.L^{-1} compared with the control treatment, which had a concentration rate of 0.62 mg.L^{-1} The results of the interaction between the level of water stress CQ and a significant increase in the rate of MDA level, where the highest value of an increase in MDA levels at stress level of 10 days and concentration of 250 mg, reaching 4.08 µg.g^{-1} compared to the lowest level of MDA 0.30 µg.g1 concentration at 0 mg.L^{-1} of CQ and without stress (control treatment).

Table 4. MDA levels under concentrations of chloroquine CQ for the *Vigna radiata* meristematic tissue affected by water stress (µg.g^{-1}).

Stress levels	Chloroquine (CQ) con. (mg))			Stress level mean
	0	125	250	
days 5 (control)	0.30	1.30	2.91	1.50
days 10	4.08	2.70	4.07	2.58
Chloroquine(CQ) (mean)	0.62	2.00	3.49	.....
Stress levels (LSD)				0.07 at (0.05)
Chloroquine(CQ) LSD				0.06 at (0.05)
interaction LSD				0.17 at (0.05)

Catalase activities under concentrations of chloroquine CQ for the Vigna radiata meristematic tissue affected by water stress (µmol.ml^{-1}). The results are have shown in Table 5 confirm that the effect of water stress has a significant effect on the activity of the catalase enzyme at 10 days of water stress. The activity of the catalase is 37.71 µmol.ml^{-1} when the control (5 days) to 18.35 µmol.ml^{-1}. The effect of CQ spraying significantly increased the level of catalase activity with the concentration of CQ. At the concentration of 125 mg.L^{-1} of the above CQ the activity of the catalase enzyme increased to 29.39 µmol.ml^{-1} concentration at 125 mg.L^{-1} of CQ and the activity of the enzyme increased by 33.81 µmol.ml^{-1} concentration at 250 mg.L^{-1} compared with the control treatment of 19.93 µmol.ml^{-1} and an increased rate of 61.29 %, the results in the interaction between stress and concentrations of CQ have shown a significant increase. The highest value of the increase in the enzyme activity at the interaction between the 10 days stress period at the concentration of 250 mg.L^{-1} of CQ with a concentration of 45.44 µmol.ml^{-1}, while the lowest activity of the enzyme was 19.91 µmol.ml^{-1} concentration at the duration of 5 days and 0 concentration of CQ (control treatment).

Table 5. Catalase activities under different concentrations of chloroquine CQ for the *Vigna radiata* meristematic tissue affected by water stress (µmol.ml^{-1}).

Stress levels	Chloroquine(CQ) con. (mg)			Stress level mean
	0	125	250	
days 5 (control)	17.91	18.95	22.19	19.35
days 10	25.95	39.83	45.44	37.71
Chloroquine(CQ) (mean)	19.93	29.39	33.81	.....
Stress levels (LSD)				0.25 at (0.05)
Chloroquine(CQ) con LSD				0.20 at (0.05)
LSD interaction				0.57 at (0.05)

Activities of superoxide dismutase enzyme under the stimulation of the antioxidant system of Chloroquine (CQ) for the apical meristem tissue affected by water stress (µmol .ml $^{-1}$). The results of Table (6) have shown a significant increase in the mean activity of Superoxide Dismutase at exposure to 10 days of water stress, with the enzyme activity increasing from 36.58 to 46.71 µmol .ml $^{-1}$ and the increase of 26.70% , the effect of CQ increased the activity of the enzyme superoxide dismutase increase the concentration of CQ at the concentration of 125mg.L^{-1}, the activity of the superoxide dismutase to 43.36 µmol .$ml^{-1}$when spraying with a concentration of 125 mg.L^{-1} of CQ, The activity of

the enzyme increased by CQ concentration to 54.54 μmol.ml^{-1} concentration at 250 mg.L^{-1} compared with the control treatment of 27.03 μmol.ml^{-1},The results of the interaction between stress and concentrations of CQ have shown a significant increase with the highest value of the increase in the enzyme at the interface between the 10 day stress period and the concentration of 250 mg, reaching 62.14μmol.ml^{-1} compared with the lowest activity SOD enzyme of 21.72μmol.ml^{-1} concentration at Nill concentration of CQ without stress.

Table 6. Superoxide dismutase activities under diffrents concentrations of chloroquine CQ for the *Vigna radiata* meristematic tissue affected by water stress (μmol.ml^{-1}).

Stress levels	Chloroquine(CQ) con. (mg)			Stress level mean
	0	125	250	
days 5 (control)	21.72	41.08	46.95	36.58
days 10	32.34	45.65	62.14	46.71
Chloroquine(CQ) (mean)	27. 03	43.36	54.54	.....
LSD)) Stress levels				0.26 at (0.05)
. Chloroquine(CQ) con. LSD				0.18 at (0.05)
LSD interaction				0.56 at (0.05)

4. Discussion

The Free radicals concentrations under the stimulation of the antioxidant system of the Chloroquine (CQ) effect of the Oxidative factors. The effect of water stress increase the concentration of hydrogen peroxide and it is believed that the increase of oxidizing enzymes is produced when the plant is exposed to oxidative stress and the production of free radicals from the effective oxygen group. Hydrogen peroxide also has a common role with protease by analyzing proteins to release energy when exposed to stress [22]. The increase of the hydrogen peroxide root is due to the increase in the production of the single oxygen root of the photodynamic process in the process of photosynthesis where the accumulation of the oxygen root and the non-spasm leads to the transition from the activation phase of the free root to the more serious stage, the toxic hydrogen peroxide root [23], the increase in peroxide concentration is due to the primary activity of the superoxide root and the water stress results in the oxidation of NADPH NADPH by the enzyme NADPH Oxidase in Strom The plastids release hydrogen peroxide, increasing its concentration at stress [24]. The results were agreed with [25]. in its study on the Canola plant. Chloroquine (CQ) spraying also increasing of hydrogen peroxide and induce proton fluxes and free radicals leakage [26]. the levels of high MDA because of the water stress effect on lipid peroxidation of the cell membrane and loss of the flexibility of membranes functions [12]. Water stress has increased the effectiveness of the enzymatic oxidation system, which includes the enzymes SOD, CAT,. These enzymes are more effective as an anti-stress reaction resulting from the free radical activity and oxidative enzymes with stress effect and low inhibition Hydrogen peroxide that accumulates in the plastids, mitochondria, the endoplasmic reticulum, and peroxisomes, and their development into the activation stage to the interactions between the other free radicals, which stimulates the plant to activate the enzymatic these free radicals [27] this is due to the increased effectiveness of enzymatic antioxidants and increased oxidation of compounds. It is also believed that the lack of stabilization of CO2 resulting from increased effectiveness of photosynthesis and free radicals accumulation The increase in the effectiveness of the enzyme superoxide Dismutase result in response to increasing the production of superoxide radical in plastids and mitochondria, The effect of the catalytic enzyme (CAT) resulted from the increased activity and accumulation of the hydrogen peroxide and single oxygen oxides by the effect of water stress [28, 29]. The results were agreed with [30],the levels of antioxidant enzymes were reduced because the effect of chloroquine cannot balance between free radical production and the antioxidants enzymes inhibition activity and the CQ induce the toxic oxidative factors with the effect of free

radicals and Hydrogen peroxide protease Enzyme and damage in lipids metabolism and reduced the antioxidant system in cells [31].

5. Conclusion

The present study has reported that the exposure of water stress and chloroquine stimulates the production of Oxidative factors of the membranes permanent division and effectiveness as they mainly induce the production of hydrogen peroxide and protease enzyme and loss of membranous lipids metabolism with increasing the levels of Malondialdehyde compound and reduce the Free Radicals scavenging activity of antioxidants of SOD and CAT. .

6. References

[1] Al-Bari MA 2015 Chloroquine analogs in drug discovery: New directions of uses, mechanisms of actions, and toxic manifestations from malaria to multifarious diseases. *J. Antimicrob. Chemother*. **70** 1608.
[2] Kapoor KM and Kapoor A. 2020 Role of Chloroquine and Hydroxychloroquine in the Treatment of COVID-19 Infection- A Systematic Literature Review *MedRxiv* 1.
[3] Liu J, Cao R, Xu M, Wang X, Zhang H, Hu H, Li Y, Hu Z, Zhong W and Wang M 2020 Hydroxychloroquine, a less toxic derivative of chloroquine, is effective in inhibiting SARS-CoV-2 infection *in vitro Cell Discov*. **6** 16.
[4] Yazdany J and Kim AHJ 2020 Use of Hydroxychloroquine and Chloroquine During the COVID-19 Pandemic: What Every Clinician Should Know *Ann. Int. Med*. **2** 22.
[5] Singh AK, Singh A, Shaikh A, Singh R and Misra A 2020 Chloroquine and hydroxychloroquine in the treatment of COVID-19 with or without diabetes: A systematic search and a narrative review with a special reference to India and other developing countries *Diabetes Metab. Syndr*. **14** 241.
[6] Vincent MJ, Bergeron E, Benjannet S, Erickson BR, Rollin PE, Ksiazek TG, Seidah NG and Nichol ST 2005 Chloroquine is a potent inhibitor of SARS coronavirus infection and spread. *Virol. J*. **2** 69.
[7] Mattos LM and Moretti CL 2015 Oxidative Stress in Plants Under Drought Conditions and the Role of Different Enzymes *Enz. Eng*. **5** 1.
[8] Pospisil P and Parsad A 2014 Formation of singlet oxygen and protection against its oxidative damage in Photosystem II under abiotic stress *J Photochemistry Photobiol. B Biol.* **137** 373.
[9] Scandalios JG 2005 Oxidative stress: molecular perception and transduction of signals triggering antioxidant gene defenses *Braz. J. Med. Biol. Res*. **38** 995.
[10] Labudda M 2013 Lipid peroxidation as a biochemical marker for oxidative stress during drought, an effective tool for plant breeding *E-Wydawnictwo*.**1** 1.
[11] Nimse SB and Pal D 2015 Free radicals, natural antioxidants, and their reaction mechanisms *RSC Adv*. **15** 27986.
[12] Jaafar HZE, Ibrahim MH and Fakri NFM 2012 Impact of soil field water capacity on secondary metabolites, Phenylalanine Ammonia-lyase (PAL), Malondialdehyde (MDA), and photosynthetic responses of Malaysian Kacip Fatimah (*Labisia pumila* Benth) *Molecules* **17** 7305.
[13] Anjum NA, Umar S, Iqbal M and Khan NA 2011 Cadmium causes oxidative stress in mung bean by affecting the antioxidant enzyme system and ascorbate glutathione cycle metabolism *Russian J Plant Physiol* **58** 92.
[14] Kanatt SR, Arjun K and Sharma A 2011Antioxidant and antimicrobial activity of legume hulls *Food Res. Int.* **44** 3182.

[15] Velikova, V., Yordanov, I. and Edreva, A. (2000) Oxidative stress and some antioxidant systems in acid rain Treated Bean Plants: Protective Role of Exogenous Polyamines. Plant Science, 151: 59-66.
[16] Kunitz, M. (1947). J. Gen. Physiol. 30: 291-296 (Cited by Subramanian, A.R. and Kalnitsky, G 1964. The major alkaline protease of Aspergillus oryzae, Aspergilopeptidase B.I. Isolation in homogenous form. Biochemistry. 3 (12) : 1861-1867.
[17] Radha, P. (2010) . Antioxidants Responses Evoked in vitro and in vivo by Bacopa monnieri leaf extract. Ph.D. thesis , Department of Biochemistry, Vinashilingam Deemed University.
[18] Carmack, I. and Horst, J. H. (1991). Effect of aluminum on lipid peroxidation, superoxide dismutase, catalase, and peroxidase activities in root tips of soybean (Glycine max). Physiologia Plantarum, 83(8): 463-468.
[19] Aebi, M. (1974). Catalase. In: Bergmeyer HU, ed. Methods of Enzymatic Analysis. New York: Verlag Chemie-Academic Press. 2: 673–684.
[20] Beyer, F. W., and Fridowich, I. (1987). Assaying for superoxide dismutase activity. Some Large Consequences of minor changes in conditions. Anal. Biochem., 161(2): 559-566.
[21] S.A.S, (2012).Statistical Analysis System,Users Guide Statistical Version 9.1th ed ., SAS.Institute Inc. Cary N.C.,USA.
[22] Taiz, L., and Zeiger, E. (2010). Plant Physiology, 5th edition. Sinauer Associates, Inc., Canada. 782P.
[23] Das, K., and Roychoudhury, A. (2014). Reactive oxygen species (ROS) and the response of antioxidants as ROS-scavengers during environmental stress in plants. Front. Environ. Sci., 2(53): 1-13..
[24] Demidchik, V. (2015). Mechanisms of oxidative stress in plants: From classical chemistry to cell biology. Environ. and exper. bot. 29: 212 – 228..
[25] Mirzaee, M.; Moieni, A. and Ghanati, F. (2013). Effects of drought stress on the lipid peroxidation and antioxidant enzyme activities in two Canola (Brassica napus L.) cultivars. J. Agr. Sci. Tech., 15: 593-602.
[26] C. B. Klouda; W. L. Stone(2020). Oxidative Stress, Proton Fluxes, and Chloroquine/HydroxychloroquineTreatment for COVID-19. MDPI. Antiox. (9): 894.1-19.
[27] Rabiei, Z.; Pirdashti, H. and Hosseini, S.J. (2015). Effect of drought stress on growth parameters and antioxidative activity of coriander (Coriandrum sativum). Inter. J. Biol. Pharm., 4(7): 230-243..
[28] Rao, N.K.S. ; Shivashankara , K.S. and Laxman , R.H. (2016). Abiotic Stress Physiology of Horticultural Crops. Springer, India. 368P..
[29] Shanker, A.K., and Shanker, C. (2016). Abiotic and Biotic Stress in Plants – Recent Advances and Future Perspectives. Intech. Croatia. 768P.
[30] Saeedfar, S.; Negahban , M. and Soorestani, M.M. (2015). The effect of drought stress on the essential oil content and some of the Biochemical Characteristics of Anise Hyssop (Agastache foeniculum [Pursh] Kuntze). Euro. J. Mole. Biotech., 8(2): 103-114..
[31] E. Uzar, R. Ozay, O. Evliyaoglu, A. Aktas, M.B. Ulkay, M.E. Uyar, A. Roy, A.Z. Burakgazi, C. Turkay, and A. Ilhan (2012).Hydroxychloroquine-induced oxidative stress on the sciatic nerve and muscle tissue of rats: A stereological. Human and Experimental Toxicology..

Histological structure of the Tongue in Mongoose (*Herpestes javanicus*)

Histological structure of the Tongue in Mongoose (*Herpestes javanicus*)

Iman Sami Ahmed Al-Jumaily[1*], Marwa Khalil Ibrahim[1]and Wijdan Bashir Abid[1]

[1]Department of Biology, College of Education for Pure Science, University of Baghdad, Baghdad, Iraq.

*E-mail: memo_aljumaily@yahoo.com

Abstract. The aim of the present study was to investigate the histological structure of the tongue in Mongoose (*Herpestes javanicus*) and its related to the feeding pattern. Five adult animals were used in this study . The tongues were dissected and fixed in 10% formalin, then prepared by following stages (dehydration, clearing, and embedding).The serial section(5µ) were stained with(H&E) and some special stains.The histological examination showed that the tongue consists of three tunicae (mucosa, submucosa and musclaris) and the lining epithelium of the filiform papillae is composed of keratinized stratified squamous epithelial tissue. The cylindrical papillae are covered with a highly keratinized stratified squamous epithelial tissue, whereas the keratinized stratified squamous epithelium tissue is weakly keratinized at fungiform papillae, whilst circumvallate papillae are non-keratinized. The medullary of the papillae consists of a loose connective tissue which is considered as the lamina propria of the tongue, while the tunica submucosa consists of dense connective tissue. The muscularis is composed of skeletal muscle fibres arranged in three direction longitudinal, transverse and obliquate. The lingual glands(Von-Ebner and Weber) placed on both sides of the lingual root at the tunica submucosa and extend to the tunica muscularis .This study pointed out that the secretion of glands is mixed and the mucin is more neutral than acid.

Keywords. Mongoose , Histology, Tongue, Mucin histochemistry.

1. Introduction

The mongoose (*Herpestes javanicus*) is a mammal that belongs to the order carnivora from family of Herpstidae [1].The tongue as taste organ has important role in digestion and swallowing of food in all vertebrates [2, 3, 4]. Tongue's has been studied in different mammals, such as hedgehog (*Hemiechinus auritus*) [5] ,local mice (*Mus musculus*) [6],wild rabbit (*Oryctolagus cunculus*) [7], bat (*Pipistrillus kuhli*) [8] and Lesser hedgehog tenrec (*Echinops telfari*) [9]. The scarcity of studies in endangered wild Iraqi mammals have been a stimulant suggestion of the current study involving mongoose that no data investigated. There is no information on the structures of histological and histochemical features of the tongue in this species of wild animal in Iraq. The present study was designed to describe the microstructure of the tongue and histochemical structure of the lingual glands in mongoose and this results were compared with those of other mammals.

2. Materials and Methods

Five adult mongoose were used in this study .The animals were dissected and removed the tongues. The specimens were fixed in 10% formalin for 72 hours and processed routinely by following stages (dehydration, clearing and embedding).Serial sections(Transverse and Longitudinal) were obtained at 5µ thickness for a rotary microtome. The section were stained in haematoxylin and eosin for general histological examination and some special stains such as shiffs reaction periodic acid (PAS) for demonstrate neutral mucins, Alcian Blue (AB) (pH 2.5) for acidic mucins, PAS/AB to assess the neutral from acidic mucins and Masson's trichrome for detect collagenous fibers [10]. The slides (sections) were mounted and examined with light microscope and photomicrograph by (MEIJI TECHNO) microscope with Omax camera.

3. Results and Discussion

The histological study of the mongoose the subject of the current study showed that the tongue consists of the three tunicae ,the tunica mucosa, which consists of two layers (lining epithelium and lamina propria), tunica submucosa and tunica muscularis (Fig. 1) and this result agree with [11] while the current results contradict some studies [7, 12, 13] because their study described connective tissue as a single layer placed within the tunica submucosa- lamina propria. This difference seems to be related to the structural composition based on functional requirements. The lining epithelium consists of keratinized stratified squamous epithelial tissue and contains lingual papillae and unlike the ventral surface which is non- keratinized and free of papillae (Fig. 2) and this result corresponds to previous studies [13, 14].

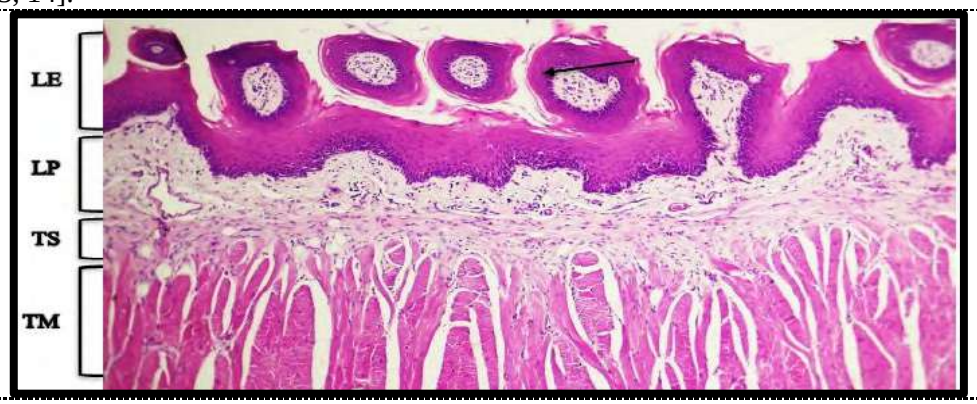

Figure 1. Cross section of lingual root in mongoose showing their components, lining epithelium (LE), lamina propria (LP), tunica submucosa (TS), tunica muscularis (TM). (H&E, 10x).

Figure 2. Cross section of lingual body in mongoose showing keratinized layer (KL). (H&E, 10x).

While lamina propria consists of loose connective tissue (Fig. 1) and this result corresponds to some studies [7] and contradict other studies which have shown that the lamina propria is composed of dense connective tissue [12, 15]. This variation is due to the pattern in the histological composition that based on function. The submucosa consists of dense connective tissue (Fig. 1) and this result is consistent with some studies [11, 16]. The presence of lingual glands in this tunica, which extends to the tunica muscularis (Fig. 3) was noted and this result is contrary to the study conducted on two species of wild rats (*Rattus wistar* and *Rattus norvegicus*) [11] because this result showed the position of the lingual glands in the lamina propria and perhaps the reason for the discrepancy is due to the fact that the animal in current study belong to carnivora order, while the mentioned study belongs to the rodents order, which vary in the pattern of nutrition. The tunica muscularis consists of skeletal muscle fibers arranged in three direction longitudinal, transvers and obliquate (Fig. 4) and this result corresponds to previous studies [5, 6, 17, 18]. This may be due to increased efficiency of the tongue in flipping and chewing food. The current study showed that the arrangement of muscle fibers varies between the three areas of the tongue, at the apex the arrangement of fiber takes an occasional direction at the medullary of the tongue and it is surrounded entirely by muscle fibers that take a longitudinal and transverse arrangement alternately (Fig. 5).

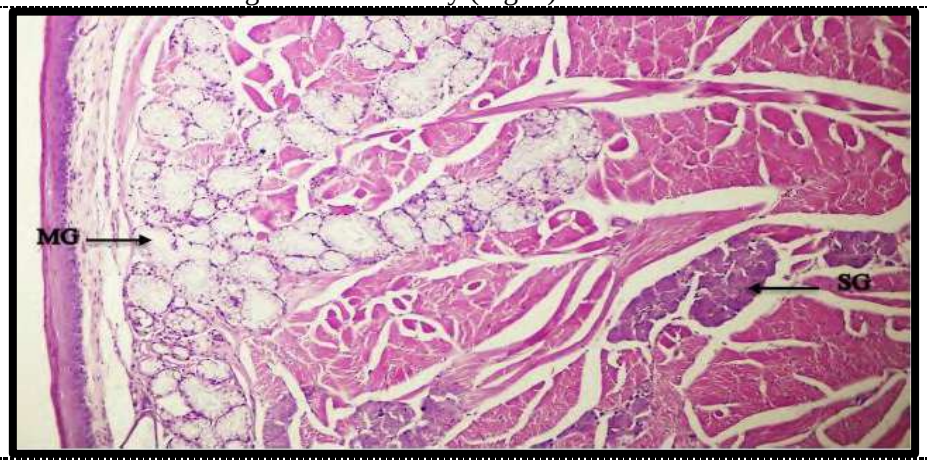

Figure 3. Lateral-cross section of lingual root in mongoose showing located of lingual glands within tunica submucosa and extened into tunica muscularis, mucous glands (MG), serous glands (SG). (H&E, 10x).

Figure 4. Cross section of lingual root in mongoose showing the tunica muscularis components and arrangement of longitudinal fibers (LF), transverse fibers (TF), obliquate fibers (OF). (H&E, 4x).

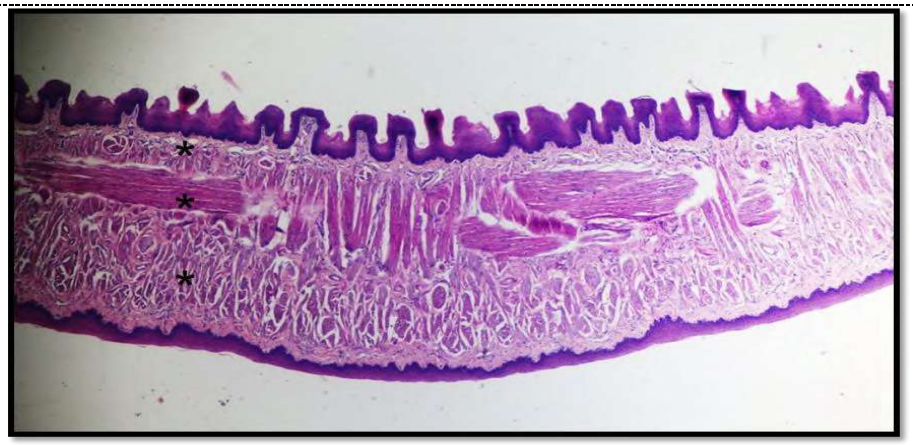

Figure 5. Cross section of lingual apex in mongoose showing the arrangement of muscle fibers (*) (H&E, 4x).

It was also noted that the surface layer of tunica muscularis at the dorsal and lateral surface in each body and root of the tongue is the arrangement of the fiber with a longitudinal and transverse exchange, while the muscular fibers at the core of the tongue are transverse as they take a radial form adjacent to the both sides the transverse fiber arrangement form in the shape of V letter (Fig. 6). While surface layer's fiber of tunica muscularis in the ventral side of tongue takes a longitudinal arrangement and there are blood vessels and nerves (Fig. 7). These results are in line with the results of [17] and this complexity in the arrangement of fiber is due to this animal depends on tongue largely during feeding as well as the fact that the muscle fibers form a basic mechanics to achieve different and precise movements of the tongue during chewing.

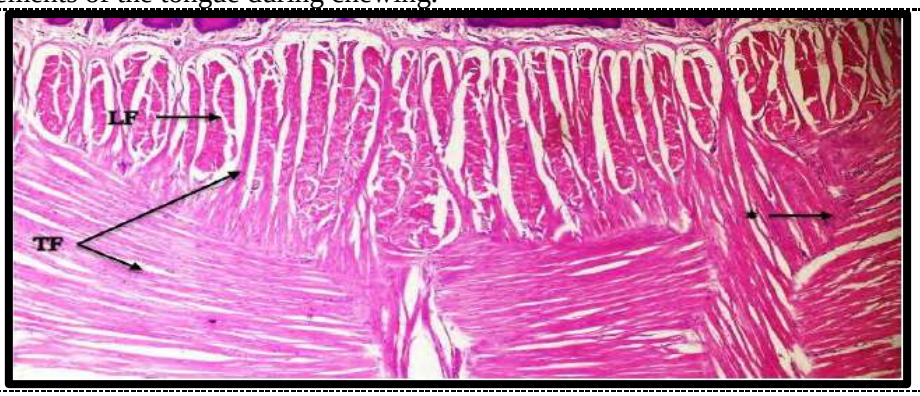

Figure 6. Cross section of lingual body in mongoose showing longitudinal fibers (LF), transverse fibers (TF) alternately, muscle fibers in form of V letter (*). (H&E, 10x).

Figure 7. Cross section of lingual body in mongoose showing keratinized layer (KL). (H&E, 10x).

This study showed that the lingual glands are positioned on both sides of the lingual root in the tunica submucosa and extend to the tunica muscularis (Fig. 3) and this result is contrary to the result of Lesser hedgehog tenrec (*Echinops telfairi*) [9] because the lingual glands are placed between the skeletal muscle fibers of tunica muscularis. The current study showed the presence of two types of glands first is the serous glands (von-Ebners) that fall forward (Fig. 8), the other type is mucous gland and seromucous gland (Weber's) which are positioned backwards (Fig 9), and this result is in line with many studies [5, 13, 18, 20]. Moreover, at the current study used some special stains to detect the type of secretions resulting from these glands. It was noted that the mucous glands give a positive result when stained with PAS, as they appear in a reddish purple color and this indicates that neutral mucin (Fig.10) and also give a positive result when stained with AB, pH: 2.5 and appear in a blue color, this indicated that the resulting secretion is acidic mucin material (Fig. 11) and these results correspond to some studies [13, 20]. But when stained in (PAS/AB, pH: 2.5) it is noted that many cells appear in a reddish purple color (implying that the secreted mucins are neutral) with a small number of cells in blue color (evidence of acidic mucins). We can conclude that the secretion of the glands is mixed mucins that are more neutral than acidic (Fig. 12) and these results are relatively consistent with the result of [13] and that this variation in the type of glandular secretions depends on the nature of the food eaten by the animal as mucous secretions of Weber's glands help to swallow food as well as facilitate the movement of the tongue, but the serous secretions of von-Ebners glands are centered in the partial digestion of food because it contains digestive enzymes.

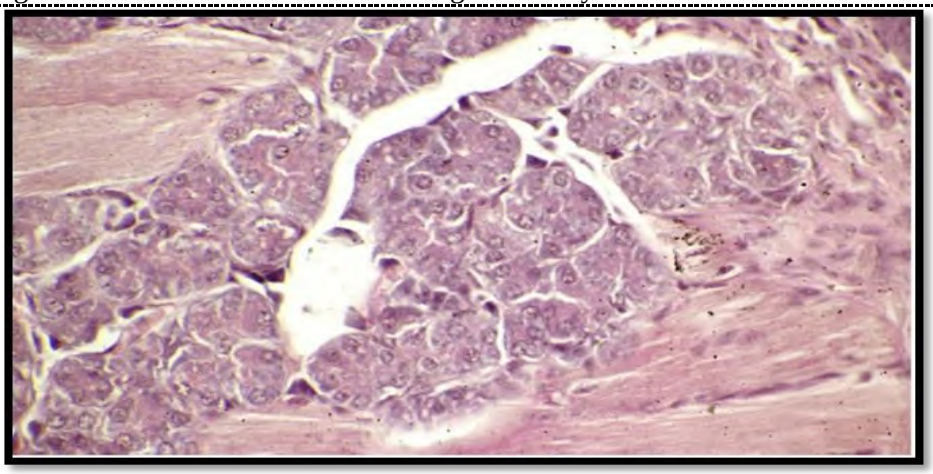

Figure 8. Cross section of lingual root in mongoose showing serous glands (von-Ebners). (H&E, 40x).

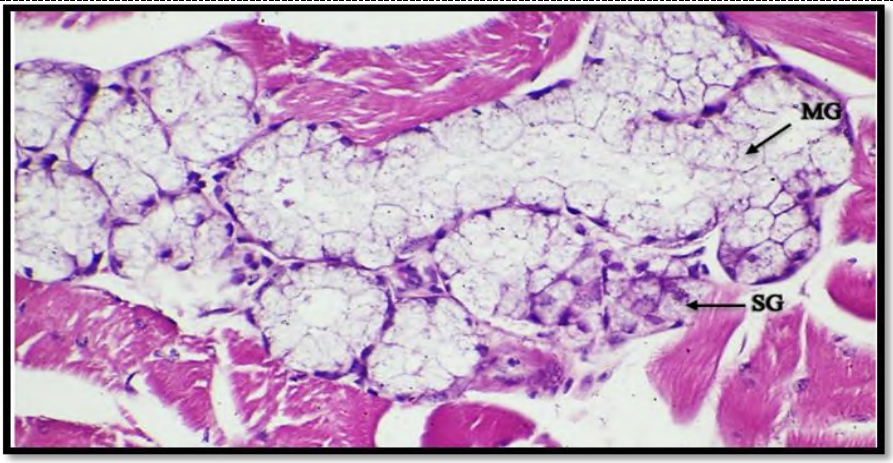

Figure 9. Cross section of lingual root in mongoose showing mucous glands (MG), serous glands (SG) (H&E, 40x).

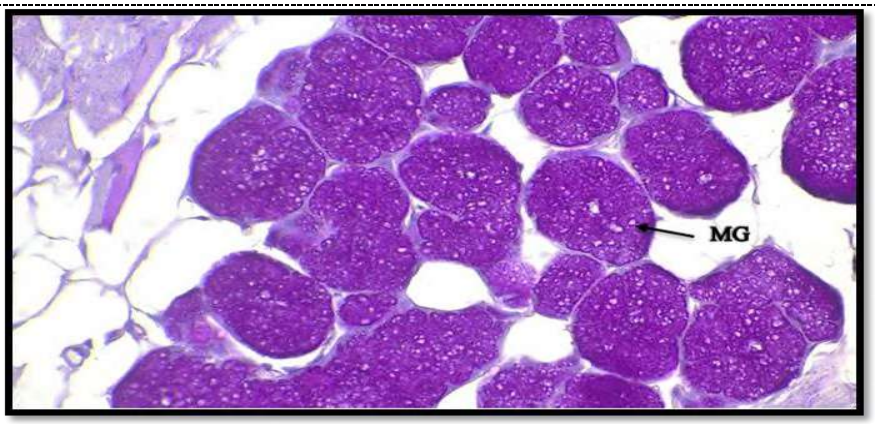

Figure 10. Cross section of lingual root in mongoose showing the positive reaction of mucin with PAS stain, mucous glands (MG). (PAS stain, 40x).

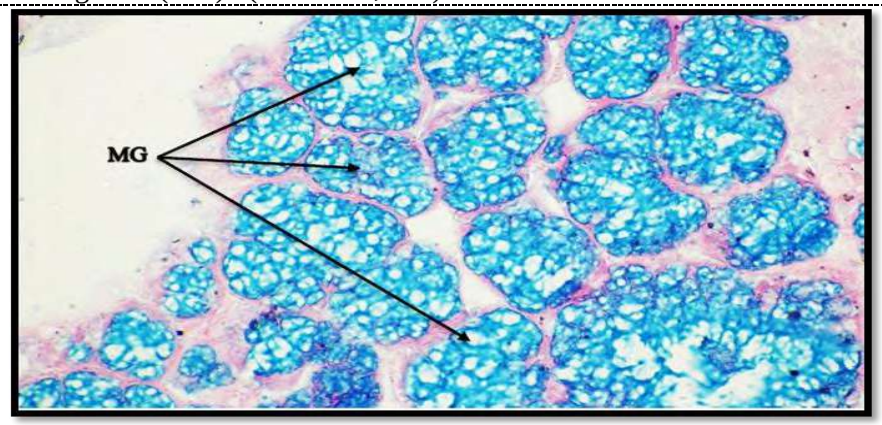

Figure 11. Cross section of lingual root in mongoose showing the positive reaction with AB stain, mucous glands (MG). (AB stain, 40x).

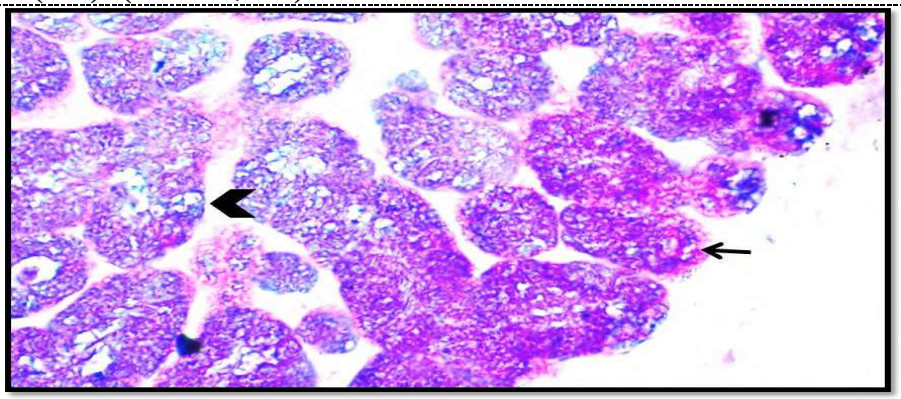

Figure 12. Cross section of lingual root in mongooe showing mucous glands and the positive reaction with PAS/AB stain, the purple color is dominant (arrow) while a little blue color (arrow head) is observed which means that the mucin is a mixed type (PAS/AB stain, 40x).

The dorsal surface of tongue's mongoose differs from the ventral surface as it contains lingual papillae, while the ventral surface is devoid of papillae, but it is characterized by the presence of rod like structure a called Lyssa [21] that consisting of skeletal muscle fibers penetrating between them the connective tissue to form bundles (Fig. 13) and this result is consistent with some studies that indicated the presence of this structure in their study animals [18, 22, 23]. While some studies are contrary in terms of the histological composition of Lyssa, the study of [24] showed that the

composition of Lyssa in the tongue of both the cat and the dog consists of a dense connective tissue, while the study of [18] stated that this composition in persian leopard consists of hyaline cartilage surrounded by connective tissue, and Lyssa's function may be that increases the efficiency of tongue movement, making it easier to flip and swallow the bite. The dorsal surface of tongue's mongoose is characterized by presence of lingual papillae that divided into mechanical papillae (filiform, cylindrical) and gustatory (fungiform, circumvallate) [21],who described the morphology of the tongue in general and , in addition, that shape, situated and distribution of papillae. The histological examination showed that the filiform papillae are covered with keratinized stratified squamous epithelial tissue and medullary of papillae composed of a loose connective tissue (Fig. 14). This result is consistent with other studies [12, 18, 20]. But it was noted that cylindrical papillae is covered with highly keratinized stratified squamous epithelial tissue and papillae's medulary composed of loose connective tissue (Fig. 15) and this result is consistent with previous references [2, 4, 18] and the role of these two types of lingual papillae (filiform and cylindrical) revolves around their mechanical function that represented by holding food and preventing it from slipping because the food of the mongoose is soft. Where the fungiform papillae is covered with a narrowly keratinized stratified squamous epithelial tissue and the dorsal surface of the papilla contains taste buds, while the medullary of papillae consists of a loose connective tissue (Fig. 14). This result is consistent with other studies [9, 12, 13, 25], while disagreement with the study of local mouse (*Mus musculus*) [6] because of their fungiform papillae lacks taste buds.

Figure 13. Cross section of lingual body in mongoose from ventral side showing: Lyssa (Ly), ventral side (V) ,Connective Tissue(CT). (Masson's trichrome, 4x).

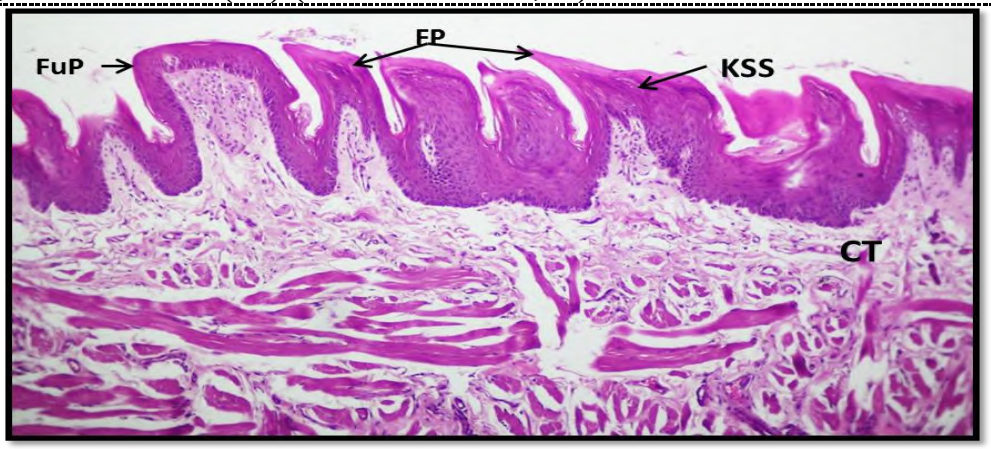

Figure 14. Cross section in tongue of mongoose showing: filiform papillae (FP), fungiform papillae (FuP), Keratinized Stratifed Squamous (KSS), Connective Tissue(CT) (H&E 10x).

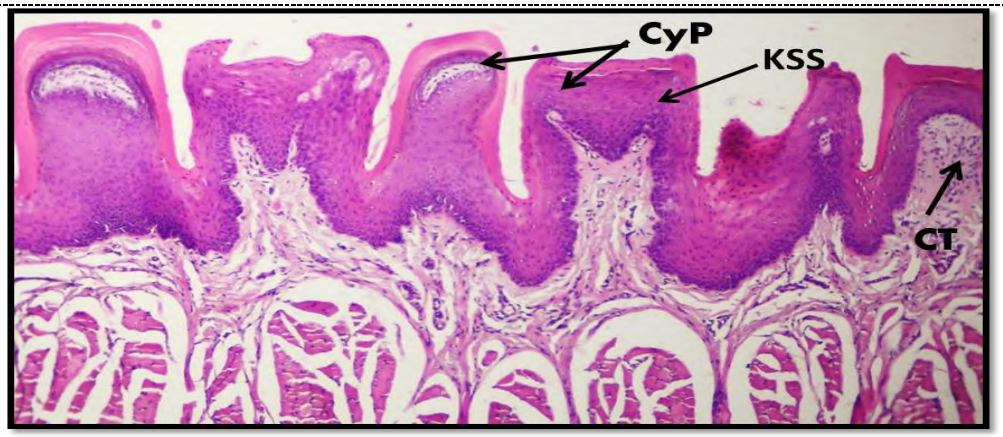

Figure 15. Cross section of lingual body in mongoose showing: cylindrical papillae (CyP) , Keratinized Stratifed Squamous (KSS), Connective Tissue(CT) (H&E, 10x).

The circumvallate papillae are covered with non-keratinized stratified squamous epithelium tissue and contain taste buds on the dorsal and lateral surface of the papillae, the medullary consisting of loose connective tissue, and surrounded by a groove and pad (Fig. 16) and this result corresponds to other studies [6, 18, 26, 27] and the reason of free these papillae from keratinized are allow the growth of taste buds and the performance of their function. The histological study showed that taste buds look like barrels in shape and consist of gustatory-sensory cells and are immersed in the epithelial tissue of gustatory papillaes (fungiform, circumvallate) and this result is agree with previous studies [5, 13]. Many references also showed that the cells of the taste bud consist of three types represented by gustatory cells, supporting cells and basal cells (Fig. 17) and this results is a compatibility with some studies [6, 12, 26]. The histological structure of these buds is associated with their taste function by receiving nutrients through their openings after the dissolving food elements are melted by the digesting enzymes of the serous glands (von-Ebners) to be distributing them over the surface of the tongue in general, including taste buds.

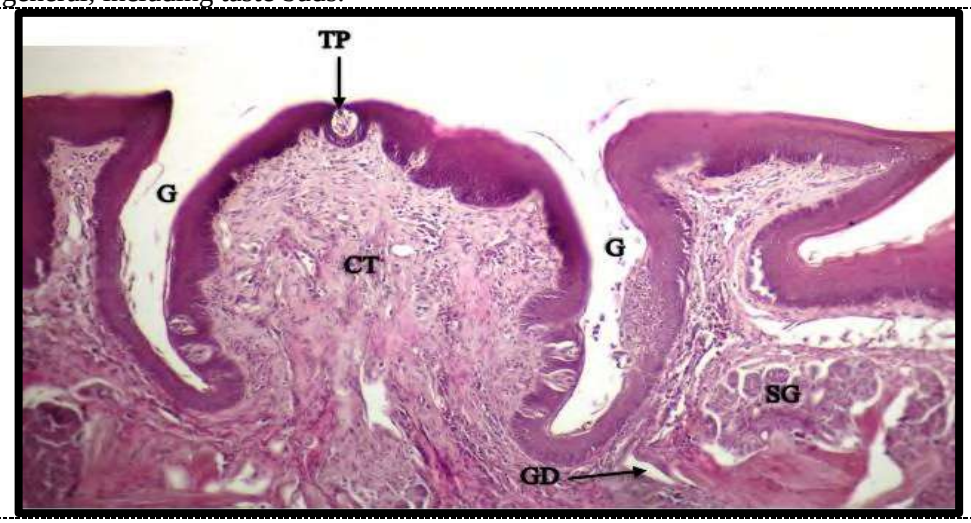

Figure 16. Longitudinal section of lingual root in mongoose showing circumvallate papillae components (CP), taste buds (TB), glosbe (G), serous glands (SG), gland duct (GD), connective tissue (CT). (H&E, 10x).

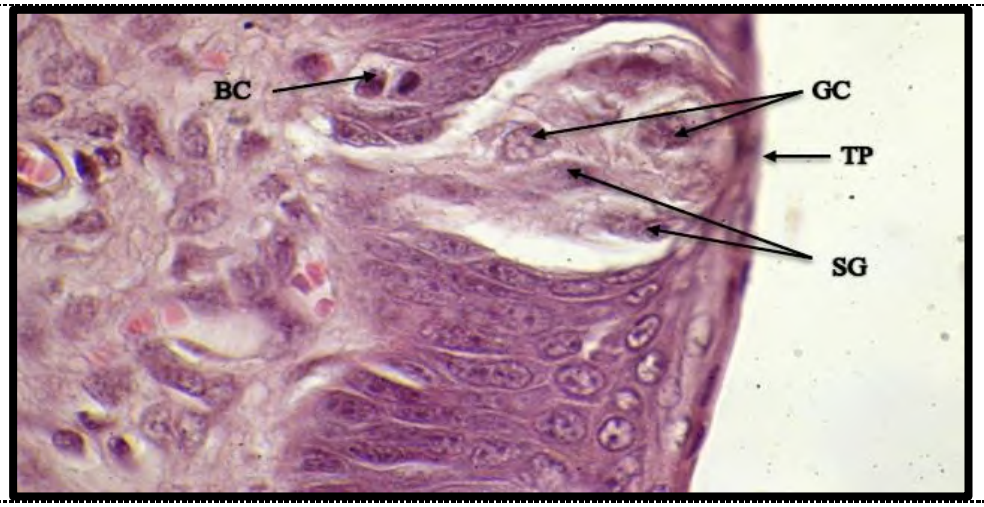

Figure 17. Longitudinal section of circumvallate papillae of lingual root in mongoose showing components of taste buds, gustatory cells (GC), supporting cells (SC), basal cells (BC), taste pore (TP). (H&E, 100x).

4. References

[1] Al-Sheikhly OF and Haba MK 2014 *Field Manual for wild mammals in Iraq* Publications of the College of Science for women / University of Baghdad 89.
[2] Emura S, Hayakawa D, Chen H and Shomura S 2004 Morphology of the lingual papillae in the tiger *Okajimas Folia Anat. Jpn*. **81** 39.
[3] Emura S, Okumura T and Chen H 2007 Morphology of the lingual papillae in the Japanese Marten *Okajimas Folia Anat. Jpn.* **84** 77.
[4] Emura S, Okumura T and Chen H 2013 Morphology of the lingual papillae in the jaguar *Okajimas Folia Anat. Jpn*. **89** 93.
[5] Jabbar AI 2014 Anatomical and histological study of tongue in the hedgehog (*Hemiechinus auritus*) *IJRSR*. **5** 760.
[6] Abd Al-Rhaman SA, Al-Fartwsy AR and Shuaily EH 2016 Morphohistological study of the tongue in local mice species by using special stain *J. Amer. Sci*. **12** 13.
[7] Al-Mahmodi AMM 2016 Anatomical and histological study of the tongue of wild adult male rabbit (*Oryctologus cuniculus* f. *domestica*) in Al-Najaf province *Kufa. J. Vet. Med. Sci*. **7** 79.
[8] Mutlak BH, Mnati IM and Al-Jumaily IS 2017 The morphological description and histological study of lingual papillae in the tongue bat (*Pipistrillus khuli*) *IJSR*. **6** 827.
[9] Cizek P, Hamouzova P, Gozdziewska-Hartajczuk K, Kleckowska-Nawrot J and Kvapil P 2020 Microscopic structure of the tongue in the lesser hedgehog tenrec (*Echinops telfairi*, Afrosoricida) and its relation to phylogenesis *Anat. Sci. Int*. 1.
[10] Bancroft JD and Stevens A 2010 *Theory and Practice of Histological techniques* 4th ed .Churchill Livingston, London 726.
[11] Ghassemi F and Cheshmi G 2014 Comparative histological study of tongue in two species of rat (*Rattus norvegicus* and *Rattus wistar*) *Cibtech. J. Zool*. **3** 13.
[12] Al-Jebori JGA 2007 *Anatomical and histological study of the tongue in Buffaloes (Bubalus bubalis) in middle of Iraq* MSc. Thesis, Medicine College, University of Baghdad 102.
[13] Sadeghinezhad J, Tootian Z and Javadi F 2018 Anatomical and histological structure of the lingual salivary glands in the Persian squirrel (*Sciurus anomalus*) *Anat. Sci. Int*., **93** 58.
[14] Ghassemi F and Jahromi HK 2013 Histological study of tongue in *Rousettus aegyptiacus* in the southwest of Iran (Jahrom) *Int. J. Res. Appl. Nat. Soc. Sci*. **1** 41.

[15] Wannaprasert T 2017 Morphological characteristics of the tongue and lingual papillae of the large bamboo rat (*Rhizomys sumatrensis*) *Anat. Sci. Int*. **93** 323.
[16] Taki-EL-Deen FMA, Sakr SM and Shahin MA 2013 Comparative histological study on the tongue of three species of Egyptian bats *Life. Sci. J.* **10** 633.
[17] Abayomi TA, Ofusori DA, Ayoka OA, Odukoya SA, Omotosa EO, Amegor FO, Ajayi SA, Ojo GB and Oluwayinka OP 2009 A comparative histological study of the tongue of rat (*Rattus norvegicus*), Bat (*Eidolon helvum*) and Pangolin (*Manis tricuspis*) *Int. J. Morphol*. **27** 1111.
[18] Sadeghinezhad J, Sheibani T, Memarian I and Chiocchetti R 2017 Morphological study of the Persian leopard (Panthera pardus saxicolor) tongue *Ant. Histol. Embriol*. **46** 240.
[19] Okada H, Suemitsu M, Kanno T, Tomamura R, Kuyama K, Murakami H, Kato T, Wakamatsu Y and Suzuki K 2013 Morphological features of the posterior lingual gland in the Gary Short-Tailed Opossums (*Monodelphis domestica*) *J. Hard Rissue. Biol*. **22** 489.
[20] Gozdziewska-Hartajczuk K, Kelckowska-Nawrot J, Barszcz K, Marycz K, Nawara T, Modlinska K and Stryjek R 2018 Biological aspects of the tongue morphology of wide-captive WWCPS rats: Ahistological, histochemical and ultrastructural study *Anat. Sci. Inter*. **93** 514.
[21] Ibrahim MK and Al-Jumaily IS 2020 Morphological study of the tongue in Mongoose (*Herpestes javanicus*). *Biochem. Cell. Arch*. **20**.
[22] Jackowiak H, Godynicki S, Skieresz-szewczyk K and Trzcielinska- Lorych J 2009 Scanning electron microscopic study of lingual papillae in the Arctic fox (*Alopex lagopus* L., 1758). *Ant. Histol. Embryol*. **38** 377.
[23] Shoeib MB, Rizk AZ and Hassanin AM 2014 Comparative morphological studied on lyssa in carnivores and camels with special reference to its surgical resection *J. Adv. Vet. Res*. **4** 135.
[24] Besoluk K, Eken E and Sur E 2006 Morphological studies on lyssa in cats and dogs *Vet. Med*. **51** 485.
[25] Yoshimura K, Hama N, Shindo J, Kobayoshi K and Kageyamal I 2008 Light and scanning electron microscopic study on the lingual papillae and their connective tissue core of the cape hyrax (*Procavia capensis*) *J.Anat*. **213** 573.
[26] Arora N 2013 *Gross and histological studies on the tongue of indigenous goat (Capra hircus)* MSc. thesis, College of Veterinary and animal sciences, Rajasthan university 139.
[27] Goodarzi N and Azarhoosh M 2016 Morphological study of the brandts headgehog, *Parechinus hypomelas* (Eulipotyphla, Erinaceidae) tongue *Vest. Zool*. **50** 457.

Quality study of the piped water of state company for drugs industry of Samarra and matching with the Iraqi and international drinking specification

Quality study of the piped water of state company for drugs industry of Samarra and matching with the Iraqi and international drinking specification

Rafah Talal Ahmed Alsamaraay[1*], Riadh Abbas Abdul Jabbar[1] and Tawos Mohammed Alshawany[1]

[1]Department of Biology, Collage of Sciences, Tikrit University, Iraq.

*E-mail: mtawis@yahoo.com

Abstract. The research aimed to evaluate piped water that supply the general company for pharmaceutical industry of Samarra and its suitable for drinking through the comparison with Iraqi and international standard for drinking. The study started from May (2015) until January (2016). Moreover, know the physical, chemical and bacterial properties piped water. The results showed that the piped water was matching of the drinking water by WHO and Iraqi standard. Only calcium quantity was higher than determination. The values rate for: Air and water temperature (29.44, 21.33) Cº respectively, EC (431.11) µs /cm. TDS (430) mg/L, the pH (7.7). DO (4.75) mg/L, while the BOD5 (1.25) mg/L, while Alkalinity hardness (157.77) mg/L, total hardness (155.55) mg/L, calcium and magnesium hardness (78.66, 72) mg/L Respectively. While chloride (68.22) mg/L, as for the phytonutrient, Nitrate concentration were (1.902) Mg/L, the phosphate concentration values rate (0.050) Mg/L, and silica concentration (1.981) Mg/L. The heavy metals, Cu (0.028) ppm, Iron (0.121) ppm, Zinc (0.203) ppm, Lead (Nil) ppm. And it was free from bacterial growth. Thus, quality of piped water, (completely purity).

Keywords. Piped water, Drugs industry, Samarra, Iraq.

1. Introduction

Water is the most vulnerable environments to pollution because of their distinguished quality, the negative effects of water pollution, are not only on humans, but also on trees and forest surrounding the world. Air and soil pollution is also the destination to watercraft, whether directly or indirectly [1]. In each country its importance, because it is the first coalition of a comprehensive reunion, aspiring to that country, according to professional and integrated development plans. In our Arab world the theme of water is very series, for more than reason, Arab world is the most arid areas and desertified in the world. In the other hand some Arab world are characterized by rain, and snow and many watercraft. Using water properly is a major problem in Arab world [2]. Water has also the potential to purify itself from its implications, with the help of the environmental purposes of self-purification, these pollutants are in the capacity of the source of affected to be affiliated with and processing [3]. Using contaminated water, caused many problems and disease moved to human such as cholera, typhoid and

dysentery as well as different chemicals accumulated in the soil [4]. Tigris river basement, which is electrical conductivity, and it's freshwater with a low salinity. The concentration of plant nutrients are less than organism needs [5]. Moreover, the research aims to study the environmental and biological factors of the piped water that provide the state company for drugs industry of Samarra.

2. Materials and Methods

Samples of the piped water were collected for 9 months, starting from May (2015) until January (2016). The samples collected monthly during that period. Three repetitions taken for each sample of piped water, to determine the properties of each sample according to standard methods are globally durable [6]. Air and water temperature measurement was measured using Mechanical mercury (0-120) C°, Measurement of Electrical conductivity by using Digital conductivity model WTW German origin, results expressed by µs /cm, Use the pH meter model JENWAY England origin to measurement pH, after calibration with Buffer solution [3, 5, 7]. At the beginning of measurement process. Using Winkler Azid modification method to determine the concentration of Dissolved oxygen in water according to described method [8] results expressed by mg/L. as the same method to measurement BOD_5 using dark bottles. Measurement Total Dissolved Salts by using Digital conductivity model WTW German origin, after filtration the sample, results expressed by mg/L. Measured total hardness, calcium, magnesium and chloride according to described method (9]. As well as Measured total alkalinity according to described method [10]. As followed method (11) to determine the nitrate, the active phosphate according to published method [12]. Depending on the American Society, for determine the concentration of active silica by using Spectrophotometer. In addition, heavy metals were determine by using Atomic absorption spectrum (AAS) [13]. The bacteriological testes by Total Plate Count as described in [14].

3. Results and Discussion

The physical properties of piped water as showed in Table (1) that air temperatures were variation and ranged between (10-40) C°, while water temperatures values between (7-31) C°, the high and low temperature surface water is affected by the air temperature [15]. EC values between (350-500) µs /cm, and it has related to the quality and concentration of the solvent ions in the water and increase with increased salinity [16]. TDS values between (350-500) mg/L, this increase maybe due to water containment on organic molecules or useful metals when it has found in the water such as nutrients or maybe cause water pollution by containing harmful material [17]. The physical properties of piped water matched with standard specification of Iraqi and international drinking water [18, 19, 20, 21].

Table 1. Monthly changed for physical test of piped water during the study period.

Months / Variables	May	June	July	August	September	October	November	December	January	Rate
Air temperature C°	35	36	37	40	38	34	23	12	10	29.44
Water temperature C°	25	22	25	31	23	26	20	7	13	21.33
Electrical conductivity µs /cm	370	450	500	440	460	350	450	360	500	431.11
Total dissolved salts mg/L	370	450	500	440	460	350	450	360	500	431.11

Table 2. Iraqi and International physical standard specification for drinking water [18, 19, 20, 21].

References / Determination	Central device of the standardization and Quality Control (1996)	US-EPA (2002)	CEOH (2003)	WHO (2004)
Water temperature C°	-	15-35	15	-
Electrical Conductivity µs /cm	-	1600	1600	1350
Total Dissolved Salts mg/L	1000	1000	450	1000

The chemical properties showed in Table (2), the pH values ranges between (7.3-8.2), and when compared pH values rate with the Iraqi and International properties in Table (4) which determinate that pH for natural water between (6.5-8.5), so it found within allowed range therefore not cause any problem in natural water [22]. DO values ranges between (4-5.9) mg/L, which suits a reflective with BOD5 that values ranges between (1-1.5) mg/L. As evaluate BOD5 values are typically with the pollution and temperature and inversely with DO concentration [23], that consistent by the Iraqi and International properties for drinking water Table (4). Thus, the water is excellent according to water resources that classified according to BOD5 values to excellent (1-75) mg/L, good (1.5-2.5) mg/L and poor (<2.5) mg/L [24]. The results of total alkalinity values showed between (120-250) mg/L, so it's within the Iraqi and international standard specification for drinking water. The higher of total alkalinity than the total hardness maybe belong to the high concentration of carbon dioxide from the air to water or moderation temperature, helping to soluble CO_2 in the water therefore increase of total alkalinity [25]. The total hardness values between (100-230) mg/L, so it's within the Iraqi and international standard specification for drinking water. The total hardness is close linked with magnesium and calcium salts, and these ions caused the hardness [26]. the results showed of high calcium values comparison with magnesium values, its maybe due to interact CO_2 with calcium more than its interact with magnesium [27], as the calcium values between (60-115)mg/L, which wasn't within the standard specification for drinking water. While magnesium values between (46-100) mg/L, the reason for low concentration of soluble magnesium than the calcium due to tends the magnesium to precipitation in large quantities [28]. Chloride values between (62-125) mg/L. notes the high quality of chloride in the winter compared to the summer, as well as the chloride levels are a factor for water quality, in the fresh water the flow of chloride is low levels and increasing in concentration in winter clearly, because the drift and ruining that washing the soil [29]. it's found within the Iraqi and international standard specification for drinking water, Table (4).

Table 3. Monthly changed for chemical test of piped water during the study period.

Months / Variables	May	June	July	August	September	October	November	December	January	Rate
pH	7.5	7.3	7.7	7.6	7.9	7.8	8.2	7.8	7.9	7.7
DO mg/l	5.6	5.1	4.2	4	4.6	4.3	4.8	5.9	4.3	4.7
BOD_5 Mg/l	1.1	1	1.3	1.2	1.2	1.3	1.4	1.3	1.5	1.2
Total Alkalinity mg/l	250	150	120	140	120	200	160	120	160	157.77
Total Hardness mg/l	180	100	160	150	230	100	165	155	160	155.55
Calcium Hardness mg/l	80	75	80	65	60	64	85	84	115	78.66
Magnesium Hardness mg/l	100	81	40	80	70	46	80	71	80	72
Chloride Ion mg/l	125	65	74	62	68	76	70	76	74	68.22

Table 4. Iraqi and International chemical standard specification for drinking water (18, 19, 20, 21).

References / Determination	Central device of the standardization and Quality Control (1996)	US-EPA (2002)	CEOH (2003)	WHO (2004)
pH	8.5-6.5	8.5-6.5	8.5-6.5	8.5-6.5
DO mg/l	—	—	6.5-4	—
BOD_5 Mg/l	1	—	—	—
Total Alkalinity mg/l	170	250	250	200
Total Hardness mg/l	500	250	250	500
Calcium Hardness mg/l	50	50	25	75
Magnesium Hardness mg/l	50	125	50	125
Chloride Ion mg/l	250	500	250	250

As for the phytonutrient results that showed in Table (5), the nitrate values shown between (1.102-2.702) Mg/L, it was noted increase nitrate concentration in winter, that's belong to the running and high watercraft that would be increase nitrate concentration by strong currents which causes mixing the sediments in water [30]. It's found within the Iraqi and international standard specification for drinking water, Table (6). The active phosphate values between (0.013-0.140) Mg/L, so it's found within the Iraqi and international standard specification for drinking water, Table (6). Silica values between (0.15-3.28)Mg/L, notes an increase silica comparison with the other studied phytonutrients, perhaps this increase to be more than (60%) from the earth's crust rocks and its soil contains silica, so its expected found as suitable mounts in natural water between (1-10) mg/L [7].

Table 5. Monthly changed for phytonutrients test of piped water during the study period.

Months / Variables	May	June	July	August	September	October	November	December	January	Rate
Nitrate Mg/l	1.102	1.981	2.486	2.101	1.310	1.479	2.702	1.590	2.465	1.902
Active phosphate Mg/l	0.140	0.027	0.013	0.015	0.026	0.021	0.016	0.120	0.076	0.050
Active Silica Mg/l	3.28	1.24	1.21	3.15	2.20	2.33	0.15	1.26	3.01	1.981

Table 6. Iraqi and International phytonutrients standard specification for drinking water (18, 19, 20, 21).

References / Determination	Central device of the standardization and Quality Control (1996)	US-EPA (2002)	CEOH (2003)	WHO (2004)
Active Phosphate Mg/l	0.4	0.5	—	0.4
Nitrate Mg/l	50	45	10	—

The results showed low of heavy metals values in piped water as shown in Table (7); the reason may be tend the heavy metals to adsorb on the surfers of sedimentation or forming complexes with the organic matters [31]. Cupper values between (Nil-0.099) Mg/L. Iron values between (Nil- 0.214)

Mg/L, so the heavy metals found less in pH more than 4 [32]. Zinc values between (Nil-0.811) Mg/L. Lead is most effective elements in the health, it has also proved several studies from which study [33]. The results showed free piped water during the study, As well as the heavy metals studied were low from the Iraqi and international standard specification for drinking water [18, 19, 20, 21] (Table 8).

Table 7. Monthly changed for heavy metals test of piped water during the study period.

Months / Elements	May	June	July	August	September	October	November	December	January	Rate
Cu Mg/l	0.070	0.045	Nil	0.053	Nil	Nil	0.099	Nil	0.084	0.028
Fe Mg/l	Nil	0.211	0.181	0.172	Nil	Nil	0.101	0.214	0.212	0.121
Zn Mg/l	0.034	0.712	0.023	0.811	Nil	Nil	0.053	0.115	0.081	0.203
Pb Mg/l	Nil	Nil	Nil	Nil	Nil	Nil	Nil	Nil	Nil	Nil

Table 8. Iraqi and International heavy metals standard specification for drinking water [18, 19, 20, 21].

References / Elements	Central device of the standardization and Quality Control (1996) Mg/l	US-EPA (2002) Mg/l	CEOH (2003) Mg/l	WHO (2004) Mg/l
Lead Mg/l	50	50	10	10
Cupper Mg/l	1000	1000	–	2000
Zinc Mg/l	1000	5000	5000	3000
Iron Mg/l	500	–	300	3000

The bacterial testing for water is the important testing, because its indicator for founding or absent the harmful microorganisms for health [34]. Therefore, the total bacterial count that studied, and didn't record any bacterial growth during the study. So TPC found within the Iraqi and international standard specification for drinking water, which is mount (50) cfu /ml, therefore the piped water is (completely pure), depending on the bacterial properties [35].

4. References

[1] Alhaag HA 2010 *Biology human* Department of biology sciences- Jordan University, Dar almaesar for publishing, distribution and printing, Amman, Jordan 467.
[2] Allkam FM, Alassady RK and Alkhanmy HA 2008 Algae content and underground water for two well from Alrahba wells/ sowth Najaf see/Iraq- accepted for publishing in *The-Qhar Univ. J*.
[3] Almashhadany YD and Alsangary MN 2007 Some of quantity properties for Tigris river water in Mosel, *The first scientific conference for environmental researching center and control on the contamination- Mosel University 5-6 June*.
[4] Saatumoinen K 2006 Reuse of purified wastewater in agriculture *Adv. Stud. Environ. Microbiol. Biotic*.
[5] Altaay RSA 2000 *Study the primary production for phytoplankton and some physical chemical properties in Tigris river water in Salah-Alden province* MSc. thesis, education college-Tikrit University.
[6] Abawy SM and Hassn MS 1990 *Scientific engineering of ecology water tests*. High education ministry and scientific research, Dar al hekma for printing and publishing. Mosel University-Iraq.

[7] Alsamaraay BAM 2009 *Environmental and microbial study for piping water in Salah- Alden* MSc. thesis, Science college- Tikrit University.
[8] Mackereth FJH 1963 Some Methods of water analysis for Limnologists *Fresh. Wat. Boil. Assoc. Sci. Pub*. **21** 70.
[9] (ASTM) American Society for testing and Materials 1984 *Annual Book of ASTM standard Water Printed in Easton* Md. U.S.A. 1129.
[10] Lind OT 1979 *Hand Book of Common methods in Limnology* C.V. Mos by Co., St. Louis 199.
[11] (ASTM) American Society for testing and Materials 1989 *Annual Book of ASTM standards (American Society for Testing and Materials)*. Philadelphia, USA. 1110.
[12] Strickland JDH and Parsons TR 1972 *A practical handbook of seawater analysis-Ottawa* Fisheries Research Board of Carada. 310.
[13] APHA (American Public Health Association) 1975 *AWWA and WPCF "Standard Methods for Examination of water and waste water* 14th Edition.
[14] APHA (American Public Health Association) 2003 *Standard Methods for the Examination of water and wastewater*, 20th Edition..
[15] Almindeel FAMS 2005 *Ecological study/limnology of phytoplankton in regulatory lake of Mosel dam* MSc thesis, Science college- department of biology science- Mosel University..
[16] Wetzel RG 2001 *Limnology, lake and river ecosystems* 4th ed. Academic press, An Elsevier Science imprint, San Francisco, New York, London 224.
[17] Hassan FM, Hadi R, Kassim TI and Al-Hassany JS 2012 Systematic study of epiphytic algal after restoration of al-Hawizah marshes, southern of Iraq *Int. J. Aquat. Sci.* **3** 1.
[18] Central device of the standardization and Quality Control 1996 *The Iraqi standard specification for drinking water* Iraqi specification number 417.
[19] US-EPA (United State–Environmental Protection Agency) 2002 *Office in Spector general status Report land Application of biolsoilds* No.2002-s-000004. Retrived May 15.200.
[20] CEOH (Federal-Provicial-Territorial Committec of Environmental and Occupational Health). 2003 *Summary of Guidelines for Canada Drinking Water Quality*. Healthy Environments and Consumer Safety Branch. Health Canada..
[21] WHO (World Health Organization) 2004 *Guide lines for Drinking Water Quality 2004* (3rd Ed.) .Geneva..
[22] EPA (Environment Protection Agency) 2004 *Ground water and drinking water* 19th Edition, List of Drinking Water Contaminates 70.
[23] Sundaran SM and Pandey M 2002 Trend of eater Quality of river Ghana at Varanasi using WQI Approach *Int. J. Ecol. Environ Sci.* **28** 139.
[24] Iraqi environmental Legislation 1988 *Protection and improve Iraqi environmental* Ministry of health. Baghdad- Iraq.
[25] Hassn FM, Alsharefy AN, Hindy AK and Saleh MM 2000 *Scientific assistant of ecological measurements* Biology science- Babel University.
[26] Alssafawy AYT 2007 Study of quantity and quality for liquid wastes that raised from Mosel city and its impact in quantity of Tigris river water. *The first scientific conference for environmental researching center and control on the contamination- Mosel University* 5-6 June.
[27] Salman JM 2006 *Ecological study for probability contamination in Euphrates river between Alhindia Blockage and Alkofa region-Iraq* PhD thesis, science college- Babel University.
[28] Allen J, Robert DRBR and Jonathan W 2000 *Partial skills in environmental science* Pearson Education Asidptelted, Singapre.
[29] Alrubaey AAH 2007 *Studying of organic contamination problem and biological effective on some of limnology organisms in Baghdad city* PhD thesis, education college- Ibn-Alhaetham-Baghdad University.
[30] Alfatlawy YFK 2007 *Evaluation of Efficiency projects for piped water in Baghdad* PhD thesis, Science college- Baghdad University.

[31] Kaiser E, Arscott DB, Tockner K and Sulzberger B 2004 Sources and distribution of organic carbon and nitrogen in The Tagliamento River Italy *Aquat. Sci*. **66** 103.
[32] Bochnke DN and Delumyea RD 2000 *Lab Experiments in Environment Ch*emistry Prentice hall, Inc., U.S.A .279.
[33] Avci Halim 2015 *Heavy Metal in Vegetables with Irrigated Waste water in Gaziantep, Turkey: A review of Causes and Potential for Human Health Risks*. Kilis 7, Aralik University, Science and Art Faculty, Kilis, Turkye.
[34] Aljubouri AHA 2005 *Study Germanic indicator for biological contamination and some physical chemical factors for Tigris river and the down zab river in Hawegaa city and Tikrit* MSc. thesis, education college- Tikrit University.
[35] Prescott C, Winslow CE and Mccrady MH 1950 *Water Bacteriology* John wily and Sons. Inc. New York.

First record of *Myxobolus insignis* Eiras, Malta, Varella, Pavanelli, 2005 (Myxozoa: Myxobolidae) in Iraq from gills of the common carp *Cyprinus carpio*

First record of *Myxobolus insignis* Eiras, Malta, Varella, Pavanelli, 2005 (Myxozoa: Myxobolidae) in Iraq from gills of the common carp *Cyprinus carpio*

Kefah Naser Abdul-Ameer[1] and Rana Saheb Shalal[1*]

[1]Department of Biology, College of Education for Pure Science (Ibn Al-Haitham), University of Baghdad, Baghdad, Iraq.

*E-mail: rana.shalal19@gmail.com

Abstract. The Myxozoan parasite, *Myxobolus insignis* Eiras, Malta, Varella, Pavanelli, 2005 is recorded in the present study from gills of the common carp *Cyprinus carpio* for the first time in Iraq. The fishes were caught from the Al-Ataifiya location on the Tigris River at Baghdad city during the period from January to October 2020. The measurements and description of this external parasite in addition to its illustrations were given.

Keywords. Myxozoa, *Myxobolus insignis*, *Cyprinus carpio*, Tigris River, Baghdad.

1. Introduction

Myxozoans are highly specialized metazoan parasites of aquatic hosts with a very wide host range. This diverse group of organisms is characterized by multicellular spores with polar capsules containing extrudable polar filaments. Interest in this group has intensified along with the development of aquaculture since many species cause serious disease outbreaks in farmed fish species, in both freshwater and marine environments [1]. Different fish-parasitic myxosporean is characterized by varying degrees of host specificity, while most Myxosporeans species are tissue-specific parasites, includes an intracellular stage and form spore within the cell [2]. *Myxobolus* species develop in large plasmodia which on the surface or in organs such as gills, fins, skin, eyes, heart, muscles, gall-bladder, kidneys, spleen, liver, a wall of the intestine, urinary bladder, testis and Ovaries [2,3]. The presence of myxosporea was related to epithelial hyperplasia, the fusion of lamellae, hyperplasia of mucous cells, inflammation and other pathological changes [4]. The prevalence and intensities of myxosporeans infestations were affected by the host's size, sex, organs and seasons [5]. Among the Myxozoan, species of the genus *Myxobolus* Bütschli, 1882 infects fishes with 856 nominal species throughout the world [6, 7].The first study on fish parasites in Iraq described three myxozoan parasites, namely *Myxobolus muelleri*, *M. multiplicatus* (reported as *Myxosoma multiplicata*), and M. oviformis [8]. Hence, many studies were performed that showed a record of 97 *Myxobolus* species [9]. For this, it is important to conduct more studies on fish parasites to registration more species and increase information on the parasitic fauna of freshwater fishes of Iraq.

2. Materials and Methods

Between January to October 2020, 40 specimens of the common carp *Cyprinus carpio* were collected weekly from Tigris River near Al-Ataifiya region north of Baghdad city (33°21'37.4"N 44°21'49.2"E). Fish were classified according to an account on freshwater fishes of Iraq [10]. Fresh smears the external parts (gills and surface of the body) and all internal organs (intestine, gallbladder, kidneys and liver) of fishes were examined macroscopically for visible plasmodia. Smears were made from the external and internal organs of the fish and examined with a microscope for spores. Fresh spores were photographed by a digital camera and draw with the aid of a Camera Lucida. For further examination, some spores were put into glycerol-gelatin to get permanent slides, while some other spores were fixed in absolute methanol for 2-8 minutes, and then staining them with Giemsa solution for about 25- 30 minutes in accordance [11]. Spores were described and measured according to the guidelines [12]. The scientific name of the parasite was used in accordance. [7]. All measurements are given here in μm as: minimum-maximum (mean) values. The information on the previous records of myxozoans of fishes of Iraq was obtained from the index-catalogue of parasites and disease agents of fishes of Iraq [13].

3. Results and Discussion

3.1. Myxobolus insignis Eiras, Malta, Varella & Pavanelli, 2005

Two out of 40 of common carp *Cyprinus carpio* Linnaeus, 1758 were infected with this parasite which was found on the gills of the infected fishes. The following is the description and measurements (in μm based on five specimens) of this parasite. Plasmodia of *M. insignis* appeared as small, white, irregular cysts which occurred in different size at the base of the secondary lamellae of gills. Spore Description (Figure 1). The spores are subspherical in frontal view with slightly tapering anterior end, its length is greater than the width, length 13.8-14.6 (14.2), width 11.6-12.2 (11.9), thickness 7. Polar capsules large, oval, equal in size, extend beyond the mid-length of the spore and converge at their anterior points, length 7.2-7.8 (7.5) and width 3.8-4.4 (4.2). There is a small intercapsular process at the frontal tip of the spore.

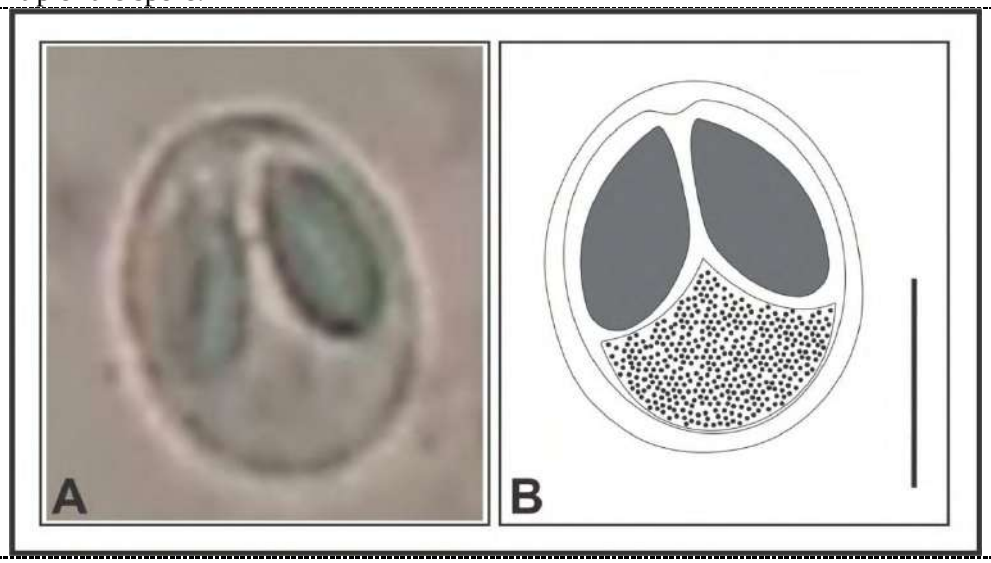

Figure 1. Myxobolus insignis: A- Photomicrograph (400 x) B- Diagrammatic drawing (Scale bar = 7.5 μm)

The descriptions and measurements of the present *M. insignis* are in agreement with those of the holotype of these parasites from secondary gill lamellae of *Semaprochilodus insignis* in Amazon River, near Manaus, Brazil [14]. Depending on the index-catalogue of parasites and disease agents of

fishes of Iraq [13], the current record of M. insignis represents its first record in Iraq, as no previous record was given for this parasite from fishes of Iraq. Previously, 14 species belonging to the genus *Myxobolus* were reported from different fish species collected from Tigris river at Al-Ataifiya location, including only *M. squamae* from *C. carpio* [15]. Although 97 *Myxobolus* species were registered recently from fishes of the different water bodies in Iraq [9], only 16 species belonging to the genus Myxobolus so far, reported from *C. carpio*. The following is a chronologically arranged list of these species with the mention of only the first record from *C. carpio* in Iraq: *M. pfeifferi* [16], *M. cyprinicola* and *M. parvus* [17], *M. muelleri* and *M. oviformis* [18], *M. dispar* [19], *M. punctatus* [20], *M. dogieli* [21] *M. intrachondrealis* [22], *M. musculi* [23], *M. squamae* [24], *M. drjagini*, *M. gigi*, *M. koi*, *M. poljanski* and *M. sphaericus* [25], besides one unidentified species [26]. With the present record of a new species *M. insignis*, the number of *Myxobolus* species from fishes of Iraq so far reaches 98 species, among which 17 species were reported from *C. carpio*.

4. Conclusion

The Myxozoan parasite, *Myxobolus insignis* Eiras, Malta, Varella, Pavanelli, 2005 for the first time in Iraq. It is the 17th species from this genus recorded from the gills of *Cyprinus carpio* Linnaeus, 1758.

5. Acknowledgement

Thanks and appreciation to Prof. Dr. Furhan T. Mhaisen for providing necessary information concerning the records of *Myxobolus* species so far known from *C. carpio* in his index-catalogue of parasites and disease agents of fishes of Iraq.

6. References

[1] Feist SW and Longshaw M 2006 *Phylum Myxozoa* In: Woo, T.K.P. (ed.) Fish diseases and disorders, Vol. 1: Protozoan and Metazoan infections, 2nd Edition. CAB International, Wallingford: 130-279.

[2] Molner K 1994 Cmments on the host, organ and tissue specificity of fish myxosporeans and on the type of their intrapiscine development *Parasit. Hung*. **27** 05.

[3] Fomena A and Bouix G 1997 Myxosporea (Protozoa: Myxozoa) of freshwater fishes in Africa: keys to genera and species *Syst. Parasitol*. **37** 161.

[4] Teixeira RJ, Eiras JC, Spadacci-Morena DD, José Guilherme Xavier JG and Lallo MA 2018 Infecção das brânquias de tilápia do Nilo (Oreochromis niloticus) por Myxosporea. *Pesq. Vet. Bras*. **38** 1085.

[5] Georges F, Timoléon T, Elysée N and Joseph T 2017 Structure and population dynamics of Myxosporeans (Myxozoa: Myxosporea), parasites of Barbus callipterus Boulenger, 1907(Cyprinidae) in the Soudano-guinean zone of Cameroon. *Int. J. Multidiscipl. Curr. Res*. **5** 1416.

[6] Eiras JC, Molnár K and Lu YS 2005 Synopsis of the species of Myxobolus Bütschli, 1882 (Myxozoa: Myxosporea: Myxobolidae) *Syst. Parasitol*. **61** 1.

[7] Eiras JC, Zhang J and Molnár K 2014 Synopsis of the species of Myxobolus Bütschli, 1882 (Myxozoa: Myxosporea, Myxobolidae) described between 2005 and 2013 *Syst. Parasitol*. **88** 11.

[8] Herzog PH 1969 Untersuchungen über die parasiten der süßwasserfische des Irak. *Arch. Fischereiwiss*. **20** 132.

[9] Mhaisen FT and Al-Jawda JM 2020 Checklists of the Species of Myxobolus Bütschli, 1882 (Cnidaria: Myxozoa: Myxobolidae) from Fishes of Iraq *Biol. Appl. Environ. Res*. **4** 127.

[10] Coad BW 2010 *Freshwater fishes of Iraq* Pensoft Publ. Sofia: 274 pp. + 16 pls. www.briancoad.com.

[11] Saha M and Bandyopadhyay PK 2017 Parasitological and histological analysis of a new species of the genus Thalohanellus and description of a myxozoan parasite (Myxosporea: Bivalvulida) from cultured ornamental goldfish, *Carassius auratus* L. *Aquac. Rep*. **8** 8.
[12] Lom J and Arthur JR 1989 A guideline for the preparation of species descriptions in Myxosporea *J. Fish Dis*. **12** 151.
[13] Mhaisen FT 2020 *Index-catalogue of parasites and disease agents of fishes of Iraq* (Unpublished: mhaisenft@yahoo.co.uk).
[14] Eiras JC, Malta JCO, Varella AMB and Pavanelli GC 2005 *Myxobolus insignis* sp. n. (Myxozoa, Myxosporea, Myxobolidae), a parasite of the Amazonian teleost fish *Semaprochilodus insignis* (Osteichthyes, Prochilodontidae) *Mem. Inst. Oswaldo. Cruz Rio de Janeiro* **100** 245.
[15] Abbas JA 2019 *The parasitic fauna of some species of fishes from Tigris river at Al-Autaifia region, Baghdad province, Iraq*. MSc. Thesis, Coll. Educ. Pure Sci. Ibn Al-Haitham, Univ. Baghdad: 140 pp. (In Arabic).
[16] Ali NM., Salih NE and Abdul-Ameer KN 1987 Parasitic fauna of some freshwater fishes from Tigris river, Baghdad, Iraq I: Protozoa *J. Biol. Sci. Res*. **18** 11.
[17] Abdullah SMA 1997 *First record of five species of Myxobolus of some fishes from Dokan Lak*e. Zanco, Spec. Issue (1). Proc. 3rd Sci. Conf. Univ. Salahaddin, Erbil: 3-4 June 1997: 14-21. (In Arabic).
[18] Al-Zubaidy AB 1998 *Studies on the parasitic fauna of carps in Al-Furat fish farm, Babylon province, Iraq* PhD. Thesis, Coll. Sci., Univ. Babylon: 141 pp. (In Arabic).
[19] Mohammad-Ali NR, Balasem AN, Mhaisen FT, Salih AM and Waheed IK 1999 Observations on the parasitic fauna in Al-Zaafaraniya fish farm, south of Baghdad. *Veterinary* **9** 79.
[20] Al-Daraji SAM, Salim YAK, Jori MM and Nasir AM 1999 Endoparasites of some cultured fishes from Basrah *Basrah J. Sci., B*, **17** 81.
[21] Al-Rubaie IA, Mohammad-Ali NR, Balasem AN and Al-Jawda JM 2003 Study on fish diseases in Diyala river *Iraqi J. Agric.* **8** 40. (In Arabic).
[22] Bannai MAA, Al-Daraji SAM, Jarallah HM and Hussian NA 2005 *Three new parasites recorded from the common carp, Cyprinus carpio L., 1758, captured from southern part of Al-Hammar marshes* 1st Sci. Conf. Rehabilit. South. Iraq Marshes. Basrah: 11-12 April 2005. (Abstract)..
[23] Al-Jawda JM and Asmar KR 2013 Myxosporeans (phylum Myxozoa) parasitic on some fishes from Tigris river at north, mid and south of Baghdad province, Iraq *Basrah J. Agric. Sci*. **26** 106.
[24] Atwan FK 2016 *Parasitic infections in some fishes from Tigris river, Al-Graiat location in Baghdad province, Iraq*. MSc. Thesis, Coll. Educ. (Ibn Al-Haitham), Univ. Baghdad: 136 pp. (In Arabic).
[25] Mansoor NT 2019 *Morphological and histopathological investigation of myxozoan parasites in some fish species in Tigris river/ Baghdad city*. PhD. Thesis, Coll. Sci., Univ. Tikrit: 160 pp.
[26] Abdullah SMA 2004 Comparison between the parasitic infections of fishes caught in two of each of small natural habitats and fish farms in Erbil city *Zanco* **16** 43 (In Arabic).

Detection of *Bacillus cereus* genes responsible for diarrheal and emetic toxins

Detection of *Bacillus cereus* genes responsible for diarrheal and emetic toxins

Ban M.S. Saeed[1*], Basil A. Abbas[2] and Shaker A. N. Al-Jadaan[3]

[1]Al-Zahraa Medical College, University of Basrah, Basrah, Iraq.
[2]Department of Microbiology, College of Veterinary Medicine, University of Basrah, Basrah, Iraq.
[3]Almaaqal University, Basrah, Iraq.

*E-mail: ban.saeed@uobasrah.edu.iq

Abstract. *Bacillus cereus* isolated from different food sources. The diarrheal toxin genes such as *cytK*, hemolytic enterotoxin (*hblA*, *hblC* and *hblD*), non-hemolytic enterotoxin (*nheA*, *nheB* and *nheC*), *bceT* and *entFM* in addition to emetic toxin gene were detected by PCR. The *cyt K* gene was observed in 94.87 % of the isolates. *entFM* and emetic toxin gene were found very rare in all food samples at the percentage 2.56% and 7.69% respectively. Uncooked rice which has a highest number of bacterial isolation, also showed relatively high percentage of the *cytK* and *bceT* genes (90%). These two genes present in 100% of *Bacillus cereus* isolates in most food samples. Bacteria isolated from burger meat contain all investigated genes.

Keywords. *Bacillus cereus*, diarrheal toxin, emetic toxin.

1. Introduction

Bacillus cereus is a Gram-positive, facultative anaerobic, spore-producing, motile, bacterium in the form of a rod. Enterotoxins produced by bacteria in intestine can cause diarrhea. 10^5–10^7 cells or spores if ingested with food, heat labile toxins are produced. Incubation period of this bacterium is range between 8-16 hours. The sign of toxicity of *B. cereus* toxins appears as nausea, vomiting, diarrhea and abdominal pain [1, 2]. Three toxins produced during the vegetative cell growth of *B. cereus* in the intestine that caused diarrheal syndrome, Cyt K, NHE and HBL [4, 5, 6]. The first enterotoxin-hemolysin BL (HBL) was discovered by [7]. NHE toxin on three molecular types A, B, and C. Bacteria need these proteins for cytotoxicity of multi-component enterotoxins [5]. The HBL complex is encoded by genes on a single operon. The B, L1 and L2 proteins are encoded by the *hblA*, *hblD* and *hblC* genes [8, 9]. NHE toxin is a major cause of cytotoxicity in *B. cereus* [10]. The emetic disease is caused by a toxin produced by *B. cereus* called cereulide. This toxin showed stability against heat, acid, and trypsin. Several studies have been done previously for bacterial food contamination [11, 12 13, 14, 15]. This study was done to investigate the *B. cereus* that responsible for food poisoning by detecting the presence of diarrheal and emetic toxin genes.

2. Materials and Methods

2.1. Bacterial strains

Bacillus cereus isolates from different food sources were previously described [16]. The DNA of all isolates was extracted by genomic DNA kit (company and origin). The identification of the isolates was done by DNA sequencing using 16S *rRNA* gene [16].

2.2. Detection of diarrheal and emetic toxin genes by polymerase chain reaction

The primers used in this study for the detection of diarrheal and emetic toxin genes with the anticipated size of the amplified product were listed in Table 1.

Table 1. Primers of diarrheal and emetic toxins genes.

Genes	Primers 5`-3`	Program cycling	Product (bp)	References
entFM	**F;** ATGAAAAAA GTA ATT TGC AGG **R;** CGT GCA TCT GTT TCA TGAAA	Initial denaturation 94°C 5min, denaturation 94°C 30sec, annealing 50°C 45 sec, extension 72°C 45 sec , final extension 72°C 5 min , 35 cycles	1269	[17]
hblA	**F;** AAG CAA TGG AAT ACA ATG GG **R;** AGA ATC TAA ATCATGCCA CTG C	Initial denaturation 95°C 15min, denaturation 95°C 30sec, annealing 60°C 30 sec, extension 72°C 1min, final extension 72°C 5 min , 40 cycles	1154	[18]
hblC	**F;** GAT AC(T,C) AAT GTG GCA ACT GC **R;** TTG AGA CTG CTC G(T,C)T AGT TG	Initial denaturation 94°C 2min, denaturation 94°C 15sec, annealing 55°C 45 sec, extension 72°C 2min, final extension 72°C 5 min , 35 cycles	740	[18]
hblD	**F;** ACC GGT AAC ACT ATT CAT GC **R;** GAG TCC ATA TGC TTA GATGC	Initial denaturation 94°C 2min, denaturation 94°C 15sec, annealing 55°C 45 sec, extension 72°C 2min, final extension 72°C 5 min , 35 cycles	829	[18]
nheA	**F;** TAC GCT AAG GAG GGG CA **R;** GTT TTT ATT GCT TCA TCG GCT	Initial denaturation 94°C 2min, denaturation 94°C 15sec, annealing 55°C 45 sec, extension 72°C 2min, final extension 72°C 5 min , 35 cycles	499	[19]
nheB	**F;** CTA TCA GCA CTT ATG GCA G **R;** ACT CCT AGC GGT GTT CC	Initial denaturation 94°C 2min, denaturation 94°C 15sec, annealing 55°C 45 sec, extension 72°C 2min, final extension 72°C 5 min , 35 cycles	769	[19]
nheC	**F;** CGG TAG TGA TTG CTG GG **R;** CAG CAT TCG TAC TTG CCA A	Initial denaturation 94°C 2min, denaturation 94°C 15sec, annealing 55°C 45 sec, extension 72°C 2min, final extension 72°C 5 min , 35 cycles	581	[19]
bceT	**F;** CGT ATC GGT CGT TCA CTC GG **R;** TTT CTT TCC CGC TTG CCT TT	Initial denaturation 94°C 2min, denaturation 94°C 15sec, annealing 56°C 45 sec, extension 72°C 2min, final extension 72°C 5 min , 35 cycles	924	[19]
cytK	**F;** CGA CGT CAC AAG TTG TAA CA **R;** CGT GTG TAA ATA CCC CAG TT	Initial denaturation 94°C 1min, denaturation 94°C 45sec, annealing 54°C 1 min, extension 72°C 2min, final extension 72°C 5 min , 35 cycles	565	[20]
Emetic Toxin gene	**F;** GAC AAG AGA AAT TTC TAC GAG CAA GTA CAA T **R;** GCA GCC TTC CAA TTA CTC CTT CTG CCA CAG T	Initial denaturation 95°C 15min, denaturation 95°C 30sec, annealing 60°C 30 sec, extension 72°C 1min, final extension 72°C 5 min , 40 cycles.	635	[21]

3. Results

3.1. Detection of diarrheal toxin genes

3.1.1. Detection of cyt K gene

cyt K gene was found in 94.87% of the isolated bacteria. No significant differences (P > 0.05) in rate of detection of this gene in the investigated samples (Table 2, Figure 1).

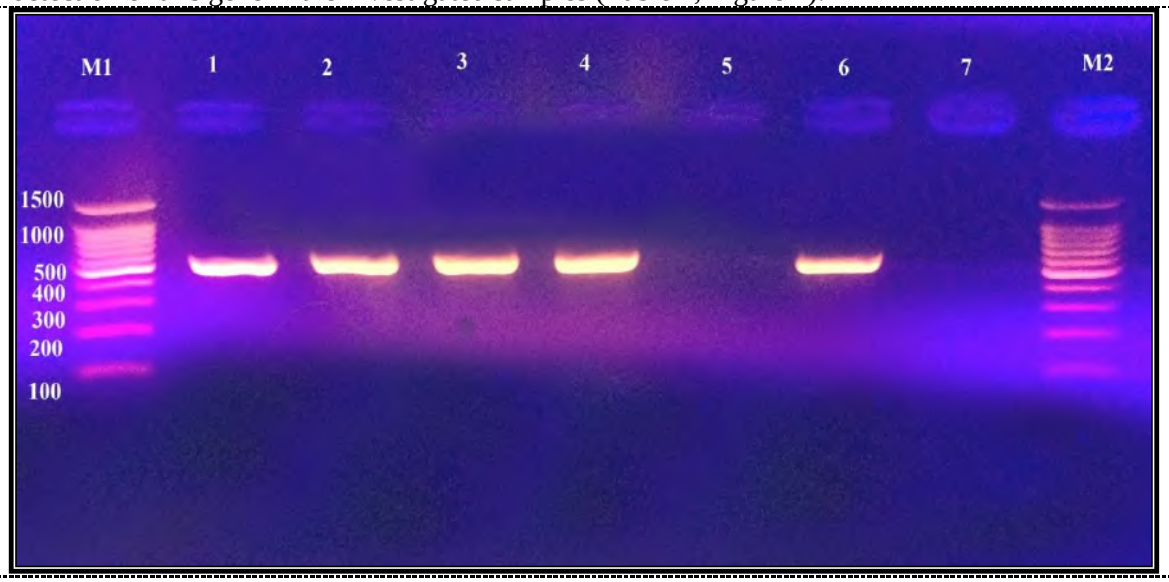

Figure 1. PCR amplification of *cytK* gene of *Bacillus cereus* isolates. M1 = Ladder; 1-4 & 6 = *cyt K* gene approximately 565 bp.; 5 = negative for *cyt K* gene; 7 = control negative.

3.1.2. Detection of (hbl and nhe) genes by multiplex PCR

Bacillus cereus isolated from different food were tested for presence of genes code for enterotoxin such as *hblA, hblC, hblD, nheA, nheB,* and *nheC* by multiplex PCR (Table 2, Figure 2). In cream isolates, the genes were detected in 6 isolates. *hblC* gene had the highest percentage 100.00 % followed by *hblA, hblD, nheA, nheB* and *nheC* genes were found in 50.00, 16.66, 50.00, 66.66 and 50.00%, respectively. In beef isolates, the genes were detected in 6 isolates. *hblC* gene had the highest percentage 66.66 % followed by *nheB* 50% and *hblD, nheA* and *nheC* genes were found as 33.33% for each one. The gene *hblA* was not found. In frozen beef isolates, the genes were detected in 5 isolates. *hblC* and *nheB* genes had the highest percentage 60.00 % followed by *nheA* and *nheC* genes were found in 40.00 % . The lowest percentage was found in *hblA* gene. The *hblD* gene was not found in all of the isolates. In burger isolates, the genes were detected in 7 isolates. *hblC* and *nheB* genes had the highest percentage 57.14 % followed by *hblD, nheC* genes were found in 42.85%. The lowest percentage was found in hblA and nheA in 28.57%. In cooked rice isolates, the genes were detected in 5 isolates. hblC, hblD and nheC genes had the highest percentage 40.00 % followed by *hblA, nheA* and *nheB* genes were found in 20.00 % for each one. In uncooked rice isolates, the genes was detected in 10 isolates. *hblC, hblD* and *nheC* genes had the highest percentage 40.00 % followed by *hblA, nheA* and *nheB* genes were found in 20.00 % for each one.

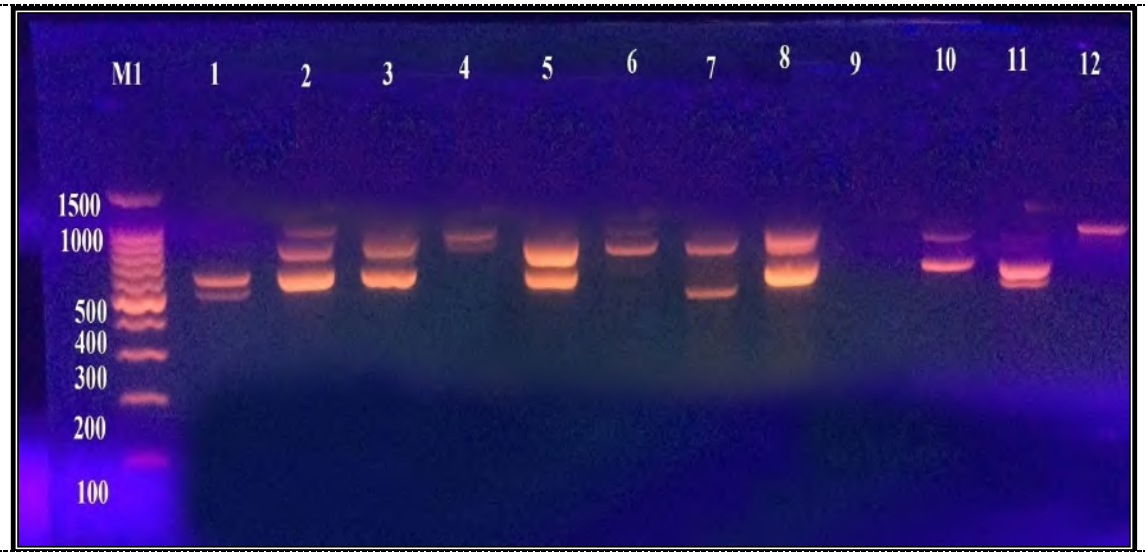

Figure 2. PCR amplification of *hblACD* and *nheABC* genes of *Bacillus cereus* isolates. Lane (M1)= Ladder, Lane 1 =*nheB, nhe* (769 and 581) bp, Lane 2 = *hblA*, hblD and *nheB*, (1154, 829 and 769) bp, Lane 3 = *hblA, hblD, nheB* and *hblC* (1154, 829, 769 and 740) bp, Lane 4 = *hblD* and *nheB* (829 and 769) bp, Lane 5 = *hblA, nheB* and *hblC* (1154, 769 and 740) bp, Lane 6 = *hblA, hblD, nheB* and *hblC* (1154, 829, 769 and 740) bp, Lane 7 = *nheB* and *nheC* (769 and 581) bp, Lane 8 = *nheB* and *hblC* (769 and 740) bp, Lane 9 = negative for genes. Lane 10 = *hblD, nheB* and *hblC* (829, 769 and 740) bp, Lane 11 = *nheB, hblC* and *nheC* (769, 740 and 581) bp, Lane 12 = *nheB* (769 bp).

3.1.3. Detection of bce T gene

The *bce* T gene was detected in 37 isolates (94.87 %) out of 39 isolates. The high rate (100%) found in beef, burger, frozen beef, and cooked rice. The lowest percentage was found in cream 83.33%. Results showed differ significantly ($P < 0.05$) in the detection of this gene in tested samples (Table 2, Figure 3).

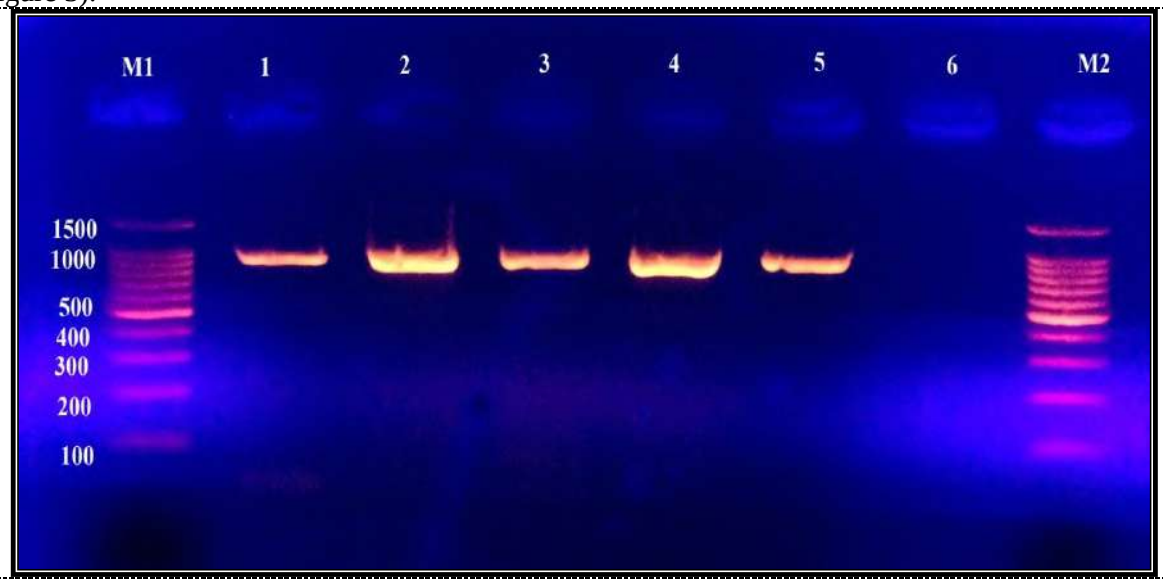

Figure 3. PCR detection of enterotoxin *bceT* gene M =Ladder; 1- 5 =positive for enterotoxin *bceT* gene approximately 924 bp.; 6= negative control.

3.1.4. Detection of enterotoxin (ent FM) gene

The *entFM* gene was detected in 1 isolate (2.5%) out of 39 isolates, it was found in burger 16.66%. The difference is non-significant (P > 0.05) in the detection of this gene in the tested samples (Table 2, Figure 4).

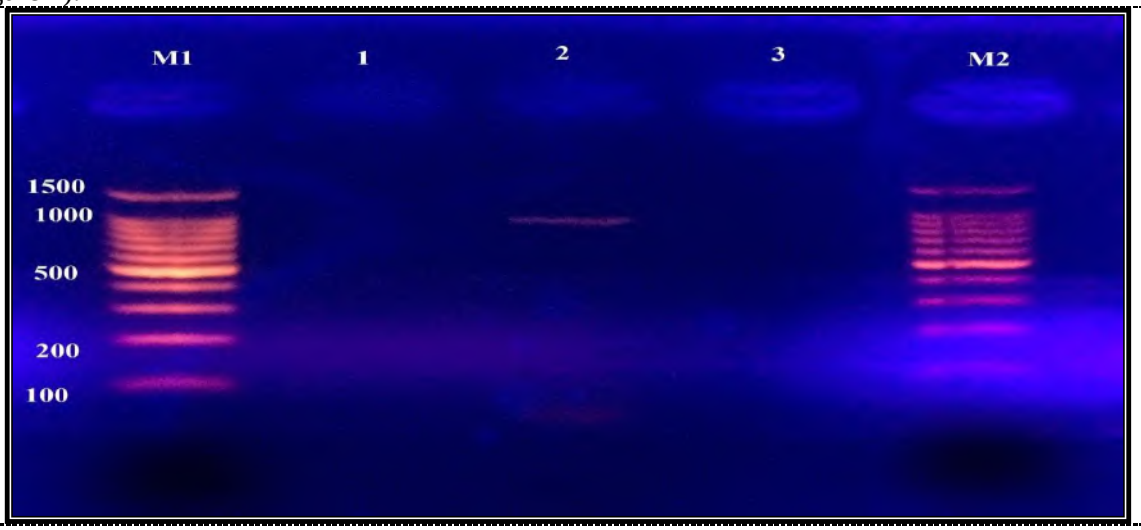

Figure 4. Detection of enterotoxin ent FM gene. M1, M2=Ladder; Lane 2=positive for *ent (FM)* gene approximately 1269 bp.

3.1.5. Detection of emetic toxin gene in Bacillus cereus

The emetic gene was detected in 3 isolates (7.6 %), distributed in cream and frozen beef and burger in 16.66, 20 and 14.28 %, respectively but was not detected in beef, cooked rice, and uncooked rice. The differences is non-significant found in the detection of emetic gene in the tested samples at (P > 0.05), (Table 2, Figure 5).

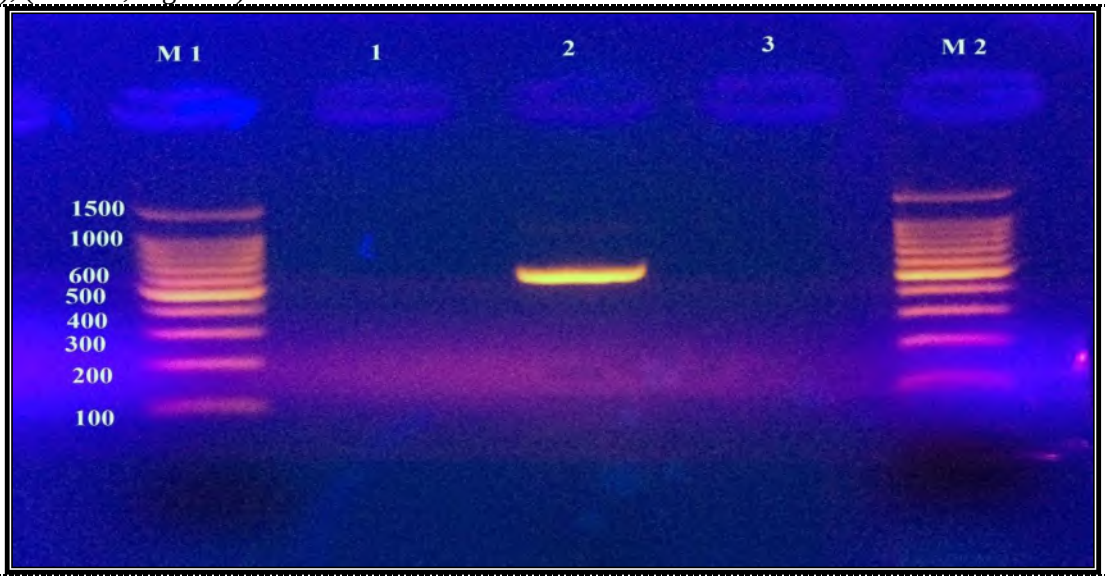

Figure 5. PCR Amplification of emetic toxin gene. M= Ladder; 2 positive for emetic gene approximately 635 bp.; 1 negative for emetic toxin gene; 3 control negative

3.2. The occurrence of diarrheal and emetic toxins genes in Bacillus cereus isolates

The presence of diarrheal and emetic toxins genes in *B. cereus* isolated from food sources are shown in (Table 2).

Table 2. The occurrence of diarrheal enterotoxin and emetic toxins genes in *Bacillus cereus* isolates.

Sample No. of isolates	*hblA* No.(%)	*hblC* No. (%)	*hblD* No. (%)	*nheA* No.(%)	*nheB* No.(%)	*nheC* No. (%)	*cytK* No. (%)	*bceT* No. (%)	*entFM* No.(%)	Emetic toxin No. (%)
Cream(6)	3 (50)	6 (100)	1 (16.66)	3 (50)	4 (66.66)	3 (50)	5 (83.33)	5 (83.33)	0(0)	1(16.66)
Beef (6)	0 (0)	4 (66.66)	2 (33.33)	2 (33.33)	3 (50)	2 (33.33)	6 (100)	6 (100)	0(0)	0(0)
Frozen beef (5)	1 (20)	3 (60)	0 (0)	2 (40)	3 (60)	2 (40)	5 (100)	5 (100)	0 (0)	1 (20)
Burger(7)	2 (28.57)	4 (57.14)	3 (42.85)	2 (28.57)	4 (57.14)	3 (42.85)	7 (100)	7 (100)	1 (14.28)	1 (14.28)
Cooked rice(5)	1 (20)	2 (40)	2 (40)	1 (20)	1 (20)	2 (40)	5 (100)	5 (100)	0 (0)	0 (0)
Uncooked rice(10)	2 (20)	7 (70)	5 (50)	2 (20)	6 (60)	5 (50)	9 (90)	9 (90)	0 (0)	0 (0)
Total (39) (%)	9 (23.07)	26 (66.6)	13 (33.3)	12 (30.7)	21 (53.8)	17 (43.5)	37 (94.87)	37 (94.87)	1 (2.5)	3 (7.6)

4. Discussion

The *Bacillus cereus* spoilage depends on two main factors: bacterial concentration in dairy products and cytotoxicity of isolates [22]. Several studies reported isolates produced cytotoxins and caused spoilage of milk, while others reported that cytotoxin production was not required for spoilage. As noted earlier, several factors affected toxin production, including environment and temperature signals [22]. The *cyt K* gene was detected in 37 isolates (94.87 %) out of 39 isolates. In cream sample, *hblC* gene had the highest percentage 100% while in beef samples, *hblC* gene had the highest percentage (66.66). On the other hand, the gene *hblA* was not found in beef. In frozen beef samples, hblC and *nheB* genes have the highest percentage of 60% (for each) followed by *nheA* and *nheC* genes which were found in 40% for each. In burger samples, each *hblC* and *nheB* genes had the highest percentage (57.14%) followed by *hblD, nheC* genes were found in 42.85% for each. The lowest percentage (28.57%) was found in each of *hblA* and *nheA*. In cooked rice samples, each of *hblC, hblD* and *nheC* genes had the highest percentage (40%) followed by each of *hblA, nheA* and *nheB* genes which were found in 20% of samples isolates. In uncooked rice samples, *hblC, hblD* and *nheC* genes had the highest percentage 40% for each, followed by *hblA, nheA* and *nheB* genes which were found in 20% for each one. [20, 23, 24, 25] detected the gene *cytK* in 50, 88, 70.40 and 65.98% of their isolates. [26] found the *cytK* gene in 27 (87.09%) out of 31 isolates. *nhe, hbl, ceses, ctyK* and *cry* genes also reported in the 92 isolates of *B. cereus* which were isolated in the previous study [16]. The rate is higher than the presence of nhe and hbl in *B. cereus* from Korea's food [27]. The positive rates for *nhe* and *hbl* in twenty raw milk samples were higher than those found for fifty four milk samples in China. In the study of [28], the positive rates of *nhe* and *hbl* were 62.0% and 37.0%, respectively.[29] found that the haemolysin gene *hblA, hblC* and *hblD* found in in most isolates. Haemolytic enterotoxin gene was isolated from vegetables [30, 31]. While haemolytic enterotoxin gene of *B. cereus* not reported from milk [30, 32]. Enterotoxin gene *bceT* gene was detected in 37 isolates (94.87%). This agreed with other studies [33, 34]. Whereas [31] found that all isolates were negative for this gene. *entFM* gene was found in one bacterial isolate (2.5%) out of 39 isolates, it was found in burger. Other studies were indicated that this gene was specific for entotoxigenic *B. cereus* [17, 35, 36]. Whereas other workers noticed that the *entFM* gene was found in 27 (93 %) *B. cereus* isolates [37]. In this study, 3 isolates (7.6%) detected the emetic toxin gene. While [38] found the emetic gene at percentage of

41.6%. Analysis of PCR is quick and easy to identify foods suspected of causing enterotoxigenic *Bacillus cereus* food poisoning.

5. Conclusion

It can be concluded that most investigated food have *Bacillus cereus* bacteria and these bacteria harboring different types of genes that can be harmful for man when ingested with food. The genes are relatively highly occurred in studied samples especially *cytK* and *bceT*.

6. References

[1] Granum PE 1994 *Bacillus cereus* and its toxins *J. App. Bacteriol. Symp. Suppl*. **76** 61S.
[2] Arnesen LPS, Fagerlund A and Granum PE 2008 From soil to gut: *Bacillus cereus* and its food poisoning toxins *FEMS Microbiol Rev*. **32** 579.
[3] Logan NA 2011 *Bacillus* and relatives in foodborne illness *J. App. Microbiol*. **112** 417.
[4] Heinrichs J, Beecher D, MacMillan J and Zilinskas B 1993 Molecular cloning and characterization of the *hblA* gene encoding the B component of hemolysin BL from *Bacillus cereus J. Bacteriol*. **175** 6760.
[5] Lund T and Granum PE 1997 Comparison of biological effect of the two different enterotoxin complexes isolated from three different strains of *Bacillus cereus Microbiology* **143** 3329.
[6] Lund T, De Buyser ML and Granum PE 2000 A new cytotoxin from *Bacillus cereus* that may cause necrotic enteritis *Mol. Microbiol*. **38** 254.
[7] Beecher D and MacMillan J 1991 Characterization of the components of hemolysin BL from *Bacillus cereus Infect. Immun*. **59** 1778.
[8] Ryan PA, Macmillan JD and Zilinskas BA 1997 Molecular cloning and characterization of the genes encoding the L1 and L2 components of hemolysin BL from *Bacillus cereus J. Bacteriol.* **179** 2551.
[9] Granum PE, O'Sullivan K and Lund T 1999 The sequence of the non-hemolytic enterotoxin operon from *Bacillus cereus FEMS Microbiol. Lett*. **177** 225.
[10] Moravek M, Dietrich R, Buerk C, Broussole V, Guinebretiere M, Granum PE, Hguyen C and Maertlbauer E 2006 Determination of the toxin potential of *Bacillus cereus* isolates by quantitative enterotoxin analysis *FEMS Microbiol. Lett*. **257** 293.
[11] Abbas BA and Jaber GM 2012 Occurrence of *Listeria monocytogens* in raw milk of ruminants in Basrah province *Iraqi J. Vet. Sci.* **26** 47.
[12] Abbas BA, Ghadban MK and Alghanim AM 2017 Microbial evaluation of milk and milk products during a past two decades, in Basrah southern Iraq: A Review *Ann. Res. Rev. Biol.* **14** 1.
[13] Abbas BA, Khudaier BY and Amaal MK 2017 Studies on *mecA* gene in methicillin resistant *Staphylococcus aureus* isolates *Jokull* **67** 58.
[14] Saeed BM, Al-Jadaan SA and Abbas BA 2019 Synthesis of a Novel 4, 4'-[1, 4-phenylenebis (1, 3, 4-thiadiazole-5, 2-diyl)] bis (azaneylylidene) bis (methaneylylidene) diphenol and Determination of Its pharmacological and antimicrobial Activities. *In J. Physics: Conference Series* (**1279** 012037). IOP Publishing..
[15] Saeed BM, Al-Jadaan SA and Abbas BA 2019 Pharmacological and Biological Evaluation of 5, 5'[(1, 4-Phenelene) bis (1, 3, 4-thiadiazol-2-amine)]. *J. Physics: Conference Series* (**1279** 012038). IOP Publishing..
[16] Saeed BMS, Abbas BA and Al-Jadaan SAN 2018 Molecular Detection of Tetracycline Resistance Genes in *Bacillus cereus* Isolated from Food Sources. *Bas. J. Vet. Res*. **17** 223.
[17] Martinez-Blanch JF, Sanchez G, Garay F and Aznar R 2009 Development of real-time PCR assay for detection and quantification of enterotoxigenic members of *Bacillus cereus* group in food samples *Int. J. Food Microb*. **135** 15.

[18] Guinebretiere MH, Broussolle V and Nguyen-The C 2002 Enterotoxigenic profiles of food-poisoning and food-borne *Bacillus cereus* strains *J. Clin. Microbiol*. **40** 3053.
[19] Hansen BM and Hendriksen NB 2001 Detection of enterotoxic *Bacillus cereus* and *Bacillus thuringiensis* strains by PCR analysis *Appl. Environ. Microbiol*. **67** 185.
[20] Ngamwongsatit P, Buasri W, Pianariyanon P, Pulsrikarn C, Ohba M, Assavanig A and Panbangred W 2008 Broad distribution of enterotoxins genes (hblCDA, nheABC, cytK and entFm) among Bacillus thuringiensis and *Bacillus cereus* as shown by novel primers *Int. J. Food Microbiol*. **121** 352.
[21] Ehling-Schulz M, Fricker M and Scherer S 2004 *Bacillus cereus*, the causative agent of an emetic type of food-borne illness *Mol. Nutr. Food Res*. **48** 479.
[22] Kohneshahri SM, Deilami Khiabani Z, Ghasemian A, Reza Shapoury R, Javid Taghinejad J, Majid Eslami M and Heidarzadeh S 2016 Detection of *hbla* and *bal* genes in *Bacillus cereus* isolates from cheese samples using the polymerase chain reaction. *Avicenna J. Clin Microb*. *Infec*. **3** 36033.
[23] Wijnands LM, Dufrenne JB, Rombouts FM, Veld PH and Leusden FM 2006 Prevalence of potentially pathogenic *Bacillus cereus* in food commodities in The Netherlands *J. Food Prot.* **69** 2587.
[24] Chitov T, Dispan R and Kasinrerk W 2008 Incidence and diarrheagenic potential of *Bacillus cereus* in pasteurized milk and cereal products in Thailand *J. Food Saf*. **28** 467.
[25] Rather MA, Aulakh RS, Gill JPS and Ghatak S 2012 Enterotoxin gene profile and antibiogram of *Bacillus cereus* strains isolated from raw meats and meat products *J. Food Saf*. **32** 22.
[26] Khudor MH, Abbas BA and Saeed BMS 2012 Molecular detection of enterotoxin (*cyt k*) gene and antimicrobial susceptibility of *Bacillus cereus* isolates from milk and milk products *Bas. J. Vet. Res*.**11** 164.
[27] Forghani F, Kim JB and Oh DH 2014 Enterotoxigenic profiling of emetic toxin and enterotoxin-producing *Bacillus cereus*, isolated from food, environmental, and clinical samples bymultiplex PCR *J. Food Sci*. **79** M2288.
[28] Zhou GP, Liu, HZ, He J 2008 The occurrence of *Bacillus cereus*, *B. thuringiensis* and *B. mycoides* in Chinese pasteurized full fat milk *Int. J. Food Microbiol*. **121** 195.
[29] Sood B, Sahota PP and Hunjan M 2017 Multidrug Resistant *Bacillus cereus* in Fresh Vegetables: A Serious Burden to Public Health *Int. J. Curr. Microbiol. App. Sci*. **6** 649.
[30] Banerjee M, Nair GB and Ramamurthy T 2011 Phenotypic and genetic characterization of *Bacillus cereus* isolated from the acute diarrhoeal patients *Indian J. of Med. Res*. **133** 88.
[31] Chon JW, Yim JH, Kim HS, Kim DH, Kim H, Oh DH, Kim SK and Seo KH 2015 Quantitative Prevalence and Toxin Gene Profile of *Bacillus cereus* from Ready-to-Eat Vegetables in South Korea *Foodborne Pathog. Dis*. **12** 795.
[32] Abbas BA, Khudor MH and Saeed BMS 2014 Detection of *hbl*, *nhe* and *bceT* toxin genes in *Bacillus cereus* isolates by multiplex PCR *Int. J. Curr. Microbiol. App. Sci*. **3** 1009.
[33] Hsieh YM, Sheu SJ, Chen YL and Tsen HY 1999 Enterotoxigenic profiles and polymerase chain reaction detection of *Bacillus cereus* group cells and *B. cereus* strains from foods and food-borne outbreaks *J. Appl. Microbiol*. **87** 481.
[34] Ombui JN, Schmieger H, Kagiko MM and Arimi SM 1997 *Bacillus cereus* may produce two or more diarrheal enterotoxins *FEMS Microbiol. Lett*. **149** 245.
[35] Nooratiny I and Sahilah AM 2013 Detection of enterotoxin targeted *entFM* and *hblA* genes by inoculating *Bacillus cereus* (Strain BC1) into ready-to-eat food (RTF) and drink samples using polymerase chain reaction (PCR) *Int. Food Res. J.* **20** 1895.
[36] Granum PE, Anderson A, Gayther C, Giffel ML, Lund T and O'Sullivan K 1996 Evidence of further enterotoxin complex produced by *Bacillus cereus FEMS Microb. Lett.* **141** 145.
[37] Tewari A, Singh SP and Singh R 2015 Incidence and enterotoxigenic profile of *Bacillus cereus* in meat and meat products of Uttarakhand, India *J. Food Sci. Technol*. **52** 1796.

[38] Aubaid AH and Dakel KM 2010 Detection of emetic toxin genes in *Bacillus cereus* isolated different types of Foods. *J. Coll. Education Pure Sci*. **2** 111.

Detection of antibiofilm formation by sliver nanoparticles created by tetracycline antibiotic

Detection of antibiofilm formation by sliver nanoparticles created by tetracycline antibiotic

Alaa Z. Hameed[1] and Nehia N. Hussein[1*]

[1]Division of Biotechnology , Department of Applied science, University of Technology, Baghdad, Iraq.

*E-mail: 100103@uotechnology.edu.iq

Abstract. Silver conjugated Tetracycline, was created and characterized by ultraviolet visible spectrophotometry (UV-vis), Fourier transform infrared (FT-IR), X-Ray Diffraction Patterns (XRD). Using antibacterial assays, the effects of tetracycline alone and drugs-conjugated with silver nanoparticles were tested against Gram-ve *Pseudomonas aeruginosa* isolates by well diffusion assay. The UV-vis spectra of silver-drug Nano conjugates showed a characteristic surface Plasmon resonance band in the range of 400–450 nm. FTIR analysis demonstrated the involvement of Hydroxyl groups in both drugs in the stabilization of silver nanoparticles. (XRD) showed that they cubic structure of silver and, antibacterial assays showed that biosynthesis silver nanoparticle conjugation enhanced antibacterial potential of Tetracycline compared with drug alone.

Keywords. Antibiotics, Anti biofilm, Nanoparticles, Antibacterial activity.

1. Introduction

Drug-resistant microbes are a main reason producing microbial re-emergence [1]. *P. aeruginosa* is main human pathogens causative to urinary tract infections [2]. Nanoparticles has shown abundant possible led to effectiveness of numerous Nano conjugates towered pathogenic microbes [3]. Nanoparticles have been often used as effective coatings to inhibit bacterial adhesion to surfaces as well as bactericidal agents [4]. Among these (AgNPs) have shown growth inhibitory as well as bactericidal effects [5].The high surface area of AgNPs leads to high antimicrobial activity in compared with the silver metal [6]. This study aimed to create AgNPs by tetracycline antibiotic, and evaluation the anti-biofilm activity and cytotoxicity against red blood cells.

2. Materials and Methods

2.1. Synthesis of AgNPs by Drug

Five mL (0.1 mM) Tetracyclin solution was added to five mL (0.1 mM) silver nitrate aqueous solution, the mixture was magnetically stirred for 10 min. 20 µL of 5 mM freshly prepared $NaBH_4$ was

added in mixture. Turned color from yellow to Greenish from transparent upon addition of a reducing agent indicating the reduction of silver ions and the formation of Tetra-AgNPs [7].

2.2. Characterization of AgNPs

Tetr.-AgNPs were exposed to whole analysis (UV-vis, FT-IR, SEM, and XRD) (8,9) UV-Vis spectral analysis this was done by using UV-Vis spectrophotometer (PG- T80+ UV/Vis spectrophotometer, England) from 350-700 nm at a resolution of 1 nm. XRD measurements of the silver nanoparticles solution drop-coated on glass were done on Shimadzu XRD-6000 model with 40 kv, 30 mA with Cu k α radiation at 2 θ angel. X- Ray powder diffraction is a rapid analytical technique primarily used for phase identification of a crystalline material and can provide information on unit cell dimensions. The crystallite domain size was calculated from the width of the XRD peaks, assuming that they are free from non-uniform strains, using the Scherer formula:

$D= 0.94 \lambda / \beta \cos \theta$

FT-IR analysis demonstrated the involvement of Hydroxyl groups in both drugs in the stabilization of silver nanoparticles.

2.3. Test pathogen

The cultures of 10 bacterial isolates of *P. aeruginosa* were obtained from the Microbiology Laboratory at Al Azizya-Hospital.

2.4. Antibiotics sensitivity test

Eleven different antibiotics were selected. Ciprofloxacin, Tobramycin, Azithromycin, Ceftraxime, Trimethoprim, chloramphenicol, erythromycin, gentamicin, and Clindamycin. Tests for antibacterial activity were performed with standard antibiotic discs. The inhibition zone was measured after incubation period at 37°C [8].

2.5. Antibacterial assay

Antibacterial potential of AgNPs synthesized by Tetracyclin. Was done by agar well diffusion assay towered *P. aeruginosa*. Nutrient broth was inoculated with isolates of *P.aeruginosa* bacterium for 3hours at 370C ,and the turbidity was compared with 0.5 McFarland standard. The culture (100µL)was poured on the Muller Hinton Agar(MHA) and spread using a spreader and left for 10 min to settle down .well with 8mm in diameter were made using gel puncture, nanoparticles solution (50 µL) was poured in each well and incubated for 24 hr at 370C. The diameter of zone inhibition was measured in millimetre after incubation period, and was recorded as mean ± SD of the triplicate experiment [9].

2.6. Biofilm formation, Tube method

This method was carried out by growing one colony at 24 hours in TSB medium for 24 hours in test tubes with a volume of 5 ml per tube with adding 1 ml of each concentration of silver nanoparticles concentrations (20 ,60, 100) mg / ml, to each tube in When the positive control tube was containing the medium inoculated with bacteria and the negative control tube contained the medium that was not inoculated with bacteria, and after the incubation period for 24 hours, the medium was discarded and the tubes were washed with a phosphate buffer solution of pH 7.3, and the tubes were left to dry, then stained with 0.1% of dye crystal violet for 5 minutes, then the dye was removed from the tubes and

washed with tap water to get rid of the remaining dye and the tubes were left in an upside down position to dry, and the results were recorded as follows:

- The result is given (-) if there is no biofilm production (negative control).

- A score of (+) is given if the biofilm composition is weak.

- The result was given (+ +) if the membrane formation was moderate.

- The result is given (+ + +) if the membrane formation is biotic-dense [10].

2.7. Cytotoxicity assay

The agar-well diffusion method was adopted and the concentrations 20, 60, 100 mg / ml. well with a diameter of 8 mm were made on the surface of the blood agar medium and the prepared concentrations were poured in wells while the physiological solution was added as control, after incubation period (18-24 hours, and 37 ° C) and the effectiveness of the AGNPS was determined by measuring the haemolysis area around each well [11].

3. Results and Discussion

3.1. Characterization of biosynthesized AgNPs

This The results in (Figure 1) show the change in color of cell filtrate of Tetracycline solution from pale yellow color to Greenish color after addition the Ag+ ions at 28 h.

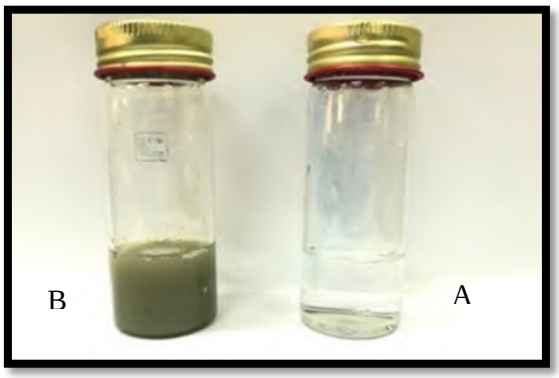

Figure 1. Synthesis of AGPS Tetracycline Coated Silver Nanoparticles (A) before treatment. (B) After treatment of silver nitrate.

Figure 2 shows the UV-vis absorption spectra of silver- nano particles, which showed absorbance peak at 390nm.

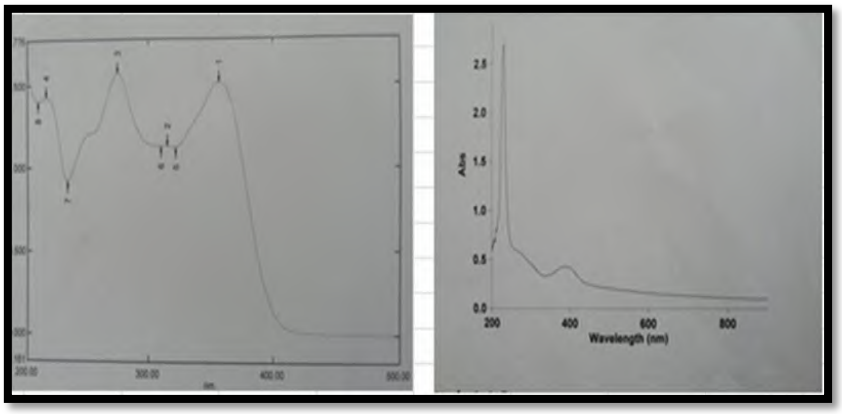

Figure 2. Uv-Vis spectrum of Silver nanoparticles for (A) Tetracycline antibiotic only, (B) Silver nanoparticles by tetracycline antibiotic**.**

FTIR of spectrum of tetracycline antibiotic showed the absorption peaks for N-H stretching at 3344 cm^{-1} and aromatic C-H stretching at 3095.75 cm^{-1}. The vibrational peaks at 2989.66cm-1 and 1352.10 cm^{-1} were assigned to CH3 stretching .and1662.64 cm^{-1} refer to C=C stretching, respectively. Aromatic C-H bending was appeared at 1456.26 cm^{-1}.The aromatic in plane and out plane deformation peaks were appeared at 1286.52 cm^{-1} (Figure3A) [12]. The results of the spectral absorption of silver nanoparticles showed the disappearance of some bonds at certain ranges that were present in (Figure3 B), and the emergence of some bonds in other ranges and this is evidence of the formation of new compounds upon the synthesis of nanoparticles, and this is very clear at the range 3387.00cm^{-1} evidence for the presence of O-H and N-H bonds. The disappearance of the C = C and CH3 bonds is observed upon the formation of the nanoparticles, after they were present in the drug alone.

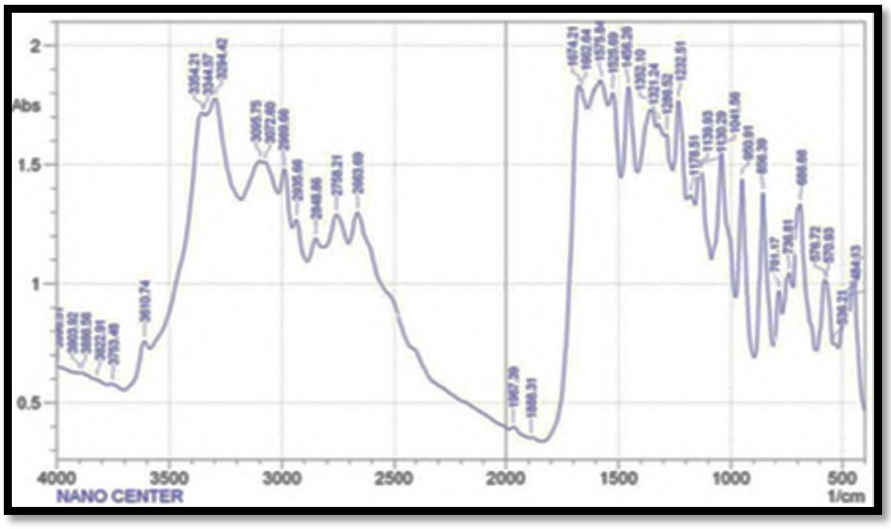

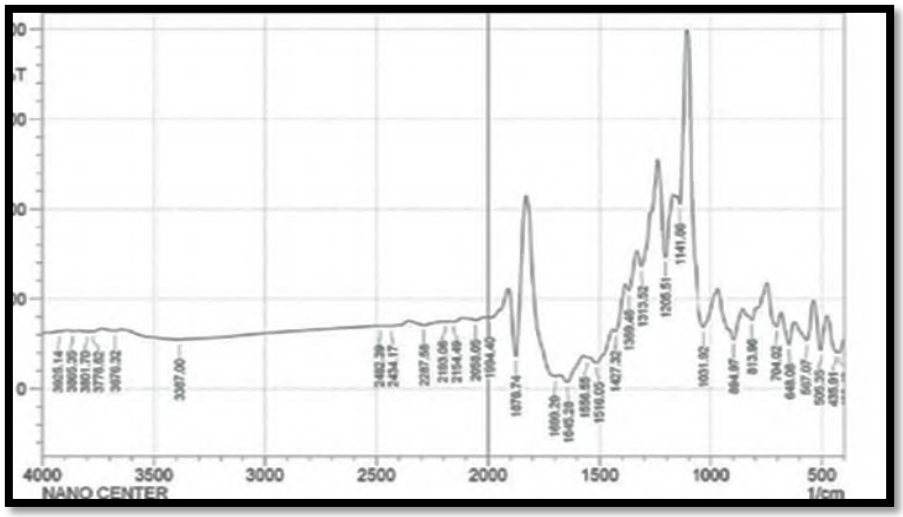

Figure 3. FTIR analysis of Silver Nanoparticles synthesized for tetracycline antibiotic (A), and (B) for to the silver nanoparticles

XRD pattern shows three strong peaks in the total spectrum of 2θvalues in 20–60, as obvious from the peaks at 2θstandards of, 35.48, 29.23, 28.03, respectively for silver. The particle size was 57.55, calculated by using Scherer equation where (Figure4).

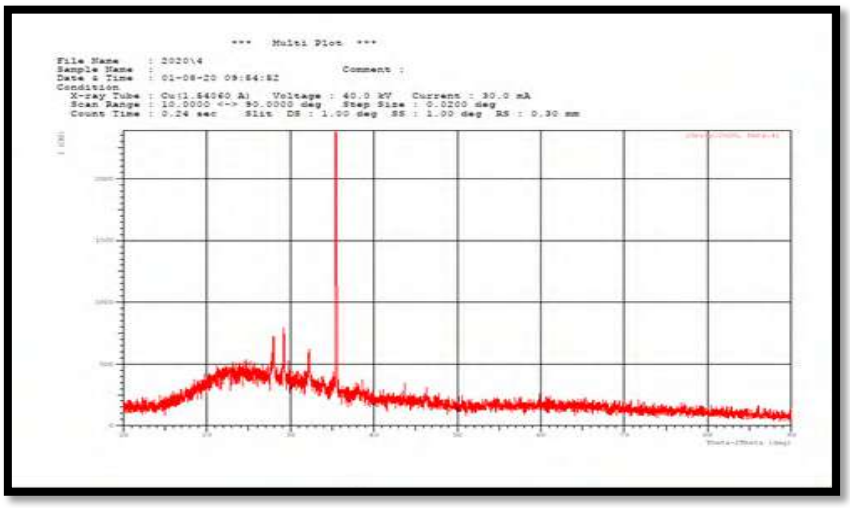

Figure 4. XRD of silver nanoparticles.

3.2. Antibiotics Susceptibility test

The result in (Table 1), shows of the antibiotics sensitivity test against the bacterial isolates, the highest recorded effect of the antibiotic Cip in the growth of isolate no. 8 with a diameter of the inhibition region reached (30 mm), followed by isolate no. 6 with a diameter of the inhibition region reached (22 mm), and the diameter of the inhibition region reached (20 mm) for each isolates (4,7,9), followed by the isolation no.3 with a diameter of the inhibition region reached (19 mm), and the isolate no. 5 with a diameter of the inhibition region reached (18 mm), while the antibiotic showed no significant effect in the growth of each of the isolates (1,2,10). As for the other isolates, the antibiotics varied in their effect. (Tob, C, AK, CN) antibiotics showed a different effect in the growth of bacterial isolates, whereas the antibiotics (Az, TMP, CTX E, DA, Tet). There was no significant effect.

Table1. Antibiotics activity test against bacterial isolates.

Isolates no. / ***Antibiotics***	Inhibition zone diameter in mm									
	1	2	3	4	5	6	7	8	9	10
Cip	6	6	19	20	18	22	20	30	20	6
Tob	6	6	9	6	10	10	10	13	11	6
Az	6	6	6	6	6	6	6	6	6	6
C	6	6	10	15	6	6	6	14	20	6
TMP	6	6	6	6	6	6	6	6	9	6
CTX	6	6	6	6	6	6	6	6	6	6
E	6	6	6	6	6	6	6	6	6	6
DA	6	6	6	6	6	6	6	6	6	6
Tet	6	6	6	6	6	6	6	6	6	6
AK	6	6	10	6	6	6	6	13	12	6
CN	6	6	10	6	10	12	10	20	10	6

3.3. Antibacterial Activity of the AgNPs

The results showed that the biosynthesized AgNPs by antibiotic has a strong inhibitory effect on the growth of pathogenic bacteria. The effect of biosynthesized silver nanoparticles was the highest inhibition on the grow thin all isolates of *P. aeroginosa* at concentration of 100%, the highest of inhibition zone reached to of24.83 mm in isolate no. 10,followed by 24.33mm in isolate no 1 (Table2). The present investigation supports the use of biosynthesized AgNPs by Tet. Elicited a strong antibacterial activity. Thus, the biological approach could be an economical alternative to conventional chemical and physical assays of AgNP synthesis and would be suitable for the development of a biological process for commercial large-scale creation. AgNPs have wide application in different fields, such as antibacterial. Therefore, the improvement of their synthesis for nanoparticle production is the main objective of nanotechnology [13]. But the biosynthesized silver nanoparticles by Tet. Have a strong inhibitory effect because silver nanoparticles have a very effective against bacterial and fungal infections. These properties are due to silver nanoparticles having a large surface area of the volume ratio which increase their association with bacterial cell well causing changes in the membrane and thus cell death [14]. That can also release silver ions that interfere with thiol groups in biomass enzymes, which inhibit them. Silver ions also inhibit respiratory enzymes and during the inhibition process reactive oxygen species are generated. (ROS) attack the cell itself and thus die [15]. Silver nanoparticles have the ability to interfere with the sulfur and phosphorus bases of DNA and thus lead to the breakdown of DNA and cell death due to a disturbance in the DNA replication of bacteria and microbes [5]. This agreement with that AgNPs has wide application in different fields, such as antibacterial. Therefore, the improvement of their synthesis for nanoparticle production is the main objective of nanotechnology [16].

Table 2. Antibacterial activity of biosynthesis of AgNPs created by Tetracycline antibiotic.

Isolates no.	Inhibition zone of different Conc. of AgNPs		
	0.2	0.6	1
1	18.16 ±0.61	19.8 ±0.6	24.33 ± 0.4
2	14.5 ±0.5	16±1.0	0.7± 18.8
3	15 ±0.81	15.33 ±0.23	18.33±0.47
4	12.6±0.94	12.9 ± 0.69	16.5 ± 0.40
5	14±1.04	15.2±0.40	16 ± 0.28
6	11.83±0.62	14.5±0.40	14.16±0.23
7	13.16±1.02	14.83±0.23	15.0 ±0.7
8	14.5±0.40	16.33±0.47	17.16±0.23
9	15.5±0.40	15.33±0.47	20.83±0.62

10	15.5±0.40	16.0±0.40	24.83±0.23

3.4. Determination the anti-biofilm activity for AgNPs

We explored the possibility of using the Ag+-tetracycline combinatorial therapy to treat biofilms grown in vitro. *P.aeruginosa* biofilms grown overnight were treated with Ag^{+} and tetracycline combination in different concentration, control positive, and control negative. In the present study, biofilm forming potential of *P. aeruginosa* strains (Figure 5) was assessed by test tube method. Biofilms are microbial networks of living beings follower to one another and an objective surface. Biofilm arrangement shields microscopic organisms from hydrodynamic stream conditions, for instance in the against phagocytosis, urinary tract and host resistance instruments, just as anti-infection agents. Over half of every bacterial disease detailed includes biofilm arrangement [17] (. The results appear a difference in the amount of pigment in which the tubes were formed. The positive control tube produced a dense biological membrane (+++). The negative control tube did not have a dynamic membrane (-), the 80% (+), the tubes treated with nanoparticles with a concentration of 100%, formed a weak biological membrane (+).

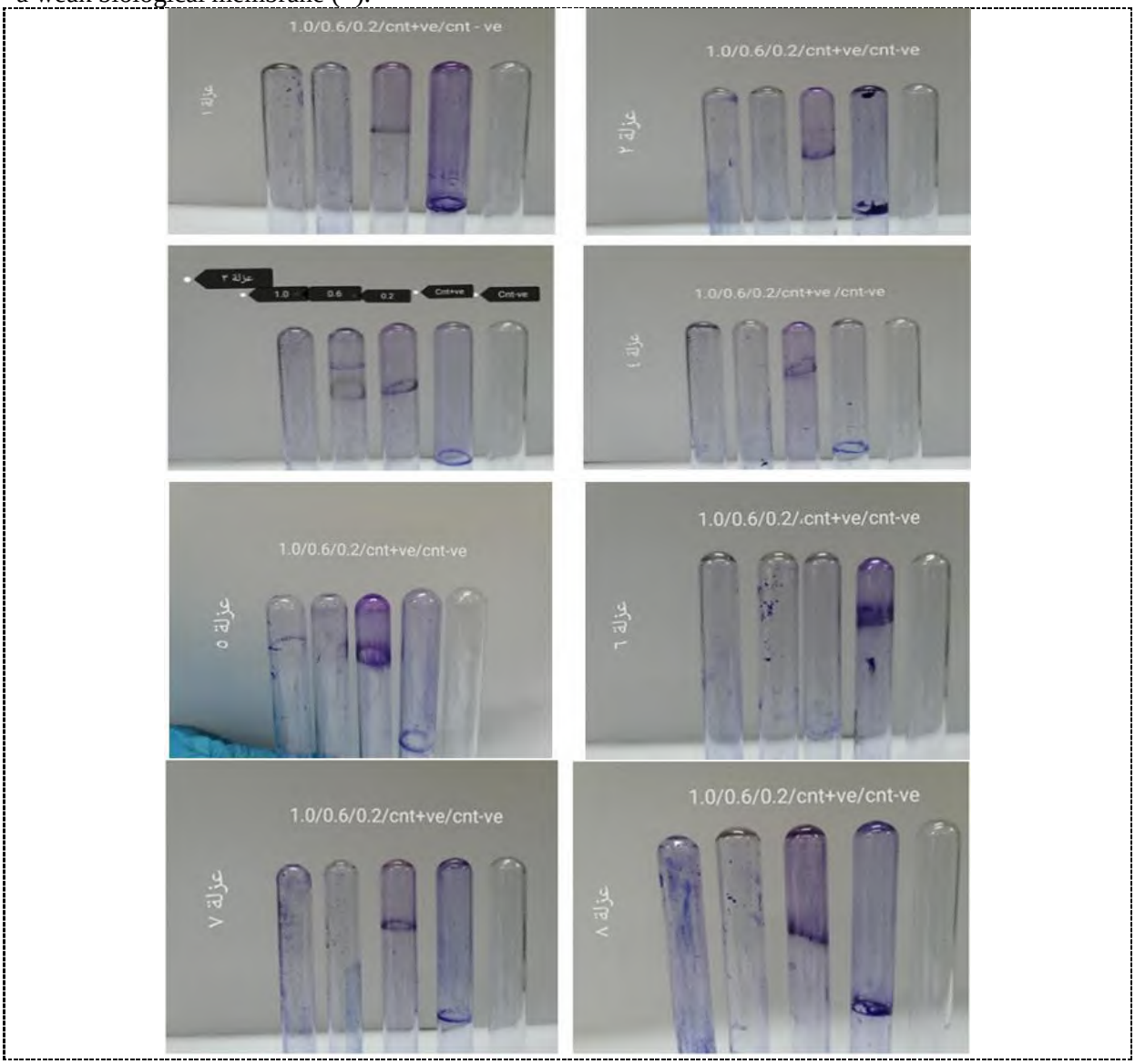

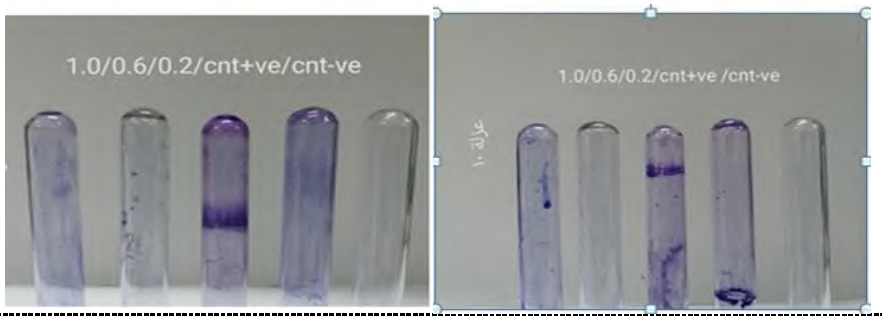

Figure 5. Anti-biofilm activity of AgNPs –tetracycline combination in different concentration.

3.5. Determination the toxicity of AgNPs on blood human

The effect of silver nanotubes in human blood on blood agar was studied at concentrations (20, 60, 100) mg / ml, through the results show there is no inhibition area (Figure 6). Which means that the silver nanoparticles are not able to cause blood cell degradation? The absorption of red blood cells and platelets of silver nanoparticles depends on the size and charge of those particles [18]. It is known that silver nanoparticles are toxic to erythrocytes at high concentrations only. Therefore, care should be taken when using silver nanoparticles at high concentrations [19].

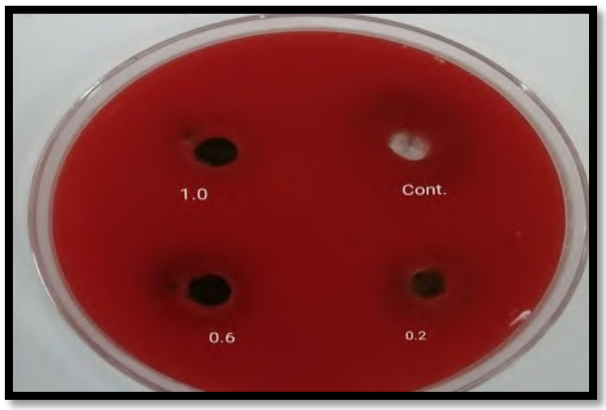

Figure 6. The effect of bio fabricated nanoparticles on human blood.

4. Conclusion

Tetr-AgNPs showed bactericidal effects against all tested isolates, and anti-biofilm activity. The exact mechanism of action of these nanoparticles is not precisely understood and it is the subject of future studies along with testing their potential *in vivo*.

5. Acknowledgement

The authors are appreciative to the Biotechnology department, and University of technology.

6. References

[1] Anuj SA, Gajera HP, Hirpara DG and Golakiya BA 2018 Bactericidal assessment of nano-silver on emerging and re-emerging human pathogens *J. Trace Elem. Med. Biol*. **51** 219.
[2] Lee K, Silva EA and Mooney DJ 2011 Growth factor delivery-based tissue engineering: General approaches and a review of recent developments *J. R. Soc. Interface* **8** 153.

[3] Naqvi SZ, Kiran U, Ali MI, Jamal A, Hameed A, Ahmed S and Ali N 2013 Combined efficacy of biologically synthesized silver nanoparticles and different antibiotics against multidrug-resistant bacteria *Int. J. Nanomed*. **8** 3187.
[4] Grace JL, Elliott AG, Huang JX, Schneider EK, Truong NP, Cooper MA, Li J, Davis TP, Quinn JF and Velkov T 2017 Cationic acrylate oligomers comprising amino acid mimic moieties demonstrate improved antibacterial killing efficiency *J. Mater. Chem. B* **5** 531.
[5] Morones JR, Elechiguerra JL, Camacho A, Holt K, Kouri JB, Ramírez JT and Yacaman MJ 2005 The bactericidal effect of silver nanoparticles. *Nanotechnology* **16** 2346.
[6] Shahverdi AR, Fakhimi A, Shahverdi HR and Minaian S 2007 Synthesis and effect of silver nanoparticles on the antibacterial activity of different antibiotics against *Staphylococcus aureus* and *Escherichia coli Nanomed. Nanotechnol. Biol. Med*. **3** 168.
[7] Ahmed D, Shah MR, Perveen S and Ahmed S 2018 Cephradine Coated Silver Nanoparticle their Drug Release Mechanism, and Antimicrobial Potential against Gram-Positive and Gram-Negative Bacterial Strains through AFM *J. Chem. Soc. Pak.* **40** 388.
[8] Reller LB, Weinstein M, Jorgensen JH and Ferraro MJ 2009 Antimicrobial Susceptibility testing: a review of general principles and contemporary practices *Clin. Inf. Dis*. **49** 1749.
[9] Nehia NH and Ameen HM 2019 Detection of the Antibacterial activity of AgNPs biosynthesized by *Pseudomonas aeruginosa Iraqi J. Agric*. **50** 617.
[10] Deka N 2014 Comparison of tissue culture plate method, tube method and Congo red agar method for the detection of biofilm formation by coagulase negative *Staphylococcus aureus* isolated from non-clinical isolates *Int. J. Curr. Microbiol. Appl. Sci*. **3** 810.
[11] Nehia NH and Noor A 2017 The antimicrobial activity of some medical plants extracts used against some types of bacteria that causes urinary tract infection. *Al-Mustansiriyah J. Sci*. **28** 72.
[12] Gunasekaran S, Varadhan SR and Karunanidhi N 1996 Qualitative analysis on the infrared bands of tetracycline and ampicillin *Proc. Indian Natl. Sci. Acad. Part A* **62** 309.
[13] Zhang Y, Yang D, Kong Y, Wang X, Pandoli O and Gao G 2010 Synergetic antibacterial effects of silver nanoparticles@ aloe vera prepared via a green method *Nano Biomed. Eng*. **2** 252.
[14] Thomas R, Viswan A, Mathew J and Radhakrishnan EK 2012 Evaluation of antibacterial activity of silver nanoparticles synthesized by a novel strain of marine *Pseudomonas* sp, *Nano Biomed. Eng*. **4** 139.
[15] Mazzola PG, Jozala AF, Novaes L, Moriel, P and Penna, TCV 2009 Minimal inhibitory concentration (MIC) determination of disinfectant and/or sterilizing agents. *Braz. J. Pharmac. Sci.* **45** 241.
[16] Lu TK and Collins JJ 2007 Dispersing biofilms with engineered enzymatic bacteriophage *Proc. Natl. Acad. Sci. U. S. A.* **104** 11197.
[17] Gavanji S, Sayedipour SS Doostmhammadi M and Larki B 2014 The effect of different concentration of silver nanoparticles on enzyme activity and liver tissue of adult male Wistar rats *in vivo* condition *IJSRK*. **4** 182.
[18] Chi Z, Lin H, Li W, Zhang X and Zhang Q 2018 *In vitro* assessment of the toxicity of small silver nanoparticles and silver ions to the red blood cells *Environ. Sci. Pollut. Res.* **25** 32373.
[19] Huang H, Lai W, Cui M, Liang L, Lin Y, Fang Q and Xie L 2016 An evaluation of blood compatibility of silver nanoparticles *Sci. Rep.* **6** 25518.

Morphological characterization and its relation with yield traits of *Oryza sativa* L. genotypes in Iraq

Morphological characterization and its relation with yield traits of *Oryza sativa* L. genotypes in Iraq

Balqees Hadi Al-Musawi[1*] and Mohammed A. Al- Anbari[2]

[1]Department of Biology, College of Science, Kerbala University, Iraq.
[2]Department of Field crops, College of Agricultural, Kerbala University, Iraq.

*E-mail: balqees.hadi@uokerbala.edu.iq

Abstract. In the current study we reported for agronomic traits and yield of fifteen rice genotypes in season during 2018 and investigated at the field experimental of Al-Mashkab research station (AMRR)**,** Najaf- Iraq . The experiment was conducted following Randomized Complete Block Design (RCBD) with having three replications. These data related days to 50% flowering and heading , plant height (cm), leaf area index (LAI) , panicle length (cm), number of tiller per panicle, 1000 grain weight (g) and biological yield ,harvest index and grain yield (kg ha-1) were evaluated. The results indicated that the rice genotypes differed in plant growth characteristics and yield and yield components. 1000 grain weight and grain yields both were highest in Gohar genotype. Shiroudi genotype required shorter days to maturity and Anber33 longest days to maturity. Some of the rice genotypes particularly (Gohar) showed high promise with grain yield. Recommended, intensification of introducing more genotypes to select the best rice genotype for Iraqi condition could maximize the benefits of genotype cultivation. Agronomic data collected in the current study would be significant to realize the suitability of an individual rice genotypes of the farmer field, also were found more appropriate of the agro climatic status of Iraq.

Keywords. *Oryza sativa* L.**,** Field experiment, Yield traits.

1. Introduction

Rice (*Oryza sativa* L.) is the serves as the staple food for more than half of the globe's population, belongs to family Graminea (Poaceae) [1]. More than 90 percent of the world's rice is mature and used in Asia, where 60 percent of the earth's people and two thirds of world's needy live [2]. Different morphological characters play very significant role for most rice production with new plant type characteristics related with the plant yield [3]. Morphological property of rice also related with the yield possibility of the different rice genotypes for the selection of the best genotypes that further interested in rice breeding program [4]. Thousand rice genotypes have been developed by selection from the cultivated material many centuries ago, which are well proper to the local climate, grain yield regard a complex trait, quantitative in nature and a collective function of a number of constitutive traits. Thus, chosen for yield present may not be much pleasing unless other yield complex traits are possessed into discernment [5]. Grain yield of rice is a quantitative polygenic trait and much influenced by climate . Range and importance of

combination of yield with yield components should be believed, while determining the chosen criteria of germplasm on the basis of available genetic diversity [6]. The success of breeding program also consist onto the value of genetic variability current in the population and range to which the desired traits are heritable. Maintenance in the current search entitled of assessment of different rice (*Oryza sativa* L.) genotypes for agronomic traits and yield traits to fulfil the following objective and to detect appropriate high yielding genotype for Iraqi regions..

2. Materials and Methods

2.1. Plant materials

Current search included 15 genotypes of rice, were collected of the Al-Mushkab Rice Research Station (AMRR), Najaf, Iraq. The source of this genotypes as given in (Table 1).

2.2. Methods

This search was carried at the experimental field of Al-Mushkab research station during rice growing season from 2018. The trial was prepared in a Randomized Complete Block Design (RCBD) with three replications, the date of planting was 17/06/2018, and the seedlings were planted after 22 days old. Cultivated of the seedlings were at spacing of 20 x 20 (cm) line. Whole cultivation exercise were used approving to the proceedings recommended of rice crop in research . The recommended amount of chemical fertilizer (CF) were used : 280 kg ha-1 of urea and 120 kg ha-1 of NP as DAP fertilizer 18-46 [7].

2.3. Genetic parameters

The following genetic parameters were studied during trial which traits: days to 50% heading, days to heading , plant height (cm), Leaf area index, panicle length (cm), number of panicles/plant, number. of filled grains/panicle, sterility (%), 1000-grain weight (g), biological yield, harvest index and grain yield/plant (kg ha^{-1}).

Table 1. Summarized of 15 rice genotypes and their source applied in this research.

Genotypes' name	Pedigree	Breeding Institute
1. Amber 33	Local (Iraqi)	AMRRS
2. Amber al-Baraka	Introduced from India	AMRRS
3. Amber Furat	Technology& Science Ministry/ Baghdad	AMRRS
4. Amber Baghdad	Technology& Science Ministry/ Baghdad	AMRRS
5. Amber Menathera	Technology& Science Ministry/ Baghdad	AMRRS
6. Sumar	Technology& Science Ministry/ Baghdad	AMRRS
7. Dijlah	Introduced from China	AMRRS
8. Ghadeer	Introduced from IRRI (Philippines).	AMRRS
9. Brnamge -4	Introduced from IRRI(Philippines).	AMRRS
10. Dorfak	Sepidrood/Salari- Iran	AMRRS
11. Gohar	Pusa1238-1/Pusa1238-81-6-Iran	AMRRS
12. Khazar	IR2071-625-1-52/TANU7456-Iran	AMRRS
13. Shiroudi	Khazar / Deylamani – Iran	AMRRS
14. Neda	Amol3/Hassansarayee/sangetarom-Iran	AMRRS
15. Nemat	Amol3/sangetarom - Iran	AMRRS

AL-Mashkhab Rice Research Station (AMRRS).

2.4. Statistical analysis

The data famed on several genetic parameters were presented to the analysis of variance (ANOVA) method to detect the difference among all genotypes. In states where difference were begin important, averages were identified for differences employ least significant variance (LSD) test, ($P \leq 0.001\%$). The software (Genstat) was utilized for calculated both LSD and the ANOVA [8]. Variability for all the agronomic traits as shown in (Table 2).

3. Results and Discussion

3.1. Analysis of variance

The results presented in this manuscript were acquired of an trial carried during 2018 in AMRRS, the literal of this trial was to study the estimation of selected rice genotypes for agronomic traits and yield traits under ecological situation of Iraq. These results related for days to 50% flowering and heading , plant height, leaf area index , panicle length, number panicle /plant, sterility , 1000 grains weight and grain yield are given and discuss . These genotypes for the studied 12 quality as current in Table 2.

Table 2. Summary mean squares (M.S.) and analysis of variance of collective data for agronomic & yield traits in fifteen genotypes from rice grown in the field at Rice Research Station, Najaf-Iraq.

S.O. V. Traits	Reps.	Genotypes	Error
Df	2	14	28
Days to 50% heading	15.76	**150.66	3.68
Days to heading	7.62	**128.80	5.36
Plant height	8.16	663.31**	50.16
Leaf area index	9.63	**107.83	7.72
Panicle length.	5.64	19.87	11.31
No .of tiller/panicle	0.59	11.63**	0.62
No of panicles	455.3	**10657	761.3
No. of filled grains/panicle	1447	**7655	412
Sterility (%)	50.61	**98.21	29.07
1000 grain weight	7.27	**21.13	0.81
Biological yield	4453129	**9730076	812724
Harvest Index (%)	51.72	**129.51	7.79
Grain yield/plant	719796	**2426113	243672

**significantly at 0.01 probability level.

3.2. Plant growth characteristics

3.2.1. Days to panicle initiation

The vegetative growth parameters of the different genotypes and the data related days to panicle initiation included day number to 50% flowering and day number to physiological maturity are presented in (Table 3). Analysis of the data exhibited that all genotypes studied are significantly several with relate to days 50% flowering and heading. The number of days required to 50% flowering stage differed. significantly among the rice genotypes studied. The lowest number of days required to 50% flowering was observed in 86.33 days with Neda, while the maximum number of days required to 50% flowering was for Anber33 was 105.67 days, also days to physiological maturity

stage also varied significantly among the genotypes studied. Shiroudi, Dorfak and Neda took the lowest duration for maturity days, while Anber33 took the longest duration days.

Table 3. Day numbers to 50% flowering, and physiological maturity stages, plant high and leaf area index per plant.

Genotypes	Day number to 50% flowering	Day number to physiological maturity	Plant high (cm)	Leaf area index
Amber 33	105.67	142.67	139.33	19.05
Amber al-Baraka	100.00	136.67	124.67	5.93
Amber Furat	104.33	141.67	139.00	17.01
Amber Baghdad	104.00	140.67	142.00	22.43
Amber Menathera	105.67	142.67	135.67	14.27
Sumar	93.67	127.33	103.67	5.81
Dijlah	105.33	140.67	112.00	6.70
Ghadeer	98.00	137.33	119.33	6.49
Brnamge -4	96.00	137.00	108.00	7.48
Dorfak	88.00	127.33	103.33	3.63
Gohar	93.00	130.67	123.00	6.05
Khazar	98.67	138.00	116.00	5.11
Shiroudi	89.00	125.00	109.00	4.47
Neda	86.33	127.67	100.33	5.44
Nemat	88.00	127.00	101.00	5.73
LSD 0.01	3.21	3.87	11.84	4.65

The breeding efforts are underway to develop short plant cycle with high yield potential. The variation in the plant growth characteristics between rice genotypes are due to variability in their genotype composition. Similar result was reported by [9, 10].

3.2.2. Plant height (cm), leaf area index per plant

variation between genotype of rice were significant presented in (Table 3). There plant height , Leaf area index per plant was higher in Anber33 compared with the other genotypes which also differed among themselves in this parameter as shown in above. It is apparent from the table 3 that the plant height was lead significantly several between the genotypes. The result display that highest (142.00cm) plant height was showed in Amber Baghdad genotype directed significantly by Amber33, Amber Furat and Amber Menathera genotype having (139.33cm, 139.00 and 135.67) respectively in plant height on record, whereas least (100.33cm) plant height was showed in Neda genotype .Also differences in leaf area index among genotype of rice are given in Table 3. It was found significantly several between them, The result show that highest (22.43) leaf area index was found in Amber Baghdad genotype follow significantly by Amber33 genotype have (19.05) recorded. The difference among genotypes in plant height is may be referred to variation climatic requirements of among genotypes, also accomplished that there is different climatic requirements of each genotype. Yet , it has been notified that plant height was influenced by numerous factors such as plant density , fertilizer employments and plantation method, [11, 12]. The yield indices for number of tiller per panicle, filled grain number per panicle, sterility ratio (%), Table 4.

Table 4. Panicle length (cm), number tillers of panicle, number panicles, filled grain number/ panicle, sterility ratio(%).

Genotypes	Panicle Length (cm)	Number Tillers/panicle	Number of panicles	Filled Grain number/panicle	Sterility Ratio (%)
Amber 33	29.07	10.43	333.3	160.2	19.96
Amber al-Baraka	26.30	9.43	361.0	75.2	21.69
Amber Furat	29.43	10.00	246.0	165.2	15.51
Amber Baghdad	23.30	9.90	370.3	171.4	19.18
Amber Menathera	28.92	9.96	363.0	154.6	14.10
Sumar	23.10	10.47	372.3	133.4	18.88
Dijlah	31.80	15.77	268.7	275.2	9.24
Ghadeer	29.17	11.40	350.0	183.6	17.97
Brnamge -4	26.97	12.83	362.0	184.9	9.90
Dorfak	25.13	8.90	388.3	79.9	30.37
Gohar	27.83	11.37	396.0	174.6	14.61
Khazar	25.10	13.77	197.0	152.1	23.10
Shiroudi	28.60	9.20	329.3	107.5	19.86
Neda	23.87	9.20	412.7	188.6	8.75
Nemat	25.73	9.07	371.0	100.9	18.46
LSD 0.01	N.S.	1.31	46.15	33.94	9.02

3.2.3. The Panicle length (cm), number tiller /panicle, filled grain number and sterility ratio (%)

The results in this (table 4) indicated that the panicle length was count of the all rice genotype no differed significantly between them at (p = 0.01). The number tillers per panicle was significantly, the highest in Dijlah reached to 15.77, while the lowest in Dorfak reached to 8.90. Filled grain number per panicle was significantly highest in the Dijlah (275.2). while recorded the lowest in the Amber al-Baraka genotype (75.2). The results in this table showed that the significant variation in sterility ratio among genotypes , the Dorfak genotype showed significantly highest ratio, and the lowest in Neda genotype. Number of tillers / panicles and number of reproductive tiller / panicle supply valuable information for the rice breeders and these traits have direct influence on yield / plant [13].

3.3. Yield components

3.3.1. 1000 grain weight (g), biological yield, Harvest Index and grain yield (kg.ha^{-1})

This analysis of the data shows in table 5 that 1000 grain weight are significantly different among genotypes. The highest (29.33g) 1000 grain weight was on record in Amber al-Baraka genotype while recorded lowest weight reached to (19.67 g) in Sumer and Brnamge-4 genotypes. 1000 weight was influenced by agriculture methods . According to [12, 14, 15] notified that agriculture methods didn't have this influence on 1000-grain weight. The genotypes also showed significant differences in the biological yield was highest reached to 17860 kg.ha^{-1} Amber33 genotypes while other genotypes Sumer in biological yield. The harvest index showed significant differences among genotypes, the Sumar gave highest index reached to 49.29 % followed by Dijlah, Gohar and Shiroodi while the Anber33 gave the lowest index reached to 27.57%. Variations among genotype of rice in grain yield are given in Table 5. The apparent from that table was found significantly several among genotypes in grain yield (kg. ha^{-1}). There result shows Gohar genotype reached to maximum (7553.33) kg.ha^{-1} with producing the highest paddy yield followed by Ghadeer and Dijlah while other genotype Khazar had lowest paddy yield reached to 4116.67 kg. ha^{-1}. The variation in the yield and yield components between rice genotypes are due to variability in their genotype composition, and differed adapted to current environmental conditions. Similar result was reported by [16, 17, 18, 19, 20].

Table 5. 1000-grain weight (g), biological yield, harvest index (%) and grain yield (kg.ha^{-1}).

Genotypes	1000 Grain Weight (g)	Biological yield	Harvest Index (%)	Grain Yield (kg.ha^{-1})
Amber 33	21.00	17860	27.57	4930.00
Amber al-Baraka	29.33	14337	37.52	5383.33
Amber Furat	21.67	14097	43.51	6113.33
Amber Baghdad	21.33	16247	34.08	5530.00
Amber Menathera	21.00	17747	33.66	5930.00
Sumar	19.67	12590	49.29	6190.00
Dijlah	23.33	14140	48.73	6856.67
Ghadeer	22.33	17210	42.05	7226.67
Brnamge -4	19.67	17617	33.97	5976.67
Dorfak	24.00	13787	37.94	5220.00
Gohar	26.67	15790	47.81	7553.33
Khazar	23.33	12700	32.42	4116.67
Shiroudi	21.33	14357	45.09	6456.67
Neda	25.33	15557	42.38	6590.00
Nemat	22.00	13960	39.95	5593.33
LSD 0.01	1.51	1507.8	4.67	825.60

4. Conclusion

The Advancement grain yield for rice is the major objective of breeding program to improve genotypes . Grain yield regard is a complex trait, controlled through many genes and very influenced by climate . Supplement, grain yield as well attached to other traits like as growth duration, plant kind and yield compound [21]. Traits like as number of reproductive tillers and number of tiller / panicle are immediately responsible for the ultimate yield while trait like as plant height, leaf area index and numbers of total tillers are not very important as yield determinants. All these traits are possessed in to seeing when the rice genotypes are choose for the commercial cultivation. However, some of rice genotypes particularly (Gohar) showed high promise with grain yield and Integrating the promising genotype into the farming system could boost rice productivity and provide the basis for national food security as well as generate sustainable income. Further, intensification of introducing more genotypes to select the best rice genotype for Iraqi condition could maximize the benefits of genotype cultivation. In the current search gives average values for each genetic parameter and these data can be employed when different genotypes are screened for future breeding programs.

5. Acknowledgement

Al-Musawi, well thanks to Al-Mashkhab Rice Research Station (AMRRS).Najaf-Iraq of provided that rice grain specimen and experiment managed in field.

6. References

[1] Khan AS, Imran M and Ashfaq M 2013 Estimation of Genetic Variability and Correlation for Grain Yield Components in Rice (*Oryza sativa* L.) *American-European J. Agric. Environ. Sci.* **6** 585.

[2] Khush GS and Virk PS 2000 Rice breeding achievements and future strategies *Crop Improv.* **27** 115.

[3] Yu HG, Zhu FQ and Wang CL 2008 Preliminary report of the application of the high-yielding techniques of SRI in single cropping hybrid rice *Hybrid Rice.* **19** 33.

[4] Shahidullah SM, Hanaf MM and Ashrafuzzaman M 2009 Phenological characters and genetic divergence in aromatic rice's *African J. Biotech*. **8** 3199.
[5] Satheeshkumar P and Saravanan K 2012 Geneticvariability, correlation and path analysis inrice (*Oryza Sativa* L.) *Int. J. Curr. Res*. **4** 082.
[6] Habib SH, Bashar MK and Khalequzzaman M 2005 Genetic analysis and morpho-physiological selection criteria for traditional biroin Bangla desh rice germplasm *J. Biol. Sci.* **5** 315.
[7] Al-Musawi BH and Al-Anbari MA 2019 Comparative study of new rice genotypes (*Oryza sativa* L.) Introduced in middle of Iraq *Biochem. Cell. Arch.* **19** 2453.
[8] Steel RG and Torrie JH 1984 *Principle and Procedure of Statistics, A biometrical Approach* Seconded Mc Claw-Hill Book Co. Inc., New York. 633pp..
[9] Sudha RM and Jayalakshm V 2008 Evaluation of rice (*Oryza sativa* L.) genotypes in saline soils of Krishna delta of Andhra Pradesh *Agric. Sci. Digest*. **28** 225.
[10] Vange T and Obi I U 2006 Effect of planting date on some agronomic traits and grain yield of upland rice varieties at Makurdi, Benue State, Nigeria. *J. Sustain. Develop. Agric Enviro.* **2** 0794.
[11] Beser N and Genctan T 1999 Effects of different plantation methods on some agricultural features and productivity in the rice (*Oryza sativa* L.) *Turk. 3rd Field Crop Cong*. **1** 462.
[12] Aide M and Beighley D 2006 Hyperspectral reflectance monitoring of rice varieties grown under different nitrogen regimes. *Transact. Missouri Acad. Sci.* **40** 6.
[13] Sadeghi SM 2011 Heritability, Phenotypic correlation and path coefficient studies for some agronomic characters in Landrace rice varieties *J. W. Applied Sci*. **13** 1229.
[14] Surek, H. and Beşer N 1996 A Research to Determine the Suitable Rice (*Oryza Sativa* L.) Harvesting Time *J. Agric Forestry* **22** 391.
[15] Manzoor Z, Ali RI Awan TH, Khalid N and Mushtaq A 2006 Appropiate time of nitrogen application of fine rice (O*ryza sativa*) *J. Agric. Res.* **44** 261.
[16] Akram M, Rehman A and Cheema AA 1982 Correlation between yield and yield attributing characters in some induced dwarf mutants of rice (*Oryza Sati*va L,) *Pak. J. Agric. Res*. **3** 141.
[17] Asad MA, Bughio HR, Odhano MA and Bughio MS 2009 interactive effect of genotype and environment on the paddy yield in sindh province *Pak. J. Bot*. **4** 1775.
[18] Khalifa AABA 2009 Physiological evaluation of some hybrid rice varieties under different sowing dates *Aust. J. Crop Sci*. **3** 178.
[19] Steven D, David L, Ann B and Ryan P 2004 Rice response to planting date differs at two locations in Louisiana *Crop Manag*.
[20] Vange T and Obi IU 2009 Influence of sowing date on rice grain yield in Benue State of Nigeria *Crop Manag*.
[21] Yoshida S 1981 *Fundamentals of Rice Crop Science* IRRI, Los Banos, the Philippines. 269.

Epidemiology of hydatid disease in Najaf province/Iraq

Epidemiology of hydatid disease in Najaf province/ Iraq

Raja Jawad Mohamed[1], Alyaa Neamah Najm Alsaedi[2]and Jasim Hameed Taher[1*]

[1]Departmentof Medical Laboratory Techniques, Technical Institute, Kufa
Al-Furat Al-Awsat Technical University, 31003 Al Kufa, Iraq.
[2]Presidency of Karbala University, Central Library Department, Karbala,Iraq.

*E-mail: rajajawad@atu.edu.iq

Abstract. It was clinically and surgically proven that sixty- four patients were infected with a hydatid cyst. Follow up was done in Al-Sadder Medical City, Najaf/Iraq during the period between January and December 2018.The incidence of the prevalence of hydatidosis female was higher than that of males. The youngest patients infected was five years, and oldest was over than 70 years old. The age group 21-30 years old had the highest percentage of hydatidosis infections. The rate of infection in females 64 (61%) more than males 25 (39%). Compared to males, there was a substantial rise ($P < 0.05$) in females. The percentage of liver hydatidosis relative to other organs was higher (67.18%). There were many patients with big cyst size (>5cm) than those with small cyst sizes (<5cm).

Keywords. Hydatid cyst, *Echinococcus granulosus*, Najaf, Iraq.

1. Introduction

Human *Echinococcus granulosus* infections occur as zoonoses mainly in sheep-raising areas where domestic dogs are used for herding [1].This parasite may potentially exist in all area as of the world, but the Mediterranean and Middle East countries, including Iran, parts of Africa. In addition to, Latin America and China are the primary sources of human infection [2]. Adults of *Echinococcus granulosus* and worm living in the intestine of the dog, eggs which are eaten by intermediate hosts (cows, dogs, rodents, deers and human) release the embryo into the duodenum. Then from there into the portal circulation; some of these embryos are stuck in the liver, the others migrate through the liver and spread, to other organs and turn into a hydatid cyst [3]. There are three layers of the liver hydatid cyst; the first is the pseudocyst (adventitia), composed of fibrous tissue, which product of the livers response to the parasite it is grey and closely attached to the liver, indistinguishable from it. The whitish and elastic ectocyst (laminated membrane) formed by the parasite itself contains a single layer of cells lining the cyst that internally secretes the hydatid fluid and externally the laminated membrane [4]. Hydatid fluid is colorless or yellowish and contains a complexity of protein, lipid, glucose, minerals and enzymes [5]. Hydatid cysts are usually well-tolerated in humans before their formation results in a strain on neighboring tissues or organs [6]. In humans, the hydatid cyst normally involves a single cyst in one organ, about 20-40% of patients have multiple cysts and usually, it involves multiple organs. The liver is the most prominent hydatid cyst site (50-70%) followed by the lungs (25%) but

less frequently in the spleen, kidney, heart, bones, and CNS around 25% of the patients had both lung and liver cysts [2].

In Iraq, hydatidosis is one of the main endemic diseases and has been recognized in both humans and animals [7, 8]. The occurrence of hydatid disease was 8 per 1000 patients admitted to the medical City Teaching Hospital in Baghdad for various cases [8]. It has been shown to be more frequent in young and middle age groups [9], 90 patients with hepatic hydatid cyst were confirmed to have been surgically treated in the first surgical unit at Baghdad Teaching Hospital since May 2009,among them,55 female (61.3%) and 35 male (38.7%). The purpose of the research was to determine the prevalence of hydatidosis parasite infection in the Province of Najaf /Iraq.

2. Materials and Methods

Sixty -four patients (25 males and 39 females), age range (5- > 70 years) with hydatidosis were confirmed surgically from Al-sadder Medical City in Najaf / Iraq, during the period between January and December 2018. The cysts were in the liver, lungs, omentum, and peritoneal cavity. Each individual patient filled a questionnaire sheet, shown in the appendix in this study.

3. Results and Discussion

3.1. Gender distribution

In this study, the total number of hydatidosis patients was 64 females (61%) and 25 males (39%), there was a significant increase ($P<0.5$) in females compared to males (Table1).

3.2. Age distribution

The age range of the patients included in this study is between 5-70 years old. In most cases, 18(28.12 %) both (male and female) were in the age group 21-30 years. There was a significant ($P < 0.05$) increase in age group 21-30 compared to other age groups.

3.3. Site of infection

Different organs were infected with hydatid disease, but the number of patients with liver hydatidosis had the highest percentage 43(67.18%) when compared to other sites of infection, followed by lung14 (21.89 %).The other organs were omentum and peritoneal cavity 1(1.56%) and 4(6.25 %) respectively. Compared to other tissues, there was a significant increase ($P<0.05$) in liver infection (Table 3).

3.4. Size and site of the cyst

Only 50 cysts were measured from the total of 64 patients.11 (45.83%) had cysts less than 5 cm in diameter, whereas the remaining13 (54.16%) cyst larger than 5cm in diameter, (Table 4). From a total of 20 liver cyst, 9(45%) has less than 5cm in diameter and 11(55%) has more than 5cm, whereas from a total of 9 lungs cyst, 3(33.33%) were less than 5cm in diameter, 6(54.54%) were more than 5 cm in size (Table 5).

Table 1. Gender distribution of 64 hydatidosis in Najaf/Iraq.

Female (%)	Male (%)	Ratio	Total
39(61 %)	25(39%)	1:1.56	64

Table 2. Distribution of 64 patients' according to age and sex with hydatidosis in Najaf/Iraq.

Ag(year)	Male No.%	Female No.%	Total
1-10	4 (50)	4(50)	8
11-20	5 (38.46)	8 (61.5)	13
21-30	9 (50)	9 (50)	18
31-40	3 (30)	7 (70)	10
41-50	4 (50)	4 (50)	8
51-60	0 (0.0)	3 (100)	3
61-70	0 (0.0)	1 (100)	1
71 - >	0 (0.0)	3 (100)	3
Total	25	39	64

Table 3. Distribution of 64 hydatidosis patients according to site and gender Najaf/Iraq.

Site of infection	Male No. (%)	Female No. (%)	Total %
Liver	15 (34.8)	28 (82.3)	43 (67.18)
Lung	7 (50)	7 (50)	14 (21.89)
Peritoneal cavity	1 (25)	3 (75)	4 (6.25)
Omentum	1 (100)	0(0.00)	1 (1.56)
Mixed	1(50)	1 (50)	2 (3.12)
Total	25	39	64

Table 4. Distribution of 64 hydatidosis patients according to the size of cysts and gender in Najaf/Iraq.

Size of cyst (cm)	Male No. (%)	Female No. (%)	Total (%)
<5	2 (18.18)	9 (81.81)	11 (45.83)
>5	4 (30.76)	9 (69.23)	13(54.16)
Total	6	18	24

Table 5. Distribution of 64 hydatidosis patients according to the size of cysts and organs infection in Najaf/Iraq.

Size of cyst (cm)	Liver No. (%)	Lung No.(%)	Total(%)
<5	6 (66.66)	3 (33.33)	9 (45)
>5	5 (45.45)	6 (54.54)	11 (55)
Total	11	9	20

4. Discussion

The occurrence of hydatid disease in the Province of Najaf is dramatically increased in this study, this may be due to the lack of appropriate personal hygiene practices to prevent ingestion of the eggs. The practice of feeding dogs potentially contaminated viscera and poor educational program for inhabitant in the area (at risk) for the transmission of the parasite [10]. Insufficient meat inspection, poor dog management and inappropriate legislation [11] no active collaboration between veterinarians and public health workers [13] and the high number of stray dogs or sheep dogs [14]. All these rare responsible for transmission of disease. The gender distribution shows that the prevalence of hydatidosis was higher in females (78.3%) relative to males (21.7%). This has been also observed by [8, 15, 16], where they found that the infection rate was higher in females than in males. This may be due to the social life in our district where the females are confined to house working and this will make them more exposed to the source of infection especially in a rural area. The age range of the case

studies was from five years up to 70 years. The highest prevalence with regard to age distribution was between 21-30 years. It was shown that the age range between 11-40 years was the age of highest incidence [17, 18], while [8] and [16] found that the greatest prevalence of infection was between 20 and 30 years of age. The study showed that most of the patients had hydatidosis of the liver followed by the lungs peritoneal cavity and omentum. This finding is well documented by [2, 18]. This is probably because most frequently, the oncosphere enters the portal vein in the liver and then to the first capillary filter. If it passes the liver, it reaches the lung and other distant foci [17]. *Echinococcus granulosus* cysts never infiltrate or invade the tissue of the host and therefore remain as a foreign entity. In this study, a high percentage of patients had a large cyst size (more than 5cm in diameter). These wide cysts have been found more in the lung than in the liver. The cyst morphological features are primarily determined by the resistance of the organs concerned. In the soft parenchymatous tissues of the lungs, the cysts grow quickly and can become very large. In contrast, the firm liver texture exerts a definite restraining effect on the cysts growth, so it remains very limited in size [18].

5. References

[1] Ruth L and Russel F 2016 Medical parasitology, A Self-Instructional Text 6th ed., F. A Davis Company Philadelphia.
[2] Taherkhani H and Rogan M 2000 General characterization of laminated layer of *Echinococcus granulosus Iran J. Med. Sci.* **25** 95.
[3] Langer JC, Rose DB and Kestone JS 1984 Diagnosis and management of hydatid disease of liver *Ann. Surg*. **199** 412.
[4] Dziric C 2001 Hydatid disease: continuing serious public health problem *World J.Surg*. **25** 1-3.
[5] Hag A 1992 The trace elements in hydatid disease *Health Dis.* **6** 75.
[6] Permin A and Hansen J W 1994 Review of echinococcosis /hydatidosis A zoonotic parasitic disease *World Anim. Rev*. **78** 67.
[7] Babero BB and Al-Dabagh MA 1963 The zoonosis of animal parasites in Iraq.IV.An experimental infection of adog with *Echinococcus* of human origin *J. Fac. Med. Baghdad* **5** 79.
[8] Al-Jeboori TI 1976 Hydatid disease: A study of the records of the Medical City Hospital *J. Fac. Med. Baghdad* **18** 65.
[9] Mahmoud SS 1980 *Studies on hydatid disease in Mosul* MSc. Thesis Coll. Medicine Univ. Mosul.
[10] Al-Aubaidi TE 2010 Surgical Treatment of hydatid cyst of the liver *Iraqi Postgradu.Med. J.* **9** 189.
[11] Elizabeth AZ 2002 *Clinical parasitology. A Practical Approach* W.B. SAUNDERS COMPANY, Philadelphia.
[12] Schwabe CW 1986 *Current status of hydatid disease : a zoonosis of in increasing importance. In: The biology of Echinicoccus and hydhydatid* Thompson, R.C.A. (ed.) George Allen and Unwin, London 81.
[13] Thompson RCA. and Allsop CE 1988 *Hydatidosis: Veterinary perspectives and annotated bibliography* R. C. A. Thompson and C. E. Allsopp 246.
[14] Lymbery AL and Thompson RCA 1996 Species of *Echinococcus*: pattern and Process *Parasitol. Today* **129** 486.
[15] Molan AL and Zangana FM 1989 Human hydatidosis in Mosul. Pro. 5th Sci. *Conf. ISRC Iraq Baghdad* **18** 5.
[16] Al-Qadhi BA 2005 *Study of Some immunological and biochemical aspects of patients infected with Hydatidosis* PhD. Thesis College of Science, University of Baghdad.
[17] Belding DL 1965 *Textbook of Parasitology*,3rd ed. PP: Appleton Century Croft, New York.
[18] Hicken NF, Allister A, Carlquist J and Madsem F 1966) Echinococcosis of the liver and lungs: analysis of nineteen cases *Am.J.Surg*. **112** 823.

Effect of ginger alcoholic extract on the ovary tissue in quail

Effect of ginger alcoholic extract on the ovary tissue in quail

Mohammed Hayder Hamad[1], Nahla Al-Bakri[2] and Abdul-Razak Labi[3]

[1]Al-Mustaqbal University College, Babylon, Iraq.
[2]Department of Biology, College of Education for Pure Science (Ibn Al-Haitham), University of Baghdad, Baghdad, Iraq.
[3]National university for science and technology, Dhi Qar, Iraq.

*E-mail: haidermohammed031@gmail.com

Abstract. This research was carried out in quail in the laboratory of histopathology diseases during four months . The objectives of this study was to detecting the effects of the addition of the alcohol extract of ginger to ovary tissue of quail. The two groups of birds were in almost similar weights and were placed in cages. Each group consisted of 8 quails. The first group (control group) fed on regular feeding without adding alcoholic extract of ginger .The second group (treated group) fed on the same normal food after adding the alcohol extract of ginger at a concentration of 300 mg / kg. The results indicated that ginger have positive effects on folliculogenesis.

Keywords. Ginger, Ovary, Flliculogenesis.

1. Introduction

The cultivation of medicinal and aromatic plants and herbs has spread in most parts of the world and has been used for their medicinal effectiveness and quick cure for diseases which are used as whole herbs, powders, or aqueous or aquatic or oily extracts [1, 2, 3]. Zinger is a plant that is found in the warm regions. Rizhomes are used under the soil and contain volatile oils with pungent smells and pungent taste.. They contain the ginger root nodes, which are the most important parts of the plants [4, 5, 6].

2. Materials and Methods

2.1. Preparation of the alcoholic extract of ginger

The ginger bought from the local markets and cut the raw ginger into very small pieces, dissolve 30 g of raw material in alcohol to get the ginger extract in 70 ml of 96% of ethyl alcohol and place in a clean glass jar in a dark place for at least two weeks, the solution is then filtered with Whatman1 filter paper , the solution is then placed in the rotary evaporator, at a temperature of 45 ° C for the purpose of extracting .The solution was then placed in an electric oven at 45 ° C for 20 minutes to dispose of the remaining alcohol. After extracting the extract weighed by a sensitive balance and stored in clean containers [7].

2.2. Dissection of birds

A total of 16 quail birds at ages 15 weeks , divided into two groups of 8 birds each , the first as a control group and the second treated with alcoholic extracts of ginger concentration (300 mg / kg) (treated group). The birds were dissected and the ovary removed and fixed in 10% formaldehyde.

2.3. Histological preparation

The methods of [8, 9, 10] were employed in the histological technique of the present study, the chemical and stain used: 10% Formaldehyde, Ethyl alcohol; ascending concentrations of ethyl alcohol 30%, 50%, 70%, 80%, 90% and 95% using distilled water. Alcoholic eosin stain. Harris Hematoxylin stain. Paraffin wax methods used according to [9, 10] as the following; Fixation of the specimens in a 10% formalin solution for 24 hours. Washing with tap water, dehydration by ascending concentrations of ethyl alcohol, clearing with xylene, infiltration and embedding with paraffin wax, melting point 58° C, sectioning at 7 micrometer using Rotary Microtome. Staining with routine stain (H&E) then Dextrin Plasticizer Xylene (D.P.X) used as a mounting media. Finally, microscopic examination and photography; Histological slides were examined using a light microscope at various magnification powers suit for the current study requirements. The microscopic slides were selected with a digital microscope equipped with a digital camera and a standard 12-megapixel Canon camera was used.

3. Results and Discussion

This The results of the current study showed some effects of alcohol extract of ginger in the ovary tissue of the quail (Figure 1, 2, 3). Birds fed on a standard diet with an alcoholic extract of ginger at a concentration of 300 mg / kg, showed some changes represented by an increase in the size of the ovaries, improvement in the fertility rate, as well as an increase in sexual receptivity and early ovulation by the birds [2, 11].

Figure 1. Transverse section passes through the ovary of quails treated with alcoholic extracts of ginger concentration (300 mg /kg): shows more Immature follicles (IMF), numbers of primary follicles (PF), secondary follicles (SF), medulla (M), (H&E) (40X).

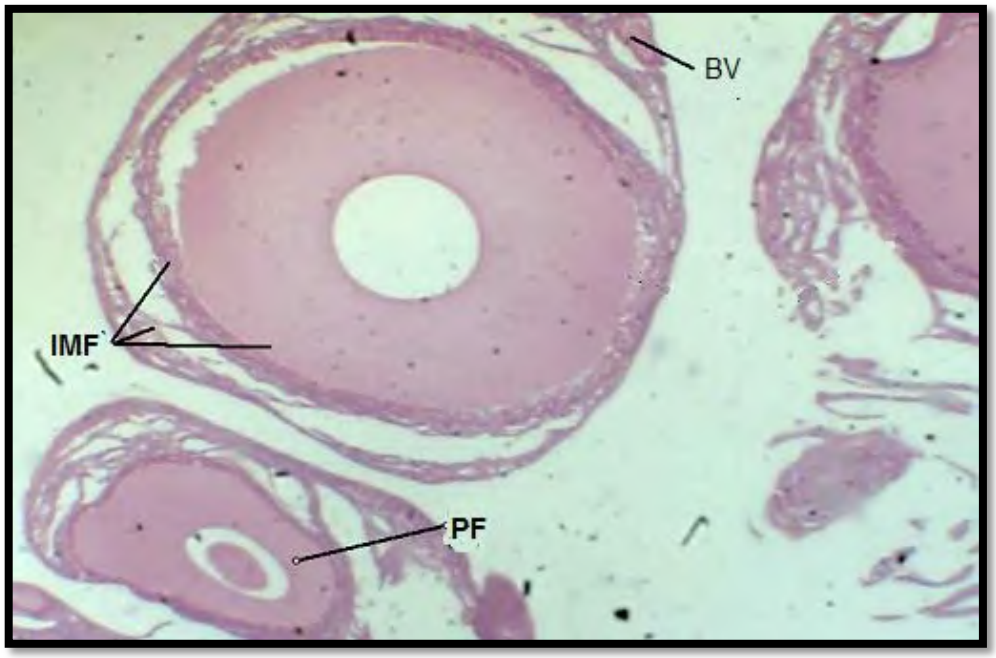

Figure 2. Transverse section passes through the ovary of quails treated with alcoholic extracts of ginger concentration (300 mg / kg): shows the Immature follicles (IMF), numbers of primary follicles (PF), Blood vessels (BV), (H&E) (40X).

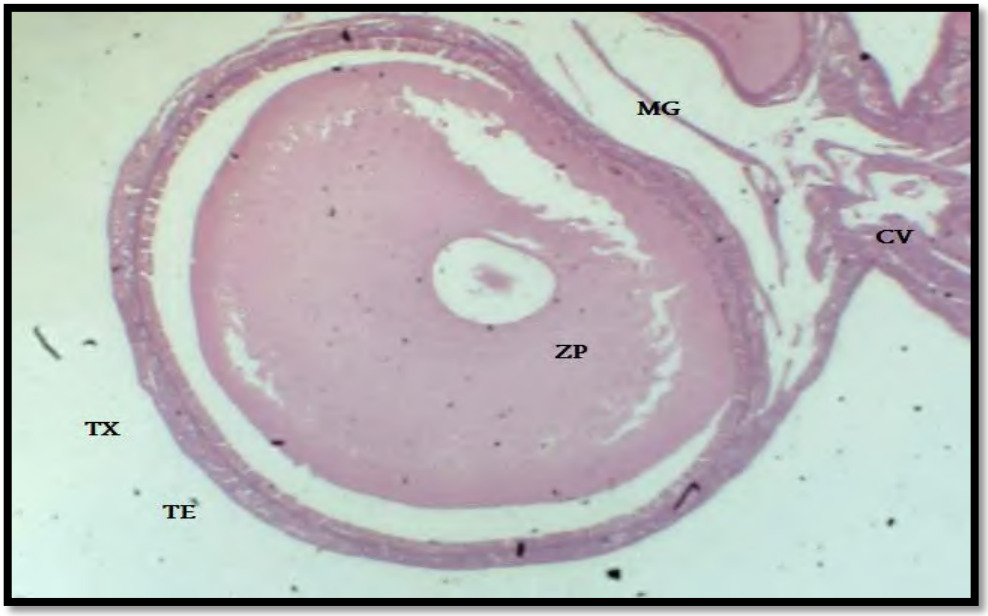

Figure 3. Transverse section passes through the ovary of quails treated with alcoholic extracts of ginger concentration (300 mg / kg): shows the Mature Follicles (MF), Blood vessels(BV), Theca Interna (TI), Theca Externa (TE), Oocyte (O), Zona Pellucida (ZP), (H&E) (40X).

The histological sections showed an increase in the growth and differentiation of ovarian follicles and the presence of several distinct follicles early in growth balanced with the control treatment and this is due to the fact that the alcoholic extract of ginger contains physiologically active substances ,these substances are similar to steroid hormones by their association with hormone receptors and estrogen receptors and with proteins that transport those hormones, and that substances also have an effect on

the metabolism of estrogen hormones and support its action which has the main role in accelerating the growth and differentiation of the follicles in early stages because ginger contains volatile oils [12]. and the proliferation of tissue the ovarian stroma has a greater degree of control, and increased ovarian cellularity and the presence and congestion of the blood vessels in the ovarian wall observed, this proportion fed by alcoholic extract led to early differentiation in the primary and secondary follicles, during folliculogenesis, also [13] stated that the ginger indicate positive effects on folliculogenesis. Ginger play an important role in goodness fertilization as it contain high level of vitamin C and A, minerals and some amino acids which are related with the activation of the endocrine gland and growth increasing [14], this foundation probably explain the activity of the ovary and increasing the number of primary and secondary follicles in quail birds treated with ginger alcoholic extract in this study. The ginger rhizomes essential oil enhances bird reproductive performances , proteins and reproductive hormone levels and hatchability traits in treated female quails [12,15].

4. References

[1] Ekwenye UN and Elegalam NN 2005 Antibacterial activity of ginger (*Zingiber officinale*) Roscoe and Grlic (*Allium sativum* L.) Extracts on *Esherichia coli* and *Salmonella typhi*. *Mycoses* **46** 12.

[2] Mascolo N, Jain R, Tain SC and Capasso FG 1989 Ethnopharmacologic investigation of ginger (*Zingiber officinale*) *J. Ethano Pharmacol*. **27** 129.

[3] Bahandari U, Kanojia R. and Pillai K 2005 Effect of ethanolic extract of Zingiber officinale on dyslipidaemia in diabetes rats *J. Ethenopharmacol.* **97** 227-230.

[4] Al-Qattan K, Thomson M and Ali M 2008 Garlic (*Allium sativum*) and ginger (*Zingiber officinale*) attenuate structural nephropathy progression in streptozotocin-induced diabetic rats. *Europ. J. Clin. Nut. Metab.* **3** e62.

[5] Ali BH, Blunden G, Tanira MO and Nemmar A 2008 Some phytochemical, Pharmac-ological and toxicological properties of ginger (*Zingiber officinale roscoe*) *Food Chem. Toxicol*. **46** 409.

[6] Ahmet T, Hasan RK and Ladine C 2011 Effects of *Zingiber officinale* and propolis extracts on the performance, carcass and some blood parameters of broilers chicks. *Res. Poult. Sci*. **1** 12.

[7] Shalmany SK and Shivazad M 2006 The effect of diet propolis supplementation on ross broiler chicks performance. *Int. J. Poul. Sci*. **5** 84.

[8] Vacca L 1982 Laboratory manual of histochimistry Raven press, New York. 328.

[9] Bancroft J and Stevens A 1982 Theory and practice of histological techniques. 2nd ed., Churchill Livingstone, London: 662.

[10] Luna LG 1968 Manual of histological staining methods,3rd ed , MC Graw–Hill book Co., Inc., New York: 258.

[11] Fuhrman B, Rosenblat M, Hayek T, Coleman R and Aviram M 2000 Ginger Extract Consumption Reduces Plasma Cholesterol, Inhibits LDL Oxidation and Attenuates Dev. E Deficient Mice *J. Nutr.* **130** 1124.

[12] Tchoffo H, Ngoula F, Kana JR, Kenfact A, Ngoumtsop VH and Vemo NB 2017 Effects of Ginger (*Zingiber officinale*) Rhizomes Essential Oil on Some Reproductive Parameters in Laying Japanese Quail (*Coturnix coturnix japonica*) *Adv. Reprod. Sci.* **5** 64.

[13] Yilmaz N, Seven B, Timur H, Yorganci A, Inal HA, Kalem MN, Kalem Z, Han O and Bilezikci B 2018 Ginger (*Zingiber officinale*) might improve female fertility: A rat model *J. Chinese Med. Med. Assoc.* **81** 1.

[14] Al-Kattan MM, Abdul-Fattah JH, Al-Hadidy AA 2008 Effect of *Zingiber officinale* Rhizomes powder on some physiological, Histological and Biochemical features in white Male Rabbits *J. Elom Al-Rafidain* 19 72.

[15] Chrubasik S, Pittler MH and Roufogalis BD 2005 Zingiber is rhizome: A comprehensive review on the ginger effect and efficiency profiles *Phytomedicine* **12** 684.

Journal of Physics: Conference Series

Physiological and histological protective role of *Astragalus spinosus* root alcoholic extract against oxidative stress induced by H_2O_2 in rabbits

Physiological and histological protective role of *Astragalus spinosus* root alcoholic extract against oxidative stress induced by H_2O_2 in rabbits

Moafaq Mutlak Zeidan[1*] and Qussay Noori Raddam[2]

[1]Department of Biology, College of Science, Tikrit University, Iraq.
[1]Department of Biology, College of Education, Al-Iraqia University,Iraq.

*E-mail: m-m.zedaan@tu.edu.iq

Abstract. This study amid to evaluate the role of plant's root (*Astragalus spinosus*), in biochemical parameters and histological sections effect in reduce the oxidative stress induced by hydrogen peroxide in rabbits *Oryctalagus cuniculus*, 7-9 months age and (1300-1500 g) of weight. Animals were distributed to three groups, every group were included five rabbits; group (1) control received water and diet. Group (2): animals treated with H2O2 (0.05) and drinking water. Group (3): animals treated with H2O2 and alcoholic extract of the plant root (5mg /kg body weight) for period one month. Study showed high significant increasing in Creatinine and ALP, LDH concentrations of animals treated with H2O2 alone (1.74±0.40) (9.900±1.058), (260.40±26.66) respectively, in compared with control (0.838±0.08) (8.420±1.132), (154.0±49.79) respectively while the concentration of Creatinine, ALP and LDH had been decreased with high significant (P≤ 0.05) in group treated with H2O2 and extract of the plant roots (0.79±0.09), (9.220±0.801) and (166.2±36.08) respectively in compared with H_2O_2 group. And the result of histological sections of liver, kidneys and heart, which showed an improvement of cells in group treated with the extract of the plant which had been induced by oxidative stress.

Keywords. Oxidative, Antioxidants, *Astragalus*, liver.

1. Introduction

Oxidative stress represents a situation in which the production of active oxygen varieties (ROS) increases in number that exceeds the ability of antioxidants to get rid of them, which results in an imbalance in the delicate balance between the production of free radicals and the body's ability to remove them or repair their destructive effects, resulting in damage to the various tissues in the body due to fat oxidation by the action of free radicals [1] of the active oxygen varieties is the negative superoxide root (O2-), which is one of the most toxic free radicals, hydrogen peroxide (H2O2) and hydroxyl radical (OH-) [2]. As for antioxidants, they are substances that prevent or slow down the generation of free radicals and oxidative processes in the body. Therefore, they form a line of defense against free radical activity and reactions [3]. Antioxidants are a substances that work to prevent or slow down the generation of free radicals and oxidative processes in the body. Therefore, they

constitute a line of defense against the destructive activity of free radicals in chain reactions [4] primary role of antioxidants of various types is work on giving an electron to the free root to prevent its reactions and stop its destructive activity, or it works on materials that scavenge free radicals, such as the superoxide dismutase (SOD) enzyme that captures the negative superoxide root, or it acts as metal chelating agents [5]. Genus *Astragalus*, consisting of about 3000 species, is a valuable reference of herbal drugs. The review article comprises scientific data concerning morphological, distribution and phytochemical characters of the genus. Polysaccharides, saponins, and flavonoids are considered main active principles. *Astragalus*. have long been used as medicinal plants in folk medicine as cardiovascular, antihypertensive, diuretic, choleretic, as well as antimicrobial and antiviral agents, this plants of the exhibit a broad spectrum of pharmacological effects, among which major include anti-inflammatory diuretic, antibactericidal, and hypotensive [6]. Plants of the genus *Astragalus* have been used in traditional medicine in many countries for centuries, which the genus *Astragalus* being the largest in the family Fabaceae. It is known to contain various metabolites such as saponins flavonoids and polysaccharides. Flavonoids, which possess a wide range of pharmacological activities [7, 8]. The present study aimed to test the effectiveness of the alcoholic extract of *Astragalus* plant's root through its protective and antioxidant role on experimental animals by measuring creatinine, basal phosphatase, lactic dehydrogenase, and a histological study of the kidneys, liver and heart to clarify the effect of oxidative stress induced by hydrogen peroxide and the protective role of the plant's root of *Astragalus spinosus*.

2. Materials and Methods

2.1. Experience Design

The animals were divided randomly into three groups (5 animals in each group), and the experiment was designed as follows; first group G1: the control group was given only water and food. Second group G2: were given water containing hydrogen peroxide (0.05) and food only. Third group G3: were dosed orally with alcoholic extract at a concentration of 5 mg /kg body weight. The amount was given according to the weight of the animal, and hydrogen peroxide was added to the drinking water at a concentration of (0.05) in addition to the food. After the ending of one-month dosing period, the animals were forbidden from food for 24 hours, after which the blood was collected by cutting the jugular vein and placing the blood in test tubes. The blood was separated by using of a centrifuge at a speed of 3000 rpm for 15 minutes to obtain serum, and then prepared blood serum was withdrawn by micropipette and placed in tubes and kept at -20 °C.

2.2. Collection and preparation of the plant root

The roots of the *Astragalus* plant were obtained from the desert areas in the west of the Tigris River between Samarra and Tikrit.

2.3. Preparation of extract

The alcoholic extract was prepared from the plant roots according to the method mentioned by [9]. The amount of extract obtained from every 100 g of the plant's root was 2 g.

2.4. The active dose of the plant

Twenty one animals were used to know The effective dose of plant, animals were randomly divided into 7 groups (3 animals for each group), and in the table below was determined the effective dose of the alcoholic extract .The experiment was carried out during three days, and the animals were dosed orally at a single dose every 24 hours, and after 3 days, blood samples were collected through the

ear's vein, and the concentrations of sugar and cholesterol were measured, and the effective alcohol dose was concentration (5 mg / kg body weight).

2.5. Determination of Lactate Dehydrogenase (LDH) and Alkaline Phosphatase (ALP) Enzymes

The activities of LDH were determined spectrophotometncally by measuring the oxidation rate at 340 nm [10]. The activity of ALP enzyme was determined according to the colour method, as the amount of liberated phenol is measured after its reaction with potassium free cyanide and 4-aminoantipyrine to produce a coloured complex with the highest absorption at the wavelength 510 nm.

2.6. Determination of Serum Creatinine

The concentration of creatinine was estimated by using of an analysis kit (BIOLABO SA, France) kit [11]. The microscopial and histological slides were prepared according to [12] for histological study.

2.7. Statistical analysis

For a statistical data, Statistical Package Social Science (spss) version 22 was used, and Student's t-test, the level of significance was $P \leq 0.05$.

3. Results

The results finding (Table 1) show significant increasing ($P \leq 0.05$) in the level of Lactate dehydrogenase (LDH), ALT, and Creatinine in group G2 which were treated with H2O2 when compared with control group G1, while group G3 which treated with plant's root alcoholic extract showing significantly decreasing in the level of LDH, ALT and Creatinine when compared with group G2 and showed no significant differences when compared with control group G1.

Table 1. The parameters of study groups.

Groups	Parameters		
	LDH	ALP	Creatinine
G1 control	154.0±49.79	8.420±1.132	0.838±0.08
G2	260.40±26.66	9.900±1.058	1.74±0.40
G3	166.2±36.08	9.220±0.801	0.79±0.09

N+5, P $P \leq 0.05$, ± = Standard error

Results in the present study showed increasing in the level of LDH significantly ($p \leq 0.05$) in group G2 giving H_2O_2 ,while group G3 showed no significant differences when compared with control group G1 (Figure 1).

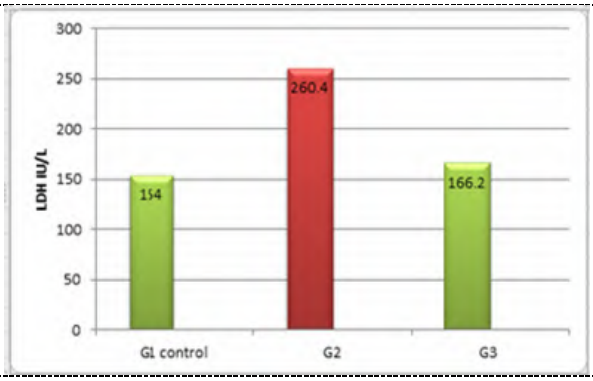

Figure 1. LDH level for study groups.

Results preserved increasing in the level of ALT significantly ($p \leq 0.05$) in group (G2) were treated with H_2O_2 ,while group G3 showed no significant differences when compared with group control (Figure 2).

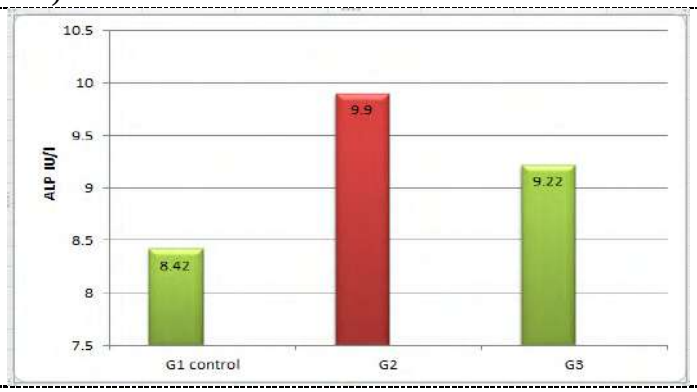

Figure 2. ALP level for Study groups.

(Figure 3) Results showed increasing in the level of Creatinine level significantly ($p \leq 0.05$) in group (G2) were treated with H_2O_2, while group G3 showed no significant differences when compared with group control G1.

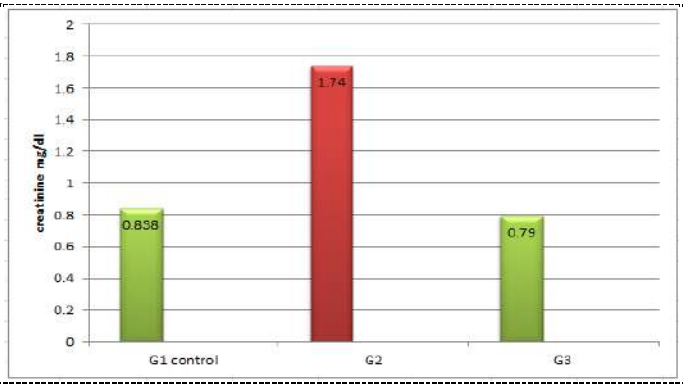

Figure 3. Creatinine level for study groups.

Histological study results in (Figures 4, 5, 6) showed the changes in the heart tissues of study animals in the group G1,G2 and the group G3.Fgures (7, 8, 9) that show the changes in liver tissues. Figures (10, 11, 12) show the changes in kidney tissues.

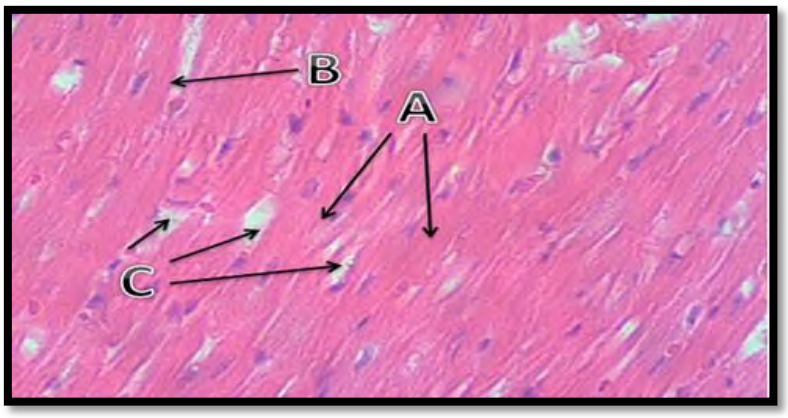

Figure 4. Histological section in the heart of control group G1. Show:A- cardiac of muscle fibres

(CMF), B- nuclei (N), C- Endomysium.

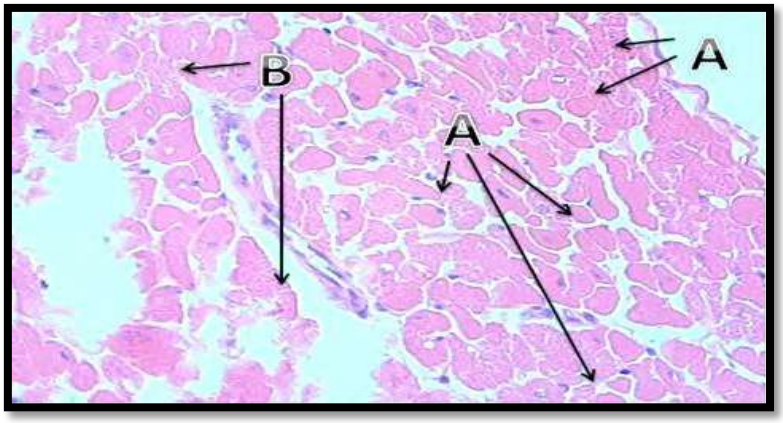

Figure 5. Cross section of heart in animal treated with hydrogen peroxide (0.05) G2 show :
A- heart, atrophy of cardiac muscle, B- Degeneration of sarcoplasm with disappearance of its nuclei (H&E stain 400x)

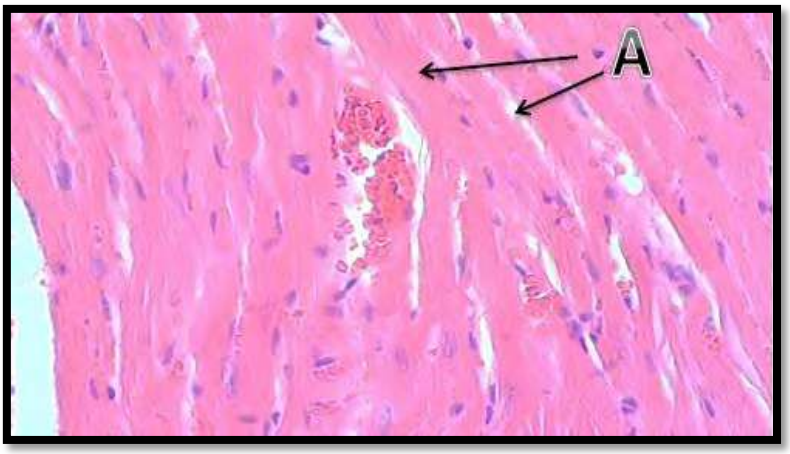

Figure 6. Longitudinal section of heart in animal treated with hydrogen peroxide (0.05) using dose of (5mg/k body weight) of the plant's root extract, group G3 show: A- cardiac muscle fibres with its normal archete chare (sarcoplasm and nuclei).

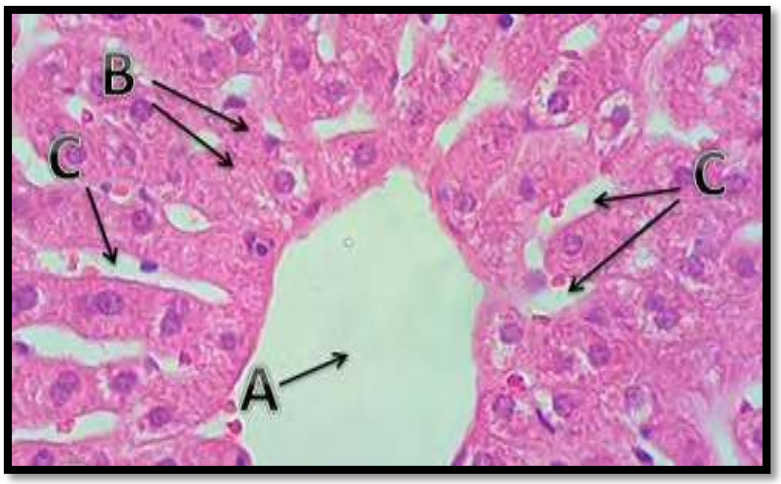

Figure 7. Histological section of liver in control group G1 show: A- central vein (CV) B- Columns of hepatic cells with its spherical nuclei (HC), C- Blood sinusoids with Kuepfer cells (BS) (H&E stain

400X).

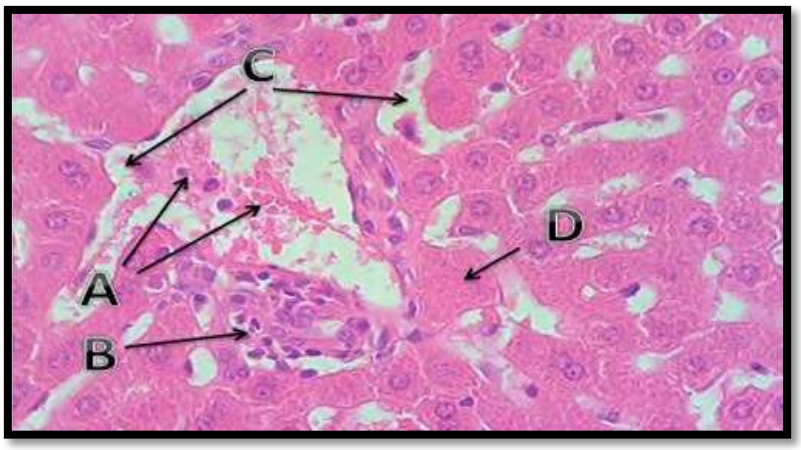

Figure 8. Cross section of liver in animal treated with hydrogen peroxide (0.05) G2 show: A- blood clot in the in the central vein, B- Lymphocytic nodular aggregation , C- Hypertrophy of Kuepfer cells in sinusoid, D- Disappearance of nuclei Frome certain number of hepatic cells (H&E stain 400X).

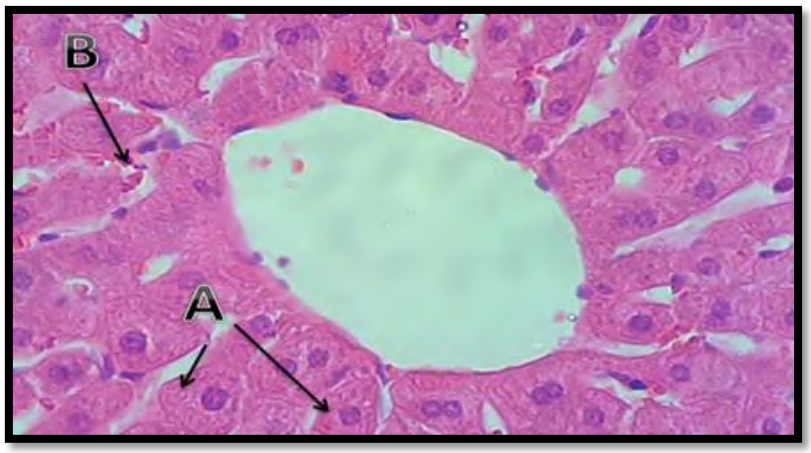

Figure 9. Histological section of liver in animal treated with hydrogen peroxide (0.05) and dose of (5mg/k body weight) of the alcoholic extract of the plant's root group G3 show: A- normal Architecture of hepatic cells with its spherical nuclei, B- Kuepfer cell in the blood sinusoid (H&E stain 400X).

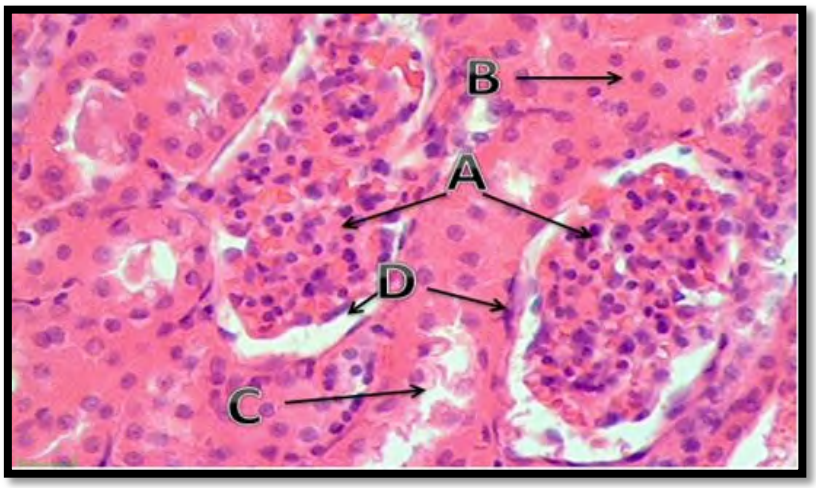

Figure 10. Figure (10) Histological section of kidney in control group G1 show: A- renal cortex ;

glomerulus G, B- proximal convoluted tubule PCT, C- Distal convoluted tubule DCT D- Bowman's capsule BC (H&E stain 400X).

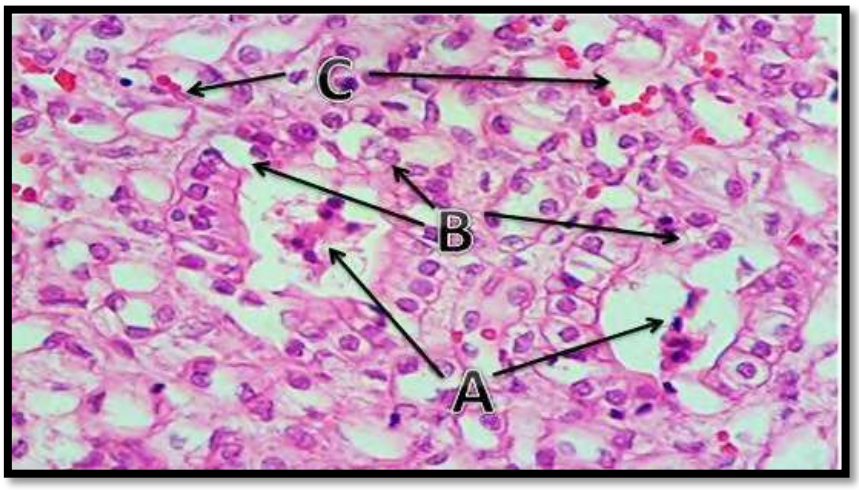

Figure 11. Histological section of kidney in animal treated with hydrogen peroxide (0.05) group G2 showing: Renal medulla, epithelia, desquamation inside the lumen of collecting ducts (A), degeneration of epithelial cells of collecting ducts (B) RBC present in between Henle loop (C) (H&E stain 400X).

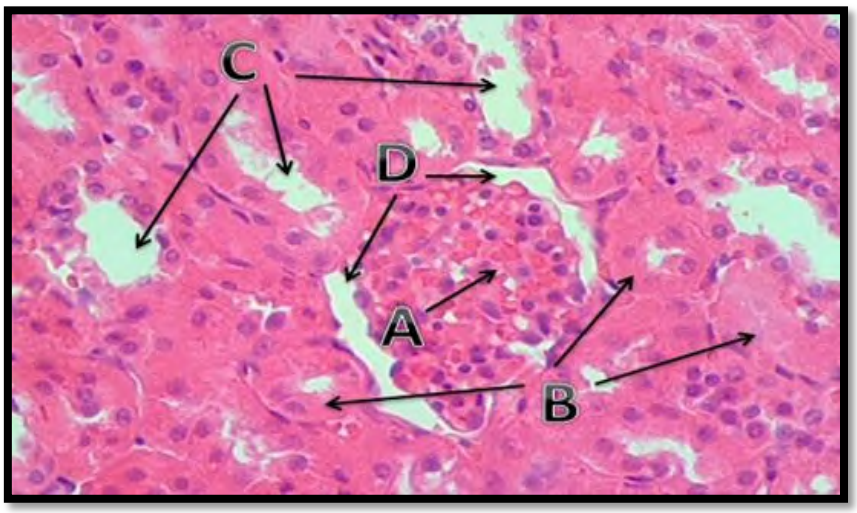

Figure 12. Histological section of kidney in animal treated with hydrogen peroxide (0.05) and dose of (5 mg/k body weight) of alcoholic extract of the plant root G3 show: A- renal cortex, hyperplasia of glomerular epithelia cell, B- Proximal convoluted tubule, C- distal convoluted tubule, D- Capsule space.

4. Discussion

The results showed a significant increase p ($P \leq 0.05$) in the LDH enzyme concentration in the blood serum of animals exposed to oxidative stress mediated by hydrogen peroxide, the results were (260.40±26.66) in compared with the control group (154.0±49.79) and the reason is due to the increase in oxidative stress resulting from the free radicals generated by H_2O_2, which damage the cells and tissues of the body, so the increase in the activity of this enzyme in the blood serum is an indication of the breakdown of the cells of the body organs, Histological section in the heart of treated with hydrogen peroxide (0.05) showing atrophy of cardiac muscle and degeneration of sarcoplasm with

disappearance of its nuclei compared with control group which show histological section in the heart of myocardium; degeneration cardiac muscle fibers. The oval nuclei in the sarcoplasm, endomysium. The cause of the high LDH is attributed to the harmful physiological effects of free radicals and stress on the heart muscle cells, which leads to its destruction and damage, and consequently damage to the cell membranes and the release of enzymes into the circulation [13]. And when the plant extract was treated, it led to a significant decrease in the total LDH level in the blood serum (166.2±36.08) compared to the H_2O_2 group (260.40±26.66). Also, a clear improvement was observed showing cardiac muscle fibers with its normal architected (sarcoplasm and nuclei) RBC outside the blood vessel. The results are in agreement with [14] where isoflavonoids were isolated from the *Astragalus* roots where the protective roles and antioxidant effects and increased the antioxidant enzymes, prevented the release of LDH from cells and stabilized the cell membrane structure. The results of ALP were (9.900±1. IU/l) in the group treated with hydrogen peroxide compared with control group (8.420±1.132 IU/l). It is evident from above results that the level of ALP increased in the serum of the group treated with hydrogen peroxide in compared with control, and this is an indication of the occurrence of liver damage as a result of the effect of free radicals, while the groups treated with plant extract show a significant decrease on probability ($P \leq 0.05$) of the level of the enzyme ALP (9.220 ± 0.801 IU / l) in compared to the group treated with hydrogen peroxide (9.900±1 IU / l). This indicates an improvement in liver cells and as shown in the Figure (7) Histological section in the liver of animal treated with hydrogen peroxide (0.5%) showing: blood clot with WBC in the Blood clot in CV with WBC Lymphocytic nodular aggregation, Hypertrophy of Kupffer cells in sinusoid, Disappearance of nuclei from certain number of hepatic cell compared with control Figure (8) showing: hepatic lobule central vein, Columns of hepatic cells with its spherical nuclei, Blood sinusoids with Kuepfer cells, Draining of blood from blood sinusoid to CV this result is agreed with [14, 15] indicated oxidative tissue damage and acute infections caused by the drug by increasing lipid peroxidation, and this leads to an increase in the permeability of the cell membrane and thus increases the movement of enzymes and their infiltration into the blood, which leads to an increase and decrease in the level of enzymes in the blood serum. In the liver, the study [16] indicated that the presence of such toxic substances leads to self-degradation of hepatocytes as a result of the increased activity of the lysosomes, which leads to the death of hepatocytes that cause an increase in the level of the three enzymes in the blood serum, and here the protective role of *Astragalus* appears spinous. Because it contains antioxidants, flavonoids can neutralize different types of oxidizing species including superoxide anion($O^{\bullet}{}_2^-$), hydroxyl radical (OH), or peroxyl radicals ($ROO.^-$) [17] Figure (9) showing section of liver of animal treated with hydrogen peroxide (0.5%) and treated with daily dose of (5mg/k body weight) of the extract of the plant sho normal Architecture of hepatic cell with its spherical nuclei , Kupffer cell in the blood sinusoid with WBC, total flavonoids, obtained from Radix Astragali showed significant antioxidant activity and inhibited the lipid peroxidation caused by $O\bullet{}_2^-$, H_2O_2[18, 19] and total flavonoids in *Astragalus* showed Protective effect from against DNA strand breaks, caused by (OH.) [20]. Flavanonols from *Astragalus sinicus* showed potent antioxidant activity determined by 2,2-diphenyl-1-picrylhydrazyl (DPPH) assay [21]. Flavonoid fraction obtained from the seeds of *Astragalus complanatus* showed significant radioprotective effect against injury induced by γ-irradiation in mice, flavonoids increased fraction on survival rate of the experimental animals and made the damaged organs recover normal appearance because of enhancing immunity [8]. Observed effect of flavonoid of *Astragalus* m against reperfusion hepatic injury in hemorrhagic shock [22]. Figure 3 shows a high increase ($P<0.05$) of creatinine (SCR) of animals exposed to oxidative stress with hydrogen peroxide, where the results were (1.74±0.4 mg / dL) compared to the control group (0.838±0.08mg / dL) and the cause may be due to increased oxidative stress, which leads to impaired renal function, leading to an increase in creatinine in the blood and less excretion in the urine levels of serum creatinine (SCR) manifest the ability of renal tissue to remove the creatinine from blood and gather it in the urine. However, kidney dysfunction could lead to the levels of SCR increased through weaken the ability to filter creatinine. In addition, the injured kidneys could cause the levels of serum urea nitrogen (SUN) elevated on account of the kidney tissue have no ability to remove the urea from

the blood [23, 24], demonstrated that astragalosides, especially astragalo- side V isolated from the root of *Astragalus* radix, inhibited the formation of advanced glycation end products in vitro. In rats induced diabetes, and treatment with *Astragalus membranaceus* improved renal function [25]. And when treating animals exposed to oxidative stress mediated by H_2O_2 with *Astragalus* extract, there was a significantly decrease in the SCR, as the results in figure 1 were (0.784 ± 0.050 mg / dL) compared to the control exposed to oxidative stress with H_2O_2 only (1.526 ± 0.260 mg / dL). While the groups treated with plant extract decreased significant on p ($P \leq 0.05$) of the activity enzyme ALP (0.79±0.09IU/l) compared to the group treated with hydrogen peroxide (1.74±0.40IU/l). Figure (10) Histological section in the kidney of animal treated with hydrogen peroxide (0.05) showing: renal medulla ; epithelia; desqumation inside the lumen of collecting ducts, degeneration of epithelial cells of collecting ducts , RBC present in between Henle loop , compred with control Figure (11) showing: renal cortex; glomerulus, proximal tubule convoluted, distal convoluted This indicates an improvement in liver cells and as shown in Figure (12), animal treated with hydrogen peroxide (0.05) and treated with daily oral dose (5 mg/kbody weight) of the extract of the plant show : renal cortex ; hyperplasia of glomerular epithelia cell , proximal convoluted tubule, distal c.t , Capsule space. The reason is due to *Astragalus* contains the high capacity of antioxidants that inhibits oxidative processes in the biological system, *Astragalus membranaceus* has a complex chemicals. Its major active constituents include *Astragalus* flavonoids, saponins, and polysaccharides [26]. Result is in accordance with [27] with cisplatin induced in mice kidney. The flavonoids made the damaged organ recover normal appearance [20].

5. Conclusion

From our results we can conclude that alcoholic extract *of Astragalus spinosus* root have a protective role against the oxidative stress effects on biochemical parameters include LDH, ALT, and Creatinine, and have a histological protective from harm effect of hydrogen peroxide and free radicals.

6. References

[1] Sikka S 1996 Oxidative stress and role of antioxidants in normal and abnormal sperm function *Front Biosci*. **1** 78.
[2] Betteridge DJ 2000 What is oxidative stress *Metabol. Clin. Exper.* **49** 1.
[3] Noguchi N, Watanabe A and Shi H 2000 Diverse functions of antioxidants *Free Radical .Res*. **33** 809.
[4] Parkash S and Joshi YK 2004 Assessment of Micronutrient Anti-oxidants Total antioxidant capacity and lipid peroxidation level in liver cirrhosis *Asia. Pac. J. Clin. Nutr*. **13** S110.
[5] Coskun O, Ocakci A, Bayraktaroglu T and Kater M 2004 Exercise training prevents and protects streptozocin-induced oxidative stress and β-cell damage in rat pancreas *Tohoku J. Exp. Med*. **203** 145.
[6] Bratkov VM, Shkondrov AM, Zdraveva PK and Krasteva IN 2016 Flavonoids from the genus Astragalus: phytochemistry and biological activity. *Pharmacog. Rev.* **10** 11.
[7] Pistelli A *2002 Secondary Metabolites of Genus Astragalus: Structure and Biological Activity* in: Atta-Ur-Rahman (Ed.), Studies in Natural Products Chemistry, Elsevier Science B.V., Vol. 27 443-545.
[8] Safar KN, Osaloo SK and Maassoumi AA 2014 Re-assessment of subspecific taxa in Astragalus section Anthylloidei (Fabaceae) based on molecular evidence *Progr. Biol. Sci*. **4** 219.
[9] Harborne JB 1985 *Phytochemical methods*. 2nd ED, New York, USA. Chapman and Hall.
[10] Bergmeyer HU and Bernt E *1974 Lactate- dehydrogenase, UV-assay with pyruvate and NADH* In: Bergmeyer HU (ed.) Methods of enzymatic analysis, 2. Academic Press, New York,574-579.

[11] Young DS 1995 *Effects of drugs on Clinical Laboratory tests* 4th ed., 3-498a.3-511.
[12] Luna LG 1968 *Manual of Histologic Staining Methods* 3rd ed., M c Graw- Hill Book Co., New York 2-38.
[13] Aslan R, Sekeroglu MR, Tarakioglu M, Bayiroglu F and Meral I 1998 The effect of acute regular exercise on antioxidant tissue damage markers and membrane peroxidation of erythrocytes in sedentary students *Tr. J. Med. Sci*. **28** 411.
[14] Yu D, Duan Y, Bao Y, Wei C and An L 2005 Isoflavonoids from Astragalus mongholicus protect PC12 cells from toxicity induced by L-glutamate *J. Ethnopharmacol.* **98** 89.
[15] Sikand M, Malik S, Parveen K and Ahmad M 2013 Hepatoprotective effect of *Origanum vulgare* in Wistar rats against carbon tetrachloride-induced hepatotoxicity *Protoplasma* **250** 483.
[16] Vardi N, Parlakpinar LH, Cetin A, Erdogan A and Ozturk IC 2010 Protective effect of Carotene on methotrexate –induced oxidative liver damage *Toxicol. Path*. **38** 592.
[17] Rawat AKS, Methrotra S, Tripothi SC and Shome U. 1997 Hepatoprotective activity of Boerhavia diffuse L-roots a popular *Indian Ethn. Med. J. Ethno*. **56** 61.
[18] Harborne JB and Williams CA 2000 Advances in favonoid research since 1992. *Phytochemistry* **55** 481.
[19] Wang D, Shen W, Tian Y, Sun Z, Yuan S and Jiang C. 1994 The effects of the three components isolated from *Astragalus mongholicus bunge* on scavenging free radicals *Chin Pharmacol. Bull*. **10** 129.
[20] Wang D, Shen W, Tian Y, Sun Z, Jiang C and Yuan S. 1996 Protective effect of active components extracted from radix Astragali on human erythrocyte membrane damages caused by reactive oxygen species *Zhongguo Zhong Yao Za Zhi*. **21** 746.
[21] Wang D, Shen W, Tian Y, Liu G, Yang S and Zhou S 1995 The protective effect of total flavonoids *Astragalus* on DNA strand break in V-(79) cell caused by hydroxyl radicals *Chin. Pharm. Bull*. **11** 311.
[22] Qi L, Liu CY, Wu WQ, Gu ZL and Guo CY 2011 Protective effect of flavonoids from Astragalus complanatus on radiation induced damages in mice *Fitoterapia* **82** 383.
[23] Shen WM, Wang CB, Wang DQ, Tian YP, Yan GT and Hao XH 1997 The protective effects of TFA on reperfusion induced hepatic injury in hemorrhagic shock *Zhongguo Yaolixue Tongbao*. *13* 532.
[24] Roulard R, Petit E, Mesnard F and Rhazi L 2016 Mo- lecular investigations of flaxseed mucilage polysaccharides. *Int. J. Biol. Macromol*,. **86** 840.
[25] Motomura K, Fujiwara Y, Nohara T, Kiyota N, Tsurushima K and Takeya M 2009 Astragalosides isolated from the root of *Astragalus* radix inhibit the formation of advanced glycation end products *J. Agric. Food Chem*. **57** 7666e72.
[26] Zhang Y, Wu C and Cheng J. 2007 Merit of Astragalus polysaccharide in the improvement of early diabetic nephropathy with an effect on mRNA expressions of NF-kappaB and IkappaB in renal cortex of streptozotocin-induced diabetic rats *J. Ethnopharmacol*. **114** 387e92.
[27] Auyeung KK, Han QB and Ko JK 2016) *Astragalus membranaceus*: a review of its protection against inflammation and gastrointestinal cancers *Re. Am. J. Chin. Med.* **44** 1.

Evaluation effect of different concentration of povidone Iodine on skin wound healing in rabbits

Evaluation effect of different concentration of povidone Iodine on skin wound healing in rabbits

Falah Mahmood Hameed[1*], Hayder Mohammed Mohsen Al-Tomah[1], Ali J. AL-Nuaimi[1] and Ail Wasfi Sadeq[1]

[1]Veterinary Medicine College, University of Kerbala, Iraq.

*E-mail: falahsurgeon1976@gmail.com

Abstract. The goal of the current study was to assess the effects of povidone iodine 10% in comparison with 5% of povidone iodine on full-thickness cutaneous wounds healing in rabbits. This was on twenty-four healthy male rabbits, weighing from (1.5–1.8 kg). Under the effect of intramuscular administration of a mixture of xylazine hydrochloride 5mg / kg, ketamine hydrochloride 35mg / kg and diazepam 1 mg / kg. On each animal, in the dorsal back area, one square (2 x 2) cm full-thickness skin wounds were made. The animals were divided into two groups, group (A) as the treatment group was treated with 10% povidone iodine daily for 1 time for day 7 post operation. While, at the same time in group (B), the rabbits were treated with 5% povidone iodine. For clinical evaluation, each group was divided into four subgroups (two wounds/subgroup) on 3rd, 5th, 7th, 9th, 14th and 21th days post-wound induction and treatment. Clinically, the result showed that 10 % of iodine was more effective than 5 % of iodine, and the wound healing rate in group (A) was faster than group (B). This was followed by statistical analysis results showing the wound healing process ((20%, 40%), (70%, 85%) contraction) and ((10%, 20%), (50%, 70%) re-epithelization).Respectively, there were significantly more ($P \leq 0.05$) than the iodine 5% during the study period. Conclusion; Povidone-iodine solution 10% is more efficient than iodine 5% so that lead to acceleration and enhancement of full-thickness cutaneous wounds healing.

Keywords. Iodine, Wounds healing, Rabbits.

1. Introduction

The wound healing in skin is an all-around coordinated endurance instrument that can be impacted by different conditions prompting a superior or worse course of healing [1]. As of late, there is an equally mounting proof that mental impacts (for example stress, social help, positive effect, and environmental enhancement) may also connect with wound healing [2]. In any case, infection and sepsis can be caused by spoiling with a pathogenic microbial agent, which disturbs the repair continuum [3, 4]. Infection evolution is driven by a dynamic relationship between the host and microorganisms, and further affected naturally and medicinal interventions [5]. There are a few germ-free skin-purging specialists accessible to the specialist to use for patients experiencing perfect, clean, clean-contaminated, contaminated, and dirty surgery. The conventional sterile purifying operator of decision is povidone iodine (PI). It is modest, viable, and the most regularly utilized operator of decision

around the world [6]. Disinfectants are valuable choices for managing the bioburden in wounds with a wider range of antimicrobial adequacy, lower risk of anti-microbial obstruction progression, and minimal blowback to tissues. For that reason, the purpose of this study include assess and compare the effects of iodine in both concentrations, on full-thickness cutaneous wounds healing.

2. Materials and Methods

2.1. Experimental animals

Twenty four adult male rabbits (1.5- 1.8 kg) divided into 2 groups (12 rabbits each) were used in this study. The rabbits were kept in the animal house of the College of Veterinary Medicine, University of Karbala, maintained in individual cages along the period of the experiment under normal environment including climate, management and feeding.

2.2.Surgical operation

In the dorsal back area of each animal, a square (2 × 2) cm full-thickness skin wound was induced. The animals were divided into two groups, group (A) as the treatment group was treated with 10% povidone iodine daily for once a day for day 7 post induction. While, in group (B), the rabbits were treated with 5% povidone iodine at the same style and for the same period.

2.3. Clinical evaluations

A total clinical assessment was performed on all animals at regular intervals along the time of the examination. Advanced photos were taken for all injuries after the zone had been shaved to envision the injury edge. The scab of each wound was deliberately evacuated for better imagination of the epithelization and granulation tissue zone by utilizing saline.

2.4. Statistical Analysis

The Statistical Analysis System [7] was used. Least Significant Difference –LSD test was used to determine the significance between groups.

3. Results and Discussion

3.1. Clinical Evaluation

In fact, the clinical statement of wounds seemed to indicate that through the current analysis, both treated wounds were rapidly reduced in size. The change began on day 3 in both treatment groups, which became evident on day 9, especially in wounds treated with10 % povidone iodine. This variation continued to occur until this research was completed. Clear differences emerged between the two treatment groups in total wound healing, mostly at the end of the study (Figure 1). During the 21 days of the study, the following-up of wound healing process appeared that the percentages of effect of concentration and day in length and width of wound contraction at 3rd, 5^{th} and 7th without significant difference. While in the day of 9^{th}, 14^{th} and 21th of this study, the significant difference was clear with progress for 10% povidone iodine more than 5% povidone iodine(Table 1). At the same time, in the (Table 2) appeared the effect of concentration and day in the length and width of re-epithelization, which gave the same results that observed in the (Table 1).

Table 1. Effect of concentration and day in Length and Width of Wound contraction.

Days	Length (Cm)		LSD value	Width (Cm)		LSD value
	Conc.10%	Conc.5%		Conc.10%	Conc.5%	
Day 3	1.50 ± 0.00	1.50 ± 0.00	0.00 NS	2.00 ± 0.03	2.00 ± 0.00	0.00 NS
Day 5	1.40 ± 0.00	1.50 ± 0.00	0.113 NS	1.90 ± 0.00	2.00 ± 0.00	0.113 NS
Day 7	1.30 ± 0.00	1.50 ± 0.00	0.175 *	1.80 ± 0.02	1.90 ± 0.00	0.113 NS
Day 9	0.90 ± 0.00	1.40 ± 0.10	0.430 *	1.30 ± 0.00	1.80 ± 0.00	0.337 *
Day 14	0.50 ± 0.10	1.00 ± 0.00	0.430 *	0.60 ± 0.00	1.40 ± 0.10	0.430 *
Day 21	0.20 ± 0.00	0.70 ± 0.00	0.255 *	0.40 ± 0.00	0.85 ± 0.05	0.215 *
LSD value	0.141 *	0.207 *	---	0.252 *	0.217 *	---
			* (P≤0.05).			

Table 2. Effect of concentration and day in Length and Width of Epithelization.

Days	Length (Cm)		LSD value	Width (Cm)		LSD value
	Conc.10%	Conc.5%		Conc.10%	Conc.5%	
Day 3	1.50 ± 0.00	1.50 ± 0.00	0.00 NS	1.80 ± 0.02	1.90 ± 0.00	0.113 NS
Day 5	1.30 ± 0.00	1.40 ± 0.00	0.113 NS	1.80 ± 0.00	1.90 ± 0.00	0.113 NS
Day 7	1.20 ± 0.00	1.40 ± 0.00	0.164 *	1.70 ± 0.00	1.80 ± 0.00	0.113 NS
Day 9	0.80 ± 0.00	1.30 ± 0.00	0.175 *	1.20 ± 0.00	1.70 ± 0.00	0.307 *
Day 14	0.50 ± 0.00	0.90 ± 0.00	0.268 *	0.40 ± 0.01	1.30 ± 0.10	0.430 *
Day 21	0.10 ± 0.00	0.50 ± 0.00	0.252 *	0.20 ± 0.00	0.70 ± 0.10	0.430 *
LSD value	0.141 *	0.157 *	---	0.271 *	0.199 *	---
			* (P≤0.05).			

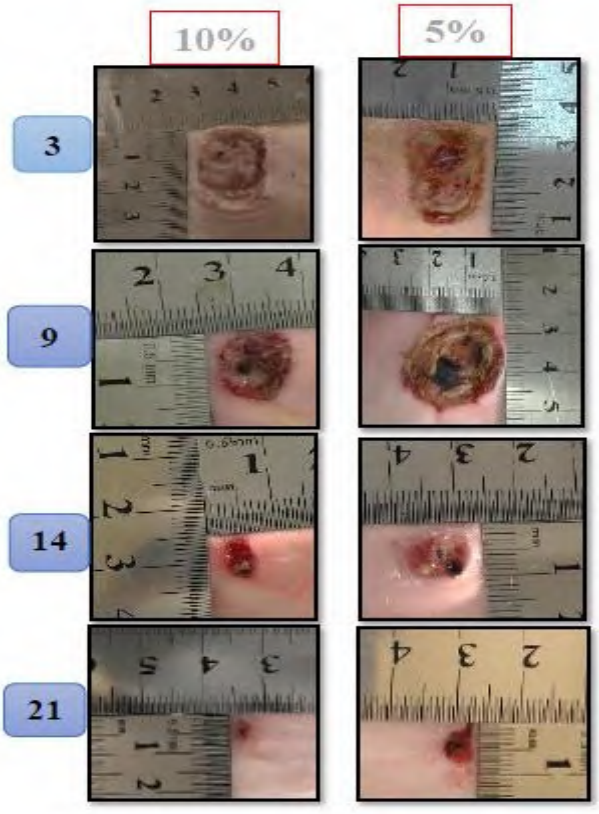

Figure 1. The study showed the difference in the wound contraction and re-epithelization between wounds treated with 5% and 10% iodine, at 3rd, 9th,14th and 21st days post-treatment.

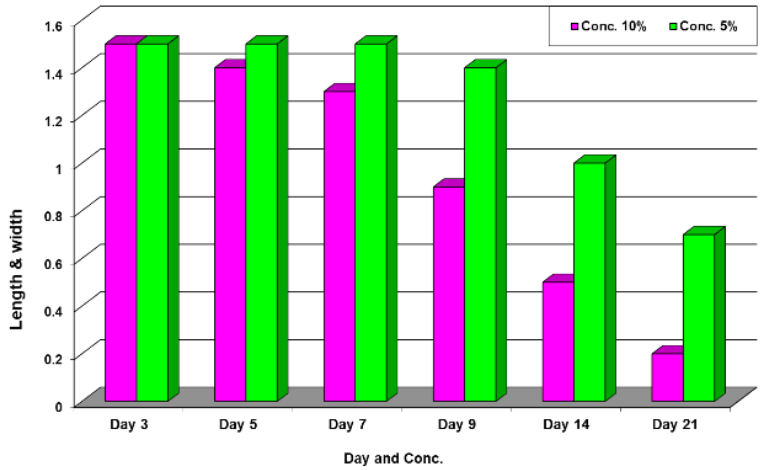

Figure 2. Effect of concentration and day the wound contraction.

4. Discussion

4.1. Clinical evaluation

In povidone iodine, the iodine factor is carried by aggregation (or micelles) and is gradually released into the solution to verify its antiseptic effect [9, 10]. Exposure to povidone iodine leads to induces cell death by destroying the cell wall, cell membrane, and cytoplasm [11]. The solution of 10% povidone iodine is widely used and does not induce resistance to microorganisms [11, 12]. The effect of PVP-1 on microbial cells was also studied by [8] and found that it affects the structure and function of enzymes and cell proteins. It damages the function of bacterial cells by preventing hydrogen bonding and altering membrane structure. The rapid death of microbes is ensured by these numerous modes of action and helps prevent the production of bacterial resistance. Since the microbicidal activity of iodine is associated with many directly toxic effects on the cell wall rather than complex molecular pathways (as used by antibiotics), tolerance is highly unlikely and there are unusually rare reports of iodine-resistant strains [8]. In the current study, the assess and compare the effects of povidone iodine solution on the healing of full-thickness skin wounds in rabbits provided by several mechanisms, including bacterial growth prevention, acceleration of the formation of granulation tissue 3–7, on all post-treated groups. The clinical observations of wounds in the present study appeared that the level of development of healing process was started rapidly in both treatment wounds. But the progression was high in the 10% povidone iodine treated groups & than those in 5% povidone iodine treated groups significantly were continued to be present until the end of the study. These results are in agreement with other animal studies in which the effect of povidone iodine on wound microcirculation has also been studied. In rabbit ear chamber wounds, the use of a 5% povidone iodine solution was associated with an early but increasingly transient reduction in blood flow [13,14]. However, wounds showed faster neovascularization with povidone iodine treatment compared to silver nitrate, sodium hypochlorite, and untreated controls in the 10 %povidone iodine study mentioned earlier[15]. Another rat model showed no adverse effects on capillary blood flow after up to 60 minutes of exposure to 1% povidone iodine solution [13]. Interestingly, povidone iodine has been shown in a recent study to enhance wound healing through TGF b, not only by increasing granulation but also by enhancing neovascularization [16]. These results are very similar to the results obtained by Cooper, 2007, with increased bacterial activity in the diluted solution due to increased free iodinelevel (up to 26 ppm in 1% to 0.1% povidone iodine solution). On the other hand, some in vitro studies have shown that povidone iodine may have a measure of cytotoxic effect [18] and no consistent deleterious effects have been shown in in vivo studies on various wound healing measures, especially at lower

concentrations of povidone iodine[17,19]. Research has also shown that a number of animal studies on povidone iodine in wound healing, were published more than thirty years ago [17, 20]. Most have shown that concentrations of up to 10% do not necessarily inhibit granulation and epithelialization processes [17].

5. References

[1] Sorg H, Tilkorn DJ, Hager S, Hauser JR and Mirastschijski U 2017 Skin wound healing: an update on the current knowledge and concepts *Eur. Surg. Res.* **58** 81.
[2] Broadbent E and Koschwanez HE 2012 The psychology of wound healing *Curr. Opin. Psychiatry* **25** 135.
[3] Edwards R and Harding KG 2004 Bacteria and wound healing, *Curr. Opi. Infect. Dis.* **17** 91e96.
[4] Leaper DJ, Schultz G, Carville K, Fletcher J, Swanson T and Drake R 2012.Extending the TIME concept: what have we learned in the past 10 years *Int. Wound J*. **9** 1e19.
[5] Konig B, Reimer K, Fleischer W and Konig W 1997 Effects of Betaisodona on parameters of host defense *Dermatology* **195** 42e48.
[6] Hemani ML and Lepor H 2009 Skin preparation for the prevention of surgical site infection which agent is best? *Rev. Urol*. **11** 190.
[7] SAS 2012 Statistical Analysis System, User's Guide. Statistical. Version 9.1th ed. SAS. Inst. Inc. Cary. N.C. USA
[8] Schreier H, Erdos G and Reimer, K 1997 Molecular effects of povidone-iodine on relevant micro-organisms: an electron-microscopic and biochemical study *Dermatology* **195** 111.
[9] Chang FY, Chang MC, Wang ST, Yu WK, Liu CL and Chen TH 2006 Can povidone-iodine solution be used safely in spinal surgery *Eur. Spine J*. **15** 1005.
[10] Cooper RA 2007 Iodine revisited *Int. Wound J* **4** 124.
[11] Schreier H, Erdos G, Reimer K, Konig B, Konig W and Fleicher W 1997 Molecular effects of povidone-iodine on relevant microorganisms: an electron-microscopic and biochemical study *Dermatology* **195** 111.
[12] Kunisada T, Yamada K, Oda S and Hara O 1997 Investigation into the efficacy of povidone-iodine against antiseptic-resistant species *Dermatology* **195** 14.
[13] Burks RI 1998 Povidone-iodine solution in wound treatment *Phys. Ther*. **78** 212e218.
[14] Brennan SS and Leaper DJ 1985 The effect of antiseptics on the healing wound: astudy using the rabbit ear chamber *Br. J. Surg*. **72** 780e782.
[15] Kjolseth D, Frank JM, Barker JH, Anderson GL, Rosenthal AI, Acland RD, Schuschke D, Campbell FR, Tobin GR and Weiner LJ 1994 Comparison of the effectsof commonly used wound agents on epithelialization and neovascularization *J. Am. Coll. Surg*. **179** 305e312.
[16] Wang L, Qin W, Zhou Y, Chen B, Zhao X, Zhao H, Mi E, Wang Q and Ning J 2017 Transforming growth factor b plays an important role in enhancing woundhealing by topical application of Povidone-iodine *Sci. Rep*. **9** 991.
[17] van Meurs SJ, Gawlitta D, Heemstra KA, Poolman RW, Vogely HC and Kruyt MC 2014 Selection of an optimal antiseptic solution for intraoperativeirrigation: an in vitro study *J. Bone Jt. Surg. Am*. **96** 285e291.
[18] Balin AK and Pratt L 2002 Dilute povidone-iodine solutions inhibit human skinfibroblast growth *Dermatol Surg*. **28** 210e214.
[19] Burks RI 1998 Povidone-iodine solution in wound treatment *Phys. Ther*. **78** 212e218.
[20] Vermeulen H, Westerbos SJ and Ubbink DT 2010 Benefit and harm of iodine in wound care: a systematic review *J. Hosp. Infect*. **76** 191e199.

Journal of Physics: Conference Series

PAPER • **OPEN ACCESS**

In vitro study of the effect of zinc oxide nanoparticles on *Streptococcus mutans* isolated from human dental caries

To cite this article: Arshad Mahdi Hamad and Qanat Mahmood Atiyea 2021 *J. Phys.: Conf. Ser.* **1879** 022041

In vitro study of the effect of zinc oxide nanoparticles on *Streptococcus mutans* isolated from human dental caries

Arshad Mahdi Hamad[1*] and Qanat Mahmood Atiyea[2]

[1]Department of Biology, College of Science, Tikrit University, Iraq.

*E-mail: arshadmnh1995@gmail.com

Abstract. Dental caries is a public health concern worldwide for which *Streptococcus mutans* has been reported Known as the potential etiology of infection. In recent years, nanotechnology has applied to Creation of novel material properties. The research was studying the effects of Nanoparticles of Zinc Oxide on *Streptococcus mutans* isolate from dental caries. In this research, Different ZnO NPs concentrations were studied as its anti-bacterial effects on *Streptococcus mutans* was isolated from dental caries cases. 27 *Streptococcus mutans* isolates were obtained, which is equivalent to 20% of the total number of 135 isolates. This nanomaterial was chosen because it has a high affinity for human cells and does not cause harm compared to other nanoparticles. The nanoparticles are those very fine materials that can be produced so that their dimensions or the dimensions of their grains range from (1-100) nanometers, and because of the small size of the nanomaterials, which made them behave differently from large-sized materials whose size exceeds 100 nanometers, and because of the small size of the particles. Nanoparticles, which gave them electrical and magnetic properties that differ from large particles of the same compounds. The well diffusion method and the MIC experiment were conducted, and the results were good, as in the well diffusion method the efficacy increased with increasing the concentration of ZnO NPs. In the MIC experiment, it was observed that MIC in the sixth tube, meaning that the MIC of ZnO NPs towards *Streptococcus mutans* equals 0. 312 mg / ml.

Keywords. ZnO NPs, *Streptococcus mutans*, MSB agar, Inhibition Zone, Dental caries.

1. Introduction

The Nanoparticales effects on human health are quite different from the macromolecules they are made from [1]. The increased nanoparticles activity may have a beneficial advantage or harmful effect, or both at the same time[2,3]. In recent times, Nanotechnology has attracted the world's attention greatly due to its characteristics compared to the giant molecules from which it is derived. The nanoparticles of zinc oxide, copper oxide and silver are used extensively industrially, including textile industries, dyes, motor oils, cosmetics, detergents and sprays [4]. A common feature of these nanocomposites is antimicrobial activity[5] . The antimicrobial effects of nanoparticles on pathogenic bacteria such as *E. coli*, *S. aureus* have been extensively studied[6]. The antimicrobial behavior of inorganic oxide metals particles such as magnesium oxide, titanium oxide, silicon oxide, titanium oxide and zinc oxide indicate that they can be used as antimicrobial treatments as possible. Use them

surgically under the heading of so-called nanomedicine [7]. One of the advantages of using inorganic oxide nanoparticles as antimicrobial agents is that they are highly effective against antibiotic-resistant pathogenic strains and are more heat resistant and less toxic [8]. ZnO NPs have a very Good safety and non-toxicity profile was Watched while taking different nanoscale sizes of The Particles of zinc oxide [9]. Tooth decay is Among the most famous oral diseases in the Oral cavity in humans [10]. It is one of the main oral problems that affect the health of all ages (children, adolescents, adults, the elderly) [11]. *Streptococcus mutans*, one of the natural flora in the mouth, is the main factor causing tooth decay and has the ability to form biofilm, and it is one of the most popular types of bacteria in this aspect [12]. The aim of this study is to investigate The directly effect of nanoparticles of zinc oxide on *Streptococcus mutans* that cause tooth decay.

2. Materials and Methods

2.1. Samples collection and isolation of bacteria

The samples were collected from the surfaces of the decaying teeth of the 135 patients attending the dental caries clinics at Tikrit city from both sexes, with different age stages between 8 to 65 years . The samples were collected using a sterile cotton swab, where the focus of this research was on isolating and diagnosing two genus of bacteria: *Staphylococcus* and *Streptococcus*, where a portion of the bacterial culture for each sample was transferred to Mannitol salt agar and MSB agar base in a plate by streaking on surface of agar, The plates were then incubated for 24 hours at 37°C. with leaving one plate from each medium as a control plate to detect the presence of contamination in the preparation of the medium. All the plates were diagnosed on the second day and the colonies growing on the agricultural media were diagnosed according to their phenotypic characteristics in terms of diameter, color, texture, shape and edge, then the characteristics of the cells and their shapes after staining them with a Gram stain as belonging to the genera *Staphylococcus* and *Streptococcus* [13]. Special biochemical tests were performed for genus discrimination *Staphylococcus* and *Streptococcus* bacteria at the age of 18-24 hours, according to the method used in to [13] to different between both genus and tests ability to produce of Catalase, Coagulase, Carbohydrate fermentation and Hemolysis. 27 *Streptococcus mutans* isolates were obtained, which is equivalent to 20% of the total number of isolates, which 135 isolates. As for other isolates, they are other bacterial types.

2.2. Preparation of Mitis Salivarius Bacitracin Agar (MSB) medium

MSB medium which observed in Figure 1 is the specific Selective Medium for *Streptococcus mutans*. This medium was prepared according to Hi-media's guidance which contained 20(w/v)% total percentage of sucrose in the medium with the addition of 200IU / L of the antibiotic Bacitracin and this ratio was prepared based on that each gram of Bacitracin it contains a number of international units and it's installed on the counter box according to the manufacturer. 0.0001 Potassium tellurite solution and 1% agar was added to ensure that the medium remained solid [14, 15, 16]. The method of preparation is by dissolving 90 grams of the medium in 1000 milliliters of distilled water and mixing well using hotplate with magnetic stirrer (zhongxing, taiwan, china) to ensure that solubility occurs well and then, to increase the selectivity of the medium for *Streptococcus mutans*, 150 grams / liter of substance was added. Sucrose for the medium so that the final percentage of sucrose is 20% in 1 liter of MSB, and after that, when the color of the medium is noticed to transparent blue, the conical flask is transferred to the autoclave to be sterilized at a temperature of 121 Celsius for 15 minutes and at a pressure of 15 pound per square inch psi, and when the medium is cooled to a temperature of 45 Celsius, potassium tellurite 0.0001, which has been sterilized by millipore filter 0.20 mm (Fisher Scientific, Wien, Austria), is added[14]. As for the solution containing the antagonist bacitracin, 1 ml of it was added after preparation as follows: By dissolving 0.364 of the powder in 100 ml of D.W, the stock solution of bacitracin was prepared. and mixed well by magnetic stirrer without any heat, and

after mixing it well, sterilize with a millipore filter (0.20Mm). The bacitracin solution is sterile at a concentration of 200IU / L . 1 ml of this solution was added to each liter of prepared medium and cooled at 45 ° C to ensure that the bacitracin is not damaged so that the ratio of this antagonist in the medium is 200 IU / L [14].

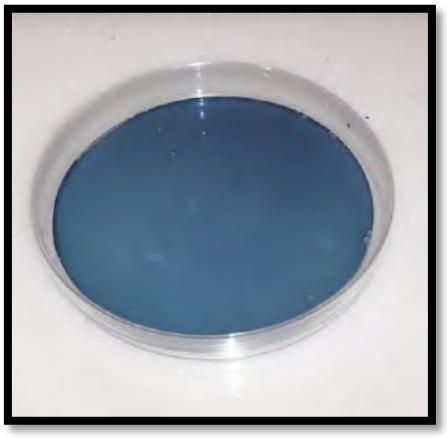

Figure 1. MSB Agar plate.

2.3. Muller Hinton Agar (MHA) preparation

Muller Hinton Agar (MHA) (Hi-media) was prepared according to the manufacturer's instructions [17] by dissolving 38 grams of powder in 1000 ml of sterile distilled water and then placed on a hot plate with magnetic stirrer until the powder completely dissolves in distilled water and the medium is clear. After that, the medium is transferred to an autoclave for sterilization at a temperature of sterilization at 121°C and a pressure of 15 pis for 15 minutes, finally it is poured into the sterilized Petri dishes , after it cools to 45-50 °C then left to harden until it is ready to cultivate the bacteria and test its sensitivity to antibiotics and zinc oxide on it.

2.4. Isolation of Streptococcus mutans

Streptoccocus mutans was isolated according to method of [18] which is summarized as follows: -

- Samples were collected using cotton swabs by passing them into the caries area and in the saliva surrounding the gums.

- The swabs were mapped on a selective culture medium (MSB) that was previously prepared.

- The plates were incubated under anaerobic conditions for 48 hours at 37°C.

- After the emergence of growth, the loop campaign of the growth appears on the surface of the medium (MSB), specifically the colonies to which the morphological characteristics are applied, are transferred and then streaked over the blood agar in order to activate the *Streptococcus mutans* bacteria, and the incubation was done at 37°C and in an anaerobic jar for a period of 24 hours.

- After the growth appeared on the medium of the blood agar, the single colony was transferred again to the MSB medium, and was streaked on the surface of the medium and then incubated in an Anaerobic jar at a temperature of 37°C for 48 hours. The benefit of last two steps is the activation of *Streptococcus mutans* bacteria as well as purification through Repeat the implantation on the selective medium (MSB).

2.5. Streptococcus mutans identification

2.5.1. Morphological feature

Streptococcus mutans was diagnosed phenotypically directly under light microscope with magnification level x15, the phenotypic diagnosis was based on colony shape on (MSB) agar plates, characteristics and based on Explanation cited by [18, 19]. Also, Hemolysis on blood agar plate , which must be (α) alpha-type, has been observed in *Streptococcus mutans* [20].

2.5.2. Gram Staining

Under aseptic conditions 1or 2 colonies were transferred from the surface of MSB Agar and exposed to Gram stain (SYR BIO, England) according to the known and scientific methods of work [21].

2.5.3. Biochemical tests

2.5.3.1. Catalase test

Colonies of *Streptococcus mutans* were taken from the MSB Agar plate by a sterile loop and transferred onto a sterile glass slide(Citotest ,Nantong , China) on the surface of which there is a drop of 3% H_2O_2 (Panreac, Barcelona, Spain). These colonies were mixed with a drop of hydrogen peroxide and the positive result of this test is bubbles [22, 23].

2.5.3.2. Test for carbohydrate fermentation (mannitol fermentation test)

Cystine trypticase agar CTA-Mannitol medium was used to the detect *Streptococcus mutans* ability to ferment mannitol sugar and convert the medium from red to yellow, which represents the positive result of the test [24]. The procedure of the test and media preparation was done according to [24]. Mannitol was added to medium cystine trypticase agar (Hi-media, India) at a concentration of 1% to form cystine trypticase manitol agar, which is used to detect the capacity of *Streptococcus mutans* bacteria to ferment manitol, ,where this medium after its preparation and autoclave sterilization at 121°C and a pressure of 15 psi for 15 minutes and after it gets cold it pours in screw capped bottles with a volume of 10 ml and keeping in the refrigerator at a temperature of 2-8 ° C until use. Later Inoculate each bottle of this medium by adding 0.1 ml of *Streptococcus mutans* bacteria samples grown on Brain Heart Infusion Broth and incubate at a temperature of 37 °C for 48 hours. The coloring change of media from red to yellow, was the indicator that the bacteria have the ability to ferment mannitol and produce acid in this reaction.

2.5.4. Diagnosis of Streptococcus mutans by VITEK-2

The diagnosis of *Streptococcus mutans* isolates was done using VITEK-2 after growing the samples on MSB Agar medium, using VITEK-2 (BIO meriex) according to the company's instructions [25].

2.6. Zinc oxide nanoparticle characterization

Zinc oxide nanoparticle was obtained from U.S Research Nanomaterial, Inc. (USA) Diameter 20-30nm, purity 99.98%, and the stock solution was made at a concentration of 10mg / ml and was diluted according to c1v1 = c2v2 [18]. The nanocomposite test was performed using scanning Electron Microscope (SEM) as shown in Figure 2.

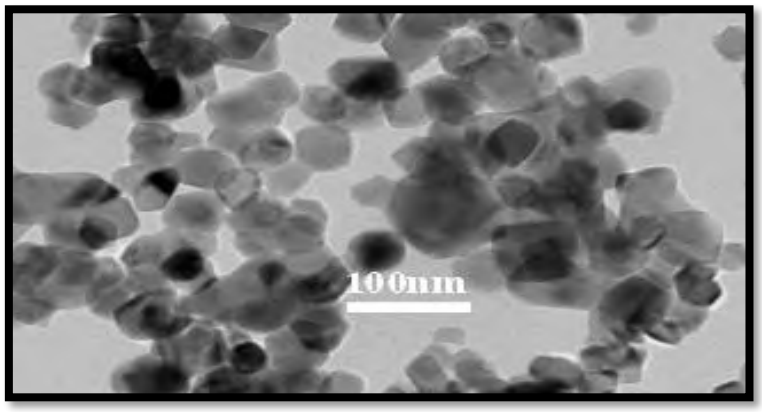

Figure 2. Zinc Oxide nanoparticles under a Scanning Electron Microscope (SEM).

In order to ensure the effectiveness of the zinc oxide nanoparticles solution, an examination was done with the UV-V device, as shown in Figure 3, and the absorption must be at its highest value at the wavelength (400–500 nm), and this is what was observed when examining these particles with UV/visible spectroscopy.

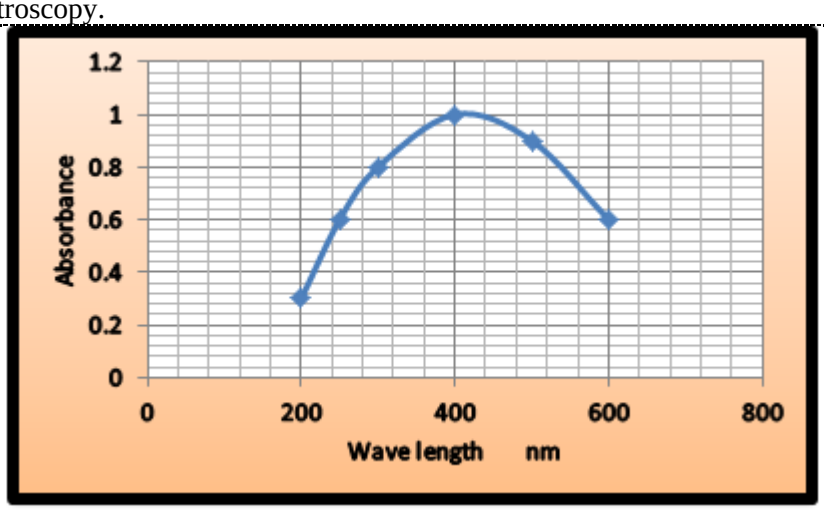

Figure 3. UV/visible spectroscopy of the ZnO NPs.

2.7. Determination of Streptococcus mutans susceptibility to various concentration of solution ZnO NPs and de-ionized water (In vitro)

The effectiveness of ZnO NPs was evaluated against Streptococcus mutans which was isolated from cases of dental caries according to method of NCCLS [26], which included the following: Greening of a bacterial suspended from *S.mutans* isolates, which we want to treat with ZnO NPs solution of different concentrations, and the bacterial suspension was made by transferring 3 colonies by sterile loop to 5 ml of Normal Saline and then compare the bacterial suspension with standard McFarland solution (0.5) to stabilize the cell numbers at 1.5×10^{8} cells /ml, then 100 µl of the prepared bacterial suspension was withdrawn and placed on a surface of Muller Hinton agar plates and were spread over the surface of MHA by a sterile swab and were planned length and width to ensure that the suspension was completely spread on the surface of the agar plate. Then, make holes in MHA by using the cork puncher (HI-Media, India) with a diameter of 5 mm and drilling serial concentrations of ZnO

NPs nanoparticles were placed. Prepared (w/v) with as a negative control, de-ionized water and the concentrations were as follows: 10 mg /ml, 5 mg /ml, 3 mg /ml, 1 mg /ml, 0.5 mg /ml, 0.1 mg /ml.

2.8. Measuring the Minimum Inhibitory Concentration (MIC) of ZnONPs

The lowest inhibitory concentration is important in the process of determining the lowest inhibitory concentration of zinc oxide in the nanoscale method by method of broth dilution. The bacterial suspension was prepared by taking 4-5 colonies from the MSB plate and transfer to the broth for 15 minutes. After mixing the bacterial suspension well, 0.1 ml of the bacterial suspension was added to each test tube containing 4.8 ml of the nutrient broth and 0.1 ml of zinc oxide solution that was prepared and added as the fellow of the concentrations 10, 5, 2.5,1.25, 0.625, 0.312, 0.156 mg / ml with a positive control tube containing broth and inoculum of bacteria to detect the ability of bacteria to grow on the nutrient broth, and a negative control tube containing only the nutrient broth and ZnONPs without bacteria was mixed well. The inoculated tubes were incubated for 24 hours at a temperature of 37°C. After that, the growth in the tubes was compared with the control tube not containing Nano-Zinc Oxide, where the lowest inhibitory concentration is the first tube with no turbidity that can be seen by eye [27].

3. Results and Discussion

3.1. Morphological Characteristic

Streptococcus mutans were examined morphologically using a light Microscope lenses (Olympos, Japan), where the colonies appeared under the microscope in blue color, 1-2 mm in diameter and have a spherical or oval shape with a little height, meaning they are convex and adherent to the surface of MSB Agar and in its center is a pool of polysaccharides, as shown in the Figure 4.

Figure 4. Shape growth colonies of *S. mutans* on MSB Agar plate.

3.2. Microscopic examination

The microscopic inspection in the oily lens Indicated that bacteria *Streptococcus mutans* Gram Positive, avoid edge and Spherical in shape and short chains to medium in length , as shown in the Figure 5.

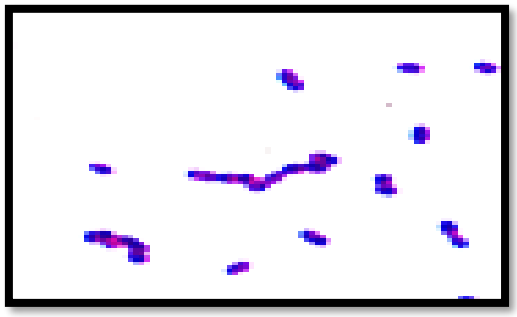

Figure 5. *S.mutans* cells with gram positive stain under light microscopic examination

3.3. Biochemical tests

Biochemical tests include the following:

3.3.1. Catalase test

All *Streptococcus mutans* are negative for catalase, meaning that they do not form bubbles when tested with H_2O_2 3%, which means that they do not have the ability to produce the catalase enzyme, It was noticed that *Streptococcus mutans* when performing the examination in the laboratory did not form any bubbles as shown in Figure 6.

Figure 6. Catalase test, shows that *S. mutans* are negative for catalase test.

3.3.2. Carbohydrate fermentation test (mannitol fermentation test)

Each *Streptococcus mutans* has the ability to ferment mannitol. The experiment was conducted in the laboratory and the result was positive, where the color of the medium changed from red to yellow, and negative control and positive control were used, and the result was positive as in Figure 7.

Figure 7. *Streptococcus mutans* - mannitol fermentation examination. A: Negative control tube (agar and mannitol without bacteria). B: Study tube (agar and mannitol inoculated with *Streptococcus mutans*). C: Positive control tube (agar and bacteria without mannitol).

3.4. Diagnosis of Streptococcus mutans by VITEK-2

VITEK2 tests showed that the Probability of *Streptococcus mutans* is 96%, and this is an excellent percentage that confirms that the bacteria isolated from caries are *Streptococcus mutans*, as noted in Figure 8.

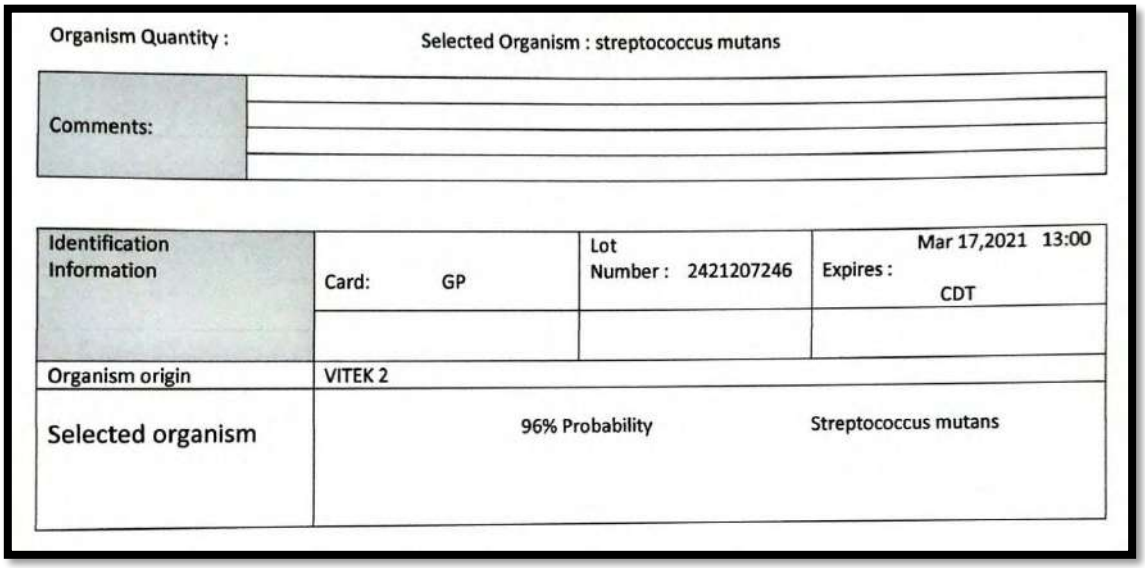

Figure 8. VITEK-2 test results.

3.5. Determination of Streptococcus mutans susceptibility to various concentration of solution Zn ONPs and de- ionized water (In vitro)

The results of the *Streptococcus mutans* susceptibility test to ZnO NPs appeared at a concentration of 0.5 mg / ml. This was the lowest inhibitory range, and it was highest at a concentration of 10 mg /ml. The highest inhibition zone appeared in Figure 9.

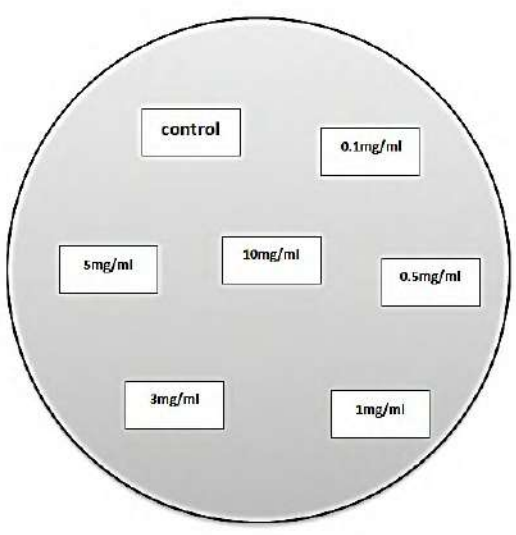

Figure 9. *Streptococcus mutans* sensitivity to different concentrations of ZnO NPs.

3.6. Measuring the Minimum Inhibitory Concentration (MIC) of ZnO NPs

MIC was determined after 24 hours of tube incubation, and where it was observed that the lowest concentration in which the growth disappeared and the tube became clear is Tube No.6, which contains a concentration of 0.312 mg/ml of ZnO NPs. For further clarification, the Table 1 below can be noted.

Table 1. Minimum Inhibitory Concentration (MIC) of ZnONPs on *Streptococcus mutans*.

Tube number	C+	C^-	1	2	3	4	5	6	7
Concentration ZnO NPs	0 mg/ml	0.078 mg/ml	10 mg/ml	5 mg/ml	2.5 mg/ml	1.25 mg/ml	0.625 mg/ml	0.312 mg/ml	0.156 mg/ml
Growth	+	–	–	–	–	–	–	–	+

= There is no growth , + = There is growth , - C = Negative Control , + C = Positive Control –

3.7. Statistical research check for Inhibition zone of ZnO Nanoparticle on Streptococcus mutans.

The arithmetic mean and arithmetic Median of inhibition zone for each conc. The inhibition zone by ZnO NPs was calculated for each of the concentrations that were used on *Streptococcus mutans* isolates. 25 isolates were selected from the diagnosed isolates and the different concentration of ZnO NPs which tested on them. The arithmetic mean of the inhibition zone was calculated for each concentration (0, 0.1, 0.5, 1, 3, 5, 10) mg\ ml which used on the 25 samples and the results were as in Table 2.

Table 2. Statistical calculations of areas of growth retardation according to the different concentrations of ZnO NPs.

ZnO NPS conc.	0mg/ml	0.1mg/ml	0.5mg/ml	1mg/ml	3mg/ml	5mg/ml	10mg/ml
Arithmetic Mean of inhibition zone for each conc. Of ZnO NPs	0mm	0mm	8 mm	11 mm	14 mm	17 mm	23 mm
Arithmetic Median of inhibition zone for each conc. Of ZnO NPs	0mm	0mm	7.6mm	12.1mm	13.5mm	15 .4mm	21 mm

4. Discussion

The quantitative evaluation of the antibacterial nanoparticle was observed by diffusion in the pits and it was observed that, the area of inhibition depends mainly on the concentration and agreement with results by the [28] which showed that the bacterial inhibition was increased with increasing the concentration of ZnO NPs and ,also the results was an agreement with [18] who are observed that zinc particles Nanoparticles have the highest effective against Gram-positive and Gram-negative bacterial activity, and ZnO NPs have excellent antibacterial activity. The increase in the zone of inhibition with the increase in concentration may be attributed to ZnO NPs the higher surface to volume ratio is due to which gives better ion exchange. The lowest concentration of ZnO NPs was 0.1 mg / ml and this concentration did not show any efficacy against *S. mutans* bacterial isolated from dental caries, many mechanisms of anti-microbial effect by ZnONPs and the activity of these molecules by generating harmful oxygen compounds to the living cell, which is H_2O_2, and when increasing the concentration of zinc oxide nanoparticles, it leads to an increase in the production of H_2O_2 and thus increase the anti-

bacterial effect. This effect occurs because of damage to the cell membranes and also causes a defect in the components of the cell, which were resulted in the cell's death permanently [18]. Another study showed that the anti-bacterial ability of ZnO NPs is due to their small size, which is 250 times smaller than a bacterial cell, and this facilitates for these particles to bind to the microorganisms' wall, which leads to their destruction and the death of living cells [18]. There is another possible mechanism for ZnO NPs activity against the bacteria through the release of Zn^{+2} ions that have the ability to break down cell membranes and interact with intracellular components[18]. The electron microscopy images showed that the effect of ZnO NPs was on the bacterial cell wall and also increased the permeability of the cell membranes as well as changing the cell morphology [18]. This was presumed to be caused by the interaction of ZnO NPs with the bacterial cell membrane, leading to a defect in the membrane function [18]. Which leads to a change in the permeability of the membrane and the leakage of intracellular components [18], then leads to cell death [18]. This interaction was likely due Electrostatic consequences attributable to the contrary charges of the nanoparticles and the cell membrane. A study by[18] showed that when ZnO NPs come into contact with bacteria, the toxic behaviour of ZnO NPs leads to the rupture of the bacterial bilayer lipid layer, which leads to leakage of the cytoplasmic contents, and there is another possible mechanism to inhibit the bacterial isolates of *S.mutans*. A weak DNA damage was observed in the treated bacteria [18]. It is believed that micro-nanostructures carry a negative charge while metal oxides carry a positive charge, and this leads to the modulation of the electromagnetic attraction between the microbe and the surface of the zinc nanoparticles. Once this attraction occurs, the microbe is oxidized and dies immediately, and in general it is believed that the production of ions by nanomaterials that interact with the dependent SH-groups. For proteins on the surface of the bacterial cell [29].

5. Conclusion

The findings indicate that nanoparticles of zinc oxide have an excellent anti-bacterial benefit., and the effectiveness of these particles increases by increasing the solution concentration that contains the nanoparticles.

6. References

[1] Albrecht MA, Evans CW, Raston CL 2006 Green chemistry and the health implications of nanoparticles *J. Green Chem*. **8** 417.
[2] Koziara JM, Lockman PR, Allen DD and Mumper RJ 2003 *In situ* blood-brain barrier transport of nanoparticles *Pharmac. Res*. **20** 1772.
[3] Oberdorster G, Sharp Z, Atudorei V, Elder A, Gelein R and Kreyling, W 2004 Translocation of inhaled ultrafine particles to the brain *Inhal Toxicol*. **16** 437.
[4] Ibrahim NA and Muhammad AA Z 2020 *Nanomaterials in detergents and cosmetics products: the mechanisms and implications* Handbook of Nanomaterials for Manufacturing Applications Elsevier, 23.
[5] Baler SA, Scheringer M, Macleod M and Hunger BK 2008Estimation of cumulative aquatic exposure and risk due to silver: contribution of nano-functionalized plastics and textiles *Sci. Total Environ*. **390** 396.
[6] Jones N, Ray B, Ranjit KT and Manna AC 2008 Antibacterial activity of ZnO nanoparticle suspensions on a broad spectrum of microorganisms *FEMS Microbiol. Lett*. **279** 71.
[7] Mohsen J and Zahra B 2008 Protein nanoparticle: A unique system as drug delivery vehicles *Afr. J. Biotechnol*. **7** 4926.
[8] Zakaria ZA, Matpesa A, Ramasamy K, Ahmat N, Mohamad AS, Jsraf DA and Sulaiman MR 2010 Lack of antimicrobial activities of Dicranopteris linearis extracts and fractions *Afr. J. Microbiol. Res*. **4** 71.

[9] Jiang W, Mashayekhi H and Xing B 2009 Bacterial toxicity comparison between nano- and micro-scaled oxide particles. *Environ. Poll.* **157** 1619.
[10] Damle S 2009 *Textbook of pediatric dentistry*. 3rd ed. Arya.
[11] Patini R 2020 Culturomics: A New Approach for the Diagnosis of the Oral Microbiota *Dental Hypoth.* **11** 72.
[12] Lévesque CM, Voronejskaia E, Huang YC, Mair RW and Ellen RP 2015 Involvement of sortase anchoring of cell wall proteins in biofilm formation by *Streptococcus mutans Infect. Immun*. **73** 3773.
[13] Brown AE 2015 *Benson's Microbiological Applications Laboratory Manual in General Microbiology* (13th ed., pp. 230-280). McGraw-Hill Companies, Inc., New York. 60.
[14] Hailan SY and Al-Khatieeb MM 2019 Antimicrobial efficacy of silver, zinc oxide, and titanium dioxide nanoparticles incorporated in orthodontic bonding agent *J. Baghdad Coll. Dent.* **31** 10.
[15] Tale V, Jadhav A and Kulkarni K 2020 Biofilm forming ability of bacteria isolated from dental caries: with reference to Streptococcus species *Fut. Dent. J. Egypt* **5** 2.
[16] Nagamine Y 2020 D-Tagatose Effectively Reduces the Number of *Streptococcus mutans* and Oral Bacteria in Healthy Adult Subjects: A Chewing Gum Pilot Study and Randomized Clinical Trial *Acta Medica Okayama* **74** 307.
[17] http://himedialabs.com/TD/M173.pdf.
[18] Abd ST and Abbas FA. 2016 The Effect of Zinc Oxide Nanoparticles on *Streptococcus mutans* of Human Saliva (*In Vitro* Study) *J. Baghdad Coll. Dent*. **28** 158.
[19] Edwardsson S 1970 The caries inducing property of variants of *Streptococcus mutans Odontologisk Revy* **21** 154.
[20] Luis M, Pezzlo MT, Bittencourt CE and Peterson EM 2020 *Color atlas of medical bacteriology* John Wiley & Sons.
[21] Procop GW 2020 *Koneman's color atlas and textbook of diagnostic microbiology* Jones & Bartlett Publishers.
[22] Wu Y, Jiang S and Fu Z 2020 Employment of teicoplanin-coated magnetic particles for quantifying gram-positive bacteria via catalase-catalyzed hydrolysis reaction of H_2O_2 *Talanta* **211** 120728.
[23] Ahmad F, Muhmood T and Mahmood A 2020 *Deciphering the mechanism of hafnium oxide nanoparticles perturbation in the bio-physiological microenvironment of catalase* Nano Express.
[24] Finegold S and Baron E 2017 *Methods for identification of etiologic agents of infectious disease. In: Bailey and Scott's Diagnostic microbiology* 14th ed. St. Louis: The CV Mosby Co.
[25] Jubair HH 2015 The Relationship Between Biofilm Forming and Antibiotics Resistance of *Streptococcus mutans* Isolated From Dental Caries *Int. J. Curr. Microbiol. App. Sci*. **4** 568.
[26] National Committee for Laboratory Standards 2004 *Performance standards for antimicrobial susceptibility testing,14thInformational supplement* M,100-513.Vol.24 No,1,NCCLS, Wayne, P A, USA.
[27] Owuama CI 2017 Determination of minimum inhibitory concentration (MIC) and minimum bactericidal concentration (MBC) using a novel dilution tube method *Afr. J. Microbiol. Res*. 978.
[28] Negahdary M, Arabi F, Imandar M , Imandar M, Noughabi M T, Akbari-dastjerdi HM and Fazilati F 2012 Investigation anti-bacterial effect of zinc oxide nanoparticles upon life of *Listeria monocytogenes Ann. Biol. Res*. **3** 3679.
[29] Thi, TUD 2020 Green synthesis of ZnO nanoparticles using orange fruit peel extract for antibacterial activities *RSC Adv.* **10** 23899.

Journal of Physics: Conference Series

PAPER • **OPEN ACCESS**

Response of model plant *Arabidopsis thaliana* to Plant growth promoting rhizobacteria & phosphate concentration

Response of model plant *Arabidopsis thaliana* to Plant growth promoting rhizobacteria & phosphate concentration

Sulaiman Abdulhusein Mashkoor[1] and Mushtak F. Karomi Kisko[2]

[1]Department of Horticulture, College of Agriculture, University of Kufa, Najaf, Iraq.
[2]Department of Biology, College of Science for women, University of Baghdad, Baghdad, Iraq.

*E-mail: sulaiman.aldhalimi@uokufa.edu.iq.

Abstract. Several reports have shown that various rhizobia can interact with non-hosted plant species, enhancing mineral nutrition and promoting plant growth. To further investigate the effects of such non-host interactions on plant growth and phosphate nutrition, we inoculated *Arabidopsis thaliana* with the model rhizobacterium *Pseudomonas fluorescens* at three phosphate concentrations in the nutrient medium. *In vitro*, we showed that root colonization by *Pseudomonas fluorescens* contributes to an increase in the amount of available phosphate that is important in plant growth, especially in the shoots, in all concentrations used in the study. In addition to improving plant growth as well as increasing plant biomass production.

Keywords. *Arabidopsis thaliana*, rhizobacteria, phosphate concentration.

1. Introduction

Arabidopsis thaliana belong to Brassicaceae is a world famous model in plant biology and genetics. It was the first plant to have its genome sequenced as it has a relatively small genome, which makes it a very useful model, as it is considered a popular tool for understanding the molecular biology of many plant traits [1]. Therefore, scientists consider it a vegetarian test mouse. Its popularity stemmed from the smallness of its genomic component. It has many sites for this plant on the World Wide Web and it is the most published plant for scientific research. The Arabidopsis thaliana plant is distinguished by its short life cycle, as the plant grows rapidly to reach maturity in six weeks, and produces thousands of seeds, and the plant is self-pollinating, so the genetic makeup of the plant is not affected by the succession of its generations, and hybrid seeds are not expensive and available, as well as can be stored. The seeds are for a long period of up to five years, as they are relatively small genome of approximately 135 mega base pairs (Mbp), and they can be cultivated easy (in vitro or in the field) and inexpensive, making the genetic testing of tens of thousands of plants easy [2]. Plant growth is affected by many external and internal factors that may improve or inhibit growth due to the interference of these factors with the plant's physiological processes. Among the factors that are in relationships with other organisms such as microorganisms that have a relationship with plants roots. The great richness of a rhizosphere in organic matter promotes the development of an abundant population of microorganisms. There is an abundant population of bacteria. It is estimated that the

density of bacteria present in a rhizosphere is on average 107-109 CFU / gr soil [3]. They develop either near the roots, in contact with the roots (which colonized the rhizoplane) or inside the roots (between cells and more rarely in a cell: endophytes). This enrichment in microorganisms attracts other animals (earthworms) which will feed on bacteria or fungi [4]. The rhizosphere is a small-scale model of the primary role that a plant plays in the structuring and functioning of an ecosystem. Types of symbiosis are classified according to the degree to which each species benefits from the interaction between plant and microorganisms [5]. There are beneficial bacteria and on the other hand, pathogenic bacteria, for example certain plants establish a symbiotic relationship with rhizobacteria, enabling them to produce nodules that facilitate the conversion of atmospheric nitrogen to ammonia [6]. Plants are also affected by other factors such as nutrition, which directly contribute to the improvement and growth of plants, especially the availability of Macro-elements, many Plant Growth Promoting Rhizobacteria (PGPRs) can influence the acquisition of macro and microelements, for example, some PGPRs are free fixers of atmospheric nitrogen (*Azospirillum brasilensee* Sp245) [7]. Present near the roots, their activated will help to provide the plant with inorganic nitrogen. In some PGPRs belonging to the *Pseudomonas fluorescens* species, there is production of a non-ribosomal oligopeptide, pyoverdin (at the origin of the fluorescence of the strains), which acts as a siderophore and which promotes the iron nutrition of plants [8]. Finally, others are able to solubilize phosphate by excreting organic acids in the medium [5]. Their presence in the rhizosphere improves the solubilization of phosphate for the benefit of bacteria as well as plant obviously, the activity of these different microorganisms contributes to modifying the organization of the soil in the vicinity of the roots and consequently, the development of the roots [9]. PGPRs on nutrition can be more extensive and include plant harvesting activity, for example, an increase in the influx of nitrate is observed in rapeseed plants inoculated with PGPRs belonging to the rhizobial family [10]. The effects of PGPRs on plants may also include carbonaceous nutrition. However, interpreting this effect is difficult because if the inoculation with Bacillus subtilis GB03 improves the photosynthesis of Arabidopsis, cultivated in vitro [11], the inoculation of Arabidopsis thaliana plantlets by the PGPR Phyllobacterium brassicacearum STM196 on the contrary decreases photosynthesis [12]. The indirect effects that PGPR can have on plants also fall into two categories. Either the effect is obtained when PGPR restricts the progression of a pathogenic microorganism, or the effect is obtained by activating the defense reactions of plants [13]. In the genome of many PGPR strains belonging to the Pseudomonas family, there are genes encoding the synthesis of 2, 4-diacetylphloroglucinol (DAPG; for review [14]). It is a compound with an antimicrobial power that can limit the growth of one or more phytopathogenic bacteria. Finally, many PGPRs also it can stimulate the activity of antioxidant defense system of plants against attacks from phytopathogenic bacteria. This is called ISR (Induced Systemic Resistance [13]. This mechanism relies on the activation of a signaling pathway involving ethylene and jasmonic acid which often results in the activation of expression of genes encoding Defensins, which have an antimicrobial function [15]. Numerous bacteria which are beneficial to plant growth and present in their rhizosphere have phosphate solubilization activity. It is mainly dependent on the activity of microorganisms to secrete protons and organic acids [16]. Gulonic acid by fixing cations such as Ca2 is arguably the one that is most directly involved in the solubilization of phosphate. This is what makes gram-negative bacteria, such as for example Pseudomonas fluorescens which directly oxidize glucose to gulonic acid in the presence of glucose dehydrogenase (GCD), excellent solubilizers of inorganic Phosphate (Pi). Also, their use is gradually popularizing in agriculture. An important component of the plant environment is formed by microorganisms. They can be pathogenic / parasitic, commensal or so beneficial (symbiosis) [17]. Studying the effect of symbioses on plants is a way to study how plants interact with their environment, but also a way to see how these symbioses could help plants better protect and adapt to climate change. This is why the study of all types of symbiosis is important today [18]. The main objective of our work was to unravel potential cross talks in the control of growth of the model plant Arabidopsis thaliana in response to different concentrations Pi and in response to the presence of *Pseudomonas fluorescens*.

.

2. Materials and Methods

2.1. Biological material

The experiments were carried out using a biological system composed by the model plant Arabidopsis thaliana as the wild type (WT) and gpt2 mutant (glucose6-Phosphate/phosphate transporter2), and at the same time by strains of rhizobacteria PGPR *Pseudomonas fluorescens*.

2.2. Culture medium and plant culture

All of the experiments were conducted in-vitro. The plants are cultivated on a minimum solid mineral medium (0,5 mM $CaSO_4(H_2O)_2$, 2 mM KNO_3, 0,5 mM $MgCl_2(H_2O)_6$, 1 mM KH_2PO_4, 0,05 mM $Na_2FeEDTA$, 2,5 mM MES, 0,03 µM $(NH_4)_6Mo_7O_{24}(H_2O)_5$, 1 µM $CuSO_4(H_2O)_2$, 1 µM $ZnSO_4(H_2O)_7$, 15 µM $MnCl_2(H_2O)_4$, 50 µM H_3Bo_3) supplemented by 1.2% (p/v) agar. The pH of the medium is adjusted to 5.7 with a KOH solution then aliquoted in the bottle and finally autoclaved at 120 °C for 15 min. Before sowing, the seeds are mixed in a disinfection solution (40 mL of osmosed water, 3 drops of tween, and 2 mL of sodium hypochlorite) for 15 min. They are then rinsed 5 times with sterile water. The seeds are sown one by one and spaced 1 cm apart under laminar air flow host in square Petri dishes containing solid culture medium, using a pipette. The cover closed with thick of adhesive plaster microporeTM 1.25 cm wide. The sown boxes are placed in the dark at 4°C for at least 2 days to promote uniform germination. At the end of this treatment, the boxes are placed vertically in the culture chamber set for long days (16h day / 8h night) at 21 °C and delivering a light output of 20,000 lux.

2.3. Preparation of the inoculum and inoculation of the plants

The strains of rhizobacteria PGPR Pseudomonas fluorescens were cultivated in the culture media which was most suitable KingB (20g bacto-tryptone, 10 glycerol, 1.5g K_2HPO_4 (anhydrous) 1.5g $MgSO_4$,) at 28 ° C for at least 3 days. The plants are inoculated by contact during their growth in the culture medium. For this, a known amount of inoculum is included in plant culture medium which has been kept liquid by incubation at 52 °C after autoclaving. The inoculum is obtained by adding 8 ml of sterile plant culture medium to the Petri dishes containing the bacteria culture. The medium is incubated under this condition for 15 min. The bacteria growing on the culture medium are then resuspended. The inoculum thus formed is taken using a sterile pipette and collected in a falcon tube. The number of bacteria contained in the inoculum is determined by measuring the turbidity of the 600nm solution. The plant culture medium is inoculated with the necessary amount of inoculum to obtain a final optical density of 0.07, which corresponds on average to 108CFU/ml of culture medium. Once the plant culture medium has cooled and been solid, eight-day-old seedlings are transferred to it. Each Petri dish then containing 10 seedlings is sealed with MicroporeTM type tape, then installed in a semi-vertical position in the culture chamber.

2.4. Plant growth

The shoot fresh weight and the root fresh weight were measured separately on a precision balance (ACL SBS-LW-300A, USA). To measure the fresh weight, all the root systems present in one plate (10 in total) were carefully collected (to avoid any sampling of agar). The result was normalized the number of root system sampled. Shoot fresh weights were measured one by one. For each genotype, the root and shoot fresh weight, and the content of soluble Pi has been repeated independently at least 5 times (50 seedlings).

2.5. Soluble phosphate content quantification

The amount of soluble/inorganic Pi was determined in the shoot, root and in aliquots of the different media 10 days after transfer. All individual samples were weighed, collected in 2 ml Eppendorf tubes, and suspended in 1ml of ultrapure water. All the samples were then heated during 1h at 95°C. We measured the amount of soluble Pi in 50 µl aliquots of each extract using the standard molybdenum blue method in conjugation with UV-visible spectrophotometer [19].

2.6. Statistical analysis

All data were collected on spreadsheets and standard statistics methods were used to describe the samples. The significance of the effect of a treatment on a variable has been tested by one - way ANOVA. The existence of differences between the observed means was tested by an LSD test at the threshold of P = 0.05. On the histograms presented in the result, the bars bearing the same letter are not considered to be significantly different. Arabidopsis thaliana seedlings were inoculated with a rhizobacteria *Pseudomonas fluorescens*. Ten days after inoculation, we measured the effect of the inoculation on the growth of the plant shoot and root at different concentrations of phosphate.

3. Results and Discussion

3.1. The presence of P. fluorescens in the Arabidopsis rhizosphere does affect the amount of soluble Pi present in plants

It is also noted in figure. 1 that the presence of Rhizobacterium Pseudomonas fluorescens an effect on the amount of phosphate absorbed by the plant after 10 days of inoculation into the agricultural medium for plant growth, as the presence of Rhizobacterium Pseudomonas fluorescens increased the amount of phosphate present in the shoot system in all phosphate levels used in the study and even at the level of deficient phosphate compared to the absence of Rhizobacteria in wild type plants (Figure 1. A), but at the level of roots, there are no significant differences at the level of normal phosphate and phosphate deficiency in both the presence and absence of Rhizobacteria in the phosphate content for the roots of wild plants, while there is a significant difference in the level of concentration 3 times phosphate by the presence of rhizobacteria (Figure 1. B).

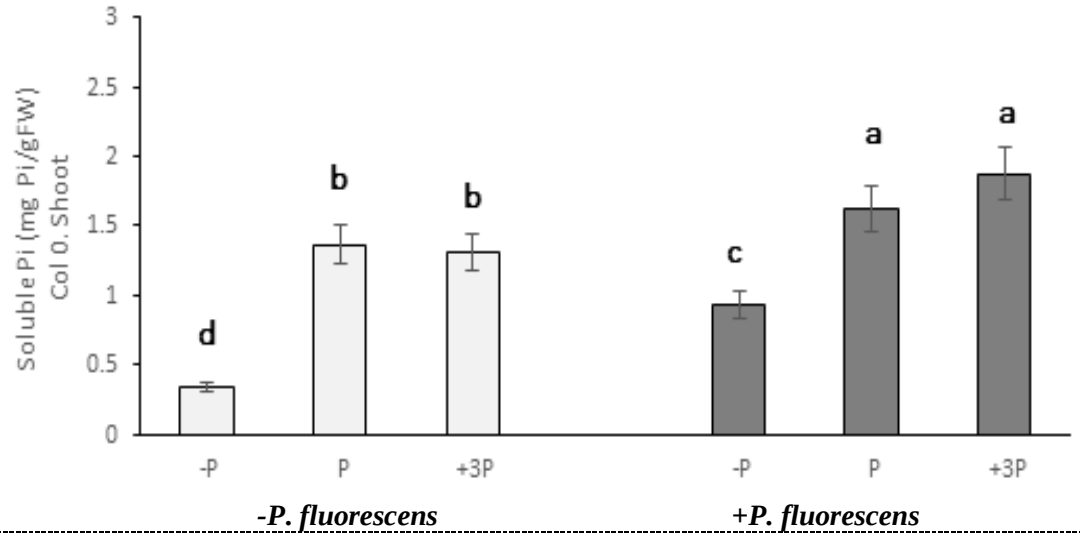

A

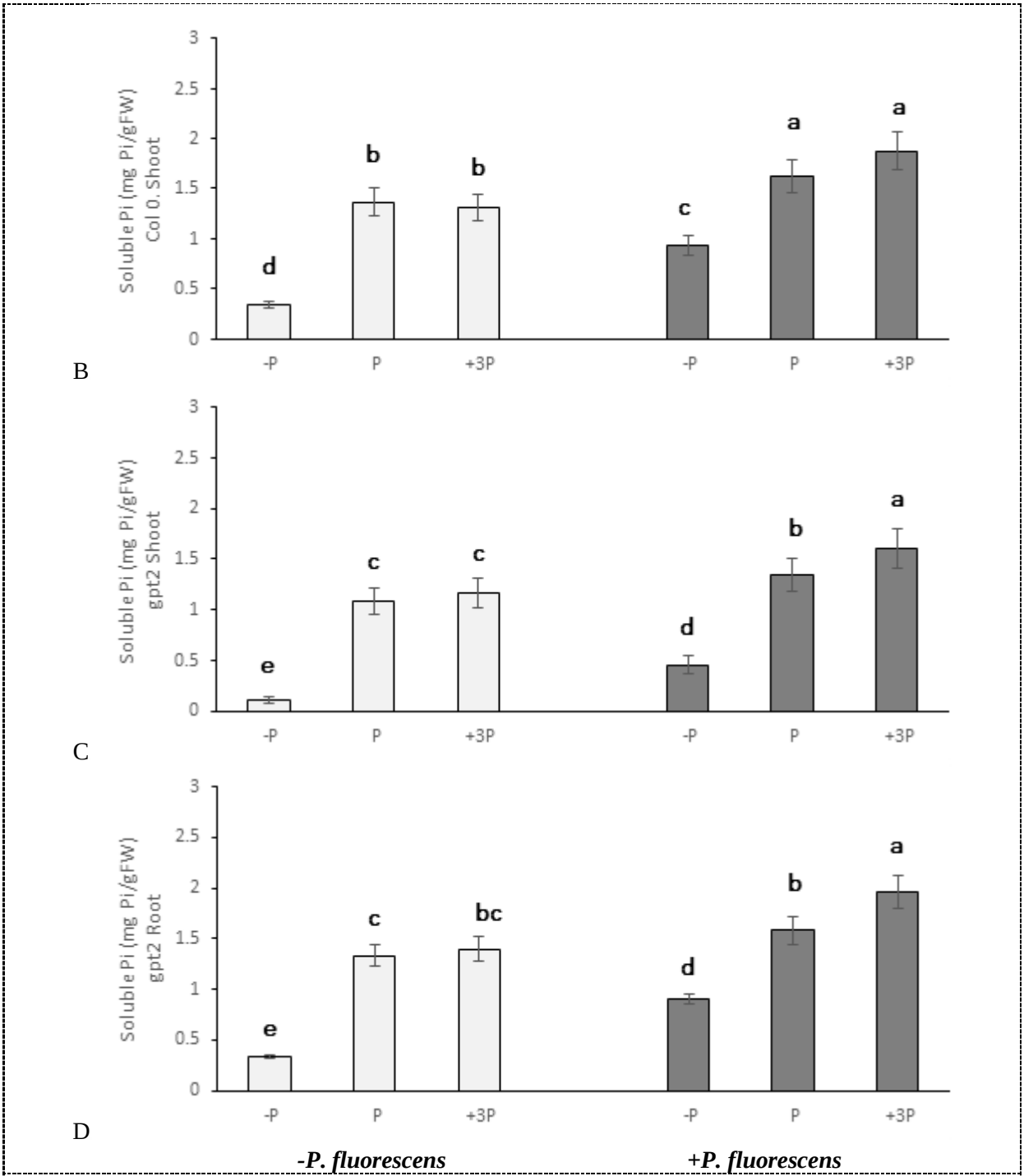

Figure 1. Phosphate content in shoot and root of Arabidopsis depends on Pi availability, Plants were transferred on different type of media: standard medium (2mM Pi), Pi deficiency medium (- Pi), and 3 time phosphate concentration medium, either with non-inoculated (- *P. fluorescens*) or inoculated (+ *P. fluorescens*). Ten days after the transfer, we measured the amount of soluble Pi. (A) Average (± SD) soluble Pi concentration in the shoot of wild type (Col 0), (B), average (± SD) soluble Pi concentration in the root of wild type (Col 0), (C) Average (± SD) soluble Pi concentration in the shoot of mutant (gpt2), (B), average (± SD) soluble Pi concentration in the root of mutant (gpt2).

Also, the effect of Rhizobacteria *Pseudomonas fluorescens* was observed with the amount of phosphate present in the mutant plants (gpt2), the presence of *Pseudomonas fluorescens* led to increase in the phosphate content present in the triple concentration of phosphate significantly and greatly, as well as the normal concentration and the level of phosphate deficiency compared to the amount of phosphate present in the shoot. In the absence of rhizobacteria (Figure 1. C), at the root level of this mutant (gpt2), it can also be seen that the rhizobacteria led to a significant increase in all phosphate levels used in the study (Figure 1. D). From all these data, it can be confirmed that the presence of Rhizobacteria *Pseudomonas fluorescens* contributes to an increase in the amount of dissolved phosphates in the plant, but the mechanics are uncertain, it may have been by producing substances that contribute to increase the phosphates availability for absorption and converting complex phosphates into simple forms that can be absorbed through channels on the roots, thus increase its quantity within the shoot system, because phosphate has a great role in the biological processes inside the plant [20].

3.2. Inoculation with Pseudomonas fluorescens stimulates plant growth

After 10 days of culture under the different conditions, it was found that the Pi and inoculation with Pseudomonas fluorescens led to beneficial effects on the growth of the plant. For Col - 0, Pi deficiency decreases the growth of the shoot whereas, on the contrary, inoculation stimulates the growth of the shoot (Figure 2. A). Whether the plants grew in the medium depleted in Pi or on the contrary enriched in Pi, the magnitude of this stimulation is similar. However, the reverse is not true: in the presence of *Pseudomonas fluorescens*, we observe that the Pi deficiency has a slightly inhibitory effect on the shoot while the excess Pi has a slightly stimulating effect. The root is directly affected by the concentration of phosphate in the nutrient medium, and we did not notice any effect of rhizobacteria *Pseudomonas fluorescens* in increasing or improving its growth (Figure 2. B).

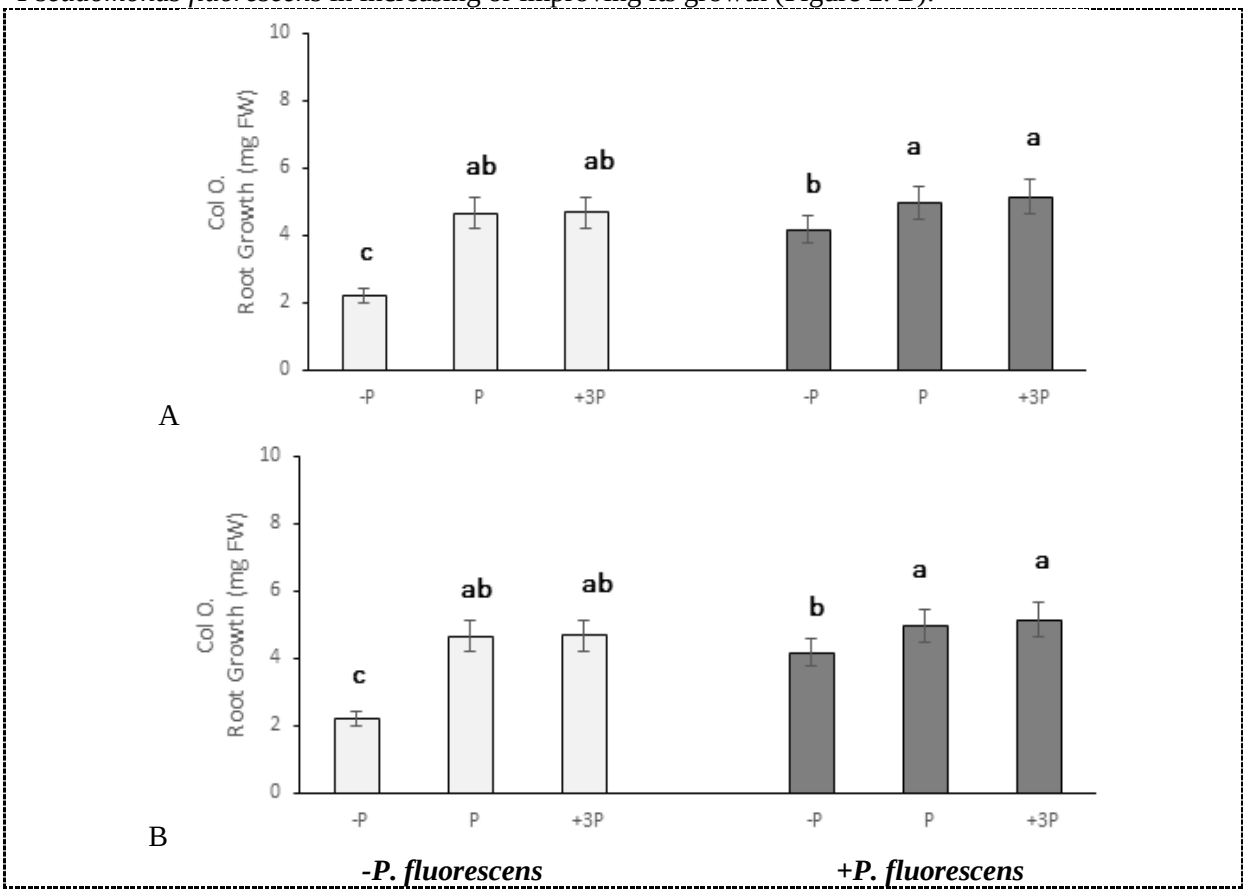

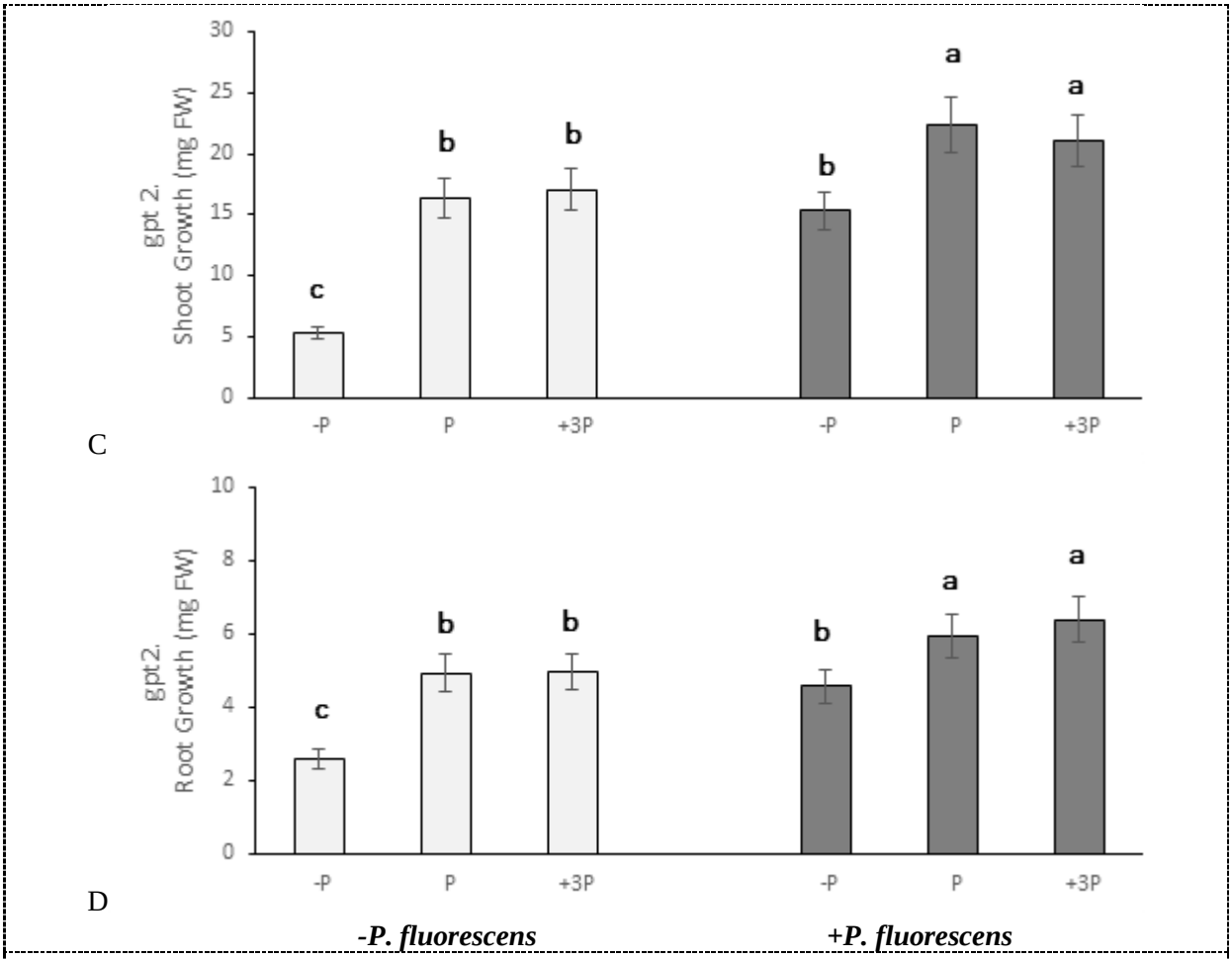

Figure 2. *P. fluorescens* promotes plant growth in vitro, regardless of Pi availability, eight days old WT Arabidopsis plantlets were. Plants were grown as described in Figure 1, ten days after the transfer, we measured the amount of soluble Pi. (A) average (± SD) shoot fresh weights of wild type (Col 0), (B), average (± SD) root fresh weights of wild type (Col 0), (C) Average (± SD) shoot fresh weights of mutant (gpt2), (B), average (± SD) root fresh weights of mutant (gpt2).

Purely additive mechanism with regard to the gpt2 mutant, it is observed that, as for Col-0, the medium with low Pi reduces the growth of the shoot (Figure 2. C). On the other hand, the presence of *Pseudomonas fluorescens* stimulates the growth of the shoot. While we noticed that the roots of the mutant gpt2 had an increased concentration of dissolved phosphate when the bacteria were present in the col-0 roots, and this increase was also affected by the concentration of phosphate directly with the nutrient medium (Figure 2. D). this is due to the capability of *Pseudomonas fluorescens* to solubilize insoluble P via two possible mechanisms: proton extrusion by ammonium assimilation and production of organic acids [21].

3.3. Correlation analysis reveals a dichotomy between plant growth and accumulation of Pi

To determine whether there are relationships between free Pi content in plants and fresh weight gains, we set out to systematically look for both linear (Pearson) correlations in all of our data. The goal was to represent the data as a network in which each node is a measured variable and each link is the correlation. For this type of analysis to provide information, it is necessary to have both dependent and independent variables. These variables must be in large number (to constitute a network with enough nodes so that the figure is interpretable) and be easily measurable. These variables must also be

measured under a very large number of conditions, if possible contrasting. In our case, these conditions are distributed between discrete characters (one mutant and a wild type plant in the same genetic background, treatment or not by a microorganism), but also continuous characters (3 different diets of phosphate nutrition). All these conditions do not necessarily have very strong contrasting effects. The analysis that we carried out allows us to identify strong relationships between the content of Pi in the leaves and the fresh weight of the shoot (Figure 3. A) Whereas at the roots level and the fresh weight there is no significant correlation (Figure 3. B). each of these correlations is expected because they are variables that are partly dependent on each other. For example, it is logical to observe that the P deficiency will be even more stress on the plant. In addition, some of the relationships confirm observations reported in the literature. For example, it is widely described that, in a situation of Pi deficiency, the main root stops growing [22]. These expected relationships, or so known in the literature, can be considered as positive witnesses.

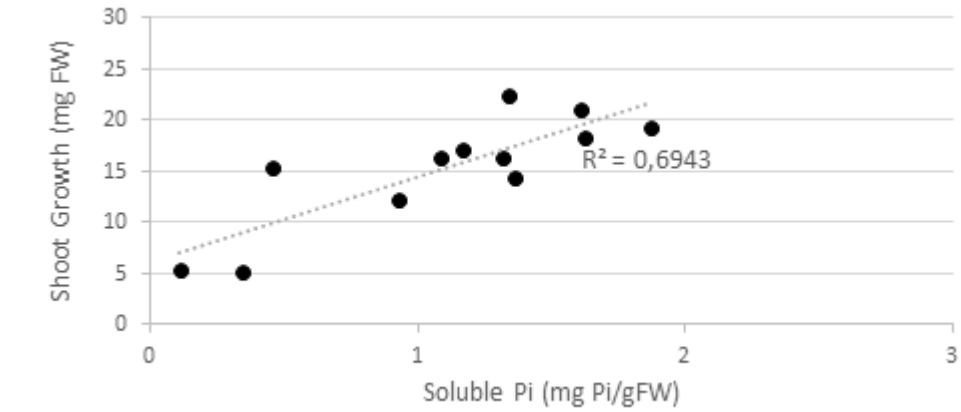

A

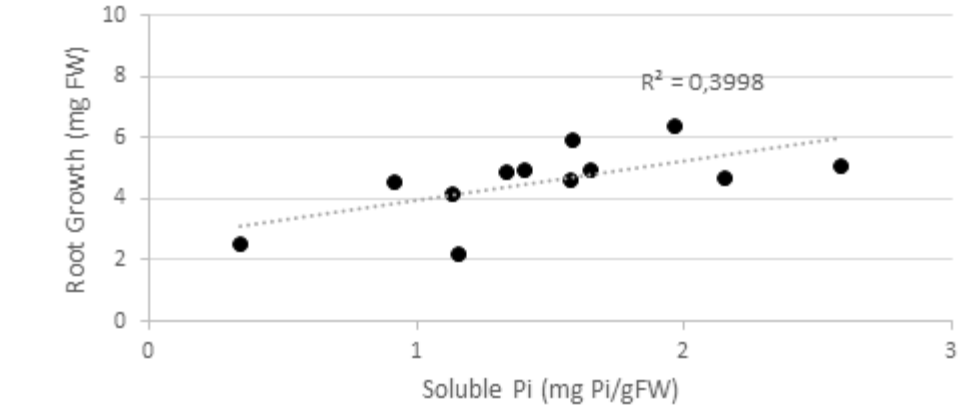

B

Figure 3. Correlations between plant growth (fresh weight) and phosphate concentration in the plant. For the shoot part (A) and the root part (B). These variables were correlated with the phosphate concentration in the plant calculating the r of a Pearson correlation (linear correlation). To test the significance of each treatment, their p-value was also calculated. The calculations were performed using R using the Base package.

4. Conclusion

In conclusion, a medium with low Pi inhibits root and shoot growth while the presence of *Pseudomonas fluorescens* stimulates the shoot growth. The gpt2 gene plays no role in the shoot and root response.

5. References

[1] Woodward AW and Bartel B 2018 Biology in Bloom: A Primer on the *Arabidopsis thaliana Model Syst*. **208** 1337.
[2] Wintermans PCA and Bakker PAHM 2016 Natural genetic variation in Arabidopsis for responsiveness to plant growth-promoting hizobacteria *Plant Mol Biol*. **90** 623.
[3] Benizri E, Baudoin E and Guckert A 2001 Biocontrol Science and Technology Root Colonization by Inoculated Plant Growth- Promoting Rhizobacteria *Biocont. Sci. Technol*. **11** 557.
[4] Compant S, Saikkonen K and Mitter B 2016 Editorial special issue: soil, plants and endophytes *Plant Soil* **1**.
[5] Vacheron J, Desbrosses G, Bouffaud M-L, Touraine B, Moënne-Loccoz Y, Muller D, Legendre L, Wisniewski-Dyé F and Prigent-Combaret C 2013 Plant growth-promoting rhizobacteria and root system functioning *Front Plant Sci*. **4** 356.
[6] Zgadzaj R, Garrido-oter R, Bodker D, Koprivova A and Schulze-lefert P 2016 Root nodule symbiosis in *Lotus japonicus* drives the establishment of distinctive rhizosphere, root and nodule bacterial communities *Proc. Natl. Acad. Sci*. U S A. **113** E7996.
[7] Fibach-Paldi S, Burdman S and Okon Y 2012 Key physiological properties contributing to rhizosphere adaptation and plant growth promotion abilities of *Azospirillum brasilense FEMS Microbiol. Lett*. **326** 99.
[8] Cornelis P 2010 Iron uptake and metabolism in pseudomonads *Appl. Microbiol. Biotechnol*. **86** 1637.
[9] Elhaissou W, Khourchi S, Ibnyasser A and Ghoulam C 2020 Phosphate Solubilizing Rhizobacteria Could Have a Stronger Influence on Wheat Root Traits and Aboveground Physiology Than Rhizosphere P Solubilization *Front. Plant Sci*. **11** 1.
[10] Bertrand H, Plassard C, Pinochet X, Touraine B, Normand P and Cleyet-Marel JC 2000 Stimulation of the ionic transport system in Brassica napus by a plant growth-promoting rhizobacterium (*Achromobacter* sp.) *Can J Microbiol*. **46** 229.
[11] Zhang H, Sun Y, Xie X, Kim MS, Dowd SE and Paré PW 2009 A soil bacterium regulates plant acquisition of iron via deficiency-inducible mechanisms. *Plant J*. **58** 568.
[12] Bresson J, Varoquaux F, Bontpart T, Touraine B and Vile D 2013 The PGPR strain *Phyllobacterium brassicacearum* STM196 induces a reproductive delay and physiological changes that result in improved drought tolerance in Arabidopsis *New Phytol*. **200** 558.
[13] Pieterse CMJ, Zamioudis C, Berendsen RL, Weller DM, Van Wees SCM and Bakker PAHM 2014 Induced Systemic Resistance by Beneficial Microbes *Ann. Rev. Phytopathol*. **52** 347.
[14] Weller DM, Landa BB, Mavrodi O V., Schroeder KL, De La Fuente L, Blouin Bankhead S, Allende Molar R, Bonsall RF, Mavrodi D V and Thomashow LS 2007 Role of 2,4-diacetylphloroglucinol-producing fluorescent *Pseudomonas* spp. in the defense of plant roots *Plant Biol*. **9** 4.
[15] Penninckx IA, Thomma BP, Buchala A, Métraux JP and Broekaert WF 1998 Concomitant activation of jasmonate and ethylene response pathways is required for induction of a plant defensin gene in Arabidopsis *Plant Cell* **10** 2103.
[16] Alori ET, Glick BR and Babalola OO 2017 Microbial Phosphorus Solubilization and Its Potential for Use in Sustainable Agriculture *Front. Microbiol*. **8** 1.
[17] Hirsch AM 2004 Plant-microbe symbioses: a continuum from commensalism to parasitism *Symbiosis* **37** 345.
[18] Grover M, Ali SZ, Sandhya V, Rasul A and Venkateswarlu B 2011 Role of microorganisms in adaptation of agriculture crops to abiotic stresses *World J. Microbiol. Biotechnol*. **27** 1231.
[19] Ames BN 1966 *Assay of inorganic phosphate, total phosphate and phosphatases* In: Methods in enzymology (Vol. 8, pp. 115-118). Academic Press.

[20] Kumar S and Sudhaker B 2020 Role of Phosphate in Biomineralization *Calcif Tissue Int*. doi: 10.1007/s00223-020-00729-9.
[21] Park KH, Lee CY and Son HJ 2009 Mechanism of insoluble phosphate solubilization by Pseudomonas fluorescens RAF15 isolated from ginseng rhizosphere and its plant growth-promoting activities *Lett. Appl. Microbial*. **49** 222.
[22] Godon C, Mercier C, Wang X, David P, Richaud P, Nussaume L, Liu D and Desnos T 2019 Under phosphate starvation conditions, Fe and Al trigger accumulation of the transcription factor STOP1 in the nucleus of Arabidopsis root cells *Plant J*. **99** 937.

Use of ultraviolet-light mutagenesis to generate a mutant with elevated cadmium resistance, *B. agri* C15 Cd^R

Use of ultraviolet-light mutagenesis to generate a mutant with elevated cadmium resistance, *B. agri* C15 Cd^R

Nadia Jebril[1,2*], Rich Boden[2] and Charlotte Braungardt[3]

[1]Department of Biology, College of Sciences for Women, University of Babylon, Iraq.
[2]School of Biological and Marine Sciences, University of Plymouth, Drake's Circus, Plymouth PL4 8AA, United Kingdom.
[3]School of Geography, Earth and Environmental Sciences and Plymouth University, Drake Circus, Plymouth, PL4 8AA, United Kingdom.

*E-mail: nadia.jebril@students.plymouth.ac.uk

Abstract. Cadmium (Cd) is toxic to living organisms; however, bacteria are adaptable to severe conditions, including Cd contamination. Bacteria can develop in the natural environment, as they generate resistant strains that can be used to remove Cd, but getting such adaptive strains usually takes a long time. In this study, ultraviolet (UV) light mutagenesis was used to accelerate the strain-resistant ability of *Brevibacillus agri* C15 to generate Cd^R mutant with high resistance to Cd. Its maximum tolerable concentration (MTC) to Cd was 15.00 mM. The UV light mutagenesis process resulted in the generation of the mutant *B. agri* C15 Cd^R (MTC: 20.00 mM Cd). Morphological and biochemical tests showed that there were no major differences between *B. agri* C15 Cd^R and *B. agri* C15. This study provides a basis for developing microbial Cd resistance and facilitating the application of Cd remediation.

Keywords. Cadmium, *Brevibacillus*, bioremediation, ultraviolet radiation, mutant, maximum tolerable concentration.

1. Introduction

Bioremediation is the process of transfer, forming contaminants into less harmful substances and, depending on the type of pollutant, and different approaches can be employed. One approach is the development of bacterial resistance to the pollutant with the aim of enhancing remediation efficiency. At this moment, engineering strategies are being investigated to increase further the Cd resistance of microbes, such as cloning the gene for metallothioneins, over-expressing metal-binding proteins, such as poly-histidine [1] or poly-cysteines [2]. Chemical mutagenesis approaches have been widely applied to develop bacterial detoxification systems for Cd, such as *Lactobacillus plantarum* ATCC 8014 and *Enterobacter cloacae* TU [3] . An alternative approach to increase bacterial resistant ability is the use of ultraviolet (UV) light mutagenesis. The advantages of using UV light are its simplicity, safety, and cost-effectiveness; there is also no need to establish a genetic system for the target organism, which can be useful when using it to create a mutant from a newly isolated strain. Ultraviolet (UVC) causes direct DNA damage due to the induction of the formation of DNA lesions

(photoproducts), most notably pyrimidine dimers, which block DNA replication, and RNA transcription [4]. Cd-resistant bacteria are often used as one of the remediation technologies for Cd. The main aims of this study were to generate a mutant with elevated resistance to Cd using UV-light mutagenesis. The objectives of this study were to induce mutations in wild type *B. agri* C15, a mutant screen, and to determine the effects on their specific growth rate and maximum amount of biomass formed.

2. Materials and Methods

2.1. Strain

Brevibacillus agri C15 was obtained from our previous study [4] (Jebril et al., 2020).

2.2. Mutagenesis of B. agri C15 and screening of mutant Cd^R

The *B. agri* C15 was mutagenized using UV light, according to [5] with some modifications. To obtain large quantities of *B. agri* C15, which were exposed to Cd and needed for the mutagenesis assay, the specific growth rate was first determined in 500 mL. Three thoroughly mixed 50 mL batch cultures from the late exponential phase were inoculated into 500 mL of EBS/pyruvate in Erlenmeyer flasks (2000 mL), in triplicate and with a nominal concentration of 10 mM Cd. This concentration of Cd was chosen as the possible concentration for achieving high biomass of the cells under Cd stress. The cultures were grown at 37 °C in a rotary shaking incubator at 100 rpm, and the amount of biomass was estimated as described in our previous study [4] . The effect of Cd (10 mM) on the growth of *B. agri* C15 was evaluated for the comparison of the specific growth rate values. These experiments were carried out with control in 50 mL and 500 mL of EBS without Cd. After determining the specific growth rate of *B. agri* C15 in 500 mL of batch cultures supplemented with 10 mM Cd, 50 mL culture of *B. agri* C15 was grown in a new fresh 500 mL of EBS /pyruvate in an Erlenmeyer flask (2000 mL) in triplicate, with a nominal concentration of 10 mM Cd, and incubated shaking at 100 rpm, 37 °C. The amount of biomass was determined, and from the late exponential phase, the cells were cooled in ice for an hour, centrifuged, and washed with and suspended in 0.5 EBS (two folds of diluted EBS with sterilised ddH2O, without pyruvate). The cell suspension was snap-frozen in liquid nitrogen. The counting of colony-forming units (CFUs) was used to estimate the survival of frozen cells using the serially diluting bacterial suspensions up to 1X106 CFU/mL. Each dilution was then spread on the nutrient agar plates in triplicate and incubated at 37 °C for 16 h. A CFU was determined from three sequential dilutions, and the mean was taken from all three. During the actual experiment, UV exposure was optimized by determining a survival time of *B. agri* C15 under UV exposure, a 90% drop of CFU required to increase the chance of mutant isolation. Five mL of cell suspensions of 500-1000 CFU/mL was transferred into empty plates in triplicate and exposed to a UV light lamp of 340 nm, with a distance of 50 cm from the plate to the light. The plates were irradiated for the set times (0, 5, 10, 15, 20, 25, 30, 35, 40, 45, 50, and 60 mins) using a digital timer. For each UV-exposure time point, three plates were randomly removed. For determination, the number of dead CFUs, which were killed by incubation rather than by the UV light, 500-1000 CFU/mL was transferred into empty plates in triplicate, covered with aluminium foil, and incubated on the bench at constant room temperature (22 °C). At the same time, three plates were collected as before. The removed plates were recovered on ice in the dark for 10 mins, then, 100 µL of the cell from each suspension was spread directly on nutrient agar, in triplicate. All nutrient agar plates were incubated at 37 °C for 16 h, and CFU was determined, plotted as survivors vs exposure times. The lethal time for 50% mortality (LT_{50}) was estimated from the survival curve and the time, which kills 90% of the total CFU, was determined as 20 mins. Therefore, for mutation experiments, 5 mL of cell suspension having 500-1000 CFU/mL were irradiated for 20 mins, in triplicate. The exposed cells were recovered, and then screened for mutants with elevated resistance to Cd. 100 µL of exposed, recovered cells of *B. agri* C15 were

inoculated into 50 mL of EBS/ pyruvate in Erlenmeyer flasks (250 mL), in triplicate and with different nominal concentrations of Cd. The concentrations were below MTC of *B. agri* C15 (7 mM), equal (15 mM), and above (18, 20, 22, and 24 mM). The control of EBS broth without Cd was used to determine whether there was growth at each concentration of the screening process. The batch flasks were incubated at 37 °C for 72 h. The isolation of mutants was done in terms of MTC to Cd [6] . 100 µL from each batch culture was transferred and spread onto EBS agar/ pyruvate and with the same nominal concentrations of Cd that were used in the exposed batch cultures. After growing, the colonies of the mutants were purified and the mutant amongst several mutants, which had the highest MTC to Cd, was selected and coded as the mutant Cd^R. The selected mutant was further screened for its MTC to Cd. The nominal concentrations of Cd in the broth were MTC and 0.1 MTC of the selected mutant (increases of 2 µM). MTC value obtained was tested up to three separate occasions, followed by the confirmation on EBS agar.

2.3. Characteristics of B. agri C15 and B. agri C15 Cd^R

Several experiments were performed to evaluate whether the mutant had lost some of its physical characterisations identified in *B. agri* C15 due to UV mutagenesis.

2.4. Identification analyses and optimising growth conditions

The morphological test, including Gram stain and biochemical tests (IMVIC) was performed, in triplicate, with control. Optimal temperature, carbon, and nitrogen sources were also studied for the mutant *B. agri* C15 Cd^R, according to the previous protocol described for the wild type [4]. Different pH (4.0, 4.6, 5.8, 6.4, 7.7, 8.8, and 9.0) in EBS/pyruvate was adjusted to obtain the optimum environmental conditions of these strains. The pH (4.0 and 4.6) was adjusted using acetic acid and sodium acetate. K2HPO4 and KH2PO4 were also used to acquire pH between 5.0 and 8.5, while pH 8.6 and 9.0, HCl, Trise-base were used. According to the ratio of each solution, 2 mL was added in a Falcon tube (50 mL) containing 20 mL of EBS/pyruvate. The bacterial culture was inoculated in triplicate and incubated at the optimal temperature (37 °C) for 72 h. Turbid growth was observed, and the results were recorded.

2.5. Measurement of core kinetic parameters

The growth curve, specific growth rate, and pyruvate utilised with its respective values of specific growth yields were studied for *B. agri* C15 and *B. agri* C15 Cd^R. The experiments were carried out by inoculating 1 mL of overnight culture into 50 mL of EBS/pyruvate in Erlenmeyer-flasks (250 mL), in triplicate, incubated at 37 °C and shaken at 100 rpm. 1 mL of growth culture was collected at interval times, and the dry biomass was measured; the culture was then centrifuged, and the supernatants were kept in Eppendorf tubes and stored at -20 °C until being analysed for pyruvate concentration using a pyruvate kit assay as described in our previous study [4] .

2.6. Inhibition effects of cadmium on the specific growth rate and maximum amount of biomass formed

The effect of Cd on specific growth rate and the maximum amount of biomass formed *B. agri* C15 and *B. agri* C15 Cd^R were investigated under different concentrations of Cd according to the method used by [7] . One mL of the culture was inoculated into 50 mL of EBS/pyruvate in Erlenmeyer-flasks (250 mL), in triplicate, and with different nominal concentrations of Cd: 2.5, 5, 7.5, 9, 10, 11, 12.5, 15, 16, 17.5, and 20 (mM), while the control was without Cd. Then, flasks were incubated at 37 °C for 72 h shaken at 100 rpm. The samples were collected at intervals, the amount of biomass formed was determined, and the growth curve was plotted, followed by the determination of the specific growth rate and the maximum amount of biomass formed.

2.7. Statistical analysis

Statistical analysis for these data was performed. All values were expressed as the mean and standard error of the mean (SEM). The bacterial growth curves were fitted with nonlinear regression (global curve fitting, four parameters) of the mean data utilising the SigmaPlot (version 13). The specific growth rates on the bacterial growth curves were subjected to the Student's t-test

3. Results

3.1. UV-mutagenesis of B. agri C15 and screening of mutant Cd^R

It was essential to keep the cells of *B. agri* C15 in EBS/ pyruvate completely frozen at -20°C for three weeks until the UV-mutagenesis was complete. Frozen cell beads have been known to be stable against freezing damage. It is not expected that the variable number of frozen cells will be affected for three months at -20 °C [8] . To obtain large quantities of the cells, the specific growth rate of *B. agri* C15, grown in a 500 mL of batch culture, was determined with a nominal concentration of 10 mM Cd. This experiment was carried out along with growth in a 50 mL batch culture with 10 mM Cd for the comparison in the specific growth rate between both volumes of cultures. The growth of *B. agri* C15 in 50 mL and 500 mL without Cd was studied. The specific growth rate of *B. agri* C15 grown under the effect of Cd in 500 mL was significantly low (μ= 0.11 ± 0.07 h^{-1}, Figure 1D, $^{b}p<0.05$) compared to growth in 500 mL without Cd, which showed a higher specific growth rate (0.19 ± 0.1 h^{-1}, Figure 1C, $^{a}p<0.05$). Similarly, specific growth rates were decreased from 0.12 ± 0.01h-1 (Figure 1A, $^{b}p<0.05$) when grown in 50 mL of batch culture without Cd to 0.11 ± 0.03 h^{-1} (Figure 1D, $^{b}p<0.05$) when grown in 50 mL of batch culture under the effect of Cd. However, there were no significant differences observed between specific growth rates when grown under Cd effects in 50 or 500 mL (Figure 1B, D, $^{b}p<0.05$).

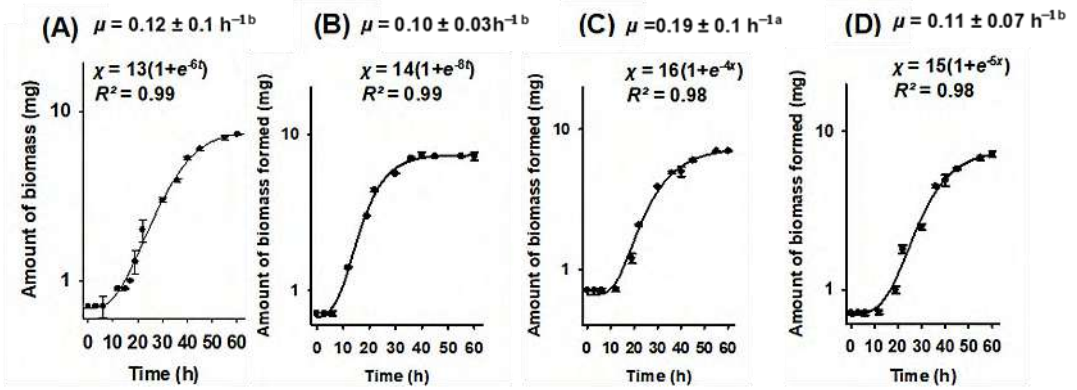

Figure 1. The growth scale of *B. agri* C15 under the effects of Cd. *B. agri* C15 was inoculated into EBS/pyruvate, incubated at 37 °C and shaken at 100 rpm. The growth was studied in different batch volumes (A) 50 mL (control) and (B) 50 mL with a nominal concentration of 10 mM Cd, (C) 500 mL (control), and (D) 500 mL with a nominal concentration of 10 mM Cd. The specific growth rate ( ) is shown. The error bars indicate the standard error of the mean of three batch cultures.

After the determination of the specific growth rate during growth at 500 mL of EBS under Cd effects, the growth of *B. agri* C15 in EBS broth (500 mL) was performed; the cells were harvested and suspended in 0.5 EBS without pyruvate to make the cell suspension form as beads to keep the cells of frozen at -20°C until the UV-mutagenesis was complete. After forming the frozen cells as beads, CFU/mL of *B. agri* C15 in these beads was estimated at 1×10^6 CFU/mL. The length of UV light

exposure that would kill 90% of cells (as CFU) to increase the chance of mutant isolation was determined at a fixed distance. Controls for CFU death just by incubation at room temperature were performed; 90% of *B. agri* C15 cells were killed after 20 mins of UV exposure (Figure 2). Thus, this was chosen as the length of exposure to induce the mutagenesis. The 50% mortality (LT_{50}), which was the time for 50% of *B. agri* C15 CFU to die, was 5.92 mins.

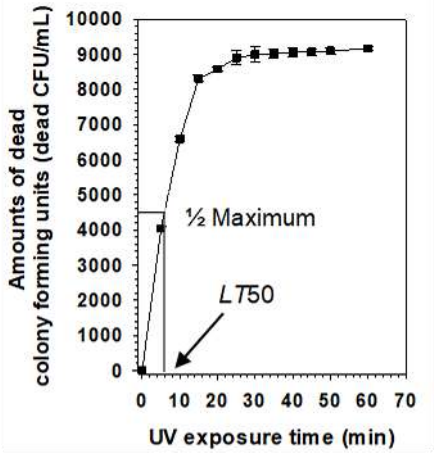

Figure 2. The lethal time curve for *B. agri* C15 after UV light exposure. 5 mL of 500–1000 CFU/mL in empty plates in triplicate were exposed to UV light (340 nm, brand Pisces, watt 13) at a 50 cm distance. The control plates were incubated on the bench at a constant room temperature of 22 °C (data not shown, used to get the final amounts of CFU death). The error bars represent the standard error of the three plates. The lethal time for 50% mortality (LT_{50}) after UV light exposure was estimated to be at 5.92 mins.

UV-mutagenesis of *B. agri* C15 was done for 20 mins, followed by the growth of exposed cells in batch cultures, with nominal concentrations of Cd: 7, 15, 18, 20, 22, and 24 mM Cd. The selection of putative mutants on EBS/pyruvate agar supplemented with the same concentrations of Cd was performed. The mutant selection was based on the growth of exposed cells at a given concentration of Cd in the plates. This showed no growth on plates with > 20 mM Cd, with few colonies at 15, 18, and 20 mM Cd. Among these, the most resistant colony to Cd was selected and considered a Cd-resistant mutant strain due to its ability to grow at 20 mM Cd and was termed as '*B. agri* C15 Cd^R'. The MTC of this mutant was 20.00 mM Cd, giving a higher MTC value than the wild type (15.00 mM).

3.2. Characteristics of B. agri C15 and B. agri C15 Cd^R

Several experiments were carried out to compare the different characteristics between *B. agri* C15 and *B. agri* C15 Cd^R.

3.2.1. Identification analyses and optimising growth conditions

Optimal growth conditions were studied to investigate whether *B. agri* C15 Cd^R had major phenotypic changes other than *B. agri* C15. Gram-stained smears of the *B. agri* C15 and the *B. agri* C15 Cd^R showed no key morphological changes. Both remained Gram-stain-positive (Figure 3A, B). Basic chemotaxonomic characters (IMVIC test) showed the same results for *B. agri* C15 Cd^R, as reported for *B. agri* C15 earlier in our previous study [4]. This data and the morphological data gave a preliminary indication of no major phenotypic changes and that *B. agri* C15 Cd^R was a bona fide mutant, not a contaminate. Amounts of biomass formed by both strains under various conditions are compared in Table 1. The statistical analysis of the biomass values showed the significant biomass obtained at 37 °C, using pyruvate and ammonia as carbon and nitrogen sources, respectively. These

biomasses were not significantly different between the two strains ($^{*}p<0.05$). The growth at a different range of pH showed that both strains could grow within a range of 4.00 to 7.70, with no significant differences between them.

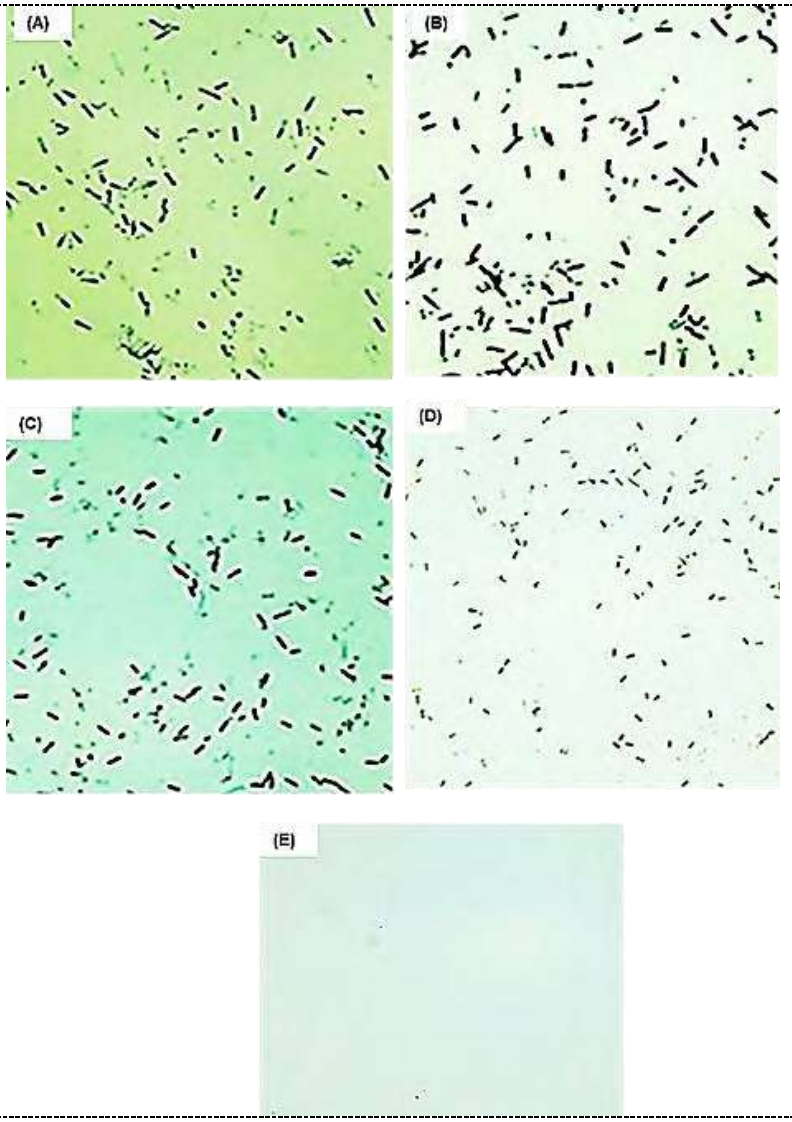

Figure 3. Morphological characterisation using Gram stain of (A) *B. agri* C15, (B) *B. agri* C15 Cd^{R}, (C) Bacillus subtilis (Gram-stain-positive control), (D) C. metallidurans DSM 2839^{T} (Gram-stain-negative control) and (E) uninoculated slide. Stains were performed symultaneously in triplicate on three separately grown nutrient agar plates. Gram-stain-positive: purple to the blue colour; Gram-stain-negative: orange to brown colour, Bismarck brown

Table 1. The growth conditions of the wild type *B. agri* C15 and the mutant *B. agri* C15 Cd^{R}. ± represents the standard errors of the mean (n = 3, batch experiments). The biomass values for the growth conditions of each strain were subjected to a t-test to analyse the difference within each growth condition, and *show a significant difference in growth values resulting from different temperature, carbon source or nitrogen source, respectively within the strain. **No biomass was obtained.

Growth conditions	Growth conditions values of :	
	B. agri C15	*B. agri* C15 Cd^{R}
Temperature	(amount of biomass formed (mg)	
4 °C	**	**

18 °C	**	**
25 °C	0.3 ± 0.8	2.1 ± 0.6
30 °C	6.6 ± 0.1	6.5 ± 0.3
30 °C	9.9 ± 0.1*	11 ± 0.5*
42 °C	6.1 ± 0.08	8.8 ± 0.2
44 °C	6.0 ± 0.7	3.9 ± 0.6
50 °C	**	**
60 °C	**	**
Carbon source	(amount of biomass formed (mg)	
Glucose (10 mM)	3.3 ± 0.8	3.9 ± 0.1
Fructose (10 mM)	2.8 ± 0.2	6.6 ± 0.6
Acetate (20 mM)	1.3 ± 0.4	2.9 ± 0.1
Pyruvate (20 mM)	4.3 ± 0.5*	9.8 ± 0.1*
Sucrose (20 mM)	3.5 ± 0.08	1.9 ± 0.01
Nitrogen	(amount of biomass formed (mg)	
Ammonium	6.4 ± 0.1*	8.7 ± 0.3*
Urea	2.3 ± 0.2	5.9 ± 0.1
Thiocyanate	1.5 ± 0.2	1.6 ± 0.6
Cyanate	4.7 ± 0.3	4.3 ± 0.6
Nitrate	4.4 ± 0.8	3.9 ± 0.2
Glycine	3.2 ± 0.2	3.2 ± 0.6
Dinitrogen	0.5 ± 0.02	1.2 ± 0.06
pH	4.00 ± 7.70	4.00 ± 7.70

3.2.2. Measurement of core kinetic parameters

Specific growth rates for *B. agri* C15 and *B. agri* C15 Cd^R are 0.12 ± 0.07 h-1 and 0.11 ± 0.02h-1, respectively, with no statistically significant differences (Figure 4A, B, respectively). Mutant *B. agri* C15 Cd^R formed a specific growth yield higher than the wild type *B. agri* C15 (Figure 4C).

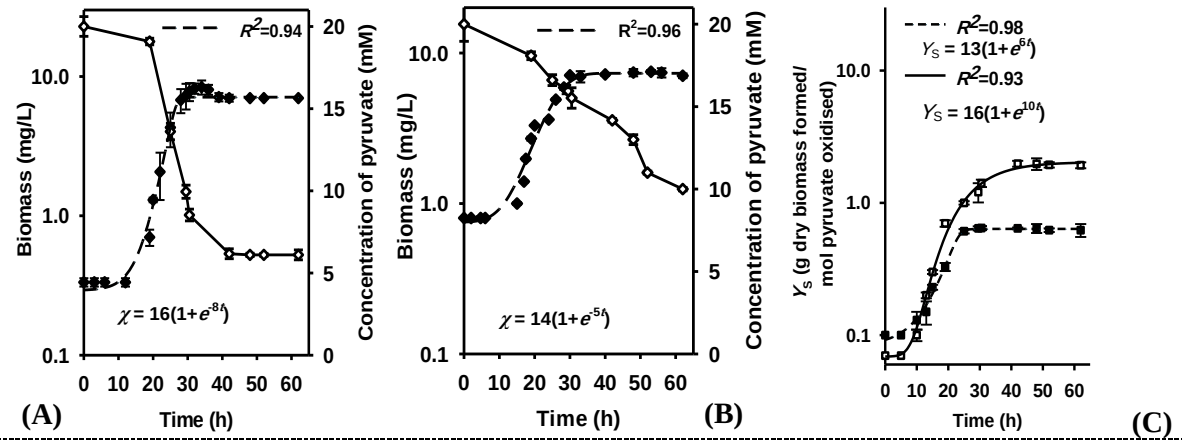

Figure 4. The amount of dry biomass formed (ϕ) and pyruvate utilisation (◊) of (A) *B. agri* C15 and (B) *B. agri* C15 Cd^R, and their respective (C) Y_S of (■) *B. agri* C15 and (□) *B. agri* C15 Cd^R. The specific growth rate ($\int$) is shown. The error bars indicate the standard error of the mean of three batch cultures

3.3. Inhibition effects of cadmium on the specific growth rate and maximum amount of biomass formed

The effects of Cd on the specific growth rate and maximum amounts of biomass formed *B. agri* C15 and *B. agri* C15 Cd^R were compared. Both strains showed a Cd-dependent fall in a specific growth rate, and the significant rate was for *B. agri* C15 (Figure 5A). The maximum amount of biomass under different concentrations of Cd showed that the lethal doses for *B. agri* C15 and *B. agri* C15 Cd^R were 15.80 and 20.00 mM Cd, respectively (Figure 5B).

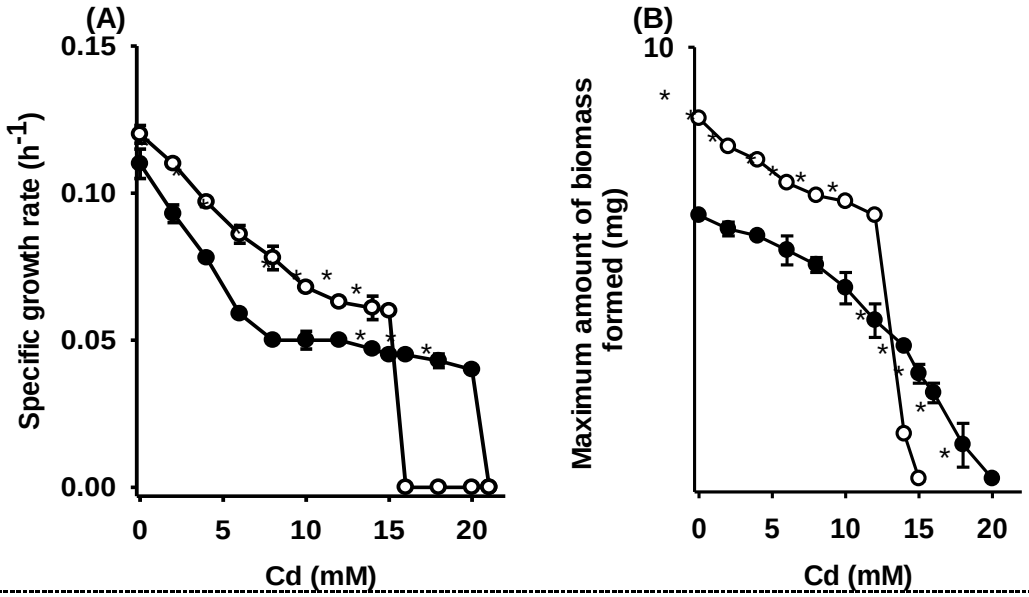

Figure 5. The inhibition effects of Cd on (A) specific growth rate and (B) maximum amounts of biomass formed of (○) *B. agri* C15 and (●) *B. agri* C15 Cd^R. The error bars indicate the standard error of the mean of three batch cultures at each Cd concentration. *Significant difference between strains at each Cd concentration.

4. Discussion

In this study, a distinct approach was carried out to achieve increased resistance in the *B. agri* C15. Isolate *B. agri* C15, which has an intrinsic ability to resist Cd (MTC: 15.00 mM), was used to increase its natural resistance to Cd. [9] found that growing a bacterium with Cd induces a mutant with elevated resistance to Cd. Using this process, several mutants were successfully generated from the wild type *B. agri* C15 by UV light mutagenesis; one of these mutants *B. agri* C15 Cd^R was able to grow in the highest Cd concentration (20.00 mM) and was chosen. The generation of Cd-resistant mutants in the growth medium can be affected by the concentration of Cd, the steps to isolate the mutants and the increase of the Cd concentrations in the medium during each step. Exposing cells, cultivating in the medium (with a high Cd concentration), and spreading exposed cells on agar plates containing Cd may have increased the resistance of the *B. agri* C15 by an MTC value of 0.25 fold. However, if the process was used repeatedly with increasing Cd concentrations in the low fold [10] , it could generate a mutant with higher MTC value (eightfold). Mutant *B. agri* C15 Cd^R had improved resistance to Cd, tolerant to 20.00 mM, and showed no key morphological or biochemical characteristics compared to wild type *B. agri* C15. Mutant *B. agri* C15 Cd^R had higher biomass than the wild type and exhibited slower growth when grown with Cd than wild type *B. agri* C15. The inhibition of the bacteria's growth led to a diminished specific growth yield; these results are similar to the results of the study performed by [11] on the Cd- mutant *P. aeruginosa* G-1.After three days of Cd exposure, it was found that wild type *B. agri* C15 was less likely to respond to Cd compared to mutant *B. agri* C15 Cd^R. Also, the inhibition appeared Cd-dependent, and both strains showed similar responses in specific growth rate and biomass under different Cd concentrations. Still, mutant *B. agri* C15 Cd^R had less specific growth rates and biomass with addition Cd concentrations (15-20 mM). Few

studies have investigated Cd effects on mutants. The mutants of Escherichia coli were found to be less responsive to a concentration of 6 mM Cd [10]. [7] found that the mutants of *E. coli* had slower growth rates when exposed to a tolerant Cd concentration of 0.7 mM. These results, together with this study, suggest that Cd concentrations influence mutant growth.

5. Conclusion

The *B. agri* C15 Cd^R mutant was generated from isolated *B. agri* C15 by UV light mutagenesis, and this mutant showed enhanced resistance to Cd and had a MTC value of 20.00 mM to Cd, which was higher than the MTC of the wild type (15 mM). Thus, it is concluded that this mutant could be suitable for the development of a Cd-bioremediation process; therefore, further studies are needed to investigate this possibility.

6. References

[1] Sousa C, Cebolla A and de Lorenzo V 1996 Enhanced metalloadsorption of bacterial cells displaying poly-His peptides *Nat. Biotechnol*. **14** 1017.
[2] Wu CH, Wood TK, Mulchandani A and Chen W 2006 Engineering plant-microbe symbiosis for rhizoremediation of heavy metals *Appl. Environ. Microbiol*. **72** 1129.
[3] Xu C, He S, Liu Y, Zhang W and Lu D 2017) Bioadsorption and biostabilization of cadmium by Enterobacter cloacae TU *Chemosphere* **173** 622.
[4] Jebril N, Boden R and Braungardt C 2020 The isolation and identification of cadmium-resistant *Brevibacillus agri* C15. 2nd *IHISC*, accepted.
[5] Yuan XW, Xie XH, Fan FX, Zhu WX, Na L and Liu JS 2013 Effects of mutation on a new strain *Leptospirillum ferriphilum* YXW and bioleaching of gold ore *T Nonferr. Metal Soc*. **23** 2751.
[6] Schmidt T and Schlegel HG 1994 Combined nickel-cobalt-cadmium resistance encoded by the ncc locus of *Alcaligenes xylosoxidans* 31A *J. Bacteriol*. **176** 7045.
[7] Helbig K, Grosse C and Nies D H 2008 Cadmium toxicity in glutathione mutants of *Escherichia coli JB.* **190** 5439.
[8] Rindala S, Jean-Ralph Z, Carbonnelle E and Lescat M 2019 Aerobic bacteria as Escherichia coli can survive in ESwab TM medium after a 3 month-freezing at-80°C but not after multiple thawing *BioRxiv* **53** 7647.
[9] Wu J, Kamal N, Hao H, Liu Z, Qian C, Shao Y, Zhong X and Xu B 2019 Endophytic *Bacillus megaterium* BM18-2 mutated for cadmium accumulation and improving plant growth in Hybrid Pennisetum *Biotechnol. Rep* e00374.
[10] Qin W, Yu X, Liu X, Chu X, Tian J and Wu N 2019 Improving Cadmium Resistance in *Escherichia coli* Through Continuous Genome Evolution *Front Microbiol* **10** 278.
[11] Horitsu H and Kato H 1980 Comparisons of characteristics of cadmium-tolerant bacterium, Pseudomonas aeruginosa G-1 and its cadmium-sensitive mutant strain *Agri. Biol. Chem*. **44** 777.

Morphological study of bronchial tree and lung in Iraqi weasel (*Herpestes javanicus*)

Morphological study of bronchial tree and lung in Iraqi weasel (*Herpestes javanicus*)

Baydaa H. Mutlak[1*], Ahmed A. Al-Jawadi[1] and Intidhar M. Mnati[1]

[1]Department of Biology, College of Education for Pure Science Ibn Al-Haitham, University of Baghdad, Baghdad, Iraq.

*E-mail: baydaahussein@gmail.com

Abstract. The current study aimed to identify the morphological description and branches of the bronchial tree and lung for the weasel *Herpestes javanicus* as one of the Iraqi mammals inhabiting the Iraqi environment. In the current study, 10 samples with an mean weight of 288-564 g were used, trachea and lung were removed from the samples and confirmed using proven solutions and laboratory tests were conducted on 5 samples of the study to identify the branches of the bronchial tree using the technique of casting resin and then exposing the samples to erosion. Weasel has a pair of bright pink sponge lungs that occupy most of the thoracic cavity. The lungs look similar to the clover leaf have a top and three surfaces represented by the costal surface that is convex, and the middle surface, characterized by a narrow and diaphragm surface and is identical to the diaphragm. The right lung is larger than the left lung and the right lung consists of four lobes: apical, middle, caudal and an accessory lobe, while the left lung consists of three lobes: apical, middle, caudal lobes the top of the right lung appeared small and semi-sharp, while the left lung is round and blind. The right primary trachea branched into two branches, the upper branch enters into the apical lobe and branches in turn into two secondary branches, while the lower branched into three branches, the first of which enters into the middle lobe and the second to the middle lobe, the third branch into two branches enter the accessory lobes, while the primary left trachea branch into three secondary or lobe branches before entering the left lung branch, where the first branch enters into apical lobe when the second enters the middle lobe while the third section enters the caudal lobe.

Keywords. *Herpestes javanicus,* Lung, bronchial tree, Iraqi weasel.

1. Introduction

The Weasel is small animals widespread, carnivores and lives in different environments and he belongs to the family of Herpestidae of order carnivores, there are two types of this family in Iraq, namely the weasel *Herpestes javanicus* that lives in the areas extending along the strand of the Tigris and Euphrates rivers, which is the most widespread, the second type is the Indian grey mongoose (*Herpestes edwardsi*) found in central and northern Iraq and is less prevalent than the first type [1]. Studies have shown that mammalian lungs are a complex of composition organ that shows a variation in form, location and composition in different species, as each lung has its triangular shape and possesses a cranial apex, caudal base and the two sides of costal and middle with three border: dorsal,

ventral and basal [2]. The color of the lung varies according to the amount of blood it contains, as it is pink during life and in cats appear bright red [3]. The lungs of the carnivores are divided into lobes, where the right lung consists of four lobes, apical or cranial lobe, middle or cardiac lobe, caudal lobes and accessories lobes, which are larger than the left lung consisting of apical and caudal lobes [4]. While [3] study in *Cats domesticus* L. showed the right lung is larger than the left lung by size and weight, the right lung is consist of four lobes as well as accessory lobes, while the left lung is composed of two apical and caudal lobes, dividing the apical lobe into two parts of a cranial or apical and another part of caudal with deep notch. The study of [5] in long-eared hedgehog *Hemiechinus auritus* reported that the lungs are in the form of a spongy pair of organs located inside the thoracic cavity and not directly connected to the ribs, covered with two layers of pleura inside the visceral pleura. Many studies have dealt with weasel in many ways, such as [6] study of the digestive and respiratory system of the grey Indian weasel and [7] study of thyroid gland, and study of a comparison of the appearance and anatomical length and weight of the body and lung and some organs of the digestive system between two types of weasel [8]. The current study aims to identify the morphological description of the bronchial tree and lung in the weasel.

2. Materials and Methods

The study included 10 samples of *Herpestes javanicus* weasel with different ages and weights ranging from 288-565 g obtained from Najaf province and the hunting process was carried out using special nets, the samples of the study was anatomized and removed the trachea and lungs and put them in the normal saline solution 9% and then put in the fixative solution until the completion of other work procedures.

2.1. Morphological study using methylene blue stains

The samples were placed in methylene blue for 1.5 minutes. Left until the lungs lobes are clear and the possibility of counting them accurately. Then transferred to ethyl alcohol 70% for 2 minutes until the samples are clear for study.

2.2. Bronchial tree study

This study was carried out on the bronchial tree by the process of resin cast and then exposing the sample to erosion according to [9]. In this study, five samples of both sexes were obtained and the samples of the trachea and lung were obtained in the same anatomy manner referred to in above with the note taking parts of the neighboring organs to avoid rupture of the tissues that may lead to the ejection of resin during injection and the samples are kept freezing until use. In this study was selected for the proper resin, which is characterized by its viscosity at room temperature and at the same time possesses solidification to give the required results after the process of maceration.

2.3. Injection technique

The injection was performed as follows: Prepare the resin by dissolving 1 g of resin powder in 12 ml of liquid resin 12 min before the injection. The samples were removed from the freezer and melted before the injection. A 4 mm plastic feeding tube was inserted through the larynx and fixated by a surgical suture wire to prevent resin from being ejected during injection. The injection was done by hand using a 20 ml plastic syringe. The first sample was injected with 6 ml, the second sample was injected with 8 ml and the third injected by 12 ml and the fourth sample by 15 ml and the fifth sample injected by 20 ml and then closed the trachea opening by a thick thread, and the sample was left all night at room temperature 30-25 ºC to complete the hardening of the resin. The maceration was performed by placing the samples in a suitable plastic tank containing 500 ml of potassium hydroxide

KOH at a concentration of 40% for 5-4 days. After the maceration process is completed, the samples were washed thoroughly and carefully with water running for at least an hour. The samples were then dried using hot air so that the sample would be ready for examination. The samples were examined with the naked eye or using an anatomy microscope and then the samples were photographed using a digital camera.

3. Results

The results of the macroscopic examination of the weasel *Herpestes javanicus* lungs showed that it is possess a pair of lungs similar to clover leaf pattern and each lung looks in the form of a bright pink sponge organ and occupy most of the thoracic cavity similar to the shape of the thoracic cavity, and extends from the third rib to the twelfth rib. While anatomically, the results of the current study showed that each lung in the weasel has an apex and three surfaces represented by the costal surface which is convex, and the middle surface and characterized by its narrow and diaphragmatic surface and is identical to the diagram (Figure 1). The results showed that the right lung is larger than left lung and the right lung is composed of four lobes represented by cranial or apical lobe, middle or intermediate lobe, caudal or basal lobe and accessory lobe (Figure 2, 4). While the left lung consists of three lobes represented by the cranial or apical lobe, intermediate lobe, caudal or basal lobe (Figure 3, 4).

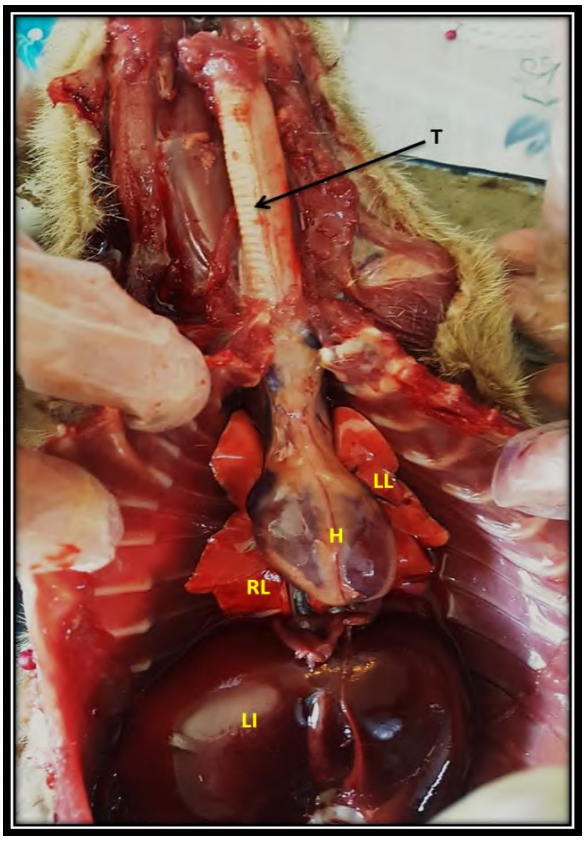

Figure 1. The internal anatomy of weasel *Herpestes javanecus* shows the location of the trachea (T) in general and the location of the lung (L), the heart (H), the liver (Li).

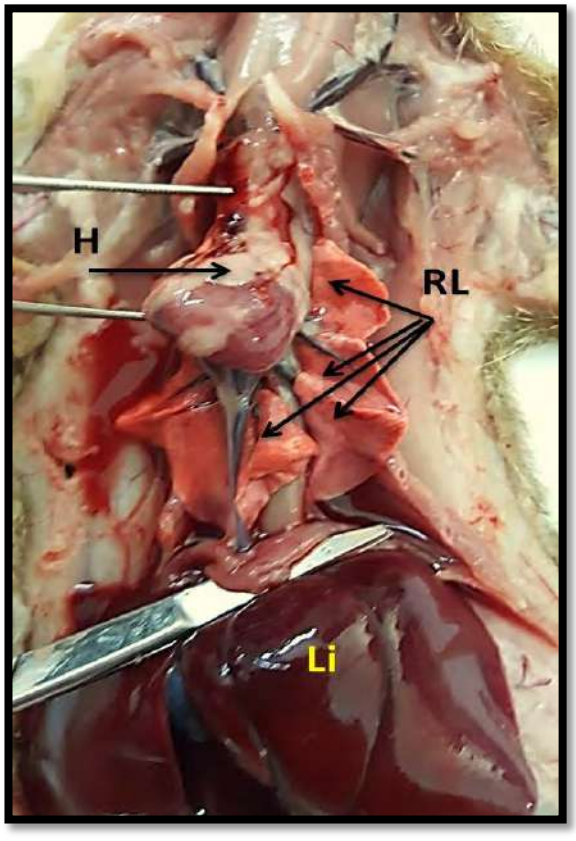

Figure 2. Figure 2: The internal anatomy of weasel *Herpestes javanecus* shows the lobes of right lung (RL),Trachea(T) ,the heart (H), the liver (Li).

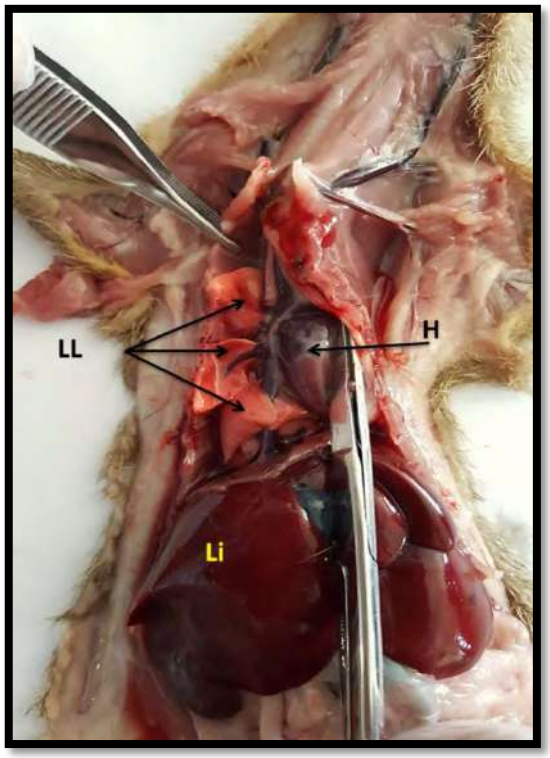

Figure 3. The internal anatomy of weasel *Herpestes javanecus* shows the lobes of left lung (LL) ,Trachea(T) ,the heart (H), the liver (Li).

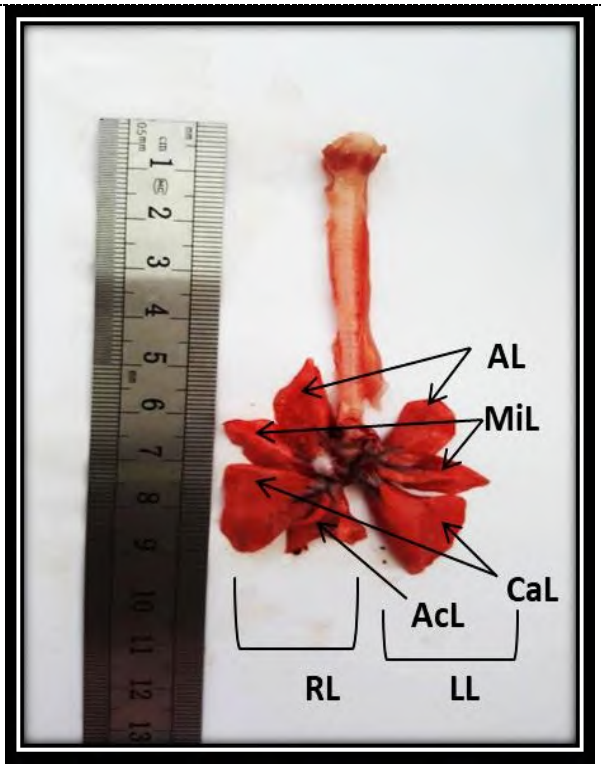

Figure 4. Shows the shape of the lungs in the weasel and its lobes, the apical lobe(AL), middle lobe (MiL), caudal lobe (CaL), accessory lobe (ACL), right lung (RL), left lung (LL).

The results also showed that the right lung top is small and semi-sharp compared to the left lung, which shows its top round and blind (Figure 4, 5). The mean length of the right lung is 4.9 cm and the mean length of the left lung is 4.4 cm, and the results showed that the total lung width was 5.9 cm (Table 1). The results of the morphological study using resin cast technology showed that the trachea in the weasel appears as a long tube branching into two main branches represented by the right primary bronchus and the left primary bronchus. It was noted that the right primary branched into two secondary branches; secondary or lobular (Lobar) bronchi after entering the right lung represented by a superior branch that enters the cranial or apical lobe, which in turn branches into two secondary branches representing the first branch tertiary bronchi, the latter also branched into a number of bronchioles, which as a result end with alveoli, while the second branch (inferior branch) of the right primary bronchus is divided into three branches: superior enters the middle lobe, and the medial enters the caudal lobe, while the third branch in turn is divided into two secondary branches entering each of its branches into the accessory lobes. The results of the current study showed that the primary left bronchus branched into three secondary or lobar before entering the left lung, as the first branch enters the apical lobe while the second branch enters the middle branch while the third branch enters the caudal lobe (Figure 6).

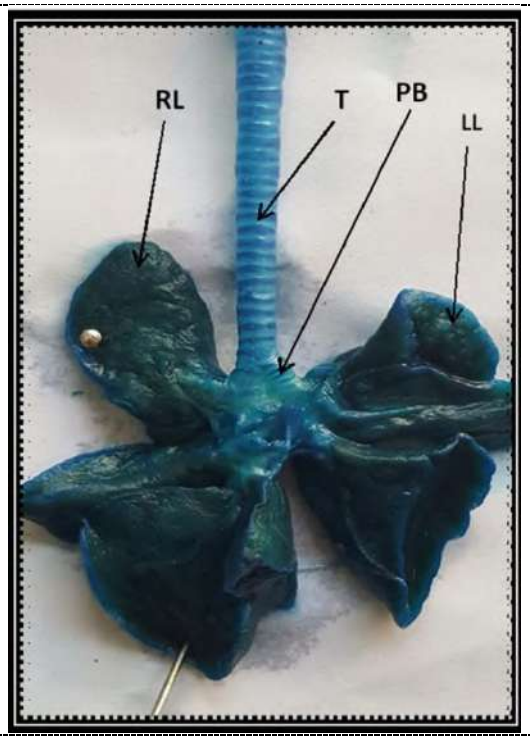

Figure 5. : Shows the branching of the trachea (T) into two branches of the primary bronchi (PB), the entry of a branch to the right lung (RL) and a branch to the left lung (LL), (Methylene blue stain).

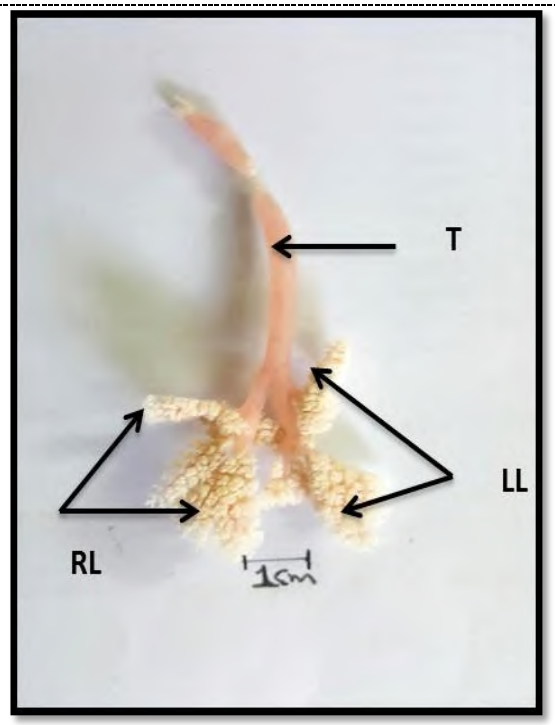

Figure 6. Whole preparation of the lung using resin casting technique shows the branches of the bronchi, trachea (T), right lung (RL), left lung (LL).

Table 1: Shows the rate of length and weight of lung for study samples.

Sample number	Real length/ cm	standard length/ cm	animal weight/ g	Length of left lung/ cm	Length of right lung/ cm	Total width of lung. cm
1	56	28	341.26	4.5	5	5.5
2	60	30	435.81	4.5	5	5.5
3	61	32	564.14	4.5	5	6
4	60	32	396.32	4.5	4.5	6
5	54	26	288.17	4	5.2	6.5
Mean	58.2	29.6	405.14	4.4	4.94	5.9

4. Discussion

The macroscopic examination showed that weasel *Herpestes javanicus* has a pair of bright pink sponge lungs that surround the heart and occupy most of thoracic cavity and shows its shape identical to the thoracic cavity it occupies and these results are fully consistent with references for the study about domestic animals [10, 11]. The results of the current study showed that the lungs of the weasel are in the form of clover leaf pattern and this result of appearance is contrary to the lungs of naked-bellied tomb bat [12] whose appearance is pyramidal in shape because the structural of the lung fits with the thoracic cavity that contains it. The lung is smooth-surface and each lung has a cranial apex that resembles the apical lobe and caudal base, which similar to the diaphragmatic surface of the caudal lobe, and each lung has three borders: dorsal and ventral abdominal, caudal (Basel) borders. The results of the anatomical study of weasel's lungs were consistent with the results of [13, 14] in

Canis lupus and [15] in ruminants, as it was found that the top of the right lung looks small and semi-sharp while the top of the left lung is round and blind. The results are contrary to what was shown by the results of [16] about the local rabbits *Oryctolagus cuniculus*, as mentioned study explained that the top of the left lung is sharp and small, while the top of the right lung is large, rounded and blind, these results are partly consistent with same study in the cats *Feils catus*, this study showed that the right lung top is sharp as it is contrary to the lung of the naked-bellied tomb bat [12] because the top of the right lung is sharp but folded down, while [17] study on *Feils catus* showed that the right lung was contained on a pointed top, which is not consistent with the results of the weasel study because the right lung contains a semi-pointed top. The left lung of the weasel in the current study showed smaller than the right lung and consists of three lobes represented by the cranial lobe, the middle lobe and the caudal lobe, while the right lung is larger than the left lung and consists of four lobes, a cranial, middle, caudal, accessory lobes. This result is consistent with the results of the study of the guinea pig *Cavia porcellus*, which showed that the right lung contains four lobes and the left lung contains three lobes [18]. The results of the current study were also contrary to the results of [16] on the local rabbit *Oryctolagus cuniculus*, as the anatomical results showed that both lungs have two lobes; one of which is apical lobe and the other is caudal lobe, and the left lung is divided into two lobes unequal in shape and the apical lobe is smaller than the caudal lobe. In addition, it disagreement with [19] study in *Cryptotis parva*, as it has a right lung containing four lobes represented by a cranial, middle, caudal and accessory lobes, while its left lung has one caudal large lobe, which is fully integrated with the small cranial lobe so that no clear dividing line between the lobes appears.

5. References

[1] Al Sheikhly OF, Haba MK, Barbanera F, Csorba G and Harrison D 2015 Checklist of the mammals of Iraq (Chordata: Mammalia) *Bon. Zool. Bul.* **64** 33.
[2] Hare WCD 1975 *Respiratory system In: The Anatomy of the Domestic Animals* 5th Ed., Getty R.W.B. Saunders Company 511.
[3] Mirhish SHM and Nassar RM 2013 Anatomical Study of the tracheal cast and lung in local breed Felis Cactus domesticus L Department of Anatomy, Histology and Emberyology Vet *Med. College. Bas. J. Vet. Res*. **12** 1.
[4] Oliveira FS, Borges EM, Machado MRF, Canola JC and Riberio AA 2001 Anatomical surgical arterial segmentation of the cat lungs (*Felis catus domesticus*, L., 1758). *Braz. J. Vet. Res. Anim. Sci*. **38** 1.
[5] Ibrahim TA 2017 Morphological Characterization and Histological composition of the lungs in the long ear hedgehog (*Hemiechinus auritus*). *Anbar Univ. J. Pure Sci.* **2** 11.
[6] Shil SK, Das BC, Uddin M, Rahman ML and Quasem MA 2012 Anatomy of digestive and respiratory system of Indian grey mongoose (*Herpestes edwardsii*) *Uni. J. of Zool*. **31** 83.
[7] Al-Amiri RAAH 2009 *An anatomical, histopathological, and chemotherapy study in comparison of the thyroid and parathyroid glands in two types of Iraqi vertebrates (biz weasel, Herpestes javanecus and long-eared hedgehog, Hemiechinus auritus) using the tag Anti-Calcitonin, code 140778)* Thesis. PhD, College of Education for Pure Sciences, University of Baghdad 180.
[8] Mahmood T, Fazal F, Akrim F, Fatima, H and Nadeem MS 2018 Comparative morphology and anatomy of two sympatric mongoose species (*Herpestes javanicus* and *H. edwardsii*) from *Potohar Plateau Pakistan J. Zool*. **52** 1129.
[9] Tompsett DH 1970 *Anatomical techniques* 2nd ed. E. and S. Livingstone 105.
[10] Reece WO 2009 *Functional Anatomy and Physiology of Domestic Animals* 4th ed. Wiley-Blackwell 273.
[11] Nassar RA 2012 *Anatomical and histological study on the lower respiratory system in the local cats* MSc. thesis. Coll. Vet. Med. Baghdad Univ.

[12] Al-Hayani HIA 2019 *Morphological description and histological composition of the trachea and lung in a naked-bellied tomb bat, (Taphozous nudiventris)* MSc. Thesis, College of Education for Pure Sciences (Ibn al-Haitham), University of Baghdad: 115 pp
[13] Getty R 1975 *Aves respiratory system* In : Anatomy of domestic animals W. S . Saunders . Co. Philadelphia .191-1884.
[14] Ishaq M 1980 A morphological study of the lungs and bronchial tree of the dog :with a suggested system of nomenclature for bronchi *J. Anat.* 131 589.
[15] Thrall DE 2002 *Text book of Veterinary Diagnostic Radiology* 4th ed. W.B. Saunders Company 312.
[16] Al-Anbaki AA 2013 *Anatomical and histological and radiological study of trachea and lungs in domestically rabbits* MSc. Thesis, Vet. Med. Collage, University. of Baghdad 94.
[17] Nickel R, Schummer A and Seiferle E 1979 The viscera of the Domestic Mammals *Trans. British Med. J. 1* 309.
[18] Khalid S and Jawad J 2017 *Histomorphological study of trachea and lungs in male and female guinea pigs (Cavia procellus)* MSc Thesis collage of university of Qadysiha 77.
[19] Arodaki F, Khamas W, Darmani N and Al-Tikriti M 2017 Histological characteristics of the tracheobronchial tree of the Least Shrew (*Cryptotis parva*). *Anatomia Histologia Embryologia* **46** 405.

Study of chemical content in *Pimpinella armena* and *Pimpinella kotschyana*: tribe Pimpinelleae/Apiaceae

Study of chemical content in *Pimpinella armena* and *Pimpinella kotschyana*: tribe Pimpinelleae /Apiaceae

Zahra B. Muhammad[1*] and Talib O. Al-Khesraji[2]

[1]Department of Biology, College of Education (Al-Haweja), University of Kirkuk, Iraq.
[2]Department of Biology, University of Tikrit, Iraq.

*E-mail: zahrabiology@gmail.com

Abstract. The flavonoid and alkaloid content in the alcoholic extract of the shoots and flowers were identified in two species of the tribe Pimpinelleae / Apiaceae: *Pimpinella armena* and *Pimpinella kotschyana*, and the flavonoids that were detected in this study are: (Apigenin, Coumarin, Kaempferol and Quercetin). The total alkaloids are estimated for these two species. It has been noticed that the species *Pimpinella armena* is a new record on the Iraqi flora, as it was identified through the genetic analysis of nucleotide sequences and registered in the National Center of Biotechnology (NCBI).

Keywords. Apiaceae, *Pimpinella*, flavonoids, alkaloid.

1. Introduction

The Apiaceae family is considered one of the most important families of flowering plants at the functional level, as its inflorescences had a great role in diagnosing them long before they are described scientifically for the first time [1]. Researchers disagreed about the number of genera and species belonging to this family, as [2] indicated that it includes (200) genera and (2900) species. [3] indicated that this family is widespread and spreads in tropical to temperate regions and that it includes (400) genera and (4250) species. In Iraq, this family is represented wildly by about (60) genera and (143) species [4]. The largest genera by the number of species *Pimpinella* genus, which includes about 15 species ,while [5] indicated that there are (130) wild species and (9) cultivated species. [6] also mentioned that this family is the fifth largest plant family in Iraq and that it is represented by approximately (67) genera and (155) species. The plants of this family contain many important chemical compounds that have contributed to strengthening their role as medicinal plants and a source of treatment for diseases, and the most important of these compounds are flavonoids [7, 8]. This family is considered to be one of the most economically important families, as many of its species are used as food or flavorings such as the *Foeniculum vulgare* Mill. , and *Anethum graveolens* L. In addition, many of the species are medicinal plants, such as Pimpinella. Pimpinella plants have been used in the treatment of several medical conditions due to their containment of very important effective compounds such as essential oils, volatile oils, flavonoids and alkaloids [9, 10, 11]. A review of the available scientific references revealed that the current study is the first local study in which the

flavonoid and alkaloid contents of the two studied species are identified. The species *Pimpinella armena* is a new record on the Iraqi flora, as it is identified through the genetic analysis of nucleotide sequences and registered in the National Center of Biotechnology (NCBI).

2. Materials and Methods

2.1. Collection of Plant Specimens

Fresh plant specimens are collected during the flowering time and then labelled with the necessary herbal information such as (place of collection, collector's name, common name of the plant, and date of collection). These samples are dried and pressed with the aforementioned herbal information recorded. The taxonomic keys and the Iraqi flora / fifth volume are used for the diagnosis of the samples, and it is confirmed by comparing the collected samples with the herbal samples kept in the Kurdistan Botanical Foundation herbarium in Sulaymaniyah and the Iraqi national herbarium in Abu Ghraib.

2.2. Chemical Study

2.2.1. Extraction of plant samples

The most common procedures used to analyse polyphenols' and simple phenolic in natural plants are Liquid-liquid and solid-liquid extraction. The main reasons behind this widely usage are their ease of use, effectiveness, and wide ranging applicability. Commonly used extraction solvents are alcohols (methanol, ethanol), acetone, diethyl ether, and ethyl acetate. Milling and homogenization are the first steps in preparation process. Extraction is the major step for recovering and isolating the bioactive phytochemicals from plant materials, before analysis. The main factors that influence extractions are their chemical nature, the extraction method employed, sample particle size, as well as the availability of interfering substances. Additional steps would be of such importance if the removal of unwanted phenolic and non-phenolic substances just like waxes, fats, terpenes, and chlorophylls. Thirty grams of plant powdered was extracted using 15 ml chloroform with constant stirring for 24 hours at the ambient temperature. The extract was placed in an ultrasonic device for 15 minutes. Then 100 ml of butanol was added and then transferred to the separation funnel. The polar organic layer (butanol) is collected and transferred to the rotary evaporator device to obtain a dry extractor. The operation is repeated three times to gain an adequate amount prior to analysis.

2.2.2. Condition of HPLC for analysed phenolic and flavonoid components

Samples are analysed by using high performance liquid chromatography HPLC model (SYKAM) Germany. Pump model: S 2100 Quaternary Gradient Pump, Auto sampler model : S 5200, Detector: UV (S 2340) and Column Oven model : S 4115. The mobile phase is = (Methanol : D.W : acetic acid) (85 : 13 : 2), the column is C18-ODS (25 cm * 4.6 mm) and detector UV – 360 nm at flow rate 1ml/min.

2.2.3. Total alkaloid content

Extraction: The 20 gm of each plant material was ground and then extracted with methanol for 24 hours in a continuous extraction (Soxholet) apparatus. The extract was faltered and methanol was evaporated on a rotary evaporator under vacuum at a temperature of 45°C until dryness.

2.2.4. Qualitative estimation (Test for alkaloids)

Presence of alkaloid was confirmed by Dragendroff's method .A part of extract was dissolved in diluted HCL and 2 drops of Dragon drops are added, presence of alkaloid is indicated by the presence of crystalline precipitate. The sample which has showed positive alkaloid is then subjected to further quantitative evaluation.

2.2.5. Separation of alkaloid

A part of extract residue is dissolved in 2N HCL and then faltered. 1 ml of this solution is transferred to reparatory funnel and washed with 10 ml chloroform. The pH of this solution is modulated to neutral with 0.1 N NaOH. This step is followed by adding 5 ml of Bromocresol Green (BCG) solution and 5 ml of phosphate buffer to the solution.

2.2.6. Standard carve

Carefully-measured aliquots of Atropine standard solution (0.4, 0.6, 0.8, 1 and 1.2 ml) is altered into various reparatory funnels. After that 5 ml of pH 4.7 phosphate buffer and 5 ml of BCG solution are taken, then the outcome mixture is shaken with extract of 1, 2, 3, and 4 ml of chloroform. These extracts have been collected later in 10 ml volumetric flask and then have mixed to adjust solution with chloroform. The absorbance of the complex in chloroform is measured at spectrum of 470 nm in UV-Spectrophotometer (SHIMADZU UV-1800) against the blank that is prepared according to the method mentioned above but without Atropine.

3. Results and Discussion

The results of the chemical study (Table 1) have showed the presence of four types of flavonoid compounds in the alcoholic extract of the shoots. These compounds are: Coumarin, Catchine, Kaempferol and Quercetin. The results of the chemical analysis have showed that the shoots are free of the flavonoid compound Apigenin. The concentration of Coumarin in the shoots is 361.4µg. ml^{-1} in *P.armena*, and the concentration of this compound reached 404.1µg / ml in *P.kotschyana*. As for the compound Catchine, the concentration reached 71.9 µg. ml^{-1} in the species *P.armena*, while the species *P.kotschyana* recorded higher concentration of this compound, which is 121.8µg /ml. It should be noted that the concentrations of Kaempferol is 39.6 µg / ml in species *P.armena* =, while the concentration is lowest in species *P.kotschyana* which is 28.64µg. ml^{-1} (Table1). Regarding Quercetin, the highest concentration is 55.14µg. ml^{-1} in species *P.armena*, and the lowest concentration is 51.2 4µg. ml^{-1} in *P.kotschyana*. It is also found from this study that the flavonoid compound Coumarin is the highest concentration compound in the alcoholic extract of the shoot of all the studied species (Table 1). As for the total content of flavonoids in the alcoholic extract of the shoots in the studied species, the highest value of it is in the *P.kotschyana* and reached 606.6 µg. ml^{-1}, while the lowest value for the total content of flavonoids is 528 µg. ml^{-1} in *P.armena* (Table 1). Concerning the total content of flavonoids in the alcoholic extract of flowering inflorescences in the studied species (Table 2), the highest value is recorded in *P.kotschyana* as it is 2625.4 µg. ml^{-1}, while the lowest total value is 418.6 µg. ml^{-1} in *P.armena*. It is revealed through this study that only Apigenin and Coumarin are present in the alcoholic extract of the flowers of *P.kotschyana* which have showed the highest concentration of these two compounds (120.8 and 2504.6) µg.ml^{-1}, respectively. The flavonoid compound Apigenin is absent from the flowers of *P.armena*. The lowest concentration of Coumarin is 261.4 µg. ml^{-1} in *A.visgana* (Table 2). It should be noted that the species *P.kotschyana* has recorded the highest concentration of compounds Apigenin, Catchine and Coumarin for the whole plant (both the vegetative and flowering parts). While the species *P.armena* has the highest concentration of Kaempferol and Quercetin in the vegetative and flowering (Table 3). It is worth noting that coumarins are the most abundant flavonoids in the studied species, and this is in agreement with [3] who has indicated that coumarins are among the compounds most present in the plants of the Apiaceae family.

Table 1. Flavonoid concentrations measured in µg. ml^{-1} in the shoot parts of the studied species.

no.	Flavonoides / Sp.	Apigenin	Coumarin	Catchine	Kaempferol	Quercetin	total
1	***P.armena***	0	361.4	71.9	39.6	55.1	528
2	***P.kotschyana***	0	404.1	121.8	28.6	51.2	606.6
	Total	0	765.5	193.7	68.2	106.3	1134.6

Table 2. Flavonoid concentrations measured in µg. ml^{-1} in the flowering parts of the studied species.

no.	Flavonoides / Sp	Apigenin	Coumarin	Catchine	Kaempferol	Quercetin	total
1	***P.armena***	0	261.4	0	0	0	261.4
2	***P.kotschyana***	120.8	2504.6	0	0	0	2625.4
	Total	120.8	2766.0	0	0	0	2886.8

Table 3. Total group of flavonoids (vegetative and flowering parts) measured in µg. ml^{-1} in each of the studied species.

no.	Flavonoides / Sp	Apigenin	Coumarine	Catchine	Kaempferol	Quercetin	total
1	***P.armena***	0	622.8	71.9	39.6	55.1	789.4
2	***P.kotschyana***	120.8	2908.7	121.8	28.6	52.1	3232
	Total	120.8	3531.5	193.7	68.2	106.3	4021.4

Regarding to the total alkaloids, it is found from this study that the highest percentage of alkaloids in the shoot system is 6.3% in *P.armena,* while *P.kotschyana* recorded the lowest percentage, reaching 5.3% (Table 4). The highest percentage of alkaliod content recorded in the Inflorescences is in *P.armena* and is 16.5%, while the lowest percentage recorded is 12.5% in *P.kotschyana*. It is evident from the observation of Table (4) that the species *P.armena* possesses the highest percentage of total alkaloid in the vegetative and flowering systems and of the studied species, which reaches 22.8%. Whilst, the species *P.kotschyana* recorded the lowest total percentage, which is 17.8% (Table 4). The flowering system is higher in its total alkaloid content than the shoots of the species under study, and the percentages are close in the studied species, which are sort of a few percentages and do not exceed 30% in each species. Perhaps these few percentages are the reason for the little attention of researchers in studying these important chemical compounds.

Table 4. Percentages of total alkaloids in shoots and Inflorescences of the studied species.

No	Sp	Shoots %	Inflorescent%	Total %
1	***P.armena***	6.3	16.5	22.8
2	***P.kotschyana***	5.3	12.5	17.8
	Total	11.6	29.0	40.6

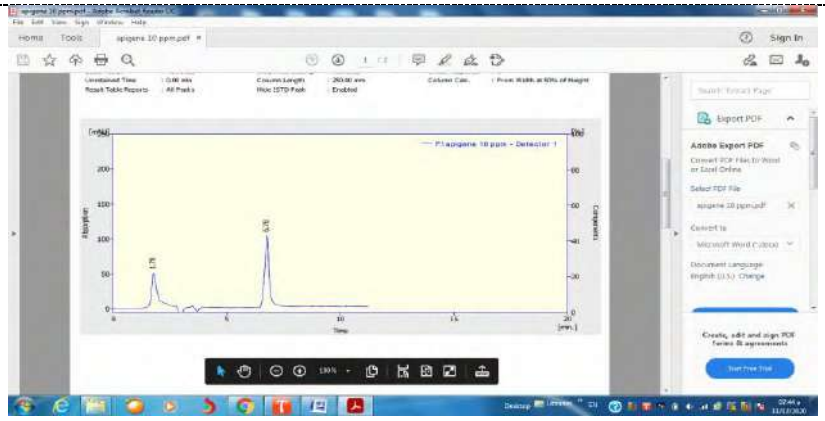

1

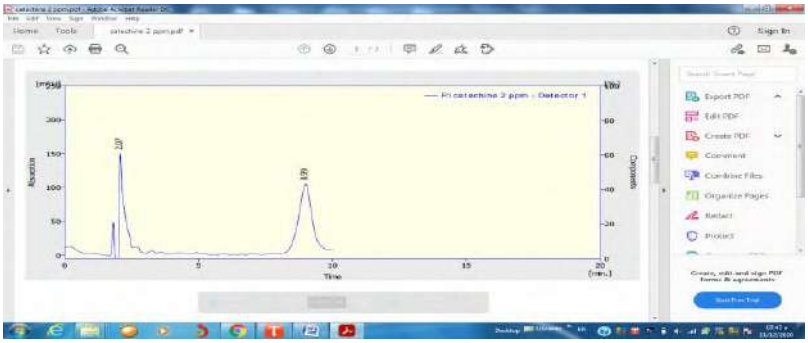

2

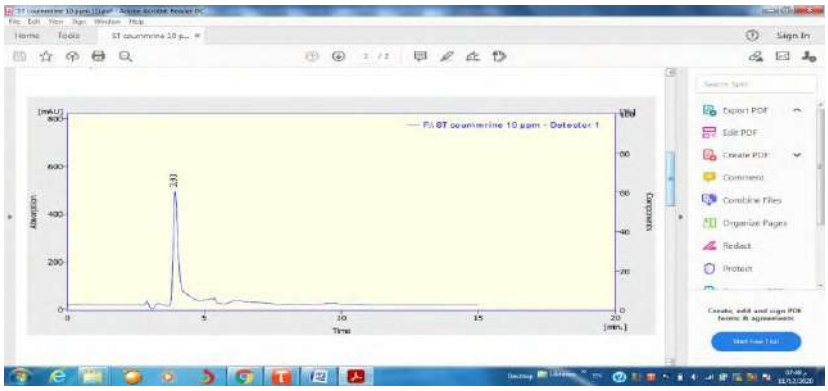

3

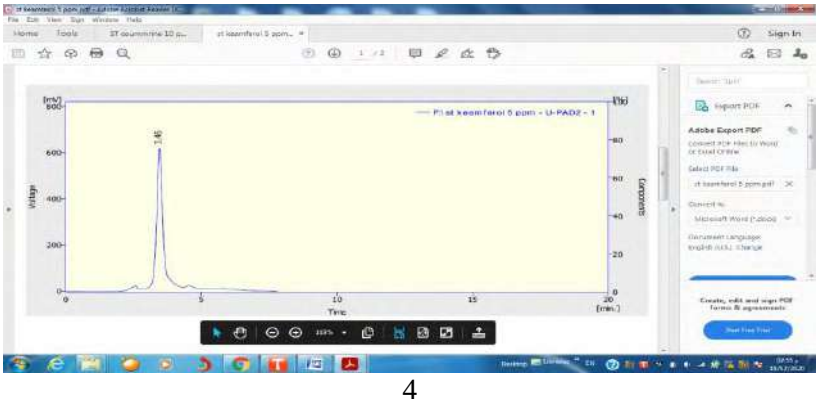

4

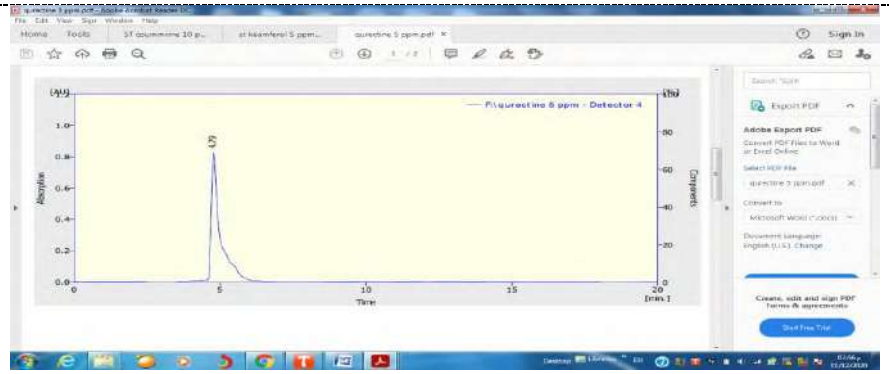
Absorption
Time
Components

5

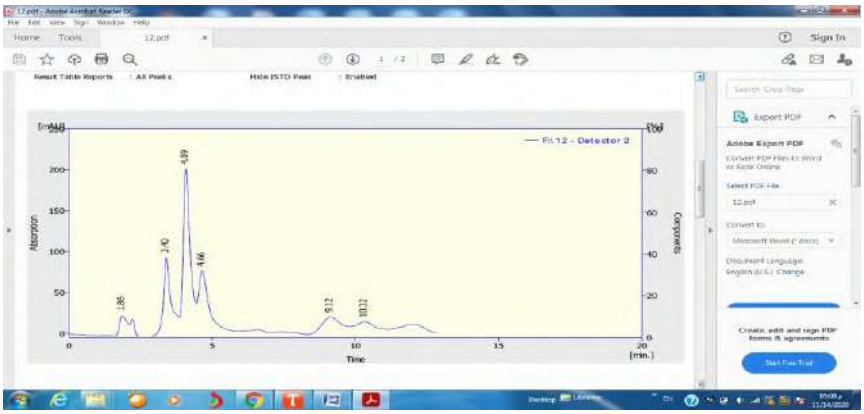
Absorption
Time
Components

6.a

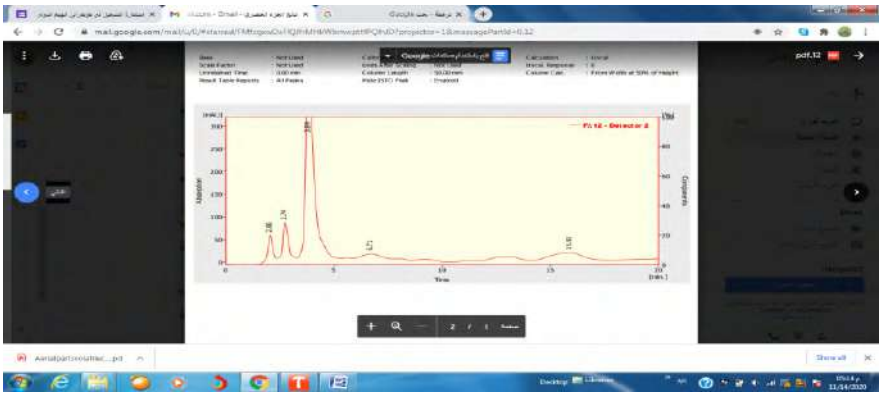

6.b

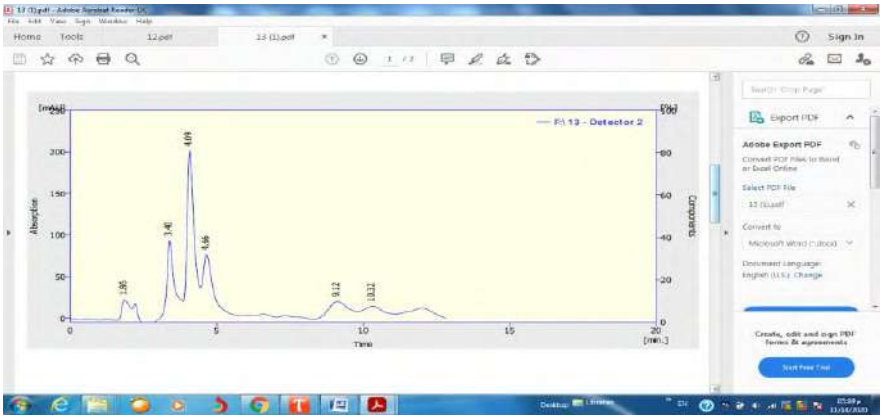
Absorption
Time
Components

7.a

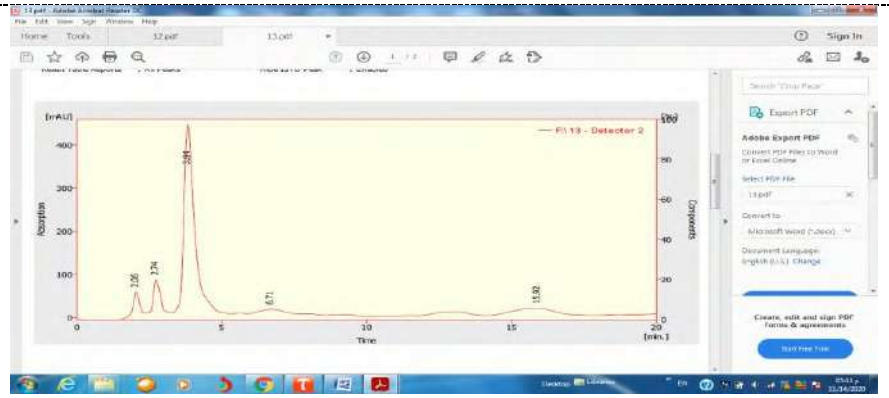

7.b

Figure 1. Standard curves of shoots and flowers extract of the studied species. (Standards: 1: Apigenin, 2. Catchine, 3: coumarin, 4: Kaempferol, 5: Quercetine) (Species: a. shoot, b. flowers 6.*P.armena*, 7. *P.kotschyana*.

P.armena *P.kotschyana*

Figure 2. Studied species with their flowers.

4. References

[1] Heywood VH 1976 *Plant Taxonomy*. 2nd Ed. Edward Arnold, London.
[2] Lawrence GHM 1951 *Taxonomy of vascular plants* The Macmillan Company New York. 823.
[3] Judd, WS, Campbell, CS, Kellogg EA and Stevens PF 1999 *Plant systematics* Sinauer associates, Inc., Sunderland, Massachusetts, U. S. A. 464 pp.
[4] Al-Mousawi AH 1987 *Plant Taxonomy* Books House for Printing and Publishing. University of Al Mosul 379.
[5] Al-Katib YM 1988 *Classification of seed plants* Baghdad University Ministry of Higher Education and Scientific Research, Iraq 243.
[6] Ghazanfar SA and McDaniel T 2016 Flora of the middle east: quantitative analysis biogeography of the flora of Iraq *Edinburgh J. Bot.* **73** 1.
[7] Askari F, Sefidkon F and Teimouri M 2011 Chemical Composition and Antimicrobial Activity of *Pimpinella kotschyana* Boiss. Oil in Iran *J. Essential Oil Bear. Plants (Jeobp)* **14** 124.
[8] Trovato A, Monforte MT, Rossito A and Forestieri AM 1996 *In vitro* cytotoxic effect of some medicinal plants containing flavonoids *Boll. Chim. Farm.* **135** 263.
[9] Amiri MS and Joharchi MR 2016 Ethnobotanical knowledge of Apiaceae family in Iran: A review *Avicenna J. Phytomed*. 1.
[10] Özdemir E and Alpınar K 2015 An ethnobotanical survey of medicinal plants in western part of central Taurus Mountains: Aladaglar (Nigde-Turkey) *J. Ethnopharmacol*. **166** 53.
[11] Al-Mayah AA 2013 *Medicinal plants and herbal remedies* Al-Basaer Press Beirut, Lebanon 358.

Effect of application of Chitosan in skin grafting surgeries in rabbits

Effect of application of Chitosan in skin grafting surgeries in rabbits

Hayder Mohammed Mohsen Al-Tomah[1*] , Falah Mahmood Hameed[1], Ali J. AL-Nuaimi[1] and Ail Wasfi Sadeq[1*]

[1]University of Kerbala, Karbala, Iraq.

*E-mail: haider.mohammed@uokerbala.edu.iq

Abstract. A study was done at the theatre of department of veterinary Surgery & obstetrics, College of Veterinary Medicine, University of Kerbala, Karbala, Iraq which performed to compare the effect of application of chitosan action as scaffold with collagen fibers. The histopathological findings in operation's sites showed the developments of skin graft's healing which was the guide to monitoring the healing. The results showed that the chitosan-treated grafts was healed more controllable with less scar tissue than non-treated grafts which indicates that the chitosan was coordinated the healing.

Keywords. Chitosan, Skin grafting, rabbits.

1. Introduction

Chitosan is derived from chitin which is the second maximum copious biopolymer after cellulose so it is biodegradable polymer and it accelerates wound healing [1]. It has been described that chitosan authorized regeneration of tissue elements in skin wounds and has affected positively in healing of wounds. Also it appear many benefits for topical applications, including non-irritancy and some anti-bacterial actions [2]. This study was aimed to study the availability of the applications of chitosan in healing of skin. Skin grafting a technique mainly used or reconstruction of skin defects at the last decades. The techniques of flaps and grafts considered are the two common surgeries utilized for restoration of losing of the tissue. Simple skin graft used as a thin layer harvested with a special scalpel called dermatome [3]. A free skin graft is a piece of skin that completely separated from normal area and transferred to a wound to a wound at another site that establish new vascular connections to survive. Skin grafting consider the best consideration for the wide wound closure or deep burns of wide body areas [4]. Skin grafting had been contraindicated if inosculation from receiver bed is unconfident or unpredictable or n wound infection [5]. Chitosan was discovered in 1859 by Rouget . Since then, it has been used as a pharmaceutical excipient and to promote wound healing [6]. Chitosan has been able to bind to substances, including acids, lipophilic materials and minerals [7] as well as inhibit fat absorption. The origin of chitosan is a fiber product that is obtained from deacetylated chitin. Chitin is naturally occurring substance found in the shells of crustaceans, invertebrates and fungi [6]. Chemical composition of chitosan consider as a copolymer which comprises of β – (1→4) – linked 2- acetamino- 2-deoxy-D-glucopyranose and 2-amino-2-deoxy-D-

glucopyranos units that obtained by alkaline deacetylation of chitin which is the main component of the exoskeleton of crustaceans [8]. Chitosan has a structure too similar to cellulose; which is fairly reactive compounded its formed in many forms such as powder, paste, film and fiber. The solubility of chitosan in dilute aqueous acetic, lactic, succinic and formic acids [9] (Shakeel et al , 2014) . Commercial production of chitosan by deacetylation of chitin [10]. Wound dressing, trauma, burns, dermatitis, purulent diseases, septic pod dermatitis, interdigitalphlegmon, interdigital hyperplasia, canker [11, 12, 13]. Wound infections are manifestations of disturbed host bacteria equilibrium in a traumatized tissues condition in a favor of the bacterium, the wound infection not only have the possibility to emerge a systemic restraint (sepsis) but it was highly probable to prevent the multiple processes involved in the orchestrated progression of normal wound healing, each process involved in healing are affected when bacterium proliferated in the wound [2]. Chitosan considered as non-toxic antibacterial polymer have the ability to prohibit a wide variety of fungi, bacteria, viruses and yeastswhich its interaction had been experimented in vitro and in vivo [14]. The accurate mechanism of the antimicrobial actions of chitosan are still hesitating, it has been suggested that is interactions between negatively charged microbial cell membrane and positively charged chitosan molecules can lead to the disturbance of microbial membrane, and thereafter infiltrate intracellular ingredients [15, 16]. Chitosan has exert as anti-inflammatory effects by restrain cyclooxygenase-2 protein expression and prostaglandin E2 and decline pro-inflammatory cytokines (e.g. interleukine-1β tumor necrosis-α). Otherwise, chitosan treatment raises the expression of the interleukin-10 [17]. Skin grafting is classified depending on the relation between the donor site and the recipient bed as: Autograft or autologus, which the skin grafted from different site on same body (man or animal). Isograft, syngraft or isogenic,which the grafting performed between animals or men are genetically identical (e.g. monozygotic twins). Allograft or allogenic, which the grafting performed between animals with same species, or men but genetically non-identical. Xenograft, heterograft or xenogenic, which the grafting performed between different speicies.[18].

2. Materials and Methods

2.1. Experimental design

Eighteen adult female rabbits divided randomly to two groups; the first group (A) which compel to skin grafting by transplantation from forelimb to hind limb using chitosan as pad under the graft and the second group(B) which compel to same grafting in (groupA) without addition of chitosan application on grafting area.

2.2. Chitosan

The chitosan which used in this experiment is manufactured Vitex Pharmaceuticals ®; Australia. The experiment done at the theatre of department of veterinary surgery and obstetrics, college of veterinary medicine / University of Kerbala, Karbala, IRAQ. Study parameters were hematological parameters and histopathological findings 21days post graftings and compare the healing of the skin according to gross findings and histopathology.

2.3. Surgical operation

2.3.1. Preoperative preparation

The animals of this study were prepared to surgery by fasting for 12 hours withheld of food and 6 hours of water before the operation, the area of medial tibial region was clipped and shaved and prepared aseptically. The skin was scrubbed by bovidine – iodine 2.5%. The rabbits were put at a lateral recumbency and covered with surgical drapes which fixed to the skin with towel clips.

2.3.2. Anesthesia

All the operations were performed under general anesthesia by intramuscular administration the combination of Xylazine and Ketamine at the dose (3:35 mg per kg B.W.) with additional dose of Xylazine to increase depth and prolong anesthesia [19, 20, 21].

2.4. Surgical technique

2.4.1. Group A

The technique which performed in this experiment was the transplantation of a square – shape of skin with 1cm×1cm in diameter from forelimb transplanted to a gap made in hind limb filled with chitosan powder then the borders of graft sutured with original skin by simple interrupted suturing covered by gauze pad changed every two days with 5 postoperative days of treatment with penicillin-streptomycin mixture to prevent any type of infection (Figure 1).

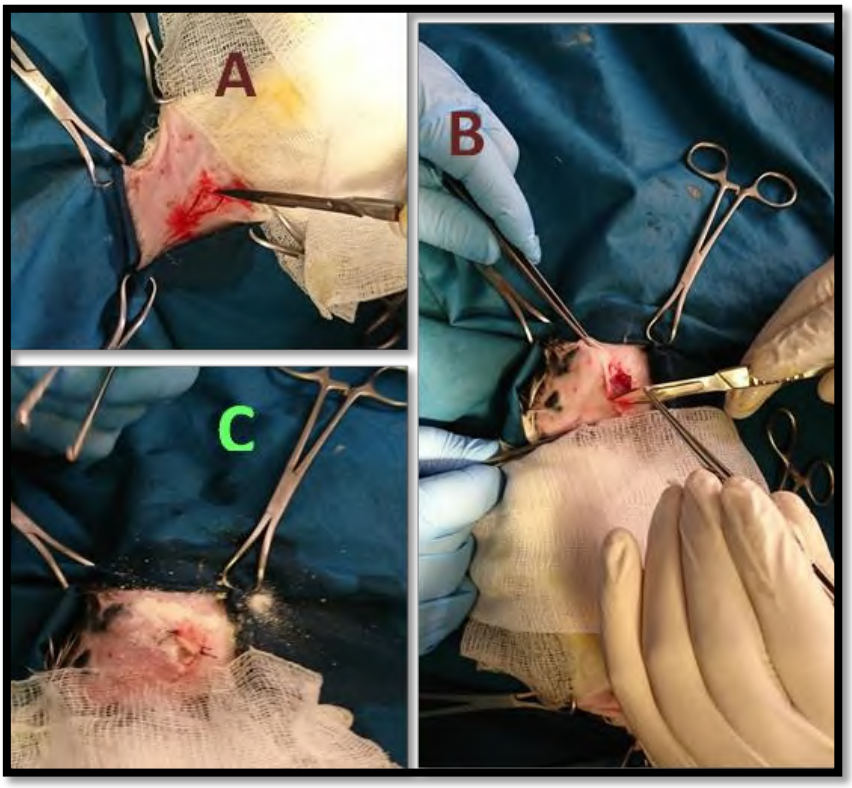

Figure 1. Shows the stages of experiment's operation: (A) Ablation of the graft from intact skin. (B) Preparation of grafting site. (C) Implanting of graft with application of chitosan.

2.4.2. Group B

The technique had been done same as in group A without adding of Chitosan at the site of operation. Other provisions was done consequently.

2.5. Postoperative care

The treated animals were housed in semi-opened house as confine within house garden fed with grain and vegetables along the period of experiment receiving freely water and food (containing green grass and grain). Experimented animals were administrated with mixture of Penicillin and streptomycin with a dose of (20000 I.U. : 10 mg per kg B.W.) for three days post operatively. Diclofinac*sodium in a dose of 1mg/kg B.W. were administered intramuscularly for 3 days post operatively. Rectal temperature, respiratory rate and heart rate were recorded daily for three days post operation.

3. Results and Discussion

The study showed that usage of chitosan as application with skin grafting was possible and useful . A total of 18 rabbits underwent successful healing with or without chitosan application , and it was observed that the normal clinical progress was without any clinical sign of complication or death due to the skin grafting and animals were in good general health and clinical condition, unless a mild signs of inflammatory signs in chitosan treating animals at first 2 days. The animals continued food intake directly after surgery with normal intensification of body weight. Understanding of the clinically and patience were very important for success of technique. However our previous experience showed that the chitosan-treated animals showed, in post mortem finding, most successful skin healing compare with non-treated animals, in addition to that there were reduce time of operation site's injury healing in chitosan-treated animals, reduced recovery time and postoperative wound complications.

3.1. Postoperative observation

The surgical phase of anesthesia was attained by administering Xylazine + Ketamine in all the animals . Injectable anesthesia was the method of choice for maintaining anesthesia during the procedure. It was perfectively done in rabbits in this experiment , and the animals completely lost consciousness without response to pinprick with excellent muscle relaxation. The post-surgical recovery from anesthesia in the two experimental groups were uneventful. The intramuscular administration of Xylazine with a dose of 3mg/kg B.W. and Ketamine with a dose of 35 mg/kg B.W. were given one by one injection produced about 45 minutes duration of general anesthesia with additional Xylazine could be added if depth of anesthesia was not adequate without any significant complication that might occur as regurgitation, delayed recovery. The surgery of indication of skin grafting in both groups were preformed successfully in all experimental animals. During the transplantation of skin graft; no trauma or injury to any muscle, blood vessels or nerve that could happen. At the beginning of the study consumed longer duration time for the chitosan- treatment's technique, but with more experience, the time became shortened, the maximum time required to obtain the chitosan application skin grafting 35- 45 while the duration time of non-treated animals 30-40 minutes.

3.2. Post-operative findings

3.2.1. Zero time

The Post-operative findings showed normal traumatic reactions with clear edges of wounds at the site of operation in both of groups immediately after the operation (Figure. 2).

Group A

Group B

Figure 2. Fig.2: shows the site of operation in both groups (time zero)

Twenty first days Post-operatively; the site of operation appear the complete healing with appearance of hair growth in grafting area. Hematological parameters shows no significant differences between both groups or within each group.

3.3. Histopathological findings

Group (A); a good healing signs with many hear follicles which grows within grafting tissue, with a thin line of scar tissue, Although, an accumulation of few inflammatory cells (Figure 3).

Group (B) ; the healing signs shows the hear follicles which grows within grafting tissue but less the which appeared in group A, with marked line of scar tissue, However, a negligible accumulation of inflammatory cells (Figure 4).

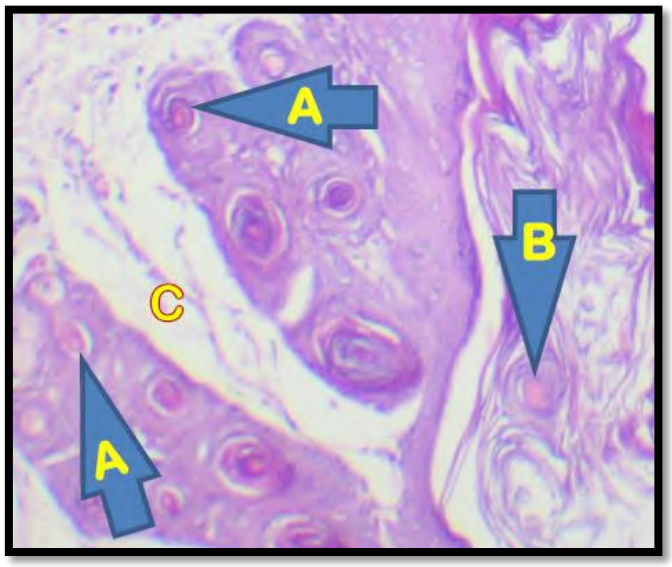

Figure 3. Shows the healing in group (A) which appear the growth of hair follicles (A) revascularization (B) with perfect scar formation(C), (X10). (C is not visible in both picture, make it like A and B). (C) refer to the area of scar tissue area which histologically classified as granulation and fibrous tissue (appear as white area).

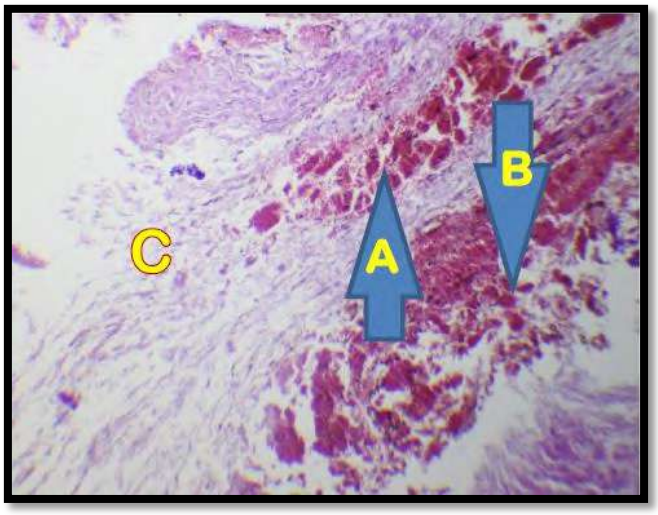

Figure 4. Shows the healing in group (B) which not appear the hair follicles (A), no marked revascularization (B) with huge margin of scar formation (C), (X4).

4. Discussion

In this study; it was appeared that Chitosan play a significant role in skin grafting healing similar with [22] that chitosan accelerate wound healing, as well as controlled the healing because the chitosan shared with other materials to scaffold the wound gap. this findings agreed with [23] and same with [24] who appeared its effect on bone marrow stromal cell osteogenesis and angiogenic factor secretion. Totally the organization of skin grafting healing which showed in chitosan-treated group in rabbits is followed the conclusion of [1] that chitosan, the biodegradable polymer, is enhance wound healing. In conclusion, the application of chitosan as filling the gap under graft can be done successfully in rabbits, despite the fact that Chitosan act as raw fibers in collagen-coated under the skin. Although, the chitosan accelerate healing of the skin grafting as well as it coordinate and controlled the scar formation .

5. References

[1] Conti B, Giunched IP, Genta I and Conte U 2000 The preparation and in vivo evaluation of the wound-healing properties of chitosan microspheres *S T P Pharm. Sci*. **10** 101.
[2] Kumar S, Swapan KM, Kumar N, Malik MS, Ninu AR, Ashok KB and Dayamon DM 2014 Effect of medical grade chitosan powder in full thickness skin wound healing in rat model *Adv. Anim. Vet. Sci.* **2** 270.
[3] Coban YK, Aytekin AH and Tenekec G 2011 *Skin Graft Harvesting and Donor Site Selection. Marcia Spear*, 1-15.
[4] Rudolph R and Ballantyne DL 1990 *Skin grafts* In: McCarthy JG, ed. Plastic Surgery Philadelphia Saunders 221.
[5] Paletta CE, Pokorny JJ and Rumbolo P 2006 *Skin grafts* In: Mc- Carthy JG, ed. Plastic Surgery. Philadelphia: Saunders Elsevier 293.
[6] Colombo P and Sciutto AM 1996 Nutritional aspects of chitosan employment in hypocaloric diet. *Acta Toxicol. Ther*. **17** 278.
[7] Jing S, Li L, Ji D, Takiguchi Y andYamaguchi T 1997 Effect of chitosan on renal function in patients with chronic renal failure *J. Pharm. Pharmacol*. **49** 721.
[8] Ahmed S, Ahmad M, Jayachandran M, Qureshi MA and Ikram S 2015 Chitosan Based Dressings for Wound Care *Immunochem. Immunopathol*. **1** 106.

[9] Shakeel A, Mudasir A. and Saiqa I 2014 Chitosan: a natural antimicrobial agent-a review *J. Appl. Chem*. **3** 493.
[10] Bedian L, VillalbaRodríguez AM, HernándezVargas G, ParraSaldivar R and Iqbal HM 2017 Biobased materials with novel characteristics for tissue engineering applications A review Candlish JK What you need to know *Singapore Med. J.* **40** 550.
[11] Minami S, Okamoto Y, Matsuhashi A, Sashiwa H, Saimoto H, Shigemasa Y, Tanjiawa T, Tanaka Y and Tokura S 1992 *Application of chitin and chitosan in large animal practice* 61. In Advances in chitin and chitosan (Brine CJ, Sandford PA and Zikakis JP Eds), Elssevier Applied Science, London and New York.
[12] Minami S, Okamoto Y, Fukumoto Y, Shigemasa Y and Matsuhashi A 1994 *Chitosan Bring lethal response in Chitin world* (Karnicicki ZS Eds), pp. 402. Wirtschafsverlag NW, Germany.
[13] Okamoto Y 2002)Analgesic effects of chitin and chitosan *Carbohydr. Polym*. **49** 249.
[14] Shakeel A, Mudasir A, Megha J, Mohammad Amir Q and Saiqa I 2015 Chitosan based dressings for wound care *Immunochem. Immunopathol*. **1** 2dx.
[15] Tang H, Zhang P and Kieft TL 2010 Antibacterial action of a novel functionalized chitosan arginine against Gram negative bacteria *Acta Biomater*. **6** 2562.
[16] Li P, Poon YF, Li W, Zhu HY, Yeap SH, Cao Y, Qi X, Zhou C, Lamrani M, Beuerman RW, Kang ET, Mu Y, Li CM, Chang MW, Leong SS and Chan Park MB 2011 A polycationic antimicrobial and biocompatible hydrogelwith microbe membrane suctioning ability *Nat Mater*. **10** 149.
[17] Spindola H, Fernandes J, De Sousa V, Tavaria F, Pintado M, Malcata X and Carvalho JE 2009 Anti-inflammatory effect of chitosan oligomers *New Biotechnol*. **25** S9.
[18] Weerda H 2001 Reconstructive Facial Plastic Surgery *Thieme*. **2** 9.
[19] Quesenberry KE and Carpenter JW 2004 *Anesthesia, Analgesia, and Sedation of Small Mammals* In: Ferrets, Rabbits, and Rodents, 2nd ed. Saunders, St. Louis., Flecknell, P.A., 356.
[20] Suckow MA, Stevens KA and Wilson RP 2012 *The laboratory rabbit, guinea pig, hamster and other rodents* (1st Ed.); Elsevier 32 Jamestown Road, London NW1 7BY, UK 34.
[21] Grimm KA, Lamont LA, Tranquilli WJ, Greene SA and Robertson SA 2015 *Veterinary Anesthesia and Analgesia* Fifth Edition of Lumb and Jones. John Wiley & Sons, Inc. 222 Rosewood Drive, Danvers, MA 01923.USA 755.
[22] Ishihara M, Nakanishi K, Ono K, Sato M, Kikuchi M and Saito Y 2002 Photo cross linkable chitosan as a dressing for wound occlusion and accelerator in healing process *Biomaterials* **23** 833.
[23] Hong-Ru L, Ko-Shao C, Su-Chen C, Chih-Hung L, Shih-Hwa C, Ta-Li C andTe-Hsing W 2006 Attachment of stem cells on porous chitosan scaffold cross linked by Na5P3O10 *Mat. Sci. Eng. C* **27** 280.
[24] Guzmán-Morales J, El-Gabalawy H, Pham M, Tran-Khanh N and McKee M 2009 Effect of chitosan particles and dexamethasone on human bone marrow stromal cellosteogenesis and angiogenic factor secretion *Bone* **45** 617.

Metal complexes of 1,6-bis(1-benzimidazolyl) hexane: synthesis, characterization and biological activity against some soil-borne fungi

Metal complexes of 1,6-bis(1-benzimidazolyl) hexane: synthesis, characterization and biological activity against some soil-borne fungi

Abbas Washeel Salman[1*], Jawadayn Talib Alkooranee[2], Hayder Dawood Arkawazi[3], Haitham Kadhim Alsharifi[4] and Michaele Hardie[5]

[1]Department of Production, College of Agriculture, Wasit University, Kut, Wasit, Iraq.
[2]Department of Plant Protection, College of Agriculture, Wasit University, Kut, Wasit, Iraq.
[3]Department of Chemistry, College of Science, Wasit University, Kut, Wasit, Iraq.
[4]Department of Food Technology, College of food science. Al-Qasim Green University, Al-Qasim, Babylon, Iraq.
[5]School of Chemistry, University of Leeds Woodhouse Lane, Leeds, LS2 9JT (UK).

*E-mail: aws.chem@gmail.com

Abstract. Metal complexes Mn(II), Co(II), Cu(II), Zn(II) and Ag(I) of the ligand 1,6-bis(1-benzimidazolyl)hexane were synthesized by the reaction of the ligand and appropriate metal salts in 1:1 mole ratio. The ligand and its complexes were characterized using IR, Uv-Vis, 1H and 13C NMR, Mass spectroscopy, and elemental analysis CHN. Depending on the abovementioned techniques, a polymeric structure was proposed to the prepared complexes. Further, all the synthesized compounds were tested against some of the soil-borne fungi namely; *Rhizoctonia solani*, *Fusarium oxysporum*, *Fusarium solani* and *Pythium aphanidermatum*. The results showed that the tested compounds have an effect on the growth of pathogenic fungi. This leads to thinking that these compounds could be used one day as new chemical pesticides as an alternative to chemical compounds that have been shown to be resistant to pathogens.

Keywords. Benzimidazole, NMR, Metal complexes, *Rhizoctonia solani*, *Fusarium oxysporum*, *Fusarium solani*, *Pythium aphanidermatum*.

1. Introduction

The use of synthetic chemical pesticides is still the most widely used method by farmers in the control of plant diseases. But, unfortunately, over the years and because of the ability of some fungi to develop their resistance, some of these pesticides became inactive and a major problem in agriculture [1]. Despite continuing the research to control the various diseases, many phytopathogens fungi have developed multiple mechanisms of resistance where fungicides are becoming challenged increasingly [2]. At the same time, alternative chemicals pesticides are synthesized, investigated, and then used

successfully to prevent fungal pathogens from growing and spreading in different environments. The introduction of inorganic fungicides such as copper, sulfur, or mercury compounds, followed by organic fungicides such as phthalimides (e.g., captan) dithiocarbamates (e.g., maneb) was the first milestone in the development of fungicide [3]. Many important chemical fungicides used extensively in the last 50 years in the protection of plants such as dicarboximide, benzimidazoles, strobilurin, phenylpyrrole, anilinopyrimidine, Q. respiration inhibitors, and demethylation inhibitors (DMI) [4]. But, over time some of them lost their importance as a result of the resistance of fungi strains [5]. A new class of fungicides was discovered during the 1960s offered curative of plant disease control, ability to longer-lasting protection, and lower application rates. The benzimidazoles were welcomed enthusiastically by farmers and plant pathologists, but the farmers soon reported great resistance to pesticides and large losses in field crops [3].Imidazole, benzimidazole and their metal complexes are exhibited different coordination modes [6] with a wide variety of applications, especially the biological [7-13], and catalytical ones [14-16]. Both copper and sulfur elements are used from the 1940s until present in integrated and organic farming. Only a few years after used them, resistance development in the pathogen fungi and the loss of fungicide activity were observed [5]. Excessive spraying programs of fungicides have resulted in appearing of multi-resistant strains of gray mold fungus Botrytis cinerea in several fields, particularly in strawberry ones [5]. Although quinol oxidation inhibitors (QoIs) are the most successful in fungicides, it was proved that they were resistant to fungi through mutations in the cytochrome b gene CYTB in some fungi pathogens [17]. To produce high-quality and quantitatively yield crops, researchers should provide optimal growth conditions for plants and protected from damage caused by pests, including insects, weeds, and fungi pathogens. Also, it is necessary to find new active compounds against the pests, at least at the moment. Therefore, this study aimed to use some synthetic compounds for the first time in the control of plant diseases caused by some soil-borne fungi. It is worth to be mentioned that the tested fungi are causing significant economic losses. In the present study, new transition metal complexes derived from the ligand 1,6-bis(1-benzimidazolyl) hexane were synthesized. The ligand and its complexes are tested against some soil-borne fungi namely *Rhizoctonia solani*, *Fusarium oxysporum*, *Fusarium solani* and *Pythium aphanidermatum*. According to the results obtained, we think that these compounds could be used as alternatives for chemical pesticides after more studies and experiments.

2. Materials and Methods

2.1. Materials and Instrumentations

All the chemicals used in the present work were purchased from commercial sources and used as it is without further purifications processes. 1H and 13C NMR spectra were recorded using Bruker UltraShield TM 500MHz spectrometer, Switzerland in d6-DMSO. Dionex Ultimate 3000 spectrometer, Germany, was used to record the mass spectrum of the ligand. The abovementioned techniques are available at School of Chemistry, University of Leeds, UK. CHN analysis was carried out using Euro EA elemental analyzer CHNS, EA3000 analyzer, Germany. Infra-Red spectra were recorded using a SHIMADZU spectrometer, Japan, on potassium bromide disks in the range 4000-400 cm-1. These techniques are available at the department of chemistry- College of science, Al-Mustansiriyah University, Baghdad, Iraq. Furthermore, the spectrophotometer Sp-3000 nano OPTIMA, South Korea, was used to record uv-vis spectra in the range 200-800 nm, which is available in the department of chemistry- college of science- University of Wasit, Iraq.

2.2. Synthesis

2.2.1. Synthesis of the ligand 1,6-bis (1-benzimidazolyl) hexane

The method used in synthesis of the ligand 1,6-bis(1-benzimidazolyl)hexane is described in our previous works [18, 19], except using of 1,6-dibromohexane instead of 1,4-dibromobutane. The resulted light beige precipitate was left standing for 2 hrs, then filtrated, washed with plenty of distilled water and dried at room temperature. The yield percentage was 95 %. Anal. Cal. For $C_{20}H_{22}N_4$: C, 75.44; H, 6.96; N, 17.60 %, found: C, 75.12; H, 7.18; N, 17.43 %. IR: ν(C-$H_{aromatic}$): 3091-3043 cm^{-1}, δ(C-$H_{aromatic}$): 767-634 cm^{-1}, ν(C-$H_{aliphatic}$): 2933-2852 cm^{-1}, ν(C=C): 1496-1670 cm^{-1}, ν(C=N): 1506 cm^{-1}. M_S: 319.198 [M^+]. ^{1}H NMR (DMSO-d^6, 500MHz): δ 1.242 (t, 4H, 2×CH_2), 1.738 (m, 4H, 2×CH_2), 4.181 (t, 4H, 2×CH_2-N), 7.159-7.235 (m, 4H, 2×Ar-H), 7.534 (d, 2H, 2×Ar-H), 7.627 (d, 2H, 2×Ar-H), 8.179 (s, 2H, NCHN). ^{13}C NMR (DMSO-d^6, 125 MHz): δ 25.54 (CH2), 29.15 (CH2), 43.91 (CH2-N), 110.31, 119.37, 121.35, 122.18, 133.74, 143.37 (Ar-C), 143.93 (NCHN) ppm.

2.2.2. Synthesis of the metal complexes

2.2.2.1. General method

To a solution of the ligand 1,6-bis(1-benzimidazolyl)hexane prepared by dissolving 1 mmol in 10 ml of ethanol, 1 mmol of the appropriate metal salts dissolved in 10 ml of ethanol was added dropwise. The resulting mixture was heated with stirring for 1 hr at ≈ 60 oC. The obtained precipitates were filtered and washed with fresh ethanol and distilled water and left to dry at ambient temperature

2.2.2.2. Synthesis of Mn (II) Complex

The complex was prepared by the reaction of the ligand with $MnCl_2.2H_2O$. The reaction produced the complex as a white precipitate with a yield of 74 %. Anal. Cal. for $(C_{20}H_{22}Cl_2MnN_4)_n$ (H_2O): C, 51.96; H, 5.23; N, 12.12 %, found: C, 51.32; H, 5.47; N, 11.83 %. IR: ν(C=N): 1492 cm^{-1}.

2.2.2.3. Synthesis of Co (II) Complex

The complex was prepared by the reaction of the ligand with $CoCl_2$. The reaction produced the complex as a blue precipitate with a yield of 69 %. Anal. Cal. for $(C_{20}H_{22}Cl_2CoN_4)_n$: C, 53.59; H, 4.95; N, 12.50 %, found: C, 53.41; H, 5.11; N, 12.39 %. IR: ν(C=N): 1494 cm^{-1}.

2.2.2.4. Synthesis of Cu(II) Complex

The complex was prepared by the reaction of the ligand with $CuCl_2$. The reaction produced the complex as a light-green precipitate with a yield of 66 %. Anal. Cal. for $(C_{20}H_{22}Cl_2CuN_4)_n$: C, 53.04; H, 4.90; N, 12.37 %, found: C, 53.22; H, 5.08; N, 12.15 %. IR: ν(C=N): 1468 cm^{-1}. IR: ν(C=N): 1494 cm^{-1}.

2.2.2.5. Synthesis of Zn(II) Complex

The complex was prepared by the reaction of the ligand with $ZnCl_2$. The reaction produced the complex as a white precipitate with a yield of 76 %. Anal. Cal. for $(C_{20}H_{22}Cl_2ZnN_4)_n$: C, 52.83; H, 4.88; N, 12.32 %, found: C, 52.52; H, 4.94; N, 11.96 % IR: ν(C=N): 1494 cm^{-1}. ^{1}H NMR (DMSO-d^6, 500M Hz): δ 1.217 (t, 4H, 2×CH_2), 1.749 (m, 4H, 2×CH_2), 4.281 (t, 4H, 2×CH_2-N), 7.271-7.333 (m, 4H, 2×Ar-H), 7.646 (d, 2H, 2×Ar-H), 7.824 (d, 2H, 2×Ar-H), 8.455 (s, 2H, NCHN). ^{13}C NMR (DMSO-d^6, 125 MHz): δ 25.35 (CH2), 28.89 (CH2), 44.41 (CH2-N), 111.06, 118.71, 122.52, 123.15, 133.15, 141.14 (Ar-C), 144.45 (NCHN) ppm.

2.2.2.6. Synthesis of Ag(I) Complex

The complex was prepared by the reaction of the ligand with $AgNO_3$. The reaction produced the complex as a light-grey precipitate with a yield of 72 %. Anal. Cal. for $(C_{30}H_{33}AgN_6)_n(NO_3)_n$: C, 55.65; H, 5.14; N, 15.14 %, found: C, 55.37; H, 5.31; N, 15.02 %. IR: ν(C=N): 1495 cm^{-1}. ^{1}H NMR (DMSO-d^6, 500M Hz): δ 1.203 (t, 4H, 2×CH_2), 1.734 (m, 4H, 2×CH_2), 4.261 (t, 4H, 2×CH_2-N), 7.293-7.303 (m, 4H, 2×Ar-H), 7.625 (d, 2H, 2×Ar-H), 7.80 (d, 2H, 2×Ar-H), 8.426 (s, 2H, NCHN). ^{13}C NMR (DMSO-d^6, 125 MHz): δ 25.33 (CH2), 28.69 (CH2), 44.38 (CH2-N), 110.86, 118.59, 122.50, 123.19, 133.11, 141.15 (Ar-C), 144.47 (NCHN) ppm.

2.3. Pathogen fungi materials

The pathogens soil-borne fungi *R. solani*, *F. oxysporum*, *F. solani*, *P. aphanidermatum* isolates were obtained from the field crops department, College of Agriculture, Wasit University, Iraq and maintained and cultured on autoclaved potato dextrose agar (P.D.A) medium (200 g peeled potato, 20 g dextrose, 15 g agar to 1 liter distilled water) in the dark at 25±2°C. The laboratory experiments were conducted in the microbiology laboratory of field crops department in the winter season of 2019.

2.3.1. In vitro inhibition of mycelia length growth

To determine the effects of the tested compounds on mycelial length growth of pathogens fungi in dual-culture techniques, 0, 10, and 20 ppm of each compound were added as 1-20 ml to Petri dish contain molten P.D.A media (40˚C ± 2˚C) (autoclaved at 121°C 15 psi for 30 min) separately, and mixed properly prior to plating. One mycelium of 5-mm of each pathogen was inoculated at the center of each Petri dish, separately. For the control, a set of plates was inoculated similarly, but with the pathogen only. Three replicate dishes per fungus strain with each concentration combination were set up and incubated at 25˚C ± 3˚C for 6 days. The radial mycelial growth of the pathogens (measured in centimeters) was assessed after 6 days, and the percent mycelial growth inhibition of each pathogen was calculated using the following growth inhibition equation:

Percent inhibition = R - r / R x 100

Where R (a control value) represents the radial growth of fungus pathogen in control sets, and r is the radial growth of the fungus in sets with tested compounds.

2.4. Statistical analysis

GenStat software was used to analyze the significant differences between different treatments using least significant difference (LSD) tests and the means ($P < 0.05$).

3. Results and Discussion

3.1. Synthesis and Characterization

In the synthesis of the ligand 1,6-bis(1-benzimidazolyl)hexane, an equimolar of benzimidazole and NaOH were reacted in DMSO at 80-90 °C for 2 hr. After cooling the mixture to about 40 °C, a half equivalent of 1,6-dibromohexane was added with constant stirring for more 2 hr. Then, the resulted mixture was poured into cooled distilled water to give instantly the product as an off-white precipitate which was filtered and washed with plenty of distilled water and left to dry at ambient temperature. For the complexes, an equimolar of ethanolic solution of the ligand and appropriate metal salt was heated with stirring between 50-60 °C for about 1 hr. The resulted precipitates were filtered, washed with fresh ethanol and water and left to dry (Scheme 1).

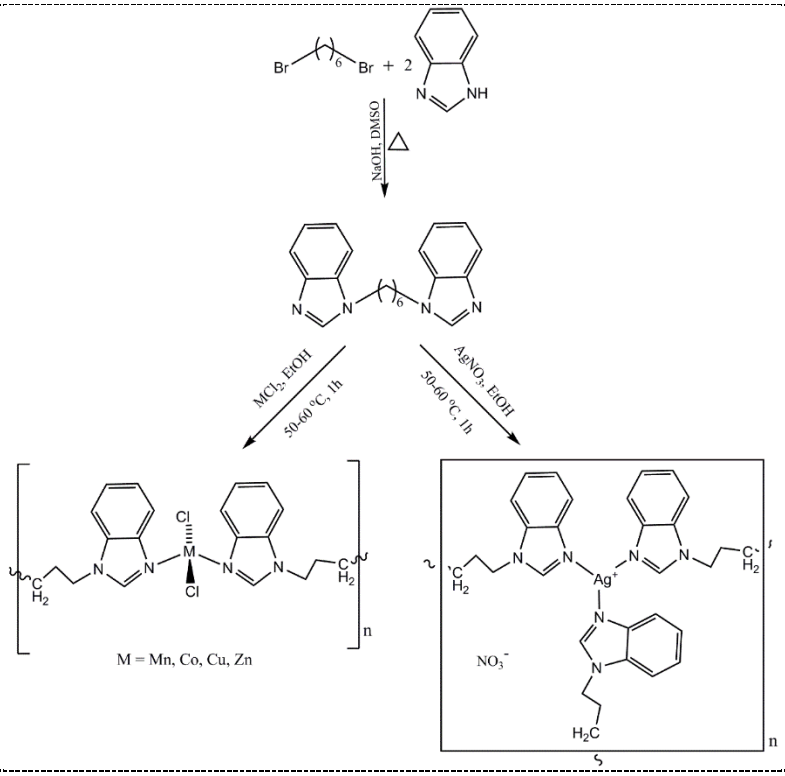

Scheme 1. Synthesis of the ligand and its metal complexes.

FT-IR spectrum of the ligand showed different bands at the range 3091-3043 cm^{-1}. These bands can be assigned to the stretching of aromatic C-H bond and to the vibration of benzimidazole ring. The bending of same groups appeared at the range 767-634 cm^{-1}. The stretching of aliphatic groups appeared at the range 2933-2852 cm-1, while the starching of C=C bond appeared at the range 1670-1496 cm-1. Last but not least, a characteristic band of ν(C=N) of benzimidazole is appeared at 1506 cm^{-1}. It is worth to be mentioned that most of the abovementioned bands are appeared too in complexes spectra, but in different positions or shapes or intensities. Particularly, the stretching vibration of benzimidazole ν(C=N) which shifted to lower frequency in all complexes (Figures 1 and 2). These changes assigned to the coordination of tertiary nitrogen in azoles with the metal ions [20-22].

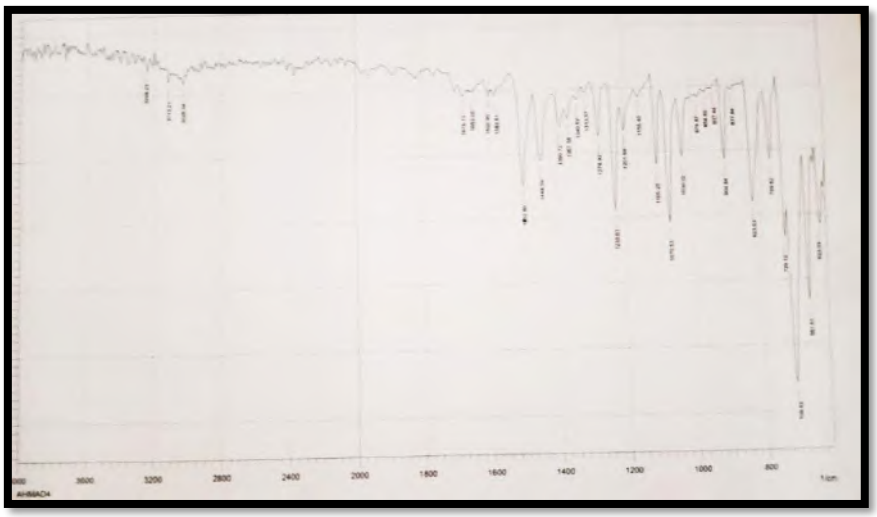

Figure 1. IR spectrum of the ligand.

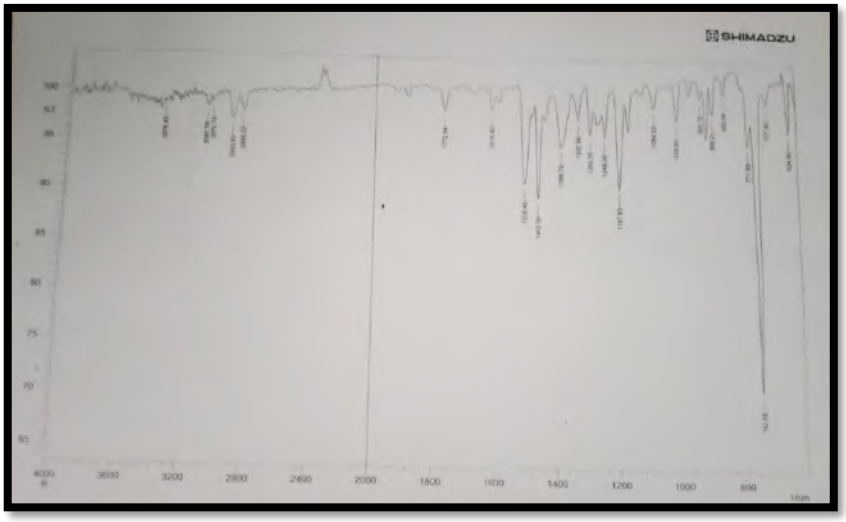

Figure 2. IR spectrum of Mn^{+2} complex.

In uv-vis spectra, the free ligand showed a broad band with two shoulders in the range 250-300 nm. These peaks are belongs to the transitions n→π* and π→π*, respectively. In complexes spectra, the mentioned peaks are slightly shifted to higher wave length, which is another evidence for complexation with metal ions [19]. ^{1}H and ^{13}C NMR spectra for the ligand and their Zn(II) and Ag(I) are recorded in DMSO-d^{6}. In the ^{1}H NMR spectrum, the ligand showed the characteristic signals which consistent with its proposed structure. The signals at δ 1.242, 1.738 and 4.181 are belongs to (-CH_2-), (-CH_2-) and (-CH_2-N), respectively (Figure 3). The signals of the benzimidazole appeared in the range δ 7.159-7.627. Further, the signal of the proton (NCHN) is appeared as singlet at δ 8.179. In the ^{13}C NMR spectrum (Figure 4), the signals appeared at δ 25.54, 29.15 and 43.91 are assigned to the carbon of (CH_2), (CH_2) and (CH_2-N), respectively. The signals of fused benzene ring appeared at δ 110.31, 119.37, 121.35, 122.18, 133.74, and 143.37. Last but not least, the signal appeared at δ 143.93 is belongs to the carbon of (NCN) group.

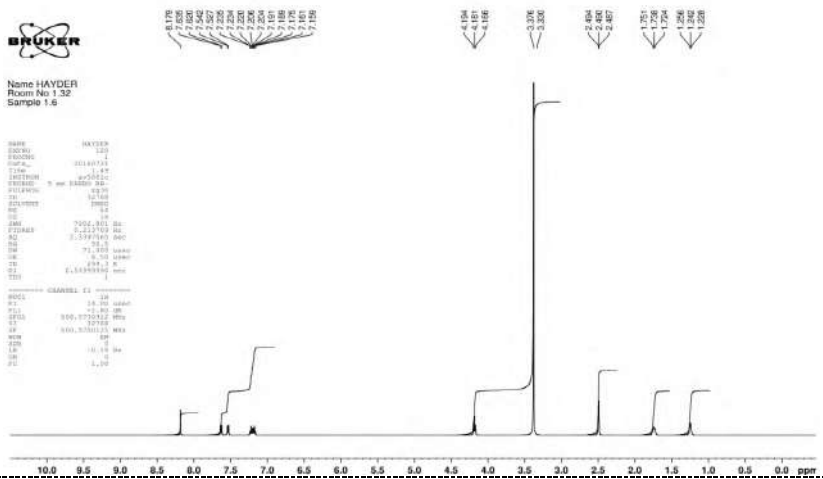

Figure 3. ^{1}H NMR spectrum of the ligand.

In Zn(II) and Ag(I) complexes, the signal of (NCHN) proton in benzimidazole is appeared at δ 8.455 and δ 8.426, respectively (Figure 5). While, the carbon signal of (NCN) is appeared at δ 144.45 and δ 144.47, respectively. Depending on the references, the observed shifting is a good signal for the coordination with metal ions [20, 22]. Unfortunately, no NMR spectra have been recorded for other

complexes due to their paramagnetism. Mass spectroscopy also confirmed the molecular weight of the synthesized ligand [M+] = 319.198 which is in fully agreement with the calculated theoretically (Figure 6).

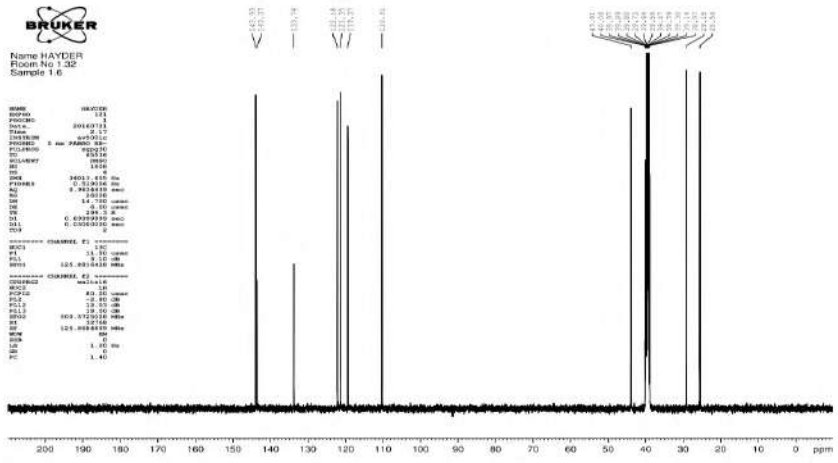

Figure 4. ^{13}C NMR spectrum of the ligand.

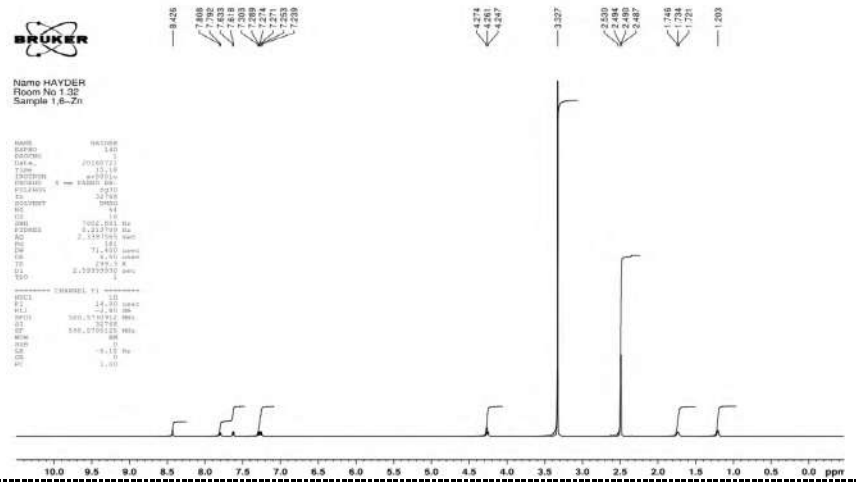

Figure 5. ^{1}H NMR spectrum of the Zn(II) complex.

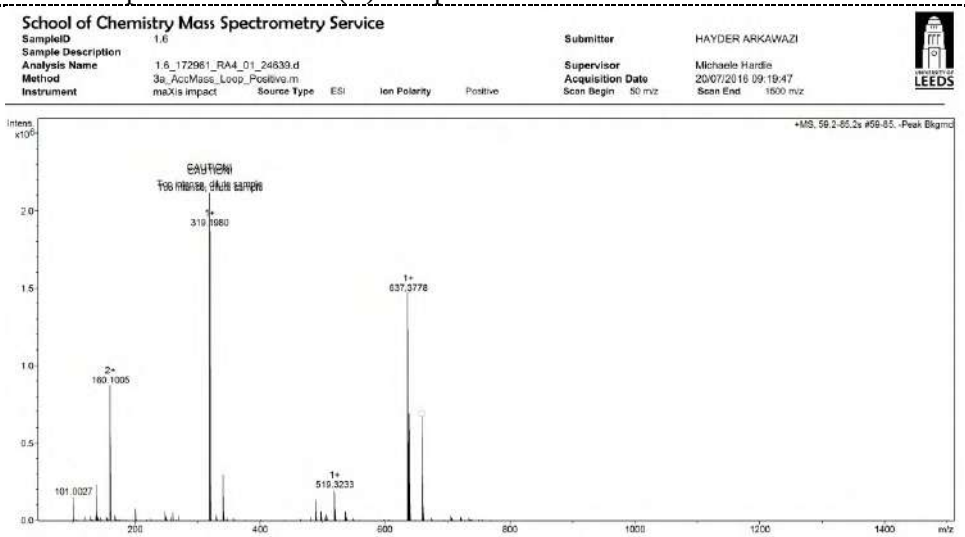

Figure 6. Mass spectrum of the ligand.

3.2. Antifungal activity

To maintain the increase of agricultural production, new possible fungicides should be diagnosed and deeply studied to know their antifungal activity. So, this study aimed to evaluate the efficiency of some new compounds towards some pathogenic fungi. The results obtained in the present study are shown in Tables (1-4). It is clear that the radial growth of all fungi was adversely affected by the tested compounds. Also, it was shown that the inhibitory effect on the growth of mycelium fungi was increased with increasing of concentrations from 10 ppm to 20 ppm of all compounds. Amongst the tested compounds, Cu^{+2} complex proved to be the most effective against all pathogens fungi with 100% inhibition in radial growth at 20 ppm.

Table 1: reveals that the R. solani fungus was affected with all tested compounds, with highest reduction in fungal growth at 20 ppm which was 100%, while, it was 64.44% at 10 ppm. On the other hand, for the tested compounds, Co^{+2} complex caused the highest reduction in growth 46.33 and 90.0 % at 10 and 20 ppm, respectively.

Compounds	Growth of *R. solani*					
	0 ppm		10 ppm		20 ppm	
	Growth rate cm	% inhibition	Growth rate cm	% inhibition	Growth rate cm	% inhibition
Ligand	*9.00	0.00	9.00	0	6.34	29.56
Mn^{+2} complex	9.00	0.00	7.56	16.00	3.88	56.89
Co^{+2} complex	9.00	0.00	4.83	46.33	0.90	90.00
Cu^{+2} complex	9.00	0.00	3.20	64.44	0	100
Zn^{+2} complex	9.00	0.00	7.75	13.89	2.35	73.89
Ag^{+} complex	9.00	0.00	6.00	33.33	4.48	50.22
L.S.D	NS	NS	1.33	4.79	0.65	6.25

*Each number represents three replicates

In case of *F. oxysporum* (Table 2), Cu+2 complex again showed the highest inhibition of mycelial growth with 76.67% at 10 ppm and 100% at 20 ppm. While, the ligand showed the lowest inhibition with 9.5 % and 31.10 % at 10 ppm and 20 ppm, respectively. Co^{+2} and Zn^{+2} complexes showed inhibition of 36.11 and 48.89% at 10 ppm, whereas at 20 ppm, they showed 87.75 and 85.0%, respectively.

Table 2. Effect of different concentrations of the compounds on the growth of Fusarium oxysporum

Compounds	Growth of *F. oxysporum*					
	0 ppm		10 ppm		20 ppm	
	Growth rate cm	% inhibition	Growth rate cm	% inhibition	Growth rate cm	% inhibition
Ligand	*9.00	0	8.14	9.56	6.20	31.10
Mn^{+2} complex	9.00	0	5.74	36.22	2.12	76.44
Co^{+2} complex	9.00	0	3.32	63.11	1.10	87.75
Cu^{+2} complex	9.00	0	2.10	76.67	0	100
Zn^{+2} complex	9.00	0	4.60	48.89	1.35	85.00
Ag+ complex	9.00	0	7.34	18.44	4.58	49.11
L.S.D	NS	NS	2.11	6.13	0.78	9.65

*Each number represents three replicates

The inhibitory effect of the compounds on the mycelial growth of *F. solani* isolate are shown in Table 3. In general, all the tested compounds showed more than 50% mycelial growth inhibition at a concentration of 20 ppm. Significantly, Cu^{+2} and Co^{+2} complexes were the most effective than others, showing 100% growth inhibition. While, Ag+ and Mn+2 complexes showed 86.22 and 82.22 % growth inhibition at the same concentration. At 10 ppm, the inhibitory effect of the compounds was ranging from 23.71% to 65.00%.

Table 3. Effect of different concentrations of the compounds on the growth of *Fusarium solani*.

Compounds	Growth of *F. solani*					
	0 ppm		10 ppm		20 ppm	
	Growth rate cm	% inhibition	Growth rate cm	% inhibition	Growth rate cm	% inhibition
Ligand	*9.00	0	7.10	23.71	4.29	52.33
Mn^{+2} complex	9.00	0	5.38	40.22	1.60	82.22
Co^{+2} complex	9.00	0	3.90	56.67	0	100
Cu^{+2} complex	9.00	0	3.15	65.00	0	100
Zn^{+2} complex	9.00	0	6.65	26.11	2.85	68.33
Ag^{+} complex	9.00	0	5.78	35.78	1.24	86.22
L.S.D	NS	NS	1.56	7.78	1.02	6.81

*Each number represents three replicates

Presented data in Table 4 reveals that tested *P. aphanidermatum* fungus was also affected with all compounds. Again, Cu^{+2} and Co^{+2} complexes were the most effective compounds, showing 100% growth inhibition, followed by Mn+2 where growth inhibition of pathogen reached 93.67% at 20 ppm. The ligand was the least effective one, showing 30.33 and 63.56% growth inhibition at 10 ppm and 20 ppm, respectively. Generally, the inhibitory effect of compounds increased as the concentration increased from 10 ppm to 20 ppm, showing more than 50% growth inhibition for the fungus pathogen.

Table 4. Effect of different concentrations of the compounds on the growth of *Pythium aphanidermatum*.

Compounds	Growth of *P. aphanidermatum*					
	0 ppm		10 ppm		20 ppm	
	Growth rate cm	% inhibition	Growth rate cm	% inhibition	Growth rate cm	% inhibition
Ligand	*9.00	0	6.27	30.33	3.28	63.56
Mn^{+2} complex	9.00	0	3.62	59.78	0.57	93.67
Co^{+2} complex	9.00	0	1.45	83.89	0	100
Cu^{+2} complex	9.00	0	1.11	87.67	0	100
Zn^{+2} complex	9.00	0	5.83	35.22	3.37	68.30
Ag^{+} complex	9.00	0	2.84	68.44	0	100
L.S.D	NS	NS	1.17	13.81	0.64	5.06

*Each number represents three replicates.

These results are consistent with [23] reported that the tested concentrations of 12.5, 25, 50 and 75 ppm of six fungicides of Techigaren 30%, Monceren 25%, Hymexate 30.0%, Moncut 25%, Topsin M70% and Aracur 72.7% led to significantly inhibition of mycelial growth of *R. solani* and *F. solani* isolates in Potato dextrose agar (PDA) medium. Godswill and co-workers [24] were determined the antifungal of two synthetic fungicides (SF1) and (SF2), at different doses against *F. oxysporum* and *P. microspora*. One of the tested compounds (SF1) showed 100% inhibition against both fungi, while

SF2 was less effective at all doses. Three pesticides Benomyl (fungicide) and Karate (insecticide) Galex (herbicide) were lead to significant inhibition, and reduction of mycelial weights of growth of some fungi, *Aspergillus flavus*, *Fusarium oxysporum* and *Fusarium monilliforme* at 0, 100, 200, 400 and 500 mg L -1 rate [25]. [26] studied several fungicides including carbindazim (BCM) for inhibiting the growth of *S. sclerotiorum* fungus, where the percentage of inhibition reached 100% when adding different concentrations of the fungicide from 50, 100, 200, 500 and1000 ppm. Youssef et al [27] reported ability of some chemical to reduce the mycelium growth of *S. sclerotiorum*, the colony diameter of fungus inhibited by 100% at 8 days after being treated with 0.1 % SA and prevented formation of new sclerotia until 21.

4. Conclusion

The ligand 1,6-bis(1-benzimidazolyl) hexane and its respective metal complexes Mn(II), Co(II), Cu(II), Zn(II) and Ag(I) are synthesized and characterized. Depending on the results obtained in this work and the literature, a polymeric structure was proposed for the synthesized complexes. Furthermore, the ligand and its complexes are tested against some soil-borne fungi namely; *Rhizoctonia solani*, *Fusarium oxysporum*, *Fusarium solani* and *Pythium aphanidermatum*. In general, all the tested compounds showed an activity against the studied pathogens. Significantly, Cu^{+2}, Co^{+2} and Mn^{+2} complexes were the most effective on mycelial growth of soil born fungi pathogen isolates. The effective compounds acts as anti-fungal agents and inhibits their growth possibly because they negatively affect the metabolic process of these pathogenic fungi.

5. References

[1] Wilson C and Tisdell C 2001 Why farmers continue to use pesticides despite environmental, health and sustainability costs *Ecol. Economics* **39** 449.
[2] Brown TM 1996 *ACS Symposium Series* American Chemical Society Washington 1.
[3] Köller, W and Scheinpflug H 1987 Fungal resistance to sterol biosynthesis inhibitors: A new challenge *Plant Dis*. **71** 1066.
[4] Yang L, Xie JT, Jiang DH, Fu YP, Li GQ 2008 Antifungal substances produced by Penicillium oxalicum strain PY-1-potential antibiotics against plant pathogenic fungi *World J. Microb. Biot.* **24** 909.
[5] Hahn M 2014 The rising threat of fungicide resistance in plant pathogenic fungi: Botrytis as a case study *J Chem Biol*. **7** 133.
[6] Sundberg RJ and Martin RB 1974 Interactions of histidine and other imidazole derivatives with transition metal ions in chemical and biological systems *Chem. Rev*. **74** 471.
[7] Mansour AM, El Bakry EM and Abdel-Ghani NT 2016 Co (II), Ni (II) and Cu (II) complexes of methyl-5-(Phenylthio) benzimidazole-2-carbamate: Molecular structures, spectral and DFT calculations *J. Mol. Struct*. **1111** 100.
[8] Haque RA, Salman AW, Budagumpi S, Abdullah AAA and Abdul Majid AMS 2013 Sterically tuned Ag(I)- and Pd(II)-N-heterocyclic carbene complexes of imidazol-2-ylidenes: synthesis, crystal structures, and in vitro antibacterial and anticancer studies *Metallomics* **5** 760.
[9] Sarı Y, Akkoç S, Gök Y, Sifniotis V, Özdemir İ, Günal S and Kayser V 2016 Benzimidazolium-based novel silver N-heterocyclic carbene complexes: synthesis, characterisation and in vitro antimicrobial activity *J. Enzyme Inhib. Med. Chem*. **31** 1527.
[10] Haque RA, Ghdhayeb MZ, Budagumpi S, Salman AW, Ahmed MBK and Abdul Majid AMS 2013 AMSA: Non-symmetrically substituted N-heterocyclic carbene-Ag(I) complexes of benzimidazol-2-ylidenes: Synthesis, crystal structures, anticancer activity and transmetallation studies *Inorg. Chim. Acta* **394** 519.

[11] McCann M, Curran R, Ben-Shoshan M, McKee V, Devereux M, Kavanagh K and Kellett A 2013 Silver(i) complexes of 9-anthracenecarboxylic acid and imidazoles: synthesis, structure and antimicrobial activity *Polyhedron* **56** 180.
[12] McGinley J, McCann M, Ni K, Tallon T, Kavanagh K, Devereux M, Ma X and McKee V 2013 Imidazole Schiff base ligands: Synthesis, coordination complexes and biological activities *Polyhedron* **55** 169.
[13] Haque RA, Salman AW, Budagumpi S, Abdullah AAA, Al-Mudaris ZAH and Abdul Majid AMS (2013 Silver(I)-N-heterocyclic carbene complexes of bis-imidazol-2-ylidenes having different aromatic-spacers: synthesis, crystal structure, and *in vitro* antimicrobial and anticancer studies *App. Organomet. Chem*. **27** 465.
[14] Salman AW, Rehman GU, Abdullah N, Budagumpi S, Endud S, Abdullah HH, Wong WY 2014 Sterically modulated palladium(II)-N-heterocyclic carbene complexes for the catalytic oxidation of olefins: Synthesis, crystal structure, characterization and DFT studies *Polyhedron* **81** 499.
[15] Yılmaz U, Küçükbay H, Deniz S and Şireci N 2013 Synthesis, characterization and microwave-promoted catalytic activity of novel N-phenylbenzimidazolium salts in Heck-Mizoroki and Suzuki-Miyaura cross-coupling reactions under mild conditions *Molecules* **18** 2501.
[16] Salman AW, Rehman GU, Abdullah N, Budagumpi S, Endud S and Abdullah HH (2015 Synthesis, characterization, density function theory studies and catalytic performances of palladium(II)-N-heterocyclic carbine complexes derived from benzimidazol-2-ylidenes *Inorg. Chim. Acta* **438** 14.
[17] Fernández-Ortuño D and Torés JA, Vicente A. and Pérez-García A. 2010 *The QoI Fungicides, the Rise and Fall of a Successful Class of Agricultural Fungicides* 203.
[18] Al-Saadi ZN, Salman AW, Arkawazi HD and Hardie, M.J 2019 Synthesis, characterization and antibacterial activity of some transition metal complexes derived from the ligand N-Benzylimidazole against methicillin-resistant *Int. J. Drug Delivery Technol*. **9** 666.
[19] Salman, AW, Al-Mayahie SM, Shallal ZS, Arkawazi HD, Al-Obaidi ZHK and Hardie MJ 2018 *J. Glob. Pharm Tech*. **10** 305.
[20] Kücükbay H, Mumcu A, Tekin S and Sandal S 2016 Synthesis and evaluation of novel N,N'N,N'*N*,*N*′-disubstituted benzimidazolium bromides salts as antitumor agents *Turk. J. Chem*. **40** 393.
[21] Küçükbay H, Yilmaz Ü, Akkurt M and Büyükgüngör O 2015 Synthesis and characterization of substituted benzimidazole Co(II), Fe(II), and Zn(II) complexes and structural characterization of dichlorobis{1-[2-(1-piperidinyl)ethyl]-1H-benzimidazole-KN3} zinc(II) *Turk. J. Chem*. **39** 108.
[22] Apohan E, Yilmaz U, Yilmaz O, Serindag A, Küçükbay H, Yesilada O and Baran Y 2016 Synthesis, cytotoxic and antimicrobial activities of novel cobalt and zinc complexes of benzimidazole derivatives *J Organomet. Chem.* **828** 52.
[23] Haggag, KHE and El-Gamal NG 2012 Isolation and identification of fungi associated with tomato root at Misurata region and testing their pathogenicity *Nat. Sci*.**10** 16.
[24] Godswill NN, Bernadette-Sorele NT, Ulrich DDC and Aoudou Y 2020 *J. Agric. Studies* **8** 111.
[25] Dare M D and Fawole O 2009 *In vitro* effects of some pesticides on pathogenic fungi associated with legumes *Austr. J. Crop Sci*. **3** 137.
[26] Rakesh, Rathi AS and Kumar A 2016 Singh Evaluation of fungicides for the control of Sclerotinia stem rot of Indian mustard caused by *Sclerotinia sclerotiorum* (Lib.) de Bary *J. Appl.Nat. Sci. JANS* **8** 441.
[27] Youssef SAM, Ezzat SM and El-Ghareeb NR 2015 Ecofriendly Strategy for Inhibition of Sclerotia formation of *Sclerotinia Sclerotiorum* (Lib.) De Bary in vitro. *Int. J. Sci. Res. Agric. Sci.* **2** 100.

Laboratory evaluation of two isolates of *Meterhizium anisopliae* and *Beauvaria bassiana* to control infesting by *Trogoderma granarium* (Coleoptera: Dermestidae) larvae

Laboratory evaluation of two isolates of *Meterhizium anisopliae* and *Beauvaria bassiana* to control infesting by *Trogoderma granarium* (Coleoptera: Dermestidae) larvae

Nawal S. Mehdi[1] and Aymen W. Al-Fadili[2]

[1]Department of Biology, College of Education for Pure Science (Ibn Al-Haitham), University of Baghdad, Baghdad, Iraq.
[2]Mesopotamia State Company for Seeds, Ministry of Agriculture.

*E-mail: nawalsadiq59@yahoo.com

Abstract. *Trogoderma granarium* Everts (Khapra beetle) is a serious pest of stored barley and wheat worldwide. The current research evaluates the efficacy of local isolates of *Meterhizium anisopliae* and *Beauvaria bassiana* compared to an imported isolates when khapra larvae sprayed with concentration of later isolates under laboratory condition, mortalities were recorded for more than two weeks after treatment. Results demonstrated that the larvae were more susceptible to the local isolates of the two fungi than the imported isolates. Cumulative mortalities were 86.67 and 50 when larvae sprayed with 10^9 conidia/ml of local and imported isolates of *M. anisopliae* respectively, and 86.67 and 66.67 when larvae sprayed with 10^9 conidia/ml of laocal and imported isolates of *B. bassiana* respectively after two weeks. The findings of the current study clearly showed that the local isolates caused higher mortalities than the imported one so they may be used as a good candidates for pragmas of integrated pest management of stored grain pests.

Keywords. *Meterhizium anisopliae*, *Beauvaria bassiana*, *Trogoderma granarium*, Larvae, Barely.

1. Introduction

Khapra beetle, *Trogoderma granarium* Evert (Coleoptera, Dermastidae) is a serious pest of stored grain product especially under warm dry condition, it is considered to be one of the worst invasive pests worldwide [1]. Weight losses and damage by sever infesting can be up to 30% and in extreme cases 73% [2]. Grains that heavily infested become unpalatable and unmarketable by consumers, high infestation by khapra beetles reduces content of fats, sugar protein and carbohydrates, of the grains along with increase of level of uric acid [3]. Moreover this pest was responsible for health problem for man like asthma and dermatitis caused by its skin [4]. Khapra beetle undergoes five larval instars and the development period for these instars may range between 30-50 days depending on relative humidity and temperature of storage conditions, but under un adversed conditions these larvae may enter into diapause where it may molt but does not feed while keep inactive, and larval period prolonged up to four years, therefore the infested food products are vulnerable to their attack, the

diapaused larvae are tolerant to common insecticides and other control methods that are very effective against other pests of stored grains [5, 6]. Fumigations the stored products by methyl bromide was the most promising way against khapra beetle since it acts as suffocating against. Killing the insects by blocking its breathing. Recent studies reveled that methyl bromide was a major ozone depleting agent there for many countries minimize its usage under strong controlled conditions [7]. Previous concerns led to look out for other alternate ways to control khapra beetles such as biological control methods [8]. Controlling khapra beetles by using predators such as *Xylocoris flavipes* (Hemiptera: Anthocoridae) had been studies [9]. Potential of the larval parasitoid *Anisopteromalus calandra* (Hymenoptera: Pteromalidae) and *Laelius pecdatus* (Hymenoptera: Bethylidae) to control larvae of khapra beetles in cereal had been studied [10, 11]. Entomopathogenic agents such as bacteria and fungi investigated to control this pest, [12] reported that the *Bacillus thuringiensis* was very effective against larvae of khpra beetles. Entomopathogenic fungi were applied and used to control many pests, one of them khapra, since these fungi infects the insect topically (by contact) then it penetrates its cuticle and kills it by the toxins and enzymes that they secret inside the insects body, so these fungi considered to be a good alternatives to control these pests [13]. Moreover entomopathogenic fungi are specific to the hosts that they infected, therefore they have no effect on mammalian animals and fishs since it is a natural enemies of insects [14]. Many species of entomopathogenic fungi such as *Meterhizium anisopliae*, *Beauvaria bassania* and *Isaria farinosa* were known to be good natural enemies of many species of stored grain pests, there for these fungi seem to be the most promising and native strategy to control these pests, especially they are available and registered for using and commercially produced. It is safe to treat the grains directly without any decreasing of its quality and marketability [15]. The aim of this study is to examine the efficacy of *M. anisopliae* and *B. bassiana* (Two isolates of each one introduced while the other local) against the larvae of *T. granarium* under lab conditions.

2. Materials and Methods

2.1. Rearing of rest insects

Infested barely with *T. granarium* (one Kg) was brought from the local market to the laboratory of entomology in Department of Biology, College of Education for Pure Science (Ibn-Al-Haitham) at September 2018, fifty adult beetles were collected than added to a sterilized plastic jar (1L) containing 500 gm of sterilized barely, two replicates were done, Jars kept in an incubator at 30±5C° and 50±5% relative humidity. The emerged second-third instar larvae of *T. granarium* was used for the later experiments, adults beetles were identified by Iraqi natural history museum, University of Baghdad [16].

2.2. Entomopathogenic isolates and preparation of fungal suspensions

Two isolates of each *M. anisopliae* and *B. bassiana* were examined against *T. granarium* larvae each of fungus were isolated from soil of Baghdad area and marked as a local isolate, so we have two local isolates one is the a local isolate of *B. bassiana* and the other is a local isolate of *M. anisopliae*. The other fungus isolate was marked as imported by Agricultural research center-Ministry of Science and Technology so we have two imported isolates, one of them *B. bassiana* imported isolates and the other *M. anisopliae* imported isolate. All isolates (The four isolates) were cultivated and suspension concentrations (10^7, 10^8, 10^9 conidia/ml) were prepared as in [16].

2.3. Bioassays

Ten larvae of *T. granarium* were placed in a petri dish, then sprayed topically by hand sprayer with two ml of each fungal suspension sprayed, larvae transferred to another petri dish containing 10 gm of

sterile barely grins. Three replicates of each of the three concentration, for the four fungal isolates were done for control treatment larvae were spread with sterile distilled water with tween-20 (0.01%). Experimental petri dishes kept in an incubator at 28±2C° and 55% relative humidity [17]. Larvae were monitored every 24 hr to record number of dead insects, and photographed them by camera fitted with a simple microscope (Dissecting). Cumulative mortality were calculated.

2.4. Statistical analysis

Percentages of mortalities were recorded and corrected according to Abott's equation [18]. Subsequently SAS was used to analyze the data which show the sensitivity of the concentrations of the fungal isolates in larvae mortalities [19]. The significant differences were compared between mean and least significant differences.

3. Results and Discussion

Insects infected by many kinds of pathogens, which cause a deadly disease fungi are one of these pathogens, infections may be by a direct contact, after the conidia/spores land on the body wall of the insects they will start to germinate and penetrate forcely through the cuticle into the insects body which kill the insects, in case of the conditions are suitable the fungus start to sporulate and make more spores which continue the infection, finally caused a slowly death to the insects. These fungi can be used as a biological control agents by causing natural epizooties diseases and reduced insects populations [20]. Laboratory assessments of isolates of *M. anisopliae* and *B. bassian* (Imported and local) against *T. granarium* larvae were done under laboratory conditions to decide whether these isolates are good candidates for biological control of *T. grananrium* larvae. Many researches had been done by the local isolates of *M. anisopliae* and *B. bassiana* and proved to be effective against many species of insects [16, 21, 22, 23] . Our study proved that the local isolate of *M. anisopliae* was very effective against larvae of khapra beetles. Table (1) shows that 109 and 108 conidia/ml led to cumulative mortality by 86.67%, and this isolate was more effective than the imported ones which have the concentrations 10^9 and 10^8 conidia/ml led to cumulative mortality by 50 and 26.67% respectively. Figure (1) shows that mortalities depend on time, insects death started after about four days of treatment since the fungus takes time to penetrate through the body wall of the larvae and invade the cavities of its body, producing hyphal mass and many kinds of toxins and secondary metabolites such as Destruxin, conidial growth demonstrated that the larvae died by the fungus which appeared greenish (Figure 2).

Table 1. Cumulative mortalities of *Trogoderma granarium* larvae sprayed by concentrations of *Meterhizium anisopliae* (Imported and local isolates).

Concentration Conidia/ml	Cumulative mortalities %	
	Imported isolate Mean%±S.E	Local isolate Mean%±S.E
Control	3.33±3.33	3.33±3.33
10^7	10.00±0.00	56.67±8.81
10^8	26.67±12.02	86.67±6.67
10^9	50.00±5.77	86.67±3.33

*S.E.: Standard error.

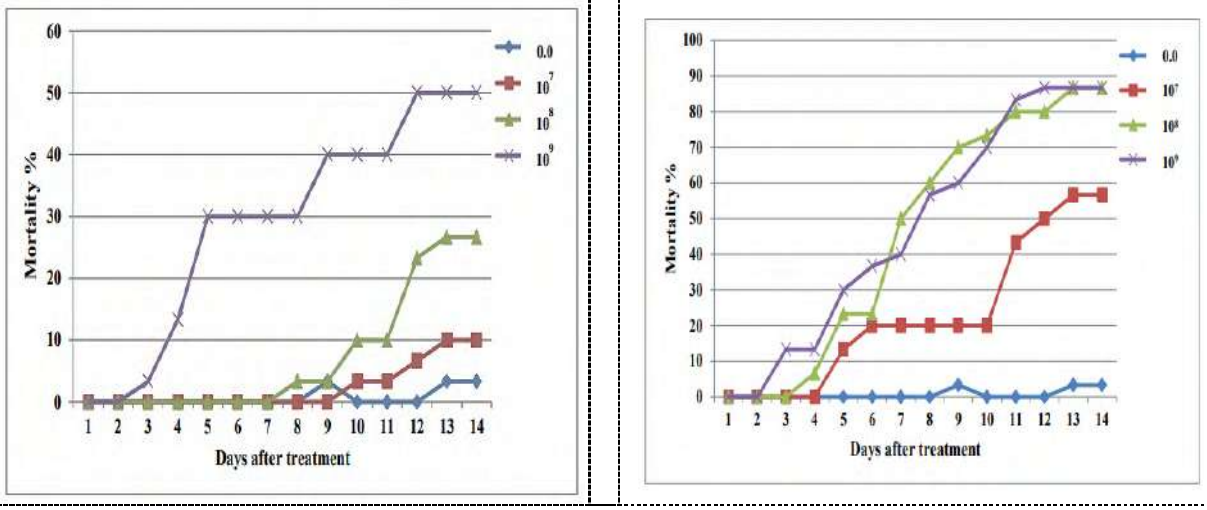

Figure 1. Mortality percentage mean of *Trogoderma granarium* sprayed by *Meterhizium anisopliae* days after treatment (A: Imported isolate ; B: Local isolate).

Figure 2. Postmortal mycelia and fungus growth on *Trogoderma granarium* infected by *Meterhizium anisopliae* (A: Imported isolate ; B: Local isolate).

Since *M. anisopliae* had known to cause the green muscardin disease. The current finding of our study confirm with [23] who proved that the some local isolate of *M. anisopliae* was effective against *Chrysomya megacaphalo* larvae. Similar result was reported by [16] when they revealed that the same local isolate of *M. abisopliae* was very effective against Tribolium castanum adult and 10^9 conidia/ml caused 80% cumulative mortality after about two weeks and they revealed that the local isolate was more effective than the imported isolate. Another research had proved that the local isolates very effective against pest of storage grain, [24] proved that Iranian isolates of *M. anisopliae* were effective against *T. castanum* and *Oryzaephilus surinamensis* when they evaluated these isolates through bioassays and found that 8.5×107 conidia/ml of one of these isolates led to 77.8% mortality percent of *O. surnamensis* and 89.9% mortality percent of *T. castanum* after ten days. The final finding of our study about *M. anisopliae* is that the local isolate was more effective against larvae of *T. granarium* than the imported isolate so it may use as a promising microbial against to control this pest. *B. bassiana* was known to be one of the most effective entomopathogenic fungi since it has high ability to infect and kill as host of many different insect species, our finding listed in Table (2) shows that 10^9 conidia/ml of the imported and local isolates led to 66.67 and 96.67 respectively as accumulative mortality percent when *T. granarium* larvae were sprayed with, after about two weeks (Figure 3), these results refer that the local isolate was more effective than the imported isolate against the larvae.

Dead larvae appeared distorted and growth of fungal hyphae spinning above then and their bodies were covered with white fungal growth (Figure 4).

Table 2. Cumulative mortalities of *Trogoderma granarium* larvae sprayed by concentrations of *Beauvaria bassiana* (Imported and local isolates).

Concentration Conidia/ml	Cumulative mortalities %	
	Imported isolate Mean%±S.E	Local isolate Mean%±S.E
Control	10.00±0.00	10.00±0.00
10^7	46.67±12.02	46.67±6.67
10^8	60.00±0.00	50.00±15.28
10^9	66.67±15.28	86.67±6.67

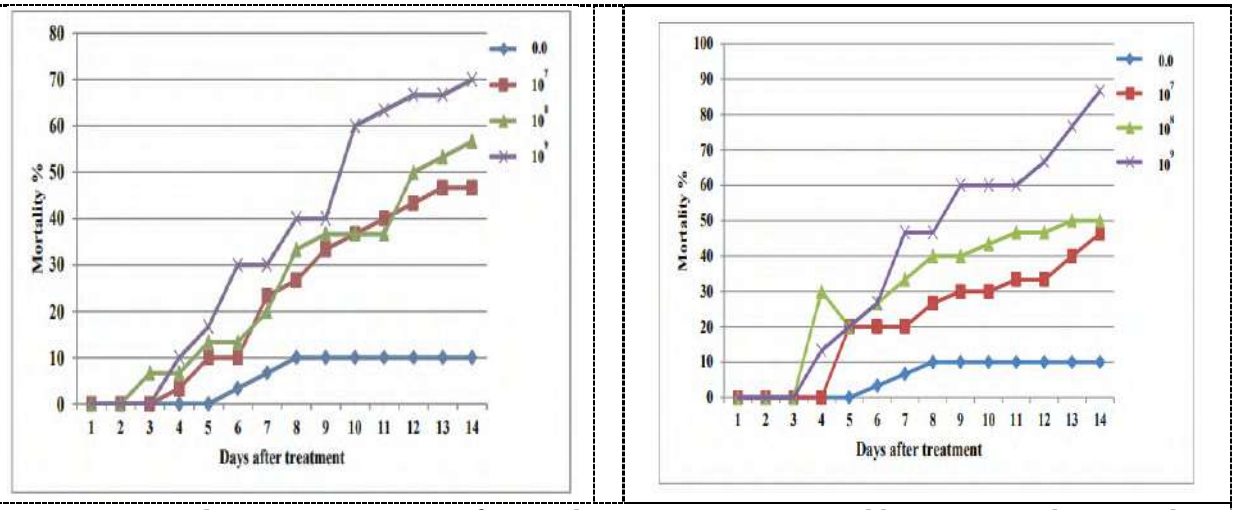

Figure 3. Mortality percentage mean of *Trogoderma granarium* sprayed by *Beauvaria bassiana* days after treatment (A: Imported isolate ; B: Local isolate).

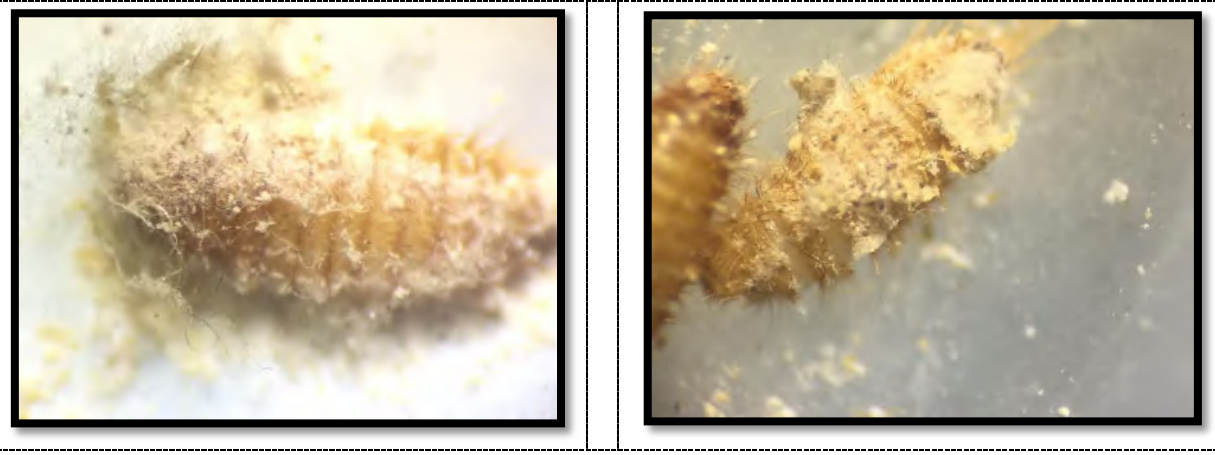

Figure 4. Postmortal mycelia and fungus growth on *Trogoderma granarium* infected by *Beauvaria bassiana* (A: Imported isolate ; B: Local isolarte).

These results were in a good agreement with those of [21, 22]. Also these results agreed with [25] who revealed that the treatment of larvae of *Agrotis ipsilon* with a concentration of *B. bassiana* (2×10^8 conidia/ml) led to mortalities after one week and hyphal fungi emergence from dead larval bodies, after 10-13 days. Mortality rates of the treated larvae were attributed to the growth of the fungus inside

the insect body which was accompanied by secretion of toxin and enzymes that finally led to destruction and decaying the host body, the most effective enzyme of the fungus were protease and chitinase which analyzed the insects body and allowed the fungus to enter inside the larval body, then the fungus started to grow inside the insects hemocole. Some toxins such as Beauverien was secreted by the fungus, followed by a growth of hyphae outside the dead insect body that carry spores/conidia of the fungus, which considered to be source of infection [26]. The present findings are in line with [27] who revealed that local isolates of entomopathogenic fungi *B. bassiana* and *M. anisopliae* which recovered from samples of soil fields (Crops, Orchards and Vegetables) were very effective against *Rhynchophorus ferrugineus*, therefore these isolates would be the most promising biocontrol agent against *R. ferrugineus* which is a serious date palm orchard pest. Similar results recorded by [28] who assessed five Iraqi isolates of entomopathogenic fungi including *B. bassiana* against *T. granarium* larvae, found that the younger larval instars were more susceptible to the fungus than the last larval instar and adult, and mortalities percentages were recorded after 10 days post treatment, these results demonstrate that these isolates (*B. bassiana*) have a good potentials biological control agent against larvae of *T. granarium*. Further investigations are required to determine the virulence of the local isolates which may be play an important role for the safer management of pests that attack stored grains since it is environment friendly agents instead of chemical insecticides.

4. Conclusion

This study shows higher susceptibility of *T. granarium* larvae to the tested concentration of the local isolates of *M. anisopliae* and *B. bassiana* than the imported isolates. Thus they can be used as promoting biocontrol insecticides agents in terms of practical application that verified from similar studies

5. References

[1] Lowe S, Browne M, Boudjelas S and Depoorter M 2000 *100 of the world's worst invasive alien species: a selection from the global invasive species* specialist Group Hollands Printing Ltd 1.
[2] Annonymous 2005 *Plant health Australia grain industry bio-security* plan 1.
[3] Jood S and Kapoor AC 1993 Protein uric acid contents of cereal grains as affected by insect infestation *Plant Food Human Nut.* **43** 45.
[4] Parashar MP 2006 *Post-harvest of black gram* Gov. India, Ministry of Agric. Dept. Agric. & Coop. Directorate of Marketing and inspection Nagpur-440001.
[5] Nair KSS and Desai AK 1972 Some new findings on factors inducing diapause in *Trogoderma granarium* Everts (Coleoptera: Dermastidae) *J. Stored Prod. Res*. **8** 27.
[6] Athanassiou CG, Phillips TW and Wakil W 2019 Biology and control of the khapra beetle, Trogoderma granarium a major quarantine threat to global food security *Ann. Rev. Entomol.* **64** 131.
[7] MBTOC 2010 *United nations environment program (UNEP) methyl bromide technical options committee (MBTOC) report of the methle bromide technical options committee assessment. United nations environment program* Nairobi, Kenya.
[8] Traynier RMM, Schumacher RK and Lau DM 1994 Oviposition site selection by *Tineola bisselliella, tinea* spp. (Lepidopetra: Tineidae) and *Anthrenus flavipes* (Coleopetra: Dermastidae) *J. Stored. Prod. Res*. **30** 321.
[9] Rahman MM, Islam W and Ahmad KN 2009 Functional response of the predator Xylocoris flavipes to three stored product insect pests *Int. J. Agric. Biol.* **11** 316.
[10] Kapil RP and Chaudhary JP 1973 Record of nine new hymenpterous parasites for khapra beetle *Trogoderma granarium* Everts. *Indian J. Entomol*. **35** 353.

[11] Al-Kirish A, Gabbar A, Reichmuth G and Bochow H 1997 Potential of the larval parasitoid Lalius pedatus for the control of the khapra beetle *Trogoderma granarium* Everts in grain *Mitt. Dtch. Ges. Allg. Angrew. Entomol*. **111** 367.
[12] Ahmedani MS, Shaheen N, Ahmedani MY and Aslam M 2007 Status of phosphine resistance in khapra beetle *Trogoderma granarium* (Everts) strains collected from remote village of Rowalpindi district *Pak. Entomol*. **29** 95.
[13] Monlar I, Gibson DM and Krasnoff SB 2010 Secondary metabolites from entomopathogenic hycrealean fungi *Nat. Prod. Rep.* **27** 1241.
[14] Jaronski, ST 2010 Ecological factors in the inundative use of fungal entomopathogens *Biocontrology* **55** 159.
[15] Khashaveh A, Ghosta Y, Saforalizadeh MH and Ziace M 2011 The use of entomopathogensic fungus *Beauvaria bassiana* (Bals.) Vuill. In assays with storage grain beetles *J. Agr. Sci. Tech*. **13** 35.
[16] Mehdi NS and Al-Fadili AW 2020 Laboratory assessment of *Beauvaria bassiana* and *Meterhizium anisopliae* isolates against Rust-Red flour beetle *Tribolium castanum* (Herbst) (Coleoptera: Tenebrionidae) *Ann. Trop. Med. Public Health* (In press).
[17] Kavallieratos NG, Athanassrou CG, Aountala MM and Kontodimas DC 2014 Evaluation of the entomopathogenic fungi *Beauvaria bassiana, Meterhizium anisoplia* and *Isaria fumosorosea* for control of *Sitophilus oryzaei J. Food.* **77** 87.
[18] Abott WS 1925 A method of computing the effectiveness of an insecticide *J. Econ. Entomol*. **18** 265.
[19] SAS 2012 *SAS/STAT users guide for personal computer release 3.12 SAS institute*. Inc. Cary. NC. USA.
[20] Safavi SA, Kharrazi A, Rosoulian GR and Bandour AR 2010 Virulence of some isolates of entomopahtogenic fungus *Beauvaria bassiana* on *Ostrinia nubilalis* (Lepidoptera: Pyralidae) Larvae *J. Agricul. Sci. Technol*. **12** 13.
[21] Al-Fadili AW 2015 *Evaluation the efficiency of some isolated entomopathogenic fungi from soil of citrus orchard infested with fruit fly Ceratilis capitata (Wiedemann) (Diptera: Tephretidae)* MSc. thesis, College of Agriculture, University of Tikrit. (In Arabic).
[22] Mehdi NS 20015 Efficacy of *Beauvaria bassiana* (Bals) Vuil against Chrysomya magecephala (Fabricius) Larvae (Diptera: Calliphoridae) via contact and ingestion *Int. J. Sci. Res*. **7** 1202.
[23] Al-Samaraee AA 2017 *Integration in controlling of big headed secondary myiasis fly Chysomya megacephala (Fabrisius, 1794) (Diptera: Calliphoridae) using two different isolates of the fungus Meterhizium anisopliae (Metschikoff) Sorokin in Baghdad city, and botanical insecticide supernemic* PhD thesis, College of Education for Pure Science (Ibn-Al-Hathiam) Baghdad University., 173 (In Arabic).
[24] Khashavch A and Chelav HS 2013 Laboratory bioassay for Iranian isolates of entomopathogenic fungus *Meterhizium anisopliae* (Metsch.) Sorokin (Ascomycota: Hypocrea) against two species of storage pest *Agric. Conspec. Sci*. **78** 35.
[25] Gabarty A, Salem HM, Foudab MA, Abasb AA and Ibrahim AA 2014 Pathogenecity induced by the entomopthogenic fungi *Beauvaria bassiana* and *Meterhizium anisopliae* in *Agrotis ipsilon* (Hufn.) *J. Red. Res and App. Sci*. **7** 95.
[26] Pendland JC, Hung SY and Boucias DG 1993 Evasion of host defense by in vivo-produced protoplast-like cells of the insect mycopathogen *Beauvaria bassiana J. Bactriol*. **175** 5962.
[27] Yasin M, Wakil W, Ghazanfar MU, Qayyum MA, Tahir M and Bedford GO 2017 Virulence of entomopathogenic fungi *Beauvaria bassiana* and *Meterhizium anisoplia* against red palm weevil, *Rhynchophorus ferrugineus* (Olivier) *Entomomogical. Res*. **2** 1.
[28] Mohammed AA, Khadim JH and Hasan AMH 2019 Laboratory evaluation of entomopathogenic fungi for control of khapra beetle (Coleoptera: Dermastidae) and their effect on beetles fecundity and longevity *J. Agric. Urban Entomol*. **35** 1.

Diversity of Mollusca in some sites of Euphrates River

Diversity of Mollusca in some sites of Euphrates River

Feryal Ameen Merza[1*]

[1]Department of Biology, Faculty of Sciences, Kufa University, Iraq.

*E-mail: firyala.hussein@uokufa.edu.iq

Abstract. This investigation of molluscs was carried out at some sites on the river of the Euphrates. Samples of molluscs were collected monthly from June 2019 to November 2019. Fourteen species were investigated which belonged to two Classes: Bivalvia (three species) and Gastropoda (eleven species). The species *Corbicula fluminalis*, *Pisidium dubium*, *Melanoides tuberculata*, *Physa acuta*, *Gyraulus convexiusculus*, and *Gyraulus intermixtus* seemed in all sites. According to the index of Shanon-Weiner, species diversity ranged from 0.5 to 2.5 bits/individual. Index of Jaccard's similarity showed that the highest similarity was recorded between site one and site two with 60 %.

Keywords. Molluscs, Taxa, River, Euphrates.

1. Introduction

Molluscs is variable and distributed phylum in the kingdom of the animal. Their members are the heights in animals phyla behind the Arthropoda, about 85,000 existing species are renowned [1]. Fossil species are appraised between 60,000 and 100,000 species [2]. The percentage of undescribed species is great, although many taxa endure languidly studied [3]. Mollusca are the biggest number of creatures of marine phyla, involving around 23% of total marine creatures. Various members likewise live in non-salty waters. Some molluscs are utilized like bioindicators to observe the health of locations in waters, as they are characteristic of the setting where they are sampled or place because they are sessile. [4]. Molluscs contains only two classes viva in freshwater, while other classes viva in salty waters. There are several surveys concerning molluscs in Iraq, as [5] studied two species in Shatt Al-Arab. [6] investigated 20 species for the first time in Gharaf River, while [7] identified 10 taxa in Kufa river. The local studies are so significant to investigating mollusca in Iraq.

2. Materials and Methods

Three sites in the river of Euphrates were selected: Site one established (after passing the river along Hindiya barring city), site two sited (after passing the river sideways city of Hindiya), and site three sited around 2500 m away from site two. Monthly, three replicates were handling from every site from June to November 2019 via Ekman Dredge, and they were conserved in four percent of Formalin, and then calculated and recognized via using a compound microscope. The molluscs member were identified via the keys of classification [8, 9, 10, 11]. Shanon-Weiner index and Jaccard equation were

calculated as described in [12, 13] respectively, while calculation of relative abundance index was depending on [14].

3. Results and Discussion

Table (1) displays the taxa of molluscs identified throughout the period. Fifteen taxa were recognized in this investigation. They were categorized into two classes: Bivalvia which contained three families and four taxa, and Gastropoda which contained ten families and eleven taxa. The number of taxa in class (Gastropoda) was higher than in taxa in (Bivalvia), this agrees with the earlier studies as [6, 7]. Among taxa, *Corbicula fluminalis*, *Pisidium dubium*, *Melanoides tuberculata*, *Physa acuta*, *Gyraulus convexiusculus*, and *Gyraulus intermixtus* seemed in all sites. *Melanoides tuberculata* showed abundant species, whereas other species were frequent or rare species. Local investigations displayed that the species of molluscs select moderate waters in its running with a content of organic supplies [15]. The quantity of taxa designated in this research was low. This might be conferred to the inadequate investigated parts or the dissimilarities in the nature in the investigated ecosystems. There are several Iraqi investigations which recorded various numbers of taxa due to differences in investigated aquatic areas. Various strategies of the gathering of taxa and the differences in the taxonomic aspects of connecting with non-diagnosis of some taxonomic levels [16, 17]. [18] identified 17 Mollusca species which live in the Shatt Al-Arab. [19] recorded 13 mollusca in their investigation in Lake of Al-Habbaniyah. Whereas, [7] identified 10 taxa in the river of Al-Kufa. The densities of mollusca ranged between (100-2340) Ind./ m2 in July and September, consecutively (Figure 1). It was exhibited that there was a decrease in densities through summer. Whereas it was exhibited a rise in the mollusca densities through autumn (Table2). The source for that might be the increases of temperate temperature and suitability of the environmental conditions which might be appropriate for its eggs to hatch; likewise, low water levels, current water through autumn might be cause change in densities [20, 21, 22]. Index of Shanon-Weiner presented site one in July was the highest diversity, whereas site one in August was the lowest diversity (Figures 2). If the values of Index of Shannon-Weiner >3 bit/Ind. that designates clean waters and biodiversity was excessive; if the value was <1 bit/Ind appoints contaminated environment that causes decline of some taxa [23]. Index of Jaccared similarity fluctuated between 60% in sites one and two; 42.86% in sites one and three. There were noteworthy numbers of taxa shared among the sites possibly, because of these taxa have the similar source of original environment. In addition to their ability to familiarize in their environment, this reveals the relative conjunction of qualitative conformation of molluscs in the sites (Figures 3).

Table 1. Relative abundant at the study area.

Taxa	Site1	Site2	Site3
Phylum: Mollusca			
Class1: Bivalvia			
Family:Corbiculidae			
***Corbicula* sp.**	=	=	*
Corbicula fluminalis	*	*	*
Family: Sphaeriidae			
Pisidium dubium	*	*	*
Family: Dreisseniidae			
Dreissena polymorpha	=	=	*
Class2: Gastropoda			
Family: Bulimidae			
Amnicola limosa	*	=	=
Family: Thiaridae			
Melanoides tuberculata	***	**	**
Family: Vivaparidae			

Taxa	Site1	Site2	Site3
Viviparus intertextus	=	=	*
Family: Ampullariidae			
Family: Naticidae			
Polynices ampla	=	*	=
Family: Neritidae			
Neritina schlaeflii	=	=	*
Family: Lymnaeidae			
Lymnaea abrussa	=	=	*
Lymnaea palustris	*	=	=
Family: Physidae			
Physa acuta	*	**	**
Family: Planorbidae			
Gyraulus convexiusculus	*	*	*
Gyraulus intermixtus	*	*	*
Family: Pyramidellidae			
Odostomia laevis	*	=	=

(***) Abundant species: 40 - 70 %, (**)Frequent species:10 - 40 %, (*) Rare species: 10 < %.

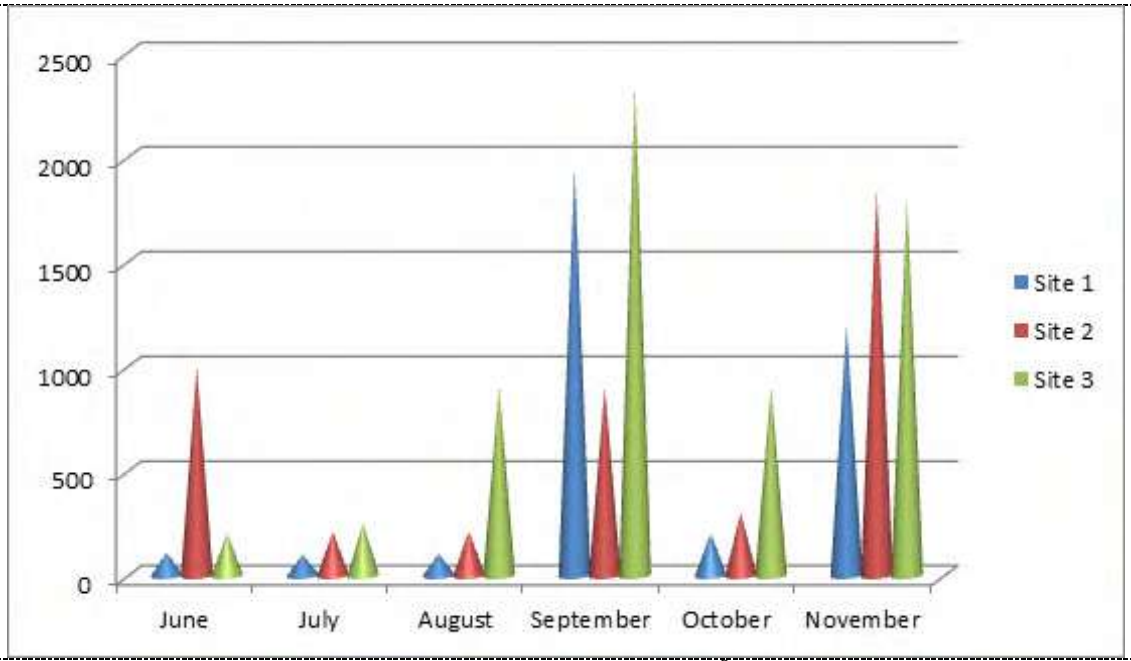

Figure 1. Seasonal variations of a total mollusca density (Ind./m^2) during period study.

Table 2. The Seasonal total density of mollusca (Ind./m^2) during period study.

Sites	Site 1	Site 2	Site 3
summer	315	1422	1349
autumn	3350	3050	5040

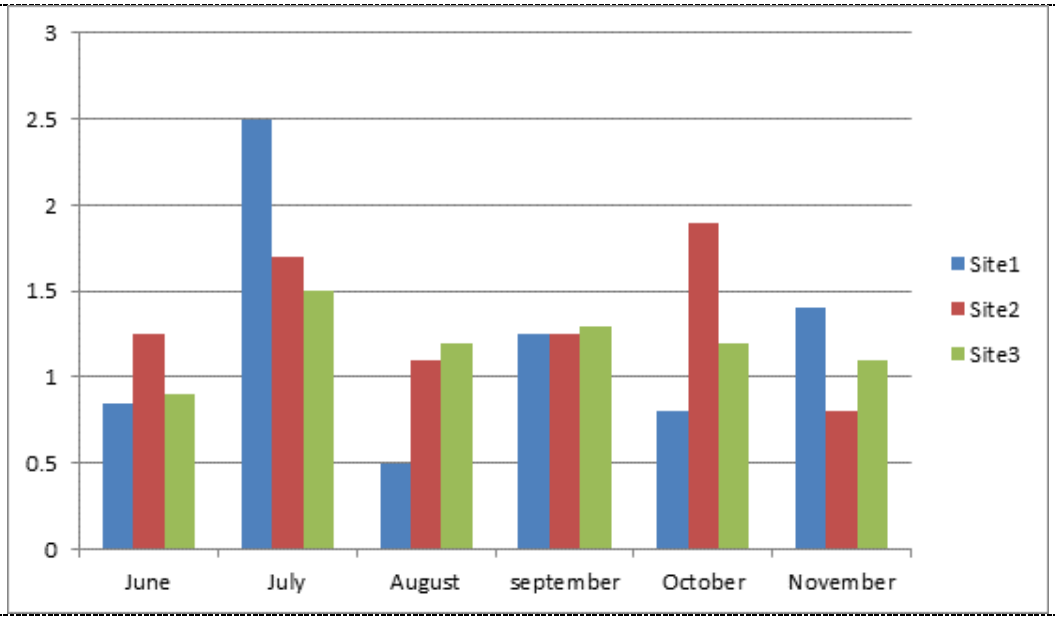

Figure 2. Variation of Shannone-Weiner values for Mollusca during period study.

Table 3. Jaccared similarity index of Mollusca during period study.

	St.1	St.3
St.2	60%	50%
St.3	42.86%	

4. References

[1] 1- Rosenberg, G. (2014). A new critical estimate of named species-level diversity of the recent mollusca. American Malacological Bulletin. 32 (2): 308–322.
[2] 2- Taylor, P.D.; Lewis, D.N. (2005). Fossil Invertebrates. Harvard University Press.
[3] 3- Fedosov, Alexander E.; Puillandre, Nicolas (2012). "Phylogeny and taxonomy of the Kermia–Pseudodaphnella (Mollusca: Gastropoda: Raphitomidae) genus complex: A remarkable radiation via diversification of larval development" (PDF). Systematics and Biodiversity. 10 (4): 447–477.
[4] 4- Université Bordeaux (2017) MolluSCAN eye project. Retrieved 2017-01-28.
[5] 5- Abdul Saheb,I. M. 1989. "The history of life and productivity of two types of freshwater molluscs Corbicula fluminea and Corbicula fluminalis in Shat-Al- Arab". MSc. Thesis, Marine Research Center, Al- Basrah University.
[6] 6- Mirza, N.A., Nashaat, M. R. (2019) Abundance, Diversity and Distribution of Mollusca in the Gharaf River, Southern Iraq. Iraqi Journal of Science. Vol. 60, No.3, pp: 469-485.
[7] 7- Al-Ameen F A (2018) An Ecological Survey of Benthic Invertebrates in Three Sites in Shatt-Al-Kufa at Al-Najaf Province, Iraq. Journal of University of Babylon for Pure and Applied Sciences, 26(8): 230-239. https://www.journalofbabylon.com/index.php/JUBPAS/article/view/1691.
[8] 8- Edmondson, W. T., (1959), Freshwater biology. 2nd Ed. John Wiley and Sons, New York, Freshwater Ecol. 18: 383-393.
[9] 9- Plaziat, J.C.& Younis, W.R. (2005). The modern environments of Molluscs in southern Mesopotamia, Iraq: A guide to paleogeographical reconstructions of Quaternary fluvial, palustrine and marine deposits. CG. Notebooks on Geology-A01: 1-18.

[10] Dobson, M., Pawley, S. ,Fletcher, M. and Powell, A., (2012). Guide to Freshwater Invertebrates. Freshwater Biological Association, Scientific Publication, 68,UK.
[11] Clench, W. J. 1976. "Mollusca". (In:) Freshwater Biology, Edmondson, W. T. (Eds.), 2nd Edition, United States of America, 1117-1160.
[12] Floder, S. and Sommer, U. (1999). "Diversity in planktonic communities: An Experimental test of the intermediate disturbance hypothesis". Limnol. Oceanogr. , 44(4): 1114-119.
[13] 13- Stilling, p. (1999) Ecology: Theories and application, 3rd Ed. Prentice Hall, New York: 638 pp.
[14] 14- Omori, M. and Ikeda, T. 1984. "Methods in marine zooplankton ecology". Wiley and Sons, New York.
[15] 15- Baloch, W. A., Memon, U. N., Burdi, G. H., Soomro, A. N., Tunio, G. R. and Khatian, A. A. 2012. "Invasion of channeled apple snail Pomacea canaliculata, Lamarck (Gastropoda: Ampullariidae) in Haleji Lake, Pakistan". Sindh Univ. Res. Jour. (Sci. Ser.), 44 (2): 263-266.
[16] Salman, S.D.; Marina, B.A. and Ali, M.H. (1990). The zooplankton of Khor Abdullah, North-West Arabian Gulf. Marina Mesopotomica,5(1):1126.
[17] Amri , N., Jamili, S. and Abdolbaghian, S. 2014. "Diversity of macrobenthos communities and their Relationships with Environmental factors in Jajroud River". Iran Resources and Environment., 4(2): 95- 103.
[18] Al- Khafaji, K. K. S., Al-Essa, S. A. K. and Hashem, A. A. 2015. "The Diversity, Abundance and Distribution of Macroinvertebrates Community in the intertidal zone of the Shatt- Al-Arab, South- Iraq". Thi- Quar J. of Science, 5(2): 54- 64.
[19] Al- Lami, A.A., Nashaat, M. R. and Radhi, A. G. 2002. "Zoo-Benthos Diversity in Habbaniya lake– Iraq". Iraq. J. of Biol., 2(2): 316- 324.
[20] Martel, A. L., Lauriault, J. and Madill, J. 2011. "Mollusca (Bivalves and Gastropods) as part of a biodiversity inventory of the Frenchman River, Southwest Sakatchewan". Canadian Museum of Nature, life Science.
[21] Al-Ameen F A (2013) An Ecological study of zooplanton in Al-kufa River/ Euphrates, Iraq. (MSc. Thesis) – niversity of Kufa, Iraq. https://www.researchgate.net/publication/335773367_An_Ecological_Study_of_Zooplankton_in_ Al-Kufa_RiverEuphrates_Iraq.
[22] Amar, Y., Djahedl. B., Lebid, S., Anani, M., Moueddene, K. and Mathieu, C. (2012). "Impact of Industrial pollution on the zooplankton population density of the Hammam Boughrara Dam". J. of Enviro. Sci. Engin., A1: 527- 532.
[23] Goel, P.K. (2008). "Water pollution causes, Effects and Control ".2nd Ed., Reprint New Age International (P) limited. Publishers, New Delhi.

Diagnostic study to detect toxoplasmosis in some Iraqi sheep

Diagnostic study to detect toxoplasmosis in some Iraqi sheep

Hiba Riyadh Al-abodi[1*]

[1]Department of Environment, College of Science, University of Al-Qadisiyah, Iraq.

*E-mail: hiba.Al-abodi@qu.edu.iq

Abstract. Parasites are cause a lot of important and serious diseases which widespread to peoples and animals all over the world, vector for disease to humans by consumption of meat sheep fresh as liver or not cooked well meat, so in this way the toxoplasmosis in sheep considered one of the causes economic and social damage and important sources of transfer this infection human, for this fact we must value economic and social damage by investigate the incidence of this disease in sheep, and using accurate methods for detection of this infection in blood fluids or tissue of sheep, so in this study we using immunological and molecular methods to detection of the parasite in sheep blood specimens in Al-Shamiya city/ Al-Qadisiyah government/Iraq, the results explained presence that antibodies in 14 samples (14%) below level significant (P≤ 0.05) by using Rapid Test Cassette, while the results depending on (RT PCR) for detection of specific gene of parasite B1 gene in blood specimens showed to (9 of 100)(9%) positive infection results in examined sheep. from these results, we can give simple picture ensured rule the infected sheep in transmission the disease to human although a low percentage of positive infection, presence the disease in sheep indicator to role sheep to transfer the disease to the human an achieved the economic and social damage.

Keywords. Toxoplasmosis, sheep, R.T PCR.

1. Introduction

Toxoplasmosis is zoonotic disease; it is widespread all over the world, it causes dangerous complications of the fetus loss, and the individuals with an immune disorder exposed to acute symptoms of this disease [1, 2]. *T. gondii* is one of a unicellular parasite; it causes infertility and abnormal embryos [3]. The incidence of the disease in small ruminants not limited to abortion but it's cross to consumption of injured flesh [4]. Sheep and goat are constituting the major sources of meat for food human in Iraq. Toxoplasmosis disease causes large loss of growing to goat and sheep as a result of abortion status and embryonic damage as well as maternal infertility in the female [5]. The diagnosis of this disease depends on the body's various fluids such as (blood, tissue, the amniotic fluid, etc.) by immunological and molecular methods [6, 7]. Investigation method is an important step advance to prevent of toxoplasmosis in animals and human. The disease can be a discovery of *T. gondii* in tissues or liquids of body in by intensification of particular nucleic acid sequences by molecular methods as (RT-PCR), or its antigens, or by the segregation of the parasite [8]. This study showed to diagnose *T. gondii* in sheep depending of serological-molecular tests. The nuclear genome of this parasite is reached nearly (87 kb), and the mitochondrial genome (6 kb), an episomal is (35 kb)

plastid-like genome, a congruence of genetic and karyotype linkage mapping are reproduced (14) nuclear chromosomes for *T. gondii* parasite [9]. B1 gene is a 2214 bp on IX chromosome with unknown function, that is repeated 35 times in the genome of this parasite [9, 10], these methods used to explain the incidence of this pathogenic parasite in infected the sheep and produce a negative impact on the economic and pathogenic side with economic and social damage.

2. Materials and Methods

One hundred blood specimen were collected from different sheep herds, every specimen were divided into two parts, for immunological and molecular diagnostic methods; the immunological method represented in kit Rapid Test Cassette (Toxo-IgG / IgM) from(PLASMATEC) [6, 11]. Real Time Polymerase Chain Reaction is a modern scientific technique combining the amplification of the genetic DNA sample and the detection of the amount and quality of the amplification product in a single reaction tube [6]; it has been used to detect *T. gondii* parasite based on the specific gene B1 (399bp), this molecular test was conducted and processed by BIONEER depending on primers based on [12], used primers sequence The primers: TOXO-F (5'-TCCCCTCTGCTGGCGAAAAGT-3', 5 µM), TOXO-R (5'-AGCGTT CGTGGTCAACTATCGATTG-3', 5 µM) (12), DNA extracted by support AccuPrep ® Genomic DNA Extraction, kit is (Bioneer, Korea) depending on the protocol of manufacturer instructions. Data analyzed by the statically 10.5 SPSS version software and X2- Square test was used to determine a significant difference with a probability ($P \leq 0.05$) [13].

3. Results and Discussion

Toxoplasmosis is a serious infectious disease that affects a lot of mammalian species; infections in this disease are caused by *T. gondii* parasite when taking inadequately cooked meat or from feces of infected cats. depending on the type of antibodies in blood serum of examined sheep by using Rapid test cassette. Results were indicated that 14 samples out of 100 (14%) were positive infection results, however IgG IgM antibodies and IgG plus IgM antibodies were found in (30.31%),(17.61) and (41.23) respectively, the statically analytic of this results referred to no significance difference between this values, as in Figure (1):

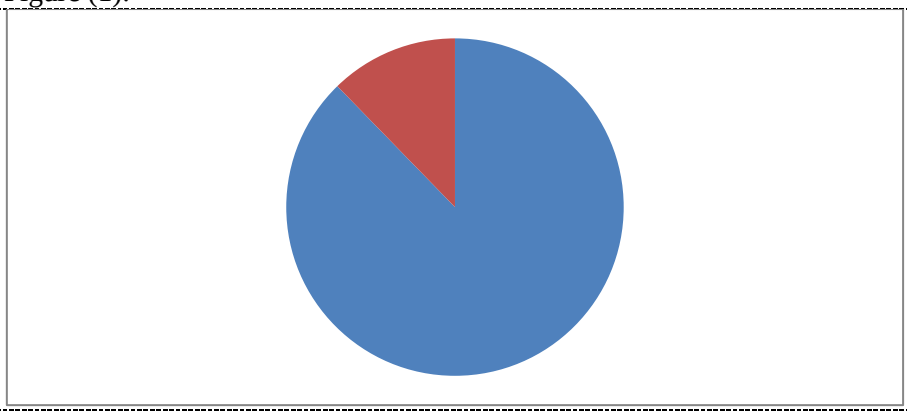

Figure 1. Positive infection rate 14% according to serological test.

This results are lower than [14] in the seroprevalence investigation of toxoplasmosis for sheep in Nepal country by collected 235 samples from sheep in different eco-zones in their country and investigate of *T. gondii* parasite with using the serological tests (commercial ELISA kit) and recorded these values: 36.17%, 32.94% as well as 9.41% positive results infection, they referred to spread infection sheep with *T. gondii* in different regions of Nepal, as well as lower than [15] in serological study for sheep when showed to 13/50 positive samples of toxoplasmosis. The Differences in positive seroprevalence results between the regions may be due to the weather and climatic in the same

country, also environmental and risk factors which affect the animal's health [5, 16]. Serological tests play a clear role in investigating and diagnosing *T. gondii* parasite through the antibodies IgG and IgM which can appear and recorded in about 8 days after infection incidence, but IgM antibodies disappear completely after a few months, IgG antibodies stay and present for lifelong of mammals [2, 6]. Real Time Polymerase Chain Reaction for investigating for B1 specific gene with infection as in Figure (2):

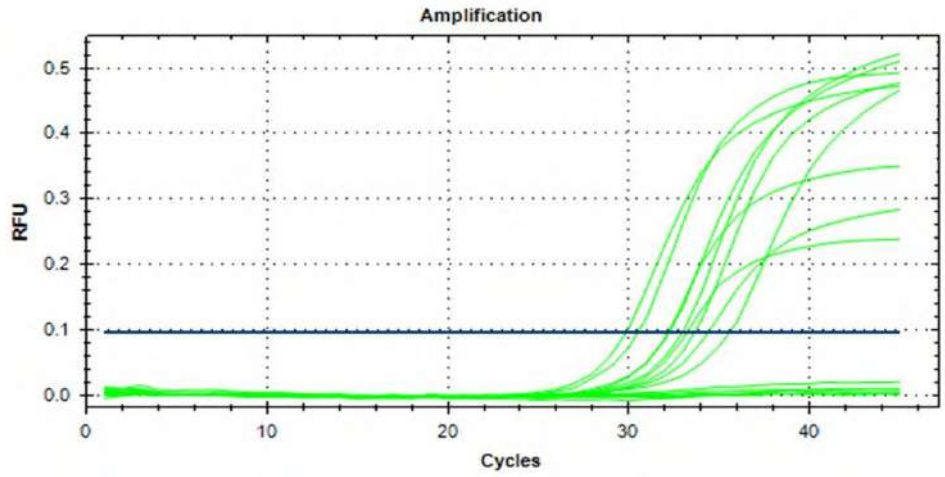

Figure 2. Amplification plot for real-time PCR assay of the positive results.

All this lower than what recorded in [15] as 26% positive infections when investigated to *T. gondii* DNA in the uterus samples, tubes, and the ovaries in the naturally sheep slaughtered in Pernambuco city in Brazil, and study of [17] when recorded 35.3% positive infections by seropositive study for abortion sheep. Some studies to spontaneous abortions in sheep due to *T. gondii* infection, for example [18] in Germany(10.6%) positive results when they used molecular method Polymerase chain reaction to detect genomic material of *T. gondii* parasite in tissues for fetal and placental for 47 samples from ovine abortions (Baden-Württemberg, Rhineland, Hesse), the amplification the specific gene B1, in this study in Germany the results explained in that toxoplasmosis infection sheep should be considered as important possible infection cause of abortions. (18.1%) positive results recorded in [19] in Italy, and (14.3%) in Brazil [20], the differences between this positive infection due to difference number of samples examined under study, so uncontrolled conditions to the laboratory that causes error in results of the polymerase chain reaction [6, 11]. This disease is one of the most important diseases of the last years, because of its widespread spread around the world and the serious human rights consequences of it, especially for pregnant women and newborn children, where many cases of miscarriage or childbirth occur for fetus during pregnancy even if the child is born after the completion of the pregnancy months, it shows serious symptoms such as damage to the retina of the eye and brain and brain hypertrophy where the head of the embryo is deformed or the head may be smaller [21, 22]. This study concluded that sheep in Al-Shamyah city in Al-Qadisiyah governorate are infected with *T. gondii* parasite, which causes the transfer the parasite to humans due to the consumption the raw meat, so it makes easy incidence the toxoplasmosis disease, and effects on the public health. Detection of small ruminant who have Toxoplasmosis infection considered important step towards preventing *T. gondii* in this animals and decreasing losses in the livestock especial abortion, and an end of the road preventing transfer to human, so it's an important step to progress in control through monitored (molecular/serologically) and depending on detect early estimated epidemiologically.

4. References

[1] Al-Ammash MSJ, Al-Shaibani KTM and Al-Abodi HRJ 2018 Investigation of toxoplasmosis in sheep in Al-Diwaniya city by using modern technique *Plant Arch*. **18** 2501.
[2] Al-Abodi HRJ 2019 Use of immunological methods to the detection of toxoplasmosis and heat shock protein HSP70 in men *J. Parasit. Dis*. **43** 234.
[3] Aspinall TV, Marlee D, Hyde JE and Sims PF 2002 Prevalence of Toxoplasma gondii in commercial meat products as monitored by polymerase chain reaction-food for thought? *Int. J. Parasitol.* **32** 1193.
[4] Bisson A, Maley S, Rubaire-Akiiki CM and Wasling JM 2000) The seroprevalence of antibodies to *Toxoplasma gondii* in domestic goats in Uganda *Acta Tropica*. **76** 33.
[5] Al-Hatami1 AO, Al-Kardhi IK and Al-Mosa MA 2018 Prevalence of seropositive toxoplasma cases in association with the frequency of abortion in sheep and goat *Kufa J. Veter. Med. Sci.* **9**.
[6] Al-Abodi HRJ 2018 Suspicion in the form of infection is the basis for selecting the appropriate method for examining the toxoplasmosis disease of bends that have no symptoms from patients *Int. J. Adv. Res*. **6** 655.
[7] Singh S, Munawwar A, Rao S, Mehta S and Hazarika NK 2014 Serologic prevalence of Toxoplasma gondii in Indian women of child bearing age and effects of social and environmental factors *PLoS Negl Trop Dis*. **8** e2737.
[8] Remington JS, McLeod R, Thulliez P and Desmonts G 2001 *Toxoplasmosis* In: Remington, J.S., Klein, J. (Eds.), Infectious Diseases of the Fetus and Newborn Infant. WB Saunders, Philadelphia 205.
[9] Jalal S and Nord CE 2004 Rapid and sensitive diagnosis of *Toxoplasma gondii* infections by PCR *Clin. Microbiol. Infect*. **10** 937.
[10] Wilson RJ and Williamson DH 1997 Extrachromosomal DNA in the Apicomplexa *Microbiol. Mol. Biol. Rev*. **61** 1.
[11] Al-Abodi HRJ2017 Serological and molecular detection of *Toxoplasma gondii* in *Columba livia* hunting pigeons of Al- Qadisiyah province *Al-Qadisiyah J. Vet. Med. Sci*. **16** 128.
[12] Sroka J, Karamon J, Dutkiewicz J, Wójcik-Fatla, AW and Cencek T 2018 Optimization of flotation, DNA extraction and PCR methods for detection of *Toxoplasma gondii* oocysts in cat faeces *Ann. Agric. Environ.Med.* **25** 680.
[13] Niazi AD 2001 *Statistical analysis in medical research* Univ. Nahrei Republic of Iraq 148.
[14] Subedi S, Sharma B, Singh S and Bindari YR 2018 Sero-prevalence of Toxoplasma gondii in sheep in different geographical regions of Nepal. *Veter. Anim. Sci.* **5** 7.
[15] Bezerra MJG, Cruz JALO, Kung ES, Silva JG, Santos AS, Moraes EPBX, Pinheiro Junior JW and Mota RA 2014 Occurrence of *Toxoplasma gondii* DNA in sheep naturally infected and slaughtered in abattoirs in Pernambuco, Brazil *Pesquisa Vete¬rinária Brasileira* **34** 329.
[16] Al-Abodi, HRJ 2018 Use of rapid cassette test and polymerase chain reaction technique to investigate toxoplasmosis in *Columba livia* birds in Al-Muthanna governorate. Proceeding of 6th International Scientific Conference, College of Veterinary Medicine, University of Basrah, Iraq *Basrah J. Veter. Res.* 17, No.3: 45-50.
[17] Silva AV, Cunha ELP, Meireles LR, Gottscchalk S, Mota RA and Langoni H 2003 Toxoplasmose em ovinos e caprinos: estudo soroepidemiológico em duas regiões no Estado de Pernambuco, Brasil *Ciência Rural* **33** 115.
[18] Steuber S, Niu A, Bauer C, Reetz J, Roth A and Janitschke K 1995 The detection of Toxoplasma gondii in abortion tissues of sheep using the polymerase chain reaction. *Dtsch Tierarztl Wochenschr*. **102** 91.

[19] Masala G, Porcu R, Daga C, Denti S, Canu G, Patta C and Tola S 2007 Detection of pathogens in ovine and caprine abortion samples from Sardinia, Italy, by PCR *J. Vet. Diagn. Invest*. **19** 96.
[20] Moraes EPBX, Costa MM, Dantas AFM, Silva JCR and Mota RA 2011 *Toxoplasma gondii* diagnosis in ovine aborted fetuses and stillborn in the State of Pernambuco, Brazil. *Vet. Parasitol*. **183** 152.
[21] Abd-Al-Hameed AS 2007 Seroepidemiological study on Ovine toxoplasmosis in Baghdad & Diyala provinces. MSc. thesis .Coll. of veterinary Medicine University of Baghdad, Iraq.
[22] Al-Abodi, HRJ 2018 Pathological Effects Associated with Parasitic Infections. *Indian J. Nat. Sci*. **9** 16146.

Molecular study to detect *bla*$_{TEM}$ and *bla*$_{CTx-M}$ genes in ESpL *Escherichia coli* and their antimicrobial resistance profile

Molecular study to detect *bla$_{TEM}$* and *bla$_{CTX-M}$* genes in ESβL *Escherichia coli* and their antimicrobial resistance profile

May Abdul Jaleal Raoof[1] and Mohammed A. Fayidh[1*]

[1]Department of Biology, College of Education for Pure Science (Ibn Al-Haitham), University of Baghdad, Baghdad, Iraq.

*E-mail: mohammedcbt66@gmail.com

Abstract. The common use of beta-lactam antibiotics resulted in the emergence of bacterial strains capable of spreading and extended-spectrum beta-lactamase (ESβL). Up to 70 of clinical samples, 30 of *Escherichia coli* (*E. coli*) were investigated as ESβL isolates. These isolates collected from inpatients and outpatients to some hospitals in Baghdad. The samples include urine, pus, stool, and blood from both genders, different age groups. The VITEK2 was used to check production of ESβL and for the automated diagnosis of rapid antimicrobial susceptibility experimentation and to the identification of the target bacteria. Technique of PCR was applied to detect the presence of *bla$_{TEM}$* and *bla$_{CTX-M}$* genes. The results demonstrated that 30(43%) isolates of the current study were ESβL producers. The gel electrophoresis of DNA for positive ESβL isolates gives differentiate results of both *bla$_{TEM}$* and *bla$_{CTX-M}$* genes were observed in 15(50%) and 29(96%) isolates respectively. The antibiotic resistance pattern to 20 antibiotics were showed majority of isolates have the multi-drug resistant (MDR) phenotypes and susceptible to carbapenems of antibiotic. Furthermore, the results of the genetic analysis, along with the pattern of isolates for antibiotic resistance, it may give an acceptable explanation for the higher presence of the *bla$_{CTX-M}$* gene compared with the proportion of the *bla$_{TEM}$* gene in the same isolates.

Keywords. *Escherichia coli*, ESβL, *bla $_{TEM}$*, and *bla$_{CTX-M}$* genes, antibiotic resistance.

1. Introduction

Escherichia coli is a various group of facultative anaerobic Gram-negative bacilli related in Enterobacteriaceae, and consist of variety strains ranging from commensal organisms to extremely pathogenic variants especially the intestine and urinary tract [1, 2]. Extended-spectrum beta Lactamase (ESβL) has been produced by several bacterial genes and noticed an increased rate after using the β-Lactam group of antibiotics has been extensively applied in human and veterinary medicine against several bacterial pathogenic infections [3]. [4] reported that the unconsidered use of antibiotics led to the evolution of many bacterial strains resistant to beta-lactam antagonists. On the other hand, the excess in the incidence of β-lactam resistance in Gram-negative bacteria has become a major clinical problem worldwide and then limits therapeutic choice, this reduces the chances of identifying appropriate antibiotic options for the resistance of newer isolates of beta-lactam in an Enterobacteriaceae [5]. The ESβLs are a series of enzymes that lead to resistance increase in

Aztreonam, Ceftazidime, Cefotaxime related oxyimino-β-lactams, Cephalosporins, and penicillins, but Clavulanic acid can be effected on them [6]. In the present work, more than 400 different ESβL variants have been identified [7]. Moreover, *TEM*, *SHV*, and *CTX-M* are three main types of ESβLs genes were known to mediate by chromosomes, plasmids, and transposons, which can effortlessly spread from one organism to another [8], and they are sporadically described all over the world, while *CTX-M* type is the master type in some countries [9] and *TEM* gene has become more spread than another genes [10]. Also, TEM β-lactamase (‘‘Temoniera’’) was isolated from recovered a Greece patient called Temoniera who infected by one strain of E coli and first reported plasmid-mediated β-lactamase which was isolated [11]. Another commonly accruing (ESβL) is the *CTX-M* was first discovered in an *E. coli* isolate recovered from Munich, German in1989. Bacterial strains that produce ESβL often demonstrate the resistance to antibiotics belongs to other classes which make strategies of treatment more complex [12], especially prevalent among a wide range of clinically important bacteria Widespread in the world [6]. Due to the lack of studies on the prevalence of beta-lactam genes, the current study was conducted to discuss the range of the prevalence of bla_{TEM} and $bla_{CTX\text{-}M}$ genes and the presence of extended-spectrum beta Lactamase in clinical *E. coli* isolates collected from different hospitals in Baghdad, to determine characteristics and patterns of antibiotic resistance among isolates of *E. coli* clinical specimens. The aims of the current study to investigate the extent of spread two ESβL genes (bla_{TEM} and $bla_{CTX\text{-}M}$) as well as investigating the antimicrobial resistances in the clinical isolates of E coli producing beta-lactamase.

2. Materials and Methods

2.1. Bacterial isolates

A total 70 bacterial isolates were collected from different clinical specimens includes urine, wound swab, stool, pus and blood samples from both genders patients with different ages and were collected from some Baghdad hospitals between the period 9/10/2019 to 20/12/2019. Standard microbiological techniques were depended for isolation [13] and Conventional microbiological procedures were employed to identify the isolates. The VITEK 2 compact system was used to re-identify them (BioMerieux, France) [14], and applied for the bacterial identification at the species level to determine antimicrobial susceptibility test (AST) of rapid clinically significant human bacterial pathogens.

2.2. Identification of E.coli isolates

All *E. coli* Isolates were identified and tested for their susceptibility profile using the VITEK 2 compact system by different antimicrobial susceptibility test cards (AST- cards), according to the expected bacterial pathogens. The regarding cards were inoculated and incubated in the instrument according to the manufacturer's instructions. A VITEK 2 susceptibility tests outcome were obtained as MIC values and shown as susceptible, intermediate, or resistant and estimate according to the periodical values of the National Committee for Clinical Laboratory Standard's breakpoint [13]. Final results were explicate according to the instructions of [15] CLSI (2019) using advanced expert system (AES), according to [16]. A total 17 different antibiotics were used and tested in AST-GN71 (bioMérieux) card that included ampicillin (AMP), ampicillin / sulbactam (SAM), aztreonam(ATM), cefazolin (CFZ), cefepime (FEP), trimethoprim / sulfamethoxazole (SXT), ciprofloxacin (CIP), Ceftriaxone (CRO), tigecycline (TGC), imipenem (IPM), meropenem (MEM), tobramycin (TOB), amikacin (AMK), ertapenem (ETP), gentamicin (GEN),moxifloxacin (mxf), nitrofurantoin (NIT)[17].

2.3. Detection of ESβLs

All isolates were tested using the VITEK 2 system with the antimicrobial susceptibility texted AST-GN71 card. This system was used to carry out both screening and confirmatory tests for phenotypic

notice of ESβL at the same plate [18]. All isolates of *E.coli* were confirmed as ESβL producing using double disc synergy (DDST) test using 30mg of aztreonam, ceftazidime, cefotaxime, ceftriaxone, and 20mg amoxicillin with10M clavulanic acid. Four discs of antibiotic were placed at 15mm apart from each other with amoxicillin /clavulanic acid disc which is placed at the centre (Figure l). Isolates of ESβL production was considered positive when the zone of inhibition around any antibiotic disc was Overlap With the amoxicillin/clavulanic acid disc [19].

2.4. Dtection of bla_{TEM} and bla_{CTX-M} genes coding for ESβL production

Only the *E. coli* isolates considered positive for ESβL, were selected for the genotypic study. The detection of bla_{TEM} and bla_{CTX-M} resistance genes were performed after extraction of total DNA of *E. coli* using the PCR and gel electrophoresis techniques isolated as maintained by the manufacturer's instruction using the ABIO pure kit (USA). The concentration and the purity of the DNA was determined by a Quantus fluorometer (Promega, USA).

Table 1. Primers details of ESβLs genes used in this study.

Genes	Primer name and sequences (5`-3`)	Expected amplicon size (bp)	Annealing temp (°C)	Reference
$\boldsymbol{bla\text{-}_{TEM}}$	TEM. Forward 5`ATAAAATTCTTGAAGACGAAA3` TEM. Reverse 5`GACAGTTACCAATGCTTAATCA3`	1080	50	[20]
$\boldsymbol{bla_{CTX-M}}$	CTX-M.Forward 5`GACGATGTCACTGGCTGAGC3` CTX-M. Reverse 5`AGCCGCCGACGCTAATACA3`	499	55	[21]

Analysis of PCR technique was applied for encoding two genes of the β-lactamase family: TEM and CTX –M. Primers were supplied by Macrogen Company for the oligonucleotide primer sets (Table 1), Which is used as a specific for the bla_{TEM} and bla_{CTX-M} genes, and the cycling conditions in PCR assay have been adopted and which was described by [22]. The PCR was performed in a PCR Thermal Cycler (BioRad, USA).

3. Results

A total 30 isolates of positive ESβL Out of 70 collected isolates of *E. coli* were identified from different clinical specimens in the patients of both genders and at different ages in all hospitals of Baghdad city. The investigation of isolates was determined up to species level using the VITEK2 automated microbiology system [23]. The isolates were confirmed as ESβL producing E.*coli* using method of double-disc synergy test (DDST), as outlined in the Figure 1. The results of DDST for 70 isolates showed that 30 isolates (43%) had been ESβL producers and 40(57%) were non-producers.

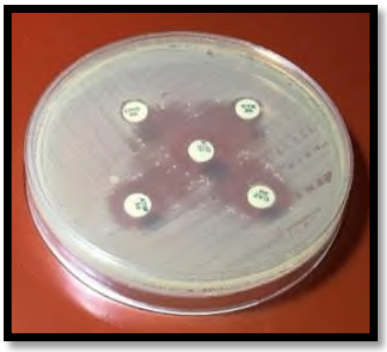

Figure 1. Photograph showing DDST.

A total of 30(43%) clinical isolate of ESβL producing in bacterial isolated from various infections was showing that 18(60%) isolates in urine tract infections and 2(6.0%) isolates in stool 4(12.1%) isolates in pus samples and 6(18.1%) isolates in the wound swab samples and these results showing in the Table 2.

Table 2. Type and number of positive samples for ESβLs.

Samples	Number of samples	Male%	Female%
Urine	18(60%)	7(23.3%)	11(36.6%)
Stool	2(6.6%)	1(3.3%)	1(3.3%)
Pus	4(13.3%)	5(16.6%)	1(3.3%)
Wound swab	6(20%)	3(10%)	1(3.3%)
Total	30	16(53.4%)	14(46.6%)

3.1. Sensitivity of antibiotic

The resistant pattern of 30 ESβL producers isolates have been detected with 17 different antibiotic using AST-GN71 card of antimicrobial agent (Table3). The results were showed that all isolates of the present study were susceptible to imipenem, ertapenem, meropenm, tigecycline, and (96 %) of isolates susceptible to amikacin and nitrofurantion and showed a high of resistance (P value) (100%) to (ampicillin, cefazolin, ceftriaxone and aztreonam) and 96% to cefepime and 90 % to ampicillin/sulbactam whereas resistance to other antibiotic was moderate.

Table 3. Showing the percentage of antimicrobial resistant for ESβL producing *E.coli*.

No.	**Antibiotics**	NO. of resistant isolates	Rat of resistant %
1	**Ampicillin**	30	100%
2	**Ampicillin/Sulbactam**	27	90%
3	**Cefazolin**	30	100%
4	**Ceftriaxone**	30	100%
5	**Cefepime**	29	96%
6	**Aztreonam**	30	100%
7	**Ertapenem**	0	0%
8	**Imipenem**	0	0%
9	**Meropenem**	0	0%
10	**Amikacin**	1	3.3%
11	**Gentamicin**	13	43.3%
12	**Tobrmycin**	15	50%
13	**Cioroflxacim**	21	70%
14	**Moxifloxacin**	21	70%

15	**Tigecycline**	0	0%
16	**Nitrofurantion**	1	3.3%
17	**Trinethoprim/Sulfamethoxazole**	20	66.6%

3.2. Gel Electrophoresis Analysis of ESβLs gene

Polymerase chain reaction (PCR) technique was conducted to detect the ability to produce and Expression on 30 ESβL recognized as positive isolates of *E. coli*, were selected. The *bla*$_{TEM}$ gene was detected for the 30 ESβL positive isolates shown in (Figure 2 A and B). The bands of the expected size (1080bp) using the TEM-F and TEM-R primers were seen as positive TEM genotype and observed in 15 (50%) of total 30 *E. coli* isolates.

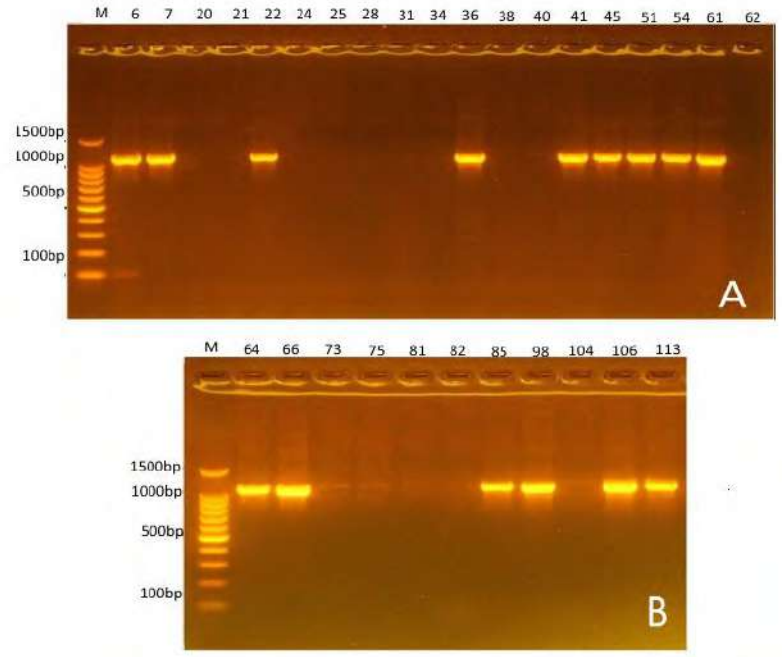

Figure 2. Gel electrophoresis analysis for PCR amplified fragment products of *bla*$_{TEM}$ (1080 bp) genes for 30 bacterial isolates of study using 1.5% agarose and DNA markers (1500 -100bp) are shown in lane M.

On the other hand, results of *bla*$_{CTX-M}$ gene was showing in the (Figure3 A and B). The bands of expected size 499bp using CTX-M-F and CTX-M-R primers were seen as a positive samples the genotype and observed in 29 (96.6%) of a total 30 *E.coli* isolates.

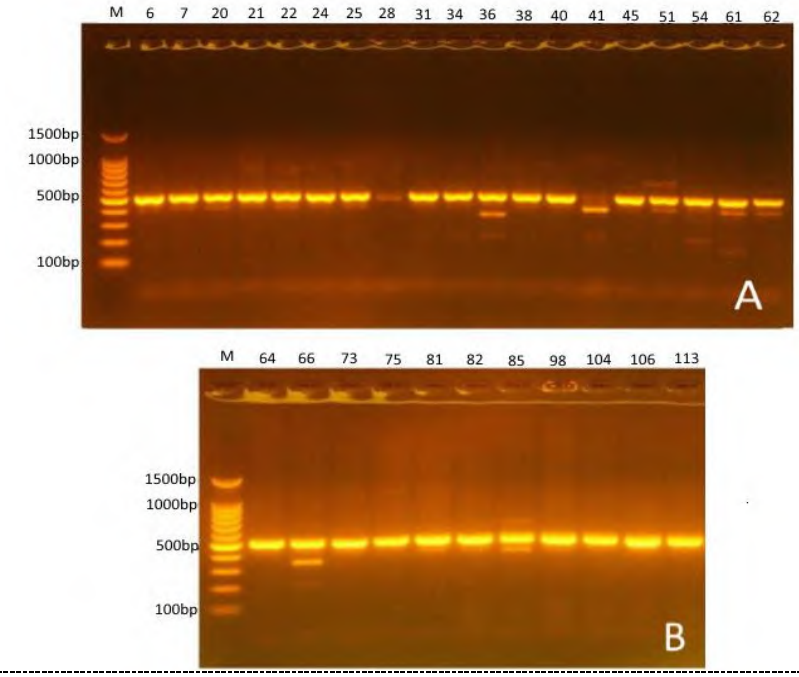

Figure 3. Gel electrophoresis analysis for PCR amplified fragment products of *bla*$_{CTX-M}$ (ca. 499 bp) genes for 30 bacterial isolates of study using 1.5% agarose and DNA markers (1500 -100bp) are shown in lane M.

3.3. Genotype patterns of ESβLs

Analysis of the PCR amplified DNA fragment of 30 *E. coli* ESβLs producers using the specific primers revealed that the two genotype patterns were obtained in (Table 4). These results also showed that predominant genotype rate was CTX - M (50%) then genotype amalgamation of TEM + CTX - M (46.6%). The commonness rate of the two different ESβL genes in the present study demonstrated that *bla*$_{CTX-M}$ gene was the most predominant type (29/30; 96.6%) while TEM gene was less dominant type (15/30; 50% respectively).

Table 4. Showing ESβLs genotype patterns among *E. coli* isolates.

ESβLs Genotype	No. of isolates	Percentage (%)
***bla*$_{TEM}$ only**	1	3.3%
***bla*$_{CTX-M}$ only**	15	50%
***bla*$_{TEM+CTX-M}$**	14	46.6%
Total	30	100

4. Discussion

The increasing rate with the progression of ESβL producing by Enterobacteriaceae has threatened the entire world. However, nowadays the main challenge to infection control is entailing continuous monitoring systems for the emergence and spared isolates of Enterobacteriaceae that produce of ESβLs. In the present study, a total 30 bacterial isolates of *E. coli* from total samples (43%) were identified as ESβLs producers. These results give a dangerous indication of public health in Iraq and the need to take caution from the excessive use of antibiotics. Also, *E. coli* and other genera of gram-negative bacteria have possessed a naturally occurring, chromosomally mediated β- lactamase and plasmid-mediated of β–lactamase [24]. The unconstrained use of these antibiotics in developing countries, poor dosing, ineffective empiric antibiotic therapy, prolonged antibiotic treatment, and

antibiotic misuse are the most reasons for the development and high resistance rates in bacterial infections [25]. Although Phenotypic tests, such as DUST method it's commonly used, for detection of ESβLs and confirm whether an ESβL is produced by bacterial isolates but cannot detect the ESβL subtype easily. Furthermore, [26] reported that although molecular methods appear sensitive, but the time consuming, expensive and require specialized equipment and expertise. Definitive identification is possible only by molecular detection methods. On the hands, the techniques, that are necessary for the task of the exact ESβL subtype, are available only in research facilities. Also, PCR fragments products for bla_{TEM} and bla_{CTX-M} genes produce expected bands of 1080 bp and 499 bp respectively. Moreover, using the same primers in the present study, the amplified DNA products of comparable molecular weight were obtained in the different worldwide studies and showed the same results of [22]. Also, some studies performed in some countries, such as Iraq, Iran, and Turkey to detect other ESβLs genes using different primer sequences gave amplified products with various molecular weights [27], which confirms that there are many genes responsible for producing of ESβLs. The covariance in the molecular weights of the amplified products could be indicating the differentiation in primer sequences or in the type of the gene that detects, currently, more than 150 gene TEM types are recognized are there [28]. For example, CTX-M gene is divided into five subgroups that have more than 80 enzymes. This variety supplies an auxiliary way to follow the prevalence of individual resistance genes. Interestingly, that 96.6% of ESβLs producer *E. coli* have sheltered the CTX - M gene. Furthermore, TEM gene was found in 50% of bacterial isolates and that consistent with the present study and with diffusion worldwide including the Middle East area, where CTX- M- type has replaced, and therefore the TEM type and became the predominating ESβL among isolates of Enterobacteriaceae [29]. Different studies that conducted in Iraq and adjacent countries have declared that the CTX-M type was the predominant gene type in *E. coli* [30], while the studies in Turkey and India showed that the TEM type was the dominant type [31]. Data analysis revealed that there are six genotype patterns of ESβLs exist among the 70 isolates. CTX - M was the most prevalent genotype (50%) followed by the genotype combination TEM + CTX - M (46.6%). This genotype combination has also been published to be the most dominant genotype in Japan, India, and Arabia Saudi kingdom [32, 33] said that in some isolates means that the ESβL producing strains may be regarding to a complex antimicrobial resistance. Finally, the results were demonstrated that the TEM gene is a broad spectrum ß- lactamase that is always concerted with CTX - M on the same plasmid. The release of TEM+CTX-M collection can cause resistance to carbapenems; this is worrisome and more serious for the community [34].

5. Conclusion

In the present study, a 43 % of the uro-pathogenic isolates of E. coli were identified as ESβLs producers. All isolates were certain by PCR to have one or more ESBL genes. Type of CTX - M was the dominant ESβL in the isolated E. coli and followed by the genotype of TEM+CTX-M combination. So, it is very important to highlight on antimicrobial resistance must be perceiving as an healthy as well as ecological problems and increase efforts to monitor and control the spread of antimicrobial-resistant strains in hospitals and communities.

6. References

[1] Mos I, Micle O, Zdrâncă M, Mureşan M and Vicaş L 2010 Antibiotic sensitivity of the *Escherichia coli* strains isolated from infected skin wounds Farmacia, **58** 637.

[2] Fayidh MA, Kalleary S, Kasirajan S and Muthusamy S 2015 Isolation of a unique Phenol degrading bacterial strain *Escherichia coli moh 1* from effluent of an edible oil industry in Chennai, India *Res. J. Biotechnol.* **10** 36.

[3] Warnke PH, Lott AJ, Sherry E, Wiltfang J and Podschun R 2013. The ongoing battle against multi-resistant strains: in-vitro inhibition of hospital-acquired MRSA, VRE, Pseudomonas,

ESBL *E. coli* and *Klebsiella* species in the presence of plant-derived antiseptic oils *J. Cranio-Maxillofac. Surg.* **41** 321.

[4] El-Badawy MF, Tawakol WM, Maghrabi IA, Mansy MS, Shohayeb MM and Ashour MS 2017 Iodometric and molecular detection of ESBL production among clinical isolates of E. coli fingerprinted by ERIC-PCR: the first Egyptian report declares the emergence of E. coli O25b-ST131clone harboring bla GES *Microb. Drug Resist.* **23** 703.

[5] Mawlood AH, Omer SA, Jalal ST and Haji SH 2018 Molecular detection of SHV-Type ESBL in *E. coli* and K. pneumoniae and their antimicrobial resistance profile *Zanco J. Med. Sci.* **22** 262.

[6] Paterson DL and Bonomo RA 2005 Extended-spectrum β-lactamases: a clinical update *Clin. Microbiol. Rev.* **18** 657.

[7] Gholipour A, Soleimani N, Shokri D, Mobasherizadeh S, Kardi M and Baradaran A 2014 Phenotypic and molecular characterization of extended-spectrum β-lactamase produced by *Escherichia coli*, and *Klebsiella pneumoniae* isolates in an educational hospital *Jundishapur J. Microbiol.* **7** 10.

[8] Nakamura T, Komatsu M, Yamasaki K, Fukuda S, Miyamoto Y, Higuchi T, Ono T, Nishio H, Sueyoshi N, Kida K and Satoh K 2012 Epidemiology of *Escherichia coli*, Klebsiella species, and Proteus mirabilis strains producing extended-spectrum β-lactamases from clinical samples in the Kinki Region of Japan *Amer. J. Clin. Pathol.* **137** 620.

[9] Akpaka PE, Legall B and Padman J 2010 Molecular detection and epidemiology of extended-spectrum beta-lactamase genes prevalent in clinical isolates of *Klebsiella pneumoniae* and *E. coli* from Trinidad and Tobago *West Indian Med. J.* **59** 591.

[10] Sharma M, Pathak S and Srivastava P 2013 Prevalence and antibiogram of Extended Spectrum β-Lactamase (ESBL) producing Gram negative bacilli and further molecular characterization of ESβL producing *Escherichia coli* and *Klebsiella* spp. *J. Clin. Diagn. Res.* **7** 2173.

[11] Rawat D and Nair D 2010 Extended-spectrum β-lactamases in Gram Negative Bacteria. *J. Global Infect. Dis.* **2** 263.

[12] Liao K, Chen Y, Wang M, Guo P, Yang Q, Ni Y, Yu Y, Hu B, Sun Z, Huang W and Wang Y 2017 Molecular characteristics of extended-spectrum β-lactamase-producing *Escherichia coli* and *Klebsiella pneumoniae* causing intra-abdominal infections from 9 tertiary hospitals in China *Diagn. Microbiol. Infect. Dis.* **87** 45.

[13] Dashti AA, West P, Paton R and Amyes SGB 2006 Characterization of extended-spectrum β-lactamase (ESBL)-producing Kuwait and UK strains identified by the Vitek system, and subsequent comparison of the Vitek system with other commercial ESBL-testing systems using these strains *J. Med. Microbiol.* **55** 417.

[14] Kazemnia A, Ahmadi M and Dilmaghani M 2014 Antibiotic resistance pattern of different *Escherichia coli* phylogenetic groups isolated from human urinary tract infection and avian colibacillosis *Iranian Biomed. J.* **18** 219.

[15] CLSI (Clinical and Laboratory Standards Institute) 2019 *Performance Standards for Antimicrobial susceptibility testing*, 29th ed CLSI supplement M100.Wayne, PA: Clinical and Laboratory Standards Institute 32.

[16] Hassan H and Abdalhamid B 2014 Molecular characterization of extended-spectrum beta-lactamase producing Enterobacteriaceae in a Saudi Arabian tertiary hospital *J. Infect. Develop. Countr.* **8** 282.

[17] Sugiartha IGE 2016 *Perbandingan Hasil Identifikasi Metode Analytical Profile Index (API) dan Tes Kepekaan Antibiotika Konvensional dengan Metode Technical Dedicated Reasonable (TDR)-300B* (Doctoral dissertation, Universitas Airlangga).

[18] Batarseh A, Soneah S, Mardeni R, Elmadni K, Noor M. and Abu Ashour N 2013 Antibiotic Resistance Patterns of Multidrug Resistant and Extended-Spectrum B-Lactamase Producing *Eshcherichia coli* Urinary Isolates at Queen Rania Al-Abdullah Hospital for Children, Jordan *Zagazig Univ. Med. J.* **19** 1.

[19] Saha M.R and Jhora ST 2018 Detection of extended spectrum beta-lactamase producing Gram-negative organisms: hospital prevalence and comparison of double disc synergy and E-test methods *J. Med. Sci.* **12** 32.
[20] Kouadio IK, Guessennd N, Dadié A, Konaté A, Gbonon V, Tiékoura B and Djè M 2017 Characterization of the Genetic Supports for Betalactam Resistance in *Escherichia coli* Strains of Porcine Origin Producing Extended-spectrum Beta-Lactamase (ESBL) *Microb. Res. J. Int.* **1** 9.
[21] Yavuz B, Ozer B, Inci M and Duran N 2015 Determination of CTX-M beta-lactamase in *Escherichia coli* strains isolated from clinical samples. *Le infezioni Med. Rivista Periodica di Eziologia, Epidemiologia, Diagn., Clin. Terapia Delle Patologie Infettive* **23** 23.
[22] Jdoana D, Sacha P, Wieczorek P, Czaban S, Michalska A, Jaworowska J, Jurczak A, Poniatowski B and Tryniszewska E 2014 The Occurrence of *blaCTX*-M, *blaSHV*, and *blaTEM* genes in extended-spectrum β-lactamase-positive strains of *Klebsiella pneumoniae*, *Escherichia coli*, and *Proteus mirabilis* in Poland *Int. J. Antibiot.* **2014**.
[23] Wibisono FJ, Sumiarto B, Untari T, Effendi MH, Permatasari DA and Witaningrum AM 2020 Resistance Profile of Extended Spectrum Beta Lactamase-Producing *Escherichia coli* Bacteria using Vitek® 2 Compact Method *Buletin Peternakan* **44** 1.
[24] Dhillon RHP and Clark J 2012 ESBLs: A clear and present danger Critical care research and practice, Dhillon RH. Clark J. ESBLS: A clear and present *Danger. Care Res. Pract*. **2012** 625170.
[25] Assafi MS, Ibrahim NM, Hussein NR, Taha AA and Balatay AA 2015 Urinary bacterial profile and antibiotic susceptibility pattern among patients with urinary tract infection in duhok city, kurdistan region, Iraq *Int. J. Pure Appl. Sci. Technol.* **30** 54.
[26] Nüesch-Inderbinen MT, Hächler H and Kayser FH 1996 Detection of genes coding for extended-spectrum SHV beta-lactamases in clinical isolates by a molecular genetic method, and comparison with the E test *Europ. J. Clin. Microbiol. Infect. Dis.* **15** 398.
[27] Goudarzi M, Sabzehali F, Tayebi Z, Azad M, Boromandi S, Hashemi A and Seyedjavadi SS 2014 Prevalence of *blaCTX-M* gene in multi-resistant *Escherichia coli* isolated from Urinary Tract Infections, Tehran, Iran *Novelty Biomed.* **2** 107.
[28] Harada S, Ishii Y and Yamaguchi K 2008 Extended-spectrum β-lactamases: implications for the clinical laboratory and therapy *Korean J. Lab. Med.* **28** 401.
[29] Livermore DM 2012 Current epidemiology and growing resistance of gram-negative pathogens *Korean J. Internal Med.* **27** 128.
[30] Barguigua A, El Otmani F, Talmi M, Bourjilat F, Haouzane F, Zerouali K and Timinouni M 2011 Characterization of extended-spectrum β-lactamase-producing *Escherichia coli* and *Klebsiella pneumoniae* isolates from the community in Morocco *J. Med. Microbiol.* **60** 1344.
[31] Bali EB, Accedil L and Sultan N 2010 Phenotypic and molecular characterization of SHV, TEM, CTX-M and extended-spectrum-lactamase produced by *Escherichia coli*, *Acinobacter baumannii* and *Klebsiella* isolates in a Turkish hospital *African J. Microbiol. Res.* **4** 650.
[32] Bindayna K, Khanfar HS, Senok AC and Botta GA 2010 Predominance of CTX-M genotype among extended spectrum beta lactamase isolates in a tertiary hospital in Saudi Arabia *Saudi Med. J.* **31** 859.
[33] Harada Y, Morinaga Y, Yamada K, Migiyama Y, Nagaoka K and Migiyama Y 2013 Clinical and molecular epidemiology of extended-spectrum β-lactamase-producing *Klebsiella pneumoniae* and *Escherichia coli* in a Japanese tertiary hospital *J. Med. Microb. Diagn.* **2** 2161.
[34] Manoharan A, Premalatha K, Chatterjee S, Mathai D and SARI Study Group 2011 Correlation of TEM, SHV and CTX-M extended-spectrum beta lactamases among Enterobacteriaceae with their *in vitro* antimicrobial susceptibility *Indian J. Med. Microbiol.* **29** 161.

First record of *Thelohanellus wuhanensis* Xiao & Chen, 1993 (Myxozoa: Myxosporea) in Iraq on the gills of *Carassius auratus* (Linnaeus, 1758)

First record of *Thelohanellus wuhanensis* Xiao & Chen, 1993 (Myxozoa: Myxosporea) in Iraq on the gills of *Carassius auratus* (Linnaeus, 1758)

Kefah Naser Abdul-Ameer[1] and Aisha Sulaiman Obaid[1*]

[1]Department of Biology, College of Education for Pure Science (Ibn Al-Haitham), University of Baghdad, Baghdad, Iraq.

*E-mail: aishaalkubaissi@gmail.com

Abstract. In the current study, the myxobolid, *Thelohanellus wuhanensis* Xiao & Chen, 1993 was recorded for the first time in Iraq from the gills of *Carassius auratus* (Linnaeus, 1758) that was caught from Tigris river near Al-Shawwaka location in Baghdad city during the period from May to October 2020. With this registration, *T. wuhanensis* become the fourth species of the genus *Thelohanellus* so far recorded from the Iraqi fish**.** The description and measurements of this external parasite as well as its illustrations are given.

Keywords. *Thelohanellus wuhanensis*, *Carassius auratus*, Myxozoa, Tigris river, Iraq.

1. Introduction

Myxozoans are microscopic metazoan parasites of marine and freshwater fishes from natural and aquaculture resource, this group is important from an economic point as it causes losses of production and makes fishes unfit for human consumption [1]. The phylum Myxozoa includes over 2,180 species belonging to 60 genera of Class Myxosporea of the Phylum [2]. *Thelohanellus* (Kudo, 1933) the sixth most species genus with 108 nominal species reported worldwide [3], 52 nominal species of this genus infected freshwater fishes in India up to 2015 [4]. Species of *Thelohanellus* are mostly histozoic, bivalvular myxosporeans, tear-shaped or pyriform to broadly ellipsoidal in valvular view, more slender in sutural view, and have a single polar capsule either pyriform or tear-shaped with a single coil of polar filament [2]. These myxozoan parasites are mainly plasmodia-forming parasites of freshwater fish with a great diversity of sites of infection such as gills, fins, scales, skin, muscles, gallbladder, kidneys [3, 4]. *Thelohanellus* species have strict tissue specificity and shown inclined to the epithelium, connective tissue, cartilage, or vascular tissue that usually occurs within the gill apparatus [5]. The plasmodia of this genus are classified according to their location in the gill filament, the interfilamentous vascular type which occupying the tip, and intralamellar vascular type which occupying the side [6]. The present paper documents the first record in Iraq of *T. wuhanensis* Xiao & Chen, 1993 from gills of *Carassius auratus* (Linnaeus, 1758) from Tigris river near Al-Shawwaka location in Baghdad city.

2. Materials and Methods

In this study, nine live specimens of *Carassius auratus* (Linnaeus, 1758) were caught from Tigris river near Al-Shawwaka location in Baghdad city between May to October 2020. The lives fishes were brought to the laboratory and classified according to an account on freshwater fishes of Iraq [7], then investigated for myxozoan infection. To detect the plasmodia, fresh smears the external parts such as the skin, fins, gills, and operculum and all internal organs such as kidneys, spleen, liver, the wall of the intestine, urinary bladder, gall-bladder, eyes, heart, muscles, testes and ovaries of fishes were examined under a dissecting microscope. A smear using fresh spores were made from the external parts and internal organs of the fish and examined with a compound microscope. Spores were freshly photographed by a digital camera. The spore was drawn using a Camera Lucida. For permanent specimens, the spores were fixed in absolute methanol for two to eight minutes and then stained with Giemsa solution for about 25-30 minutes, then washed in tap water and dried [8]. Myxosporian spores were measured and described according to the guidelines [9].The scientific name of the parasite was checked with lists [3]. All measurements are presented (in μm) as minimum-maximum followed by mean values. The information on the previous records of myxozoans of fishes of Iraq was obtained from the index-catalogue of parasites and disease agents of fishes of Iraq [10].

3. Results and Discussion

3.1. Thelohanellus wuhanensis Xiao & Chen, 1993

This parasite found in the skin and gills of two out of nine of *Carassius auratus*. The infection of these fishes was not severe, the plasmodia were not found during the examination. Groups of spores distributed in the tissues examined were obtained, so the identification has been based on the characters of spores. Description and measurements (in μm) based on five fresh spores are listed below and shown in Figures 1 and 2. Spores large-sized, oval elongated slightly tapering anteriorly in frontal view, lemon-shaped in lateral view with the straight sutural line, the anterior end slightly narrow, a pit near on the anterior end, asymmetric valves, length of spore 22.6-24.2 (22.9) and width 12.3-12.6 (12.45), thickness 10.8-11.4 (11.1). One subspherical polar capsule with triangle protrusion at the upper end near the anterior end of the spore and occupies almost half the size of the spore, measuring 11.1-11.9 (11.5) long and 7.9-8.3 (8.1) wide. Sporoplasma occupying most of the extracapsular space behind the polar capsules with the small dark granules.

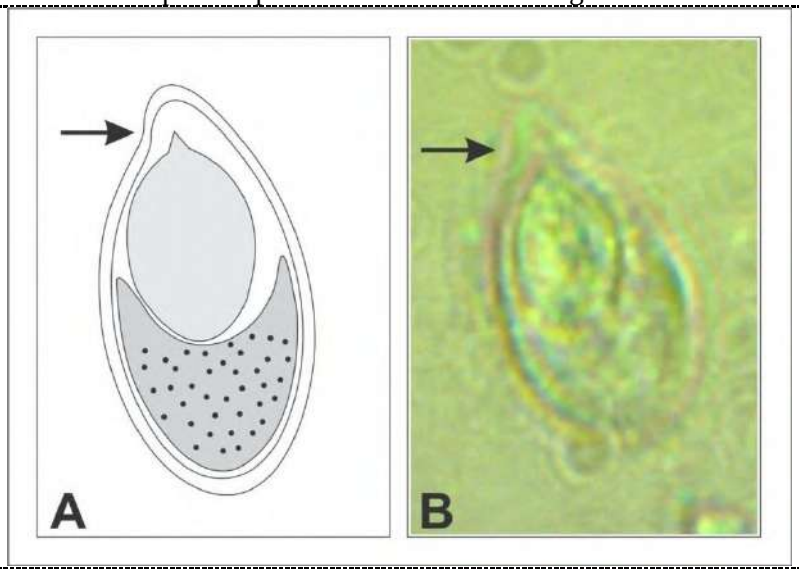

Figure 1. *Thelohanellus wuhanensis* in frontal view. A-Diagrammatic drawing (Scale bar = 11.5 μm), A: Photomicrograph (4 00 x). The arrows appear in the pit on the anterior end of the spore.

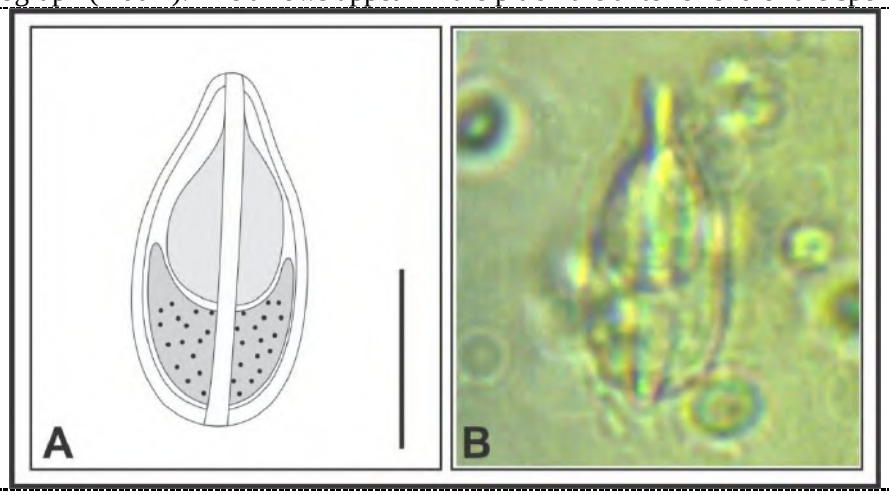

Figure 2. *Thelohanellus wuhanensis*, Lemon-shaped in lateral. A- Diagrammatic drawing (Scale bar = 11.5 μm), B- Photomicrograph (4 00 x).

The descriptions and measurements of *T. wuhanensi* in this study are corresponded with those of the holotype of the parasite from on the skin of silver crucian carp *Carassius gibelio* (Bloch, 1782) (= *Carassius auratus gibelio*) in Wuhan City and Jingshan County of Hubei Province, China [3]. This is the first record of *T. wuhanensis* in Iraq, as it has not been recorded in any studies of the parasites of Iraqi freshwater fish [10]. *T. wuhanensis* Xiao & Chen, 1993 was first identified on the skin of allogynogenetic silver crucian carp in Wuhan City and Jingshan County of Hubei Province, China. Subsequently, this parasite was described and supplements its ultrastructural and histological characteristics from the same fish host from a pond in Honghu City, Hubei Province, China [11]. Although many species of the genus *Thelohanellus* showed less pathogenicity to their hosts, *T. wuhanensis*, caused the mortality of infected fish [3], for being leads to the formation of obvious swellings on the skin of infected fishes, and severe epidemic thelohanellosis and mortality of the heavily infected fish [12]. In Iraq, three *Thelohanellus* species have been described from freshwater fishes from different water bodies. The first species, *T. catlae* (Chakrawarty and Basu, 1958) was registered from the gills of *Cyprinion macrostomum* for the first time in Iraq from the Tigris river within the limits of Baiji city [13). Then, three other host fish species are so far known as hosts for this parasite: *Planiliza abu* (= *Liza abu*) [14], *Carasobarbus luteus* [15] and *Carassius auratus* [16]. The second one, T. dogieli (Akhmerov, 1955) was reported for the first time from Iraq in gills of *Cyprinus carpio* from Tigris river near Al-Zaafaraniya region at Baghdad province [16].The third one, T. misgurni (Kudo, 1919) registered for the first time in Iraq from the gills of *Garra rufa* from the Tigris river within the city limits of Al-Ataifiya [17]. Accordingly, *T. wuhanensis* is the fourth species of the genus *Thelohanellus* so far recorded from the Iraqi fish.

4. Conclusion

The Myxozoan parasite *Thelohanellus wuhanensis* Xiao & Chen, 1993 was recorded from gills of *Carassius auratus* (Linnaeus, 1758) for the first time in Iraq and becomes the fourth species of the genus Thelohanellus so far recorded from the Iraqi fish.

5. Acknowledgement

Thanks to Prof. Dr. Furhan T. Mhaisen for providing previously recorded species of the genus *Thelohanellus* species in Iraq.

6. References

[1] Singh R and Kaur H 2012 *Thelohanellus* (Myxozoa: Myxosporea: Bivalvulida) infections in major carp fish from Punjab wetlands (India) *Protistology* **7** 178.
[2] Lom J and Dykova´ I 2006 Myxozoan genera: definition and notes on taxonomy, life-cycle terminology and pathogenic species *Folia Parasitologica* **53** 1.
[3] Zhang JY, Gu ZM, Chaganti K, Eiras J, Liu Y, Guo QY and Molnár K 2013 Synopsis of the species of *Thelohanellus* Kudo, 1933 (Myxozoa: Myxosporea: Bivalvulida) *Syst. Parasitol*. **86** 235.
[4] Kaur H, Singh R, Katoch A, Attri R, Dar SA and Gupta A 2017 Species diversity of the genus *Thelohanellus* Kudo, 1933 (Myxozoa: Bivalvulida) parasitizing fishes in Indian subcontinent *J Parasit. Dis*. **41** 305
[5] Molnár K 2002 Site preference of fish myxosporeans in the gill *Dis Aquat Org*. **48**197.
[6] Kaur H and Katoch A 2014 Gill disease caused by *Thelohanellus bifurcata basu* and *haldar*, 1999 a pathogenic myxozoan parasite in cultured Indian carp, *Labeo rohita* (Hamilton, 1822) in Punjab India *J. Anim. Health Prod*. **2** 19.
[7] Coad BW 2010 *Freshwater fishes of Iraq* Pensoft Publ., Sofia: 274 pp.+16 pls. www.briancoad.com.
[8] Saha M and Bandyopadhyay PK 2017 Parasitological and histological analysis of a new species of the genus *Thalohanellus* and description of a myxozoan parasite (Myxosporea: Bivalvulida) from cultured ornamental goldfish, *Carassius auratus* L. *Aquac. Rep*. **8** 8.
[9] Lom J and Arthur JR 1989 A guideline for the preparation of species descriptions in Myxosporea *J. Fish Dis*. **12** 151.
[10] Mhaisen FT 2020 *Index-catalogue of parasites and disease agents of fishes of Iraq* (Unpublished: mhaisenft@yahoo.co.uk)..
[11] Liu Y, Yuan J, Jia L, Huang M, Zhou Z and Gua Z 2014 Supplemental description of *Thelohanellus wuhanensis* Xiao & Chen, 1993 (Myxozoa: Myxosporea) infecting the skin of *Carassius auratus gibelio* (Bloch): Ultrastructural and histological data. *Parasitol. Int*. **63** 489.
[12] Wang G T, Yao W J, Wang JG and Lu YS 2001 Occurrence of thelohanellosis caused by *Thelohanellus wuhanensis* (Myxosporea) in juvenile allogynogenetic silver crucian carp, *Carassius auratus gibelio* (Bloch), with an observation on the efficacy of fumagillin as a therapeutant *J. Fish Dis*. **4** 57.
[13] Abdul-Ameer KN 1989 *Study of the parasites of freshwater fishes from Tigris River in Salah Al-Dien province, Iraq*. MSc. Thesis, Coll. Sci., Univ. Baghdad 98. (In Arabic)..
[14] Balasem AN, Mhaisen FT, Adday TK, Al-Jawda JM ans Asmar KR 2003 A second survey of parasitic infections in freshwater fishes from Al-Qadisiya Dam Lake, Euphrates River, Iraq *Mar. Mesopot*. **18** 123. (In Arabic).
[15] Mohammed HJ 2017 *Parasitic fauna of some fish species from Diyala River in Diyala province*. MSc. Thesis, College of Education Pure Sci., Ibn Al-Haitham, Univ. Baghdad 122. (In Arabic).
[16] Bdair AT 2018 *Diagnosis of ectoparasitic infestation in some fishes in the Tigris river at Al-Zaafaraniya region from Baghdad city* MSc. Thesis, Coll. Vet. Med., Univ. Baghdad: 118 (In Arabic).
[17] Abbas JA and Abdul-Ameer KN 2020 *Thelohanellus misgurni* (Kudo, 1919) (Myxozoa: Myxobolidae) in gills of the cyprinid fish *Garra rufa*: first record in Iraq *Biochem. Cell. Arch.* **20** 3281.

Arabidopsis thaliana L. Seeds are A novel source of somatic embryos

Arabidopsis thaliana L. Seeds are A novel source of somatic embryos

Rasha Fawzi Al-Jirjees[1*], Shifa Mahdi Salih[1] and Mozahim Kasim AL- Mallah[1]

[1]Department of Biology, Biotechnology Lab, College of Education for Pure Sciences, University of Mosul, Iraq.

*E-mail: rasha.fawzi2016@uomosul.edu.iq

Abstract. Somatic embryogenesis is a valuable tool for investigating the totipotency of plant cells. A simple and efficient protocol for inducing somatic embryogenesis from seeds of *Arabidopsis thaliana* were established. Surface sterilized seeds were placed on agar-solidified Murashige and Skoog (MS) medium free from growth regulators. Callus initiation began7days after seeds culture and became visible with the naked eye within 10-14 days. It was friable and yellowish white in color. Within 20 days, callus was transferred to Gamborg's B5 medium containing 1.0 mgL-1 2, 4-D (2, 4-dichlorophenoxyacetic acid) and 0.05 mgL^{-1} Kin for multiplication. The results indicated that somatic embryos had been recorded only in B5 medium supplemented with 0.4 mgL^{-1} TDZ (N-phenyl-N'-1,2, 3-thidiazol-5-ylurea) and it was the best one. Through our observation, different stages of somatic embryos have been found. The results revealed that the continuous transfer of small masses containing several embryos at different stages to the same induction medium subsequently formed a large cluster of shoots, which were rooted in MS medium free from growth regulators and MS hormone-free medium with 0.2activated charcoal. The percentages of rooting were 63% and 51% respectively. This study proved that Arabidopsis thaliana seeds are a novel source for somatic embryos.

Keywords. *Arabidopsis thaliana*, Seeds, Somatic Embryos, TDZ, Plant regeneration.

1. Introduction

Somatic embryogenesis (SE) is a method of differentiating cells to bipolar structures similar to zygotic embryos in plants [1]. The (SE) process shows that plants' specific development capabilities have already evolved to move to embryogenic development program in somatic cells [2]. Plant cells have been recognized for their ability to be reprogrammed into embryogenesis [3]. Somatic embryos (SEs) formation has been demonstrated as evidence of plant cell totipotency since the development of SEs was observed from colonies of single cell origin [4]. In addition to being a tool for studying and understanding early embryonic growth, SE is also a key plant biotechnology tool used for the asexual propagation of (hybrid) plants and it is also important to rapidly reproduce, preserve, or regenerate genetically modified plants during transformation processes [5]. SEs may grow into whole plants and since the 1960s; numerous protocols have been developed that allow the efficient regeneration, through *in vitro* cultivation conditions, of dozens of plant species through SEs [6]. Although hormones and stress are common treatments that can encourage SE [7, 8], there is little understanding as to how

these causes contribute to SEs formation, including mechanisms interacting to align the SEs with regulatory networks of transcription factors [9].The detection of exogenous and endogenous factors facilitating embryogenic transfer to *in vitro* cultured somatic cells contributes to a deeper understanding of the totipotency of plant cells. Unlike advanced tissue culture experience which encourages the SEs induction [10]. Much less are known the endogenous factors that determine the capability of the tissue to an embryogenic response. However, in the last decade there were strong progress in deciphering the molecular mechanism regulating the embryogenic transformation of somatic plant cells and extensive molecular analysis of the functioning of auxins in SEs induction [2]. The Somatic embryogenesis process is usually divided into two major phases: one phase of the induction and one development. During the induction process, isolated somatic cells undergo conditions that facilitate cell proliferation and dedifferentiation and are assumed to have the capacity to undergo SE and some of the cultivated cells begin to differentiate in somatic embryos during the developmental phase [11]. A host of factors, including cell-to - cell signaling, have been involved in SE induction [12], modification of the wall composition [13]. The alteration in hormones [14,15] and the epigenetic shifters [16,17]. In plant biology, due to lack of early cytological or morphological markers for SE the key experimental factor was the impossibility to precisely isolate and study the cells reacting to SE-induction. As a result, the molecular processes that affect exactly the fate and embryogenicity of such cells in the callus are not known yet. Many plant species like *Arabidopsis thaliana* (*Arabidopsis*), well respond to somatic embryogenesis [18,19]. *Arabidopsis* has been instrumental in disclosing fundamental molecular pathways for regulating *in vitro* plant somatic cell developmental plasticity. Recently it has built a rather good framework for the study, among others, of functional genomics, biology systems, synthetic biology and *in vitro* embryogenesis [20]. SE has earned the most recognition, due to its cognitive as well as functional importance in the field of plant biotechnology, among the various morphogenic pathways induced by cultivated plant explants [21].The goal of this study was to obtain plants from somatic embryos of *Arabidopsis thaliana* seeds which represent a novel source of SEs.

2. Materials and Methods

2.1. Plant material and callus formation

Arabidopsis thaliana col-0 seeds were supplied from Nottingham Arabidopsis Stock Center (NASC),UK. These seeds were surface sterilized by submerging in ethanol alcohol 96% for 3 min, then rinsed three times with sterilized distilled water under a laminar flow hood. Dried seeds were germinated on agar- solidified MS medium [22] free from growth regulators and incubated in the culture room in the dark at 25∓ 2℃. Once callus was induced from the intact specimens seeds, they were transferred to 16 h light/8 h dark photoperiod provided by cool-white fluorescent tubes. The callus induction frequency was recorded after 3 weeks of culturing. For calculating the callus induction frequency, the following equation has been used:

$$\text{Calli induction frequency} = \frac{(\text{Number of seed with calli})}{(\text{Number of incubated seeds})} \times 100\ \% \quad \ldots\ldots\ldots\ldots\ldots\ldots\ [1]$$

2.2. Somatic embryogenesis and plant regeneration

During 20 days, callus was transferred to Gamborg's B5 medium [24] containing 1.0 mgL^{-1} 2,4-D and 0.05 mgL^{-1} Kin for multiplication. Sub culturing of this callus was carried out at 3-4 week intervals at the same medium. To enhance proliferation and plant regeneration, clumps of about 0.5 gm. of callus were cultivated on B5 medium supplemented with four different combinations of plant growth regulators as shown below:

1-5.0 mgL^{-1} BA

2-5.0 mgL^{-1} BA + 0.9mgL^{-1} IAA

3-0.4 mgL^{-1} TDZ

4-0.4 mgL^{-1} TDZ+ 0.1mgL^{-1} IBA

All the samples were kept in the growth chamber at 25∓ 2℃ (16h Light/8h dark). A binocular dissecting microscope was used to investigate different phases of somatic embryos.

2.3. Rooting and acclimatization

Shoots originating from germinated embryos were individually removed, and transplanted in 100 ml volume glass jars containing agar solidified hormone-free MS0 medium which was also used with 0.2% activated charcoal for rooting. Subsequently, rooted shoots were removed from the medium washed from the agar carefully, and each plantlet was transferred to small pot with a diameter of 6.5cm and 5cm height containing peat-moss for adaptation.

3. Results and Discussion

The results of this study showed that *Arabidopsis thaliana* seeds which were placed on MS hormonal-free (MS0) germination media, seven days after cultivation, can form callus rather than seedlings. Recent transcriptomic data confirm that calli can form through different initial routes, whereby a coordinating stress, hormone and evolved responses converge into a single gene regulatory network [25]. This callus became visible with the naked eye within 10-14 days and the callus induction frequency was 100%. In general, It was yellowish white in color with friable texture (Figure 1, A).It was recognized that calli are highly diverse and can be grouped according to their macroscopic properties calli without obvious organ regeneration, for example, are usually known as friable or compact callus [26]. In one hand, we don't find any previous study referred to callus induction from *Arabidopsis thaliana* seeds on MS medium free from growth regulators. On the other hand, [27] have suggested a potential callus induction from *Arabidopsis thaliana* seeds on Gamborg's B5 media with 20 g /l sucrose, 0,5 mgL^{-1} (2,4-D) and 0,05 mgL^{-1} kinetine. Also callus formation from seeds, stems and leaf pieces of *Arabidopsis thaliana* was observed on B5 medium and modified B5 medium [28]. Addition of auxin and cytokinin promotes callus in various plant species. In general, an intermediate proportion of auxin and cytokinin facilitates induction of callus [26]. Since the seeds of *Arabidopsis* are very small and delicate, forceps may have damaged them when they are being carried to the cultivated medium, so callus induction occurred. Iwase and his colleagues [29] pointed out that wounding promotes callus formation in various parts of *Arabidopsis* seedlings and they showed that an AP2/ERF transcription factor, WOUND INDUCED DEDIFFERENTIATION 1 (WIND1), is participates in the control of *Arabidopsis* cell differentiation. At the wound site WIND1 is immediately induced and facilitates cell de-differentiation and subsequent cell proliferation to form a mass of pluripotent callus cells. As a consequence, cell dedifferentiation is genetically regulated mechanism. The results obtained showed that somatic embryos were recovered only in B5 medium supplemented with 0.4mgL-1TDZ, and it was the best one, and through our careful observation, different stages of somatic embryos have been found (Table1).

Table1. Number of somatic embryos stages produced from seeds callus of *Arabidopsis thaliana*.

Media	*No. embryos stage			
	Globular	Heart	Torpedo	Cotyledonary
B_5 + 0.4 mgL^{-1} TDZ	117	87	73	72
B_5+0.4 mgL^{-1} TDZ+ 0.2 mgL^{-1} IBA	100	0	0	0
B_5+1.0 mgL^{-1} 2,4D+0.05mgL^{-1} Kin	0	0	0	0
B_5 + 5 mgL^{-1} BA + 0.9 mgL^{-1} IAA	0	0	0	0
B_5 + 5 mgL^{-1} BA	0	0	0	0

*Average of 6 replicate \ treatment

Cell differentiation and initiation of embryogenesis may be regulated by hormones [30, 31, 32]. In the induction of somatic embryos in *Paeonia Ostii* [33] a combination 0.5 mgL^{-1} thidiazuron (TDZ) and 0.5 mgL-1 2,4-D was found to be successful. Thidiazuron has received considerable attention over recent decades because of its prominent significance in *in vitro* culture with Auxin as well as cytokinin like effects in various plant species [34]. There are some available theories that describe the mode of action of TDZ, but it is still unclear. The TDZ action mechanism can be described as helping in accumulate and/or synthesize endogenous growth hormones [35]. Our study showed that the callus is easily divided and formed abundant green nodules. These nodules developed and emerge repeatedly in this callus to embryogenic masses after 15 days (Figure 1.B) which produced globular stage after 45 days (Figure 1.C), then developed after 60 days to heart stage (Figure 1.D). High numbers of these heart embryos were started elongation and transformed to torpedo stage (Figure 1.E). Subsequently after 3th sub cultures majority of them transform to the differentiated cotyledonary stage (Figure 1.F).

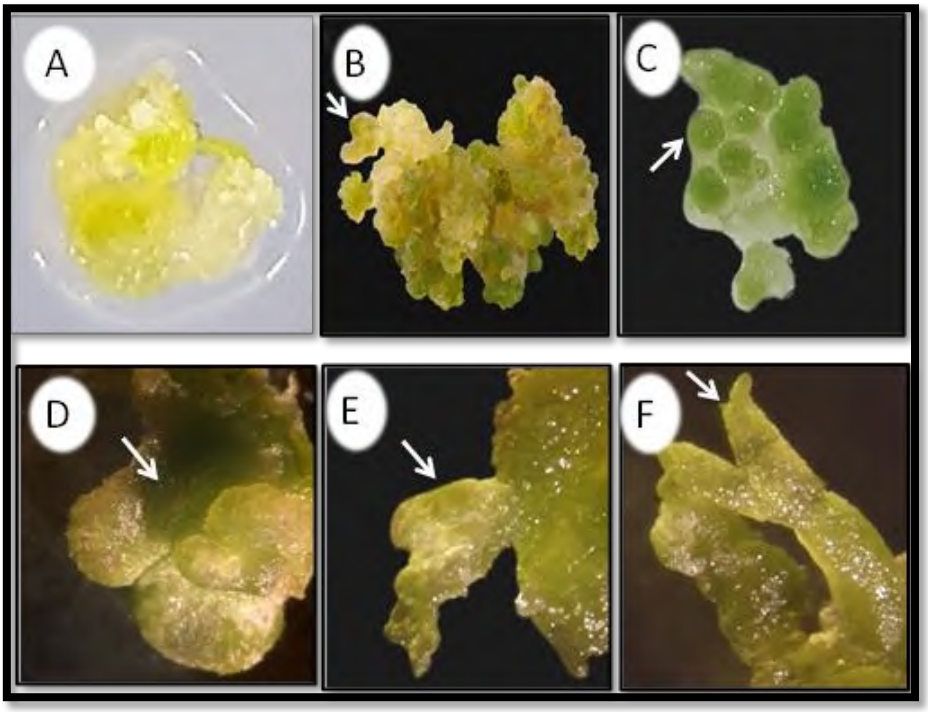

Figure 1. Somatic embryo developmental stages from nodule-like structure produced in callus of Arabidopsis thaliana L: (A) Callus initiation from seeds on MS0 medium. (B) Embryogenic masses formed on B5 medium + 0.4 mgL^{-1} TDZ after 15 days of culture (arrows) (C) Development of globular stage embryos in (a) (arrows). (D)Heart stage embryos (arrows). (E)Torpedo stage (arrows).

(F) Cotyledonary stage (arrows).

Additionally, subculture of the embryogenic masses at the same medium (B5 + 0.4 mgL^{-1} TDZ) led to the emergence of a new variety of nodules (Figure 2.A). It was followed by its development into secondary embryo: globular, heart and torpedo that have basic roots (Figure 2.B). When these structures were left at the same medium, leaf-like structures appeared within 4 weeks (Figure 2.C) ,easy to separate and subsequently transferred to the MS0 medium for additional 3 weeks that allowed the complete development of the leaves (Figure 2.D) which were finally formed plants. In addition, to increasing root system growth.

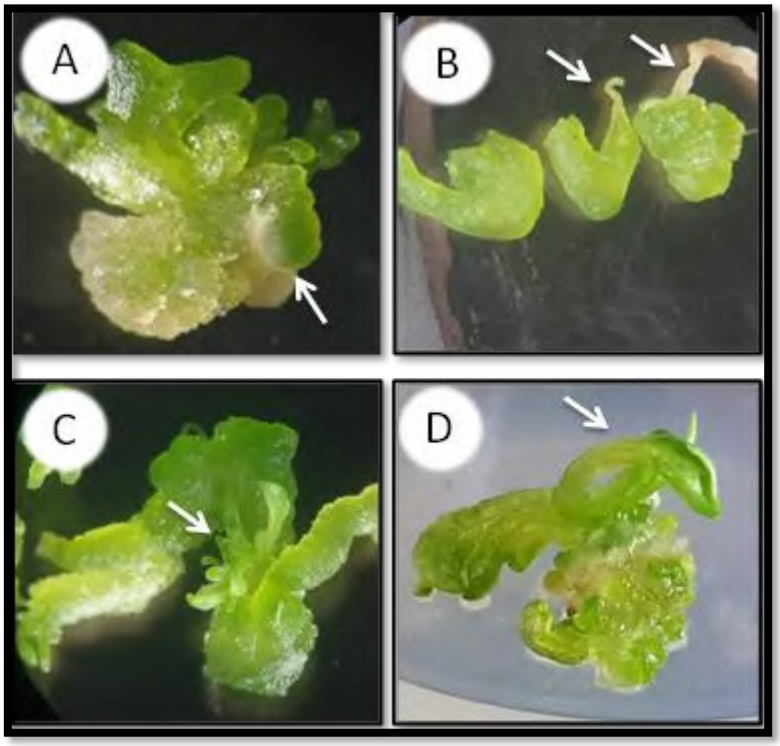

Figure 2**.** Secondary embryos developmental stages from subculture of *Arabidopsis thaliana L.* callus on B_5 + 0.4 mgL^{-1} TDZ: (A) Formation of abundant green nodules and development of globular stage embryos. (B) Embryo-genic masses development and shine Heart, Torpedo stages embryos. (C)After 4weeks cotyledonary stage embryos (arrows). (D) Separation and subsequently transferring of shoot to MS0 medium.

When the cell lines reach the point of moderation, somatic embryogenesis can be formed, and this will involve the addition of Cytokinins, which prevent the polar transfer of auxin while raising hormone levels within the cell because keeping the auxin in the medium prevents the development of embryos that is, the spherical phase does not produce auxin during the formation of primitive embryogenesis masses, after which embryos continue to develop and function like somatic embryogenesis masses [27]. *Arabidopsis thaliana* is known by its high capacity to form somatic embryos directly and indirectly, and this is depending on the type and age of the explant [36, 37, 38]. Indirect somatic embryos formation is more efficient and less stable as mutant plants may form [39]. The results indicated that the continuous transfer of a small masses containing several embryos and secondary embryos at different stages to the same induction medium subsequently formed a large cluster of young and small shoots (Fig 3.A) and upon transfer100 branch, some of them had roots (Figure 3.B) separately to the MS0 media. These branches had the ability to grow and configure them for the root

system (Figure 3.C) after 15 days (Table.2). After that the regenerated plants adapted to the soil conditions (Figure 3.D).

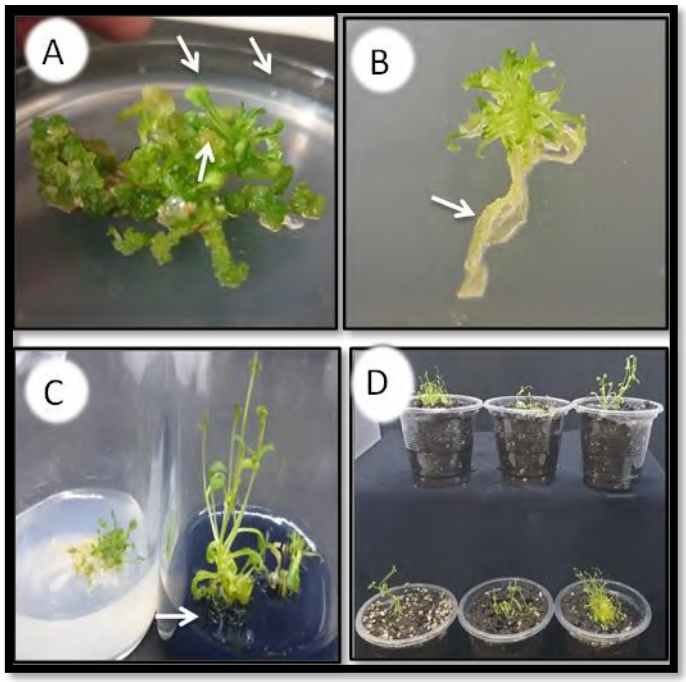

Figure 3**.** Evolution of the vegetative branches of the *Arabidopsis thaliana L*. embryos. (A)Somatic embryos on stimulation media. (B) Rooted derived shoots in A. (C) Rooting of shoots in MS0. (D) Hardening of regenerated plants in the soil.

Although TDZ is grouped under cytokinin because of its natural cytokinetic response in *in vitro* culture, there are evidence in different plant species such as soybeans which refer that TDZ has both auxin and cytokinin-like activities [40].

Table 2. Rotting of *Arabidopsis thaliana L*. shoots regenerated from somatic embryos.

Media	No. Shoot regeneration/ No. Shoot regeneration from secondary embryos		Rooting%
	Transferred shoots	No. rooted shoots	
MS0	100/20	36/5	36/25
MS with 0.2 charcoal	100/20	51/10	51/50

Generally TDZ at low concentrations induces somatic embryogenesis in different plant species such as olive [41] blume orchid [42], the geranium [43]. TDZ induced the synthesis and accumulation of purines [44], moreover it alters cytokinin metabolism [45]. Somatic embryogenesis is characterized by their capability to grow simultaneously and to give a large number of foetuses, and by their capacity to repeat the production of embryos until a full year after the transference to new media [46]. Finally, the protocol of this paper is easy and very efficient to produce large quantities of SEs which considered a very attractive system for studying plants development. Also this method could be used as helpful tool to explain various biochemical and physiological embryogenesis events.

4. Acknowledgement

The authors are very grateful to the University of Mosul, College of Education for Pure Sciences for their provided facilities which help to improve the quality of this works.

5. **References**

[1] Hu R, Sun Y, Wu B, Duan H, Zheng H, Hu D, Lin H, Tong Z, Xu J and Li Y 2017 Somatic Embryogenesis of Immature *Cunninghamia lanceolata* (Lamb.) Hook Zygotic Embryos *Sci. Rep.* **7** 1.

[2] Wojcik AM, Wojcikowska B and Gaj MD 2020 Current Perspectives on the Auxin-Mediated Genetic Network that Controls the Induction of Somatic Embryogenesis in Plants *Int. J. Mol. Sci*. **21** 1333.

[3] Egertsdotter U, Ahmad I and D. Clapham D 2019 Automation and scale up of somatic embryogenesis for commercial plant production with emphasis on conifers *Front. Plant Sci*. **10** 109.

[4] Kadokura, S, Sugimoto K, Tarr P, Suzuki T and Matsunaga S 2018 Characterization of somatic embryogenesis initiated from the Arabidopsis shoot apex *Develop. Bio*. **442** 13.

[5] Ikeda-Iwai M and Kamada H 2005 *Comparison of molecular mechanisms of somatic and zygotic embryogenesis* In: Mujib A and Samaj J eds., Plant Cell Monographs: Somatic Embryogenesis. Springer-Verlag, Berlin 51.

[6] Monja-Mio, KM, Herrera-Alamillo MA and Robert ML 2016 *Somatic embryogenesis in temporary immersion bioreactors*. In Somatic Embryogenesis: Fundamental Aspects and Applications, 1st ed.; Loyola-Vargas V and Ochoa-Alejo N, Eds.; Springer International Publishing: Cham, Switzerland 435.

[7] Feher A 2015 Somatic embryogenesis D Stress-induced remodeling of plant cell fate *Biochim. Biophys. Acta* **1849** 385-402.

[8] Karami O, Rahimi A, Mak P, Horstman A, Boutilier K, Compier M, Zaal B and Offringa R *2010 An Arabidopsis AT-hook motif nuclear protein mediates somatic embryogenesis and coinciding genome duplication* (2010).

[9] Zheng Q, Zheng Y and Perry SE 2013 AGAMOUS-Like15 Promotes Somatic Embryogenesis in Arabidopsis and Soybean in Part by the Control of Ethylene Biosynthesis and Response *Plant Physiol.* **161** 2113.

[10] Gaj MD 2004 Factors influencing somatic embryogenesis induction and plant regeneration with particular reference to *Arabidopsis thaliana* (L.) Heynh. *Plant Growth Regul*. **43** 27.

[11] Luo Y and Koop HU 1997.Somatic embryogenesis in cultured immature zygotic embryos and leaf protoplasts of Arabidopsis thaliana ecotypes *Planta* **202** 387.

[12] Hecht V, Vielle-Calzada JP, Hartog MV, Schmidt K, Boutilier E, Grossniklaus U and de Vries SC 2001 The Arabidopsis SOMATIC EMBRYOGENESIS RECEPTOR KINASE 1 gene is expressed in developing ovules and embryos and enhances embryogenic competence in culture *Plant Physiol*. **127** 803.

[13] Malinowski R and Filipecki M 2002 The role of cell wall in plant embryogenesis *Cell Mol. Bio. Lett.* **7** 1137.

[14] Su, YH , Zhao XY, Liu Y, Zhang B, O'Neill CL and Zhang XS 2009 Auxin-induced WUS expression is essential for embryonic stem cell renewal during somatic embryogenesis in Arabidopsis *Plant J*. **59** 448.

[15] Zheng Q, Zheng Y, Ji H, Burnie W and Perry SE 2019 Gene regulation by the AGL15 transcription factor reveals hormone interactions in somatic embryogenesis *Plant Physiol*. **172** 2374.

[16] De-la-Pena C, Nic-Can GI, Galaz-Avalos RM, Montalvo RA and Loyola- argas VM 2015The role of chromatin modifications in somatic embryogenesis in plants *Front Plant Sci*. **6** 635.

[17] Mozgova I, Munoz-Viana R and Henni L 2017 PRC2 represses hormone-induced somatic embryogenesis in vegetative tissue of *Arabidopsis thaliana PLoS Genet*. **13** e1006562.
[18] Magnani,E , Jiménez-Gómez J, Soubigou-Taconnat L, Lepiniec L and Fiume E 2017 Profiling the onset of somatic embryogenesis in *Arabidopsis* Genomics **18** 998.
[19] Gaj M 2001 Direct somatic embryogenesis as a rapid and efficient system for *in vitro* regeneration of Arabidopsis thaliana. *Plant Cell Tiss. Org. Cult.* **64** 39.
[20] Pais MS 2019 Somatic Embryogenesis Induction in Woody Species: The Future After OMICs Data Assessment *Front. Plant Sci*. **10** 240.
[21] Wójcikowska B and Gaj M 2016 *Somatic Embryogenesis in Arabidopsis* Springer International Publishing Switzerland. Chapter 11, 185.
[22] Murashige T and Skoog F 1962 A revised medium for rapid growth and bioassays with tobacco tissue cultures *Physiol. Plant.* **15** 437.
[23] Mostafiz SB and Wagiran A 2018 Efficient Callus Induction and Regeneration in Selected Indica Rice. *Agronomy* **8** 1.
[24] Gamborg OL, Miller RA and Ojima K 1968 Nutrient requirement of suspension cultures of soybean root cells *Exp. Cell Res*. **50** 151.
[25] Fehér AC 2019 Dedifferentiation, Totipotency, Somatic Embryogenesis: What These Terms Mean in the Era of Molecular Plant Biology Front *Plant Sci*. **10** 536.
[26] Ikeuchi M, Shibata M, Rymen B, Iwase A, Ba A and Watt L 2018 A gene regulatory network for cellular reprogramming in plant regeneration *Plant Cell Physiol*. **59** 770.
[27] Huang B and Yeoman M 1984 Callus Proliferation and Morphogenesis in Tissue Culture of *Arabidopsis thaliana* L., *Plant Sci. Lett.* **33** 353.
[28] Negrutiu, I, Beeftink F and Jacobs M 1975 Arabidopsis thaliana as a model system in somatic cell genetics I. Cell and tissue culture *Plant Sci. Lett.* **5** 293.
[29] Iwase A, Mitsuda N, Koyama T, Hiratsu K, Kojima M, Arai T, Inoue Y, Seki M, Sakakibara H and Sugimoto K 2011 The AP2/ERF transcription factor WIND1 controls cell dedifferentiation in *Arabidopsis Curr. Biol*. **21** 508.
[30] Shiota H, Satoh R, Watabe KI, Harada H and Kamada H 1998 C-ABI3, the carrot homologue of the Arabidopsis ABI3, is expressed during both zygotic and somatic embryogenesis and functions in the regulation of embryo-specific ABA-inducible genes *Plant Cell Physiol*. **39** 1184.
[31] Fehér A, Pasternak TP and Dudits D 2003 Transition of somatic plant cells to an embryogenic state *Plant Cell Tiss. Org*. Cult. **74** 201.
[32] Rose RJ and Nolan KE 2006 *In vitro* review: Genetic regulation of somatic embryogenesis with particular reference to Arabidopsis thaliana and *Medicago truncatula*. *In Vitro Cell. Dev. Biol. Plant* **42** 473.
[33] Ren X, Liu Y and Jeong BR 2020 Enhanced Somatic Embryo Induction of a Tree Peony, Paeonia ostii 'Fengdan', by a Combination of 6-benzylaminopurine (BA) and 1-naphthylacetic Acid (NAA) *Plants* **9** 1.
[34] Ghosh A, Igamberdiev AU and Debnath SC 2018 Thidiazuron-induced somatic embryogenesis and changes of antioxidant properties in tissue cultures of half-high blueberry plants *Sci. Rept* **8** 16978.
[35] Guo B, Abbasi BH, Zeb A, Xu LL and Wei YH 2011 Thidiazuron: a multi-dimensional plant growth regulator *Afr. J. Biotechnol.* **10** 8984.
[36] Kurczyńska EU, Gaj M, Ujczak A and Mazur E 2007 Histological analysis of direct somatic embryogenesis in *Arabidopsis thaliana* (L.) *Heynh. Planta* **226** 619.
[37] Gaj MD 2011 Somatic embryogenesis and plant regeneration in the culture of Arabidopsis Thaliana (L.) Heynh. Immature zygotic embryos *Methods Mol Biol.* **710** 257.
[38] Jenik PD, Gillmor CS and Lukowitz W 2007 Embryonic patterning in *Arabidopsis thaliana Ann. Rev. Cell Dev. Biol*. **23** 207.

[39] Ikeda-Iwai M, Satoh S and Kamada H 2002 Establishment of reproducible tissue culture system for the induction of Arabidopsis somatic embryos *J. Exp. Bot*. **53** 1575.
[40] Radhakrishnan R, Ramachandran AE and Ranjitha Kumari BD 2009 Rooting and shooting: dual function of thidiazuron in *in vitro* regeneration of soybean (*Glycine max* L) *Acta Physiol. Plant* **31** 1213.
[41] Narváez I, Martín C, Jiménez-Díaz RM, Mercado J and Pliego-Alfarom F 2019 Plant regeneration via somatic embryogenesis in mature wild olive genotypes resistant to the defoliating pathotype of *Verticillium dahlia Front Plant Sci*. **10** 1471.
[42] Mose W, Indrianto A, Purwantoro A and Semiarti E 2017 Somatic embryo formation from various types of explant in *Phalaenopsis amabilis* L. blume orchid *Hayati J. Biosci*. **24** 201.
[43] Qureshi JA and Saxena PK 1992 Adventitious shoot induction and somatic embryogenesis with intact seedlings of several hybrid seed geranium (Pelargonium X hortorum Biley) Varieties. *Plant Cell Rep*. **11** 443.
[44] Capelle SC, Mok DW, Kirchnerandand SC and Mok MC 1983 Effects of Thidiazuron on Cytokinin Autonomy and the Metabolism of N6-(Δ2-Isopentenyl)[8-14C]Adenosine in Callus Tissues of *Phaseolus lunatus* L *Plant Physiol*. **73** 796.
[45] Mok MC, Mok DW, Armstrong DJ, Shudo K, Isogai Y and Okamoto T 1982 Cytokinin activity of N-phenyl-N- 1, 2, 3-thiadiazol-5- ylurea (thidiazuron) *Phytochemistry* **21** 1509.
[46] Kobayashi T, Nagayama Y, Higashi K and Kobayashi M 2020 Establishment of a tissue culture system for somatic embryogenesis from germinating embryos of Arabidopsis thaliana. *Plant Biotech*. **27** 359.

Antibacterial, antivirulence and antifungal activity of silver nanoparticles synthesized using alkhal mother shae

Antibacterial, antivirulence and antifungal activity of silver nanoparticles synthesized using alkhal mother shae

Esam J. Al-Kalifawi[1*], Yasamine. J. Al-Azzawi[1] and Mohammed A. Feaza[1]

[1]Department of Biology, College of Education for Pure Science (Ibn Al-Haitham), University of Baghdad, Baghdad, Iraq.

*E-mail: aesam365@yahoo.com

Abstract. Silver nanoparticles were biosynthesized using alkhal mother shae. Nanoparticles were characterized using four methods. The results of the fourth methods proved that silver nanoparticles are spherical shape with a size ranging between 30-40 nm. AMS-AgNPs has antibacterial and antibiofilm activity against gram negative and gram positive tested bacteria, and it has antifungal and antivirulence activity against five types of fungi. Results declare the effect of AMS-AgNPs on the fungus, it can disrupt the integrity fungal cell wall, promoting the permeability and the leakage of the cell constituents, and eventually induce cell death, which is reached from the Congo red dye absorption test and the formation of swelling in the hyphae of the fungal. This study revealed that AMS-AgNPs can be used as an alternative medicin for pathogenic bacteria and fungi.

Keywords. Alkhal Mother Shae, Silver nanoparticles, antibacterial, antifungal, antivirulence.

1. Introduction

Alkhal Mother is a substance composed of yeast and acetic acid bacteria especially, Acetobacter xylinum which forms a cellulose pellicle on shae broth. It is produced by fermenting shae using a "symbiotic 'colony' of bacteria and yeast" (SCOBY). Actual contributing microbial populations in SCOBY cultures vary, but the yeast component generally includes Saccharomyces and other species, and the bacterial component almost includes A. xylinus to oxidize yeast-produced alcohols to acetic and other acids [1]. Tea is the oldest and cheapest health beverage in the world next to water [2]. Today, tea is produced in over 20 countries in tropical, sub-tropical and temperate regions. It is the most widely consumed beverage after water, due to its health, sensory, stimulant, relaxing and cultural properties [3]. The beneficial effects of tea are owing to its polyphenolic compounds. Among the shae polyphenols, flavonoids, especially catechins, are the leading functional components, which accounts for 30% of the dry weight of green tea leaves. Fresh tea leaves are very rich in catechins, which include mainly epicatechin (EC), epicatechin-3-gallate (ECG), epigallocatechin (EGC), epigallocatechin-3-gallate (EGCG), and gallocatechin (GC). EGCG is the most abundant catechin in green tea which accounts for at least 65% of the total catechin [4]. Black tea which grows in many parts of world, is used as an herbal tea for Drinking. *Camellia sinensis* leaves (Black tea) have been reported to contain considerable amounts of tannin products [5]. In Iraq, mats of personally are

individually circulated among those people seeking for health remedy. So, this mat is called "Alkhal mother" as an acquired local traditional Iraqi name, however, it has little scientific studies. The goal of this study is to examine the antibacterial and antifungal activities of silver nanoparticles synthesized using Alkhal Mother Shae (AMS).

2. Materials and Methods

2.1. Collection of bacteria

The bacteria were isolated from patients with infection wounds and burns attending to Al-Yarmouk Teaching Hospital for the period from October to December, 2019. and used as an antimicrobial.

2.2. Collection of fungi

Five types of fungi isolates from Mycotoxins laboratory. Faculty of Sciences, University of Baghdad.

2.3. Alkhal Mother SCOBY

Alkhal Mother SCOBY was obtained from (Dr. Al-Kalifawi, Esam J.), as described by [6].

2.4. Cultivation of Alkhal Mother SCOBY

Alkhal Mother cultured as described by [7].

2.5. Extracellular synthesis of silver nanoparticles

AMS-AgNPs synthesized as described by [8].

2.6. Properties of AgNPs

2.6.1. UV-Vis analysis

The silver nanoparticle colloidal was examined for the absorption peak, which falls within the range 350-450 nm

2.6.2. FT-IR Spectroscopy

The active biological groups present in Alkhal Mother Shae, which serve to reducing and capping the resulting silver nanoparticles, have been identified as described by [8].

2.6.3. XRD analysis

The peaks of the AgNPs were determined using the XRD device as described by [9].

2.6.4. SEM Analysis

The silver nanoparticles were scanned to find out the shape and clustering of the particles.

2.6.5. Antibacterial activity determination

The effect of AMS-AgNPs was determined as described by [10].

2.6.6. Antibiofilm activity determination

Detection of antibiofilm activity of AMS-AgNPs against *Pseudomonas aeruginosa* and *Staphyloccocus aureus* isolates using Microtiter plate method as mentioned in [11].

2.6.7. Antifungal activity determination

The antifungal activity of AMS-AgNPs was tested by the radial growth of tested fungi, after the addition of different concentration of silver nanoparticles to potato dextrose agar medium. The media inoculated with the tested fungi and incubated at 25±2°C [12].

2.6.8. The effect of AMS-AgNPs on cell wall function

The effect of AMS-AgNPs on cell wall efficacy was studied by phenotypic changes and congo-red dye test [13].

3. Results and Discussion

The fresh suspension of (AMS) was bright brown but it turned reddish brown after adding it to the silver nitrate solution. This color change indicates the completion of the reaction and the formation of silver nanoparticles Figure 1.

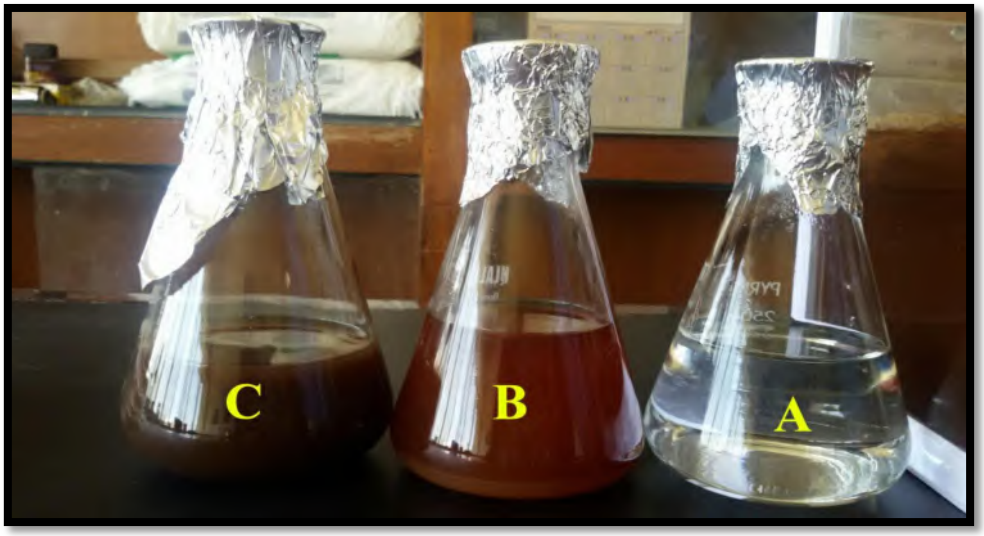

Figure 1. Synthesis of AMS-AgNPs: A- Solution of silver nitrate. B- (AMS), and C- AMS-AgNPs colloidal.

3.1. UV-Vis Spectrophotometry

UV-Vis absorption spectrum of AMS-AgNPs is shown in figure 2. It's at 430 nm.

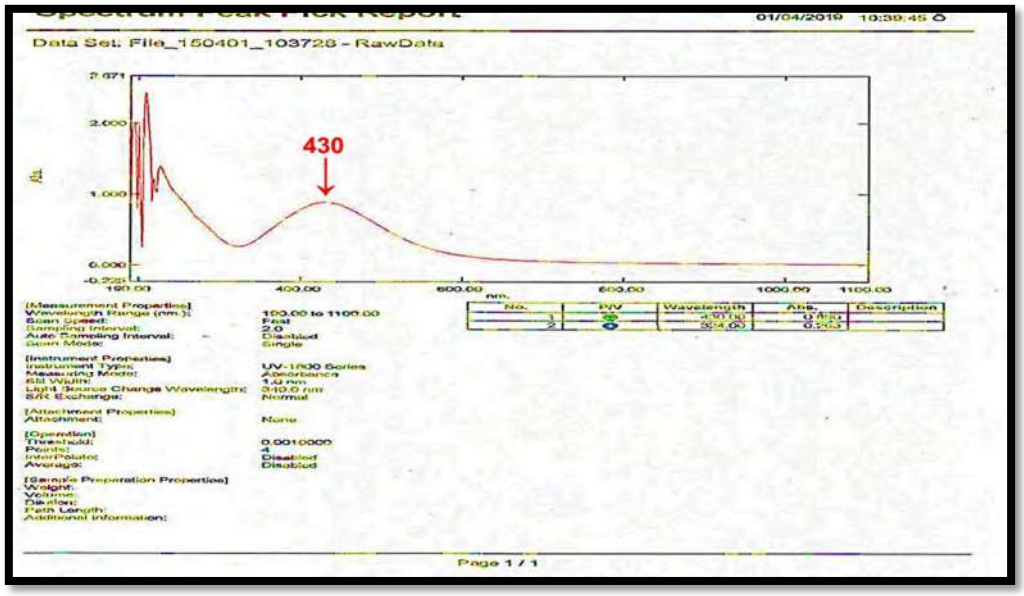

Figure 2. UV-Vis absorption spectra of AMS-AgNPs.

3.2. Fourier Transform Infra-Red Spectroscopy

Figure 3 shows the spectra for Alkhal Mother Shae were obtained using an FTIR spectrophotometer. Several peaks were observed indicating the Alkhal Mother Shae is composed of various functional groups. The broad band at about 3448.72 cm^{-1} can be attributed to bond –OH groups. The band at about 2356.89 cm^{-1} can be attributed to C=N bond Amine I groups are also observed at 1635.64 cm^{-1}. The peak at 1543.05 cm-1 is attributed to secondary amine groups. The peaks at 1458.18 and 1396.46 cm-1 are both related to the symmetric bending of CH3. While the peak at about 1107.14 cm^{-1} can be attributed to C=O stretching vibrations groups. The peak at 470.63 cm-1 correspond to stretching vibration of amine groups.

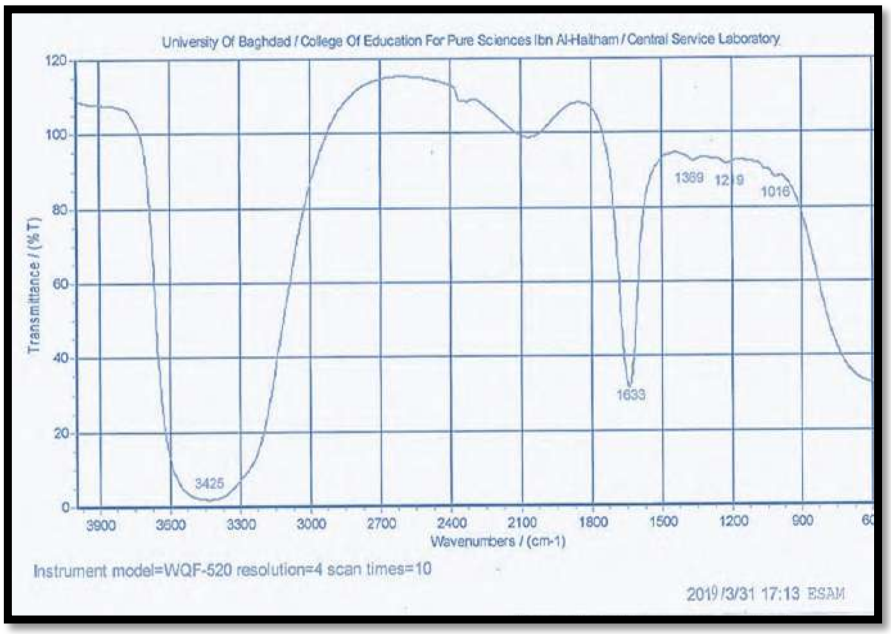

Figure 3. Fourier Transform Infra-Red Spectroscopy image of AMS-AgNPs.

3.3. XRD pattern of AMS-AgNPs

Figure 4 shows the main peaks obtained at 111, 200, 220, and 311 correspond to reflections with 2θ values of the Bragg angles 38.12°, 44.31°, 64.46 °, and 76.98 °, respectively. These results confirm that the material tested are AgNPs and are of high purity. The average crystallite size of AMS-AgNPs in arrange (30-40 nm).

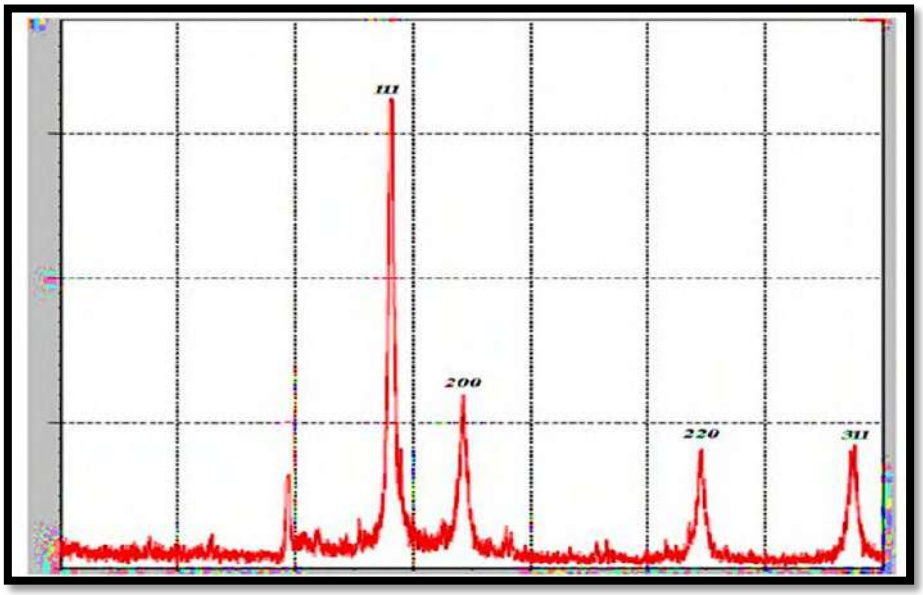

Figure 4. X ray diffraction of AMS-AgNPs.

3.4. SEM analysis of AMS-AgNPs

The scanning showed that the AMS-AgNP s are spherical in shape and are aggregated in clusters Figure 5.

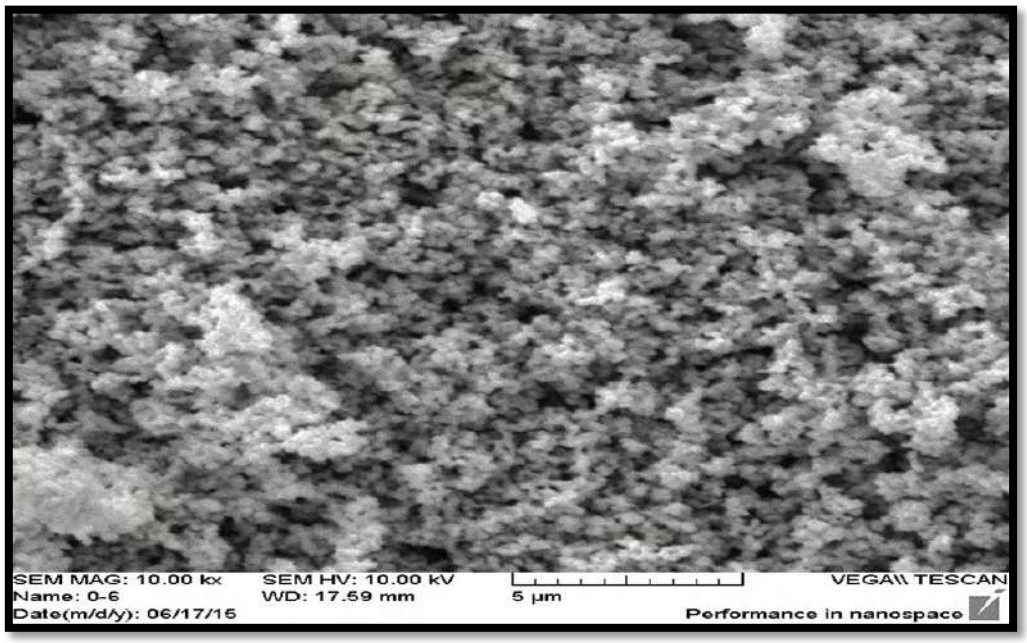

Figure 5. SEM micrographs of AMS-AgNPs.

The results in Table (1) and Figures (6 and 7) shows the inhibition zone was 18 mm for *P. aeruginosa* No.1, 3, 4, 7, 9, 10 and *S. aureus* No.3, 5, 6, 9. 16 mm for *P. aeruginosa* No.2, 8 and *S. aureus* No.4, 10. 14 mm for *P. aeruginosa* No. 5, 6 and *S. aureus* No.1, 2, 7. The IZ was 10 mm for *P. aeruginosa* No.1, 4, 6, 8, 9, 10 and *S. aureus* No.2, 3, 7, 8, 9. 11 mm for *P. aeruginosa* No.2, 5 and *S. aureus* No.1, 5, 10. 12 mm for *P. aeruginosa* No.3, 7 and *S. aureus* No.4, 6.

Table 1. Activity of the AMS-AgNPs against the tested bacteria.

Isolated bacteria	Zone of Inhibition (mm)		
	Silver nitrate solution	Alkhal mother tea	Silver nanoparticles colloidal
***P. aeruginosa* No.1**	0	10	18
***P. aeruginosa* No.2**	0	11	16
***P. aeruginosa* No.3**	0	12	18
***P. aeruginosa* No.4**	0	10	18
***P. aeruginosa* No.5**	0	11	14
***P. aeruginosa* No.6**	0	10	14
***P. aeruginosa* No.7**	0	12	18
***P. aeruginosa* No.8**	0	10	16
***P. aeruginosa* No.9**	0	10	18
***P. aeruginosa* No.10**	0	10	18
***S. aureus* No.1**	0	11	14
***S. aureus* No.2**	0	10	14
***S. aureus* No.3**	0	10	18
***S. aureus* No.4**	0	12	16
***S. aureus* No.5**	0	11	18
***S. aureus* No.6**	0	12	18
***S. aureus* No.7**	0	10	14
***S. aureus* No.8**	0	10	14
***S. aureus* No.9**	0	10	18
***S. aureus* No.10**	0	11	16

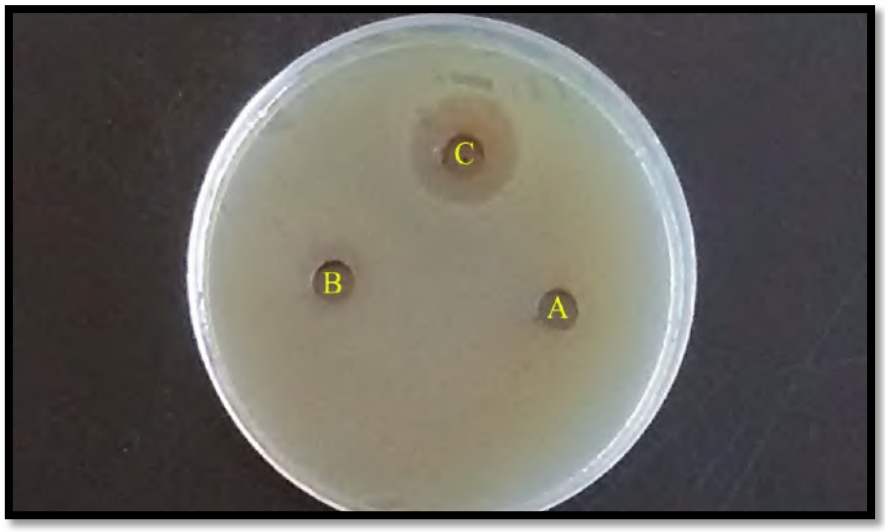

Figure 6. Figure 6. Antibacterial of AMS-AgNPs using the test bacterium Pseudomonas aeruginosa No 4. A- Solution of silver nitrate, B- Alkhal Mother Shae, C- AgNPs colloidal.

Figure 7. Antibacterial of AMS-AgNPs using the test bacterium *Staphylococcus aureus*. No.3. A-Solution of silver nitrate, B- Alkhal Mother Shae, C- AgNPs colloidal.

The results showed the inhibition of biofilm formation for *P. aeruginosa* and *S. aureus* was 70% and 60%, respectively when using AMS-AgNPs at 0.1 concentration. While the inhibition of biofilm formation for *P. aeruginosa* and *S. aureus* was 80% and 70%, respectively when using AMS-AgNPs at 0.5 concentration table 2 and figures 8 and 9.

Table 2. Inhibition of biofilm formation of *Pseudomonas aeruginosa* and *Staphylococcus aureus* using AMS-AgNPs.

Isolate number	The value of biofilm	The value of biofilm after addition 0.1 mg/ml AgNPs	The value of biofilm after addition 0.5 mg/ml AgNPs
***P. aeruginosa* No.1**	0.176	0.90	0.80
***P. aeruginosa* No.2**	0.169	0.75	0.62
***P. aeruginosa* No.3**	0.188	0.95	0.86
***P. aeruginosa* No.4**	0.179	0.88	0.75
***P. aeruginosa* No.5**	0.295	0.280	0.200
***P. aeruginosa* No.6**	0.289	0.222	0.210
***P. aeruginosa* No.7**	0.170	0.89	0.78
***P. aeruginosa* No.8**	0.187	0.170	0.91
***P. aeruginosa* No.9**	0.200	0.93	0.85
***P. aeruginosa* No.10**	0.199	0.87	0.70
***S. aureus* No.1**	0.274	0.200	0.192
***S. aureus* No.2**	0.217	0.195	0.187
***S. aureus* No.3**	0.223	0.102	0.89
***S. aureus* No.4**	0.224	0.188	0.171
***S. aureus* No.5**	0.193	0.88	0.76
***S. aureus* No.6**	0.184	0.90	0.83
***S. aureus* No.7**	0.234	0.210	0.200
***S. aureus* No.8**	0.310	0.304	0.298
***S. aureus* No.9**	0.198	0.84	0.71
***S. aureus* No.10**	0.186	0.160	0.90

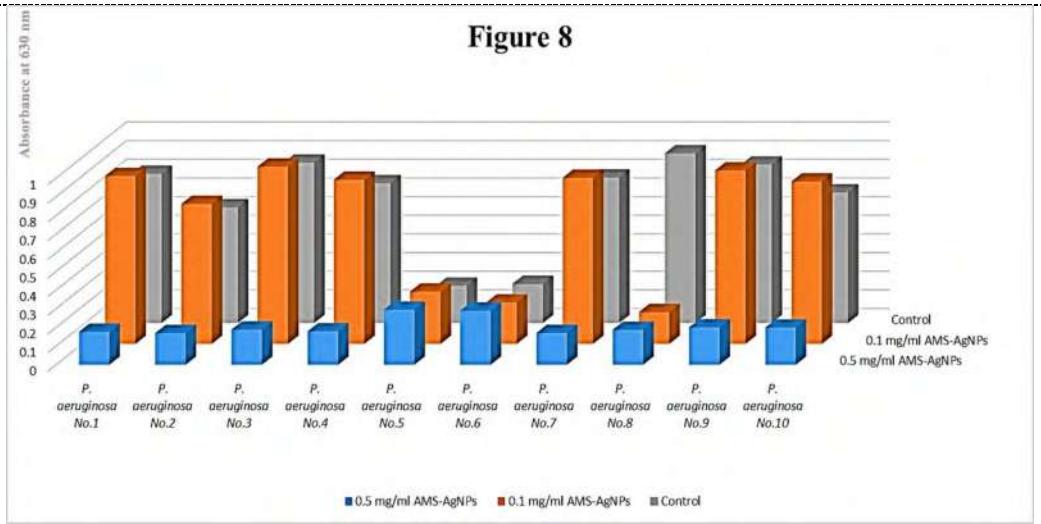

Figure 8. Inhibition of biofilm formation of Pseudomonas aeruginosa using AMS-AgNPs.

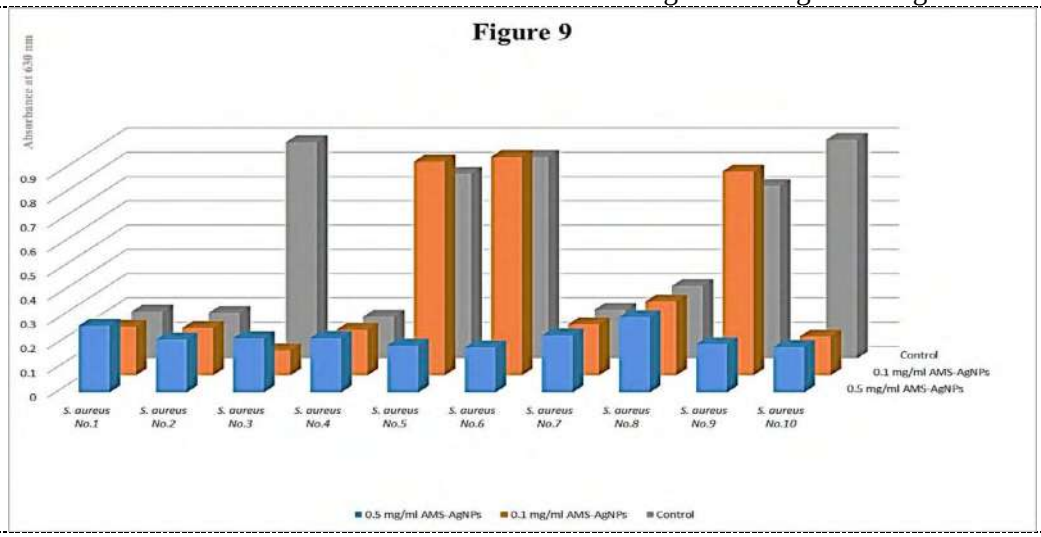

Figure 9. Inhibition of biofilm formation of Staphylococcus aureus using AMS-AgNPs.

The results in Table (3) and Figure (10, 11) shows that AMS-AgNPs has effective antifungal activities on the *Aspergillus flavus*, *Aspergillus parasiticus*, *Aspergillus niger*, *Fusarium oxysporum* and *Fusarium verticillioides* as indicated by the diameter of their radial growth. The radial growth of *Aspergillus flavus*, *Aspergillus parasiticus* and *Aspergillus niger* reduce from 9 cm for control to 2cm at 15% concentration of silver nanoparticles in the culture media. Whereas the radial growth of *Fusarium oxysporum* and *Fusarium verticillioides* reduce from 7 cm for control to 1cm at 15% concentration of silver nanoparticles in the culture media.

Table 3. The antifungal effect of the AMS-AgNPs.

Isolated microbes	Diameter of growth*			
	control	5%	10%	15%
Aspergillus flavus	9	7	4	2
Aspergillus parasiticus	9	7	4	2
Aspergillus niger	9	7	3	2
Fusarium oxysporum	7	2	1.5	1
Fusarium verticillioides	7	3	2	1

* Radial growth of fungi (cm).

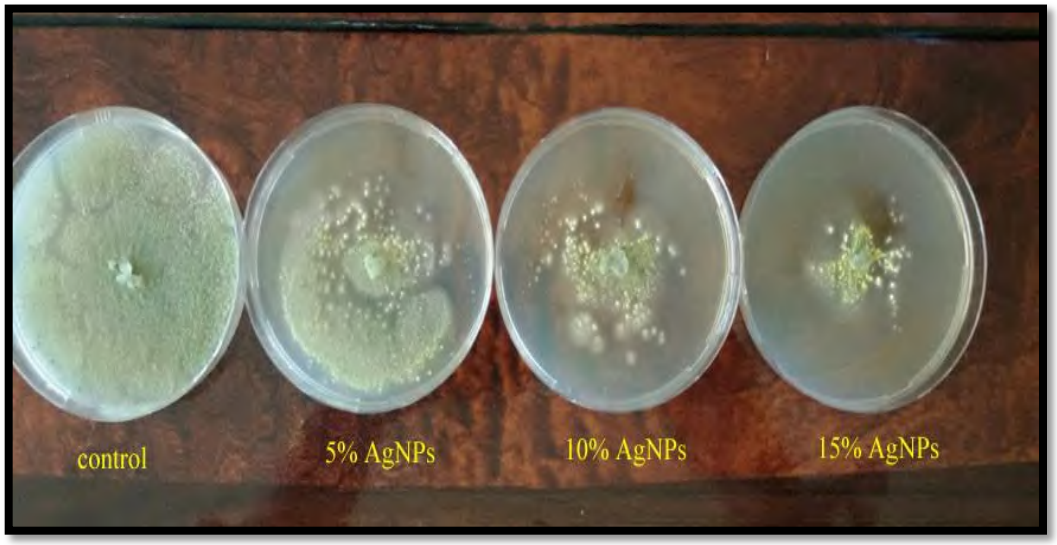

Figure 10. Antifungal activity of AMS-AgNPs against *Aspergillus flavus*.

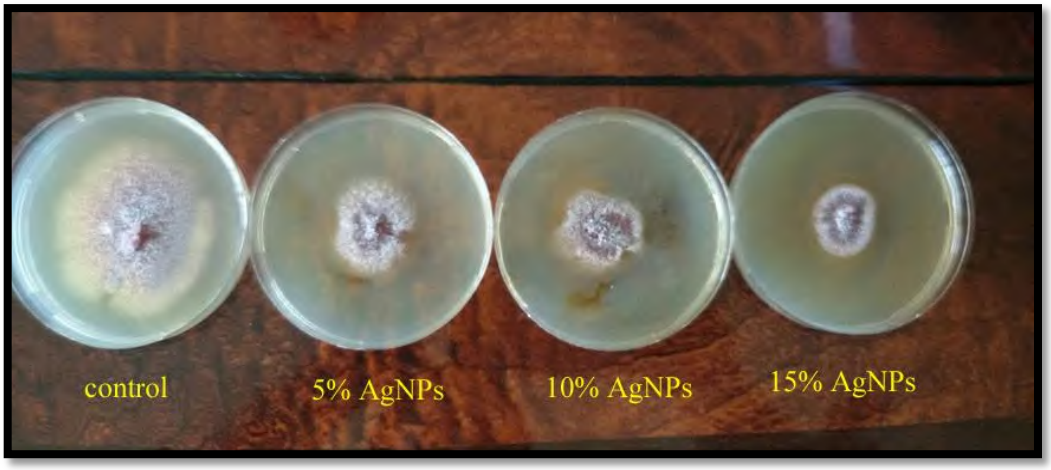

Figure 11. Antifungal activity of AMS-AgNPs against *Fusarium oxysporum*.

The effect of silver nanoparticles on the fungus was also studied and it was found that AMS-AgNPs lead to swelling in the fungal hyphae Figure 12. These swelling effect on permeability of hyphae cell and thus kill it, which is reached from the Congo red dye absorption test Figure 13.

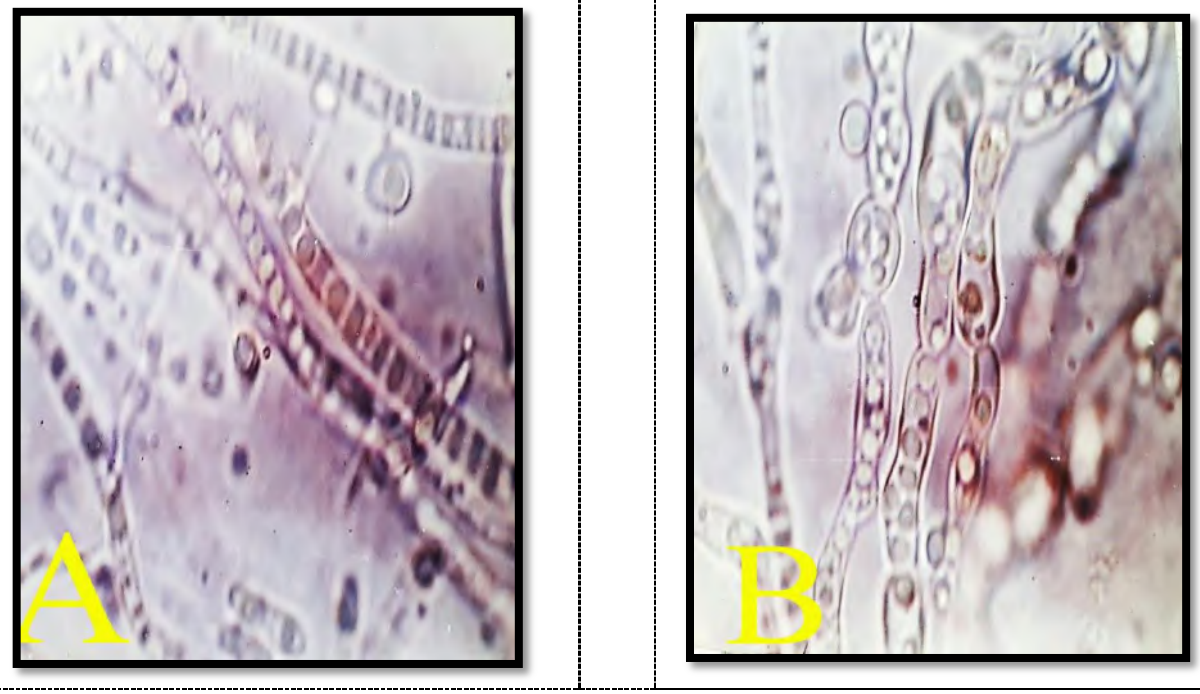

Figure 12. Show the effect of AMS-AgNPs on the *Fusarium verticillioides* hyphae. A- Control. B- treated with AMS-AgNPs. Power of magnification 100X.

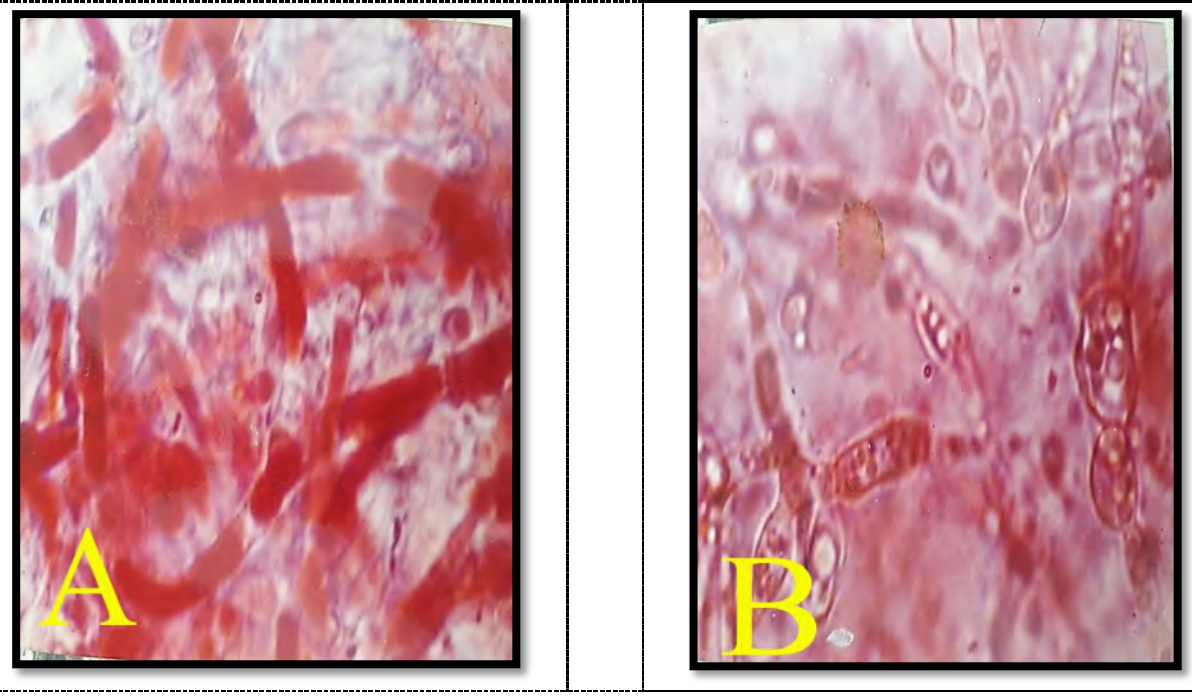

Figure 13. Show the Congo red dye absorption test. A- Normal hypha of *Fusarium verticillioides*. B- treated with AMS-AgNPs. Power of magnification 100X.

4. Discussion

In the present study, AgNPs was biosynthesized using alkhal mother shae. Production of AgNPs was confirmed by the change in colour and formation of gray aggregates of AgNPs. This result is in agreement with many studies [16, 17, 18] which found that the formation of gray aggregates is

evidence of completeness of reaction and formation of AgNPs. The crystalline AgNPs were confirmed by UV absorption spectrum at 430 nm. This result is accordance with several studies [19, 20, 21] which reported that the peak absorption of AgNPs is around 300-500nm. The functional groups associated with the process of reducing and stabilizing AgNPs were analyzed using Fourier Transform Infrared Spectroscopy. Several peaks were observed indicating that the alkhal mother shae is composed of various functional groups are attributed to secondary amine groups. These finding are acceptable with many studies [22, 23, 24] which found these groups are responsible for reducing and capping of AgNPs. The results of X-ray Diffraction spectrum with 2θ values was at Bragg angles 38.12, 44.31, 64.46 and 76.98, respectively. These results are consistent with several studies in which biosynthesis of nanoparticles of silver molecules using tea leaf extract and kombucha tea [25, 26, 27]. Particle size causes the broadening of peaks in the XRD patterns and by using Debye-Scherrer's equation, the average particles size were arrange 30-40 nm. Results of the present study show that AMS-AgNPs have antibacterial activity against Gram positive and Gram negative bacteria which tested. The antimicrobial activity of alkhal mother shae has less effect against tested isolates. These finding are in agreement with several studies [28, 29, 30, 31]. Who's found that the silver nanoparticles synthesized by leaf tea extract had antibacterial activity against Gram-negative and Gram-positive bacteria. The inhibition of biofilm formation for *P. aeruginosa* and *S. aureus* was 70% and 60%, respectively when using AMS-AgNPs at 0.1 concentration. While the inhibition of biofilm formation for *P. aeruginosa* and S. aureus was 80% and 70% respectively when using AMS-AgNPs at 0.5 concentration. These finding are in agreement with several studies [32, 33, 34] which found that the antibiofilm activity of AgNPs was between 50 to 90 in Gram negative bacteria and about 50 to 80 in Gram positive bacteria. AMS-AgNPs has antifungal activity on the *Aspergillus flavus*, *Aspergillus parasiticus*, *Aspergillus niger*, *Fusarium oxysporum* and *Fusarium verticillioides* as indicated by the diameter of their radial growth. The radial growth of *Aspergillus flavus*, *Aspergillus parasiticus* and *Aspergillus niger* reduce from 9 cm for control to 2cm at 15% concentration of silver nanoparticles in the culture media. Whereas the radial growth of *Fusarium oxysporum* and Fusarium verticillioides reduce from 7 cm for control to 1cm at 15% concentration of silver nanoparticles in the culture media these finding are in agreement with several studies which found the effect of silver nanoparticles against various plant pathogenic fungi [35, 36, 37]. The two species have been selected because they are producers of the mycotoxins. The *Aspergillus*, especially A. flavus and A. parasiticus, which produce aflatoxins and *Fusarium*, which produces *Trichothecenes*. Aflatoxins is the leading cause of cancer. *Trichothecenes* is used in chemical warfare [38, 39]. For these reasons, the eradication of these fungi protects plants, from the infection of and animals, humans from their toxins [40, 41]. The effect of silver nanoparticles on the fungus was also studied and it was found that silver nanoparticles lead to swelling in the fungal hyphae and thus kill it, which is reached from the Congo red dye absorption test [42]. These finding are in agreement with several studies [43, 44, 45] in which found AMS-AgNPs disrupt the integrity fungal cell wall, promoting the permeability and the leakage of the cell constituents, and eventually induce cell death.

5. Conclusions

We concluded that the AMS-AgNPs can be used as an alternative medicin for pathogenic bacteria and fungi.

6. Acknowledgement

We would like to thanks Dr. Nehmeh, Mycotoxins laboratory. Faculty of Sciences, University of Baghdad for supplying us with fungal isolates.

7. References

[1] Al-Kalifawi E J and Hassan IA 2014 Factors Influence on the yield of bacterial cellulose of Kombucha (Khubdat Humza) *Baghdad Sci. J.* **11** 1420.
[2] Rahman MM, Kalam MA Salam MA and Rana MR 2013 Aged leaves effect on essential components in green and oolong tea *Int. J. Agril. Res. Innov. Tech*. **3** 54.
[3] Ahmed S and Stepp JR 2012 Green tea: plants, processing, manufacturing and production *Tea Health Dis. Prev.* **1** 19.
[4] Zaveri NT 2006 Green tea and its polyphenolic catechins: medicinal uses in cancer and noncancer applications *Life Sci*. **78** 2073.
[5] Gramza A, Korczak J and Amarowicz R 2005 Tea polyphenols-their antioxidant properties and biological activity-a review *Pol. J. Food Nutr. Sci*. **14** 219.
[6] Al-Kalifawi EJ 2014 Produce bacterial cellulose of kombucha (Khubdat Humza) from honey. J. Genet. Environ *Resour. Conserv*. **2** 39.
[7] Chen C and Liu BY 2000 Changes in major components of tea fungus metabolites during prolonged fermentation *J. Appl. Microbiol*. **89** 834.
[8] Moosa AA, Ridha AM and Allawi MH 2015 Green Synthesis of Silver Nanoparticles using Spent Tea Leaves Extract with Atomic Force Microscopy *Int. J. Curr. Eng. Technol.* **5** 3233.
[9] Bykkam S, Ahmadipou M, Narisngam S, Kalagadda VR and Chidurala SC 2015 Extensive Studies on X-Ray Diffraction of Green Synthesized Silver Nanoparticles *Adv. Nanopart.* **4** 1.
[10] Valgas C, de Souza SM, Smânia EFA and Jr. AS 2007 Screening Methods to Determine Antibacterial Activity of Natural Products *Braz. J. Microbiol.* **38** 369.
[11] Sharma BK, Saha A, Rahaman L, Bhattacharjee S. and Tribedi P 2015 Silver Inhibits the Biofilm Formation of *Pseudomonas aeruginosa Adv. Microbiol*. **5** 677.
[12] Kim SW, Jung JH, Lamsal K, Kim YS, Min JS and Lee YS 2012 Antifungal Effects of Silver Nanoparticles (AgNPs) against Various Plant Pathogenic Fungi *Mycobiology* **40** 53.
[13] Linder T 2018 Evaluation of the chitin-binding dye Congo red as a selection agent for the isolation, classification, and enumeration of ascomycete yeasts *Arch. Microbiol.* **200** 671.
[14] Loo YY, Chieng BW, Nishibuchi M and Radu S 2012 Synthesis of silver nanoparticles by using tea leaf extract from *Camellia sinensis Int. J. Nanomed*, **7** 4263.
[15] Langford JI and Wilson AJC 1978 Scherrer after sixty years: A survey and some new results in the determination of crystallite size *J. Appl. Cryst*. **11** 102.
[16] Al-Kalifawi EJ, Al-Saadi TM, Al-Dulaimi SA and Al-Obodi EE 2015 Biosynthesis of silver nanoparticles by using onion (*Allium cepa*) extract and study antibacterial activity *J. Gene c Environ. Resour. Conserv*. **3** 1.
[17] Shihab RN, Al-Kalifawi EJ and Al-Haidari SHJ 2016 Environmental Friendly Synthesis of Silver Nanoparticles Using Leaf Extract of Mureira Tree (*Azadirachta indica*) cultivated in Iraq and Efficacy the Antimicrobial Activity *J. Nat. Sci. Res.* **6** 47.
[18] Al-Kalifawi EJ, Hasan SAR, Al-Saadi TM and AlObodi EE 2015 Green synthesis of silver nanoparticles by kumquat (*Fortunella margaarita*) fruit extract and efficacy the antimicrobial activity *J. Al-Fath* 1.
[19] Panda SK, Chakraborti S and Basu RN 2018 Size and shape dependences of the colloidal silver nanoparticles on the light sources in photo-mediated citrate reduction technique *Bull. Mater. Sci*. **41** 1.
[20] Hamouda RA, Hussein MH,. Abo-elmagd RA and Bawazir SS 2019 Synthesis and biological characterization of silver nanoparticles derived from the cyanobacterium *Oscillatoria limnetica Sci. Rep.* **9** 1.
[21] Anandalakshmi K, Venugobal J and Ramasamy V 2016 Characterization of silver nanoparticles by green synthesis method using *Pedalium murex* leaf extract and their antibacterial activity *Appl. Nanosci*. **6** 399.

[22] Narasimha G, Alzohairy JM, Khadri H and Mallikarjuna K 2013 Extracellular synthesis, characterization and antibacterial activity of silver nanoparticles by *Actinomycetes* isolative *Int. J. Nano Dimens*. **4** 77.
[23] Narasimha G, Praveen B, Mallikarjuna K and Raju BDP 2011 Mushrooms (*Agaricus bisporus*) mediated biosynthesis of sliver nanoparticles, characterization and their antimicrobial activity *Int. J. Nano Dim*. **2** 29.
[24] Prabakaran M., Subha K, Thennarasu V and Merinal S 2012 Biosynthesis of silver nanoparticles using Sphaerulina albispiculata and evaluation of antibacterial activity *Europ. J. Exper. Biol.* **2** 297.
[25] Shameli K, Ahmad MB, Zamanian A, Sangpour P, Shabanzadeh P, Abdollahi Y and Zargar M 2012 Green biosynthesis of silver nanoparticles using Curcuma longa tuber powder *Int. J. Nanomed.* **7** 5603.
[26] Kandakumar S, Sathya V and Manju V 2014 Synthesis and Characterization of Silver Nanoparticles Using Hydnocarpus Alpina, Its Application as a Potent Antimicrobial and Antioxidant Agent–A Novel Study *Int. J. ChemTech Res.* **6** 4770.
[27] Jyoti K, Baunthiyal M and Singh A 2016 Characterization of silver nanoparticles synthesized using Urtica dioica Linn. Leaves and their synergistic effects with antibiotics *J. Rad. Res. Appl. Sci.* **9** 217.
[28] Al-Kalifawi EJ 2018 Silver Nanoparticles Synthesis by Hamza's Khubdat (A.S.) (Kombucha) Tea and used in Burn Wounds Treatment *J. Glob. Pharma Technol.* **10** 489.
[29] Al-Kalifawi EJ 2016 Green Synthesis of Silver Nanoparticles Using Leaf Extract of Al-Rawag tree (Moringa oleifera Lamarck) Cultivated in Iraq and Efficacy the Antimicrobial activity *Mesopot. Environ. J.,* **A** 39.
[30] Vaseeharan B, Ramasamy P and Chen JC 2010 Antibacterial activity of silver nanoparticles (AgNPs) synthesized by tea leaf extracts against pathogenic *Vibrio harveyi* and its protective efficacy on juvenile *Feneropenaeus indicus Lett. Appl. Microbiol.* **50** 352.
[31] Al-Kalifawi EJ 2014 Bacterial isolated from burn wound patients, study resistance to antimicrobials and effect of Kombucha (Khubdat Humza) tea on isolates bacteria *J. Genet. Environ. Resour. Conserv*. **2** 159.
[32] Ebrahimia A, Jafferib H, Habibianc S and Lotfalian S 2018 Evaluation of Anti biofilm and Antibiotic Potentiation Activities of Silver Nanoparticles against Some Nosocomial Pathogens *IJPS*. **14** 7.
[33] Gurunathan S, Han JW, Kwon DN and Kim JH 2014 Enhanced antibacterial and anti-biofilm activities of silver nanoparticles against Gram-negative and Gram-positive bacteria *Nanosc. Res. Lett.* **9** 1.
[34] Ramachandran R and Sangeetha D 2017 Antibiofilm efficacy of silver nanoparticles against biofilm forming multidrug resistant clinical isolates *Pharma Innov. J.* **6** 36.
[35] Al-Kalifawi EJ, Al-Azzawi YJ and Hassan FF 2018 Biosynthesis of silver nanoparticles using Al-Ankabut's home extract and its antimicrobial activity. *Acad. J. Agric. Res.* **6** 33.
[36] Jo, YK, Kim B.H and Jung G 2009 Antifungal Activity of Silver Ions and Nanoparticles on Phytopathogenic Fungi *Plant Dis.* **93** 1037.
[37] Abdelmalek JAMA and Salaheldin TA 2016 Silver Nanoparticles as a Potent Fungicide for Citrus Phytopathogenic Fungi *J. Nanomed. Res.* **3** 1.
[38] Al-Abdalall AHA 2009 Production of aflatoxins by *Aspergillus flavus* and *Aspergillus niger* strains isolated from seeds of pulses *J. Food, Agric. Environ.***7** 33.
[39] Kimura M, Tokai T, Takahashi-Ando N, Ohsato S and Fujimura M 2014 Molecular and Genetic Studies of Fusarium Trichothecenes Biosynthesis: Pathways, Genes, and Evolution. *Biosci. Biotechnol. Biochem*. **71** 2105.
[40] Michael C and Kew MC 2013 Aflatoxins as a Cause of Hepatocellular Carcinoma *J. Gastrointestin. Liver Dis*. **22** 305.

[41] Kankkunen P, Rintahaka J, Aalto A, Leino M, Majuri ML, Alenius H, Wolff H and Matikainen S 2018 *Trichothecenes* Mycotoxins activate inflammatory response in human macrophages *J. Immunol*. **182** 6418.
[42] Slifkin M and Cumbie R 1988 Congo red as a Fluorochrome for the Rapid Detection of Fungi *J. Clin. Microbiol.* **26** 827.
[43] Hwang IS, Lee J, Hwang JH, Kim KJ and Lee DG 2012 Silver nanoparticles induce apoptotic cell death in *Candida albicans* through the increase of hydroxyl radicals *FEBS J.* **279** 1327.
[44] Matei PM, Iacomi BM, Martín-Gil J, Pérez-Lebeña E, Ramos-Sánchez MC, Barrio-Arredondo MT and Martín-Ramos P 2018 In vitro antifungal activity of composites of AgNPs and polyphenol inclusion compounds against *Fusarium culmorum* in different dispersion media *Agronomy* **8** 1.
[45] Al-Zubaidi S, Al-Ayafi A and Abdelkader H 2019 Biosynthesis, Characterization and Antifungal Activity of Silver Nanoparticles by *Aspergillus niger* Isolate *J. Nanotechnol. Res*. **1** 23.

Anatomical study of the *Carissa macrocarpa* (Apocynaceae family) in Iraq

Anatomical study of the *Carissa macrocarpa* (Apocynaceae family) in Iraq

Feryal K. Khalaf[1*]

[1]Department of Biology, College of Education for Pure Science (Ibn Al-Haitham), University of Baghdad, Baghdad, Iraq.

*E-mail: firial.k.k@ihcoedu.uobaghdad.edu.iq

Abstract. This study was conducted to examine the anatomical aspects of *Carissa macrocarpa*, of stem, leaf and leaf venation. The results obtaind showed that the tissue of the studied parts have important anatomical characteristics in terms of the shape of the cross-sectional of stem and vertical-sectional of leaves. The stem section appeared in circular and the midrib was crescent shape and the stomata appeared on the upper surface of the leaf only, Tetracytic in type. Druses crystals and Aleurone granules appeared on both surfaces of leaves. The venation type was Brochidodromous in which the secondary veins do not end at the edge of the leaf, and each secondary race is connected with the higher race and linked together with a series of prominent arches.

Keywords. *Carissa macrocarpa*, Anatomical study, Apocynaceae, Iraq.

1. Introduction

The Apocynaceae family consists of 300 genera and more than 1300 species spread all over the world and in Iraq have 4 wild species and 7 cultivated species [1]. The species is considered domestic in South Africa and is grown in Egypt [2]. Most of the plants in this family were herbs or shrubs or trees with milky juice, the leaves were simple, bracelet or alternate with smooth edge, the flowers radial symmetry and the seeds are often covered with hairs [3]. Most of the plants are grown for decoration, but many species are poisonous to humans and animals if they eat the fruit and their vegetative compositions, extracting a number of drugs and tanning materials [4]. We did not find published data provides clarify anatomical information to describe the species under study in Iraq, so the aim of this study provide and description anatomical features and enhanced measurements and forms which can be adopted the morphological studies of this species and applications of phylogenic relationships [3, 5, 6, 7].

2. Materials and Methods

The present study relied on the fresh samples of the species Carissa macrocarpa (Figure 1) collected at the flowering stage from the Botanical Garden of the College of Education for pure sciences-Ibn Al-Haitham, parks, public parks and some office located within the areas of AL-Adhamiya, Alkraiat, and

Al-Ameriya in the Baghdad at the period from (20/12/2017 - 20/3/2018). The diagnosed of the species by taxonomic keys and fluorescent Arabic and international as well as Internet sources. The fresh samples of the stem and leaf were cut up to 2-3 cm from the middle of each part [8]. The samples were fixing by formalin acetic acid alcohol (F.A.A.) for 24 hours at room temperature according to [9] and then washed with alcohol concentration 70% to remove traces of the fixative solution and then kept in the same concentration of alcohol in the refrigerator until used. Several samples of preserved samples were selected to prepare the epidermal of leaves to study the stomata and the other Accessories of the epidermis. The epidermis of the leaf was peeling by a razor blade also the samples of stems and leaves have cut off by using the hand sectioning method follows by [10] were the parts of stem sectioned into thin pieces by a razor blade too. All the samples of the stem, leaf, and epidermis of leaf were put in the 0.5% sodium hypochlorite for 5 mints to remove the chlorophyll pigments, then the samples were transported to Petry Dish with Safranin pigment to gives color to the tissue of stems. Finally, the samples of the stem were put on the slides and mounted by cover slides with D.P.X. and fixed by Olympus light microscope then photographed using the Omax camera. The measurements of tissue were made using the Ocular micrometer and the characters were studied that are, the epidermis features, the cross-section of the stem and the cross-section of leaves also the dimensions of the stomata were measured and the stomatal index was calculated according to [11].

$$\text{Stomatal index} = \frac{Number\ of\ stomata}{Number\ of stomata + Number\ of\ ordinary\ epidermal\ cells} \times 100$$

Also doing clearing of vegetative leaves to identify the system of venation as followed [12]. The study also relied on the terms contained in [3, 5, 6, 13].

Figure 1. General shape of the species C*arissa macrocarpa by* digital camera.

3. Results and Discussion

3.1. Cross section of stem

The cross-section of the stem circular shape (Figure 2). The epidermis of stem consists of small cells, simple, uniseriate and cubical shape with straight walls, the thickness of it reached 13.4 µm. the epidermis covered by cuticle except for the position of stomata. The cortex consists from two layers the first layer it's the collenchyma tissue under the epidermis consists from 5 rows free of intercellular

spaces and the thickness of it reached to 75 µm, the second layer it's chlorenchyma tissue consist from parenchyma cell riches of chlorophyll, the cell were very thin circular to polygonal shape and throw it the intercellular spaces, the thickness of it reached to 133 µm. the average thickness to all cortex reached 210 µm. The vascular bundles open and collateral ensue as a wavy circular ring around the pith, the thickness of it 20 µm consist of phloem and xylem. the phloem consists of sieve tubes and companion cells have a transparent area being responsible for the milky white secretions that come out when the stem is broken and this is agreed with [2]. The thickness of phloem reached to 8 µm and the xylem thickness reached to 10 µm, also the number of vessels rows in xylem reached to 8-10 rows (Table 1). The pith consists of many layers of parenchyma cells storage, circular to polygonal shape with thin walls throw it intercellular spaces, the pith occupied the central part with solid tissue, the Druses crystals diffuse in the cortex and pith, and this is agreed with [2].

Table 1. characters cross section of stem in the species *Carissa macrocarpa* (µm).

Epidermis thickness	Collenchyma thickness	Chlorenchyma thickness	Cortex thickness	Phloem thickness	Xylem thickness	Number of xylem rows	Vascular bundles thickness
7.5-15.2 (13.4)	70.4-78 (75)	125.9-135.8 (133)	200-215 (210)	6-10 (8)	8-12 (10)	8-10 (8)	15-26 (20)

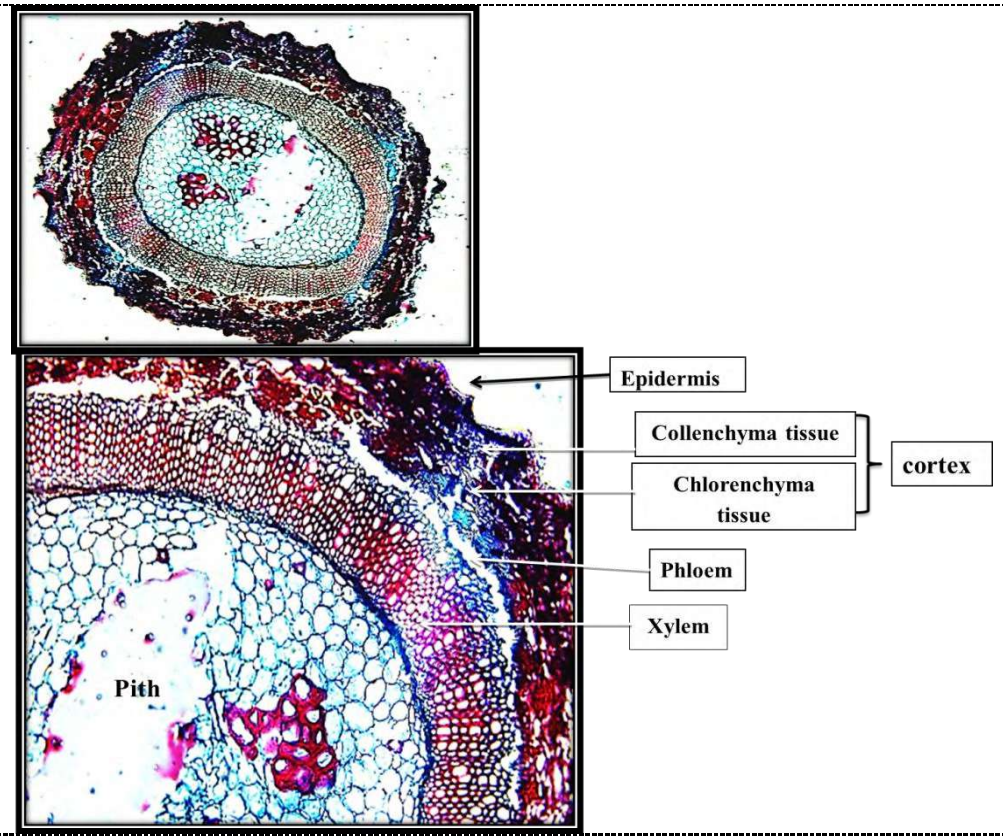

Figure 2. Cross section of stem in the species C*arissa macrocarpa* X40.

3.2. Leaves

3.2.1. Service view of leaves

The ordinary epidermal cells on both sides of leaf consist from oblong to-coordinate cells like bee cells with straight walls to semi-wavy on the side (Figure 3) this is due to changes in the shape of the outer tangential walls and the inner tangential walls of the cells [14]. The average of cell long on the upper epidermis of leaf reached to 46.2 µm and the average of width 43.2 µm also the average of cell long on the lower epidermis reached to 32 µm and the average of width 29 µm.

3.2.2. The Complex of stomata of leaves

The stomata appeared on the lower surface only and these results agree with [1]. Their diffused on that surface varied as they appeared in high density, were circular in shape, and the stomatal model was Tetracytic type, which is surrounded by four normal cells on that surface (Figure 3). It is possible to rely on the variation in the dimensions of stomata and stomatal evidence as an important anatomical characteristic that helps in the diagnosis and isolation of the species, it is also a demonstration of plant efficiency in photosynthesis [2].

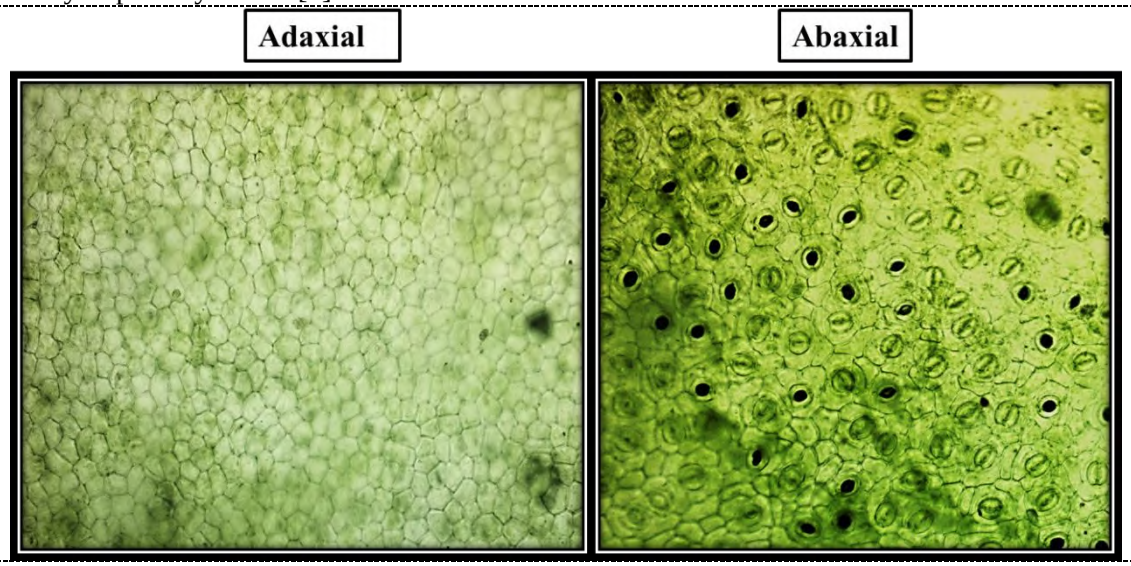

Figure 3. Characters of the epidermis and stomata of leaves in the species C*arissa macrocarpa* X100.

3.2.3. Longitudinal section of leaves

The epidermis of blade was characterized by upper epidermis and lower epidermis, but they were almost identical, were consist from simple and uniseriate epidermal cells, with square shapes to polygonal ridges, stacked together, and straight walls have low wavy, and the lower epidermis appeared thinner and more stomata than the upper epidermis, the average thickness of upper epidermis reached to 22 µm, while the average thickness of the lower epidermis was 10 µm. The epidermal cells covered a layer of the thick-toothed cuticle (Figure 4). The mesophyll tissue, which follows the upper epidermal layer, appears to consist of the upper Palisade parenchyma and the lower spongy parenchyma, the type of this arrangement of mesophyll known bifacial and this type is a common form in the most leaves of plants. The palisade layer consist from 1-2 rows of oblong cells with narrow intercellular space between cells, its longitudinal axis is perpendicular to the leaf surface and contains chloroplasts, the average thickness of palisade layer reached to 62 µm, so the spongy layer of mesophyll consists from loose tissue have air lacunae between the cells and the cells irregular shape

consist from druses crystals and ailerons grains, the rows of it reached to 2-3 rows and the average thickness of spongy layer reached to 94 µm, so the average of thickness of blade reached to 120.8 µm (Table 2). The result of the study of appeared that the midrib has almost straight from the upper to the zigzag from the lower (Figure 4) the tissue of midrib consist from two types of cells, the Angular collenchyma, occupied the corners of the middle race against the vascular bundle and exchanged with chlorenchyma cells, spherical to polygonal shape, containing an abundance of chloroplasts. The Crystals were also observed in the tissue and around the vascular bundles. The study showed that the vascular tissue in the midrib is only an extension of the vascular strand from the stem to the blade. Therefore, the vascular tissue retained its components of xylem and phloem elements. The vascular tissue appeared in the midrib in the form of veins, consisting of vascular bundles branching into several intertwined branches and thus the main vascular bundle showed the largest bundles in the middle ovate broad shape, and the average thickness of the vascular bundle was 33 µm. In addition to the emergence of sub-vascular bundles spread in the leaf blade less in size as we move away from the midrib, 1-2 rows of parenchyma cells surrounded by the vascular bundle compose the bundle sheath. The results of the present study confirmed that there are differences in the anatomical characteristics shown by the leaves of the species under study and the leaf consider is the most plant-specific part of the anatomical characteristics and the most consistent, this agrees with [8] that appeared the leaf has been used extensively to solve the most difficult taxonomic problems between different genus and species.

Table 2. Characters of longitudinal section of baled and midrib of leaves in the species *Carissa macrocarpa* (µm).

Upper Epidermis thickness	Lower Epidermis thickness	Palisade layer thickness	Spongy layer thickness	Blade thickness	Vascular bundles thickness
18-24 (22)	9.2-13.1 (10)	220-305 (62)	260-300 (94)	115-130 (120.8)	20-38 (33)

*The number between parentheses refer to average

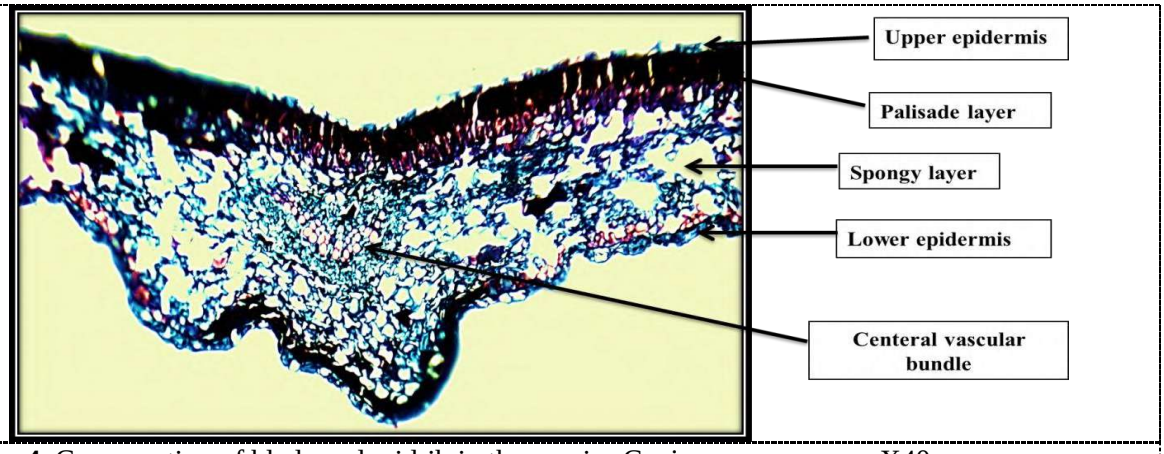

Figure 4. Cross section of blade and midrib in the species C*arissa macrocarpa* X40.

3.3. Crystals

The results of the present study showed crystals and their forms, and that one plant species may contain two or more types of crystals of different shapes and sizes and this is due to the form and nature of the isolated cell Idoblast, which acts as a template responsible for the shape of the crystal, the

crystals consist from calcium oxalate is a toxic acid which is produced by the plant's biological activity. Oxalic acid is a toxic acid and is therefore transformed by cells into insoluble compounds in the form of crystals that minimize their toxic effect [1]. The druses crystals appeared as a diffuse on the upper and lower leaves surfaces and appeared within the spongy layer and parenchyma tissue of their blade, as well as in the tissue of the cortex and pith of stem (Figure 5).

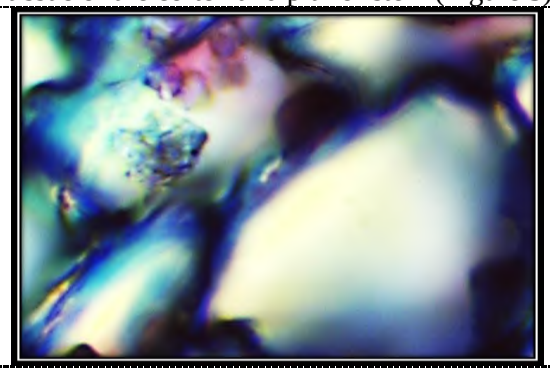

Figure 5. Druses crystals of the leaves in the species *Carissa macrocarpa* X100.

3.4. Starch grains

The starch is one of the most important materials stored in plant cells and the composition of these granules depends on the physiological conditions associated with the plant [15]. The phenotypic characteristics of these plants vary depending on the location and shape of the starch grains like the center of the grain formation (hilum), and the presence or absence of layers as well as the nature of those granules layers of being simple or complex or semi-complex [16]. The starch grains appeared in the parenchyma tissue as complex types have two hilum and the arrangement of the layers around each of them, the hilum circular shape un-centric location (Figure 6) also showed the Aleurone grains in the epidermis of leaves (Figure 7). Starch grains are an important anatomical characteristic in isolating plant species [17].

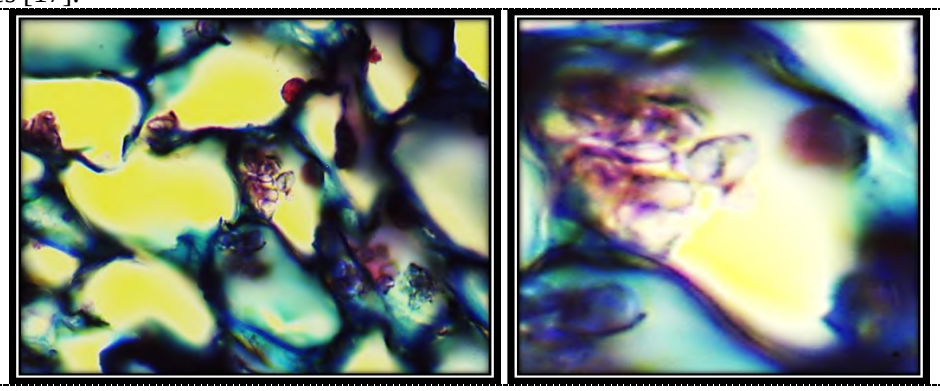

Figure 6. starch grains of the leaves in the species *Carissa macrocarpa* (X100).

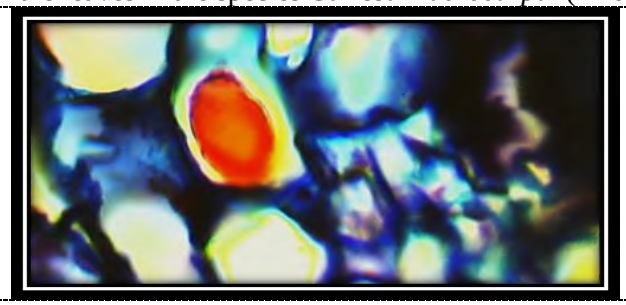

Figure 7. Aleurone grains of the leaves in the species *Carissa macrocarpa* (X100).

3.5. Venation system of leaves

The type of venation in the leaves of this species has a reticulate system, a characteristic of Dicotylidone [18], which was a type of Camptodromous, in this type the midrib penetrates the blade longitudinally, characterized by being larger than the rest of the veins, thicker and longer than the rest veins, the secondary veins. Branching from the midrib don't reach to the margin of leaf and this veins branching and bifurcate and come back together to form a brochidodromous network type, in this type the veins do not end at the edge of the leaf and each secondary veins is connected with the higher vein and linked to each other composes prominent arches (Figure 8).

Figure 8. Venation pattern of the leaves in the species *Carissa macrocarpa* (cm).

4. References

[1] Allam KM, Abd El-Kader AM, Mostafa MA and Fouad MA 2016 Botanical studies of the leaf, stem and root of Carissa macrocarpa, (Apocynaceae), cultivated in Egypt *J. Pharmacogn. Phytochem*. **5** 106.

[2] Sennblad B and Bremer B 2002 *Classification of Apoceynaceae s.l. According to a New Approach Combining Linnaean and phylogenetic Taxonomy*; Department of Systematic Botany Evolutionary Biology Center (EBC), Uppsala University, Uppsela, Sweden. 752.

[3] Metcalfe CR and Chalk L 1950 *Anatomy of dicotyledones* Clarendon press, Oxford, 2 1067.

[4] Al-Mashhadani AN 1992 *Comparative Taxonomic Study of Onosma L. (Boraginaceae) Species in Iraq*. PhD thesis, College of Science, University of Baghdad.

[5] Johansen DA1940 *Plant microtechnique* Mc.Grow-Hill book Company-New York and London: 523pp.

[6] Radford AE, Dikison WC, Massey JR and Bell CR 1974 *Vascular plants systematic* Harper and Row, New York and London 891.

[7] Heywood VH 1978 *Flowering plants of the world*. Oxford University press 335.

[8] Al-Khafaji BA 2004 *Taxonomic Study of Crepis L (Compositae) in Iraq*. Master Thesis College of Science. University of Babylon.

[9] Al-Obeidi BMRK 2014 *Comparative anatomical study of the vegetative and some reproductive parts of mattresses of the Cucurbitaceae family in Iraq* Master Thesis, College of Education Ibn Al-Haitham, University of Baghdad.

[10] Al-Hadeethi MA 2016 Anatomical and palynological study of *Myrtus communis* L. *Diyala J. Pure Sci.* **12** 1.
[11] Esau K 1965 *Plant anatomy* 2nd edition, John Wiley and Sons, New York, USA: 767pp.
[12] Al-Lamy ZA.K 2018 *Comparative Anatomical study of some Cassia L. species (Fabaceae) from middle and south of Iraqi districts* Thesis of Master. College of Education for Pure Sciences / Ibn Al-Haitham. University of Baghdad.
[13] Le-Houerou HN 1993 *Salt- tolerant Plants for the arid regions of the Mediterranean isoclimatic zone* Towards the rational use of high salinity tolerant plants 403-422.
[14] Esau K 2006 *Esau's Plant anatomy: meristems, cells, and tissues of the plant body, their structure, function, and development*. Ray F. Evert. (3rd Ed.). Hoboken, New Jersey. Canada, 607.
[15] Al-Duaiji AR 2000 *Practical Plant Anatomy* King Saud University, Scientific Publishing and Printing Press, Saudi Arabia: 49.
[16] Esau K 1953 *Plant anatomy* John Wiley and Sons, New York, USA 735.
[17] Al-Katib Y 2000 *Taxonomy of seeds plants. Ministry of high education and science research* Dar alkutb, University of Musel 407. (In Arabic).
[18] Hickey L 1973 Classification of architecture dicotyledonous leaves. *Amer. J. Bot.* **60** 17.

Design, Synthesis and Biological Screening of New Benzimidazole Derivatives

Design, Synthesis and Biological Screening of New Benzimidazole Derivatives

Ali Mohammed Sabur [1], **Muayad Ahmed Rdaiaan** [2, *]

[1,2]Department of Chemistry, College of education for pure sciences, University of Diyala, Iraq

E-mail: mredayan@gmail.com

Abstract. In this study, we synthesized a series of benzimidazole compounds containing. 1,3,4-thiadiazole ring from many reaction steps. The obtained benzimidazole series were characterized by melting point, Data from FT-IR and 1H-13C-NMR and In vitro screening of antibacterial activity against strains of selected pathogenic Gram-positive (*Staphylococcus aureus, Bacillus subtilis*) and Gram-negative (*Acinetobacter baumannii, Pseudomonas aeruginosa*) bacteria relative to (Amoxicillin) and (Ciprofloxacin) as standard antibacterial agents has shown high pharmacological activity.

Keywords: benzimidazole, 1,3,4-thiadiazole, antibacterial activity, 1,2-*o*-phenylenediamine

1. Introduction

Benzimidazoles remain one of the most robust classes of antimicrobial agents, despite several attempts to create a new structural template in the search for more effective antimicrobials. [1–8]. Benzimidazoles are considered to be a possible class of heterocyclic bioactive compounds with a wide range of biological activities. In fact, this nucleus is a component of vitamin B12 [9]. As a consequence, benzimidazoles have diverse biological properties, such as antifungal.[4], antitumor[10–12],antiviral[13,14] ,antihistaminic[15]. benzimidazole and its derivatives have also been used as optical lasers and polymer dyes in optoelectronics.[16,17], For the identification of biologically important molecules such as DNA, RNA or proteins and enzymes, organic luminophores, fluorescent fags [18]. In a large spectrum of therapeutically important agents, The nucleus of 1,3,4-thiadiazole has been incorporated. Which mainly provides antimicrobial operations [19]. In many fields, There are enough applications for 1,3,4-thiadiazole. As antibacterial medicines, the first applications of the medicinal industry were [20].

2. Experimental

2.1. Materials and physical measurements

Without purification from Aldrich, many of the starting materials and solvents were collected and used.On the SHIMADZU model FT-IR-8400S, the FT-IR spectrum was registered, 1H and 13C-NMR spectra were recorded on the BRUKER model Ultra Shield 500 MHz spectrophotometer using DMSO-d6 as solvent and TMS as internal comparison. The melting points were registered and are unreliable by the Stuart smp3 electronic system.

2.2. Methods of preparation and physical data of synthesised compounds 1(a,b), 2(a–e), 3(a-e), and 4(a-j).

2.2.1. Common method for synthesizing 1(a-b) of compounds.
Mixing (20) mmol of *o*-phenylene diamine derivatives, (20 mmol) of CS_2, (20) mmol of KOH, (25) mL of EtOH and (5) mL of reflux-heated H2O in a 100 ml circular flask for 3 hours, carefully inserted (0.5 g) of (charcoal) and continued reflux for 10 minutes, Filtered charcoal was extracted by filtration and (25 mL) of hot water was added.. In order to complete the crystallization, the mixture obtained was held in an ice bath for (3 h), the material obtained was distilled, dried and recrystallized from ethanol, and TLC(mobile phase: $CH_3(CH_2)_4CH_3$: $CH_3COOCH_2CH_3$ (1:1))

2.2.1.1. 2-mercaptobenzimidazole (1a).

Light beige powder, m.p 305-307 °c, FT- ir (cm^{-1}) 3155 (NH), 3093 (CH, aromatic), 2569 (S-H), 1620 (C=N), 1585 and 1462 (C=C, aromatic) was obtained.

2.2.1.2. 2-mercapto-5-methylbenzimidazole (1b).

Light brown powder, yield (80%), m.p 286-288 °C, FT-ir (cm^{-1}) 3132 (N-H), 3041 (C-H, aromatic), 2968-2862 (C-H, aliphatic), 2573 (S-H), 1625 (C=N), 1593 and 1469 (C=C, aromatic) was obtained.

2.2.2. Specific protocol for compound synthesis 2(a-e).
For 3 hours, The resultant mixture of (ArCOOH) (20 mmol), ($NH_2NHCSNH_2$) (1.82 g, 20 mmol) and $POCl_3$ (10 mL) was refluxed gently. H_2O (50 mL) was applied slowly after cooling and The mixture of reactions was refluxed and purified for 4 h. The distilled KOH solution neutralized the solvent and the precipitate was purified and recycled from EtOH,and TLC was tested for the completion of the reaction and for the purity of the compounds (mobile phase: $CH_3(CH_2)_4CH_3$: $CH_3COOCH_2CH_3$(1:3)).

2.2.2.1. 2-Amino-5-(phenyl)-1,3,4-thiadiazole (2a).

Pale yellow powder, yield (76%), m.p 224-227 °C, FT- ir (cm^{-1}) 3275 and 3113 (NH_2), 3043 (C-H, aromatic), 1631 (C=N), 1581 and 1469 (C=C, aromatic) was obtained.

2.2.2.2. 2-Amino-5-(4-chlorophenyl)-1,3,4-thiadiazole (2b).

Yellow powder, yield (80%), m.p 226-229 °C, FT- ir (cm^{-1}) 3271 and 3105 (NH_2), 3047 (C-H, aromatic), 1631 (C=N), 1597 and 1462 (C=C, aromatic) was obtained.

2.2.2.3. 2-Amino-5-(2-chlorophenyl)-1,3,4-thiadiazole (2c).

Yellow powder, yield (70%), m.p 214-216 °C, R_f = 0.58; FT- ir (cm^{-1}) 3282 and 3105 (NH_2), 3028 (C-H, aromatic), 1635 (C=N), 1597 and 1458 (C=C, aromatic) was obtained.

2.2.2.4. 2-Amino-5-(4-nitrophenyl)-1,3,4-thiadiazole (2d).

Dark yellow powder, yield (78%), m.p 244-247 °C, FT- ir (cm^{-1}) 3259 and 3113 (NH_2), 3066 (C-H, aromatic), 1627 (C=N), 1597 and 1458 (C=C, aromatic), 1508 and 1346 (NO_2) was obtained.

2.2.2.5. 2-Amino-5-(3,5-dinitrophenyl)-1,3,4-thiadiazole (2e).

Dark yellow powder, yield (75%), m.p 265-268 °C, FT- ir (cm^{-1}) 3275 and 3116 (NH_2), 3055 (C-H, aromatic), 1624 (C=N), 1593 and 1419 (C=C, aromatic), 1539 and 1350 (NO_2) was obtained.

2.2.3. Common method for synthesizing 3(a-e) compounds.
Compounds 2(a-e) (5 mmol) were dissolved in DMF, and the reaction mixtures were added to TEA (5 mmol). The reaction mixtures were slowly applied to chloroacetyl chloride (10 mmol). The mixture of reactions was

heated under reflux for 2 h. The solution was then applied to crushed ice, filtering the substance collected, Washed with H_2O, dried and recrystallized from C_2H_5OH.

2.2.3.1. 2-chloro-N-(5-phenyl-1,3,4-thiadiazol-2-yl)acetamide (3a)

Pale yellow powder, yield (82%), m.p 233-235 °C, FT- ir (cm^{-1}) 3182 (N-H), 3043 (C-H, aromatic), 2947, 2835 (C-H, aliphatic), 1705 (C=O), 1627 (C=N), 1573 and 1438 (C=C, aromatic) was obtained.

2.2.3.2. 2-chloro-N-(5-(4-chlorophenyl)-1,3,4-thiadiazol-2-yl)acetamide (3b)

Beige powder, yield (85%), m.p 254-256 °C, FT- ir (cm^{-1}) 3170 (N-H), 3043 (C-H, aromatic), 2943, 2835 (C-H, aliphatic), 1705 (C=O), 1631 (C=N), 1570 and 1442 (C=C, aromatic) was obtained.

2.2.3.3. 2-chloro-N-(5-(2-chlorophenyl)-1,3,4-thiadiazol-2-yl)acetamide (3c)

Beige powder, yield (84%), m.p 230-232 °C, FT- ir (cm^{-1}) 3174 (N-H), 3032 (C-H, aromatic), 2939, 2831 (C-H, aliphatic), 1708 (C=O), 1624 (C=N), 1581 and 1438 (C=C, aromatic) was obtained.

2.2.3.4. 2-chloro-N-(5-(4-nitrophenyl)-1,3,4-thiadiazol-2-yl)acetamide (3d)

Dark beige powder, yield (80%), m.p 250-252 °C, R_f = 0.47; FT- ir (cm^{-1}) 3163 (N-H), 3032 (C-H, aromatic), 2943, 2839 (C-H, aliphatic), 1708 (C=O), 1627 (C=N), 1593 and 1438 (C=C, aromatic), 1519 and 1346 (NO_2) was obtained.

2.2.3.5. 2-chloro-N-(5-(3,5-dinitrophenyl)-1,3,4-thiadiazol-2-yl)acetamide (3e)

Pale brown powder, yield (86%), m.p 240-243 °C, FT- ir (cm^{-1}) 3182 (N-H), 3035 (C-H, aromatic), 2943, 2877 (C-H, aliphatic), 1712 (C=O), 1624 (C=N), 1593 and 1438 (C=C, aromatic), 1543 and 1350 (NO_2) was obtained.

2.2.4. The general protocol for compound synthesis 4(a-j).

A mixture of 2-chloro-N- (5-((un)substituted phenyl)-1,3,4 thiadiazole-2-yl) acetamide (5 mmol), compouds 1(a,b) (5 mmol) and K_2CO_3 (5 mmol) in DMF (25 mL) was refluxed for 10 h. The solvent was then added into the crushed ice, refining and recrystallizing the liquid derived from ethanol, TLC tested the end of the reaction and the compounds' purity. (mobile phase: $CH_3(CH_2)_4CH_3$: $CH_3COOCH_2CH_3$ (2:3)).

2.2.4.1. 2-((benzimidazol-2-yl)thio)-N-(5-phenyl-1,3,4-thiadiazol-2-yl)acetamide (4a)

Beige powder, yield (60%), m.p 188-190 °C, FT- ir (cm^{-1}) 3336 (N-H), 3155 (N-H, benzimidazole),3035 (C-H, aromatic), 2951, 2881 (C-H, aliphatic), 1670 (C=O), 1616 (C=N), 1558 and 1435 (C=C, aromatic); ^{1}H-NMR (DMSO-d_6, 500 MHz, δ) 4.45 (s, 2H, CH_2), 7.15-7.75 (m, 9H, Ar-H), 8.58 (s, 1H, NH), 12.55 (s, 1H, benzimidazole-NH); ^{13}C-NMR (DMSO-d_6, 125 MHz, δ) 36.74, 114.35, 121.88, 122.97, 127.08, 129.66, 130.42, 131.47, 139.97, 150.62, 161.08, 162.57, 169.43 was obtained.

2.2.4.2. 2-((5-methylbenzimidazol-2-yl)thio)-N-(5-phenyl-1,3,4-thiadiazol-2-yl)acetamide (4b)

Dark brown powder, yield (71%), m.p 222-225 °C, FT- ir (cm^{-1}) 3317 (N-H), 3167 (N-H, benzimidazole),3028 (C-H, aromatic), 2908, 2808 (C-H, aliphatic), 1674 (C=O), 1627 (C=N), 1570 and 1438 (C=C, aromatic); ^{1}H-NMR (DMSO-d_6, 500 MHz, δ) 2.37 (s, 3H, CH_3), 4.43 (s, 2H, CH_2), 6.95-7.52 (m, 8H, Ar-H), 8.59 (s, 1H, NH), 13.14 (s, 1H, benzimidazole-NH); ^{13}C-NMR (DMSO-d_6, 125 MHz, δ) 21.62, 35.33, 120.04, 123.35, 125.50, 127.36, 129.78, 130.54, 131.07, 149.03, 158.81, 162.50, 167.55 was obtained.

2.2.4.3. 2-((benzimidazol-2-yl)thio)-N-(5-(4-chlorophenyl)-1,3,4-thiadiazol-2-yl)acetamide (4c)

Dark brown powder, yield (62%), m.p 190-192 °C, FT- ir (cm^{-1}) 3298 (N-H), 3163 (N-H, benzimidazole),3051 (C-H, aromatic), 2900, 2819 (C-H, aliphatic), 1678 (C=O), 1620 (C=N), 1593 and 1438 (C=C, aromatic); ^{1}H-

NMR (DMSO-d_6, 500 MHz, δ) 4.34 (s, 2H, CH_2), 7.12-7.91 (m, 8H, Ar-H), 8.55 (s, 1H, NH), 12.60 (s, 1H, benzimidazole-NH); ^{13}C-NMR (DMSO-d_6, 125 MHz, δ) 35.40, 119.71, 122.71, 128.29, 128.96, 129.55, 129.77, 130.27, 132.70, 134.40, 135.63, 149.68, 159.01, 162.73, 169.30 was obtained.

2.2.4.4. 2-((5-methylbenzimidazol-2-yl)thio)-N-(5-(4-chlorophenyl)-1,3,4-thiadiazol-2-yl)acetamide (4d)

Dark beige powder, yield (58%), m.p 190-194 °C, FT- ir (cm^{-1}) 3305 (N-H), 3159 (N-H, benzimidazole),3047 (C-H, aromatic), 2939, 2873 (C-H, aliphatic), 1678 (C=O), 1624 (C=N), 1593 and 1438 (C=C, aromatic) was obtained.

2.2.4.5. 2-((benzimidazol-2-yl)thio)-N-(5-(2-chlorophenyl)-1,3,4-thiadiazol-2-yl)acetamide (4e)

Dark beige powder, yield (68%), m.p 217-219 °C, FT-IR (KBr disk, cm^{-1}) 3325 (N-H), 3155 (N-H, benzimidazole),3035 (C-H, aromatic), 2962, 2897 (C-H, aliphatic), 1674 (C=O), 1620 (C=N), 1573 and 1435 (C=C, aromatic); ^{1}H-NMR (DMSO-d_6, 500 MHz, δ) 4.38 (s, 2H, CH_2), 7.12-7.81 (m, 8H, Ar-H), 8.62 (s, 1H, NH), 12.38 (s, 1H, benzimidazole-NH); ^{13}C-NMR (DMSO-d_6, 125 MHz, δ) 36.31, 114.35, 121.91, 128.17, 130.02, 130.94, 131.18, 131.40, 131.80, 139.94, 150.36, 157.45, 163.26, 169.06 was obtained.

2.2.4.6. 2-((5-methylbenzimidazol-2-yl)thio)-N-(5-(2-chlorophenyl)-1,3,4-thiadiazol-2-yl)acetamide (4f).

Pale brown powder, yield (55%), m.p 225-227 °C, FT- ir (cm^{-1}) 3282 (N-H), 3167 (N-H, benzimidazole),3032 (C-H, aromatic), 2920, 2823 (C-H, aliphatic), 1678 (C=O), 1631 (C=N), 1577 and 1435 (C=C, aromatic); ^{1}H-NMR (DMSO-d_6, 500 MHz, δ) 2.36 (s, 3H, CH_3), 4.42 (s, 2H, CH_2), 6.94-7.62 (m, 7H, Ar-H), 8.53 (s, 1H, NH), 12.47 (s, 1H, benzimidazole-NH); ^{13}C-NMR (DMSO-d_6, 125 MHz, δ) 21.62, 35.47, 120.49, 123.32, 126.03, 128.25, 129.42, 130.98, 131.23, 131.48, 132.16, 149.14, 158.21, 160.94, 167.96 was obtained.

2.2.4.7. 2-((benzimidazol-2-yl)thio)-N-(5-(4-nitrophenyl)-1,3,4-thiadiazol-2-yl)acetamide (4g).

Brown powder, yield (59%), m.p 193-196 °C, FT- ir (cm^{-1}) 3317 (N-H), 3155 (N-H, benzimidazole),3074 (C-H, aromatic), 2935, 2866 (C-H, aliphatic), 1670 (C=O), 1624 (C=N), 1589 and 1431 (C=C, aromatic), 1516, 1342 (NO_2) was obtained.

2.2.4.8. 2-((5-methylbenzimidazol-2-yl)thio)-N-(5-(4-nitrophenyl)-1,3,4-thiadiazol-2-yl)acetamide (4h).

Dark brown powder, yield (63%), m.p 189-192 °C, FT-IR (KBr disk, cm^{-1}) 3329 (N-H), 3167 (N-H, benzimidazole),3074 (C-H, aromatic), 2927, 2862 (C-H, aliphatic), 1681 (C=O), 1627 (C=N), 1593 and 1435 (C=C, aromatic), 1523, 1346 (NO_2) was obtained.

2.2.4.9. 2-((benzimidazol-2-yl)thio)-N-(5-(3,5-dinitrophenyl)-1,3,4-thiadiazol-2-yl)acetamide (4i).

Dark brown powder, yield (66%), m.p 246-249 °C, FT-IR (KBr disk, cm^{-1}) 3321 (N-H), 3174 (N-H, benzimidazole),3089 (C-H, aromatic), 2981, 2885 (C-H, aliphatic), 1685 (C=O), 1631 (C=N), 1589 and 1423 (C=C, aromatic), 1539 and 1346 (NO_2) was obtained.

2.2.4.10. 2-((5-methylbenzimidazol-2-yl)thio)-N-(5-(3,5-dinitrophenyl)-1,3,4-thiadiazol-2-yl)acetamide (4j)

Dark brown powder, yield (60%), m.p 215-218 °C, FT- ir (cm^{-1}) 3348 (N-H), 3167 (N-H, benzimidazole),3101 (C-H, aromatic), 2951, 2873 (C-H, aliphatic), 1662 (C=O), 1624 (C=N), 1589 and 1423 (C=C, aromatic), 1543 and 1346 (NO_2); ^{1}H-NMR (DMSO-d_6, 500 MHz, δ) 2.31 (s, 3H, CH_3), 4.52 (s, 2H, CH_2), 6.93-7.76 (m, 6H, Ar-H), 8.61 (s, 1H, NH), 12.47 (s, 1H, benzimidazole-NH); ^{13}C-NMR (DMSO-d_6, 125 MHz, δ) 21.38, 36.23, 123.59, 125.94, 126.19, 128.52, 130.60, 132.06, 132.87, 136.05, 148.70, 159.16, 162.74, 168.17 was obtained.

3.Results and discussion

3.1.Synthesis

The synthetic route of title compounds 4(a-j) is presented in Scheme 1. Cyclization of 5-(un)-substituted-*o*-phenylenediamine with CS_2 The compounds 1(a, b) were given in The existence of KOH in the EtOH medium. These synthesized compounds were characterized by FT-IR. In the IR spectra of the compounds, stretching band belonging to (N-H), (S-H) and (C=N) were observed at the range (3155-3132 cm-1),(2573-2569 cm-1) and (1625-1620 cm-1) respectively.

In the presence of phosphorous oxide chloride, 2-amino-5-(substituted)-1,3,4-thiadiazole 2(a-e) was synthesized by the reaction of different carboxylic acid derivatives with thiosemicarbazide. Compound 2(a-e) FT-IR spectra demonstrated the presence at (1635-1624 cm-1) of a group of C = N and two bands at (3282-3259 cm-1) and (3116-3105 cm-1) that may be attributed to asymmetric and symmetric stretching vibrations of the NH2 group.

Compounds 3(a-e) were synthesized by a reaction of compounds 2(a-e) with chloroacetyl chloride in the presence of TEA in the DMF medium to yielded compounds 3(a-e). The chemical structures of these compounds were elucidated via FT-IR. In the IR spectra of all compounds, the occurrence of amide group (N-H) bonds was confirmed through bands in the region of (3182-3163 cm-1). Due to the occurrence of a sharp peak at (1712-1705 cm-1), the inclusion of the carbonyl group (C = O) in the structure is confirmed. Also confirmed by the existence of a sharp absorption band at (1631-1624 cm-1) was the existence of C = N in the 1,3,4-thiadiazole nucleus. Compounds 1(a, b) were reacted with compounds (3a-e) in the DMF medium in the anhydrous K_2CO_3 to give the target compounds 4(a-j) in the final step. FT-IR, 1H NMR, and 13C identified the chemical structures of all target compounds. The IR data acquired for the final compounds 4(a-j) allow us to a large degree to validate their formation. By analyzing data for both synthesized compounds and absorption peaks at (3348-3282 cm-1), (3174-3155 cm-1) and (1685-1662 cm-1) the presence of N-H amide, N-H benzimidazole and C=O groups was confirmed, respectively. The presence of C-H bonds in the final products was allocated to a steep peak at (2981-2808 cm-1). sharp absorption band at(1631-1616)confirmed the presence of C=N in the benzimidazole and 1,3,4-thiadiazole nucleus In the ^{1}HNMR spectra of all compounds, the methylene protons have resonated at δ (4.52-4.34) ppm and this down filed value can be attributed to the inductive effect of the carbonyl group. The singlet NH signal of benzimidazole has appeared at δ (13.14-12.38) in all compounds. The signals belonging to the aromatic region was seen at δ (7.91-6.93) ppm. In the ^{13}CNMR spectra, the methylene carbon between the sulfur atom and carbonyl group was observed at δ (36.74-35.33) ppm. Two carbons on the thiadiazole ring were observed at δ (163.26-157.45) ppm. While the carbonyl carbon was observed at δ (169.43-167.55) ppm. All other aromatic carbons were recorded between δ (139.97) and δ (114.35).

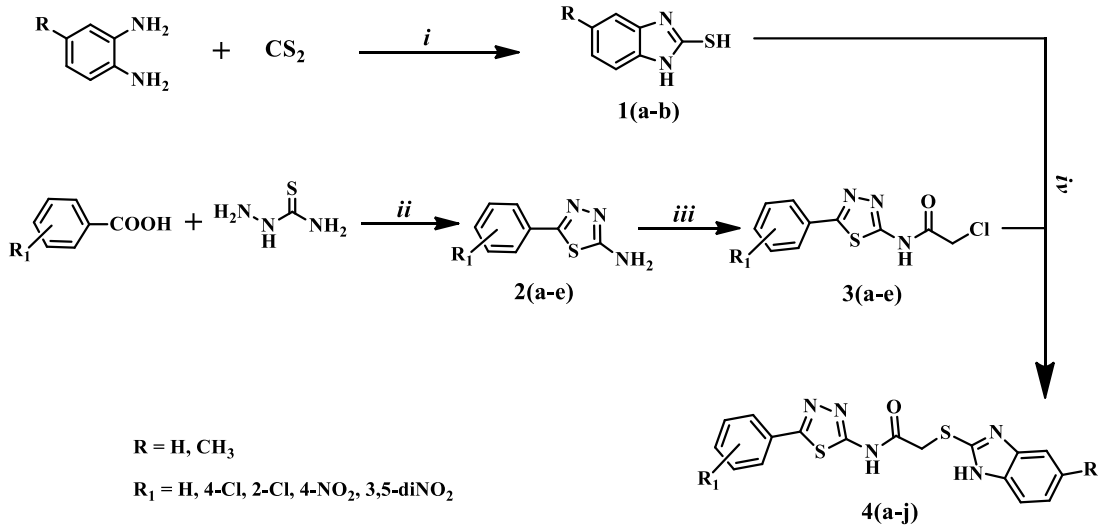

Reagents and condition: (i) KOH, EtOH, reflux 3h; (ii) $POCl_3$, reflux 3h; H_2O, reflux 4 h; KOH; (iii) $ClCH_2COCl$, TEA, DMF, reflux 2h; (iv) K_2CO_3, DMF, reflux 10 h

Scheme 1. General scheme of the prepared compounds

Table 1. Physical properties of molecules that are synthesized

Comp. No.	R	R_1	Molecular Formula	M.wt	Color	M.P (°C)	Yield %	Rf
1a	H		$C_7H_6N_2S$	150.20	Light beige	305-307	78	0.57
1b	CH_3		$C_8H_8N_2S$	164.23	Light brown	286-288	80	0.59
2a		H	$C_8H_7N_3S$	177.23	Pale yellow	224-227	76	0.46
2b		4-Cl	$C_8H_6ClN_3S$	211.67	Yellow	226-229	80	0.51
2c		2-Cl	$C_8H_6ClN_3S$	211.67	Yellow	214-216	70	0.58
2d		4-NO_2	$C_8H_6N_4O_2S$	222.22	Dark yellow	244-247	78	0.45
2e		3,5-diNO_2	$C_8H_5N_5O_4S$	267.22	Dark yellow	265-268	75	0.62
3a		H	$C_{10}H_8ClN_3OS$	253.70	Pale yellow	233-235	82	0.48
3b		4-Cl	$C_{10}H_7Cl_2N_3OS$	288.15	Beige	254-256	85	0.54
3c		2-Cl	$C_{10}H_7Cl_2N_3OS$	288.15	Beige	230-232	84	0.48
3d		4-NO_2	$C_{10}H_7ClN_4O_3S$	298.70	Dark beige	250-252	80	0.47
3e		3,5-diNO_2	$C_{10}H_6ClN_5O_5S$	343.70	Pale brown	240-243	86	0.53
4a	H	H	$C_{17}H_{13}N_5OS_2$	367.45	Beige	188-190	60	0.43
4b	CH_3	H	$C_{18}H_{15}N_5OS_2$	381.47	Dark brown	222-225	71	0.46
4c	H	4-Cl	$C_{17}H_{12}ClN_5OS_2$	401.89	Dark brown	190-192	62	0.48

4d	CH_3	4-Cl	$C_{18}H_{14}ClN_5OS_2$	415.91	Dark beige	190-194	58	0.49
4e	H	2-Cl	$C_{17}H_{12}ClN_5OS_2$	401.89	Dark beige	217-219	68	0.46
4f	CH_3	2-Cl	$C_{18}H_{14}ClN_5OS_2$	415.91	Pale brown	225-227	55	0.50
4g	H	4-NO_2	$C_{17}H_{12}N_6O_3S_2$	412.44	Brown	193-196	59	0.44
4h	CH_3	4-NO_2	$C_{18}H_{14}N_6O_3S_2$	426.47	Dark brown	189-192	63	0.41
4i	H	3,5-diNO_2	$C_{17}H_{11}N_7O_5S_2$	457.44	Dark brown	246-249	66	0.47
4j	CH_3	3,5-diNO_2	$C_{18}H_{13}N_7O_5S_2$	471.47	Dark brown	215-218	60	0.51

3.2.Biological evaluation

The antibacterial operation in vitro was carried out against Gram-positive bacteria, including S. For aureus, B. And Gram-negative bacteria, including A, subtilis. P. aeruginosa, Baumannii. Many of the synthesized compounds 4(a-j) have been tested for antibacterial activity by calculating the inhibition zone in mm using the cup-plate agar diffusion method[22]. (Amoxicillin and Ciprofloxacin) have been used as a typical antibacterial activity medication. The observations are illustrated in Table 2.

If we display the (inhibition zone) data of some synthesized compounds 4(a-j) in Table (2), some significant findings are observed:

The first showed good activity against (P. aeruginosa) compounds (4d) (4 g), while only compounds (4d) (4 g) showed good activity against (B. subtilis). We also showed that some of the compounds (4b) (4h) have strong activity against (S. aureus), while no antibacterial activity against (A. baumannii) was seen in all compounds 4(a-j).

Table 1. The antibacterial efficacy of compounds synthesized

Comp. No.	Concentration (mg / ml)	Zone of inhibition (in mm)			
		Gram-positive		Gram-negative	
		B. subtilis	*S. aureus*	*A.baumannii*	*P. aeruginosa*
4a	100	-	10	-	12
	50	-	7	-	8
4b	100	-	15	-	12
	50	-	8	-	9
4c	100	11	-	-	13
	50	10	-	-	12
4d	100	28	-	-	20
	50	17	-	-	15
4e	100	-	-	-	13
	50	-	-	-	15

4g	100	22	10	-	18
	50	14	11	-	10
4h	100	17	18	-	15
	50	14	14	-	14
Amoxicillin	25	22	11	-	-
Ciprofloxacin	10	29	29	28	14
DMSO solvent		-	-	-	-

4.Conclusion

Benzimidazole compounds of thiadiazole moiety have been formed and structurally characterized using spectroscopic techniques.. Pharmacological research has been conducted to examine the replacement effects on antibacterial function, with some variants exhibiting high to moderate activity against bacteria.

Acknowledgment

The writers express their gratitude and appreciation to the Department of Chemistry, the College of Pure Science Education, and the University of Diyala for their encouragement and assistance.

References

[1] Vaidya S D, Kumar B V S, Kumar R V, Bhise U N and Mashelkar U C 2007 *J. Heterocycl. Chem.* **44** 685.
[2] Mohamed B G, Hussein M A, Abdel-Alim A A M and Hashem M 2006 *Arch. Pharm. Res.* **29** 26.
[3] Pawar N S, Dalal D S, Shimpi S R and Mahulikar P P 2004 Studies of antimicrobial activity of N-alkyl and N-acyl 2-(4-thiazolyl)-1H-benzimidazoles *Eur. J. Pharm. Sci.* **21** 115–8
[4] Göker H, Kuş C, Boykin D W, Yildiz S and Altanlar N 2002 Synthesis of some new 2-substituted-phenyl-1H-benzimidazole-5-carbonitriles and their potent activity against Candida species *Bioorganic Med. Chem.* **10** 2589–96
[5] Göker H, Tunçbilek M, Süzen S, Kus C and Altanlar N 2001 Synthesis and Antimicrobial Activity of Some New 2-Phenyl-N-substituted Carboxamido-1H-benzimidazole Derivatives *Arch. Pharm. (Weinheim).* **334** 148–52
[6] Tunçbilek M, Göker H, Ertan R, Eryigit R, Kendi E and Altanlar N 1997 Synthesis and antimicrobial activity of some new anilino benzimidazoles *Arch. Pharm. (Weinheim).* **330** 372–6
[7] NS H, R S, FA A and M el-T 1997 Synthesis and antimicrobial testing of novel oxadiazolylbenzimidazole derivatives. *Pharmazie* **52** 746–9
[8] Bishop B C, Chelton E T J and Jones A S 1964 The antibacterial activity of some fluorine-containing benzimidazoles *Biochem. Pharmacol.* **13** 751–4
[9] Budavari S, O'Neil M J, Smith A, Heckelman P E and Kinneary J F 2001 The Merck Index, 13th *Merck*

Co. Inc. Whitehouse Station. New Jersey

[10] Hranjec M, Kralj M, Piantanida I, Sedić M, Šuman L, Pavelić K and Karminski-Zamola G 2007 Novel cyano- and amidino-substituted derivatives of styryl-2-benzimidazoles and benzimidazo[1,2-a]quinolines. Synthesis, photochemical synthesis, DNA binding, and antitumor evaluation, part 3 *J. Med. Chem.* **50** 5696–711

[11] Hranjec M, Piantanida I, Kralj M, Šuman L, Pavelić K and Karminski-Zamola G 2008 Novel amidino-substituted thienyl- and furylvinylbenzimidazole: Derivatives and their photochemical conversion into corresponding diazacyclopenta[c] fluorenes. Synthesis, interactions with DNA and RNA, and antitumor evaluation *J. Med. Chem.* **51** 4899–910

[12] Hranjec M, Pavlović G, Marjanović M, Kralj M and Karminski-Zamola G 2010 Benzimidazole derivatives related to 2,3-acrylonitriles, benzimidazo[1,2-a]quinolines and fluorenes: Synthesis, antitumor evaluation in vitro and crystal structure determination *Eur. J. Med. Chem.* **45** 2405–17

[13] Starčević K, Kralj M, Ester K, Sabol I, Grce M, Pavelić K and Karminski-Zamola G 2007 Synthesis, antiviral and antitumor activity of 2-substituted-5-amidino-benzimidazoles *Bioorganic Med. Chem.* **15** 4419–26

[14] Rida S M, El-Hawash S A M, Fahmy H T Y, Hazzaa A A and El-Meligy M M M 2006 *Archives of Pharmacal Research* vol 29 (Springer) pp 826–33

[15] Velík J, Baliharová V, Fink-Gremmels J, Bull S, Lamka J and Skálová L 2004 Benzimidazole drugs and modulation of biotransformation enzymes *Res. Vet. Sci.* **76** 95–108

[16] Baista R M F, Costa S P G, Belsley M and Raposo M M M 2007 *Tetrahedron* **63** 9842–9

[17] Nurulla I, Tanimoto A, Shiraishi K, Sasaki S and Yamamoto T 2002 Preparation of π-conjugated polymers consisting of 2-decylbenzimidazole and thiophene units and chemical properties of the polymers *Polymer (Guildf).* **43** 1287–93

[18] Jäger A, Stefani V, Guterres S S and Pohlmann A R 2007 Physico-chemical characterization of nanocapsule polymeric wall using fluorescent benzazole probes *Int. J. Pharm.* **338** 297–305

[19] Bharti S K, Nath G, Tilak R and Singh S K 2010 Synthesis, anti-bacterial and anti-fungal activities of some novel Schiff bases containing 2,4-disubstituted thiazole ring *Eur. J. Med. Chem.* **45** 651–60

[20] Vasoya S L, Paghdar D J, Chovatia P T and Joshi H S 2005 Synthesis of some New Thiosemicarbazide and 1,3,4-Thiadiazole Heterocycles Bearing Benzo[b]Thiophene Nucleus as a Potent Antitubercular and Antimicrobial Agents *J. Sci. Islam. Repub. Iran* **16** 33–6

Purification and Determination of The Arginase Enzyme Activity from Kidney Patients

Purification and Determination of The Arginase Enzyme Activity from Kidney Patients

Nuha Ali Hadi al-Samarrai1 [1*] and Nadia Ahmed Salih[2]

[1]Chemistry Department, College of Education, Samarra University.
[2]Chemistry Department, College of Education for Pure Sciences, Tikrit University.

* E-mail: Nuhaali922@gmail.com

Abstract. The current study measuring the effectiveness and purification of the enzyme (arginase) in the serum of kidney diseases samples were collected from Samarra General Hospital from October to December 2019, 60 samples were collected from the infected and 25 samples from he healthy people control group of ages 30-55 years, the effectiveness of the control group was 6.87 ± 2.95, and the patient group was 25.71 ± 8.39., the purification process was carried out using Sephadex G-200 and EDEA cellulose - using a column of separation with dimensions (32 x 1.5nm), the molecular weight of the enzyme was 245 kDa. The study included measuring the level of urea 83.7 ± 23.4mg/dl, Creatinine 2.85 ± 1.19 mg/dl, Total protein 3.8 ± 0.6 mg/dl, Albumin 4.120 ± 0.02 mg/dl, Uric acid 5.19 ± 1.52 mg/dl and Globulin was 1.29 ± 0.01 mg/dl. at P≤0.01.

Keywords: Arginase enzyme, purification, activity,Kidney.

1.Introduction

Arginase (EC 3.5.3.1, Arginine amidinase, canavanase, L-arginase, arginine transamidinase) is an enzyme containing manganese. This enzyme catalyzes the following reaction: arginine H_2O → ornithine+ urea. This enzyme is considered the last enzyme in the urea cycle. It is widely present in all areas of life. It is ubiquitous to all domains of life.Arginase stimulates the fifth step and is the final step in the urea cycle, which are chain biochemical reactions that occur in mammals that aim to rid the body of harmful ammonia. Specifically, arginine converts L-arginine to L-ornithine and urea [1,2] Mammalian arginase is active as a trimer, except that some bacterial arginases form hexmeric arginases. [3] In order to maintain proper function, the enzyme needs a two-molecule metal cluster of manganese. These ions coordinate Mn^{2+} with water, directing the molecule and fixing it. They also allow water to act as a nucleophilic antipyretic and attack L-arginine, breaking it down into ornithine and urea [4] In most mammals, there are two types of this type of enzyme; the first is Arginase I, which functions in the urea cycle, and its location is in the cytoplasm of the liver cells. The second isozyme, Arginase II, is involved in the regulation of arginine / ornithine levels within cells. And its place in the mitochondria in many different tissues of the body, and it is very abundant in both the prostate and the kidneys. They may also be found, at lower levels, in macrophages, lactating mammary glands, and the brain. [5] We can find a second isozyme even in the absence of other urea cycle enzymes [4]

Arginases catalyze the divalent cation-dependent hydrolysis of L-arginine as it synthesizes the non-protein amino acids L-ornithine and urea. This reaction is the last step in the biogenesis of urea in the liver. flux during this reaction is very large, that an adult person excretes about

10 kg of urea/year. The urea cycle arginase (arginase I or liver arginase) is considered cytosolic, and is the best characterized of the mammalian arginases. A second isozyme, arginase II or kidney arginase, it is location is mitochondria. The type I and type II arginases in human are related by 58% sequence identity [(6)], and they are immunologically distinct. Comparative properties of 2 arginase enzymes have been discussed in a number of new reviews [2-4]. With it, the activity of arginase has been detected in many non-hepatic tissues that lack the complete urea cycle; This reaction is thought to be a source of ornithine, the biosynthetic precursors of proline and polyamines. For example, in the lactating mammary glands, the activity of arginase is increased to about 25% found in the liver in order to provide proline needed for milk protein (prolactin) synthesis [5]. Ornithine is also a biosynthetic precursor of polyamine [6], the muscular activity of arginine is increased by 25-fold during pregnancy to provide the fast-growing fetus with polyamines to enable cell proliferation [7]. It has become evident that the rapidly dividing tissue requirement to enhance polyamine biosynthesis is achieved through increased arginase activity as found in gastric cancers [8-10] and in breast cancer [9]. Recently, arginase activity has been detected in some human colon cancer and human breast cancer cell lines [10].

2.Material and Methods

25 blood samples were collected for normal cases of both sexes as control, their ages ranged between 30-55 years Samples were collected from Samarra General Hospital for the period from October to December after being diagnosed by specialized doctors on the basis of urea and creatinine examination, as 60 blood samples were collected for both sexes, whose ages ranged between 30-55 years.

• The blood was drawn the vein using a single-use 5 ml plastic syringe and the blood was placed in clean plastic tubes with a size of the blood serum separated from the coagulated part, and then the serum was withdrawn by a micropipette, after which the enzyme activity was measured directly and the sample was kept in freezing for the purpose of Make other required measurements

a- Measuring the activity of the arginase enzyme for kidney disease samples and healthy samples, using the ready-made kit for the arginase enzyme ELISA, as mentioned[11].

b- Purification of the arginase enzyme in samples with kidney disease: it was done according to the stages[12](saturation ammonium sulphate , Dialysis, Gel filtration, Ion exchange)

Enzyme unit: It is the amount of enzyme that catalyzes a reaction of 1 µl of the substrate in per minute

2.1.Saturation of ammonium sulphate

The serum proteins were precipitated using graduated concentrations of ammonium sulphate until reaching a saturation rate of 60%, as 3 gm of ammonium sulfate was added to 5 ml of serum during a period of (60 - 45) minutes by placing the serum in an ice bath with continuous stirring, usually thawing after freezing. Precipitate with 4ml of 0.1M Tris buffer - HCl pH 7.2.

2.2.Dialysis

It is one of the most important and oldest methods used in purifying enzymes, and the aim of which is to remove the remainder of the added ammonium sulfate to precipitate the proteins by placing the dissolved protein in the above step in the dialysis bag after measuring the activity (arginase enzyme) and protein concentration, and dipping the bag in 0.1M buffer solution Tris - HCl pH 7.2 The buffer solution was changed from time to time for an entire night. This step was performed at 4 ° C to maintain the enzyme effectiveness, and after the end of the membrane separation process, the effectiveness (arginase enzyme) and protein concentration were measured.

2.3.Gel filtration

The basis for the work of this technique is the difference in the molecular weight, as it was used to purify the symmetric separated by gel filtration chromatography using a Sephadex G200 gel filtration column, as 20 fraction collected the volume of each fraction was 4 ml where the effectiveness of (arginase enzyme) was measured and the total protein level of all the separated parts was measured.

2.4.Ion exchange

A separation column with dimensions (32 x 1.5) cm was used that contains DEAE cellulose-25 gel, which separates the compounds depending on the charge, and the gel material was placed at a height of 20 cm by pouring the gel on the walls of the separation column quietly and diagonally to prevent the formation of bubbles, after placing a suitable piece of glass wool at the end of the column, The blood serum was injected into the separator column in a circular motion and on the walls of the separator column, followed by ashake prosses using the buffer solution with a pH of 7.2, and the collection process was carried out at a flow rate of 0.63 ml/min, i.e. at a rate of 1.09 ml/ minute for each part, by a manual method, as was followed up. Calculation of the protein concentration by measuring the absorbance of the separated parts, where the activity of arginase enzyme was measured and the total protein level was measured for all the separated parts at 450nm wavelength.

-Estimation of the enzyme molecular weight: the molecular weight of the enzyme was estimated by filtering at [13,14].

2.5. Biochemical tests

The level of urea, creatinine, albumin, total protein and uric acid was measured using a ready-made assay (Kit) supplied by Biolab Corporation. The globulin was calculated from the following equation Globulin concentration = total protein - albumin

3.Results and discussion

1- The Effectiveness of (arginase enzyme) was measured in the serum of patients have kidney diseases compared with healthy patients, according to the following table kidney and healthy patients, according to the following table

Table 1. shows the Effectiveness of the arginase enzyme in the blood serum of kidney diseases and healthy people at the probability level P≤0.01

Arginase Enzyme activity (unit)	Total and standard deviation	P-Value
Control group	6.87±2.95	≤0.01
Patient group	25.71±8.39	

It is evident from the table above that the activity of arginase enzyme in the serum of kidney patients increased compared to healthy people at the probability level P≤0.01, and this is consistent with what was mentioned (Alshamaa and. Al-Obaidi) [15], where a significant increase in the activity of the arginase enzyme was observed. In all the studied age stages, as well as the current study consistent with what was mentioned (Scalia) [16]

Those who have hypothesized that this elevation is caused by histopathology, tumors, and pathological changes such as apoptosis, kidney infection and oxidative fatigue (disruption of the balance between the production of reactive oxygen types (free radicals) and antioxidant defenses, are discussed in relation to their potential role in the production of tissue damage) that increases The nitrogen oxide ranges that block the transit of urea and creatinine throughout the liver.

The high activity of arginase associated with acute kidney disease, therefore, alters the epithelial cell function in heart disease and kidney disease. (Heisel et al.) [17] Arginase also reduces the excretion of sodium from the kidneys when consuming small amounts of salt, but stimulates sodium excretion in the case of high salt amounts (Lakowicz). [18]

Table 2. shows the stages of purification (arginase enzyme) in serum of kidney patients

Steps of purifications	Volume (ml)	Activity	Total Activity	Protein Conc (mg/ml)	Specific activity (mg)	Yield %	Folds	Total protein (mg)
Crude serum	5	10.1	50.05	7.3	1.32	100	1	36.5
Ammonium sulphate	3.5	10.19	35.36	6.2	1.64	74.2	1.2	21.7
Dialysis	4	10.3	41.2	4.1	2.5	84.9	1.8	16.4
Gel filtration	4	10.7	42.8	2.5	4.28	88	3.2	10

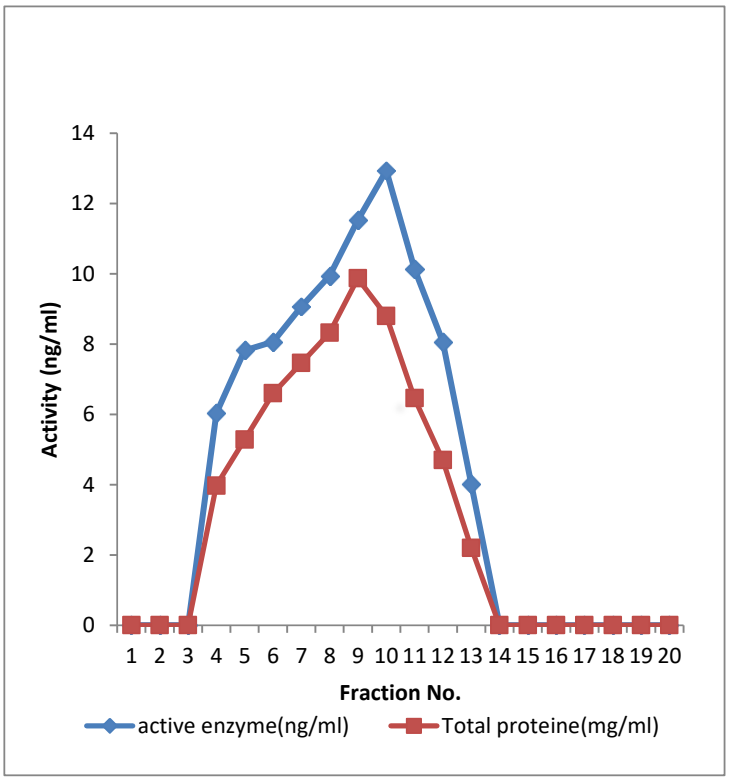

Figure 1 shows the purification of the enzyme arginase using Sephadex G-200

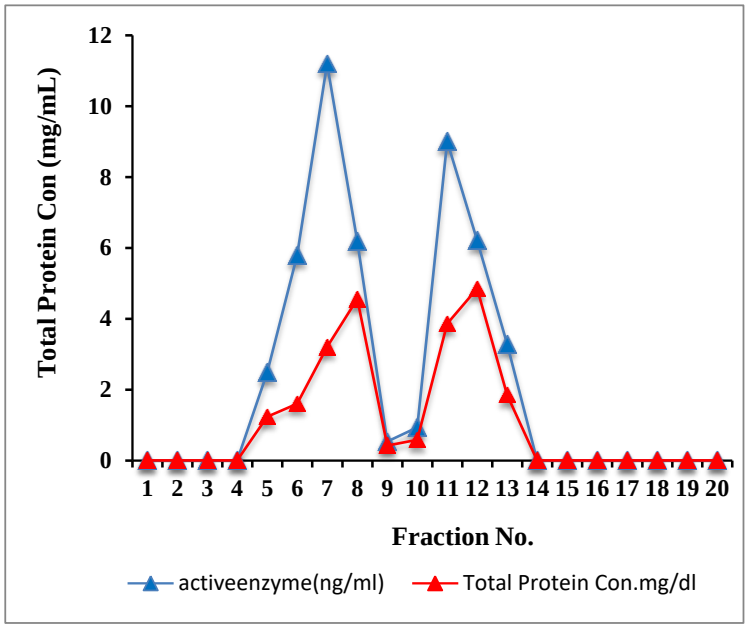

Figure 2 also shows ion exchange chromatography using EDEA-cellulose for the separated fractions versus the total protein.

The electrolysis revealed that the molecular weight of the enzyme is high and reaches 245 kDa, according to the figure below

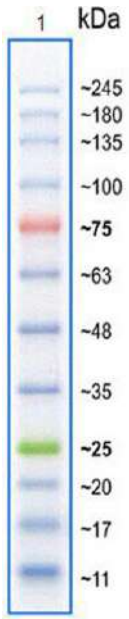

Figure 3 Electrolysis analysis showing the molecular weight of the enzyme, up to 245 kDa, using the acrylamide gel.

'Figure (3) ' shows the molecular weight of the arginase enzyme separated by electrophoresis [14,15],the electrophoresis analysis revealed the presence of two arginase peaks, according to the figure below

Figure (4) Highest effective electrophoresis of separated fractions by chromatography using Sephadex G-200 to isolate the arginase enzyme.

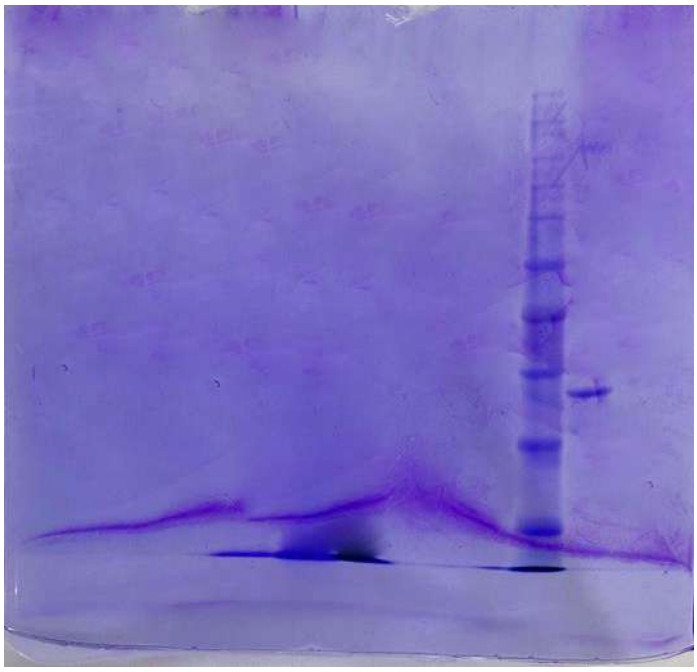

Figure 4 Electrophoresis to isolate the enzyme arginase in serum of kidney patients [13]
The literature indicates that the arginase enzyme contains two isotopes, one in red blood cells of the liver (ARGI) at a high level and the other (ARGII) at a lower level in mitochondria in many tissues [5].

Table 3. shows the level of urea in the serum of patients compared with healthy subjects measured in units (mgldL) at the probability level P≤0.01

Urea level in units (mgldL)	Mean ± standard deviation	P-Value
Control group	27.92±3.2	≤0.01
Patient group	83.7±23.4	

The above table shows a significant increase in the level of urea in the blood serum of patients with kidney disease compared to healthy people, This is in agreement with (**Hasan**) [19]
Where he found a significant increase in the level of urea in patients with renal impairment, as well as the current results are consistent with the findings of (**Al-gharaghouly**) [20] that refers to the significant increase in the level of urea in patients with renal impairment. The current result is consistent with what was mentioned by Loughridge L., [21]. The reason for this increase is the weakening of kidney function with age, as this is due to the reduction of glomerular filtrate after the age of thirty.

Table 4. shows the level of creatinine in the blood serum of people with kidney disease (mgldL) compared to healthy people with the p ≤ 0.01 level.

Creatinine level In units (mg dL)	Mean ± standard deviation	P-Value
Control group	0.83±0.7	≤0.01
Patient group	2.85±1.19	

The table above shows a significant increase in the level of creatinine in the serum of kidney diseases compared to healthy people, and these results were consistent with the result of (Hababi) [22], (Philip et al.)[23]. The reasons for the increase in the level of creatinine in the blood indicate the fact that creatinine is waste of nitrogen metabolism processes, which are excreted with urine in the normal state, but in the case of a kidney disorder that may lead to a

gradual loss of kidney function and a failure in filtration, which leads to an increase in the concentration of creatinine in the body. The patients who suffer from chronic renal failure and diabetic nephropathy suffer from a decrease in the value of glomerular filtration(Hasan) [19]

Table 5. shows the level of total protein (mg/dL) in the serum of kidney patients compared with healthy people with a probability level P≤0.05

Total protein level In units (mg/ dL)	Mean ± standard deviation	P-Value
Control group	6.53±0.2	≤0.05
Patient group	3.8±0.6	

Table 5 the level of total protein in the serum of kidney patients compared with healthy people, where it was found that there are significant differences at the level of probability P≤0.05 and this is consistent with (**Al-gharaghouly**) [20], where it was mentioned that there is a decrease in the level of total protein at all ages. In patients with renal insufficiency, and also agrees with(Muthu), [24] that the reason for this decrease is inflammation in the renal glomeruli, which leads to its appearance in the urine.

Table 6. shows the level of albumin in kidney disease serum compared to healthy people with the probability level P≤0.01

The level of albumin unit (mgldL)	Mean ± standard deviation	P-Value
Control group	4.120±0.02	≤0.01
Patient group	2.51±0.39	

Table 6 The level of albumin in kidney disease serum compared to healthy people, where a significant difference was found at the probability level P≤0.01. The result of the current study is consistent with what was found by**(Hasan)** [(19),] where a significant decrease was observed compared with The result is also consistent with the findings of healthy people (Junlin et al) [25], The reasons for the decrease refer to kidney damage resulting from chronic renal failure and diabetic nephropathy, which leads to loss of albumin through damaged filter units and glomeruli, the amount of albumin in the urine increases and there is a decrease in the concentration of albumin in the blood, which ultimately leads to a state of hypoalbuminemia. Roche, M.;] [26], or that the possible cause is due to poor nutrition and the increased need for albumin in the body [Maher Borai @eta] [27].

Table 7. shows the level of globulin in serum of kidney disease compared to healthy people with the probability level P≤0.01.

Globulin level (mgldL)	Mean ± standard deviation	P-Value
Control group	2.41±0.06	≤0.01
Patient group	1.29±0.01	

Table 8. shows the level of uric acid in the blood serum of kidney patients compared with healthy people with no significant differences.NS = 0

Uric acid level in units (mg dL)	Mean ± standard deviation	P-Value
Control group	4.7±0.28	NS
Patient group	5.19±0.28	

It can be seen from Table 8 uric acid is one of the non-protein organic compounds in the blood and represents in humans the final product of the metabolism of purines, a substance that is difficult to dissolve in water. The majority of it must be excreted through urine, as 20% of it is filtered through the kidneys (Salih) [28]. The formation of uric acid depends on the extent to which the food contains nucleoproteins, as well as on the extent to which the food

contains free purine bases, as is the case in tea and coffee, as well as on the process of destruction that occurs in the cells of the body, Its level in the blood increases due to a decrease in the percentage of renal filtration of uric acid as a result of renal failure as well as in the case of lytic anemia and pernicious anemia as well as gout (Fiedman@eta) [29]

References

[1] Di CCostanzo L, Pique M E and Christianson D W 2007 *J. Am. Chem. Soc.* **129** 6388 .
[2] Wu G and Morris S M 1998 *Biochem. J*. **336** 1.
[3] Dowling D P, Di Costanzo L, Gennadios H A and Christianson DW 2008. *Cell. Mol. Life Sci*. **65** 2039.
[4] Di Costanzo L, Moulin M, Haertlein M, Meilleur F and Christianson DW 2007 *Arch. Biochem. Biophys*. **465** 82.
[5] Morris S M 2002 *Annu. Rev. Nutr*. **22** 87.
[6] Reczkowski R S and Ash D E . *Arch. Biochem. Biophys*. 1994. **312** 31.
[7] Cox J D, Kim N N, Traish A M ,etal 1999 *Nat. Struct. Biol*. **6** 1043.
[8] Cama E , Colleluori D M , Emig FA, etal . 2003 *Biochemistry*. **42** 8445.
[9] Moody J A, Vernet D, Laidlaw S, etal 1997 *J. Urol.* **158** 942
[10] Iyer R K, Yoo P K and Kern R M, . 2002 *Mol. Cell .Biol*. **22** 4491.
[11] Coulomble J J and Favreau L 1963 *Clin. Chem*. 9.
[12] Pierre C , Claude B 1978 *Biochem. J.* **175** 449.
[13] Chang G G , Wang J K , Huang T M , etal, 1991 *Eur. J Biochem.* **202** 681.
[14] Hames B D and Rickwood D 1990 *Gel Electrophoresis of Proteins: A Practical Approach* . 2nd ed(Oxford University Press, Oxford) p 383.
[15] Chang G G, Wang J K and Huang T M 1991 *Eur J Biochem.* **202** 681.
[16] Alshamaa S D, Al-Obaidi S H . 2018 *Raf. J. Sci*. **27** 1.
[17] Scaglia F , Lee B 2016 . *Am J. Med Genet C Semin Med Genet*.**142** 113.
[18] Hezel M P , Liu M and Schiffer T A .2015 *J. Redox Biol*. **5** 234.
[19] Lakowicz J R *Principles of Fluorescence Spectroscopy* (Springer Publisher. New York), 2006,chapter 10.
[20] Hasan S M. , Maher F T and Kadhim N Q 2018 *Tikrit Journal of Pure Science*. **23** 10.
[21] Al-gharaghouly J M 2015. *Biochemical study of partially purified glutathione peroxidase from sera of patients with renal failure* . Master Thesis.
[22] Loughridge L and Lewis M G 2008 *Nephrotic syndrome in malignant disease , Lancet,* Willimam J Marshall. clinical chemistry 6thed p 70-82.
[23] Al-Ahbabi M Y K . *Study of Chronic Kidney Disability Patients in Salahuddin Province Biochemical and Molecular* (Master Thesis, College of Education for Pure Sciences, Tikrit University). 2018.
[24] Philip M F, David C and Richard E G 2018 *Can. J .Diabetes* .**42** S201.
[25] Muthu K M 2003 *Kidney Int Suppl*. **83** S86.
[26] Zhang J , Zhang R and Wang Y 2019 *J. Diabetes Res*.**9** 1.
[27] Roche M , Rondeau P , singh M , ,etal. 2008. **582** -1783.
[28] Maher B M B, Manar M A, Hala A A 2016 *Int. J. Curr. Adv. Res*. **4** 1337.
[29] Salih N A 2010 *Determination of Urea, Creatinine , Uric acid and Alkaline phosphatase activity , Phosphorous, Calcium and total protein in the blood of Acute Renal Failure Patients in Tikrit city*. (College of pharmacy, Tikrit University, Tikrit , Iraq).

Synthesis, Theoretical Treatment and Investigation of Adsorption of 4,4'-((1E,1'E)-(Methylenebis(4,1-phenylene))bis(diazene-2,1-diyl))bis(naphthalen-1-ol) on Olive Peel

Synthesis, Theoretical Treatment and Investigation of Adsorption of 4,4'-((1E,1'E)-(Methylenebis(4,1-phenylene))bis(diazene-2,1-diyl))bis(naphthalen-1-ol) on Olive Peel

Zainab J. Khudair [1*], Khawla K. Jassim [2] and Ameena N. Seewan [3]

[1,3] Science Dept., College of Basic Education, Al-Muthanna University, Samawah, Iraq
[2] Chemistry Dept., College of Science, Al-Muthanna University, Samawah, Iraq

E-mail: chemistry.zainb@mu.edu.iq

Abstract. In this study, the compound 4,4'-((1E,1'E)-(methylenebis(4,1-phenylene))bis (diazene-2,1-diyl))bis (naphthalen-1-ol) synthesized by reaction of 4,4'-Diaminodiphenylmethane with Alpha-naphthol. This compound was identified by using an element C.H.N analyzer, Infra-Red spectrum, Ultraviolet and Visible spectrum, and GC-Mass spectrometry. We used olive peels to adsorb the synthesized dye from an ethanol solution. The results obtained showed that olive peel has a good adsorption on the bis-azo dye. Temperature and pH effect were studied under multiple conditions. The result showed that the adsorption increased with temperature increasing, and adsorption efficiency according to pH as 7<4<9. Theoretical treatment was studied in gas phase for molecular mechanics and semi-empirical computations using the hyper chem8 program. Dipole moment, formation heat and binding energy were done via the methods (PM_3 and ZINDO/S) at 25 ºC. Electrostatic potential of active sites were also studied for the newly synthesized bis-azo dye. Vibrational values were evaluate using PM_3 method, the theoretical frequencies obtained from the calculations were consistent with the experimental values. HOMO & LUMO (frontier orbitals) were studied by PM_3 method, electronic spectrum was also studied using ZINDO/S method and compared with experimental spectrums. The results obtained were closely related between the theoretical and experimental spectrum.

Keywords: Bis-azo, Olive peel, Adsorption, Theoretical study.

1.Introduction

More than one million tons of dyes are produced annually, 60-70% of them are azo dyes. The use of dyes has increased over the years, and widely used in various industries such as textiles, paint, paper, cosmetics, pharmaceuticals, printing, and foodstuffs [1]. Dyes are one of the main pollutants [2-4]. A literature survey identified adsorption as a potential technique for purifying wastewater from dyes. Adsorption is the most preferred method for treating liquid waste in textile industry compared to other available physical, biological and chemical methods, due to its simple, flexible design and ease of use [5]. Some side products may be produced from the adsorption process, some of which may be beneficial or at least non-toxic, The adsorption process is also considered to involve lower operating costs. Moreover, it has no environmental problems, don't produce any sludge and produce high quality treated water. Although adsorption is an excellent dye removal technique, it has significant limitations to its application due to the limited availability of low-cost adsorbents [6,7]. One of the most commonly used adsorbent is activated carbon, as it is characterized by its high surface area and great adsorption capacity. Due to the high cost and lack of reusability of activated carbon, the need to explore new adsorbents with low cost, reusable, biodegradable and the possibility of regeneration, as well as the high efficiency of removing dyes, has increased. Many adsorbents have been implemented to adsorb dyes from wastewater with low cost and high efficiency, most of them are natural and

modified clays, modified agricultural by-products, bagasse, chitosan ash, industrial waste, coconut pulp, charcoal, peat and neem leaves [8, 9]. The cost of adsorbents is usually unstable and frequently changing depending on the changes in prices in the markets, and it varies greatly according to the manufacturing companies, even if they contain exactly the same material. The material chosen for a specific application should preferably be less expensive and more suited to specifications to achieve its intended use. The variation and diversity of adsorbents and the expansion in their spread and manufacture make the selection process difficult [10]. In the present work, a new dye was synthesized and its adsorbent effects on olive peels were identified, along with the theoretical study of some properties of the synthesized dye.

2.Experimental

2.1. Chemicals and Instruments

The materials and solvents that used were supplied by Sigma Aldrich, Fluka, and BDH. C.H.N elementals were measured by EM - 017. FT-IR spectra were recorded on an FT-IR—8400S plus spectrometer operating from (4000—400 cm^{-1}) in KBr pellets. UV—Visible spectra were recorded by UV—1800 PC Shimadzu, Al-Muthanna University, Semawa, Iraq. The GC-Mass spectra were recorded on at 70 eV using Agilent technologies mass selective detector 5973 watt work in the department of chemistry, Technology Shareef University, Tehran, Iran.

2.2.Preparation of (MBN) compound

The compound of 4,4'-((1E,1'E)-(methylenebis(4,1-phenylene))bis (diimide -2,1-diyl))bis (naphthalen-1-ol) (MBN) diazotized by following the method described in literature [11], 4,4'-Diaminodi phenylmethane (0.01mol) was dissolved in conc. HCl (3 mL) and (10 mL) of distilled water, after that the mixture cooled in an ice bath, after the temperature reached less than 5 °C, (10 mL) of cooled solution of (0.01 mole) sodium nitrite was added dropwise to keep the temperature below 5 °C for 15 minutes. After that, the reaction mixture was added to an alkaline solution of (0.02 mole) alpha-naphthol slowly and left for 20 minutes, the reaction mixture irradiated with a microwave at 700 W for 5 minutes, after the reaction was completed, the precipitate was collected by filtration, washed with distilled water and dried**.** Physical data of MBN are described in Table 1.

Table1. Physical data of MBN compound

Color	melting point (°C)	yield %	m.wt (g/mol)	Found (calc.)%		
				C	H	N
Dark red	232-234	90	508.57	78.51 (77.93)	4.82 (4.76)	10.30 (11.02)

2.3. Olive peel surface preparation

A surface of olive peel used as an adsorbent was prepared from fresh olives picked and cut into small pieces, washed several times with distilled water to remove dust, dried in the air and grinded into a fine powder, then washed the powder with distilled water and making sure that the impurities were removed and then dried in an oven at a temperature of 60 °C for two hours.

2.4.Preparation of Stock solution

A stock aqueous solution of the synthesized bis-azo dye was prepared at a concentration of 125 ppm by dissolving 125 mg of the dye in 1000 mL of ethanol. Using UV-visible spectrophotometer for determining the maximum absorbance wavelength of MBN at 250-700 nm. To plot the standard curve, several concentrations of MBN dye were prepared from (2-10 ppm), which were used to measure the different dye concentrations in ethanolic solution.

2.5.Study pH effect on Adsorption of MBN

0.1N of hydrochloric HCl and 0.1N of NaOH was added to different concentrations of MBN dye to justify pH, to study the effect of pH changing on adsorption efficiency of MBN dye on 0.05 g of the powdered olive

peel. The mixture stirred at 5 °C for one hour, MBN dye concentrations were determined by measuring the absorbance at wavelength of 488.00 nm of the solution.

2.6.Study the temperature effect on the bis-azo compound adsorption

A volume solutions of 10 mL were used with different concentrations with pH 7 of the MBN dye which was added to 0.05 g of olive peel. The mixture stirred for one hour to be exposed to the same temperature at 298, 308, 318 K, MBN dye concentrations were also determined by measuring the absorbance at wavelength of 488.00 nm of the solution.

3. Results and Discussion

3.1. Synthesis of MBN dye.

MBN was prepared according to the following Scheme:

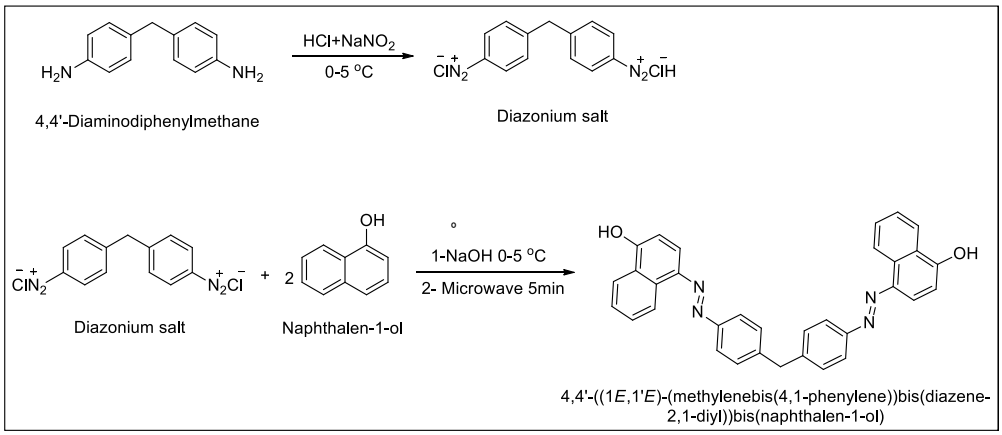

Figure 1. scheme for the synthesis route of MBN compound

The prepared compound was characterized by FT-IR spectroscopy, GC-Mass spectrometry and C.H.N. analysis.

3.2.Spectroscopic Studies:

3.2.1.Infrared Spectral Study:

FT-IR spectrum of MBN showed the disappearance of NH_2 stretching bands at 3354 cm^{-1} and appearance of broad peak for phenolic OH at 3444 cm^{-1}. FT-IR spectrum also showed the appearance of strong peaks at 1618 and 1498 cm^{-1} for C=C and N=N groups, respectively (Figure 2) [12,13].

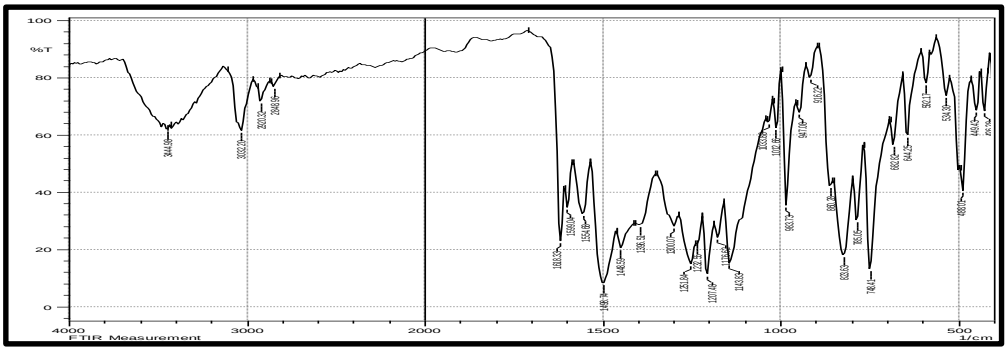

Figure 2.FTIR spectrum of MBN compound

Table 2. FT-IR spectra of MBN compound.

N=N	C=C	C-H aromatic	O-H

1498 s	1618 s	3032 m	3444 b

Where: m: medium, s: strong and b: broad

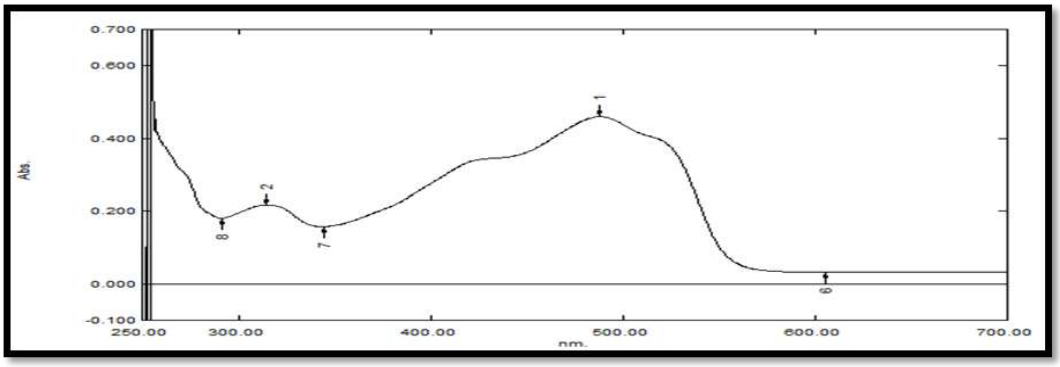

Figure 3 . UV-Visible spectrum of MBN compound

3.2.2.UV–Vis spectral data for MBN compound:

The azo functional group (-N=N-) usually absorb at the wavelength range from (350 - 370) nm [13]. The electronic spectrum of MBN compound exhibits transitions at (488, 314.5 and 253) nm respectively, these bands probably belong to n-π * and π-π* transition of N=N group [14].

3.2.3.Analysis of mass spectrum:

The mass spectrum of MBN compound showed the molecular ion peak at m/z = 508(R%55), the important fragmentation peaks shown at m/z = 466(R%1), m/z = 367(R%5), m/z = 353(R%20), m/z =337(R%10), m/z = 171(R%15), m/z = 157(R%5), m/z = 143(R%100), m/z =129(R%10), m/z = 115(R%50), as shown in 'Figure 4'.

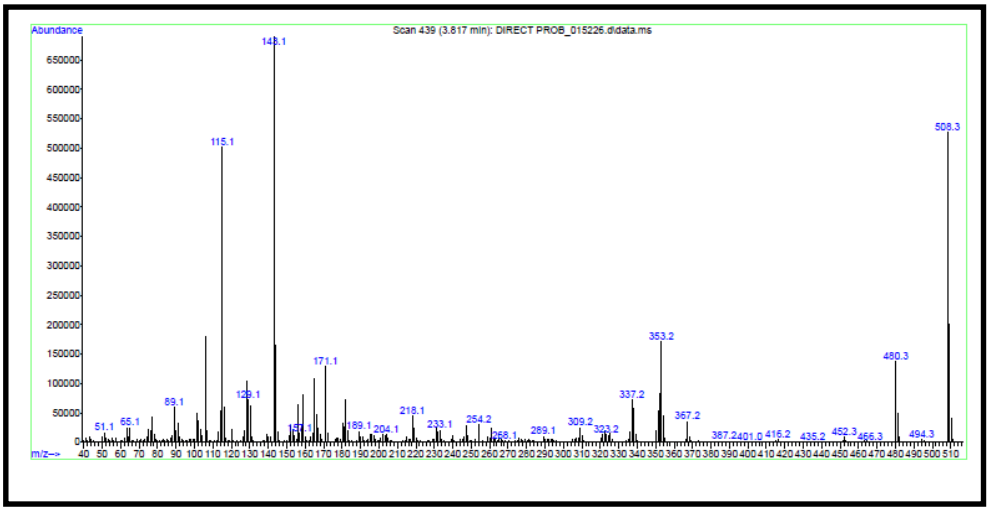

Figure 4 . Mass spectrum of MBN compound

3.3.Study of Adsorption of MBN compound

The study of adsorption of MBN on the surface olive peel at temperature 298 K was calculated and the amount of absorbent material drawn against equilibrium concentration to give the general form of isotherm adsorption

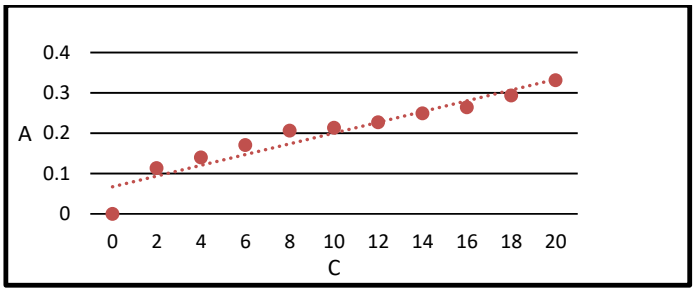

Figure 5 . The amount of adsorbent material against concentration

3.3.1.Effect of Temperature

The effect of temperature on the adsorption of synthesized MBN dye at different temperatures, which are 298, 308 and 318 K was studied at a constant pH. The temperature changes showed an obvious change in the efficiency of dye adsorption on the olive peel, it was found that the adsorption of MBN increases with increasing the temperature, so the reaction is endothermic [15], as it shown in Figure 6.

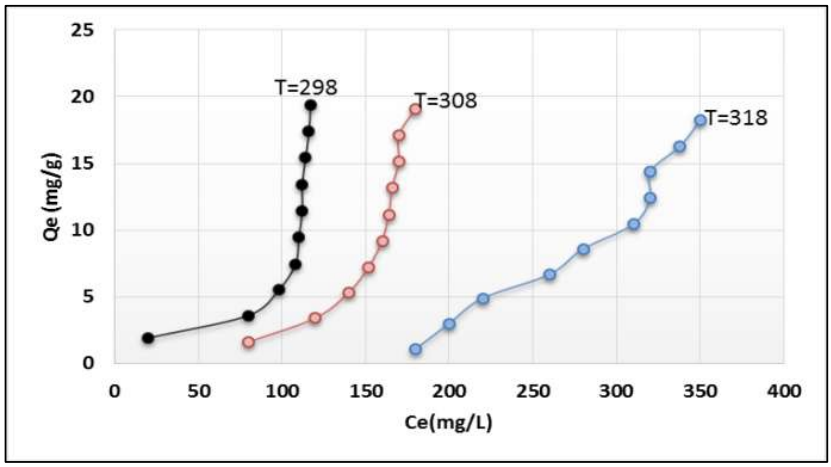

Figure 6. Adsorption of MBN on olive peel at different temperatures

3.3.2.The Effect of Initial pH

The effect of changing pH on the efficiency of adsorption of the dye on the surface of the olive peels was studied at different pH ranges (4 – 9) by adding acidic or basic solutions, it was found that the adsorption efficiency decreases when the pH is reduced, reaching its highest level at 9 PH value to decrease and reach its lowest levels at 4 pH value and this change can be explained by the fact that at basic medium the efficiency of adsorption increases because positive charges have a tendency to bond with the surface greater than the association with the solvent molecules [16], as shown in Figure 7.

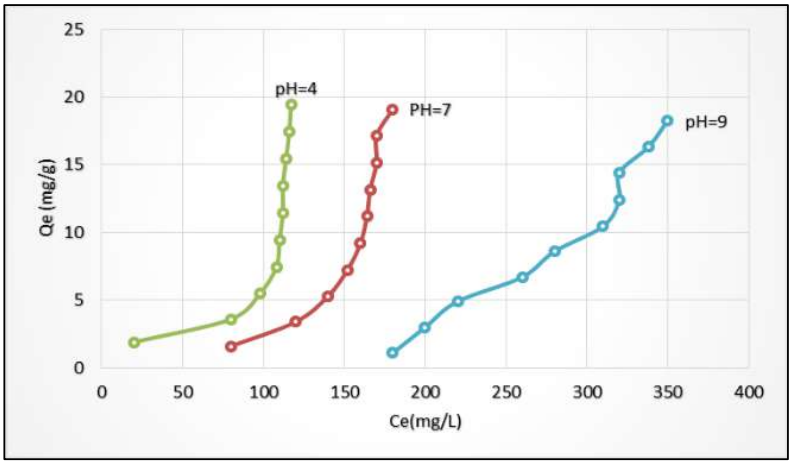

Figure 7. Adsorption of MBN on olive peel at different pH values

3.4.Theoretical Studies

3.4.1.Energies and Dipole Moment

The study of energetic theoretically could predict the occurrence of molecular processes or not. Low energy systems are the most stable in all computational chemistry techniques, so their molecular structure is compatible with the structure with the minimum energy [17]. Dipole moment was used to measure the charge density of the dye. The accuracy of the overall distribution of electrons in the molecule is difficult to assess because it contains all of the multiple dipole moments. In this study, standard enthalpy of formation (ΔH_f^o), dipole moment (μ) and binding energy (ΔE_b) of MBN compound were calculated theoretically by PM_3 method and HOMO & LUMO (frontier orbitals) were calculated also by using PM_3 method.

Table 3. Formation, binding energies and dipole moment for MBN dye

ΔH°_f (KJ.mol^{-1})	ΔE_b (KJ.mol^{-1})	μ (debye)	HOMO	LUMO	ΔE_{gab} (KJ.mol^{-1})
-61922.91	-93139.47	4.54	-8.54	-0.85	7.69

3.4.2.Theoretical Vibration Frequencies

PM_3 method was used to evaluate vibrational frequencies of MBN compound following literature [18]. The theoretical spectra from the semi-empirical computation help explain peaks of the experimental spectrum of MBN. The most characteristic calculated vibrational frequencies were chosen for the bis-azo dye assignment. The theoretical wave number of the synthesized dye showed some differences against experimental values, and these differences are mostly acceptable in computational chemistry.

Table 4. Theoretical and experimental frequencies in cm^{-1} of MBN compound

C=C	N=N	C-H	O-H
1684.65*	1508.60*	3084.92*	3144.36*
1618.33**	1498.74**	3032.20**	3444.98**
(3.9)***	(0.6)***	(1.7)***	(9.6) ***

Where:

* : Theoretical value

** : Experimental value

***: Error %

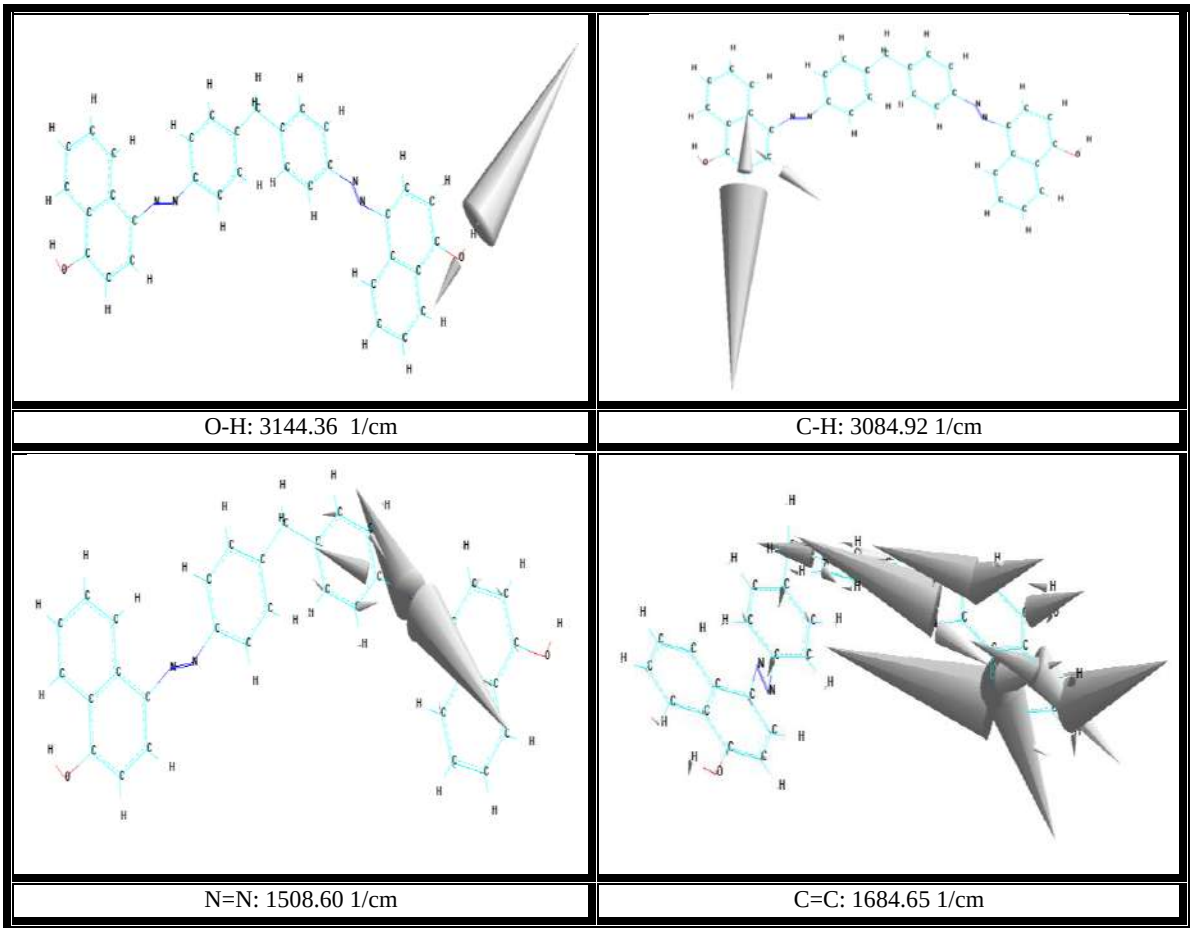

Figure 8. Theoretical vibrational frequencies of MBN compound

3.4.3.Theoretical UV-Spectrum

Theoretical electronic data of MBN dye was evaluated by ZINDO / S method, the results showed that there is high acceptable between the experimental and theoretical data.

Table 5. Theoretical and experimental electronic data of MBN compound

Transitions	Theoretical	Experimental
n→π*	355.05 nm	488.00 nm
π→π*	338.73 nm	314.50 nm
π→π*	271.89 nm	253.00 nm

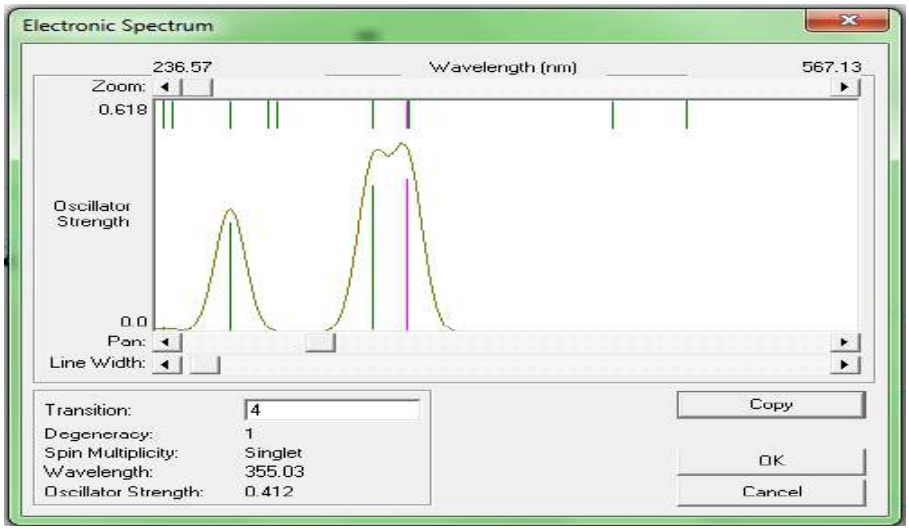

Figure 9. Theoretical electronic spectrum of MBN compound.

4.Conclusion

1- The results showed the ability of olive peels to adsorb the synthesized dye with high efficiency under normal conditions of temperature and pH.
2- Adsorption efficiency of MBN dye on olive peel increases with the increasing of temperature as it follows: 298<308<318 K.
3- Adsorption efficiency of MBN dye on olive peel according to pH values, increases in basic and decreases in acidic mediums as it follows: 4<7<9 pH values.
4- The theoretical results of formation and binding energies showed that the synthesized dye was a stable compound.
5- MBN dye structure was confirmed by the experimental spectra and found that it is almost similar with the theoretical results calculated by PM_3 and ZINDO / S methods.
6- Active sites of MBN dye were evaluated theoretically using semi-empirical methods.

Acknowledgement

The authors would like to thank Dept. of Science / College of Basic Education/AL-Muthanna University for the facilities during this work.

References

[1] Dai Q, Zhang S, Liu H, Huang J, and Li L 2020 *Bioelectrochemistry*, 131 107349.
[2] Sarkheil H , Noormohammadi F, Rezaei A.R. and Borujeni M.K 2014. In *International Conference on Agriculture, Environment and Biological Sciences*.
[3] El- Haddad M, Regti A , Laamari M.R , Slimani R , Mamouni R, El- Antri S and Lazar S 2014 *J. Taiwan. Inst .Chem. Eng*, 45 533.
[4] Tsui L S , Roy W R and Cole M A 2003 *Color. Technol*, 119 14.
[5] Crini G.2006 *Bioresour. Technol*, 97 1061.
[6] Choy K K , McKay G and Porter J F 1999 *Resour .Conserv .Recycl*, 27 57.
[7] Reffas A 2010 *Étude de adsorption de colorants organics (rouge nylosan et bleu de méthylène) sur des carbons actifs préparés à partir du marc de café*,PhD.thsis.
[8] Lora-Wainwright A 2009 *Soc . Anthropol.* **17** 56.
[9] Al-Qodah Z, Yahya M and Al-Shannag M 2017 *Desalin Water Treat*, **85** 339.
[10] Cao X , Huang X , Liang P , Xiao K., Zhou Y., Zhang X and Logan B E 2009 *Environ. Sci. Technol*, **43** 7148 .

[11] Wu T Y , Mohammad A W, Lim S L , Lim P N and Hay J X W 2013. *Wastewater reuse and management* ,(Springer, Dordrecht) p 47-103 .
[12] Purohit D H, Dodiya B L , Ghetiya R M , Vekariya P B and Joshi H S 2011 *Acta Chim. Slov*, **58** 53.
[13] Pavia D L , Lampman G M , Kriz G S and Vyvyan J A 2008 , *Introduction to spectroscopy*. (Cengage Learning) .
[14] Jasim K K , Kadhim Z Y , and Khudair Z J 2018 *Jour Adv Res. Dyn. Control Syst.*, **10** 159.
[15] Geçgel Ü , Üner O , Gökara G. and Bayrak Y 2016 *Adsorp .Sci .Technol*, **34** 512.
[16] Vijayakumar G , Tamilarasan R and Dharmendirakumar M 2012 *J. Mater. Environ. Sci*, **3** 157.
[17] Atkins P W 1997 *The periodic kingdom: A journey into the land of the chemical elements*. Science Masters.
[18] Seewan A N and Alias M F 2013 *Baghdad. Sci. J,* **10** (Special issue in Chemistry Conference).

Synthesis and DNA binding study of Co (II) and V(IV) complexes with O, N, O tridentate 3-methoxysalicylaldehyde-semicarbazide based ligand

Synthesis and DNA binding study of Co (II) and V(IV) complexes with O,N,O tridentate 3-methoxysalicylaldehyde -semicarbazide based ligand

Suher M. Dawoud [1]

[1]Department of Chemistry, Environmental science and technology College University of mosul, mosul, Iraq

E-mail: suher.alsaaty@uomosul.edu.iq

Absract. Cobalt and vanadium complexes with (E)-2-(2-hydroxy-3-methoxybenzylidene)hydrazine-1-carboxamide were synthesized. The ligand was structurally characterized by FTIR, ^{1}HNMR and ^{13}CNMR spectroscopy. The interaction activity of ligand and complexes was investigated with DNA by spectroscopical and physical methods. The results showed an intercalative binding between the synthesized compounds and DNA.

Keywords: Methoxysalicylaldehyde, Semicarbazide, EDX, DNA, Viscosity

1.Introduction

Sulfur and nitrogen donor ligands have received particular attention as one of the essential fields in coordination chemistry. Semicarbazones are among the main nitrogen/oxygen compounds which are provide variable binding modes, structural variety and biological applications [1-3]. The atoms coordination modes allow flexibility to semicarbazone ligands to coordinate with the metal ion that giving one or multi-nuclear complexes [4-7]. Semicarbazone metal complexes show perfect stability that can support the biological activity, reduces the toxicity and become a dependable source for creating novel biologically active compounds [8, 9].

Cobalt and vanadium are essential elements in biological systems [10]. The presence of cobalt in vitamin B12 makes it a regulator for the DNA synthesis. Cobalt uses as a supplement of the B12 vitamin due to it participates in the coenzyme of this vitamin [11]. In the other hand, vanadium complexes are described as therapeutic agents and promising drugs against diabetes, cancer and parasitic diseases [12, 13].

DNA has an important role in the biological processes because of its responsibility about intelligence and directed synthesis of biomolecules of enzymes and proteins during duplication and reproduction for genetic intelligence in living cells. Metal complexes are reported an attractive binding sites with DNA [14, 15]. Three noncovalent binding modes are well known; electrostatic, groove and intercalation [16–18]. Transition metal complexes have been received the large part of attention to create new nonradioactive tests of DNA construction [19, 20], new curative agents capable to cleave DNA, and DNA-mediated electron transfer reactions [21-23].

The biological properties of semicarbazones depend on the way that the metal ion is coordinated which determines the lipophilic properties that are responsible on the rate of entry into the cell [24]. The reported studies revealed that the complexes are higher bioactivities, lower side effects and lower drug-resistance than that of free ligand [25]. This work has

described the synthesis, characterization and DNA binding of vanadium and cobalt complexes based on semicarbazone which are explaining in scheme 1.

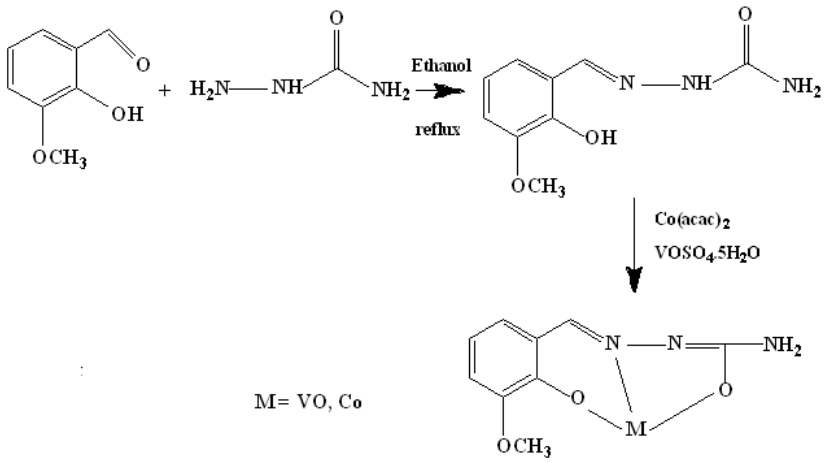

Scheme 1. Ligand and complexes general synthetic procedure

2.Experimental

2.1.Material and Instruments

All chemicals were obtained from Sigma Aldrich and used without more purification. DNA was obtained from human blood. FTIR spectra were conducted on a Shimadzu (FTIR -8400S, Japan) spectrometer using KBr pellets. Energy dispersive X-ray spectrometry (EDX) were recorded at room temperature. Electronic spectra were recorded by UV-Vis double-beam spectrophotometer (Spectroscan-80D, England). ^{1}HNMR and ^{13}CNMR recorded spectra by using DMSO-d_6 as solvent on a BRUKER 500 MHz spectrometer.

2.2. Synthesis of (E)-2-(2-hydroxy-3-methoxybenzylidene) hydrazine-1-carboxamide

A solution of 3-methoxysalicylaldehyde in (15 ml) ethanol dissolving (0.3735 g , 2.25 mmol) adding to semicarbazide solution in (15 ml) ethanol dissolving (0.25 g, 2.25 mmol). The resulting yellow solution was stirring for 2h with refluxing, filtered the solution with washing the precipitate by ethanol, then left to dried. Yield: 85%, mp:189-190 ˚C

2.3.Synthesis of vanadium complex

A solution of $VOSO_4$ $5H_2O$ (0.985 mmol, 0.25 g) dissolving in (20 ml) ethanol added to a solution of 3-methoxy-2 hydroxybenzaldehyde hydrazinecarboamide in (20 ml) ethanol dissolving (0.985 mmol, 0.2195 g). The red solution for 2h was refluxed, with filtration, by ethanol washing the precipitate, then left to dried. Yield: 80%, mp: 234-236 ˚C

2.4.Synthesis of cobalt complex

A solution of $Co(acac)_2$ in (20 ml) ethanol dissolving (0.25 g, 1.00 mmol) has been added to a solution of 3-methoxy-2- hydroxybenzaldehyde hydrazinecarboamide in (20 ml) ethanol dissolving (0.2195 g, 0.985 mmol) . The brown solution for 2 h was refluxed with filtration, and washed the precipitate with ethanol , then left to dried. Yield: 77%, mp: 243-245 ˚C

2.5.DNA binding assay

The DNA binding was performed in NaCl buffer (pH= 7.2), 6.3 mM Tris-HCl/50 mM. We prepared DNA stock solution in 6.3 mM Tris-HCl/50 mM of (pH= 7.2) buffer NaCl by dissolving a suitable amount of DNA at room temperature. For 48 h the product was stored in the refrigerator. A DNA buffered solution showed two UV absorbance at (260 and 280) nm a

ca.1.9: 1, ratio indicating the DNA was free of protein. The concentration of DNA was determined by the UV absorbance at 260 nm by using known molar absorption coefficient (6600 $M^{-1}cm^{-1}$) value [26], the reference (Tris/HCl buffer solution) was scanned from 230 nm to 600 nm.

measurements viscosity were achieved using a Cannon Manning Semi-Micro viscometer which is immersed in a water bath a thermostatic at 37 ^{0} C. By using digital stopwatch flow times were conducted manually. Calculating values viscosity from the observing the flow time DNA-containing solutions (t) using (t_0) for correcting the solvent mixture , $\eta = t - t_0$. The data viscosity were presented as $(\eta / \eta_0)^{1/3}$ versus [complex]/[DNA] where η and η_0 are the complex viscosity in presence of DNA and the viscosity of DNA alone respectively [27].

3.Results and Discussion

V(IV) and Co(II) complexes were synthesized with salicylaldehyde derivative based on semicarbazones. The complexes and ligand are strongly soluble in DMSO, air-stable, and strongly stable in aqueous solutions. UV and ^{1}H NMR spectra recording after preparation, (3, 30) days and 3 months, showing a high stability at room temperature.

The ligand showed^{1}H NMR , FTIR , and ^{13}C NMR spectra. In FTIR, the band of 3351 cm^{-1} to 3451 cm^{-1} due to υ (N–H) stretching, bands at about 3146 cm^{-1} corresponding to υ (O – H) group, ligand band at about 1585 cm^{-1} is due to υ (C=N) group, the bands at about 1600 cm^{-1} to 1612 cm^{-1} attributed to υ (C=N-N-C). band at about 1550 cm^{-1} to 1559 cm^{-1} is assigned to the stretching frequency of the phenolic bond (C – O). The chelation of semicarbazone ligand can easily be detected by monitoring the ligand position bands which are shifted to low or high energy upon complexation. The stretching phenolic(C–O) band has upward shifted to appeared in the region 1560-1568 cm^{-1}. In both complexes, υ (C=N) underwent a change in intensity and frequency, caused by complexation and downshifted to higher frequency to appeared in the region (1580 cm^{-1}). In ^{1}H NMR spectrum 'Figure 1 '.The signal appeared at (3.80) ppm attributed to the CH_3 protons of CH_3O group. doublet signals at (6.91) ppm and (7.34) ppm are due to the aromatic protons 4 and 6, respectively. The triplet signal at (6.74) ppm is due to the aromatic proton 5. a singlet signal emerged at 8.16 ppm is attributed to the proton of CH=N group. The broad signal emerged at (6.37) ppm is due to the NH_2 protons, whereas, the singlet signal emerged at (10.18) ppm is due to OH proton. In ^{13}C NMR spectrum, the carbon of the CH_3 group is appeared at 56.30 ppm, Figure 2. The signals in the range 112.65 ppm to 145.76 ppm are due to the aromatic carbons and the signals at 148.32 and 157.04 ppm are due to the carbons of (C=N) and (C=O), respectively.

The complexes were identified by the energy dispersive X-ray spectrometry (EDX) which confirmed that the ligands were successfully chelated with Co and V, Figure 3.

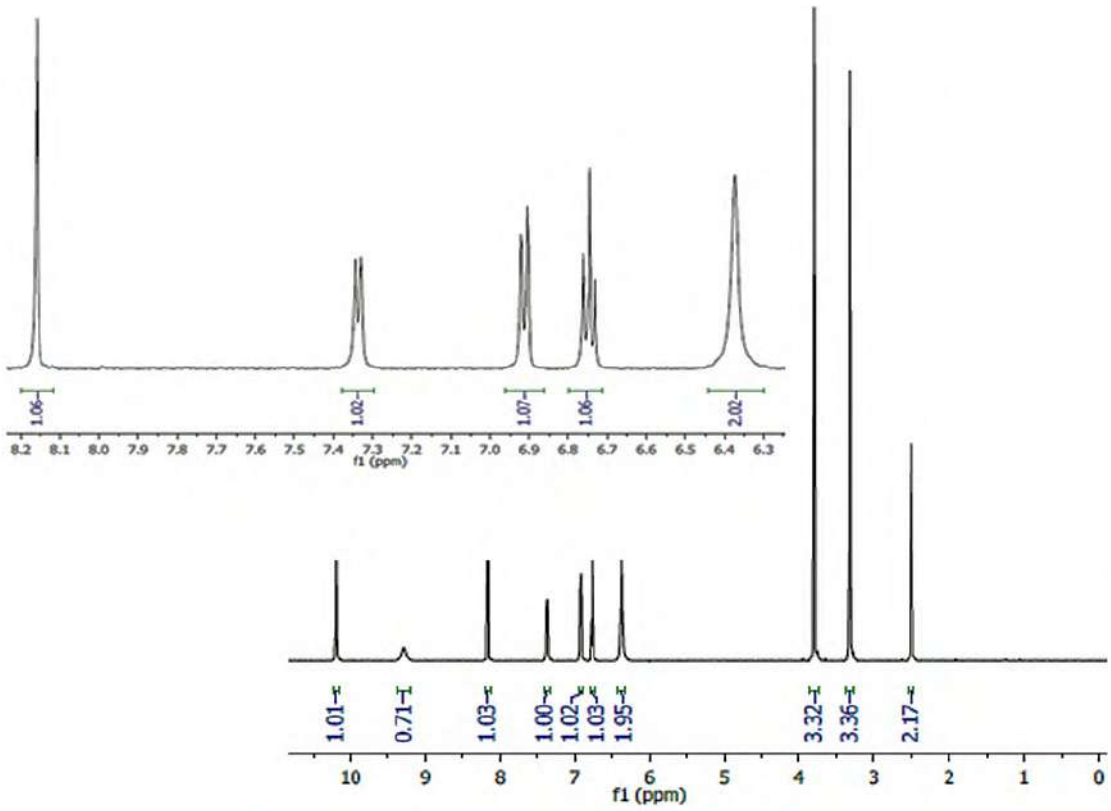

Figure 1. [1]HNMR spectrum of ligand.

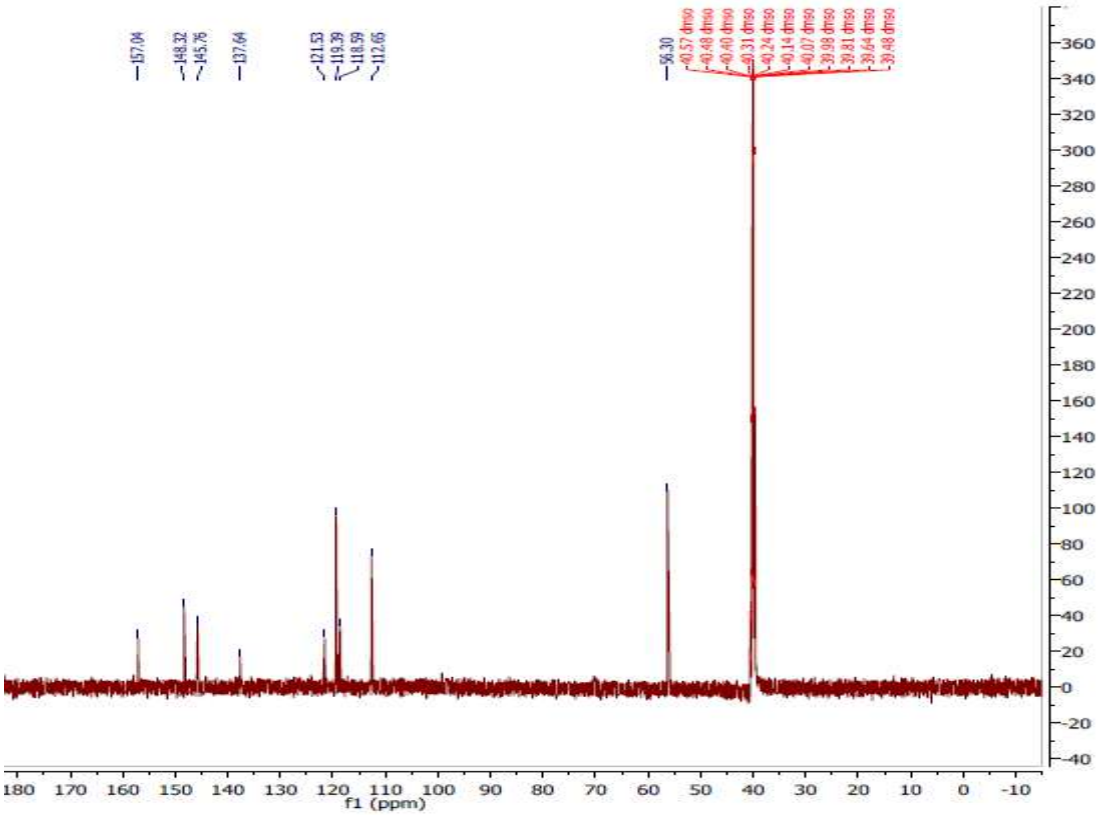

Figure 2. [13]CNMR spectrum of ligand.

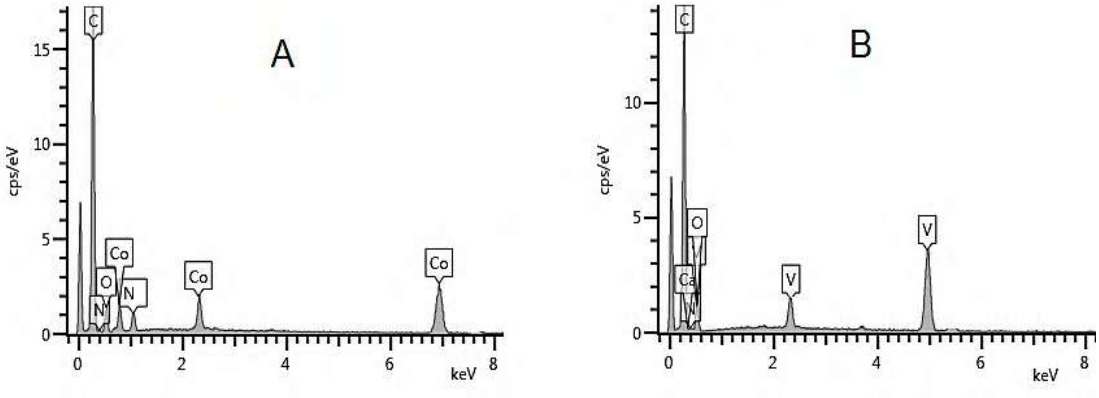

Figure 3. EDX analysis of cobalt complex (A) and vanadium complex (B).

3.1.Interaction with the DNA

3.1.1. studies of Electronic absorption

The electronic absorptions result studies are shown in (Figure 4). Ligand is exhibits two band absorptions at (245 nm and 352 nm) are attributed to transitions π-$\pi^*$and n- π^*, respectively. In addition, the complexes exhibited new bands at 403 nm and 670 nm are attributed to d-d transitions for the vanadium and cobalt complexes, sequentively. The π-π^* absorption bands is chosen to track the DNA interaction with complexes and ligands . spectroscopic titrations revealed that the increased amounts of (DNA) are lead to decreasing in absorptions intensity (hypochromism) of the complexes and their ligands, Figure 4. This spectral behavior are suggests DNA intercalative binding, since lead to the hypochromism in spectral bands [28, 29].

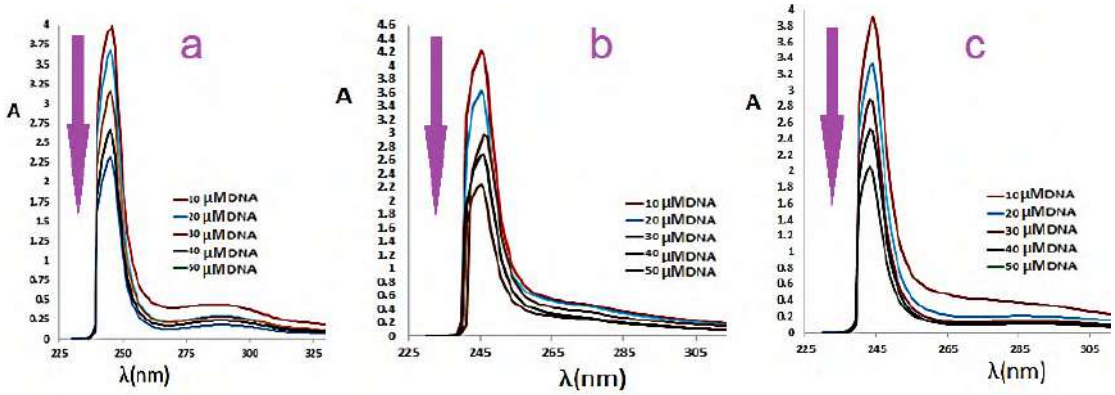

Figure 4. UV spectra of ligand (a) and its complex with cobalt (b) and vanadium (c). The arrows show the absorbance changes with DNA amounts .

3.1.2.Viscosity studies

Viscosity is one of the most important experiment that can be utilized to explain binding of compounds modes to DNA . . The results showed increases viscosity with increases amounts of ligand or complexes, Figure 5. These results have confirmed the intercalation of the compounds into DNA because the intercalation leads an stiffing and extension helix of DNA which consequently guide to increases viscosity of DNA solutions [30].

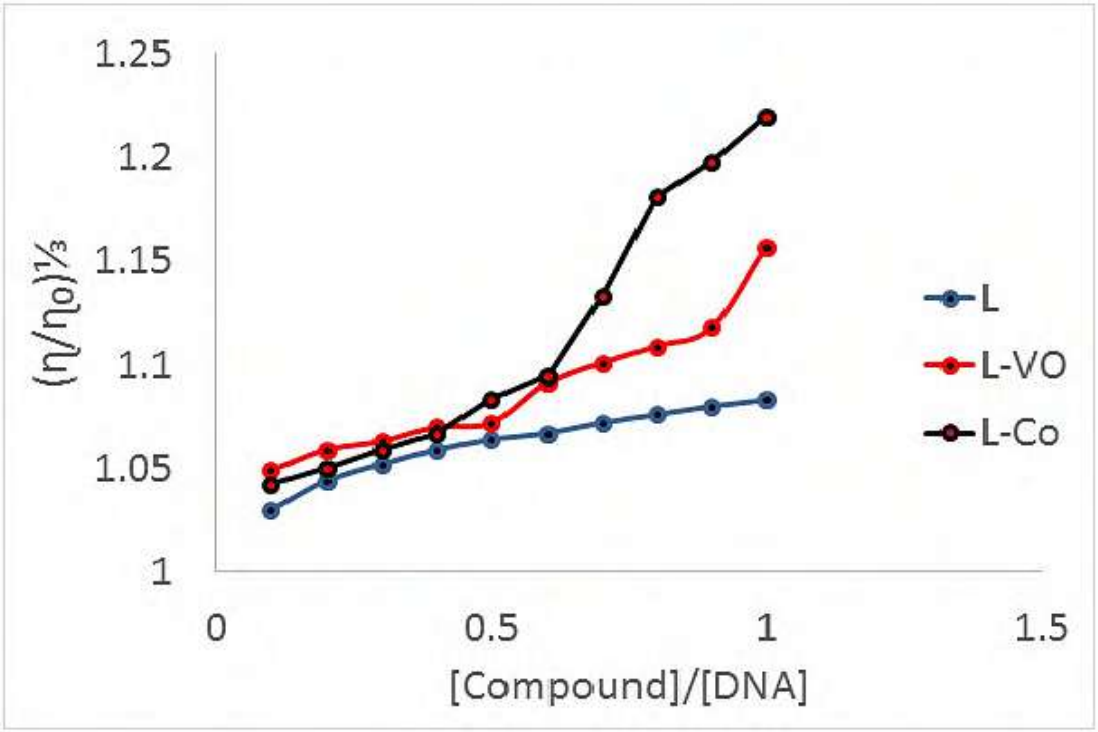

Fig. 5. Ligands and complexes viscometric results at 37 °C.

4.CONCLUSION

Two complexes of cobalt and vanadium with (E)-2-(2-hydroxy-3-methoxybenzylidene)hydrazine-1-carboxamid ligand were synthesized. The compounds were characterized by FTIR, ^{1}HNMR, ^{13}CNMR and EDX techniques. The interaction between the compounds and DNA was investigated. The results of UV–Vis spectroscopy and viscosity measurement showed a hypochromic shift and an intercalative mode. The obtained results have offering a promising therapeutic reagent for cancerous diseases.

References

[1] Alam O, Mallick P, Verma SP, Gilani SJ, Khan SA, Siddiqui N and Ahsan W 2010 *Chem. Eur. J. Med.* **45** 2467.
[2] Dilworth JR and Hueting R. 2012 *Inorg. Chim.* **389** 3.
[3] T.S. Lobana, R. Sharma, G. Bawa and S. Khanna. 2009 *Coord. Chem. Rev*. **253** 977.
[4] Mouayed, A. H., Teoh, S. G., Rosenani, A. H., Mohamed, B. K. A. and Amin, M. S. A 2015 Polyhedron. **85** 93.
[5] Savithri K and Revanasiddappa H D 2018 *Bioinorg. Chem. Appl.* 1.
[6] Kowol C R, Miklos W, Pfaff S, Hager S, Kallus S, Pelivan K, Kubanik M, Enyedy E A, Berger W, Heffeter P and Keppler B K 2016 *Med. Chem.* **59** 6739.
[7] Richards A D and Rodgers A 2007 *Chem. Soc. Rev*. **36** 471.
[8] Mouayed A H , Teoh S G, Rosenani A H, Mohamed B K A and Amin M S A 2014 *J. Coord. Chem*. **67** 714.
[9] Hancock R D 2013 *Chem. Soc. Rev*. **42** 1500.
[10] Fekri R , Salehi M, Asadi A and Kubicki M 2017 . Appl. Organomet. **32** 1.
[11] Thamilarasan V, Sengottuvelan N, Sudha A, Srinivasan P and Chakkaravarthi G 2016 *J. Photochem. Photobiol .B .Biol* **162** 558.
[12] Abyar F and Tabrizi L 2019 *J. Biomol .Struct .Dyn.* **4** 1.

[13] Mohamed S S and Adam H E 2018 *J. Photochem. Photobiol .B .Biol.* **184** 34.
[14] Kosiha A, Parthiban C, Kuppanagounder P and Elango J C 2018 *Studies Chem.* **71** 1560.
[15] Komor A C and Barton J K 2013 Chem.Comm. **49** 3617.
[16] Chandra A, Singh K, Singh S, Sivakumar S, and Patra A K 2016. *Dalton Trans*.**45** 494.
[17] Ngan N K, Lo K M and Wong C S R 2012 *Polyhedron.* **33** 235.
[18]Strekowski L and Wilson B 2007 *Mutat. Res*. **623** 3.
[19] Chetana P R, Rao R, Saha S, Policegoudra R S, Vijayan P and Aradhya M S 2012 *Polyhedron*. **48** 43.
[20] Zhou W, Saran R and Liu J 2017 *Chem. Rev.* 2017, 117(12), 8272–8325.
[21] Dolatabadi J. 2011 *Int J Biol Macromol*. **48** 227.
[22] Karthikeyan M S, Prasad D J, Poojary B, Bhat K S, Holla B S and Kumari N S 2006 *Chem. Bioorg. Med*. **14** 7482.
[23] Satyanarayana D, Kalluraya B and George N 2002 *J. Saudi Chem. Soc.* **6** 459.
[24] Ying L, Shun Y Z, Hong Z, Cao B J, Wang F D, Zhang Y, Shi Y L, Yang J, Wu B A 2003 *Med. Chem.* **11** 4363.
[25] Isloor A M, Kalluraya B, Shetty P and Eur J 2009. *Med. Chem*. **44** 3784.
[26] Malhotra M, Sharma G and Deep A 2012.. *Acta. Pol. Pharm*. **69** 355.
[27] Mouayed A H, Teoh S G, Rosenani A H, Mohamed B K A and Amin M S A 2014 *Chimica. Acta.* **421** 270.
[28] Baskaran S, Murali K M and Arumugham M N 2015 *J .Coord .Chem.* **68** 4395.
[29] Ooms K J, Bolte S E, Smee J J, Baruah B, Crans D C, and Polenova T 2007 *Inorg. Chem*. **46** 9285.
[30] Hancock R D 2013 *Chem. Soc. Rev*. **42** 1500.

Assessment The Suitable of The Groundwater for Civil uses in Kakhirta Village, Al-Ayadiyah Subdistrict, Iraq

Assessment The Suitable of The Groundwater for Civil uses in Kakhirta Village, Al-Ayadiyah Subdistrict, Iraq

Mohammed Hazim Sabry Al-Mashhadany

College of Education for Pure Sciences ,University of Mosul, Iraq

E-mail: mohammedhazemm@uomosul.edu.iq

Abstract. The current research describes the application of the water quality index (WQI) based on the collection of 50 samples of water sample for 10 wells for five months in the village of Kakhirta in Al-Ayadiyah subdistrict, northwest of Nineveh Governorate. The model was applied using 13 parameters (pH, TDS (total dissolved salts), DO (dissolved oxygen), T.A (Total Alkaline), Cl, Ca, Na, Mg, K, PO_4, SO_4, TPC (Total Plate Count), and F. Colif. (Faecal coliform) depending on the results obtained from the model. The groundwater quality ranged between (218 - 765), which indicates deterioration in water quality due to the high numbers of bacteria TPC and F. Colif., as well as the high total alkaline T.A and hypoxia in the water more the recommended limits for drinking water.

1.Introduction

Water enters the soil naturally because of the hydrological cycle of water in nature. The quality of groundwater changes during its movement inside the soil and its cohesion with rocks, as the water interacts with some of its constituent elements and melts from them and deposits others according to the quality of the rocks, the quality of water and the nature of its movement[1]. As a result of natural factors, it is very little compared to the pollution that occurs from human intervention, as human activity affects water quality in one way or another on water quality, and humans have a direct and indirect influence in changing the quality and quantity of groundwater[2].

Groundwater is one of the most important parts of water resources as it constitutes 71.7% of the world's drinkable water. Groundwater contains calcium, magnesium, and sodium salts. in high concentrations to make this water hardness due to its exposure to soluble substances in geological formations in addition to the salts transported in it [3]. The tremendous development in the development of agricultural and animal fields and the establishment of industrial and population gatherings around the wells have increased their pollution problems and have become a health threat to the consumers of these wells' water[4].

The influence of sewage and industrial waste through the soil into the water layers is a source of danger for groundwater pollution and deterioration of its quality, which made it more exposure to contamination[5]. Therefore, the current study aimed to know the quality of groundwater by collecting groundwater samples for ten wells in the village of Kakhirta, analyzing them, and then determining their suitability for drinking water purposes Depending on the standard parameters applicable internationally.

Many researchers have been studied the qualitative characteristics of groundwater in various regions of Iraq, Al-Shanona and others[6] have studied the water wells of Abu Maria village of Tal Afar district to determine its suitability for drinking and household uses, The results of the study showed a high concentration of salts, as the total hardness concentration reached 2020 mg. l^{-1}, and sulfates

reached 2136 mg. l^{-1}. The results also showed a decrease in WQI that water was of very poor quality for drinking and is not suitable for household uses according to the classification. Al-Saffawi[7] also studied the quality of the groundwater in the Al-Mahlabiah sub-district northwest of the city of Mosul, to evaluate it for drinking purposes. The results of the study reached a high concentration of some measured characteristics, especially solid dissolved salts and calcium ions. (3390, 673, 2271) mg. l^{-1}, respectively, which will affect the values of the Water Quality Index, this indicates that 83% of the studied water samples are of poor class after applying the Canadian model[7], and this is attributed to the geological formations that the water passes through, It requires some simple treatments, such as slow freezing and melting, to improve its quality before using it for drinking.
Jaafar and others[8] assessed the quality of water wells in the Rashidiya area, north of the city of Mosul, for drinking and domestic use, as water samples were collected from ten wells scattered in the study area for bacteriological and chemical examinations using the log. model to Evaluation the quality of well water using 11 parameters, the results of the Water Quality Index indicated that all well water is not suitable for domestic use and drinking this deterioration because of bacterial contamination. (Total number of TPC and F. coliform bacteria), high salt concentration, total hardness, and sulfate ions.

1.1.Geology of the study area

The region consists of the formation of the Fat´ha (the middle Miocene), the sediments of this formation were characterized by being periodic and containing different stones such as limestone. This formation's thickness ranges from (64-818) m. The containment of this formation on a large number of cracks and fractures filled with sand made it have a high capacity on the storage of groundwater, but its containment of gypsum in large quantities had a negative impact on the quality of the water contained within it, as the dissolution of the elements of limestone rocks in the water makes them rich in magnesium and calcium compounds[9,10].

1.2.Description of the study area

The study area included the selection of 10 wells in the village of Kakhirta, affiliated to Al-Ayadiyah subdistrict in Nineveh governorate, in the area Trapped between latitudes (36˚55´06´´) and (36˚55´90´´) to the north and between longitudes (42˚34´45´´) and (42˚35´01´´) to the east (Table 1, 'Figure 1')). This choice came because this village does not contain stations to purify drinking water, and the people depend on well water[11].

Table 1. Coordinates, Altitude, and depth of the studied wells

Well	E	N	Altitude (m)	Depth (m)
1	42˚34´88´´	36˚55´90´´	406	45
2	42˚34´71´´	36˚55´87´´	406	61
3	42˚34´93´´	36˚55´73´´	407	40
4	42˚34´45´´	36˚55´68´´	406	35
5	42˚34´59´´	36˚55´45´´	407	50
6	42˚34´95´´	36˚55´60´´	407	63
7	42˚35´01´´	36˚55´34´´	407	38
8	42˚34´68´´	36˚55´31´´	407	55
9	42˚34´70´´	36˚55´12´´	407	67
10	42˚35´00´´	36˚55´06´´	407	43

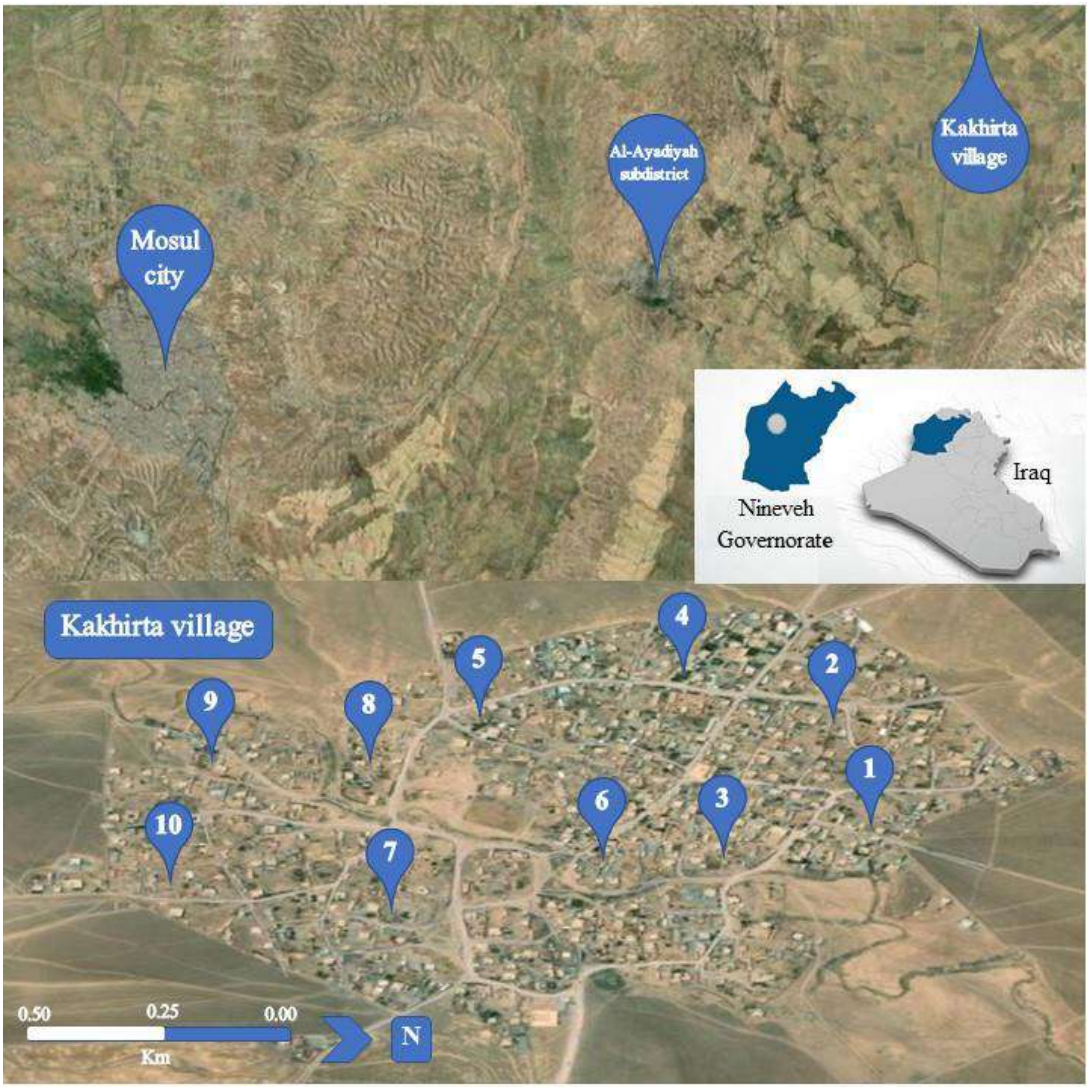

Figure 1. Map of Kakhirta village in Nineveh governorate showing the studied wells

2.Materials and Methods

In the study, 50 water samples were collected from ten wells spread all over Kakhirta village using cleaned polyethylene bottles, and homogenized with each a sample before Filling. As for oxygen, samples were collected from them Water using special bottles installed in the field by Addition of a solution of manganese sulfate (Winkler A) and Alkaline iodide azide solution (Winkler B), as in Bacteriological examination samples and sterile vials used and samples were kept out of light Container until reaching the laboratory. It measures the pH of water and TDS values using the field device and, in the lab, every variable like O_2, TA, phosphate, Sulphate, Na, Ca, K, Cl, Mg, TDS, TPC, and F. colif. were measured. Based on international standard methods[12.13]. The following devices were used in the analyzes: spectrophotometer, flame photometer, pH meter, TDS meter, and turbidity meters.

2.1.WQI calculation

Several variables have been selected that have an impact on the use of drinking water for their use in finding the quality of water for drinking purposes. These variables pH, O_2, TDS, T.A, Ca, Mg, Cl, Na, K, PO_4, SO_4, TPC, and F. Colif. And has been computed using the following equation[14-17]:

$$K = 1/\sum_{i=1}^{n} \frac{1}{S.TDS} + \frac{1}{S.O_2} + + \quad (1)$$

$$Wn = K / Si \quad (2)$$

$$qn = 100 \times [Vn - Vi] / [Si - Vi] \quad (3)$$

$$WQI = \sum qn \times Wn / \sum Wn \quad (4)$$

Where to:

K: proportionality constant., Wn weight value for each property., Si: permissible normal concentration as seen in the Table 2, qn: consistency ranking for each parameter., Vn: calculated value., Vi: ideal values.

The WQI values are categorized into five categories: excellent quality water (IWQI 0-25), good (IWQI 26-50), poor (IWQI 51-75), very poor (IWQI 76-100), and Unfit for drinking (IWQI> 100)[18-20].

Table 2. standard values and Wn for parameters

parameters	Standard limit (Si)	Wn
pH	6.5 -8.5	0.207792208
TDS	1000	0.001558442
O_2	5	0.311688312
T.A	150	0.010389610
Ca	50	0.007792208
Mg	50	0.010389610
Cl	200	0.006233766
Na	200	0.007792208
K	12	0.12987013
PO_4	10	0.155844156
SO_4	400	0.003896104
TPC	10	0.155844156
F. Colif.	0	0
	∑	1.019516

3.Results and Discussion

The health concerns associated with the chemical components of drinking water differ from those associated with microbial contamination and primarily stem from the ability of these chemical components to cause harm to health after long periods of drinking the water. Chemical composition of water can lead to health problems as a result of a single exposure, except for their effects through accidental, widespread contamination of the drinking water supply. Moreover, experience shows that in many such incidents, the water becomes unfit for drinking as a result of the unacceptable taste, smell, and appearance[21].

The most common and widespread health risk associated with drinking water is biological contamination, the effects of which mean that great attention must always be paid for monitoring. Priority needs to be given to improve and develop drinking water supplies, which represent the greatest public health risk[22].

The pH values recorded in the study were moderate and within the permissible limits for drinking water, which ranged between (7.01 – 7.76) as in table (3), due to the distance of its water from the direct air changes that caused the dissolution of carbon dioxide in the water. In addition to the high regulatory capacity of hard and Alkaline water rich in bicarbonate, which resists change in pH[23].

The results shown in Table 3 indicated a decrease in the concentration of DO in well water, as 50% of the studied samples were less than the standard permissible limits for drinking water, which ranged between (2.40-8) mg. l^{-1}, and the reason for the decrease in values is The percentage of oxygen saturation decreases due to the high salinity, as well as the lack of contact of water wells with the air. The great deficiency of this factor has a very negative impact on the aquatic ecosystem, as it leads to an increase in the activity of anaerobic microorganisms and changing the interaction paths for organic materials to produce substances harmful to the aquatic environment, and this explains for us the

emission of unpleasant odors from some water wells in the study area as shown in the equations The following[24].

Table 3 shown that all values of TDS in the groundwater of wells were within the permissible limits except for well No. (8) whose values exceeded 1000 mg. l^{-1}. This is because the concentration of total dissolved salts in groundwater depends on the type of rocks and soils that are in contact with them, and on the period that the contact process, movement, and source of groundwater take[25].

The results of the T.A in the water of the study wells did not come within the standard specifications for drinking and for all wells, which means ranged between (248 - 444) mg. l^{-1}. The high T.A of well water in the current study shown in Table 3 is due to alkaline bicarbonate, due to its abundance and resulting from the dissolution of lime materials, which is the main source for it[26]. High concentrations of the alkaline of drinking water reduce the secretion of gastric juice (inhibit the action of the enzyme pepsin), which results in an imbalance in the digestive process, vomiting, and nausea, as well as some research indicates delayed growth and weight loss[27].

High concentrations of sodium ions in drinking water lead to health problems for heart and kidney disease[28]. The results of the levels of sodium and potassium concentrations in this study were within the standard specifications for drinking water, which ranged between (48 - 97) mg. l^{-1} and (2.20 – 9.2) mg. l^{-1} except for well No. 2, 8, and 10 for sodium, and well No. 5 and 7 for potassium which exceeded the permissible limits for drinking.

Chlorides enter the human digestive system through drinking water and their taste is unpalatable if it exceeds its limits and also affects the osmotic pressure of the person. The concentration of chloride ions in groundwater depends on the type of rocks and geological layers in which the groundwater passes[27] and since 90% of the study wells found that the chloride ion is within the standard specifications of drinking water, which did not exceed 200 mg. l^{-1} except for well No. (8.)

The results of the calcium and magnesium ion concentration mean in well water was not within the drinking water standard specifications, which ranged between (80 - 129) mg. l^{-1} and (55 - 87) mg. l^{-1} respectively. The presence of dolomite and calcite rocks in the Fat´ha layer was attributed to the high values of ionic concentration in the study area[9].

The sulfate ion present in the groundwater and formed as a result of the dissolution and Disintegration of gypsum and anhydrite rocks. High concentrations of sulfates in drinking water produce a noticeable taste and can also degrade the piping system[29]. The recommended upper limit is 400 mg. l^{-1} in water intended for human use, and the values of the studied well water ranged between (80-880) mg.l^{-1} where 50% of the well water was outside the recommended limits for drinking, the high concentrations of sulfates in the groundwater in the research area are attributed to the presence of mucin deposits that contain gypsum and limestone[9], as in the Table 4.

Table 3. Summary results of the present study chemical analyses mg. l^{-1}

wells		pH	TDS	O_2	T.A	Cl	Na	K
1	Min	7.16	470	4.00	270	62	92	2.50
	Max	7.49	779	6.40	370	84	96	4.90
	Mean	7.28	649	5.04	328	69	94	3.16
	SD±	0.14	128	0.88	38	9	2	0.98
2	Min	7.36	329	2.40	296	76	48	2.70
	Max	7.52	545	6.40	400	170	245	5.70
	Mean	7.44	476	4.32	342	112	189	3.46
	SD±	0.06	93	1.53	40	38	80	1.26
3	Min	7.29	591	3.60	380	60	90	5.50
	Max	7.76	765	6.80	430	86	93	9.20
	Mean	7.50	666	5.04	408	70	92	6.88
	SD±	0.20	70	1.28	19	10	1	1.52
4	Min	7.25	384	2.40	368	38	71	3.80
	Max	7.54	497	6.80	410	44	75	6.40
	Mean	7.39	433	5.44	388	41	74	4.62

	SD±	0.12	45	1.80	17	2	2	1.02
5	Min	7.08	760	4.40	344	116	90	5.90
	Max	7.46	978	8.00	420	128	93	19.00
	Mean	7.20	885	5.44	389	124	91	9.40
	SD±	0.15	79	1.46	31	5	1	5.45
6	Min	7.03	588	4.00	400	70	77	4.90
	Max	7.32	685	6.00	416	88	81	8.20
	Mean	7.15	631	4.72	407	79	79	5.86
	SD±	0.14	35	0.87	7	7	2	1.35
7	Min	7.08	545	4.00	412	62	86	2.20
	Max	7.38	735	7.20	470	68	88	30.50
	Mean	7.20	625	5.36	444	65	87	8.78
	SD±	0.12	73	1.25	21	3	1	12.27
8	Min	7.25	1111	3.20	120	210	180	5.20
	Max	7.49	1405	6.00	400	374	375	8.20
	Mean	7.39	1237	4.72	248	285	273	6.20
	SD±	0.09	107	1.15	104	58	78	1.32
9	Min	7.01	456	3.60	344	50	94	3.00
	Max	7.57	534	5.20	400	58	97	5.30
	Mean	7.35	491	4.24	382	53	95	4.06
	SD±	0.21	29	0.61	26	3	1	1.11
10	Min	7.08	732	3.20	224	70	82	3.70
	Max	7.43	940	6.40	450	124	235	5.90
	Mean	7.22	803	5.36	368	94	115	4.88
	SD±	0.14	84	1.37	90	22	67	0.94

As for phosphate ions PO_4, studies indicate that it is non-toxic to humans and animals unless it is present in high levels, which may cause digestive problems. The results in table (4) showed a decrease in the content of phosphate ions in the studied well water, which ranged between (0.00 - 1.54) mg. l^{-1}. It is also noted that the phosphate concentrations decreased compared to the negative ions studied, which is due to the ability to precipitate phosphate in the form of calcium phosphate in addition to its adsorption by surfaces mud minutes, which reduces its transfer to the water environment, and the frequent use of phosphate fertilizers and detergents is the main source of phosphates in groundwater, and in general, the concentration of phosphate ions is within the permissible limits for drinking[30].

Table 4. Summary results of the present study chemical analyses mg. l^{-1}

wells		PO_4	SO_4	Ca	Mg	TPC*	F. Colif*
1	Min	0.00	220	80	17	20	0
	Max	0.26	510	138	77	508	23
	Mean	0.05	360	104	62	231	5
	SD±	0.12	110	21	25	186	10
2	Min	0.00	200	64	7	66	0
	Max	1.05	820	125	91	1632	7
	Mean	0.21	504	87	58	640	1
	SD±	0.47	267	23	32	604	3
3	Min	0.00	110	80	19	88	3
	Max	0.00	320	130	96	1440	240
	Mean	0.00	210	109	68	545	108
	SD±	0.00	80	21	30	528	121
4	Min	0.00	80	80	30	112	0
	Max	0.15	220	120	82	2720	15
	Mean	0.03	146	96	55	801	8
	SD±	0.07	59	16	23	1083	7
5	Min	0.00	170	88	20	41	0
	Max	0.49	470	189	115	3040	4
	Mean	0.10	300	127	87	899	2
	SD±	0.22	113	37	38	1227	2

6	Min	0.00	180	104	40	181	0
	Max	0.00	390	152	101	2352	93
	Mean	0.00	244	129	81	935	21
	SD±	0.00	84	18	24	839	40
7	Min	0.00	200	88	47	152	0
	Max	0.86	310	104	96	2000	460
	Mean	0.31	236	99	77	738	122
	SD±	0.36	44	7	19	783	200
8	Min	0.00	330	112	42	97	0
	Max	0.60	880	136	120	1616	4
	Mean	0.15	660	122	87	771	1
	SD±	0.26	241	11	29	610	2
9	Min	0.00	140	64	10	54	0
	Max	0.75	320	122	86	1440	4
	Mean	0.17	204	80	56	766	2
	SD±	0.33	71	23	28	622	2
10	Min	0.30	240	96	3	5	0
	Max	1.54	404	144	110	1760	23
	Mean	0.84	297	128	69	822	6
	SD±	0.56	70	19	47	710	10

* 10^2 cell. ml^{-1}

Water is contaminated with microbes as a result of the infiltration of human or animal waste into it. This bacterial contamination leads to an increase in infectious diseases. It is one of the most important types of bacteria that are considered evidence of water pollution with F. colif. bacteria, which is one of the causes of disease, foremost among which is diarrheal diseases that kill approximately 5500 people around the world, most of them children under the age of five[31]. Through the results of the detection of TPC and F. Colif bacteria and their comparison with standard specifications, whose rates ranged between (231-935) 10^2 cell. ml^{-1} and (1-122) 10^2 cell. ml^{-1}, it appears that all well water is not suitable for drinking, which means contamination of groundwater with samples of sewage or leakage in septic tanks for the study area[7].

3.1.WQI

The WQI model was applied on 13 parameters as shown in Table 2 to evaluate the water of the studied wells for drinking and household uses, and the results are shown in Table 5 indicate that the values of WQI ranged between (218 - 765), When comparing the results of water classification, we found that 100% of the groundwater of the study area was of unfit for drinking quality for drinking and household uses, and this deterioration was mainly due to the studied standards exceeding the permissible limits according to the standard specifications, especially oxygen and TPC, which affects the high (qn×Wn) values. Which is directly proportional to the WQI values.

Table 5. Results of overall WQI calculation with corresponding water quality status Wells

para.		1	2	3	4	5	6	7	8	9	10
pH	qn	52	63	67	60	47	43	47	60	56	48
	qn×Wn	10.76	13.01	13.85	12.40	9.69	9.00	9.70	12.39	11.73	9.96
TDS	qn	31	9	33	4	61	29	28	105	11	50
	qn×Wn	0.05	0.01	0.05	0.01	0.09	0.04	0.04	0.16	0.02	0.08
O_2	qn	99	123	99	85	85	109	88	109	125	88
	qn×Wn	30.75	38.23	30.75	26.60	26.60	34.08	27.43	34.08	39.06	27.43
T.A	qn	357	383	516	475	478	514	587	195	463	435
	qn×Wn	3.71	3.98	5.36	4.94	4.96	5.34	6.10	2.03	4.81	4.52
Cl	qn	18	45	19	1	52	24	16	153	8	34
	qn×Wn	0.11	0.28	0.12	0.00	0.33	0.15	0.10	0.95	0.05	0.21
Ca	qn	217	149	236	184	309	317	197	288	121	312
	qn×Wn	1.69	1.16	1.84	1.43	2.41	2.47	1.53	2.24	0.95	2.43
Mg	qn	48	32	73	20	146	124	106	149	23	75

	qn×Wn	0.50	0.33	0.75	0.20	1.52	1.29	1.11	1.54	0.24	0.78
Na	qn	18	91	17	3	16	7	13	156	19	35
	qn×Wn	0.14	0.70	0.13	0.02	0.13	0.05	0.10	1.20	0.15	0.27
K	qn	12	15	49	26	74	39	68	42	21	29
	qn×Wn	1.51	1.90	6.34	3.40	9.61	5.01	8.81	5.45	2.68	3.74
PO_4	qn	1	2	0	0	1	0	3	2	2	8
	qn×Wn	0.08	0.33	0.00	0.05	0.15	0.00	0.48	0.23	0.27	1.31
SO_4	qn	85	140	27	2	62	40	37	200	25	60
	qn×Wn	0.33	0.55	0.10	0.01	0.24	0.16	0.14	0.78	0.10	0.23
TPC	qn	1104	3152	2674	3954	4445	4623	3642	3807	3782	4059
	qn×Wn	172.0	491.22	416.7	616.21	692.7	720.5	567.5	593.3	589.4	632.57
F. Colf.	qn	27	7	541	41	11	104	610	4	11	32
	qn×Wn	0.067	0.017	1.355	0.102	0.025	0.260	1.525	0.010	0.025	0.080
WQI		218	542	468	654	736	765	613	643	639	672
Water Quality		Unfit for drinking	Unfit for drinking	Unfit for drinking	Unfit for drinking	Unfit for drinking	Unfit for drinking	Unfit for drinking	Unfit for drinking	Unfit for drinking	Unfit for drinking

4.Conclusions

The study has concluded the following:

1. The TDS was suitable for drinking water for all well water except for Well No. 8.
2. The T.A is above the permissible limits for drinking water for all wells.
3. Low DO values up to 50% of well water at standard specifications.
4. A large increase to TPC for all well water is considered one of the most influential parameters in the results that all well water is not suitable for drinking and household uses.
5. The potential health consequences of bacterial contamination must be of great importance and not be tolerated.

Reference

[1] Abdullah M, Al-Ansari N and Laue J 2020 *J .Earth. Sci .Geotech. Eng* , **10** 199.
[2] Adejumo R O , Adagunodo T A, Bility H , Lukman A F and Isibor P O 2018 *Int. J. Civ.* 8 903.
[3] Ahmad S , Singh N and Mazhar S N 2020 *Appl. Water Sci*. **10** 2.
[4] L-Bassam F B and Taher R K 2015 *D.J.E.S*, 8(4): 37-45 .
[5] Al-Mansori N J 2017 *J. Univ. Babylon eng. sci.*, **25** 81.
[6] Al-Shanona R A, Sadeq N M and Al-Saffawi A Y 2018 *E.D.U.S.J*, **27** 81.
[7] Al-Saffawi A Y 2018 *R.J.S*, **27** Botany Special Issue of the Third Scientific Conference of Biology.
[8] Jaafer A J And al-saffawi A Y 2020. *Plant .Arch* **20** 3221.
[9] Al-Youzbaky K T and Eclimes Y F M 2018 *The Proceeding of the 9th Periodical Scientific Conference for Dams & Water resources Res*. 165.
[10] Al-Mashhadany M H S , Al-Mamaree J A and Al- Saffawi A Y 2020 *Plant .Arch*. **20** 3924.
[11] AL-Saffawi A Y T, InAubbakar B S V and Abbass L Y 2020. *Niger. J. Technol*. **39** 632.
[12] APHA 1998 *Standard method for the examination of water and waste water*. (American Public Health Association 20th ed . Washington D.C, USA).
[13] APHA 2017 *Standard Method for Examination of water and wastewater* (American public Health Association 23th ed. Washington, DC, USA).
[14] Bhat M A, Wani S A , Singh V K, Sahoo J ,Tomar D and Sanswal R 2018 *J. Agri. Sci. Food Res.* **9** 1.
[15] Chebet E C, Kibet J K and Damaris M D 2020. *Appl. Water Sci*. **10** 92.
[16] Issa H M and Alrawi R A 2018 *UKH-JSE*. **2** 39.
[17] KOÇ C 2018 *ÖHÜ Müh. Bilim. Derg. / OHU J. Eng. Sci.*, **7** 694.
[18] Shobha B S 2018 *American J. of Civil and Env. Eng*. **3** 68.
[19] Xu P , Feng W , Qian H and Zhang Q 2019 *Int. J. Environ. Res. Public Health*. **16** 1.
[20] Yasmin G , Islam D, Islam M T, Ullah M S and Adham A K M 2019 . *Fund. and Appl. Agric*. **4** 632.

[21] Adekanmi A T 2020 *Res. J. Appl. Sci*. **1** 7.
[22] Kareem U H and Tariq A H 2015. *Iraqi J. of science,* **56** 3203.
[23] Kablan A Y H 2018 *Qualitative status assessment of groundwater of some quarters of Mosul city by using water quality index models (WQI)*. MSC thesis. (College of Science, University of Tikrit. Iraq).
[24] Al- Hamdany N A 2020 *Application of water quality index to assess the quality of some wells water in the left side of Mosul city / Iraq.* MSC thesis (College of Environmental Technicality, University of Mosul).
[25] Hussin A 2017 *M.J.A.S,* **5** 32.
[26] Mahmood A A, Eassa A M, Mohammed M H and Shubbar I Y 2013 *J.U.B.P.A.S,* **21** 2531.
[27] Al-Mashhadany M H 2019 *Study the environmental status for khosar river water and the application of some mathematical models*. Ph. D. Thesis (chemistry, College of education for pure science, University of Mosul) .
[28] Kumari M and Rai S C 2020 *J. Geol. Soc. India,* **95** 159.
[29] Saffawi A Y T, Al-Asaaf A Y R and Talat R A 2020. *Nipp. J. Env. Sci*.**1** 1.
[30] Ramadhan O M, Saffawi A Y and Al-Mashhadany M H 2018 *I.J.E.R.S.T.E* , **7** 1.
[31] Enitan-Folami A M , Mutileni N , Odiyo J O, Swalaha F M and Edokpayi J N 2020. *Hum .Ecol. Risk .Assess*, **26** 2044.

Journal of Physics: Conference Series

Study of Corrosion Inhibition for Mild Steel in Hydrochloric Acid Solution by a new furan derivative

Study of Corrosion Inhibition for Mild Steel in Hydrochloric Acid Solution by a new furan derivative

Israa M H Al-mousawi[1*], Rana S Ahmed[2], Nafeesa J Kadhim[3] and Ahlam M Farhan[3]

[1]Department of Chemistry, College of Science, University of Baghdad,
[2] Department of pharmacy Al-Esraa University College,
[3]Department of Chemistry /College of Science of Women /University of Baghdad, Iraq.

*E-mail : israamousawi@gmail.com

Abstract. The corrosion inhibition effect of a new furan derivative (furan-2-ylmethyl sulfanyl acetic acid furan-2-ylmethylenehydrazide) on mild steel in 1.0 M HCl was investigated using corrosion potential (ECORR) and potentiodynamic polarization. The obtained results indicated that the new furan derivative (furan-2-ylmethyl sulfanyl acetic acid furan-2-ylmethylenehydrazide) (FSFD) has a promising inhibitive effects on the corrosion of mild steel in 1.0 M HCl across all of the conditions examined. The density functional theory (DFT) study was performed on the new furan derivative (FSFD) at the B3LYP/6-311G (d,p) basis set level to explore the relation between their inhibition efficiency and molecular electronic structure. The final experimental results showed that FSFD act as a good corrosion inhibitor in the acidic solution for mild steel which is in agreement with the results of the theoretical study.

Keywords: Furan derivative, FSFD, Mild Steel, Corrosion inhibitor.

1. Introduction

Corrosion is a fundamental property of metals and alloys in an acidic or saline solution. Studies on corrosion represent a growing field due to substantial financial losses in various sectors and require extensive efforts to limit its impact [1-3]. Recent years have witnessed a growing academic interest in studies on inhibitor corrosion in many ways. Corrosion inhibitor is an increasingly important area particularly in industria [4-6]. Recent years have shown interest in using organic compounds containing sulfur, oxygen, and nitrogen atoms to inhibit corrosion process [7-9]. Organic compounds with heteroatoms are among the most widely used in inhibitor corrosion due to the effect of the polar groups and Pi-electrons on the iron surface and minimizing the effect of corrosion [10-11]. In this work, we used a new furan derivative FSFD with molecular formula ($C_{12}O_3N_2SH_{12}$) as show in Figure 1. FSFD was synthesized and characterized by Luma S.A. [12]. A new furan derivative was applied as corrosion inhibitor by investigated in the mild steel in acidic solution (1.0 M HCl) with different concentrations using electrochemical measurements and theoretical treatment using Gaussian 05 in two media (vacuum and ethanol solvent).

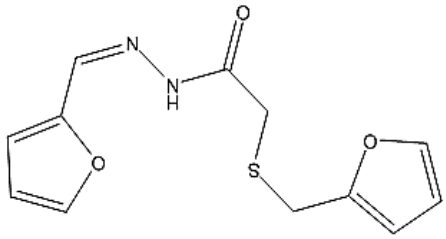

Figure 1. Structure of (furan-2-ylmethyl sulfanyl acetic acid furan-2-ylmethylenehydrazide)

2. Experimental

2.1 Preparation of carbon steel sample

Mild steel which has the configuration percentages as shown in Table 1 was used.

Table 1. Structure of carbon steel [13].

Metal	Amount	Metal	Amount
Fe%	99.579	P%	0.002
S%	0.0154	C%	0.03
Cu%	0.065	Mo%	0.002
Mn%	288	C%	0.0199
Zn%	99.989	V%	0.0005

The sample of mild steel was subjected to surface cleaning by absolute ethanol and drying in acetone. The specimen material was fabricated in circular samples with dimensions of 2.5 cm in diameter and used as working electrode.

2.2 Preparation solutions

2.2.1 Blank solution

Corrosive solution (1.0 M HCl) was prepared. Dilution of analytical grade 35.4% HCl with purified water up of to 1 liter. Blank solution consisted of 990 ml of 1.0 M HCl and completed to 1 L with 10 ml ethanol solvent.

2.2.2 Corrosion Inhibitor FSFD solution

Three different concentrations (100, 200, 300 ppm) were prepared by dissolving FSFD powder in the ethanol solvent and transferred to a volumetric flask of 10 ml.

2.3 Corrosion Potential (ECORR) Measurements

The electrochemical system consisting of a potentiostate, three electrodes, with a controlled computer and standard corrosion cell was used. The thermostat was among the most widely, used to control the temperature of (1.0 M HCl) which flows through the external vessel at 30 ^{o}C. Figure 2 shows the corrosion cell, and the three electrodes were:

1-The first is the reference electrodes which based on its potential consist of AgCl, Ag, KCl, and the outer solution filled with the prepared hydrochloric acid solution (1.0 M HCl). The reference electrode, a lugging tube placed at the distance 2mm from working electrode.

2- The second electrode is auxiliary consists of high purity platinum rod with 0.6 mm in diameter and 10 cm in length.
3- The third is working electrode (mild steel) which was mounted in the working electrode load with 1 cm2 surface area the opening uncovered to the acidic solution.

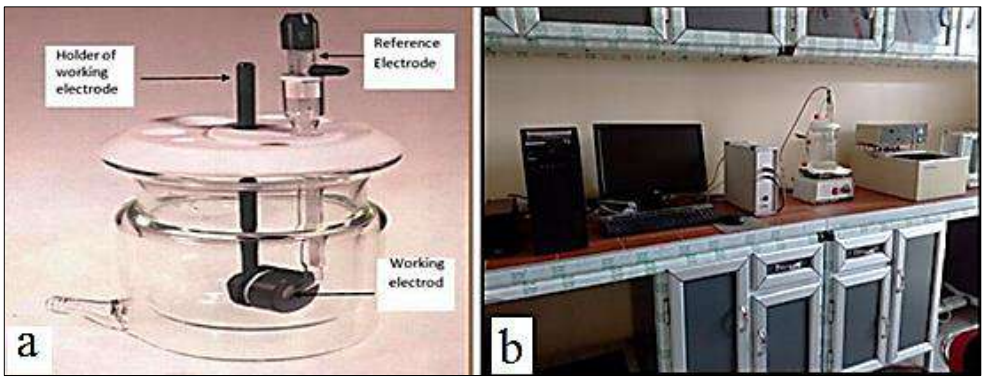

Figure 2. (a) The corrosion cell and the three electrodes.
(b) Experimental set up.

2.4 Experimental Procedure

The corrosion rate calculation protocol was carried out in compliance with the following steps:

1- One liter of corrosive media has been applied to the corrosion cell (see paragraph 2.3).
2- The temperature of the solution has been raised to the desired value with the use of the circulator of the water bath.
3- The first programmed step in this measurement is the open-circuit potential and the polarization curve starts at an open-circuit potential of approximately ± 200 mV from the open-circuit.
4- Measurements of corrosion for mild steel were assessed at 1.0 M. HCl with potentiostatic and blank solution followed by an inhibitor at different concentrations.
5- Corrosion current density (I mA) and corrosion potential (E mV) are calculated from the polarization curve as seen in Table (2) and in Figures (3-5).

3. Results and Discussion

3.1 Potentiostatic Polarization Measurement

In order to investigate the effects of electronic structure of FSFD compound as inhibitor corrosion, the theoretical study was conducted for FSFD compound [14]. The potentiostatic polarization curves for mild steel without and with FSFD immersed in 1.0 M HCl solution at temperatures range 303K are show in Figures 3, 4, 5 and the results are listed in Table 2.

Table 2. Polarization parameters for different concentrations of the FSFD at mild steel in acidic solution at 303 K.

Conc (ppm)	-Ecorr.(Mv)	Icorr.(µA.cm^{-2})	-bc (mv/Dec)	ba (mV/Dec)	W(Lg.m^{-2}.d^{-1})	P(Lmm.y^{-1})	Rp(Ω.cm^{2})	IE%	CR (mpy)
0	490.1	872.24	87.5	100.2	12.45	3.44	23	0	403
100	467.1	410.46	86.4	88.1	6.99	1.98	46	53	190
200	476.5	234.66	49.5	87.6	3.67	1.54	59	73	108
300	448.8	201.15	79.8	72.0	1.74	0.99	82	77	92

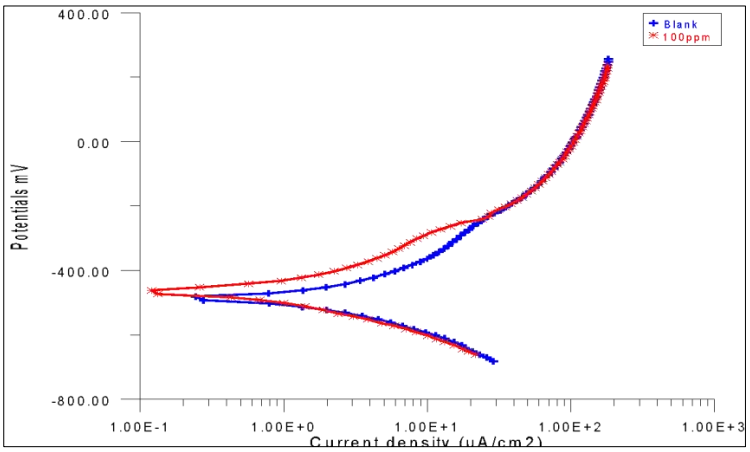

Figure 3. Potentioatatic Polarization curves for uncoated and coated mild steel with 100pp of FSFD in 1.0 M HCl Solution at 303 K.

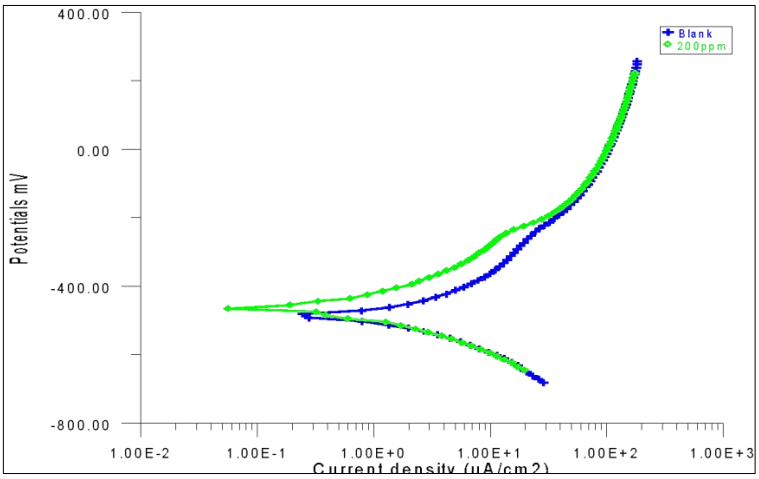

Figure 4. Potentioatatic Polarization curves for uncoated and coated mild steel with 200ppm of FSFD in 1.0 M HCl Solution at 303 K.

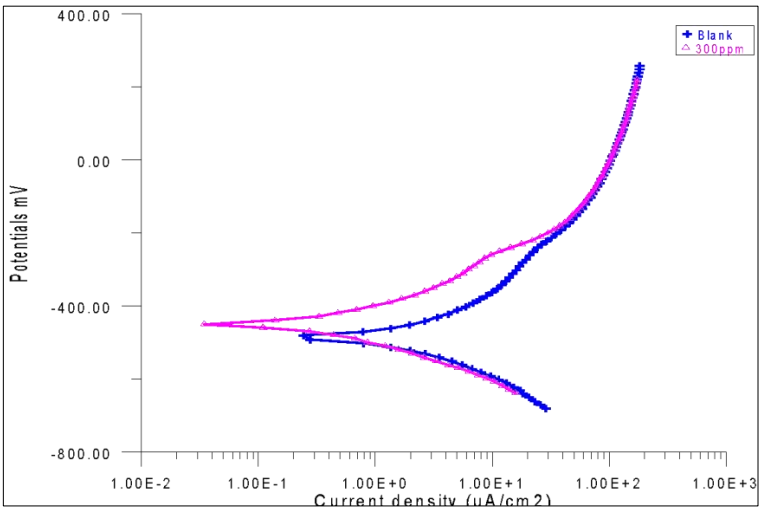

Figure 5. Potentioatatic Polarization curves for uncoated and coated mild steel with 300ppm of FSFD in 1.0 M HCl Solution at 303 K.

Values of corrosion potentials Ecorr, corrosion current densities icorr, cathodic and anodic Tafel slopes bc and ba. Rp polarization resistance which determination by equation (1), CR corrosion rate determination by equation. (2), the inhibition efficiency of FSFD can calculated from equation (3),

$$R_P = \left(\frac{B}{icorr}\right) \quad (1)$$

$$R_P = \frac{\beta a\, \beta c}{2.303\,(\beta a + \beta c)icorr}$$

$$CR = 0.13\left(\frac{e}{\rho}\right) icorr \quad (2)$$

e: Chemical equivalent

p: density of mild steel

$$I(\%) = \left(\frac{i\,corr - iinh\,corr}{i\,corr}\right) \times 100 \quad (3)$$

where $icorr$ and $i_{inh}corr$ are referred to the corrosion current density without and with the addition of the inhibitor, respectively.

Result shows that corrosion current density were decreased with increased the concentration of the **FSFD** compound and the inhibition efficiency increased due to the **FSFD** effect on the anodic and cathodic the electrochemical corrosion reaction because **FSFD** contain heteroatoms like nitrogen, sulfur and oxygen atoms as well as lone pairs of electrons present on N, S and O atoms and the planarity are the important structural features that rule to adsorption of these molecules onto the surface of the iron and prevent the continued corrosion [15-16].

3.2 Computational study

3.2.1. Molecular geometry

All the work on the computer was carried out using Gaussian-05 series of programs at the DFT and (B3LYP)/ 6-311G (d, p) basis set level as so to explore the connection among their inhibition efficiency and molecular electronic structure of a new furan derivative (furan-2-ylmethyl sulfanyl acetic acid furan-2- ylmethylenehydrazide) (FSFD) in ethanol and without solvent (vacuum) as seen in Figure 6. The computational structural parameters such as bond length and dihedral angles were calculated by ChemDraw of Mopac program (ver. 10) as shown in Tables 3 and 4.

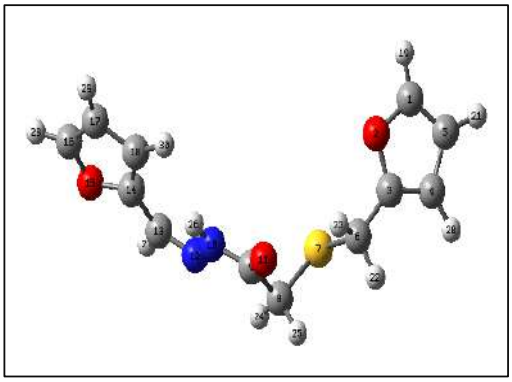

Figure 6. Optimized molecular structure of FSFD compound.

Table 3. Bond length of FSFD compound.

Bond	Actual (A^o)	Optimal (A^o)	Bond	Actual(A^o)	Optimal (A^o)
C(1)-O(2)	1.3631	1.4210	S(7)-C(8)	1.8197	1.8150
C(1)-C(5)	1.3611	1.3370	C(8)-C(9)	1.5230	1.5090
C(1)-H(19)	1.0944	1.1000	C(8)-H(24)	1.1133	1.1130
O(2)-C(3)	1.3670	1.4210	C(8)-H(25)	1.1148	1.1130
C(3)-C(4)	1.3656	1.3370	C(9)-N(10)	1.3690	1.3673
C(3)-C(6)	1.5012	1.4970	C(9)-O(11)	1.2067	1.2080
C(4)-C(5)	1.4305	1.5030	N(10)-N(12)	1.3507	-
C(4)-H(20)	1.0962	1.1000	N(10)-H(26)	1.0096	1.0120
C(5)-H(21)	1.0961	1.1000	N(12)-C(13)	1.2776	1.2600
C(6)-S(7)	1.8188	1.8150	C(13)-C(14)	1.4640	1.5030
C(6)-H(22)	1.1142	1.1130	C(13)-H(27)	1.1044	1.1000
C(6)-H(23)	1.1135	1.1130			

Table 4. Dihedral angles of FSFD compound.

Atoms	Dihedral Angle (deg.)	Atoms	Dihedral Angle (deg.)
C(1)-O(2)-C(3)-C(6)	179.049	H(20)-C(4)-C(5)-H(21)	0.029
C(1)-O(2)-C(3)-C(4)	0.191	H(20)-C(4)-C(5)-C(1)	-179.702
C(6)-C(3)-C(4)-H(20)	0.814	H(23)-C(6)-S(7)-C(8)	-67.095
C(6)-C(3)-C(4)-C(5)	-179.049	H(22)-C(6)-S(7)-C(8)	53.027
O(2)-C(3)-C(4)-H(20)	179.644	H(24)-C(8)-C(9)-O(11)	132.787
O(2)-C(3)-C(4)-C(5)	-0.219	H(24)-C(8)-C(9)-N(10)	-47.504
C(4)-C(3)-C(6)-H(23)	148.686	S(7)-C(8)-C(9)-O(11)	-103.631
C(4)-C(3)-C(6)-H(22)	31.787	S(7)-C(8)-C(9)-N(10)	76.076

C(4)-C(3)-C(6)-S(7)	-89.238	O(11)-C(9)-N(10)-H(26)	2.324
O(2)-C(3)-C(6)-H(23)	-29.983	O(11)-C(9)-N(10)-N(12)	-170.172
O(2)-C(3)-C(6)-H(22)	-146.887	C(16)-C(17)-C(18)-H(30)	177.943
O(2)-C(3)-C(6)-S(7)	92.086	H(29)-C(17)-C(18)-C(14)	179.794
C(3)-C(4)-C(5)-H(21)	179.893	H(29)-C(17)-C(18)-H(30)	-1.644
C(3)-C(4)-C(5)-C(1)	0.161		

3.2.2 Calculation of the main quantum parameters

The quantum chemical properties such as total energy, energy gap (ΔE_{gap}), softness (S), dipole moment (μ), hardness (η), E_{HOMO} (highest occupied molecular orbital energy), E_{LUMO} (lowest unoccupied molecular orbital energy), ionization energy (I), the absolute electronegativity (χ), the fractions of electrons transferred (ΔN), the electrophilicity index (ω), and electron affinity (A) were completed using (DFT) at the (B3LYP) / 6-311G (d, p) basis set as shown in Table 5. Quantum chemical parameters were estimated by using the following equations (1-7):

$I = - E_{HOMO}$ (1)

$A = - E_{LUMO}$ (2)

$\eta = \frac{I-A}{2}$ (3)

$\chi = \frac{I+A}{2}$ (4)

$S = \frac{1}{\eta}$ (5)

$N = \frac{\chi_{Fe} - \chi_{inh}}{[2(\eta_{Fe}+\eta_{inh})]}$ (6)

$\omega = \frac{\chi^2}{2\eta}$ (7)

Table 5. Quantum chemical parameters for inhibitor FSFD calculated using DFT / B3LYP/ 6-311G (d,p) in ethanol and vacuum solvent.

Parameters	Ethanol solvent	Vacuum
Total Energy (eV)	-32599.730	- 32599.395
E_{HOMO} (eV)	- 6.286	- 6.122
E_{LUMO} (eV)	-1.793	-1.793
ΔE_{gap} (eV)	4.493	4.329
μ (Debye)	3.5493	2.8168
I (eV)	6.286	6.122
A (eV)	1.793	1.793
η (eV)	2.247	2.165
ω (eV)	3.631	3.618
χ (eV)	4.0395	3.958
S $(eV)^{-1}$	0.445	0.462
ΔN (eV)	0.658	0.703

Table 5 shows the theoretical data for FSFD. It is obvious that the values of HOMO energy was increased in ethanol than in vacuum, the HOMO energy is often associated with the electron donating ability of the molecule. So inhibitor with high value of HOMO energy have a tendency to donate electrons to appropriate acceptor with low empty molecular orbital energy. The decrease in the E_{LUMO} value leads to higher inhibitory efficiency due capability of the FSFD compound to accept electrons from metal iron.

The ΔE_{gap} is an important parameter that should be considered. When the energy gap value decreases the reactivity of molecular system increases [17]. Moreover, the ΔE_{gap} is a part of the reactivity of the inhibitor molecule towards the adsorption on the metal surface.

As well as, the dipole moment (μ) is the maximum parameter that could be applied to describe the polarity of a molecule [18]. Where an increase in the dipole moment of the molecules leads to an increase in the inhibition efficiency. The inhibitor FSFD has 3.5493 Debye which reflects the increase of the reactivity more than the media without solvent. The electron density distributions, molecular optimization of the frontier molecular orbitals, highest occupied molecular orbital energy and lowest unoccupied molecular orbital energy of the inhibitor FSFD in ethanol solvent and vacuum are presented in Figure (7).

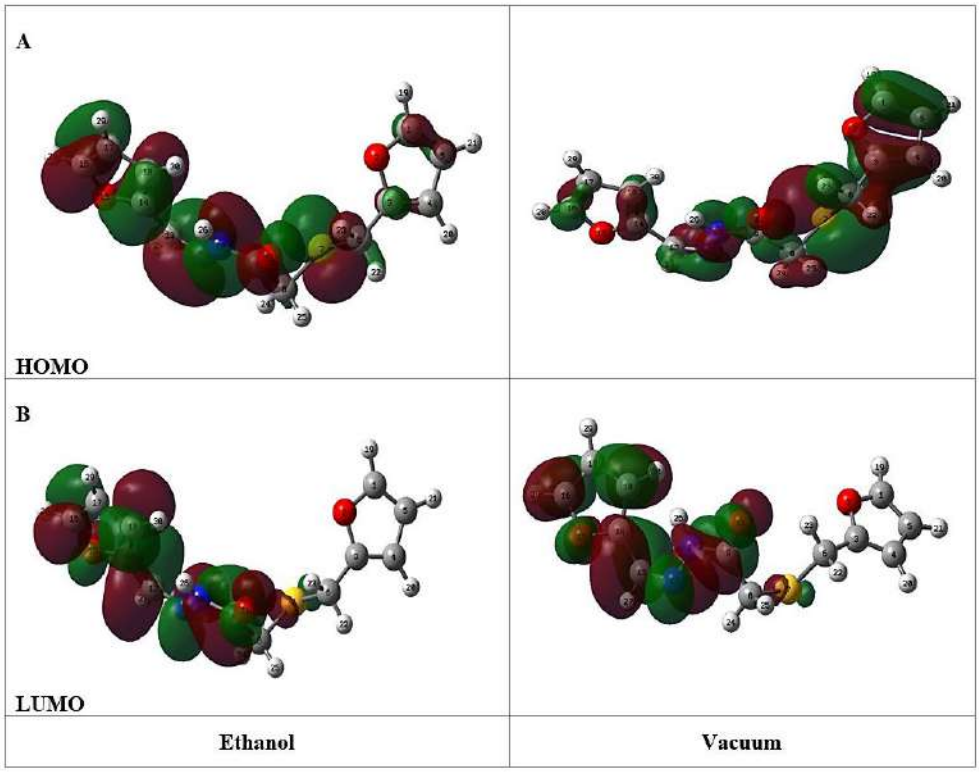

Figure 7 .**(A) HOMO** in ethanol solvent and vacuum and **(B) LUMO** in ethanol solvent and vacuum of the inhibitor FSFD using DFT / B3LYP / 6-311 G (d, p).

Molecular orbitals HOMO shows that the electronic density is totally centered on the heteroatoms oxygen, nitrogen, sulfur and the furan ring, the LUMO present an important electronic density distributed over most of molecule. This result agrees with the distribution of the Mulliken charges and the direction of the polar direction (moment) are presented in Figure 8 and listed in Table 6.

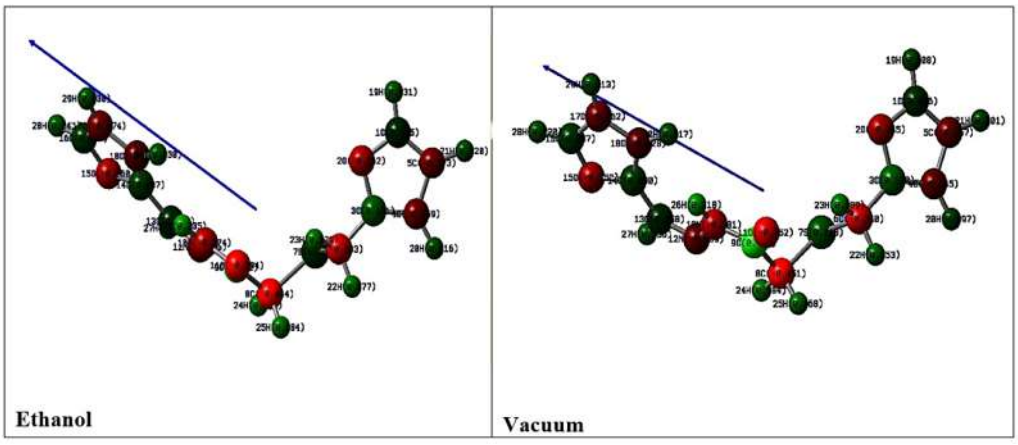

Figure 8. Mulliken charge distribution (MCD) of the FSFD inhibitor.

Table 6. MCD values (10^{-3}) of the inhibitor FSFD

Atom	1C	2O	3C	4C	5C
Mulliken charge	548* 65.6**	-262 -245	131 138	-159 -145	-173 -156
Atom	6C	7S	8C	9C	10N
Mulliken charge	333 -340	668 118	-444 -451	412 410	-274 -280
Atom	11O	12N	13C	14C	15O
Mulliken charge	-394 -352	-182 -159	59 584	87 90	-259 -251
Atom	16C	17C	18C	19H	20H
Mulliken charge	85 866	-174 -162	-126 128	131 108	116 971
Atom	21H	22H	23H	24H	25H
Mulliken charge	120 100	177 153	179 188	190 183	184 168
Atom	26H	27H	28H	29H	30H
Mulliken charge	235 218	148 136	142 120	130 112	130 117

*Ethanol solvent, **Vacuum

Figure 8 and Table 6 display Mulliken charge distribution values. It can be realized that the some C atoms and heteroatoms, N, O, S have maximum charge intensity. The large electronic intensity regions are mostly the sites that electrophiles can attack through [19]. Thus, some C atoms, S, O and N are the active cores that easily the atom gives away its electrons to the unoccupied orbital of the metal [20]. Several reports have shown that some heteroatoms with more negatively charged is the more it can be hold as a thin film on the mild steel surface through the donor-acceptor style reaction [21].

4. Conclusions

A new synthesized furan derivative FSFD was investigated using electrochemical measurements and quantum chemical calculations as corrosion inhibition. Experimental results exhibited good corrosion inhibition impact on iron metal surface with maximum inhibition efficiencies of 77% in acidic solution (1.0 M) at 303 K. The contribution of theoretical results has been to confirm with the experimental results.

References

[1] Rani, B.E.A. and Basu, B.B.J., 2012, *Int. J. Corros*., **2**, 1.
[2] Bin, X., Wenzhong, *Y., Ying, L., Xiaoshuang, Y., Weinan, G. and Yizhong*, C., 2014, Corros. Sci., **78**, 260.
[3] Kosari, A., Moayed, M.H., Davoodi, A., Parvizi, R., Momeni, M.,Eshghi, H. and Moradi, H., 2014, *Corros. Sci*., **78**, 138.
[4] Bobina, M., Kellenberger, A., Millet, J., Muntean, C. and Vaszilcsin, N., 2013, *Corros. Sci*., , **69**, 389.
[5] Fragoza-Mar, L., Olivares-Xometl, O., Domí nguez-Aguilar, M., Flores, E., Lozada, P. and Jimé nez-Cruz, F., 2012,, *Corros. Sci*., **61**, 171.
[6] Yohai, L., Vá zquez, M. and Valcarce, M. B., 2013, *Electrochim. Acta*, , **102,** 88.
[7] Saravanamoorthy, S. and Velmathi, S., 2013, *Prog. Org. Coat*., **76**, 1527.
[8] Nam, N.D., Bui, Q.V., Mathesh, M., Tan, M.Y.J. and Forsyth, M., 2013, *Corros. Sci*., **76,** 257.
[9] Arab, S.T. and Noor, E.A., 1993, *Corrosion*, , **49**, 122.

[10] Belghiti M.E., Bouazama S., Echihi S., Hammouti B. and Tabyaoui M., 2020 , *ARAB J CHEM*, **13**, 1499.
[11] Scendo, M. and Uznanska, 2011, *J., Int. J. Corros*., **1**, 1.
[12] Luma S. Ahamed 2018, J. *Glob. Pharma Technol*., **11**, 298.
[13] Arouji S. EL., Ismaili K. A., El Assyry A. and Rais Z., 2015, *Der Pharma Chem*., **7** (10), 23.
[14] Sekine, I., Nakahata, Y. and Tanabe, H., 1988, *Corros. Sci*., **28**, 987.
[15] Laamari, M.R., Benzakour, J., Berrekhis, F., Bakasse, M. and Villepin, D.. 2012, *J. Mater. Environ. Sci.*, **3,** 485.
[16] Wang, L., 2001, *Corros. Sci*., **43**, 1637.
[17] Kraka E. and Cremer D., 2000, *J*. Am. *Chem. Soc*., **122,** 8245 .
[18] Al Hamzi AH., Zarrok H., Zarrouk A., Salghi R., Hammouti B. and AlDeyab SS., 2013, Int. *J. Electro. Sci*., **8**, 2586.
[19] Hsissou R, Abbout S, Berisha A, Berradi M, Assouag M. and Hajjaji N. ,2019, J. *Mol. Struct*., **1182**, 340.
[20] Obi-Egbedi N., Essien K., Obot I and Ebenso E., 2011, Int. *J. Electro. Sci.*, **6**, 913.
[21] Fergachia O., Benhibae F., Rbaab M., Touira,d R. and Ouakkic M., 2018,*Mater. Res*., **21**, 1.

Journal of Physics: Conference Series

PAPER • **OPEN ACCESS**

Biochemical Aspect, Antimicrobial and Antioxidant Activities of *Melaleuca* and *Syzygium* Species (Myrtaceae) Grown in Egypt

To cite this article: Omar M. Khalaf *et al* 2021 *J. Phys.: Conf. Ser.* **1879** 022062

Biochemical Aspect, Antimicrobial and Antioxidant Activities of *Melaleuca* and *Syzygium* Species (Myrtaceae) Grown in Egypt

Omar M. Khalaf [1*], Mohamed S. Abdel-Aziz [2], Ali M. El-Hagrassi [3], Abeer F. Osman [4] and Mosad A. Ghareeb [5]

[1]Chemistry of Natural Product Department, Ministry of Education, Anbar Education Directorate, Iraq.
[2]Department of Microbial Chemistry, Division of Genetic Engineering and Biotechnology, National Research Centre, Giza, Egypt.
[3]Medicinal Chemistry Department, Theodor Bilharz Research Institute, Kornaish El-Nile, Warrak El-Hadar, Imbaba (P.O. 30), Giza 12411, Egypt.

[*] E-mail: Omarro44@gmail.com; Tel.: 07807855656-07700005967

Abstract. The objective of the present work was to establish the antimicrobial activity of four species of Melaleuca (i.e. Melaleuca leucandron, Melaleuca armillaris, Melaleuca linarifolia, & Melaleuca ericifolia) methanolic extracts and five species of Syzygium (i.e., Syzygium samaragense, Syzygium jambos, Syzygium gratum, Syzygium paniculatum & Syzygium malaccense). To research the chemical composition of the most promising extracts, as well. The antimicrobial activity was evaluated against four pathogenic microbial strains, namely Staphylococcus aureus, Escherichia coli, Candida albicans and Aspergillus niger, the antioxidant activity was evaluated by 2,2'-diphenyl-1-picrylhydrazyl radical (DPPH), while the chemical composition was calculated by gas chromatography coupled to a mass spectrometry method (GC/MS). For the genus of Melaleuca, S. After therapy, aureus pathogens were inhibited with their methanolic extracts with an 8.0-20.0 mm range of inhibition zones, E. Coli with a 0.0-21.0 mm inhibition zone size, C. Albicans with an inhibition zone size of 9.0-18.0 mm, and A. Niger with an inhibition zone scale of 0.0-15.0 mm. Whereas, for the genus Syzygium, S. After treatment with their methanolic extracts, aureus pathogens were inhibited with a 10.0-20.0 mm range of inhibition zones, E. Coli, with an inhibition zone size of 0.0-14.0 mm, C. Albicans with an inhibition zone size of 0.0-21.0 mm, and A. Niger with a range of inhibition zones of 0.0-9.0 mm. The IC50 values in the DPPH assay ranged from 34.60 to 60.97µg/ml for the species Melaleuca. The IC50 values for the Syzygium species ranged from 29.81 to 52.95µg/ml compared to 7.35µg/ml for the normal ascorbic acid. GC/MS research showed that Syzygium gratum's methanolic extract consists of 39 compounds comprising 99.08 percent, with Veridiflorol (7.16 percent) and 2-methyl, 3-Hexanone being the main compounds (5.74 percent). While Melaleuca armillaris' methanolic extract consists of 30 compounds comprising 97.66%, with Veridiflorol (18.36%) and Globulolol compounds being the key compounds (12.57 percent).

Keywords: Myrtaceae; *Melaleuca* sp.; *Syzygium* sp.; Antimicrobial, DPPH, GC/MS.

1. Introduction:

The resistance to the presence of antibiotics by pathogenic microbial strains remains a major challenge. Infectious diseases caused by bacterial and fungal infections are, however, known to be a great health concern. Microbial resistance to antimicrobial agents has increased dramatically recently, so it is very important to look for alternative antimicrobial agents from natural sources, such as plants or herbs, in order to address this challenge[1,2]. A variety of plant, fungal and marine extracts have therefore been screened for their antimicrobial activity [3-12]. In addition, due to their biomedical properties against microbes, plants develop a high diversity of secondary metabolites with a prominent role for defense against predators and microbial pathogens[13.[

During normal oxygen metabolism, reactive oxygen species (ROS) are produced as secondary products. The over-production of such organisms, including DNA, proteins, and lipids, contributes to damage to essential cells and tissues in the human body. This phenomenon is considered to be associated with oxidative stress and is associated with chronic diseases such as cancer, coronary artery disease, hypertension, and diabetes[14-20.[

Involved in the Myrtales Order, the Myrtaceae family has approximately 130 genera and approximately 3800-5800 species, primarily tropical and subtropical, concentrated in the Neotropics and Australia[21]. The Melaleuca L. genus. (Myrtaceae) primarily occurs in Australia and contains around 250 species. The most common chemical constituents of this genus are essential oils[22], as well as flavonoids[23, 24], phenolic acids[25] and tannins[25, 26.[

In addition, the genus Syzygium (Myrtaceae) includes around 1200-1800 species, especially flowering plants. Species of this genus are widely distributed in Africa and Southeast Asia[27, 28]. The efficacy of Syzygium species against various bacterial strain types has been demonstrated in several studies [29, 30]. In the various Syzygium species, numerous groups of secondary metabolites have been identified, including flavonoids[31], proanthocyanidins[32], chalcons[33], and phenolic acids[34, 31]. In this context, the chemical profiles, antimicrobial activities and antioxidant activities of some species of Melaleuca and Syzygium grown in Egypt have been described in the current study.

2. Materials and Methods:

2.1. Plants materials

Fresh leaves of four *Melaleuca* (i.e., *Melaleuca leucandron*, *Melaleuca armillaris*, *Melaleuca linarifolia*, and *Melaleuca ericifolia*) and five *Syzygium* (i.e., *Syzygium samaragense*, *Syzygium jambos*, *Syzygium gratum*, *Syzygium paniculatum* and *Syzygium malaccense*) species were collected from different locations including; Zoo Garden, El-Orman Garden and Mazhar Botanical Garden, Giza, Egypt during April, 2019. The plant was taxonomically identified by Dr. Tearse Labib, Department of Flora and Taxonomy, El-Orman Botanical Garden, Giza, Egypt.

2.2. Extraction

The dried leaves were grinded and extracted with methanol (50 gm for each plant sample) at room temperature for four days (8×500 ml). The combined extracts were filtered evaporated under vacuum until becoming dry at 40°C.

2.3. In vitro antimicrobial evaluation

The antimicrobial activities were evaluated by using disc agar plate assay against four different pathogenic microbial strains, *Staphylococcus aureus*, *Escherichia coli*, *Candida albicans* and *Aspergillus niger* according to the reported procedures [35,36]. Neomycin (100 µg/disc) and Cyclohexamide (100 µg/disc) were used as antibacterial and antifungal standards, respectively

2.4. Antiradical activity:

The antiradical action of the tested samples was evaluated according to the reported methodology illustrated by [37], briefly different dilutions of each sample (2 ml) were added to (2 ml) solution of 0.1 mmol/l 2,2'-diphenyl-1-picrylhydrazyl radical (DPPH). An equal amount of methanol and DPPH were acted as a regulator. After 20 min of incubation at 37^{o}C in the dark, the absorbance was registered at 517 nm. The test was accomplished in triplicate. The antiradical action was estimated and the SC_{50} (concentration of analyte needed to sweep fifty percent of the

radical) value was calculated. The reduction in the absorbance of DPPH solution reveals an increase of the DPPH radical masking potential. The DPPH radical scavenging activity was estimated according to the following equation:

$$\% \text{ DPPH radical scavenging activity} = [(1- A_{sample} / A_{control})] \times 100 \quad (1)$$

Where A_{sample} and $A_{control}$ are the absorbance of the sample and control.

2.5. GC/MS analysis

GC/MS investigation of the most active samples was carried out according to the reported procedures [7], using a Thermo Scientific, Trace GC Ultra/ISQ Single Quadrupole MS,TG-5MS fused silica capillary column (30 m, 0.251 mm, 0.1 mm film thickness). For GC/MS detection, an electron ionization system with ionization energy of 70 eV was used, Helium gas was used as the carrier gas at a constant flow rate of 1ml/min. The injector and MS transfer line temperature was set at 280°C. The oven temperature was programmed to an initial temperature of 50°C (hold 2 min) to 150 °C at an increasing rate of 7°C/min. then to 270 at an increasing rate of 5°C/min (hold 2 min) then to 310°C as a final temperature at an increasing rate of 3.5°C/min (hold 10 min). The quantification of all the identified components was investigated using a percent relative peak area. A tentative identification of the compounds was performed based on the comparison of the irrelative retention time and mass spectra with those of the NIST, WILLY library data of the GC/MS system.

3. Results and Discussion:

3.1. In vitro evaluation of the antimicrobial activities of Melaleuca species

Table 1 and 'Figure 1' show the results linked to antimicrobial inhibition zones of methanolic leaf extracts of four Melaleuca species against four pathogenic microbial strains. The areas of inhibition for M. It was between 10 and 20 mm of leucandron. While, because of M. There were between 8 and 18 mm of armillaris, for M. There were between 8 and 15 mm of linarifolia, and for M. There were 8 and 21 mm of ericifolia. The microbial strains which are most susceptible to the M. S. was leucandron extract. S. Aureus, as well as A. Niger, with 20 and 15 mm inhibition areas, respectively. While, the most vulnerable microbial strains to the M. The extract from Armillaris was C. Albicans with an 18 mm inhibition zone. The most potent activity for M. was also reported. Against E ericifolia. 21 mm coli with an inhibition zone. To date, very few studies in the literature describe the antimicrobial activity of extracts of the Melaleuca species, but the most frequently published papers deal with the antimicrobial activity of their essential oils.

Antimicrobial activity of the extract of M. crude leaf. Five microbial strains were tested against Quinquenervia. The 10 mg concentration inhibition zones were 13.4 mm against S. Aureus, against B 11.5 mm. 14.1 mm against E, cereus. Coli, and any action against C is registered. S. and Albicans. [38]. Typhimurium

Antibacterial activity of the leaves and flowers of M methanolic extracts. Eight pathogens, namely Staphylococcus aureus, Escherichia coli, Bacillus cereus, Staphylococcus epidermidis, Salmonella typhimurium, Klebsiella pneumoniae, Streptococcus pneumoniae, and Pasteurella multocida, have been tested against cajuputi. The extracts showed activity against bacterial strains of Gram+ve; B. 6.33 mm/12.33 mm (leaves/flowers) cereus, S. 12.33 mm/ 12.33 mm (leaves/flowers) of aureus, and S. Epidermidis 13.66 mm/ 17.33 mm (leaves/flowers), while no activity against Gram-negative bacterial strains has been reported[39]. In addition, a recent analysis has discovered that the aqueous extract of M. Alternifolia grown in Australia demonstrated antimicrobial activity with a MIC of 0.25 mg/ml against P. aeruginosa [40].

Table 1. The antimicrobial activity of the methanolic extracts of four *Melaleuca* species using four pathogenic microbes

Sample	Clear zone (φmm)			
	S. aureus	***E. coli***	***C. albicans***	***A. niger***
M. leucandron	20	0	10	15
M. armillaris	8	0	18	9
M. linarifolia	10	15	11	8
M. ericifolia	8	21	9	0

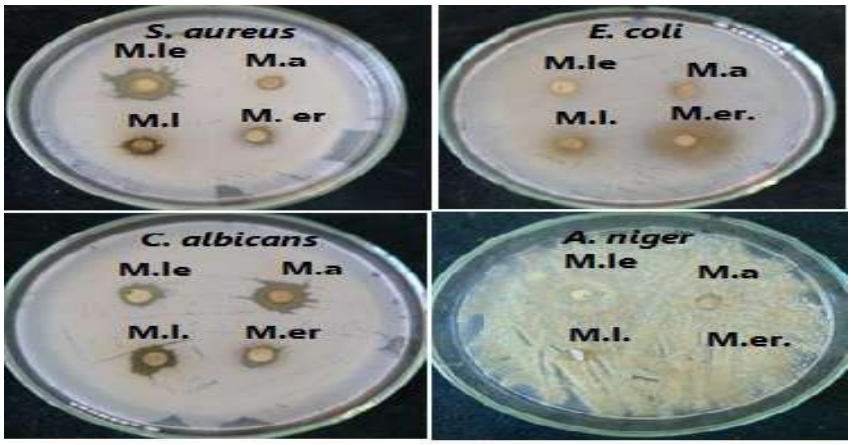

Figure 1. Antimicrobial inhibition zones of the methanolic extracts of four *Melaleuca* species against four pathogenic microbes. M.le: *Melaleuca leucandron*; M.a: *Melaleuca armillaris*; M.l: *Melaleuca linarifolia*; M.er: *Melaleuca ericifolia*.

3.2. In vitro evaluation of the antimicrobial activities of Syzygium species

The methanolic extracts from the leaves of five *Syzygium* species were subjected to *in vitro* antimicrobial activity test against four pathogenic microbial strains, i.e., *S. aureus*, *E. coli*, *C. albicans*, and *A. niger*. Results presented in Table 2 and‘Figure 2’ revealed the antimicrobial activity of these extracts. It has been found that *S. jambos* and *S. paniculatum* showed a remarkable activity against all test microbes except the fungus. However, *S. jambos* showed almost the highest antimicrobial activity against *S. aureus* (20 mm), *E. coli* (8 mm), *C. albicans* (21 mm), and *A. niger* (7 mm). Our findings are in agreement with some extent with several previous studies [41-42].

A present study has reported that the inhibition zones of *S. polyanthum* leaves extract against There were 7.00 mm, 9.33 mm, 9.67 mm, 7.00 mm, 6.67 mm, 9.33 mm, 6.67 mm, 8.33 mm, and 6.67 mm of foodborne pathogens on E. For coli, K. Pneumoniasis, L. P. aeruginosa, monocytogenes, P. mirabilis, S. With aureus, S. Typhimurium, V. cholerae and, respectively, V. parahaemolyticus[42]. In addition, the acetone bark extract of Syzygium cordatum showed an inhibition zone diameter of 22 mm for Staphylococcus aureus, 19 mm for Bacillus subtilis and 18 mm for each of Enterococcus fecalis, Enterobacter cloacae and Proteus mirabilis[43.[

Interestingly, a previous study showed that the extract of hydroalcoholic leaves from S. Cumini demonstrated antimicrobial activity against six microbial pathogenic strains, viz., S. Mutans, S. Mutans Yeah. Oralis, S. From Parasanguis, S. For salivarius, S. L and sp. Casei with 15 mm, 15 mm, 19 mm, 13.5 mm, 15.5 mm and 15.5 mm inhibition zones respectively [44]. The antimicrobial activity was evaluated for the different solvent extracts of Syzygium alternifolium leaves. The inhibition zones ranged between 4-8 mm (Staphylococcus aureus), 4-7 mm (Escherichia coli), 3-15 mm (Staphylococcus aureus), and 3-15 mm (Escherichia coli),

respectively. (*Pseudomonas aeruginosa*), 3-9 mm (*Candida albicans*), 5-10 mm (*Pencillium notatum*), and 2-6 mm (*Enterococcus*) [45].
The antimicrobial activity of the hydroalcoholic extract of *Syzygium cumini* leaves was evaluated via agar diffusion method. The inhibition zones were 12.0 mm, 14.7 mm, 9.7 mm, 8.7 mm, 10.0 mm, 9.0 mm, and 8.3 mm against *Candida albicans*, *Candida krusei*, *Enterococcus faecalis*, *Kocuria rhizophila*, *Pseudomonas aeruginosa*, *Staphylococcus aureus*, *Shigella flexneri*, respectively [46].

The ethanol extracts of the fruits and seeds parts of *Syzygium samaragense* were evaluated for their antimicrobial activities against certain clinical isolates, the inhibition zones were 16 mm fruits, 25 mm seeds, 10 mm fruits, 18 mm seeds, 11 mm fruits, 23 mm seeds, and 9 mm fruits, 21 mm seeds, respectively against *S. aureus*, *S. typhi*, *P. aeruginosa* and *E. coli*. While, the aqueous extracts showed low antimicrobial activities with inhibition zones of 7 mm fruits, 11 mm seeds, 0 mm fruits, 9 mm seeds, 0 mm fruits, 10 mm seeds, and 0 mm fruits, 9 mm seeds, respectively against *S. aureus*, *S. typhi*, *P. aeruginosa* and *E. coli* [47].
In accordance with a recent study, the aqueous methanol extract (85% MeOH) of *Syzygium jambos* leaves grown in Egypt showed antimicrobial activity against four microbial strains with inhibition ones of 13.5 mm, 11.0 mm, 13.5 mm, and 11.5 mm, respectively for *Staphylococcus aureus*, *Methicillin-resistant Staphylococcus aureus*, *Pseudomonas aeruginosa* and *Candida albicans* [41].

Table 2. The antimicrobial activity of the methanolic extracts of five *Syzygium* species using four pathogenic microbes

Sample	**Clear zone (φmm)**			
	S. aureus	***E. coli***	***C. albicans***	***A. niger***
S. samaragense	15	14	10	0
S. jambos	20	8	21	7
S. gratum	10	0	0	0
S. paniculatum	12	13	8	9
S. malaccense	13	9	12	0

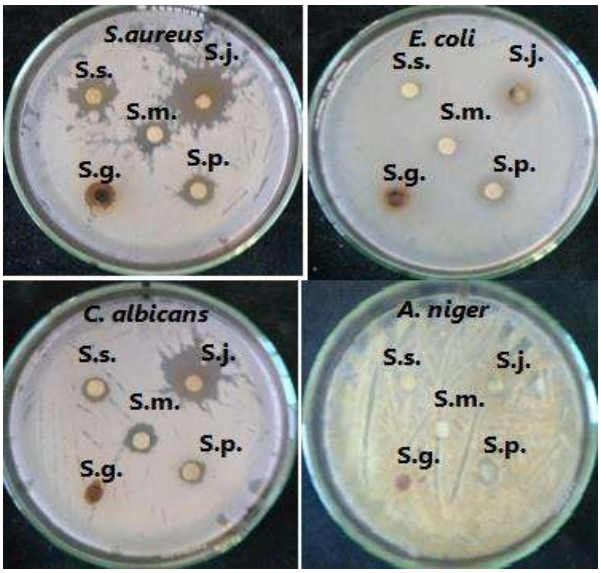

Figure 2. Antimicrobial inhibition zones of the methanolic extracts of five *Syzygium* species against four pathogenic microbes. S.s.: *Syzygium samaragense*; S.j.: *Syzygium jambos*; S.g.: *Syzygium gratum*; S.p.: *Syzygium paniculatum*; S.m.: *Syzygium malaccense*.

3.3. DPPH free radical scavenging biochemical activity

The DPPH free radical masking properties of the crude methanolic extracts of four *Melaleuca* and five *Syzygium* species are reported in Table 3. For *Melaleuca* species, the IC_{50} values for the tested extracts ranged from 34.60 to 60.79 µg/ml compared to ascorbic acid with IC_{50} equal to 7.35 µg/ml. The results are in the order: *Melaleuca armillaris* (IC_{50}: 34.60 µg/ml) > *Melaleuca ericifolia* (IC_{50}: 49.92 µg/ml) > *Melaleuca linarifolia* (IC_{50}: 59.54 µg/ml) > *Melaleuca leucandron* (IC_{50}: 60.97 µg/ml). While for *Syzygium* species, the *Syzygium gratum* extract showed the highest antioxidant activity with IC_{50} value of 29.81µg/ml, followed by *Syzygium paniculatum* (IC_{50}: 40.95 µg/ml), *Syzygium samaragense* (IC_{50}: 41.50 µg/ml), *Syzygium jambos* (IC_{50}: 48.13 µg/ml), and *Syzygium malaccense* (IC_{50}: 52.95 µg/ml), respectively, compared to ascorbic acid with IC_{50} equal to 7.35 µg/ml.

In this regard, a recent study dealt with the DPPH antiradical activity of the methanolic extracts of the leaves parts of seven *Syzygium* species from Indonesia has suggested that IC_{50} values were in the order; *S. jambos* (7.90 µg/ml), *S. malaccences* (10.77 µg/ml), *S. samarangense* (13.85 µg/ml), *S. cumini* (16.91µg/ml), *S. aqueum* (20.24 µg/ml), *S. aromaticum* (21.51 µg/ml), and *S. polyanthum* (26.03 µg/ml). The obtained results were matched to some extent with our current findings [48].

IC_{50} values of DPPH free radical scavenging activities of *M. leucadendron* solvents extracts were 5.1, 55.7, 4.8 and 60.0 µg/ml, respectively for methanol, chloroform, butanol and water extracts [49]. Also, free radical masking antioxidant activity of the methanolic extract of the leaves part of *Melaleuca leucadendra* from Indonesia was evaluated and IC_{50} value was 22.46 µg/ml [48]. The methanolic extract from flowers and leaves parts of *Melaleuca cajuputi* were evaluated for their DPPH free radical scavenging antioxidant activity, the leaves extract showed a higher scavenging activity with IC_{50} value of 10 µg/ml, while the flower extract showed an IC_{50} value of 25 µg/ml [50, 57]. Also, the Inhibition percent's of DPPH radical by the aqueous leaves extract of *Syzygium cumini* were 62.23%, 82.6%, and 87.13% at 100, 150 and 200 µg/ml, respectively. While, for the ethanolic extract 6%, 9%, and 25% were 100, 150 and 200 µg/ml, respectively [51]. IC_{50} values of DPPH free radical scavenging activities of aqueous and methanolic extracts of *S. cumini* were 24.77, and 9.97 µg/ml, respectively for aqueous and methanolic extracts [52].

Table 3. DPPH free radical scavenging activity of the methanolic extracts of four *Melaleuca* and five *Syzygium* species

Sample	DPPH free radical scavenging activity SC_{50} (μg/ml)[a]
Melaleuca leucandron	60.97 ± 0.59
Melaleuca armillaris	34.60 ± 0.15
Melaleuca linarifolia	59.54 ± 0.38
Melaleuca ericifolia	49.92 ± 0.13
Syzygium samaragense	41.50 ± 0.36
Syzygium jambos	48.13 ± 0.24
Syzygium gratum	29.81± 0.27
Syzygium paniculatum	40.95 ± 0.17
Syzygium malaccense	52.95 ± 0.20
Ascorbic acid	7.35 ± 0.47

[a]SC_{50}: concentration in μg/ml required for scavenging the DPPH radical (100 μg/ml) by 50 %, it was calculated by probit-graphic interpolation for ten concentration levels.

3.4.GC/MS analysis of the methanolic extract of Syzygium gratum

GC/MS analysis of the methanolic extract of *Syzygium gratum* comprises 39 ingredients. The overall peak areas of the identified components constitutes 99.08 %, the prospects of the chemical skeletons of the identified components are recorded in table (4): The main biochemical compounds are Veridiflorol $C_{15}H_{26}O$ (7.16%), 2-methyl, 3-Hexanone $C_7H_{14}O$ (5.74%), Pentadecanoic acid, 14-methyl-, methyl ester $C_{17}H_{34}O_2$ (4.98%), Nonadecane $C_{19}H_{40}$ (4.77%), 2,6,10,15-tetramethyl, and Heptadecane $C_{21}H_{44}$ (4.12%), collectively represented 26.77 % of the total peak areas ‘Figure 3’. The identification was accomplished using computer search user-generated reference libraries, incorporating mass spectra [53-55]. Peaks were examined by single-ion chromatographic reconstruction to confirm their homogeneity. Occasionally, when identical spectra have not been found, only the structural type of the isomer component was proposed on the bases of its mass spectral fragmentation. Reference compounds were co-chromatographed when possible to confirm GC retention times. 3-Piperidinamine, 1-ethyl-, N-[3-[n-aziridyl]propylidene]-3-methylaminopropylamine, Carbamic acid, hydroxy-, ethyl ester, and 3-Oxabicyclo[3.3.0]octan-2-one,7-methylene were detected by GC/MS analysis as major constituents in the methanolic extract of *Syzygium calophyllifolium* [56].

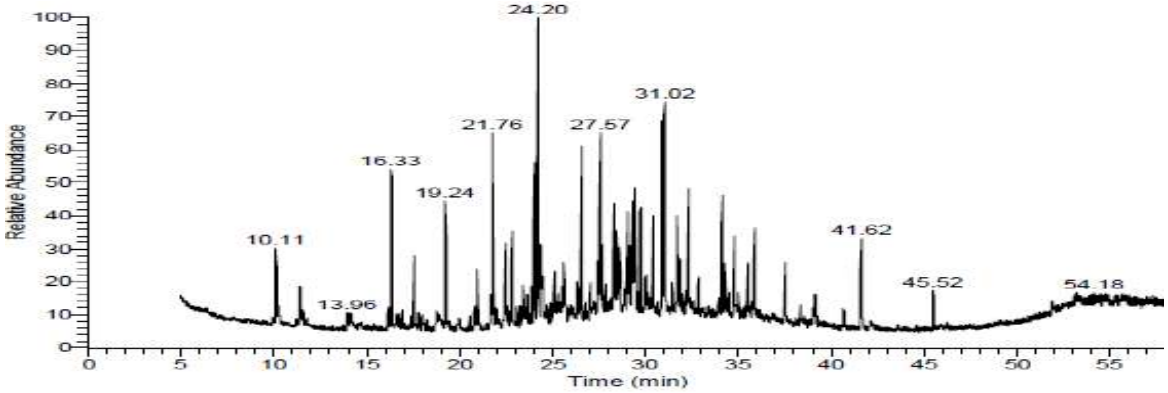

Figure 3. GC/MS profile of the methanolic extract of *Syzygium gratum*.

Table 4. GC/MS investigation of the methanolic extract of *Syzygium gratum*

Peak No.	R_t (min.)	M.W.	M.F.	Area %	Identified compounds
1	10.11	184	$C_{13}H_{28}$	2.02	2, 4, 6, Trimethyl, Decane
2	11.40	160	$C_9H_{20}O_2$	1.14	(2RS,3RS)-2-Butyl-3-methylbutane-1,4-diol
3	16.33	156	$C_{11}H_{24}$	3.30	2,6,6-trimethyl, Octane
4	17.55	212	$C_{15}H_{32}$	1.49	2,6,11-trimethyl, Dodecane
5	19.24	196	$C_{14}H_{28}$	2.65	3-Tetradecene
6	20.95	184	$C_{13}H_{28}$	1.37	2,3,7-trimethyl, Decane
7	21.76	198	$C_{14}H_{30}$	3.84	2,3,5,8-tetramethyl, Decane
8	22.47	206	$C_{14}H_{22}O$	2.17	2,4-bis(1,1-dimethylethyl), Phenol
9	22.82	226	$C_{16}H_{34}$	2.17	Hexadecane
10	24.01	238	$C_{17}H_{34}$	3.93	1-Heptadecene
11	24.20	222	$C_{15}H_{26}O$	7.16	Veridiflorol
12	24.35	192	$C_{13}H_{20}O$	2.14	α-Ionone
13	25.12	220	$C_{15}H_{24}O$	1.19	Aromadendrene oxide-(1)
14	25.61	222	$C_{15}H_{26}O$	1.21	α-Cadinol
15	26.57	296	$C_{21}H_{44}$	4.12	2,6,10,15-tetramethyl, Heptadecane
16	27.49	268	$C_{19}H_{40}$	4.77	Nonadecane
17	27.57	150	$C_{10}H_{14}O$	3.98	1-carboxaldehyde,4-(1-methyletheny), 1-Cyclohexene
18	27.67	234	$C_{15}H_{22}O_2$	1.48	7-(1,3-Dimethylbuta-1,3-dienyl)-1,6,6-trimethyl-3,8-dioxatricyclo[5.1.0.0(2,4)]octane
19	28.31	242	$C_{16}H_{34}O$	2.71	1-Hexadecanol
20	28.44	254	$C_{18}H_{38}$	2.35	2,2,4,9,11,11-hexamethyl, Dodecane
21	28.62	236	$C_{16}H_{28}O$	2.02	7,11-Hexadecadienal
22	29.04	270	$C_{17}H_{34}O_2$	2.03	Isopropyl myristate
23	29.14	306	$C_{20}H_{34}O_2$	1.32	Butyl, 6,9,12-hexadecatrienoate

24	29.33	208	$C_{14}H_{24}O$	2.29	à,2,6,6-tetramethyl,1-Cyclohexene-1-butanal
25	29.42	268	$C_{18}H_{36}O$	3.25	6,10,14-trimethyl-2-Pentadecanone
26	29.74	258	$C_{15}H_{14}O_4$	3.77	4-(3-Hydroxyphenoxy)benzoic acid ethyl ester
27	30.90	114	$C_7H_{14}O$	5.74	2-methyl, 3-Hexanone
28	31.02	270	$C_{17}H_{34}O_2$	4.98	Pentadecanoic acid,14-methyl-, methyl ester
29	31.46	292	$C_{18}H_{28}O_3$	1.15	Benzenepropanoic acid,3,5-bis(1,1-dimethylethyl)-4-hydroxy-, methyl ester
30	31.70	282	$C_{20}H_{42}$	1.07	2,6,11,15-tetramethyl, Hexadecane
31	32.32	282	$C_{20}H_{42}$	2.52	Eicosane
32	34.14	394	$C_{28}H_{58}$	2.43	Octacosane
33	34.27	282	$C_{18}H_{34}O_2$	1.25	dihydro-5-tetradecyl, 2(3H)-Furanone
34	34.79	380	$C_{27}H_{56}$	2.06	Heptacosane
35	35.52	408	$C_{29}H_{60}$	1.33	Nonacosane
36	35.87	422	$C_{30}H_{62}$	1.90	Triacontane
37	37.54	310	$C_{22}H_{46}$	1.42	Docosane
38	41.62	390	$C_{24}H_{38}O_4$	2.28	1,2-Benzenedicarboxylicacid, bis(2-ethylhexyl) ester
39	45.51	410	$C_{30}H_{50}$	1.08	Squalene
T%				**99.08 %**	

R_t: Retention time; M.W.: Molecular Weight; M.F.: Molecular Formula

3.5. GC/MS investigation of the methanolic extract of Melaleuca armillaris

The GC/MS study of Melaleuca armillaris methanolic extract consists of 30 ingredients. Table 5 shows the prospects of the chemical skeletons of the identified components in the overall peak areas of the identified components: the main biochemical compounds are Veridiflorol C15H26O (18.36 percent), Globulol C15H26O (12.57 percent), (+) spathulenol C15H24O (7.53 percent), Cyclopropa[c,d]pentalene-1,3-dione, hexahydro-4(2-methyl-2-propenyl)-2,2,4-t. The identification was achieved by using user-generated reference libraries for computer search, integrating mass spectra[53-55]. Ethanone, 4H-1-Benzopyran-4-one, 1,4-Naphthalenedione, Alpha.-Tetralone, Caryophyllene Bicyclo,[7.2.0]undec-4ene, 1H-Cycloprop[e]azulen-7-ol, 2-Naphthalenemethano, Squalene, and Stigmast-5-en-3-ol[57] were detected by GC/MS study of the methanolic extract of Melaleuca cajuputi grown in Malaysia.

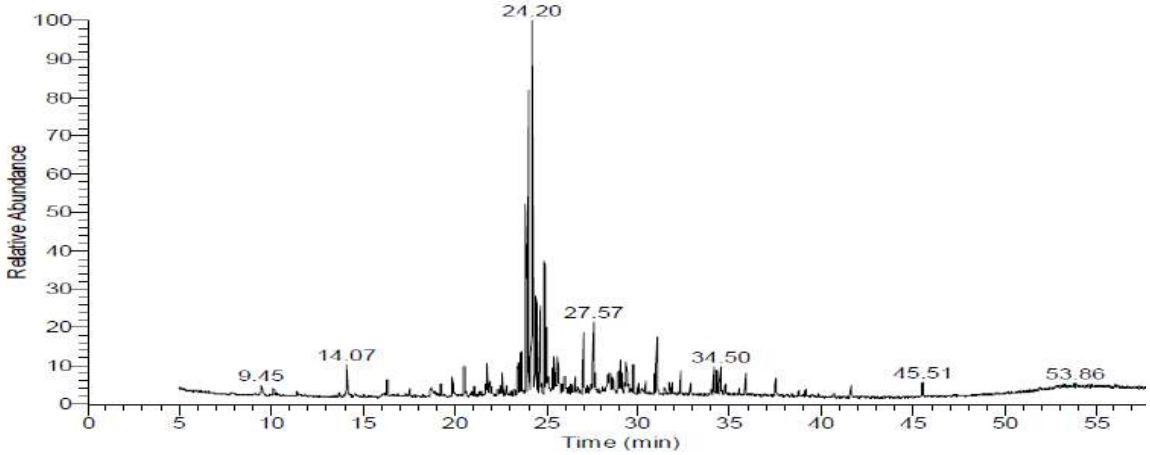

Figure 4. GC/MS profile of the methanolic extract of *Melaleuca armillaris*.

Table 5. GC/MS investigation of the methanolic extract of *Melaleuca armillaris*

Peak No.	R_t (min.)	M.W.	M.F.	Area %	Identified compounds
1	14.07	154	$C_{10}H_{18}O$	1.62	3-Cyclohexene-1-methanol, à,à,4-trimethyl
2	19.85	178	$C_{11}H_{14}O_2$	1.10	2-Butanone,4-(4-methoxyphenyl)-
3	20.52	204	$C_{15}H_{24}$	1.96	trans-Caryophyllene
4	22.85	202	$C_{15}H_{22}$	0.90	trans-calamenene
5	23.45	222	$C_{15}H_{26}O$	3.21	Epiglobulol
6	23.88	220	$C_{15}H_{24}O$	7.53	(+) spathulenol
7	24.02	222	$C_{15}H_{26}O$	12.57	Globulol
8	24.20	222	$C_{15}H_{26}O$	18.36	Veridiflorol
9	24.35	177	C_9H_7NOS	1.03	5-(2'-Thienyl)pyrrole-2-carbaldehyde
10	24.44	232	$C_{15}H_{20}O_2$	4.71	Cyclopropa[c,d]pentalene-1,3-dione,hexahydro-4-(2-methyl-2-propenyl)-2,2,4-trimethyl
11	24.65	222	$C_{14}H_{22}O_2$	3.62	2-Heptanone,6-(3-acetyl-2-methyl-1-cyclopropen-1-yl)-6-methyl
12	24.90	164	$C_{12}H_{20}$	5.35	1H-Indene,1-ethylideneoctahydro-7a-methyl
13	25.01	222	$C_{15}H_{26}O$	2.95	Cubenol
14	25.11	290	$C_{19}H_{30}O_2$	0.69	Methyl 8,10-octadecadiynoate
15	25.32	222	$C_{15}H_{26}O$	2.35	1,4-Methanoazulen-7-ol, decahydro-1,5,5,8a-tetramethyl
16	25.61	222	$C_{15}H_{26}O$	1.36	α-acorenol
17	27.02	220	$C_{15}H_{24}O$	2.79	Isoaromadendrene epoxide
18	27.57	232	$C_{15}H_{20}O_2$	3.33	(-)-oxidoselina-1,3,7(11)- trien-8-one
19	27.67	324	$C_{23}H_{32}O$	0.70	2-[4-methyl-6-(2,6,6-trimethylcyclohex-1-enyl)hexa-1,3,5-trienyl]cyclohex-1-en1-Carboxaldehyde
20	28.31	254	$C_{16}H_{30}O_2$	0.76	9-Hexadecenoic acid
21	28.43	310	C22H46	5.31	Docosane
22	28.62	254	$C_{15}H_{26}O_3$	1.08	Perhydrocyclopropa[e]azulene-4,5,6-triol,1,1,4,6-tetramethyl
23	29.04	270	$C_{17}H_{34}O_2$	1.56	Isopropyl myristate
24	29.14	292	$C_{19}H_{32}O_2$	2.52	Methyl3-cis,9-cis,12-cis-octadecatrienoate
25	29.42	268	$C_{18}H_{36}O$	1.07	2-Pentadecanone, 6,10,14-trimethyl-
26	29.73	285	$C_{19}H_{14}O$	1.92	6-methyl-7(12h)-benz[a]anthracenone
27	31.03	270	$C_{17}H_{34}O_2$	2.50	Pentadecanoic acid, 14-methyl-, methyl ester
28	34.13	422	C30H62	1.18	Triacontane
29	34.28	314	$C_{19}H_{38}O_3$	1.59	Octadecanoic acid,4-hydroxy-, methyl ester
30	34.50	296	$C_{20}H_{40}O$	1.28	Phytol
T%				**97.66 %**	

R_t: Retention time; M.W.: Molecular Weight; M.F.: Molecular Formula

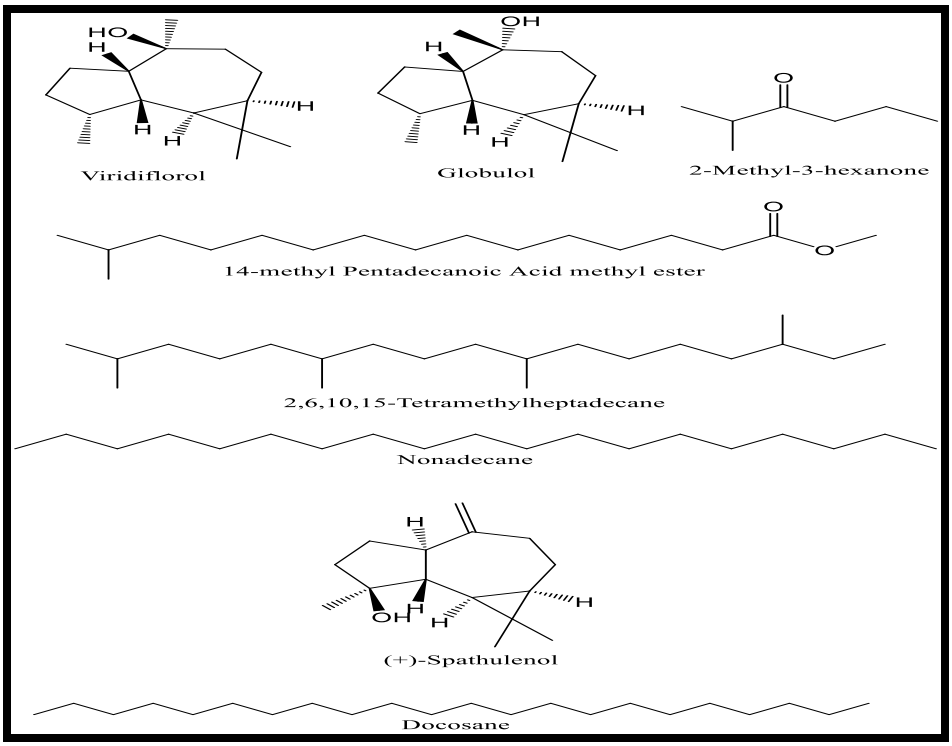

Figure 5. Chemical structures of the major biochemical compounds identified by GC/MS analysis from the methanolic extract of *Syzygium gratum* and *Melaleuca armillaris*.

References:

[1] Ghareeb M A, Habib M R, Mossalem H S, and Abdel-Aziz M S 2018 *Bull. Natl. Res. Cent. (Egypt)*. **42** 1.
[2] Hamed M M, Ghareeb M A, Shafei A A, Abdel-Aziz M S, and Tolba S S 2019 *PharmacologyOnline*. **1** 221.
[3] Ghareeb M A, Saad A M, Abdel-Aleem A H, Abdel-Aziz M S, Hamed M M, and Hadad A H 2016 *Der Pharma Chem.* **8** 277.
[4] Ghareeb M A, Ahmed W S, Refahy L A, Abdou A M, Hamed M M, and Abdel-Aziz M S 2016 *Pharmacologyonline*. **3** 157.
[5] Hathout A S, EL-Neekety A A, Abdel Aziz M S, Sabry B A, Hamed A A, Ghareeb M A, and Aly S E. 2016 *J. Appl. Pharm. Sci.* **6** 001.
[6] El-Neekety A A, Abdel-Aziz M S, Hathout A S, Hamed A A, Sabry B A, Ghareeb M A, Aly S E, and Abdel-Wahhab M A. 2016 *Der Pharma Chem*. **8** 121.
[7] Madkour H M F, Ghareeb M A, Abdel-Aziz M S, Khalaf O M, Saad A M, El-Ziaty A K, and Abdel-Mogib M. 2017 *J. Appl. Pharm. Sci.* **7** 023.
[8] Saad A M, Abdel-Aleem A H, Ghareeb M A, Hamed M M, Abdel-Aziz M S, and Hadad A H. 2017. *J. Appl. Pharm. Sci.* **7** 141.
[9] Abdel-Aziz M S, Ghareeb M A, Saad A M, Refahy L A, and Hamed A A, 2018 *Acta Chromatogr.* **30** 243.
[10] Khalaf O M, Ghareeb M A, Saad AM, Madkour H M F, El-Ziaty A K, and Abdel-Aziz M S 2019 *Acta Chromatogr.*. **31** 138.
[11] Ghareeb M A, Hamed M M, Saad A M, Abdel-Aziz M S, Hamed A A, and Refahy L A. 2019 *Pharmacognosy. Res*. **11** 162.
[12] Ghareeb M A, Khalaf O M, Abdel-Aziz M S, Saad A M, Madkour H M F, El-Ziaty A K, and Refahy L A 2020 *Curr. Bioact. Compd*. **16** 308.
[13] Bassolé I H N and Juliani H R. 2012 *Molecules*. **17** 3989.
[14] Hasan N , Al Mamun , Belal H, Rahman A, Ali H, Tasnin N, Ara T, Rabbi A, Asaduzzaman M and Islam A 2016 *Int. J. Pharm. Sci. Res*. **1** 36.

[15] Ghareeb M A, Mohamed T , Saad A M, Refahy L A, Sobeh M and Wink M 2016 *J. Pharm. Pharmacol.* **70** 133.
[16] Ghareeb M A, Saad A M, Ahmed W S, Refahy L A, and Nasr S M 2018 *Pharmacognosy Res*. **10** 368.
[17] Ghareeb M A, Sobeh M , Rezq S , El-Shazly A M, Mahmoud M F, and Wink M. 2018. *Molecules*. **23** 3238.
[18] Sobeh M , Mahmoud M F, Hasan R A, Abdelfattah M A O, Sabry O M, Ghareeb M A, El-Shazly A M and Wink M 2018 *Sci. Rep*. **8** 9343.
[19] Boulanouar B, Gherib A, Bronze M R, and Ghareeb M A 2019 *Turk. J .Pharm Sci.* **16** 234.
[20] Ghareeb M A, Sobeh M , El-Maadawy W H, Mohammed H S, Khalil H, Botros S S, and Wink M . 2019 *Antioxidants*. **8** 415.
[21] Barbosa L C A, Silva C J, Teixeira R R, Meira R M S A and Pinheiro A L. 2013. *Agric. Conspec. Sci*.**78** 11.
[22] Silva J C, Barbosa L C A, Demuner A J, Montanari R M, Pinheiro A L, Iara Dias L and Andrade N J. 2010 *Quim. Nova*. **33** 104.
[23] Yao L , Jiang Y, Singanusong R , D'arcy B , Datta N, Caffin N and Raymont K. 2004 *Food Res. Int.* **37** 166.
[24] Yoshimura M , Ito H , Miyashita K , Hatano T, Taniguchi S, Amakura Y and Yoshida T. 2008 *Phytochemistry*. **69** 3062.
[25] Yao L, Jiang Y, Singanusong R, Datta N and Raymont K. 2005 *Food Res. Int*. **38** 651.
[26] Hussein S A M, Hashim A N M, El-Sharawy R T, Seliem M A, Linscheid M, Lindequist U and Nawwar M A M. 2007 *Phytochemistry*. **68** 1464.
[27] Tuiwawa S H, Crave L A, Sam C, and Crisp M D. 2013 *Blumea.* **58** 53.
[28] Chen J and Craven L A. *2015. Fruct. Sem. Pl*. **13** 1788.
[29] Djipa C D, Delmée M and Quetin-Leclercq J 2000 *J. Ethnopharmacol*. **71** 307**.**
[30] Chandrasekaran M and Venkatesalu V. 2004 *J. Ethnopharmacol*. **91** 105.
[31] Ghareeb M A, Hamed M M, Abdel-Aleem A H, Saad A M, Abdel-Aziz M S and Hadad A H 2017 *Asian. J .Pharm .Clin .Res.* **10** 194.
[32] Gordon A , Jungfer E , da Silva B A, Maia J G and Marx F. 2011 *J. Agric. Food Chem.* **59** 7688.
[33] Simirgiotis M J, Adachi S , To S , Yang H, Reynertson K A, Basile M J, Gil R R, Weinstein I B, and Kennelly E J. 2008 *Food .Chem*. **107** 813.
[34] Kasetti R, Nabi S, Swapna S and Apparao C. 2012 *Food Chem. Toxicol*. **50** 1425.
[35] Bauer A W, Kirby W M, Sherris J C, and Turck M. 1966 *Am. J. Clin. Pathol*. **45** 493.
[36] Ghareeb M A, Refahy L A, Saad A M, Osman N S, Abdel-Aziz M S, El-Shazly MA and Mohamed A S. 2015 *J. Appl. Pharm. Sci*. **5** 045.
[37] Shirwaikar A, Rajendran K and Punitha ISR. 2006 *Biol. Pharm. Bull*. **29** 1906.
[38] Soonthornchareonnon N, Wiwat C and Chuakul W 2012 *Mahidol University Journal of Pharmaceutical Science*. **39** 9.
[39] Al-Abd N M, Nor Z M, Mansor M, Azhar F, Hasan M S and Kassim M. 2015 *BMC Complement Altern. Med.* **15** 385
[40] Wigmore S M, Naiker M and Bean D C. 2016 *Phcog Commn*. **6** 80.
[41] Ghareeb M A, Saad A M, Abdel-Aleem A H, Abdel-Aziz M S, Hamed M M and Hadad A H. 2016 *Der Pharma Chem*. **8** 277.
[42] Ramli S, Radu S, Shaari K and Rukayadi Y. 2017 *Biomed Res. Int*. 1.
[43] Samie A, Obi CL, Bessong P O and Namrita L. 2005 *Afr. J. Biotechnol*. **4** 1443.
[44] Vieira T I, Gondim B L C, Santiago B M and Valença A M G. 2012. *RGO - Rev Gaúcha Odontol.,* **60** 359.
[45] Kumar M S and Yasmeen N. 2013 *Am. J. Adv. Drug Deliv*. **1** 628.
[46] de Oliveira G F, Furtado N A J C, Filho A A D, Martins C H G, Bastos J K, Cunha W R and Silva M L D. 2007 *Braz. J. Microbiol*. **38** 381.
[47] Abah K A, Owolabi A O and Oranusi S. 2017 *Journal of Industrial Research and Technology*. **6** 136.

[48] Ramadhania Z M, Insanu M, Gunarti N S, Wirasutisna K R, Sukrasno S and Hartati R. 2017 *Asian. J. Pharm. Clin. Res.* II-Indonesian Conference on Clinical Pharmacy. 5.
[49] Surh J and Yun J. 2012 *Prev. Nutr. Food. Sci.* **17** 22.
[50] Ghareeb M A, Refahy L A, Saad A M, Osman N S, Abdel-Aziz MS, El-Shazly MA, and Mohamed A.S. 2015 *J. Appl. Pharm. Sci*. **5** 045.
[51] Bhati G S, Vaidya X, Sharma P and Agnihotri A. 2017 *Int. J .Curr .Pharm. Res*. **9** 180.
[52] Eshwarappa R S B, Iyer R S, Subbaramaiah S R, Richard S A, and Dhananjaya B L. 2014 *BioImpacts.* **4** 101.
[53] Madkour H M F, Ghareeb M A, Abdel-Aziz M S, Khalaf O M, Saad A M, El-Ziaty A K, and Abdel-Mogib M 2017. *J. Appl. Pharm. Sci*. **7**: 023.
[54] Abdel-Wareth M T A, El-Hagrassi A M, Abdel-Aziz M S, Nasr S M and Ghareeb M A. 2019 *Int. J. Environ. Stud*. **76** 780.
[55] Shawky B T, Nagah M , Ghareeb M A, El-Sherbiny G M, Moghannem S A M , and Abdel-Aziz M S. 2019 *J. Renew. Mater*. **7** 667.
[56] Sathyanarayanan S, Chandran R, Thankarajan S, Abrahamse H and Thangaraj P 2018. *J. Food Sci. Technol.* **55** 341.
[57] Al-Abd N M, Nor Z M, Mansor M, Azhar F, Hasan M S and Kassim M. 2015 *BMC Complement Altern. Med.* **15** 385.

Adsorption Studies of Cobalt (II) Complex By Bentonite clay surface

Adsorption Studies of Cobalt (II) Complex By Bentonite clay surface

Sahira S. Abd-Ulrazzaq[1], Farah A. Dawood[2], Ahmed T. Numan[1]

[1]Department of Chemistry, College of Education for Pure Science-Ibn Al-Haitham, University of Baghdad.
[2]Department of Medical Laboratory Technique, Al-Nisour University college.

*E-mail: farah.a.path@nuc.edu.iq

Abstract. This paper is summarized with one of the applications of adsorption behavior; A UV-Vis method has been applied to survey the isotherm of adsorption. Results for experimental showed the applicability of Langmuir equation. The effect of temperature on the adsorption of cobalt (II) Complex by bentonite surface was studied. The results shown that the amount of adsorption was formed to increase, such as the temperature increase (Endothermic process). Cobalt (II) Complex has adsorption studies by bentonite surface at different pH values (1.6-10); these studies displayed an increase in adsorption with increasing pH.
ΔG, ΔH, and ΔS thermodynamic functions of the cobalt (II) Complex for their adsorption have been calculated.

Keywords: Adsorption, Langmuir , cobalt (II) Complex, ethanol, bentonite.

1. Introduction

Heavy metals have a high effect on plants, animals, and public health. Heavy metals are also more toxic than other metals [1]. Harmfulness of heavy metals is a part of being dangerous for living organisms when overdoing the particular limits. The existence of heavy metals in nature may be influence biodegraded, producing health problems for animals, plants, and humans [2,3].

Inorganic waste of the industries always has heavy metals like Co, Ni, Cu, Zn, and Cd, etc., which tend to collect in the chain for food [4]. That is related to their high solubility in the aquatic medium, as well as; toxic metals can be adsorbed by living organism. When these metals come into the food chain for one time which it may be concentrate and collect in the human body [5].

The removal of toxic metals, like cobalt, from wastewater, is fundamental and good for human health and the environment. Sharp effects of acute cobalt injuring on humans life which can contain (asthmatic symptoms and harm for heart, thyroid, and liver). At higher concentrations of (cobalt), it

may be too caused (genetic mutations in living cells), accenting the requirement for increasing consciousness of the problems related to cobalt toxicity [6].

The removal processes of metal, such as adsorption, it is too important. This process is inexpensive, simple, and more active than the other techniques, like (solvent extraction, electrolytic processes, chemical precipitation, ion-exchange, membrane separation, reverse osmosis, or biological systems) [7]. The molecule formula of bentonite is ($Mg_2Al_{10}Si_{24}O_{60}(OH)_{12}$[Na, Ca]), [8].

In this paper, we have examined the probability of the adsorption of various concentrations of cobalt (II) complex on to (bentonite) clay surface in various (pH solution), and the various temperature was studied.

2. Materials & Methods

2.1. Synthesis:

2.1.1. Synthesis of the ligand [(H_2L)[4-(5,5-dimethyl-3-oxocyclohex-1-enylamino)-N-(5-methylisoxazol-3-yl) benzene sulfonamide].

The preparation of the ligand (H_2L) was carried out according to the published procedure in literature [9], by fusing of sulfamethoxazole and dimedone at (140) ºC for 1/2 hour.

2.1.2.Synthesis of cobalt (II) Complex [Co(H_2L)(HA)]

The metal solution of $CoCl_2.6H_2O$ (0.061g,0.26mmole) was dissolved in (10) ml ethanol, and it was stirred for ten minutes. The H_2L ligand solution (0.1g, 0.026mmole) in (10) ml ethanol after accustomed for pH=8 using few drops of KOH solution was added to the metal solution. Finally, a solution of 3-amino phenol(HA) (0.03g,0.027mmole) in (10) ml ethanol was also added to the above metal solution. These results of the mixture were heated under reflux for (3) hrs. After that, the mixture was filtered. However, the precipitate was washed with an extra of ethanol and dried at room temperature for twenty-four hours. A bluish-green solid was acquired. Weight (0.13 g), yield (93.5%), m.p (>350 C°) dec. The synthesis route of the complex is shown in Figure 1. The microanalysis of results for the complex and some of its physical properties is given in Table 1.

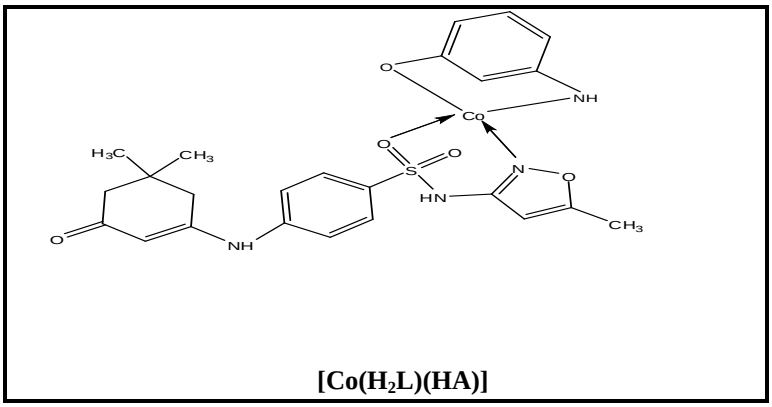

[Co(H_2L)(HA)]

Figure 1. A proposed structure of cobalt (II) Complex

Table 1. Microanalysis results and some physical properties for the cobalt(II) Complex

Empirical Formula	M.wt	Color	M.P (°C)	M Found, (Calc)%	Yield %	Λ_m S.cm^2 (molar^{-1})
[Co(H_2L)(HA)]	556.52	Bluish green	112	9.98 , (10.59)	93.5	17.02

M.P= melting point, Calc=calculated, M.wt = molecular weight,

2.2. Preparation of Clay Powder:

Bentonite clay sample having the (montmorillonite mineral). It was used as an adsorbent; it was obtained from (The General Company for Geological Survey and Mining, Baghdad, Iraq). Bentonite dried in an oven for 4 hours at 200ºC. The clay was ground and sieved by using (0.75 mesh). The results are listed in Table 2.

Table 2. the chemical analysis of bentonite

Constituent	SiO_2	Al_2O_3	CaO	Fe_2O_3	MgO	Na_2O	So_3	Losson ignition
Wt %	(54.66)	(14.65)	(4.77)	(4.88)	(6)	0.65	1.2	13.06

2.3. Preparation of Solutions:

2.3.1.Standard Stock Solution of cobalt (II) Complex solution (100 mg/L)

A standard stock solution of cobalt (II) Complex (100mg/L) was prepared by dissolving (0.01g) of [Co(H_2L)(HA)]in (3mL) of ethanol. The volumetric flask (100mL) was completed to the mark with an ethanol solvent.

2.3.2.Calibration Curve:

Cobalt (II) Complex solution of different concentration was prepared as mentioned in (3-4) by serial dilution absorbance values of these solutions were measured at the specified (λ_{max} = 477 nm) value for cobalt (II) Complex and plotted versus the concentration values as in Figure (2). These results were treated by (Least Square method). Concentration (2.5-100 mg / L) that obeys Beer- Lambert's law was then used in subsequent quantitative estimation of the concentration. Quantities of cobalt (II) Complex adsorbed were determined by Visb-spectrophotometric technique.

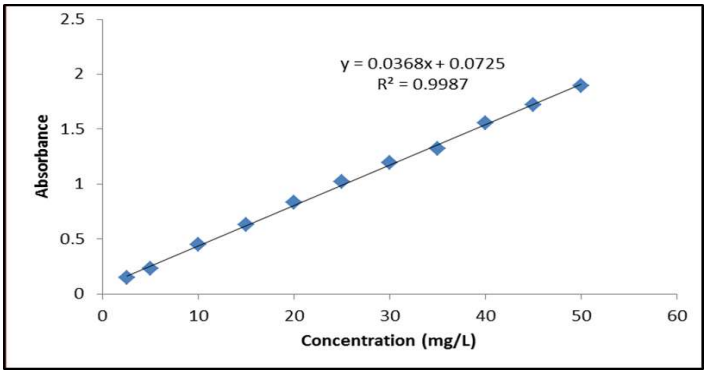

Figure 2, Calibration curve of cobalt (II) Complex solution

3. Results and Discussion

The synthesized cobalt (II) Complex [Co(H2L)(HA)] has been characterized by FT-IR, (C.H.N), UV-Vis spectroscopic methods[10-12]**.** [IR spectra of complex exhibited bands with convenient shifts due to complex figuration table (3) and (U.V-Vis) spectrum for the complex, Table 4 and Figure3.

Table 3. FT-IR spectral data (wave number υ) cm^{-1} of the cobalt(II) Complex

COMPOUND	υ(OH) PHENOL	υ(NH_2)	υ(S-NH)	υ(C-NH)	υ(C=N)	υ(C=O)	υ_{AS}(S=O) υ_{S}(S=O)	υ(CO–N)	υ(CO–O)
[H_2L]	–	_	3302	3205	1612	1571	1363 1137	_	–

LIGAND [HA]	3548	3362 3298	–	–	–	–	–	–	–
$[CO(H_2L)(HA)]$	–	_	**3301**	**3201**	**1629**	**1572**	**1328** **1163**	**543** **514**	**474** **437**

Table 4. Electronic spectral data of the cobalt(II) Complex

COMPOUND	WAVENUMBER		ε_{MAX} MOLAR^{-1} CM^{-1}	ASSIGNMENT	SUGGESTED STRUCTURE
	Nm	cm^{-1}			
$[CO(H_2L)(HA)]$	268	37313	1425	L.F	
	353	28328	1897	L.F	
	477	22371	1985	C.T	
	613	16313	685	$^4A_2 \rightarrow {}^4T_2$ (F)	
	679	14727	913	$^4A_2 \rightarrow {}^4T_1$ (F)	

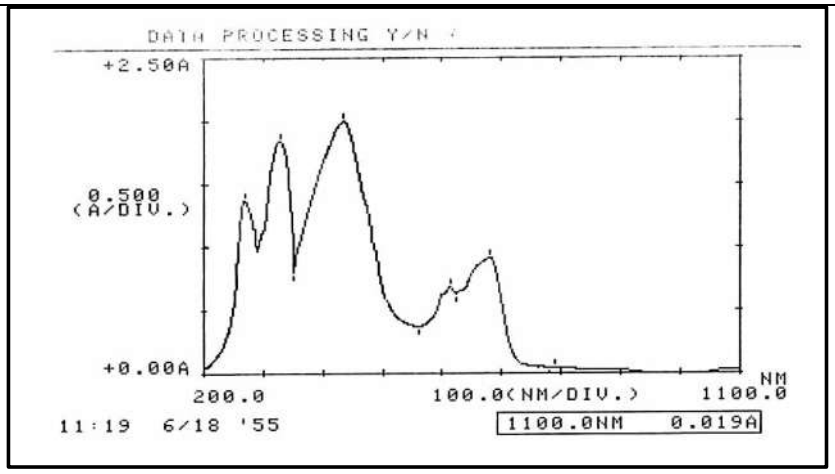

Figure 3. Spectrum of cobalt(II) Complex solution shows λ_{max} at(477) nm

3.1.Effect of shaking time on equilibrium adsorption system

The time that is sufficient for the adsorption operation to reach equilibrium at 25 C°, $C_\circ$ = 50 mg /L and Particle size = 75 µm has been studied. Table (5) shown the time intervals needed for each pair of adsorbent – adsorbant to attain equilibrium.

Table 5. Equilibrium time for each adsorbent –adsorbant pair

C_o (mg/L)	Time (minute)	C_e (mg/L)	Equilibrium Time (minute)
50	15	15.29	75
	30	11.92	
	45	10.69	
	60	10.67	
	75	11.68	
	90	11.68	
	120	11.68	

3.2.Adsorption of cobalt (II) Complex $[Co(H_2L)(HA)]$

The adsorption cobalt (II) Complex from ethanol solution on bentonite has been studied initially at room temperature (25)C° as well as at (10,37.5 and 50) C°**.** Table 6 shown the related results by the first concentration of cobalt (II) Complex, the equilibrium concentration (C_e), and the quantity adsorbed on clay (Q_e).The results shown an increase in adsorptive capacities of the clay as the concentration of cobalt(II) Complex Increased until reaching a limited value [13].

Table 6. adsorption values of cobalt (II) Complex ,on bentonite surface at various temperatures

C_o (mg/L)	10°C			25°C			37.5°C			50°C		
	C_e (mg/L)	Q_e (mg/g)	C_e/Q_e (g/L)	C_e (mg/L)	Q_e (mg/g)	C_e/Q_e (g/L)	C_e (mg/L)	Q_e (mg/g)	C_e/Q_e (g/L)	C_e (mg/L)	Q_e (mg/g)	C_e/Q_e (g/L)
5	0.0211	0.1659	0.127185	0.0135	0.1662	0.081227	0.1766	0.1607	1.098942	0.6114	0.1462	4.181943
10	0.5298	0.3156	1.678707	0.0679	0.3311	0.205074	0.3941	0.3201	1.231178	0.7744	0.3075	2.518374
15	2.1603	0.4279	5.048609	0.6282	0.479	1.311482	0.9987	0.4796	2.08236	2.0027	0.3999	5.008002
20	3.7635	0.5412	6.953991	1.5941	0.6135	2.59837	2.1875	0.5937	3.684521	3.6821	0.5439	6.769811
25	5.8016	0.6399	9.066417	3.2364	0.7254	4.461538	3.2744	0.7241	4.522027	5.4755	0.6508	8.413491
30	8.1611	0.7279	11.21184	5.0701	0.8309	6.101938	4.7146	0.8428	5.593972	6.9429	0.7685	9.034353
35	9.8854	0.8371	11.8091	7.1321	0.9289	7.678006	5.8288	0.9723	5.994858	8.6548	0.8781	9.856281
40	11.3862	0.9537	11.93897	9.2114	1.0262	8.976223	7.4222	1.0792	6.877502	10.0951	0.9968	10.12751
45	12.7635	1.0412	12.25845	10.8016	1.1399	9.475919	8.9733	1.2142	7.390298	11.6441	1.1118	10.4732
50	14.4972	1.1834	12.25046	12.6821	1.2439	10.19543	10.6114	1.3129	8.082413	13.6005	1.2133	11.20951

3.3.Adsorption Isotherm

In figure (4) the general shape of cobalt (II) Complex adsorption isotherms, when (Q_e) is a function to (C_e) among (10- 50 C^o)]**.** The isotherm of cobalt (II) Complex on bentonite consistent with shape (L_1- type) on (Giles classification). The isotherm of the mentioned system obeyed Langmuire equation leading to the assumption of high adsorption affinity between the cobalt (II) Complex and the clay surface in addition to the formation of one adsorption layer of cobalt (II) Complex on the clay surface[14]. The data of experimental adsorption were applied to both the empirical Freundlich equation and the theoretical Longmuir isotherm equation]. These results indicated the applicability of Longmuir isotherm as shown by the linear relationship of (C_e / Q_e) versus (C_e), Figure (5). The Langmuir constant empirical values (Qmax) (maximum adsorption capacity), (Ka) (energy of adsorption), and correlation coefficients of cobalt(II) Complex by bentonite surface was obtained from the linear equation at different temperatures. The values are summarized in Table 7. The results showed that the maximum adsorption capacity (Qmax) of cobalt(II) Complex by bentonite (increased when temperature increase), showing that (Qmax) enhanced at higher (T). The energy of adsorption (Ka) is enhanced (10 and 25 C^o) more than (37.5 and 50 C^o) by bentonite surface.[15-16].

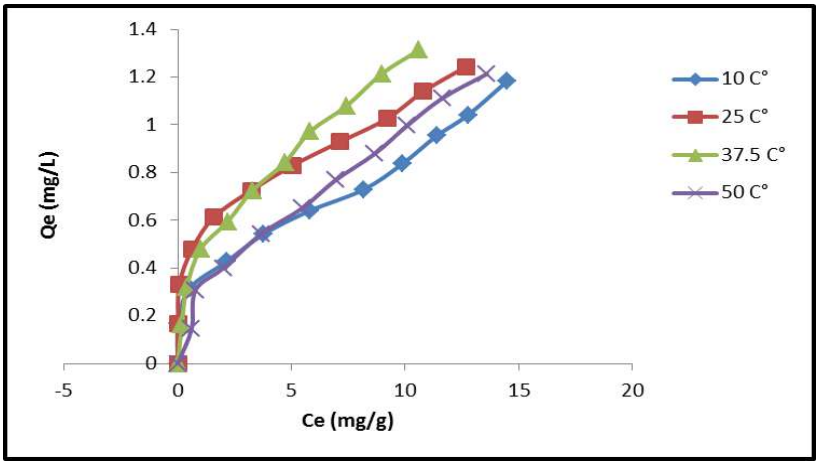

Figure 4. Adsorption isotherm of cobalt (II) Complex on bentonite surface at various T

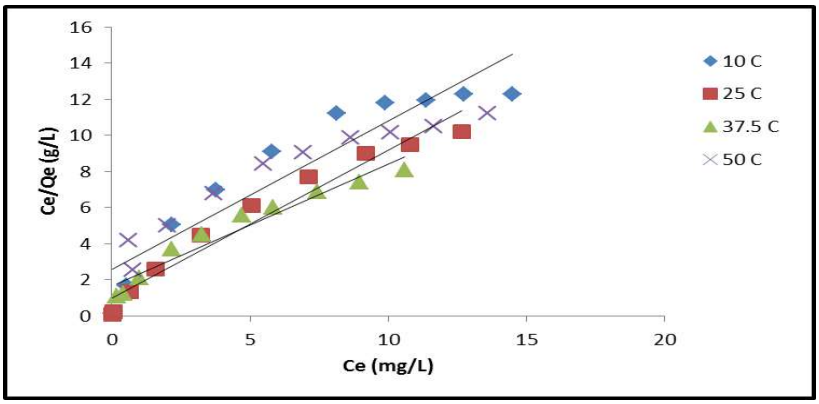

Figure 5. the linear form of Langmuir isotherm of cobalt (II) Complex on bentonite surface at different temperatures

Table 7. the Longmuir constant empirical values and the correlation coefficients for the adsorption of cobalt (II) Complex by bentonite surface at different temperature

Temperature (°C)	Q_{max} (mg/g)	Ka (L/g)	R^2
10.0	1.2153	0.3215	0.8752
25.0	1.2235	0.8288	0.9586
37.5	1.4830	0.4087	0.9468
50.0	1.6246	0.1598	0.9034

3.4.Effect of temperature on adsorption

The effect of temperature on the adsorption extent of cobalt (II) Complex by bentonite has been studied. Table (6) and Figure (4) illustrate data and general shapes of cobalt (II) Complex adsorption at (10, 25, 37.5, and 50 C°). The results showed an increase in the amount of cobalt (II) Complex adsorbed by bentonite with increasing temperature.Hence the adsorption process appeared endothermic. This means the interaction between bentonite and the cobalt (II) Complex requires appreciable energy in order to take place [17].Endothermic cobalt (II) Complex uptake may also be explained as a result of probable (absorption process), in which the ions diffuse inside the crystal lattice of the clay and (the diffusing speed increase with increasing of temperature). (This behavior referred to the absorption process, which means that the absorption process may come accompanied by an adsorption process) [18]. It can also explain the increase in the amount of cobalt (II) Complex adsorbed by bentonite with increasing temperatures according to the effect of temperature on the weak bonds between the

clay platelets. Bentonite is consist of three platelets of aluminum –silicate connect to one another by weak bonds, so the increase in the temperature may be broken these weak bonds that lead to a change in the geometry of the pore of the clay, causing an increase in adsorption extent as a result of an increase in surface area of the clay [13].The study of the temperature effect on adsorption of cobalt (II) Complex by bentonite will help in evaluating the basic thermodynamic function Free energy (ΔG), Enthalpy (ΔH), and Entropy (ΔS) of the adsorption process.

The change in free energy (ΔG^o) could be determined from the equation [19].

$$\Delta G^o = -RT\ln K \quad (1)$$

Where

ΔG^o : the standard free energy of change ($K.J.mole^{-1}$).

R: the gas constant ($8.314\ J.mol^{-1}.deg^{-1}$).

K: the thermodynamic equilibrium constant [20].

$$K = \frac{Q_e(mg/g)}{C_e(mg/g)} \quad (2)$$

Xm: the maximum value of the equilibrium concentration (Ce) (mg of adsorbate per liter of solution).

Ce: the equilibrium concentration of the adsorbate expressed in (mg) per one liter of solution

Q_e : the quantities adsorbed on bentonite

The heat of adsorption (ΔH^o) may be obtained from the equation [20].

$$\ln k = \frac{-\Delta H}{RT} + \text{Constant} \quad (3)$$

The change in entropies (ΔS^o) was calculated from the Gibbs equation:

$$\Delta G^o = \Delta H^o - T\Delta S^o \quad (4)$$

Table (8) gives K values at different temperatures plotting (lnK) versus (1/T) should produce a straight line with a slop = (-ΔH/R) as shown in Figure (6).Table (9) shown the basic thermodynamic values of cobalt (II) Complex adsorption by bentonite surface at different temperatures.[The positive values of (ΔH^o) indicate the endothermic nature of the process while the positive (ΔS^o) corresponds to increase the disorder of the system increase, the negative values of (ΔG^o) confirm the feasibility of the process and the spontaneous nature of sorption][8].

Table 8. effect of temperature on the thermodynamic equilibrium constant for adsorption of cobalt (II) Complex by bentonite surface

C_e (mg/L)	T(°C)	T(K)	1/T (K^{-1})	Q_e (mg/g)	Equilibrium constant (K)	l n Q_{max}	LnK
10.6	10.0	283.0	0.003534	0.96	72.4528	-0.0408	4.2829
	25.0	298.0	0.003356	1.12	84.5283	0.1133	4.4370
	37.5	310.5	0.003221	1.32	99.6226	0.2776	4.6013
	50.0	323.0	0.003096	1.08	81.5094	0.0769	4.4007

Table 9. [values of a thermodynamic function for the adsorption of cobalt (II) Complex by bentonite surface at different temperatures]

ΔG ($kJ.mol^{-1}$)	ΔH ($kJ.mol^{-1}$)	ΔS ($J.mol^{-1}.K^{-1}$)
-8.7227	+ 2.3559	+ 39.1471
-10.2541		+ 42.3154
-10.3499		+ 40.9204
-10.3335		+ 39.2860

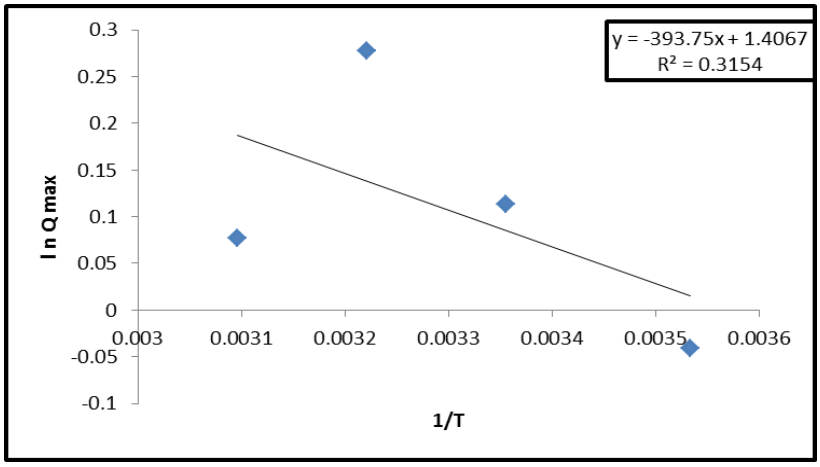

Figure 6 . plot of ln K against reciprocal absolute temperature for adsorption of cobalt (II) Complex by bentonite surface

3.5.Effect of pH on the adsorption

The effect of pH on the adsorption of cobalt (II) Complex with the clay (bentonite) in different media (pH =1.6-10) has been studied using a fixed concentration at 25 C^{o} . Figure (7) (demonstrate the influence of pH on the adsorption).

The results showed an (increase in adsorption quantities of cobalt (II) Complex on clay surface with increasing pH values of the solution).The amount of absorbent material is low in the acid medium and then increases in the base medium. This was due to the fact that the complex was unstable in the strong acid circles. The complex tends to decompose and thus reduces the amount of adsorption. In the base medium, the complex was stable, and thus the amount of adsorption increases (the surface becomes saturated) [13].

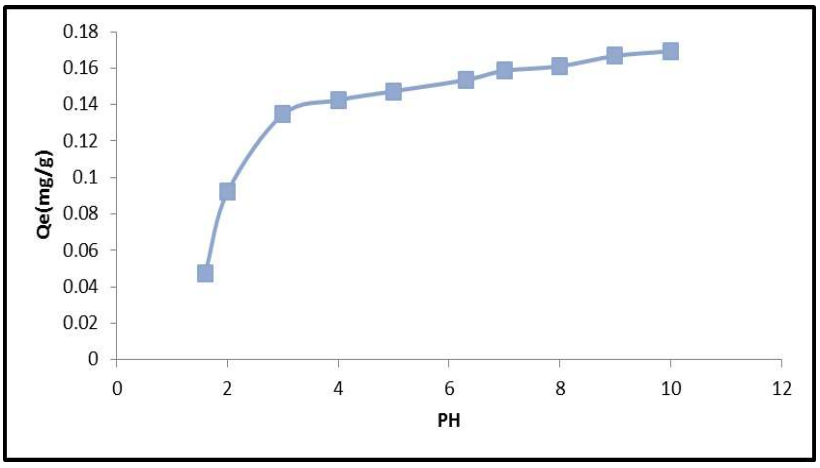

Figure 7 . Effect of pH on adsorption of cobalt (II) Complex by bentonite surface at 25 ^{o}C

References

[1] Muthukrishnan, M.; Guha, B.K.; 2006,"Heavy metal separation by using surface modified nanofiltration membrane"; Desalination, 200, pp:351.
[2] Saravanan, A.; Brindha, V.; Manimekalai, R.; Krishnan, S;2009 ,*Indian J. Sci. Tech*., **2** (1), pp:53.
[3] Ong, S.; Seng, C.; Lim, P.; 2007,*J. Environ. Agric. Food Chem*., **6** (2), pp:1764.
[4] Kurniawan, T.A.; Chan, G; 2006, *Chem. Eng. J*., **118**, pp:83.
[5] Panneerselvam, P.; Bala, V.S.S.; Thiruvengadaravi, K.V.; Nandagobal, J.; Palanichamy, M.; Sivanesan, S.; 2009, *Indian J. Sci. Tech.*, **2** (2), pp:63.
[6] Rengaraj S, Moon SH. 2002 ,*Water Res*. **36**,pp:1783.
[7] Eleonora ,S, Jan,K, 2013 , *J. Environ. Chem. Eng.*,.**1** ,pp:581.
[8] Asmaa ,K.A, 2011, Baghdad Sci. J., **8**(4).
[9] Ahmed T. N, Sahira S. A, Farah A. D, 2016 , *IHJPAS.*, **29** (1) .
[10] Jaina ,B. Malikb,S. Sharmaa, N. and Sharma,S.,2013, *Der Chemica Sinica*, **4**(5),pp:40.
[11] kindeel, A.S.,Dawood, I.J. and Aziz, M.R.,2013" *J. Baghdad for Sci*., **110**(2), pp:396 .
[12] Halli, M.B., Patil, V.B., Sumathi R.B. and Mallikarjun,K,2012, Der Pharma *Chem*,**4**(6), pp:2360.
[13] Alaa.F. H, Moen .I.Al-Jeboori , Hamsa, M.Y, 2008, *Iraqi National Journal of Chemistry*, **30**,pp:229.
[14] Giles, C.H,and Smith D. 1974, *J. Colloid and Interface Science*, **47**, 3, pp:755 .
[15] Yavus et al 2003,*water Res*., **37**, pp:948.
[16] Hors fall et al 2003, *waste Biomass* "1994 Afr .J.Biotechnol., **2**(10), pp:360.
[17] Kapoor K.L. "A Text Book of Physical Chemistry ", Macmillam India Limited , India ,pp:449.
[18] Rozaini, C.A.; Jain, K.; Oo, C.W.; Tan, K.W.; Tan, L.S.; Azraa, A.; Tong, K.S.;2010 , *Int. J. Chem. Eng. Appl.*, **1** (1), pp:84.
[19] Areej. A. J, Mahasin. F. A and Karim. H. H, 2014, *ANJS*,**17** (1),pp:32.
[20] Moreno, J.C.; Gomez, R.; Giraldo, L.; 2010 ,*Materials*, **3**, p:452.

Preparation of Mixed ligand Complexes of Heterocyclic Azo Quinoline Ligand and Imidazole Molecule with Some of Divalent Transition Ions and their Biological Activity Against Multi Drug Resistance Pathogenic Bacteria

Preparation of Mixed ligand Complexes of Heterocyclic Azo Quinoline Ligand and Imidazole Molecule with Some of Divalent Transition Ions and their Biological Activity Against Multi Drug Resistance Pathogenic Bacteria

Israa N.Witwit [1*], Hawraa M.Farhan [2] Zahraa Y.Motaweq[3]

[1,2] Dept. of Chemistry, Faculty of Science, University of Kufa , Najaf , Iraq
[3] Dept. of Biology, Faculty of Science, University of Kufa , Najaf , Iraq

*E-mail :israa.witwit@uokufa.edu.iq

Abstract. Heterocyclic azo compound 2-(8-quinolyl azo)-4,6-dimethyl phenol as a primary ligand and imidazole molecule as a secondary ligand in the basic medium were prepared with novel mixed ligand complexes of Hg(II), Mn(II), Ni(II), Co(II) and Cu(II) ions, these compounds were characterized by Mass, 1HNMR, IR, UV-Vis, Magnetic susbtibility and Molar Conductivity, which suggested octahedral conductivity. Free ligands and five mixed ligand complexes of Hg(II), Mn(II), Ni(II), Co(II) and Cu(II) metal ions with a general formula of [M(L1)(L2)2Cl] against eight pathogenic multidrug resistance bacteria, six G-ve bacteria (Pr. mirabilis, S. typhi, E. coli, P. aeroginosa, A. baumanii and K. pneumoniae) and two G+ve bacteria (E. faecalis and S. aureus) were capable of antimicrobial efficacy. The findings show that free ligands have had stronger antibacterial activity on S. Bacterial isolation of typhi and P. aeroginosa relative to other isolates. As for the effectiveness of metal complexes, compared to G+ve bacteria, they usually have a large antibacterial effect on G-ve bacteria, whereas the Hg(II) ion complex has a higher antibacterial effect on most bacterial isolates compared to other metal complexes. Compared with other metal complexes, Mn (II) ion complexes demonstrated poorer antibacterial activity..

Key words: Imidazole, azo, mixed ligand complexes, MDR bacteria, biological activity.

1.Introduction :

In recent years, researchers have seen an interesting increase in the preparation of mixed ligand complexes, especially in the biological fields**[1].** These complexes contained high bioavailability ligands that prove their value, such as the imidazole molecule, known to be included in the structure of several biological systems such as histidine, in addition to its anti-bacterial and antifungal activity, imidazole was considered a monodintate ligand that coordinated through nitrogen number with various metal ions (3) [**2-4] .**

In several areas, such as quantitative, qualitative and biological research, Azo compounds have demonstrated their potential and significance**[5.6].** They were characterized by their stability and sensitivity, and also showed their skill in the field of coordination chemistry, especially heterocyclic azo ligands that are considered to be a remarkable form of quinoline compounds that act as di and tridentate ligands**[2,7.8].**

A global issue that threatens our ability to kill common infectious diseases is resistance to antimicrobial agents. It occurs naturally over time through genetic alterations or can occur in lower growth due to the

liveliness of unkilled bacteria [**9].** The guidelines recommended by the WHO are to prevent infections and prevent the prevalence of resistance, pathway resistant bacteria, to increase the use of current antibiotics and to promote the emergence of new antibiotics and to develop new diagnostic tests for resistant bacteria in order to avoid lethal diseases due to antibiotic-resistant bacteria. While several studies have been conducted in recent years to tackle multidrug-resistant microorganisms, further advances are still required to develop new and effective molecules in order to extend the antibiotic treatment options**[10].**
The goal of this study is to prepare new mixed ligand complexes by primarily using azo quinoline ligand and imidazole molecule as secondary ligand with five divalent ions Mn(II), Co(II), Ni(II), Cu(II) and Hg(II) than by testing their biological activity against eight pathogenic bacteria isolated from different clinical specimens that are multi-drug resistance.

2.Instruments and chemicals :
AB SCIEX 3200 QTRAP Mass Analyzer reported mass spectrum, while Shimadzu UV-1650 UV-Vis Spectrophotometer, Japan, and IR spectra performed electronic spectra on Shimadzu FTIR8400 by KBr disk in the region (400-4000) cm-1, Costech ECS Elemental 4010 measured element analysis, and 720(WTW) measured molar conductivity, 1HNMR spectra in the DMM spectra.

2.1. Main Ligand (QADMP) Preparation and Complexes:
The primary ligand (QADMP) was prepared by diazonation of 8-amino quinoline with 4,6-dimethyl phenol in the presence of (NaNO2) and hydrochloric acid at temperatures between (0-5)oC [11] as shown in scheme (1), while the complexes of metal ions were prepared by mixing (10) mmol of each metal ion chloride with (10) mmol of (QADMP) (L1) and (20) mmol of each metal ion chloride with (10) mmol of (M:L1:L2) (1:1:2) Table 1 describes the percentage of complexes and some of their physicochemical properties.

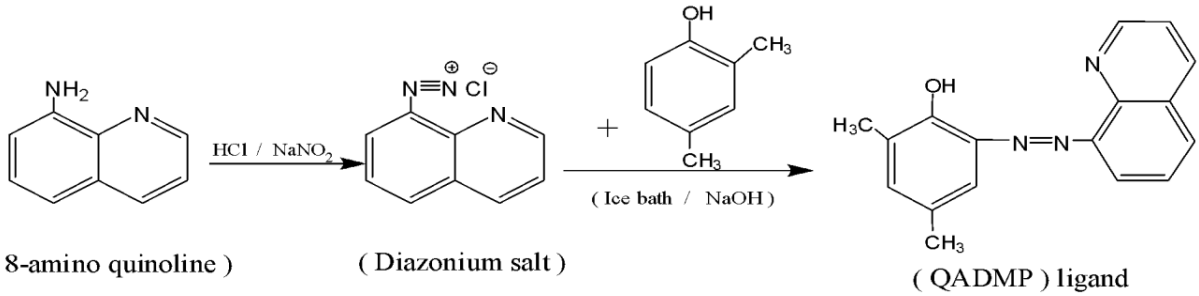

Scheme 1. Preparation reaction of primary ligand (QADMP)

2.2.Biological Activity
2.2.1.Collection and diagnosis of bacterial isolates:

The following multidrug resistance pathogenic bacterial isolates (MDR): six grams of bacteria (Proteus mirabilis, Salmonella typhi, Escherichia coli, Pseudomonas aeroginosa, Acinetobacter baumanii and Klebsiella pneumoniae) and two grams of bacteria (Staphyllococcus aureus and Enterococcus faecalis) were isolated from various clinical samples, such as burns, stools, synovial fluids, wounds, vomit, A variety of morphological as well as biochemical tests were used to diagnose isolates **[12],** which were later recently verified using the Vitek-2 compact system GP and GN card automatic bacterial recognition instrument. BHI broth supplemented with (15 percent) glycerol at (-20 °C) was stored on all bacterial isolates. On BHIA, the isolates were sub-cultivated and incubated for 24 hours at 37 ° C before use.

2.2.2.Preparation of ligands (L1) ,(L2), and the Complexes Concentrations:
The concentrations below were utilized in the biological activity test:
1- Free ligands concentrations: (0.02) gram of the powder of every ligands (L1) and (L2) has been dissolved in (1) ml of DMSO to yield (20) mg/ml concentration.
2- Mixed ligand complexes concentrations: (0.02) gram of powder of every mixed ligand complexes of the studied ions were dissolved in (1) ml of DMSO to yield concentration (20) mg/ml.

2.2.3.Antibacterial activity experimental

The preparation of bacterial suspensions was as Ramalivhana, *et al*. **[13]** explained. Agar well diffusion method was utilized to evaluate free ligand and mixed ligand ion complexes antibacterial activity versus bacterial isolates **[14] ..** MHA medium was utilized to evaluate the biological activity of free ligand and mixed ligand complexes of ions versus bacterial isolates.

2.2.4.Agar well diffusion assay

Bacterial isolate suspensions were prepared to match the normal 0.5 McFarland. Distribution of 100 µl of the BHIB bacterial suspension using the micropipette on the surfaces of the MHA layer. Wells were punctured using a sterile cork borer on all the culture plates. One of the wells was perforation in the center of the plate, adding 100 µl of Gentamicin as a positive control; adding 100µl of DMSO as a negative control in the other well; adding 100µl of free ligand and mixed ligand ion complexes alone, adding five wells to the [M(L1)(L2)2]Cl complexes in the residual wells. Then the cultivation plates were incubated at 37 ° C for 24 h. The clear inhibition zone around wells has been measured in mm. Testing was performed in triplicate **[15]** .

Table 1. Some of the physicochemical properties of ligands and their complexes

			Elemental Analysis Calcl. (Found)				
Empirical Formula	M.wt.	Yield(%)	C%	H%	N%	M%	m.p (°C)
$C_{17}H_{15}ON_3$ (L_1)	277	85	73.63	5.45	15.15	------	56-58
			(73.61)	(5.47)	(15.13)		
$C_3H_4N_2$ (L_2)	68.07	-	52.93	5.92	41.15	-------	90 - 92
			(52.91)	(5.90)	(41.14)		
$C_{23}H_{24}ClMnN_7O$	504.88	502.87	54.72	4.79	19.42	10.88	245-247
			(54.71)	(4.81)	(19.45)	(10.86)	
$C_{23}H_{24}ClCoN_7O$	508.88	84	54.29	4.75	19.27	11.58	259-261
			(54.30)	(4.73)	(19.25)	(11.61)	
$C_{23}H_{24}ClNiN_7O$	508.64	71	54.31	4.76	19.28	11.54	265-267
			(54.35)	(4.78)	(19.26)	(11.54)	
$C_{23}H_{24}ClCuN_7O$	513.49	81	53.80	4.71	19.09	12.38	271-273
			(53.82)	(4.70)	(19.05)	(12.40)	
$C_{23}H_{24}ClHgN_7O$	651.14	76	42.47	3.72	15.07	30.83	284-286
			(42.50)	(3.74)	(15.10)	--------	

3.Results and Discussion

Mass spectra of the (QADMP) (L_1) show molecular peak at m/z= 277.26 which is agreed with the molecular weight of the free ligand , mass fragmentation take two paths the first one started by losing (N_2) molecule at (250.24) that represented the mother peak , while the second path started by cleavage (-N=N-) bond to give two peaks at (m/z = 144.19) and (m/z=137.17) that due to the fragments which have molecular formula ($C_9H_8N_2$) and ($C_8H_{11}NO$) respectively , molecular peak in mass spectrum of Ni(II) complex appeared at m/z = 508.46 which was concerted with molecular weight of this complex the initial fragmentation was started by berk Cl^- ion from it , as shown in Figures 1 , 2 and schemes 2 , 3 **:**

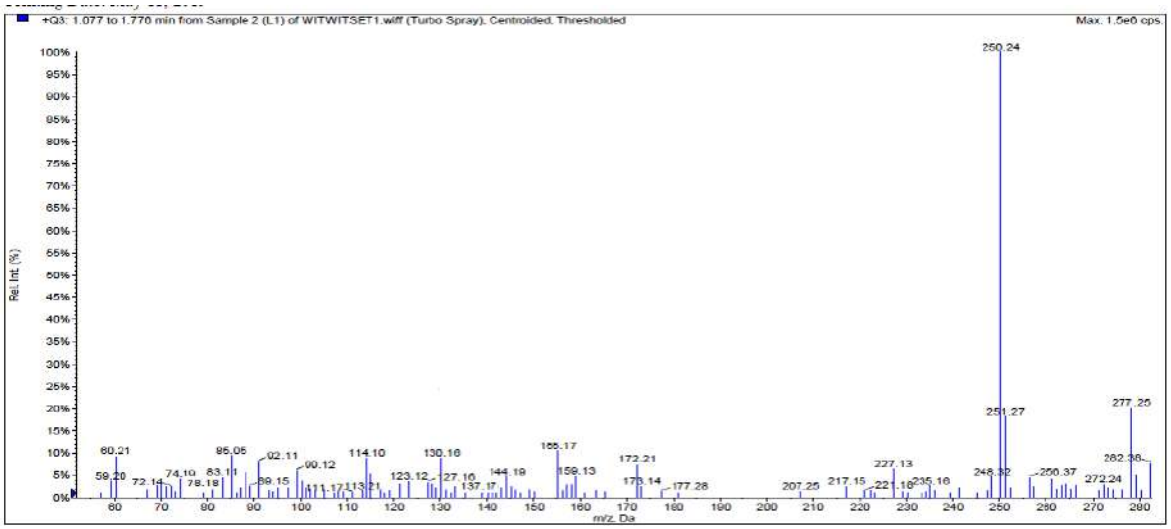

Figure 1. Mass spectrum of (QADMP) ligand

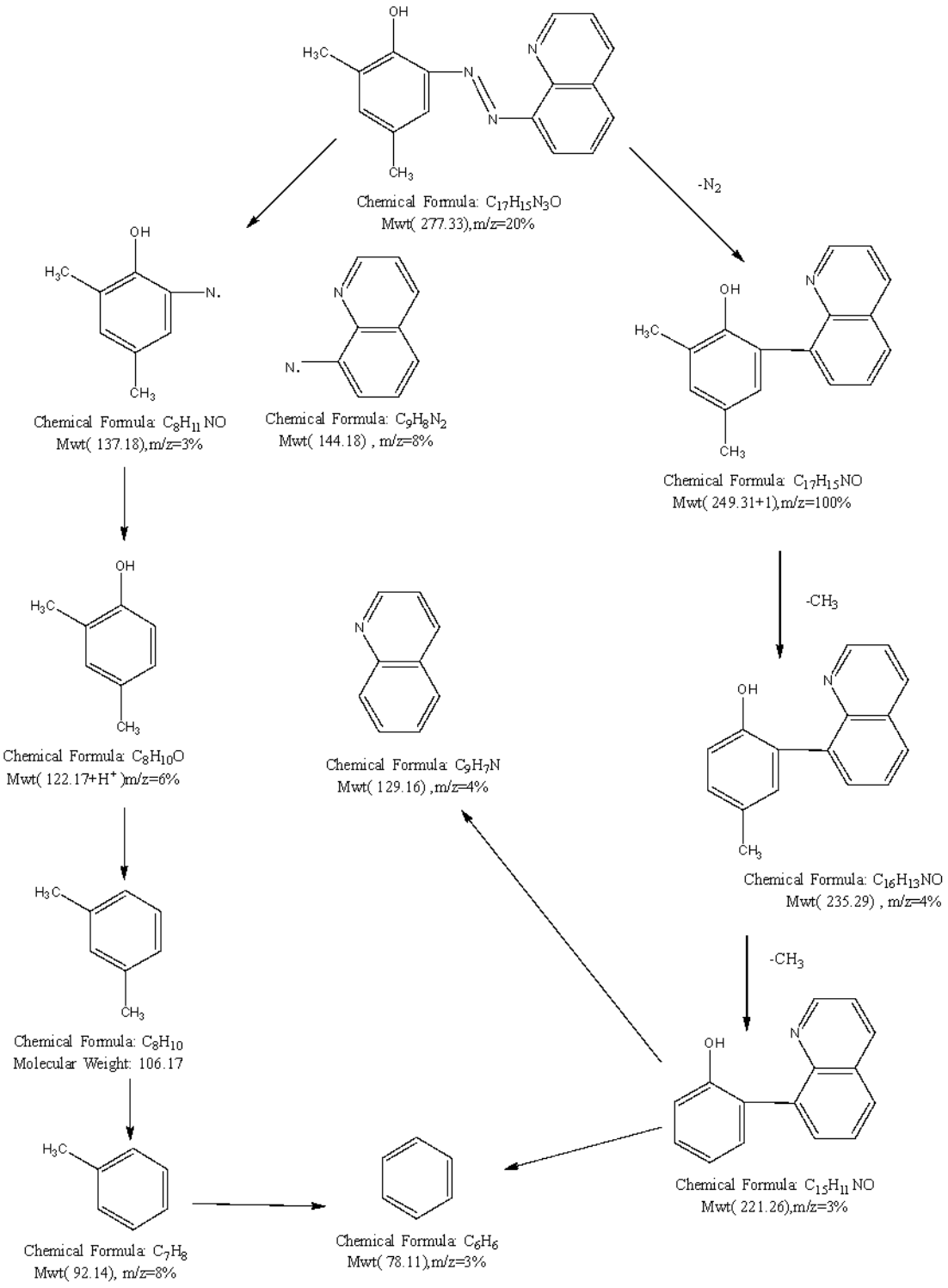

Scheme 2. Mass fragmentation of (QADMP) ligand

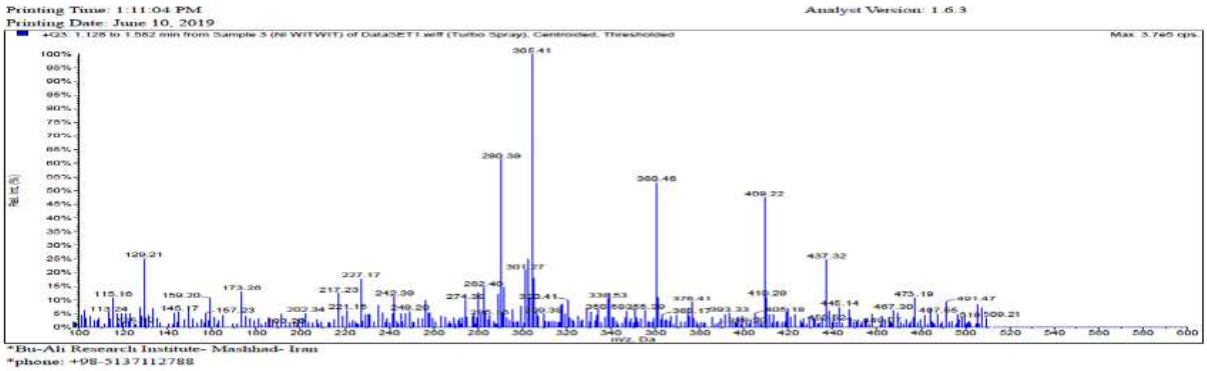

Figure 2. Mass Spectrum of Nickel (II) Complex

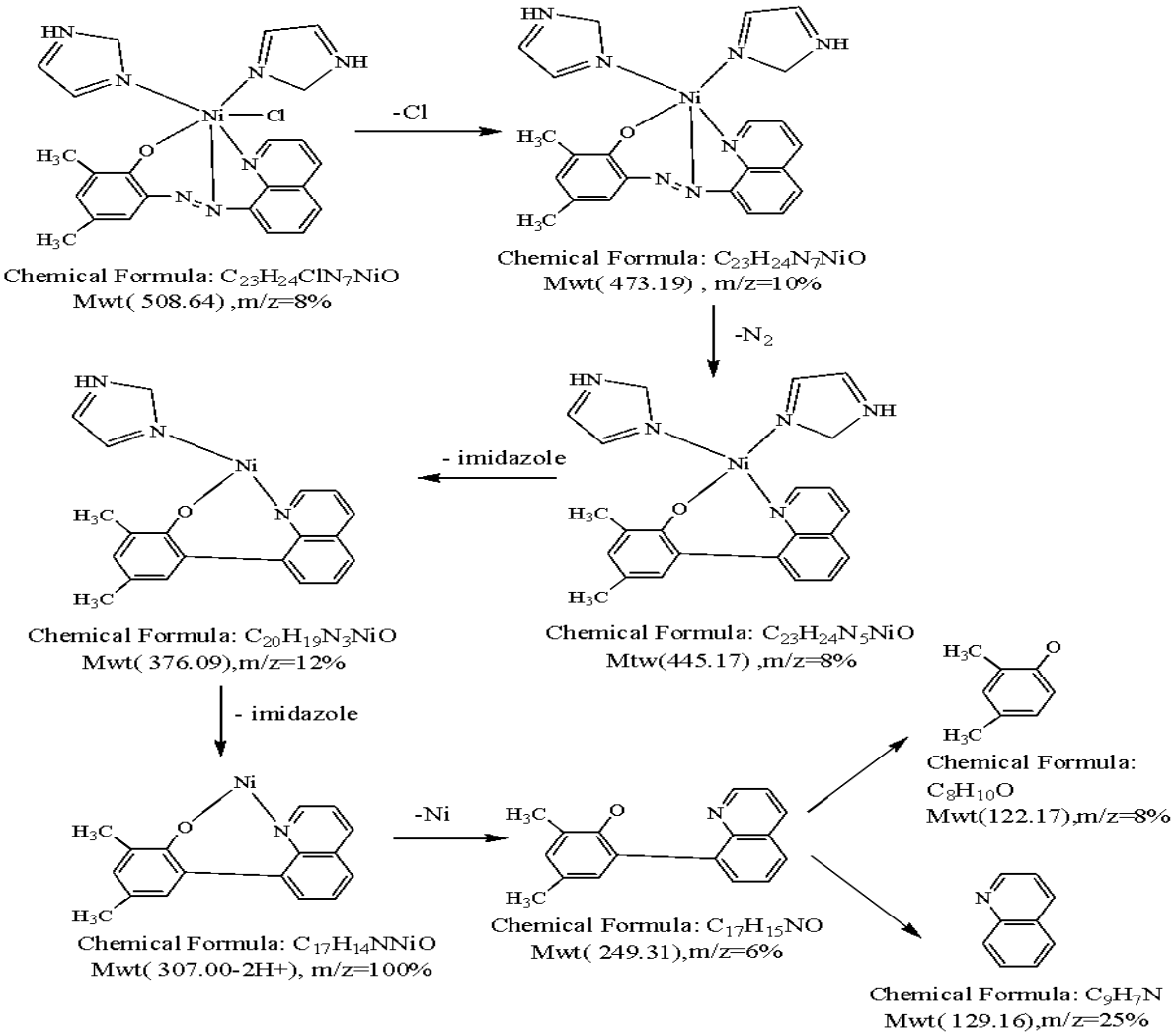

Scheme 3. Mass fragmentation of Ni(II) Complex

1HNMR spectra of primary ligand (QADMP) in DMSO solvent showed two singlet peaks at (2.46) ppm , and (2.62) ppm due to the protons of methyl groups (-CH3) , singlet peak at (5.58) ppm of (-OH) [11], while the peaks of aromatic protons appeared between (6.87-7.64) ppm **[16]** , Some changes found in 1HNMR spectra of Hg(II) complex a singlet peaks at (1.36) and (12.36) ppm for (H2) , and (H1) protons of imidazole ring appeared and absence of (-OH) peak as a result of it's coordination with metal ion after deprotonation , as shown in Figures (3 , 4 ') .

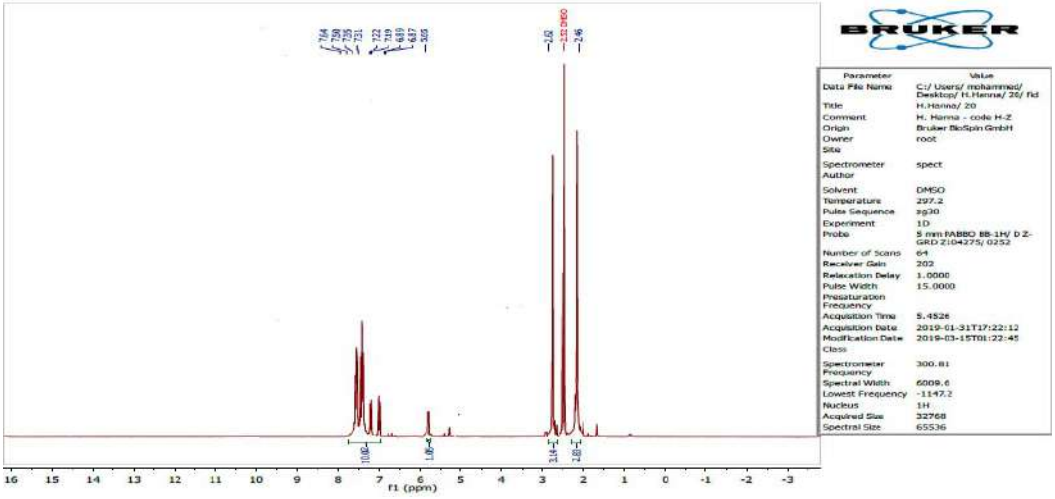

Figure 3 . [1]HNMR Spectra of primary ligand (QAMPD) in DMSO

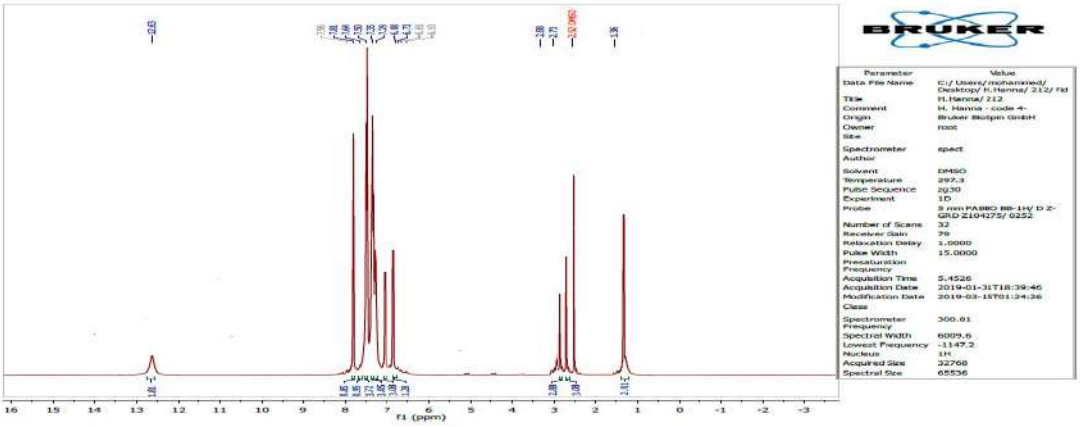

Figure 4. [1]HNMR Spectra of Hg (II) complex in DMSO

IR spectrum of free ligand (QADMP) (L_1) showed the v(C-O) [17] of phenolic group at (1265) cm^- which was shifted to lower wave numbers in the complexes , also the change in position and intensity of this bond in plane and out of plane was appeared in the complexes , these changes give an indicating of participation of (-OH) group after deprotonation in coordination process . The wave number in (1498)cm^- in (L_1) spectra due to *ν*(C-N=N-C) group [18] also shifted to lower wave numbers in the complexes which was indicted the coordination of this ligand through one of nitrogen atoms of azo group with each of metal ions , also the *ν* (C=N) of imidazole (L_2) [19] at (1541) cm^- showed red shift in the complexes that considered as an evidence for coordination of this ligand by (N3) atom , New peaks were appeared in the complexes refers to *ν*(M-O) and *ν*(M-N) considered as additional proof of the coordination of the two ligands , as shown in Table 2 .

Table 2. IR wavenumber (cm^{-}) values of free ligands and their complexes

Compound	*v*(C=N) imidazole	*v*(C=N) Quinoline	*v*(C-N=N-C)	*v*(C-O) Phenolic	*v* (C-O) phenolic In plane	*v*(C-O) phenolic Out of plane	v(M-O)	v(M-N)
(QADMP) (L_1)	-----	1506 m	1498 m	1265 m	684 m	856 m	-----	-----
Imidazole(L_2)	1541m	------	-------	-------	------	-------	-----	-----
[Mn(L_1) (L_2)$_2$Cl]	1524 m	1454 s	1409 m	1213 m	638 m	867 m	509 w	476 w
[Co(L_1) (L_2)$_2$Cl]	1530 m	1471 s	1433 m	1294 m	659 m	894 m	528 w	445 w
[Ni(L_1) (L_2)$_2$Cl]	1533 m	1469 s	1440 m	1255 m	672 m	869 m	584 w	472 w
[Cu(L_1) (L_2)$_2$Cl]	1530 m	1467 m	1444 m	1236 m	667 m	867 m	507 w	439 w
[Hg(L_1) (L_2)$_2$Cl]	1525 m	1473 s	1442 m	1257 m	661 m	879 m	549 w	457 w

UV-Vis. Spectra of (QADMP) (L1) in ethanol shows three bands at (219,226,266) nm due to (π –π*) transitions of the aromatic rings , Intra charge transfer , and one band in (375) nm for (n-π*) transitions all of these bands appears red shift in the complexes spectra as a result of coordination , the values are explained in the 'Figures 5-7 ' and Table 3.

Conductivity measurements of the complexes in (DMSO) solvent showed the non-ionic character [20] , also it was observed that the silver chloride salt was not deposited when added when adding drops of silver nitrate solution to solution of soluble complexes in ethanol and (DMSO) solvents confirming the absence of chloride ion outside the coordination sphere . Magnetic susbtibility showed that the complexes of Mn(II) , Co(II) , Ni(II) , and Cu(II) have octahedral geometry with high spin values while the complex of Hg(II) is diamagnetic due to absence of single electrons in the electronic configuration as shown in Table 3.

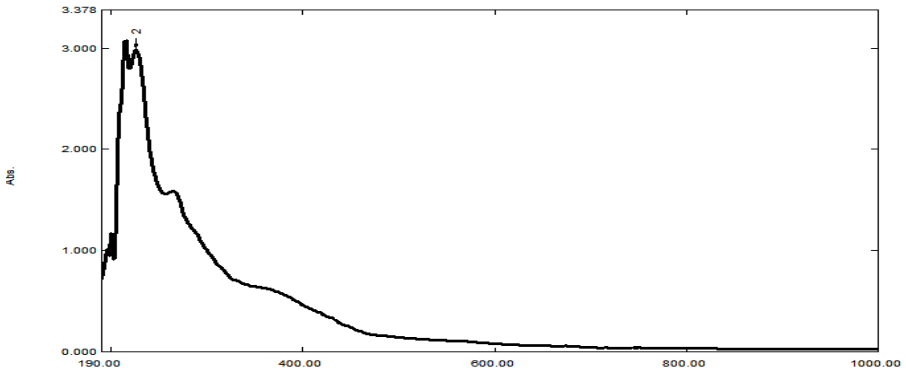

Figure 5 . UV-Vis. Spectra of primary ligand (QAMPD)

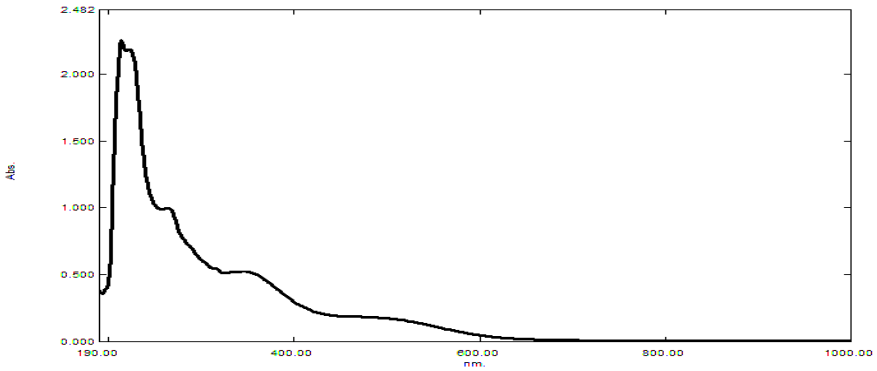

Figure 6 . UV-Vis. Spectra of Mn(II) Mixed ligand complex

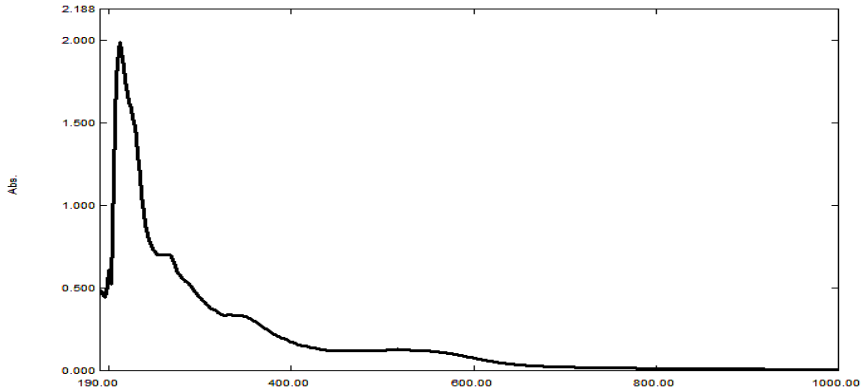

Figure 7 . UV-Vis. Spectra of Cu(II) Mixed ligand complex

Table 3 . Electronic transitions , and conductivity measurements of free ligands and their complexes

Compound	λ_{max} (nm)	Transitions	Molar Conductivity $S.Cm^2.mole^-$	μ.eff. (B.M.)	Geometry
(QADMP) (L1)	375	n-π*	-------	--------	------
	266	Intra C.T			
	226	π-π*			
	219	π-π*			
Imidazole(L2)	278	n-π*	--------	--------	-------
	227	π-π*			
$[Mn(L_1)(L_2)_2Cl]$	498	MLCT	19.2	5.74	Octahedral
	346	C.T			
	268	π-π*			

	214	π-π*			
	584	MLCT			
	342	C.T			
$[Co(L_1)(L_2)_2Cl]$			17.5	4.76	Octahedral
	266	π-π*			
	214	π-π*			
	536	MLCT			
	346	C.T			
$[Ni(L_1)(L_2)_2Cl]$			17.4	2.83	Octahedral
	266	π-π*			
	212	π-π*			
	541	MLCT			
		C.T			Distorted
$[Cu(L_1)(L_2)_2Cl]$			16.6	1.73	
		π-π*			Octahedral
		π-π*			
	546	MLCT			
	350	C.T			
$[Hg(L_1)(L_2)_2Cl]$			21.7	------	Octahedral
	266	π-π*			
	224	π-π*			

From the results presented suggested that the complexes have octahedral geometry where the primary ligand (QADMP) coordinated with each metal ion as a tridentate from oxygen atom of hydroxyl group after deprotonation, one nitrogen atom of azo group , and nitrogen atom of quinoline ring while the secondary ligand (imidazole) coordinated through nitrogen atom number (3) of heterocyclic ring., as shown in **'**Figure 8 '**.**

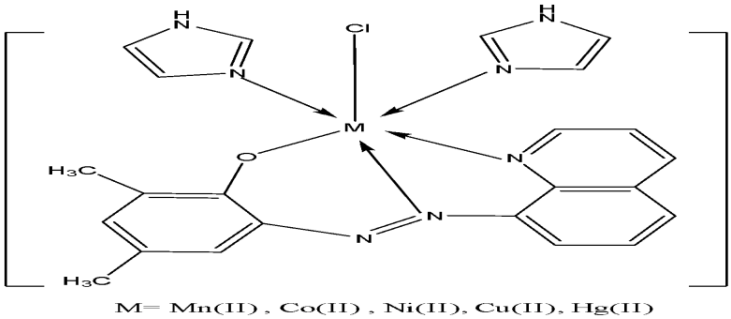

Figure 8. Suggested general formula of the mix ligand complexes

3.1.Antibacterial efficiency of free ligand and ligand complexes:

The ability of antibacterial efficiency of free ligand (QADMP) (L1) and five mixed ligand complexes of studied ions which have a general structure [M(L1)(L2)2Cl] to each ion toward eight MDR bacteria, two G +ve bacteria (E. faecalis and S. aureus) and six G –ve bacteria (Pr. mirabilis, S. typhi, E. coli, P. aeroginosa, A. baumanii and K. pneumoniae) were evaluated by the present or absence of inhibition zone around the holes. The results of the antibacterial effectiveness of various ingredients in solutions are listed in Table, and Figure. The study proves that free ligand is best at killing the bacteria Staphylococcus. typhi and P. aeroginosa isolates were better than the other isolates.

As for the efficacy of the metal complexes, they typically have a strong antibacterial efficacy on G-ve bacteria comparison to G +ve bacteria, whereas Hg (II) ion complexes had greater biological efficacy on most bacterial isolates than other metal complexes while Mn (II) ion complex had weaker antibacterial efficacy comparing to other metal complexes Table (5). The results in this paper conflict with the result of [2] that found the complexes to have strong antibacterial activity against gram-negative bacteria.The free ligand (L_1) showed high antibacterial efficiency on *S. typhi* and *P. aeroginosa* than other mixed ligand complexes of ions. Hg (II) ion complexes had higher biological efficacy on *E. faecalis*, *S. aureus* , *Pr. mirabilis, E. coli, A. baumanii* and *K. pneumonia*.

Preliminary studies of antimicrobial activity showed which the azo dye containing 1,3,4- benzothiozole moiety had a possible antibacterial efficacy [21].

The improvement of antimicrobial efficacy of the free ligand might be related to transient metal chelation along with it. Complicated reduction of metal ion polarity by ligand coordination and increased lipophilicity of the metals [22] . This makes it easy for the novel prepared complex to penetrate the bacterial lipoid cell membrane and inhibit its growing.

Some studies showed the potential of methyl nitro imidazole to reduce the growth of G-ve bacteria including *K. pneumoniae, Proteus merablis*, *E. coli and P. auroginosa* in addition to reducing effects on G+ve bacteria. This ligand could release free radicals which destroy and kill bacteria [23] .

In addition, the azo compounds are reported to have a variety of biological functions, including nucleic acid inhibition, protein synthesis, nitrogen fixation and carcinogenesis [24]. Azo derivatives and their metal combinations are too extremely essential pigments for artificial leather and vinyl polymers [25]. They are the strong pharmaceutical agents with adaptable therapeutic efficiency such as antimicrobial [26-29] efficiency, DNA, RNA, and protein synthesis, nitrogen fixation, and cancer [30].

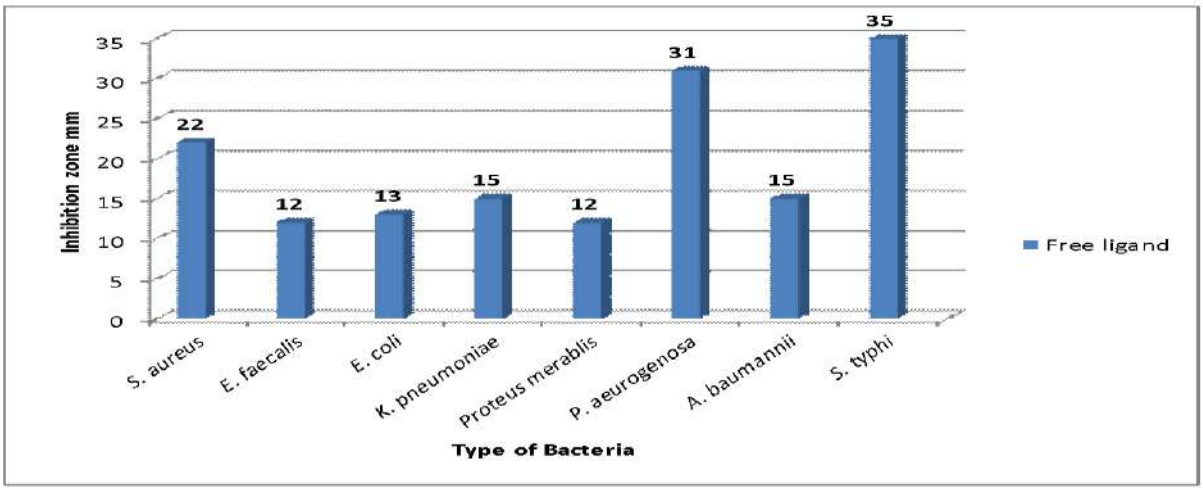

Figure 9 : Comparison of inhibition zone measurement (mm) of free ligand (QADMP) (L_1) against multidrug resistance bacteria**.**

Table 4 Inhibition zone measurements (antibacterial activity) of free ligand against multidrug resistance bacteria

Type of bacteria	Inhibition zone(mm) [Free ligand (L_1)]
Staphylococcus aureus	22
Enterococcus faecalis	12
Escherichia coli	13
Klebsiella pneumoniae	15
Proteus mirabilis	12
Pseudomonas aeroginosa	31
Salmonella typhi	35
Acinetobacter baumannii	15

Table 5 . Inhibition zone measurements (antibacterial activity) of mixed ligand complexes of Hg(II), Co(II), Mn(II), Cu(II) and Ni(II) ions against multidrug resistance bacteria

Compound	Inhibition zone (mm)							
	S. aureus	*E. faecalis*	*E. coli*	*A. baumannii*	*S. typhi*	*K. pneumoniae*	*P. mirabilis*	*P. aeroginosa*
Mn $(L_1)(L_2)_2Cl$	12	0	15	18	18	12	0	15
Co $(L_1)(L_2)_2Cl$	24	13	14	15	15	14	17	25
Ni $(L_1)(L_2)_2Cl$	18	0	20	12	13	17	13	20
Cu $(L_1)(L_2)_2Cl$	18	13	14	13	12	15	14	13
Hg $(L_1)(L_2)_2Cl$	25	20	24	22	26	23	16	17

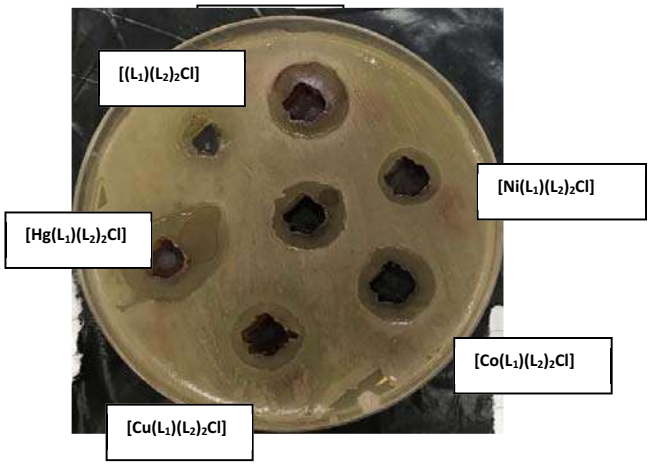

Figure 10. Antibiogram pattern of free ligand and five mixed ligand complexes of Hg(II), Mn(II), Ni(II), Co(II) and Cu(II) ions against *Acinetobacter baumannii*.

4.Conclusions :

For primary azo ligand (QADMP) (L1) and imidazole molecule (L2) as a secondary molecule with a general formula [M(L1) (L2)2Cl] and octahedral geometry, new mixed ligand complexes of Mn(II), Co(II), Ni(II), Cu(II) and Hg(II) have been prepared. Biologically active molecules possessing antimicrobial properties are proposed in this study. These new complexes of free and mixed ligands show essential antimicrobial activities. A strong antimicrobial efficacy of azo dye with 1,3,4-thiadiazole moiety was shown in preparatory antimicrobial activity studies. Therefore, it can be concluded that this new class of compounds certainly provides a greater promise to discover a potent antimicrobial agent.

References :

[1] Shimaa H S, Hazem S E, Ippolito C and Sadeek A S 2018 *Molecules* , **23** 1182 .
[2] Israa N W , Zahraa Y M and Husham M M 2018 *J. Pharm. Sci. & Res.* **10** 3074.
[3] Evgenii P and Plotnikov V P 2018 *Antiinfect Agents*, **16** 100.
[4] M.Sivasankaran N and M.Santappa P N 1980 *Inorganica Chimica Acta* , **41** 7.
[5] Ghulam H , Nasir A , Ghulam S, Makshoof A , Aamer S , Rashid S , Farman A and Misbahul A K 2017 *J. Appl. Res. Technol.,* **15** 346.
[6] Gafar S M , El-Kelany M A and El-Shawadfy S R 2018 *J. Radiat. Res. Appl.,* **11** 190.
[7] Kaulage M H , Maji B , Pasadi S , Bhattacharya S and Muniyappa K 2017 *Eur J Med Chem.* **20** 1016 .
[8] Amer J J , Muna A K and Shahryar A J h 2012 **,** *Baghdad Sci. J,* **9** 178.
[9] http://www.tufts.edu/med/apua/consumers/personal_home_5_1451036133.
[10] Albrecht M, Fiege M and Osetska O 2008 *Coord Chem Rev*.**252** 812.
[11] Hawraa M F 2013**,** *JUBPAS* 21 **1**.
[12] Macfaddin J F 2009 *Biochemical tests for identification of medical Bacteria.* 3rd ed (williium and Wilkins, U. S. A).
[13] Ramalivhana J N, Obi C L, Samie A , Iweriebor B C, Uaboi-Egbenni P ,Idiaghe J E and Momba M N B 2014 *Afr. J. Biotechnol*, **13** 616.
[14] Murray P R , Baron E J , Pfaller M A, Tenover F C and Yolken H R 1995 *Manual of clinical microbiology*, 6th ed (ASM press , WashingtonDC) p 15-18.
[15] Olurinola P F 1996 *A laboratory manual of pharmaceutical microbiology*.(Idu, Abuja, Nigeria) p 69-105.
[16] Ganesh M , Darshana R, .Aruna K and Sakina B 2017 *J. Saudi Chem. Soc.* **21** 954.
[17] Omar H S A 2012 *Bioinorg Chem Appl*, 1.
[18] Saad M M and Ali K I 2018 *J. Pharm. Sci. & Res*. **10** 2175.
[19] John M G, Malachy M C, Kaijie N , Theresa T, Kevin K, Michael D , Xiaomei M and Vickie M K 2013 *Polyhedron* , **55** 169.
[20] Reddy K H , Reddy M R and Raju K M 1997 *Polyhedron* , **16** 2673.
[21] Chinnagiri T K K, Jathi K , Tantry N R, Sanehalli K P and Angadi R S A 2013. *Org. Chem. Int*. 1.
[22] Franz A M, Roland C F, Mark S, Andres R A, Diana H T and Salah S M 2016 *Crystals* ,**6** 91.
[23] Shahid H A, Jahangir S, Yousuf S, Hanif M and Sherwan S K 2016 *Arab J Chem* ,**9** 668.
[24] Nejati K , Rezvani Z and Seyedahmadian M 2009 *Dyes Pigm*. **83** 304.
[25] Abdallah S M 2012 *Arabian J Chem*. **5** 251.
[26] Khalid A, Arshad M and Crowley D E 2008 *Appl Microbiol Biotech*. **78** 361.
[27] Sahoo J and 2017 *J Taibah Univ Med Sci*. **12** 115.
[28] Motaweq Z Y , Sadiq H M , Alsallami N Y and AL-Rufaie M M *2017 World J. Pharm. Res.* **6** 1425.
[29] Sahoo J, Parween G, Sahoo S, Mekap S K, Sahoo S and Paidesetty S K 2016 *Ind J Chem.* **55B** 1267.
[30] Badea M , Olar R , Cristurean E , Marinescu D, Emandi A, Budrugeac P and Segal E 2004 *J Therm Anal Calor.***77** 815.

Preparation of Polystyrene/Polyacrylonitrile Blends by Electrospinning Technique

Preparation of Polystyrene/Polyacrylonitrile Blends by Electrospinning Technique

Ahmed H Oleiwi*[1,2], Akram R Jabur[2] and Qusay F Alsalhy[3]

[1,] Wasit University /College of Engineering /Wasit,Iraq
[2] University of Technology/ Materials Engineering Department /Baghdad, Iraq
[3] University of Technology /Chemical Engineering Department, /Baghdad, Iraq

* E-mail: ahmedhashim.tech@gmail.com

Abstract: New blend material membranes as fibers produced by electrospinning technology and these membranes were characterized and evaluated their properties in this research. Polyacrynitrile polymer mixed physically with polystyrene to produce the blend membranes. FTIR confirm the occurrence of polymeric blends by establishing the absence of new chemical reactions occurs. The hydrophobicity of the membrane was reduced by increase the PAN percent in the blend. Field emission scanning electron microscopy used to study the morphologies of the membranes and illustrated the average diameters of produced fibers which found about 1.68-0.73 µm. The average pore size found about 1.28 – 0.31 µm for blend membranes. The result showed an increasing in fibers diameter and pore size with increasing of the PAN percent while the membranes porosity still high percentage about 98%.

KeyWords: Blend materials, Electrospinning technique, FE-SEM, Polyacrnitrile.

1. Introduction:

Polymeric blends are a member of a class of materials similar to alloys in metals; where at least two polymers were mixed together in order to produce a new material that has various properties [1]. Reason of blending include the formation of new with low cost materials, development materials with wide range properties, increasing their performance, Adjusting the composition of materials, and conceder as recyclable method for polymeric scrap [2, 3].

Polyacrylonitrile is a thermoplastic polymer with useful properties such as good strength and modulus of elasticity with thermal stability [4]. Polyacrylonitrile prepared as films, fibers, foams, and other forms and the polyacrylonitrile have a significant property that related to absorb of toxic metal ions [5]. Polystyrene is also a human synthesis polymeric material, with properties such as transparent to light, stiff and have high modulus. It has wide range applications and considered an economic polymer with high volume production. Blend formation from polystyrene and polyacrylonitrile have present good dispersion with thermal stability, and superior physical properties [6].Electrospinning technology consider adaptable and effectively method for producing polymeric fibers with wide range of diameters from nano to micro scale [7]. Electrospinning had been used to produce fibers since 1934 and applied for various polymeric materials and composites [8]. Electrospun fibers membrane have

3D structure with high specific surface and surface roughness, produced membranes have special fields application such as sensors [9], filters [10], solar cells [11], catalysts [12], tissues [13], hydrophobicity surfaces [14],etc. Also the electrospinning had special features like low cost, high production rate, high degree of flexibility that provide a good control on the membranes, so controlling on formed fibers properties like membrane morphology, degree of homogeneity, porosity percent, structure type (hollow, parallel, network fibers) by changing the process parameters [15].The present work for produce new blend materials from polystyrene and polyacrynitrile in different ratios using electrospinning technique and produced the blend in the form of nano, submicron fibers diameter from polystyrene/polyacrynitrile. This approach will provide to prepare the samples with relatively high surface area and low cost.

2. Experimental Part:

2.1. Materials that used in this study were:

2.1.1. Polystyrene with molecular weight of Mw = 250,000 gm/mol purchased from (Sigma Aldrich, USA). N,N-dimethylformamide purchased from (Central Drug House (P) Ltd, India). Polyacrylonitrile with molecular weight of Mw = 150,000 gm/mol purchased from (MACKLIN, Chine).

2.1.2. Polystyrene Solution preparation was done by solving polystyrene (Mw=250000, USA) in dimethylformamide by stirring for 2 hours at ambient temperature to form 20 wt. % PS solution. Polyacrylonitrile Solution preparation was done by solving polyacrylonitrile (Mw=1500000, China) in dimethylformamide by stirring for 1 hour at ambient temperature to form 10 wt. % PAN solution.

2.1.3. Polystyrene solution at a concentration of (20 %) and polyacrylonitrile solution at a concentration of (10 %) were mixed to produce blends as follows: The PAN solution was added to PS solution in ratio (1:9, 2:8, 3:7 and 4:6), then mixed together by using magnetic stir the both solutions under laboratory temperature for 30 minutes to form a good dispersion solution.

2.1.4. Electrospinning process was done by (Bio-electrospinning/ Electrospray system ESB-200, South Korea) [16]. The prepared blend solutions were feeding over a needle (diameter = 0.7mm) using a syringe (10 ml). The power supply was fixed to a syringe needle tip and the collector. Where the operating parameters of electrospinning device were: 20 KV voltage, 1 ml/hour flow rate, 15 cm distance between electrodes and 2 hour operating time at ambient temperature with (25-30%) humidity, these parameters will be fixed for all following solutions.

2.2. Characterization

2.2.1. FE-SEM (Model: MIRA 3-XMU) was used to obtain the morphology of electrospinning membranes. The fibrous membranes were cutting into small piece then coating with a thin layer of gold by sputtering. The fibers diameter and distribution of the electrospinning membranes were carried by the FE-SEM images using the Auto CAD 2010 software.

2.2.2. EDX spectroscopy analysis was done using FE-SEM device, used X-rays to emit from electrospinning membranes surface during bombing by electrons to investigate the basic constitution of membranes.

2.2.3. FT-IR Spectroscopy device (Model: BRUKER, TENSOR-27) for elecrospinning membranes were done using wavenumber ranging from 4000 cm^{-1} to 400 cm^{-1} in order to sure of the blending concept happened.

2.2.4. Wettability of the electrospinning membranes surface was measured in the term of contact angle (type: CAM 110, Germany) at ambient conditions. Contact angle was measuring by drop method. A liquid droplet (5 µL volume) was dropping on the membranes and measured in all sides then takes the average value, contact angle take the average of five values at different positions on the surface.

3. Results and Discussion:

3.1. Field Emission Scanning electron microscopy:

'Figure 1'. Presented the morphology of the 20wt.% polystyrene electrospinning film and showed a bead structure because of an uncompleted stretching in polymer chains that result broken of polymeric solutions as droplets in elecrospinning process [17].

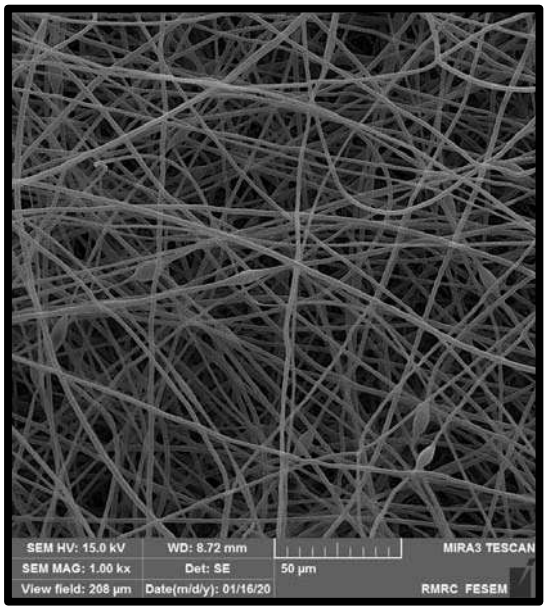

Figure 1. FE-SEM images for 20% polystyrene membrane

'Figure 2'. Illustrated the analysis of FE-SEM image, and showed the average fibers diameter, pores size and their distributions, also some fibers diameter might appear in micron scale due to fast solution feeding that occur in the beginning of the electrospinning. 20% wt. polystyrene has chosen to produce the electrospun composite membranes because it's easy to spin in electrospinning and present thin and smooth fibers, high porosity and surface area.

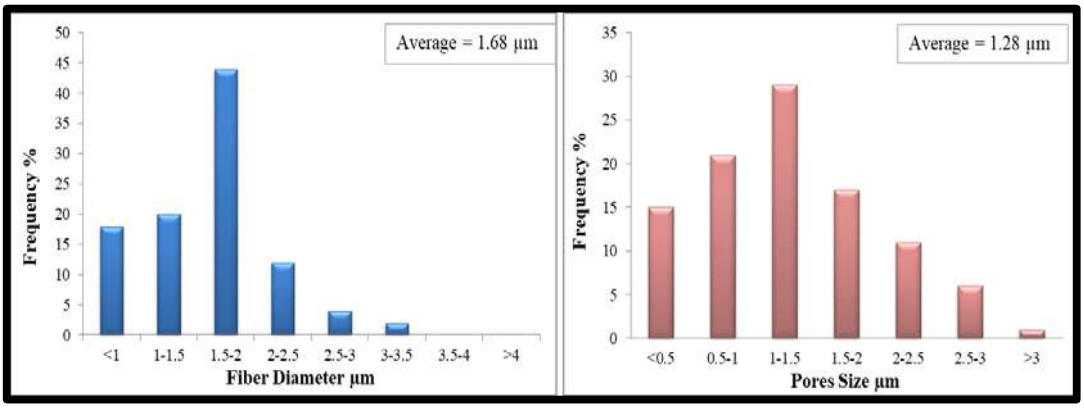

Figure 2. Illustrated (A) fiber diameter distributions (B) pores size distributions for 20% polystyrene

'Figure 3'. Showed the morphology of the electrospun PS/PAN membranes and presents a significant reducing in beads formation with increasing the incorporation of polyacrylonitrile in the polystyrene polymers, predominantly due to that the expansion of polyacrylonitrile results in a higher electric charge density on the surface of ejected jet conveyed by electrospinning [18].

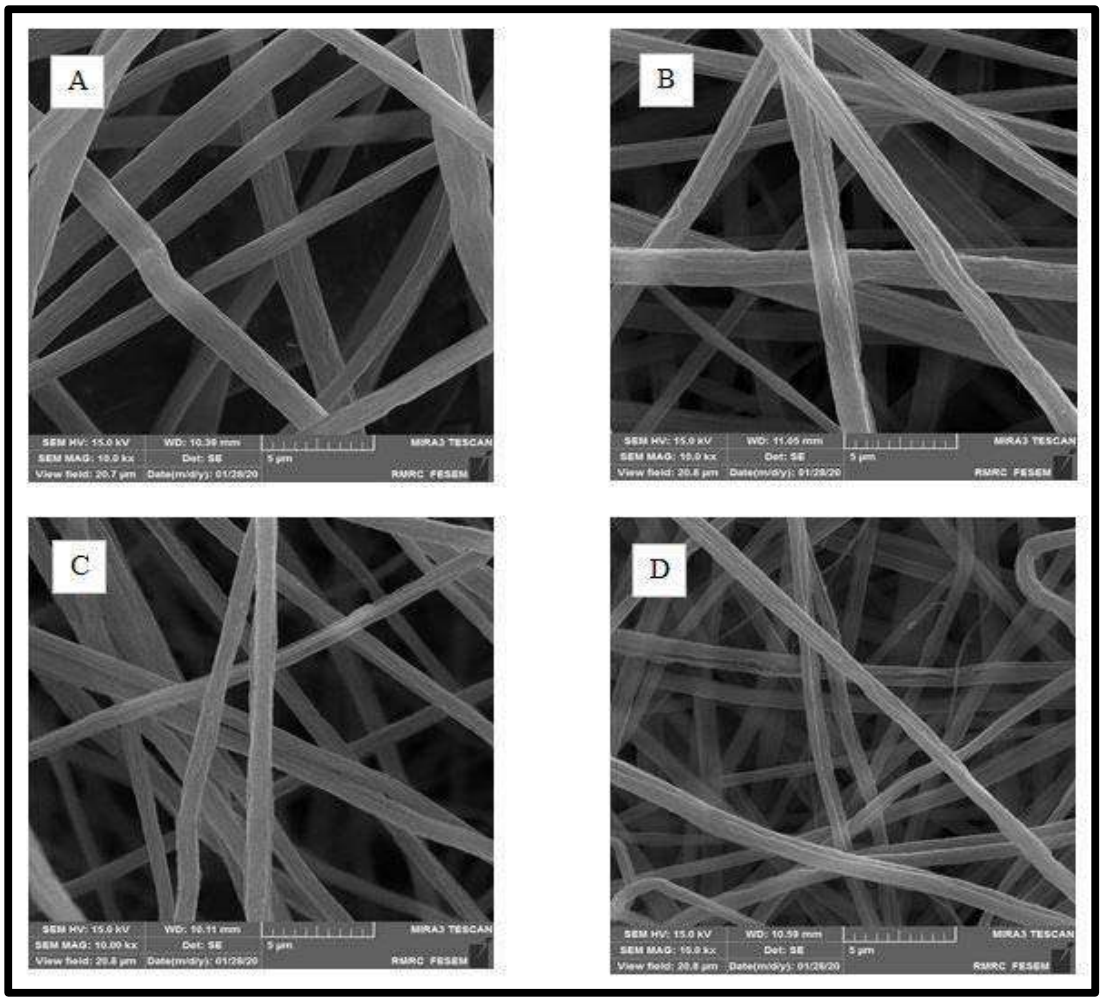

Figure 3. FE-SEM images for polystyrene membranes with different PAN concentration (10, 20, 30 and 40%) respectively

High solution surface tension and viscosity are not encouraging to ejected, while the repulsive force encouraging the droplets to eject. When used a small force the feeding of the jet decrease, while the jet split increased [19]. PAN solution works to obstruct droplets splitting, so resulting to produce in thinner fibers with small pore size as shown in 'figure 4'.

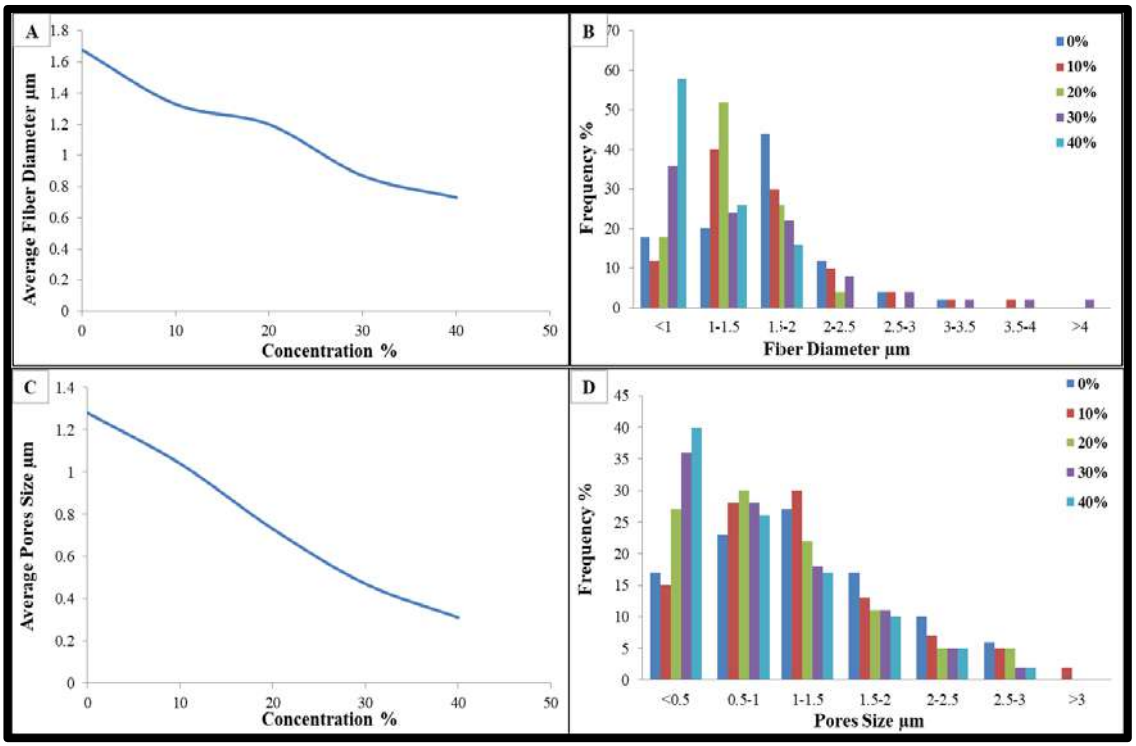

Figure 4. Illustrated the effect PAN concentration on fiber diameter, fiber diameter distribution, pores size and pores size Distribution

This result concurs with Li Peng [20], who illustrated that when increase the PAN concentration in other polymeric material will lead to raise viscosity and conductivity of solutions. And explain the effect of repulsive forces when its consider main factor, cause reducing in fiber diameters with increased the PAN concentrations.

3.2 Energy Dispersive X-ray spectroscopy

Figure 5. Showed the EDX chart for 20% wt. polystyrene electrospinning membrane and present the composition of the membrane that formed basically from carbon and oxygen, confirming founds of carbon in fiber structure besides to find gold due to coat process .

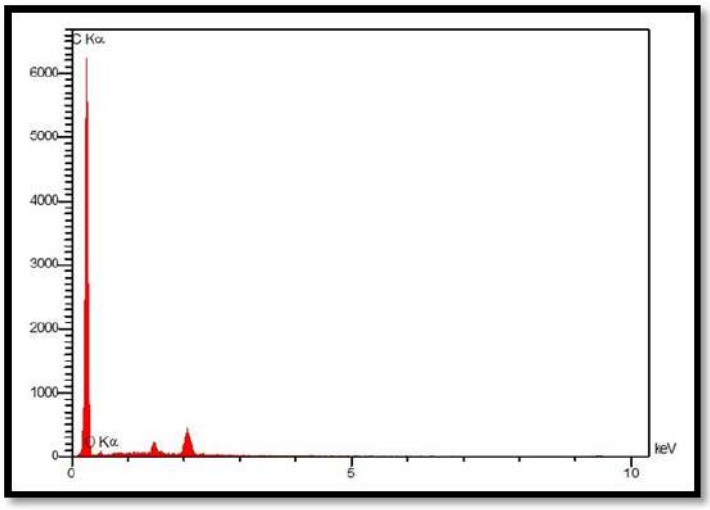

Figure 5. EDX for 20% polystyrene electrospun membrane

'Figure 6'. Illustrated the EDX spectrum for polystyrene with (10, 20, 30 and 40%) PAN membranes which suggest that the chemical composition consists mainly from mainly carbon and oxygen, confirming founds of carbon in fiber structure due to chemical composition of polyacrynitrile besides to gold due to coat process.

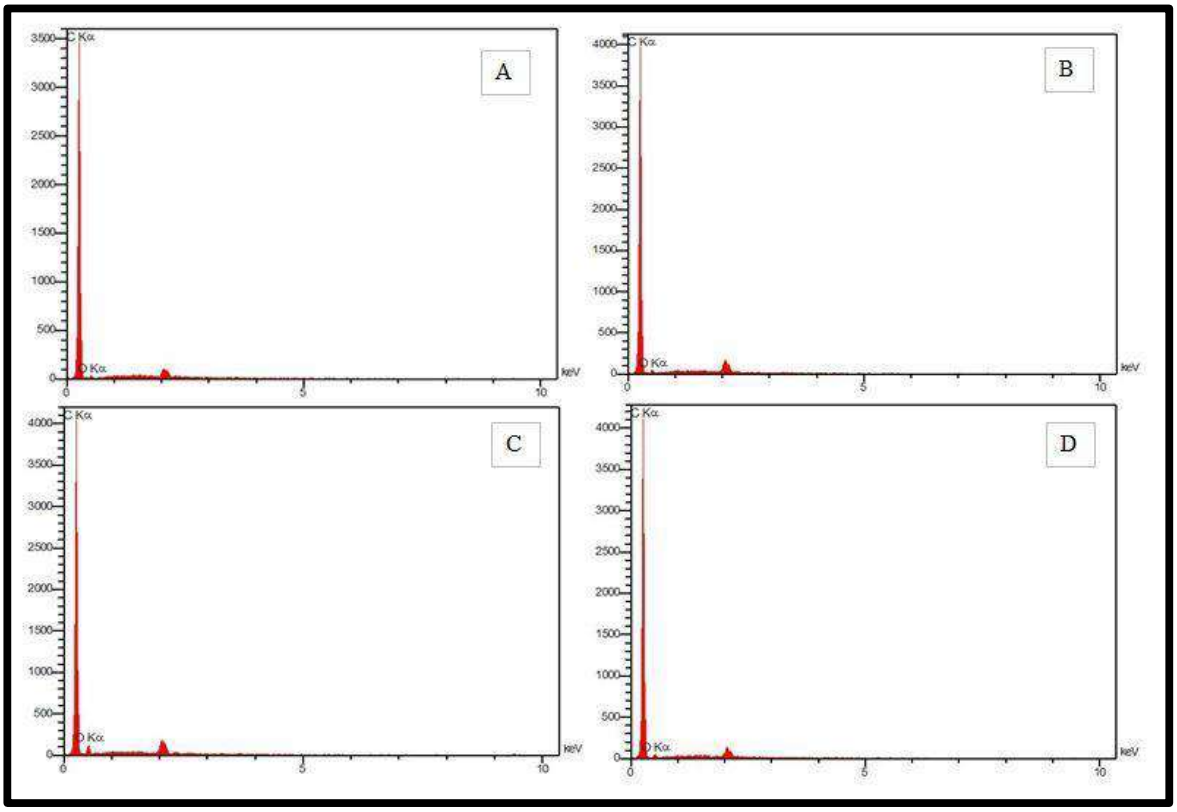

Figure 6. EDX for polystyrene membranes with different PAN concentration (10, 20, 30 and 40%) respectively

3.3 Fourier Transform Infrared Spectroscopy

'Figure 7'. showed FTIR spectra for polystyrene 20% concentration electrospinning films with the principle peaks. The peaks at the wavenumbers of 3082.44 and 3025.74 related to aromatic C-H bond, while the peaks at the wavenumbers of 1601.23, 1492.73, and 1451.83 related to aromatic C=C bond, these peaks represent the benzene ring. The peaks at the wavenumbers of 753.69 and 696.43 related to C-H bond out-of-plane and indicate that benzene ring has only one substituent side, also there are peaks at the wavenumbers of 2921.77 and 2850.39 caused by existing of methylene group. All the peaks agreed with Noor M. Jalal [21].

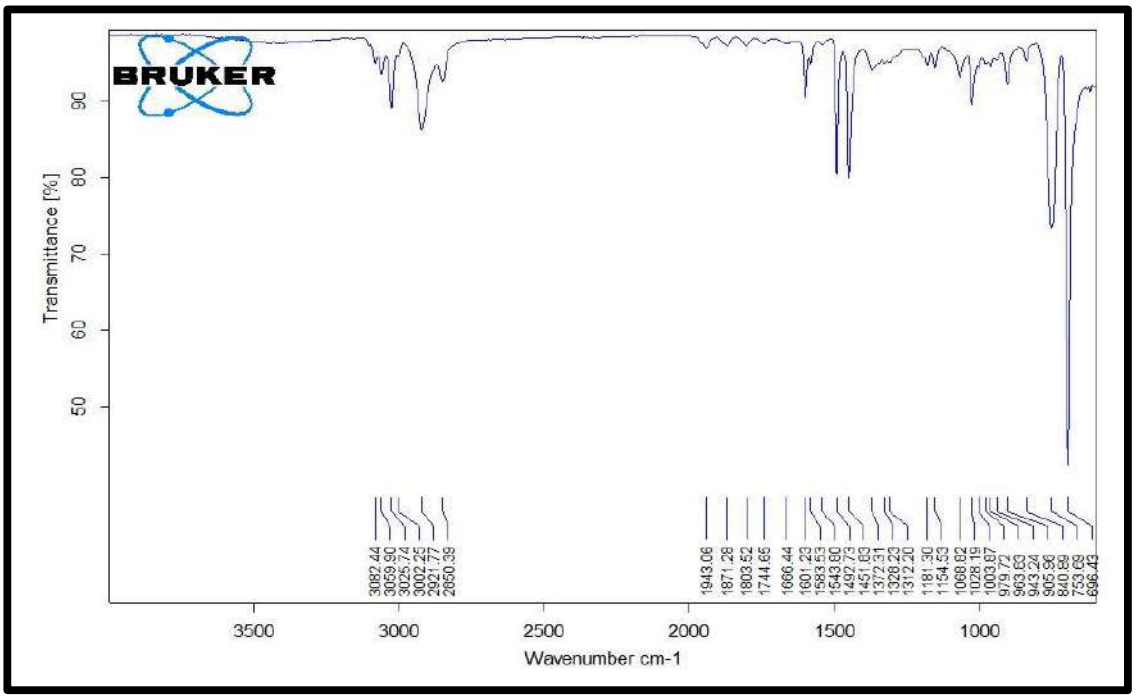

Figure 7. FTIR for 20 % polystyrene membranes

'Figure 8'. presents the (FTIR) spectrum of polystyrene and polystyrene with (10, 20, 30 and 40%) PAN. The presence of generally small decease in intensity in C-H Aromatic ring and CH_2 of methylene bonds peaks followed by increasing the intensity until reach high intensity in C-H out-of-plane bonds peaks as compare to the FTIR spectrum polystyrene electrospinning membrane when decrease in the infrared wavelength. While, there is a new (C≡N stretching of nitrile) bonds was formed in (2243.5 cm^{-1}) where in 20% polystyrene membrane not formed that represent the side group of polyacrynitrile. This result agreed with Pan Wi [22], who present the peaks of polystyrene and polyacrynitrile and notice the absence in effect of the two polymers that caused to lack in intermolecular interaction.

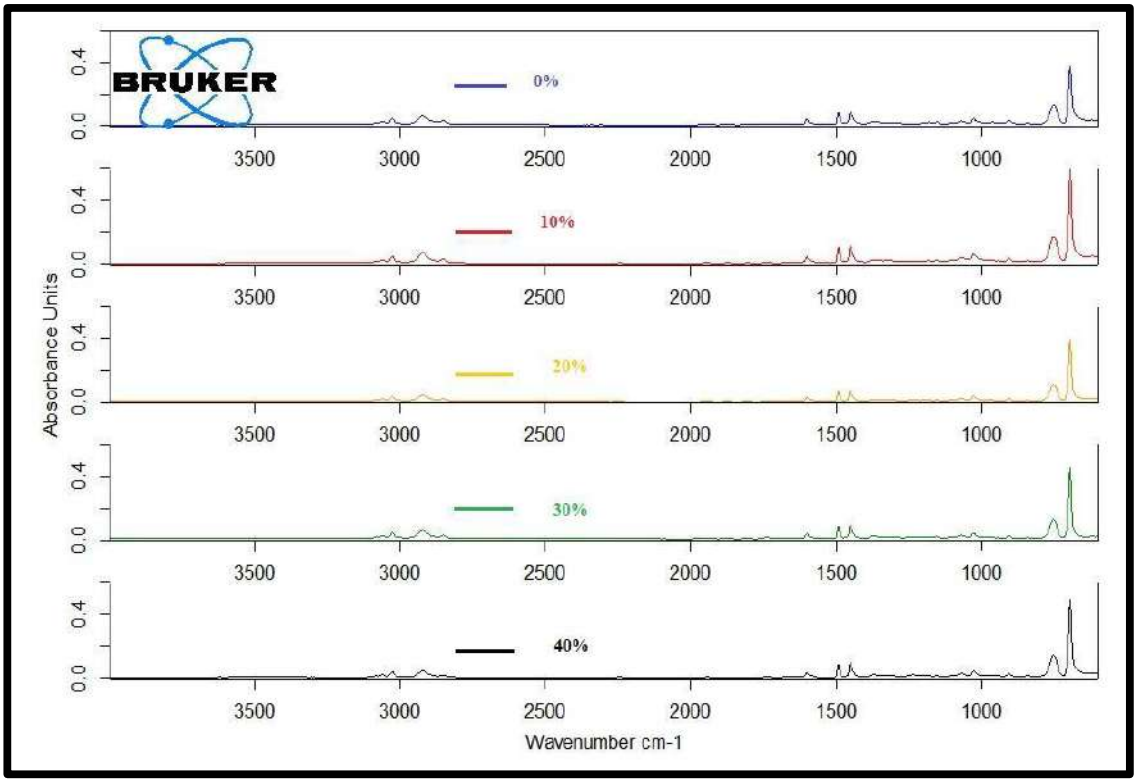

Figure 8. FTIR for polystyrene membranes with different PAN concentration (10, 20, 30 and 40%) respectively

3.4 Contact Angle Measurement

'Figure 9'. showed the effect of increase PAN concentration in 20 % polystyrene on water contact angle which observed the increased from 128° to 106° as the PAN concentration increased due to the polyacrylnitrile hydrophobic nature with contact angle about 80 to 90 for pure membranes, that cause to reduce the hydrophobicity for polystyrene [23].

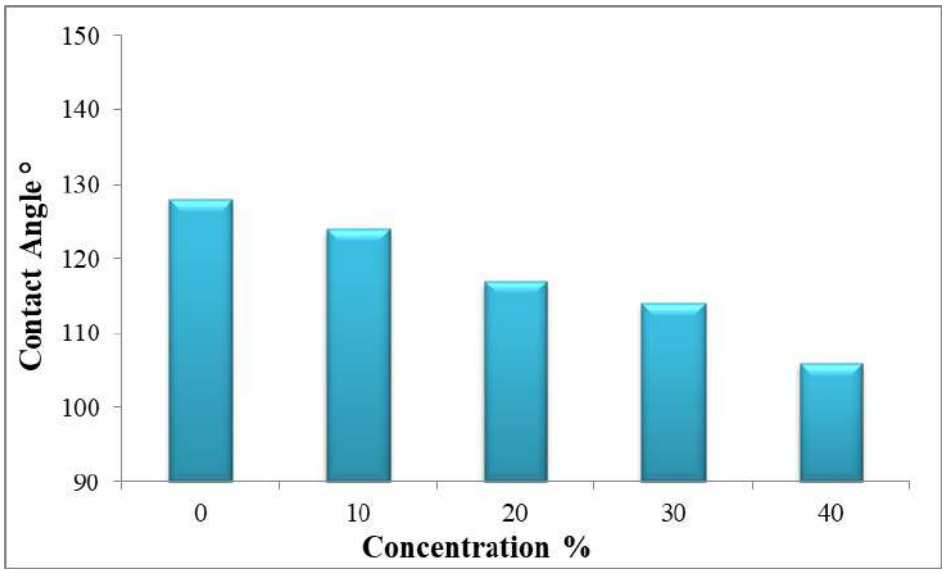

Figure 9. Illustrated the effect of PAN concentrations on the contact angle

4 Conclusions

electrospinning method used for preparing polymeric blends from polystyrene with polyacrylonitrile in form of micro/nano-fibers. FE-SEM used to characterize the morphological changes and the reducing in fibers diameter with increasing of PAN concentrations. FTIR approved the blend concept by there is no chemical reaction occurred. Also observed a decreasing in membranes wettability with increasing of PAN concentrations since the polyacrylonitrile has hydrophobic properties but lower than polystyrene hydrophobicity.

References

[1] Bahjat B K, Ridha H R, Auday H Sh and Kareem A J 2019 *AIP Conf. Proc.* **2123,** 1
[2] Martinova L and Daniela L 2012 *AIP Conf. Proc* **1502** 115
[3] Kareem A J, Rihab N F, Auday H Sh, Harith I J, Bushra K.H M, Suad H A and Ebtisam M T 2019 *IJAIP* **13** 163.
[4] Partovi A P J and Kaghazchi P S 2018 *Phys. Rev. Appl* **9** 014012.
[5] Li P , Wang Z, Yang L, Zhao S, Song P and Khan B 2018 *J. Membr. Sci*. **555** 56.
[6] Tuli S K, Roy A L, Elgammal R A, Tian M, Zawodzinski TA and Fujiwara T 2018 *J. Membr. Sci.* **565** 213.
[7] Chayad F A , Akram R J and Noor M J 2016 *J. Eng. Technol.* **34** 1265.
[8] Akram R J ,Laith K A and Saja A M 2015 *JKU* **11** 200.
[9] Sen R, Zhao B, Perea D, Itkis M E ,Hu H, Love J, Bekyarova E and Haddon R.C 2004 *Nano Lett*. **4** 459.
[10] Wang X F , Ding B, Yu J Y, Wang M R and Pan F K 2010 *Nanotechnology* **21** 055502.
[11] C. Shin J, 2006 *J.Colloid Interface Sci.* **302** 267.
[12] Onozuka K , Ding B , Tsuge Y, Naka T, Yamazaki M, Sugi S, Ohno S, Yoshikawa M and Shiratori S 2006 *Nanotechnology* **17** 1026.
[13] Madhugiri S, Sun B, Smirniotis P, Ferraris J and Balkus K 2004 *Microporous Mesoporous Mater.* **69** 77.
[14] Zhang Y , Feng Y , Huang Z and Ramakrishna S 2006 *Nanotechnology* **17** 901.
[15] Jabur A R, Fadhil A Ch and Noor M J 2016 *Int. J. Thin Film. Sci. Tec.* **5** 1.
[16] Jabur A R, Laith K A and Saja A M 2017 *Al-Khwarizmi Engineering Journal* **13** 84.
[17] Palaniswamy S K, Jayaraman S, Sundarrajan S, Veluru J B, Gurdev S, Suleyman I A and Seeram R *2014 Energy Environ. Sci* **00–00 10.1039**/C4EE00612G.
[18] Jabur A R 2018 *international journal of hydrogen energy* **43** 530
[19] Eda G and Shivkumar S 2006 Bead structure variations during electrospinning of polystyrene, *J. Mater. Sci.* **41** 5704.
[20] Li P, Qiao Y, Zhao L, Yao D, Sun H and Hou Y, Li Q 2015 *Mar. Pollut. Bull.* **93** 75.
[21] Jalal N M et al 2020 *Energy Rep.* **6** 287.
[22] Pan W, Zhang Q and Chen Y 2011 *Adv Mat Res.***332-334** 235.
[23] Jabur A R, Laith K A and Saja A M 2016 *Adv. Mater. Sci.* **2016**.

Evaluation of Ceruloplasmin ferroxidase activity and lipid profiles in patients with Valvular heart diseases

Evaluation of Ceruloplasmin ferroxidase activity and lipid profiles in patients with Valvular heart diseases

H K Sacheat[1], S Z Hussein[1*] and S S Al-Mudhaffar[2]

[1] Department of Chemistry, College of Sciences, University of Baghdad
[2] Ibn Al-Bitar Specialized Cardiac Surgery Centre / Baghdad - Iraq
*E.mail : sa78ba2016@sc.uobaghdad.edu.iq

Abstract. One of the major health problems causing defects or damage to one or more of the four heart valves [aortic, mitral, pulmonary, and tricuspid] is valvular heart disease [VHD]; it occurs due to congenital abnormalities or acquired pathology. It is a defect that results in weak heart valves and is therefore unable to function as precise pathways of the blood. The aim of the current study was to evaluate the ferroxidase activity of ceruloplasmin (Cp) and the lipid profile of valvular heart disease patients in sera. Ninety subjects were included in this study and 60 patients with HDV were divided into two subgroups according to the affected valve: 33 patients with aortic valve disease (AV) and 27 patients with mitral valve disease (MV group). In addition, 30 healthy individuals were registered in all groups as control(C) group Serum copper (Cu), total protein (TP), activity and specific activity of ferroxidase Cp, and lipid profile were measured. The results showed that there was a highly significant increase in patient (AV & MV) groups compared to the C group in activity, specific Cp and Cu activity levels. In addition, compared to the C group, triglyceride (TG) and very low density lipoprotein (VLDL) levels showed a highly significant increase in the AV and MV groups. No significant differences were found between patients and control groups in TP, Total Cholesterol (TC), Low Density Lipoprotein Cholesterol (LDL-C) & High Density Lipoprotein Cholesterol (HDL-C) levels. Likewise, for all parameters, there were no significant differences between the AV and MV groups. In conclusion, the high serum level of Cu and the activity of Cp ferroxidase may be considered to be a risk factor for VHD.

Keywords: Heart valve disease, Ceruloplasmin, copper, lipid profile

1. Introduction

Valvular heart disease (VHD) is a pathological situation correlated with heart valves. The affected valve may be inefficient to close fully, led to not opening and closing of the heart properly, this allows an amount of blood to leak backward. Also, this may happen due to the stiffened, thickened or fused leaflets causing the improper opening of the valve [1]. Valves that are involved in VHD, including: on the left (aortic and mitral) and the right (pulmonary and tricuspid) [2].

VHD can evolve before birth or acquired during the life due to some infection such as: a rheumatic fever; while acquired VHD is more common. Sometimes the reason is unknown, but often the valves structure changes as a result of mineral deposits, either all over it or its surrounding tissues [3].

Unfortunately, all functional disorders of heart valves may not lead directly to specific symptoms. The injured may remain undetected the disease for a long period of time that may extend to years. Because the disease is not discovered and neglected, the heart will suffer from real damage and thus all fuse disorders are a rotational burden on the heart and eventually lead to heart failure [4].

Ceruloplasmin (Cp) [EC 1.16.3.1, Ferroxidase; Iron (II): O2 oxidoreductase] can be defined as the major blue copper containing glycoprotein which has a molecular weight of 132 kDa. It is consists of a single polypeptide chain of (1046) amino acid residues with carbohydrate content (between 7% and 8%). Essentially, Cp is synthesized and secreted by the liver as well as its expression was also found in numerous organs such as: heart, lung, kidney, brain and lymphocytes [5].
Ceruloplasmin, the multifunctional copper containing enzyme, possesses significant functions such ferroxidase activity, oxidase activity, transport, mobilization, and homeostasis of copper, serum antioxidant, and endogenous modulator of the inflammatory response [6,7]. Interestingly, the copper (Cu) in Cp plays an important role in iron oxidation before it is transported to the plasma. In recent years, it has become increasingly evident that the essential metal plays critical roles in a wide range of physiological processes, Fe, Zn, Mn, and Cu. Remarkably, Cu importance is apparent in human physiology [8].
Lipid profile is about tests group which are often requested together to determine the heart disease risk. Therefore, these tests are considered good indicators which someone is possible to have a heart attack or stroke due to blockage of blood vessels or arteries hardening. It is typically comprises: [9] (i) total cholesterol [TC] that strongly associated with progression of heart disease [10]; (ii) High density lipoprotein-cholesterol [HDL-C] which is also known as good cholesterol, and its function to protect from atherosclerosis [11]; (iii) Triglycerides [TG] are a form of bloodstream fat that derived from glycerol and fatty acids [12]. It has several functions, such: an excellent insulation material which forms a layer around the body that conserves heat and converts toxic excess of the sugars required for brain functions [13]; (iv) Low density lipoprotein-cholesterol [LDL-C] which is also called bad cholesterol, and its Cholesterol-rich lipoproteins that result from the breakdown and removal of TG from intermediate-density lipoproteins. However, elevated LDL-C levels in blood increase the risk of artery and heart disease [14].
Thus, the current study aims to determine the Cp ferroxidase activity, Cu level and evaluate the lipid profile parameters in sera of Iraqi patients with VHD.

2. Materials and Methods

2.1 Topics for Research

This research enrolled participants who attended the Baghdad, Iraq, Ibn Al-Bitar Center for Cardiac Surgery. Group 1 consists of 33 aortic valve (AV) patients (17 male and 16 female) with an age (55.5±13.3 years) and BMI (28.73±6.26) kg/m2. Ninety individuals were classified into three classes. Group 2: consists of 27 patients with mitral valve (MV) (10 male and 17 female) aged (53.81±10.00 years) and BMI (28.99±4.01) kg/m2 respectively. Group 3: a control group (C) composed of 30 healthy individuals (16 male and 14 female) with age (46.63 ± 8.79 years) and BMI (28.35 ± 3.79) kg/m2. Patients with diabetes, kidney and liver disorders were the criterion for exclusion. The body mass index (BMI) was measured in kilograms by weight, divided into square meters by length.
The study protocol was accepted by the College of Sciences/ University of Baghdad Ethical Committee.

2.2. Samples

In the plane tube, blood samples (10 ml) were obtained from all participant (patient and control) groups. The tubes were left at room temperature for coagulation for 10 minutes. The blood samples were then centrifuged at 4000 rpm for 10 min. The serum was isolated, aliquoted and processed for analysis at (-20 ° C).

2.3 Cp Activity of ferroxidase and Total protein levels

The Cp (U/L) ferroxidase activity was calculated using the Erel[15] process. Results at a wavelength of 600 nm were measured using the Colorimetric method and absorbance. Using a total protein reagent kit (AGAPPE, Switzerland), serum total protein levels (g/dl) were calculated by observing a Biuret reaction to determine the basic activity of Cp ferroxidase. The basic Cp activity was expressed in protein U per g[6].

2.4 Copper concentration determination in serum

A direct colorimetric assay kit (LTA, Milano, Italy) without sample deproteinization[16] was used to evaluate copper in serum. The 3,5-DiBr-PAESA chromogen reacts with cupric ions (Cu2+Cu+) and forms a blue-violet compound. The absorbance was then measured at a wavelength of 580 nm. The strength of the color is proportional to the sample concentration of Cu.

2.5 Lipid Profile Determination

For quantitative in vitro diagnostic measurements, serum total cholesterol (TC) was calculated using the colorimetric method Cholesterol Oxidase Phenol 4-Amino antipyrine peroxidase {CHOD-PAP} method [17], whereas triglycerides (TG) levels were assessed using the GPO-PAP enzyme assay [17,18]. A two-step assay was used to estimate HDL-C: (1) precipitation and then (2) enzymatic determination [17]. Using Friedwald's formula[19], serum LDL-C and VLDL levels were calculated.

2.6 Review of Statistics

SPSS version 21 (One-Way ANOVA) performed data analysis in this study, where the difference is considered to be highly significant at P<0.001, meaningful at P<0.05 and non-significant at P>0.05. The data is expressed as mean ± norm (mean ± SD) variance.

P>0.05. The data is expressed as mean ± norm (mean ± SD) variance.

3. Results

The mean ± SD of age, gender and BMI for all AV, MV & C groups is shown in Table 1. There was a large difference in age between patients (AV & MV) and control (p<0.05), as shown in Table (1). In addition, there were no substantial variations (P>0.05) in BMI between the patients and the control groups.

Table 1. Age, gender and BMI of all studied groups**.**

Parameters		Groups C (n=30)	AV (n=33)	MV (n=27)
Age (years)		46.63±8.79	55.50±13.3*	53.81±10.0*
Gender	Male (%)	16 (53.3%)	17 (51.5%)	10 (37.0%)
	Female (%)	14 (46.6%)	16 (48.4%)	17 (70.8%)
BMI (Kg/m^2)		28.35±3.79	28.73±6.26	28.99±4.01

* p<0.05, ** p<0.001

Table 2 presents the Cp ferroxidase function, TP and Cp specific activity in both patients (AV & MV) and C groups. Cp activity and specific activity were found to be highly significant changes in the AV and MV groups relative to the C group (p<0.001), although no significant differences between AV and MV were observed. The findings, meanwhile, showed no major differences in TP levels in all the groups examined.

Table 2. Mean values ± SD of total protein, Cp ferroxidase and specific activities in the serum of patients and control groups.

Parameters	***Groups***		
	C n=30	***AV n=33***	***MV n = 27***
Cp ferroxidase activity (U/L)	836.53± 50.11	1735.59 ± 101.61**	1735.33± 75.95**

Total protein (g/dl)	6.380 ± 0.449	6.685 ± 0.988	6.815 ± 0.769
Cp specific activity (U/g)	13.179 ± 1.245	26.50 ± 4.101**	25.763 ± 2.99**
Cu µg/dl	113.7±17.871	182.4±17.609**	190.8±13.771**

* $p<0.05$, ** $p<0.001$

In addition, the serum Cu concentration of both patient groups (AV & MV) showed a highly significant increase ($p<0.001$) relative to the C group, while there were no significant differences between AV and MV.

Comparing the two patient groups (AV&MV) with the C group in Table 3, the findings showed that there was a highly significant increase in TG and VLDL levels ($p<0.001$) in the patient group relative to the C group. Furthermore, the findings in Table 3 showed no substantial differences ($p>0.05$) in the levels of TC, LDL-C and HDL-C in the AV and MV groups with respect to the C group. The findings also showed no major variations in all parameters between the AV and MV classes (TC, TG, HDL-C, LDL-C and VLDL).

Table 3. Mean values ± SD of lipid profiles parameters levels in the serum of patients and control groups.

Parameters	*Groups*		
	C *n=30*	*AV* *n=33*	*MV* *n = 27*
TC (mg/dl)	176.33±17.91	178.74±16.77	185.44±15.83
TG (mg/dl)	118.6±19.13	178.9±16.44**	185.44±12.87**
HDL-C (mg/dl)	46.57±6.35	47.82±6.35	48.96±4.71
LDL-C (mg/dl)	106.0±17.29	97.72±13.14	99.41±18.43
VLDL (mg/dl)	23.72±3.83	35.79±3.21**	37.07±2.57**

* $p<0.05$, ** $p<0.001$

4. Discussion

Ceruloplasmin (Cp) is a human serum protein that holds about 95% of the total Cu plasma in healthy individuals. It is synthesized in the liver [95% in the hepatocyte], but other forms of cells, such as astrocytes, monocytes, and sertoli, are also formed [20]. A number of studies on several forms of cardiovascular diseases [CVD] have reported a near link between increasing serum Cp and an increased risk of myocardial infarction (MI), arteriosclerosis, angina and coronary artery disease (CAD) [21-23], while there are few studies on Cp in rheumatic patients and VHD [20]. This is the first research, to the best of our knowledge, to deal with the relationship between Cp and VHD activity, which showed that Cp ferroxidase activity was significantly elevated in patients with VHD. A previous study carried out in children with acute rheumatic fever documented elevated levels of Cp at the time of diagnosis [24]. Similarly, Petelenz et al. also revealed that Cp levels were significantly increased relative to safe controls in acquired VHD patients [25].

Ceruloplasmin (Cp) is the most enzymatic contributor to the antioxidant protection of human plasma, which acts as an antioxidant through various mechanisms, such as: inhibition of iron-dependent lipid peroxidation and formation of hydroxyl radical [OH] from hydrogen peroxide through its involvement in

ferroxidase, reaction and scavenging of H2O2 and superoxide anion, and inhibition of copper-induced lipid peroxidation

Unfortunately, there is no clear explanation of the function and status of Cp in cardiovascular pathophysiology. One of the mechanisms shown by Cp to have major oxidase activities, including the ability to catalytically consume NO through NO oxidase activity, resulting in decreased bioavailability of NO plasma as well as enhancing oxidation of low-density lipoprotein [22, 27]. NO also plays an important role in heart contraction and alteration in the secretion of endogenous NO may lead to heart failure (HF)[22,28]. The key proatherogenic role of oxidized low-density lipoprotein in the arterial wall, however, is that reduced NO bioavailability promotes endothelial dysfunction, which also leads to atherosclerosis[22]. In vitro and in vivo studies in humans with aceruloplasminemia showed a decrease in the activity of plasma NO oxidase following Cp immunodepletion [27,29]. Thus, via increased NO oxidase activity, high Cp levels can decrease the available NO in the heart; then leading to increased oxidative stress (OS) causes further dysfunction, which would explain the correlation between higher Cp levels and heart disease incidents.

Essentially, Cu, which plays a vital role in the oxidant/antioxidant, is one of the significant trace elements for humans. Cu dyshomeostasis can result in cardiovascular disease (CVD). Several studies therefore support the possibility that high Cu levels can increase the risk of CVD [30]. The current study showed a higher than safe control level of Cu in VHD. In particular, there are no studies in the literature to examine the degree of Cu in VHD; we compared our findings with other forms of CVD, however. In a study conducted in patients with HF, serum Cu levels were found to be higher than in healthy individuals, finding an important correlation between high serum Cu and HF [31]. It is also increasingly recognized that Cu is an important mediator in MI, CAD and atherosclerosis development and progression [30,32].

In addition, the high serum Cu in VHD is likely to represent a highly significant increase in Cp, which binds approximately 95% of the serum's circulating Cu [33]. Cp has also been shown to have many functions in the transportation of Cu, coagulation, angiogenesis, oxidant stress defense, and iron homeostasis. In addition, Cp oxidizes the {ferroxidase function} of Fe2+ to Fe3+ to be connected to transferrin, exerts the activity of antioxidant glutathione peroxidase, and scavenges reactive oxygen species {ROS}. It is also likely to be mainly involved in iron-mediated free radical injury protection [34,35].

Several studies have shown several parallels between atherosclerosis and calcific aortic stenosis (CAS) histopathologic features [36-38]. Atherosclerosis risk factors and CAS also interfere; one of them is dyslipidemia [39,40]. In AV and MV situations, as well as controls, the lipid profile was carried out in the present analysis. The findings showed a highly significant rise in the amount of TG in patients as opposed to controls. This result is in line with Peltier et al.[41], who documented higher levels of TG in patients with CAS. Another study carried out in patients with VHD showed that the amount of TG in patients was substantially higher compared to normal individuals. Hypertriglyceridemia is therefore caused by excess TG in the blood, and elevated TG in the blood has been linked to atherosclerosis[14]. Mean TC, HDL-C and LDL-C levels in this sample, meanwhile, showed no substantial difference in both patients and control groups. Our findings are consistent with the results of previous studies by Afaq et al. and Ortlepp et al. [42,43]. In comparison to the other studies reported by Peltier et al. who found that there was a rise in TC level (hypercholesteremia) in patients with CAS[41] and Hasan et al. who found that there were significantly higher LDL-C and TC levels, while significantly lower HDL-C levels were observed in patients with VHD compared with normal individuals [14]. Regarding the level of LDL-C, our research was in line with the study which showed insignificant levels of LDL-C between patients with calcific valvular heart disease and controls [44].

5. Conclusion

There is no research that discusses the enzymatic behavior of Cp in patients with VHD to date by reviewing the literature. The current findings concluded that changes in Cp ferroxidase activity and Cu levels were found to be highly important in groups of VHD patients and could be used as risk factors for disease prognosis and diagnosis. The Cp value can also be used as an independent biomarker related to

the level of VHD. For all factors, except for triglycerides (TG), there were no variations in the lipid profile that could be used as a predictor for predicting the early occurrence of VHD

References

[1] Zakaria M S, Ismail F, Tamagawa M, Aziz A F A, Wiriadidjaja S, Basri A A and Ahmad K A 2017 *Med Biol Eng Comput.* **55** 1519.
[2] Cömert, Z and Kocamaz A F 2016 *Int. J. Comput. Appl*. **156** 26.
[3] Watkins D A, Beaton A Z, Carapetis J R, Karthikeyan G, Mayosi B M, Wyber R, Yacoub M H and Zühlke L J 2018 *J. Am. Coll. Cardiol*. **72** 1397.
[4] Floriani M A, Glaeser A B, Dorfman L E, Agnes G, Rosa R F and Zen P R 2020 *J. Pediatr. Genet*.
[5] Samygina V R, Sokolov A V, Bourenkov G, Schneider T R, Anashkin V A, Kozlov S O and Vasilyev V B 2017 *Metallomics*, **9** 1828.
[6] Zainulabdeen J A and Sami M M 2017 *I.J.P.H*. **1** 47.
[7] Mukhopadhyay B P 2018 *J. Biomol. Struct. Dyn,* **36** 3829.
[8] Fukai T , Ushio-Fukai M and Kaplan J H 2018 *Am. J. Physiol. Cell Physiol.* **315** C186.
[9] Madziga H, Sanni S and Sandabe U 2010 *Am. J. Sci.* **6** 510.
[10] Hasan H R and Dawood R M 2013 *Baghdad Sci. J.* **10** 934.
[11] Porth C 2014 *Essentials of pathophysiology: concepts of altered health states*. 4th ed (*Lippincott Williams & Wilkins*).
[12] Nelson D L , Lehninger A L and Cox M M 2008 *Lehninger principles of biochemistry*. 5th ed. (Palgrave Macmillan).
[13] Leiß O 2016 *Verdauungskrankheiten*, **34** 229.
[14] Hasan R , Ahmad M , Javaid A and Zaka F 1998 *I.J.B.M.R*. **4** 3414.
[15] Erel O 1998 *Clin. Chem*. **44** 2313.
[16] Voynova I V, Kostevich V A, Elizarova A Y, Karpenko M N and Sokolov A V 2019 *Acad. Med.* **19** 37.
[17] Bishop M L, Fody E P and Schoeff L E 1996 *Clinical Chemistry. Techniques, Principles, Correlations*. 6th ed (Lippincott Williams and Wilkins) 313-318.
[18] Werner M, Garberielson D G, Estman J. 1981 *Clin. Chem*. **27** 268.
[19] Friedewald W T , Levy R I and Fredrickson D S 1972 *Clin. Chem*. **18** 499.
[20] Sezen H. and Sezen Y 2018 *Koşuyolu Heart J.* **21** 61.
[21] Berntsson J, Östling G , Persson M , Smith J G , Hedblad B and Engström G 2016. *Stroke,* **47** 1858.
[22] Arenas de Larriva A P, Limia-Pérez L , Alcalá-Díaz J F , Alonso A , López-Miranda J and Delgado-Lista J 2020 *Nutrients,* **12** 3219.
[23] Grammer T B , Kleber M E , Silbernagel G, Pilz S , Scharnagl H and Lerchbaum E 2014 *Free Radic. Res.* **48** 706.
[24] Shanidze E and Zhvania M 2005 *Georgian Med. News* **127** 38.
[25] Petelenz T , Drózdz M , Słomińska-Petelenz T, Jendryczko A, Kucharz E and Drazkiewicz U 1989 *Materia Medica Polona*. **21** 199.
[26] Hasan S H , Hasan H R and Melconian A K 2018 *J. Pharm. Sci.* **10** 3321.
[27] Hughan K S , Wendell S G, Delmastro-Greenwood M , Helbling N , Corey C , Bellavia L, Shiva S 2017 *Hypertension,* **70** 634.
[28] Michel T 2010 *Circulation*. **121** 484.
[29] Frieden E and Hsieh H S 1976 *Adv. Exp. Med. Biol.* **74** 505.
[30] Kang Y J 2011 *Pharmacol. Ther.* **129** 321.
[31] Huang L , Shen R , Huang L, Yu J and Rong H 2019 *Asia Pac. J. Clin. Nutr.* **28** 761.
[32] Chen A , Li G and Liu Y 2015 *Inhal. Toxicol.* **27** 237.
[33] Hammadah, M , Fan Y , Wu Y, Hazen S L Tang W H 2014 *J. Card. Fail.* **20** 946.
[34] Alexanian I, Parissis J , Farmakis D , Athanaselis S , Pappas L , Gavrielatos G 2014 *Clin. Res. Cardiol.* **103** 938.
[35] Cabassi A, Binno S M , Tedeschi S , Ruzicka V , Dancelli S , Rocco R 2014 *Circ. Res.* **114** 1723.
[36] Kamath A R and Pai R G 2008 *Int J Angiol* **. 17** 63.

[37] Liberman M , Evo B, Martinatti M K , Lario F b C, Wosniak J O, Pomerantzeff P M A. 2008 . *Arterioscler. Thromb. Vasc. Biol.* **28** 463.
[38] Rajamannan N M , Evans F J , Aikawa E , Grande-Allen K J , Demer L L and Heistad D D 2011 *Circulation*. **124** 1783.
[39] Ljungberg J , Johansson B , Engström K G , Albertsson E , Holmer P and Norberg M 2017 *J. Am. Heart Assoc.* **6** e005133.
[40] Freeman R V and Otto C M 2005 *Circulation*. **111** 3316.
[41] Peltier M , Trojette F , Sarano M E , Grigioni F, Slama, M A and Tribouilloy C M 2003. *Am. J. Card.* **91** 97.
[42] Afaq E , Hafeezul-Hassan S , Nisar M K , Afaq H and Naheed K 2017 *J. Islamabad Med. Dent*. **6** 141.
[43] Ortlepp J R , Pillich M , Mevissen V , Krantz C , Kimmel M and Autschbach R 2006 *Heart*. **92** 1463.
[44] Novaro G M , Sachar R , Pearce G L, Sprecher D L and Griffin B P 2003 *Circulation*. **108** 1804.

Regeneration of Used Oils by Red Mud and DESs (Reline)

Regeneration of Used Oils by Red Mud and DESs (Reline)

W M Saleh[1], R Z Al-Khayat[2],S h M Saied[3] ,A M SYassin[4] and F fadil[5]

[1,2,4,5] Dept. of Chemical Industries, Institute of Technical, Mosul,
[3]Dept. of Medical Laboratories Technique/Al-Noor University College, Mosul

Email: [1] wijdan.m.salih@ntu.edu.iq

Abstract To regeneration of oils which are used in cars engines to lubricate its moving parts, and to get rid of highly contaminants which must be separated to reuse the engine oils. In the column chromatography, the waste oil was treaded as mobile phase (eluent) with petroleum ether (40-60ºC), while the red mud (alhuor) is a stationary phase for adsorbed the impurities. The effect of the new method using deepeutectic solvent (DESs Reline) as a kind of ionic liquids to help extract impurities by adsorption (choline chloride and urea). Moreover, some thermal and physicochemical properties like density, thermal and electrical conductivity, ash percentages, viscosity, specific gravity and pH values were determined. Values were determ.using TGA for blank oil for comparison and differential scanning calorimetric analyses (DSC).

Keywords: Reline, oils ,choline chloride, physicochemical properties, waste oils

1.Introduction

Enormous amount of cars oils is considered as destructive waste into the environment in Mosul (the main city in Nenavah/ Iraq), and discarding of used oil in Tigris river, which produces complications not only the water contamination (the only source of people drinking in the area) but also destructive to river life. One gallon of engine oil approximately pollute a million gallon of water including plants [1]. Waste oil used in cars engines to lubricate the moving parts of engine, but it picks up highly contaminants compounds which must be separated in order to reuse the engine oil [2]. So to prevent undesirable properties in engine oil, many additives are used. The laboratory recycling of waste oils depends on the procedures of the refining and chemicals used in these procedures and depend on the type of used oil also, in this paper we will use deep fusion solvent which is a new method (DESs) as a kind of ionic liquid is used to help extract impurities by adsorption. Deep eutectic solvents (DESs) are extensively recognized as a novel type of ionic liquids (ILs) since they share many features and properties with ILs. Deep eutectic solvents (DESs) and ILs have been used mutually in the literature though it is essential to indicate that these are really two different types of solvent [3]. DESs are formed from a eutectic mixture of Lewis or Brønsted acids and bases which can include anionic and/or cationic species; in disparity, ILs are formed from systems composed primarily of one type of discrete anion and cation. It is explain here that the chemical properties of DESs and ILS suggest

application areas which are significantly different although the physical properties of DESs are similar to other ILS [4]. The investigation into DESs has intensified in this decade, eversince the possible for new chemical knowledges was grasped, they have recommended that choline chloride based DESs and Bronsted-Loury acid (hydrogen donor) were effective to remove free glycerol from palm-oil [5]. This waste oil can be distilled into diesel fuel or marine fuel in a process similar to oil re-refining, but without the final hydrotreating process [6]. Paul [7] define the used oil re-refining as the process of restoring used oil to new oil by removing chemical impurities and heavy metals using reclaimed waste lubricating by hydro treating after washing with a polyglycol ether [8]. In 1998, Al-Khazraji used different thermally activated clays which gave best results of reclaiming of used lubricating oils when they were treated with diluted hydrochloric acid [9]. In current work it is the first time to use ionic liquid type of DESs (Reline) in recycle process of oil re-refining, which was only used by modelling and simulation of CO_2 removal from model shale gas along with the physicochemical properties of DES**s**, which were employed for the modelling and simulation of CO_2 removal studies [10].

2. Materials and Methods

Iraqi Red mud (alhuor), Petroleum ether 40-60 ^{O}C, Urea, Choline chloride and Engine oil (new) and used.

2.1 Instruments

The instruments used are electrical conductivity, Weiss – Techn. Werk Statlen, WTW). LBR and pH meter, Philips. TGA and DSC analysis were done by scanning TGA using Horizontal balance and carried out using Mettler-Toledo TGA/ DSC star system in pottery (silica) crucibles at temperatures ranging from (25 to 600◦C) with heating rate of (20◦C/min) under air atmosphere.

2.2 Preparation of choline chloride – urea DESs (Reline)

A mixture of choline chloride (1 mole) and urea (2 mole) is heated and stirred at 80-100 °C until a clear solution is beginning to form[11]. The product was cooled and used without any purification. The freezing point of the product is 12ºC [12].

2.3 Activation of red mud (Al-Khazraji,1998)

The red mud is grinding very well, then it is washed in a sink with water for many times. The resulting mud is draying in microwave oven, then grinding again and is saved in 80 mesh size save. The resulting particles are washed with water, heated in oven at (100 – 120 ºC) and then heated in another oven at (600- 800ºC).

2.4 Setting the column chromatography

A column was packed with the red mud (absorbent)(about 30 gm) into a cylindrical glass with size (2*30 cm) [13]. The base of the tube contains a glass wool pad to grip the solid phase in place. A solution of oil (20ml.) and DESs (Reline) in petroleum ether (50ml.) ‘Table 1’ was added. Then, the used oil was eluted from the top of the column and 90% of the mixture solvent (64ml. was received from the tap control. This is a simple laboratory column which runs by gravity flow which can be increased by extending the solvent (petroleum ether) filled column above the top of the stationary phase or decreased by the stopcock controls’ Figure 1’.

Table 1. The amounts of DESs (Reline) used.

Sample No.	Type of oil	Weight of DESs (Reline) (gm)
1	fresh	-------
2	fresh	1.5
3	fresh	2.5
4	fresh	3.5
5	regenerated	-------
6	Regenerated	1.5
7	Regenerated	2.5
8	Regenerated	3.5

Table 2. DSC results for analyzed with(without)DESs (Reline) oil samples (which isolated from oxygen).

Sample No.	DSC Results (°C)	
	Exothermic peaks	Endothermic peaks
5	275	313
6	282	328
7	290	328
8	294	340

3. Results and Discussion

The reaction of quaternary ammonium salt choline chloride and urea is atom efficient since all the atoms present in the starting materials are incorporated in the products DESs (Reline), as in equation 1, the preparation of DES in ethanol [14].

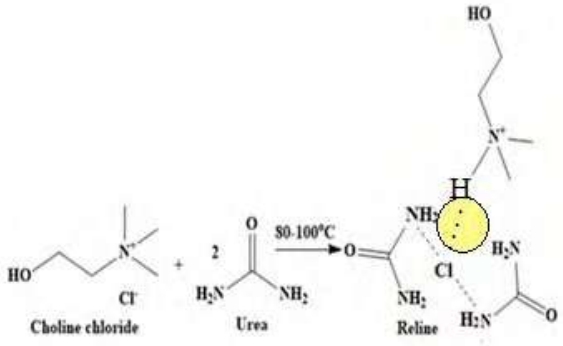

Figure 1. Preparation of DESs (Reline)

While red mud is a stationary phase for adsorbed the impurities, mobile phase (eluent) is petroleum ether (40-60ºC) because it is a solvent used to move the recycle oil through the column. It is selected for two reasons. First, it's retention factor value of approximately 0.2 - 0.3 for diminish the time and the amount of eluent to run the chromatography, and the latter is the different impurities in the used oil can be separated effectively. Chromatography is an important characteristic that affects the oil's ability to transfer heat from the engine is its thermal properties, the increasing of the values of thermal conductivity (k) of recycle oil samples (5-8) (which is the measure of their abilities to conduct heat) to 35.83211267×10^5 cal.cm^{-2}.sec^{-1} for sample No (8) of the highest amount of Reline (3.5 gm) than that of standard (new) oil $33.73493976 * 10^5$ cal.cm^{-2}.sec^{-1}. Also, specific heats of recycle oil samples (5-8) were only less than the unused samples 1-4 by only less than 0.03ºC cm^{-3}(25ºC) 'Table 3'the oil transfers heat more efficiently, the higher the thermal conductivity and specific heat**[15]**

Table 3. The Physical properties of the new and used oil:

Sample No.	Density (gm .cm^{-2})	Thermal conductivity (cal.cm^{-2}.sec^{-1}. ^{o}C *10^{5})	Electrical Conductivity (Ohm.cm^{-1} *10^{8})	Ash content %	Viscosity Poise (25^{O}C)	Specific heat ^{o}C. cm^{3} (25^{O}C)	pH
1	0.830	33.73493976	0.65	0.18	3.1428	0.50049	6.51
2	0.826	33.88000	0.66	0.0	3.233	0.498078	6.89
3	0.8.6	34.72069479	0.85	0.0	3.210	0.486018	6.59
4	0.81	34.45923457	0.75	0.0	2.998	0.48843	6.98
5	0.8.5	34.763822609	1.08	1.23	2.778	0.485415	8.14
6	0.784	35.69500000	0.93	1.03	2.861	0.472752	8.10
7	0.798	35.06877193	0.92	0.39	2.911	0.481194	6.91
8	0.781	35.83211267	0.82	0.54	2.678	0.470943	6.70

Heat transfer happens at a lesser degree in sample (5) of low thermal conductivity than in other samples (6-8) of high thermal conductivity. For instance, samples typically have high thermal conductivity and are very efficient at conducting heat. Sample No. 7 had the best neutralizing value of pH = 6.91 of all other regenerated samples. The acidity of engine oils favorites the neutral pH. The polar nature of DESs (Reline) has therefore shown to decrease the electrical conductivity of waste oil 0.26-0.15-ohm cm$^{-1,}$ Also, as amount of DESs (Reline), the polar nature increases from 1.5-2.5 gm as viscosity increase from 2.861 to 2.911 Poise, more viscosity means thicker the oil (at higher temperatures, thick oils have more renitence to shearing and losing film strength and these best values indicate that the regenerated oils show minimum contamination). These results come with agreement of ash content percentage which is also 0.39% for sample (7) which is the best oil purity (ash content is very important factors).. Specific gravity in cal. / gm °C. Thermal gravimetric analysis (TGA) is measure the change in weight during heating or cooling, it studies of recycle samples show that sample No (5) without DESs (Reline) and sample No. (6) with 1.5 gm verifies less stability at 279^{o}C and 281^{o}C, respectively, with only 10% of weight loss at these temperatures as shown in 'Figure 2' and 'Figure 3'. The same study indicates that samples (7 and 8) of only (1.5 and 2.5 gm) DESs respectively, 'Figure 4' and 'Figure 5' verified more stability at 300^{O}C with only 10% of weight loss at this temperature.

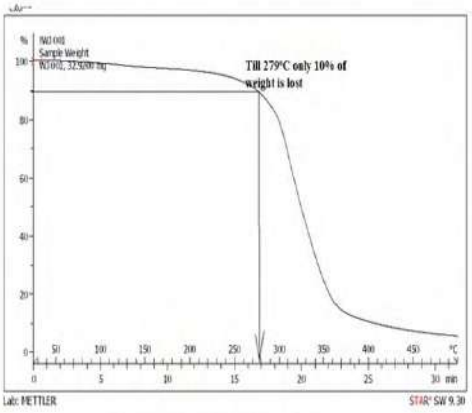

Figure 2. TGA of Sample (5)

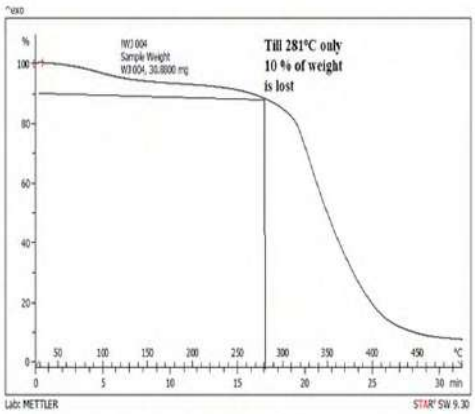

Figure 3. TGA of Sample (6)

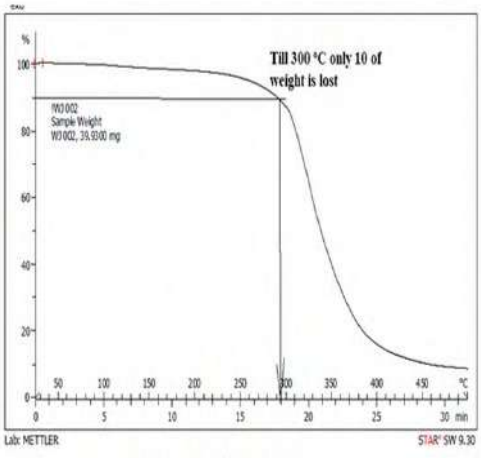

Figure 4 . TGA of Sample (7)

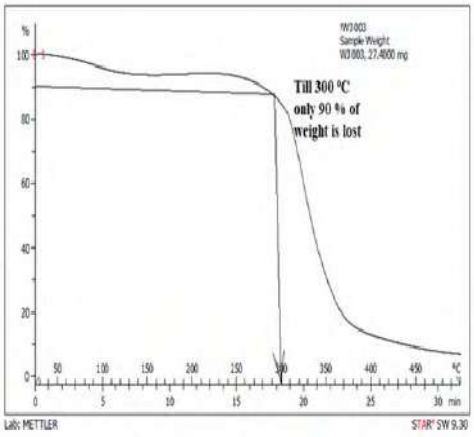

Figure 5 . TGA of Sample (8)

Similar to TGA, differential scanning calorimetric analyses (DSC) are valid tools in the study of the thermal and oxidative stability of drying oils [16]. DSC analysis can be fit for the estimate the sample stability and the calculation of the film formation (the very first stages) since oil layers have been painted out. The differential scanning calorimetry (DSC) is measuring the absorbed or released heat during heating or cooling. The DSC data shows Table 2, 'Figure5-8' an exothermic and endothermic peaks and the decreases in the heat generation is due to decreasing of unburned impurities (such as aromatic hydrocarbons) in the recycle oil. the maximum amount of DESs with sample No (8) gives larger peak of endothermic heat 340^{o}C[17].The results of these regenerated samples, Sample No(7) of (2.5gm) of DESs (Reline) gives the best result.

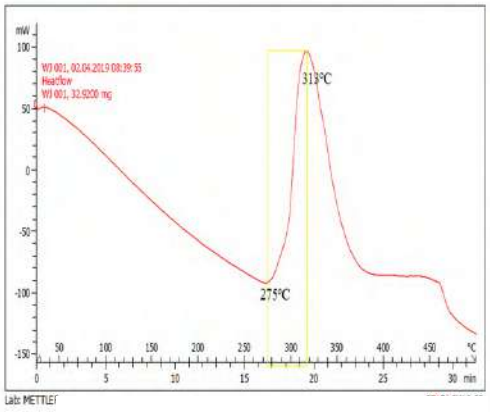

Figure 6. DSC of Sample No. (5)

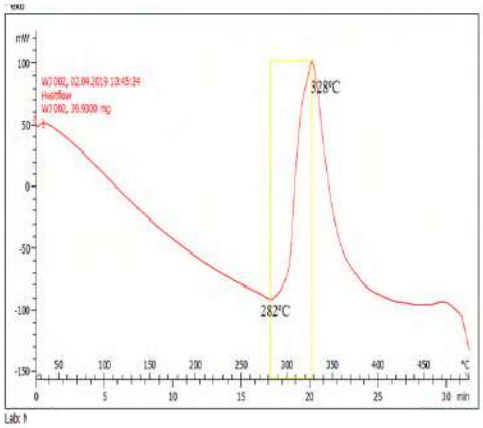

Figure 7. DSC of Sample No. (6)

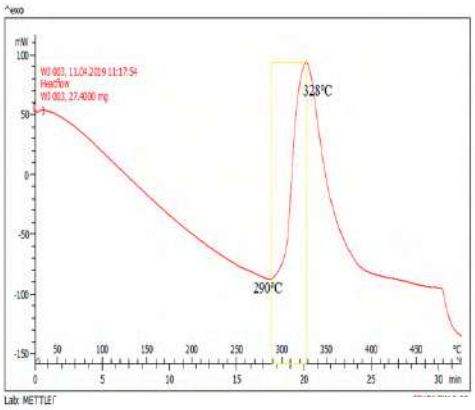

Figure 8. DSC of Sample No. (7)

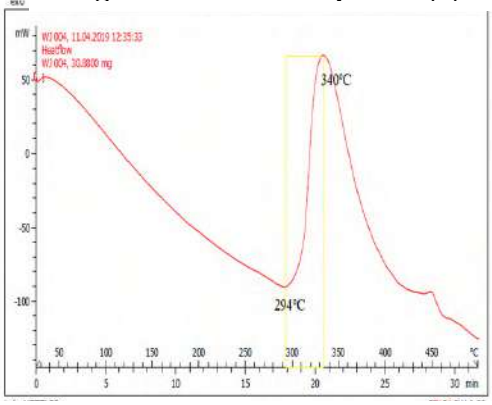

Figure 9. DSC of Sample No. (8)

4. Conclusion

The methodology presented in this work wass succeeded in the removal of waste materials and thus regenerate most properties of the engine lubricating synthetic oil for its reuse. This was achieved by using column chromatography, the waste oil was treated as mobile phase (eluent) with petroleum ether (40-60ºC), while the red mud is a stationary phase for adsorbed the impurities. The effect of this new method of using deep-eutectic solvent (DESs Reline) as a kind of ionic liquids to help extract impurities by adsorption (choline chloride and urea). Moreover, sample No (7) of (2.5gm) of DESs (Reline) showed the best result.

Acknowledgements

We are grateful to the department of Chemical Industries, Institute of Technical, Mosul, for the facilities given to perform this work. Thanks are also to College of Science, University of Mosul and Al-Noor University College to support this research.

References

[1] Filho J L A, Moura L G M. and Ramos A C S 2010 *Braz. J. Chem. Eng.* **27** 687.
[2] Abro R**,** Chen Z, Harijan K, Dhakan Z A and Ammar M 2013 *Chem. Eng. Sci.* Article ID 952589 p. 5.
[3] Abbott A P, Capper G,Davies D.L, Rasheed R K and Tambyrajah v 2003 *Commun. Chem.* **0** 70.
[4] Smith E L, Abbott A P and Ryder K S 2014 *Chem. Rev.* **114** 11060.
[5] Shahbaz K, Mjalli F S and Hashim M A AlNashef I M 2011 Energy Fuels , **25**, 2671.
[6] Liz S 2003 *Environmenta Encyclopedia* **II** 1178.
[7] Paul A 2012 *Greenville Online. com*.
[8] Tomi K 1971 *Nitto Seiyn Co., Ltd* **49** 809.
[9] Al-Khazraji A A H 1998 *Reclaiming of Spent Lubricating Oils by Clay Treatment*.Thesis MSc(College of Education, University of Mosul)
[10] Haider M B, Jha D 2019 *J. Environ. Chem. Eng* **7** 1.
[11] Lobo H R, Singh B S and Shankar L G S 2012 *Catal. Commun.* **27** 179.
[12] Zhang Q, Oliveira V K.D, Royer S and Jerome F 2012 *Chem. Soc. Rev.,* **41** 7108.
[13] Nyul G, Vamos E and Foldva I 1960 Magyar Asvanyoloj Foldgas Kiser Int., **106** 591.
[14] Shamsuri A A and Dzulkefly K A. *Singapore Journal of Scientific Research* **1** 246
[15] Scott W, Paul S, Harold P and Schwarz E S. 2005 Washington, D.C., USA.
[16] Izzo F C, Zendri E, Biscontin G and Balliana E 2011 *J Therm Anal Calorim* **104** 541.
[17] Brown M E 2007 *Introduction to thermal Techniques and Application* 2nd edd.

Conductometric Study of Proline-Mn (II) Complex in Some Solvents at Various Temperatures, with Computational Factors Calculation

Conductometric Study of Proline-Mn (II) Complex in Some Solvents at Various Temperatures, with Computational Factors Calculation

Fanar M Al-Healy[1], Shayma H Abdulrahman[1*] and Anfal R Mahmoud[1]

Department of Chemistry, College of Science, University of Mosul.

[*]E-mail: shaymaa.hashim@uomosul.edu.iq

Abstract: The equivalent conductivities of proline in water, methanol were studied in the temperature range of 288.15 to 313.15 K at 5 K intervals, in mixtures of methanol and water at percentages of10 %, 20%, 30%, 40% and, 50% of methanol at 37°C. The experimental data were treated by the Lee-Wheaton conductivity equation of unsymmetrical electrolytes (1:2) (1 molecule of metal with 2 molecules of ligand) derived to calculate the conductivity parameters, equivalent conductance at infinite dilution Λ_o, ionic conductivity, association constant Ka and the main distance between ions in solution(R) at best fit values of ($\sigma\Lambda$). Thermodynamic quantities for the ion-association reaction (ΔG^o, ΔH^o and ΔS^o) have been also measured. The results of the analysis showed that the ions of the complex can be separated by solvent molecules (SSIP). The values of Ka, Λ_o and R were found to be different from one solvent to another depending on the interactions in the solution. Furthermore, the chemical structure of the Proline-Mn complex was optimized by using of Gaussian interface version 16.0 program of chem3D to optimiz the features of complex molecule. The suggested statistical model possesses only two parameters with excellent values of the square regression coefficient (r^2) and cross-validation (q^2) are equal to 0.999 and 0.994, respectively, which refers to the perfect relationship between Ka value and the physical properties of the solvent.

Keywords: Proline Complex, Electrical Conductivities, Lee-Wheaton equation, Thermodynamic parameter, Gaussian program, Semi-empirical.

1. Introduction:

Proline (Pro), composed of an amino group and a carboxylic acid, is an amino acid. It is the only amino acid with a secondary alpha-amino group that naturally exists, which explains its more basic character with respect to many other alpha-amino acids. Pro and its derivative in organic reaction are also used as asymmetric catalysts. It is an osmoprotectant and is also used in many biotechnological and medicinal applications [1]. The biological function of several transition metals with mixed amino acid complexes have been revealed, putting them in many biochemical processes [2–5]. Pro has been estimated in different ways such as HPLC [6-8], flow-injection analysis [9], kinetic study [10], capillary electrophoresis [11] in addition to theoretical study [12,13]. The complexes of amino acids

with metals are interesting to be studied by electrical methods especially by conductivity methods. For example, the Tyrosine conductivity has been studied in aqueous solutions at 310.16 K, also Co(II)-, Mn(II)-, Ni(II)-, Fe(II)-prepared tyrosine complexes to form [Ni(tyr)3]Cl2, [Co(tyr)3]Cl2, [Fe(tyr)3]Cl2, and [Mn(tyr)3]Cl2 complexes at various temperatures. Numerous complexes of Co(II), Ni(II) and Fe(II) with different ligands of amino acids (e.g. Glycine, Histidine, Cysteine and Arginine) were prepared and diagnosed using various techniques and then studying their electrochemical conductivity in several solvents [14-15].

The electrical conductivity of solutions depends on the nature of the solute and solvent. For a solvent, the main parameter is the dielectric constant [16]. It is interest to study the effect of temperature and solvent on the electrical conductivity of complexes [17]. In this study, Molar conductivities of dilute solutions for the complex: Mn(II)(Proline) in water, methanol and mixture of them were measured in the temperature range (288.15 - 313.15 K). The ionic molar conductivity (Λ), association constant (Ka) and distance parameter (R), were determined by treating experimental data with Lee-Wheaton conductivity equation.

Hence, the ion-association thermodynamic quantities (ΔG^{o}, ΔH^{o} and ΔS^{o}) are a very useful study of intermolecular interactions, geometric influences of solutions structural, thermo-physical and bulk properties. The study of the transport properties (conductance, viscosity,density and ionic mobility) of electrolytes in aqueous and partly aqueous media, It provides us more detail about ion-ion and ion-solvent interactions in these solutions especially from thermodynamic point of view [18,19].

All Computational Details using semi-empirical methods with the Gaussian'09 software package were carried out. Semi-empirical approaches adopt what are sometimes referred to as empirical techniques where there is no clear using of the two-electron component of the Hamiltonian. Roald Hoffmann suggested the expanded Huckel approach for all valence electron systems. Chem 3D ultra-program were used for a graphic presentation, and to optimized using semi empirical quantum chemical computation [20].

2. Experimental

The Mn(II) complex with proline was prepared by mixing 0.001mole (0.1258g) of $MnCl_2.4H_2O$ in 25ml of conductivity water, its conductivity was equal (2μS), with 0.003 mole (0.3439g) of the proline in 25 ml of conductivity water and refluxed for two hours. On cooling, the complex was precipitated. Magnetic electronic spectra, IR measurement were used to investigate composition of complex [21]. Conductivity water was prepared by redistilling water three times with the addition of 1.5g/L KmnO4 and 0.05g/L KOH [22]. A general method eas used for measuring the conductivity of the electrolytes. The conductivity cell was washed , dried and then weighted empty and kept at a constant temperature (± 0.1ºC) using a water circulating ultra thermostat . A certain amount of solution was injected into the conductivity cell and the conductivity of solution was measured by (WTW) Inolab (740) computerized conductivity meter. Another known amount of solution was injected by a syringe (1ml) and the measurement was repeated. Generally about (15) addition have been made by weighting the amount for each one.

2.1.Computational details

Theoretical calculations were carried out using GAUSSIAN 09 package software implemented on a Lenovo-PC computer with a 2.6 GHz processor. Initial estimation of the structural geometry of the prolin complex was obtained by a molecular mechanic methods (MM2, MD), and for further optimization of geometry, we used the AM1 then PM3 method**.** Finally, Statistical analysis of the experimental results was performed, using Minitab software release 14.1 to find a mathematical equation that describe the relationship between the Ka and the important solvent properties (dielectric constant and viscosity) of the mix methanol and water at different percentages.

3. RESULTS AND DISCISSION

3.1. Molecular Geometry Optimization

Geometry optimization was carried out to determine the best atomic arrangement that makes the molecule more stable. Optimized geometrical parameters such as bond lengths and bond angles and dihedral angles of proline-Mn(II) complex were calculated by semi empirical methods using

parameter PM3[23].The optimized structures with atom labeling and number labeling of complex are shown in Figure 1.

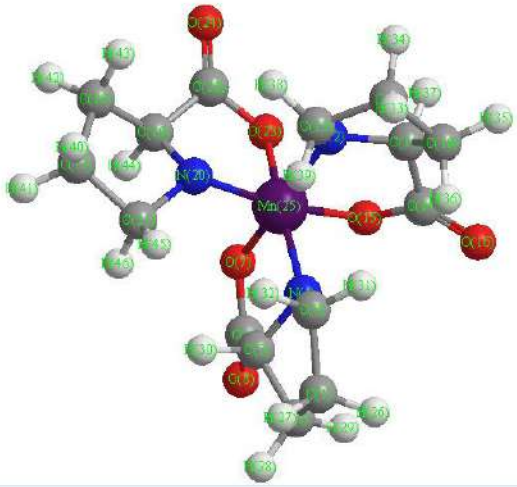

Figure 1. Semi-empirical-calculated optimized structure (at PM3 level of theory) of Proline-Mn complex

After minimizing the energy, the molecule will be in minimum energy level (more stable), then was determine the internal coordinates of atoms of the complex molecule as shown in the Table 1. After that measured the Huckel charge, from the Huckel charge measurement on each atom of complex molecule, we can deduce that the manganese atom have the largest amount of charge, followed by the three nitrogen atoms.

Table 1. PM3-calculated bond lengths and angles between all atoms of the complex molecule.

Atom	Bond atom	bond length atom (A˚)	Angle Atom (A)	Angle (˚)	2nd Angle Atom (A˚)	2nd Angle (˚)	2nd Angle Type
C(3)							
N(4)	C(3)	1.438					
Mn(25)	N(4)	1.846	C(3)	104			
N(12)	Mn(25)	1.846	N(4)	90	C(3)	-127.488	Dihedral
N(20)	Mn(25)	1.846	N(4)	90	N(12)	90	Pro-R
C(11)	N(12)	1.438	Mn(25)	104	N(4)	63.433	Dihedral
C(19)	N(20)	1.438	Mn(25)	104	N(4)	127.21	Dihedral
C(5)	N(4)	1.438	C(3)	104	Mn(25)	109.5	Pro-S
O(7)	Mn(25)	1.81	N(4)	90	N(12)	90	Pro-S
C(13)	N(12)	1.438	C(11)	104	Mn(25)	109.5	Pro-R
O(15)	Mn(25)	1.81	N(4)	90	O(7)	90	Pro-R
C(21)	N(20)	1.438	C(19)	104	Mn(25)	109.5	Pro-R
O(23)	Mn(25)	1.81	N(4)	90	O(7)	90	Pro-R
C(6)	C(3)	1.509	N(4)	104	C(5)	-179.161	Dihedral
C(2)	C(3)	1.523	N(4)	104	C(6)	107.8	Pro-S
C(14)	C(11)	1.509	N(12)	104	C(13)	154.66	Dihedral
C(10)	C(11)	1.523	N(12)	104	C(14)	107.8	Pro-R
C(22)	C(19)	1.509	N(20)	104	C(21)	179.973	Dihedral

C(18)	C(19)	1.523	N(20)	104	C(22)	107.8	Pro-R
C(1)	C(5)	1.951	N(4)	90.278	C(3)	53.812	Dihedral
C(9)	C(13)	1.523	N(12)	104	C(11)	-41.253	Dihedral
C(17)	C(21)	1.523	N(20)	104	C(19)	-40.289	Dihedral
O(8)	C(6)	1.208	C(3)	131.989	O(7)	131.989	Pro-S
O(16)	C(14)	1.208	C(11)	161.472	O(15)	161.472	Pro-R
O(24)	C(22)	1.208	C(19)	131.694	O(23)	131.694	Pro-R
H(30)	C(3)	1.113	C(2)	112.303	N(4)	115.659	Pro-R
H(37)	C(11)	1.113	C(10)	112.303	N(12)	115.659	Pro-S
H(44)	C(19)	1.113	C(18)	112.303	N(20)	115.659	Pro-S
H(26)	C(1)	1.113	C(2)	111.843	C(5)	111.843	Pro-R
H(27)	C(1)	1.113	C(2)	115.113	C(5)	115.113	Pro-S
H(28)	C(2)	1.113	C(1)	110.797	C(3)	110.797	Pro-R
H(29)	C(2)	1.113	C(1)	112.642	C(3)	112.642	Pro-S
H(31)	C(5)	1.113	C(1)	114.005	N(4)	114.005	Pro-R
H(32)	C(5)	1.113	C(1)	120.26	N(4)	120.26	Pro-S
H(33)	C(9)	1.113	C(10)	110.543	C(13)	110.543	Pro-S
H(34)	C(9)	1.113	C(10)	112.043	C(13)	112.043	Pro-R
H(35)	C(10)	1.113	C(9)	110.641	C(11)	110.641	Pro-S
H(36)	C(10)	1.113	C(9)	112.275	C(11)	112.275	Pro-R
H(38)	C(13)	1.113	C(9)	110.797	N(12)	110.797	Pro-S
H(39)	C(13)	1.113	C(9)	112.642	N(12)	112.642	Pro-R
H(40)	C(17)	1.113	C(18)	111.147	C(21)	111.147	Pro-S
H(41)	C(17)	1.113	C(18)	113.468	C(21)	113.468	Pro-R
H(42)	C(18)	1.113	C(17)	114.708	C(19)	114.708	Pro-S
H(43)	C(18)	1.113	C(17)	121.948	C(19)	121.948	Pro-R
H(45)	C(21)	1.113	C(17)	110.797	N(20)	110.797	Pro-S
H(46)	C(21)	1.113	C(17)	112.642	N(20)	112.642	Pro-R

3.2 Conductivity analysis

The equivalent conductivity ($\Lambda_{equiv.}$) at each concentration of each electrolyte solution was calculated by the following equation:

$$(\Lambda_{equiv.}) = 1000\sigma / C1C2 \quad (1)$$

Where σ is the specific conductance obtained experimentally, C1 and C2 are the equivalent concentration of 2:1 and 1:1 electrolytes used respectively[24]. Table 2a, 2b,and 2c shows the values of the equivalent conductivity and concentrations of the two electrolytes salts (2:1) determined experimentally. The Kohlrausch equations was used to discover types of electrolyte through plot the relation between equivalent conductivity against the square root of concentration [25] at different temperature (288.16 -313.16 K) and different solvent (water ,methanol, and their mixtures) as shown in the Figures 2a, 2b and 2c.

Table 2a. Molar concentration (M) and Equivalent conductance of $[Mn(pro)_3]Cl_2$ in water at different temperatures

Conc. Mole/L $*10^{-7}$	√Conc. (mole/L) $*10^{-4}$	Λ (Ohm^{-1}. equive^{-1} .cm^2) 288.16 K	Λ (Ohm^{-1}. equive^{-1} .cm^2) 293.16 K	Λ (Ohm^{-1}. equive^{-1} .cm^2) 298.16 K	Λ (Ohm^{-1}. equive^{-1} .cm^2) 303.16 K	Λ (Ohm^{-1}. equive^{-1} .cm^2) 308.16 K	Λ (Ohm^{-1}. equive^{-1} .cm^2) 313.16 K
2.5643	7.1990	194.9821	210.0046	195.0748	192.9125	257.3206	189.5213
5.0213	10.2689	165.9666	190.9497	190.9014	164.2526	230.0771	184.239
7.5435	12.5406	154.5371	185.9497	173.0658	152.9858	196.8279	172.8288
9.8325	14.3921	152.4805	177.9343	166.0891	150.9934	184.6956	166.3414
12.2964	16.0571	149.0946	170.0499	159.5157	147.6829	174.6973	160.2151
14.7457	17.4490	147.4802	168.6692	144.1688	146.1662	168.166	156.3808
16.9542	18.6958	147.0327	169.5794	135.1085	145.589	165.8528	150.961
19.2708	20.0543	146.9388	165.0565	127.3933	137.1891	163.1273	149.8349
21.5852	21.1831	146.9516	162.1295	126.3367	130.1396	158.3273	146.3369
23.8737	22.3235	146.6762	161.2595	125.9081	129.9399	155.9928	140.0646
26.2474	23.2902	146.0461	160.3251	122.3702	128.704	153.8403	133.8626
28.2739	24.3409	141.4737	157.021	120.1549	127.0049	149.8012	130.5831
30.4031	25.2974	140.0465	151.9279	120.873	124.2806	148.8608	127.3397
32.6374	26.1169	139.665	150.9272	120.4697	121.4671	146.9295	124.0498

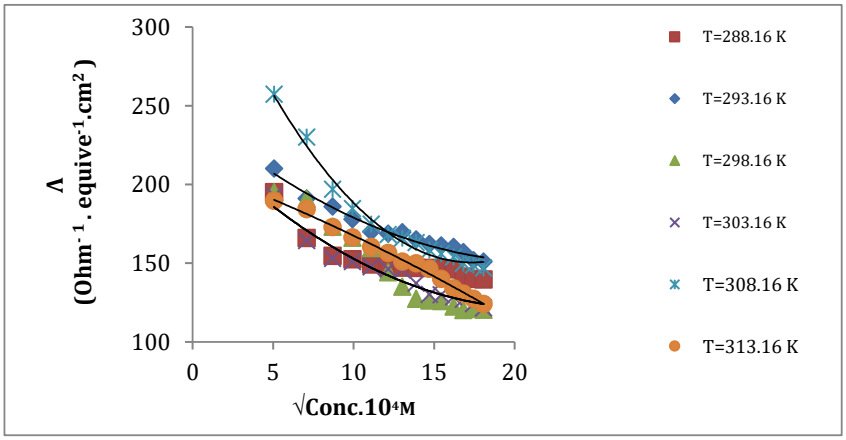

Figure 2a. The relation between the square root of concentration and the equivalent conductance of $[Mn(pro)_3]Cl_2$in water at different temperatures

Table 2b. Molar concentration (M) and Equivalent conductance of $[Mn(pro)_3]Cl_2$ in methanol at different temperatures

Conc. Mole/L $*10^{-7}$	√Conc. (mole/L) $*10^{-4}$	Λ ($Ohm^{-1}.equive^{-1}.cm^2$) 288.16 K	Λ ($Ohm^{-1}.equive^{-1}.cm^2$) 293.16 K	Λ ($Ohm^{-1}.equive^{-1}.cm^2$) 298.16 K	Λ ($Ohm^{-1}.equive^{-1}.cm^2$) 303.16 K	Λ ($Ohm^{-1}.equive^{-1}.cm^2$) 308.16 K	Λ ($Ohm^{-1}.equive^{-1}.cm^2$) 313.16 K
6.55604	8.0969	77.7410	77.5926	75.4429	75.5798	76.1726	78.6841
12.8632	11.3416	76.2651	77.2447	74.0047	64.2040	64.7040	76.1726
19.3808	13.9215	68.7964	76.1236	66.7687	59.6598	60.1211	69.6153
25.3026	15.9068	65.8691	65.7373	63.9330	58.7554	52.6280	66.6383
31.6924	17.8023	63.1065	62.9772	61.2569	57.3355	47.2685	63.8290
38.0817	19.5145	61.2716	61.1434	59.4811	56.9934	43.7078	57.5337
43.8606	20.9429	60.7986	60.6685	59.0265	56.4978	41.7432	53.7839
49.9570	22.3510	60.0514	59.9202	58.3060	52.9118	39.9800	50.5822
56.0792	23.6810	59.4396	59.3069	57.7168	50.0831	38.5826	48.0535
61.9826	24.8963	56.4674	59.0214	57.4462	47.9801	37.5924	46.1840
68.4457	26.1621	53.5704	58.3046	56.7561	45.8649	36.4736	44.2733
73.8580	27.1768	51.9013	58.5320	56.9842	44.7424	36.0535	43.2991
79.5650	28.2072	50.2732	56.4208	54.9356	43.6111	35.5585	42.2996
85.6442	29.2650	48.6508	54.3548	52.9308	42.4462	34.9770	41.2530

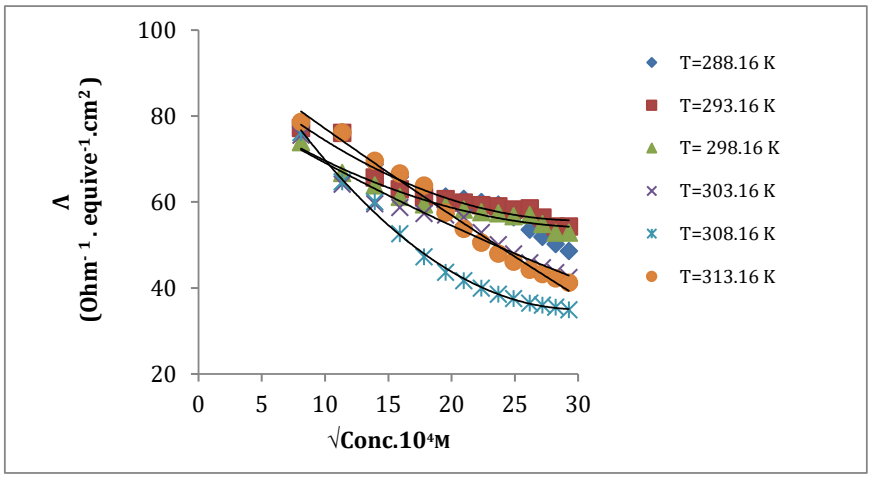

Figure 2b. The relation between the square root of concentration and the equivalent conductance of $[Mn(pro)_3]Cl_2$ in methanol at different temperatures

Table 2c. Molar concentration (M) and Equivalent conductance of $[Mn(pro)_3]Cl_2$ at different percentage of methanol in water

Conc. Mole/L $*10^{-7}$	√Conc. (mole/L) $*10^{-4}$	Λ (Ohm^{-1}. $equive^{-1}$ .cm^2) 10%	Λ (Ohm^{-1}. $equive^{-1}$ .cm^2) 20%	Λ (Ohm^{-1}. $equive^{-1}$ .cm^2) 30%	Λ (Ohm^{-1}. $equive^{-1}$ .cm^2) 40%	Λ (Ohm^{-1}. $equive^{-1}$ .cm^2) 50%
2.6646	5.1620	375.2790	258.8416	244.8986	234.5255	239.1073
5.2282	7.2308	286.8876	230.8790	208.7791	186.9101	182.7888
7.8743	8.8760	253.8579	197.0221	184.6778	165.3729	161.7446
10.2086	10.1419	226.8457	184.4627	176.7567	158.3136	154.8570
12.8855	11.3510	206.9663	174.0534	169.2722	151.6456	148.3508
15.4832	12.4431	193.7569	155.9976	164.2815	147.2094	133.7389
17.8329	13.3541	186.9163	145.1320	162.9573	146.0531	125.0464
20.1315	14.2524	180.5070	135.9232	160.8930	144.2348	117.6217
22.8384	15.1009	175.4092	128.6584	151.2318	142.7413	111.7597
25.2536	15.8761	171.9211	123.2607	143.9772	135.5834	107.4304
27.8625	16.6841	167.6471	117.8233	136.8409	128.6017	102.9995
30.3722	17.3312	160.9114	114.9500	132.8120	129.9980	100.7538
32.5904	17.9886	154.5163	112.0496	128.8455	125.6846	98.4460
34.8368	18.6637	148.3239	109.0575	124.8550	121.4132	96.0249

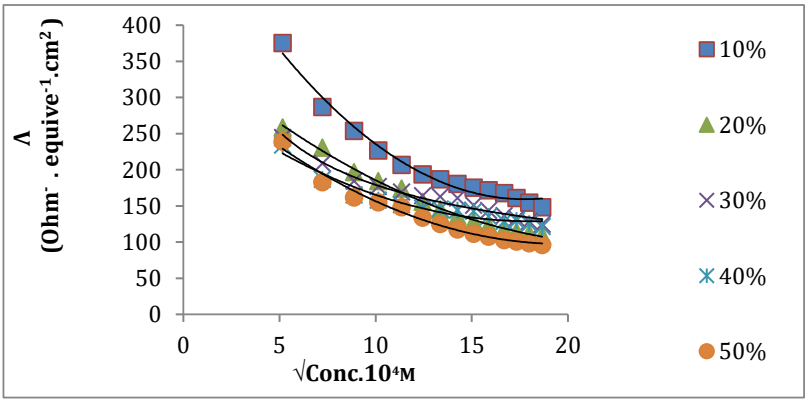

Figure 2c. The relation between the square root of concentration and Equivalent conductance of $[Mn(pro)_3]Cl_2$ at different percentage of methanol in water

Figures 2a and 2b show the relations between (Λ) and concentration (√c) for the studied complex at different temperatures. Gave a curved line, these relationships which indicate that complex of amino acid was weakly associated in different solvents and temperatures [26]. Moreover, Figure 2c shows the relation between (Λ) and the square root of concentration (√c) for the studied complex at different percentages of methanol to water which also gave a curve line. The Lee-Wheaton equation (LW) for unsymmetrical electrolytes is used for analyses of the conductance data for mixed electrolyte solutions using a computer program (AM1).
The theoretical equivalent conductance is given by the following equation.

$$\Lambda e_{quiv.} = \Sigma |Zi| \, mi \, \lambda i / \Sigma Cn \qquad (2)$$

Where Zi is the charge, mi: molar concentration, λi: equivalent conductivity for each

ionic species present in the solution and Cn is the stoichiometric equivalent concentration of electrolyte species n. It was found earlier that Ka and λ°s value for single ion and for ion-pair are constant from one system to another for symmetrical, asymmetrical and mixed electrolytes by using LW equation[27].The input data of the computer program (AM1) are: solvent parameters (T, D, η), charges Zi and limiting conductivities λ°i for each ionic species. $K_{association}$ for each ion association equilibrium as shown in tables (3a, 3b and 3c); for mixture as an example and the experimental data which are the stoichiometric concentration of the two electrolytes solution within the experimentally determined equivalent conductivities calculated from equation (1). The computer program (AM1) calculated the minimum standard deviation σs(Λ) between $\Lambda_{equiv.}$ (found experimentally) using equation (1) and $\Lambda_{equiv.}$ (Calculated by using equation (2) as

$$\sigma s(\Lambda) = (\Lambda e_{quiv.} - \Lambda_{experi.})^3 \ldots\ldots\ldots (3)$$

at the appropriate (R) values (R: the overall distance parameter), where R is only the variable parameter, for each set of the data of each experiment done[28]. Tables 3a, 3b and, 3c show the results of proline complex analysis in water and methanol at different temperatures and at mixtures.

Table 3a. The values at constant Ka, Λ,the distance between R(A°) and σΛ of the$[Mn(pro)_3]Cl_2$ at different temperatures in water solvent.

T (K)	Ka	Λ° (Ohm^{-1} .equive^{-1} .cm^2)	R (A°)	бΛ
288.16	30	90	7.4	0.072
293.16	25	110	7.1	0.112
298.16	72	74	7.5	0.171
303.16	92	78	7.4	0.127
308.16	82	98	7.0	0.168
313.16	122	92	7.0	0.128

Table 3b. The values at constant Ka, Λ,the distance between R(A°) and σΛ of the$[Mn(pro)_3]Cl_2$ at different temperatures in methanol solvent.

T (K)	Ka	Λ° (Ohm^{-1} equive^{-1} cm^2)	R (A°)	бΛ
288.16	6	18	5.4	0.07
293.16	10	15	5.8	0.061
298.16	10	12	4.5	0.057
303.16	8	11	5.2	0.085
308.16	6	10	5	0.151
313.16	4	6	5.9	0.102

Table 3c. The values at constant Ka, Λ,the distance between R(A°) and σΛ of the $[Mn(pro)_3]Cl_2$ in different percentage of methanol in water.

%	Ka	Λ° (Ohm^{-1} . equive^{-1}. cm2)	R (A°)	бΛ
10	52	122	5.5	0.209
20	71	120	7.9	0.21
30	92	91	7.2	0.161
40	110	82	8.1	0.112
50	132	62	8.2	0.169

It is noted that the Ka values of complex increase with increasing temperature because the electronic density of the solvent decrease, associations will decrease that the solvent molecules will be attracted and thus ion association increase. The results of distance parameter R show that complexes electrolytes form solvent separated ion pairs (R is between 4-8) these high values of R indicated that cations and anions are separated by many solvent molecules since the association was high with increased temperatures [29]. The values of σΛ give an indication of good best-fit values [30].

3.3 Calculation of the thermodynamic parameters (ΔH, ΔG, ΔS)

Thermodynamic functions of proline complex were estimated through the value of the equilibrium constant at different temperatures by the Vant-Hoff equation. ΔH values were calculated from the relation between lnKa against 1/T as shown in Figures 3a and 3b. The relation gives a straight line for complex solutions [31] .

$$\ln Ka = -\frac{\Delta H}{RT} + C \qquad (4)$$

While ΔS values were calculated from the equation :

$$\Delta G = \Delta H - T\,\Delta S \qquad (5)$$

and ΔG from the equation :

$$\Delta G = -R\,T\,\ln Ka \qquad (6)$$

The values of thermodynamic parameters (ΔH, ΔG, ΔS) shows in Table (4a and 4b)

Table 4a. Thermodynamic parameters of $[Mn(pro)_3]Cl_2$ in water.

T (K)	ΔS (J.mol-1.K-1)	ΔG (KJ.mol-1)	ΔH (KJ.mol-1)	Ln ka
288.16	28.26	-8.1444	-5.59	3.401
293.16	26.74	-7.84163		3.219
298.16	35.54	-10.5963		4.277
303.16	37.58	-11.3917		4.522
308.16	36.62	-11.2850		4.407
313.16	39.93	-12.5021		4.804

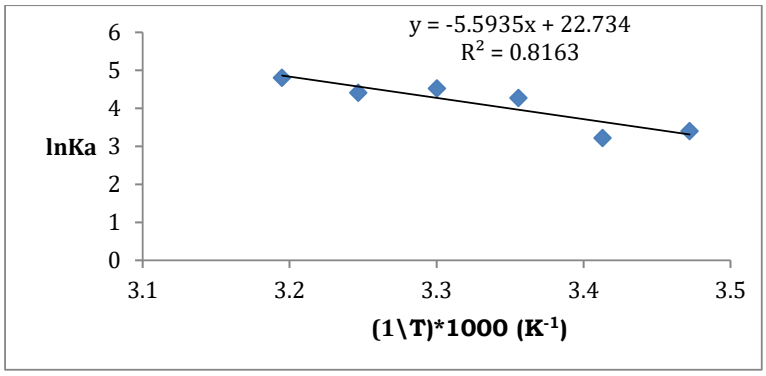

Figure 3a. The relation between the ln Ka &1/T of $[Mn(pro)_3]Cl_2$ in water.

Table 4b. Thermodynamic parameters of $[Mn(pro)_3]Cl_2$ in methanol.

T (K)	ΔS (J.mol-1.K^{-1})	ΔG (KJ.mol^{-1})	ΔH (KJ.mol^{-1})	Ln ka
288.16	28.8	-8.299	-3.41	3.466
293.16	31.26	-9.163		3.761
298.16	32.68	-9.742		3.932
303.16	34.57	-10.48		4.159
308.16	35.55	-10.95		4.277
313.16	36.83	-11.53		4.431

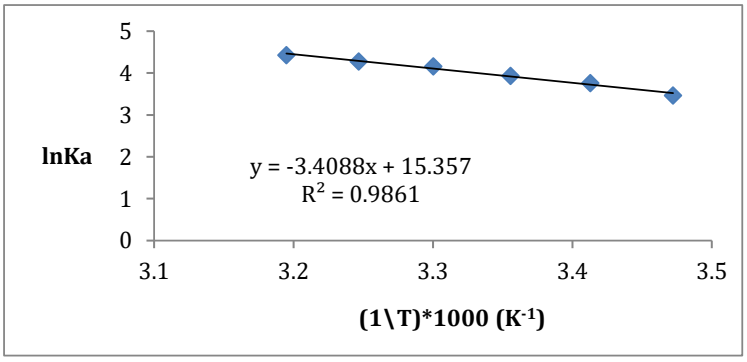

Figure 3b. The relation between the ln Ka &1/T of $[Mn(pro)_3]Cl_2$ in methanol

The values of ΔH (enthalpy of association) were negative(exothermic) which show that the operation was hydration, while ΔG (Gibbs free energy) had negative values which depend upon the kind of ions and in agreement with the relation, which means that the reaction was spontaneous towards the association and the values of ΔS were also positive (increase the random with increase the temperature) [32].

3.4 Statistical analysis

After completing the analysis of conductivity results and determining the Ka and R, the statistical analysis used to find the relationship between the parameters by suggesting an intensive model that is nearly close to accurate mathematical methods with excellent regression parameters. Thus, the first descriptor was selected in accordance with the simple correlation between the Ka and the adjusted parameters as exhibited in Table 5. Below the model equation (eq.7), which was obtained by multiple

linear regression, with r^2 and q^2 equal to 0.999 and 0.994 respectively. The suggested model can be used to predict the Ka value from the dielectric constant and viscosity of solvents before experiments.

Ka = 531 - 0.6 dielectric const. - 65472 Viscosity (7)

Table (5):physical parameters and Ka in different mixture solvents

% MeOH	Ka	Viscosity (Poise)	Density (g/cm^3)	Dielectric Const.	R (A°)	Λ° (Ohm^{-1}. $equive^{-1}$ .cm^2)
10	52	0.00664	0.9737	69.64	5.5	122
20	71	0.00638	0.9534	65.2	7.9	120
30	92	0.00612	0.9331	60.8	7.2	91
40	110	0.00586	0.9128	56.418	8.1	82
50	132	0.0056	0.8925	52	8.2	62

Table (6): Theoretical and expermental value of Ka according to the suggested model

Obs	Ka expermentaly	Ka theoriticaly
Training set		
1	52	51.647
2	71	71.065
3	110	111.213
4	132	131.075
Test set		
5	92	93.83

4.Conclusions:

The present work reports conductivity data for proline-Mn solutions in water, methanol at different temperatures and in mixtures of methanol in water, which were measured by assisting the lee-Wheaton equation at the best fit values of standard deviled (σ Λ) for analyzing the data of unsymmetrical electrolytes included. The values of conductivity parameters such as association constant Ka, Λo, and distance parameter R, were differ from one solvent to another depending on dielectric constant and viscosity and interactions in solution. An indication of the above can be said that the electrophoretic effect or asymmetric effect. The Affected Ka values were in the following order [mixture> methanol> water], due to the difference in the density, viscosity and, dielectric constant which decreases with the increase of alcohol content. Consequently, increased intermolecular interaction and ionic hydration between the methanol and water molecules are responsible for the decrease in density which is in coherence with the available literature values. Therefore, the mixture results are better than those of methanol or water alone. Also, from theoretical results, the effect of the solvent property upon the Ka is in matching with the experimental results.

5. Acknowledgments

The authors are very grateful to the University of Mosul / College of Science, for their provided facilities, which helped to improve the quality of this work.

References

[1] Lu J, Meng D , Li F, Guo M and Li Y 2020 *Russ. J. Phys. Chem.* **A,**. **94** 1427.
[2] Lahsasni S A, Ammar R A and Amin M F *INT J ELECTROCHEM SC,*. **7** 7699.
[3] Sigel H, Operschall B P, Massoud S S, Song B and Griesser R 2006 Dalton Transactions, **46** 5521.
[4] Udhayakumar S, Shankar K G, Sowndarya S , Venkatesh S , Muralidharan C and Rose C 2017 *RSC Advances*, 7 25070.
[5] Datta P K, Chandra M and Dey A K 1980 *Transition Metal Chemistry***, 5** 1.

[6] Long D , Wilkinson K L , Poole K, Taylor D K , Warren T, Astorga A M and Jiranek V 2012 J. Agric. Food Chem,.60 4259.
[7] Ábrahám E , Hourton-Cabassa C, Erdei L and Szabados L *Methods Mol Biol* **, 639** 317.
[8] Lv Z, Zhang H , Zhang Y , Guan Y J and Chengyin W 2016 *JCS*. **54**(10) 1743.
[9] Costin J W , Barnett N W and Lewis S W 2004 *Talanta*. **64**(4) 894.
[10] Kuntz A F , Boynton A W , David G A, Colyer K E and Poutsma J C 2002 *JASMS*, **13**(1) 72.
[11] Dominguez M A , Jacksén J, Emmer Å and Centurión M E 2016 *Microchemical Journal*, **129** 1.
[12] Wang Y, Shang Z C, Wu T X, Fan J C and Chen X 2006 *J Mol Catal A Chem*. **253** (1-2) 212.
[13] Huang X Y, Wang H J and Shi J 2010 *J. Phys. Chem. A*,**114**(2) 1068.
[14] Al-Healy F and Hamed Y 2019 ***EPSTEM*** .**7** 48.
[15] Al-Allaf Y O , Al-Tamer M Y and Abdulfattah M N *Raf.J.Sci*.**24** 45.
[16] Petruhina V A , Kurnaleva T A, Egorova D A and Koltsov N I 2016 *Butlerov Communications*.**45** 107.
[17] Petrukhina V A , Kirillova T A , Tcareva L Y, Andreeva E V and Koltsov N I 2019 *Butlerov Communications*.**57** 54.
[18] Wagner H 2012 *Power Plant Chemistry*,**14** 455.
[19] Boškovi p , Sokol v, Tomaš R and Prkic A *Int. J. Electrochem. Sci*.. **8** 10961
[20] Itte P , Amshumali M K and Mussavir P K M 2017 *Univers. J. Chem*.**5** 48.
[21] Hummodat M Z and Mustafa I 2013 *Synthsis and Characterization of Mixed ligand Complexes of Nikal(II) Copper(II) Palladium(II) Platinum(IV) and Gold(III) with Some Amino Acid and Dithiocarbamates or Dithiophosphat in Thetriphenylphosphine Adducts with some of the Nickal(II) Complexes* , Ph.D., University of Mosul ,College of Science.
[22] Palmer, W.G. (1954). *Experimental Physical Chemistry.* (Cambridge at the University Press**,** London) 186.
[23] Abdulrahman S H and Khalil R A 2020 *Statistical Treatment for study the Relationship between the Chemical Structure and Activity of some biologically Active Isatin Derivatives Using Quantum Mechanics Methods,* Ph.D., University of Mosul ,College of Science.
[24] Akrawi B A, Al-Nuri I J and Khalil S M 1991 *Iraqi J.Chem*.**16** 67.
[25] Lee W H and Wheaton R J 1978 *J.C.S.Farady II*,. **74**, pp.743.
[26] AL-Bashar M.N., Jamil A. M.; (2016), "Determination of Thermodynamic Functions for Ion Association of Hippuric Acid in 20% Aqueous Ethanol'' ***Res. J. Chem. Sci***.,. **6**, No.2, pp.15.
[27] Lee, W.H.; Wheaton, R.H. (1979). The conductivity of dilute aqueous solutions of magnesium chloride at 25C◦. ***J. Chem. Soc., Faraday II***,**75** 1128.
[28] Akrawi B A and Hameed Y O 2005 . *IASJ*. **16** 165.
[29] Radhika V and Manikyamba P 2008 . *Indian J. Chem*. **47**[A] 1814.
[30] Al-Alallaf Y O , Ahmed S A and Ahmed,R.H *Raf.J.Sci*. **27** 58.
[31] Eggers D F , Gregory N W , Halsey G D , Rabinovitch B S 1964 *Physical Chemistry*,(John Wiley and Sons, Inc. New York) p. 198
[32] Robert G M 2008 *Physical Chemistry*. 3rd ed., (Elsevier Inc., Burlington, USA) p 1**.**

Journal of Physics: Conference Series

Levels of Heavy Metal and Trace Element Among Children with Autism Spectrum Disorders

Levels of Heavy Metal and Trace Element Among Children with Autism Spectrum Disorders

Furqan Moein Auda*, Amar M .Ali and Shaymaa Dhyaa

University of Kufa /College of Science/ Department of Chemistry , Iraq.

*E- mail: furqan.chmala@uokufa.edu.iq

Abstract. The aim of this study was estimation the concentration of heavy and trace element in blood samples for autism spectrum disorder *material and method*: sixty patients with autism participated in the present study, all of these patients are registered in an autism center in Basrah province(Iraq). At the same time, 30 healthy children contributed in the study as a control group. The heavy levels were estimated and trace elements (chromium , zinc, selenium, copper, lead, mercury and iron) in the patient and control groups by used energy dispersive X-ray spectroscopy (EDS). The basic principle should appear in the X-rays emitted by the different energies coming from the sample at the same time as a beam of an electron is moving its factors. *Conclusion*: The results showed that there was no significant difference between patients and the control group in all trace elements except zinc. On the other hand, the study showed that there was no significant change between male and female in all levels of trace elements except selenium.

Key words: Trace elements , Autism Spectrum Disorder ,Energy dispersive X-ray spectroscopy.

1. Introduction

Autism spectrum disorder is a disorder that affects children at an early age, characterized by difficulty in communicating with others, slow speech, aggression and isolation, the causes of which are unknown [1]. Hereditary and ecological reasons were involved within the disease [2]. Trace elements are existing in several forms in the nature, and these elements are actual necessary for the body to achieve different functions, where this elements acting as cofactors for various enzymes. Serum iron level showed correlation with oxidative stress markers in several disease such as beta thalassemia major [3]. On the other hand, the scientist was explained the effect of some elements in function of more glands which was that effect on the some hormones [4]. In addition, the researchers have shown that the high level concentration of some trace elements consider an important factors for increase oxidative stress [5]. Researchers have also shown that there is a significant relationship between trace elements and genetic factors, as a result of this relationship, oxidative stress is impaired [6]. In addition ,the researchers explained the relationship of iron with oxidative stress and consequently the effect of oxidative stress on glands and production of hormones, which in turn regulate the vital activities of the human body [6].Despite the importance of these elements in the human function, an increase in their concentrations in the blood is considered toxic, On the other hand, any lack of concentration causes a defect in many life processes studies have proven a correlation between the accumulation of heavy elements in the blood and memory impairment [7], Mental disorders. In addition, the researcher explained the effect of trace elements including iron, on the oxidation of fats and consequently its negative effect

on oxidative stress and on steroid hormones and neurons [7,8], neurological and behavioral abnormalities and neurotoxicity [9-12].

Objective: The aim of the current study was to compare the level of trace elements in patients with autism and control group.

2. Subject and Method

Sixty patients with autism were contributed in this study. Their ages were between 3 and 6 years. These patients are listed at a specialized autism center in Basrah province (Iraq). Blood sample was taken from them after the agreement of their parents. To estimate the concentration of trace elements, a technique was used energy dispersive X-ray spectroscopy (EDS). Primary precept needs to have an appearance at of released X-rays of different energies coming from the sample at the similar time as a beam of electron moves its factors. The amount and composition of metal nanoparticles can without difficulty be identified from the floor of the given sample [13].

3. Statistical Analysis

The data collated after biochemical analysis were subjected to statistical calculation using statistical software (Megastat). The mean, standard deviation of mean and F-distribution test were obtained. Critical value or test of probability less than 0.05 ($p< 0.05$) was regarded significant and microsoft excel (2010) and Minitab v. 14 was also used**.**

4. Result and discussion

Table 1. shows the level of chromium , zinc, selenium, copper, lead, mercury and iron for autism patients and their control group .

Table 1. level of chromium , zinc, selenium, copper, lead, mercury and iron for autism spectrum disorder and their control group.

Parameter	Patients	Control	P-value
Chromium ng/mL	2230.4 ± 1796.2	2745.7 ± 1497.7	0.155214
Zinc ng/mL	24072.3 ± 7359.8	33952.3 ± 15533.7	0.002182*
Selenium ng/mL	23297.6 ± 9813.8	27441.9 ± 8833.4	0.047508*
Copper ng/mL	26818.4 ± 11359	29626.3 ± 8657.2	0.196874
Lead ng/mL	65012.9 ± 23703.6	64568.5 ± 17341.9	0.919859
Mercury ng/mL	48341.8 ± 10280.1	48309.3 ± 8753.8	0.98759
Iron ng/mL	4686.3 ± 4059	6827.2 ± 6169	0.092182

The results in Table 1 show there is no significant change in all trace elements($p>0.05$) except zinc and selenium which have a significant decrease ($p\leq0.05$). These results are consistent with study of Knutson & Mitchell(2019), Where they studied the effect of trace elements on neurons in vitro they found that the effect of these trace elements very little except when the concentration of a very high level. On the other hand, Knutson & Mitchell explained that zinc is the most important elements that affect the function of neurons and brain [14].

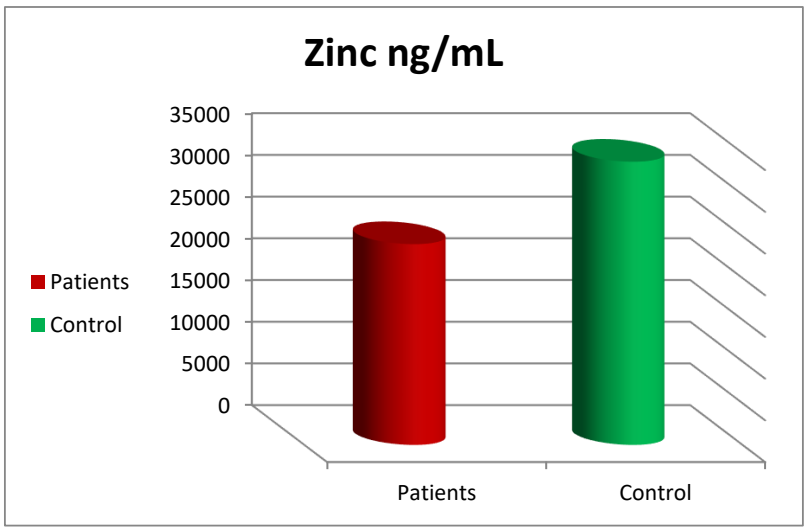

Figure 1. The level of zinc in autism patients and control group

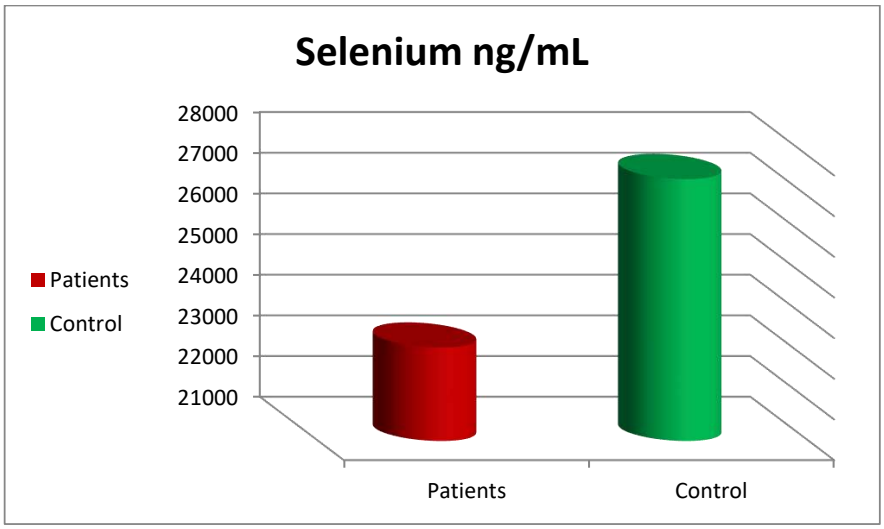

Figure 2. The level of selenium in autism patients and control group

In the other hand, the results showed non –significant change in chromium, Copper, lead, mercury and iron in ASD samples as compare control group. These results are consistent with a study of (14),which they proved that that most trace elements have a normal level in autism patients.

Table 2. level of chromium , zinc, selenium, copper, lead, mercury and iron in male with autism spectrum disorder **.**

Parameter	Patients/Male	Control/Male	P-value
Chromium (ng/mL)	2315.8±1812.2	2763.4±1567.1	0.351
Zinc (ng/mL)	24769.4±7134.5	38385.4±12591.3	0.0004*

Selenium (ng/mL)	25019.4±9905.7	25926.4±7658.5	0.709
Copper (ng/mL)	26951.4±11296.1	29020.4±9736.5	0.487
Lead (ng/mL)	66515.4±23227.6	67736.1±5143	0.751
Mercury (ng/mL)	47558.7±11956.6	50246.5±3309.5	0.192
Iron (ng/mL)	4623.4±4145.4	7767.9±6580.2	0.081

The results refers to no significant change in male with ASD for all parameters($p>0.05$) except zinc($p\leq0.05$).

Table 3. level of chromium , zinc, selenium, copper, lead, mercury and iron in female with autism spectrum disorder .

Parameter	Patients/Female	Control/Female	P-value
Chromium (ng/mL)	2046.2±1795.8	2722.6±1464.9	0.251941
Zinc (ng/mL)	22568±7806.3	28155.1±17535.5	0.297741
Selenium (ng/mL)	19582.3±8735.8	29423.7±10142	0.009*
Copper (ng/mL)	26531.5±11799.9	30418.6±7316	0.259
Lead (ng/mL)	61771±25029.7	60426.2±25665.6	0.884
Mercury (ng/mL)	50031.6±4929.1	45776.2±12582.5	0.265
Iron (ng/mL)	4822.1±3973.3	5597.1±5598.6	0.672

The results refers to no significant change in female with ASD for all parameters ($p>0.05$) except selenium($p\leq0.05$).

Table 4. Comparison between male and female with autism spectrum disorder for level of chromium , zinc, selenium, copper, lead, mercury and iron.

Parameter	Male	Female	P-value
Chromium (ng/mL)	2315.8±1812.2	2046.2±1795.8	0.593
Zinc (ng/mL)	24769.4±7134.5	22568±7806.3	0.304
Selenium (ng/mL)	25019.4±9905.7	19582.3±8735.8	0.038*
Copper (ng/mL)	26951.4±11296.1	26531.5±11799.9	0.897
Lead (ng/mL)	66515.4±23227.6	61771±25029.7	0.489
Mercury (ng/mL)	47558.7±11956.6	50031.6±4929.1	0.262

Iron (ng/mL)	4623.4±4145.4	4822.1±3973.3	0.859

The results in Table 4 have shown there is no significant change between male and female with ASD for all parameters ($p>0.05$) except selenium($p\leq0.05$). Pfaender, *et al*., 2017 compared the current results with his findings and show that the most of the trace elements have a high level for the comparison group such as such as copper, mercury, lead, and others suffered from a decrease in their level such as iron, selenium and zinc the contradiction between this research and current research. The research group measured these trace elements during the sampling of hair and nails for ASD, while the current research took blood samples only, knowing that trace elements are more stable in tissues than in blood due to the persistence of heavy elements in those tissues. The second reason is the environmental and regional variances between the two researches, where environmental pollution plays an important role in the levels of trace elements in individuals. At the same time, the size of pollution varies from region to another [15]. Researchers have proven that the level of zinc in men is higher than the level of zinc in women, as zinc is affected by many factors, the most important of which is BMI, TG, Metabolic Syndrome, and since autistic people suffer from problems in absorption and metabolism. It also suffers from the variation in zinc levels between men and women[16]. The results in Figure 2 and Figure 3 do not show any change in the levels of trace elements which were listed in this figure in male and female. (Baker.,2016) The difference that occurs in the levels of trace elements is not affected by gender, but it is affected by the environment in which the person lives as there is no difference between men and women in the concentrations of trace elements. There is a difference in the concentrations of these elements between male and female because of the geographical environment in which the person lives, this explains the results of the current research. Differential expression of a big range of genes has proven to correlate with blood degrees of lead and mercury in children with ASD (2). High blood concentration of mercury in the course of diverse developmental tiers consequent to genetically decreased capacity to excrete mercury is shown to reason immunological, neurological and behavioral abnormalities very much like the ones seen in ASDs [17]. The chance of an aggregate of genetic and environmental elements specifically exposure to metals inside the etiology of ASDs. Therefore, appears to be sturdy and cannot be omitted because of the large environmental. Cadmium is a xenobiotic of high toxicity. It has neurotoxic, hepatotoxic, mutagenic, carcinogenic and teratogenic effects (it is protected with the aid of the international agency for research on cancer IARC into the group 1 of sellers of a showed carcinogenic impact on humans). Moreover, Cd impairs metabolism of Ca, Mg, Fe, Zn, Se and Cu, which causes morphological and functional modifications specially organs[18]. Cd is absorbed into a human body in particular via the digestive tract and respiratory gadget. As regards Cd in meals within the digestive tract, it's miles absorbed in approximately 6% in adults and up to 60% in kids [18]. Although Zn may be an environmental pollutant in addition to the cause of sideroblastic anemia in instances of excessive exposure, it's miles an vital trace element for human beings. Zn is vital in the synthesis of nucleic acids, cell replication in addition to tissue boom and repair, particularly in toddlers. Zinc deficiency negatively affects immunity, neuropathy, and difficulty in wound healing [19]. Zn also deficiency effects in excessive absorption of poisonous metals together with Cd and Pb, and enhances the formation of their deposits inside the body. Deficiency of Zn and Mg blended with an extended burden of poisonous metals may additionally play the main epigenetic position inside the pathogenesis of sicknesses from the autism spectrum [20]. Apart from the Mg deficiency, a number of autistic kids additionally show that the deficiency of Zn and Ca. Moreover, a courting among the deficiency of Zn and Mg were found. Every fourth baby suffers from the deficiency of each factors concurrently [19]. Most of the research concerned with studying the effect of selenium on autism disorder on children proves that the level of selenium decreases significantly in autistic children and this supports the current results of the current research. As for the high level of selenium in boys more than that of girls, there are no clear and compelling physiological reasons that explain the reason for the difference, but

perhaps the reason is due to the special care enjoyed by boys but not girls.cFor example, give them some nutritional supplement that contains trace elements important to treat the autism [21].

5. Conclusion

It can be concluded from this study that the levels of trace elements such as chromium ,copper, lead, mercury, selenium and iron are normal in children with autism spectrum disorders. While the level of zinc is significantly lower in patients compared to the control group. Also concluded no significant change between male and female in all levels of trace elements except selenium which showed a significant decrease in female patients compared to male patients.

Reference

[1] American Psychiatric Association (APA) 2013. *Diagnostic and Statistical Manual DSM-5*, 5th ed, p: 501-504.
[2] Tian Y, Green P G, Stamova B, Hertz P I, Pessah IN and Hansen R 2011 *Neurotox. Res*. **19** 1
[3] Al-Hakeim H K, Furqan M A and Basim M A 2014 *J Clin Biochem Nutr* **55** 203.
[4] Basim M 2016 *Int. J. Sci. Res.* **5** 2033.
[5] Basim M , Alassadi J I, Zearah S A 2020 *Indian J Med Forensic Med Toxicol* **14** 1681.
[6] Furqan M, Afrodet A. S and Dawood S A 2019 *Gene Rep* **17** 100516.
[7] Furqan M A 2013 *Journals kufa for chamical* **8** 22.
[8] Furqan M and Al-Hakeim H K 2012 *Al-Kufa University Journal for Biology* **4** 253.
[9] Golub, N, Winters P, van W E 2010 *Int. Arch. Occup. Environ. Health* **83** 771.
[10] Weisskopf M G, Proctor S P; Wright R O, Schwarts J, Spiro A, Sparrow D,Nie H, Hu H 2007 *Epidemiology* **18** 59.
[11] Weisskopf M G, Wright R O, Schwartz J, Spiro A, Aro A, Hu H 2004 *Am. J. Epilemiol* **160** 1184.
[12] Tchounwou P B, Ayensu W K, Ninashvili N, Sutton D 2003 *Environ Toxicol* **18** 149.
[13] Manna A and Ramkrishna M 2018 *Geosci. Front*. **9** 1577.
[14] Chen, Jingying, et al. 2019 *Comput. Hum. Behav.* **90** 204.
[15] Stefanie P 2017 *Sci. Rep* **7** 45190.
[16] Ghasemi A ,Saleh Z , Firoozeh H E and Azizi F 2014 *Annals of human biology* **41** 436.
[17] Furqan M. A, Basim M A , Maha S R and Marhoon H M 2014 *IJSRP* **4**.
[18] Boakye P 2011 *A Study of the Effects of Chemicals Used to Control Diseases and Pests of Cocoa on the Users: A Case Study of Atwima Nwabiagya District. Diss.*
[19] Wojtunik K, Karolina A O and Monika W H 2019 *Biomed. Pharmacother*. **111** 1277.
[20] Al-Zurfi S , Ali B M, Abojassim A A , Albanon R and Qazmooz H A 2016 *Rasayan J. Chem.* **9** 405.
[21] El-Ansary A 2017 *Metab. Brain Dis.* **32** 1073.

Synthesis and Study Antibacterial Activity of Some New Polymers Containing Maleimide Group

Synthesis and Study Antibacterial Activity of Some New Polymers Containing Maleimide Group

Ruwaidah S.Saeed [1], Fatimah Ali Hussein [2], Sana Hitur Awad [3] and Muna S.Al-rawi [*4]

[1,4]University of Baghdad, College of Education for Pure Science [Ibn Al-Haitham,Department of Chemistry] , Baghdad , Iraq.
[2] University of Babylon , College of Science, Department of Chemistry, Babylon, Iraq.
[3] University of Baghdad ,College of science for women Iraq , Baghdad , Iraq.

[*]E-mail: muna.samir67@gmail.com

Abstract. By condensation of benzaldehyde with thiourea in absolute ethanol in the presence of glacial acetic acid as a catalyst, the Schiff base(1-benzylidenethiourea)[I] was synthesized by synthesis of 4-(3-benzylidenethioureido)-4-thioxobut-2-enoic acid compound[II] by reaction of maleic anhydride with schiff base [I] in DMF. When treating compound [II] with ammonium persulfate (NH4)2S2O8 (APS) as an ethanol initiator to obtain polymer [III], compound [III] reacted to polymer [IV] with SOCl2 in benzene. Sulfamethizole, celecoxib, salbutamol, 4-aminoantipyrine to yield polymers [V-VIII], compound [IV] reaction with different drugs. Spectral evidence established the structure of synthesized compounds: FTIR and 1HNMR, UV-Vis Spectroscopy and Elemental Analysis (C.H.N-S) . These synthesized derivatives [V-VIII] were tested for their antibacterial activity against Bacillus subtilis (G+) and Escherichia coli (G-) by agar well diffusion process, and the results showed that all polymers had a greater diameter of the growth inhibition region. This may be relative to the presence of sulfamethizole medication, maleimide group and Schiff bases, Polymer[V] demonstrated excellent inhibition against Bacillus subtilisa and E.coli.

Keyword : Schiff base , Antibacterial activity, Salbutamol , Celecoxib , Maleimide , sulfamethizole.

1. Introduction

Schiff bases are a group of compounds containing (-HC=N-) formed from condensing products of aromatic aldehydes or primary amine ketones [1]. Schiff bases are commonly used in various fields, such as medical chemistry [2], antibacterial, antiviral, pharmacological, antioxidant and cancer activities [3-5]. In addition, the Schiff base enhances the biopolymer's stability[6]. A generic formula, $H_2C_2(CO)_2NH$, has maleimide compounds. The name 'maleimide' derives from the maleic acid and imide combination [7]. Maleimides are an essential type of heterocyclic compounds contained in natural products[8] and are used in organic and medicinal chemistry[9]. In pharmaceutical products with biological specific functions, such as antibacterial, anticancer, antitumor, tuberculostatic activity, anti-microbial, antiviral and antigenic activities, maleimides have important significance [10,11]. In order to be able to use multiple macromolecule systems, such as thermostability materials[12], self-healing systems[13], click reactions[14] and antibody-drug conjugates[15], Chemistry's

Maleimide[MI] has acquired a senior interest in both polymer and biological sciences. The structure of the alpha,β-unsaturated imide allows Maleimide to be extremely versatile. First, the two carbonyl groups have hydrogen bonding interaction power that can be used to modify the behavior of polymerization[16]. The feasibility of preparing higher and thermally stable polymers[17] is the copolymerization of maleimides with Schiff base supply. In addition to the process ability of maleimide polymer, flexible units within the polymer backbone can also be increased.

2. Experimental

Materials : *All chemicals supplied from Merck and Aldrich.*

Techniques : FTIR spectra recorded using KBr , discs on a 8400s Shimadzu spectrophotometer and FTIR spectrophotometer , Shimadzo [Ir prestige-21] . ^{1}HNMR spectra carried out by : Bruker , ultra shield 300 MHz , : Switzerland and are reported in ppm.

2.1.Synthetic Procedures:

2.1.1.Preparation of Schiff base[1-benzylidenethiourea] [I] [18]*:*

This compound was prepared from the reaction of benzeldehyde [1.06 g. , 0.01 mol] with thiourea [0.76 g. , 0.01 mol] in (30 ml.) ethanol and [3]drops of glacial acetic acid , the mixture refluxing at 70°C for 12h. . The course of the reaction was followed up using a technique TLC. When the reaction was completion , separated as yellow-colored product which was filtered , dried and recrystallized by methanol . Yield 85% ; m.p[129-131]^{0}C. Elemental Analysis , Calcd : C% = 58.53; H% = 4.87; N% = 17.07; S%= 19.51 , Found: C% = 58.67; H% = 4.98 ; N% =17.27 S% = 18.98.

2.1.2.Synthesis of 4-[3-benzylidenethioureido]-4-thioxobut-2-enoic acid[II] [19]

Mix Maleic anhydride [0.98 g. , 0.01mol] and [1.64 g. , 0.01mol] Schiff base [I] in 25ml DMF then refluxed about 4hr. , the viscous result washed with diethyl ether and then dried at room temperature. Yield 73% ; m.p[198-200]^{o}C**.** Elemental Analysis , Calcd : C% =54.96 ; H% = 3.81; N% = 10.68 ; S% = 12.21
Found: C% = 55.99 ; H% =3.90 ; N% =10.15; S% = 12.87

2.1.3.Synthesis of polymer[III] [20] *:*

[0.27g ,0.001mol] of compound [II] was mixed with (0.22gm) of ammonium per sulfate [APS] as initiator of polymerization in (15 ml.) of ethanol . The mixture stirring for 2-3 hrs at room temperature , then refluxed about 12hr. Filtered , washed with cold EtOH absolute , dried and recrystallized with ethanol to gave the required product [III].

2.1.4.Synthesis of polymer[IV] [21]

0.01 mol of compound [III] mixed with 0.01mol of thionyl chloride in 25ml. of dry benzene and reflux for (6hr) The Amount of $SOCl_2$ and benzene separated under vacuum after cooling.

2.1.5.*Synthesis of polymers [V-VIII]* [22]

A mixture [0.01mol] of compound [IV] and [0.01 mol] of drug [sulfamethizole or celecoxib or salbutamol or 4-aminoantipyrine] in 20 ml. of DMF . The mixture refluxed about 3 hr. Filtered , wash with ethanol absolute , dried and recrystallized from EtOH to gave the required product[V-VIII].

3. Result and Discussion

-1benzylidenethiourea[I] was prepared to give good yield to compound[I] by reaction of benzaldehyde with thiourea in absolute ethanol. FTIR and 1HNMR spectroscopy were used to identify this Schiff base [I]. The FTIR spectra, Fig.(1) shown at (1647)cm-1 appearance band refers to the azomethine group and two (3325,3149)cm-1 appearance bands attributable to NH2 . 1HNMR (DMSO) spectrum, Fig.(2) showed a signal at δ(2.11) ppm attributable to the NH2 group, a sharp singlet at δ(8.1) ppm for one proton attributed to CH=N and several signals for aromatic protons at δ(7.32-7.83) ppm. Compound [II] produces maleic anhydrides with Schiff base [I] in DMF from the reaction. FTIR spectroscopy detected the compound

[II]. 3400-2400 (OH), 3184 (NH) group, 3041 (C-H arom.) group, 1739 (C=O) of carboxylic acid, 1654(C=O-NH), 1641(C=N), 1591(C=C)Aromatic and 1126(C=S). FTIR absorption[a,cm-1]: Polymer [III] was synthesized with ethanol using ammonium per sulfate (APS) as the initiator via the reaction compound [II]. The stretching band referred to the O-H of the COOH moiety in the area (3406-2800)cm-1, the stretching band of the N-H group appeared at (3170) cm-1-, 3007 (C-H arom.)-, 2941,2856 (C-H aliph.) and the stretching band to (C=O) for COOH appeared at 1735cm-1.

In order to achieve transformation to a new function group, acid chloride was considered a very active intermediate, so we aimed at synthesizing compound[IV] by reaction compound[III] with thionyl chloride, the acid chloride[IV]formed as residue was used in the next reaction without further purification. Polymers [V-VIII] is synthesized with drugs (sulfamethizole or celecoxib or salbutamol or 4-aminoantipyrine) from the reacted polymer [IV] . FT-IR spectrum for compound [VII], acyl chloride absorption band disappearance and absorption band appearance at (1729) cm-1 refer to (C=O-O), N-H group stretch band appeared at (3214) cm-1 and OH, C=O-NH and C=N stretch bands appeared at(3438), (1687), (1630) cm-1 respectively. 1H NMR (δ ppm): sharp singlet signal at δ (1.17) refers to nine C(CH3)3 protons, signal at δ (2.01) due to proton NH of [NH-C(CH3)3] group, -CH=CH chemical shift disappears and shows chemical shift at δ (2.73-2.98) due to-[CH-CH]n-, doublet signal at (3.17-3.40) connected to CH2 proton and triplet signal at δ(4.47) due to CH proton signals at δ(5.65),(5.77) due to proton CH2O and (5.77) Compound FT-IR spectrum [VIII] (200, cm-1): reveals the current absorption band due to amide (C=O) in the area (1687)cm-1 and absorption band disappearance due to acyl chloride. A signal at δ (2.73) due to protons of [C[CH3]] group, -CH=CH chemical shift disappears and shows chemical shift at δ (2.98-3.23) ppm due to-(CH-CH)n-, signal at δ(3.45) refer to protons of [N(CH3)] group, signal at δ(6.02) refer to proton of (NH-C=O) group, multiple signals at δ(6.91-7.25) attributable to aromatic protons, signal at δ(7.97) attributable to CH=N, multiple signals at δ(6.91-7.25) The UV-Vis compound spectrum[VII,VIII] displays the peaks of absorption at(280-332), (290-2320) that can be attributed to(π-π*) and (n-π*).

Table1.FT-IR of polymers[V-VIII]

Comp. No.	υ (N-H)	υ (C-H) aliph.	υ (C=O) amide	υ (C=O) ester.	υ (C=N)	υ (C=S)
[V]	3351	2933-2872	1670	-	1627	1141
[VI]	3329	2924-2856	1680	-	1637	1132
[VII]	3214	2920-2850	1687	1729	1630	1157
[VIII]	3190	2964-2804	1687	-	1631	1193

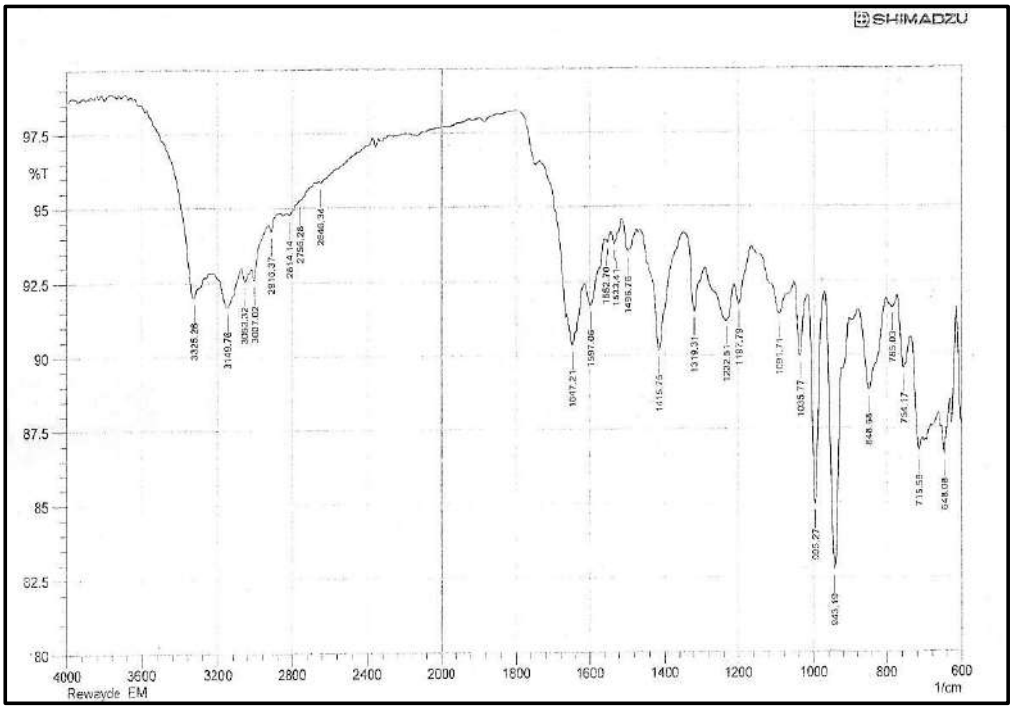

Figure1.FT-IR of compound[I]

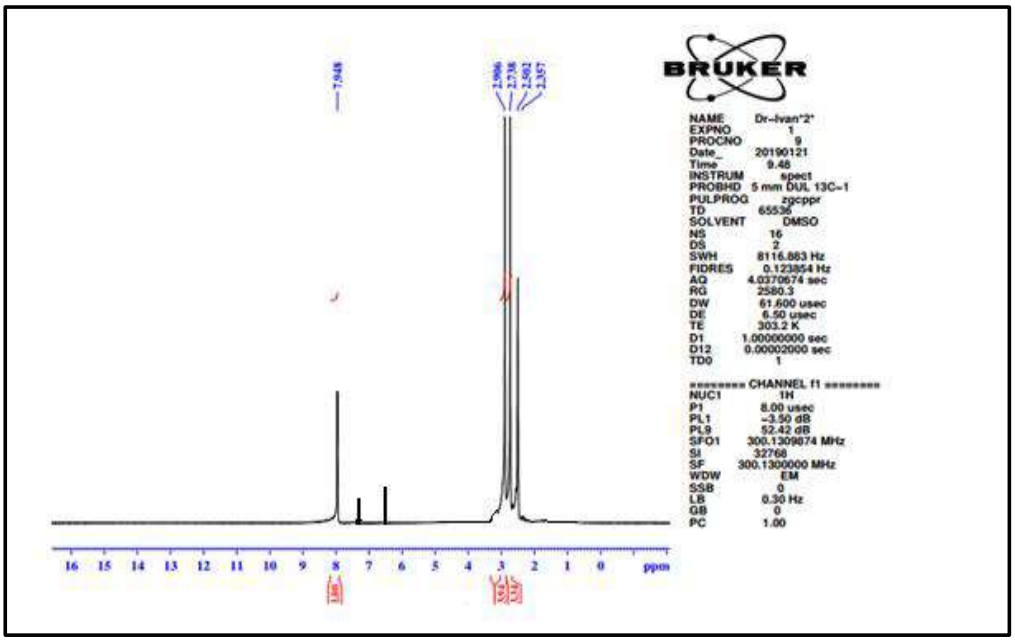

Figure 2 . [1]H-NMR of compound [I]

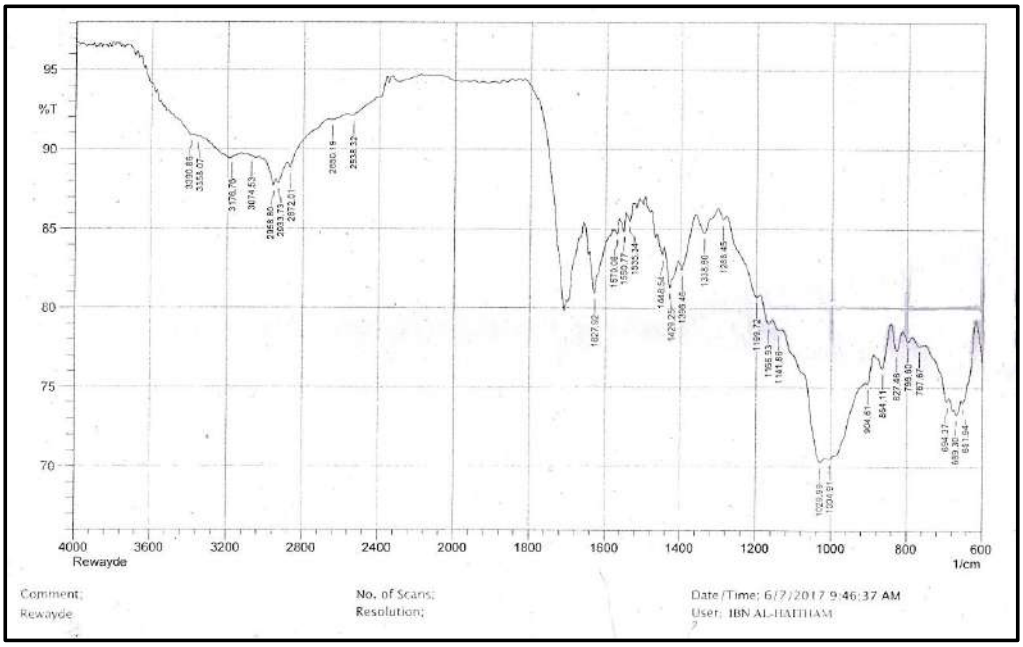

Figure 3. FT-IR of compound[V]

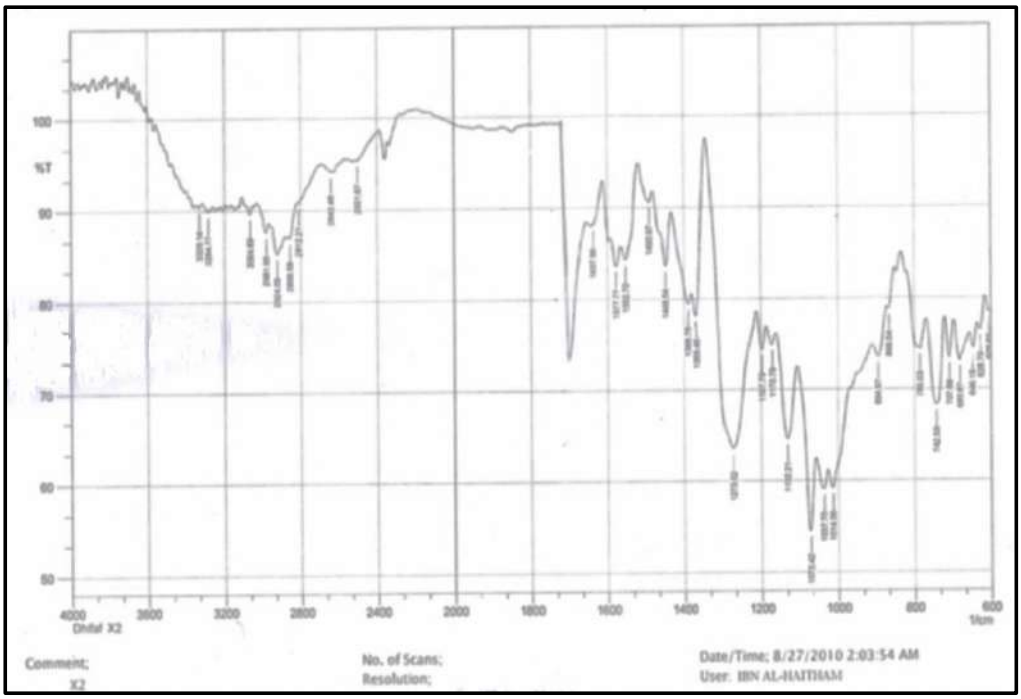

Fig.(4).FT-IR of compound[VI]

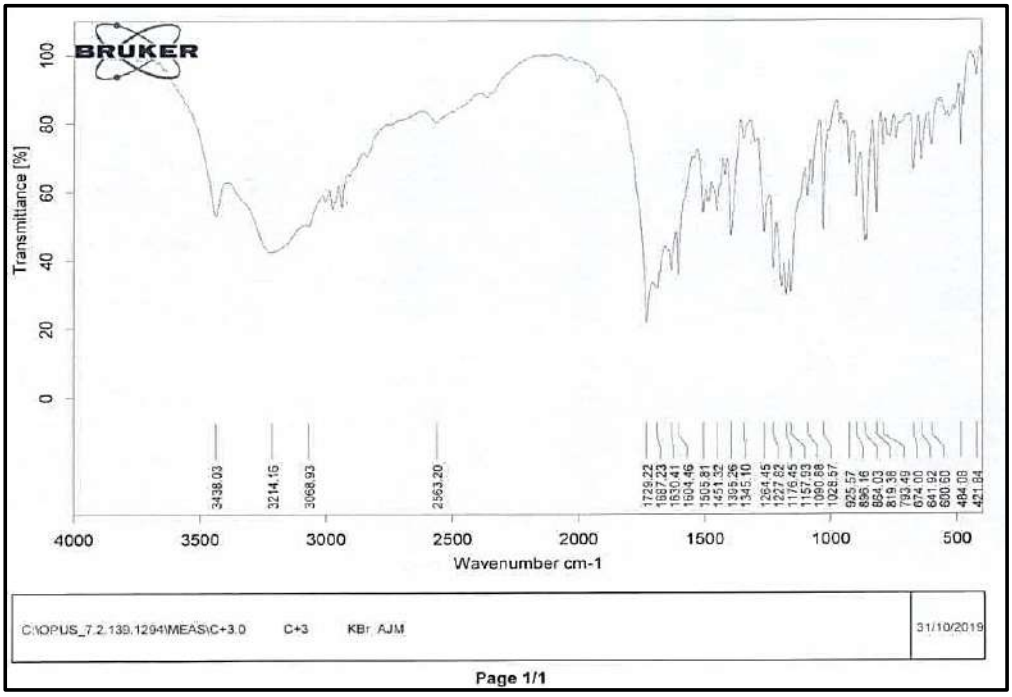

Figure 5. FT-IR of compound[VII]

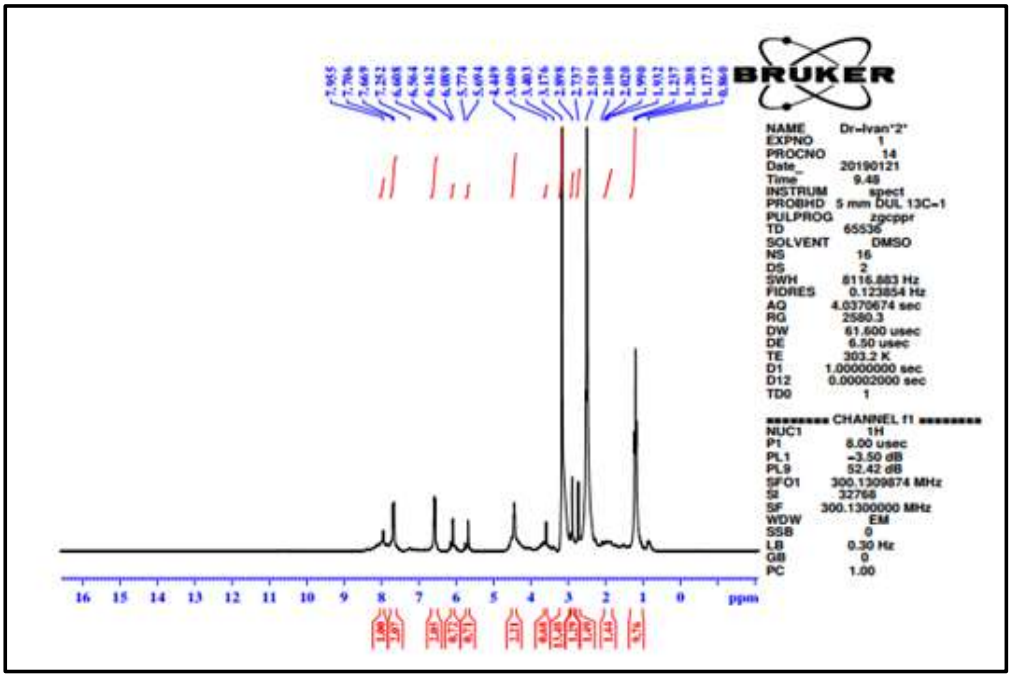

Figure 6 . ^{1}H-NMR of compound [VII]

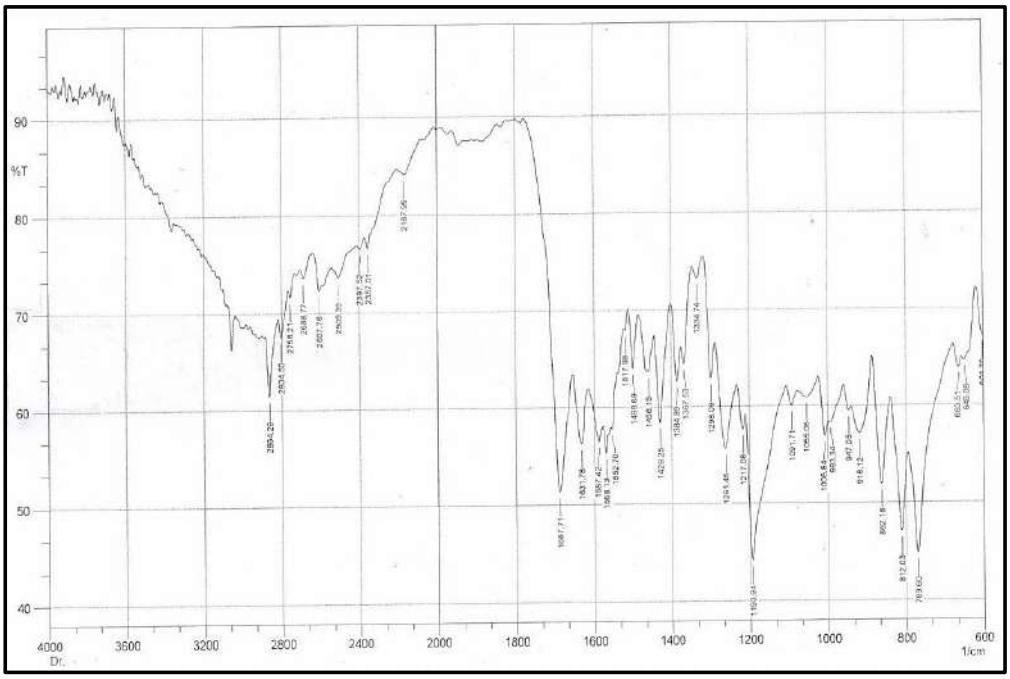

Figure 7 . FT-IR of compound[VIII]

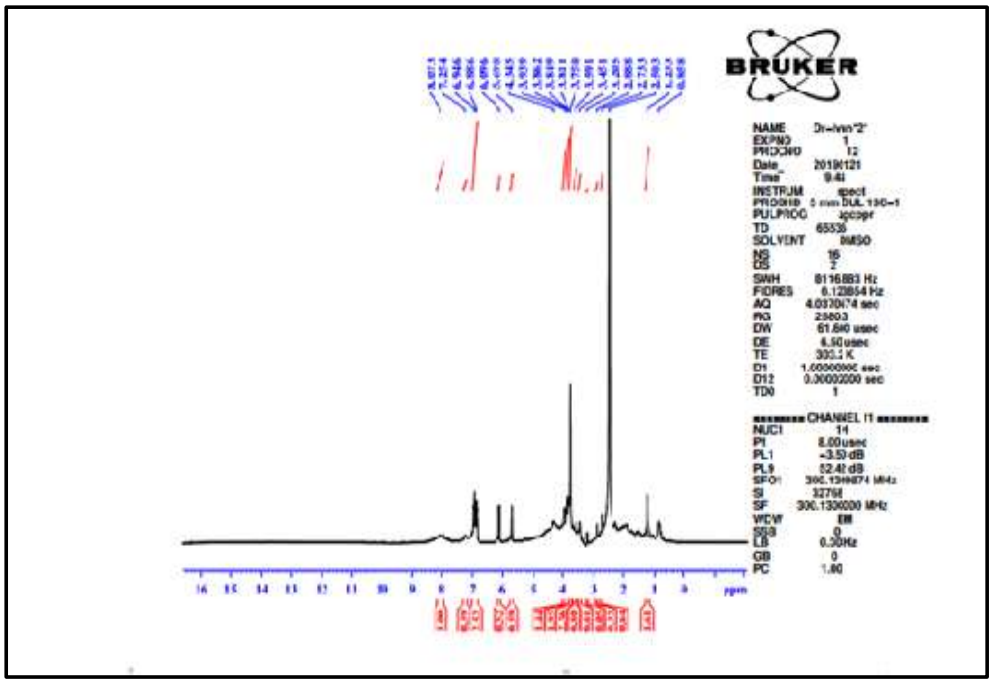

Figure 8 . ^{1}H-NMR of compound [VIII]

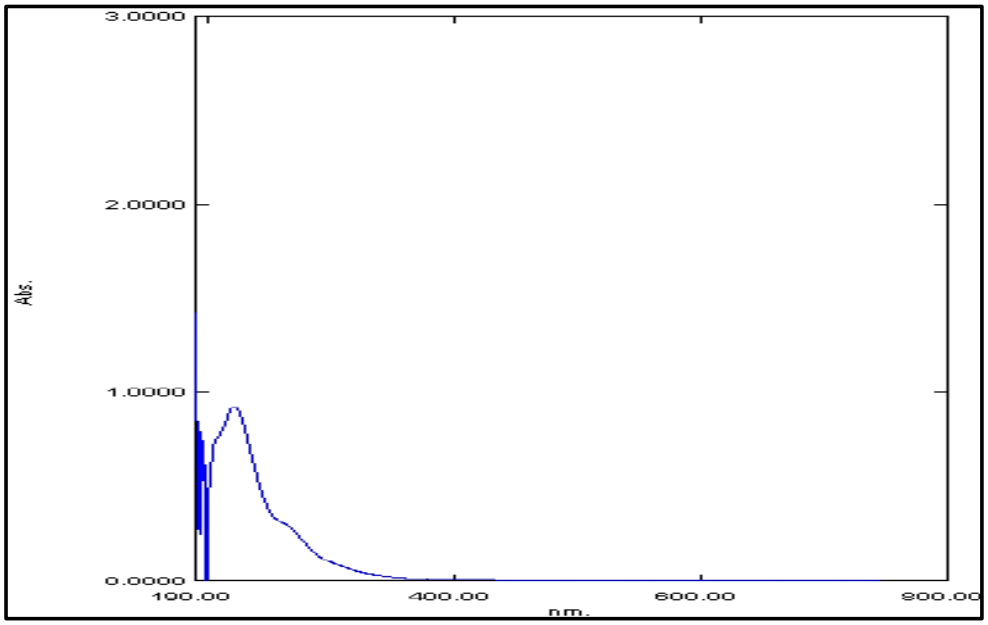

Figure 9. U.V. spectrum of compound [VII]

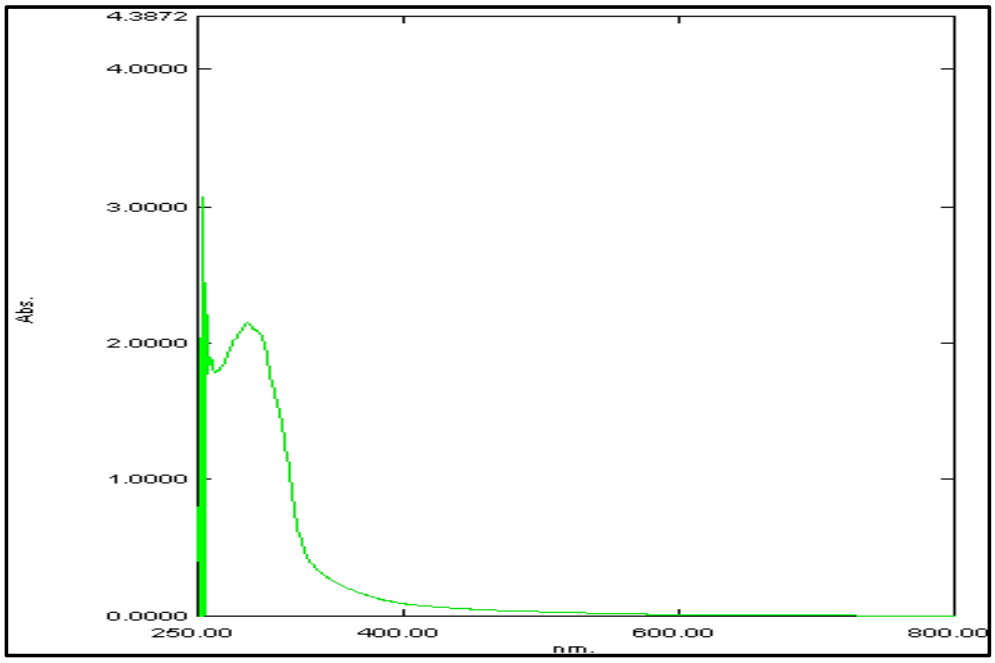

Figure 10. U.V. spectrum of compound [VIII]

4. Biological Activity:

The polymers [V-VIII] were tested by the agar well diffusion method (Barry, 1977) for their antibacterial activity against Bacillus subtilis [G+] and Escherichia coli [G-] (in vitro), the standard drug used to compare the synthesized polymers with penicillin (50µg / ml) . The results showed that the growth inhibition zone diameter of all polymers was higher. Compound[V] demonstrated strong inhibition against Bacillus subtilisa and E.coli, which may be linked to the existence of the drug sulfamethizole, since this drug is a sulfonamide-derived antibacterial. It is effective against a wide variety of gram-negative and gram-positive bacteria as an antibiotic. The polymer[V] also includes Maleimide group and Schiff bases that have strong antibacterial activity.

Table2. The inhibition zone of some synthesized compounds[V-VIII].

Comp.	E .coli	Bacillus cereus
Penicillin	17	23
[V]	28	22
[VI]	14	15
[VII]	23	20
[VIII]	16	16

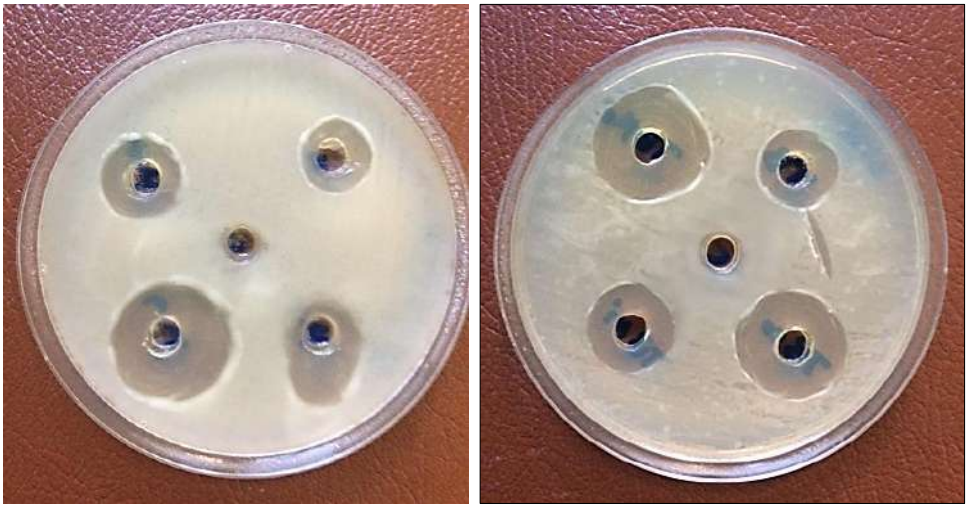

Figure 11 . Antibacterial activities of polymers

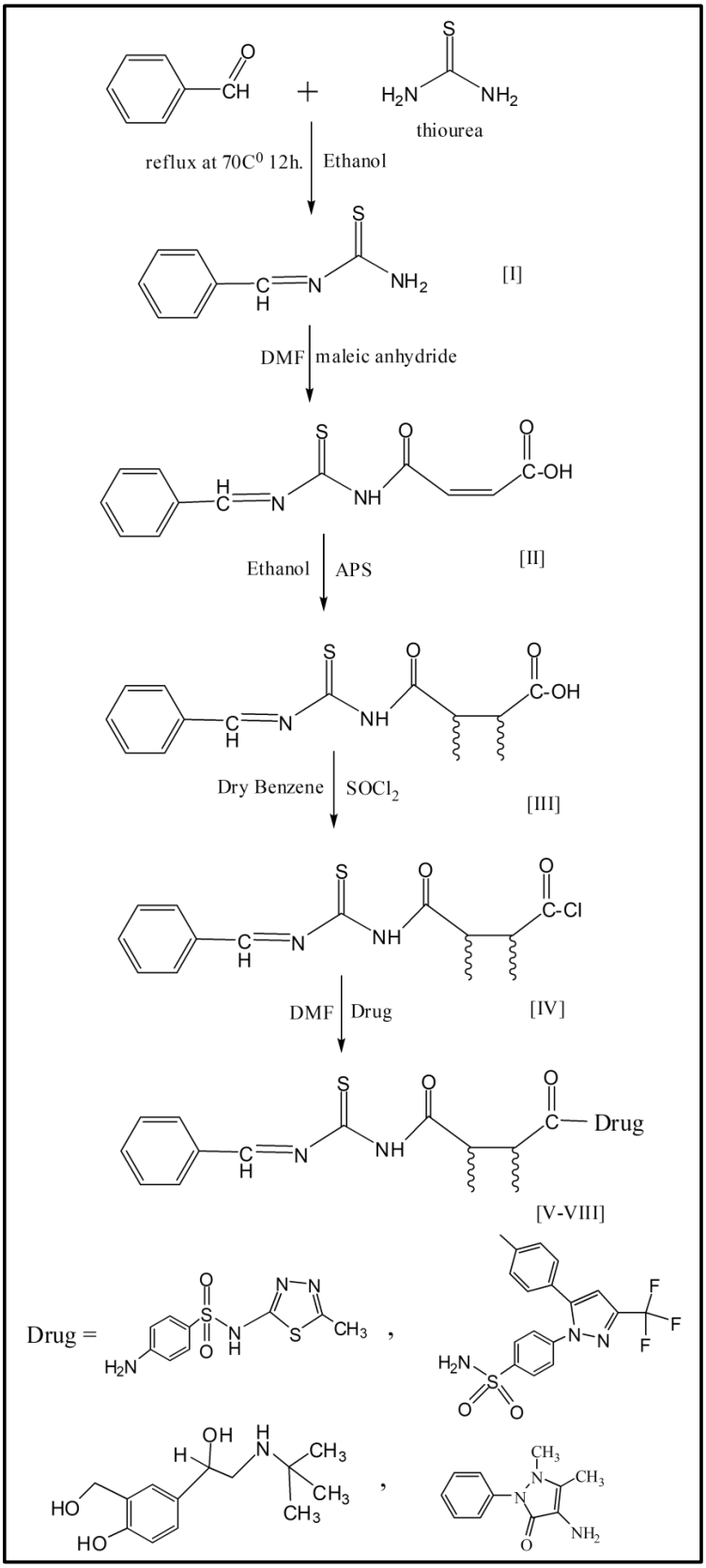

Scheme 1. The synthetic route for target derivatives[I-VIII]

References

[1] Ishraq J. Hasan1, Rasha K. Khudhur , Ihsan S. Sahi 2019, *Drug Invention Today*, **11**, 7009.
[2] Khalida Al-Azawi1, Dunya Lafta AL-Duhaidahawi , Ahmed Al-Amiery , Abdul Amir Hassan Kadhum 2019, *Free Radicals and Antioxidants*.; **9**,1.
[3] Mohammad Muzammil Y. Kuddushi , Mohammed Abrar H. Malek , Vinod L. Patidar , Mihir S.Patel , Roma K.Patel and Rohit H.Dave 2018, *Int*. J. *Recent Sci. Res.,* ; **9**, (4G), 26026–26030.
[4] Ali A. Sabah , Muna S. Al-Rawi and Jumbad H. Tomma , 2020 , *Indian J. Forensic Med. Toxicol*., **14**, 1
[5] Fiadh A. Neshan , Muna S. Al-Rawi and Jumbad H. Tomma ,2019, J *Drug Deliv Sci Technol,* **9** ,4
[6] K P R Chowdary , B Suresh , B Sangeeta and G Kamalakara Reddy , 2003, *Saudi Pharm J*, **11**,4.
[7] Hermanson Greg , Bioconjugate Techniques. Elsevier , 2013 , 299-339.
[8] Bakat Ali, Léonard D. Kanda Kupa , Cíntia S. Heluany , Carine C. Drewes , Stanley N.S. Vasconcelos , Sandra H.P. Farsky , Hélio A. Stefani , 2017, *Bioorg. Chem*., **72** ,199-207.
[9] P. Chauhan , J. Kaur, S.S. Chimni , 2013, *Chem Asian J*, **8** (2) : 328-346.
[10] Kumar M. M. K. ; Naik J. D. ; Satyavathi K ; Ramana H Varma , P. R. ; Nagasree , K. P.; Smitha D. , 2014; *Rao D. V. Nat Prod. Res*., **28** , 888
[11] Alexey A. Panov , Alexander Yu. Simonov, Sergey N. Lavrenov , Sergey A. Lakatosh , Alexey S. Trenin , 2018 ,*Chemistry of Heterocyclic Compounds*, **54**(2), 103-113
[12] Liu C , Mao H , Zheng J , Zhang S. , Tight ultrafiltration membrane 2017, *J. Membr. Sci*. ; **530** :1.
[13] Billiet S , Camp WV , Hillewaere XKD , Rahier H , Du Prez F. 2012 , *Polymer* ; **53** : 2320-2326.
[14] Hoyle CE , Lowe AB , Bowman CN. 2010. *Chem Soc Rev*. ; **39** : 1355-1387.
[15] Beck A, Goetsch L , Dumontet C, Corvaïa N. 2017, *Rev Drug Discov*; **16**:315-337.
[16] Balkenende D.W.R. , Winkler S.M. and Messersmith P.B. , 2019, *Eur. Polym. J*., **116**, 134-143.
[17] Tasdelen M. A. Diels–Alder , 2011, *science polym . Chem.* , **2** , 2133.
[18] Samarasinghe W.M.P. , Sithambaresan M. and Mahendranathan C. , 2018 , *International Journal of Current Innovations in Advanced Research*, 1(4) :59-68
[19] J. Chaudhary , S.Purohit , S. Jngerand and R.Chaudhary, 2017, *J. Sci. Ind .Res.*,**76** : 570-574.
[20] Xia Li , Yun Huang and Yi Dan , 2020, *Colloid Polym Sci* , **298**: 225-232.
[21] Fouad MS, Redha I, Al-Bagati, Araa Al –Juboori , 2006, *Al- Mustansiriya Journal of Science*, **17** (3):15-26.
[22] Ahamed L. S. 2011, *ANJS*, **14** (2): 29-42.
[23] Smith J.G., Organic Chemistry,1st ed , MC Graw Hill , New York , 2006 , 522.
[24] Ali H. Samir , Khalid F. Ali and Ruwaidah S. Saeed, 2014, *Ibn Al-Haitham Jour. for Pure & Appl. Sci*., , **27** (3) :350-364.
[25] Ruwaidah S. Saeed , Fadhel S. Matty and Ali H. Samir, 2019, *J. Pharm. Sci. Res*, **11**(3) : 733-740.
[26] Fatimah Abdul Razzak Mageed , Mohanad Musa Kareem and Mohammad N. AL-baiati , 2019, *ASIAN J CHEM*; **31**(3):569-574.
[27] Abdul-Jabbar A. Mukhlis , Muna S. Al-Rawi , Jumbad H Tomma , Ammar H. Al-Dujaili , 2012, *Ibn Al-Haitham Jour. for Pure & Appl. Sci*, **25** (2) : 293-307.
[28] Barry A.L. , The Antimiccrobial Susceptibility Test 1977, *BiolAbstr* , **180** (64) , 25183 .
[29] Ahlam Marouf AL- Azzawi and Suroor Abdul Rhahman Mahdi , 2013, *Baghdad Sci. J.*, **10**(3).
[30] Ruwaidah S. Saeed , 2020, *Int. J. Drug Deliv. Technol* , **10** (3):402-407.
[31] Wurood Ali Jaafar and Ruwaidah S. Saeed, 2020, *Sys Rev Pharm*, **11**, 134.
[32] Ruwaidah S. Saeed and Muna S.Al-rawi 2020, *J. Pharm. Sci. Res*. , 12 , 2.

A Novel Coated Wire Electrode And Coated Graphite Electrode for Potentiometric Determination of Amitriptyline Hydrochloride in its pharmaceutical preparations, urine and blood plasma

A Novel Coated Wire Electrode And Coated Graphite Electrode for Potentiometric Determination of Amitriptyline Hydrochloride in its pharmaceutical preparations, urine and blood plasma.

Muthana Saeed Ali [1] and Ali Ibraheem Khaleel [1]

[1] Chemistry Departmment ,College of Science,University of Tikrit , Sallah Al-Den,Iraq.

*E-mail: mothanasaeedali@gmail.com

Abstract . This paper uses the potentiometric method to evaluate (amitriptyline hydrochloride, AM) by creating selective electrodes for AM drugs with the active ingredient (Ammonium Reinackate, AR) using a plasticizer (Dibutyl phthalate, DBP). The results showed that for (Coated Wire Electrode (CWE)) and Coated Graphite Electrode (CGE) respectively, the Nernstian slope of the prepared Am-AR-DBP electrodes is (57.293, 58.803 mV / decade). With a pH range of (4-7) and a concentration range of 1 ?? 10 ?? ^(-6)-1 ?? 10 ?? ^(-1) M for both electrodes, the upper and lower limit of detection for the Am-AR-DBP CGE is 0.2042M, 4.8 ?? 10 ?? ^(-7) M, and the upper and lower limit of detection for the Am-AR-DBP CWE electrode is 0.2051M, 4.91 ?? 10^(-7) M, respectively. The response time ranges from 20-83 sec, 14-76 sec for CWE and CGE electrodes respectively. For the CWE electrode, the age of the electrodes is 26 days, and for the CGE electrode, 42 days. The research included calculating the selectivity with the presence of interferers of these electrodes where the K(i,j)^pot values for all ions were less than 1. In the estimation of the drug Amitriptyline Hydrochloride in the pharmaceutical preparation (Amitriptyline tablets), the manufactured electrodes were used by following the direct process, the standard method of additions, the possible titration method and the homogeneity of the material sample, as well as the drug was estimated in urine and blood plasma with a recovery of not less than 100.57 for urine and 99.46 f for urine.

Keywords :Amitriptyline hydrochloride, Ion selective electrodes, Coated Wire Electrod; Coated Graphite Electrode, Ion pair.

1. Introduction:

Electrochemical sensors are one of the smallest chemical tools that can give instant and direct information when a specific compound or ion is present in complex samples. Among the different classes of chemical sensors, ion selective electrodes used in potential sensors are one of the most widely used. Potential detection by ion selective electrodes (ISEs) provide several advantages over other analysis methods such as speed, ease of operation, simple instrumentation, relatively fast response, wide dynamic range, reasonable selectivity, and low cost [1]. A selective electrode is generally known as a chemical sensor capable of converting the activity of a particular ion dissolved in a solution into an electrical potential that can be measured with a voltmeter or pH meter [2,3] The formula for amtriptyline hydrochloride is [4]

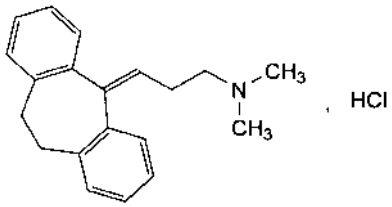

The molecular formula [4] is $C_{20}H_{23}N$, HCl, and its molecular weight is 313.9 g / mol, and the scientific name for the drug [5] is

3-(10,11-Dihydro-5H-dibenzo[a,d][7]annulen-5-ylidene)-N,Ndimethyl propan -1- amine hydrochloride.It is in the form of white powder or colorless crystals, easily dissolved in water, alcohol, and dichloromethane [6]. Amitriptyline hydrochloride is used to treat mental / mood problems such as depression. It may help improve mood and feelings of well-being, relieve anxiety and tension, aid in a better sleep, and increase the patient's energy level. This medication belongs to a class of drugs called tricyclic antidepressants[7]. Due to the medical importance of this drug, it has been determined by many different analytical methods, such as spectroscopy [8,9], HPLC [10,11], (RP-HPLC) [12], Voltmeter technology[13], and gas Liquid chromatography [14], capillary electrophoresis method [15], LC-MS technique [16], liquid chromatography [17], flow injection technique [18], thin-layer chromatography [19], fluorometry (20), and atomic absorption spectroscopy [21]. In this study, several selective electrodes were manufactured for the determination of Amitriptyline hydrochloride in its pure form, in its pharmaceutical preparations, and in biological fluids. Two types of electrodes were prepared (Coated Graphite Electrode (CGE) and Coated Wire Electrode (CWE).

2. Experimental Section

2.1. Apparatus

Jenway 3310 pH Meter, HANNA Instruments pH Meter 211, calomel electrode Swiss source, JENWAY Hot Plate with Stirrer-Germany, C.H.N Perkin Elmer USA 2400 Series II element analyzer.

2.2. Materials and Reagents

All chemicals used were of a high degree of purity and supplied by SDI, BDH, and Fluka

1.solution of Amitriptyline hydrochloride, AM 10^{-1} M.

Prepared the standard solution of Amitriptyline hydrochloride at a concentration of 10^{-1} M by dissolving 3.1390 grams in deionized distilled water using a 100 mL volumetric flask and complete the volume with deionic distilled water to the mark and the other standard solutions (10^{-2}-10^{-8}) M were prepared by dilution With deionized distilled water.

2.3 .Ammonium reinackate solution, AR 10^{-1} M.

Prepared the solution by dissolving 3.5444 g of the substance in a 100 mL volumetric flask and complete the volume with deionized distilled water to the mark.

2.4 Hydrochloric acid at a concentration of approx 0.1 M.

0.8 mL of concentrated hydrochloric acid (12 N) was transferred by a graduated pipette to a 100 mL volumetric flask containing 50 mL deionized distilled water and the volume was completed with deionized distilled water to the mark.

2.5 Sodium hydroxide at a concentration of approx 0.1 M.

Dissolved 0.4 g of the substance in a 100 mL volumetric flask and complete the volume with deionized distilled water to the mark.

2.6 Amitriptyline Tabletes preparation solution 25 mg.

Ten tablets containing 0.25 g of the basic substance Amitriptyline hydrochloride developed by the State Medicines and Medical Supplies Company of Samarra were crushed in an agate mortar and 1,025 grams was the average weight of one tablet. When 1,2867 g of the pharmaceutical preparation was taken and then dissolved with an ultrasonic system in deionized distilled water with Shake to ensure full dissolution and filtered with Whatman filter paper, the filtrate was then diluted in a 100 mL volumetric flask and the volume was

completed with deionized distilled water to the mark, so the result was a solution with a concentration of 10-2 M and a concentration of 100 mL.

2.7 Biological fluid solutions (urine, blood plasma) 0.01 M

In a stopper test tube, 4.5 mL of human plasma or urine were Then added, 0.5 mL was added at a concentration of 0.1 M amtriptyline hydrochloride, and the tube was shaken for 1 minute. Other solutions of different concentrations were prepared by dilution with deionized distilled water.

2.8 Preparation of the ion-pair

The ion pair was prepared by combining 10 ml of AM drug solution at 10-1 M concentration with 10 ml of AR solution at 10-1 M concentration with stirring to form a light red AM-AR precipitate, then the precipitate was filtered and washed several times with deionized distilled water and left for two days at the temperature of the laboratory until dehydration and the precipitate was dehydrated and washed several times with deionized distilled water (1).

Table 1. Element Analysis for the AM-AR ion pair

Element analysis	AM-AR		
	%C	%H	%N
Found	43.24	5.38	16.76
Calculated	43.13	5.43	16.75
Formula	$[C_{20}H_{24}NCl][C_4H_{10}CrN_7S_4].H_2O$		

2.9. Preparation of the Electrodes

2.9.1. Coated Graphite Electrode (CGE)

Through a series of preliminary experiments, the selective membrane was prepared by mixing its components according to weight ratios, which gave the best membranes in terms of the nature of the membrane and its response according to the following: The coated graphite electrode was prepared by encapsulating a pure carbon rod (5.5 cm in length, 8 mm in diameter) with a tight polyethylene tube. A mixture consisting of (10% AM-AR, 30% PVC, 60% DBP as plasticizer) was prepared. And then dissolve the mixture in (5 ml) of THF, which is considered a good solvent and adhesive, and then continue stirring until we get a thick solution at a volume of 2-3 ml of the mixture. 1cm of the uncoated graphite rod was immersed (5) times each immersion for 10 seconds, between each immersion and another (2-3) minutes, then left in the air for an hour to dry. The electrode was immersed in a 1×10^{-2} M solution of amtriptyline hydrochloride for different periods, then the other end of the coated carbon rod was connected with an insulated copper wire and connected to a Potentiometer recorder [22].

2.9.2. Coated Wire Electrode (CWE)

Via a series of preliminary experiments, the selective membrane was prepared by mixing its components according to the weight ratios given by the best membranes in terms of the nature of the membrane and its reaction according to the following: when the silver wire was washed with nitric acid, rinsed with distilled water, dried with acetone, and then left to dry. The silver wire should be insulated well (8 cm long and 2 mm in diameter). We leave the silver wire 1 cm from both ends exposed and uninsulated. A mixture was prepared consisting of (10% AM-AR, 30% PVC, 60% DBP as plasticizer). And then dissolve the mixture into (5 ml) THF, which is known to be a strong solvent and adhesive, and then continue stirring until 2-3 ml of the mixture has a thick solution. 1 cm of unwrapped silver wire (5) was submerged every 10 seconds between each dip and another (2-3) minutes, then left in the air to dry for an hour. For different times, the electrode was submerged in an amtriptyline hydrochloride solution of 1 ?? 10^(-2) M, then the other end of the silver wire was attached to the potentiometer recorder[23].

3. Results and Discussion

3.1. Study the optimal components of (CWE, CGE)

In a 50 ml glass beaker, the AM-AR electrode (CWE, CGE) was immersed with a calomel electrode, and the potential difference was recorded for the pharmaceutical solutions at concentrations of 10^{-8} - 10^{-1} M and a corresponding graph of (-) the logarithm of the solutions concentration and the results are shown in Table (2). Solutions concentrations that are less than 1×10^{-6} M did not show a linear response in the (CWE, CGE) electrodes and were therefore neglected in the subsequent experiments. Two types of electrodes were prepared, CWE and CGE, with different proportions. The electrode (No. 1) is the best AM-AR-DBP CGE electrode, with the Nirnste slope being about 58.62 mV.decade^{-1}, and the electrode (No. 4) the best Am-AR-DBP CWE electrode, where the Nirnesty slope gives about 56.85mV.decade-1 , This can be seen from Table (2). The properties and specifications of these selective electrodes that are manufactured for the medicinal substance have been studied according to the following Table (2):

Table 2. Improvement of CWE and CGE electrode components

Electrode No.	PVC (%)	plasticizer (%)	Am-AR (%)	Slope $\frac{mV}{decade}$	Linear range M	R^2
			AM-AR-DBP, CGE			
1	**30**	**60**	**10**	**58.62**	**1×10^{-6} - 1×10^{-1}**	**0.9998**
2	30	63	7	53.29	1×10^{-6} - 1×10^{-1}	0.9951
3	30	65	5	52.22	1×10^{-6} - 1×10^{-1}	0.9876
			AM-AR-DBP, CWE			
10	**30**	**60**	**10**	**56.85**	**1×10^{-6} - 1×10^{-1}**	**0.9996**
11	30	63	7	54.66	1×10^{-6} - 1×10^{-1}	0.9991
12	30	65	5	53.91	1×10^{-6} - 1×10^{-1}	0.9993

3.2 Effect of pH

In order to research the effect of the pH on the electrode's potential response, the potential was determined by adding NaOH or HCl to a constant concentration of 1 ?? 10 ?? ^(-4) M of amtriptyline hydrochloride solution and to different pH values ranging from (1-10). As a function of pH in Fig., the potential shift was plotted. 1. The results indicated that the potential of the electrode is constant between the pH (4-7). In this range, no interference from hydrogen ions or hydroxyl ions was observed. Fluctuations in the potential value at a pH of more than 7 can be due to the formation of soluble and insoluble complexes with hydroxyl ions in the solution of the medication amtriptyline hydrochloride. As for the fluctuations at a pH below 4, it is likely to be due to the partial protonation of the formed complex. The results of this research are shown in Figure 5 (1).

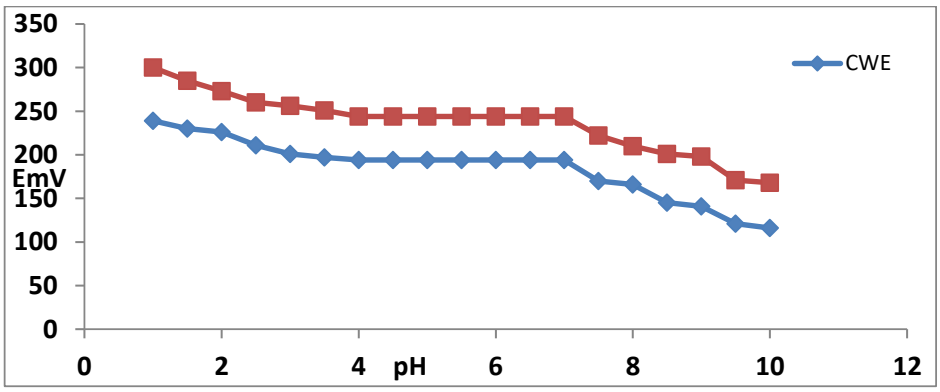

Figure 1. Effect of pH on the potential response of AM-AR-DBP Electrodes

3.3. Effect of Temperature

The potential change was measured by changing the temperature of the solution from (5-85) C for a concentration of 1×10^{-4} M, and the relationship between the temperature and the measured potential difference was plotted, and it was found that the best temperature range in which the electrodes would operate is between (10-50) ºC for (CWE, CGE) electrodes. which was used in the subsequent experiments, and the results are shown in Fig. 2. It shows a significant increase in the potential difference values at higher temperatures, which can be attributed to the increase in the movement of drug solution particles inside and outside the electrode. The temperature that is less than 5 °C was neglected due to the freezing of the solution, as the phenomenon of water anomalies occurs at a temperature of 4 °C, so the surface of the solution becomes freezing, preventing the electrode from performing its work, which makes measuring the potential difference of the solution at a temperature less than 5 °C is not possible.

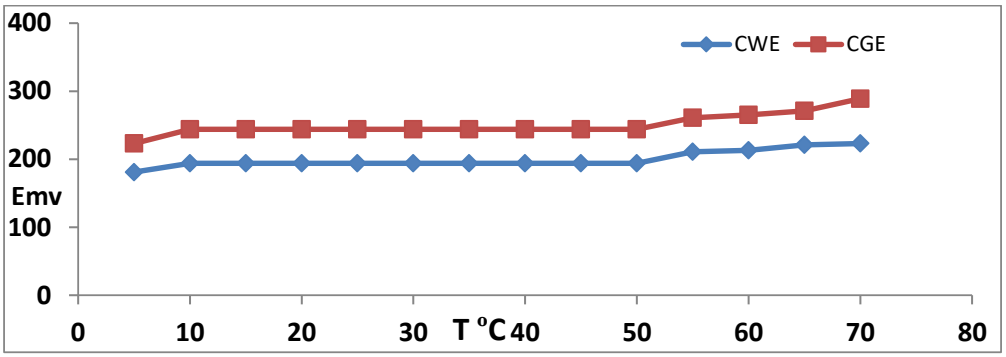

Figure 2. Effect of Temperature on the potential response of AM-AR-DBP Electrodes

3.4. Effect of electrode immersion time on electrode performance

The effect of submerging the AM-AR-DBP electrodes in a 1×10^{-2} M solution of Amitriptyline hydrochloride was studied for different periods by measuring and following the slope values until the readings stabilized and the highest value of the Nernstatic slope was obtained. The slope values reached their maximum values for the prepared AM-AR-DBP electrodes (58.62, 56.85) mV / (decade) after continuous immersion for (12, 24 hours) CWE and CGE electrodes respectively.

3.5. Calibration Curve and Detection limit

After determining the optimal conditions of the pH and temperature in several experiments, a calibration curve was drawn, and it is evident in Figure 3 how linear the calibration curve is. The upper and lower detection limit of the prepared AM-AR-DBP electrodes were calculated and the upper and lower detection limit of the CGE electrode was 0.2042M, 4.8×10^{-7} M respectively, and the upper and lower detection limit of the CWE electrode was 0.2051M, 4.91×10^{-7} M respectively.

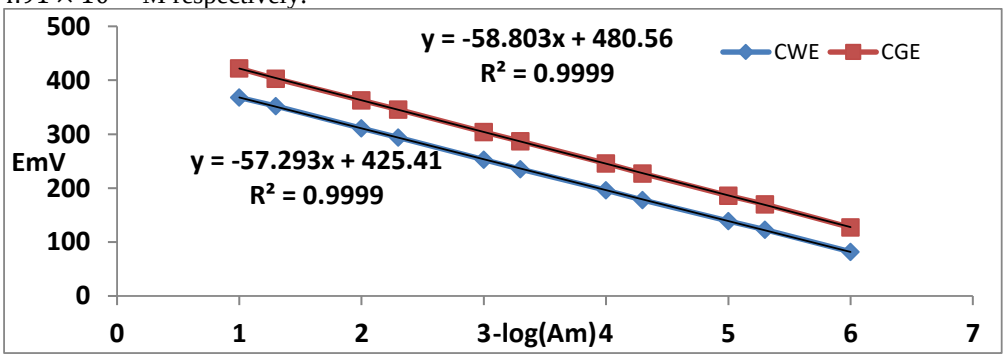

Figure 3. calibration curve of AM-AR-DBP Electrodes

3.6.Precision and accuracy

After drawing the calibration curve for the AM-AR-DBP electrodes, precision and accuracy were studied by calculating the potential of different drug concentrations to be tested within the linear range of the calibration curve for (7) consecutive readings and at the optimal selected conditions, and the results are shown in the Table (3).

Table 3. Precision and accuracy of results for AM-AR-DBP electrodes

Sample	Taken [AM] M	Found [AM] M	%Recovery	%RE
CGE	1×10^{-1}	1.0095×10^{-1}	100.95	0.95
	1×10^{-2}	1.0018×10^{-2}	100.18	0.18
	1×10^{-3}	9.941×10^{-4}	99.41	- 0.59
	1×10^{-4}	1.0258×10^{-4}	102.58	2.58
	1×10^{-5}	9.788×10^{-6}	97.88	- 2.12
	1×10^{-6}	9.71×10^{-7}	97.10	-2.90
%Mean ± SD		99.683 ± 2.0120		
n		6		
Variance		4.0483		
%RE		-1.9		
%RSD		2.0183		

Sample	Taken [AM] M	Found [AM] M	%Recovery	%RE
CWE	1×10^{-1}	9.9530×10^{-2}	99.53	-0.47
	1×10^{-2}	1.007×10^{-2}	100.70	0.70
	1×10^{-3}	$9.7.880 \times 10^{-4}$	97.88	- 2.12
	1×10^{-4}	9.9040×10^{-5}	99.04	- 0.96
	1×10^{-5}	1.002×10^{-5}	100.20	0.20
	1×10^{-6}	1.0140×10^{-6}	101.40	1.40
%Mean ± SD		99.7916 ± 1.145		
n		6		
Variance		1.311		
%RE		- 0.2083		
%RSD		1.1473		

In addition to good recovery and relative error values, Table (3) shows a value for the relative standard deviation of the AM-AR-DBP electrodes which are 2.0183% and 1.1473% for the CGE and CWE electrodes respectively for the concentrations selected from the calibration curve. These results indicate that the prepared electrodes can be used. To estimate the drug with high accuracy and Precision.

3.7. Response Time

The Response Time of the electrodes was studied by immersing the electrode in the solution of the drug to be analyzed at concentrations of 10^{-6}-10^{-1} M and measuring the potential difference for each solution and determining the response time and the results are shown in Figure (4) and it is clear that the response time of the prepared AM-AR-DBP electrodes ranges Between 20-83 seconds, 14-76 seconds for CWE and CGE electrodes respectively.

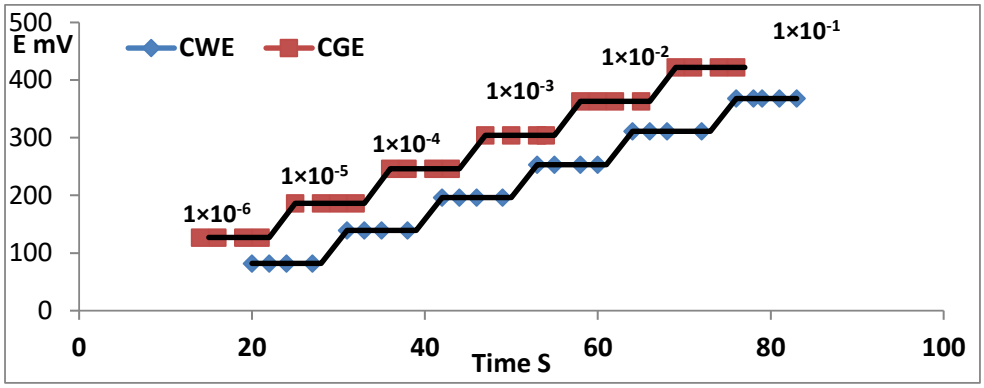

Figure 4. Response Time of AM-AR-DBP Electrodes

3.8. Study the life time of the Electrode

The lifetime of the AM-AR-DBP electrode was calculated by repeating the calibration two or three times a week for each prepared electrode, with Nernstatic slope follow-up values, as no deviation or decrease in Nernstatic slope was observed for 26 days, 42 for CWE and CGE electrodes, respectively. After that, a negative deflection was shown by the electrodes. In general, the explanation for the end of the electrode's existence could be due to the leakage of the electrode material (the active substance).

3.9. Selectivity

The electrodes showed high selectivity in the direction of the drug without the potential being affected by the interfering ions selected through the selectivity coefficient values that are less than one and shown in Table (4). The selectivity was measured by the separate solutions method [24], where the potential of the drug solution was measured at a concentration of 1×10^{-3} M without adding the interfering ion (E_i), then the potential of the interfering ion solution was measured at a concentration of 1×10^{-3} M Alone (E_j).

Table 4. selectivity coefficient values

the interfering ion $\mathbf{1 \times 10^{-3}}$ M	Selectivity coefficient values $K_{i,j}^{pot}$	
	AM-AR-DBP	
	CWE	CGE
Na^{1+}	5.001×10^{-1}	4.444×10^{-1}
K^{1+}	4.878×10^{-1}	4.100×10^{-1}
$NH_4{}^{1+}$	4.099×10^{-1}	3.911×10^{-1}
Ba^{2+}	4.111×10^{-3}	5.998×10^{-3}
Ca^{2+}	9.0012×10^{-3}	60333×10^{-3}
Mg^{2+}	4.111×10^{-3}	7.321×10^{-3}
Cl^{1-}	9.678×10^{-2}	8.008×10^{-2}
Br^{1-}	6.321×10^{-2}	7.191×10^{-2}
I^{1-}	3.665×10^{-2}	2.900×10^{-2}
$NO_3{}^{-1}$	2.988×10^{-2}	3.434×10^{-2}
$CO_3{}^{1-}$	4.432×10^{-2}	8.801×10^{-2}
$SO_4{}^{2-}$	2.200×10^{-2}	3.120×10^{-2}
Glucose	1.922×10^{-3}	2.222×10^{-3}
Fructose	8.004×10^{-3}	6.990×10^{-3}
Starch	7.777×10^{-3}	5.000×10^{-3}

3.10. Robustness and Ruggedness

The robustness of the analytical method used for the AM-AR-DBP electrodes prepared for both types CWE and CGE was examined by using ethanol as a solvent instead of water in the preparation of drug solutions for the concentration range $1 \times 10^{-6} - 1 \times 10^{-1}$ M. As for the rigidity of the method, it was studied by using another Potentiometer recorder (HANNA Instruments 211 pH Meter) with changing the laboratory used, and the results are shown in Table (5).

Table 5. Robustness and Ruggedness of the analytical method used for AM-AR-DBP electrodes

Parameter	Robustness	
	CGE	CWE
%Mean ± SD	101.015 ± 2.3942	101.2466 ± 2.0018
n	6	6
Variance	5.7324	4.0072
%RE	1.0150	1.2466
%RSD	2.3701	1.9771

Parameter	Ruggedness	
	CGE	CWE
%Mean ± SD	100.01 ± 1.6865	99.800 ± 1.6015
n	6	6
Variance	2.8445	2.5648
%RE	0.0100	-0.2000
%RSD	1.6863	1.6047

3.11. Applications of drug Amitriptyline hydrochloride in pharmaceutical preparations

3.11.1. The direct method

The drug was estimated in the pharmaceutical formulation, Amitriptyline tablets, using the prepared AM-AR-DBP electrodes, and the results are shown in Table (6).

Table 6. Estimating the drug by the direct method

Sample AM-AR-DBP	Taken [AM] M	Found [AM] M	%Recovery	%RE	%RSD*
CWE	5×10^{-2}	5.0261×10^{-2}	100.522	0.522	0.2548
	5×10^{-3}	5.0857×10^{-3}	101.71	1.714	0.3042
CGE	5×10^{-2}	4.9891×10^{-2}	99.7827	- 0.217	0.1565
	5×10^{-3}	4.9508×10^{-3}	99.0160	-0.984	0.3175

The good recovery values using the prepared AM-AR-DBP electrodes and the relative standard deviation values for the CWE, CGE electrodes confirm that the estimation using these electrodes is of high Precision and accuracy.

3.11.2. Standard Additions Method

The calibration curves for the standard additions method of AM on the pharmaceutical preparation Amitriptyline tablets of the prepared AM-AR-DBP electrodes are shown in Fig. (5). Depending on the straight-line equation and when y = 0, x = -2.0064 for the CWE electrode and x = -2.0247 for the CGE electrode, it represents the volume of the standard solution Vs with a concentration of 1×10^{-3}M, and using the relationship:

$C\ V = -V_s\ X$

Since C = concentration of the pharmaceutical preparation solution (required), V = volume of Amitriptyline tablet preparation solution = 10 ml, X = standard solution concentration of the pure drug additive = 1×10^{-3}M, Vs = volume of standard solution Of the drug.

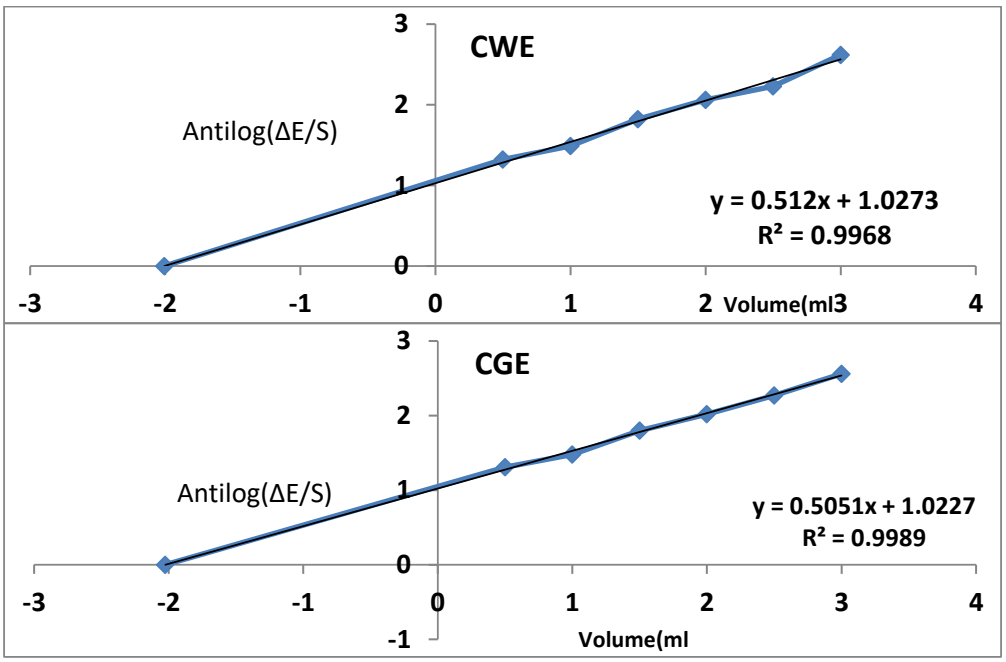

Figure 5. Standard Additions Curves for Estimation of AM in (Amitriptyline Tablet) using the prepared AM-AR-DBP electrodes.

Table 7. Estimating the drug by the Standard Additions method

Sample AM-AR-DBP	Taken [AM] M	Found [AM] M	%Recovery	%RE
CWE	2×10^{-4}	2.0064×10^{-4}	100.32	0.32
CGE	2×10^{-4}	2.0247×10^{-4}	101.23	1.23

The recovery values of the amitriptyline hydrochloride concentration using AM-AR-DBP electrodes prepared after application for the pharmaceutical preparation of amitriptyline tablets are shown in Table (7). We infer from these good results of recovery values and relative error that the electrodes developed and used in the determination of amitriptyline hydrochloride in the amitriptyline tablet pharmaceutical preparation are electrodes that give good precision results.

3.11.3. potentiometric titration method

The drug was estimated in the pharmaceutical preparation amitriptyline tablets using the prepared AM-AR-DBP electrodes and the results are shown in Table (8) after the graph of the values of the potential of the solution AM, its concentration 1×10^{-3} M and its volume of 10 ml against the titrant solution AR Its concentration is 1×10^{-3} M, and the end point is defined as a bisection of the steeply sloping portion of the curve which is analogous to the inverse of the letter S.

Table 8 . Estimating the drug by the potentiometric titration method

Sample AM-AR-DBP	Taken [AM] M	Found [AM] M	%Mean* ± SD	%Recovery	%RE	%RSD
CWE	1×10^{-3}	1.0083×10^{-3}	100.83 ±2.5000	100.83	0.83	2.4794
CGE	1×10^{-3}	1.0027×10^{-3}	100.27± 2.6352	100.27	0.27	2.6281

Average of nine potential readings *

3.11.4. Study the homogeneity of content

The drug was measured using the prepared AM-AR-DBP electrodes in the pharmaceutical formulation, amitriptyline tablets, and the results are shown in the table (9). After a series of bakers had been prepared and one tablet was dissolved in 100 ml of deionized distilled water in each baker, then the potential was measured and the concentration of the solution was determined by the calibration curve.

Table 9. Estimating the drug by the homogeneity of content method

Sample AM-AR-DBP	Taken [AM] M	Found [AM] M	%Recovery*	%RE
CWE	7.9643×10^{-4}	7.8595×10^{-4}	98.6800	-1.32
CGE	7.9643×10^{-4}	8.0068×10^{-4}	100.5341	0.5341

Average of six potential readings *

3.11.5. Determination of drug in urine and blood plasma

amitriptyline hydrochloride was estimated in urine and blood plasma in the pharmaceutical formulation Amitriptyline tablets using AM-AR-DBP electrodes prepared and the results are shown in Table (10).

Table 10 . Estimating the drug in urine and blood plasma

Sample Urine AM-AR-DBP	Taken [AM] M	Found* [AM] M	%Recovery	%RE
CWE	2×10^{-3}	2.0179×10^{-3}	100.89	0.89
CGE	2×10^{-3}	2.0115×10^{-3}	100.57	0.57
Sample Urine AM-AR-DBP	Taken [AM] M	Found* [AM] M	%Recovery*	%RE
CWE	2×10^{-3}	1.9945×10^{-3}	99.7274	-0.2725
CGE	2×10^{-3}	1.9892×10^{-3}	99.4600	- 0.5399

Average of seven potential readings *

4. Conclusion

In the presence of DBP as a plasticizer, Ion-selective electrodes consisting of an electrically active material resulting from the interaction of AM with AR were produced. A linear response range (10-6-10-1 M) with a slope equal to (57.293, 58.803 mV / decade) was achieved by the prepared AM-AR-DBP electrodes. The CGE electrode's upper and lower detection limit was 0.2042M, 4.8 ?? 10 ?? ^(-7) M, and the CWE electrode's upper and lower detection limit was 0.2051M, 4.91 ?? 10^(-7) M. For both CWE and CGE electrodes, the lifetime of the electrodes was (26 days, 42 days). This new technique has been shown to be highly accurate and successfully applied to pharmaceutical preparation (Amitriptyline tablets), urine and plasma blood.

References

[1] Bagotsky V S 2006 *Fundamentals of Electrochemistry* ,2nd Ed., John Wiley and Sons, New Jersey ,694,402.
[2] Zdrachek E and Bakker E 2019, *Anal. Chem*., **91** 2.
[3] Mikhelson., 2010**,** *J. Anal. Chem*., **65**, 112.
[4] U.S. pharmacopeia on CD-ROM",1965, 2013 36th ed. NF 25, system simulation ltd. The stationary office, America.
[5] British pharmacopeia in CD-ROM", 1827, 2013, 7th ed., by system simulation ltd., The stationary office, London.
[6] Moffat A C , Osselton M D and Widdop B 2011 *Clarke's Analysis of Drugs and Poisons* ,4th ed . (pharmaceutical press, London UK).
[7] Sweetman S C , Martindale 2014 *The complete drug reference* ,38th ed. (Pharmaceutical Press. London).
[8] Susmitha K , Thirumalachary M , Singh T C and Venkateshwarlu G 2014 *J. Chil. Chem. Soc*., **59**, 2265.
[9] Reddy T V B, Ramu G and Rambabu C 2014, *J. Pharm. Sin*. **5**, 9**.**
[10] Farag R S , Darwish M Z , Fathy W M and Hammad H A 2013.,*Int. J. Chemical and Anal. Scie*., **4**, 120.
[11] Mosavian M T H , Es'haghi Z , Razavi N and Banihashemi S 2012, *J. Pharma. Anal*., **2**, 361.
[12] Thejaswini C G and Gurupadayya B 2014. *J. Pharma. Res*., **4,** 3597.
[13] Beitollahi H , Nejad F G , Tajik S , Jahani S and Biparva P 2017, *Int. J. Nano Dimens*., **8**, 197.
[14] Ulrich S, Isensee T and Pester U, 1996, *J. Chroma. B: Biomedical Scie. and Appl*., **685**, 81,**.**
[15] Wu S M , Wu H L , Ko W K and Chen S H 2000, *Anal. Chim. Acta*., **413**, 125.
[16] Shen Y, Zhu R H , Li H D , Liu Y W and Xu P 2010, *J. Pharma. and Biomed*., **53**, 735
[17] Karpinska J and Starczewska B 2002, *J. Pharma. and Biomed. Anal*., **29**, 519.
[18] El-Nashar R M , Abdel Ghani N T and Bioumy A A 2004, *J. Microchem.*, **78**, 107.
[19] Patel S.K. and N.J. Patel. 2009, *Chroma.*, **69**, 393.
[20] Kaur K and Malik A K 2013, *J. Fluoresce.*, **23**, 533**.**
[21] Elnemma E M , El Zawawy F M and Hassan S S M 1993**,** *Microchimica. Acta*., **110**, 79.
[22] Khalil M M , Issab Y M and Mostafa S M 2015, *Int. J. Eng. Res. and Gen. Sci.*, **3**, 1191.
[23] Abdallah N A 2016, *Sens. Mater*. **28**, 797.
[24] Bakker E and Pretsch E 2007, *J. Angew. Chem. Int. Ed*. **46**, 5660.

Influence of ultrasonic pre-treatment on Pyrolysis and Combustion of Sewage Sludge by TG

Influence of ultrasonic pre-treatment on Pyrolysis and Combustion of Sewage Sludge by TG

Ruaa O. Taha [1,*] and Farah Ali Mohammed[2]

University of Technology, Department of chemical engineering, Baghdad, Iraq.

[1]E-mail: rtosse581@gmail.com

Abstract. The combustion and pyrolysis processes of sewage sludge were studied in the current report. Two kinds of sewage sludge(SS) were used, SS the sewage sludge was not treated, while SS-U90KHz the ultrasonic bath pre-treated sewage sludge with a frequency of 90KHz was not treated. Wastewater treatment plants are the origins of waste sludge. Analyses were performed roughly and finally. Thermogravimetric research analyzed the thermal behaviour of the analysed sewage bucket (TGA). The samples were heated at a constant rate of 25 to 800 Celsius by air (combustion) and nitrogen flow (pyrolysis). For sludges which have been investigated. In the TG/DTG curves, comparable thermal profiles were available. All of the TG/curves DTG's were divided into three periods. At the same time, during the combustion stage, the sewage sludge decomposition occurred in the 180-580 0C range. The pyrolysis procedure took place at a lower rate, but less weight loss..

1. Introduction

Wastewater sludge is a by-product of wastewater treatment comprising organic compounds, microorganisms and harmful substances, including heavy metals[1], weakly biodegradable organic compounds, microbes, viruses, pharmaceuticals and dioxins that are not easily disposable[2,3]. At least 20 metals are dangerous and half of them are released into the atmosphere to the point of posing a danger to public health[4]. When the waste sludge is treated, a number of operations are performed which rapidly decompose the concentrations of organic materials. The safe removal of wastewater sludge is one of the world's greatest environmental issues [5]. As sludge has a relatively high "calorific value," it is particularly fascinating to have energetic processing technologies, including thermal pyrolysis and combustion. The main advantages of combustion are the decreasing volumes provided by the centimeters relative to the initial commodities. This waste can be transformed by combustion into heat energy [6]. On the other hand, pyrolysis is a promising technique that makes it a valuable fuel that can be developed for the manufacture of fuels of a different sort, such as oil and gas[7]. Since most of the hazardous components are partially stored in the monkey[8], it seems that this process is less polluting than combustion. Like gas produced by the gasification of waste [9]. Coal combustion is a value for gaseous gas filtered pyrolysis as well as an understanding of the process of sludge pyrolysis is a first step in developing our combustion knowledge during the time of explosive combustion. Other methods have been followed[10], and sludge has been used in compound adsorbents[11,12,13] for the extraction of poisons such as NO2 and SH2. The sludge is, in other words, still very useful. Sewage sludge pyrolysis studies and documents have been released. Pyrolysis and drying methods were examined by Kasakura and Hiraoka, taking into account the economies of various choices. Seggiani et al.[14] studied the decomposition of four wastewater sludge sites, showing that sewage sludge pyrolysis was prone to small quantities of organic salt and to the decomposition of two different reactions. An significant research method for the biomass

conversion of electricity[15] has been the alteration of multiple wastewater treatment plant sludge (WWTP) to modify the fuel properties of sludge and its actions during pyrolysis and combustion using ultrasound waves as pre-treatment[15]. This will build up energy through cavitation and then quickly discharge the energy through the immediate collapse of a cavitation bubble, which will break up the chemical connection and kill the interface constraints of the multi-phase system and increase the heat and mass flow[16]. About Subhedar et.al. [17] clarified some of the multiple findings of lignocellulose ultrasound. In certain cases, the ultrasound had a remarkable capacity to sever the chemical bonds of the biomass materials, allowing it to eliminate compounds of interest such as cellulose, hemicellulose or lignin. This research is being carried out to compare two samples of sandstone with pyrolysis and combustion in drainage plants. In pyrolysis and sludge combustion, TG results were achieved in N2 and O2 atmospheres in the 25 800C temperature range of the ultrasonic wave 90 K Hz. Compared to other papers, the research carried out in this study is relevant for both of the two activities found, as it analyzes pyrolysis and combustion for the same sludge form.

2. Material and Techniques

2.1 Sample collection

The samples of sewage sludge have been taken from a factory of treating waste water plant (Al– Rustumiya, Baghdad, Iraq).

2.2 Techniques

2.2.1. Prior-treating Techniques

An ultrasonic bath processor was used to treat (100 g) of sewage sludge powder which melted, scattered in a good way with 200 millilitres of filtered water, after that the mix sample settled in ultrasonic bath for 1 hr at 180 W power and exposed to 90 KHz frequency at steady temperature 80°C. as a final point, the mixture has been gathered by using filtrating sucked and drained off at one hundred and five°C for twenty-four hr.

2.2.2.Using TGA analysing Device for High Temperature Decomposition:

SS and SS-U90KHz samples have been analysed utilizing an analyser of thermal properties (Linseis STA PT1000) for creating thermo-graphs in a flowing of nitrogen and oxygen . the specimen has been put under a heat rate of 10°C per minute. the primary sample weight has been nearly at (seven – ten) milligrams for every single run, besides the losing in weight data have been noticed at a degree of heat constant reach to 800 degrees.

3. Results and Discussion

In the inert atmosphere (pyrolysis) and in the oxidative atmosphere (combustion), the experimental variations in weight fraction vs. temperature were established in active runs at a temperature of 10 ° C min-1 as shown in 'Figure. 1 'for two samples of SS and SS-90KHz, define the following differences.

Table 1: Approximate and ultimate analysis for SS and SS – U90KHz samples.

	SS	**SS-U90 KHz**
Humidity (wt%)	3.9	4.1
Volatile matter (wt%)	53.9	65.9
Fixed carbon (wt%)	2.9	8.8
Ash content (wt%)	45.3	30.0
C total (wt%)	26.42	40.56
H (wt%)	3.9	5.5
O (wt%)	26.0	28.3
N (wt%)	3.10	6.65
S total (wt%)	0.71	1.25

3.1 Pyrolysis results on thermographer and derivative thermogravimetry TG/DTG analysis

Sludge pyrolyzing is an inert thermal method, where organic material is subject to a sequence of complicated reactions, causing explosive production and organic condensation, which eventually contribute to the formation of carbon dioxide. The processes of devolatilization of sludge follow.

Sludge ---------- volatile material (H2, CO, CO2, H2O, CxHy, etc) + Char

Directed thermogravimetry (DTG) of the samples of sludge pyrolysis confirmed a paralyse of sludge elements (biodegradable organic and bacterial substances and nondegradable substances) at two peaks partly overlapping or one peak and one shoulder of 180, 550 C. Specimens for sludges pyrolysis derivative thermogravimetry (DTG) A pyrolysis of sludges explained a top and a shoulder between 180 and 550 C. Two primary periods in this temperature range were regarded: (a) The bulk of reactive pyrolysis was considered for the first cycle (from around 180 to 385 C). Components (organic material biodegradable) were collected along with less reactive partial pyrolysis of the (bacterial components, the pyrolysis of which was initiated further at higher temperatures. (b) Less reactive portion (most usually bacterial) pyrolysis [18] was carried out in the second era (385-550 C). In addition, a light char devolatilization (secondary pyrolysis) causing the breakdown of the C-C terminal bonds in a concentrated organic composition in the char was detected at temperatures greater than 550 C. The end was observed. Other scientists [19,20,21] suggested that the above devolatilization has risen due to the non-biodegradable pyrolysis of the material. Moisture loss along with certain volatiles at temperatures below 200 C The high temperature was between 90 ^{0}C and 97 ^{0}C because of the lack of humidity. In Table 2 for pyrolysis and burning, the percentages of weight loss for each stage are shown to compare the weight loss of pyrolysis between these two methods, and to remember the ultrasound effect of pyrolysis and combustion. The lost weight is referred to in the same foundation for each sludge. The pyrolysis data thus contains a char production as a weight loss percentage. The profile and the two contrasting peaks vary from the sample of SS-U90KHz ‘Figure 1’ Due to ultrasound waves breaking up the chemical bond and disrupt the interface constraint of the multi-phase device, and boost heating and mass transfer, SS samples loss mass lower (36.2 wt. percent) than SS-U90KHz (59.1 wt. percent) If soaked samples were applied to the bath, biomass would well, resulting in lower crystallinity and a higher surface area, which increased structural interruption, moreover the lignin-carbohydrate bond decreased, lowering lignin percentage and digestibility of cellulose greater than previously during longer periods of treatment [22, 23, 24].

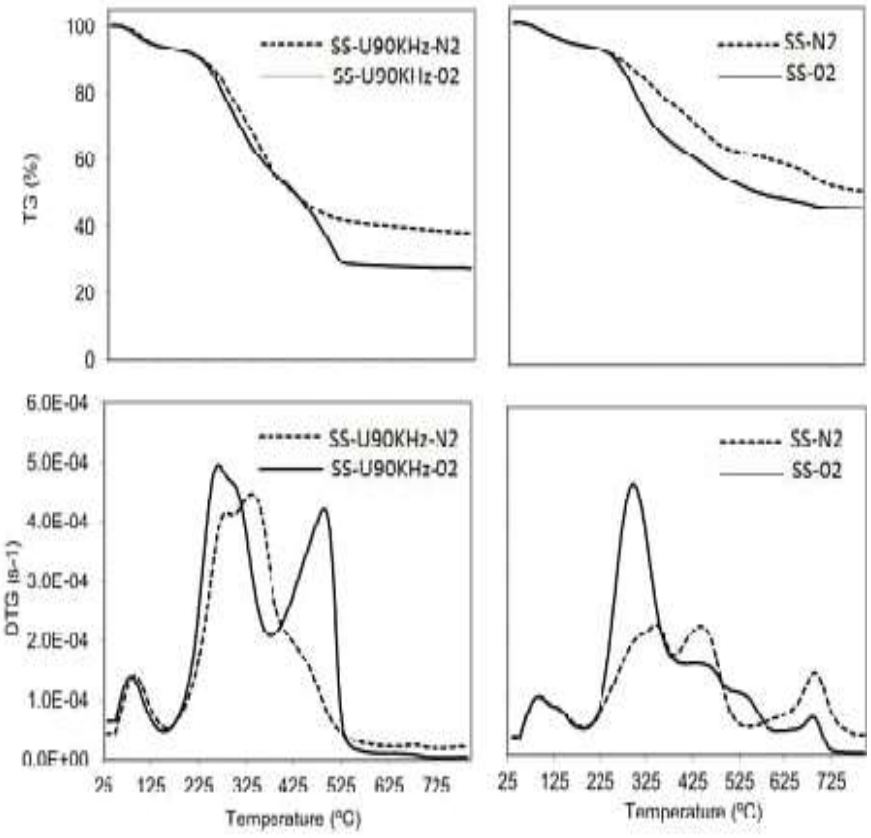

Figure 1. Comparison between pyrolysis and combustion sketch (TG and DTG) of SS and SS-U90KHz.

3.2 Combustion results on thermographmetry and Derivative thermogravimetry TG/DTG analysis

The combustion of sludge is a complicated process that occurs in many phases. A pyrolysis loop begins the combustion process along with a fuel gas and a solid cargo. The gas generated burn when it comes to O2. Finally, the expanding O2 oxidizes the char. The reactions involved during combustion are the following:
Pyrolysis period: Sludge ---------- volatile material (H2, CO, CO2, H2O, CxHy, etc) + char

Volatile combustion: volatile material + O2 ---------CO2 + H2O

Char combustion: char + O2 --------CO2

These partly agree with the reactions observed in Table 2 during each cycle. The SS sludge's combustion sketch was different from that of the SS-U90KHz batch, similar to the DTG combustion sketches of pyrolysis 'Figure 1' consisting of two partly overlapping peaks between 180 and 550 C of approximately SS-90KHz. For SS sludge and the plateau, one top and two shoulders of 200 and 600C can be found due to carbonate decomposition at 685 C. Eventually, the sludge combustion cycle was divided into three main stages. Two sub-periods were seen for SS in the second cycle and only carbon decomposition was used in the third cycle in the combustion of the SS sample. Table 2 displays the percentages of weight loss during sludge sample combustion during different times.
In the first step, in contrast to the pyrolysis analysis of combustion and pyrolysis profiles of SS-U90KHz sludge, the DTG combustion profile was similar in nature. On the other hand, several differences in DTG combustion may be noted in the case of pyrolysis (table 2). The

first combustion cycle deteriorated in relation to pyrolysis. A lower peak temperature and high mass velocity loss were exhibited in the resulting DTG combustion peak. Data in Table 2 indicate that during the initial combustion process, only a volatile part of that formed in the first and second pyrolysis cycles was burnt (70.9 percent). This implies that the process of devolatilization/volatile combustion overlapped and lasted in the 2nd century. Starting from the 2nd one. A plateau loss (differing from the shoulder of the pyrolysis skirt) was confirmed by the combustion profile. Mass losses occurred on the 2nd table according to the results of Table 2 due to both the combustion of the chariot and the end of the devolatilization/volatile combustion process of the portion of bacterial matter initiated in the first stage of the SS-U90KHz sludge. The SS-U90KHz was 27.9 percent through instability / combustion and 15.2 percent through carbohydrate combustion.

For SS burning, first. A period between 200 C and 375 C was identified, with a single limit of about 59.5 Wt percent weight loss, which was greater than that obtained in pyrolysis (36.2 Wt percent). The drawing identified two small shoulders between 375 C and 600 C associated with the combustion of carbohydrates in the 2nd century. The shoulders were 3 to 515 centimeters by 70 centimeters and 5 to 600 centimeters by 515 centimeters. Beginning with the seventh. With a high of 685 C, the weight loss was 7.0Wt percent (See Table 2) due to the carbon division between 60C and 800 C. The rate of devolatilization/volatile combustion (59.5 percent wt) was high in the former, according to the data from Table 2. Compared to 66.8 percent and the Second Pyrolysis Stage of the SS, period of the first volatile produced. In the entire SS sludge combustion process, the following processes were also used: superficial water loss, decomposition and auto-gasification reactions, combustion of flux and carbon, and combustion of charcoal.

Table 2. wt% loss for both samples (SS and SSu90KHz) in each period in pyrolysis and combustion processes.

Sludge (period)	1st period	2nd period	3rd period	Char[a]
Pyrolysis				
SS (200-380-550-800 C°)	36.2	30.6	22.5	10.7
SS-u90KHz (180-385-550-800 C°)	59.1	19.6	4.3	17
Combustion				
SS (200-375-515-600-800 C°)	59.5	24[b] 9.5[c]	7.0	
SS-u90KHz (180-370-550-800 C°)	55.4	43.1	1.5	

[a] Char obtained also regard as a wt % loss.
[b] 1st sub period.
[c] 2nd sub period.

4. Conclusions

To evaluate the effect of sludge treatment on pyrolysis and combustion, thermographmetric analysis was used. First, two samples were used for waste sludge SS without treatment and the second was used as a pretreatment with a frequency of 90 KHz for SS-U90KHz using ultrasonic baths. The combustion and pyrolysis were considered for two forms of sewage sludge. there is Some variations were found between the drawings of the combustion and pyrolysis phase of sewage sludge samples generated by the chemical composition. Combustion under a controlled oxidizing atmosphere is a mechanism that turns any carbonaceous feed into a functional heating value gaseous substance, leaving solid remains behind. The only pyrolysis discrepancy that is done under the inert atmosphere. The main process of devolatilization associated with the degradation of protein and soluble polysaccharides occurred during pyrolysis between 200 and 550 C. The oxidation of the sample was over 500 C during combustion. The char oxidation switched to lower temperatures as the concentration of oxygen rose. We will note the influence of the presence of oxygen on thermal decomposition by comparing the combustion and pyrolysis DTG diagrams.

References

[1] Bi LW, Zhao Z D and Vinatrovu 2007 *Chem.Ind.for.Prod.* **27** 138
[2] Bussemaker M J, Zhang D 2013 *Ind.Eng.Chem.Res*.**52** 3563.
[3] Kalisz S, Pronobis M and Baxter D, *Energy J* **33** 1770.
[4] Kasakura T and Hiraoka M ,1982 *Water Res*. **16** 1335.
[5] Kistler RC and Widmer F,1987 *Environ. Sci.* Technol. **21** 704.
[6] Leckner B 2007 . *Therm. Sci*. **11** 5.
[7] Lin Y , Liao Y ,Yu Z,Fang S,Lin Y ,Fang Y ,Peng X and Ma X 2016 *Energy Convers. Manag.***118** 345..
[8] Methrath L N A, Muley P O,Aita G and Boldor D 2016 *Bioresour. Technol.* **200** 262.
[9] Nzihou A, Flamant G and Stanmore B 2012. *Energy* **42** 121.
[10] Pietrzak R and Bandosz TJ 2008 *J. Hazard. Mater* **154** 946
[11] Pietrzak R and Bandosz TJ 2007 *Carbon* **45** 2537.
[12] Rulkens W 2008 Energy Fuels **22** 9.
[13] Sanchez M M A, Mondini C, Nobili M De, Leita L and Roig A 2004 Waste Manage **24** 325.
[14] Seggiani M ,Puccini M,Raggio G,Vitolo S 2012 waste Manage.**32** 1826.
[15] Shao J, Yang R, Chen H, Wang B, Lee DH and Liang DT 2008 Energy Fuels **22** 38.
[16] Noor A J and Jathwa A I 2020 *JAARU* **27** 165.
[17] Subhedar P B and Gogate P R 2015 *Ultrason.sonochem*. **27** 37.
[18] Sumner M E 2000 *Commun Soil Sci Plant Anal* **31** 1701.
[19] Tabasova A, Kropac J, Kermes V, Nemet A, Stehlik P 2012 *Energy* **44** 146.
[20] Urban D L , Antal Jr M J 1982 *Fuel* **61** 799.
[21] Wang Z,He Z,Zhao Z,Yi S,Mu J 2017 Influence of ultrasonic –assisted extraction on the pyrolysis characteristics and kinetic parameters of eucalyptus ultrason. *Ultrason Sonochem* **37** 47.
[22] Yuan W, Bandosz TJ 2007 *Fuel* **86** 2736
[23] Salman M S *Ibn Al Haitham J. for Pure and Appl. Sci* **22** 45.
[24] Musa S A 2009 *Ibn Al Haitham J. for Pure and Appl. Sci* **22** 1.

Pretreated Fishbone as Low Cost-Adsorbent for Cationic Dye Adsorption from Aqueous Solutions: Equilibrium, Optimization, Kinetic and Thermodynamic Study

Pretreated Fishbone as Low Cost-Adsorbent for Cationic Dye Adsorption from Aqueous Solutions: Equilibrium, Optimization, Kinetic and Thermodynamic Study

Muna Abd Ul Rasool Al-Kazragi [1] and Dhafir T.A.Al-Heetimi [*1]

[1]University of Baghdad, College of Education for pure science Ibn-Al-Haitham, Iraq

* E-mail: dhafir1973@gmail.com

Abstract. The present study investigated the use of pretreated fish bone (PTFB) as a new surface, natural waste and low-cost adsorbent for the adsorption of Methyl green (MG, as model toxic basic dye) from aqueous solutions. The functional groups and surface morphology of the untreated fish bone (FB) and pretreated fish bone were characterized using Fourier transform infrared (FTIR), scanning electron microscopy (SEM) and Energy dispersive X-ray spectroscopy (EDS),respectively. The effect of operating parameters including contact time, pH, adsorbent dose, temperature, and inorganic salt was evaluated. Langmuir, Freundlich and Temkin adsorption isotherm models were studied and the results showed that the adsorption of basic dye followed Freundlich isotherm. Kinetic modeling of the data at different temperatures confirmed pseudo-second-order(P-2-O) model, along with calculated thermodynamic parameters depicted that the adsorption process is spontaneous and endothermic in nature. Diffusion studies suggested that intra-particle diffusion is not the singular rate-controlling factor. The results indicated that 92% of MG capable of being sequestered under optimum adsorption conditions: pH 10.64, adsorbent dose 0.1 g/L, and 60 min contact time. Finally, the results showed that the pretreated fish bone can be effectively used as a proper adsorbent for the adsorption of cationic dye from aqueous solutions.

Keywords: Fishbone, Methyl green, Temkin isotherm, Thermodynamic parameters,Intra-particle diffusion

1. Introduction

The pollution of water stands for a serious environmental problem for human and aquatic systems. Many applications such as printing, tanning, food, textile, and cosmetics industries typically employ biological molecules as dyes to color their products. It has been supposed that cationic dyes have been in general more toxicity levels as compared with anionic dyes [1]. Cationic (basic) dyes have typically employed in silk, nylon, acrylic and wool dyeing in textile production owing to noble solubility of synthetic dyes, and may be existing in trace quantities in built-up wastewaters. The existence of cationic dyes in aquatic streams averts light from water penetrating and has a passive influence on photosynthesis. Features like poisonousness and non-biodegradability stand for the consequence of complex dyes structures. Consequently, they represent against risk to environmental health and human. Therefore, the removal of cationic dye from aquatic system before discharging into water bodies is needed [2]. Methyl green (MC), a cationic dye, is one of the most frequently used dye stuff and it causes hazardous problems both water environments and human life.

Many treatment systems have been used for the removal of different kinds of dyes from aqueous solutions such as, flocculation [3], photocatalytic degradation [4], microbiological decomposition [5], fungus biosorbent [6], and adsorption [7].

Recently, adsorption method has been initiated as being economical and more effectual as compared with physical and chemical techniques. Its process has succeeded in eliminating organic and inorganic pollutants [8], as a result of being cost-effective, astraight forward process and simple design.

Recently, diverse adsorbent materials were employed for removing organic material and color. Naturally, cheap and in effect materials like agronomic materials, food manufacturing by-products and animal bones like fish bones were employed as adsorbents for the removal of organic and inorganic contaminates in recent times. Several economical absorbents in the literature were used for dyes removal including lignocellulosic material [9], sunflower seed hull [10], coconut coir [11], bauxite clay [12], and fish bone [13]. Bones have 70 % inorganic and 30 % organic phases by weight [14]. The hydroxyl apatite Ca10(PO4)6(OH)2 creates the foremost portion of inorganic phase and it is an effectual adsorption material as a result of its capability or removing completely charged contaminates based on ion exchange reacting with calcium ions on a bone surface [2].
The main objective of the present research is to use fish bone (FB) as new adsorbent and to study its capability for the adsorption of cationic dye from aqueous solutions. As a model dye, methyl green was selected for the adsorption analyses. In our current study, the surface categorization of PTFB will be examined using Fourier transform infrared (FTIR) , scanning electron microscopy (SEM) and Energy dispersive X-ray spectroscopy(EDS). Additionally, contact time of adsorption, adsorbent dose, temperature, pH, and salt effect parameters were investigated. The adsorption kinetic, isotherm behaviors were compared and the thermodynamic parameters were determined as well.

2. Experimental

2.1 Pretreatment of fish bones sorbent

Fish bones was collected from a local fish shops in Al-Kadhumyia city, Iraq. Firstly, the fish bones were washed for a number of times with hot purified water for removing the soluble and residue impurities from the bones. Then, the washed fish bones was dried up in the oven at 90 ºC and ground into fine powder by a mortar.

2.2. Pretreatment of fish bones sorbent

Fifteen gram of ground fish bones was treated with100 mL of 0.1 M aqueous solution of NaOH and stirred at room temperature for 4 hours. Then, 3g ofAl_2O_3 gradually added and stirred at room temperature for 5 hours. The treated fish bones were filtered, washed several time with distilled water, and then dried in an oven at 80ºC for 6 hours; milled and sieved in the size ≤75µm. Lastly, the treated fish bones powder was kept in the air tight container to be ready for a use.

2.3. Adsorption experimental method

Basic dye, Methyl green (MG), was employed without additional purification. The dye features and chemical structure are listed in Table 1. The stock solution was prepared by dissolving 1 g of dye in 1000 mL distilled water. The pH solution was adjusted to 7.42 for MG as optimum value obtained from the optimization study conducted in our previous study[15].NaOH (Merck) and HCl (Merck) have employed for adjusting the pH of the solutions. NaCl that have employed for studying the influence of mineral salt on dye removal has as well gotten from Merck. To examine the effect of temperature, 0.1 g of fish bones with 10mL MG dye solutions of known concentration (60-140mg.L^{-1}) in 100 mL Erlenmeyer flasks, shaken on a temperature-controlled shaker at 25, 35 and 45 ºC. After the equilibrium time elapsed, the suspension was centrifuged at 3000 rpm for 5 min., then filtered to be analyzed for MG concentration using UV–Vis spectrophotometer (double beam, T-80, England) at a maximum wavelength of 618 nm. The MG uptake loading capacity (mg/g) of fish bones for each concentration at equilibrium was determined as follows:

$$q_e = (C_o - C_e) \times V / W_t \quad (1)$$

Here, C_o and C_e (mg/L) are for the initial and equilibrium solution concentrations of MG, respectively, V (L) is for the volume of the dye solution, and W_t (g/L) represents the dose of used adsorbent. The MG removal percent was calculated for each run by the following equation:

$$R\% = (C_o - C_e)/C_o \times 100 \quad (2)$$

Table 1. Dye structure and characteristics.

IUPAC Name	Molecular Formula	Molecular Weight	Synonyms	color
[4-[[4-(dimethylamino)phenyl]-(4-dimethylazaniumylidenecyclohexa-2,5-dien-1-ylidene)methyl]phenyl]-trimethylazanium;dichloride	$C_{26}H_{33}N_3Cl_2$	458.471 g/mol	Basic Blue 20, Methyl green chloride	Blue-green

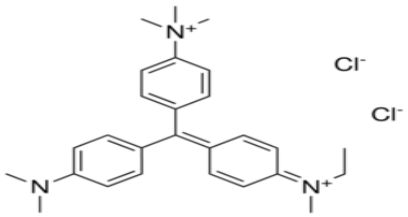

2.4. fish bondes Characterization

Characterization of the fish bones has investigated using scanning electron microscopy (T-SCAN Mira3 France) and Energy dispersive X-ray spectroscopy (EDS, Hitachi, Ltd., Tokyo, Japan)to investigate the surface morphology of fish bones. Fourier transform infrared (FTIR) analysis (Shimadzu 8400, Japan) in the scanning range of(4000–500 cm^{-1})was used to identify the functional groups of fish bones surface.

3. Results and Discussion

3.1. FTIR spectroscopy analysis

The FTIR analysis of untreated Fish bones and PTFB is given in (Figure 1.a,b). The band in 'Figure1a' observed at 3344.68 cm^{-1} can be assigned to the O–H stretching bond. The two bands at 2922.55 and 2852.81 cm^{-1} were attributed to the C-H stretching bond. The stretching band of C=O groups is placed at 1741.78 cm^{-1} [2]. The bands at 1020.38 and 960.58 cm^{-1} are related to vibrations of $–PO4^{-3}$ groups. The stretching mode of N=O is attributed to band at 1456.30 cm^{-1}. The band at 871.85 cm^{-1} is assigned to C-C stretching [16]. After treatment with NaOH and Al_2O_3 'Figure1 b', the band at 3344.68 cm^{-1} shifted and changed the intensity of this band at around 3473.91 cm^{-1}. The band at 981.80 cm^{-1} is assigned to Al–O bond vibrations. The bands at 848.71 and 642.32cm^{-1} are characteristics of vibrational modes of alumina O–Al–O bond [17].

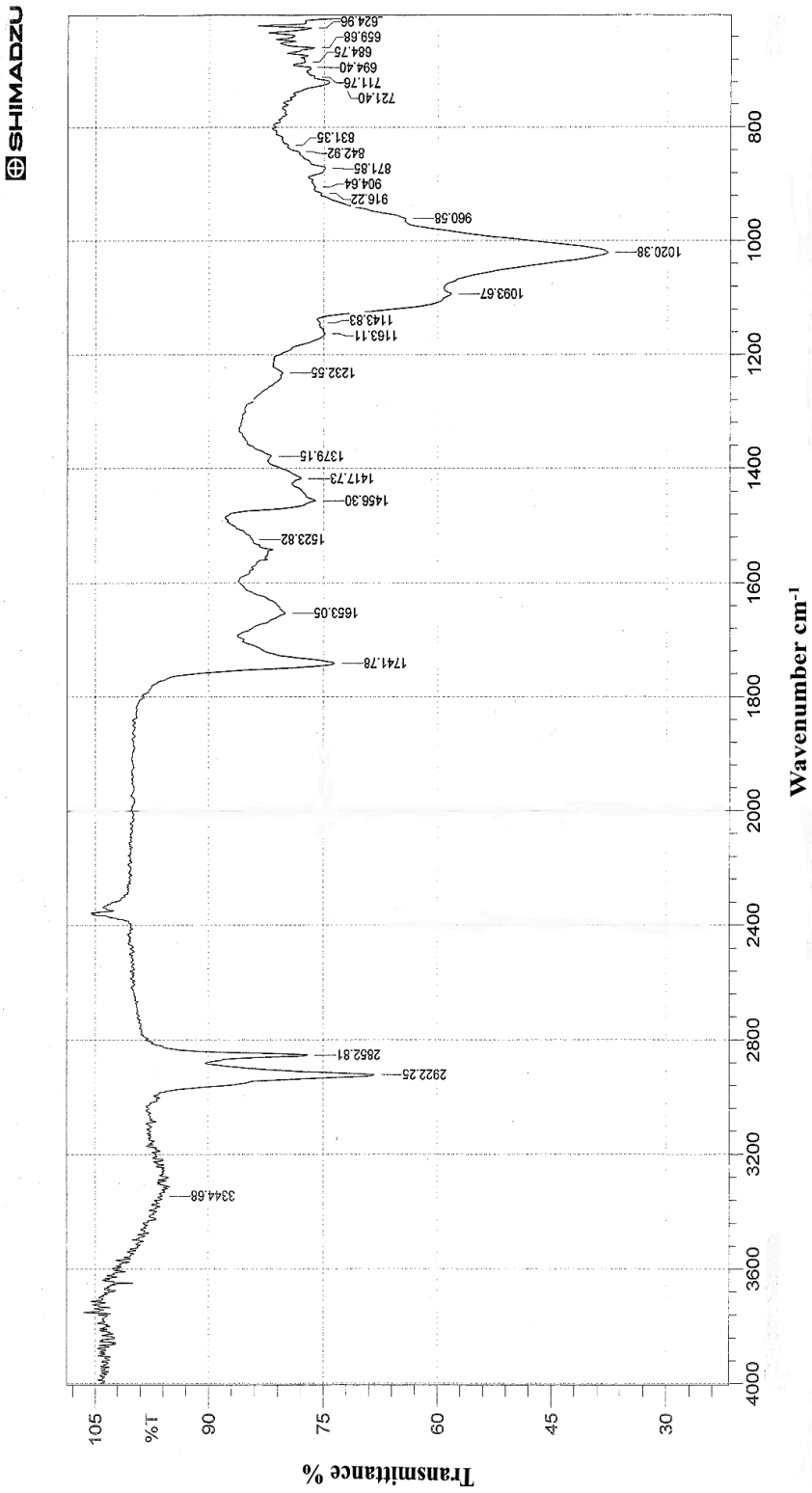

Figure 1 a. FTIR spectra of untreated fish bones surface (FB).

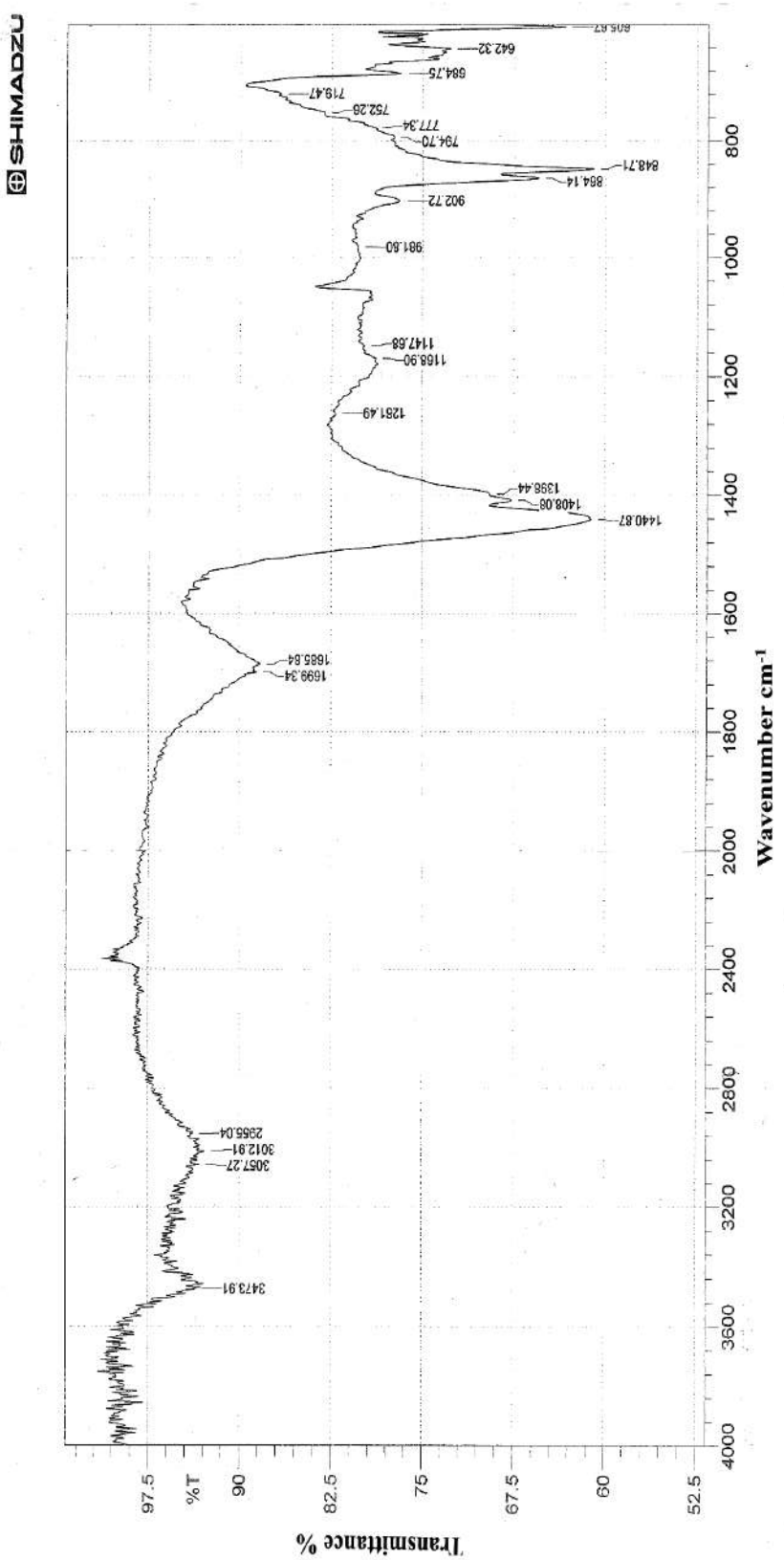

Figure 1b. FTIR spectra of pretreated fish bones surface (PTFB).

3.2. SEM analysis

The SEM images for characterizing fish bones surface before and after treatment are depicted in ʻFigure2 a,bʼ. Before treatment ʻFigure2aʼ, the fish bone shows a clean surface with several numbers heterogeneous pores and holes, which create a huge free surface area [2]. After treatment ʻFigure2bʼ, the morphology of fish bones has roughness surfaces and the distinct openings of pores as well enable the dye ions accessibility into the internal bones part [16,18].

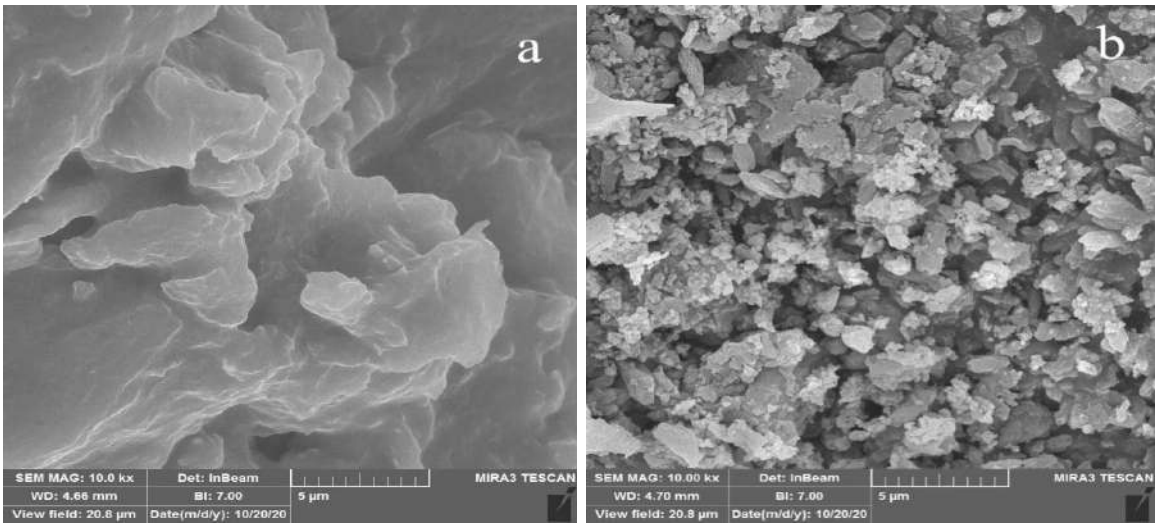

Figure 2.SEM images of fish bones surface(a) untreated FB (b) PTFB.

3.3. Elemental analysis

Elemental analysis of untreated FB and PTFB surfaces was examined by energy dispersive X-ray spectroscopy (EDS) analysis. Detailed composition of untreated FB and PTFB samples with EDS diagram is given in ʻFigure3a, bʼ. In the EDS spectrum ʻFigure 3 aʼ of untreated FB (C, O, Ca and P) were detected. The EDS spectrum after treatment with NaOH and Al_2O_3 revealed the existence of Al element (17.58 W_t%) of FB surface ʻFigure 3 bʼ. The content of O, P and Ca increased from 34.29 W_t%, 8.59 W_t% and 10.31 W_t% to 37.08 W_t%, 12.62 W_t% and 15.62 W_t%, respectively, while the content of C declined from 46.45 W_t% to 17.10 W_t%. It was an evident that most of Al is deposited on the fish bones surface.

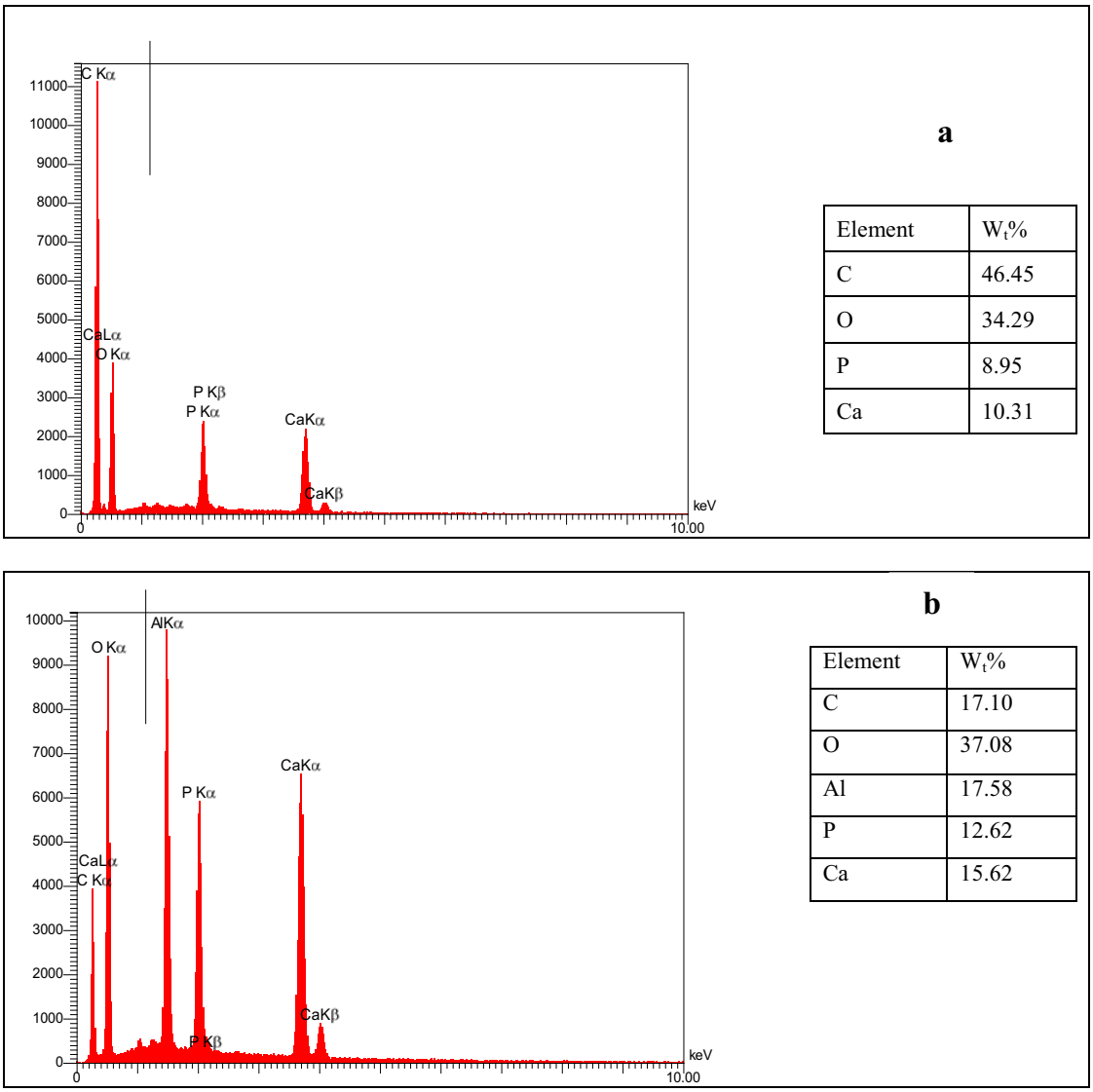

Element	W_t%
C	46.45
O	34.29
P	8.95
Ca	10.31

Element	W_t%
C	17.10
O	37.08
Al	17.58
P	12.62
Ca	15.62

Figure 3. Energy dispersive X-ray analysis images and composition of fish bones surface (a) untreated FB (b) PTFB.

3.4. Effect of sorbent dose

Regulating the influence of adsorbent dose in experiments, one of the useful significant parameters influencing adsorption, have accomplished with a primary dye concentration of 80 mg/L and adsorbent dose in the interval 0.05-0.8g/L at 25º C. The experiment consequences have illustrated in'Figure4'. As the adsorbent dose has increased, the MG dye removal efficiencies have raised from 79.3% to 98.6 %. Actually, the amount of existing adsorption sites rises by raising the adsorbent dose and volume of pores wherever adsorption takes a place. Accordingly, the highly applicable adsorbent dose for MG dye removal has adjusted to 0.8 g/L[19]. Similar observations have been made earlier [20, 21].

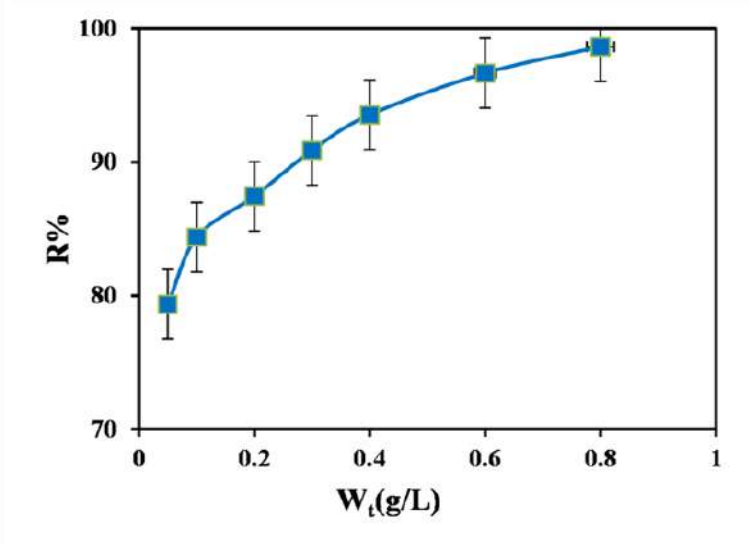

Figure 4. Effect of adsorbent dose on adsorption of MG onto PTFB surface(initial MG conc. 80 mg/L, pH 7.42 and 25 ºC).

3.5. Salt effect

The effect of inorganic salt (i.e. NaCl) on adsorption capacity of MG on PTFB surface is shown in Figure 5.The dye adsorption increased from 7.11 to 7.94 mg/g with the increasing NaCl concentration ranging from 0.1 to 0.3 M.This MG attachment to the solid can be regulated through electrostatic interactions increasing along with its adsorption capacity. The increased MG adsorption capacity under salt adding is based on the dye molecules aggregation generated by the salt ion actions, and this raises the adsorption capacity of dye onto PTFB surface [22].

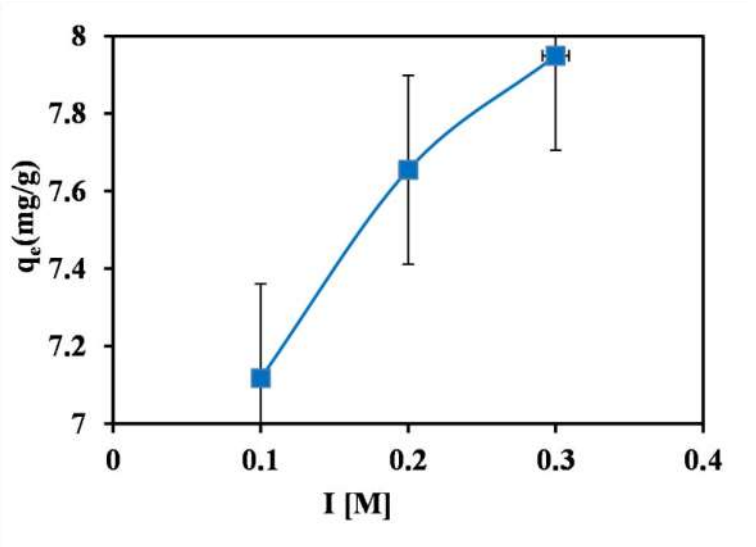

Figure 5. Effect of ionic strength on MG adsorption (initial MG conc. 80 mg/L, pH 7.42 and 25 ºC).

3.6. Effect of pH

The pH effect on MG adsorption by PTFB surface was studied at 25ºC, initial concentration of 80 mg/L and adsorbent dose of 0.1 g. To obtain the desired pH a few drops of 0.1 M NaOH or HCl was added. Figure6 explains the influence of pH on the adsorption of MG at pH range of 1.88–10.64. The dye removal was increased with increasing pH. The low value of dye removal at pH 1.88 is may be as a result of the protonation of functional groups that creates the adsorbent surface in more positive and investigate the repulsion among dye cations and adsorbent [2]. When the pH is increased, the amount of negatively charged sites on the surface of adsorbent surface increased and the removal percentage of MG as well rises. This might be due to the increasing in electrostatic attractions among the MG cation and the adsorbent's functional groups [23]. Related performance has stated by other scholars for the adsorbing basic dye in [24, 25].

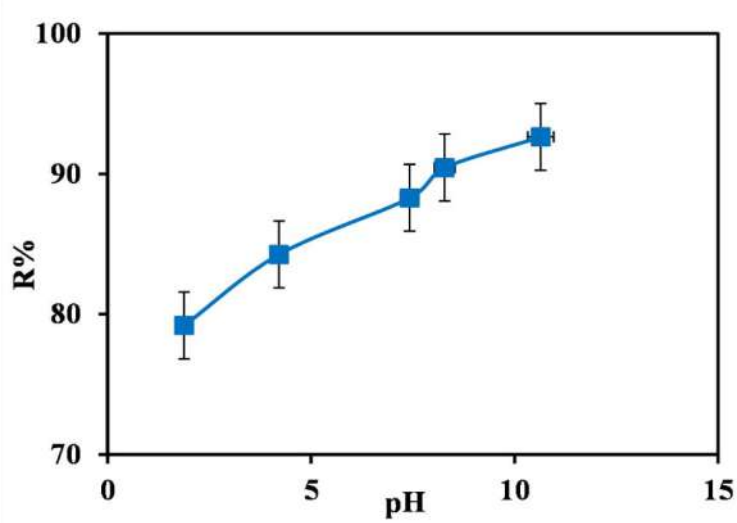

Figure 6. Effect of pH on MG adsorption(initial MG conc. 80 mg/L and 25ºC).

3.7. Kinetic modeling

A kinetics study of adsorption was necessary to investigate the effect of contact time. The resulting parameters of adsorption kinetic, as shown in 'Figure 7', after a contact time of 30min, there was no change in cationic dye (MG) adsorption capacity on PTFB surface. Thus, we selected 60 min as the best contact time for all the MG adsorption experiments on the adsorbent surface [26]. The rapid uptake of MG dye molecules from aqueous solution refers to the adsorption process efficiency. Moreover, it is evident that the adsorption capacity of PTFB surface increased rapidly with increasing of contact time due to the availability of active sites on the surface [27].

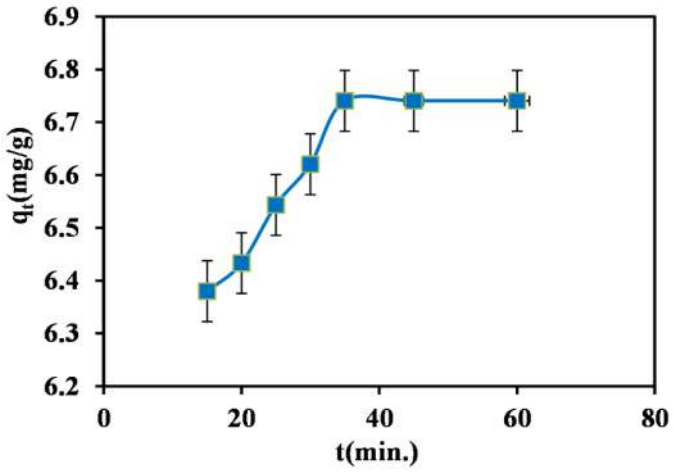

Figure 7. The effect of contact time of MG adsorption onto PTFB surface (initial MG conc. 80 mg/L, pH 7.42 and 25 ºC).

The adsorption process kinetics were studied using the pseudo-first-order (P -1-O)equation 3 [28], and the pseudo-second-order(P-2-O) equation 4 [29] models

$$\ln(q_e-q_t) = \ln q_e - k_1 t \quad (3)$$

$$\frac{t}{qt} = \frac{1}{k_2 q_t^2} + \frac{1}{q_e} t \quad (4)$$

Here, k_1(min^{-1}) and k_2 (g·mg^{-1}·min^{-1}) are the kinetic rate constants, respectively. q_e and q_t (mg/g) are the MG adsorbed concentrations at equilibrium and at time of adsorption t (min), respectively. The P -1-O constants ($k_1$and q_e) were calculated from slopes and intercepts as given in Figure 8a. P -2-O constants $k_2$and q_e were determined from the slopes and intercepts from 'Figure 8 b', respectively. The results of experimental data with the (P -1-O) and (P -2-O) for adsorption of MG onto PTFB have shown in Table2.Consequences indicated great correlation coefficient magnitudes by ranging (0.9999-0.9997) for system and a good agreement between ($q_e$cal.) and ($q_e$exp.) magnitudes specifying the applicability of the P-2-O kinetic model for PTFB system.[30].Related consequences have found in [31,32].

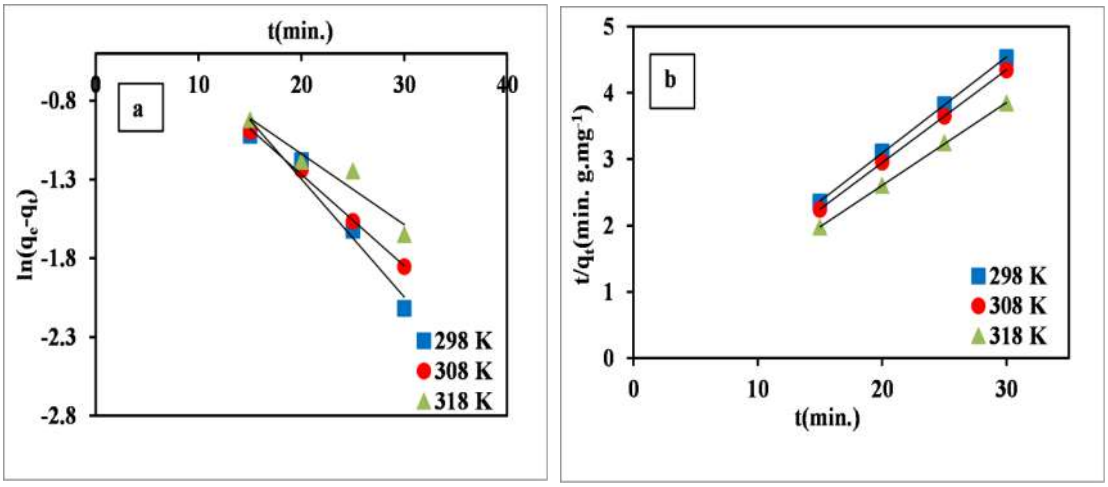

Figure 8. Pseudo-first order (a) and Pseudo-second order(b) kinetics for MG dye adsorption onto PTFB surface at different temperatures.

Table2. Kinetics parameters for the adsorption of MG onto PTFB surface (C_o= 80 mg/L).

Adsorbent	T(K)	Pseudo-first order				Pseudo-second order		
		K_1 (min^{-1})	$q_{e,exp}$ mg/g	$q_{e,calc}$ mg/g	R^2	K_2($g \cdot mg^{-1} \cdot min^{-1}$)	$q_{e,calc}$ mg/g	R^2
PTFB	298	0.0747	6.7381	0.5387	0.9578	0.1112	6.8965	0.9997
	308	0.0579	7.0686	2.6093	0.9970	0.1361	7.1428	0.9999
	318	0.0448	7.9889	2.4783	0.9266	0.1547	8.0000	0.9998

3.8. Kinetic model validity

The fitting and applicability of the isotherm model to the kinetic parameters have compared through judging from the R^2 magnitudes and the normalized standard deviation Δq_t (%) determined from equation 5. The normalized standard deviation, Δq_t (%) has employed for confirming the used kinetic model to refer to the adsorption process. It is given as:

$$\Delta q_t = 100 \frac{\sqrt{\sum(\frac{q_{exp}-q_{cal}}{q_{exp}})^2}}{n-1} \quad (5)$$

Where n is the data points number, q_{exp} and q_{cal} (mg/g) stand for the experimental and calculated adsorption capacity magnitudes. Lower magnitude of Δq_t specifies very well agreement between experimental and calculated data. The Δq_t magnitudes for p-2-O are 4.2666%, 3.3900% and 2.7166% at 25ºC, 35ºC and 45ºC, respectively. Thus, the pseudo-second-order kinetic model appears to be the best fitting model for adsorption of MG dye onto PTFB surface[33].

3.9. Adsorption mechanism

Adsorption kinetics can be typically controlled by various mechanisms. The highly general ones are based on the diffusion mechanisms that can be clarified by intraparticle diffusion model suggested by Weber and Morris [34]. Intraparticle diffusion model is given as

$$q_t = k_{id} t^{0.5} + I \quad (6)$$

k_{id}, the intra-particle diffusion rate constant (mg/g $min^{0.5}$) can be obtained from the slope of the linear plot of q_t versus $t^{1/2}$and I (mg/g) is a constant'Figure9'.The interceptions of plot reveals the boundary layer influence. Greater magnitudes of intercept means bigger contribution of surface sorption in the rate-controlling step. If the regression of q_t against $t^{0.5}$ is linear and passes through the origin, then intraparticle diffusion is the solitary rate-limiting step. In the case of linear plots at every concentration didn't pass through the origin, it shows that the intraparticle diffusion wasn't only rate controlling step [35]. The magnitudes of k_{id} and I and the resultant regression coefficients have recorded in Table 3.The magnitudes of K_{id} and I listed in Table3 explain that the constants I values are not zero. This specified that the intraparticle diffusion is not the only rate-limiting step but other process is feasibly be involved in the adsorbing process [8].

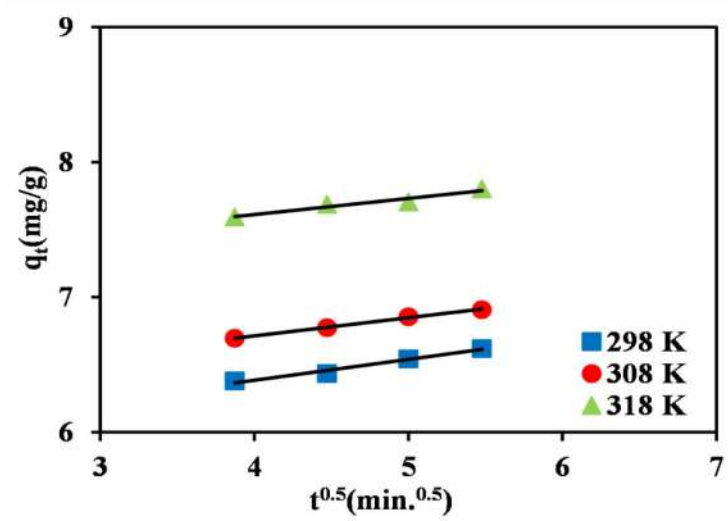

Figure 9. The intra-particle diffusion for MG dye adsorption onto PTFB surface at different temperatures.

Table 3.intraparticle diffusion rate constants for the adsorption of MG onto PTFB surface at different temperatures.

Adsorbent	T(K)	k_{id} (mg/g $min^{0.5}$)	I (mg/g)	R^2
PTFB	298	0.1548	5.7654	0.9747
	308	0.1347	6.1739	0.9969
	318	0.1187	7.1374	0.9435

3.10. Equilibrium study

For optimizing the design of adsorption system for the adsorbates adsorption, it is essential to create the most suitable correlation for the equilibrium curves. Diverse isotherm models have been reported to refer to the equilibrium features of adsorption. Several of these models are Langmuir, Freundlich, and Temkin models.

Langmuir isotherm is effective for monolayer adsorption. The linearized equation can be represented as follow [36]:

$$\frac{C_e}{q_e} = \frac{1}{K_L q_m} + \frac{C_e}{q_e} \quad (7)$$

Where, C_e(mg/L) is equilibrium concentration of MG in solution, q_m (mg/g) is the Langmuir monolayer adsorption capacity and K_L(L/mg) is Langmuir constant. q_m and K_L values can be determined from the slope and intercept of the linear plots of C_e/q_e against C_e.

The Freundlich isotherm model, which is frequently employed for describing non-specific adsorption, was employed to clarify the adsorption data. The linear form of the Freundlich equation as given as below [37]:

$$logq_e = logK_f + \frac{1}{n} loqC_e \quad (8)$$

Where, K_F is Freundlich coefficient related to adsorption capacity(mg/g) and n(related to adsorption intensity) were obtained from the values of slope and intercept of the plots of log q_e against log C_e

Regarding Temkin adsorption isotherm, the energy of adsorption is in a linear function of the surface coverage because of adsorbent-adsorbate interactions. Temkin isotherm equation has in general been adopted as [38]:

$$q_e = B\ ln\ lnA_T + B\ ln\ lnC_e \quad (9)$$

Where B = RT/b, b stands for Temkin constant and associated with heat of adsorption (J/mol), A represents Temkin isotherm constant (L/g), R for the gas constant (8.314 J/mol K), and *T* is the absolute temperature (K). The magnitudes of (B) and (A_T) can be determined from the slope and interception by the graph plotted between q_e and lnC_e.

The isotherm parameters for the three models are introduced in Table 4. In terms of R^2 values, Freundlich isotherm skwed the highest values for dye within the temperature range used.

Table 4. Isotherm parameters for MG adsorption onto PTFB surface.

Isotherm	298 K	308 K	318 K
Langmuir			
K_L(L/mg)	-0.0362	-0.0321	12.3456
q_m(mg/g)	-8.1967	-17.2413	13.5135
R^2	0.9751	0.9043	0.9930
Freundlich			
K_F	0.0492	0.2513	10.6340
1/n	1.9555	1.5170	1.0267
R^2	0.9919	0.9925	0.9952
Temkin			
B_T(J/mol)	15.6479	12.7073	1.3572
A_T(L/g)	0.1262	0.1969	2921.9310
R^2	0.9597	0.9683	0.9820

3.11. Thermodynamic analyses

The uptake of MG dye by the PTFB rises with raising the temperature ratifying the endothermic nature of the adsorption step. The variation in standard free energy (ΔG°), enthalpy (ΔH°) and entropy (ΔS°) of adsorption have computed by [39]

$$\Delta G^\circ = -RT \ln K^o \quad (10)$$

Where R is the gas constant ($8.314 J \cdot mol^{-1} K^{-1}$) and T is the absolute temperature.
The distribution adsorption coefficient (K_d) [40] is determined by the following equation:

$$K_d = \frac{C_o - C_e}{C_e} \times \frac{V}{W} \quad (11)$$

Where C_o is the initial MG concentration and C_e is the equilibrium MG concentration in (mg/L). V is the sample volume (mL) and W_t is the weight of the adsorbent (g/L).

The standard enthalpy change (ΔH°) and the standard entropy change (ΔS°) were calculating using equation 12:

$$\ln K^o = (\Delta S^o / R) - (\Delta H^o / RT) \quad (12)$$

The equilibrium constant (K^o) was determined by plotting $\ln K_d$ against C_e and extrapolating $C_e$to. The value of the intercept is that of $\ln K^o$ [12].

Thermodynamic parameters obtained are summarized in Table5. The negative values of ΔG° obtained reveal that the adsorption process is favorable and that it is spontaneous and is observed to decrease with increase in the temperature, signifying that the adsorption process of MG on PTFB surface is more advantageous under higher temperatures [41]. Positive magnitude of ΔH° indicates endothermic features of the adsorption process. The positive ΔS° magnitude for MG adsorption on PTFB indicates the randomness and reveals the affinity of adsorbent surface concerning MG[42].

Table5. Thermodynamic parameters for the adsorption of MG.

Adsorbent	T(K)	ΔG° (kJ.mol^{-1})	ΔH^{o} (kJ. mol^{-1})	ΔS^{o} (J. K^{-1}. mol^{-1})
PTFB	298	-13.3819	214.0082	757.5908
	308	-15.8513		
	318	-28.7596		

4. Conclusions

Fish bones, one of the most numerous fish-processing industry waste and natural products, were used for MG adsorption. With many specific advantages such as low- cost, availability, natural origin, and high adsorption capacity. In this study, the adsorption of basic dye (methyl green) from aqueous solutions was based on pretreated fish bone as a new adsorbent surface. Kinetic, isotherm, and thermodynamic parameters of the adsorption process were investigated. The resultant data of adsorption process are fitted in good manner to Freundlich isotherm. The second-order-model has been in highly agreed to the acquired results. The adsorption process has been spontaneous and endothermic in nature in relation to the negative and positive magnitudes of ΔG° and ΔH°, respectively. The influence of different parameters including, pH, contact time, temperature, inorganic salt and adsorbent dose was studied. The resultant has depicted that pretreated fish bones can be efficiently employed as a low-cost adsorbent for the adsorption of basic dyes from aqueous solutions and could contribute to the protection of the environment.

References

[1] KizilkayaB andTemkinay A 2015*IJMS* **44(1)** 37.
[2]Ebrahimi A,Arami M, Bahrami H and Pajootan E 2013*Environ. Model. Assess.***18(6)** 661.
[3] MohanS, Sailaja P, Srimurali M andKarthikeyan J 1998 *Environ Eng Pol* **1(3)** 149.
[4] Sheshdeh K, Nikou K, Badii K andSoroush M2013 *Chem. Eng. Technol*. **36(10)** 1713.
[5]Wu J,Eiteman M andLaw S 1998 *J.Environ. Eng.***124** 272.
[6]Vlyssides A, Loizidou M, Karlis P , ZorpaA and Papaioannou D 1999 *J. Hazard. Mater.***70** 41.
[7]Khalighi R, KhosraviM, Badii K, Limaee N and GolkarnarenjiG 2014 *J Taiwan InstChemEng* **45** 1792.
[8] Aichour A,Zaghouane-BoudiafH,Viseras C and Sanchez M 2018 *J. Mol. Liq.***256** 533.
[9] DidarG,De –Germenci N, AyvaoV,Durmaz E,ÇakirD and Akan E 2019 *J. Clean. Prod.***225** 1220.
[10] Oguntimein G 2015 *J. Environ. Chem. Eng.***3 (4)** 2647.
[11] Etim U, Umoren S and Eduok U2016 *J SAUDICHEM SOC* **20** S67.
[12] Al-Kazragi M, Al-Heetimi D and Al-KhazrajyO 2019 *Desalination Water Treat.***145** 369.
[13] KizilkayaB 2012 *J DispersSciTechnol* **33** 1429.
[14] Kizilkaya B, Tekinay A and Dilgin Y 2010 *Desalination* **264(1–2)** 37.
[15] Wakkel M, Khiari B and Zagrouba F 2019 *J Taiwan InstChemEng* **96** 439.
[16] KhimH, Tow T, HakimiM, Ahmad A and Teng H 2012 *APCBEE Procedia* **1** 96.
[17] Webber J, Zorzi J, Perottoni C, Mourae S and Cruz R 2016 *J. Mater. Sci.* **51(11)** 5170.
[18] Nurhadi M, Kusumawardani R, Widiyowati I and Wirhanuddin H 2018 *J. Phys. Conf. Ser.***1022** 1.
[19] Degermenci G, De N,Germenci,Ayvao-Glu V, DurmazE,ÇakirD and Akan E 2019 *J. Clean. Prod.***225** 1220.
[20] Kurczewska J, Cegłowski M and Schroeder G 2019 *Int. J.BiolMacromol* **123** 398.
[21] SatlaouiY, Trifi M, Romdhane D, Charef A and Azouzi R 2019 *J. Chem.***2019** 1.
[22] Salima A, Benaouda B,Noureddine B and DuclauxL 2013 *water Res.***47(10)** 3375.

[23] Fayouda N, Tahirib S,YounssiS, AlbizaneA,Gallart-Mateu D,Cervera M and Guardia M 2016 *Desalination Water Treat.***57(35)** 16611.
[24] MekhalifT, GuediriK,Reffas A,ChebliD,Bouguettoucha A and Amrane A 2017 *JDispersSciTechnol* **38(4)** 463.
[25] Alardhi S,Alrubaye J andAlbayati T 2020 *Desalination Water Treat.***179** 323.
[26] RajabiM ,MahanpoorK and Moradi O 2019 *ComposB* **167** 544.
[27] Kannan C, Muthuraja K and Devi R 2013 J. Hazard. Mater. **244– 245** 10.
[28]Lagergren S 1898 Sven. Vetenskapsakad. Handingarl **24** 1.
[29]Ho Y andMckay G 1999*Process Biochem* **34** 451.
[30] Gupta N, KushwahaA and Chattopadhyaya M 2016 *Arab. J. Chem.***9** S707.
[31] Farghali A, Bahgat M, El Rouby W and Khedr M 2013 *J. Alloys Compd* **555** 193.
[32] Sharma P, Saikia B and Das M 2014*Colloids Surf, A PhysicochemEngAsp* **457** 125.
[33] Ahmad M, Puad N and Bello O 2014 *Water Resour. Ind.***6**1 8.
[34] Weber W and Morris1963 *J.Sanit.Eng.Div.* **89(2)** 31.
[35] WuF,Tseng R and Jung R 2001 Water Res. **35** 613.
[36] Langmuir I 1918*J. Am. Chem. Soc.***40** 1361.
[37] Freundlich H 1906 *J. Phys. Chem.***57A** 385.
[38] BiswasK, Saha S and Ghosh U 2007 *Ind. Eng. Chem. Res* .**46(16)** 5346.
[39] Constantin M, Asmarandei I, Harabagiu V, Ghimici L, Ascenzi P and Fundueanu G 2013*Carbohydr. Polym.* **91** 74.
[40] Bouraada M, Ouali M and Menorval L 2016*J. Saudi Chem. Soc.***20**397.
[41] Kulkarn I, Revanth T, Acharya A and BhatP 2017 Res.Efficient Tech. **3** 71.
[42] Agarwal, S, Tyagi I, Gupta V, Mashhadi S and Ghasemi2016 *J.Mol.Liq.***223** 1340.

Metal Complexes of Multidentate N_2S_2 Heterocyclic Schiff-base Ligands;Formation, Structural Characterisation and Biological Activity

Metal Complexes of Multidentate N_2S_2 Heterocyclic Schiff-base Ligands;Formation, Structural Characterisation and Biological Activity

Baidaa K Al-Rubaye [1], Mohamad J. Al-Jeboori [1*] and Herman Potgieter [2]

[1] Department of Chemistry, College of Education for Pure Science (Ibn Al-Haitham), University of Baghdad, Baghdad, Iraq.
[2] Division of Chemistry and Environmental Science, Manchester Metropolitan University, Manchester, M1 5GD, UK.

*E-mail: mohamadaljeboori@yahoo.com

Abstract: The synthesis of ligands with N_2S_2 donor sets that include imine, an amide, thioether, thiolate moieties and their metal complexes were achieved. The new Schiff-base ligands; N-(2-((2,4-diphenyl-3-azabicyclo[3.3.1]nonan-9-ylidene)amino)ethyl)-2-((2-mercaptoethyl)thio)- acetamide (H_2L^1) and N-(2-((2,4-di-p-tolyl-3-azabicyclo[3.3.1]nonan-9-ylidene)amino)ethyl)-2-((2-mercaptoethyl)thio) acetamide (H_2L^2) were obtained from the reaction of amine precursors with 1,4-dithian-2-one in the presence of triethylamine as a base in the $CHCl_3$ medium. Complexes of the general formula $K_2[M(Ln)Cl_2]$, (where: M = Mn (II), Co(II) and Ni(II)) and [M(Ln)], (where: M = Cu(II), Zn(II) and Cd(II); n =1-2, expect $[Cu(HL^2)Cl]$) were isolated. The entity of ligands and complexes including their purity were confirmed using elemental microanalysis (C.H.N.S), atomic absorption (A.A), chloride content, conductivity measurement's, melting point and thermal analysis technique. The molecular structures were elucidated with FT-IR, UV-Vis, magnetic susceptibility, ^{1}H- and ^{13}C-NMR and mass spectroscopy. The synthesised compounds were evaluated for their activity against bacterial strains (G+ and G-) and fungi species. The tested compounds indicated that; the ligands have not shown any antimicrobial activity against *Escherichia coli*. The Cd(II) complexes, for ligands H_2L^1 and H_2L^2, display the higher antimicrobial activity, compared with the other complexes. The H_2L^1 and H_2L^2 have not shown any activity against *Candida albicans*. All complexes for ligands (H_2L^1 and H_2L^2) exhibited less activity against *Candida albicans*, compared with other types of fungi.

Keywords: Schiff-bases, N_2S_2 ligand system, Metal complexes, Structural characterisation, Biological activity.

1. Introduction

Compounds incorporate nitrogen and sulfur in their frameworks are a class of organic species that attracted a range of chemist researchers (organic, inorganic and bioinorganic chemists) [1]. The impact of these species on chemistry stimulated researches to investigate and implementing a range of synthetic protocols to increase yields and stability of these materials. These species have shown a range of potential applications, including their role as useful chelating agents for radio-metals of transition and representative elements [2]. They have also used as biomedical agents, in radiopharmaceutical [2], medicine [3] and as a mimic for bioactive molecules, in catalysis, analytical chemistry, coordination chemistry [4], environmental, materials and supramolecular chemistry [5]. Mannich-bases are an important organic species that pronounced a range of uses and applications in chemistry. Compounds derived from 2,4-bis(R-phenyl)-3-azabicyclo[3.3.1]nonan-9-one are interesting materials that used as organic reagents in the fabrication of natural-based blocks including the synthesis of

phenanthridine-based compounds [6,7]. Further, compounds include N_2S_2 systems are remarkable materials that played a part in the expansion of chemistry and nuclear medicine [8]. Thus, the formation of functionalised Mannich-bases with N, S atoms should be an important class of compounds. They provide a flexible *hard*/*soft* system, upon acting as a chelating ligand to the metal centre. In this work, we describe the synthesis and characterisation of two multidentate N_2S_2 heterocyclic ligands N-(2-((2,4-diphenyl-3-azabi cyclo[3.3.1] nonan-9-ylidene)amino)ethyl)-2-((2-mercapto ethyl)thio)acetamide (H_2L^1) and N-(2-((2,4-di-p-tolyl-3-azabicyclo[3.3.1]nonan-9-ylidene)amino)ethyl)-2-((2-mercapto ethyl)thio)acetamide (H_2L^2) and their metal complexes. The anti-bacterial and anti-fungi behaviour of ligands and their complexes were also investigated.

2. Experimental

2.1. Materials and methods

All reagents in this work were commercially available and used without further purification. 1,4-Dithian-2-one and ligands were obtained by a reported method [8,9].

2.2. Physical measurements

A Heraeus instrument (Vario EL) and a Perkin-Elmer 2400 Series-II analyser were used to obtain elemental analyses (C.H.N.S) at Materials Research Centre, Ministry for Science and Technology, Baghdad, IRAQ. Uncorrected melting points were recorded using an electro-thermal Stuart SMP40 apparatus. FT-IR spectra were measured as KBr discs using a Biotic 600 FT-IR spectrophotometer in the range 4000-400 cm^{-1} FTIR and as CsI discs in the range 4000-200 cm^{-1} on a Shimadzu 8400s FT-IR at College of Science, University of Baghdad. Electronic spectra were measured from 200-1100 nm for 10^{-3} M solutions in DMSO at room temperature with (UV-Vis) spectrophotometer type Shimadzu 1800, using quartz cell of 1.0 cm length. The measurements were obtained at Ibn Sina Company, Ministry of Industry, Baghdad, Iraq. Mass spectra were obtained as Electrospray (ES) using an LTQ-FT mass spectrometer (Thermo Fisher Scientific). The spectra were recorded at the University of Manchester Metropolitan, UK. The spectral data were recorded in the positive mode. NMR spectra (^1H, ^{13}C-NMR) were recorded in DMSO-d_6 solutions using a Brucker-400 MHz and a JEOL-400 MHz for ^{1}HNMR and 100.61 MHz for ^{13}C-NMR, respectively, and TMS was used as an internal standard for ^{1}HNMR measurement. The samples were recorded at the University of Manchester Metropolitan, UK and Isfahan University, Islamic Republic of Iran. Metals were determined using a Shimadzu atomic absorption spectrophotometer (F.A.A) 680G. Chloride was determined using a 686-titro processor-665 Dosimat-Metrohm Swiss. in Ibn Sina Company, Ministry of Industry Baghdad, Iraq. Conductivity measurements were made with DMSO solutions using a Eutech Instruments Co, 150 digital conductivity meter, and magnetic moments were determined at 298 k with a Sherwood Scientific magnetic susceptibility balance. Thermal analyses were performed under an argon atmosphere on an STA PT-1000 Linseis company /Germany with a heating rate of 10 ºC/min. at College of Education for Pure Science (Ibn Al-Haitham), University of Baghdad. The evaluation of ligands and their metal complexes against four bacterial strains *(Escherichia coli, Pseudomonas aeruginosa, Staphylococcus aureus and Bacillus stubtilis)* and four fungi species (*Candida albican*s, *Candida glabrat*a, *Candida tropicali*s and *Candida parapsilsis*) were performed using agar-well diffusion. The results were recorded at College of Science, Baghdad University and at College of Education for Pure Science (Ibn Al-Haitham), University of Baghdad.

2.3. Synthesis

2.3.1. Preparation of precursors (M_1, M_2, A_1 and A_2)

The preparation of M_1 and M_2 was performed according to a published method [10,11] and the preparation of A_1 and A_2 was achieved using a reported method [12].

2.3.1.1. Preparation of (1R,2R,4R,5S)-2,4-diphenyl-3-azabicyclo[3.3.1]nonan-9-one (M_1)

A solution of benzaldehyde (1.33ml, 13mmol), ammonium acetate (0.5g, 6.500mmol) and cyclohexanone (0.674ml, 6.500mmol) [2:1:1] in ethanol (20ml) was mixed together. The reaction mixture was allowed heating between 30-40 ºC for 6h, during which time a yellow solid was formed. However, upon using MeOH medium for 4h reflux the reaction yielded an identical compound. The solid was collected by filtration, washed with ethanol (5ml), and diethylether (10ml) and then dried under vacuum. Yield: 1.26g (93%), m.p = 108-110 ºC. FT-IR data (cm^{-1}), 3313 ν(N–H), 3032 $\nu(C–H)_{arom}$, 2920 and 2850 $\nu(C–H)_{alip}$, 1716 ν(C=O), 1581 and 1558 ν(C=C), 1492 ν(N–H). NMR data (ppm), ^{1}H (400 MHz, DMSO-d_6): δ_H = 1.60 (2H, m, C_{10}-H); 1.76 (4H, quar, 3.6 Hz, J_{HH} = 9.6 Hz, $C_{9,9}$`-*H*); 2.60 (2H, dd, $J_{HH}$ = 6 Hz, $C_{8,8}$`-*H*); 2.80 (2H, t, J_{HH} = 4.8 Hz, $C_{7,7}$`-*H*); 7.80 ppm (1H, s, *N*-*H*); 7.02 and 7.11 ($C_{1,1}$`-*H*; 2H, t, J_{HH} = 5.2 Hz) and ($C_{2,2}$`, $_{6,6}$`-*H*; 4H, t, J_{HH} = 5.2 Hz), respectively; 7.43 ppm (4H, d, J_{HH} = 6 Hz) was assigned to (C3,3`, 5,5`-H); ^{13}C NMR (100.63 MHz, DMSO-d_6): δ_c = 22.89 (C_{10}), 25.61 ($C_{9,9}$`), 55.69 ($C_{7,7}$`), 58.93 ($C_{8,8}$`), 124.09 ($C_{1,1}$`), 131.08 ($C_{2,2}$`, $_{6,6}$`) and ($C_{3,3}$`, $_{5,5}$`), 139.37 ($C_{4,4}$`), 203.40 (C=O). The electrospray (+) mass spectrum of M_1 shows no molecular ion peak for M_1. Peak detected at m/z = 266.2844 amu assigned to $[M-(C_2H_2)+H)]^+$ for $C_{18}H_{20}NO$, requires = 266.1539. The other peaks detected at m/z = 240.2844, 174.1106 and 107.0409 were assigned to $[(M-C_2H2+C_2)]^+$, $[(M-C_2H+C_2+C_6H)]^+$ and $[(M-C_2H+C_2+C_6H+C_4H_{14})]^+$.

2.3.1.2. Preparation of (1R,2R,4R,5S)-2,4-di-p-tolyl-3-azabicyclo[3.3.1]nonan-9-one (M_2)

The method used to prepare M_2 was analogous to the starting material M_1, but with the used of 4-methylbenzaldehyde instead of benzaldehyde. The amounts of other reagents used were adjusted accordingly, and a similar workup procedure was used to give compound M_2 as a pale-yellow solid. Yield: 1.53g (54 %) , m.p. = 168-170 ºC. FT-IR data (cm^{-1}), 3298 ν(N–H), 3020 $\nu(C–H)_{arom}$, 2858 and 2927 $\nu(C–H)_{alip}$, 1705 ν(C=O), 1577 and 1550 ν(C=C), 1512 ν(N–H). NMR data (ppm), ^{1}H (400 MHz, DMSO-d_6): δ_H = 1.57 (2H, m, C_{10}-H); 1.67 (4H, m, $C_{9,9}$`-*H*); 1.77 and 1.79 (2H, d, $J_{HH}$ = 6 Hz, $C_{8,8}$`-*H*); 2. 71 (2H, t, J_{HH} = 5.6 Hz, $C_{7,7}$`-*H*); 2.91 ppm (6H, s, *2CH$_3$*); 4.36 (1H, s, *N*-*H*); 7.38 (4H, d, $J_{HH}$ = 7.2 Hz, ($C_{2,2}$`, $_{6,6}$`-*H*); and 7.43 ppm (4H, d, $J_{HH}$ = 7.2 Hz ($C_{3,3}$`, $_{5,5}$`-*H*). $^{13}$C NMR (100.63 MHz, DMSO-$d_6$): $\delta_c$ = 23.75 ($C_{10}$); 25.98 ($C_{9,9}$`); 44.61 (C methyl); 56.19 ($C_{8,8}$`); 58.79 ($C_{7,7}$`); 124.93 ($C_{3,3}$`, $_{5,5}$`); 126.71 ($C_{2,2}$`, $_{6,6}$`); 135.61($C_{1,1}$`); 138.93 ($C_{4,4}$`) and 209.69 (C=O). The electrospray (+) mass spectrum of M_2 shows the molecular ion peak for M_2 at m/z = 319.0421 amu for $C_{22}H_{25}NO$, requires = 319.1936. Peaks recorded at m/z = 275.1434 and 151.4732 amu attributed to $[M-(CH_3CH_2CH_3)]^+$ and $[M-(CH_3CH_2CH_3)+(C_{10}H_4)]^+$.

2.3.1.3. Preparation of 2-(((1R,2S,4R,5S,E)-2,4-diphenyl-3-azabicyclo[3.3.1]nonan-9-ylidene)amino)ethan-1-amine (A_1)

A solution of ethylenediamine (0.160g, 2.663mmol) dissolved in ethanol (20ml) was added to a mixture of M_1 (0.8g, 2.747mmol) in ethanol (20ml). The reaction mixture was treated with 2ml of concentration hydrochloride acid, and then allowed to reflux for 6h. The reaction mixture was left for a slow evaporation and yellow crystals were obtained that isolated by filtration, washed with cold ethanol (5ml) and diethylether (10ml) and then dried under vacuum. Yield: 0.104g (65%), m.p = 194-196 ºC. FT-IR data (cm^{-1}), 3309 and 3248 ν(N–H), 1639 ν(C=N), 1504 δ(N–H), 119 ν(C–N). NMR data (ppm), ^{1}H NMR (400 MHz, DMSO-d_6): δ_H = 1.24 (6H, m, $C_{9,9}$` and $C_{10}$-*H*); 1.75 (2H, m, $C_{12}$-*H*); 2.28-2.41 (5H, m, $C_{8,8}$`,C_{11}-*H* and N-*H*); 3.16 (2H, d, J_{HH} = 7.6 Hz, $C_{7,7}$`-*H*); 7.25 ($C_{1,1}$`-*H*; 2H, t, J_{HH} = 4.4 Hz); 7.35 ($C_{2,2}$`, $_{6,6}$`-*H*; 4H, t, J_{HH} = 4.4 Hz); 7.46 (4H, dd, J_{HH} = 3.6 and 7.3 Hz) ($C_{3,3}$`, $_{5,5}$`-*H*). ^{13}C NMR (100.63 MHz, DMSO-d_6): δ_c = 23.80 ($C_{9,9}$`); 27.83 ($C_{10}$); 28.80 ($C_{8,8}$`); 35.39($C_{7,7}$`); 46.82 ($C_{12}$); 49.44($C_{11}$); 122.35 ($C_{1,1}$`); 127.08 ($C_{3,3}$`, $C_{2,2}$`); 127.24 ($C_{6,6}$`); 142.49 ($C_{4,4}$`);152.49 (C=N). The electrospray (+) mass spectrum of A_1 revealed a peak at m/z = 333.1042 amu assigned to $(M)^+$ for $C_{22}H_{27}N_3$, requires = 333.2205 and the following fragments at 304.1548 and 264.1742 amu were related to $[M-CH_3N]^+$ and $[M-(CH_3N+C_3H_4)]^+$, respectively.

2.3.1.4 Preparation of 2-(((1R,2S,4R,5S,E)-2,4-di-p-tolyl-3-azabicyclo[3.3.1]nonan-9-ylidene)amino)ethan-1-amine (A_2)

An analogues method for the isolation of precursor A_1 was used to prepare A_2, but M_2 was used in place of M_1 and other reagents were adjusted accordingly. A yellow solid was obtained, yield = 0.2155g (75 %), m.p. = 113-115 ºC. FT-IR data (cm^{-1}), 3421 ν(N–H), 1658 ν(C=N), 1508 δ(N–H), 1311 ν(C–N). NMR data (ppm), ^{1}H NMR (400 MHz, DMSO-d_6): δ_H = 1.18 (6H, m, $C_{9,9`}$, $C_{10}$ -H); 1.55 (2H, m, $C_{12}$-H); 2.20-2.25 (5H, m, $C_{8,8`}$, C_{11}-H) and N-H; 3.10 (2H, d, J_{HH} = 5.2 Hz $C_{7,7`}$-H); 3.76 (6H, s, 2 x $CH_3$); = 7.02 (4H, d, $J_{HH}$ = 7.6 Hz, $C_{2,2`}$, $_{6,6`}$-H); 7.70 (4H, d, $J_{HH}$ = 7.6 Hz, $C_{3,3`}$, $_{5,5`}$-H). $^{13}$C NMR (100.63 MHz, DMSO-$d_6$): $\delta_c$ = 21.82 ($C_{methyl}$); 22.02 ($C_{9,\ 9`}$); 24.50 (C_{10}); 29.84 ($C_{8,\ 8`}$); 39.28 ($C_{7,7`}$); 43.41 (C_{12}); 51.36 (C_{11}); 124.58 ($C_{2,2`}$,$C_{6,6`}$); 126.43 ($C_{3,3`}$, $C_{5,5`}$); 134.34 ($C_{1,1`}$); 137.75 ($C_{4,4`}$); 153.39 (C=N). The electrospray (+) mass spectrum of A_2 showed the mass ion peak at m/z = 347.0251 amu assigned to $(M-(CH_3)+H)^+$ for $C_{23}H_{29}N_3$. Peaks detected at m/z = 303.1755 and 169.1104 were correlated to $[(M-(CH_3)+(CH_4N_2)]^+$ and $[(M-(CH_3)+(CH_4N_2)]+(C_{12}H_{14})]^+$.

2.3.2. Synthesis of ligands (H_2L^1 and H_2L^2)

2.3.2.1. Synthesis of N-(2-(((1R,2R,4R,5S,Z)-2,4-diphenyl-3-azabicyclo[3.3.1]nonan-9-ylidene)amino)ethyl)-2-((2-mercaptoethyl)thio)acetamide (H_2L^1)

A mixture of 1,4-dithian-2-one (0.080g, 0.597mmol) in $CHCl_3$ (10ml) was added dropwise, under N_2 atmosphere, to a mixture of precursor A_1 (0.233g, 0.699mmol) in $CHCl_3$ (10ml). The reaction mixture was stirred under nitrogen atmosphere for 3h. A white solid that formed was collected by filtration, washed with diethylether (10ml) and then allowed to dry under vacuum. Yield: 0.056 g (70 %), m.p. = 312-315 ºC. Ft-IR data (cm^1), 3417 $\nu(N-H)_{amide}$, 1662 $\nu(C=O)_{amide}$, 1604 ν(C=N), 2555 ν(S-H), 1531 and 1492 $\nu(C=C)_{arom}$, 1346 ν(C-N), 1056 and 914 ν(C-S). NMR spectra (ppm), ^{1}H (400 MHz, DMSO-d_6), see Figure 1; δ_H = 1.23 (3H, m, H_{10}, S-H); 1.60 (2H, t, J_{HH} = 8.8 Hz, H_{14}); 1.81 (9H, m, $H_{8,8`}$, $H_{9,9`}$, H_{11} and N-H); 2.61 (2H, t, H_{15}, J_{HH} = 6.4 Hz); 2.87(2H, d, $H_{7,7`}$ , $J_{HH}$ = 5.2 Hz); 3.16 (2H, t, $H_{12}$, $J_{HH}$ = 6.4 Hz); 3.63(2H, s, $H_{13}$); 7.44 (2H, t, $J_{HH}$ = 5.2 Hz, $H_{1,1`}$); 7.57 (4H, t, J_{HH} = 5.2 Hz, H $_{2,2`;\ 6,6`}$); 7.77 (4H, d, J_{HH} = 4.8 Hz, $H_{3,3`;\ 5,5`}$); 8.09 (1H, s, N-*H*)$_{amide}$.), ^{13}C (100 MHz, DMSO-d_6), Figure 2; δc= 24.49 (C_{10}); 25.52 ($C_{9,9`}$); 28.80 ($C_{8,8`}$); 32.56 (C_{15}); 41.18 (C_{14}); 46.42 (C_{13}); 48.13 (C_{12}); 56.79 (C_{11}); 60.97 ($C_{7,7`}$) 125.10($C_{1,1`}$); 126.95($C_{2,2`}$, $_{6,6`}$);127.11 ($C_{3,3`}$, $_{5,5`}$); 138.28 ($C_{4,4`}$); 157.79 (C=N); 175.86 (C=O). The electrospray (+) mass spectrum of H_2L^1 showed the parent ion peak at m/z = 467.3040 amu corresponding to $(M)^+$, requires; 467.2065 and the following fragments at 374.2201, 261.1360 and 160.8401 amu were assigned to $[M-(C_2H_6S_2)+H]^+$, $[M-(C_2H_6S_2+C_9H_5)]^+$ and $[M-(C_2H_6S_2+C_9H_5+C_5H_{11}NO)]^+$, respectively.

2.3.2.2. Synthesis of N-(2-(((1R,2R,4R,5S,Z)-2,4-di-p-tolyl-3-azabicyclo[3.3.1]nonan-9-ylidene)amino)ethyl)-2-((2-mercaptoethyl)thio)acetamide(H_2L^2)

The method adopted to prepare H_2L^2 was similar to that for H_2L^1, but with precursor A_2 instead of A_1. Other reaction reagents were adjusted accordingly and an analogues workup procedure that implemented resulted in the isolation of the required ligand. Yield: 0.2155g (75 %), m.p. = 320-322ºC. IR data (cm^1), 3398 $\nu(N-H)_{amide}$, 1674 $\nu(C=O)_{amide}$, 1616 ν(C=N), 2619 ν(S-H), 1577and 1523 $\nu(C=C)_{arom}$, 1323 ν(C-N), 1033 and 9254 ν(C-S). NMR data (ppm), Figure 1; ^{1}H (400 MHz, DMSO-d_6), see Figure 1; δ_H = 1.02 (3H, m, H_{10}, S-H);1.582 (2H, t, J_{HH} = 8.8 Hz, H_{14}); 1.44 (9H, m, $H_{8,8`}$, $H_{9,9`}$, H_{11} and N-H); 1.71 (2H, t, H_{15}, J_{HH} = 6.4 Hz); 2.73(2H, d, $H_{7,7`}$ , $J_{HH}$ = 5.2 Hz); 2.86 (2H, t, $H_{12}$, $J_{HH}$ = 6.4 Hz); 3.09(2H, s, $H_{13}$); 3.59 (2H, t, $J_{HH}$ = 5.2 Hz, 2x $CH_3$); 3.70 (4H, t, $J_{HH}$ = 5.2 Hz, H $_{2,2`;\ 6,6`}$); 7.15 (4H, d, $J_{HH}$ = 4.8 Hz, $H_{3,3`;\ 5,5`}$); 7.45 (1H, s, N-*H*)$_{amide}$. ): 8.12. $^{13}$C (100 MHz, DMSO-$d_6$), Figure 2; $\delta$c= 20.40 ($C_{methyl}$); 23.19 ($C_{9,9`}$); 26.35 ($C_{10}$); 28.75 ($C_{8,8`}$); 32.26 ($C_{15}$); 35.46 ($C_{7,7`}$); 41.15 ($C_{14}$); 44.79 ($C_{13}$); 46.14 ($C_{12}$); 54.37 ($C_{11}$); 126.35 ($C_{2,2`}$, $_{6,6`}$);128.26 ($C_{3,3`}$, $_{5,5`}$); 134.69 ($C_{4,4`}$); 136.69 ($C_{1,1`}$); 146.84 (C=N); 177.69 (C=O). The electrospray (+) mass spectrum of H_2L^1 recorded a peak at m/z = 495.2304 amu related to $(M)^+$, requires; 495.2378. Fragments at 403.3873, 374.2201 and 261.1360 amu correspond to $[M-(SCH_2SCH_2)]^+$, $[M-(SCH_2SCH_2)+(CH_2NH)]^+$ and $[M-(SCH_2SCH_2)+ (CH_3NH_2)+(NHCCOCHCHCHCH)]^+$, respectively. Elemental microanalyses of precursors and ligands, colours, yields and melting points are placed in Table 1.

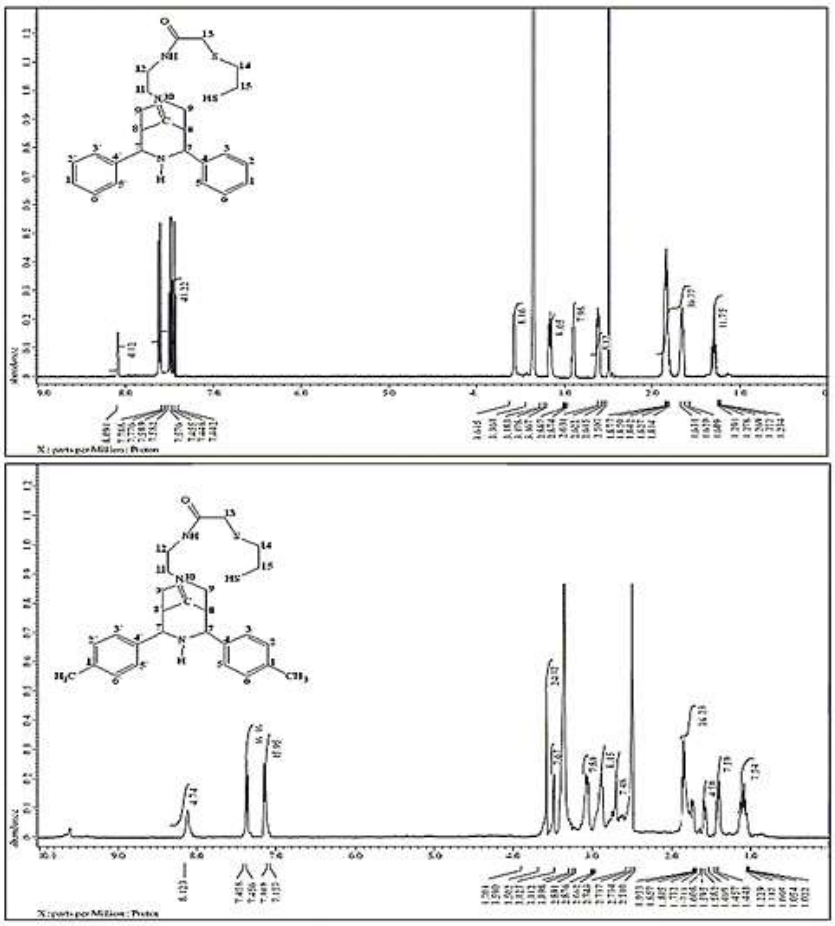

Figure 1. ^{1}HNMR spectra of H_2L^1 and H_2L^2 in DMSO-d_6.

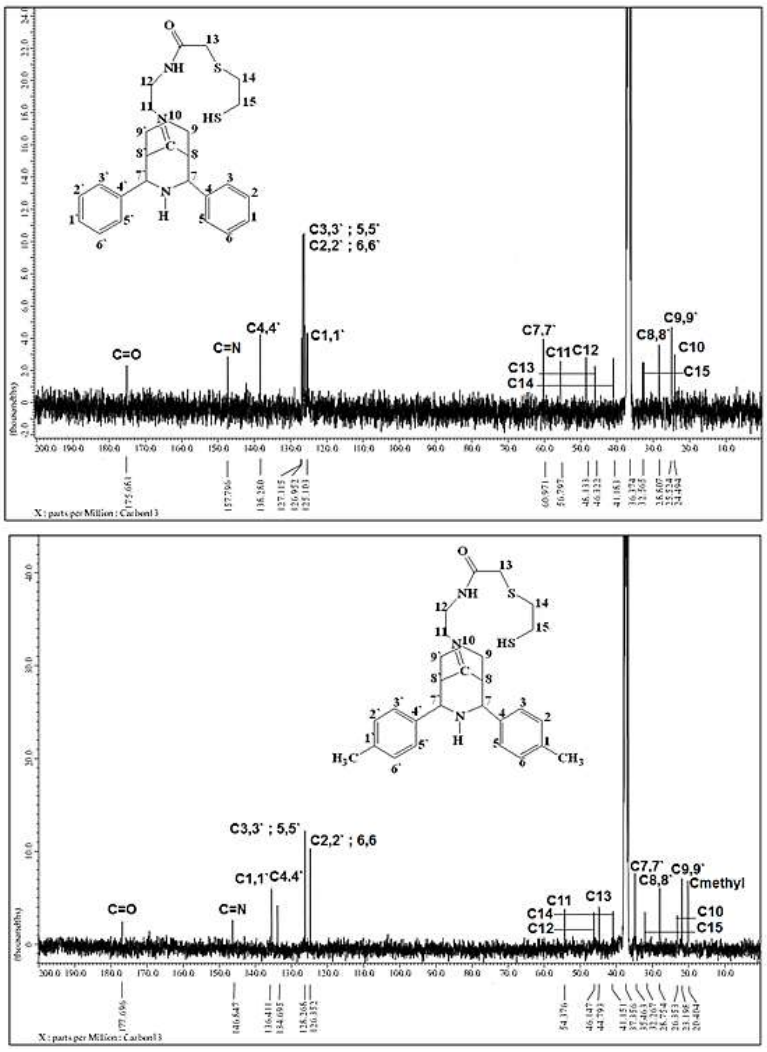

Figure 2. ^{13}CNMR spectra of ligands H_2L^1 and H_2L^2 in DMSO-d_6.

Table 1. Microanalyses data and physical properties for precursors and ligands**.**

Comp.	Empirical formula	M.wt g/mol	Yield (%)	m.p. ºC	Colour	Found/(Calc.)% C	H	N	S
M_1	$C_{20}H_{21}NO$	291.38	93	108-110	White	82.69 (82.44)	7.83 (7.26)	5.03 4.81)	-
M_2	$C_{22}H_{25}NO$	319.44	54	168-170	Pale-yellow	82.24 (82.72)	8.23 (7.89)	4.95 (4.38)	-
A_1	$C_{22}H_{27}N_3$	333.46	65	194-196	Off-white	79.47 (79.24)	8.75 (8.16)	12.98 (12.60)	-
A_2	$C_{24}H_{31}N_3$	361.52	75	113-115	Yellow	80.02 (79.73)	8.17 (8.64)	11.82 (11.62)	-
H_2L^1	$C_{26}H_{33}N_3OS_2$	467.68	70	312-315	White	66.22 (66.77)	7.75 (7.11)	8.44 (8.98)	13.48 (13.71)
H_2L^2	$C_{28}H_{37}N_3OS_2$	495.74	75	320-322	White	67.11 (67.84)	7.95 (7.52)	8.27 (8.48)	12.11 (12.94)

2.3.3. Synthesis of the complexes with H_2L^1 and H_2L^2

A mixture of the title ligand (0.1g, 0.180mmol) in 20ml of a mixture solution of ethanol:chloroform 1:1 and potassium hydroxide (0.03g, 0.541mmol) in ethanol (5ml) was stirred for 10 min. To the above mixture was added dropwise an ethanolic solution (10ml) of the metal chloride (0.043g, 0.180mmol). The resulting mixture was refluxed under N_2 atmosphere for 3h. A solid that formed was filtered, washed by ethanol and diethyl ether, and dried under vacuum. Elemental analysis data, colours, and yields for the ligands and their complexes are given in Table (2).

2.4. Determination of biological activity

The evaluation of compounds (ligands and complexes) against four bacterial strains *(Escherichia coli, Pseudomonas aeruginosa, Staphylococcus aureus and Bacillus)* and four fungi species (*Candida albican*s, *Candida glabrat*a, *Candida tropicali*s and *Candida parapsilsis*) were performed using agar-well diffusion. In this method, the wells were dug in the media with the help of a sterile metallic borer with centres at least 6 mm. A 100 μL concentration of the title specimen 1 mg/mL in DMSO was placed in the individual wells [13]. The Petri dishes were incubated in the incubator for 24h at 37 ºC. The biological activity was observed by measuring the diameter of inhibition zones (mm).

Table 2. Elemental analyses, some physical properties, yields and colours of (H_2L^1 –H_2L^2) complexes.

Chemical Formula	M.wt g/mol	Yield (%)	Colour	m.p. ºC	μ_{eff} per one atom	Microanalysis Found, (Calc.)% C	H	N	S	M	Cl
$K_2[Mn(L^1)Cl_2]$	699.70	56	Brown	310*	1.85	46.39 (46.58)	4.21 (4.43)	6.68 (6.27)	9.87 (9.55)	8.30 (7.85)	10.02 (10.58)
$K_2[Co(L^1)Cl_2]$	673.70	40	Dark-blue	295*	4.96	46.63 (46.31)	4.36 (4.60)	6.74 (6.23)	9.73 (9.48)	8.11 (8.74)	10.74 (10.52)
$K_2[Ni(L^1)Cl_2]$	673.46	62	Pale-blue	285*	3.83	46.80 (46.32)	4.22 (4.60)	6.64 (6.23)	9.71 (9.50)	8.97 (8.71)	10.67 (10.52)
$[Cu(L^1)]$	529.22	73	Pale-green	250*	1.78	58.39 (58.95)	5.53 (5.85)	8,03 (7.93)	12.71 (12.09)	12.62 (12.00)	0 0
$[Zn(L^1)]$	531.05	66	White	305*		58.67 (58.75)	5.88 (5.83)	7.92 (7.90)	12.08 (12.05)	12.35 (12.31)	0 0
$[Cd(L^1)]$	578.09	68	White	315*		54.23 (53.97)	5.82 (5.36)	7.72 (7.26)	11.23 (11.07)	9.86 (9.64)	0 0
$K_2[Mn(L^2)Cl_2]$	697.76	42	Brown	275*	1.79	48.67 (48.51)	5.27 (5.01)	5.76 (6.01)	9.43 (9.17)	7.48 (7.87)	10.43 (10.16)
$K_2[Co(L^2)Cl_2]$	701.75	71	Green-blue	280*	4.90	47.61 (47.87)	4.51 (4.98)	5.24 (5.98)	9.30 (9.11)	8.82 (8.39)	9.89 (10.10)
$K_2[Ni(L^2)Cl_2]$	701.51	85	Pale-blue	290*	3.31	47.33 (47.89)	4.80 (4.70)	5.22 (5.98)	9.31 (9.12)	8.90 (8.36)	10.23 (10.10)
$[Cu(HL^2)]Cl$	558.28	41	Blue	310*	1.69	60.51 (60.18)	6.65 (6.44)	7.27 (7.52)	11.70 (11.46)	11.72 (11.48)	6.16 6.34

[Zn(L^2)]	559.11	50	White	310*	60.71 (60.09)	6.62 (6.25)	7.72 (7.51)	11.22 (11.44)	11.40 (11.69)	0 0
[Cd(L^2)]	606.14	68	White	315*	55.17 (55.43)	5.29 (5.77)	6.54 (6.92)	10.29 (10.55)	18.85 (18.54)	0 0

*= Decomposition temp.

3. Results and discussion

Ligands were prepared from the reaction of amine precursors with 1,4-dithian-2-one. The preparation of the precursors was achieved into two steps; the first step includes Mannich-reaction of benzaldehyde or its derivative with ammonium acetate and cyclohexanone in the presence of ethanol to isolate precursors M_1 and M_2. The second step focused on the reaction of precursors with ethylenediamine to obtain amine compounds A_1 and A_2. The ligands were synthesised from the reaction of 1,4-dithian-2-one and amine precursors in the presence of triethylamine as a base in $CHCl_3$ medium, which gave the title ligands (H_2L^1 and H_2L^2), see Scheme (1). Elemental analysis Table 1, FT-IR (Table 3), NMR (^{1}H- and ^{13}C-NMR) and mass spectra were implemented to determine the entity of compounds (precursors and ligands).

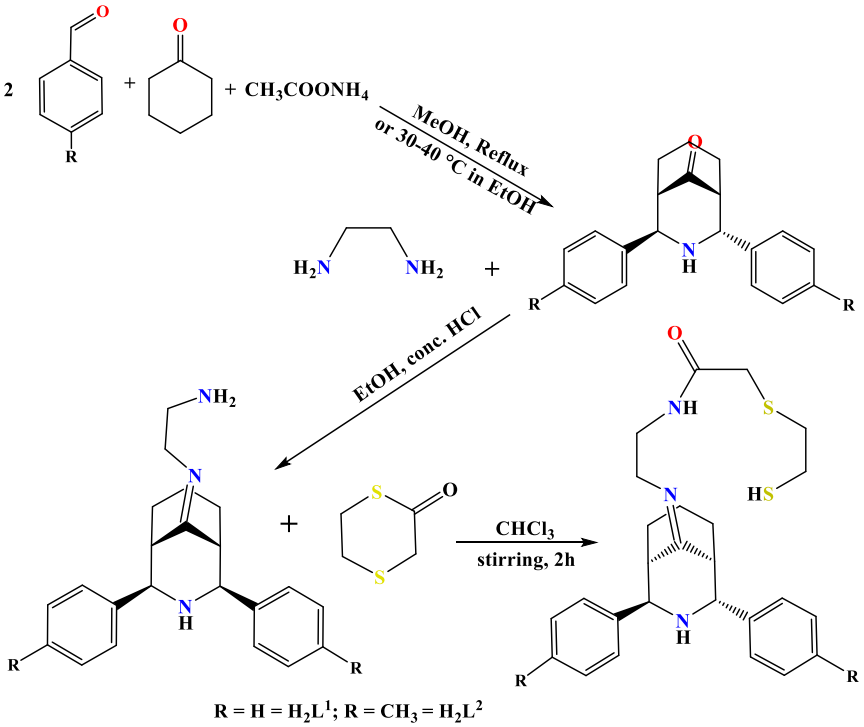

Scheme 1. Synthetic route for precursors and ligands H_2L^1 and H_2L^2.

Complexes of the ligands with Mn(II), Co(II), Ni(II), Cu(II), Zn(II) and Cd(II) ions were synthesised by heating 1 mmole of each ligand with 1 mmole of metal chloride using a mixture of ethanol/chloroform medium at reflux using KOH as a base. In the ethanol/chloroform solution of KOH, the deprotonation of the ligands is occurred that facilitated the formation of $K_2[Co(HL^n)Cl_2]$, $K_2[Mn(HL^n)Cl_2]$, $K_2[Ni(HL^n)Cl_2]$, $[Cu(HL^n)]$, $[Zn(HL^n)]$ and $[Cd(HL^n)]$ **(**M = Mn(II), Co(II), Ni(II), Cu(II), Zn(II), and Cd(II), $L^n = L^1$ or L^2), Scheme 2. The complexes are air-stable and soluble in DMSO (bar other organic solvents). Elemental analysis and other physical properties of the complexes are placed in Table 4. Physico-chemical data agree well with the proposed formulas. The prominent infrared peaks and their assignments for the ligands and complexes are included in Table 3. The electronic data (UV-Vis) with their assignments for ligands and complexes are placed in Table 4.

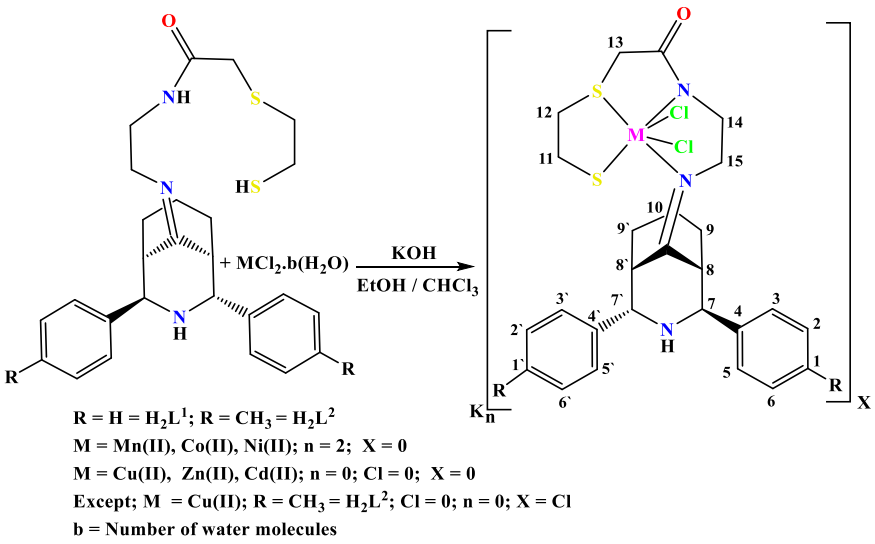

Scheme 2. General synthetic route of ($H_2L^1$and H_2L^2) complexes.

3.1. FT-IR and NMR spectra

The FT-IR spectra of free ligands display bands due to $\nu(C=O)_{amide}$, $\nu(C=N)_{imine}$ and ν(C-N) groups. The distinct frequency around 2555-2619 cm^1 related to ν(S–H), confirms the presence of the ligands in the thiol form [14]. The FT-IR spectra of the complexes exhibited H_2L^1 and H_2L^2 bands with the proper shifts due to complex formation (Table 3). Band assigned to ν(S-H) in the free ligands was disappeared in the spectra of complexes, due to the involvement of sulfur atom, as a thiolate moiety, in complex formation. The $\nu(C=O)_{amide}$ and $\nu(C=N)_{imine}$ at ca. 1662,1674 cm^1 and at ca. 1604-1616 cm^1 in the free ligands were recorded at lower frequencies, indicated a reduced bond order, and observed around 1631-1651; 1600 and 1639-1651; 1600 cm^1 for H_2L^1 and H_2L^2 complexes, respectively. This shift confirmed the involvement of the N atoms of these moieties in the coordination to the metal centre. Bands detected around 1056-1029; 898-855 cm^{-1} and 1083-1033; 898-855 cm^{-1} were attributed to ν(C-S) for complexes of H_2L^1 and H_2L^2, respectively indicating the involvement of sulfur atoms upon coordination to metal centre [15]. At lower frequency, the complexes exhibited bands around 416-493 and 333-383 cm^1 attributed to ν(M-N) and ν(M-S), respectively. Bands observed around 244-262 and 243-277 cm^1 in the spectra of $K_2[Mn(L^1)Cl_2]$, $K_2[Co(L^1)Cl_2]$, $K_2[Mn(L^2)Cl_2]$ and $K_2[Ni(L^2)Cl_2]$ are related to ν(M-Cl) [16]. The appearance of two bands indicated the coordination of the Cl atoms in the *cis* conformation.

Table 3. Infrared spectral data (wavenumber, $\bar{\nu}$) cm^{-1} of (H_2L^1 - H_2L^1) and their complexes

Compound	ν(N-H)	ν(C=O) amid	ν(C=N) imine	ν(C=C) arom	ν(C-N)	ν(C-S)	ν(M-N)	ν(M-S)	ν(M-Cl)
H_2L^1	3417	1662	1604	1531 1492	1323	1056 914	-	-	-

$K_2[Mn(L^1)Cl_2]$	3490	1651	1600	1585	1342	1033	470	362	262
				1508		864	428	347	244
$K_2[Co(L^1)Cl_2]$	3485	1631	1600	1581	1338	1029	466	370	254
				1492		891	443	339	248
$K_2[Ni(L^1)Cl_2]$	3500	1651	1600	1504	1342	1033	464		
				1489		860	447		
$[Cu(L^1)]$	3495	1651	1600	1577	1342	1033	493		
				1504		855	455		
$[Zn(L^1)]$	3500	1643	1600	1577	1334	1045	455		
				1500		857	416		
$[Cd(L^1)]$	3500	1647	1600	1585	1330	1064	459		
				1543		898	447		
H_2L^2	3398	1674	1616	1577	1323	1033	-	-	-
				1523		925			
$K_2[Mn(L^2)Cl_2]$	3490	1651	1600	1558	1342	1060	462	383	277
				1508		891	439	333	243
$K_2[Co(L^2)Cl_2]$	3495	1639	1600	1504	1342	1053	479		
				1454		887	439		
$K_2[Ni(L^2)Cl_2]$	3500	1651	1600	1504	1342	1056	462	366	248
				1489		855	439	339	244
$[Cu(HL^2)]Cl$	3302	1647	1600	1570	1342	1083	474		
	3232			1504		879	443		
$[Zn(L^2)]$	3455	1651	1600	1570	1338	1083	466		
				1504		891	443		
$[Cd(L^2)]$	3485	1651	1600	1543	1330	1064	474		
				1504		898	459		

The ^{1}H and ^{13}C NMR spectra of ligands revealed peaks related to the various proton and carbon nuclei consistent with the proposed structural formula. The ^{1}HNMR spectrum of $[Cd(L^1)]$ Figure 3; in DMSO-d_6 solution indicated two characteristic sets of chemical shifts in the aliphatic and aromatic regions. In the aromatic region, the spectrum indicated signals at; 7.57 ppm (4H, d, J_{HH} = 4 Hz, $H_{3,3`;\ 5,5`}$); 7.17 (4H, t, J_{HH} = 8 Hz, $H_{2,2`;6,6`}$); 7.02 ppm (2H, t, J_{HH} = 8 Hz, $H_{1,1`}$). The aliphatic region shows chemical shifts at 3.99 (2H, s, $H_{13}$); 3.41 (2H, t, $H_{12}$, $J_{HH}$ = 8 Hz); 2.68 (2H, s, $H_{7,7}$); 2.34 (2H, t, $H_{15}$); 1.60 (9H, m, $H_{8,8`}$, $H_{9,9`}$, H_{11} and N-*H*); 1.14 (2H, t, H_{14}, J_{HH} = 8 Hz); 1.01 (2H, m, H_{10}). The spectrum indicated no signals may attribute to N-H of the amide groups and S-H of thiol, confirming the involvement of these moieties in complexation, and making the ligand behaves as -2 species upon complexation. 22.61 (C_{10}); 23.50 ($C_{9,9`}$); 28.36 ($C_{8,8`}$) 29.61 (C_{15}); 38.07(C_{14}); 39.81(C_{13}); 41.10(C_{12}) 44.27 (C_{11}); 67.52 ($C_{7,7`}$); 128.27($C_{1,1`}$); 128.60 ($C_{2,2`}$, $_{6,6`}$); 131.63 ($C_{3,3`}$, $_{5,5`}$); 137.43 ($C_{4,4`}$); 167.06 (C=N); 188.12 (C=O). The $^{13}$C-NMR spectrum of $[Cd(L^2)]$ displayed signals at; 22.30 ($C_{methyl}$); 23.80 ($C_{9,9`}$); 28.24 (C_{10}); 28.55 ($C_{8,8`}$); 34.49 ($C_{15}$); 43.95 ($C_{7,7`}$); 50.28 (C_{14}); 55.42 (C_{13}) and (C_{12}); 55.76 (C_{11}); 128.21($C_{2,2`}$, $_{6,6`}$); ($C_{3,3`}$, $_{5,5`}$) 132.55; 134.45 ($C_{4,4`}$); 135.17 ($C_{1,1`}$); 159.76 (C=N); (C=O) 188.87 ppm. The chemical shift for the imine and amide groups by ca. 10-13 and 11-13 ppm, respectively in comparison with that in the free ligand confirmed the involvement of the nitrogen atoms of the imine and amide groups in complexation. This shift is related to the deshielding occurred to these moieties by the Cd(II) centre upon complexation.

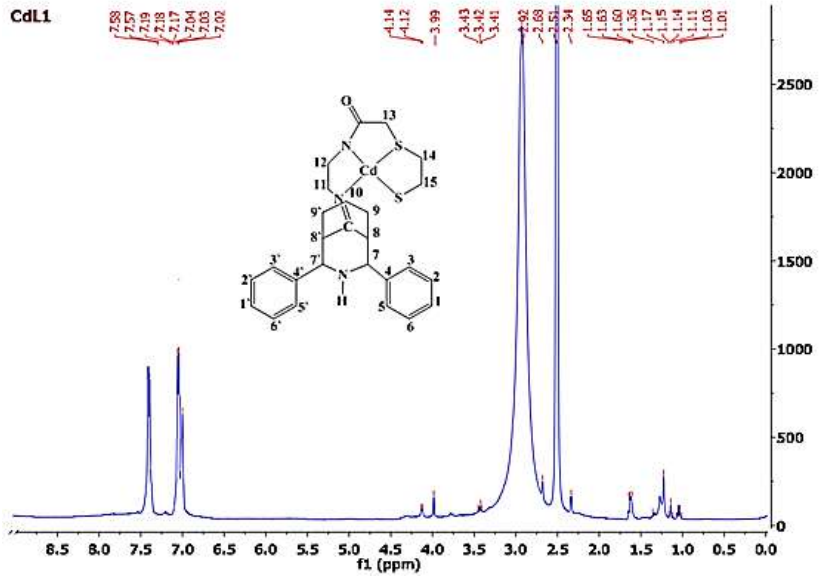

Figure 3. ^{1}HNMR spectrum of [Cd(L^{1})] complex in DMSO-d_6.

3.2. Mass spectra

The obtained mass spectra of the ligands agreed with the suggested structural formula (see experimental section and 'Figure 4'.

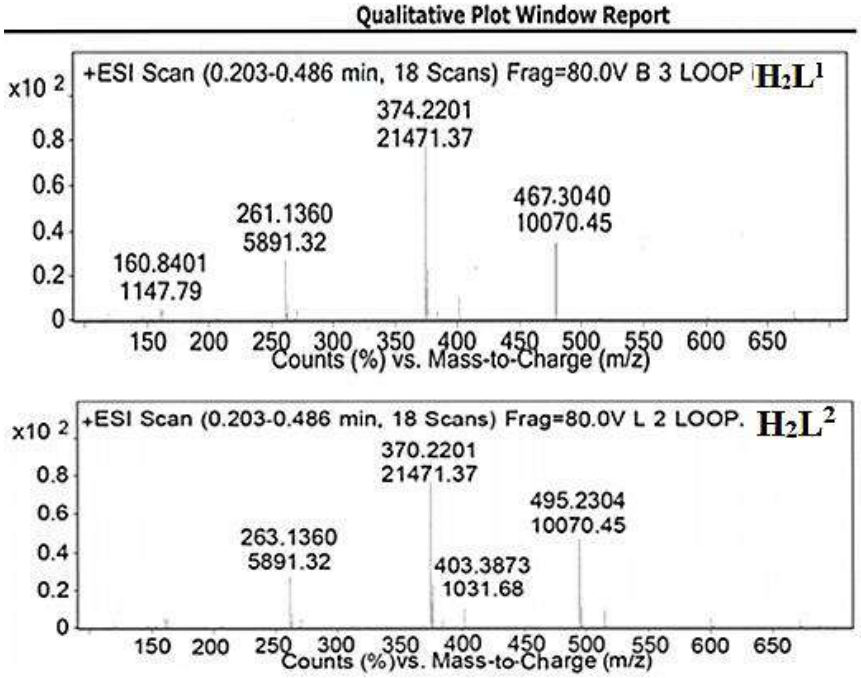

Figure 4 . ESI (+) mass spectra of H_2L^1 and H_2L^2

The accurate electrospray (+) mass spectrum of $K_2[Ni(L^1)Cl_2]$ Figure 5; indicated a peak at m/z = 671.4532 amu, requires = 670.9913 corresponding to $(M)^+$. The successive fragments at 487.3041, 374.2202, 261.1360 and 160.8402 were assigned to $[M-(C_5H_6S)+(C_4H_2S)]^+$,$[M-(C_5H_6S)+(C_4H_2S)+(CHCl_2NO)]^+$, $[M-(HCN)+(2HCl)+(C_4H_8S_2)+(HCN)+(C_6H_4O)+(C_5H_2C_5H_6S)+(C_4H_2S)+(CHCl_2NO)+(HCN)+(C_7H_2)]^+$ and $[M-(C_5H_6S)+(C_4H_2S)+(CHCl_2NO)+(HCN)+(C_8H_3N)+(C_6H_{13}N)]^+$, respectively.

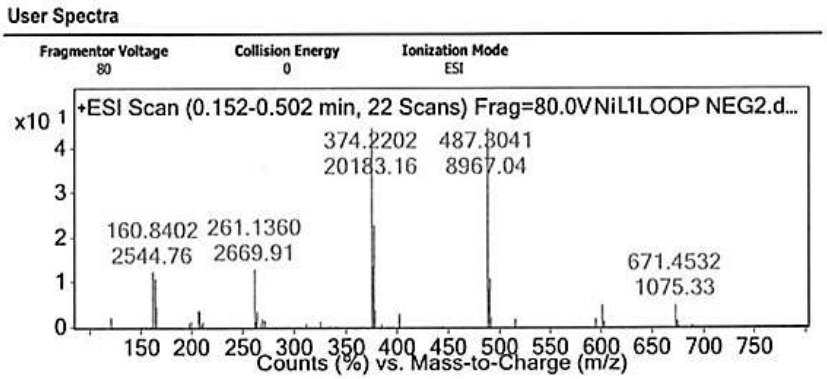

Figure 5. ESI (+) mass spectrum of $K_2[Ni(L^1)Cl_2]$.

3.3. Electronic spectra, magnetic moments, and conductivity measurements

The electronic data of H_2L^1 and H_2L^2 display absorption peak at 260, 265 and 345, 360 nm, respectively related to overlaps of $\pi \rightarrow \pi^*$ and $n \rightarrow \pi^*$ transitions. The spectra of H_2L^1 complexes showed hypsochromic shift peaks correlated to the ligand field transitions ($\pi \rightarrow \pi^*$ and $n \rightarrow \pi^*$) [17-19], bar Cu(II) complex that exhibited a bathochromic shift. The electronic spectrum of Mn(II) complex revealed peaks in the d-d region at 441 and 762 nm assigned to $^6A_1g^{(F)} \rightarrow {}^4T_2g^{(G)}$ and $^6A_1g \rightarrow {}^4T_1g^{(G)}$ transitions, respectively indicating a distorted octahedral geometry about Mn(II) ion [20-21]. These data with the magnetic moment value confirmed an octahedral geometry around the Mn(II) atom. The Co(II) complex displays more peaks in the d-d region at 413, 537 and 674 nm due to $^2Eg \rightarrow {}^2T_1g$ or ^2T_2g, $^2Eg \rightarrow {}^4T_1g^{(F)}$ and $^4T_1g^{(F)} \rightarrow {}^4A_2g^{(F)}$, respectively. This spectrum is characteristic for Co(II) complexes with distorted octahedral geometries around Co atom [22-24]. The μ_{eff} value for this complex is included at the range of octahedral confirming octahedral geometry about metal centre. The Ni(II) complex showed peaks at 417, 610 and 681 nm related to $^3A_2g \rightarrow {}^1T_1g^{(P)}$, $^3A_2g \rightarrow {}^3T_1g^{(p)}$ and $^3A_2g \rightarrow {}^3T_1g^{(F)}$ transitions, respectively confirmed a distorted octahedral geometry around Ni atom [16]. The paramagnetic behaviour of the Ni(II) complex suggested a distorted octahedral geometry. The Cu(II) complex displayed a peak in the d-d region at 828 nm attributed to d-d transition attributed to $^2B_1g \rightarrow {}^2A_2g$, confirming a distorted square planar arrangement about Cu atom [25-27]. The proposed distorted square planar arrangement for the pale-green Cu(II) complex is supported by its magnetic measurement value and other analytical data. The spectra of the Zn(II) and Cd(II) complexes revealed peaks related to ligand field ($\pi \rightarrow \pi^*$ and $n \rightarrow \pi^*$). These diamagnetic complexes (d^{10} system) normally prefer tetrahedral structures. The conductance values of the Mn(II), Co(II), Ni(II), Cu(II), Zn(II) and Cd(II) complexes were in the range of 13.1-76.99 $\Omega^{-1}cm^2mol^{-1}$ indicating 2:1 electrolytic behaviour of the Mn(II), Co(II) and Ni(II), while those of the Cu(II), Zn(II) and Cd(II) complexes were indicating nonelectrolytes [27-28]. The electronic spectra of H_2L^2 complexes revealed peaks that attributed to the ligand field ($\pi \rightarrow \pi^*$ and $n \rightarrow \pi^*$ transitions) [16-18]. The electronic spectrum of Mn(II) complex displayed peaks at 434 and 639 nm correlated to $^6A_1g^{(F)} \rightarrow {}^4T_2g^{(G)}$ and $^6A_1g \rightarrow {}^4T_2g^{(G)}$ transitions, respectively confirming a distorted octahedral structure around Mn atom [23]. These data with the value of magnetic moment support an octahedral geometry around the Mn atom. The Co(II) complex displays additional peaks in the d-d area at 438 and 680 nm due to $^4T_1g^{(F)} \rightarrow {}^4A_2g^{(F)}$ and $^4T_1g \rightarrow {}^4T_2g^{(F)}$ transitions, respectively. This spectrum is characteristic for Co(II) complexes that adopt distorted octahedral structures [23]. The magnetic moment value of the Co(II) complex is in the agreement of octahedral structure with a high spin configuration around Co(II) ion. The Ni(II) complex displayed a peak at 641 nm related to $^3A_2g \rightarrow {}^3T_1g$ transition, confirming a distorted octahedral sphere about Ni atom [23]. The Ni(II) complex is paramagnetic with a value consists of the distorted octahedral geometry. The electronic spectrum of this complex was in agreement with this assignment. Cu(II) complex showed a peak in the d-d region at 794 nm attributed to d-d transition $^2B_1g \rightarrow {}^2B_2g$ demonstrating a distorted square planar geometry about Cu atom [14]. The suggested distorted square planar geometry of the blue Cu(II) complex is supported by magnetic moment value

and other analytical data. The spectra of the Zn(II) and Cd(II) compounds indicated peaks attributed to ligand field ($\pi\rightarrow\pi^*$ and $n\rightarrow\pi^*$). These diamagnetic complexes (d^{10} system) normally prefer tetrahedral structures. The molar conductance values of the Mn(II), Co(II), Ni(II), Cu(II), Zn(II) and Cd(II) complexes were in the range of 7.07-78.21 $\Omega^{-1}cm^2mol^{-1}$ indicating 2:1 electrolytic behaviour of the Mn(II), Co(II) and Ni(II), while those of the Cu(II), Zn(II) and Cd(II) complexes were indicating nonelectrolytes, except Cu(II) complex that indicated a 1:1 electrolytic behaviour [27-28].

Table 4. Electronic spectral data of (H_2L^1- H_2L^2) complexes in DMSO solutions.

Comp.	Band Position λ_{nm}	Wavenumber (cm^{-1})	Extinction coefficient $\varepsilon_{max}(dm^3 mol^{-1} cm^{-1})$	Assignment	$_M(\Omega^{-1}cm^2mol^{-1})$	Suggested geometry
H_2L^1	285	35087	2197	$\pi\rightarrow\pi$		
	360	27777	545	$n\rightarrow\pi^*$		
$K_2[Mn(L^1)Cl_2]$	275	36363	1146	$\pi\rightarrow\pi^*$	75.08	Distorted
	345	28985	33	$n\rightarrow\pi^*$		Octahedral
	441	22675	32	$^6A_1g\rightarrow{}^4T_2g^{(G)}$		
	762	13123	20	$^6A_1g\rightarrow{}^4T_2g$		
$K_2[Co(L^1)Cl_2]$	269	37174	1724	$\pi\rightarrow\pi^*$	76.99	Distorted
	350	28571	70	$n\rightarrow\pi^*$		Octahedral
	413	24213	72	$^4T_2g^{(F)}\rightarrow{}^4A_2g$ (F)		
	537	18621	71			
	674	14836	51	$^4T_2g^{(F)}\rightarrow{}^4A_2g$ (F)		
				$^4T_2g^{(F)}\rightarrow{}^4A_2g$ (F)		
$K_2[Ni(L^1)Cl_2]$	265	37735	1033	$\pi\rightarrow\pi^*$	74.65	Distorted
	350	28571	36	$n\rightarrow\pi^*$		Octahedral
	417	23980	126	$^3A_2g\rightarrow{}^1T_1g^{(P)}$		
	610	16393	120	$^3A_2g\rightarrow{}^3T_1g^{(F)}$		
	681	14684	206	$^3A_2g\rightarrow{}^3T_1g^{(F)}$		
$[Cu(L^1)]$	290	34482	2312	$\pi\rightarrow\pi^*$	16.77	Distorted
	828	12077	78	$^2B_1g\rightarrow{}^2A_2g$		Square Planar
$[Zn(L^1)]$	264	37878	646	$\pi\rightarrow\pi^*$	14.11	Distorted
	350	28571	48	$n\rightarrow\pi^*$		Tetrahedral
$[Cd(L^1)]$	270	37037	1484	$\pi\rightarrow\pi^*$	13.1	Distorted
	341	29325	53	$n\rightarrow\pi^*$		Tetrahedral
H_2L^2	265	37735	1254	$\pi\rightarrow\pi^*$		
	345	28985	45	$n\rightarrow\pi^*$		
$K_2[Mn(L^2)Cl_2]$	268	37313	1696	$\pi\rightarrow\pi^*$	78.21	Distorted
	350	28571	300	$n\rightarrow\pi^*$		Octahedral
	434	23041	308	$^6A_1g\rightarrow{}^4T_2g^{(G)}$		
	639	15649	25	$^6A_1g\rightarrow{}^4T_2g^{(G)}$		
$K_2[Co(L^2)Cl_2]$	270	37037	1957	$\pi\rightarrow\pi^*$	76.01	Distorted
	438	22831	123	$^4Tg^{(F)}\rightarrow{}^4A_2g($ F)		Octahedral
	680	14705	102			
				$^4T_1g^{(F)}\rightarrow{}^4A_2g$ (F)		
$K_2[Ni(L^2)Cl_2]$	268	37313	1684	$\pi\rightarrow\pi^*$	74.54	Distorted
	350	28571	195	$n\rightarrow\pi^*$		Octahedral
	641	15600	188	$^3A_2g\rightarrow{}^3T_1g^{(F)}$		
$[Cu(HL^2)]Cl$	266	37594	1469	$\pi\rightarrow\pi^*$	32.27	Distorted
	300	33333	45	$n\rightarrow\pi^*$		Square
	794	12594	36	$^2B_1g\rightarrow{}^2B_2g$		Planar
$[Zn(L^2)]$	267	37453	1600	$\pi\rightarrow\pi^*$	13.77	Distorted
	350	28571	75	$n\rightarrow\pi^*$		Tetrahedral
$[Cd(L^2)]$	269	37174	1832	$\pi\rightarrow\pi^*$	7.07	Distorted
	350	28571	85	$n\rightarrow\pi^*$		Tetrahedral

3.4. Thermal gravimetric analysis

This technique was implemented to study the thermal properties of compounds (stability and chemical composition of ligands and some complexes). TGA analysis supported the determination of the melting points of compounds and identifying their decomposition steps, see Table (5). The TGA peak of the ligand Figure 6; observed at 399.9 ºC indicated the loss of ($C_{20}H_{22}N_2$) fragment, (det. = 12.364 mg, 60.904 %; calc. = 12.357 mg). The other step occurred at 521.8 ºC revealed the loss of (CH_3NO) portion, (det. = 1.941 mg, 9.562 %; calc. = 1.921 mg). The third step of the decomposition of the compound at 593.3 ºC is linked to the evolving of (CH_2S) segment, (obs. = 1.956 mg, 9.633 %; calc. = 1.958 mg). The remaining deposit of the compound above 598.0 ºC is associated with the loss of (C_4H_6S), (obs. = 4.040 mg, 19.901%; calc. = 3.668 mg). The differences in the weight may be related to a sublimation process that occurred at high temperature. The DSC curve recorded peaks at 317.1, 337.0, 524.1 and 593.3 ºC, which refer to an endothermic decomposition process. While the peak at 344.0 ºC was referred to an exothermic decomposition process. The exothermic and endothermic peaks may specify combustion of the organic ligand in an argon environment [29-30]. The thermogram for $K_2[Co(L^1)Cl_2]$ Figure 7; which confirmed the Co(II) complex is stable up to 285.0 ºC. In the TGA curve, peak detected at 408.6 ºC is related to the loss of (C_7H_4, C_7H_7NO and 2HCl) segments, (det. = 9.954 mg, 54.997 %; calc. = 9.941 mg). The second step at 594.0 ºC that indicated the loss of (2C) fragment, (obs. = 0.619 mg, 3.429%; calc. = 0.646 mg). The final residue of the compound that recorded above 598.0 ºC is correlated to the (Co, 2K, N_2, $2H_2S$, CH_4 and C_2H_6), (det. = 7.534 41.573 %; calc. = 7.512 mg). The DSC curve indicated peaks at 283.0, 325.4, 353.6, 419.2 and 594.0 ºC correlated to an endothermic decomposition process. The endothermic peaks may show combustion of the organic ligand in the inert atmosphere [29-30]. The last endothermic peak may indicate the braking of the metal-ligand bond. The thermogram for $[Cu(L^1)]$ Figure 8; which shows the Cu(II) complex is stable up to 220.0 ºC. The TGA peak at 259.9 ºC attributed to the loss of (C_2H_2) group, (det. = 0.835 mg, 4.347 %; calc. = 0.946 mg). The differences between the observed and calculated weight may be related to the sublimation process. The second step occurred at 391.9 ºC account for the loss of ($C_4H_6S_2$, C_6H_6 and NH_3) portions, (det. = 7.698 mg, 40.092 %; calc. = 7.711 mg). The third step of the decomposition of the compound is observed at 515.5 ºC, which attributed to the loss of ($2H_2$ and NH_3) fragments, (obs. = 0.771 mg, 4.016 %; calc. = 0.765 mg). The final residue of the compound recorded above 598.0 ºC is assigned to the (Cu, HCN and $C_{12}H_5NO$), (obs. = 9.896 mg, 51.543 %; calc. = 9.778 mg). The DSC curve indicated endothermic decomposition processes at temperatures 220.4, 280.4, 334.6 and 515.5 ºC. Peaks at 436.1 and 459.4 ºC attributed to exothermic decomposition steps. The exothermic and endothermic curves may relate to the combustion of the organic ligand in the inert atmosphere [29-30]. The last endothermic peak may signify the metal-ligand bond breaking. While the thermogram for H_2L^2 is shown in Figure 9; The analysis chart indicated the ligand is intact up to 325.0 ºC. The TGA curve measured at 336.9 ºC attributed to the mass loss of (C_5H_7NO) segment, (obs. = 3.845 mg, 19.612 %; calc. = 3.844 mg). The second step took place at 399.3 ºC confirmed the loss of ($C_5H_6S_2$, C_5H_5N and C_3H_4) portions, (obs. = 12.979 mg, 66.217 %; calc. = 12.985 mg). The third decomposition step of the compound at 577.5 ºC is assigned to the mass loss of (C_2H_4) fragment, (obs. = 1.146 mg, 5.8471 %; calc. = 1.110 mg). The final residue that observed above 598.0 ºC is attributed to the elimination of (C_3H_6) portion, (obs. = 1.631 mg, 8.322 %; calc. = 1.664 mg). In the DSC curve, peaks at 331.3, 363.1 and 577.5 ºC indicate endothermic decomposition processes. Peaks at 535.0 and 568.8 refer to exothermic decomposition processes. The exothermic and endothermic curves may relate to the pyrolysis of the organic ligand in the inert atmosphere [29-30]. The thermogram for $K_2[Mn(L^2)CL_2]$ Figure 10; that revealed the Mn(II) complex is steady up to 272.0 ºC. The TGA curve observed at 399.3 ºC related to the loss of (C_5H_6, 2HCl, NH_3, H_2S, $C_5H_{10}S$ and C_7H_8) portions, (obs. = 11.014 mg, 55.0305 %; calc. = 11.010 mg). The second and third steps occurred at 485.3 and 580.28 ºC indicated the evolving of (HCN) compound, (obs. = 0.779 mg, 3.894 %; calc. = 0.779 mg). The final residue of the compound at 598.0 ºC is related to the loss of (Mn, 2K, N_2, and C_9O), (obs. = 8.215 mg, 41.0755 %; calc. = 8.186 mg). The DSC curve displayed peaks at 272.0, 351.8, 418.3, 449.2, 504.3 and 580.2 ºC refer to endothermic decomposition processes. The endothermic peaks may relate to the combustion of the organic ligand in an argon environment [29-30]. The last endothermic peak may signify the metal-ligand bond breaking. The thermogram for $K_2[Ni(L^2)Cl_2]$, Figure 11; which revealed the Ni(II) complex is stable up to 288.8 ºC. The TGA peak observed at 411.9 ºC

confirmed the loss of ($C_7H_{11}N$, $C_4H_8S_2$ and C_8H_{10}) segments, (obs. = 10.070 mg, 47.952 %; calc. = 10.069 mg). The second and third step occurred at 443.9 and 594.8 ºC indicated the loss of (C_2H_4 and HCN) fragments, (det. = 1.663 mg, 7.919 %; calc. = 1.655 mg). The remaining residue above 598.0 ºC related to the (NiO, 2K, Cl_2, HCN and 4C), (det. = 9.267 mg, 44.128 %; calc. = 8.978 mg). The DSC analysis shows peaks at 288.8, 347.7, 502.7 and 594.8 ºC refer to endothermic decomposition processes. The peak at 477.0 ºC refers to an exothermic decomposition step. The exothermic and endothermic peaks may conclude combustion of the organic compound in the inert atmosphere [29-30]. The final endothermic peak attributed to the metal-ligand bond breaking.

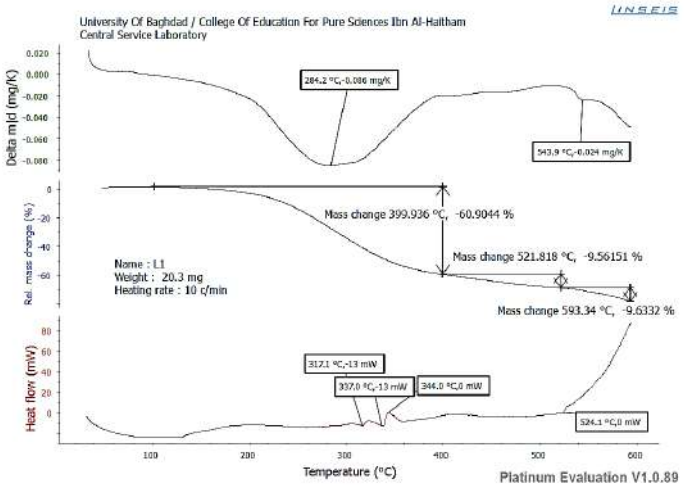

Figure 6. (TGA/ DTA and DSC) thermogram of H_2L^1 in an argon atmosphere.

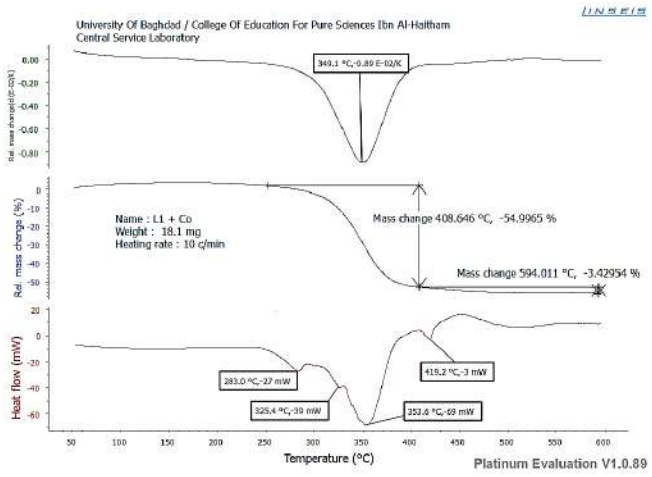

Figure 7 . (TGA/ DTA and DSC) thermogram of $K_2[Co(L^1)Cl_2]$ in an argon atmosphere**.**

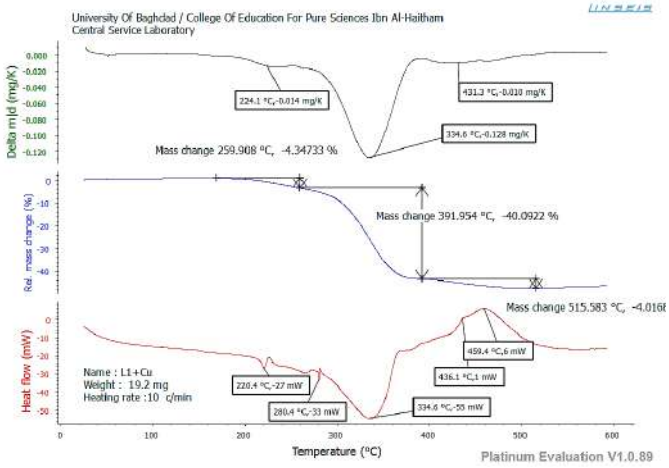

Figure 8. (TGA/ DTA and DSC) thermogram of [Cu(L^1)] in an argon atmosphere.

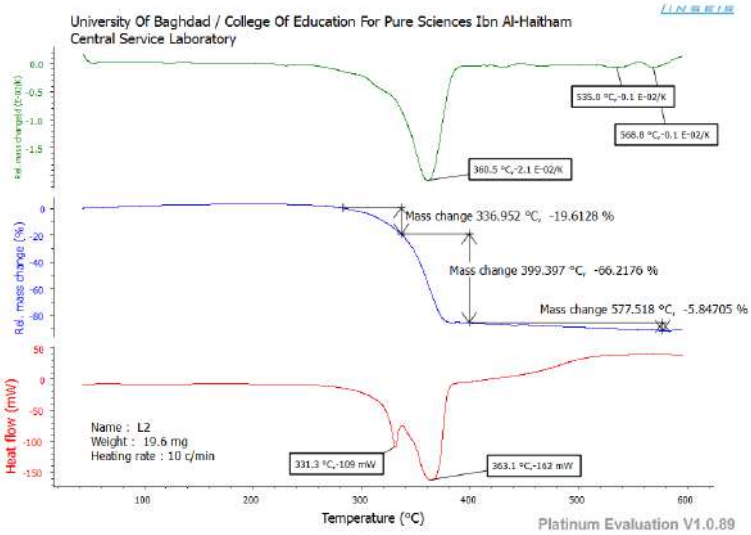

Figure 9. (TGA/ DTA and DSC) thermogram of ligand H_2L^2 in an argon atmosphere.

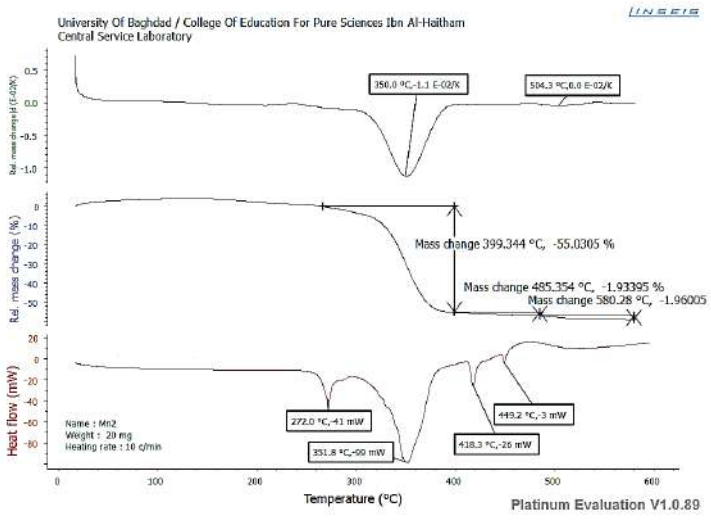

Figure 10. (TGA/ DTA and DSC) thermogram of $K_2[Mn(L^2)Cl_2]$ in an argon atmosphere**.**

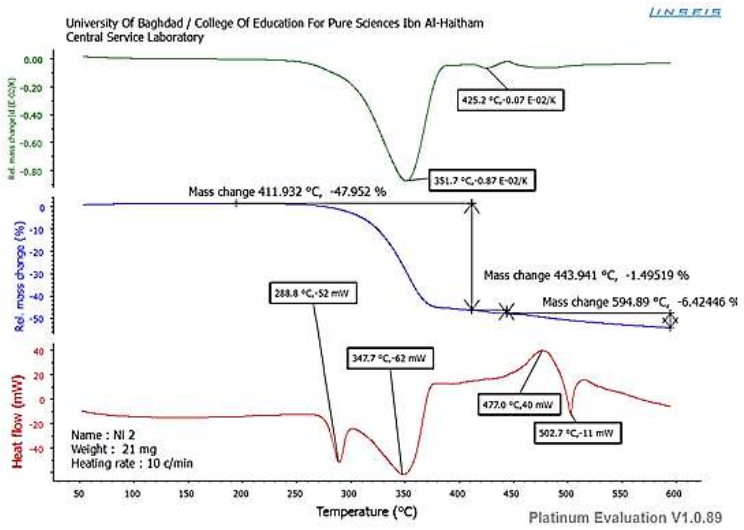

Figure 11. (TGA/ DTA and DSC) thermogram of $K_2[Ni(L^2)Cl_2]$ in an argon atmosphere**.**

Table 5. TGA/DTA/DSC data for ligands (H_2L^1-H_2L^2) and complexes**.**

Compound	Stable up to °C	Stage	Decomposition temperature °C	Nature of transformation/intermediate formed% mass found (calc.)	Nature of DSC peak and temp. °C	DTG peak temp. °C
H_2L^1	317.1	1	399.9	12.364 (12.357)	317.1 Endo 337.0 Endo 344.0 Exo	593.3
		2	521.1	1.941 (1.921)		
		3		1.956 (1.958)	524.1 Endo	
$K_2[Co(L^1)Cl_2]$	285.0	1	408.6	9.954 (9.941)	283.0 Enod 325.4 Endo 353.6 Endo 419.2 Endo	594.0
		2	594.0	0.619 (0.646)		
$[Cu(L^1)]$	220.0	1	259.9	0.835 (0.946)	220.4 Endo 280.4 Endo 334.6 Endo	515.5
		2	391.9	7.698 (7.711)	436.1 Exo 459.4 Exo	
		3	515.5	0.771 (0.765)		
H_2L^2	325.0	1	336.9	3.845 (3.844)	331.3 Endo	577.7
		2	399.3	12.979 (12.985)	363.1 Endo	
		3	577.7	1.146 (1.110)	Endo	
$K_2[Mn(L^2)Cl_2]$	272.0	1	393.3	11.014 (11.010)	272.0 Endo 351.8 Endo 418.3 Endo 449.2 Endo	580.2
		2+3	485.3 and 580.2	0.779 (0.779)	504.3 Exo	
$K_2[Co(L^2)Cl_2]$	284.8	1	406.2	9.774 (9.784)	284.8 Endo 325.8 Endo	595.7
		2	595.7	0.619 (0.621)	419.0 Endo 513.8 Endo	
$K_2[Ni(L^2)Cl_2]$	288.8	1	411.9	10.070 (10.069)	288.8 Endo 347.7 Endo	594.3
		2+3	443.9 and 594.3	1.663 (1.655)	477.0	

								Exo 502.7 Endo		

4. Antimicrobial activity

The compounds (ligands and complexes) were screened against four bacterial strains *(Escherichia coli, Pseudomonas aeruginosa, Staphylococcus aureus and Bacillus)* and four fungi species (*Candida albican*s, *Candida glabrat*a, *Candida tropicali*s and *Candida parapsilsis*). The measured areas of inhibition against the growth of different microorganisms were listed in Tables (6 and 7). These data show the inhibition capacity of the prepared compounds on the tested bacteria and fungi species. It is found that metal complexes have antimicrobial activity against bacterial strains and fungi species. This attributed to the complexation influence that allows the participation of the inherent positive charge of the metal ion in complexes with the negative charge provided by the donor atoms of the ligand. Subsequently, the π-electron will distribute over the entire chelate ring resulting in the increases of the lipophilic character of the metal chelate system. This shall help its mobility through the cell membranes [31-32].

Table 6. The bacterial activity of (H_2L^1 - H_2L^2) and their complexes.

		Gram-negative (G−)				***Gram-positive (G+)***			
No.	**Compound**	***Escherichia coli***		***Pseudomonas aeruginosa***		***Bacillus stubtilis***		***Staphylococcus aureus***	
		Av.	SD±	Av.	SD±	Av.	SD±	Av.	SD±
1	Control	---		---		---		---	
2	H_2L^1	---	0	11.67	1.65	10	7.07	10	0
3	$K_2[Mn(L^1)Cl_2]$	5	1.18	9.33	0.24	12	2.83	17.33	1.18
4	$K_2[Co(L^1)Cl_2]$	14.5	0	14.33	0.47	0	0	0	0
5	$K_2[Ni(L^1)Cl_2]$	19.67	0.24	12.00	0.71	4	5.66	10.33	0.24
6	$[Cu(L^1)]$	13.67	2.36	11.33	0.94	9.67	3.77	13.67	2.36
7	$[Zn(L^1)]$	14	1.41	0	0	14.33	0.47	11.33	1.15
8	$[Cd(L^1)]$	44.67	2.01	21.33	1.08	25	0	36.67	0.76
9	H_2L^2	0	1.65	16.67	1.02	16.67	0	17	0.71
10	$K_2[Mn(L^2)Cl_2]$	6.67	9.43	6.67	0.24	6.67	2.36	16.67	0.24
11	$K_2[Co(L^2)Cl_2]$	3.67	2.60	3.67	0	4.33	3.06	0	0
12	$K_2[Ni(L^2)Cl_2]$	15.67	2.60	15.67	0.24	3	4.24	9.33	0.47
13	$[Cu(HL^2)]Cl$	14.67	6.60	14.67	4.01	0	0	9	1.41
14	$[Zn(L^2)]$	15	0	15	0	10	2.83	14	1.41
15	$[Cd(L^2)]$	23.67	0.94	23.67	1.18	12	0.71	15.67	3.77

5. Conclusions

In the present publication, we have investigated the synthesis, structural characterisation and coordination bonding mode of metal complexes isolated from the reaction of multidentate N_2S_2 heterocyclic ligands (H_2L^1 and H_2L^2) with a range of metal ions. The coordination chemistry and overall structure of the complexes were concluded using a range of analytical and spectroscopic techniques. Further, thermal properties of the ligands and some complexes were established using TGA, DTA and DSC analyses. Biological activities revealed that the ligands and their metal complexes showed different

activity effect on both types of the Gram-positive (G+) and Gram-negative (G-) of the tested bacteria and four species of fungi.

Table 7. Fungi activity of ligands and their complexes**.**

No.	Compound	*Candida albicans*	*Candida glabrata*	*Candida tropicalis*	*Candida parapsilsis*
1	Control	0	0	0	0
2	H_2L^1	0	13	10	13
3	$K_2[Mn(L^1)Cl_2]$	0	14	10	10
4	$K_2[Co(L^1)Cl_2]$	0	10	18	20
5	$K_2[Ni(L^1)Cl_2]$	8	22	19	16
6	$[Cu(L^1)]$	0	14	11	15
7	$[Zn(L^1)]$	0	10	18	0
8	$[Cd(L^1)]$	8	24	33	30
9	H_2L^2	0	0	0	0
10	$K_2[Mn(L^2)Cl_2]$	0	13	15	16
11	$K_2[Co(L^2)Cl_2]$	0	0	18	12
12	$K_2[Ni(L^2)Cl_2]$	9	11	0	10
13	$[Cu(HL^2)]Cl$	0	0	16	12
14	$[Zn(L^2)]$	0	12	10	15
15	$[Cd(L^2)]$	13	22	22	22

Acknowledgment

The authors would like to thank the Iraqi Ministry for Higher Education, University of Baghdad and College of Education for Pure Science (Ibn Al-Haitham) for the providing of the funding and Labs facilities for the project.

References

[1] Asatkar A K, Tripathi M, Panda S, Pande R and Zade S S 2017 *Spectro Chimica Acta Part A: Molecular and Biomolecular Spectroscopy*, **171**, 18.
[2] Thaddeus J W , Edward H W, Gary R W and Carolyn J 2010 *A. Chem. Rev.*, **110**, 3, 2858.
[3] Abram U and Alberto R 2006 *J. Braz. Chem. Soc.*, **17**, 8, 1486.
[4] Yokoi A , Yoshinari N and Konno T 2015 *J. Incl. Phenom. Macrocycl Chem.*, **82**, 123.
[5] Bilgin A, Ertem B, Gok Y 2009 *Dyes and Pigments*, **80**, 1, 187.
[6] Al-Rubaye B K, Brink A, Miller G J, Potgieterd H Al-Jeboori M J 2017 *Acta Cryst*. **E73**, 1092.
[7] Al-Rubaye B K, Potgieter H and Al-Jeboori M 2017 *J Der Chemica Sinica*, **8** (3)**,** 365.
[8] Al-Jeboori M J 1996 , Novel Rhenium, *Technetium and Nickel Complexes as Radiopharmaceuticals in Nuclear Medicine*, Technical University of Munich. *Germany*, PhD.
[9] Archer C M, Dilworth J R, Griffiths D V, Al-Jeboori M J, Kelly J D, Lu C, Rossera M J and Zheng Y 1997 *J. Chem. Soc., Dalton Trans.*,1403.
[10] Al-Jeboori M J , Al-Fahdawi M S and Sameh A A 2009 *J. Coord. Chem.*, **62**, 3853.
[11] Umamatheswari S and Kabilan S 2011 *J. Enzyme Inhib. Med. Chem.* **26**, 430.
[12] Sampath N, Malathy S S M, Ponnuswamy M N and Nethaji M 2004 *Cryst. Res. Technol.*, **39**, 821.
[13] Rahman A, Choudhary M and Thomsen W 2001 *Bioassay Techniques For Drug Developmen*", Harwood Academic. Amsterdam. The Netherlands.
[14] Al-Jeboori M J, Al-Tawel H H and Ahmad R M 2010 *Inorganica Chimica Acta*, **363**, 1301.
[15] Ferreiraa G B, Comerlatoa N M , Wardell J L and Hollauer E 2004 *J. Braz. Chem. Soc.*, **15**, 951.
[16] Abdul-Gganiy A J , AL-Jeboori M J and Al-karawi J A 2009 *Journal of Coordination Chemistry*, **62**, 2736.
[17] Orescanin V , Mikelic L , Roje V and Lulic S 2006 *Anal. Chim. Acta.*,**570**, 277.
[18] Jowit T R N and Mitchell P C H 1970 *J. Chem. Soc.* part A, 1702.

[19] Ronconi L , Giovagnini L, Marzono C, Bettio F , Graziani R , Pilloni G and Fregona D 2005 *Inorg. Chem,* **44** 1867.
[20] El-Sonbati A Z , Al-Shihri A S and El-Bindary A A 2004 *Spectro chimica Acta Part A: Molecular and Biomolecular Spectroscopy,* **60**(8-9) 1763.
[21] Al-Jeboori F H A, Hammud K K , Al-Jeboori M J 2014 *Iranian Journal for Science & Technology*, **38A (**4) 489.
[22] Yousif N S , Hegab K H and Eid A E 2003 , *Inorganic and nano- metal chemistry*, **33** 1647.
[23] Ahmad R M 2012 *Synthesis, Characterisation and Theoretical Studies of Polymeric Chain-Assemblies of Transition Metal Complexes with Mixed Azido-Carboxylato Bridges*, University of Baghdad, College of Education - Ibn-Al-Haitham, PhD .
[24] Lever A B P 1984 *Inorganic Electronic Spectroscopy* 2nd ed., New York.
[25] Baghlaf A O , Ishaq M , Ahmed O A and Al-Julani M A 1985 *Polyhedron*, **4** 853.
[26] Jowitt R N and Mitchell P C H 1970 *J. Chem. Soc.* part A, 1702.
[27] Canpolat E and Kaya M 2005 *J. Coord. Chem.*, **31** 511.
[28] Geary W J 1971 *Russian J. Coord. Chem. Rev.*,**7** 81.
[29] Yousif E I, Hasan H A , Ahmad R M , Al-Jeboori M J 2016 *Der Chemica Sinica*, 7(2) 53.
[30] Muat T H , Al-Jeboori M J 2016 *Chem Xpress*, **9** 156.
[31] Singh R V , Dwivedi R and Joshi S C 2004 , *Trans .Met .Chemi*, **29** 70.
[32] Tweedy B G 1964 *Phytopathology*, **55** 910.

Removal Congo Red Dye on Surface of Nano Charcoal Activated by Used Central Composite Chemometric Method

Removal Congo Red Dye on Surface of Nano Charcoal Activated by Used Central Composite Chemometric Method

Aayad Ammar Sayhood[1], Noor Hassan Abdulrudha[1]and Mohanad Hazim Halboos[2]*

[1]Department of Basic Sciences, Faculty of Dentistry, University of Kufa, Najaf, Iraq
[2]Department of Ecology, Faculty of Science, University of Kufa, Najaf, Iraq

*E-mail: muhaned.halbus@uokufa.edu.iq

Abstract. In this paper; the modern method was used to remove the congo red dye (CR) from its aqueous solutions by chemometric separation. The nano charcoal activated (NCA) was used to remove the CR and the factors affecting the adsorption process were studied simultaneously to reduce the number of experiments followed and to rely on central composite design and the method of response surface by used statistica 12 program. This gives the relationship between all the variables simultaneously. It was found that the removal efficiency reached to 98.371%.

Keyword: Chemometric Method, Congo Red Dye, Nano Charcoal Activated, Adsorption, and Simultaneously.

1.Introduction:

Environmental pollution in general and water pollution in particular is a problem of significant importance in many countries [1]. Water pollution hurts human health [2] as liquid pollutants such as heavy metal ions and dyes are among most critical diseases [3]. These dyes are used in many vital industries such as paper, fabric, tanning and painting [4]. Congo red dye (CR) is one of the known industrial dyes and it is one of the oldest dyes used, Figure (1) [5]. The molecular formula for this dye is ($C_{32}H_{22}N_6Na_2O_6S_2$) [6]. Despite the benefits of its use in the medical field and the food field, but when discharged into water it causes pollution [7]. There are many techniques to remove the dyes from water including the adsorption method as one of the most crucial methods [8]. Adsorption is used to remove dyes from water because it is simple to operate, cheap, and highly efficient [9]. Nano charcoal activated (NCA) is widely used as an adsorbent in separation processes due to its large surface area, low price and painless preparation [10].

(NCA) had stimulated research society to solve the problems of the environment [11]. This nano is very useful for removing by adsorption of various water, air and soil contaminants [12]. Moreover, the decline in water quality has led researchers to use new adsorbents to treat water with charcoal activated [13]. NCA is an excellent adsorbent as its surface that can be adjusted with the addition of other materials and has a high ratio of the volume to the surface area. In addition, it is relatively low cost of production and it is able to reuse [14]. Using coating, stabilizing, and functionalization (NCA) can be modified surface [15]. In the (NCA) surface coating process, clusters are not formed due to the particle dispersion when water molecules containing contaminants (hydrophilicity) are attracted [16]. Therefore, the surface modification of (NCA) will improve its ability to adsorb many pollutants such as dyes and ions of heavy metals [17]. The coating of surface phenomenon helps convert the geometry of closely-packed cubic to nanoparticles in compacts and robust [18].

In this study, the nano charcoal activated (NCA) was used to remove congo red dye (CR) from its aqueous solutions by chemometric separation, making the process less expensive, more productive and environmentally friendly after determining the optimum adsorption conditions.

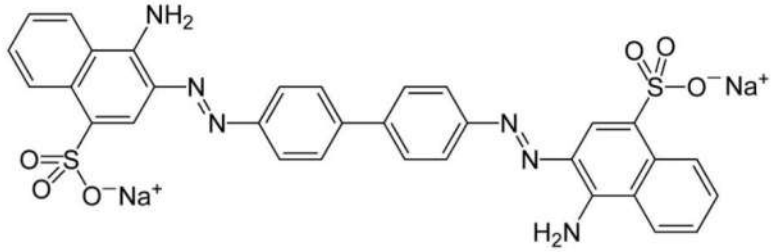

Figure 1. Chemical Structure of Congo Red Dye (CR)

2.The experimental part:

2.1.Chemicals and instruments:

Throughout this study, a high pure and analytical grade was used for all chemical substances and reagents, including nano charcoal activated (NCA) from (BDH), positive congo red dye (CR) from Sigma-Aldrich with purity 99.5%. During the experiments, ultra-pure water was used. Shimadzu UV-Vis Spectrophotometer 1650Pc was used for specifying the residual (CR) in the experiments. Adjusted pH by adding 0.01 M NaOH or 0.01 M HCl and measured by WTW pH meter InoLab 730. A shaker water bath from Amerexa was used to maintain a steady mixing temperature, and it was set to 150 rpm throughout the experiments.

The stock solution of 100 mg/L of (CR) was prepared by dissolving 0.01000 g in a small volume of ultra-pure water and transferred to a 100 mL volumetric flask, diluted with water to a mark. Every day freshly prepares in the range of 30-0.05 mg/L solutions to create a calibration curve. The dye concentration in the aqueous solution was measured via the absorbance (Abs.) at λ_{max} equal to 522 nm by the Least-squares method.

$$[CR]_{mg/L} = \frac{\text{Abs.} - Intercept}{\text{Slope}} \quad (1)$$

2.2.The methodology of experiments:

In this study, all experiments were performed after an added amount of (CR) with nano charcoal activated in the Erlenmeyer flask, placed in the shaker water bath. In order to obtain the optimum conditions for the process of removing (CR) from its aqueous solutions, the effect of five different factors was studied simultaneously and at three levels as shown in table (1); the initial concentration of (CR), the amount of nano charcoal activated, pH, shaking time, and the temperature depended on central composite design [19] and the method of response surface [20] by used STATISTICA 12 program.

Table 1. Factors, Symbol and Coded level to Natural Level by Chemometric Separation

Factors	Symbol	-1	0	+1	Coded level to natural level
The initial concentration of (CR) (mg/L)	X1	10	20	30	10
Amount of Nano charcoal activated(g)	X2	0.2	0.4	0.6	0.2
pH	X3	2	6	10	4
Shaking time (min)	X4	15	25	35	10
Temperature (K)	X5	290	310	330	20

For the passage from coded variable level to natural variable level, the following equations were used: X1 = $([CR]_{mg/L}$ - 20)/10; X2 = (NCA - 0.4/0.2); X3 = (pH−6)/4; X4 = (Time - 25/10) and X5 = (Temperature - 310)/20.

The adsorption process behaviour can be explained based on the empirical second-order polynomial model below [21]:

$$Response = \beta_0 + \sum_{i=1}^{n} \beta_i X_i + \sum_{i=1}^{n} \beta_{ii} X_i^2 + \sum_{i=1}^{n-1} \sum_{j=i+1}^{n} \beta_{ij} X_i X_j \quad (2)$$

Where β_0 is a constant, β_i is the linear coefficient, β_{ii} is the quadratic coefficient, and β_{ij} is the interaction effect coefficient. X_i and X_j are the symbolic values of the factors.
The amount of residual dye was measured at λ_{max}. The quantity (CR) adsorbed onto nano charcoal activated q_e (mg/g) and the removal efficiency R%, which were determined by the following equations:

$$q_e = (C_0 - C_e) \times \frac{V_L}{m_g} \quad (3)$$

$$R\% = \frac{C_0 - C_e}{C_0} \times 100 \quad (4)$$

If the initial concentration (CR) is C_0 (mg/L), the equilibrium concentration C_e (mg/L) of (CR), the Nano charcoal activated mass is m (g), and the solution volume is V(L).

3.Result and Discussion:

3.1.Calibration curve for (CR):

Concentrations of (CR) ranged between (30.0-0.05) mg/L in their aqueous solutions were measured at λ_{max} = 522 nm for creating the calibration curve, as in 'Figure 2' by the Least-squares method.

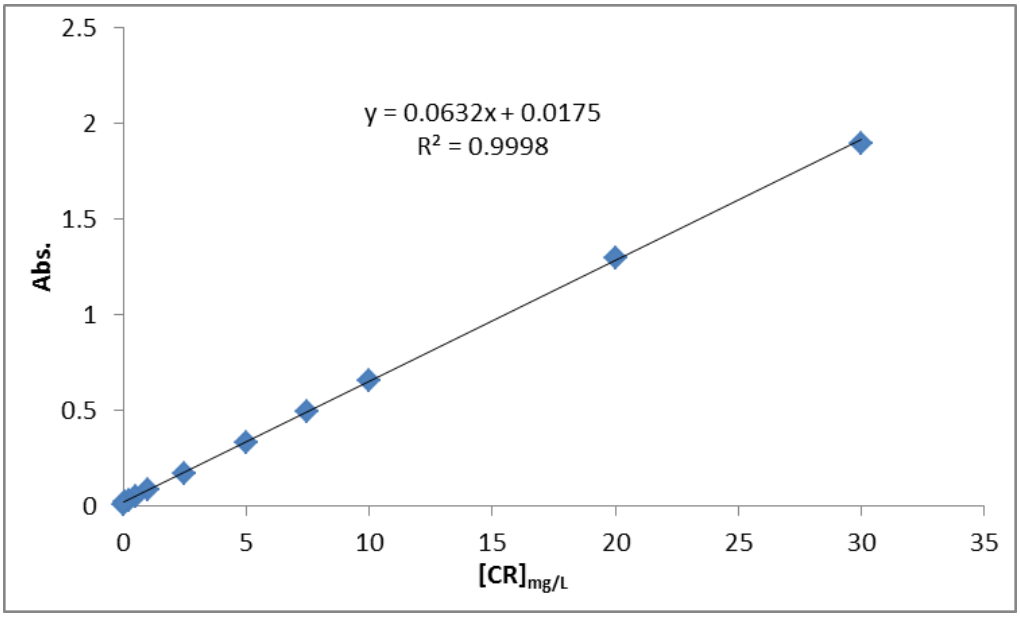

Figure 2. Calibration Curve for Congo Red Dye (CR)

3.2.The optimum conditions:

After studying simultaneously for Nano charcoal activated (NCA) to remove Congo Red dye (CR) from its aqueous solutions by chemometric separation in different conditions [22]; The following results were obtained in 'Figures 3-12' .

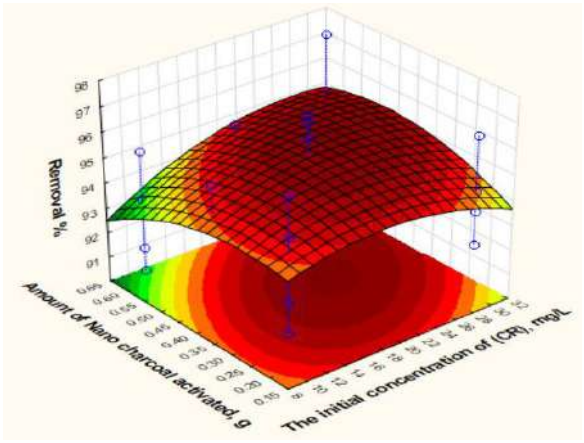

Figure 3. The relationship between the initial concentration of (CR) and amount of nano charcoal activated

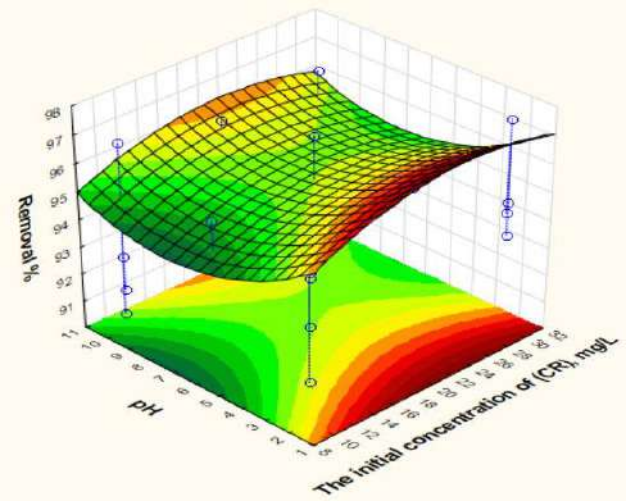

Figure 4. The relationship between the initial concentration of (CR) and pH

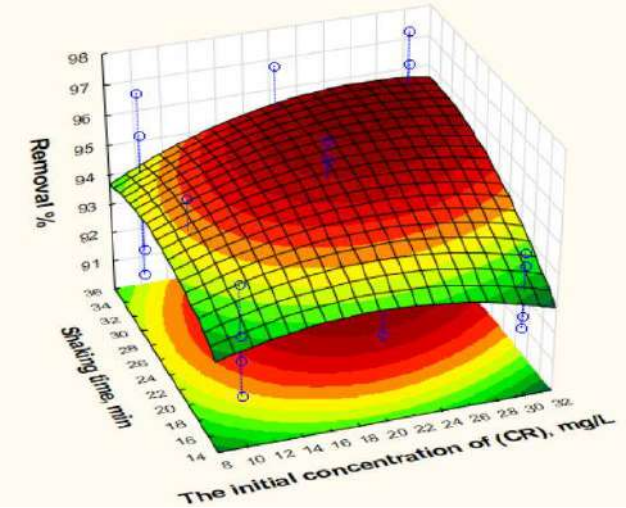

Figure 5. The relationship between the initial concentration of (CR) and Time

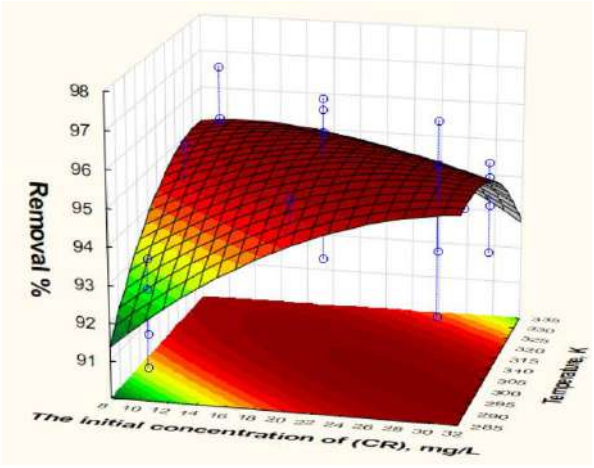

Figure 6. The relationship between the initial concentration of (CR) and temperature

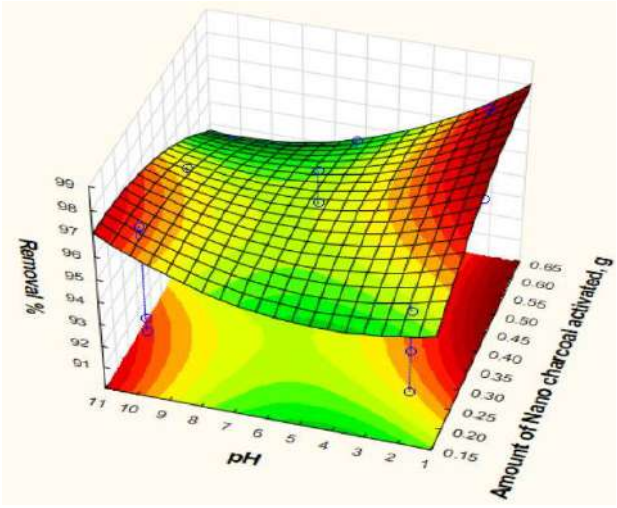

Figure 7. The relationship between amount of nano charcoal activated and pH

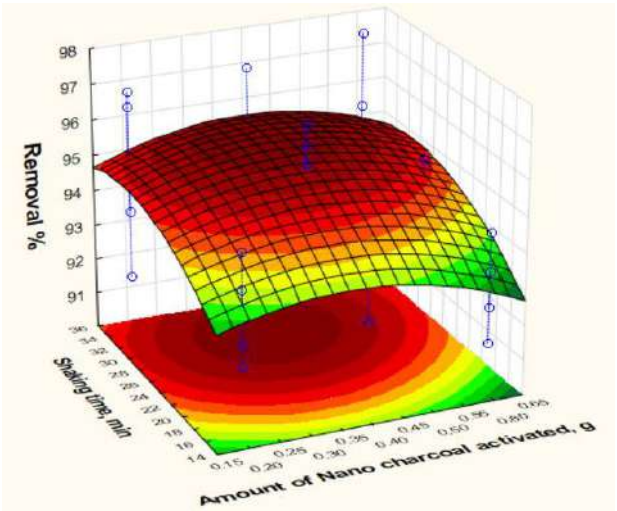

Figure 8. The relationship between amount of nano charcoal activated and Time

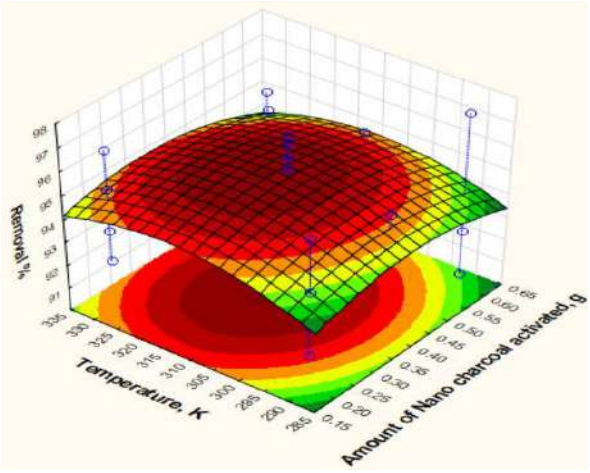

Figure 9. The relationship between amount of nano charcoal activated and temperature

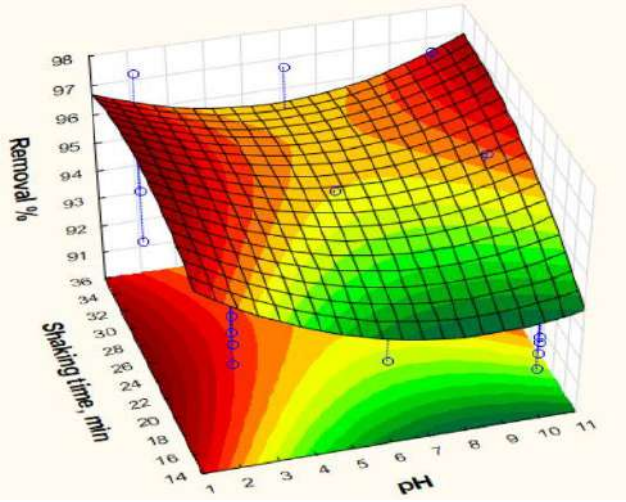

Figure 10. The relationship between pH and time

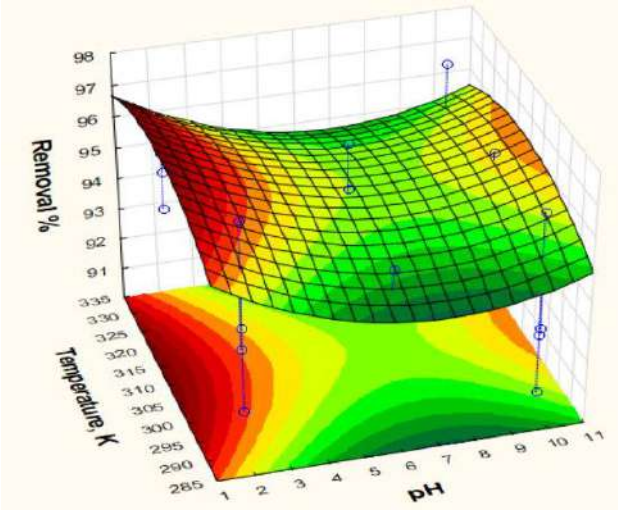

Figure 11. The relationship between pH and temperature

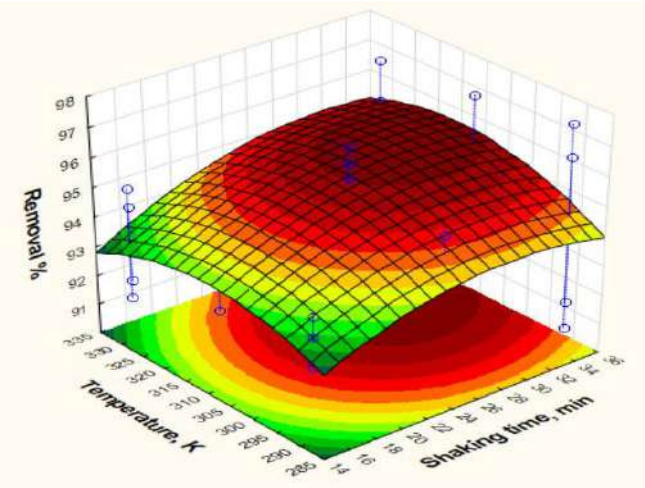

Figure 12. The relationship between time and temperature

By studying the relationship between the five variables with each other and using the statistica 12 program, optimal conditions were found for each factor [23] as shown in Table 2.

Table 2. Optimal conditions by chemometric separation for (CR)

Factors	Symbol	Optimal Conditions
The initial concentration of (CR) (mg/L)	X1	15.341
Amount of Nano charcoal activated (g)	X2	0.258
pH	X3	4.671
Shaking time (min)	X4	20.470
Temperature (K)	X5	309.455

When applying this model to the (CR) dye, it was found that the removal efficiency R% reached 98.371%, as shown in ‘ Figure 13 ’.

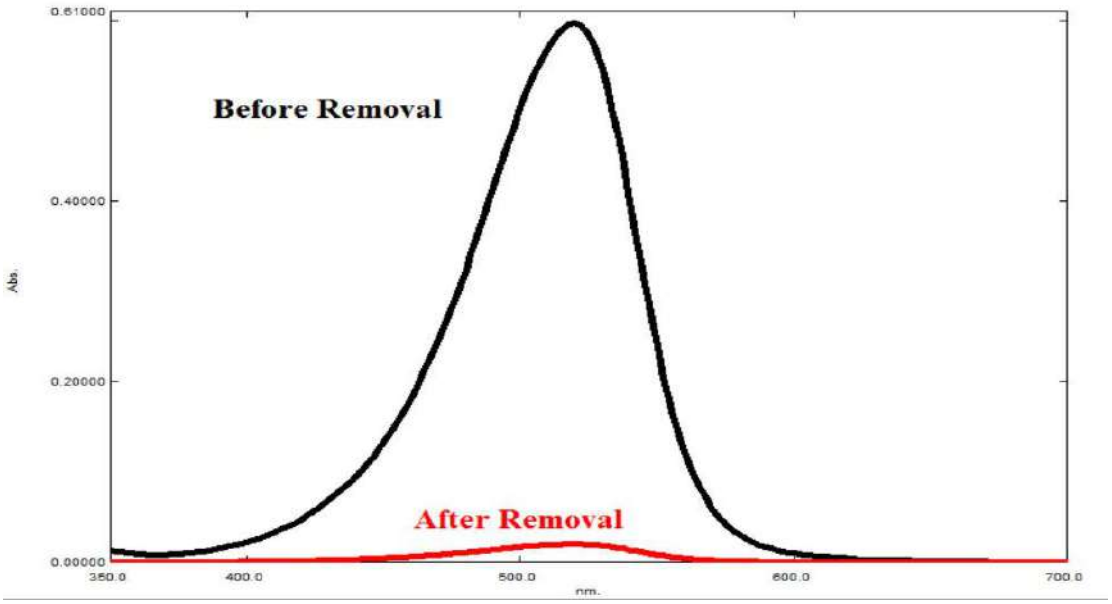

Figure 13. The removal efficiency of congo red dye (CR)

4.Conclusions:

The chemometric separation method is one of the modern, easy and inexpensive methods as it depends on reducing the number of experiments and thus reducing pollution inside the laboratory. The method relied on the use of nano charcoal activated to remove the congo red dye (CR) from its aqueous solutions based on five factors which are the initial concentration of (CR), the amount of nano charcoal activated, pH, shaking time and the temperature depended on Box-Behnken design and the method of response surface by used statistica 12 program and to study the effect of these factors on each other at the same time. The obtained results are satisfactory and compared to the classic methods used in the process of removing dyes.

References:

[1] Wang X, Zhang C and Zhang Z 2019 *J. Environ. Manage.* **248** 109248
[2] Sayhood A A and Mohammed H J 2015 *Der Pharma Chem.* **7** 50
[3] Aljafery A M A, Sayhood A, Abdulridha W M and Yousif A M 2018 *Indian J. Public Heal. Res. Dev.* **9** 917.
[4] Vankar P S and Shukla D 2019 *Newer Natural Dyes for Various Textiles New Trends in Natural Dyes for Textiles* (Elsevier) p 1–69
[5] Guler U A, Ersan M, Tuncel E and Dügenci F 2016 *Process Saf. Environ. Prot.* **99** 194.
[6] Kaur S, Rani S, Mahajan R K, Asif M and Gupta V K 2015 *J. Ind. Eng. Chem.* **22** 19.
[7] Mohamed F, Abukhadra M R and Shaban M 2018 *Sci. Total Environ.* **640**–**641** 352.
[8] Sahoo T R and Prelot B 2020 *Adsorption processes for the removal of contaminants from wastewater Nanomaterials for the Detection and Removal of Wastewater Pollutants* (Elsevier) p 161–222
[9] Hokkanen S and Sillanpää M 2020 Nano- and microcellulose-based adsorption materials in water treatment *Advanced Water Treatment* (Elsevier) pp 1–83
[10] Cukierman A L, Nunell G V. and Bonelli P R 2019 *Removal of emerging pollutants from water through adsorption onto carbon-based materials Emerging and Nanomaterial Contaminants in Wastewater: Advanced Treatment Technologies* (Elsevier) p 159–213
[11] Ciambelli P, La Guardia G and Vitale L 2019 *Nanotechnology for green materials and processes Studies in Surface Science and Catalysis* vol 179 (Elsevier Inc.) p 97–116
[12] Bhateria R and Singh R 2019 *J. Water Process Eng.* **31** 100845
[13] Halboos M H, Ammar Sayhood A and Ala'a Hussein T 2019 *J. Phys. Conf. Ser.* **1294** 052035
[14] Sayhood A A and Mohammed H J 2015 *Int. J. Chem. Sci.* **13** 1123.
[15] Dutta B, Rawoot Y A, Checker S, Shelar S B, Barick K C, Kumar S, Somani R R and Hassan P A 2020 *Nano-Structures and Nano-Objects* **22** 100466
[16] Al-Shirifi A N M, Dikran S B and Halboos M H N 2018 *J. Glob. Pharma Technol.* **10** 143.
[17] Sayhood A A, Hussein B J and Halboos M H 2020 *Syst. Rev. Pharm.* **11** 1478.
[18] Jain M, Yadav M, Kohout T, Lahtinen M, Garg V K and Sillanpää M 2018 *Water Resour. Ind.* **20** 54.
[19] Salman M, Shahid M, Sahar T, Naheed S, Mahmood-ur-Rahman, Arif M, Iqbal M and Nazir A 2020 *Biocatal. Agric. Biotechnol.* **24** 101542
[20] Vakili-Azghandi M, Fattah-alhosseini A and Keshavarz M K 2018 *Meas. J. Int. Meas. Confed.* **124** 252.
[21] McNamee J M and Pan V Y 2013 Nearly Optimal Universal Polynomial Factorization and Root-Finding *Studies in Computational Mathematics* vol 16 (Elsevier B.V.) p 633–717
[22] Halboos M H, Hussein B J and Sayhood A A 2020 *Period. Tche Quim.* **17** 569.
[23] Faris A, Hussain A and Halboos M H 2020 *J. Phys. Conf. Ser.* **1660** 12080.

Loading and Activating a Carbon Surface and Applied for Congo Red Adsorption, Kinetic Study

Loading and Activating a Carbon Surface and Applied for Congo Red Adsorption, Kinetic Study

Russol Abdul Salam Faraj[1] and Ahmed Mohammed Abbas [1*]

[1] Department of Chemistry, College of Education for pure science (Ibn-Al - Haitham), university of Baghdad, Baghdad, Iraq

*** E: mail:Ahmed.phychem@gmail.com**

Abstract. this paper contains preparation of Active carbon surface (AC) from pro so millet grain husks and Loading and activating by Iron oxide and hydrogen peroxide sequentially to obtain surface (ACIPE). The changes of previous processes on Active carbon surface were diagnosed by Fourier transform infrared spectroscopy (FTIR) and Scanning electron microscopy (SEM) . These surfaces (AC and ACIPE) were using as adsorbent for removing of congo red dye from aqueous solutions under certain conditions through batch system .More than one kinetic model was applied to congo red dye adsorption process and it was found that the most kinetic model applied to it is a model (pseudo second order model). In addition to the adsorption efficiency of the surface after activation and loading, it was much better than the main surface where the adsorption efficiency of the first and second surface was equal (27% , 85%) sequentially at higher temperatures .

Keyword: Active carbon; waste plant; Adsorption; Conge red.

1.Introduction

Industrial waste dumped in water is a serious environmental issue in the world, especially developing countries. [1-3]. The presence of many organic and inorganic pollutants in water areas by different industries stimulated the world's attention because of its harmful effects on the environment and human health [4,5].

Dyes are one of the most dangerous pollutants, which are produced in large quantities in the form of liquid waste from several different industries such as textiles, paper, rubber, leather, cosmetics and food industries. The unacceptable treatment of these colored wastes of water has negative effects on living organisms in nature in addition to harmful health effects on humans [6,7]. Therefore, it is important to remove the dyes from the waste before releasing it into the environment [8]. Among these dyes is the Congo red dye (CR) , an anion dye, (4-aminonaphthalene-1-sulphonic acid) is a benzidine-based anionic diazo dye, which is generated by some industries, They are toxic to many organisms and suspect they are carcinogenic and mutagenic [6]. Several physical, chemical and microbial methods have been used to remove CR from colored water [7,9]. Adsorption technology is preferred among several techniques, as it is simple, easy and efficient, and it uses environmental friendly adsorbents— such as activated carbon [10], montmorillonite [11], rice husk [12], bentonite [13],

Activated carbon has a high surface area and this qualifies it to adsorb many pollutants, including organic pollutants, but it is also characterized by its high cost and inability to recover it [2,10]. Use Aloe Vera leaf shells as a cheap absorbent material to produce activated

carbon to absorb the CR dye from industrial wastewater. Particle sizes of 300 to 500 micrometer were carbonized in an oven at 550 ° C [14].
One of the recent studies included the synthesis of activated carbon by collecting leaves and trunks of the Bambusa plant. Then they were thermally and chemically treated with nitric and phosphoric acids. The properties of the resulting carbon surface have been diagnosed with several techniques (FTIR, EDX, SEM and BET). The adsorption of the methylene blue dye on the activated carbon surface has been studied due to its relatively large surface area and a high degree of porosity.[15] The aim of this study was to prepare new surface (activated carbon) from Millet crusts, loaded with oxidized iron particles and use as adsorbent surfaces of Congo red dye.

2.Experiments part

2.1.Materials and methods

2.1.1. Congo red dye

Congo red dye the sodium salt of 3,3'-(biphenyl-4,4'-diyldidiazene-2,1-diyl)bis(4-aminonaphthalene-1-sulfonate) (chemical formula :$C_{32}H_{22}N_6Na_2O_6S_2$,M.wt: 696.66 g/mol) was obtained from Merck (Darmstadt, Germany) ,
Used in this study as an adsorbent material without any purification. Use distilled water twice to prepare all required solutions and reagents.. chemical structure of Congo red dye was shown as 'Figure 1' , Congo red [3, 9- bis dimethylaminophenazo thionium chloride], λ_{max} = 498 nm.

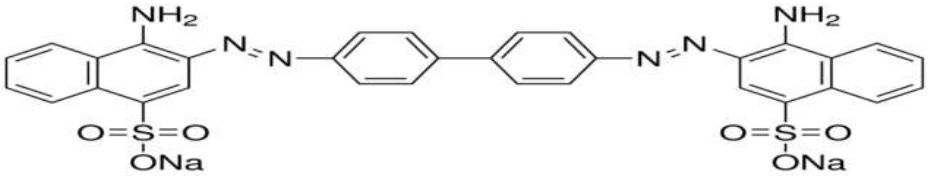

Figure 1. chemical structure of Dye

2.2. Preparation of activated carbon

2.2a. Iron loading on carbon surface

Millet husks were collected from a famous Iraqi market for birds (algazel market) in Baghdad, Iraq, where the crusts were washed several times from the liquefied water and distilled water to remove the dust and foreign bodies, then the crusts were burned after being wrapped with silicon sheets in a burning oven (Furnaces oven Vindon Scientific LTD, OLDHAM, England) at a temperature (500ºC) for an (3) hour, Then the grinding process was done with a home mill,A certain amount of the resulting carbon surface was suspended in (400) ml of water under the influence of ultrasound and continuous stirring for a period of (90) minutes interspersed with the gradual addition of (0.5) gram of iron oxide, and then the filtering and drying process was completed in an oven (Daihan Labtech Oven , LDO-60e,south korea**)** at a temperature (80ºC) Then grinding., the result was a carbon surface with the symbol (AC).

2.2b. Activation of loaded crbon surface

Amount of the modified carbon surface was taken with iron particales and added to (300) ml of hydrogen peroxide with constant stirring and dispersion by ultrasound for one hour and then the carbon surface It was washed with distilled water many times and then filtered and dried at a temperature (80ºC) after grinding and sieving at size of 150 µm to produce the modified carbon surface, symbol (ACIPE).

2.3. Sorption Experiment of Congo red (CR)

Adsorption of the Congo red dye was carried out with an initial concentration (55 mg/L) and its factors were studied in terms of the adsorbent dose, contact time and the temperature in the batch system, which includes direct contact between the dye solution with the weight of the

surfaces(AC,ACIPE) studied in round flask (50 ml) placed in shaker water bath (Labtech ,South korea) at a thermal range (288 , 298 , 308 , 318) K and at A period of time (5-120)min , then separated of adsorbent surface for the dye solution by a centrifuge (Hettich EBA-20,Germany) and then the absorbance of the dye solution was measured by the UV-vis spectrophotometer (Shimadzu 1800,Japan) the amount of adsorbed dye (mg/g) is calculated through the following equation:[16]

$$q_t=V(C_0-C_t)/m \quad (1)$$

where q_t = the amount of solute adsorbed from the solution at time. V = Volume of the adsorbate (L), C_0= the concentration before congo red adsorption, C_t= the concentration after Congo red adsorption and m = the weight of the adsorbent(g).

3.Result and discussion

3.1.Characterization of AC and ACIPE surfaces

3.1.1.FTIR analysis

'Figures 2 , 3' shown the FTIR spectra of (AC) and (ACIPE) surfaces respectively ,We noticed from the 'Figures 2,3 ' the presence of peaks for (ACIPE) surface after the loading and activation process more than the (AC) surface before loading and activation, which indicates the reorganization of surface oxides after being exposed to heat in high temperatures in addition to its treatment with iron oxides and hydrogen peroxide, and this leads to changes in the peaks locations, intensity and shape in addition to disappearance And the emergence of new peaks, which indicates the success of the process of loading and activation to cause changes in the carbon surfaces studied.Where we note the presence of a weak and wide peak that is within the range (3300-3000) cm^{-1} stretch vibration returns to the (OH) group in addition to the vibration of aliphatic compounds already present in the cellulosic tissue of the carbon surface (AC),Also found at (1699 cm^{-1}) return to the (C=O) group and also the presence of a peak at (1576 cm^{-1}) returns to the bend vibration of the (NH) group for primary amine compounds with a peak at (1367cm^{-1}) returns to the vibration of the(C-O)group For alcoholic and carboxylic compounds as well, these compounds contain a peak at(1211cm^{-1}) which is due to the bend vibration of (OH) group in addition to the vibration of the group CH at frequencies within the area of (1100-550cm^{-1}) as well as the presence of weak peaks at frequencies less than(500cm^{-1}) which are due to the bend patterns of the aromatic compounds in the cellulosic tissue. These peaks give a less sharp and more homogeneous spectrum, which gives a less active characteristic in terms of functional groups,While we observe a spectrum 'Figure 2' that includes sharper and more pronounced peaks, especially those that appear at (3160 cm^{-1}) and which are due to the vibration of (OH) group of the carbon surface (ACIPE) after treatment with hydrogen peroxide and iron oxide this gives a less homogeneous spectrum which gives a more effective characteristic in terms of totals Effective functionality compared to the first surface.[17,18]

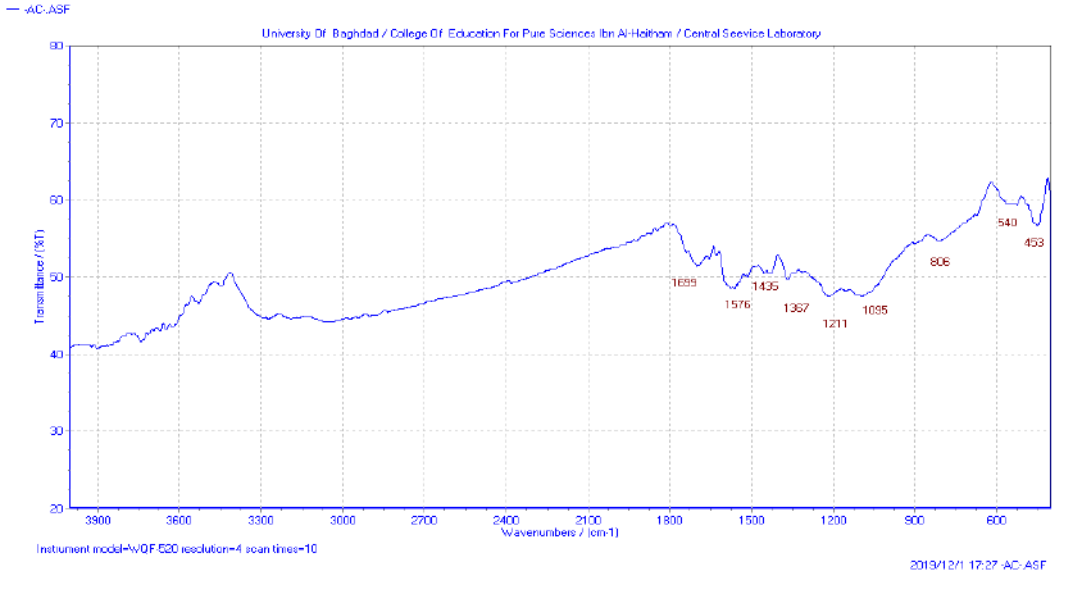

Figure 2. FTIR spectrum of AC surface

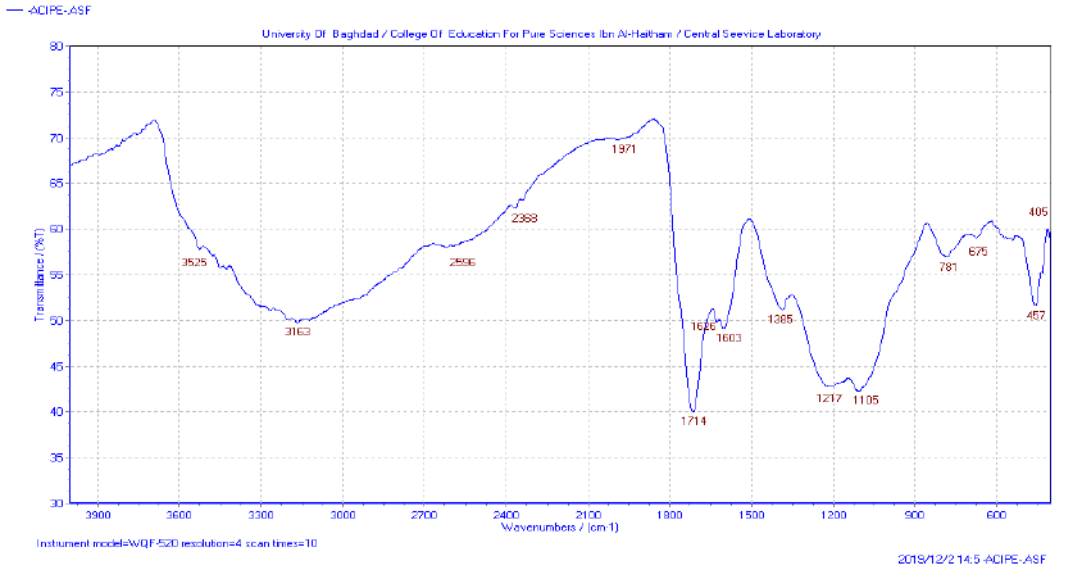

Figure 3. FTIR spectra of ACIPE surface

3.1.2.FESEM analysis

The FESEM images exhibited a description of the morphology of the surfaces of the studied materials with specific enlarging dimensions and forces (100 nm) from the figure. The surface morphologies of (AC) and (ACIPE) surfaces were observed, the FESEM image 'Figure 4 ' of the first surface shown surface particles in the form of individual longitudinal particles that are more than (200nm) intermittently interfering with each other to give Irregular clusters, this in the end gives heterogeneous surfaces, not at the level of their surfaces or at the end, which may cause a kind of obstruction in the reception of any of the materials to be loaded to it, and thus this affects his efficiency when using it in a specific field, as the 'Figure 5' (FESEM) includes On the second surface, surfaces are more flat, in addition to large cavities

On the whole, it given more uniform, homogenous and porous scarves, which greatly improves its surface properties.[19]

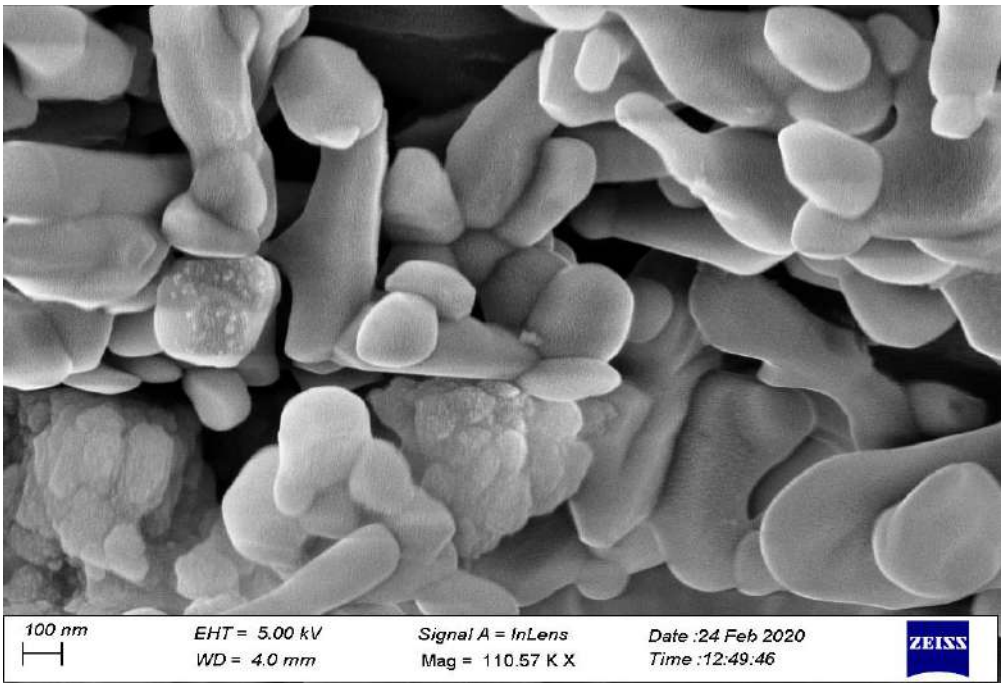

Figure 4. SEM micrographs of (AC)surface

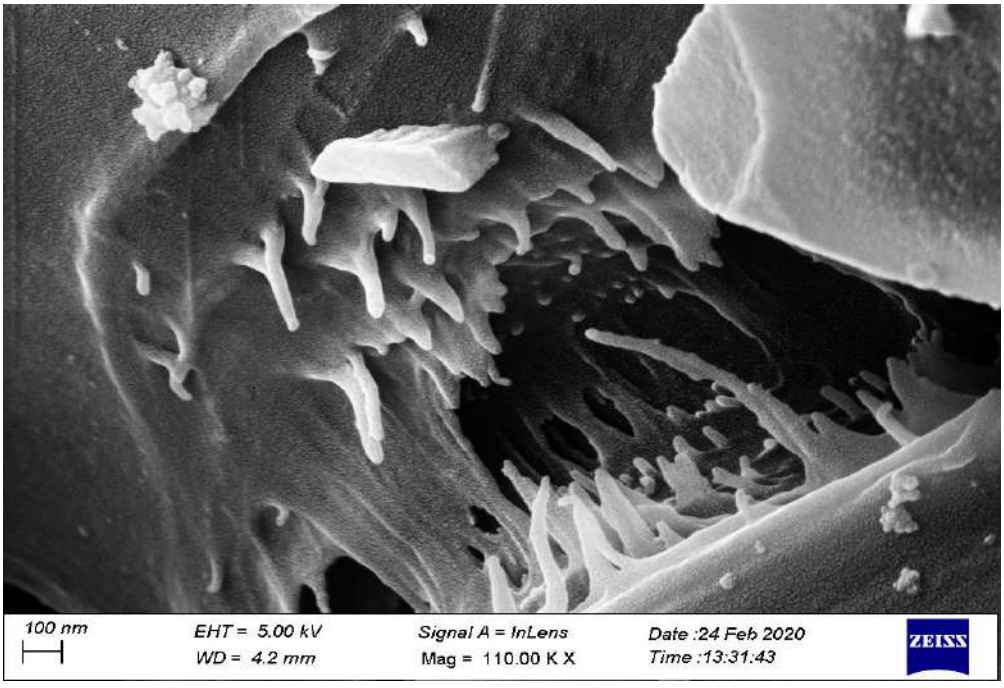

Figure 5. SEM micrographs of (ACIPE)surface

3.2.Study of (CR) adsorption

3.2.1.Effect of adsorbent dose

Absorption dose is an important parameter that strongly influences the adsorption process by affecting the adsorption capacity. Therefore, the influence of adsorbent dose on (CR) dye adsorption by (AC,ACIPE) surfaces were investigated in the range of (0.01-0.05) g . We noticed from the 'Figure 6' that the greatest adsorbing amount of dye for both surfaces was at weight (0.01 g) and then after that either they are relatively stable or decrease with the increase in the weight of the adsorbed surface and this was due to more than the reason that the surfaces may have reached the level of saturation and there are no places for more adsorbed dye particles, which pushes the escape from surface to solution [20]

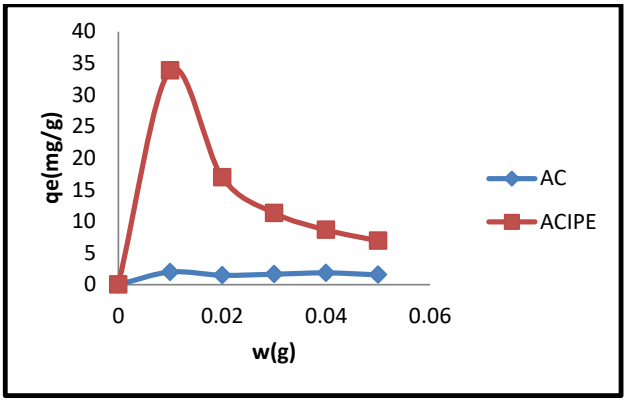

Figure 6. Effect of adsorbents dose on adsorption of (CR) dye

3.2.2.Effect of contact time on (CR) dye adsorption

'Figure 7 ' shown the time effect on initial concentration (55 mg/L) adsorption of (CR) dye by adsorbents (AC,ACIPE) . 'Figure 7 ' shown an increase in the amount of adsorbed dye with increasing time. This increase was rapid during (10), and then the adsorption speed of the dye on both surfaces slows down to a constant amount of adsorption at the time (45 min) and (60 min) of the surfaces (AC) and (ACIPE) sequentially. This time represents The equilibriminum time for adsorption of the dye on both surfaces. This time and beyond represents the saturation area of the two surfaces with this dye. [21,22]

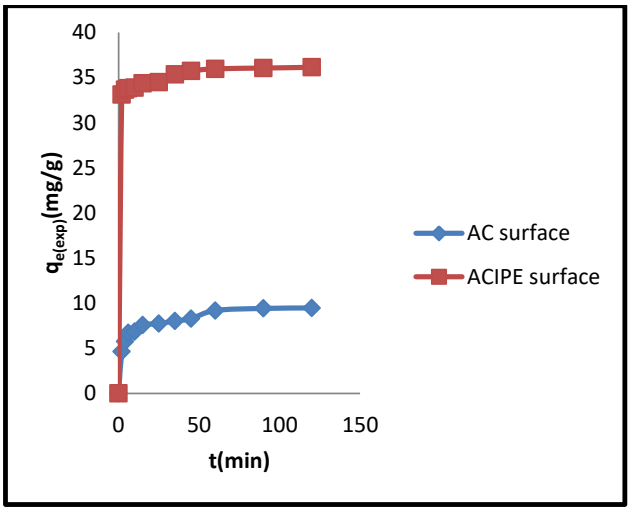

Figure 7. Effect of contact time on the adsorption of (CR) dye on both adsorbents

3.2.3.Effect of temperature on (CR) dye adsorption

'Figures 8 , 9 ' Explained the effect of temperature on the dye adsorption rate (CR) on adsorbents (AC, ACIPE), researched at four different temperatures (288, 298,308 and 318) K , using the initial concentration of (55 mg/L) . It was observed that the removal percentage of (CR) increases with increasing temperature for both adsorbents studied. An increase in temperature increases the rate of diffusion of the adsorbate molecules across the external boundabotry layer and within the internal pores of the adsorbent particles, due to a decrease in the viscosity of the solution. The obtained results revealed that an increase in temperature from 288 to 318 K increased the (AC) surface adsorption efficiency from 16%.1 to 27% while at same range temperatures K increased the (ACIPE) surface adsorption efficiency from 65%. to 85% . This phenomenon indicates that the adsorption process was of a endothermic nature. This may be due to the movement of the particles, which generally increases with increasing temperature, which facilitates the formation of mono layers.[23,24]

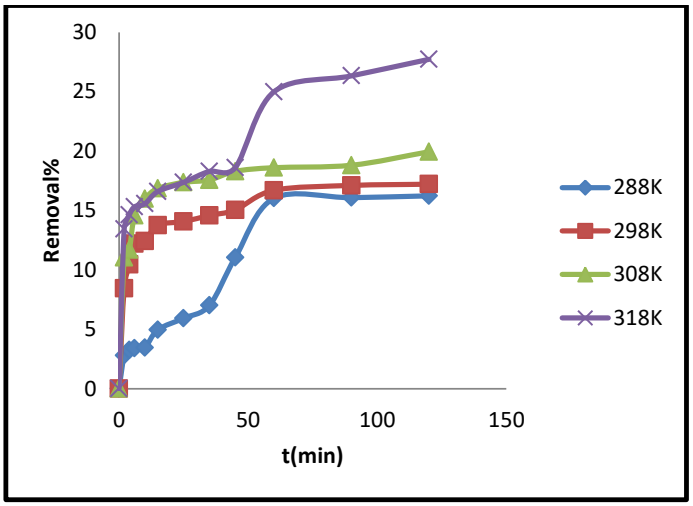

Figure 8. Effect of temperature on the adsorption efficiency of (CR) dye on (AC) surface

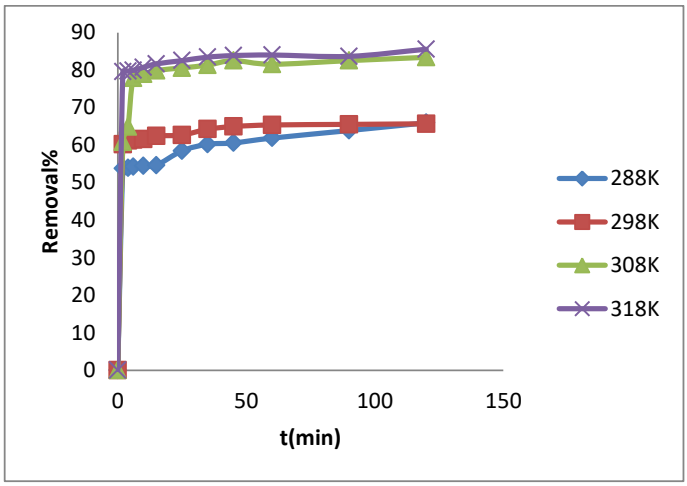

Figure 9. Effect of temperature on the adsorption efficiency of (CR) dye on (ACIPE) surface

3.2.4.Kinetic study

A study was conducted Kinetics of the (CR) dye adsorption process on both surfaces (AC,ACIPE) from the application of the most famous kinetic models (pseudo first order [25] and pseudo second order [26]) which were recorded in Tables 1,2 where they were represented graphically to obtain ' Figures 10a,b ' for the pseudo first order for (AC ,ACIPE) surfaces and 'Figures 11a,b ' for the pseudo second order for (AC ,ACIPE) surfaces and from these figures are calculated coefficients of the two orders and included in the Tables 1,2.

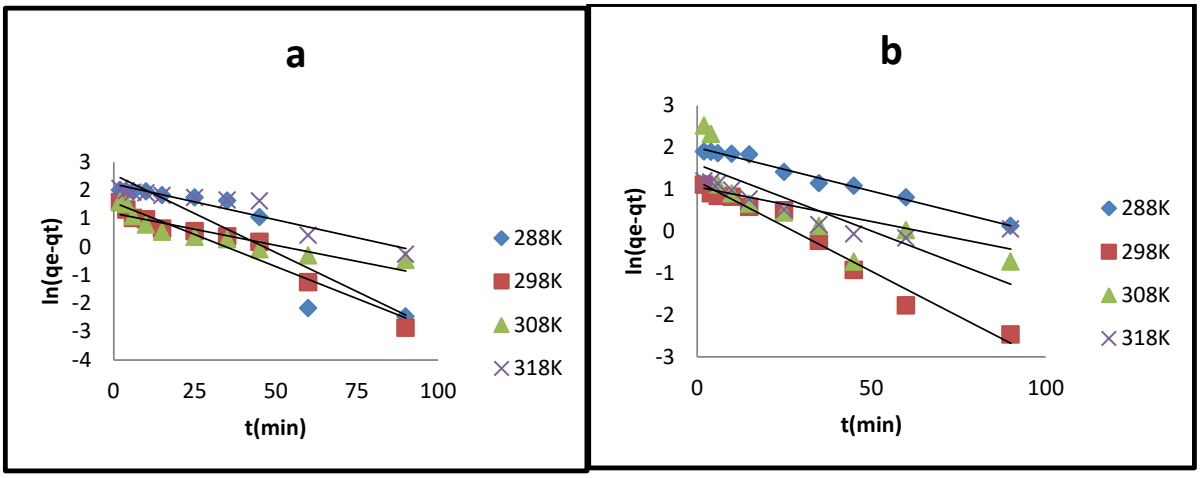

Figure 10.the graphical representation of first order of (CR) dye adsorption on a)AC ,b) ACIPE surfaces at different temperatures

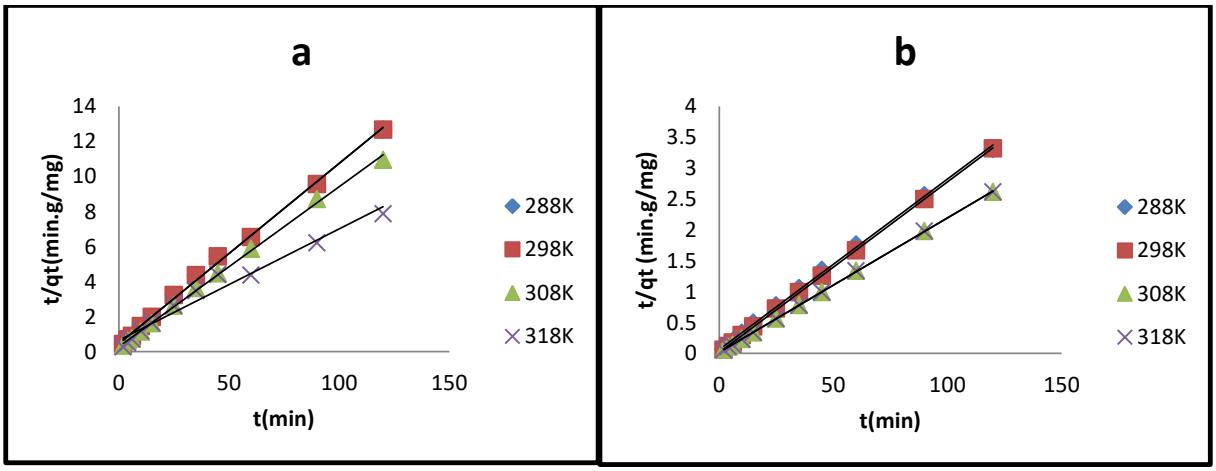

Figure 11. the graphical representation of second order of (CR) dye adsorption on a) AC ,b) ACIPE surfaces at different temperatures

Table 1 . Kinetic parameters for adsorption of (CR) dye onto AC surface based on Pseudo (first and second) order equations

Model kinetic		Parameter	Temperature / K			
			288	298	308	318
Pseudo-first order	$\ln(q_e-q_t) = \ln q_e - k_1 t$	$k_1(min^{-1})$	0.0553	0.0455	0.0227	0.0254
		q_e(mg/g)	12.9461	4.8235	3.2713	9.2202

Pseudo-second order	$t/q_t=1/k_2q^2_e + (1/q_e)t$	R^2	0.8282	0.9448	0.8217	0.8897
		k_2(g/mg.min)	0.0020	0.0237	0.0295	0.0063
		q_e(mg/g)	11.976	9.727	10.964	15.723
		R^2	0.805	0.997	0.998	0.967

Table 2 . Kinetic parameters for adsorption of (CR) dye onto ACIPE surface based on Pseudo (first and second) orders equations

Model kinetic		Parameter	Temperature / K			
			288	298	308	318
Pseudo-first order	$\ln(q_e-q_t) = \ln q_e-k_1t$	$k_1(min^{-1})$	0.0207	0.0429	0.0318	0.0165
		q_e(mg/g)	7.3419	3.2828	4.9170	2.8688
		R^2	0.9844	0.9714	0.676	0.7561
Pseudo-second order	$t/q_t=1/k_2q^2_e + (1/q_e)t$	k_2(g/mg.min)	0.0121	0.0432	0.0260	0.0374
		q_e(mg/g)	36.231	36.231	46.082	46.948
		R^2	0.998	0.999	0.999	0.999

Where $q_{t(exp)}$ ($mg.g^{-1}$) and $q_{e(theo)}$ ($mg.g^{-1}$) were the adsorption capacity of dye at time t and at equilibrium, k_1 (min^{-1}) and k_2 ($g.mg^{-1}.min^{-1}$) are the rate constants of pseudo-first order and pseudo-second order models respectively.

From the Tables 1,2 shown the applicability of the pseudo second order equation more than the pseudo first order to the (CR) dye adsorption process for both adsorbents because the values of (R^2) for the second order were higher than their values for the first order and on the other hand the values of (q_e) (practical and theoretical) for the second rank are closer more than the The first order.[27]

4.Conclusion

In this study we concluded that the process of activating and modifying the carbon surface (AC) with iron particles and hydrogen peroxide was introduced through diagnostic tools (FESEM,FTIR) in addition to this process led to improving the adsorption efficiency of the ACIPE surface and was (85 %) while it was for the (AC) surface (27 %) and the nature of both processes was endothermic. adsorption (CR) dye follows a pseudo-second kinetics, which follows the mechanism of monolayer chemical adsorption.

Acknowledgments: The authors wish to thank and acknowledge the college of education for pure science (ibn al-haitham), University of Baghdad.

References

[1] Nourmoradi H , Nikaeen M and Khiadani H M 2012 *Chem. Eng. J.* **191** 341.
[2] Omidi-Khaniabadi Y, Jafari A, Nourmoradi H , Taheri F and Saeedi S 2015 *J Adv Environ Health Res* , **3** 120.
[3] Basiri H, Nourmoradi H, Moghadam F M, Moghadam K F, Mohammadian J and Khaniabadi Y O 2015 *Der Pharma Chem*., **7** 149.
[4] Jourvand M, Shams K G, Omidi-Khaniabadi Y, Godini H and Nourmoradi H 2015 *JBRMS*, **2** 32 .
[5] Cheng Z, Zhang L, Guo X, Jiang X and Li T 2015 *Spectrochim Acta A Mol Biomol Spectrosc*, **137** 1126.
[6] Omidi K Y , Heydari R, Nourmoradi H , Basiri H and Basiri H 2016 *J Taiwan Inst Chem Eng* , **68** 90 .
[7] Arumugam A and Saravanan M 2015 *Der Pharm. Lett*, **7** 332.
[8] Wasti A and Ali A M 2016 *J. Assoc. Arab Univ. Basic Appl. Sci*. **20** 26.
[9] Khodadadi M, Saghi M , Azadi N A and Sadeghi S 2016 *JMUMS***. 26** 70.
[10] Chen H and Zhao J 2009 *Adsorption*, **15** 381 .
[11] Wang L and wang A 2007 *J. Hazard. Mater*, **147** 979 .
[12] Han R, Ding D, Xu Y, Zou W, Wang Y and Li Y 2008 *Bioresour. Technol*, **99** , 2938 .

[13] Bulut E, Özacar M O and Şengil İ A 2008 *J. Hazard. Mater*,**154** 613.
[14] Khaniabadi Y O, Mohammadi M J, Shegerd M , Sadeghi S, Saeedi S and Basiri H 2017 *Environ. Health Eng. Manag*. **4** 29 .
[15] Daniel K, Chubaakum P and Rao K S 2017 *J. Mater. Environ. Sci.* **8** 2494.
[16] Raposo F, De La Rubia M A and Borja R 2009 *J. Hazard. Mater*, **165** 291.
[17] Manjeet B, Diwan S, Garg V K and Pawan R 2009 Int. *J. Environ. Sci. Technol*, **1** 1084.
[18] Rao R M, Ahmedna M and Marshall W E 2000 *Bioresour. Technol*, **71** 103.
[19] Sumrit M , Phansiri M, Wanwimon P and Sataporn K 2015 *Sci. World J.*, 1.
[20] Hu Z, Chen H, Ji F and Yuan S 2010 *J. Hazard. Mater*,173(1-3) ,292-297(2010).
[21] Saeed A, Sharif M and Iqbal M 2010 *J. Hazard. Mater*,**179** 564 .
[22] Chanzu H A, Onyari J M and Shiundu P M 2012 , *J Polym Environ*. **20** 665.
[23] Abbas A M , Abdulrazzak F H and Himdan T A 2018 *J. Mater. Environ. Sci.* **9** 2652.
[24] Geçgel Ü, Üner O, Gökara G and Bayrak Y 2016 *Adsorp Sci Technol*, **34** 512.
[25] Damiyine B, Guenbour A and Boussen R 2017 *J Mater Environ Sci* ,**8** 345 .
[26] Fayoud N, Alami Y S, Tahiri S and Albizane A 2015 *J. Mater. Environ. Sci*, **6** 3295.
[27] Lairini S, El Mahtal K, Miyah Y, Tanji K, Guissi S, Boumchita S and Zerrouq F 2017. *J. Mater. Environ. Sci*, **8** 3252.

Audio source separation using supervised deep neural network

Audio source separation using supervised deep neural network

Riham J. Issa and Yusra F.Al-Irhaym

College of Computer Sciences and Mathematics
University of Mosul, Mosul, Iraq

E-mail: rihamjassim11@gmail.com

Abstract. The speech signals inserted in the computer may be mixed as a result of interference with signals from other sources. These signals may be speech signals or noise. One of the most famous examples of this problem when a group of people speaking in the same time is the "Cocktail Party". This problem produces a mixture of different speech signals, called the mixed signal. To solve this problem, the audio signals that make up the mixed-signal must be restored to their sources. This task is called separating audio sources. In this paper, supervised Deep Recurrent Neural Networks with Bi-directional Long Short Term Memory (Supervised DRNN-BLSTM) were used. To achieve a monaural source separation, we build a model to separate audio signals from a monaural mixed signal. This mixed signal consists of two different audio signals (male-female). We predict two types of time-frequency masks (Ideal Ratio Mask (IRM), and Optimal Ratio Mask (ORM). They are used to achieve the separation of the target audio sources from the mixed signal. We test the model on a dataset with (500) mixed signals. Each mixed signal three seconds in length and consists of two speaker signals (Female-Male). They are recorded in a stereo format at 8192kHz, our approach achieves Signal-to-Distortion ratio (SDR) (0.183.db), Source-to-interference Ratio (SIR) (0.198.db), and Source-to-Artifacts Ratio (SAR) (0.13.db) gain using (ORM) mask compared to the existing model using (IRM) mask.

Keywords: Monaural source separation, Ideal ratio mask (IRM), Optimal Ratio Mask (ORM), Deep Neural Network, Cocktail party problem.

1.Introduction

In the field of sound processing, separation methods are used to extract the interfering sounds of speakers in a mixture of different audio signals. The term (Source) is used on the signals forming the mixture, while the task is called Blind Source Separation (BSS)[1]. The process of separating single-channel audio sources is a special case of separating audio sources because the separation is done using a single mixed-signal. This adds another challenge as the different signals overlap in time and frequency, making the separation process more difficult [2]. Recent researches on supervised single-channel source separation as in [3,4,5], have enhanced the (BSS) techniques by merging the sources training to generate linear and nonlinear models. These models achieve an efficient source separation. The development of deep learning techniques in recent years has a significant impact on the evolution of the performance of source separation algorithms, where deep learning techniques have been used to separate different types of audio

signals, including mixed musical signals, speech signals from noise, separating interfering and synchronous speech signals[6]. The models based on Deep Neural Networks(DNN) have improved the source separation tasks because their learning capacity allows effective modeling of the interaction between the source signal and the acoustic environment in a nonlinear manner as well as the dynamic structure of speech. Discriminative features are also important[6,14].(DNNs) are usually used to predict time-frequency mask that contributes to determining the contribution of each source in the mixed signal. The Ideal mask estimation shouldn't be hard to estimate by learning machine and should obtain good separation results[10]. Separation task carried out in the time-frequency domain(TF-domain) as recovering the Short-Time Discrete Fourier Transformation (STFT) of the source signals $X_n(t,f)$ for each time frame t and frequency f , as follow[11]:

$$X(t,f) = \sum_{n=1}^{N} x[n+tL]w[n] \exp\left(-\frac{j2\pi nf}{N}\right) \quad (1)$$

The input to the network is the magnitude spectrogram of the mixed-signal assigned to training ($x_{n,f}$), and the original signals for each source ($S_{1(n,f)}$) and($S_{2(n,f)}$)[5]. After training the output prediction of the network are ($\hat{S}_{1(n,f)}$) and ($\hat{S}_{2(n.f)}$) [12].

To reconstruct estimated time-domain frames, an inverse Discrete Fourier Transform (DFT) can be used from the estimated STFT ($\hat{S}_{(n,f)}$) of each source signal. The overlap-add operation with the synthesis window v[n] is used to reconstruct the estimate ($\hat{S}_{(n,f)}$) of the target signal[11]

$$\hat{S}_{(n,f)}[n] = \frac{1}{N}\sum_{f=1}^{N} \hat{S}_s(t,f) \exp\left(\frac{j2\pi nf}{N}\right) \quad (2)$$

$$\hat{S}_{(s)}[n] = \sum_{t=1}^{T} v(n-tL)\, \hat{S}_{(s,t)}(n-tL) \quad (3)$$

2. Methodology of the Problem

The process of separating the audio source signals from single-channel mixed signal requires an estimation of (S) sources from the mixed-signal, as in equation (4).

$$x(t) = \sum_{i=1}^{S} y_i(t) \quad (4)$$

Where $y_i(t), i = 1 \ldots S$, is i^{th} of sources to be estimated, while $x(t)$ is the observed mixture[7]. For simplicity, we assume that the mixed signal is consisting of two different signals $s_1(t), s_2(t)$ as in Equation (5)

$$x(t) = s_1(t) + s_2(t) \quad (5)$$

This problem can be solved in the (STFT) Domain. Let $X(n,f)$ be the corresponding (STFT) of the mixed-signal $x(t)$, where t denotes the time domain, n represents the frames index and f is the frequency-index of the STFT domain of the signal. This problem can be formulated as follows:

$$X(n,f) = S_1(n,f) + S_2(n,f) \quad (6)$$

Where $S_1(n,f)$ and $S_2(n,f)$ are the unknown (STFTs) of the sources in the mixed signal. Given $X(n,f)$ the aim of monaural source separation is to recover one or more desired signals from the mixed signal[8]. The typical setup assumed that only (STFT) magnitude spectra is available and differences between the phase angles of the (STFT) of the sources are ignored during the separation task. This is used only when reconstruct the time domain waveforms of the sources. [9]. The magnitude spectrogram of the measured audio signal can be written as the sum of source signals magnitude spectrograms as follows:

$$|X_n| \approx |S_1(n,f)| + |S_2(n,f)| \quad (7)$$

We use the matrix form to represent the magnitude spectrograms where n and f denote the spectral frame and frequency index respectively, as follows:

$$X(n,f) \approx S_1(n,f) + S_2(n,f) \quad (8)$$

Where $S_1(n,f)$ and $S_2(n,f)$ are the unknown magnitude spectrograms of the sources that need to be estimated[8]. The magnitude spectrogram of the mixture signal $|X(n,f)|$, together with spectral features are fed into (DNN) to predict time-frequency mask for each speaker. The masks are multiplied by the mixture using (element-wise multiplication operation) to estimate the magnitude STFT of the desired speaker. The separated waveforms of the estimated speaker are resynthesized using inverse(STFT), the estimated magnitude of the speaker, and noisy phase information.[10]

3. Bi-directional Long Short Term Memory (BLSTM)

The (BLSTM) combines long short-term memory (LSTM) and bi-directional iterative recurrent neural network (BI-RNN**).** The recurrent neural network (RNN) is a special development of artificial neural networks to process continuous data. Due to the problem of gradient vanishing or explosion, the (LSTM) was created, which consists of three gates (input - forget - output). Both (RNN) and (LSTM) can obtain information from the previous context only. To solve this problem(BLSTM) was used [10]. The (BLSTM) consists of two hidden recurrent layers, receive the input string separately in two opposite directions, one in the forward direction, and the other in the backward direction. Both layers are connected to the same output layer. Thus enabling access to long contexts in two different directions [12]. In a single cell (LSTM), the hidden serial vector is calculated by calculating the output of each gate as in the following equations:

$$f_t = \sigma\left(W_f x_t + R_f h_{t-1} + b_f\right) \quad (9)$$
$$i_t = \sigma(W_i x_t + R_i h_{t-1} + b_i) \quad (10)$$
$$o_t = \sigma(W_o x_t + R_o h_{t-1} + b_o) \quad (11)$$
$$j_t = tanh\left(W_j h_t + R_j h_{t-1} + b_j\right) \quad (12)$$
$$c_t = c_{t-1} \odot f_t + j_t \odot i_t \quad (13)$$
$$h_t = \tanh(c_t) \odot o_t \quad (14)$$

Where x_t is cell's input, c_t and h_t the state and output respectively, at time t. f_t, i_t and o_t are forget gate, input gate and output gate, respectively. W, R denote the trainable weight matrices, b the bias vectors and σ the activation function of the hidden layer. In (BLSTM) the equation (14) cannot be used directly, instead, the forward hidden sequence h1 and backward hidden sequence h2 is computed as shown in equation(15) and (16) respectively[13].

$$\overrightarrow{h_1} = f(W_{x\vec{h}} x_t + W_{\vec{h}\vec{h}} \vec{h}_{t+1} + b_{\vec{h}} \quad (15)$$

$$\overleftarrow{h_2} = f(W_{x\overleftarrow{h}} x_t + W_{\overleftarrow{h}\overleftarrow{h}} \overleftarrow{h}_{t+1} + b_{\overleftarrow{h}} \quad (16)$$

4. Mask Estimation Using Deep Neural Network(DNN)

Deep neural networks are usually used to predict a mask. This mask is used to determine the contribution of each source in the training mixed signal. The input to the network is the magnitude spectrogram of the training mixed-signal (X_{tr}), the original signals for each source (S_{tr1}) and(S_{tr2})[7]. After training, the output prediction of the network are ($\hat{S}_{tr1}$) and ($\hat{S}_{tr2}$) [13]. To smooth the spectra results, two types of masks are estimated separately by the model, the first mask is the ideal ratio mask (IRM) which is a smooth form of an ideal binary mask (IBM),(IRM) mask represented in equation (17)

$$IRM_s = \left(\frac{S_1(t,f)^2}{S_1(t,f)^2 + S_2(t,f)^2}\right)^{\beta} \qquad (17)$$

Where $S_1(t,f)^2$ and $S_2(t,f)^2$ are the energy of each speech signal in mixed-signal, in each (TF Unit). (β) is the square root value used as a tunable parameter, which is usually set to (0.5). (IRM) the mask used to conserve the speech energy of each (TF unit), assuming $S_1$and S_2 are uncorrelated[14]. The second mask is the optimal ratio mask (ORM) which can be derived by minimizing mean square error(MSE) between the clean speech signal and the target speech signal that has been estimated and can be defined by equation (18).

$$M(t,f) = \frac{|S_1(t,f)^2 + R(S_1(t,f)S_2{}^*(t,f))}{|S_1(t,f)|^2 + |S_2(t,f)|^2 + 2R(S_1(t,f)S_2{}^*(t,f))} \qquad (18)$$

Where S_1 and S_2represent the spectrum of the two speech signals in the mixed-signal at frame (t) and frequency(f). The symbol (*) indicates the conjugate operation, while R (°) represents the real component of the spectrum. The ORM differs from the IRM in the presence of the coherent part by $R(S(t,f)N^*(t,f))$, whose value is equal to zero in the IRM. The (ORM) achieves high efficiency in the separation process in the case of a high correlation between the speech signal and the noise signal. The mask ORM values range from (-∞, + ∞), which makes the estimation process more difficult. So the values of the ORM mask are determined using the hyperbolic tangent function as in equation (19).

$$ORM(t,f) = K\frac{1 - e^{-cy(t,f)}}{1 + e^{-cy(t,f)}} \qquad (19)$$

Where c=0.1 is the steepness, while K is equal to 10, it restricts the values of the ORM between (-10, + 10). Equation (18) is the basic equation of the ORM mask[14].

5. Network architecture

The (DRNN_BLSTM) architecture based on monaural speech separation was used in this paper. To estimate the mask that can determine the contribution of each source in the mixed signal. We adopt the magnitude spectrogram of the mixed-signal, using (STFT) with Hann window the size is set to (512)), and the reference masks of the clean sources (male-female). The network trained to predict the mask closest to the reference masks by minimizing the mean squared error between the predicted and the reference mask, the predicted mask is then used for separation. The (DRNN-BLISTM) model consists of two sub-networks, the first network is used to estimate masks for the male signal, while the other is used to estimate masks for the female signal. Each sub-network consists of three hidden layers (BLSTM) (128cell),followed by (dense layer) (64cell),and

(BLSTM) layer with (512cell). The activation function is used to train the model type (Tanh). The architecture of the proposed model is shown in figure (1).

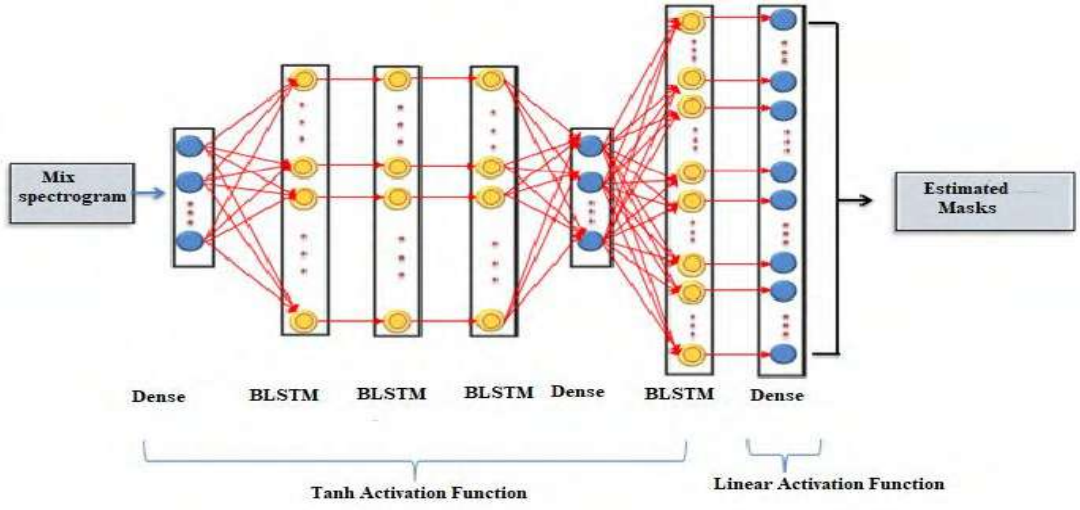

Figure (1) DRNN-BLSTM Model

6. Dataset and Results

The dataset used to train the network consists of (500) preprocessed mixed-signal consists of two different signals (female-male) with (3) seconds length and frequency (8192Hz). These audio files are collected from the internet and combined to form the mixed signals. The trained model was tested on (10) mixed signals for each mask and the results of the separation process differ according to the used mask. So the efficiency of the network performance was measured using three types of metrics: signal to distortion ratio (SDR), the signal to interference ratio (SIR) addition to signal to artifact ratio (SAR) in the signal generated by the separation process. Figure (2) shows the combined signal and the source signal, as well as the separated signal using the (IRM) mask, and Figure (2) shows the separation process for the same signal using the (ORM) mask. The performance of the separation model is evaluated based on SDR, SIR and SAR calculated using the BSS evaluation toolbox, Table(1), show the results of these three metrics when use (IRM) and (ORM) in separation task. The separating results show that the signal separation process using the (ORM) mask achieved (SDR) slightly higher (0.183.db) than it is when using the (IRM). As well as for (SIR) by (0.198 .db) is higher when using the (IRM). While (SAR) in both (IRM) and (ORM), its percentage is high, but the difference between the two masks is (0.13 .db). The efficiency of separation using (ORM) is high in the case of a high correlation between the combined signals, and the loss function represented by the learning curve of the neural network using the root mean square. Propagation (RMSprop) optimizer reduces the value of the error function to reach the best value in which the error function is lower. As in Figure (3), which shows the loss function when training the network to predict each of the filters (IRM) and (ORM) using the hyperbolic tangent function as activation function with a range of [1, -1]. We achieved the best results for both masks

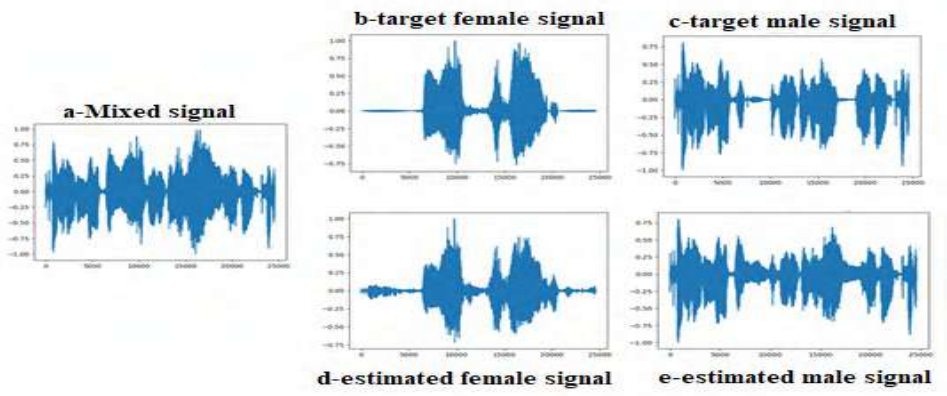

Figure (2) the original source signal and the estimated signal Using IRM Mask

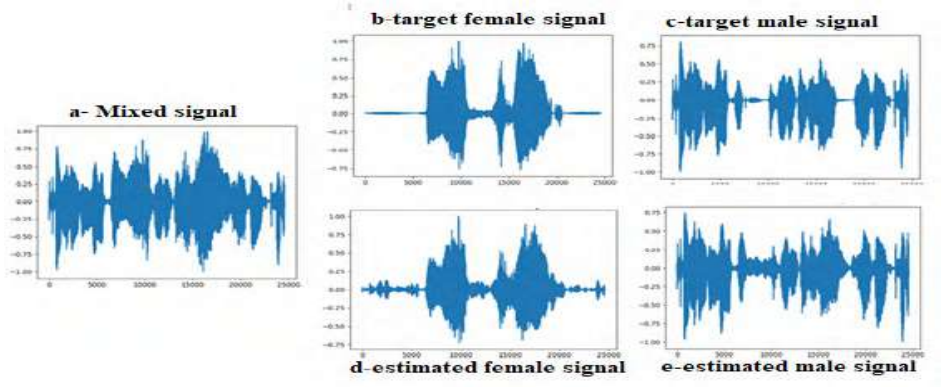

Figure (3) the original source signal and the estimated signal Using ORM Mask

Table(1) performance comparison of two masks measures

Masks	SDR	SIR	SAR
(IRM)	6.164	7.189	14.020
(ORM)	6.347	7.387	14.150

.

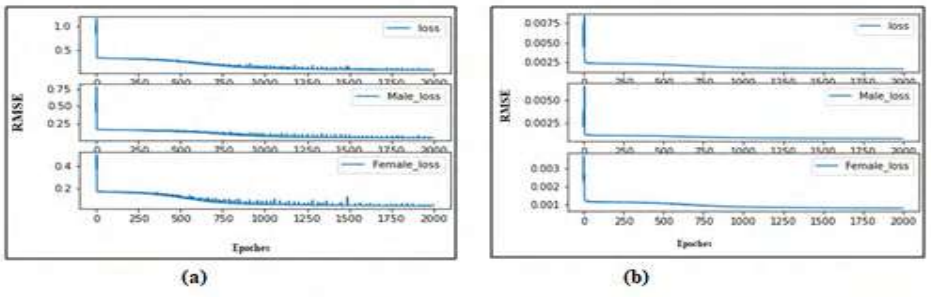

Figure (4) loss function (a) (IRM) (b) (ORM) using (Tanh)

7. Conclusions

The use of Supervised (DNN) in monaural source separation has effectively contributed to achieving separation results, especially in the case of separating large data such as audio signals. As the network extracts the characteristics from the data automatically the (TF masks) showed improvement in separation results better than the use of direct mapping, where the resulted mask was directly used to perform the separation. The (IRM) mask depend on the information of the magnitude spectrogram for both mix and source signal, the results of separation using (IRM) mask has improved good performance and the estimated signal improves high quality and intelligibility, but less than the efficiency when using (ORM) mask due to the correlation between the source signal and signals in the mixed signal.

References

[1] Rolet , Antoine ; Seguy, Vivien ; Blondel , Mathieu; awada , Hiroshi; 2018 ; **"Blind Source Separation with Optimal Transport Non-negative Matrix Factorization"**; **(**EURASIP) Journal on Advances in Signal Processing; No.53; https://doi.org/10.1186/s13634-018-0576-2.

[2] Bhargava , S.; 2017; **" Vocal source separation using spectrograms and spikes, applied to speech and birdsong"**, M.sc. thesis ; ETH Zurich, india .https://doi.org/10.3929/ethz-b-000175085.

[3] E. M. Grais, M. U. Sen, and H. Erdogan,2014, "Deep neural networks for single channel source separation," IEEE International Conference on Acoustics, Speech and Signal Processing (ICASSP), pp. 3734–3738.

[4] Gao, W. L. Woo, and S. S. Dlay, 2011 , "Adaptive sparsity nonnegative matrix factorization for single-channel source separation" , IEEE Journal of Selected Topics in Signal Processing, vol. 5, no. 5, pp. 989–1001.

[5] P. S. Huang, M. Kim, M. Hasegawa-Johnson, and P. Smaragdis, 2015 ,"Joint optimization of masks and deep recurrent neural networks for monaural source separation", IEEE/ACM Transactions on Audio, Speech, and Language Processing, vol. 23, no. 12, pp. 2136– 2147.

[6] E. M. Grais ; M. D. Plumbley ; 2017; **" Single Channel Audio Source Separation Using Convolutional Denoising Autoencoders"**; 5th IEEE Global Conference On Signal And Information Processing (Globalsip); Pp.1265-1269; arXiv:1703.08019V2 .

[7] Gang , Arpita ; Biyani , Pravesh; Soni, Akshay ; 2018 ; **" Towards Automated Single Channel Source Separation using Neural Networks"** ; Interspeech; pp. 3494-3498 ; arXiv:1806.08086

[8] E. M. Grais , ; Roma , Gerard ; J.R. Simpson , Andrew ; Plumbley, D. Mark; 2017;**" Single Channel Audio Source Separation using Deep Neural Network Ensembles"**; 140th Audio Engineering Society Convention; No. 9494; pp: 236–246.

[9] Yulitaa , N. Intan; Fananya , I. Mohamad ; Arymuthya , M. Aniati; 2017; **"Bi-directional Long Short-Term Memory using Quantized data of Deep Belief Networks for Sleep Stage Classification"**; 2nd International Conference on Computer Science and Computational Intelligence; (ICCSCI) ; Procedia Computer Science Vol. 116 ; pp: 530–538.

[10] Brueckner , Raymond ; Schuller, Bj¨Orn ; 2014; **" Social Signal Classification Using Deep BLSTM Recurrent Neural Networks"**; Proceedings 39th IEEE International Conference on Acoustics, Speech, and Signal Processing, ICASSP; pp.4856-4859; Florence; Italy .

[11] Kolbæk, Morten; Yu , Dong; Tan,Zheng-Hua; Jensen,Jesper; 2017," **Multi-Talker speech Separation With Utterance-Level Permutation Invariant Training of Deep Recurrent Neural Networks"** , IEEE/ACM Transactions on Audio, Speech, and Language Processing, vol. 25, no. 10, pp. 1901-1913.

[12] Ray, Anupama ; Rajeswar, Sai; Chaudhury, Santanu; 2015; **"Text Recognition using Deep BLSTM Networks"** ; Eighth International Conference on Advance in Pattern Recognition (ICAPR) ; pp. 1- 6 ; DOI: 10.1109/ICAPR.2015.7050699.

[13] Fan , Zhe-Cheng ; Lai , Yen-Lin ; Jang ,R. Jyh-Shing ; 2017 ; **"SVSGAN: Singing Voice Separation Via Generative Adversarial Network"**; IEEE International Conference on Acoustics ; Speech and Signal Processing (ICASSP); **DOI:** 10.1109/ICASSP.2018.8462091.

[14] Xia , Shasha ; Li , Hao; Zhang, Xueliang; 2017; **"Using Optimal Ratio Mask as Training Target for Supervised Speech Separation"**; IEEE; Asia-Pacific Signal and Information Processing Association Annual Summit and Conference (APSIPA ASC); arXiv:1709.00917.

A Parallel Adaptive Genetic Algorithm for Job Shop Scheduling Problem

A Parallel Adaptive Genetic Algorithm for Job Shop Scheduling Problem

Wathiq N. Abdullah[1] and Salwa A. Alagha[2]

[1] Department of Computer Science, College of Education for Pure Science/Ibn-Al Haitham/University of Baghdad, Iraq
[2] Department of Electrical Engineering, University of Technology, Iraq

E-mail: wathiq.n.aa@ihcoedu.uobaghdad.edu.iq

Abstract. In order to enhance the production efficiency, scheduling problem of job-shop has used that thought of complex problem with complicated constraints and structure . This problem is characterized as NP-hard. In most cases, the excessive complexity of the problem makes it difficult to discover the best solution within affordable time. Hence, searching for estimated solutions in polynomial time rather than precise solutions at excessive cost is favored for challenging situations of the problem. In this paper, a parallel genetic algorithm with proposed adaptive genetic operators and migration operation is applied for job-shop scheduling problem . Through tests on numerous different experimental cases, the adaptive operator of genetic algorithm and the parallelism strategy are considerably improving the results effectively while decreasing the computation time. Also, the migration operation gives a greater effect on the performance of the algorithms.

Keywords: Job-Shop, Scheduling, Genetic Algorithm, Adaptive Genetic Operators, Migration Operation, Parallel Algorithm

1. Introduction

Job-Shop Scheduling Problem is a conventional combinational optimization problem. It is common in present day production industries in which numerous processing machines need to be allocated fairly and operation orders of the jobs order need to be sorted well to enhance manufacturing efficiency. Its most important characteristic includes numerous machines with same function but distinct operation time [1].Efficient methods of solving scheduling problems can have major effects on profitability product quality. The big matter is the minimization of the whole elapsed time between the start of the first operation and the completion of the last operation (the makespan). The shortest makespan is the simplest and most extensively used criterion among any other measures of scheduling quality. In general, the difficulty of the Job-Shop Scheduling problem makes it very difficult for conventional search-based approaches to find near-optima in reasonable time. This has led to recent interest to adopt genetic algorithms to deal with these problems [2].Genetic algorithm (GA) is a flexible in dealing with complicated problems and normal attribute of parallel processing, that randomly and successfully pattern and search at big state space, and rapidly converge to the optimal or near-optimal solution, so it gets extensively interest in the discipline of scheduling. Experimental tests showed GAs' scheduling performances in a several different criterions are better than heuristic and stochastic hill-climbing approaches. All these illustrate that GAs are so appropriate to solve scheduling problem [3].The remainder of this paper is organized as follows: the job-shop scheduling problem, the design of the

system of solving job-shop scheduling problem using parallel genetic algorithm, and finally, the results of the system and some concluding remarks are given.

2. Job-Shop Scheduling Problem Description

Scheduling for the adaptable activity shop is essential in the two fields of creation administration and combinatorial improvement. Be that as it may, it is very hard to accomplish an ideal answer to this issue in medium and genuine size issue with conventional improvement approaches inferable from the high computational unpredictability [4].

2.1. Problem Description

The JSSP is a scheduling problem that assumes M various machines and N various jobs. Each job consists of Q operations and each operation needs a different machine. The jobs' operations are handled in a fixed processing order which specifies the precedence restrictions. The job's operations are completely ordered so that no job's operation can begin earlier than the completion of its predecessor [5]. The operation sequence of every job is predetermined whereas each operation will be processed on any a machine from a group of candidate machines [6]. To achieve optimal performance, the system should satisfy the scheduling goals, which include: selection of the most appropriate machine for every process, and approve the optimal sequence of processing and time of every work process on every machine [3].

2.2. Problem Formulation

The JSSP is defined by:

- J = {J1 , J2, … , Jn } the set of n independent jobs,
- O = {(O11 , O12 , ...), (O21 ,O22 , ...) ... (On1 On2, ...)} the set of operations, where Oji is operation i of job j.
- M = {m1, m2 ,... mk } a set of machines.

The goal is to find a schedule of operations that minimizes the completion times of all jobs (MakeSpan of the schedule):

$$\text{Makespan} = \text{Min}(\text{Max}(T1, T2, \ldots, Tn)) \quad \ldots\ldots\ldots (1)$$

where, Tj is the completion time of job J.

2.3. Parallel Genetic Algorithm for JSSP

The following sections illustrate the application of parallel GA for solving JSSP:

2.4. Parallel GA

GA is a powerful approach used in many various areas to search for a near-optimal solution when searching for the optimal solution is too expensive[7]. Though, parallelization is also an appropriate way to enhance the process time and the efficiency in the exploration of the search space. Certainly, GAs are 'naturally parallelizable', for example, their population-based features enable us to assess in a parallel manner the fitness of each individual [7]. To exploit parallelism in GAs, various ways exist; these include: master–slave models, fine-grained models, island models, and hybrid models. Island models are the foremost known to consider on parallel GAs. Populations on islands are free to converge toward totally different sub-optima with a quicker improvement of the average fitness and a migration operator will facilitate combine good features that emerge from different local islands [8]. The advantages of the parallel design are as follows:

• Since more than GA work together, GA get new search points in exploring space via various techniques, this strategy increases the searching process range and decreases the probability of premature convergence.
• Because of the independent evolution, individuals from heterogeneous islands gain different characters from a range of different solutions. Thus, the migration performance is improved [9].
In this paper, three Genetic Algorithms are used in parallel mode. Each GA consists of two main keys: choosing an encoding representation of the problem; and defining the genetic operators [7].

2.5. Encoding and Fitness Evaluation for JSSP

• Encoding Representation of a schedule
As a schedule consists of a sequence of total operations *OP*, it can be represented as follows:

$$OP = \{op\ ij \mid i = 1, 2, \ldots, N \text{ and } j = 1, 2, \ldots, M \quad \ldots (2)$$

Where: *op* is the operation, *i* is the job number, *j* indicates the operation number of job *i*, *N* is the set of jobs, and *M* is the set of available machines. The *ij* indices of the operation *op* are encoded as a sequence number (*index*) of a chromosome's gene which can be represented by two fields: the first field consists of the machine's number and the second field of a gene is the completion time of the operation [2].
The chromosome length is equal to the product of the number of jobs and the total number of machines in a given problem [10].

• Evaluation of Fitness Function
The fitness value can be evaluated by summing the total completion time of the operations on each machine (TCT). The total completion time with maximum value is the chromosome's fitness value [2], as follows:

$$\text{Fitness Value} = \text{Maximum of (TCTx)} = \text{Max (TCTx)} \quad \ldots (3)$$

Where:
x : is the machine number, $1 \leq x \leq M$,
M: is the no. of machines.

2.6. The Operators and the Proposed Adaptive Operators of GA
The three genetic algorithms adopted in this paper use several types of GA operators. Some of them are the same as original GA operators and the other are improved and adapted to give best results.

• Original GA Operators
For selection operator, the system uses tournament selection technique with tournament of two and three. For crossover operator, one-point crossover and two-point crossover operator are used. For mutation operator, random selection of chromosome and randomly replace a position in it with random value [11].

• The Proposed Adaptive Operators of GA
i. Adaptive Selection Operator:

Because of the size of the population of every generation is constant ,each time one individual chosen, there is an excessive possibility that individuals with high fitness are selected over

and over whereas individuals with low fitness aren't selected at all. However, when the generation number increased, the population will contain many good but identical individuals.

The proposed selection operator is as follows: in each tournament selection, the individual having the greater fitness is added to the new population and removed from the parent population. Such that, every individual can be chosen solely as soon as such that the population's diversity is ensured.

ii. Adaptive Crossover Operator

In this paper, a special crossover operator is adopted which randomly selects two individuals, and then checks whether they have common points (i.e., common machine number within a schedule). If not, then the crossover will not be performed and the two parents from the population are copied to the population of the next generation. If they have only one common point, then that point is the crossover point. If there are more than one common points, then the crossover point is randomly selected.

iii. Adaptive Mutation Operator

The mutation operator is improved as follows: after a random selection of an operation within a schedule, this operation is reassigned to a machine away from the original machine in two locations in circular style. That is, if the machine number is x, then reassign to machine number x+2, and if the original machine is the last machine then reassign to machine 2.

2.7. The Migration Operation

The migration operation is the process of swapping individuals amongst the subpopulations of the GA. The operation of migration improves the population's genes and consequently will increase the diversity and speed up the convergence of the algorithm.

The essential migration's parameters are the interval of migration, rate of migration, the technique for choosing migrating individuals, the technique for changing an individual by the new one in the receiving subpopulation, and the type of topology.

The migration topology adopted in this paper is based on the unidirectional ring topology by which the communications between islands are done on a unidirectional ring, and hence an island can send migrants to its next neighbors and receive migrants only from its previous neighbors.

Each sub-population sends and receives the best individual from the neighbor sub-population, and exchanges the worst one in its pool by the received individual. The rate of migration was determined as a fixed number of the best individuals in the population in each interval. The interval in terms of generations in GA [12].

3. The Implementation of The System

The system uses three genetic algorithms (GA1, GA2, and AGA which stands for Adaptive Genetic Algorithm) work in parallel mode. It starts by dividing the initial population into three parts. GA1 is applied on the first part, GA2 is applied on the second part, and AGA is applied on the third part.

The types of genetic operators used in each genetic algorithm are shown in Table (1).

Table (1): GA Operators Used in GAs

GA Operators	GA1	GA2	AGA
Selection	Tournament (Size= 2)	Tournament (Size= 3)	Adaptive selection
Crossover	One-point	Two-point	Adaptive Crossover
Mutation	Classical (random change)	Classical (random change)	Adaptive Mutation

The detailed steps of the system are shown in Figure (1).

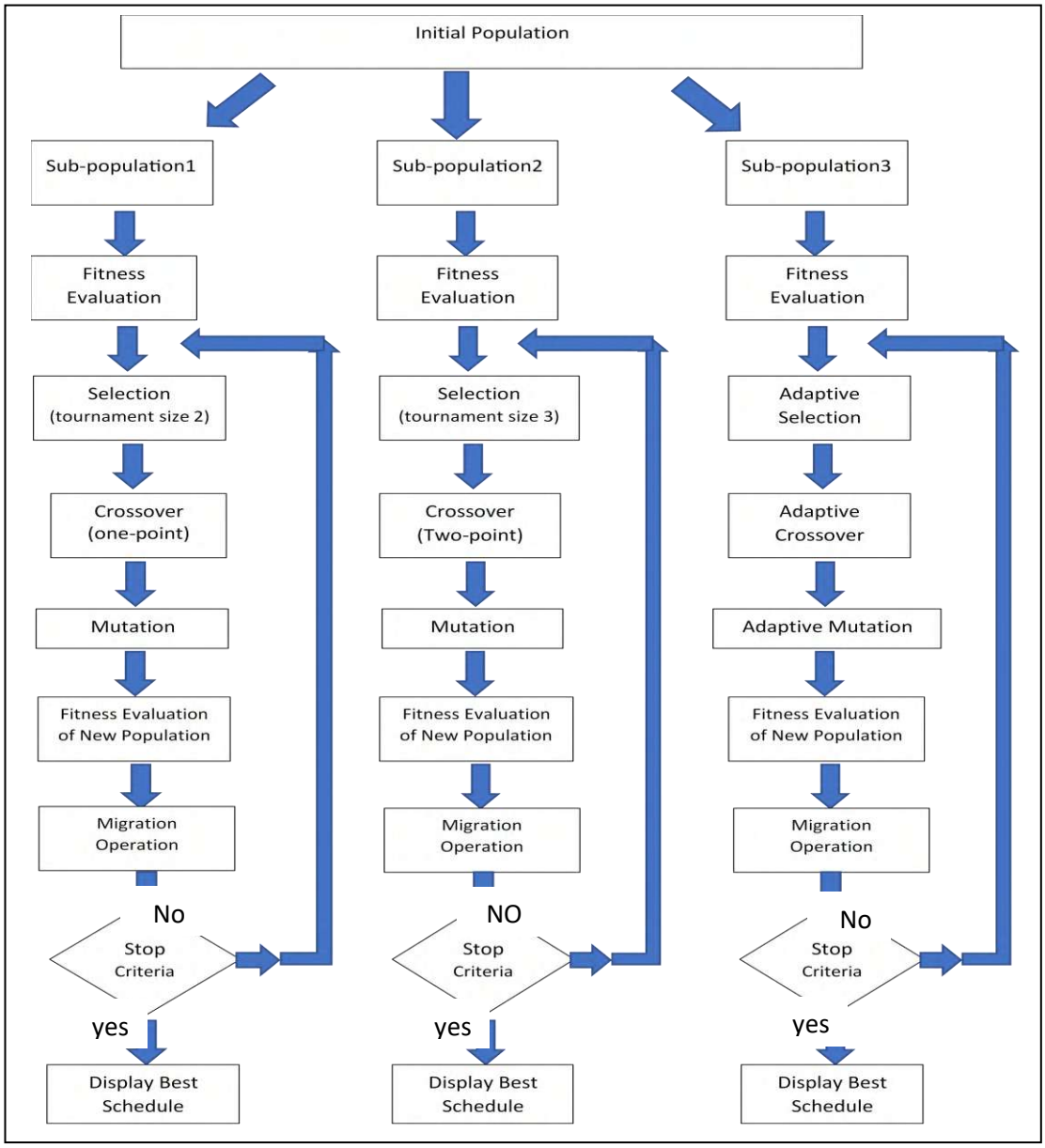

Figure (1): The Steps of The System of The Parallel GA.

4. Experimental Settings and Results

Various cases of different job-shop problem are taken. However, All the three genetic algorithms use the same case instances in order to compare the implementation results among them.

Firstly, Table (2) shows various problem instances. These instances are different in the number of machines in the system and the number of jobs.

Table (2): The Problem Instances Used by The System

Instance number	No. of Machines	No. of jobs
1	6	6
2	10	10
3	8	8
4	10	4
5	10	5

The system specifications and the parameters used with their assigned values are described in Table (3).

Table (3): The System's Parameters Settings

Parameter Name	Value
Sub-population size	50 individuals
Max No. of Generations	500
Crossover Rate (pc)	0.7
Mutation Rate (pm)	0.1
No. of Migrant Individuals	4

The adopted migration policy is done by the selection of the best individuals from the sending island and the replacement of the worst individuals in the destination island.
The result of applying each genetic algorithm on any of the problem instances is a schedule having a minimum *makespan* of a schedule. The Table (4) and Figure (2) show the makespans from GA1, GA2, and AGA.

Table (4): The resultant makespan from GA1, GA2, and AGA

Instance Number	Makespan of GA1		Makespan of GA2		Makespan of AGA	
	Without Migration	With Migration	Without Migration	With Migration	Without Migration	With Migration
1	68	54	70	50	62	48
2	196	112	185	88	86	75
3	107	89	101	84	84	61
4	240	205	232	194	190	172
5	181	167	177	155	154	128

From Table (4) and Figure (2), it is obvious that the best makespan is from the schedule resulted from AGA with migration operation, while the worst makespan resulted from GA1.

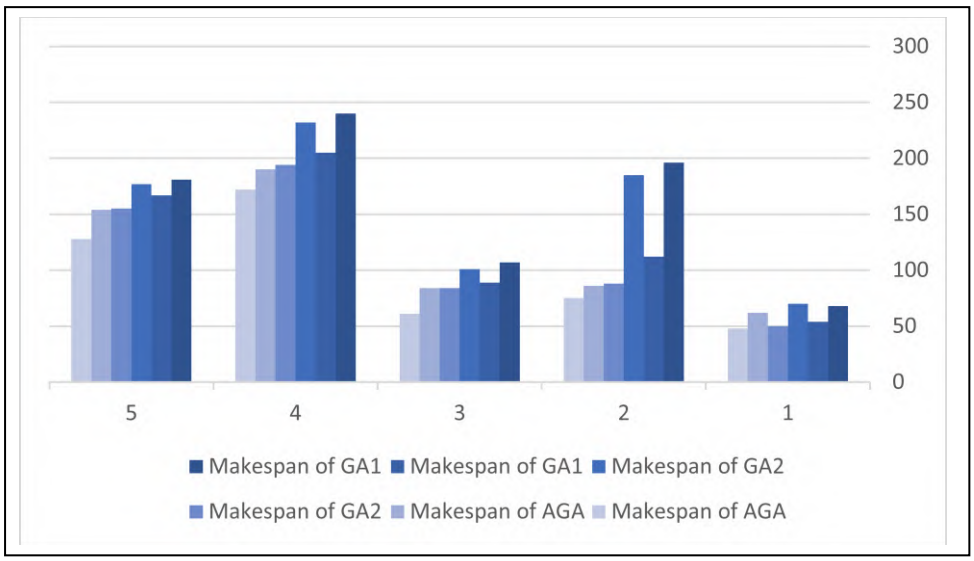

Figure (2): The makespans from GA1, GA2, and AGA.

The converged generation numbers for GA1, GA2, and AGA at which the algorithms reach the best schedule are shown in Table (5). Table (5) and Figure (3) show the converged generation number with and without applying the migration operation.

Table (5): The Converged Generation Number from GA1, GA2, and AGA

Instance Number	Gen. No. of GA1		Gen. No. of GA2		Gen. No. of AGA	
	Without Migration	With Migration	Without Migration	With Migration	Without Migration	With Migration
1	165	144	146	142	90	77
2	254	219	202	197	132	101
3	137	130	129	111	107	85
4	277	215	238	221	134	120
5	116	103	108	106	98	95

The results displayed in Table (4) and Table (5) showed that the GA2 gives better makespan and better converged generation number than the GA1. This is due to: (i) the larger tournament size of selection operator adopted in GA2 than that in GA1, (ii) the two-point crossover operator used in GA2 that provides more diversity than one-point crossover in GA1.

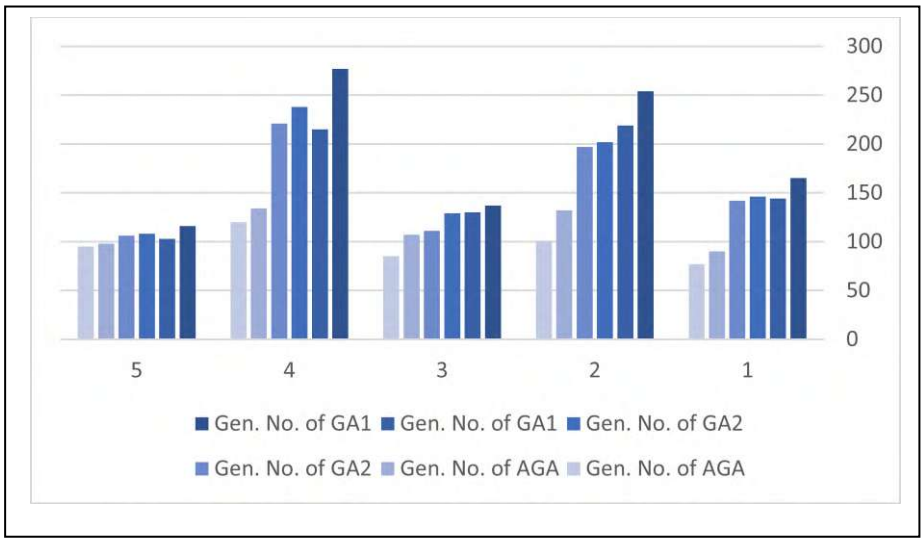

Figure (3): The Converged Generation Number from GA1, GA2, and AGA

Also, the applying of the migration operation significantly enhanced the performance (makespan and converged generation number) in GA1, GA2, and AGA.
However, Table (4) and Table (5) show that the AGA gives a better performance than GA1 and GA2 in all problems' instances.

5. Conclusions

In this paper, we present a system of implementation of a parallel genetic algorithm to find the best schedule of a job-shop scheduling problem. The system proposes adaptations for the three GA operators. It demonstrates that by dividing the initial population and uses adaptive GA operators in parallel mode give best schedule, and less computation time.
The system uses three genetic algorithms each with different type of genetic operators. The use of adaptive selection operator, adaptive crossover operator, and adaptive mutation operator in the third algorithm has significantly improves the system performance in terms of the resulted schedule and time it takes to find the best solution. The application of migration operation among the three genetic algorithms greatly enhanced the system performance.

References:

[1] Zhang, M., et al., *A competitive and cooperative Migrating Birds Optimization algorithm for vary-sized batch splitting scheduling problem of flexible Job-Shop with setup time.* Simulation Modelling Practice and Theory, 2020. **100**: p. 102065.

[2] Abdullah, W.N., *Solving Job-Shop Scheduling Problem Using Genetic Algorithm Approach.* 2011(70): p. 241-253.

[3] Hu Li, Z.L., Ruiduan Yang, Huawei Lu, Youchao Zhang, *A Flexible Job-shop Scheduling for Small Batch Customizing.* 2016: p. 2179-2201.

[4] *Solving Flexible Job Shop Scheduling Problem Using Meerkat Clan Algorithm.* Iraqi Journal of Science, 2018. **59**(2A).

[5] Abdullah, W.N., *Solving Job-Shop Scheduling Problem Using a Developed Particle Swarm Optimization Algorithm.* International Journal of Science and Research (IJSR), 2018. **7**(1): p. 1845-1848.

[6] Huizhi Ren, H.X., Shenshen Sun, *Immune Genetic Algorithm for Multi-objective Flexible Job-shop Scheduling*
Problem. 28th Chinese Control and Decision Conference (CCDC), 2020: p. 2167-2171.

[7] Salza, P. and F. Ferrucci, *Speed up genetic algorithms in the cloud using software containers.* Future Generation Computer Systems, 2019. **92**: p. 276-289.

[8] Luo, J., et al., *GPU based parallel genetic algorithm for solving an energy efficient dynamic flexible flow shop scheduling problem.* Journal of Parallel and Distributed Computing, 2019. **133**: p. 244-257.

[9] Luo, J., et al., *Solving the dynamic energy aware job shop scheduling problem with the heterogeneous parallel genetic algorithm.* Future Generation Computer Systems, 2020. **108**: p. 119-134.

[10] Kaouther Ben Ali, A.J.T., Said Gattoufi, *Stochastic Cases of the Dynamic Job Shop Problem Based on the Genetic Algorithm to minimize Cmax.* Proceedings of 2017 4th International Conference onControl, Decision and Information Technologies (CoDIT'17), 2017: p. 0760-0765.

[11] Goldberg, D.E., *Genetic Algorithms in Search, Optimization and Machine Learning*1989: Addison-Wesley Longman Publishing Co., Inc.

[12] Abdelhafez, A., E. Alba, and G. Luque, *Performance analysis of synchronous and asynchronous distributed genetic algorithms on multiprocessors.* Swarm and Evolutionary Computation, 2019. **49**: p. 147-157.

Human Activity Diagnosis System Based on the Internet of Things

Human Activity Diagnosis System Based on the Internet of Things

Mohammed Khammas Jabar and Ali Kadhum M. Al-Qurabat

Department of Computer Science, College of Science for Women, University of Babylon, Babylon, Iraq.

E-mail: alik.m.alqurabat@uobabylon.edu.iq

Abstract. The Cognitive Internet of Things (CIoT) is the next step in enhancing the accuracy and reliability of the Internet of Things (IoT) technology used for Cognitive Computing, which plays a main role in health and disease diagnosis. The study was suggested a diagnosis method to sound sensitivity by developing a framework with IoT and cloud based on a facial expression recognition system. It was achieved through the creation of a cognitive IoT hardware-based environment and the elements of the programs that are implemented to test the behaviour of people suffering from sound sensitivity, this operation is done by using a camera and image processing and it used Convolutional Neural Network (CNN) as a facial recognition software to track human facial emotions through live video. The sentiment values were analysed that they were collected and stored in a cloud using Transmission Control Protocol (TCP) protocol. These emotions were categorized as abnormal or normal. Normal states represented by happy or natural feelings that give the impression that the environment is suitable for people's senses and that they do not suffer from discomfort towards this environment, therefore; the system operates on a mechanism to increase the volume in this environment by using an Arduino microcontroller. Although the device operates automatically in the event of hypersensitivity detection, it reduces this severity. The obtained results showed the efficiency of the proposed system in recognizing facial emotions with 80% accuracy.

1. Introduction

The Significant advancements in telecommunications networks and the advent of the Internet of Things (IoT) paradigm have resulted in remarkable improvements in the everyday usage of computer resources and applications. The IoT is an evolving model of communication in which computers, cameras and sensors act as objects or 'things' capable of sensing their environment, communicating with each other, and sharing knowledge over the Internet [1, 2]. IoT key purpose is to allow us to define, signify, navigate and monitor items individually at any time and everywhere by the use of the Internet. A large number of intelligent and autonomous applications and resources will result from interconnected system networks, bringing substantial personal, technical and economic benefits [3, 4].

More recently, the Internet of Things paradigm has been used to build information ecosystems such as smart communities and diagnostic networks for human operation, with various functional fields and similar facilities in the medical industry, for example. The aim of creating such smart environments is to make human life more prosperous and convenient by resolving the problems of living conditions, energy use and industrial needs [5]. This purpose is clear, and is reflected in the significant increase in

applications for open and IoT-based services across various networks. IoT technology can be used in order to create a human behaviour diagnostic system. In order to provide the medical personnel with information, good medical diagnosis and control, proper care and comfort. The use of IoT technology puts together doctors and patients in new health care applications for real-time tracking and hospital management. One of the core technologies of IoT improvements in the healthcare monitoring system is the emotions recognition system based on the Internet of Things [6].

In this paper, a Human Activity Diagnosis System is proposed. The system consists of three essential entities: first, physical elements, smart sensors and actuators; secondly, a communication network (wired/wireless) typically interconnecting the physical compounds; third, intelligent processing of information, for the management and control of the human activity diagnostic system, using the Artificial Intelligence algorithms (e.g. CNN).

The contributions made by this paper are as follows:

- Cognitive IoT for smart diagnosis systems: this paper provides prototyping of smart diagnosis systems (hardware and software) for measuring sound sensitivity.
- Designing a face and emotion recognition system: the paper using Convolution neural network (CNN) as a software to detect faces and emotions signs.
- TCP protocol-based sound management system: the paper includes a control system that uses Arduino to publish and subscribe to cloud server features using the TCP protocol.

2. Related Works

The Human Activity Diagnosis System Based on the Internet of Things has become a highly developed research in the field of healthy intelligence, various approaches were proposed for designing such systems.

Söhsten and Murilo, in 2013, proposed performance evaluations on a neighboring Emgu CV multi-facial detection system and versions communicating with Windows Azure, calculating in real time the amount of facial information processed and the classification element. The greater the number of faces processed is better in terms of reliability [5].

Diego Castro et al., in 2017, presented a new method for Human Activity Recognition (HAR) based on the Internet of Things (IoT) by remotely tracking vital signs. To assess the activities conducted within four pre-established categories (lie, sit, walk, and jog), they use machine learning algorithms. Meanwhile, using a remote monitoring component with remote visualization and programmable alarms, it is able to provide input during and after the operation is completed [6].

Martin Magdin, et al., in 2019, presented the study of reactions recorded by the face analysis method. The experiment was performed on a group of 50 students from universities. 100 random images were presented to each student and the student's response to the image was registered. The reactions reported were subsequently compared to the predicted image response. Several imperfections in the face recognition method have been illustrated by the findings of the experiment. The machine has trouble classifying gestures and is unable to identify and understand inner emotions that an individual may experience when the picture is seen. Only feelings conveyed externally on a face through hormonal changes in some areas of the face can be identified through facial recognition systems [7].

Stefan Oniga and József Sütő in 2012, discussed studies using IoT technology for autonomous everyday life support for aged people or people with disabilities. The aim is to build a system that makes it possible to remain in a familiar atmosphere for as long as possible. The larger spread of assistive devices and the Internet of Things (IoT) would make this possible. In order to build a dynamic assistive device with functional capabilities and learning behavior, the authors plan to bring

together the current achievements in the area of the Internet of Things and Assistive Technology. In order to be eventually evaluated for a medical diagnosis, they used IoT technology to track the status of a patient in real-time or to get critical details [8].

Fadhil and Mandeel, in 2018, a remote tracking system for children with autism has been developed to help experts track the success of their patients and interpret the analysis of data. This method monitors the cases' reactions to different emotions such as sorrow, enthusiasm, nervousness, appetite, trepidation and relaxation, and then logs this detail [9].

3. Proposed System

In this paper, a diagnosis method to sound sensitivity by developing a framework using IoT and cloud computing for a facial expression recognition system is suggested. In the following subsections the face recognition and emotion detection algorithms are discussed in detail.

3.1. *System Parameters*

The proposed system depends on many parameters:

- **Emotion:** It is a case of mindfulness link with the nervous system. The emotions can be categorized as normal (i.e. happy) and abnormal (i.e. sad). Emotions parameter is represented by e_i, where $(i = 1,2)$.
- **Sound Intensity:** It is the power that sound waves hold per unit area in a direction vertical to that area, International System of Units defined intensity of sound - as watts per square meter $(watts/m^2)$, s_i represents the parameter of sound intensity where $(i = 1,2, \dots m)$, and s_0 and s_m denote the initial and maximal sound intensity respectively.
- **Levels of Sensitivity**: Experience many levels to find a human sensitivity to sound. The sensitivity level is placed through the symbol n_i where $(i = 1,2, \dots m)$, n_0 is the first sensitivity level and n_m is the highest sensitivity level.

3.2. *System Model*

The mechanism of the system can be specifically created based on the diagnostic process performed at multiple sensitivity levels. Figure 1 shows the diagram of the diagnostic system. The sentiment detection system can interpret the captured data that represent the video frames and produce the emotions to describe the person's reaction to the sound. Sentiment collected from the previous stage, which was processed in the patient's computer to determine if the person is in a normal state or abnormal and choose the appropriate volume level for each condition. The results are then sent to the cloud that uses Internet protocols. Objects Encapsulated in a TCP Datagram. The results uploaded in the cloud can be accessed by the other party for checking if the emotions values are normal or not.

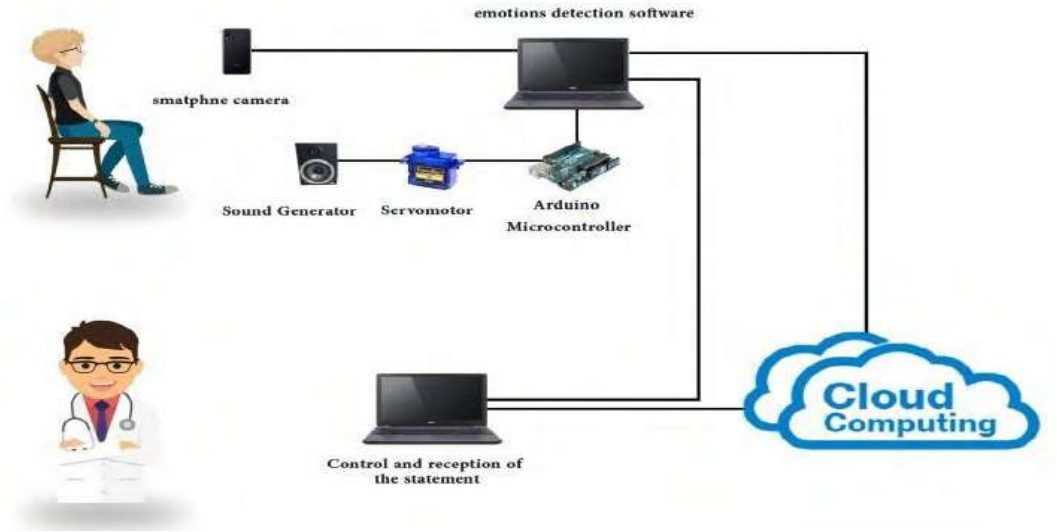

Figure 1. The diagram of proposed diagnosis system.

3.3. *System Work*

The value of sound intensity s_i, which decreases or increases depending on the equations and conditions described below, is calculated by the control system of the diagnostic system for acoustic sensitivities as follows:

1. The system of diagnosis determines the range of the levels of sensitivity ni.
2. The maximal intensity of sound s_m is set by the diagnostic system and the test begins with s_0, the initial intensity of sound.
3. The intensity of sound difference value Δs which increases/decreases at each stage can be determined from the following equation:

$$\Delta s = \frac{s_m - s_0}{n_m} \quad \text{..... (1)}$$

4. Diagnosis system regulates the ei at each level.
5. e_i normality is an indicator to raise the intensity of sound and vice versa.
    1. The intensity of sound is determined from the following equation for normal emotions:

$$s_i = s_{i-1} + \Delta s \quad \text{..... (2)}$$

    2. The intensity of sound is determined from the following equation for abnormal emotions:

$$s_i = s_{i-1} - \Delta s \quad \text{..... (3)}$$

6. When it notices abnormal feelings or when n_i equals n_m, the system stops.

The flowchart for the diagnostic sound sensitivity method displayed in Figure 2.

3.4. *Facial Emotion Detection*

In human life, emotions play a significant role. Human face represents at different times or moments how he feels or in what mood he is. Emotional factors have an enormous effect on social intelligence,

such as understanding interaction, making decisions, and helping to understand human behavioural aspects. The processing of facial emotion recognition passes through three stages [10]:

1. Facial Detection: Face position in any photo can be identified, offline video or live video.
2. Facial Recognition: Comparing various faces to define which faces belonging to the same individual. This is achieved by comparing the embedding vectors of the face.
3. Emotion Detection: Classifying the emotion as being on the forehead happy, angry, sad, neutral, surprise, disgust or fear.as shown in Figure 3.

In this paper, facial emotions recognition will be used to support the faces and emotions detection of autism people and patients with sensitivity to sound.

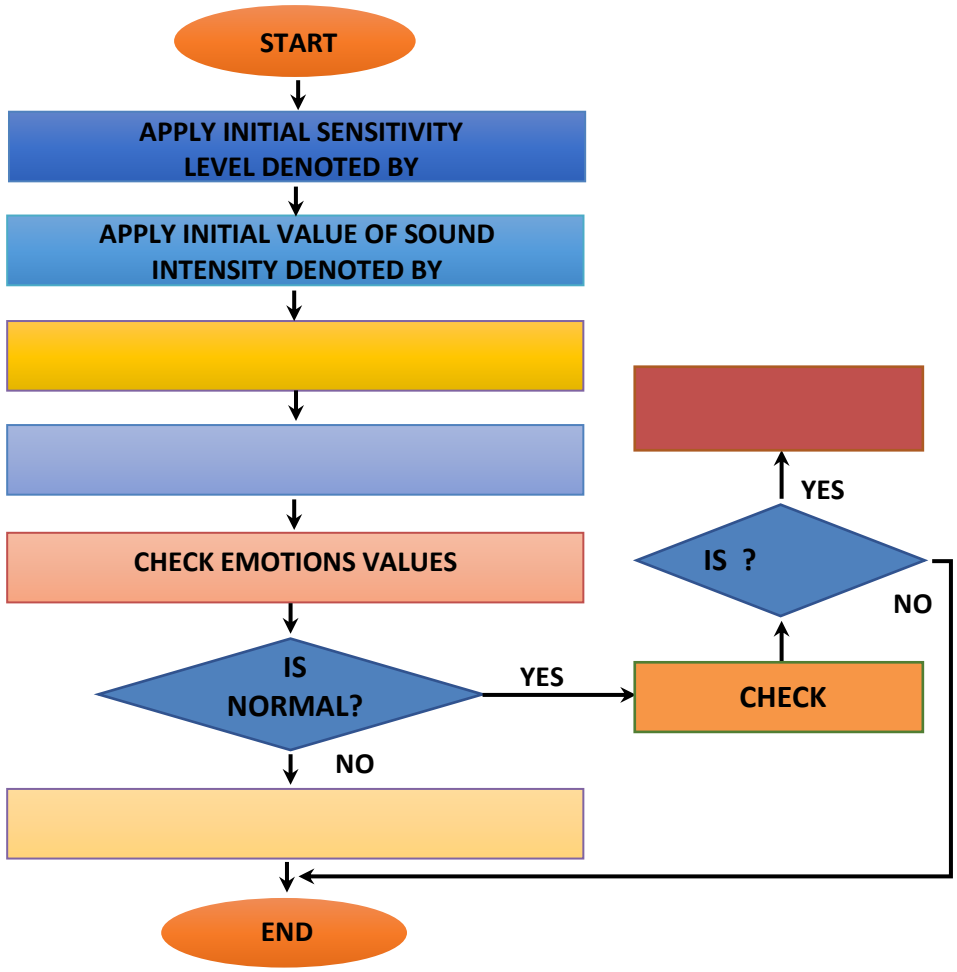

Figure 2. Sound Sensitivity Diagnostic Flowchart.

Figure 3. Example for Emotions Detection.

The mechanism used for emotion detection in this project is based on Deep learning. Convolutional Neural Networks (CNN) is one of the deep learning algorithms specialized in the images that have the best high resolution. The CNN, as well as other hidden layers, it consists of an input and output node. These layers are usually categorized into four forms: convolution, max pooling, flattening and full connection (short for fully-connected) [11] as shown in Figure 4.

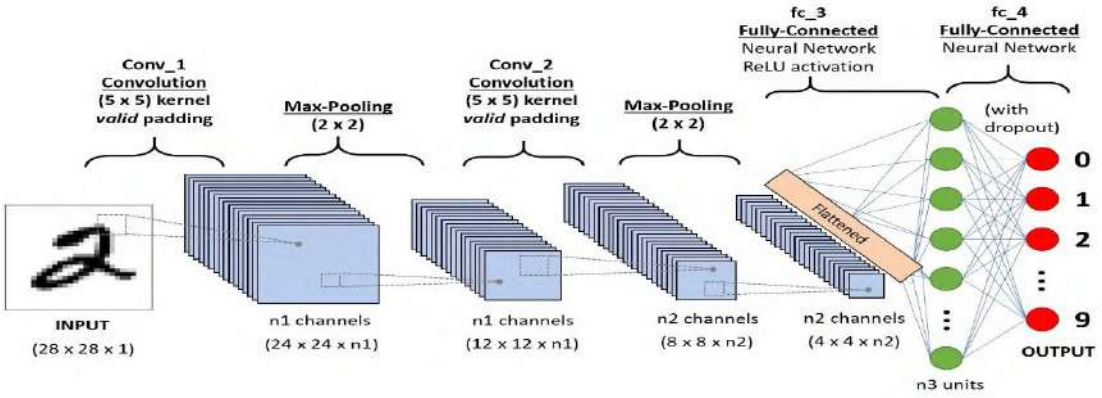

Figure 4. CNN sequence to classify handwritten digits [11].

4. Design and Implementation

The software/hardware components of the system and the detailed description of its implementation is given in this section. The components that need to build the proposed system are Arduino Uno, Arduino WiFi Shield, Servomotor, Micro USB cable, breadboard, jumper wires, Smartphone, two laptops and sound generator. Figure 5 illustrates the system components.

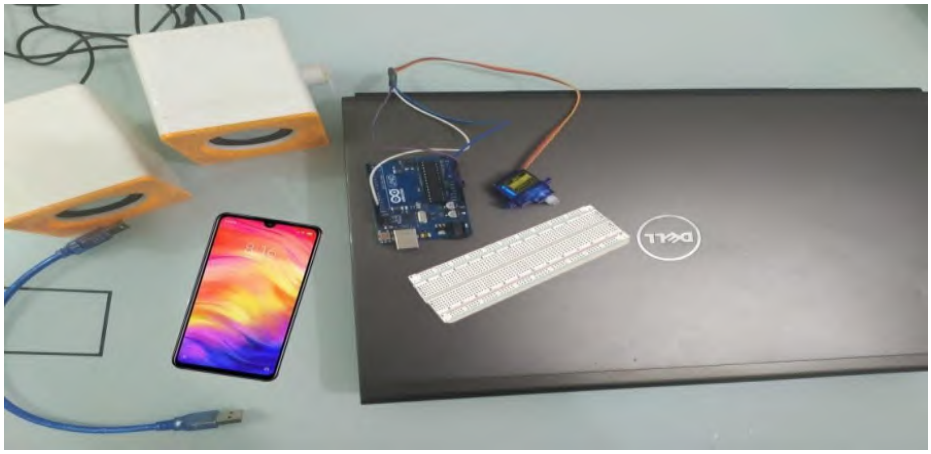

Figure 5. Components needed for Human Activity Diagnosis System.

4.1. *Live Video Processing System*

A smartphone (Redmi note 7) was utilized to recognize the patient's face during live video capturing mode for the purpose of detecting and examining his emotions. DroidCam software was used for both interfaces of emotion detection system (smartphone and laptop) that are connected via Wi-Fi using Wi-Fi IP and DroidCam port 4747 4.3. DroidCam software was connected to reprogrammed software written by python 2.7 language using. PyCharm Community Edition 2020.2 x64 for face and emotion detection in laptop.

4.2. *Emotions Detection*

After taking the picture through the smartphone the image enters the analysis algorithm (as shown in Figure 6) which is as we mentioned in the third section convolutional neural network in which the patient's condition is (happy, angry, sad, neutral, surprise, disgust or fear). Currently, only these cases are taken into account due to limited time.

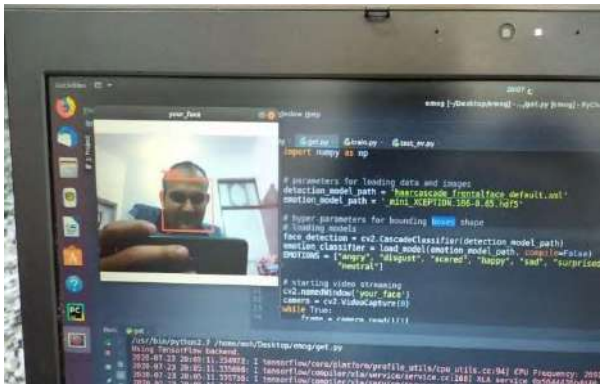

Figure 6. Emotions detection

This algorithm relies on training the network by entering more than 1792 emotional images for training and nearly 20 emotional images to test the neural network, the dimensions of the input image are 48 * 48, it is implemented using Kiras Library, which is a Python compiler used in TensorFlow library including machine learning tools and algorithms.

Inserting images into the convolution layer, whose size is the size of the input image, which creates very important features and by applying the filter that determines the edges of the image where the

images wanted for training were entered into the convolution layer four times to find the desired, then enter the Max pooling layer which is 24 * 24 in the first layer and continues to decrease each time, this layer is repeated four times as well. Then enter the Max pooling layer.
The size is 24 * 24 in the first layer then continues to decrease each time and repeat this layer four times also, after that flattening layer which flattens the matrices emerging from the previous two layers. We have repeated this layer three times then the image or arrays enter the neural network for training.
The emotions results are extracted from the input image as follows:

1. If the percentage of normal features inside the output matrix increases, the output value is normal
2. If a decrease in the percentage of normal features and an increase in abnormal features is observed within the trained network, the output will be abnormal. As shown in Figure 7.

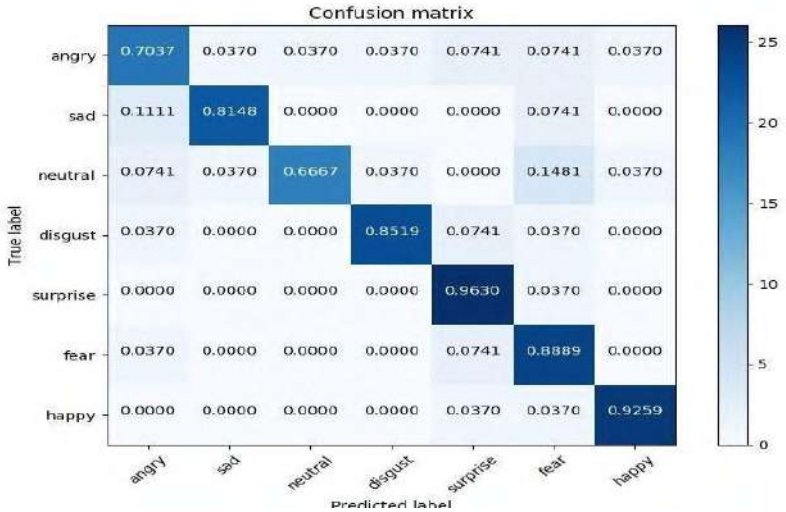

Figure 7. Output matrix of the CNN.

4.3. Cloud Implementation

After completing the processing on the patient's computer, the edge node (i.e. PC) sends the complete results to the cloud, which can be accessed from anywhere. The results and patient photos are displayed on the cloud as shown in Figure 8.

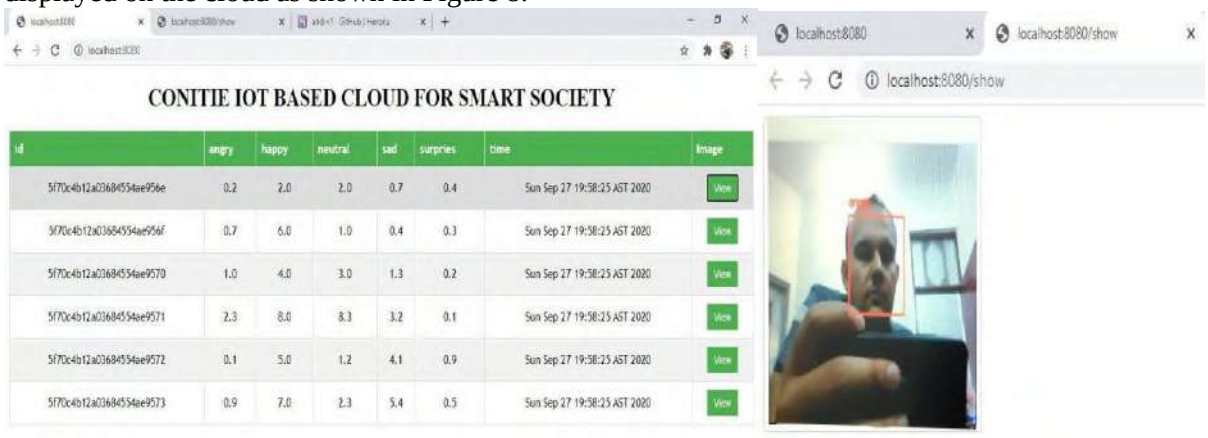

Figure 8. Uploaded results on Cloud.

4.4. Devices of Sound Control

The sound control system contains the sound control knob (micro kigdom Q280) Arduino, servo engine, board and wires integrating to control the rotation of the sound volume control knob. The sound frequency of the sound generator should be between 0 dB and 70 dB. The control knob of sound volume is connected to the servomotor in order to increase or decrease the volume of sound through rotating it clockwise or counter-clockwise. To connect the Arduino Uno (low-level language) with Python (high-level language) we need to use the Firmata firmware from Arduino Uno.

4.5. System Implementation

After the completion of the configuration and installation of the software/hardware components of the system will look as shown in Figure 9. The practical implementation of the system will be as follows:

Figure 9. Circuit Connections for the proposed system.

1. The patient sits in front of the mobile camera that connected to the first computer through the Wi-Fi network.
2. Providing internet service to ensure that the results are sent to the cloud, which in turn reaches the doctor in any place.
3. When clicking from the controller's computer, an instruction is sent to the patient's computer on the second party via the TCP protocol to take a picture of the patient.
4. The facial recognition algorithm determines the patient's condition.
5. And then the computer sends the results to the cloud, at the same time the computer sends an instruction to the motor to move according to the results.

5. Results

Each case was examined to determine his/her sensitivity to sound using Nostalgia music for Yanni (it is adjusted in terms of duration to be appropriate for examination) for sensitivity ranging from 1 to 5 levels system works to increase this intensity within certain periods ranging from 106 sec to 636 sec depending on the patient sensitivity and examination situation. At each sensitivity level the case was examined to detect his/her emotions to find out if he is in a normal situation or suffers from sensitivity toward this sound intensity. This intensity was automatically increased when the case was confirmed to be normal and stable and vice versa if he turns out to be disturbed.

In figure 10 four cases are examined. Case 1 in Figure 10-A displays a normal emotional reaction for all levels of the heard sound. While the other cases in Figure 10 (B, C and D) illustrate a

hypersensitivity to a specific level of sound intensity. After the patient suffers from hypersensitivity, the sound intensity is reduced automatically to the previous level.

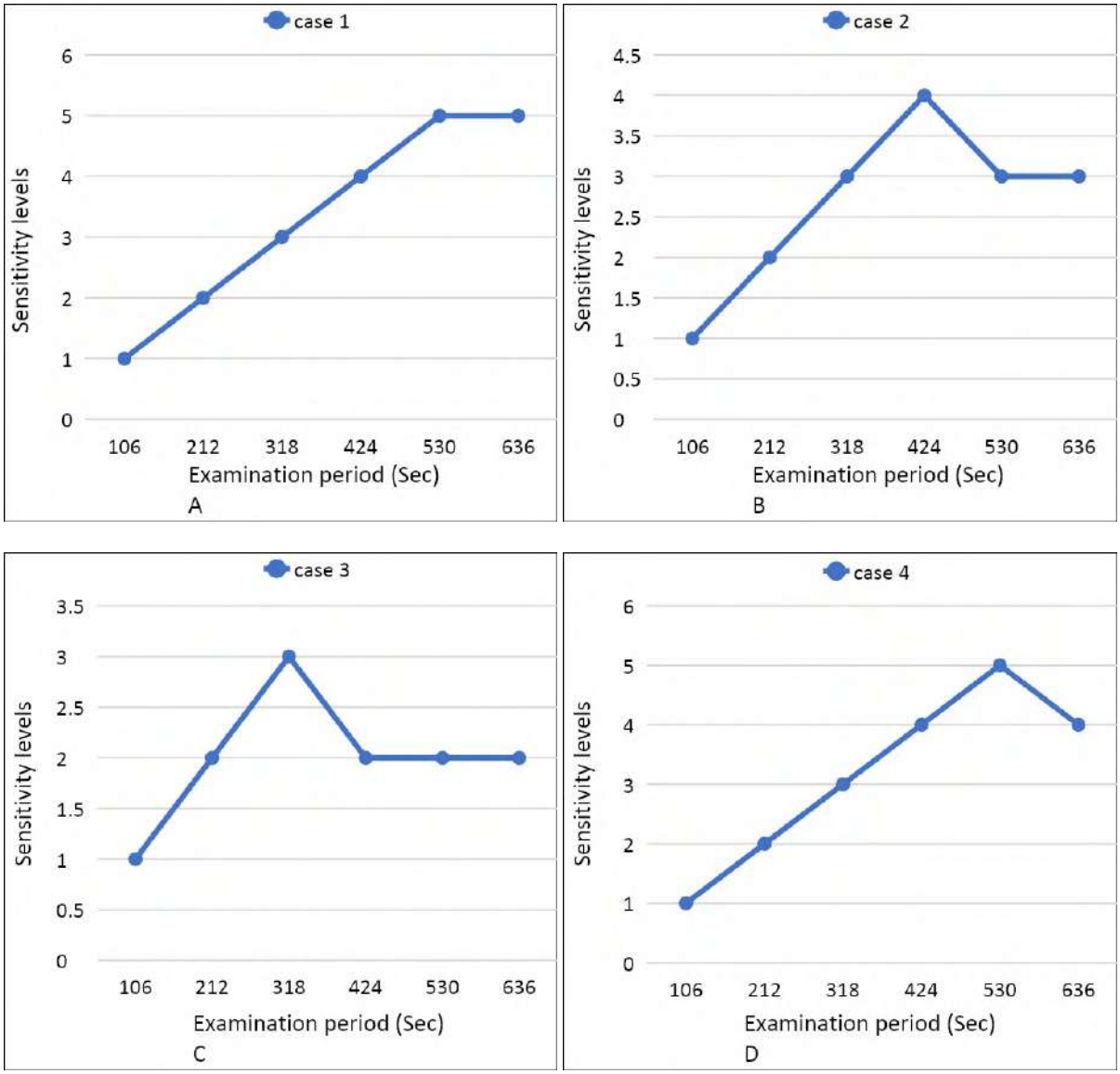

Figure 10. The sound sensitivity examination.

6. Conclusion

This paper introduced a smart diagnostic device to detect sound sensitivity to the effects of the surrounding atmosphere using cloud computing and cognitive IoT. The system prototype can be adopted as an effective system in medical centres dealing with the diagnosis of hypersensitivity toward environmental parameters. Several experiments have been conducted using different algorithms as fuzzy algorithm. These experiments showed that a convolutional neural network is 80% more accurate than as fuzzy algorithm but requires more time in training. Also, this system applies the idea of social spacing, especially in the context of the spread of the new Coronavirus. The proposed system is effective in diagnosing and responding to autistic patients with sound sensitivity.

As a suggestion for future works, hands and head motion detection can be added to the proposed system to support emotion detection. Also, with the training of many networks and the introduction of

all aspects of body language, can be converted into a polygraph system in criminal cases, with many factors such as light and sound and manipulation of guilty room temperature and other factors.

7. References

[1] Idrees A.K., Al-Qurabat A.K.M., Energy-Efficient Data Transmission and Aggregation Protocol in Periodic Sensor Networks Based Fog Computing. *J Netw Syst Manag*. 2020, 29(1):1-24.

[2] Al-Qurabat A.K.M., Idrees A.K., Data gathering and aggregation with selective transmission technique to optimize the lifetime of Internet of Things networks. *Int J Commun Syst*. 2020, 33(11):e4408.

[3] Al-Qurabat A.K.M, Idrees A.K., Abou Jaoude C. Dictionary-Based DPCM Method for Compressing IoT Big Data. In 2020 International Wireless Communications and Mobile Computing (IWCMC). 2020 (pp. 1290-1295). IEEE.

[4] Al-Qurabat A.K.M, Abou Jaoude C, Idrees A.K., Two tier data reduction technique for reducing data transmission in IoT sensors. In *2019 15th International Wireless Communications & Mobile Computing Conference (IWCMC).* 2019 (pp. 168-173). IEEE.

[5] von Söhsten D, Murilo S. Multiple face recognition in real-time using cloud computing, Emgu CV and Windows Azure. In *2013 13th International Conference on Intelligent Systems Design and Applications*. 2013 (pp. 137-140). IEEE.

[6] Castro D, Coral W, Rodriguez C, Cabra J, Colorado J. Wearable-based human activity recognition using an iot approach. *Journal of Sensor and Actuator Networks*. 2017 Dec;6(4):28.

[7] Magdin M, Benko Ľ, Koprda Š. A case study of facial emotion classification using affdex. *Sensors*. 2019;19(9):2140.

[8] Oniga S, Sütő J. Human activity recognition using neural networks. In *Proceedings of the 2014 15th International Carpathian Control Conference (ICCC)*. 2014 (pp. 403-406). IEEE.

[9] Fadhil TZ, Mandeel AR. Live Monitoring System for Recognizing Varied Emotions of Autistic Children. In *2018 International Conference on Advanced Science and Engineering (ICOASE)* 2018 (pp. 151-155). IEEE.

[10] Deshmukh R, Scholar ME. A Comprehensive Survey on Techniques for Facial Emotion Recognition. *International Journal of Computer Science and Information Security*. 2017;15(3).

[11] Simonyan, K., and Zisserman, A. (2014) "Very deep convolutional networks for large-scale image recognition". arXiv preprint arXiv:1409.1556.

Personal identification system based on multi biometric depending on cuckoo search algorithm

Personal identification system based on multi biometric depending on cuckoo search algorithm

Ansam Nazar Younis

Collage Of Computer Sciences And Mathematics, University Of Mosul, Mosul, Iraq

E-mail: anyma8@uomosul.edu.iq

Abstract. In modern devices, many personal identification systems are used using various biometrics to confirm the identity of an individual and identify him for several purposes. Some of these essential biometrics are used in this paper to help identify a person while attaining social distance because of the widespread epidemics. The features of the face, eyes, nose, and finally, the features of the mouth are used in this article. The work begins by detecting the parts of multibiometric from the input images using Viola-Jones face detection algorithm with a modification to it then segment them. After that, various initial treatment processes begin which helps clarify them to facilitate subsequent operations. Also, a Histogram of oriented gradient method(HOG) is used to extract the significant features of those image segments. The extracted features from these segments are entered into the developed cuckoo search algorithm(DCSA), the best image segment within the used dataset is searched for similar in terms of characteristics to the entered image segment. The work has also been developed so that the system is executed on two cores using parallel processing technology to utilize the processor as much as possible and reduce the time it takes to implement the system and identify the person concerned. A high identification rate has been reached, reaching 99.25%, and overall speed up 1.40323 sec relative to serial execution
.

Keywords: Multi biometric, Cuckoo Search Optimization Algorithm, Preprocessing, Viola-Jones Face Detection Algorithm, HOG, DCSA, Parallel Processing.

1. **Introduction**.

The emergence of some epidemic diseases such as the recently introduced Corona disease, which is transmitted rapidly through contact, has led to a reduction in the use of systems and techniques that are used to confirm the identity and which require touching the associated devices. Such as the use of fingerprints, palm prints, or even the use of live signatures, as these techniques were rapid methods of spreading diseases among people. Also, the needing for social distancing has led most people to carry out their activities, work, and lessons through computer services and the Internet, which has increased the needing for institutions and official departments to confirm the identity of the people who communicate with them. Therefore, experts have recently resorted to advocating the development and use of personal identification techniques that reduce contact between people by focusing on safer biometrics that have strong characteristics to distinguish people at the same time.

Multibiometric Systems mean systems that rely on multiple biometric characteristics are systems that use more than one physiological or behavioral characteristic for the same person[1], and the most striking biometric solution is facial identification[2].

In [3] the authors suggested a mapping technique for Using deep convolutional neural recognition(DCNNs) networks consists of the proposed architecture for two branches of DCNNs to map the high and low-resolution face images, [4] build a deep neural network for deeply encoding the face regions, also [5],[6]built an application for facial recognition for a Convolutional Neural Networks Biometric Network-Based, While [2]A facial classification strategy was proposed using the support vector machine algorithm,[7] Propose a multi-biometric face recognition technique to extract deep features from various facial regions using multiple convolutional neural networks (CNNs). A system that uses KELM to identify normalized face images is proposed in [8] to compensate for the effects of light variations.

In this paper, the clearest multibiometric for digital camera capture, the simplest availability and the most accurate and recognizable for individuals were adopted, Where the work relied on using the characteristics of the face, eyes, nose, and mouth separately using modified Viola-Jones face detection algorithm, as these characteristics express the person clearly. Where the algorithm (Histogram of oriented gradient algorithm) is used in the process of extracting important characteristics, reducing the dimensions, and developing an algorithm(Cuckoo Search Algorithm CSA) one of the metaheuristic algorithms, to make the algorithm better in the process of searching for the ideal solution and reaching the desired goal. Also proposed an algorithm for the execution of work on 2 cores to achieve optimum utilization of the processor inside the computer and achieve a high speed of execution. So that the work aims to achieve the identification of people by using multiple biometric features with a high recognition rate and short execution time.

2. Traditional cuckoo search optimization algorithm:

It is an intelligent algorithm that is considered one of the metaheuristic algorithms for optimization and random searching, first introduced in 2009[9] that simulates the behavior of one of the cuckoo bird family types in finding the nest and raising the young. Where this bird searches for a suitable nest randomly from the nests of other birds to lay its eggs in it so that the owner of the nest does not suspect the host, and each egg from the original nest represents a solution, while the cuckoo's egg represents a new solution[10].

3. Proposed work:

3.1. Creating dataset :

In the first stage of the system's work, the original dataset is created, which consists of 180 diverse natural images for a large group of people. The number of models varies for each person, as some people have some changes in taking pictures, for example changing the state of the mouth (silence, laughing, taking out the tongue, changing movement The mouth is in a different direction.) Also, some changes may occur to the type and shape of the covering over the head. It may also change at times from the shape of the eyes by adding different medical glasses, as well as other changes such as the background and the distance from the camera. For this purpose, a smartphone camera is used, Also some standard datasets are used, some pictures can be seen in Figure 1.

Figure 1. Examples of the dataset of the proposed system.

3.2.Preprocessing:

To facilitate smooth implementation of the algorithm steps, the input images are preprocessed at this stage, These preprocessed include unifying the input image sizes for all images into a single size, then converting it from (RGB) color space images to gray-level color space images.

3.3. Detect the segments of the multibiometric for each facial image:

Here at this stage, the multibiometric segments are identified and cut from the original image separately and stored in a special matrix, which is done by using a detection algorithm based on the Viola-Jones face detection algorithm[11]. Besides, a special programmatic section was used to modify the algorithm, whereby the nose area is used to obtain the mouth area easily. After the nose is determined, the square of dimensions by which the nose was defined is shifted downwards to easily identify the mouth without making mistakes with a small amount of enlargement of those dimensions, this is because the nose area is stronger in the detection process with this algorithm, that will help to get the segments correctly while not allowing false possibilities or segments that are out of place. Whenever the square of the nose contour is shifted by the length of the nose of the person (the length of the vertical side of the square) while expanding the square by the width of the nose of the person (the length of the horizontal side of the square) to show us the square that correctly defines the mouth area of the person. The mechanism of action is thus shown in Figure 2. The method of detecting and segmenting an image from the images entered into the device is shown in figure 3.

Figure 2. Defining the mouth area by shifting and enlarging the square that determines the nose

Figure3. Detecting and segmenting Multibiometric(Face, Eye, Mouth, Noise) of an image

3.4. Feature extraction:

The Feature extraction process was carried out using the Histogram of oriented gradient (HOG) method to obtain the best characteristics and features of each segment of multibiometric that belong to one of the images in the dataset. In most systems for recognizing objects or people, a strong set of extracted properties is relied upon. This method relies on studying edge descriptors based on gradation[12]. It uses a gradient of local intensity or distribution in the direction of the edge to describe an object's appearance. So effectively, HOG features will be resolving the issues of classification and identification systems[13], First of all, HOG is calculated, usually by convolution, by finding the horizontal gradients and vertical gradients in the image. For both the horizontal direction and vertical direction, use the (One_Dimention)point discrete derivative mask for, which is(-1,0,1) in the horizontal direction and(-1,0,1) in the vertical direction, The value of the gradient can be calculated according to the value of each pixel in the image using the equation:

$$G = \sqrt{g_y^2 + g_x^2} \quad (1)$$

It is also possible to measure the angle of the gradient for each pixel of the image by using the equation:

$$\theta = \arctan(\frac{g_y}{g_x}) \quad (2)$$

Where g_y represents the result of the convolution in the vertical direction, while g_x represents the result of the convolution in the horizontal direction[14].

3.5. Developing Cuckoo search Algorithm (DCSA):

The process of extracting the previously mentioned traits was applied to each of the biometric segments that were segmented from all the images, whether in the dataset or entered into the system, which were later used as inputs to the cuckoo search algorithm, and this represents a hybridization of the algorithm so that it deals with the extracted properties and not with the images and segments directly.

The goal of the basic search optimized cuckoo algorithm is to replace the bad (solution) individuals with the good individuals in the nest. This is done by using the fitness function [10],[15]. Therefore, the algorithm has been developed to suit the work in searching for the optimal solution, which represents the best match of the properties of the biometric segments with the corresponding segments in the dataset. Therefore, the Euclidean distance equation was used as a function of fitness for all individuals or solutions available in each generation which is can be defined as the following equation:[16][17]

$$D(x,y) = \sqrt{(x_1 - y_1)^2 + (x_2 - y_2)^2} \quad (3)$$

Where D is the distance between x which has(x1,x2)coordinates, and y which has(y1,y2) point. Thus, the pseudo-code of the DCSA algorithm can be written as follows in figure 4[18][19], where:s is the solution(egg), m is the nests, pr the probability of egg laid by a cuckoo is discovered by host bird with pr ∈[0, 1], D is the fitness value which calculated by equation 3.

Input: host nests m**,** cuckoo egg s.
Output: best nest.
Begin
1. Objective function : $f(s), s = (s_1, s_2, \dots\dots, s_d)^t$
2. Initial population created of m host nests $s_i = (i = 1,2, \dots\dots, m)$
3. **while** (t <Max number of Generation)
4. Randomly get a cuckoo
5. Evaluate cuckoo fitness (D_i)
6. Choosing a nest randomly among m(say, j)
7. if ($[D_i > D_j$)
8. Replace the solution j with the current new solution i;
9. **end**
10. A fraction (pr) are left worse nests and new ones are created;
11. Hold the best solution
12. Rank all the solutions then find the current best
13. **end while**
14. Post-process results and visualization

end

Figure 4. DCSA Algorithm Pseudo Code

3.6. Parallel Processing Method:

Parallel processing implies faster execution of the program by breaking the main program into several components and running simultaneously as each component operates on a separate processor or kernel[20][21]. The program is divided into two separate parts, so that each part is executed on a different core in the processor, to implement this method I used : (Intel ® Core TM i5-7200U, CPU @ 2.50GHZ 2.70GHZ) computer, Windows10 Processor OS. figure 5 represents a system execution by using two cores(kernels) which are called workers in MATLAB programming language.

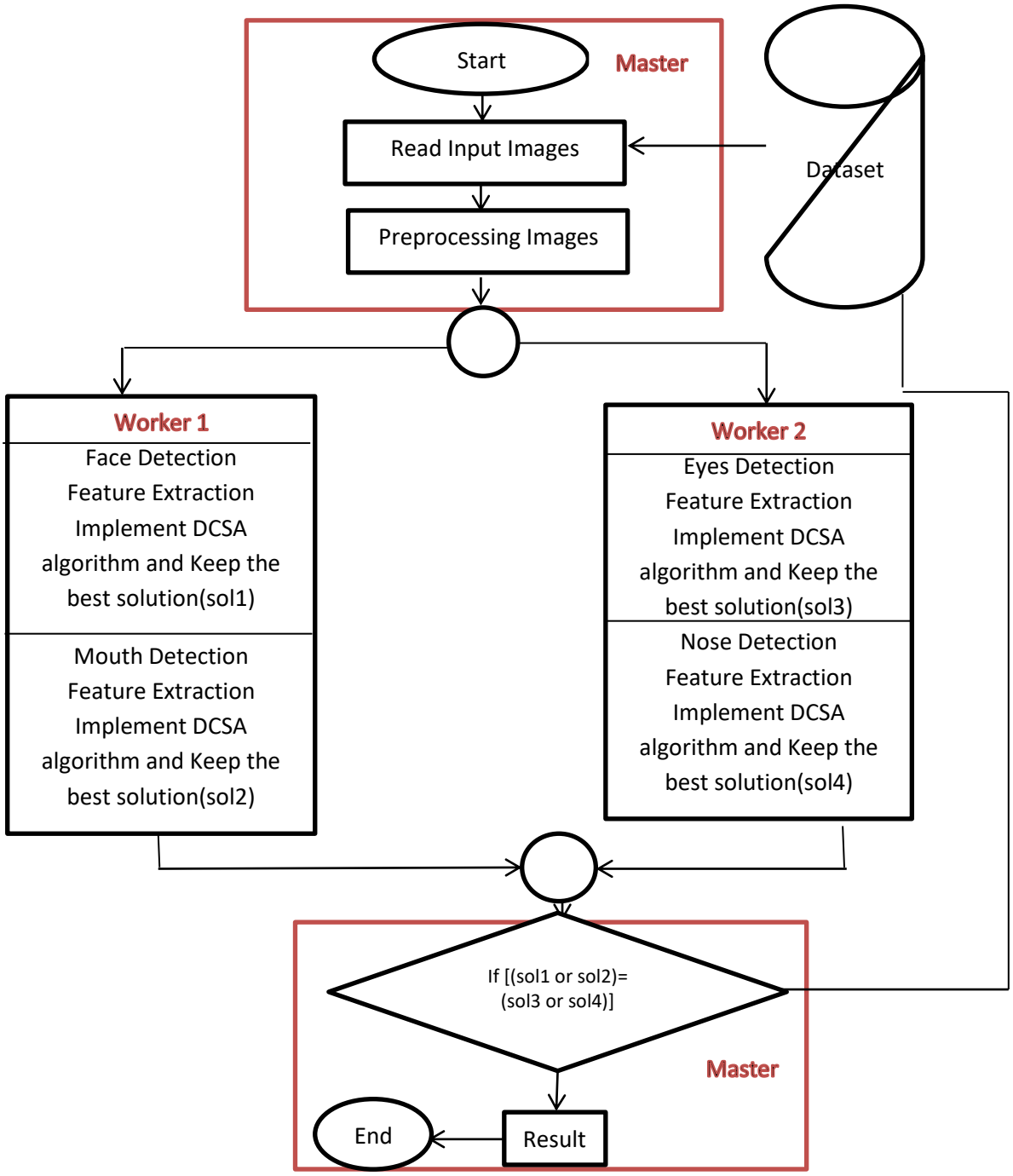

Figure 5. Flowchart of the Parallel Processing Method

Where the Master responsible for:

a. It provides the possibility of choosing the method used in the implementation and works to prepare the work environment as a whole in the case of parallel implementation.
b. Calling the necessary functions for parallel execution.
c. Process the input image as preliminary processing and then pass it on to the workers later.
d. Open parallel environment.
e. Preparing the workers and giving each worker his data and functions that it will work on.
f. Close the parallel environment.
g. Collecting and arranging the results and examining the solutions obtained to find the best.
h. Output results.

While the worker will responsible for:

a. Receive the data the worker needs from the master, including the target image that he wants to identify.
b. Implementation of the feature extracting method and developed cuckoo algorithm and searching for the best solution for two types of the biometric segment.
c. Return the best solutions to the master.

4. Measures Used To Calculate System Results:

To calculate the results obtained after implementing the developed algorithm and applying the aforementioned work steps, a set of important measures are used. These measures are divided into two main types, one that calculates the results of the system's accuracy in identifying people through its biometric characteristics and the success of the proposed algorithm for that purpose. As for the second type, it is concerned with measuring the speed and efficiency obtained from the implementation of the proposed algorithm in identifying people after implementing it in a parallel manner. The first type includes two measures, so The following measures can be used to calculate the identification results[21][22]:

1) $$\text{Identification Rate IR} = \frac{\text{Number of sample correctly identified}}{\text{Total number of images}} * 100 \quad (4)$$

Which represents the percentage of the number of people who have been identified in the system successfully, and the higher the value of this scale, the stronger the system will be in identifying people.

2) $$\text{Wrong Identification Rate(WIR)} = \frac{\text{Number of images identified error}}{\text{Total number of images}} * 100 \quad (5)$$

Which represents the percentage of the number of people who have been not identified in the system, and the lower value of this scale, the stronger the system will be in identifying people.

As for the second type, as seen in the following two equations, the measure of the increasing speed and the measure of the increase in the efficiency was used to prove the efficiency and performance of the system.

1) $$\text{Speed Up} = \frac{\text{The execution time of serial execution(one core)}in\ second}{\text{The execution time on n cores(in second)}} \quad (6)$$

This scale represents the acceleration factor of the system when we use parallel processing, which helps increase the execution speed of the intelligent system and depends on the execution time spent. Whenever the output value of this equation is greater than 1, the system is considered to be better in terms of execution speed.

2) Speed up Efficiency $= \frac{\textbf{Speed Up}}{c}$ (7)

The measure of increased efficiency depends on the scale of the acceleration factor, and that c represents the number of cores used in the execution. In terms of speed-up efficiency, the greater value of the output for this equation, the system is considered better.

5. Results and Analysis.

Practical experiments were conducted and the system was tested in identifying images of people in two ways (parallel execution and sequential execution). The input images were identified by finding the best solutions in recognizing the face, eyes, nose, and mouth, which represent the multibiometric for each image of a person. The result is calculated in favor of the image of the optimal solution that emerged from the implementation of the algorithm of cuckoos developed four times each time for a specific type of multibiometric and the detection of the solution closest to it. if the solutions returned from the four algorithms(DCSA algorithm for face identification, DCSA algorithm for mouth identification, DCSA algorithm for nose identification, DCSA algorithm for eyes identification) do not match, then the facial recognition solution with the mouth recognition solution is considered and must match with the nose recognition solution with the eye recognition dependent solution. This is because the biometric characteristics of the face and the nose are stronger than the biometric characteristics of the eyes and mouth. This is due to the possibility that the person will wear eyeglasses, use colored lenses, or make some striking movements of the mouth that cause the inability to recognize them.
Table 1 shows the most important results obtained from implementing the system on 180 images. We note from the results of the table that the strongest biometric characteristics are the facial and nose characteristics due to the lack of their changes even with changing the headcover sometimes, where the face and nose biometric identification ratio was 100%. It also appears that the IR of biometric for the eyes is 98.6% which is stronger than the biometric for the mouth that the IR of it is 98.4%, that is because the addition of glass glasses does not affect the results to a large extent as it affects moving the mouth or opening and closing it. Also, notice that the use of two cores to implement the system is much faster 1.40323 times compares to serial execution, as well as the efficiency of the system has achieved high efficiency estimated at 0.701615, which is considered to be very good even though the parallel execution needs to do a lot of additional executive operations that are not needed by the sequential execution. Figure 5 shows the implementation of the system as an example and the results with the data information of the person. Table 2. demonstrates a comparison of the recognition results using previously used algorithms with the proposed algorithm DCSA.

Table 1. Results of the system execution

No.	Type of Multibiometric	Type of Execution		IR	WIR	Speed Up times(in seconds)	Speed Up Efficiency
1	Face	Serial Execution		100	0.0	1	1
2	Nose	Serial Execution		100	0.0	1	1
3	Eyes	Serial Execution		98.6	1.4	1	1
4	Mouth	Serial Execution		98.4	1.6	1	1
5	Face	Parallel Execution Using 2 cores		100	0.0	1.40323	0.701615
6	Nose	Parallel Execution Using 2 cores		100	0.0	1.40323	0.701615
7	Eyes	Parallel Execution Using 2 cores		98.6	1.4	1.40323	0.701615
8	Mouth	Parallel Execution Using 2 cores		98.4	1.6	1.40323	0.701615
Total				99.25	0.75	1.40323	0.701615

Figure 6. Example of system execution

Table 2. A comparison between Algorithms(among works)

No.	Algorithm	Biometric Type	Recognition Rate
1	Two-Branch Deep Convolutional Neural Network Architecture[3]	Face	80.8% to 98.8%
2	deep neural networks [4]	Face	98.52%
3	Convolutional Neural Networks [5]	Face	98.75%
4	Convolutional Neural Network (CNN)[6]	Face	98.75
5	support vector machine[2]	Face	94% to 99 %
6	deep learning[7]	Face, Nose, Eyes, Mouth	93.77% to 97.94
7	light variations [8]	Face	98.89%
8	Proposed Algorithm(DCSA)	Face, Nose, Eyes, Mouth	99.25

6. Conclusion and future work.

The adoption of the developed cuckoo search algorithm along with the trait extraction algorithm used in the Persons identification system has proven its worth in reducing the possible solutions and reaching the optimal solution at a high speed. Also, the adoption of multiple biometrics has given power in identifying people while achieving social distancing, so a person who relies on this type of system does not need to touch devices for this purpose. Although the camera used to take pictures is a non-fixed camera, so the total IR reached 99.25, which is an excellent value in personal identification ratio, This can be seen by observing the outcome of identification obtained in Table 1, and the comparison made with other algorithms shown in Table 2. The great results that have been achieved give high confidence in using the system with established verification systems in institutions and official departments. Also, the use of parallel execution has given importance to this kind of exploitation of available computer capabilities, which helps in developing systems specialized in identifying people quickly where the speed up reached 1.40323 times compares to serial execution and the Speed Up Efficiency 0.701615 which is high.

As future work, we can develop the work to include another type of biometric in addition to the one used in the research. Also, additional other algorithms can be used in the trait extraction process to reduce the possibility of error such as PCA, LDA,.. etc. Also, with the increase in the number of dataset images, more than two cores can be used in the execution of the system to increase the utilization of the processor and ensure the utilization of the time spent.

Some limitations may appear in this algorithm, which is not identifying a specific area of the biometric areas used by the method, and this may be due to the lack of clarity of the taken image or to the rapid movement of the person during the capture, which distorts the image completely, or to some external environmental influences that affect the clarity of the image such as the presence of blur On the lens or taking the photo in a relatively dark place, etc., which negatively affects the identification results.

ACKNOWLEDGEMENTS
The author is very thankful for the facilities provided by the Mosul University / College of Computer Science and Mathematics, which helped to enhance the quality of this work.

References

[1] Imran, M., Rao, A., & Kumar, G. H. (2010). Multibiometric systems: A comparative study of multi-algorithmic and multimodal approaches. Procedia Computer Science, 2, 207-212.
[2] VenkateswarLal, P., Nitta, G. R., & Prasad, A. (2019). Ensemble of texture and shape descriptors using support vector machine classification for face recognition. Journal of Ambient Intelligence and Humanized Computing, 1-8.
[3] Zangeneh, E., Rahmati, M., & Mohsenzadeh, Y. (2020). Low resolution face recognition using a two-branch deep convolutional neural network architecture. Expert Systems with Applications, 139, 112854.
[4] Zhao, F., Li, J., Zhang, L., Li, Z., & Na, S. G. (2020). Multi-view face recognition using deep neural networks. Future Generation Computer Systems.
[5] Pranav, K. B., & Manikandan, J. (2020). Design and Evaluation of a Real-Time Face Recognition System using Convolutional Neural Networks. Procedia Computer Science, 171, 1651-1659.
[6] Said, Y., Barr, M., & Ahmed, H. E. (2020). Design of a Face Recognition System based on Convolutional Neural Network (CNN). Engineering, Technology & Applied Science Research, 10(3), 5608-5612.
[7] Abdellatef, E., Ismail, N. A., Abd Elrahman, S. E. S., Ismail, K. N., Rihan, M., & Abd El-Samie, F. E. (2020). Cancelable multi-biometric recognition system based on deep learning. The Visual Computer, 36(6), 1097-1109.
[8] Vishwakarma, V. P., & Dalal, S. (2020). A novel approach for compensation of light variation effects with KELM classification for efficient face recognition. In Advances in VLSI, Communication, and Signal Processing (pp. 1003-1012). Springer, Singapore.
[9] Fister, I., Yang, X. S., & Fister, D. (2014). Cuckoo search: a brief literature review. In Cuckoo search and firefly algorithm (pp. 49-62). Springer, Cham.
[10] Al-Asadi, H. A. A. (2016). Cuckoo Search Algorithm and Discrete Wavelet Transform for Iraqi Road Signs Recognition System. The ICSES Journal on Evolutionary and Metaheuristic Algorithms (IJEMA).
[11] Dabhi, M. K., & Pancholi, B. K. (2016). Face detection system based on viola-jones algorithm. International Journal of Science and Research (IJSR), 5(4), 62-64.
[12] Déniz, O., Bueno, G., Salido, J., & De la Torre, F. (2011). Face recognition using histograms of oriented gradients. Pattern recognition letters, 32(12), 1598-1603.
[13] Tian, S., Lu, S., Su, B., & Tan, C. L. (2013, August). Scene text recognition using co-occurrence of histogram of oriented gradients. In 2013 12th International Conference on Document Analysis and Recognition (pp. 912-916). IEEE.
[14] Stokka, M. J. M. N. Faculty of Science and Technology Master's Thesis, Jun. 15, 2013. University of Stavanger.
[15] MAHBUB, H. Voice Recognition Based On Cuckoo Search Algorithm Using Artificial Intelligence System.
[16] Dokmanic, I., Parhizkar, R., Ranieri, J., & Vetterli, M. (2015). Euclidean distance matrices: essential theory, algorithms, and applications. IEEE Signal Processing Magazine, 32(6), 12-30.
[17] Liberti, L., Lavor, C., Maculan, N., & Mucherino, A. (2014). Euclidean distance geometry and applications. SIAM review, 56(1), 3-69.
[18] Yang, X. S., & Deb, S. (2009, December). Cuckoo search via Lévy flights. In 2009 World congress on nature & biologically inspired computing (NaBIC) (pp. 210-214). IEEE.
[19] Kaur, H., & Kaur, G. Cuckoo Search based Optimization for Multimodal Biometrics (Signature, Speech and Palmprint). International Journal of Computer Applications, 975, 8887.

[20] B. Basil, (2017)"New Platform for Mobile Cloud Computing," M.Sc. Thesis, University of Mosul/Computer and Mathematics College.
[21] Younis, A. N., & Ramo, F. M. A new parallel bat algorithm for musical note recognition. International Journal of Electrical & Computer Engineering (2088-8708), 11(1).
[22] Younis, A. N., & Remo, F. M. Distinguish Musical Symbol Printed using the Linear Discriminant Analysis LDA and Similarity Scale. International Journal of Computer Applications, 975, 8887.

Predictions of COVID-19 Spread by Using Supervised Data Mining Techniques

Predictions of COVID-19 Spread by Using Supervised Data Mining Techniques

Wid Akeel Awadh[1], Ali Salah Alasady[2] and Hadeel Ismail Mustafa[3]

[1, 3] Dep. of Computer Information System, College of Computer Science and Information Technology
[2] Dep. of Computer science, College of Computer Science and Information Technology
University of Basrah - Iraq

E-mail: umzainali@gmail.com

Abstract. In the wake of the outbreak of the new coronavirus, the countries in the world have fought to combat the spread of infection and imposed preventive measures to compel the population to social distancing, which led to a global crisis. Important strategies must be studied and identified to prevent and control the spread of coronavirus COVID-19 disease 2019. In this paper, the effect of preventive strategies on COVID-19 spread was studied, a model based on supervised data mining algorithms was presented and the best algorithm was suggested on the basis of accuracy. In this model, three classifiers (Naive Bayes, Multilayer Perceptron and J48) depended on the questionnaires filled out by Basra City respondents. The questionnaires consisted of 25 questions that covered fields most related to and that affect the prevention of COVID-19 spread, including demographic, psychological, health management, cognitive, awareness and preventive factors. A total of 1017 respondents were collected. This model was developed using Weka 3.8 tool. Results showed that quarantine played an important role in controlling the spread of the disease. By comparing the accuracy of the algorithms used, the best algorithm was found to be J48.

Key words: Supervised Data Mining, COVID-19, Predictions, Accuracy, NB, MLP, J48.

1. Introduction

A new type of coronavirus has been discovered recently after it has been identified as the cause of the spread of one of the diseases that started in China from December 2019. The resulting disease is called coronavirus 2019 (COVID-19). In March 2020, the World Health Organization declared COVID-19 as a pandemic [1]. Evidence that men are more likely to die from COVID-19 than women is growing. People who suffer from aging diseases, weak immunity and lung-related diseases are the most affected [2]. The signs and symptoms of the disease may appear 2–14 days after exposure and may include the following: fever, coughing, shortness of breath, runny nose, headache, diarrhoea, vomiting and loss of sense of smell and taste. For protection from this epidemic, people must avoid contact with others and surfaces; avoid touching eyes, nose or mouth; wash hands frequently with soap and water; and maintain social distancing by 1–3 m [3]. The two important stages of COVID-19 are stages 2 and 3. Stage 2 involves infection from one person to another, whilst stage 3 involves infection from society. In accordance with COVID-19 stages,

the action plan could be determined by different countries. In Basra, the first case of COVID-19 was documented on 24 February 2020, originating from Najaf-Iraq. After 3 months, this disease spread in almost all areas of the city. A total of 22,926 cases have been recorded thus far. Among them, 16,817 recovered and 630 died. In this research, the following questions were answered: first, what are the most important factors that reduce the spread of COVID-19? Second, among the supervised data mining (DM) algorithms used, which could best predict the prevention of the spread of the disease? These questions were answered using DM techniques.

2. DM Technique

DM is a computational process applied in many areas; it aims to obtain useful and hidden predictive knowledge. DM techniques are used to construct a model where new information could be identified by unknown information [4]. One popular feature of all DM techniques is automated learning that recognises new patterns in the observed datasets [5]. DM specialists have devoted their careers to enhance the understanding on how to process and draw conclusions from huge quantities of knowledge depending on the techniques from the intersection of database management, machine learning and statistics. Thus, they divided the algorithms into two simple groups: supervised and unsupervised algorithms [6] [7]. Supervised DM is used to build models by using training data with a familiar class to which the data belong. The training data are composed of a series of training examples. Each example is a pair consisting of a vector of attribute value and a desired output class. A supervised learning algorithm analyses the training data and generates a feature inferred, which could be used to map new examples. This algorithm allows to determine the classes labels correctly for unseen instances. Classification methods belong to this group. The most popular classification methods are decision trees, classification rules, Bayesian networks and neural networks [8] [9]. The role of unsupervised learning is more complex than that of supervised learning because its only aims at searching the data for interesting connections and attempts to group elements by postulating class descriptions for sufficient numbers of classes to cover all objects in the database [10]. These tasks range from the identification of potentially useful regularities among the data couched in the language of description given to the discovery of concepts by conceptual clustering and constructive inference and further discovery of empirical laws relating to concepts developed by the method. Clustering and association rule methods belong to this group [8] [11]. Several different classifier models are available in the literature and determining the best method is not possible as they vary from each other in several aspects, such as learning rate, amount of training data, speed of classification and accuracy. In this paper, the effect of three algorithms, namely, Naive Bayes (NB), Multilayer Perceptron (MLP) and J48, on data analysis was discussed. These three classifier algorithms were used to predict the final class (prevention of COVID-19 spread) that some new unlabelled attributes belong to. The selected algorithms were also used to find the most convenient method to predict the final class.

2.1 Naive Bayes

NB algorithm is one of the most popular machine learning methods, specifically data analysis and classification. This method relies on the statistical concept of Bayes' theorem, which calculates the probability of a specific result by using available information [12]. This classifier is called naive because it relies on the principle of independence assumptions, that is, the relationship among all attributes and features is considered independent of one another [13]. The NB classifier model is characterised by the ease of construction and development and the ability to process large data, outperforming a number of sophisticated and sophisticated algorithms. The model is trained with the data and its available properties in databases, determines the type of new records and then classifies them on the basis of data and statistics previously available [14]. It is used in many systems, such as for identifying harmful messages; classifying documents, such as in news sites, to anticipate the type of document (e.g. politics, sports and technology);

recognising the views and feelings in the text content (negative, positive or optimistic) and in face recognition in pictures [15].

2.2 Multilayer Perceptron

MLP algorithm is one of the most popular neural networks algorithms. It consists of a perceptron, an input layer for receiving the signal, an output layer for making a decision or prediction about the data and an infinite number of hidden layers, which are MLP's true computational engine between the two layers [16]. MLP is also applied to supervised machine learning problems; they train on a collection of pairs of input–output and learn to model the correlation between those pairs. Network training requires adjusting the model's parameters (weights) to reduce error [17] [18]. This network could also be used for unsupervised machine learning by using auto-associative structure, where similar values are set for the network inputs and outputs. This method is intensive in computational terms. For any fair representation, the MLP network must have at least three hidden layers, thus requiring a long time [19] [20].

2.3 J48

J48 algorithm is an extension of ID3 algorithm. It was developed by Ross Quinlan in 1993 to generate a tree-like hierarchy and construct classification trees that represent a flowchart structure, in which the non-terminal nodes indicate the attribute tests and the terminal nodes represent the decision outcomes [21] [22]. This classifier is one of the most widely used machine learning language processing domains. The main advantages of this algorithm are easy construction of graphical classification and low-cost formal generation. However, this algorithm does not generate multiple redundant attributes and modules and it is quite susceptible to noise in the data [23].

3. Model

3.1 Data Discerption

Quantitative method relies on the use of questionnaire survey. In this work, questionnaires were built on Google Docs to collect data online. These questionnaires were used to collect data of the real direction and challenges of the respondents in Basra City on the basis of on their different experiences, allowing for collection of more accurate coded data. The research data, a total of 1017 samples, were collected in March of 2020. The six main parts of the questionnaire were demographic, psychological, health management, cognitive, awareness and preventive factors. Table 1 shows the questionnaire parts, question number and question description and the respondents' answers. These answers were shortened and converted from nominal to numeric type for ease of use and understanding. The answers were classified on the basis of Likert scale as follows: 1 for strongly agree, 2 for agree, 3 for not applicable, 4 for disagree and 5 strongly disagree. The initial step in data pre-processing involved preparing the data and converting them for evaluation and processing using MS Excel. In the second step, the collected responses were converted carefully using Weka 3.8 tool.

Table 1. Questionnaire Description

Part	No.	Distribution	Rank
Demographic Data	Q1	Gender	Male
			Female
	Q2	Age (years)	15–24
			25–34
			35–44
			45–54
			> 54
	Q3	Job	Healthcare field
			Engineering field
			Teaching field
			Student
			Earner
			Unemployed
	Q4	Address	City centre
			City outskirts
	Q5	Level of Education	Ph. D.
			MS. C.
			BS. C.
			Diploma
			Secondary
			Middle
			Primary
Psychological Factors	Q6	Social media is the most influencing factor of my psychological state.	1, 2, 3, 4, 5
	Q7	I suffer from nervous tension and anxiety during this period.	1, 2, 3, 4, 5
	Q8	I consider storing goods and food items a necessity in this period.	1, 2, 3, 4, 5
	Q9	Seeking help from psychologists is necessary during this period.	1, 2, 3, 4, 5
Health Management Factors	Q10	Basra is one of the healthiest cities to fight COVID-19.	1, 2, 3, 4, 5
	Q11	The medical personnel from the province are ready to deal with the virus.	1, 2, 3, 4, 5
	Q12	The crisis could be overcome by connecting health institutions with international scientific research centres.	1, 2, 3, 4, 5
	Q13	I support receiving medical personnel from outside Iraq, such as China.	1, 2, 3, 4, 5
Cognitive Factors	Q14	One of the most important transmission routes of infection is inhalation of the droplets produced when an infected person sneezes or coughs.	1, 2, 3, 4, 5
	Q15	Contact with surfaces contaminated with droplets from an infected person is a typical way to catch the disease.	1, 2, 3, 4, 5
	Q16	COVID-19 one of the most dangerous infectious viruses in recent times.	1, 2, 3, 4, 5
	Q17	Taking nonsteroidal anti-inflammatory drugs, such as Provin and Punestan, reduce the severity of symptoms.	1, 2, 3, 4, 5
Awareness Factors	Q18	Staying away from markets, restaurants and gatherings is a good way to prevent the spread of the virus.	1, 2, 3, 4, 5-
	Q19	I support the compulsory quarantine of all expats from abroad.	1, 2, 3, 4, 5
	Q20	I support curfews and disruption of circuits and schools and I encourage e-learning.	1, 2, 3, 4, 5
	Q21	I support isolating infected people in hospitals far from residential areas.	1, 2, 3, 4, 5
Preventive Factors	Q22	Meat and eggs should be cooked well.	1, 2, 3, 4, 5
	Q23	It is necessary to wear masks and paws when leaving the house.	1, 2, 3, 4, 5
	Q24	The immune system is strengthened by taking high doses of zinc and vitamin C.	1, 2, 3, 4, 5
	Q25	Washing hands with soap and water for at least 20 seconds and using sterilisers containing 70% alcohol are the basic information that I know.	1, 2, 3, 4, 5
Total of all items			25

3.2 Questionnaire Reliability

Reliability is the extent to which an instrument would produce the same results, whether the measurement under the same conditions was to be taken again. For example, measuring people's height and weight is also extremely reliable [24]. Cronbach's alpha is statistically one of most effective methods to measure internal consistency and reliability; it is used to calculate the extent to which the questions in the survey all measure the same underlying construct. When Cronbach's alpha > 0.7, its internal reliability performance is satisfactory [25]. Table 2 shows that the Cronbach's alpha was 0.8 for the scaled variables, which consisted of 21 items (parts 2–5) and 1017 respondents.

Table 2. Questionnaire Reliability

Reliability Statistics			
Cronbach's alpha	***No. of items***	***No. of respondents***	***% of respondents***
0.8	21	1017	100%

4. Results and Discussions

A Weka software package developed at Waikato University in New Zealand was used to implement this study. This package is run on Java, and it stands out as perhaps the most professional and extensive package of machine learning algorithms [26]. Analysing the effect of attributes is necessary to obtain an enhanced insight into the importance of the attributes. Thus, the effect of certain attributes of the model on the final class was analysed in the present study. This analysis discussed the most correlated attributes (respondents) to the final class (prevention of COVID-19 spread) and how they may affect the final class. This stage revealed the average correlation of the attributes with the final class. The respondents with high correlation could be regarded as points of advice for interested parties in this field. Weka provides several filters that could be used to clean up the data before invoking a classifier. In this stage, a filter (CorrelationAttributeEval) was used to find the correlation between attributes and the final class. This filter evaluated the value of an attribute by calculating the correlation (Pearson's) between it and the final class.

Table 3. Correlation Rate of Responses

Sequence	**Respondent**	**Average**	**Sequence**	**Respondent**	**Average**
1	Q19	0.15624	13	Q3	0.04214
2	Q16	0.14841	14	Q6	0.03534
3	Q24	0.13699	15	Q8	0.03149
4	Q22	0.10039	16	Q5	0.03136
5	Q25	0.0961	17	Q17	0.02950
6	Q15	0.09046	18	Q14	0.01748
7	Q20	0.08735	19	Q1	0.0159
8	Q11	0.07532	20	Q2	0.01316
9	Q4	0.0587	21	Q9	0.00743
10	Q10	0.05505	22	Q7	0.00483
11	Q23	0.04537	23	Q12	0.00414
12	Q18	0.04358	24	Q13	0.00352

Table 3 displays the correlation rate with the evaluation mode between the attributes and the final class (10-fold cross validation) to ensure accuracy. This analysis aimed to determine the importance of each attribute

individually. The responses were ranked from the highest to the lowest correlation rate with the final class. Those with the highest correlation rates represent the value most correlated with the final class. The results showed that Q19 affected the final class the most, followed by Q16, Q24, Q22 and Q25, whereas Q9, Q7, Q12 and Q13 had the smallest output effect. Some experiments were also conducted to evaluate the performance and usefulness of the different classification models of the prevention of COVID-19 spread. The results are summarized in Tables 4–6.

Table 4. Predictive Results of Classifier Models

Evaluation Criteria	Classifier Models		
	NB	***MLP***	***J48***
Timing to Build Model (in seconds)	0.05	25.49	0.05
Correctly Classified Instances	906	934	953
Incorrectly Classified Instances	110	82	64
Prediction Accuracy	89.17%	91.92%	93.79%

Table 5. Comparison of Performance

Evaluation Criteria	Classifier Models		
	NB	***MLP***	***J48***
Kappa Statistics	0.2017	0.1542	0.1368
Mean Absolute Error	0.122	0.0835	0.099
Root Mean Squared Error	0.2975	0.2676	0.2412
Relative Absolute Error	114.27%	78.23%	92.73%
Root Relative Squared Error	192.29%	116.26%	104.80%

Table 6. Comparison of Evaluation Measures

Classifier Model	TP	FP	Precision	Recall
NB	0.925	0.667	0.959	0.925
MLP	0.964	0.825	0.952	0.175
J48	0.987	0.895	0.0.949	0.987

The performance of the three models was measured on the basis of three criteria: prediction accuracy, building time and error average, as shown in Figures 1–3, respectively.

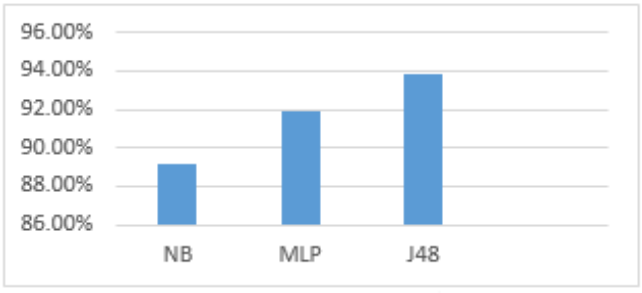

Figure 1. Prediction Accuracy

Figure 1 illustrates the classifier models used in the experiment; the accuracy average of NB algorithm was the lowest.

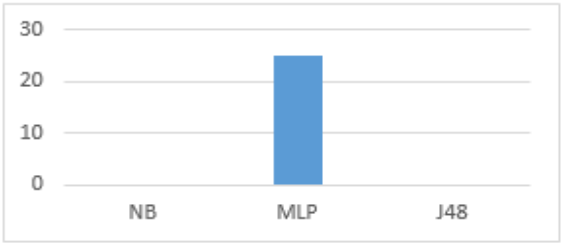

Figure 2. Building Time of Classifier Models

Figure 2 illustrates the building time of the three models under consideration. Amongst them, the MLP classifier took the longest time to build a model, whereas the NB and J48 classifiers learned to construct a model quickly for the given data. Figure 3 displays the correctly and incorrectly classified instances.

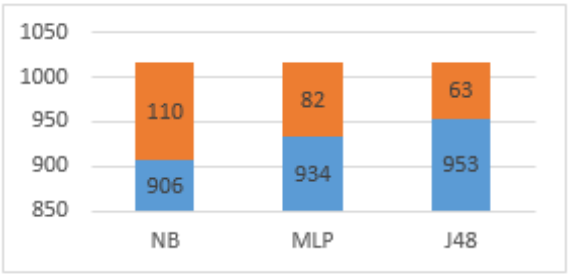

Figure 3. Error average

The performance of machine learning techniques is highly dependent upon the quality of the training data. Confusion matrices are extremely useful for evaluating the classifier models. A confusion matrix is a table used to define a classification model's output on a collection of training data for which the true values are known. In table 7 there are two possible predicted classes: "A" and "B". "A = yes" would mean they predicating the prevention of COVID-19 spread, and "B = no" would mean they do not . For example, The classifier made a total of 1017 predictions . Out of those 1017 cases, the classifier "NB" predicted "A" 981 times, and "B" 36 times. In reality, 998 respondents in the sample have the prevention, and 19 respondents do not. Briefly, the columns in table7 represent the predictions, whilst the rows indicate the final class.

.

Table 7. Confusion Matrices

Classifier Model	A	B	
NB	969	29	A
	12	7	B
MLP	992	6	A
	14	5	B
J48	983	15	A
	10	9	B

In general, the experiments proved that cross validation was statistically good in the classifier performance. Good results lead to large numbers and small down the main diagonal, perfectly zero off-diagonal elements. As shown in Table 7, the classifier algorithms (MLP, NB and J48) demonstrated good results, indicating that DM methods could effectively help in the prevention of COVID-19 spread.

Figure 4 demonstrates the tree of the J48 classifier algorithm, which was the best method to show the most connected questions to the final class. Each node represent a question and its branches are drawn in accordance with the answers.

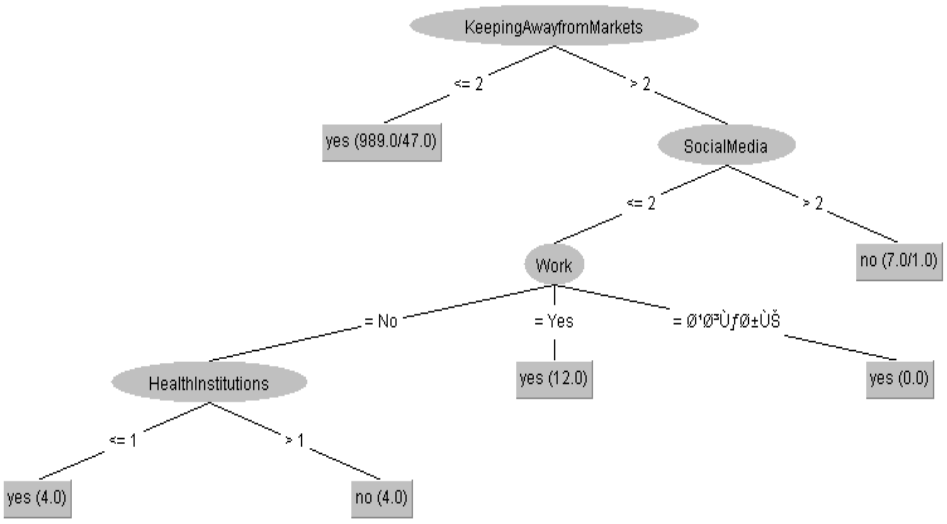

Figure 4. J48 Classifier Algorithm

5. Conclusion

In this paper, the problem of COVID-19 spread in Basra City was studied by applying three supervised DM algorithms to predict the prevention of COVID-19 spread. The performance of the learning methods was evaluated on the basis of their prediction accuracy. The results indicated that the J48 classifier outperformed the NB and MLP methods. A good classifier model must be accurate and comprehensible. This study was based on the questionnaires filled out by respondents from Basra City and the DM techniques were applied after the data were collected. This method could help medical departments by limiting the spread of the disease and reducing infection by taking necessary precautions in a timely manner and improve the quality of health institutions. For future works, the experiment could be expanded with more special attributes to obtain more accurate results. Many specific technologies could also be used when using different factors.

References

[1] Lauer, S.A., et al., The incubation period of coronavirus disease 2019 (COVID-19) from publicly reported confirmed cases: estimation and application. Annals of internal medicine, 2020. 172(9): p. 577-582.
[2] Arti, M. and K. Bhatnagar, Modeling and Predictions for COVID 19 Spread in India. ResearchGate, DOI: DOI. 10.
[3] Yu, H., et al., Reverse logistics network design for effective management of medical waste in epidemic outbreaks: Insights from the coronavirus disease 2019 (COVID-19) outbreak in Wuhan (China). International Journal of Environmental Research and Public Health, 2020. 17(5): p. 1770.
[4] Wu, H., et al., Type 2 diabetes mellitus prediction model based on data mining. Informatics in Medicine Unlocked, 2018. 10: p. 100-107.
[5] Amin, M.S., Y.K. Chiam, and K.D. Varathan, Identification of significant features and data mining techniques in predicting heart disease. Telematics and Informatics, 2019. 36: p. 82-93.
[6] Kostopoulos, G., et al. Predicting student performance in distance higher education using active learning. in International Conference on Engineering Applications of Neural Networks. 2017. Springer.
[7] Awadh, W.A., A.S. Hashim, and A.K. Hamoud, A REVIEW ON INTERNET OF THINGS ARCHITECTURE FOR BIG DATA PROCESSING. Iraqi Journal for Computers and Informatics, 2020. 46(1): p. 11-19.
[8] Cattral, R., F. Oppacher, and D. Deugo. Supervised and unsupervised data mining with an evolutionary algorithm. in Proceedings of the 2001 Congress on Evolutionary Computation (IEEE Cat. No. 01TH8546). 2001. IEEE.
[9] Murphy, K.P., Machine learning: a probabilistic perspective. 2012: MIT press.
[10] Abd Ulkareem, M., W.A. Awadh, and A.S. Alasady. A comparative study to obtain an adequate model in prediction of electricity requirements for a given future period. in 2018 International Conference on Engineering Technology and their Applications (IICETA). 2018. IEEE.
[11] Zhu, X. and A.B. Goldberg, Introduction to semi-supervised learning. Synthesis lectures on artificial intelligence and machine learning, 2009. 3(1): p. 1-130.
[12]. Hamoud, A., et al., Students' success prediction based on Bayes algorithms. International Journal of Computer Applications, 2017. 178(7): p. 6-12.
[13] Wildani, I. and I. Yulita. Classifying Botnet Attack on Internet of Things Device Using Random Forest. in IOP Conference Series: Earth and Environmental Science. 2019. IOP Publishing.
[14] Panda, M., Developing an Efficient Text Pre-Processing Method with Sparse Generative Naive Bayes for Text Mining. International Journal of Modern Education & Computer Science, 2018. 10(9).
[15] Hassan, M.K., et al., EoT-driven hybrid ambient assisted living framework with naïve Bayes–firefly algorithm. Neural Computing and Applications, 2019. 31(5): p. 1275-1300.
[16] Heidari, A.A., et al., An efficient hybrid multilayer perceptron neural network with grasshopper optimization. Soft Computing, 2019. 23(17): p. 7941-7958.

[17]. Ploj, B., R. Harb, and M. Zorman, Border Pairs Method—constructive MLP learning classification algorithm. Neurocomputing, 2014. 126: p. 180-187.
[18] Janani, V., et al., Dengue Prediction Using (MLP) Multilayer Perceptron-A Machine Learning Approach. 2020, EasyChair.
[19] Jain, A., S. Sharma, and M.S. Sisodia, Network intrusion detection by using supervised and unsupervised machine learning techniques: a survey. International Journal of Computer Technology and Electronics Engineering, 2011. 1.
[20] Khan, A.N., et al. Learning from Privacy Preserved Encrypted Data on Cloud Through Supervised and Unsupervised Machine Learning. in 2019 2nd International Conference on Computing, Mathematics and Engineering Technologies (iCoMET). 2019. IEEE.
[21] Hong, H., et al., Landslide susceptibility mapping using J48 Decision Tree with AdaBoost, Bagging and Rotation Forest ensembles in the Guangchang area (China). Catena, 2018. 163: p. 399-413.
[22] Hamoud, A., A.S. Hashim, and W.A. Awadh, Predicting student performance in higher education institutions using decision tree analysis. International Journal of Interactive Multimedia and Artificial Intelligence, 2018. 5: p. 26-31.
[23] Kaur, R. and R. Gangwar, A Review on Naive Baye's (NB), J48 and K-Means Based Mining Algorithms for Medical Data Mining. Int. Res. J. Eng. Technol, 2017. 4: p. 1664-1668.
[24] Carson, B., The transformative power of action learning. Chief Learning Officer. Retrieved, 2017.
[25] Sekaran, U. and R. Bougie, Research methods for business: A skill building approach. 2016: John Wiley & Sons.
[26] Hashima, A.S., A.K. Hamoud, and W.A. Awadh, Analyzing students' answers using association rule mining based on feature selection. Journal of Southwest Jiaotong University, 2018. 53(5).

Knowledge management model to enhance Enterprise Resource Planning system in Green software development process

Knowledge management model to enhance Enterprise Resource Planning system in Green software development process

Sarah M Yahya[1] and Mustafa S Khalefa[1]

[1]Computer science department education college of education for pure science, University of Basrah

E-mail: bathrat.amal88@gmail.com

Abstract. The global economy is constantly evolving and corporate technology and business are an important factor in this development and because of the accompanying negative impact on the environment and society, the role of sustainability and sustainable development highlights. To further investigate the scope of the green software development process and its integration with information systems such as the Enterprise Resource Planning (ERP) system, we presented this study due to its importance in minimizing the negative effects of information technology on our natural environment. In this connection, there is a have to combine sustainability and information technology allow organizations to behave in a manner to going greener. Comprehending that the Enterprise Resource Planning (ERP) system is one of the very effective commercial enterprise solutions for organizations, it is necessary to align its use with sustainability factors through the utilization of green IT practices, the objective of this research study is to provide a design model to enhance ERP system in green software development process. So every company must look into the impact of the utilization of Information and communications technology (ICT) on our natural environment and take care to adopt methods to decrease the effects negative on its. Therefore, knowledge management (KM) can be used as the facilitation tool. This research paper presents the results of qualitative research, which proposes a model that to the possibility of enhancing the implementation of the ERP system in the Green Software Development Process by using green IT practices and knowledge management as facilitation tools.

1. Introduction

The global economy is constantly evolving and corporate technology and business are an important factor in this development and because of the accompanying negative impact on the environment and society, the role of sustainability and sustainable development highlights. This actually is the place the sustainability idea is needed, with the purpose to make a balanced interplay between economic investments, useful resource utilization, and social advancement for modern wishes and future potentials[1], [2]. In this connection, there is a have to combine sustainability and information technology allow organizations to behave in a manner to going greener [3]. The green or Greenness has become an important topic that goes into all aspects of life around the world including information technology and business. In general, Merriam-Webster (An American Dictionary of the English Language) defined a green is "tending to preserve environmental quality (as by being recyclable, biodegradable, or non-polluting)" [4].

In 2018, Hayri ACAR consider sustainable software at the outside of the green software. Therefore, that mean the green must respect sustainable criteria. In this regard, UN cited the sustainability criteria only have three main dimensions, which are economic growth, environmental protection, and social equality[5].

Because the globalization changing very speedily in business, competition increased, and information technology rapidly growths, companies have to undertake enterprise resource planning (ERP) systems furnished with software program and hardware amenities[6][7] to typically meet the technical data necessities of companies along with the desire of owner to strengthen corporate competitiveness[8].

Comprehending that the Enterprise Resource Planning (ERP) system is one of the very effective commercial enterprise solutions for organizations, In doing so, it have now been an important contributor to environmental degradation brought on by resource consumption, greenhouse (carbon) emissions, and wastage[9]. As a consequence, it's essential to align its use with sustainability elements through the utilization of green information technology (IT) [3], So every company must look into the impact of the utilization of Information and communications technology (ICT) on our natural environment and take care to adopt methods to decrease the effects negative on its [3][9][10].

2. Related work

The development of information and communication technologies has an impact on the development of all types of software and applications in the organization. At the same time, the phenomenon of globalization and the external environment were more complex with the new need and conditions for institutions in terms of reducing the negative effects on the environment[11]. For this reason, a high-quality information system is now a necessity for every enterprise to be capable to make bigger competitiveness with the aid of decreasing fees via higher logistics. Previous reviews of the literature need more research in the scope of the green software development process, as well as little research on the topic of green software development process with ERP system, so we focused on this as shown in (Figure 1) where we note that the ERP system and the software development process and knowledge management are all within the environment of the green software development process, and this leads to a high quality of data and software in the enterprise. In these circumstances, companies have two challenges: to generate and put in force an infrastructure for information technologies with purposes for storing and sharing information and to successfully use this information for the decision-making process[11].

Because of the negative effects on the environment resulting from its software, systems, and applications in organizations[3], the objective of this study is to the possibility of enhancing the implementation of the ERP system in Green SDP by using green IT practices and knowledge management as a facilitation tools. Moreover, knowledge can also being a significant intangible asset to attain success in the situation of green sustainable development [12]. The organization can take advantage of the benefits of ERP systems and knowledge management and achieve success in the competition globally[11]. In this regard, In 2003 Darshana Sedera et al. propose a model to empirically assessing the impact of KM on the success of ERP systems.

In 2007 Rosemary and Sukunesan show there is an opportunity that may be explored, are the many companies that undertake IT implementation towards sustainable development and many of those companies have a basis in KM[13]. Currently, organizations have assigned very significance to the knowledge, which is generated internal and external the company, think about it an priceless asset to acquire sustainable benefits and due to the have an effect on enhancing their processes, rendering it fundamental to generate techniques focused at knowledge management[14].

In this regard, Pattarin and Vichita in 2019 developed a framework by means of integrating the essential concepts from sustainability and knowledge management [1]. In 2019, Minodora, et al. proposed a framework to explore the connection between green IT practices and ERP to check how green IT provides a chance for organizations to enhance ERP in greater environmentally answerable initiatives [3]. However, they published that the connection between ERP and green IT practices is now not relevant, specifically due to the fact of the low stage of environmentally friendly lifestyle inside companies. So they advised that organizations should start to provoke an massive layout now not simply addressing the

operational stage of these systems, however moreover the integration of sustainability factors in software program quality, administration elements of ERP implementation, or enterprise attitudes to going green[3].

In this regard, the objective of this study is to possibility of enhance the implementation of ERP system in Green SDP by using green IT practices and knowledge management as a facilitation tools. This leads to new knowledge in this field that combines ERP, Green SDP, SDP and KM, as well as focusing on the quality factor of data and software.

3. Methodology

The objective of this research study is to provide a design model to enhance ERP system in green software development process by using green IT practices and knowledge management as a facilitation tools , to achieve this objective, we conducted are:

1. Reconnoitering of previous studies on the subject of the research study based on keywords such as Green Process Software Development (GSDP), Software Development (SDP) or it is also called Software Development Lifecycle (SDLC), Project Planning (ERP) and Knowledge Management (KM).
2. Analysis (filtering and summarizing) the existing researches, provide a systematic review.
3. Propose and design a model to enhance the ERP system in the green software development process.

4. Propose model

Based on the literature review and to achieve the goal of this paper, we propose a design model to enhance ERP system in GSDP. This model consists of five components: ERP, software development process, green software development process, green IT practices, and knowledge management. The importance of this model comes from the green software development process, which is about producing nature-friendly software products with the aim of reducing the terrible environmental impacts on our environment, using green IT practices in SDLC that can be successfully implemented. (Figure 1) shows the model proposed.

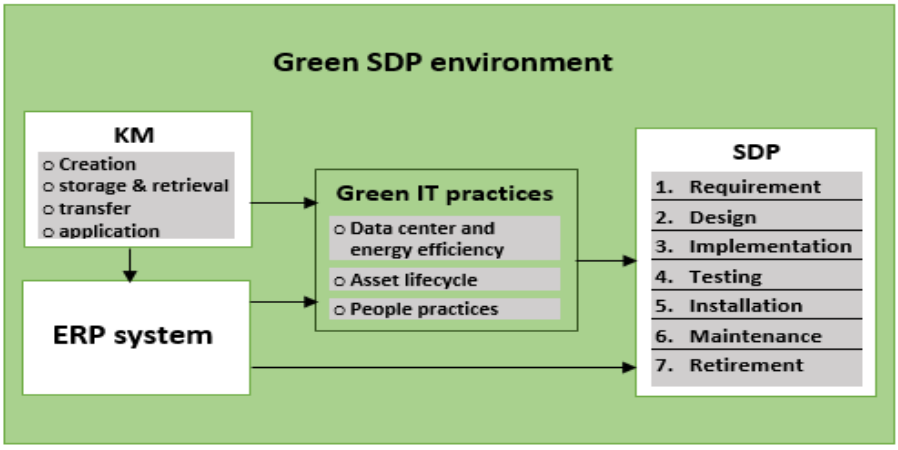

Figure1. ERPs in Green SDP model

4.1. ERP system

ERP system is one of the integrated information systems, which continues to evolve as information technologies evolve and business requirements continue to diversify [8], [15]. The opinions about ERP evolution are different; Rashid et al. (2002) described that evolution as follows: in the 1960s the

organizations were used inventory control packages to automating systems, were using programming languages to writing like COBOL and FORTRAN. In the 1970s, Material requirement and planning (MRP) structures had been used to sketch the requirements of product and components inside a process of production[16]. After that, at 1980s, manufacturing resource planning (MRPII) was evolved to enhance the process of production; it added modules to include business planning, production planning, finance, engineering, human resources, distribution, and shop floor in one computer system (Wallace, 1990). Then these concepts expanded, were appeared ERP systems in the 1990s, which have the ability to integrate the business processes throughout a company[8][17].

Irwan et al. 2018, defined ERP "is a software for business management system which integrates all business functions, processes, and information between different departments inside the company. This business software system will allow companies to automate and integrate the majority of their business processes, share common data and practices across the entire enterprise, and produce and access information in a real-time environment"[18].

ERP systems may provide a company with multiple benefits. However, it is very important these benefits outweigh the expenses of the system and they need to provided that the proper system for the company is chosen and the system is implemented properly[7]. According to Deloitte 1998, the ERP system is a software system package for business[19] that lets in the enterprise to: automate and combine the majority of its enterprise processes, share common practices and data throughout the whole enterprise produce, and get admission to information in real-time.

There are many vendors, which provide an ERP system like SAP, Oracle, Microsoft et al.; they have relied on various ERP software programs according to customer needs. Most ERP solutions run along with Unix and Linux operating systems or Windows platform[20] [21]. We will take SAP ERP system as a case study. SAP word abbreviation means "Systems Applications and Products" in Data Processing. (SAP AG) by using definition, can be the title of the ERP software program alongside the title of the organization. SAP AG Software is absolutely a European multinational, established in 1972 by five engineers were worked at the IBM company are Plattner, Wellenreuther, Hector, Tschira, and Hopp. They improve software program solutions for client relationships and managing enterprise operations[22]. In practice, this business enterprise software program is known as (SAP), and the professional name is SAP ERP. (SAP AG) is the world's greatest provider of business enterprise software program that, in 2017, served extra than 345,000 clients in over a hundred ninety nations (SAP AG, 2017b). The Enterprise Software section of the organization has developed industry-specific features in the software product for over twenty-five industries to client relations and manage commercial enterprise operations for organizations [23].

SAP provides ERP solutions, to all enterprise areas, inclusive of midsize and small businesses. Where SAP launched its first ERP software program in 1979 as R/2, then redesigned the software program in 1992 the usage of a client-server architecture. R/3 used to be the ensuing software; it grew to be an immediately hit. With the assertion of it a client-server SAP R/3 system, SAP AG, which already the greatest issuer in the ERP market, brought a system that used to be attractive to small-sized and medium organizations in addition to the large organizations that already make use of SAP software program [24]. The key features of SAP R/3 software are:

1. SAP R/3 software runs on truly any software/hardware platform and may use numerous database management systems.
2. The programing code of SAP R/3 is wrote in an interpretive language known as ABAP. (ABAP is a German abbreviation that, translate as loosely, mean "Advanced Business Application Programming"). ABAP is very comparable in its syntax to COBOL. Use of the ABAP language permits SAP clients to increasing the functions of the software product.

SAP presents a massive array of widespread reports and a report writer, "Advanced Business Application Programming" (ABAP). ABAP programming language is an object-oriented environment that generates reports or transactions. The ABAP surroundings limited in offers some automatic report generation and query tools. To obtain the total advantage of the ABAP surroundings, one should be a proficient programmer [20].

Generally SAP ERP is primarily based on a database that treats with numerous commercial enterprise features interior exclusive modules like finance, sales, purchase, human resources, inventory, and manufacturing [23]. However, SAP ERP is a commercial enterprise system designed to assist the optimization of business processes within an enterprise and associated process management activities[25][26].

4.2. Software development process

SDP is also called SDLC "Software development life cycle" is a procedure that produces a software program with the very best high-quality and lowest price in a short time. SDLC consists of a detailed sketch for how to develop, maintain, replace, and alter a software system[27]. However, SDP is a systematic technique for developing software program applications. Introducing any idea early in the SDLC can make sure that the idea is propagated via a number of phases [28].
Below are the software development lifecycle stages:

1. Requirement: gather all the information and requirements to conceive a concrete expectation to the software product.
2. Design: is a phase do a clear and expert design of the system and software to obtain all the requirements of the preceding phase with the aid of the developers and architects of the system.
3. Implementation: The software design will now be translated into code.
4. Testing: each module will be tested to make sure that the software product is completely free of any defects.
5. Installation: install the product up to be ready for customer use.
6. Maintenance: fine-tuning and enhancements of the system and begin planning to the feasible features and functionalities that should be inserted into the software.
7. Retirement: is the removal of a software release from production, it is also known as system decommissioning.

4.3. Green software development process

Green or Greenness has become an important topic that goes into all aspects of life around the world including information technology and business. In general, Merriam-Webster (An American Dictionary of the English Language) defined a green is tending to reserve environmental qualities (such as by being biodegradable, recyclable , or non- contaminating)[4]. In 2018, Hayri ACAR consider sustainable software at the outside of the green software. Therefore, that mean the green must respect sustainable criteria. In this regard, UN cited the sustainability criteria only have three main dimensions, which are economic growth, environmental protection, and social equality[5].
GSD is a methodical processes which allow a disciplined, systematic and well-organized development of green software products[12]. Green SD is concerning to use green finest practices during SDLC process. The Key idea of Green SD is regarding manufacturing of nature-friendly software products with the aim of minimizing negative ecological impacts to our natural environment[29][30]. The main goal of GSD is about using green practices in SDLC for making greener software products, including any kinds of application software and system software products[31][32][28].

GSD includes seven phases: 1) Requirement, 2) Design, 3) Implementation, 4) Testing, 5) Installation, 6) Maintenance, and 7) Retirement [33]. Consciousness of environmental concerns and green practices must certainly be promoted at the starting of the software development [31][34]. Alike, building a secure software, security concepts should be presented in the initial SDLC phases. Likewise, presenting energy awareness early confirms that the energy-related expenditures could be minimized in later SDLC phases[28]. McXin Tee, Rusli Abdullah, J. Din, S. Abdullah, and L. Wu (2017) proposed a framework to explore relations between five independent variables (ethical motivation, competitive motivation, managerial motivation, financial motivation, and regulatory motivation) and Green SD adoption through using KM acts as simplification tools[29]; But the result of the empirical analysis showed the only motivating factor that expressively contributes to motivate software practitioners in adopting Green SD is the ethical motivation.

4.4. Green IT practices

Green practices are expressed as collections of knowledge about green policies and activities that gather the most common environmental issues[35][31]. To do make work environment harmful and decreasing the overall expense of ownership, green IT proposes some of the main pros that can be done if green policies and frameworks based on green IT should be implemented correctly. Some of these benefits are[36]:

1. Green IT reduces total energy costs of the organizations.
2. It extends or elongate the life of existing data center kit by cleverly revitalizing equipment, taking benefit of energy efficiencies.
3. It lowers IT maintenance actions and costs and improves over- all impression of the organization.
4. It reduces environmental stewardship and saves money and by appropriate disposal of discarded and toxic hardware, by suggesting new hardware's which are environment friendly, consume less energy and easy to get rid of.
5. It reduce global warming effects by reducing overall carbon footprints.
6. It reduces smog, Acid rains and global climate change effects.
7. It reduces the emanation of CO2, thereby reducing the respirational problems faced by different types.
8. It reduces the straining on the electricity grid.
9. Free up spaces on data center floors.

Thus, based on the green IT maturity model suggested by Foogooa et al. [37], the next three focal points are contained in the model in our research: energy efficiency and data centers, asset lifecycle, and people practices[3].

4.5. Knowledge management

KM is defined as a cyclical process concerning to phases of collecting knowledge from varied sources, then storing the knowledge in an appropriate format and place, and finally upgrading the present knowledge with the goal of making new values to organizations[29], [38], [39]. Knowledge is really a melted mixture of experience, related information, and expert insight that provides a construction for evaluating and combining new experiences and information. It initiates and is applied in the awareness of a knower[40][14].

Knowledge could be split into two kinds: explicit knowledge and tacit knowledge. The tacit knowledge is the better practices, intuitions, heuristic, special know-how, practical skills, and so on. Its individual

knowledge that's difficult to formalize or expressive. The explicit knowledge could be transmitted and codified in recognized and systematic language[40].

The utilization of KM can upraise sustainability through its essential processes and activities[1]. KM processes are composed of four groups of activities working with the management of explicit and tacit knowledge within the organization[41] .

1. Knowledge creation: could be the improvement of new knowledge or replacement of the existing one, where inventions and solutions are generated.
2. Knowledge retrieval and storage: are described the memory that preserves, keep and share knowledge across time and space, which supports reduce replication of work and wastefulness of resources.
3. Knowledge transfer: could be the exchange of knowledge at different levels between individuals, groups, or organizations using various communication methods.
4. Knowledge application: is the process that knowledge is utilized in practice to be able to bring competitive advantage to life.

And the knowledge evolution cycle consists of five phases [42]:

1. Originate/create knowledge: members of an organization develop knowledge through learning, problem solving, innovation, creativity, and importation from outside sources.
2. Capture/acquire knowledge: members acquire and capture information about knowledge in the explicit forms.
3. Transform/organize knowledge: in written material and knowledge bases.
4. Deploy/access knowledge: organizations distribute through education, training program, and automated knowledge base system or expert networks.
5. Apply knowledge: KM aims to make knowledge available whenever it is needed.

5. Discussion

In this paper, We got to know the ERP system (definition, stages of development, importance and suppliers... etc.) of many research papers, as well as identifying the most important practices applied in the software development lifecycle to get a practical environment for the development of green software, which must be without or less an impact on the environment. In addition, we got know the importance of knowledge management in the organization and its relationship with the project planning system and the green software development environment.

The proposed model for improving the implementation of ERP system in the green software development process environment is important in improving software quality as well as knowledge quality because it requires the implementation of ERP in a pure, environmentally friendly environment, with less of (energy consumption, carbon emissions and waste of resources).

6. Conclusion

The adoption of ERP system is important for companies around the world, and the implementation of ERP continues to face many problems. There are many studies in this regard, but there is no framework that demonstrates the possibility of improving the implementation of the ERP system in a green software development process environment as it is pure and environmentally friendly.

In this paper we propose a model to improve the implementation of the ERP system in a green software development process environment based on knowledge management and IT practices as support tools. The result model shows how knowledge management has been used as a management to enhance the green software development process environment.

In the future, we will provide a questionnaire for specialists in this field to verify the validity of the model, and we suggest that there should be a field study of some companies that use ERP system in Iraq/Basra and urge them to implement the system in a friendly environment. One of the limitations of this study is that it is a theoretical study, not an application, as well as the ability to develop an algorithm for the model.

7. Acknowledgments

We would like to express our thanks to everyone who helped us complete this research.

8. References

[1] P. Sanguankaew and V. V. Ractham, 'Bibliometric review of research on Knowledge Management and sustainability, 1994-2018', *Sustain.*, vol. 11, no. 16, 2019.
[2] C. More and C. More, 'Environment, economy and society', *Ind. Age*, vol. 196, pp. 208–212, 2019.
[3] M. Ursacescu, D. Popescu, C. State, and I. Smeureanu, 'Assessing the Greenness of Enterprise Resource Planning Systems through Green IT Solutions: A Romanian Perspective', *Sustainability*, vol. 11, no. 16, p. 4472, Aug. 2019.
[4] 'Green | Definition of Green by Merriam-Webster'. [Online]. Available: https://www.merriam-webster.com/dictionary/green. [Accessed: 07-Jul-2020].
[5] H. Acar, 'Software development methodology in a Green IT To cite this version : Software development methodology in a Green IT environment', 2018.
[6] W. H. Tsai, K. C. Lee, J. Y. Liu, S. J. Lin, and Y. W. Chou, 'The influence of enterprise resource planning (ERP) systems' performance on earnings management', *Enterp. Inf. Syst.*, vol. 6, no. 4, pp. 491–517, 2011.
[7] H. M. Beheshti and C. M. Beheshti, 'Improving productivity and firm performance with enterprise resource planning', *Enterp. Inf. Syst.*, vol. 4, no. 4, pp. 445–472, 2010.
[8] S. Y. Huang, A. A. Chiu, P. C. Chao, and A. Arniati, 'Critical success factors in implementing enterprise resource planning systems for sustainable corporations', *Sustain.*, vol. 11, no. 23, 2019.
[9] J. Vom Brocke, S. Seidel, and J. Recker, 'Green business process management: Towards the sustainable enterprise', *Green Bus. Process Manag. Towar. Sustain. Enterp.*, vol. 9783642274, no. June 2016, pp. 1–251, 2013.
[10] T. Butler, 'Compliance with institutional imperatives on environmental sustainability: Building theory on the role of Green IS', *J. Strateg. Inf. Syst.*, vol. 20, no. 1, pp. 6–26, 2011.
[11] I. Vrdoljak, 'ERP Concept for Enterprise Management and Knowledge Management Era', *New Trends Technol. Control. Manag. Comput. Intell. Netw. Syst.*, 2010.
[12] R. Abdullah, S. Abdullah, J. Din, and M. Tee, 'A S YSTEMATIC L ITERATURE R EVIEW OF G REEN S OFTWARE D EVELOPMENT IN C OLLABORATIVE'.
[13] R. Van Der Meer and S. Sinnappan, 'The Role of Knowledge Management in an Organisation ' s Sustainable Development', pp. 450–454, 2007.
[14] L. Fernando, S. Joya, L. Eduardo, B. Ardila, L. Eduardo, and B. Ardila, 'Model for Knowledge Management in Software Project Planning in University Research Groups', vol. 9, no. 16, pp. 58–64, 2014.
[15] A. Gholamzadeh Chofreh, F. A. Goni, S. Ismail, A. Mohamed Shaharoun, J. J. Klemeš, and M. Zeinalnezhad, 'A master plan for the implementation of sustainable enterprise resource planning systems (part I): concept and methodology', *J. Clean. Prod.*, vol. 136, no. July 2018, pp. 176–182, 2016.
[16] A. mike, 'Analysing the Impact of Enterprise Resource Planning', *Www.Ejise.Com*, pp. 103–113, 2001.

[17] M. Rashid, L. Hossain, and J. Patrick, *Enterprise Resource Planning*. IGI Global, 2002.
[18] I. Ibrahim, N. A. Jamil, and I. A. Halin, 'Green Enterprise Resource Planning and Green Logistics Performance', *SIJ Trans. Ind. Financ. Bus. Manag.*, vol. 06, no. 03, pp. 01–06, Jun. 2018.
[19] E. Processes, 'ERP ' s Maximizing the Value of Erp-Enabled Processes', *Business*, p. 28, 1998.
[20] G. T. Timbrell, 'A meta-study of SAP financials in the Queensland Government', 2006.
[21] F. Alizai, 'A model for the implementation of ERP systems in midsize businesses', no. November, pp. 1–391, 2014.
[22] 'What is SAP? Definition of SAP ERP Software'. [Online]. Available: https://www.guru99.com/what-is-sap-definition-of-sap-erp-software.html. [Accessed: 09-Jul-2020].
[23] M. Grube, 'The impact of SAP on the utilisation of business process management (BPM) maturity models in ERP projects', *CEUR Workshop Proc.*, vol. 2196, no. February, pp. 6–10, 2018.
[24] J. M. Esteves de Souza, 'Definition and analysis of Critical Success Factors for ERP implementation projects', *Thesis*, pp. 1–313, 2004.
[25] N. Dechow, M. Granlund, and J. Mouritsen, 'Management Control of the Complex Organization: Relationships between Management Accounting and Information Technology', *Handbooks Manag. Account. Res.*, vol. 2, pp. 625–640, 2006.
[26] N. Williams, 'IT Service Management in SAP Solution Manager', 2013.
[27] S. Ray, 'Journal of Global Research in Computer Science[[Elektronische Ressource]] JGRCS', *J. Glob. Res. Comput. Sci.*, vol. 4, no. 1, pp. 25–29, 2013.
[28] N. S. Chauhan and A. Saxena, 'A green software development life cycle for cloud computing', *IT Prof.*, vol. 15, no. 1, pp. 28–34, 2013.
[29] M. Tee, R. Abdullah, J. Din, S. Abdullah, and L. Wu, 'Green SD adoption using knowledge mangement facilitation – A motivational perspective', *J. Theor. Appl. Inf. Technol.*, vol. 95, no. 17, pp. 4291–4303, 2017.
[30] B. Penzenstadler and H. Femmer, 'A generic model for sustainability with process- and product-specific instances', *GIBSE 2013 - Proc. 2013 Work. Green Softw. Eng. Green by Softw. Eng.*, pp. 3–7, 2013.
[31] M. Tee, R. Abdullah, and L. Wu, 'Towards Developing Agent-Based KMS In Managing Knowledge of Green SD For Community of Practice', vol. 9, no. 2, pp. 71–76.
[32] C. Calero and M. Piattini, 'Green in software engineering', in *Green in Software Engineering*, 2015, pp. 1–327.
[33] M. Dick and S. Naumann, 'Enhancing Software Engineering Processes towards Sustainable Software Product Design', *EnviroInfo 2010, Integr. Environ. Inf. Eur. Proc. 24th Int. Conf. Informatics Environ. Prot.*, vol. 2010, pp. 706–715, 2010.
[34] C. Barth and S. Koch, 'Critical success factors in ERP upgrade projects', 2019.
[35] C. Calero and M. Piattini, 'Green in software engineering', in *Green in Software Engineering*, no. January 2015, 2015, pp. 1–327.
[36] M. Uddin and A. A. Rahman, 'Energy efficiency and low carbon enabler green IT framework for data centers considering green metrics', *Renew. Sustain. Energy Rev.*, vol. 16, no. 6, pp. 4078–4094, 2012.
[37] R. Foogooa, C. Bokhoree, and K. Dookhitram, 'Green ICT Maturity Models', *Ieee*, 2015.
[38] R. Lu and J. Liu, 'The research of the knowledge management technology in the education', *Proc. - 2008 Int. Symp. Knowl. Acquis. Model. KAM 2008*, pp. 551–554, 2008.
[39] R. Abdullah, H. Ibrahim, R. Atan, S. Napis, M. H. Selamat, and N. Haslina, 'The Development of Bioinformatics Knowledge Management System with Collaborative Environment The Development of Bioinformatics Knowledge Management System with Collaborative Environment', no. January, 2008.

[40] M. Personal and R. Archive, 'Munich Personal RePEc Archive The Roles of Knowledge Management for the Development of Organizations', no. 83038, 2017.
[41] M. Alavi and D. E. Leidner, 'Review : Knowledge Systems : Management Knowledge and Foundations Conceptual', *MIS Q.*, vol. 25, no. 1, pp. 107–136, 2001.
[42] I. Rus and M. Lindvall, 'Knowledge management in software engineering', *IEEE Softw.*, vol. 19, no. 3, pp. 26–38, 2002.

The Prediction of COVID 19 Disease Using Feature Selection Techniques

The Prediction of COVID 19 Disease Using Feature Selection Techniques

Rasha H. Ali[1] and Wisal Hashim Abdulsalam[2]

[1]Computer Science Department/College of Education for Women/University of Baghdad, Iraq
[2]Computer Science Department/College of Education for Pure Science/Ibn-Al Haitham/University of Baghdad, Iraq

E-mail: wisal.h@ihcoedu.uobaghdad.edu.iq

Abstract. COVID 19 has spread rapidly around the world due to the lack of a suitable vaccine; therefore the early prediction of those infected with this virus is extremely important attempting to control it by quarantining the infected people and giving them possible medical attention to limit its spread. This work suggests a model for predicting the COVID 19 virus using feature selection techniques. The proposed model consists of three stages which include the preprocessing stage, the features selection stage, and the classification stage. This work uses a data set consists of 8571 records, with forty features for patients from different countries. Two feature selection techniques are used in order to select the best features that affect the prediction of the proposed model. These are the Recursive Feature Elimination (RFE) as wrapper feature selection and the Extra Tree Classifier (ETC) as embedded feature selection. Two classification methods are applied for classifying the features vectors which include the Naïve Bayesian method and Restricted Boltzmann Machine (RBM) method. The results were 56.181%, 97.906% respectively when classifying all features and 66.329%, 99.924% respectively when classifying the best ten features using features selection techniques.

Keywords: Feature selection, COVID 19, Recursive Feature Elimination, Extra Tree Classifier, Restricted Boltzmann Machine, Naïve Bayesian.

1. Introduction

COVID 19 is an infectious disease that spreads through the air. Besides, it can live on rooftops for about two days, and it was initially called the Wuhan virus because of its origin from Wuhan, China, where the first human case was recorded [3]. Then the disease spreads rapidly and within a month turned into a pandemic affecting people all over the world in a negatively way. This prompted the World Health Organization (WHO) to declare a general global health emergency by the end of January 2020. Symptoms may appear on the infected person or not, but in either cases, the infected person can spread the virus. The incubation period ranges from two days to two weeks. The symptoms are different, such as fever,

shortness of breath, cough, chest pain, loss of sense of smell and taste, vomiting, headache, nausea, laziness, and others [4, 5].
In general, there is no vaccine available for **COVID 19** and information about it remains limited. There are several clinical trials to understand how the virus could be redeveloped in an attempt to produce a vaccine [6].
To limit the virus spread, governments around the world have taken various measures such as closing borders and commercial complexes, suspending education in universities and schools and converting them to e-learning, and suspending gatherings, etc., which affected various aspects of life, especially the economic aspect. People have been made aware of the importance of practicing simple steps such as staying home, regularly washing and sterilizing hands, social distancing, and wearing masks. Figure (1) gives **COVID 19** cases distribution worldwide, in November 2020 [2].

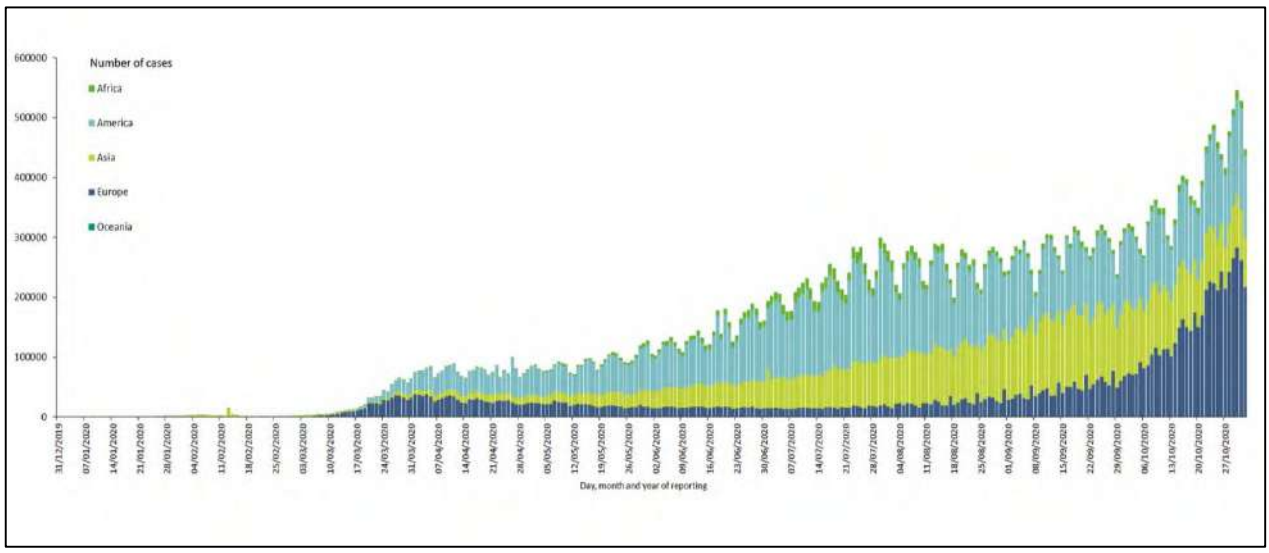

Fig. (1) **COVID 19** cases distribution worldwide, in November 2020 [2].

The goal of this work is to suggest a model for predicting the disease of **COVID 19** using feature selection techniques. The feature selection techniques are used for selecting the important features which affect the accuracy of the classification for the model.
The main contribution of this work is the prediction of the COVID 19 disease using two types of feature selection techniques, which are REF as wrapper feature selection method and ETC as embedded feature selection method and comparing between them by the results in order to select the most important features, then extracted the optimal number of features in the dataset contained different information, different types of data (text, number, and date), missing value, and large numbers. Two types of classification techniques are used including the Naïve Bayesian and RBM which are applied on different number of features for comparing the results.
This paper is ordered as follows: Section 2 presents the literature review. Section 3 describes the proposed work including the dataset used, basic preprocessing operations, feature selection, and classification. Section 4 presents the results and discussion while section 5 gives the conclusions.

2. Literature Review

This section presents the work related to **COVID 19** prediction based on feature selection techniques.

Warda M. Shaban et al. [5] suggested a strategy to diagnosis **COVID 19** using a hybrid feature selection that used filter method as a rapid feature selection and then used genetic algorithm as a wrapper method to select the most important features from those extracted from chest Computed Tomography (CT) images and then an Enhanced K-Nearest Neighbour (EKNN) classifier was used. This method achieved 96% of accuracy.

Liang Sun et al. [7] proposed an Adaptive Feature Selection guided Deep Forest (AFS-DF) for **COVID 19** classification based on chest CT images. AFS-DF was evaluated on a dataset with 1495 patients of **COVID 19** and 1027 patients of community and gained an accuracy of 91.79%.

Bejoy Abraham, and Madhu S. Nair [8] investigated the effectiveness of a combination of several pre-trained Convolutional Neural Networks (CNNs) for **COVID 19** detection from X-ray images. The method used a combination of features extracted from multi-CNN with correlation based feature selection technique in combination with subset size forward selection, and a linear forward selection based search technique to determine the optimal feature subset and Bayesnet classifier. They achieved an accuracy of 91.16% when tested on a dataset with 453 **COVID 19** images and 497 non-COVID images, and 97.44% on a dataset consisting of 71 **COVID 19** images and 7 non-COVID images.

Mohammad Pourhomayoun, and Mahdi Shakibi [9] applied different filter and wrapper methods for feature selection to select 42 features out of 112 features. Then they used several machine-learning algorithms to predict mortality in patients with **COVID 19**. They used a dataset of more than 117,000 laboratory-confirmed **COVID 19** patients from76 countries. The Neural Network algorithm achieved the best performance and accuracy of 93%.

3. The Proposed Work The proposed work consists of three stages. These are pre-processing stage, features selection stage, and finally the classification stage. In each stage, more than one step and techniques are used for achieving the goal of each stage. Figure (2) shows the structure of the proposed model.

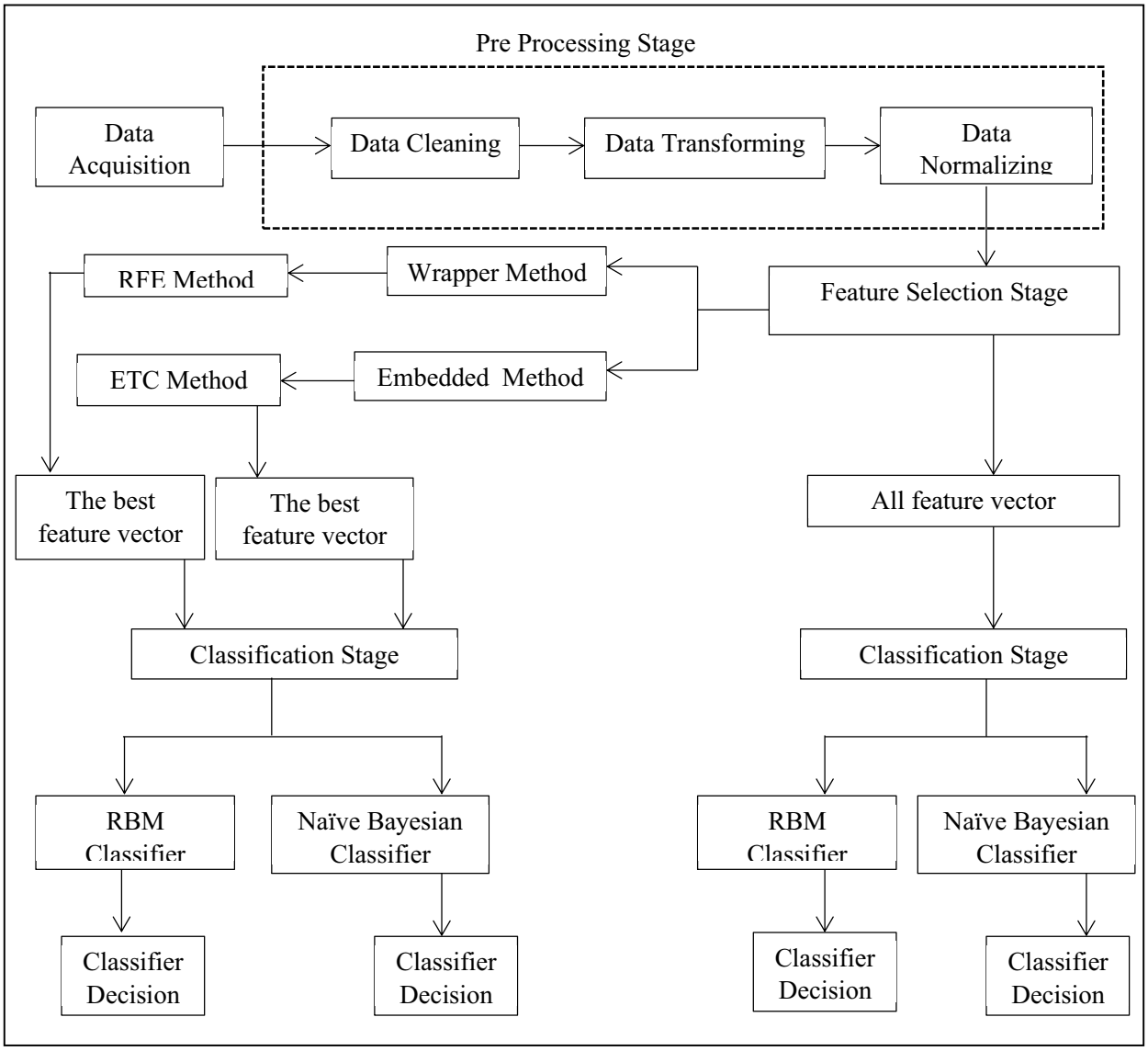

Fig. (2) The structure of the proposed model.

3.1 The Pre-processing Stage

This stage is also known as data preparation. It is a very important stage to build a good model and enhance the accuracy [10]. The dataset used in this work had been collecting by the WHO, which contained 8571 records from thirty-eight countries.

Figure (3) shows the number of records for each country in the dataset. The dataset included forty features with different types (time, text, and number), with type (CSV) file. The proposed model undergoes pre-processing in three steps, namely data cleaning, transforming and normalization

- **Data cleaning processing.** The data set may have insufficient data, missing data, too much data in rows or in columns, duplicate data and outlier values. In this work, the data has been cleaned through processing the missing value by fill each missing value with the nearest value.
- **Data transforming process** has been applied through transforming data into numeric forms.
- **Data normalizing** has been performed by applying min max scalar using the following equation

$$z = (x - \min) / (\max - \min) \quad \ldots(1)$$

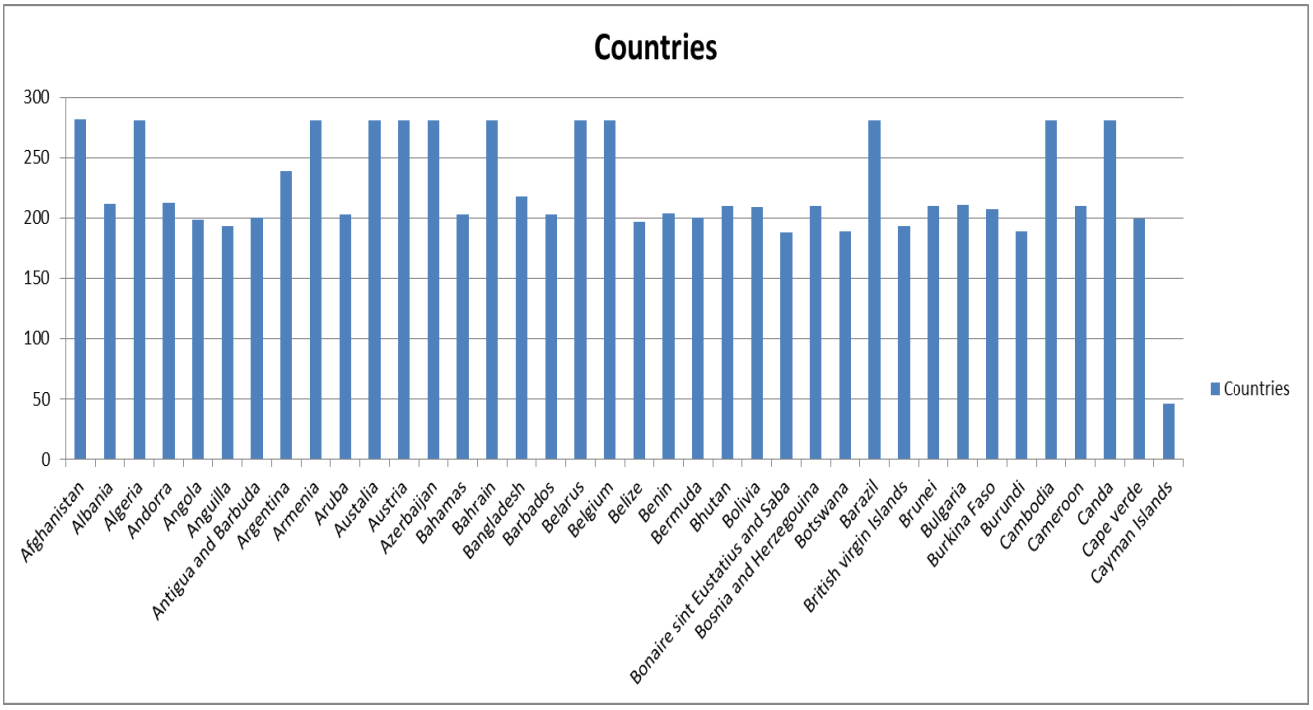

Fig. (3) The number of records and countries in the dataset.

3.2 The Feature Selection Stage

To improve learning performance, dimensionality reduction was used when there are a large number of input features, which divided into feature extraction and feature selection techniques. Feature extraction extracts a new set of features that is smaller than that resulting from feature selection, so the discriminative power is better. Because of that, it is more useful for signal processing, information retrieval, and image analysis, but a combination of features may have no physical meaning, so feature extraction is not a good approach in respect of transparency, interpretability, and readability. Feature

selection builds a subset of the original features. This is useful when interpretability knowledge extraction is crucial, as in medicine, and since this work is based on a medical problem, we will concentrate on feature selection. There are three types of feature selection: filters, wrappers, and embedded. Filters concentrate on the general characteristics of the data. So they are independent of any learning method, not computationally costly and have a good generalization capacity. Wrappers and embedded methods both are required for selecting features. For wrappers, an induction method evaluates candidate subsets of features. They are more computationally costly than filters but perform better. Embedded methods lie between filters and wrappers because the selection is part of the training process for the induction method. The search for the best subset of features is performed during the training of the classifier and, because of that; embedded methods are less computationally costly than wrappers. There is also a hybrid method, which combines different feature selection algorithms in a sequential manner [11].
In this work, the number of features in the dataset is forty. Table (1) presents the features of the dataset. The goal of this stage is selecting the important features which affect the prediction of the model. Two methods are used for selecting features: Recursive Feature Elimination (RFE) method and the Extra Tree Classifier (ETC) method. The RFE is one of the wrapper feature selection method. It works by recursively removing attributes and building a model on those attributes that remain. It uses accuracy metric to rank the feature according to their importance. It takes the model to be used and the number of required features as input and gives the ranking of all the variables, the value (one) being most important. It also gives its support, the value (True) being a relevant feature and (False) value being an irrelevant feature. Algorithm (1) shows the steps of the RFE.

Algorithm (1) The steps of the RFE method.

Step1:- Train the logistic regression model using training set.

Step2:- Calculate the performance of the model.

Step3:- Calculate the variable ranking.

Step4:- For each subset size S_i do

1. keep the S_i most important variable
2. preprocessing the data
3. train the model using S_i predictors
4. calculate the performance of the model.
5. recalculate the ranking for each predictors.

End

Step5:- Calculate the performance for all S_i

Step6:- Determine the number of the predictors.

Step7:- END.

The (ETC) method is an embedded feature selection method. It depends on decision trees where each decision tree is created from the unusual training sample. Then, at each test node, each tree is provided with a random sample of N features from the feature set from which each decision tree must select the best feature to split the data based on the Gini Index using equation (2) as a mathematical criterion [12]. This random sample of features leads to the creation of multiple de-correlated decision trees.

$$I_G = 1 - \sum_{j=1}^{c} p_j^2 \quad \ldots(2)$$

Table (1) The features of the dataset [1].

No.	Feature's Name	No.	Feature's Name
1	iso_code	21	new_tests_smoothed_per_thousand
2	Continent	22	tests_per_case
3	Location	23	positive_rate
4	Date	24	tests_units
5	total_cases	25	stringency_index
6	new_cases_smoothed	26	population
7	total_deaths	27	population_density
8	new_deaths	28	median_age
9	new_deaths_smoothed	29	aged_65_older
10	total_cases_per_million	30	aged_70_older
11	new_cases_per_million	31	gdp_per_capita
12	new_cases_smoothed_per_million	32	extreme_poverty
13	total_deaths_per_million	33	cardiovasc_death_rate
14	new_deaths_per_million	34	diabetes_prevalence
15	new_deaths_smoothed_per_million	35	female_smokers
16	new_tests	36	male_smokers
17	total_tests	37	handwashing_facilities
18	total_tests_per_thousand	38	hospital_beds_per_thousand
19	new_tests_per_thousand	39	life_expectancy
20	new_tests_smoothed	40	human_development_index

3.3 The Classification Stage

Also, it is known as decision making. The goal of this stage is to classify the feature vector [13]. In this stage, the feature vector is classified using two methods: the Naïve Bayesian (NB) method and Restricted Boltzmann Machine (RBM) method. NB is a simple classifier based on the Bayes theorem which assumes that the features are independent. This classifier has worked well in many real-world situations. It is a very fast and has a good performance. The main advantages of this classifier are the conditional independence assumption, which helps to obtain a quick classification, and the probabilistic hypotheses. Parameters of probability distributions are obtained from the training material [14].

RBM is an algorithm useful for dimensionality reduction, feature learning, regression, classification, and collaborative filtering. RBM is a two-layered stochastic recurrent neural network capable of unsupervised learning and feature extraction [15]. It is an energy based model that can be viewed as a single layer undirected neural network which consists of two binary layers, the visible layer, and hidden layers. There are no effects between nodes in a single layer of RBM[16].

4 The Results and Discussion

This paper suggests a model for predicting the **COVID 19** disease using features selection techniques and two methods for classifying the features vector. The implementation of the proposed work was achieved using Python (V.3.5) as programming language, Jet Brains Pycharm (V.2018.2) as framework. As described earlier, the suggested method consists of three main stages. Firstly, the data pre-processing which was contained more than one process because of the nature of the collected dataset which has missing values, extra data, and different types of data. Secondly, the features selection was achieved by using two models for selecting features (the wrapper method and the embedded method). In this stage, the number of features selected was: ten features and twenty features. The RFE is one of the wrapper methods which was applied for selecting the 10 features and 20 features. Figure (4) presents the sorting of ten important features using RFE. The true value means the relevant feature while the false value means the irrelevant feature. Also, it can be viewed as ranking; the value (one) is the most important feature while the remainder values mean the rank of each feature depending on its importance.

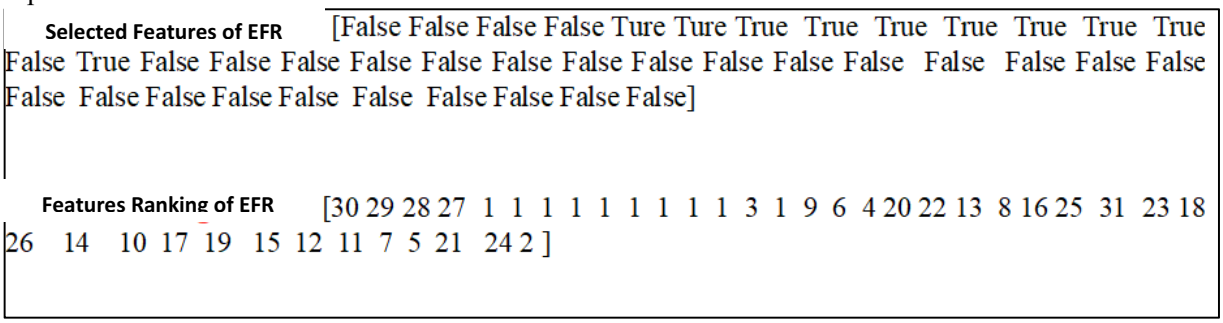

Fig. (4) The results of RFE method.

The second method applied for selecting features was ETC. Table (2) shows the values of features depend on their importance. While Figure (5) and (6) show the sorting of features depends on the importance of features for (10 most important features and 20 most important features respectively).

Table (2) The values of importance for features

Feature's Name	The value	Feature's Name	The value
iso_code	0.0000	new_tests_smoothed_per_thousand	0.017507
Continent	0.0000	tests_per_case	0.017407
Location	0.0000	positive_rate	0.015329
Date	0.0000	tests_units	0.0000
total_cases	0.075913	stringency_index	0.037782
New_deaths	0.040493	population	0.004229
new_cases_smoothed	0.075071	population_density	0.002263
total_deaths	0.047183	median_age	0.006317
new_deaths_smoothed	0.044856	aged_65_older	0.008087
total_cases_per_million	0.071144	aged_70_older	0.016779
new_cases_per_million	0.180063	gdp_per_capita	0.005155
new_cases_smoothed_per_million	0.076830	extreme_poverty	0.004050
total_deaths_per_million	0.047108	cardiovasc_death_rate	0.004266
new_deaths_per_million	0.036282	diabetes_prevalence	0.008391
new_deaths_smoothed_per_million	0.040993	female_smokers	0.002974
new_tests	0.016462	male_smokers	0.004460
total_tests	0.016644	handwashing_facilities	0.005238
total_tests_per_thousand	0.016404	hospital_beds_per_thousand	0.005043
new_tests_per_thousand	0.014537	life_expectancy	0.005591
new_tests_smoothed	0.019729	human_development_index	0.009421

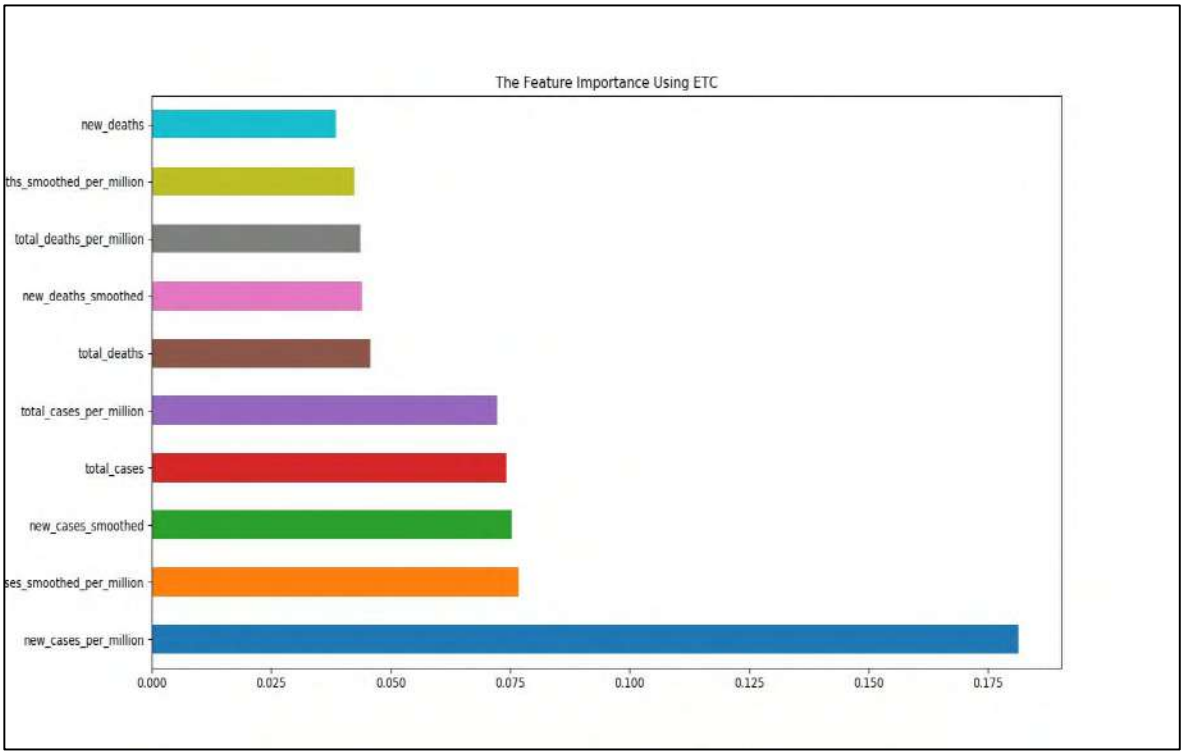

Fig. (5) The sorting of important ten features using ETC.

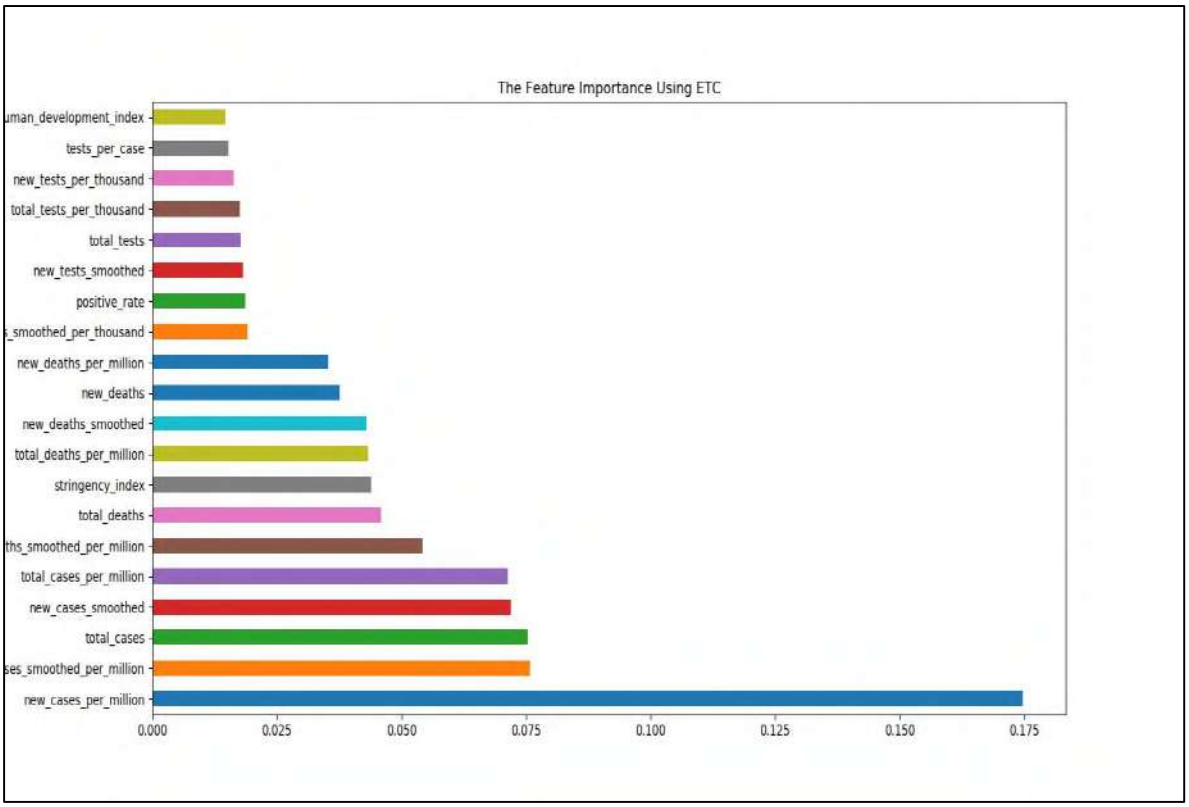

Fig. (6) The sorting of important twenty features using ETC.

Finally, the classification stage aimed to classify the features vector. In this stage, two methods were applied including the NB method and RBM method. The dataset was split into 70% for training and 30% for testing to predicate the disease of **COVID 19**. The equation (3) was used for computing the accuracy of the proposed work.

$$Accuracy = \frac{Number\ of\ correct\ predictions}{Total\ number\ of\ predictions} \quad \ldots(3)$$

Table (3) presents the results of classification using two methods (NB and RBM) with three cases: firstly, for all features, secondly, for the best 20 features, and finally, for 10 best features which selected in features selection stage. The results show that there is an improvement in accuracy when using the techniques of selecting features. Also, the RBM classifier got a good accuracy comparing with (NB) classifiers.

Table (3) The accuracy of the methods.

The Method	The accuracy for all features	The accuracy for best 20 features	The accuracy for best 10 features
NB	56.181%	61.780%	66.329%
RBM	97.906%	98.949%	99.924%

As shown in figures (4) and (5), the results of the RFE method and ETC method in selecting the important features are approximate. As shown in table (3), the accuracy when using the best ten features is more than the accuracy of the best twenty features. This is because of the correlation between these features. So, it can eliminate the correlated features which may cause a decrease the accuracy and performance as all. By comparing the results of this work with the results of the related works, this work had more accuracy especially when using RBM method comparing with the related works in spite of increasing the size of the dataset except for the work in Reference [8], but this work got more accuracy comparing with that study. The features selection techniques had a more positive impaction on the classification of the feature vector.

5 The Conclusion

In this work, the prediction of **COVID 19** disease using the techniques of feature selection had been achieved. The dataset contained different information about the disease from different countries. The proposed system contains three stages. More than one steps has been applied for preparing the data for the next stage. In the features selection stage, two types of techniques (RFE and ETC) were used for selecting the important features from forty features. The results of the two methods for the important features were approximate. The selecting of the important features affected the accuracy of the proposed work. The accuracy was very good when used RBM technique more than the NB technique.

REFERENCES

[1] https://www.who.int/emergencies/diseases/novel-coronavirus-2019?gclid=CjwKCAiA_Kz-BRAJEiwAhJNY7zTX-h33i5Ty1mcFi-XXcMl7cjj7J9FFESmnKgvHxk7JcoynYR5oAhoCcVMQAvD_BwE#2020
[2] https://www.ecdc.europa.eu/en/publications-data/download-todays-data-geographic-distribution-covid-19-cases-worldwide
[3] Cohen, J.: 'Wuhan seafood market may not be source of novel virus spreading globally', Science, 2020, 10
[4] Huang, C., Wang, Y., Li, X., Ren, L., Zhao, J., Hu, Y., Zhang, L., Fan, G., Xu, J., and Gu, X.: 'Clinical features of patients infected with 2019 novel coronavirus in Wuhan, China', The lancet, 2020, 395, (10223), pp. 497-506
[5] Shaban, W.M., Rabie, A.H., Saleh, A.I., and Abo-Elsoud, M.: 'A new COVID-19 Patients Detection Strategy (CPDS) based on hybrid feature selection and enhanced KNN classifier', Knowledge-Based Systems, 2020, 205, pp. 106270
[6] Chen, N., Zhou, M., Dong, X., Qu, J., Gong, F., Han, Y., Qiu, Y., Wang, J., Liu, Y., and Wei, Y.: 'Epidemiological and clinical characteristics of 99 cases of 2019 novel coronavirus pneumonia in Wuhan, China: a descriptive study', The Lancet, 2020, 395, (10223), pp. 507-513
[7] Sun, L., Mo, Z., Yan, F., Xia, L., Shan, F., Ding, Z., Song, B., Gao, W., Shao, W., and Shi, F.: 'Adaptive feature selection guided deep forest for covid-19 classification with chest ct', IEEE Journal of Biomedical and Health Informatics, 2020
[8] Abraham, B., and Nair, M.S.: 'Computer-aided detection of COVID-19 from X-ray images using multi-CNN and Bayesnet classifier', Biocybernetics and biomedical engineering, 2020, 40, (4), pp. 1436-1445
[9] Pourhomayoun, M., and Shakibi, M.: 'Predicting mortality risk in patients with COVID-19 using artificial intelligence to help medical decision-making', medRxiv, 2020
[10] Abdulsalam, W.H., Alhamdani, R.S., and Abdullah, M.N.: 'Emotion Recognition System Based on Hybrid Techniques', International Journal of Machine Learning and Computing, 2019, 9, (4)
[11] Remeseiro, B., and Bolon-Canedo, V.: 'A review of feature selection methods in medical applications', Computers in biology and medicine, 2019, 112, pp. 103375
[12] Tangirala, S.: 'Evaluating the Impact of GINI Index and Information Gain on Classification using Decision Tree Classifier Algorithm'
[13] RASHA H. ALI, D.M.N.A.A.D.B.F.A.: 'SPEAKER IDENTIFICATION AND LOCALIZATION USING FUSION OF FEATURES AND SCORE LEVEL FUSION ', Journal of Theoretical and Applied Information Technology, 2018 96, (21), pp. 11
[14] Urbano Romeu, Á.: 'Emotion recognition based on the speech, using a Naive Bayes classifier', Universitat Politècnica de Catalunya, 2016
[15] Nasrin, S., Drobitch, J.L., Bandyopadhyay, S., and Trivedi, A.R.: 'Low power restricted Boltzmann machine using mixed-mode magneto-tunneling junctions', IEEE Electron Device Letters, 2019, 40, (2), pp. 345-348
[16] Hu, H., Gao, L., and Ma, Q.: 'Deep restricted boltzmann networks', arXiv preprint arXiv:1611.07917, 2016

The Classification of Fetus Gender Based on Fuzzy C-Mean Using a Hybrid Filter

The Classification of Fetus Gender Based on Fuzzy C-Mean Using a Hybrid Filter

Ahmed S Aljuboori[1], Firas A.Abdullatif [2]and Duraid Y.Mahmmed[3]

[1,2]College of Education for Pure Science /Ibn Al-Haitham, University of Baghdad, Baghdad, Iraq.
[3]Al-Iraqia University, Baghdad, Iraq.

E-mail: a.s.aljuboori@ihcoedu.uobaghdad.edu.iq

Abstract. This paper proposes a new approach, of Clustering Ultrasound images using the Hybrid Filter (CUHF) to determine the gender of the fetus in the early stages. The possible advantage of CUHF, a better result can be achieved when fuzzy c-mean FCM returns incorrect clusters. The proposed approach is conducted in two steps. Firstly, a preprocessing step to decrease the noise presented in ultrasound images by applying the filters: Local Binary Pattern (LBP), median, median and discrete wavelet (DWT), (median, DWT & LBP) and (median & Laplacian) ML. Secondly, implementing Fuzzy C-Mean (FCM) for clustering the resulted images from the first step. Amongst those filters, Median & Laplace has recorded a better accuracy. Our experimental evaluation on real data from the Kadhimiya teaching hospital shows that the proposed CUHF is a better method when compared to the accuracy of the other integrated filters.
Keywords: Fuzzy C-mean, Filters Integration, Noise Reduction, Fetus Gender.

1. Introduction.

Many studies have focused on the use of fuzzy logic techniques to improve medical diagnostics [1]. The fuzzy c-mean algorithm (FCM) [2] is one of the most famous algorithms which can assist in decision-making [3]. [4] Proposed a novel approach to measure the muscle thickness from ultrasound images of the lumbar area to diagnose low back pain effectively. [5] Used robust Optimal GLCM features linked to FCM segmentation algorithm which is employed to cluster the kidney cysts and tumor from the ultrasound kidney images. However, others applied filters before implementing FCM to reduce the speckle in ultrasound images to obtain better results.

Filters play a major role in the pre-processing step which could assist researchers to reduce the noise of images [6]. Other studies also used filters for enhancing ultrasound images [7]. [8]Adopted a special study on "noise reduction" by using a wiener filter and discrete wavelet transform in a homomorphic region. The use of the Weiner filter and wavelet conversion is utilized to reduce the noise of ultrasound [8]. Besides, (LBP) local binary pattern operator to provide the classification Ultrasonic Thyroid of HOG Features[9]. A median filter is used in artifact removal in radiological ultrasound images [10]. In addition, several studies reported that filters can be useful to improve the FCM algorithm. For example, [11] used LBP with fuzzy c-mean to extract features in underwater images. [12] Integrated wavelet into FCM for

reconstructing morphological grayscale of sparse regularization. Moreover, improved malignant diagnosis using FCM based on the improved median of lung images [13].

In this study, we propose CUHF a new approach for improving the performance of FCM by using such an algorithm that tries different applied filters as preprocess on Ultrasound images. The proposed approach uses single and combination filters until the CUHF records the highest accuracy. The design of our approach was to detect the gender of the fetus by extracting selected features. Many difficulties were challenged such as the complexity of uterine tissue and the similarity of the fetus features were difficult to distinguish. Kadhimiya teaching hospital was selected because pregnancies attend the sonar department to do regular checks. The test of pregnant mothers was conducted to obtain the source of medical images for educational purposes. The images include related features from the ultrasound device (UD) during the second and third trimester of pregnancy. Our initial experimental results show that the CUHF approach achieves a better accuracy when the ML filter is applied and compared to those obtained when using FCM and other used filters.

2. Pre-Processing & Filters Applied to CUHF Approach

This section describes the used filters to reduce the noise of ultrasound images. These filters are applied to reduce the noise to enhance the performance of the FCM algorithm. Ultrasound images contain a noise which may cause damage conditions because of variation of the velocity with beam frequency. Therefore the preprocess step contains a series of image enhancement stages that can be listed as follows: noise removal, segmentation, and normalization. To remove the noise associated with the ultrasound image, a suitable filter will be applied to reduce the noise and maintain the original details of the image. Images are next partitioned into multiple segments for object recognition. Ultimately, the images are normalized into the range of pixel intensity of 256 x 256. The difference between the edges and the noise will produce a frame (3*3) into the next candidate filter.

2.1 Local Binary Pattern (LBP)

LBP is a local binary pattern that works as a character revealer can be executed on ultrasound images. The basic algorithm idea can be described as two-parent surface textures. The native operator classifies pixels of the image by specifying the 3 x 3 (LBP) of each pixel with the value of the center and a result is a binary number, (LBP) as classification or fragmentation properties by applying a summation of the probability of fabric pattern in the histogram [14]. The reason for the failure of the LBP in the classification is because it is influenced by the contour, which is often a "high contrast".

First, When LBP is applied to the ultrasound images; the proposed CUHF approach converts them into greyscale. Secondly, it divides the examined frame into cells 3x3 pixels. Third, compare the pixel to each of its 8 neighbors" .Follow the pixels clockwise or counterclockwise. If the center pixel's value is greater than the neighbor's value", then the value is 1 else value is 0. "After computing this for every neighbor pixel, the values are listed in a clockwise manner and the equivalent decimal value is calculated". Finally "Once done for every pixel, the values are grouped in 256 bins and the histogram is created", the output is the enhanced filter.

2.2 Discrete Wavelet Transform (DWT)

Is an easy-to-implement conversion in which wavelets are sampled instead of separate DWT. It is important to use because the transform uses a Fourier transform instead of using a fixed-width frame, DWT as well as the time it takes to calculate a conversion very quickly compared to a Fourier transform that takes more time, the conversion depends mainly on the wavelet matrix, which can be calculated faster than the Fourier matrix. The method of hiding information can also be used as DWT [15], [16]. The process of converting wavelets is a simple idea. The original image is divided into 4 new sub-images. Each sub-image is (25%) the original image by analyzing each image in different frequency bands with varying degrees of accuracy.

Each image is decomposed by four levels using the separate wavelet conversion at each level. (HH, HL, LH) and Details (LL) Transactions, Rounding The sub picture appears in the upper right, lower left, and lower right as an approximation of the original image because it contains high-frequency components of the original image. As for the upper left sub-picture, it appears as the original image and looks smoother, with the lower frequency components of the original image [17].

2.3 Median Filtering

Median and Nonlinear digital filtering is mostly used for noise removal of "spots" from ultrasound images [18]. This method is effective and widely used in digital image processing because it maintains sharp edges when noise is removed [19]. It calculates the median by sorting all pixel values from surrounding neighborhoods in the numerical approach and then replaces corresponding pixels with the pixel value. The median is also provided the simplicity of eliminating noise when compared with other filters. Especially for ultrasound images, this filter is very important [18].

Table1 Unsorted Vectors

1	0	0
0	8	7
5	29	14

Taken the above example, unsorted vectors are (1, 0, 5, 0, 8, 29, 0, 7, 14), sorted vector are (0, 0, 0, 1, 5, 7, 8, 14, 29) Median value is 5. It is noted in Figure 1 that the images contain a higher percentage of noise than the image (B) resulting in the results as shown below:

(A) (B)

Figure 1 Applying Median Filter

(A) The original image before the implementation of the median filter
(B) Filtered image after the implementation of the median filter

When the median filter is applied to the proposed CUHF, an Input of 256*256 ultrasound images is obtained. In the first step, the entire matrix of the image pixel is padded with zeros or ones on all sides. Second, the frame will be an array, store the 3*3 neighbor value in the array, and sort the neighboring pixels into order. Finally, replace the value of a center pixel with the median value from the list, the enhanced filter is obtained.

2.4 Laplacian Filtering

Laplacian is considered as a two-dimension isotropies' measure of the second spatial derivative of an image. It highlights areas of fast intensity change and consequently often utilized for edge detection with the technique of zero-crossing edge detectors. This filter is frequently applied on images that have first been smoothed with something approximating a Gaussian filter to reduce its sensitivity to noise. Therefore the two variants will be labeled together. A single gray level image is normally taken as an input and generates another gray level of the image as output [20]. The Laplacian $L(x,y)$ of an image with pixel intensity values is, x & y are random variables, ə= an integral transform that converts a function of a real

variable, I = integral maps a function from original to function space, the equation of Laplacian is given below :

$$L(x,y) = \frac{\partial^2 I}{\partial x^2} + \frac{\partial^2 I}{\partial y^2} \quad (1)$$

Equation 1 Laplacian Intensity Metric [21]

Because the input of the image appears as a set of discrete pixels, a discrete convolution kernel can be approximated as second derivatives. Thus, in the definition of the Laplacian, small kernels could be relatively sensitive to noise. The image is preferably Gaussian smoothed before applying the Laplacian filter. This pre-processing step decreases the high-frequency noise contents before the differentiation step. The combination of filters could lead to better results. [22] Proposed hybrid filter of image processing approach which improves the Gabor function to execute the image classification. [23] Suggested a new speckle-noise reduction algorithm in medical ultrasound images by combining a wavelet transform and Laplacian filter. [24] suggested a hybrid median filter as a noise removal based non-liener filter for image enhancement. It is suggested for Gaussian noise removal from the medical image. The introduced hybrid filtering technique is for the removal of Gaussian noise from medical images. The research conducted on extracting skeleton on Kinect images [25] supported the idea of combining filters to reduce the noise and obtain better performance. This encouraged the researcher to try combining median and Laplacian filters to remove the noise and detect edges of ultrasound images.

2.5 Feature Extraction

Extracting features is the most important step in image classification. It helps to extract the attribute of the image as perfect as possible. [26] Described that the extraction of features of visual information from the image and saves properties oriented in the database features. The feature extracting is originated to extract visual information from the image and save oriented properties in the database features. Extract feature finds the image description in the form value feature for each pixel. For a given image, the GLCM (Gray-Level Co-Occurrence Matrix) works by calculating how often pairs of pixels are made in images and then extracting statistical measures from that matrix, in a given space relationship. Features can be derived from the original image to be combined with the GLCM features. The derived from an image that has been optimized and used as features to cluster the fabric of digital images [27]. The features are useful for clustering and retrieving similar images and provide information on the distribution properties of the density level of the Image. The tissue attributes are extracted from the common presence matrix and the mathematical equations are given the textile profiles as shown in the algorithm of [28].

In addition, the original selected features of the fetuses are bi-parietal diameter (BPD), femur length (FL), Liquor, Placenta, FH+ve, uterine wall contraction, congenital anomaly, longitudinal lie, single or twin, contrast, entropy, diabetes. Moreover, the age of pregnancies was taken between (15 - 40) weeks of pregnancy.

Feature Extraction Algorithm:
Input: Number of image of (mxn) gray scale image.
Output: 12 features.
Step 1: Select data set of image.
Step 2: Construct GLCM for images.
Step 3: Calculate feature from GLCM.
Step 4: Put all feature in matrix.
Step 5: Normalize feature.
Step 5.1: Calculates mean, variance, standard deviation, skewness for each feature.

2.6 Fuzzy C – Mean Algorithm

Data mining algorithms have been used for improving many fields [29]. One of the most useful algorithms is FCM. It is a method of clustering in which each data can be assigned to more than one cluster. It involves allocating data points to clusters for instance items in the same cluster are as similar as possible, while items fitting to different clusters are as dissimilar as possible. These similarity measures contain distance, connectivity, and intensity. In hard clustering, data belong to different clusters, where each point can only belong to precisely one cluster. In fuzzy clustering, data points can belong to many clusters. Membership scores are allocated to each of the dataset points (tags). These membership scores refer to the degree to which data points fit each group. Therefore, points on the edge of a cluster, with higher membership scores, could be in the cluster to higher scores than refers in the center of the cluster. FCM has been a very significant approach for image processing in clustering objects in images. In the last decades, mathematicians presented the spatial term into the FCM algorithm to develop the accuracy of clustering under noise [30].

Enhanced FCM has been utilized to distinguish between different actions using image-based features [31]. As a result, FCM is still the most spread for its practical success which can discover the basic skeletons of data that are used in many engineering and scientific fields for example medical images and search for biological data [32].

3. Proposed approach: CUHF to Enhance the Performance of Clustering.

This stage was performed through collecting images after the ethical approval is obtained of pregnancies in the maternity hospital. An experimental methodology has been utilized to obtain the best results. The used filters in the first experiments were produced unsatisfactory results because of low accuracy. All filters are applied before implementing the FCM algorithm to remove noise as shown in Figure 2. We first applied the LBP filter but undesirable results were obtained. Thus, to improve the performance of FCM, we second applied the Median filtering technique on these images as a pre-processing step of noise reduction. Afterward, Median & DWT are applied to the CUHF approach, the accuracy went slightly better. (Median, DWT & LBP) are examined to obtain good results but undesirable accuracy is gained by this integration. As shown in CUHF Algorithm, the attempt was to try one or a combination of the determined filters to obtain the best results. After the selected features are extracted the CUHF allocates the number of clusters i.e. Cn. In addition, the approach chooses the appropriate level of membership of fuzziness m > 1. After initializing the partition matrix randomly U, the Calculation of the centers of Vector (C^ ((k)) will be completed. Calculate the Euclidean distance ($\mathbf{D_{ij}}$) to update fuzzy membership matrix Uij, if the distance is less than the membership ε the approach must be stopped otherwise it should return to the step of calculating the centers of Vectors. The best results are obtained by the proposed (Median & Laplacian) ML when compared to other applied filters. The combination of filters is to enhance the performance of clustering. ML is an integration of non-linear and linear filters. The attempt was to remove the noise using the Median filter and then pass the result to the Laplacian filter to allocate the fetus's edges. ML produces better results for noise reduction, preservation of structures and key details. The Hybrid Filter is used for de-noising and smoothing images as shown in

Figure 3 (B), whereas in the same figure (A) the image is still distorted. The filter fits in with the local variation and the performance of the smoothing feature extraction.

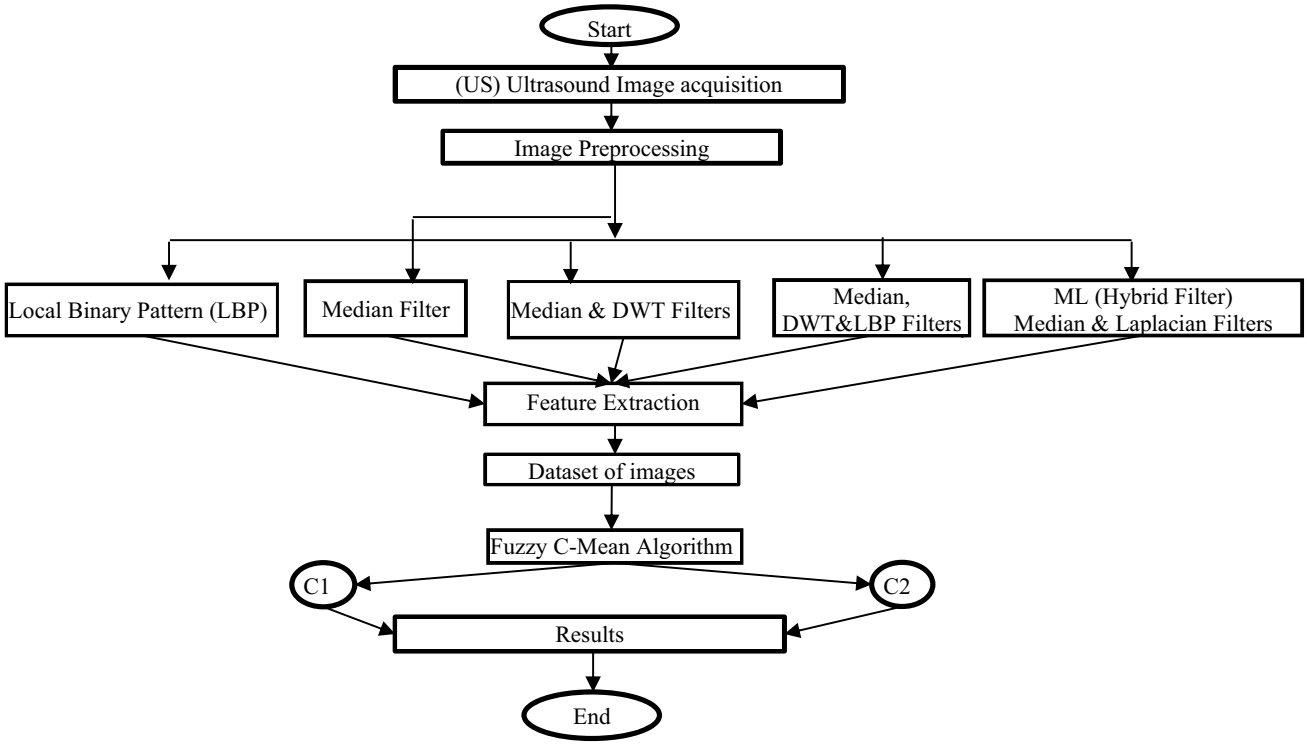

Figure 2 The Proposed System CUHF

4. Results and Discussions

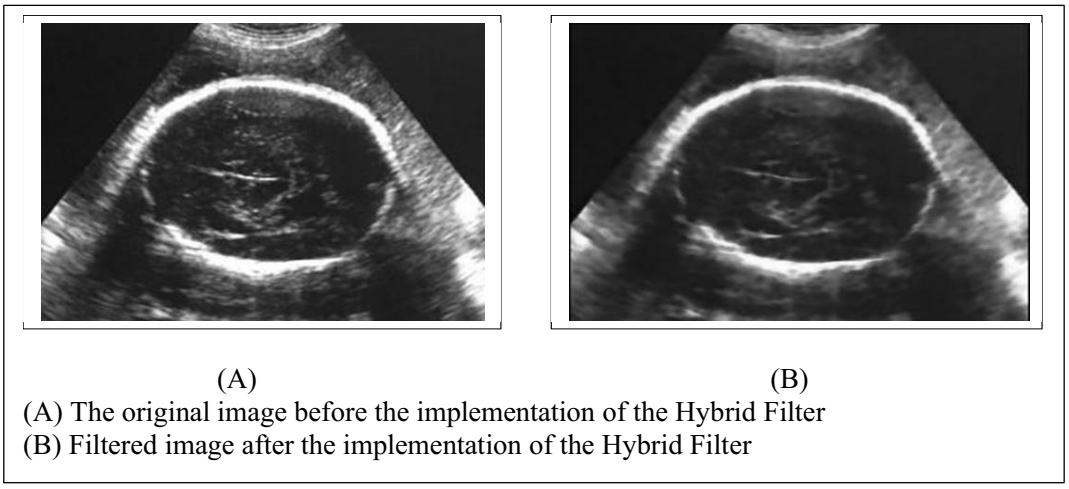

(A) (B)

(A) The original image before the implementation of the Hybrid Filter
(B) Filtered image after the implementation of the Hybrid Filter

Figure 3 Applying Hybrid Filter

To examine the accuracy of CUHF, tests were carried out using a dataset gained from Kadhimiya teaching hospital.

Algorithm: CUHF
Input dataset: 100 ultrasound images.
Preprocess (Try filters):

1- LBP.
2- Median.
3- Median & DWT.
4- Median, DWT & LBP.
5- Median & Laplacian (ML).

Feature Extraction (FL, BPD, Liquor, Placenta, FH+ve, uterine wall contraction, congenital anomaly, longitudinal lie, single or twin).
Dataset of images.
Fuzzy c-mean:
1: select the data set of feature extraction.
2: Select the number of clusters Cn.
3: Select an appropriate level of cluster fuzziness m > 1.
4: Initialize the partition matrix randomly, such that $U = [u_{ij}]\ matrix\ , U^{(0)} \in$ Mf c.
5: Calculate the cluster centers Vector $C^{(k)} = [C_j]\ with\ U^{(k)}$, using the expression given below:
6: Calculate the Euclidean distance
7: Update fuzzy membership matrix. $U\ according\ to\ D_{ij}\ .if\ D_{ij} > 0,$
then STOP; otherwise return to step 5
Results: c1 or c2

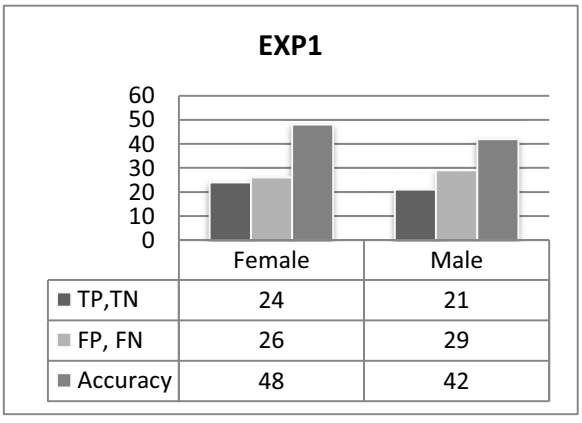

Figure 4 LBP Results

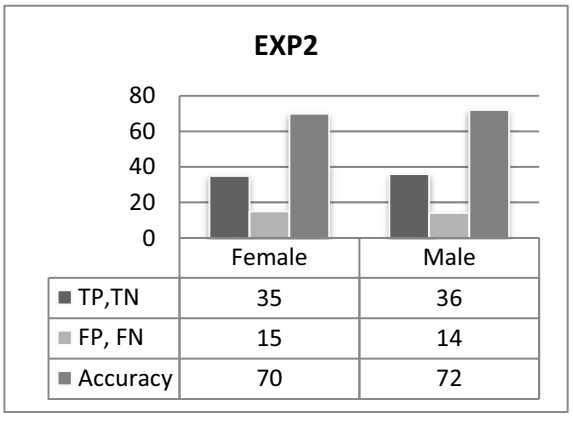

Figure 5 Median Filtering Results

In the conducted experiments, the results of CUHF approach will be illustrated as a clustering of the fetal sex, the determination of the ultrasound images is divided into 2 clusters. In addition, a total of 100 images of the ultrasound device were used to measure the features dimensions 50 males and 50 female. This section highlights the implementation of LBP, DWT, and combination of (Median & DWT), (Median, DWT&LBP) and (Median & Laplacian) filters, and how the best results are obtained.
Figures displayed in the results section are to show the outcomes of the experiments conducted on the proposed approach. It starts with the experiments of LBP and ends with the hybrid ML filter till the research reached reasonable outcomes. For all charts, The "Accuracy" recaps the evaluation of FCM after applying a filter of LBP, Median, Median & DWT, (Median, DWT & LBP), and proposed ML. TP, FP, TN, FN refer to True Positive, False Positive, True Negative, and False Negative respectively. In addition, Cluster1 and Cluster2 represent the images of the females and males respectively.

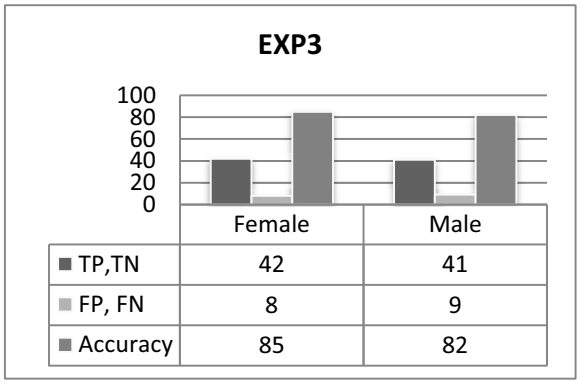

Figure 6 Median & DWT' Filtering

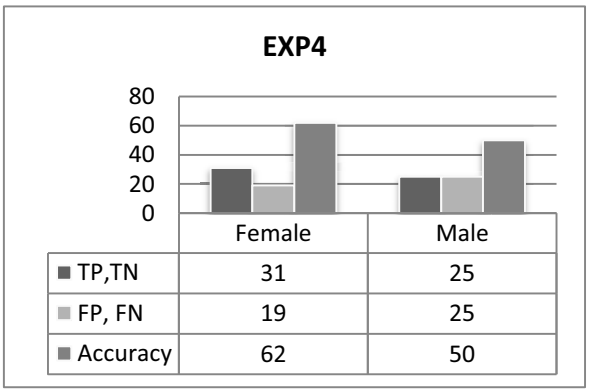

Figure 7 Median, DWT& LBP Filtering

The initial experiment was conducted on the FCM algorithm to obtain reasonable clusters. FCM algorithm on its own returns 20 TP & 19 FP which records 40% and 38% respectively. This research attempts to enhance the performance of FCM by improving accuracy.
Experiment1: the bar chart in Figure 4 shows the accuracy of the LBP filter. From the chart, it clear that cluster1 consists of (24) images which are clustered as a TP, whereas 26 of them are clustered as a FP wrongfully. The Accuracy summarizes the evaluation of LBP respectively 48%, which is lowest among the conducted experiments. Also, Cluster2 returned a 21 TN and 29 FN of males with an accuracy of 42% which gave unsatisfactory results. Therefore more experiments are needed to obtain better results.
Experiment 2: From the chart in Figure 5, it is noticed that the accuracy of Median Filtering is 70% with 35 TP and 15 FP wrongfully clustered images, cluster1. In addition, in Cluster 2, 36 are clustered as a TN and 14 FN with an accuracy of 72%. This gave a better accuracy compared to Experiment 1.

The third experiment is conducted using Median & DWT filters. The outcomes show that cluster1 consists of 42 TP whereas 8 are categorized as FP with an accuracy 85% as shown in Figure 6. Also, 41 TN and 9 FN of males are clustered with an accuracy of 82%, this gave a better accuracy compared to experiments 1 and 2.
The Fourth experiment (Median, DWT&LBP) is integrated. Figure 7 shows the results of cluster1 which consists of 31 TP images, 19 FP with an accuracy of 62%. Clusters contained 25 TN and 25 FN which indicates 50% accuracy. This outcome refers to the worst results compared to experiments 2 and 3 but better than 1, which indicates that LBP could cause non-preferred results due to produce rather long histograms, which slow down the recognition especially on image database.
In the fifth experiment, when the Median & Laplacian filter is applied to the CUHF approach, the outcomes of cluster1, cluster2 consist of 45 TP, 5 FP, 47 TN, and 3 FN with the accuracy of 90% and 94% respectively as shown in Figure 8. This gives the highest accuracy when compared to all the conducted experiments in this study.

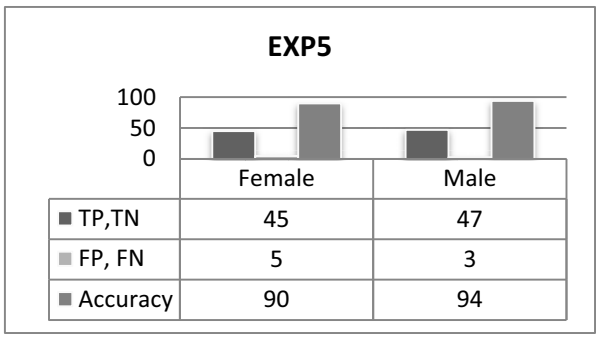

Figure 8 ML Hybrid Filtering

The result in experiment 5 showed that the best method of clustering was obtained from the application of the ML hybrid filter. The implementation of the median filter and Laplacian filter has directed the experiments to the highest accuracy. In experiment 5, total accuracy in both Claster1 and Claster2 was higher than the results obtained in experiments 1, 2, 3 and 4.
Besides, when using the median filter, the results were fairly good compared to LBP. (Median & DWT) filter, the results were better compared to the accuracy when using the (Median, DWT & LBP), because it is affected by the contours that are often (High Contrast). The greatly improved accuracy rate is obtained in the proposed ML filter when the union of median and discrete wavelet was employed to match a target of enhanced ultrasound images. The CUHF approach is presented with a path to take this research further.

5. Conclusion and Recommendations

This paper has presented a new approach, CUHF, to improve the performance of FCM clustering. The CUHF approach uses a new hybrid filter ML as a process that produces far fewer clustered images than would be produced from basic FCM. It uses a new approach to extracting important features to determine the gender of the fetus in ultrasound images. The best ratings were obtained from the images for the ML filter and the inability of the LBP images to give correct clustering. The experimental results have shown that the advantages of CUHF over classic FCM when unrelated images are clustered. The outcome of the

CUHF approach, cluster1, cluster2 returned 45 TP, 5 FP, 47 TN, and 3 FN with the accuracy of 90% and 94% respectively. This gives the highest accuracy when compared to all the conducted experiments in this study. It is recommended to consider other methods such as Fourier Transform as well as the adoption of other prediction algorithms e.g. SIFT to reduce the dimension in the field of clustering. Also, the Fuzzy Neural Network for clustering fuzzy images can be used for a training net that can predict the gender of the fetus in the early stages to obtain better results.

References

[1] A. T. Azar and A. E. Hassanien, "Dimensionality reduction of medical big data using neural-fuzzy classifier," *Soft Comput.*, vol. 19, no. 4, pp. 1115–1127, 2015.

[2] S. S. Basha and K. S. Prasad, "AUTOMATIC DETECTION OF BREAST CANCER MASS IN MAMMOGRAMS USING MORPHOLOGICAL OPERATORS AND FUZZY C--MEANS CLUSTERING.," *J. Theor. Appl. Inf. Technol.*, vol. 5, no. 6, 2009.

[3] B. L. Gledhill, "Gender preselection: Historical, technical, and ethical perspectives," in *Seminars in reproductive endocrinology*, 1988, vol. 6, no. 04, pp. 385–395.

[4] K.-B. Kim, H.-J. Lee, D. H. Song, and Y. W. Woo, "Extracting fascia and analysis of muscles from ultrasound images with FCM-based quantization technology," *Neural Netw. World*, vol. 20, no. 3, p. 405, 2010.

[5] P. Raju, V. M. Rao, and B. P. Rao, "Optimal GLCM combined FCM segmentation algorithm for detection of kidney cysts and tumor," *Multimed. Tools Appl.*, pp. 1–23, 2019.

[6] S. K. Amirgholipour and A. R. Naghsh-Nilchi, "Robust digital image watermarking based on joint DWT-DCT," *Int. J. Digit. Content Technol. its Appl.*, vol. 3, no. 2, pp. 42–54, 2009.

[7] J. Zhang and Y. Cheng, "Despeckle Filters for Medical Ultrasound Images," in *Despeckling Methods for Medical Ultrasound Images*, Springer, 2020, pp. 19–45.

[8] R. Dass, "Speckle noise reduction of ultrasound images using BFO cascaded with wiener filter and discrete wavelet transform in homomorphic region," *Procedia Comput. Sci.*, vol. 132, pp. 1543–1551, 2018.

[9] Y. Wu and P. Liu, "A Classification Algorithm of Ultrasonic Thyroid Standard Planes Using LBP and HOG Features," in *2019 IEEE 13th International Conference on Anti-counterfeiting, Security, and Identification (ASID)*, 2019, pp. 103–107.

[10] A. Nugroho, R. Hidayat, and H. A. Nugroho, "Artifact removal in radiological ultrasound images using selective and adaptive median filter," in *Proceedings of the 3rd International Conference on Cryptography, Security and Privacy*, 2019, pp. 237–241.

[11] M. Somasekar and S. S. Murugan, "Feature Extraction of Underwater Images by Combining Fuzzy C-Means Color Clustering and LBP Texture," in *Proceedings of the Fourth International Conference in Ocean Engineering (ICOE2018): Volume 1*, 2019, vol. 22, p. 453.

[12] C. Wang, W. Pedrycz, M. Zhou, and Z. Li, "Sparse Regularization-Based Fuzzy C-Means Clustering Incorporating Morphological Grayscale Reconstruction and Wavelet Frames," *IEEE Trans. Fuzzy Syst.*, 2020.

[13] G. G. N. Geweid, M. A. Abdallah, and A. M. Hassan, "Improved Malignant Diagnosis Using Fuzzy C-means Based on Histopathological of PET-CT Lung Images," in *Proceedings of the 2020 12th International Conference on Bioinformatics and Biomedical Technology*, 2020, pp. 99–105.

[14] A. Porebski, V. Truong Hoang, N. Vandenbroucke, and D. Hamad, "Combination of LBP Bin and Histogram Selections for Color Texture Classification," *J. Imaging*, vol. 6, no. 6, p. 53, 2020.

[15] N. Attlas and S. Gupta, "Reduction of speckle noise in ultrasound images using various filtering techniques and discrete wavelet transform: comparative analysis," *Int. J. Res.*, vol. 1, no. 6, pp. 112–117, 2014.

[16] A. Gutub and F. Al-Shaarani, "Efficient Implementation of Multi-image Secret Hiding Based on LSB and DWT Steganography Comparisons," *Arab. J. Sci. Eng.*, pp. 1–14, 2020.
[17] M. M. Altuwaijri, A. Bahanshal, and M. Almehaid, "Implementation of computerized physician order entry in National Guard Hospitals: assessment of critical success factors," *J. Fam. Community Med.*, vol. 18, no. 3, p. 143, 2011.
[18] M. A. Gungor and I. Karagoz, "The effects of the median filter with different window sizes for ultrasound image," in *2016 2nd IEEE International Conference on Computer and Communications (ICCC)*, 2016, pp. 549–552.
[19] P. Patidar, M. Gupta, S. Srivastava, and A. K. Nagawat, "Image de-noising by various filters for different noise," *Int. J. Comput. Appl.*, vol. 9, no. 4, pp. 45–50, 2010.
[20] W. G. Besio and A. K. Kota, "Laplacian ECG moment of activation detection algorithm during pacing," in *The 26th Annual International Conference of the IEEE Engineering in Medicine and Biology Society*, 2004, vol. 1, pp. 948–951.
[21] S. Paris, S. W. Hasinoff, and J. Kautz, "Local Laplacian filters: edge-aware image processing with a Laplacian pyramid," *Commun. ACM*, vol. 58, no. 3, pp. 81–91, 2015.
[22] B. He *et al.*, "Local receptive fields based extreme learning machine with hybrid filter kernels for image classification," *Multidimens. Syst. Signal Process.*, vol. 30, no. 3, pp. 1149–1169, 2019.
[23] S. Gai, B. Zhang, C. Yang, and L. Yu, "Speckle noise reduction in medical ultrasound image using monogenic wavelet and Laplace mixture distribution," *Digit. Signal Process.*, vol. 72, pp. 192–207, 2018.
[24] L. K. Baghel and R. K. Sunkaria, "High density fixed valued impulse noise removal using improved decision based hybrid median filter and its application on medical images," in *2018 Second International Conference on Inventive Communication and Computational Technologies (ICICCT)*, 2018, pp. 523–530.
[25] E. Ozbay, A. Cinar, and Z. Guler, "A hybrid method for skeleton extraction on Kinect sensor data: Combination of L1-Median and Laplacian shrinking algorithms," *Measurement*, vol. 125, pp. 535–544, 2018.
[26] I. Matthews, T. F. Cootes, J. A. Bangham, S. Cox, and R. Harvey, "Extraction of visual features for lipreading," *IEEE Trans. Pattern Anal. Mach. Intell.*, vol. 24, no. 2, pp. 198–213, 2002.
[27] A. Suresh and K. L. Shunmuganathan, "Image texture classification using gray level co-occurrence matrix based statistical features," *Eur. J. Sci. Res.*, vol. 75, no. 4, pp. 591–597, 2012.
[28] D. Bariamis, D. K. Iakovidis, and D. Maroulis, "Dedicated hardware for real-time computation of second-order statistical features for high resolution images," in *International Conference on Advanced Concepts for Intelligent Vision Systems*, 2006, pp. 67–77.
[29] A. S. Aljuboori, F. Coenen, M. Nsaif, and D. J. Parsons, "Performance of case-based reasoning retrieval using classification based on associations versus Jcolibri and FreeCBR: a further validation study," in *Journal of Physics: Conference Series*, 2018, vol. 1003, no. 1, p. 12130.
[30] M. N. Ahmed, S. M. Yamany, N. Mohamed, A. A. Farag, and T. Moriarty, "A modified fuzzy c-means algorithm for bias field estimation and segmentation of MRI data," *IEEE Trans. Med. Imaging*, vol. 21, no. 3, pp. 193–199, 2002.
[31] P. Wu, M. Bedoya, J. White, and C. L. Brace, "Feature-Based Automated Segmentation of Ablation Zones by Fuzzy C-mean Clustering During Low-dose Computed Tomography," *Med. Phys.*, 2020.
[32] H.-Y. Lin, "Feature clustering and feature discretization assisting gene selection for molecular classification using fuzzy c-means and expectation–maximization algorithm," *J. Supercomput.*, pp. 1–17, 2020.

Air Pollution Monitoring based Fuzzy Controller with Embedded System

Air Pollution Monitoring based Fuzzy Controller with Embedded System

Saja Sattar Hasanh , Abbas Hussein Miry and Tariq M. Salman

Electrical Engineering Department AL-Mustansiriyah University

E-mail: eng.sajasattar@yahoo.com

Abstract. Air pollution has a wide and great influence on the concentration of constituents of the atmosphere, which leads to many effects such as acid rains and global warming. In order to avoid such unwanted adverse imbalances in the nature, designing an air pollution monitoring system (APMS) is very important. This paper discussed the development of an effective solution for monitoring the air pollution by making an Arduino-Based Air Pollution Monitoring System (APMS) . Carbon monoxide and Carbon Dioxide concentration levels in air were measured and monitored using MQ4 and MQ7 gas sensors and Arduino atmega microcontroller. These sensors can detect many harmful gases and can be used for measuring their amount very accurately .The concentrations of CO and CO2 in particle per million (PPM) will be monitored and displayed on the LCD very easily. based on these measurements the pollution level could be monitored, determined, and displayed .The experiments were carried out using the developed wireless APMS under various physical conditions. The results showed that the designed system collects reliable and reasonable real time pollution data .Three hour sampling time was executed in each location. One of the logical functions that are widely used is fuzzy logic . A fuzzy logic artificial intelligence for gas sensors is used which clarifies the presence as well as the concentration of CO and CO2 efficiently. Fuzzy logic will gives the decision about whether the air is polluted or unpolluted. This logic function we can process some existing data into a form of output which can be in the form of a status or state of action that will be performed by a tool .This proposed system will contribute in the construction of an APMS in the outdoor or even in the indoor environment.

Keywords: Air pollution, Carbon monoxide, Carbon dioxide, Arduino, Gas sensors, Fuzzy Logic, Membership Function

1. Introduction.

One of the world's unembellished environment issues is air pollution. World Health Organization (WHO) reported that, in developing countries there are about 3 million people died annually due to air pollution [1]. The emergence of air pollution in many countries all over the world is a result of the industrial growth and road transport [2]. Air pollution contributes in the climate change. Exposure to CO gas leads to various and different health effects. This gas affects the central nervous systems, the cardiovascular system, blood, and lungs [2]. Effect of CO depends on the physiological status, the health of exposed person, exposure time and the pollutant concentration [3]. On the other hand CO2 gas can be considered as a basic indication for air quality. The concentration of CO2 is about 350 PPM

in the outdoor atmosphere [4]. The main profits of APMS are improving the environment, reducing costs, better risk control, better pollution detection, and reduced errors. The main artificial intelligence methods of soft computing namely fuzzy logic, neural network and genetic algorithm have shown great ability in solving complex non-linear system identification and control problems. Several research efforts have been expended to use evolutionary methods as effective tools for system identification. Among these methodologies, fuzzy rule based systems have been an active research field for their unique ability to build models based on experimental data [4]. This paper is arranged as follows: Section 2 contains the related works and Section 3 explains background theory. It also explains the implementation of the system. Section 4 presents, demonstrates, and discusses the results obtained from the developed system while Section 5 presents the conclusions of this proposed system.

2. Related works:

There are many studies and researches that have been proposed, analyzed, and published on the subject of air pollution monitoring systems (APMS), such as [3], where concentrations of carbon monoxide in indoor and outdoor air of Ghalyun cafes were measured using a portable gas meter (Honeywell BW MAX XTII, Brandt Instruments, Inc. Canada). In [5], shows a Novel Fuzzy Logic Model for Multiple Gas Sensor Array where the outputs from an integrated multiple gas sensor was used to specifically select the presence and concentration of four gases namely Hydrogen, methane, LPG and Carbon monoxide. In [6], the concept of IoT is used to monitor the air pollution using MQ135 Gas sensor through Arduino Uno. In [7], the author attempts to develop an effective solution for pollution monitoring using wireless sensor networks (WSN) on a real time basis namely real time wireless air pollution monitoring system. Each of these studies has different methods, number of sensors, types of machine learning, microcontrollers to realize of the APMS. In this paper, the carbon dioxide (CO_2) concentration and carbon monoxide (CO) concentration were monitored, and then the readings were analyzed using fuzzy logic with several rules and memberships to decide the degree of risk according to air pollution, and display the results and measurements of CO and CO_2 and the output of fuzzy logic. The Atmega microcontroller was used in this system. This proposed APMS may participate in the development process of a comprehensive outdoor air pollution monitoring systems in the future. It may also support indoor air pollution monitoring.

3. Background theory

3.1. Carbon monoxide (CO): It is a non–irritating, colorless, odorless, tasteless, poisonous and Pollutant gas [7][8]. It may be emitted by anthropogenic or natural sources into the environment [3]. It is formed when carbon (C) in fuels such as petrol, wood, coal, and natural gas hasn't burned completely. Air quality may be affected by emitting sources of CO such as tobacco smoke, gas stoves, fireplaces, and other types of fuel burners [2]. CO produces carboxyhemoglobin (COHb) through reacting with blood hemoglobin molecules; this will reduce oxygen (O_2) supplied to the body organs. The concentration of COHb in blood is considered as an indicator for exposure to CO [2][9]. In this article CO concentrations had been surveyed in the outdoor air in Baghdad; the capital of Iraq.

3.2. Carbon dioxide (CO_2): It is a non-toxic, non-flammable, colorless, odorless, and non-reactive gas. It is a naturally sub product of cellular respirational process and a as a result of burning the fossil fuels. Exposure to high concentrations of CO_2 may cause a risk to life [7]. In this article CO_2 concentrations had been surveyed in the outdoor air in Baghdad; the capital of Iraq.

3.3. MQ7 Gas Sensor (CO Sensor): This is a low cost, simply used with extremely high sensitivity for sensing Carbon Monoxide (CO) concentrations in the air. This sensor has the ability to sense and detect CO-gas concentrations within a range from 20 to 2000 PPM wherever the sensor is placed. MQ7 has fast time of response. The output of the sensor is the analog resistance of it. MQ7 sensor consumes not more than 150 mA at a voltage of 5 V. It is very stable sensor with the characteristic of long life. It is an ideal sensor to use for a CO alarm [7]. MQ7 Gas Sensor is shown in fig.1.

Figure 1 MQ7 Gas Sensor (CO Sensor)

The sensitive material of MQ7 is SnO_2 is. It has a low conductivity in the clean air. MQ7 can detect CO at low temperatures when heated by 1.5V. The conductivity of MQ7 sensor is high along whenever the gas concentration is rising. At high temperatures when the sensor is heated by 5.0V, it will clean the gases which had been adsorbed at low temperatures. MQ7 can detect various gases that contains CO. This sensor is very suitable to use for different applications [7].

3.4. MQ4 Gas Sensor (CO_2 Sensor): The MQ4 gas sensor is using SnO_2 as a sensitive material to sense and detect combustible gasses which includes methane, propane, and butane. This gas sensor can detect concentrations of methane / natural gas in the range of 200 PPM to 10,000 PPM. This range is very suitable to detect gas leaks. MQ4 is simple and analog voltage interface that requires one analog input pin only from the microcontroller. MQ4 is a perfect gas sensor for Air Pollution Monitoring System (APMS) can sense CO_2, smoke, NH3, Benzene, alcohol, and other gases. MQ4 is a low cost gas sensor and it's suitable for many different applications [7]. MQ4 Gas Sensor is shown in fig.2.

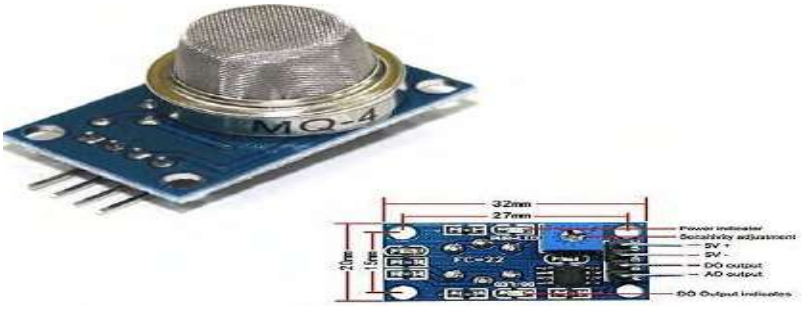

Figure 2 MQ4 Gas Sensor (CO2 Sensor)

MQ4 is a sensitive gas sensor to the changes in temperature. The variations in the readings of CO_2 are small if it happened according to temperature changes. It's (<100 PPM) on the low range, and it's (<1000 PPM) on the high range. These variations in the readings of CO_2 due to the change in temperature may become negligible as compared to the whole changes in concentration of CO_2 if the design was good. Sensor's accuracy can be improved to make the entire experiments in a constant temperature if the sensor is calibrated at the desired temperature. MQ4 operates in temperatures within the range 20-30°C, but it may be used outside this range [5].

3.5 Arduino:

Arduino is a flexible micro-controller and a development environment that is used for controlling devices and reading data from all types and categories of sensors. It's simple, extensible; also it has a great success, wide adoption and spread between users. The previous properties of Arduino lead to continuous development of several software libraries and hardware extensions which enable it to

communicate wirelessly as well as using wires with the Internet. Arduino is an open hardware platform. Sensors do the function of collecting data from the surrounded environment and generating information to raise awareness about the context by monitoring any change in the environment, then the corresponding things will make the needed responses. Here, using the MQ4 and MQ7 gas sensor gives the ability to monitor various kinds of dangerous gases and Arduino mega 2560 microcontroller considered as the heart of Air Pollution Monitoring System (APMS) because it controls the entire monitoring process. Arduino mega 2560 is a microcontroller board based on the ATmega2560. It has 54 digital input / output pins where 15 of them can be used as PWM outputs, 16 analog inputs, 4 UARTs (hardware serial ports), a 16 MHz crystal oscillator, a power jack, a USB connection, an ICSP header as well as a reset button. Arduino contains all the things that are needed for supporting the microcontroller. It can be connected simply and easily to a computer using a USB cable. Arduino also can be powered with a battery or an AC-to-DC adapter to get started [6]. The tracking APMS was developed in order to monitor air pollution even at the remote and far sites accurately. APMS is very helpful for those who are involved in monitoring the environment. Arduino-Based APMS uses the required data to adjust air parameters on time and to update the risk of environmental parameters during the standard period of time. In addition to that, Arduino-Based APMS and its sensors readings of measurements relevant to environmental parameters can be employed in a very efficient manner to detect the carbon monoxide concentration (CO) and carbon dioxide concentration (CO_2). Arduino Mega is shown in fig.3.

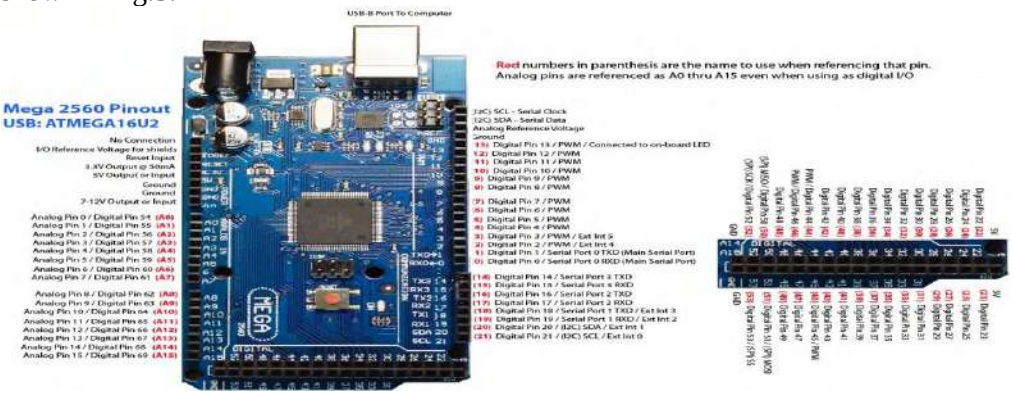

Figure 3 Arduino Mega

3.6. Fuzzy Logic:

The approach of Fuzzy logic (FL) has been introduced by the artificial intelligence researcher Lotfi A. Zadeh in 1965. FL methodology focuses on the purpose of making a decision for deficient data with a concept named true or false and the degrees of truth. The fuzzy logic set includes the classical set [9][10]. The fuzziness of elements had been implemented using membership functions in the set of solution which is based on experiment regardless knowledge. The membership function is implemented using the methodology of weighted rate inside fuzzy logic interference system [11][12][13].

4. The designed system and implementation

4.1 Proposed system architecture:

In this paper an Arduino-Based Air Pollution Monitoring System (Arduino-Based APMS) was designed and implemented with the use of Fuzzy logic as a type of artificial intelligence as shown in Fig 4. The data collected using MQ4 and MQ7 sensors is analyzed by the method of FL and graphs based on the fuzzy inferences had been also generated using this method. Using FL has many advantages like there isn't any need for many data sets for analyzing the collected data. The second advantage of using FL is its power of interpretation as well as its simplicity [10][14][15]. The approach of

Mamdani Fuzzy Inference (MFI) is a simple and a commonly used Fuzzy methodology [13]. The MFI structure depends on the operations of min-max. MFI method has a wide spread acceptance. It is a well suited method for human inputs. The output of MFI can be transferred easily to a linguistic form [13]. In this system we can monitor air pollution using Arduino and gas sensors that available locally to monitor gases such as Carbon monoxide (CO) and Carbon dioxide (CO_2) which considered so dangerous and harmful gases to people. This APMS will display the concentration of CO and CO_2 in PPM on LCD so we can observe and monitor them very easily. Measurements of CO and CO_2 concentration levels were taken in the Iraqi capital, Baghdad. Different measurements were made within different times during day and night. The reading were recorded and displayed such that there is 2 minutes between each reading and another. The information obtained from these gas sensors is recorded then will be sending to the destination device through the Arduino atmega microcontroller. The level of air pollution can be viewed by people wirelessly using this method. APMS will reduce cost, it's reliable and a very comfortable system to use it for any place to monitor these gases.

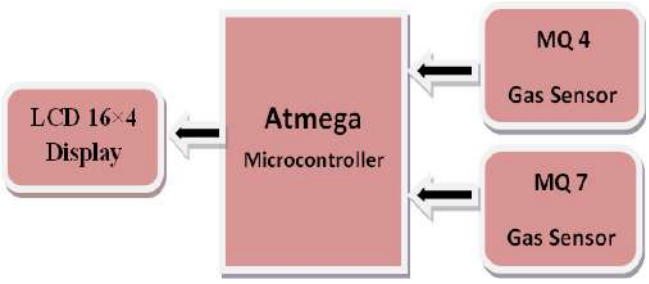

Figure 4 APMS architecture

In this paper the outputs were produced using a fuzzy rule based system according to the inputs for the system. Two input parameters had been entered to the APMS. The first input is CO concentration and it consists of 2 membership functions. The second input is CO_2 concentration and it consists of 3 membership functions. The output of APMS is the degree of pollution and it consists of 3 membership functions.

All the membership functions of inputs and output were graphed in Matlab using the trapezoidal function. The membership function for CO concentration is demonstrated in Fig. 5 with the parameters low and high to analyze CO concentration whereas Fig. 6 shows the membership function for CO_2 concentration with the parameters low, medium and high for analyzing CO_2 concentration. In Fig. 7 the membership function for output is shown with the parameters low, medium and high to analyze it.

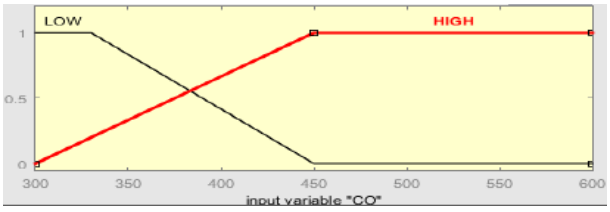

Figure 5 membership function of CO concentration

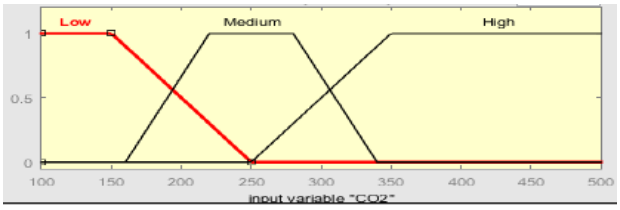

Figure 6 membership function of CO2 concentration

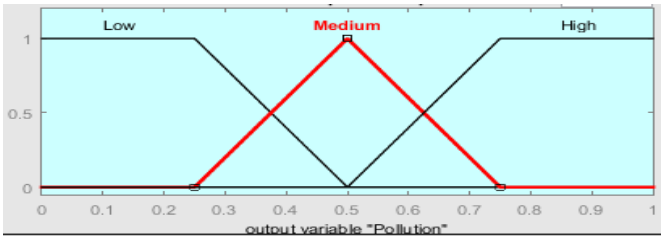

Figure 7 membership function of the output

The number of fuzzy rules that governed the APMS is 6 and it's determined according to the given membership function of the parameters as shown in Table 1.

Table 1. Fuzzy rules of the APMS input and output parameters

No.	Input		Output
	CO concentration	CO_2 concentration	degree of pollution
1	Low	Low	Low (Normal air)
2	High	Low	High (Low level of pollution)
3	Low	Medium	Medium (Low level of pollution)
4	High	Medium	High (Air is polluted)
5	Low	High	High (Low level of pollution)
6	High	High	High (Air is polluted)

Fig. 8 shows the Fuzzy Logic Inference System where CO and CO_2 concentrations are the inputs of the system. Fuzzification and Defuzzification methods were carried out and the degree of pollution is the output of APMS.

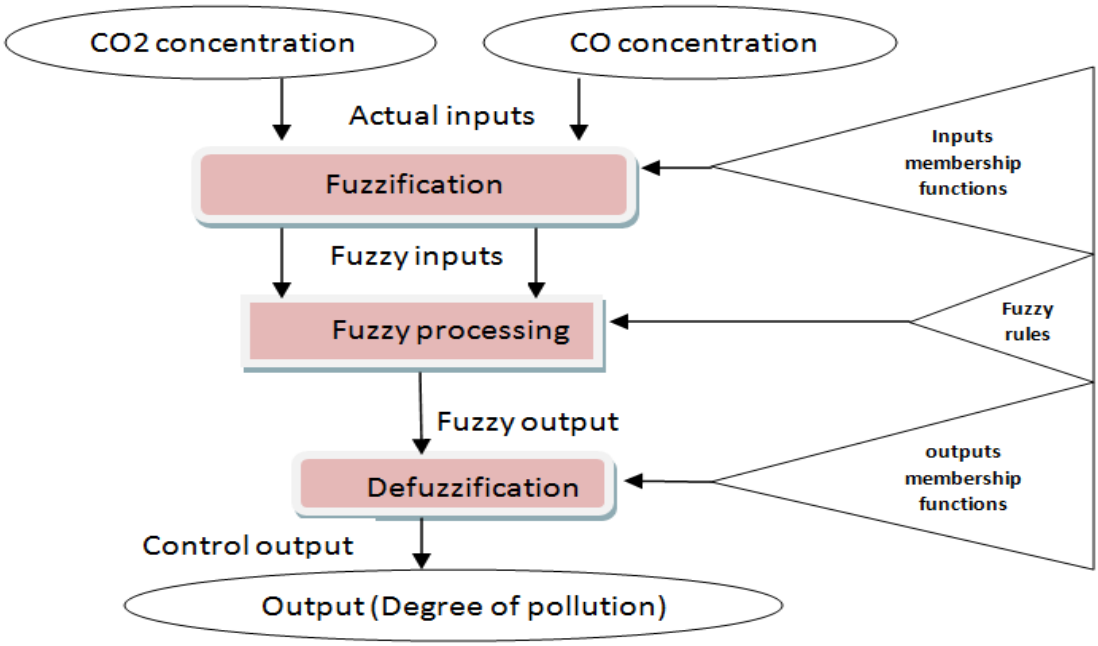

Figure 8 Fuzzy Inference System

4.2 Implementation of APMS:

Figure 9 shows the connections between of the LCD and the Arduino microcontroller board through the VCC, GND, SDA and SCL pins also the figure shows how to connect the sensors MQ4 and MQ7 to the power (5v) and ground through wires, while the wire that transfers information of the CO concentration sensor was connected to one of the analog pins (A0) and the information wire of the CO2 concentration sensor was connected by wire to the analog pin (A1) of the Arduino. The power of the Arduino microcontroller can be supplied in the following three ways, the 1st way is by laptop using the USB port and the 2nd way is by using an external adapter which connected to the power jack in the microcontroller and the 3rd way is by using batteries that are connected to Vin port.

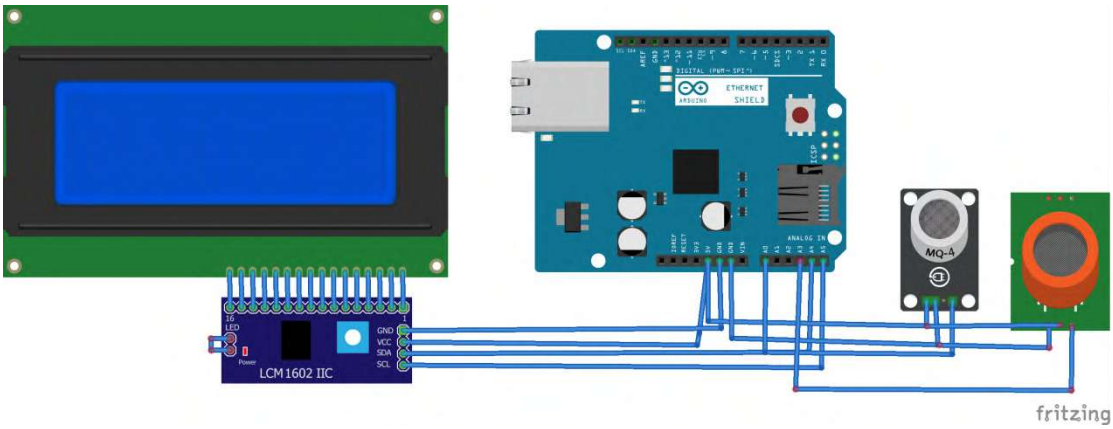

Figure 9 Installation of Arduino-Based APMS circuit

5. Results and discussion.

The developed Arduino-Based Air Pollution Monitoring System (APMS) is checked using different measurements in different situations and conditions from normal and common states to abnormal and uncommon states of air. These different tests and results shows minimum error rate and high accuracy in sensing CO and CO_2.

Through the experiments that had been carried in several times and conditions, it had been noticed that when the levels of air pollutions (CO and CO_2 concentrations) are within the normal range, APMS gives a low risk notification whereas if one of the levels of CO and CO_2 concentrations is not within the normal range and the pollution is in risky levels, APMS will give a risk notification which is appropriate to the data as shown in fig.10, so people who involves with air pollution will be able to know how dangerous the situation is, in very easy and high speed way, in order to do the necessary measurements.

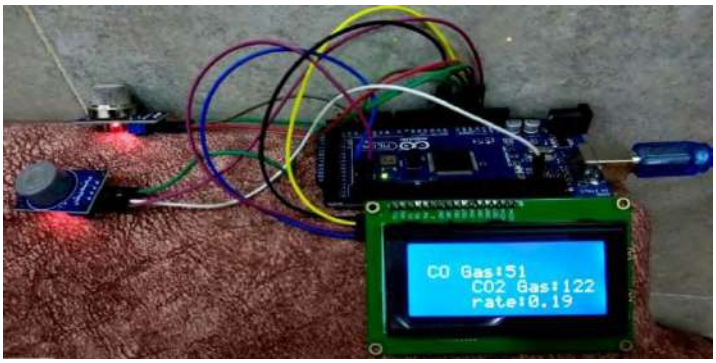

Figure 10 Implementation of Arduino-Based APMS circuit

6. Conclusion and future work.

The risk of environmental pollution can be reduced when Arduino and gas sensors are used in detecting air pollution with the aid of an intelligent fuzzy logic system. Arduino can enable easy and simple integration with air pollution monitoring sensors (MQ4 and MQ7 gas sensors). This paper demonstrates a very simple and easy-to-use system. The libraries of fuzzy logic system which is found in the Arduino mega microcontroller software was used to analyze the data and information recorded from MQ4 and MQ7 sensors, and then it gives the decision about the risk directly. Using Arduino made the information of the APMS to be recorded for all of those who are involved with environmental monitoring. It's appeared from this experiment that using APMS gives good results that one can rely on it. APMS is easy, quick, and accurate system. It can be used for monitoring everywhere and for any period of time without any obstacles or problems.

Acknowledgement.

The authors would like to thank Al-Mustansiriyah University (www.uomustansiriyah. edu.iq), Baghdad-Iraq for supporting the present work.

References:

[1] "Air pollution," World Health Organization, [Online]. Available: who.int [Accessed 17 April 2018].
[2] Chowdhury, Z., Campanella, L., Gray, C., Al Masud, A., Marter–Kenyon, J., Pennise, D., Charron, D., Zuzhang, X., 2013. Measurement and modeling of indoor air pollution in rural households with multiple stove interventions in Yunnan, China. *Atmospheric Environment* 67, 161–169.
[3] Reboul, C., Thireau, J., Meyer, G., Andre, L., Obert, P., Cazorla, O., Richard, S., 2012. Carbon monoxide exposure in the urban environment: An insidious foe for the heart? *Respiratory & Physiology& Neurobiology*, 184, 204–212.
[4] Schell, M.; Hinthout, D. Demand Control Ventilation Using CO2. Ashrae J. 2001, 43, 18–29.
[5] Parthasarathy, R.; Kalaichelvi, V.; Sundaram,S., 2015.Novel Fuzzy Logic Model for Multiple Gas Sensor Array,1143-1146.
[6] K.Nirosha, B. Durgasree, N. Shirisha, 2017. IOT BASED AIR POLLUTION MONITORING SYSTEM, VOLUME-4, ISSUE-6, 40-42.
[7] V.S.Revathy, K.Ganesan, K.Rohini, S.Tamil Chindhu , T.Boobalan, 2016. Air Pollution Monitoring System, Volume 11, Issue 2, 27-40.
[8] Langston, J.W., Widner, H., Brooks, D., 2010. Carbon monoxide poisoning. Encyclopedia of Movement Disorders 1, 187.
[9] ATSDR (Agency for Toxic Substances and Disease Registry), 2009. Toxicological Profile for Carbon Monoxide. Atlanta, Georgia.
[10] Bahaa S. Mostafa, Abbas Hussain Miry, Tariq M. Salman, 2020.Healthcare Monitoring and Analytic System Based Internet of Thing, The 3rd Scientific Conference of Electrical and Electronic Engineering Researches (SCEEER), 31-35.
[11] Bahaa S. Mostafa, Abbas Hussain miry, Tariq M. Salman, 2020. PERSONAL HEALTHCARE SYSTEM BASED ON ARTIFICIAL INTELLIGENCE, First Online Scientific Conference for Graduate Engineering Students.
[12] H. N. Saha, D. Paul, S. Chaudhury, S. Haldar, and R. Mukherjee, "Internet of Thing based healthcare monitoring system," ,*IEEE Annual Information* Technology, Electronics and Mobile Communication Conference (IEMCON), 2017, pp. 531-535.
[13] K. Vani and R. R. Neeralagi, "IoT based health monitoring using fuzzy logic," International Journal of Computational Intelligence Research, vol. 13, pp. 2419- 2429, 2017.
[14] M. Bansal and B. Gandhi, "IoT Based Development Boards for Smart Healthcare Applications," in 2018 4th International Conference on Computing Communication and Automation (ICCCA), 2018, pp. 1-7.
[15] K. Bylykbashi, E. Qafzezi, M. Ikeda, K. Matsuo, and L. Barolli, "Fuzzy-based Driver Monitoring System (FDMS): Implementation of two intelligent FDMSs and a testbed for safe driving in VANETs," Future Generation Computer Systems, vol. 105, pp. 665-674, 2020.

An Automated Mammals Detection Based on SSD-Mobile Net

An Automated Mammals Detection Based on SSD-Mobile Net

Elham Mohammed Thabit A. Alsaadi[1] and Nidhal K. El Abbadi[2]

[1]College of Information Technology, University of Babylon, Iraq
[2]Computer Science Department, College of Science, University of Kerbala,

E-mail: elham.thabit@uokerbala.edu.iq

Abstract. Animal detection techniques are one of the researcher's interests and challenge. There are many difficulties faces by the researchers in this field that reduce the detection performance and efficiency, such as variation of image illumination, animal occlusion, the similarity of animal colors with background environment, etc.
Multi-label Image Detection and classification of Mammals animals is the goal of this paper which we proposed to achieve in this proposal by using Single Shot Multi-Box Detector (SSD) and MobileNet v1 coco_2017 model. Localizing and classifying multiple objects (animals) of the Mammal category in digital images is another goal. The suggested SSD is regarded as a more accurate, fast, and efficient way to detect objects of different sizes based on deep learning technology.
In this proposal, we used 2000 images in the network were collected from the standard dataset (such as Caltech 101) and the net. The SSD framework improves the detection and recognition processes of Convolution Neural Network (CNN). During the prediction time, the network introduces scores to the presence of every object class and bounded each object in the image with a box. Each box has a label that indicates the type of the object and the score represents the probability of the relationship of the object to that type. Boxes during the process are modified for getting the best matching to the object's shape. The experimental results of this work proved the efficiency of classifying and detecting animals even in the variation of illumination, pose, and occlusion. Detection and classification accuracy is up to 98.7 %. This suggestion is more reliable and accurate than other similar works and detects a wide range of Mammals animals, unlike other similar works.

Keywords: Deep Learning, Convolutional Neural Networks, Animals Classification, Mammals, Reptiles.

1. Introduction

Visual monitoring in animal scenes is currently one of the most distinguished research issues in the field of Computer Vision (CV), but the ways of detecting and understanding dynamic objects are still inaccessible [1], [2]. Animal detection methods are helpful to solve various problems such as prevent risky animal intrusion in a residential area [3]. It is also a part of a large work for a robot to detect and classify objects in critical situations such as natural disasters or other accidents which need to different objects such as human, animal and other [4]. Another example is self-driving cars, for which accurately detecting pedestrians, animals, street signs, or other vehicles, is a crucial feature when maximizing the safety of such systems. As well, it provides a great value in biomedical laboratories by monitoring laboratory animals using a powerful following method which can extract a rodent from a

frame under an uncontrolled environment [5]. Furthermore, it increases the efficiency and productivity of laboratory staff by reducing the time spent in direct monitoring of animals, also, to have a better understanding of animal behavior. Deep (CNN) or ConvNet has accomplished important success in the computer vision field, like target detection, target tracking, image classification, and semantic image segmentation [6]. It is a multi-layered neural network with a special architecture to detect complex features in data. Object detection means to predict the location of an object along with its category in static images which is one of the most critical computer vision problems [7], [8]. It often uses extracted characteristics and learning algorithms to identify the object belonging to a certain category of objects in a static image [9]. Several types of CNNs are existing; MobileNet is considered as one of the important applications for this type of CNN networks [10]. The architecture of "Depthwise Separable Convolutions" greatly decreases the number of parameters compared to the normal CNN that has the same depth. This results in lightweight neural networks. The MobileNet-SSD Model is a Single-Shot Multibox Detection (SSD) used as the pre-trained models for detecting and classification multi animals in difficult cases like detect part of an animal in lighting/illumination conditions [11], [8]. This combining between them gives us fast and sufficient performance to detect and classify the object. This architecture is more suitable for mobile and vision-based mobile applications where there is a lack of computing power [12]. SSD approach utilizes deep neural network technique to detect and classify the target objects and this limits the output area for bounding boxes in the default boxes set over different aspect ratios and scales per each spatial position of the feature map. At the prediction time, the network introduces scores to the presence of each object class in every default box. As well, it inserts modification to these boxes for getting the best matching of the object's shape. Then, the current network collects predictions from multi-feature maps with various scales for handling objects of different volumes.

1.1. Research Problem

Animal detection and recognition is still a challenging task at the moment and there is no distinctive technique that provides a strong and efficient solution to all situations.
To summarize some of these challenges as follows:
1. The great variation in the appearance and the size of animals belonging to a particular category.
2. Lighting / Illumination Conditions: The image color of the picture is highly susceptible to light intensity and light direction variations.
3. Detect and classify animals are placed in arbitrary poses in the cluttered and the occluded environment, and in rotate states.

1.2. Paper Contributions

The contributions of this paper are presented in this section as follows:
1. Detecting the single and multi-animals of the Mammals category and also no animal category in case there is no mammal animal inside the image.
2. Detecting all types of the mammals' category.
3. Detecting and classifying the animals when the variation of image light/illumination, in a blurry and dark image.

2. Related Work

This section briefly presents the existing related works on the classification and tracking of animals.
Norouzzadeh, et al. (2018) trained Deep Convolutional Neural Networks (DCNNs) to recognize, amount, and describe behaviors of 48 species in 3.2 million images (Dataset Snapshot Serengeti). This neural network automatically recognized animals with 93.8% accuracy. Their results suggested that Deep Learning (DL) enables an inexpensive, large-scale, unobtrusive, and real-time gathering of wealth information around large numbers of wild animals. To test how best DL can automatic information elicitation from images of the camera trap, they collected millions of labeled data from the

Snapshot Serengeti (SS) dataset, the latest development of (DNN) engineering, and modern supercomputing [13].

Verma and Gupta (2018) focused on monitoring and analysis of wildlife through detection of the animal from natural scenes obtained by camera trap networks. They implemented a model of animal recognition using a self-learned feature of feature Deep CNN. Then this set of features was used for the process of classification using the state of art algorithms of Machine Learning (ML), which supported k-nearest neighbor, vector machine, and ensemble tree. Their results presented an accuracy of 91.4% [14].

(Schneider, et al. 2018) proposed network to train and compare two classifiers of deep learning object detection, Faster YOLO v2.0, and R-CNN to recognize, classify, and localize species of animals within images of camera-trap using datasets. The results were with average accuracies of 93.0% and 76.7% on the two datasets [15].

Xuefeng Liu et al. (2019) suggested a MobileNetV2-based embedded system combined with deep learning and learning transfer. This model aims to classify images of marine animals in an efficient way and in real-time. Firstly, these images were collected by using a robot equipped with a built-in device underwater. Subsequently, the proposed model has been created depending on CNN according to the images of "marine animals" which could guarantee the requirements in real-time.

Then, for further enhance rankings, learning transfer was used. After that, the model was trained using selected images of marine animals. Lastly, this trained model has been applied in the embedded devices and categorized underwater images of marine animals in real-time [16].

Deboleena Roy, et al. (2020) proposed an adaptive hierarchical network architecture made up of DCNNs which can evolve and learn as new data becomes available. This network organized the incrementally accessible data into feature-oriented super-classes and enhanced it by applying self-growth functionality to existing hierarchical CNN models. Compared to fine-tuning a deep network, the proposed hierarchical model achieved an important reduction in training effort while retaining competitive accuracy on CIFAR-10, and CIFAR-100 [17].

3. SSD MobileNet Pre-Trained Model

MobileNet SSD model is one of the pre-trained models which includes integrating the SSD and MobileNet model [18]. SSD is a popular algorithm used as an object detector while Mobilenet is a convolutional neural network used as a features extractor to produce high-level features [19]. It is pre-trained on some public datasets like the Common Objects in Context (COCO) dataset for detecting and classifying multi-objects. The architecture of the SSD MobileNet model is lightweight in its architecture which is more suitable for mobile and embedded based vision applications where there is a lack of computing power. This architecture was proposed by Google. It uses depthwise separable convolutions which basically means it performs a single convolution on each colour (input) channel rather than combining all three and flattening it.

The pointwise convolution then applies a 1×1 convolution to combine the outputs of the depthwise convolution. This factorization has the effect of drastically reducing computation and model size [20], [21].

This type of convolution divides the resulting output into two layers: a separate filtration layer, and a combination layer. The combination of these two layers will reduce the size of the model, thereby decreasing computational power requirements. A pre-trained model transfers the learned features or weights to begin the tuning process, and it allows the object detector to be trained with a limited amount of training. It is a very common and powerful method for the technique of deep learning of small image datasets which is to usage a pre-trained network [18].

4. SSD MobileNet Architecture

CNN in SSD is fully convolutional, based on MobileNet which serves as the backbone network [22]. Next, many additional CONV layers gradually decrease in size [23]. To detect smaller objects, the SSD uses extra shoaly layers with higher accuracy. For objects of various sizes, SSD detects multi metrics

by working on multiple convolution feature maps, each of which has the appropriate bounding boxes that predict dozens of categories and box offsets [24], [25]. In SSD, for the primacy of every object category inside each bounding box, a score is generated, followed by adjusting the bounding box to best match the shape of the object before detection [11]. SSD accomplishes its goal with the help of the multi-tasking loss function which represents the difference between the predicted and actual values [24]. It is created for getting the minimal of that function for optimizing the model and improving the accurate predictions. SSD is a feed-forward CNN. it associates each cell in the feature maps used for prediction with a set of the default bounding boxes (it is called also anchors) [24]. The algorithm predicts the offsets relative to a default box in the cell and a confidence score that expresses the presence of a target object class inside the default box [22]. For making the bounding box detectors particular, so each detector tries to predict just one object and various detectors will find various objects. SSD assigns each bounding box's detector to a particular position in the image. In this manner, detectors learn to specify objects at specific locations. MobileNet SSD model is shown in figure 1.

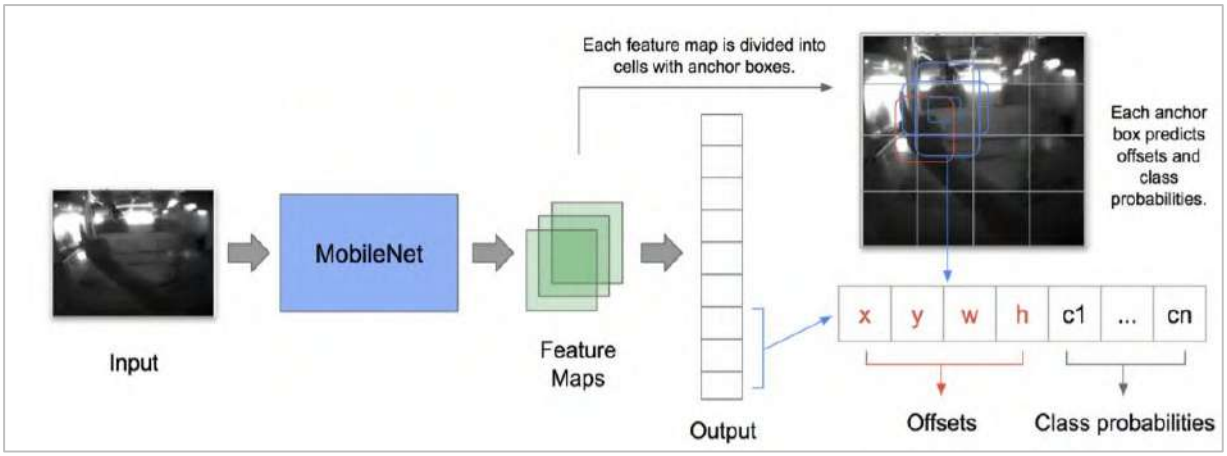

Figure 1: MobileNet SSD Model [26]

5. Research Methodology

The multi-label image classification model is proposed for detecting and classifying multiple objects (animals) of the Mammal category in static images. SSD MobileNet v1 model is used in this work, figure 2 illustrates the block diagram of the proposed model.

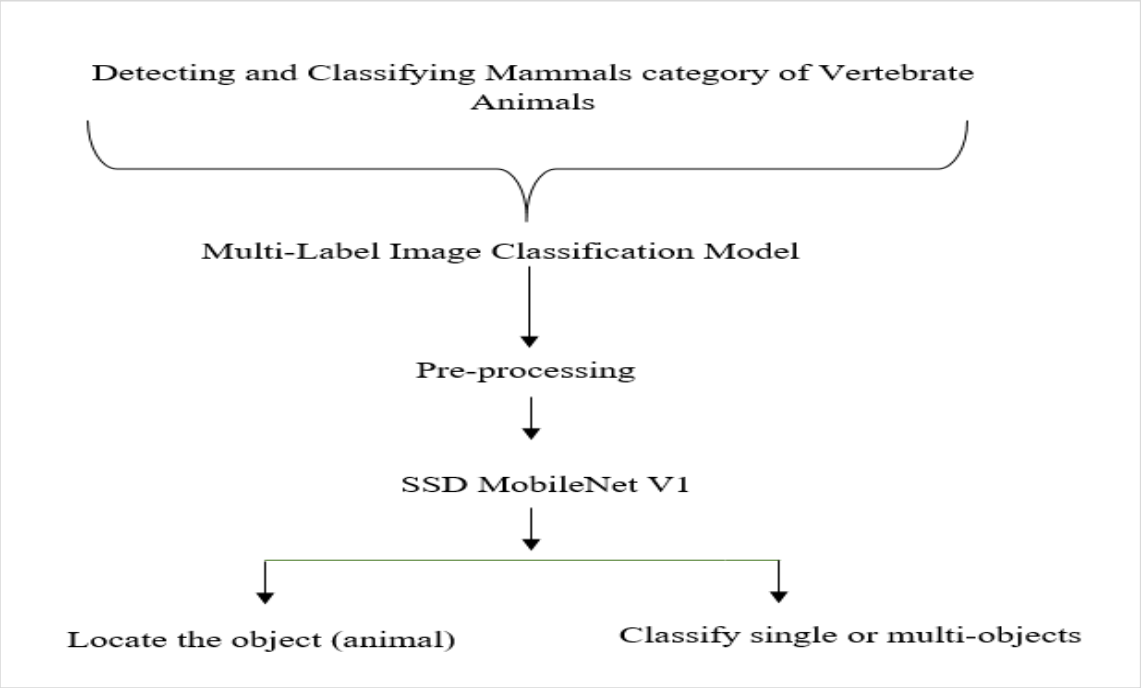

Figure 2: Block diagram of the proposed model

5.1. Pre-processing Stages for Deep Learning

The most common parameters for input image data are the number of images, number of channels, image height, and image width. Several steps of images pre-processing should be implemented before using it in deep learning:

a. Standard aspect ratio image scaling

b. Normalize the input image to the range of (0, 1) and reduce the dimension of the image to meet the standard range value and dimension for the SSD network.

c. Image Augmentations Techniques are used in this work to solve some of the challenges facing the detection and classification of the animal in static images, for example, when the animal may appear truncated or partially occluded, the animals may change their shape, or problem of Lighting/Illumination Conditions.

5.2. Proposed Method of Multi-Label Image Classification

The proposed method of Multi-Label Image Classification is used for the following:

1. Classification + Localization: Classifying an image as a mammal category or no animal, also, localizing the target object inside the image to locate the main object in an image.

2. Object Detection: Detecting all types of mammal categories and drawing bounding boxes around them. Figure 3 shows the localization, classification, and detection of two samples of our results by this method.

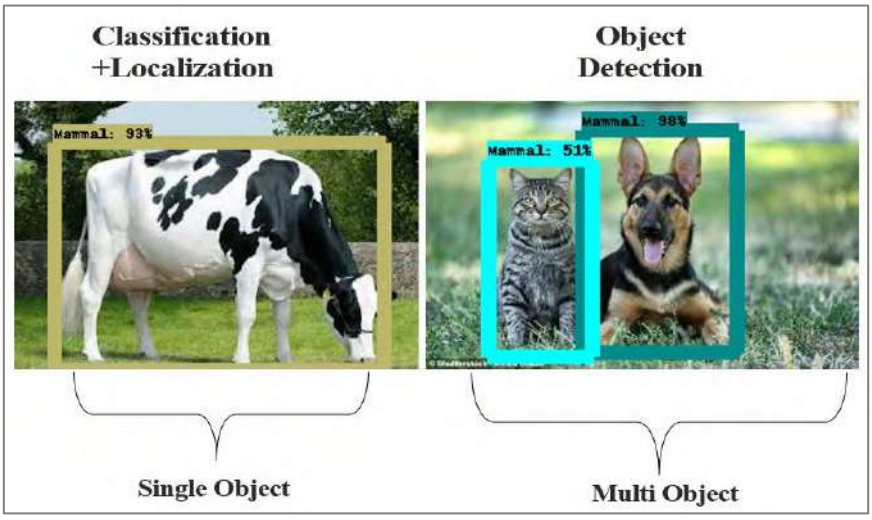

Figure 3: Localization, classification, and detection object (animal)

In this research, the SSD MobileNet v1 model is used to detect and classify multiple (objects) animals of mammal's class even in difficult cases like detecting part of the animal in lighting/ illumination conditions. Both MobileNets and Single Shot Multibox Detection (SSD) are combined and pre-trained on the COCO_2017 dataset for detecting and classifying multiple objects in difficult cases. It is an efficient CNN architecture for mobile and applications of embedded vision [19].

The Common Objects in Context (COCO) dataset is the public dataset used widely to address the issue of large training datasets and to train models to depend on the image and to overcome of data limitations problem provided by Microsoft. Presently, this dataset performs like some of the best object detection data. It includes (300,000) segmented images with (80) various object categories with highly accurate location labels. This combination of SSD and MobileNet has achieved fast detection speed while maintaining high detection quality. The dataset used in this work includes 2000 colored images in different sizes like (128 x 128, 256 x 256, 512 x 512, 1024 x 1024) pixels of two categories (Mammal category and no animal category).

This model pre-processes the images by resizes the input image sizes into 300×300 pixels to meet the requirements of the SSD mobile net model. This new size of images is used for the process of detection. Detection performs with localizing and classifying multiple objects in still images.

The outputs of the proposed model represent four matrixes which mapped to the indices 0 - 3, (Locations, Classes, Scores, and No. of detections) as shown in table 1. 20 epochs have been selected during the network training.

Table 1. The model outputs

Index	**Name**	**Description**
0	Locations	They represent (floating-point values which fall in the range [0 – 1]), where object location represents the "top, left, bottom, right" of the bounding boxes at the model.
1	Classes	A matrix of two integers is output as floating-point values [0 – 1], every index referring to the class label index for the labels file.
2	Scores	An array of two floating values which are between 0 and 1 represents the probability of detecting a class.
3	No. of detections	A matrix of length one implicates the term "floating-point value" which is the entire No. of detection results for two objects detected.

5.3. Algorithm of SSD Detection

The steps of the SSD algorithm which used in this work are as follow:

Input: RGB image.

Output: Represent four matrices that are mapped to the indices 0 - 3 (Locations, Classes, Scores, and No. of detections).

1. Apply CONV Layers to extract features at different sizes using various filters to get Feature Maps.
2. Get various feature maps at different sizes as output to fed SSD.
3. From each spatial location in Feature Maps, generate MultiClass Classification and Bounding Box Regression.
4. Add CONV layers to get smaller feature maps and continue the steps of detection.
5. Filter the bounding boxes by using IoU metrics, and the hard negative mining.
6. Compute the loss using a collection of classification (softmax), and detection (smooth L1).

5.4. Proposed Model Architecture

Our architecture of the Single Shot MultiBox Detector MobileNet model is based on (Depthwise Separable Convolutions) which is divided into two CONV layers, one layer for the filtering and the other for combining. The MobileNet model implements a single default filter for each neural input channel to initiate feature extraction. After the Depthwise Convolution, a (1 × 1) Pointwise Convolution follows to incorporate the Depthwise Convolution output. All these separable layers are followed by the batch norm, and ReLU nonlinearity expects the last (FC) layer that feeds into a softmax layer to classify as having no nonlinearity.

Filters on Mobilenet work for each color channel separately unlike the traditional CNN, and later combine the three results in one value. This factorization has the effect of drastically reducing computation and model size.

In this proposed model, (32, 64) filters with sizes (5 x5) are used to extract features from the input images followed by 2 max-pooling (pool size=2). Figure 4 illustrates the proposed model SSD MobileNet.

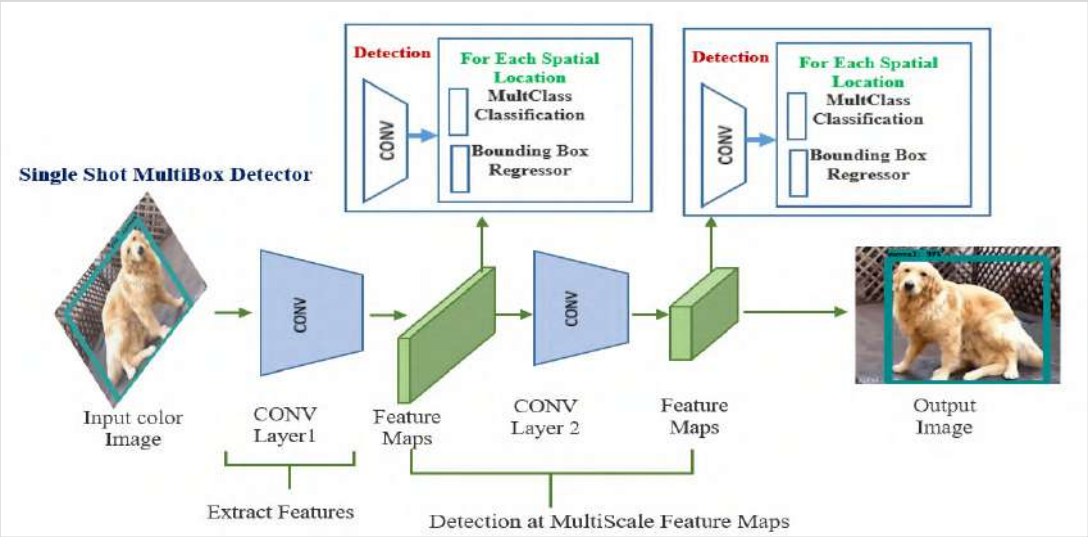

Figure 4: Proposed model SSD MobileNet V1

The model is extended by many convolutional layers. In SSD, the priority of creating a bounding box is to the target object with a high score. And then adjusting the bounding box according to the

location, scale, and aspect ratios to get the best match to the shapes of the object (to the ground truth boxes).

During training time, each feature map is used for predicting bounding boxes and the variety in the size of the feature map allows object detection with various accuracy. Boxes are filtered by IoU metrics and Hard Negative Mining. IoU is a perfect metric to measure the overlap between the predicted box and the ground-truth as computed in equation (1) and as shown in figure 5. The ideal value between them has a 100% IoU, but particularly, the result over 50% is commonly considered a correct prediction. Finally, the predicted box will be determined with maximum overlap with ground truth.

$$IoU = \frac{area\ of\ overlap}{area\ of\ union} \qquad (1)$$

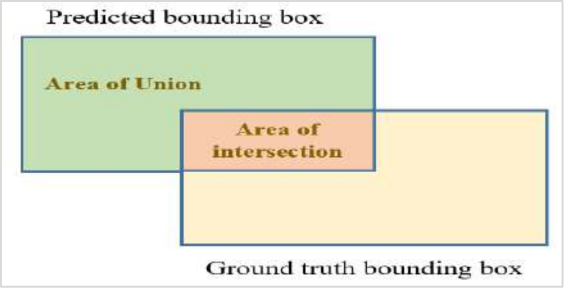

Figure 5: Intersection over union (IOU)

Loss Function is used in this model which is the weighted sum of the loss of confidence “L_{conf}” and loss of localization “L_{loc}”, as shown in equation 2.

$$L(x, c, l, g) = \frac{1}{N}(L_{conf}\ (x, c) + aL_{loc}\ (x, l, g)) \qquad (2)$$

Where:

L_{conf}: loss of confidence
L_{loc}: loss of localization
N: number of matched default bounding boxes.
α: the weight for the localization loss.
l: predicted box
g*: ground truth box*
c: *class score*
X: Input image

6. Experiment Results

The input images used in this model is RGB, and the dataset used consists of 2000 different images. 1000 images were selected for each category (mammals, and no animal). The proposed method was evaluated by the following tests:

6.1. Detection and Classification Single Animal from Different Types of Mammals

In this test, 1000 images of mammals included different types of mammals such as a dog, cat, deer, bear, rabbit, etc. have been selected. This proposed model has detected and classified all types of mammal categories in images and bounded them by a box successfully as shown in figure 6.

Figure 6: Detection and classification of the single animal from different types of Mammals

6.2. Detection and Classification Single Object of no animal Category

In this test, 1000 images of no animal category which include different types of objects belong to no animal category have been used. This model has detected and classified the objects of this category in images and bounded them by a box successfully as shown in figure 7.

Figure 7: Detection and classification of a single object of no animal's category

6.3. Detection and Classification Multi animals of Mammals Category

In this test, the model has detected and classified the multi similar and different animals of mammals in one image successfully and bounded them by a box as shown in figure 8.

Different animals **Similar animals**

Figure 8: Detection and classification multi animals of mammals Category

6.4. Detection and Classification Multi Objects of no animal Category

In this test, the model has detected and classified multi objects of no animal category and bounded them by a box successfully as shown in figure 9.

Figure 9: Detection and classification multi objects of no animal category

6.5. Detection and Classification Parts of Mammals in Image

In this test, the model has been detected and classified parts of animals displayed in the image successfully, figure 10 shows samples of the detected cut parts of animals.

Figure 10: Detection and classification cut parts of animal

6.6. Detection and Classification Mammals with Rotate Their Shapes

In this test, the proposed model has detected and classified the Mammals even in case of rotating their shapes in image and bounding them by box successfully as shown in figure 11.

Figure 11: Detection and Classification Mammals with Rotate Their Shapes

6.7. Detection and Classification the Animals from Dark Images

In this test, the model has detected and classified the animals from dark images successfully and bounding them by a box successfully as shown in figure 12.

Figure 12: Detection and classification of the Animals from Dark Images

6.8. Detection and Classification of the Animals from Blurry Images

This model tested to detect and classify the animals from blurry images; the model successfully detected and classified the animals in the blurry image as shown in figure 13.

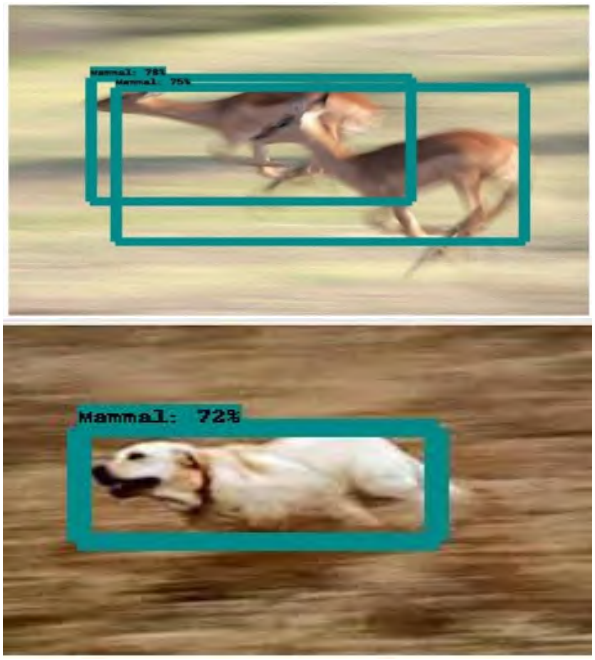

Figure 13: Detect and classify animals from blurry images

7. Comparison Between the Proposed Work Against the Others

Most studies are only detecting the specific types of a certain category but they are not detecting all types of animals that belong to a certain category. These studies also are not detecting a part of (object) animal in image, and are not detecting the objects in the dark images or under variation of illumination conditions. Most of them have not collected images; they used the online ImageNet dataset. Table 2 shows a comparison between the proposed work against the other works.

Table 2: Comparison between the proposed work against the other works

No.	Research Goal	Method	Test Accuracy
[27]	Detecting of large fauna in the open savannah of "Maasai Mara National Reserve, Kenya from very altitude resolution GeoEye-1 satellite" images.	By combining the features of "pixels based and object-based approaches of image classification".	90-96%
[28]	Identifying, and recognizing the animal images for Monitoring of Automated Wildlife" Bird, Rat, Bandicoot, Rabbit, Mouse, Cat".	Using Deep CNNs.	94.2 %
[29]	Recognizing and classifying animals located in "Slovak country" which is called "wolf, fox, brown bear, deer, and wild boar".	Using a collection of some approaches "SIFT - Scale-invariant feature transform, SURF - Speeded Up Robust Features".	(50 , 80, 86)%
[13]	Detecting animals in images, identifying species, and counting them.	Applying DNNs to automatically extract features from the images in the wild animal's dataset called "Snapshot Serengeti (SS) dataset".	93.8%

[30]	Detecting and monitoring cattle with a drone.	Using (CNNs) for recognizing the objects taken in the images.	87%
[6]	Tracking a group of unmarked zebrafish.	Suggesting a "semi-automatic multi-organism tracking method" for dealing with partial blockages by using Kalman Filter to keep tracking of every animal.	87.85%
[**7**]	Detecting and classifying “bear, hog, fox, deer, and wolf”, in the image.	Using CNN, this model is compared to high image recognition approaches like, “Principal Component Analysis, Local Binary Patterns Histograms, Linear Discriminant Analysis, and Support Vector Machine”.	97%
[33]	Monitoring pets as dogs in smart cities utilizing animal biometrics.	Using the Learning Technique “One-Shot Similarity (OSS) via distance metric.	96.87%
[12]	Developing a detector that analyses the images of video from camera traps in real-time. These images are related to "rhinoceros, humans and a set of six common large animals in the African savannah".	Using CNN “ SSD MobileNet V2”.	90%
The proposed work	Detecting, localizing, and classifying mammal in an image. Also, solve the problems of detecting animals in case of part of an animal in image, various illumination environment, and blurry image.	The proposed method used a “CNNs training, combine with pre-trained Single Shot Detector (SSD) MobileNet v1 architecture”.	98.7%

8. Conclusions

In this work, the SSD and Mobilenet-v1 are proved as an accurate and fast method for detection, classification, and localization the animal in static images.
Most other studies are only detecting the specific types of a certain category but they are not detecting all types of animals that belong to the Mammals category as we did in the current proposal.
Several tests have been done in the SSD MobileNet v1 model, and the model has achieved good results in the detection and classification of the object (animal). The results were very effective, the accuracy of detection using 20 epochs was up 98.7% which is promising compared with the other works.
This model successfully detected and classified the single and multiple objects in the static images. Moreover, this model successfully detected and classified the animal in different illumination such as dark and blurry images. Also, it could detect and classify the animal when there is a part of the animal in the image. Each object in the image was detected and bounded by boxes, besides labeling it.

References

[1] Z. He *et al.*, “Visual informatics tools for supporting large-scale collaborative wildlife monitoring with citizen scientists,” *IEEE Circuits Syst. Mag.*, vol. 16, no. 1, pp. 73–86, 2016.
[2] A. J. Shepley, G. Falzon, P. Meek, and P. Kwan, “Location Invariant Animal Recognition

Using Mixed Source Datasets and Deep Learning," *bioRxiv*, 2020.
[3] C. Zhu, T. H. Li, and G. Li, "Towards automatic wild animal detection in low-quality camera-trap images using two-channeled perceiving residual pyramid networks," in *Proceedings of the IEEE International Conference on Computer Vision*, 2017, pp. 2860–2864.
[4] H. Dong, G. Sun, W.-C. Pang, E. Asadi, D. K. Prasad, and I.-M. Chen, "Fast ellipse detection via gradient information for robotic manipulation of cylindrical objects," *IEEE Robot. Autom. Lett.*, vol. 3, no. 4, pp. 2754–2761, 2018.
[5] A. C. Coelho and J. García Díez, "Biological risks and laboratory-acquired infections: a reality that cannot be ignored in health biotechnology," *Front. Bioeng. Biotechnol.*, vol. 3, p. 56, 2015.
[6] W. Wang, Y. Li, T. Zou, X. Wang, J. You, and Y. Luo, "A Novel Image Classification Approach via Dense-MobileNet Models," *Mob. Inf. Syst.*, vol. 2020, 2020.
[7] G. Rogez, P. Weinzaepfel, and C. Schmid, "Lcr-net: Localization-classification-regression for human pose," in *Proceedings of the IEEE Conference on Computer Vision and Pattern Recognition*, 2017, pp. 3433–3441.
[8] S. Tang and Y. Yuan, "Object detection based on convolutional neural network," in *International Conference-IEEE–2016*, 2015.
[9] E. M. T. A. ALSAADI, "Auto Animal Detection and Classification among (Fish, Reptiles and Amphibians Categories) Using Deep Learning."
[10] A. G. Howard and M. Zhu, "Mobilenets: Open-source models for efficient on-device vision," *Google AI blog*, 2017.
[11] L. Leal-Taixé and S. Roth, *Computer Vision–ECCV 2018 Workshops: Munich, Germany, September 8-14, 2018, Proceedings, Part VI*, vol. 11134. Springer, 2019.
[12] A. Tydén and S. Olsson, "Edge Machine Learning for Animal Detection, Classification, and Tracking." 2020.
[13] M. S. Norouzzadeh *et al.*, "Automatically identifying, counting, and describing wild animals in camera-trap images with deep learning," *Proc. Natl. Acad. Sci.*, vol. 115, no. 25, pp. E5716–E5725, 2018.
[14] A. Joly *et al.*, "Lifeclef 2017 lab overview: multimedia species identification challenges," in *International Conference of the Cross-Language Evaluation Forum for European Languages*, 2017, pp. 255–274.
[15] P. Badre, S. Bandiwadekar, P. Chandanshive, A. Chaudhari, and M. S. Jadhav, "Automatically Identifying Animals Using Deep Learning," *Int. J. Recent Innov. Trends Comput. Commun.*, vol. 6, no. 4, pp. 194–197, 2018.
[16] X. Liu, Z. Jia, X. Hou, M. Fu, L. Ma, and Q. Sun, "Real-time Marine Animal Images Classification by Embedded System Based on Mobilenet and Transfer Learning," in *OCEANS 2019-Marseille*, 2019, pp. 1–5.
[17] D. Roy, P. Panda, and K. Roy, "Tree-CNN: a hierarchical deep convolutional neural network for incremental learning," *Neural Networks*, vol. 121, pp. 148–160, 2020.
[18] A. G. Howard *et al.*, "Efficient convolutional neural networks for mobile vision applications," *arXiv Prepr. ArXiv1704.0486*, 2017.
[19] Z.-Q. Zhao, P. Zheng, S. Xu, and X. Wu, "Object detection with deep learning: A review," *IEEE Trans. neural networks Learn. Syst.*, vol. 30, no. 11, pp. 3212–3232, 2019.
[20] E. Suharto, A. P. Widodo, and E. A. Sarwoko, "The use of mobilenet v1 for identifying various types of freshwater fish," in *Journal of Physics: Conference Series*, 2020, vol. 1524, no. 1, p. 12105.
[21] S. GHOURY, C. SUNGUR, and A. DURDU, "Real-Time Diseases Detection of Grape and Grape Leaves using Faster R-CNN and SSD MobileNet Architectures."
[22] R. Verma and C. Arora, "Modeling and implementation of real-time animal detection module for mobility assistant for visually impaired (MAVI) system." 2017.
[23] W. Liu *et al.*, "Ssd: Single shot multibox detector," in *European conference on computer vision*, 2016, pp. 21–37.

[24] J. L. Masache Narvaez, "Adaptation of a Deep Learning Algorithm for Traffic Sign Detection," 2019.
[25] A. Younis, L. Shixin, S. Jn, and Z. Hai, "Real-Time Object Detection Using Pre-Trained Deep Learning Models MobileNet-SSD," in *Proceedings of 2020 the 6th International Conference on Computing and Data Engineering*, 2020, pp. 44–48.
[26] R. Pandey, M. White, P. Pidlypenskyi, X. Wang, and C. Kaeser-Chen, "Real-time Egocentric Gesture Recognition on Mobile Head-Mounted Displays," *arXiv Prepr. arXiv1712.04961*, 2017.
[27] Z. Yang, T. Wang, A. K. Skidmore, J. de Leeuw, M. Y. Said, and J. Freer, "Spotting east African mammals in open savannah from space," *PLoS One*, vol. 9, no. 12, p. e115989, 2014.
[28] H. Nguyen *et al.*, "Animal recognition and identification with deep convolutional neural networks for automated wildlife monitoring," in *2017 IEEE international conference on data science and advanced analytics (DSAA)*, 2017, pp. 40–49.
[29] S. Matuska, R. Hudec, P. Kamencay, M. Benco, and M. Zachariasova, "Classification of wild animals based on SVM and local descriptors," *AASRI Procedia*, vol. 9, pp. 25–30, 2014.
[30] A. Rivas, P. Chamoso, A. González-Briones, and J. Corchado, "Detection of cattle using drones and convolutional neural networks," *Sensors*, vol. 18, no. 7, p. 2048, 2018.
[31] G. de Oliveira Feijó, V. A. Sangalli, I. N. L. da Silva, and M. S. Pinho, "An algorithm to track laboratory zebrafish shoals," *Comput. Biol. Med.*, vol. 96, pp. 79–90, 2018.
[32] T. Trnovszký, P. Kamencay, R. Orješek, M. Benčo, and P. Sýkora, "Animal recognition system based on convolutional neural network," 2017.
[33] S. Kumar and S. K. Singh, "Monitoring of pet animal in smart cities using animal biometrics," *Futur. Gener. Comput. Syst.*, vol. 83, pp. 553–563, 2018.

Image Steganography using Dynamic Threshold based on Discrete Cosine Transform

Image Steganography using Dynamic Threshold based on Discrete Cosine Transform

Namar A Taha, Amna Al Saffar, Alaa A Abdullatif and Firas A Abdullatif

University of Baghdad, College of Education for Pure Science-Ibn Al-Haitham, Computer Science Department

E-mail: namar.t@ihcoedu.uobaghdad.edu.iq

Abstract. The art of preventing the detection of hidden information messages is the way that steganography work. Several algorithms have been proposed for steganographic techniques. A major portion of these algorithms is specified for image steganography because the image has a high level of redundancy. This paper proposed an image steganography technique using a dynamic threshold produced by the discrete cosine coefficient. After dividing the green and blue channel of the cover image into 1*3-pixel blocks, check if any bits of green channel block less or equal to threshold then start to store the secret bits in blue channel block, and to increase the security not all bits in the chosen block used to store the secret bits. Firstly, store in the center of the block and then store another bit in the write or left bit depended on differences between them.
The proposed method was applied to many color images and many measurement terms used to show the efficiency of it. The experiment result showed good result that the PSNR = 53.76, MSE = 0.273, SSIM= 0.999, with embedding rates 0.55

Key Words: Steganography, DCT, and Least Significant Bit (LSB)

1. Introduction

Steganography is the technique of covered writing [1] it tends to hide the digital message with the digital data of different carriers' media, the carrier's media may be audio, image, movie, etc. [2,3]. For hiding secret information inside an image, several algorithms have been proposed. The main important element used in image steganography is carrier image also known as cover-image; it is the media to hide the secret information by using some embedding algorithms. Embedding algorithm: it is combining the cover image with the secret information. Stego -image: it is the image obtained after embedding the secret message that is the goal of the image steganography technique. The two images (the stego -image and cover image) must have the same quality and without distorting the quality of the cover image [4].

Steganography techniques can be done into two types of domains: spatial and frequency domain. In the spatial domain technique, the secret information is embedded directly in pixels of the image. Where in the frequency domain also known as the transform domain, the image is transformed, and then the secret information is embedded in it [5].

The most common and simplest steganography method is the Least Significant Bit. It is a spatial domain substitution process where the secret message is hidden in the least significant bit pixels of the

cover image [6]. Various algorithms for steganography hide a large number of secret information in the first least significant bits of the cover-image pixels. Because the sensitivity of the human visual system is very weak, the Presence of the hidden secret information unable to be noticed [7]. If the message is simply hidden in the least significant bits of the Sequential pixels, it can be easily destroyed by filtering, compression, or a less than size transmutation to get the original hidden message. So, this technique must be modified and combined with another transform to resist any stego-analysis methods [8] transformation technique based on the covert the cover image from the spatial domain into frequency coefficients by manipulation of the orthogonal transform of the image through using different transformation techniques like Discrete Cosine Transformation DCT [9].

This paper proposed a method that combines the Least Significant Bit (LSB) and Discrete Cosine Transform (DCT). This is done by separate the color image into RGB channels and then applying DCT transform on the green channel to find the dynamic threshold by using the DCT coefficient. The dynamic threshold used to select the block to hide text data in the blue channel based on the absolute differences between the value on the pixels in the block, The pixels in the block of cover image satisfying the threshold condition are not in Sequential locations makes this proposed method stronger and secured. The rest of the research is ordered as follows; Section 2 illustrated the discrete cosine transform with its general equation. Section 3 described the proposed algorithm with its block diagram, performance measurement explained in Section 4 and the corresponding simulations and discussions are done in section5. Finally, the conclusion of the paper was given in section 6.

2. Discrete Cosine Transform (DCT)

For image and signal processing DCT is orthogonally transformed with many advantages such as little in bit error rate and high compression ratio with good in both synthetic effects of calculation complexity and information integration ability. It broke the image into three frequency bands the low, high, and mid as in Fig1 [8,9].

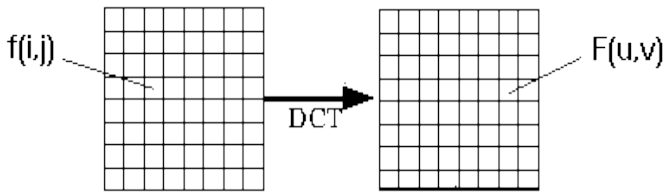

Fig 1. The DCT transform of An Image

The one-dimension DCT equation (k data items) is:

$$F(u)=\alpha(u)\sum_{x=0}^{k-1} f(x)cos\left[\frac{(2x+1)u\pi}{2k}\right] \qquad (1)$$

for u = 0, 1, 2, . . . , K-1.

The two-dimension DCT equation (k by L image) is [10]:

$$F(u,v)=\alpha(u)a(v)\sum_{x=0}^{k-1}\sum_{y=0}^{K-1} f(x,y)\cos\left[\frac{(2x+1)u\pi}{2K}\right]cos\left[\frac{(2y+1)u\pi}{2K}\right] \qquad (2)$$

for u,v = 0, 1, 2, . . . , K-1 Here, the input image is of size K × L. The pixel intensity is f(i, j); and DCT coefficient is F(u,v).

Broken the image into 8 by 8 blocks pixels and applying DCT to each block Through working left to right, top to bottom is how to used DCT in steganography [11].

3. Proposed algorithm

The proposed algorithm used the discrete cosine transform on the cover image. The DCT transform was applied on the green of the color cover image, calculate the threshold for each row, divide the blue channel and green channel into non overlapping block 1*3 and then check if any bits of green channel block less or equal to threshold then store one of the secret bits in center of blue channel block and the other in right or left according to the differences between the pixels. This way is ensuring secret bits is non embedding in consecutive pixels, which increase the security. Final step in the proposed method applied inverse DCT transform on green channel and combined it with blue channel after embedding and red channel to get the stego- image as shown in Fig 2 and explain the hiding for two bit of secret text in example as shown in Fig 3.

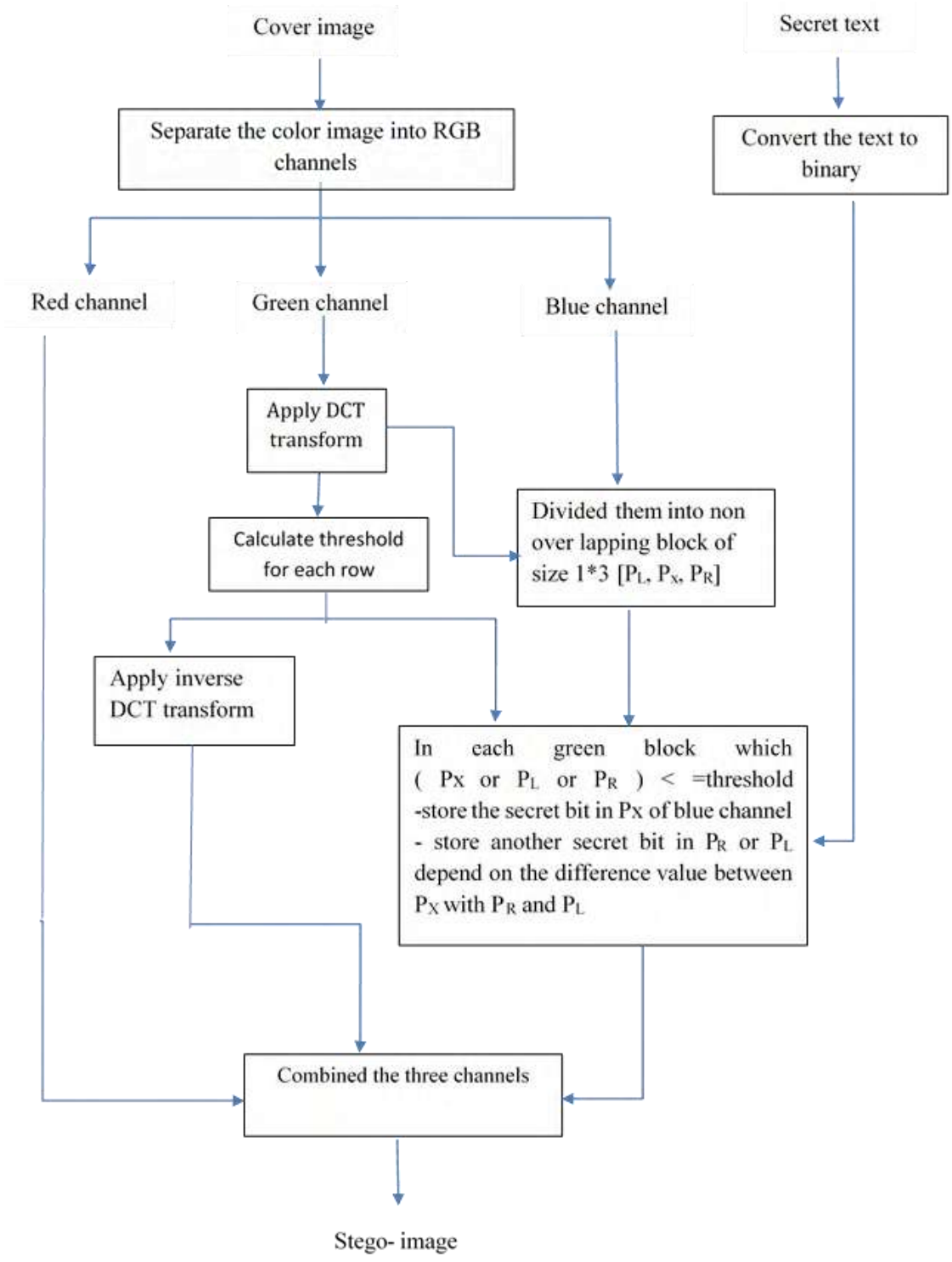

Fig 2. The main block diagram of the proposed method

An embedded and extracts algorithm are shown in 3.1 & 3.2

3.1. Embedded data process

The embedding algorithm

Input: color image with the size [M x N], secret text.

Output: stego_image.

Begin

Step 1: Read the color image and separate it into three channels R, G, and B.
Step 2: Apply DCT transform on G channel.
Step3: Calculate the dynamic threshold by the following equation (3) $\mathrm{Ti} = 1/(N-1)\sum_{j=1}^{N-1} |(\mathrm{Ci,j} - \mathrm{Ci,j+1})|$, i= 1 to M (3)
Where
$C_{i,j}$ is the DCT coefficient in i row, j column
Step 4: Apply inverse DCT on G channel
Step 5: Divide B and G channels into non overlapping blocks of size 1 x 3, P_L, P_X, and P_R.
Step 6: Convert the secret text into binary bits.
Step 7: i=1, L=1
While (i≤ M and L≤ length of secret bits) do
j=1 // the counter of blocks in each row
While (j≤ N/3 and L≤ length of secret bits) do
If (P_L, P_X, and P_R) in block [i, j] in G channel ≤ Ti then
- Store secret bit in LSB of P_X in block [i, j] in B channel
- If $|(P_X - P_L)| \geq |(P_X - P_R)|$ of B channel
- store another secret bit in LSB of P_R
Else
- store another secret bit in LSB of P_L
L= L+2;
End //
- j= j+1
End // end of j
i=i+1
End // end of i
Step 8: Reconstruct the stego-image by combination the three-color channels of the image to produce stego-image
End.

3.2. Extraction Secret text process, the extracting algorithm

Input: stego_image
Output: secret text
Begin
Step 1: Read the color image and separate it into three channels R, G, and B.
Step 2: Apply DCT transform on G channel.
Step3: Calculate the dynamic threshold by using eq. (3)
Step 4: Divide G and B channel into non overlapping block of size 1 x 3, P_L, P_X, and P_R.
Step 5: i=1, L=1
While (I ≤ M) do
j=1 // the counter of blocks in each row
While (j ≤ N/3) do
If (P_L, P_X, and P_R) in block [i, j] of G channel ≤ Ti then
- extract secret bit from LSB of P_X in block [i, j] of B channel
- If $|(P_X - P_L)| \geq |(P_X - P_R)|$ of B channel
- extract another secret bit in LSB of P_R
Else
- extract another secret bit in LSB of P_L
End //
j= j+1
End // end of j
i=i+1
End // end of i

Step 6: Convert the extracted bits to Ascii then to text
End

An Implementation example for the proposed algorithm is as follows:
After applying DCT on the green channel and calculate the dynamic threshold for each row, divide the blue and green channel into non overlapping blocks of size 1 x 3, (P_L, P_X, and P_R).
Suppose the threshold of row **i** in green channel = 151
If any pixel (P_L or P_X or P_R) in the block (i, j) of green channel < =151

Store secret bit in LSB of P_X in the block (i, j) of blue channel

Calculate the difference between the center pixel and the right, left pixels in block (i, j) of blue channel

$|Px-P_L|= |165-170| =5$

$| Px-P_R|=|165-162|= 3$

$$| (P_X - P_L) | \geq | (P_X - P_R) | \qquad (4)$$

Store another secret bit in LSB of P_R of blue channel.

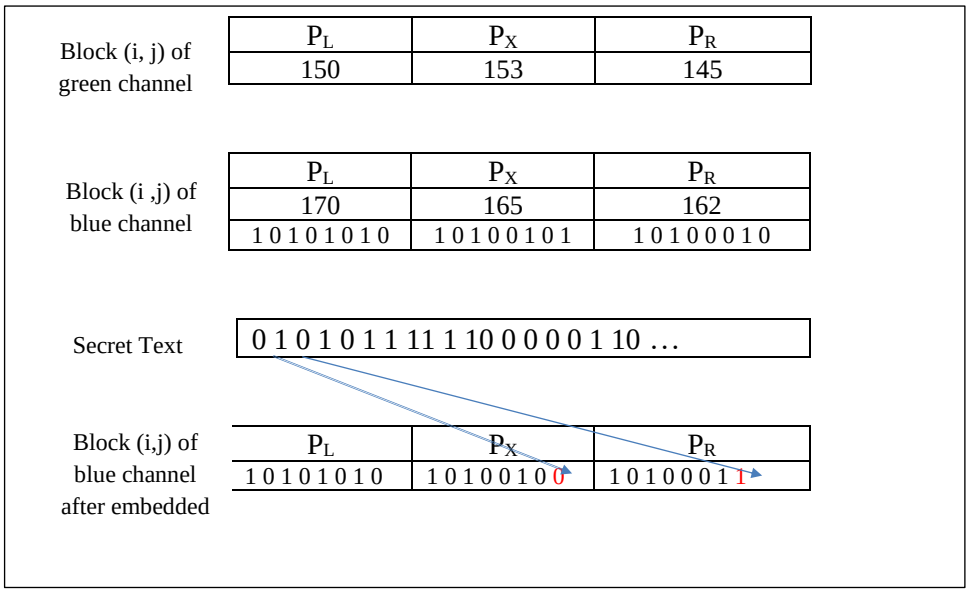

Fig 3. shows the blocks of the green and blue channel of the implemented example.

4. Performance measurement

The digital quality of an image can be calculated by using many parameters to measure the performance of the proposing method:

4.1. *Peak Signal to Noise Ratio (PSNR)*

The peak signal-to-noise ratio between two images is computed using PSNR the ratio is used to measure the quality between the cover-image and a stego- image. When PSNR is high, good quality of stego-image is obtained. (MSE) mean square error represents the differences between the pixels of two images (cover image (CI) and stego-image (SI)). The PSNR equation is [13,14].

$$\text{PSNR} = 10 \text{ Log10 } \frac{\text{RI}^2}{\text{MSE}} \qquad (5)$$

$$\text{MSE} = \frac{1}{\text{mn}} \sum_{\text{k}=1}^{\text{m}} \sum_{\text{l}=1}^{\text{n}} [\text{CI}(\text{k},\text{l}) - \text{SI}(\text{k},\text{l})]2 \qquad (6)$$

Where *m* and *n* are representing the image size, RI is the maximum value of the image's pixels.

4.2. *Structural Similarity Index Measure (SSIM)*

SSIM is an improvement method of the classical PSNR & MSE methods which is used to determine the resemblance between two images. [0,1] is the range value of the SSIM index. If the index is high then it means more similarity of two images (cover image (CI), and stego-image (SI)), and it's calculated as the follows:

$$SSIM\ (x_1,y_1) = \frac{(2\mu_{x1}\mu_{y1} + c_1)(2\sigma_{x1y1} + c_2)}{(\mu_{x1}^2 + \mu_{y1}^2 + c_1)(\sigma_{x1}^2 + \sigma_{y1}^2 + c_2)} \qquad (7)$$

Where x_1 and y_1 are two windows of common size, μ_{x1} is the average of $x1$, μ_{y1} is the average of y_1, $\sigma x_1{}^2$ is the variance of x_1, $\sigma y_1{}^2$ is the variance of y_1 and $\sigma x_1 y_1$ is the covariance of x_1 and y_1 [15].

4.3. *Image histogram*

One of the important criteria of security analysis is histogram. The security for the encrypt message is more guaranteed as the histogram of the image being is more uniform [16]. The x axis and y axis of the histogram graph explains the pixel difference between each pair and the number of occurrences, respectively. Comparing the histogram of cover and the stego-image to monitor unusual shapes as a result of an embedding algorithm or to identify pixels distribution, it is considered as one of the effective experiments of a stego-image identify the pixels distribution [17, 18].

5. Results and Discussion

The proposed algorithm was implemented and tested on several standard images. The cover images with the size (256 × 256) color – scale are used such as (a) Lena, (b) Baboon, (c) pepper, (d) monarch, (e) sails and (f) tulips as shown in Fig. 4. Fig 5 shows the stego image after embedding 36000 secret bits with embedded rate ER =0.55.

Many metrics are used to measure the performance of proposed method such as PSNR, MSE and SSIM and the result shown in table -1, High value of PSNR indicates good perceptual quality of stego-image and the high value of SSIM indicate that have more similarity between cover image and stego-image

(a) (b) (c)

(d) (e) (f)

Figure 4. The cover image (a) Lena, (b) Baboon, (c)pepper, (d) monarch, (e) sails and (f) tulips

(a) (b) (c)

(d) (e) (f)

Figure 5. the stego-images (a) Lena, (b) Baboon, (c)pepper, (d) monarch, (e) sails and (f) tulips

Table 1. PSNR, MSE and SSIM values for different cover images

Image	PSNR	MSE	SSIM
Lena	53.750	0.274	0.998
Pepper	53.764	0.273	0.998
Baboon	53.730	0.275	0.999
Monarch	53.720	0.276	0.997
Sails	53.770	0.272	0.999
Tulips	53.731	0.275	0.999

The histogram for the blue channel to the cover images and the stego images are shown in Fig. 6. It can be seen the high correlation between cover and stego- images.

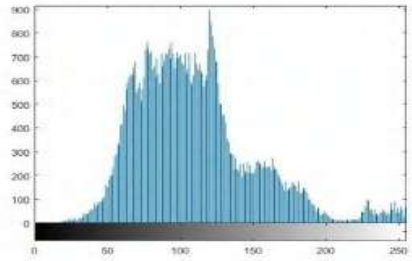

(a)

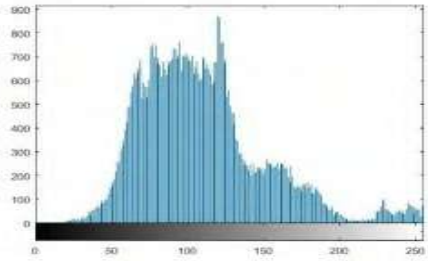

(b)

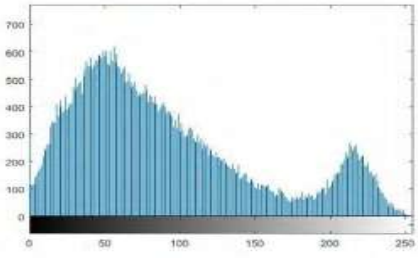

(c)

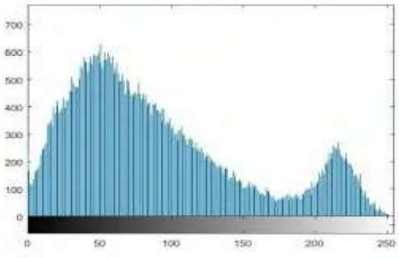

(d)

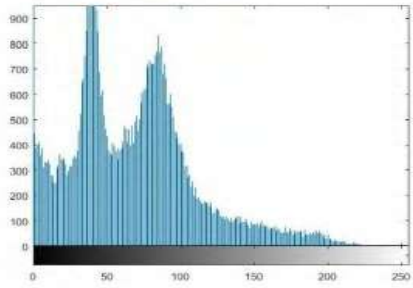

(e)

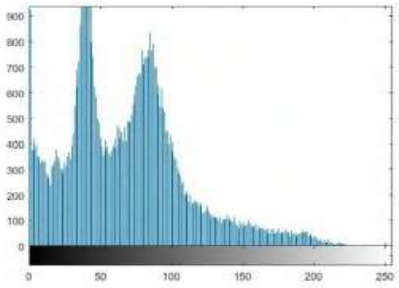

(f)

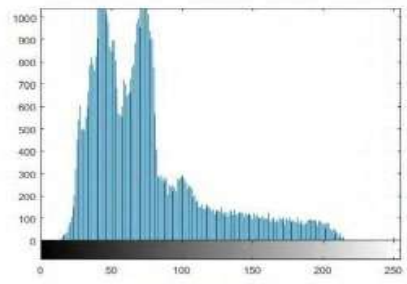

(g)

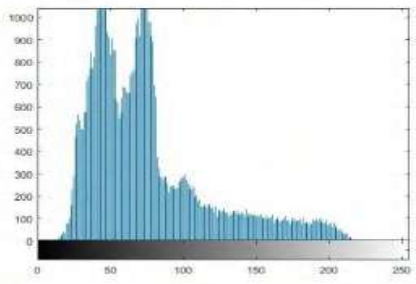

(h)

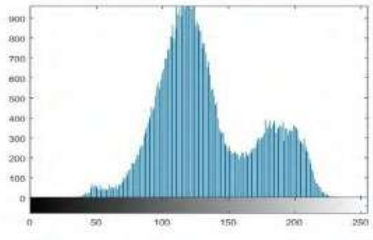

(i)

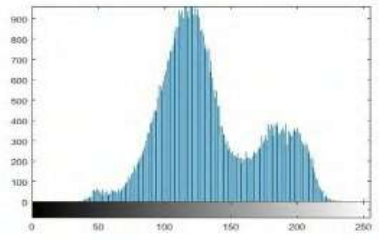

(j)

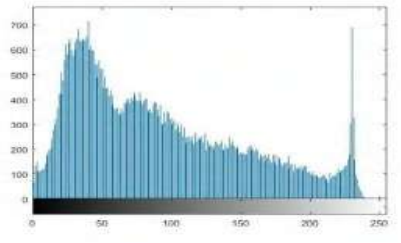

(k)

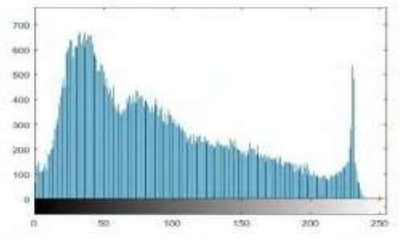

(l)

Figure 6. histogram for cover and stego images: (a) Cover Lena image, (b) Stego -Lena image, (c) Cover Baboon image, (d) Stego -Baboon image , (e) cover pepper image (f) stego- pepper image, (g) cover monarch image (h) stego -monarch image , (i) cover sails image (j) stego -sails image (k) cover tulips image, and (l) stego -tulips image

6. Conclusion

To increase the security in the steganography methods, the process of hiding the secret bits must not in a consecutive manner. In this proposed method the dynamic threshold was produced based on DCT coefficient in the green channel of the cover. The blue channel was divided into blocks of size 1*3. The block is selected to hide the secret data depend on the dynamic threshold. Two pixels only in each selected block were used to hide the secret bit to increase the security, these two pixels are the center pixel in the block and the right or left pixel of the center. The proposed method maintained good result depend on the high value of PSNR and SSIM

Reference

[1] B. Della T. Jitha A. Gisny G. Elsa R. Neenu 2015 A Novel DWT based Image Securing Method using Steganography *Procedia Computer Science* **Vol.46** pp. 612 – 618
[2] H. Nagham Y. Abid R. Ahmad M. Osamah 2012 Image Steganography Techniques: An Overview *(IJCSS)* **Vol.6** : Issue (3) pp. 168-187
[3] A. Firas, A. Alaa, A. Amna 2018 Hiding Techniques for Dynamic Encryption Text based on Corner Point *Journal of Physics* **Conf. Series 1003**
[4] M. Mohammed S. Mohd A. Fadil S. Mustafa S. Hassan 2018 Performance evaluation measurement of image steganography techniques with analysis of LSB based on variation image formats *International Journal of Engineering & Technology* **Vol.7** (4) pp. 3505-3514
[5] Parul Manju R. Harish 2014 Optimized Image Steganography using Discrete Wavelet Transform (DWT) *IJRDET* **Vol.2** Issue 2
[6] M. Oudah A. Abed R. Khudhair S. Kaleefah 2020 Improvement Of Image Steganography Using Discrete Wavelet Transform *Engineering and Technology Journal* **Vol.38** Part A No.1 pp. 83-87
[7] A. Khalid K. Ahlam, F. Iyad 2017 A New Steganographic Algorithm Based on Multi Directional PVD and Modified LSB *ITC*, **Vol.46** (1) pp. 16-36
[8] D. Ajit A. Preethi 2010 Randomized Embedding Scheme Based on DCT Coefficients for Image Steganography *IJCA* Special Issue on **RTIPPR (2)** pp.97-103
[9] K. Manal N. Aqeela S. Rula M. Saad 2020 Improvement of Image Steganography using Discrete Wavelet Transform *Engineering and Technology Journal* **Vol. 38** Part A No. 1 pp. 83-87

[10] W. Ekta J. Payal Navdeep 2010 An Analysis of LSB & DCT based Steganography *Global Journal of Computer Science and Technology* **Vol. 10** Issue 1 (Ver 1.0) pp.4-8
[11] B. Kaur A. Kaur , J. Singh 2011 Steganographic Approach For Hiding Image In DCT Domain *IJAET* **Vol.1** Issue 3 pp.72-78
[12] A. Amna, 2011 Proposed Steganography Method Based on DCT Coefficients *IHJPAS* **Vol.24**
[13] A. Firas A. Alaa A. Namar 2020 Data Hiding Using Integer Lifting Wavelet Transform And DNA Computing *Periodicals of Engineering and Natural Sciences* **Vol.8** No.1 pp.58-66
[14] S. Ali M. Ali L. Abd Z. Qudr S. Ali 2019 PDA : A Private Domains Approach for Improved msb Steganography Image *Period. Eng. Nat. Sci.* **vol.7** no. 3 pp. 1405–1411
[15] A. Bovik Z. Wang H. Sheikh 2005 Structural Similarity Based Image Quality Assessment. Digital Video Image Quality and Perceptual Coding *Series in Signal Processing and Communications* chap. 7
[16] M. Melika B.Reza 2014 CVC: Chaotic Visual Cryptography to Enhance Steganography *DOI: 10.1109* **ISCISC.2014.6994020** pp.44-48
[17] M. Mohammed S. Mohd A. Fadil S. Mustafa S. Hassan 2018 Performance Evaluation Measurement Of Image Steganography Techniques With Analysis Of LSB Based on Variation Image Formats *International Journal of Engineering & Technolog* **Vol.7** pp.3505-3514.
[18] T. A. Al-asadi and A. J. Obaid, "Object detection and recognition by using enhanced speeded up robust feature," International Journal of Computer Science and Network Security (IJCSNS), vol. 16, no. 4, pp. 66-71, 2016.

Impact of Feature Selection for Data Classification Using Naive Bayes Classifier

Impact of Feature Selection for Data Classification Using Naive Bayes Classifier

Eman Hato

Computer Science Department, College of Science, Al-Mustansiriyah University

Email: emanhatto@gmail.com

Abstract. In the field of data processing and analysis, the dataset may be a large set of features that restrict data usability and applicability, and thus the dimensions of data sets need to be reduced. Feature selection is the process of removing as much of the redundant and irrelevant features as possible from the original dataset to improve the mining process efficiency.This paper presented a study to evaluate and compare the effect of filter and wrapper methods as feature selection approaches in terms of classification accuracy and time complexity. The Naive Bayes Classifier and three classification datasets from the UCI repository are utilizing in the classification procedure. To investigate the effect of feature selection methods, they are applied to the different characteristics datasets to obtain the selected feature vectors which are then classified according to each dataset category. The datasets used in this paper are the Iris, Ionosphere, and Ovarian Cancer dataset.Experimental results indicate that the filter and wrapper methods provide approximately equal classification accuracy where the average accuracy value of the Ionosphere and Ovarian Cancer dataset is 0.78 and 0.91 for the same selected feature vectors respectively. For Iris dataset, the filter method outperforms the wrapper method by achieving the same accuracy value using only half number of selected features. The results also show that the filter method surpasses when considering the execution time.

Keywords: Feature selection, Naive Bayes classifier, Iris, Ionosphere, Ovarian cancer.

1. Introduction

Data Classification is an analysis technique used to categorize data into different classes. Classification process is carried out in two phases which are training phase and testing phase. In the first phase, also known as learning phase, the classifier model is trained using a classification algorithm with a pre-determined set of data inputs called the training data set. The classifier model, in the second phase, is employed for the classification process with another set of data, called the testing data set. The training and testing data sets are prepared by dividing the general data set by a certain percentage, noting that testing data samples are not included in the training data set [1].

The classification process depends on two main factors which are the classifiers used and the feature vectors extracted [2]. Different advanced classifiers have a powerful learning ability and high performance such as Convolution Neural Networks (CNN), K- Nearest Neighbor (KNN), Support Vector Machine (SVM), Naive Bayes Technique, and Random Forest [3, 4]. Feature extraction is an important step for multimedia processing such as video retrieval, image classification and object recognition. Feature extraction aims to extract relevant information from the data to obtain a robust descriptor and reduce huge data content. Massive data will produce a high dimensionality of the feature vector, which greatly decreases the efficiency of the classification process [5].

Feature selection is always discussed with feature extraction; it is a procedure in machine learning to selects a useful sub-features set that helps in finding the most important features of model

construction. Feature selection eliminates redundant and irrelevant features as much as possible [6]. The motivation for feature selection is dimensionality reduction of feature vectors to decrease the time complexity, as well as remove irrelevant features that lead to false prediction and thus reduce the performance of classifier [7].

Researchers attempt to extract important features or minimize noise and redundant features from the high dimensions of feature vectors utilizing diverse feature selection techniques.

In [8] Torija and Ruiz proposed prediction model for urban environments based on machine learning regression and feature selection techniques. Three feature selection methods were used which are correlation based feature subset selection, wrapper for feature subset selection and the principal component analysis to reduce time complexity and resources cost for the large number of variables involved in urban environments.

Imtiaz et al. in [9] designed brain tumor segmentation method using multi planar superpixel level features extracted from magnetic resonance imaging. A histogram based consistency analysis was applied as a feature selection method to reduce the feature vectors. In [10] Haidar and Verma proposed a method for selecting optimal input features and network parameters based on a hybrid genetic algorithm for artificial neural networks which was applied for rainfall forecasting.

In [11] Bolon-Canedo and Remeseiro give a detailed survey of feature selection techniques using in image analysis process, they considered four fields in the review which are image classification, image segmentation, image annotation and image retrieval. Silva et al. in [12] combined the feature selection methods applied on training data and machine learning algorithms to identify predictors of prediabetes for enhancing predictive performance of prediabetes. Tumar et al. in [13] Binary Moth Flame Optimization (BMFO) was used as feature selection algorithm to reduce data dimensions for improving the performance of Software fault prediction (SFP) model.

Magesh and Swarnalatha employed Decision Tree (TD) for optimal feature selection in [14]. After identifying a subset of the features, classification algorithms such As Random Forest (RF), Support Vector Machine (SVM), Linear Model (LM) and DT were applied for heart disease prediction and their performances are evaluated. Feature dimensions were reduced by approximately 61% without affecting classification accuracy. In [15] Liu et al. presented feature selection method based on independent feature space search to improve the text classification performance.

The summary from previous studies is that feature selection methods aim to reduce the feature dimensions as much as possible while maintaining the predictive accuracy of the classifiers. The objective of this paper is to evaluate and compares the effect of feature selection methods in term of classification accuracy and time complexity.

2. Feature Selection Approaches

Feature selection methods aim to reduce the data dimensionality by selecting a subset of extracted features to create a classification models. Feature selection methods search for a subset of features that achieve an optimal response from the classification algorithms so that the learning algorithms can focus on the relevant features that are more useful for the prediction process. Improving the performance of prediction and providing more faster and cost effective predictors are the main advantages of feature selection methods. Using too many features can degrade performance of prediction even when all features are relevant and contain information about the response variable [16, 17].

The feature selection methods can be classified into three approaches [18]:

1. Filter approach aim to measure features importance based on the general features characteristics such as features variance and features relevance to the response. The important features are selected as a step in pre-processing the data and then the model is trained using the selected features. Therefore, this approach is not related to the training algorithm.
2. Wrapper approach aims to select better subsets of features to enhance the performance of the learning algorithm. It starts training model using a subset of features and then removes or add a features based on a selection criterion. The selection criterion directly evaluates the model performance that results from removing or adding a feature. Model training and improving is repeated until the stopping criteria are met.

3. Embedded approach learns importance of feature as part of the model learning process. When the model is trained, the importance of the features is obtained in the trained model. Often the embedded approach cannot achieve better learning performance than wrapper approach.

3. Naive Bayes Classifier

Naive Bayesian classifier is a probabilistic classifier that applies the Bayes' theorem along with Naive assumptions about feature independence. Assume that each instance in the learning set is defined by attribute vector X = (x1, x2, x3,……xn), and the m classes C = (C1, C2, …,Cm,) exist. The naive Bayes classifier assigns the X to the class of maximum probability. The maximized probability can be defined as the follows [19, 20]:

$$P(C_i|X) = \frac{P(X|C_i)\ P(C_i)}{P(X)} \quad (1)$$

Where
P(Ci | X): The probability of Ci in case X occurs.
P(X | Ci): The probability of X in case Ci occurs.
P(X): The probability of X.
P(Ci): The probability of Ci.
The classification problem according to equation (1) is calculating the P(Ci | X) since it finds the probability that the given X belongs to class Ci. Because P(X) is a constant and generally assumed P(Ci) have the same probability, only the maximum value of P(X | Ci) must be determined. Assuming that the relationships of attribute in each class are statistically independent of each other, P (X | Ci) can be estimated as follows [19, 20]:

$$P(X|C_i) = \prod_{k=1}^{n} P(x_k|C_i) \quad (2)$$

This assumption results in efficient data classification process and simpler computation cost.

4. Methodology and Materials

In this section, details of methodology, classification datasets and performance evaluation measures are described.

4.1. The Methodology

The method in this paper is designed for comparison and finding the most appropriate feature selection methods for classification task. Their effects are evaluated based on performance of Naive Bayes classifier according to classification accuracy and time complexity.
The paper method consists of several steps. First, three popular datasets are collected from the UCI repository to conduct the experiments. Each dataset is divided into two subsets including training data and testing data. Second, the features selection methods are applied to select essential features. The next, Naive Bayes classifier is employed for classification process. Further, the comparison is performed to highlight the strengths and effectiveness of features selection methods in data classification.
The feature selection approaches employed in this paper are filter and wrapper method. The filter method rank importance of features using Relief algorithm. Whereas, wrapper method defines a subset of the training data that best predict the testing data by sequentially selecting features until there is no change in defined criterion value. The criterion adopted is mean squared error.

4.2. Classification Datasets

Three classification datasets from the UCI Machine Learning Database Repository were used in the process of evaluating the impact of feature selection methods for data classification. Datasets vary in the number of instances, the number of attributes, and the number of classes, which allows testing the effect of feature selection in different cases.

- **Iris Dataset**: represent data describing Iris flower of three related species. The dataset consists of 150 instances belonging to three classes which are "Iris Setosa", "Iris Virginica" and "Iris Versicolor". Each instance consists of 4 attributes measured in centimeters which are the sepal length, sepal width, petal length and petal width [21].
- **Ionosphere Dataset**: represent data receiving from the classification of radar returns from the ionosphere. The dataset consists of 351 instances belonging to two classes which are "Good" and "bad" and each instance consists of 34 attributes [22].

- **Ovarian Cancer Dataset**: the dataset exemplify the information on cancer of ovarian for different patients. The dataset consists of 261 instances belonging to two classes which are "Cancer" and "Normal" and each instance consists of 4000 attributes [23]. Table 1 gives a summary describing the three datasets.

Table 1. The datasets summarization

Dataset Name	Attribute Characteristics	Instances Number	Attributes Number	Associated Task
Iris	Real	150	4	Classification
Ionosphere	Integer, Real	351	34	Classification
Ovarian Cancer	Real	261	4000	Classification

4.3. Performance Evaluation Measures

The evaluation measure is based on the classification accuracy that summarizes the classification performance as the percentage of the number of correctly classified instances out of the total number of instances. The measure values are based on the statistical values of True Positive (TP: actual and predicted values are correct positive), True Negative (TN: actual and predicted values are correct negative), False Positive (FP: actual value is negative while predicted value is positive), and False Negative (FN: actual value is positive while predicted value is negative) [24, 25].

$$\text{Accuracy} = \frac{TP+TN}{TP+FP+TN+FN} \quad (3)$$

The error classification can be calculated from classification accuracy because they are complements of each other. The classification error measured as the percentage of the number of incorrectly classified instances out of the total number of instances [1].

$$\text{Error Rate} = \text{Accuracy} - 1 \quad (4)$$

A confusion matrix is a visual summary of the predictions made by a classification model organized as a matrix. It provides a clear picture of which classes are being correctly and incorrectly predicted and what type of errors are being made. Matrix rows represent the actual classes, and matrix columns indicate the predicted classes. The cell values represent the number of predictions made for a class that are actually for a given class. Classification accuracy can be calculated by computing by averaging the values across the main diagonal of confusion matrix. High score refers to high classification accuracy [6, 24].

Computational complexity is an important aspect of an effective classification model. Since features selection helps reduce the time consumed, execution time is also used to evaluate performance; it measures the response speed of the classification model.

5. Experimental Results

Initially, from each dataset, 70% of samples are selected randomly for training data and 30% of samples are also selected randomly for testing data. The method implementation and experiments are performed on Hp PC with an Intel Core i7–5500 4.40GHz CPU and 12GB RAM running Matlab 2018a.

The filter method is applied to three datasets, where the importance of each feature attribute is calculated. To get an accurate assessment, Naive Bayes performs the classification process using the most important feature attribute, and then gradually increases the feature attributes used in the classification process according to their importance. The classification accuracy, error rate and execution time are recorded with each addition.

Table2 shows the classification performance of Iris dataset for different cases, starting with the first case that uses the most important attribute feature, which is the fourth attribute, and ending with the last case that uses all the features attribute. Table 3 shows confusion matrixes of the predictions made by a classification model to the four cases.

Table 2. Effect of the filter method for Iris dataset classification

Cases	Selected Attributes	Accuracy	Error Rate	Execution Time in sec.
Case 1	4^{th}	0.944	0.055	0.1162
Case 2	4^{th},3^{th}	0.972	0.027	0.1361
Case 3	4^{th},3^{th},1^{th}	0.972	0.027	0.1512
Case 4	4^{th},3^{th},1^{th},2^{th}	0.972	0.027	0.1812

Table 3. Confusion matrixes of filter method for Iris dataset.

Case 1			
Classes Name	**Setosa**	**Versicolor**	**Virginica**
Setosa	1	0	0
Versicolor	0	1	0
Virginica	0	0.083	0.916

Case 2			
Classes Name	**Setosa**	**Versicolor**	**Virginica**
Setosa	1	0	0
Versicolor	0	1	0
Virginica	0	0.0833	0.916

Case 3			
Classes Name	Setosa	Versicolor	Virginica
Setosa	1	0	0
Versicolor	0	1	0
Virginica	0	0.083	0.916

Case 4			
Classes Name	**Setosa**	**Versicolor**	**Virginica**
Setosa	1	0	0
Versicolor	0	1	0
Virginica	0	0.166	0.833

The effects of filter method are clear, it can correctly determine the most important feature attribute. It can be noted that the classification accuracy based on only one feature attribute is very close to the accuracy using more than one feature attribute and with less execution time.
With the same procedure, the filter method is applied to the Ionosphere and Ovarian Cancer dataset, taking into account that the number of feature attributes is large in these datasets, so larger numbers of feature attributes are used by the classifier in each time for brevity.
The performance results are presented in Table 3 and Table 4 for Ionosphere and Ovarian Cancer dataset respectively, while Table 5 and Table 7 show the corresponding confusion matrixes.

Table 4. Effect of the filter method for Ionosphere dataset classification

Cases	Selected Attributes	Accuracy	Error Rate	Execution Time in sec.
Case 1	The first 4^{th} attributes	0.784	0.215	0.3030
Case 2	The first 8^{th} attributes	0.874	0.125	0.3273
Case 3	The first 16^{th} attributes	0.899	0.100	0.3696
Case 4	The first 24^{th} attributes	0.923	0.076	0.4340
Case 5	The first 32^{th} attributes	0.927	0.072	0.4831
Case 6	All attributes	0.912	0.087	0.5159

Table 5. Confusion matrixes of filter method for Ionosphere dataset

Case 1		
Classes Name	**Good**	**Bad**
Good	0.585	0.414
Bad	0.015	0.984

Case 2		
Classes Name	**Good**	**Bad**
Good	0.780	0.219
Bad	0.031	0.968

Case 3		
Classes Name	**Good**	**Bad**
Good	0.829	0.170
Bad	0.031	0.968

Case 4		
Classes Name	**Good**	**Bad**
Good	0.878	0.121
Bad	0.031	0.968

Case 5		
Classes Name	**Good**	**Bad**
Good	0.902	0.097
Bad	0.0468	0.953

Case 6		
Classes Name	**Good**	**Bad**
Good	0.902	0.097
Bad	0.078	0.921

.

Table 6. Effect of the filter method for Ovarian Cancer dataset classification

Cases	Selected Attributes	Accuracy	Error Rate	Execution Time in sec.
Case 1	The first 5^{th} attribute	0.907	0.092	8.7709
Case 2	The first 500^{th} attribute	0.858	0.141	11. 4085
Case 3	The first 1000^{th} attribute	0.839	0.160	14.2684
Case 4	The first 1500^{th} attribute	0.839	0.160	17.8197
Case 5	The first 2000^{th} attribute	0.858	0.141	19.4085
Case 6	The first 2500^{th} attribute	0.858	0.141	21.9515
Case 7	The first 3000^{th} attribute	0.858	0.141	25.1981
Case 8	The first 3500^{th} attribute	0.839	0.160	27.3748
Case 9	All attribute	0.826	0.173	31.1855

Table 7. Confusion matrixes of filter method for Ovarian Cancer dataset.

Case 1		
Classes Name	**Cancer**	**Normal**
Cancer	1	0
Normal	0.185	0.814

Case 2		
Classes Name	**Cancer**	**Normal**
Cancer	0.864	0.135
Normal	0.148	0.851

Case 3		
Classes Name	**Cancer**	**Normal**
Cancer	0.864	0.135
Normal	0.185	0.814

Case 4		
Classes Name	**Cancer**	**Normal**
Cancer	0.864	0.135
Normal	0.185	0.814

Case 5		
Classes Name	**Cancer**	**Normal**
Cancer	0.864	0.135
Normal	0.148	0.851

Case 6		
Classes Name	**Cancer**	**Normal**
Cancer	0.864	0.135
Normal	0.148	0.851

Case 7		
Classes Name	**Cancer**	**Normal**

Case 8		
Classes Name	**Cancer**	**Normal**

Case 9		
Classes Name	**Cancer**	**Normal**

Cancer	0.864	0.135
Normal	0.148	0.851

Cancer	0.864	0.135
Normal	0.185	0.814

Cancer	0.837	0.162
Normal	0.185	0.814

For Ionosphere dataset, the accuracy is improving every time a new feature attribute is added and correspondingly execution time increases as shown in Table 3.
Referring to Table 4, fluctuations in the accuracy values can be observed. Where the accuracy values are expected to have a uniform increase when the feature attribute used are also increased, as in previous datasets. This is due to the variousness and heterogeneity of the Ovarian Cancer dataset, which influenced the process of determining the importance of each feature attribute.
The wrapper method is applied on the training data only from each dataset to determine the feature attributes that can be used in the classification process as explained earlier. The results of criterion values and the final features attributes selected are listed in Table 5, Table 6 and Table 7 for Iris, Ionosphere and Ovarian Cancer dataset respectively.

Table 8. Wrapper feature selection for Iris dataset

Steps	Added Attributes	Criterion Value
1	4^{th}	0.00457491
2	2^{th}	0.00456496
3	3^{th}	0.00449546
4	1^{th}	0.00308608
Final Attributes	1^{th}, 2^{th}, 3^{th}, 4^{th}	

Table 9. Wrapper feature selection for Ionosphere dataset

Steps	Added Attributes	Criterion Value
1	5^{th}	0.00704117
2	1^{th}	0.00434487
3	10^{th}	0.00416756
4	24^{th}	0.00401223
Final Attributes	1^{th}, 5^{th}, 10^{th}, 24^{th}	

Table 10. Wrapper feature selection for Ovarian Cancer dataset

Steps	Added Attributes	Criterion Value
1	3032^{th}	0.00748559
2	2337^{th}	0.00432453
3	2680^{th}	0.00218727
4	2735^{th}	0.00085638
5	2236^{th}	0.00045620
Final Attributes	2236^{th} , 2337^{th}, 2680^{th} , 2735^{th} , 3032^{th}	

It is noticeable that the feature dimensions of Ionosphere and Ovarian Cancer dataset were reduced by wrapper method, while the Iris dataset was not affected**.**
The classification was performed by Naive Bayes algorithm based on the selected attributes feature only. The results are presented in Table 8 details the classification accuracy, error rate and execution

time of the three datasets, while Table 11 illustrate the classification performance as confusion matrixes.

Table 11. Effect of the wrapper method for datasets classification

Dataset Name	Attributes Included	Accuracy	Error Rate	Execution Time in sec.
Iris	4^{th}, 2^{th}, 3^{th}, 1^{th}	0.972	0.027	4.5212
Ionosphere	1^{th}, 5^{th}, 10^{th}, 24^{th}	0.793	0.206	37.654
Ovarian Cancer	2236^{th}, 2337^{th}, 2680^{th}, 2735^{th} , 3032^{th}	0.917	0.082	2400.106

Table 12. Confusion matrixes of wrapper method for datasets classification

Iris Dataset			
Classes Name	**Setosa**	**Versicolor**	**Virginica**
Setosa	1	0	0
Versicolor	0	1	0
Virginica	0	0.083	0.916

Ionosphere Dataset		
Classes Name	**Good**	**Bad**
Good	0.634	0.365
Bad	0.046	0.953

Ovarian Cancer Dataset		
Classes Name	**Cancer**	**Normal**
Cancer	0.945	0.054
Normal	0.111	0.888

.

Although the accuracy classification achieved by applying the wrapper method or filter method appears to be similar to the same number of selected feature attributes as shown in Table 8. But the execution time increased exponentially when using a large dataset, which is consistent with the expected results.

It should be noted that the wrapper method was able to identify the most related feature attributes from Ovarian Cancer dataset. Whereas the five selected feature attributes employed in the classification process can achieve 0.917 accuracy classification. This indicates the efficiency and ability of the wrapper method to deal with heterogeneous and varied datasets.

A clear picture was presented by visualizing the comparison of the filter and wrapper method according to the classification accuracy and execution time in a graphical representation illustrated in Figure 1 and Figure 2.

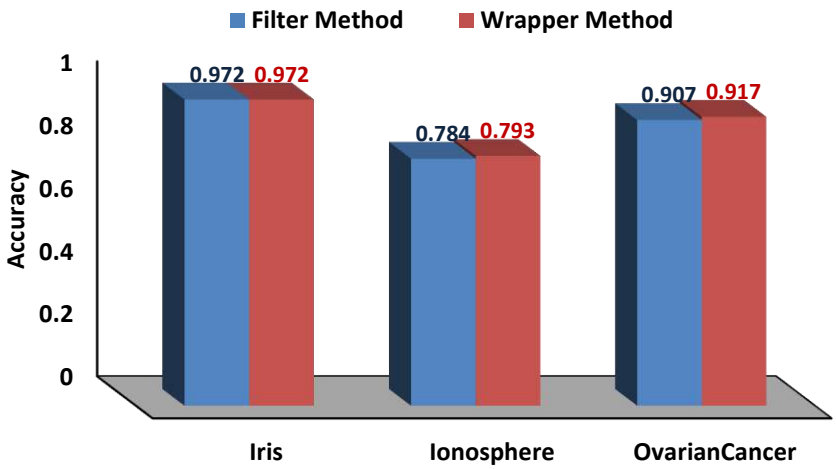

Figure 1. The Accuracy comparison

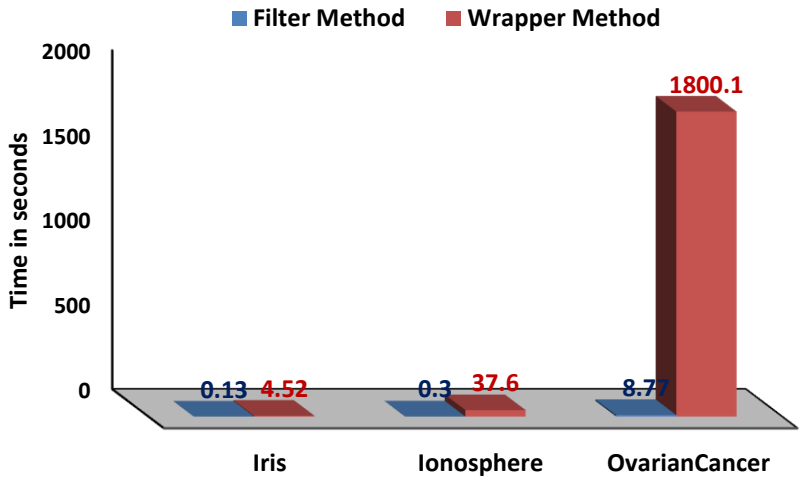

Figure 2. The execution time comparison

The comparison was made and it can be inferred from the accuracy values that applying the filter and wrapper method has almost the same accuracy value, but the wrapper method consumed more time.

6. Conclusions

Feature selection methods aim to find the most relevant features to the problem domain resulting in improved prediction accuracy and computational speed. The effect of two feature selection methods was assessed in this paper depended on the time consuming for determining the selected feature vectors and the classification accuracy of Naive Bayes algorithm for different datasets.

It is noted upon examining the results obtained that the wrapper method achieved almost the same classification accuracy as the filter method, but at the cost of time consumption. The exaction time required to determine the selected feature vectors increases dramatically with the volume of the dataset. Regardless of the extraction time, the wrapper method specified the most relevant features than the filter method when using heterogeneity dataset.

On the other hand, the filter method gave flexibility in choosing the appropriate features that helped to achieve high classification accuracy while maintaining a reasonable execution time. This makes the filter method more suitable for datasets of various sizes.

Acknowledgments

The work presented in this paper was supported by Al-Mustansiriyah University (www. uomustansiriyah.edu.iq), which is gratefully acknowledged.

References

1. Raychaudhuri, K., Kumar, M. and Bhanu, S. "A Comparative Study and Performance Analysis of Classification Techniques: Support Vector Machine, Neural Networks and Decision Trees." Singh M., Gupta P., Tyagi V., Sharma A., Oren T., Grosky W. (Eds.), Advances in Computing and Data Sciences, Communications in Computer and Information Science, In proceedings of International Conference on Advances in Computing and Data Sciences, Springer, Singapore, vol. 721, pp. 13-21, **2016**.
2. Wu, C., Li, Y., Zhao, Z., and Liu, B. "Image Classification Method Rationally Utilizing Spatial Information of the Image." Multimedia Tools and Applications, vol. 78, no. 14, pp.19181-19199, **2019**.
3. Xin, M., and Wang, Y. "Research on Image Classification Model Based on Deep Convolution Neural Network." EURASIP Journal on Image and Video Processing 2019, vol. 1, no. 40, pp. 1-11, **2019**.

4. Noi, P. T., Kappas, M. "Comparison of Random Forest, K-Nearest Neighbor, and Support Vector Machine Classifiers for Land Cover Classification Using Sentinel-2 Imagery." Sensors, vol. 18, no. 1, pp. 1-20, **2018**.
5. Zhang, L., and Lu, X. "Feature Extraction Based on Support Vector Data Description." Neural Processing Letters, vol. 49, no. 2, pp. 643-659, **2019**.
6. Chen, R., Dewi, C., Huang, S. "Selecting critical features for data classification based on machine learning methods." Journal of Big Data, vol. 7, no.52, pp. 1-26, **2020**.
7. Azhar, M. A., and Thomas, P. A. "Comparative Review of Feature Selection and Classification Modeling." In 2019 International Conference on Advances in Computing, Communication and Control (ICAC3), IEEE, pp. 1-9. **2019**.
8. Torija, A. J., and Ruiz, D. P. "A General Procedure to Generate Models for Urban Environmental-Noise Pollution Using Feature Selection and Machine Learning Methods." Science of the Total Environment, vol.505, pp.680-693, **2015**.
9. Imtiaz, T., Rifat, S., Fattah, S. A, and Wahid, K. A. "Automated Brain Tumor Segmentation Based on Multi-Planar Superpixel Level Features Extracted From 3D MR Images." IEEE Access, vol. 4, pp. 25335-25349. **2019**.
10. Haidar, A., and Verma, B. "A Novel Approach for Optimizing Climate Features and Network Parameters in Rainfall Forecasting." Soft Computing, vol. 22, no. 24, pp. 8119-8130, **2018**.
11. Bolon-Canedo, V., Remeseiro, B. "Feature Selection in Image Analysis: a Survey." Artificial Intelligent Review, vol.53, pp. 2905-2931, **2020**, https://doi.org/10.1007/s10462-019-09750-3.
12. De Silva, K., Jönsson, D., and Demmer, R. T. "A Combined Strategy of Feature Selection and Machine Learning to Identify Predictors of Prediabetes." Journal of the American Medical Informatics Association, vol. 27, no. 3, pp. 396-406, **2020**.
13. Tumar, I., Hassouneh, Y., Turabieh, H., and Thaher, T. "Enhanced Binary Moth Flame Optimization as a Feature Selection Algorithm to Predict Software Fault Prediction." IEEE Access, vol.8, pp.8041-8055, **2020**.
14. Magesh, G., and Swarnalatha, P. "Optimal Feature Selection through a Cluster-Based DT Learning (CDTL) in Heart Disease Prediction." Evolutionary Intelligence, pp. 1-11, **2020**, https://doi.org/10.1007/s12065-019-00336-0.
15. Liu, Y., Ju, S., Wang, J., and Su, C. "A New Feature Selection Method for Text Classification Based on Independent Feature Space Search." Mathematical Problems in Engineering, vol. 2020, no. 6076272, pp. 1-14, **2020**.
16. Balogun, A. O., Basri, S., Abdulkadir, S. J., and Hashim, A. S. "Performance Analysis of Feature Selection Methods in Software Defect Prediction: a Search Method Approach." Applied Sciences, vol. 9, no. 13. pp. 1-20, **2019**.
17. Hoque, N., Singh, M., and Bhattacharyya, D. K. "EFS-MI: an Ensemble Feature Selection Method for Classification." Complex and Intelligent Systems, vol. 4, no. 2, pp. 105-118, **2018**.
18. Hancer, E., Xue, B., and Zhang, M. "A Survey on Feature Selection Approaches for Clustering." Artificial Intelligence Review, vol. 53, pp. 4519–4545, 2020, https://doi.org/10.1007/s10462-019-09800-w.
19. Nitta, G. R., Rao, B. Y., Sravani, T., Ramakrishiah, N., and Balaanand, M. "LASSO-Based Feature Selection and Naïve Bayes Classifier for Crime Prediction and Its Type." Service Oriented Computing and Applications, vol. 13, no. 3, pp. 187-197, **2019**.
20. Lin, C., Lin, S., Liu, H., and Tseng, K. "Applying the Naïve Bayes Classifier to HVAC Energy Prediction Using Hourly Data." Microsystem Technologies, pp.1-15, **2019**, https://doi.org/10.1007/s00542-019-04479-z.
21. Halakatti, S.T., Halakatti, S.T. "Identification of Iris Flower Species Using Machine Learning." International Journal of Computer Science, vol.5, no. 8, pp. 59- 69, **2017**.
22. Ala'raj, M., Majdalawieh, M. and Abbod, M.F. "Improving Binary Classification Using Filtering Based on K-NN Proximity Graphs." Journal of Big Data, vol. 7, no. 15, pp. 1-18, **2020.**

23. Conrads, T. P., Fusaro, V. A., Ross, S., Johann, D., Rajapakse, V., Hitt, B. A., Steinberg, S.M. "High-Resolution Serum Proteomic Features for Ovarian Cancer Detection." Endocrine-related cancer, vol. 11, no. 2, pp.163-178, 2004.
24. Dalianis, H. "Evaluation Metrics and Evaluation." In: Clinical Text Mining. Springer, Cham, **2018**, https://doi.org/10.1007/978-3-319-78503-5_6.
25. T. A. Al-asadi and A. J. Obaid, "Object Based Image Retrieval Using Enhanced SURF," Asian Journal of Information Technology, vol. 15, no. 16, pp. 2756-2762, 2016.

An Improved Data Hiding using Pixel Value Difference Method and Hyperchaotic System

An Improved Data Hiding using Pixel Value Difference Method and Hyperchaotic System

Sameera Abbas Fadhel[1], Zeena N. Al-Kateeb[2] and Muna Jaffer AL-Shamdeen [3]

[1,2,3] Computer Sciences Department, College of Computer Science and Mathematics, University of Mosul, Mosul, Iraq

E-mail: sameeraabbas84@gmail.com

Abstract. The present paper builds a security system to encrypt and hide important text data. The system utilized an AES method to conduct an encryption process, followed by hiding the encrypted data using an improved Pixel Value Difference (PVD) technique. The method works to builds a map to hide data in a non-sequential way by relying on a hyperchaotic system to increase the security level. The system methodology proposed that the data embedding process is in one of the three levels of the colour image (Red, Green, and Blue), where the embedding level will determined based on the coordinates of the PVD pair points that is increase the efficiency of performance. A set of measures was used to measure the quality of steganography where we used MSE, PSNR, SNR, and Corr, and the results are well and satisfactory. The proposed method records the least MSE value with 0.85348784908256, while the Corr values did not decrease about 0.994145776227782. The proposed method also proved successful and effective in retrieving and decoding data, where the BER scale was equal to zero for all retrieved text.

Keywords: Data hiding, AES, Pixel Value Difference, hyperchaotic.

1. Introduction

In the last era, the Internet has been seen as a suitable manner for transferring digital data, as it can be considered an inexpensive manner to transfer digital quickly [1]. Using the internet has many disadvantages, one of them is the weakness of data security due to all forbidden users from accessing data can monitor and detect the data, and that's why steganography was used[2].Steganography is a way to keep communication protected and minimize the risk of attack while moving through the channel. In general, different kinds of files, such as text, photos, video, and sound can be used as covers to hide information. However, the cover with high redundancy will be more appropriate, so the sound and image files are the typical format used to hide information [3].The classic steganography included a confidential text in the original file to enhance the level of security. Moreover, the use of keys makes the removal or detection of original embedded text very hard when the user keys are not known.Steganography and cryptography are two ways of protecting confidential data. However, they are different, steganography hides the existence of secret data, but cryptography hides the meaning of secret data. These are important technologies that work on the internet to provide security [4], [5]. Many authors proposed methods that used the chaotic system to verify encryption and information hiding [6], [7], [8]. In our paper, a method that combined cryptography and steganography was used by relying on a hyperchaotic system.

2. Related work

In the last era, a large number of authors have proposed different methods for encrypting and hiding secure data. In [9] Das and Basak propose a scheme of data hiding, focusing on the security of message, and uses the pixel value difference to hide confidential data where the bitstream has altered before hiding in each block of the pixel. The cover image is split into non-overlapping blocks, then these blocks are distinguished with specific ranks, evaluated from the pixel value difference of every specific block. In the process of embedding, the secret data are chosen from different bins that are identified rely on the array of rank. A new data hiding method has been proposed using pixel-value differencing (PVD) in dual images. In this method, more secret data can be embedded with the increase in the value of the difference from neighboring pixels. In the suggested method, the original image is split into non-overlapping blocks and the maximum pixel value difference is computed to embed confidential data. On the sender's side, the secret data length that can be embedded is computed by using the maximum difference value of a pixel and the log function, convert the bits of confidential text to decimal, and then embedded them into the two stego-images after applying the floor function and ceil function. On the receiver's side, confidential text can be extracted and the original image restored by using correlation between two stego-images. After restoring the original image from two stego-images, the confidential text can be obtained using the maximum value difference (PVD) and the log function [10]. A new steganography technique was proposed to hide secret data and produce the stego-image. To estimate the smoothness and contrast of the pixels, we examine the relationship between adjacent pixels. In this technique, the pixels are first arranged in an ascending manner, then take the value of the highest pixel common with the other two pixels, after that apply Pixel Value Difference (PVD) method in each block. To obtain the three-pixel components, should be readjusting the two overlapping blocks. After that calculate the block of the new stego-pixel. In this method, take the lowest and middle pixel as the common pixel and perform the same procedure [11]. A new method was proposed that combined compression of data with the data hiding technique. To enhance the quality after embedding and the flow of data processing signal, the neural network was used in the communication channel. Compression of Data enhances the capacity when hiding a large amount of data. Steganography of Image that relying on neural network ensure that the size and quality of the stego-image do not change after hiding the secret data [12]. A method of improved reversible image steganography is proposed to rely on the ordering of pixel value to enhance the capacity of steganography. Before the process of steganography, one group of three continuous and adjacent pixels are considered, where the minimum and maximum values are used for calculating the value of difference and the values of difference are registered. The method determines the pixels in rows and columns that have more steganography difference values, after that steps of cipher text retrieval are implemented in the rows and columns of the image. It replace the block in the selected frame with groups of pixels that are read continuously, thus improve the capacity of steganography effectively [13]. Swain in [14] suggested a method of steganography in two variables using a combination of modified LSB substitution and pixel value difference (PVD). The first variable uses blocks of 2 × 3 pixels and the second uses blocks of 3× 3 pixels. In one of a block of the pixels, pixel value difference with other adjacent pixels are computed. This method exploited the edges in more than one direction, so analysis of pixel difference histogram (PDH) cannot find out this steganography. The substitution of LSB is performed in one pixel of the block, so this steganography cannot be detected by RS analysis also. To address the fall-off boundary problem (FOBP), appropriate equations must be used during the embedding process. In [15] the proposed method found a solution to the problem of detection of pixel value differencing (PVD) by analysis of pixel difference histogram (PDH). The resolution for this problem could be (1) using vertical, horizontal, and diagonal edges and (2) utilizing adaptive quantization ranges. This displays an adaptive pixel value difference (PVD) method utilizing blocks of 6-pixels. There are two variants. Variant1 operates on blocks of 2×3-pixels, and variant 2 operates on blocks of 3×2-pixels. For each block in variant1, secret data are hidden utilizing the four

pixels of the corner utilizing the pixels of the column in the middle for discovering the horizontal and diagonal edges. In the same way, for each block in variant2, secret data are hidden utilizing the four pixels of the corner utilizing the pixels of the row in the middle for discovering the vertical and diagonal edges. In [16] Rojali and et al show that the concealment of secret data is utilizing the Multi Pixel Value Differencing (MPVD) algorithm, using the pixel value difference. The improvement was done by utilizing tables of six intervals. This method aims to increase the capacity of steganography and to maintain the level of security.

3. The proposed algorithm:

The proposed algorithm contains three stages (i) Encryption of secret data using Advanced Encryption Standard (AES) algorithm, (ii) Selection the locations of the pixels that will be used to hide the encrypted secret data by relying on the hyperchaotic system to enhance the level of security and the efficiency of performance, (iii) Hiding the encrypted secret data in the cover image using Pixel Value Difference (PVD) method in order to enhance the capacity of information hiding.

The process of encryption is done using AES. AES is an asymmetric encryption algorithm, encryption and decryption operations include a number of rounds, and the number of rounds is depending on the length of the key. Each round performs four transformations in the encryption process. Decryption in AES includes reverse of the processes using in the encryption process [17], [18].

Hyperchaotic system: Chaos is the science of the nonlinear, unexpected, and unpredictable. Therefore, it has recently been used in a lot of research to enhance the security level and confidentiality. We used the Hyperchaotic system to select the locations of the pixels that the encrypted secret data will be hidden in them. This system shows us to expect the unexpected. Chaos Theory deals with things that are nonlinear and impossible to control or predict effectively [19], [20]. Theory of Chaos is one of the branches of physics and mathematics, rely on the manner of dynamical systems that are effected to initial conditions highly. That is defined as the effect of a butterfly. The chaos is useful in hiding secret data because: (i) nonlinear behaviours and complexity, (ii) Sensibility rely on initial values. When the initial value is specified in any system, it is easy to expect the new state of the system, but in the chaos system is impossible to predict the long term [21].

We used a 4D hyperchaotic system is derived from the famous 3D Lorenz system [19], [20] which is depicted as:

$$\begin{cases} \dot{x} = a(y - x) \\ \dot{y} = cx - y - xz + w \\ \dot{z} = xy - bz \\ \dot{w} = -dx \end{cases} \quad \dots\dots\dots\dots\dots\dots\dots\dots\dots\dots (1)$$

In which x, y, z, w are state variable, and $a, b, c, d > 0$ are control parameters. The above system is exhibiting hyperchaotic behaviour under the initial parametersa $= 10, b - \frac{8}{3}, c = 28, d = 5$. Figure (1) shows the system attractors. In our method, we use the hyperchaotic system to determine the positions of the pixels that are used to hide secret data.

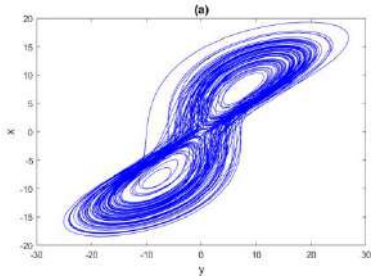

Figure (1): The attractors of hyperchaotic system

Hiding of encrypted secret data is rely on the Pixel Value Difference (PVD) method, but in a style that ensures a type of distributed diffusion depending on the x-axis coordinate and y-axis coordinate of the pair of pixels that are used in the hiding process, hiding three bits from the encrypted confidential data in the red layer, green layer and blue layer in a specified manner.

3.1 **Suggested method steps at a sender's side:**

1. Select the cover image.
2. Enter the important secret text to be encrypted.
3. Make the important text encryption process using AES to get the encrypted text.
4. Convert the encrypted text to Binary code.
5. Calculate the size of encrypted text.
6. Enter the initial values for the hyperchaotic system.
7. Build a hiding map based on a hyperchaotic system.
8. Comparing the capacity of the resulting map with the size of the encrypted text to be hidden, If the capacity is sufficient, go to step 9, else go back to 6 to update the initial values of hyperchaotic system.
9. Determine which layer will be used to hide data (Red layer, or Green, or Blue) depending on the x-axis coordinate and y-axis coordinate of the pair of pixels that are used in the hiding Process:
   If $(X_i * Y_{i+1})\%3$
   - =0 Then the hidden process will be Red layer.
   - =1 Then the hidden process will be the Green layer.
   - =2 Then the hidden process will be the Blue layer.
10. Calculate the number of bits that will be hidden in any layer using the PVD method, this process is done according to the range table that was used to find the number of bits depends on the difference of pixels.
11. Repeat step 9 until all encrypted text has been hidden.
12. Get the stego-image that contains the encrypted text data.

3.2 Suggested method steps at a receiver's side:

1. Enter the stego-image.
2. Enter the initial values for the hyperchaotic system.
3. Build an extraction map based on a hyperchaotic system.
4. Determine which layer will hold the hidden data (Red layer, or Green, or Blue) depending on the x-axis coordinate and y-axis coordinate of the pair of pixels that are used in the extraction process:
   If $(Xi * Y_{i+1}) \%3$
   - =0 Then the extraction process will be Red layer.
   - =1 Then the extraction process will be the Green layer.
   - =2 Then the extraction process will be Blue layer.
5. Calculate the number of bits drawn from any layer using the PVD method, this process is done according to the range table that was used to find the number of hidden bits depends on the difference values of pixels.
6. Retrieve all cipher hidden text.
7. Decrypt cipher text using AES algorithm.
8. Get the important secret text.

Fig (1). Is the Block diagram clear the sender processes encryption & embedding and the receiver processes extracting & decryption in the proposed algorithm.

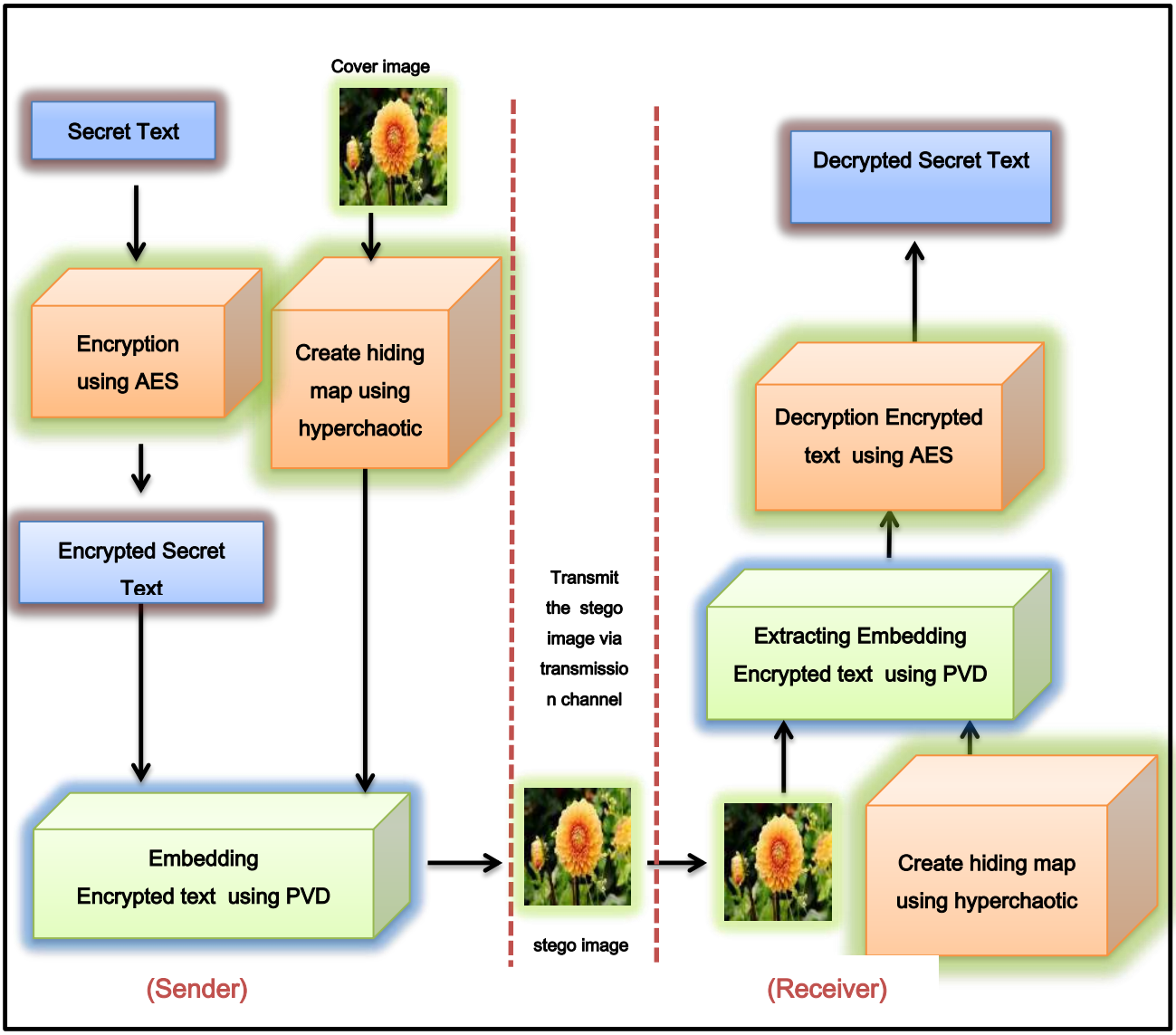

Figure (2). The block diagram of the proposed algorithm

4. Results and Analysis:

The Suggested method was implemented in Matlab 2019, and it has implemented to different size images to show the capability of using it for all different images sizes and the results were shown in table.1 which is below.

Table 1. The Used Cover & Stego images

Name of Image	Cover Image	Stego Image
Img 1		
Img 2		
Img 3		
Img 4		
Img 5		
Img 6		

Img 7	

Table 2. The histogram of images before and after Hiding

Name of Image	Cover Image histogram Stego Image histogram
Img 1	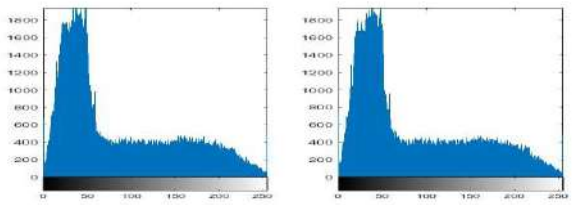
Img 2	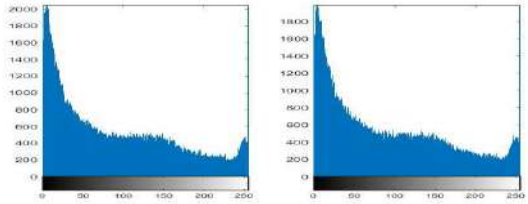
Img 3	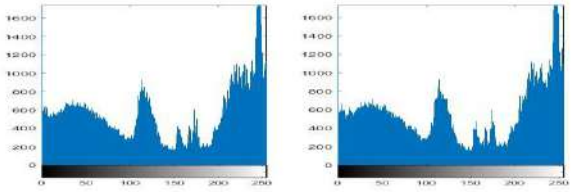
Img 4	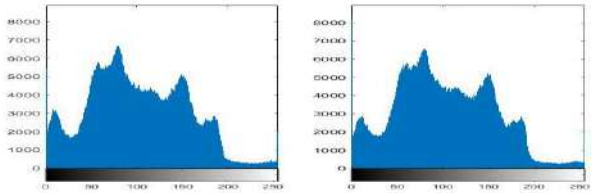
Img 5	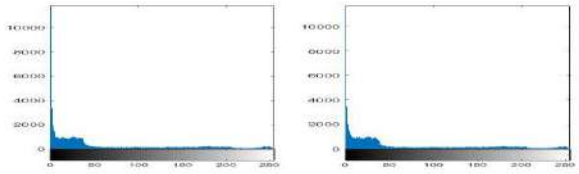
Img 6	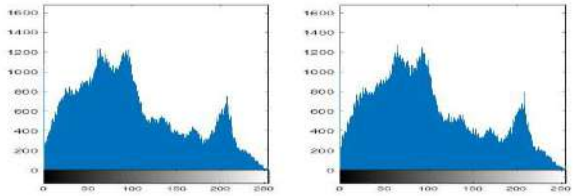

Img 7	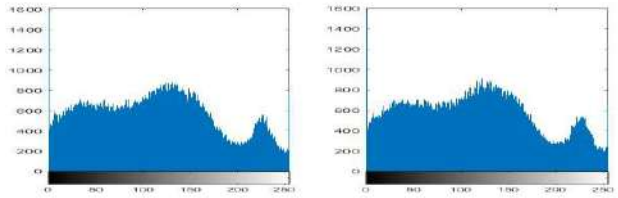

We are used many metrics to show the efficiency, the Mean Square Error (MSE), the Peak Signal to Noise Ratio (PSNR) and the Signal to Noise Ratio (SNR), correlation coefficient (Corr).
MSE is used to calculate the amount of distortion in the image, whereas PSNR is a measure of the stego image quality by comparing the cover image with the stego-image. MSE, PSNR and SNR can be calculated as follows: [22], [23], [24].

$$PSNR = 10 \log_{10}\left(\frac{C_{max}^2}{MSE}\right) \dots\dots\dots\dots\dots\dots\dots\dots\dots\dots\dots\dots (2)$$

Where $C_{\_max}$ represents the max value in the image.

$$MSE = \frac{1}{MN} \sum_{i=1}^{M}\sum_{j=1}^{N}(x_{ij} - y_{ij})\,2 \dots\dots\dots\dots\dots\dots (3)$$

$$SNR = 10 \log_{10} \frac{\sum_{i=1}^{N}\sum_{j=1}^{M} x_{ij}^2}{\sum_{i=1}^{N}\sum_{j=1}^{M}[x_{ij} - y_{ij}]\,2} \dots\dots\dots\dots\dots\dots\dots (4)$$

Where M, N Represents row and column of the image, $x_{\_(ij)}$ represents the cover image and $y_{\_ij}$ represents an image that includes secret text.

Also, it could compare the two images by using the correlation. The better value of correlation is to be near to one [25],[26],[27].

$$Corr = \frac{\sum_{i=1}^{N}\sum_{j=1}^{M}(x_{ij} - \bar{x})\,(y_{ij} - \bar{y})}{\sqrt{\sum_{i=1}^{N}\sum_{j=1}^{M}(x_{ij} - \bar{x})2}\ \sqrt{\sum_{i=1}^{N}(\sum_{j=1}^{M}(y_{ij} - \bar{y})2}} \dots\dots\dots\dots\dots (5)$$

Where $\bar{x}$, $\bar{y}$ Represents the mean of images x and y and can be calculated as follows:

$\bar{x} = \sum_{i=1}^{N}\sum_{j=1}^{M}\frac{x_{ij}}{NM}$ …….. (6) And $\bar{y} = \sum_{i=1}^{N}\sum_{j=1}^{M}\frac{y_{ij}}{NM}$…….. (7)

Bit error rate (BER) It is a measure of the accuracy of the retrieved information calculate as the actual number of bit positions which are varied in the stego-image compared with the original image [5].

Table 3. The Values of metrics on different Images

Image name	MSE	Corr	SNR	PSNR	BER
Image 1	2.42928299387316	0.999463019629443	33.9135498071767	41.3058183398367	0

Image 2	2.84100851187182	0.999436178520677	33.0398631471044	39.8278753104839	0
Image 3	1.93450888296249	0.999704386489412	37.9550318696187	41.7862567233412	0
Image 4	1.69615192209505	0.994145776227782	25.9174259673571	32.9150448252477	0
Image 5	0.85348784908256	0.999717801954953	33.5559859881410	44.8064898245093	0
Image 6	1.43589641645462	0.999595710880613	36.5437518677764	43.3625274094347	0
Image 7	3.26398121243482	0.999161047633477	33.4770570635068	39.2480536436209	0

After noticing the values in table 3, we find that the values of the MSE are small amount, the maximum value is 3.26398121243482, and this gives a good idea aboutthe algorithm quality. And find that the values of Corr between two images is very near to one, which indicates a high correlation between two images. The PSNR values between the cover image and the stego-image were large, so that no noticeable distortions occurred, meaning that the algorithm achieved a high percentage in the inability to distinguish the cover image from the stego-image, or in other words the inability to detect. And as shown by the (BER) values, the algorithm was able to retrieve the hidden secret data completely without errors.

Table 4. Comparison between previous methods that used PVD and Suggested method

Method name	MSE	PSNR
Our method	0.853487849082563	44.8064898245093
Ref9	4.926098000000000	41.2057720000000
Ref12	3.532000000000000	44.5273000000000

In Table 4 the values of best results were compared in the three methods (In this comparison, we compared between the best results in our method, Ref9 and Ref12). We note from the table that the proposed method achieved the best results.

Conclusion

The combination of encryption and hiding is one of the successful ways to protect confidential data from exposure to any detection or disclosure by unauthorized persons or entities. The system suggested using the AES method to perform the encryption process. Moreover, the system also suggested using the PVD method to perform the concealment process, but using this method for traditional masking may lead to the easy discovery of the hidden data. So we used it differently than the usual manner, where we suggested that the selection of the pixel pairs for the PVD method depends on a very turbulent system, which adds to the method's complexity and the inability to guess the locations of the data hiding. The research also suggested using all three levels of the image to perform the hiding process, where hiding is done at one of the levels for each pixel, and the level is determined depending on the location of the hiding, which increases the level of security provided by the proposed method. And because the success rate of the work can only be determined through metrics, we have tested the quality of our work through metrics MSE, PSNR, SNR, and Corr, and all of them have proven the good quality of the hiding process. The BER standard also confirmed the validity of the hiding and encryption process, which indicates that the proposed method can be adopted to protect important data.

Acknowledgments

The authors thank the University of Mosul/ College of Computer Science and Mathematics for providing facilities and support, which led to the development of the quality of this work.

References

[1] K. Joshi, S. Gill, and R. Yadav, 2018, "A New Method of Image Steganography Using 7th Bit of a Pixel as Indicator by Introducing the Successive Temporary Pixel in the Gray Scale Image", Journal of Computer Networks and Communications, (8),1-10, Article ID 9475142.

[2] P. Chandarana, P. Ahirao, 2018, "ADVANCED IMAGE STEGANOGRAPHY", International Journal Of Innovative Research in Information Security (IJIRIS), 5(7).

[3] A. S. Ansar, M. S. Mohammadi, and M. T. Parvez, 2019, "A Comparative Study of Recent Steganography Techniques for Multiple Image Formats", I.J. Computer Network and Information Security, 11(1), 11-25.

[4] A. AL-Shaaby, T. AlKharobi, 2017,"Cryptography and Steganography: New Approach", TRANSACTIONS ON NETWORKS AND COMMUNICATIONS, 5(6), 25-38.

[5] Z. Al-Kateeb, M. Al-Shamdeen, & F. Al-Mukhtar, 2020, " Encryption and Steganography a secret data using circle shapes in colored images," In Journal of Physics: Conference Series 1591(1), 012019, IOP Publishing.

[6] S. F. Al-Azzawi and M. M. Aziz, "Chaos Synchronization of Nonlinear Dynamical Systems via a Novel Analytical Approach," Alexandria Engineering Journal, vol. 57, no. 4, pp. 3493-3500, Dec 2018.

[7] S. F. Al-Azzawi, et al., "Chaotic Lorenz System and it's Suppressed," Journal of Advanced Research in Dynamical and Control Systems, vol.12, no. 2, pp. 548-555, 2020.

[8] A. S. Al-Obeidi and S. F. AL-Azzawi, "Chaos Synchronization in a 6-D Hyperchaotic System with Self-Excited Attractor," TELKOMNIKA Telecommunication, Computing, Electronics and Control, vol. 18, no 3, pp. 1483-1490, June 2020.

[9] D. Das, and R. K. Basak, 2020, "Rank Based Pixel-Value-Differencing: A Secure Steganographic Approach", Proceedings of the Global AI Congress 2019. Springer, Singapore, 2020.

[10] P. H. Kim, K. W. Ryu and K. H. Jung, 2020, "Reversible data hiding scheme based on pixel-value differencing in dual images", International Journal of Distributed Sensor Networks, 16(7), 1550147720911006.

[11] J. Majumder and C. Pradhan, 2020, "A Steganographic Method with an Overlapping of Three Pixel Block of Image", International Journal of Innovative Technology and Exploring Engineering (IJITEE) ISSN: 2278-3075, Volume-9 Issue-4, February 2020.

[12] J. Majumder and C. Pradhan, 2019, "High Capacity Image Steganography using Pixel Value Differencing Method with Data Compression using Neural Network", International Journal of Innovative Technology and Exploring Engineering (IJITEE) ISSN: 2278-3075, Volume-8 Issue-12, October 2019.

[13] H. H. Liu and C. M. Lee, 2019, "High-capacity reversible image steganography based on pixel value ordering". EURASIP Journal on Image and Video Processing, 2019(1), 54.

[14] G. Swain, 2018, "High capacity image steganography using modified LSB substitution and PVD against pixel difference histogram analysis". Security and communication networks.

[15] A. Pradhan, K. R. Sekhar, and G. Swain, 2017, "Adaptive PVD steganography using horizontal, vertical, and diagonal edges in six-pixel blocks". Security and Communication Networks.

[16] Rojali, I. S. R. Siahaan and B. Soewito, 2017, August. "Steganography algorithm multi pixel value differencing (MPVD) to increase message capacity and data security". In AIP Conference Proceedings, Vol. 1867, No. 1, p. 020035. AIP Publishing LLC.

[17] A. M. Abdullah, 2017, "Advanced Encryption Standard (AES) Algorithm to Encrypt and Decrypt Data". Cryptography and Network Security, 16.

[18] Sh. Wadehra, Sh. Goel and N. Sengar, 2018, April, "AES Algorithm: Encryption and Decryption", International Journal of Trend in Scientific Research and Development (IJTSRD), Volume 2, Issue 3, pp.1075-1077, , ISSN No: 2456 - 6470.
[19] Z. Sh. Al-Talib and S. F. Al-Azzawi: Projective and hybrid projective synchronization of 4-D hyperchaotic system via nonlinear controller strategy, TELKOMNIKA Telecommunication, Computing, Electronics and Control, 18(2), (2020), 1012-1020.
[20] S. Y. Al-hayali and S. F. Al-Azzawi: An optimal control for complete synchronization of 4D Rabinovich hyperchaotic systems, TELKOMNIKA Telecommunication, Computing, Electronics and Control, 18(2), (2020), 994-1000.
[21] S. Y. Al-hayali and S. F. Al-Azzawi: An optimal nonlinear control for anti-synchronization of Rabinovich hyperchaotic system. Indonesian Journal of Electrical Engineering and Computer Science. 19(1), (2020), 379-386.
[22] A.Sundar, V. Pahwa, C. Das, M. Deshmukh, N. Robinson, 2016, "A Comprehensive Assessment of the Performance of Modern Algorithms for Enhancement of Digital Volume Pulse Signals ", International Journal of Pharma Medicine and Biological Sciences, 5(1), 91.
[23] Y. Inan, 2018, "Assesment of the Image Distortion in Using Various Bit Lengths of Steganographic LSB ", Near east University, Computer Engineering Department, Nicosia, TRNC, Mersin 10 Turkey, ITM Web of Conferences 22, 01026.
[24] E. Noroozi, S. B. M. Daud, A. Sabouhi, 2011, "Critical Evaluation on Steganography Metrics ", In Advanced Materials Research,748, 927-931, Trans Tech Publications Ltd.
[25] Z. N. Al-Khateeb, M. F. Jader, 2020, "Encryption and Hiding Text Using DNA Coding and Hyperchaotic System," Indonesian Journal of Electrical Engineering and Computer Science, 19(2)Aug 2020.
[26] Z. N. Al-kateeb , M. R. Al-Bazaz, 2019,"Steganography in Colored Images Based on Biometrics," Tikrit Journal of Pure Science, 24(3), 111-117.
[27] Z. N. Al-Khateeb, S J. Mohammed, 2020, "A Novel Approach for Audio File Encryption Using Hand Geometry," Multimedia Tools and Applications,Mar 2020.

Multi-Camera Collaborative Network Experimental Study Design of Video Surveillance System for Violated Vehicles Identification

Multi-Camera Collaborative Network Experimental Study Design of Video Surveillance System for Violated Vehicles Identification

Hasan Thabit Rashid [1] and Israa Hadi Ali [2]

[1, 2] Department of Software, college of Information Technology, University of Babylon, Iraq
[1]Computer Department, Education College for Women, University of Kufa, Iraq

E-mail: hasant.kurmasha@uokufa.edu.iq

Abstract: In this paper, we propose an experimental study of multi-camera collaborative network for surveillance the highway traffic turn in real life scenario, the target of surveillance based offline video processing is capturing the violated vehicles that driving violated paths in many cases specified by user-defined rules. Best topology of the experiment zone is considered and covered by four pillars; each has two (fixed and motorized) cameras that casing the entire specific effective field of view. As to author knowledge, there is no such available experiment, and hence, it could serve researchers that interested in. However, the experiment is done for around 180 recorded hours for 8 videos during 9 days, each video for one camera. It is designed based on the collaborative cameras principle for intelligent video surveillance systems and the outcomes show that the surveillance and the tracking of violated vehicles have been successes in most user-defined rules cases for more than 90 % cases.

Keywords: Traffic violations; Area topology; Multi-camera collaborative network; Video analysis; Intelligent video surveillance systems.

1. Introduction

Nowadays, the cameras in use not only respond on the basis of the sensed data, but also support each other by their information, through multi-camera collaborative network MCCN. Coupling between two cameras may be affected geometrically and kinematic connections are the principal forms of coupling. To analyze low and higher resolution events, cooperation between static and dynamic cameras with their specific parameters is important. Field of view FOV is the maximum viewable angle from a camera. Spatial resolution is the ratio of the total number of pixels on its image element excited by the projection of an object in the real world. Higher spatial resolution may capture more data and makes pictures clearer. Depth of field is called the sum of distance between nearest and farthest objects that appear in an acceptably sharp focus of an image. To automatically extract valuable information from video data, intelligent video surveillance systems IVSSs is required with more scalability, flexibility and efficiency. IVSSs technology was used to monitor traffic, identify road collisions and control crowd activity in public spaces. The primary aim for surveillance is to retain understanding of the situation by fusing information from various cameras into a cohesive model of people, actions, and events to help a remote user understand anomalous and irregular activities [1, 2].

Single camera is weaker for tracking because it is covering a small area of such environment. It has problems such as segmentation of objects, occlusion of objects, etc. Multi-camera coordination had, until recently, allowed overlapping FOV. MCCN Setup works more efficiently with occlusion. Occlusion can be managed as the job of monitoring every single object by switched to another camera which can clearly realize it. Coordination and monitoring of MCCN performs many tasks; capturing and analyzing videos obtained from multiple cameras; Fuses the important information gained from different network cameras; it carries out the control actions necessary for the monitoring task in question [3-6]. However, we introduce short introduction at first section, and the traffic experimental considerations with weaknesses is arranged on second. The methodology and the topology of the experiment showed at the third section. The results and discussions, and conclusion have been explained consequently at last two sections.

2. Traffic experimental considerations

According to [7], many situations need to be addressed as to the surveilled area as following. The state transportation departments also maintain traffic cameras which simply track vehicle flows on roads and major arteries to conclude the valuable data. As well as monitoring the roads for collisions or significant delays, traffic camera footage is instrumental in future road growth and construction decisions. Monitor rules, cameras used to monitor speed and red light rules efficiently record driving violations and issue tickets. Promote safe driving, the visible intersection security cameras will encourage healthy driving practices and prevent moving violations. Weather-Traffic cameras are vulnerable to weather harm when they are tracking intersections or checking for traffic jams. The traffic security camera can damage, or destroy, heating, wind, rain, snow and ice. Accidents, there is also the risk that accidents will damage traffic cameras as they are placed on busy roads and intersections. Traffic surveillance cameras and red light or speed cameras have different functions and should therefore be regarded separately during set-up. For installing traffic control in right way, one may need to answer the following questions, what are your area's main roads? When is traffic the heaviest in your area (Rush Hour) at what time? Is traffic actually congested by other features on the roads? However, you need to install cameras to overlook specific areas of congestion and to make certain that all camera lanes are clearly clear and have a good view. Camera bodies can help protect the sensor from weather conditions by temperature and humidity. All above situations are considerations for specific surveillance systems which is very important to be taken into account when such system designs.

3. Methodology

3.1. Experiment design and considerations

Wired video system design is reliability and confidence; the ensuring to mix and match the most appropriate system components from different vendors as well as the power to optimize or expand the system to any size which demands quite knowledge. We need to know what the different components and how they work, and how they interact to construct a good reliable and perfect system. At the same time, the appropriate network and storage solutions depend greatly on the selected cameras, the camera settings such as resolution, compression, frame rate, and the number of cameras. One advantage of such wired system is to avoid the bandwidth and storage problems over complex and dynamic scenes on the applied scenario, so you may have to work on easy solutions, reducing the frame rate, lowering the resolution, or increasing the compression as to your proposed system requirements and best performance [8]. The considerations of our experiment include the following. We use outdoor-ready bullet cameras in general because of the environment of our scenario is noisy on traffic highway road. We use fixed cameras to keep all field of view FOV in watching, and (motorized, or PTZ) cameras with a large optical zoom to give us high-quality images for an effective zone in the work area especially for capturing the platelet numbers of vehicles, and to balance the cost of the budgets. Other considerations are involved within the devices such as day and night light-

sensitivity measurements, tamper- proof requirements, discreet installation, covering the area, FOV detection with high-details images for objects like license platelet recognition, analytic the system in general. To represent one meter of a scene, you need to 70-100 pixels in general, but for more details images such as human faces recognition or license platelets numbers' capturing and identification, operations like this needs to increase as many as 500 pixels per one meter. For license platelet numbers identification on vehicle with size 2×2 meters, we need to use one megapixel camera resolution or more. As to Fredrik Nilsson [8] in chapter (17), practices for indoor dome camera 2.8 mm lens mounted at 3 meters with straight FOV founded that the 125 pixels per meter is for face recognition while more than 250 pixel per meter is for face identification as to figure 1.

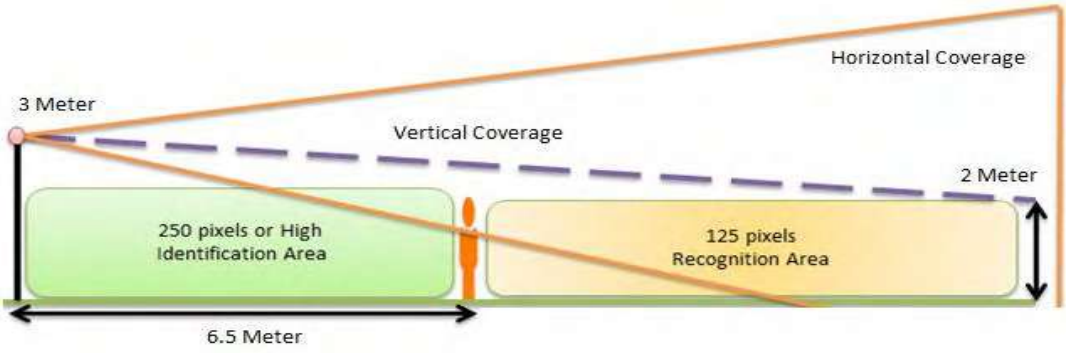

Figure 1. Person standing 6.5 meters away can be identified when the camera is mounted at a height of 3 meters. The horizontal coverage of the camera is shown in (a) and the vertical coverage in (b).

For positive identification of such small details of license platelets numbers or human faces and based on pixel density of horizontal dimension, Swedish National Laboratory of Forensic Science SKL recommend 80 pixels across a face for identification, while the international standard published by CELENEC, recommend a sufficient 40-100 pixels [9]. Because of most license platelets have the same width which is around 0.16 meter, then measuring its pixels will be easy as to the following figure 2.

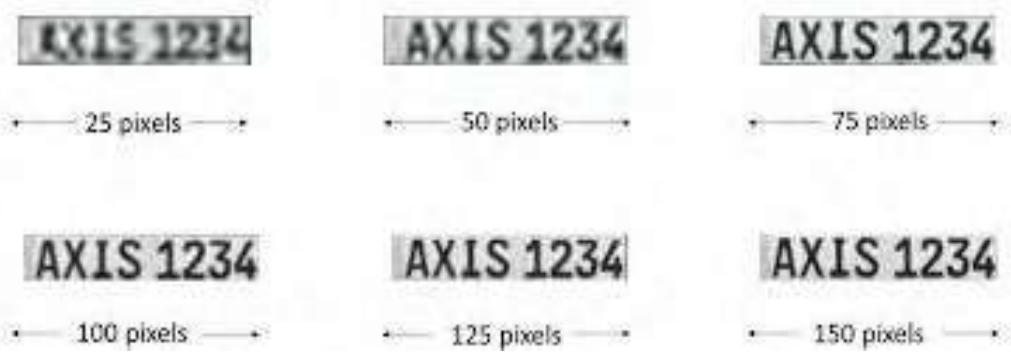

Figure 2. The impact of resolution increasing over different pixels number.

For calculation, we need the surveillance area dimensions which are scene width SW, scene high SH, the number of pixels needed for platelet resolution PR, and platelet width PW. Now, we can compute the number of pixels for the scene resolution horizontally SRH and vertically SRV as to the following Equation (1) and (2).

$$SR(H) = \frac{SW}{PW} \times PR\ (width) \qquad (1)$$

$$SR(V) = \frac{SH}{PH} \times PR(high) \qquad (2)$$

Now, to calculate SRH as to Equation (1), the general platelet dimensions are (20×10) (width×high) cm and assume that SW equal to (4 m ×125 pixel /20 cm) × 80, the result is 2,000 pixels. For SRV calculation, by assume SW equal to (0.70 m ×250 pixel/10 cm) × 40, the result is 700 pixels. In the scene, to identify the platelet number with high resolution based on above, we need 2000×700 pixels resolution which stands for 1080p to PTZ or Motorize cameras (optical zooming) while fixed 5MP 2560×1920 pixels (digital zooming) over the entire scene resolution to identification the vehicles. The general dimensions measures as standard for high definition HD videos are as following. 720p (1 MP) 1280×720 HD equal to 921.600 pixels (resolution = 922 of kilo pixels), 1080p (2MP) 1920×1080 Full HD (FHD) equal to 2.07 million pixels, 2048 × (unspecified) (2 K) equal to more than 2.000.000 pixels (cinema resolution), 1440p (4MP) 2560×1440 Quad HD (QHD) equal to 3.686.400 pixels, 2560×1920 (5MP) equal to 4.915.200 pixels, 2160p (4 K) (3480×2160) Ultra HD (UHD) equal to 7.516.800 pixels, and 4680p (8K) (7680×4320) as in figure 3[10]. However, by determining the required resolutions, the calculation of the number of cameras needed to cover the surveillance area can be identified. Number of cameras needed is equal to horizontal scene resolution divided by camera resolution. For our experiment, the vehicles size more than 2×1.5 meters and then 5MP camera will be more quite enough.

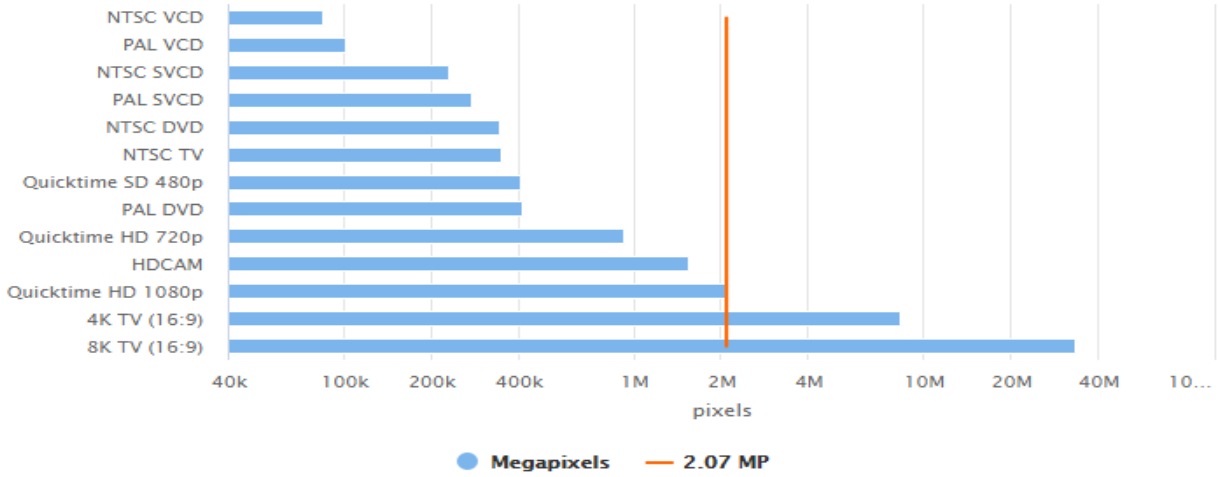

Figure 3. 1080p (2MP) specifications.

3.2. Experiment topology

We test and select the best topology of cameras positions of our experimental system by four pillars, two cameras for each, four rules to detect the violated vehicles as in figure 4. The first rule is rule 1, vehicles that take the violated path (inverse direction) for cross over to the opposite side of the road straight from the area of pillar 1 to the best topology of cameras positions of our experimental system area of pillar 3 and vice versa. The second rule is rule 2, vehicles that take the violated path (inverse direction) for cross over to the opposite side of the road straight from the area of pillar 2 to the area of pillar 4 and vice versa. The third rule is rule 3, vehicles that take the violated path (inverse direction) for moving on the same side of the road straight from the area of pillar 2 to the area of pillar 1 and vice versa. The forth second rule is rule 4, vehicles that take the violated path (inverse direction) for moving on the same side of the road straight from the area of pillar 4 to the area of pillar 3 and vice versa.

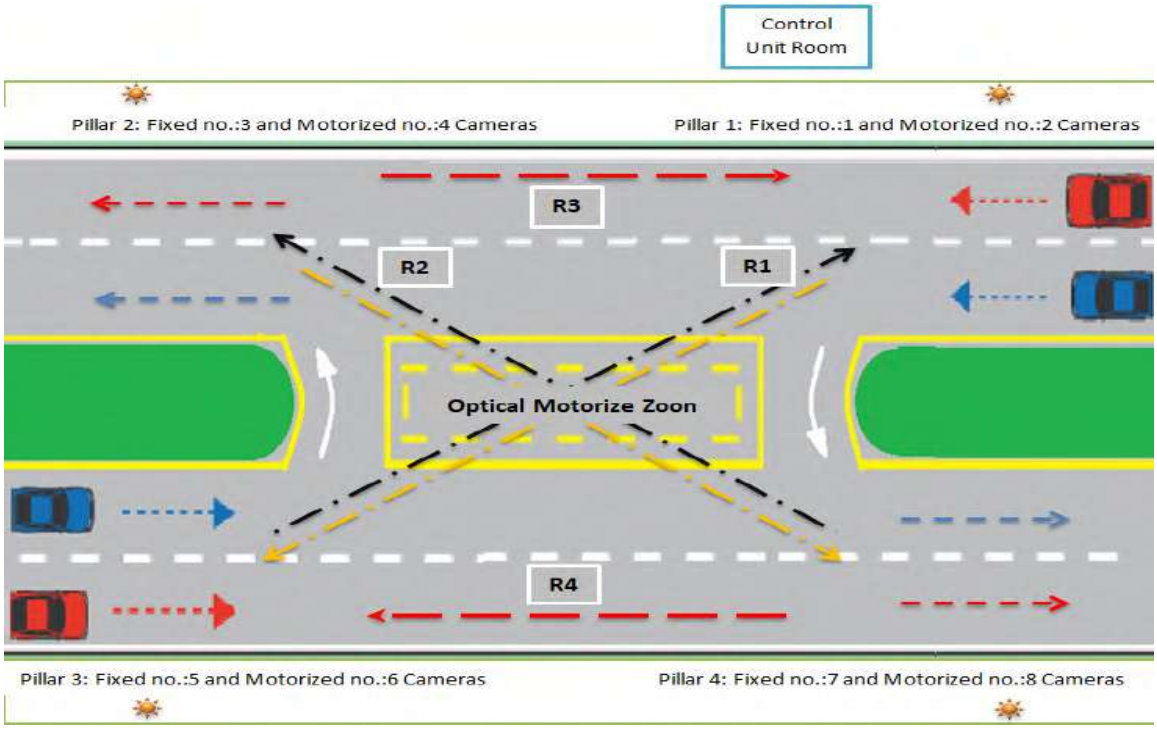

Figure 4. Applied topology based the proposed user-defined rules (R1: rule one, R2: rule two, R3: rule three, and R4: rule four) of our scenario. Yellow rectangle: effective FOVs (optical motorized zone) watched by all four motorized cameras in the pillars.

For achieving that, we cooperates four fixed and four motorized cameras to capture the violated vehicles and its plate late numbers for identification purposes. Based on that, the vehicles tracking will be done based on birth and death zones and trajectories of them will be analyzed based on above rules to report each violated one. Each violated vehicle will be reported with its specific properties and metadata such as (time, numbers of frames, front side images of vehicle, rear side images of vehicle, platelets licenses images, etc.) using video processing and machine learning techniques such as Haar cascade classifier. Also, it is important to consider the relations of effective FOVs time and objects appearances between cameras over the scene cameras' motion, and scene structure for any applied tracking algorithm. Several relationships exist between the images with different views are very important for the construction of vehicles tracking. However, the performance of any IVSS is subject to the performance of its cameras, hardware costs, installation costs, maintenance costs and operating costs [11, 12, 13].

3.3. Experiment Setting up

The purpose of our experiment is to detect all violated vehicles such as car, bus, truck, and scooter that take a violated path to be turned on double inverse side of highway road. The detection will be done based on the conception of MCCNs on single device video recording DVR system via RG59 coaxial cable based on two stages. The first stage is for measuring the distances between each pillar that will carry up two cameras as in figure 5. Four pillars positioned on the rectangle figure, each carried up two cameras, the upper camera is fixed 5MP (at 3 meters of height) to covering the entire area while the lower one is a motorized or PTZ 2MP (at 2.75 meters of height) which set to capture platelets of vehicle. This scenario will help in covering the front and rear of the vehicle at same time. Capturing platelets of vehicles over specific recorded frames is done by setting the optical lens for the better length (4 – 5 meters) to be wider (catch misleading vehicles) and clear when recovering the

frames from both two opposite pillars. The fixed 5MP cameras are settled as to covering the same FOV for each pillar. DVR unit is used to control and simultaneous the time ticks and dates on frames of different recorded videos, and however, many positions and situations are tried and studied until the best setting up and shooting video is accomplished. However, the following Figure 5 shows all first stage representations.

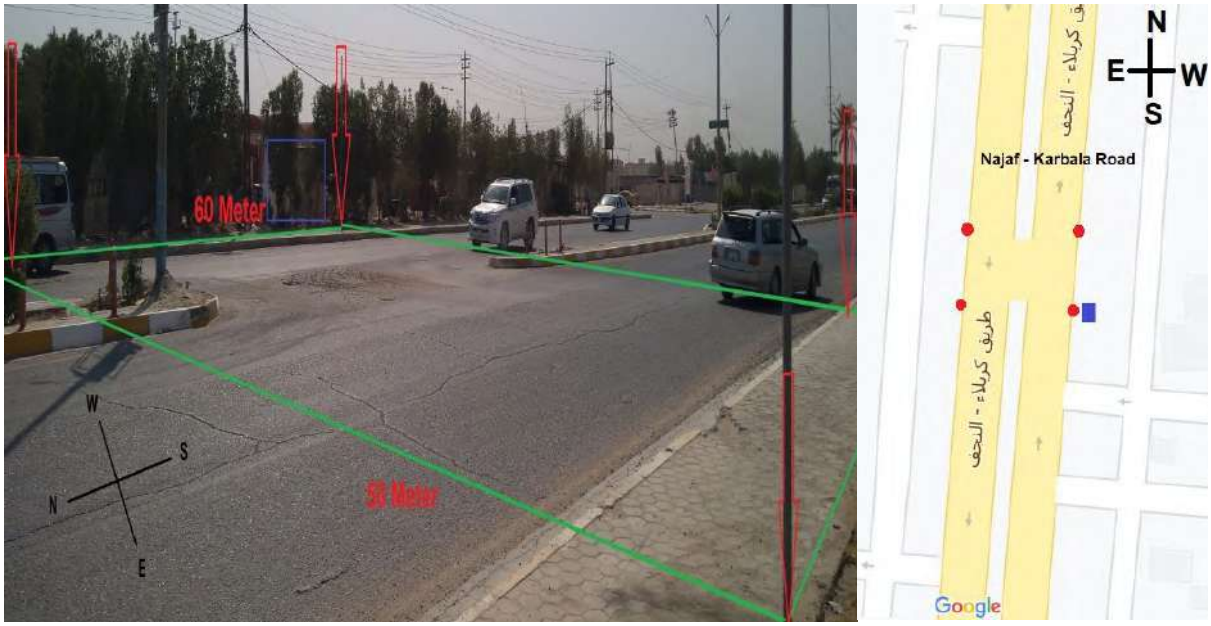

Figure 5. First stage representations: area topology with distances and directions. Red arrows: pillars positions, blue box: control unit position.

The second stage is for DVR software installation and setting up different properties for all eight cameras where all viewed in one control monitor. For best recording process, we choose one hour time duration of each video (to be saved), 11 frame per second FPS for fixed cameras, and 13 (manufacturing setting) FPS for motorized or PTZ cameras. Table 1 below shows the setting options used in practices.

Table 1. The applied setting for cameras and video information.

Camera	Frame rate	Width × Height	Video Type and Duration
Fixed Cameras	11 FPS	1920×1080	MPEG-4 / H.264 / 1 hour
	11 FPS	2560×1920	
Motorize or PTZ Cameras	25 FPS	1920×1080	
	13 FPS	1920×1080	

Figure 6. Second stage representation: setting process of experiment tools and DVR software.

4. Results and Discussions

We show how the recording videos are cooperated for the purpose of capturing the violated vehicles based on the proposed user-defined rule one (R1) and rule two (R2) with its platelets information identification, the times of violation, and other important metadata from all cameras as to their specific purposes into scenario and generating them as new reports. We present the cooperating benefits for avoiding the problems of overlapping effective E-FOVs such as full and partial occlusions, technology mistakes during recording time, and other situations.

4.1. Overall Scene

One violated vehicle based user-defined rule one (R1) of scene number 1926.jpg from all four fixed 5MP cameras (11 fps) and its corresponding 2276.jpg from all four motorized cameras (13 fps) on (29/09/2019 1:02:59 PM) as to the following figures 7, and 8.

Figure 7. Background scene over four fixed cameras at frame 1926.jpg. Top left: fixed camera installed on pillar 3. Top right: fixed camera installed on pillar 1. Bottom left: fixed camera installed on pillar 2. Bottom right: fixed camera installed on pillar 4.

Figure 8. Capturing platelets of violated vehicle (2276.jpg) that detected by R1. First row: two frames of PTZ cameras on optical motorized zone. Second row: two frames of motorised cameras on optical motorized zone. Third row: zoomed PTZ frames of first row. Note that platelets license form in Arabic language and numbers (50972 M / Baghdad, Iraq).

4.2. Occluded Scene

The following situations in figures 9 and 10 are for occluded scenes, the first one is harmed platelets case and the second one is for misleading vehicles case. It solved by other cooperated cameras on different positions.

Figure 9. Harmed Platelet of violated vehicle captured by rule two (R2) from one rear side only at frame (15412.jpg) in 29/09/2019 on 1:19:45 PM. Note that platelets license form in Arabic language and numbers (6406, Iraq, Basra).

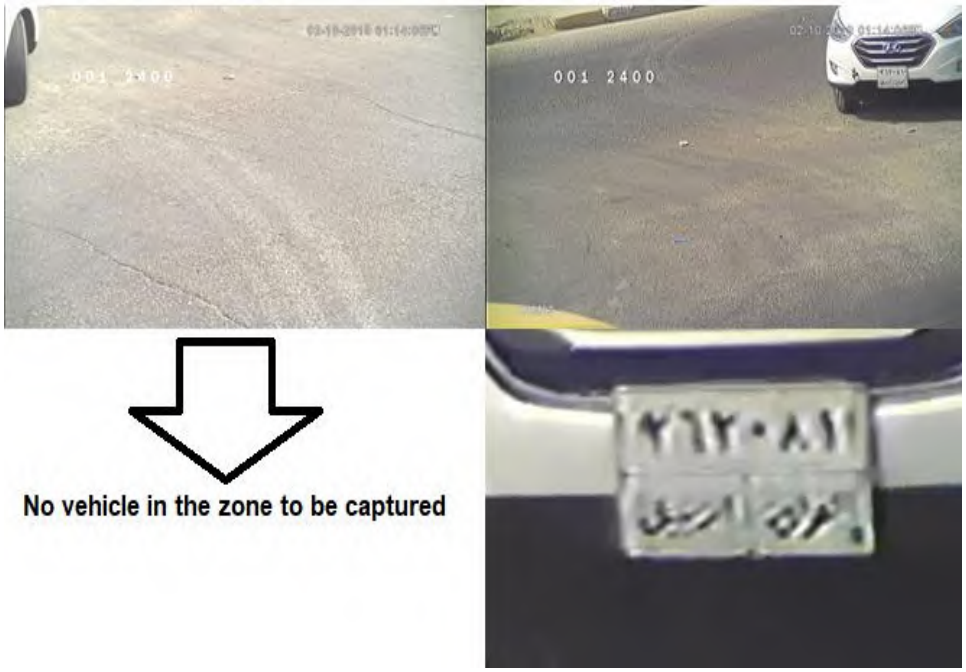

Figure 10. Violated vehicle of inverse rule one (R1) from one front side only at frame 14802.jpg. Note that only one tire is present on PTZ motorized zone by pillar 3 camera while it is captured by PTZ camera of pillar 1 clearly. Date of recording is 2/10/2019 on 1:14:06 PM. Note that platelets license form in Arabic language and numbers (362081, Irbil, Iraq).

4.3. Technical and emerged mistakes

The founded noisy camera video output (factory errors) as in fixed camera of pillar 4 can be avoided by other cooperated cameras' videos based MCCN principle and video processing techniques. The number of each frame for each camera should be equal but in the PTZ and motorized cameras and based on factory setting; they have 13 FPS while it is 11 FPS in fixed cameras. This problem is solved

as the calculation of the following Equations (3), (4), and (5) for fixed cameras and Equation (6) for motorize or PTZ cameras.

$$Current\ second\ (CS) = \frac{Frame\ Number(fixed)}{11} \quad (3)$$

$$First\ Frame\ at\ CS = CS\ \times 11 \quad (4)$$

$$Fixed\ Current\ Frame\ (FCF) = Frame\ Number - First\ Frame\ at\ CS \quad (5)$$

$$Motorize\ Current\ Frame\ (MCF) = CS\ \times 13 + FCF \quad (6)$$

As an example of above figures 8 and 9, the current second (1926÷11) equal to 175 seconds as to Equation (3) while the current frame in the current second is 1926 - (175×11) equal to 1 as to Equation (4) and Equation (5). The current frame in motorize camera is (175×13) +1 which equal to frame number 2276.jpg as to Equation (6). The fixed cameras on pillars 3 and 4 (both are 5MP) have noisy appearance video output (company errors) and they need to be processed, therefore the problem is solved by the opposite and cooperated cameras as to the same rules of violated. Over all the recorded videos of different daytimes, there are more than 90% cases are successes in capturing the violated vehicles among the user-defined rules. This will help effectively in vehicles detection and tracking using video processing and machine learning techniques. However, by solving and avoiding the technical and emerge errors of experiment setting; there will achieving 100 % success.

5. Conclusion

We propose a methodology of using techniques and technologies in cooperate with MCCN and area topology principles by explain how to take the important criteria into account for achieving a good IVSS results. Based on that, we design an experimental study following the mentioned scenario of traffic turn on highway in real life environment; the resulted recorded videos will be very helpful and serve in design and test IVSS over video processing and machine learning techniques. The topology of the experiment has been set as best as possible to eliminate the costs of financial, technical, and operational equipment's and hence; the four settled user-defined rules summarize the surveillance process of the violated vehicles by allowing to detect objects initially and tracking it over specific regions of interests in offline processing (to be identified) finally. However, the gathered raw data set will be available online for researchers to use and generate perfect IVSS for object detection, tracking, and identification.

References

[1] Kolekar, M. H. (2018). Intelligent video surveillance systems: an algorithmic approach. *CRC Press*. Chapter 7, pp 152-157.
[2] Andrew P. Tarko (2020), Techniques and technologies of observing traffic conflicts, Measuring Road Safety Using Surrogate Events, *Elsevier,Chapter 4*, Pages 47-65.
[3] Silva, T. C., Laiz, M. T., & Tabak, B. M. (2020). Traffic campaigns and overconfidence: an experimental approach. *Accident Analysis & Prevention*, 146, 105694.
[4] Zhang, J., Perloff, J. M., & Lu, F. (2020). Informing and inquiring: Experimental evidence on reducing traffic violations. *Journal of Development Economics*, 147, 102534.
[5] Landowski, M., & Landowska, A. (2019). Knowledge extraction from the experimental data of the vehicle traffic volume. *Transportation Research Procedia*, 39, 270-279.
[6] Natarajan, P., Atrey, P. K., & Kankanhalli, M. (2015). Multi-camera coordination and control in surveillance systems: A survey. *ACM Transactions on Multimedia Computing, Communications, and Applications (TOMM)*, 11(4), 1-30.
[7] Website of videosurveillance (01/09/2020), Advantages of Traffic Surveillance Cameras, *https://www.videosurveillance.com/traffic.asp.*
[8] Nilsson, F. (2016). Intelligent network video: Understanding modern video surveillance systems. *CRC Press*.Chapter 17, pp 301-304.
[9] European Committee for Electrotechnical Standardization CENELEC Guides (10/08/2020), *https://www.cenelec.eu/membersandexperts/referencematerial/cenelecguides.html.*
[10] Website of Megapixel calculator (16/09/2020), *https://toolstud.io/photo/megapixel.php*.
[11] Hasan Th. & Israa H. A. (2019), Varying Techniques for Vehicles Violations over Intelligent Surveillance Systems: A Short Review. *Jour of Adv Research in Dynamical & Control Systems*, Vol. 11, 10-SP.
[12] Han, Z., Li, S., Cui, C., Song, H., Kong, Y., & Qin, F. (2019). Camera planning for area surveillance: A new method for coverage inference and optimization using location-based service data. *Computers, Environment and Urban Systems*, 78, 101396.
[13] Zahra Arbabi et al 2020 J. Phys.: Conf. Ser. 1530 012111.

Hasan Thabit Rashid Kurmasha is currently a lecturer with University of Kufa, Najaf, Iraq. He received his Bachelor degree in Computer Science from Babylon University, Hillah, Iraq in 2005, and his Master degree in Information Technology from UNITEN University, Malaysia in 2013. He is currently a PhD candidate in Babylon University. His research interests include Intelligent Video Surveillance Systems, Image and Video Analysing, Computer Vision.

Prof. Dr. Israa H. Ali received her PhD degree from University of Babylon in 2013. She is currently a Professor in Software Department, College of Information Technology, Babylon University, Iraq. Her main areas of research interest are Video Tracking and Analysis, Image Processing, Data Mining, Machine Learning, Multimedia and Information Hiding.

Higher Education's Certificates Model based on Blockchain Technology

Higher Education's Certificates Model based on Blockchain Technology

Mustafa A. Ali[1] and Wesam S. Bhaya[2]

[1]College of Science, University of Kerbala
[2]College of Information Technology, University of Babylon

E-mail: Mustafa.a@uokerbala.edu.iq

Abstract. Blockchain technology has revolutionized economic transactions, and it is expected to spread and influence other fields. It can create innovative and destructive effects on the systems that need to be executed, store, verified, and continually update digital data among participating parties. Moreover, it provides security, privacy, trust, and transparency. In the education field, there is a shy presence of some blockchain applications, and the majority of them have a pilot character. Hence, a model based on blockchain is introduced in this study, which aims to provides easy to apply for certificates, as well as share and verify these certificates with a third party. Moreover, the mechanism of the proposed model proposes permanent distributed hashes records of students' certificates in Higher Education to reduce forgery. In conclusion, the study discussed the opportunities, benefits, features, and challenges are represented by deploying this model in the Higher Education field.

Keywords. Blockchain Applications, Consensus, Automated Certificate Educational Systems, University Digital Certificate.

1. Introduction

In our increasingly interconnected world and with the constantly increasing and evolving use of computer systems in various areas of contemporary life. In addition to the rapid increase in the speed of internet connections and with the fact that most computer users are novice or untrusted, who have sophisticated computers with high-speed internet connection [1]. Consequently, all that lead to facilitate and increase of security threats and abuse rises that facing the digital systems. Therefore, it is necessary to replace or develop other technologies to preserve digital systems from many security threats and adds layers of protection and trust. A powerful opportunity can emerge from utilizing new blockchain technology. This technology is expected to develop various industries objectives such as economic, society, medical, businesses, and education. As a result, it is necessary to explore and identify the advantage and challenges of blockchain technology [2].

Blockchain technology can be defined as a time-stamped and tamper-resistant distributed digital ledger. It can allow validate and secure the transactions and update records in a transparent, synchronized, and decentralized with the consensus of a majority scheme and is considered a part of the fourth industrial revolution.

[3]. This mechanism for generating and managing digital data can be effective across sectors, for instance, when it moves toward increasing productivity and automating processes, reducing cost, or promote new organizational and business models [4].

Blockchain technology has numerous advantage, it enables known and unknown parties who do not have a specific trust in each other to exchange any kind of digital assets such as educational and medical records, services, money, goods, or contracts on a peer-to-peer network without the need to central authorize to provide the trust [5]. On the other hand, blockchain faces many underlying technical challenges such as bottlenecks, scalability and performance, interoperability, high-energy consumption, and protection of personal and sensitive data, which are, depending on the type of blockchain [5]. Moreover, regulatory and standardization uncertainties about the formal status of this technology also lead to more risks and ambiguity for companies and other organizations that are interested in deploying blockchain or experimenting with it [6].

At present, many of the potential advantages of blockchain are unrealized or yet to be fully examined. Blockchain evolution faces critical questions about the potential effect, added value, or the specific direction of adoption [7]. However, blockchain technology has seen a burst of interest in recent years and it is expected that it will lead to a revolution that will significantly disrupt the way that the data are shared and create prominence in the evolution of the digital world. It is a highly promising field that requires further researches, experiments, and implementation in different areas [8].

This study objectives not only to explorer blockchain technology and its features but also to provide a view on the opportunities and challenges for it's used within the Higher Education context. So, we designed a model that utilized blockchain features that could be applicable used to secure, fast, online, and accurately generate and verify academic certificates with a few manual work and without the chance to certificates forgery. After this introduction, the study reviews in section 2, the most related works that discuss the document forgery problem. Section 3 presents the proposed model. In section 4, the outputs of the proposed model based on a set of theoretical points are discussed and lastly the conclusion.

2. Background

The origin of prevalent academic fraud can be traced back to people without educational qualifications who want to become rich, powerful, honor, or being employed in a short period. Unemployed youth, graduates, and potential college students soon learned that intellectual effort and the need for serious study is not required to achieve their wish, instead, seek connections and then obtain forgery credentials by any means [9]. However, hired fraudulent means became broad.

In [10], the researcher explains that academic fraud consists of a broad range of suspicious activities in the academic field, among them is mutating of the content of the certificates, which originated from a legitimate issuer to suit the holder's need. Researchers in [11] defined academic fraud as the intended misrepresentation of academic achievement that may have a harmful consequence on other parties. Another definition of fake degrees has been introduced by [12,13] which describes it as a certificate obtained from a bogus institution (diploma mills) that holds an

original establishment but has not been issued by the claimed institution. Furthermore, another type of academic fraud is both the origin and content of the certificate are fake; however, it may be difficult to disclose them [13]. According to [14], there are various sources of fake degrees including unaccredited degree-granting institutions, degree mills, and corrupt officials at academic foundations.

Document verification is the process taken to ensure that the documents received from the owner are genuine and that the owner is legitimate [15, 16]. The verification of the certificate removes suspicion about the certificate content and the issuer educational institution. Whether the certificate issued by the alleged institution, as well as, the issuing institution is authentic[15,17]. This always validates the issuing institution and the qualifications provided. The goal of verification is also to ensure that the certificate has not been altered by the holder and whether it has been truly issued to the owner [11, 16- 17]. Certificate verification is steps to seeks and trace to ensuring that the certificate is authentic from its source, means of issuance, and other details about the basis for issuance. It is the process that establishes the originality of something using a confirmed technique. [18].

Electronic verification was used, to facilitate and automation of some processes, as well as, the authentication can be accomplished instantly, which saves time for all parties. Furthermore, certificates are shared more easily and securely [18, 19]. It is automation and uses some of the appropriate tools such as verification through a web portal without making a central database to ensure data privacy. This technique operates within a digital certificate and facilitates automatic verification of a degree by a third party without the need of the issuing institution [18.19].

An online certificate system is a web-based system that contains a secure database that can be viewed by three levels of users - the issuing institution, the degree holder, and the third party. The institution issues a digital certificate to a graduate student after fulfilling the academic requirements. On the other hand, the student applied the affirmation to access and share the electronic certificate. Meanwhile, a third party (verifier) also inquires into the system webpage to verify the certificate.

Blockchain technology is a distributed digital ledger with the consensus of a majority scheme that promotes systems that need to be executed, store, verified, and continually update digital data among participating parties. Distributed ledger technology protects and retains the transaction recording and asset tracking and sharing in a decentralized manner [20].

Through the previous studies, it can be noted the there are big problems with forging official documents and the methods to verify these documents. This research aims to propose a model based on permission blockchain that stores compact data proofs of academic certificates in a decentralized database that enables students easy to apply certificates and easy methods to verify and share with a third party.

3- The Proposed Model

In this section, we will describe and illustrate the phases and workings steps of the proposed model. We start with a high-level overview of the main phases in the proposed model. The research aims to

design a model for a trust system to exporting, securing, and ensure the validity of the higher certifications of graduate students.

The main advantage of the proposed model is to ensure the validity of students' certificates in a safe, direct, trust, and fast manner. It also allows students to electronically request a copy of the certification. The proposed model store the validity of academic certificates in a safely electronically compact method depending on blockchain technology. Furthermore, it allows ensuring the validity of students' academic certificates by any interested verifier and from anywhere. This model proposed a permission blockchain distributed system to deployed verifications of students' certificates to prevent the process of forgery certificates, as well as to add transparency and trust in the issuing and export process by ensuring the authenticity of the issuance of those documents. The permission blockchain proposed by the model involved in all student affairs departments belongs to universities of the Ministry of Higher Education. It allows the network participating to add, update, and confirm the student's certifications by a consensus mechanism.

The hash function was used to obtain a one-way encrypted and compressed copy of the students' certifications, and these hashes are stored on the blockchain after the verification processes by participants parties are done. As a result of using the proposed techniques above in the proposed model, we prevent the process of issuing a tampered certificate. Furthermore allowing non-participants parties of blockchain networks such as other companies and organizations to securely and instantaneously check the validity of the student's certificate that is provided to it.

The proposed system includes three main stages, which are issuing certificates, demanding the creation of certification, and verifying the validity of the certifications. Each one of these phases

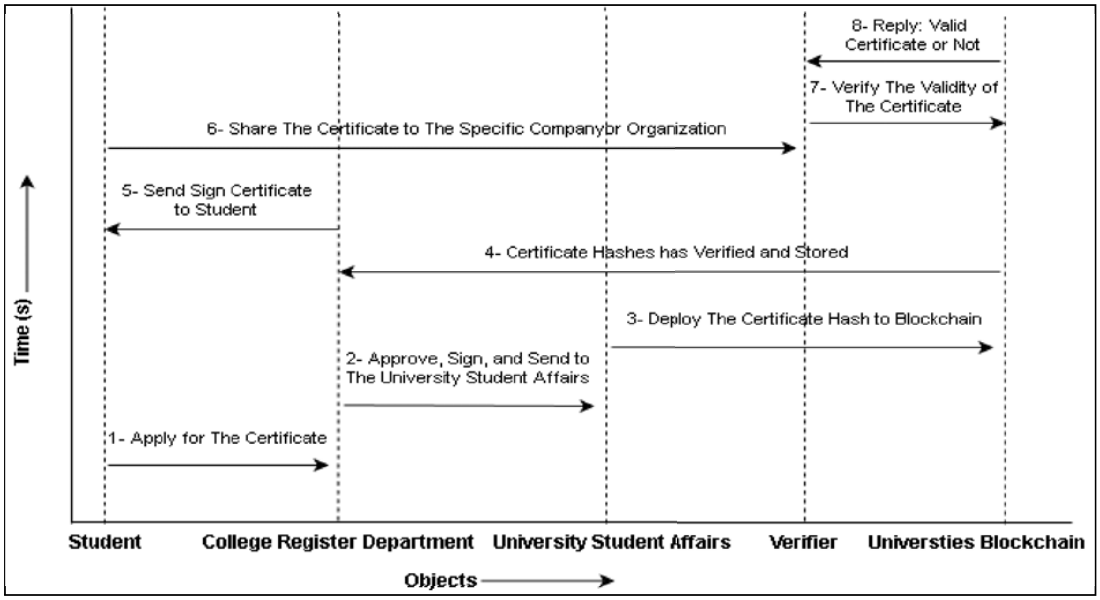

will be explained in the following sections. Fig. 1. Show workflow of research proposed model.

Fig. 1. Proposed Model Work Flow

3.1 Students Certificates Issuer

The first phase of the proposed model work begins with the process of submitting the graduating student's grades by the department's examination committee to the proposed central system of the university. After completing this process, the system directs these results to the dean of the faculty, the person who in charge, or the person with authority and here there are two cases. The first case is returning the results to the examination committee for modification within the terms and conditions. The second case agrees to approval (consider as a signed) and issue students' grades and certificates. Then the each signed students' certificate is hashed by the system and forwarded with the hashes to the college's registration department. As well as the same copy of these certificates is sent to the student affairs department at the university. The output of the hash function is a string of a certain length, which is the hash value. The proposed model extracting the hash value for each student's certificate separately which is considered a verification checksum for each certificate.

After receiving certificates carried out by the approval of the authority holder, these certificates with their hashes are stored in a local database individually by the college's registration department and the student affairs department at the university. The system sent and deploy only hash values on the universities' blockchain network if the match of hash values occurs between the Student Affairs Department compared with the College Register Department for the same certificates, and if no match means suspicious altering has occurred in certificates, and a person with authority revisions are required. Fig.2. show the steps of certifications issuer.

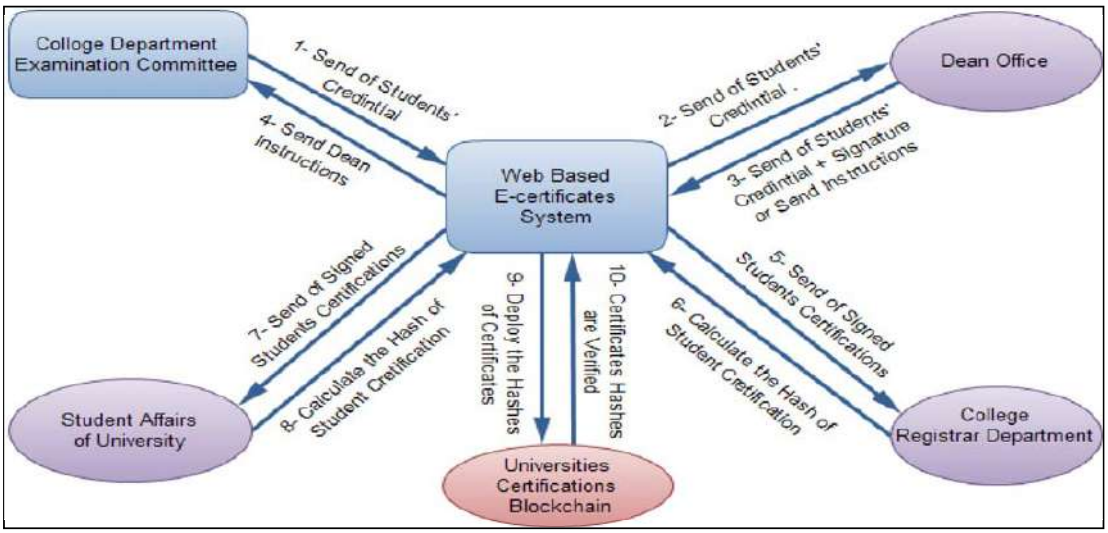

Fig.2. Steps of Certificates Issuer

3.2 Request the Student's Certificate

The proposed system allows any graduated students from any one of the participating universities in this system to request a graduation certificate from anywhere in the world at any time. It provides a portal or application based on the Internet that allows the student to request an addressed certificate to the desired destination according to the rules. In the case of using the portal, the student should enter important information such as the full name, college, department, and the destination to which the certificate is to be addressed in addition to a valid email address. The certificate issued is sending to the student's email address. In the case of using the application, it will be an electronic wallet in which the student receives and save all the certificates issued to him. Furthermore, by this wallet, all the details of the student can be identified through a specific serial number or a public key when contacting the system or when requesting the certificate. It also saves all previously issued certificates.

Upon receiving the application submitted by the student to get the academic certificate, the system will verify the student's identity and whether he has the right to apply for the certificate. If the information provided by the student is correct, the system will direct the application to the registration department in the specified college for the required procedure. The Registration Department performs a first validity check by extracts the student's information and grades stored locally and calculates the hash value for this information and compares it with the hash value stored on the blockchain network to ensure that there is no tampering with locally stored certificate information. Upon completion of the verification of the validation process of the students' information, this information with the destination to which the certificate is to be addressed that taken as requested from the student shall be submitted as an unsigned student certificate issued to the Dean's office for approval (signing).

After obtaining the approval of the dean, the date and number of the certificate issued are given by the system. To deploy the newly created certificate information, it is sent to the Student Affairs Department that performs a second validity check by calculating the hash value of the new certificate's main information and comparing it with the stored hash value in the universities blockchain network. When a match occurs, it means that there is no tampering with the newly created certificate main information and sends a newly created hash value of the new student certificate to the blockchain network to be approved and stored.

After obtaining the approval of the members participating in the network to publish and store the value of the new hash, the process of storing the new hash is performed and a confirmation message sends to the system. Upon completion of the storage process, a copy of the certificate required by the system is sent to the student's electronic wallet or via the electronic email, as mentioned previously. Students can also go to the college's registration department to receive the hard copy of that attested certificate.

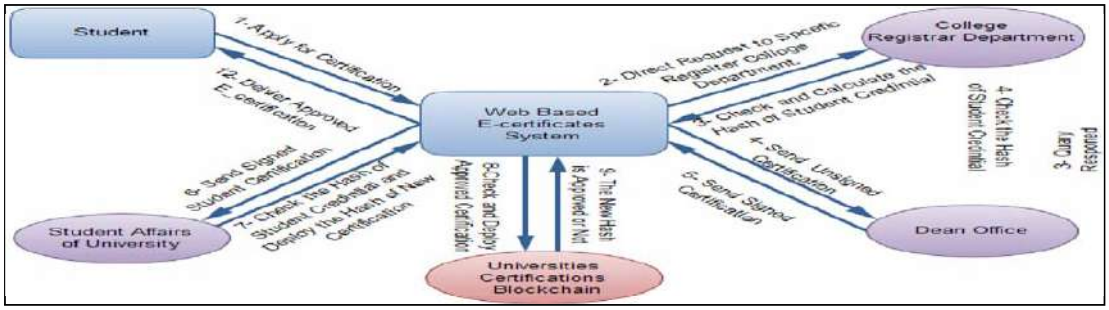

Fig. 3. Steps to Apply for Certificate

3.3 Validations of Certificates

This phase is considered the practical and actual result of the system, as it represents the benefit of applying the proposed model. Actual works of this phase begin when an institution or a company wanted to verify the validity of the certificates submitted to it to obtain the advertised position. As the proposed system provides a webpage or application that can be accessed from anyone, any time, and anywhere in the world without the need to participate or pay for the system. The gate could be a portal or an application based on the Internet, which enables anyone to verify the correctness of the students' certification instantly. Even when the absence of the institution that granting this certificate for any reason, such as stopping its work or being exposed to any natural or intentional disaster such as fires or floods.

When the graduate student provides his gained higher certificate information to obtain a specific position within a specific company(get hire). Therefore, the company or organization needs to verify the validity of the submitted certificate from the concerned person. In this case, the company employer can verify the validity of the provided certificate in a real, reliable, and safe way through a portal belong to the system.

The work of this phase begins when enters only the important information of the certificate which is the name, average grade, date, issue number, agency, or the certificate is uploaded electronically (if the certificate is submitted to the company electronically) through the portal by an employer in the company. The received information of the certificate submit to the portal is entered at the same hash function used when creating and stored the original certificate hash on the blockchain network. Then a query is created to perform a search for a match of the generated hash within universities blockchain network stored hashes. If a match is found means that the certificate information is correct and the validity message will be shown.

If there is no match for any reason such as a mistake in the entry process or a process that changes any information from the certificate information (forging the certificate). In this case, there will be no match of the stored hashes on the blockchain network and the system will be shown a message of failure or error through the portal. Fig.4. show steps to verify the certificate.

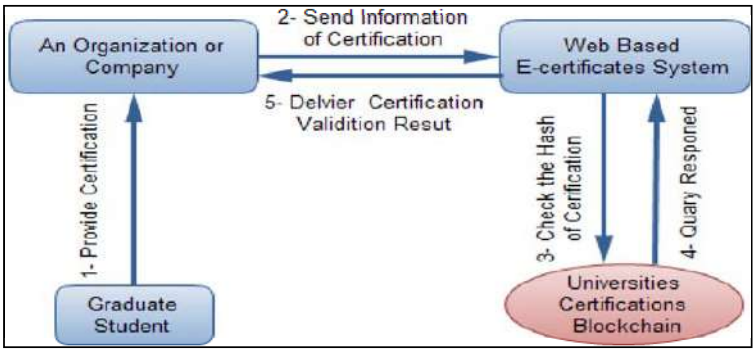

Fig.4. Steps of Certificate Verification

4. Results and Discussion

To understand the expected outputs from applying this model to the certificates system, it must be compared with the current systems of the issuer the paper and electronic certificates. Moreover, explain the problems and weaknesses to solve or enhance them using blockchain technology. This section describes the most important problems in the current systems.

Certifications acquired over a long period from different accredited educational institutions throughout the country or the world, need to be approved for their originality. The verified process is becoming more difficult and takes long periods due to the increase in the number of universities, colleges, courses, and students. Educational institutions spend a lot of time, effort, and resources in creating academic certificates for students as well as verifying transcripts and data starting from their date's births, records of accomplishment, and capabilities.

The trust, security, transparency, and speed along with automation through digitization are offered by blockchain technology that comes as leverage to the education industry across the world. The results of adopting the proposed model are summarized below:

1- Easy Verification Mechanism and Accurate Information: A portal can be used by the third-party who want to verify the certificate.

2- Convenient**:** The students need to no longer provide many papers with proof of their originality each time they use to apply for a job.

3- Cost-effective: The digitization of the process of the creation and validation of the certificates reduces the costs for all parties.

4- Time-efficient: The increased speed of creating and verifying the certificates as the certificates can be delivered and verified digitally.

5- Data Privacy and Security: Students' academic achievement is stored in the local and private database of an educational institution, as well as store hashes of those credentials, which are stored on the blockchain that is cryptographically protected. As result, prevent the issuance of forgery certificates and at the same time, students' creational is safe and reliable.

6-. Secure Transactions, Transparent, and Immutable Data: The hashes are approved and authorized by a consensus mechanism. Moreover, all blockchain participants store the same transactional data that vastly improve the trust in the whole system.

7- Availability: The verification of certificate is there at any time and from anywhere even when the problem of unavailability of the educational institution such stops using the network, that their equipment malfunctions, or even stop institution work.

On the other hand, to develop a reliable and secure blockchain certificate system with high functionality and usability, a group of solid technical and mathematical foundation experts of blockchain is needed. This presents a shortcoming for practitioners and researchers in the field of

education. Blockchain technology is difficult to comprehend by educators, learners, and other professional parties. Universities need to know how the adoption of the blockchain will affect their privacy, database rights, and other confidential information. This study aims to establish a model for blockchain technology accreditation for certificate verification systems but does not address the technical aspects of implementation. Further studies will be necessary to realize the implications of adopting this technology for enhanced implementation.

5. CONCLUSION

The development of distributed and secure electronic systems has become an important subject in line with the development of the digital world. The application of blockchain technology is an excellent example of these systems that provides exciting features such as transparency, trust, and decentralization with untampered and permanents data records. The implementation of such technology to systems for issuing students' certificates, especially when the individuals are subject to many academic studies and training from several different institutions and they obtain several certificates, is critical. The process of preserving these certificates in a way that is permanent, not tampered with, or forged is very important. Moreover, it is important to presents an opportunity for third parties to verify shared certificates quickly, securely, and independently. The proposed model fulfills for preventing forgery certificates and managing digital academic credentials mainly in terms of the trust, high outputs, availability, transparency, low costs, and resource consumption, especially with the existence of many educational institutions nowadays. This study does not address the technicalities of implementation. Further studies to design and facilitate the creation and implementation of the blockchain solution in education are recommended.

References

[1] Bhaya, W. S., & Ali, M. A. (2017). Review on Malware and Malware Detection Using Data Mining Techniques. *Journal of University of Babylon for Pure and Applied Sciences*, *25*(5), 1585-1601.

[2] Schwab, K. (2017). *The fourth industrial revolution*. Currency.

[3] Bozic, N., Pujolle, G., & Secci, S. (2016, December). A tutorial on blockchain and applications to secure network control-planes. In *2016 3rd Smart Cloud Networks & Systems (SCNS)* (pp. 1-8). IEEE.

[4] Chang, S. E., Chen, Y. C., & Lu, M. F. (2019). Supply chain re-engineering using blockchain technology: A case of smart contract based tracking process. *Technological Forecasting and Social Change*, *144*, 1-11.

[5] Niranjanamurthy, M., Nithya, B. N., & Jagannatha, S. (2019). Analysis of Blockchain technology: pros, cons and SWOT. *Cluster Computing*, *22*(6), 14743-14757.

[6] De Filippi, P. D. F. (2018). *Blockchain and the law: The rule of code*. Harvard University Press.

[7] Hughes, L., Dwivedi, Y. K., Misra, S. K., Rana, N. P., Raghavan, V., & Akella, V. (2019). Blockchain research, practice and policy: Applications, benefits, limitations, emerging research themes and research agenda. *International Journal of Information Management*, *49*, 114-129.

[8] Yli-Huumo, J., Ko, D., Choi, S., Park, S., & Smolander, K. (2016). Where is current research on blockchain technology?—a systematic review. *PloS one*, *11*(10), e0163477.

[9] Murray, D. E. (1993). Letters of credit and forged and altered documents: some deterrent suggestions. *Com. LJ*, *98*, 504.

[10] Effiong, M. E. A FRAMEWORK FOR THE ADOPTION OF BLOCKCHAIN TECHNOLOGY IN ACADEMIC CERTIFICATE-VERIFICATION SYSTEMS: A CASE STUDY OF NIGERIA.

[11] du Plessis, L., Vermeulen, N., van der Walt, J., & Maekela, L. (2015). *Verification of Qualifications in Africa*. Research report on the Verification of Qualifications in Africa, Northwest University, South Africa supported by the South African Qualifications Authority.

[12] Haciyakupoglu, G., Hui, J. Y., Suguna, V. S., Leong, D., & Rahman, M. F. B. A. (2018). Countering fake news: A survey of recent global initiatives.

[13] Johnson, D. A. (2020). 'An Underworld in Education': The Demise of Missouri's Medical Diploma Mills. *Social History of Medicine*, *33*(1), 106-131.

[14] Garwe, E. C. (2015). Qualification, award and recognition fraud in higher education in Zimbabwe. *Journal of studies in education*, *5*(2), 119-135.

[15] Houser, P. B., & Adler, J. M. (1997). *U.S. Patent No. 5,606,609*. Washington, DC: U.S. Patent and Trademark Office.

[16] Balsubramanian, S., Prashanth, I. R., & Ravishankar, S. (2009, August). Mark sheet verification. In *2009 3rd International Conference on Anti-counterfeiting, Security, and Identification in Communication* (pp. 359-362). IEEE.

[17] Beattie, D. D., Creighton Jr, N. L., Bailey, C. T., Remy, D. L., & Hamandi, H. (2006). *U.S. Patent No. 7,003,661*. Washington, DC: U.S. Patent and Trademark Office.

[18] Badr, A., Rafferty, L., Mahmoud, Q. H., Elgazzar, K., & Hung, P. C. (2019, June). A permissioned blockchain-based system for verification of academic records. In *2019 10th IFIP International Conference on New Technologies, Mobility and Security (NTMS)* (pp. 1-5). IEEE.

[19] Saleh, O. S., Ghazali, O., & Rana, M. E. (2020). Blockchain based framework for educational certificates verification. *Journal of critical reviews*, *7*(3), 79-84.

[20] Laurence, T. (2019). *Blockchain for dummies*. John Wiley & Sons.

Brain Computer Interface using EEG Based Sequential Minimal Optimization algorithms

Brain Computer Interface using EEG Based Sequential Minimal Optimization algorithms

Batool Abd Alhade[1], Israa Safaa Ahmed[2] and Baidaa Zahid Kamil [3]

[1]Al-Qasim green University. Babylon.Iraq
[2]University of Diyala, College of Science, Diyala, Iraq
[3]University of Diyala, Al-Muqdad College of Education, Diyala, Iraq

E-mail: batoolabd1985@gmail.com

Abstract. The concept of interfacing brains with robots/machines has been capturing human interests for a long time. The technology of the Brain-computer interface (BCI) has been aimed at building an interface between the brain and any electronic/electrical device (such as, smart home appliance, a wheelchair, and robotics devices) with the use of the electroencephalogram (EEG) that can be defined as a non-invasive approach for the measurement of the electrical potentials from the electrodes that have been placed on the scalp, produced by the activity of the brain. Over the past years, pattern classification was a highly challenging research field. Presently, the tasks of the pattern classification. In this paper, we chose motor imagery with the use of the single trial EEG signal, the SOM has been utilized to classify the signal processing algorithm (FICA). In comparison to other algorithms of the EEG signal analyses. It has achieved a classification accuracy of up to 88.% in comparison with the other method where the reported accuracy has been 65%. The SOM classification algorithm has been fast, simple, efficient, and easy to use. It achieved satisfactory results at the BCI

Keywords: brain computer interface (BCI), FICA, SMO,

1. Introduction

BCI can be defined as a direct connection between an animal or human brain (or brain cell culture) and an external device that has the ability the directly conducting of some external actions, based on signals provided by the brain. Before that, a team of researchers at Tsinghua Univ. have developed a set of internationally advanced approaches for pattern classification and signal processing, they have utilized this group of approaches for the successful implementation of BCI for the real-time brain activity cortical signal interpretations [1].

The EEG method was utilized for establishing portable asynchronous and synchronous controls for the applications of the BCI.

BCI may also be known as the Mind-Machine Interface (MMI), BMI or the direct neural interface. Those terms have led to the recognition of the BCI as a tube of direct communication between the brain and an external device as can be seen in Fig1 [2].

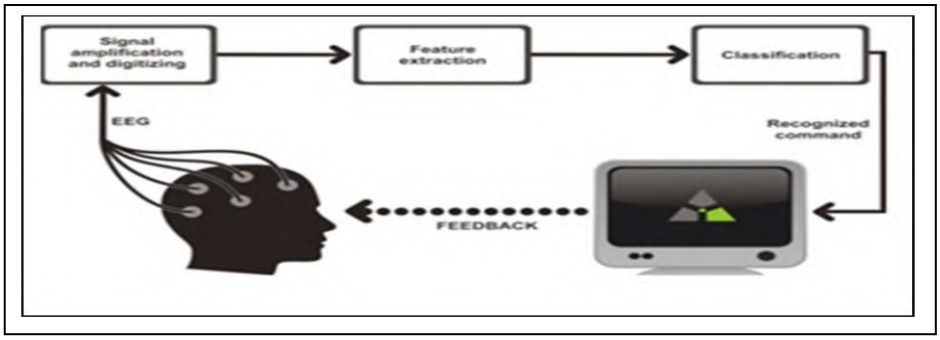

Figure1 Brain computer interface system

The technology of the BCI has been divided mainly into 2 brain activity measurement types, which are: the invasive BCI, and the non-invasive BCI, according to the way that the electrodes to record the electrical brain activity.

The non-invasive EEG-based BCIs can be defined as the best interface for space of the applications for the people who have severe motor disabilities due to their non-invasiveness, practicality, low cost, simplicity to use and portability. For some of the disabled patients that have paralysis or physical disabilities whereas the brain functions normally, even though they have the consciousness and thought of a normal large brain, they are not capable of communicating with the external environment by severely damaged nervous system and muscle and independently complete daily works. Which resulted in serious mental and physical trauma, and they live very painful lives that will have an impact on their process of recovery to some degree. The way of restoring or enhancing their communication and control abilities to outside world was the aim which was pursued for years in the medical rehabilitation area[3].

Invasive BCI can result in immune reactions, causing dangerous harm to a user, and it's barely accepted by the disabled people due to the method's invasiveness, requiring a special surgery, and its cost with the equipment is quite high and not yet covered by most of the governments. Even though the non-invasive BCI has a lower accuracy compared to invasive BCI, which remains rather less expensive in comparison to all of the other approaches and everyone can accept it easily [4][5].

There is a number of the models for controlling computer or machine with the use of the signal characteristics of the human brain and most popular ones are the motor imagery [6][7][8] [9]. P300 wave[10][11][12], steady state visual evoked potentials (SSVEP) [13].

The commonly utilized signal processing and classification approaches of the motor imagery with the use of the single trial EEG signal. Which include fast Fourier transformation (FFT), canonical correlation analysis (CCA), wavelet transformation, support vector machine (SVMs), and linear discriminant analysis (LDA).

In some previous research, the EEG has been used for various tasks [26].

In [8] it is seen that authors suggested new deep NNs like the Convolutional Neural Network (CNN) and Multi-Layer Perceptron (MLP) have been utilized for the classification of right- and left-hand motor imagery. after analyzation with Wavelet Transform.

In [14]: They have utilized an FFT for the extraction of the important features from a signal. After that, the obtained features are input signals of an FNN based classifier, the BCI for Controlling Wheelchairs they have discovered that using FFN is of a high effectiveness in classifying the signals of the EEG.

In[15]: have suggested an innovative model of classification, which has been referred to as multi-modal fuzzy fusion-based brain-computer interface system. There have been 10 volunteers who have carried out a motor imagery-based BCI experimentation, the system accomplished the maximum accuracy, of up to 78.45% and 78.81% with Sugeno and Choquet integrals, respectively. The authors have presented a new idea for the enhancement BCI systems that adopt fuzzy integrals
In[16]: This study implemented algorithms that have the ability of separating and classifying the task-associated EEG signal from the ongoing signals of EEG. This separation has been carried out through the hybridization between a classical approach which is represented by the process of filtering and a modern approach which is represented by Stone's BSS method to their ability of the isolation and deletion of the artefacts have an impact on system efficiency, as well as the task-related EEG signal have been categorized with the use of the NB. The obtained recognition rate results have been 82%
The remainder of this paper was arranged as: the important topics are discussed in the following section. In part3, the proposed model is discussed. Experimental results are presented in part4. Finally, the conclusions of this research are presented in part5.

2. Features extraction and dimension reduction

Raw EEG this raw was not used as a feature to identify patterns in the interfaces between the brain and the computer (BCI) due to the large amount of data generated from it. One second of an EEG recording containing 8000 features, it needs a method to reduce the dimensions or extract Important information only.
(FFT) As in a raw EEG, the Fourier transform contains a large amount of data,
(Autoregressive AR) In regression techniques, the model is modeled so that a voltage is predicted from a voltage N that precedes it. Regression coefficients are used as features for pattern recognition,
(wavelet) Wavelet shifting features of the (time-domain) and (frequency- domain) due to the fact that it allows the user to view the change in frequency bands over time. In the case of an intermittent wave transfer,
(Transform wavelet Discrete) The maximum number of conversion parameters is equal to the number of samples in the basic signal, While (a continuous Wavelet transfer) creates a lot of additional transactions.
Several methods have been utilized for the extraction of the features from the EEG signals like the independent component analysis (ICA), principal component analysis (PCA), wavelet Packet Decomposition(WPD), and genetic algorithms.

3. Fast Independent Component Analysis (FICA).

Fast ICA is an efficient implementation of ICA technique and a technique of popularly utilized BSS approach [17]. It has computational efficiency and needs a smaller amount of memory compared to other algorithms due to the fact that it is capable of estimating independent components one after the other. It additionally has the benefit of multi-component extracting, and the performance of the system does not degrade [18]. The ICA modeling is performed with the use of Equation (1):

$$Z = A_M . s_D \quad (1)$$

Here, Z indicates the observed matrix, Am represents the separating matrix, and sD represents determined sources. ICA is mainly utilized for the identification of separating matrix X for the sake of attaining the independent components in independent criteria pre-requisites.

$$s_D^* = X.Z \quad (2.)$$

$$X = A_m^{-1} \quad (3)$$

FastICA uses kurtosis for the independent components estimation Whitening is usually performed on data before the execution of the algorithm[19].
Before applying a FICA algorithm on the data, it is necessary to perform some pre-processing techniques, like the centering and whitening of the data that makes the issue of the estimation of ICA

better and simpler conditioned [20]

1**. Centering**: the most necessary and basic pre-processing is centering observed variables through the subtraction of their sample average, that is:

$$x = x' - E\{x'\} \ldots \quad (4)$$

where x represents centered signal,

x' is the observed signal, and

E{x'} represents the expectation of x'.

Also the independent components have been made 0-mean, since

$$E\{s\}=A\text{-}1E\{x\}$$

After the estimation of mixing matrix as well as independent components for 0-mean data, this subtracted mean may be re-constructed simply through the addition of the A-1E{x'} to 0-mean independent component.

2. **Whitening**: whitening the observed data is another useful preprocessing strategy in FICA. The purpose of whitening is to transform the observed vector x to another vector z, so that its components have not been correlated and their variance equal to unity. In another word the covariance matrix of z equals the identity matrix:

$$E\{z\,zT\}=I \ldots (5)$$

The whitening is a linear transformation that transforms the observed vector x by linearly multiplying it with some matrix V

$$z(k)=Vx(k) \ldots 6)$$

where z is the whitened vector, and

V represents the whitening matrix.

The whitening matrix has been obtained by using Eigen value decomposition (EVD) approach of covariance matrix:

$$Cx=E\{xxT\}=EDET \ldots (7)$$

where Cx represents covariance matrix of x,

D represents the diagonal Eigen values matrix of Cx.

E represents orthogonal Eigen vectors matrix of Cx,

Thus, whitening matrix has been given as

$$V=D\text{-}1/2\ ET$$

Sequential Minimal Optimization (SMO) Algorithm

SMO can be defined as one of the algorithms, which improve SVMs algorithm for the purpose of tackling QP problem. It performs the reduction of large amounts of the time, which is consumed by the SVMs throughout the phase of the training due to the QP optimization problem solution. The concept of the SMO is that it performs the separation of QP problem to smaller problems and analytically solves them. SMO has more capability for handling larger training sets due to the fact that it requires a linear memory amount on the training set. Therefore, the SMO is more appropriate for the EEG signal, which involves large size feature vectors. Moreover, it scales with large training sets and its implementation is quite simple [21][22].

3.The Proposed Classification System

The formation of a system of interfaces between the brain and the proposed computer includes three main steps that are included in Fig (2). The first step: obtaining the signal, the second step: processing the signal using a FICA, JADE algorithm, in the third step: classifying the data by SOM algorithm to classify the movement the left or right index finger.

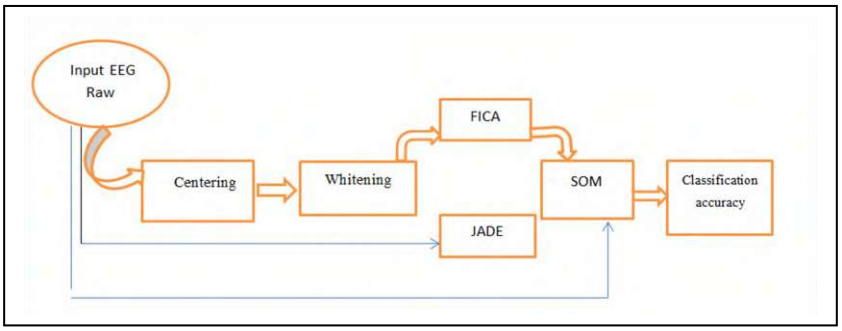

Figure2 Block diagram of the proposed system

3.1 Data Recording

EEG signals data were collected using computerized EEG device at a sampling rate of 256Hz according to computerized EEG device specifications. The scalp was covered by 19 electrodes that were based on 10-20 international system, as can be seen from (Fig3). The were been acquired from [12]

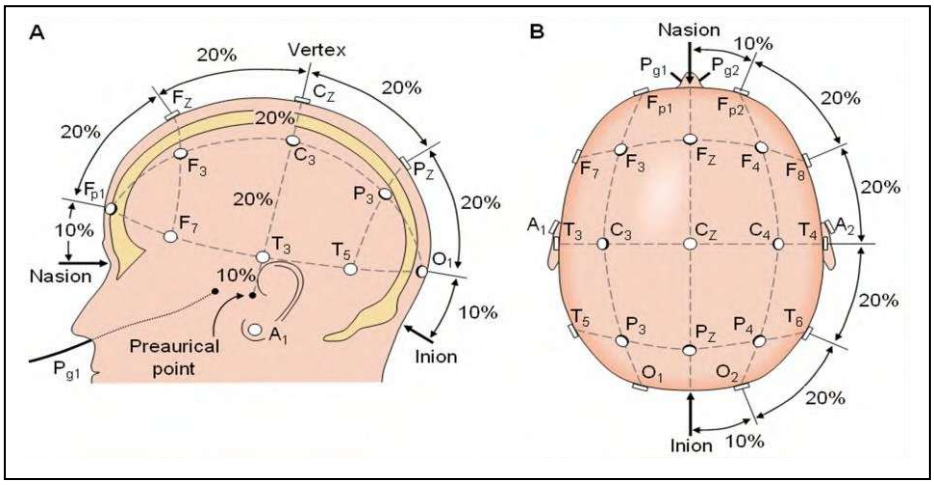

Figure3 Location of the EEG channels based upon the international 10-20 system [23].

This step includes obtaining the information that has been gathered from the EEG device and arrange it into excel sheet for additional processing. Table1. illustrates the basic data specifications. Data recording in 2 sessions one for the left index finger and the second one for the right movements each one of the sessions consists of numerous trails, every one of which is 10sec long, 19 channel signals and every one of the signals includes 256 samples in Hz.

TABLE1 DATA SET SPECIFICATIONS.

Gender	***age***	***position***	***motion***	***Medical condition***	***situation***
male	24	1meter from computer monitor	static	healthy	**Sit on chair**

3.2 Processing signals

3.2.1 **Attribute extraction and proposed algorithms**

In the original articles, the datasets have been pre-processed in a variety of ways. In order to gain fair comparison of the performance, to eliminate noises. in this work, we using FICA to analyses signal EEG raw To improve the system.

Steps of FICA Algorithms

Step1: Centering

Step2: Whitening

Step3: data have been centered through the subtraction of the average value of every one of the data matrix columns X.

Step4: data matrix will be 'whitened' through the projection of data on its principal component orientations in other words, X -> XK where K stands for a pre-whitening matrix. The number of the components may be identified by a user.

Step5: ICA algorithm performs an estimation of a matrix W s.t XKW = S . W has been selected for the maximization of neg-entropy approximation under constraints that W represents orthonormal matrix. Such constraint makes sure that estimated components are not correlated. This algorithm has been based upon a fixed-point scheme of iteration for the maximization of neg-entropy.

3.2.2 Classification

The classification procedures were performed In the presented study, through the use of Sequential Minimal Optimization algorithms (SMO): As shown by the algorithm below[22].

Algorithm: Simplified SMO

Input

C=regularization parameter

tol: numerical tolerance

max- passes: max # of times to iterate over α' s without changing

$(x^1,y^1),\ldots\ldots(x^m,y^m)$:training date

Out put

$\alpha \in R^m$: Lagrange multipliers for solution

b $\in$R: threshold for solution

- Initialize $\alpha_i = 0, \forall_i$, b = 0.
- Initialize passes=0
- **While** (passes < max- passes)
    - num-changed -alphas = 0
    - for i = 1, . . . m,

Calculate $E_i = f(x^{(i)}) - y^{(i)}$ using (2).

if $((y^{(i)}E_i < -tol \;\&\&\; \alpha_i < C) \;||\; (y^{(i)}E_i > tol \;\&\&\; \alpha_i > 0))$

- Select j ≠ i randomly.
- Calculate $E_j = f(x^{(j)}) - y^{(j)}$ using (2).
- Save old α′s: $\alpha_i^{(old)} = \alpha_i$, $\alpha_j^{(old)} = \alpha_j$.
- Compute L and H by (10) or (11).
- if (L == H)

continue to next i.

4. Results

Classification Accuracy

The present section includes a discussion of results in the case of using 2 algorithms, which are (FICA, JADE) and a SOM Classifier in the system of the brain interface between computer. Comparing them in the case of using the same classifier, we noticed that the classification accuracy when using the SOM algorithm with the FICA algorithm reached 88% and it led to the improvement of the system where the classification accuracy without processing was 64%, and when it was processed using the JADE algorithm, the classification accuracy was 65%.. The results are shown in tables (2)-(4).

Table (2) illustrates the Detailed Accuracy by movement Right index finger

EEG RAW	Preprocessing	Classification	precision	F-Measure	Recall
Right index finger	Without processing	SOM	0.792	0.069	0.036
	With JADE		0.750	0.667	0.66
	with FICA proposed work		1.000	0.800	0.667

Table (3) illustrates the Detailed Accuracy by movement Left index finger

EEG RAW	Preprocessing	Classification	precision	F-Measure	Recall
Left index finger	Without processing	SOM	0.495	0.660	0.990
	With JADE		0.500	0.571	0.667
	with FICA proposed work		0.800	0.889	1.000

Table (4): results of the suggested study and table numbers have shown that the suggested work performs better and provides higher accuracy of the rating. Where it represents Results of weighted Average classification And the time it takes to build the classifier model

Table 4. Results of weighted Average classification and time utilizing the suggested methods

	Pre-processing	Classification	precision	F-Measure	Recall	Time
EEG data	With no processing	SOM	0.647	0.358	0.502	0.13 seconds
	With JADE		0.656	0.631	0.625	0.05 seconds
	with FICA proposed work		88.6	0.851	0.857	0.05 seconds

In general, the suggested study has been providing more sufficient performance: compared to other methods through the experimentation whit, which is why, the FICA was chosen to be enhanced due to the fact that it has been more sufficient already, compared to other utilized blind source separation approaches with the SOM method. Results have given gave better rating accuracy equal to 88% . as can be seen from Fig (4)

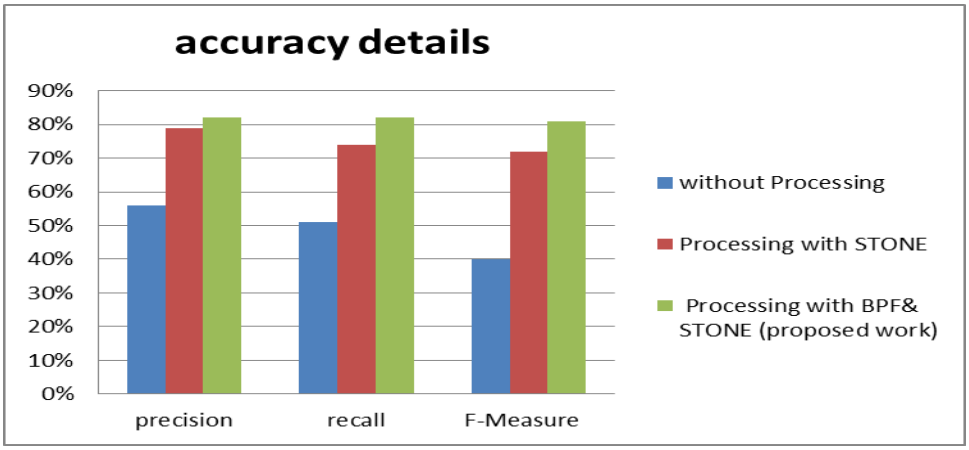

Fig 4. accuracy using proposed techniques.

The thesis presented by Salem 2007 [20] under the title (Design and The implementation of an AI control unit based on the 'brain-computer interface) is the closest research in this study. Use the same dataset (19) channels and FICA algorithm for analyses the EEG of signal the BCI. Signal was classified using an adaptive pattern classifier Consists of a set of Kohonen Self-Organization Map (SOM) And LVQ While we used classifier Sequential Minimal Optimization (SMO). The results of the comparison between the system in the proposed study and the thesis [20] were shown in table (5) and Fig (5).

Table 5. Results of comparing the proposed techniques with previous technologies

input data	data analysis	Classifier	Precision %	
			Left index finger	right index finger
	RAW EEG	(SOM) And LVQ	25	45.8
		Sequential Minimal Optimization	49	79
	FICA	(SOM) And LVQ	53.3	75
		Sequential Minimal Optimization	80	100

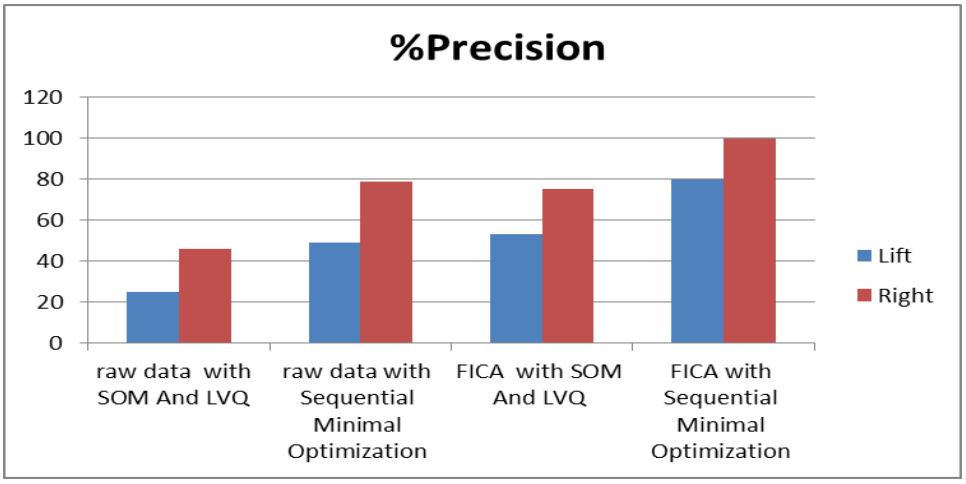

fig (5). comparing the proposed techniques with previous technologies

5. Conclusions

In the present research, the impact of the EEG -BCI performance enhancement has been shown by employing a suitable classifier. There are numerous sparse characteristics with dimensions that exceed 2,650. Training a massive amount of data with the use of traditional approaches is insufficient and expensive. This is why SMO has been chosen which operates best on the sparse data with the high dimensions. The results of the classification have been enhanced by utilizing it. The SMO speeds up the process of training, as well as reducing the classification errors. The precision which has been obtained from the use of the SMO has been 88%

.

References

1. Andruseac, G.G., Paturca, S.V., Banica, C.K., Costea, I.M., Rotariu, C.: A novel method of teaching information technology applied in health monitoring. J. Biotechnol. 239, 1–3 (2016).

2. A, F., El-KhoriMousabi, R.A., Shoman, M.E.: An integrated classification method for brain computer interface system. In: 2015 Fifth International Conference on Digital Information Processing and Communications (ICDIPC). pp. 141–146. IEEE (2015).

3. Edelman, B.J., Meng, J., Suma, D., Zurn, C., Nagarajan, E., Baxter, B.S., Cline, C.C., He, B.: Noninvasive neuroimaging enhances continuous neural tracking for robotic device control. Sci. Robot. 4, (2019).

4. Shao, L., Zhang, L., Belkacem, A.N., Zhang, Y., Chen, X., Li, J., Liu, H.: EEG-Controlled Wall-Crawling Cleaning Robot Using SSVEP-Based Brain-Computer

Interface. J. Healthc. Eng. 2020, (2020).

5. Somandepalli, K.: A Therapy for Nightmares through Invasive Brain Computer Interface (BCI). (2019).

6. Frolov, A., Bobrov, P., Biryukova, E., Isaev, M., Kerechanin, Y., Bobrov, D.: Using Multiple Decomposition Methods and Cluster Analysis to Find and Categorize Typical Patterns of EEG Activity in Motor Imagery Brain–Computer Interface Experiments. Front. Robot. AI. 7, 88 (2020).

7. He, L., Hu, D., Wan, M., Wen, Y., Von Deneen, K.M., Zhou, M.: Common Bayesian network for classification of EEG-based multiclass motor imagery BCI. IEEE Trans. Syst. man, Cybern. Syst. 46, 843–854 (2015).

8. Janković, M.: EEG classification for left and right hand motor imagery, (2019).

9. Joadder, M.A.M., Rahman, M.K.M.: Classification of Motor Imagery signal using wavelet decomposition: A study for optimum parameter settings. In: 2016 International Conference on Medical Engineering, Health Informatics and Technology (MediTec). pp. 1–6. IEEE (2016).

10. Martínez-Cagigal, V., Gomez-Pilar, J., Álvarez, D., Hornero, R.: An asynchronous P300-based brain-computer interface web browser for severely disabled people. IEEE Trans. Neural Syst. Rehabil. Eng. 25, 1332–1342 (2016).

11. Allison, B.Z., Kübler, A., Jin, J.: 30+ years of P300 brain–computer interfaces. Psychophysiology. 57, e13569 (2020).

12. Fouad, I.A., Labib, F.E.-Z.M., Mabrouk, M.S., Sharawy, A.A., Sayed, A.Y.: Improving the performance of P300 BCI system using different methods. Netw. Model. Anal. Heal. Informatics Bioinforma. 9, 1–13 (2020).

13. Saravanakumar, D., Reddy, R.: A Brain Computer Interface based Communication System using SSVEP and EOG. Procedia Comput. Sci. 167, 2033–2042 (2020).

14. Abiyev, R.H., Akkaya, N., Aytac, E., Günsel, I., Çağman, A.: Brain-computer interface for control of wheelchair using fuzzy neural networks. Biomed Res. Int. 2016, (2016).

15. Ko, L.-W., Lu, Y.-C., Bustince, H., Chang, Y.-C., Chang, Y., Ferandez, J., Wang, Y.-K., Sanz, J.A., Dimuro, G.P., Lin, C.-T.: Multimodal Fuzzy Fusion for Enhancing the Motor-Imagery-Based Brain Computer Interface. IEEE Comput. Intell. Mag. 14, 96–106 (2019).

16. Abass, Z.K., Hasan, T.M., Abdullah, A.K.: Brain Computer Interface Enhancement Based on Stones Blind Source Separation and Naive Bayes Classifier. In: International Conference on New Trends in Information and Communications Technology Applications. pp. 17–28. Springer (2020).

17. Ngarianto, H., Gunawan, A.A.S., Budiharto, W.: Separating Multi Speeches in Intelligent Humanoid Robot using FastICA. IPTEK J. Technol. Sci. 29, (2018).

18. Mishra, A., Bhateja, V., Gupta, A., Mishra, A.: Noise Removal in EEG Signals Using SWT–ICA Combinational Approach. In: Smart Intelligent Computing and Applications. pp. 217–224. Springer (2019).

19. Langlois, D., Chartier, S., Gosselin, D.: An introduction to independent component analysis: InfoMax and FastICA algorithms. Tutor. Quant. Methods Psychol. 6, 31–38 (2010).

20. Salim, M.H.: Design and implementation of AI controller based on brain computer interface, (2007).

21. Hassen, H., Al-Maadeed, S.: Arabic handwriting recognition using sequential minimal optimization. In: 2017 1st International Workshop on Arabic Script Analysis and Recognition (ASAR). pp. 79–84. IEEE (2017).

22. Rusmee, K., Chumuang, N.: Predicting System for the Behavior of Consumer Buying Personal Car Decision by Using SMO. In: 2019 14th International Joint Symposium on Artificial Intelligence and Natural Language Processing (iSAI-NLP). pp. 1–6. IEEE.

23. GomeNicolas-Alonso, L.F., Z-Gil, J.: Brain computer interfaces, a review. sensors. 12, 1211–1279 (2012).

Digital Modulation Classification Based On Chicken Swarm Optimization and J48 Algorithm

Digital Modulation Classification Based On Chicken Swarm Optimization and J48 Algorithm

Zainab Kadhm Obeas[2], Shaimaa Safaa Ahmed Alwaisi[2] and Nadie Kadom Abd[3]

[1,3]Al-Qasim Green University. Babylon.Iraq
[2] Ministry of water resources, Iraq

E-mail: zainabkadhm10@gmail.com

Abstract. Automatic Modulation Recognition (AMR) has a significant impact in the military as well as civil applications. Recognizing the modulation of the received signal has been considered as an intermediate step between the detection and demodulation of the signal. Which is why, in many military and communication systems, the AMR is considered as part of the system. Presently, due to increasing digital modulations in military and civil applications. Digital modulation recognition is especially important. Usually for the AMR a small number of the received signal features are obtained and utilized. The choice of the suitable feature plays an important part in the increase of AMR efficiency. The presented paper indicates hybrid intelligent system for the recognitions of digital signal types, consisting of 3 major modules: classifier module, feature extraction module and J48 Classifier that was used for the first time in our research in the field of classification of modulated signals and optimization module by Chicken Swarm Optimization (CSO) . To get better results of the system suggested optimization the features to discard weak or irrelevant features in the system and keep only strong relevant features Chicken Swarm Optimization. The results of simulation confirm the high accuracy of recognition that is related to the suggested system even at low SNR.

keywords: Hybrid System, Automatic modulation recognition, Chicken Swarm Optimization Algorithm, J48 Algorithm

1.Introduction.

Automatic Modulation Recognition the second stage which is used after detection of the embedded signals to demodulate them [1] is capable of recognizing the received signal's modulation type between the pre-supposed modulation numbers. The automatic modulation recognition is of a significant impact on the military and civil applications in the present day, as a result of the increase in the digital modulations in the military and civil applications the recognition of the digital modulation is particularly important. Generally, for the automatic modulation recognition, a few features of the received signal will be obtained and utilized. The choice of suitable features is of a significant impact on the increase of recognition efficiency [2]. In [3] used the neural network algorithm choosing 10 modified signals (2-ASK, 4-ASK, 2-FSK, 4-FSK, 2-PSK, 4-PSK, 4-QAM, 16-QAM, 64-QAM). The existence of the Gaussian noise -5dB to 20dB. Results have shown an increase in the accuracy of recognition of the modification type. In [4] This study uses 2 convolutional neural network (CNN)-based DL models. The experimental results have demonstrated the considerable advantage of the performance and the feasibility of the applications of the DL-based method for the classification of the modulation. In [5] Suggested novel algorithm for distinguishing six types of digital: modulation approaches (2ASK, 2FSK, 2PSK,4 ASK,4 FSK, and 4 PSK) High-resolution result for new algorithms have been demonstrated even when SNR = 4dB. In [6] They proposed a data-based model to classify automatic settings without relying on expert features such as high-frequency moments. The accuracy of the results was 90% in the SNR variance ranging from 0dB to 20d In this research, the following

digital signals have been considered: (2ASK, 2PSK, 4PSK, 8PSK, 8QAM,16QAM,32QAM, 64 QAM, 128QAM, and 256QAM) is enhancing modulated signal features, which leads to the reduction of the properties of the signal by the increase of system accuracy in detections and identifications of the signal type with the use of the Chicken Swarm optimization algorithm . In The general outline of the present paper is: After introduction, features extraction and algorithms of the optimization will be reviewed in Section2 the classification will be provided in Section3. Section4 provides some of the simulation results, and finally, the conclusions of the present research will be provided in section5.

2. Feature Extraction and Optimization

The standard system of pattern recognition after carrying out some operations of the pre-processing usually decreases the raw data set size through the extraction of a group of the distinctive attributes that are referred to as features. The necessity for the feature extraction results from the potential incapability of using raw data. In the field of signal recognition, selecting good features results in enabling the classifier from distinguishing higher and more digital signals, as well as helping the reduction of the classifier's complexity. A variety of digital signal types are known for different characteristics which is why they find the accurate features to identify them (particularly in the cases of the higher-order moment, cumulant) is a complicated task.. according to the researches, statistical features present a good way to discriminate the types of the considered digital signals [7] .

2.1. **Moments**

Probability distribution moments can be defined as a model of expected value and defining the character of the probability density function. Concerning digital signals the specification for i^{th} the moment for finite length is specified via:

$$\mu_i = \sum_{K=1}^{N} (s_k - \mu)^i f(s_k) \quad (1)$$

Where N can be defined as the data length, s_k is the random variable, subscript (k) is integer-valued, μ is the mean value of a random variable. Let the signal has a zero mean (μ= 0), thus equation (1) becomes:

$$\mu_i = \sum_{K=1}^{N} S_k^i \ f(s_k) \quad (2)$$

The auto-moment regarding random variable is:

$$E_{s,p+q,p} = E[S^P (S^*)^q] \quad (3)$$

The (p) represents the number of the non-conjugated terms (q) represents the number of conjugated terms, (p+q) represent moment order, and (S) is a discrete random variable[8]

2.2 **CUMULANTS**

Cumulants are also statistical features If the characteristic equation of a random variable S with zero mean is :

$$\mathrm{F}(t) = E\left[e^{jts}\right] \quad (4)$$

Expanding the Logarithm of equation (4) by applying a Taylor series we obtain
$:g(t)\ log\left\{E\left[e^{jts}\right]\ \sum_{n=1}^{\infty} k_n\ \frac{(jt^n)}{n!}\right\}$

Where(k_n) is called the cumulant, (t) is time The nth-order cumulant is comparable to nth order moment thus

$$C_{s,p+q,p} = Cum\left[\underbrace{s(t),\dots,s(t),}_{pterms}\ \underbrace{S^*(t),\dots,S^*(t),}_{qterms}\right] \quad (5)$$

The cumulants can be derived from moment :

$$cum[s_1,\dots.s_n] = \sum_{\forall v}(-1)^{q-1} \quad (q-1)!\,E\left[\prod_{j\epsilon v_1} s_j\right]\dots E\left[\prod_{j\epsilon v_q} s_j\right] \quad (6)$$

The summation will be implemented on partitions $v = (v_1,\dots.,v_q)$ for the indexes (1, 2, ..., n), (q) represents the number of elements in partition [1].

2.3 **Optimization**

To get better results of the system optimization is suggested to the features to discard weak or irrelevant features in the system and keep only strong relevant features, to check the accuracy of the system and comparing the results obtained from applying the feature optimization algorithm and without applying it .algorithm used for feature optimization (BAT swarm).

2.4 **Chicken Swarm Algorithm (CSO)**

CSO may be characterized as an advanced intelligent approach that has been proposed to a lot of behaviors related to chickens cocks and hens in their process when they search for food. In the CSO the chicken swarm in the search space is mapped as a specific individual of the particle. The chicken particle swarm, cock particle swarm, and hen particle swarm have been organized according to the fitness value of the particle, and a variety of the search modes will be utilized by every one of the sub-swarms [9]**.** In this algorithm, more than a few particles with the best fitness are selected as the cock particle swarm which can be characterized as:

$$(x)_{i,j}^{t+1} = (x)_{i,j}^{t} + randn(0,\sigma^2) \quad (7)$$

where $x_{i,j}^{t+1}$ and $x_{i,j}^{t}$ represents the position regarding j-the dimension of a particle i in t+1 and t iterations respectively rand n (0, σ^2) represents the random number of Gauss distribution whose variance is σ^2The parameter σ^2 could be computed via

$$\sigma^2 = \begin{cases} 1, & fit_i < fit_k \\ \exp\left(\dfrac{(fit_k - fit_i)}{(|fit_i| + \xi)}\right), & fit_i \geq fit_k \end{cases} \quad (8)$$

where i, $k \in [1, r\ \text{size}]$ and $i \neq k$. $r$size can be defined as the number of cock swarms. fit_i and fit_k represents the values of the fitness regarding cock particle i & k, respectively; ξ can be defined as a fairly small number. Moreover, most particles with the best fitness will be selected as the hen swarm**.** Its random search will be carried out by population cocks of **.**hen and that of others, which may be given as**:**

$$X_{i,j}^{t+1} = X_{i,j}^{t} + s2rand.\left(X_{r1,j}^{t}, X_{i,j}^{t}\right) + ..s2\ rand.\left(X_{r2,j}^{t}, X_{i,j}^{t}\right) \quad (9)$$

where $X_{r1,j}^{t}$ and $X_{r1,j}^{t}$ represents the position related to cock individual $r1$ in a population of the hen X_j and cock individual $r2$ in other populations, respectively. rand can be defined as a uniform random number over [0, 1]. $S1$ & $S2$ indicate the weight that is estimated by

$$S1 = exp\left(\frac{(fit_{i-fit_{r1}})}{(|fit_i|+\xi)}\right)$$

$$S2 = exp(fit_{r2} - fit_i) \quad (10)$$

where fit_{r1} and. fit_{r2} represents, fitness value regarding the cock individual $r1$ in hen population X_j and the cock individual $r2$ in other populations. Each one of the individuals, apart from a hen**.** swarm and cock swarm will be specified as chick swarm. Its mode of search follows the search mode of the hen swarm which has been provided as:

$$X_{i,j}^{t+1} = X_{i,j}^{t} + FL.\left(X_{m,j}^{t} - X_{i,j}^{t}\right), FL \in [0,2] \quad (11)$$

where FL**.** represents a parameter, indicating that a chick will follow its mother to search for food. $X_{m,j}^{t}$ indicates the *i*th chick's mother's position ($m \in [.1,N]$) [9]**.**

3. CLASSIFIER

3.1 Classification Algorithms

Classification can be defined as a very important problem of data mining. Its input can be described as a data-set of the training record, where every one of the records got several attributes. Numerical attributes can be defined as the attributes that have numerical domains and categorical attributes, which are attributes that have non-numerical domains. In addition to that, there has been as well, a distinguished attribute which has been referred to as Class label. Such classification has been intended for the construction of a console model that may be utilized for the prediction of the future of the class label [10] unlabeled records. Numerous models of classification have been utilized and a method which is referred to as the called decision tree has been utilized in the present paper.

3.2 . Decision trees

Decision trees are used for delineating the process of decision-making. It is a classifier that is embodied with a tree construction that is similar to a flowchart, which was used extensively for embodying the models of association, as a result of its graspable nature which holds to mind human reasoning. They have been used for categorizing the instances through sorting those instances down the 3 from origin to a small leaf node, running the instance association. Each one of the nodes is specifying an instance examination and each one of the divisions is corresponding to a potential advantage of that attribute. The decision tree in [11] performs the building of the regression or classification models as a tree structure. It performs a division of the data-set to smaller and smaller sub-sets as at a similar period a related decision tree has been developed incrementally. The final result is a tree alongside the leaf and the decision nodes. The decision node has 2 or more divisions and the leaf node embodies a decision or association. The topmost decision node in the tree, corresponding to the optimal predictor produced the origin node

3.3 DECISION TREE (J48)

One of the best algorithms of machine learning to examine the data continuously and categorically. J48 is utilized for the classification of a variety of applications and provide precise classification results: J-48 is a highly sufficient algorithm of machine learning which is utilized for the categorical and continuous examination of data C 4.5 (J-48) is one of the algorithms utilized for the generation of the decision tree, it has been advanced by R. Quinlan. C 4.5 is an extension of the earlier ID-3 algorithm by Quinlan. The C 4.5 actualizes (J 48) for the creation of a trimmed C 4.5 decision tree. All information aspects are split into smaller sub-sets to base a decision. J 48 considers the standardized data gain which is the result of splitting information through the selection of an attribute. In a summary, attribute extreme standardized data gained has been deployed. The smaller sub-sets are gathered again by the algorithm. Split strategies are stopped in the case where a sub-set has an index that has a similar class in every instance. J-48 produces a decision node with the use of expected class (J 48) estimations, the decision tree is capable of dealing with certain properties, the missing or lost data attribute estimations, and different attribute costs. Here the precision may be expanded with pruning [12, 13].

4. The Step of J48

Step1// Labeling of the leaf with a similar class in the case where instances are part of the same class.
Step2// For every one of the attributes, the possible data is figured and data gain will be obtained from the attribute test.
Step3// Ultimately, the optimal attribute is selected according to the current parameter of selection:

4.1 THE PROPOSED MODULATION CLASSIFICATION SYSTEM

The System which has been presented in This paper consists of 2 phases: Phase one: the electromagnetic signals. HOMs and HOCs were used for feature extraction (FE). MATLAB programs were designed to fulfill the tasks. the extracted HOMs and HOCs were obtained as a matrix of the dataset. Output FE was improved using the Chicken swarm optimization algorithm Phase 2: The outputs of the first stage are applied as inputs into the J48 to classify the signal and predict the signal type Fig. (1) demonstrates the -diagram of the Proposed System.

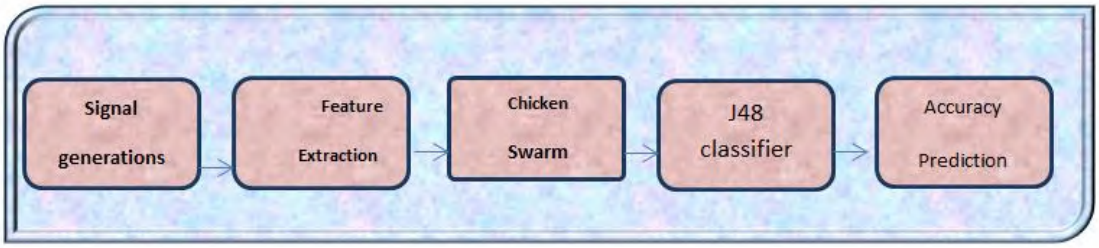

Figure 1 . A diagram of the proposed method

4.2 IMPLEMENTATION AND RESULT:

This section discusses the Results of using the Algorithm chicken Swarm Optimization and (J48) to classify 10 types of The modified signal (8 QAM, 16QAM, 32 QAM, 64QAM, 128 QAM, 256 QAM, 2PSK, 4 PSK, 8 PSK, 2 ASK Within the level of SNR (-2, -1,0,1,2,3,4,5,6,7, 8,910,11and 12) dB and comparing these results when classifying without optimization the feature of signals in an algorithm (J48 decision tree) is for each type of signal and the accuracy of the rating as shown in Table 1 Each type of signal. The success rate in identifying signals after using the CSO algorithm is higher as indicated in Table 3which means more system efficiency.
Results of classification accuracy using (J48 decision tree) without optimization where the accuracy ratio was 87% to the proposed methodology.

Table1. Represents Classification criteria of the suggested algorithm's without optimization

Signal Type-	Criteria of Classification		
	Classification Accuracy	**Re-call**	**F-Measure**
8 QAM	**%100**	**100**	**100**
16 QAM	**%100**	**100**	**100**
32QAM	86	83	83
64 QAM	86	83	83
128QAM	86	83	83
256QAM	**%100**	**100**	**100**
2 ASK	**%100**	100	100
2 PSK	**71**	**73**	**75**
4PSK	**75**	**100**	**100**
8PSK	**86**	**86**	**83**

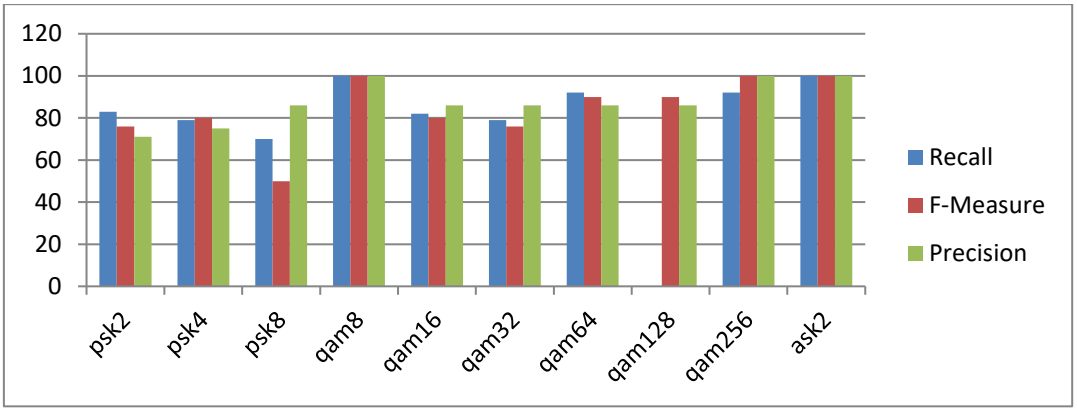

Figure 2 The classification Accuracy without optimization

Represents results Accuracy using (J48 decision tree) with CSO where the accuracy ratio was 95 % to the proposed methodology.

Signal Type	Criteria of Classification		
	Classification Accuracy	Re-call	F-Measure
8QAM	**%90**	**100**	**100**
16QAM	**%100**	**100**	**100**
32QAM	95%	91	90
64QAM	88%	88	86
128QAM	**%100**	**100**	**100**
256QAM	**%100**	**100**	**100**
2ASK	**%100**	**100**	**100**
2PSK	**88%**	**83**	**82**
4PSK	**93%**	**93**	**92**
8PSK	**%88**	**87**	**86**

Table- 2. Represents Rresult's Classification criteria of the Proposed algorithm's with optimization

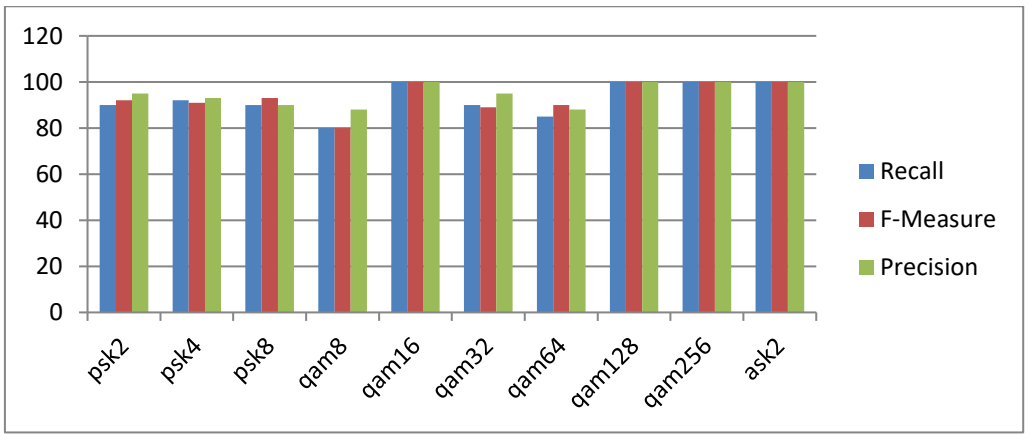

Figure 3 The classification Accuracy with optimization

Conclusions

In the present research, Ten digital signal types Modulated were generated in the MATLAB program in an SNR level that ranges within (-2, - 1,0,1,2,3,4,5,6,7,8,9,10,11,12) dB . after that, statistical features have been extracted (Moment, Cumulant) of signals, above. optimizing features with (CSO algorithm) Using the (J48 decision tree) as a classifier The results showed higher classification accuracy when optimization the features by CSO up to 95% even at low noise levels compared to the classification accuracy without Optimize.

References

[1] M. Azarbad, S. Hakimi, and A. Ebrahimzadeh, "Automatic recognition of digital communication signal," *Int. J. energy, Inf. Commun.*, vol. 3, no. 4, pp. 21–34, 2012.

[2] W. Su, J. L. Xu, and M. Zhou, "Real-time modulation classification based on maximum likelihood," *IEEE Commun. Lett.*, vol. 12, no. 11, pp. 801–803, 2008.

[3] S. Almaspour and M. R. Moniri, "Automatic modulation recognition and classification for digital modulated signals based on ANN algorithms," *nine*, vol. 3, no. 12, 2016.

[4] S. Peng *et al.*, "Modulation classification based on signal constellation diagrams and deep learning," *IEEE Trans. neural networks Learn. Syst.*, vol. 30, no. 3, pp. 718–727, 2018.

[5] P. K. HL and L. Shrinivasan, "Automatic digital modulation recognition using minimum feature extraction," in *2015 2nd International Conference on Computing for Sustainable Global Development (INDIACom)*, 2015, pp. 772–775.

[6] S. Rajendran, W. Meert, D. Giustiniano, V. Lenders, and S. Pollin, "Deep learning models for wireless signal classification with distributed low-cost spectrum sensors," *IEEE Trans. Cogn. Commun. Netw.*, vol. 4, no. 3, pp. 433–445, 2018.

[7] A. A. Khurshid and A. P. Gokhale, "Classification system for digital signal types using neuro fuzzy system and PSO," in *2009 World Congress on Nature & Biologically Inspired Computing (NaBIC)*, 2009, pp. 373–378.

[8] S. B. Sadkhan-Smieee, A. Q. Hameed, and H. A. Hamed, "Digitally modulated signals recognition based on adaptive neural-fuzzy inference system (ANFIS)," *Int. J. Adv. Comput. Technol.*, vol. 7, no. 5, p. 57, 2015.

[9] C. Qu, S. Zhao, Y. Fu, and W. He, "Chicken swarm optimization based on elite opposition-based learning," *Math. Probl. Eng.*, vol. 2017, 2017.

[10] S. N. Chary and B. Rama, "A survey on comparative analysis of decision tree algorithms in data mining," in *International Conference On Innovative Applications In Engineering and Information Technology (ICIAEIT-2017)*, 2017, vol. 3, no. 1, pp. 91–95.

[11] P. Kapoor, R. Rani, and R. JMIT, "Efficient decision tree algorithm using J48 and reduced error pruning," *Int. J. Eng. Res. Gen. Sci.*, vol. 3, no. 3, pp. 1613–1621, 2015.

[12] N. Saravana and D. V Gayathri, "Performance and Classification Evaluation of J48 Algorithm and Kendall's Based J48 Algorithm (KNJ48)," *Int. J. Comput. Trends Technol. (IJCTT)–Volume*, vol. 59, 2018.

[13] T. A. Al-asadi, A. J. Obaid, R. Hidayat and A. A. Ramli, "A survey on web mining techniques and applications," International Journal on Advanced Science Engineering and Information Technology, vol. 7, no. 4, pp. 1178-1184, 2017.

TSCO: Trust-based secure and cooperative opportunistic resource utilization networks

TSCO: Trust-based secure and cooperative opportunistic resource utilization networks

Abduljaleel Al-Hasnawi

College of Technical Al-Mussaib, Al-Furat Al-Awsat Technical University, Iraq

E-mail: abduljaleel.alhasnawi@atu.edu.iq

Abstract. An opportunistic resource utilization network (denoted as Oppnet) is a type of network that enables its node to cooperate in an opportunistic and ad hoc manner. Cooperation in oppnet includes sharing node computational resources, rather than only opportunistic communication in the traditional opportunistic networks. The key idea of oppnet is its ability to grow from seed node (initiator) to expanded oppnet via joining more nodes until getting the desired resources in a timely manner. This expansion raises the security risk of joining malicious nodes and threatens the oppnet including nodes and data. Besides, uncontrolled oppnet expansion might allow joining nodes with low computational capabilities or limited resources that have delayed responses, and hence affect the performance of oppnet. This study aims to mitigate these two problems by proposing a new oppnet paradigm (an enhanced version of original oppnet) called Trust-based Secure Cooperative Oppnet (TSCO) that utilizing a trust as a foundation for security and cooperation. Trust foundation is the major aspect of TSCO, which relies mainly on establishing trust value for each oppnet node and updating these values based on cooperation experience with those nodes. In TSCO, oppnet nodes have classified based on their trust values in which the highest trust value has the priority to join oppnet, if it exists within the specific range. Otherwise, the second-highest trust value takes priority, and so on. To test the feasibility of TSCO in realistic systems, a framework of using TSCO as an oppnet expansion control regarding security and cooperation is simulated. The experimental results show that TSCO has a better performance in terms of secure, success expansion, and cooperation. The success rate of TSCO is higher than the success rate of the original oppnet (our experimental baseline). In addition, regarding the time of satisfying oppnet tasks, TSCO shows less average latency than the baseline.

Keywords: Trust, Security, Cooperation**,** Opportunistic Networks

1. Introduction

Opportunistic resource utilization networks (oppnets) considered in this study are categories of ad hoc networks where diverse nodes, not originally designed as oppnet nodes, join it dynamically to perform certain tasks they have been called to participate in. Oppnets use opportunistically all kinds of resources including computation, communication, storage, sensing, actuation, etc.

Trust considered in this study is an aspect of security and reliability. In other words, trust is formulated and integrated within oppnet architecture to assure that only secure nodes with a sufficient level of trust, resources, reliability, and past cooperation experience can join the oppnet. If a node does not has an experience, an initial trust value assigns for it, and then this value is updated based on the new experience with oppnet. This section provides a theoretical background about the major aspects and terms considered in this research including oppnet, trust, security, and cooperation. Section 2 reviews

the literature and outlines a selected set of works that have similarity with our work and distinguishes our work in the literature. Section 3 describes the proposed Trust-based Secure Cooperative Oppnet (TSCO) static and dynamic architectures. Section 4 presents an evaluation framework for testing the feasibility and efficiency of the proposed TSCO model. Section 5 shows the experimental results and discusses the results in terms of the satisfying the goals of the study. Finally, section 5 concludes the paper and draws the directions for future work.

2. Background

2.1. Opportunistic Resource Utilization Networks

Opportunistic resource utilization network (Oppnet) is a special kind of ad hoc networks that enables opportunistic use of all kinds of resources, services, or capabilities (incl. hardware, software, applications, etc.), and opportunistic communications which happen to be within the oppnet's reach [1]. Oppnet starts as a relatively small network, known as seed network, which grows into an expanded oppnet. It should be noted that the more pervasive is the environment in which the oppnet operates the more benefits they can provide (the higher interoperability, with more heterogeneous software and hardware components). Oppnets can be consider collaborative distributed systems [2], since integration of resources can only be achieved through collaboration. Entities collaborate with an oppnet, by sharing diverse resources, to help it achieving a certain goal. Oppnets can also be consider ad hoc networks, peer-to peer (P2P) systems, and self-organizing networks (SONs) since they share many of their capabilities and characteristics. In particular, they share node localization and self-organization qualities with ad hoc networks; growth-by-joining abilities with P2P systems and forming, organization, and management.

Oppnet consists of three major components: seed, Decentralized Command Center (DCC), helpers, and Oppnet Virtual Machine (OVM) [3]. Seed is a single node or multiple neighboured nodes that initiated the oppnet deployment (expansion) process due to a need for resources. DCC is a controller, which can include an arbitrary subset of seed, works on inviting foreign nodes to help in reaching oppnet goals. The initial seed oppnet grows into an expanded oppnet. Helpers are foreign or oppnet entities that accept the DCC invitation. The OVM is a set of primitives that create a universal platform for application-level communication within and among oppnets. This communication is the basis for opportunistic utilization of all resources. OVM primitives can be downloaded to any system or device to make it oppnet-enabled, that is, able to communicate and share resources with other oppnets or oppnet-enabled nodes. Oppnet operation, illustrated in Figure 1, initiated by the seed oppnet when it declares the need for help by other surrounding nodes. The DCC notified by this declaration, via command sent by the seed, and starts the growth process. The growth consists of three steps: discovering enough candidate helpers, admitting them into oppnet, and integrating their resources into oppnet. This process prepare helpers to cooperate. Once the cooperation has done and the goal of an oppnet has achieved, DCC releases helpers' resources and finalizes the oppnet process. Note that the oppnet DCC presides over the operations of the oppnet throughout its lifecycle.

2.2. Trust

Trust is an abstract concept, which combines many complicated factors. It can be reflected by utility, availability, reliability, confidence, and quality of services, reputation, and other concepts [4]. Trust can be defined as a particular level of subjective probability which an agent will perform a particular action for a specified period within a specified context. In opportunistic networks, trust of a specific node is a subjective estimation done by another peer node on the reliability and accuracy of information received from or traversing through that node [5]. The Level of trust is a probability varying from 0 (complete distrust) to 1 (complete trust). In this sense, trustworthiness is a measure of the actual probability that the trustees will behave as expected. Trustworthiness defined as the objective probability that the trustee performs a particular action on which the interests of the trustor depend. If the trustor ignores the difference between the believed (i.e., trust) and the actual (i.e., trustworthiness) probability, there is a risk of trust miscalculation. There is misplaced trust when the perceived trust is higher than the actual trustworthiness. Misplaced trust increases risk and thus

enhances the chance of deceit as well. On the other hand, when the perceived trust is lower than the actual trustworthiness, the trustee is distrusted more than warranted. Hence, the trustor may lose potentially good opportunities to cooperate with partners with high trustworthiness [6].

2.2.1. **Trust Properties**. Due to the unique characteristics of oppnets environments and the inherent unreliability of the wireless channels, the concept of trust in oppnets should be carefully defined. The main properties of trust in such environments can be defined in many directions. Trust is dynamic: In mobile environments, information is typically incomplete and can change rapidly due to node mobility, so building trust in such environments is based on temporally and spatially local information [7]. In order to capture the dynamicity of trust, it should be expressed as a continuous variable, rather than as a binary or even discrete-valued entity. Trust is subjective: Different level of trust can be determined by a trustor node against the same trustee node due to different experiences derived from a dynamically changing network topology. Trust is not necessarily transitive: If A trusts B, and B trusts C, it does not guarantee A trusts C. Transitivity of trust between two entities to a third party requires two types of trust to be done by a trustor: trust in a trustee and trust in the trustee's recommendation of the third party [8]. Trust is asymmetric: Node A with higher capability (e.g., more energy or computational power) may not trust node B with lower capability at the same level that node B trusts node A.

2.2.2. **Establishment of Trust.** Two common ways to establish trust are through using policies or reputation. Hard evidence trust used in policies, and the estimation of trust used in reputation systems [9]. Policies determine specifically the conditions necessary to obtain trust, and can predetermine the actions and outcomes if certain conditions are met. Using policies to establish trust is based on managing and exchanging credentials and enforcing access policies. Reputation is an assessment based on the history of observations of or interactions with an entity. This assessment can be done either directly with the evaluator (subjective experience) or as reported by others (recommendations or third party verification). Using reputation to establish trust, focusing on the past performance or interactions for an entity which are combined to assess its future behavior. English et al. [10] defines four steps for establishing trust: trust formation, trust evolution, and trust exploitation. Trust formation is the process of establishing the initial trustworthiness value of each cooperator, then using the available trust evidences of the principal to set the initial trust value. If no evidence available for a principal regarding the specific action, it is possible use available trust evidence from other actions with the principal. Trust evolution is the evolution of trust values over time. New evidence from experience can modifies the stored trust value directly, producing a new trust value. Trust update is the process of adding experience evidence to the store of trust after each evaluation. The store contains the set of all trust evidences, and it is possible to re-evaluate trust values based on the most recent evidence. Trust exploitation is the process of determining the expected behavior of cooperator based on trust values of that cooperator.

2.3. Security

One of the major challenges of an oppnet is to timely detect and identify the malicious devices, and to prevent them from joining the network and ensure the privacy and security of the oppnet. Based on the standard ISO 7498-24 [11], there are eight security services with acronym CIA-AANN-A that define security are confidentiality, integrity, availability, authentication, access control, non-repudiation, notarization, auditability. Confidentiality is the property that information is not made available or disclosed to unauthorized individuals, entities, or processes. Integrity is the property that data has not been altered or destroyed in an unauthorized manner. Availability is the property of being accessible and useable upon demand by an authorized entity. Authentication is the corroboration that an entity is the one claimed, and the source of data received is as claimed. Access control is the prevention of unauthorized use of a resource. It includes the prevention of use of a resource (by an authorized entity) in an unauthorized manner. Non-repudiation is the prevention of entities' denial to be involved in all

or part of a communication. Notarization is the registration of data with a trusted third party that allows (to assure) the accuracy of its characteristics such as content, origin, time, and delivery. Auditability is the ability of a system to trace all actions related to a given asset.

2.4. Cooperation

Cooperation can be defined as a joint collaboration interaction between two or more principals (Ps), to perform one or more actions (As) on one of the principals' resources. There are five services for cooperation process, outlined in Figure 2, are cooperation request analyzer, cooperative risk assessment, cooperation decision, cooperation monitoring, and cooperation evaluation [10]. Functionally, cooperation services process the cooperation request denoted by *Req(P, A),* where *P* determines which node has to participate, *A* determines which action has to be done by *P* in cooperative processing. Cooperation services work in a sequence manner to determine whether the action *A* can take place by using the principal's *P* resources. In cooperation request analyzer service, the contents of the received cooperation request *Req(P, A)* is analyzed to determine whether *P* has the necessary resources to allow the action *A* to take place. The request analyzer provides cooperative risk assessment with the results of request analysis. Cooperative risk assessment determines whether the risks are acceptable to enable cooperation to proceed. It estimates the risk of interacting with a particular principal P for a particular action A based on the outcomes from cooperation request analyzer and trust exploitation. In cooperation decision service the decision about enabling cooperation process takes place. The cooperation decision made based on the outcomes from cooperative risk assessment. In cooperation monitoring service, the progress of the individual cooperation actions is monitored to ensure that the interaction is progressing towards the desired outcome, and a negative outcome predicted during the cooperative risk assessment for that interaction. In cooperation evaluation service, trust foundation is provided with the evaluation of the interactions. The evaluation based on the range of outcomes established during cooperative risk assessment.

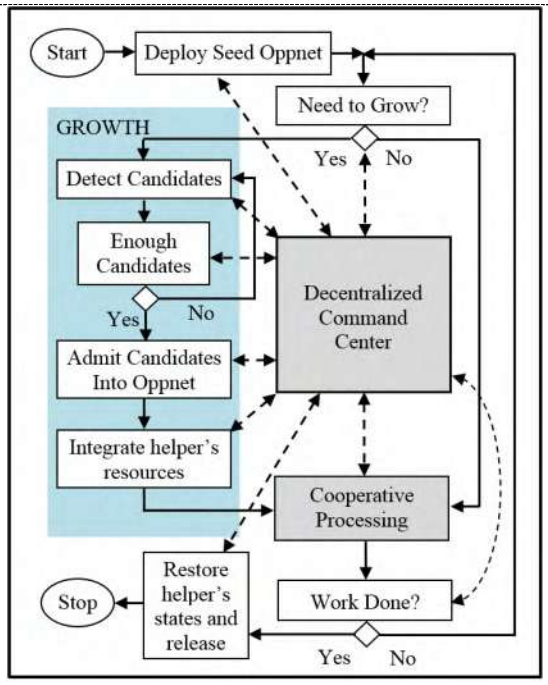

Figure 1. Oppnet operation flow diagram.

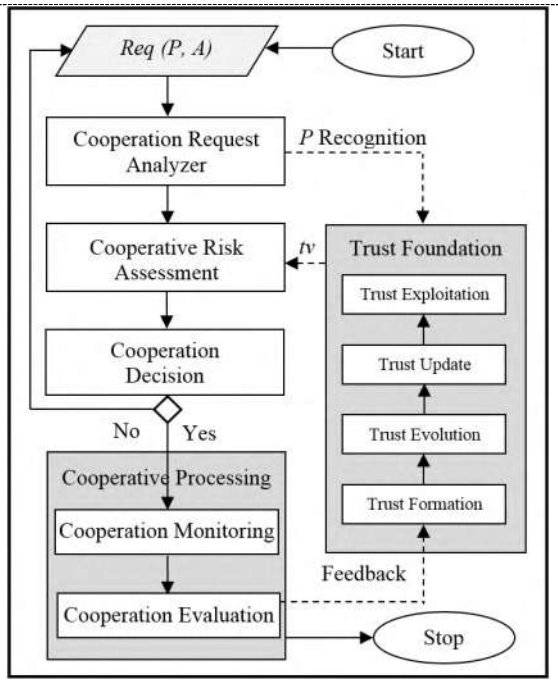

Figure 2. Cooperation process flow diagram.

3. Literature Review

Message forwarding opportunistic networks are wider investigated in the literature than opportunistic resource utilization networks. Although, they share that same opportunistic principle unless the latter is more general and includes opportunistic communication. This section outlines researchers' work in the literature regarding trust, security, and cooperation in opportunistic networks or opportunistic resource utilization networks and distinguishes our work from them.

In [3], the author proposed a virtual machine for opportunistic resource utilization networks as a universal standard for the application-level of oppnet resource sharing. Oppnet virtual machine (OVM) is defined as a set of primitives that are designed to create a middleware for application-level resource acquisition by oppnet-enabled devices and systems. Any computational entity can be oppnet-enabled by downloading and installing the OVM primitives that enables those entities acquire and communicate computational resources in an opportunistic manner. The author improved the original OVM primitives by developing non-monolithic OVM-based oppnet middleware to support a very broad and diverse set of applications. This work improved oppnet in terms of primitives and applications. While, our work improves oppnet in terms of security and cooperation. Wu et al. [12] provided a systematic description of security threats in opportunistic networks. They also proposed a general security architecture of opportunistic networks and analyzed many security aspects including access control and authentication, privacy protection, secure routing, cooperation mechanisms, and trust management. In addition, they surveyed various trust and security solutions for opportunistic networks. This work investigated security and trust management in opportunistic communication rather than opportunistic resource utilization, as we do. Yao et al. [13] proposed the incorporating social trust concept for the routing decision opportunistic networks. They presented a Trust Routing based on Social Similarity (TRSS) scheme based on the common interests or social similarities of nodes. Social features are extracted from the social history record of a given node in opportunistic network. They established social trust based on observed nodes' trustworthiness and based on direct or indirect recommendations. This work utilized social similarities to establish trust. While, we utilize actual cooperation experience to establish and maintain trust values for nodes. Kumar et al. [14] proposed altruism-dependent trust-based data forwarding mechanism, denoted ATDTN. In ATDTN, altruism value associated with each node representing its trust in the opportunistic network and determining its participation in forwarding messages or sharing resources. This study relied on altruism, which is established by social interactions, as a major factor of trust. While, we classify oppnet nodes based on their calculated trust values and manage their task assignment in opportunistic recourse utilization based on the calculated trust. Alajeely et al. [15] provided an overview of the major security issues in opportunistic networks and surveyed various security protection approaches to mitigating these issues. They described different types of attacks that can specifically affect routing in opportunistic networks, such as Blackhole attacks Wormhole attacks, Sybil attacks, Selective Dropping attacks, and Selfish attacks. Then, they outlined the defense against each type of attacks in terms of trust as a factor used in the defense process. Trust calculated mutually by interactive nodes through direct and indirect reputation and recommendation. This study utilized trust for security only. While, we utilize trust for security and cooperation to assure secure, effective, and efficient oppnet.

4. The Proposed TSCO Model

This section presents the proposed Trust based Secure and Collaborative Oppnet (TSCO) by outlining its static and dynamic architectures as well as the way of establishing trust based on the helpers classification described in Ref. [16].

4.1. Static TSCO Architecture

Figure 3 illustrates the static TSCO architecture, which includes four major components: oppnet, cooperation blocks, security services, and trust foundation. TSCO architecture components built in the matter that follows the basic oppnet operations to keep the functionality of oppnet. Security block consists of eight sub blocks; each represents a single security services (as explained in Subsection 2.3). Cooperation block consists of five sub blocks; each represents a single cooperation service in the cooperation process (as explained in Subsection 2.4). Trust Foundation acts as a basis for both cooperation services and security services. It sends *tv* for *P* to cooperative risk assessment to help determining risk level of *P* and to ensure that P satisfies security services. It also update trust value of an admitted helper based on information from cooperative processing unit that includes cooperation monitoring and cooperation evaluation.

4.2. Dynamic TSCO Architecture

Figure 4 shows the basic TSCO operations. DCC can grow the oppnet into the expanded oppnet by admitting other nodes. After determining enough candidates by DCC, cooperation request analyzer can analyze each cooperation request *Req(P, A)* to determine whether the helper *P* has the required resources to participate doing the action *A*. Then it feeds this information to the cooperative risk assessment. In this stage, cooperative risk assessment estimates every helper's risk with respect to its trust value; it also helps DCC to make decision about the admission of the candidate helpers. Once candidate helper admitted, this means it passed cooperative risk assessment, and it is expected to be cooperative. Then DCC integrates helper's resources in oppnet to start cooperative process. In this stage, the admitted helper will be under cooperation monitoring and evaluation stages to provide the information needed for trust calculation. Based on the cooperation monitoring and evaluation information, trust foundation starts calculating trust value for the admitted helper, and supplies cooperative risk assessment with this information. All the security, cooperation, and trust information about a specific helper stored in the DCC record for future references. In Figure 4, DCC controls every single block. However, control interactions by CC are not shown to avoid "crowding the picture." The solid arrows indicate control flow between architecture blocks, and broken lines indicate data flow.

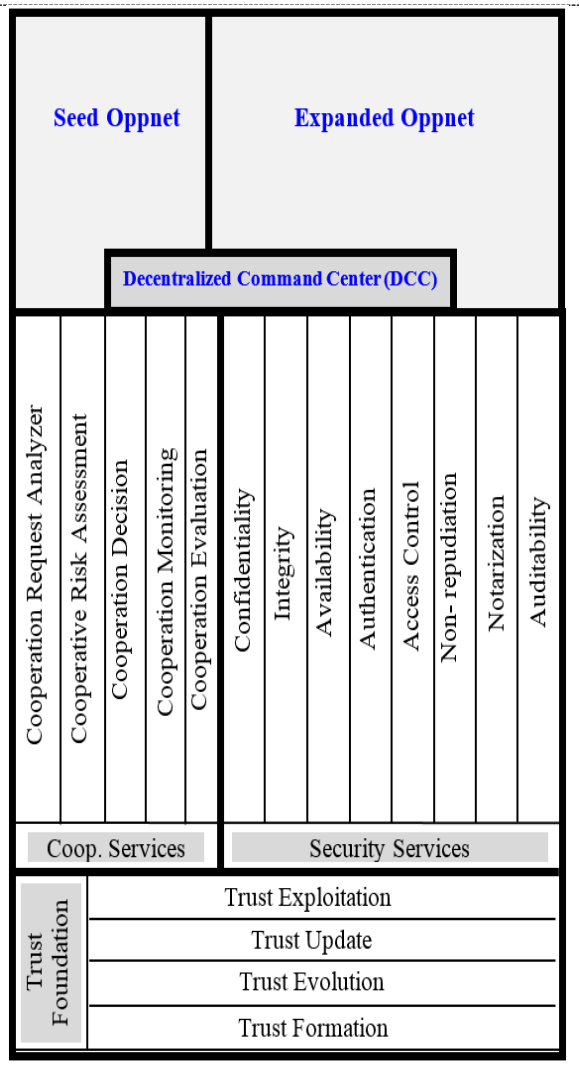

Figure 3. Static TSCO architecture.

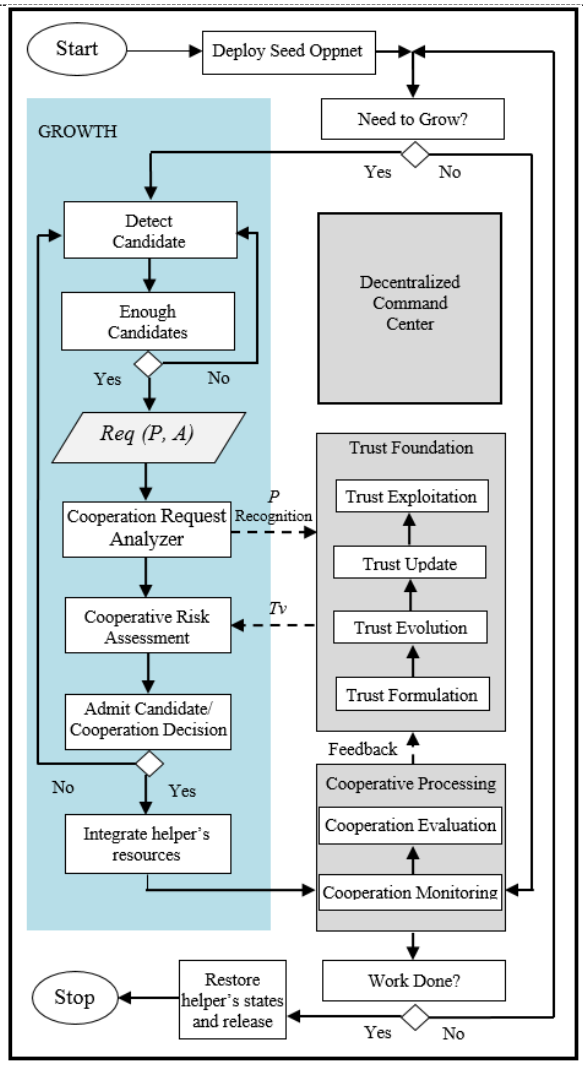

Figure 4. Dynamic TSCO architecture.

4.3. Establishment of Trust in TSCO

In TSCO system, DCC maintains trust value (*Tv*) for each helper *P* based on the set of all evidence values (EV) that related to the helper *P* including *first-hand experience* (EX) values and *second-hand reputation* (RP) values. Each of these sets of evidence has two subsets, positive and negative. For instance, EX represents the set of possible experience values for Helper *P*. Experience values consists of two subsets, $EX_{pos.}$ (positive experience) and $EX_{neg.}$ (negative experience) for the interactions. If there is no evidence related to the admitted helper *P*, DCC has to establish an Initial Trust Value (ITv) for *P*. Establishing an ITv in TSCO system depends on the helper type, based on the classification of helpers [16]. Table 1 illustrates estimate interval values for each helper type that can be establish as ITv. The evolution of a stored *Tv* value over time is important in TSCO system to ensure accuracy of *Tv*. For this reason, Trust Evolution takes a new piece of evidence and modifies the stored trust value *Tv* directly, producing a new trust value *Tv′*. After cooperative processing, new evidence outcome is an experience evidence that shoud be added to the stored trust information. This information contains all trust evidence, EV. When new ev′∈EV arrives as the latest experience of the helper, Trust Update

modifies EV to produce an updated set of trust evidence, EV′ [10].

Table 1. Initial and evolution of helpers' trust values.

Helper Type	Initial tv Range	tv Evolution	tv Change	Resulting tv Range
Private Unknown	0 - 50%	Up / Down	Large	0 - 70%
Public Unknown	50 - 70%	Up / Down	Medium	30 - 90%
Trusted Known	70 - 90%	Relatively Constant	Small	60 - 100%
Oppnet Reservists	90-100%	Constant	None	90 - 100%

5. Evaluation Framework

This section presents an evaluation framework for testing the feasibility and efficiency of the proposed TSCO model. The evaluation framework including experimental setup, simulation parameters, and evaluation metrics.

5.1. Experimental Setup

Simulation experiments are conducted for original oppnet model, which considered as a baseline in which a performance of TSCO compared with, and TSCO model. For the purpose of accurate comparison, experiments are designed to be implemented for both models (baseline and TSCO) simultaneously and within the same network configuration. The simulation is conducted using SimPy, a process-based discrete event simulation package based on standard Python. The simulation is implemented in the PyCharm IDE (Integrated Development Environment). The simulation runs on an Intel Core i7-4710 HQ 250 GHz processor with 8 GB RAM. To test TSCO performance on different network topology sizes, we have varied the size of expanded oppnet by considering five levels of scalable oppnet, namely, L_1, L_2, L_3, L_4, and L_5. These levels starting from small scale to a larger scale and so on. We consider these levels to simulate the realistic oppnet scenarios. Note that, within each level, many oppnet tasks can be done locally at the edge level. While, other oppnet tasks might require more communications to be done at fog or cloud levels [17].

5.2. Simulation Parameters

Three major types of nodes are defined and configured in the simulation are SEED, DCC, and HLPR. These nodes are the major actors in the simulation where the SEED (defined in Subsection 2.1) initiates oppnet growth process, the DCC (defined in Subsection 2.1) manages the growth and the cooperation processes, HLPR (helper) participates in the oppnet cooperation process. As a network node, we define two simulation parameters, CPU speed and the number of processing cores. The CPU speed is the maximum number of instructions in which a node's CPU can process per second. CPU speed defined in MIPS (Million Instructions Per Second) [18]. Note that DCC has higher computation power that both SEED and HLPR nodes due to the management tasks required by it. In addition, typically, SEED nodes have the lowest computation power in oppnet environment since they always need resources from others so they initiate oppnet to get help. Helper resources are defined in the simulation using two parameters: capacity, which define the number of computational resource a helper has; and queuing type, which defines how helper node handle multiple help request based on network queuing theory [19]. Three major types of packets are defined in the simulation are Help Request (HR), Normal Help (NH), and TSCO Help (TH). These packet types are configured using two parameters: packet size, which simulated as a random variable with Poisson distribution [20]; and packet processing efforts, which simulated as a random variable with Binomial distribution [21]. The type of carried packet into three types defines the network links: Help Request Link (HR-Link),

Normal Help Link (NH-Link), and TSCO Help Link (TH-Link). These link types are configured using two parameters: bandwidth, which is the maximum number of bits per second that can be transmitted via the link, defined by Mbps (Megabits per second) [22]; and propagation delay, which is a period from the instant when the last bit of a packet is placed onto a transmission link by the sending node till the instant when the last bit of the packet is received by the receiving node [23]. Trust value for each type of oppnet helpers (outlined in Table 1) is defined in the simulation for four classes of oppnet helpers: Private Unknown Helper (PrUH), Public Unknown Helper (PuUH), Trusted Known Helper (TKH), and Oppnet Reservists Helper (ORH). Each helper class is configured in the simulation using two parameters: Trust Value Range, which determines the minimum and maximum trust value this helper class can have; and Trust Value Probability, which simulated as a random variable with Uniform distribution [24]. Table 2 lists the simulation the abovementioned parameters.

Table 2. Simulation Parameters.

Parameter	Instance	Type	Value	Type	Value
Node	SEED DCC HLPR	CPU Speed (MIPS)	4000 10000 6000	Number of Cores	2 4 2
Resource	HLPR_REC	Capacity	2	Queuing Type	FIFO
Packet	HR NH TH	Packet Size (Poisson)	$\lambda = 10$ $\lambda = 20$ $\lambda = 20$	Processing Effort (Binomial)	$n = 30, p = 0.75$ $n = 30, p = 0.75$ $n = 30, p = 0.75$
Link	HR-Link NH-Link TH-Link	Bandwidth (Mbps)	50 100 120	Propagation Delay (ms)	2 4 4
Trust	PrUH PuUH TKH ORH	Trust Value Range	0 - 49 50 - 69 70 - 89 90 - 100	Trust Value Probability (Uniform)	$l = 0, h = 0.49$ $l = 0.5, h = 0.69$ $l = 0.7, h = 0.89$ $l = 0.9, h = 1$

5.3. Evaluation Metrics

Two metrics are considered in the simulation experiments are latency and success rate. The latency (LAT) for an oppnet task is defined as the period between the moment of submission of help request by seed node and the moment when competing the oppnet task. More specifically, LAT is the period from the instant when the *first* bit of HR is sent by a given SEED for a task till the instant when either the *last* bit of NH packet is delivered to SEED or the *last* bit of TH packet for this task is delivered to the SEED oppnet via DCC-HLPRs hope of communications. The success rate is defined as a number of successfully performed oppnet tasks to the number of total tasks in the experiment. We conducted two ways to accurately calculate success rate for oppnet task. First, we define a threshold in term of response time by helper to help request. The motivation for that is the mobility nature of oppnet helper, if a helper A within the seed oppnet reach at time t_1 and it receives the help request, there is no guarantee that at time t_{1+n}, the helper A is still in the reach of oppnet or it successfully forwarded the help request to other candidate helper. Second, we use the hypergeometric distribution [25], which is a discrete probability distribution that describes the probability of successes within a scale of events. Where uniform distribution used to calculate the probable range of success helps for the baseline and TSCO models and similarly the probable range of fail helps. Then, the binomial distribution used to calculate the probability of good samples (successes) and bad samples (fails) from the total sample size. Finally, hypergeometric distribution utilized to find the success rate of an experiment.

6. Results and Discussion

This section shows and discusses the experimental simulation results of using the proposed TSCO model as compared with the baseline (original oppnet model outlined and illustrated in Section 2.1 and Figure 1, respectively). According to our evaluation metrics (Subsection 5.3), experimental results have shown and discussed for each metric separately in a separate subsection.

6.1. Success Rate

Figure 5 shows the simulation experimental results regarding the absolute success rate . The simulation experiments are conducted for five levels of expanded oppnet are L_1, L_2, L_3, L_4, and L_5. For each level, the chart shows the total number of helps happened at that level of network configuration as well as the number of normal (baseline) success helps, which is used as the base in which the number of TSCO success helps compare with. The results show that with increasing the scale of oppnet from L_1 to L_5, the number of helps increase as well as the number of successes for both baseline and TSCO models. This is a normal phenomenon since based on the nature of oppnet structure and operation, the victims increases the probability of helps happened and hence increases the number of successes, accordingly. However, TSCO shows a higher number of success rate than the baseline for all levels. In the baseline oppnet, only 47% of total helps happened in the system are succeeded. While, in the TSCO system, 75% of total helps happened in the system are succeeded. Hence, TSCO shows a better performance than the baseline with 28% regarding the absolute success rate.

Figure 6 shows the simulation experimental results regarding the relative success rate. For each level, the chart shows the relative success rate at that level both the baseline and TSCO models. The experimental results show that with increasing the scale of oppnet from L_1 to L_5, the success rate is relatively stays stable with slightly increasing for both baseline and TSCO models. This is also a normal phenomenon since the success rate calculated relatively with the scale of victims. However, TSCO shows a higher success rate than the baseline for all levels. The average success rate for baseline is 44%. While, The average success rate for TSCO is 76%. Hence, TSCO over performances the baseline with 32% regarding the relative success rate.

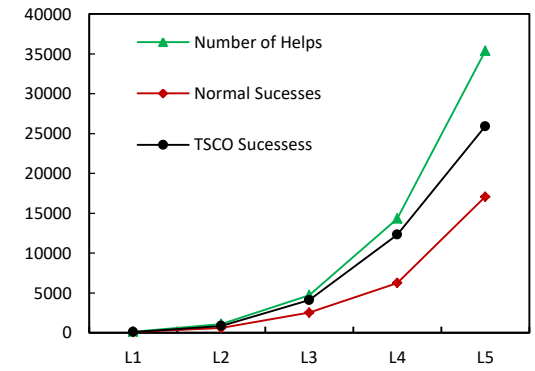

Figure 5. Absolute success rate .

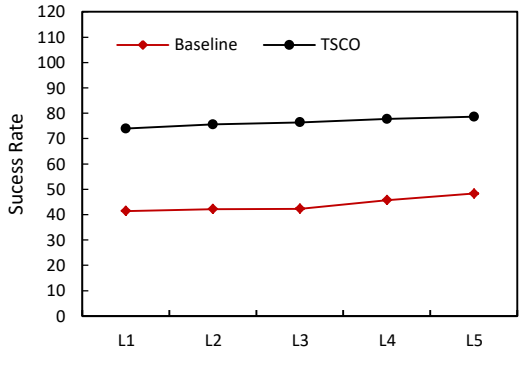

Figure 6. Relative success rate.

6.2. Latency

Figure 7 shows the simulation experimental results regarding the absolute latency. The simulation experiments are also conducted for five levels of expanded oppnet are L_1, L_2, L_3, L_4, and L_5. For each level, the chart shows the absolute latency at that level for both the baseline and TSCO models. The results show that with increasing the scale of oppnet from L1 to L5, the absolute latency increases slightly for both baseline and TSCO models. This is a normal phenomenon since the latency in this experiment is calculated as an accumulative quantity. Hence, increasing the scale of oppnet victims

increases the absolute latency, accordingly. However, TSCO shows a lower latency than the baseline for all levels. In average, TSCO has 35% less absolute latency than the baseline.

Figure 8 shows the simulation experimental results regarding the relative latency. For each level, the chart shows the relative latency at that level for both the baseline and TSCO models. The experimental results show that with increasing the scale of oppnet from L1 to L5, the relative latency is sharply decreasing for both baseline and TSCO models. This is a normal phenomenon since the latency is calculated relatively with the scale of victims. The absolute latency divided by the number of helps happened at each level and with increasing the scale by levels, the relative latency decreases accordingly. TSCO shows a lower relative latency than the baseline for all levels. In average, TSCO has 26% less relative latency than the baseline.

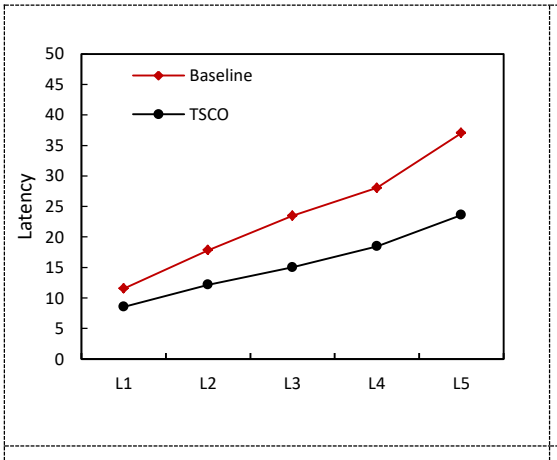

Figure 7. Absolute latency.

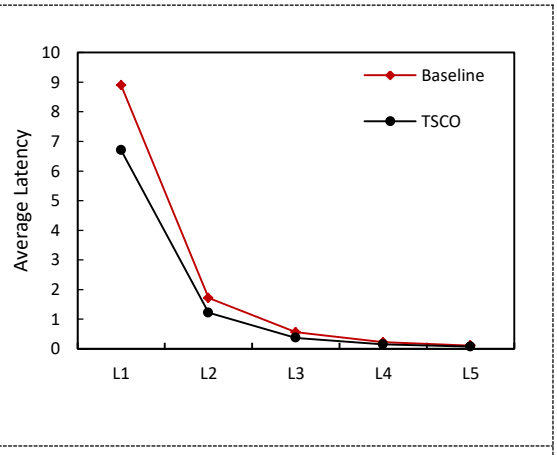

Figure 8. Relative latency.

7. Conclusions

Opportunistic resource utilization networks can be significantly optimized by increasing their performance in terms of security and cooperation. Adding security control to the oppnet architecture assures the protection from selfish or malicious helpers. Furthermore, adding cooperation control improves the reliability of oppnet performance. In our perspective, the common key to improve both security and cooperation in oppnet is Trust.

In this paper, we proposed a new oppnet paradigm denoted TSCO, which integrate security and cooperation controls based on trust with the original oppnet architecture. A theoretical background on the major research terminologies, including oppnet, trust, security, and cooperation, is provided. Then, we distinguished our work in the literature. A conceptual design is presented for the proposed TSCO model including its static and dynamic architectures.

To prove the feasibility and efficiency of the proposed TSCO model, we have introduced a framework of performance evaluation including simulation experimental setup, simulation parameters, and evaluation metrics. Experiments are conducted for both TSCO and the original oppnet, simultaneously. The experimental results show that TSCO over performed the original oppnet (as a baseline) regarding absolute and relative success rate with 28% and 32%, respectively. TSCO also have shown a better performance than the original oppnet regarding absolute and relative latency with 35% and 26%, respectively.

References

[1] M. A. Alduailij and L. T. Lilien, (2015). A collaborative healthcare application based on opportunistic resource utilization networks with OVM primitives. *International Conference on Collaboration Technologies and Systems (CTS)*, Atlanta, GA, 426-433.

[2] Yasmin, S., Qayyum, A., & Rais, R. N. B. (2017). Cooperation in opportunistic networks: an overlay approach for destination-dependent utility-based schemes. *Arabian Journal for Science and Engineering*, 42(2), 467-482.
[3] Alduailij, M. A. (2015). Design of Oppnet Virtual Machine for opportunistic resource utilization networks: A universal standard for application-level resource sharing. A Dissertation at Western Michigan University.
[4] Ciobanu, R. I., Marin, R. C., Dobre, C., & Cristea, V. (2017). Trust and reputation management for opportunistic dissemination. *Pervasive and Mobile Computing*, *36*, 44-56.
[5] Qin, X., Wang, X., Lin, Y., Wang, L., & Zhang, L. (2017, October). An efficient routing algorithm based on interest similarity and trust relationship between users in opportunistic networks. In *China Conference on Wireless Sensor Networks* (pp. 273-284). Springer, Singapore.
[6] Dhananjayan, G., & Subbiah, J. (2016). T2AR: trust-aware ad-hoc routing protocol for MANET. *SpringerPlus*, *5*(1), 995.
[7] Muhammad, S., Wang, L., & Yamin, B. (2017, October). Trust model based uncertainty analysis between multi-path routes in MANET using subjective logic. In *China Conference on Wireless Sensor Networks* (pp. 319-332). Springer, Singapore.
[8] Tong, X., Zhang, W., & Wang, Y. (2016, August). Research on the transitivity closure of trust network. In *2016 12th International Conference on Natural Computation, Fuzzy Systems and Knowledge Discovery (ICNC-FSKD)* (pp. 2070-2074). IEEE.
[9] Luo, T., Kanhere, S. S., Huang, J., Das, S. K., & Wu, F. (2017). Sustainable incentives for mobile crowdsensing: Auctions, lotteries, and trust and reputation systems. *IEEE Communications Magazine*, *55*(3), 68-74.
[10] English, C., Wagealla, W., Nixon, P., Terzis, S., Lowe, H., & McGettrick, A. (2003, May). Trusting collaboration in global computing systems. In *International Conference on Trust Management* (pp. 136-149). Springer, Berlin, Heidelberg.
[11] ISO, ISO/IEC 10181-2:1996, "Information technology - Open Systems Interconnection - Security frameworks for open systems: Authentication framework - Part 2," Last Accessed Feb. 2015. Available at: https://www.iso.org/obp/ui/#iso:std:iso-iec:10181:-2:ed-1:v1:en
[12] Wu, Y., Zhao, Y., Riguidel, M., Wang, G., & Yi, P. (2015). Security and trust management in opportunistic networks: a survey. *Security and Communication Networks*, *8*(9), 1812-1827.
[13] Yao, L., Man, Y., Huang, Z., Deng, J., & Wang, X. (2015). Secure routing based on social similarity in opportunistic networks. *IEEE Transactions on Wireless Communications*, *15*(1), 594-605.
[14] Kumar, A., Dhurandher, S. K., Woungang, I., Obaidat, M. S., Gupta, S., & Rodrigues, J. J. (2017). An altruism-based trust-dependent message forwarding protocol for opportunistic networks. *International Journal of Communication Systems*, *30*(10), e3232.
[15] Alajeely, M., Doss, R., & Ahmad, A. A. (2016). Security and trust in opportunistic networks–a survey. *IETE Technical Review*, *33*(3), 256-268.
[16] Tamez, E. B., Woungang, I., Lilien, L., & Denko, M. K. (2009, August). Trust management in opportunistic networks: A semantic web approach. In *2009 World Congress on Privacy, Security, Trust and the Management of e-Business* (pp. 235-238). IEEE.
[17] Al-Hasnawi, A., Carr, S. M., & Gupta, A. (2019). Fog-based local and remote policy enforcement for preserving data privacy in the Internet of Things. *Internet of Things*, *7*, 100069.
[18] "Instructions per second," Wikipedia. Accessed on Oct. 10, 2020, from: https://en.wikipedia.org/wiki/Instructions _ per _ second.
[19] Memon, R. A., Li, J. P., & Ahmed, J. (2019). Simulation model for blockchain systems using queuing theory. *Electronics*, *8*(2), 234.
[20] "Poisson Distribution." 2008–2018. Accessed on Oct. 15, 2020, from: https://docs.scipy.org/doc/numpy/reference/generated/numpy.random.poisson.html/numpy.random.poisson.

[21] "Binomial Distribution." 2008–2018. Accessed on Oct. 15, 2020, from: https://docs.scipy.org/doc/numpy/reference/generated/numpy.random.binomial.html#numpy.random.binomial.
[22] Cohen, M. A., Dennett, D. C., & Kanwisher, N. (2016). What is the bandwidth of perceptual experience?. *Trends in cognitive sciences*, *20*(5), 324-335.
[23] Appasani, B., & Mohanta, D. K. (2018). Co-optimal placement of PMUs and their communication infrastructure for minimization of propagation delay in the WAMS. *IEEE Transactions on Industrial Informatics*, *14*(5), 2120-2132.
[24] "Discrete Uniform Distribution." 2008–2018. Accessed on Oct. 15, 2020, from: https://docs.scipy.org/doc/scipy/reference/tutorial/stats/discrete _ randint. html.
[25] "hypergeometric Distribution." 2008–2018. Accessed on Oct. 20, 2020, from: https://docs.scipy.org/doc/scipy/reference/generated/scipy.stats.hypergeom.html.

Using Chebyshev Polynomials in Solving Diffusion Equations

Using Chebyshev Polynomials in Solving Diffusion Equations

Ghuson S Abed

University of Information Technology and Communications, Iraq

E-mail: Ghsonabed.2019@uoitc.edu.iq

Abstract. In this work, we modified Chebyshev polynomials of the first kind to match the characteristics of a second order differential equation that is a result of a separation of the variable technique used to solve a partial differential diffusion equation. The resultant polynomials solution in one spatial dimension is found and the corresponding changing parameters for the first order differential equation in time are extracted accordingly. The method is tested for applicability, stability, and convergence.

1. Introduction

Differential Equations (DEs) are widely used as models for variables behavior in many phenomena in different fields of science. While setting DE to the model certain phenomenon can be achieved if all the variables, parameters, and relations are known, the solution of this DE is another story. An only a small fraction of different types of DEs can be solved analytically and exactly, while most of them have no known analytical exact solution. Partial Differential Equations (PDEs) represent a special type of DEs, where two or more independent variables exist, and they have special importance in the fields of engineering and physics. PDEs have no analytical exact solution in most cases; so many techniques are used to find an approximate solution instead. These techniques can be classified into two major types: numerical solution and series solution. Each technique has its advantages and disadvantages. The numerical solution, mainly by using a finite difference technique, has the advantages of both simplicity and wide applicability if convergence criteria are followed. The disadvantage of the numerical solution is the non function results representation, the result is only values of the variables at the limited number of nodes specified by the solution. The series solution has the advantage of representing the solution as a sum of analytical functions applied at all the space of the problem, but to achieve this task more complicated steps and different approaches are needed for different DEs.One of the most powerful methods used to solve PDEs is using Orthogonal Polynomials (OPs) together with the separation of variables technique [17, 18, 3, 19, 9]. Different other techniques also used such as the Fokas method [6, 1, 2]. There are different types of OPs, most of them were used for solving DEs. Among them, Fourier series are widely used, due to their characters that their second derivatives are a constant multiple of their values that match, widely used, second order DEs [26, 25, 15, 12]. But when the Fourier series is not compatible with the problem symmetry and\or boundary values, then other OPs can be used, where they can be matched to the problem boundary conditions [7,4,21,24,16,5], or they can be matched to the problem symmetry [20] and develop a correct solution. Chebyshev Polynomials CPs are OPs, which have many interesting properties [22, 29, 11]. CPs are widely used in fitting due to their high efficiency in reducing the error of interpolation [27], and for that, they are used to find the particular solution of different types of DEs [23].CPs are also used in solving different types of DEs [8,13,10,28].

In this work we used CPs of the first kind [22] and the separation of variables technique, to solve the diffusion equation. CPs is modified to match the diffusion equation characteristics and boundary conditions. The strategy is tested for convergence and stability, and the results are compared with that of well-known method of using the Fourier series and separation of variables that compatible with the chosen examples.

2. Problem definitions:

2.1 Diffusion equation

The diffusion equation represents a time varying, the spatial balance of specific particles that are generated, absorbed, and leaked out/in due to non field diffusion [14].

Diffusion equation in a homogeneous medium can be written as:

$$\frac{1}{v}\frac{\partial \emptyset(\bar{r},t)}{\partial t} - \mathrm{D}\,\nabla^2\emptyset(\bar{r},t) = s(\bar{r},t) - \sum_a .\emptyset(\bar{r},t) \tag{1}$$

Where:
First term: Particles flux rate of change with time
Second term: Particles leakage rate
Third term: Particles generation rate
Fourth term: particles absorbing rate

2.2 Orthogonal series

Any continuous function can be expanded in an infinite series as:

$$f(x) = \sum_{i=0}^{\infty} a_i . s_i(x) \tag{2}$$

An orthogonal series is a special type, with the property:

$$\int_{x1}^{x2} s_i(x) \times s_j(x) \times w(x) = \begin{cases} 0 & i \neq j \\ constant & i = j \end{cases} \tag{3}$$

Chebyshev Polynomials $\sum_{i=0}^{\infty} a_i . T_i(x)$, and trigonometric polynomials $\sum_{i=0}^{\infty} a_i . \cos(ix)$, are examples of orthogonal polynomials.

2.3 Problem setting and examples

Normalizing the problem, eq. (1), by setting: $v = 1,\ D = 1,\ \sum_a = 1$ and let: $s(x,t) = K.\sum_a \emptyset(x,t)$, $K: constant$. Equation (1) in one spatial dimension will be

$$\frac{\partial \emptyset(x,t)}{\partial t} - \frac{\partial^2 \emptyset(x,t)}{\partial x^2} = (k-1)\,\emptyset(x,t) \tag{4}$$

The method will be tested for two examples:
Example A, have a spatial symmetrical initial condition:

$$\emptyset(x,0) = 4x(1-x);\ \emptyset(0,t) = 0;\ \emptyset(1,t) = 0 \tag{5A}$$

Example B, asymmetrical initial condition:

$$\emptyset(x,0) = x(1-x)(2-x)(3-x);\ \emptyset(0,t) = 0;\ \emptyset(1,t) = 0 \quad (5B)$$

3. Solution using Fourier analysis and Separation of Variables (SFASV).

Let

$$\emptyset(x,t) = \emptyset x(x).\emptyset t(t) \quad (6)$$

Equation (4) will be:

$$\emptyset x(x)\frac{d\emptyset t(t)}{dt} - \emptyset t(t)\frac{\mathrm{d}^2\emptyset x(x)}{\mathrm{dx}^2} = (k-1)\,\emptyset x(x).\emptyset t(t) \quad (7)$$

$$\frac{1}{\emptyset t(t)}\frac{d\emptyset t(t)}{dt} - \frac{1}{\emptyset x(x)}\frac{\mathrm{d}^2\emptyset x(x)}{\mathrm{d}x^2} = (k-1) \quad (8)$$

Equation (8) can be split to two equations:

$$\frac{1}{\emptyset t(t)}\frac{d\emptyset t(t)}{dt} = a_1 \quad (9)$$

$$\frac{1}{\emptyset x(x)}\frac{d^2\emptyset x(x)}{dx^2} = -(b_1)^2 \quad (10)$$

Where their solutions are:

$$\emptyset t(t) = A2.e^{a_1.t} \quad (11)$$

$$\emptyset x(x) = B1.cos(b_1.x) + B2.sin\,(b_1.x) \quad (12)$$

The general solution will be

$$\emptyset(x,t) = [C1.cos(b_1.x) + C2.sin\,(b_1.x)].e^{a_1.t} \quad (13)$$

From the boundary condition $\emptyset(0,t) = 0$, one can find that C1=0.
From the boundary condition $\emptyset(1,t) = 0$, one can find that:$b_1 = n.\pi,\ \ n = 1(1)\infty$
Note that $a_1 + (b_1)^2 = (k-1)$, hence $a_1 = (k-1) - (n\pi)^2$
Then the solution will be:

$$\emptyset(x,t) = \sum_{n=1(1)\infty} C_n.sin\,(n\pi.x)\,.e^{\left((k-1)-(n\pi)^2\right).t} \quad (14)$$

And from the initial condition: $\emptyset(x,0) = 4x(1-x)$

$$\emptyset(x,0) = \sum_{n=1(1)\infty} C_n.sin\,(n\pi.x) \quad (15)$$

This will give:

$$C_n = 2\int_0^1 \emptyset(x,0).sin(n\pi.x)\,.dx \quad (16)$$

Moreover, for the given examples:

$$C_n = 2\int_0^1 4x(1-x).\sin(n\pi.x)\,.dx \tag{17A}$$

$$C_n = 2\int_0^1 x(1-x)(2-x)(3-x).\sin(n\pi.x)\,.dx \tag{17B}$$

$$C_n = \left[\frac{32}{(n\pi)^3}\right], \quad n = 1(2)\infty\,, odd \tag{18A}$$

$$C_n = 0, \quad n = even$$

$$C_n = \left[\frac{48}{(n\pi)^3}\right], \quad n = 2(2)\infty\,, even \tag{18B}$$

$$C_n = \left[\frac{40}{(n\pi)^3} - \frac{96}{(n\pi)^5}\right], \quad n = 1(2)\infty\,, odd$$

Then (14) will be:

$$\emptyset(x,t) = \sum_{n=1(2)\infty}\left[\frac{32}{(n\pi)^3}\right].\sin(n\pi.x).\exp\left(\left((k-1)-(n\pi)^2\right).t\right) \tag{19A}$$

$$\emptyset(x,t) = \sum_{n=2(2)\infty}\left[\frac{48}{(n\pi)^3}\right].sin(n\pi.x).exp\left(\left((k-1)-(n\pi)^2\right).t\right) + \sum_{n=1(2)\infty}\left[\frac{40}{(n\pi)^3} - \frac{96}{(n\pi)^5}\right].sin(n\pi.x).exp\left(\left((k-1)-(n\pi)^2\right).t\right) \tag{19B}$$

4. Solution using Chebyshev Polynomials and Separation of Variables (SCPSV).
Chebyshev polynomials of the first kind have the following recurrence relations [22].

$$T_1(x) = 1, \qquad T_2(x) = x, \quad T_{n+1}(x) = 2x.T_n(x) - T_{n-1}(x)$$

They are listed with their second derivatives up to i=9 in Table1.

Table1: Some Chebyshev first kind polynomials, and their second derivatives.

i	$T_i(x)$	$T_i''(x)$
1	1	0
2	X	0
3	$2x^2$-1	4
4	$4x^3$-3x	24x
5	$8x^4$-$8x^2$+1	$96x^2$-16
6	$16x^5$-$20x^3$+5x	$320x^3$-120x
7	$32x^6$-$48x^4$+$18x^2$-1	$960x^4$-$576x^2$+36
8	$64x^7$-$112x^5$+$56x^3$-7x	$2688x^5$-$2240x^3$+336x
9	$128x^8$-$256x^6$+$160x^4$-$32x^2$+1	$7168x^6$-$7680x^4$+$1920x^2$-64

We have equation (4): $\frac{\partial\emptyset(x,t)}{\partial t} - \frac{\partial^2\emptyset(x,t)}{\partial x^2} = (k-1)\,\emptyset(x,t)$, and the boundaries are: x= [0,1], and $t_{initial}$ =0.

Note that for the problem {x=[0,1], t=[0,∞)}, while Chebyshev polynomials are defined in the interval {y=(-1,1)}. Therefore, axis transformation is required. Let: $x = \frac{y+1}{2},\ y = 2x - 1$. Then (4, 9, and 10) will be:

$$\frac{\partial \emptyset(y,t)}{\partial t} - 4\frac{\partial^2 \emptyset(y,t)}{\partial y^2} = (k-1)\,\emptyset(y,t) \tag{4.1}$$

$$\frac{1}{\emptyset t(t)}\frac{d\emptyset t(t)}{dt} = a_1 \tag{4.2}$$

$$\frac{d^2 \emptyset y(y)}{dy^2} = -\left(\frac{b_1}{2}\right)^2 \emptyset y(y) \tag{4.3}$$

The boundaries are y= [-1,1], and $t_{initial}$=0, and where for example (A):
$\emptyset(y,0) = (1-y^2);\ \emptyset(-1,t) = 0;\ \emptyset(1,t) = 0$
And for example (B):$\emptyset(y,0) = \left(\frac{15-8y-14y^2+8y^3-y^4)}{16}\right);\ \emptyset(-1,t) = 0;\ \emptyset(1,t) = 0$
Let the solution of (10.1) is:

$$\emptyset y(y) = \sum_{i=1}^{\infty} c_i . \emptyset y_i(y) \tag{20}$$

$$\emptyset y_i(y) = (T_i(y) - T_{i+2}(y)) + EP \tag{21}$$

And the total solution is:

$$\emptyset(y,t) = \sum_{i=1}^{\infty} c_i . \emptyset y_i(y) . \exp(a_{1i} . t)$$
$$a_{1i} = (k-1) - (i\pi)^2 \tag{22}$$

Where Equation Polynomial is an extension to $(T_i(y) - T_{i+2}(y))$ that will make the second derivative of $\emptyset y_i(y)$ a constant, $\left(-\left(\frac{b_i}{2}\right)^2\right)$, multiple of $\emptyset y_i(y)$ itself, and matching the characteristics of (10.1). To find the *EP(extended polynomial)*, multiply the second term in the function $(T_i(y) - T_{i+2}(y))$ by the value of $\left(-\left(\frac{b_i}{2}\right)^2\right)$, and add it to the second derivative, and add its double integral to the function, and so on. Some $\emptyset y_i(y)$, their second derivatives, and the corresponding $\left(-\left(\frac{b_i}{2}\right)^2\right)$ values are shown in Table2.

Table2: Some $\emptyset y_i(y)$, their second derivatives, and $\left(-\left(\frac{b_i}{2}\right)^2\right)$ values.

i	$T_i(y)$	$\emptyset y_i(y) = T_i(y) - T_{i+2}(y)$ + EP	$\frac{d^2 \emptyset y(y)}{dy^2}$	$-\left(\frac{b_i}{2}\right)^2$
1	1	$-y^{10}/56700+y^8/1260-y^6/45+y^4/3-2y^2+2$	$-y^8/630+2y^6/45-2y^4/3+4y^2-4$	-2
2	y	$-3y^{11}/3850+y^9/70-6y^7/35+6y^5/5-4y^3+4y$	$-3y^9/35+36y^7/35-36y^5/5+24y^3-24y$	-6
3	$2y^2-1$	$3125y^{14}/13621608-625y^{12}/149688+125y^{10}/2268-125y^8/252+25y^6/9-y^4/3-8y^4+10y^2-2$	$3125y^{12}/74844-625y^{10}/1134+625y^8/126-250y^6/9+250y^4/3-4y^2-96y^2+20$	-10

4	$4y^3-3y$	$-59049\ y^{17}/238238000 +6561\ y^{15}/1751750 -8(18)^7\ y^{13}/(13!) +8(18)^5\ y^{11}/(11!) -8(18)^4\ y^9/(9!) +8(18)^3\ y^7/(7!) -28\ y^5/5-16y^5+24y^3-8y$	$-59049\ y^{15}/875875 +19683\ y^{13}/25025 -13122\ y^{11}/1925 +1458\ y^9/35 -5832\ y^7/35 +1944\ y^5/5-112\ y^3-320\ y^3+144y$	-18

Note that:

$(b_i)^2(s)=4*s^2+4,$ s=odd (23)

$(b_i)^2(s)=4*s^2+8,$ s=even (24)

$$\emptyset y_s(odd)(y) = \sum_{j=1,3,5}^{\infty} (-1)^{\frac{s-1}{2}} (2) \left(\frac{b_s^2}{4}\right)^{\frac{j-1}{2}} \cdot \frac{y^{j-1}}{(j-1)!} \quad (25)$$

$$\emptyset y_s(even)(y) = \sum_{j=2,4,6}^{\infty} (-1)^{\frac{s+2}{2}} (2s) \left(\frac{b_s^2}{4}\right)^{\frac{j}{2}-1} \cdot \frac{y^{j-1}}{(j-1)!} \quad (26)$$

Note that the solution in (22), SCPSV, is a floating solution with respect to the boundary conditions. This represents an advantage, that it can be used for any boundary conditions while SFASV is limited to zero boundary conditions. To match the solution to the problem boundary conditions, the stated boundary conditions and that obtained from the floating solution are matched by a quadratic function in the spatial dimension, since it is the order of $\emptyset y_1(y)$. This show reasonable stability and convergence.

5. Results and discussion:

The (SFASV) is found according to (19) for the two examples. The solutions are modeled using Matlab, and it is found that the results are stable for N=7 (n truncated at 7). The (SCPSV) are also found according to (22) using Matlab, for different values of N (series truncation value of i), where $\emptyset y_i(y)$ are found according to (25 &26) and where j truncated at different (M_i) values (M=1, 2, &3 are used), and where for M>3 there are no effective changes in the results. (bi) values are found by (23&24) and C_i values are found by a least-square fitting of $\emptyset y_i(y)$ to the initial condition, according to (20).The total transient solutions for (k=20, t_{final}= 0.1) by SFASV with N=7 and by SCPSV with N=25, M=3 are shown in Fig. (1) for example A and in Fig. (2) for Example B. While total transient solution figures show no differences between the two methods, one can use better descriptive comparisons. Fig. (3&4) shows the solutions by SCPSV for different N&M values compared to the solution by SFASV with N=7, for examples A & B respectively. Fig. (5) shows an average of the absolute difference of the whole solutions between SFASV with N=7 and SCPSV for different N & M values, for example, B. Example A shows the same behavior. Figures (3, 4 &5) show clearly the SCPSV stability and convergence with N & M values.

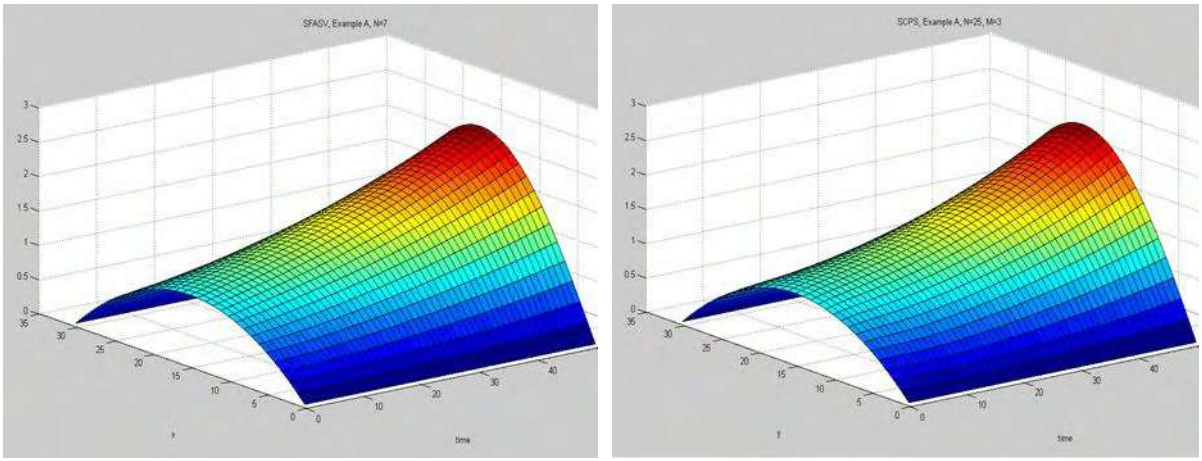

Fig (1): Comparison between SFASV & SCPSV for examples A

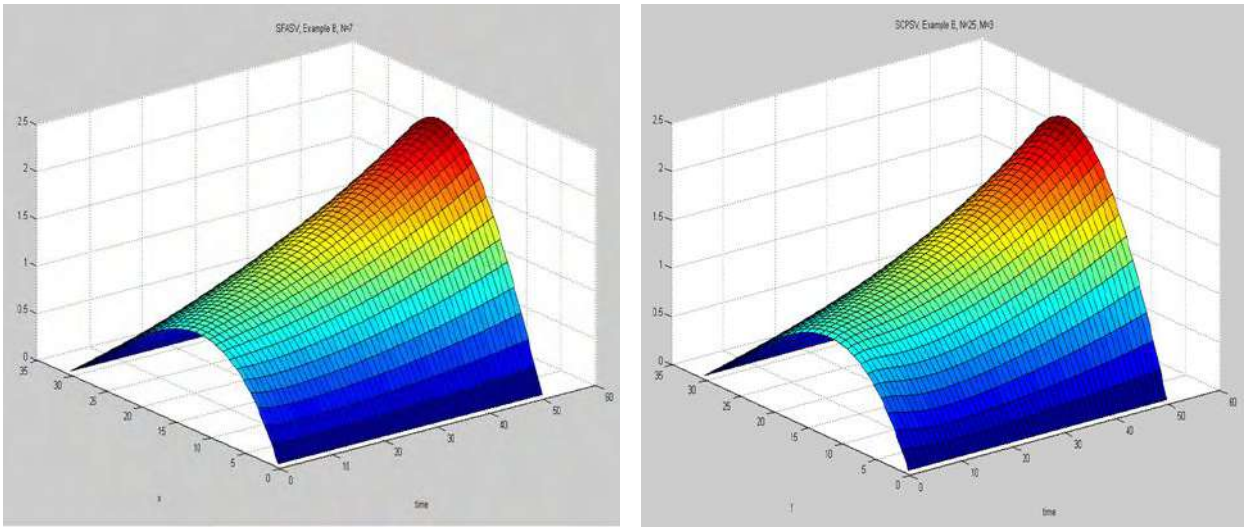

Fig (2): Comparison between SFASV & SCPSV for examples B

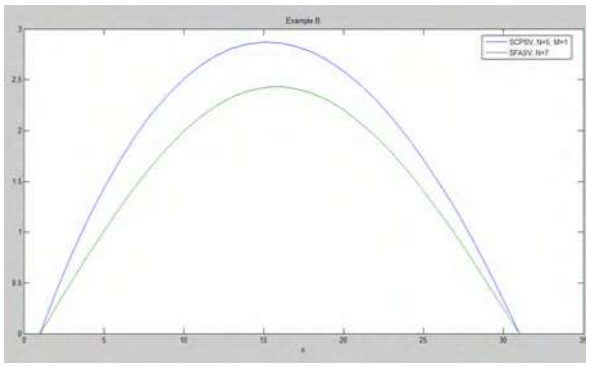

N=5, M=1

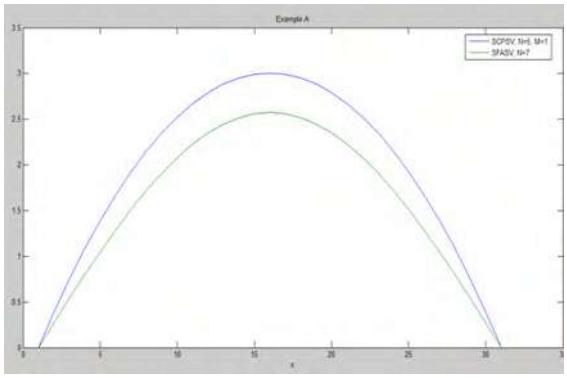

N=5, M=1

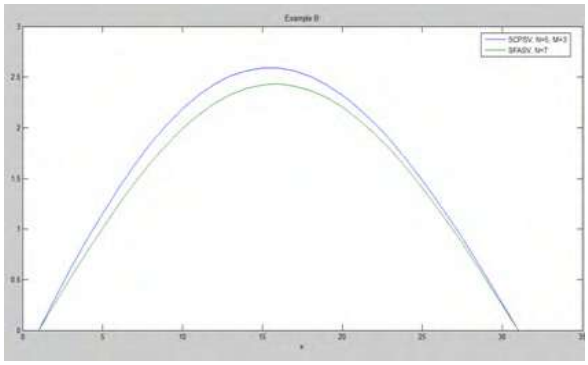

N=5, M=3

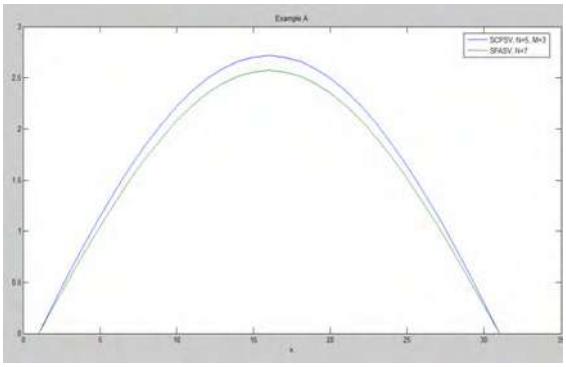

N=5, M=3

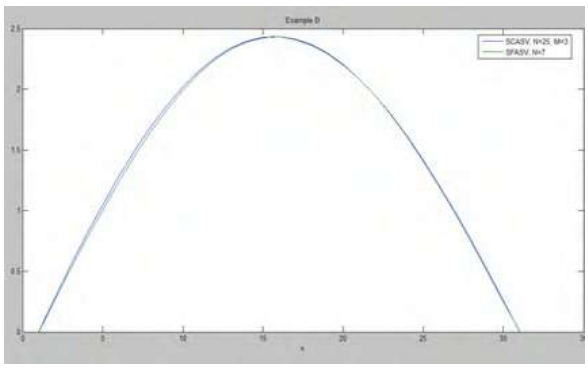

N=25, M=3

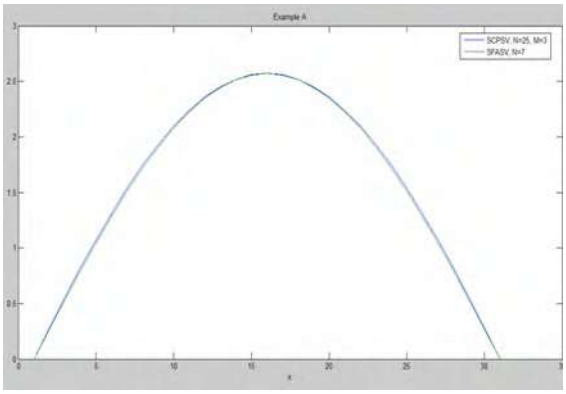

N=25, M=3

Fig (3): The solution at $t_{ini.}$= 0.1, by SCPSV for different N &M values compared to SFASV solution with N=7, for Example B.

Fig (4): The solution at $t_{ini.}$=0.1, by SCPSV for different N &M values compared to SFASV solution with N=7, for Example A

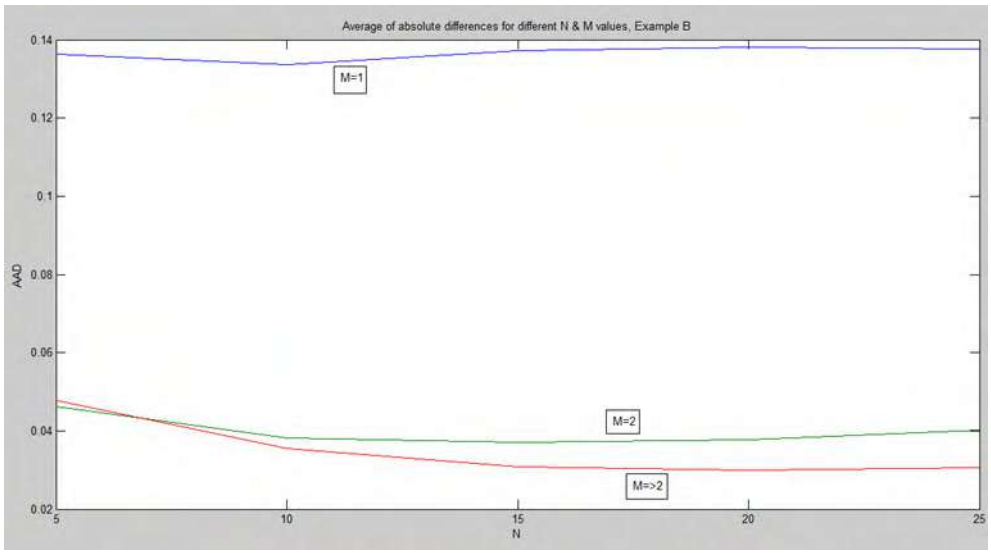

Fig(5): Average of the absolute difference of the whole solutions between SFASV with N=7 and SCASV, for different N & M values, for example B.

References

[1] A. S. Fokas2002 A new transform method for evolution partial differential equations *IMA J Appl. Math.***67**(6) 559-590
[2] A. S. Fokas and B. Pelloni 2005 A transform method for linear evolution PDEs on a finite interval *IMA J. Appl. Math*, **70**(4) 564-587
[3] A. S. Fokas and B. Pelloni 2014 Unified transform for boundary value problems: (eds*) Applications and advanced, Society for Industrial and Applied Mathematics*.
[4] J. M. Kosterlitz, 2017 Nobel lecture: Topological defects and phase transitions *Reviews of Modern Physics* **89** (4) 040-501
[5] A. Zenginoglu 2011 Hyperboloidal layers for hyperbolic equations on unbounded geometris *J. Comp. Phys.*, **230** 2286-2302
[6] B. Deconinck, T. Trogdon, and V. Vasan 2014 The method of Fokas for solving linear partial differential equations *SIAM Review* **56** 159-186
[7] D. Givoli 2004 High order local non-reflecting boundary conditions: a review *wave motion* **39** 319-326
[8] G. M. Caporale, M. Cerrato 2010 Using Chebyshev polynomials to approximate partial differential equations *Computational Economics* **35**(3) 235-244
[9] G. M. Vasil, K. J. Burns, D. Lecoanet, S. Olver, B. P. Brown, and J. S. Oishi 2016 Tensor calculus in polar coordinates using Jacobi polynomials *J. Comp. Phys.* **325** 53-73
[10] Hornr, T. S., Chebyshev 1977 Polynomials in the solution of ordinary and partial differential equations, *PhD Thesis* Department of Mathematics University of Wollongong
[11] Y.Tian 2006 Reducing order of derivatives and derivation of coefficients for chebyshev polynomial approximation, *preprint*
[12] H. F. Weinberger 1995 A first course in partial differential equations with complex variables and transform methods Dover Publications *Inc., New York, NY*
[13] J. Ding, H. Y. Tian and C. S. Chen 2009 The recursive formulation of particular solutions for inhomogeneous elliptic PDEs with chebyshev basis functions *Communications in Computational Physics* **5** 942-958
[14] J. R. Lamarsh 1983 Introduction to Nuclear Engineering *Addison-Wesley Publishing Company*
[15] J. Kevorkian1990 Partial differential equations *The Wadsworth & Brooks/Cole Mathematics Series. Wadsworth & Brooks/Cole Advanced Books & Software, Paci_c Grove, CA*
[16] J. Szeftel 2006 A nonlinear approach to absorbing boundary conditions for the semi-linear wave equation, *Math. Comput* **75** 565-594
[17] K. Atkinson, D. Chien and O. Hansen 2010 A spectral method for elliptic equations: the Dirichlet problem *Advances in Computational* Mathematics **33** 169-189
[18] K. Atkinson, D. Chien and O. Hansen 2011 A spectral method for elliptic equations: the Neumann problem *Advances in Computational Mathematics* **34** 295-317
[19] K. H. Kwon, D. W. Lee and L. L. Littlejohn 1997 Differential equations having orthogonal polynomial solutions *Journal of Computational and Applied Mathematics*
[20] K. H. Kwon, L. L. Littlejohn and B. H. Yoo 1994 Characterization of orthogonal polynomials satisfying differential equations, *SIAM J. Math. Anal* **25**(3) 976-990
[21] L. L. Littlejohn and A. M. Krall 1989 Orthogonal polynomials and higher order singular strum Liouville systems *Acta Appl. Math* **17** 99-170
[22] F. W. J. Olver, A. B. Olde Daalhuis, D. W. Lozier, B. I. Schneider, R. F. Boisvert, C. W. Clark, B. R. Miller, and B. V. Saunders 2019 NIST Digital Library of Mathematical Functions *http://dlmf.nist.gov/, release* **1**.0.22, eds
[23] Robertson and Amber Sumner 2013 Chebyshev Polynomial Approximation to Solutions of Ordinary Differential Equations *Undergraduate Theses*, Paper **1**
[24] R. M. Slevinsky 2018 On the use of Hahn's asymptotic formula and stabilized recurrence for a fast, simple, and stable Chebshev-Jacobi transform *IMA J. Numer. Anal* **38** 102-124

[25] R. B. Guenther and J. W. Lee 1996 Partial differential equations of mathematical physics and integral equations *Dover Publications Inc., Mineola, NY*
[26] S. J. Farlow 1993 Partial differential equations for scientists and engineers *Dover Publications Inc., New York, NY*
[27] S. Reutskiy and C.S. Chen 2006 Approximation of multivariate functions and evaluation of particular solutions using chebyshev polynomial and trigonometric basis functions, International *Journal for Numerical Methods in Engineering* **67** 1811-1829
[28] S. Reutskiy, C. S. Chen and H. Y. Tian 2008 A boundary mesh-less method using chebyshev interpolation and trigonometric basis functions for solving heat conduction problems, International *Journal for Numerical Methods in Engineering* **74** 1621-1644
[29] Theodore J. Rivlin 1990 Chebyshev Polynomials: From Approximation Theory to Algebra and Number Theory *Wiley and Sons Copyright (C) by Wiley-Inter-science.*

Three Weighted Residuals Methods for Solving the Nonlinear Thin Film Flow Problem

Three Weighted Residuals Methods for Solving the Nonlinear Thin Film Flow Problem

Areej Salah Mohammed* and
Majeed A Al-Jawary

Department of mathematics, college of education for pure sciences (Ibn AL-Haitham) / University of Baghdad, Baghdad, Iraq.

E-mail: areej.s.m@ihcoedu.uobaghdad.edu.iq

Abstract. In this paper, the methods of weighted residuals: Collocation Method (CM), Least Squares Method (LSM) and Galerkin Method (GM) are used to solve the thin film flow (TFF) equation. The weighted residual methods were implemented to get an approximate solution to the TFF equation. The accuracy of the obtained results is checked by calculating the maximum error remainder functions (MER). Moreover, the outcomes were examined in comparison with the 4th-order Runge-Kutta method (RK4) and good agreements have been achieved. All the evaluations have been successfully implemented by using the computer system Mathematica®10.

1. Introduction

Physical phenomena and engineering problems are often formulated in the form of ordinary differential equations with initial or boundary conditions. Many researchers have studied the exact or approximate solution of these types of equations [1, 2].

Thin liquid films are important in many applications, for example, the non-Newtonian fluids are polymer, oils, and greases, melts, blood and drilling muds. Solving the nonlinear problems is still not an easy task, and the exact solution cannot be obtained for many problems, therefore, either approximate or numerical solutions can be achieved. Many researchers have studied and addressed non-Newtonian fluid behavior problems with a wide range of applications [3, 4].

During the past few years many researchers have been interested to study the non-Newtonian fluids, thin film equation and treated by using different analytic methods such as: He [5] has solved the TFF equation by using the variational iteration method (VIM), AL-Jawary [6] solved the TFF equation by Temimi and Ansari method (TAM), Al-Jawary *et al*.[7] applied the Banach contraction principle method (BCPM) to find the approximate solutions of the nonlinear TFF equation and made a comparison with the solutions obtained from the variational iteration method and the homotopy perturbation method. Moreover, Sajid and Hayat [8] applied the homotopy perturbation method to provide the analytic solutions to two TFF equations of third order. Also, Manafian and Sindi [9] have solved the TFF equation by the optimal homotopy asymptotic method (OHAM).

On the other hand, there are accurate and reliable approximate techniques used to solve differential equations: the Collocation method, least square method and Galerkin method. Arnau et al. [10] introduced and used a new method constructed on a polynomial collocation to solve the models of one-dimensional flow in the systems of intake and exhaust of interior combustion engines. Also, Aswhad [11] applied the collocation method with the Bernstein polynomials as a basis function to solve the first

order linear delay differential equations approximated. Moreover, Vaferi *et al*. [12] presented the transient pressure response study by using the method of orthogonal collocation to solve the diffusion equation in the system of radial transient flow, Raghad *et al*. [13] obtained the approximate solutions for nth-order retarded by using Collocation method with the aid of B-Spline functions and Weddle method, Ahuja [14] obtained the solution using the technique of normal modes and weighted residual Galerkin approximation. Also, Ganji and Hatami [15] have been applied the collocation, Galerkin and least square methods for solving Jeffery-Hamel Flow. Daşcioğlu and Acar [16] used the collocation method for approximate solutions of initial and boundary value problems. Furthermore, Al-Hawasy and Jaber [17] used the Galerkin method to demonstrate the existence and uniqueness theorem of the state vector solution, Al-Hawasy and Jawad [18] applied the Galekin finite element method for the equations of the nonlinear parabolic boundary value problem, Tufekci *et al*.[19] studied the forced vibration characteristics of the rotating disk by using the Galerkin method.

This paper aims to apply the weighted residuals methods (WRMs): Collocation Method (CM), Least Squares Method (LSM) and Galerkin Method (GM) to find the approximate solutions of the TFF equation.

This paper is arranged as follows: In section 2, the nonlinear TFF problem will be presented. The basic concepts of the methods of weighted residuals are introduced in section 3. In section 4, solving the nonlinear TFF equation will be introduced by the weighted residuals methods. Finally, the conclusion is given in section 5.

2. The Nonlinear TFF Problem

In this section, the flow of thin film of the non-Newtonian fluid will be presented on a moving belt [20]. The flow is fixed, laminar and uniform. The thickness of the film is uniform as well as the flow. We can introduce the governing equations of this problem as follows

$$\frac{d^2u}{dx^2}+\frac{6(k_2+k_3)}{\mu}\left(\frac{du}{dx}\right)^2\frac{d^2u}{dx^2}-\frac{\rho g}{\mu}=0, \tag{1}$$

$$u(0)=k, \text{ and } \frac{du}{dx}=0, at\ \ x=\delta, \tag{2}$$

where u is the velocity, k_2 and k_3 are the third degree fluid materiality constants, μ symbolize the dynamic viscosity, ρ present a density, g is gravitational acceleration, δ describes the thickness of the film and k is the belt speed.

We can write the dimensionless variables as below

$$\check{x}=\frac{x}{\delta}\ ,\check{u}=\frac{u}{k}\ ,\gamma=\frac{(k_2+k_3)k^2}{\mu\delta^2}, \text{ and } \sigma=\frac{\rho g\delta^2}{\mu k} \tag{3}$$

By removing (ˇ) from equation (3) and substituting equation (3) in equations (1) and (2), the equation of dimensionless form for the nonlinear boundary value problem is

$$\frac{d^2u}{dx^2}+6\gamma\left(\frac{du}{dx}\right)^2\frac{d^2u}{dx^2}-\sigma=0, \tag{4}$$

$$u(0)=1, \text{ and } \frac{du}{dx}=0, x=1. \tag{5}$$

Equation (4) is considered to be a well-posed problem because it is a second order nonlinear ODE and it has two boundary conditions.

By integrating equation (4) twice and using the boundary conditions given in equation (5), we get:

$$\frac{du}{dx}+2\gamma\left(\frac{du}{dx}\right)^3-\sigma x=a, \tag{6}$$

where a is the constant of integration process. To calculate the constant in equation (6), we used the 2nd condition given in equation (5), and then the value of $a = -\sigma$. Thus, we can write the nonlinear system in equations (4) and (5) as follows

$$\frac{du}{dx} + 2\gamma(\frac{du}{dx})^3 - \sigma(x-1) = 0, \text{ where } u(0) = 1. \quad (7)$$

3. Weighted Residuals Methods (WRMs) [12, 15]

The basic idea of the weighted residuals method is to find the approximate solution in the form of a polynomial to the differential equation of the formula

$$D[u(x)] = \varepsilon(x). \quad (8)$$

Let us assume that $\tilde{u}$ is approximate to u, and $\tilde{u}$ is a linear combination of basis functions selected by a linearly independent set that must satisfy the boundary conditions, that is:

$$u \cong \tilde{u} = \sum_{i=1}^{n} c_i \varphi_i. \quad (9)$$

Substituting equation (9) in equation (8), when the differential operator *D* is linear or nonlinear, the result of the operation is generally $\varepsilon(x)$. So, there will be an error or residual:

$$R(x) = D\big(\tilde{u}(x)\big) - \varepsilon(x) \neq 0. \quad (10)$$

The idea in the WRMs is to impose the error to zero. That is:

$$\int_X R(x) W_i(x) dx = 0, \ i = 1,2, \dots, n \quad (11)$$

The number of weight functions W_i is similar to the number of unknown constants c_i in $\tilde{u}$. The results will be the set of *n* algebraic equations of c_i. Three methods of WRMs will be presented in the next subsections to solve these equations and get the values of unknown constants.

3.1. Collocation Method(CM)

This method is based on the weighting functions, which depend on the Dirac δ functions in the domain. Such that

$$\delta(x - x_i) = \begin{cases} 1 & x = x_i \\ 0 & otherwise \end{cases}. \quad (12)$$

Thus, the integral of the weighted residual results in the residual equals zero at some selected points in the domain. That is, insert equation (12) in equation(11), results in $R(x_i) = 0$.

3.2. Least Squares Method(LSM)

This method depends on the minimization of the continuous summation of all the squared residuals. That is, a minimum of

$$S = \int_X R(x) R(x) dx = \int_X R^2(x) dx, \quad (13)$$

The derivatives of equation (13) must be zero with respect to all the unknown parameters, in order to obtain a minimum of a scalar function. That is,

$$\frac{\partial S}{\partial c_i} = 2 \int_X R(x) \frac{\partial R}{\partial c_i} dx = 0. \quad (14)$$

Then, compared equation (14) to equation (11), the weight functions can be

$$W_i = 2\frac{\partial R}{\partial c_i}. \quad (15)$$

However, the "2" will be canceled from the equation (15), we can neglect it. Then, the LSM weight functions are just the residual derivatives for the unknown constants:

$$W_i = \frac{\partial R}{\partial c_i}. \quad (16)$$

3.3. Galerkin Method (GM)

This method can be considered as a modification of the LSM. The derivative of the approximate function is used instead of the residual derivative for the unknown c_i. In other words, if the function is approximated as in equation (9), then the weight functions are given by

$$W_i = \frac{\partial \tilde{u}}{\partial c_i}, \quad (17)$$

$$\int_X W_i R(x)dx = 0, \ i = 1,2,\dots,6. \quad (18)$$

By substituting equation (17) in equation (18) and putting the weighted residual integration equal to zero, then the unknown coefficients in the approximate solution will be determined.

4. Solving The Nonlinear TFF Equation by The Method of Three Weighted Residuals

Before solving the nonlinear TFF equation, we recall the Weierstrass theorem [21]:

Theorem 4.1: If $u: [a, b] \to \mathbb{C}$ is continuous and $\epsilon > 0$ then there exists a polynomial p such that $|u(x) - p(x)| < \epsilon$, for all $x \in [a, b]$.

4.1. CM for Solving TFF Equation

The trial function is considered as [22]:

$$\tilde{u}(x) = 1 + \sum_{i=1}^{n} c_i x_i^n \qquad n = 6\,. \quad (19)$$

Where, equation (19) satisfies the initial condition. By replacing equation (19) in equation (10) and using equation (7), then we get the residual function:

$$R(x) = -\sigma(-1 + x) + c_1 + 2xc_2 + 3x^2c_3 + 4x^3c_4 + 5x^4c_5 + 6x^5c_6 + 2\gamma(c_1 + 2xc_2 + 3x^2c_3 + 4x^3c_4 + 5x^4c_5 + 6x^5c_6)^3, \quad (20)$$

Furthermore, the residual function should be tend to zero, to reach this goal, we first collocate equation (20) at $n - 1$ suitable points and choosing by [23]:

$$x_i = \left(\frac{1}{2}\right)\left(cos\ \left(\frac{i\pi}{n}\right) + 1\right), \ i = 1, 2, \dots, n \quad (21)$$

By substituting equation (21) and choosing the values of $\gamma = 0.5$ and $\sigma = 0.3$ as proposed in [24] in equation (20), then a set of six equations and six unknown coefficients were obtained by replacement these points into the residual function $R(x)$ with $n = 6$. After solving these unknown parameters c_1, c_2, c_3, c_4, c_5 and c_6, the formula of the $\tilde{u}(x)$ will be determined

$$\tilde{u}(x) = 1. - 0.2784179903218099x + 0.12170283596956218x^2 + 0.013323650734029828x^3 + 0.00064163429638052 9x^4 - 0.0012608938213647149x^5 - 0.00020578092642242158x^6. \quad (22)$$

4.2. LSM for Solving TFF Equation

The trial function in equation (19) must satisfy the initial condition, and the residual will be defined by equation (20). By replacing the residual function *R(x)* given in equation (14) with taking into account equation (16), a set of six equations will be obtained. We will solve this system of equations to find the values of coefficients c_1, c_2, c_3, c_4, c_5 and c_6, we get:

$$\tilde{u}(x) = 1. - 0.2784200109488398x + 0.12174092145386706x^2 + 0.013114374195112015x^3 + 0.0011173100601081297x^4 - 0.00173639971405525 5x^5 - 0.00003254002646081224 4x^6. \quad (23)$$

4.3. GM for Solving TFF Equation

In this method, the approximate function $\tilde{u}(x)$ is derived with respect to the unknown coefficients c_i to obtain the weight function W_i as mentioned in the equations (17) and (18), the weight functions will be:

$$W_1 = x\,, W_2 = x^2, W_3 = x^3, W_4 = x^4, W_5 = x^5\,, W_6 = x^6. \quad (24)$$

$$\int_a^b (1 + W_i) R(x) dx = 0,\ i = 1,2, \dots ,6. \quad (25)$$

By substituting equation (24) into equation (25), and applying equation (14), we getting a system of algebraic equations that will be solved to get the values of unknown coefficients, and substituting these values into equation (19), we have:

$$\tilde{u}(x) = 1. - 0.2784269835482562x + 0.12180368394378813x^2 + 0.012886759804023607x^3 + 0.0015069962962708115x^4 - 0.00205157568378486x^5 + 0.00006458861736018161x^6. \quad (26)$$

To check the accuracy of the approximate solutions and since the exact solution is unknown, we define the following maximal error remainder function

$$MER_n = |ER_n|\,, \quad (27)$$

where

$$ER_n(x) = \frac{d}{dx}\left(\tilde{u}(x)\right) + 2\gamma\left(\frac{d}{dx}\left(\tilde{u}(x)\right)\right)^3 - \sigma(x-1) = 0. \quad (28)$$

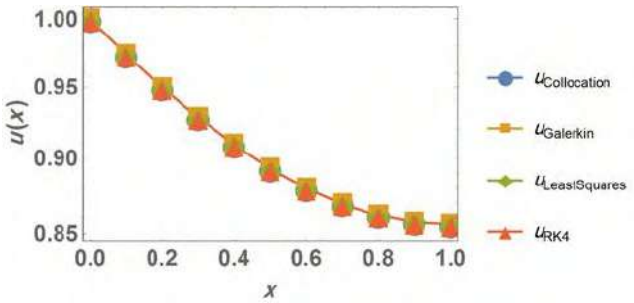

Figure 1. Comparison between ũ(x) obtained by the WRMs and the RK4 for $0 \le x \le 1$ when $\gamma = 0.5$ and $\sigma = 0.3$.

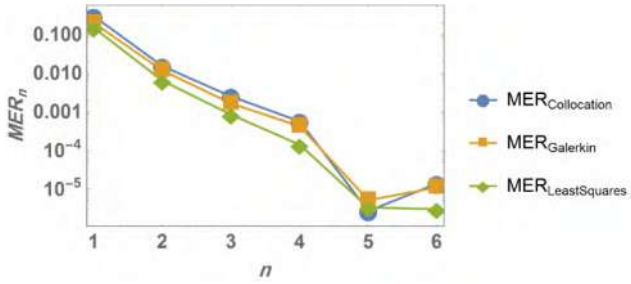

Figure 2.The logarithmic plots for the curves of the $MER_{Collocation}$,$MER_{Galerkin}$ and $MER_{LeastSquares}$ when $\gamma = 0.5$ and $\sigma = 0.3$.

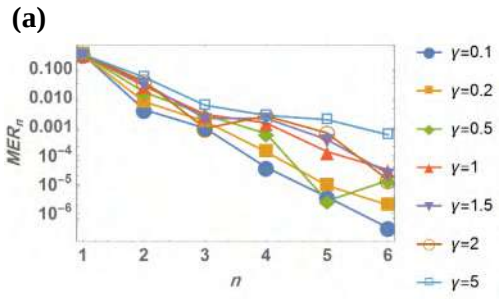

Figure 3. (a) $MER_{Collocation}$ with various value of γ when $\sigma = 0.3$

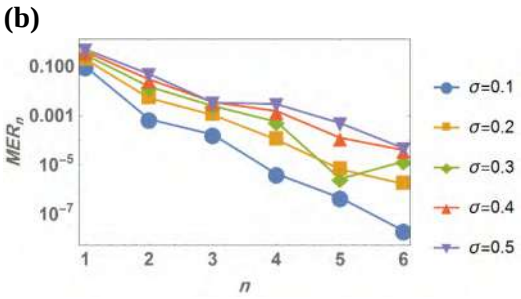

(b)$MER_{Collocation}$ with various values of σ when $\gamma = 0.5$

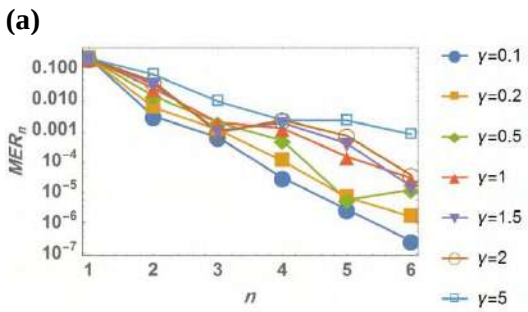

Figure 4. (a) $MER_{Galerkin}$with various values of γ when $\sigma = 0.3$

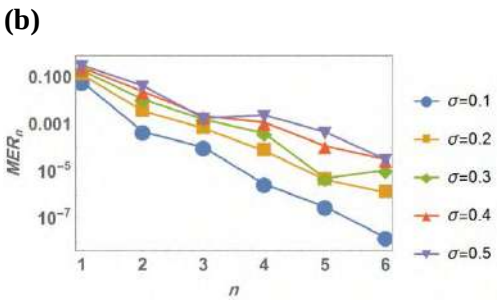

(b) $MER_{Galerkin}$with various values of σ when $\gamma = 0.5$.

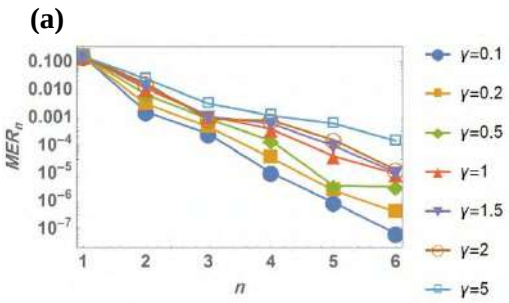

Figure 5. (a) $MER_{LeastSquares}$with various values of γ when $\sigma = 0.3$.

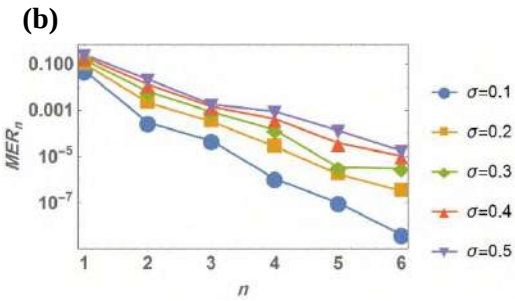

(b)$MER_{LeastSquares}$ with various values of σ when $\gamma = 0.5$.

Figure 1 shows good agreements have been obtained between the approximate solution from the use of WRMs as shown in the equations (22), (23) and (26) and the numerical solution obtained by the RK4 method. Also, Figure 2 shows the approximate solution obtained by the LSM has a lower error and good accuracy compared to the other methods.

Moreover, figures 3, 4 and 5 are present the effects of γ and σ values on the error of MER_n of the WRMs of the CM, GM and LSM, respectively that calculated according to the equations (27) and (28). An additional numerical examination can be performed by studying the influence of the non-Newtonian parameter γ and the value σ on the velocity given in equation (7). The differences are shown in figures 6(a), 7(a), and 8(a), when the γ value is stationary, the velocity tends to the Newtonian state when σ values increase. On the other side, figures. 6(b), 7(b), and 8(b) show that the non-Newtonian parameter γ is decreased when σ is kept fixed; the solution approaching the Newtonian case.

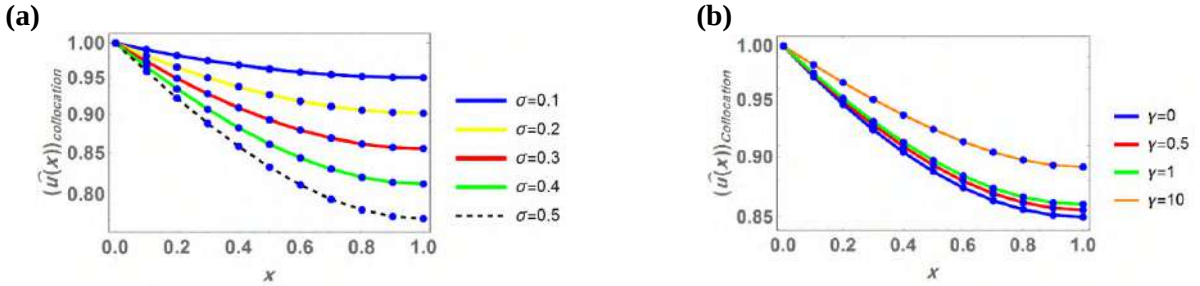

Figure 6. (a)Impact of σ on ũ(x) when $\gamma = 0.5$. (b)Impact of γ on ũ(x)when $\sigma = 0.3$.

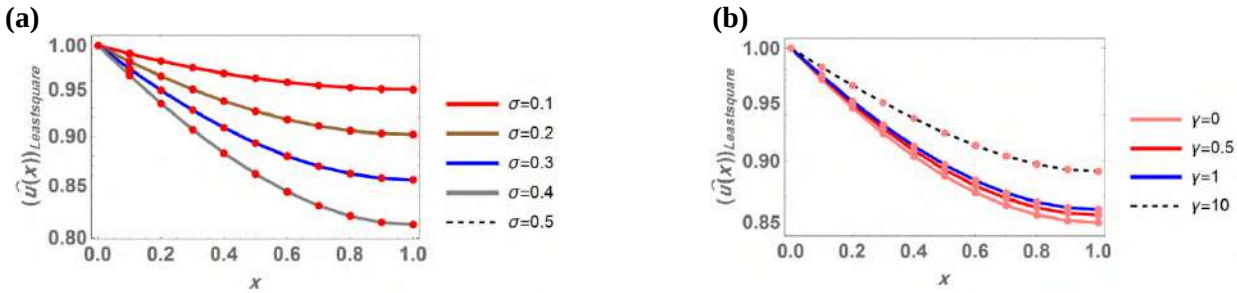

Figure 7. (a) Impact of σ on ũ(x) when $\gamma = 0.5$. (b) Impact of γ on ũ(x)when $\sigma = 0.3$.

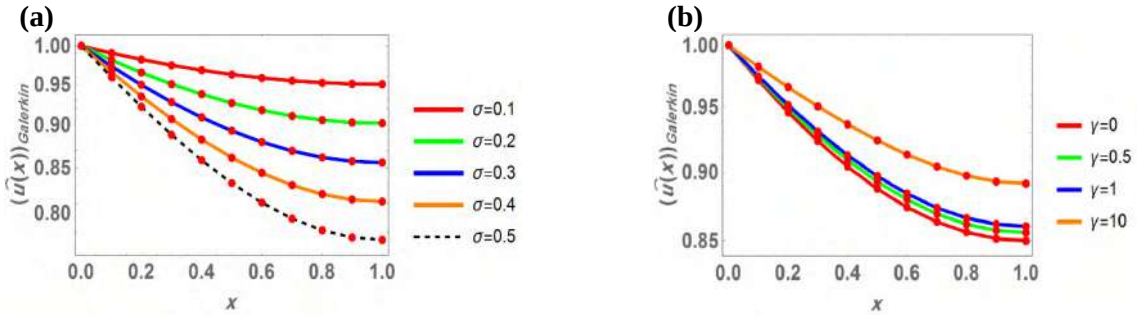

Figure 8. (a) Impact of σ on ũ(x) when $\gamma = 0.5$. (b) Impact of γ on ũ(x) when $\sigma = 0.3$.

Table 1 presents the values of $\tilde{u}(x)$ when $\gamma = 0.5$ and $\sigma = 0.3$ which are obtained by applying the CM, LSM, GM and RK4 method, a good agreement between the approximate solution obtained by the proposed methods and RK4 method. Furthermore, table 2 presents the numerical values of the MER functions for the three proposed methods, and the errors will be reduced when the values of *n* are increased, and the errors of the LSM are less than others which state that the LSM provides the best approximate solution.

Table 1. The numerical values of $\tilde{u}(x)$of the WRMs and the RK4 when $0 \leq x \leq 1$

x	Collocation method	Least squares method	Galerkin method	RK4 method
0	1	1	1	1
0.1	0.973388604326959	0.9733886168283186	0.9733883554928777	0.97338860199038
0.2	0.949291714539164	0.9492917796275736	0.9492916035500591	0.94929173866873
0.3	0.927789579962055	0.9277895747879666	0.9277894474313629	0.92778960206722
0.4	0.908960642679965	0.9089605521220884	0.9089603841643205	0.90896060771800
0.5	0.892879654057870	0.892879582613215	0.8928793589128667	0.89287957663844
0.6	0.879615643100865	0.879615692734783	0.8796154658498363	0.87961562345976
0.7	0.869229736651382	0.869229875341048	0.8692296955332617	0.86922984013857
0.8	0.861772831424131	0.8617728771289226	0.8617727287864787	0.86177292659036
0.9	0.857283117878783	0.8572829626709952	0.8572827770820347	0.85728297544108
1	0.855783455930375	0.8557836550197314	0.8557834694294016	0.85578364908701

Table 2. The numerical values of the MERof the WRMs when $m = 0.3$ and $\beta = 0.5$

	$MER_{Collocation}$	$MER_{Least\ squares}$	$MER_{Galerkin}$
1	0.29999999999999993	0.15	0.2
2	0.015253981352280344	0.006405659219384741	0.011817721123391134
3	0.002520086249197119	0.0008507902995215852	0.0016576442422136968
4	0.0005682077594781135	0.00014125376564085024	0.00042630589671925623
5	0.00002715662320165648	0.00000343758328659685	0.0000051585839074067
6	0.00013983660434798394	0.00000304394437825906	0.0000110846664006687

5. CONCLUSION

In this paper, we obtained the approximate solution to the TFF equation by applying the WRMs which are the CM, LSM, and GM. The approximate solutions obtained that provided the WRMs are reliable and effective methods. A good agreement has been achieved by comparing the numerical solution obtained by using the 4th-order Runge-Kutta method and the proposed methods. It can be concluded from the figures and tables, that the maximal error remainder will be reduced when the values of polynomial power *n* are increased. Moreover, the LSM provided the best approximate solution with less error. Finally, we found that selecting the parameters had an influence on convergence as well.

References

[1] Abdul N Z and Al-Jawary M A 2019 Reliable iterative methods for solving convective straight and radial fins with temperature-dependent thermal conductivity problems *Gazi University Journal of Science* **32** pp 967-89
[2] Al-Jawary M A and Adwan M I 2020 Reliable iterative methods for solving the Falkner-Skan equation *Gazi University Journal of Science* **33** pp 168-86
[3] Wang C Pop L 2006 Analysis of the flow of a power-law fluid film on an unsteady stretching surface by means of homotopy analysis method *Journal of Non-Newtonian Fluid Mechanics* **138** pp 161-72
[4] Waheed S E 2016 Flow and heat transfer in a Maxwell liquid film over an unsteady stretching sheet in a porous medium with radiation *Springer Plus* **5** 1061

[5] He J H 1999 Variational iteration method – a kind of non-linear analytical technique: some examples *International Journal of Non-Linear Mechanics* **34** pp 699-708
[6] Al-Jawary M A 2017 A semi-analytical iterative method for solving nonlinear thin film flow problems *Chaos, Solitons and Fractals* **99** pp 52-6
[7] Al-Jawary M A, Radhi G H and Ravnik J 2018 Development of the banach contraction method for the solution of nonlinear thin film flows of non-Newtonian fluids *Arab Journal of Basic and Applied Science* **25** pp 122–31
[8] Sajid M and Hayat T 2008 The application of homotopy analysis method to thin film flows of a third order fluid *Chaos, Solitons and Fractals* **38** 506–15
[9] Manafian J and sindi C T 2018 An optimal homotopy asymptotic method applied to the nonlinear thin film flow problems *International Journal of Numerical Methods for Heat & Fluid Flow* **28** pp 2816-41
[10] Arnau J M, Company R, Rosello M D and Climent H 2004 A collocation method to compute one-dimensional flow models in intake and exhaust systems of internal combustion engines *Mathematical and Computer Modelling* **40** pp 995-1008
[11] Aswhad A A 2011 Approximate solution of delay differential equations using the collocation method based on Bernstien polynomials *Baghdad Science Journal* **8** 820-5
[12] Vaferi B, Salimi V, Baniani D D, Jahanmiri A and Khedri S 2012 Prediction of transient pressure response in the petroleum reservoirs using orthogonal collocation *Journal of Petroleum Science and Engineering* **98-99** pp156-63
[13] Salih R K, Hassan I H and Kadhim A J 2014 An Approximated Solutions for nth Order Linear Delay Integro-Differential Equations of Convolution Type Using B-Spline Functions and Weddle Method *Baghdad Science Journal* **11** pp166-77
[14] Ahuja J 2019 Rayleigh-Bénard Convection for nanofluids for more realistic boundary conditions (Rigid-Free and Rigid-Rigid) using darcy model *International Journal of Mathematical, Engineering and Management Sciences* **4** pp 139-56
[15] Ganji D D and Hatami M 2014 Three weighted residual methods based on Jeffery-Hamel flow *International Journal of Numerical Methods for Heat & Fluid Flow* **24** pp 654-68
[16] Akyüz-Daşcioğlu A and Acar N I 2013 Bernstein collocation method for solving linear differential equations *Gazi University Journal of Science* **26** pp 527-34
[17] Al-Hawasy J A and Jaber M A K 2020 The Continues Classical Optimal Control Governing by Triple Linear Parabolic Boundary Value Problem *Ibn Al Haitham Journal for Pure and Applied sciences* **33** pp 129-42
[18] Al-Hawasy J A and Jawad M A 2018 The Approximation Solution of a Nonlinear Parabolic Boundary Value Problem Via Galerkin Finite Elements Method with Crank-Nicolson *Ibn Al Haitham Journal for Pure and Applied sciences* **31** pp 126-34
[19] Tufekci M ,Genel O E, Koc H, Oldac, O and Tufekci E 2019 Vibrations of a rotating disk under perpendicular space fixed forces *Gazi University Journal of Science* **32** pp 273-84
[20] Siddiqui A M, Mahmood R and Ghori Q K 2006 Thin film flow of a third grade fluid on a moving belt by He's homotopy perturbation method *International Journal of Nonlinear Sciences and Numerical Simulation* **7** pp 7-14
[21] Výborný R 2005 The Weierstrass theorem on polynomial approximation *Mathematica Bohemica* **130** pp 161-6
[22] Finlayson B A 1972 *The Method of Weighted Residuals and Variational Principles, With Application in Fluid Mechanics* 1st ed (United States: Academic Press Inc).
[23] Pirabaharan P and Chandrakumar R D 2016 A computational method for solving aclass of singular boundary value problems arising in science and engineering *Egyptian Journal of Basic and Applied Sciences* **3** pp 383-91
[24] AL-Jawary M A, Radhi G H and Ravnik J 2018 Daftardar-Jafari method for solving nonlinear thin film flow problem *Arab Journal of Basic and Applied Sciences* **25** pp 20–7

Improving Flower Pollination Algorithm for Solving 0–1 Knapsack Problem

Improving Flower Pollination Algorithm for Solving 0 –1 Knapsack Problem

Ghalya Tawfeeq Basheer[1]and Zakariya Yahya Algamal[2*]

[1]Department of Operations Research and Intelligent Techniques, University of Mosul, Mosul, Iraq
[2]Department of Statistics and Informatics, University of Mosul, Mosul, Iraq

E-mail: zakariya.algamal@uomosul.edu.iq

Abstract: Binary knapsack problem has received considerable attention in combinational optimization. Various meta-heuristic algorithms are dedicated to solve this problem in the literature. Recently, a binary flower pollination algorithm (BFPA) was proposed, which has been successfully applied to solve 0-1 knapsack problem. In this paper, two new time-varying transfer functions are proposed to improve the exploration and exploitation capability of the BFPA with the best solution and short computing time. Based on small, medium, and high-dimensional scales of the knapsack problem, the computational results reveal that the proposed time-varying transfer functions not only to find the best possible solutions but also to have less computational time. Compared to the standard transfer functions, the efficiency of the proposed time-varying transfer functions is superior, especially in the high-dimensional scales.

1. Introduction

The process of optimization is searching and finding the optimal solution of a given problem [1, 2]. In general, based on the nature of the search space and decision variables, an optimization problem can be divided into three main classes: continuous, discrete and mixed integer optimization problem [3, 4]. The binary optimization problems are a set classes of the discrete optimization problem in which the decision variable is a set of bits.

The knapsack problem is an optimization problem that can be modelled as a discrete binary optimization problem. The knapsack problem has widely studied in many real world applications, such as project selection, cutting stock problems, scheduling problems, resource allocation, and investment decision making [5-7].

There are several methods that have been developed to solve knapsack problem which can be divided into two types: exact methods, such as branch and bound method and dynamic programming. These methods can give the exact solution, but it is effective for small sized problems. The second type includes approximate methods that can give an approximate solution, but at reasonable times compared to exact methods [8-10].

In recent years, several meta-heuristic methods were proposed for tackling 0-1 knapsack problem, such as monarch butterfly optimization (MBO)[11], bat algorithm (BA)[12,13], particle swarm optimization (PSO)[14-16], monkey algorithm (MA)[17], ant colony optimization (ACO)[18], amoeboid organism algorithm (AOA)[19], and harmony search (HS)[20].

The flower pollination algorithm is a bio-inspired algorithm that mimics the pollination characteristics of flowers in plants. Flower pollination algorithm is first proposed by Yang [21] for solving single objective optimization problems. In (2014) Yang et al.[22] extended flower pollination algorithm for solving multi objective optimization problems. In (2015) Yang [23] proposed a binary flower pollination algorithm to tackle a feature selection problem. Abdel-Basset et al. [9] proposed a binary version of flower pollination algorithm for solving both small and large scale knapsack problem. Compared with some other algorithms, the flower pollination algorithm can perform better in terms of the global convergence and the convergence speed.

In the binary flower pollination algorithm, a transformation function is used to convert the continuous values generated from the algorithm into binary ones, and, therefore it is able to provide a binary flower pollination algorithm a sufficient amount to balance between exploration and exploitation [24].

In this paper, two efficient time-varying transfer functions are proposed to solve the 0 –1 knapsack problem. The proposed transfer functions are based on combining the S-shaped and V-shaped transfer functions with time-varying concept.

The remainder of this paper is organized as follows. Section 2 describes the basic 0 –1 knapsack problem. Section 3 introduces binary flower pollination algorithm. In Section 4, the proposed time-varying transfer functions are presented. Section 5 presents and discusses the experimental results. In section 6, conclusion is drawn.

2. Knapsack problem

Knapsack problem is a NP-hard combinatorial optimization problem and defined as follows [8, 25]:

Given a set of n items, each item i has a profit c_i and weight w_i. The objective is to select a subset of the items such that the total profit is maximized without exceeding the knapsack's capacity M. Mathematically, the knapsack problem can be formulated as follows:

$$Max\ f\left(x\right)=\sum_{i=1}^{n}c_i x_i \qquad (1)$$

s.t.

$$\sum_{i=1}^{n}w_i x_i \le M \qquad (2)$$

where

$$x_i=\begin{cases}1 & \text{if item i is selecled}\\ 0 & \text{otherwise}\end{cases}$$

To solve knapsack problem, we select a subset of the items of the binary vector x_i such that the optimal solution satisfies the constraint in Eq. (2) and maximizes the objective function in Eq.(1).

In such a constrained optimization problem, the penalty function is used to handle the constrained knapsack problem. As known, the knapsack problem is a maximization problem that can be converted into minimization by multiplying Eq. (1) by -1. As a result, the penalty function can be written as follow:

$$Min\phi\left(x\right)=-f\left(x\right)+\lambda Max\left(0,h\right) \qquad (3)$$

Where $h=\sum_{i=1}^{n}w_i x_i - M$ and λ represents the penalty coefficient. In this paper λ set to 10^{10} for all tests. The penalty function can be described in Figure1.

Penalty function

- **input** solution x_i
- Calculate total weight of x_i by $\left(\sum_{i=1}^{n} w_i x_i\right)$
- **if** $\left(\sum_{i=1}^{n} w_i x_i \le M\right)$
- $\phi(x) = -\sum_{i=1}^{n} c_i x_i$
- **else**
- $\phi(x) = -\sum_{i=1}^{n} c_i x_i + \lambda\left(\sum_{i=1}^{n} w_i x_i - M\right)$
- **end**

Figure 1: Penalty function

A Repair operator is treated the infeasible solutions which violates the constraint in Eq. (2) by converting them into feasible solutions and also improve the feasible solutions. The repair operator algorithm can be applied in two stages. The first stage is to convert the infeasible solution into feasible by taking out the items of the lower c_i / w_i ratio so as the constraint in Eq. (2) is not to exceed the knapsack capacity. The second stage is to improve the feasible solution by adding the items of the high c_i / w_i ratio to the knapsack with the keeping of the constraint.

3. Binary flower pollination algorithm(BFPA)

Yang (2012) proposed a new algorithm for global optimization called flower pollination algorithm [21]. It is a meta-heuristic algorithm that mimics nature, inspired of the pollination process in flowers.

Pollination in flowers can be taken two forms: biotic pollination and abiotic pollination. In the first type, the pollen is transferred by pollination like insects and animals. While the second form based on wind and diffusion in the water.

Pollination can be divided into self-pollination and cross-pollination. Self-pollination is transferring the pollens from one flower to the same flower or different flowers in the same plant. Cross-pollination is transferring the pollens from one flower to another flower of a different plant. A flower and its pollen represented a solution to the optimization problem. In the flower pollination algorithm, four basic rules are used[21, 26, 27]:

1. The global pollination includes biotic and cross-pollination, the pollinators move in a way that follows a lévy flight distribution.
2. The local pollination includes abiotic and self-pollination.
3. Flower constancy can be considered as the reproduction probability that is proportional to the similarity of two flowers involved.
4. We use a switch probability $p \in [0,1]$ to switch between global pollination and local pollination.

Rules 1 and 3 can be expressed mathematically as:

$$x_i^{t+1} = x_i^t + \gamma L(\lambda)\left(x_i^t - g^*\right) \quad (4)$$

where x_i^t is the solution vector or the pollen i at iteration t, g^* is the current best solution that is found at the current iteration, γ is a scaling factor to control the step size, $L(\lambda)$ is the step size in the lévy flights which is representing the strength of the pollination. Since pollinators move over a long distance with various distance steps, a lévy flight can be used to mimic this behaviour. That is, $L > 0$ from a lévy distribution as

$$L \sim \frac{\lambda\Gamma(\lambda)\sin\left(\frac{\pi\lambda}{2}\right)}{\pi}\left(\frac{1}{S^{1+\lambda}}\right)(S >> S_0 > 0) \quad (5)$$

Yang (2012) proposed $\Gamma(\lambda)$, the standard gamma function, and $\lambda = 1.5$. This distribution is valid for large steps $S > 0$. In (1994), Mantegna used the Gaussian distribution for generating the step size S by generating two random numbers U and V as follows [26]:

$$S = \frac{U}{|V|^{1/\lambda}} \quad U \sim N\left(0,\sigma^2\right),\ V \sim N(0,1) \quad (6)$$

$$\sigma^2 = \left(\frac{\Gamma(1+\lambda)}{\lambda\Gamma\left[(1+\lambda)/2\right]} * \frac{\sin(\pi\lambda/2)}{2^{\frac{\lambda-1}{2}}}\right)^{1/\lambda} \quad (7)$$

For local pollination, rules 2 and 3 can be expressed as:

$$x_i^{t+1} = x_i^t + k\left(x_j^t - x_k^t\right) \quad (8)$$

where x_j and x_k are the pollens (solution vectors) from different flowers of the same plant. k is the parameter draws from a uniform distribution in $[0,1]$. To switch between common global pollination to intensive local pollination, we used rule 4. In 2012,Yang suggested that switch probability or proximity probability $p = 0.8$ for most applications. The flower pollination algorithm can be presented in Figure 2.

Flower Pollination Algorithm

Begin

- Define the objective function max or min $f(x)$, and switch probability $p \in [0,1]$
- Initialize the population of n random flowers
- Evaluate each flowers in the population
- Find the best solution
- **while** (stopping criterion)
- **for** i=1:n
- **if** (r<p)
- New solution =global pollination Eq. (4)
- **else**
- New solution = local pollination Eq. (8)
- **end if**
- Evaluate new solution
- If new solution is better , update the population
- **end for**
- Find current best solution
- **end while**

Figure 2: Flower pollination algorithm

4. The proposed time-varying transfer functions

The knapsack problem can be modeled as a discrete problem in which the solution vector is binary, where 1 corresponds to that an item will be selected in the knapsack and 0 otherwise. In any binary algorithm, where one uses the step vector to calculate the probability of changing positions, the transfer functions significantly impact the balance between exploration and exploitation[24, 28].

In BFPA, the transfer function is used to map a continuous search space to a binary one, and the updating process is designed to switch positions of pollens between 0 and 1 in binary search spaces. In order to build this binary vector, a transfer function in Eq. (9) can be used after Eq. (8), in which the new solution is constrained to only binary values:

$$x_i^t = \begin{cases} 1 & if \quad T(x) > r \\ 0 & o\,w \end{cases} \tag{9}$$

where $r \in [0,1]$ is a random number, $T(x)$ is the transfer function.

Mirjalili and Lewis [29] introduced eight transfer functions and divided them into two families: S-Shaped transfer functions and V-Shaped transfer functions. These transfer functions are listed in Table 1. The transfer function was tested by Mirjalili and Lewis on 25 benchmark functions. The results show that V-shaped transfer functions are useful for the binary particle swarm optimization, especially V_4 function has merit for solving these functions. Teng et al.[30] has demonstrated the effect of V-shaped transfer function using binary particle swarm optimization on the feature selection problem. The experimental tests reveal that the efficiency of the proposed method.

In optimization algorithm, it is expected that the focus of the early stages of the implementation the algorithm will be on exploration to avoid falling into the local point, but in later stages of implementing the algorithm focuses more on exploitation to improve the quality of the solution[24, 28].

In this paper, two dynamic transfer functions are adapted form Mafarja, Aljarah [28] and Islam, Li [24], and proposed to improve the BFPA with the following considerations [24]:

1. In the early stages of the implementation, the transfer function should provide a high probability of flipping all the bits of x_i so that the BFPA can provide a stronger exploration.
2. In the intermediate stages of the implementation, the BFPA should start shifting from exploration to exploitation. This can achieved by using a transfer function that can reduce the probability of flipping all the bits of x_i .
3. In the final stages of the implementation, the transfer function should provide a low probability of flipping all the bits of x_i , so that the BFPA can provide a stronger exploitation capability.

In our proposed time-varying transfer function (TV), a new control parameter τ is added in the original transfer function. This τ is a time varying variable which starts with large value and gradually decreases over time. Two types of τ are proposed as follow:

$$\tau_1 = \left(1 - \frac{t}{T}\right)\tau_{1,\max} + \frac{t}{T}\tau_{1,\min} \tag{10}$$

and

$$\tau_2 = \tau_{2,\max} - t\left(\frac{\tau_{2,\max} - \tau_{2,\min}}{T}\right) \tag{11}$$

where $\tau_{\max}$ and $\tau_{\min}$ are the minimum and maximum values of the control parameter τ , and T is the maximum iteration of the BFPA. Table 2 lists the two proposed time-varying transfer functions.

Table 1: Families of transfer functions

	S-Shaped family		V-Shaped family
S1	$T(x)=\frac{1}{1+e^{-2x}}$	**V1**	$T(x)=\left\lvert erf\left(\frac{\sqrt{\pi}}{2}x\right)\right\rvert$
S2	$T(x)=\frac{1}{1+e^{-x}}$	**V2**	$T(x)=\lvert\tanh(x)\rvert$
S3	$T(x)=\frac{1}{1+e^{-\frac{x}{2}}}$	**V3**	$T(x)=\left\lvert\frac{x}{\sqrt{1+x^2}}\right\rvert$
S4	$T(x)=\frac{1}{1+e^{-\frac{x}{3}}}$	**V4**	$T(x)=\left\lvert\frac{2}{\pi}\arctan\left(\frac{\pi}{2}x\right)\right\rvert$

Table 2: The two proposed time-varying transfer functions.

	Time-varying 1		Time-varying 2
T1S1	$TVS(x)=\frac{1}{1+e^{\frac{-2x}{\tau_1}}}$	**T2S1**	$TVS(x)=\frac{1}{1+e^{\frac{-2x}{\tau_2}}}$
T1S2	$TVS(x)=\frac{1}{1+e^{\frac{-x}{\tau_1}}}$	**T2S2**	$TVS(x)=\frac{1}{1+e^{\frac{-x}{\tau_2}}}$
T1S3	$TVS(x)=\frac{1}{1+e^{-\frac{x}{2\tau_1}}}$	**T2S3**	$TVS(x)=\frac{1}{1+e^{-\frac{x}{2\tau_2}}}$
T1S4	$TVS(x)=\frac{1}{1+e^{-\frac{x}{3\tau_1}}}$	**T2S4**	$TVS(x)=\frac{1}{1+e^{-\frac{x}{3\tau_2}}}$

Table 3: The two proposed time-varying transfer functions.

T1V1	$TVV(x)=\left\lvert erf\left(\frac{\sqrt{\pi}x}{2\tau_1}\right)\right\rvert$	**T2V1**	$TVV(x)=\left\lvert erf\left(\frac{\sqrt{\pi}x}{2\tau_2}\right)\right\rvert$
T1V2	$TVV(x)=\left\lvert\tanh\left(\frac{x}{\tau_1}\right)\right\rvert$	**T2V2**	$TVV(x)=\left\lvert\tanh\left(\frac{x}{\tau_2}\right)\right\rvert$
Γ1V3	$TVV(x)=\left\lvert\frac{x/\tau_1}{\sqrt{1+x^2/\tau_1}}\right\rvert$	**Γ2V3**	$TVV(x)=\left\lvert\frac{x/\tau_2}{\sqrt{1+x^2/\tau_2}}\right\rvert$
Γ1V4	$TVV(x)=\left\lvert\frac{2}{\pi}\arctan\left(\frac{\pi x}{2\tau_1}\right)\right\rvert$	**Γ2V4**	$TVV(x)=\left\lvert\frac{2}{\pi}\arctan\left(\frac{\pi x}{2\tau_2}\right)\right\rvert$

5. Computational results

5.1. Parameter setting

For the binary flower pollination algorithm, the parameters were setting as follows: the population size =50, $\lambda = 1.5$, $p = 0.8$. In this paper, we use linear decreasing time varying where $\tau_{\max} = 4$, $\tau_{\min} = 0.1$, and T represents the maximum number of iterations.

5.2 Comparison results

To verify the feasibility and effectiveness of the proposed time-varying transfer functions method for solving 0–1 Knapsack problem, three scales of the knapsack problem are considered: low, medium, and high-dimensional scales. In this paper, all the results are obtained from 50 independent trials. The best solution, the worst solution, the mean and the standard deviation (SD) values, Mean iterations are reported as evaluation criteria. All of the computational experiments were conducted in Matlab 13a on a PC with an Intel Pentium Core i7-7500 processor (2.9 GHz) with 16GB of RAM in the Windows 10 OS.

5.2.1 Low scale 0-1 KP

The performance of the improved algorithm is investigated to solve ten low scale 0-1 KP instances (kp-1 to kp-10), which are taken from [9, 13]. The dimensions in this case are ranging from 4 to 23. The information dimension, capacity, weights and profits for these ten instances are described in Table S1 (Appendix). Table 4 shows the comparison results for all the used different transfer functions for the kp1 and kp10. The rest instances are listed in Table S2 (Appendix).

As observed from the results in Table 4 and Table S2, for the low scale knapsack problems, there is no difference among the results of using the proposed time-varying transfer functions and the standard transfer functions in terms of the best, worse, mean, and SD values. The major difference among the performance of the proposed time-varying transfer functions and the standard transfer functions in not expected because of relatively small numbered items. Contrary, the proposed time-varying transfer functions give optimal results with less number of iterations. The mean iterations of the proposed time-varying transfer functions are obviously better than the standard transfer functions for kp8, kp9, and kp10 where the number of items is higher than the others. Moreover, comparing between the two proposed transfer function, the required iterations to get the optimal solution using Eq. (11) is less than of Eq. (10) for kp8, kp9, and kp10.

Table 4: Results obtained by the transfer functions for the low scale 0–1 KP

Instance	Transfer function	Best	Mean	Worst	SD	Mean iterations
kp-1	S1	35	35	35	0	1
	S2	35	35	35	0	1
	S3	35	35	35	0	1
	S4	35	35	35	0	1
	V1	35	35	35	0	1
	V2	35	35	35	0	1
	V3	35	35	35	0	1
	V4	35	35	35	0	1
	T1S1	35	35	35	0	1
	T1S2	35	35	35	0	1
	T1S3	35	35	35	0	1
	T1S4	35	35	35	0	1

	T1V1	35	35	35	0	1
	T1V2	35	35	35	0	1
	T1V3	35	35	35	0	1
	T1V4	35	35	35	0	1
	T2S1	35	35	35	0	1
	T2S2	35	35	35	0	1
	T2S3	35	35	35	0	1
	T2S4	35	35	35	0	1
	T2V1	35	35	35	0	1
	T2V2	35	35	35	0	1
	T2V3	35	35	35	0	1
	T2V4	35	35	35	0	1
kp-10	S1	9767	9767	9767	0	2.28
	S2	9767	9767	9767	0	4.44
	S3	9767	9767	9767	0	9.8
	S4	9767	9767	9767	0	15.64
	V1	9767	9767	9767	0	1.2
	V2	9767	9767	9767	0	1.2
	V3	9767	9767	9767	0	1.24
	V4	9767	9767	9767	0	1.12
	T1S1	9767	9767	9767	0	4.39
	T1S2	9767	9767	9767	0	1.95
	T1S3	9767	9767	9767	0	7.19
	T1S4	9767	9767	9767	0	15.19
	T1V1	9767	9767	9767	0	1.12
	T1V2	9767	9767	9767	0	1.08
	T1V3	9767	9767	9767	0	1.15
	T1V4	9767	9767	9767	0	1
	T2S1	9767	9767	9767	0	2.95
	T2S2	9767	9767	9767	0	2.17
	T2S3	9767	9767	9767	0	8.42
	T2S4	9767	9767	9767	0	12.76
	T2V1	9767	9767	9767	0	1.15
	T2V2	9767	9767	9767	0	1
	T2V3	9767	9767	9767	0	1.04
	T2V4	9767	9767	9767	0	1

5.2.2 Medium scale 0-1 KP

To further evaluate the performance of proposed time-varying transfer functions in medium scale 0-1 Knapsack problem, ten medium size 0-1 KP instances (kp-11 to kp-20) are taken from [9, 13] in which the items are between 30 and 75. The description of these ten instances is described in Table S3 (Appendix). Table 5 summarizes the comparison results for all the used different transfer functions for the kp15 and kp20. The rest instances results are reported in Table S4 (Appendix).

Obviously, it is evident from Table 5 and Table S4 that the proposed time-varying transfer functions obtained the same best, worse, mean, and SD values as the standard transfer functions. From Tables 5 and S4, for the mean iterations, the proposed time-varying transfer functions are superior to the other eight standard transfer functions on kp11 to kp20. This indicates that the proposed time-varying transfer functions is comparatively fast. For example, in kp20, the reduction in mean iteration of T1S2 and T2S2

functions was 37.61% and 49.81% lower than that of S2, respectively. On the other hand, the reduction in mean iteration of T1V4 and T2V4 functions was 40.08% and 60.32% lower than that of V4, respectively.

Further, it was noted that the v-shaped transfer functions are usually yielded the least iterations compared to S-shaped transfer functions. On the other hand, comparing between the two proposed transfer functions, the required iterations to get an optimal solution using Eq. (11) is less than of Eq. (10) for all the 0-1 Knapsack problems. Additionally, the number of iterations of T2V1, T2V2, T2V3, and T2V4 are obviously small than T1V1, T1V2, T1V3, and T1V4.

Table 5: Results obtained by the transfer functions for the medium scale 0–1 KP

Instance	Transfer function	Best	Mean	Worst	SD	Mean iterations
kp-15	S1	2440	2440	2440	0	9.72
	S2	2440	2440	2440	0	29.4
	S3	2440	2440	2440	0	21.64
	S4	2440	2440	2440	0	15.6
	V1	2440	2440	2440	0	5.56
	V2	2440	2440	2440	0	3.4
	V3	2440	2440	2440	0	2.44
	V4	2440	2440	2440	0	1.8
	T1S1	2440	2440	2440	0	19.84
	T1S2	2440	2440	2440	0	17.04
	T1S3	2440	2440	2440	0	12.12
	T1S4	2440	2440	2440	0	8.48
	T1V1	2440	2440	2440	0	1.08
	T1V2	2440	2440	2440	0	1.16
	T1V3	2440	2440	2440	0	1.16
	T1V4	2440	2440	2440	0	1.12
	T2S1	2440	2440	2440	0	25.16
	T2S2	2440	2440	2440	0	16.8
	T2S3	2440	2440	2440	0	15.56
	T2S4	2440	2440	2440	0	9.92
	T2V1	2440	2440	2440	0	1.04
	T2V2	2440	2440	2440	0	1.04
	T2V3	2440	2440	2440	0	1.04
	T2V4	2440	2440	2440	0	1
kp-20	S1	3614	3614	3614	0	48.53
	S2	3614	3614	3614	0	125.41
	S3	3614	3614	3614	0	115.36
	S4	3614	3614	3614	0	137.4
	V1	3614	3614	3614	0	18.54
	V2	3614	3614	3614	0	8.46
	V3	3614	3614	3614	0	6.82
	V4	3614	3614	3614	0	4.89
	T1S1	3614	3614	3614	0	50.18
	T1S2	3614	3614	3614	0	78.24
	T1S3	3614	3614	3614	0	82.13
	T1S4	3614	3614	3614	0	92.74
	T1V1	3614	3614	3614	0	10.21

T1V2	3614	3614	3614	0	4.18
T1V3	3614	3614	3614	0	4.53
T1V4	3614	3614	3614	0	2.93
T2S1	3614	3614	3614	0	46.65
T2S2	3614	3614	3614	0	62.94
T2S3	3614	3614	3614	0	91.6
T2S4	3614	3614	3614	0	69.34
T2V1	3614	3614	3614	0	7.26
T2V2	3614	3614	3614	0	3.62
T2V3	3614	3614	3614	0	3.98
T2V4	3614	3614	3614	0	1.94

5.2.3 High-dimensional scale 0-1 KP

To further highlight the benefits of our proposed time-varying transfer functions, three cases have been investigated. The first case handles the uncorrelated problem (kp21 – kp25) where the weights w_i are uncorrelated with the profits c_i. Each w_i and c_i is randomly chosen from 5 to 20 and from 5 to 40, respectively. The second case handles the weakly correlated problem (kp26 – kp30). In this case, the weights w_i and the profits c_i can be expressed as follows: $w_i \in [5,20]$ and $c_i \in [w_i - 5, w_i + 5]$. The third case handles the strongly correlated problem (kp31 – kp35). In this case, w_i and c_i can be calculated as: $w_i \in [5,20]$ and $c_i \in [w_i + 5]$. The knapsack capacity for the kp-21-kp35 can be calculated as $M = 0.75 \times \sum_{i=1}^{n} w_i$. The dimension sizes varying from 100 to 2000 items. For all used transfer functions, the maximum iteration is set to 10000. Tables 6 – 8 reports the comparison results for all the used different transfer functions for the kp22, kp25, kp27, kp30, kp32, and kp35. The rest problems are listed in Tables S5 – S7 (Appendix). Based on the obtained results, several points are concluded.

(1) It can be seen that the proposed time-varying transfer functions significantly outperform the standard transfer functions on all evaluation measures including the best, mean, worst, and standard deviations.
(2) As observed from the results, the proposed time-varying V-shaped transfer functions, T1V1 – T2V4, can easily find the optimal values with small SD in all uncorrelated, weakly correlated, and strongly correlated problems.
(3) It is obvious that there is an improvement for searching the global optimal solution when using T2V1, T2V2, T2V3, and T2V4 compared to T1V1, T1V2, T1V3, and T1V4. This leads to the performance dominance of T2V1, T2V2, T2V3, and T2V4 against those performed on the T1V1, T1V2, T1V3, and T1V4.
(4) The mean iteration values of time-varying V-shaped transfer functions, T1V1 – T2V4, are obviously superior to S1, S2, S3, S4, V1, V2, V3, and V4 for all high-dimensional scale problems. The performance of T2V1, T2V2, T2V3, and T2V4 is better than that of T1V1, T1V2, T1V3, and T1V4.
(5) Compared to the proposed time-varying V-shaped transfer functions, T2V4 is significantly improving the performance metrics with lower SD and mean iterations.

Table 6: Comparison results of uncorrelated high-dimensional scale 0–1 KP

Instance	Dimension	Transfer function	Best	Mean	Worst	SD	Mean iterations

kp-22	500	S1	10340	10338	10335	2.739	1038
		S2	10338	10302.2	10225	25.46	2394
		S3	10338	10306.6	10225	26.923	2187
		S4	10338	10311	10225	20.01	2541
		V1	10345	10345	10345	0	185
		V2	10345	10345	10345	0	103
		V3	10345	10345	10345	0	161
		V4	10345	10345	10345	0	94
		T1S1	10345	10345	10345	0	1074
		T1S2	10343	10333.4	10319	13.145	1851
		T1S3	10343	10328.6	10319	13.145	2018
		T1S4	10343	10323.8	10319	10.733	1932
		T1V1	10345	10345	10345	0	110
		T1V2	10345	10345	10345	0	95
		T1V3	10345	10345	10345	0	104
		T1V4	10345	10345	10345	0	73
		T2S1	10345	10345	10345	0	1022
		T2S2	10343	10325	10319	10.392	1915
		T2S3	10343	10327.2	10319	9.96	1893
		T2S4	10343	10328.4	10319	9.044	1801
		T2V1	10345	10345	10345	0	100
		T2V2	10345	10345	10345	0	94
		T2V3	10345	10345	10345	0	99
		T2V4	10345	10345	10345	0	69
kp-25	2000	S1	40612	40598.2	40589	12.674	6285
		S2	40610	40554.8	40525	33.945	8136
		S3	40610	40549	40525	37.259	7985
		S4	40610	40544.9	40525	38.157	7612
		V1	40615	40611.8	40610	15.375	3485
		V2	40615	40612.4	40610	14.281	2952
		V3	40615	40611.2	40610	16.158	3624
		V4	40615	40612.8	40610	14.825	2531
		T1S1	40616	40610.6	40595	9.521	4258
		T1S2	40614	40599.5	40590	20.98	6395
		T1S3	40614	40611.8	40590	19.353	5927
		T1S4	40614	40610.2	40590	21.97	6042
		T1V1	40616	40614.6	40611	8.34	2493
		T1V2	40616	40615	40611	7.921	2051
		T1V3	40616	40614.2	40611	8.95	2964
		T1V4	40616	40615.2	40611	6.56	1950
		T2S1	40616	40611.2	40595	8.536	4381
		T2S2	40614	40610.6	40590	19.561	6134
		T2S3	40614	40611.4	40590	17.562	5630
		T2S4	40614	40610.8	40590	20.315	6729
		T2V1	40616	40614	40611	7.65	2654
		T2V2	40616	40614.8	40611	6.98	1983
		T2V3	40616	40614.6	40611	6.551	2452
		T2V4	40616	40615.4	40611	5.439	1875

Table 7: Comparison results of weakly correlated high-dimensional scale 0–1 KP

Instance	Dimension	Transfer function	Best	Mean	Worst	SD	Mean iterations
kp-27	500	S1	5197	5185.2	5175	8.624	1002
		S2	5190	5186.2	5184	9.943	1980
		S3	5190	5185.4	5184	8.67	1542
		S4	5190	5185.6	5184	8.24	1834
		V1	5197	5193.4	5190	4.96	162
		V2	5197	5193	5190	5.63	90
		V3	5197	5194.2	5190	5.176	166
		V4	5197	5194.6	5190	4.641	75
		T1S1	5197	5197	5197	0	995
		T1S2	5197	5194.8	5194	2.67	1091
		T1S3	5197	5195.4	5194	1.954	1124
		T1S4	5197	5194.2	5194	1.37	1387
		T1V1	5197	5197	5197	0	123
		T1V2	5197	5197	5197	0	84
		T1V3	5197	5197	5197	0	98
		T1V4	5197	5197	5197	0	61
		T2S1	5197	5197	5197	0	981
		T2S2	5197	5195	5194	1.095	1192
		T2S3	5197	5194.8	5194	2.04	1184
		T2S4	5197	5194.4	5194	1.93	1207
		T2V1	5197	5197	5197	0	111
		T2V2	5197	5197	5197	0	88
		T2V3	5197	5197	5197	0	93
		T2V4	5197	5197	5197	0	56
kp-30	2000	S1	21044	21036.5	21018	20.652	6018
		S2	21025	21005.2	20890	44.67	9820
		S3	21025	21004.8	20890	46.391	9453
		S4	21025	21005.1	20890	45.752	9572
		V1	21068	21057	21033	17.297	3091
		V2	21068	21057.4	21033	18.632	2735
		V3	21068	21056.8	21033	15.348	3120
		V4	21068	21057.8	21033	14.982	2493
		T1S1	21081	21079.2	21070	12.358	5304
		T1S2	21078	21074	21062	27.291	7659
		T1S3	21078	21073	21062	28.9	7362
		T1S4	21078	21074.6	21062	25.367	7710
		T1V1	21081	21079	21075	9.452	2514
		T1V2	21081	21079.2	21075	8.651	2183
		T1V3	21081	21078	21075	10.12	2907
		T1V4	21081	21079.2	21075	8.654	2061
		T2S1	21081	21079	21070	11.92	5297
		T2S2	21078	21074.8	21062	29.381	7640
		T2S3	21078	21075	21062	25.648	7193
		T2S4	21078	21074	21062	28.31	7684
		T2V1	21081	21078	21075	11.51	2761
		T2V2	21081	21079	21075	8.372	2031
		T2V3	21081	21078.6	21075	9.62	2897
		T2V4	21081	21079.4	21075	8.05	2005

Table 8: Comparison results of strongly correlated high-dimensional scale 0–1 KP

Instance	Dimension	Transfer function	Best	Mean	Worst	SD	Mean iterations
kp-32	500	S1	6783	6783	6783	0	978
		S2	6779	6775.6	6768	5.681	1862
		S3	6779	6776	6768	6.16	1734
		S4	6779	6775	6768	5.935	1815
		V1	6783	6781.5	6779	3.94	138
		V2	6783	6782	6779	4.67	105
		V3	6783	6781.9	6779	4.914	133
		V4	6783	6782.4	6779	3.952	100
		T1S1	6783	6783	6783	0	1086
		T1S2	6783	6780	6776	3.68	1273
		T1S3	6783	6780.2	6776	2.942	1360
		T1S4	6783	6780.9	6776	4.37	1109
		T1V1	6783	6783	6783	0	97
		T1V2	6783	6783	6783	0	57
		T1V3	6783	6783	6783	0	96
		T1V4	6783	6783	6783	0	50
		T2S1	6783	6783	6783	0	1050
		T2S2	6783	6781.2	6776	4.518	1241
		T2S3	6783	6780.8	6776	5.63	1293
		T2S4	6783	6782	6776	4.09	1113
		T2V1	6783	6783	6783	0	101
		T2V2	6783	6783	6783	0	55
		T2V3	6783	6783	6783	0	90
		T2V4	6783	6783	6783	0	51
kp-35	2000	S1	27285	27279.6	27246	15.162	5506
		S2	27292	27276	27230	30.37	6931
		S3	27292	27277.2	27230	35.61	6654
		S4	27292	27276.1	27230	29.49	6837
		V1	27356	27349	27344	10.34	2741
		V2	27356	27350	27344	12.57	2652
		V3	27356	27349.8	27344	11.31	2903
		V4	27356	27351	27344	11.94	2511
		T1S1	27362	27359	27350	9.58	6347
		T1S2	27362	27358	27349	16.54	5028
		T1S3	27362	27357	27349	18.36	5391
		T1S4	27362	27357.6	27349	15.29	5727
		T1V1	27362	27360	27358	3.67	1890
		T1V2	27362	27361	27358	2.94	1682
		T1V3	27362	27360.2	27358	3.05	1954
		T1V4	27362	27361.6	27358	3.58	1509
		T2S1	27362	27358.2	27350	10.17	3583
		T2S2	27362	27357.6	27349	14.89	5126
		T2S3	27362	27358	27349	16.52	6084
		T2S4	27362	27357	27349	17.13	5737
		T2V1	27362	27361	27358	2.34	1903
		T2V2	27362	27360.9	27358	3.61	1530
		T2V3	27362	27361.4	27358	2.57	1827

	T2V4	27362	27361.8	27358	2.09	1493

6. Conclusion

In this paper, two time-varying transfer functions are proposed to improve the exploration and exploitation capability of the binary flower pollination algorithm in solving the 0–1 KP problem efficiently. The experimental results show that the introduction of time-varying parameter in the transfer function can improve the performance of BFPA in solving small, medium, and high-dimensional scales 0–1 KP problems. Additionally, the experimental results show that proposed time-varying V-shaped transfer functions outperform the other S-shaped transfer functions in terms of the best, worse, mean, SD values, and the mean iterations.

Appendix

Table S1: The description of the low scale 0-1 KP instances

Instance	dimension	capacity M	weights W	profits C
kp-1	4	20	w=[6 5 9 7]	c=[9 11 13 15]
kp-2	4	11	w=[2 4 6 7]	c=[6 10 12 13]
kp-3	5	80	w=[15 20 17 8 31]	c=[33 24 36 37 12]
kp-4	7	50	w=[31 10 20 19 4 3 6]	c=[70 20 39 37 7 5 10]
kp-5	10	269	w=[95 4 60 32 23 72 80 62 65 46]	c=[55 10 47 5 4 50 8 61 85 87]
kp-6	10	60	w=[30 25 20 18 17 11 5 2 1 1]	c=[20 18 17 15 15 10 5 3 1 1]
kp-7	15	375	w=[56.358531 80.874050 47.987304 89.596240 74.660482 85.894345 51.353496 1.498459 36.445204 16.589862 44.569231 0.466933 37.788018 57.118442 60.716575]	c=[0.125126 19.330424 58.500931 35.029145 82.284005 17.410810 71.050142 30.399487 9.140294 14.731285 98.852504 11.908322 0.891140 53.166295 60.176397]
kp-8	20	879	w=[84 83 43 4 44 6 82 92 25 83 56 18 58 14 48 70 96 32 68 92]	c=[91 72 90 46 55 8 35 75 61 15 77 40 63 75 29 75 17 78 40 44]
kp-9	20	878	w=[92 4 43 83 84 68 92 82 6 44 32 18 56 83 25 96 70 48 14 58]	c=[44 46 90 72 91 40 75 35 8 54 78 40 77 15 61 17 75]
kp-10	23	10000	w=[983 982 981 980 979 978 488 976 972 486 486 972 972 485 485 969 966 483 964 963 961 958 959]	c=[981 980 979 978 977 976 487 974 970 485 485 970 970 484 484 976 974 482 962 961 959 958 857]

Table S2: Results obtained by the transfer functions for the low scale 0–1 KP

Instance	Transfer function	Best	Mean	Worst	SD	Mean iterations
kp-2	S1	23	23	23	0	1
	S2	23	23	23	0	1
	S3	23	23	23	0	1
	S4	23	23	23	0	1
	V1	23	23	23	0	1
	V2	23	23	23	0	1

	V3	23	23	23	0	1
	V4	23	23	23	0	1
	T1S1	23	23	23	0	1
	T1S2	23	23	23	0	1
	T1S3	23	23	23	0	1
	T1S4	23	23	23	0	1
	T1V1	23	23	23	0	1
	T1V2	23	23	23	0	1
	T1V3	23	23	23	0	1
	T1V4	23	23	23	0	1
	T2S1	23	23	23	0	1
	T2S2	23	23	23	0	1
	T2S3	23	23	23	0	1
	T2S4	23	23	23	0	1
	T2V1	23	23	23	0	1
	T2V2	23	23	23	0	1
	T2V3	23	23	23	0	1
	T2V4	23	23	23	0	1
	S1	130	130	130	0	1
	S2	130	130	130	0	1
	S3	130	130	130	0	1
	S4	130	130	130	0	1
	V1	130	130	130	0	1
	V2	130	130	130	0	1
	V3	130	130	130	0	1
	V4	130	130	130	0	1
	T1S1	130	130	130	0	1
	T1S2	130	130	130	0	1
	T1S3	130	130	130	0	1
	T1S4	130	130	130	0	1
kp-3	T1V1	130	130	130	0	1
	T1V2	130	130	130	0	1
	T1V3	130	130	130	0	1
	T1V4	130	130	130	0	1
	T2S1	130	130	130	0	1
	T2S2	130	130	130	0	1
	T2S3	130	130	130	0	1
	T2S4	130	130	130	0	1
	T2V1	130	130	130	0	1
	T2V2	130	130	130	0	1
	T2V3	130	130	130	0	1
	T2V4	130	130	130	0	1
	S1	107	107	107	0	1
	S2	107	107	107	0	1.08
	S3	107	107	107	0	1.04
	S4	107	107	107	0	1.04
kp-4	V1	107	107	107	0	1
	V2	107	107	107	0	1
	V3	107	107	107	0	1
	V4	107	107	107	0	1

	T1S1	107	107	107	0	1
	T1S2	107	107	107	0	1
	T1S3	107	107	107	0	1
	T1S4	107	107	107	0	1
	T1V1	107	107	107	0	1
	T1V2	107	107	107	0	1
	T1V3	107	107	107	0	1
	T1V4	107	107	107	0	1
	T2S1	107	107	107	0	1
	T2S2	107	107	107	0	1
	T2S3	107	107	107	0	1
	T2S4	107	107	107	0	1
	T2V1	107	107	107	0	1
	T2V2	107	107	107	0	1
	T2V3	107	107	107	0	1
	T2V4	107	107	107	0	1
	S1	295	295	295	0	1.12
	S2	295	295	295	0	1.92
	S3	295	295	295	0	1.32
	S4	295	295	295	0	1.16
	V1	295	295	295	0	1.16
	V2	295	295	295	0	1.04
	V3	295	295	295	0	1.04
	V4	295	295	295	0	1.04
	T1S1	295	295	295	0	1
	T1S2	295	295	295	0	1
	T1S3	295	295	295	0	1
	T1S4	295	295	295	0	1
kp-5	T1V1	295	295	295	0	1
	T1V2	295	295	295	0	1
	T1V3	295	295	295	0	1
	T1V4	295	295	295	0	1
	T2S1	295	295	295	0	1
	T2S2	295	295	295	0	1
	T2S3	295	295	295	0	1
	T2S4	295	295	295	0	1
	T2V1	295	295	295	0	1
	T2V2	295	295	295	0	1
	T2V3	295	295	295	0	1
	T2V4	295	295	295	0	1
	S1	52	52	52	0	1
	S2	52	52	52	0	1
	S3	52	52	52	0	1
	S4	52	52	52	0	1
kp-6	V1	52	52	52	0	1
	V2	52	52	52	0	1
	V3	52	52	52	0	1
	V4	52	52	52	0	1
	T1S1	52	52	52	0	1
	T1S2	52	52	52	0	1

	T1S3	52	52	52	0	1
	T1S4	52	52	52	0	1
	T1V1	52	52	52	0	1
	T1V2	52	52	52	0	1
	T1V3	52	52	52	0	1
	T1V4	52	52	52	0	1
	T2S1	52	52	52	0	1
	T2S2	52	52	52	0	1
	T2S3	52	52	52	0	1
	T2S4	52	52	52	0	1
	T2V1	52	52	52	0	1
	T2V2	52	52	52	0	1
	T2V3	52	52	52	0	1
	T2V4	52	52	52	0	1
	S1	481.07	481.069	481.07	0	1
	S2	481.07	481.069	481.07	0	1
	S3	481.07	481.069	481.07	0	1
	S4	481.07	481.069	481.07	0	1
	V1	481.07	481.069	481.07	0	1
	V2	481.07	481.069	481.07	0	1
	V3	481.07	481.069	481.07	0	1
	V4	481.07	481.069	481.07	0	1
	T1S1	481.07	481.069	481.07	0	1
	T1S2	481.07	481.069	481.07	0	1
	T1S3	481.07	481.069	481.07	0	1
	T1S4	481.07	481.069	481.07	0	1
kp-7	T1V1	481.07	481.069	481.07	0	1
	T1V2	481.07	481.069	481.07	0	1
	T1V3	481.07	481.069	481.07	0	1
	T1V4	481.07	481.069	481.07	0	1
	T2S1	481.07	481.069	481.07	0	1
	T2S2	481.07	481.069	481.07	0	1
	T2S3	481.07	481.069	481.07	0	1
	T2S4	481.07	481.069	481.07	0	1
	T2V1	481.07	481.069	481.07	0	1
	T2V2	481.07	481.069	481.07	0	1
	T2V3	481.07	481.069	481.07	0	1
	T2V4	481.07	481.069	481.07	0	1
	S1	1025	1025	1025	0	1.36
	S2	1025	1025	1025	0	1.68
	S3	1025	1025	1025	0	1.24
	S4	1025	1025	1025	0	1.68
	V1	1025	1025	1025	0	1.68
	V2	1025	1025	1025	0	1.56
kp-8	V3	1025	1025	1025	0	1.52
	V4	1025	1025	1025	0	1.28
	T1S1	1025	1025	1025	0	1.95
	T1S2	1025	1025	1025	0	1.22
	T1S3	1025	1025	1025	0	1.15
	T1S4	1025	1025	1025	0	1.56

kp-9	T1V1	1025	1025	1025	0	1.49
	T1V2	1025	1025	1025	0	1.23
	T1V3	1025	1025	1025	0	1.07
	T1V4	1025	1025	1025	0	1.04
	T2S1	1025	1025	1025	0	2.14
	T2S2	1025	1025	1025	0	1.02
	T2S3	1025	1025	1025	0	1.04
	T2S4	1025	1025	1025	0	1.32
	T2V1	1025	1025	1025	0	1.59
	T2V2	1025	1025	1025	0	1.14
	T2V3	1025	1025	1025	0	1.04
	T2V4	1025	1025	1025	0	1
	S1	1024	1024	1024	0	1.6
	S2	1024	1024	1024	0	1.72
	S3	1024	1024	1024	0	1.16
	S4	1024	1024	1024	0	1.92
	V1	1024	1024	1024	0	1.92
	V2	1024	1024	1024	0	2
	V3	1024	1024	1024	0	2.04
	V4	1024	1024	1024	0	1.48
	T1S1	1024	1024	1024	0	2.5
	T1S2	1024	1024	1024	0	1.04
	T1S3	1024	1024	1024	0	1.04
	T1S4	1024	1024	1024	0	1.21
	T1V1	1024	1024	1024	0	1.07
	T1V2	1024	1024	1024	0	1.94
	T1V3	1024	1024	1024	0	1.83
	T1V4	1024	1024	1024	0	1.08
	T2S1	1024	1024	1024	0	1.91
	T2S2	1024	1024	1024	0	1.29
	T2S3	1024	1024	1024	0	1.12
	T2S4	1024	1024	1024	0	1.67
	T2V1	1024	1024	1024	0	1.54
	T2V2	1024	1024	1024	0	1.44
	T2V3	1024	1024	1024	0	1.75
	T2V4	1024	1024	1024	0	1

Table S3: Medium size 0–1 KP test problems

Instance	dimension	capacity M	weights W	profits C
kp-11	30	577	w=[46 17 35 1 26 17 17 48 38 17 32 21 29 48 31 8 42 37 6 9 15 22 27 14 42 40 14 31 6 34]	c=[57 64 50 6 52 6 85 60 70 65 63 96 18 48 85 50 77 18 70 92 17 43 5 23 67 88 35 3 91 48]
kp-12	35	655	w=[7 4 36 47 6 33 8 35 32 3 40 50 22 18 3 12 30 31 13 33 4 48 5 17 33 26 27 19 39 15 33 47 17 41 40]	c=[35 67 30 69 40 40 21 73 82 93 52 20 61 20 42 86 43 93 38 70 59 11 42 93 6 39 25 23 36 93 51 81 36 46 96]

kp-13	40	819	w=[28 23 35 38 20 29 11 48 26 14 12 48 35 36 33 39 30 26 44 20 13 15 46 36 43 19 32 2 47 24 26 39 17 32 17 16 33 22 6 12]	c=[13 16 42 69 66 68 1 13 77 85 75 95 92 23 51 79 53 62 56 74 7 50 23 34 56 75 42 51 13 22 30 45 25 27 90 59 94 62 26 11]
kp-14	45	907	w=[18 12 38 12 23 13 18 46 1 7 20 43 11 47 49 19 50 7 39 29 32 25 12 8 32 41 34 24 48 30 12 35 17 38 50 14 47 35 5 13 47 24 45 39 1]	c=[98 70 66 33 2 58 4 27 20 45 77 63 32 30 8 18 73 9 92 43 8 58 84 35 78 71 60 38 40 43 43 22 50 4 57 5 88 87 34 98 96 99 16 1 25]
kp-15	50	882	w=[15 40 22 28 50 35 49 5 45 3 7 32 19 16 40 16 31 24 15 42 29 4 14 9 29 11 25 37 48 39 5 47 49 31 48 17 46 1 25 8 16 9 30 33 18 3 3 3 4 1]	c=[78 69 87 59 63 12 22 4 45 33 29 50 19 94 95 60 1 91 69 8 100 32 81 47 59 48 56 18 59 16 45 54 47 84 100 98 75 20 4 19 58 63 37 64 90 26 29 13 53 83]
kp-16	55	1050	w=[27 15 46 5 40 9 36 12 11 11 49 20 32 3 12 44 24 1 24 42 44 16 12 42 22 26 10 8 46 50 20 42 48 45 43 35 9 12 22 2 14 50 16 29 31 46 20 35 11 4 32 35 15 29 16]	c=[98 74 76 4 12 27 90 98 100 35 30 19 75 72 19 44 5 66 79 87 79 44 35 6 82 11 1 28 95 68 39 86 68 61 44 97 83 2 15 49 59 30 44 40 14 96 37 84 5 43 8 32 95 86 18]
kp-17	60	1006	w=[7 13 47 33 38 41 3 21 37 7 32 13 42 42 23 20 49 1 20 25 31 4 8 33 11 6 3 9 26 44 39 7 4 34 25 25 16 17 46 23 38 10 5 11 28 34 47 3 9 22 17 5 41 20 33 29 1 33 16 14]	c=[81 37 70 64 97 21 60 9 55 85 5 33 71 87 51 100 43 27 48 17 16 27 76 61 97 78 58 46 29 76 10 11 74 36 59 30 72 37 72 100 9 47 10 73 92 9 52 56 69 30 61 20 66 70 46 16 43 60 33 84]
kp-18	65	1319	w=[47 27 24 27 17 17 50 24 38 34 40 14 15 36 10 42 9 48 37 7 43 47 29 20 23 36 14 2 48 50 39 50 25 7 24 38 34 44 38 31 14 17 42 20 5 44 22 9 1 33 19 19 23 26 16 24 1 9 16 38 30 36 41 43 6]	c=[47 63 81 57 3 80 28 83 69 61 39 7 100 67 23 10 25 91 22 48 91 20 45 62 60 67 27 43 80 94 47 31 44 31 28 14 17 50 9 93 15 17 72 68 36 10 1 38 79 45 10 81 66 46 54 53 63 65 20 81 20 42 24 28 1]
kp-19	70	1426	w=[4 16 16 2 9 44 33 43 14 45 11 49 21 12 41 19 26 38 42 20 5 14 40 47 29 47 30 50 39 10 26 33 44 31 50 7 15 24 7 12 10 34 17 40 28 12 35 3 29 50 19 28 47 13 42 9 44 14 43 41 10 49 13 39 41 25 46 6 7 43]	c=[66 76 71 61 4 20 34 65 22 8 99 21 99 62 25 52 72 26 12 55 22 32 98 31 95 42 2 32 16 100 46 55 27 89 11 83 43 93 53 88 36 41 60 92 14 5 41 60 92 30 55 79 33 10 45 3 68 12 20 54 63 38 61 85 71 40 58 25 73 35]
kp-20	75	1433	w=[24 45 15 40 9 37 13 5 43 35 48 50 27 46 24 45 2 7 38 20 20 31 2 20 3 35 27 4 21 22 33 11 5 24 37 31 46 13 12 12 41 36 44 36 34 22 29 50 48 17 8 21 28 2	c=[2 73 82 12 49 35 78 29 83 18 87 93 20 6 55 1 83 91 71 25 59 94 90 61 80 84 57 1 26 44 44 88 7 34 18 25 73 29 24 14 23 82 38 67 94 43 61 97 37 67 32 89 30 30 91

			44 45 25 11 37 35 24 9 40 45 8 47 1 22 1 12 36 35 14 17 5]		50 21 3 18 31 97 79 68 85 43 71 49 83 44 86 1 100 28 4 16]	

Table S4: Results obtained by the transfer functions for the medium scale 0–1 KP

Instance	Transfer function	Best	Mean	Worst	SD	Mean iterations
	S1	1437	1437	1437	0	2.48
	S2	1437	1437	1437	0	7.8
	S3	1437	1437	1437	0	6.96
	S4	1437	1437	1437	0	4.92
	V1	1437	1437	1437	0	1.84
	V2	1437	1437	1437	0	2.04
	V3	1437	1437	1437	0	1.24
	V4	1437	1437	1437	0	1.12
kp-11	T1S1	1437	1437	1437	0	5.7
	T1S2	1437	1437	1437	0	3.56
	T1S3	1437	1437	1437	0	5.81
	T1S4	1437	1437	1437	0	4.17
	T1V1	1437	1437	1437	0	1.14
	T1V2	1437	1437	1437	0	1.94
	T1V3	1437	1437	1437	0	1.08
	T1V4	1437	1437	1437	0	1.04
	T2S1	1437	1437	1437	0	3.87
	T2S2	1437	1437	1437	0	3.92
	T2S3	1437	1437	1437	0	4.91
	T2S4	1437	1437	1437	0	2.55
	T2V1	1437	1437	1437	0	1.04
	T2V2	1437	1437	1437	0	1.37
	T2V3	1437	1437	1437	0	1
	T2V4	1437	1437	1437	0	1
	S1	1689	1689	1689	0	3.8
	S2	1689	1689	1689	0	7.96
	S3	1689	1689	1689	0	4.88
	S4	1689	1689	1689	0	3.76
	V1	1689	1689	1689	0	2.2
	V2	1689	1689	1689	0	1.92
kp-12	V3	1689	1689	1689	0	1.68
	V4	1689	1689	1689	0	1.36
	T1S1	1689	1689	1689	0	4.24
	T1S2	1689	1689	1689	0	3.6
	T1S3	1689	1689	1689	0	3.48
	T1S4	1689	1689	1689	0	3.8
	T1V1	1689	1689	1689	0	1.04

	T1V2	1689	1689	1689	0	1.16
	T1V3	1689	1689	1689	0	1.04
	T1V4	1689	1689	1689	0	1.04
	T2S1	1689	1689	1689	0	4.88
	T2S2	1689	1689	1689	0	3.8
	T2S3	1689	1689	1689	0	4.64
	T2S4	1689	1689	1689	0	3.16
	T2V1	1689	1689	1689	0	1.24
	T2V2	1689	1689	1689	0	1
	T2V3	1689	1689	1689	0	1.08
	T2V4	1689	1689	1689	0	1
kp-13	S1	1821	1821	1821	0	8.28
	S2	1821	1821	1821	0	37.8
	S3	1821	1821	1821	0	22.2
	S4	1821	1821	1821	0	17.92
	V1	1821	1821	1821	0	4.56
	V2	1821	1821	1821	0	3.72
	V3	1821	1821	1821	0	2.68
	V4	1821	1821	1821	0	1.96
	T1S1	1821	1821	1821	0	11.56
	T1S2	1821	1821	1821	0	22.41
	T1S3	1821	1821	1821	0	16.63
	T1S4	1821	1821	1821	0	12.65
	T1V1	1821	1821	1821	0	3.47
	T1V2	1821	1821	1821	0	2.34
	T1V3	1821	1821	1821	0	1.94
	T1V4	1821	1821	1821	0	1.04
	T2S1	1821	1821	1821	0	9.53
	T2S2	1821	1821	1821	0	19.3
	T2S3	1821	1821	1821	0	18.66
	T2S4	1821	1821	1821	0	10.06
	T2V1	1821	1821	1821	0	1.94
	T2V2	1821	1821	1821	0	1.15
	T2V3	1821	1821	1821	0	1.35
	T2V4	1821	1821	1821	0	1.23
kp-14	S1	2033	2033	2033	0	3.28
	S2	2033	2033	2033	0	22
	S3	2033	2033	2033	0	25.28
	S4	2033	2033	2033	0	22.88
	V1	2033	2033	2033	0	3.52
	V2	2033	2033	2033	0	2.32
	V3	2033	2033	2033	0	2.08
	V4	2033	2033	2033	0	1.48
	T1S1	2033	2033	2033	0	5.19
	T1S2	2033	2033	2033	0	14.55
	T1S3	2033	2033	2033	0	20.12

	T1S4	2033	2033	2033	0	19.49
	T1V1	2033	2033	2033	0	1.42
	T1V2	2033	2033	2033	0	1.42
	T1V3	2033	2033	2033	0	1.19
	T1V4	2033	2033	2033	0	1.04
	T2S1	2033	2033	2033	0	3.92
	T2S2	2033	2033	2033	0	12.95
	T2S3	2033	2033	2033	0	17.88
	T2S4	2033	2033	2033	0	14.94
	T2V1	2033	2033	2033	0	1.08
	T2V2	2033	2033	2033	0	1.12
	T2V3	2033	2033	2033	0	1.04
	T2V4	2033	2033	2033	0	1.04
kp-16	S1	2651	2651	2651	0	13.56
	S2	2651	2650.2	2647	1.69	524.3
	S3	2651	2651	2651	0	423.53
	S4	2651	2650.2	2643	2.53	360.6
	V1	2651	2651	2651	0	11.36
	V2	2651	2651	2651	0	9.12
	V3	2651	2651	2651	0	5.04
	V4	2651	2651	2651	0	3.2
	T1S1	2651	2651	2651	0	20.82
	T1S2	2651	2651	2651	0	347.16
	T1S3	2651	2651	2651	0	279.31
	T1S4	2651	2651	2651	0	318
	T1V1	2651	2651	2651	0	8.94
	T1V2	2651	2651	2651	0	6.78
	T1V3	2651	2651	2651	0	3.92
	T1V4	2651	2651	2651	0	1.9
	T2S1	2651	2651	2651	0	15.34
	T2S2	2651	2651	2651	0	328.5
	T2S3	2651	2651	2651	0	223.96
	T2S4	2651	2651	2651	0	6.95
	T2V1	2651	2651	2651	0	7.15
	T2V2	2651	2651	2651	0	4.52
	T2V3	2651	2651	2651	0	2.94
	T2V4	2651	2651	2651	0	1.08
kp-17	S1	2917	2917	2917	0	6.08
	S2	2917	2917	2917	0	81.88
	S3	2917	2917	2917	0	43.44
	S4	2917	2917	2917	0	42.88
	V1	2917	2917	2917	0	3.52
	V2	2917	2917	2917	0	2.88
	V3	2917	2917	2917	0	2.16
	V4	2917	2917	2917	0	1.8
	T1S1	2917	2917	2917	0	8.5
	T1S2	2917	2917	2917	0	50.73

	T1S3	2917	2917	2917	0	40.95
	T1S4	2917	2917	2917	0	39.27
	T1V1	2917	2917	2917	0	1.93
	T1V2	2917	2917	2917	0	1.96
	T1V3	2917	2917	2917	0	1.04
	T1V4	2917	2917	2917	0	1
	T2S1	2917	2917	2917	0	6.94
	T2S2	2917	2917	2917	0	48.33
	T2S3	2917	2917	2917	0	35.97
	T2S4	2917	2917	2917	0	31.94
	T2V1	2917	2917	2917	0	1.26
	T2V2	2917	2917	2917	0	1.75
	T2V3	2917	2917	2917	0	1.23
	T2V4	2917	2917	2917	0	1
	S1	2818	2818	2818	0	24.28
	S2	2818	2817.1	2817	0.32	978.5
	S3	2818	2817.1	2817	0.32	965.5
	S4	2818	2817.1	2817	0.32	905.5
	V1	2818	2818	2818	0	94.76
	V2	2818	2818	2818	0	39.6
	V3	2818	2818	2818	0	30.36
	V4	2818	2818	2818	0	18.52
	T1S1	2818	2818	2818	0	30.65
	T1S2	2818	2818	2818	0	766.3
	T1S3	2818	2818	2818	0	598.5
	T1S4	2818	2818	2818	0	832.9
kp-18	T1V1	2818	2818	2818	0	71.2
	T1V2	2818	2818	2818	0	23.9
	T1V3	2818	2818	2818	0	19.43
	T1V4	2818	2818	2818	0	8.69
	T2S1	2818	2818	2818	0	27.83
	T2S2	2818	2818	2818	0	515.8
	T2S3	2818	2818	2818	0	691.6
	T2S4	2818	2818	2818	0	536.4
	T2V1	2818	2818	2818	0	74.9
	T2V2	2818	2818	2818	0	21.95
	T2V3	2818	2818	2818	0	15.35
	T2V4	2818	2818	2818	0	6.94
	S1	3223	3223	3223	0	95.68
	S2	3223	3221.2	3221	0.632	985.5
	S3	3223	3221.2	3221	0.632	589.5
	S4	3223	3221.2	3221	0.632	765.3
kp-19	V1	3223	3223	3223	0	13.1
	V2	3223	3223	3223	0	9.43
	V3	3223	3223	3223	0	7.93
	V4	3223	3223	3223	0	4.1
	T1S1	3223	3223	3223	0	120.6

	T1S2	3223	3223	3223	0	645.35
	T1S3	3223	3223	3223	0	428.6
	T1S4	3223	3223	3223	0	594.82
	T1V1	3223	3223	3223	0	9.72
	T1V2	3223	3223	3223	0	9.18
	T1V3	3223	3223	3223	0	4.38
	T1V4	3223	3223	3223	0	2.14
	T2S1	3223	3223	3223	0	89.5
	T2S2	3223	3223	3223	0	583.8
	T2S3	3223	3223	3223	0	357.91
	T2S4	3223	3223	3223	0	455.91
	T2V1	3223	3223	3223	0	8.16
	T2V2	3223	3223	3223	0	6.28
	T2V3	3223	3223	3223	0	6.13
	T2V4	3223	3223	3223	0	1.91

Table S5: Comparison results of uncorrelated large size 0–1 KP

Instance	Dimension	Transfer function	Best	Mean	Worst	SD	Mean iterations
kp-21	100	S1	2060	2060	2060	0	142
		S2	2060	2038.4	2023	19.756	350
		S3	2060	2036.8	2023	17.387	353
		S4	2060	2043	2023	18.886	351
		V1	2060	2060	2060	0	95
		V2	2060	2060	2060	0	88
		V3	2060	2060	2060	0	90
		V4	2060	2060	2060	0	76
		T1S1	2060	2060	2060	0	169
		T1S2	2060	2049	2045	6.519	153
		T1S3	2060	2049.8	2045	6.14	215
		T1S4	2060	2048.4	2045	7.092	201
		T1V1	2060	2060	2060	0	57
		T1V2	2060	2060	2060	0	45
		T1V3	2060	2060	2060	0	62
		T1V4	2060	2060	2060	0	39
		T2S1	2060	2060	2060	0	185
		T2S2	2060	2049.6	2048	6.542	162
		T2S3	2060	2049	2048	6.633	224
		T2S4	2060	2049.6	2048	5.941	240
		T2V1	2060	2060	2060	0	61
		T2V2	2060	2060	2060	0	42
		T2V3	2060	2060	2060	0	59
		T2V4	2060	2060	2060	0	34
kp-23	1000	S1	20348	20339.6	20334	7.668	2859
		S2	20340	20327.2	20308	17.527	4781
		S3	20340	20329.4	20308	15.027	4618
		S4	20340	20326.8	20308	17.181	4237

		V1	20350	20347.6	20346	2.19	531
		V2	20350	20348	20346	2	498
		V3	20350	20348.4	20346	2.19	562
		V4	20350	20349.2	20346	1.789	415
		T1S1	20350	20344.8	20342	3.899	2094
		T1S2	20349	20338.8	20332	9.311	3586
		T1S3	20349	20339.4	20332	8.848	3428
		T1S4	20349	20338.8	20332	7.12	4057
		T1V1	20350	20348.8	20348	1.095	463
		T1V2	20350	20349.4	20348	0.894	401
		T1V3	20350	20348.8	20348	0.837	443
		T1V4	20350	20349.4	20348	0.894	381
		T2S1	20350	20346	20342	3.742	2099
		T2S2	20349	20342.2	20332	9.3	3308
		T2S3	20349	20343.6	20332	7.8	3258
		T2S4	20349	20340.2	20332	8.526	3974
		T2V1	20350	20349.2	20348	1.095	492
		T2V2	20350	20349.2	20348	0.837	391
		T2V3	20350	20349	20348	1	412
		T2V4	20350	20349.6	20348	0.894	328
		S1	31255	31247.8	31241	6.686	4289
		S2	31250	31224.2	31198	26.04	6722
		S3	31250	31222	31198	23.63	5983
		S4	31250	31224	31198	25.76	5347
		V1	31257	31249.8	31245	5.215	1025
		V2	31257	31250.8	31245	4.49	992
		V3	31257	31250.4	31245	4.67	1349
		V4	31257	31252.2	31245	4.38	903
		T1S1	31257	31254.6	31253	2.19	2951
		T1S2	31256	31237.6	31228	13.45	4228
		T1S3	31256	31235.4	31228	14.69	3984
kp-24	1500	T1S4	31256	31236.4	31228	15.646	4129
		T1V1	31257	31255.8	31255	1.095	751
		T1V2	31257	31256	31255	1	694
		T1V3	31257	31256.2	31255	0.837	789
		T1V4	31257	31256.4	31255	0.821	562
		T2S1	31257	31255	31253	2	2493
		T2S2	31256	31237.4	31228	12.605	4059
		T2S3	31256	31238.6	31228	12.954	4286
		T2S4	31256	31238.4	31228	11.06	4178
		T2V1	31257	31255.8	31255	0.837	842
		T2V2	31257	31256	31255	0.707	697
		T2V3	31257	31255.6	31255	0.894	981
		T2V4	31257	31256.4	31255	0.821	509

Table S6: Comparison results of weakly correlated large size 0–1 KP

Instance	Dimension	Transfer function	Best	Mean	Worst	SD	Mean iterations
kp-26	100	S1	1016	1016	1016	0	120

		S2	1016	997.2	989	11.278	325
		S3	1016	994.2	989	9.952	298
		S4	1016	998	989	10.677	337
		V1	1016	1016	1016	0	86
		V2	1016	1016	1016	0	79
		V3	1016	1016	1016	0	83
		V4	1016	1016	1016	0	62
		T1S1	1016	1016	1016	0	157
		T1S2	1016	1004	999	7.661	129
		T1S3	1016	1007	999	6.166	194
		T1S4	1016	1009.4	999	7.057	173
		T1V1	1016	1016	1016	0	65
		T1V2	1016	1016	1016	0	49
		T1V3	1016	1016	1016	0	64
		T1V4	1016	1016	1016	0	30
		T2S1	1016	1016	1016	0	160
		T2S2	1016	1009.6	1008	3.578	122
		T2S3	1016	1012	1008	4	188
		T2S4	1016	1011.2	1008	3.347	169
		T2V1	1016	1016	1016	0	64
		T2V2	1016	1016	1016	0	39
		T2V3	1016	1016	1016	0	61
		T2V4	1016	1016	1016	0	31
kp-28	1000	S1	10352	10345.4	10340	9.631	2156
		S2	10351	10348.2	10338	13.964	3924
		S3	10351	10347.8	10338	14.57	3615
		S4	10351	10348	10338	13.238	4025
		V1	10356	10353.6	10350	5.613	492
		V2	10356	10354	10350	4.679	385
		V3	10356	10353.8	10350	5.348	477
		V4	10356	10354.4	10350	4.069	336
		T1S1	10357	10354.2	10352	2.15	2294
		T1S2	10357	10352.1	10344	7.281	2960
		T1S3	10357	10351.6	10344	6.823	3458
		T1S4	10357	10351.4	10344	6.134	3512
		T1V1	10357	10355.1	10354	2.36	418
		T1V2	10357	10356	10354	1.068	304
		T1V3	10357	10355.4	10354	2.06	393
		T1V4	10357	10356.2	10354	0.985	300
		T2S1	10357	10354	10352	2.01	2341
		T2S2	10357	10351.8	10344	7.328	3001
		T2S3	10357	10351.2	10344	7.054	2923
		T2S4	10357	10532	10344	6.832	3194
		T2V1	10357	10355.4	10354	2.456	407
		T2V2	10357	10356.1	10354	1.37	318
		T2V3	10357	10356	10354	1.254	371
		T2V4	10357	10356.2	10354	0.895	303
kp-29	1500	S1	15446	15441.6	15432	7.627	4091
		S2	15400	15383.4	15365	21.975	5906
		S3	15400	15384	15365	19.713	5213

		S4	15400	15383.6	15365	20.668	5194
		V1	15496	15486	15454	10.634	1395
		V2	15496	15486.4	15454	9.248	1082
		V3	15496	15486.2	15454	11.573	1267
		V4	15496	15486.8	15454	8.275	990
		T1S1	15507	15491	15470	5.382	3924
		T1S2	15507	15495.6	15460	13.627	4615
		T1S3	15507	15494.8	15460	14.351	4208
		T1S4	15507	15495	15460	12.01	4792
		T1V1	15507	15502	15490	5.617	971
		T1V2	15507	15503.2	15490	4.319	898
		T1V3	15507	15502.6	15490	4.065	919
		T1V4	15507	15503.2	15490	4.319	805
		T2S1	15507	15491.6	15454	5.915	3902
		T2S2	15507	15494.2	15460	12.951	4593
		T2S3	15507	15494	15460	13.986	4321
		T2S4	15507	15495.4	15460	13.035	4435
		T2V1	15507	15502.6	15490	4.972	850
		T2V2	15507	15503	15490	3.658	777
		T2V3	15507	15502	15490	5.349	882
		T2V4	15507	15503.4	15490	4.568	692

Table S7: Comparison results of strongly correlated large size 0–1 KP

Instance	Dimension	Transfer function	Best	Mean	Worst	SD	Mean iterations
kp-31	100	S1	1332	1332	1332	0	95
		S2	1332	1332	1332	0	184
		S3	1332	1332	1332	0	176
		S4	1332	1332	1332	0	190
		V1	1332	1332	1332	0	54
		V2	1332	1332	1332	0	31
		V3	1332	1332	1332	0	50
		V4	1332	1332	1332	0	29
		T1S1	1332	1332	1332	0	109
		T1S2	1332	1332	1332	0	123
		T1S3	1332	1332	1332	0	125
		T1S4	1332	1332	1332	0	120
		T1V1	1332	1332	1332	0	40
		T1V2	1332	1332	1332	0	25
		T1V3	1332	1332	1332	0	33
		T1V4	1332	1332	1332	0	19
		T2S1	1332	1332	1332	0	137
		T2S2	1332	1332	1332	0	114
		T2S3	1332	1332	1332	0	122
		T2S4	1332	1332	1332	0	108
		T2V1	1332	1332	1332	0	47
		T2V2	1332	1332	1332	0	27
		T2V3	1332	1332	1332	0	30
		T2V4	1332	1332	1332	0	25
kp-33	1000	S1	13410	13405.2	13395	7.391	1945

		S2	13390	13386	13370	18.62	3026
		S3	13390	13385.9	13370	19.28	2915
		S4	13390	13386.4	13370	17.54	3108
		V1	13448	13441	13436	12.68	1154
		V2	13448	13442	13436	10.25	1093
		V3	13448	13441.6	13436	11.39	1251
		V4	13448	13442.4	13436	10.09	1001
		T1S1	13454	13449	13440	9.52	2397
		T1S2	13454	13448.5	13440	10.27	2108
		T1S3	13454	13448	13440	9.35	2293
		T1S4	13454	13447.2	13440	11.24	2604
		T1V1	13454	13454	13454	0	938
		T1V2	13454	13454	13454	0	756
		T1V3	13454	13454	13454	0	849
		T1V4	13454	13454	13454	0	720
		T2S1	13454	13447	13440	10.14	2253
		T2S2	13454	13448	13440	8.37	2204
		T2S3	13454	13447.8	13440	9.63	2157
		T2S4	13454	13448.2	13440	8.921	2384
		T2V1	13454	13454	13454	0	961
		T2V2	13454	13454	13454	0	770
		T2V3	13454	13454	13454	0	902
		T2V4	13454	13454	13454	0	738
kp-34	1500	S1	20295	20284	20252	10.692	3157
		S2	20289	20277.2	20246	25.34	5089
		S3	20289	20276	20246	27.137	4975
		S4	20289	20276.8	20246	26.821	5013
		V1	20310	20306	20302	9.38	1085
		V2	20310	20306.8	20302	8.937	1020
		V3	20310	20306.4	20302	9.036	1017
		V4	20310	20307	20302	10.02	1003
		T1S1	20314	20312	20300	6.35	3681
		T1S2	20314	20310	20296	16.93	3054
		T1S3	20314	20310.6	20296	18.37	3376
		T1S4	20314	20311	20296	20.589	3128
		T1V1	20314	20314	20314	0	984
		T1V2	20314	20314	20314	0	793
		T1V3	20314	20314	20314	0	980
		T1V4	20314	20314	20314	0	751
		T2S1	20314	20312.6	20300	5.83	3507
		T2S2	20314	20311	20296	19.34	3182
		T2S3	20314	20310.6	20296	15.61	3259
		T2S4	20314	20310.4	20296	13.29	3204
		T2V1	20314	20314	20314	0	901
		T2V2	20314	20314	20314	0	800
		T2V3	20314	20314	20314	0	826
		T2V4	20314	20314	20314	0	748

References

[1] Wang G, Guo L, Wang H, Duan H, Liu L and Li J 2012 Incorporating mutation scheme into krill

herd algorithm for global numerical optimization *Neural Computing and Applications* **24**(3-4) pp 853-871
[2] Feng Y, Yang J, Wu C, Lu M and Zhao X 2016 Solving 0–1 knapsack problems by chaotic monarch butterfly optimization algorithm with Gaussian Mutation *Memetic Computing* **10**(2) pp 135-150
[3] Tilahun S L and J M T Ngnotchouye 2017 Firefly algorithm for discrete optimization problems: A survey *KSCE Journal of Civil Engineering* **21**(2) pp 535-545
[4] Parsopoulos K E and Vrahatis M N 2010 Particle Swarm Optimization and Intelligence Advances and Applications *IGI Global*
[5] Abdel-Basset M, El-Shahat D and Sangaiah A K 2017 A modified nature inspired meta-heuristic whale optimization algorithm for solving 0–1 knapsack problem *International Journal of Machine Learning and Cybernetics*
[6] Abdel-Basset M, El-Shahat D and El-Henawy I 2017 Solving 0–1 Knapsack Problems by Binary Dragonfly Algorithm *Springer International Publishing AG* 10363 pp 491-502
[7] Cao J, Yin B, Lu X, Kang Y and Chen X 2017 A modified artificial bee colony approach for the 0-1 knapsack problem *Applied Intelligence* **48**(6) pp 1582-1595
[8] Layeb A 2013 A hybrid quantum inspired harmony search algorithm for 0–1 optimization problems *Journal of Computational and Applied Mathematics* 253 pp 14-25
[9] Abdel-Basset M, D El-Shahat and I El-Henawy 2018 Solving 0–1 knapsack problem by binary flower pollination algorithm *Neural Computing and Applications*
[10] Zouache D, A Moussaoui and F Ben Abdelaziz 2018 A cooperative swarm intelligence algorithm for multi-objective discrete optimization with application to the knapsack problem *European Journal of Operational Research* **264**(1) pp 74-88
[11] Feng Y, Wang G, Deb S, Lu M and Zhao X 2015 Solving 0–1 knapsack problem by a novel binary monarch butterfly optimization *Neural Computing and Applications* **28**(7) pp 1619-1634
[12] Zhou Y, L Li, and M Ma 2015 A Complex-valued Encoding Bat Algorithm for Solving 0–1 Knapsack Problem *Neural Processing Letters* **44**(2) pp 407-430
[13] Rizk-Allah R M and A E Hassanien 2017 New binary bat algorithm for solving 0–1 knapsack problem *Complex & Intelligent Systems* **4**(1) pp 31-53
[14] Haddar B, Khemakhem M, Hanafi S and Wilbaut C 2015 A hybrid heuristic for the 0–1 Knapsack Sharing Problem *Expert Systems with Applications* **42**(10) pp 4653-4666
[15] Haddar B, Khemakhem M, Rhimi H and Chabchoub H 2014 A quantum particle swarm optimization for the 0–1 generalized knapsack sharing problem *Natural Computing* **15**(1) pp 53-164
[16] Bansal J C and K Deep 2012 A Modified Binary Particle Swarm Optimization for Knapsack Problems *Applied Mathematics and Computation* **218**(22) pp 11042-11061
[17] Zhou Y, X Chen and G Zhou 2016 An improved monkey algorithm for a 0-1 knapsack problem *Applied Soft Computing* **6(**38) pp 817-830
[18] Changdar C, G S Mahapatra and R K Pal 2013 An Ant colony optimization approach for binary knapsack problem under fuzziness *Applied Mathematics and Computation* 223 pp. 243-253
[19] Zhang X, Huang S, Hu Y, Zhang Y, Mahadevan S and Deng Y 2013 Solving 0-1 knapsack problems based on amoeboid organism algorithm *Applied Mathematics and Computation* **219**(19) pp 9959-9970
[20] Zou D, Gao L, Li S and Wu J 2011 Solving 0–1 knapsack problem by a novel global harmony search algorithm *Applied Soft Computing* **11**(2) pp 1556-1564
[21] Yang X S 2012 Flower pollination algorithm for global optimization Unconventional *Computation and Natural Computation* 7445 pp 240-249
[22] Yang X S, M Karamanoglu and H Xingshi 2014 *Flower pollination algorithm: A noval approach for multiobjective optimization* Engineering Optimization
[23] Yang X S 2015 *Recent Advances in Swarm Intelligence and Evolutionary Computation* Springer International Publishing Switzerland

[24] Islam M J, X Li and Y Mei 2017 A time-varying transfer function for balancing the exploration and exploitation ability of a binary PSO *Applied Soft Computing* **59** pp 182-196
[25] Kulkarni A J and H Shabir 2014 Solving 0–1 Knapsack Problem using Cohort Intelligence Algorithm *International Journal of Machine Learning and Cybernetics* **7**(3) pp 427-441
[26] Abdel-Basset M, El-Shahat D, El-Henawy I and Sangaiah A A 2017 modified flower pollination algorithm for the multidimensional knapsack problem: human-centric decision making *Soft Computing* **22**(13) pp 4221-4239
[27] Bozorg-Haddad O 2018 *Advanced Optimization by Nature-Inspired Algorithms* Springer Nature Singapore Pte Ltd
[28] Mafarja M, Aljarah I, Heidari A, Faris H, Fournier-Viger P, Li X and Mirjalili S 2018 Binary dragonfly optimization for feature selection using time-varying transfer functions *Knowledge-Based Systems* 161 pp 185-204
[29] Mirjalili S and A Lewis 2013 S-shaped versus V-shaped transfer functions for binary Particle Swarm Optimization *Swarm and Evolutionary Computation* 9 pp 1-14
[30] Teng X, H Dong and X Zhou 2017 Adaptive feature selection using v-shaped binary particle swarm optimization *PLoS One* **12**(3) pp e0173907

The Syriac Letters and e-Abacus Diagram II

The Syriac Letters and e-Abacus Diagram II

Shukriyah S Ali[1], Mohammed K Ahmed[2], Hadil H Sami[*,٢] and Ammar S Mahmood[٣]

[1]Department. Specialized Supervision, General Dirctorate of Education in Kirkuk, Kirkuk, Iraq
[2]Department of Computer Science, College of Education, University of Al-Hamdaniya, Mosul, Iraq
[٣]Department of Mathematics, College of Education for Pure Science, University of Mosul, Mosul, Iraq

E-mail: hadilhazem29@yahoo.com

Abstract. The Syriac language is one of the oldest languages in the world. So far, some people speak it, for example in Iraq, Syria, southeastern Turkey and other countries. In this work, the Syriac letters were coded according to what was adopted by Sami and Mahmood in 2017 using the e-abacus diagram. More than one method is used to encode the English letters or diagrams that follow the concepts of partition theory. Each of them was taking its own path and the vision was to start with what Mohommed et al looked like in 2015 through the orbit concept. Then make the comparisons to observe the most efficient, fastest and most accurate method that could be followed.

1. Introduction

Let r be a nonnegative integer. The composition $\delta = (\delta_1, \delta_2, \dots, \delta_n)$ of r is a sequence of non-negative integers such that $|\delta| = \sum_{j=1}^{n} \delta_j = r$. The composition is called a partition of r if $\delta_j \geq \delta_{j+1} \ \forall\, j \geq 1$. Fix δ is a partition of r and defining $\beta_i = \delta_i + b - i$, $1 \leq i \leq b$. The set $\{\beta_1, \beta_2, \cdots \beta_b\}$ is said to be the set of β - number for δ, see [1]. Let e be a positive integer number greater than or equal to 2, we can represent numbers by a diagram called e-abacus diagram, see [2], as shown in Table 1:

Table 1. e-Abacus Diagram

run.1	**run.2**	**...**	**run. e**
0	1		$e-1$
e	$e+1$	...	$2e-1$
2e	$2e+1$	...	$3e-1$
⋮	⋮	⋮	⋮

Where every β-numbers will be represented by a (●) which takes its location in e-abacus diagram and in case of non-existence of β- numbers then the value in e-abacus diagram will be represented by a

blank. For example, if $\delta = (7,7,6,5,5,5,4,2,1)$ and $e = 4, b = 9$ then the set of β – number is $\{1,3,6,8,9,10,12,14,15\}$ then e-abacus diagram for this partition is:

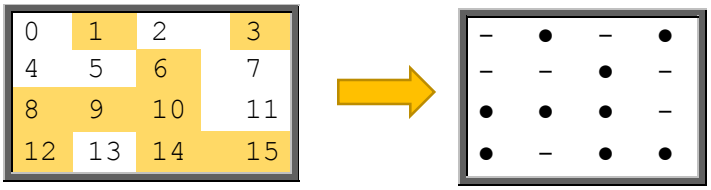

Figure 1. e-Abacus Diagram for $\delta = (7,7,6,5,5,5,4,2,1)$

Fayers is one of the creators who added a lot to this topic so much so we might refer here to [3-5]. Sami and Mahmood [6] developed a design for the shape of the 22 Syriac letters; (to learn more about this language see [7,8], through the e-abacus diagram technology and $e = 7$ in order to ensure that the shape becomes more accurate and clear if we choose e less than 7. We mention, the following example:

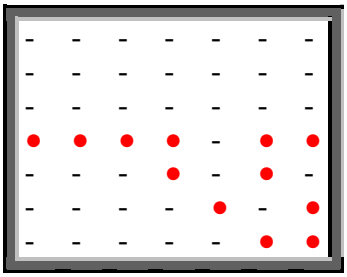

Figure 2. The Partition of 3rd - Syraic letter is$(37^2, 32,31,26,25, 22^2, 21^4)$ where e=7.

The problem that, we want to solve is how we change the parameters of the Syraic letters (to become unreadable as if I were sending a secret message), so we had the concept of "Orbits" presented in 2015 by Mohommed et al the best assistant to solve this dilemma.

2. The Orbits

The movement in orbits that were presented by Mohommed et al [9-11] and later on [12], made a major impact on the research that followed on the e-abacus diagram as it lads here to many ideas such as [13,14]. A new coding idea for the English letters which adopted $e = 5$ was introduced [15]; (these comparisons are possible, especially since there is a lot of research dealing with more than one language, for example we mention each of them [15], Based on [16] there are four orbits in e-abacus if $e = 7$ as shown in Figure3:

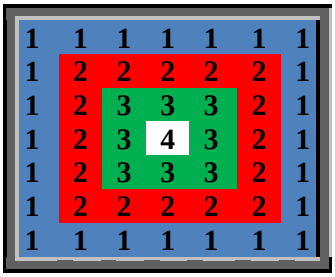

Figure 3. The four orbits.

The first (**1**), is the external path, where we do not change anything as a result of our need for the first site to be empty, see [17]. The Second (**2**), which is immediately following the first and here we will notice the presence of 16 sites that have not been fully studied in [11]. The third (**3**), this path contains 8 possible movements, and the fourth (**4**), is the last orbit that is usually fixed in place, because it contains only one location (site), then this orbit has no effect.

In this work we would like to point out here that we will move only on the second orbit without the rest, because the third orbit is the same movements that were addressed in [11]. We denoted by any move in each orbit by m_k, where $1 \leq k \leq 4$.

2.1. Movement on the Second Orbit

It is normal to move in the movement from the first until the arrival of the possible movements, in order to formulate this work easily, the James abacus diagram is converted to matrix form [12] as shown in Figure4.:

	a_{22}	a_{23}	a_{24}	a_{25}	a_{26}	
	a_{32}				a_{36}	
	a_{42}				a_{46}	
	a_{52}				a_{56}	
	a_{62}	a_{63}	a_{64}	a_{65}	a_{66}	

Figure 4. The locations of 2nd-orbit.

Rule (2.1.1): When choosing a partition for any Syriac letter where $e = 7$ and the value of β_i is equal to the location $a_{\tau\rho}$ within $[m_1;1; m_3; m_4]$ where ρ be column number, and τ the number of rows in the James abacus diagram then:

$$a_{\tau\rho} \rightarrow \begin{cases} a_{\tau(\rho\mp1)} & \text{if} \quad (\tau = 2\ (\text{or } 6)) \wedge (\rho = 2, \dots, 5\ (\text{or } 3, \dots, 6)) \text{resp.}, \\ a_{(\tau\mp1)\rho} & \text{if} \quad (\tau = 2, \dots, 5\ (\text{or } 3, \dots, 6) \wedge (\rho = 6\ (\text{or } 2))\ \text{resp.}, \end{cases} \quad (1)$$

Proof: Here is the ideal movement (with clockwise and the amount of movement is equal to one), we have one path, it will start from a_{22} up to a_{26} (respectively from a_{66} to a_{62}) provided it does not exceed it; we mean that does not go to a_{27} (respectively a_{61}) where this is outside the scope of the second orbit. Also form $a_{26} \rightarrow a_{36} \rightarrow \cdots \rightarrow a_{66}$ (respectively from $a_{62} \rightarrow a_{52} \rightarrow \cdots \rightarrow a_{22}$). This movement is not complicated and therefore the possibilities are limited.

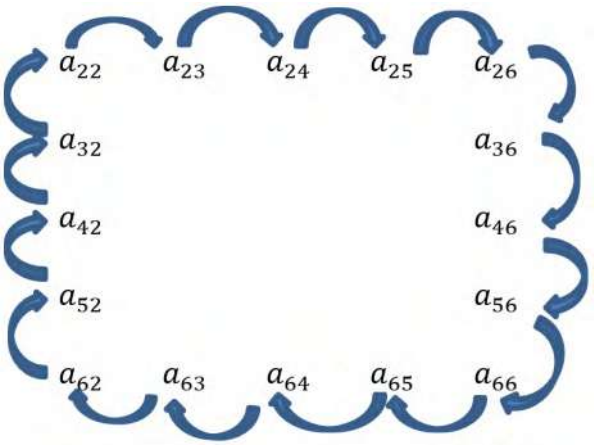

Figure 5. The movement when $m_2 = 1$

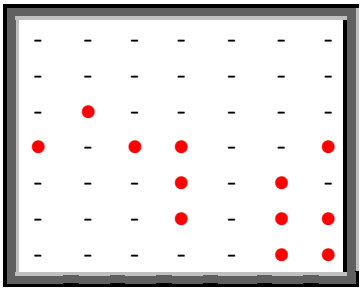

Figure6. The new partition of 3rd-Syriac letter is $(37^2, 32^2, 31,27,26,23, 21^2, 20,15)$

Then we have a new partition for each Syriac letter after using this method, the movement will generate a new table and a new partition as show in Table 2:

Table2. Syriac Letters

Letter	Origin partition	Letter	After one move
ܙ	(43,37,31,25, 19,13)	$ܙ^{[m_1,1,m_3,m_4]}$	(43,37,31,25, 19,13)
ܒ	$(30^8, 24^4)$	$ܒ^{[m_1,1,m_3,m_4]}$	$(30, 29^7, 26,25, 24^2)$
ܠ	$(37^2, 32,31,26, 25, 22^2, 21^4)$	$ܠ^{[m_1,1,m_3,m_4]}$	$(37^2, 32^2, 31,27,26, 23, 21^2, 20,15)$
ܪ	$(37,32,26, 20^3, 16,15, 11^3)$	$ܪ^{[m_1,1,m_3,m_4]}$	$(37,32, 26^2, 21,20, 16^3, 12^2)$
ܓ	$(29, 27^3, 26,24, 23, 22^6)$	$ܓ^{[m_1,1,m_3,m_4]}$	$(29, 26^2, 25^2, 24,23,22 , 21^4, 15)$
ܕ	$(30^5, 29, 24^2, 19^2, 14^2, 9, 8^5)$	$ܕ^{[m_1,1,m_3,m_4]}$	$(30^5, 29, 24^2, 19^2, 14^3 , 10, 9^4)$
ܐ	(42,37,31,25,19 13)	$ܐ^{[m_1,1,m_3,m_4]}$	(42,37,31,25,19,13)
ܝ	(39^3)	$ܝ^{[m_1,1,m_3,m_4]}$	$(39,38^2)$
ܟ	$(34^2, 31, 30^5, 29, 28, 23^2, 17)$	$ܟ^{[m_1,1,m_3,m_4]}$	$(34^2, 31^2, 30^4, 27,26, 23^2, 17)$
ܗ	(40^2)	$ܗ^{[m_1,1,m_3,m_4]}$	(40,39)
ܚ	$(32^8, 31,26)$	$ܚ^{[m_1,1,m_3,m_4]}$	$(32, 31^8, 29)$
ܛ	$(32^7, 31,24,17)$	$ܛ^{[m_1,1,m_3,m_4]}$	$(32^7, 27,24,17)$
ܟ̣	$(29^8, 28, 24^2, 23 , 16)$	$ܟ̣^{[m_1,1,m_3,m_4]}$	$(29, 28^8, 26,25,23 , 16)$
ܠ̣	$(32^8, 26,20)$	$ܠ̣^{[m_1,1,m_3,m_4]}$	$(32^8, 26,20)$
ܡ	$(28^8, 27,26, 24^2, 23$	$ܡ^{[m_1,1,m_3,m_4]}$	$(28,27^8$

	$,20)$		$,26^2,25,23,20)$
ح	$(33^7,32,25)$	$_{ح}^{[m_1,1,m_3,m_4]}$	$(33^7,28,25)$
ط	$(30^8,24^2,19^2)$	$_{ط}^{[m_1,1,m_3,m_4]}$	$(30,29^7,26,25^2,20)$
ي	$(42^3,38,31,26^2)$	$_{ي}^{[m_1,1,m_3,m_4]}$	$(42^3,38^2,32,27)$
ك	$(30^8,29,25^3)$	$_{ك}^{[m_1,1,m_3,m_4]}$	$(30,29^8,27,26,$ $25)$
ل	$(38,32,26^3,22,21$ $,17^3,6)$	$_{ل}^{[m_1,1,m_3,m_4]}$	$(38,,32^2,27,26,22^3,$ $18,17,6)$
م	$(31^7,30^3,25)$	$_{م}^{[m_1,1,m_3,m_4]}$	$(31^7,29^2,28,25)$
ن	$(35^4,29,23,17)$	$_{ن}^{[m_1,1,m_3,m_4]}$	$(35,34^3,29,23,17)$

Rule (2.1.2): When choosing a partition for any Syriac letter where $e = 7$ and the value of β_i is equal to the location $a_{\tau\rho}$ within $[m_1;2; m_3; m_4]$ will be:

$$a_{\tau\rho} \rightarrow \begin{cases} a_{\tau(\rho\mp2)} & \text{if } (\tau = 2 \text{ (or 6)}) \wedge (\rho = 2,\dots,4 \text{ (or 4,}\dots\text{,6)) resp.,} \\ a_{(\tau\mp2)\rho} & \text{if } (\tau = 2,\dots,4 \text{ (or 4,}\dots\text{,6)}) \wedge (\rho = 6 \text{ (or 2)}) \text{ resp.,} \\ a_{(\tau\mp1)(\rho\mp1)} & \text{if } (\tau = 2 \text{ (or 6)}) \wedge (\rho = 5 \text{ (or 3)}) \text{resp.,} \\ a_{(\tau\mp1)(\rho\pm1)} & \text{if } (\tau = 5 \text{ (or 3)}) \wedge (\rho = 6 \text{ (or 2)}) \text{resp.,} \end{cases} \quad (2)$$

Proof: The reason for the many relationships here is that there are two paths that never cross between them.
The calculating all cases of each path separately, we will be in front of all the cases mentioned in the text of the theorem.

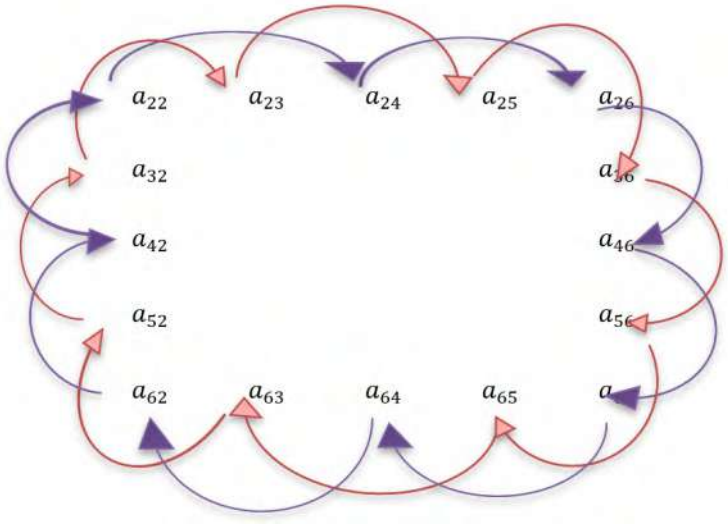

Figure 7. The movement when m_2=2.

For example, if we have the 3rd - Syriac letter then the new partition when $m_2 = 2$ it will be:

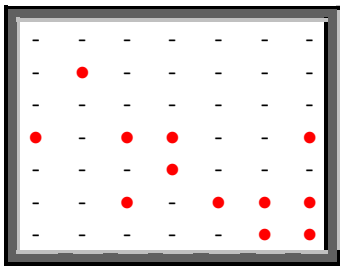

Figure 8. The new partition when $m_2 = 2$ is $(37^2 32^3, 31,26,23, 21^2, 20,8)$

It is important to say that whenever the value of m_2 exceeds 1 or 2, we will have completely different paths for each of the rules (2.1.1) and (2.1.2), meaning that we will inevitably have completely different possibilities, as the following relationship shows:

Rule (2.1.3): When choosing a partition for any Syriac letter where $e = 7$ and the value of β_i is equal to the location $a_{\tau\rho}$ within $[m_1; m_2; m_3; m_4]$ will be:

(i) When $m_2 = 3$, then we have:

$$a_{\tau\rho} \rightarrow \begin{cases} a_{\tau(\rho\mp 3)} & \text{if } (\tau = 2 \text{ (or } 6)) \wedge (\rho = 2,3 \text{(or } 5,6)) \text{resp.,} \\ a_{(\tau\mp 3)\rho} & \text{if } (\tau = 2,3 \text{ (or } 5,6)) \wedge (\rho = 6 \text{ (or } 2)), \text{resp.,} \\ a_{(\tau\mp 2)(\rho\mp 1)} & \text{if } (\tau = 2 \text{ (or } 6)) \wedge (\rho = 5 \text{ (or } 3)) \text{resp.,} \\ a_{(\tau\pm 2)(\rho\mp 1)} & \text{if } (\tau = 4) \wedge (\rho = 2 \text{ (or } 6)) \text{resp.,} \\ a_{(\tau\mp 1)(\rho\mp 2)} & \text{if } (\tau = 2 \text{ (or } 6)) \wedge (\rho = 4) \text{ resp.,} \\ a_{(\tau\mp 1)(\rho\pm 2)} & \text{if } (\tau = 5 \text{ (or } 3)) \wedge (\rho = 6 \text{ (or } 2)) \text{ resp.,} \end{cases} \quad (3)$$

(ii) If we take $m_2 = 4$:

$$a_{\tau\rho} \rightarrow \begin{cases} a_{\tau(\rho\mp 4)} & \text{if } (\tau = 2 \text{ (or } 6)) \wedge (\rho = 2 \text{ (or } 6)) \text{ resp.,} \\ a_{(\tau\mp 4)\rho} & \text{if } (\tau = 2 \text{ (or } 6)) \wedge (\rho = 6 \text{ (or } 2)) \text{resp.,} \\ a_{(\tau\mp 1)(\rho\mp 3)} & \text{if } (\tau = 2 \text{ (or } 6)) \wedge (\rho = 3 \text{ (or } 5)) \text{resp.,} \\ a_{(\tau\pm 1)(\rho\pm 3)} & \text{if } (\tau = 5 \text{ (or } 3)) \wedge (\rho = 6 \text{ (or } 2)) \text{ resp.,} \\ a_{(\tau\mp 2)(\rho\mp 2)} & \text{if } (\tau = 2 \text{ (or } 6)) \wedge (\rho = 4) \text{ resp.,} \\ a_{(\tau\mp 2)(\rho\pm 2)} & \text{if } (\tau = 4) \wedge (\rho = 6 \text{ (or } 2)) \text{ resp.,} \\ a_{(\tau\mp 3)(\rho\mp 1)} & \text{if } (\tau = 2 \text{ (or } 6)) \wedge (\rho = 5 \text{ (or } 3)) \text{resp.,} \\ a_{(\tau\mp 3)(\rho\pm 1)} & \text{if } (\tau = 3 \text{ (or } 5)) \wedge (\rho = 6 \text{ (or } 2)) \text{ resp.,} \end{cases} \quad (4)$$

(iii) If we take $m_2 = 5$, then we have:

$$a_{\tau\rho} \rightarrow \begin{cases} a_{(\tau\mp1)(\rho\mp4)} & \text{if} \quad (\tau = 2 \text{ (or } 6)) \quad \wedge \quad (\rho = 2 \text{ (or } 6)) \text{ resp.,} \\ a_{(\tau\pm1)(\rho\mp4)} & \text{if} \quad (\tau = 3 \text{ (or } 5)) \quad \wedge \quad (\rho = 2 \text{ (or } 6)) \text{ resp.,} \\ a_{(\tau\mp4)(\rho\mp1)} & \text{if} \quad (\tau = 2 \text{ (or } 6)) \quad \wedge \quad (\rho = 5 \text{ (or } 3)) \text{resp.,} \\ a_{(\tau\mp4)(\rho\pm1)} & \text{if} \quad (\tau = 2 \text{ (or } 6)) \quad \wedge \quad (\rho = 6 \text{ (or } 2)) \text{resp.,} \\ a_{(\tau\pm2)(\rho\pm3)} & \text{if} \quad (\tau = 6 \text{ (or } 2)) \quad \wedge \quad (\rho = 5 \text{ (or } 3)) \text{resp.,} \\ a_{(\tau\pm3)(\rho\pm2)} & \text{if} \quad (\tau = 6 \text{ (or } 2)) \quad \wedge \quad (\rho = 4) \text{ resp.,} \\ a_{(\tau\mp3)(\rho\pm3)} & \text{if} \quad (\tau = 2 \text{ (or } 5)) \quad \wedge \quad (\rho = 6) \quad \text{resp.,} \\ a_{(\tau\pm2)(\rho\mp3)} & \text{if} \quad (\tau = 4) \quad \wedge \quad (\rho = 2 \text{ (or } 6)) \text{ resp.,} \end{cases} \tag{5}$$

(iv)When $m_2 = 6$, then we have the following formula:

$$a_{\tau\rho} \rightarrow \begin{cases} a_{(\tau\mp2)(\rho\mp4)} & \text{if} \quad \big(\tau = 2 \text{ (or } 6)\big) \quad \wedge \quad \big(\rho = 2 \text{ (or } 6)\big) \text{resp.} \\ a_{(\tau\pm2)(\rho\pm4)} & \text{if} \quad (\tau = 4) \quad \wedge \quad (\rho = 6 \text{ (or } 2)) \text{ resp.,} \\ a_{(\tau\mp4)(\rho\mp2)} & \text{if} \quad (\tau = 2 \text{ (or } 6)) \quad \wedge \quad (\rho = 4) \text{ resp.,} \\ a_{(\tau\pm4)(\rho\mp2)} & \text{if} \quad (\tau = 6 \text{ (or } 2)) \quad \wedge (\rho = 2 \text{ (or } 6)) \text{resp.,} \\ a_{(\tau\mp3)(\rho\mp3)} & \text{if} \quad (\tau = 2 \text{ (or } 6)) \quad \wedge \quad (\rho = 3 \text{ (or } 5)) \text{resp.,} \\ a_{(\tau\pm3)(\rho\mp3)} & \text{if} \quad (\tau = 5 \text{ (or } 3)) \quad \wedge \quad (\rho = 2 \text{(or } 6)) \text{resp.,} \\ a_{\tau(\rho\pm4)} & \text{if} \quad (\tau = 5 \text{ (or } 3)) \quad \wedge \quad (\rho = 6 \text{ (or } 2)) \text{ resp.,} \\ a_{(\tau\mp4)\rho} & \text{if} \quad (\tau = 2 \text{(or } 6)) \quad \wedge \quad (\rho = 5 \text{ (or } 3)) \text{ resp.,} \end{cases} \tag{6}$$

(v) When $m_2 = 7$, we have:

$$a_{\tau\rho} \rightarrow \begin{cases} a_{(\tau\mp3)(\rho\mp4)} & \text{if} \quad (\tau = 2 \text{ (or } 6)) \quad \wedge \quad (\rho = 2 \text{ (or } 6)) \text{ resp.,} \\ a_{(\tau\mp4)(\rho\mp3)} & \text{if} \quad (\tau = 2 \text{ (or } 6)) \quad \wedge \quad (\rho = 3 \text{ (or } 5)) \text{ resp.,} \\ a_{(\tau\pm1)(\rho\pm4)} & \text{if} \quad (\tau = 5 \text{ (or } 3)) \quad \wedge \quad (\rho = 6 \text{ (or } 2)) \text{resp.,} \\ a_{(\tau\pm4)(\rho\pm1)} & \text{if} \quad (\tau = 6 \text{ (or } 2)) \quad \wedge \quad (\rho = 4) \quad \text{resp.,} \\ a_{(\tau\pm1)(\rho\mp4)} & \text{if} \quad (\tau = 4) \quad \wedge (\rho = 2 \text{ (or } 6)) \text{resp.,} \\ a_{(\tau\mp4)(\rho\pm1)} & \text{if} \quad (\tau = 2 \text{ (or } 6)) \quad \wedge \quad (\rho = 5 \text{(or } 3)) \text{resp.,} \\ a_{(\tau\mp3)(\rho\pm4)} & \text{if} \quad (\tau = 3 \text{ (or } 5)) \quad \wedge \quad (\rho = 6 \text{ (or } 2)) \text{ resp.,} \\ a_{(\tau\pm4)(\rho\mp3)} & \text{if} \quad (\tau = 6 \text{(or } 2)) \quad \wedge (\rho = 2 \text{ (or } 6)) \text{ resp.,} \end{cases} \tag{7}$$

(vi) When $m_2 = 8$, we have:

$$a_{\tau\rho} \rightarrow \begin{cases} a_{(\tau\mp4)(\rho\mp4)} & \text{IF} \quad (\tau = 2 \text{ (OR } 6)) \quad \wedge \quad (\rho = 2 \text{ (OR } 6)) \text{ RESP.,} \\ a_{(\tau\pm4)(\rho\pm2)} & \text{IF} \quad \big(\tau = 6 \text{ (OR } 2)\big) \quad \wedge \quad \big(\rho = 5 \text{ (OR } 3)\big) \text{RESP.} \\ a_{(\tau\mp4)\rho} & \text{IF} \quad (\tau = 2 \text{ (OR } 6)) \quad \wedge \quad (\rho = 4) \text{ RESP.,} \\ a_{(\tau\mp4)(\rho\pm2)} & \text{IF} \quad (\tau = 2 \text{ (OR } 6)) \quad \wedge \quad (\rho = 5 \text{ (OR3)}) \text{RESP.,} \\ a_{(\tau\pm4)(\rho\mp4)} & \text{IF} \quad (\tau = 6 \text{ (OR } 2)) \quad \wedge \quad (\rho = 2 \text{ (OR } 6)) \text{RESP.,} \\ a_{(\tau\mp2)(\rho\pm4)} & \text{IF} \quad (\tau = 3 \text{ (OR } 5)) \quad \wedge \quad (\rho = 6 \text{(OR } 2)) \text{RESP.,} \\ a_{\tau(\rho\pm4)} & \text{IF} \quad (\tau = 4) \quad \wedge \quad (\rho = 6 \text{ (OR } 2)) \text{ RESP.,} \\ a_{(\tau\mp2)(\rho\mp4)} & \text{IF} \quad (\tau = 3 \text{(OR } 5)) \quad \wedge \quad (\rho = 2 \text{ (OR } 6)) \text{ RESP.,} \end{cases} \tag{8}$$

Finally, (vii) if $m_2 = 9, \ldots, 15$, then we have the same cases as $m_2 = 7, \ldots, 1$ respectively but with changing rows by columns in additions to reversing the values of τ and ρ.

Table 3. The partition of two letters after application $3 \leq m_2 \leq 15$.

Letter	Partition	Letter	Partition
ט	$(30^8, 24^4)$	ר	$(37^2, 32, 31, 26, 25, 22^2, 21^4)$
$ט^{[m_1,3,m_3,m_4]}$	$(30, 29, 28^4, 24, 23, 22^2, 21, 15)$	$ר^{[m_1,3,m_3,m_4]}$	$(37^2, 32, 31^2, 30, 26, 23, 21^2, 20, 9)$
$ט^{[m_1,4,m_3,m_4]}$	$(30, 28, 27^3, 23, 22, 21^2, 20, 14, 8)$	$ר^{[m_1,4,m_3,m_4]}$	$(37^2, 32, 30^2, 25, 24, 23, 21^2, 20, 10)$
$ט^{[m_1,5,m_3,m_4]}$	$(30, 27, 26^2, 22, 21, 20^2, 19, 13, 8^2)$	$ר^{[m_1,5,m_3,m_4]}$	$(37^2, 32, 29^2, 25, 22, 20^4, 11)$
$ט^{[m_1,6,m_3,m_4]}$	$(30, 26^3, 20, 19^2, 18, 12, 8^3)$	$ר^{[m_1,6,m_3,m_4]}$	$(37^2, 32, 28, 24, 23, 22, 20^2, 19, 14, 12)$
$ט^{[m_1,7,m_3,m_4]}$	$(30, 25^2, 21, 20, 19^2, 11, 8^4)$	$ר^{[m_1,7,m_3,m_4]}$	$(37^2, 32, 23, 22, 21, 19^4, 18, 8)$
$ט^{[m_1,8,m_3,m_4]}$	$(30, 25^2, 19, 18^2 17, 8^5)$	$ר^{[m_1,8,m_3,m_4]}$	$(37^2, 32, 23, 20^2, 19^4, 14, 9)$
$ט^{[m_1,9,m_3,m_4]}$	$(30, 25^2, 19, 18^2, 14, 11, 9^4)$	$ר^{[m_1,9,m_3,m_4]}$	$(37^2, 32, 25, 24, 21\ 19^2, 18, 13, 9, 8\ )$
$ט^{[m_1,10,m_3,m_4]}$	$(30, 25^2, 19^4, 15, 9^3, 8)$	$ר^{[m_1,10,m_3,m_4}$	$(37^2, 32^2, 24, 21, 19^2, 18, 9,)$
$ט^{[m_1,11,m_3,m_4]}$	$(30, 25^3, 20^4, 16, 10^2, 9)$	$ר^{[m_1,11,m_3,m_4}$	$(37^2, 32, 31, 24, 214, 19^2, 18, 10, 9^2)$
$ט^{[m_1,12,m_3,m_4]}$	$(30^2, 26^3, 21^4 17, 11, 10)$	$ר^{[m_1,12,m_3,m_4}$	$(37^2, 32, 30, 24, 21, 19^2, 18, 17, 10^2)$
$ט^{[m_1,13,m_3,m_4]}$	$(30^3, 27^3, 22^4, 18, 11)$	$ר^{[m_1,13,m_3,m_4}$	$(37^2, 32, 29, 24, 21^2, 20^2, 19, 11^2)$
$ט^{[m_1,14,m_3,m_4]}$	$(30^4, 28^3, 23^4, 12)$	$ר^{[m_1,14,m_3,m_4}$	$(37^2, 32, 28, 26, 25, 22, 20^2, 19, 18, 12)$
$ט^{[m_1,15,m_3,m_4]}$	$(30^5, 29^3, 24, 23^2, 19)$	$ר^{[m_1,15,m_3,m_4}$	$(37^2, 32^2, 24, 23, 22^2, 21^2, 20, 19)$

3. Computer Solution

In this work we used mohommed et al method [9,10] to encode any Syriac letter by using Microsoft Visual Studio 2017 and C#. The Program starts by creating two (1-D) arrays with 49 values each (index starts from 0 to 48 because C# is a zero-based array indexing language). The first array is the ***nodes*** array. By default, all values of nodes array are set to zero. The other array is the ***modified-nodes*** array. This is where the values of nodes are stored after applying the movement steps.

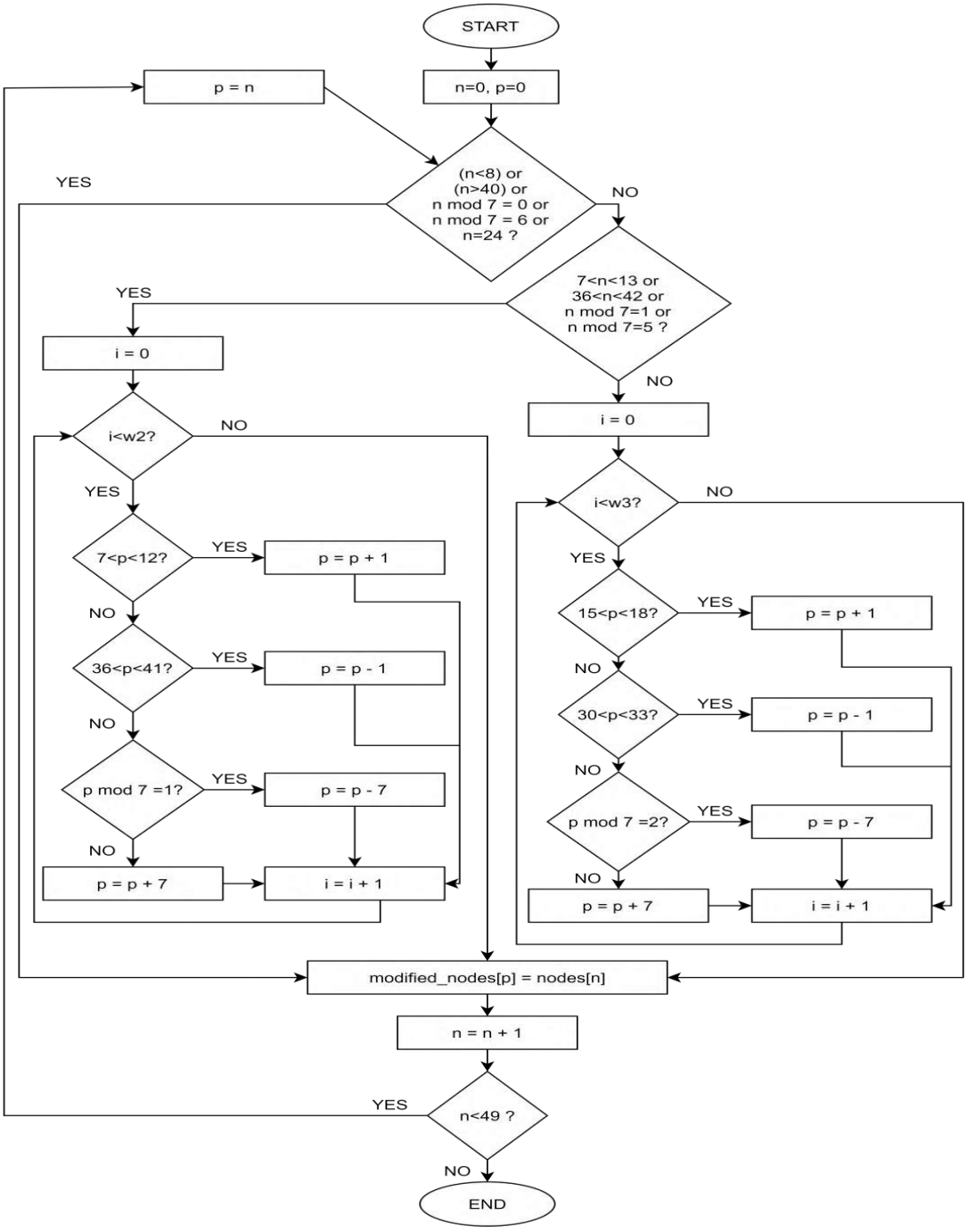

Figure 9. Chart illustrates the values of an array (modified- nodes) of an array (nodes).

The first step of this algorithm is to choose the nodes that form the most similar shape to the desired letter. When a cell at row R and column C is selected to be a node; the ***nodes*** array value of address (R*7+C) is set to1. After selecting all nodes values, the next step is the orbital movement. To avoid data loss, the modified array is stored in a separate array called ***modified-nodes***. Values of first orbit and forth orbit are moved directly from ***nodes*** array to ***modified-nodes*** array. Values of second and third orbit are displaced depending on m_2 and m_3 values respectively.

Note that the same chart can be used to copy values from ***modified-nodes*** array back into ***nodes*** array (in case of receiving coded data and trying to retrieve the original layout). The only differences in that case will be replacing values of (m_2 with $16 - m_2$) and ($m_3$with $8 - m_3$) and the equation (modified-nodes[p] = nodes[n]) will be (nodes[p] = modified-nodes[n]).

The last step of the algorithm is to number the partitions based on the (Partition theory). One important point to mention is that the *modified-nodes* array is a one-dimensional array used to store data of a two-dimensional array. The addresses of the *modified-nodes* are converted into 2-D array addressing by dividing the address of modified-nodes by 7. For each modified-nodes index i, the row index of the corresponding 2-D array address r is $i/7$ (ignoring the reminder) while the column index r is i mod 7; (this method can change if the formulas used in [18,19].

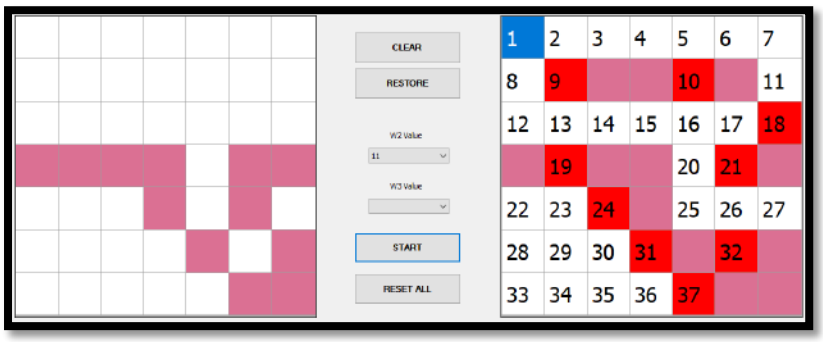

Figure 10. Illustrates The 3rd Syriac letter After Applying $[m_1;11;m_3;m_4]$.

4. Results and Discussion

It is quite natural to study the basics of the subject matter of coding, for examples we mention each of them [20-22], let's understand how we deal with developing ideas here. Perhaps it is important to note that, this coding note that, this coding used for Syriac letters is completely different from how the coding of these letters was handled by Sami and Mahmood [6] which was by extended Vigenere Cipher; (more on this technology can see [22,23], in the sense of using another medium and not died through the scheme itself, also [24,25].

We also have to add that the technology prepared by [26, 27] has a benefit that can be combined with the idea of this paper to become more difficult to reveal or infer the origin of the letter.

5. Conclusion

From the foregoing it becomes quite clear that each method followed was useful for changing the features of the letter and each time according to a specific mechanism completely different from the other. Some of it is easy and it changes a simple part of the shape, and another is complicated, so I have a case whose details are not easy to reveal, especially if more than one case is combined. For this, we suggest that if we want a very difficult message, we should use merging more than one method.

Acknowledgments

The authors are very grateful to the (Kirkuk Education Directorate), (University of Al-Hamdaniya, College of Education) and (University of Mosul, College of Education for Pure Science) for their provided facilities, which helped to improve the quality of this work.

References

[1] Mathas A 1999 Iwahori-Hecke algebras and Schur Algebras of the Symmetric Group *American Mathematical Soc*. **l.15**
[2] James G D 1978 Some combinatorial results involving Young diagrams *Math. Proc. of the Cambridge Phil. Soc*. **83** pp1-10
[3] Fayers M 2006 Weight two blocks of Iwahori-Hecke algebras of type B *J. algebra* **303** (1) pp 154-201
[4] Fayers M. 2007 Another runner removal theorem for v-decomposition numbers of Iwahori-Hecke algebras and q-Schur algebras *J. algebra* **310 (**1) pp 346-367
[5] Fayers M 2010 On the irreducible representations of the alternating group which remain irreducible in characteristic p *Representation Theory of the American Mathematical Society* **14** (16) pp 601-626
[6] Sami H H and Mahmood A S 2017 Syriac letters and James diagram (A) *Int. J. of Enhanced Research in Science, Technology Engineering* **6** (12) pp 53-62
[7] Dweik B S and Al-Obaidi T A 2014 Syriac language maintenance among the Assyrian of Iraq *J. of Sociology and Scoial Work* **2(**1) pp 269-282
[8] Rollinger R 2006 The terms "Assyria" and "syria" again *J. of Near Eastern Studies* **65(**4) pp 283-287
[9] Mohommed E F, Ahmed N, I H and Mahmood A S 2015 Embedding chain movement in James diagram for partitioning β-numbers *AIP Conference Proc* 1691 (040019)
[10] Mohommed E F, Ahmed N, Ibrahim H and Mahmood A S 2016 Nested chain movement of length 1 of β-numbers in James abacus diagram *Global J. of Pure and Applied Mathematics* **12** pp 2953-2969
[11] Mohommed E F, Ibrahim H, Ahmed N and Mahmood A S 2016 Embedding the outer chain movement for main partition of β-number with length [1,0,0,...] *Proc. of the International conference on Applied Sc. and Technology (ICAST'16)*
[12] Shareef R J and Mahmood A S 2019 The movement of orbits and their effect on the encoding of letters in partition theory *Open Access Library J.* **6(**11) pp 1-7
[13] Shareef R J and Mahmood A S 2020 The movement of orbits and their effect on the encoding of letters in partition theory II *Open Access Library J.* **7**(3) pp 1-7
[14] Mahmood A B and Mahmood A S 2019 Secret-word by e-abacus diagram I *Iraqi J. of Science* **60**(3) pp 638-646
[15] Mahmood A B and Mahmood A S 2019 Secret-text by e-abacus diagram II *Iraqi J. of Science* **60**(4) pp 840-846
[16] Mahmood A S 2011 On the intersection of Young's diagrams *Journal of Education and Science* **24** pp 149-157
[17] Mahmood A S, Mahmood S M and Naoum F S 2012 Remarks of the intersection of Young diagrams core *Iraqi J. of Science* **53**(1) pp 156-160
[18] Ahmed M K, Aziz S F, Alsaleem N Y A, Sielivanov K and Moskalets M 2020 Method for determining the responses from a non-linear system using the Volterra series *Eastern-European journal of Enterprise Technologies* **4**(9-106) pp 34-44
[19] Stallings W 2017 *Cryptography and Network Security Principles and Practices* 7th Edition *Pearson Education* 767
[20] Mohommed E F, Ibrahim H and Ahmed N 2017 Enumeration of n-connected ominous inscribed in an abacus *JP J. of Algebra, Number Theory and applications* **39**(6) pp 843-874
[21] Richardson T 2008 *Modern Coding Theory* Cambridge University Press
[22] Biswas S 2014 Encoding and decoding of file to image *Int. J. of Innovative Research and Development* **3**(9) pp 172-176

[23] Sami H H and Mahmood A S 2020 Encoding Syriac letters in partition theory using extended Vigenere cipher *Eastern-European J. of Enterprise Technologies* 1/2 (103) pp 37-46
[24] Singh Y K 2012 Generalization of Vigenere Cipher *ARPN J. of Engineering and Applied Sciences* **7**(1) pp 39-44
[25] Mahmood A S and Baker R I 2019 The hybrid Morse code *J. of Education and Science* **28**(1) pp 171-188
[26] Mahmood A S 2020 Replace the content in e-abacus diagram *Open Access Library J.* **7**(4) pp 1-6
[27] Mahmood A S and Al-Hussaini A T 2020 e-Abacus diagram rows rearranging technology *Open Access Library Journal* **7**(6) pp 1-5

Application of Fixed Point in Algebra Fuzzy Normed Spaces

Application of Fixed Point in Algebra Fuzzy Normed Spaces

Jehad R Kider

Branch of Mathematics and Computer Applications, Department of Applied Sciences, University of Technology, Baghdad, Iraq

Email:10046@uotechnology.edu.iq

Abstract. In the present paper first we recall the definition of algebra fuzzy metric space and some basic properties of algebra fuzzy metric space are introduced. Our goal is to prove the fixed point theorem in fuzzy complete algebra fuzzy metric space. Finally, the application to this theorem introduced.

1.Introduction

Kider in 2011 [1] introduced a fuzzy normed space. Also he proved this fuzzy normed space has completion in [2]. Again Kider introduced a new fuzzy normed space in 2012 [3]. Kider and Hussain in 2014 [4] introduced a new type of fuzzy metric space called standard fuzzy metric space and they study continuous, uniform continuous mappings on a standard fuzzy metric spaces. Again Kider in 2014 [5] study completeness of Hausdorff standard fuzzy metric spaces.

Kider and Kadhum in 2017 [6] introduced the fuzzy norm for a fuzzy bounded operator on a fuzzy normed space and proved its basic properties then other properties were proved by Kadhum in 2017 [7]. Ali in 2018 [8] proved the basic properties of complete fuzzy normed algebra. Kider and Ali in 2018 [9] introduced the notion of fuzzy absolute value and study properties of finite dimensional fuzzy normed space. Again Kider and Ali in 2019 [10] introduced a new type of fuzzy normed algebra and they study properties of a complete fuzzy normed algebra.

The concept of general fuzzy normed space was presented by Kider and Gheeab in 2019 [11] [12] also they proved basic properties of this space and the general fuzzy normed space GFB (V, U). Kider and Kadhum in 2019 [13] introduce the notion of fuzzy compact linear operator and proved its basic properties a gain Kider and Kadhum in 2019 [14] study properties of fuzzy closed linear operator. For more information about fuzzy metric spaces also see [15, 16].

In 2020 Kider [17] introduced the notion of fuzzy soft metric space after that he investigated and proved some basic properties of this space again Kider in 2020 [18] introduced a new type of fuzzy metric space he called it algebra fuzzy metric space after that the basic properties of this space is proved.

In the present paper first we recall the notion of algebra fuzzy metric space which is a new type of fuzzy metric space then we recall basic properties of this space that will be used later in this paper. After that we introduce the main result in this paper it is the fixed point theorem with which prove to show that the important of this theorem and application to system of linear equation, solution of the differential equation, Fredholm integral equation and Volterra integral equation are introduced.

2. Basic Properties of Algebra fuzzy metric space

Definition 2.1: [18]

Let $\otimes: I \times I \to I$ be a binary operation function then $\otimes$ is said to be continuous t-conorm (or simply t-conorm) if it satisfies the following conditions $s, r, z, w \in I$ where $I = [0,1]$
(i)$s \otimes r = r \otimes s$
(ii) $s \otimes [r \otimes z] = [s \otimes r] \otimes z$
(iii) $\otimes$ is continuous function
(iv)$s \otimes 0 = 0$
(v) $(s \otimes r) \leq (z \otimes w)$ whenever $s \leq z$ and $r \leq w$.

Lemma 2.2: [18]
If $\otimes$ is a continuous t-conorm on I then
(i)$1 \otimes 1 = 1$
(ii)$0 \otimes 1 = 1 \otimes 0 = 1$
(iii)$0 \otimes 0 = 0$
(iv)$a \otimes a \geq a$ for all $a \in [0,1]$.

Example 2.3: [18]
The algebra product $a \otimes b = a + b - ab$ is a continuous t-conorm for all $a, b \in I$.

Definition 2.4: [18]
Assume that $S \neq \emptyset$, a fuzzy set $\widetilde{D}$ in S is represented by $\widetilde{D} = \{(s, \mu_{\widetilde{D}}(s)): s \in S, 0 \leq \mu_{\widetilde{D}}(s) \leq 1\}$ where $\mu_{\widetilde{D}}(s): S \to [0,1]$ is a membership function.
The following definition the main definition

Definition 2.5: [18]
A triple $(S, m, \otimes)$ is said to be the algebra fuzzy metric space if S$\neq \emptyset$, $\otimes$ is a continuous t- conorm and $m: S \times S \to [0,1]$ satisfying the following conditions:

(1)$0 \leq m(s,r) \leq 1$;

(2) $m(s,r) = 0$ if and only if $s = r$;

(3) $m(s,r) = m(r,s)$;

(4) $m(s,t) \leq m(s,r) \otimes m(r,t)$
For all s, r, t $\in$ S then the triple $(S, m, \otimes)$ is said to be the algebra fuzzy metric space
Example 2.6:[18]
If (S,d) is a metric space and $t \otimes r = t + r - tr$ for all t, r $\in$ [0, 1]. Put $m_d(s,u) = \frac{d(s,u)}{1+d(s,u)}$ for all s, u $\in$ S. Then $(S, m_d, \otimes)$ is algebra fuzzy metric space. m_d is known as the algebra fuzzy metric comes from d.

Example 2.7: [18]
If $S \neq \emptyset$ put $m_D(s,u) = \begin{cases} 0 & if\ s = u \\ 1 & if\ s \neq u \end{cases}$
Then $(S, m_D, \otimes)$ is algebra fuzzy metric space known as the discrete algebra fuzzy metric space.

Definition 2.8: [18]
If $(S, m, \otimes)$ is algebra fuzzy metric space then $fb(s,j) = \{u \in S: m(s,u) < j\}$ is known as an open fuzzy ball with center s$\in$S and radius j $\in$(0, 1). Similarly closed fuzzy ball is defined by $fb[s,j] = \{u \in S: m(s,u) \leq j\}$.

Definition 2.9: [18]

If $(S, m, \otimes)$ is algebra fuzzy metric space and W⊆S is known as fuzzy open if $fb(w, j) \subseteq W$ for any arbitrary w∈W and for some j ∈(0, 1).
Also $D \subseteq S$ is known as fuzzy closed if D^C is fuzzy open then the fuzzy closure of D, $\overline{D}$ is defined to be the smallest fuzzy closed set contains D.

Definition 2.10: [18]
If $(S, m, \otimes)$ is algebra fuzzy metric space then $D \subseteq S$ is known as fuzzy dense in S whenever $\overline{D}$=S.

Theorem 2.11: [18]
If $fb(s, j)$ is open fuzzy ball in algebra fuzzy metric space $(S, m, \circledcirc)$ then it is a fuzzy open set.

Proposition 2.12: [18]
In algebra fuzzy metric space $(S, m, \otimes)$ $s_n \to s$ if and only if $m(s_n, s) \to 0$.

Definition 2.13: [18]
In algebra fuzzy metric space $(S, m, \otimes)$ a sequence (s_n) is fuzzy Cauchy if for each r∈(0, 1) then we can find N such that $m(s_n, s_m) < r$, for each m, n ≤ N.
Definition 2.14: [18]
An algebra fuzzy metric space $(S, m, \otimes)$ is known as fuzzy complete if (s_n) is fuzzy Cauchy sequence then $s_n \to s \in$ S.

Theorem 2.15: [18]
In algebra fuzzy metric space $(S, m, \otimes)$ $if\ s_n \to s \in S$ then (s_n) is fuzzy Cauchy sequence.

Definition 2.16: [18]
Anon empty set D in algebra fuzzy metric space (S, m, ⊗) is known as fuzzy bounded whenever we can find s∈(0, 1) with $D \subset fb(d, s)$ for some d ∈S. Also a sequence (d_n) in algebra fuzzy metric space $(S, m, \otimes)$ is fuzzy bounded if we can find s∈(0, 1) with $\{d_1, d_2, \dots, d_n, \dots\} \subseteq fb(d, s)$ for some d ∈S.

Lemma 2.17:[18]
In algebra fuzzy metric space $(S, m, \otimes)$ If the sequence (s_n) ∈S with $s_n \to s$ ∈S. Then (s_n) is fuzzy bounded.

Lemma 2.18: [18]
In algebra fuzzy metric space $(S, m, \otimes)$ if $(s_n) \in$ S with $s_n \to$s ∈S and $s_n \to$ d ∈S as n→ ∞. Then s=d.

Theorem 2.19: [18]
In algebra fuzzy metric space $(S, m, \otimes)$ when D⊂S then d∈$\overline{D}$ if and only if there is $(d_n) \in$ D with $d_n \to$ d.

Definition 2.20: [18]
If $(S, m_S, \otimes)$ and $(V, m_V, \otimes)$ are two algebra fuzzy metric spaces and W ⊆ S. Then a function $T: S \to V$ is called fuzzy continuous at w∈W. If for every $0 < r < 1$, we can find some $0 < t < 1$, with $m_V[T(w), T(s)] < r$ as s∈W and $m_S(w, s) < t$.
Also f is said to be fuzzy continuous on W if it is fuzzy continuous at every point of W.

Theorem 2.21: [18]
If $(S, m_S, \otimes)$ and $(V, m_V, \otimes)$ are two algebra fuzzy metric spaces and $W \subseteq S$. Then a function $T: S \to V$ is fuzzy continuous at w∈W if and only if whenever $w_n \to w$ in W then $T(w_n) \to T(w)$ in V.

Theorem 2.22: [18]
The function $T: S \to V$ is fuzzy continuous on S if and only if $T^{-1}(D)$ is fuzzy open in S for all fuzzy open subset D of V where $(S, m_S, \otimes)$ and $(V, m_V, \otimes)$ are algebra fuzzy metric spaces.

3.Fixed Point Theorem

Definition 3.1:
If $(U, m, \otimes)$ is algebra fuzzy metric space then the function $S: U \to U$ is known as a fuzzy contraction on U if we can find r∈(0, 1) with $m[S(u), S(v)] \leq r\, m(u, v)$ for all u, v ∈U. The constant r is called the fuzzy contraction constant.
The proof of the next result is clear and hence is omitted.

Theorem 3.2:
Suppose that $(U, m, \otimes)$ is algebra fuzzy metric space. If the function $S: U \to U$ is a fuzzy contraction on U then S is fuzzy continuous.
The following theorem is the key of all results in this section
Theorem 3.3:
Suppose that $(U, m, \otimes)$ is fuzzy complete algebra fuzzy metric space where $U \neq \emptyset$, $a \otimes b = a + b - ab$ for all a, b∈I and assume that the function $S: U \to U$ is a fuzzy contraction on U that is we can find r∈(0, 1) with $m[S(u), S(v)] \leq r\, m(u, v)$ for all u, v ∈U. Then S has exactly one fixed point.

Proof: The construction of the iterative sequence (u_k) follows by Choosing u_0 ∈U and define
$S(u_0) = u_1, S(u_1) = S^2(u_0) = u_2, \dots, S^k(u_0) = u_k, \dots$ (1)
Now (u_k) is a fuzzy Cauchy sequence follows from the next steps

$$m(u_{n+1}, u_n) = m[S(u_n), S(u_{n-1})] \leq r\, m(u_n, u_{n-1}) = r\, m[S(u_{n-1}), S(u_{n-2})]$$
$$\leq r^2\, m(u_{n-1}, u_{n-2}) = r^2\, m[S(u_{n-2}), S(u_{n-3})]$$

And so on we have
$m(u_{n+1}, u_n) \leq r^n\, m(u_1, u_0)$ (2)
Therefore if we take n>j ≥N for some N ∈ ℕ we have

$$m(u_j, u_n) \leq m(u_j, u_{j+1}) \otimes m(u_{j+1}, u_{j+2}) \otimes, \dots, \otimes m(u_{n-1}, u_n)$$
$$\leq m(u_j, u_{j+1}) + m(u_{j+1}, u_{j+2}) +, \dots, m(u_{n-1}, u_n) - [m(u_j, u_{j+1}) m(u_{j+1}, u_{j+2}) \dots m(u_{n-1}, u_n)]$$
$$\leq [r^j + r^{j+1} + \dots + r^{n-j}]\, m(u_0, u_1) - [r^j\, r^{j+1} \dots r^{n-j}]\, m(u_0, u_1)$$

$m(u_j, u_n) \leq [(r^j \frac{1-r^{n-j}}{1-r}) - (r^{[(n-j)j+(n-j)]})]\, m(u_0, u_1)$ (3)

Now choose t ∈(0, 1) so that $[(r^j \frac{1-r^{n-j}}{1-r}) - (r^{[(n-j)j+(n-j)]})]\, m(u_0, u_1) < t$.
Thus $m(u_j, u_n) < t$ for all n>j ≥N that is (u_k) is a fuzzy Cauchy sequence but U is fuzzy complete so we can find u∈U such that (u_k) is fuzzy converges to u.
The proof of u is a fixed point of S follows from the following steps

$$m(u, S(u)) \leq m(u, u_n) \otimes m(u_n, S(u))$$
$$\leq m(u, u_n) + m(u_n, S(u)) - m(u, u_n)\, m(u_n, S(u))$$
$$\leq m(u, u_n) + r\, m(u_{n-1}, u) - m(u, u_n)\, r\, m(u_{n-1}, u)$$

By taking limit to both sides as n→ ∞ and using u_k →u getting $m(u, S(u)) = 0$ which implies that S(u)=u.
Finally, to show that u is the only fixed point of S. Assume that S(u)=u and S(y) = y that is S has two fixed points u and s. Now
$m(u, y) = m(S(u), S(y)) \leq r\, m(u, y)$. Thus $m(u, y) = 0$ since r ∈(0, 1). Hence u=y.

Corollary 3.4:

In Theorem 3.3 the iterative sequence (u_k) where u_0 is arbitrary fuzzy converges to the unique fixed point u of S. Error estimates are the prior

$$m(u_j, u) \leq [\frac{r^j}{1-r}]\, m(u_0, u_1) \quad (4)$$

and the posterior estimates

$$m(u_j, u) \leq [\frac{r}{1-r}]\, m(u_{j-1}, u_j) \quad (5)$$

Proof: The inequality (4) follows from inequality (3)

$m(u_j, u_n) \leq [(r^j \frac{1-r^{n-j}}{1-r}) - (r^{(n-j)j+(n-j)})]$ m(u_0, u_1). Since r ∈(0, 1) we have $(1 - r^{n-j}) \in (0, 1)$ hence by letting n→ ∞ we have inequality (4)

$$m(u_j, u) \leq [\frac{r^j}{1-r}]\, m(u_0, u_1).$$

Now we derive (5) by taking j=1 and writing y_0 for u_0 and y_1 for u_1 we have from (4) m$(y_1, u) \leq [\frac{r}{1-r}]$ m(y_0, y_1). Putting $y_0 = u_{j-1}$ we have $y_1 = S(y_0) = u_j$thus we obtain (5).

Theorem 3.5:
Suppose that $S: U \to U$ is a function where $(U, m, \otimes)$ is algebra fuzzy metric space and $a \otimes b = a + b - ab$ for all a, b∈I. Assume that $m(u_0, S(u_0)) < (1 - r)t$ and S is a fuzzy contraction on the closed fuzzy ball $fb[u_0, t]$ that is we can find r∈(0, 1) with $m[S(u), S(v)] \leq r\, m(u, v)$ for all u, v ∈ $fb[u_0, t]$. Then the iterative sequence (u_k) fuzzy converges to $u \in fb[u_0, t]$, this u is fixed point of S and it is the only fixed point of S in $fb[u_0, t]$.

Proof:
$(u_k) \in fb[u_0, t]$ follows from the next step. In inequality (3) put j=0 and use $m(u_0, S(u_0)) < (1 - r)t$ we have

$$m(u_0, u_n) \leq [\frac{1}{(1-r)} - r^n] m(u_0, u_1)$$
$$= [\frac{1}{(1-r)}]\, m(u_0, u_1) - r^n m(u_0, u_1)$$
$$< t - (1 - r)\, r^n t < t.$$

Hence $(u_k) \in fb[u_0, t]$ also $u \in fb[u_0, t]$ since (u_k) is fuzzy converges to u and $fb[u_0, t]$ is closed. Now from the proof of Theorem 3.3 the other assertion of the theorem follows.

Definition 3.6:
Let ℝ be the field of real numbers and ⊗ be a continuous t-norm. A fuzzy set $a_{\mathbb{R}}$ is a function from ℝ to I is called algebra fuzzy absolute value on ℝ if it satisfies the following conditions for all r, s ∈ ℝ**;**
(1) $a_{\mathbb{R}}(r) \in I$
(2) $a_{\mathbb{R}}(r) = 0$ if and only if r=0
(3) $a_{\mathbb{R}}(sr) \leq a_{\mathbb{R}}(s) \cdot a_{\mathbb{R}}(r)$
(4) $a_{\mathbb{R}}(s + r) \leq a_{\mathbb{R}}(s) \otimes a_{\mathbb{R}}(r)$
Then the triple $(\mathbb{R}, a_{\mathbb{R}}, \otimes)$ is called algebra fuzzy absolute value space.

Example 3.7:
Let $U=C[a, b]$ and $t \otimes s = t + s - ts$ for all t, s ∈I. Define $m(f, g) = max_{t \in [a,b]}\, a_{\mathbb{R}}[f(t) - g(t)]$ then $(U, m, \otimes)$ is algebra fuzzy metric space.

Proof:
(1)Since $a_{\mathbb{R}}[f(t) - g(t)] \in (0, 1)$ for all t∈[a, b] it is clear that m(f, g) ∈(0, 1)

(2)m(f, g) = 0 if and only if $max_{t\in[a,b]}a_{\mathbb{R}}[f(t)-g(t)] = 0$ if and only if $a_{\mathbb{R}}[f(t)-g(t)] = 0$ for all t ∈ [a, b] if and only if f(t) –g(t) =0 for all t ∈ [a, b] if and only if f(t) =g(t) for all t ∈ [a, b] if and only if f=g.
(3)it is clear that $m(f,g) = m(g,f)$.

$$(4)m(f,g) = max_{t\in[a,b]}\, a_{\mathbb{R}}[f(t)-h(t)+h(t)-g(t)]$$
$$\leq max_{t\in[a,b]}\, a_{\mathbb{R}}[f(t)-h(t)] \otimes max_{t\in[a,b]}\, a_{\mathbb{R}}[h(t)-g(t)]$$
$$\leq m(f,h)\otimes m(h,g)$$

For all f, g, h ∈U. Hence (U, m, ⊗) is algebra fuzzy metric space.

Theorem 3.8:
If $a\otimes b = a + b - ab$ for all a, b ∈I define m: $\mathbb{R}^2$ →I by $m(u,v) = a_{\mathbb{R}}(u-v)$ for all u, v∈ ℝ. Then $(\mathbb{R},m,\otimes)$ is algebra fuzzy metric space.

Proof:
(1)it is clear that m(u, v) ∈I for all u, v∈ ℝ.
(2) $m(u,v) = 0$ if and only if $a_{\mathbb{R}}$(u−v)=0 if and only if u−v=0 if and only if u=v.
(3)it is clear that $m(u,v) = m(v,u)$

$$(4)m(u,z) = a_{\mathbb{R}}(u-z) = a_{\mathbb{R}}(u-v+v-z)$$
$$\leq a_{\mathbb{R}}(u-v)\otimes a_{\mathbb{R}}(v-z)$$
$$\leq m(u,v)\otimes m(v,z)$$

Hence $(\mathbb{R},m,\otimes)$ is algebra fuzzy metric space

Theorem 3.9:
If $s\otimes r = s + r - sr$ for all s, r ∈I then $(\mathbb{R},m,\otimes)$ is a fuzzy complete where $m(u,v) = a_{\mathbb{R}}(u-v)$ for all u, v∈ ℝ.

Proof:
Let (r_n) be a fuzzy Cauchy sequence in ℝ then (r_n) has a monotonic subsequence (r_{n_j}) but (r_n) is a fuzzy bounded hence (r_{n_j}) is a fuzzy bounded thus (r_{n_j}) fuzzy approaches to r∈ ℝ that is every s∈(0, 1) we can find N ∈ ℕ with $a_{\mathbb{R}}(r_{n_k} - r_k) \leq s$. Since (r_n) is a fuzzy Cauchy sequence in ℝ so $a_{\mathbb{R}}(r_m - r_n) \leq s$ for all m, n ≥N. That is for k ≥N,
$a_{\mathbb{R}}(r_{n_k} - r_k) \leq s$. Now for all k≥N

$$a_{\mathbb{R}}(r_k - r) \leq a_{\mathbb{R}}(r_k - r_{n_k} + r_{n_k} - r)$$
$$\leq a_{\mathbb{R}}(r_k - r_{n_k})\otimes a_{\mathbb{R}}(r_{n_k} - r)$$
$$\leq s\otimes s$$

Now we can find t∈(0, 1) with s ⊗ s <t that is $a_{\mathbb{R}}(r_k - r) \leq$ t. Thus (r_n) approaches to r∈ ℝ. Hence (ℝ, m, ⊗) is a fuzzy complete.

Example 3.10:
If $s\otimes t = s + t - st$ for all s, t ∈I define m: $\mathbb{R}^n \to I$ by $m(u,v) = max_j\, a_{\mathbb{R}}(\alpha_j - \beta_j)$ for all $u = (\alpha_1,\alpha_2,\dots,\alpha_n)$, $v = (\beta_1,\beta_2,\dots,\beta_n) \in \mathbb{R}^n$. Then $(\mathbb{R}^n,m,\otimes)$ is algebra fuzzy metric space.

Proof:
(1)it is clear that m(u, v) ∈I for all u, v∈ $\mathbb{R}^n$.
(2) $m(u,v) = 0$ if and only if max_j $a_{\mathbb{R}}(\alpha_j - \beta_j)$ if and only if $a_{\mathbb{R}}(\alpha_j - \beta_j)$ for all j=1, 2, …,n if and only if $\alpha_j - \beta_j$=0 for all j=1, 2, …,n if and only if $\alpha_j = \beta_j$ for all j=1, 2, …,n if and only if u=v.
(3)it is clear that $m(u,v) = m(v,u)$

$$(4)\, m(u,z) = max_j\, a_{\mathbb{R}}(\alpha_j - \gamma_j)$$
$$= max_j\, a_{\mathbb{R}}(\alpha_j - \beta_j + \beta_j - \gamma_j)$$

$$\leq max_j\ a_{\mathbb{R}}(\alpha_j - \beta_j)\ \otimes\ max_j\ a_{\mathbb{R}}(\beta_j\ - \gamma_j)$$
$$\leq m(u,v)\ \otimes\ m(v,z)$$

Where $z\ = (\gamma_1, \gamma_2, \dots, \gamma_n)\ \in \mathbb{R}^n$.
Hence $(\mathbb{R}^n, m, \otimes)$ is algebra fuzzy metric space

Example 3.11:
If $s \otimes t = s\ +\ t\ - st$ for all s, t ∈I then $(\mathbb{R}^n, m, \otimes)$ is fuzzy complete where m: $\mathbb{R}^n \to$I is defined by $m(u,v) =\ max_j\ a_{\mathbb{R}}(\alpha_j\ - \beta_j)$ for all $u = (\alpha_1, \alpha_2, \dots, \alpha_n),\ v\ = (\beta_1, \beta_2, \dots, \beta_n)\ \in\ \mathbb{R}^n$.

Proof:
Consider a fuzzy Cauchy sequence (u_k) in $\mathbb{R}^n$ putting $u_k = (r_{1k}, r_{2k}, \dots r_{nk})$. Since (u_k) is fuzzy Cauchy so for any s∈ (0, 1) we can find N∈ ℕ with
$m(u_k, u_j) =\ max_i\ a_{\mathbb{R}}(r_{ik} - r_{ij})\ <\ s$ (6)
for all k, j ≥N and i=1, 2, …, n. This implies that $a_{\mathbb{R}}(r_{ik} - r_{ij}) < r$.
This shows that for any fixed i, 1≤ i ≤n the sequence $(r_{i1}, r_{i2}, \dots)$is a fuzzy Cauchy sequence in $(\mathbb{R}, m, \otimes)$. But $(\mathbb{R}, m, \otimes)$ is fuzzy complete by Theorem 3.10 so it fuzzy converges that is $r_{ik} \to r_i$ as k→ ∞. Now we use these n limits to define u=$(r_1, r_2, \dots, r_n)$ it is clear that u∈ $\mathbb{R}^n$. From (6) by letting j→ ∞ we have

$$m(u_k, u) = m(u_k, \lim_{j\to\infty} u_j) =\ max_i\ a_{\mathbb{R}}(r_{ik} - r_i)\ <\ s$$

Thus (u_k) is fuzzy converges to u. Hence $(\mathbb{R}^n, m, \otimes)$ is fuzzy complete.

Example 3.12:
Let $U = C[a,b]$ and $t \otimes s = t\ +\ s\ - ts$ for all t, s ∈I. then $(U, m, \otimes)$ is fuzzy complete where

$$m(f,g)\ =\ max_{t\in[a,b]}\ a_{\mathbb{R}}[f(t) - g(t)]$$

Proof:
Let (f_k) be a fuzzy Cauchy sequence in *C[a, b]*. Then for any s ∈ (0, 1)we can find N∈ ℕ such that for m, n ≥N we have
$m(f_k, f_n)\ =\ max_{t\in[a,b]}\ a_{\mathbb{R}}[f_k(t) - f_n(t)]\ <\ s$ (7)
Hence for fixed t=t_0 ∈[a, b], $a_{\mathbb{R}}[f_k(t_0) - f_n(t_0)] < s$. This shows that $(f_1\ (t_0),\ f_2(t_0), \dots)$ is fuzzy Cauchy sequence in $(\mathbb{R}, m, \otimes)$. But $(\mathbb{R}, m, \otimes)$ is fuzzy complete by Example 3.9 so it is fuzzy converge to f(t_0). In this way we can associate with each t ∈[a, b] a unique f(t) ∈ ℝ. This defines a function f on [a, b] and we show that f ∈C[a, b] and (f_k) fuzzy converges to f. From (7) with n→ ∞ we have $max_{t\in[a,b]} a_{\mathbb{R}}[f_{k(t)} - f(t)] < s$ for all k≥N. Hence for every t∈[a, b],
$a_{\mathbb{R}}[f_k(t) - f(t)]\ <\ s$ for all k≥N.
This shows that $(f_k(t))$ fuzzy converge to f(t) uniformly on [a, b]. Since all members of (f_k) are fuzzy continuous on [a, b] and the fuzzy convergence is uniform the limit function f is fuzzy continuous on [a, b]. Hence $f\ \in C[a,b]$. Also (f_k) fuzzy converges to f. Hence $(C[a,b], m, \otimes)$ is fuzzy complete.

4.Application of Fixed Point Theorem

The following result is an application of Theorem 3.3 to system of linear equations

Theorem 4.1:
If the system of n linear equations
$u\ =\ Cu\ +\ b$ $(C = (c_{jk}), b$ given) (8)
in n unknowns $\alpha_1, \alpha_2, \dots, \alpha_n$, (the component of u) satisfies
$\sum_{k=1}^{n} a_{\mathbb{R}}(c_{jk}) < 1, (j = 1, 2, \dots, n)$ (9)
It has only one solution u. This solution can be obtained as the limit of the iterative sequence $(u^{(0)}, u^{(1)}, u^{(2)}, \dots)$ where $u^{(j)}$ is arbitrary and

$u^{(j+1)} = Cu^{(j)} + b, (\ j = 0, 1, , , ,)$ (10)

Error bounds are

$$m(u^{(j)}, u) \ \leq \ [(\frac{r}{1-r})]m(u^{(j-1)}, u^{(j)}) \ \leq \ [(\frac{r^j}{1-r})]m(u^{(0)}, u^{(1)})$$

Proof:

Let $v = (\beta_1, \beta_2, \dots, \beta_n), w = (\gamma_1, \gamma_2, \dots, \gamma_n) \ \in \ \mathbb{R}^n$. From Example 3.10 and Example 3.11, $(\mathbb{R}^n, m, \otimes)$ is fuzzy complete algebra fuzzy metric space.

Now define S: $\mathbb{R}^n \to \mathbb{R}^n$by v= S(u)=Cu+b where C=$(c_{jk})$ is a fixed n×n real matrix and b∈ $\mathbb{R}^n$. First we will show that S is a fuzzy contraction $\beta_j = \sum_{k=1}^{n} c_{jk}\, \alpha_j + \sigma_j$ where b=(σ_1, σ_2, …, σ_n). Putting S(w)=z where z=(δ_1, δ_2, …, δ_n). Now

$$m(v,z) = m(S(u), S(w)) = max_j a_{\mathbb{R}}(\beta_j \ - \ \delta_j) \ = \ max_j a_{\mathbb{R}}(\sum_{k=1}^{n} c_{jk}\ (\alpha_j - \delta_j))$$
$$\leq \ max_j[a_{\mathbb{R}}(\alpha_j \ - \ \delta_j)\ a_{\mathbb{R}}(c_{jk})] \ \leq \ max_j a_{\mathbb{R}}(\alpha_j \ - \ \delta_j)\ max_j a_{\mathbb{R}}(c_{jk})$$

Thus $m(v,z) \ \leq \ r\ m(u,w)$ where $r = max_j a_{\mathbb{R}}(c_{jk})$.

Now the assertion of the theorem follows from the proof of Theorem 3.3.

Definition 4.2:

Suppose that $(\mathbb{R}, a_{\mathbb{R}}, \otimes)$ is algebra fuzzy absolute value space. The function $f: \mathbb{R} \to \mathbb{R}$ is said to be satisfying a fuzzy Lipschitz condition if $a_{\mathbb{R}}$[f(t) – f(s)] ≤ k $a_{\mathbb{R}}$(t – s) for all t, s ∈ $\mathbb{R}$ where the constant k is called fuzzy Lipschitz constant.

The next result is an application of Theorem 3.3 to differential equations.

Theorem 4.3:

Let f be fuzzy continuous function on the rectangle $D = \{(t,u): |t - t_0| \leq a, |u - u_0| \leq b\}$and fuzzy bounded on D that is $a_{\mathbb{R}}(f(t,u)) \leq c$ for all (t, u)∈D**.** Suppose that f satisfies a fuzzy Lipschitz condition on D with respect to its second argument, that is there is a constant k such that for (t, u), (t, v) ∈D, $a_{\mathbb{R}}(f(t,u) - f(t,v)) \leq k a_{\mathbb{R}}(u - v)$. Then the initial value problem $\frac{du}{dt} = f(t,u),\ u(t_0) = u_0$ has a unique solution. This solution exists on an interval $[t_0 - \beta, t_0 + \beta]$ where β <min{a, $\frac{b}{c}$, $\frac{1}{k}$}

Proof:

Let $C(J)$ be the algebra fuzzy metric space of all real-valued continuous functions on the interval $J = [t_0 - \beta, t_0 + \beta]$ with fuzzy metric defined by $m(f,g) = \ max_{t \in J} a_{\mathbb{R}}[f(t) - g(t)]$. Then by Example 3.7 and Example 3.12 (C(J), m, ⊗) is fuzzy complete algebra fuzzy metric space. Let $\acute{C}$ be the subspace of C(J) consisting of all those functions u ∈C(J) that satisfy $a_{\mathbb{R}}$(u(t)− u_0) ≤ cβ, It is clear that $\acute{C}$ is closed in C(J). $\acute{C}$ is fuzzy complete.

By integration we see that $\frac{du}{dt}$=f(t, u) can be written u=S(u) where S: $\acute{C} \to \acute{C}$ is defined by $S(u(t)) = \ u_0 \ + \ \int_{t_0}^{t} f(\tau, u(\tau))d\tau$. S is defined for all u ∈ $\acute{C}$ since cβ <b so that if u ∈ $\acute{C}$ then τ ∈J and (τ, u(τ))∈ D and the integration exists since f is fuzzy continuous on D. To see S maps $\acute{C}$ into itself

$$a_{\mathbb{R}}[S(u(t)) - u_0] \leq \ a_{\mathbb{R}}[\int_{t_0}^{t} f(\tau, u(\tau)d\tau] \leq c a_{\mathbb{R}}[t - t_0] \leq c\beta.$$

Now we will show that S is a fuzzy contraction on $\acute{C}$. By the fuzzy Lipschitz condition, we have

$$a_{\mathbb{R}}[S(u(t)) - \ S(v(t)] \ = a_{\mathbb{R}}[\int_{t_0}^{t} [f(\tau, u(\tau)) - f(\tau, v(\tau)]d\tau$$
$$\leq a_{\mathbb{R}}[t - t_0]\ max_{\tau \in J} k\ a_{\mathbb{R}}[u(\tau) - \ v(\tau)]$$
$$\leq k\beta m(u,v)$$

But the last expression does not depends on t. we can take the maximum on the left and have $m[S(u), S(v)] \leq r\, m(u, v)$ where r=kβ. Thus S is a fuzzy contraction on $\acute{C}$. Then Theorem 3.3 implies that S has a unique fixed point u ∈ $\acute{C}$ that is a fuzzy continuous function u on J satisfying $u = S(u)$. Or

$$u(t) = u_0 + \int_{t_0}^{t} f(\tau, u(\tau) d\tau \quad (11)$$

Since $(\tau, u(\tau))$ ∈D where f is fuzzy continuous (8) may be differentiated.

Hence u is even differentiable and satisfies $\frac{du}{dt}$=f(t, u), u(t_0)= u_0.

Conversely every solution of $\frac{du}{dt}$=f(t, u), u(t_0)= u_0 must satisfy (11).

The next result is an application of Theorem 3.3 to integral equations

Theorem 4.4:

Suppose k and v in the Fredholm integral equation

$$u(t) - \mu \int_a^b k(t, \tau) u(\tau) d\tau = v(t) \quad (12)$$

are fuzzy continuous on J×J where J=[a, b] respectively and assume that μ satisfies

$$a_{\mathbb{R}}(\mu) < \frac{1}{c(b-a)} \quad (13)$$

Where c is defined in

$$a_{\mathbb{R}}(k(t, \tau)) \leq c \text{ for all } (t, \tau) \in G \quad (14)$$

Then (12) has a unique solution u on J. This function u is the limit of the iterative sequence (u_0, u_1, …) where u_0 is any fuzzy continuous function on J for n=0, 1, …

$$u_{n+1}(t) = v(t) + \mu \int_a^b k(t, \tau) u_n(\tau) d\tau \quad (15)$$

Proof:

The kernel function k of (12) is a given function on the square G=J×J and v is a given function on J. We assume that v∈C[a, b] and k is fuzzy continuous on G. Then k is fuzzy bounded on G by (14). Now (12) can be written S(u)=u where

$$S(u) = v(t) + \mu \int_a^b k(t, \tau) u(\tau) d\tau \quad (16)$$

Formula (16) defines an operator $S: C[a, b] \to C[a, b]$. Now

$$m(S(u), S(y)) = max_{t \in J}\, a_{\mathbb{R}}[Su(t) - Sy(t)]$$

$$= a_{\mathbb{R}}(\mu) \max_{t \in J} a_{\mathbb{R}}[\int_a^b k(t, \tau)[u(\tau) - y(\tau)] d\tau$$

$$\leq a_{\mathbb{R}}(\mu) max_{t \in J} \int_a^b a_{\mathbb{R}}\{k(t, \tau)[u(\tau) - y(\tau)]\} d\tau$$

$$\leq a_{\mathbb{R}}(\mu) max_{t \in J} \int_a^b a_{\mathbb{R}}\{k(t, \tau)\} a_{\mathbb{R}}\{[u(\tau) - y(\tau)]\} d\tau$$

$$\leq a_{\mathbb{R}}(\mu) c max_{\sigma \in J} a_{\mathbb{R}}[u(\sigma) - y(\sigma)] \int_a^b d\tau$$

$$\leq a_{\mathbb{R}}(\mu)\, c\, m(u, y)(b - a)$$

This can be written $m(S(u), S(y)) \leq r\, m(u, y)$ where $r = a_{\mathbb{R}}(\mu)\, c(b - a)$

We see that S becomes a fuzzy contraction from (13). Then Theorem 3.3 implies that S has a unique fixed point u on J. This function u is the limit of the iterative sequence (u_0, u_1, …) where u_0 is any fuzzy continuous function on J for n=0, 1, … $u_{n+1}(t) = v(t) + \mu \int_a^b k(t, \tau) u_n(\tau) d\tau$.

Theorem 4.5:

Suppose that v in Volterra integral equation

$$u(t) - \mu \int_a^t k(t, \tau) u(\tau) d\tau = v(t) \quad (17)$$

is fuzzy continuous on J and the kernel k is fuzzy continuous on the

triangular region D in the tτ-plane by a$\leq \tau \leq$t, a$\leq$t$\leq$b. Then equation (17) has a unique solution u on J for every μ.

Proof:
We see that equation (16) can be written u=S(u) with $S: C(J) \to C(J)$defined by

$$S(u(t)) = v(t) + \mu \int_a^t k(t,\tau)u(\tau)d\tau \quad (18)$$

since k is fuzzy continuous on R and R is fuzzy closed also k is fuzzy bounded function on D so

$$a_{\mathbb{R}}(k(t,\tau)) \leq c \text{ for all } (t,\tau) \in D \quad (19)$$

Now for all u, v ∈C(J) we have

$$a_{\mathbb{R}}[Su(t) - Sv(t)] = a_{\mathbb{R}}(\mu)a_{\mathbb{R}}[\int_a^t k(t,\tau)(u(\tau) - v(\tau))d\tau]$$

$$a_{\mathbb{R}}[Su(t) - Sv(t)] \leq a_{\mathbb{R}}(\mu)c\, m(u,v) \int_a^t d\tau = a_{\mathbb{R}}(\mu)\, c\, m(u,v)\, (t-a) \quad (20)$$

We show by induction that

$$a_{\mathbb{R}}[S^m u(t), S^m v(t)] \leq a_{\mathbb{R}}(\mu)\, {}^m c^m \frac{(t-a)^m}{m!} m(u,v) \quad (21)$$

For m=1 this is (20). Assume that (21) holds for any m we obtain

$$a_{\mathbb{R}}\,[S^{m+1}u(t), S^{m+1}v(t)] = a_{\mathbb{R}}(\mu)a_{\mathbb{R}}[\int_a^t k(t,\tau)(S^m u(\tau) - S^m v(\tau))d\tau]$$

$$\leq \mathrm{a}_{\mathbb{R}}(\mu)c \int_a^t \mathrm{a}_{\mathbb{R}}(\mu)\, {}^m c^m\, \frac{(t-a)^m}{m!} d\tau\, m(u,v)$$

$$\leq \mathrm{a}_{\mathbb{R}}(\mu)\, {}^{m+1}c^{m+1} \frac{(t-a)^{m+1}}{(m+1)!} m(u,v)$$

Which complete the inductive proof of (21). Using (t−a) ≤(t−b) on the right hand of (21) then taking the maximum over t∈J on the left we obtain from (20)

m(S^mu, S^mv) ≤ r_mm(u, v) where $r_m = \mathrm{a}_{\mathbb{R}}(\mu)\, {}^m c^m \frac{(t-a)^m}{m!}$

For any fixed μ and sufficiently large m we have r_m <1. Hence the corresponding S^m is a fuzzy contraction on *C(J)*. The assertion of our theorem now follows from Theorem 3.3.

Lemma 4.6:
Let $S: U \to U$ be a function where $(U, m, \otimes)$ is a fuzzy complete algebra fuzzy metric spaces. Suppose that S^m is a fuzzy contraction on U for some m∈ ℕ. Then S has a unique fixed point.

Proof:
By assumption S^m=T is a fuzzy contraction on U by Theorem 3.3 this function T has a unique fixed point y that is T(y)=y. Hence T^n(y)=y. Now Theorem 3.3 also implies that for every u∈U T^n(u) →y as n→ ∞. For the particular u=S(y) since $T^n = S^{nm}$ we obtain

$$y = \lim_{n\to\infty} T^n Sy = \lim_{n\to\infty} ST^n y = \lim_{n\to\infty} Sy = Sy.$$

This shows that y is a fixed point of S. Since every fixed point of S is also a fixed point of T we see that S cannot have more than one fixed point.

References

[1] Kider J 2011 On fuzzy normed spaces *Eng. & Tech. Journal* **29**(9) 1790
[2] Kider J 2011 Completion of fuzzy normed spaces *Eng. & Tech. Journal* **29**(10) 2004
[3] Kider J 2012 New fuzzy normed spaces *J. Baghdad Sci.* **9** 559
[4] Kider J and Hussain Z 2014 Continuous and Uniform Continuous Mappings on a Standard Fuzzy Metric Spaces *Eng. & Tech. Journal* **32**(B6) 1111
[5] Kider J 2014 Completeness of Hausdorff Standard Fuzzy Metric Spaces *Al- Mustansiriyah J. Sci.* **25**(3) 85
[6] Kider J and N Kadhum N 2017 Properties of fuzzy norm of fuzzy bounded operators *Iraqi Journal of Science* **58**(3A) 1237

[7] Kadhum N 2017 *On fuzzy norm of a fuzzy bounded operator on fuzzy normed spaces* M.Sc. Thesis University of Technology Iraq
[8] Ali A 2018 *Properties of Complete Fuzzy Normed Algebra* M.Sc. Thesis University of Technology, Iraq
[9] Kider J and A. Ali A 2018 Properties of fuzzy absolute value on and properties finite dimensional fuzzy normed space *Iraqi Journal of Science* **59**(2B) 909
[10] Kider J and Ali A 2019 Properties of a Complete Fuzzy Normed Algebra *Baghdad Science Journal* **16**(2) 382
[11] Kider J and M. Gheeab M 2019 Properties of a General Fuzzy Normed Space **Iraqi Journal of Science 60**(4) 847
[12] Kider J and M Gheeab M 2019 Properties of The Space GFB (V, U) *Journal of AL-Qadisiyah for computer science and mathematics* **11**(1) 102
[13] Kider J and N Kadhum N 2019 Properties of Fuzzy Compact Linear Operators on Fuzzy Normed Spaces *Baghdad Science Journal* **16**(1) 104
[14] Kider J Kadhum N 2019 Properties of Fuzzy Closed Linear Operator *Eng. & Tech. Journal* **37**(B1) 25
[15] Šostak A and George-Veeramani 2018 Fuzzy Metrics Revised, Axioms 7 60
[16] Gregori V Crevillén l Morillas S and Sapena A 2009 On convergence in fuzzy metric Spaces *Topology and its Applications* 156 3002
[17] Kider J 2020 Some Properties of Fuzzy Soft Metric Space *Al-Qadisiyah Journal of Pure Science* **25**(2) 1
[18] Kider J 2020 Some Properties of Algebra Fuzzy Metric Space *Journal of Al-Qadisiyah for Computer Science and Mathematics* **12**(2) 43

Some convergence results by using K — iteration process in $CAT(H)$spaces

Some convergence results by using$K-$ iteration process in $CAT(H)$spaces

Shahla Abd Al-Azeaz Kadhim

Directorate General of Education Baghdad′ s Karkh Third/Ministry of Education

Email: ousamastat@gmail.com

Abstract: In this paper, we study the convergence and$\Delta-$convergence results of $K-$iteration process for Lipschizian self-mapping with $L \geq 1$in $CAT(H)$ spaces , $H > 0$.

1 −Introduction

Let D a positive number . A metric space (E,d) is said to be a$D-$geodesic space if any two points of E with the distance less than D are joined by a geodesic .If $H > 0$,then E is said to be a $CAT(H)$ space if and only if it is D_H- geodesic and any geodesic triangle$\Delta(x,y,w)$ in $E$with$d(x,y)+d(y,w)+d(w,x) < 2\,D_H$ satisfies the $CAT(H)$ inequality .If $H < 0$,then E is said to be a$CAT(H)$ space if and only if it is a geodesic space such that all of its geodesic triangle satisfy the $CAT(H$ inequalitysee ([1]). He et al .[2]definedMann iteration in$CAT(H)$spaces ,$H > 0$ for self mapping V as follows , for any $x_1 \in E$

$$x_{n+1} = (1-\gamma_n)x_n \oplus \gamma_n V x_n \;; n \geq 0 \quad \ldots(i)$$

Where $\{\gamma_n\}$is sequence in $(0,1)$ and proved the sequencedefined by (i) converges in $CAT(H)$ spaces.

Kifayat U., Kashif I. and Muhammed A. [3] introdused$K-$ iteration in $CAT(0)$, space for Suzuki generalized nonexpansive self mapping V as follows , for any $x_1 \in E$

$$\begin{aligned} x_{n+1} &= Vy_n \\ y_n &= V(1-\sigma_n)Vx_n \oplus \sigma_n V z_n \\ z_n &= (1-\gamma_n)x_n \oplus \gamma_n V x_n \;; n \geq 0 \end{aligned} \quad \ldots(ii)$$

Where $\{\sigma_n\}$and$\{\gamma_n\}$ are sequences in $(0,1)$ and proved the sequence defined by (ii) converges in $CAT(0$ space .

Raweerots S . [4] denote the set of fixed points of the mapping V by $F(V) = \{x \in E; Vx = x\}$.

On the other hand A sequence $\{y_n\}$ in the space A is said to be $\Delta-$ converges to y if y is the unique asymptotic center of $\{v_n\}$for everysubsequence $\{v_n\}$of $\{y_n\}$. we write $\Delta-\lim_{n\to\infty} y_n = y$. where the asymptotic center $C(\{y_n\})$of $\{y_n\}$is the set

$C(\{y_n\}) = \{x \in A: r(\{y_n\}) = r(y,\{y_n\})\}$ .see ([5])

Das and Debata [6]introdused Ishikawa iteration in $CAT(0)$ space for two nonexpansiveself mappings V and Was follows, forany$x_1 \in E$

$$\begin{aligned} x_{n+1} &= (1-\sigma_n)x_n \oplus \sigma_n W y_n \\ y_n &= (1-\gamma_n)x_n \oplus \gamma_n V x_n \;; n \geq 0 \end{aligned} \quad \ldots(iii)$$

Where $\{\sigma_n\}$and $\{\gamma_n\}$ are sequences in (0,1) and proved the sequence defined by $(iii)\Delta-$ converges in $CAT(0)$ space . Jun[7]defined Ishikawa iteration in$CAT(H), H>0$ space for self mapping Vas follows , for any $x_1 \in E$

$$x_{n+1} = (1-\sigma_n)x_n \oplus \sigma_n V y_n$$
$$y_n = (1-\gamma_n)x_n \oplus \gamma_n V x_n \ ; n \geq 0 \quad \ldots(v)$$

Where $\{\sigma_n\}$and$\{\gamma_n\}$ are sequences in (0,1) and proved the sequencedefined by $(v)\Delta-$ converges to a fixed point of$V$ in $CAT(H)$ space .

2- Preliminaries

In this section ,we provide some definitions and lemmas which will be used Lemma (2.1)[8]: Let $H>0$ and(E,d) is a complete $CAT(H)$ spacewith diam (E) $=\frac{\pi/2-\mu}{\sqrt{H}}$for some $\mu \in (0,\pi/2)$. Then

$$d\big((1-\sigma)x \oplus \sigma y, w\big) \leq (1-\sigma)d(x,w) + \sigma d(y,w)$$
for all $x,y,w \in E$ and $\sigma \in (0,1)$.

Definition (2.2)[3]: Let G be a non−empty and convex subset of a CAT(H)spaceand $V: G \to G$ is a mapping for any $x_1 \in E$, the sequence $\{x_n\}$ define by

$$x_{n+1} = Vy_n$$

$$y_n = V((1-\sigma_n)Vx_n \oplus \sigma_n V z_n)$$

$$z_n = (1-\gamma_n)x_n \oplus \gamma_n V x_n \ ; n \geq 0 \quad \ldots(1)$$

is said to be $K-$ iteration sequence$CAT(H)$space,$\{\sigma_n\}$and $\{\gamma_n\}$ are sequences in (0,1).

Definition (2.3)[9]: Let G be a non−empty and convex subset of $CAT(H)$. A mapping $V: G \to G$ is said to be
(i) Lipschizian if $d(Vx,Vy) \leq L\, d(x,y)$ ... (2)
for all $x,y \in G$ and $L \geq 1$

Definition (2.4)[4]: A point $y \in E$ is a $\Delta-$ cluster point of $\{y_n\}$ if there exist asubsequence of $\{y_n\}$that $\Delta-$ converges to$y$,for a sequence$\{y_n\}$in A .

Lemma(2.5), [2] : Let(E,d) is a complete $CAT(H)$space . $q \in E$
Suppose that a sequence$\{y_n\}$ in A $\Delta-$ converges to$y$such that $r(q,y_n) < \frac{D_H}{2}$. Then $d(y,q) \leq \lim_{n\to\infty} \inf d(y_n, q)$

Definition (2.6)[4] : Let (E,d) be a complete metric space and Gbe a non−empty subset of E . Then a sequence $\{y_n\}$ in E isFej é r monotone with respect to G . If $d(y_{n+1}, q) \leq d(y_n, q)$, $n \geq 0$ andfor all $q \in G$.

Lemma(2.7), [2] :Let $H>0$ and(E,d) is a complete $CAT(H)$ space , G is a nonempty subset of E . Suppose that the sequence $\{y_n\}$ in EisFejér monotone with respect to G and the asymptotic radius $r(\{y_n\})$ of$\{y_n\}$ is less than $\frac{\pi}{2}$ .If any$\Delta-$cluster point of$\{x_n\}$ in G. Then$\{y_n\}$ $\Delta-$ converges to a point in G .

Definition (2.8)[1]: Let G be a non−empty and convex subset of $CAT(H)$space. A sequence$\{y_n\}$inG issaid to be an approximate fixed point sequence for G if $\lim_{n\to\infty} d(y_n, Vy_n) = 0$.

3 −Main Theorem

In this section , The convergence and $\Delta-$convergenceresults of $K-$ iteration process has been proved .

Theorem(3.1): Let $H>0$ and(E,d) is acomplete $CAT(H)$ space with diam (E) $=\frac{\pi/2-\mu}{\sqrt{H}}$for some$\mu\in(0,\pi/2)$, G is a nonempty and convex subset of E and $V:G\to G$is Lipschizian mapping with$L\geq 1$, $F\neq\emptyset$.Let$\{x_n\}$define by condition (1) withγ_n and$\sigma_n\in(0,1)$. If G is complete and $\lim_{n\to\infty}\inf d(x_n,F)=0$ or $\lim_{n\to\infty}\sup d(x_n,F)=0$, then $\{x_n\}$converges to a unique point in F .

Proof: Let $q\in F$, from lemma (2.1), condition(1)and(2),

$$\begin{aligned} d(z_n,q)=\ d((1-\gamma_n)x_n\ \oplus\gamma_n Vx_n,q) &\leq(1-\gamma_n)d(x_n,q)+\gamma_n d(Vx_n,q)\\ &\leq(1-\gamma_n)d(x_n,q)+\gamma_n\ L\ d(x_n,q)\\ &=(1-\gamma_n+\gamma_n\ L)d(x_n,q)\\ &\leq(1+\gamma_n\ L)d(x_n,q)\ldots(3)\end{aligned}$$

From lemma (2.1), condition(1), (2)and(3), we get

$$\begin{aligned} d(y_n,q)=\ d(V(1-\sigma_n)Vx_n\ \oplus\sigma_n Vz_n,q) &\leq L\ d((1-\sigma_n)Vx_n\ \oplus\sigma_n Vz_n,q)\\ \leq\ L[(1-\gamma_n)d(Vx_n,q)+\sigma_n d(Vz_n,q)] &\leq L[(1-\sigma_n)\ L\ d(x_n,q)+\sigma_n\ L\ d(z_n,q)]\\ &=[L^2+\sigma_n\gamma_n\ L^3]d(x_n,q)\\ &=L^2[1+\sigma_n\gamma_n\ L]d(x_n,q)\ldots(4)\end{aligned}$$

From lemma (2.1), condition(1), (2), (3)and(4), we get

$$\begin{aligned} d(x_{n+1},q)=d(Vy_n,q) &\leq L\ d(y_n,q)\\ &=\ L^3[1+\sigma_n\gamma_n\ L]d(x_n,q)\end{aligned}$$

Hence , for all$n,m\ \epsilon\ N$ and every $q\in F$, there exists $W>0$ such that,

$$d(x_{n+m},q)\leq W\ d(x_n,q).$$

Now we show that$\{x_n\}$ is acaushysequence in G,since $\lim_{n\to\infty}d(x_n,F)=0$, so for each $\delta>0$, $there\ e\ n_1\in N$ such that

$d(x_n,F)<\frac{\delta}{W+1}$for all $n>n_1$

Thus , there exists $\rho\in F$ such that

$d(x_n,\rho)<\frac{\delta}{W+1}$for all $n>n_1$, we get

$$\begin{aligned} d(x_{n+m},x_n)\leq\ d(x_{n+m},\rho)+d(x_n,\rho)&\leq\ Wd(x_n,\rho)+d(x_n,\rho)\\ &\leq(W+1)d(x_n,\rho)\\ &\leq(W+1)\frac{\delta}{W+1}=\delta,\end{aligned}$$

therefore$\{x_n\}$ is a caushysequence in G . From the completeness of G , we get $\lim_{n\to\infty}\{x_n\}$existsand equals$\rho\in G$, thereforefor all$\delta_1>0$

$$\text{there exists } n_1\in N\text{such that } d(x_n,\rho)<\frac{\delta_1}{3(2+3\vartheta_1)}$$

Now , $\lim_{n\to\infty}\inf d(x_n,F)=0$ or $\lim_{n\to\infty}\sup d(x_n,F)=0$

gives that$\lim_{n\to\infty}d(x_n,F)=0$.So there exists $n_2\in N$with$n_2>n_1$

$d(x_n,\rho)<\frac{\delta_1}{3(2+3\vartheta_1)}$.

Thus there exists $\theta\in F$ such that

$d(x_{n_2}, \theta) < \frac{\delta_1}{3(4+3\vartheta_1)}$, we obtain

$$d(V\rho, \rho) \le d(V\rho, \theta) + d(\theta, x_{n_2}) + d(x_{n_2}, \rho)$$
$$\le L\, d(\rho, \theta) + d(\theta, x_{n_2}) + d(x_{n_2}, \rho)$$
$$\le \frac{\delta_1}{3(4+3\vartheta_1)\mathrm{L}} + \frac{\delta_1}{3(4+3\vartheta_1)} + \frac{\delta_1}{3(2+3\vartheta_1)}$$
$$\le L\,(4+3\vartheta_1)\frac{\delta_1}{3(4+3\vartheta_1)\mathrm{L}} + (4+3\vartheta_1)\frac{\delta_1}{3(4+3\vartheta_1)}$$
$$+(2+\vartheta_1)\delta_1/3(2+\vartheta_1)$$
$$= \frac{\delta_1}{3} + \frac{\delta_1}{3} + \frac{\delta_1}{3} = \delta_1$$

Since δ_1 is arbitrary so $d(V\rho, \rho)$, so thus$V\rho = \rho$, there fore$\rho \in F$.

Corollary (3.2) Let (E, d) is a complete $CAT(0)$ space , G is a nonempty and convex subset of E and $V: G \to G$ is Lipschizian mapping with $L \ge 1$, $F \neq \emptyset$. Let $\{x_n\}$define by condition(1) with $\gamma_n$and$\sigma_n \in (0,1)$. If G is complete and $\liminf_{n\to\infty} d(x_n, F) = 0$ or $\limsup_{n\to\infty} d(x_n, F) = 0$, the$\{x_n\}$converges to a unique point in F.

Corollary(3.3) Let E, G, V and$\{x_n\}$ be as in theorem(3.1) with $F(V) \neq \emptyset$ if

$(i)\{x_n\}$ is an approximate fixed point sequence for V
(ii)there exists a function $\tau: [0,\infty[\to [0,\infty[$ which is right continuous at 0, $\tau(0) = 0$ and$\tau(d(x_n, Vx_n) \ge d(x_n, F)$, for all $n \in N$
then $\{x_n\}$converges to a unique point in F .

proof ;From (i) and (ii) , we get

$$\lim_{n\to\infty} d(x_n, F) \le \lim_{n\to\infty} \tau(d(x_n, Vx_n)$$
$$= \tau \lim_{n\to\infty} (d(x_n, Vx_n)$$
$$= \tau(0) = 0$$

Thus $\lim_{n\to\infty} d(x_n, F) = 0$.

$$\text{Thus } \liminf_{n\to\infty} d(x_n, F) = 0 \text{ and } \limsup_{n\to\infty} d(x_n, F) = 0 .$$

By theorem(3.1) , $\{x_n\}$converges to a unique point in$F$.

Corollary (3.4) Let E, G, V and $\{x_n\}$ be as inCorollary(3.2) with $F(V) \neq \emptyset$ if
$(i)\{x_n\}$ is approximate fixed point sequence for V
(ii)there exists a function $\tau: [0,\infty[\to [0,\infty[$ which is right continuous at 0, $\tau(0) = 0$ and$\tau(d(x_n, Vx_n) \ge d(x_n, F)$, for all $n \in N$
then $\{x_n\}$ converges to a unique point in F .

Theorem(3.5)Let E, G, V and$\{x_n\}$ be as in theorem(3.1) with $F(V) \neq \emptyset$if
(i) $d(x_0, F) < \frac{T_H}{4}$ for $x_0 \in G$. $(ii)\{x_n\}$ is Fej é r monotone with respect to G. $(iii)\{x_n\}$ is an approximate fixed point sequence for V. then$\{x_n\}$ $\Delta-$converges to a point in F .

proof :Set $F_0 = F \cap B_{\frac{\pi}{2}}(x_0)$.

Let $\{x_n\}$ is Fejér monotonewith respect to $F_0$and$q \in F$ such that $d(x_0, q) < \frac{\pi}{4}$. Then $q \in F_0$we get

$$d(x_{n+1}, q) \leq d(x_n, q) \leq d(x_0, q) < \frac{\pi}{4} \quad \text{, for all } n \geq 0. \qquad \ldots (5)$$

Hence $r(\{x_n\}) < \frac{\pi}{4}$

from lemma (2.7) ,let$\overline{q} \in G$be a $\Delta -$ cluster point of $\{x_n\}$, then there exists asubsequence $\{x_{n_l}\}$of$\{x_n\}$ which $\Delta -$ converges to $\overline{q}$. By (5) , we obtain $r(q, \{x_{n_l}\}) \leq d(x_0, q) < \frac{\pi}{4}$.

Using lemma (2.5) , we get

$d(\overline{q}, x_0) \leq d(\overline{q}, q) + d(x_0, q) \leq \lim_{l\to\infty} \inf d(x_{n_l}, q) + d(x_0, q) < \frac{\pi}{4}$.

That is $\overline{q} \in B_{\frac{\pi}{2}}(x_0)$. From condition (iii), we obtain

$$\lim_{l\to\infty} \sup d(V\overline{q}, x_{n_l}) \leq \lim_{l\to\infty} \sup d(V\overline{q}, Vx_{n_l}) + \lim_{l\to\infty} \sup d(Vx_{n_l}, x_{n_l})$$
$$\leq \lim_{l\to\infty} \sup d(\overline{q}, x_{n_l})$$

Hence $V\overline{q} \in C(\{x_{n_l}\})andV\overline{q} = \overline{q}$. Then$\overline{q} \in F_0$ and using lemma (2.7) , we get$\{x_n\}$ $\Delta -$ converges to a point in F .

Corollary (3.6) Let E, G, V and$\{x_n\}$ be as in corollary(3.2) with $F(V) \neq \emptyset$ if
(i) $d(x_0, F) < \frac{T_H}{4}$ for $x_0 \in G$. $(ii)\{x_n\}$is Fejér monotone with respect to H. $(iii)\{x_n\}$ is an approximate fixed point sequence for$V$. then$\{x_n\}$ $\Delta -$ converges to a point in F .

4- Conclusions

The convergence and $\Delta -$convergenceresults of $K -$ iteration process has been proved when used Lipschizian self mapping with $L \geq 1$ in $CAT(H)$, $H > 0$ spaces . alsoe stablished the convergence and $\Delta -$convergence results has been in $CAT(0)$spaces .

5- Suggestion

$1 -$ we can useuniformly Lipschizian mapping to established the convergence and $\Delta -$ convergesresults of$K -$ Iteration .

$2 -$ we can use another iteration to established the convergence and $\Delta -$ convergesresults .

References

[1] Gurucharan S S, Mihai P and Alia K 2015Convergence of three – step iterations for nearly asymptotically non expansive mappings in CAT(K) spaces *J of Inequalities and Applications* **156**
[2] He J S, Fang D H, Lopez G and Li C 2012 Mann′s algorithm for nonexpansive mappings CAT(K) spaces *Nonlinear Anal.* **75** 445-452
[3] Kifayat U Kashif I and Muhammad A 2018 Some convergence results using K iteration process in CAT(0) spaces *Spring Open J.*
[4] Raweerote S and Prasit Ch 2016 The modified S- iteration process for non expansive mappings in CAT(K) spaces Springer Open J. **25**
[5] Lim T C 1976 Remarks on some fixed point theorems *Proc . Am. Math. So .* **60** 179-182
[6] Das G and Debata J P 1986 Fixed points of quasi –non expansive mappings *Indian J. Pure Appl. Math.* **17** 1263-1269
[7] Jun C Ishikawa iteration process in CAT(K) spaces *arXiv* , 1303.6669v1 [math . MG]
[8] Bridson M R and Haefliger A 1999 Metric Spaces of Non –positive Curvature *Grundlehren der Mathematisc henwissenschaften* **319** Springer Berlin
[9] Rafiq A 2006 Modified Noor Iteration for nonlinear equations in Banach spaces Applied Mathematics and Computation **182** 589-595.1

Radiative peristaltic transport of Ree-Eyring fluid through porous medium in asymmetric channel subjected to combined effect of inclined MHD and convective conditions

Radiative peristaltic transport of Ree-Eyring fluid through porous medium in asymmetric channel subjected to combined effect of inclined MHD and convective conditions

Hayat A Ali

Department of Applied Science, Mathematics and Application of Computer, University of Technology, Baghdad, Iraq

E-mail: 100048@uotechnology.edu.iq

Abstract. This study emphasizes the flow phenomenon of trapped bolus traveling along the interior walls of asymmetric inclined channels contains a non-Newtonian Ree-Eyring. The flow was exposed to influenced by inclined MHD field, thermal heat radiative, and porous media. Further, no slip and convective thermal conditions are considered. Mathematical expression for governing equations are reformulated and in accordance with lubrication approximations, nonlinear partial differential equations of the flow reduced into a system of ordinary differential equations associated with boundary conditions an approximate solution is deduced by implementing perturbation strategy for tiny A Ree-Eyring fluid parameter. Finally, a graphical description is presented to figure out the elevation behavior of flow quantities i.e. velocity profile, temperature distribution, pressure rise, and streamlines formulation due to variation of emerging involved parameters. The study analyzed that the velocity profile reveals mixed behavior via increment of Ree-Eyring parameters η, A as well as Hartman number H and Darcy number Da. whereas the thermal radiative parameter Rn accelerates the temperature distribution profile. The study calculations are made by the "Mathematica 11.3" package.

1. Introduction

Peristaltic pumping is a type of fluid motion that appears when a progressive wave of area clasping and compressing propagates along the wall of a distensible channel. Bolus development through the esophagus, movement of blood in small vessels, intrauterine fluid motion, lymph transport, and embryo motion through the uterine cavity are the biological applications of the peristaltic mechanism. Moreover, it is an inherent property of many modern industrial applicable such as the ceramic and porcelain industry, nuclear industry, pharmaceutical industry, and heart-lung machines [1]. After the first attempt on peristaltic transport given by Latham [2]. Fung and Yih [3] introduced the peristaltic mechanism in the laboratory frame. Nowadays many pieces of literature are available on peristalsis considering different fluids models and flow configurations see Refs. [4,5,6].

Incited by the fact that enormous fluids in nature have an immense impact in modern industry, science, and technology is non-Newtonian like paints, cosmetic products, colloidal fluids, certain oils, and shampoo known by their behavior cannot be predicted by a single constitutive equation [7,6]. Inspired by the aforementioned applicable literature survey, many researchers presented various models to visualize the non-Newtonian fluid models. Recently the most considerable non-Newtonian fluid

gained the attraction of many researchers due to its wide medical and scientific application. Furthermore, its constitutive equation is derived from the kinetic theory of liquids, not from empirical relations alike the power-law model, and it properly reduced into the Newtonian fluid model at high shear stress known by Ree-Eyring fluid [8,9]. numerous scientific literature outlined the peristaltic transport of Ree-Eyring with different effects and flow situations in Refs. [10-12].

On other hand, a flow through magneto hydrodynamic (MHD) field has vigorous attention in recent years via its vastly applicable in metallurgy processes, engineering, geophysics, and industry. Plasma confinement, nuclear reactor, bleeding reduction during surgeries, stirring, crystal growth process, and MRI (magnetic resonance imaging) to diagnose the disease are several utilization of electrically fluid flows in the presence of (MHD) field [13]. In view of these diverse, many studied considering the peristaltic transport of MHD various fluid models are mentioned through the studies [7,14-16].

Thermal radiation can control the excess heat generation inside the body since high temperatures pose serious stresses for the human body which leads to injury or even death. This effect occurs in many physiological, technological, and industrial processes like plasma tissue heat conduction, MHD generators, laser surgery, destruction of cancer tumors, polymer processing industry, etc. However, the rate of heat or energy transfer between two bodies via thermal radiation essentially depends on the absolute temperature difference this means that the influence of thermal radiation on fluid flow has major coverage at high temperatures. Motivated by these developments some modern attempts have been devoted to investigating the influence of thermal radiation on the peristaltic mechanism for different non-Newtonian fluid. Nikiforov [17] elevate an electromagnetic hyperthermia technique in which the undesired cancer cells are exposed to a higher temperature field of more than 41 °C with aid of thermal radiation. In such a technique, a magnetic liquid is injected into the malignant tissues and then exposing the framework to an alternating current. So, the temperature is produced in the infused magnetic fluid and hence the cancer cells will be destroyed see also [14]. Hayat et al. [18] analyzed numerically heat transfer due to viscous dissipation and radiation on peristaltic flow of Sutter by fluid in a vertical channel. While Bhatti et al. [19] explored theoretically nonlinear thermal radiation impact on EMHD peristaltic propulsion of non-Newtonian fluid-particle (dusty) suspensions in a planar channel including a homogenous porous media. Naveed Imrana et al. [20] discuss the influence of heterogeneous-homogenous effect in the peristaltic flow of non-Newtonian Rabinowitsch fluid considering thermal radiation effects and viscous dissipation for more knowledge in this aspect see Refs.[21-26].

From the aforementioned survey, we conclude that no attempt has been made to examine the combined impact of heat radiative, and inclined (MHD) on peristaltic transport of Non-Newtonian Ree-Eyring fluid yet and the current study will fill this gap. In this article, we explore the peristaltic transport of Ree-Eyring fluid past through inclined asymmetric porous channel subjected to the combined influence of thermal radiation and inclined (MHD) field. Velocity no-slip and convective boundary conditions are taken into account. The flow is illustrated in the laboratory frame which is transformed into a wave frame. The flow mathematical system was simplified by considering the assumption of infinite wave length and low Reynolds number. Analytical solution for stream function and temperature distribution function is evaluated by implementing the regular perturbation method. The impact of impeded physical parameters on the flow quantities is discussed in detail through figures.

2. Mathematical Model

Reconsidering the peristaltic transport of an incompressible electrically conducting Ree-Eyring fluid in asymmetric an inclined channel at an angle (α_1) and width $(d_1 + d_2)$ through porous media see Figure 1. The flow is incident to inclined uniform magnetic field of strength $\vec{B} = (\beta_0\, Sin\alpha_2, \beta_0\, Cos\alpha_2)$. The induced magnetic field is neglected by taken a small magnetic Reynolds number. The flow is propagating by the sinusoidal waves of length λ with different amplitudes and phases moving with a constant speed (c) along the walls of the channels.

The geometry of the walls surfaces is given by [4]

$$Y_1 = H_1(X,t) = d_1 + a_1 Cos\left(\frac{2\pi(X-ct)}{\lambda}\right), \quad (1)$$

$$Y_2 = H_2(X,t) = -d_2 - a_2 Cos\,(2\pi(X-ct)/\lambda + \emptyset), \quad (2)$$

Where Y_1, Y_2 are the upper and lower wall respectively a_1, a_2 are the wave amplitudes, t is the time, and (X,Y) the Cartesian coordinates in a fixed frame. $\emptyset$ is the phase different and $\emptyset \in [0,\pi]$ such that when $(\emptyset = 0)$ corresponds to asymmetric channel with waves out of phase, while $(\emptyset = \pi)$, the waves in phase. Further a_1, a_2, d_1, d_2 *and* $\emptyset$ satisfy the condition.

$$a_1{}^2 + a_2{}^2 + a_1 a_2 d_1 d_2\, cos\emptyset \le (d_1 + d_2)^2, \quad (3)$$

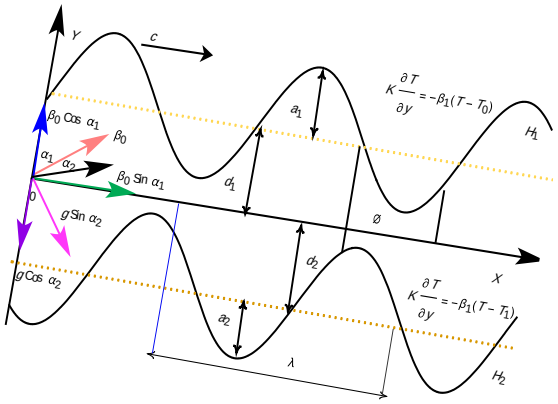

Figure 1. The geometry of the Inclined Asymmetric Channel [4]

To calculate the Lorentz force applying the following Ohm's formula [27] as below

$$\vec{F} = \sigma[\vec{V} \times \vec{B}] \times \vec{B}, \quad (4)$$

We have

$$\vec{F} = \left(-\sigma\beta_0{}^2 Cos\alpha_1(\bar{U}Cos\alpha_1 - \bar{V}Sin\alpha_1), \sigma\beta_0{}^2 Sin\alpha_1(\bar{U}Cos\alpha_1 - \bar{V}Sin\alpha_1)\right), \quad (5)$$

$\vec{F}$ is the magnetic force, $\vec{J}$ is the current density vector, $\vec{V} = (\bar{U}, \bar{V}, 0)$ the velocity field, σ the electrical conductivity.

The governing equations of continuity, motion, and energy can be constructed as

$$\frac{\partial \bar{U}}{\partial X} + \frac{\partial \bar{V}}{\partial Y} = 0, \quad (6)$$

$$\rho\left(\frac{\partial \bar{U}}{\partial t} + \bar{U}\frac{\partial \bar{U}}{\partial X} + \bar{V}\frac{\partial \bar{U}}{\partial Y}\right) = -\frac{\partial \bar{P}}{\partial X} + \frac{\partial \check{S}_{XX}}{\partial X} + \frac{\partial \check{S}_{XY}}{\partial Y} - \sigma\beta_0{}^2 Cos\alpha_1(\bar{U}Cos\alpha_1 - \bar{V}Sin\alpha_1) - \frac{\mu}{\kappa_0}\bar{U} + \rho g Sin\alpha_2, \quad (7)$$

$$\rho\left(\frac{\partial \bar{V}}{\partial t} + \bar{U}\frac{\partial \bar{V}}{\partial X} + \bar{V}\frac{\partial \bar{V}}{\partial Y}\right) = -\frac{\partial \bar{P}}{\partial Y} + \frac{\partial \check{S}_{XY}}{\partial X} + \frac{\partial \check{S}_{YY}}{\partial Y} + \sigma\beta_0{}^2 Sin\alpha_1(\bar{U}Cos\alpha_1 - \bar{V}Sin\alpha_1) - \frac{\mu}{\kappa_0}\bar{V} - \rho g Cos\alpha_2, \quad (8)$$

$$\rho c_P\left(\frac{\partial T}{\partial t} + \bar{U}\frac{\partial T}{\partial X} + \bar{V}\frac{\partial T}{\partial Y}\right) = K\left(\frac{\partial^2 T}{\partial X^2} + \frac{\partial^2 T}{\partial Y^2}\right) + \check{S}_{XX}\frac{\partial \bar{U}}{\partial X} + \check{S}_{YY}\frac{\partial \bar{V}}{\partial Y} + \check{S}_{XY}\left(\frac{\partial \bar{U}}{\partial Y} + \frac{\partial \bar{V}}{\partial X}\right) - \frac{\partial q_r}{\partial Y} + \sigma\beta_0{}^2(\bar{U}Cos\alpha_1 - \bar{V}Sin\alpha_1)^2, \quad (9)$$

Where σ is the electrical conductivity, K is thermal conductivity, κ_0 posity parameter, ρ density, c_P specific heat, T is the temperature vector, $\bar{P}$ the pressure.

Using Rosseland approximation for radiation, the radiative heat flux $q_r$is given by

$$q_r = -\frac{4\sigma_1}{3k_1}\frac{\partial T^4}{\partial Y}, \quad (10)$$

σ_1 is the Stefan-Boltzman constant and $k_1$is the mean absorption coefficient. By assuming a sufficiently small temperature difference in the flow, the term

the Taylor series approximation for T^4in terms of T_0 take the following form

$$T^4 \cong 4{T_0}^3 T - 3{T_0}^4, \tag{11}$$

placement of equation (10) and equation (11) into equation (9), the energy equation will take the form

$$\rho c_P \left(\frac{\partial T}{\partial t} + \bar{U}\frac{\partial T}{\partial X} + \bar{V}\frac{\partial T}{\partial Y}\right) = K\left(\frac{\partial^2 T}{\partial X^2} + \frac{\partial^2 T}{\partial Y^2}\right) + \check{S}_{XX}\frac{\partial \bar{U}}{\partial X} + \check{S}_{YY}\frac{\partial \bar{V}}{\partial Y} + \check{S}_{XY}\left(\frac{\partial \bar{U}}{\partial Y} + \frac{\partial \bar{V}}{\partial X}\right) + \frac{16{T_0}^3\sigma_1}{3k_1}\frac{\partial T}{\partial Y} + \sigma{\beta_0}^2\left(\bar{U}Cos\alpha_1 - \bar{V}Sin\alpha_1\right)^2, \tag{12}$$

With the boundary conditions

$$\left.\begin{aligned} &\bar{U} = 0, \quad \psi = \frac{F}{2}, \quad K\frac{\partial T}{\partial y} = -\beta_1(T - T_0), at\ Y = H_1 \\ &\bar{U} = 0, \quad \psi = -\frac{F}{2}, \quad K\frac{\partial T}{\partial y} = -\beta_1(T - T_1), at\ Y = H_2 \end{aligned}\right\} \tag{13}$$

The stress tensor for Ree-Eyring fluid is given as follows [28]:

$$\check{S}_{ij} = \mu\frac{\partial \bar{V}_i}{\partial X_j} + \frac{1}{\beta}Sinh^{-1}\left(\frac{1}{c}\frac{\partial \bar{V}_i}{\partial X_j}\right) \quad i,j = 1,2 \tag{14}$$

$$Sinh^{-1}\left(\frac{1}{c}\frac{\partial \bar{V}_i}{\partial X_j}\right) \approx \frac{1}{c}\frac{\partial \bar{V}_i}{\partial X_j} - \frac{1}{6}\left(\frac{1}{c}\frac{\partial \bar{V}_i}{\partial X_j}\right)^3, \ \left|\frac{1}{c}\frac{\partial \bar{V}_i}{\partial X_j}\right| \ll 1, \tag{15}$$

Then

$$\check{S}_{ij} = \mu\frac{\partial \bar{V}_i}{\partial X_j} + \frac{1}{\beta c_1}\frac{\partial \bar{V}_i}{\partial X_j} - \frac{1}{6\beta{c_1}^3}\left(\frac{\partial \bar{V}_i}{\partial X_j}\right)^3 \tag{16}$$

Where $\bar{V}_1 = \bar{U}, \bar{V}_2 = \bar{V}$, $x_1 = X$, $x_2 = Y$.

$\check{S}_{ij}$ represents the extra stress tensor, β, c_1 are the fluid parameter, and μ is the dynamic viscosity.

In view of equation (16), the laboratory frame components of extra stress tensor become

$$\left.\begin{aligned} \check{S}_{XX} &= \mu\frac{\partial \bar{U}}{\partial X} + \frac{1}{\beta c_1}\frac{\partial \bar{U}}{\partial X} - \frac{1}{6\beta{c_1}^3}\left(\frac{\partial \bar{U}}{\partial X}\right)^3 \\ \check{S}_{XY} &= \mu\frac{\partial \bar{U}}{\partial Y} + \frac{1}{\beta c_1}\frac{\partial \bar{U}}{\partial Y} - \frac{1}{6\beta{c_1}^3}\left(\frac{\partial \bar{U}}{\partial Y}\right)^3 \\ \check{S}_{YX} &= \mu\frac{\partial \bar{V}}{\partial X} + \frac{1}{\beta c_1}\frac{\partial \bar{V}}{\partial X} - \frac{1}{6\beta{c_1}^3}\left(\frac{\partial \bar{V}}{\partial X}\right)^3 \\ \check{S}_{YY} &= \mu\frac{\partial \bar{V}}{\partial Y} + \frac{1}{\beta c_1}\frac{\partial \bar{V}}{\partial Y} - \frac{1}{6\beta{c_1}^3}\left(\frac{\partial \bar{V}}{\partial Y}\right)^3 \end{aligned}\right\}, \tag{17}$$

By the following transformations, we furnished the relationship between laboratory frame (X, Y) and wave frame $(\check{x}, \check{y})$ coordinates

$$\check{x} = X - c\bar{t}\ ,\ \check{y} = Y\ ,\bar{u} = \bar{U} - c\ ,\bar{v} = \bar{V}, \bar{p}(\check{x},\ \check{y}) = \bar{P}(X, Y, t), \tag{18}$$

Employing the above equation, we transform equations (1), (2) and (6) - (17) in wave frame and then normalize the resulting equations by considering the following dimensionless quantities [25,27]

$$x = \frac{\check{x}}{\lambda}\ , y = \frac{\check{y}}{d_2}\ ,\ u = \frac{\bar{U}}{c}\ , v = \frac{\bar{V}}{c}\ , h_1 = \frac{H_1}{d_2}, h_2 = \frac{H_2}{d_2}\ , p = \frac{{d_2}^2\bar{p}}{\lambda\mu c}, \delta = \frac{d_2}{\lambda}\ , u = \frac{\partial\psi}{\partial y}\ , v = -\delta\frac{\partial\psi}{\partial x}, S = \frac{d_2\check{S}(\check{x})}{\mu c}\ , Re = \frac{\rho c d_2}{\mu},\ \theta = \frac{T - T_0}{(T_1 - T_0)}, Pr = \frac{\mu c_P}{k}\ , H = \beta_0 d_2\sqrt{\frac{\sigma}{\mu}}\ , E_c = \frac{c^2}{c_P(T_1 - T_0)}\ , Br = E_c Pr\ ,\ Fr = \frac{c}{\sqrt{g d_2}}\ , a = \frac{a_1}{d_2}\ , b = \frac{a_2}{d_2}\ , d = \frac{d_1}{d_2}, Da = \frac{\kappa_0}{{d_2}^2}, \eta = \frac{1}{\mu\beta c_1}, A = \frac{\eta}{6}\left(\frac{c}{c_1 d}\right)^2, Rn = \frac{16\sigma_1{T_0}^3}{3k_1\mu c_P}, \omega_1 = \frac{\beta_1}{K}, \tag{19}$$

Where Re is Renolds number, δwave number, Pr Prandtl number, H Hartman number, E_c Eckret number, Br Brinkman number, Fr Froude number, Da Darcy number, Rn is the thermal radiation parameter, η, A are the Ree- Eyring fluid parameters, ω_1 is the heat Biot number a, b the amplitude ratio of the upper and lower wall, and $\psi(x, y, t)$ is the stream function.

Using the assumptions of long wavelength and low Renolds number approximation and equation (19), the flow equations reduced and simplified to the forms

$$Re\ \delta\left(\psi_y\psi_{xy} - \psi_x\psi_{yy}\right) = -p_x + \delta\frac{\partial}{\partial x}S_{xx} + \frac{\partial}{\partial y}S_{xy} - H^2 Cos\alpha_1\left(\psi_y Cos\alpha_1 - \delta\psi_x Sin\alpha_1\right) - \frac{1}{Da}\psi_y + \frac{Re}{Fr}Sin\alpha_2, \tag{20}$$

$$Re\,\delta^3(-\psi_y\psi_{xx}-\psi_x\psi_{xy}) = -p_y+\delta^2\frac{\partial}{\partial x}S_{xy}+\delta\frac{\partial}{\partial y}S_{yy}-\delta H^2 Sin\alpha_1(\psi_y Cos\alpha_1+\ \delta\psi_x Sin\alpha_1)-\frac{\delta}{Da}\psi_x-\delta\frac{Re}{Fr}Cos\alpha_2, \quad (21)$$

$$PrRe\,\delta(\psi_y\theta_x-\psi_x\theta_y) = (\delta^2\theta_{xx}+\theta_{yy})+\mathrm{Pr}\,Rn\,\theta_{yy}+\delta S_{xx}\psi_{yx}+S_{xy}(-\delta^2\psi_{xy}+\psi_{yy})-\delta S_{yy}\psi_{xy}+H^2Br(\psi_y Cos\alpha_1+\delta\psi_x Sin\alpha_1)^2, \quad (22)$$

By applying($Re \ll 0, \delta \to 0$) we finally get

$$0 = -p_x+\frac{\partial}{\partial y}S_{xy}-H^2\psi_y(Cos\alpha_1)^2-\frac{1}{Da}\psi_y+\frac{Re}{Fr}Sin\alpha_2, \quad (23)$$

$$0 = -p_y, \quad (24)$$

$$(1+\mathrm{Pr}\,Rn)\,\theta_{yy}+S_{xy}\psi_{yy}+H^2Br(\psi_y Cos\alpha_1)^2 = 0, \quad (25)$$

Eliminating p from equations (23) and (24), we have the following equation

$$0 = \frac{\partial^2}{\partial y^2}S_{xy}-H^2\psi_{yy}(Cos\alpha_1)^2-\frac{1}{Da}\psi_{yy}, \quad (26)$$

Where $S_{xy} = (1+\eta)\psi_{yy}-A(\psi_{yy})^3$.

Associated with the following dimensionless boundary conditions

$$\left.\begin{array}{l}\psi_y = 0,\ \ \psi = \frac{F}{2},\quad \theta_y = -\omega_1\theta,\quad at\ y = h_1\\ \psi_y = 0,\ \ \psi = -\frac{F}{2},\quad \theta_y = -\omega_1(\theta-1),\quad at\ y = h_2\end{array}\right\}, \quad (27)$$

In which $y = h_1 = d + a\,Cos(x)$ and $y = h_2 = -1 - b\,Cos(x+\emptyset)$ dimensionless upper and lower walls and F is the non-dimensional mean flow which related to the non-dimensional time- mean flow ϑ by following dimensionless relationship

$$F = \vartheta - 1 - d, \quad (28)$$

And the pressure rise per wavelength is

$$\Delta p_\lambda = \int_0^1 \frac{dp}{dx}dx, \quad (29)$$

3. Methodology of solution

Dimensionless equations (25) and (27) are highly complicated, non-linear and thus the closed form solution for arbitrary values of all parameters is impossible hence we adopt the perturbation method for the analytical solution of the problem. Inserting the following expressions

$$\psi = \psi_0 + A\,\psi_1 + O(A)^2, \quad (30)$$

$$\theta = \theta_0 + A\,\theta_1 + O(A)^2, \quad (31)$$

$$F = F_0 + A\,F_1\ + O(A)^2, \quad (32)$$

Substituting equations (30) - (32) into equations (25) - (28) and then comparing the coefficients of the same power of A up to the first order we obtain the following systems

3.1. Zeroth order system

The general form of the zeroth-order system is

$$(1+\eta)\psi_{0yyyy}-\left(H^2(Cos\alpha_1)^2+\frac{1}{Da}\right)\psi_{0yy} = 0, \quad (33)$$

$$(1+Pr\,Rn)\,\theta_{0yy}+(1+\eta)(\psi_{0yy})^2+H^2(Cos\alpha_1)^2Br{\psi_{0y}}^2 = 0, \quad (34)$$

the boundary conditions are

$$\left.\begin{array}{l}\psi_{0y} = 0,\ \ \psi_0 = \frac{F_0}{2}, \theta_{0y} = -B_1\theta_0,\ at\ y = h_1\\ \psi_{0y} = 0, \psi_0 = -\frac{F_0}{2},\ \theta_{0y} = -B_1(\theta_0-1), at\ y = h_2\end{array}\right\}, \quad (35)$$

3.2. First order system

The first- order system is

$$(1+\eta)\psi_{1yyyy}-\left(H^2(Cos\alpha_1)^2+\frac{1}{Da}\right)\psi_{1yy}-\frac{\partial^2}{\partial y^2}(\psi_{1yy})^3 = 0, \quad (36)$$

$$(1 + Pr\,Rn)\,\theta_{1yy} + Br(1+\eta)\left((\psi_{1yy})^2 - \left(\psi_{0yy}\right)^4\right) + BrH^2(Cos\alpha_1)^2 Br{\psi_{1y}}^2 = 0, \quad (37)$$

With the respect to the boundary conditions

$$\left.\begin{array}{l} \psi_{1y} = 0, \quad \psi_1 = \frac{F_1}{2}, \quad \theta_{1y} = -\omega_1\theta_1, \quad at\ y = h_1 \\ \psi_{1y} = 0, \quad \psi_1 = -\frac{F_1}{2}, \quad \theta_{1y} = -\omega_1(\theta_1 - 1), \quad at\ y = h_2 \end{array}\right\}, \quad (38)$$

Solving both systems using Mathematica program, the closed form for stream function ψ, and temperature field θ will be obtained

$$\psi = \frac{e^{-\frac{vy}{\sqrt{1+\eta}}}(1+\eta)(e^{\frac{2vy}{\sqrt{1+\eta}}}\mathrm{c}_1+\mathrm{c}_2)}{v^2} + \mathrm{c}_3 + yc_4 + A\left(\frac{A_1+A_2+A_3}{8v(1+\eta)^{3/2}} + c_7 + yc_8\right),$$

$$\theta_0 = \mathrm{r}_1 + y\,\mathrm{r}_2 - \frac{Br(A_4+A_5+A_6)}{2(v+PrRnv)},$$

$$\theta_1 = r_3 + yr_4 + \frac{\mathrm{Br}}{128(1+PrRn)v(1+\eta)^2}\left(A_7 - A_8 - 4e^{\frac{2vy}{\sqrt{1+\eta}}}(-18c1^4c2^2vy^2(1+\eta) - \frac{A_9+A_{10}+A_{11}}{v} + 4e^{-\frac{2vy}{\sqrt{1+\eta}}}(-18\mathrm{c}1^2\mathrm{c}2^4vy^2(1+\eta) - \frac{A_{12}+A_{13}}{v}) + A_{14} + A_{15} - A_{16}\right),$$

$$A_1 = \frac{{c_2}^3 e^{-\frac{3vy}{\sqrt{1+\eta}}}(1+\eta)^{3/2}}{v} + \frac{{c_1}^3 e^{\frac{3vy}{\sqrt{1+\eta}}}(1+\eta)^{3/2}}{v},$$

$$A_2 = 2e^{\frac{vy}{\sqrt{1+\eta}}}(6{c_1}^2c_2y(1+\eta) + \frac{(1+\eta)^{3/2}(-15{c_1}^2c_2+4*c_5+4\eta*c_5)}{v}),$$

$$A_3 = e^{-\frac{vy}{\sqrt{1+\eta}}}(-12c_1{c_2}^2y(1+\eta) + \frac{2(1+\eta)^{3/2}(-15c_1{c_2}^2+4*c_6+4\eta*c_6)}{v}),$$

$$v = \left(H^2(Cos\alpha_1)^2 + \frac{1}{Da}\right)^{1/2},$$

$$A_4 = \frac{c2^2e^{-\frac{2vy}{\sqrt{1+\eta}}}(1+\eta)^2}{2v} + \frac{c1^2e^{\frac{2vy}{\sqrt{1+\eta}}}(1+\eta)^2}{2v},$$

$$A_5 = -\frac{2c2e^{-\frac{vy}{\sqrt{1+\eta}}}H^2(1+\eta)^{3/2}Cos[\alpha_1]^2}{v^2} + \frac{2c1e^{\frac{vy}{\sqrt{1+\eta}}}H^2(1+\eta)^{3/2}Cos[\alpha_1]^2}{v^2},$$

$$A_6 = \frac{1}{2}vy^2(c_4H^2 + 4c_1c_2(1+\eta) + c_4H^2Cos[2\alpha_1]),$$

$$A_7 = (48c1^3c2^3v^3y^4 + 64c1c2(c2c5 - c1c6)v^2y^3(1+\eta)^{3/2} - \frac{9c2^6e^{-\frac{6vy}{\sqrt{1+\eta}}}(1+\eta)^2}{2v} - \frac{9c1^6e^{\frac{6vy}{\sqrt{1+\eta}}}(1+\eta)^2}{2v} + c1^3e^{\frac{4vy}{\sqrt{1+\eta}}}(1+\eta)(-27c1^2c2y\sqrt{1+\eta} + \frac{(1+\eta)(8c1+27c1^2c2-18c5+8c1\eta-18c5\eta)}{v}),$$

$$A_8 = c2^3e^{-\frac{4vy}{\sqrt{1+\eta}}}(1+\eta)(-27c1c2^2y\sqrt{1+\eta} - \frac{(1+\eta)(8c2+27c1c2^2-18c6+8c2\eta-18c6\eta)}{v}),$$

$$A_9 = (1+\eta)^2(-32c1^3c2 + 63c1^4c2^2 - 36c1^2c2c5 + 8c5^2 + 18c1^3c6 - 32c1^3c2\eta,$$

$$A_{10} = -36c1^2c2c5\eta + 16c5^2\eta + 18c1^3c6\eta + 8c5^2\eta^2),$$

$$A_{11} = 3y(-27c1^4c2^2v\sqrt{1+\eta} + 8c1^2c2c5v\sqrt{1+\eta} - 27c1^4c2^2v\eta\sqrt{1+\eta} + 16c1^2c2c5v\eta\sqrt{1+\eta} + 8c1^2c2c5v\eta^2\sqrt{1+\eta}),$$

$$A_{12} = (1+\eta)^2(-32c1c2^3 + 63c1^2c2^4 + 18c2^3c5 - 36c1c2^2c6 + 8c6^2 - 32c1c2^3\eta + 18c2^3c5\eta - 36c1c2^2c6\eta + 16c6^2\eta + 8c6^2\eta^2),$$

$A_{13} = 3y(-27c1^2c2^4v\sqrt{1+\eta} + 8c1c2^2c6v\sqrt{1+\eta} - 27c1^2c2^4v\eta\sqrt{1+\eta} + 16c1c2^2c6v\eta\sqrt{1+\eta} + 8c1c2^2c6v\eta^2\sqrt{1+\eta})$,

$A_{14} = \frac{16c2^3 e^{-\frac{3vy}{\sqrt{1+\eta}}} H^2(1+\eta)^{5/2}Cos[\alpha_1]^2}{3v^2} - \frac{16c1^3 e^{\frac{3vy}{\sqrt{1+\eta}}} H^2(1+\eta)^{5/2}Cos[\alpha_1]^2}{3v^2}$,

$A_{15=} -\frac{32e^{\frac{vy}{\sqrt{1+\eta}}} H^2(1+\eta)(6c1^2c2y(1+\eta)+\frac{(1+\eta)^{3/2}(-21c1^2c2+4c5+4c5\eta)}{v})Cos[\alpha_1]^2}{v}$,

$A_{16=}\frac{32e^{-\frac{vy}{\sqrt{1+\eta}}} H^2(1+\eta)(-6c1c2^2y(1+\eta)+\frac{(1+\eta)^{3/2}(-21c1c2^2+4c6+4c6\eta)}{v})\mathrm{Cos}[\alpha_1]^2}{v}$,

$A_{17=}2vy^2(1+\eta)(117c1^3c2^3 - 48c1c2^2c5(1+\eta) - 48c1^2c2(4c2+c6)(1+\eta) + 16(1+\eta)(c8H^2 + 4c5c6(1+\eta)) + 16c8H^2(1+\eta)Cos[2\alpha_1]))$,

Where $c_1, c_2, c_3, c_4, c_5, c_6, c_7, c_8, r_1, r_2, r_3, r_4$ can be found using simple calculations.

4. Result and discussions

In this part of the work, graphical results are illustrated in order to figure out the impact of various emerging parameters such as $\kappa, H, \eta,$ and A on velocity, temperature profiles, pressure rise, and trapping phenomenon.

4.1. Velocity profile

The effect of Darcy number Da , Hartman number H , Ree-Eyring fluid parameters η, A , phase difference parameter ϕ, and lower wall amplitude parameter b respectively on the velocity curve quantifies in figure 2(a)-(f). we attributed an enhancement in the velocity field at the center of the channel due to the rise in Darcy number Da, whereas it decreases over the rest of the channel cross-section by increasing Darcy number Da via figure 2(a). However, ascending values of Hartman number H directly related to Lorentz force that resists the fluid flow and consequently decreases its velocity see figure 2(b). Whereas From figures 2(c) and (d) two opposite behaviors are seen for the higher magnitude of Ree-Eyring fluid parameters η and A respectively on velocity profile i.e. the magnitude of velocity is an increment in η resulted in an increase of $u(y)$ in the central part of the channel and decreases toward the walls whereas this result is revers with A impact. In figures, 2(e) and (f) two opposite reactions are noticed on the velocity profile via increment of ϕ magnitude. It depicts $u(y)$ decays at the region($0 \leq y \leq 0.22$), while it reflects increasing behavior for the rest channel. Larger values of b parameter lead to a reduction in velocity profile at the central part of the channel while this result is reversed toward the boundaries.

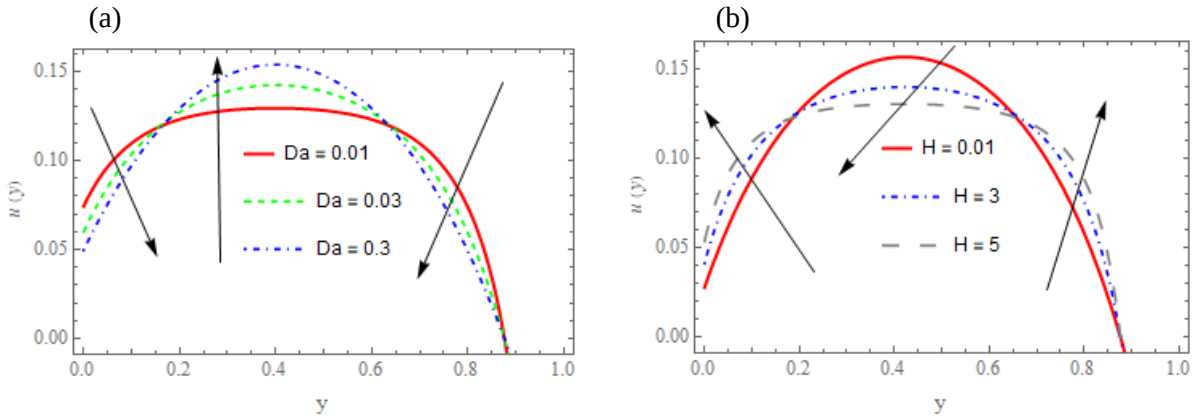

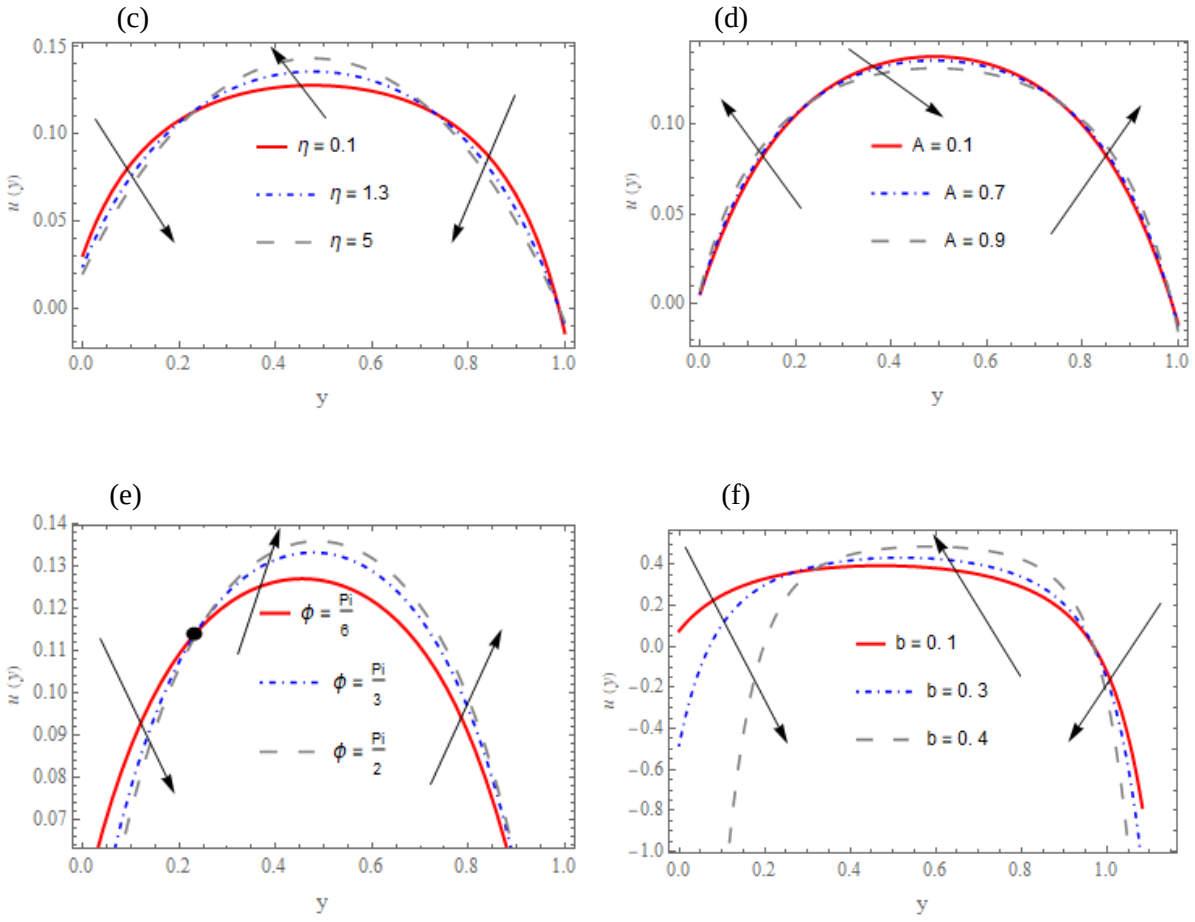

Figure 2. Velocity profile for different values of (a) permeability parameter κ (b) Hartman number H (c) Ree- Eyring parameter η (d) Ree- Eyring parameter A (e) phase difference parameter ϕ (f) lower wall amplitude parameter b and for fixed values of parameters$\{a = 0.04, d = 0.3, \vartheta = 1.4, x = 0.3, \alpha_1 = \frac{\pi}{6}\}$

4.2. Temperature distribution

In this part, we characterize graphical behavior of temperature distribution profile against variation of Prandtl number Pr, Brinkman number Br, thermal radiation parameter Rn, Hartman number H, Darcy number Da, heat generation parameter B_1. figure 3(a) reveals the direct reaction of Pr on temperature profile $\theta(y)$. Whereas increment of Br tends to drop in $\theta(y)$ field see figure 3(b). The impression of $\theta(y)$ against the ascending value of Rn is considered in figure 3(c). We observed that $\theta(y)$ behaves as an increasing function upon Rn rises since it increases the surface heat flux so $\theta(y)$ is developed. It reveals from figure 3(d) that increment of Hartman number causes markedly resistance to temperature distribution profile. Due to enhancement in Darcy number,$\theta(y)$ tends to raise near the boundary regions whereas fluid temperature remains stable in the central part of the channel see figure 3(e). It is visualized from figure 3(f) that the heat generation parameter $B_1$is directly proportional to the temperature distribution profile.

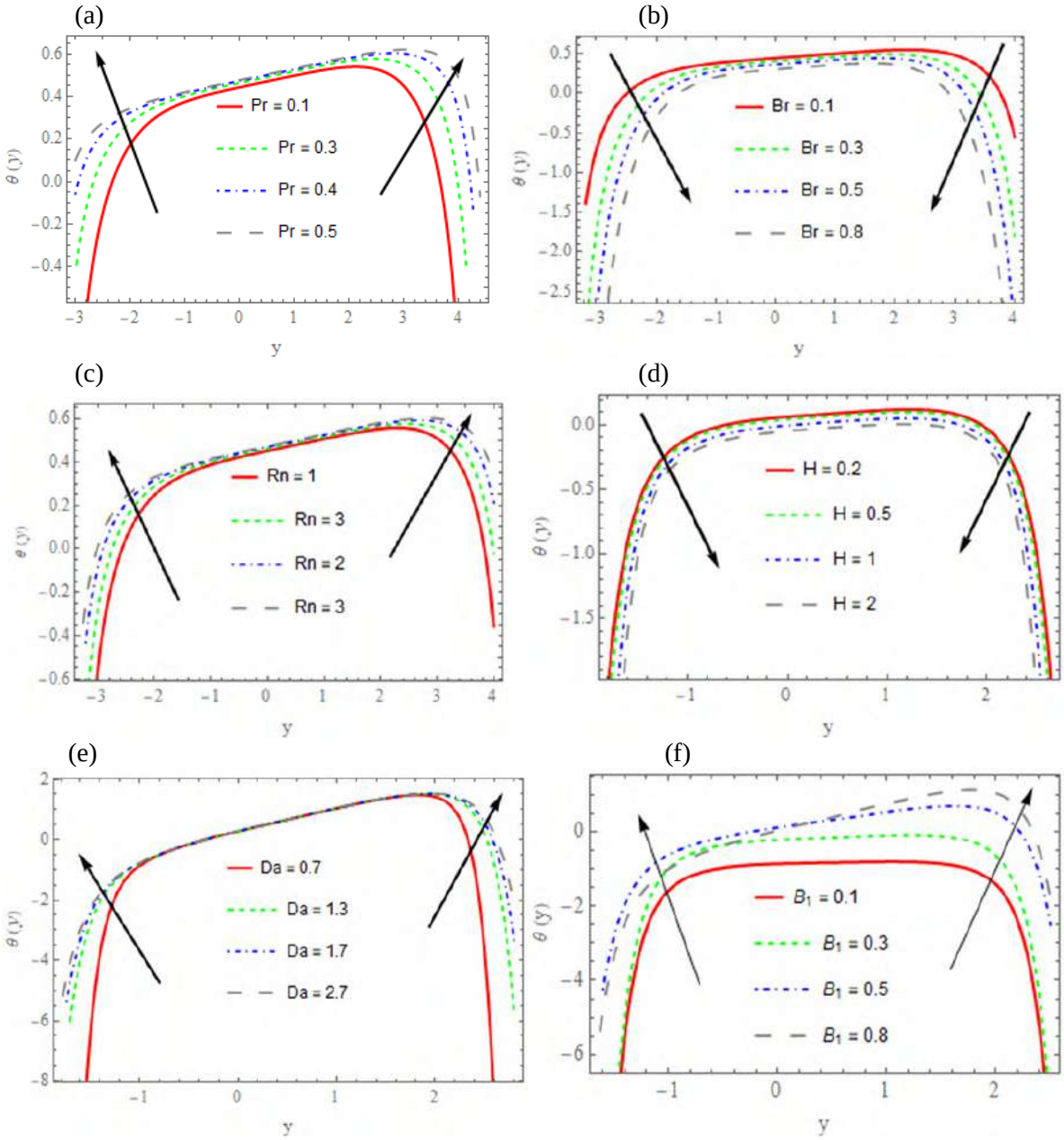

Figure 3. Temperature profile for different values of (a) Prandtl number Pr (b) Brinkman number Br (c) Thermal radiative number Rn (d) Hartman number H (e) Darcy number Da (f) Heat generation parameter B_1 and for fixed parameters $\{a = 0.3, b = 0.1, d = 0.3, \phi = \frac{\pi}{2}, x = 0.1, \eta = 0.2, A = 0.02, \vartheta = 0.71, \alpha_1 = \frac{\pi}{2}\}$.

4.3. Pumping phenomenon

The most interesting phenomenon that is used to visualize the physiological behavior of fluids in the peristaltic mechanism is characterized by pumping phenomena. figure 4 illustrates the consequence of pressure rise Δp_λ against the averaged flow rate ϑ via variation of the following pertinent parameters Hartman number H , Darcy number Da, Ree- Eyring parameters η, and A. The figures portrayed the parabolic behavior for Δp_λ profile. Furthermore, we noticed that the whole pumping region varied into four regions, the peristaltic pumping where$(\Delta p_\lambda > 0, \vartheta > 0)$, augmented pumping where $(\Delta p_\lambda < 0, \vartheta > 0)$ and $(\Delta p_\lambda < 0, \vartheta < 0)$ and retrograde pumping where $(\Delta p_\lambda > 0, \vartheta < 0)$ while free pumping

is recognized for($\Delta p_\lambda = 0$). Figure 4(a) prepared to visualize the variation of Δp_λ against ϑ for various values of H. It is obvious that higher values of H cause the augmented and retrograde pumping regions to decreases whereas growth in peristaltic pumping is witnessed. However, the completely opposite response on pumping flow is appeared due to enhance Da magnitude which means the flow can pass easily without imposing higher pressure shown in figure 4(b). One can contemplate from figures 4(c) and 4(d), the dissimilar action for η, and A parameters respectively on pumping characteristic i.e. η is developing the augmented and retrograde pumping regions while the peristaltic pumping has a depressing function whereas this situation is absolutely reversed for enhancing A parameter further free pumping is recognized where ($\vartheta > 0.55$).

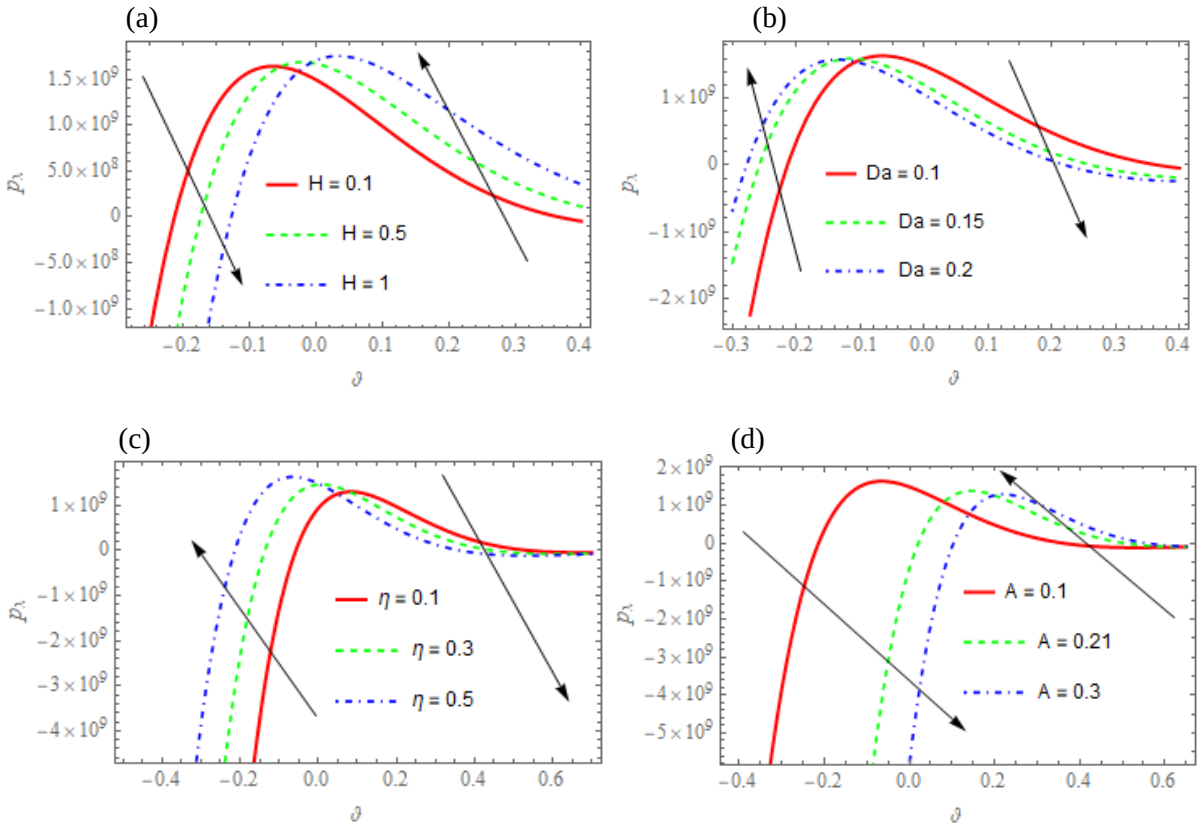

Figure 4. Pressure rise ΔP_λ versus ϑ via various values of (a) Hartman number$H$ (b) Darcy number Da (c) Ree- Eyring parameter η (d) Ree- Eyring parameter A with $\{a = 0.1, b = 0.3, d = 0.3, \phi = \frac{\pi}{2}, y = 0.1, t = 0.1, \alpha_1 = \frac{\pi}{6}, \alpha_2 = \frac{\pi}{2}, \mathrm{Re} = 0.1, \mathrm{Fr} = 0.1\}$.

4.4. Trapping characteristic

Formation of a circular path or bolus interior the flow streamlines along the peristaltic wave is known by trapping, we highlighted in this subsection upon the influences of some interesting pertinent parameters like Hartman number H, Darcy number Da, angle inclination parameter α_1, phase difference parameter ϕ, Ree-Eyring parameters η and A , and time flow rate parameter ϑ with respect to fixed parameters $\{a = 0.3, b = 0.1, d = 0.3, t = 0.1\}$ on the trapping phenomenon. figure 5 captured the diminished behavior for the streamlines contours in size and number due to a rise in H magnitude which leads to enhance Lorentz force that opposite the flow in return. Whereas figure 6 identifies the direct influences of Darcy's number on the magnitude and number of moving trapping bolus. No remarkable

changes on the streamlines pattern were seen for ascending variation in α_1 values i.e. the trapping bolus developed very slowly with α_1 see figure 7. The significant impact of emerging parameter ϕ on trapping bolus is outlined in figure 8, it is noticed that the size and number of trapped bolus declines for higher values of ϕ . Figures 9 and 10 recorded enhancement impact for the two Ree- Eyring embedded parameters η and A on trapping bolus phenomenon. An elevation of flow rate parameter ϑ produces more bolus as well as their size enhance see figure 11.

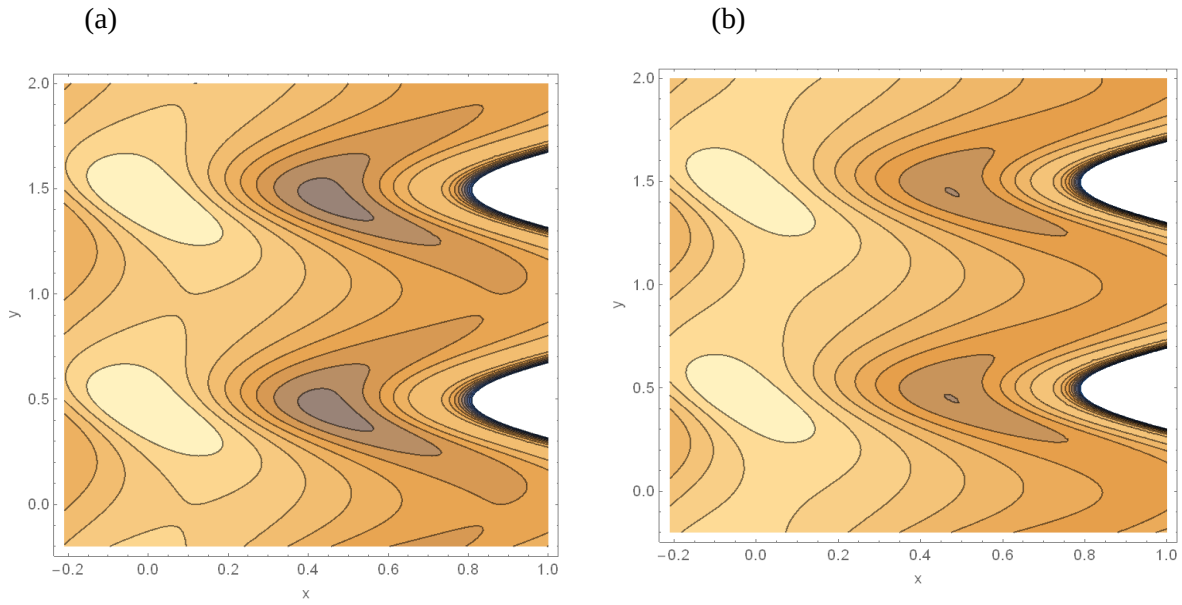

Figure 5. Streamlines contours for multiple values of Hartman number $H = \{1, 1.5\}$

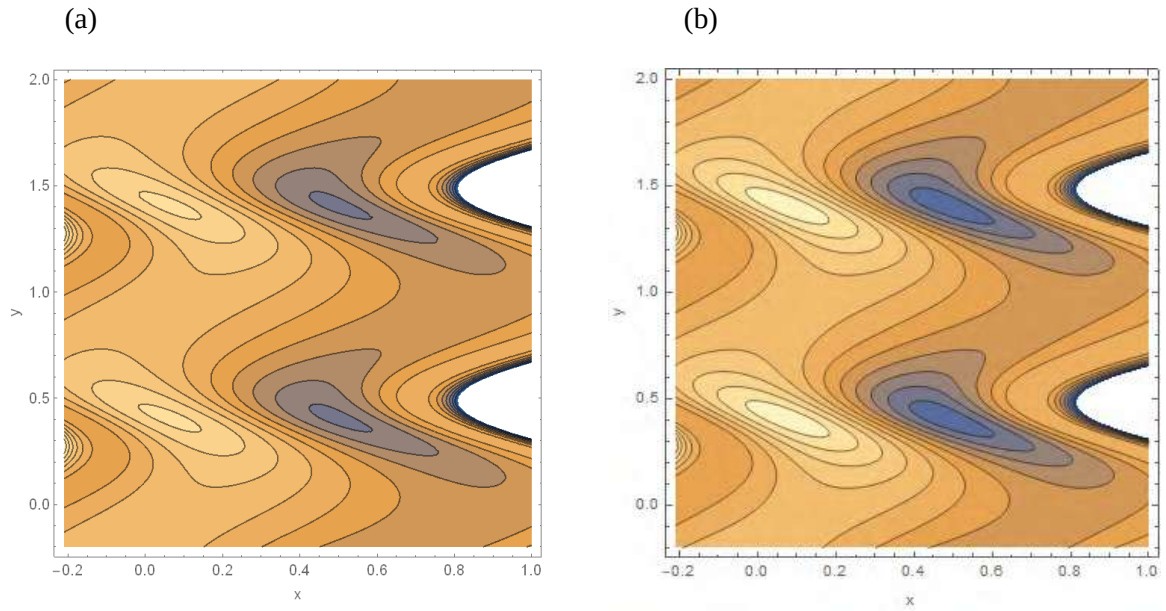

Figure 6. Streamlines contours for multiple values of Darcy number $Da = \{0.3, 0.8\}$.

(a) (b)

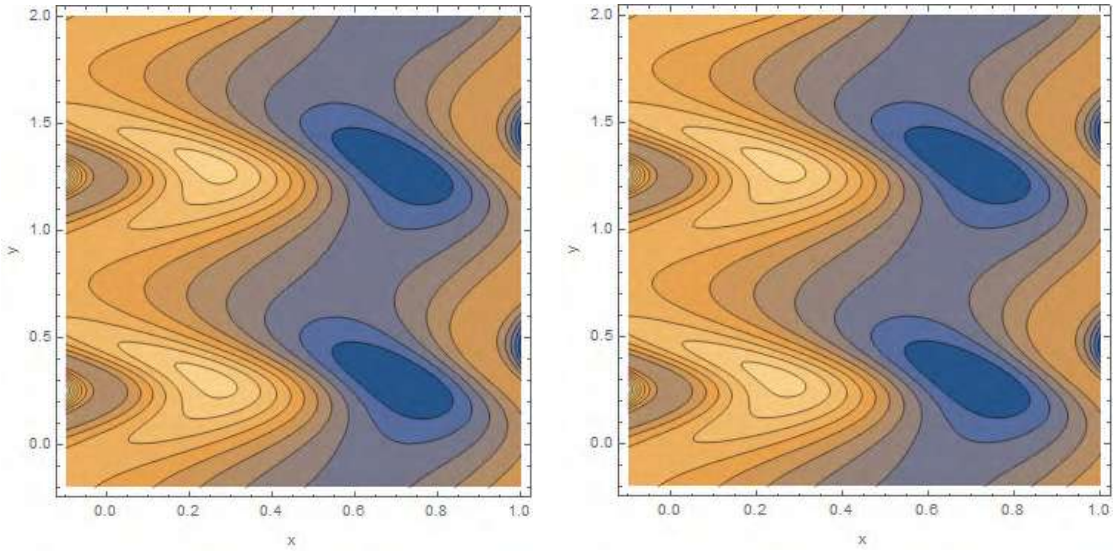

Figure 7. Streamlines contours for multiple values of angle inclination parameter $\alpha_1 = \{\pi/3, \pi\}$.

(a) (b)

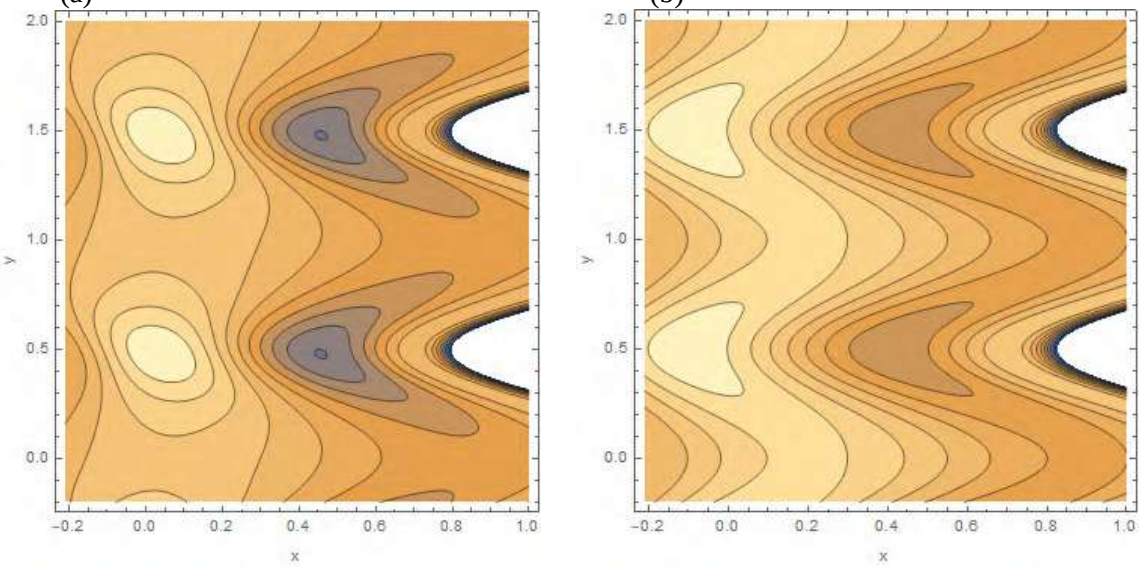

Figure 8. Streamlines contours for multiple values of phase difference parameter $\emptyset = \{\frac{\pi}{6}, \pi\}$.

(a) (b)

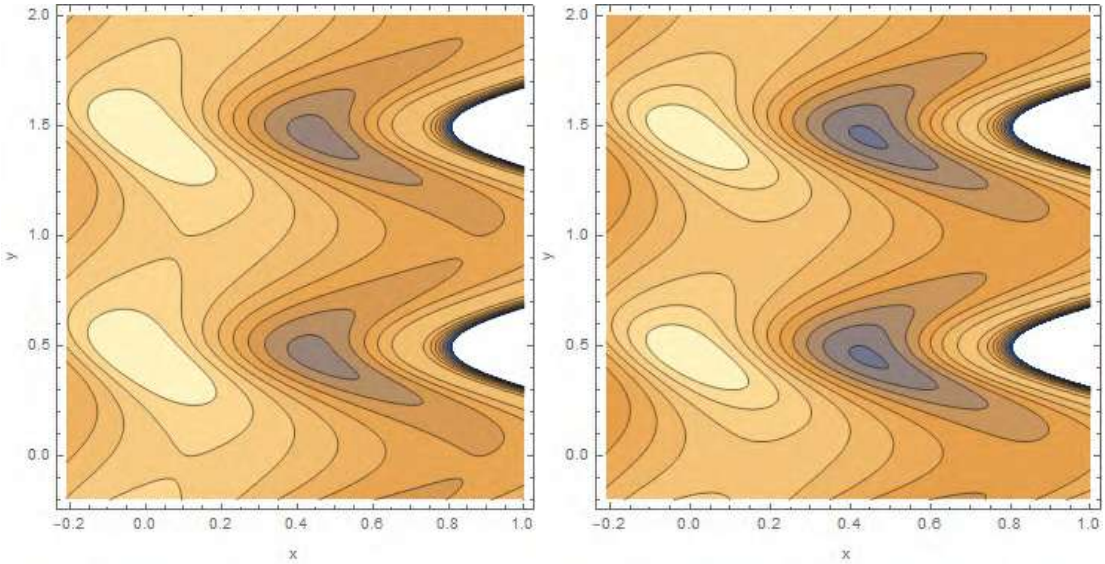

Figure 9. Streamlines contours for multiple values of Ree-Eyring fluid parameter $\eta = \{0.2, 0.6\}$.

(a) (b)

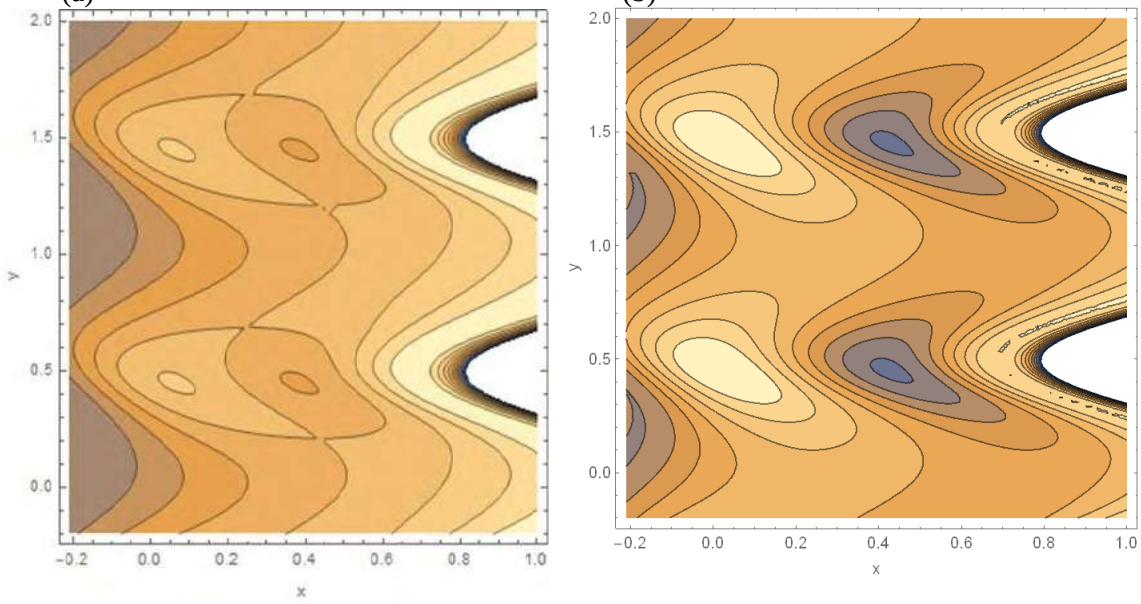

Figure 10. Streamlines contours for multiple values of Ree-Eyring fluid parameter $A = \{0.1, 0.3\}$.

(a) (b)

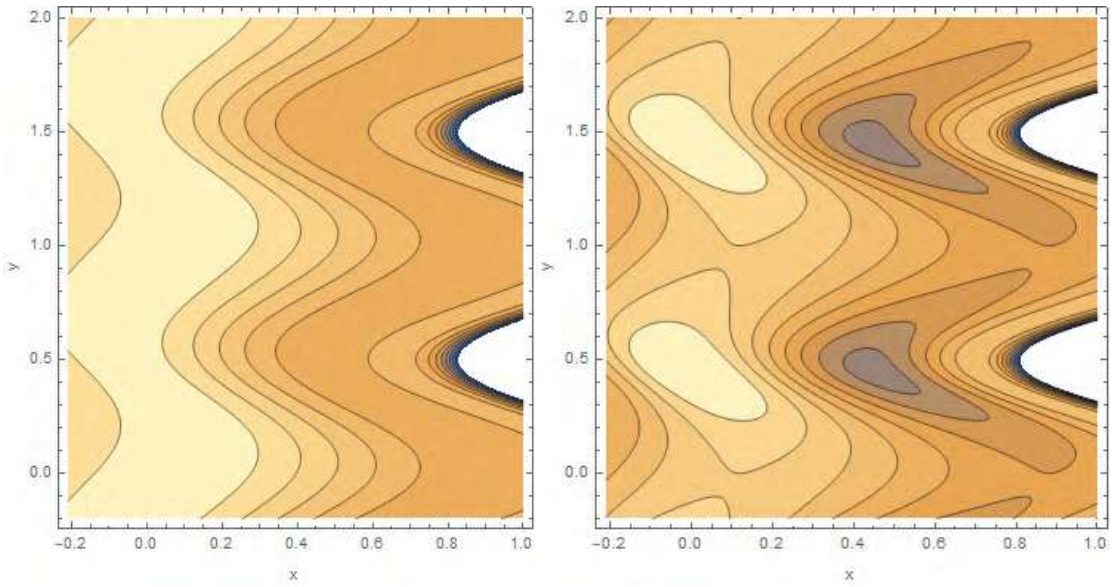

Figure 11. Streamlines contours for multiple values of time flow rate parameter $\vartheta = \{1, 1.8\}$.

5. conclusions

In this investigation, several effects like inclined MHD, convective conditions, porous media, and radiative thermal on the peristaltic transport of Ree-Eyring fluid through the asymmetric channel are presented. The dimensionless nonlinear partial differential equations are simplified by adopting the restriction of infinite wavelength and small Renold numbers and then solved exactly using the perturbation technique. Some major outcomes from the graphical analysis of this study are listed below:

1.The velocity profile showed mixed responses throughout the channel via increasing all pertinent interesting physical parameters $H, Da, \emptyset, \eta, A, b$.
2. The Effect of Hartman number$H$, Ree-Eyring fluid parameter$A$, and lower wall amplitude parameter b on the velocity distribution is totally same and completely opposite $Da, \emptyset, \eta$ impact.
3. It is noticed from figures that Brinkman number oppositely affected on temperature distribution profile whereas Prandtl number directly affected on $\theta(y)$.
4. Hartman number H shows a decreasing behavior on temperature profile while $\theta(y)$ is increasing function with radiative thermal parameter Rn .
5. The temperature distribution axial greatly affected by risen up heat generation parameter B_1 however, one can be noticed that $\theta(y)$ enhanced near the walls and remains stable in the central part of the channel due to increasing Darcy number Da .
6. The pressure rise profile shows a parabolic nature moreover growth in peristaltic pumping is noticed for H whereas the opposite result is found via ascending magnitude of Da.
7. The graphical discussion portrayed totally opposite behavior for Ree-Eyring parameters η and A on pressure rise.
8. Two asymmetric regions observed for the trapping phenomenon as well as the figures pretend to increase the trapped bolus magnitude and the number of circulation with Da, η, A, ϕ , and flow rate parameter ϑ, in other hands a diminished function for H on trapped bolus is seen.
9. No remarkable effect of α_1 on trapping, phenomena is noticed.

References

[1] Nasir A and Zaheer A 2019 Mixed convective heat transfer analysis for the peristaltic transport of visco plastic fluid: perturbation and numerical study *J. Aip. Advances* **9** 095001 pp1-9
[2] Latham T 1996 Fluid motion in a peristaltic pump *M.Sc. Thesis* Cambridge MA: MIT
[3] Fung T and Yih C 1968 Peristaltic transport Trans ASME *J. Appl. Mech.* pp 669 –75

[4] Hasona W M, Almalki N H ElShekhipy A A and Ibrahim M G 2020 Combined effects of variable thermal conductivity and electrical conductivity on peristaltic flow of pseudoplastic nanofluid in an inclined non uniform asymmetric channel: applications to solar collectors *J. Thermal Sci. Eng. Appl.* **12** 021018 pp 1-10
[5] Hayat T, Farooq S, Mustafa M, Ahmed B, Ahmed B 2017 Peristaltic transport of Bingham plastic fluid considering magnetic field Soret and Dufour effects *J. Results in physics* **7** pp 2000-11
[6] Shapiro A H, Jaffrin M Yand Weinberg S L 1969 Peristaltic pumping with long wavelengths at low Reynolds number *J. Fluid. Mech.* **37** pp 799–825
[7] Hayat T, Zahir H, Alsaedi A and Ahmad B 2017 Heat transfer analysis on peristaltic transport of Ree-Eyring fluid in rotating frame Chinese *Journal of Physics* **55** pp 51894-1907
[8] Ijaz N, Zeeshan A and Bhatti M M 2018 Peristaltic propulsion of particulate non-Newtonian Ree-Eyring fluid in a through duct through constant magnetic field *J. Alex. Eng.* **57** (2) pp 1055-60
[9] Ijaz N , Bhatti M M and Zeeshan A 2019 Heat transfer analysis in magnetohydrodynamic flow of sold particles in non-Newtonian Ree-Eyring fluid due to peristaltic wave in a channel *Vinča Institute of Nuclear Sciences, Belgrade, Serbia* **23**(2B) pp 1017-26
[10] Taha S 2016 Variational approach for the flow of Ree-Eyring and Casson fluid in the pipes. Int. J. Modling Simulation and Scientific Computing 7 1650007
[11] Tanveer A and Malik M Y 2020 Slip and porosity effects on peristalsis of MHD Ree-Eyring nanofluid in curved geometry Ain Shams Engineering Journal https://doi.org/10.1016/j.asej.2020.04.008
[12] Tanveer A, Khan M, Salahuddin T, Malik M Y and Khan F 2020 Theoretical investigation of peristaltic activity in MHD based blood flow of non-Newtonian material. *J. Computer Methods and Programs in Biomedicine* **187**
[13] Jordan A, Wust P, Scholz R, Tesche B, Fahling H, Mitrovics T, Vogl T, Carvos-Navarro J and Felix R 1996 Cellular uptake of magnetic fluid particles and their effects on human adenocarcinoma cells exposed to AC magnetic fields in vitro *Int. J. Hyperth* **12** 6 pp 705–22
[14] Kumar H 2018 Homotopy perturbation method analysis to MHD flow of a radiative nanofluid with viscous dissipation and Ohmic heating over a stretching porous plate *Thermal. Sci. J.* **22**(1B) pp 413–22
[15] Khan A A, Farooq A and Vafai K 2018 Impact of induced magnetic field on synovial fluid with peristaltic flow in an asymmetric channel *J. Magn. Magn. Mater.* **15** pp 54–67
[16] Noreen S 2017 Magneto-thermo hydrodynamic peristaltic flow of Eyring-Powell nanofluid in asymmetric channel *J. Nonlinear Engineering* https://doi.org/10.1515/nleng-2017-0069
[17] Nikiforov V N 2007 Magnetic induction hyperthermia *Russ. Phys. J.* **50(**9) pp 913–24
[18] Hayat T, Zahir H, Mustafa M and Alsaedi A 2016 Peristaltic flow of Sutterby fluid channel with radiative heat transfer and compliant walls: a numerical study *J. Results in Physics* **6** pp 805-10
[19] Bhatti M M, Zeeshan A, Ijaz N, Anwar B O and Kadir A 2017 Mathematical modelling of nonlinear thermal radiation effects on EMHD peristaltic pumping of viscoelastic dusty fluid through a porous medium duct *Eng. Sci. & Tech. Int. J.* **20** pp 1129-39
[20] Imrana N, Javeda M, Sohail M and Tlili I 2020 Simultaneous effects of heterogeneous-homogeneous reactions in peristaltic flow comprising thermal radiation: Rabinowitsch fluid model *J. Mater. Res. Technol.* **9**(3) pp 3520–29
[21] Ayub S, Hayat T, Asghar S and Ahmad B 2017 Thermal radiation impact in mixed convective peristaltic flow of third grade nano fluid *J. Results in Physics* **7** pp 3687-95
[22] Akbar Y, Abbasi F M and Shehzad S A 2020 Thermal radiation and Hall effects in mixed convective peristaltic transport of nanofluid with entropy generation *J. Appl.Nano. sci.* https://doi.org/10.1007/s13204-020-01446-3.
[23] Bhatti, M M, Zeeshan A and Ellahi R 2017 Heat transfer with thermal radiation on MHD particle-fluid suspension induced by metachronal wave J. Pramana .Phy 89

[24] Elbashbeshy E M A 2018 Effects of pressure stress work and thermal radiation on free convection flow around a sphere embedded in a porous medium with Newtonian heating *J.Thermal. Sci.* **22**(1B) pp 401-12
[25] Hayat T, Iqbal R, Tanveer A and Alsaedi A 2016 Influence of convective conditions in radiative peristaltic flow of pseudo plastic nano fluid in a tapered asymmetric channel *J. Magn. Magn. Mater.***408**
[26] Khan Z, Shah R A, Altaf M, Islam S and Khan A 2018 Effect of thermal radiation and MHD on non-Newtonian third grade fluid in wire coating analysis with temperature dependent viscosity *Alex. Eng. J.* **57** 3 pp 2101–12
[27] Ramesh K 2016 Infuence of heat and mass transfer on peristaltic fluid of a couple stress fluid through porous medium in the presence of inclined magnetic field in an inclined asymmetric channel *J. Mol. Liq* **219** pp 256–71
[28] Khan I, Kadry M S, Chu Yu M, Khan W A and Kumar A 2020 Exploration of Lorentz force on a paraboloid stretched surface in flow of Ree-Eyring nanomaterial *J. Mat. Res. Tech.* **9**(5) pp 10265-75

A reduction of Dynamic Fault Tree to a Simple Form

A reduction of Dynamic Fault Tree to a Simple Form

Ali Salman Abdulkadhim

Babylon Education Directorate

E-mail: alisalmanabudalk77@gmail.com

Abstract. The dynamic fault tree expands fault tree by giving the design of complex system components' actions and crossings. Because DFT is high grade design and simple to use it is proving a rising not fail through reliability researchers. Unluckily, an issue of problems as yet stays when we using DFT These problems are (1) There are no formalities, (2) restriction in symbolic analysis and thus sensitiveness to increasing the trouble, and (3) there is a few of modular type- structure. Chain of Markov (I/O-IMC) input/output formularization are used to analyse DFT. I/O-IMC have accurate semantics and are expansion of uninterrupted-time Markov chains with output and input conducts.

1. Introduction

There are many diverse items of the dynamic fault tree analysis which are: dynamic gates, static gates and basic event. The determining the gates on dynamic fault tree analysis we become strong analysis of action and reaction through member of complex system which produce a dynamic fault tree analysis more developed than static fault tree analysis. Through figuring a DFT three major dynamic gates: stand by (spare) gate, primacy (priority) gate (PAND) and functional dependency gate which are usually used. FT were evolved to accelerate unreliability analysis of the minuteman skyrocket system, which stock a precise, schematic, conjectural procedure to construe reliability. Conventional FT used Boolean gates to illustrate how the component fiascos fuse together make system fiasco which are analyze utilizing cut sets (or Boolean algebraic technique) or Monte Carlo emulation.

2. Preliminaries

In this Section some definitions about fault tree, dynamic fault tree, static fault trees are given

2.1 Definition [8]: A fault tree is formulation fugue impersonation of certain relationships which effect a system hazard backwards to search for all its possible causes.

2.2 Definition [5]: Static Fault Trees (briefly SFT or FT) are consisting of gates OR, AND, and K-out-of-N, they are combinatorial or fixed (static) gates.

2.3 Definition [5]: Dynamic Fault Trees (briefly DFT) consisting of in addition to the static gates (OR, AND, and K-out-of-N), basic events, and dynamic gates (PAND, FDEP, WSP, and SEQ).

2.4 Definition [7**]:** A fault tree is a figural exemplification of specific connections which effect a system hazard back terms for all its potential causes.

2.5 Definition [7]: A path set is a collection of fault tree commences which if none of them exist will surety that the top event not exist.

2.6 Definition [8]: A cut set is collection of synthesizes which that when the synthesizes in the cut are taken away the system there is no route from one station to the other.

2.7 Definition [8]: A minimal cut set is a least set of fault tree commences which if all happen, will give rise to the top event to happen

3. Dynamic gates

Pictorial display and explications of most usually used dynamic gates are presented in figure (1). Spare gates have one mine and one or several stand by (spare) inputs. When initial input event was fail, spare input substitutes it. Stand by gates make output when elementary and all stand by events fail. There are many kinds of spare gates: cool gates(CSP), snug (warm) gates (WSP) and spicy (hot) gates (HSP). If the amount of fault eventuality of particular component is equal to γ, in state when component actions as stand by, value of failure probability equal to $\delta\gamma$, if $\delta = 0$, gate is cool(CSP) and it is inactive (quiescent) state. If $\delta = 1$, gate is spicy (HSP). In other hands if $0 < \delta < 1$ gate is snug (WSP). Functional dependency gate(FDEP) contains of causative event (basic event or output for rational gate) and vassal events. All vassal (dependent) events rely on causative (trigger) event. When causative event occurs, all vassal events have occur. Output of gate (FDEP) is not taking into reckoning in computation of fiasco likelihood. Primacy gate (PAND) which has two input A and B, both of them can be basic or outputs of other logical gates. Primacy gates unsuccessful if all input components failure in the coincided row.

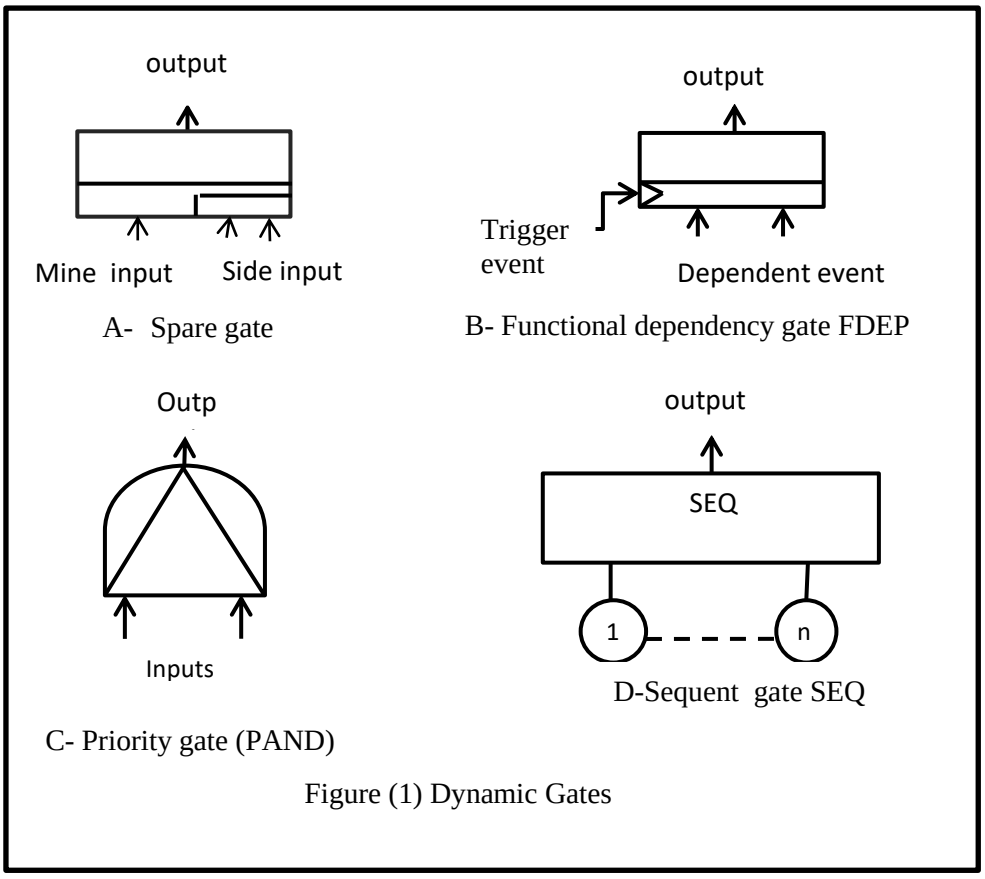

A- Spare gate

B- Functional dependency gate FDEP

C- Priority gate (PAND)

D-Sequent gate SEQ

Figure (1) Dynamic Gates

4. Reduction method:

In this section we introduce a method to calculate the failure of some systems once in fault tree and in dynamic fault tree.

4.1 Reduction fault tree: Consider that the fault tree in the figure (2):

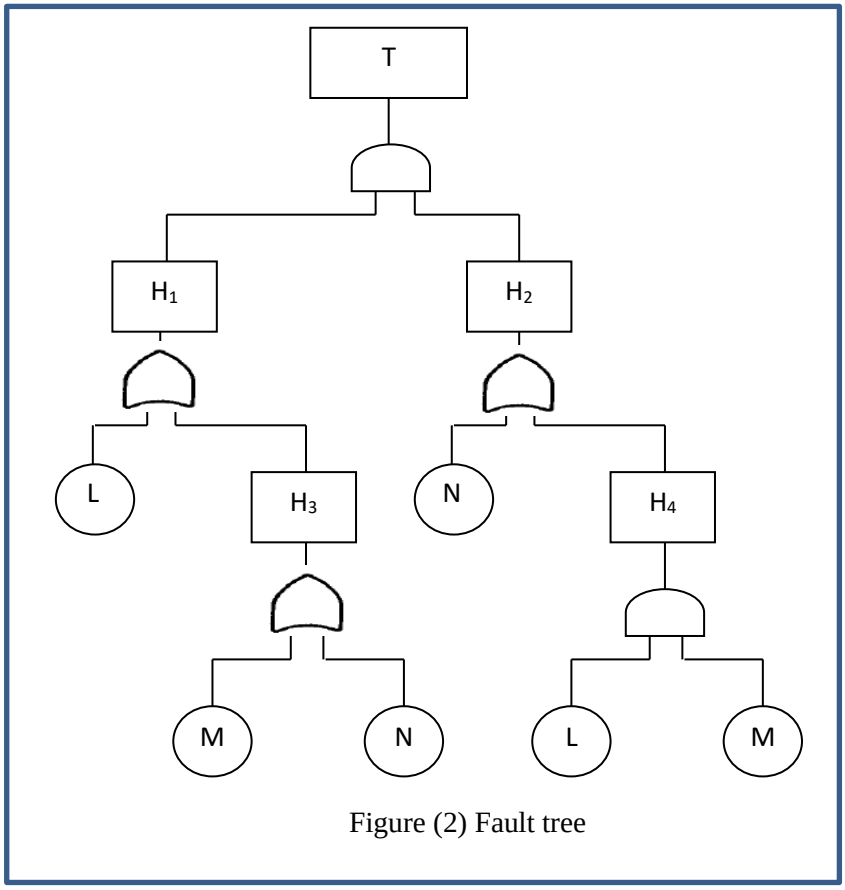

Figure (2) Fault tree

By using Boolean algebra:

$T = H_1 . H_2$, $H_1 = L + H_3$, $H_2 = N + H_4$, $H_3 = M + N$, $H_4 = L . M$

$T = H_1 . H_2$

$= [L + H_3] [N + H_4]$

Substitute H_3 by $M + N$

$= [L + (M + N)] [N + H_4]$

$= L . N + L H_4 + N . H_3 + H_3 . H_4$

$= L . N + L . H_4 + N . M + N . N + M . H_4 + N . H_4$

$= (L . N + N . M + N + N . H_4) + L . H_4 + M . H_4$

$= N + L . H_4 + M . H_4$ $= N + L (L . M) + (L . M) = N + L . M + L . M$

$= N + L . M$

New the equivalent fault tree is:

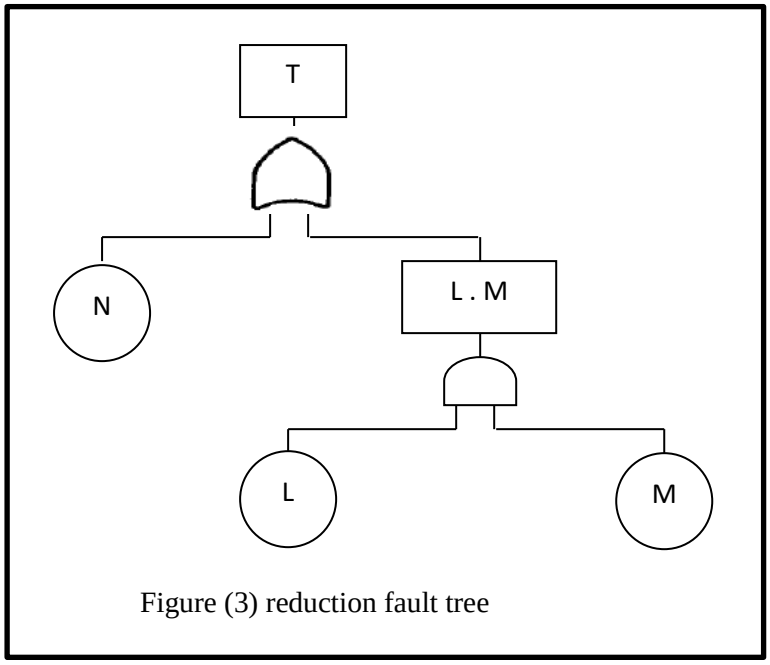

Figure (3) reduction fault tree

4.2 Example (1):
Suppose that the fault tree in the figure (2) and assume that each component (L, M and N) has reliability (0.9) then the reliability of a system is as follow:
T = H_1. H_2 ,then from 5.1 we get that :$T = N + L.M$

$$T = 0.9 + (0.9 * 0.9) = 0.729$$

4.3 Reduction dynamic fault tree:
Assume that dynamic fault tree as showing in figure (4):

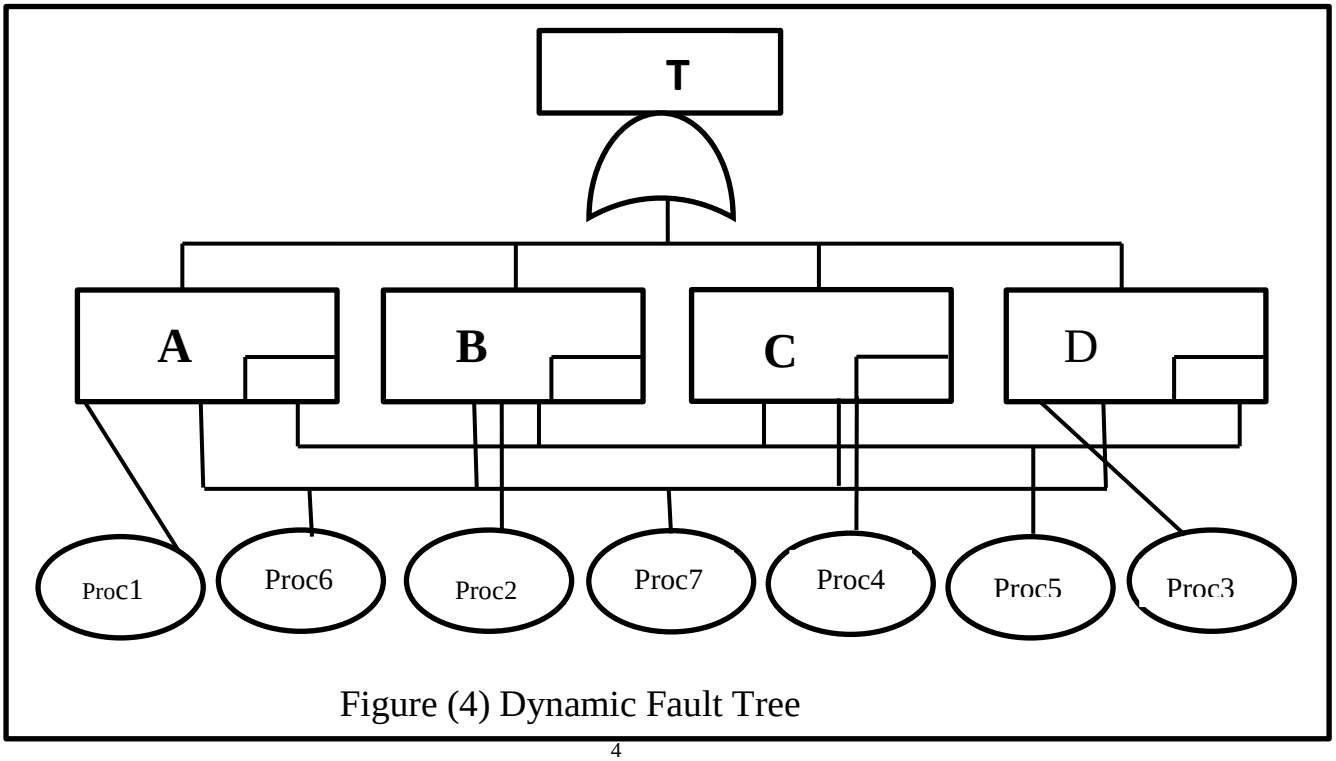

Figure (4) Dynamic Fault Tree

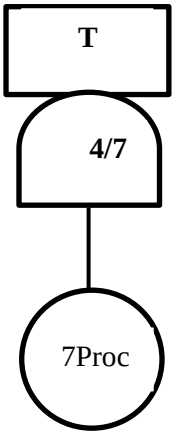

Figure (5)

The Dynamic fault tree (DFT) in figure (4) can be consider as a Fault tree of type k-out-of –n or (4 out-of 7) as in figure (5) by replacing a set of OR gates one for each basic event instead of the functional dependency gate (FDFP) which easier in calculation of system reliability.
The fault tree in figure (5) can be represented as a parallel series system contains (35) paths since the combination $\frac{7!}{(7-4)!\ 4!} = \frac{7\times6\times5\times4!}{3!\ \times\ 4!} = 35$
We get the same numerical results for the two fault trees in figure (4) and (5).

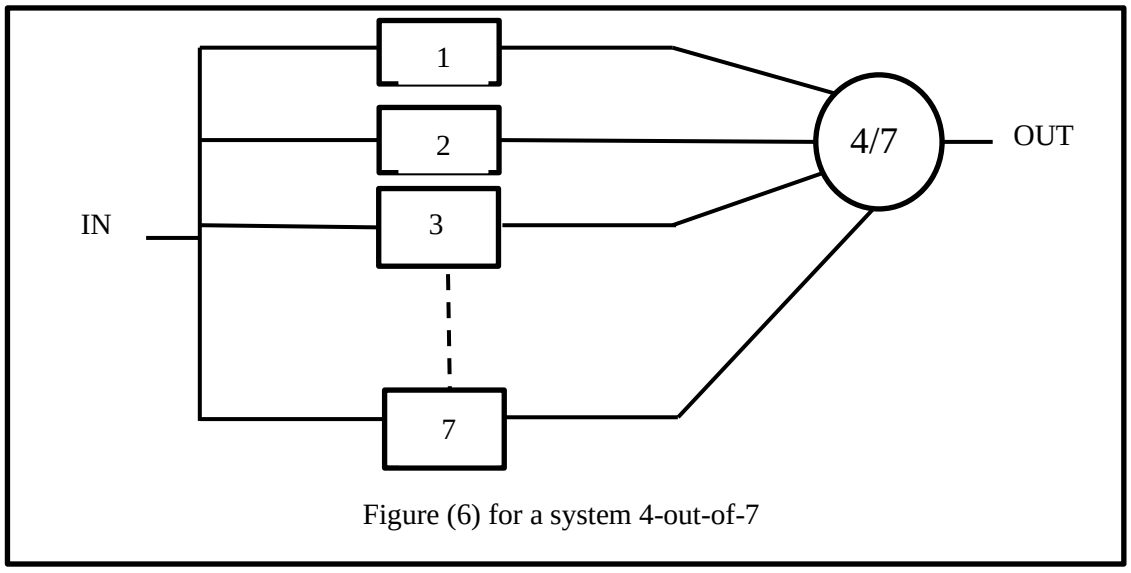

Figure (6) for a system 4-out-of-7

For simplicity to engineers and technologists we can change DFT into equivalent SFT via replacing a set of OR gates one for each basic event instead of the dynamic gate (FDEP) i.e.$M_i, i = 1,2,3,4,5,6,7$ as shown in Figure (7) below :

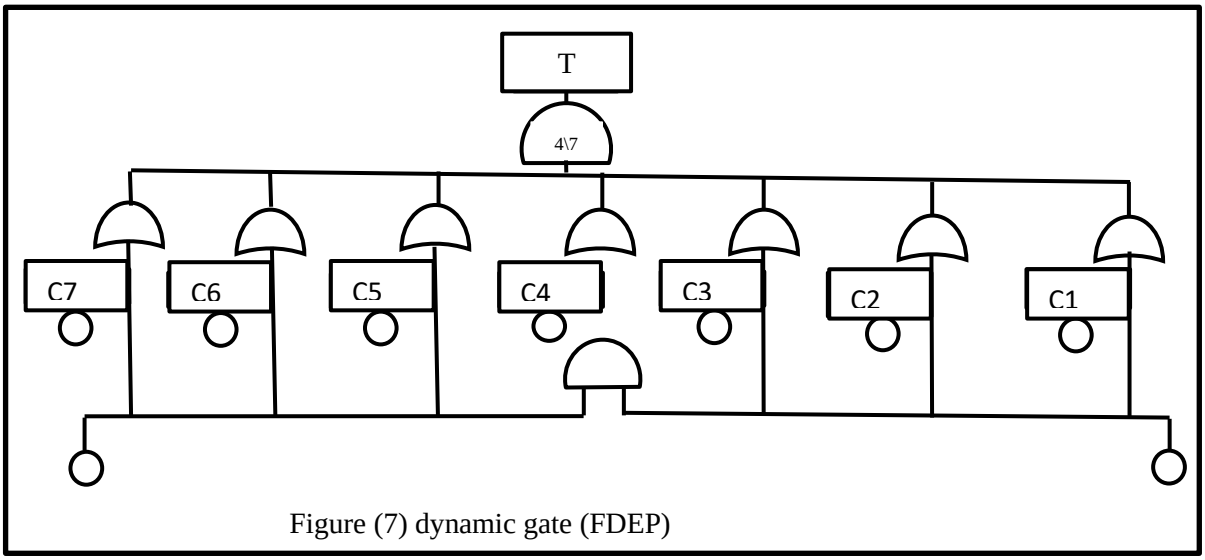

Figure (7) dynamic gate (FDEP)

For getting r successes out of n trials the reliability of $r-out-of-n$ system R_S is :

$$R_S = \sum_{x=r}^{n} \binom{n}{r} (R)^r (1-R)^{n-r}$$

4.4 Example (2):

A space vehicle need three out of four engines to operate to achieve orbit. If every engine has a reliability of 0.97, then to calculate the reliability of achieving orbit.

Sol:

$$R_S = \binom{4}{3}(0.97)^3(0.03)^{4-3} + \binom{4}{4}(0.97)^4(0.03)^{4-4}$$
$$= 4(0.97)^3(0.03) + (0.97)^4$$
$$= 4(0.912673)(0.03) + (0.88529281)$$
$$= 0.10952076 + 0.88529281$$
$$Then \quad R_S = 0.99481357$$

Conclusion

In this study a reduction method is used for a dynamic fault tree (DFT) to a simpler fault tree and we get the same numerical result since the DFT is an important too in reliability of complex system for the analysis is of two cases quantitative and qualitative which have a great role to determine the system failure.

References

[1] Penttinen J P, Lehtinen T 2015 Advanced Dynamic Fault Tree Analysis using Fault Tree Analysis for Improved Quality and Risk Assessment advanced-fta-paper

[2] Delic M, Ilic S, Glisovic J, Catic D 2015 Dynanic Fault Tree of Lawnmower *9th International Quality Conference Center for Quality* Faculty of Engineering, University of Kragujevac

[3] Lindhe A, Norberg T, Rosen L 2012 Approximate dynamic fault tree calculations for modeling water supply risks *Reliability Engineering and system Safety* **106**

[4] Merle G, Roussel J M and Jean-Jacques Lesage 2011Dynamic Fault Tree Analysis Based on The Structure Function *Annual Reliability and Maintainability Symposium* Orlando, FL, United States pp 462-467

[5] Merle Guillaume 2010 Algebraic modelling of Dynamic Fault Trees *contribution to qualitative and quantitative analysis. Automatic. École normale supérieure de Cachan - ENS Cachan*, English
[6] Nan Yu, Zhou J L 2005 Extended Dynamic Fault Tree Algorithm Based on Stochastic Petri Net and Micro-Satellite On-Board Computer Case Analysis *the open Automation and Control System Journal* **7** 1051-1056
[7] Limnios N 2007 Fault Tree ISTELTD
[8] Srinath L S 2005 Reliability Engineering *4thedtion Affiliated East* Wast Press Private Limited - New –Delhi
[9] H. Boudali J.B.Dugan 2005 A discrete-time Bayesian network reliability modeling and analysis framework *Reliability Engineering and system Safety* **87** 337-349
[10] Dugan B J, Sullivan J K and Coppit D 2000 Developing a Low-Cost High-Software Tool for Dynamic Fault-Tree Analysis *IEEE Transaction on Reliability* **49** (1)

Paths and Cycles in Alpha Topological Spaces

Paths and Cycles in Alpha Topological Spaces

Balqees K Mahmoud* **and Yousif Y Yousif**

Department of Mathematics, College of Education for Pure Sciences Ibn Al-Haitham, University of Baghdad, Baghdad, Iraq

E-mail: balqees.khaleel1003a@ihcoedu.uobaghdad.edu.iq

Abstract. This paper presents the concepts of prepaths, paths, and cycles in α-topological spaces and studies them in orderable spaces. Also, many relationships are proved with their equivalences using some properties in topological spaces like compactness and locally connectedness.

1. Introduction

Graph theory is an important part of mathematics, so many sciences are interested in the applications of graphs in multiple aspects [1]. Paths and cycles are some of basic combinatorial properties of graphs which are defined in [2, 3, 4] in addition in general topology in [5, 6, 7]. Cyclically orderable spaces are defined and studied in [8], and some new concepts are presented in [9].

Many years ago, many concepts had been studied in topological spaces, like α-open (α-closed) sets [10] and they have generalized and developed to get another new concept with new relationships to extend the mathematics knowledges [11, 12, 13].

In this paper, we introduce the concepts of prepaths, paths, and cycles with the topological viewpoint in α-topological space. Also, we study their equivalence relationships with convexity and intervals in an orderable space. In addition compactness, order-complete, and locally connectedness.

2. Preliminaries and basic definitions

Through this section, any graph G contains the set of vertices V_G and the set of edges E_G. The non-empty set $X = V_G \cup E_G$ used to define a topology τ on it which satisfied the general topological conditions, and for simplest (X, τ) refers to the topological space that we constructed it. For $A \subseteq X$, the interior and the closure of A in X with respect to τ are denoted by Int(A) and Cl(A). A sub set A is said to be an α-open set, if it satisfied $A \subseteq Int(Cl(Int(A)))$ for all $A \subseteq X$, and the complement of A in X is an α-closed set. It is clear that every open set is α-open, but in general the reverse is not true. We obtain an α-topology τ_α by taking all α-open sets, and (X, τ_α) is an α-topological space. Furthermore, the interior of A in this space with respect to τ_α is denoted by $\alpha\text{-Int}(A) = \cup \{ B \mid B \subseteq A, B \text{ is } \alpha\text{-open}\}$, while the closure of A denoted by $\alpha\text{-Cl } A) = \cap \{ B \mid A \subseteq B, B \text{ is } \alpha\text{-closed}\}$.

We recall some basic definitions, remarks and facts in topology and graph.

Definition 2.1: Let X be a topological space, then:

1) X is called connected space if there do not exist two disjoint, nonempty, open sets A and B such that $X = A \cup B$. Otherwise, X is disconnected [7].

2) X is called separated space if there are two unordered disjoint subsets of X such that each one is the complement of the other [7].

3) if A is a subset of X, then the intersection of Cl(A) and Cl(X - A) is called the boundary points of A [5].
4) the component of X is the largest connected subspace of X, and an adherent component denoted as K(x) \ {x} is the component of X contains x without x itself [3].
5) X is said to be S_1-space if every singleton is either open or closed [3].
6) an α-topological space X is called an α-separated space if there are two unordered disjoint subsets of X, such that each one is the complement of the other [9].
7) any family of X has the finite intersection property if the intersection is non-empty of any finite subfamily [7].
8) if B ⊆ X , then the intersection of all α-open sets contained B is called α-surrounding set of B, and denoted by $B^{\alpha\diamond}$ [9].

Definition 2.2 [3]: If x is any point in a connected topological space X, and X \ {x} is not connected, then x is called a cutpoint of X . Otherwise x is a non-cutpoint (that is an endpoint).

Theorem 2.3 [3]: Let X be a topological space, then the next statements are equivalence:
(A) ∀ x, y, z ∈ X: x < y < z, there exists a total order ≤ on X such that y disconnects x from z.
(B) for each triple of points S in X, there exists a point in S which disconnects the other two.
(C) ∀ x ∈ X, every adherent component of x denoted by K(x) \ {x}, has at most one endpoint, also any cutpoint is strongly cutpoint.

Corollary 2.4 [3]: Let X be a connected topological space has at least four points, then X is S_1-space, and any two non-incident points disconnect the others, but no one do.

Definition 2.5 [3]: Let X be a connected topological space, then :
1) X is a prepath denoted by P if |X| ≤ 2 with any topology except the indiscrete one, otherwise, X satisfies theorem (2.3) when |X| ≥ 3.
2) a prepath is called a path if it is locally connected.
3) X is a precycle if it satisfies corollary (2.4).
4) a locally connected precycle is called a cycle.

Facts 2.6 [3,7]:
A) Let A be a connected subset of a connected topological space X, and K a component of X \ A. Then X \ K is connected.
B) Let Y be a subspace of a topological space X, then any component of Y is contained in a component of X.
C) let X be a topological space with exactly two components, then $\{K_1, K_2\}$ is a separation of X if and only if K_1, K_2 are the components of X.
D) If C is a connected subset of a topological space, and A is a subset such that C ⊆ A ⊆ Cl(C), then A is connected.
E) A topological space X is locally connected if and only if each component of each open set is open.

Definition 2.7 [3]: If P is a prepath, then the interval topology on P is the collection of intervals of P which is a base for a this topology on P.

Theorem 2.8 [3]: A prepath is locally connected if and only if the topology concurs with the interval topology.

Definition 2.9 [3]: Let ≤ be a binary relation on X with a ∈ X, then ω(x) = {x ∈ X | x > a}, Ω (x) = {x ∈ X | x ≥ a}, δ(x) = {x ∈ X | x < a} and Δ(x) = {x ∈ X | x ≤ a}.

Definition 2.10 [11]: Let $\leq$ be a total order on X, a subset of X of the form $L \cap U$ is an interval where U and L are taking one of the following forms:
1. X.
2. $\omega(a)$, for some $a \in X$ and ($\delta(b)$, for some $b \in X$).
3. $\Omega(a)$, for some $a \in X$ and ($\Delta(b)$, for some $b \in X$).

Definition 2.11 [3]: Let X be a totally ordered space. A subset S of X is said to be convex if for all a, b $\in$ S, and $a < x < b$, then $x \in S$ for all $x \in X$.

Theorem 2.12 [3]: Let S be a subset of a complete totally ordered set, then it is convex if and only if S is an interval.

Definition 2.13 [3]: A convex subset containing exactly two points is called a jump.

Definition 2.14 [3]: A convex subset S of a totally ordered space X is said to be a chain, if S is order isomorphic onto a convex subset of Z.

Corollary 2.15 [3]: Every chain in a totally ordered space is contained in a maximal one.

Corollary 2.16 [3]: Any two maximal chains in a totally ordered set are disjoint.

Definition 2.17 [3]: Let X be any set, $S \subseteq X$ with a binary relation on X, S is said to be strongly upper-bounded (lower-bounded) if S has a maximum (respectively, minimum) M (respectively, m), where M (respectively, m) is strictly bounded from above (respectively, below). Also, S is strongly bounded if it is both strong (upper-bounded and lower-bounded). However, S is partially strongly bounded if it satisfies one of them.
We notice that a chain is finite if it has both minimum and maximum.

Corollary 2.18 [9]: Let X be an α-topological space, and x, y, z $\in$ X. If y α-separates x and z, then y α-disconnects x and z.

Corollary 2.19 [9]: Let X be an α-connected topological space, x is an α-cutpoint of X, then only one of the next statements are holding for any α-separation $\{B_1, B_2\}$of $X \setminus \{x\}$:
1. $\{x\}$ is α-closed, B_i is α-open in X, and $\alpha\text{-Cl}(B_i) = B_i \cup \{x\}$ is α-closed, for i = 1,2
2. $\{x\}$ is α-open, B_i is α-closed in X, and $B_i^{\alpha\diamond} = B_i \cup \{x\}$ is α-open, for i = 1, 2.

Theorem 2.20 [9]: Let X be an α-connected topological space, x be an α-cutpoint of X, then there exist two nonempty α-closed sets F_1, F_2 in X, such that $F_1 \cup F_2 \cup \{x\} = X$, $\{F_1 \setminus \{x\}, F_2 \setminus \{x\}\}$ is an α-separation of $X \setminus \{x\}$ and only one of the following statements are holding:
1. $\{x\} = (F_1 \cap F_2)$ with $\{x\}$ is an α-closed.
2. $\{F_1, F_2, \{x\}\}$ is a partition of X with $\{x\}$ is an α-open.

Theorem 2.21 [9]: If X is an α-connected topological space, h is an α-hyperedge of X with finite number of α-boundary points, then each α-component of $X \setminus \{h\}$ includes an α-boundary point of h. Specifically, $X \setminus \{h\}$ contains at most two α-connected components, when h is an edge.

Corollary 2.22 [9]: Let X be an α-connected topological space, x is a cutedge, then an α-adherent component $K_\alpha(x) \setminus \{x\}$ contains exactly two α-connected components, each α-component consisting of one α-boundary point of x.

Definition 2.23 [3]: An ordered pair (A, B) is said to be a gap, if A and B have no maximum and no minimum respectively.

Fact 2.24 [3]: Any total order has no gaps if and only if it is order-complete.

Definition 2.25 [3]: Let X be any set, a triplex relation $S \subseteq X^3$ is said to be a cyclic order on X if:
* (a, b, c) $\notin$ S where a $\neq$ b $\neq$ c $\neq$ a if and only if (c, b, a) $\in$ S
* if (a, b, c) $\in$ S, then (b, c, a) $\in$ S
* if (a, b, c) $\in$ S and (a, c, d) $\in$ S, then (a, b, d) $\in$ S

If S is a cyclic order on X and Y is a subset of X, then there exists a cyclic order $S^* = S \cap Y^3$ inherited on Y by the classes contains all its elements in Y.
Furthermore, the ordered space S^* is called a cyclic subsequence of S, where S is finite.

3. Prepaths in Alpha Topological Spaces

In this section, we introduce some concepts of α-topological spaces and investigate the relationships between them.

The first important theorem can be proven in the same way as in [3], we need it here to define an α-prepath and in the proof of theorem (3.4).

Theorem 3.1: Let X be a topological space, then the next statements are equivalents:
(A) $\forall$ x, y, z $\in$ X: x $<$ y $<$ z, there exists a total order $\leq$ on X such that y α-disconnects x from z.
(B) For each triple of points S in X, there exists a point in S which α-disconnects the other two.
(C) $\forall$ x $\in$ X, every α-adherent component of x denoted as $K_\alpha(x) \setminus \{x\}$, has at most one endpoint, also any α-cutpoint is strongly α-cutpoint.
(*) if X is an α-connected in this theorem, then the 3rd statement means that for all x $\in$ X, $X \setminus \{x\}$ has mostly two α-component contains one endpoint in each one.

Definition 3.2: An an α-connected topological space X is said to be an α-prepath denoted by P_α if $|X| \leq 2$ with any α-topology except the indiscreet one, otherwise $|X| \geq 3$ and X satisfies the conditions of theorem (3.1).

Definition 3.3: An α-topological space X is said to be α-topologized graph if:
* any singleton is either α-open or α-closed.
* X has at most two α-boundary points, for all x $\in$ X.

The next theorem shows that an α-prepath is always an α-topologized graph.

Theorem 3.4: Let X be an α-connected topological space, if X is an α-prepath then:
1. X is an α-topologized graph.
2. Every edge in X is a cutedge or a loop which is an endpoint.

Proof: Suppose X is an α-prepath, then X has many cases. Firstly, X is trivially an α-topologized graph if it is an empty set because it is α-clopen . Secondly, When X is a singleton element, so it has a unique point and it is α-open and α-closed. Thirdly, when X have two points, we can get exactly two α-connected topologies, the first one is the indiscrete α-topology which excepted in definition (3.2) and the second one is an α-topologized graph with exactly one vertex with one loop.
Finally, when X has at least three points, we must prove it is an α-topologized graph by satisfying the conditions of definition (3.3). Now, we discuss being x is an α-cutpoint or an α-endpoint. Suppose that x is an α-cutpoint, it is either α-open or α-closed by corollary (2.19). Furthermore, all α-cutpoints are strong α-cutpoints by theorem (3.1 part C). Thus, when x is an α-open, we have that an α-boundary of

x contains exactly two points by theorem (2.21). So, x is a proper edge, that is a cutedge because x is an α-cutpoint.

Now, suppose that x is an endpoint, so X must has at least one α-cutpoint, and mostly two endpoints because it has at least three points. Let y be any α-cutpoint in X, and A_y, B_y be the α-connected components of X \ {y}. Define C as the set of all α-cutpoints, and $= \bigcap_{y \in C} \overline{A_y}$, so $x \in A_y$ implies that $x \in W$.

Now, assume that y is another endpoint in W, such that $y \neq x$, and take another point to be an α-cutpoint like w. Since y ∈ W, we have that $y \in \overline{A_w}$, by theorem (2.20) which leads to either $y \in A_w$ or y = w. That means x and y lie in the same α-connected component of X \ {w}, that is a contradiction with (*) of theorem (3.1) since the component contains two endpoints together. Also the second choice impossibly hold, because y an endpoint and w is an α-cutpoint. Hence, W does not contain any endpoints excepting x.

Suppose that $y_1 \neq y_2$ are two α-cutpoints in W. Clearly, x cannot α-disconnect y_1 and y_2 because it is an endpoint. So, for the three elements {x, y_1, y_2}, if y_1 α-disconnects x with y_2, then $y_2 \notin A_{y_1}$ implies $y_2 \notin W$ (otherwise if y_2 α-disconnects x with y_1, then $y_1 \notin A_{y_2}$ implies $y_1 \notin W$), by using (3.1B) is a contradiction. So, W contains mostly one element besides x, and it is an α-cutpoint. If W = {x}, then {x} is α-closed, since it is the intersection of α-closed sets. Otherwise, when W = {x, y} for some α-cutpoint y, $y \in A_y$. Hence A_y = {x} is α-open and α-Cl(x) = {x, y} by corollary (2.19), (that is a loop).

Corollary 3.5: Let X be an α-connected topological space, x, y, z ∈ X, then only one of them α-disconnects the others.
Proof: Suppose that y α-disconnect x and z, and assume that $K_\alpha(x)$ define the α-component of X \ {y} which contains x. So X \ $K_\alpha(x)$ is an α-connected set containing y and z without x by (2.6A). So x can not α-disconnect y from z. By the same way, z cannot α-disconnect x from y.
The next theorem is proved in [9], and it is very useful in our proofs.

Theorem 3.6: If X be an α-connected topological space, x is an α-cutpoint of X. If {A, B} is an α-separation of X \ {x}, then A ∪ {x} is an α-connected (so as B).
The next theorem shows that α-disconnected and α-separated are equivalent in α-connected prepaths.

Theorem 3.7: Let X be an α-connected topological space, then the following statements are equivalent:
(1) ∀ x, y, z ∈ X, there exists a total order ≤ on X such that, if x < y < z, then y is a strong α-cutpoint and α-disconnects x from z.
(2) ∀ x, y, z ∈ X, there exists a total order ≤ on X such that, if x < y < z, then y α-separates x from z.
(3) ∀ x, y, z ∈ X, there exists a total order ≤ on X such that, if x < y < z, then y α-disconnects x from z.
(4) For any three disjoint points, there exists exactly one of them that α-disconnects the others.
(5) For any three disjoint points, there exists exactly one of them that α-separates the others.
(6) For any three disjoint points, there exists exactly one strong α-cutpoint of them that α-disconnects the others.

Proof: Firstly, we should prove the equivalent of the first three statements, and later we should prove the last three of them.
(1) ⇒ (2) ⇒ (3) ⇒ (1)
(1) ⇒ (2); Let x < y < z, then X \ {y} has exactly two α-connected components, K_x, K_z such that x ∈ K_x, z ∈ K_z. So we obtain that $\{K_x, K_z\}$ is an α-separation of X \ {y}, and y α-separates x and z by facts (2.6C)
(2) ⇒ (3); This prove is coming immediately from corollary (2.18).

(3) ⇒ (1); Since y α-disconnects x from z by (3), implies that y is an α-cutpoint, and a strong α-cutpoint by using theorem (3.1).
(6) ⇒ (5) ⇒ (4) ⇒ (6)
(6) ⇒ (5); Take any three disjoint points such that one of them is strong α-cutpoint, so it α-disconnects the others. Also it α-separetes them.
(5) ⇒ (4); This prove is coming immediately from corollary (2.18).
(4) ⇒ (6); Since there exists one point that α-disconnects the others, implies that it is an α-cutpoint, and a strong α-cutpoint by using theorem (3.1).
Now to prove the equivalent between the two sets of statements, we shall prove that (3) and (4) are coincides.
(3) ⇔ (4): This proves is direct from conditions of theorem (3.1).

Corollary 3.8: Let X be an α-connected topological space, and the total order $\leq$ on X is satisfying the 2nd condition of theorem (3.7). If y α-separates x from z, then either $x < y < z$, otherwise $z < y < x$.
Proof: Since y α-separates x from z, then there exists an α-separation {H, K} of X \ {y} such that $x \in H$ and $z \in K$. So $x < y < z$. But, if the result not hold, assume that $y < x < z$, ($x < z < y$). Then x should α-separate y and z (z should α-separate x and y). But by theorem (3.6) {y} ∪ K (H ∪{y}) is an α-connected subset containing y and z but not x (containing x and y but not z), this is contradiction.

Definition 3.9: Let P_α be any α-prepath, then every total order defined on P_α is said to be α-compatible with $P_\alpha$when it is satisfying conditions of theorem (3.7).

Theorem 3.10: Any subset B of an α-prepath P_α is an α-connected if and only if B is an α-prepath. Moreover, any compatible total order of an α-connected subset of P_α is exactly this one inherits from P_α.

Proof: Let B be an α-prepath subset of an α-prepath X, if B is an α-disconnected, then that is contradiction with theorem (3.1), so B is an α-connected.
Conversely, let B is an α-connected subset, and $\leq_B$ is inherited total order by B from a compatible one $\leq$ on P_α. Let x, y, z ∈ B and $x <_B y <_B z$, implies that $x < y < z$ and y α-disconnects x from z, that is mean, each of x and z belong to different α-components of X \ {y}, so they belong to different α-connected components of B \ {y}. Hence $\leq_B$ on B satisfies the 3rd condition of the theorem (3.7).

Definition 3.11: Let P_α be an α-prepath, a point $x \in P_\alpha$ is internal if it is not extremum with respect to a compatible total order, and terminal otherwise, so the α-cutpoints are the internal points, and the endpoints are the terminal.

Definition 3.12: An α-prepath is said to be α-bounded, if the compatible total orders are α-bounded. That means, it is an α-prepath with two terminal points. Moreover, some compatible total order is α-bounded from above (respectively, below) but not from below (respectively, above), the α-prepath is said to be one-sided.

Definition 3.13: Let X be an α-topological space, a, b ∈ X, a subset P_α of X is said to be an ab- α-prepath if it is a (bounded) α-prepath with two terminal points a minimum point and b maximum point.

Definition 3.14: Let X be an α-topological space, X is said to be an ab-α-prepath connected space, if X contains an α-prepath for every a, b ∈ X.

Theorem 3.15: Let P_α be α-prepath, then a point $x \in P_\alpha$ is an endpoint if and only if it is an extremum with respect to a compatible total order. Furthermore, very α-prepath has at most two endpoints.

Proof: Let x ∈ P_α be an endpoint, to prove x is extremum. Assume that x is not extremum (not minimum nor maximum) with respect to a compatible total order ≤, then there exist two points a, b such that a < x < b, so we obtain that x is an α-cutpoint. That is a contradiction, hence every non α-cutpoint is a maximum or a minimum. Conversely, if x is not an endpoint, it is an α-cutpoint, then there exists at least two points a, b such that x α-separates them. So we get a < x < b (b < x < a) by corollary (3.8), implies that x is not maximum nor minimum (not extremum). That is contradicting the hypothesis, hence X is an endpoint.

Let P_α be α-prepath, and has three distinct endpoints a, b, c in X. Then any two of them must be α-disconnected by the third one, which became an α-cutpoint. That is contradiction. Therefore, P_α must has at most two endpoints.

The next corollary shows that if x is an α-cutpoint, then either δ(x) or Δ(x)((ω(x) or Ω(x)) is α-open.

Corollary 3.16: Let P_α be α-prepath, x ∈ P_α be an internal point with a fixed compatible total order. Then one of the following must satisfy:
(1) x is an edge, Δ(x) and Ω(x) are α-open, δ(x) and ω(x) are α-closed, $(\delta(x))^{\alpha\diamond}$ = Δ(x) and $(\omega(x))^{\alpha\diamond}$ = Ω(x).
(2) x is a vertex, Δ(x) and Ω(x) are α-closed, δ(x) and ω(x) are α-open, α-Cl(δ(x)) = Δ(x) and α-Cl(ω(x)) = Ω(x).

Proof: Assume x is an internal point, and fixed ≤ as a compatible order, then x is an α-cutpoint and a strong α-cutpoint by theorem (3.1). Suppose that K_1, K_2 are the two α-components of P_α\ {x}. So we can prove that {K_1, K_2} = {δ(x), ω(x)}, by using definition (2.17). But, if not, then there exist two points a ∈ K_1, b ∈ K_2 such that a < x < b. Hence x is α-disconnected a from b. This is contradiction, since K_1, K_2 are two α-connected sets containing a and b respectively but not x.

Definition 3.17: Let P_α be an α-prepath with a fix compatible order, and let a ∈ P_α. The α-open tail from a upwards (respectively, downwards) is the largest α-open subset of P_α contained in Ω(a) (Δ(a)).
- If a is a terminal point, we have two cases: when a is maximum then the α-open tail from a upwards is P_α, and when a is minimum the α-open tail from a downwards is {a} where {a} is α-open or equal ∅ if not.
- If a is an α-cutpoint, the α-open tail from a upwards (downwards) is ω(x) (δ(x)) or Ω(x) (Δ(x)) depending on what condition is satisfied from corollary (3.16).

Definition 3.18: Let x_1, x_2 be any two points in an α-topologized hypergraph H, then{x_1, x_2} is said to be an edge-vertex incident pair if any one of them is a vertex and the other is an incident edge.

Theorem 3.19: If P_α is an α-prepath, then:
1. {x, y} is an edge-vertex incident pair if and only if it is a jump with respect to a compatible total order.
2. any terminal edge exactly has one endvertex, and any internal edge has exactly two endvertices.

Proof: Suppose that e is an edge with an incident vertex v, and {e, v} is not a jump. If e < v or (v < e), this leads to the existence of a point x such that e < x < v or (v < x < e) . So we obtain y is an α-cutpoint, by using theorem (3.15), and (x,∞) is an α-open set containing v but not e, by corollary (3.16) and definition (3.17).That is a contradiction, since e and v are incident.
Conversely, Let ≤ be an compatible total order, and {x, y} a jump. Assume that x < y or (y < x), then P_α = Δ(x) ∪ Ω(y), where they are disjoint. If x, y are both edges, then both these sets are α-open, but if they are both vertices, then both these sets are α-closed, by corollary (3.16). Hence, {Δ(x), Ω(x)} is an α-separation of P_α, which contradiction with being P_α is α-connected.

Since every edge is a cutedge or a loop from theorem (3.4). So an internal edge is a cutedge, by theorem (3.15). Therefore, it has exactly two endvertices by corollary (2.22), and since terminal points are not α-cutpoints, then they are loops. Therefore, they are incident with exactly one vertex.

Corollary 3.20: Let P_α be an α-prepath, A be a convex subset of P_α with at least two points. If a $\in A \backslash A^{\alpha^\circ}$, then a is an extremum point for A, but not for P_α.

Proof: Let $\leq$ be an compatible total order for P_α. Assume that there exist two points in A such that a between them, (that is $\exists$ x, y $\in$ A, where x $<$ a $<$ y). Then $\langle x, y\rangle$ is α-open contains a, but A is convex, then a is contained in A, so a $\in A^{\alpha^\circ}$, that is a contradiction. Therefore, a is an extremum point of A. To prove that a is not an extremum point of P_α let b be another point in A. By contradiction, let a be a minimum point of P_α, then [a, $b\rangle$ = (-∞, $b\rangle$ is an α-open subset of A containing a. That is contradiction, hence a cannot be a minimum for P_α. By the same way a can not be a maximum. Therefore, a is not an extremum for P_α.
The following theorem can be proven similarly as in [3], and we need it in the subsequence details of proofs.

Theorem 3.21: A subset of an α-prepath is an α-connected if and only if it is convex.
Corollary 3.22: If P_α is an α-prepath and $\leq$ a compatible total order, then $\leq$ is an order-complete.

Proof: By way of contradiction, we must prove that there are no gaps, let (A, B) be a gap, and A must be convex, since (A, B) is a cut. If A is not α-open, then there exists some point a $\in A \backslash A^{\alpha^\circ}$ by corollary (3.20). So a is an extremum for A, and the same as B, which is contradicting the definition of a gap definition (2.23). Therefore A and B are α-open, then {A, B} is an α-separation of the α-connected space P_α, that is contradiction.

Corollary 3.23: Let X be an α-prepath, M $\subseteq$ X, then the next statements are equivalent:
(1) M is α-connected.
(2) M is an α-prepath.
(3) M is convex.
(4) M is an interval.
Proof: We prove (1) $\leftrightarrow$ (2) by using theorem (3.10), and (2) $\leftrightarrow$ (3) by using theorem (3.21), and (3) $\leftrightarrow$ (4) by using theorem (2.12), so to prove (4) $\leftrightarrow$ (1) we use corollary (2.22) and corollary (3.22).

Theorem 3.24: Let X be an α-topological space, a, b $\in$ X, then the following statements are equivalent:
(1) For all x $\in$ X \ {a, b}, x α-disconnects a from b.
(2) For all S $\subset$ X, such that {a, b}$\subseteq$ S, S is α-disconnected.

Proof: Suppose that (1) satisfies, assume that S $\subset$ X contains {a, b}. Take x $\in$ X \ S, and define W = X \ {x}. Let a $\in S_a$, b $\in S_b$ be the α-connected components of S containing a, b. So a $\in W_a$, b $\in W_b$ is the α-connected components of W containing a, b. Since S $\subseteq$ W, we get that $S_a \subseteq W_a$ and $S_b \subseteq W_b$ by the fact that α-connected components form a partition of the point set of an α-topological space and facts (2.6B). But, W_a and W_b are different, then S_a and S_b are disjoint. So, S is α-disconnected, we get (2).
Now suppose that (2) holds, Assume that x $\in$ X \ {a, b}. So, if S = X \ {x} $\subset$ X contains a, b, then S is α-disconnected. Assume that a, b are in the same α-connected component K of X \ {x}. So K is a subset of X \ {x} containing a, b, and hence K is α-connected, that is a contradiction. So a and b must contain in a different α-connected components of X \ {x}.

4. Paths and Cycles in Alpha Topologica Spaces

In this section, we introduce some basic definitions and facts on α-topological spaces which we need it to define our new concepts. Moreover, we study some important relationships in α-space.

Definition 4.1: Let P_α be an α-prepath, we can define the interval α-topology on P_α by taking a subbase contains X and all open intervals $(-\infty, x)$, (x, ∞) on P_α for some vertex x and we can obtain (the base, the topology, and the α-topology) of P_α. We should refer to that the α-open sets in the interval α-topology are α-open sets in general topology on P_α.

Corollary 4.2: An α-topological space X is a locally α-connected if and only if each component of each α-open set in X is α-open.

Proof: Let K be a component of α-open set U in a locally α-connected space X, $x \in K$. So there is an α-open connected set V such that $x \in V \subset U$, and $V \subset K$, therefor K is α-open.
Conversely, assume that the components of every α-open set is α-open in X. Let U be any α-open neighborhood containing x in X, then there is an α-component K containing x of U which is an α-open connected neighborhood in U. That is, $x \in K \subset U$. Hence, X is locally α-connected.

Theorem 4.3: An α-prepath is locally α-connected if and only if the α-topology concurs with the interval α-topology.

Proof: Let P_α be an α-prepath, and let U be an α-open set in P_α containing x, assume that P_α is locally α-connected. We have to show that U contains an α-open interval containing x. By corollary (3.23), we obtain that $K_U(x)$ is an interval, because it is an α-connected of P_α. Since P_α is locally α-connected and U is α-open, the components $K(U)(x)$ is α-open by corollary (4.2).
Conversely, assume that P_α has the interval α-topology and $U \subseteq P_\alpha$ is α-open. Then the union of every α-open intervals is α-open, means, $\bigcup_{i\in I} J_i$ where the J_i are α-open intervals. Now, if $x \in K$, where K is any α-component of U, is an α-open interval. So we get $x \in J_i$ for some i. But J_i is an α-connected subset of U, therefore $J_i \subseteq K$. Hence, P_α is locally α-connected.

Definition 4.4: Let X be an α-connected topological space, an α-prepath is called an α-path if it is locally α-connected.
If we have an α-prepath say ab, we can express it by ab-α-prepath, and it is an ab-α-path if it is locally α-connected. If there exists an α-topology on X such that X is an α-prepath(α-path) with a total order $\leq$ is compatible with X, then $\leq$ on X is an α-prepath(α-path) compatible.

Theorem 4.5: Let X be an α-connected topological space with the interval α-topology ${\tau_\alpha}^*$, and X is an α-prepath, then X is an α-path with compatible orders, and it has the same α-connected subsets.

Proof: Let ${\tau_\alpha}^*$ be the interval α-topology on X, then any α-separation in ${\tau_\alpha}^*$ should be an α-separation in τ_α, Since ${\tau_\alpha}^* \subseteq \tau_\alpha$. Hence, X is α-connected with respect to ${\tau_\alpha}^*$.
Assume that $\leq$ is a compatible total order on X with respect to τ_α. Let x, y, z be any three points on X such that $x < y < z$. If y is a vertex, then we have an α-separation $\{(-\infty, y), (y, \infty)\}$ of $X \setminus \{y\}$, and y α-separates x from z. But, if y is an edge (not external), then it has a previous vertex a and a latter vertex b. So we have an α-separation $\{(-\infty, b) \setminus \{y\}, (a, \infty) \setminus \{y\}\}$ of $X \setminus \{y\}$. Hence, X is an α-prepath compatible with the same total order $\leq$ with respect to ${\tau_\alpha}^*$. That is implying that the intervals with respect to the orders compatible with ${\tau_\alpha}^*$ are exactly the intervals with respect to the original α-topology τ_α. Hence, X is locally α-connected with respect to ${\tau_\alpha}^*$, by (4.3), that is, $(X, {\tau_\alpha}^*)$ is an α-path.
The next definition was introduced in [13].

Definition 4.6: An α-topological space X is said to be α-compact if every α-open cover has a finite subcover.

Corollary 4.7: If X is an α-topological space, then the following statements are equivalent:
(1) X is α-compact.
(2) If every family of α-closed sets has the finite intersection property, then it has a non-empty intersection.
Proof: (1) → (2) Let X be an α-compact space, by contradiction, let $\{F_i | \ i \in I\}$ be a collection of α-closed sets such that $\bigcap_{i\in I} F_i = \emptyset$. Then we have an α-open cover $\{X - F_i | \ i \in I\}$. Since X is α-compact, then there exists a finite subcover $\{X - F_i\}_{i=1}^{n}$, and $\bigcap_{i=1}^{n} F_i = \emptyset$. That is contradicting with the finite intersection property, hence $\bigcap_{i\in I} F_i \neq \emptyset$.
(2) → (1) Let $\{U_i | \ i \in I\}$ be an α-open cover of X such that $X = \cup \{U_i | \ i \in I\}$ and does not have a finite subcover, then $X - \{U_i | \ i \in I\} = \{F_i | \ i \in I\}$ is a nonempty α-closed sets. Hence $\bigcap_{i=1}^{n} F_i \neq \emptyset$ when $\bigcap_{i\in I} F_i \neq \emptyset$ because of the finite intersection property by (2). So $X - \cap \{F_i | \ i \in I\} = \cup \{U_i | i \in I\}$, moreover $X - \bigcap_{i=1}^{n} F_i = \bigcup_{i=1}^{n} U_i$ which is a finite subcover of $\{U_i | \ i \in I\}$. Hence, X is an α-compact.
The next theorem is very important because it shows the relation between compactness and locally connectedness in α-topological spaces. Therefore, we take it here without proof, so we can write its proof in another place.

Theorem 4.8: If P_α is an α-bounded prepath, then P_α is α-compact if and only if it is locally α-connected.
From the above theorem, we can conclude the next corollary.

Corollary 4.9: Let P_α be an α-bounded prepath, then the next statements are equivalent:
(1) P_α is α-compact.
(2) P_α is locally α-connected.
(3) The α-topology of P_α concurs with the interval α-topology.

Proof: we can see the equivalence the above statements directly by using theorem (4.8) and theorem (4.3).

Definition 4.10: An α-topological space X is said to be α-S_1 space if every singleton is either α-open or α-closed.
We introduced the next theorem to use it when we define precycle and cycle.

Theorem 4.11: If X is an α-connected topological space with at least four points, then the following statements are equivalent:
1. For every four points, no one α-disconnects the remaining, however, some two α-disconnect, and are α-disconnected by the others.
2. There exists a cyclic order on X such that for every four points a, b, c, d, we have that a, c α-separate(α-disconnect) b and d if and only if $\langle w, x, y, z\rangle$ is a cyclic subsequence for some choice of w, $y \in \{a, c\}$ and $x, z \in \{b, d\}$.
3. X is α-S_1, and for every finite subset A, the complement of A and A have the same number of α-connected components.
4. X is α-S_1 and every two non-incident points α-disconnects, but no one point do.

Proof: (1) → (2) Let S be a cyclic order on X, and a, b, c, d, be disjoint points with a, c α-separate(α-disconnect) b and d. Now suppose that $Y \subseteq X$, then Y inherits a cyclic order $S^* = S \cap Y^4$ such that all quadruple with entries in Y. Since S is finite, then the obtaining ordered space is a cyclic subsequence of S. By (1), since a, c α-separate(α-disconnect) b and d, that means they are belong to different component. So, there is four points w, x, y, z in Y such that $\{w, y\} = \{a, c\} \cap Y$, and $\{x, z\} = \{b, d\} \cap$

Y, since Y is a subspace of X. That leads to w, y ∈ {a, c} and x, z ∈ {b, d}, because they belong to the intersection.
(2) → (3) from (2) we have a cyclic subsequence ordered space such that w, y ∈ {a, c} and x, z ∈ {b, d} which makes an α-separation any four points into two disjoint finite sets. Each one of them is being the complement of the other by definition (2.1). Hence, any one of these sets have the same number of α-connected components by facts (2.6A).
(3) → (4) X is α-S_1space, and A is a finite subset that has the same number of α-component with its complement. So there is an α-separation of X into two α-connected subsets by facts (2.6C). If A contains only one elemen, t then it is an α-open(α-closed) connected which can not α-disconnect the other points in X. However, if it contains two elements, it is a jump. So, it is an edge-vertex incident pair by theorem (3.19). Therefore, the two points can not α-separate the two others points. Hence, they are non-incident to α-separate the others.
(4) → (1) we have X is α-S_1space, for every four points on X, any two points which non-incident are α-disconnect the other two, so they are α-disconnected. Since X is α-S_1 and α-connected, then there has not any point that α-disconnect the other three points in X.

Definition 4.12: An α-connected topological space X is said to be an α-precycle, if |X| = 2, and X is an α-topolgized graph contains one vertex and one edge (a loop) only. Otherwise, If |X| ≥ 4, and X satisfies the statements of theorem (4.11).

Definition 4.13: An α-precycle is called an α-cycle if it is locally α-connected.
The following simple example shows the idea of precycles and cycles by using the above definitions.

Example 4.14: Let $X = V_G \cup E_G = \{v, e\}$ be a set consists of one vertex and one edge (loop), with $\tau_X = \{\emptyset, X, \{v\}\}$, then (X, τ) is a topological space such that the elements of τ are open sets and their complements are closed sets. So the α-topology of X is $\tau_{\alpha X} = \{\emptyset, X, \{\mathrm{v}\}\}$ which contains an α-open sets and their complements are α-closed set. We can see that X is an α-connected space, therefore it is an α-precycle by definition (4.12). Moreover, it is an α-cycle since it is locally α-connected by definition (4.13).

5. Conclusion

Through this paper, alpha-prepaths, alpha-paths, and alpha-cycles have been formulated and some relationships have been discussed. Moreover, several theorems and corollaries have been proved to continuum the future searches and works to define a new concepts which are related with them like cycle spaces.

References

[1] Harary F 1969 *Graph Theory* (USA: Addison – Wesley, Reading, Mass)
[2] Bondy J and Murty U 1976 *Graph Theory with Applications* (London: Macmillan Press)
[3] Vella A 2005 A Fundamentally Topological Perspective on Graph Theory *Ph. D. Thesis* (Canada: Uni. Waterloo, Ontaio)
[4] Keevash P, K¨uhn D, Mycroft R and Osthus D 2011 Loose Hamilton Cycles in Hypergraphs *Discrete Mathematics* **311** pp 544–59
[5] Gemignani M 1972 *Elementary Topology* Buffalo: State University of New York
[6] Kelley J 1955 *General Topology* New York: Van Nostrand company
[7] Willard S 1970 *General topology* London: Addison-Wesley Publishing Co. Reading Mass
[8] Kok H 1973 *Connected Orderable Spaces* Amsterdam: Mathmematish Centrum
[9] Mahmoud B and Yousif Y 2020 Cutpoints and Separations in Alpha Topological Spaces *Iraq J. Sci.* to appear
[10] Njastad O 1965 On Some Classes of Nearly Open Sets *Pacific J. Math.* **15** pp 961-70
[11] Andrijevic D 1984 Some Properties of the Topology of α-Sets *Math. Vesink* **36** pp 1-10

[12] Levine N 1970 Generalized Closed Sets in Topology *Rend. Circ. Math. Palermo* **19** 89-96
[13] Maheshawari S and Thakur S 1985 On α-compact Spaces *Bulletin of The Institute of Mathematics Academia Sinice* **13**(4) 341-47

The Transmuted Topp Leone Flexible Weibull (TTLFW) distribution with applications to reliability and lifetime data

The Transmuted Topp Leone Flexible Weibull (TTLFW) distribution with applications to reliability and lifetime data

Mizal H Alobaidi[1], Pelumi E Oguntunde[2] and Mundher A Khaleel[1]

[1]Department of Mathematics, Faculty of Computer Science and Mathematics, University of Tikrit, Tikrit, Iraq.
[2] Department of Mathematics, Covenant University, Ota, Ogun State, Nigeria

Email: mun880088@tu.edu.iq

Abstract. The Transmuted Topp Leone Flexible Weibull distribution was developed in this paper using the Transmuted Topp Leone family of distributions and its basic statistical properties were established. Estimation of model parameters was considered using the maximum likelihood estimation (MLE) method and three real life applications were provided. The TTLFW distribution is a promising model as its performance relative to other compounds probability models like the Exponentiated Flexible Weibull, Weibull Flexible Weibull, Kumaraswamy Flexible Weibull, Beta Flexible Weibull, Gamma Flexible Weibull, and Exponentiated Generalized Flexible Weibull distributions is quite credible.

1 Introduction

Probability models have played important roles in many areas of study like finance, biology, engineering, and so on. Many of these probability models have been modelled extended and/or generalized using families of distributions; these families of distributions give room for the introduction of additional shape parameters into the existing probability models. Examples of the existing families of distributions include Kumaraswamy-G family of distribution [1], Gompertz family of distribution [2], Weibull-G family of distribution [3], and a host of others which are mentioned in [4 - 7], and the references therein. However, developing families of distributions have taken a new dimension where two families of distributions are combined to produce a more robust family. For instance, Kumaraswamy Transmuted-G family of distribution [8], exponentiated Weibull-H family of distribution [9], Beta Transmuted {H family of distribution [10], Generalized Transmuted-G family of distribution [11], Transmuted Topp-Leone G family of distribution [12], Marshall-Olkin Topp Leone-G family of distributions [13], and some other ones are notable examples. These families have been used in the literature to extend several existing standard probability models and their potentials have been recorded. The performance of these families is impressive when fitted to real-life events, and this is a major motivation for this present research.

This research aims to explore the work of [12] who combined the Topp Leone family of distributions [14] and Transmuted family of distributions [15]. Particularly, this research considered extending the Flexible Weibull distribution using the Transmuted Topp-Leone G family of distributions. Flexible Weibull (FW) distribution is one of the medications of the well-known Weibull distribution which caters for the disadvantage of not being able to model datasets with a non-monotonic failure rate. The FW distribution exhibits increasing, decreasing, or bathtub shaped failure rate, it has also received

consideration in clinical studies, life testing experiments, reliability analysis and applied statistics ([16], [17], and [18]). In the next section, the Transmuted Topp-Leone Flexible Weibull distribution is developed and its basic statistical properties are explicitly derived including estimation of model parameters while real life applications are provided in section 3.

2. The Transmuted Topp Leone Flexible Weibull (TTLFW) Distribution

For a random variable y, the Transmuted Topp-Leone family of distribution is defined by the following densities:

$$F(y) = (1+\lambda)\{1-[1-G(y)]^2\}^{\alpha} - \lambda\{1-[1-G(y)]^2\}^{2\alpha} \quad (1)$$

and

$$f(y) = 2\alpha g(y)[1-G(y)]\{1-[1-G(y)]^2\}^{\alpha-1}\{1+\lambda-2\lambda\{1-[1-G(y)]^2\}^{\alpha}\} \quad (2)$$

where y ≥ 0. $\alpha > 0$ and $|\lambda| \leq 1$ are shape parameters, $F(y)$ and $f(y)$ are regarded as the cumulative distribution function (c.d.f) and probability density function (p.d.f) respectively.

Also, the densities of the Flexible Weibull distribution are:

$$G(y) = 1 - exp\left(-e^{\beta y-\frac{\theta}{y}}\right) \quad ; y>0, \beta>0, \theta>0 \quad (3)$$

and

$$g(y) = \left(\beta+\frac{\theta}{y^2}\right)e^{\beta y-\frac{\theta}{y}} exp\left(-e^{\beta y-\frac{\theta}{y}}\right) \quad ; y>0, \beta>0, \theta>0 \quad (4)$$

To derive the c.d.f of the Transmuted Topp-Leone Flexible Weibull distribution, equation (3) is substituted into equation (1) as follows:

$$F(y) = (1+\lambda)\left\{1-\left[exp\left(-e^{\beta y-\frac{\theta}{y}}\right)\right]^2\right\}^{\alpha} - \lambda\left\{1-\left[exp\left(-e^{\beta y-\frac{\theta}{y}}\right)\right]^2\right\}^{2\alpha} \quad (5)$$

Similarly, the corresponding pdf is obtained by substituting equations (3) and (4) into equation (2) as follows:

$$f(y) = 2\alpha\left(\beta+\frac{\theta}{y^2}\right)e^{\beta y-\frac{\theta}{y}}\left[exp\left(-e^{\beta y-\frac{\theta}{y}}\right)\right]^2\left\{1-\left[exp\left(-e^{\beta y-\frac{\theta}{y}}\right)\right]^2\right\}^{\alpha-1}$$

$$\times\left((1+\lambda)\left\{-2\lambda\left\{1-\left[exp\left(-e^{\beta y-\frac{\theta}{y}}\right)\right]^2\right\}^{\alpha}\right\}\right) \quad (6)$$

for y ≥ 0. $\alpha > 0$ and $|\lambda| \leq 1$, $\beta > 0, \theta > 0$.

The plots for the p.d.f and c.d.f of TTLFW distribution are presented in figures 1 and 2 respectively.

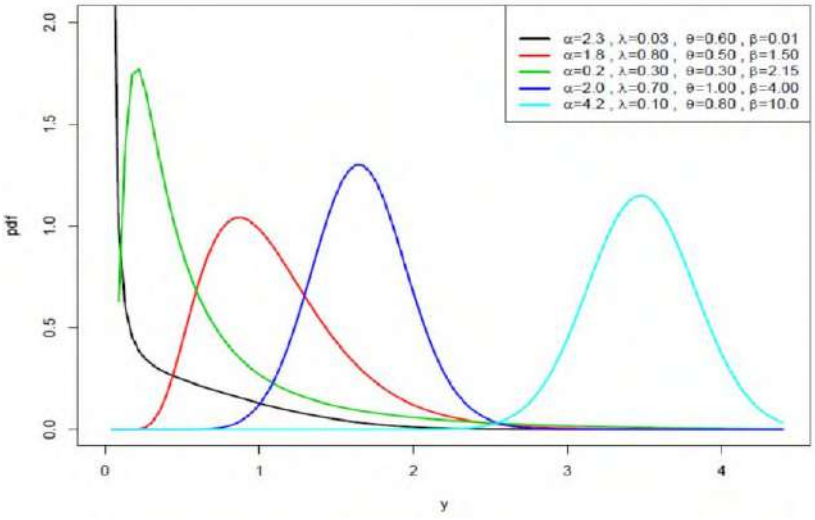

Figure 1: PDF of Transmuted Topp Leone Flexible Weibull Distribution

The plot in figure 1 suggests that the shape of the TTLFW distribution is decreasing and unimodal

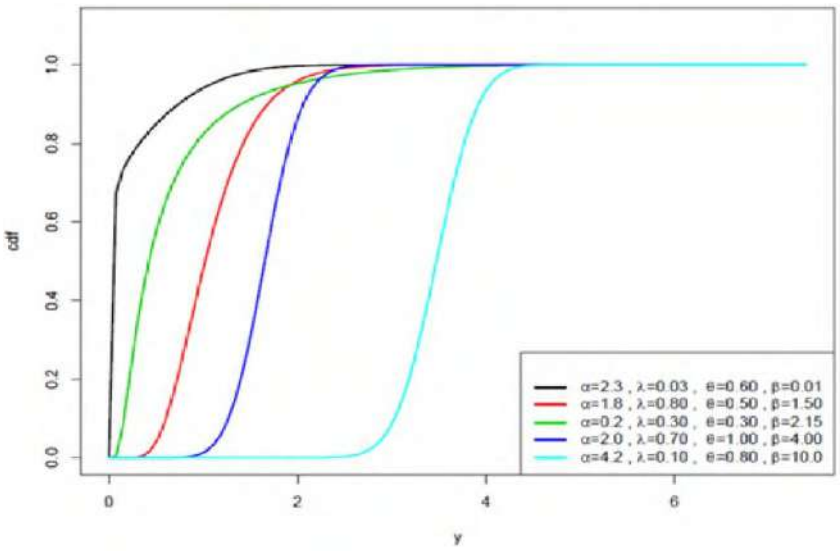

Figure 2: The c.d.f plot for the TTLFW Distribution

2.1 Reliability Analysis

Survival Function is obtained as:

$$S(y) = 1 - F(y)$$

Thus, the survival function for TTLFW distribution is:

$$S(y) = 1 - \left((1+\lambda)\left\{1 - \left[exp\left(-e^{\beta y - \frac{\theta}{y}}\right)\right]^2\right\}^{\alpha} - \lambda\left\{1 - \left[exp\left(-e^{\beta y - \frac{\theta}{y}}\right)\right]^2\right\}^{2\alpha} \right) \quad (7)$$

The Failure rate is obtained as:

$$h(y) = f(y)/S(y)$$

Thus, the failure rate for TTLFW distribution is:

$$h(y) = 2\alpha\left(\beta + \frac{\theta}{y^2}\right)e^{\beta y - \frac{\theta}{y}}\left[exp\left(-e^{\beta y - \frac{\theta}{y}}\right)\right]^2\left\{1 - \left[exp\left(-e^{\beta y - \frac{\theta}{y}}\right)\right]^2\right\}^{\alpha-1} \times \frac{\left((1+\lambda)\left\{-2\lambda\left\{1-\left[exp\left(-e^{\beta y - \frac{\theta}{y}}\right)\right]^2\right\}^{\alpha}\right\}\right)}{\left[1-\left((1+\lambda)\left\{1-\left[exp\left(-e^{\beta y - \frac{\theta}{y}}\right)\right]^2\right\}^{\alpha} - \lambda\left\{1-\left[exp\left(-e^{\beta y - \frac{\theta}{y}}\right)\right]^2\right\}^{2\alpha}\right)\right]} \quad (8)$$

$$For\ y > 0, \alpha > 0, |\lambda| \leq 1, \beta > 0, \theta > 0$$

The plot for the failure rate of TTLFW distribution is presented in figure 3.

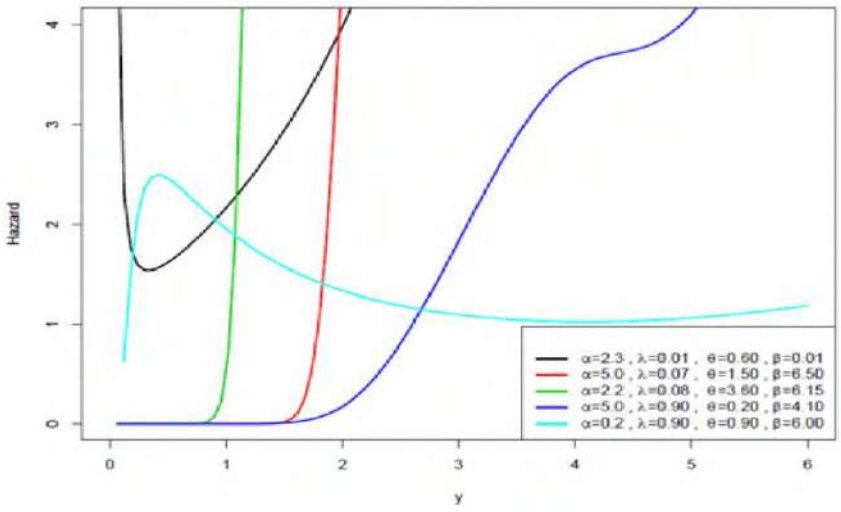

Figure 3: Plot for the failure rate of the TTLFW Distribution

Figure 3 suggests that the shape for the failure rate of TTLFW distribution is uni-antimodal, unimodal, and increasing.

2.2 Quantile Function

The quantile function of the TTLFW distribution can be obtain by find the inverse equation (5) with some algebra. The quantile function is obtained as:

$$Q(u) = F^{-1}(u)$$

$$Q(u) = \frac{ln\ ln\ [-\ ln\ ln\ (\rho)\ ] + \sqrt{\{ln[-ln(\rho)]\}^2 + u\beta\theta}}{2\beta} \quad (9)$$

where

$$\rho = \left\{1 - \left[\frac{1+\lambda-\sqrt{(1+\lambda)^2 - u\lambda u}}{2\lambda}\right]^{\frac{1}{2}}\right\}^{\frac{1}{2}}$$

and $U \sim Uniform(0,1)$

The median can be obtained when 'u' is set at 0.5. Random samples are generated from the TTLFW distribution using:

$$y = \frac{ln \mid -ln(\rho)] + \sqrt{\{ln \mid -ln(\rho)]\}^2 + u\beta\theta}}{2\beta} \quad (10)$$

2.3 Estimation of Parameter

Let $y_1, y_2, \ldots, y_n$ represent random samples from the TTLFW distribution. By the method of maximum likelihood estimation (MLE), the likelihood function of the TTLFW distribution is:

$$f(y_i \mid \alpha, \beta, \lambda, \theta) = \prod_{i=1}^{n}[f(y_1, y_2, \ldots, y_n; \alpha, \beta, \lambda, \theta)]$$

$$f(y_i \mid \alpha, \beta, \lambda, \theta) = \prod_{i=1}^{n} 2\alpha\left(\beta + \frac{\theta}{y_i^2}\right)e^{\beta y_i - \frac{\theta}{y}}\left[exp\left(-e^{\beta y_i - \frac{\theta}{y_i}}\right)\right]^2$$

$$\times\left\{1 - \left[exp\left(-e^{\beta y_i - \frac{\theta}{y_i}}\right)\right]^2\right\}^{\alpha-1}\left\{1 + \lambda - 2\lambda\left\{1 - \left[exp\left(-e^{\beta y - \frac{\theta}{y}}\right)\right]^2\right\}^{\alpha}\right\}$$

The log-likelihood function say; $l(\alpha, \beta, \lambda, \theta|y_i)$= log $[f(y_i|\alpha, \beta, \lambda, \theta)]$ is then given as:

$$l(\alpha, \beta, \lambda, \theta \mid y_i) = nlog(2) + nlog(\alpha) + \sum_{i=1}^{n} log\left(\beta + \frac{\theta}{y_i^2}\right) + \beta\sum_{i=1}^{n} y_i - \theta\sum_{i=1}^{n}\left(\frac{1}{y_i}\right) -$$

$$2e^{\beta\sum_{i=1}^{n} y_i - \theta\sum_{i=1}^{n}\left(\frac{1}{y_i}\right)} + (\alpha-1)\sum_{i=1}^{n} log\left\{1 - \left[exp\, exp\left(-e^{\beta y_i - \frac{\theta}{y_i}}\right)\right]^2\right\} + \sum_{i=1}^{n} log\left\{1 + \lambda -$$

$$2\lambda\left\{1 - \left[exp\, exp\left(-e^{\beta y_i - \frac{\theta}{y_i}}\right)\right]^2\right\}^{\alpha}\right\} \quad (11)$$

The partial derivatives of $l(\alpha, \beta, \lambda, \theta|y_i)$ for each of the model parameters are equated to zero; $\frac{dl(\alpha,\beta,\lambda,\theta|y_i)}{d\alpha} = 0, \frac{dl(\alpha,\beta,\lambda,\theta|y_i)}{d\beta} = 0, \frac{dl(\alpha,\beta,\lambda,\theta|y_i)}{d\lambda} = 0$, and $\frac{dl(\alpha,\beta,\lambda,\theta|y_i)}{d\theta} = 0$.

The expressions are solved simultaneously to give the maximum likelihood estimates of the parameters. Since the solutions cannot be obtained in closed forms, numerical methods can be used to obtain the estimates using software like R, MAPLE, and so on. In particular, R software was used in this research to obtain the parameter estimates using iterative methods and with the aid of datasets.

3. Applications

To demonstrate the potentials of the TTLFW distribution, two different datasets are used and models like the Exponentiated Flexible Weibull (EFW), Weibull Flexible Weibull (WFW), Kumaraswamy Flexible Weibull (KuFW), Beta Flexible Weibull (BFW), Gamma Flexible Weibull (GaFW) and Exponentiated Generalized Flexible Weibull (EGFW) distributions are used as the basis for comparison.

The following selection criteria; Negative Likelihood function (NLL), Bayesian Information Criteria (BIC), Akaike Information Criteria (AIC), Consistent Akaike Information Criteria (CAIC), Hannan and Quinn Information Criteria (HQIC) are used to determine the model with the best fit. The Saphiro Wilk (W) statistic, Kolmogorov Smirnov (KS) statistic, and the Anderson Darling statistic are also obtained. It is preferable to have low values for these selection criteria; therefore, the probability model with the lowest value for these criteria is selected as the distribution with the best fit. R software was used for all the analyses.

First Data: The dataset on time to failure for 40 suits of turbochargers in diesel engines was considered. [19] has previously used the dataset, the observations are:

1.6, 2.0, 2.6, 3.0, 3.5, 3.9, 4.5, 4.6, 4.8, 5.0, 5.1, 5.3, 5.4, 5.6, 5.8, 6.0, 6.0, 6.1,
6.3, 6.5, 6.5, 6.7, 7.0, 7.1, 7.3, 7.3, 7.3, 7.7, 7.7, 7.8, 7.9, 8.0, 8.1, 8.3, 8.4, 8.4,
8.5, 8.7, 8.8, 9.0

The result corresponding to the time to failure dataset is presented in table 1.

Table 1: Estimates, NLL, AIC, CAIC, BIC, and HQIC for the time-to-failure data

Model	Estimates	NLL	AIC	CAIC	BIC	HQIC
TTLFW	$\hat{\alpha} = 0.1517$ $\hat{\lambda} = 0.577$ $\hat{\theta} = 0.6165$ $\hat{\beta} = 48.938$	**78.95826**	**165.9165**	**167.0594**	**172.672**	**168.3591**
EFW	$\hat{\alpha} = 14.49$ $\hat{\lambda} = 0.182$ $\hat{\theta} = 0.0806$	83.300	172.601	173.268	177.668	174.433
WFW	$\hat{\alpha} = 1.6144$ $\hat{\lambda} = 10.67$ $\hat{\theta} = 0.361$ $\hat{\beta} = 1.425$	79.790	167.584	168.724	174.336	170.024
KuFW	$\hat{\alpha} = 17.774$ $\hat{\lambda} = 24.933$ $\hat{\theta} = 0.086$ $\hat{\beta} = 0.1653$	81.100	170.200	171.343	176.955	172.642
BFW	$\hat{\alpha} = 34.432$ $\hat{\lambda} = 6.397$ $\hat{\theta} = 0.1019$ $\hat{\beta} = 0.0187$	82.714	173.425	174.564	180.181	175.686
GaFw	$\hat{\alpha} = 4.7806$ $\hat{\lambda} = 0.2434$ $\hat{\theta} = 0.3497$	81.339	168.675	169.346	173.746	170.511
EGFW	$\hat{\alpha} = 0.1022$ $\hat{\lambda} = 1.9209$ $\hat{\theta} = 0.4057$ $\hat{\beta} = 0.9977$	80.706	169.412	170.555	176.162	171.855

The result for the goodness of fit test is presented in table 2.

Table 2: The W, A, KS Statistics, and p-value using the time-to-failure data

Models	**W − Statistic**	**A − Statistic**	**KS − Statistic**	**K S p − value**
TTLFW	**0.0222**	**0.1880**	**0.0942**	**0.8690**
EFW	0.0918	0.6668	0.1071	0.7481
WFW	0.0313	0.2363	0.0910	0.8645
KuFW	0.0498	0.3789	0.0979	0.8372
BFW	0.0778	0.5742	0.1050	0.7697
GaFW	0.0536	0.4071	0.0999	0.8192
EGFW	0.0444	0.3385	0.0907	0.8970

The histogram plot for the data set with the competing models is displayed in figure 4 while the empirical cdf (ecdf) plot is presented in figure 5.

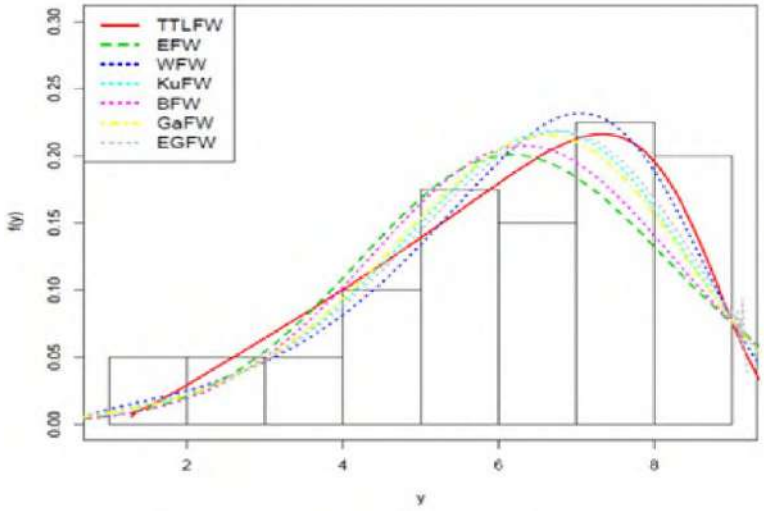

Figure 4: The histogram plot for the time-to-failure dataset

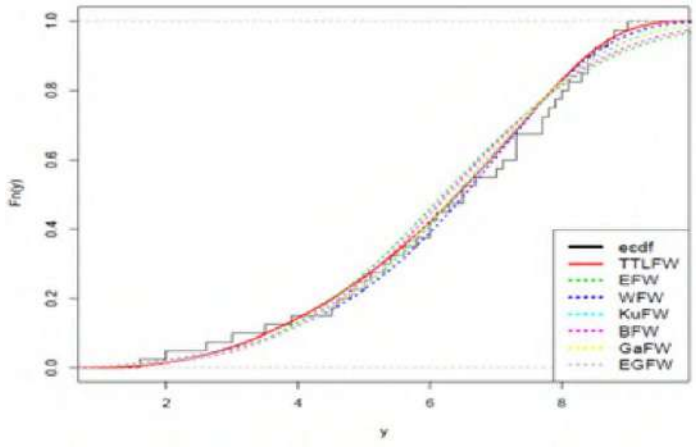

Figure 5: The ecdf plot for the time-to-failure dataset

Second Data: The dataset on the exceedances of the Wheatson river was also considered. The dataset has been analyzed previously by [20]. The observations are: 1.7, 1.4, 0.6, 9.0, 5.6, 1.5, 2.2, 18.7, 2.2, 1.7, 30.8, 2.5, 14.4, 8.5, 39.0, 7.0, 13.3, 27.4, 1.1, 25.5, 0.3, 20.1, 4.2, 1.0, 0.4, 11.6, 15.0, 0.4, 25.5, 27.1, 20.6, 14.1, 11.0, 2.8, 3.4, 20.2, 5.3, 22.1, 7.3, 14.1, 11.9, 16.8, 0.7, 1.1, 22.9, 9.9, 21.5, 5.3, 1.9, 2.5, 1.7, 10.4, 27.6, 9.7, 13.0, 14.4, 0.1, 10.7, 36.4, 27.5, 12.0, 1.7, 1.1, 30.0, 2.7,2.5, 9.3, 37.6, 0.6, 3.6, 64.0, 27.0. The result corresponding to the exceedances of the Wheatson river dataset is presented in table 3.

Table 3: Estimates, NLL, AIC, CAIC, BIC and HQIC for the exceedances of the Wheatson river dataset

Model	Estimates	NLL	AIC	CAIC	BIC	HQIC
TTLFW	$\hat{\alpha} = 4.231$ $\hat{\lambda} = 0.883$ $\hat{\theta} = 0.025$ $\hat{\beta} = 0.243$	**252.018**	**512.0**	**512.6**	**521.1**	**515.6**
EFW	$\hat{\alpha} = 2.215$ $\hat{\lambda} = 0.035$ $\hat{\theta} = 0.475$	253.786	513.7	514.1	522.5	516.8
WFW	$\hat{\alpha} = 1.333$ $\hat{\lambda} = 1.554$ $\hat{\theta} = 0.033$ $\hat{\beta} = 0.740$	254.367	516.7	517.3	525.8	520.3
KuFW	$\hat{\alpha} = 4.252$ $\hat{\lambda} = 2.727$ $\hat{\theta} = 0.024$ $\hat{\beta} = 0.2.63$	253.757	515.1	515.8	524.8	518.8
BFW	$\hat{\alpha} = 2.457$ $\hat{\lambda} = 1.097$ $\hat{\theta} = 0.034$ $\hat{\beta} = 0.432$	253.876	515.7	516.4	524.8	519.4
GaFw	$\hat{\alpha} = 1.596$ $\hat{\lambda} = 0.037$ $\hat{\theta} = 0.636$	254.153	514.3	514.6	521.1	517.0
EGFW	$\hat{\alpha} = 1.045$ $\hat{\lambda} = 2.370$ $\hat{\theta} = 0.035$ $\hat{\beta} = 0.446$	253.877	515.7	516.3	524.8	519.5

The result for the goodness of fit test is presented in table 4.

Table 4: The W, A, KS and p - value using the exceedances of the Wheatson river dataset

Models	**W − Statistic**	**A − Statistic**	**K S − Statistic**	**K Sp – value**
TTLFW	**0.0845**	**0.6457**	**0.0816**	**0.7229**
EFW	0.1259	0.9205	0.0964	0.5140
WFW	0.1516	1.0732	0.1040	0.4172

KuFW	0.1153	0.8482	0.0959	0.5217
BFW	0.1242	0.9098	0.0966	0.5119
GaFW	0.1396	1.0033	0.0989	0.4808
EGFW	0.1245	0.9124	0.0969	0.5084

The histogram plot for the data set with the competing models is displayed in figure 6 while the empirical cdf (ecdf) plot is presented in figure 7.

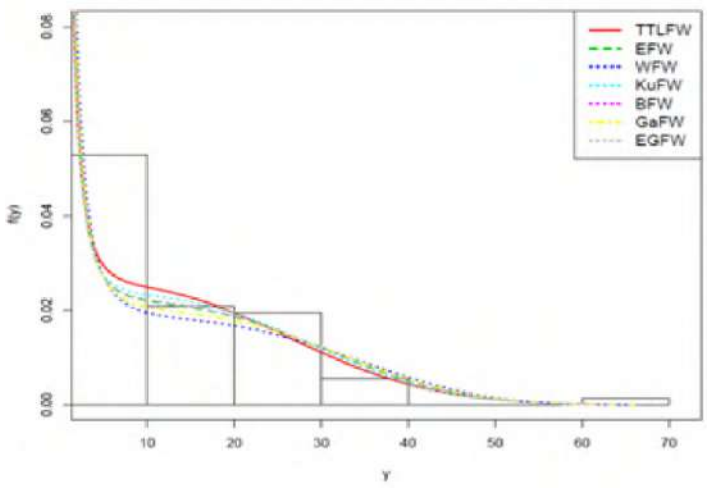

Figure 6: Histogram of the exceedances of the Wheatson river dataset with the competing models

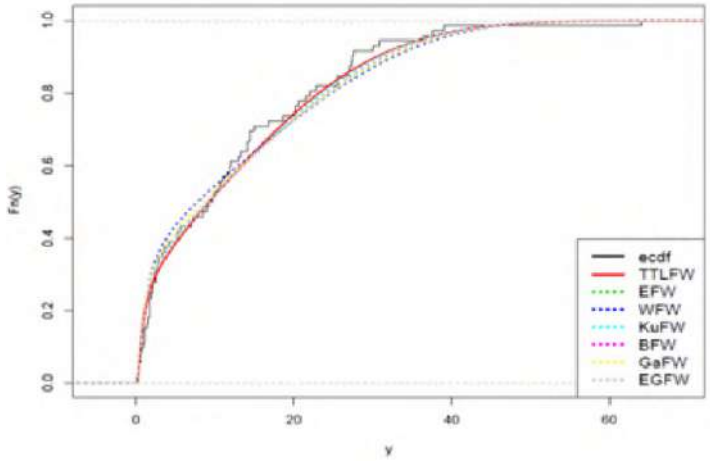

Figure 7: The ecdf plot of the exceedances of the Wheatson river dataset with the competing models

Clearly, all the two applications provided indicate that the TTLFW distribution is better than the other models based on the values of the criteria used. It has lower values for the NLL, AIC, CAIC, BIC, and HQIC. The histogram and ecdf plots also support all the results presented in tables 1 to 4.

4. Conclusion

The Transmuted Topp-Leone Flexible Weibull (TTLFW) distribution has been successfully derived in this research. It's properties have been established and applications to two real datasets have been provided. The TTLFW distribution exhibits decreasing and unimodal shapes while its failure rate exhibits increasing, unimodal and uni-antimodal shapes. The applications provided reveal that the TTLFW distribution is a good competitor as it performs creditably well than the Exponentiated Flexible Weibull, Weibull Flexible Weibull, Kumaraswamy Flexible Weibull, Beta Flexible Weibull, Gamma Flexible Weibull, and Exponentiated Generalized Flexible Weibull distributions under the considered selection criteria.

References

[1] Cordeiro G M and de Castro M 2011 *Journal of Statistical Computation and Simulation* **81** pp 883-898
[2] Alizadeh M, Cordeiro G M, Bastos Pinho L G and Ghosh I 2017 *Journal of Statistical Theory and Practice* **11** pp 179-207
[3] Bourguignon M, Silva R B and Cordeiro G M 2014 *Journal of Data Science* **12** pp 53-68
[4] Owoloko E A, Oguntunde P E and Adejumo A O 2015 *SpringerPlus*, **4**, 818 pages
[5] Cordeiro G M, Alizadeh M, Nascimeto A D C and Rasekhi M 2016 *Chilean Journal of Statistics* **7** pp 29-50
[6] Oguntunde P E, Khaleel M A, Okagbue H I and Odetunmibi O A 2019 *Wireless Personal Communication* **109** pp 349-360
[7] Ahmed M T, Khaleel M A and Khalaf E K 2020 *Periodicals of Engineering and Natural Sciences **8*** pp 684-692
[8] Afify A Z, Cordeiro G M, Yousof H M, Alzaatreh A and Nifal Z M 2016 *Journal of Data Science* **14** pp 245-270
[9] Cordeiro G M, Afify A Z, Yousof H M, Pescim R R and Aryal G R 2017 *Mediterrenian Journal of Mathematics* **14** 155 https://doi.org/10.1007/s00009-017-0955-1
[10] Afify A Z, Yousof H M and Nadarajah S 2017 *Statistics and Inference* **10** pp 505-520
[11] Nofal Z M, Afify A Z, Yousouf H M and Cordeiro G M 2017 *Communications in Statistics: Theory and Methods* **46** pp 4119-4136
[12] Yousof H M, Alizadeh M, Jahanshahi S M A, Ramires T G, Ghosh I, Hamedani G G 2017 *Journal of Data Science* **15** pp 723-740
[13] Khaleel M A, Oguntunde P E, Al-Abbasi J N, Ibrahim N A and Abujarad M H 2020 *Scientific African* **8** e00470
[14] Al-Shomrani A, Arif O, Shawky A, Hanif S and Shahbaz M Q 2016 *Pakistan Journal of Statistics and Operation Research* **12** pp 443-451
[15] Shaw W T and Buckley I R C 2007 *Research Report*
[16] Bebbington M, Lai C D and Zitikis R 2007 *Reliability Engineering and System Safety* **92** pp 719-726
[17] El-Desouky B S, Mustafa A and Al-Garash S 2017 *Open Journal of Modelling and Simulation* **5** pp 83-97
[18] Khaleel M A, Oguntunde P E, Ahmed M T, Ibrahim N A and Loh Y F 2020 *Malaysian Journal of Mathematical Sciences* **14** pp 169-190
[19] Xu K, Xie M, Tang L C and Ho S L 2003 *Applied Soft Computing* **2** pp 255-268
[20] Akinsete A, Famoye F and Lee C 2008 *Statistics* **42** pp 547-563

Estimate the Parallel System Reliability in Stress-Strength Model Based on Exponentiated Inverted Weibull Distribution

Estimate the Parallel System Reliability in Stress-Strength Model Based on Exponentiated Inverted Weibull Distribution

Eman A Abdulateef [1,*], Abbas N Salman[1] and Adil Abdulkadhim Hussein[1]

[1]Department of mathematics, college of education for pure sciences (Ibn AL-Haitham) University of Baghdad, Baghdad, Iraq.

E-mail: eman.a.al@ihcoedu.uobaghdad.edu.iq

Abstract. In this paper, we employ the maximum likelihood estimator in addition to the shrinkage estimation procedure to estimate the system reliability (R_k) contain K^{th} parallel components in the stress- strength model, when the stress and strength are independent and non-identically random variables and they follow two parameters Exponentiated Inverted Weibull Distribution (EIWD). Comparisons among the proposed estimators were presented depend on simulation established on mean squared error (MSE) criteria.

1. Introduction

The parallel stress-strength model occurs when a system has a mixture of k independent component with the strengths $X_1, X_2, \dots\dots, X_k$ and each component of this system is subject to a common stress Y. the system works successfully if at least one of the components survives, it is termed parallel in the analogy with electric circuits [4].

The reliability of the above system denoted by R_k take the attention in this work and the formula of such stress - strength reliability when the stress and strength are independent random variable can be expressed as follow:

$$R_k = P(Y < \max(X_1, X_2, \dots\dots, X_k) \quad (1)$$

In (2006), Mokhlis estimated the reliability system contains two parallel components via four different methods based bivariate exponential distribution [1]. In (2013), Ali estimated the reliability of the parallel stress-strength system with a non-identical component using Lomax distribution using estimation methods namely: MLE, LS, PCE and MOM [2]. In (2017), Fatima estimated three types of system reliability (one component, k^{th} parallel component and multicomponent in the stress-strength model for Exponentiated Weibull distribution using; MLE, MOM, and three shrinkage methods and made a comparison among them [3]. And in (2018) Cheng estimated the system reliability in S-S models based on Exponentiated Pareto distribution using different estimation methods [4].

The aim of the present paper is to estimate the reliability (R_k) of the system contain K^{th} parallel components have strengths $(X_1, X_2, \dots\dots, X_k)$ subjected to common stress Y (stress-strength model) based on Exponentiated Inverted Weibull distribution with unknown shape parameter θ and known shape β (β =4) via different estimation methods like MLE, as well as some shrinkage estimation methods and

make a comparison among the proposed estimator methods using simulation depends on mean squared error.

The probability density function pdf of a r.v. X distributed as Exponentiated Inverted Weibull distribution (EIWD) is as below [5].

$$f(x;\theta,\beta) = \beta\theta x^{-(\beta+1)}\left(e^{-x^{-\beta}}\right)^{\theta};\ x>0,\theta>0 \quad (2)$$

And the cumulative distribution function (c.d. f.) of X will be:

$$F(x;\theta,\beta) = \left(e^{-x^{-\beta}}\right)^{\theta};\ x>0,\theta>0 \quad (3)$$

Assume $X_1,X_2,\ldots,X_k$ arises strength have (EIWD) with parameter α_i, i=1,2,..., k and Y refer to common stress follow (EIWD) with parameter α_{k+1}.

The system reliability R_k of the K^{th} parallel in pre mentioned stress-strength model can be obtained as the following [6].

$$R_{(k)} = P(y < \max(x_1, x_2, \ldots\ldots, x_k))$$
$$R_k = \int_o^{\infty} \overline{F}_z(y)\, f(y)\, dy$$

Where, $z = \max(x_1, x_2, \ldots\ldots, x_k)$

$$F_z(z) = P(Z<z) = \left(e^{-z^{-\beta}}\right)^{\sum_{i=1}^{k}\theta_i}$$

$$Rk = \int_o^{\infty}\left[1-\left(e^{-y^{-\beta}}\right)^{\sum_{i=1}^{k}\theta_i}\right]\theta_{k+1}\beta y^{-(\beta+1)}\left(e^{-y^{-\beta}}\right)^{\theta_{k+1}} dy$$

$$Let\ w = e^{-y^{-\beta}} \rightarrow dy = \frac{1}{\beta w}(-lnw)^{-\frac{1}{\beta}-1}dw$$

$$Rk = \int_o^1 \theta_{k+1}\left(1-w^{\sum_{i=1}^{k}\alpha_i}\right)(w)^{\theta_{(k+1)}-1}dw$$
$$= \int_o^1 \theta_{k+1}(w)^{\theta_{(k+1)}-1}dw - \int_o^1 \theta_{k+1}(w)^{\sum_{i=1}^{k+1}\theta_i-1}dw$$
$$= \theta_{k+1}B(\theta_{k+1},1) - \theta_{k+1}B(\sum_{i=1}^{k+1}\theta_i,1)$$

Where, $B(.,.)$ denote to Beta function.

And by simplification, R_k became:

$$R_k = \frac{\sum_{i=1}^{k}\theta_i}{\sum_{i=1}^{k+1}\theta_i} \quad (4)$$

2. Estimation Methods of R_k

2.1. Maximum Likelihood Estimator (MLE)

Let $x_{11},x_{12},\ldots,x_{1n}$; $x_{21},x_{22},\ldots,x_{2n}$; $x_{k1},x_{k2},\ldots,x_{kn}$ form EIWD(θ_i,β), respectively, for i=1,2,..,k and $y_1, y_2,\ldots, y_m$ follows EIWD (θ_{k+1},β). Then the likelihood functions:

$$l = l(\alpha_i,\lambda;x_i,y) = \prod_{i=1}^{n_i}\left(\prod_{i=1}^{k} f(x_{ij})\right)\prod_{t=1}^{m} g(y_t)$$

$$= \prod_{j=1}^{n_i}\prod_{i=1}^{k}\beta\theta_i x_{ij}^{-(\beta+1)}\left(e^{-x_{ij}^{-\beta}}\right)^{\theta_i}\prod_{t=1}^{m}\beta\theta_{k+1}\,y_t^{-(\beta+1)}\left(e^{-y_t^{-\beta}}\right)^{\theta_{k+1}}$$

$$\ln(l) = \sum_{i=1}^{k} n_i ln\theta_i + \sum_{i=1}^{k} n_i ln\beta - (\beta-1)\sum_{i=1}^{k}\sum_{j=1}^{n_i} lnx_{ij} - \sum_{i=1}^{k}\sum_{j=1}^{n_i}\theta_i x_{ij}^{-\beta} + mln\beta + mln\beta + mln\theta_{k+1} - (\beta-1)\sum_{t=1}^{m} ln\, y_t - \theta_{k+1}\sum_{t=1}^{m} y_t^{-\beta}$$

$$\frac{d\ln(l)}{d\theta_i} = \frac{n_i}{\theta_i} - \sum_{j=1}^{n_i} x_{ij}^{-\beta} = 0 \quad ;\ i=1,2,\ldots,k$$

$$\frac{d\ln(l)}{d\theta_{k+1}} = \frac{m}{\theta_{k+1}} - \sum_{t=1}^{m} y_t^{-\beta} = 0$$

Thus, the maximum likelihood estimator of the parameters θ_i, $i=1,2,\ldots,k,k+1$ will be as follows:

$$\widehat{\theta_i}_{mle} = \frac{n_i}{\sum_{j=1}^{n_i} x_{ij}^{-\beta}} \quad ;\ i=1,2,\ldots,k \quad (5)$$

$$\hat{\theta}_{k+1mle} = \frac{m}{\sum_{t=1}^{m} y_t - \beta} \tag{6}$$

Noted that, $\hat{\theta}_{\iota_{mle}}$ is biased estimator for all i , i=1,2,…,k+1, since $E(\hat{\theta}_{\iota\text{mle}}) \neq \theta_i = \frac{\mathfrak{Z}}{\mathfrak{Z}-1}$

Hence, $\hat{\theta}_{\iota\text{ub}} = \frac{\mathfrak{Z}-1}{\mathfrak{Z}}\hat{\theta}_{\iota_{mle}}$ will be unbiased estimators of θ_i, i=1,2,..,k+1, and $\mathfrak{Z}$ may refers to n_i , i=1,…,k or refer to m .

Also, it is known that the $Var(\hat{\theta}_{i_{ub}}) = \frac{(\theta_i)^2}{\mathfrak{Z}-2}$; $i = 1, \dots, k+1$

By substituting $\hat{\theta}_{\iota\text{mle}}$; i=1,2….,k+1 in equation (4), we get the reliability estimation $\hat{R}_{k_{mle}}$model as bellow:

$$\hat{R}_{k_{mle}} = \frac{\sum_{i=1}^{k} \hat{\theta}_{\iota_{mle}}}{\sum_{i=1}^{k+1} \hat{\theta}_{\iota_{mle}}} \tag{7}$$

2.2. Shrinkage Estimation Method

Thompson in 1968, proposed the problem of shrink a usual estimator $\hat{\theta}$ of the parameter θ to prior information θ_0 using shrinkage weight factor $k(\hat{\alpha})$, such that $0 \leq k(\hat{\alpha}) \leq 1$. He believes that θ_0 is closed to the true value of θ or θ_0 maybe near the true value of θ. Thus, the form of Thompson - Type shrinkage estimator of θ_i say $\hat{\theta}_{i\,sh}$ will be [7].

$$\hat{\theta}_{i\,sh} = k\hat{\theta}_{ub} + (1-k)\theta_0 \tag{8}$$

One of the most important methods of finding the value of k it can be made by minimizing of MSE($\hat{\theta}_{sh}$).[11]

$$\begin{aligned}
MSE(\hat{\theta}_{i\,sh}) &= E(\hat{\theta}_{i\,sh} - \theta)^2 \\
&= E(k_i\hat{\theta}_{i_{ub}} + (1-k_i)\theta_{i_0} - \theta)^2 \\
&= E\big(k_i(\hat{\theta}_{i_{ub}} - \theta_{i_0}) - (\theta - \theta_{i_0})\big)^2 \\
\frac{dMSE(\hat{\theta}_{i\,sh})}{dk_i} &= 2k_iE(\hat{\theta}_{i_{ub}} - \theta_{i_0})^2 - 2(1-k_i)(\hat{\theta}_{i_{ub}} - \theta_{i_0})^2 \\
0 &= 2k_iE(\hat{\theta}_{i_{ub}} - \theta_{i_0})^2 - 2(1-k_i)(\hat{\theta}_{i_{ub}} - \theta_{i_0})^2 \\
0 &= k_iVar(\hat{\theta}_{i_{ub}}) - (\hat{\theta}_{i_{ub}} - \theta_{i_0})^2 + k_i(\hat{\theta}_{i_{ub}} - \theta_{i_0})^2 \\
k_i &= \frac{(\hat{\theta}_{i_{ub}} - \theta_{i_0})^2}{(\hat{\theta}_{i_{ub}} - \theta_{i_0})^2 + var(\hat{\theta}_{i_{ub}})}
\end{aligned} \tag{9}$$

Then, by compensating in an equation (7), we get $\hat{\theta}_{i_{sh}}$ it also comes:

$$\hat{\theta}_{i_{sh}} = \frac{(\hat{\theta}_{i_{ub}} - \theta_{i_0})^2}{(\hat{\theta}_{i_{ub}} - \theta_{i_0})^2 + var(\hat{\theta}_{i_{ub}})}\hat{\theta}_{i_{ub}} + \left(1 - \frac{(\hat{\theta}_{i_{ub}} - \theta_{i_0})^2}{(\hat{\theta}_{i_{ub}} - \theta_{i_0})^2 + var(\hat{\theta}_{i_{ub}})}\right)\theta_{i_0} \text{ ; for i=1,2,....,k+1}$$

Thus, based on equation (4), the reliability estimation of k components parallel system in (S-S) model using shrinkage estimation methods will be:

$$\hat{R}_{k_{sh}} = \frac{\sum_{i=1}^{k} \hat{\theta}_{\iota_{sh}}}{\sum_{i=1}^{k+1} \hat{\theta}_{\iota_{sh}}} \tag{10}$$

2.3. Preliminary Test Single Stage Shrinkage Estimator

The preliminary test single stage shrinkage estimator (SS) introduced in this article as an estimator of the level of significance (Δ) for test the hypotheses H_0: $\theta = \theta_0$ vs. H_1: $\theta \neq \theta_0$ if H_0 accepted we use the shrinkage estimator. However; if H_0 rejected, we choose $\hat{\theta}_{i_{ub}}$, then the form of preliminary test single stage shrinkage estimator as below [8].

$$\hat{\theta}_{i_{ss}} = \begin{cases} \Psi(\hat{\theta}_i)\,\hat{\theta}_{i_{ub}} + \left(1 - \Psi(\hat{\theta}_i)\right)\theta_0 & ,if \;\; H_0 \in R \\ \hat{\theta}_{i_{ub}} & ,if \;\; H_0 \notin R \end{cases} \tag{11}$$

Assume that: $\Psi(\hat{\theta}_i) = e^{-n_i}$ and $\Psi(\hat{\theta}_{k+1}) = e^{-m}$; i=1,…k. (12)

Where, R is the preliminary test region for acceptance of size Δ for testing the hypothesis H_0: θ = θ_0 against the hypothesis H_A: θ ≠ θ_0 using the test statistic $T(\hat{\theta}/\theta) = {2n\theta_0}/{\hat{\theta}_i}$.

$$R = \left[\chi^2_{\frac{\Delta}{2},2n} \leq \frac{2n\theta_0}{\hat{\theta}_i} \leq \chi^2_{1-\frac{\Delta}{2}}\right]$$

where, $\chi^2_{\frac{\Delta}{2},2n}$ and $\chi^2_{1-\frac{\Delta}{2}}$ are respectively the lower and upper 100(Δ/2) percentile point of Chi-square distribution with (2n) degree of freedom [9].

Hence, via equation (4), the reliability estimation of k components parallel system in (S-S) models using single stage shrinkage estimator become:

$$\hat{R}_{k\,ss} = \frac{\sum_{i=1}^{k}\hat{\theta}_{i_{ss}}}{\sum_{i=1}^{k+1}\hat{\theta}_{i_{ss}}} \quad (13)$$

3. Simulation Experiments

In this section, numerical results were studied to compare the performance of the different estimators of reliability using different sample sizes (20, 60 and 100) based on 1000 replication via MSE criteria. For this purpose, Monte Carlo simulation was employed by generating the random sample from the continuous uniform distribution defined on the interval (0,1) as $u_{i1}, u_{i2}, \ldots, u_{in_i}$;i=1,2, and $v_1, v_2, \ldots, v_m$. Transform uniform random samples to follows some distributions special case of n using (c. d. f.) [10,11].

$$F(x_{i_t}) = \left(e^{-x_{i_t}{}^{-\beta}}\right)^{\theta_i}$$

$$U_{i_t} = \left(e^{-x_{i_t}{}^{-\beta}}\right)^{\theta_i}$$

$$x_{it} = -(ln(U_i)^{\frac{1}{\theta_i}})^{-\frac{1}{\beta}}, \text{ i=1,2}$$

And, by the same method, we get y_j, $y_j = -(ln(V_j)^{\frac{1}{\theta_{k+1}}})^{-\frac{1}{\beta}}$

The following steps, Compute the real value of R_k in equation (4) and the value of estimation methods of all proposal methods $\hat{R}_{k_{mle}}$, $\hat{R}_{k_{sh}}$, $\hat{R}_{kss}$ in equations (6), (10), and (13) respectively.

Based on (L=1000) replication, we calculate the MSE for all proposed estimation methods of $\hat{R}_k$ as follows:

$$MSE = \frac{1}{L}\sum_{i=1}^{L}\left(\hat{R}_{k_i} - R_k\right)^2$$

At this instant, the estimation of reliability parallel system of stress- strength model for some different assumption parameters $of\ \theta_1, \theta_2, \theta_3$and $\beta = 4$ through the following tables:

Table1.Values of the $\hat{R}_k$when $R_k = 0.700000000$, $\theta_1 = 1, \theta_2 = 2.5, \theta_3 = 1.5$ and $\beta = 4$.

(n_1, n_2, m)	$\hat{R}_{k_{mle}}$	$\hat{R}_{k_{sh}}$	$\hat{R}_{k_{SS}}$
(20,20,20)	٠,٧٠٠٣٠٩٦٥٢٦٠٤١٧٧	٠,٧٠٠٣١٦٨٤٩٨٥٦٦٥١	٠,٦٩٩٩٨٠٠١١٩٩٥٤٤٨
(20,20,60)	٠,٧٠٢٢٣٤٠١٤٢٤٧٢٤٢	٠,٦٩٥٣١٤٦٩٩٠٤٠١٠٠	٠,٦٩٩٩٨٠٠١١٩٨٨٩٥٢
(20,20,100)	٠,٧٠٣٢٩٥٢٦١٩٠٥١٨١	٠,٦٩٤٩٦٥٥٥٧٣١٠٥٠١	٠,٦٩٩٩٨٠٠١١٩٩٠٠٥٦
(20,60,20)	٠,٦٩٦١٠٠٣٨٥٢٥٦٢٥٨	٠,٧٠١٠٦٧٩٩٤٨٢١٤٩١	٠,٦٩٩٩٨٠٠١١٩٩٢٥٥٣
(20,60,60)	٠,٧٠٠٢٣٤١٠٧٤٩٤٦٧٥	٠,٦٩٨٢٢٤٥٦٥٦٨٤٨٥١	٠,٦٩٩٩٨٠٠١١٩٩١٤٩٤

(20,60,100)	٠,٧٠٣٠٦٥٣٠٦٦٧٧٠٥٧	٠,٦٩٩٦١٧٧٨٠٥١٨٧٦٠	٠,٦٩٩٩٨٠٠١١٩٩٥٥٣٠
(20,100,20)	٠,٦٩٣٨٠٧٨٦٢٥٥٧٩٢٠	٠,٦٩٩٧٩٨٣٣١٧٣٦٥٣٠	٠,٦٩٩٩٨٠٠١١٩٨٧٩٢٨
(20,100,60)	٠,٧٠٣٤٨١٨٥٧١٠٦٢١٤	٠,٧٠٢٤٥٤٣٢٢٦٨٧٣٩٥	٠,٦٩٩٩٨٠٠١١٩٩٣٢٤٦
(20,100,100)	٠,٧٠١٩٦٩٥٨٦٧٥٣٦٢٧	٠,٦٩٩٥٦٦٠٧٩٣٦٤٣٦٦	٠,٦٩٩٩٨٠٠١١٩٩٢٦٣٢
(60,20,20)	٠,٦٩٥٣٢٨٣٣٧٦٠٣١١١	٠,٦٩٧٤٠٩٦٧٩٣١٤٢١٢	٠,٦٩٩٩٨٠٠١١٩٨٩٣٤٣
(60,20,60)	٠,٧٠١١٥١٥٨١٦٨٧٤١٤	٠,٦٩٦٢٦٤١٤٢٢٤٥٠٦٧	٠,٦٩٩٩٨٠٠١١٩٩٠٨١٥
(60,20,100)	٠,٧٠٣١٣٩٩٥٣٤٩٦٠٤٤	٠,٦٩٦٧٩٩٠٧٦١٨٥٨٦٢	٠,٦٩٩٩٨٠٠١١٩٩٤٣٨٣
(60,60,20)	٠,٦٩٣٧٦٤٤٦٧٩٢٢٧٠٧	٠,٧٠٠٧٧٥٧٠٣١٣١٨٩٥	٠,٦٩٩٩٨٠٠١١٩٩١٦٣٥
(60,60,60)	٠,٦٩٩٠٢٤٤٠٥٦٦٤١٣٥	٠,٦٩٩٠٣٠٢٣٨٠٣٨٣١٢	٠,٦٩٩٩٨٠٠١١٩٩٢٨٠٧
(60,60,100)	٠,٦٩٩٤٠٨٥٥١٤٢٣٠٤٧	٠,٦٩٨٠١٥٢٢٩٣٩٨٠٦٠	٠,٦٩٩٩٨٠٠١١٩٩٢٨٠٧
(60,100,20)	٠,٦٩٤٨٤٩٤٩٥٢٥٧٥٢٢	٠,٧٠٢٧٨٧٠٢٦١١٥٣٤٤	٠,٦٩٩٩٨٠٠١١٩٩٤٤٥٨
(60,100,60)	٠,٦٩٩١٢٤٠٦٢٣٣٨٧١١	٠,٧٠٠١١٨٨٣٠٥٨٩٣٦٠	٠,٦٩٩٩٨٠٠١١٩٩٢٨٠٧
(60,100,100)	٠,٦٩٩٧٨٠١٦٩٣٩٨٨٤٤	٠,٦٩٩٣٨٢٨٨١٤١٧٨٩٢	٠,٦٩٩٩٨٠٠١١٩٩٢٨٠٧
(100,20,20)	٠,٦٩٤٩٧٥٠٩٠٤٠٥١٠٤	٠,٦٩٧٤٩١٨٢٥٩١٧١٧٣	٠,٦٩٩٩٨٠٠١١٩٩٠٢٢٦
(100,20,60)	٠,٧٠٢٢٥٤٦٠٤٩٢١٥٨٠	٠,٦٩٧٧٥٩٦٧٢٦٢٠٨٧٠	٠,٦٩٩٩٨٠٠١١٩٩٣٣٣٧
(100,20,100)	٠,٧٠٣٤٥٨١٦٢٧٨٦٨٣٠	٠,٦٩٧٥٤٨٩٠٢٦١١٩٣٣	٠,٦٩٩٩٨٠٠١١٩٩٣٧٧٥
(100,60,20)	٠,٦٩٦٠٤٢٠٩٣٩٨٣٢٢٤	٠,٧٠٣٣٨٣٠١٥٥٢٩٤٢٧	٠,٦٩٩٩٨٠٠١١٩٩٥٩٦٠
(100,60,60)	٠,٧٠٠٢٥٥٥١٧١٢٧٣٣٠	٠,٧٠٠٦٥٦٥٥٩٣٤٤٢٩٧	٠,٦٩٩٩٨٠٠١١٩٩٢٨٠٧
(100,60,100)	٠,٧٠٠٩٣٥٢٧٨٣٥٦٦٢٣	٠,٦٩٩٩٤٢٠٩٦٢٥٧٩٥٩	٠,٦٩٩٩٨٠٠١١٩٩٢٨٠٧
(100,100,20)	٠,٦٩٤٠٩٨٥٠٢٦٩٧١٥١	٠,٧٠٢٤٤٥٦٨٤٨٤٠٧٠٨	٠,٦٩٩٩٨٠٠١١٩٩٤٧٧٢
(100,100,60)	٠,٦٩٩١١١٦٤٦٦٧٤٦١٠	٠,٧٠٠٥٠٨٥٨٣٩٠٥٢٠٢	٠,٦٩٩٩٨٠٠١١٩٩٢٨٠٧
(100,100,100)	٠,٦٩٩٩٨٣٠٢٨١١٥٨٨٠	٠,٦٩٩٩٨٣٢٥٥٠٣٦٠٣٠	٠,٦٩٩٩٨٠٠١١٩٩٢٨٠٧

Table2. MSE of the $\hat{R}_{\mathrm{k}}$when $R_k = 0.7000000000$, $\theta_1 = 1, \theta_2 = 2.5, \theta_3 = 1.5$ and $\beta = 4$

(n_1, n_2, m)	$\hat{R}_{k_{mle}}$	$\hat{R}_{k_{sh}}$	$\hat{R}_{k_{SS}}$
(20,20,20)	٠,٠٠٣٢٥٩٠٦٢٣٢٧٠٠٣	٠,٠٠٣١٦٣٧١٧٨١٠٩٢٣	٠,٠٠٠٠٠٠٠٠٣٩٩٥٢٠
(20,20,60)	٠,٠٠١٩٤١٦٢٧٧٩٠٦٣٢	٠,٠٠١٩٦٤١٩٩٤٠٥٨٦٠	٠,٠٠٠٠٠٠٠٠٣٩٩٥٢١
(20,20,100)	٠,٠٠١٦٩٥٠٤٨٣٤٣٨٠٩	٠,٠٠١٧٢٣٣٧٨٧٦٨٨٩٣	٠,٠٠٠٠٠٠٠٠٣٩٩٥٢١
(20,60,20)	٠,٠٠٢٧٣٣٦١٣٣٨٠٢٧٧	٠,٠٠٢٦٠١٠٧٠٣٣٣٥٧٦	٠,٠٠٠٠٠٠٠٠٣٩٩٥٢٠
(20,60,60)	٠,٠٠١٢٤٤٢٣٧٤٥١٩٥٢	٠,٠٠١٢٣٩٠٩٦٢٢٤٧٥٥	٠,٠٠٠٠٠٠٠٠٣٩٩٥٢٠
(20,60,100)	٠,٠٠١٠٤٤٩١٠٧١٢٨٢٠	٠,٠٠١٠٣٥٥٨٩٧٥٥٩٨٦	٠,٠٠٠٠٠٠٠٠٣٩٩٥٢٠
(20,100,20)	٠,٠٠٢٦٩٧٦٢١١٦٣٤٣٠	٠,٠٠٢٥٢٧٥٥٨٥٧٣٢٠٨	٠,٠٠٠٠٠٠٠٠٣٩٩٥٢1
(20,100,60)	٠,٠٠١١٧٩٧٦٤٠٣٣٥٤٦	٠,٠٠١١٥٧٦٣٩٨٣٣٢٧٥	٠,٠٠٠٠٠٠٠٠٣٩٩٥٢٠
(20,100,100)	٠,٠٠٠٩٤٦٥٦٥٧٠٥٢٦٢	٠,٠٠٠٩٣٥٢٢١٣٢٤٤٦١	٠,٠٠٠٠٠٠٠٠٣٩٩٥٢٠
(60,20,20)	٠,٠٠٣٨٩٧٥٥١٩٢٢٤٦١	٠,٠٠٣٧٣٠٤٥٦٦٧٦٦٢٣	٠,٠٠٠٠٠٠٠٠٣٩٩٥٢١
(60,20,60)	٠,٠٠١٨٣٨٣٦٣٦٧٩٨٢١	٠,٠٠١٨٢٩٨٥٧٨١٦٥٧٦	٠,٠٠٠٠٠٠٠٠٣٩٩٥٢١
(60,20,100)	٠,٠٠١٠٥٦٤١٤١٩٩٥٨٦	٠,٠٠١٠٤٤٨٨٦٣٣٩٥٣٢	٠,٠٠٠٠٠٠٠٠٣٩٩٥٢٠
(60,60,20)	٠,٠٠٢٥١٠٩٥٥٥٧٧٦٦٦	٠,٠٠٢٣٥٤٥٧٢٨٢٨٧٩٦	٠,٠٠٠٠٠٠٠٠٣٩٩٥٢٠
(60,60,60)	٠,٠٠١٢٢٦٣٣٤٨٨٨٠٤٣	٠,٠٠١٢١٥٤٩٨٢٤٧٦٦٩	٠,٠٠٠٠٠٠٠٠٣٩٩٥٢٠
(60,60,100)	٠,٠٠٠٩٣١١٦٧٣٤٥٨٥٩	٠,٠٠٠٩٣٣٠٩٠٩٥٤٤٠٢	٠,٠٠٠٠٠٠٠٠٣٩٩٥٢٠
(60,100,20)	٠,٠٠٢٦٦٩٧٩٨٩١٠٨١٣	٠,٠٠٢٥٠٩٦٨٣١١٥١٠٩	٠,٠٠٠٠٠٠٠٠٣٩٩٥٢٠
(60,100,60)	٠,٠٠١٠٩٩٦٥١٠٨١٦٩٢	٠,٠٠١٠٨٦٣١٠٠٥٢٣٨١	٠,٠٠٠٠٠٠٠٠٣٩٩٥٢٠
(60,100,100)	٠,٠٠٠٧٤٦١٤٢٣١٠١١٠	٠,٠٠٠٧٤٣٧٤٣٠٩٢٤٦	٠,٠٠٠٠٠٠٠٠٣٩٩٥٢٠
(100,20,20)	٠,٠٠٣٤٦١٦٢٧٨٥٣٦٢٢	٠,٠٠٣٢٩١٣٣٧٦٦٥١٣١	٠,٠٠٠٠٠٠٠٠٣٩٩٥٢١
(100,20,60)	٠,٠٠١٧٩٠٩٢٦٩٣٣٥٠٤	٠,٠٠١٧٦٠٣٦٠٥٥٢٢٨٦	٠,٠٠٠٠٠٠٠٠٣٩٩٥٢٠
(100,20,100)	٠,٠٠١٥٩٦٥٤٦١٣٦٢٩٨	٠,٠٠١٥٧٠٥٧١٥٩٧٢٠٩	٠,٠٠٠٠٠٠٠٠٣٩٩٥٢٠
(100,60,20)	٠,٠٠٢٤١٥٦٣٣٤٨٨٩٨٠	٠,٠٠٢٢٨٦٧٢٠٥٨١٤٨٥	٠,٠٠٠٠٠٠٠٠٣٩٩٥٢٠
(100,60,60)	٠,٠٠١١٥٣٨٧٨١٤٨٧٠٠	٠,٠٠١١٤١٤٠٤٣٧٤٤٩٣	٠,٠٠٠٠٠٠٠٠٣٩٩٥٢٠
(100,60,100)	٠,٠٠٠٨٣٦٨٨٨٢٢٣٥٢٩	٠,٠٠٠٨٣٢٥١٤٣٩١١٣	٠,٠٠٠٠٠٠٠٠٣٩٩٥٢٠
(100,100,20)	٠,٠٠٢٥٣٠٤٣٥١٥٦٠٤٢	٠,٠٠٢٣٦٨٤٣٠٣٠١٣٥١	٠,٠٠٠٠٠٠٠٠٣٩٩٥٢٠
(100,100,60)	٠,٠٠١٠٤٤٢٠٥١٤٥٥٩٣	٠,٠٠١٠٣٠٢٩٥٨٥٦٥٩٨	٠,٠٠٠٠٠٠٠٠٣٩٩٥٢٠
(100,100,100)	٠,٠٠٠٧١٢٩٨٣٠٨٧٤٦٩	٠,٠٠٠٧٠٩٣٣٥٧٨٤٤٦٠	٠,٠٠٠٠٠٠٠٠٣٩٩٥٢٠

Table3.Values of the $\hat{R}_{\mathrm{k}}$when $R_k = 0.80000000$, $\theta_1 = 2.5, \theta_2 = 1.5, \theta_3 = 1$and $\beta = 4$.

(n_1, n_2, m)	$\hat{R}_{k_{mle}}$	$\hat{R}_{k_{sh}}$	$\hat{R}_{k_{SS}}$
(20,20,20)	٠,٧٩٧٠٤٣٧٧٠٩٨٩٩٤٥	٠,٧٩٧١١٤٩١٢٤٠١٤٧٢	٠,٧٩٩٩٢٠٠٤٧٩٦٩١٦٣
(20,20,60)	٠,٨٠٢١٩٤٩٢٦٦٠٥٧٩٥	٠,٧٩٦٩١٤٧٩٧٧٥٩٥٣٢	٠,٧٩٩٩٢٠٠٤٧٩٦٨٩٠٩
(20,20,100)	٠,٨٠٢٥٤٠٨٦٤١٥٠٥١٢	٠,٧٩٦١٨٨٧٣٩١٤٣٥٩٩	٠,٧٩٩٩٢٠٠٤٧٩٦٩٢٧٢
(20,60,20)	٠,٧٩٧٠٣٥٨٦٧٢٩٣٥٧٠	٠,٧٩٩٠٩٨٢٩٤٠٦٣٤٩٣	٠,٧٩٩٩٢٠٠٤٧٩٧٢٧٢٠
(20,60,60)	٠,٨٠٠٨٩٥٨٧٠٢٥٣٣٣٨	٠,٧٩٧٦١٩٧٣١٩٠٨٢٣٧	٠,٧٩٩٩٢٠٠٤٧٩٧١٨٧٦
(20,60,100)	٠,٨٠٢٥٧٧٤٢٤٦٤٨٢٧٤	٠,٧٩٨٢٣٣١٢٢٤٧٦٧٩٩	٠,٧٩٩٩٢٠٠٤٧٩٧٣١٤٥
(20,100,20)	٠,٧٩٥٨٠٨٦٣٧٤١٥٨٩٠	٠,٧٩٨٣٠٣٧٦٥٧١٠٧١٧	٠,٧٩٩٩٢٠٠٤٧٩٧٠٢٥٤
(20,100,60)	٠,٨٠٢٥٦٣٩٩٩١١٨٣٥٧	٠,٧٩٩٧٠٢١١٠٦٠٣٥٨٣	٠,٧٩٩٩٢٠٠٤٧٩٧٢٥٥٣

(20,100,100)	٠,٨٠١٨٣٧٤٥٤٠١٥٩٣٢	٠,٧٩٧٩٠٠٧٥٥٣٥٣٦٦٨	٠,٧٩٩٩٢٠٠٤٧٩٧٠١٣٩
(60,20,20)	٠,٧٩٦١٣٢٣٤٢٦٠٢١٥٢	٠,٧٩٩٥٠٥٤١٨٧١٢٢٢٣	٠,٧٩٩٩٢٠٠٤٧٩٧١٢٩٧
(60,20,60)	٠,٧٩٩٤٦٦٤٠٦٨١٦١٧٩	٠,٧٩٧٤٧٨٠١٦٤٩٨٨٠٧	٠,٧٩٩٩٢٠٠٤٧٩٦٩٥٥٨
(60,20,100)	0.801179751899114	0.798038813579648	0.799920047972490
(60,60,20)	٠,٧٩٣٦٣٥٦٨٤٣٣٤٣٥٣	٠,٧٩٩٠٤٣٤٩٨٥٣٥٧٨٠	٠,٧٩٩٩٢٠٠٤٧٩٦٨٦٩١
(60,60,60)	٠,٧٩٨٦٧٦٣٩٥٦٦٢٠٥٤	٠,٧٩٨٦٨٣١٩٤٩٦٧١٤٦	٠,٧٩٩٩٢٠٠٤٧٩٧١٢٢٥
(60,60,100)	٠,٨٠٠١٠٦٨٨٦٩٦٢٦٢٣	٠,٧٩٩٠٤٤٦٨٥٩٤٣٩٣٥	٠,٧٩٩٩٢٠٠٤٧٩٧١٢٢٥
(60,100,20)	٠,٧٩٥٨٥٣٦٣٩٣٢٦٨٦٠	٠,٨٠١٦٠٣٠٧٣٩٩١١٤١	٠,٧٩٩٩٢٠٠٤٧٩٧٢٩٢٣
(60,100,60)	٠,٧٩٩٧٦٤٥٨٠٩٧٦٨٣٢	٠,٨٠٠١٦٧٥٧٢٦٠٣٦٣٣	٠,٧٩٩٩٢٠٠٤٧٩٧١٢٢٥
(60,100,100)	٠,٧٩٩٨٤٣٦٦٧٤١٣٣٥٥	٠,٧٩٩١٨٢٠٤٥٤٥٣٨٣٣	٠,٧٩٩٩٢٠٠٤٧٩٧١٢٢٥
(100,20,20)	٠,٧٩٧٢٥٧٧٦٧٦٥٠١٩٩	٠,٨٠١٢٤٢٨٩١٣٥٣٠٣٧	٠,٧٩٩٩٢٠٠٤٧٩٧٣٩٦٣
(100,20,60)	٠,٨٠١١٨٣٧١٨٧٣٧٦١٧	٠,٧٩٩٨٣٨٠٩٠٢٦٣٠٢٦	٠,٧٩٩٩٢٠٠٤٧٩٧١٨٧٧
(100,20,100)	٠,٨٠٠٧٣٩٣٨١٥٢٣٩٥٢	٠,٧٩٨٣٢٧٣٨٨٨٦٨٨٠٣	٠,٧٩٩٩٢٠٠٤٧٩٧١٣٧٤
(100,60,20)	٠,٧٩٥٣٧١٠٧٧٠٨٥٨٥٧	٠,٨٠١٣٨٢٥٠٥٢٦٢٠٠٣	٠,٧٩٩٩٢٠٠٤٧٩٧٢١٤٦
(100,60,60)	٠,٧٩٩٩٧٦٦٣٢٢٢٤٧٣٣	٠,٨٠٠٦٣٨٧٣٢٣٨٦٨٣٢	٠,٧٩٩٩٢٠٠٤٧٩٧١٢٢٥
(100,60,100)	٠,٧٩٩٨٦٢٤٦٩٥٧٢٩٤٨	٠,٧٩٩٤٦٢٥١٢٨٩٧٢٨٠	٠,٧٩٩٩٢٠٠٤٧٩٧١٢٢٥
(100,100,20)	٠,٧٩٦٤٥٦١٩٢٢١٣٧٥٨	٠,٨٠٢٨٣١٨٩٤٦٩٩٤٧٥	٠,٧٩٩٩٢٠٠٤٧٩٧٥٠١٠
(100,100,60)	٠,٧٩٨٦١٠٤٥٥٨١٨٩٢٥	٠,٧٩٩٦٨٢٦٤٣٦٢١٢٤٩	٠,٧٩٩٩٢٠٠٤٧٩٧١٢٢٥
(100,100,100)	٠,٧٩٩٧٩٩٢٦١٠٣٢٦٠١	٠,٧٩٩٨٠٠١٦٦٤٧٠٥٥٠	٠,٧٩٩٩٢٠٠٤٧٩٧١٢٢٥

Table4. MSE of the $\hat{R}_{\mathrm{k}}$when $R_k = 0.80000000$, $\theta_1 = 2.5, \theta_2 = 1.5, \theta_3 = 1$and $\beta = 4$.

(n_1, n_2, m)	$\hat{R}_{k_{mle}}$	$\hat{R}_{k_{sh}}$	$\hat{R}_{k_{SS}}$
(20,20,20)	٠,٠٠٢١٧١٤٩١٢٠٥٦٢٣	٠,٠٠٢١٠٩٩٩١٥٣٨٨٦٤	٠,٠٠٠٠٠٠٠٦٣٩٢٣٢٧
(20,20,60)	٠,٠٠١١١٢٨٩٥٣١٥٧٨٨	٠,٠٠١١٣٤٨٥٨٩٠٦٢٣٣	٠,٠٠٠٠٠٠٠٦٣٩٢٣٢٧
(20,20,100)	٠,٠٠٠٩٨٣٨٩٠٧٨٧٠٥٥	٠,٠٠١٠١٤٩٦٧٦٤٢٨٣٠	٠,٠٠٠٠٠٠٠٦٣٩٢٣٢٧
(20,60,20)	٠,٠٠١٩٤١٣٠٥١٨٩٦١٧	٠,٠٠١٨٤١٦٥٤٠٥٦٢١٨	٠,٠٠٠٠٠٠٠٦٣٩٢٣٢٧
(20,60,60)	٠,٠٠١٠٠٠٨٧٦٢٣٢٨١٥	٠,٠٠١٠٠٠٧٩٤٥٧٠٨٠٤	٠,٠٠٠٠٠٠٠٦٣٩٢٣٢٧
(20,60,100)	٠,٠٠٠٨٢١٤٤٧٦٠٥٢٧٨	٠,٠٠٠٨١٧٧٩٨٩٧٣٤٣٧	٠,٠٠٠٠٠٠٠٦٣٩٢٣٢٦
(20,100,20)	٠,٠٠٢٠٣٦٥٩٨٦٥٦٦٠٦	٠,٠٠١٩١٩٣٦٨٥٧٢٢٠٤	٠,٠٠٠٠٠٠٠٦٣٩٢٣٢٧
(20,100,60)	٠,٠٠١٠١٠٥٨٩٦١٣١٩٦	٠,٠٠٠٩٩٣١٨٨٤٣٣٤١٧	٠,٠٠٠٠٠٠٠٦٣٩٢٣٢٧
(20,100,100)	٠,٠٠٠٧٥١٧٣٥٧٩٢٧٦٩	0.000٧٤٧٢٧٥٦٧٣٨٩٧	٠,٠٠٠٠٠٠٠٦٣٩٢٣٢٧
(60,20,20)	٠,٠٠١٦٢٦٤٨٧٤٥٥٠٢٩	٠,٠٠١٥٢٨٦٣٧٢٧٨٠١٣	٠,٠٠٠٠٠٠٠٦٣٩٢٣٢٧
(60,20,60)	٠,٠٠٠٧٥٧٨٥٨٨٠١٨٥٧	0.000761049088573	٠,٠٠٠٠٠٠٠٠٦٣٩٢٣٢٧
(60,20,100)	٠,٠٠٠٦١٦٢٩١١٧٦١٦٧	٠,٠٠٠٦٢١٩٤٤٦٥٨٦٣٦	٠,٠٠٠٠٠٠٠٠٦٣٩٢٣٢٦
(60,60,20)	٠,٠٠١٧٧٥٤٠٦٥٤٧٣٦٧	٠,٠٠١٦٢٩٢١٨٣٦٢٥٨٠	٠,٠٠٠٠٠٠٠٠٦٣٩٢٣٢٧
(60,60,60)	٠,٠٠٠٦٤٣٩٦١٣٧٧٥٤٣	٠,٠٠٠٦٣٨٤٣٣٨٢٢٥١٥	٠,٠٠٠٠٠٠٠٠٦٣٩٢٣٢٦
(60,60,100)	٠,٠٠٠٥٠٦٨٩٢٩٨٨٢١٩	٠,٠٠٠٥٠٨٢٨٧٧٧٨٦١٩	٠,٠٠٠٠٠٠٠٠٦٣٩٢٣٢٦
(60,100,20)	٠,٠٠١٥٩١٦٨٦٥٧٢٦٠٣	٠,٠٠١٤٧٤٥٧٦٨٦١٨٩٠	٠,٠٠٠٠٠٠٠٠٦٣٩٢٣٢٧
(60,100,60)	٠,٠٠٠٦٢٤٥٠٥٠٩٢٦٩٢	٠,٠٠٠٦١٦٨٣٢٨٦٦٨٥٤	٠,٠٠٠٠٠٠٠٠٦٣٩٢٣٢٦
(60,100,100)	٠,٠٠٠٥٠٦٥٥٩٨١٨٥٤٢	٠,٠٠٠٥٠٥٩٤٩٧٦١١٢٧	٠,٠٠٠٠٠٠٠٠٦٣٩٢٣٢٦
(100,20,20)	٠,٠٠١٦٣٦١٧٧٨٠٠٢١٦	٠,٠٠١٥٣٣٣٥١٤١٤٦٢٤	٠,٠٠٠٠٠٠٠٠٦٣٩٢٣٢٦
(100,20,60)	٠,٠٠٠٧٠١٤٩٣٥٠٦٦٦٧	٠,٠٠٠٦٩٢٦٧٣٩٧٣٨٣٤	٠,٠٠٠٠٠٠٠٠٦٣٩٢٣٢٦
(100,20,100)	٠,٠٠٠٥٦٣٠٨٥٦٤٥٨١٨	٠,٠٠٠٥٦٢٨٢٨٠٩٩٢٨١	٠,٠٠٠٠٠٠٠٠٦٣٩٢٣٢٦

(100,60,20)	٠,٠٠١٦١٨٦٥٢٣٢٥٨٦٨	٠,٠٠١٤٩٤٩٦٤٩٩٠٧٤٦	٠,٠٠٠٠٠٠٠٦٣٩٢٣٢٧
(100,60,60)	٠,٠٠٠٦٢٠٤١٤٢٠٦٩٢٨	٠,٠٠٠٦١٢٩٠٤٠٨٥٣٤٠	٠,٠٠٠٠٠٠٠٦٣٩٢٣٢٦
(100,60,100)	٠,٠٠٠٤٤٢٣١١٣٧٥٨٠٣	٠,٠٠٠٤٤١٣٠٨٩٨٣٥٩٩	٠,٠٠٠٠٠٠٠٠٦٣٩٢٣٢٦
(100,100,20)	٠,٠٠١٤٧٥٠٦٥٨٦٠٨١١	٠,٠٠١٣٦٦٠٥٥٦٩٨٧٢٤	٠,٠٠٠٠٠٠٠٠٦٣٩٢٣٢٦
(100,100,60)	٠,٠٠٠٥٧١٤٥٣١٤٩٩١٤	٠,٠٠٠٥٦٠٦٦٦٨٠٧٩٠٨	٠,٠٠٠٠٠٠٠٠٦٣٩٢٣٢٦
(100,100,100)	٠,٠٠٠٣٧٦٠٨٦٤٩١٧٩٢	٠,٠٠٠٣٧٤١٠٨٠٢٥٠٣٩	٠,٠٠٠٠٠٠٠٠٦٣٩٢٣٢٦

Table5.Values of the $\hat{R}_{\mathrm{k}}$when $R_k = 0.50000000$, $\theta_1 = 1.5, \theta_2 = 1, \theta_3 = 2.5$ and $\beta = 4$.

(n_1, n_2, m)	$\hat{R}_{k_{mle}}$	$\hat{R}_{k_{sh}}$	$\hat{R}_{k_{SS}}$
(20,20,20)	٠,٥٠١٤١١٢٤٧٦٤١٦٧٢	٠,٥٠١٣٦٤٩٤٩٨٨٩٨٨٢	٠,٥٠٠٠٩٩٩٤٠٠٣٣٣٦١
(20,20,60)	٠,٥٠٨٣٣٨١٨٦٥٣١٦٠٣	٠,٥٠٠٠٢٦١٩٢٧٧٥٩٢٥	٠,٥٠٠٠٩٩٩٤٠٠٣٧٣٩٦
(20,20,100)	٠,٥٠٦٦١٥٦٢٨٤٢٦٤٠٢	٠,٤٩٦٦٦٤٤٢٨٨٨٣٨٨٢	٠,٥٠٠٠٩٩٩٤٠٠٣٣١٢٥
(20,60,20)	٠,٥٠٠٤٥٤٢٥١٦١٤٧٢٣	٠,٥٠٣٦٩٠٢٩٦٥١١٢٥٢	٠,٥٠٠٠٩٩٩٤٠٠٣٥٦٦٦
(20,60,60)	٠,٥٠٤٦٤١٨٧٦٩٨٢٥٤٠	٠,٤٩٩٦٦٦٦٣٥٢٧٣٣٠٠	٠,٥٠٠٠٩٩٩٤٠٠٣٧٧٢٥
(20,60,100)	٠,٥٠٣٧٠٩٩٢٩٣٠٤٥٤٧	٠,٤٩٧١٣٨٤١٩٢٣٦١٣٦	٠,٥٠٠٠٩٩٩٤٠٠٣١٣٩٣
(20,100,20)	٠,٥٠٢٥٦٢٧٤٨١٨٢٤٧٤	٠,٥٠٦٣٧٥٠٧٤٨٥٩١٢٦	٠,٥٠٠٠٩٩٩٤٠٠٤١٢٣١
(20,100,60)	٠,٥٠٢٤٢٨٣٦٩٥٦٨٣٢٦	٠,٤٩٨١٢٤٨٠٠١٣٠٩٨٣	٠,٥٠٠٠٩٩٩٤٠٠٣٥٧٤٢
(20,100,100)	٠,٥٠٦٣٥٨١٣٥٧١٧٦٠٧	٠,٥٠٠٣٤٦٧٥٠٣٥٨٩٣٤	٠,٥٠٠٠٩٩٩٤٠٠٣٨٦٢٥
(60,20,20)	٠,٤٩٨٩٧٤٣٩١٤١٣٢٥٩	٠,٥٠٣٨٢٩٣٧٠٨٥٣٣٦٩	٠,٥٠٠٠٩٩٩٤٠٠٣٣٨٤٣
(60,20,60)	٠,٥٠٣٩٧٦٩٤٤٨٢٢٢٢٣	٠,٥٠٠٦٣٧٩٥٤١٧١٧٠٨	٠,٥٠٠٠٩٩٩٤٠٠٣٥٢٦١
(60,20,100)	٠,٥٠٦١٥٨٦٧٩٨٦١٩٤٤	٠,٥٠١١٦٠٩٧٣٥٤٩٧٢٦	٠,٥٠٠٠٩٩٩٤٠٠٣٥٢٥٩
(60,60,20)	٠,٤٩٥٩٣٠٨٤٠٢١٢٨٢٨	٠,٥٠٤١٢٠٠٥٧٥٩٥٢٦٣	٠,٥٠٠٠٩٩٩٤٠٠٣٣١١٧
(60,60,60)	٠,٤٩٨٧٠١١٣٥١٤٥٤٩٤	٠,٤٩٨٧٠١٩٩٦٤٠٩٨١٠	٠,٥٠٠٠٩٩٩٤٠٠٣٥٩٦٩
(60,60,100)	٠,٥٠١٥٣٥٠٠٢٧٣٨١٨٢	٠,٤٩٩٨٧٠٠٦٨٧٤٦٥٩٥	٠,٥٠٠٠٩٩٩٤٠٠٣٥٩٦٩
(60,100,20)	٠,٤٩٦٤٠٢١٠٩٣٩٠٠٤١	٠,٥٠٥٢١٣٠٢٤٦٦٢٦٠٠	٠,٥٠٠٠٩٩٩٤٠٠٣٧٥٩٦
(60,100,60)	٠,٤٩٨٥٦٢٩٣٨٤٣٢١٠٠	٠,٤٩٩٢٢٧١٣٦٨٧٧٦٧٩	٠,٥٠٠٠٩٩٩٤٠٠٣٥٩٦٩
(60,100,100)	٠,٥٠١٩٩٦٧٧٥٠٩٨٩٧٨	٠,٥٠٠٩٩٢٨١٦٢١٩٨٩٧	٠,٥٠٠٠٩٩٩٤٠٠٣٥٩٦٩
(100,20,20)	٠,٥٠١١٤٥١١٩٠٦٦٦٧٣	٠,٥٠٦٩٨٣٣٤١٦٦٥٠٣٤	٠,٥٠٠٠٩٩٩٤٠٠٣٦٦١٠
(100,20,60)	٠,٥٠٢٧٦٧٩٩٤٦٥٩٣٩٧	٠,٥٠٠٤٣٥١٣٢٢٩٩٤٨٩	٠,٥٠٠٠٩٩٩٤٠٠٣٣٣٨٦
(100,20,100)	٠,٥٠٣١٧٠٧١٧٨٠٦٨٤٦	٠,٤٩٩١٣٧١٧٩٤٢٩٧٤٧	٠,٥٠٠٠٩٩٩٤٠٠٣٦٧٣١
(100,60,20)	٠,٤٩٨٦٠١٩٧٦٦٥٢٩٣١	٠,٥٠٧٧٥٠٨٦٥١٨١٧٣٧	٠,٥٠٠٠٩٩٩٤٠٠٤٠٥٢٢
(100,60,60)	٠,٤٩٩٦٤١٤٢٣٨٥٤٨٦٠	٠,٥٠٠٦٢٣٢٦١٥٩٩٦٩٠	٠,٥٠٠٠٩٩٩٤٠٠٣٥٩٦٩
(100,60,100)	٠,٥٠٠٢٦٩٥٣٢٩٠٩٣٤٥	٠,٤٩٩٦٠٦٣٣٨١٠٩٨٩٩	٠,٥٠٠٠٩٩٩٤٠٠٣٥٩٦٩
(100,100,20)	٠,٤٩٩٥٧٥٩٢١٢٨٥٦٨٨	٠,٥٠٩٣٩٤٦٥٠٦٧٥٧٥٤	٠,٥٠٠٠٩٩٩٤٠٠٤٣٩٥٧
(100,100,60)	٠,٤٩٩٠٧٠٤٧٧٢٢٠٢٥٢	٠,٥٠٠٧٢٥٥٥٩٠٥٨٨٧٦	٠,٥٠٠٠٩٩٩٤٠٠٣٥٩٦٩
(100,100,100)	٠,٤٩٩٢١١٧٠٠٥١٥٥٦٧	٠,٤٩٩٢١٢٣٠٤٩٢٤٠٦٨	٠,٥٠٠٠٩٩٩٤٠٠٣٥٩٦٩

Table6. MSE of the $\hat{R}_{\mathrm{k}}$when $R_k = 0.50000000$, $\theta_1 = 1.5, \theta_2 = 1, \theta_3 = 2.5$ and $\beta = 4$.

(n_1, n_2, m)	$\hat{R}_{k_{mle}}$	$\hat{R}_{k_{sh}}$	$\hat{R}_{k_{SS}}$
(20,20,20)	٠,٠٠٤٦١١١٦٤١٢٨١٨٤	٠,٠٠٤٤٧٨٥٨١٨٨٢٨٢٨	٠,٠٠٠٠٠٠٠٠٩٩٨٨٠١٠
(20,20,60)	٠,٠٠٢٨١٤٨٧٣٢٣٢٤٥٦	٠,٠٠٢٦٨٩٧٥٤٨٣٩٤٦٥	٠,٠٠٠٠٠٠٠٠٩٩٨٨٠١١

(20,20,100)	٠,٠٠٢٣٣١٧٢٧٢٠٠٢٦٠	٠,٠٠٢٢٤٨٠٦٩٠٧٠٠٧٣	٠,٠٠٠٠٠٠٠٩٩٨٨٠١٠
(20,60,20)	٠,٠٠٤٦١٩٥٨٥٨٥٣٨٤٦	٠,٠٠٤٤٨٢١٥٠٢٩٥٦٣٢	٠,٠٠٠٠٠٠٠٩٩٨٨٠١١
(20,60,60)	٠,٠٠٢٤٩٢٣٣٧١٩٦٧٧٩	٠,٠٠٢٤٠٤٠٧٤١٨٢٠٢٠	٠,٠٠٠٠٠٠٠٩٩٨٨٠١١
(20,60,100)	٠,٠٠١٩٤٨٩٤١٧٢٠٥٦٩	٠,٠٠١٨٨٥٧٨٥٣٨١٦٢٣	٠,٠٠٠٠٠٠٠٩٩٨٨٠١٠
(20,100,20)	٠,٠٠٤٤٩٨١٧٣٥٣٢٠٨٨	٠,٠٠٤٣٧١٩٥٠١٠٨١٩١	٠,٠٠٠٠٠٠٠٩٩٨٨٠١٢
(20,100,60)	٠,٠٠٢٢٧٢٥٦٣٤٦٠٢١١	٠,٠٠٢٢٠٢٧٠٣٧٢٣٥٧٣	٠,٠٠٠٠٠٠٠٩٩٨٨٠١١
(20,100,100)	٠,٠٠١٨٥٣٢١٠٣١٧١٢٢	٠,٠٠١٧٤٨٤٧٤٧٣٤٥٤٣	٠,٠٠٠٠٠٠٠٩٩٨٨٠١١
(60,20,20)	٠,٠٠٤٠١٢٣٧٢٢٠٣٨٠٩	٠,٠٠٣٩١١٣٨٨٤١٥٩٢٣	٠,٠٠٠٠٠٠٠٩٩٨٨٠١٠
(60,20,60)	٠,٠٠٢٠٠٩٣١٧٤٢٩١٦١	٠,٠٠١٩٥٤٦١١٥٧٠٠٤٢	٠,٠٠٠٠٠٠٠٩٩٨٨٠١١
(60,20,100)	٠,٠٠١٦٠٤٣٥٧٣٣٠٣٨٣	٠,٠٠١٥٣٥٢٧٥٣١٥١٨٩	٠,٠٠٠٠٠٠٠٩٩٨٨٠١١
(60,60,20)	٠,٠٠٣٦٩٨٤٠١٧٢٨٢٢٠	٠,٠٠٣٦٠٤٩٣٠٧٧٥٢٣٢	٠,٠٠٠٠٠٠٠٩٩٨٨٠١٠
(60,60,60)	٠,٠٠١٧٨٩٦٦٧٧٨٧١٦٧	٠,٠٠١٧٧٤٣٨٨٥٨٣٥٥٠	٠,٠٠٠٠٠٠٠٩٩٨٨٠١١
(60,60,100)	٠,٠٠١٠٨٣٨٠٥٨٨٠٣٣٨	٠,٠٠١٠٧٣٩٦٧٦٧٨٢٦٤	٠,٠٠٠٠٠٠٠٩٩٨٨٠١١
(60,100,20)	٠,٠٠٣٦٥٨٠٣٥٨٠٣٩٤٠	٠,٠٠٣٥٧١٤٠٢٩٣٦٩٦٣	٠,٠٠٠٠٠٠٠٩٩٨٨٠١١
(60,100,60)	٠,٠٠١٤٩٠٧٢٢٧٤٤٨١٠	٠,٠٠١٤٧٥٦٠٩٢٣٣٨٠٨	٠,٠٠٠٠٠٠٠٩٩٨٨٠١١
(60,100,100)	٠,٠٠١٠٨٠٨١٣٣٤٢٧٥٢	٠,٠٠١٠٧٠٠٥٦١٩٧٥٨٩	٠,٠٠٠٠٠٠٠٩٩٨٨٠١١
(100,20,20)	٠,٠٠٤٠٤٠١٤١٣٥٢٧٦٦	٠,٠٠٣٩٥٢٩٧٨٠٠١٥١٤	٠,٠٠٠٠٠٠٠٩٩٨٨٠١١
(100,20,60)	٠,٠٠١٨١٠٠٧٥١٥٤٤٢٤	٠,٠٠١٧٦١٤٢٥٢٢٨٩٥٢	٠,٠٠٠٠٠٠٠٩٩٨٨٠١٠
(100,20,100)	٠,٠٠١٤٥٢٨٣٤٠٢٣٣٥١	٠,٠٠١٤٠٥٨٣٣٢٤٠٧٧٨	٠,٠٠٠٠٠٠٠٩٩٨٨٠١١
(100,60,20)	٠,٠٠٣٣٣٣٠٦٨٦٤٢٦٨٣	٠,٠٠٣٢٩٥٩٢١٠٢١٤٠٤	٠,٠٠٠٠٠٠٠٩٩٨٨٠١٢
(100,60,60)	٠,٠٠١٤٣١١٠٨٣٠٥١٨٠	٠,٠٠١٤١٩١٣٠٩٩٦٣٠٣	٠,٠٠٠٠٠٠٠٩٩٨٨٠١١
(100,60,100)	٠,٠٠٠٩٨٤٤٩٣٣٠١٩٤١	٠,٠٠٠٩٧٨٧٥١٤٦٤٣٢٢	٠,٠٠٠٠٠٠٠٠٩٩٨٨٠١٠
(100,100,20)	٠,٠٠٣٠٦٨٨٤٥٨٤٣٢٥٢	٠,٠٠٣٠٧٢٨٦٨٨٦١٤١٩	٠,٠٠٠٠٠٠٠٩٩٨٨٠١٢
(100,100,60)	٠,٠٠١٤٣٢٧٦٨٨٤٣٩٤٧	٠,٠٠١٤٢١٠٥٧٥٢٣٦٠٩	٠,٠٠٠٠٠٠٠٩٩٨٨٠١١
(100,100,100)	٠,٠٠٠٩٥٣٧٩٦١٠٥٠٧٣	٠,٠٠٠٩٤٨٨٧٨٠٩٥٨٧٠	٠,٠٠٠٠٠٠٠٠٩٩٨٨٠١٠

Table7.Values of the $\hat{R}_{\mathrm{k}}$when $R_k = 0.538461538461538$, $\theta_1 = 2, \theta_2 = 1.5, \theta_3 = 3$and $\beta = 4$.

(n_1, n_2, m)	$\hat{R}_{k_{mle}}$	$\hat{R}_{k_{sh}}$	$\hat{R}_{k_{SS}}$
(20,20,20)	٠,٥٣٩٢٤١٠٢٥٩١٣٨١٨	٠,٥٣٩٢١٢٨٣٦٤٣٨١١١	٠,٥٣٨٥٢٠٦٨٢٧٥٩٣٥٣
(20,20,60)	٠,٥٤٣٩٧٠٠٠٥٣٢٢٩٨٠	٠,٥٣٥٧٥٢٤٦٧٦٨٥٧٠١	٠,٥٣٨٥٢٠٦٨٢٧٥٩١٨٢
(20,20,100)	٠,٥٤٦٨٨٦٤٩٢٥٨٤٨٩٣	٠,٥٣٦٩٦٠٣٧٥٦٢٦٢٨٧	٠,٥٣٨٥٢٠٦٨٢٧٦٢٦١٩
(20,60,20)	٠,٥٣٦١٥٧٩٦٠٨٤٢٨٧١	٠,٥٣٩٦٦٦٩٦٥٤٢٨١٢٨	٠,٥٣٨٥٢٠٦٨٢٧٥٧٣٦٠
(20,60,60)	٠,٥٤٣٨٣٩٤٧٣٦٢٧٤٢٨	٠,٥٣٩١١٥٦٤٣١٤٣٣٢٧	٠,٥٣٨٥٢٠٦٨٢٧٦٣٧٠٨
(20,60,100)	٠,٥٤٢٥٠٠٨٠١١٠١٣٣٤	٠,٥٣٦١٤٦٥٦٠١٦١٤٠٦	٠,٥٣٨٥٢٠٦٨٢٧٥٩٦٦٥
(20,100,20)	٠,٥٣٦٥٧٩٢٩٢٤٧٧٤٥١	٠,٥٤٠٧٩٥٤٦٩٣٤٢٩٦٠	٠,٥٣٨٥٢٠٦٨٢٧٥٩٤٨٥
(20,100,60)	٠,٥٤١٨٧٨٦٧٢٢٢٧٤١٤	٠,٥٣٧٨٦٩٨٥٣٧٢٧٩١٦	٠,٥٣٨٥٢٠٦٨٢٧٦٣٦٩٧
(20,100,100)	٠,٥٤١٨٠٨٥٩٦٢٦٩٣٠٢	٠,٥٣٦١٦٣٦٤٢٧٨٤٥٧٨	٠,٥٣٨٥٢٠٦٨٢٧٦٢٨١٠
(60,20,20)	٠,٥٣٣١٠٧٩٧٥٩٨٠٩٤٦	٠,٥٣٧٧٦٦٩٩٠٢٠٣٣٦١	٠,٥٣٨٥٢٠٦٨٢٧٥٦٠١٧
(60,20,60)	٠,٥٤٠٦٢٥٧٦١٨٧٨١٣٧	٠,٥٣٧٠٤٤٢٤٩١١٢٥٥٧	٠,٥٣٨٥٢٠٦٨٢٧٦٢٨٤٠
(60,20,100)	٠,٥٤٢١٥٣٨٨٦١٢٩١٠٥	٠,٥٣٦٩٥٢٣٢١٤٠١٨٩٩	٠,٥٣٨٥٢٠٦٨٢٧٦٢٠٧٨
(60,60,20)	٠,٥٣٣٧٠٧٢٣١١١٨٨٠٧	٠,٥٤١٨٤٢٣٤٥٠٣٧٥٣٧	٠,٥٣٨٥٢٠٦٨٢٧٦٠٩٧٩

(60,60,60)	٠,٠٥٣٧٦٣٥٦٢٢١٦٣٦٤٦	٠,٠٥٣٧٦٣٧٨٣٠٢٩٩٠١٥	٠,٠٥٣٨٥٢٠٦٨٢٧٦١٨١٤
(60,60,100)	٠,٠٥٣٩٨٢٢٥٨٣٢١٢٧٣١	٠,٠٥٣٨١٦٥٥٩٣٣٢٥٦٦٩	٠,٠٥٣٨٥٢٠٦٨٢٧٦١٨١٤
(60,100,20)	٠,٠٥٣٥٨٦٣٣٤٨٤٥٨١٨٩	٠,٠٥٤٤٦٩٩٨٠٣٥٦٩٩٤٦	٠,٠٥٣٨٥٢٠٦٨٢٧٦٦٧٦٧
(60,100,60)	٠,٠٥٣٦١٥٦٨٤٣٢٠٦٩٣١	٠,٠٥٣٦٨٧٧٥٤٦١٦٢٠١٧	٠,٠٥٣٨٥٢٠٦٨٢٧٦١٨١٤
(60,100,100)	٠,٠٥٣٩٨٧٦٧١٩٨٤٠٢٤٤	٠,٠٥٣٨٩٣٠٥٠٩٢١٥٥٠٢	٠,٠٥٣٨٥٢٠٦٨٢٧٦١٨١٤
(100,20,20)	٠,٠٥٣٥٥٢١١٤٧٢٣١٦٨٥	٠,٠٥٤١٠٩٠٨٠٥٥٧٣٧٦٤	٠,٠٥٣٨٥٢٠٦٨٢٧٦٠٩١٤
(100,20,60)	٠,٠٥٣٩١٢٩٥١١٩٤٨٨٢١	٠,٠٥٣٦٥٢٩٠٦٦٩٦١٦٧٥	٠,٠٥٣٨٥٢٠٦٨٢٧٦٠٤٢٨
(100,20,100)	٠,٠٥٤٣١٥٠٧٤١١٤٧٠٨٤	٠,٠٥٣٨٨٤٤٠٥٢٣٥٨٣٨٤	٠,٠٥٣٨٥٢٠٦٨٢٧٦٣٦٩٣
(100,60,20)	٠,٠٥٣٨١٨٠١٩٣٧٢٥٢٦٤	٠,٠٥٤٧١٨١٤٨٦٩٥١٩١٣	٠,٠٥٣٨٥٢٠٦٨٢٧٧٠١٩١
(100,60,60)	٠,٠٥٣٨٨٤٤٥٩٥٦٨٠٢٢٥	٠,٠٥٣٩٧٨٣٠٩٣٢٩٨٨٧٦	٠,٠٥٣٨٥٢٠٦٨٢٧٦١٨١٤
(100,60,100)	٠,٠٥٣٨٩٥٣٨٥٤٥٥٠٦٦٣	٠,٠٥٣٨٢٤٤٧٤٢٢٢٤٥٦١	٠,٠٥٣٨٥٢٠٦٨٢٧٦١٨١٤
(100,100,20)	٠,٠٥٣٣١٩٥٠٠٨٠٦٨٤٩٦	٠,٠٥٤٢٩٥٦٤٢٢٤١٤١١٢	٠,٠٥٣٨٥٢٠٦٨٢٧٦٣٦٠٨
(100,100,60)	٠,٠٥٣٨٩٨١٨٠٩٧٥٤٣٠٢	٠,٠٥٤٠٦٢١٣٦٣٨٦١٠٤٥	٠,٠٥٣٨٥٢٠٦٨٢٧٦١٨١٤
(100,100,100)	٠,٠٥٣٧٧١٧٧٦٦٨٠٨٤٧٥	٠,٠٥٣٧٧١٨٢٩٨٠٣٥٨٩٤	٠,٠٥٣٨٥٢٠٦٨٢٧٦١٨١٤

Table8. MSE of the $\hat{R}_{\mathrm{k}}$when $R_k = 0.538461538461538$, $\theta_1 = 2, \theta_2 = 1.5, \theta_3 = 3$and $\beta = 4$.

(n_1, n_2, m)	$\hat{R}_{k_{mle}}$	$\hat{R}_{k_{sh}}$	$\hat{R}_{k_{SS}}$
(20,20,20)	٠,٠٠٤٥٥٤٦٩٩٥٥٨٧٢٤	٠,٠٠٤٤٢٤٤٦٤٣١٢٩٢٣	٠,٠٠٠٠٠٠٠٣٤٩٨٠٤٨
(20,20,60)	٠,٠٠٢٧٥٥٤٢٤٧٥٧٧٦٩	٠,٠٠٢٦٩١٥٢٥٣٧٢٩٧٧	٠,٠٠٠٠٠٠٠٣٤٩٨٠٤٨
(20,20,100)	٠,٠٠٢١٥٧٧٩١٧٨٨٤٧٧	٠,٠٠٢٠٦٠٠١٢٦٨٩٥٥٧	٠,٠٠٠٠٠٠٠٣٤٩٨٠٤٨
(20,60,20)	٠,٠٠٤١٠٨٧٥٧٩٥٩٦٤٩	٠,٠٠٣٩٦٥٢٧٢٢٦٩٦١١	٠,٠٠٠٠٠٠٠٣٤٩٨٠٤٨
(20,60,60)	٠,٠٠٢٢٠٣٠٣٢٥٨٥٥٠٣	٠,٠٠٢١٢٣١٥٣٢٧٦٨٦٥	٠,٠٠٠٠٠٠٠٣٤٩٨٠٤٨
(20,60,100)	٠,٠٠١٦٩٦٥٨٣٦٤٣٢٩٨	٠,٠٠١٦٤٤٠٩١٣٦٨٨٦٠	٠,٠٠٠٠٠٠٠٣٤٩٨٠٤٨
(20,100,20)	٠,٠٠٤٠٠٩١٢٣٨١١٥٥٤	٠,٠٠٣٨٦٧٦٠٧٤١٤٩٨٣	٠,٠٠٠٠٠٠٠٣٤٩٨٠٤٨
(20,100,60)	٠,٠٠٢٢٤٥١٩٤٠٢٩٦١٨	٠,٠٠٢١٦٨٢٤٨٧٦٥٣٣٧	٠,٠٠٠٠٠٠٠٣٤٩٨٠٤٨
(20,100,100)	٠,٠٠١٩٢٧١٠٨٤٣٩٥٥٥	٠,٠٠١٨٦٢٢٨٠٤٤٣٣١٢	٠,٠٠٠٠٠٠٠٣٤٩٨٠٤٨
(60,20,20)	٠,٠٠٣٧٨٢١٢١٦٣١٢٨٨	٠,٠٠٣٦٣١٣٦٦٢٠٣٩٨٨	٠,٠٠٠٠٠٠٠٣٤٩٨٠٤٨
(60,20,60)	٠,٠٠٢٠٥٥٦٣٤٦٣٣٢٤٨	٠,٠٠٢٠١٧٦١٠٠٠٣٦٥٨	٠,٠٠٠٠٠٠٠٣٤٩٨٠٤٨
(60,20,100)	٠,٠٠١٥٥٠١٩٥٣٨١٨٩٤	٠,٠٠١٥٠٧١٧١٥١٢٦٥٤	٠,٠٠٠٠٠٠٠٣٤٩٨٠٤٨
(60,60,20)	٠,٠٠٣٧٦١٣٦٨٨٧٠٥٦٨	٠,٠٠٣٦٣٤١٩٧٠٧٦٨٦٧	٠,٠٠٠٠٠٠٠٣٤٩٨٠٤٨
(60,60,60)	٠,٠٠١٤٤٦٣٩٤٥١٨٢٨٥	٠,٠٠١٤٣٣٨٨٩٤١٦١٣٠	٠,٠٠٠٠٠٠٠٣٤٩٨٠٤٨
(60,60,100)	٠,٠٠١١٥٥٨٣٩١٩٦٥١٢	٠,٠٠١١٤٧٦٦٢٣٣٥٢٦٨	٠,٠٠٠٠٠٠٠٣٤٩٨٠٤٨
(60,100,20)	٠,٠٠٣٣٤٦٩٤٠٦٢٤٧٢١	٠,٠٠٣٢٧٠٠٢٤٣٢٣٥٠٠	٠,٠٠٠٠٠٠٠٣٤٩٨٠٤٩
(60,100,60)	٠,٠٠١٤١٥٠٣٠٥٩٧٨٨٩	٠,٠٠١٣٩٨٣٦٤٧١٩٠٥٤	٠,٠٠٠٠٠٠٠٣٤٩٨٠٤٨
(60,100,100)	٠,٠٠١٠٤٢٤٩٥٤٠٦٩٢٠	٠,٠٠١٠٣٤٠٤٣٢٨٥٥٣١	٠,٠٠٠٠٠٠٠٣٤٩٨٠٤٨
(100,20,20)	٠,٠٠٣٥٤٢٢٧١٤٨٩٦١٥	٠,٠٠٣٤١٢٩٥٥١٨٨٠٠٤	٠,٠٠٠٠٠٠٠٣٤٩٨٠٤٨
(100,20,60)	٠,٠٠١٨١٥٢١٥٤٨٩٨٩٢	٠,٠٠١٧٧٥٤٣٢٣٥٠٠٢٤	٠,٠٠٠٠٠٠٠٣٤٩٨٠٤٨
(100,20,100)	٠,٠٠١٥٠٣٢٧٣٤٥٤١٨٤	٠,٠٠١٤٤٣٢٦١٣٣٦٠٠٩	٠,٠٠٠٠٠٠٠٣٤٩٨٠٤٨
(100,60,20)	٠,٠٠٣٥٤٦٥٨٨١٧٣٣٢١	٠,٠٠٣٤٩٩٧٣٥٨٥٦٩٨٣	٠,٠٠٠٠٠٠٠٣٤٩٨٠٤٩
(100,60,60)	٠,٠٠١٤٤٢١٢٧٣٠٧٤٦٧	٠,٠٠١٤٣٠٥٩٣٨٢١٢٤١	٠,٠٠٠٠٠٠٠٣٤٩٨٠٤٨
(100,60,100)	٠,٠٠١٠٢٥٠٢٩٨١٥٢٧٨	٠,٠٠١٠١٨٩٢٨٩٨٨٧٥٠	٠,٠٠٠٠٠٠٠٣٤٩٨٠٤٨
(100,100,20)	٠,٠٠٣٥١٥٧٣١٥٦٦٤٨٣	٠,٠٠٣٣٩٦٢٤٥٧٦٣٦٥٨	٠,٠٠٠٠٠٠٠٣٤٩٨٠٤٨
(100,100,60)	٠,٠٠١٣٣٥٩٦١٦٣٢٨١١	٠,٠٠١٣٢٨١٤٠٢٠٨٩٨٧	٠,٠٠٠٠٠٠٠٣٤٩٨٠٤٨

(100,100,100)	٠,٠٠٠٩٤٨٤٣٥٩٢٤٥٦٩	٠,٠٠٠٩٤٣٥٤٩٦٧٧٧٣٩	٠,٠٠٠٠٠٠٠٣٤٩٨٠٤٨

Table 9.Values of the $\hat{R}_k$when $R_k = 0.692307692307692$, $\theta_1 = 1.5, \theta_2 = 3, \theta_3 = 2$and $\beta = 4$.

(n_1, n_2, m)	$\hat{R}_{k_{mle}}$	$\hat{R}_{k_{sh}}$	$\hat{R}_{k_{SS}}$
(20,20,20)	٠,٦٨٩٤٦٦٥٨٦٨٠٤٣٧٤	٠,٦٨٩٥٢٥٠٠٨٧١٣٢٤٦	٠,٦٩٢٢٩٥٨٦٣٤٤٣١٢٩
(20,20,60)	٠,٦٩٦٥٨٤٢٣٠٩٦٨٢٣٦	٠,٦٨٩٥٨٧٣٨٣٦٧٠٦٢٧	٠,٦٩٢٢٩٥٨٦٣٤٤٦٣٨٢
(20,20,100)	٠,٦٩٩٠٩٤٤٨٩٦٨١٨٧٢	٠,٦٩٠٦٥٨٢٦٥٨٧١٤٧٥	٠,٦٩٢٢٩٥٨٦٣٤٥٠٥٨٧
(20,60,20)	٠,٦٨٨٨٩٤١٦٣١١٥٥٠٦	٠,٦٩٣٥٥١٩١٥٠٢٤٨٦٨	٠,٦٩٢٢٩٥٨٦٣٤٤٨٦١٦
(20,60,60)	٠,٦٩٥١٢٣٣٦٥٠٨٢٣٨٢	٠,٦٩٢٧٥٢٥١٢٧٧١٣٠٨	٠,٦٩٢٢٩٥٨٦٣٤٤٧٠٣١
(20,60,100)	٠,٦٩٥٠٤٤٠٧١٠٩٢٩٨٠	٠,٦٩١٢٧٧٤٦٥٨١٧٣٤٥	٠,٦٩٢٢٩٥٨٦٣٤٤٦٥٦٥
(20,100,20)	٠,٦٨٩٠٩٢٥٦٤٢٨٧٣١٠	٠,٦٩٤٧١٢٩٥٨٦٥١٢٩٧	٠,٦٩٢٢٩٥٨٦٣٤٤٩١٠١
(20,100,60)	٠,٦٩٤٠١٤٠٩٦٠٦٥٩٠٨	٠,٦٩٢٥٧٦٠٨٣٤٠٧٢٤٧	٠,٦٩٢٢٩٥٨٦٣٤٤٨٤٢٤
(20,100,100)	٠,٦٩٢٧٩٩٨٦٦٦٩٥٨٠٠	٠,٦٨٩٩٦٠٣١٢٩٠٢٣٠١	٠,٦٩٢٢٩٥٨٦٣٤٤٦٥٨٣
(60,20,20)	٠,٦٨٨٩٤٩١١١٦٠٥٥٣٥	٠,٦٩١٣٥٧٠٤٨٠٦٩٢٦٩	٠,٦٩٢٢٩٥٨٦٣٤٤٦١١٠
(60,20,60)	٠,٦٩٤٥١٦٨٠٢٥٢٨٦٥٥	٠,٦٨٩٨٦٤٠٥٤٠٣٨٤٦٦	٠,٦٩٢٢٩٥٨٦٣٤٤٧٥٠٠
(60,20,100)	٠,٦٩٦٤٦٨٦٤٢٦٤٠٦٣٤	٠,٦٩٠٣٨٠٧١٠٣١٤٢٣٢	٠,٦٩٢٢٩٥٨٦٣٤٤٨٩٥١
(60,20,20)	٠,٦٨٨٤٠١٨٤١٦٦٩٨١١	٠,٦٩٥٤١٢٩٨٨٦٤٧٨٢٧	٠,٦٩٢٢٩٥٨٦٣٤٥١٣٩٣
(60,60,60)	٠,٦٩٢٧٨١٠٤٣٠٤٢٤٧٩	٠,٦٩٢٧٨٠٧١٧٣٥٣٠٩٦	٠,٦٩٢٢٩٥٨٦٣٤٤٧٦٢٢
(60,60,100)	٠,٦٩٢٩١١٢٤٠٦١٧٣١٣	٠,٦٩١٤٩٧٠٥٦٥٧٤٣١٦	٠,٦٩٢٢٩٥٨٦٣٤٤٧٦٢٢
(60,100,20)	٠,٦٨٥٦٩٣٧٢٤٤٠٤٩٩٠	٠,٦٩٣٧٠٦٢٥٤٦٠٠٦٠٦	٠,٦٩٢٢٩٥٨٦٣٤٤٦١٤٢
(60,100,60)	٠,٦٩٢٣٨٩٦٧٢٢٢٧٧٢٧	٠,٦٩٣٣٢٩٩١٧٨٧٠٦٢١	٠,٦٩٢٢٩٥٨٦٣٤٤٧٦٢٢
(60,100,100)	٠,٦٩٢١٥٤٢٩١٥٨٢٢١٩	٠,٦٩١٦٨٣٩٧٠٦٦٠٣٠٥	٠,٦٩٢٢٩٥٨٦٣٤٤٧٦٢٢
(100,20,20)	٠,٦٨٩١١٤٢٢٦٥٠١٦٩٢	٠,٦٨٩١١٤٢٢٦٥٠١٦٩٢	٠,٦٩٢٢٩٥٨٦٣٤٤٧٧٧٣
(100,20,60)	٠,٦٩٢٧٤٢٩٦٧٠٣٢٢٣٣	٠,٦٨٨٥٨٤٧٢٧٠٥٣٢٩٢	٠,٦٩٢٢٩٥٨٦٣٤٤٦٠٨٦
(100,20,100)	٠,٦٩٣٩٧٧٨٥٠٥٢٨٠٥٣	٠,٦٨٨٣٨١٣٧٧٦٩٧١٦٥	٠,٦٩٢٢٩٥٨٦٣٤٤٥٧٢٤
(100,60,20)	٠,٦٨٧٤١٦٣٣٢٦٧٨٢٢٥	٠,٦٩٤٩٤٠٩٢٤٧٩٩٠٠٦	٠,٦٩٢٢٩٥٨٦٣٤٥١٢٩٩
(100,60,60)	٠,٦٩٢٠٩٩٨٩٦٨٢٠١٦٠	٠,٦٩٢٥٧٣٥٠٩٠٥٩١٢٥	٠,٦٩٢٢٩٥٨٦٣٤٤٧٦٢٢
(100,60,100)	٠,٦٩٢٧٤٥٨٣٩٤٠٠٦٦٩	٠,٦٩١٨٠٥٦٩٦٩٢٨٢١٨	٠,٦٩٢٢٩٥٨٦٣٤٤٧٦٢٢
(100,100,20)	٠,٦٨٨٤٩٣٨٣٢٣٨٣٣٩٦	٠,٦٩٦٩١٩٠٧٧١٨٠٠١٦	٠,٦٩٢٢٩٥٨٦٣٤٥٢٧٧٣
(100,100,60)	٠,٦٩١٧٩٧٩٣٧٧٥٣٩٥٠	٠,٦٩٣٢٠٩٠٧٥٣٨١٥٠٨	٠,٦٩٢٢٩٥٨٦٣٤٤٧٦٢٢
(100,100,100)	٠,٦٩١٠٥٤٨٥١٤٢٥٨١٨	٠,٦٩١٠٥٧٩٥٠٤٤٥٠٩٧	٠,٦٩٢٢٩٥٨٦٣٤٤٧٦٢٢

Table10. MSE of the $\hat{R}_k$when $R_k = 0.692307692307692$, $\theta_1 = 1.5, \theta_2 = 3, \theta_3 = 2$and $\beta = 4$.

(n_1, n_2, m)	$\hat{R}_{k_{mle}}$	$\hat{R}_{k_{sh}}$	$\hat{R}_{k_{SS}}$
(20,20,20)	٠,٠٠٣٥٠٠٩٧٣٥٠٥٩٧٨	٠,٠٠٣٤٠١٤٦٦٩٨٩٠٢٢	٠,٠٠٠٠٠٠٠٠١٣٩٩٢٢
(20,20,60)	٠,٠٠٢٢٠٤٠٨٦٥٦٨٦٠٦	٠,٠٠٢١٩٨٤٠٧٥٨٤٥٠٧	٠,٠٠٠٠٠٠٠٠١٣٩٩٢٢
(20,20,100)	٠,٠٠١٨٣٠١٧٧٣٤٩٧٠٧	٠,٠٠١٨٠٠٣٦١٩٠٥٦٥١	٠,٠٠٠٠٠٠٠٠١٣٩٩٢٢
(20,60,20)	٠,٠٠٣٠٩٣١٠٢٤٣٧٩٤٢	٠,٠٠٢٩٥١٨٧١٧٢١٦١٥	٠,٠٠٠٠٠٠٠٠١٣٩٩٢٢
(20,60,60)	٠,٠٠١٤١٤٢٢١٢٤٥٧٤٧	٠,٠٠١٣٩٦١٠٣٤٩٨٠٤٨	٠,٠٠٠٠٠٠٠٠١٣٩٩٢٢
(20,60,100)	٠,٠٠١١٢٢٤٥١٣٩٢٨٤٠	٠,٠٠١١١٣١١٠٢٣٣١٧١	٠,٠٠٠٠٠٠٠٠١٣٩٩٢٢
(20,100,20)	٠,٠٠٢٧٩٨٣٦١٥٩٤٦٠٣	٠,٠٠٢٦٥٦٥٤٨٧٧٣٧٧٢	٠,٠٠٠٠٠٠٠٠١٣٩٩٢٢

(20,100,60)	٠,٠٠١٢٥٦٢٢٧٠٩١٣٣٩	٠,٠٠١٢٣٥١٤٠٠٨٠٧١٩	٠,٠٠٠٠٠٠٠٠١٣٩٩٢٢
(20,100,100)	٠,٠٠٠٩٧٨١٩٧٠٦٥٠٩٧	٠,٠٠٠٩٧٤١٨٠١٠٠٧١٠	٠,٠٠٠٠٠٠٠٠١٣٩٩٢١
(60,20,20)	٠,٠٠٣٦٠٥٤٦٣٤٣٤٨٦١	٠,٠٠٣٤٤٨٧٧١١٢٦٢١٤	٠,٠٠٠٠٠٠٠٠١٣٩٩٢٢
(60,20,60)	٠,٠٠١٦٨٨٢٢٧٨٤٨١٦١	٠,٠٠١٦٦٨٤١٤٤٦٣٥٥٦	٠,٠٠٠٠٠٠٠٠١٣٩٩٢٢
(60,20,100)	٠,٠٠١٤٤٧٥٤٣٥٨٥٩٦٣	٠,٠٠١٤٢١٤٧٢٢١٦٥٦٦	٠,٠٠٠٠٠٠٠٠١٣٩٩٢٢
(60,60,20)	٠,٠٠٢٩١٥٩٩٩٤٦٦٠٦١	٠,٠٠٢٧٦٧٧٢٠٧٤٨٤٥٦	٠,٠٠٠٠٠٠٠٠١٣٩٩٢٢
(60,60,60)	٠,٠٠١٢٧٢٥١٧٠٣٧٠٩٣	٠,٠٠١٢٦١٥٧٥٥٩٧٠٨٥	٠,٠٠٠٠٠٠٠٠١٣٩٩٢٢
(60,60,100)	٠,٠٠٠٨٦٩٩٢٣٦٩٧١٦٨	٠,٠٠٠٨٦٨٥٧٥٤٤١٧٧٩	٠,٠٠٠٠٠٠٠٠١٣٩٩٢١
(60,100,20)	٠,٠٠٢٨٢١٨٧١٩١٣٣٢٧	٠,٠٠٢٦٣٩٢٥١١٨٠٤٢٠	٠,٠٠٠٠٠٠٠٠١٣٩٩٢٢
(60,100,60)	٠,٠٠١٠٣٣٩٧٦٥٩٤٤٣2	٠,٠٠١٠٢٣٥٠٥٠٧٤٦٨٩	٠,٠٠٠٠٠٠٠٠١٣٩٩٢٢
(60,100,100)	٠,٠٠٠٧٧٧٩٨٩١٨٠٨٢٧	٠,٠٠٠٧٧٥٣٩٩٠٠٠٦٢٨	٠,٠٠٠٠٠٠٠٠١٣٩٩٢١
(100,20,20)	٠,٠٠٣٥١٨٧٤٣١٠٢٣٣٠	٠,٠٠٣٣٥٧١٣٦٣٧٤٤٧٠	٠,٠٠٠٠٠٠٠٠١٣٩٩٢٢
(100,20,60)	٠,٠٠١٧٦٤٨٣٣٦٥٣٦١٧	٠,٠٠١٧٤٥٢٢٩٥٢٦٩٧٠	٠,٠٠٠٠٠٠٠٠١٣٩٩٢٢
(100,20,100)	٠,٠٠١٣٨١٧٢٥٩٦٣٠٣٤	٠,٠٠١٣٧٠٦٧١٩٥٥٦٦٣	٠,٠٠٠٠٠٠٠٠١٣٩٩٢٢
(100,60,20)	٠,٠٠٢٦١٤٥٠٦٧٢٣٠١٧	٠,٠٠٢٤٦٣٣٥٢٥٢٠٠٨٣	٠,٠٠٠٠٠٠٠٠١٣٩٩٢٢
(100,60,60)	٠,٠٠١١١٨٨٧١٠٣٢٨٢٨	٠,٠٠١١٠٦٦٢٨٩٨٣٧٥١	٠,٠٠٠٠٠٠٠٠١٣٩٩٢٢
(100,60,100)	٠,٠٠٠٩٠٨٢٩٠٣٠٧٩٩٩	٠,٠٠٠٩٠٤٣١٩٨٩٠٥١٦	٠,٠٠٠٠٠٠٠٠١٣٩٩٢١
(100,100,20)	٠,٠٠٢٥٧٠٤٣٦٠٣٩٨٢٤	٠,٠٠٢٤٣٩٤٦٩٦٧٣٠٦١	٠,٠٠٠٠٠٠٠٠١٣٩٩٢٢
(100,100,60)	٠,٠٠١١٦٨١٨٥٦٨٩٥٢١	٠,٠٠١١٥٣٩١٧٤٠٠٥٠٧	٠,٠٠٠٠٠٠٠٠١٣٩٩٢٢
(100,100,100)	٠,٠٠٠٧٥٢٧٣١٨٨١٢٧٠	٠,٠٠٠٧٤٨٨٦٩١٧٢٦٧٨	٠,٠٠٠٠٠٠٠٠١٣٩٩٢١

Table11.Values of the $\hat{R}_{\mathrm{k}}$when $R_k = 0.769230769230769$, $\theta_1 = 3, \theta_2 = 2, \theta_3 = 1.5$and $\beta = 4$.

(n_1, n_2, m)	$\hat{R}_{k_{mle}}$	$\hat{R}_{k_{sh}}$	$\hat{R}_{k_{SS}}$
(20,20,20)	٠,٧٦٨٨٧٩٨٥٣٢٥٧٦١٩	٠,٧٦٨٩٠٣٣٨٤٩٥١٢٥٤	٠,٧٦٩١٨٣٤٥٣٧٩٢٨٠٦
(20,20,60)	٠,٧٧١٤٩٥١٣٩٢٦١٦٧٩	٠,٧٦٥٦٢٢٧٩٥٠١١٣٦٦	٠,٧٦٩١٨٣٤٥٣٧٨٩٦٨٢
(20,20,100)	٠,٧٧٣٠١٦٦٠٩٧٢٥٣٣١	٠,٧٦٥٩٦٢٩١٣٣٣٧٨٠١	٠,٧٦٩١٨٣٤٥٣٧٩٠٩٧٦
(20,60,20)	٠,٧٦٥٩٠١٨٨٩٣٤١١١٠	٠,٧٦٨٣٢٩١٣٩٣٤٣٣٩٩	٠,٧٦٩١٨٣٤٥٣٧٨٨٩٠٠
(20,60,60)	٠,٧٧١٠٩١٠٠٣١٥٤٠٥٩	٠,٧٦٧٥٩٣٩٠١٧٤٤٩٧٤	٠,٧٦٩١٨٣٤٥٣٧٩٠٢٥٩
(20,60,100)	٠,٧٧١٣٧٣٣١٦٥٦٦٢٧٣	٠,٧٦٦٦٩٣٣٢٤٠٩٠٢٠٨	٠,٧٦٩١٨٣٤٥٣٧٩٠٠٣٠
(20,100,20)	٠,٧٦٧٩١٩٣٩٠٨٥٨٤٧٤	٠,٧٧٠٧٦٠٣٢٠٥٣٢٤٨١	٠,٧٦٩١٨٣٤٥٣٧٩٥٩٥٤
(20,100,60)	٠,٧٧٠٩٦١٤٩٩٤٠٩٠٥٥	٠,٧٦٧٩٢٧٠٣٢٩٤٨٨٨٣	٠,٧٦٩١٨٣٤٥٣٧٩٣٠٢١
(20,100,100)	٠,٧٧٠٧١٨٧١٩١٨٩٧٧٤	٠,٧٦٦٥٢٢٨٣٨٨٣٤٨٠٣	٠,٧٦٩١٨٣٤٥٣٧٨٩٣٥١
(60,20,20)	٠,٧٦٤٢٧٠٦٠٢٦١٦٤٣٦	٠,٧٦٧٨٨٧٦٣٣٤٤١٣٠٠	٠,٧٦٩١٨٣٤٥٣٧٨٧٣٥٠
(60,20,60)	٠,٧٧٢٠٣٧٥٩٥١٥٥٠٤٩	٠,٧٦٩٦٨٦٠٤٧٢٤٠٦٤٩	٠,٧٦٩١٨٣٤٥٣٧٩٠٥٦٩
(60,20,100)	٠,٧٧١٤٢٣٥٥٠٥٦٥١٩٨	٠,٧٦٧٨٩٤٢٣٠٨٥١٩٢١	٠,٧٦٩١٨٣٤٥٣٧٩٠٢٢٦
(60,60,20)	٠,٧٦٤٠٤٤٤١٠٨٦٩٧١٢	٠,٧٦٩٩٦٤٧١٣٢٣٢٥٤١	٠,٧٦٩١٨٣٤٥٣٧٩١٦٧٧
(60,60,60)	٠,٧٦٨١٨٥٠١٥٨٢٣٧٩٩	٠,٧٦٨١٩١٧٩٢١٥٩٣٩٣	٠,٧٦٩١٨٣٤٥٣٧٩٠٥٦٠
(60,60,100)	٠,٧٦٨٩٠٥٤٣٧٣١٥٤٨٧	٠,٧٦٧٧٢٦٧٣٣٤٠٤٥١٥	٠,٧٦٩١٨٣٤٥٣٧٩٠٥٦٠
(60,100,20)	٠,٧٦٤٨٥٩٣١٤٥٠٧١٠٧	٠,٧٧١٢٣٧٦٧٠٠١٠٦١٤	٠,٧٦٩١٨٣٤٥٣٧٩٣٤٧٦
(60,100,60)	٠,٧٦٩٩١٣١٥٠٠٣٤٥٨٧	٠,٧٧٠٣٨١٢٩٢٦٨٧٧٢٧	٠,٧٦٩١٨٣٤٥٣٧٩٠٥٦٠
(60,100,100)	٠,٧٧٠١٠١٦٨٦٢٤٤٣٠٦	٠,٧٦٩٣٩٦٠٨٠١١٥٤١٤	٠,٧٦٩١٨٣٤٥٣٧٩٠٥٦٠
(100,20,20)	٠,٧٦٤٥٥١١٨٣١٦٣٣٨٥	٠,٧٦٨٨٤٩٨٨٩٩٨٨٢١٧	٠,٧٦٩١٨٣٤٥٣٧٨٩٠٠٧
(100,20,60)	٠,٧٦٩٣٦٢٩٢٤٦٣٠٤٨٣	٠,٧٦٧٧٢١٨٨٦٣٨٦٢٦٠	٠,٧٦٩١٨٣٤٥٣٧٨٩٨٣٥

(100,20,100)	٠,٧٧٠٨١٩٣٨٢٦٨٨٥٢١	٠,٧٦٧٩٦٣٧٧٠٦٣٦٣٤٠	٠,٧٦٩١٨٣٤٥٣٧٩٢٥٥٣
(100,60,20)	٠,٧٦٢٦٧٩٧٠١٤٣٩٥٨٨	٠,٧٦٩٣٥٥٣٤١٨٥٤٠٣١	٠,٧٦٩١٨٣٤٥٣٧٨٩٠٤٥
(100,60,60)	٠,٧٦٧٢٤٦٥٩٨٢٩٥٤٤٥	٠,٧٦٧٩٦٨٥١٩٣٣٥٠٠٧	٠,٧٦٩١٨٣٤٥٣٧٩٠٥٦٠
(100,60,100)	٠,٧٦٨٣٩٠٣٠٦٣٥٠٤٩٢	٠,٧٦٧٩١٩٣٨٩١٨٨١٣١	٠,٧٦٩١٨٣٤٥٣٧٩٠٥٦٠
(100,100,20)	٠,٧٦٢٧٨٤٥٧٧٧٠٣٣٦٥	٠,٧٦٩٩٣١٧٢٧١٣٤٧٥٠	٠,٧٦٩١٨٣٤٥٣٧٨٩٩٨٤
(100,100,60)	٠,٧٦٧١٩٣٣٩٩١٨٠٨٤٠	٠,٧٦٨٣٨٧٠٢٥٣٤٤٨٤٢	٠,٧٦٩١٨٣٤٥٣٧٩٠٥٦٠
(100,100,100)	٠,٧٦٩٠٣٨٧٧٠٦٥٧٨٨٤	٠,٧٦٩٠٣٩٩٠٦٥٢٧٠٧٥	٠,٧٦٩١٨٣٤٥٣٧٩٠٥٦٠

Table12. MSE of the $\hat{R}_{\mathrm{k}}$when $R_k = 0.769230769230769$, $\theta_1 = 3, \theta_2 = 2, \theta_3 = 1.5$ and $\beta = 4$.

(n_1, n_2, m)	$\hat{R}_{k_{mle}}$	$\hat{R}_{k_{sh}}$	$\hat{R}_{k_{SS}}$
(20,20,20)	٠,٠٠٢٤٣٥٧٨٥٣٠٧٧١٠	٠,٠٠٢٣٦٣٦٦٤٥٣٣٤٣٣	٠,٠٠٠٠٠٠٠٠٢٢٣٨٧٥١
(20,20,60)	٠,٠٠١٣١٤٠١٠١٣٤١٣٥	٠,٠٠١٣٣٨٩٢٨٢٨١٩٨٨	٠,٠٠٠٠٠٠٠٠٢٢٣٨٧٥١
(20,20,100)	٠,٠٠١١٤٣١٨٤٩٢٦٩٨٣	٠,٠٠١١٦٠٥٩٦٢٥٨٤٤٤	٠,٠٠٠٠٠٠٠٠٢٢٣٨٧٥١
(20,60,20)	٠,٠٠٢٤٤٢٧٠٨٩٤٦٦٥٨	٠,٠٠٢٣٢٠٦٤٩٧٠١٢٣٥	٠,٠٠٠٠٠٠٠٠٢٢٣٨٧٥١
(20,60,60)	٠,٠٠١٢٣٧٣٣٣٩٢٥٥٤٦	٠,٠٠١٢٢٨٢١٠٩٩٨٩٥٣	٠,٠٠٠٠٠٠٠٠٢٢٣٨٧٥١
(20,60,100)	٠,٠٠٠٩٨٢١٣٧٧٨٩٩٦٣	٠,٠٠٠٩٨٢٦٠٤١١٥٤٦٩	٠,٠٠٠٠٠٠٠٠٢٢٣٨٧٥٠
(20,100,20)	٠,٠٠٢٤٣٨٧٧٣١٥٦٥٢٠	٠,٠٠٢٣١٧٩٩٠٩٦١٤٧٩	٠,٠٠٠٠٠٠٠٠٢٢٣٨٧٥٠
(20,100,60)	٠,٠٠١٢٦٦٤١٥٢٨٨٦١٥	٠,٠٠١٢٥٠٤٦٩٢٧٦٩٢١	٠,٠٠٠٠٠٠٠٠٢٢٣٨٧٥١
(20,100,100)	٠,٠٠٠٩٢١٧٦٢٣٣٥٥٧٥	٠,٠٠٠٩١٨٥٩١٨٣٩١١٦	٠,٠٠٠٠٠٠٠٠٢٢٣٨٧٥٠
(60,20,20)	٠,٠٠٢١٩٩٣٣٩١٩٧٣٩٣	٠,٠٠٢٠٧٠٠٠٢٦١٧٨٢٤	٠,٠٠٠٠٠٠٠٠٢٢٣٨٧٥١
(60,20,60)	٠,٠٠٠٩٧٦٨١٥٧٧١١٧٢	٠,٠٠٠٩٦٤٨٠٢٨٦٧٦٤٧	٠,٠٠٠٠٠٠٠٠٢٢٣٨٧٥٠
(60,20,100)	٠,٠٠٠٧٧٧٦٧٩٨٩٣٠٥٤	٠,٠٠٠٧٧٥٣٧٥٧٩٤٥٦٧	٠,٠٠٠٠٠٠٠٠٢٢٣٨٧٥٠
(60,60,20)	٠,٠٠٢١٢٧٨٢٠٦٦٥٤٠١	٠,٠٠١٩٨١٧٩٣٣٣٣٠٦	٠,٠٠٠٠٠٠٠٠٢٢٣٨٧٥١
(60,60,60)	٠,٠٠٠٨٨٤٥٨٩٦٥٧٨٠٩	٠,٠٠٠٨٧٧٠٢٨٥٤٨٦٦٣	٠,٠٠٠٠٠٠٠٠٢٢٣٨٧٥٠
(60,60,100)	0.000586706327036	0.000589015710074	0.000000002238750
(60,100,20)	٠,٠٠١٩٣٧٠٤٤٧٧٦٢٦٠	٠,٠٠١٨٠٥٣٦٢٩١٢١٢٢	٠,٠٠٠٠٠٠٠٠٢٢٣٨٧٥١
(60,100,60)	٠,٠٠٠٨١٢٩٤٧٤٨٧٧٨٥	٠,٠٠٠٨٠٤١٢٧٤٥١٠٩٤	٠,٠٠٠٠٠٠٠٠٢٢٣٨٧٥٠
(60,100,100)	٠,٠٠٠٥٣٤٣١٨٠٨٠٩٠٣	٠,٠٠٠٥٣١٨٧٩٤٢٠٠٦٧	٠,٠٠٠٠٠٠٠٠٢٢٣٨٧٥٠
(100,20,20)	٠,٠٠٢١٠٠٨٠٨٥٨٦٤٥٢	٠,٠٠١٩٦٥٩١٦٦٣٩٥٨٠	٠,٠٠٠٠٠٠٠٠٢٢٣٨٧٥١
(100,20,60)	٠,٠٠٠٨٩٠٥٠٦٩٢٠٤٤٩	٠,٠٠٠٨٨٠٨٦٧٨٦٣٦٨٩	٠,٠٠٠٠٠٠٠٠٢٢٣٨٧٥٠
(100,20,100)	٠,٠٠٠٨١٢٣٥٢١٢٢٣٣٣	٠,٠٠٠٨٠٤١٦٢٦٢٨٤٨٥	٠,٠٠٠٠٠٠٠٠٢٢٣٨٧٥٠
(100,60,20)	٠,٠٠١٩٦٨٢٣٠٤٥٧٠٠٧	٠,٠٠١٨٠٤٧٦٠٧١١٤٨٩	٠,٠٠٠٠٠٠٠٠٢٢٣٨٧٥١
(100,60,60)	٠,٠٠٠٧٣٧٥٣٤٩٥٧١٧٠	٠,٠٠٠٧٢٥٩٧٣٢٦١١٤٧	٠,٠٠٠٠٠٠٠٠٢٢٣٨٧٥٠
(100,60,100)	٠,٠٠٠٥١٧٠٣٦٠٩٧٦٦٢	٠,٠٠٠٥١٦٣٤١٥٩٣٢١٠	٠,٠٠٠٠٠٠٠٠٢٢٣٨٧٥٠
(100,100,20)	٠,٠٠١٨٧٤٢٢٣١٨٨٨٨٨	٠,٠٠١٧١٦٢٢٣٤١١٧٨٨	٠,٠٠٠٠٠٠٠٠٢٢٣٨٧٥١
(100,100,60)	٠,٠٠٠٦٦٥٦٥٣٢١٢٥٧٣	٠,٠٠٠٦٥٢٤٣٥٢٤٨٨٣٤	٠,٠٠٠٠٠٠٠٠٢٢٣٨٧٥٠
(100,100,100)	٠,٠٠٠٥١٦٨٦٤٨١١٠٩٨	٠,٠٠٠٥١٤١٦٧٤١٩٤٨٨	٠,٠٠٠٠٠٠٠٠٢٢٣٨٧٥٠

4. Results Analysis

From the tables above, for all n_1= (20,60,100), n_2= (20,60,100) and m=(20,60,100), we conclude that when Δ=0.05 ,the minimum (MSE) for $\hat{R}$kss held using single stage shrinkage estimator (SS) so it is the best for all $n_i, i = 1,2$ and m, follow by the shrinkage methods using $\hat{R}$ksh and finally by the Maximum

Likelihood estimator $\hat{R}$kMLE , but in case, when $(n_1, n_2, m) = (20,20,60), (20,20,100), (60,60,100)$ and $(\theta_1, \theta_2, \theta_3) = (1,2.5,1.5)$, $(2.5,1.5,1)$ and $(3,2,1.5)$ seen that the second best methods using Maximum Likelihood estimator and follows the shrinkage methods and seen that the MSE for the preliminary test single stage shrinkage estimator (SS) is equal for all n_1, n_2 and m , when we used $K = e^{-n_i}$.

5. Conclusion

The simulation results exhibited that, the preliminary test single stage shrinkage estimator (SS) is the best way. Then the resulting estimator $\hat{R}_{k_{SS}}$ perform well and will be the best estimator than the other in the sense of MSE, and the shrinkage estimator using in this paper near on the Maximum Likelihood estimator.

References

[1] Mokhlish N M 2006 Reliability of Strength Models with Bivariate Exponential distribution *Journal of the Egyptian Mathematical Society* **14**(1) pp 69-78
[2] Ali H M 2013 *Comparison of some methods to estimate some of stress-strength Lomax models* M.Sc.thesis Al-Mustansiriya University
[3] Sail F H 2017 *On Reliability Estimation of Stress-Strength Models* M. Sc. thesis Baghdad University College of Education Ibn-AL-Haitham
[4] Cheng C 2018 Reliability of Parallel stress-strength models *Journal of Mathematical Research with Application* **38**(4) pp 427-440
[5] A Flaih, H Elsalloukh, E Mendi and M. Milanova 2012 The Exponentiated Inverted Weibull Distribution *Applied Mathematics & Information Sciences* **6**(2) pp167-171
[6] Hanagle D D 1998 On the Estimation of System Reliability in Stress-Strength models *Economic Quality Control* **13 pp** 17-22
[7] Thompson J R 1968 Some shrinkage Techniques for Estimating the mean *J. Amer. Statist. Assoc* **63** pp113-122
[8] Abbas N S and else 2014 Preliminary Test Single Stage Shrinkage Estimator for the scale parameters of Gamma distribution *American Journal of Mathematics and Statistics* **4**(3) pp 131-136
[9] Abbas N S and Hadi R A 2016 Preliminary Test Single Stage Shrinkage Estimator for the shape parameters of generalized exponential distribution *International Journal of Applied Mathematical Research* **5**(4) pp 162-166
[10] Rubinstein R Y and Kroese D P 1981 *Simulation and the Monte Carlo Method* John Wiley and Sons
[11] Abbas N S and Taha T A 2017 On Reliability Estimation for the Exponential Distribution Based on Monte Carlo Simulation *Baghdad University College of Education Ibn-AL-Haitham* **Spec Vol** pp 409-419

Some Properties of Regular and Normal Space on Topological Graph Space

Some Properties of Regular and Normal Space on Topological Graph Space

Rasha A Isewid[1], Nabila I Aziz[2], Samer R Yaseen[3,*] and Mahera Rabee Qasem[3]

[1] Department of Mathematics, College of Physical Education and sport science Al-qadisya University, Iraq
[2] Department of Physics, College of Education -Tuzkhurmatu, Tikrit University, Tikrit, Iraq
[3] Department of Mathematics, College of pure science, Tikrit University, Iraq

E-mail: samer2017@tu.edu.iq

Abstract. The goal of this article is to give the concepts of Regular space and Normal space in the topological graph space also generalize α and β that to Regular space and Normal space where the relationship between these concepts were given. Finally, some characteristics of these concepts were investigated.

1. Introduction

Graph theory [3] is one of the fundamental topics of modern mathematics. This theory is also used in most branches of knowledge, as it has applications and uses of great benefits in topics of scientific and economic importance such as game theory, mathematical programming, connection theory and electrical networks in addition to its use in physics, organic chemistry, economics, civil engineering, biology and many other fields.

Kosterlitz [5] given the relationship between graph theory and topology. The topology is created by graph theory and the study of topological properties in graph theory. Some researchers make the relationship only on the vertices of the graph, while others make it on the edges. But the process is to create a schematic diagram of a particular topology that was not interested before ([6] and [8].

2. Preliminaries

Definition 2.1 [3]: A graph H is a set $l \neq \emptyset$ of elements called vertices graph with a family L from unarranged pairs of vertices a graph is called an edge. It is called set vertices graph l(H) and family edge m(H) and We express a graph of ordered pairs H(l, M).

Definition 2.2 [7]: A directed graph or digraph D as set w that is non-empty of elements called vertices I and edges M with a family of ordered pairs of vertices denoted by (l, M).
A directed graph is expressed as an ordered pair (l, D) and denoted set vertices l(D) and family directed edge M(D).

Definition 2.3 [6]:
Let H(l, m) be a graph, we call K is a sub graph from H and can write by $K \subseteq H$ if

$l(K) \subseteq l(H), m(K) \subseteq m(H)$. The spanning sub graph from a graph is a sub graph acquired by edge deletions only.

Definition 2.4 [4]: A topological space (S,σ) is called regular space if for every non-empty closed set F and a point m which does not belong to F, there are open sets U_1, U_2 s.t. $m \in U_1$ $F \notin U_2$ and $U_1 \cap U_2 = \emptyset$.

Definition 2.5 [4]: A topological space (S,σ) is called normal space iff for every non-empty closed set F_1 , F_2 , there is a pair U_1, U_2 of open set s.t. $F_1 \subseteq U_1$ $F_2 \subseteq U_2$ and $U_1 \cap U_2 = \emptyset$.

Definition 2.6: A subset K of a space S is called:
(4) α-open [2] if K ⊆int(cl(int(K))).
(5) β-open [9] if K ⊆cl(int(cl(K))).

Definition 2.7[1]: Let (L, H) be a graph, $l \in L(H)$ then we define the post stage is the set of all vertices which is not a neighborhood of l. QH is the collection of (lR) is called sub basis of graph $B_H = \cap^{n}_{j=1} QH_j$ is called bases of the graph. Then the union of $B_H$is form a topology on H and $(L(H), \sigma_H)$ is called a topological graph.

Example 2.8[1]: Let (L, H) be a graph, We'll create a topology via graph as follows:
$l_1(H) = \{l_1, l_2\}, l_2(H) = \{l_3, l_4\}, l_3(H) = \{l_1\}, l_4(H) = \{l_2\}, l_5(H) = \{l_2, l_5\}$. Then a subbase is a topology is $S_H = \{\{l_1, l_2\}, \{l_3, l_4\}, \{l_1\}, \{l_2\}, \{l_2, l_5\}\}$. The base is $B_H = \{L(H), \emptyset, \{l_1, l_2\}, \{l_3, l_4\}, \{l_3\}, \{l_1\}, \{l_2\}, \{l_2, l_5\}\}$. Therefore, the topological graph of H is $\sigma_H = \{L(H), \emptyset, \{l_1, l_2\}, \{l_3, l_4\}, \{l_3\}, \{l_1\}, \{l_2\}, \{l_2, l_5\}, \{l_1, l_3\}, \{l_1, l_2, l_3, l_4\}, \{l_1, l_2, l_3\}, \{l_1, l_3, l_4\}, , \{l_2, l_3, l_4\}, \{l_1, l_2, l_5\}, \{l_3, l_2, l_5\}, \{l_3, l_4, l_2, l_5\}\}$

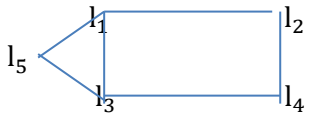

Figure 1 Topology via graph

3- Regular and Normal Space on Topological Graph Space

In this section, we give new definitions of Regular and Normal space on topological graph space with relation among them.

Definition 3.1: A topological graph $(L(H), \sigma_H)$ is called H-Regular space if for any vertices l from L(H) and F is closed set vertices s.t, $l \notin F$, there exist post two stages from any vertices U_1, U_2 s.t. $l \in U_1$ $F \notin U_2$ and $U_1 \cap U_2 = \emptyset$.

Definition 3.2: A topological graph $(L(H), \sigma_H)$ is called H-Normal space if for any two closed vertices F_1, F_2 from L(H), there exists two post stage from any vertices U_1, U_2 s.t. $F_1 \in U_1$ $F_2 \notin U_2$ and $U_1 \cap U_2 = \emptyset$.

Definition 3.3: A topological graph $(L(H), \sigma_H)$ is called H-α-Regular space if for any vertices l from L(H) and F is α-closed vertices s.t, $l \notin F$, there exist α-post two stages from any vertices U_1, U_2 s.t. $l \in U_1$ $F \notin U_2$ and $U_1 \cap U_2 = \emptyset$.

Definition 3.4: A topological graph $(L(H), \sigma_H)$ is called H-β-Regular space if for any vertices l from L(H) and F is is β-closed set vertices s.t, $l \notin F$, there exist two β-post stage from any vertices U_1, U_2 s.t. $l \in U_1$ $F \notin U_2$ and $U_1 \cap U_2 = \emptyset$.

Definition 3.5: A topological graph $(L(H), \sigma_H)$ is called H-α-Normal space if for any two α-closed vertices F_1, F_2 there exist two α-post stage from any vertices U_1, U_2 s.t. $F_1 \in U_1$ $F_2 \notin U_2$ and $U_1 \cap U_2 = \emptyset$.

Definition 3.6: A topological graph $(L(H), \sigma_H)$ is called H-β-Normal space if for any two β-closed vertices F_1, F_2 , there exist two β-post stage from any vertices U_1, U_2 s.t. $F_1 \in U_1$ $F_2 \notin U_2$ and $U_1 \cap U_2 = \emptyset$.

Theorem 3.7. Let $(L(H), \sigma_H)$ be a topological graph space. Then L(H) is satisfied following:

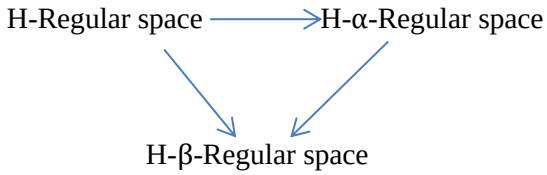

Proof: H-regular space $\Longrightarrow$ H-α-Regular space: Let $(L(H), \sigma_H)$ be H-Regular space and let each of l is vertices and F is closed vertices s.t, $l \notin F$, since $(L(H), \sigma_H)$ be H-Regular space, then F is α-closed vertices (every closed vertices are α-closed vertices). Thus, there exist α-post two stages from any α vertices U_1, U_2 s.t. $l \in U_1$ $F \notin U_2$ and $U_1 \cap U_2 = \emptyset$. Therefore $(L(H), \sigma_H)$ is H-α-Regular space.
H-regular space $\Longrightarrow$ H-β-Regular space: It is clear.
H-regular space $\Longrightarrow$ H-β-Regular space: Let $(L(H), \sigma_H)$ be H-α-Regular space and let each of l is vertices and F is α-closed vertices s.t, $l \notin F$, since $(L(H), \sigma_H)$ be H-α-Regular space, then F is β-closed vertices (every α - closed vertices is β-closed vertices). Thus, there exist β-post two stages from any β vertices U_1, U_2 s.t. $l \in U_1$ $F \notin U_2$ and $U_1 \cap U_2 = \emptyset$. Therefore $(L(H), \sigma_H)$ is H-β-Regular space.

Example 3.8: Let $(L(H), \sigma_H)$ be a topological graph space. We'll create a topology via a graph.
We take $l_1(H) = \{l_1, l_2\}, l_2(H) = \{l_3, l_4\}, l_3(H) = \{l_1\}, l_4(H) = \{l_2\}, l_5(H) = \{l_2, l_3\}$.
Then a subbase is a topology is $S_H = \{\{l_1, l_2\}, \{l_3, l_4\}, \{l_1\}, \{l_2\}, \{l_2, l_3\}\}$. The base is $B_H = \{L(H), \emptyset, \{l_1, l_2\}, \{l_3, l_4\}, \{l_3\}, \{l_1\}, \{l_2\}, \{l_2, l_3\}\}$. Therefore, the topological graph on H is $\sigma_H = \{L(H), \emptyset, \{l_1, l_2\}, \{l_3, l_4\}, \{l_3\}, \{l_1\}, \{l_2\}, \{l_2, l_3\}, \{l_1, l_3\}, \{l_1, l_2, l_3, l_4\}, \{l_1, l_2, l_3\}, \{l_1, l_3, l_4\}, , \{l_2, l_3, l_4\}, \}$.
Then $(L(H), \sigma_H)$ is H-α-Regular space, but $(L(H), \sigma_H)$ is not H-Regular space, because there is not exist disjoint post two stages for any vertices and closed set vertices in this graph.

Example 3.9: Let $(L(H), \sigma_H)$ be a topological graph space We'll create a topology via a graph.
We take $l_1(H) = \{l_1, l_2\}, l_2(H) = \{l_3, l_4\}$. Then a sub base is a topology is $S_H = \{\{l_1, l_2\}, \{l_3, l_2\}\}$. The base is $B_H = \{L(H), \emptyset, \{l_1, l_2\}, \{l_3, l_4\}, \{l_2\}\}$. Therefore, the topological graph on H is $\sigma_H = \{L(H), \emptyset, \{l_1, l_2\}, \{l_3, l_4\}, \{l_2\}, \{l_2, l_3, l_4\}\}$.
Then $(L(H), \sigma_H)$ is H-β-Regular space, but $(L(H), \sigma_H)$ is not H- α-Regular space, because there is not exist disjoint post two stages for any vertices and α-closed set vertices in this graph. Also $(L(H), \sigma_H)$ is not H-Regular space, because there is not exist disjoint post two stages for any vertices and closed set vertices in this graph.

Proposition 3.10. Let $(L(H), \sigma_H)$ be a topological graph space. Then L(H) is satisfied the following:

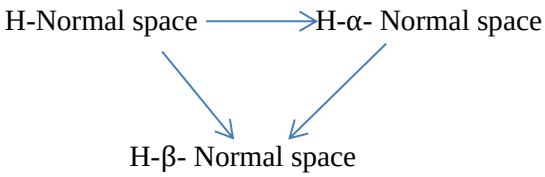

Proof: H-Normal space $\Longrightarrow$ H-α- Normal space: Let $(L(H),\sigma_H)$ be H-normal space and let and two αclosed vertices F_1, F_2 , since $(L(H),\sigma_H)$ then F is α-closed vertices (every closed vertices are α-closed vertices). Thus, there exist α-post two stages from any vertices U_1, U_2 s.t. $F_1 \in U_1$ $F_2 \notin U_2$ and $U_1 \cap U_2 = \emptyset$. Therefore $(L(H),\sigma_H)$ is H-α-Normal space.
H-Normal space $\Longrightarrow$ H-β-Normal space: it is same above.
H- α-Normal space $\Longrightarrow$ H-β-Normal space: it is same above.

Example 3.11: Let $(L(H),\sigma_H)$ be a topological graph space. We'll create a topology via a graph. We take

$$l_1(H) = \{l_1\}, l_2(H) = \{l_2, l_4\}, l_3(H) = \{l_3\}, l_4(H) = \{l_4\}.$$

Then a subbase is a topology is $S_H = \{\{l_2, l_4\}, \{l_1, l_3\}, \{l_3\}, \{l_4\}\}$. The base is $B_H = \{L(H), \emptyset, \{l_2, l_4\}, \{l_1, l_3\}, \{l_3\}, \{l_4\}\}$. Therefore, the topological graph on H is $\sigma_H = \{L(H), \emptyset, \{l_2, l_4\}, \{l_1, l_3\}, \{l_3\}, \{l_4\}, \{l_1, l_3, l_4\}, \{l_2, l_3, l_4\}, \{l_3, l_4\}\}$.
Then $(L(H),\sigma_H)$ is H-αnormal space, but $(L(H),\sigma_H)$ is not H- normal space, because there is not exist disjoint post two stages contain two closed vertices for any two vertices in this graph.

Example 3.12: Let $(L(H),\sigma_H)$ be a topological graph space . We'll create a topology via a graph.
We take $l_1(H) = \{l_1\}, l_2(H) = \{l_2, l_4\}, l_3(H) = \{l_1, l_3\}$.Then a sub base is a topology
$S_H = \{\{l_1\}, \{l_2, l_4\}, \{l_2, l_3\}\}$. The base is $B_H = \{L(H), \emptyset, \{l_1\}, \{l_2, l_4\}, \{l_2, l_3\}, \{l_2\}\}$.
Therefore, the topological graph on L(H) is $\sigma_H = \{L(H), \emptyset, \{l_1\}, \{l_2, l_4\}, \{l_2, l_3\}, \{l_2\}, \{l_1, l_2, l_4\}, \{l_1, l_2, l_3\}, \{l_1, l_2\}, \{l_2, l_3, l_4\}\}$.
Then $(L(H),\sigma_H)$ is H- β-Normal space, but $(L(H),\sigma_H)$ is not H- α-Normal space, because there is not exist disjoint post two stages contain two β-closed vertices for two α-vertices in this graph.

Remark 3.13. The relation between H-Normal space with H-Regular space (H-α-Normal space with H-α-Regular space, and H-β-Normal space with H-β-Regular space) are independent relations. We show this following:
1- Recall Example 3.8.We see that $(L(H),\sigma_H)$ is H-α-Regular space, but it is not H-α-Normal space.
2- Recall Example 3.11.We see that $(L(H),\sigma_H)$ is H- β-Regular space, but it is not H-β-Normal space.
3- Recall Example 3.8.We see that $(L(H),\sigma_H)$ is H- H-α-Normal space, but it is not H-α-Regular space.
4- Recall Example 3.8.We see that $(L(H),\sigma_H)$ is H- β-Normal space, but it is not H-β-Regular space.

Example 3.14: Let $(L(H),\sigma_H)$ be a topological graph space. We'll create a topology via a graph.
We take $l_1(H) = \{l_1\}, l_2(H) = \{l_2, l_3\}$. Then a sub base is a topology is
$S_H = \{\{l_1\}, \{l_2, l_3\}\}$. The base is $B_H = \{L(H), \emptyset, \{l_1\}, \{l_2, l_3\}\}$. Therefore, the topological graph on L(H) is $\sigma_H = \{L(H), \emptyset, \{l_1\}, \{l_2, l_3\}\}$. Then $(L(H),\sigma_H)$ is H-Normal space, but $(L(H),\sigma_H)$ is not H-Regular space, because there is not exist disjoint post two stages for any two α-vertices in this graph.

Example 3.15: Let $(L(H),\sigma_H)$ be a topological graph space. We'll create a topology via a graph.
We take $l_1(H) = \{l_2\}, l_2(H) = \{l_2, l_3\}, l_2(H) = \{l_3\}$.
Then a sub base is a topology is $S_H = \{\{l_2\}\{l_2, l_3\}, \{l_3\}\}$. The base is $B_H = \{L(H), \emptyset, \{l_2\}, \{l_2, l_3\}, \{l_3\}\}$.
Therefore, the topological graph on L(H) is $\sigma_H = \{L(H), \emptyset, \{l_2\}\{l_2, l_3\}, \{l_3\}\}$. Then $(L(H),\sigma_H)$ is H-

regular space, but $(L(H), \sigma_H)$ is not H- normal space, because there is not exist disjoint post two stages for any two α-vertices contain two closed vertices in this graph.

4-Some Properties of Regular and Normal Space on Topological Graph

In the section, we introduce some properties of Regular and Normal Space on Topological Graph. We start by the following proposition:

Proposition 4.1. Let $(L(H), \sigma_H)$ be a topological graph space. Then the following are equivalents:
1) L(H) is H-Regular space.
2) For each $l \in l(H)$, F is closed a post stage and $F \subseteq M(F)$, there exists a post stage K s.t, $l \in l(H) \subseteq cl_H(l(H)) \subseteq M(F)$.

Proof: (1) $\Longrightarrow$ (2) Assume that L(H) is H-Regular space, F is closed a post stage and $l \in M(F)$, then there exists a post stage K s.t, $l \in l(H) \subseteq cl_H(l(H))$,so that $M\left(cl_H(l(H))\right)$ and $cl_H(l(H)) \subseteq M(F)$. Thus $l \in l(H) \subseteq cl_H(l(H)) \subseteq M(F)$.
(2) $\Longrightarrow$ (1) Assume that F is closed a post stage, $l \in M(F)$, so that there exists a post stage K s.t. $l \in l(H) \subseteq cl_H(l(H)) \subseteq M(F)$. Thus $l \in l(H) \subseteq cl_H(l(H)) \subseteq M(F)$, so $F \subseteq M\left(cl_H(l(H))\right)$ which is a disjoint post stage. Thus L(H) is H-Regular space.

Remark 4.2. The converse of above Proposition is not true. The following example shows that the opposite of the above theorem is incorrect.

Example 4.3. Let (L, H) be a graph, We'll create a topology via graph as follows:
$l_1(H) = \{l_1\}, l_2(H) = \{l_3\}, l_3(H) = \{l_2\}$. Then a sub base is a topology is
$S_H = \{\{l_1\}, \{l_3\}, \{l_2\}\}$. The base is $B_H = \{L(H), \emptyset, \{l_1, l_2\}, \{l_1, l_3\}, \{l_3, l_2\}, \{l_3\}, \{l_1\}, \{l_2\}\}$. Therefore, the topological graph on H is $\sigma_H = \{L(H), \emptyset, \{l_1, l_2\}, \{l_1, l_3\}, \{l_3, l_2\}, \{l_3\}, \{l_1\}, \{l_2\}\}$
Then $\{l_1, l_2\}$ is closed a post stage and $\{l_1, l_2\} \subseteq M(\{l_1, l_2\})$, there exists a post stage K s.t, $\{l_1, l_2\} \in l(H) \subseteq cl_H(\{l_1, l_2\}) \subseteq M(\{l_1, l_2\})$, but L(H) is not H-Regular space.

Proposition 4.4. Let $(L(H), \sigma_H)$ be a topological graph space. Then the following are equivalents:
1) L(H) is H-α-Regular space.
2) For each $l \in l(H)$, F is α-closed a post stage and $F \subseteq M(F)$, there exists a post stage αK s.t. $l \in l(H) \subseteq \alpha cl_H(l(H)) \subseteq M(F)$.

Proof: it is obvious.

Remark 4.5 the converse of above Proposition is not true. The following example shows that the opposite of the above theorem is incorrect.

Example 4.6: Recall Example 3.3. Then $\{l_1\}$ is α-closed a post stage and $\{l_1\} \subseteq M(\{l_1\})$, there exists a post stage K s.t, $\{l_1\} \in l(H) \subseteq cl_H(\{l_1\}) \subseteq M(\{l_1\})$, but L(H) is not H-α-Regular space.

Proposition 4.7. Let $(L(H), \sigma_H)$ be a topological graph space. Then the following are equivalents:
1) L(H) is H- β regular space.
2) For each $l \in l(H)$, F is β -closed a post stage and $F \subseteq M(F)$, there exists a post stage βK s.t, $l \in l(H) \subseteq \beta cl_H(l(H)) \subseteq M(F)$.

Proof: it is obvious.

Remark 4.8 the converse of above Proposition is not true. The following example shows that the opposite of the above theorem is incorrect.

Example 4.9: Recall Example 3.3. Then $\{l_1, l_3\}$ is β-closed a post stage and $\{l_1, l_3\} \subseteq M(\{l_1, l_3\})$, there exists a post stage K s.t, $\{l_1, l_3\} \in l(H) \subseteq cl_H(\{\{l_1, l_3\}\}) \subseteq M(\{\{l_1, l_3\}\})$, but L(H) is not H-β-Regular space.

Proposition 4.10. Let $(L(H), \sigma_H)$ be H-Regular topological graph space and $l_1, l_2 \in l(H), l_1 = l_2$. Then $cl_H(l_1) = cl_H(l_2)$.

Proof: Assume that $(L(H), \sigma_H)$ be H-Regular and $l_1, l_2 \in l(H), l_1 = l_2$. Suppose that $cl_H(l_1) \neq cl_H(l_2)$. Then $l_1 \notin cl_H(l_2)$ and $l_2 \notin cl_H(l_1)$, since $l_1 \notin cl_H(l_2)$
then there exists a post K s.t, $cl_H(l_1) \subseteq K$, so $l_1 \in M(cl_H(l_2))$ and $l_1 \in M(K)$,
which is a closed post stage. So $cl_H(l_1) \subseteq M(K)$. Thus$cl_H(l_1) = cl_H(l_2)$.

Proposition 4.11. Let $(L(H), \sigma_H)$ be H- α-Regular topological graph space and $l_1, l_2 \in l(H), l_1 = l_2$. Then $\alpha cl_H(l_1) = \alpha cl_H(l_2)$.

Proof: it is clear.

Proposition 4.12. Let $(L(H), \sigma_H)$ be H- β-Regular topological graph space and $l_1, l_2 \in l(H), l_1 = l_2$. Then $\beta cl_H(l_1) = \beta cl_H(l_2)$.

Proof: it is clear.

Proposition 4.13. Let $(L(H), \sigma_H)$ be a topological graph space. Then the following are equivalents:
1) L(H) is H-Normal space.
2) For each $l \in l(H)$, F is closed a post stage and $F \subseteq M(F)$, there exists a post stage K s.t, $l \in l(H) \supseteq int_H(l(H)) \subseteq M(F)$.

Proof: (1) $\Longrightarrow$ (2) Assume that L(H) is H-Regular space, F is closed a post stage and
$l \in M(F)$, then there exists a post stage K s.t, $l \in l(H) \supseteq int_H(l(H))$, so that
$M\left(int_H(l(H))\right)$ and $int_H(l(H)) \subseteq M(F)$. Thus $l \in l(H) \supseteq int_H(l(H)) \subseteq M(F)$.
(2) $\Longrightarrow$ (1) Assume that F is closed a post stage, $l \in M(F)$,so that there exists a post stage K s.t, $l \in l(H) \supseteq int_H(l(H)) \subseteq M(F)$ .Thus $l \in l(H) \supseteq int_H(l(H)) \subseteq M(F)$, so $F \subseteq M\left(int_H(l(H))\right)$ which is a disjoint post stage.Thus L(H) is H-Normal space.

Remark 4.14 the converse of above Proposition is not true. The following example shows that the opposite of the above theorem is incorrect.

Example 4.15: Recall Example 3.15. Then $\{l_1\}$ is closed a post stage and $\{l_1\} \subseteq M(\{l_1\})$, there exists a post stage K s.t, $\{l_1\} \in l(H) \subseteq cl_H(\{\{l_1\}\}) \subseteq M(\{\{l_1\}\})$, but L(H) is not H- Normal space.

Proposition 3.16. Let $(L(H), \sigma_H)$ be a topological graph space. Then the following are equivalents:
1) L(H) is H-α-Normal space.
2) For each $l \in l(H)$, F is α-closed a post stage and $F \subseteq M(F)$, there exists a post stage αK s.t, $l \in l(H) \supseteq \alpha int_H(l(H)) \subseteq M(F)$.

Proof: it is obvious.

Remark 4.17 the converse of above Proposition is not true. The following example shows that the opposite of the above theorem is incorrect.

Example 4.18: Recall Example 3.8. Then $\{l_2\}$ is α-closed a post stage and $\{l_2\} \subseteq M(\{l_2\})$, there exists a post stage K s.t, $\{l_2\} \in l(H) \subseteq cl_H(\{\{l_2\}\}) \subseteq M(\{\{l_2\}\})$, but L(H) is not H-α-Regular space.

Proposition 4.19. Let $(L(H), \sigma_H)$ be a topological graph space. Then the following are equivalents:
1) L(H) is H- β-Normal space.
2) For each $l \in l(H)$, F is β-closed a post stage and $F \subseteq M(F)$, there exists a post stage βK s.t. $l \in l(H) \supseteq \beta\, int_H(l(H)) \subseteq M(F)$.

Proof: it is obvious.

Remark 4.20 the converse of above Proposition is not true. The following example shows that the opposite of the above theorem is incorrect.

Example 4.21: Recall Example 3.11. Then $\{l_1, l_2\}$ is β-closed a post stage and $\{l_1, l_2\} \subseteq M(\{l_1, l_2\})$, there exists a post stage K s.t. $\{l_1, l_2\} \in l(H) \subseteq cl_H(\{\{l_1, l_2\}\}) \subseteq M(\{\{l_1, l_2\}\})$, but L(H) is not H-β-Regular space.

Proposition 4.22. Let $(L(H), \sigma_H)$ be H- normal topological graph space and $l_1, l_2 \in l(H), l_1 = l_2$. Then $int_H(l_1) = int_H(l_2)$.

Proof: Assume that $(L(H), \sigma_H)$ be H-Normal and $l_1, l_2 \in l(H), l_1 = l_2$. Suppose that $int_H(l_1) \neq int_H(l_2)$.Then $l_1 \notin int_H(l_2)$ and $l_2 \notin int_H(l_1)$, since $l_1 \notin int_H(l_2)$
then there exists a post K s.t, $int_H(l_1) \supseteq K$, so $l_1 \in M(int_H(l_2))$ and $l_1 \in M(K)$,
which is a closed post stage. So $int_H(l_1) \supseteq M(K)$. Thus $int_H(l_1) = int_H(l_2)$.

Proposition 4.23. Let $(L(H), \sigma_H)$ be H- α-Normal topological graph space and $l_1, l_2 \in l(H), l_1 = l_2$. Then $\alpha int_H(l_1) = \alpha int_H(l_2)$.

Proof: it is clear.

Proposition 4.24. Let $(L(H), \sigma_H)$ be H- β-Normal topological graph space and $l_1, l_2 \in l(H), l_1 = l_2$. Then $\beta int_H(l_1) = \beta int_H(l_2)$.

Proof: it is clear.

5. Conclusion

The regular space and the normal space were generalized to the space of the topological graph statement, as well as the α and β were generalized to both spaces, and we studied the relationships among these generalizations and gave us opposite examples of cases in which the opposite is not valid. We also obtained cases for all these generalizations.

References

[1] Abdu K A and Kilicman A 2018 Topologies on the edges set of directed graphs *International Journal of Mathematical Analysis* **12** (2) 71-84
[2] Andrijevic D 1986 Semi-preopen sets *Mat. Vesnik* **38** (1) 24-32

[3] Bonikowski Z 2004 A representation theorem for codiangonalizable al-gebras *Reports on Mathematical Logic* **38** 13-22
[4] Galton A 2003 A generalized topological view of motion in discrete space *Theoretical Computer Science* **305** 111-134
[5] J. M. Kosterlitz, 2017 "Nobel lecture: Topological defects and phase transitions," *Reviews of Modern Physics* **89** (4) 040-501
[6] Mahdi A H and Saba N F 2013 Construction A Topology On Graphs *Journal of Al-Qadisiyah for computer science and mathematics* **5** 39-46
[7] Radwan A, Nayle M S and Nasir A I 2012 New Rough Sets Properties on Graph Theory *Int. J. Contemp. Math. Sciences* 7 1217–1232
[8] Shokry M 2015 Generating topology on graphs by operations on graphs *Applied Mathematical Sciences* **9** 2843-2857
[9] Stadler B M R and Stadler P F 2002 Generalized topological spaces in evolutionary theory and combinatorial chemistry *Journal of Chemical Information and Computer Sciences* **42**(3) 577-585

Separation Axioms with Grill-Topological Open Set

Separation Axioms with Grill-Topological Open Set

R B Esmaeel[1,*] and M O Mustafa[2,3]

[1]Department of Mathematics, Ibn Al-HaithamCollege of Education, University of Baghdad, IRAQ
[2]Department of Mathematics, College of Computers Science And Mathematics, University of Mosul, IRAQ
[3]Department of Mathematics, College of Basic Education, University of Telafer, IRAQ

E-mail: ranamumosa@yahoo.com

Abstract. The concepts 𝔾-g-closedness and 𝔾-g-openness were used to popularize presented modern classes of separation axioms in grill topological spaces. Many relationships between multiple kinds of these classes are summarized, too.

1. Introduction

A nonempty collection 𝔾 of nonempty subsets of a topological space 𝕏 is named a Grill if

i. $\mathcal{A} \in \mathbb{G}$ and $\mathcal{A} \subseteq \mathcal{B} \subseteq \mathbb{X}$ then $\mathcal{B} \in \mathbb{G}$

ii. $\mathcal{A}, \mathcal{B} \subseteq \mathbb{X}$ and $\mathcal{A} \cup \mathcal{B} \in \mathbb{G}$ then $\mathcal{A} \in \mathbb{G}$ *or* $\mathcal{B} \in \mathbb{G}$ [1]. Let 𝕏 be a nonempty set. Then the following families are grills on 𝕏. [1-3]

- $\{\emptyset\}$ and $P(\mathbb{X})\backslash\{\emptyset\}$ are trivial examples of grills on 𝕏.
- $\mathbb{G}_{\infty}$ the grill of all infinite subsets of 𝕏.
- $\mathbb{G}_{co}$ the grill of all uncountable subsets of 𝕏.
- $\mathbb{G}_p = \{ \Lambda : \Lambda \in P(\mathbb{X}), p \in \Lambda \}$ is a specific point grills on 𝕏.
- $\mathbb{G}_{\mathcal{A}} = \{ \mathcal{B} : \mathcal{B} \in P(\mathbb{X}), \mathcal{B} \cap \mathcal{A}^c \neq \emptyset \}$, and

If $(\mathbb{X},\mathfrak{t})$ is a topological space, then the family of all non-nowhere dense subsets called $\mathbb{G}_{\varsigma} = \{ \mathcal{A} \subseteq \mathbb{X} : \mathrm{int}_{\mathfrak{t}}\, \mathrm{cl}_{\mathfrak{t}}(\mathcal{A}) \neq \emptyset \}$. Is the one of kinds of grill on 𝕏.

Let 𝔾 be a grill on a topological space$(\mathbb{X},\mathfrak{t})$. The operator $\varphi: P(\mathbb{X}) \to P(\mathbb{X})$ was defined by $\varphi(\mathcal{A}) = \{x \in \mathbb{X} \setminus U \cap \mathcal{A} \in \mathbb{G}$, for all $U \in \mathfrak{t}(x)\}$, $\mathfrak{t}(x)$ denotes the neighborhood of x. A mapping $\Psi: P(\mathbb{X}) \to P(\mathbb{X})$ is defined as $\Psi(\mathcal{A}) = \mathcal{A} \cup \varphi(\mathcal{A})$ for all $\mathcal{A} \in P(\mathbb{X})$ [4-6].

The map Ψ satisfies Kuratowski closure axioms: [3,4]

(i) $\Psi(\emptyset) = \emptyset$,
(ii) If $\mathcal{A} \subseteq \mathcal{B}$, then $\Psi(\mathcal{A}) \subseteq \Psi(\mathcal{B})$,
(iii) If $\mathcal{A} \subseteq \mathbb{X}$, then $\Psi(\Psi(\mathcal{A})) = \Psi(\mathcal{A})$,
(iv) If $\mathcal{A}, \mathcal{B} \subseteq \mathbb{X}$, then $\Psi(\mathcal{A} \cup \mathcal{B}) = \Psi(\mathcal{A}) \cup \Psi(\mathcal{B})$.

In this research, we presented 𝔾-g-closed set and it is complement 𝔾-g-open set some notions have been presented by new kinds of separation axioms like: 𝔾-g-$\mathbb{T}_0$-space, 𝔾-g-$\mathbb{T}_1$-space, 𝔾-g-$\mathbb{T}_2$-space. ■

2. Separation Axioms with Grill-Topological Open Set

Definition 2. 1: In grill topological space $(\mathbb{X}, \mathbb{t}, \mathbb{G})$, let $\mathbb{D} \subseteq \mathbb{X}$. $\mathbb{D}$ is said to be grill-g-closed set denoted by "$\mathbb{G}$-g-closed", if $(\mathbb{D} - \mathbb{U}) \notin \mathbb{G}$ then, $(cl(\mathbb{D}) - \mathbb{U}) \notin \mathbb{G}$ where every, $\mathbb{U} \subseteq \mathbb{X}$ and $\mathbb{U} \in \mathbb{t}$.
Now, D^c is a grill-g-open set denoted by "$\mathbb{G}$-g-open" .The family of all "$\mathbb{G}$-g-closed" sets denoted by $\mathbb{G}\mathbf{g}C(\mathbb{X})$. The family of all "$\mathbb{G}$-g-open" sets denoted by $\mathbb{G}\mathbf{g}O(\mathbb{X})$.

Example 2. 2: Consider the space $(\mathbb{X}, \mathbb{t}, \mathbb{G})$, where $\mathbb{X} = \{ \mathbb{f}_1, \mathbb{f}_2, \mathbb{f}_3\}$, $\mathbb{t} = \{\mathbb{X}, \emptyset, \{ \mathbb{f}_1\}, \{ \mathbb{f}_2\}, \{ \mathbb{f}_1, \mathbb{f}_2\}\}$, and $\mathbb{G} = \{\mathbb{X}, \{ \mathbb{f}_1\}, \{ \mathbb{f}_1, \mathbb{f}_2\}, \{ \mathbb{f}_1, \mathbb{f}_3\}\}$. So,
$P(\mathbb{X}) = \{ \mathbb{X}, \emptyset, \{ \mathbb{f}_1\}, \{ \mathbb{f}_2\}, \{ \mathbb{f}_3\}, \{ \mathbb{f}_1, \mathbb{f}_2\}, \{ \mathbb{f}_1, \mathbb{f}_3\}, \{ \mathbb{f}_2, \mathbb{f}_3\}\}$
$\mathbb{G}gC(\mathbb{X}) = \{ \mathbb{X}, \emptyset, \{ \mathbb{f}_1\}, \{ \mathbb{f}_2\}, \{ \mathbb{f}_3\}, \{ \mathbb{f}_1, \mathbb{f}_2\}, \{ \mathbb{f}_1, \mathbb{f}_3\}, \{ \mathbb{f}_2, \mathbb{f}_3\}\}$, $\mathbb{G}gO(\mathbb{X}) = \{ \mathbb{X}, \emptyset, \{ \mathbb{f}_1\}, \{ \mathbb{f}_2\}, \{ \mathbb{f}_3\}, \{ \mathbb{f}_1, \mathbb{f}_2\}, \{ \mathbb{f}_1, \mathbb{f}_3\}, \{ \mathbb{f}_2, \mathbb{f}_3\}\}$.

Remark 2. 3: For any $(\mathbb{X}, \mathbb{t}, \mathbb{G})$ then
i. Every closed set is a $\mathbb{G}$-g-closed set.
ii. Every open set is a $\mathbb{G}$-g-open set.
The converse of Remark 2. 3 is not true. See Example 2. 2.
$\{\mathbb{f}_1\}$ is a $\mathbb{G}$-g-closed set, but $\{\mathbb{f}_1\}$ is not closed set.
$\{\mathbb{f}_1, \mathbb{f}_3\}$ is a $\mathbb{G}$-g-open set, but $\{\mathbb{f}_1, \mathbb{f}_3\}$ is not open set.

Definition 2. 4: The space $(\mathbb{X}, \mathbb{t}, \mathbb{G})$ is a $\mathbb{G}$-g-$\mathbb{T}_0$-space shortly "$\mathbb{G}g$-$\mathbb{T}_0$-space" if for each $\mathbb{m} \neq \mathbb{n}$ and $\mathbb{m}, \mathbb{n} \in \mathbb{X}$, there exist $\mathbb{U} \in \mathbb{G}g\text{-}o(\mathbb{X})$ whenever, $\mathbb{m} \in \mathbb{U}$ and $\mathbb{n} \notin \mathbb{U}$ or $\mathbb{m} \notin \mathbb{U}$ and $\mathbb{n} \in \mathbb{U}$.

Example 2. 5: Consider the space $(\mathbb{X}, \mathbb{t}, \mathbb{G})$, where $\mathbb{X} = \{ \mathbb{f}_1, \mathbb{f}_2 \}$, $\mathbb{t} = \{\mathbb{X}, \emptyset, \{ \mathbb{f}_1\}\}$ and $\mathbb{G} = \{\mathbb{X}, \{ \mathbb{f}_2\}\}$. $\mathbb{G}gC(\mathbb{X}) = \{ \mathbb{X}, \emptyset, \{ \mathbb{f}_2\}\}$, $\mathbb{G}gO(\mathbb{X}) = \{ \mathbb{X}, \emptyset, \{ \mathbb{f}_1\}\}$. Hence $(\mathbb{X}, \mathbb{t}, \mathbb{G})$ is a $\mathbb{G}g$-$\mathbb{T}_0$-space.

Proposition 2. 6: If $(\mathbb{X}, \mathbb{t})$ is a $\mathbb{T}_0$-space then $(\mathbb{X}, \mathbb{t}, \mathbb{G})$ is a $\mathbb{G}g$-$\mathbb{T}_0$-space.
Proof: By Remark 2. 3. (ii).For each $\mathbb{U} \in \mathbb{t}$, then $\mathbb{U}$ is a $\mathbb{G}g$-open set ,so the proof is over.

Definition 2. 7: The space $(\mathbb{X}, \mathbb{t}, \mathbb{G})$ is a $\mathbb{G}$-g-$\mathbb{T}_1$-space shortly "$\mathbb{G}g$-$\mathbb{T}_1$-space" if for each $\mathbb{m}, \mathbb{n} \in \mathbb{X}$ and $\mathbb{m} \neq \mathbb{n}$. Then there are $\mathbb{G}g$-open sets $\mathbb{U}_1, \mathbb{U}_2$ whenever $\mathbb{m} \in \mathbb{U}_1$, $\mathbb{n} \notin \mathbb{U}_1$ and $\mathbb{n} \in \mathbb{U}_2$, $\mathbb{m} \notin \mathbb{U}_2$.

Example 2. 8: A space $(\mathbb{X}, \mathbb{t}, \mathbb{G})$ when $\mathbb{X} = \mathbb{N}$, where $\mathbb{N}$ is the set of all natural numbers, $\mathbb{t} = \mathbb{t}_{cof} = \{ \mathbb{U} \subseteq \mathbb{N}, \mathbb{U}^c$ is a finite set$\} \cup \emptyset$ *and* $\mathbb{G} = P(\mathbb{X})\backslash\{\emptyset\}$. So $(\mathbb{X}, \mathbb{t}, \mathbb{G})$ is a $\mathbb{G}g$-$\mathbb{T}_1$-space. Since for each $\mathbb{m}, \mathbb{n} \in \mathbb{X}$ and $\mathbb{m} \neq \mathbb{n}$. Then there are $\mathbb{G}g$-open sets $(\mathbb{N} - \{\mathbb{n}\})$, $(\mathbb{N} - \{\mathbb{m}\})$ whenever $\{\mathbb{n}\}$ and $\{\mathbb{m}\}$ are two finite sets such that $(\mathbb{m} \in (\mathbb{N} - \{\mathbb{n}\}))$, $(\mathbb{n} \notin (\mathbb{N} - \{\mathbb{n}\}))$ and $(\mathbb{m} \notin (\mathbb{N} - \{\mathbb{m}\}))$, $(\mathbb{n} \in (\mathbb{N} - \{\mathbb{m}\}))$.

Proposition 2. 9**:** If $(\mathbb{X}, \mathbb{t})$ is a $\mathbb{T}_1$-space then $(\mathbb{X}, \mathbb{t}, \mathbb{G})$ is a $\mathbb{G}g$-$\mathbb{T}_1$-space.
Proof: By Remark 2. 3.(ii).For each $\mathbb{U} \in \mathbb{t}$, then $\mathbb{U}$ is a $\mathbb{G}g$-open set ,so the proof is over.

Proposition 2. 10: If $(\mathbb{X}, \mathbb{t}, \mathbb{G})$ is a $\mathbb{G}g$-$\mathbb{T}_1$-space then it is a $\mathbb{G}g$-$\mathbb{T}_0$-space.

Proof: Let $\mathbb{m}, \mathbb{n} \in \mathbb{X}$ such that $\mathbb{m} \neq \mathbb{n}$ since $(\mathbb{X}, \mathbb{t}, \mathbb{G})$ is a $\mathbb{G}g$-$\mathbb{T}_1$-space, then there exists $\mathbb{U}_1, \mathbb{U}_2 \in \mathbb{G}g\text{-}o(\mathbb{X})$ such that, $\mathbb{m} \in \mathbb{U}_1$, $\mathbb{n} \notin \mathbb{U}_1$ and $\mathbb{n} \in \mathbb{U}_2$, $\mathbb{m} \notin \mathbb{U}_2$. Then there exist $\mathbb{U} \in \mathbb{G}g\text{-}o(\mathbb{X})$ whenever, $\mathbb{m} \in \mathbb{U}$, $\mathbb{n} \notin \mathbb{U}$ and $\mathbb{m} \notin \mathbb{U}$, $\mathbb{n} \in \mathbb{U}$.
The converse of proposition 2. 10 is not true for example 2. 11.

Example 2. 11: The grill topological space $(\mathbb{X}, \mathbb{t}, \mathbb{G})$ is a $\mathbb{G}g$-$\mathbb{T}_0$-space, where $\mathbb{X} = \{\mathbb{f}_1, \mathbb{f}_2\}$, $\mathbb{t} = \{\mathbb{X}, \emptyset, \{ \mathbb{f}_2\}\}$ and $\mathbb{G} = \{\mathbb{X}, \{ \mathbb{f}_1\}\}$. $\mathbb{G}gC(\mathbb{X}) = \{ \mathbb{X}, \emptyset, \{ \mathbb{f}_1\}\}$, $\mathbb{G}gO(\mathbb{X}) = \{ \mathbb{X}, \emptyset, \{\mathbb{f}_2\}\}$. The grill topological space $(\mathbb{X}, \mathbb{t}, \mathbb{G})$ is not $\mathbb{G}g$-$\mathbb{T}_1$-space, since for any elements $\mathbb{f}_1 \neq \mathbb{f}_2$, there is no $\mathbb{G}g$-open set $\mathbb{U}$ containing $\mathbb{f}_1$ which does not contain $\mathbb{f}_2$.

Definition 2. 12: The space $(\mathbb{X}, \mathbb{t}, \mathbb{G})$ is a $\mathbb{G}$-g-$\mathbb{T}_2$-space shortly "$\mathbb{G}$g-$\mathbb{T}_2$-space" if for each $\mathbb{m} \neq \mathbb{n}$. There are $\mathbb{G}$g-open sets $\mathbb{U}'_1, \mathbb{U}'_2$ whenever $\mathbb{m} \in \mathbb{U}'_1$, $\mathbb{n} \in \mathbb{U}'_2$ and $\mathbb{U}'_1 \cap \mathbb{U}'_2 = \emptyset$.

Example 2. 13: Consider the space $(\mathbb{X}, \mathbb{t}, \mathbb{G})$, where $\mathbb{X} = \{ \mathbb{f}_1, \mathbb{f}_2, \mathbb{f}_3\}$, $\mathbb{t} = \{\mathbb{X}, \emptyset, \{ \mathbb{f}_1\}, \{\mathbb{f}_2\}, \{ \mathbb{f}_1, \mathbb{f}_2\}\}$, and $\mathbb{G} = \{\mathbb{X}, \{ \mathbb{f}_1\}, \{ \mathbb{f}_1, \mathbb{f}_2 \}, \{ \mathbb{f}_1 , \mathbb{f}_3\}\}$. So, $\mathbb{G}gC(\mathbb{X}) = P(\mathbb{X}) = \mathbb{G}gO(\mathbb{X})$. Hence $(\mathbb{X}, \mathbb{t}, \mathbb{G})$ is a $\mathbb{G}$g-$\mathbb{T}_2$-space.

Proposition 2. 14: If $(\mathbb{X}, \mathbb{t})$ is a $\mathbb{T}_2$-space then $(\mathbb{X}, \mathbb{t}, \mathbb{G})$ is a $\mathbb{G}$g-$\mathbb{T}_2$-space.

Proof: By Remark 2. 3. (ii).For each $\mathbb{U}' \in \mathbb{t}$, then $\mathbb{U}'$ is a $\mathbb{G}$g-open set ,so the proof is over.

Proposition 2. 15: If $(\mathbb{X}, \mathbb{t}, \mathbb{G})$ is a $\mathbb{G}$g-$\mathbb{T}_2$-space then it is a $\mathbb{G}$g-$\mathbb{T}_1$-space.

Proof: Let $\mathbb{m}, \mathbb{n} \in \mathbb{X}$ whenever, $\mathbb{m} \neq \mathbb{n}$ since $(\mathbb{X}, \mathbb{t}, \mathbb{G})$ is a $\mathbb{G}$g-$\mathbb{T}_2$-space, then there are $\mathbb{G}$g-open sets $\mathbb{U}'_1, \mathbb{U}'_2$ such that $\mathbb{m} \in \mathbb{U}'_1$, $\mathbb{n} \in \mathbb{U}'_2$ and $\mathbb{U}'_1 \cap \mathbb{U}'_2 = \emptyset$. Implies $\mathbb{m} \in \mathbb{U}'_1$ and $\mathbb{n} \notin \mathbb{U}'_1$ or $\mathbb{n} \in \mathbb{U}'_2$ and $\mathbb{m} \notin \mathbb{U}'_2$.
The converse of proposition 2. 15 is not true see example 2. 8.
A space $(\mathbb{X}, \mathbb{t}, \mathbb{G})$ is a $\mathbb{G}$g-$\mathbb{T}_1$-space. Which is not $\mathbb{G}$g-$\mathbb{T}_2$-space, since there is no two $\mathbb{G}$g-open sets, $\mathbb{U}'_1, \mathbb{U}'_2$ such that $\mathbb{U}'_1 \cap \mathbb{U}'_2 = \emptyset$.

Remark 2. 16: We have formerly noted that $(\mathbb{X}, \mathbb{t}, \mathbb{G})$ is a $\mathbb{G}$g-$\mathbb{T}_i$-space whenever, it is a $\mathbb{T}_i$-space (for every $i \in \{ 0, 1, 2 \}$).
The converse of Remark 2. 16 is not true in general for example 2. 17.

Example 2. 17: Consider the space $(\mathbb{X}, \mathbb{t}, \mathbb{G})$, where $\mathbb{X} = \{ \mathbb{f}_1, \mathbb{f}_2, \mathbb{f}_3\}$, $\mathbb{t} = \{\mathbb{X}, \emptyset\}$, and $\mathbb{G} = P(\mathbb{X})\backslash\{\emptyset\}$. So, $\mathbb{G}gC(\mathbb{X}) = P(\mathbb{X}) = \mathbb{G}gO(\mathbb{X})$. Then the space $(\mathbb{X}, \mathbb{t}, \mathbb{G})$ is a $\mathbb{G}$g-$\mathbb{T}_i$-space (for every $i \in \{ 0, 1, 2 \}$). But the space $(\mathbb{X}, \mathbb{t})$ is not $\mathbb{T}_i$-space (for every $i \in \{ 0, 1, 2 \}$).
The following diagram shows the relations between the various kinds of concepts of our formerly mentioned.

Diagram (2. 1)

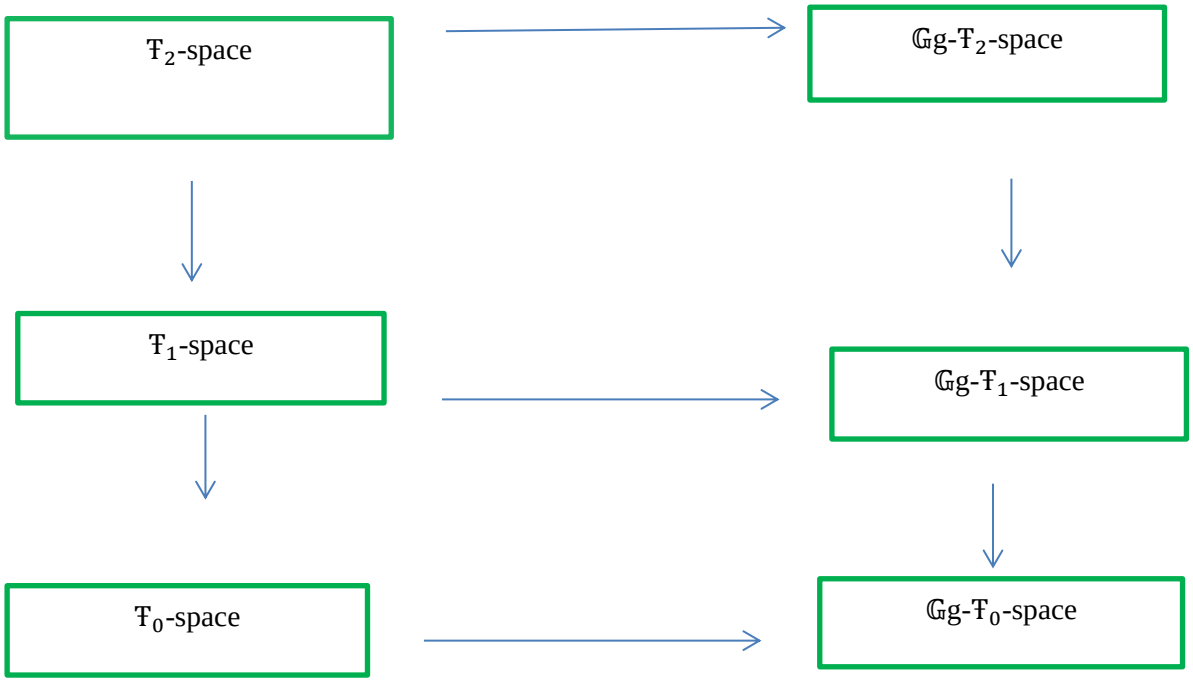

Relationships among $\mathcal{T}_i$-space and $\mathcal{G}$g-$\mathcal{T}_i$-space

3. Separation Axioms with Some Types of Open Functions

Definition 3. 1: The function $\mathcal{F}$: ($\mathcal{X}$, $\mathcal{t}$, $\mathcal{G}$) →($\mathcal{Y}$, $\mathcal{t}$, $\mathcal{G}$) is called
i. $\mathcal{G}$-g-open function, shortly "$\mathcal{G}$go-function" if $\mathcal{F}$ ($\mathcal{U}$) ∈ $\mathcal{G}$g-o($\mathcal{Y}$) whenever, $\mathcal{U}$ ∈ $\mathcal{G}$g-o($\mathcal{X}$).
ii. $\mathcal{G}^*$-g-open function, shortly "$\mathcal{G}^*$go-function" if $\mathcal{F}$ ($\mathcal{U}$) ∈ $\mathcal{G}$g-o($\mathcal{Y}$) whenever, $\mathcal{U}$ ∈ $\mathcal{t}$.
iii. $\mathcal{G}^{**}$-g-open function, shortly "$\mathcal{G}^{**}$go-function" if $\mathcal{F}$ ($\mathcal{U}$) ∈ $\mathcal{t}$ whenever, $\mathcal{U}$ ∈ $\mathcal{G}$g-o($\mathcal{X}$).

Proposition 3. 2: If ($\mathcal{X}$, $\mathcal{t}$, $\mathcal{G}$) is a $\mathcal{G}$g-$\mathcal{T}_i$-space and $\mathcal{F}$ is an onto, $\mathcal{G}$go-function from ($\mathcal{X}$, $\mathcal{t}$, $\mathcal{G}$) to ($\mathcal{Y}$, $\mathcal{t}$, $\mathcal{G}$) then $\mathcal{Y}$ is a $\mathcal{G}$g-$\mathcal{T}_i$-space (for every $i \in \{ 0, 1, 2 \}$).

Proof: If $i = 0$: Let $\mathcal{m}$, $\mathcal{n} \in \mathcal{Y}$ such that $\mathcal{m} \neq \mathcal{n}$. Since $\mathcal{F}$ is an onto function, then $\mathcal{F}^{-1}(\mathcal{m}) \neq \emptyset \neq \mathcal{F}^{-1}(\mathcal{n})$ and $\mathcal{F}^{-1}(\mathcal{m})$, $\mathcal{F}^{-1}(\mathcal{n}) \in \mathcal{X}$ and $\mathcal{F}^{-1}(\mathcal{m}) \neq \mathcal{F}^{-1}(\mathcal{n})$. Since ($\mathcal{X}$, $\mathcal{t}$, $\mathcal{G}$) is a $\mathcal{G}$g-$\mathcal{T}_0$-space, then there exist $\mathcal{U} \in \mathcal{G}$g-o($\mathcal{X}$) whenever $\mathcal{F}^{-1}(\mathcal{m}) \in \mathcal{U}$, $\mathcal{F}^{-1}(\mathcal{n}) \notin \mathcal{U}$ or $\mathcal{F}^{-1}(\mathcal{m}) \notin \mathcal{U}$, $\mathcal{F}^{-1}(\mathcal{n}) \in \mathcal{U}$. Since $\mathcal{F}$ is a $\mathcal{G}$go-function, then $\mathcal{F}(\mathcal{U})$ is a $\mathcal{G}$g-open set such that $\mathcal{m} \in \mathcal{F}(\mathcal{U})$ and $\mathcal{n} \notin \mathcal{F}(\mathcal{U})$ or $\mathcal{m} \notin \mathcal{F}(\mathcal{U})$ and $\mathcal{n} \in \mathcal{F}(\mathcal{U})$. Hence $\mathcal{Y}$ is a $\mathcal{G}$g-$\mathcal{T}_0$-space. If $i = 1$: Let $\mathcal{m}$, $\mathcal{n} \in \mathcal{Y}$ such that $\mathcal{m} \neq \mathcal{n}$. Since $\mathcal{F}$ is an onto function, then $\mathcal{F}^{-1}(\mathcal{m}) \neq \emptyset \neq \mathcal{F}^{-1}(\mathcal{n})$ and $\mathcal{F}^{-1}(\mathcal{m})$, $\mathcal{F}^{-1}(\mathcal{n}) \in \mathcal{X}$ and $\mathcal{F}^{-1}(\mathcal{m}) \neq \mathcal{F}^{-1}(\mathcal{n})$. So ($\mathcal{X}$, $\mathcal{t}$, $\mathcal{G}$) is a $\mathcal{G}$g-$\mathcal{T}_1$-space, then there exists $\mathcal{U}_1, \mathcal{U}_2 \in \mathcal{G}$g-o($\mathcal{X}$) such that $\mathcal{F}^{-1}(\mathcal{m}) \in \mathcal{U}_1$, $\mathcal{F}^{-1}(\mathcal{n}) \notin \mathcal{U}_1$and $\mathcal{F}^{-1}(\mathcal{n}) \in \mathcal{U}_2$, $\mathcal{F}^{-1}(\mathcal{m}) \notin \mathcal{U}_2$. By the condition $\mathcal{F}$ is a $\mathcal{G}$go-function, $\mathcal{F}(\mathcal{U}_1)$, $\mathcal{F}(\mathcal{U}_2)$ are $\mathcal{G}$g-open sets in $\mathcal{Y}$ such that $\mathcal{m} \in \mathcal{F}(\mathcal{U}_1)$, $\mathcal{n} \notin \mathcal{F}(\mathcal{U}_1)$ and $\mathcal{n} \in \mathcal{F}(\mathcal{U}_2)$, $\mathcal{m} \notin \mathcal{F}(\mathcal{U}_2)$. Hence ($\mathcal{Y}$, $\mathcal{t}$, $\mathcal{G}$) is a $\mathcal{G}$g-$\mathcal{T}_1$-space.
If $i = 2$: The same proof above , but $\mathcal{F}(\mathcal{U}_1) \cap \mathcal{F}(\mathcal{U}_2) = \emptyset$. Hence ($\mathcal{Y}$, $\mathcal{t}$, $\mathcal{G}$) is a $\mathcal{G}$g-$\mathcal{T}_2$-space.

Corollary 3. 3: If ($\mathcal{X}$, $\mathcal{t}$) is a $\mathcal{T}_i$-space and $\mathcal{F}$ is an onto, $\mathcal{G}^*$go-function from ($\mathcal{X}$, $\mathcal{t}$, $\mathcal{G}$) to ($\mathcal{Y}$, $\mathcal{t}$, $\mathcal{G}$) then ($\mathcal{Y}$, $\mathcal{t}$, $\mathcal{G}$) is a $\mathcal{G}$g-$\mathcal{T}_i$-space, where $i \in \{ 0, 1, 2 \}$.

Proof: Follows from $\mathcal{F}(\mathcal{U})$ is a $\mathcal{G}$g-open in ($\mathcal{Y}$, $\mathcal{t}$, $\mathcal{G}$) for all open set $\mathcal{U}$ in $\mathcal{X}$.

Corollary 3. 4: If ($\mathcal{X}$, $\mathcal{t}$, $\mathcal{G}$) is a $\mathcal{G}$g-$\mathcal{T}_i$-space and $\mathcal{F}$ is an onto, $\mathcal{G}^{**}$go-function from ($\mathcal{X}$, $\mathcal{t}$, $\mathcal{G}$) to ($\mathcal{Y}$, $\mathcal{t}$, $\mathcal{G}$) then $\mathcal{Y}$ is a $\mathcal{T}_i$-space, where $i \in \{ 0, 1, 2 \}$.

Proof: Follows from $\mathcal{F}(\mathcal{U})$ is an open set in $\mathcal{Y}$ for all $\mathcal{G}$g-open set $\mathcal{U}$ in ($\mathcal{X}$, $\mathcal{t}$, $\mathcal{G}$).

Corollary 3. 5: If $\mathcal{F}$ is an onto and open function from ($\mathcal{X}$, $\mathcal{t}$) to ($\mathcal{Y}$, $\mathcal{t}$) and ($\mathcal{X}$, $\mathcal{t}$) is a $\mathcal{T}_i$-space, then ($\mathcal{Y}$, $\mathcal{t}$, $\mathcal{G}$) is a $\mathcal{G}$g-$\mathcal{T}_i$-space, where $i \in \{ 0, 1, 2 \}$, for any grill $\mathcal{G}$ on ($\mathcal{Y}$, $\mathcal{t}$, $\mathcal{G}$).

Definition 3. 6: The function $\mathcal{F}$: ($\mathcal{X}$, $\mathcal{t}$, $\mathcal{G}$) →($\mathcal{Y}$, $\mathcal{t}$, $\mathcal{G}$) is called
i. $\mathcal{G}$-g-continuous function, shortly "$\mathcal{G}$g-continuous function" if $\mathcal{F}^{-1}(\mathcal{U}) \in \mathcal{G}$g-o($\mathcal{X}$) for all $\mathcal{U} \in \mathcal{t}$.
ii. Strongly-$\mathcal{G}$-g-continuous function, shortly "Strongly-$\mathcal{G}$g-continuous function" if $\mathcal{F}^{-1}(\mathcal{U}) \in \mathcal{t}$ for every, $\mathcal{U} \in \mathcal{G}$g-o($\mathcal{Y}$).
iii. $\mathcal{G}$-g-irresolute function, shortly "$\mathcal{G}$g-irresolute function" if $\mathcal{F}^{-1}(\mathcal{U}) \in \mathcal{G}$g-o($\mathcal{X}$) for every, $\mathcal{U} \in \mathcal{G}$g-o($\mathcal{Y}$).

Proposition 3. 7: If ($\mathcal{Y}$, $\mathcal{t}$) is a $\mathcal{T}_i$-space and $\mathcal{F}$: ($\mathcal{X}$, $\mathcal{t}$, $\mathcal{G}$) → ($\mathcal{Y}$, $\mathcal{t}$, $\mathcal{G}$) is an injective, $\mathcal{G}$g-continuous function then ($\mathcal{X}$, $\mathcal{t}$, $\mathcal{G}$) is a $\mathcal{G}$g-$\mathcal{T}_i$-space, where $i \in \{ 0, 1, 2 \}$.

Proof: If $i = 0$: Let $\mathcal{m}$, $\mathcal{n} \in \mathcal{X}$ such that $\mathcal{m} \neq \mathcal{n}$. Since $\mathcal{F}$ is an injective function, then $\mathcal{F}(\mathcal{m}) \neq \mathcal{F}(\mathcal{n})$, where, $\mathcal{F}(\mathcal{m})$, $\mathcal{F}(\mathcal{n}) \in \mathcal{Y}$. So, ($\mathcal{Y}$, $\mathcal{t}$) is a $\mathcal{T}_0$-space, then there exist $\mathcal{U} \in \mathcal{t}$ whenever, $\mathcal{F}(\mathcal{m}) \in \mathcal{U}$, $\mathcal{F}(\mathcal{n}) \notin \mathcal{U}$ or $\mathcal{F}(\mathcal{m})$

$\notin U'$, $\mathfrak{f}(\mathfrak{n}) \in U'$. By $\mathfrak{f}$ is a $\mathbb{G}$g-continuous function, then $\mathfrak{f}^{-1}(U') \in \mathbb{G}$g-o($\mathbb{X}$) whenever, $\mathfrak{m} \in \mathfrak{f}^{-1}(U')$, $\mathfrak{n} \notin \mathfrak{f}^{-1}(U')$ or $\mathfrak{m} \notin \mathfrak{f}^{-1}(U')$, $\mathfrak{n} \in \mathfrak{f}^{-1}(U')$. Hence ($\mathbb{X}, \mathfrak{t}, \mathbb{G}$) is a $\mathbb{G}$g-$\mathbb{T}_0$-space.
If i = 1: Let $\mathfrak{m}, \mathfrak{n} \in \mathbb{X}$ such that $\mathfrak{m} \neq \mathfrak{n}$. Since $\mathfrak{f}$ is an injective function, then $\mathfrak{f}(\mathfrak{m}) \neq \mathfrak{f}(\mathfrak{n})$, where, $\mathfrak{f}(\mathfrak{m})$, $\mathfrak{f}(\mathfrak{n}) \in \mathbb{Y}$. So, ($\mathbb{Y}, \mathfrak{t}$) is a $\mathbb{T}_1$-space, then there exists U'_1, $U'_2 \in \mathfrak{t}$ whenever, $\mathfrak{f}(\mathfrak{m}) \in U'_1$, $\mathfrak{f}(\mathfrak{n}) \notin U'_1$ and $\mathfrak{f}(\mathfrak{n}) \in U'_2$, $\mathfrak{f}(\mathfrak{m}) \notin U'_2$. Since $\mathfrak{f}$ is a $\mathbb{G}$g-continuous function, then $\mathfrak{f}^{-1}(U'_1)$ and $\mathfrak{f}^{-1}(U'_2)$ are $\mathbb{G}$g-open sets whenever, $\mathfrak{m} \in \mathfrak{f}^{-1}(U'_1)$, $\mathfrak{n} \notin \mathfrak{f}^{-1}(U'_1)$ and $\mathfrak{n} \in \mathfrak{f}^{-1}(U'_2)$, $\mathfrak{m} \notin \mathfrak{f}^{-1}(U'_2)$. Hence ($\mathbb{X}$, $\mathfrak{t}$, $\mathbb{G}$) is a $\mathbb{G}$g-$\mathbb{T}_1$-space.
If i = 2: The same proof above but $\mathfrak{f}(U'_1) \cap \mathfrak{f}(U'_2) = \emptyset$. Hence ($\mathbb{Y}$, $\mathfrak{t}$, $\mathbb{G}$) is a Gg-$\mathbb{T}_2$-space.

Remark 3. 8: Let $\mathfrak{f}$: ($\mathbb{X}, \mathfrak{t}, \mathbb{G}$) →($\mathbb{Y}$, $\mathfrak{t}$, $\mathbb{G}$) is a function
If $\mathfrak{f}$ is a continuous function, then $\mathfrak{f}$ is a $\mathbb{G}$g- continuous function

Corollary 3. 9: If ($\mathbb{Y}$, $\mathfrak{t}$) is a $\mathbb{T}_i$-space and $\mathfrak{f}$: ($\mathbb{X}, \mathfrak{t}, \mathbb{G}$) →($\mathbb{Y}$, $\mathfrak{t}$, $\mathbb{G}$) is an injective continuous function, then ($\mathbb{X}, \mathfrak{t}, \mathbb{G}$) is a $\mathbb{G}$g-$\mathbb{T}_i$-space, where $i \in \{ 0, 1, 2 \}$.

Proof: Since every continuous function is a $\mathbb{G}$g-continuous function by Proposition 3. 7, then Corollary 3. 5, is applicable

Proposition 3. 10: If ($\mathbb{Y}$, $\mathfrak{t}$, $\mathbb{G}$) is a $\mathbb{G}$g-$\mathbb{T}_i$-space and $\mathfrak{f}$: ($\mathbb{X}, \mathfrak{t}, \mathbb{G}$) → ($\mathbb{Y}$, $\mathfrak{t}$, $\mathbb{G}$) is an injective strongly-$\mathbb{G}$g-continuous function then ($\mathbb{X}, \mathfrak{t}$) is a $\mathbb{T}_i$-space, where $i \in \{ 0, 1, 2 \}$.

Proof: Follows from, $\mathfrak{f}^{-1}(U') \in \mathfrak{t}$ for each $U' \in$ Gg-o($\mathbb{Y}$).

Proposition 3. 11: If ($\mathbb{Y}$, $\mathfrak{t}$, $\mathbb{G}$) is a $\mathbb{G}$g-$\mathbb{T}_i$-space and $\mathfrak{f}$: ($\mathbb{X}, \mathfrak{t}, \mathbb{G}$) → ($\mathbb{Y}$, $\mathfrak{t}$, $\mathbb{G}$) is an injective $\mathbb{G}$g-irresolute function then ($\mathbb{X}, \mathfrak{t}, \mathbb{G}$) is a $\mathbb{G}$g-$\mathbb{T}_i$-space, where $i \in \{ 0, 1, 2 \}$.

Proof: Since $\mathfrak{f}^{-1}(U') \in \mathbb{G}$g-o($\mathbb{X}$) for each $U' \in$ Gg-o($\mathbb{Y}$).

4. Gg-Convergence Sequence
Definition 4. 1: Let ($\mathbb{X}, \mathfrak{t}, \mathbb{G}$) be a grill topological space, where $\mathfrak{x}_0 \in \mathbb{X}$ and $(\mathfrak{S}_\mathfrak{n})_{\mathfrak{n} \in \mathbb{N}}$ be a sequence in $\mathbb{X}$. Then $(\mathfrak{S}_\mathfrak{n})_{\mathfrak{n} \in \mathbb{N}}$ is called Gg-Convergence to $\mathfrak{x}_0$ shortly $\mathfrak{S}_\mathfrak{n} \rightsquigarrow \mathfrak{x}_0$ if for every Gg-open set U' where, $\mathfrak{x}_0 \in U'$ there exist $\mathfrak{K} \in \mathbb{N}$ where, $\mathfrak{S}_\mathfrak{n} \in U'$ for every $\mathfrak{n} \geq \mathfrak{K}$. A sequence $(\mathfrak{S}_\mathfrak{n})_{\mathfrak{n} \in \mathbb{N}}$ is called Gg-divergence, if it is not Gg-Convergence.

Theorem 4. 2: If ($\mathbb{X}$, $\mathfrak{t}$, $\mathbb{G}$) is a $\mathbb{G}$g-$\mathbb{T}_2$-space then every Gg-Convergence sequence in $\mathbb{X}$ has a unique limit point.
Proof: Let $(\mathfrak{S}_\mathfrak{n})_{\mathfrak{n} \in \mathbb{N}}$ be a sequence in $\mathbb{X}$ where, $\mathfrak{S}_\mathfrak{n} \rightsquigarrow \mathfrak{x}_1$ and $\mathfrak{S}_\mathfrak{n} \rightsquigarrow \mathfrak{x}_2$; $\mathfrak{x}_1 \neq \mathfrak{x}_2$ where, $\mathfrak{x}_1, \mathfrak{x}_2 \in \mathbb{X}$. Since ($\mathbb{X}$, $\mathfrak{t}$, $\mathbb{G}$) is a $\mathbb{G}$g-$\mathbb{T}_2$-space then there exists $U'_1, U'_2 \in \mathbb{G}$go($\mathbb{X}$) such that $\mathfrak{x}_1 \in U'_1$ and $\mathfrak{x}_2 \in U'_2$ where $U'_1 \cap U'_2 = \emptyset$. Since $\mathfrak{S}_\mathfrak{n} \rightsquigarrow \mathfrak{x}_1$ and $\mathfrak{x}_1 \in U'_1 \in \mathbb{G}$go($\mathbb{X}$) implies there exist $\mathfrak{K}_1 \in \mathbb{N}$; $\mathfrak{S}_\mathfrak{n} \in U'_1$ for all $\mathfrak{n} \geq \mathfrak{K}_1$. So, $\mathfrak{S}_\mathfrak{n} \rightsquigarrow \mathfrak{x}_2$ and $\mathfrak{x}_2 \in U'_2 \in \mathbb{G}$go($\mathbb{X}$) implies there exist $\mathfrak{K}_2 \in \mathbb{N}$; $\mathfrak{S}_\mathfrak{n} \in U'_2$ for all $\mathfrak{n} \geq \mathfrak{K}_2$. Hence, $U'_1 \cap U'_2 \neq \emptyset$, that is contradiction.
The prerequisite that a space $\mathbb{X}$ is a $\mathbb{G}$g-$\mathbb{T}_2$-space is very necessary to make Theorem 4. 2 is proper.

Example 4. 3**:** Let ($\mathbb{X}$, $\mathfrak{t}$, $\mathbb{G}$) be a grill topological space, where, $\mathbb{X} = \{ \mathfrak{f}_1, \mathfrak{f}_2, \mathfrak{f}_3 \}$, $\mathfrak{t} = \{\mathbb{X}, \emptyset\}$, and $\mathbb{G} = \{\mathbb{X}, \{ \mathfrak{f}_3\}, \{ \mathfrak{f}_1, \mathfrak{f}_3 \}, \{ \mathfrak{f}_2, \mathfrak{f}_3\}\}$. Then $\mathbb{G}$gC($\mathbb{X}$) = $\{ \mathbb{X}, \emptyset, \{ \mathfrak{f}_3\}, \{ \mathfrak{f}_1, \mathfrak{f}_3\}, \{ \mathfrak{f}_2, \mathfrak{f}_3\}\}$, $\mathbb{G}$gO($\mathbb{X}$) = $\{ \mathbb{X}, \emptyset, \{ \mathfrak{f}_1\}, \{ \mathfrak{f}_2\}, \{ \mathfrak{f}_1, \mathfrak{f}_2\}\}$.The sequence $(\mathfrak{S}_\mathfrak{n})_{\mathfrak{n} \in \mathbb{N}}$ in $\mathbb{X}$, where $\mathfrak{S}_\mathfrak{n} = \mathfrak{f}_3$ for all $\mathfrak{n} \in \mathbb{N}$. The sequence $(\mathfrak{S}_\mathfrak{n})_{\mathfrak{n} \in \mathbb{N}}$ has one limit point such that $\mathfrak{S}_\mathfrak{n} \rightsquigarrow \mathfrak{f}_3$, but ($\mathbb{X}$, $\mathfrak{t}$, $\mathbb{G}$) is not $\mathbb{G}$g-$\mathbb{T}_2$-space.

Proposition 4. 4: If a sequence $(\mathfrak{S}_\mathfrak{n})_{\mathfrak{n} \in \mathbb{N}}$ is a Gg-convergence to $\mathfrak{x}_0$ in ($\mathbb{X}, \mathfrak{t}, \mathbb{G}$), then it is a convergence to $\mathfrak{x}_0$.

Proof: Let U' be an open set in X where, $x_0 \in U'$. By Remark 2. 3. (ii). U' is a Gg-open set in X where, $x_0 \in U'$. Since $(S_n)_{n \in \mathbb{N}}$ is a Gg-convergent to x_0, then there exist $K \in \mathbb{N}$ where, $S_n \in U'$ for every $n \geq K$. Hence $(S_n)_{n \in \mathbb{N}}$ is a convergent to x_0.
The converse of Proposition 4. 4 is not true for example 4. 5.

Example 4. 5: Let (X, t, G) be a grill topological space, where, $X = \mathbb{N}$ set of all natural numbers $t = \{X, \emptyset\}$, and $G = P(X)\backslash\{\emptyset\}$, $GgC(X) = P(X) = GgO(X)$. The sequence $(S_n)_{n \in \mathbb{N}}$ where $S_n = n$ for all $n \in \mathbb{N}$ is a convergent to n for all $n \in \mathbb{N}$, which is not Gg-convergence for any element in $\mathbb{N}$.

Proposition 4. 6: Let $f: (X, t, G) \to (Y, t, G)$ be an injective and Gg-irresolute function and $(S_n)_{n \in \mathbb{N}}$ be a sequence in X. Then $f(S_n) \rightsquigarrow f(x_0)$ in (Y, t, G) whenever, $S_n \rightsquigarrow x_0$ in (X, t, G).

Proof: Let U' is a Gg-open set in Y where $f(x_0) \in U'$. Since f is a Gg-irresolute function, then $f^{-1}(U')$ is a Gg-open set where, $x_0 \in f^{-1}(U')$. Since $(S_n)_{n \in \mathbb{N}}$ is a Gg-convergent to x_0, then there exist $K \in \mathbb{N}$ where, $S_n \in f^{-1}(U')$ for all $n \geq K$. Since f is an injective function, then there exist $K \in \mathbb{N}$ where, $f(S_n) \in U'$ for all $n \geq K$. Hence $f(S_n)$ is a Gg-convergent to $f(x_0)$.

Theorem 4. 7: Let $f: (X, t, G) \to (Y, t, G)$ be an injective and Gg-continuous function and $(S_n)_{n \in \mathbb{N}}$ be a sequence in X. Then $f(S_n) \to f(x_0)$ in (Y, t, G) whenever, $S_n \rightsquigarrow x_0$ in (X, t, G).

Proof: Let U' is an open set in (Y, t, G) where, $f(x_0) \in U'$. Since f is a Gg- continuous function, then $f^{-1}(U')$ is a Gg-open set in (X, t, G) where, $x_0 \in f^{-1}(U')$. Since $(S_n)_{n \in \mathbb{N}}$ is a Gg-convergent to x_0, then there exist $K \in \mathbb{N}$ where, $S_n \in f^{-1}(U')$ for all $n \geq K$. Since f is an injective function, then there exist $K \in \mathbb{N}$ where, $f(S_n) \in U'$ for all $n \geq K$. Hence $f(S_n)$ is a convergent to $f(x_0)$.

Proposition 4. 8: Let $f: (X, t, G) \to (Y, t, G)$ be an injective and strongly-Gg-continuous function and $(S_n)_{n \in \mathbb{N}}$ be a sequence in X. Then $f(S_n) \rightsquigarrow f(x_0)$ in (Y, t, G) whenever, $S_n \to x_0$ in (X, t, G).

Proof: Let U' is a Gg-open set in (Y, t, G) where $f(x_0) \in U'$. Since f is a strongly-Gg-continuous function, then $f^{-1}(U')$ is an open set in X where, $x_0 \in f^{-1}(U')$. Since $(S_n)_{n \in \mathbb{N}}$ is a convergent to x_0, then there exist $K \in \mathbb{N}$ where, $S_n \in f^{-1}(U')$ for all $n \geq K$. Since f is an injective function, then there exist $K \in \mathbb{N}$ where, $f(S_n) \in U'$ for all $n \geq K$. Hence $f(S_n)$ is a Gg-convergent to $f(x_0)$.

References

[1] Choquet G 1947 Sur les notions de filter et grille *Comptes Rendus Acad. Sci. Paris* **224** 171-173
[2] Roy B and Mukherjee M N 2007 On a type of compactness via grills *Matematicki Vesnik*. **59** 113-120
[3] Roy B and Mukherjee M N 2007 on a typical topology induced by a grill *Soochow J. Math* **33** (4) 771-786
[4] Shawqi A Hazza, Sobhy A EL-Sheikh, Ali Kandil and Mohamed Ahmed Abdelhakem 2015 on ideals and grills in topological spaces *South Asian Journal of Mathematics* **5** (6) 233-238
[5] Thenmozhi P, Kaleeswari M and Maheswari N 2015 Regular Generalized Closed Sets in Grill Topological Spaces *International Journal of Science Research* 2319-7064
[6] Mustafa M O and Esmaeel R B 2020 Some Properties in Grill–Topological Open and Closed Sets Ready to be Published in *Journal of Physics: Conference Series (6th International Conferen of Iraqi AL-Khwarizmi Association)*

Generalizations of Fuzzy k-ideals in a KU-algebra with Semigroup

Generalizations of Fuzzy k-ideals in a KU-algebra with Semigroup

Fatema F. Kareem[1] and Majid Mohammed Abed[2]

[1]Department of mathematics, college of education for pure sciences (Ibn AL-Haitham) University of Baghdad, Baghdad, Iraq
[2]Department of Mathematics, College of Education, University of Anbar, Iraq

E-mail: fatma.f.k@ihcoedu.uobaghdad.edu.iq

Abstract. We present the notion of bipolar fuzzy k-ideals with thresholds (θ,λ) of a KU-algebra with semigroup and give some basic properties of this ideal. Also, we study some relations about a bipolar fuzzy k-ideal with thresholds (θ,λ) and a k-ideal of a KU-semigroup.

1.Introduction

The idea of a fuzzy set was initialed in 1965 by the author Zadeh [12]. Since, the fuzzy set has been applied to most mathematical fields and other sciences. The notion of fuzzy KU-ideals of ·KU-algebras was introduced by Mostafa et al [6] they given some properties related to fuzzy KU-ideals. In [4] Lee introduced an extension of ·fuzzy sets namely, bipolar fuzzy· sets. This concept is an extension of fuzzy sets from[0, 1] to [-1, 1]. Some authors introduced a bipolar fuzzy set on different algebraic structures, see [3], [5], [7] , [8],[10] and [11]. In this paper, the bipolar ·fuzzy set with· thresholds (θ,λ) to·k-ideal of KU-algebra with semigroup is introduced and some basic relations between a bipolar fuzzy k-ideal with thresholds (θ,λ) and a k-ideal are proved.

2. Basic concepts

To complete this work, we collect some essential definitions and properties related to KU-algebra with semigroup and bipolar fuzzy logic.

Definition2.1 [9]. Algebra$(\aleph,*,0)$ is called a KU-algebra if, for all$\chi,\gamma,\tau \in \aleph$,
$(\mathrm{k}u_1)\ (\chi*\gamma)*[(\gamma*\tau)*(\chi*\tau)]=0$
$(ku_2)\ \chi*0=0$
$(ku_3)\ \ 0*\chi=\chi$
$(ku_4)\chi*\gamma=0$ and$\gamma*\chi$ implies $\chi=\gamma$ and
$(ku_5)\chi*\chi=0$

A binary relation $\leq$on $\aleph$ is define by$\chi\leq\gamma \Leftrightarrow \gamma*\chi=0$. It follows that $(\aleph,\leq)$is a partially ordered set. It follows that $(\aleph,*,0)$ is satisfies the following statements. For all $\chi,\gamma,\tau\in\aleph$,

$(^{ku_{1}}) \ (\gamma * \tau) * (\chi * \tau) \leq (\chi * \gamma)$,
$(^{ku_{2}}) \ 0 \leq \chi$,
$(^{ku_{3}}) \ \chi \leq \gamma, \gamma \leq \chi$ implies $\chi = \gamma$
$(^{ku_{4}}) \ \gamma * \chi \leq \chi$.

Theorem2.2[6]. Let$(\aleph,*,0)$ be a KU-algebra. Then, for all$\chi,\gamma,\tau \in \aleph$,
(1) if $\chi \leq \gamma$ imply $\gamma * \tau \leq \chi * \tau$
(2) $\chi * (\gamma * \tau) = \gamma * (\chi * \tau)$
(3) $((\gamma * \chi) * \chi) \leq \gamma$.

Example 2.3 [9]. Let $\aleph = \{0, a, b, c\}$ be a set and $*$ a binary operation defined in the following table

$*$	0	a	b	c
0	0	a	b	c
a	0	0	0	b
b	0	b	0	a
c	0	0	0	0

It is easy to see that$(\aleph,*,0)$ is a KU-algebra.

Definition 2.4 [9]. Let$(\aleph,*,0)$ be a KU-algebra and I be a non- empty subset of $\aleph$. Then I is called an ideal of $\aleph$ if for any$\chi,\gamma \in \aleph$, then
(i) $0 \in I$and
(ii) If $\chi * \gamma \in I$ and $\chi \in I$ imply $\gamma \in I$.

Definition 2.5 [6]. Let I be a subset of a KU-algebra$(\aleph,*,0)$ and $I \neq \varphi$. Then I is named a *KU*-ideal of $\aleph$, if
(I_1) $0 \in I$ and
$(I_2)\forall \chi,\gamma,\tau \in \aleph$, if $(\chi * (\gamma * \tau)) \in I$, $\gamma \in I$, then $\chi * \tau \in I$.

Definition2.6[2]. A KU-semigroup is a nonempty set $\aleph$ with two binary operations $*,\circ$ and a constant 0 satisfying the following
(I) $(\aleph,*,0)$ is a KU-algebra
(II) $(\aleph,\circ)$is a semigroup
(III) The operation$\circ$is distributive (on both sides) over the operation$*$, i.e.
$\chi \circ (\gamma * \tau) = (\chi \circ \gamma) * (\chi \circ \tau) and (\chi * \gamma) \circ \tau = (\chi \circ \tau) * (\gamma \circ \tau)$, for all$\chi,\gamma,\tau \in X$

Example 2.7[2]. Let $\aleph = \{0,1,2,3\}$be a set. Define$*$ -operation and $\circ\odot$-operation by the following tables

*	0	1	2	3
0	0	1	2	3
1	0	0	0	2
2	0	2	0	1
3	0	0	0	0
| |	0	1	2	3
0	0	0	0	0
1	0	1	0	1
2	0	0	2	2
3	0	1	2	3

Then $(\aleph,*,\circ,0)$ is a KU - semigroup.

Definition 2.8[2]. A *sub*KU-*semigroup* is a non-empty subset A of a KU-semigroup $\aleph$ and it is satisfied $\chi * \gamma, \chi \circ \gamma \in A$, for all $\chi,\gamma \in A$.

Definition2.9[2]. Let $(\aleph,*,\circ,0)$ be a KU-semigroup and $\varphi \neq I\aleph$. Then

I is named an *S-ideal* of $\aleph$, if

(i) I is an ideal of a KU-algebra$(\aleph,*,0)$.
(ii) For all $\chi \in \aleph$, $a \in I$, we have$\chi \circ a \in I$ and $a \circ \chi \in I$.

Definition2.10[2]. Let $(\aleph,*,\circ,0)$ be a KU-semigroup and $\varphi \neq A\aleph$. Then$A$ is said to be a *k-ideal* of $\aleph$ X, if

i) A is an *KU*-ideal of a KU-algebra $(\aleph,*,0)$,
ii) For all$\chi \in X$,$a \in A$, we have $\chi \circ a \in A$ and $a \circ \chi \in A$.

Now, we review some concepts of fuzzy logic.

Let $\aleph$ be the collection of objects and a fuzzy set is a function $\mu : \aleph \to [0,1]$, then $\mu(\chi)$ is called the membership value of χ in $\aleph$ and $0 \le \mu(\chi) \le 1$.

The set $U(\mu,t) = \{\chi \in \aleph : \mu(\chi) \ge t\}$, where $0 \le t \le 1$ is said to be a level set of $\mu(\chi)$.

Defintion2.11[1]. Let $\mu(\chi)$ be a fuzzy set in $\aleph$, then $\mu(\chi)$ is called a fuzzy sub KU-semi group of $\aleph$, if for all $\chi,\gamma \in \aleph$. Then

i) $\mu(\chi * \gamma) \ge \min\{\mu(\chi), \mu(\gamma)\}$

ii) $\mu(\chi \square \gamma) \ge \min\{\mu(\chi), \mu(\gamma)\}$.

Defintion2.12[1]. A fuzzy set $\mu(\chi)$ in $\aleph$ is called a fuzzy *k*-ideal, if for all $\chi,\gamma,\tau \in \aleph$, the following conditions are satisfied

(k_1) $\mu(0) \geq \mu(\chi)$,

(k_2) $\mu(\chi * \tau) \geq \min\{\mu(\chi * (\gamma * \tau)), \mu(\gamma)\}$,

(k_3) $\mu(\chi \square \gamma) \geq \min\{\mu(\chi), \mu(\gamma)\}$.

Example2.13[1]. Let $\aleph = \{0, a, b, c, d\}$ be a set with two operations $*$ and $|$ $\odot$ are defined by the following tables

$*$	0	a	b	c	d
0	0	a	b	c	d
a	0	0	b	c	d
b	0	c	0	c	d
c	0	a	b	0	0
d	0	a	b	c	0

	0	a	b	c	d
0	0	0	0	0	0
a	0	0	0	0	0
b	0	0	0	0	b
c	0	0	0	b	c
d	0	a	b	c	d

Then $(\aleph, *, \circ, 0)$ is a KU-semigroup. Define a fuzzy set $\mu: \aleph \to [0,1]$ by $\mu(0) = \mu(a) = 0.4$, $\mu(b) = \mu(c) = 0.2$, $\mu(d) = 0.1$. Then $\mu(\chi), \forall \chi \in \aleph$ is a fuzzy *k*-ideal.
In the following, we recall some basic concepts about a bipolar fuzzy set.

Definition2.14[4]. The concept (a bipolar fuzzy set B) in a set $\aleph$ is an object having the form $\mathrm{B} = \{(\chi, \mu^-(\chi), \mu^+(\chi)) : \chi \in \aleph\}$, where $\mu^-(\chi): \aleph \to [-1,0]$ $\mu^-: \aleph \to [-1,0]$and $\mu^+(\chi): \aleph \to [0,1]$ are two fuzzy mappings. The two membership degrees $\mu^+(\chi)$ and $\mu^-(\chi)$ $\mu^+(\chi)$denotes the fulfillment degree ofχ $\aleph$ to the property corresponding of B and the fulfillment degree of χ $\aleph$ to some implicit counter-property of B, respectively. The symbol $B = (\chi, \mu^-, \mu^+)$ $\mathrm{B} = (\chi, \mu^-, \mu^+)$ is used instead of $B = \{(\chi, \mu^-(\chi), \mu^+(\chi) | \chi \in \aleph\}$ $\mathrm{B} = \{(\chi, \mu^-(\chi), \mu^+(\chi)) : \chi \in \aleph\}$ and the concept of a bipolar fuzzy set instead of the concept of bipolar-valued fuzzy set.

Definition2.15[4]. Let $B = (\chi, \mu^-, \mu^+)$ $\mathrm{B} = (\chi, \mu^-, \mu^+)$ be a bipolar fuzzy set. Then

(1) For any $(s,t)\in[-1,0]\times[0,1]$, $(s,t)\in[-1,0]\times[0,1]$. the set $B_s^- = \{\chi\in\aleph : \mu^-(\chi)\le s\}$ $B_S^- = \{\chi\in\aleph: \mu^-(\chi)\le s\}$ is named a negative s-cut of $B=(\chi,\mu^-,\mu^+)$ B and the set $\mathrm{B}_t^+ = \{\chi\in\aleph : \mu^+(\chi)\ge t\}$ $B_t^+ = \{\chi\in\aleph: \mu^+(\chi)\ge t\}$ is called the positive t-cut of B.

(2) The set $\aleph_B^{(t,s)} = \{\chi\in\aleph : \mu^-(\chi)\le s, \mu^+(\chi)\ge t\}$ is called a $(s,t)-$ level subset of B.

(3) The set $^{<}\mathrm{B}_s^- = \{\chi\in\aleph : \mu^-(\chi)< s\}$ is called a strong negative s-cut of B and $^{>}\mathrm{B}_t^+ = \{\chi\in\aleph : \mu^+(\chi)> t\}$ is named a strong positive t-cut of B.

(4) The set $^{\perp}\aleph_B^{(t,s)} = \{\chi\in\aleph : \mu^-(\chi)< s, \mu^+(\chi)> t\}$ is called a strong (s,t) -level subset of B.

Kareem and Hasan [3] introduced the bipolar fuzzy *k*-ideal of KU-semigroup as follows:

Definition2.16[3]. A fuzzy set μ in $\aleph$ is called a bipolar fuzzy sub KU-semi group of $\aleph$ if it is satisfies the following condition : for all $\chi,\gamma\in\aleph$ $\chi,\gamma\in\aleph$

i) $\mu^-(\chi*\gamma)\le\max\{\mu^-(\chi),\mu^-(\gamma)\}$ and $\mu^+(\chi*\gamma)\ge\min\{\mu^+(\chi),\mu^+(\gamma)\}$ $\mu^-(\chi*\gamma)\le\{\mu^-(\chi),\mu^-(\gamma)\}$.

ii) $\mu^-(\chi\square\gamma)\le\max\{\mu^-(\chi),\mu^-(\gamma)\}$ and $\mu^+(\chi\square\gamma)\ge\min\{\mu^+(\chi),\mu^+(\gamma)\}$.

Defintion2.17[3]. Let $(\aleph,*,\square 0)$ be a KU-semigroup. A set $B=(\chi,\mu^-,\mu^+)$ $\mathrm{B}=(\chi,\mu^-,\mu^+)$ of $\aleph$ is called a bipolar fuzzy *k*-ideal if, for all $\chi,\gamma,\tau\in\aleph$ $\chi,\gamma,\tau\in\aleph$. The following conditions are satisfied

(BF_1) $\mu^-(0)\le\mu^-(\chi)$ and $\mu^+(0)\ge\mu^+(\chi)$ $\mu^+(0)\ge\mu^+(\chi)$,

(BF_2) $\mu^-(\chi*\tau)\le\max\{\mu^-(\chi*(\gamma*\tau)),\mu^-(\gamma)\}$ $\mu^-(\chi*\tau)\le\{\mu^-(\chi*(\gamma*\tau)),\mu^-(\gamma)\},$, $\mu^+(\chi*\tau)\ge\min\{\mu^+(\chi*(\gamma*\tau)),\mu^+(\gamma)\}$.

(BF_3) $\mu^-(\chi\square\tau)\le\max\{\mu^-(\chi),\mu^-(\gamma)\}$, $\mu^+(\chi\square\tau)\ge\min\{\mu^+(\chi),\mu^+(\gamma)\}$ $\mu^-(\chi\gamma)\le\{\mu^-(\chi),\mu^-(\gamma)\}$, $\mu^+(\chi\gamma)\ge\{\mu^+(\chi),\mu^+(\gamma)\}$.

3. (BF) ideals with Thresholds (θ,λ) of a KU-semigroup

We will define the notion of bipolar fuzzy *k*-ideal with thresholds (θ,λ) of a KU-semigroup and proved some of its properties

In what follows, we denote a bipolar fuzzy by (BF) and let $\theta,\lambda\in[0,1]$ such that $0<\theta<\lambda<1$, where θ and λ are arbitrary values.

Definition 3.1. A (BF) subset $B=(\chi,\eta^-,\eta^+)$ in $\aleph$ is called a (BF) sub KU-semigroup with thresholds (θ,λ) if, for all $\chi,\gamma\in\aleph$,

(1) $\min\{\eta^-(\chi*\gamma),-\theta\}\le\max\{\eta^-(\chi),\eta^-(\gamma),-\lambda\}$ and $\max\{\eta^+(\chi*\gamma),\theta\}\ge\min\{\eta^+(\chi),\eta^+(\gamma),\lambda\}$.

(2) $\min\{\eta^-(\chi\square\gamma),-\theta\}\le\max\{\eta^-(\chi),\eta^-(\gamma),-\lambda\}$ and $\max\{\eta^+(\chi\square\gamma),\theta\}\ge\min\{\eta^+(\chi),\eta^+(\gamma),\lambda\}$

Remark 3.2. A (BF) sub KU-semigroup of $\aleph$ is a (BF) sub KU-semigroup with thresholds (θ,λ) with $\theta=0$ and $\lambda=1$.

Corollary 3.3. Every (BF) sub KU-semigroup of $\aleph$ is a (BF) sub KU-semigroup with thresholds (θ,λ).

The reverse of Corollary 3.3 is incorrect. The example 3.4 shows the reverse

Example 3.4. Let $\aleph$ = {0, 1, 2, 3} be a set with two operations $*$ and $|$ $\odot$ are defined by the following tables

$*$	0	1	2	3
0	0	1	2	3
1	0	0	0	2
2	0	2	0	1
3	0	0	0	0

	0	1	2	3
0	0	0	0	0
1	0	1	0	1
2	0	0	2	2
3	0	1	2	3

Then ($\aleph$, *, 0) is a KU-semigroup. Now, we define $\mathrm{B}=(\chi,\eta^-,\eta^+)$ by

$$\eta^+(\chi)=\begin{cases}0.29 & if \quad \chi=0\\ 0.26 & if \quad \chi=1\\ 0.25 & if \quad \chi=3\\ 0.20 & if \quad \chi=2\end{cases} \quad \text{and} \quad \eta^-(\chi)=\begin{cases}-0.30 & if \quad \chi=0\\ -0.25 & if \quad \chi=1\\ -0.24 & if \quad \chi=3\\ -0.22 & if \quad \chi=2\end{cases}$$

It is clear that $\mathrm{B}=(\chi,\eta^-,\eta^+)$ is a (BF) sub KU-semigroup with thresholds $(0.1,0.2)$ of $\aleph$ but not a (BF) sub KU-semigroup since $\eta^+(1*3)=\eta^+(2)=0.20\le\min\{\eta^+(1),\eta^+(3)\}=0.25$ and $\eta^-(1*3)=\eta^-(2)=-0.22\ge\max\{\eta^-(1),\eta^-(3)\}=-0.24$.

Defintion3.5. A (BF) set $B=(\chi,\mu^-,\mu^+)$ $\mathrm{B}=(\chi,\eta^-,\eta^+)$ in $\aleph$ is named a (BF) *S*-ideal with thresholds (θ,λ) of $\aleph$ if, for all $\chi,\gamma\in\aleph$ $\chi,\gamma\in\aleph$

(Bi$_1$) $\min\{\eta^-(0),-\theta\}\le\max\{\eta^-(\chi),-\lambda\}$ and $\max\{\eta^+(0),\theta\}\ge\min\{\eta^+(\chi),\lambda\}$

(Bi$_2$) $\min\{\eta^-(\gamma),-\theta\}\le\max\{\eta^-(\chi*\gamma),\eta^-(\chi),-\lambda\}$ and $\max\{\eta^+(\gamma),\theta\}\ge\min\{\eta^+(\chi*\gamma),\eta^+(\chi),\lambda\}$

(Bi$_3$)) $\min\{\eta^-(\chi\square\gamma),-\theta\}\le\max\{\eta^-(\chi),\eta^-(\gamma),-\lambda\}$ and $\max\{\eta^+(\chi\square\gamma),\theta\}\ge\min\{\eta^+(\chi),\eta^+(\gamma),\lambda\}$.

Definition 3.6. A (BF) set $B=(\chi,\eta^{-},\eta^{+})$ of $\aleph$ is named a (BF) *k*-ideal with thresholds (θ,λ), if, for all $\chi,\gamma,\tau\in\aleph$. Then

(BI$_1$) $\min\{\eta^{-}(0),-\theta\}\le\max\{\eta^{-}(\chi),-\lambda\}$ and $\max\{\eta^{+}(0),\theta\}\ge\min\{\eta^{+}(\chi),\lambda\}$,

(BI$_2$) $\min\{\eta^{-}(\chi*\tau),-\theta\}\le\max\{\eta^{-}(\chi*(\gamma*\tau)),\eta^{-}(\gamma),-\lambda\}$,

$\max\{\eta^{+}(\chi*\tau),\theta\}\ge\min\{\eta^{+}(\chi*(\gamma*\tau)),\eta^{+}(\gamma),\lambda\}$.

(BI$_3$) $\min\{\eta^{-}(\chi\square\gamma),-\theta\}\le\max\{\eta^{-}(\chi),\eta^{-}(\gamma),-\lambda\}$ and

$\max\{\eta^{+}(\chi\square\gamma),\theta\}\ge\min\{\eta^{+}(\chi),\eta^{+}(\gamma),\lambda\}$.

Example 3.7. Let $\aleph$ = {0, 1, 2, 3} be a set with the following tables

*	0	1	2	3
0	0	1	2	3
1	0	0	0	2
2	0	2	0	1
3	0	0	0	0

	0	1	2	3
0	0	0	0	0
1	0	1	0	1
2	0	0	2	2
3	0	1	2	3

Then ($\aleph$, *, 0) is a KU-semigroup. Define $B=(\chi,\eta^{-},\eta^{+})$ by

$$\eta^{+}(\chi)=\begin{cases}0.5 & if \quad \chi=0\\ 0.3 & if \quad \chi=1,2,3\end{cases}\qquad \eta^{-}(\chi)=\begin{cases}-0.6 & if \quad \chi=0\\ -0.4 & if \quad \chi=1,2,3\end{cases}$$ and

Then $B=(\chi,\eta^{-},\eta^{+})$ is a (BF) *k*-ideal with thresholds $(0.1,0.2)$ of $\aleph$.

Remark 3.8. If $\theta=0$ and $\lambda=1$, then a (BF) *k*-ideal of $\aleph$ is a (BF) *k*-ideal with thresholds (θ,λ).

Lemma 3.9. Every (BF) *k*-ideal of $\aleph$ is a (BF) *k*-ideal with thresholds (θ,λ).

Proof. Clear.

The reverse of Lemma3.9 is incorrect. The example 3.10 shows the reverse

Example 3.10. Let $\aleph=\{0,a,b,c\}$ $\aleph=\{0,1,2,3\}$ with $*$ defined as in Example (3.6), we can define $B=(\chi,\eta^{-},\eta^{+})$ by

$$\eta^{+}(\chi)=\begin{cases}0.8 & if \quad \chi=0\\ 0.7 & if \quad \chi=1\\ 0.6 & if \quad \chi=2\\ 0.3 & if \quad \chi=3\end{cases}\qquad \eta^{-}(\chi)=\begin{cases}-0.5 & if \quad \chi=0\\ -0.4 & if \quad \chi=1\\ -0.3 & if \quad \chi=2\\ -0.2 & if \quad \chi=3\end{cases}$$ and

It is clear that $B=(\chi,\eta^-,\eta^+)$ is a (BF) *k*-ideal with thresholds $(0.4,0.2)$ of $\aleph$ but it is not a (BF) *k*-ideal, since $\eta^+(0*3)=\eta^+(3)=0.3\le\min\{\eta^+(0*(2*3)),\eta^+(2)\}=0.6$ and $\eta^-(0*3)=\eta^-(3)=-0.2\ge\max\{\eta^-(0*(2*3)),\eta^-(2)\}=-0.3$.

Proposition 3.11. Let $B=(\chi,\eta^-,\eta^+)$ be a (BF) *k*-ideal with thresholds (θ,λ) of $\aleph$. If $\chi\le\gamma$, then $\min\{\eta^-(\chi),-\theta\}\le\max\{\eta^-(\gamma),-\lambda\}$ and $\max\{\eta^+(\chi),\theta\}\ge\min\{\eta^+(\gamma),\lambda\}$.

Proof. If $\chi\le\gamma$, then $\gamma*\chi=0$ and by (ku_3) $0*\chi=\chi$, since $B=(\chi,\eta^-,\eta^+)$ is a (BF) *k*-ideal with thresholds (θ,λ) of $\aleph$,we get

$$\min\{\eta^-(0*\chi),-\theta\}=\min\{\eta^-(\chi),-\theta\}\le\max\{\eta^-(0*(\gamma*\chi)),\eta^-(\gamma),-\lambda\}$$
$$=\max\{\eta^-(0*0),\eta^-(\gamma),-\lambda\}=\max\{\eta^-(0),\eta^-(\gamma),-\lambda\}=\max\{\eta^-(\gamma),-\lambda\}.$$

And

$$\max\{\eta^+(0*\chi),\theta\}=\max\{\eta^+(\chi),\theta\}\ge\min\{\eta^+(0*(\gamma*\chi),\eta^+(\gamma),\lambda\}$$
$$=\min\{\eta^+(0*0),\eta^+(\gamma),\lambda\}=\min\{\eta^+(0),\eta^+(\gamma),\lambda\}=\min\{\eta^+(\gamma),\lambda\}.$$

Proposition 3.12. Let $B=(\chi,\eta^-,\eta^+)$ is a (BF) *k*-ideal with thresholds (θ,λ) of $\aleph$. Then the following condition is hold, for all $\chi,\gamma\in\aleph$

$\min\{\eta^-(\chi*\gamma),-\theta\}\le\max\{\eta^-(\gamma),-\lambda\}$ and $\max\{\eta^+(\chi*\gamma),\theta\}\ge\min\{\eta^+(\gamma),\lambda\}$.

Proof.

Let $B=(\chi,\eta^-,\eta^+)$ be a (BF) *k*-ideal with thresholds (θ,λ) of $\aleph$. If we put $\gamma=\tau$ in (BI_2) and by using ku_2 and ku_5. We get:

$$\min\{\eta^-(\chi*\gamma),-\theta\}\le\max\{\eta^-(\chi*(\gamma*\gamma)),\eta^-(\gamma),-\lambda\}$$
$$=\max\{\eta^-(\chi*0),\eta^-(\gamma),-\lambda\}$$
$$=\max\{\eta^-(0),\eta^-(\gamma),-\lambda\}$$
$$=\max\{\eta^-(\gamma),-\lambda\}$$

And

$$\max\{\eta^+(\chi*\gamma),\theta\}\ge\min\{\eta^+(\chi*(\gamma*\gamma)),\eta^+(\gamma),\lambda\}$$
$$=\min\{\eta^+(\chi*0),\eta^+(\gamma),\lambda\}$$
$$=\min\{\eta^+(0),\eta^+(\gamma),\lambda\}$$
$$=\min\{\eta^+(\gamma),\lambda\}$$

Proposition 3.13. Let $B=(\chi,\eta^-,\eta^+)$ be a (BF) *k*-ideal with thresholds (θ,λ) of $\aleph$. If the inequality $\chi*\gamma\le\tau$ holds in $\aleph$, then $\min\{\eta^-(\gamma),-\theta\}\le\max\{\eta^-(\chi),\eta^-(\tau),-\lambda\}$ and $\max\{\eta^+(\gamma),\theta\}\ge\min\{\eta^+(\chi),\eta^+(\tau),\lambda\}$, for all $\chi,\gamma,\tau\in\aleph$.

Proof. Assume that the inequality $\chi*\gamma\le\tau$ holds in $\aleph$, then $\tau*(\chi*\gamma)=0$ and by (BI_2)

$$\min\{\eta^-(\chi*\gamma),-\theta\} \le \max\{\eta^-(\chi*(\tau*\gamma)),\eta^-(\tau),-\lambda\} =$$
$$\max\{\eta^-(\tau*(\chi*\gamma)),\eta^-(\tau),-\lambda\} = \max\{\eta^-(0),\eta^-(\tau),-\lambda\}...(1)$$

But

$$\min\{\eta^-(0*\gamma),-\theta\} = \min\{\eta^-(\gamma),-\theta\} \le \max\{\eta^-(0*(\chi*\gamma)),\eta^-(\chi),-\lambda\} =$$
$$\max\{\eta^-(\chi*\gamma),\eta^-(\chi),-\lambda\} \le \max\{\eta^-(\tau),\eta^-(\chi),-\lambda\}$$

by (1) i.e. $\min\{\eta^-(\gamma),-\theta\} \le \max\{\eta^-(\tau),\eta^-(\chi),-\lambda\}$ and

$$\max\{\eta^+((\chi*\gamma)),\theta\} \ge \min\{\eta^+(\chi*(\tau*\gamma)),\eta^+(\tau),\lambda\} = \min\{\eta^+(\tau*(\chi*\gamma)),\eta^+(\tau),\lambda\}$$
$$= \min\{\eta^+(0),\eta^+(\tau),\lambda\}...(2)$$

But

$$\max\{\eta^+(0*\gamma),\theta\} = \max\{\eta^+(\gamma),\theta\} \ge \min\{\eta^+(0*(\chi*\gamma)),\eta^+(\chi),\lambda\}$$
$$= \min\{\eta^+(\chi*\gamma),\eta^+(\chi),\lambda\} \ge \min\{\eta^+(\tau),\eta^+(\chi),\lambda\} \text{ by } (2)$$

i.e. $\max\{\eta^+(\gamma),\theta\} \ge \min\{\eta^+(\chi),\eta^+(\tau),\lambda\}$.

Theorem 3.14. Let $\aleph\aleph$ be a KU-semigroup, a (BF) set $B = (\chi,\mu^-,\mu^+)$ $B=(\chi,\eta^-,\eta^+)$ of $\aleph\aleph$ is a (BF) *k*-ideal with thresholds (θ,λ) of $\aleph$ if and only if B $B=(\chi,\eta^-,\eta^+)$ is a (BF) *S*-ideal with thresholds (θ,λ) of $\aleph$.

Proof. (⇒) Let $B = (\chi,\mu^-,\mu^+)$ $B=(\chi,\eta^-,\eta^+)$ be a (BF) *k*-ideal with thresholds (θ,λ) of $\aleph$. If we put $\chi = 0$ $\chi=0$ in (BI_2), then $\min\{\eta^-(0*\tau),-\theta\} \le \max\{\eta^-(0*(\gamma*\tau)),\eta^-(\gamma),-\lambda\}$ is $\min\{\eta^-(\tau),-\theta\} \le \max\{\eta^-(\gamma*\tau),\eta^-(\gamma),-\lambda\}$ and $\max\{\eta^+(\tau),\theta\} \ge \min\{\eta^+(\gamma*\tau),\eta^+(\gamma),\lambda\}$.

Also, since $B = (\chi,\mu^-,\mu^+)$ $B=(\chi,\eta^-,\eta^+)$ is a (BF) *k*-ideal with thresholds (θ,λ) of $\aleph$, then (BI_3) is true. Hence $B = (\chi,\mu^-,\mu^+)$ $B=(\chi,\eta^-,\eta^+)$ is a (BF) *S*-ideal with thresholds (θ,λ) of $\aleph$.

(⇐) Let $B = (\chi,\mu^-,\mu^+)$ $B=(\chi,\eta^-,\eta^+)$ be a (BF) *S*-ideal with thresholds (θ,λ) of $\aleph$, then $\min\{\eta^-(\chi*\tau),-\theta\} \le \max\{\eta^-(\gamma*(\chi*\tau)),\eta^-(\gamma),-\lambda\}$ and $\max\{\eta^+(\chi*\tau),\theta\} \ge \min\{\eta^+(\gamma*(\chi*\tau)),\eta^+(\gamma),\lambda\}$. And by Theorem (2.2)(2), we get $\min\{\eta^-(\chi*\tau),-\theta\} \le \max\{\eta^-(\chi*(\gamma*\tau)),\eta^-(\gamma),-\lambda\}$ and $\max\{\eta^+(\chi*\tau),\theta\} \ge \min\{\eta^+(\chi*(\gamma*\tau)),\eta^+(\gamma),\lambda\}$. Also, since $B = (\chi,\mu^-,\mu^+)$ $B=(\chi,\eta^-,\eta^+)$ is a (BF) *S*-ideal with thresholds (θ,λ) of $\aleph$, then (Bi_3) is true. Hence $B = (\chi,\mu^-,\mu^+)$ $B=(\chi,\eta^-,\eta^+)$ is a (BF) *k*-ideal with thresholds (θ,λ) of $\aleph$.

Theorem 3.15. The set $B=(\chi,\eta^-,\eta^+)$ of $\aleph$ is a (BF) *k*-ideal with thresholds (θ,λ) if and only if $\aleph_B^{(t,s)} \ne \phi$ is a *k*-ideal of $\aleph$. For any $(s,t) \in [-\lambda,-\theta]\times[\theta,\lambda]$

Proof. ($\Rightarrow$) Let $(s,t)\in[-\lambda,-\theta]\times[\theta,\lambda]$, $\aleph_B^{(t,s)}\neq\phi$ and $\chi,\gamma\in\aleph$ such that $\chi\in\aleph_B^{(t,s)}$, then $\eta^+(\chi)\geq t$ and $\eta^-(\chi)\leq s$, so by(BI$_2$),

$\max\{\eta^+(\gamma*0),\theta\}=\max\{\eta^+(0),\theta\}\geq\min\{\eta^+(\gamma*(\chi*0)),\eta^+(\chi),\lambda\}\geq\min\{\eta^+(0),\eta^+(\chi),\lambda\}$

$=\min\{\eta^+(0),t,\lambda\}=t$

and

$\min\{\eta^-(\gamma*0),-\theta\}=\min\{\eta^-(0),-\theta\}\leq\max\{\eta^-(\gamma*(\chi*0)),\eta^-(\chi),-\lambda\}\leq\max\{\eta^-(0),\eta^-(\chi),-\lambda\}$

$=\max\{\eta^-(0),s,-\lambda\}=s$, *which implies that* $\eta^+(0)\geq t$ *and* $\eta^-(0)\leq s$, *hence* $0\in\aleph_B^{(t,s)}$.

Let $\chi,\gamma,\tau\in\aleph$, and $(\chi*(\gamma*\tau)),\gamma\in\aleph_B^{(t,s)}$. Then $\eta^+(\chi*(\gamma*\tau))\geq t$ and $\eta^+(\gamma)\geq t$, also $\eta^-(\chi*(\gamma*\tau))\leq s$ and $\eta^-(\gamma)\leq s$. since $\mathrm{B}=(\chi,\eta^-,\eta^+)$ is a (BF) *k*-ideal with thresholds (θ,λ) of $\aleph$. Then

$\max\{\eta^+(\chi*\tau),\theta\}\geq\min\{\eta^+(\chi*(\gamma*\tau)),\eta^+(\gamma),\lambda\}\geq\min\{t,t,\lambda\}=t$ and

$\min\{\eta^-(\chi*\tau),-\theta\}\leq\max\{\eta^-(\chi*(\gamma*\tau)),\eta^-(\gamma),-\lambda\}\leq\max\{s,s,-\lambda\}=s$. This implies that, $\eta^+(\chi*\tau)\geq t$ and $\eta^-(\chi*\tau)\leq s$. Thus $\chi*\tau\in\aleph_B^{(t,s)}$. Also Let $\chi,\gamma\in\aleph_B^{(t,s)}$, then $\eta^+(\chi)\geq t$ and $\eta^+(\gamma)\geq t$, also $\eta^-(\chi)\leq s$ and $\eta^-(\gamma)\leq s$. As $\mathrm{B}=(\chi,\mu^-,\mu^+)$ is a (BF) *k*-ideal with thresholds (θ,λ) of $\aleph$, then $\min\{\eta^-(\chi\square\gamma),-\theta\}\leq\max\{\eta^-(\chi),\eta^-(\gamma),-\lambda\}=\max\{s,s,-\lambda\}=s$ and $\max\{\eta^+(\chi\square\gamma),\theta\}\geq\min\{\eta^+(\chi),\eta^+(\gamma),\lambda\}=\min\{t,t,\lambda\}=t$. Then $\eta^+(\chi\square\gamma)\geq t$ and $\eta^-(\chi\square\gamma)\leq s$. Thus $\chi\square\lambda\in\aleph_B^{(t,s)}$. Hence $\aleph_B^{(t,s)}$ is a *k*-ideal of $\aleph$.

($\Leftarrow$) Let $\chi,\gamma,\tau\in\aleph$ such that $\max\{\eta^+(\chi*\tau),\theta\}<\min\{\eta^+(\chi*(\gamma*\tau)),\eta^+(\gamma),\lambda\}$ and $\min\{\eta^-(\chi*\tau),-\theta\}>\max\{\eta^-(\chi*(\gamma*\tau)),\eta^-(\gamma),-\lambda\}$ then there exist $(s,t)\in[-\lambda,-\theta]\times[\theta,\lambda]$ such that $\max\{\eta^+(\chi*\tau),\theta\}<t\leq\min\{\eta^+(\chi*(\gamma*\tau)),\eta^+(\gamma),\lambda\}$ and $\min\{\eta^-(\chi*\tau),-\theta\}>s\geq\max\{\eta^-(\chi*(\gamma*\tau)),\eta^-(\gamma),-\lambda\}$. This shows that $\eta^+(\chi*(\gamma*\tau))\geq t$, $\eta^+(\gamma)\geq t$ and $\eta^+(\chi*\tau)<t$, also $\eta^-(\chi*(\gamma*\tau))\leq s$, $\eta^-(\gamma)\leq s$ and $\eta^-(\chi*\tau)>s$. Thus $\chi,\gamma,\tau\in\aleph_B^{(t,s)}$, since $\aleph_B^{(t,s)}$ is a *k*-ideal of $\aleph$. Then $\chi*\tau\in\aleph_B^{(t,s)}$, but this is a contradiction to $\eta^+(\chi*\tau)<t$ and $\eta^-(\chi*\tau)>s$. Thus

$\max\{\eta^+(\chi*\tau),\theta\}\geq\min\{\eta^+(\chi*(\gamma*\tau)),\eta^+(\gamma),\lambda\}$ and

$\min\{\eta^-(\chi*\tau),-\theta\}\leq\max\{\eta^-(\chi*(\gamma*\tau)),\eta^-(\gamma),-\lambda\}$. Also, suppose that $\max\{\eta^+(\chi\square\gamma),\theta\}<\min\{\eta^+(\chi),\eta^+(\gamma),\lambda\}$ and $\min\{\eta^-(\chi\square\gamma),-\theta\}>\max\{\eta^-(\chi),\eta^-(\gamma),-\lambda\}$, then there exist $(s,t)\in[-\lambda,-\theta]\times[\theta,\lambda]$ such that $\max\{\eta^+(\chi\square\gamma),\theta\}<t\leq\min\{\eta^+(\chi),\eta^+(\gamma),\lambda\}$ and $\min\{\eta^-(\chi\square\tau),-\theta\}>s\geq\max\{\eta^-(\chi),\eta^-(\gamma),-\lambda\}$. This shows that $\eta^+(\chi)\geq t$, $\eta^+(\gamma)\geq t$ and $\eta^+(\chi\square\gamma)<t$, also $\eta^-(\chi)\leq s$, $\eta^-(\gamma)\leq s$ and $\eta^-(\chi\square\gamma)>s$. Thus $\chi,\gamma\in\aleph_B^{(t,s)}$, and since $\aleph_B^{(t,s)}$ is a *k*-ideal of $\aleph$. Therefore $\chi\square\gamma\in\aleph_B^{(t,s)}$, but this is a contradiction to $\eta^+(\chi\square\gamma)<t$ and $\eta^-(\chi\square\gamma)>s$. Thus $\max\{\eta^+(\chi\square\gamma),\theta\}\geq\min\{\eta^+(\chi),\eta^+(\gamma),\lambda\}$ and

$\min\{\eta^-(\chi \square \gamma), -\theta\} \le \max\{\eta^-(\chi), \eta^-(\gamma), -\lambda\}$. The proof is completed

Theorem 3.16. If $\mathrm{B} = (\chi, \eta^-, \eta^+)$ is a (BF) *k*-ideal with thresholds (θ, λ) of $\aleph$, then $\mathrm{B}_\theta = ({}^{<}B^-_{-\theta}, {}^{>}B^+_\theta)$ is a *k*-ideal of $\aleph$, where ${}^{<}B^-_{-\theta} = \{\chi \in \aleph : \eta^-(\chi) < -\theta\}$ and ${}^{>}B^+_\theta = \{\chi \in \aleph : \eta^+(\chi) > \theta\}$.

Proof. Suppose that $\mathrm{B} = (\chi, \eta^-, \eta^+)$ is a (BF) *k*-ideal with thresholds (θ, λ) of $\aleph$, then $0 \in B_\theta$. Now, for all $\chi, \gamma, \tau \in \aleph$. Let $(\chi * (\gamma * \tau)) \in B_\theta$ and $\gamma \in B_\theta$. Then $\eta^+(\chi * (\gamma * \tau)) > \theta, \eta^+(\gamma) > \theta$ and $\eta^-(\chi * (\gamma * \tau) < -\theta, \eta^-(\gamma) < -\theta$. Since $\mathrm{B} = (\chi, \eta^-, \eta^+)$ is a (BF) *k*-ideal with thresholds (θ, λ) of $\aleph$, then $\max\{\eta^+(\chi * \tau), \theta\} \ge \min\{\eta^+(\chi * (\gamma * \tau), \eta^+(\gamma), \lambda\} > \min\{\theta, \theta, \lambda\} = \theta$ and $\min\{\eta^-(\chi * \tau), -\theta\} \le \max\{\eta^-(\chi * (\gamma * \tau), \eta^-(\gamma), -\lambda\} < \{-\theta, -\theta, -\lambda\} = -\theta$. Hence $\eta^+(\chi * \tau) > \theta$ and $\eta^-(\chi * \tau) < -\theta$. This show that $\chi * \tau \in B_\theta$. Also, for any $\chi \in B_\theta$ and $\gamma \in B_\theta$, then $\eta^+(\chi) > \theta, \eta^+(\gamma) > \theta$ and $\eta^-(\chi \square \gamma) \le -\lambda, \eta^-(\gamma) < -\theta$. Since $\mathrm{B} = (\chi, \eta^-, \eta^+)$ is a (BF) *k*-ideal with thresholds (θ, λ) of $\aleph$, then $\max\{\eta^+(\chi \square \gamma), \theta\} \ge \min\{\eta^+(\chi), \eta^+(\gamma), \lambda\} > \min\{\theta, \theta, \lambda\} = \theta$ and $\min\{\eta^-(\chi \square \gamma), -\theta\} \le \max\{\eta^-(\chi), \eta^-(\gamma), -\lambda\} < \{-\theta, -\theta, -\lambda\} = -\theta$. Hence $\eta^+(\chi \square \gamma) > \theta$ and $\eta^-(\chi \square \gamma) < -\theta$. Thus $\chi \square \gamma \in B_\theta$. Hence the set $\mathrm{B}_\theta = ({}^{<}B^-_{-\theta}, {}^{>}B^+_\theta)$ is a *k*-ideal of $\aleph$.

Theorem 3.17. A nonempty subset A of $\aleph$ is a *k*-ideal if and only if a (BF) subset $\mathrm{B} = (\chi, \eta^-, \eta^+)$ of $\aleph$ defined as follows:

$$\eta^+(\chi) = \begin{cases} \ge \lambda & if \quad \chi \in A \\ \theta & if \quad \chi \notin A \end{cases} \quad \text{and} \quad \eta^-(\chi) = \begin{cases} \le -\lambda & if \quad \chi \in A \\ -\theta & if \quad \chi \notin A \end{cases}$$ is a (BF) *k*-ideal with thresholds (θ, λ) of $\aleph$.

Proof. Since A is a *k*-ideal of $\aleph$, then $0 \in A$, hence $\eta^+(0) \ge \lambda$ and $\eta^-(0) \le -\lambda$.

Now, we have

$$\max\{\eta^+(\gamma * 0), \theta\} = \max\{\eta^+(0), \theta\} \ge \lambda = \min\{\eta^+(\gamma * (\chi * 0)), \eta^+(\chi), \lambda\}$$
$$= \min\{\eta^+(0), \eta^+(\chi), \lambda\} = \min\{\eta^+(\chi), \lambda\}$$

And

$$\min\{\eta^-(\gamma * 0), -\theta\} = \min\{\eta^-(0), -\theta\} \le -\lambda = \max\{\eta^-(\gamma * (\chi * 0)), \eta^-(\chi), -\lambda\}$$
$$= \max\{\eta^-(0), \eta^-(\chi), -\lambda\} = \max\{\eta^-(\chi), -\lambda\}$$

Hence $0 \in \mathrm{B} = (\chi, \eta^-, \eta^+)$

Let $\chi, \gamma, \tau \in \aleph$ be such that $(\chi * (\gamma * \tau)) \in A$ and $\gamma \in A$, then $(\chi * \tau) \in A$. Hence $\eta^+(\chi * \tau) \ge \lambda$ and $\eta^-(\chi * \tau) \le -\lambda$. Therefore $\max\{\eta^+(\chi * \tau), \theta\} \ge \lambda = \min\{\eta^+(\chi * (\gamma * \tau)), \eta^+(\gamma), \lambda\}$ and $\min\{\eta^-(\chi * \tau), -\theta\} \le -\lambda = \max\{\eta^-(\chi * (\gamma * \tau)), \eta^-(\gamma), -\lambda\}$. If $\chi \notin A$, $\gamma \notin A$ or $\tau \notin A$, then $\min\{\eta^+(\chi * (\gamma * \tau)), \eta^+(\gamma), \lambda\} = \theta$ and $\max\{\eta^-(\chi * (\gamma * \tau)), \eta^-(\gamma), -\lambda\} = -\theta$. Thus $\max\{\eta^+(\chi * \tau), \theta\} \ge \theta = \min\{\eta^+(\chi * (\gamma * \tau)), \eta^+(\gamma), \lambda\}$ and

$\min\{\eta^-(\chi*\tau),-\theta\} \le -\theta = \max\{\eta^-(\chi*(\gamma*\tau)),\eta^-(\gamma),-\lambda\}$. Also, let $\chi \in \aleph$ and $\gamma \in A$, then $(\chi \square \gamma) \in A$. Hence $\eta^+(\chi \square \gamma) \ge \lambda$ and $\eta^-(\chi \square \gamma) \le -\lambda$. Therefore $\max\{\eta^+(\chi \square \gamma),\theta\} \ge \lambda = \min\{\eta^+(\chi),\eta^+(\gamma),\lambda\}$ and $\min\{\eta^-(\chi*\tau),-\theta\} \le -\lambda = \max\{\eta^-(\chi*(\gamma*\tau)),\eta^-(\gamma),-\lambda\}$. If $\chi \notin A$, $\gamma \notin A$ or $\tau \notin A$, then $\min\{\eta^+(\chi*(\gamma*\tau)),\eta^+(\gamma),\lambda\} = \theta$ and $\max\{\eta^-(\chi*(\gamma*\tau)),\eta^-(\gamma),-\lambda\} = -\theta$. Thus $\max\{\eta^+(\chi \square \gamma),\theta\} \ge \theta = \min\{\eta^+(\chi),\eta^+(\gamma),\lambda\}$ and $\min\{\eta^-(\chi \square \gamma),-\theta\} \le -\theta = \max\{\eta^-(\chi),\eta^-(\gamma),-\lambda\}$. Consequently $\mathrm{B} = (\chi,\eta^-,\eta^+)$ is a (BF) *k*-ideal with thresholds (θ,λ) of $\aleph$.

Conversely, let $(\chi*(\gamma*\tau)) \in A$ and $\gamma \in A$. Then $\eta^+(\chi*(\gamma*\tau)) \ge \lambda$, $\eta^+(\gamma) \ge \lambda$ and $\eta^-(\chi*(\gamma*\tau)) \le -\lambda, \eta^-(\gamma) \le -\lambda$. As $\mathrm{B} = (\chi,\eta^-,\eta^+)$ is a (BF) *k*-ideal with thresholds (θ,λ) of $\aleph$. Therefore $\max\{\eta^+(\chi*\tau),\theta\} \ge \min\{\eta^+(\chi*(\gamma*\tau)),\eta^+(\gamma),\lambda\} \ge \min\{\lambda,\lambda,\lambda\} = \lambda$

And $\min\{\eta^-(\chi*\tau),-\theta\} \le \max\{\eta^-(\chi*(\gamma*\tau)),\eta^-(\gamma),-\lambda\} \le \{-\lambda,-\lambda,-\lambda\} = -\lambda$. This implies that $\eta^+(\chi*\tau) \ge \lambda$ and $\eta^-(\chi*\tau) \le -\lambda$. Hence $(\chi*\tau) \in A$. Also, let $\chi,\gamma \in A$, then $\mu^+(\chi) \ge \lambda$, $\mu^+(\gamma) \ge \lambda$ and $\mu^-(\chi) \le -\lambda, \mu^-(\gamma) \le -\lambda$. As $\mathrm{B} = (\chi,\eta^-,\eta^+)$ is a (BF) *k*-ideal with thresholds (θ,λ) of $\aleph$. Therefore $\max\{\eta^+(\chi \square \gamma),\theta\} \ge \min\{\eta^+(\chi),\eta^+(\gamma),\lambda\} \ge \min\{\lambda,\lambda,\lambda\} = \lambda$

And $\min\{\eta^-(\chi \square \gamma),-\theta\} \le \max\{\eta^-(\chi),\eta^-(\gamma),-\lambda\} \le \{-\lambda,-\lambda,-\lambda\} = -\lambda$. This implies that $\eta^+(\chi \square \gamma) \ge \lambda$ and $\eta^-(\chi \square \gamma) \le -\lambda$. Hence $(\chi \square \gamma) \in A$. It follows that A is a *k*-ideal of $\aleph$.

ACKNOWLEDGEMENT
The authors are thankful to the referees for a careful reading of the paper and for valuable comments and suggestions.

References

[1] E R Hasan and F F Kareem 2018 Fuzzy KU-Semi-Groups and Investigate Some Basic Properties *Journal of Engineering and Applied Science* **13** (18) pp 7739-7744
[2] F F Kareem and E R Hasan 2018 On KU-semigroup *Int. J.Sci.Nat.* **1(13)** 79-84
[3] F F Kareem and E R Hasan 2019 Bipolar Fuzzy k-ideals in KU-semigroups *journal of New Theory* **29** pp 71-78
[4] M K Lee 2000 Bipolar -valued Fuzzy sets and their operations *Proc. Int. Conf. on Intelligent technologies* Bangkok Thailand
[5] K M Lee and K J Cios 2001 Comparison of interval-valued fuzzy sets, Intuitionistic Fuzzy sets, and Bipolar-valued Fuzzy sets *Computing and Information Technologies* pp 433-439
[6] S M Mostafa, M A Abd-Elnaby and M M M Yousef 2011 Fuzzy ideals of KU-Algebras *Int. Math. Forum* **6** (63) pp 3139-3149
[7] S M Mostafa and F F Kareem 2014 Bipolar Fuzzy n-fold KU-ideals of KU-algebra *Mathematica Aeterna* **4** (6) pp 633-650
[8] G Muhiuddin 2014 Bipolar Fuzzy KU-subalgebra\ ideals of KU-algebras *Fuzzy Math. Inform* **8** (3) pp 409-418
[9] C Prabpayak and U Leerawat 2009 On ideals and congruence in KU-algebras *Scientia Magna* **5** (1) pp 54-57

[10] A B Saeid 2009 Bipolar-valued Fuzzy BCK\ BCI-algebras World Applied Sciences Journal **7** (11) pp 1401-1411
[11] N Yaqoop and M A Ansari 2013 Bipolar (λ,δ)-fuzzy ideals in ternary semigroups International Journal of mathematical Analysis **7** (36) pp 1775-1782
[12] L A Zadeh 1965 Fuzzy sets Information and control **8**(3) pp 338-353

Solution BBM-Burger Equation via Quartic Trigonometric B-spline Approach

Solution BBM-Burger Equation via Quartic Trigonometric B-spline Approach

Hamad Salih

Department of Mathematics, University of Anbar, Al-anbar, Iraq

E-mail: hamadm1969@uoanbar.edu.iq

Abstract. In the present work, the new quartic trigonometric B-spline approach based on finite difference scheme is described to solve the one dimensional non-linear equation of (Benjamin – Bona-Mahony- Burger). Dirichlet boundary with the help of applying the von-Neumann stability analysis is also used in this description. While the time derivative part is discretized by using the finite difference scheme. In the space dimension, the quartic trigonometric B-spline is also used as an interpolation function. The execution of this method which is used in the present work showed that the quartic trigonometric B-spline method is a more efficient and effective tool and gives better results according to the comparisons that are made with the precise solution for a different time and some other published numerical methods.

1. Introduction

Nonlinear phenomena have important roles in physical and engineering issues in addition to that in applied mathematics they take different parameters depending on various factors. The mathematics model of propagation of small amplitude long waves in nonlinear dispersive media is described by the following (B-B-M-B) equation [3].

$$\frac{\partial \varpi}{\partial t}+\delta\frac{\partial \varpi}{\partial x}+\varpi\frac{\partial \varpi}{\partial x}-\lambda\frac{\partial \varpi}{\partial xx}-\frac{\partial \varpi}{\partial xxt}=0 \qquad x\in[\psi,\tau]\,,t\in[0,T] \tag{1}$$

For both δ and λ are constants, and applying the flowed initial and boundary conditions

$$u(x,0)=g(x) \qquad x\in[\psi,\tau] \tag{2}$$

$$u(\psi,t)=u(\tau,t)=0 \tag{3}$$

In the case of physical applications, the dispersive effect of Equation 1 same as (B-B-M-B) equation, while the dissipative effect is similar to Burgers equation that is an alternative sample for Korteweg-de Vries Burger's equation.

In the previous studies, many researchers are focused to solve same these equations by applying different numerical methods'. Arora et al. [1] solved the BBM-Burger by used the quartic B-spline approach, and he got good results as compared with the exact solution and the other researchers' solutions. Omrain & Ayadi [2] are used the Crank-Nicolson-type finite difference method to prove the stability and uniqueness of the corresponding approaches by the means of the discrete energy method. Salih et al. [3] presented the cubic trigonometric B-spline approach to solve (B-B-M-B) equations. They have obtained good results with high rate of accuracy and efficiency when they have compared the fining results with those ones obtained by Zarebnia & Parvaz [4], where they have used the cubic B-spline collection method to solve the same equation. Yin & Piao [5] solved the equation by using the

quadratic B-Spline finite element method. The predicted numerical solutions give that the scheme is efficient and feasible when compared with the exact solution.

Because of the effectiveness of the B-spline method in a numerical solution for different linear partial and non-linear differential equations, it has great attention on interest in its use in many previous works that are mentioned in the literature. It also has many geometric properties such as local support and the ability to deal with local phenomena, which makes it used in a solution of partial non-linear differential equations effortlessly and easily. The trigonometric B-spline (T-BS) gives more accurate results than the T-BS functions for solving the non-linear initial boundary value problems [6].

In the present work, the (QT-BS) method will represent to obtain the approximate solution of the (B-B-M-B) equation. Zin et al [7] used this approach to obtain a numerical solution to the Korteweg-de Vries equation. The detailed outline of this work deals with the following: In section2, discuss the (QT-BS) method will explain. In section 3, discussing the proposed numerical solution. In section 4, investigate the stability of the method. In section 5, the obtained results of approximate experiments will present and then compared with the obtained results for some of the previous methods. Finally, in section 6, the conclusions of the current work will write down.

QT-BS Method

In this section, we give the QT basis function based on [7, 8].

$$TB_{5,j}(x)=\frac{1}{z}\begin{cases}\eta^4(x_j), & x\in[x_j,x_{j+1})\\ \eta^3(x_j)\sigma(x_{j+2})+\eta^2(x_j)\sigma(x_{j+3}) & x\in[x_{j+1},x_{j+2})\\ +\eta(x_j)\sigma(x_{j+4})\eta^2(x_{j+1})+\sigma(x_{j+5})\eta^3(x_{j+1}),\\ \eta^2(x_j)\sigma^2(x_{j+3})+\eta(x_j)\sigma(x_{j+4})\eta(x_{j+1})\sigma(x_{j+3})\\ +\eta(x_j)\sigma^2(x_{j+4})\eta(x_{j+2})+\sigma(x_{j+5})\eta^2(x_{j+1})\sigma(x_{j+3}) & x\in[x_{j+2},x_{j+3})\\ +\sigma(x_{j+5})\eta(x_{j+1})\sigma(x_{j+4})\eta(x_{j+2})+\sigma^2(x_{j+5})\eta^2(x_{j+2}),\\ \eta(x_j)\sigma^3(x_{j+4})+\sigma(x_j+5)\eta(x_{j+1})\sigma^2(x_{j+4}) & x\in[x_{j+3},x_{j+4}]\\ +\sigma^2(x_{j+5})\eta(x_{j+2})\sigma(x_{j+4})+\sigma^3(x_{j+5})\eta(x_{j+3}),\\ \sigma^4(x_{j+5}), & x\in[x_{j+4},x_{j+5}]\\ 0 & otherwise\end{cases} \tag{4}$$

where $\eta(x_j)=\sin\left(\frac{x-x_j}{2}\right)$, $\sigma(x_j)=\sin\left(\frac{x_j-x}{2}\right)$ and $z=\sin\left(\frac{h}{2}\right)\sin(h)\sin\left(\frac{3h}{2}\right)\sin(2h)$

Due to the B-spline's domestic support characteristics, there are only four non-zero functions, $B_{5,j-4}(x_j), B_{5,j-3}(x_j), B_{5,j-2}(x_j)\ and\ B_{5,j-1}(x_j)$ over subinterval $[x_j, x_{j+1}]$.

Where $h=(\tau-\psi)/n$ and values of $TB_{5,j}(x)$ are tabulated in Table 1

Table 1: Values of $TB_i^4(x)$

x	x_{j-4}	x_{j-3}	x_{j-2}	x_{j-1}	x_j
$TB_{5,j}$	κ_1	κ_2	κ_2	κ_1	0
TB'_j	κ_3	κ_4	κ_4	κ_3	0
TB''_j	κ_5	κ_5	κ_5	κ_5	0

TB_j'''	κ_6	κ_7	κ_7	κ_6	0

Where

$$\kappa_1=\frac{\sin^3(\frac{h}{2})}{\sin(h)\sin(\frac{3h}{2})\sin(2h)} \quad ,\kappa_2=\frac{5+6\cos(h)}{8\cos^2(h)\cos(h)(1+2\cos(h))}$$

$$\kappa_3=\frac{1}{2\sin(h)\cos(h)(1+2\cos(h))} \quad ,\kappa_4=-\frac{1}{\sin(2\mathrm{h})},\kappa_5=\frac{1}{\sin(h)\sin(2h)}$$

$$\kappa_6=\frac{\cos(\frac{h}{2})(1-4\cos(h))}{\sin(h)\sin(\frac{3h}{2})\sin(2h)} \quad , \quad \kappa_7=\frac{1+2\cos(h)}{2\sin^2(\frac{h}{2})\sin(2h)}$$

3. Numerical Approach

The QT-BS method will be discussed in this section for solving the (B-B-M-B) equation numerically. The solution domain will be divided equally in the knots into subintervals. Our aim for (B-B-M-B) equation is using QT-BS to find an approximate solution like [8, 9].

$$\varpi_j=\sum_{j=-4}^{n-1}C_jTB_{5,j}(x) \tag{5}$$

where $C_j(t)$ is a time dependent unknown to be determined where $j=0,1,2,...,n$. In order to obtain approximate estimates of the solution, the values of $B_{5,j}(x)$ and its derivatives at the node points are required and these derivatives are tabulated by using approximate functions (4) and (5). The values at the U_i^j node and its derivatives up to second order are

$$\begin{cases}(\varpi)_j^i=\kappa_1C_{j-4}^i+\kappa_2C_{j-3}^i+\kappa_2C_{j-2}^i+\kappa_1C_{j-1}^i,\\(\varpi_x)_j^i=\kappa_3C_{j-4}^i+\kappa_4C_{j-3}^i-\kappa_4C_{j-2}^i-\kappa_3C_{j-1}^i\\(\varpi_{xx})_j^i=\kappa_5C_{j-4}^i-\kappa_5C_{j-3}^i-\kappa_5C_{j-2}^i+\kappa_5C_{j-1}^i\\(\varpi_{xxx})_j^i=\kappa_6C_{j-4}^i+\kappa_7C_{j-3}^i-\kappa_7C_{j-2}^i-\kappa_6C_{j-1}^i\end{cases} \tag{6}$$

The approximations for the solutions of (B-B-M-B) equation at t_{j+1} th time level can be as

$$[\frac{(\varpi-\varpi_{xx})^{n+1}-(\varpi-\varpi_{xx})^n}{\Delta t}]+\theta\kappa_j^{n+1}+(1-\theta)\kappa_j^n=0 \tag{7}$$

Where $\kappa_j^n=[-\lambda(\varpi_{xx})_j^n+(\varpi\varpi_x)_j^n+\delta(\varpi_x)_j^n]$ and the subscripts n and $n+1$ are successive time levels, $n=0,1,2,..$ and Δt is the time step. By using the following formula:

$$(\varpi\varpi_x)^{n+1}=\varpi^{n+1}\varpi_x^n+\varpi^n\varpi_x^{n+1}-\varpi^{n+1}\varpi_x^n \tag{8}$$

The scheme equation (7) with the placement of the nodal w and derivatives using (6) becomes the following difference equation with variable C_j, $j=-4,...,\mathrm{n}-1$ and noted the crank-Nicolson scheme when $\theta=0.5$

$$\dagger_1C_{j-4}^{n+1}+\dagger_2C_{j-3}^{n+1}+\dagger_3C_{j-2}^{n+1}+\dagger_4C_{j-1}^{n+1}=\lambda_1C_{j-4}^{n+1}+\lambda_2C_{j-3}^{n+1}+\lambda_3C_{j-2}^{n+1}+\lambda_4C_{j-1}^{n+1} \tag{9}$$

Where

$$\dagger_1 = (1+\frac{\Delta t}{2}\varpi_x^n)\kappa_1 + \frac{\Delta t}{2}(\varpi^n+\delta)\kappa_3 - (1+\frac{\alpha\,\Delta t}{2})\kappa_5$$
$$\dagger_2 = (1+\frac{\Delta t}{2}\varpi_x^n)\kappa_2 + \frac{\Delta t}{2}(\varpi^n+\delta)\kappa_4 + (1+\frac{\lambda\,\Delta t}{2})\kappa_5$$
$$\dagger_3 = (1+\frac{\Delta t}{2}\varpi_x^n)\kappa_2 - \frac{\Delta t}{2}(\varpi^n+\delta)\kappa_4 + (1+\frac{\lambda\,\Delta t}{2})\kappa_5$$
$$\dagger_4 = (1+\frac{\Delta t}{2}\varpi_x^n)\kappa_1 - \frac{\Delta t}{2}(\varpi^n+\delta)\kappa_3 - (1-\frac{\lambda\,\Delta t}{2})\kappa_5$$
$$\lambda_1 = \kappa_1 - \frac{\Delta t\delta}{2}\kappa_3 + (\frac{\Delta t}{2}\lambda - 1)\kappa_5 \qquad (10)$$
$$\lambda_2 = \kappa_2 - \frac{\Delta t\delta}{2}\kappa_4 + (1-\frac{\Delta t}{2}\lambda)\kappa_5$$
$$\lambda_3 = \kappa_2 - \frac{\Delta t\delta}{2}\kappa_4 + (1-\frac{\Delta t}{2}\lambda)\kappa_5$$
$$\lambda_4 = \kappa_1 + \frac{\Delta t\delta}{2}\kappa_3 + (\frac{\Delta t}{2}\lambda - 1)\kappa_5$$

On simplification (9) the system consists of a linear equation $(N+1)$ in $(N+4)$ unknown $C^n = [C_{j-4}^n, ..., C_{N-1}^n]$ at the time level $t = t_{i+1}$. In order to obtain the unique solution to the system, adds three equations obtained from the boundary conditions. The system consists $(N+4)\times(N+4)$ as follows:

$$\vartheta_{(N+4)\times(N+4)}\, C_{1xN+4}^{n+1} = \zeta_{(N+4)\times(N+4)}\, C_{1xN+4}^{n}$$

From the initial conditions and its derivatives, we will compute initial vector by use it get approximate solution

$$\begin{cases} (\varpi_j^0)_x = g'(x_j) & j = 0 \\ (\varpi_j^0)_{xx} = g''(x_j) & j = 0 \\ \varpi_j^0 = g(x_j) & j = 0,1,..N \\ (\varpi_j^0)_x = g'(x_j) & j = N \end{cases} \qquad (11)$$

From equation (11), we obtain the system consist $(N+4)\times(N+4)$ which can be solved by Gauss-Jordan elimination method [8].

4. Stability Analysis

In this section, the investigation was performed to stability analysis of the proposed scheme using the von Neumann method. The nonlinear term $\varpi\varpi_x$ is linearized as considering a constant as α in equation (1). Therefore, the equation that is got is the same as of [1].

$$\varpi_t + \delta\varpi_x + \alpha\varpi_x - \lambda\varpi_{xx} - \varpi_{xxt} = 0$$

The linearized form of proposed scheme as following:

$$\hbar_1 C_{j-4}^{n+1} + \hbar_2 C_{j-3}^{n+1} + \hbar_3 C_{j-2}^{n+1} + \hbar_4 C_{j-1}^{n+1} = \Omega_1 C_{j-4}^{n+1} + \Omega_2 C_{j-3}^{n+1} + \Omega_3 C_{j-2}^{n+1} + \Omega_4 C_{j-1}^{n+1} \qquad (12)$$

where

$$\hbar_1 = \kappa_1 + \frac{\Delta t}{2}(\alpha+\delta)\kappa_3 - (1+\frac{\lambda\Delta t}{2})\kappa_5 \ ,$$

$$\hbar_2 = \kappa_2 + \frac{\Delta t}{2}(\alpha+\delta)\kappa_4 + (1+\frac{\lambda\Delta t}{2})\kappa_5 \ ,$$

$$\hbar_3 = \kappa_2 - \frac{\Delta t}{2}(\alpha+\delta)\kappa_4 + (1+\frac{\lambda\Delta t}{2})\kappa_5 \ ,$$

$$\hbar_4 = \kappa_1 - \frac{\Delta t}{2}(\alpha+\delta)\kappa_3 - (1+\frac{\lambda\Delta t}{2})\kappa_5 \ ,$$

$$\Omega_1 = \kappa_1 - \frac{\Delta t}{2}(\alpha+\delta)\kappa_3 + (-1+\frac{\lambda\Delta t}{2})\kappa_5 \ ,$$

$$\Omega_2 = \kappa_2 - \frac{\Delta t}{2}(\alpha+\delta)\kappa_4 + (-1+\frac{\lambda\Delta t}{2})\kappa_5 \ ,$$

$$\Omega_3 = \kappa_2 + \frac{\Delta t}{2}(\alpha+\delta)\kappa_4 + (1-\frac{\lambda\Delta t}{2})\kappa_5 \ ,$$

$$\Omega_4 = \kappa_1 + \frac{\Delta t}{2}(\alpha+\delta)\kappa_3 + (-1+\frac{\lambda\Delta t}{2})\kappa_5 \ ,$$

Substitution of $D_j^n = \delta^n \exp(imh\eta)$ into equation (12) where $= \sqrt{-1}$, after simplifying the equation (12), we get

$$\xi = \frac{A_1 + iB_1}{A_2 + iB_2} \tag{13}$$

where

$$A_1 = (\kappa_2 + \frac{\Delta t}{2}(\alpha+\delta)\kappa_4) + (\kappa_1 - \frac{\Delta t}{2}(\alpha+\delta)\kappa_3 +)(\cos(2\eta h))$$

$$+((\kappa_2 - \frac{\Delta t}{2}(\alpha+\delta)\kappa_4 + 2(-1+\frac{\lambda\Delta t}{2})\kappa_5) + (\kappa_1 + \frac{\Delta t}{2}(\alpha+\delta)\kappa_3 +))(\cos(\eta h))$$

$$B_1 = (((\kappa_1 + \frac{\Delta t}{2}(\alpha+\delta)\kappa_3) - (\kappa_2 - \frac{\Delta t}{2}(\alpha+\delta)\kappa_4))(\sin(\eta h))$$

$$-(\kappa_1 - \frac{\Delta t}{2}(\alpha+\delta)\kappa_3 + (-1+\frac{\lambda\Delta t}{2})\kappa_5)(\sin(2\eta h))$$

$$A_2 = (\kappa_2 - \frac{\Delta t}{2}(\alpha+\delta)\kappa_4) + ((\kappa_1 + \frac{\Delta t}{2}(\alpha+\delta)\kappa_3)(\cos(2\eta h)))$$

$$+((\kappa_2 + \frac{\Delta t}{2}(\alpha+\delta)\kappa_4) + (\kappa_1 - \frac{\Delta t}{2}(\alpha+\delta)\kappa_3))(\cos(\eta h))$$

$$B_2 = (\kappa_1 - \frac{\Delta t}{2}(\alpha+\delta)\kappa_3 - 2(1+\frac{\lambda\Delta t}{2})\kappa_5) - \kappa_2 - \frac{\Delta t}{2}(\alpha+\delta)\kappa_4))(\sin(\eta h))$$

$$-(\kappa_1 + \frac{\Delta t}{2}(\alpha+\delta)\kappa_3 - (1+\frac{\lambda\Delta t}{2})\kappa_5)(\sin(2\eta h))$$

simplifying the equation (13), we obtain

$$0 \le \frac{g_5}{-2+g_5} \le \cos(\eta h) - 1$$

So the linear numerical diagram of the (B-B-M-B) equation is unconditionally stable.

5. Test problem and discussion

The efficiency and accurateness of the proposed method can be illustrated in the following two examples in this section with L_∞ and L_2 being the error criteria that are computed by $L_\infty = \max_i \left|\varpi_j^{exact} - \varpi_i^{num}\right|$ and $L_2 = \sqrt{h\left(\sum_i^n \left|\varpi_j^{exact} - \varpi_j^{num}\right|^2\right)}$

The conservation laws apply on equation (1) as follows [9].

$$C_1 = \int_\psi^\tau \varpi(x,t)dx,\ C_2 = \int_\psi^\tau \varpi(x,t)^2 dx,\ C_3 = \int_\psi^\tau [\varpi(x,t)^2 + \frac{1}{3}\varpi(x,t)^3]dx$$

Where C_1, C_2, C_3 match mass, momentum and energy, respectively.

Then for validation, the numerical solutions obtained by testing the QT-BS method of equation (B-B-M-B) (1) are compared with the precise solutions and with the results of numerical methods that have been found in the literature. It was noted that numerical results are expected at different time scales.

Example 5.1

Consider the (B-B-M-B) problem [3] with $\delta = 1.0$ and $\lambda = 1.0$,

$$\varpi_t + \varpi_x + \varpi\varpi_x - \varpi_{xxt} - \varpi_{xx} = 0 \qquad x \in [-12,12]\ , t \in [0,T]$$

with initial condition

$$\varpi(x,0) = g(x) = \sec h^2\left(x/4\right),\ -12 \le x \le 12$$

boundary conditions as follows:

$$\varpi(-12,t) = \sec h^2\left(-3 - t/3\right), \varpi(12,t) = \sec h^2\left(3 - t/3\right)$$

The precise solution of this problem is $\varpi(x,t) = \sec h^2\left(x/4 - t/3\right)$. The QT-BS method is employed to calculate the numerical solutions of this problem. For the purpose of comparison, the numerical results obtained in this paper are found to be more accurate as compared to CuBS [4]. The absolute errors at different time levels with $h = 1/200$ and $\Delta t = 0.01$ at different time levels in Table 2 and Table 3. Figuer1 shows a graph of approximate space-time and a good agreement with their precise solutions at $0.2 \le t \le 1$. Figuer2 depicts the error at T=2 and A=200.

Table 2: Absolute errors for Example5.1

x	Present method			CuBS [4]		
	$t = 0.2$	$t = 0.5$	$t = 0.7$	$t = 0.2$	$t = 0.5$	$t = 0.7$
-12	2.1164-16	6.9389E-17	1.1015E-16	3.33E-11	2.23E-10	3.33E-11
-10	1.2931E-03	2.6551E-03	3.2522E-03	2.29E-02	1.98E-02	1.79E-02
-5	6.0445E-03	1.4880E-02	2.0122E-02	2.56E-01	2.24E-01	2.06E-01
0	1.7425E-02	3.9343E-02	4.9853E-02	9.78E-01	9.33E-01	8.97E-01
5	5.816E-03	1.2295E-02	1.4373E-02	3.19E-01	3.80E-01	4.23E-01
10	1.6463E-03	4.8198E-03	7.4331E-03	3.04E-02	3.97E-02	4.72E-02
12	0	0	3.4694E-18	2.00E-10	6.66E-11	2.66E-10

Table 3: Absolute errors for Example5.1

x	Present method			CuBS [4]		
	$t = 1.0$	$t = 1.5$	$t = 2.0$	$t = 1.0$	$t = 1.5$	$t = 2.0$
-12	1.06E-16	4.1373E-16	1.3097E-16	1.33E-11	1.26E-10	8.66E-11

-10	6.9002E-04	4.0285E-03	3.7824E-03	1.54E-02	1.19E-02	9.16E-03
-5	3.0994E-03	3.5237E-02	4.0018E-02	1.82E-01	1.49E-01	1.23E-01
0	8.9008E-03	5.2923E-02	2.8860E-02	8.38E-01	7.33E-01	6.31E-01
5	3.0181E-03	5.2377E-03	4.5119E-2	4.87E-01	5.89E-01	6.76E-01
10	7.7837E-04	2.1844E-02	3.3271E-02	6.05E-02	8.86E-02	1.25E-01
12	0	0	0	1.13E-09	-3.33E-10	-1.01E-16

Table 4: Invariants for N=200 at different time

t	C_1	C_2	C_3
0.2	7.9572	5.2432	5.1590
0.4	7.9515	5.1574	5.0775
0.8	7.9356	4.9472	4.9248
1.0	7.9251	4.9220	4.8530
1.5	7.8901	4.767	4.6850
2.0	7.8396	4.5860	4.5302

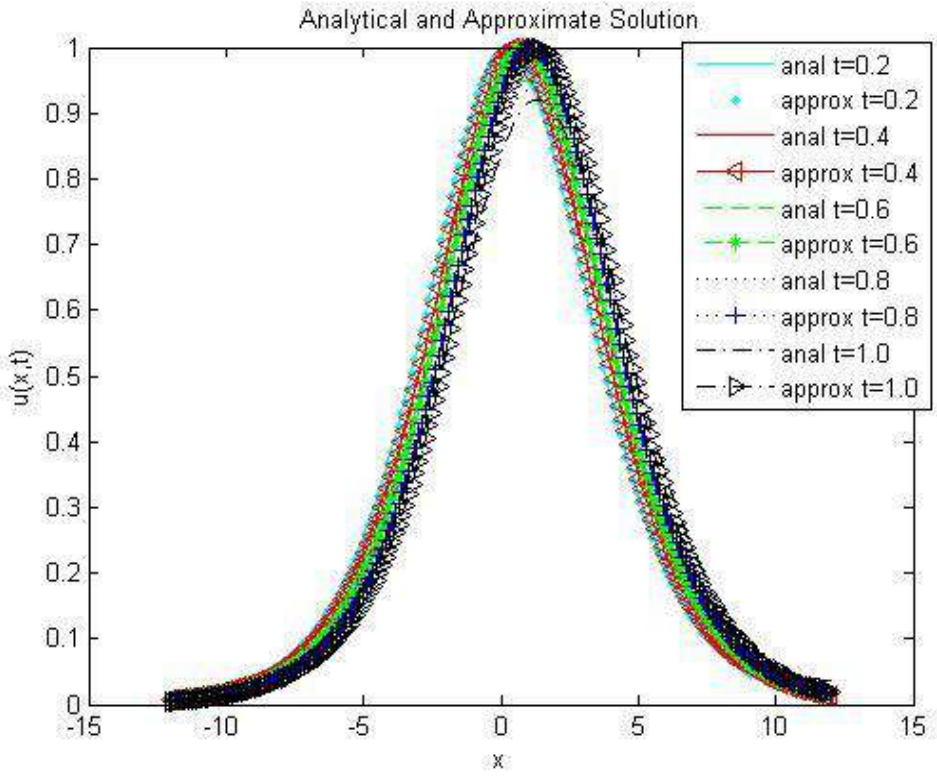

Figuer.1. Approximate solution and exact solution at different value to time level $0.2 \le t \le 1$**. problem5.1**.

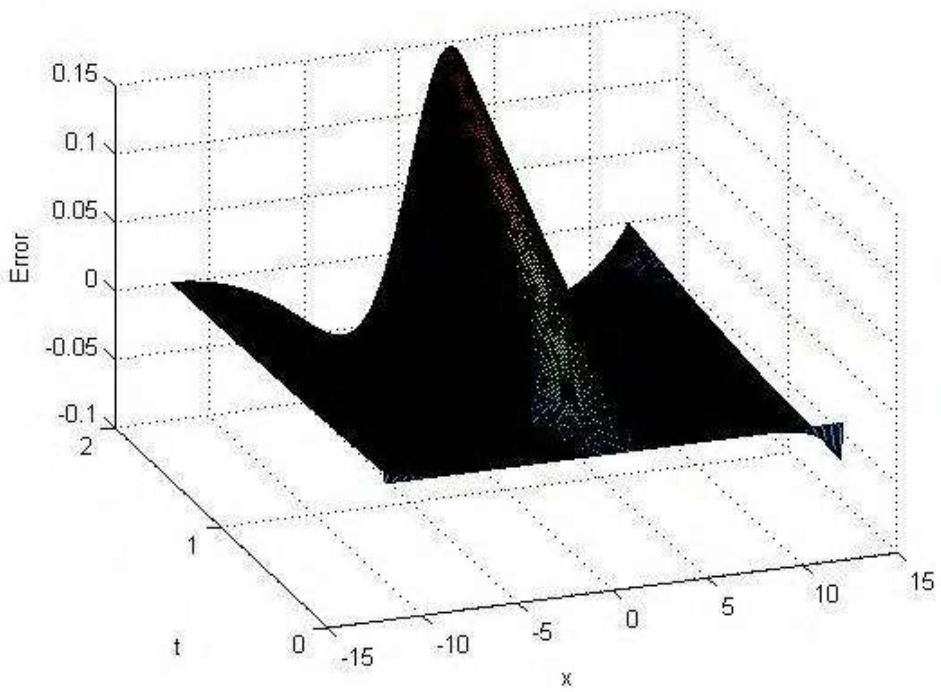

Figure.2.Erroer plot at T=2 and N=200 of problem 5.1

Example 5.2
Consider the B-B-M- B inhomogeneous problem [1] with $\delta = 1.0$ and $\lambda = 1.0$, $x \in [0, \pi]$

$$\varpi_t + \varpi_x + \varpi\varpi_x - \varpi_{xxt} - \varpi_{xx} = e^{(-t)}[\cos(x) - \sin(x) + 0.5e^{(-t)}\sin(2x)$$

initial conditions

$$\varpi(x,0) = \sin(x)$$

The boundary conditions are taken from the precise solution $\varpi(x,t) = e^{(-t)}\sin(x)$. The result for L_∞ and L_2 errors for N=121 and different value to T in table 5 are comparison with [1]. The numerical results obtained in this paper are found to be more accurate. In table 6, we take different values to N and T=10 with $\Delta t = 0.01$ and the result is comparison with [1]. We illustrate and show that the QT-BS is more accurate than the method suggested by Arora and Omarani. Figure 3 shows approximate and a good agreement with their exact solutions T.

Table 5: L_2 and L_∞ Errors at N=121 and different time-levelsa for Example5.2

Error	t=1	**present method** t=2	t=4	t=10	QuBS [1] $t=2$	t=10
$\boldsymbol{L_\infty}$	1.25801E-3	1.10980E-3	3.83346E-4	2.89577E-6	2.83801E-3	4.05946E-6
$\boldsymbol{L_2}$	1.25667E-3	1.1099E-3	3.78937E-4	2.64010E-6	1.72970E-3	4.07835E-6

Table 6: L_2 Error at T=10 and different value for N Example5.2

N	present method	QuBs[1]	[2]
10	1.0275E-4	1,7147E-4	2.200E-2
20	2.5540E-5	5.6341E-5	5.000E-3

80	2.6413E-6	7.2635E-6	3.329E-4
320	2.6826E-6	8.163E-7	2.076E-5

Table 7: Invariants for N=121 at different time

T	C_1	C_2	C_3
0.2	1.6370	1.0529	0.6954
0.4	1.3410	0.7065	0.4650
0.6	1.0985	0.4741	0.3090
0.8	0.8999	0.3182	0.2038
1.0	0.7372	0.2135	0.1332

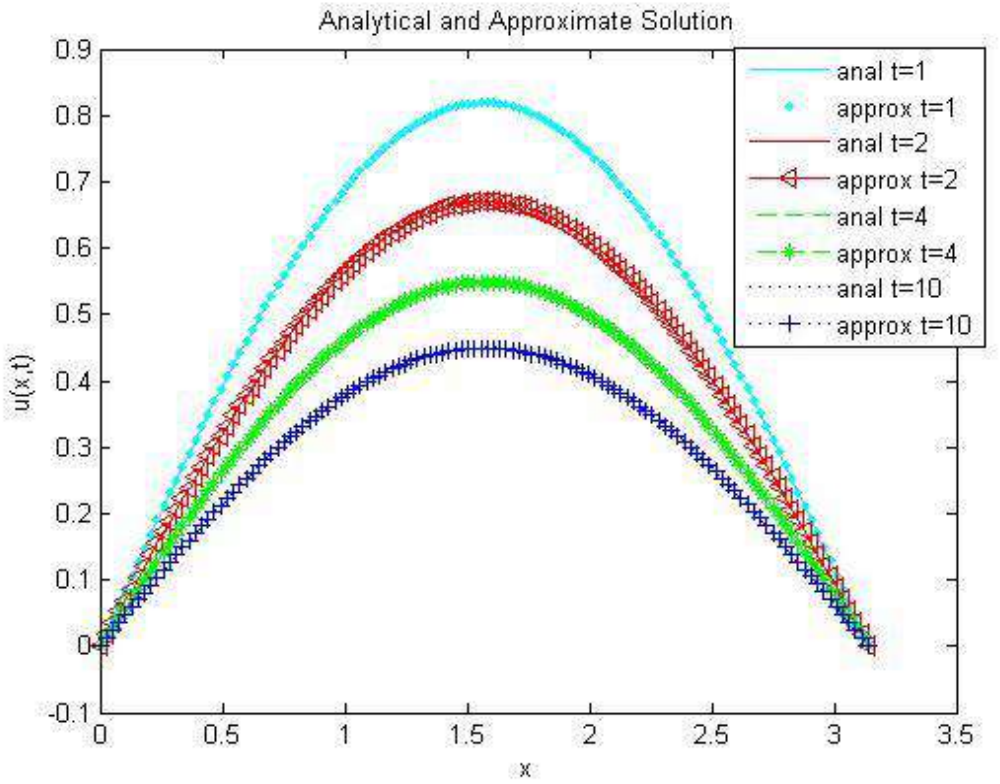

Figure.3. Approximate solution and exact solution at different value to T.problem5.2.

6. Conclusions

The quartic trigonometric B-spline method is proposed to solve the BBM-Berger equation in the present work. Applying this method is occurred by taking two examples and then compare the results with cubic B-spline method as in example one. The obtained results from the proposed method are given more accuracy than the cubic B-spline method but in example two the comparison is made with both quartic B-spline and finite difference methods. Then, the founded results from the proposed methods give high accuracy and efficiency than both of quartic B-spline and finite difference methods. Finally, the obtained results from the proposed method are validated with the von Neumann method for the purpose of checking the stability and getting unconditionally stable.

References

[1] Arora G, Mittal R C and Singh B K 2014 Numerical solution of BBM-Burger equation with quartic B-spline collocation method *J. Engg. Sci. Tech* **9**(3) pp 104-116
[2] Omrani K and Ayadi M 2008 Finite difference discretization of the Benjamin- Bona- Mahony-Burgers Equation *Numerical Methods for Partial Differential Equations* **24(1)** pp 239-248
[3] Salih H M, Tawfiq L N M and Yahya Z R 2016 Using Cubic Trigonometric B-Spline Method to Solve BBM-Burger Equation *IWNEST Conference Proceedings* **2** pp 1-9
[4] Zarebnia M and Parvaz R 2013 Cubic B-spline Collocation Method for Numerical Solution of the Benjamin-Bona-Mahony-Burgers Equation *World Academy of Science, Engineering and Technology, International Journal of Mathematical, Computational, Physical, Electrical and Computer Engineering* **7(3)** pp 540-543
[5] Yin Y X and Piao G R 2013 Quadratic B-Spline Finite Element Method for the Benjamin-Bona-Mahony-Burgers Equation *East Asian mathematical journal* **29(5)** pp 503-510
[6] Nazir T, Abbas M, Ismail A I M and Majid A A 2015 Numerical Solution of second order hyperbolic telegraph equation via new Cubic Trigonometric B-Splines Approach *arXiv preprint arXiv* pp 1510-09051
[7] Zin S 2016 *B-spline Collocation Approach for Solution Partial Differential Equation*. Thesis
[8] Zin S M, Majid A A and Ismail A I M 2014 Quartic B-spline collocation method applied to Korteweg de Vries equation *In PROCEEDINGS OF THE 21ST NATIONAL SYMPOSIUM ON MATHEMATICAL SCIENCES (SKSM21): Germination of Mathematical Sciences Education and Research towards Global Sustainability* **1605(1)** pp 292-297
[9] Salih H M, Tawfiq L N M and Yahya Z R 2016 Numerical Solution of the Coupled Viscous Burgers' Equation via Cubic Trigonometric B-spline Approach *Math Stat* **2**(011)
[10] Sajjadian M 2012 Numerical solutions of Korteweg de Vries and Korteweg de Vries-Burger's equations using computer programming *arXiv preprint arXiv* pp 1209-1782

On semi strongly (*E, F*)-convex functions and semi strongly (*E, F*)-convex optimization problems

On semi strongly (E, F)-convex functions and semi strongly (E, F)-convex optimization problems

S N Majeed and A A Enad

Department of Mathematics, College of Education for Pure Sciences Ibn-Al-Haitham, University of Baghdad, Baghdad, Iraq

E-mail: saba.n.m@ihcoedu.uobaghdad.edu.iq

Abstract. In this paper, a new class of non-convex functions called semi strongly (E, F)-convex functions are presented. This class represents a natural extension of semi strongly E-convex functions shown in the literature. Different properties of this class of functions are discussed. Optimality properties of constrained optimization problems in which the objective function or the inequality constraints functions are semi strongly (E, F)-convex are proved for this class.

1. Introduction and Preliminaries

Convex analysis studied and employed widely in applied mathematics, especially in optimization and optimal control (see e.g., [1-2]). Several attempts were made in the literature to generalize and extend convex sets and convex functions. For instance, the class of E-convex sets and E-convex functions, introduced first by Youness [3], that introduced as one class of generalized classical convex sets and convex functions in finite dimensional Euclidian space. Youness inspired many researchers to extend many concepts from convex analysis into E-convexity and applying E-convexity in optimization problems see (e.g., [4-12]). The class of E-convex sets and E-convex functions is extended into strongly E-convex sets and E-convex functions [13-14]. Moreover, E-convexity results extended to new classes such as semi E-convex functions [15-16] and semi strongly E-convex functions [17]. E-convex sets and functions are also extended to another class called (E, F)-convex sets and (E, F)-convex functions [18-19]. The results related to semi E-convexity mentioned earlier are also extended into semi (E, F)-convexity [20]. By combining semi strongly E-convexity and (E, F)-convexity, we introduce in this paper the class of semi strongly (E, F)-convex functions and studying some of their properties. In section 2, the definition of strongly (E, F)-convex functions are introduced, and some examples related to the new function are shown. In section 3, some important properties related to semi strongly (E, F)-convex functions are proved. Finally, section 4 discusses some optimality criteria of a constrained optimization problem are proved as an application of (E, F)-convexity to optimization problems in this section.

Denote by $\mathbb{R}^n$, the n-dimensional Euclidean space. Throughout the paper, the following assumption is required.

Assumption: Let $\emptyset \neq S \subseteq \mathbb{R}^n$ and $f: \mathbb{R}^n \to \mathbb{R}$ be a real valued function. Suppose that $E, F: \mathbb{R}^n \to \mathbb{R}^n$ are two mappings.

For the rest of the paper, S, f, E, and F are defined as in the Assumption. Next, some definitions and related concepts that are necessary in the sequel are recalled.

Definition 1.1 Let $S, f, E,$ and F are assumed as in the Assumption then, for each $x, y \in S$ and for each $\delta \in [0,1]$, S is called

1. E-convex if $\delta E(x) + (1-\delta)E(y) \in S$. [3]
2. Strongly E-convex set if $\delta(\alpha x + E(x))) + (1-\delta)(\alpha y + E(y)) \in S$. for all $\alpha \in [0,1]$. [13]
3. (E,F)-convex if $\delta E(x) + (1-\delta)F(y) \in S$. [18]
4. Strongly (E,F)-convex set if $\delta(\alpha x + Ex) + (1-\delta)(\alpha y + Fy) \in S$. for all $\alpha \in [0,1]$. [21]

Remark 1.2

i. For the rest of the paper, $E(x)$ and $F(y)$ are written as Ex and Fy.
ii. In [18], the mappings E and F are considered as point to set maps. As a result, the set S is called (E,F)-convex if $\delta E(x) + (1-\delta)F(y) \subseteq S$. In this paper, we deal with E and F as point to point mappings.

Proposition 1.3 If $S_i \subseteq \mathbb{R}^n$, for $i = 1,2,\dots,m$, are strongly (E,F)-convex sets, then $\bigcap_{i=1}^{m} S_i$ is a strongly (E,F)-convex set.

Proof. Let $x, y \in \bigcap_{i=1}^{m} S_i$ and $\lambda, \alpha \in [0,1]$, this means $x, y \in S_i$, for each $i = 1,2,\dots,m$. From the assumption, S_i is strongly (E,F)-convex set, we get $\delta(\alpha x + Ex) + (1-\delta)(\alpha y + Fy) \in S_i$ for all $i = 1,2,\dots,m$. This means, $\delta(\alpha x + Ex) + (1-\delta)(\alpha y + Fy) \in \bigcap_{i=1}^{m} S_i$. Hence, $\bigcap_{i=1}^{m} S_i$ is strongly (E,F)-convex set.

Definition 1.4 Let $S, f, E,$ and F are assumed as in the Assumption then, for each $x, y \in S$ and for all $\delta, \alpha \in [0,1]$, f is called

1. E-convex function if S is E-convex and $f(\delta Ex + (1-\delta)Ey) \leq \delta f(Ex) + (1-\delta)f(Ey)$. [3]
2. Strongly E-convex function if S is strongly E-convex and $f(\delta(\alpha x + Ex) + (1-\delta)(\alpha y + Ey)) \leq \delta f(Ex) + (1-\delta)f(Ey)$. [13]
3. Semi strongly E-convex function if S is strongly E-convex and $f(\delta(\alpha x + Ex) + (1-\delta)(\alpha y + Ey)) \leq \delta f(x) + (1-\delta)f(y)$. [17]
4. (E,F)-convex function if S is (E,F)-convex and $f(\delta Ex + (1-\delta)Fy) \leq \delta f(Ex) + (1-\delta)f(Fy)$. [18]
5. Semi (E,F)-convex function if S is (E,F)-convex and $f(\delta Ex + (1-\delta)Fy) \leq \delta f(x) + (1-\delta)f(y)$. [20]
6. Strongly (E,F)-convex function on S, if S is strongly (E,F)-convex and $f\big(\delta(\alpha x + Ex) + (1-\delta)(\alpha y + Fy)\big) \leq \delta f(Ex) + (1-\delta)f(Fy)$. [21]

Definition 1.5 [1] The level set of f is denoted by H_γ and defined as $H_\gamma = \{x \in S : f(x) \leq \gamma\}$.

2. Semi strongly (E,F)-convex functions

In this section, we introduce the concepts of semi strongly (E,F)-convex and provide some related examples and properties.

Definition 2.1 Let S is a strongly (E,F)-convex set. A function f is called semi strongly (E,F)-convex function on S, if for each $x, y \in S$ and $\delta, \alpha \in [0,1]$,

$f\big(\delta(\alpha x + Ex) + (1-\delta)(\alpha y + Fy)\big) \le \delta f(x) + (1-\delta) f(y)$.
The function f is called strictly semi strongly (E,F)-convex if for each $x, y \in S$ $(x \ne y)$,
$f\big(\delta(\alpha x + Ex) + (1-\delta)(\alpha y + Fy)\big) < \delta f(x) + (1-\delta) f(y)$.

Remark 2.2 Every semi strongly (E,F)-convex function is semi (E,F)-convex function [21] (when $\alpha = 0$). The converse is not true as the following example shows.

Example 2.3 Let $S = \mathbb{R}$, $f: \mathbb{R} \to \mathbb{R}$, and $E, F: \mathbb{R} \to \mathbb{R}$ such that

$$f(x) = \begin{cases} 1 & \text{if } x = 0 \\ -3 & \text{otherwise} \end{cases}, \quad E(x) = \begin{cases} 0 & \text{if } x = 0 \\ 3 & \text{otherwise} \end{cases}$$

and $F(x) = \begin{cases} 0 & \text{if } x = 0 \\ 1 & \text{otherwise} \end{cases}$.

Let $x, y \in \mathbb{R}$ and $\delta \in [0,1]$. First, we show that

$$f(\delta Ex + (1-\delta)Fy) \le \delta f(x) + (1-\delta) f(y).$$

We consider four cases:
Case 1: If $x = y = 0$, then

$$f(\delta Ex + (1-\delta)Fy) = f(\delta E(0) + (1-\delta)F(0)) = f(0) = 1, \text{ and}$$
$$\delta f(x) + (1-\delta) f(y) = \delta f(0) + (1-\delta) f(0) = \delta(1) + (1-\delta)(1) = 1.$$

Case 2: If $x \ne 0$ and $y \ne 0$, then

$$f(\delta Ex + (1-\delta)Fy) = f\big(\delta(3) + (1-\delta)(1)\big) = f(2\delta + 1) = -3, \text{ and}$$
$$\delta f(x) + (1-\delta) f(y) = \delta(-3) + (1-\delta)(-3) = -3.$$

Case 3: If $x = 0$ and $y \ne 0$, then

$$f(\delta Ex + (1-\delta)Fy) = f(\delta(0) + (1-\delta)(1))$$
$$= f(1-\delta) = \begin{cases} 1 & if\ \delta = 1 \\ -3 & if\ \delta \ne 1 \end{cases},$$

On the other hand, $\delta f(x) + (1-\delta) f(y) = \delta f(0) + (1-\delta) f(y)$
$$= \delta(1) + (1-\delta)(-3) = 4\delta - 3$$

If $\delta = 1$, then $4\delta - 3 = 1$ and if $0 \le \delta < 1$, then $4\delta - 3 \ge -3$

Case 4: If $x \ne 0$ and $y = 0$, then

$$f(\delta Ex + (1-\delta)Fy) = f(\delta(3) + (1-\delta)(0))$$
$$= f(3\delta) = \begin{cases} 1 & if\ \delta = 0 \\ -3 & \text{otherwise} \end{cases},$$

and $\delta f(x) + (1-\delta) f(y) = \delta f(x) + (1-\delta) f(0)$
$$= \delta(-3) + (1-\delta)(1) = -4\delta + 1$$

If $\delta = 0$, then $-4\delta + 1 = 1$ and if $0 < \delta \le 1$, then $-4\delta + 1 \ge -3$.

All cases imply that, $f\big(\delta(Ex) + (1-\delta)(Fy)\big) \le \delta f(x) + (1-\delta) f(y)$.
Hence, f is semi (E,F)-convex function.
Now, let $\alpha = \frac{1}{2}$, $x = -6$, $y = 1$, $\delta = 1$, then

$$f\big(\delta(\alpha x + Ex) + (1-\delta)(\alpha y + Fy)\big) = f\big(-3 + E(-6)\big)$$
$$= f(-3 + 3) = 1. \qquad (2.1)$$

On the other hand, $\delta f(x) + (1-\delta)f(y) = f(-6) = -3.$ (2.2)
From (2.1) and (2.2),

$$f\big(\delta(\alpha x + Ex) + (1-\delta)(\alpha y + Fy)\big) > \delta f(x) + (1-\delta)f(y),$$

which shows that f is not semi strongly (E,F)-convex function.

Remark 2.4 A strongly (E,F)-convex function is not necessary semi strongly (E,F)-convex function as it is illustrated in the next example.

Example 2.5 Let $S = \mathbb{R}$ and $f, E, F: \mathbb{R} \to \mathbb{R}$ such that for each $x \in \mathbb{R}$

$$f(x) = \begin{cases} 2 & if\ x \in [0,2] \\ 1 & otherwise \end{cases},$$

$E(x) = 0$ and $F(x) = \frac{1}{2}$. From [21, Example 2.9], f is a strongly (E,F)-convex function. Now, let $\alpha = \frac{1}{2}$, $x = 2$, $y = -1$, $\delta = 0$, then $f\big(\delta(\alpha x + Ex) + (1-\delta)(\alpha y + Fy)\big) = f(0) = 2.$ (2.3)
And, $\delta f(x) + (1-\delta)f(y) = (1-0)f(-1) = 1.$ (2.4)
From (2.3) and (2.4), $f\big(\delta(\alpha x + Ex) + (1-\delta)(\alpha y + Fy)\big) > \delta f(x) + (1-\delta)f(y)$.
This yield, f is not semi strongly (E,F)-convex function.

Proposition 2.6 If f is a semi strongly (E,F)-convex function on a strongly (E,F)-convex set S, then $f(\alpha x + Ex) \le f(x)$ and $f(\alpha y + Fy) \le f(y)$, for each $x, y \in S$ and $\alpha \in [0,1]$.
Proof. Suppose that f is a semi strongly (E,F)-convex function on a strongly (E,F)-convex set S, then for each $x, y \in S$ and $\alpha, \delta \in [0,1]$, we have $\delta(\alpha x + Ex) + (1-\delta)(\alpha y + Fy) \in S$ and $f\big(\delta(\alpha x + Ex) + (1-\delta)(\alpha y + Fy)\big) \le \delta f(x) + (1-\delta)f(y)$. Thus for $\delta = 1$, $f(\alpha x + Ex) \le f(x)$ and for $\delta = 0$, we obtain $f(\alpha y + Fy) \le f(y)$.

Next proposition shows the relation between strongly (E,F)-convex function and semi strongly (E,F)-convex function.

Proposition 2.7 Let S be a strongly (E,F)-convex set. Then, a strongly (E,F)-convex function f on S is semi strongly (E,F)-convex function if and only if $f(Ex) \le f(x)$ and $f(Fy) \le f(y)$, for any $x, y \in S$.
Proof. From assumptions f is a strongly (E,F)-convex function on S and $f(Ex) \le f(x)$ and $f(Fy) \le f(y)$, for all $x, y \in S$ and $\alpha, \delta \in [0,1]$, we get

$$\begin{aligned} f\big(\delta(\alpha x + Ex) + (1-\delta)(\alpha y + Fy)\big) &\le \delta f(Ex) + (1-\delta)f(Fy) \\ &\le \delta f(x) + (1-\delta)f(y) \end{aligned}$$

Thus, f is semi strongly (E,F)-convex function on S. Assume now f is semi strongly (E,F)-convex function, so from Proposition 2.6, we have
$f(\alpha x + Ex) \le f(x)$ and $f(\alpha y + Fy) \le f(y)$ for each $x, y \in S$ and $\alpha \in [0,1]$.
Take $\alpha = 0$ to obtain the required conclusion.

3. Some Properties of Semi Strongly (E,F)-convex Functions

In this section, some basic properties of semi strongly (E,F)-convex functions such as closedness, supremum and composite are discussed.

Proposition 3.1 If $f_i: \mathbb{R}^n \to \mathbb{R}$, $i = 1,2,\dots,m$ are semi strongly (E,F)-convex functions on the strongly (E,F)-convex set S such that $f(x) = \sum_{i=1}^{m} a_i f_i(x)$, then f is semi strongly (E,F)-convex function on S for each $a_i \geq 0, i = 1,\dots,n$.

Proof. From the hypothesis, for each $x, y \in S$ and for all $\delta, \alpha \in [0,1]$, we have $\delta(\alpha x + Ex) + (1-\delta)(\alpha y + Fy) \in S$ and

$$\begin{aligned} f\big(\delta(\alpha x + Ex) + (1-\delta)(\alpha y + Fy)\big) &= \sum_{i=1}^{m} a_i f_i(\delta(\alpha x + Ex) + (1-\delta)(\alpha y + Fy)) \\ &\leq \delta \textstyle\sum_{i=1}^{m} a_i f_i(x) + (1-\delta)\sum_{i=1}^{m} a_i f_i(y) \\ &= \delta f(x) + (1-\delta) f(y) \end{aligned}$$

This implies, f is semi strongly (E,F)-convex function on S.

Proposition 3.2 Let I be an index set and $f_i: \mathbb{R}^n \to \mathbb{R}$ for each $i \in I$ be a family of bounded above and semi strongly (E,F)-convex functions on the strongly (E,F)-convex set S. Then, $f(x) = \sup_{i \in I} f_i(x)$ is semi strongly (E,F)-convex on S.

Proof. From the assumptions, for each $x, y \in S$ and for each $\delta, \alpha \in [0,1]$, we have $\delta(\alpha x + Ex) + (1-\delta)(\alpha y + Fy) \in S$ and

$$\begin{aligned} f\big(\delta(\alpha x + Ex) + (1-\delta)(\alpha y + Fy)\big) &= \sup_{i \in I}\big\{f_i\big(\delta(\alpha x + Ex) + (1-\delta)(\alpha y + Fy)\big)\big\} \\ &\leq \sup_{i \in I}\{\delta f_i(x) + (1-\delta) f_i(y)\} \end{aligned}$$

where in the last inequality we used the fact that f_i is semi strongly (E,F)-convex for each $i \in I$ and f_i is bounded above for all $i \in I$. The inequality above yields

$$= \delta \sup_{i \in I} f_i(x) + (1-\delta)\sup_{i \in I} f_i(y) = \delta f(x) + (1-\delta) f(y).$$

This means f is a semi strongly (E,F)-convex on S.

Proposition 3.3 Let f be a semi strongly (E,F)-convex function on the strongly (E,F)-convex set S. Let $G: \mathbb{R} \to \mathbb{R}$ be a non decreasing convex function, then $G \circ f$ is semi strongly (E,F)-convex function on S.

Proof. Let $x, y \in S$ and $\delta, \alpha \in [0,1]$. From the assumptions on S and f, we get $\delta(\alpha x + Ex) + (1-\delta)(\alpha y + Fy) \in S$ and

$$f\big(\delta(\alpha x + Ex) + (1-\delta)(\alpha y + Fy)\big) \leq \delta f(x) + (1-\delta) f(y)$$

From the assumptions on G, the last inequality yields

$$\begin{aligned} (G \circ f)(\delta(\alpha x + Ex) + (1-\delta)(\alpha y + Fy)) &\leq G(\delta f(x) + (1-\delta) f(y)) \\ &\leq \delta\,(G \circ f)(x) + (1-\delta)(G \circ f)(y) \end{aligned}$$

This implies, $G \circ f$ is semi strongly (E,F) −convex function on S.

Proposition 3.4 Suppose f is a semi strongly (E,F)-convex function on a strongly (E,F)-convex set M, then for all $\gamma \in \mathbb{R}$ the level set H_γ is strongly (E,F)-convex set.

Proof. From the assumptions, for any $x, y \in H_\gamma$ and for each $\alpha, \lambda \in [0,1]$, $f(x) \leq \gamma$ and $f(y) \leq \gamma$. Since f is a semi strongly (E,F)-convex function on S, then $\delta(\alpha x + Ex) + (1-\delta)(\alpha y + Fy) \in S$ and

$$f\big(\delta(\alpha x + Ex) + (1-\delta)(\alpha y + Fy)\big) \le \delta f(x) + (1-\delta) f(y)$$
$$\le \delta\gamma + (1-\delta)\gamma = \gamma$$

This means, $\delta(\alpha x + Ex) + (1-\delta)(\alpha y + Fy) \in H_\gamma$. Hence, H_γ is a strongly (E,F)-convex set.

4. Optimality Properties of Semi Strongly (E,F)-convex Functions

In this section, some optimality criteria of constrained optimization problems, in which the objective function or the inequality constraints functions are semi strongly (E,F)-convex, are discussed. First, denote by (P), the following constrained optimization problem.

$$\min\ f(x)$$
$$\text{subject to}\quad x \in S,$$

where S and f are assumed as in the Assumption. Let $g_i: \mathbb{R}^n \to \mathbb{R}$ for each $i = 1, \dots, m$ such that $S = \{x \in \mathbb{R}^n : g_i(x) \le 0 \text{ for each } i = 1, \dots, m\}$.

Definition 4.1 In the Problem (P)**,** the set of optimal solutions is denoted by $argmin_S f$ and is defined as $argmin_S f = \{x^* \in S : f(x^*) \le f(x), for\ each\ x \in S\}$.

The next theorem, introduced in [21], is needed in the sequel.

Theorem 4.2 In Problem (P), let S be a strongly (E,F)-convex set and $f(\alpha x + Fx) \le f(x)$ for each $x \in S$, $\alpha \in [0,1]$. If $x^* \in S$ is a solution of the following problem denoted by (P_1)

$$\min f(\alpha x + Ex)$$
$$\text{subject to}\ x \in S$$

Then $\alpha x^* + Ex^*$ is an optimal solution of Problem (P).

Because of Proposition 2.6 and the proceeding theorem, we have the following result.

Corollary 4.3 Consider problem (P) such that S be strongly (E,F)-convex set and f is semi strongly (E,F)-convex function. If $x^* \in S$ is solution of the following problem denoted by (P_1)

$$\min f(\alpha x + Ex)$$
$$\text{subject to}\ x \in S.$$

Then $\alpha x^* + Ex^*$ is an optimal solution of problem (P).

Proof. Since f is semi strongly (E,F)-convex function on M, then from Proposition 2.6**,** $f(\alpha x + Fx) \le f(x)$. Now, from Theorem 4.2, we obtain the required result.

Next, we prove that, under simple condition, the constraint set S of Problem (P) is strongly (E,F)-convex set.

Theorem 4.4 If g_i are semi strongly (E,F)-convex functions for each $i = 1,2, \dots, m$, then M is strongly (E,F)-convex set.

Proof. By Proposition 3.4, we have $S_i = \{x \in \mathbb{R}^n : g_i(x) \le 0\}$ is strongly (E,F)-convex set for each $i = 1,2, \dots, m$. Thus, using Proposition 1.3, $S = \bigcap_{i=1}^m S_i$ is strongly (E,F)-convex set.

The following three result provides sufficient condition under which $argmin_S f$ is strongly (E,F)-convex.

Theorem 4.5 Let S be strongly (E,F)-convex set. If f is semi strongly (E,F)-convex function on S. Then, $argmin_S f$ of problem (P) is strongly (E,F)-convex set.

Proof. Let $x, y \in argmin_S f$ such that $x \ne y$. From Definition 4.1, $f(x) = f(y) = P^*$. If f is semi strongly (E,F)-convex function on S, then for each $\alpha, \delta \in [0,1]$, we have
$\delta(\alpha x + Ex) + (1-\delta)(\alpha y + Fy) \in S$ and

$$f\big(\delta(\alpha x + Ex) + (1-\delta)(\alpha y + Fy)\big) \le \delta f(x) + (1-\delta) f(y) = P^*$$

Since $\inf_{x\in S} f(x) = P^*$, this fact with the last inequality forces
$\delta(\alpha x + Ex) + (1-\delta)(\alpha y + Fy) \in argmin_S f$. Hence, $argmin_S$ is strongly (E,F)-convex set.

Theorem 4.6 Let S is strongly (E,F)-convex set. If f is strictly semi strongly (E,F)-convex function on S, then $argmin_S f$ is unique.
Proof. On the contrary, let $x, y \in S$ two different optimal solutions of problem (P), i.e., $f(x) = f(y)$. Since S is strongly (E,F)-convex set and f is strictly semi strongly (E,F)-convex function on S, we have for $x \neq y$ and $\alpha, \delta \in (0,1)$,

$$\delta(\alpha x + Ex) + (1-\delta)(\alpha y + Fy) \in S \text{ and}$$
$$f\big(\delta(\alpha x + Ex) + (1-\delta)(\alpha y + Fy)\big) < \delta f(x) + (1-\delta) f(y) = f(x),$$

which is contradiction. Thus, $argmin_S f$ of problem (P) is unique.

References

[1] Rockafellar R T 1970 *Convex Analysis (*Princeton University Press Princeton)
[2] Zalinescu C 2002 *Convex Analysis in General Vector Spaces* (World Scientific, Singapore)
[3] Youness E A 1999 E-convex sets, E-convex functions, and E-convex programming *J. Optim. Theory Appl.* **102** 439
[4] Abou-Tair I A and Sulaiman W T 1999 Inequalities via convex functions *International Journal of Mathematics and Mathematical Scienes* **22** 543
[5] Suneja S K, Lalitha C S and Govil M G 2002 E-convex and related functions *International Journal of Management and Systems* **102** 439
[6] Grace J S and Thangavelu P 2009 Properties of E-convex sets *Tamsui Oxford Journal of Mathematical Sciences* **25** 1
[7] Majeed S N and Abd Al-Majeed M I 2017 Some notions on generalized convex sets and affine sets *23th Scientific Specialized Conference, College of Education, University of Al-Mustansiryah* 30
[8] Youness E A 2001 Optimality criteria in E-convex programming *Chaos, Solitons & Fractals* **12** 1737
[9] Youness E A 2001 Stability in E-convex programming *International Journal of Mathematics and Mathematical Sciences* **26** 643
[10] Megahed A A, Gomma H G, Youness E A and El-Banna A H 2013 A study on the duality of E-convex non-linear programming problem *International Journal of Mathematical Analysis* **7** 175
[11] Megahed A E M A, Gomma H G, Youness E A and El-Banna A Z H 2013 Optimality conditions of E-convex programming for an E-differentiable function *Journal of Inequalities and Applications* **246** 175
[12] Majeed S N and Abd Al-Majeed M I 2017 On convex functions, E-convex functions and their generalizations: applications to non-linear optimization problems *Int. J. Pure Appl. Math.* **116** 655
[13] Youness E A and Emam T 2005 Strongly E-convex sets and strongly E-convex functions *J. Interdiscipl. Math.* **8** 107
[14] Majeed S N 2019 On strongly E-convex sets and strongly E-convex cone sets *Journal of AL-Qadisiyah for computer science and mathematics* **11** 52
[15] Chen X 2002 Some properties of semi-E-convex functions *J. Math. Anal. Appl.* **278** 251
[16] Chen X 2009 Some properties of semi-E-convex functions and semi-E-convex programming *The Eighth International Symposium on Operations Research and Its Applications* ***(ISORA'09)*** 20
[17] Youness E A and Emam T 2005 Semi Strongly E-convex functions *Journal of Mathematics and Statistics* **1** 51
[18] Jian J B 2003 On (E, F) generalized convexity *International Journal of Mathematical Sciences*

2 121
[19] Jian J B 2003 Incorrect results for E-convex functions and E-convex programming *Mathematical Research and Exposition* **23** 461
[20] Jian J B Hu Q J and Tang C M 2004 Semi-(E, F)-convex functions and semi-(E, F)-convex programming *International Journal of Pure and Applied Mathematics* **14** 437
[21] Enad A A and Majeed S N 2019 Strongly (E, F)-convexity with applications to optimization problems *Journal of AL-Qadisiyah for computer science and mathematics* **11** 66

A New Type of Conjugate Gradient Technique for Solving Fuzzy Nonlinear Algebraic Equations

A New Type of Conjugate Gradient Technique for Solving Fuzzy Nonlinear Algebraic Equations

Hisham M. Khudhur [1,*] and Khalil K. Abbo [2]

[1]Mathematics Department, College of Computer Science and mathematics, University of Mosul, Mosul, Iraq
[2]Department of Mathematics, College of Basic Education, University of Telafer, Tall'Afar, Iraq

Email: hisham892020@uomosul.edu.iq

Abstract. In this paper, we suggest a new method for the numerical solution of fuzzy nonlinear equations in parametric form using a new Conjugate Gradient Technique. Table of the numerical solution is given to show the efficiency of the proposed method and which is compared with classical algorithms such as (Fletcher and Reeves (FR), Polak and Ribiere (PRP), and Fletcher (CD)) techniques.

1.Introduction

Recently, Systems of simultaneous nonlinear equations have been played a major role in various areas of science such as mathematics, statistic, engineering social sciences, robotics, and medicines. The idea of fuzzy numbers and mathematic activity with these numbers were first presented and researched by[1][2][3][4][5]. One of the significant utilization of fuzzy number-crunching is nonlinear systems whose parameters are all or partially represented by fuzzy numbers [6- 8]. Standard analytical methods like Buckley and Qu method [9][10], cannot be suitable for resolving the equations such as

i- $cx^5 + bx^4 + cx^3 + dx - e = f,$

ii- $x - \sin(x) = g,$

Where x, a, b, c, d, e, f and g are fuzzy numbers. In this way, we need to build up the numerical techniques to find the roots of such equations. Here, we think about these conditions, as a rule, as $F(x) = c.$

whose parameters are all or partially represented by fuzzy numbers, [11] research the performance of Newton's scheme for getting the solve of the fuzzy nonlinear equations and reached out to the systems of fuzzy nonlinear equations by [12]. Newton's technique converges quickly if the initial point is picked near the solution point. The primary downside of Newton's strategy is figuring the Hessian matrix in each epoch. Probably the easiest variation of Newton's technique was considered by[13] for solution the double fuzzy nonlinear equations. Another type of Newton's technique known as Levenberg-Marquardt alteration was used to fathom fuzzy nonlinear equations by[14]. Authors in [15] applied also the Broyden's technique to solve the fuzzy nonlinear equations. Every one of these techniques is Newton-like which requires the calculation and storage of either Hessian matrix or approximate Hessian

matrix at every iterative of iterations. Newly, a diagonal update method for solving fuzzy nonlinear equations was proposed by[14]. A gradient based technique by [16] was applied to get the optimal value of variables of fuzzy nonlinear equations. This technique is simple and requires no Hessian matrix assessment during calculations. Be that as it may, method convergence is linear and very slow toward the optimal solution [17]. The steepest descent technique is additionally affected by ill-conditioning [18].

In this work, we developed a new conjugate gradient coefficient and applied it to solve fuzzy nonlinear equations. The conjugate gradient technique is known to be easy and high proficient in taking care of optimization problem. The plan in this work is to convert the parametric form of a fuzzy nonlinear Algebraic equation into an unconstrained optimization problem before applying the new conjugate gradient technique to get the optimal solution.

2. Preliminaries

Definition 1. A fuzzy number is a fuzzy set like $u: \mathbb{R} \longrightarrow I = [0,1]$ which satisfies[19][20],

1. u is upper semi continuous,
2. $u(x) = 0$ outside some interval $[c, d]$,
3. There are real numbers a, b such that $c \leq a \leq b \leq d$ and
   - i. $u(x)$ is monotonic increasing on $[c, a]$,
   - ii. $u(x)$ is monotonic decreasing on $[b, d]$,
   - iii. $u(x) = 1, a \leq x \leq b$.

The set of all these fuzzy numbers is denoted by E. An equivalent parametric is also given in[21] as follows.

Definition 2. A fuzzy number u in parametric form is a pair $(\underline{u}, \overline{u})$ of function $\underline{u}(r), \overline{u}(r), 0 \leq r \leq 1$, which satisfies the following requirements:

1- $\underline{u}(r)$is a bounded monotonic increasing left continuous function,

2- $\overline{u}(r)$is a bounded monotonic decreasing left continuous function,

3- $\underline{u}(r) \leq \overline{u}(r), 0 \leq r \leq 1$.

A popular fuzzy number is the trapezoidal fuzzy number $u = (x_0, y_0, \sigma, \beta)$ with interval defuzzifier $[x_0, y_0]$ and left fuzziness σ and right fuzziness β where the membership function is

$$u(x) = \begin{cases} \frac{1}{\sigma}(x - x_0 + \sigma), & x_0 - \sigma \leq x \leq x_0, \\ 1, & x \in [x_0, y_0], \\ \frac{1}{\beta}(y_0 - x + \beta), & y_0 \leq x \leq y_0 + \beta, \\ 0, & otherwise. \end{cases}$$

Its parametric form is

$\underline{u}(r) = x_0 - \sigma + r\sigma, \overline{u}(r) = y_0 + \beta + r\beta$.

Let $TF(\mathbb{R})$ be the set of all trapezoidal fuzzy numbers. The addition and scalar multiplication of fuzzy numbers are defined by the extension principle and can be equivalently represented as follows.

For arbitrary $u = (\underline{u}, \overline{u}), v = (v, \overline{v})$and $k > 0$ we define addition $(u + v)$and multiplication by scalar k as

$$\left(\underline{u} + \underline{v}\right)(r) = \underline{u} + \underline{v}, \quad (\overline{u} + \overline{v}) = \overline{u} + \overline{v}, \tag{1}$$

$$\left(\underline{ku}\right)(r) = ku(r), \quad \left(\overline{k\overline{u}}\right)(r) = k\overline{u}(r). \tag{2}$$

3. New conjugate gradient method for solving fuzzy nonlinear equations

In this section we will show some of the conjugate gradient methods and then suggest a new algorithm for conjugate gradient algorithm for solving fuzzy nonlinear equations

$$x_{k+1} = x_k + \alpha_k d_k, \quad k \geq 1 \tag{3}$$

Where α_k step-size that satisfy the standard wolfe conditions

$$f(x_k + \alpha_k d_k) \leq f(x_k) + \delta \alpha_k g_k^T d_k \tag{4}$$

$$d_k^T g(x_k + \alpha_k d_k) \geq \sigma d_k^T g_k \tag{5}$$

or strong wolfe conditions

$$f(x_k + \alpha_k d_k) \leq f(x) + \delta \alpha_k g_k^T d_k \tag{6}$$

$$|d_k^T g(x_k + \alpha_k d_k)| \leq -\sigma d_k^T g_k \tag{7}$$

$$d_{k+1} = \begin{cases} -g_1, & k = 1 \\ -g_{k+1} + \beta_k d_k, & k \geq 1 \end{cases} \tag{8}$$

The Fletcher and Reeves (FR) [22], Fletcher (CD) [23], Polak and Ribiere (PRP) [24] and β is scalar.

$\beta^{FR} = \frac{\|g_{k+1}\|^2}{\|g_k\|^2}$, see [22]

$\beta^{CD} = \frac{-\|g_{k+1}\|^2}{g_k^T d_k}$, see [23]

$\beta^{PRP} = \frac{g_{k+1}^T y_k}{\|g_k\|^2}$, see [24]

Where $g_k = \nabla f(x_k)$, and let $y_k = g_{k+1} - g_k$ $y_k = g_{k+1} - g_k$.

Now we suggest a new of conjugate gradient algorithm for solving fuzzy nonlinear equations depend basically on norm-1 instead of norm-2 in Fletcher-Reeves (FR) algorithm so we get new formula

$$d_{k+1} = -g_{k+1} + \beta_k^{NEW} d_k \tag{9}$$

$$\beta_k^{NEW} = \frac{\| g_{k+1} \|_1^2}{\| g_k \|_1^2} \tag{10}$$

4. The Descent property for a new Conjugate Gradient Method (CGM)

In this part, we have to show the descent property for our proposed new conjugate gradient method, denoted by β_k^{NEW}.

Theorem (1)

Consider the search direction given by equation (9) and (10) if α_k computed by strong wolfe condition (6) and (7) then $g_{k+1}^T d_{k+1} < 0$.

$d_{k+1} = -g_{k+1} + \beta_k^{NEW} d_k$, for all $k \geq 1$

Proof:-

The proof is by using mathematical inducement

1- If $k = 1$ then $g_1^T d_1 < 0$, $d_1 = -g_1 \rightarrow < 0$.

2- Let the relation $g_k^T d_k < -c|g_k|$ for all k where $0 < c < 1$.

3- We prove that the relation is true when $k = k + 1$ by multiplying the equation (9) in g_{k+1} we obtain

$d_{k+1} = -g_{k+1} + \beta_k^{NEW} d_k$

$\beta_k^{NEW} = \frac{\|g_{k+1}\|_1^2}{\|g_k\|_1^2}$

Multiply above equation by g_{k+1}

Using the following inequality$\| x \|_2 \leq \| x \|_1 \leq \sqrt{n} \| x \|_2$ We get

$$g_{k+1}^T d_{k+1} = -\|g_{k+1}\|^2 + \frac{\|g_{k+1}\|_1^2}{\|g_k\|_1^2} g_{k+1}^T d_k \leq -\|g_{k+1}\|^2 + \frac{\|g_{k+1}\|^2}{\|g_k\|^2} \left|g_{k+1}^T d_k\right|$$

$$\frac{g_{k+1}^T d_{k+1}}{\|g_{k+1}\|^2} \leq -1 + \frac{\left|g_{k+1}^T d_k\right|}{\|g_k\|^2}$$

By strong wolfe conditions $g_k^T d_k \leq -c|g_k|$

$$\frac{g_{k+1}^T d_{k+1}}{\|g_{k+1}\|^2} \leq -1 + \frac{\sigma\|g_k\|^2}{\|g_k\|^2} \leq -1 - \sigma c$$

$$\therefore\ g_{k+1}^T d_{k+1} \leq -(1+\sigma c)|g_{k+1}|$$

5. Global convergence study

We will display that CG method with β_k^{NEW} convergences globally. We need some assumption for the convergence of the proposed new algorithm.

Assumption (1)

1- Assume f is bound below in the level set $S = \{x \in R^n : f(x) \leq f(x_0)\}$; In some Initial point.

2- f is continuously differentiable and its gradient is Lipchitz continuous, that is there exist $L > 0$ such that [25]:

$\| g(x) - g(y) \| \leq L \| x - y \| \ \forall x, y \in N$.

On the other hand, under Assumption (1), it is clear that there exist positive constants B such

$$\|x\| \leq B, \forall x \in S \tag{11}$$

$$\| \nabla f(x) \| \leq \overline{\gamma}, \forall x \in S \tag{12}$$

Lemma (1)

Suppose that Assumption (1) and equation (11) hold. Take into consideration any conjugate gradient method in from (3) and (8), where d_k is a descent direction and α_k is obtained by the strong wolfe conditions if

$$\sum_{k>1} \frac{1}{\| d_{k+1} \|^2} \geq \infty$$

Then we have

$$\lim_{k\to\infty} inf \| g_k \| = 0$$

More details can be found in[26][27][28][29][30][31].

Theorem (2)

Assume that Assumption (1) and equation (11) and the descent condition hold. Consider a conjugate gradient scheme in the form

$$d_{k+1} = -g_{k+1} + \beta_k^{NEW} d_k$$

where α_k is computed from strong Wolfe line search condition for more details see[32][33][34] , If the objective function is uniformly on set S, then $\lim_{n\to\infty} (inf \| g_k \|) = 0$.

Proof

$$d_{k+1} = -g_{k+1} + \beta_k^{NEW1} d_k$$

$$\beta_k^{NEW1} = \frac{\| g_{k+1} \|_1^2}{\| g_k \|_1^2}$$

$$\| d_{k+1} \| = \| -g_{k+1} + \beta_k^{NEW1} d_k \|$$

$$\| d_{k+1} \| = \| -g_{k+1} + \frac{\| g_{k+1} \|_1^2}{\| g_k \|_1^2} d_k \|$$

$$\| d_{k+1} \| = \| -g_{k+1} + \frac{\| g_{k+1} \|_1^2}{\| g_k \|_1^2} d_k \|$$

$$\| d_{k+1} \| \leq \| g_{k+1} \| + \frac{\sqrt{n} \| g_{k+1} \|^2}{\| g_k \|_1^2} \| d_k \|$$

$$\| d_{k+1} \| \leq (1 + \frac{\sqrt{n} \| g_{k+1} \|}{\| g_k \|_1^2} \| d_k \|) \| g_{k+1} \|$$

Let $\omega = (1 + \frac{\sqrt{n}\|g_{k+1}\|}{\|g_k\|_1^2} \| d_k \|)$

$$\| d_{k+1} \| \leq \omega \| g_{k+1} \|$$

$$\sum_{k \geq 1} \frac{1}{\| d_{k+1} \|^2} \geq (\frac{1}{\omega^2}) \frac{1}{\gamma^2} \sum 1 = \infty$$

Therefore, we have contradiction

$\lim_{n \to \infty} (inf \| g_k \|) = 0.$

6. Numerical Examples

In this part, we present the numerical solution of some examples using the new proposed method for CG method for fuzzy nonlinear equations. All computations are carried out on MATLAB 9.0 using a double precision computer. We use the stop criterion $\| g_{k+1} \| < 10^{-6}$, and employ the new method to solve fuzzy nonlinear equations. Then, we compare with the other methods (Fletcher and Reeves (FR), Polak and Ribiere (PRP), and Fletcher (CD)).

Example 1: Consider the fuzzy nonlinear equation [9]

$(3,4,5)x^2 + (1,2,3)x = (1,2,3)$

Without any loss of generality, assume that x is positive, and then the parametric form of this equation is as follows:

$$\begin{cases} (3+r)\underline{x}^2(r) + (1+r)\underline{x}(r) - (1+r) = 0, \\ (5-r)\overline{x}^2(r) + (3-r)\overline{x}(r) - (3-r) = 0. \end{cases}$$

The above system needs initial values as follows. For $r = 1$

$$\begin{cases} 4\underline{x}^2(1) + 2\underline{x}(1) - 2 = 0, \\ 4\overline{x}^2(1) + 2\overline{x}(1) - 2 = 0, \end{cases}$$

For $r = 0$

$$\begin{cases} 3\underline{x}^2(0) + \underline{x}(0) - 1 = 0, \\ 5\overline{x}^2(0) + \overline{x}(0) - 3 = 0 \end{cases}$$

With initial values

$x_0 = (\underline{x}(0), \underline{x}(1), \overline{x}(1), \overline{x}(0)) = (0.434, 0.5, 0.5, 0.681)$

Example 2: Consider the fuzzy nonlinear equation [9]

$(4,6,8)x^2 + (2,3,4)\,x - (8,12,16) = (5,6,7)$

Without any loss of generality, assume that x is positive, and then the parametric form of this equation is as follows:

$$\begin{cases}(4+2r)\underline{x}^2(r) + (2+r)\underline{x}(r) - (3+3r) = 0,\\ (8-2r)\overline{x}^2(r) + (4-r)\overline{x}(r) - (9-3r) = 0.\end{cases}$$

The above system needs initial values as follows. For $r = 1$

$$\begin{cases}6\underline{x}^2(1) + 3\underline{x}(1) - 6 = 0,\\ 6\overline{x}^2(1) + 3\overline{x}(1) - 6 = 0,\end{cases}$$

For $r = 0$

$$\begin{cases}4\underline{x}^2(0) + 2\underline{x}(0) - 3 = 0,\\ 8\overline{x}^2(0) + 4\overline{x}(0) - 9 = 0,\end{cases}$$

With initial values

$$x_0 = (\underline{x}(0), \underline{x}(1), \overline{x}(1), \overline{x}(0)) = (0.651, 0.7808, 0.7808, 0.8397)$$

Example 3: Consider the fuzzy nonlinear equation [9]

$(1,2,3)x^3 + (2,3,4)x^2 + (3,4,5) = (5,8,13)$

Without any loss of generality, assume that x is positive, and then the parametric form of this equation is as follows:

$$\begin{cases}(1+r)\underline{x}^3(r) + (2+r)\underline{x}^2(r) - (2+2r) = 0,\\ (3-r)\overline{x}^3(r) + (4-r)\overline{x}^2(r) - (8-4r) = 0.\end{cases}$$

The above system needs initial values as follows. For $r = 1$

$$\begin{cases}2\underline{x}^3(1) + 3\underline{x}^2(1) - 4 = 0,\\ 2\overline{x}^3(1) + 3\overline{x}^2(1) - 4 = 0,\end{cases}$$

For $r = 0$

$$\begin{cases}\underline{x}^3(0) + 2\underline{x}^2(0) - 2 = 0,\\ 3\overline{x}^3(0) + 4\overline{x}^2(0) - 8 = 0.\end{cases}$$

With initial values

$x_0 = (\underline{x}(0), \underline{x}(1), \overline{x}(1), \overline{x}(0)) = (0.76, 0.91, 0.91, 1.06)$.

Table of numerical results for examples above

Examples	*FR*			*PRP*			*CD*			*NEW*		
	iter	*x_optimal*	*f_optimal*	*iter*	*x_optimal*	*f_optimal*	*iter*	*x_optimal*	*f_optimal*	*iter*	*x_optimal*	*f_optimal*
1	8	0.4343 0.5000 0.5000 0.5307	5.2505e-014	**6**	**0.4343** **0.5000** **0.5000** **0.5307**	**1.2314e-016**	8	0.4343 0.5000 0.5000 0.5307	8.1709e-014	**6**	**0.4343** **0.5000** **0.5000** **0.5307**	**1.7016e-011**
2	12	0.6514 0.7808 0.7808 0.8397	2.3998e-010	12	0.6514 0.7808 0.7808 0.8397	7.9887e-012	14	0.6514 0.7808 0.7808 0.8397	5.9506e-010	**9**	**0.6514** **0.7808** **0.7808** **0.8397**	**1.9513e-011**
3	19	0.8393 0.9108 0.9108 1.0564	2.6011e-011	16	0.8393 0.9108 0.9108 1.0564	4.6595e-012	135	0.8393 0.9108 0.9108 1.0564	1.4978e-008	**13**	**0.8393** **0.9108** **0.9108** **1.0564**	**1.6756e-013**

7.Conclusions

We presented in this research a new type conjugate gradient technique for solving fuzzy nonlinear equations, and the proposed algorithm has shown high efficiency in solving these problems with the least number of iterations and higher accuracy in reaching the approximate solution of the function.

Acknowledgements

I would like to express my sincere gratitude and appreciation to my supervisors Prof. Dr. Khalil K. Abbo for this valuable suggestion, encouragement and invaluable remark during writing this paper.

References

[1] S S L Cheng and L A Zadeh 1972 On fuzzy mapping and control *IEEE Trans. Syst. Man Cybern* **2** pp 30-34
[2] D Dubois and H Prade 1978 Operations on fuzzy numbers *Int. J. Syst. Sci.* **9** (6) pp 613-626
[3] M Mizumoto 1979 Some properties of fuzzy numbers
[4] S Nahmias 1978 Fuzzy variables *Fuzzy sets Syst* **1** (2) pp 97-110
[5] L A Zadeh 1975 The concept of a linguistic variable and its application to approximate reasoning—II *Inf. Sci. (Ny)* **8** (4) pp 301-357
[6] Y J Cho, N J Huang and S M Kang 2000 Nonlinear equations for fuzzy mappings in probabilistic normed spaces *Fuzzy Sets Syst* **110** (1) pp 115-122
[7] J Fang 2002 On nonlinear equations for fuzzy mappings in probabilistic normed spaces *Fuzzy Sets Syst* **131** (3) pp 357-364
[8] J Ma and G Feng 2003 An approach to H∞ control of fuzzy dynamic systems *Fuzzy Sets Syst*. **137** (3) pp 367-386
[9] J J Buckley and Y Qu 1990 Solving linear and quadratic fuzzy equations *Fuzzy sets Syst.* **38** (1) pp 43-59
[10] J J Buckley and Y Qu 1991 Solving fuzzy equations: a new solution concept *Fuzzy sets Syst.* **39** (3) pp 291-301
[11] S Abbasbandy and B Asady 2004 Newton's method for solving fuzzy nonlinear equations *Appl. Math. Comput.* **159** (2) pp 349-356 doi: 10.1016/j.amc.2003.10.048
[12] A Mottaghi, R Ezzati and E Khorram 2015 A new method for solving fuzzy linear programming problems based on the fuzzy linear complementary problem (FLCP) *Int. J. Fuzzy Syst*. **17** (2) pp 236-245
[13] M Y Waziri and A U Moyi 2016 An alternative approach for solving dual fuzzy nonlinear equations *Int. J. Fuzzy Syst.* **18** (1) pp 103-107
[14] I M Sulaiman, M Mamat, M Y Waziri and N S Amzeh 2018 Barzilai-Borwein gradient method for solving fuzzy nonlinear equations *Int. J. Eng. Technol*. **7** (3.28) pp 80 doi: 10.14419/ijet.v7i3.28.20972.
[15] M Mamat, A Ramli and M L Abdullah 2010 Broyden's method for solving fuzzy nonlinear equations *Adv. Fuzzy Syst.* doi: 10.1155/2010/763270.
[16] S Abbasbandy and A Jafarian 2006 Steepest descent method for solving fuzzy nonlinear equations *Appl. Math. Comput.* **174** (1) pp 669-675 doi: 10.1016/j.amc.2005.04.092.
[17] E K P Chong and S H Zak 2004 *An introduction to optimization* John Wiley & Sons
[18] W Sun and Y X Yuan 2006 *Optimization theory and methods: nonlinear programming* **1** Springer Science & Business Media
[19] D J Dubois 1980 *Fuzzy sets and systems: theory and applications* **144** Academic press
[20] L A Zadeh 1965 Fuzzy sets *Inf. Control* **8** (3) pp 338-353
[21] R G Jr and W Voxman1986 Elementary fuzzy calculus *Fuzzy sets Syst.* **18** (1) pp 31-43
[22] R Fletcher and C M Reeves 1964 Function minimization by conjugate gradients *Comput. J.* **7** (2) pp 149-154 doi: 10.1093/comjnl/7.2.149.
[23] L C W Dixon 1975 Conjugate gradient algorithms: quadratic termination without linear searches

IMA J. Appl. Math. **15** (1) pp 9-18
[24] E Polak and G Ribiere 1969 Note sur la convergence de méthodes de directions conjuguées *ESAIM Math. Model. Numer. Anal. Mathématique Anal. Numérique* **3** (R1) pp 35-43
[25] K K Abbo, Y A Laylani and H M Khudhur 2016 Proposed new Scaled conjugate gradient algorithm for Unconstrained Optimization **5** (7)
[26] Z M Abdullah, M Hameed, M K Hisham and M A Khaleel 2019 Modified new conjugate gradient method for Unconstrained Optimization *Tikrit J. Pure Sci.* **24** (5) pp 86-90
[27] H M Khudhur 2015 *Numerical and analytical study of some descent algorithms to solve unconstrained Optimization problems* University of Mosul
[28] K K Abbo and H M Khudhur 2015 New A hybrid Hestenes-Stiefel and Dai-Yuan conjugate gradient algorithms for unconstrained optimization *Tikrit J. Pure Sci*. **21 (**1) pp 118-123
[29] K K Abbo and H M Khudhur 2015 New A hybrid conjugate gradient Fletcher-Reeves and Polak-Ribiere algorithm for unconstrained optimization *Tikrit J. Pure Sci.* **21** (1) pp 124-129
[30] H N Jabbar, K K Abbo and H M Khudhur 2018 Four--Term Conjugate Gradient (CG) Method Based on Pure Conjugacy Condition for Unconstrained Optimization *kirkuk Univ. J. Sci. Stud.* **13** (2) pp 101-113
[31] H Tomizuka and H Yabe 2004 *A Hybrid Conjugate Gradient method for unconstrained Optimization*
[32] M Al-Baali 1985 Descent property and global convergence of the Fletcher—Reeves method with inexact line search *IMA J. Numer. Anal.* **5** (1) pp 121-124
[33] L Zhang and W Zhou 2008 Two descent hybrid conjugate gradient methods for optimization *J. Comput. Appl. Math* **216** (1) pp 251-264
[34] K K ABBO, Y A Laylani and H M Khudhur 2018 A NEW SPECTRAL CONJUGATE GRADIENT ALGORITHM FOR UNCONSTRAINED OPTIMIZATION *Int. J. Math. Comput. Appl. Res.* **8** pp 1-9

A Geometric Construction of Surface Complete (k, r)-cap in PG (3, 7)

A Geometric Construction of Surface Complete (k, r)-cap in PG (3, 7)

Ali Ahmed A. Abdulla[1] and Nada Yassen Kasm Yahya [2,*]

[1]Department of Mathematics, College of Computer Science and Mathematics, University of Mosul, Mosul, Iraq
[2]Department of Mathematics, College of Education for Pure Science, University of Mosul, Mosul, Iraq

E-mail: drnadaqasim1@gmail.com

Abstract
The aim of this paper is to a geometric construction of Surface Complete (k, r)-cap in PG(3,7). We found that the maximum complete (k, 2)-cap which is called an ovaloid, exists in PG (3, 7) when k = 23. Moreover the complete (k, 3)-caps, (k, 4)-caps and (k, 5)-caps,(k,6)-caps , (k,7)-caps , (k,8)-caps, and we obtain a new example for theorem(2.8).

1-Introduction

I study of finite projective spaces PG (3, q) over Galois field GF(q), it is the largest of the projective plane over Galois field, Hirschfield, 1985 [5], gives the finite projective spaces of three dimensions. Hirschfield,1998 [1], give the basic definition and theorems of projective geometries over finite fields, and Al-Mukhtar, in 2008 [4] give the complete Arcs and surfaces in Three-dimensional projective space over Galois field and give (k, r)-caps in PG(3,q) over Galois fields GF(q), q = 2,3, and 5.In 2017 [2] Kareem give the complete (k, r)-Cap in PG (3, p) Over Galois Field GF (4) . In 2019[5] thus,give the arcs, caps, generalizations: results and problems, in 50 years of Combinatorics, Graph Theory, and computing. In this work we construct the (k, r)-caps in PG (3, 4). This paper is divided into three sections, section one is the preliminaries of projective 3-space which contains some definitions and theorems for that concept and section two consists of the construction of a geometric construction of surface complete (k, r)-cap (k, r)-caps for r = 2, 3, 4, 5 in PG (3, 7). Also, we obtain a new example. In section three obtain the conclusion. This work I have done manually without using the computer program.

2- Preliminaries

2.1 Definition: "Projective 3-Space" [20], [23], [24],[25],[26]
A projective 3-space PG(3,k) over a field k is a 3-dimensional projective space with that consists of points, lines, and planes with the incidence relation between them. The projective 3-space satisfies the following axioms:
A) Any two distinct points are contained in a unique line.
B) Any three distinct non-collinear points, also any line and a point not on the line are contained in a unique plane.

C) Any two distinct coplanar lines intersect in a unique point.
D) Any line not on a given plane intersects the plane in a unique point.
E) Any two distinct planes intersect in a unique line.

A projective space PG(3,p) over Galois field GF(p), $p = q^m$ for some prime number q and some integer m, is a 3-dimensional projective space. Any point in PG(3,p) has the form of a quadruple (x_1,x_2,x_3,x_4), where x_1,x_2,x_3,x_4 are elements in GF(p) with except for the quadruple consisting of four zero elements.

Two quadruples (x_1,x_2,x_3,x_4) and (y_1,y_2,y_3,y_4) represent the same point if there exists λ in GF(p)\{0} such that $(x_1,x_2,x_3,x_4) = \lambda\ (y_1,y_2,y_3,y_4)$.

Similarly, any plane in PG(3,p) has the form of a quadruple $[x_1,x_2,x_3,x_4]$, where x_1,x_2,x_3,x_4 are elements in GF(p) with the exception of the quadruple consisting of four zero elements.

Two quadruples $[x_1,x_2,x_3,x_4]$ and $[y_1,y_2,y_3,y_4]$ represent the same plane if there exists λ in GF(p)\{0} such that $[x_1,x_2,x_3,x_4] = \lambda\ [y_1,y_2,y_3,y_4]$

Also a point $p(x_1,x_2,x_3,x_4)$ is incident with the plane $\pi\ [a_1,a_2,a_3,a_4]$ iff $a_1x_1 + a_2x_2 + a_3x_3 + a_4x_4 = 0$.

2.2 Definition: "Plan π", [21],[22]

A plan π in PG(3,p) is the set of all points $p(x_1,x_2,x_3,x_4)$ satisfying a linear equation $u_1x_1 + u_2x_2 + u_3x_3 + u_4x_4 = 0$. This plane is denoted by $\pi\ [u_1,u_2,u_3,u_4]$.

2.3 Theorem: [6],[7],[8]

Four distinct points $A(x_1,x_2,x_3,x_4)$, $B(y_1,y_2,y_3,y_4)$, $C(z_1,z_2,z_3,z_4)$ and $D(w_1,w_2,w_3,w_4)$ are coplanar iff

$$\Delta = \begin{vmatrix} x_1 & x_2 & x_3 & x_4 \\ y_1 & y_2 & y_3 & y_4 \\ z_1 & z_2 & z_3 & z_4 \\ w_1 & w_2 & w_3 & w_4 \end{vmatrix} = 0 \cdot$$

2.4 Corollary: [11],[12]

If four distinct points $A(x_1,x_2,x_3,x_4)$, $B(y_1,y_2,y_3,y_4)$, $C(z_1,z_2,z_3,z_4)$ and $D(w_1,w_2,w_3,w_4)$ are collinear, then $\Delta = 0$.

2.5 Theorem: [5]

The points of PG(3,p) have unique forms which are (1,0,0,0), (x,1,0,0), (x,y,1,0), (x,y,z,1) for all x, y, z in GF(p).

2.6 Theorem: [13]

The planes of PG(3,p) have unique forms which are [1,0,0,0], [x,1,0,0], [x,y,1,0], [x,y,z,1] for all x, y, z in GF(p).

2.7 Theorem: [10]

A projective 3-space PG(3,p) satisfies the following:

A) Every line contains exactly p + 1 points and every point is on exactly p + 1 lines.
B) Every plane contains exactly $p^2 + p + 1$ points (lines) and every point is on exactly $p^2 + p + 1$ planes.
C) There exist $p^3 + p^2 + p + 1$ of points and there exists $p^3 + p^2 + p + 1$ of planes.
D) Any two planes intersect in exactly p + 1 points and any line is on exactly p + 1 planes, and any two points are on exactly p + 1 planes.

2.8 Theorem: [14]

There exists $(p^2+1)(p^2+p+1)$ of lines in PG(3,P).

2.9 Definition: [16]
A (k,ℓ)-set in PG(3,p) is a set of k spaces π_ℓ. A k-set is a (k,0)-set that is a set of k-points.

2.10 Definition: "(k,r)-cap", [13]
A (k,r)-cap is a set of k points in PG(n,p) with $n \geq 3$, such that at most r points on any line. Thus (k,2)-cap is a set of k points in PG(3,p), such that no three of them are collinear.

2.11 Definition: "Complete (k,r)-cap", [15]
A (k,r)-cap is a complete if it is not contained in a (k+1,r)-cap.

2.12 Definition: [18]
Let C_i be the number of points of index i in PG(3,p) which are not on a (k,r)-cap, then the constants C_i of (k,r)-cap satisfy the following:

i) $\sum_{\alpha}^{\beta} C_i = p^3 + p^2 + p + 1 - k$

ii) $\sum_{\alpha}^{\beta} iC_i = \frac{k(k-1)...(k-n+1)}{n!}(p^2 + p + 1 - n)$

where α is the smallest i for which $C_i \neq 0$, β be the largest i for which $C_i \neq 0$.

2.13 Remark: [15]
The (k,r)-cap is complete iff $C_0 = 0$.

2.14 Definition: [16]
The i-secant of a (k,r)-cap is a line intersects the cap in exactly i points, that is 0-secant is an external line, 1-secant is an unisecant line, 2-secant is a bisecant line and 3-secant is a trisecant line.

2.15 Rrmark:[16]
A (k, r)-cap is maximum iff every line in PG(3,p) is a 0-secant or r-secant.

2.16 Theorem: [19],[22]
A maximum (k, 2)-cap in PG(3,p) is an ovaloid.

3. The Approximate Algorithm of (k,r)-Cap in PG(3,7):

By using theorem (1.7) we will find the number of (k,r)-cap in the projective space PG(3,7) is (k,8)-cap, A (k,r)-cap is a complete if it is not contained in a (k+1,r)-cap .

If the opposite is true that we can add {p} to the (k,r)-arc B= A $\cup${p} , and constriction A (k+1,r)-cap, that is a contradiction of assuming.

We assume that want to construct the complete (k,2)-cap having a maximum number of points, we are starting with the reference five-point (Reference points) and we will add a few points (to take attention we want to constrict one arc no more of that),also we find with all time, the points of index zero we add one of the themes, the set B become have six elements, we continue to the adding one of points (index zero) of all times. Finally, we have reached the times k that we cannot add any points to the (k,2)-cap. That is B is the required complete caps. We are repeating the method to finding the required complete (k,3)-cap and (k,4)-cap….(k , q+1)-cap, and finding his arcs in all levels, with the attention that the reference points are growing by add from the points of index zero of all levels.

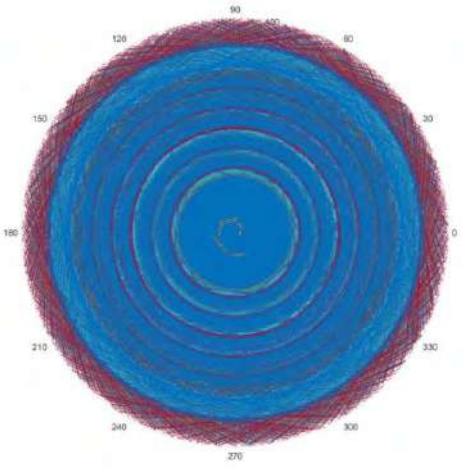

Figure 1: A representation a (k,n)-cap of projective space PG(3,7) by using computer programming.

3.1 The (k, 2)-caps in PG (3,7):

PG (3, 7) contains 400 points and 400 planes such that each point is on 57 planes and every plane contains 57 points and every line contains 8 points and it is the intersection of 8 planes, (table 1 and 2). In table (1), the set A={1,2,9,58,115} is taken which is the set of unit and reference points 1=(1,0,0,0), 2=(0,1,0,0), 9=(0,0,1,0), 58=(0,0,0,1), 115=(1,1,1,1), this set is a (5,2)-cap since no three points of A are collinear as in table (2).

A is a (5,2)-cap, which is not complete since there exists some point of index zero for it, which are

(18	19	20	21	22	24	25	26	27	28	29	31	32
33	34	35	36	38	39	40	41	42	43	45	46	47
48	49	50	52	53	54	55	56	57	67	68	69	70
71	73	74	75	76	77	78	80	81	82	83	84	85
87	88	89	90	91	92	94	95	96	97	98	99	101
102	103	104	105	106	109	110	111	112	113	121	123	124
125	126	127	128	130	131	132	133	134	135	137	138	139
140	141	142	144	145	146	147	148	149	151	152	153	154
155	157	158	159	160	161	162	163	165	166	167	168	169
170	171	173	174	175	176	177	178	179	180	181	182	183
184	185	186	187	188	189	190	191	192	193	194	195	196
197	198	199	200	201	202	203	204	206	207	208	209	210
211	212	214	215	216	217	218	219	220	221	222	223	224
225	226	227	228	230	231	232	233	234	235	236	237	238
239	240	241	242	243	244	245	246	247	248	249	250	251
252	253	255	256	257	258	259	260	261	263	264	265	266
267	268	269	270	271	272	273	274	275	276	277	278	279
280	281	282	283	284	285	287	288	289	290	291	292	293
294	295	296	297	298	299	300	301	302	304	305	306	307
308	309	310	312	313	314	315	316	317	318	319	320	321
322	323	324	325	326	327	328	329	330	331	332	333	334
335	336	337	338	339	340	341	342	344	345	346	347	348
349	350	351	353	354	355	356	357	358	359	361	362	363
364	365	366	367	368	369	370	371	372	373	374	375	376
377	378	379	380	381	382	383	384	385	386	387	388	389
390	391	392	393	394	395	396	397	398	399).			

Then, one can add some of them to A in order to obtain a complete (23,2)-cap B=A∪{18,24,33,67,73,82,109,124,132,141,147,169,170,187,203,217,247,384}={1,2,9,18,24,33,58,67,73,82,109,115,124,132,141,147,169,170,187,203,217,247,384}. B is the maximum (23,2)-cap in PG(3,7), since every line is a 0-secant or 2-secant, B is called an ovaloid

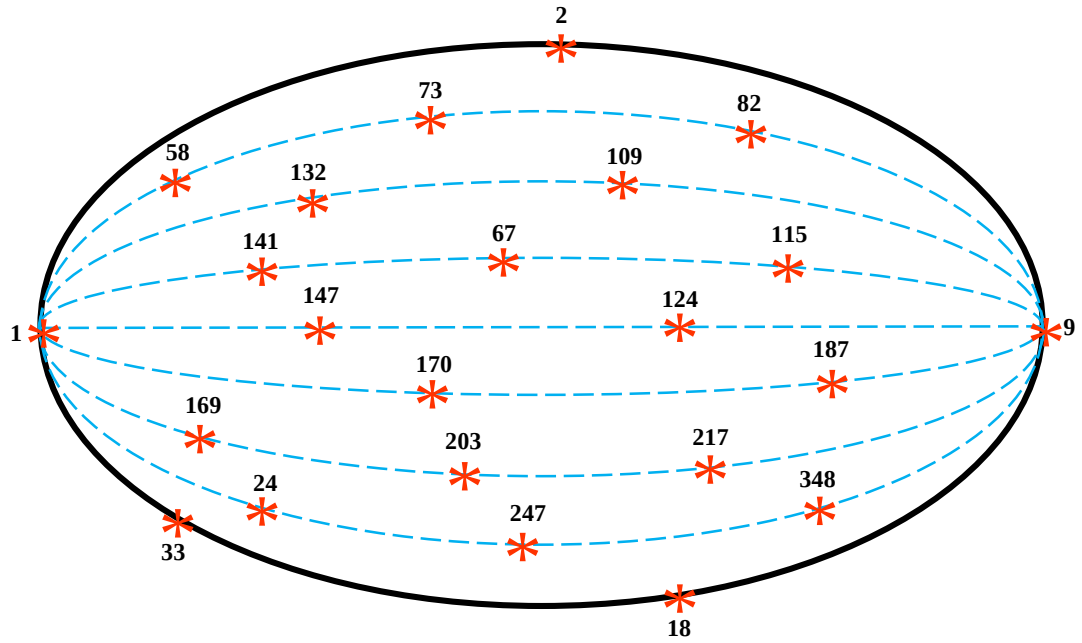

Figure 2 : Ovaloid for a (k,2)-cap in PG(3,7)

3.2 The (k, 3)-caps in PG (3, 7):

Let B={1,2,9,18,24,33,58,67,73,82,109,115,124,132,141,147,169,170,187,203,217,247,384} be a (23,2)-cap. The points of index zero are (3

4	5	6	7	8	10	11	12	13	14	15	16	17
19	20	21	22	23	25	26	27	28	29	30	31	32
34	35	36	37	38	39	40	41	42	43	44	45	46
47	48	49	50	51	52	53	54	55	56	57	59	60
61	62	63	64	65	66	68	69	70	71	72	74	75
76	77	78	79	80	81	83	84	85	86	87	88	89
90	91	92	93	94	95	96	97	98	99	100	101	102
103	104	105	106	107	108	110	111	112	113	114	116	117
118	119	120	121	122	123	125	126	127	128	129	130	131
133	134	135	136	137	138	139	140	142	143	144	145	146
148	149	150	151	152	153	154	155	156	157	158	159	160
161	162	163	164	165	166	167	168	171	172	173	174	175
176	177	178	179	180	181	182	183	184	185	186	188	189
190	191	192	193	194	195	196	197	198	199	200	201	202
204	205	206	207	208	209	210	211	212	213	214	215	216
218	219	220	221	222	223	224	225	226	227	228	229	230
231	232	233	234	235	236	237	238	239	240	241	242	243
244	245	246	248	249	250	251	252	253	254	255	256	257
258	259	260	261	262	263	264	265	266	267	268	269	270
271	272	273	274	275	276	277	278	279	280	281	282	283
284	285	286	287	288	289	290						

291 292 293 294 295 296 297 298 299 300301 302 303
304 305 306 307 308 309 310 311 312 313314 315 316
317 318 319 320 321 322 323 324 325 326327 328 329
330 331 332 333 334 335 336 337 338 339340 341 342
343 344 345 346 347 349 350 351 352 353354 355 356
357 358 359 360 361 362 363 364 365 366367 368 369
370 371 372 373 374 375 376 377 378 379380 381 382
383 384 385 386 387 388 389 390 391 392393 394 395
396 397 398 399 400) .

The distinct (k,3)-cap can be constructed by adding some points of index zero for B, which are: 3,10,16,27,35,46,55,59,65,76,84,104,110,118,121,130,157,158,166,172,185,211,216,221,224,228,240,246,273,336,369. Then,

C=B∪{3,10,16,27,35,46,55,59,65,76,84,104,110,118,121,130,157,158,166,172,185,211,216,221,224,228,240,246,273,336,369}={1,2,3,9,10,16,18,24,27,33,35,46,55,58,59,65,67,73,76,82,84,104,109,110,115,118,121,124,130,132,141,147,157,158,166,169,170,172,185,187,203,211,216,217,221,224,228,240,246,247,273,336,348,369 },C is complete (54,3)-cap ,C is a complete (k, 3)-cap.

3.3 The (k, 4)-caps in PG(3,7):

We can construct complete (k,4)-caps by adding some points of index zero for C which are (4 5
6 7 8 11 12 13 14 15 17 19 20 21 22
23 25 26 28 29 30 31 32 34 36 37 38 39
40 41 42 43 44 45 47 48 49 50 51 52 53
54 56 57 60 61 62 63 64 66 68 69 70 71
72 74 75 77 78 79 80 81 83 85 86 87 88
89 90 91 92 93 94 95 96 97 98 99 100 101
102 103 105 106 107 108 111 112 113 114 116 117
119 120 122 123 125 126 127 128 129 131 133 134
135 136 137 138 139 140 142 143 144 145 146 148
149 150 151 152 153 154 155 156 159 160 161 162
163 164 165 167 168 171 173 174 175 176 177 178 179
180 181 182 183 184 186 188 189 190 191 192 193 194
195 196 197 198 199 200 201 202 204 205 206 207 208
209 210 212 213 214 215 218 219 220 222 223 225 226
227 229 230 231 232 233 234 235 236 237 238 239 241
242 243 244 245 248 249 250 251 252 253 254 255 256
257 258 259 260 261 262 263 264 265 266 267 268 269
270 271 272 274 275 276 277 278 279 280 281 282 283
284 285 286 287 288 289 290 291 292 293 294 295 296
297 298 299 300 301 302 303 304 305 306 307 308 309
310 311 312 313 314 315 316 317 318 319 320 321 322
323 324 325 326 327 328 329 330 331 332 333 334 335
337 338 339 340 341 342 343 344 345 346 347 349 350
351 352 353 354 355 356 357 358 359 360 361 362 363
364 365 366 367 368 370 371 372 373 374 375 376 377
378 379 380 381 382 383 384 385 386 387 388 389 390
391 392 393 394 395 396 397 398 399 400),

by adding to C thirty three of these points which are {4,19,25,54,60,69,72,80,91,111,114,131,135,136,162,164,175,183,198,205,218,227,231,242,270,276,289,296,302,313,329,333,344}. Thus can get a complete (k,4)-cap call

D={1,2,3,4,9,10,16,18,19,24,25,27,33,35,46,54,55,58,59,60,65,67,69,72,73,76,80,82,84,91,104,109,110,111,114,115,118,121,124,130,131,132,135,136,141,147,157,158,162,164,166,169,170,172,175,183,185,187,198,203,205,211,216,217,218,221,224,227,228,231,240,242,246,247,270,273,276,289,296,302,313,329,333,336,344,348,369}. D is the complete (87,4)-cap.

3.4 The (k,5)-caps in PG(3,7):

In section five, D is a complete (87,4)-cap. The points of index zero for D are (5 6 7 8

11	12	13	14	15	17	20	21	22	23	26	28	29
30	31	32	34	36	37	38	39	40	41	42	43	44
45	47	48	49	50	51	52	53	56	57	61	62	63
64	66	68	70	71	74	75	77	78	79	81	83	85
86	87	88	89	90	92	93	94	95	96	97	98	99
100	101	102	103	105	106	107	108	112	113	116	117	119
120	122	123	125	126	127	128	129	133	134	137	138	139
140	142	143	144	145	146	148	149	150	151	152	153	154
155	156	159	160	161	163	165	167	168	171	173	174	176
177	178	179	180	181	182	184	186	188	189	190	191	192
193	194	195	196	197	199	200	201	202	204	206	207	208
209	210	212	213	214	215	219	220	222	223	225	226	229
230	232	233	234	235	236	237	238	239	241	243	244	245
248	249	250	251	252	253	254	255	256	257	258	259	260
261	262	263	264	265	266	267	268	269	271	272	274	275
277	278	279	280	281	282	283	284	285	286	287	288	290
291	292	293	294	295	297	298	299	300	301	303	304	305
306	307	308	309	310	311	312	314	315	316	317	318	319
320	321	322	323	324	325	326	327	328	330	331	332	334
335	337	338	339	340	341	342	343	345	346	347	349	350
351	352	353	354	355	356	357	358	359	360	361	362	363
364	365	366	367	368	370	371	372	373	374	375	376	377
378	379	380	381	382	383	384	385	386	387	388	389	390
391	392	393	394	395	396	397	398	399	400), then			

E=D∪{5,26,31,48,61,66,75,79,88,89,90,107,117,122,125,140,148,168,174,188,193,199,206,209,212,220,232,248,258,263,285,288,291,293,324,347} .
E is the complete (123,5)-cap.

3.5 The (k,6)-caps in PG(3,7):

In (2.4), E is a complete (123,5)-cap. The points of index zero for E are (6 7

8	11	12	13	14	15	17	20	21	22	23	28	29
30	32	34	36	37	38	39	40	41	42	43	44	45
47	49	50	51	52	53	56	57	62	63	64	68	70
71	74	77	78	81	83	85	86	87	92	93	94	95
96	97	98	99	100	101	102	103	105	106	108	112	113
116	119	120	123	126	127	128	129	133	134	137	138	139
142	143	144	145	146	149	150	151	152	153	154	155	156
159	160	161	163	165	167	171	173	176	177	178	179	180
181	182	184	186	189	190	191	192	194	195	196	197	200
201	202	204	207	208	210	213	214	215	219	222	223	225
226	229	230	233	234	235	236	237	238	239	241	243	244
245	249	250	251	252	253	254	255	256	257	259	260	261
262	264	265	266	267	268	269	271	272	274	275	277	278

279 280 281 282 283 284 286 287 290 292 294295 297
298 299 300 301 303 304 305 306 307 308 309310 311
312 314 315 316 317 318 319 320 321 322 323325 326
327 328 330 331 332 334 335 337 338 339 340341 342
343 345 346 349 350 351 352 353 354 355 356357 358
359 360 361 362 363 364 365 366 367 368 370371 372
373 374 375 376 377 378 379 381 382 383 384385 386
387 388 389 390 391 392 393 394 395 396 397398 399
400). Then, by adding to E thirty of these points which are {6,22,70,83,87,93,102,126,129,134,146,180,189,194,197,215,234,237,239,245,249,286,292,301,321, 323,345,346,351,399} .

F={1,2,3,4,5,6,9,10,16,18,19,22,24,25,26,27,31,33,35,46,48,54,55,58,59,60,61,65,66,67,69,70,72,73,7 5,76,79,80,82,84,87,88,89,90,91,93,102,104,107,109,110,111,114,115,117,118,121,122,124,125,126, 129,130,131,132,134,135,136,140,141,146,147,148,157,158,162,164,166,168,169,170,172,174,175,1 80,183,185,187,188,189,193,194,197,198,199,203,205,206,209,211,212,215,216,217,218,220,221,22 4,227,228,231,232,234,237,239,240,242,245,246,247,248,249,258,263,270,273,276,285,286,288,289, 291,292,293,296,301,302,313,323,324,329,333,336,344,345,346,347,348,351,369,399} is the complete (153,6)-cap**.**

3.6 The (k,7)-caps in PG(3,7):

In (2.5), F is a complete (153,6)-cap. The points of index zero for F are (7 8 11
12 13 14 15 17 20 21 23 28 29 30 32 34
36 37 38 39 40 41 42 43 44 45 47 49 50
51 52 53 56 57 62 63 64 68 71 74 77 78
81 85 86 92 94 95 96 97 98 99 100 101 103
105 106 108 112 113 116 119 120 123 127128 133 137
138 139 142 143 144 145 149 150 151 152153 154 155
156 159 160 161 163 165 167 171 173 176177 178 179
181 182 184 186 190 191 192 195 196 200201 202 204
207 208 210 213 214 219 222 223 225 226229 230 233
235 236 238 241 243 244 250 251 252 253254 255 256
257 259 260 261 262 264 265 266 267 268269 271 272
274 275 277 278 279 280 281 282 283 284287 290 294
295 297 298 299 300 303 304 305 306 307308 309 310
311 312 314 315 316 317 318 319 320 322325 326 327
328 330 331 332 334 335 337 338 339 340341 342 343
349 350 352 353 354 355 356 357 358 359360 361 362
363 364 365 366 367 368 370 371 372 373374 375 376
377 378 379 380 381 382 383 384 385 386387 388 389
390 391 392 393 394 395 396 397 398 400), then by adding to F twenty nine of these points which are

{7,28,52,56,103,112,123,128,144,150,159,160,171,186,196,214,219,222,241,251,252,282,294,300,32 7,330,358,365,375} .

G={1,2,3,4,5,6,7,9,10,16,18,19,22,24,25,26,27,28,31,33,35,46,48,52,54,55,56,58,59,60,61,65,66,67,6 9,70,72,73,75,76,79,80,82,84,87,88,89,90,91,93,102,103,104,107,109,110,111,112,114,115,117,118,1 21,122,123,124,125,126,128,129,130,131,132,134,135,136,140,141,144,146,147,148,150,157,158,15 9,160,162,164,166,168,169,170,171,172,174,175,180,183,185,186,187,188,189,193,194,196,197,198, 199,203,205,206,209,211,212,214,215,216,217,218,219,220,221,222,224,227,228,231,232,234,237,2 39,240,241,242,245,246,247,248,249,251,252,258,263,270,273,276,282,285,286,288,289,291,292,29

3,294,296,300,301,302,313,321,323,324,327,329,330,333,336,344,345,346,347,348,351,358,365,369, 375,399} is the complete (182,7)-cap.

3.7 The (k,8)-caps in PG(3,7):

In (2.6) , G is a complete (182,7)-cap. The points of index zero for G are (8 11 12 13 14 15 17 20 21 23 28 29 30 32 34 36 37 38 39 40 41 42 43 44 45 47 49 50 51 52 53 56 57 62 63 64 68 71 74 77 78 81 85 86 92 94 95 96 97 98 99 100 101 103 105 106 108 112 113 116 119 120 123 127128 133 137 138 139 142 143 144 145 149 150 151 152153 154 155 156 159 160 161 163 165 167 171 173 176177 178 179 181 182 184 186 190 191 192 195 196 200201 202 204 207 208 210 213 214 219 222 223 225 226229 230 233 235 236 238 241 243 244 250 251 252 253254 255 256 257 259 260 261 262 264 265 266 267 268269 271 272 274 275 277 278 279 280 281 282 283 284287 290 294 295 297 298 299 300 303 304 305 306 307308 309 310 311 312 314 315 316 317 318 319 320 322325 326 327 328 330 331 332 334 335 337 338 339 340341 342 343 349 350 352 353 354 355 356 357 358 359360 361 362 363 364 365 366 367 368 370 371 372 373374 375 376 377 378 379 380 381 382 383 384 385 386387 388 389 390 391 392 393 394 395 396 397 398 400), then by adding to G forty of these points which are {8,11,17,23,32,36,39,42,68,74,77,81,94,116,119,138,143,163,173,177,182,204,210,235,253,265,268, 274,278,279,283,295,299,310,328,331,356,385,398,400} .

H={1,2,3,4,5,6,7,8,9,10,11,16,17,18,19,22,23,24,25,26,27,28,31,33,32,35,39,42,46,48,52,54,55,56,58, 59,60,61,65,66,67,68,69,70,72,73,74,75,76,79,80,81,82,83,84,87,88,89,90,91,93,102,103,104,107,109 ,110,111,112,114,115,116,117,118,119,121,122,123,124,125,126,128,129,130,131,132,134,135,136,1 38,140,141,143,144,146,147,148,150,157,158,159,160,162,163,164,166,168,169,170,171,172,173,17 4,175,177,180,182,183,185,186,187,188,189,193,194,196,197,198,199,203,204,205,206,209,210,211, 212,214,215,216,217,218,219,220,221,222,224,227,228,231,232,234,237,239,240,241,242,245,246,2 47,248,249,251,252,253,258,263,265,268,270,273,274,276,278,279,282,283,285,286,288,289,291,29 2,293,294,295,296,299,300,301,302,310,313,321,323,324,327,328,329,330,331,333,336,344,345,346, 347,348,351,356,358,365,369,375,385,398,399,400}

is the complete (222,8)-cap which can be obtained for any line of PG(3,7) contains eight points and hence there are no more than eight are collinear.

3.8 Theorem:

(a)-There exists a maximum complete 23-cap in PG(3,7).
(b)- There exists a complete (54, 3)-cap in PG(3,7).
(c)- There exists a complete (87, 4)-cap in PG(3,7).
(d)- There exists a complete (123, 5)-cap in PG(3,7).
(e)- There exists a complete (153, 6)-cap in PG(3,7).
(f)- There exists a complete (182, 7)-cap in PG(3,7).
(g)- There exists a complete (222, 8)-cap in PG(3,7).

Proof:

It will be sufficient to give an example of a maximum complete 23-cap in PG(3,7) These examples were also checked on completeness using . Computer programming

A complete (23,2) in PG(3,7), A complete (54,3) in PG(3,7), A complete (87,4) in PG(3,7), A complete (123,5) in PG(3,7), A complete (153,6) in PG(3,7), A complete (182,7) in PG(3,7), A complete (222,8) in PG(3,7).
the points constituting the complete caps in the respective space in PG(n, q) are denoted with homogeneous coordinates $(x_0,x_1,x_2,\ldots\ldots,x_n)$, in accordance with the terminology used in the preceding.

An example of maximum complete 23-cap in PG(3,7)

{ (1,0,0,0) , (0,1,0,0) , (0,0,1,0) , (2,1,1,0) , (1,2,1,0) , (3,3,1,0) ,(0,0,0,1) , (2,1,0,1) , (1,2,0,1) , (3,3,0,1) , (2,0,1,1) , (3,2,1,1) , (4,3,1,1) , (6,4,1,1) , (5,5,1,1) , (6,1,2,1) , (0,2,2,1) , (3,4,2,1) , (5,6,2,1) , (5,1,3,1) , (0,6,3,1) , (4,4,6,1) } .

An example of a complete (54,3)-cap in PG(3,7).
{(1,0,0,0) , (0,1,0,0) , (1,1,0,0) , (0,0,1,0) , (1,0,1,0) , (0,1,1,0) , (2,1,1,0) , (1,2,1,0) , (4,2,1,0) , (3,3,1,0) , (5,3,1,0) , (2,5,1,0) , (4,6,1,0) , (0,0,0,1) , (1,0,0,1) , (0,1,0,1) , (2,1,0,1) , (1,2,0,1) , (4,2,0,1) , (3,3,0,1) , (5,3,0,1) , (4,6,0,1) , (2,0,1,1) , (3,0,1,1) , (1,1,1,1) , (4,1,1,1) , (0,2,1,1) , (3,2,1,1) , (2,3,1,1) , (4,3,1,1) , (6,4,1,1) , (5,5,1,1) , (1,0,2,1) , (2,0,2,1) , (3,1,2,1) , (6,1,2,1) , (0,2,2,1) , (2,2,2,1) , (1,4,2,1) , (3,4,2,1) , (5,6,2,1) , (6,0,3,1) , (4,1,3,1) , (5,1,3,1) , (2,2,3,1) , (5,2,3,1) , (2,3,3,1) , (0,5,3,1) , (6,5,3,1) , (0,6,3,1) , (5,2,4,1) , (5,4,5,1) , (3,6,5,1) , (3,2,6,1) }.

An example of a complete (87,4)-cap in PG(3,7).
{(1,0,0,0) , (0,1,0,0) , (1,1,0,0) , (0,0,1,0) , (1,0,1,0) , (0,1,1,0) , (2,1,1,0) , (1,2,1,0) , (4,2,1,0) , (3,3,1,0) , (5,3,1,0) , (2,5,1,0) , (4,6,1,0) , (0,0,0,1) , (1,0,0,1) , (0,1,0,1) , (2,1,0,1) , (1,2,0,1) , (4,2,0,1) , (3,3,0,1) , (5,3,0,1) , (4,6,0,1) , (2,0,1,1) , (3,0,1,1) , (1,1,1,1) , (4,1,1,1) , (0,2,1,1) , (3,2,1,1) , (2,3,1,1) , (4,3,1,1) , (6,4,1,1) , (5,5,1,1) , (1,0,2,1) , (2,0,2,1) , (3,1,2,1) ,(6,1,2,1) , (0,2,2,1) , (2,2,2,1) , (1,4,2,1) , (3,4,2,1) , (5,6,2,1) , (6,0,3,1) , (4,1,3,1) , (5,1,3,1) , (2,2,3,1) , (5,2,3,1) , (2,3,3,1) , (0,5,3,1) , (6,5,3,1) , (0,6,3,1) , (5,2,4,1) , (5,4,5,1) , (3,6,5,1) , (3,2,6,1) , (2,1,0,0) , (3,1,1,0) , (2,2,1,0) , (3,6,1,0) , (2,0,0,1) , (4,1,0,1) , (0,2,0,1) , (1,3,0,1) , (5,4,0,1) , (4,0,1,1) , (0,1,1,1) , (3,3,1,1) , (0,4,1,1) , (1,4,1,1) , (6,0,2,1) , (1,1,2,1) ,(5,2,2,1) , (6,3,2,1) , (0,6,2,1) , (0,0,3,1) , (6,1,3,1) , (1,3,3,1) , (5,3,3,1) , (2,5,3,1) , (2,2,4,1) , (1,3,4,1) , (0,5,4,1) , (0,6,4,1) , (6,6,4,1) , (3,1,5,1) , (5,3,5,1) , (2,4,5,1) , (6,5,5,1) }.

An example of a complete (123,5)-cap in PG(3,7).
{(1,0,0,0) , (0,1,0,0) , (1,1,0,0) , (0,0,1,0) , (1,0,1,0) , (0,1,1,0) , (2,1,1,0) , (1,2,1,0) , (4,2,1,0) , (3,3,1,0) , (5,3,1,0) , (2,5,1,0) , (4,6,1,0) , (0,0,0,1) , (1,0,0,1) , (0,1,0,1) , (2,1,0,1) , (1,2,0,1) , (4,2,0,1) , (3,3,0,1) , (5,3,0,1) , (4,6,0,1) , (2,0,1,1) , (3,0,1,1) , (1,1,1,1) , (4,1,1,1) , (0,2,1,1) , (3,2,1,1) , (2,3,1,1) , (4,3,1,1) , (6,4,1,1) , (5,5,1,1) , (1,0,2,1) , (2,0,2,1) , (3,1,2,1) ,(6,1,2,1) , (0,2,2,1) , (2,2,2,1) , (1,4,2,1) , (3,4,2,1) , (5,6,2,1) , (6,0,3,1) ,(4,1,3,1) , (5,1,3,1) , (2,2,3,1) , (5,2,3,1) , (2,3,3,1) , (0,5,3,1) , (6,5,3,1) ,(0,6,3,1) , (5,2,4,1) , (5,4,5,1) , (3,6,5,1) , (3,2,6,1) , (2,1,0,0) , (3,1,1,0) , (2,2,1,0) , (3,6,1,0) , (2,0,0,1) , (4,1,0,1) , (0,2,0,1) , (1,3,0,1) , (5,4,0,1) , (4,0,1,1) , (0,1,1,1) , (3,3,1,1) , (0,4,1,1) , (1,4,1,1) , (6,0,2,1) , (1,1,2,1) , (5,2,2,1) , (6,3,2,1) , (0,6,2,1) , (0,0,3,1) , (6,1,3,1) , (1,3,3,1) , (5,3,3,1) ,(2,5,3,1) , (2,2,4,1) , (1,3,4,1) , (0,5,4,1) , (0,6,4,1) , (6,6,4,1) , (3,1,5,1) , (5,3,5,1) , (2,4,5,1) , (6,5,5,1) , (3,1,0,0) , (3,2,1,0) , (1,3,1,0) , (4,5,1,0) , (3,0,0,1) , (1,1,0,1) , (3,2,0,1) , (0,3,0,1) , (2,4,0,1) , (2,4,0,1) , (4,4,0,1) ,(0,0,1,1) , (3,1,1,1) , (1,2,1,1) , (4,2,1,1) , (5,4,1,1) , (6,5,1,1) , (5,1,2,1) ,(4,2,2,1) , (4,4,2,1) , (2,5,2,1) , (1,6,2,1) , (1,0,3,1) , (4,0,3,1) , (0,1,3,1) ,(1,2,3,1) , (6,3,3,1) , (1,6,3,1) , (4,0,4,1) , (2,1,4,1) , (3,4,4,1) , (6,4,4,1) , (2,5,4,1) , (4,5,4,1) , (0,3,5,1) , (2,6,5,1) }.

An example of a complete (153,6)-cap in PG(3,7).
{(1,0,0,0) , (0,1,0,0) , (1,1,0,0) , (0,0,1,0) , (1,0,1,0) , (0,1,1,0) , (2,1,1,0) , (1,2,1,0) , (4,2,1,0) , (3,3,1,0) , (5,3,1,0) , (2,5,1,0) , (4,6,1,0) , (0,0,0,1) , (1,0,0,1) , (0,1,0,1) , (2,1,0,1) , (1,2,0,1) , (4,2,0,1) , (3,3,0,1) , (5,3,0,1) , (4,6,0,1) , (2,0,1,1) , (3,0,1,1) , (1,1,1,1) , (4,1,1,1) , (0,2,1,1) , (

3,2,1,1) , (2,3,1,1) , (4,3,1,1) , (6,4,1,1) , (5,5,1,1) , (1,0,2,1) , (2,0,2,1) , (3,1,2,1) , (6,1,2,1) , (0,2,2,1) , (2,2,2,1) , (1,4,2,1) , (3,4,2,1) , (5,6,2,1) , (6,0,3,1) , (4,1,3,1) , (5,1,3,1) , (2,2,3,1) , (5,2,3,1) , (2,3,3,1) , (0,5,3,1) , (6,5,3,1) , (0,6,3,1) , (5,2,4,1) , (5,4,5,1) , (3,6,5,1) , (3,2,6,1) , (2,1,0,0) , (3,1,1,0) , (2,2,1,0) , (3,6,1,0) , (2,0,0,1) , (4,1,0,1) , (0,2,0,1) , (1,3,0,1) , (5,4,0,1) , (4,0,1,1) , (0,1,1,1) , (3,3,1,1) , (0,4,1,1) , (1,4,1,1) , (6,0,2,1) , (1,1,2,1) , (5,2,2,1) , (6,3,2,1) , (0,6,2,1) , (0,0,3,1) , (6,1,3,1) , (1,3,3,1) , (5,3,3,1) , (2,5,3,1) , (2,2,4,1) , (1,3,4,1) , (0,5,4,1) , (0,6,4,1) , (6,6,4,1) , (3,1,5,1) , (5,3,5,1) , (2,4,5,1) , (6,5,5,1) , (3,1,0,0) , (3,2,1,0) , (1,3,1,0) , (4,5,1,0) , (3,0,0,1) , (1,1,0,1) , (3,2,0,1) , (0,3,0,1) , (2,4,0,1) , (2,4,0,1) , (4,4,0,1) , (0,0,1,1) , (3,1,1,1) , (1,2,1,1) , (4,2,1,1) , (5,4,1,1) , (6,5,1,1) , (5,1,2,1) , (4,2,2,1) , (4,4,2,1) , (2,5,2,1) , (1,6,2,1) , (1,0,3,1) , (4,0,3,1) , (0,1,3,1) , (1,2,3,1) , (6,3,3,1) , (1,6,3,1) , (4,0,4,1) , (2,1,4,1) , (3,4,4,1) , (6,4,4,1) , (2,5,4,1) , (4,5,4,1) , (0,3,5,1) , (2,6,5,1) , (4,1,0,0) , (6,1,1,0) ,(5,1,0,1) , (4,3,0,1) , (1,4,0,1) , (0,5,0,1) , (2,6,0,1) , (5,2,1,1) , (1,3,1,1) , (6,3,1,1) , (4,5,1,1) , (3,3,2,1) , (5,4,2,1) , (3,5,2,1) , (6,5,2,1) , (3,1,3,1) , (1,4,3,1) , (4,4,3,1) , (6,4,3,1) , (5,5,3,1) , (2,6,3,1) , (4,4,4,1) , (3,5,4,1) , (5,6,4,1) , (4,2,5,1) , (6,2,5,1) , (0,6,5,1) , (1,6,5,1) , (6,6,5,1) , (5,6,6,1) }.

An example of a complete (182,7)-cap in PG(3,7).
{(1,0,0,0) , (0,1,0,0) , (1,1,0,0) , (0,0,1,0) , (1,0,1,0) , (0,1,1,0) , (2,1,1,0) , (1,2,1,0) , (4,2,1,0) , (3,3,1,0) , (5,3,1,0) , (2,5,1,0) , (4,6,1,0) , (0,0,0,1) , (1,0,0,1) , (0,1,0,1) , (2,1,0,1) , (1,2,0,1) , (4,2,0,1) , (3,3,0,1) , (5,3,0,1) , (4,6,0,1) , (2,0,1,1) , (3,0,1,1) , (1,1,1,1) , (4,1,1,1) , (0,2,1,1) , (3,2,1,1) , (2,3,1,1) , (4,3,1,1) , (6,4,1,1) , (5,5,1,1) , (1,0,2,1) , (2,0,2,1) , (3,1,2,1) , (6,1,2,1) , (0,2,2,1) , (2,2,2,1) , (1,4,2,1) , (3,4,2,1) , (5,6,2,1) , (6,0,3,1) , (4,1,3,1) , (5,1,3,1) , (2,2,3,1) , (5,2,3,1) , (2,3,3,1) , (0,5,3,1) , (6,5,3,1) , (0,6,3,1) , (5,2,4,1) , (5,4,5,1) , (3,6,5,1) , (3,2,6,1) , (2,1,0,0) , (3,1,1,0) , (2,2,1,0) , (3,6,1,0) , (2,0,0,1) , (4,1,0,1) , (0,2,0,1) , (1,3,0,1) , (5,4,0,1) , (4,0,1,1) , (0,1,1,1) , (3,3,1,1) , (0,4,1,1) , (1,4,1,1) , (6,0,2,1) , (1,1,2,1) , (5,2,2,1) , (6,3,2,1) , (0,6,2,1) , (0,0,3,1) , (6,1,3,1) , (1,3,3,1) , (5,3,3,1) , (2,5,3,1) , (2,2,4,1) , (1,3,4,1) , (0,5,4,1) , (0,6,4,1) , (6,6,4,1) , (3,1,5,1) , (5,3,5,1) , (2,4,5,1) , (6,5,5,1) , (3,1,0,0) , (3,2,1,0) , (1,3,1,0) , (4,5,1,0) , (3,0,0,1) , (1,1,0,1) , (3,2,0,1) , (0,3,0,1) , (2,4,0,1) , (2,4,0,1) , (4,4,0,1) , (0,0,1,1) , (3,1,1,1) , (1,2,1,1) , (4,2,1,1) , (5,4,1,1) , (6,5,1,1) , (5,1,2,1) , (4,2,2,1) , (4,4,2,1) , (2,5,2,1) , (1,6,2,1) , (1,0,3,1) , (4,0,3,1) , (0,1,3,1) , (1,2,3,1) , (6,3,3,1) , (1,6,3,1) , (4,0,4,1) , (2,1,4,1) , (3,4,4,1) , (6,4,4,1) , (2,5,4,1) , (4,5,4,1) , (0,3,5,1) , (2,6,5,1) , (4,1,0,0) , (6,1,1,0) ,(5,1,0,1) , (4,3,0,1) , (1,4,0,1) , (0,5,0,1) , (2,6,0,1) , (5,2,1,1) , (1,3,1,1) , (6,3,1,1) , (4,5,1,1) , (3,3,2,1) , (5,4,2,1) , (3,5,2,1) , (6,5,2,1) , (3,1,3,1) , (1,4,3,1) , (4,4,3,1) , (6,4,3,1) , (5,5,3,1) , (2,6,3,1) , (4,4,4,1) , (3,5,4,1) , (5,6,4,1) , (4,2,5,1) , (6,2,5,1) , (0,6,5,1) , (1,6,5,1) , (6,6,5,1) , (5,6,6,1) (5,1,0,0) , (5,2,1,0) , (1,6,1,0) , (5,6,1,0) , (3,6,0,1) , (5,0,1,1) , (2,2,1,1) , (0,3,1,1) , (2,5,1,1) , (1,6,1,1) , (3,0,2,1) , (4,0,2,1) , (1,2,2,1) , (2,4,2,1) , (5,5,2,1) , (2,1,3,1) , (0,2,3,1) , (3,2,3,1) , (1,5,3,1) , (4,6,3,1) , (5,6,3,1) , (0,4,4,1) , (5,5,4,1) , (4,6,4,1) , (3,3,5,1) , (6,3,5,1) , (6,0,6,1) , (6,1,6,1) , (2,3,6,1)}.

An example of a complete (222,8)-cap in PG(3,7)
{(1,0,0,0) , (0,1,0,0) , (1,1,0,0) , (0,0,1,0) , (1,0,1,0) , (0,1,1,0) , (2,1,1,0) , (1,2,1,0) , (4,2,1,0) , (3,3,1,0) , (5,3,1,0) , (2,5,1,0) , (4,6,1,0) , (0,0,0,1) , (1,0,0,1) , (0,1,0,1) , (2,1,0,1) , (1,2,0,1) , (4,2,0,1) , (3,3,0,1) , (5,3,0,1) , (4,6,0,1) , (2,0,1,1) , (3,0,1,1) , (1,1,1,1) , (4,1,1,1) , (0,2,1,1) , (3,2,1,1) , (2,3,1,1) , (4,3,1,1) , (6,4,1,1) , (5,5,1,1) , (1,0,2,1) , (2,0,2,1) , (3,1,2,1) , (6,1,2,1) , (0,2,2,1) , (2,2,2,1) , (1,4,2,1) , (3,4,2,1) , (5,6,2,1) , (6,0,3,1) , (4,1,3,1) , (5,1,3,1) , (2,2,3,1) , (5,2,3,1) , (2,3,3,1) , (0,5,3,1) , (6,5,3,1) , (0,6,3,1) , (5,2,4,1) , (5,4,5,1) , (3,6,5,1) , (3,2,6,1) , (2,1,0,0) , (3,1,1,0) , (2,2,1,0) , (3,6,1,0) , (2,0,0,1) , (4,1,0,1) , (0,2,0,1) , (1,3,0,1) , (5,4,0,1) , (4,0,1,1) , (0,1,1,1) , (3,3,1,1) , (0,4,1,1) , (1,4,1,1) , (6,0,2,1) , (1,1,2,1) , (5,2,2,1) , (6,3,2,1) , (0,6,2,1) , (0,0,3,1) , (6,1,3,1) , (1,3,3,1) , (5,3,3,1) , (2,5,3,1) , (2,2,4,1) , (1,3,4,1) , (0,5,4,1) , (0,6,4,1) , (6,6,4,1) , (3,1,5,1) , (5,3,5,1) , (2,4,5,1) , (6,5,5,1) , (3,1,0,0) , (3,2,1,0) , (1,3,1,0) , (4,5,1,0) , (3,0,0,1) , (1,1,0,1) , (3,2,0,1) , (0,3,0,1) , (2,4,0,1) , (2,4,0,1) , (4,4,0,1) , (0,0,1,1) , (3,1,1,1) , (1,2,1,1) , (4,2,1,1) , (5,4,1,1) , (6,5,1,1) , (5,1,2,1) , (4,2,2,1) , (4,4,2,1) , (2,5,2,1)

, (1,6,2,1) , (1,0,3,1) , (4,0,3,1) , (0,1,3,1) , (1,2,3,1) , (6,3,3,1) , (1,6,3,1) , (4,0,4,1) , (2,1,4,1) , (3,4,4,1) , (6,4,4,1) , (2,5,4,1) , (4,5,4,1) , (0,3,5,1) , (2,6,5,1) , (4,1,0,0) , (6,1,1,0) ,(5,1,0,1) , (4,3,0,1) , (1,4,0,1) , (0,5,0,1) , (2,6,0,1) , (5,2,1,1) , (1,3,1,1) , (6,3,1,1) , (4,5,1,1) , (3,3,2,1) , (5,4,2,1) , (3,5,2,1) , (6,5,2,1) , (3,1,3,1) , (1,4,3,1) , (4,4,3,1) , (6,4,3,1) , (5,5,3,1) , (2,6,3,1) , (4,4,4,1) , (3,5,4,1) , (5,6,4,1) , (4,2,5,1) , (6,2,5,1) , (0,6,5,1) , (1,6,5,1) , (6,6,5,1) , (5,6,6,1) (5,1,0,0) , (5,2,1,0) , (1,6,1,0) , (5,6,1,0) , (3,6,0,1) , (5,0,1,1) , (2,2,1,1) , (0,3,1,1) , (2,5,1,1) , (1,6,1,1) , (3,0,2,1) , (4,0,2,1) , (1,2,2,1) , (2,4,2,1) , (5,5,2,1) , (2,1,3,1) , (0,2,3,1) , (3,2,3,1) , (1,5,3,1) , (4,6,3,1) , (5,6,3,1) , (0,4,4,1) , (5,5,4,1) , (4,6,4,1) , (3,3,5,1) , (6,3,5,1) , (6,0,6,1) , (6,1,6,1) , (2,3,6,1), (6,1,0,0) , (2,0,1,0) , (1,1,1,0) , (0,2,1,0) , (2,3,1,0) , (6,3,1,0) , (2,4,1,0) , (5,4,1,0) , (3,1,0,1) , (2,2,0,1) , (5,2,0,1) , (2,3,0,1) , (1,5,0,1) , (2,1,1,1) , (5,1,1,1) , (3,4,1,1) , (1,5,1,1) , (0,1,2,1) , (3,2,2,1) , (0,3,2,1) , (5,3,2,1) , (6,6,2,1) , (5,0,3,1) , (2,4,3,1) , (6,6,3,1) , (4,1,4,1) , (0,2,4,1) , (6,2,4,1) , (3,3,4,1) , (4,3,4,1) , (1,4,4,1) , (6,5,4,1) , (3,6,4,1) , (0,1,5,1) , (4,3,5,1) , (0,4,5,1) , (4,0,6,1) , (5,4,6,1) , (4,6,6,1) , (6,6,6,1) }.

Table 1. Points and Plans of PG (3, 7)

I	p_i	π_i
1	(1,0,0,0)	2 9 16 23 30 37 44 51 58 65 72 79 86 93 100 107 114 121 128 135 142 149 156 163 170 177 184 191 198 205 212 219 226 233 240 247 254 261 268 275 282 289 296 303 310 317 324 331 338 345 352 359 366 373 380 387 394
2	(0,1,0,0)	1 9 10 11 12 13 14 15 58 59 60 61 62 63 64 107 108 109 110 111 112 113 156 157 158 159 160 161 162 205 206 207 208 209 210 211 254 255 256 257 258 259 260 303 304 305 306 307 308 309 352 353 354 355 356 357 358
.	.	
400	(6,6,6,1)	8 15 21 27 33 39 45 51 59 65 78 84 90 96 102 107 120 126 132 138 144 150 162 168 174 180 186 192 198 210 216 222 228 234 240 253 258 264 270 276 282 295 301 306 312 318 324 337 343 349 354 360 366 379 385 391 397

Table 2. Plane and lines of $PG(3,7)$

2	2	2	2	2	2	2	2	9	9	9	9	9	9	9	16	16	16	16	16	16	16	23	23	23	23	23	23	23	30	30	30	30	30	30	30
9	58	107	156	205	254	303	352	58	65	72	79	86	93	100	58	65	72	79	86	93	100	58	65	72	79	86	93	100	58	65	72	79	86	93	100
16	65	114	163	212	261	310	359	107	114	121	128	135	142	149	114	121	128	135	142	149	107	121	128	135	142	149	107	114	128	135	142	149	107	114	121
23	72	121	170	219	268	317	366	156	163	170	177	184	191	198	170	177	184	191	198	156	163	184	191	198	156	163	170	177	198	156	163	170	177	184	191
30	79	128	177	226	275	324	373	205	212	219	226	233	240	247	226	233	240	247	205	212	219	247	205	212	219	226	233	240	219	226	233	240	247	205	212
37	86	135	184	233	282	331	380	254	261	268	275	282	289	296	282	289	296	254	261	268	275	261	268	275	282	289	296	254	289	296	254	261	268	275	282
44	93	142	191	240	289	338	387	303	310	317	324	331	338	345	338	345	303	310	317	324	331	324	331	338	345	303	310	317	310	317	324	331	338	345	303
51	100	149	198	247	296	345	394	352	359	366	373	380	387	394	394	352	359	366	373	380	387	387	394	352	359	366	373	380	380	387	394	352	359	366	373

All necessary verifications have been performed Utilizing a computer, so the proof of our theorems now ends. We have proven theoretically and practically that the maximum value of k such that k-cap exists is 23.

Table (3) The sizes of the known complete *k*-caps in PG(3, *q*).$Tq = (q^2 + q + 4) / 2$

q	$t_2(3,q)$	Size k of the known complete caps with $t_2(3,q)\leq k\leq m_2'(3,q)$	$m_2'(3,q)$	$m_2(3,q)$
3	8	8=Tq	8	10
4	10	10,12,13,14 =Tq+2	14	17
5	12	and **12≤k≤18** **k=20=** Tq+3	20	26
7	17	and **17≤k≤30** **k=32=** Tq+2	32	50
8	14≤	**20≤k≤41**=Tq+3	60≤	65
9	15≤	**24≤k≤48**=Tq+1	78≤	82
11	18≤	**30≤k≤70**=Tq+2	116≤	122
13	21≤	**36≤k≤93**=Tq	162≤	170
16	25≤	**41≤k≤138**=Tq	242≤	257
17	26≤	**51≤k≤157**=Tq+2	278≤	290
19	19≤	58**≤k≤192**=Tq	348≤	362
23	35≤	**72≤k≤280**=Tq+2	512≤	530

3.9 Theorem: in PG(3,7)

$$m_2(3,7)=17\text{-}30.$$

3.10 Corollary**:** in PG(3,7)

$$m'_2(3,7)=23.$$

4. Conclusions:

From the above results, the distinct complete (K,n)-caps in PG(3,7), $2\leq n\leq 8$
Is as follows:

(K, 2)-cap, where k=23 is a complete cap which is ovaloid.
(K, 3)-cap, where k=54 is a complete cap.
(K, 4)-cap, where k=87 is a complete cap.
(K, 5)-cap, where k=123 is a complete cap.
(K, 6)-cap, where k=153 is a complete cap.
(K, 7)-cap, where k=182 is a complete cap.
(K, 8)-cap, where k=222 is a complete cap, which is the whole space in PG (3, 7).

References

[1] Hirschfeld J 1998 Projective geometries over finite fields *Oxford University Press*
[2] Kareem F F 2011 A complete (k, r)-Caps in PG(3,P) Over Galois Field GF(4) *Ibn AL-HaithamJ.Pure Appl. Sci.* **2(24)**
[3] Thas J A 2019 Arcs Caps Generalisations: Results and Problems *50 years of Combinatorics Graph Theory and Computing* Chapman and Hall/*CRC* 387-407
[4] M S I and Al-Mukhtar A Sh 2008 Complete Arcs and Surfaces in three Dimensional Projective Space Over Galois Field *Ph. D. Thesis. University of Technology, Iraq*
[5] Hirschfeld J 1985 Finite Projective spaces of three dimensions *Clarendon Press Oxford*

[6] Ibrahim H Sh and Kasm N Y 2019 The Possibility of Applying Rumen Research at the Projective Plane PG (2,17) *Modern Applied Science* **13 (8)**. https://doi:10.5539/mas.v13n8p150
[7] Ibrahim H Sh and Kasm N Y 2019 The optimal size of {b, t} -blocking set When t = 3, 4 By intersection the tangents in PG (2 , q) *Modern Applied Science* **13(7)**.URL:https://doi.org/10.5539/mas.v13n7p
[8] Kasm N Y and Hamad A Z 2019 Applications of Algebraic Geometry in Cryptography *Modern Applied Science* **13(5)**. URL: https://doi.org/10.5539/mas.v13n5p130
[9] Yahya N Y K 2018 A geometric Construction of Complete (k, r)-arc in PG (2, 7) and the Related Projective [n,3, d]7 Codes *AL-Rafidain Journal of Computer Sciences and Mathematics* **12(1)** 24-40. https://doi.org/10.13140/RG.2.2.16543.25767
[10] Yahya N Y K 2014 A Non PGL (3, q) k-arcs in the projective plane of order 37 *Tikrit Journal of Pure Science* **19(1)** 135-145. https://doi.org/10.13140/RG.2.2.23254.14401
[11] Yahya N Y K 2012 Existence of Minimal Blocking Sets of Size 31 in the Projective Plane PG (2, 17) *Journal of University of Babylon/Pure and Applied Sciences* **20(4)** 1138-1146. https://doi.org/ 10.13140/RG.2.2.10146.94407
[12] Yahya N Y K 2014 The Use of 7- Blocking Sets in Galois Geometries. *Journal of University of Babylon/Pure and Applied Sciences* **22(4)** 1229-1235. https://doi.org/10.13140/RG.2.2.16857.83044
[13] Yahya N Y K and Salim M N 2018 The Geometric Approach to Existences Linear [n, k, d]13 Code. *International Journal of Enhanced Research in science Technology and Engineering*. https:// doi.org/ 10.13140/RG.2.2.16018.96960
[14] Yahya N Y K and Salim M N 2019 New Geometric Methods for prove Existence three Dimensional linear [97,3,87]11 and [143,3,131]13 codes *Journal of education and science* **28(1812-125X)** 312-333. https//:doi.org/ 10.13140/RG.2.2.29944.08965
[15] Yahya N Y K and Salim M N 2019 17 New Existences linear [n, 3, d]19 Codes by Geometric Structure Method in PG (2, 19) *AL-Rafidain Journal of Computer Sciences and Mathematics* **13(1)**. https://doi.org /10.13140/RG.2.2.18697.29284
[16] Yahya N Y K and Hamad A Z 2019 A geometric Construction of a (56, 2)-blocking set in PG (2, 19) and on three dimensional Linear $[325,3,307]_{19}$ Griesmer Code *AL-Rafidain Journal of Computer Sciences and Mathematics* **13(2)** 13-25. https://doi.org/10.33899/csmj.2020.163511
[17] Sulaimaan A E M and Kasm N Y 2019 Linear code originates from complete arc by Engineering Building methods *Applied Mathematical Science* 13(21) 1013-1020. https://doi.org/10.12988/ams.2019.99132
[18] Sulaimaan A E M and Kasm N Y 2019 Linear code related Ω-Blocking sets *Applied Mathematical Science* **13(21)**1033-1040. https://doi.org/10.12988/ams.2019.99133
[19] Sulaimaan A E M and Kasm N Y 2019 New Structural Engineering Construction methods by Remove q points in PG(2,q) *Applied Mathematical Science* **13(21)**1048 - 1041. https://doi.org/10.12988/ams.2019.99134
[20] Sulaimaan A E M and Kasm Yahya N Y 2020 The Reverse construction of complete (k,n)- arcs in three dimensional projective space PG(3,4) *Journal of Physics: Conference Series* **1591**. doi:10.1088/1742-6596/1591/1/012078
[21] Sulaimaan A E M and Kasm Yahya N Y 2020 The Reverse construction of complete (k,n)- arcs in PG(2,q) where q=2,4,8 related with linear codes *Journal of Physics: Conference Series* **1591**.doi:10.1088/1742-6596/1591/1/012079
[22] Faraj M G and Kasm N Y 2019 Reverse Building of complete (k,r)-arcs in PG(2,q) *Library Journal* **6(12)**.https:// doi.org / 10.4236/oalib.1105900
[23] Abdullah F N and Kasm Yahya N Y 2020 Bounds on Minimum Distance for Linear Codes Over GF(q) *Italian Journal of Pure and Applied Mathematics* has been Accepted on February 5 2020. For Publication in n.**45**. In press

[24] Abdulla A A and Kasm N Y 2020 Complete Arcs and Surfaces In Three Dimensional projective space PG (3,7) *Library Journal* **7(4)** . https://doi.org/10.4236/oalib.1106071
[25] Abdulla A A and Kasm Yahya N Y 2020 Application of Algebraic Geometry In Three Dimensional projective space PG (3,7) *Journal of Physics: Conference Series* **1591**. doi:10.1088/1742-6596/1591/1/01207
[26] Kasm Yahya N Y 2021 Applications Geometry of Space in PG(3,P), in Journal of Interdisciplinary Mathematics, for publication in Journal of Interdisciplinary plinary Mathematics, in press, 2021.

Stabilization study of a non-Linear self-regression model using Linear Approximation Technique

Stabilization study of a non-Linear self-regression model using Linear Approximation Technique

Kawther Abbood Neamah [1] and Safa Abood Namah [2]

[1] Department of Computer Science, Baghdad College of Economics Sciences University, Iraq
[2] Department of Computer Engineering, AL-Iraqi University, Iraq

E-mail: cs@baghdadcollege.edu.iq

Abstract. In this paper, stability in a polynomial model called a polynomial self- regression model with trigonometric boundaries was studied. A linear approximation technique was used, and the Box-Genghis method was used in data analysis, and time series modeling of numbers of people with media. Data were obtained from AL-Yarmouk Hospital in Baghdad AL-Karkh for the period (2011- 2016) shows the numbers of patients with the disease through the technique of Linear approximation. Then we found the single point and the stability of the final cycle, and we tried to apply the results that we obtained on the correct data for audit.
Keywords. stability ,dynamic ,single ,limit cycle

1. Introduction

The subject of time series is one of the important topics through which most sciences can be entered in the way of medical, natural, biological sciences, human development sociology and many other sciences. Time series analysis methods are among the most used statistical methods, where any phenomenon can be analyzed for periods. Time is equal and not equal. The high interest in the subject of time series is due to the urgent need for a reliable and highly effective forecasting system So that it can be relied upon to explain many phenomena in different Journals [4]. Our research focuses on studying the stability of a proposed model Polynomial called the polynomial self-regression model polynomial autoregressive model with trigonometric terms(PAR). This model usually has cyclic nonlinear behavior and limit cycles. And we will try to find the traits of the dross or the stability of the singular point Using the method of linear approximation for the proposed nonlinear model and some other statistical characteristics.

2. Basic concepts and principles

2.1 Time Series

time series is a collection of data a recorded for particular phenomenon during a specific period that was economical, social, or statistical, and arranged sequentially according to time. Usually, the periods between the observations anal the other are equal.

A mathematical time series defines a sequence of random variables, defined within the probability space. Multivariate and index t, which belongs to the T group and denotes the time series usually $\{x(t);\ -\infty < t < \infty, t \in T\}$or abbreviated $\{x(t)\}$.

If it takes continuous values then the time series It is called " Continuous-time" if it takes intermittent value $t = o, \mp 1, \mp 2, \ldots$ then the series is called "Time-Discrete " symbolizes the god with the symbol $\{x_t; t = o, \mp 1, \mp 2, \ldots\} or \{x_t\}$[2].

2.2 The polynomial model

To be {y(t)} Time series,$\{z_t\}$ White annoyances . Assuming that f(0) Into the equation:
y(t)=f(y(t-1),,y(t-p),z(t-1)…….,z(t-p))+z_t
A p-degree polynomial We will get a polynomial self-regression model and have the following formula:
y(t)= p(t-1),….,y(t-p),z(t-1),…..,(t-q)) +z(t) (1)
If that p(0) is degree polynomial and {z(t)} White annoyances from a degree q.[7]

2.3 Exponential Autoregressive model

In [9], the Japanese researcher Ozaki defined the exponential regression model from the rank P as follows:

$$x_t = \sum_{i=l}^{p} (\propto_i + \pi e^{-\frac{x^2}{t-1}}) x_{t-i} + Z_t \quad (2)$$

Where $\{Z_t\}$ is an independent and uniform distribution of white inconvenience, and $i = 1,2, \ldots p$ and $\propto_i, \pi_i$ Constant quantities represent model coefficients.

2.4 polynomial autoregressive model with trigonometric

This proposed model is a polynomial Self- regression model with the terms of trigonometric functions with the following form:

$$x_t = \sum_{i=l}^{p} \alpha_i [cos\left(\frac{\pi}{2} x_{t-k}\right)]^i + Z_t \; ; k = 1,2,3, \ldots$$

Where, $\{x_t\}$ is a time series, $\propto_i$ is constant, Z_t white inconveniences, and $t = o, \mp 1, \mp 2, \ldots$

3. The theoretical Side

3.1 Nonlinear Dynamical System

In dynamic systems covered by non-Linear differential equations, they have often used Approximation methods for converting it into a system of linear differential equations, and there are two methods of approximation that depend on the structure. The physical system of the kinematic system and these two methods are approximation by wise cutting and approximation to the local sin. The stability of the kinematic systems depends mainly on the behavior of the solution, whether it approaches one point or a closed curve when the solution is cyclical or not. Non-Linear systems have several characteristics, including:

1. The nature of the Jump, since $c\dot{x}(t)$are the decaying force and $\propto x(t) + Bx^3(t)$ is the reference force of the oscillating force.
2. Reliability between the amplitude of the oscillator and the frequency, which Can beseen in models of random vibrations.
3. Having the final cycle and this behavior of the solution is clearly shown in the vender POL formula that formulated:

$$\ddot{x}(t) - B(1 - x^2(t))\dot{x}(t) + \propto x(t) = 0 \quad (3)$$

Where $\dot{x}(t) = \frac{dx(t)}{dt}$

And one of the most important techniques used to bring non-linear systems closer to Linear local systems near a single point. The stationary solution to the system is to approximate the local linear technique

and to demonstrate this technique. We have a non-Linear differential equation, and it is converted into a linear differential equation with the following steps:

1. Reducing the rank of the equation.
2. Writing it in the' space form.
3. Finding the fixed solution of the system, as follows:

We do not have the following equation: (Vander pol equation):

$$\ddot{x}(t) - (1 - x^2)\dot{x} + x = 0 \tag{4}$$

And put $\dot{x} = y$ the equation (2-2) becomes as:

$$\dot{y} = (1 - x^2)y - x \tag{5}$$

By rewriting it as the state space, that $(x, y)^T$ is the state vector, and that the only fixed point in the system (2-3) is the origin point, and the fixed solution at this point is zero ($\dot{x} = o, \dot{y} = o$).
Using the Taylor (2-3) system expansion around its original point, we obtain:

$$\dot{x} = o * x + 1 * y$$
$$\dot{y} = (-1 - 2xy)x + (1 - x^2)y \tag{6}$$

The expansion of Taylor is rounded in equation (2-4) to the second term only, given that the functions $X(x, y)$ and $Y(x, y)$ are functions with two variables x, y and $x(o, o) = o, y(o, o) = o$ at the original point:

$$\begin{bmatrix} 0 & 1 \\ -1 - 2xy & 1 - x^2 \end{bmatrix} = \begin{bmatrix} \dot{x} \\ \dot{y} \end{bmatrix} \begin{bmatrix} x \\ y \end{bmatrix} \tag{7}$$

And this system has an original point becomes as follows:

$$\begin{bmatrix} 0 & 1 \\ -1 & 1 \end{bmatrix} \begin{bmatrix} \dot{x} \\ \dot{y} \end{bmatrix} = \begin{bmatrix} x \\ y \end{bmatrix} \tag{8}$$

That is:

$$\dot{x} = y$$
$$\dot{y} = -x + y$$

That is, the equation for Van DerpoL (2-3) and near to that fixed point becomes a linear equation as follows:

$$\ddot{x} - \dot{x} + x = 0 \tag{9}$$

This technique can be applied single non – zero points as well since non-Linear kinematic systems include single zero and non – zero points. The stability of these systems is determined by the behavior of the solution path when approaching these isolated $t \longrightarrow \infty$, points, or moving away from them when t and here represents time [12],[8].

3.2 Stationary and Stability

In many engineering and physical matters, we come across processes that can be described as statistically, stable, this means that if we get views of a process of this type and it is done.
Divide them into groups of periods. The different sections of these observations appear similar, and with more accurate words. The statistical characteristics are constant and do not change with time. Random operations that act in this way are called phased operations [1]. It means that there is no growth or erosion of time series data, in other words. The data are spread around a fixed medium and have a

constant variance. That means $x_1, x_2, x_3, \dots, x_t$ it must have the same probability density function, that is, $f(x_1, x_2, x_3, \dots, x_t) = f(x_{1+k}, x_{2+k}, x_{3+k}, \dots, x_{t+k})$ since k it represents a real exception. And that the Joint probability distribution does not change with the change in the period or when the displacement is carried out in a fixed number. It has been shown by the word priestly that the varied operations are usually created through a stable system that reaches the steady-state after an appropriate period. Specific output, and therefore the system is mathematically stable. if the roots of the system equation in the form of the defaults factor lie all outside the unit circle, and that the characteristics of the characteristics' equation are all located within the unit circle [1].

3.3 Singular point

The single point of the form $\in$ is defined;

$$x_t = f(x_{t-1}, \dots, x_{t-p}) \tag{10}$$

it is the one that the path of the model closes above, and the approach is either when $t \longrightarrow \infty \; ort \longrightarrow -\infty$.

If the path approach is when $t \longrightarrow \infty$ it is called single stable point. And if the path approaches a point $\in$ when $t \longrightarrow \infty$, then a single point is called unstable. And the necessary condition and what is sufficient for $\in$ is to achieve the relationship: [10] [12], $\in = f(\in)$.

3.4 Limit cycle

Let us have the following model: $x_t = f(x_{t-1}, \dots, x_{t-p})$.

Limit cycle of the above model is defined as the isolated and closed path. $x_t, x_{t+1}, x_{t+2}, \dots, x_{t+q} = x_t$ Since q represents a positive integer. The isolated path is defined as any path that begins very close to Limit cycle and approaches it either when $t \longrightarrow \infty$ or $t \longrightarrow -\infty$ifit is approaching it when $t \longrightarrow \infty$ it is called a stable Limit cycle, but if the approach is when $t \longrightarrow -\infty$ it is called an unstable limit cycle,but the closed path is if the initial values $x_1, x_2, x_3, \dots, x_p$ belong to the Limit cycle, then $(x_{1+kq}, \dots, x_{p+kq}) = (x_1, \dots, x_p)$for each positive integer K whereas P is the period to the Limit cycle, and it is the closed path points, and that q and k represent appositive integer [10].

3.5 Find the stability of non-linear models using Linear approximation

The Linear approximation method was proposed to find the stability of the non-Linear models based on the approximation technique in the previous paragraph that was applied to the non-linear exponential time series models by the researcher Ozaki. The method is summarized in two stages:

First stage: Finding the non-zero single Point of the non-Linear Model.

Second Stage: Stability test of this point using Linear approximation technique.

3.6 stability of the Polynomial self-regression model with the Limits of trigonometric functions

Let us have the following form:

$$x_t = \sum_{i=1}^{\infty} \alpha_i [cos\left(\frac{\pi}{2} x_{t-k}\right)]^i + Z_t \; ; k = 1,2, \dots \tag{11}$$

As $\propto_i$ constant and Z_t white inconveniences.

We assume that $k = 1$ (i.e. we will get Polynomials with trigonometric function and x_{t-1}) that is:

$$x_t = \sum_{i=1}^{\infty} \propto_j [cos\left(\frac{\pi}{2} x_{t-1}\right)]^j + Z_t \tag{12}$$

3.7 Find the single point of the proposed model

To have the model defined in equation (2-10), we assume the effect of $\{z_t\}$equals zero and by using the definition of a single point, and by assuming that$\in^n \longrightarrow o$For each $n \geq ,4\ and j = 1,2,3,4$ in equation (2-10) and using the decomposition of Taylor we get:

$$\Longrightarrow \in^2 + \frac{1}{B} \in -\frac{A}{B} = 0 \tag{13}$$

Where as:

$A = \propto_1 + \propto_2 + \propto_3 + \propto_4$

$B = \frac{\pi^2}{8}(\propto_1 + 2 \propto_2 + 3 \propto_3 + 4 \propto_4)$

That is:

$$\Longrightarrow \in = \frac{\frac{-1}{B} \pm \sqrt{(\frac{1}{B})^2 + 4\frac{A}{B}}}{2} \tag{14}$$

3.8 Single point of the proposed grade of rank k (k=2,3,…)

To find the single point of the proposed model (2 – 9) of rank k, we neglect the effect of Z_t on the form (2–9), so we obtain:

$$x_t = \sum_{j=1}^{\infty} \propto_j [cos\left(\frac{\pi}{2} X_{t-k}\right)]^j; k = 2,3, \ldots$$

Using the definition of a single point, we obtain:

$$\in = \sum_{j=1}^{\infty} \propto_j [cos\ (\frac{\pi}{2} \in)]^j$$

The individual points are not flogged to any rank, and we follow a formula similar to the way the single point is found when k=1.

3.9 Non–Zero single point stability of the polynomialmodel (proposed)

We will attempt to test the stability of the non – zero single point using the local linear approximation method near the single point as follows:

Let us have the model defined in (2–10) to assume the effect of Z_t non – existent and using the Taylor decoder and compensation for $x_t = \in + \in_t$ where $\in$are a very small amount and that $\forall n \geq 2;\ \in_{t-1}^n \longrightarrow o, J = 1,2,3,4$ we get:

$$\in + \in_t = A - B(\in^2 + 2 \in \in_{t-1}) \tag{15}$$

Where as:

$A = \propto_1 + \propto_2 + \propto_3 + \propto_4$

$B = \frac{\pi^2}{8}(\propto_1 + 2 \propto_2 + 3 \propto_3 + 4 \propto_4)$

Since then:

$$\in = \frac{\frac{-1}{B} + \sqrt{(\frac{1}{B})^2 + 4\frac{A}{B}}}{2}$$

With compensation in (15), we obtain:

$$\in +\in_t = A - B(\in^2 + 2 \in \in_{t-1}) \tag{16}$$

Accordingly, the model is stable if it is:

$$\left|1 - \sqrt{1 + 4AB}\right| < 1 \tag{17}$$

3.10 Limit cycle stability

We will find the stability of the limit cycle based on the following two views:

Theorem (1): the limit cycle in turn $a, x_{t+1}, x_{t+2}, \dots, x_{t+q}$,of the exponential regression from the first order is stable in orbit if the following condition is met:

$$\left|\prod_{j=1}^{q}[\emptyset_j + \pi_j(1 - 2x_{t+q-j}^2)e^{-x_{t+q-j}^2}]\right| < 1$$

The proof: Note [9]

Theorem (2): The limit cycle in turn q of the form (1 – 13) is stable if it is:

$$\left|\frac{\in_{t+q}}{\in_t}\right| < 1$$

Proof: Note [10]

3.10.1 Issue (1)

The limit cycle of the cycle q (if any) of the proposed model when p = 1 is stable if the condition is met:

$$\left|\prod_{j=1}^{q}[\alpha_j cos\,(\frac{\pi}{2}x_{t-1})]^j\right| < 1$$

The proof:

We assume that the proposed model has a limit cycle in the period q and $q > 1$ as:

$x_t, x_{t+1}, x_{t+2}, \dots, x_{t+q} = x_t$

It is a closed and isolated path.

Let us have the model defined in equation (12) below:

$$x_t = \sum_{j=1}^{\infty} \propto_j [cos\left(\frac{\pi}{2}x_{t-k}\right)]^j + z_t$$

We take a special case when k = 1, j = 1 and generalize the idea in the same way.

$$x_t = \propto_1 cos\left(\frac{\pi}{2}x_{t-1}\right) + Z_t$$

$$x_t = \sum_{j=1}^{\infty} \propto_j [cos\left(\frac{\pi}{2}x_{t-k}\right)]^j + z_t$$

We take a special case when k = 1, j = 1 and generalize the idea in the same way.

$$x_t = \propto_1 cos\left(\frac{\pi}{2}x_{t-1}\right) + Z_t$$

$$x_t = \propto_1 \sum_{k=o}^{\infty}(-1)^k \frac{(\frac{\pi}{2}x_{t-1})^{2k}}{2k!} + Z_t \tag{18}$$

Let $x_t = x_s + \in_s$ and assume that $|\in_{s-1}|^n \longrightarrow o$ for each $n \geq 2$ and neglecting the effect $\{z(t)\}$ we get study of the stability of a nonlinear self-regression model:

$$x_s + \in_s = \propto \left[1 - \frac{(\frac{\pi}{2})^2}{2!} x_{s-1}^2 + \frac{(\frac{\pi}{2})^4}{4!} x_{s-1}^4 - \frac{(\frac{\pi}{2})^6}{6!} x_{s-1}^6 + \cdots\right] - \propto \frac{2(\frac{\pi}{2})^2}{2!} x_{s-1} \in_{s-1} +$$
$$\propto \frac{4(\frac{\pi}{2})^4}{4!} x_{s-1}^3 \in_{s-1} - \propto \frac{6(\frac{\pi}{2})^6}{6!} x_{s-1}^6 \in_{s-1} + \cdots$$

That is:

$$\in_s = -\alpha_1 \frac{2(\frac{\pi}{2})^2}{2!} x_{s-1} \in_{s-1} + o(x_{s-1} \in_{s-1}) \quad (19)$$

Leads to $\in_s = \beta x_{s-1} \in_{s-1}$ (20)

Assume that:

$$\beta = -\alpha \frac{2(\frac{\pi}{2})^2}{2!}$$

$$T(x_{t-1}) = \beta x_{s-1}$$

$$\Longrightarrow \in_{t+q} = \left|\prod_{i=1}^{q} T(x_{t+q-i})\right| \in_t$$

$$\left|\frac{\in_{t+q}}{\in_t}\right| = \left|\prod_{i=1}^{q} T(x_{t+q-i})\right|$$

For the sake of zero convergence this ratio must be less than one:

$$\left|\prod_{i=1}^{q} T(x_{t+q-i})\right| < 1$$

Thus, the model has a stable orbital limit cycle if the following condition is met:

$$\left|\prod_{i=1}^{q} \beta(x_{t+q-i})\right| < 1 \quad (21)$$

And by this, the proof is made.

3.10.2 Issue (2)

The proposed model has a limit cycle if it is:

$$\left|\frac{\in_{t+q}}{\in_t}\right| < 1$$

The proof:

Let us have the model defined by the equation (18)

Neglecting the effect $\{z_t\}$ and using the assumptions in the previous paragraphs, we obtained the following form:

$$\in_t = (1 - \sqrt{1 + 4AB}) \in_{t-1}$$

Where:

$$A = \propto_1 + \propto_2 + \propto_3 + \propto_4$$

$$B = \frac{\pi^2}{8}(\propto_1 + 2 \propto_2 + 3 \propto_3 + 4 \propto_4)$$

We assume that:

$C = (1 - \sqrt{1 + 4AB})$
We get:
$\in_t = C \in_{t-1}$
$\in_{t+q} = C^q \in_t$
That is:
$\frac{\in_{t+q}}{\in_t} = C^q \Longrightarrow \left|\frac{\in_{t+q}}{\in_t}\right| = |C^q| < 1$
And this condition is fulfilled if it is $|C| < 1$. And then the proof ends.
Example 3.1
Let us have the following model:
$x_t = 0.398\ cos\left(\frac{\pi}{2} x_{t-1}\right) + z(t)$
And refer to the stability condition of the proposed model, we get the single point $\in = 0.29256$ and using the relationship (16) we get:
$\in_1 = -0.70784\ \in_{t-1}$
And since $|\lambda| < 1$ and therefore the model is stable.
The following figures show the stability of the model and by assuming different initial values.[15]

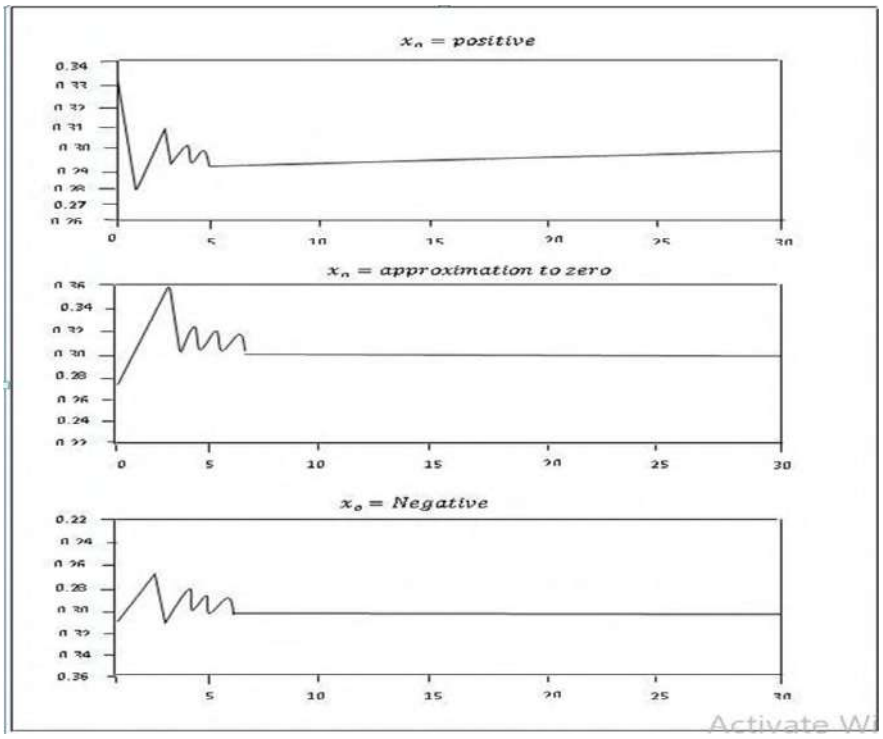

Figure (1). the serial series generated from the model

We notice from the above figures that the series generated by the model does not depend on the initial condition and that paths an approach to the limit cycle.
Example 3.2
Let us have the following model
$x_t = 2.787\ cos\left(\frac{\pi}{2} x_{t-1}\right) + z(t)$
And from it we get $\in = 1.26104$, and from the relationship (16) we get the form $\in_t = -2.44025\ \in_{t-1}$.

That is, $1 < |\lambda|$ which indicates that the stability condition has not been fulfilled, the form (2) is not stable.[15]
The following figures illustrate this:

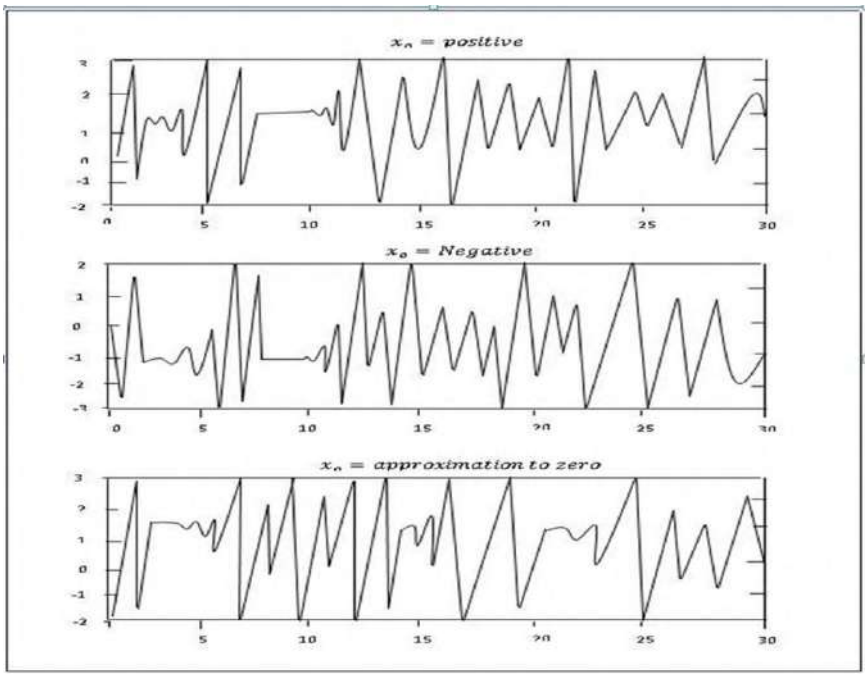

Figure (2). the serial series generated from the model(2)

4. The practical side

4.1 introduction

During this time we will try to rely on the way (Box- Genghis) in the analysis and Modeling of the time series of numbers of People with media, where data was obtained from the Yarmouk Hospital in Baghdad/ AL-karkh for the period (2011- 2016) represented by the number of patients with the disease.
1-The first stage: diagnosing the model (Model-identification)
2.The second stage: estimating the parameters of the Model (Parameters Estimation)
3- Third stage: suitability test of the personalized Model (Diagnostic checking) [3].

4.2 Data analysis

Figure (1) represents the graph of the time series. where the axis of the Years is the time t, and the axis of the antibiotics represents the numbers of patients with this disease, which represents the studied time series $\{x_t\}$. As we note that the series fluctuates irregularly, which indicates that the series is not crossed in the middle and that the series follows a periodic, irregular system, that is, it repeats itself for a specific period.

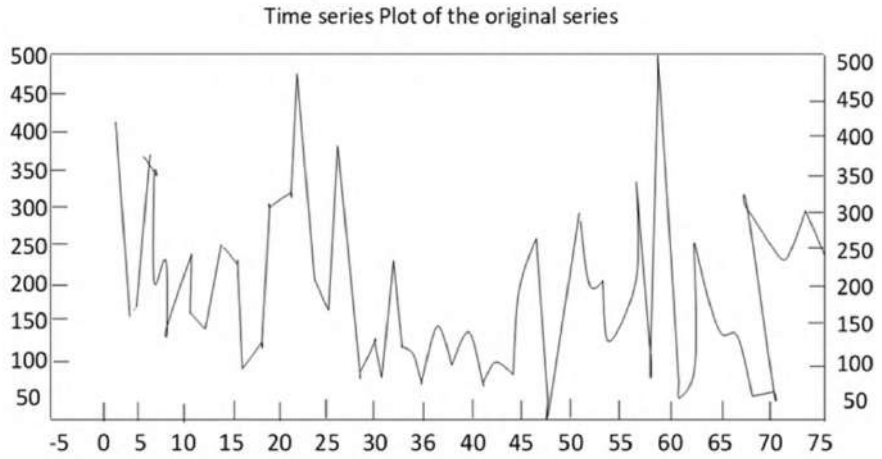

Figure(3). Diagram of the series represented by the number of cases of media

The figures (2), (3) and(4) represent the fee for the self-correlation function, the partial self-correlation function, and a drawing for the incidence of this disease.

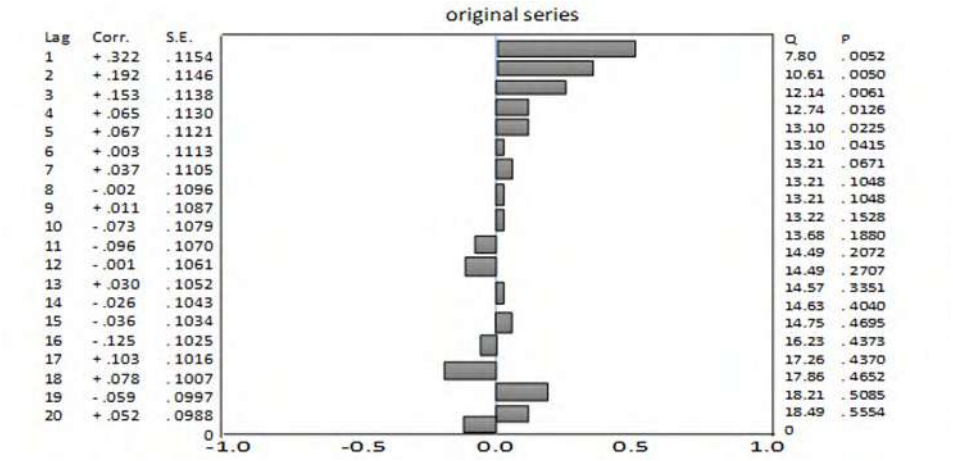

Figure(4). auto correlation function for the original data

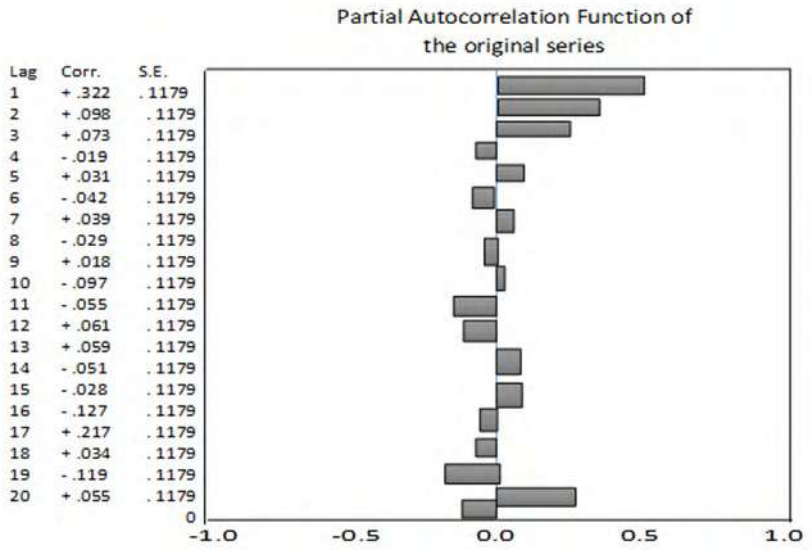

Figure(5). partial auto- link function for the original data

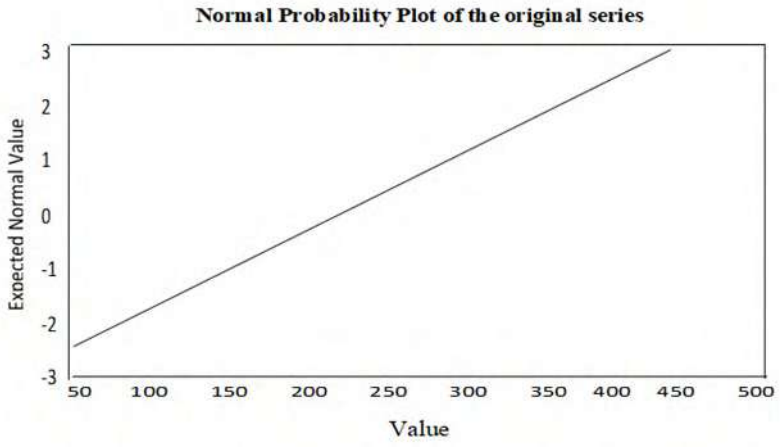

Figure(6). Charting the nature of the original data

Where we note that the sequence is not related, and we find that more than 8% approximately of the Self - Correlation coefficients are outside the constraint $\pm\frac{1.92}{\sqrt{n}}$, but they are close to the natural distribution, as we note that most of the data are close to the main axis of the nature drawing.

4.3 Modeling

From the observation of the graph of the series, figure (1) we find that the series is not arranged in the Middle, and fluctuate periodically, almost irregularly.

In order to convert it into a time series ranging in the Middle, the differences were taken for it,that is:

$Y_t = \Delta_{x_t}^d \ldots$

$d = 1,2, \ldots ; \ \Delta = (1 - B)$

x_t Represents the original series, Y_tRepresents the transformed series. And B displacementposteriortrigger, which is known as the following:

$B_{x_t}^r = x_{t-r} \, ; r = 1,2, \ldots$

And the shape (s) represents the transformed sequence (d =1), and we find that the sequence is rounded around the medium.

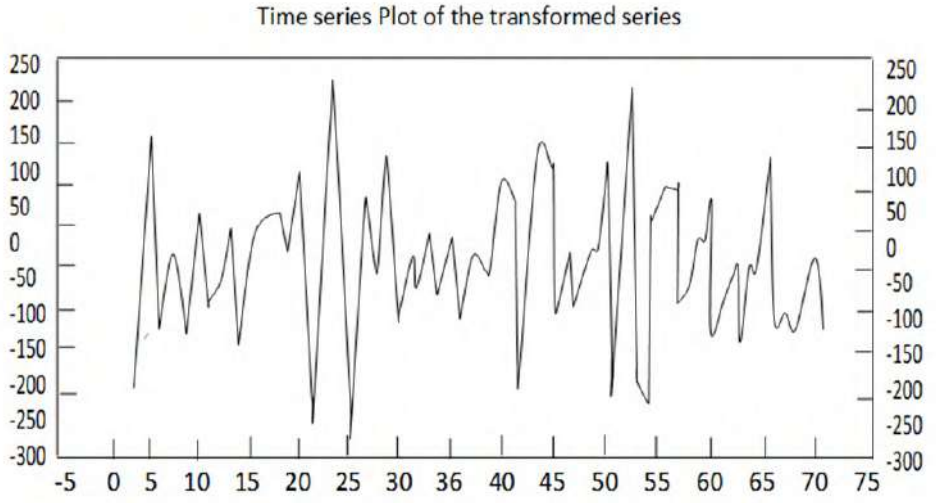

Figure(7). the serial drawing of the converted data

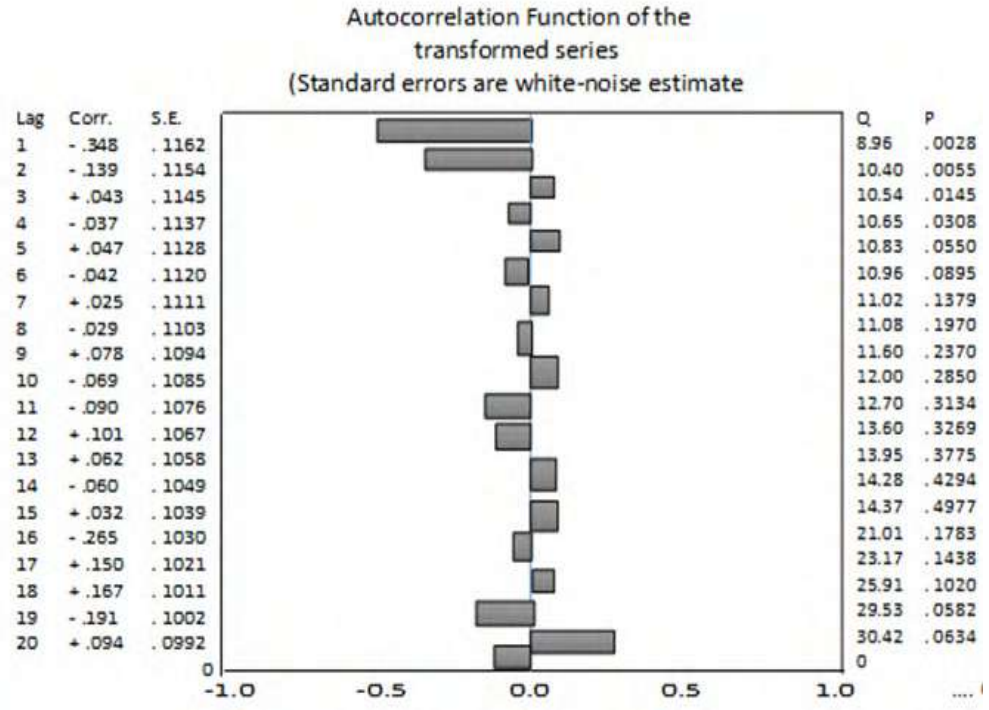

Figure (8) is a self-correlation function for the converted data

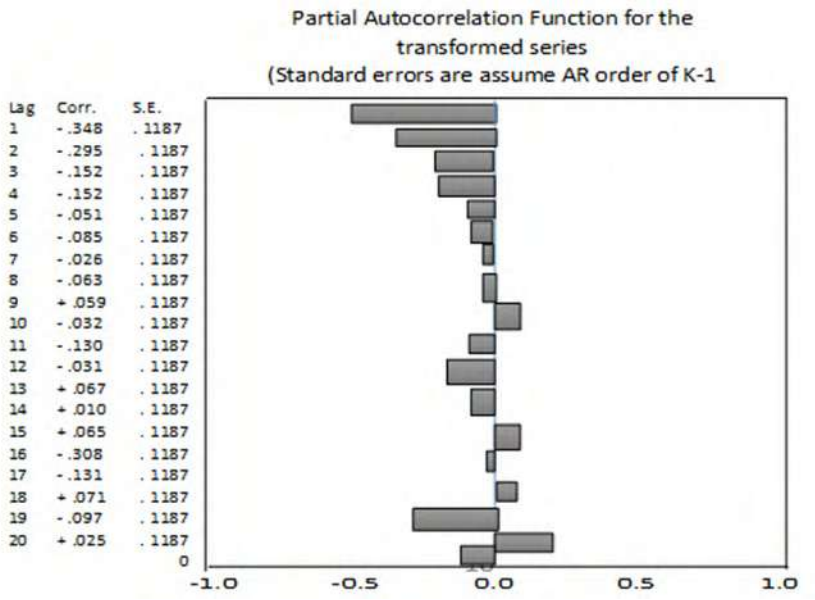

Figure(9) the partial self-correlation function for the converted data

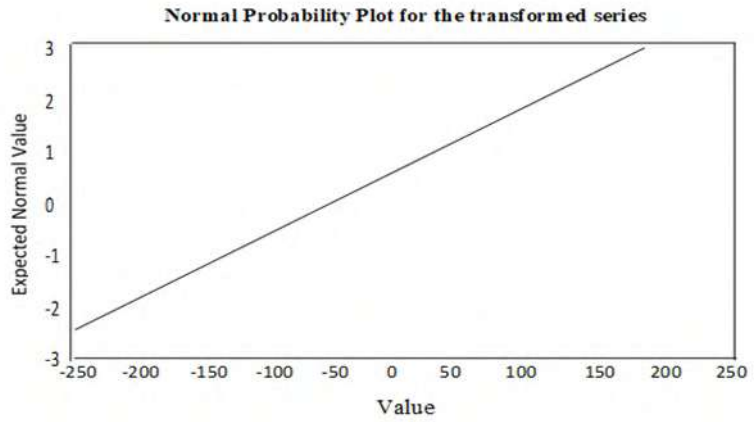

Figure(10) Charting the natural of the transferred data

As for the shapes (6), (7) and (8), the represents the drawing of the self and partial correlation function and the nature drawing, as we note that the serial data are not correlated and where we observe more than 12% of the self-correlation coefficients that are outside the constraint $\pm\frac{1.92}{\sqrt{n}}$ but they are close to the natural distribution.

Depending on the graphical description and correlation function diagram, we have noticed that the series possesses periodic, characteristics and irregular cycle swhich enables us to use non -Liner models to represent the series.

Since the model we have is a polynomial model, since:

$$y_t = \sum_{j=1}^{p} \propto_j [cos\left(\frac{\pi}{2} y_{t-1}\right)]^j + Z_t$$

We will try to construct models form the first anal second ranks to demonstrate the stability of the model above using relationships obtained in the hypothetical side of the previous paragraphs.

let p = l be in the form above:

$y_t = \propto_1 cos\left(\frac{\pi}{2} y_{t-1}\right) + Z_t$

Using the Mathlab program, we obtained the following form:

$y_t = 0.0811\ cos\left(\frac{\pi}{2} y_{t-1}\right) + Z_t$

$\sigma_z^2 = 0.1476576$

$NBIC = -1.83249$

And when p = 2 that is:

$y_t = \propto_1 cos\left(\frac{\pi}{2} y_{t-1}\right) + \propto_2 (cos\ (\frac{\pi}{2} y_{t-1}))^2 + Z_t$

We obtained the following form:

$y_t = 0.0798\ cos\left(\frac{\pi}{2} y_{t-1}\right) + 0.0373\ (cos\ (\frac{\pi}{2} y_{t-1}))^2 + Z_t$

$\sigma_z^2 = 0.1722664$

$NBIC = -1.545764$

4.4 Stability

In this paragraph, we will attempt to apply the relationships (single Point and Limit cycle stability) obtained in the theoretical side of the models that were constructed to represent the studied sequence.

EXAMPLE 4.4.1 Polynomial regression model of the first order

That is:

$y_1 = 0.0622\ cos\left(\frac{\pi}{2} y_{t-1}\right) + Z_t$

Where as:

$\sigma_z^2 = 0.168576$

$NBIC = -1.842783$

$\propto = 0.0822$

i.The single Point

of the above model is by using the relationship (14) is:

$\in = 0.06018272$

ii. single point stability:

Using relationship (16), we get the following form:

$\in_1 = -0.0348714\ \in_{t-1}$

It is a first-order self – regression model and the characteristic equation for the model is:

$v + 0.0348714 = 0$

That is $\lambda = -0.0348714$ is the root of the equation, and it is clear that the above model is stable because $|\lambda| < 1$

iii. Limit cycle stability:

The higher model has a stable orbital limit cycle if the condition is met:

$\left|\frac{\in_{t+q}}{\in_t}\right| < 1$

From the relationship (16) and the hypotheses in that paragraph we obtained:

$\in_t = A\ \in_{t-1}$

From which we obtain:

$c = -0.0348625$

Therefore, the condition for the model to have a stable limit cycle is $|C^q| < 1$, and since $|C| < 1$ the amount $|C^q| < 1$ is fulfilled for all values $q > 1$

So the model has a limit – cycles

EXAMPLE 4.4.2The polynomial regression model of the second-order that is:

$y_t = 0.0876\ cos\left(\frac{\pi}{2} y_{t-1}\right) + 0.0373(cos\ cos\left(\frac{\pi}{2} y_{t-1}\right))^2 + Z_t$

Whereas:

$\sigma_z^2 = 0.1512664$
$NBIC = -1.444782$
$\propto_1 = 0.0876$
$\propto_2 = 0.0474$
i.The single Point of the above model is by using the relationship (14) is:
$\in = 0.12848034$
ii. The stability of a single point using the relationship (16), we get the following model:
$\in_t = -0.108305263 \ \in_{t-1}$
It is a second-order subjective regression model, and the characteristic equation for the model is:
$v + 0.108305263 = 0$
That is $\lambda = -0.108305263$
The root of the equation it is clear that the model is stable above because $|\lambda| < 1$
iii. Stability limit cycle the above form have Stability limit cycle if the condition is true:
$\left|\frac{\in_{t+9}}{\in_t}\right| < 1$
It is a relationship(16) and hypotheses we get .
$\in_t = A \in_{t-1}$
From them we get.
C= -0.108305263
And so it is condition of stability limit cycle $|C^q| < 1$
Since the $|C| < 1$ the value $|C^q| < 1$ all values will be fulfilled q> 1 so the model has stability limit cycle

References

[1] Al-Bid R and Dhafer R 2002 Study on the diagnosis of systems of control with special reference to the method of space for the state and decision *PhD Thesis* Mosul University, Iraq
[2] Al-Obeidi and Abdul G S 1989 Analysis and modelling of the temperature chain in Mosul City *MSc Thesis* University of Mosul, Iraq
[3] Al- Ajili and Sondos N 2002 Building an incident model of tuberculosis infection in Salah Al-ddin governorate (1989-2000) *MSc Thesis*, University of Tikrit, Iraq
[4] Al-Azzawi and Adel A 2009 applying the emergency model to the global wheat price chain *MSc Thesis* University of Mosul, Iraq
[5] Al-Mahdawi, Haifa J 1991 "unstable, higher-grade self-regression *PhD Thesis* University of Mustansiriya, Iraq
[6] Chatfield C 1982 The analysis of time series: An introduction (2nd Ed) (Chapman and Hall)London
[7] Chen S and S A Billings 1989 Modelling and analysis of non- linear time series University of Southampton
[8] Ozaki T 1980 Nonlinear Time-series Model for Nonlinear Random Vibrations *J. APP. Prob.* **17** 84-93
[9] Ozaki T 1985 Nonlinear Time-series Models and Dynamical system *E.J. Hannan, P. R. krishnaiah, M, M. Rao, eds.*(Handbook of statistics) **5** 25-83
[10] Ozaki T 1982 Nonlinear Time-series Stochastic Processes and Dynamical system (Handbook of Statistics) **5** ltd
[11] Priestley M B 1981 Spectral Analysis and Time Series volume 1 Univariate Series (Academic Press.Inc.) London
[12] Tong H 1990 Nonlinear Time series; A Dynamical system Approach (Oxford University Press) London
[13] Wen S 2015 Introduction to Ordinary and Partial Differential Equations (Spring)

[14] William F T 2013 ELEMENTARY DIFFERENTIAL EQUATIONS WIYH BOUNDARY VALUE PROBLEM (New-york)
[15] Kawther A N 2019 NUMERICAL ANALYSIS &METHODS USING MATLAB, IRAQ

Generalized Projectivity and *Generalized Projectivity

Generalized Projectivity and *Generalized Projectivity

Mukdad Qaess Hussain[1], Ammar Saied Rasheed[1]

College of Education for pure science, Diyala University, Iraq

E-mail: mukdadqaess2016@yahoo.com

Abstract. Let R be a Ring with identity and let T be a unitary left Module over R. In this paper, we recall the concepts of generalized projectivity and *generalized projectivity. These types of projectivity are very useful for the study on direct sums of Modules to be semihollow-lifting.

1. Introduction

A Submodule H of an R-Module S is small Submodule of S ($H \ll S$) if for every Submodule D of S such that $S = H + D$ implies $D = S$[1]. A Submodule H of an R-Module S is semismall of S ($H \ll_S S$) if H = 0 or $H/F \ll S/F$ $\forall$ nonzero Submodule F of H[2]. Let S be an R-Module and H, F be Submodules of S such that $F \subset H \subset S$. F is semicoessential Submodule of H in S ($F \subseteq_{sce} H$ in S) if $\frac{H}{F} \ll_S \frac{S}{F}$[3]. An R-Module S is semihollow-lifting if for every Submodule H of S with $\frac{S}{H}$ hollow, there exists a Submodule F of S such that $S = F \oplus F^*$ and $F \subseteq_{sce} H$ in S[4].

A Module K is said to be generalized L-projective (or L cojective) if, for any epimorphism $g: L \to X$ and any homomorphism $f: K \to X$, there exist decompositions $K = K_1 \oplus K_2$, $L = L_1 \oplus L_2$, a homomorphism $h_1: K_1 \to L_1$ and an epimorphism $h_2: L_2 \to K_2$ such that $g \circ h_1 = f|K1$ and $f \circ h_2 = g|L_2$ [5].

That is, K is generalized L-projective if any diagram

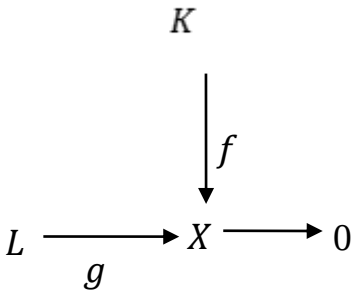

Can be imbedded in a diagram

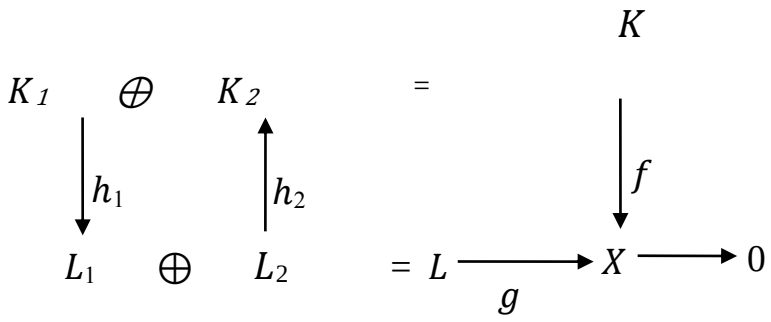

Such that h_2 is onto, $g \circ h_1 = f|K_1$ and $f \circ h_2 = g|L_2$.
The following proposition gives properties of the generalized projectivity. ■

Proposition1: [5] Let K and L be Modules with K is generalized L-projective, Thus for any direct summand L^* of L , the Module K is generalized L^*-projective.

We need the following lemma.

Lemma2: Let S= K⊕L and let L be a semihollow-lifting Module. If K is generalized L-projective, then for any Submodule N of S with $\frac{S}{N}$ hollow and S = N+L, there exists $N' \subseteq_{sce} N$ in S with $K' \subseteq K$ and $L' \subseteq L$ such that $S = N' \oplus K' \oplus L'$.

Proof: Let N be a Submodule of S with $\frac{S}{N}$ hollow and S = N+L. By second isomorphism theorem, $\frac{S}{N} = \frac{N+L}{N} \cong \frac{L}{N\cap L}$ and hence $\frac{L}{N\cap L}$ is hollow. Then by [6,Th.1], there exists a decomposition $L = L_1 \oplus L_2$ s.t $L_2 \subseteq N \cap L$ and $(N \cap L) \cap L_1 = N \cap L_1 \ll_S L_1$. S= N+L = N+L_1+L_2 = N+L_1. Since S = K⊕L, thus S = K⊕ $L_1 \oplus L_2$. By modular law, $N = N \cap S = N \cap (K \oplus L_1 \oplus L_2) = (N \cap (K \oplus L_1)) \oplus L_2$. Let A = K⊕ L_1, thus $N = (A \cap N) \oplus L_2$. Since S = N+$L_1$ and $L_1 \subseteq$ A, then $A = A \cap (N+L_1) = (A \cap N)+L_1$. Since K is generalized L-projective and L_1 is a direct summand of L, Then by Prop.1, K is generalized L_1-projective. But A= $K \oplus L_1$ and $A = (A \cap N)+L_1$, therefore there exists a decomposition $A = T \oplus K' \oplus L'_1 = T+L_1$ with $T \subseteq A \cap N$, $K' \subseteq K$ and $L'_1 \subseteq L_1$. Since $T \subseteq A \cap N$, $L_2 \subseteq$N and $T \cap L_2 = 0$, thus $L_2 \oplus T \subseteq N$. Now, S = N+L_1 = $(A \cap N)+L_2+L_1 = A+ L_2 = (T+L_2)+L_1$. Since S = $(T+L_2)+L_1$ and $N \cap L_1 \ll_S L_1$, thus by [2], $(T \oplus L_2) \subseteq_{sce}$ N in S. Since S = K⊕L = (K⊕L_1)⊕ L_2 and A = K ⊕ L_1, then $S = A \oplus L_2 = T \oplus K' \oplus L'_1 \oplus L_2$. Then S = $(T \oplus L_2) \oplus K' \oplus L'_1$, where $(T \oplus L_2) \subseteq_{sce}$ N in S, $K' \subseteq$ K and $L'_1 \subseteq$ L.

In the following proposition we give conditions to obtain the direct sum of two Modules is semihollow-lifting.

Proposition3: Let S = K⊕ L be a Module, where K is generalized L-projective and L is semihollow-lifting. If for every Submodule N of S with $\frac{S}{N}$ is hollow, S ≠ K+N. Then S is semihollow-lifting.

Proof: Let N be a Submodule of S s.t $\frac{S}{N}$ is hollow. Thus S ≠ K+N. Now, $\frac{S}{N} = \frac{K\oplus L}{N} = \frac{K+N}{N} + \frac{L+N}{N}$. Since $\frac{S}{N}$ is hollow, thus either $\frac{K+N}{N} = \frac{S}{N}$ or $\frac{L+N}{N} = \frac{S}{N}$. But S ≠ K+N, therefore $\frac{L+N}{N} = \frac{S}{N}$ and hence S = L+N. Since K is generalized L-projective and L is semihollow-lifting, thus by Lemma2, there exists $N' \subseteq_{sce} N$ in S, with $K' \subseteq$ K and $L' \subseteq$ L s.t $S = N' \oplus K' \oplus L'$. Then S is a semihollow-lifting Module.

Let T_1 and T_2 be R-Modules, recall that T_1 is h-semismall T_2- projective if every homomorphism $g: T_1 \rightarrow \frac{T_2}{W}$,(where W is a Submodule of T_2), $\frac{T_2}{W}$ is hollow and Im $g \ll_s \frac{T_2}{W}$ can be lifted to a homomorphism φ: $T_1 \rightarrow T_2$[7].

Proposition4: Let S = K⊕L has (D3). If L is a semihollow-lifting Module and K is generalized L-projective then K is h-semismall L-projective.

Proof: Let N be a Submodule of S s.t $\frac{S}{N}$ is hollow and S ≠ K+N. But, $\frac{S}{N} = \frac{K\oplus L}{N} = \frac{K+N}{N} + \frac{L+N}{N}$, therefore N $\subseteq_{sce}$ (K+N) in S and hence S = L+N. Since K is generalized L-projective and L is semihollow-lifting, thus by Lemma2, there exists N′ $\subseteq_{sce}$ N in S with K′⊆ K and L′⊆ L s.t S = N′⊕ K′⊕ L′. Since $\frac{S}{N}$ is semihollow, thus by [3,Prop.7], $\frac{S}{N'}$ is a semihollow Module. Now, $\frac{S}{N'} = \frac{L+N}{N'} = \frac{L+N'}{N'} + \frac{N}{N'}$. But N′ $\subseteq_{sce}$ N in *S*, therefore S = L + N′. Since *S* has (D_3) and L, N′ are direct summands of *S*, then L ∩ N′ is a direct summand of *S*. Since L ∩ N′⊆ N′, thus N′ = (L ∩ N′) ⊕ A, for some A ⊆ N′. Hence S = L+N′ = L+ ((L ∩ N′) ⊕ A) . this implies that S = L ⊕ A. Then K is h-semismall L-projective.

Lemma5: [8] If *S* = K + N, where K and N are supplemented Modules. Then S is supplemented, and any Submodule X of S has a supplement of the form K′ + N′ with K′ ⊆ K and N′ ⊆ N.

Assume that X is a supplement Submodule of S, thus K′ and X + N′ are mutual supplements in S and the same is true for N′ and X + K′.

Now, we prove the following proposition.

Proposition 6 : Let S = K⊕L, where K and L are supplemented Modules and L is semihollow-lifting. If K is generalized L-projective, then for every coclosed Submodule X of S such that $\frac{S}{X}$ is hollow, there exists a Submodule N of S such that either S = N ⊕ K″ or S = N ⊕ L″, where K″ ⊆ K and L″⊆ L and N $\subseteq_{ce}$ H in S such that H is a supplement Submodule in S and X ⊆ H.

Proof: Let X be a coclosed Submodule of S s.t $\frac{S}{X}$ is hollow. Since K and L are supplemented Modules, thus by Lemma 5, S is supplemented and X has a supplement K′⊕ L′, where K′ ⊆ K and L′ ⊆ L. Since S is supplemented, thus by [9, Lemma1.1], the coclosed Submodules are supplements. Then X is a supplement Submodule of S. By Lemma5, X+K′ and X+L′ are supplement Submodules of S, also X + K′ and L′ are mutual supplements in S. Thus S = (X+K′)+L′ and hence S = (X+K′)+L. Since $\frac{S}{X}$ is hollow, thus by [3,prop3], $\frac{S}{X+K'}$ is semihollow. But K is generalized L-projective and L is semihollow-lifting, so by Lemma2, there exists a Submodule N of *S* s.t N $\subseteq_{sce}$ (X+K′) in *S* and S = N⊕K″⊕ L″ , for some K″⊆ K and L″⊆ L. Let H = X+K′. Since $\frac{S}{H}$ is hollow, thus by [3,prop7], $\frac{S}{N}$ is semihollow. But by second isomorphism theorem, $\frac{S}{N} \cong K''\oplus L''$, therefore either K″ = 0 or L″ = 0. Thus either *S* = N ⊕ K″ or *S* = N ⊕ L″, where N $\subseteq_{sce}$ H, H is a supplement Submodule of *S* and X ⊆ H.

Let S = K⊕ L. Then K is *generalized L-projective (or L-*cojective), if for any supplement N of L in S, S decomposes as S = N ⊕ K′⊕ L′, with K′⊆ K and L′⊆ L[5].

The following proposition gives properties of *generalized projectivity.

Proposition 7: [10] Let L^* be a direct summand of L. If K is *generalized L-projective, thus K is *generalized L^*-projective.

Proposition 8: Let S = K⊕L be a Module, where K is *generalized L-projective and L is semihollow-lifting. If X $\subseteq_{scc}$ S such that $\frac{S}{X}$ is hollow with *S* = X+L, then *S* is decomposes S = X ⊕ K′⊕ L′ with K′ ⊆ K and L′ ⊆ L.

Proof: Let X be a semicoclosbmodule of S s.t $\frac{S}{X}$ is hollow with S = X+L. By the second isomorphism theorem, $\frac{S}{X} = \frac{X+L}{X} \cong \frac{L}{X\cap L}$. Then $\frac{L}{X\cap L}$ is hollow.Since L is semihollow-lifting, thus by [6.Th.1], there exists a decomposition $L = L_1 \oplus L_2$ s.t $L_1 \subseteq X \cap L$ and $(X \cap L)\cap L_2 \ll_S L_2$ and hence $X \cap L_2 \ll_S L_2$. Since $S = K \oplus L$, thus $S = K \oplus L_1 \oplus L_2$. Let $N = K \oplus L_2$, thus $S = N \oplus L_1$. By modular law, $X = X \cap (N \oplus L_1) = (X \cap N) \oplus L_1$, thus $X = X_1 \oplus L_1$, where $X_1 = X \cap N$. Since S = X+L, thus $S = X+L_1+L_2 = X+L_2$. Again by modular law, $N = N \cap (X+L_2) = (N \cap X)+L_2$, hence $N = X_1+L_2$. Since $X \cap L_2 \ll_S L_2$, thus $X_1 \cap L_2 \ll_S L_2$. Then L_2 is a semisupplement of X_1 in N, since X_1 is a direct summand of X and $X \subseteq_{cc} S$, thus by [10, Lemma 2.3], $X_1 \subseteq_{cc} S$. Since $X_1 \cap L_2 \ll_S S$ and $X_1 \subseteq_{cc} S$, then by [2], $X_1 \cap L_2 \ll_S X_1$ and hence X_1 is a semisupplement of L_2 in N. But K is *generalized L-projective and L_2 is a direct summand of L, thus by Prop.7, K is *generalized L_2-projective. Since X_1 is a semisupplement of L_2 in N, thus $N = X_1 \oplus K' \oplus L'_2$, where $K' \subseteq K$ and $L'_2 \subseteq L_2$. But $S = N \oplus L_1$, therefore $S = X_1 \oplus K' \oplus L'_2 \oplus L_1$ and hence $S = X_1 \oplus L_1 \oplus K' \oplus L'_2$. Since $X = X_1 \oplus L_1$, thus $S = X \oplus K' \oplus L'_2$ with $K' \subseteq K$ and $L'_2 \subseteq L$.
Remark9[11] Every hollow module is amply supplemented.
Proposition10[9] Let S be an amply supplemented Module. Thus every Submodule of S has a coclosure Submodule.

Proposition 11: [9] Let S be a weakly supplemented Module and $K \subseteq N$ be Submodules of S such that $\frac{N}{K} \subseteq_{scc} \frac{S}{K}$ and $K \subseteq_{scc} S$. Then $N \subseteq_{scc} S$.

Proposition12[11] Epimorphic image of hollow Module is hollow.

The following propositions give properties of Modules which have hollow factor Modules.

Proposition 13 **:** Let S be an R-Module, and let K and N be Submodules of S such that $K \subset N \subset S$, if $\frac{S}{K}$ is a hollow Module, thus $\frac{S}{N}$ hollow.

Proof: Suppose that $\frac{S}{K}$ is hollow, define a map f: $\frac{S}{K} \to \frac{S}{N}$ as follows $f(s+K) = s+N$, for all $s \in S$. It is clear that f is an epimorphism. Since $\frac{S}{K}$ is hollow thus by Prop.12, $\frac{S}{N}$ is hollow.

Proposition 14: Let $S = K \oplus L$ be a weakly supplemented R-Module, where K is *generalized L-projective and L is semihollow-lifting. Then for any semicoclosed Submodule X of S such that $\frac{S}{X}$ is hollow, either $S = X \oplus K'$ or $S = X \oplus L'$ where $K' \subseteq K$ and $L' \subseteq L$.

Proof**:** Let X be a semicoclosed Submodule of S s.t $\frac{S}{X}$ is hollow. Then by Remark9, $\frac{S}{X}$ is amply supplemented.Then by Prop.10, $\frac{K+X}{X}$ has a semicoclosure in $\frac{S}{X}$. That is, there exists a semicoclosed Submodule $\frac{N}{X}$ in $\frac{S}{X}$ s.t $\frac{N}{X} \subseteq_{sce} \frac{K+X}{X}$ in $\frac{S}{X}$. Thus by the third isomorphism theorem, $N \subseteq_{sce} (K+X)$ in S. Since $X \subseteq_{scc} S$ and $\frac{N}{X} \subseteq_{scc} \frac{S}{X}$ and S is a weakly supplemented Module, thus $N \subseteq_{scc} S$. Since $N \subseteq_{ce} (K+X)$ in S, thus $K+X \neq S$. But $\frac{S}{X} = \frac{K\oplus L}{X} = \frac{K+X}{X} + \frac{L+X}{X}$, therefore, $X \subseteq_{ce} (K+X)$ in S, thus S = L+X this implies that S = L+N. Since $\frac{S}{X}$ is hollow and $X \subseteq N$ thus by Prop.13, $\frac{S}{N}$ is hollow. But K is *generalized L-projective and L is semihollow-lifting, thus by Prop.8, S decomposes as $S = N \oplus K' \oplus L'$, with $K' \subseteq K$ and $L' \subseteq L$. Then by the second isomorphism theorem, $\frac{S}{N} \cong K' \oplus L'$. But $\frac{S}{N}$

is hollow, therefore, either $K' = 0$ or $L' = 0$. Thus either $S = N \oplus K'$ or $S = N \oplus L'$. If $S = N \oplus K'$, thus $\frac{S}{X} = \frac{N \oplus K'}{X} = \frac{N}{X} \oplus \frac{K' \oplus X}{X}$. Since $\frac{S}{X}$ is hollow, thus $X \subseteq_{ce} N$ in S, then $S = X \oplus K'$, where $K' \subseteq K$.
By the similar way, if $S = N \oplus L'$ then $S = X \oplus L'$, where $L' \subseteq L$.

References

[1] F.Kasch 1982 Modules and rings *Academic Press*. London
[2] Mahmood L. S., Shihab B. N.and Khalaf H. Y. 2015 Semihollow modules and semilifting modules *International Journal of Advanced Scientific and Technical* 375-382
[3] Hussain M. Q. 2017 SemiHollow Factor Modules *23 scientific conference of the college of Education Al-mustansiriya university* 350-355
[4] Salih M. A., Hussen N. A.and Hussain M. Q. 2019 SemiHollow-Lifting Module *Revista Aus* **26(4)** 222-227
[5] S. H. Mohamed and B.J. Müller 2004 Cojective modules *Egyptian J. Math*. **12** 83-96
[6] Mansour I. A., Qasem M. R., Salih M. A. and Hussain M. Q. 2019 Characterizations of semihollow-Lifting Modules *Revista Aus* **26** 249-257
[7] Dheyab A. H., Kadhim Z. J. and Hussain M. Q. Direct Sum and Projectivity of SemiHollow-Lifting Modules 1 st*International Conference of Pure and Engineering Science. Iraqi Academic Syndicate, Kerbala*
[8] Clark J., Lomp C., Vanaja N. and Wisbauer R. 2006 Lifting modules Frontiers *Mathematics, Birkhäuser*
[9] Keskin D. 2000 On lifting modules, Comm. Algebra, **28(7)** 3427-3440
[10] Dejun W. 2006 On direct sums of lifting modules and internal exchange property *Kyngpook J. Math.* **46** 11-18
[11] Payman M.H. 2005 Hollow modules and semihollow modules *M.Sc., Thesis, University of Baghdad*

Equivalence of Some Iterations for Class of Quasi Contractive Mappings

Equivalence of Some Iterations for Class of Quasi Contractive Mappings

Zena Hussein Maibed [1,*] and Ali Qasem Thajil [1]

[1]Department of Mathematics, College of Education for Pure Sciences Ibn-Al-Haitham, University of Baghdad, Baghdad, Iraq

E-mail:mrs_ zena.hussein@yahoo.com

Abstract. In this article, we recalled different types of iterations as Mann, Ishikawa, Noor, CR-iteration and, Modified $\mathcal{SP}$_iteration of quasi δ-contraction mappings, and we proved that all these iterations equivalent to approximate fixed points of δ -contraction mappings in Banach spaces.

1. Introduction:

The iterations methods are used to calculate a non-expansive mapping fixed point. Many of applied science and engineering's physical problems are commonly formulated as functional equations. These equations can conveniently be written in the form of fixed-point equations. An iterative method that approximates the solution of these equations in fewer stages is always needed. At the heart of systematic research, activity was the analysis of variational inequalities and complementarity concerns of mappings meeting those constraints. In view, fact that problems of variational inequalities are particularly useful in optimization theory, which can be found by solving an equation with some special type of nonlinear function for various forms of mappings, several studies are dealing with iterative methods, see[1-12], so it is very important to develop some faster Iterative process to find the approximate solution. Now we give some well- known Iteration methods.

The Mann iterative scheme was invented in 1953, see [13], and was used to obtain convergence to a fixed point for many functions for which the Banach principle fails. For example, the author showed that, for any continuous self map of a closed and bounded interval, the Mann iteration converges to a fixed point of the function. In 1974, Ishikawa [14] devised a new iteration scheme to establish convergence for a Lipschitzian pseudo contractive map in a situation where the Mann iteration process failed to converge. Let $(X, \|.\|)$ be a Banach space, $\mathcal{T}$ be self -mapping on $\mathcal{C}$ and $\emptyset \neq \mathcal{C}$ be a closed convex subset of X. we recalled different types of iterations as Mann, Ishikawa, Noor, CR- iteration and Modified $\mathcal{SP}$_iteration respectively:

1. Let $r_0 \in \mathcal{C}$ $r_{n+1} = (1 - a_n)r_n + a_n \mathcal{T} r_n , n \in N$, where $\langle a_n \rangle_{n=0}^{\infty}$ be a sequence in $(0, 1)$.
2. Let $c_0 \in \mathcal{C}$, $c_{n+1} = (1 - a_n)c_n + a_n \mathcal{T} d_n$,
$d_n = (1 - b_n)c_n + b_n \mathcal{T} c_n$, $n \in N$, where $\langle a_n \rangle_{n=0}^{\infty}$ and $\langle b_n \rangle_{n=0}^{\infty}$be a sequence in $(0, 1)$.
3. The third iteration process is referred to as Noor, in 2000 [15] introduced the following iterative
$u_0 \in \mathcal{C}$, $u_{n+1} = (1 - a_n)u_n + a_n \mathcal{T} q_n$,
$q_n = (1 - b_n)u_n + b_n \mathcal{T} p_n$,
$p_n = (1 - c_n)u_n + c_n \mathcal{T} u_n$, n $\in N$
where $\langle a_n \rangle_{n=0}^{\infty}$, $\langle b_n \rangle_{n=0}^{\infty}$ and $\langle c_n \rangle_{n=0}^{\infty}$ are sequences in $(0, 1)$.

4. The fourth CR- iteration, in 2012 [16] introduced the following iterative ,
   $k_0 \in \mathcal{C}$, $k_{n+1} = (1 - a_n)m_n + a_n \mathcal{T}m_n$,
   $m_n = (1 - b_n)\mathcal{T}k_n + b_n \mathcal{T}\mathcal{O}_n$
   $\mathcal{O}_n = (1 - c_n)k_n - c_n \mathcal{T}k_n$, where $\langle a_n\rangle_{n=0}^{\infty}$, $\langle b_n\rangle_{n=0}^{\infty}$and $\langle c_n\rangle_{n=0}^{\infty}$ are sequences in $(0, 1)$.
5. The fifth Modified $\mathcal{SP}$_iteration, in 2014 [17] introduced the following iterative,
   $d_0 \in \mathcal{C}$, $d_{n+1} = \mathcal{T}t_n$,
   $t_n = (1 - a_n)s_n + a_n \mathcal{T}s_n$,
   $s_n = (1 - b_n)d_n + b_n \mathcal{T}d_n$
   where $\langle a_n\rangle_{n=0}^{\infty}$ and $\langle b_n\rangle_{n=0}^{\infty}$ are sequences in $(0, 1)$.

1.1 Lemma:[18]
Let $\langle \tilde{a}_n\rangle_{n=0}^{\infty}$ and $\langle \tilde{b}_n\rangle_{n=0}^{\infty}$ be nonnegative real sequences satisfying the following condition:
$\tilde{a}_{n n+1} \le (1 - \mu_n)\tilde{a}_n + \tilde{b}_n$, where $\mu_n \in (0,1)$, for all $n \ge n_0$, $\sum_{n=1}^{\infty} \mu_n = \infty$ and $\frac{\tilde{b}_n}{\mu_n} \to 0$ as $n \to \infty$. Then $\lim_{n \to \infty} \tilde{a}_n = 0$.

1.2 Lemma:[19]
Let $\langle x_n\rangle_{n=0}^{\infty}$ be nonnegative real sequences and there exists $n_0 \in \mathbb{N}$, such that for all $a_n \ge n_0$ satisfying the following condition:
$x_{n+1} \le (1 - \mu_n)x_n + \mu_n a_n$,
Where $\mu_n \in (0,1)$ for all $n \in \mathbb{N}$, $\sum_{n=1}^{\infty} \mu_n = \infty$. Then the following inequality holds:
$0 \le \lim_{n \to \infty} \sup x_n \le \lim_{n \to \infty} \sup a_n$.

1.3 Definition:[20]
Let $(\mathcal{N}, \|\,.\,\|)$ be a normed space and $\mathcal{T}$ be self - mapping on $\mathcal{N}$. Then $\mathcal{T}$ is called quasi δ −contraction if satisfy the following inequality: For all $x, y \in \mathcal{N}$
$\|\mathcal{T}x - \mathcal{T}y\| \le \delta\|x - y\| + L m(x, y)$,for some $0 \le \delta < 1$, $L \ge 0$, where
$m(x, y) = \min\{\|x - \mathcal{T}x\|, \|y - \mathcal{T}y\|, \|x - \mathcal{T}y\|, \|y - \mathcal{T}x\|\}$.

1.4 Definition:[21]
Let $\langle a_n\rangle_{n=0}^{\infty}$ and $\langle b_n\rangle_{n=0}^{\infty}$ be two sequences converging to the same fixed point p . We say that $\langle a_n\rangle_{n=0}^{\infty}$ converges faster than $\langle b_n\rangle_{n=0}^{\infty}$ if $\lim_{n \to \infty} \frac{\|a_n - p\|}{\|b_n - p\|} = 0$.

2. Main Results

During this section, .we will study the convergence equivalent between many iterations by using quasi δ –contraction.

2.1 Theorem: Let $\mathcal{T}$ a quasi δ -contraction mapping on $\mathcal{C}$ which has a unique fixed point p . Consider the Ishikawa and Mann iterations with real sequences $\langle a_n\rangle_{n=0}^{\infty}, \langle b_n\rangle_{n=0}^{\infty}$ lies in $[0, 1]$. Then the following assertions are equivalent :

i. The Mann iteration converges to p .
ii. The Ishikawa iteration converges to p.

Proof: To show that (i) ⇒ (ii) .i.e, if the Mann iteration converges to p then the Ishikawa iteration does converge to p too.
Now Consider Mann and The Ishikawa iterations, we have

$$\begin{aligned} \|r_{n+1} - c_{n+1}\| &= \|(1 - a_n)r_n + a_n \mathcal{T}r_n - (1 - a_n)c_n - a_n \mathcal{T}d_n\| \\ &\le (1 - a_n)\|r_n - c_n\| + a_n\|\mathcal{T}r_n - \mathcal{T}d_n\| \\ &\le (1 - a_n)\|r_n - c_n\| + \delta a_n\|r_n - d_n\| + a_n L m(r_n, d_n) \end{aligned} \quad (2.1)$$

And,

$$\begin{aligned}\|r_n - d_n\| &= \|r_n - (1-b_n)c_n - b_n\mathcal{T}c_n\| \\ &\le (1-b_n)\|r_n - c_n\| + b_n\|r_n - \mathcal{T}c_n\| \\ &\le (1-b_n)\|r_n - c_n\| + b_n\|r_n - \mathcal{T}r_n\| + \delta b_n\|r_n - c_n\| + b_n L m(r_n, c_n) \quad (2.2)\end{aligned}$$

Substituting (2.2) in (2.1), we obtain

$$\begin{aligned}\|r_{n+1} - c_{n+1}\| &\le (1-a_n)\|r_n - c_n\| + \delta a_n(1-b_n)\|r_n - c_n\| + \delta a_n b_n\|r_n - \mathcal{T}r_n\| \\ &\quad + \delta^2 a_n b_n\|r_n - c_n\| + \delta a_n b_n L m(r_n, c_n) + a_n L m(r_n, d_n) \\ &\le [1 - a_n + \delta a_n(1-b_n) + \delta a_n b_n]\|r_n - c_n\| + \delta a_n\|r_n - \mathcal{T}r_n\| \\ &\quad + \delta a_n L m(r_n, c_n) + a_n L m(r_n, d_n) \\ &\le [1 - a_n(1 - \delta(1-b_n) - \delta b_n)]\|r_n - c_n\| + \delta a_n b_n\|r_n - \mathcal{T}r_n\| \\ &\quad + \delta a_n b_n L m(r_n, c_n) + a_n L m(r_n, d_n) \\ &\le [1 - a_n(1 - \delta(1 - b_n + b_n))]\|r_n - c_n\| + \delta a_n\|r_n - \mathcal{T}r_n\| \\ &\quad + \delta a_n L m(r_n, c_n) + a_n L m(r_n, d_n) \\ &\le [1 - a_n(1-\delta)]\|r_n - c_n\| + \delta a_n\|r_n - \mathcal{T}r_n\| + \delta a_n L m(r_n, c_n) + a_n L m(r_n, d_n)\end{aligned}$$

Since $\delta \in (0,1)$ and $[a_n(1-\delta)] < 1$, we have

$$\begin{aligned}\|r_{n+1} - c_{n+1}\| &\le [1 - a_n(1-\delta)]\|r_n - c_n\| + \delta a_n\|r_n - \mathcal{T}r_n\| \\ &\quad + \delta a_n L \min\{\|r_n - \mathcal{T}r_n\|, \|c - \mathcal{T}c_n\|, \|d_n - \mathcal{T}c_n\|, \|r - \mathcal{T}r_n\|\} \\ &\quad + a_n L \min\{\|r_n - \mathcal{T}r_n\|, \|d - \mathcal{T}d_n\|, \|r_n - \mathcal{T}d_n\|, \|d_n - \mathcal{T}r_n\|\}\end{aligned}$$

Let $\mu_n = a_n(1-\delta) \in (0,1)$

$\tilde{a}_n = \|r_n - c_n\|$, $\tilde{b}_n = \delta a_n\|r_n - \mathcal{T}r_n\| + \delta a_n L \min\{\|r_n - \mathcal{T}r_n\|, \|c - \mathcal{T}c_n\|, \|d_n - \mathcal{T}c_n\|, \|r - \mathcal{T}r_n\|\} + a_n L \min\{\|r_n - \mathcal{T}r_n\|, \|d - \mathcal{T}d_n\|, \|r_n - \mathcal{T}d_n\|, \|d_n - \mathcal{T}r_n\|\}$

Furthermore using $\mathcal{T}p = p$ and $\|r_n - p\| \to 0$, we have

$$\begin{aligned}\|r_n - \mathcal{T}r_n\| &= \|r_n - p + \mathcal{T}p - \mathcal{T}r_n\| \\ &\le \|r_n - p\| + \delta\|r_n - p\| + L m(r_n, p) \\ &= (1+\delta)\|r_n - p\| + L\min\{\|r_n - \mathcal{T}r_n\|, \|p - \mathcal{T}p\|, \|r_n - \mathcal{T}p\|, \|p - \mathcal{T}r_n\|\}\end{aligned}$$

Therefore $\|r_n - \mathcal{T}r_n\| \to 0$. So, we get $\check{b}_n \to 0$,

Now, by applying lemma (1.1), we obtain

$\check{a}_n = \|r_n - c_n\| \to 0$ as $n \to 0$.

Consequently ;

$\|r_{n+1} - c_{n+1}\| \to 0$ as $n \to 0$

Now we show that, (ii) ⇒ (i)

$$\begin{aligned}\|c_{n+1} - r_{n+1}\| &\le \|c_{n+1} - p\| + \|r_{n+1} - p\| \\ &= \|(1-a_n)c_n + a_n\mathcal{T}d_n - p\| + \|(1-a_n)r_n + a_n\mathcal{T}r_n - p\| \\ &\le (1-a_n)\|c_n - p\| + \delta a_n\|d_n - p\| + a_n L m(d_n, p) \\ &\quad + (1-a_n)\|r_n - p\| + \delta a_n\|r_n - p\| + a_n L m(r_n, p) \\ &\le (1-a_n)\|c_n - p\| + \delta a_n\|d_n - p\| + a_n L m(d_n, p) \\ &\quad + (1 - a_n(1-\delta))\|r_n - p\| + a_n L m(r_n, p) \quad (2.3)\end{aligned}$$

And,

$$\begin{aligned}\|d_n - p\| &= \|(1-b_n)c_n + b_n Tc_n - p\| \\ &\le (1-b_n)\|c_n - p\| + \delta b_n\|c_n - p\| + b_n L m(c_n, p) \\ &= (1 - b_n(1-\delta))\|c_n - p\| + b_n L m(c_n, p) \quad (2.4)\end{aligned}$$

Substituting (2.4) in (2.3), we obtain

$$\begin{aligned}\|c_{n+1} - r_{n+1}\| &\le (1-a_n)\|c_n - p\| + a_n L m(d_n, p) \\ &\quad + \delta a_n(1 - b_n(1-\delta))\|c_n - p\| + \delta a_n b_n L m(c_n, p) \\ &\quad + (1 - a_n(1-\delta))\|r_n - p\| + a_n L m(r_n, p) \\ \|c_{n+1} - r_{n+1}\| &\le (1-a_n) + \delta a_n\|c_n - r_n + r_n - p\| + a_n L m(d_n, p) \\ &\quad + \delta a_n L m(c_n, p) + (1 - a_n(1-\delta))\|r_n - p\| + a_n L m(r_n, p)\end{aligned}$$

$$\leq (1-a_n(1-\delta)\|c_n-p\|+a_nLm(d_n,p)$$
$$+\delta a_nLm(c_n,p)+(1-a_n(1-\delta))\|r_n-p\|+a_nLm(r_n,p)$$

Since $\delta\in(0,1)$ and $[a_n(1-\delta)]<1$, we have

$$\|c_{n+1}-r_{n+1}\| \leq (1-a_n(1-\delta)\|c_n-r_n\|+(1-a_n(1-\delta))^2\|r_n-p\|$$
$$+\delta a_nL\min\{\|c_n-\mathcal{T}c_n\|,\|p-\mathcal{T}p\|,\|p-\mathcal{T}c_n\|,\|c_n-\mathcal{T}p\|\}$$
$$+a_nL\min\{\|d_n-\mathcal{T}d_n\|,\|p-\mathcal{T}p\|,\|p-\mathcal{T}d_n\|,\|d_n-\mathcal{T}p\|\}$$
$$+a_nL\min\{\|r_n-\mathcal{T}r_n\|,\|p-\mathcal{T}p\|,\|r_n-\mathcal{T}p\|,\|p-\mathcal{T}r_n\|\}$$

Denote that $\mu_n=a_n(1-\delta)\in(0,1)$

$\check{a}_n=\|c_n-r_n\|$ and $\check{b}_n=(1-a_n(1-\delta))^2\|r_n-p\|$
$$+\delta a_nL\min\{\|c_n-\mathcal{T}c_n\|,\|p-\mathcal{T}p\|,\|p-\mathcal{T}c_n\|,\|c_n-\mathcal{T}p\|\}$$
$$+a_nL\min\{\|d_n-\mathcal{T}d_n\|,\|p-\mathcal{T}p\|,\|p-\mathcal{T}d_n\|,\|d_n-\mathcal{T}p\|\}$$
$$+a_nL\min\{\|r_n-\mathcal{T}r_n\|,\|p-\mathcal{T}p\|,\|r_n-\mathcal{T}p\|,\|p-\mathcal{T}r_n\|\}$$

Thus from lemma (1.1), we get

$\check{a}_n=\|c_n-r_n\|\to 0$ as $n\to 0$. Therefore,

$\|c_{n+1}-r_{n+1}\|\to 0$ as $n\to 0$.

2.2 Theorem: Let $\mathcal{T}$ a quasi δ -contraction mapping on $\mathcal{C}$ which has a unique fixed point p. Consider the Modified $\mathcal{SP}$_iteration and Mann iteration with real sequences $\langle a_n\rangle_{n=0}^{\infty},\langle b_n\rangle_{n=0}^{\infty}$ lies in $(0,1)$. Then the following assertions are equivalent :

i. The Mann iteration converges to p .

ii. The Modified $\mathcal{SP}$_iteration converges to p.

Proof. To show that (i) ⇒ (ii. i.e., if the Mann iteration converges to p then The Modified $\mathcal{SP}$_iteration does converge to p too. Now Consider Mann and The Modified $\mathcal{SP}$_iterations, we have

$$\|r_{n+1}-d_{n+1}\| = \|(1-a_n)r_n+a_n\mathcal{T}r_n-\mathcal{T}t_n\|$$
$$\leq (1-a_n)\|r_n-\mathcal{T}t_n\|+a_n\|\mathcal{T}r_n-\mathcal{T}t_n\|$$
$$\leq (1-a_n)\|r_n-\mathcal{T}r_n\|+\delta(1-a_n)\|r_n-t_n\|$$
$$+(1-a_n)Lm(r_n,t_n)+\delta a_n\|r_n-t_n\|+a_nLm(r_n,t_n)$$
$$=(1-a_n)\|r_n-\mathcal{T}r_n\|+\delta\|r_n-t_n\|+Lm(r_n,t_n) \quad (2.5)$$

And

$$\|r_n-t_n\| = \|r_n-(1-a_n)s_n-a_n\mathcal{T}s_n\|$$
$$\leq (1-a_n)\|r_n-s_n\|+a_n\|r_n-\mathcal{T}s_n\|+\delta a_n\|r_n-s_n\|+a_nLm(r_n,s_n)$$
$$\leq (1-a_n)\|r_n-s_n\|+a_n\|r_n-\mathcal{T}r_n\|$$
$$\leq (1-a_n(1-\delta))\|r_n-s_n\|+a_n\|r_n-\mathcal{T}r_n\|+a_nLm(r_n,s_n) \quad (2.6)$$

And,

$$\|r_n-s_n\| = \|r_n-(1-b_n)d_n-b_n\mathcal{T}d_n\|$$
$$\leq (1-b_n)\|r_n-d_n\|+b_n\|r_n-\mathcal{T}d_n\|$$
$$\leq (1-b_n)\|r_n-d_n\|+b_n\|r_n-\mathcal{T}r_n\|+\delta b_n\|r_n-d_n\|+b_nLm(r_n,s_n)$$
$$\leq (1-b_n(1-\delta))\|r_n-d_n\|+b_n\|r_n-\mathcal{T}r_n\|+b_nLm(r_n,d_n) \quad (2.7)$$

Substituting (2.7) in (2.6), we obtain

$$\|r_n-t_n\| \leq (1-a_n(1-\delta))[(1-b_n(1-\delta))\|r_n-d_n\|$$
$$+b_n\|r_n-\mathcal{T}r_n\|+b_nLm(r_n,d_n)]+a_n\|r_n-\mathcal{T}r_n\|+a_nLm(r_n,s_n)$$
$$\leq (1-b_n(1-\delta))\|r_n-d_n\|+a_nLm(r_n,s_n)$$
$$+b_n\|r_n-\mathcal{T}r_n\|+b_nLm(r_n,d_n)+a_n\|r_n-\mathcal{T}r_n\| \quad (2.8)$$

Substituting (2.8) in (2.5), we obtain

$$\|r_{n+1}-d_{n+1}\| \leq (1-a_n)\|r_n-\mathcal{T}r_n\|+Lm(r_n,t_n)$$
$$+\delta[(1-b_n(1-\delta))\|r_n-d_n\|+b_nLm(r_n,d_n)$$

$$+ a_n\|r_n - \mathcal{T}r_n\| + a_nLm(r_n, s_n)]$$
$$\leq (1 - b_n(1-\delta))\|r_n - d_n\| + (1 - a_n)\|r_n - \mathcal{T}r_n\|$$
$$+a_nL\min\{\|r_n - \mathcal{T}r_n\|, \|s - \mathcal{T}s_n\|, \|r_n - \mathcal{T}s_n\|, \|s - \mathcal{T}r_n\|\}$$
$$+b_nL\min\{\|r_n - \mathcal{T}r_n\|, \|d - \mathcal{T}d_n\|, \|r_n - \mathcal{T}d_n\|, \|d_n - \mathcal{T}r_n\|\}$$
$$+L\min\{\|r_n - \mathcal{T}r_n\|, \|t_n - \mathcal{T}t_n\|, \|r_n - \mathcal{T}t_n\|, \|t_n - \mathcal{T}r_n\|\}$$

Denote that

$\mu_n = b_n(1-\delta) \in (0,1)$, $\check{a}_n = \|r_n - d_n\|$ and $\check{b}_n = (1 - a_n)\|r_n - \mathcal{T}r_n\|$
$+a_nL\min\{\|r_n - \mathcal{T}r_n\|, \|s - \mathcal{T}s_n\|, \|r_n - \mathcal{T}s_n\|, \|s - \mathcal{T}r_n\|\}$
$+b_nL\min\{\|r_n - \mathcal{T}r_n\|, \|d - \mathcal{T}d_n\|, \|r_n - \mathcal{T}d_n\|, \|d_n - \mathcal{T}r_n\|\}$
$+L\min\{\|r_n - \mathcal{T}r_n\|, \|t_n - \mathcal{T}t_n\|, \|r_n - \mathcal{T}t_n\|, \|t_n - \mathcal{T}r_n\|\}$

Furthermore using $\mathcal{T}p = p$ and $\|r_n - p\| \to 0$, we have

$$\|r_n - \mathcal{T}r_n\| = \|r_n - p + \mathcal{T}p - \mathcal{T}r_n\|$$
$$\leq \|r_n - p\| + \delta\|r_n - p\| + Lm(r_n, p)$$
$$= (1+\delta)\|r_n - p\| + L\min\{\|r_n - \mathcal{T}r_n\|, \|p - \mathcal{T}p\|, \|r_n - \mathcal{T}p\|, \|p - \mathcal{T}r_n\|\}$$

Then $\|r_n - \mathcal{T}r_n\| \to 0$. Because of these results we get $b_n \to 0$, by applying lemma (1.1),
we obtain $\check{a}_n = \|r_n - d_n\| \to 0$ as $n \to 0$.
Consequently ; $\|r_{n+1} - d_{n+1}\| \to 0$ as $n \to 0$
Now we show that, (ii) ⇒ (i)

$$\|d_{n+1} - r_{n+1}\| \leq \|d_{n+1} - p\| + \|r_{n+1} - p\|$$
$$= \|\mathcal{T}t_n - p\| + \|(1 - a_n)r_n + a_n\mathcal{T}r_n - p\|$$
$$\leq \delta\|t_n - p\| + Lm(t_n, p) + (1 - a_n)\|r_n - p\|$$
$$+ \delta a_n\|r_n - p\| + a_nLm(r_n, p)$$
$$\leq \delta\|t_n - p\| + Lm(t_n, p) + a_nLm(r_n, p)$$
$$+(1 - a_n(1-\delta))\|r_n - p\| \quad (2.9)$$

And,

$$\|t_n - p\| = \|(1 - a_n)s_n + a_nTs_n - p\|$$
$$\leq (1 - a_n)\|s_n - p\| + \delta a_n\|s_n - p\| + a_nLm(s_n, p)$$
$$= (1 - a_n(1-\delta))\|s_n - p\| + a_nLm(s_n, p) \quad (2.10)$$

And,

$$\|s_n - p\| = \|(1 - b_n)d_n + b_nTd_n - p\|$$
$$\leq (1 - b_n)\|d_n - p\| + \delta b_n\|d_n - p\| + b_nLm(d_n, p)$$
$$= (1 - b_n(1-\delta))\|d_n - p\| + b_nLm(d_n, p) \quad (2.11)$$

Substituting (2.11) in (2.10), we obtain

$$\|t_n - p\| \leq (1 - a_n(1-\delta))[(1 - b_n(1-\delta))\|d_n - p\| + b_nLm(d_n, p)] + a_nLm(s_n, p)$$
$$\leq (1 - b_n(1-\delta))\|d_n - p\| + b_nLm(d_n, p) + a_nLm(s_n, p) \quad (2.12)$$

Substituting (2.12) in (2.9), we obtain

$$\|d_{n+1} - r_{n+1}\| \leq \delta[(1 - b_n(1-\delta))\|d_n - p\| + b_nLm(d_n, p)$$
$$+a_nLm(s_n, p)] + Lm(t_n, p) + a_nLm(r_n, p) + (1 - a_n(1-\delta))\|r_n - p\|$$
$$\leq \delta[(1 - b_n(1-\delta))(\|d_n - r_n\| + \|r_n - p\|) + b_nLm(d_n, p)$$
$$+a_nLm(s_n, p)] + Lm(t_n, p) + a_nLm(r_n, p) + (1 - a_n(1-\delta))\|r_n - p\|$$
$$\|d_{n+1} - r_{n+1}\| \leq (1 - b_n(1-\delta))\|d_n - r_n\| + (1 - a_n(1-\delta))\|r_n - p\|$$
$$+(1 - b_n(1-\delta))\|r_n - p\| + a_nLm(s_n, p) + Lm(t_n, p)$$
$$+a_nLm(r_n, p) + b_nLm(d_n, p)$$

Denote that:

$\mu_n = b_n(1-\delta) \in (0,1)$, $\check{a}_n = \|d_n - r_n\|$ and
$\check{b}_n = (1 - a_n(1-\delta))\|r_n - p\| + (1 - b_n(1-\delta))\|r_n - p\| + a_nLm(s_n, p)$
$+Lm(t_n, p) + a_nLm(r_n, p) + b_nLm(d_n, p)$

Thus from lemma (1.1), we get

$\check{a}_n = \|d_n - r_n\| \to 0$ as $n \to 0$ as a result of these inequalities,

$\|d_{n+1} - r_{n+1}\| \to 0$ as $n \to 0$.

2.3 Theorem: Let $\mathcal{T}$ a quasi δ -contraction mapping on $\mathcal{C}$ which has a unique fixed point $\mathcal{p}$. Consider the CR iteration and Mann iteration with real sequences $\langle a_n\rangle_{n=0}^{\infty}$, $\langle b_n\rangle_{n=0}^{\infty}$, $\langle c_n\rangle_{n=0}^{\infty}$ lies in $[0,1]$ .Then the following assertions are equivalent :

i.The Mann iteration converges to $\mathcal{p}$.

ii. The CR iteration converges to $\mathcal{p}$.

Proof. To show that (i) ⇒ (i, that is if the Mann iteration converges to $\mathcal{p}$ then The CR iteration does converge to $\mathcal{p}$ too. Now Consider Mann and The CR iterations, we have

$$\begin{aligned}\|r_{n+1} - k_{n+1}\| &= \|(1-a_n)r_n + a_n\mathcal{T}r_n - (1-a_n)m_n - a_n\mathcal{T}m_n\| \\ &\le (1-a_n)\|r_n - m_n\| + a_n\|\mathcal{T}r_n - \mathcal{T}m_n\| \\ \|r_{n+1} - k_{n+1}\| &\le (1-a_n)\|r_n - m_n\| + \delta a_n\|r_n - m_n\| + a_n L\mathcal{m}(r_n, m_n) \\ &= \big(1 - a_n(1-\delta)\big)\|r_n - m_n\| + a_n L\mathcal{m}(r_n, m_n) \qquad (2.13)\end{aligned}$$

And,

$$\begin{aligned}\|r_n - m_n\| &= \|r_n - (1-b_n)\mathcal{T}k_n + b_n\mathcal{T}o_n\| \\ &\le (1-b_n)\|r_n - \mathcal{T}k_n\| + b_n\|r_n - \mathcal{T}o_n\| \\ &\le (1-b_n)\|r_n - \mathcal{T}r_n\| + \delta(1-b_n)\|r_n - k_n\| + (1-b_n)L\mathcal{m}(r_n, k_n) \\ &\quad + b_n\|r_n - \mathcal{T}r_n\| + \delta b_n\|r_n - o_n\| b_n L\mathcal{m}(r_n, o_n) \\ &= \|r_n - \mathcal{T}r_n\| + \delta(1-b_n)\|r_n - k_n\| \\ &\quad +(1-b_n)L\mathcal{m}(r_n, k_n) + \delta b_n\|r_n - o_n\| + b_n L\mathcal{m}(r_n, o_n) \qquad (2.14)\end{aligned}$$

And,

$$\begin{aligned}\|r_n - o_n\| &= \|r_n - (1-c_n)k_n - c_n\mathcal{T}k_n\| \\ &\le (1-c_n)\|r_n - k_n\| + c_n\|r_n - \mathcal{T}k_n\| \\ &\le (1-c_n)\|r_n - k_n\| + c_n\|r_n - \mathcal{T}r_n\| + \delta c_n\|r_n - k_n\| + c_n L\mathcal{m}(r_n, k_n) \\ &\le \big(1 - c_n(1-\delta)\big)\|r_n - k_n\| + c_n\|r_n - \mathcal{T}r_n\| + c_n L\mathcal{m}(r_n, k_n) \qquad (2.15)\end{aligned}$$

Substituting (2.15) in (2.14), we obtain

$$\begin{aligned}\|r_n - m_n\| \le\ & \|r_n - \mathcal{T}r_n\| + \delta(1-b_n)\|r_n - k_n\| + (1-b_n)L\mathcal{m}(r_n, k_n) \\ & +\delta b_n\big(1 - c_n(1-\delta)\big)\|r_n - k_n\| + \delta b_n c_n\|r_n - \mathcal{T}r_n\| \\ & +\delta b_n c_n L\mathcal{m}(r_n, k_n) + b_n L\mathcal{m}(r_n, o_n) \qquad (2.16)\end{aligned}$$

Substituting (2.16)in (2.13), we obtain

$$\begin{aligned}\|r_{n+1} - k_{n+1}\| \le\ & \big(1 - a_n(1-\delta)\big)[\|r_n - \mathcal{T}r_n\| + \delta(1-b_n)\|r_n - k_n\| + (1-b_n)L\mathcal{m}(r_n, k_n) \\ & + \delta b_n\big(1 - c_n(1-\delta)\big)\|r_n - k_n\| + \delta b_n c_n\|r_n - \mathcal{T}r_n\| \\ & +\delta b_n c_n L\mathcal{m}(r_n, k_n) + b_n L\mathcal{m}(r_n, o_n)] + a_n L\mathcal{m}(r_n, m_n)\end{aligned}$$

Since $\delta \in (0,1)$ and $\big(1 - a_n(1-\delta)\big) < 1$, we have

$$\begin{aligned}\|r_{n+1} - k_{n+1}\| &\le (1 - a_n(1-\delta))\|r_n - \mathcal{T}r_n\| + \big[(1-b_n) + \delta b_n\big(1 - c_n(1-\delta)\big)\big]\|r_n - k_n\| \\ &\quad +(1-b_n)L\mathcal{m}(r_n, k_n) + b_n L\mathcal{m}(r_n, k_n) + b_n L\mathcal{m}(r_n, o_n) + a_n L\mathcal{m}(r_n, m_n) \\ &\le ((1 - a_n(1-\delta))\|r_n - \mathcal{T}r_n\| + [(1-b_n) + \delta b_n]\|r_n - k_n\| \\ &\quad +L\mathcal{m}(r_n, k_n) + b_n L\mathcal{m}(r_n, o_n) + a_n L\mathcal{m}(r_n, m_n) \\ &\le [(1 - b_n(1-\delta)]\|r_n - k_n\| + ((1 - a_n(1-\delta))\|r_n - \mathcal{T}r_n\| \\ &\quad +L\min\{\|r_n - \mathcal{T}r_n\|, \|k - \mathcal{T}k_n\|, \|r_n - \mathcal{T}k_n\|, \|k - \mathcal{T}r_n\|\} \\ &\quad +b_n L\min\{\|r_n - \mathcal{T}r_n\|, \|o_n - \mathcal{T}o_n\|, \|r_n - \mathcal{T}o_n\|, \|o_n - \mathcal{T}r_n\|\} \\ &\quad +a_n L\min\{\|r_n - \mathcal{T}r_n\|, \|m_n - \mathcal{T}m_n\|, \|r_n - \mathcal{T}m_n\|, \|m_n - \mathcal{T}r_n\|\}\end{aligned}$$

Let $\mu_n = a_n(1-\delta) \in (0,1)$, $\check{a}_n = \|r_n - k_n\|$ and

$\check{b}_n = (1 - a_n(1-\delta))\|r_n - \mathcal{T}r_n\| + L\min\{\|r_n - \mathcal{T}r_n\|, \|k - \mathcal{T}k_n\|, \|r_n - \mathcal{T}k_n\|, \|k - \mathcal{T}r_n\|\}$

$$+b_nL\min\{\|r_n-\mathcal{T}r_n\|,\|o_n-\mathcal{T}o_n\|,\|r_n-\mathcal{T}o_n\|,\|o_n-\mathcal{T}r_n\|\}$$
$$+a_nL\min\{\|r_n-\mathcal{T}r_n\|,\|m_n-\mathcal{T}m_n\|,\|r_n-\mathcal{T}m_n\|,\|m_n-\mathcal{T}r_n\|\}$$

Furthermore using $\mathcal{T}p=p$ and $\|r_n-p\|\to 0$, we have

$$\begin{aligned}\|r_n-\mathcal{T}r_n\| &= \|r_n-p+\mathcal{T}p-\mathcal{T}r_n\|\\ &\le \|r_n-p\|+\delta\|r_n-p\|+Lm(r_n,p)\\ &= (1+\delta)\|r_n-p\|+L\min\{\|r_n-\mathcal{T}r_n\|,\|p-\mathcal{T}p\|,\|r_n-\mathcal{T}p\|,\|p-\mathcal{T}r_n\|\}\end{aligned}$$

Then $\|r_n-\mathcal{T}r_n\|\to 0$. By applying lemma (1.1), we obtain

$a_n=\|r_n-k_n\|\to 0$ as $n\to 0$.

Consequently ; $\|r_{n+1}-k_{n+1}\|\to 0$ as $n\to 0$

Now we show that, (ii) ⇒ (i)

$$\begin{aligned}\|k_{n+1}-r_{n+1}\| &= \|k_{n+1}-p\|+\|r_{n+1}-p\|\\ &= \|(1-a_n)m_n+a_n\mathcal{T}m_n-p\|+\|(1-a_n)r_n+a_n\mathcal{T}r_n-p\|\\ &\le (1-a_n)\|m_n-p\|+\delta a_n\|m_n-p\|+a_nLm(m_n,p)\\ &\quad+(1-a_n)\|r_n-p\|+\delta a_n\|r_n-p\|+a_nLm(r_n,p)\\ &= (1-a_n(1-\delta))\|m_n-p\|+a_nLm(m_n,p)+\big(1-a_n(1-\delta)\big)\|r_n-p\|\\ &\quad+Lm(r_n,p)\end{aligned}\tag{2.17}$$

And

$$\begin{aligned}\|m_n-p\| &= \|(1-b_n)Tk_n+b_nTo_n-p\|\\ &\le \delta(1-b_n)\|k_n-p\|+(1-b_n)Lm(k_n,p)+\delta b_n\|o_n-p\|\\ &\quad+b_nLm(o_n,p)\end{aligned}\tag{2.18}$$

And

$$\begin{aligned}\|o_n-p\| &= \|(1-c_n)k_n+c_nTk_n-p\|\\ &\le (1-c_n)\|k_n-p\|+\delta c_n\|k_n-p\|+c_nLm(k_n,p)\\ &= (1-c_n(1-\delta))\|k_n-p\|+c_nLm(k_n,p)\end{aligned}\tag{2.19}$$

Substituting (2.19) in (2.18), we obtain

$$\begin{aligned}\|m_n-p\| &\le \delta(1-b_n)\|k_n-p\|+(1-b_n)Lm(k_n,p)\\ &\quad+\delta b_n\big(1-c_n(1-\delta)\big)\|k_n-p\|+\delta b_nc_nLm(k_n,p)+b_nLm(o_n,p)\end{aligned}\tag{2.20}$$

Substituting (2.20) in (2.17), we obtain

$$\begin{aligned}\|k_{n+1}-r_{n+1}\| &\le (1-a_n(1-\delta))[\delta(1-b_n)\|k_n-p\|+(1-b_n)Lm(k_n,p)\\ &\quad+b_nLm(o_n,p)+\delta b_n(1-c_n(1-\delta))\|k_n-p\|+\delta b_nc_nLm(k_n,p)]\\ &\quad+a_nLm(m_n,p)+\big(1-a_n(1-\delta)\big)\|r_n-p\|+a_nLm(r_n,p)\\ &\le \big(1-a_n(1-\delta)\big)\|r_n-k_n+k_n-p\|+(1-a_n(1-\delta))[\delta(1-b_n)\|k_n-p\|\\ &\quad+(1-b_n)Lm(k_n,p)+b_nLm(o_n,p)+\delta b_n\big(1-c_n(1-\delta)\big)\|k_n-p\|\\ &\quad+\delta b_nc_nLm(k_n,p)]+a_nLm(m_n,p)+a_nLm(r_n,p)\\ &\le \big(1-a_n(1-\delta)\big)\|r_n-k_n\|+[\big(1-a_n(1-\delta)\big)\delta(1-b_n)\\ &\quad+\delta b_n(1-c_n(1-\delta))]\|k_n-p\|+(1-b_n)Lm(k_n,p)+b_nLm(o_n,p)\\ &\quad+\delta b_nc_nLm(k_n,p)]+a_nLm(m_n,p)+a_nLm(r_n,p)\end{aligned}$$

Denote that

$\mu_n=a_n(1-\delta)\in(0,1)$, $\check{a}_n=\|r_n-k_n\|$ and

$$\begin{aligned}\check{b}_n &= [\big(1-a_n(1-\delta)\big)\delta(1-b_n)+\delta b_n(1-c_n(1-\delta))]\|k_n-p\|\\ &\quad+(1-b_n)Lm(k_n,p)+b_nLm(o_n,p)+\delta b_nc_nLm(k_n,p)]+a_nLm(m_n,p)+a_nLm(r_n,p)\end{aligned}$$

Thus from lemma (1.1), $\check{a}_n=\|r_n-k_n\|\to 0$ as $n\to 0$

Therefore, $\|k_{n+1}-r_{n+1}\|\to 0$ as $n\to 0$.

2.4 Theorem: Let $\mathcal{T}$ a quasi δ -contraction mapping on $\mathcal{C}$ which has a unique fixed point p . Consider the Noor iteration and Mann iteration with real sequences $\langle a_n\rangle_{n=0}^{\infty}$, $\langle b_n\rangle_{n=0}^{\infty}$, $\langle c_n\rangle_{n=0}^{\infty}$ lies in$[0,1]$ .Then the following assertions are equivalent :

i. The Mann iteration converges to $\mathcal{p}$.

ii. The Noor iteration converges to $\mathcal{p}$.

Proof. To show that (i) ⇒ (ii), that is if the Mann iteration converges to $\mathcal{p}$, then The Noor iteration does converge to $\mathcal{p}$ too. Now Consider Mann and The Noor iterations, we have

$$\begin{aligned}\|r_{n+1}-u_{n+1}\| &= \|(1-a_n)r_n + a_n\mathcal{T}r_n-(1-a_n)u_n-a_n\mathcal{T}q_n\|\\ &\le (1-a_n)\|r_n-u_n\| + \delta a_n\|r_n-q_n\| + a_nL\mathcal{m}(r_n,q_n) \qquad (2.21)\\ \|r_n-q_n\| &= \|r_n-(1-b_n)u_n-b_n\mathcal{T}p_n\|\\ &\le (1-b_n)\|r_n-u_n\| + b_n\|r_n-\mathcal{T}p_n\|\\ &\le (1-b_n)\|r_n-u_n\| + b_n\|r_n-\mathcal{T}r_n\| + \delta b_n\|r_n-p_n\| + b_nL\mathcal{m}(r_n,p_n) \qquad (2.22)\\ \|r_n-p_n\| &= \|r_n-(1-c_n)u_n-c_n\mathcal{T}u_n\|\\ &\le (1-c_n)\|r_n-u_n\| + c_n\|r_n-\mathcal{T}u_n\|\\ &\le (1-c_n)\|r_n-u_n\| + c_n\|r_n-\mathcal{T}r_n\| + \delta c_n\|r_n-u_n\| + c_nL\mathcal{m}(r_n,u_n)\\ &\le \big(1-c_n(1-\delta)\big)\|r_n-u_n\| + c_n\|r_n-\mathcal{T}r_n\| + c_nL\mathcal{m}(r_n,u_n) \qquad (2.23)\end{aligned}$$

Substituting (2.23) in (2.22), we obtain

$$\begin{aligned}\|r_n-q_n\| &\le (1-b_n)\|r_n-u_n\| + b_n\|r_n-\mathcal{T}r_n\|\\ &\quad +\delta b_n[(1-c_n(1-\delta))\|r_n-u_n\| + c_n\|r_n-\mathcal{T}r_n\|\\ &\quad +c_nL\mathcal{m}(r_n,u_n)] + b_nL\mathcal{m}(r_n,p_n)\\ &= (1-b_n)\|r_n-u_n\| + b_n\|r_n-\mathcal{T}r_n\| + \delta b_n\big(1-c_n(1-\delta)\big)\|r_n-u_n\|\\ &\quad +\delta b_nc_n\|r_n-\mathcal{T}r_n\| + \delta b_nc_nL\mathcal{m}(r_n,u_n) + \delta b_nL\mathcal{m}(r_n,p_n)\\ \|r_n-q_n\| &\le ((1-b_n)+\delta b_n)\|r_n-u_n\| + (b_n+\delta b_nc_n)\|r_n-\mathcal{T}r_n\|\\ &\quad +\delta b_nc_nL\mathcal{m}(r_n,u_n) + \delta b_nL\mathcal{m}(r_n,p_n)\\ &\le \big((1-b_n(1-\delta))\|r_n-u_n\| + (b_n+\delta b_nc_n)\|r_n-\mathcal{T}r_n\|\\ &\quad +\delta b_nc_nL\mathcal{m}(r_n,u_n) + \delta b_nL\mathcal{m}(r_n,p_n) \qquad (2.24)\end{aligned}$$

Substituting (2.24) in (2.21), we obtain

$$\begin{aligned}\|r_{n+1}-u_{n+1}\| &\le (1-a_n)\|r_n-u_n\| + \delta a_n\big((1-b_n(1-\delta))\|r_n-u_n\|\\ &\quad +(b_n+\delta b_nc_n)\|r_n-\mathcal{T}r_n\| + \delta b_nc_nL\mathcal{m}(r_n,u_n) + \delta b_nL\mathcal{m}(r_n,p_n)\\ &\quad +a_nL\mathcal{m}(r_n,q_n)\\ \|r_{n+1}-u_{n+1}\| &\le \Big((1-a_n)+\delta a_n\big((1-b_n(1-\delta))\big)\Big)\|r_n-u_n\|\\ &\quad +(b_n+\delta b_nc_n)\|r_n-\mathcal{T}r_n\| + \delta b_nc_nL\mathcal{m}(r_n,u_n) + \delta b_nL\mathcal{m}(r_n,p_n)\\ &\quad +a_nL\mathcal{m}(r_n,q_n)\\ &\le \big((1-a_n)+\delta a_n\big)\|r_n-u_n\| + (b_n+\delta c_n)\|r_n-\mathcal{T}r_n\|\\ &\quad +\delta b_nc_nL\mathcal{m}(r_n,u_n) + \delta b_nL\mathcal{m}(r_n,p_n) + a_nL\mathcal{m}(r_n,q_n)\\ &\le ((1-a_n(1-\delta))\|r_n-u_n\| + (b_n+\delta c_n)\|r_n-\mathcal{T}r_n\|\\ &\quad +\delta b_nc_nL\min\{\|r_n-\mathcal{T}r_n\|,\|u_n-\mathcal{T}u_n\|,\|r_n-\mathcal{T}u_n\|,\|u_n-\mathcal{T}r_n\|\}\\ &\quad +\delta b_nL\min\{\|r_n-\mathcal{T}r_n\|,\|p_n-\mathcal{T}p_n\|,\|r_n-\mathcal{T}p_n\|,\|p_n-\mathcal{T}r_n\|\}\\ &\quad +a_nL\min\{\|r_n-\mathcal{T}r_n\|,\|q_n-\mathcal{T}q_n\|,\|r_n-\mathcal{T}q_n\|,\|q_n-\mathcal{T}r_n\|\}\end{aligned}$$

Let $\mu_n = a_n(1-\delta) \in (0,1)$, $\check{a}_n = \|r_n-u_n\|$ and

$$\begin{aligned}\check{b}_n &= (b_n+\delta c_n)\|r_n-\mathcal{T}r_n\|\\ &\quad +\delta b_nc_nL\min\{\|r_n-\mathcal{T}r_n\|,\|u_n-\mathcal{T}u_n\|,\|r_n-\mathcal{T}u_n\|,\|u_n-\mathcal{T}r_n\|\}\\ &\quad +\delta b_nL\min\{\|r_n-\mathcal{T}r_n\|,\|p_n-\mathcal{T}p_n\|,\|r_n-\mathcal{T}p_n\|,\|p_n-\mathcal{T}r_n\|\}\\ &\quad +a_nL\min\{\|r_n-\mathcal{T}r_n\|,\|q_n-\mathcal{T}q_n\|,\|r_n-\mathcal{T}q_n\|,\|q_n-\mathcal{T}r_n\|\}\end{aligned}$$

Furthermore using $\mathcal{T}\mathcal{p}=\mathcal{p}$ and $\|r_n-\mathcal{p}\| \to 0$, we have

$$\begin{aligned}\|r_n-\mathcal{T}r_n\| &= \|r_n-\mathcal{p}+\mathcal{T}\mathcal{p}-\mathcal{T}r_n\|\\ &\le \|r_n-\mathcal{p}\| + \delta\|r_n-\mathcal{p}\| + L\mathcal{m}(r_n,\mathcal{p})\\ &= (1+\delta)\|r_n-\mathcal{p}\| + L\min\{\|r_n-\mathcal{T}r_n\|,\|\mathcal{p}-\mathcal{T}\mathcal{p}\|,\|r_n-\mathcal{T}\mathcal{p}\|,\|\mathcal{p}-\mathcal{T}r_n\|\}\end{aligned}$$

Then $\|r_n-\mathcal{T}r_n\| \to 0$. Because of these results we get, $\check{b}_n \to 0$, by applying lemma (1.1),

We obtain $\check{a}_n = \|r_n - u_n\| \to 0$ as $n \to 0$.
Consequently ;
$\|r_{n+1} - u_{n+1}\| \to 0$ as $n \to 0$
Now we show that, (ii) ⇒ (i)

$$\begin{aligned}\|u_{n+1} - r_{n+1}\| &= \|u_{n+1} - p\| + \|r_{n+1} - p\| \\ &= \|(1 - a_n)u_n + a_n \mathcal{T} q_n - p\| + \|(1 - a_n)r_n + a_n \mathcal{T} r_n - p\| \\ &\le (1 - a_n)\|u_n - p\| + \delta a_n \|q_n - p\| + a_n L m(q_n, p) \\ &\quad + (1 - a_n)\|r_n - p\| + \delta a_n \|r_n - p\| + a_n L m(r_n, p) \\ &= (1 - a_n)\|u_n - p\| + \delta a_n \|q_n - p\| + a_n L m(q_n, p) \\ &\quad + \big(1 - a_n(1 - \delta)\big)\|r_n - p\| + a_n L m(r_n, p) \end{aligned} \quad (2.25)$$

And,

$$\begin{aligned}\|q_n - p\| &= \|(1 - b_n)u_n + b_n T p_n - p\| \\ &\le (1 - b_n)\|u_n - p\| + \delta b_n \|p_n - p\| + b_n L m(p_n, p)\end{aligned} \quad (2.26)$$

And,

$$\begin{aligned}\|p_n - p\| &= \|(1 - c_n)u_n + c_n T u_n - p\| \\ &\le (1 - c_n)\|u_n - p\| + \delta c_n \|u_n - p\| + c_n L m(u_n, p) \\ &= (1 - c_n(1 - \delta))\|u_n - p\| + c_n L m(u_n, p)\end{aligned} \quad (2.27)$$

Substituting (2.27) in (2.26), we obtain

$$\begin{aligned}\|q_n - p\| &\le (1 - b_n)\|u_n - p\| + b_n L m(p_n, p) + \delta b_n c_n L m(u_n, p) + \delta b_n \|u_n - p\| \\ &= [1 - b_n + \delta b_n (1 - c_n(1 - \delta))]\|u_n - p\| \\ &\quad + b_n L m(p_n, p) + \delta b_n c_n L m(u_n, p)\end{aligned} \quad (2.28)$$

Substituting (2.28) in (2.25) , we obtain

$$\begin{aligned}\|u_{n+1} - r_{n+1}\| &\le (1 - a_n)\|u_n - p\| + \delta a_n([1 - b_n + \delta b_n]\|u_n - p\| \\ &\quad + b_n L m(p_n, p) + \delta b_n c_n L m(u_n, p)) + a_n L m(q_n, p) \\ &\quad + \big(1 - a_n(1 - \delta)\big)\|r_n - p\| + a_n L m(r_n, p) \\ \|u_{n+1} - r_{n+1}\| &\le (1 - a_n(1 - \delta)\|u_n - r_n + r_n - p\| \\ &\quad + b_n L m(p_n, p) + \delta b_n c_n L m(u_n, p)) + a_n L m(q_n, p) \\ &\quad + \big(1 - a_n(1 - \delta)\big)\|r_n - p\| + a_n L m(r_n, p) \\ &\le (1 - a_n(1 - \delta)\|u_n - r_n\| + b_n L m(p_n, p) + \delta b_n c_n L m(u_n, p)) \\ &\quad + a_n L m(q_n, p) + \big(1 - a_n(1 - \delta)\big)^2 \|r_n - p\| + a_n L m(r_n, p)\end{aligned}$$

Let $\mu_n = a_n(1 - \delta) \in (0, 1)$
$\check{a}_n = \|u_n - r_n\|$

$$\check{b}_n = \big(1 - a_n(1 - \delta)\big)^2 \|r_n - p\| + a_n L m(r_n, p) + b_n L m(p_n, p) + \delta b_n c_n L m(u_n, p)) + a_n L m(q_n, p)$$

Thus from lemma(1.1), we get
$\tilde{a}_n = \|u_n - r_n\| \to 0$ as $n \to 0$. So,
$\|u_{n+1} - r_{n+1}\| \to 0$ as $n \to 0$.

References

[1] Mabeed Z 2011 Strongly Convergence Theorems of Ishikawa Iteration Process With Errors in Banach Space *Journal of Qadisiyah Computer Science and Mathematics* **3** pp 1-8
[2] Maibed Z 2019 New Algorithm Method for Solving the Variational Inequality Problem in Hilbert Space *Global Journal of Mathematical Analysis* **7** pp 1-10
[3] Maibed Z 2019 Generalized Tupled Common Fixed Point Theorems for Weakly Compatible Mappings in Fuzzy Metric Space *IJCIET* **10** pp 255-273
[4] Maibed Z 2018 Strong Convergence of Iteration Processes for Infinite Family of General Extended Mappings *IOP Conf. Series: Journal of Physics: Conf. Series* **1003**, 012042 doi :10.1088/1742-6596/1003/1/012042

[5] Mabeed Z 2013 Some Convergence Theorems for the Fixed Point in Banach Spaces *Journal of the University of Anbar for pure science* **7** pp 1-4
[6] Maibed Z 2012 The Study of New Iterations Procedure For Expansion Mappings. *Journal of Qadisiyah Computer Science and Mathematics* **11** pp 11 – 18
[7] Maibed Z 2018 Some Generalized n-Tuplet Coincidence Point Theorems for Nonlinear Contraction Mappings *Journal of Engineering and Applied Sciences* **13** pp 10375-10379
[8] Maibed Z *2019* Contractive Mappings Having Mixed Finite Monotone Property in Generalized Metric Spaces *Ibn Al-Haitham Jour. for Pure & Appl.Sci* **32** pp 15-166
[9] Maibed Z 2020 Common Fixed Point problem for Classes of Nonlinear Maps in Hilbert Space *IOP Conf. Series: Journal of Physics: Conf. Series* **871** pp 12-22
[10] Maibed Z 2017 On The (G.n)_ Tupled Fixed Point Theorems In Fuzzy Metric Space Journal of Qadisiyah Computer Science and Mathematics **10** pp 15-25
[11] Mohammed K 2019 Aprallel Numerical Algorithm for Solving Some Fractional Integral Equations. *Ibn Al-Hitham Jour For pure and Appl.Sci* **32** pp 178-186
[12] Mann W 1953 Mean Value Methods in Iteration *Proc, Am.Math.soc* **4** pp 506-510
[13] Ishikawa S 1974 Fixed point by a new iteration. Method *Proceedings of the American, Soc* 44 pp 147-150
[14] Noor M 2000 New Approximation Schemes for General Variational Inequalities *Journal of Mathematical Analysis and Applications* **251** pp 217-229
[15] Change R, Kumar V and Kumar S 2012 Strong Convergence of a New Three-Step Iterative Schema in Banach Spaces *American Journal of Computational Mathematics* **2** pp 345-357
[16] Celiker F 2014 Convergence Analysis for a Modified SP Iterative Method *Hindawi Publishing Corporatione Scientific World Journal* **10** pp 1-5
[17] Weng X 1991 Fixed Point Iteration For Local Strictly Pseudocontractive Mapping *Proc. Amer. Math. Soc* 113 pp 1163-1170
[18] Soltuz S and Grosan T 2008 Data Dependence for Ishikawa Iteration When Dealing With Contractive Like Operators *Fixed Point Theory and Applications* **2008** 7 pages
[19] PopescuO S 2007 Picard Iteration Converges Faster Than Mann Iteration For a Class of Quasi-Contractive Operators *Mathematical Communications* **12** pp 195-202
[20] Pheungrattana W, Suantai R 2011 On The Rate of Convergence of Mann, IshikawNoor and SP Iterations for Continuous on an Arbitrary Interval *Journal of computational and Applied Mathematics* **235** pp 3006-3914

Some Properties of Fuzzy Compact Algebra Fuzzy Normed Spaces and Finite Dimensional Algebra Fuzzy Normed Spaces

Some Properties of Fuzzy Compact Algebra Fuzzy Normed Spaces and Finite Dimensional Algebra Fuzzy Normed Spaces

Zainab A. Khudhair and Jehad R. Kider

Branch of Mathematics and Computer Applications, Department of Applied Sciences, University of Technology.

Email: 10046@uotechnology.edu.iq

Abstract. Our goal in this article is to recall the notion of algebra fuzzy normed space and its basic properties to introduce the notion of fuzzy compact algebra fuzzy normed space. Then some properties of fuzzy compact algebra fuzzy normed spaces are proved. After that, we study a finite dimensional algebra fuzzy normed space and we proved some properties that algebra fuzzy normed spaces do not admit it.

1.Introduction

In 2009 [1] the fuzzy topological structure of a fuzzy normed space was studied by Sadeqi and Kia. In 2011 [2] Kider introduced a fuzzy normed space. Also he proved this fuzzy normed space has a completion in [3]. Again in 2012 [4] Kider introduced a new type of fuzzy normed space. In 2013 [5] Bag and Samanta study some basic results on finite dimensional fuzzy normed linear spaces.

In 2017 [6] Kider and Kadhum introduced the fuzzy norm for a fuzzy bounded operator on a fuzzy normed space and proved its basic properties then other properties were proved by Kadhum in 2017 [7]. In 2018 [8] Ali proved basic properties of complete fuzzy normed algebra. Again in 2018 [9] Kider and Ali introduced the notion of fuzzy absolute value and study some properties of finite dimensional fuzzy normed space.

The concept of general fuzzy normed space was presented by Kider and Gheeab in 2019 [10] [11] also they proved basic properties of this space and the general fuzzy normed space GFB (V, U). In 2019 [12] Kider and Kadhum introduced the notion fuzzy compact linear operator and proved its basic properties. In 2020 kider [13] introduced the notion fuzzy soft metric space after that he investigated and proved some basic properties of this space again kider in 2020 [14] introduced a new type of fuzzy metric space called algebra fuzzy metric space after that the basic properties of this space is proved.

In this paper, first we recall the notion algebra fuzzy absolute value space and its some basic properties that introduced by Khudhair and Kider in [15]. Then, we recall the notion algebra fuzzy normed space and its some basic properties that introduced by Khudhair and Kider in [15]. Our first aim is to define fuzzy compact algebra fuzzy normed space then we study this space and proved some of its basic properties.

The second aim is to assume that the algebra fuzzy normed space has a finite dimension and proved some basic results that this type of spaces must have.

2. Basic properties of algebra fuzzy normed space

Definition 2.1: [1]
Assume that S≠ ∅, a fuzzy set $\widetilde{\mathbf{D}}$ in S is represented by $\widetilde{\mathbf{D}}$ = {(s, $\boldsymbol{\mu}_{\widetilde{\mathbf{D}}}$(s)): s∈S, $0 \leq \boldsymbol{\mu}_{\widetilde{\mathbf{D}}}(s) \leq 1$} where $\boldsymbol{\mu}_{\widetilde{\mathbf{D}}}$(x): S⟶ I is a membership function where I=[0, 1].

Definition 2.2: [14]
The binary operation ⊙:I × I →I be is said to be continuous t-conorm if it satisfies
(i)r ⊙ s= s ⊙ r, (ii) r ⊙ [s ⊙ w] = [r ⊙ s] ⊙ w, (iii) ⊙ is continuous function
(iv)s ⊙ 0 = 0, (v) (r ⊙ z) ≤ (s ⊙ w) whenever r ≤ s and z ≤ w. For all r, s, z, w ∈ I=[0, 1].

Lemma 2.3: [14]
If ⊙ is a continuous t-conorm on [0, 1] then
(i)1 ⊙ 1=1, (ii)0 ⊙ 1 = 1 ⊙ 0 =1. (iii)0 ⊙ 0 = 0, (iv)p ⊙ p ≥ p for all p ∈ [0, 1].

Remark 2.4: [14]
If ⊙ is a continuous t-conorm then
(i)For any p, q ∈ (0, 1) with p > q we have w ∈ (0, 1) whenever p > q ⊙ w. In general for any p, q ∈ (0, 1) with p > q we can find $\boldsymbol{w_1}, \boldsymbol{w_2}, \ldots, \boldsymbol{w_k} \in (0, 1)$ whenever p > q ⊙ $\boldsymbol{w_1}$ ⊙ $\boldsymbol{w_2}$ ⊙ …⊙ $\boldsymbol{w_k}$ where k ∈ ℕ.
(ii) For any r ∈ (0, 1) ∃ s ∈ (0, 1) s. t. s ⊙ s ≤ r. In general for any r ∈ (0, 1) there exists $\boldsymbol{w_1}, \boldsymbol{w_2}, \ldots, \boldsymbol{w_k}$ ∈ (0, 1) such that $\boldsymbol{w_1}$ ⊙ $\boldsymbol{w_2}$ ⊙ …⊙ $\boldsymbol{w_k}$ ≤ r where k ∈ ℕ.

Example 2.5: [14]
The algebra product p ⊙ q = p + q − pq is a continuous t-conorm for all p, q ∈ [0, 1].

Definition 2.6: [15]
Let ⊙ be a continuous t-conorm and $\boldsymbol{a}_{\mathbb{R}}$:ℝ →I be a fuzzy set then a is called algebra fuzzy absolute value on ℝ if
(1)0< $\boldsymbol{a}_{\mathbb{R}}(\boldsymbol{\alpha})$ ≤1, (2) $\boldsymbol{a}_{\mathbb{R}}(\boldsymbol{\alpha})$=0 if and only if $\boldsymbol{\alpha}$=0, (3) $\boldsymbol{a}_{\mathbb{R}}(\boldsymbol{\alpha\beta}) \leq \boldsymbol{a}_{\mathbb{R}}(\boldsymbol{\alpha})$. $\boldsymbol{a}_{\mathbb{R}}(\boldsymbol{\beta})$
(4) $\boldsymbol{a}_{\mathbb{R}}(\boldsymbol{\alpha} + \boldsymbol{\beta}) \leq \boldsymbol{a}_{\mathbb{R}}(\boldsymbol{\alpha})$ ⊙ $\boldsymbol{a}_{\mathbb{R}}(\boldsymbol{\beta})$. For all $\boldsymbol{\alpha}, \boldsymbol{\beta} \in \mathbb{R}$. Then (ℝ, $\boldsymbol{a}_{\mathbb{R}}$, ⊙) is called algebra fuzzy absolute value space.

Example 2.7: [15]
Let |.| be absolute value on ℝ and $\boldsymbol{\alpha}$ ⊙ $\boldsymbol{\beta}$= $\boldsymbol{\alpha}$+ $\boldsymbol{\beta} - \boldsymbol{\alpha\beta}$ for all $\boldsymbol{\alpha}, \boldsymbol{\beta}$ ∈ I. Define $\boldsymbol{a}_{|.|}(\boldsymbol{\alpha})=\begin{cases} \frac{|\boldsymbol{\alpha}|}{1+|\boldsymbol{\alpha}|} & \boldsymbol{if\ \alpha \neq 1} \\ \mathbf{1} & \boldsymbol{if\ \alpha = 1} \end{cases}$
for all $\boldsymbol{\alpha} \in \mathbb{R}$. Then (ℝ, $\boldsymbol{a}_{|.|}$, ⊙) is algebra fuzzy absolute value space. Also $\boldsymbol{a}_{|.|}$ is called the standard algebra fuzzy absolute value on ℝ.

Example 2.8: [15]
Define $\boldsymbol{a}^{|.|}$: ℝ →I by $\boldsymbol{a}^{|.|}(r) = \begin{cases} \frac{\mathbf{1}}{|r|} & \boldsymbol{if\ r \neq 0} \\ \mathbf{0} & \boldsymbol{if\ r = 0} \end{cases}$
for all r ∈ ℝ and If s⊙r=s + r −sr for all s, r ∈I. Then (ℝ, $\boldsymbol{a}^{|.|}$, ⊙) is algebra fuzzy absolute value space. This space is called the algebra fuzzy absolute value space induced by |.|.

Definition 2.9: [15]
Let (ℝ, $\boldsymbol{a}_{\mathbb{R}}$, ⊙) be algebra fuzzy absolute value space and let $\{\mathbf{p_n}\}_{\mathbf{n=1}}^{\infty}$be a sequence in ℝ, we say that $\{\mathbf{p_n}\}_{\mathbf{n=1}}^{\infty}$ is fuzzy approaches to the limit p as n approaches to ∞ if ∀ s ∈ (0,1) ∃ N ∈ ℕ s. t. $\boldsymbol{a}_{\mathbb{R}}(\mathbf{p_n} - p)$

$<$ s, $\forall$ n$\geq$N. If $\mathbf{p_n}$ is fuzzy approaches to the limit p we write $\lim_{\mathbf{n\to\infty}} \mathbf{p_n}$= p or $\mathbf{p_n} \to$p as n approaches to ∞ or $\lim_{\mathbf{n\to\infty}} \boldsymbol{a}_{\mathbb{R}}(\mathbf{p_n} - \mathbf{p})$=0.

Definition 2.10: [15]
Let ($\mathbb{R}$, $\boldsymbol{a}_{\mathbb{R}}$, $\circledcirc$) be algebra fuzzy absolute value space and let $\{\mathbf{p_n}\}_{\mathbf{n=1}}^{\infty}$be a sequence in $\mathbb{R}$, we say that $\{\mathbf{p_n}\}_{\mathbf{n=1}}^{\infty}$ is fuzzy Cauchy sequence in $\mathbb{R}$ if $\forall$ s $\in$ (0,1) $\exists$ N $\in \mathbb{N}$ s. t. $\boldsymbol{a}_{\mathbb{R}}(\mathbf{p_k} - \mathbf{p_m}) <$ s, $\forall$ k, m $\geq$N.

Definition 2.11: [15]
Let ($\mathbb{R}$, $\boldsymbol{a}_{\mathbb{R}}$, $\circledcirc$) be algebra fuzzy absolute value space. The sequence $\{\mathbf{q_n}\}_{\mathbf{n=1}}^{\infty}$ in $\mathbb{R}$ is called fuzzy bounded if $\exists$ t $\in$ (0, 1) s. t. $\boldsymbol{a}_{\mathbb{R}}(\mathbf{q_n}) <$ t $\forall$ n $\in \mathbb{N}$

Theorem 2.12: [15]
Let ($\mathbb{R}$, $\boldsymbol{a}_{\mathbb{R}}$, $\circledcirc$) be algebra fuzzy absolute value space. If $\{\mathbf{q_n}\}_{\mathbf{n=1}}^{\infty}$ is a fuzzy Cauchy sequence in $\mathbb{R}$ then $\{\mathbf{q_n}\}_{\mathbf{n=1}}^{\infty}$ is fuzzy bounded.

Definition 2.13; [15]
The algebra fuzzy absolute value ($\mathbb{R}$, $\boldsymbol{a}_{\mathbb{R}}$, $\circledcirc$) is called fuzzy complete if every fuzzy Cauchy sequence in $\mathbb{R}$ fuzzy approaches to a real number in $\mathbb{R}$.

Definition 2.14: [15]
Let U be a vector space over $\mathbb{R}$ and let $\circledcirc$ be a continuous t-conorm. Let ($\mathbb{R}$, a, $\circledcirc$) be algebra fuzzy absolute value space and n: U$\to$I be a fuzzy set then n is called algebra fuzzy norm on U if
(1)0$<$ n(u) $\leq$ 1, (2)n(u) =0 if and only if u=0, (3)n($\boldsymbol{\alpha}$u) $\leq$ a($\boldsymbol{\alpha}$) n(u) for all 0$\neq$ $\boldsymbol{\alpha} \in \mathbb{R}$.
(4)n(u + v) $\leq$ n(u) $\circledcirc$ n(v)
For all u, v $\in$ U. Then (U, n, $\circledcirc$) is called algebra fuzzy normed space.

Example 2.15: [15]
Let U=C[p, b], t$\circledcirc$s=t + s $-$ts for all t, s $\in$I and ($\mathbb{R}$, a, $\circledcirc$) is algebra fuzzy absolute space. Define n(r) = $\boldsymbol{max}_{\boldsymbol{s\in[p,b]}}$ a[r(s)] for all r $\in$ U. Then (U, n, $\circledcirc$) is algebra fuzzy normed space

Definition 2.16: [15]
Suppose that (U, n, $\circledcirc$) is algebra fuzzy normed space and assume that $(\boldsymbol{u_k}) \in$ U, we say that $(\boldsymbol{u_k})$ is fuzzy converges to the limit u ask approaches to ∞ if $\forall$ s $\in$ (0,1) $\exists$ N $\in \mathbb{N}$ s. t. n($\mathbf{u_k} -$u) $<$ s, $\forall$ k$\geq$N. If $(\boldsymbol{u_k})$ is fuzzy approaches to the limit u we write $\lim_{\mathbf{k\to\infty}} \mathbf{u_k}$=u or $\mathbf{u_k} \to$u as k approaches to ∞ or $\lim_{\mathbf{n\to\infty}} \boldsymbol{n}(\mathbf{u_k} - \mathbf{u})$=0.

Definition 2.17: [15]
Let (U, n, $\circledcirc$) be algebra fuzzy normed space . Then the open and closed fuzzy ball with the center u $\in$U and radius t, with t $\in$ (0, 1) is defined by fb(u, r)= {v $\in$U: n(u$-$v) $<$ t} and fb[u, r]= {v $\in$ U: n(u$-$v) $\leq$ t}respectively.

Definition 2.18: [15]
Let (U, n, $\circledcirc$) be algebra fuzzy normed space and let $(\boldsymbol{u_k})$ be a sequence in U, we say that $(\boldsymbol{u_k})$ is fuzzy Cauchy sequence in U if $\forall$ s $\in$ (0, 1) $\ni$ N $\in \mathbb{N}$ s. t. n($\mathbf{u_k} - \mathbf{u_m}$) $<$ s, $\forall$ k, m $\geq$N.

Lemma 2.19: [15]
If (U, n, $\circledcirc$) is algebra fuzzy normed space then the function u $\longmapsto$ n(u) is a fuzzy continuous function from (U, n, $\circledcirc$) $\to$ ($\mathbb{R}$, n, $\circledcirc$).

Lemma 2.20: [15]
If (U, n, ⊙) is algebra fuzzy normed space then n(u−v) = n(v−u) for all u, v ∈ U.

Definitions 2.21: [15]
If (U, n, ⊙) is algebra fuzzy normed space and W⊆U is known as fuzzy open if fb(w, j) ⊆W for any arbitrary w∈W and for some j ∈(0, 1). Also D⊆U is known as fuzzy closed if $\boldsymbol{D^C}$ is fuzzy open. Moreover the fuzzy closure of D, $\overline{\mathbf{D}}$ is defined to be the smallest fuzzy closed set contains D.

Definition 2.22: [15]
If (U, n, ⊙) is algebra fuzzy normed space then D⊆U is known as fuzzy dense in U if whenever $\overline{\mathbf{D}}$ = U.
Theorem 2.23: [15]
If fb(s, j) is an open fuzzy ball in algebra fuzzy normed space (U, n, ⊙) then it is a fuzzy open set.

Definition 2.24: [15]
An algebra fuzzy normed space (U, n, ⊙) is known as fuzzy complete if $(\boldsymbol{s_k})$ is fuzzy Cauchy sequence in U then $\boldsymbol{s_k} \to$s ∈ U.

Theorem 2.25: [15]
In algebra fuzzy normed space (U, n, ⊙) if $\boldsymbol{u_k} \to$u ∈ U then $(\boldsymbol{u_k})$ is fuzzy Cauchy.

Theorem 2.26: [15]
In algebra fuzzy normed space (U, n, ⊙) when D⊂U then d∈$\overline{\mathbf{D}}$ if and only if there is $(\mathbf{d_k})$ ∈ D with $\mathbf{d_k} \to$ d.

3. Fuzzy compact algebra fuzzy normed space

Definition 3.1:
Let (U, n, ⊙) be algebra fuzzy normed space and P⊆ U. Let $\boldsymbol{\Omega} = \{\boldsymbol{O_j}: j \in J$ where $\boldsymbol{O_j}$ is fuzzy open set in U$\}$. Then $\boldsymbol{\Omega}$ is called a fuzzy open cover or a fuzzy open covering of P if $P \subseteq \bigcup_{\boldsymbol{O_j} \in \boldsymbol{\Omega}} \boldsymbol{O_j}$ that is for each p∈P there is $\boldsymbol{O_k} \in \boldsymbol{\Omega}$ such that p∈ $\boldsymbol{O_k}$ for some k ∈J. A finite sub collection of $\boldsymbol{\Omega}$ which itself is a fuzzy open cover is called a finite fuzzy open sub cover or a finite fuzzy open sub covering of P.

Definition 3.2:
An algebra fuzzy normed space (U, n, ⊙) is said to be fuzzy compact if every fuzzy open covering $\boldsymbol{\Omega}$ of U has a finite fuzzy open sub covering that is there is a finite sub collection $\{\mathbf{O_1}, \mathbf{O_2}, \mathbf{O_3}, \ldots, \mathbf{O_k}\} \subseteq \boldsymbol{\Omega}$ such that $U = \bigcup_{\mathbf{j=1}}^{\mathbf{k}} \mathbf{O_j}$.

Definition 3.3:
A nonempty subspace P of U is said to be fuzzy compact if every fuzzy open covering $\boldsymbol{\Omega}$ of P has a finite fuzzy open sub covering that is there is a finite sub collection $\{\mathbf{O_1}, \mathbf{O_2}, \mathbf{O_3}, \ldots, \mathbf{O_k}\} \subseteq \boldsymbol{\Omega}$ such that $P = \bigcup_{\mathbf{j=1}}^{\mathbf{k}} \mathbf{O_j}$.

Example 3.4:
The open interval $\{r \in \mathbb{R}: 0 < r < 1\}$ in the algebra fuzzy normed space $(\mathbb{R}, \boldsymbol{a}_{|.|}, \odot)$ where $\boldsymbol{a}_{|.|}(\boldsymbol{\alpha}) = \frac{|\boldsymbol{\alpha}|}{\mathbf{1}+|\boldsymbol{\alpha}|}$ is not fuzzy compact. Since the fuzzy open covering $\{(\frac{\mathbf{1}}{\mathbf{k}}, 1): k = 2, 3...\}$ is fuzzy open covering of (0, 1) from which no finite fuzzy open sub covering can be selected.

Remark 3.5:
If P is a finite subset of algebra fuzzy normed space (U, n, ⊙) then P is fuzzy compact.

Definition 3.6:
Assume that (U, n, ⊙) is algebra fuzzy normed space and P be a subset of U. Then P is called fuzzy totally bounded if for each $0 < r < 1$, there is a finite set of points $\{\boldsymbol{p_1}, \boldsymbol{p_2},\ldots,\boldsymbol{p_k}\} \subseteq P$ such that whenever u in U, $n(u - \boldsymbol{p_j}) < r$ for some $\boldsymbol{p_j} \in \{\boldsymbol{p_1},\boldsymbol{p_2},\ldots..,\boldsymbol{p_k}\}$. This set of points $\{\boldsymbol{p_1}, \boldsymbol{p_2},..., \boldsymbol{p_k}\}$ is called fuzzy r- net.

Proposition 3.7:
A fuzzy totally bounded algebra fuzzy normed space is fuzzy bounded.
Proof:
Let (U, n, ⊙) be fuzzy totally bounded and suppose $0 < r < 1$ is given. Then there exists a finite fuzzy r- net for U, say A. Since A is a finite set of points and $0 < n(A) < 1$, where $n(A) = \sup\{n(b-a): b, a \in A\}$. Now let $\mathbf{u_1}$and $\mathbf{u_2}$ be any two points of U. There exists points b and a in A such that $n(\mathbf{u_1} - b) < r$ and $n(\mathbf{u_2} - a) < r$. Now for n(A) and r there is t, where $0 < t < 1$ such that $r \odot n(A) \odot r \leq t$. It follows that
$n(\mathbf{u_1} - \mathbf{u_2}) \leq n(\mathbf{u_1} - b) \odot n(b-a) \odot n(a - \mathbf{u_2}) \leq r \odot n(A) \odot r \leq t$
So, $n(U) = \sup\{n(\mathbf{u_1} - \mathbf{u_2}):\mathbf{u_1}, \mathbf{u_2} \in X\} \leq t$. Hence U is fuzzy bounded.

Theorem 3.8:
Let (U, n, ⊙) be algebra fuzzy normed space and let P be a subset of U. Then P is fuzzy totally bounded if and only if ∀ $(\mathbf{p_k})$ in P contains subsequence $(\mathbf{p_{k_j}})$ which is fuzzy Cauchy.
Proof:
Let P be fuzzy totally bounded and $(\mathbf{p_k}) \in P$. Consider a finite fuzzy $\frac{\mathbf{1}}{\mathbf{2}}$ -net in P. Then we can find fuzzy open ball of radius $\frac{\mathbf{1}}{\mathbf{2}}$ with center in the fuzzy $\frac{\mathbf{1}}{\mathbf{2}}$ -net contains infinite elements of $(\mathbf{p_k})$. Let $(\mathbf{p_{1k}})$ denote the subsequence contains these element. Again consider a finite fuzzy $\frac{\mathbf{1}}{\mathbf{4}}$ -net in P. Then we can find fuzzy open ball of radius $\frac{\mathbf{1}}{\mathbf{4}}$ with center in the finite fuzzy $\frac{\mathbf{1}}{\mathbf{4}}$ -net contains infinitely many elements of $(\mathbf{p_{1k}})$.
Let $(\mathbf{p_{2k}})$ be the subsequence. After many steps we get $(\mathbf{p_k}) \supseteq (\mathbf{p_{1k}}) \supseteq (\mathbf{p_{2k}}) \supseteq \ldots$
At the jth step members of $(\mathbf{p_{jk}})$ lie in the fuzzy open ball of radius $\frac{\mathbf{1}}{\mathbf{2^j}}$ with center in the fuzzy $\frac{\mathbf{1}}{\mathbf{2^j}}$ -net.
Now $(\mathbf{p_{jj}})$ is a subsequence of $(\mathbf{p_j})$. Assume that $r \in (0, 1)$. Consider $N \in \mathbb{N}$ so large that
$(\frac{\mathbf{1}}{\mathbf{2^j}}) \odot (\frac{\mathbf{1}}{\mathbf{2^{j+1}}}) \odot \ldots \odot (\frac{\mathbf{1}}{\mathbf{2^{m-1}}}) < r$. Then for $m > j > N$, we have
$n(\mathbf{p_{jj}} - \mathbf{p_{mm}}) \leq n(\mathbf{p_{jj}} - \mathbf{p_{j+1j+1}}) \odot n(\mathbf{p_{j+1j+1}} - \mathbf{p_{j+2j+2}}) \odot \ldots \odot n(\mathbf{p_{m-1m-1}} - \mathbf{p_{mm}})$
$n(\mathbf{p_{jj}} - \mathbf{p_{mm}}) \leq (\frac{\mathbf{1}}{\mathbf{2^j}}) \odot (\frac{\mathbf{1}}{\mathbf{2^{j+1}}}) \odot \ldots \odot (\frac{\mathbf{1}}{\mathbf{2^{m-1}}}) < r$.
Thus the sequence $(\mathbf{p_{kk}})$ is a fuzzy Cauchy sequence.
To prove the converse assume that any sequence $(\mathbf{p_k})$ in P contains subsequence $(\mathbf{p_{k_j}})$ which is fuzzy Cauchy.
Let $r \in (0, 1)$ and let $\mathbf{p_1} \in P$. If $P - fb(\mathbf{p_1}, r) = \emptyset$, we have found a fuzzy r-net put it $\{\mathbf{p_1}\}$. Or consider $\mathbf{p_2} \in P - fb(\mathbf{p_1}, r)$. If $P - [fb(\mathbf{p_1}, r) \cup fb(\mathbf{p_2}, r)] = \emptyset$. We have found a fuzzy r-net put it by $\{\mathbf{p_1},\mathbf{p_2}\}$. We must prove that this process after a finite number of steps stops. If it does not stops, we get $(\mathbf{p_1}, \mathbf{p_2}, \ldots, \mathbf{p_k},\ldots)$ with $n(\mathbf{p_j} - \mathbf{p_m}) \geq r$, $j \neq m$. Thus this implies $(\mathbf{p_k})$ does not contain subsequence $(\mathbf{p_{k_j}})$ which is fuzzy Cauchy. This is a contradiction.

Proposition 3.9:
If (U, n, ⊙) is a fuzzy compact algebra fuzzy normed space then U is fuzzy totally bounded.
Proof:

Let $0 < r < 1$ then {fb(p, r) :for p∈U} is a fuzzy open cover of U. But U is fuzzy compact this implies that {fb(p, r) :for p∈U} contains {fb($\boldsymbol{p_1}$, r), fb($\boldsymbol{p_2}$, r),…, fb($\boldsymbol{p_k}$, r)} such that $U=\cup_{j=1}^{k} \mathbf{fb}(\boldsymbol{p_j}, \mathbf{r})$. Hence for $0 < r < 1$ { $\boldsymbol{p_1}$, $\boldsymbol{p_2}$. …, $\boldsymbol{p_k}$}U is a finite fuzzy r-net for U. Hence U is fuzzy totally bounded.

Proposition 3.10:
If (U, n, ⊙) is a fuzzy compact algebra fuzzy normed space then (U, n, ⊙) is fuzzy complete.
Proof:
Assume that (U, n, ⊙) is a fuzzy compact algebra fuzzy normed which is not fuzzy complete. Then we can find a fuzzy Cauchy ($\mathbf{p_k}$) in U does not has a limit in U. Let p∈U, since $\mathbf{p_k} \nrightarrow p$ ∃ $0 < r < 1$ such that n($\mathbf{p_k} - p$) ≥ r for k=1, 2, … but ($\mathbf{p_k}$) is fuzzy Cauchy ∃ N∈ ℕ s. t. n($\mathbf{p_j} - \mathbf{p_m}$) <t ∀ j, m ≥ N. Choose m ≥ N for which n($\mathbf{p_m} - p$) < t . So, the fuzzy open ball fb(p, t) contains { $\mathbf{p_1}$, $\mathbf{p_2}$, …,$\mathbf{p_k}$} where k ∈ ℕ. Now consider fuzzy { fb($\mathbf{p_1}$, t($\mathbf{p_1}$)), fb($\mathbf{p_2}$, t($\mathbf{p_2}$)),… fb($\mathbf{p_k}$, t($\mathbf{p_k}$))} where $0 < t(\mathbf{p_k}) < 1$ and $U=\cup_{j=1}^{k} \mathbf{fb}(\boldsymbol{p_j}, \mathbf{t}(\boldsymbol{p_j}))$. But each fb($\mathbf{p_j}$, t($\mathbf{p_j}$))} contains $\mathbf{p_k}$ for only a finite number of values so U, must contains $\mathbf{p_k}$ for only a finite number of values of k. This is a contradiction. Hence (U, n, ⊙) must be fuzzy complete.

Theorem 3.11:
If (U, n, ⊙) is fuzzy totally bounded and fuzzy complete algebra fuzzy normed space then (U, n, ⊙) is fuzzy compact.
Proof:
Assume that (U, n, ⊙) is not fuzzy compact. Then we can find a fuzzy open covering {$\mathbf{O_\lambda}$: $\boldsymbol{\lambda}$∈∧} of U that does not have a finite fuzzy open sub covering. But U is fuzzy totally bounded, so it is fuzzy bounded, hence consider fb(p, r) for some $0 < r < 1$ and some p∈U, clearly fb(p, r) ⊆U if U ⊆ fb(p, r) then we must have U = fb(p, r).
Put $\mathbf{t_k} = \frac{\mathbf{r}}{\mathbf{2^k}}$ but U is fuzzy totally bounded this means that U can be covered by finite fuzzy open balls of radius $\mathbf{t_1}$. By our assumption at least one of these fuzzy open balls, say fb($\mathbf{p_1}$, $\mathbf{t_1}$)≠ $\cup_{j=1}^{k} \mathbf{O}_{\lambda_j}$ since fb($\mathbf{p_1}$, $\mathbf{t_1}$) is itself fuzzy totally bounded. ∃ $\mathbf{p_2}$ ∈ fb($\mathbf{p_1}$, $\mathbf{t_1}$), s. t. fb($\mathbf{p_2}$, $\mathbf{t_2}$))≠ $\cup_{j=1}^{k} \mathbf{O}_{\lambda_j}$. After many steps we get a sequence ($\mathbf{p_k}$) has the property that for each k, fb($\mathbf{p_k}$, $\mathbf{t_k}$))≠ $\cup_{j=1}^{k} \mathbf{O}_{\lambda_j}$ and $\mathbf{p_{k+1}}$ ∈fb($\mathbf{p_k}$,$\mathbf{t_k}$). We next show that the sequence ($\mathbf{p_k}$) is convergent.
Since $\mathbf{p_{k+1}}$ ∈fb($\mathbf{p_k}$,$\mathbf{t_k}$) it follows that n($\mathbf{p_k} - \mathbf{p_{k+1}}$) < $\mathbf{t_k}$. Let $0 < t < 1$ such that $\mathbf{t_k} \circledcirc \mathbf{t_{k+1}} \circledcirc \ldots\ldots \circledcirc \mathbf{t_m} < t$
Hence n($\mathbf{p_k} - \mathbf{p_m}$) ≤ n($\mathbf{p_k} - \mathbf{p_{k+1}}$) ⊙……⊙ n($\mathbf{p_{m-1}} - \mathbf{p_m}$)
≤ $\mathbf{t_k} \circledcirc \mathbf{t_{k+1}} \circledcirc \ldots\ldots \circledcirc \mathbf{t_m} < t$
So ($\mathbf{p_k}$) is a fuzzy Cauchy sequence in U and since U is fuzzy complete, it converges to p∈U. Because p∈U ∃ $\boldsymbol{\lambda_0}$∈ ∧ s. t. p∈ $\mathbf{O}_{\lambda_0}$. Since $\mathbf{O}_{\lambda_0}$ is fuzzy open it contains fb(p, s) for some $0 < s < 1$. Let N∈ ℕ n($\mathbf{p_k} - p$) < s Then, for any u∈U such that n($u - \mathbf{p_k}$) < $\mathbf{t_k}$. It follows that
n(u−p) ≤ n($u - \mathbf{p_k}$) ⊙ n($\mathbf{p_k} - p$) ≤ $\mathbf{t_k}$ ⊙s < r,
for some $0 < r < 1$. So that fb($\mathbf{p_k}$, $\mathbf{t_n}$) ⊆ fb(p, r). Therefore fb($\mathbf{p_k}$,$\mathbf{t_k}$) has a finite fuzzy open sub covering, namely by the set $\mathbf{O}_{\lambda_0}$. Since this contradicts fb($\mathbf{p_k}$, $\mathbf{t_k}$))≠ $\cup_{j=1}^{k} \mathbf{O}_{\lambda_j}$. The proof is complete.

Proposition 3.12:
Let (U, n, ⊙) be algebra fuzzy normed space. Then every set {$\mathbf{u_1}$, $\mathbf{u_2}$, …,$\mathbf{u_k}$, …}in (U, n, ⊙) has at least one limit point in U ⇔ every sequence ($\mathbf{u_k}$) in (U, n, ⊙) contains ($\mathbf{u_{k_j}}$) such that $\mathbf{u_{k_j}} \rightarrow u \in U$.
Proof:
Assume that every set {$\mathbf{u_1}$, $\mathbf{u_2}$, …,$\mathbf{u_k}$, …}in (U, n, ⊙) has at least one limit point in U. Let ($\mathbf{u_k}$) ∈ U. If {$\mathbf{u_1}$, $\mathbf{u_2}$,…., $\mathbf{u_k}$} then take $\mathbf{u_j}$ ∈ {$\mathbf{u_1}$, $\mathbf{u_2}$,…., $\mathbf{u_k}$} and ($\mathbf{u_j}$, $\mathbf{u_j}$, …) ⊆ ($\mathbf{u_k}$), where ($\mathbf{u_j}$, $\mathbf{u_j}$, …) → $\mathbf{u_j}$. Now consider {$\mathbf{u_1}$, $\mathbf{u_2}$,…., $\mathbf{u_k}$, …}.

By our assumption the infinite set $\{\mathbf{u_1}, \mathbf{u_2},\ldots,\}$ has at least one limit point u∈U. Now we construct $(\mathbf{u_{k_j}})$ as follows: Take $\mathbf{k_1} \in \mathbb{N}$ s. t. $n(\mathbf{u_{k_1}} - u) > 0$.
Having defined $\mathbf{k_j}$, let $\mathbf{k_{j+1}}$ be the smallest integer such that $\mathbf{k_{j+1}} > \mathbf{k_j}$
and $n(\mathbf{u_{k_{j+1}}} - u) < \frac{1}{j+1}$. Then the sequence $(\mathbf{u_{k_j}})$ fuzzy converges to u.
Conversely assume that every sequence $(\mathbf{u_k})$ in (U, n, ⊙) contains $(\mathbf{u_{k_j}})$ such that $\mathbf{u_{k_j}} \to u \in U$. Let $S=\{\boldsymbol{p_1}, \boldsymbol{p_2}, \ldots\} \subseteq U$ then $\exists$ $(\mathbf{p_k})$ in U where $\mathbf{p_k} \neq \mathbf{p_j}$. By our assumption $(\mathbf{p_k})$ contains a subsequence $(\mathbf{p_{k_i}})$ where $\mathbf{p_{k_i}} \neq \mathbf{p_{k_j}}$ and $\mathbf{p_{k_i}} \to p \in U$. Thus ∀ fb(p, r) we have $\{\mathbf{p_{k_1}}, \mathbf{p_{k_2}}, \ldots, \mathbf{p_{k_j}}, \ldots\} \subseteq$ fb(p, r). But $\mathbf{p_{k_i}} \neq \mathbf{p_{k_j}}$ hence p∈U is a limit point of S.

Theorem 3.13:
Suppose that (U, n, ⊙) is algebra fuzzy normed space then the following is equivalent
(1)(U, n, ⊙) is fuzzy compact;
(2) ∀ $(\mathbf{u_k})$ in (U, n, ⊙) contains $(\mathbf{u_{k_j}})$ such that $\mathbf{u_{k_j}} \to u \in U$.
Proof:
(1)⇒(2)
Consider $(\mathbf{u_k})$ in U by using Theorem 3.12, it follows that $(\mathbf{u_{k_i}}) \subseteq (\mathbf{u_k})$ and $(\mathbf{u_{k_i}})$ is a fuzzy Cauchy. But $\mathbf{u_{k_i}} \to u \in U$ since U is fuzzy complete by Theorem 3.11.
(2)⇒(1)
Since every fuzzy convergent sequence is fuzzy Cauchy and by using Theorem 3.11 we have U is fuzzy totally bounded. Let $(\mathbf{p_k})$ be a fuzzy Cauchy sequence in U. By (2) $(\mathbf{p_{k_i}}) \subseteq (\mathbf{p_k})$ and $\mathbf{p_{k_i}} \to p \in U$. To prove that $\mathbf{p_k} \to p$. Consider $r \in (0, 1)$ by Remark 1.2, there is $0 < t < 1$ such that $r ⊙ r < t$.
Now $\mathbf{p_{k_i}} \to p$, there exist $\mathbf{N_1}$ such that $n(\mathbf{p_{k_i}} - p) < r$ for all $\mathbf{k_i} \geq \mathbf{N_1}$.
Since the sequence $(\mathbf{p_k})$ is fuzzy Cauchy, there exists $\mathbf{N_2}$ such that
$n(\mathbf{p_j} - \mathbf{p_m}) < r$ for all $m, j \geq \mathbf{N_2}$.
Let $N = \min\{\mathbf{N_1}, \mathbf{N_2}\}$ then $n(\mathbf{p_k} - p) \leq n(\mathbf{p_k} - \mathbf{p_{k_i}}) ⊙ n(\mathbf{p_{k_i}} - p) \leq r ⊙ r < t$
For all $k \geq N$. Hence U is fuzzy complete and by Theorem 3.11 U is fuzzy compact.

Corollary 3.14:
If P is a fuzzy closed subset of the fuzzy compact algebra fuzzy normed space (U, n, ⊙) then P is fuzzy compact.
Proof:
Let $(\mathbf{p_k}) \in P$. Then $(\mathbf{p_k})$ in U and $(\mathbf{p_{k_i}}) \subseteq (\mathbf{p_k})$ and $\mathbf{p_{k_i}} \to p \in U$. Thus p∈P since P is fuzzy closed. Hence by Theorem 3.13 P is fuzzy compact.

Theorem 3.15:
Suppose that (U, n, ⊙) is algebra fuzzy normed space and P ⊆U. If P is fuzzy compact then P is a fuzzy closed subset of U.
Proof:
Consider p ∈U is a limit point of P. Then $\exists$ $(\mathbf{p_k})$ in P such that $\mathbf{p_k} \to p$. But then $(\mathbf{p_k})$ is a fuzzy Cauchy sequence in P. Because P is fuzzy complete $\mathbf{p_k} \to q$ in P. Thus q = p and so q ∈P.Thus P fuzzy closed since it contains all its limit points.

4. When the dimension of algebra Fuzzy Normed Space is finite
In this section we deal with finite dimensional vector spaces with algebra fuzzy norm.
The following theorem plays the key role in the studying properties of finite dimensional algebra fuzzy normed linear spaces.

Theorem 4.1:

Let (U, n, ⊙) be algebra fuzzy normed space and ($\mathbb{R}$, $\boldsymbol{a}_{\mathbb{R}}$, ⊙) is algebra fuzzy absolute value space. Suppose that $\{\boldsymbol{u_1}, \boldsymbol{u_2}, \ldots, \boldsymbol{u_k}\}$ is linearly independent set in U . Then there is r ∈(0, 1) such that

$\boldsymbol{n_U}[\boldsymbol{\alpha_1 u_1} + \boldsymbol{\alpha_2 u_2} + \ldots + \boldsymbol{\alpha_k u_k}] \geq r[\boldsymbol{a}_{\mathbb{R}}(\boldsymbol{\alpha_1}) \odot \boldsymbol{a}_{\mathbb{R}}(\boldsymbol{\alpha_2}) \odot \ldots \odot \boldsymbol{a}_{\mathbb{R}}(\boldsymbol{\alpha_k})]$

Proof:

Assume that we cannot find r ∈(0, 1) such that

$\boldsymbol{n_U}[\boldsymbol{\alpha_1 u_1} + \boldsymbol{\alpha_2 u_2} + \ldots + \boldsymbol{\alpha_k u_k}] \geq r[\boldsymbol{a}_{\mathbb{R}}(\boldsymbol{\alpha_1}) \odot \boldsymbol{a}_{\mathbb{R}}(\boldsymbol{\alpha_2}) \odot \ldots \odot \boldsymbol{a}_{\mathbb{R}}(\boldsymbol{\alpha_k})]$.

Then we can find a sequence $(\boldsymbol{d_m})$ in U where $\boldsymbol{d_m} = \boldsymbol{\alpha_{1m} u_1} + \boldsymbol{\alpha_{2m} u_2} + \ldots + \boldsymbol{\alpha_{km} u_k}$ such that $\mathbf{n_U}(\mathbf{d_m}) \to 0$ as $\mathbf{m} \to \infty$.

Now for each fixed j we have a sequence $\boldsymbol{\alpha_{jm}} = (\boldsymbol{\alpha_{j1}}, \boldsymbol{\alpha_{j2}} \ldots, \boldsymbol{\alpha_{jm}}, \ldots)$ is fuzzy bounded since $0 \leq \mathbf{a}_{\mathbb{R}}(\boldsymbol{\alpha_{jm}}) \leq 1$ so $(\boldsymbol{\alpha_{jm}})$ has a convergent subsequence. Let $\boldsymbol{\alpha_j}$ denote the limit of the subsequence $(\boldsymbol{\alpha_{jm}})$ for each $1 \leq \mathbf{j} \leq k$. Let $(\mathbf{u_{jm}})$ denote the corresponding subsequence of $(\mathbf{d_m})$ where the corresponding subsequence of scalar $\boldsymbol{\alpha_{jm}}$ fuzzy converges to $\boldsymbol{\alpha_j}$ for each $\mathbf{1} \leq \mathbf{j} \leq k$.

Now put $d = \sum_{\mathbf{j=1}}^{\mathbf{k}} \boldsymbol{\alpha_j u_j}$ then $(\mathbf{d_m})$ has a subsequence $(\mathbf{d_{jm}})$ fuzzy converges to d since $\{\boldsymbol{u_1}, \boldsymbol{u_2}, \ldots, \boldsymbol{u_k}\}$ is linearly independent set so $d \neq 0$. Now $\mathbf{d_{jm}} \to d$ implies $\mathbf{n_U}(\mathbf{d_{jm}}) \to \mathbf{n_U}(d)$ by fuzzy continuity of the algebra fuzzy norm.

But $\mathbf{n_U}(\mathbf{d_m}) \to 0$ as $\mathbf{m} \to \infty$ by our assumption and $(\mathbf{d_{jm}})$ is a subsequence of $(\mathbf{d_m})$.Thus $\mathbf{n_U}(\mathbf{d_{jm}}, \mathbf{t}) \to 0$. Hence $\mathbf{n_U}(d) = 0$ so $d = 0$. This contradicts $d \neq 0$.

Theorem 4.2:

Consider (U, n, ⊙) is algebra fuzzy normed space. If D is a subspace of U with finite dimension, then D is fuzzy complete

Proof:

Consider that $(\boldsymbol{d_m})$ is a fuzzy Cauchy sequence in D. Let dim D=k and

B=$\{\boldsymbol{u_1}, \boldsymbol{u_2}, \ldots, \boldsymbol{u_k}\}$ be any basis for D. Then each $\mathbf{d_m}$ has a unique representation as $\mathbf{d_m} = \boldsymbol{\alpha_{1m} u_1} + \boldsymbol{\alpha_{2m} u_2} + \ldots + \boldsymbol{\alpha_{km} u_k}$ since $(\mathbf{d_m})$ is fuzzy Cauchy sequence so for every t ∈(0, 1) there is N ∈ ℕ such that $\mathbf{n_U}(\mathbf{d_m} - \mathbf{d_j}) \leq t$ for every m, j ≥N. Now by Theorem 4.1 we have some r ∈(0, 1) such that

$r[\boldsymbol{a}_{\mathbb{R}}(\boldsymbol{\alpha_{1m}} - \boldsymbol{\alpha_{1j}}) \odot \boldsymbol{a}_{\mathbb{R}}(\boldsymbol{\alpha_{2m}} - \boldsymbol{\alpha_{2j}}) \odot \ldots \odot \boldsymbol{a}_{\mathbb{R}}(\boldsymbol{\alpha_{km}} - \boldsymbol{\alpha_{kj}})] \leq \mathbf{n_U}(\mathbf{d_m} - \mathbf{d_j}) = \mathbf{n_U}\left[\sum_{\mathbf{i=1}}^{\mathbf{k}} (\boldsymbol{\alpha_{im}} - \boldsymbol{\alpha_{ij}})\mathbf{u_i}\right] \leq t$ dividing by $\mathbf{r}$ we get $a(\boldsymbol{\alpha_{im}} - \boldsymbol{\alpha_{ij}}) \leq \frac{\boldsymbol{t}}{\boldsymbol{r}}$

This show that $(\boldsymbol{\alpha_{i1}}, \boldsymbol{\alpha_{i2}}, \ldots)$ is fuzzy Cauchy sequence in ℝ. Hence $\boldsymbol{\alpha_{jm}} \to \boldsymbol{\alpha_j}$ for each $1 \leq \mathbf{j} \leq k$. Put $d = \sum_{\mathbf{j=1}}^{\mathbf{n}} \boldsymbol{\alpha_j u_j}$. Clearly d ∈D.

Also now for all m>N

$\mathbf{n_U}(\mathbf{d_m} - \mathbf{d}) = \mathbf{n_U}\left[\sum_{\mathbf{i=1}}^{\mathbf{k}} (\boldsymbol{\alpha_{im}} - \boldsymbol{\alpha_i})\mathbf{u_i}\right]$

$\leq \boldsymbol{a}_{\mathbb{R}}(\boldsymbol{\alpha_{1m}} - \boldsymbol{\alpha_1})\, \mathbf{n_U}(\boldsymbol{u_1}) \odot \boldsymbol{a}_{\mathbb{R}}(\boldsymbol{\alpha_{2m}} - \boldsymbol{\alpha_2})\, \mathbf{n_U}(\boldsymbol{u_2}) \odot \ldots \odot \boldsymbol{a}_{\mathbb{R}}(\boldsymbol{\alpha_{km}} - \boldsymbol{\alpha_k})\, \mathbf{n_U}(\boldsymbol{u_k})$

By taking limit to both sides as $\mathbf{m} \to \infty$ we get

$\lim_{\mathbf{m}\to\infty} \mathbf{n_U}(\mathbf{d_m} - \mathbf{d}) \leq 0 \odot 0 \odot \ldots \odot 0 = 0$. Hence $\mathbf{d_m} \to \mathbf{d}$ and D is fuzzy complete.

Definition 4.3:

Consider that (U, $\boldsymbol{n_1}$, ⊙) is algebra fuzzy normed space and $(\boldsymbol{u_k}) \in$ U. Then the algebra fuzzy norm $\boldsymbol{n_2}$ is said to be equivalent to $\boldsymbol{n_1}$ whenever $\boldsymbol{u_k} \to u \in$ U in (U, $\boldsymbol{n_1}$, ⊙) if and only if $\boldsymbol{u_k} \to u \in$ U in (U, $\boldsymbol{n_2}$, ⊙).

Theorem 4.4:

Suppose that (U, $\boldsymbol{n_1}$, ⊙) is algebra fuzzy normed space then the algebra fuzzy norm $\boldsymbol{n_2}$ is equivalent to $\boldsymbol{n_1}$ if there exists p, q in (0, 1) such that $p\boldsymbol{n_2}(u) \leq \boldsymbol{n_1}(u) \leq q\boldsymbol{n_2}(u)$.

Proof:

Suppose that $\boldsymbol{u_k} \to u \in$ U in (U, $\boldsymbol{n_1}$, ⊙) then for any r ∈(0, 1) ∃ N∈ ℕ such that

$\boldsymbol{n_1}(\boldsymbol{u_k} - u)) \leq r$. Now $p\boldsymbol{n_2}(\boldsymbol{u_k} - u) \leq \boldsymbol{n_1}(\boldsymbol{u_k} - u)) \leq r$. By dividing both sides by p since $p \neq 0$ and taking limit to both sides as $k \to \infty$ we get $\boldsymbol{n_2}(\boldsymbol{u_k} - u) \to 0$. Hence we have $\boldsymbol{u_k} \to u \in U$ in $(U, \boldsymbol{n_2}, \circledcirc)$
Now assume that $\boldsymbol{u_k} \to u \in U$ in $(U, \boldsymbol{n_2}, \circledcirc)$ $\forall$ r $\in (0, 1)$ $\exists$ N$\in \mathbb{N}$ such that $\boldsymbol{n_2}(\boldsymbol{u_k} - u) \leq r$. But $\boldsymbol{n_1}(\boldsymbol{u_k} - u) \leq q\boldsymbol{n_2}(\boldsymbol{u_k} - u)$ or $\boldsymbol{n_1}(\boldsymbol{u_k} - u) \leq qr$ put $qr = t \in (0, 1)$ that is $\boldsymbol{n_1}(\boldsymbol{u_k} - u) \leq t$. Hence we have $\boldsymbol{u_k} \to u \in U$ in $(U, \boldsymbol{n_1}, \circledcirc)$.

Theorem 4.5:
Suppose that U is vector space with dim U=k if $\mathbf{n_1}$ and $\mathbf{n_2}$ are two algebra fuzzy norms on U then $\mathbf{n_1}$ is equivalent to $\mathbf{n_2}$.
Proof:
Since dim U=k and $B = \{\boldsymbol{u_1}, \boldsymbol{u_2}, \ldots, \boldsymbol{u_k}\}$ be any basis for U. Then for any $u \in U$ we have $u = \sum_{j=1}^{k} \alpha_j \mathbf{u_j}$. Now

$$\mathbf{n_1}(\mathbf{u}) = \mathbf{n_1}\left(\sum_{j=1}^{k} \alpha_j \mathbf{u_j}\right) \leq \mathbf{n_1}(\alpha_1 \mathbf{u_1}) \circledcirc \mathbf{n_1}(\alpha_2 \mathbf{u_2}) \circledcirc \ldots \circledcirc \mathbf{n_1}(\alpha_k \mathbf{u_k})$$
$$\leq \boldsymbol{a}_{\mathbb{R}}(\alpha_1)\, \mathbf{n_1}(\mathbf{u_1}) \circledcirc \boldsymbol{a}_{\mathbb{R}}(\alpha_2)\, \mathbf{n_1}(\mathbf{u_2}) \circledcirc \ldots \circledcirc \boldsymbol{a}_{\mathbb{R}}(\alpha_k)\, \mathbf{n_1}(\mathbf{u_k})$$
$$\leq t[\boldsymbol{a}_{\mathbb{R}}(\alpha_1) \circledcirc \boldsymbol{a}_{\mathbb{R}}(\alpha_2) \circledcirc \ldots \circledcirc \boldsymbol{a}_{\mathbb{R}}(\alpha_k)]$$

Where $t = \max\{\mathbf{n_1}(\mathbf{u_1}), \mathbf{n_1}(\mathbf{u_2}), \ldots, \mathbf{n_1}(\mathbf{u_k})\}$ that is
$\mathbf{n_1}(\mathbf{u}) \leq t[\boldsymbol{a}_{\mathbb{R}}(\alpha_1) \circledcirc \boldsymbol{a}_{\mathbb{R}}(\alpha_2) \circledcirc \ldots \circledcirc \boldsymbol{a}_{\mathbb{R}}(\alpha_k)]$ or dividing by t
$\frac{1}{t}\mathbf{n_1}(\mathbf{u}) \leq [\boldsymbol{a}_{\mathbb{R}}(\alpha_1) \circledcirc \boldsymbol{a}_{\mathbb{R}}(\alpha_2) \circledcirc \ldots \circledcirc \boldsymbol{a}_{\mathbb{R}}(\alpha_k)]$ …….(1)
Now by Theorem 4.1
$\mathbf{n_2}(\mathbf{u}) = \mathbf{n_2}\left(\sum_{j=1}^{k} \alpha_j \mathbf{u_j}\right) \geq r[\boldsymbol{a}_{\mathbb{R}}(\alpha_1) \circledcirc \boldsymbol{a}_{\mathbb{R}}(\alpha_2) \circledcirc \ldots \circledcirc \boldsymbol{a}_{\mathbb{R}}(\alpha_k)]$ or dividing by r
$\frac{1}{r}\mathbf{n_2}(\mathbf{u}) \geq [\boldsymbol{a}_{\mathbb{R}}(\alpha_1) \circledcirc \boldsymbol{a}_{\mathbb{R}}(\alpha_2) \circledcirc \ldots \circledcirc \boldsymbol{a}_{\mathbb{R}}(\alpha_k)]$ …….(2)
Now from (1) and (2) we have
$\frac{1}{t}\mathbf{n_1}(\mathbf{u}) \leq [\boldsymbol{a}_{\mathbb{R}}(\alpha_1) \circledcirc \boldsymbol{a}_{\mathbb{R}}(\alpha_2) \circledcirc \ldots \circledcirc \boldsymbol{a}_{\mathbb{R}}(\alpha_k)] \leq \frac{1}{r}\mathbf{n_2}(\mathbf{u})$ or
$\frac{1}{t}\mathbf{n_1}(\mathbf{u}) \leq \frac{1}{r}\mathbf{n_2}(\mathbf{u})$ this implies that $\mathbf{n_1}(\mathbf{u}) \leq \frac{t}{r}\mathbf{n_2}(\mathbf{u})$ put $\frac{t}{r} = q$ we have
$\mathbf{n_1}(\mathbf{u}) \leq q\, \mathbf{n_2}(\mathbf{u})$ …….(3)
In similar way

$$\mathbf{n_2}(\mathbf{u}) = \mathbf{n_2}\left(\sum_{j=1}^{k} \alpha_j \mathbf{u_j}\right) \leq \mathbf{n_2}(\alpha_1 \mathbf{u_1}) \circledcirc \mathbf{n_2}(\alpha_2 \mathbf{u_2}) \circledcirc \ldots \circledcirc \mathbf{n_2}(\alpha_k \mathbf{u_k})$$
$$\leq \boldsymbol{a}_{\mathbb{R}}(\alpha_1)\, \mathbf{n_2}(\mathbf{u_1}) \circledcirc \boldsymbol{a}_{\mathbb{R}}(\alpha_2)\, \mathbf{n_2}(\mathbf{u_2}) \circledcirc \ldots \circledcirc \boldsymbol{a}_{\mathbb{R}}(\alpha_k)\, \mathbf{n_2}(\mathbf{u_k})$$
$$\leq s[\boldsymbol{a}_{\mathbb{R}}(\alpha_1) \circledcirc \boldsymbol{a}_{\mathbb{R}}(\alpha_2) \circledcirc \ldots \circledcirc \boldsymbol{a}_{\mathbb{R}}(\alpha_k)]$$

Where $s = \max\{\mathbf{n_2}(\mathbf{u_1}), \mathbf{n_2}(\mathbf{u_2}), \ldots, \mathbf{n_2}(\mathbf{u_k})\}$ that is
$\mathbf{n_2}(\mathbf{u}) \leq s[\boldsymbol{a}_{\mathbb{R}}(\alpha_1) \circledcirc \boldsymbol{a}_{\mathbb{R}}(\alpha_2) \circledcirc \ldots \circledcirc \boldsymbol{a}_{\mathbb{R}}(\alpha_k)]$ or dividing by s
$\frac{1}{s}\mathbf{n_2}(\mathbf{u}) \leq [\boldsymbol{a}_{\mathbb{R}}(\alpha_1) \circledcirc \boldsymbol{a}_{\mathbb{R}}(\alpha_2) \circledcirc \ldots \circledcirc \boldsymbol{a}_{\mathbb{R}}(\alpha_k)]$ (4)
Again by Theorem 4.1
$\mathbf{n_1}(\mathbf{u}) = \mathbf{n_1}\left(\sum_{j=1}^{k} \alpha_j \mathbf{u_j}\right) \geq r[\boldsymbol{a}_{\mathbb{R}}(\alpha_1) \circledcirc \boldsymbol{a}_{\mathbb{R}}(\alpha_2) \circledcirc \ldots \circledcirc \boldsymbol{a}_{\mathbb{R}}(\alpha_k)]$ or dividing by r
$\frac{1}{r}\mathbf{n_1}(\mathbf{u}) \geq [\boldsymbol{a}_{\mathbb{R}}(\alpha_1) \circledcirc \boldsymbol{a}_{\mathbb{R}}(\alpha_2) \circledcirc \ldots \circledcirc \boldsymbol{a}_{\mathbb{R}}(\alpha_k)]$ (5)
Now from (4) and (5) we have
$\frac{1}{r}\mathbf{n_1}(\mathbf{u}) \geq [\boldsymbol{a}_{\mathbb{R}}(\alpha_1) \circledcirc \boldsymbol{a}_{\mathbb{R}}(\alpha_2) \circledcirc \ldots \circledcirc \boldsymbol{a}_{\mathbb{R}}(\alpha_k)] \geq \frac{1}{s}\mathbf{n_2}(\mathbf{u})$ or $\frac{1}{r}\mathbf{n_1}(\mathbf{u}) \geq \frac{1}{s}\mathbf{n_2}(\mathbf{u})$ this implies that
$\frac{s}{r}\mathbf{n_2}(\mathbf{u}) \leq \mathbf{n_1}(\mathbf{u})$ put $\frac{s}{r} = p$ we have
$p\mathbf{n_2}(\mathbf{u}) \leq \mathbf{n_1}(\mathbf{u})$ (6)
Now from (3) and (6) we obtain
$p\mathbf{n_2}(\mathbf{u}) \leq \mathbf{n_1}(\mathbf{u}) \leq q\, \mathbf{n_2}(\mathbf{u})$
Hence by Theorem 4.4, $\mathbf{n_1}$ is fuzzy equivalent to $\mathbf{n_2}$.

Theorem 4.6:

Suppose that (U, n, ⊙) is algebra fuzzy normed space with dim U=k and D⊂U . If D is fuzzy closed and fuzzy bounded, then D is fuzzy compact.
Proof:
Since dim U=k and B={$\boldsymbol{u_1}$, $\boldsymbol{u_2}$, …,$\boldsymbol{u_k}$} be any basis for U. Consider the sequence ($\boldsymbol{d_m}$) in D then ∀ r ∈(0, 1) ∃ N∈ ℕ such that $\boldsymbol{d_m}$=$\boldsymbol{\alpha_{1m}u_1}$+$\boldsymbol{\alpha_{2m}u_2}$+…+$\boldsymbol{\alpha_{km}u_k}$, since D is fuzzy bounded so, is ($\boldsymbol{d_m}$) that is $\boldsymbol{n_U(d_m)}$ <t for all **m** and for some t ∈(0, 1). Now by Theorem 4.1
$\boldsymbol{n_U[d_m]}$= $\boldsymbol{n_U[\sum_{j=1}^{k}\alpha_{jm}u_j]}$ ≥ r[$\boldsymbol{a_{\mathbb{R}}(\alpha_1)}$ ⊙ $\boldsymbol{a_{\mathbb{R}}(\alpha_2)}$ ⊙…⊙ $\boldsymbol{a_{\mathbb{R}}(\alpha_k)}$]
Thus r[$\boldsymbol{a_{\mathbb{R}}(\alpha_{1m})}$ ⊙ $\boldsymbol{a_{\mathbb{R}}(\alpha_{2m})}$ ⊙…⊙ $\boldsymbol{a_{\mathbb{R}}(\alpha_{km})}$] ≤ $\boldsymbol{n_U[d_m]}$ <t or
$\boldsymbol{a_{\mathbb{R}}(\alpha_{jm})}$ ≤ [$\boldsymbol{a_{\mathbb{R}}(\alpha_{1m})}$ ⊙ $\boldsymbol{a_{\mathbb{R}}(\alpha_{2m})}$ ⊙…⊙ $\boldsymbol{a_{\mathbb{R}}(\alpha_{km})}$] < $\frac{t}{r}$
Hence the sequence ($\boldsymbol{\alpha_{jm}}$) for fixed **j** is fuzzy bounded so it has a limit point $\boldsymbol{\alpha_j}$ for each 1<j<k. We see that ($\boldsymbol{d_m}$) has a subsequence ($\boldsymbol{z_m}$) which converges to z = $\boldsymbol{\sum_{j=1}^{n}\alpha_j u_j}$. Since D is closed so z ∈D. But ($\boldsymbol{d_m}$) was an arbitrary sequence in D. Hence D is fuzzy compact.

Lemma 4.7:
Consider that (U, n, ⊙) is algebra fuzzy normed space and assume that D and Z two subspace of U with D⊆Z and D is fuzzy closed. Then for every t∈(0, 1) there is $\boldsymbol{z \in Z}$ such that $\boldsymbol{n_U}$(z−d)≥t for all d∈D.
Proof:
Let u∈Z−D and put s=$\boldsymbol{\inf_{d\in D} n_U}$(u−d). Clearly s>0 since D is fuzzy closed. Take t∈(0, 1) with s>t then by definition of infimum there is $\boldsymbol{d_0}$ ∈D such that s≤ $\boldsymbol{n_U(u-d_0)} \le \frac{s}{t}$. put z=u−$\boldsymbol{d_0}$. Now $\boldsymbol{n_U}$(z−d)= $\boldsymbol{n_U}$(u−$\boldsymbol{d_0}$ −d)= $\boldsymbol{n_U}$(u−$\boldsymbol{d_1}$) where $\boldsymbol{d_1}$=$\boldsymbol{d_0}$+d. Hence $\boldsymbol{n_U}$(z−d)= $\boldsymbol{n_U}$(u−$\boldsymbol{d_1}$)≥s>t.

Theorem 4.8:
Suppose that (U, n, ⊙) is algebra fuzzy normed space and if D={u∈U: 0<n(u)≤1} is a fuzzy closed in U and is compact then U must be finite dimension.
Proof:
Suppose that D is fuzzy compact and dim U is not finite. Choose $\boldsymbol{u_1}$ ∈D and let $\boldsymbol{U_1}$ be the subspace of U with basis {$\boldsymbol{u_1}$} so it is fuzzy closed. But $\boldsymbol{U_1}$ ≠U since dimU is not finite. Now by Lemma 4.7 there is $\boldsymbol{u_2}$ ∈D such that n($\boldsymbol{u_2-u_1}$)≥t=$\frac{1}{2}$. Let $\boldsymbol{U_2}$ be the subspace of U with basis { $\boldsymbol{u_1}$, $\boldsymbol{u_2}$}since $\boldsymbol{U_2}$ ≠U so there is $\boldsymbol{u_3}$ ∈D such that n($\boldsymbol{u_3-u_2}$)≥ $\frac{1}{2}$ and n($\boldsymbol{u_3-u_1}$)≥ $\frac{1}{2}$.
Now by induction we get ($\boldsymbol{u_k}$) ∈D with n($\boldsymbol{u_m-u_j}$))≥ $\frac{1}{2}$ where m≠j. This implies that ($\boldsymbol{u_k}$) does not contains a subsequence which is fuzzy converges. This contradicts the compactness of D. Hence dimU must be finite.

References

[1] Sadeqi I and Kia F 2009 Fuzzy normed linear space and its topological structure *Chaos Solutions and Fractals* **40(5)** 2576.
[2] Kider J 2011 On fuzzy normed spaces *Eng. & Tech. Journal* **29(9)** 1790
[3] Kider J 2011 Completion of fuzzy normed spaces *Eng. & Tech. Journal* **29(10)** 2004
[4] Kider J 2012 New fuzzy normed spaces J. Baghdad Sci. **9** 559
[5] Bag T and Samanta S 2013 Finite dimensional fuzzy normed spaces *Annals of Fuzzy Mathematics and Informatics* **6 (2)** 271
[6] Kider J and N. Kadhum N 2017 Properties of fuzzy norm of fuzzy bounded operators, *Iraqi Journal of Science* **58(3A)** 1237
[7] Kadhum N 2017 On fuzzy norm of a fuzzy bounded operator on fuzzy normed spaces M.Sc. Thesis *University of Technology Iraq*
[8] Ali A 2018 Properties of Complete Fuzzy Normed Algebra, M.Sc. Thesis *University of Technology, Iraq*

[9] Kider J and A. Ali A 2018 Properties of fuzzy absolute value on and properties finite dimensional fuzzy normed space *Iraqi Journal of Science* **59(2B)** 909
[10] Kider J and M. Gheeab M 2019 Properties of a General Fuzzy Normed Space *Iraqi Journal of Science* **60(4)** 847
[11] Kider J and M. Gheeab M 2019 Properties of The Space GFB (V, U), *Journal of AL- Qadisiyah for computer science and mathematics* **11(1)** 102
[12] Kider J and N. Kadhum N 2019 Properties of Fuzzy Compact Linear Operators on Fuzzy Normed Spaces *Baghdad Science Journal* **16(1)** 104
[13] Kider J 2020 Some Properties of Fuzzy Soft Metric Space *Al-Qadisiyah Journal of Pure Science* **25(2)** 1
[14] Kider J 2020 Some Properties of Algebra Fuzzy Metric Space, *Journal of Al-Qadisiyah for Computer Science and Mathematics* **12(2)** 43
[15] Khudhair Z and J. Kider J 2020 Some Properties of Algebra Fuzzy Absolute Value Space and Algebra Fuzzy Normed Space, *Al-Qadisiyah Journal of Pure Science* **25(4)** 46.
[16] S. Sharma and A. J. Obaid, "Mathematical modelling, analysis and design of fuzzy logic controller for the control of ventilation systems using MATLAB fuzzy logic toolbox," Journal of Interdisciplinary Mathematics, vol. 23, no. 4, pp. 843-849, 2020.

Q and JCPI–ings

QR and JCPI –Rings

Raida D. Mahmood, Roua S. Mohammed

Department of Mathematics, College of Computer Sciences and Mathematics, University of Mosul, Iraq.

E-mail: raida.1961@uomosul.edu.iq

Abstract. In this paper, we continue studies of several other authors, on QR (quasi-regular) and JCPI (JCP-injective) rings. In particular, we investigate some characterizations of several basic properties of QR and JCPI rings. Also, we prove that, if R is a semisimple and quasi duo, then R is strongly regular if and only if every simple singular right R-modules are JCPI. Keywords: JCPI-ring, QR-ring, MP-ring, strongly regular ring.

1. Introduction

Throughout, this paper is R denoted an associative ring with identity, and R-modules is until. For $d \in R$, $r(d)$ ($\ell(d)$) to denote the right (left), annihilator. We write $J(R)$,$y(R)$ ($z(R)$), DR for the Jacobson radical, the right singular (left singular) ideal and division ring. A right R -modules M is called P-injective, if for every principal right ideal I of R, any right R-homomorphism of I into M extends to one of R into M. R is called a right P-injective if R_R is P-injective [2]. A ring R is said to be quasi duo if every maximal right ideal of Ris a two-sided ideal [3]. Regular rings have been studied extensively by many authors (for example, [9], [5], and [8]). It is well known that a ring R is regular (strongly regular), if for any $d \in R$, there exists $b \in R$ such that $d = dbd$ ($d = d^2b$) [8]. In section 2, we give a relation between QR-rings and DR, and in section 3 gives some concepts of right JCPI-ring and the relationship between these and strongly regular rings.

2. QR -rings

Following [7], a ring R is said to be right (left) QR -ring, if $d \in dRd$ for all $d \notin y(R)$ ($d \notin z(R)$). Clearly, R is regular if and only if R is right (left) QR-ring and $y(R) = 0$ ($z(R) = 0$) ,[7].

Examples: 1) Let Z_4 be a ring of integers modulo 4. Then Z_4 is QR but not DR.

2) Let Z_5 be a ring of integers modulo 5. Then Z_5 is DR and QR. Now, we give some properties right QR -rings

Proposition 2.1**:** Let R be a ring without zero divisors. Then R is DR ring if and only if R is QR – ring.

Proof: Let a be a non-zero divisor of R. Then $r(d)=0$ and $d \notin y(R)$. Since R is QR - ring, then there exists $b \in R$ such that $d = dbd$, this implies $(1-bd) \in r(d)=0$. Hence $bd=1$. Similarly, we can show that $db=1$. Therefore d is invertible, hence it follows that R is a DR. Conversely: It is clear.

Corollary 2.2: If R is commutative and without zero divisors, then R is a field if and only if R is QR-ring.

Proof: Since R is the field, then R is DR and by (Proposition (2.1)) R is QR – ring.
Conversely: It is clear.
A ring R is called a right (left) MP- ring, if every maximal right (left) ideal is a left (right) pure [3]. A ring R is called ZC if $d'b = 0$ implies $bd' = 0$ for all $d', b \in R$. R is said to be a reduced ring if, R has no non-zero nilpotent element [1].

Lemma 2.3: Let R be a right MP- ring. Then $Y'(R) = 0$ [3].From Lemma 2.3 we get the following results:

Theorem 2.4: Let R be a right MP and QR-ring. Then J(R) =0.

Proof: Let $d' \in J(R)$. Since R is QR-ring, then there exists $b \in R$ such that $d' = d'bd'$ ($Y'(R) = 0$, Lemma 2.3). Since $d' \in J(R)$, then 1- $d'b$ is an invertible and hence (1- $d'b$) $\mu = 1$, $\mu \in R$. Consequently $d' = d'(1- d'b)\mu = 0$. Thus J(R) =0.

Proposition 2.5**:** Let R be the right MP and ZC ring. Then R is right QR –ring.

Proof: suppose that R is QR - ring, then there exist $d' \notin Y'(R)$ such that $dR + r(d') \neq R$, ($Y'(R) = 0$ Lemma (2.3)). Let M be any maximal right ideal containing $dR + r(d')$. Now since $d' \in M$ and R is MP-ring, then M is a left pure and $d' = bd'$ for some $b \in M$, $(1-b) \in \ell(d') = r(d) \subseteq M$ (R is ZC). Yielding $1 \in M$, which is a contradiction. Therefore $R = dR + r(d)$. Hence $d' = dbd'$ and consequently R is QR – ring.

3- Right JCPI Rings

A right R - modules M is JCPI if, for each $d' \notin Y'(R)$, every right R -homomorphism from $d'R$ to M can be extended to one of R into M.If R_R is JCPI, we call R is a right JCPI-ring[7]. Right ́P-injective rings are right JCPI,[7]. A ring R is said to be left (right) uniform if and only if every non-zero left (right) ideal is essential [3]. A ring R is abelian if every idempotent element is central.

Proposition 3.1: Let R be a right uniform QR -ring and $\ell(d) \subseteq r(d)$, for every $d' \in R$. Then R either a DR or a local ring and $Y'(R) = J(R)$.

Proof : If $Y'(R) = 0$, for all $0 \neq d' \in R$, hence $r(d) = 0$. Therefore by Proposition (2.1) R is DR. Now suppose that $Y'(R) \neq 0$, then for any $d' \notin Y(R)$, $r(d')$ cannot be essential. If $r(d') \neq 0$, there exist $0 \neq x \in r(d)$ and $d'x = 0$, and $r(d')$ is essential, a contradiction. Therefore $r(d') = 0$, which implies a left invertible by (Proposition (2.1))**.** Therefore every proper (maximal) left ideal is contained in $Y'(R)$ hence $J(R) \subseteq Y'(R)$. Since every QR - the ring is JCPI –ring, then $Y(R) \subseteq J(R)$ [7, Theorem 2.5]. So $Y'(R) = J(R)$ is the unique maximal left ideal, thus R is the local ring.

Proposition 3.2: Let R be an abelian ring and $r(d') = 0$, for $d' \in R$ with every principal ideal is JCPI, then R is reduced.

Proof: Let $d' \in R$ such that $d'^2 = 0$. Since $r(d) = 0$, then $d' \notin Y'(R)$. Define f: $d'R \to d'R$, by $f(d'r) = d'r$, for any $r \in R$. Since $d'R$ is JCPI, then there exists $b \in R$ such that $f(d'r) = d'bd'r$, thus $d' = d'bd'$. If we set $e = d'b$, then $d' = ed' = d'e$ (R is an abelian). So $d' = d'(d'b) = d'^2b = 0$. Hence, R is reduced.

Corollary 3.3**:** Let ℜ be an abelian and ɤ(ɗ)=0, for ɗ∈ ℜ, with every principal ideal is JCPI. Then ɣ(ℜ) =ʒ(ℜ) =0.

Theorem 3.4: If ℜ is a ring without zero divisors, ℜ/ɗℜ is JCPI and ɗℜ= ℜɗ, then ℜ is a Dℜ.

Proof: Let 0 ≠ ɗ ∈ ℜ be a non-zero divisor, then ɤ(ɗ) =0 and ɗ ∉ ɣ(ℜ), there exists any right ℜ -homomorphism of ɗℜ into ℜ/ɗℜ extended to one of ℜ into ℜ/ɗℜ. Define f: ɗℜ → ℜ/ɗℜ by f(ɗɤ)= ɤ + ɗℜ for all ɤ ∈ ℜ. So f is well defined, indeed if ɗɤ1=ɗɤ2, then ɗ(ɤ1-ɤ2) =0, (ɤ1–ɤ2) ∈ ɤ(ɗ)=0, hence f(ɗɤ1)=f(ɗɤ2). Now, since ℜ/ɗℜ is JCPI, then f(ɗɤ)= (c+ɗℜ)ɗɤ = cɗɤ +ɗℜ , for some c ∈ ℜ , In particular f(ɗ) =1+ ɗℜ =cɗ+ ɗℜ . Thus 1-cɗ∈ ɗℜ = ℜɗ implies 1 ∈ ɗℜ, and hence ɗℜ = ℜ, thus ɗƀ = 1 for some ƀ ∈ ℜ. Therefore, ℜ is Dℜ.

Following [4], a right module ɱ is called right an almost WJCPI, if, for any ɗ∉ ɣ(ℜ), there exists an S- sub module ɤɗ of ɱ such that $l_{ɱ}r_{ℜ}(ɗ)=ɱ_{ɗ}\oplus ɤ_{ɗ}$ as left S-sub module (S=End (ɱℜ)). If ℜ is almost WJCPI, then we call $ℜ_{ℜ}$ a right almost WJCPI rings.

Lemma 3.5 [6]: If ℜ is semisimple and quasi duo rings, then ℜ is reduced.

Theorem 3.6: Let ℜ be a semisimple quasi duo. Then the following conditions are equivalent:
1- ℜ is strongly regular.
2- ℜ is regular.
3- ℜ is Qℜ.
4- Every right ℜ -module is JCPI.
5- Every simple ℜ -module is JCPI.
6- Every simple singular right ℜ -module is JCPI.
7- Every simple singular right ℜ -module is almost WJCPI.

Proof: 1→ 2→ 3 → 4 → 5 → 6 →7 are trivial
6 → 1: For any 0 ≠ ɗ∈ ℜ. If ɗℜ +ɤ(ɗ) ≠ ℜ, then there exists a maximal right ideal ɱ of ℜ containing ɗℜ + ɤ(ɗ). If ɱ is not essential in ℜ , then ɱ = ɤ(e) , e^2 = e ∈ ℜ . Therefore eɗ=0, since ℜ is an abelian and ɗe =0. Hence e ∈ ɤ(ɗ) ⊆ ɱ = ɤ(e), which is a contradiction. So ɱ is essential in ℜ, By hypothesis, ℜ /ɱ is JCPI, since ɣ(ℜ) = 0 (Lemma 3.5), hence for any right ℜ - homomorphism ɗℜ → ℜ/ɱ can be extended to ℜ → ℜ/ɱ, defined by f(ɗɤ) = ɤ + ɱ, ɤ ∈ ℜ. Since ℜ is reduced, then f is a well-defined right ℜ-homomorphism. Hence, there exists c ∈ ℜ such that 1+ ɱ = f(ɗ) = cɗ+ ɱ , So 1-cɗ∈ ɱ , 1∈ ɱ, because ℜ is quasi duo. This is a contradiction. Hence ɗℜ +ɤ(ɗ)= ℜ, and then ℜ is strongly regular.
7 → 1: Let 0≠ ɗ∈ ℜ and ɗ∉ ɣ(ℜ) (ℜ is reduced). If ƀ ℜ ⊕ ɤ(ƀ) ≠ ℜ. Then ƀℜ ⊕ ɤ(ƀ) ⊆ N for some maximal right ideal of ℜ. Similarly to prove of [4, Theorem 3.11] we get ℜ is a strongly regular ring.

Acknowledgment
The authors are very grateful to the University of Mosul College of Computer Science and Mathematics for their provided facilities, which helped to improve the quality of this work**.**

References
[1] Cohn P M 1999 Reversible rings Bull *London Math*. Soc. **31** 641 -648
[2] Chen J and N Ding 1999 On general principally injective rings *Comm. In. Algebra* **27** (5) 2097-2116
[3] Mahmood R D 2000 On pure ideals and pure sub modules *Ph.D. thesis* Mosul University
[4] Mahmood R D and Ahmad S H 2019 On almost WJCP- injective rings *J Edu and sci **28***(1) 83–89
[5] Ming R Y C 1984 On Von Neumann regular rings XII *Tam*. *J. Math*. **16** (4) 67–75
[6] Jacobson N 1964 Structure of rings *Amer. Math Soc. Coll. Publ. XXXVII. Procidence, R. I*
[7] Junchao W. 2009 JCP –injective rings *Inter. Elec. J. of Algebra* **6** 1 –22

[8] Subedi T. and Ardeline M. Buhphang 2012 On strongly regular rings and generalization of semicommutative rings *Inter. Math. Forum* **7** (16) 777–790
[9] Von Neumann J. 1936 On regular ring *Proc. Nat. Sca. Sci. U. S. A.* **22** 707–713

The Analytic of Image Processing Smoothing Spaces Using Wavelet

The Analytic of Image Processing Smoothing Spaces Using Wavelet

Asma Abdulelah Abdulrahman, Mohammed Rasheed, Suha Shihab

Applied Science Department, University of Technology, Baghdad, Iraq

E-mail: rasheed.mohammed40@yahoo.com

Abstract. Image analysis took wide areas in many fields, including medicine, physics, and other areas where you need a tool to deal with it smoothly and softly without losing the original image information. Using an image of a sample of a physical atom that was analyzed and highlighting the compression and raising the noise, histogram and statistics the image statistics where the best results were recorded when using a specific threshold i.e. when pressing the methods were used the first has the threshold methods is Balance sparsity-norm, Remove near 0 and Bal-sparsity-norm(sqrt). As for the methods of raising the noise are fixed form thresholding method with soft threshold, penalize high with hard threshold, penalize medium with hard threshold, penalize low with hard threshold, Bal sparsity norm (sqrt) with soft threshold, where image parameters were divided into approximation coefficients and details coefficients. Through the analysis, a suitable threshold value was obtained, which helps to restore energy that leads to the fact that the compressed necessity did not lose much of its original information, which proves the new wavelets in the field of physical and medical imaging.

1. Introduction

Image compression helped to avoid the problem of the large size that the image needs in storage and transportation as it is one of the techniques that achieve reducing the space that the image needs for storage and transportation when analyzing the image and is considered one of the applications that are obtained by using wavelets [1-3]. Other techniques are to raise the noise, image statistics and histogram that are recognized through the use of wavelets after the effect of the wavelets used, where the image is analyzed into coefficients of the approximation and details, and the latter is divided into vertical, diagonal and horizontal [4-7]. Many of the works included types of standard wavelengths that were used in the field of image analysis, where these wavelets bear the characteristic of orthogonally and their affiliation to the fields of linear and non-linear approximation of these common wavelets families are Symlets (Level 2), coiflets (constitute a family of wavelets with an unusual property-Level 2), Daubecheis (Level 2) and Haar [8-10]. Multi Resolution Analyze (MRA) that achieves the wavelets feature of the ability to analyze the wavelets of images, which is the analysis of wavelets into two fields, is the field scaling function and wavelet function, the field to which the wavelet belongs [11-12]. Wavelets that are constructed from the mother wavelet were used, which we obtain expansion and contraction with the help of coefficients s and r such as first, second, third and fourth Chebyshev wavelets, Legendre wavelet Hermite wavelet and Laguerre wavelets [13-22]. Through which the best results were obtained to reach the optimal solution to solve many numerical problems such as variational problems, optimal problems, integral equations Fredholm and voltera and integro differential equations.

In this work, a kind of these wavelengths Second Chebyshev Wavelet Transform (SCWT) have used in the field of image analysis after demonstrating several theories that qualify them to perform this function and a technique has obtained Multi Resolution Analyze (MRA) that obtained wavelet analysis to approximation factors and details. The new wavelet has used to analyze the image that belongs to a sample of a physical atom [23-32], where image statistics have obtained and noise has removed from them using methods the first has the threshold methods are Balance sparsity-norm, Remove near 0 and Bal-sparsity-norm(sqrt) in compression image and in de noising image used methods are soft threshold, penalize high with hard threshold, penalize medium with hard threshold, penalize low with hard threshold, Bal sparsity norm(sqrt) with soft threshold, and get the best results, which shows that the Tables (1-5). The objective of the present work is new wavelets were used for the first time that was used in other works to solve problems numerically. However, in this work they have used to analyze the image as it performed its job in the best image by the filter produced from it before that many new theories have demonstrated to prove its readiness in the field of images. One of these theorems is to prove the affiliation of the new wavelets to the fields of linear and non-linear approximation because of the property that the new wavelets possess, which is the property of orthogonality and their contain Scaling function and the realization of Multi Resolution Analyze (MRA) that achieves the wavelets feature of the ability to analyse the wavelets of images.

2. Suggested Wavelet Conversions

In this section, wavelets that have been used in previous works are chosen for many numerical solutions and to reach the optimum solution or the exact solution compared to other wavelets that have been compared with them where the best is reached. These wavelets will be built on the mother waves in the Eq. 1

$$\Psi_{s,r}(x) = |s|^{\frac{-1}{2}}\Psi\left(\frac{x-r}{s}\right)\ s, r \in R,\ \ s \neq 0 \qquad (1)$$

where: $\psi(t) = [\psi_0(t), \psi_1(t), \ldots, \psi_{M-1}]^T$

The elements $\psi_0(t), \psi_1(t), \ldots, \psi_{M-1}(t)$ are the basis functions, orthogonal on the [0,1].

If you don't wish to use the Word template provided, please set the margins of your Word document as follows.

2.1. Second Kind of Chebysheve Wavelet Transform (SCWT)

These wavelets are Second Kind of Chebysheve Wavelet Transform (SCWT) [33-34], which have proven in many actions in the foreground between the sons of their generation from the first, third and fourth wavelets of the worms of Chebysheve, by comparing the results when solving many numerical problems. For example, covariance issues Discrete Second Kind of Chebysheve Wavelet Transform (SCWT), denoted by (t) $D_{s,r}(t) = D(t, s, r, n)$, the parameters s, r transformed to discrete wavelet by used $x = 2^{-(n-1)}(2^n t),\ d = 2^{-(n-1)}(2s-1),\ c = 2^{-(n-1)}$ by substituting these parameters in Eq. 1 that have obtained Discrete Second Chebysheve Wavelet Transformations (DSCWT) as shown in Eq. 2,

$$D_{s,r}(t) = \begin{cases} 2^{\frac{n}{2}}\widetilde{D}_r(2^n t - 2s + 1) & t \in \left[\frac{s-1}{2^{n-1}}, \frac{s}{2^{n-1}}\right) \\ 0 & \text{otherwise} \end{cases} \qquad (2)$$

where: $\widetilde{D}_r(t) = \sqrt{\frac{2}{\pi}}D_r(t)$ $r = 0,1,2,\ldots,M-1$ for $k = 2$ with weight function $w_r(2^n t - 2s + 1) = \sqrt{(1-(2^n t - 2s + 1)^2)}$ on the interval $[-1, 1]$, satisfied the recursive formula

$$D_0 = 1, \qquad D_1 = 2t,\ \ D_{r+1}(t) = 2tD_r(t) - D_{r-1}(t),\ \ r = 1,2,\ldots,M-1$$

$$D_{1,0} = \frac{2\sqrt{2}}{\sqrt{\pi}}$$

$$D_{1,1} = \frac{2\sqrt{2}}{\sqrt{\pi}}(8t-2)$$
$$D_{1,2} = \frac{2\sqrt{2}}{\sqrt{\pi}}(64t^2-32t+3)$$
$$D_{1,3} = \frac{2\sqrt{2}}{\sqrt{\pi}}(512t^3-384t^2+80t-4), \text{ where: } 0 \le t < \frac{1}{2}$$
$$D_{2,0} = \frac{2\sqrt{2}}{\sqrt{\pi}}$$
$$D_{2,1} = \frac{2\sqrt{2}}{\sqrt{\pi}}(8t-6)$$
$$D_{2,2} = \frac{2\sqrt{2}}{\sqrt{\pi}}(64t^2-96t+35)$$
$$D_{2,3} = \frac{2\sqrt{2}}{\sqrt{\pi}}(512t^3-1152t^2+848t-204), \text{ where: } \frac{1}{2} \le t < 1$$

With respect to SKCWT the same above have get with the coefficients the function approximation

$$X(t) \cong X_{2^{n-1},M-1} = \sum_{s=1}^{2^{n-1}} \sum_{r=0}^{M-1} X_{s,r} D_{s,r}(t) = X^T D_{s,r}(t) \quad (3)$$

where: $C, D_{s,r}$ are $2^{n-1}M \times 1$ matrices

$$D = \left[D_{1,0}, D_{1,1}, \dots, D_{1,M-1}, D_{2,0}, \dots, D_{2^n,M-1}, \dots D_{2^n,0}, \dots D_{2^n,M-1}\right]^T$$

and

$$X = \left[X_{10}, X_{11}, \dots, X_{1(M-1)}, X_{20}, \dots, X_{2(M-1)}, \dots, X_{2^n}, \dots, X_{2^nM-1}\right]^T$$

2.2. Properties of SCWT and It's Scaling Function

Theories that will be demonstrated adapt the smoothness of the proposed waves in many new uses, for example image processing, such as medical and physical images [35-43], etc. These theories are the most important mathematical aspects in the field of wavelets

Definition 2.1

For every pair of $s, r \in Z$, define the period $I_{s,r}$ by $I_{s,r} = [2^{-s}r, 2^{-s}(r+1)]$ which is familiar as dyadic period. The group of all such period is called dyadic sub periods of R.

The collection of functions

$$\{\alpha_{s,r}(t)\}_{s,r\in Z} = \frac{1}{2^s}\alpha(2^{-s}-r) \forall s, r \in Z \quad (4)$$

Definition 2.2

(SCWT scaling function): Eq. 4 is called the scaling function of Second Kind of Chebysheve Wavelet Transform (SCWT), it defines

$$\alpha(t) = \begin{cases} 2\sqrt{2} & \text{if } 0 \le t \le 1 \\ 0 & \text{otherwise} \end{cases} \quad (5)$$

The system of Second Kind of Chebysheve Wavelet Transform (SCWT), $\forall s, r \in Z$ define

$$\{D_{s,r}(t)\}_{s,r\in Z} = \frac{1}{2^s}\alpha(2^{-s}-r) \forall s, r \in Z \quad (6)$$

Let $f(t)$ is defined on $L^2[0,1]$ has an expansion in terms of Second Kind of Chebysheve functions as follows.

$$f(t) = \sum_{s=S}^{2^s} < f, \alpha_{S,r} > \omega_{S,r}(t) + \sum_{s=S}^{\infty} \sum_{r=0}^{2^s} < f, D_{s,r} > D_{S,r}(t)$$
$$= \sum_{s=S}^{2^s} a_{s,r}\, \omega_{S,r}(t) + \sum_{s=S}^{\infty} \sum_{r=0}^{s-1} d_{s,r}\, D_{S,r}(t) \quad (7)$$

$d_{s,r}$ is the details of coefficients and $a_{s,r}$ is the approximate coefficients.

2.3. Multi Resolution Analyses (MRA) With Wavelet

The main coefficients of wavelet DSCWT through a system MRA L^2 (R):

$$f = \sum\sum X_{s,r} D_{s,r} \quad (8)$$

$$f \in V_s = \{f(t) | f(t) = \frac{1}{2^{s/2}} h(2^{-s}t),\ h(t) \in V_0\},$$

$$f(t) = \sum_{s\in z} < f, \alpha(r) > \alpha(r)$$

Then a MRA of DSCWT on R is a sequence of subspaces $\{V_s\}$ $s \in Z$ of functions L^2 on R, First and foremost, in order for the new wavelets to be ready for the applications that can take place in the next sections, the following characteristics must be found.

For $\forall\, s, r \in Z, V_s \subseteq V_{s+1}$.

If f(t) is R, then $f(t) \in \text{span}\{V_s\} s \in Z$, with $\epsilon > 0$, there is an $s \in Z$ and a function $g(t) \in V_s$ such that $\|f - g\|_2 < \epsilon$.

$$\cap_{s\in Z}\ V_s = \{0\}.$$

A function $f(t) \in V_0 \leftrightarrow 2^{-s/2} f(2^{-s}t) \in V_s$.

There exists a function $\alpha(t), L^2$ on R, called the scaling function such that the collection $\alpha(t - s)$ is an orthonormal system of translates and $V_0 = \text{span}\{\alpha(t - s)\}$.

Definition 2.3

Let $\{V_S\}$ be an MRA) with scaling function $\alpha(t)$ which satisfies (9) and $h(r)$ in this definition are considered calibration colander, where

$$D_{s,r}(t) = \frac{1}{2^s} D(2^{-s}t - r) \quad (9)$$

$$h(r) = < \frac{1}{\sqrt{\pi}} \alpha\left(\frac{t}{2}\right), \alpha(t - r) > \quad (10)$$

$\alpha(r)$Is the function that has called scaling wavelet

$$g(t) = (-1)^r h(1 - r) \quad (11)$$

DSCWT is defined

$$D(x) = \sum_{t\in Z} g(r) \frac{1}{\sqrt{\pi}} \alpha(\frac{t}{2} - r) \quad (12)$$

Then $\{D_{s,r}(t)\} s, r \in Z$ is a Chebysheve wavelet orthonormal standard on R.

Definition 2.4

Obtaining the Eq. 13 representing orthogonal projection if the function f is arbitrary

$$P_s f = \sum_{s\in Z} < f, \alpha_{s,r} > \alpha_{s,r} \quad (13)$$

$f \in L^2$ when it on to V_s

3. Suggested Wavelet Conversions With Approximation Spaces [44-55]

In this section, many theories that demonstrate the affiliation of wavelets proposed in this paper have demonstrated approximation spaces.

3.1. Approximation in Space of Square Integrable Functions over R

Let $f \in L_2(R)$ is continuous then the bases of SCWT be a series

$$f = \sum_{s=0}^{\infty} \sum_{r=0}^{R-1} < f, D_{s,r} > D_{s,r}(t) \quad (14)$$

$D_{s,r}$ be in the interval $I_{s,r} = \left[\frac{r}{2^{-s}}, \frac{(r+1)}{2^{-s}}\right]$,

$$< f, D_{s,r} > = \int f(t) D_{s,r}(t) dt = 2^{s/2} \int_{r2^s}^{(r+1)2^s} f(t) D(2^s t - r) dt. \quad (15)$$

Let $S=2^T$ is the coefficients if $T \in S$ has account in finite sum s= 0, 1, 2,…, $2^T - 1 = S$, then $\sum_{s=0}^{T-1} \sum_{r=0}^{S-1} 1 + 2 + 2^2 + \cdots + 2^T - 1 = S - 1$ coefficients of in SCWT that for each s only one of the non-zero coefficients is its size$2^{-s/2}$.

E is the approximate error in $L_2(R)$, which has determined from the Eq. 16

$$\left\| f - \sum_{s=0}^{T-1}\sum_{r=0}^{R-1} < f, D_{s,r} > D_{s,r}(t) \right\|_{L_2}^2 = \left\| \sum_{s=T}^{\infty}\sum_{r=0}^{S-1} < f, D_{s,r} > D_{s,r}(t) \right\|_{L_2}^2$$
$$= \sum_{s=T}^{\infty}\sum_{r=0}^{R-1} \left| < f, D_{s,r} > \right|^2 = \sum_{s=T}^{\infty} 2^{-s} = 2^{-T} = \frac{1}{S} = \sigma(2^{-s}) \quad (16)$$

Not: σ is any approximation result.

Theorem 3.1 (Approximation in $L_P(R)$)

Let $L_P(R)$ be a partial sum of SCWT and $f \in L_P(R)$ then

$$K = \sum_{s=0}^{T-1}\sum_{r=0}^{S-1} < f, D_{s,r} > D_{s,r}(t) \rightarrow E_{app} = \sigma(2^{-s/2})$$

Proof

E_{app} is a determine the approximate error in $L_P(R)$

$$E_{app} = \|f - K\|_{L_P} = \left\| f - \sum_{s=0}^{T-1}\sum_{r=0}^{S-1} < f, D_{s,r} > D_{s,r}(t) \right\|_{L_P}$$
$$= \left\| \sum_{s=I}^{\infty}\sum_{r=0}^{S-1} < f, D_{s,r} > D_{s,r}(t) \right\|_{L_P} = \left(\sum_{s=I}^{\infty}\sum_{r=0}^{S-1} \left| < f, D_{s,r} > \right|^P \right)^{1/P}$$
$$= \left(\sum_{s=T}^{\infty} 2^{-TP/2} \right)^{1/P} = 2^{-T/2} = \sigma 2^{-T/2}$$

Theorem 3.2 (Approximation in iPM L (□,P))

Let P is a constant $1 < P \leq \infty$, $M > 0$ and if $f \in L_{iPM}(\mu, P)$ then SCWT and T⊆S then

$$K(t) = \sum_{s=0}^{T-1}\sum_{r=0}^{S-1} < f, D_{s,r} > D_{s,r}(t) \rightarrow E_{app} = \sigma(2^{-T\mu})$$

Theorem 3.3 (Approximation in Besov Space B (L (R))

In SCWT $K(t) = \sum_{s=0}^{T-1}\sum_{r=0}^{S-1} < f, D_{s,r} > D_{s,r}(t)$ $f \in F^s(R)$ then $\exists: T \in S \rightarrow E_{app} = \sigma(2^{-TS/2})$ where $S = 2^T$ and E_{app}:- is the approximate error of in $F^s L_2(R)$

Proof

$$E_{app} = \|f - K\|_{L_2} = \left\| f - \sum_{s=0}^{T-1}\sum_{r=0}^{S-1} < f, D_{s,r} > D_{s,r}(t) \right\|_{L_2} \leq \left(\sum_{s=T}^{\infty}\sum_{r=0}^{S-1} \left| < f, D_{s,r} > \right|^2 \right)^{1/2} \leq$$
$$\left(\sum_{s=T}^{\infty}\sum_{r=0}^{S-1} \frac{2^r}{2^S} \left| < f, D_{s,r} > \right|^2 \right)^{1/2} \left(2^{-S} \sum_{s=T}^{\infty}\sum_{r=0}^{S-1} 2^r \left| < f, D_{s,r} > \right|^2 \right)^{1/2}$$ from spaces's properties
$$\|f\|_{F^s}\left(L_2(R)\right) \cong \left(\left(\sum_{s=T}^{\infty}\sum_{r=0}^{S-1} 2^{Sr} \left| < f, D_{s,r} > \right|^2 \right)^{1/2} \right) \text{ then } E_{app} \leq 2^{-S/2} \|f\|_{F^s}\left(L_2(R)\right) = \sigma 2^{-S/2}$$

4. Nonlinear Approximation in L(R)

Theorem 4.1

If the partial sum of SCWT with f and let $f \in L_P(R)$

$$K = \sum_{s=0}^{T-1}\sum_{r=0}^{S-1} < f, D_{s,r} > D_{s,r}(t),\ s \in Z \rightarrow E_{app} = \sigma(2^{-s/2})$$

Proof

$$E_{app} \|f - K\|_{L_P} = \left\| f - \sum_{s=0}^{T-1}\sum_{r=0}^{S-1} < f, D_{s,r} > D_{s,r}(t) \right\|_{L_P}$$
$$= \left\| \sum_{s=T+1}^{\infty}\sum_{r=0}^{S-1} < f, D_{s,r} > D_{s,r}(t) \right\|_{L_P} = \left(\sum_{s=T+1}^{\infty}\sum_{r=0}^{S-1} \left| < f, D_{s,r} > \right|^P \right)^{1/P}$$
$$= \left(\sum_{s=T+1}^{\infty} 2^{-TP/2} \right)^{1/P} = 2^{-T/2} = \sigma 2^{-T/2}.$$

5. New Filter of SCWT

The filter is constructed for the proposed wavelets starting from scaling function for SCWT according to the Eq. 5 with the wavelength function at zero. The following two basic atoms of wavelets called the laguerre wavelet.

$$D_{s,r}(t) = 2^{\frac{n}{2}} D(2^n t - 2s + 1) \qquad \text{for } (s,r) \in Z^2 \tag{17}$$

$$\alpha_{s,r}(t) = 2^{\frac{n}{2}} \alpha(2^n t - 2s + 1) \qquad \text{for } (s,r) \in Z^2 \tag{18}$$

Eq. 17 is the wavelet equation and Eq. 18 is the scaling equation.

5.1. The Coefficients of SCWT

In this section, the proposed wavelet coefficients are created. The wavelet coefficients of a signal S, in Eqns. 19 and 20 the wavelet coefficients and scaling coefficients

$$\delta_{s,r} = \int S(t) D_{s,r}(t) dt \qquad \text{in R} \tag{19}$$

$$\varphi_{s,r} = \int S(t) \alpha_{s,r}(t) dt \qquad \text{in R} \tag{20}$$

When using the parameters, the signal is rebuilt

$$S(t) = \sum_{s\in Z} \sum_{r\in Z} \delta_{s,r} D_{s,r}(t) \tag{21}$$

From MRA the space of scaling function V_0

$V_0 = \{f \in L^2(R) | f(t) = \varphi_{0,r} \alpha(2^n t - 2n + 1) \in l^2(Z)\}$ is span $V_1, V_2, \dots., V_s = V_{s+1} + W_{s+1}$

W_s the space of wavelet function

Wavelet coefficients, when analyzed, have divided into approximate coefficients and details coefficients of SCWT and scaling function of SCWT Eqns. 22 and 23 show these coefficients from Eq. 20 to obtain Eq. 22

$$a_s(t) = \sum_{r\in Z} \varphi_{s,r} \alpha_{s,r}(t) \text{ (Approximate coefficients)} \tag{22}$$

$$d_s(t) = \sum_{r\in Z} \delta_{s,r} D_{s,r}(t) \quad \text{(Details coefficients)} \tag{23}$$

In level s, then the coefficients whine $s = 0$ is $\{\varphi_{0,r}\}$

5.2. Decision Tree of SCWT

The signal S found is from level 0 to $a_0 = S$, in level 1 $d_1 = a_0 - a_1$ then $S = d_1 + a_1$ and in level 2

$$\begin{aligned} d_2 &= a_1 - a_2 \\ &= S - d_1 - a_2 \\ &= d_2 + d_1 + a_2 \end{aligned}$$

From Eq. 3; if $f_{s,r} = S$

$$S = \sum_{s=1}^{2^{n-1}} \sum_{r=0}^{M-1} \delta_{s,r} D_{s,r}(t) = \delta^T D_{s,r}(t) \tag{24}$$

$$\text{In general} \qquad S = a_N + \sum_{s\le N} d_s \tag{25}$$

and $a_{N-1} = a_N + d_N$

5.3. Formation Packets of SCWT

By Multi Resolution Analysis with the equation if $e_r, f_r \in l^2$

$$\frac{1}{2}\alpha\frac{1}{2} = \sum_{r\in Z} e_r \alpha(t - r) \in L^2 \tag{26}$$

$D_{0,r} = D(t - r)$ $D \in W_0$ such that

$$\frac{1}{2}D\frac{1}{2} = \sum_{s\in Z} f_r \alpha(t - r) \in L^2 \tag{27}$$

In the norm space the interval $[0,1) \rightarrow \{D_{s,r}\}_{s,r\in Z} \subseteq L^2$

The following Algorithm stages explain the construction Packets steps

Algorithm 5.1: construction Packets of SCWT

Step 1: Start with the candidates $u_{r,} v_r$ the orthogonal of SCWT and scaling function of SCWT with MRA of $L^2(R)$ has been the basis of sequences $\{e_r\}_{r\in Z}$ and $\{f_r\}_{r\in Z}$ in l^2

Step 2: The sequence of functions $(D_s)_{s\in Z}$ $(L_n)_{n\in N}$ the $D_0 = \alpha$ the scaling function

$$\begin{cases} D_{2r}(t) = \frac{2\sqrt{2}}{\sqrt{\pi}} \sum_{r=0} v_r D_r(2t-s) \\ D_{2r+1=} \frac{2\sqrt{2}}{\sqrt{\pi}} \sum_{r=0} u_r D_r(2t-s) \end{cases} \quad (28)$$

$$r = 0 \rightarrow v_0 = v_1 = \frac{2\sqrt{2}}{\sqrt{\pi}}, u_0 = -u_1 = \frac{-2\sqrt{2}}{\sqrt{\pi}} \quad (29)$$

Step 3: The wavelet SCWT in [0,1) in $r = 1$ and scaling function in $r = 0$

$$D_{2r}(t) = D_r(2t) + D_r(2t-1) \quad (30)$$

$$D_{2r+1}(t) = D_r(2t) - D_r(2t-1) \quad (31)$$

Step 4: Two copies of D_r in [0, 0.5) for $D_r(2t)$ obtain D_{2r} and in [0.5, 1) obtain D_{2r+1} from $D_r(2t-1)$.

Step 5: The result of smoothed relation for regular function in the interval $[0, 2M-1]$

$$D_r(2^k t - 2s + 1)$$

Let the (j, k) is the SCWT packet $j = 0,1,2,3, \ldots . \quad j \in Z \ , k = 0,1, \ldots, 2^j - 1$

$j = 0, \ \alpha_{0,0}(t) = \frac{\sqrt{2}}{\sqrt{\pi}} D_0(t) = 1$ and $j = 1, \ D_{1,0}(t) = \frac{\sqrt{2}}{\sqrt{\pi}} D_0(t) = \frac{2\sqrt{2}}{\sqrt{\pi}}, D_{1,1} = \frac{\sqrt{2}}{\sqrt{\pi}} D_1(2t-1) = \frac{\sqrt{2}}{\sqrt{\pi}}[1 - (2t-1)] \quad j = 2, \ D_{2,0} = \alpha_{0,0}(t) = D_{1,0}(t) = \frac{\sqrt{2}}{\sqrt{\pi}} D_0(t)$

The norm in this filter is $\frac{\sqrt{2}}{\sqrt{\pi}}$ will be obtained high filter and low filter then

High pass filter is $\frac{\sqrt{2}}{\sqrt{\pi}}$ $[2 \ -2]$ and low pass filter is $\frac{\sqrt{2}}{\sqrt{\pi}}$ $[2 \quad 2]$ this filter will be used in the image analyses after add this filter in MATLAB.

W divided into low pass filter will symbolize the filter L_0_D and high pass filter H_0_D they are used in decomposition step and reconstructed with invers SCWT filter denoted by R they are L_i_R and H_i_R with SCWT the figure displays that

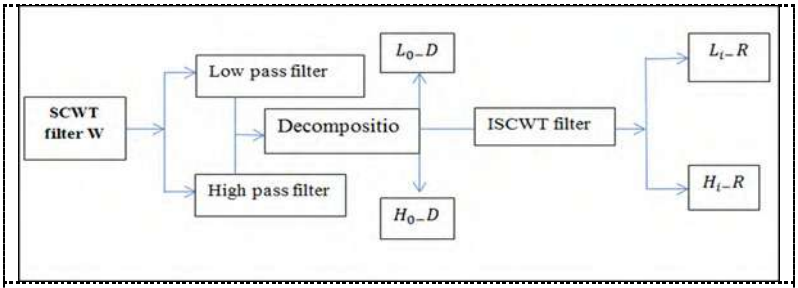

Figure 1. The four filters in second Chebyshev Wavelet Transform.

6. Applied SCWT With Image Processing

In this section, various applications in image processing such as compression and noise removal will be identified.

6.1. SCWT filter effect on analytic of image

In this section, the proposed wavelets are affected by the color image analysis. Where a physical image 256×256 was used for a specific atom, the color image is converted into a gray image. The image is divided into approximation coefficients, and the detail coefficients by which it is divided into three vertical, horizontal, and diagonal sections, so the image is divided into four blocks each Block size (16×16), Figure 2 shows the effect of SCWT filter on the proposed image, which is the physical image [37].

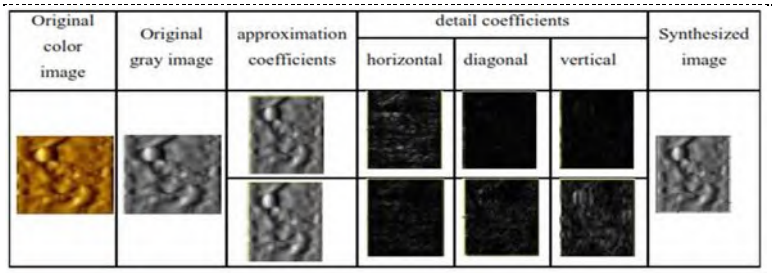

Figure 2. The effect of wavelets SCWT on the physical image.

6.2. The most Important Operations on the Physical Images

After analyzing the image using SCWT, the new wavelet faces four important operations, statistics, histograms, compress and de-noise. Figure 3 shows the statistics operation of image physical using SCWT in level 2 and the norm in statistics in level 1 is $8.91e^{+0.8}$ and in level 2 $3.22e^{+04}$ max norm 256.

6.2.1. The Statistics Image by SCWT

In this section, the effect of SCWT on the image will be displayed in terms of statistics with respect to the coefficients of approximation factors and details that are divided into vertical, horizontal and diagonal. Details are shown where the Figure 3 will display the original image with SCWT, Figure 4 shows how the effect Wavelets on approximation and rebuilding coefficients. As for the figure 5, it shows details of coefficients with rebuilding, showing the differences between them, Approximation Coefficients (AC), Approximation Reconstructed (AR), Details Horizontal Coefficients (DHC), Details Vertical Coefficients (DVC), Details Diagonal Coefficients (DDC), Details Horizontal Reconstructed (DHR), Details Vertical Reconstructed (DVR), Details Diagonal Reconstructed (DDR).

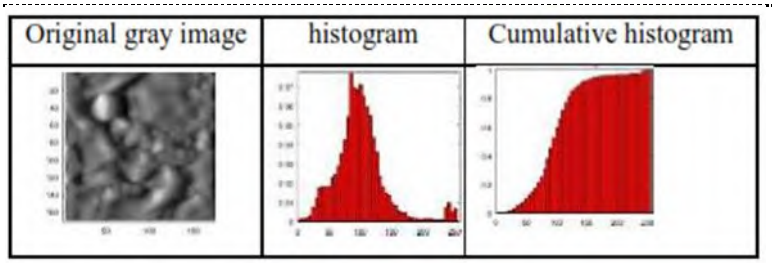

Figure 3. Original statistics image with SCWT.

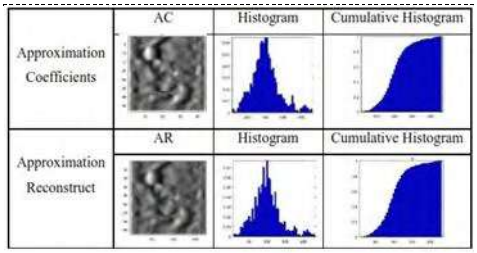

Figure 4. Approximation coefficients and reconstruct.

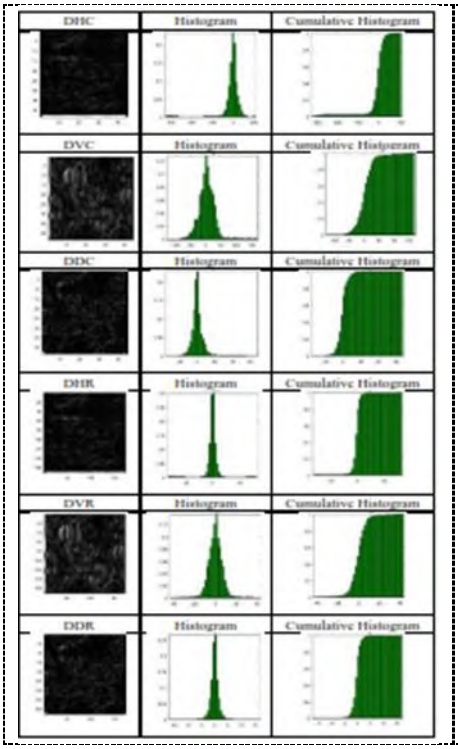

Figure 5. Details coefficients and reconstruct.

6.2.2. The histogram Image by SCWT

This section shows one of the effects of the new wavelet SCWT on the physical sample, where the signal represents and is equal to a_0 see section 5.2 the Figure 6 shows the approximation coefficients in level 1 and 2, and Figure 7 shows the details of coefficients horizontal, vertical and diagonal in level 1 and 2.

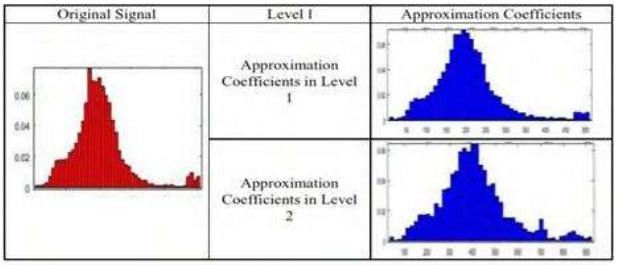

Figure 6. The approximation coefficients in level 1 and 2.

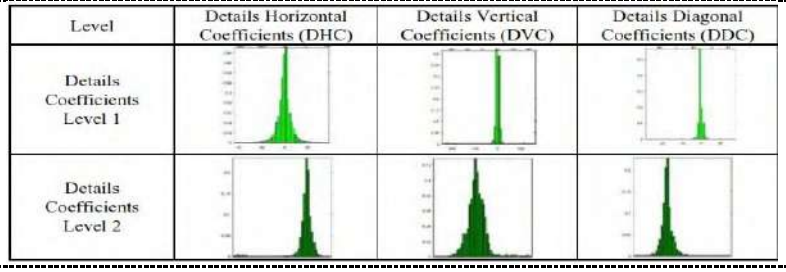

Figure 7. The details of coefficients horizontal, vertical and diagonal in level 1 and 2.

6.2.3. The Compression Image by SCWT

The appropriate technique for transferring image information without any losing of it's information. New waves will be used to compress the image. In Matlab program, the compression process is carried out using two methods, global thresholding and by level thresholding, the first has the threshold methods is Balance sparsity-norm, Remove near 0 and Bal-sparsity-norm (sqrt). Figure 8 represents the process of compression using the first method with SCWT, while Table 1 shows the results that were reached through the first method with the wavelets proposed. The second is with the methods of threshold scarce high, scarce medium, scarce low, balance sparsity-norm, remove near zero, and bal sparsity norm(sqrt), are shown in Figures 9 and 10. The results are identified from Table 2.

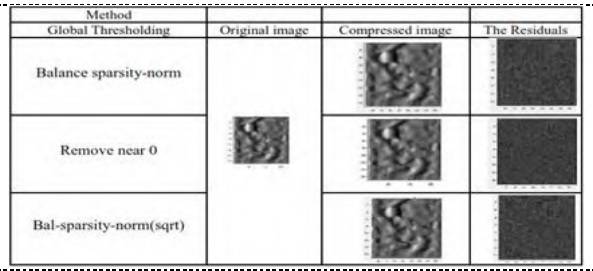

Figure 8. The compressed by global thresholding with SCWT.

Table 1. The results compressed of Global thresholding method with SCWT.

Global thresholding			
Balance spearsity-norm		Remove near zero	Bal- sparsety norm
Thresholding	6.76	6.76	5
Return energy (Information)	99.69%	99.69%	99.98
Number zero	73.38%	73.38%	65.42
L_2Norm	1.5	1.5	2.4
L_1Norm	681	681	104
Max norm	9	9	14

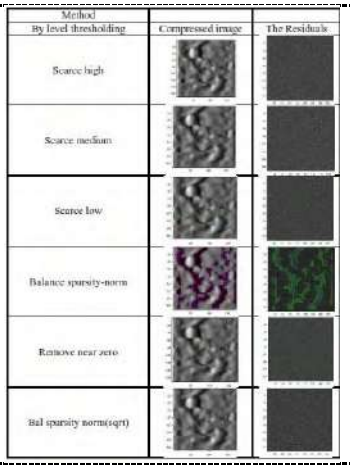

Figure 9. Details coefficients and reconstruct.

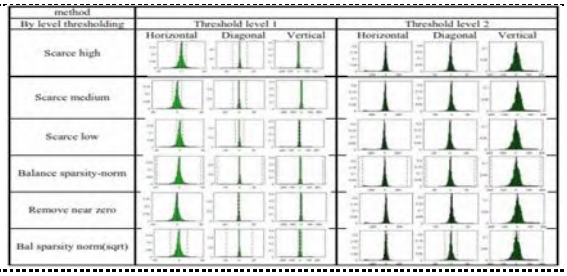

Figure 10. Threshold compressed by level method with SCWT.

Table 2. Results compressed by level thresholding with SCWT.

By level thresholding							
Thresholding method	Scarce high		Scarce medium	Scarce low	Balance sparsity-norm	Remove near zero	Bal sparsity norm(sqrt)
Thresholding	L_1	10.5	9	6	325.8	1.5	18.05
	L_2	0	0	0	47.3	1.5	18.05
Return energy (Information)		99.97%	99.99%	99.98%	99.92%	100%	96.21%
Number zero		20	22.74%	25.69%	30.85%	14.55%	35.70%
L_2Norm		575	$6.646e^{+04}$	504.5	$2.197e^{+05}$	40.14	$1.004e^{+06}$
L_1Norm		$1.273e^{+05}$	326.6	1.108	961.5	63.36	62.46
Max norm		9	5	8	17	1	100

6.2.4. De-Noising Image by SCWT

Adding new noise to the image or signal helps reduce and restore the noise of the color image or signal, the simple statistically significant relationship to noise reduction

Let F is the image to be de noised, the image to be restored, e is the noise and $\vartheta^2 I$ expressed in the following equation

$$F_{(r,s)} = l_{(s,r)} + e \qquad (32)$$

The removal of noise by wavelets consists of three stages

At the level in which the wavelets decompose the image from which the noise is to be removed.

In three directions the choice of threshold from the detail coefficients is with the absolute threshold dependent on ϑ.

This stage is to reconstruct the image after analysis and be dependent on the approximation coefficients.

The de noising image by SCWT selected thresholding method

1. Fixed form thresholding method with soft threshold.
2. Penalize high with hard threshold.
3. Penalize medium with hard threshold.
4. Penalize low with hard threshold.
5. Bal sparsity norm (sqrt) with soft threshold.

Select noise structure

1. Unscaled white noise
2. Scale white noise
3. Non scale white noise

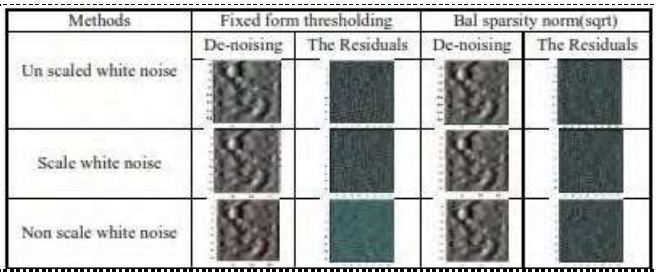

Figure 11. De-noising with soft threshold by SCWT.

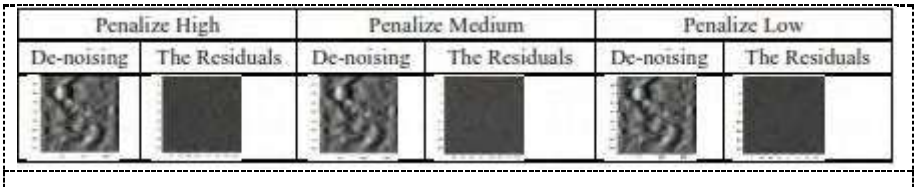

Figure 12. De-noising with hard threshold by SCWT.

Table 3. The results de noising soft threshold methods with SCWT.

	Fixed form Thresholding			Bal Sparsity Norm(sqrt)		
	Un scaled white noise	scale white noise	non scale white noise	Un scaled white noise	scale white noise	non scale white noise
Soft threshold	4.158	9.247	43.15	18.05	18.05	18.05
L^2norm	$1.431e^{+05}$	$2.791e^{+05}$	$7.668e^{+05}$	$4.522e^{+05}$	$4.522e^{+05}$	$4.522e^{+05}$
L^1norm	605.7	116.2	290.8	187.1	187.1	187.1
Max norm	6	12	21	4	23	23

Table 4. The results de noising soft threshold methods with SCWT

	Penalize High	Penalize Medium	Penalize Low
Hard threshold	8.5	4.75	4.25
L^2norm	$1.068e^{+05}$	$5.071e^{+04}$	$4.344e^{+04}$
L^1norm	488.4	265	238
Max norm	8	5	4

Table 5. Results of three different methods with the fixed form thresholding.

Method	Fixed Form Thresholding					
Hard thresold	Threshold level 1			Threshold level 2		
	Horizontal	Diagonal	Vertical	Horizontal	Diagonal	Vertical
Un Scaled white noise	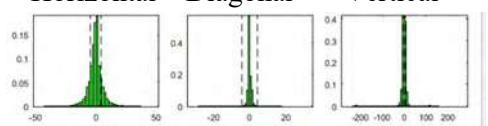			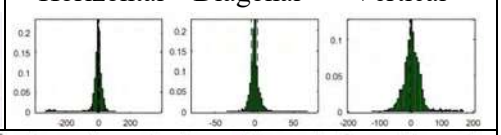		
Scale white noise	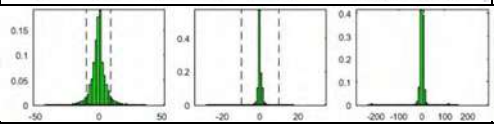			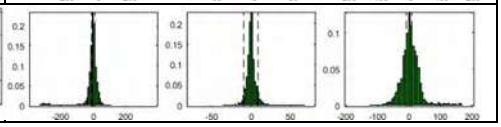		

7. Discussion of The Results

In this work, unlike the usual work, a sample of a physical image of an atom was taken to shed the proposed wavelets and was used for the first time in a physical image analysis for analysis based on the wavelet image algorithm analysis, where the image was analyzed and its statistics, pressure, and the noise raising process have obtained. Good results were compared. The standard wavelets in the second level and the tables in the above sections indicate that and compared with the results obtained, they will be shown in the Table 4, where this table shows the efficiency of the new wavelets in this research.
The above table will be compared between one of the standard wavelets in level 8, (Symlet 2) has been compared with the new proposed wavelets. Compresses and compare the image with the results obtained by the method of Set Partitioning in Hierarchical Tree and relying on the measures obtained. Table 4 shows the compassion results of wavelets according to the following

1. Peak signal to noise ratio (PSNR): $\mathrm{PSNR} = 10\log10\left(\frac{255^2}{\mathrm{MSE}}\right)$ (33)
2. Compression ratio (CR): $\mathrm{CR} = \frac{\text{Original image size in bit}}{\text{Compressed image size in bit}}$ (34)
3. Bits per pixel (BPP): $\text{Bit Per Pixel} = \frac{\text{Compressed image size in bits}}{\text{Total number of Pixel in the image}}$ (35)
4. Mean Squared Error (MSE): $\mathrm{MSE} = \alpha_q^2 = \frac{1}{L}\sum\left(I(j,k), G(j,k)\right)^2$ (36)

Table 6. Compare the results between SCWT and Symlet 2 filter with loops of true compression by Set Partitioning in Hierarchical Tree (SPIHT) on Physical image.

	Symlet 2 Wavelet Transformations				Second Chebysheve Wavelet Transformations (DSCWT)			
Loops	MSE	PSNR	CR	BPP	MSE	PSNR	CR	BPP
1	4.07e^{+04}	2.025	0.03%	0.007815	4.07e^{+04}	2.025	0.03%	0.007815
2	9928	8.162	0.03%	0.007815	9928	8.162	0.03%	0.007815
3	9928	8.162	0.03%	0.007815	9928	8.162	0.03%	0.008178
4	4324	11.77	0.04%	0.008056	5045	11.1	0.04%	0.0083008
5	3342	12.89	0.04%	0.008911	3029	13.32	0.04%	0.009511
6	1896	15.35	0.06%	0.013306	1460	16.49	0.06%	0.014282
7	1179	17.24	0.09%	0.020508	1079	17.8	0.08%	0.019409
8	622	20.19	0.17%	0.04138	702.7	19.06	0.15%	0.03686
9	337	22.85	0.35%	0.083252	351.8	22.67	0.37%	0.087769
10	154.3	26.25	0.77%	0.18384	149.2	26.39	0.76%	0.18188
11	55.93	30.65	1.53%	0.3667	66.34	29.91	1.35%	0.32446
12	23.65	34.35	2.42%	0.58179	30.82	33.24	2.44%	0.56545
13	10	38.13	3.98%	0.95422	13.52	36.82	4.37%	1.04930
14	4.526	41.57	6.43%	1.5495	5.433	40.78	7.83%	1.8795
15	2.334	44.45	10.46%	2.5096	2.054	45	12.72	3.0525
16	1.483	46.42	16.14%	3.8745	1.108	47.69	18.12%	4.3616

The above table was compared with the results. It was observed that the difference in favor of the proposed new wavelet starts from step 5, 6 and 7, and this difference is repeated 10, 15 and 16.

This means the result obtained with the new wavelet SCWT is better than the result obtained from using the standard wavelet Symlet 2.

8. Conclusion

In this work, wavelets were relied on and were used in many businesses to find the best numerical solutions. In this work, I found a suitable filter from wavelets SCWT through scaling function and wavelet function find high pass filter and low pass filter used it to analyze the image where it was obtained. Good efficiency results obtained using new wavelets compared to the results obtained from the standard wavelets. Using an image of a sample of a physical atom that was analyzed and highlighting the compression and raising the noise, histogram and statistics the image statistics where the best results were recorded when using a specific threshold i.e. when pressing the methods were used the first has the threshold methods is Balance sparsity-norm, Remove near 0 and Bal-sparsity-norm (sqrt). As for the methods of raising the noise are fixed form thresholding method with soft threshold, penalize high with hard threshold, penalize medium with hard threshold, penalize low with hard threshold, Bal sparsity norm (sqrt) with soft threshold, where image parameters were divided into approximation coefficients and details coefficients. Through the analysis, a suitable threshold value was obtained, which helps to restore energy that leads to the fact that the compressed necessity did not lose much of its original information; which proves the new wavelets in the field of physical and medical imaging.

References

[1] Farghaly S H, and Samar M I 2020 *AEU-INT. J. ELECTRON C.* **124** 153363
[2] Bruni V, Mariantonia C, and Francesca P 2020 *J. Comput. Appl.* **367** 112467
[3] Ammah P N T and Ebenezer O 2019 *IMU* 15 100183
[4] Liu X, He Z, Yu-ming C, Xinge Y and Yuan Y T 2017 *Comput Vision Image Understanding* **162** 23-33
[5] Tang L, Leida L, Kezheng S, Zhifang X, Ke G and Jiansheng Q 2017 *J. VIS. COMMUN Image R* **49** 204-212
[6] Liu G, Xiaoping Z, Fengchun T, Kadri C and Zan Z *AEU-INT. J. ELECTRON C.* **64** 6 531-539
[7] Thakur K V, Pramod G A and A. M. Sapkal A M 2016 *Procedia Comput. Sci.* **79** 499-508
[8] Golmohammadi A A T and Siahtiry M S 2020 *Compos. Struct.* **235** 111729
[9] Erfanian M and Amin M 2019 *Math. Comput. Simul.* **165** 223-237
[10] Daniel H, Gabriel V G, Marcelo V G, Alfonso J L R, and J F D P 2020 *FUTURE GENER COMP SY* **113** 318-328
[11] Chakraborty J, Abhishek M and Rinku R 2018 Expert Systems with Applications **99** 168-179
[12] Masoudnia A, Hamid S and Said B 2005 *Comput. Electr. Eng.* **31** 8 572-588
[13] Qin C, Jianfeng T, Haotian S, Dengyu X, Bingchu L and Chengliang L 2020 *Precis. Eng.* **62** 244-255
[14] Rayal A and Sag R V 2020 *CHAOS SOLITONS & FRACTALS* **139** 110076
[15] Najeh T, Abdelkader M, Kais B, Lotfi N and Hassani M 2017 *ISA trans.* **70** 93-103
[16] Brackx F, Hennie D S, Nele D S and Franciscus S 2008 *J. Math. Anal. Appl.* **341** 1 120-130
[17] Al-Faour O, Al-Ani F H D and Al-Rawi S N 2000 *Eng. Technol. J.* **17**
[18] Shihab S N, Abdulrahman A A and Mohammedali M N 2015 *Eng. Technol. J.* **33** 1493-1502
[19] Al-Rawi S N 2006 *Kirkuk Univ. J. Sci. Stud.* **1** 125-136
[20] Shihab N S and Abdalrehman A A 2012 *Eng. Technol. J.* **30** 3219-3229
[21] Shehab S N, Ali H A and Yaseen H M 2010 *Eng. Technol. J.* **28** 1893-1899
[22] Shihab S N and Abdalrehman A A 2014 *Baghdad Sci. J.* **11** 229-234
[23] Rasheed M S 2014 Baghdad Science Journal **11** 186-192
[24] Rasheed M and Barillé R 2017 *Opt. Quantum Electron.* **49** 5 1-14
[25] Rasheed M and Barillé R. 2017 *J. Non. Cryst. Solids* **476** 1-14
[26] Rasheed M and Barillé R. 2017 *J. Alloys Compd.* **728** 1186-1198

[27] Saidani T, Zaabat M, Aida MS, Barille R, Rasheed M and Almohamed Y 2017 *J. Mater. Sci. Mater. Electron.* **28** 13 9252-9257
[28] Guergouria K, Boumezoued A, Barille R, Rechemc D, Rasheed M and Zaabata M 2019 *J. Alloys Compd.* **791** 550-558
[29] Bouras D, Mecif A, Barillé R, Harabi A, Rasheed M, Mahdjoub A and Zaabat M 2018 *Ceram. Int.* **44** 17 21546-21555
[30] Saidi W Hfaidh N, Rasheed M, Girtan M, Megriche A and EL Maaoui M 2016 *RSC Adv.* **6** 73 68819-68826
[31] AUKŠTUOLIS A, Girtan M, Mousdis G A, Mallet R, Socol M, Rasheed M and Stanculescu A 2017 Proceedings of the Romanian Academy *Ser. A Math. Phys. Tech. Science Info. Science* **18** 1 34-41
[32] Dkhilalli F, Megdiche S, Guidara K, Rasheed M, Barillé R and Megdiche M 2018 *Ionics* **24** 1 169-180
[33] Abdulrahman A A, Rasheed M and Shihab S 2020 *J. Southwest Jiaotong Univ.* **55** 2
[34] Rasheed M, Abdulrahman A A and Shihab S *2020 J. Southwest Jiaotong Univ.* **55** 2
[35] Dkhilalli F, Borchani S M, Rasheed M, Barille R, Guidara K and Megdiche M 2018 *J. Mater. Sci. Mater. Electron.* **29** 8 6297-6307
[36] Dkhilalli F, Borchani SM, Rasheed M, Barille R, Shihab S, Guidara K and Megdiche M 2018 *R. Soc. open Sci.* **5** 8 1-12
[37] Enneffati M, Louati B, Guidara K, Rasheed M and Barillé R 2018 J. Mater. *Sci. Mater. Electron.* **29** 1 171-179
[38] Kadri E, Krichen M, Mohammed R, Zouari A and Khirouni K 2016 *Opt. Quantum Electron.* **48** 12 1-15
[39] Kadri E, Messaoudi O, Krichen M, Dhahri K, Rasheed M, Dhahri E. Zouari A, Khirouni K and Barillé R 2017 *J. Alloys Compd.* **721** 779-783
[40] Kadri E, Dhahri K, Zaafouri A, Krichen M, Rasheed, Khirouni K and Barillé R 2017 *J. Alloys Compd.* **705** 708-713
[41] Azaza N B, Elleuch S, Rasheed M, Gindre D, Abid S, Barille R, Abid Y and Ammar H 2019 *Opt. Mater.* **96** 109328
[42] Enneffati M, Rasheed M, Louati B, Guidara K and Barillé R 2019 *Opt. Quantum Electron.* **51** 9 299
[43] Abbas M M and Rasheed M 2020 *J. Southwest Jiaotong Univ.* **55** 2
[44] Ouda E H, Shihab S and Rasheed M 2020 *J. Southwest Jiaotong Univ.* **55** 2
[45] Sarhan A M, Shihab S and Rasheed M 2020 *J. Southwest Jiaotong Univ.* **55** 2
[46] Sarhan A M, Shihab S and Rasheed M 2020 *J. Southwest Jiaotong Univ.* **5** 3
[47] Aziz S H, Rasheed M and Shihab S 2020 *J. Southwest Jiaotong Univ.* **5** 3
[48] Mitlif R J, Rasheed M and Shihab S 2020 *J. Southwest Jiaotong Univ.* **5** 3
[49] Kashem BE, Ouda EH, Aziz SH, Rasheed M and Shihab S 2020 *J. Southwest Jiaotong Univ.* **5** 3
[50] Mohammedali M N, Sabri R I, Rasheed M and Shihab S 2020 *J. Southwest Jiaotong Univ.* **5** 4
[51] Sabri R I, Mohammedali M N, Rasheed M and Shihab S 2020 *J. Southwest Jiaotong Univ.* **5** 4
[52] Aziz S H, Shihab S and Rasheed M 2020 *Al-Qadisiyah J. Pure Sci.* **26** 1 39-54
[53] Sarhan M A, Shihab S and Rasheed M 2020 *Al-Qadisiyah J. Pure Sci.* **26** 1 55-70
[54] Rasheed M and Shihab S 2020 *Iraqi J. Phys. (IJP)* **18** 47 33-43
[55] Jalal R, Shihab S, Alhadi M A and Rasheed M 2020 J. Phys. Conf. Ser. 1660 **1** 012090 IOP Publishing

The Homomorphism of a cubic set of a semigroup in a KU-algebra

The Homomorphism of a cubic set of a semigroup in a KU-algebra

Omniat Adnan Hasan[1] , Fatema F. Kareem[1]

[1]Department of mathematics, college of education for pure sciences (Ibn AL-Haitham) University of Baghdad, Baghdad, Iraq.

E-mail: fatma.f.k@ihcoedu.uobaghdad.edu.iq

Abstract. The study of homomorphisms in cubic sets is considered one of the important concepts that transfer algebraic properties between different structures, so we study a homomorphism of a cubic set of a semigroup in a KU-algebra and defined the product of two cubic sets in this structure. Firstly, we define the image and the inverse image of a cubic set in a KU-semigroup and achieve some results in this notion. Secondly, the Cartesian product of cubic subsets in a KU-semigroup is discussed and some important characteristics are proved.

1-Introduction

A new algebraic structure which is named a KU-algebra was introduced by Prabpayak and Leerawat [9, 10]. They studied the concept of homomorphism of a KU-algebra. After that, the notions of fuzzy KU-ideals and an interval value fuzzy KU-ideals are discussed by Mostafa et al. [7,8]. In [4], Kareem and Hasan introduced the notion of a KU-algebra with semigroup which is called a KU-semigroup and defined some types of ideals in this concept. Also, they studied the fuzzy ideals of a KU-semigroup in [1]. And then, Kareem and Talib [5] introduced the notion of interval value fuzzy *k*-ideal of KU-semigroup and a few properties are investigated.

The concept of cubic subalgebras/ideals in BCK/BCI-algebras was introduced by Jun et al. [2, 3]. They discussed the relationship between a cubic subalgebra and a cubic ideal. And then, Yaqoob et al [11] introduced the notion of cubic KU-algebra which is a generalization of the concept of fuzzy KU-ideals of KU-algebras. In this paper, we study a homomorphism of a cubic set of a semigroup in a KU-algebra and defined the product of two cubic sets in this structure.

2. Preliminaries

In this section, we collect some basic definitions and theorems of KU-semigroup, which will be used in the next sections.

Definition2.1[10]. An Algebra$(\aleph,*,0)$ is called a KU-algebra if, for all$\chi,\gamma,\tau \in \aleph$,
$(\mathrm{ku}_1)\ (\chi*\gamma)*[(\gamma*\tau)*(\chi*\tau)]=0$,
$(\mathrm{ku}_2)\ \chi*0=0$,
$(\mathrm{ku}_3)\ 0*\chi=\chi$,
$(\mathrm{ku}_4)\ \chi*\gamma=0$ and $\gamma*\chi$ implies$\chi=\gamma$ and
$(\mathrm{ku}_5)\ \chi*\chi=0$.

A binary relation $\leq$ on $\aleph$ is define by $\chi \leq \gamma \Leftrightarrow \gamma * \chi = 0$. It follows that $(\aleph, \leq)$ is a partially ordered set.

Example 2.2 [9]. Let $\aleph = \{0, a, b, c\}$ be a set and $*$ a binary operation defined in the following table

*	0	a	b	c
0	0	a	b	c
a	0	0	0	b
b	0	b	0	a
c	0	0	0	0

It is easy to see that$(\aleph, *, 0)$ is a KU-algebra.

Theorem2.3[9]. Let $(\aleph, *, 0)$ be a KU-algebra. Then, for all$\chi, \gamma, \tau \in \aleph$,
(1) If $\chi \leq \gamma$ imply $\gamma * \tau \leq \chi * \tau$,
(2) $\chi * (\gamma * \tau) = \gamma * (\chi * \tau)$,
(3) $((\gamma * \chi) * \chi) \leq \gamma$.

Definition 2.4 [9]. Let $(\aleph, *, 0)$ be a KU-algebra and I be a non- empty subset of $\aleph$. Then I is called an ideal of $\aleph$ if for any $\chi, \gamma \in \aleph$, then
(i) $0 \in I$ and
(ii) If $\chi * \gamma \in I$ and $\chi \in I$ imply $\gamma \in I$.

Definition 2.5 [7]. Let I be a subset of a KU-algebra$(\aleph, *, 0)$ and $I \neq \varphi$. Then I is named a KU-ideal of $\aleph$, if
(I_1) $0 \in I$ and
$(I_2) \forall \chi, \gamma, \tau \in \aleph$, $(\chi * (\gamma * \tau)) \in I$, $\gamma \in I$ imply $\chi * \tau \in I$.

Definition2.6[4]. A KU-semigroup is a nonempty set $\aleph$ with two binary operations $*, \circ$ and a constant 0 satisfying the following
(I) $(\aleph, *, 0)$ is a KU-algebra,
(II) $(\aleph, \circ)$ is a semigroup,
(III) The operation $\circ$ is distributive (on both sides) over the operation$*$, i.e.
$\chi \circ (\gamma * \tau) = (\chi \circ \gamma) * (\chi \circ \tau)and(\chi * \gamma) \circ \tau = (\chi \circ \tau) * (\gamma \circ \tau)$, for all $\chi, \gamma, \tau \in X$.

Example 2.7[4]. Let $\aleph = \{0,1,2,3\}$ be a set. Define$*$ -operation and $\circ$-operation by the following tables

*	0	1	2	3
0	0	1	2	3
1	0	0	0	2
2	0	2	0	1
3	0	0	0	0

∘	0	1	2	3
0	0	0	0	0
1	0	1	0	1
2	0	0	2	2
3	0	1	2	3

Then $(\aleph,*,\circ,0)$ is a KU-semigroup.

Definition 2.8[4]. A *sub*KU-*semigroup* is a non-empty subset A of a KU-semigroup $\aleph$ and it is satisfied $\chi * \gamma, \chi \circ \gamma \in$ A, for all $\chi,\gamma \in$ A.

Definition2.9[4]. Let $(\aleph,*,\circ,0)$ be a KU-semigroup and $\varphi \neq I \subseteq \aleph$. Then
I is named an *S-ideal* of $\aleph$, if
(i) I is an ideal of a KU-algebra$(\aleph,*,0)$,
(ii) For all $\chi \in \aleph$, $a \in I$, we have$\chi \circ a \in I$ and $a \circ \chi \in I$.

Definition2.10 [4]. Let $(\aleph,*,\circ,0)$ be a KU-semigroup and $\varphi \neq A \subseteq \aleph$. Then A is said to be a *k-ideal* of $\aleph$, if
i) A is an KU-ideal of a KU-algebra $(\aleph,*,0)$,
ii) For all $\chi \in X, a \in$ A, we have $\chi \circ a \in$ A and $a \circ \chi \in$ A .
We recall the definition of a cubic set in a KU-semigroup as follows:
Let$(\aleph,*,\circ,0)$ be a KU-semigroup. A cubic set Θ in a set $\aleph$ is the structure
$\Theta = \{\langle x, \tilde{\mu}_\Theta(x), \lambda_\Theta(x)\rangle : x \in \aleph\}$, where $\tilde{\mu}_\Theta: \aleph \to D[0,1]$ such that
$\tilde{\mu}_\Theta(x) = [\tilde{\mu}_\Theta{}^L(x), \tilde{\mu}_\Theta{}^U(x)]$ is an interval valued fuzzy set in $\aleph$ and $\lambda_\Theta(x)$ is a fuzzy set in $\aleph$. We write a cubic set by briefly as follows $\Theta = \langle \tilde{\mu}_\Theta, \lambda_\Theta \rangle$,
We can define the level subset of $\Theta = \langle \tilde{\mu}_\Theta, \lambda_\Theta \rangle$ which is denoted by $U(\Theta, \tilde{t}, \alpha)$ as follows $U(\Theta, \tilde{t}, \alpha) = \{\chi \in \aleph : \tilde{\mu}_\Theta(x) \geq \tilde{t}, \lambda_\Theta(x) \leq \alpha\}$, for every $[0,0] \leq \tilde{t} \leq [1,1]$ and $\alpha \in [0,1]$.

Definition2.11[6]. Let$(\aleph,*,\circ,0)$ be a KU-semigroup. A cubic set $\Theta = \langle \tilde{\mu}_\Theta, \lambda_\Theta \rangle$ in $\aleph$ is called a cubic sub KU-semigroup if: for all $\chi, \gamma \in \aleph$,
(1) $\tilde{\mu}_\Theta(\chi * \gamma) \geq rmin\{\tilde{\mu}_\Theta(\chi), \tilde{\mu}_\Theta(\gamma)\}$, $\lambda_\Theta(\chi * \gamma) \leq max\{\lambda_\Theta(\chi), \lambda_\Theta(\gamma)\}$
(2) $\tilde{\mu}_\Theta(\chi \circ \gamma) \geq rmin\{\tilde{\mu}_\Theta(\chi), \tilde{\mu}_\Theta(\gamma)\}$, $\lambda_\Theta(\chi \circ \gamma) \leq max\{\lambda_\Theta(\chi), \lambda_\Theta(\gamma)\}$.

Example 2.12[6]. Let $\aleph = \{0,1,2,3\}$ be a set. We define two operations by the following tables

*	0	1	2	3
0	0	1	2	3
1	0	0	0	2
2	0	2	0	1
3	0	0	0	0

∘	0	1	2	3
0	0	0	0	0
1	0	1	0	1
2	0	0	2	2
3	0	1	2	3

Then $(\aleph,*,\circ,0)$ is a KU-semigroup. Define $\tilde{\mu}_\Theta(x)$ and $\lambda_\Theta(\chi)$ by

$$\tilde{\mu}_\Theta(x)=\begin{cases}[0.2,0.8] & if \quad \chi=\{0,1,2\}\\ [0.1,0.3] & if \quad \chi=3\end{cases},\ \lambda_\Theta(\chi)=\begin{cases}0.2 & if\ \chi=\{0,1,2\}\\ 0.4 & if\ \chi=3\end{cases},$$

And by apply definition3.1, we can prove that $\Theta=\langle\tilde{\mu}_\Theta,\lambda_\Theta\rangle$ is a cubic sub KU-semi group of $\aleph$.

Definition2.13[6]. A cubic set $\Theta=\langle\tilde{\mu}_\Theta,\lambda_\Theta\rangle$ in $\aleph$ is called a cubic ideal of a KU-semigroup $(\aleph,*,\circ,0)$ if it satisfies the following conditions: for all $\chi,\gamma\in\aleph$
(II_1) $\tilde{\mu}_\Theta(0)\geq\tilde{\mu}_\Theta(x)$ and $\lambda_\Theta(0)\leq\lambda_\Theta(x)$,
(II_2) $\tilde{\mu}_\Theta(\gamma)\geq$
$rmin\{\tilde{\mu}_\Theta(\chi*\gamma),\tilde{\mu}_\Theta(\chi)\}$, $\lambda_\Theta(\gamma)\leq max\{\lambda_\Theta(\chi*\gamma),\lambda_\Theta(\chi)\}$
(II_3) $\tilde{\mu}_\Theta(\chi\circ\gamma)\geq rmin\{\tilde{\mu}_\Theta(\chi),\ \tilde{\mu}_\Theta(\gamma)\}, \lambda_\Theta(\chi\circ\gamma)\leq max\{\lambda_\Theta(\chi)\ ,\ \lambda_\Theta(\gamma)\}$.

Example2.14[6]. Let $\aleph=\{0,1,2\}$ be a set. Define the operations $*,\circ$ by the following tables.

$*$	0	1	2
0	0	1	2
1	0	0	1
2	0	1	0

$\circ$	0	1	2
0	0	0	0
1	0	1	0
2	0	0	2

Then$(\aleph,*,\circ,0)$ is a KU-semigroup. Define $\Theta=\langle\tilde{\mu}_\Theta,\lambda_\Theta\rangle$ as follows:

$$\tilde{\mu}_\Theta(x)=\begin{cases}[0.4,0.8] & if\ \ \chi\in\{0,2\}\\ [0.1,0.3] & if\ \ \chi=1\end{cases}\ \text{and}\ \lambda_\Theta(x)=\begin{cases}0.1 & if\ \ \chi\in\{0,2\}\\ 0.3 & if\ \ \chi=1\end{cases}$$

Then $\Theta=\langle\tilde{\mu}_\Theta,\lambda_\Theta\rangle$ is a cubic ideal of $\aleph$.

Definition2.15[6]. A cubic set $\Theta=\langle\tilde{\mu}_\Theta,\lambda_\Theta\rangle$ in $\aleph$ is called a cubic *k*-ideal of a KU-semigroup$(\aleph,*,\circ,0)$ if it satisfies the following conditions:

For all $\chi,\gamma,\tau\in\aleph$
$(\boldsymbol{Ck_1})\tilde{\mu}_\Theta(0))\geq\tilde{\mu}_\Theta(\chi)$, and $\lambda_\Theta(0)\leq\lambda_\Theta(x)$
$\boldsymbol{(Ck_2)}\tilde{\mu}_\Theta(\chi*\tau)\geq rmin\{\tilde{\mu}_\Theta(\chi*(\gamma*\tau)),\tilde{\mu}_\Theta(\gamma)\}$,
$\lambda_\Theta(\chi*\tau)\leq max\{\lambda_\Theta(\chi*(\gamma*\tau)),\lambda_\Theta(\gamma)\}$
$\mathbf{(Ck_3)}\tilde{\mu}_\Theta(\chi\circ\gamma)\geq r\min\{\tilde{\mu}_\Theta(\chi)\ ,\ \tilde{\mu}_\Theta(\gamma)\}$ $,\lambda_\Theta(\chi\circ\gamma)\leq max\{\lambda_\Theta(\chi)\ ,\ \lambda_\Theta(\gamma)\}$.

3. Homomorphism of a cubic *k*-ideal

In this section we present definitions the homomorphism, image and preimage of a cubic KU-ideal, and some results on these concepts.

Definition 3.1. Let *f* be a mapping from KU-semigroup $\aleph$ into KU-semigroup $\aleph'$ if $\Theta=\langle\tilde{\mu}_\Theta(\chi),\lambda_\Theta(\chi)\rangle$ is a cubic sub set of $\aleph$, then the image of Θ under*f* is defined as follows

$$f(\tilde{\mu}_\Theta)(\gamma)=\begin{cases}rsup\ \tilde{\mu}_\Theta(\chi)_{\chi\in f^{-1}(\gamma)}, & if\quad f^{-1}(\gamma)=\{\chi\in\aleph: f(\chi)=\gamma,\gamma\in\aleph'\}\neq\emptyset\\ 0 & otherwise\end{cases}$$

And

$$f(\lambda_\Theta)(\gamma)=\begin{cases}inf\ \lambda_\Theta(\chi)_{\chi\in f^{-1}(\gamma)}, & if\ f^{-1}(\gamma)=\{\chi\in\aleph: f(\chi)=\gamma,\gamma\in\aleph'\}\neq\emptyset\\ 0 & otherwise\end{cases}$$

Definition 3.2. Let f be a mapping from $\aleph$ into $\aleph'$and $\beta = \langle \tilde{\mu}_\beta, \lambda_\beta \rangle$ be a cubic set in $\aleph'$. Then the inverse image of β, is defined as $f^{-1}(\beta) = \langle x, f^{-1}(\tilde{\mu}_\beta), f^{-1}(\lambda_\beta) \rangle$ with the membership function and non-membership function respectively are given by $f^{-1}(\tilde{\mu}_\beta(x)) = \tilde{\mu}_\beta\big(f(x)\big)$ and $f^{-1}(\lambda_\beta(x)) = \lambda_\beta\big(f(x)\big)$. It can be shown that $f^{-1}(\beta)$ is a cubic set.

Theorem 3.3. Let $f: \aleph \to \aleph'$ be an epimorphism between KU-semigroups $\aleph$ and $\aleph'$, if $\Theta = \langle \tilde{\mu}_\Theta(\chi), \lambda_\Theta(\chi) \rangle$ is a cubic *k*-ideal in $\aleph$,then $f(\Theta)$ is a cubic *k*-ideal in $\aleph'$.

Proof:
$\forall\, \chi', \gamma' \in \aleph'$, then $\exists\, \chi, \gamma \in \aleph$ such that $f(\chi) = \chi'$ and $f(\gamma) = \gamma'$. By definition of an image, we have
$f(\tilde{\mu}_\Theta)(\chi') = rsup\tilde{\mu}_\theta(\chi)_{\chi \in f^{-1}(\chi')}$, for some $\chi \in \aleph$, and
$f(\lambda_\Theta)(\chi') = \lambda_\Theta(\chi') = inf\lambda_\Theta(\chi)_{\chi \in f^{-1}(\chi')}$, for some $\chi \in \aleph$, we have
$\tilde{\mu}_\Theta(0) \geq \tilde{\mu}_\Theta(\chi), \forall\, \chi \in \aleph$, then the condition($\boldsymbol{Ck_1}$) is
$f(\tilde{\mu}_\Theta)(0') = rsup\tilde{\mu}_\Theta(0)_{0 \in f^{-1}(0')} \geq rsup\tilde{\mu}_\Theta(\chi)_{\chi \in f^{-1}(\chi')} = f(\tilde{\mu}_\Theta)(\chi)$
And
$f(\lambda_\Theta)(0') = inf\lambda_\theta(0)_{0 \in f^{-1}(0')} \leq inf\lambda_\theta(\chi)_{\chi \in f^{-1}(\chi')} = f(\lambda_\Theta)(\chi)$
($\boldsymbol{Ck_2}$)For any$\chi', \gamma', \tau' \in \aleph'$, let $\chi_0 \in f^{-1}(\chi'), \gamma_0 \in f^{-1}(\gamma'), \tau_0 \in f^{-1}(\tau')$, since f is a homomorphism, then $f(\tilde{\mu}_\Theta)(\chi' * \tau') = rsup\tilde{\mu}_\Theta(\chi_0 * \tau_0))_{\chi_0 * \tau_0 \in f^{-1}(\chi' * \tau')}$
$\geq rmin\{rsup\tilde{\mu}_\Theta(\chi_0 * (\gamma_0 * \tau_0))_{(\chi_0 * (\gamma_0 * \tau_0)) \in f^{-1}(\chi' * \gamma' * \tau')}, rsup\tilde{\mu}_\Theta(\gamma_0)_{\gamma_0 \in f^{-1}(\gamma')}\}$
$= rmin\{f(\tilde{\mu}_\Theta)(\chi' * (\gamma' * \tau'), f(\tilde{\mu}_\Theta)(\gamma')\}$
And then $f(\lambda_\Theta)(\chi' * \tau') = inf\lambda_\Theta(\chi_0 * \tau_0))_{\chi_0 * \tau_0 \in f^{-1}(\chi' * \tau')}$
$\leq max\{ inf\lambda_\Theta(\chi_0 * (\gamma_0 * \tau_0))_{(\chi_0 * (\gamma_0 * \tau_0)) \in f^{-1}(\chi' * (\gamma' * \tau'))}, inf\lambda_\Theta(\gamma_0)_{\gamma_0 \in f^{-1}(\gamma')}\}$
$= max\{f(\lambda_\Theta)(\chi' * (\gamma' * \tau')), f(\lambda_\Theta)(\gamma')$
($\boldsymbol{Ck_3}$) For any $\chi', \gamma' \in \aleph'$, let $\chi_0 \in f^{-1}(\chi'), \gamma_0 \in f^{-1}(\gamma')$ be such that
$f(\tilde{\mu}_\Theta)(\chi' \circ \gamma') = r\ sup\tilde{\mu}(\chi_0 \circ \gamma_0))_{\chi_0 \circ \tau_0 \in f^{-1}(\chi' \circ \tau')}$
$\geq rmin\{r\ sup\tilde{\mu}_\Theta(\chi_0)_{(\chi_0) \in f^{-1}(\chi')}, r\ sup\tilde{\mu}_\Theta(\gamma_0)_{\gamma_0 \in f^{-1}(\gamma')}\}$
$= rmin\{f(\tilde{\mu}_\Theta)(\chi'), f(\tilde{\mu}_\Theta)(\gamma')\}$ and
$f(\lambda_\Theta)(\chi' \circ \gamma') = inf\lambda_\Theta(\chi_0 \circ \gamma_0)_{\chi_0 \circ \tau_0 \in f^{-1}(\chi' \circ \tau')}$
$\leq max\{inf\tilde{\mu}_\Theta(\chi_0)_{(\chi_0) \in f^{-1}(\chi')}, inf\tilde{\mu}_\Theta(\gamma_0)_{\gamma_0 \in f^{-1}(\gamma')}\}$
$= max\{f(\lambda_\Theta)(\chi'), f(\lambda_\Theta)(\gamma')\}$, hence $f(\Theta)$ is a cubic *k*-ideal.

Theorem3.4. An epimorphism pre-image of a cubic *k*-ideal of a KU-semigroup$\aleph'$ also a cubic *k*-ideal of KU-semigroup $\aleph$.

Proof. Let $\beta = \langle \tilde{\mu}_\beta, \lambda_\beta \rangle$ be a cubic *k*-ideal of $\aleph'$, to prove $f^{-1}(\beta)$ is a cubic *k*-ideal of $\aleph$.
$\forall\, \chi', \gamma', \tau' \in \aleph'$, then $\exists\, \chi, \gamma, \tau \in \aleph$ such that $f(\chi) = \chi'$, $f(\gamma) = \gamma'$and $f(\tau) = \tau'$,
(Ck$_1$) we have
$f^{-1}\left(\tilde{\mu}_\beta(0)\right) = \tilde{\mu}_\beta(f(0)) = \tilde{\mu}_\beta(0') \geq \tilde{\mu}_\beta(\chi') = \tilde{\mu}_\beta(f(\chi)) = f^{-1}(\tilde{\mu}_\beta(\chi))$, and
$f^{-1}\left(\lambda_\beta(0)\right) = \lambda_\beta(f(0)) = \lambda_\beta(0') \leq \lambda_\beta(\chi') = \lambda_\beta(f(x)) = f^{-1}\left(\lambda_\beta(x)\right)$.
(Ck$_2$)$\forall\, \chi, \gamma, \tau \in \aleph$, we have
$f^{-1}\left(\tilde{\mu}_\beta(\chi * \tau)\right) = \tilde{\mu}_\beta(f(\chi * \tau)) = \tilde{\mu}_\beta(f(\chi) * f(\tau)) = \tilde{\mu}_\beta(\chi' * \tau')$
$\geq rmin\{\tilde{\mu}_\beta(\chi' * (\gamma' * \tau')),\ \tilde{\mu}_\beta(\gamma')\}$ (since β is a cubic *k*-ideal of $\aleph'$)

$= rmin\left\{\tilde{\mu}_\beta\left(f(x) * \left(f(\gamma) * f(\tau)\right),\ \tilde{\mu}_\beta(f(\gamma)\right)\right\} = rmin\{\tilde{\mu}_\beta(f\left(\chi * (\gamma * \tau)\right), \tilde{\mu}_\beta(f(\gamma))\}$
$= rmin\{f^{-1}(\tilde{\mu}_\beta\left(\chi * (\gamma * \tau)\right), f^{-1}(\tilde{\mu}_\beta(\gamma))\}$. And
$f^{-1}\left(\lambda_\beta(\chi * \tau)\right) = \lambda_\beta\left(f(\chi * \tau)\right) = \lambda_\beta\left(f(\chi) * f(\tau)\right) = \lambda_\beta(\chi' * \tau')$
$\leq ma\, x\{\lambda_\beta(\chi' * (\gamma' * \tau')), \lambda_\beta(\gamma')\} = max\{\lambda_\beta\left(f(\chi) * (f(\gamma) * f(\tau)\right), \lambda_\beta\left(f(\gamma)\right)$
$= max\{\lambda_\beta(f(\chi * (\gamma * \tau)), \lambda_\beta(f(\gamma)\}$
$= ma\, x\{f^{-1}\left(\lambda_\Theta(\chi * (\gamma * \tau)\right), f^{-1}\left(\lambda_\Theta(\gamma)\right)\}$

(Ck$_3$) $\forall\ \chi, \gamma \in \aleph$ **,** we have

$f^{-1}\left(\tilde{\mu}_\beta(\chi \circ \gamma)\right) = \tilde{\mu}_\beta\left(f(\chi \circ \gamma)\right) = \tilde{\mu}_\beta\left(f(\chi) \circ f(\gamma)\right) = \tilde{\mu}_\beta(\chi' \circ \gamma') \geq rmin\{\tilde{\mu}_\beta(\chi'), \tilde{\mu}_\beta(\gamma')\}$
$= rmin\{\tilde{\mu}_\beta\left(f(\chi)\right), \tilde{\mu}_\beta\left(f(\gamma)\right)\} = rmin\{f^{-1}(\tilde{\mu}_\beta(\chi)), f^{-1}(\tilde{\mu}_\beta(\gamma))\}$
and
$\lambda_\beta(\chi \circ \gamma) = \lambda_\beta\left(f(\chi \circ \gamma)\right) = \lambda_\beta\left(f(\chi) \circ f(\gamma)\right) = \lambda_\beta(\chi' \circ \gamma') \leq ma\, x\{\lambda_\beta(\chi'), \lambda_\beta(\gamma')\}$
$\leq max\{\lambda_\beta\left(f(\chi)\right), \lambda_\beta\left(f(\gamma)\right)\} = max\{f^{-1}\left(\lambda_\beta(\chi)\right), f^{-1}\left(\lambda_\beta(\gamma)\right)\}$, that is
$\beta = \langle\tilde{\mu}_\beta, \lambda_\beta\rangle$ is a cubic *k*-ideal of $\aleph$.

Definition3.5. Let $\Theta_1 = \langle\tilde{\mu}_{\Theta 1}(x), \lambda_{\Theta 1}(x)\rangle$ and $\Theta_2 = \langle\tilde{\mu}_{\Theta 2}(x), \lambda_{\Theta 2}(x)\rangle$ be two cubic subsets of KU-semigroup $\aleph_1$and $\aleph_2$ respectively. Then the Cartesian product of cubic subsets Θ_1 and Θ_2 is denoted by $\Theta_1 \times \Theta_2 = \langle\tilde{\mu}_{\Theta 1\times\Theta 2}(x), \lambda_{\Theta 1\times\Theta 2}(x)\rangle$ and is defined by
$\tilde{\mu}_{\Theta 1\times\Theta 2}(x_1, x_2) = rmin\{\tilde{\mu}_{\Theta 1}(x_1), \tilde{\mu}_{\Theta 2}(x_2)\}$ and $\lambda_{\Theta 1\times\Theta 2}(x_1, x_2) = max\{\lambda_{\Theta 1}(x_1), \lambda_{\Theta 2}(x_2)\}$, for all $(x_1, x_2) \in \aleph_1 \times \aleph_2$.

Remark3.6. Let $\aleph_1$, $\aleph_2$ be KU-semigroups , we define the binary operations $*$ and $\circ$ on $\aleph_1 \times \aleph_2$ by
$(x_1, x_2) * (y_1, y_2) = (x_1 * y_1, x_2 * y_2)$ and

$(x_1, x_2) \circ (y_1, y_2) = (x_1 \circ y_1, x_2 \circ y_2)$, for all $(x_1, x_2), (y_1, y_2) \in \aleph_1 \times \aleph_2$.

We can easy to prove that $(\aleph_1 \times \aleph_2, *, \circ, (0,0))$ is a KU-semigroup.

Theorem 3.7. If Θ_1 and Θ_2 are two cubic *k*-ideals of KU-semigroup $\aleph_1$and $\aleph_2$ respectively. Then the product $\Theta_1 \times \Theta_2$ is a cubic *k*-ideal of $\aleph_1 \times \aleph_2$.

Proof: Let $\Theta_1 = \langle\tilde{\mu}_{\Theta 1}(x), \lambda_{\Theta 1}(x)\rangle$, $\Theta_2 = \langle\tilde{\mu}_{\Theta 2}(x), \lambda_{\Theta 2}(x)\rangle$ be two cubic *k*-ideals.

(CK$_1$) For any $(x_1, x_2) \in \aleph_1 \times \aleph_2$

$\tilde{\mu}_{\Theta 1\times\Theta 2}(0,0) = rmin\{\tilde{\mu}_{\Theta 1}(0), \tilde{\mu}_{\Theta 2}(0)\} \geq rmin\{\tilde{\mu}_{\Theta 1}(x_1), \tilde{\mu}_{\Theta 2}(x_2)\} = \tilde{\mu}_{\Theta 1\times\Theta 2}(x_1, x_2)$

And

$\lambda_{\Theta 1\times\Theta 2}(0,0) = max\{\lambda_{\Theta 1}(0), \lambda_{\Theta 2}(0)\} \leq max\{\lambda_{\Theta 1}(x_1), \lambda_{\Theta 2}(x_2)\} = \lambda_{\Theta 1\times\Theta 2}(x_1, x_2)$

(CK$_2$) Let $(x_1, x_2), (y_1, y_2), (\tau_1, \tau_2) \in \aleph_1 \times \aleph_2$

$\tilde{\mu}_{\Theta 1\times\Theta 2}\left((x_1, x_2) * (\tau_1, \tau_2)\right) = \tilde{\mu}_{\Theta 1\times\Theta 2}(x_1 * \tau_1, x_2 * \tau_2)$
$= rmin\{\tilde{\mu}_{\Theta 1}(x_1 * \tau_1), \tilde{\mu}_{\Theta 2}(x_2 * \tau_2)\}$
$\geq rmin\{rmin\{\tilde{\mu}_{\Theta 1}\left(x_1 * (y_1 * \tau_1)\right), \tilde{\mu}_{\Theta 1}(y_1)\}, rmin\{\tilde{\mu}_{\Theta 2}(x_2 * (y_2 * \tau_2)), \tilde{\mu}_{\Theta 2}(y_2)\}\}$
$= rmin\{\ rmin\{\tilde{\mu}_{\Theta 1}\left(x_1 * (y_1 * \tau_1)\right), \tilde{\mu}_{\Theta 2}(x_2 * (y_2 * \tau_2)\}, rmin\{\tilde{\mu}_{\Theta 1}(y_1), \tilde{\mu}_{\Theta 2}(y_2)\}\}$
$= rmin\{\tilde{\mu}_{\Theta 1\times\Theta 2}\left((x_1, x_2) * \left((y_1, y_2) * (\tau_1, \tau_2)\right)\right), \tilde{\mu}_{\Theta 1\times\Theta 2}(y_1, y_2)\}$,

and

$\lambda_{\Theta 1\times\Theta 2}\left((x_1, x_2) * (\tau_1, \tau_2)\right) = \lambda_{\Theta 1\times\Theta 2}(x_1 * \tau_1, x_2 * \tau_2)$
$= max\{\lambda_{\Theta 1}(x_1 * \tau_1), \lambda_{\Theta 2}(x_2 * \tau_2)\}$

$\leq max\{max\{\lambda_{\Theta 1}(x_1 * (y_1 * \tau_1)), \lambda_{\Theta 1}(y_1)\}, max\{\lambda_{\Theta 2}(x_2 * (y_2 * \tau_2)), \lambda_{\Theta 2}(y_2)\}\}$

$= max\{max\{\lambda_{\Theta 1}(x_1 * (y_1 * \tau_1))\}, \lambda_{\Theta 2}(x_2 * (y_2 * \tau_2))\}, max\{\lambda_{\Theta 1}(y_1), \lambda_{\Theta 2}(y_2)\}\}$

$=max\{\lambda_{\Theta 1\times\Theta 2}\left((x_1, x_2) * \left((y_1, y_2) * (\tau_1, \tau_2)\right)\right), \lambda_{\Theta 1\times\Theta 2}(y_1, y_2)\}$

(CK₃) Let $(x_1, x_2), (y_1, y_2) \in \aleph_1 \times \aleph_2$

$\tilde{\mu}_{\Theta 1\times\Theta 2}((x_1, x_2) \circ (y_1, y_2)) = \tilde{\mu}_{\Theta 1\times\Theta 2}(x_1 \circ y_1, x_2 \circ y_2)$

$= rmin\{\tilde{\mu}_{\Theta 1}(x_1 \circ y_1), \tilde{\mu}_{\Theta 2}(x_2 \circ y_2)\}$

$\geq rmin\{rmin\{\tilde{\mu}_{\Theta 1}(x_1), \tilde{\mu}_{\Theta 1}(y_1)\}, rmin\{\tilde{\mu}_{\Theta 2}(x_2), \tilde{\mu}_{\Theta 2}(y_2)\}\}$,

Since both Θ_1 and Θ_2 are cubic *k*-ideal, then

$= rmin\{rmin\{\tilde{\mu}_{\Theta 1}(x_1), \tilde{\mu}_{\Theta 2}(x_2)\}, rmin\{\tilde{\mu}_{\Theta 1}(y_1), \tilde{\mu}_{\Theta 2}(y_2)\}\}$

$= rmin\{\tilde{\mu}_{\Theta 1\times\Theta 2}(x_1, x_2), \tilde{\mu}_{\Theta 1\times\Theta 2}(y_1, y_2)\}$, and

$\lambda_{\Theta 1\times\Theta 2}((x_1, x_2) \circ (y_1, y_2)) = \lambda_{\Theta 1\times\Theta 2}(x_1 \circ y_1, x_2 \circ y_2)$

$= max\{\lambda_{\Theta 1}(x_1 \circ y_1), \lambda_{\Theta 2}(x_2 \circ y_2)\}$

$\leq max\{max\{\lambda_{\Theta 1}(x_1), \lambda_{\Theta 1}(y_1)\}, max\{\lambda_{\Theta 2}(x_2), \lambda_{\Theta 2}(y_2)\}\}$,

Since both Θ_1 and Θ_2 are cubic *k*-ideal, then

$= max\{max\{\lambda_{\Theta 1}(x_1), \lambda_{\Theta 2}(x_2)\}, max\{\lambda_{\Theta 1}(y_1), \lambda_{\Theta 2}(y_2)\}\}$

$= max\{\lambda_{\Theta 1\times\Theta 2}(x_1, x_2), \lambda_{\Theta 1\times\Theta 2}(y_1, y_2)\}$, that is $\Theta_1 \times \Theta_2$ is a cubic *k*-ideal of $\aleph_1 \times \aleph_2$.

Now we discuss the converse in the following proposition.

Proposition 3.8. Let Θ_1 and Θ_2 be two cubic *k*-ideals of KU-semigroup $\aleph_1$and $\aleph_2$ respectively. If $\Theta_1 \times \Theta_2$ is a cubic *k*-ideal of $\aleph_1 \times \aleph_2$, then

(i) Either $\tilde{\mu}_{\Theta 1}(0) \geq \tilde{\mu}_{\Theta 1}(x_1)$, $\lambda_{\Theta 1}(0) \leq \lambda_{\Theta 1}(x_1)$ or $\tilde{\mu}_{\Theta 2}(0) \geq \tilde{\mu}_{\Theta 2}(x_2)$,$\lambda_{\Theta 2}(0) \leq \lambda_{\Theta 2}(x_2)$, for all $x_1 \in \aleph_1, x_2 \in \aleph_2$.

(ii) If $\tilde{\mu}_{\Theta 1}(0) \geq \tilde{\mu}_{\Theta 1}(x_1)$, $\lambda_{\Theta 1}(0) \leq \lambda_{\Theta 1}(x_1)$ for all $x_1 \in \aleph_1$. Then either $\tilde{\mu}_{\Theta 2}(0) \geq \tilde{\mu}_{\Theta 1}(x_1)$, $\lambda_{\Theta 2}(0) \leq \lambda_{\Theta 1}(x_1)$ or $\tilde{\mu}_{\Theta 2}(0) \geq \tilde{\mu}_{\Theta 2}(x_2)$, $\lambda_{\Theta 2}(0) \leq \lambda_{\Theta 2}(x_2)$.

(iii) If $\tilde{\mu}_{\Theta 2}(0) \geq \tilde{\mu}_{\Theta 2}(x_1)$, $\lambda_{\Theta 2}(0) \leq \lambda_{\Theta 2}(x_1)$, for all $x_1 \in \aleph_1$, then either $\tilde{\mu}_{\Theta 1}(0) \geq \tilde{\mu}_{\Theta 1}(x_1)$, $\lambda_{\Theta 2}(0) \leq \lambda_{\Theta 1}(x_1)$ or $\tilde{\mu}_{\Theta 1}(0) \geq \tilde{\mu}_{\Theta 2}(x_1)$, $\lambda_{\Theta 1}(0) \leq \lambda_{\Theta 2}(x_1)$.

Proof. (i) Suppose that $\tilde{\mu}_{\Theta 1}(0) \leq \tilde{\mu}_{\Theta 1}(x_1)$, $\lambda_{\Theta 1}(0) \geq \lambda_{\Theta 1}(x_1)$, and $\tilde{\mu}_{\Theta 2}(0) \leq \tilde{\mu}_{\Theta 2}(x_2)$

, $\lambda_{\Theta 2}(0) \geq \lambda_{\Theta 2}(x_2)$, for some $x_1 \in \aleph_1, x_2 \in \aleph_2$. Then

$\tilde{\mu}_{\Theta 1\times\Theta 2}(x_1, x_2) = rmin\{\tilde{\mu}_{\Theta 1}(x_1), \tilde{\mu}_{\Theta 2}(x_2)\} \geq rmin\{\tilde{\mu}_{\Theta 1}(x_1), \tilde{\mu}_{\Theta 2}(x_2)\} = \tilde{\mu}_{\Theta 1\times\Theta 2}(0,0)$

And

$\lambda_{\Theta 1\times\Theta 2}(x_1, x_2) = max\{\lambda_{\Theta 1}(x_1), \lambda_{\Theta 2}(x_2)\} \leq max\{\lambda_{\Theta 1}(0), \lambda_{\Theta 2}(0)\} = \lambda_{\Theta 1\times\Theta 2}(0,0)$

, for some $x_1 \in \aleph_1, x_2 \in \aleph_2$. This is a contradiction. Therefore, either $\tilde{\mu}_{\Theta 1}(0) \geq \tilde{\mu}_{\Theta 1}(x_1)$, $\lambda_{\Theta 1}(0) \leq \lambda_{\Theta 1}(x_1)$ or $\tilde{\mu}_{\Theta 2}(0) \geq \tilde{\mu}_{\Theta 2}(x_2)$, $\lambda_{\Theta 2}(0) \leq \lambda_{\Theta 2}(x_2)$, for all $x_1 \in \aleph_1, x_2 \in \aleph_2$.

(ii) Suppose that $\tilde{\mu}_{\Theta 2}(0) \leq \tilde{\mu}_{\Theta 1}(x_1)$, $\lambda_{\Theta 2}(0) \geq \lambda_{\Theta 1}(x_1)$ and $\tilde{\mu}_{\Theta 2}(0) \leq \tilde{\mu}_{\Theta 2}(x_2)$, $\lambda_{\Theta 2}(0) \geq \lambda_{\Theta 2}(x_2)$, for all $x_1 \in \aleph_1, x_2 \in \aleph_2$.

Then $\tilde{\mu}_{\Theta 1\times\Theta 2}(0,0) = rmin\{\tilde{\mu}_{\Theta 1}(0), \tilde{\mu}_{\Theta 2}(0)\} = \tilde{\mu}_{\Theta 2}(0)$, and

$\tilde{\mu}_{\Theta 1\times\Theta 2}(x_1, x_2) = rmin\{\tilde{\mu}_{\Theta 1}(x_1), \tilde{\mu}_{\Theta 2}(x_2)\} \geq rmin\{\tilde{\mu}_{\Theta 2}(0), \tilde{\mu}_{\Theta 2}(0)\} = \tilde{\mu}_{\Theta 2}(0) \quad = \tilde{\mu}_{\Theta 1\times\Theta 2}(0,0)$

And $\lambda_{\Theta 1\times\Theta 2}(0,0) = max\{\lambda_{\Theta 1}(0), \lambda_{\Theta 2}(0)\} = \lambda_{\Theta 2}(0)$ and $\lambda_{\Theta 1\times\Theta 2}(x_1, x_2) =$

$max\{\lambda_{\Theta 1}(x_1), \lambda_{\Theta 2}(x_2)\} \leq max\{\lambda_{\Theta 2}(0), \lambda_{\Theta 2}(0)\} = \lambda_{\Theta 2}(0) = \lambda_{\Theta 1\times\Theta 2}(0,0)$

. This is a contradiction. Therefore, either $\tilde{\mu}_{\Theta 2}(0) \geq \tilde{\mu}_{\Theta 1}(x_1)$, $\lambda_{\Theta 2}(0) \leq \lambda_{\Theta 1}(x_1)$ or

$\tilde{\mu}_{\Theta 2}(0) \geq \tilde{\mu}_{\Theta 2}(x_2)$, $\lambda_{\Theta 2}(0) \leq \lambda_{\Theta 2}(x_2)$.

(iii)The proof is similar to (ii).

The partial converse of Theorem3.7 is the following.

Theorem3.9. If $\Theta_2 \times \Theta_2$ is a cubic *k*-ideal of $\aleph_1 \times \aleph_2$, then either Θ_1 or Θ_2 is a cubic *k*-ideal of KU-semigroup $\aleph_1$, $\aleph_2$ respectively.

Proof. By Proposition (3.8) (i), without loss of generality we assume that $\tilde{\mu}_{\Theta 2}(0) \geq \tilde{\mu}_{\Theta 2}(x_2)$

, $\lambda_{\Theta 2}(0) \leq \lambda_{\Theta 2}(x_2)$, for all $x_2 \in \aleph_2$. By Proposition (3.8) (iii), then either $\tilde{\mu}_{\Theta 1}(0) \geq \tilde{\mu}_{\Theta 1}(x_1)$, $\lambda_{\Theta 2}(0) \leq \lambda_{\Theta 1}(x_1)$ or $\tilde{\mu}_{\Theta 1}(0) \geq \tilde{\mu}_{\Theta 2}(x_1)$, $\lambda_{\Theta 1}(0) \leq \lambda_{\Theta 2}(x_1)$.

If $\tilde{\mu}_{\Theta 1}(0) \geq \tilde{\mu}_{\Theta 1}(x_1)$, $\lambda_{\Theta 2}(0) \leq \lambda_{\Theta 1}(x_1)$, then
$\tilde{\mu}_{\Theta 1\times\Theta 2}(0, x_2) = rmin\{\tilde{\mu}_{\Theta 1}(0), \tilde{\mu}_{\Theta 2}(x_2)\} = \tilde{\mu}_{\Theta 2}(x_2)$……..(1)
And
$\lambda_{\Theta 1\times\Theta 2}(0, x_2) = max\{\lambda_{\Theta 1}(0), \lambda_{\Theta 2}(x_2)\} = \lambda_{\Theta 2}(x_2)$ ……(2)
Since $\Theta_2 \times \Theta_2 = \langle \tilde{\mu}_{\Theta 1\times\Theta 2}(x), \lambda_{\Theta 1\times\Theta 2}(x) \rangle$ is a cubic *k*-ideal of $\aleph_1 \times \aleph_2$, then
Let $(x_1, x_2), (y_1, y_2), (\tau_1, \tau_2) \in \aleph_1 \times \aleph_2$
$\tilde{\mu}_{\Theta 1\times\Theta 2}\big((x_1, x_2), (\tau_1, \tau_2)\big) \geq rmin\{\tilde{\mu}_{\Theta 1\times\Theta 2}\big((x_1, x_2) * ((y_1, y_2) * (\tau_1, \tau_2)\big), \tilde{\mu}_{\Theta 1\times\Theta 2}(y_1, y_2)\}$
$\tilde{\mu}_{\Theta 1\times\Theta 2}\big((x_1 * \tau_1), (x_2 * \tau_2)\big) \geq rmin\{\tilde{\mu}_{\Theta 1\times\Theta 2}\big((x_1, x_2) * ((y_1 * \tau_1), (y_2 * \tau_2)\big), \tilde{\mu}_{\Theta 1\times\Theta 2}(y_1, y_2)\}$
$= rmin\left\{\tilde{\mu}_{\Theta 1\times\Theta 2}\left(\big(x_1 * (y_1 * \tau_1)\big), (x_2 * (y_2 * \tau_2)\big), \tilde{\mu}_{\Theta 1\times\Theta 2}(y_1, y_2)\right\}\right.$
Put $x_1 = y_1 = \tau_1 = 0$, we have
$\tilde{\mu}_{\Theta 1\times\Theta 2}\big((0 * 0), (x_2 * \tau_2)\big) \geq rmin\left\{\tilde{\mu}_{\Theta 1\times\Theta 2}\left(\big(0 * (0 * 0)\big), (x_2 * (y_2 * \tau_2)\big), \tilde{\mu}_{\Theta 1\times\Theta 2}(0, y_2)\right\}\right.$
Then by using equation (1), we get
$\tilde{\mu}_{\Theta 2}(x_2 * \tau_2) \geq rmin\{\tilde{\mu}_{\Theta 2}(x_2 * (y_2 * \tau_2)), \tilde{\mu}_{\Theta 2}(y_2)\}$
And
$\lambda_{\Theta 1\times\Theta 2}\big((x_1, x_2), (\tau_1, \tau_2)\big) =$
$\leq max\{\lambda_{\Theta 1\times\Theta 2}\big((x_1, x_2) * ((y_1 * \tau_1), (y_2 * \tau_2)\big), \lambda_{\Theta 1\times\Theta 2}(y_1, y_2)\}$

$\lambda_{\Theta 1\times\Theta 2}\big((x_1 * \tau_1), (x_2 * \tau_2)\big) \leq max\{\lambda_{\Theta 1\times\Theta 2}\big((x_1, x_2) * ((y_1 * \tau_1), (y_2 * \tau_2)\big), \lambda_{\Theta 1\times\Theta 2}(y_1, y_2)\}$

$= max\left\{\lambda_{\Theta 1\times\Theta 2}\left(\big(x_1 * (y_1 * \tau_1)\big), (x_2 * (y_2 * \tau_2)\big), \lambda_{\Theta 1\times\Theta 2}(y_1, y_2)\right\}\right.$

Put $x_1 = y_1 = \tau_1 = 0$, we have

$\lambda_{\Theta 1\times\Theta 2}\big((0 * 0), (x_2 * \tau_2)\big) \leq max\left\{\lambda_{\Theta 1\times\Theta 2}\left(\big(0 * (0 * 0)\big), (x_2 * (y_2 * \tau_2)\big), \lambda_{\Theta 1\times\Theta 2}(0, y_2)\right\}\right.$
Then by using equation (2), we get
$\lambda_{\Theta 2}(x_2 * \tau_2) \leq max\{\lambda_{\Theta 2}(x_2 * (y_2 * \tau_2)), \lambda_{\Theta 2}(y_2)\}$.
also we have
$\tilde{\mu}_{\Theta 1\times\Theta 2}\big((x_1, x_2) \circ (y_1, y_2)\big) \geq rmin\{\tilde{\mu}_{\Theta 1\times\Theta 2}(x_1, x_2), \tilde{\mu}_{\Theta 1\times\Theta 2}(y_1, y_2)\}$
$\tilde{\mu}_{\Theta 1\times\Theta 2}(x_1 \circ y_1, x_2 \circ y_2) \geq rmin\{\tilde{\mu}_{\Theta 1\times\Theta 2}(x_1, x_2), \tilde{\mu}_{\Theta 1\times\Theta 2}(y_1, y_2)\}$
Put $x_1 = y_1 = 0$, then we have
$\tilde{\mu}_{\Theta 1\times\Theta 2}(0 \circ 0, x_2 \circ y_2) \geq rmin\{\tilde{\mu}_{\Theta 1\times\Theta 2}(0, x_2), \tilde{\mu}_{\Theta 1\times\Theta 2}(0, y_2)\}$ And by using equation (1), we get
$\tilde{\mu}_{\Theta 2}(x_2 \circ y_2) \geq rmin\{\tilde{\mu}_{\Theta 2}(x_2), \tilde{\mu}_{\Theta 2}(y_2)\}$. And $\lambda_{\Theta 1\times\Theta 2}\big((x_1, x_2) \circ (y_1, y_2)\big) \leq$
$max\{\lambda_{\Theta 1\times\Theta 2}(x_1, x_2), \lambda_{\Theta 1\times\Theta 2}(y_1, y_2)\}$
$\lambda_{\Theta 1\times\Theta 2}(x_1 \circ y_1, x_2 \circ y_2) \leq max\{\lambda_{\Theta 1\times\Theta 2}(x_1, x_2), \lambda_{\Theta 1\times\Theta 2}(y_1, y_2)\}$
Put $x_1 = y_1 = 0$, then we have
$\lambda_{\Theta 1\times\Theta 2}(0 \circ 0, x_2 \circ y_2) \leq max\{\lambda_{\Theta 1\times\Theta 2}(0, x_2), \lambda_{\Theta 1\times\Theta 2}(0, y_2)\}$ And by using equation (2), we get
$\lambda_{\Theta 2}(x_2 \circ y_2) \leq max\{\lambda_{\Theta 2}(x_2), \lambda_{\Theta 2}(y_2)\}$
It follows that Θ_2 is a cubic *k*-ideal of KU-semigroup $\aleph_2$.

Acknowledgement
The authors are thankful to the referees for a careful reading of the paper and valuable comments and suggestions.

References
[1] Hasan E R and Kareem F F 2018 Fuzzy KU-Semi-Groups and Investigate Some Basic Properties *Journal of Engineering and Applied Science* **13**(18) pp 7739-7744
[2] Jun Y B, Kim C S and Kang M S 2010 Cubic subalgebras and ideals of BCK/BCI-algebras *Far East Journal of Mathematical Sciences* **2**(44) pp 239–250
[3] Jun Y B, Kim C S and Yang K O 2012 Cubic sets *Annals of Fuzzy Mathematics and Informatics* **1**(4) pp 83–98
[4] Kareem F F and Hasan E R 2018 On KU-semigroup *Int. J.Sci.Nat.* **1**(13) pp 79-84
[5] Kareem F F and Talib S A 2020 Interval value fuzzy *k*-ideal of a KU-semigroup *Ibn Al-Haitham Jour for Pure & Appl. Sci.* **33** (2) pp 95-106
[6] Kareem F F and Hasan O A 2020 Cubic ideals of semigroup in KU-algebra *Accepted in IOP Journal of Physics*.
[7] Mostafa S M, Abd-Elnaby M A and Yousef M M M 2011 Fuzzy ideals of KU-Algebras *Int. Math. Forum* **6**(63) pp 3139-3149
[8] Mostafa S M, Abd-Elnaby M A and Elgendy O R 2011 Interval-valued Fuzzy KU-ideals in KU-algebras *Int. Math Forum* **6**(64) pp 3151-3159
[9] Prabpayak C and Leerawat U 2009 On ideals and congruence in KU-algebras *Scientia Magna* **5**(1) pp 54-57
[10] Prabpayak C and Leerawat U 2009 On isomorphisms of KU-algebras *scientia magna (International Book Series)* **5**(3) pp 25-31
[11] Yaqoop N, Mostafa S M and Ansari M A 2013 On cubic KU-ideals of KU-algebras *ISRN Algebra* Article **ID935905** 10 pages

A Novel Predictor-Corrector Hally Technique for Determining the Parameters for Nonlinear Solar Cell Equation

A Novel Predictor-Corrector Hally Technique for Determining the Parameters for Nonlinear Solar Cell Equation

Suha Shihab [1], Mohammed Rasheed [1], Osama Alabdali [3], Asma Abdulelah Abdulrahman [1]

[1]Applied Sciences Department, University of Technology, Baghdad, Iraq
[2]College of Education for Pure Sciences, University of Anbar, Al-Anbar, Iraq

E-mail: rasheed.mohammed40@yahoo.com

Abstract. This paper presents an iterative method Accelerated Predictor-Corrector Hally's Method (AHM) for finding the voltage of a single-diode model for a solar cell from the equivalent circuit. The purposes of the obtained results are to reduce the number of iterations. Two numerical methods are applied and compared; Newton's and Hally's methods. The results showed that the proposed is the most efficient compare with NRM. The purpose of the present work is to acquire the results of photovoltaic parameters using two numerical models and the comparison between them. The acquired results presented the suggested technique (NRM) is a sufficient tool, powerful method to solve this model with the least iteration. All the calculations are achieved using Matlab program.

1. Introduction

The topics of numerical analysis are very important topics in all different fields of science and it is indispensable for all scientific branches, especially applied from the study of numerical analysis and multiple programming languages. Therefore, scientific problems have been solved based on this science in the scientific working life [1-14]. Nowadays, many researchers have developed different types of solar cells based on cost and efficiency. These solar cells were prepared using different and easy methods of preparation, depending on the materials used and the quality of solar cells and the goal is to reduce cost and increase efficiency [15-25]. Other researchers can be utilizing the mathematical techniques in order to solving nonlinear equations of various of solar cells structures depending on the technique of fabrication for inorganic and organic materials for example ceramic materials, silicon solar cells, thin films solar cells [26-36]. Different techniques have been utilized to calculate the parameters of photovoltaic cell and mathematical algorithms for example fuzzy set and logic techniques and visual studio program [37-47]. Recently researchers can be utilizing numerical techniques to solve nonlinear equations in space depending on Kepler's and Barker equations [48-64].

This article aims is to present a new iterative method Accelerated Predictor-Corrector Hally method (AHM) for solving nonlinear equation of a solar cell. The propose of reducing the root of iteration in the numerical solution of the nonlinear equation root. Systematic as the following points: in section two characterizing the model of a solar cell type single-diode; in section three establishing the root finding of Newton Raphson technique; whereas; in section four Accelerated Predictor-Corrector Hally method has been studied; in section five discussion of the results; section six conclusions of the acquired results.

2. Properties of The equation for a Single Diode Solar Cells [50-61]

Figure 1 presents the equivalent electronic circuit of the photovoltaic cell solar cell.

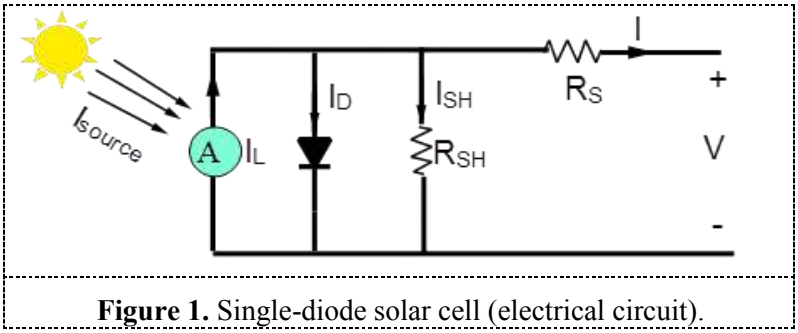

Figure 1. Single-diode solar cell (electrical circuit).

By applying Kirchhoff's current law of Figure 1; the final equation of the solar cell current can be extracted according to this equivalent as follows [52-61]

$$I = I_{ph} - I_D \quad (1)$$

$$I_D = I_0\left(e^{\frac{-V_{pv}}{nV_T}} - 1\right) \quad (2)$$

$$I = I_{ph} - I_0\left(e^{\frac{-V_{pv}}{mV_T}} - 1\right) \quad (3)$$

where:
I_{ph} : the photocurrent in (A), I_0: the diode's reverse saturation current in (A), V_{pv} and I are the delivered voltage and current in (A) and (V) respectively.

Thermic voltage can be calculated using the equation $V_T = \frac{kT}{q} = 0.0259\,V = 26$ mV, at room temperature, air-mass is 1.5; m: $(1 < m < 2)$, k: Boltzmann constant$= 1.38 \times 10^{-23}$J/K; T: the temperature of the junction $(p - n)$ (K); $q = 1.6 \times 10^{-19}$ C: the electron charge [36-37].

$$I_{ph} = I_{source} \quad (4)$$

$$I_D = I_s \times \left(e^{\frac{V_D}{nV_T}} - 1\right) \quad (5)$$

Substitute Eq. 4 in Eq. 5 yield

$$(I_{source}) - 10^{-12}\left(e^{\frac{-V}{1.2*0.026}} - 1\right) = \frac{V}{R} \quad (6)$$

where: I_s: reverse saturation current$= 10^{-12}$A. In the case of parallel, $V_D = V_{pv} = V$
By the first derivative of Eq. 6, the voltage of the cell is calculated numerically.

3. Newton's Method [50-55]

The following algorithm suggestion for solving Eq. 6 by using NRM
INPUT initial approximate solution $x_0 = 1$, ε (tolerance), N: the maximum number of iterations.
The OUTPUT for the approximate solution x_{n+1}
Step 1: Set $x = 0$
Step 2: while $i \leq x_0$
Step 3: Calculate
$x_{n+1} = x_n - \frac{f(x_n)}{f(x_n)}$ for $n = 0, 1, 2, \ldots$
Step 4: if $|x_i - x_{i-1}| < \varepsilon$; then OUTPUT x_{n+1} and stop.
Step 5: put $i = i + 1$ and $n = n + 1$; and go to Step 2.
Step 6: The OUTPUT

4. Accelerated Predictor-Corrector Hally Method (AHM)

To compare the different numerical methods of iterations, method 1 has been used against the proposed method 2. Also, Eq. 6 has been solved to demonstrate the performance of the new method, and determine the consistency and the stability of results. The results are examined using two iterative methods

Method 1: Newton Raphson Method (NRM)

$x_{n+1} = x_n - \frac{f(x_n)}{\acute{f}(x_n)}, n = 0, 1, 2, 3, \ldots$

Method 2: Accelerated Predictor- Corrector Hally Method (AHM)

$y_n = x_n - \frac{f(x_n)}{\acute{f}(x_n)}$

$x_{n+1} = y_n - \frac{2\times f(y_n)\acute{f}(y_n)}{2\times \acute{f}(y_n)^2 - f(y_n)\times \acute{\acute{f}}(y_n)}, n = 0, 1, 2, 3, \ldots$

$z_n = x_n - \frac{(x_{n+1}-x_n)^2}{x_{n+2}-2\times x_{n+1}+x_n}, \ n = 0, 1, 2, 3, \ldots$

We take $\varepsilon = 10^{-9}$ (tolerance).

For estimating the zero, the following equation is utilized

$|f(z_n)| < \varepsilon, \ \sigma = |z_{n+1} - z_n| < \varepsilon$

5. Results and Discussion

Suppose Eq. 6 is modelled has obtained the following approximate solutions and the NRM and AHM are achieved based on first initial value x_0. In Table 1 the NRM and AHM of the solution results; voltage V_{pv}; current I_{pv}; power P_{pv} of the solar cell. Table 1 shows the obtained results, $R = 1$ (load resistance).

Table 1. The obtained values using NRM and AHM.

Iterations	V_{pv} *-NRM*	I_{pv} *- NRM*	P_{pv} *- NRM*	V_{pv} *-AHM*	I_{pv} *-AHM*	P_{pv} *- AHM*
1	1	1	1	0.790453895	0.790453895	0.624817361
2	0.971416861	0.971416861	0.943650719	0.893473304	0.893473304	0.798294545
3	0.946732606	0.946732606	0.896302627	0.918974787	0.918974787	0.844514659
4	0.929865706	0.929865706	0.864650231	0.922319866	0.922319866	0.850673936
5	0.923247893	0.923247893	0.852386673	0.922422989	0.922422989	0.850864171
6	0.922434	0.922434	0.850884484	0.922423135	0.922423135	0.850864439
7	0.922423136	0.922423136	0.850864443	0.922423135	0.922423135	0.850864439
8	0.922423135	0.922423135	0.850864439			
9	0.922423135	0.922423135	0.850864439			

Figure 2 The obtained values corresponding to Table 1.

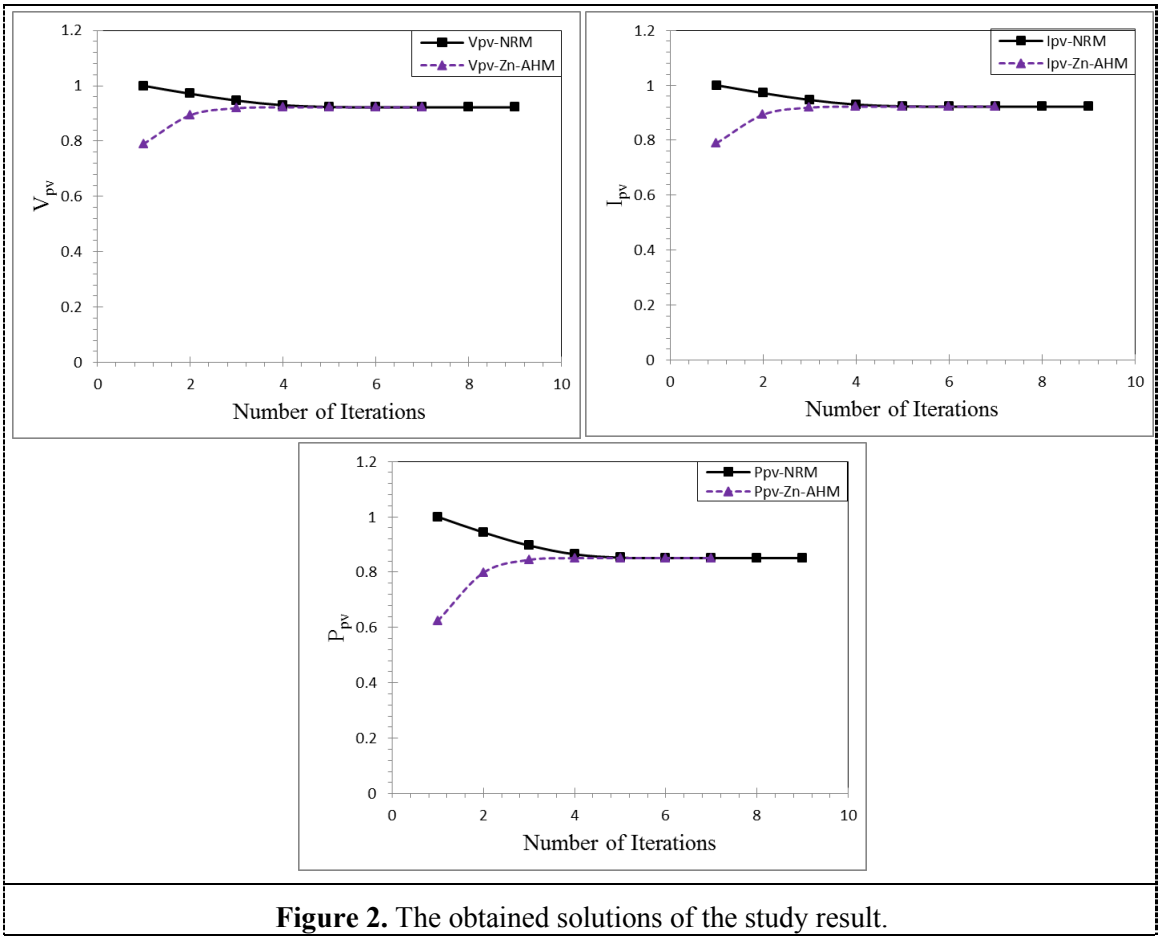

Figure 2. The obtained solutions of the study result.

Table 2 shows AHM and NRM results; voltage V_{pv}; current I_{pv}; power P_{pv} of the solar cell R = 2 (load resistance).

Table 2. The obtained values using NRM and AHM.

Iterations	V_{pv}*-NRM*	I_{pv}*- NRM*	P_{pv}*- NRM*	V_{pv}*-AHM*	I_{pv}*-AHM*	P_{pv}*- AHM*
1	1	0.5	0.5	0.750304127	0.375152064	0.281478142
2	0.97103047	0.48551524	0.47145009	0.877625808	0.438812904	0.385113529
3	0.94542197	0.47271098	0.44691135	0.911522541	0.455761271	0.415436672
4	0.92683448	0.46341724	0.42951107	0.916798941	0.45839947	0.420260149
5	0.91843875	0.45921937	0.42176486	0.917034659	0.458517329	0.420476283
6	0.91706688	0.45853344	0.42050584	0.917035382	0.458517691	0.420476946
7	0.9170354	0.4585177	0.42047696	0.917035382	0.458517691	0.420476946
8	0.91703538	0.45851769	0.42047695			
9	0.91703538	0.45851769	0.42047695			

Figure 3 The obtained values corresponding to Table 2.

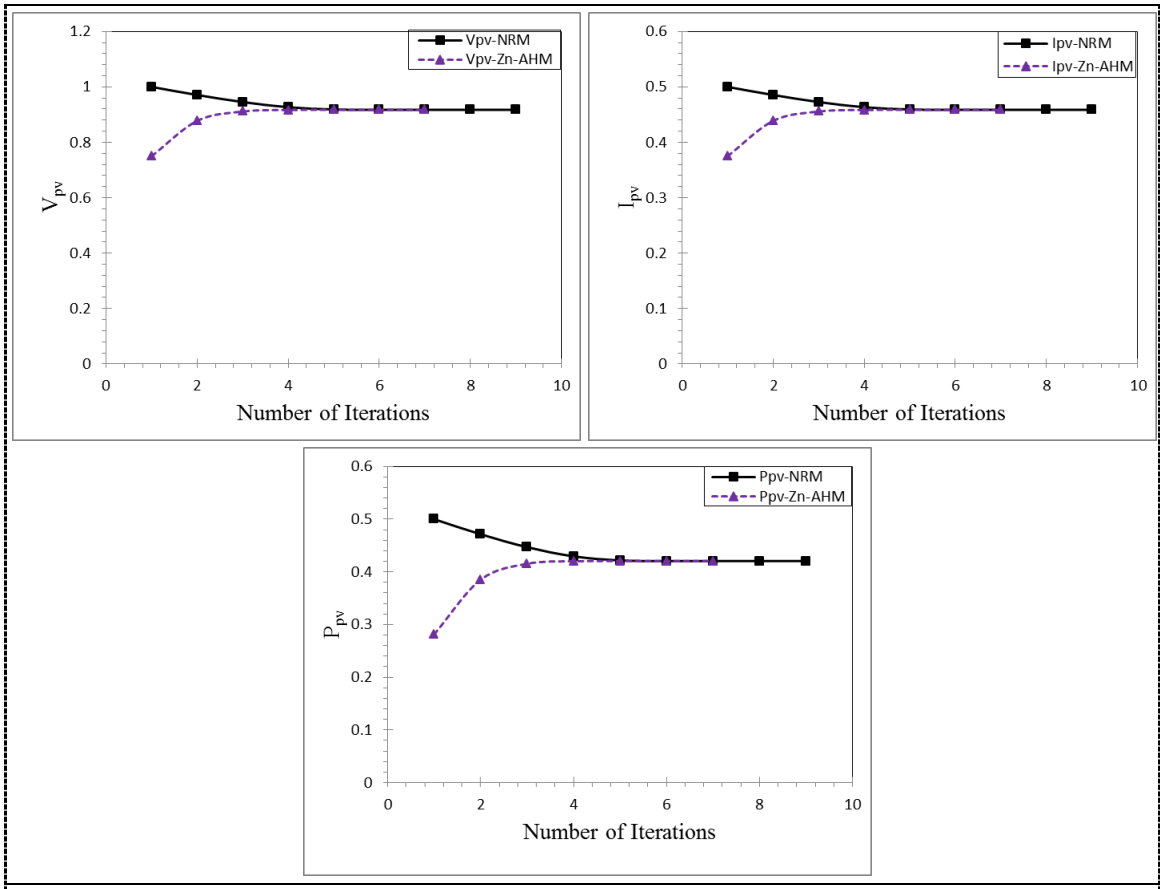

Figure 3. The obtained solutions of the study result.

In Table 3 shows AHM and NRM results; voltage V_{pv}; current I_{pv}; power P_{pv} of the solar cell R = 3 (load resistance).

Table 3. The obtained values using NRM and AHM.

Iterations	V_{pv}*-NRM*	I_{pv}*- NRM*	P_{pv}*- NRM*	V_{pv}*-AHM*	I_{pv}*-AHM*	P_{pv}*- AHM*
1	1	0.333333333	0.333333333	0.691850003	0.230616668	0.159552142
2	0.970643792	0.323547931	0.31404979	0.854423029	0.284807676	0.243346237
3	0.944084232	0.314694744	0.297098346	0.90112767	0.30037589	0.270677026
4	0.923594243	0.307864748	0.284342109	0.909824015	0.303274672	0.27592658
5	0.91287784	0.304292613	0.277781984	0.91039934	0.303466447	0.276275653
6	0.910501262	0.303500421	0.276337516	0.910403374	0.303467791	0.276278101
7	0.910403531	0.303467844	0.276278197	0.910403374	0.303467791	0.276278101
8	0.910403374	0.303467791	0.276278101			
9	0.910403374	0.303467791	0.276278101			

Figure 4 The obtained values corresponding to Table 3.

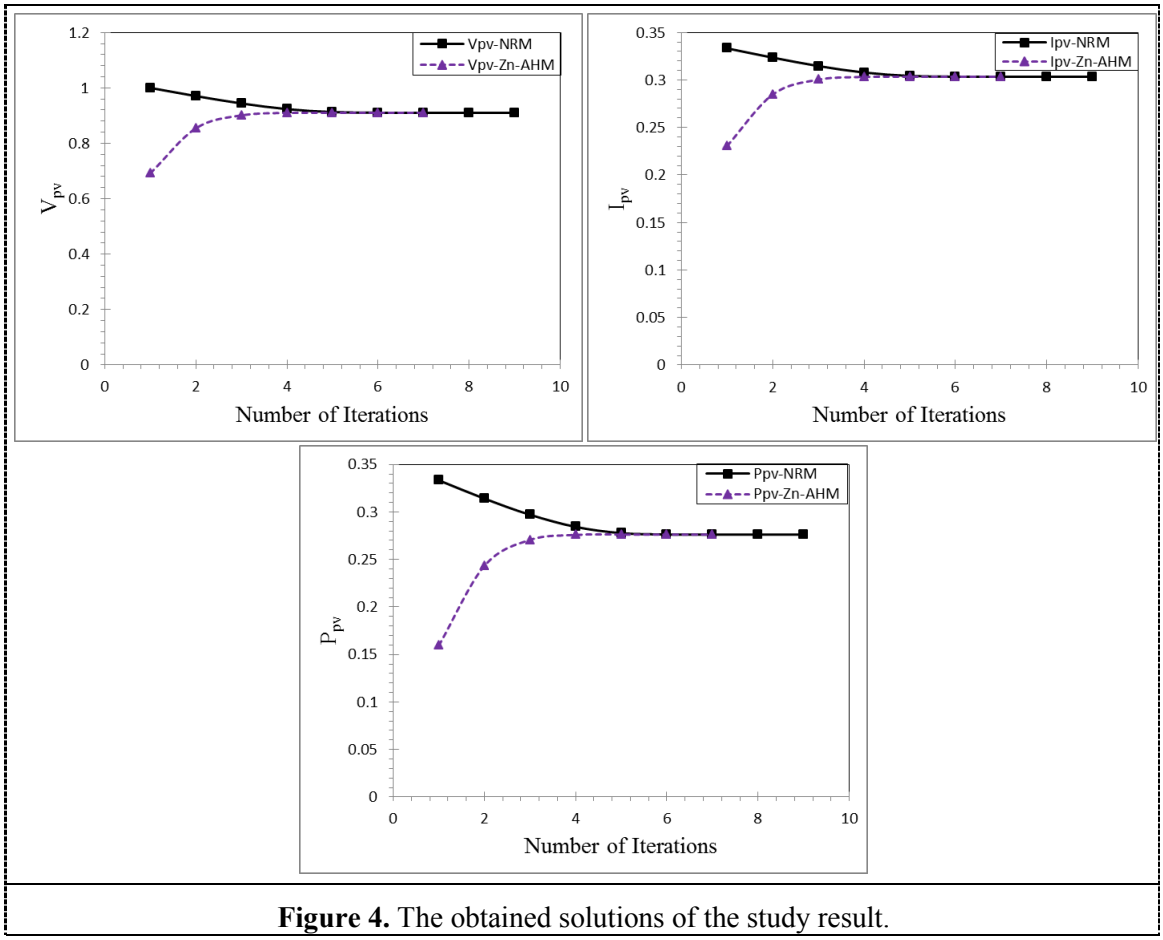

Figure 4. The obtained solutions of the study result.

In Table 4 shows AHM and NRM results; voltage V_{pv}; current I_{pv}; power P_{pv} of the solar cell $R = 4$ (load resistance).

Table 4. The obtained values using NRM and AHM.

Iterations	V_{pv}*-NRM*	I_{pv}*- NRM*	P_{pv}*- NRM*	V_{pv}*-AHM*	I_{pv}*-AHM*	P_{pv}*- AHM*
1	1	0.25	0.25	0.598809171	0.149702293	0.089643106
2	0.970256822	0.242564205	0.235349575	0.816819533	0.204204883	0.166798538
3	0.94271872	0.23567968	0.222179646	0.884826124	0.221206531	0.195729317
4	0.920123009	0.230030752	0.211656588	0.900161102	0.225040276	0.202572502
5	0.906346494	0.226586624	0.205365992	0.901713938	0.225428485	0.203272007
6	0.902077706	0.225519427	0.203436047	0.901740591	0.225435148	0.203284023
7	0.901742503	0.225435626	0.203284885	0.901740602	0.22543515	0.203284028
8	0.901740602	0.225435151	0.203284028			
9	0.901740602	0.22543515	0.203284028			

Figure 5 The obtained values corresponding to Table 4.

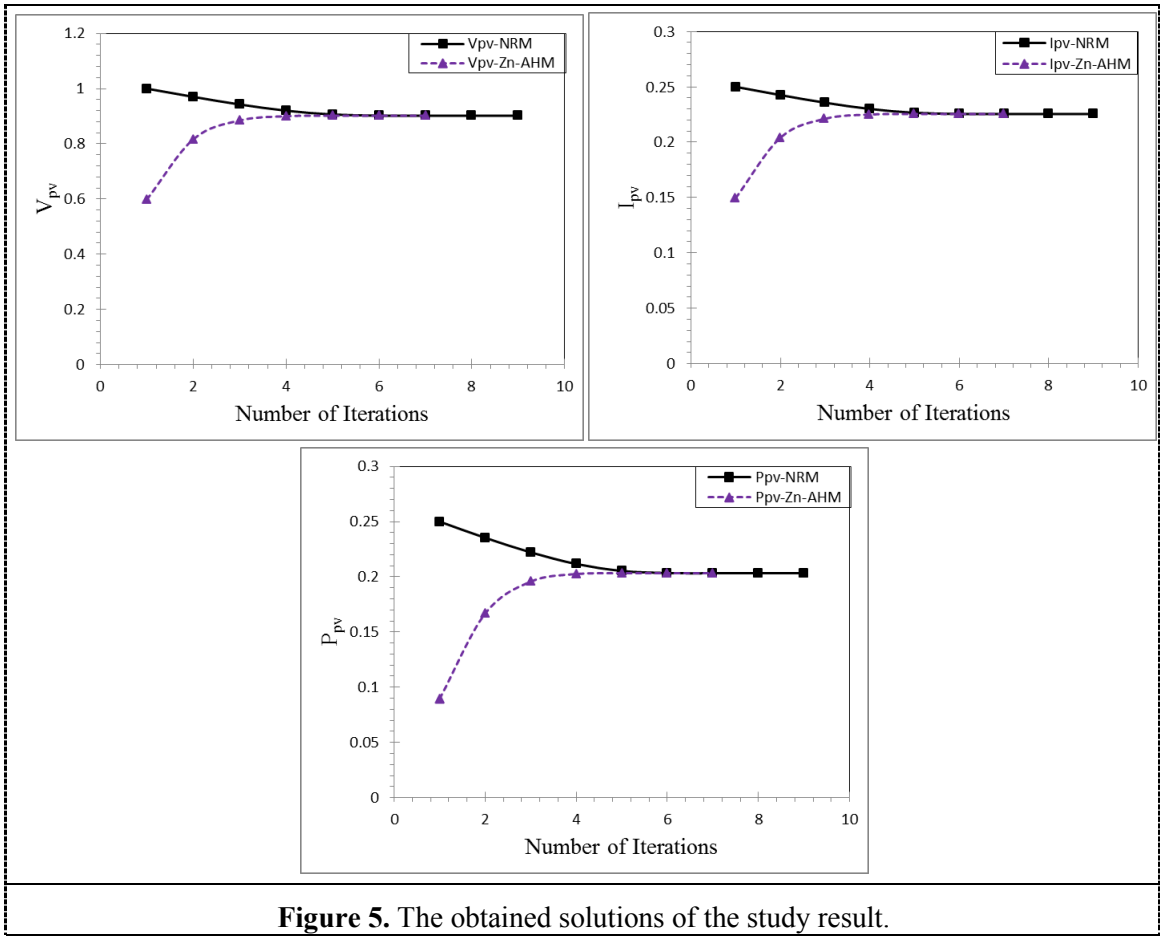

Figure 5. The obtained solutions of the study result.

In Table 5 shows AHM and NRM results; voltage V_{pv}; current I_{pv}; power P_{pv} of the solar cell $R = 5$ (load resistance).

Table 5. The obtained values using NRM and AHM.

Iterations	V_{pv}*-NRM*	I_{pv}*- NRM*	P_{pv}*- NRM*	V_{pv}*-AHM*	I_{pv}*-AHM*	P_{pv}*- AHM*
1	1	0.25	0.25	0.598809171	0.149702293	0.089643106
2	0.970256822	0.242564205	0.235349575	0.816819533	0.204204883	0.166798538
3	0.94271872	0.23567968	0.222179646	0.884826124	0.221206531	0.195729317
4	0.920123009	0.230030752	0.211656588	0.900161102	0.225040276	0.202572502
5	0.906346494	0.226586624	0.205365992	0.901713938	0.225428485	0.203272007
6	0.902077706	0.225519427	0.203436047	0.901740591	0.225435148	0.203284023
7	0.901742503	0.225435626	0.203284885	0.901740602	0.22543515	0.203284028
8	0.901740602	0.225435151	0.203284028			
9	0.901740602	0.22543515	0.203284028			

Figure 6 The obtained values corresponding to Table 5.

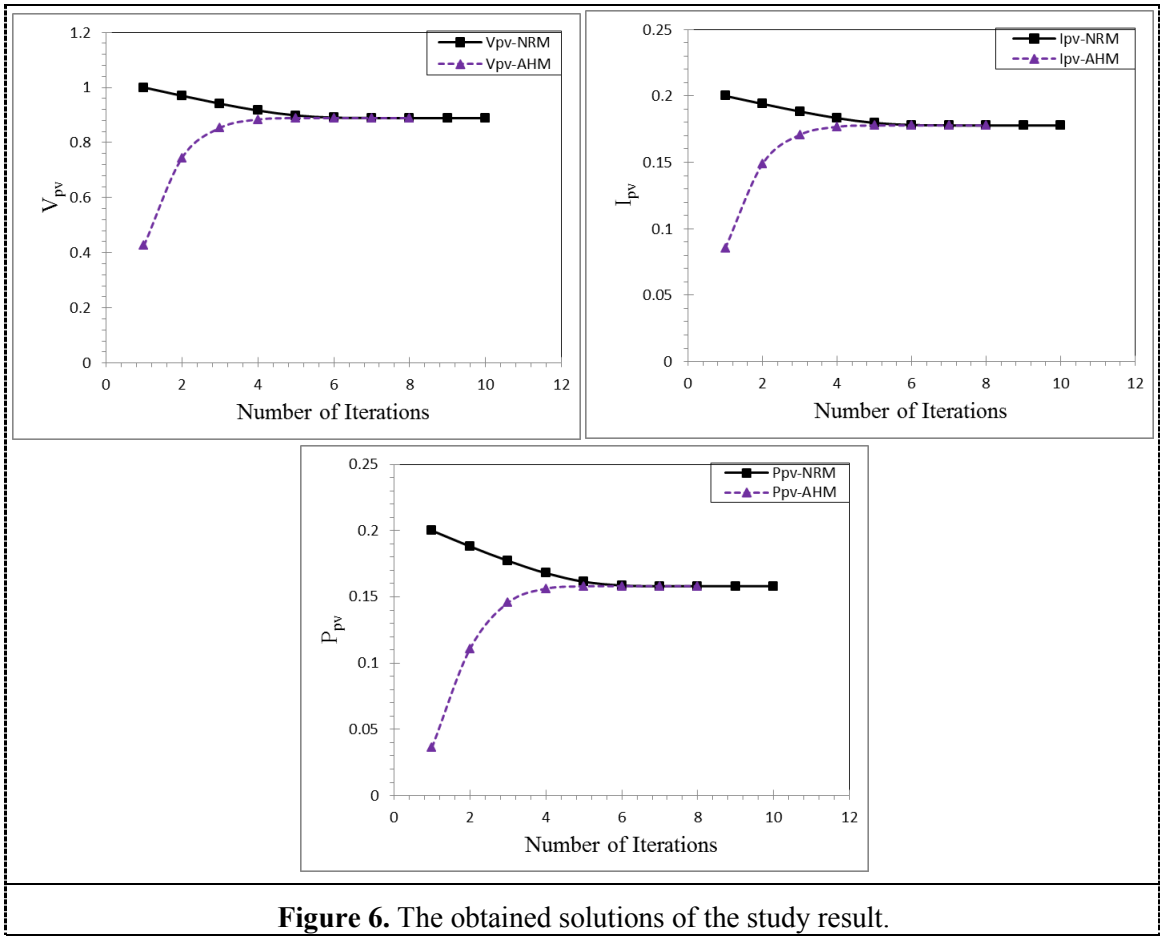

Figure 6. The obtained solutions of the study result.

Obtained results plot number of iteration V, I and P-plane and the initial-output values proves that the proposed method AHM has eight iterations indicated a fast behavior. The comparison between the two methods NRM and AHM is to acquire the results based on the least number of iterations, which confirms that the mathematical method with the least number of iterations is better and faster. The results confirmed with NRM, ten iterations were used, while using the AHM, eight iterations were utilized.

6. Conclusion

In this paper, we observed that the efficiency of the new Accelerated Predictor- Corrector Hally method considerably improve that of Newton method and the given two step method Remark that only 8 iterations are needed to reach the exact solution with small tolerance, while Newton's method requires ten iterations. Data acquired from the proposed method AHM were found to be sufficient and values for single diode solar cell were determined with fast convergence, more capable to determine these parameters and establishing towards the final values.

References

[1] Al-Faour O, Al-Ani F H D and Al-Rawi S N 2000 *Eng. Technol. J.* 17
[2] Salih A A and Shihab S 2020 *Samarra J. Pure and Appl. Sci.* **2** 2 68-78
[3] Alrawy S S and Salih A A 2020 Samarra J. Pure and Appl. Sci. **2** 1 67-75
[4] Al-Rawi S N 2006 *Kirkuk Univ. J. Sci. Stud.* **1** 125-136
[5] Shihab S N, Abdulrahman A A and Mohammedali M N 2015 *Eng. Technol. J.* **33** 1493-1502
[6] Shihab N S and Abdalrehman A A 2012 *Eng. Technol. J.* **30** 3219-3229
[7] Shihab S N, Ali H A and Yaseen H M 2010 *Eng. Technol. J.* **28** 1893-1899

[8] Shihab S N and Abdalrehman A A 2014 *Baghdad Sci. J.* **11** 229-234
[9] Shihab S N and Sarhan M A 2014 *IOSR J. Math.* **10** 2 54-58
[10] Al-Rawi S N and Al-Rubaie H R 2010 *J. Pure Appl. Sci.* **22** 1 85-97
[11] Al-Rawi S N 1992 *J. Coll. Ed.* **5** 51-60
[12] Eleiwy J A and Shihab S N 2009 *Eng. Tech. J.* **27** 14 2642-2652
[13] Shihab S N and Sarhan M A 2014 *Elixir Int. J. Appl. Math.* **69** 1 23239-23244
[14] Delphi M and SHIHAB S 2019 *Electron. Sci. Tech. Appl.* **6** 2 18-24
[15] Rasheed M S 2010 *Eng. Tech. J.* **28** 3 492-499
[16] Rasheed M S 2010 *Eng. Tech. J.* **28** 7 1316-1320
[17] Rasheed M S 2012 *Int. J. Emerg. Tech. Comput. Appl. Sci.* 1 2 91-94
[18] Rasheed M S 2012 *Int. J. Eng. Bus. Enter. Appl.* 1 2 60-63
[19] Rasheed M S 2013 *Diyala J. Pure Sci.* 9 4 31-38
[20] Rasheed M S 2013 *Int. J. Soft. Web Sci. (IJSWS)* 1 2 65-71
[21] Rasheed M S 2020 *J. Univ. Anbar Pure Sci.* **14** 1 33-37
[22] Rasheed M S 2014 *Baghdad Sci. J.* **11** 1 186-192
[23] Kadri E, Krichen M, Rasheed M, Zouari A and Khirouni K 2016 *Opt. Quantum Electron.* **48** 12 1-15
[24] Kadri E, Messaoudi O, Krichen M, Dhahri K, Rasheed M, Dhahri E, Zouari A, Khirouni K and Barillé R 2017 *J. Alloys Compd.* **721** (2017) 779-783
[25] Kadri E, Dhahri K, Zaafouri A, Krichen M, Rasheed M, Khirouni K and Barillé R 2017 *J. Alloys Compd*. **705** 708-713
[26] Rasheed M and Barillé R 2017 *Opt. Quantum Electron.* **49** 5 1-14
[27] Rasheed M and Barillé R. 2017 *J. Non. Cryst. Solids* **476** 1-14
[28] Rasheed M and Barillé R. 2017 *J. Alloys Compd.* **728** 1186-1198
[29] Saidani T, Zaabat M, Aida MS, Barille R, Rasheed M and Almohamed Y 2017 *J. Mater. Sci. Mater. Electron.* **28** 13 9252-9257
[30] Guergouria K, Boumezoued A, Barille R, Rechemc D, Rasheed M and Zaabata M 2019 *J. Alloys Compd.* **791** 550-558
[31] Bouras D, Mecif A, Barillé R, Harabi A, Rasheed M, Mahdjoub A and Zaabat M 2018 *Ceram. Int.* **44** 17 21546-21555
[32] Saidi W Hfaidh N, Rasheed M, Girtan M, Megriche A and EL Maaoui M 2016 *RSC Adv.* **6** 73 68819-68826
[33] AUKŠTUOLIS A, Girtan M, Mousdis G A, Mallet R, Socol M, Rasheed M and Stanculescu A 2017 Proceedings of *the Romanian Academy Ser. A Math. Phys. Tech. Science Info. Sci.* **18** 1 34-41
[34] Dkhilalli F, Megdiche S, Guidara K, Rasheed M, Barillé R and Megdiche M 2018 *Ionics* **24** 1 169-180
[35] Dkhilalli F, Borchani S M, Rasheed M, Barille R, Guidara K and Megdiche M 2018 *J. Mater. Sci. Mater. Electron.* **29** 8 6297-6307
[36] Dkhilalli F, Borchani SM, Rasheed M, Barille R, Shihab S, Guidara K and Megdiche M 2018 R. *Soc. open Sci.* **5** 8 1-12
[37] Enneffati M, Louati B, Guidara K, Rasheed M and Barillé R 2018 *J. Mater. Sci. Mater. Electron.* **29** 1 171-179
[38] Enneffati M, Rasheed M, Louati B, Guidara K and Barillé R 2019 *Opt. Quantum Electron.* **51** 9 299
[39] Azaza N B, Elleuch S, Rasheed M, Gindre D, Abid S, Barille R, Abid Y and Ammar H 2019 *Opt. Mater.* **96** 109328
[40] Abdulrahman A A, Rasheed M and Shihab S 2020 *J. Southwest Jiaotong Univ.* **55** 2
[41] Rasheed M, Abdulrahman A A and Shihab S *2020 J. Southwest Jiaotong Univ.* **55** 2
[42] Abbas M M and Rasheed M 2020 *J. Southwest Jiaotong Univ.* **55** 2
[43] Sarhan A M, Shihab S and Rasheed M 2020 *J. Southwest Jiaotong Univ.* **55** 2

[44] Sarhan A M, Shihab S and Rasheed M 2020 *J. Southwest Jiaotong Univ.* **5** 3
[45] Aziz S H, Rasheed M and Shihab S 2020 *J. Southwest Jiaotong Univ.* **5** 3
[46] Mitlif R J, Raseed M and Shihab S 2020 *J. Southwest Jiaotong Univ.* **5** 3
[47] Mohammedali M N, Sabri R I, Rasheed M and Shihab S 2020 *J. Southwest Jiaotong Univ.* **5** 4
[48] Sabri R I, Mohammedali M N, Rasheed M and Shihab S 2020 *J. Southwest Jiaotong Univ.* **5** 4
[49] Jalal R, Shihab S, Alhadi M A and Rasheed M 2020 *J. Phys Conf. Ser.* **1660** 1 012090 *IOP Publishing*
[50] Tahir F S, Rasheed M S and Hameed I A 2012 *J. Coll. Basic Ed.* **18** 7 173-183
[51] Tahir F S and Rasheed M S 2012 *J. Coll. Basic Ed.* **18** 75 95-111
[52] Shihab S and Rasheed M 2019 *Insight Math.* **1** 1 1-16
[53] Rasheed M and Shihab S 2019 *Insight Electron.* **1** 1 1-9
[54] Rasheed M and Shihab S 2019 *Electron. Sci. Tech. Appl.* **1** 1 1-9
[55] Rasheed M and Sarhan M A 2019 *Insight Electron.* **1** 1 1-9
[56] Rasheed M and Sarhan M A 2019 *Insight Math.* **1** 1 1-17
[57] Rasheed M and Sarhan M A 2019 *Insight Math.* **1** 1 1-8
[58] Rasheed M *Insight Electron.* **1** 1 1-17
[59] Rasheed M *Insight Electron.* **1** 1 1-7
[60] Rasheed M and Shihab S 2020 *Adv. Energ. Convers. Mater.* **1** 2 96-104
[61] Rasheed M and Shihab S 2020 *Adv. Energ. Convers. Mater.* **1** 2 70-79
[62] Aziz S H, Shihab S and Rasheed M 2020 *Al-Qadisiyah J. Pure Sci.* **26** 1 39-54
[63] Sarhan M A, Shihab S and Rasheed M 2020 *Al-Qadisiyah J. Pure Sci.* **26** 1 55-70
[64] Rasheed M and Shihab S 2020 *Iraqi J. Phys. (IJP)* **18** 47 33-43

Soft Convergence Via Soft--Pre-Generalized-Open Sets

Soft Convergence Via Soft-ļ- Pre-Generalized-Open Sets

R B Esmaeel and A A Hammood

Department of Mathematics, College of Education for Pure Sciences Ibn Al-Haitham, University of Baghdad, Baghdad, Iraq

E-mail: ranamumosa@yahoo.com

Abstract. In this paper, the concept of soft open set is inserted by using soft ideal with soft *pre* -open sets, like: soft-ļ-*pre*-*g*-open sets "*sp*ļ*g*-open" some of the characteristics of these sets are offered. New soft functions are given such as; sļ*pg*-open functions, soft ļ**pg*-open functions, soft ļ***pg*-open functions, soft ļ*pg*-continuous *functions*, strongly soft ļ*pg*-continuous functions and soft ļ*pg*-irresolute-functions. New separation axioms and convergences are introduced by using soft-ļ-*pre*-*g*-open sets like; *s*ļ*pg*-Ţ$_0$-*space*, *s*ļ*pg*-Ţ$_1$-*space*, *s*ļ*pg*-Ţ$_2$-*space*. some figures and suggestions have been introduced the relationships with near soft functions as well some examples are explained.

1. Introduction

In 2011, *Shaber* [1] introduced smooth topological space. Many studies have been presented to study several topological properties using the soft set as *derived* groups, *compactness*, *separation* axioms and other properties see [2-4]. As well, Kandil use the Soft ideal Model, which is a family of soft sets that meet the added genetic and characteristic of Ẋ, to study the ideal of a soft function [5], The concept of soft topological spaces (Ẋ, Ţ, Đ) is considered the beginning of the study of many topological concepts by using the concept of the ideal see [6-9].

In this work, and by using the concept of soft pre- open set and soft ideal, we have defined a new type of soft near open set. Many properties of this set have also been studied and new types of functions defined using the concept under study and new types of separation axioms have also been studied by using this set in (Ẋ, Ţ, Đ, ļ).

2. Preliminaries

In this section, some basic concepts about soft space $(\dot{X}, \tau, Đ)$ with soft ideal were presented.

Definition 2.1: [10] Let $\dot{X} \neq \emptyset$ and Đ be a set of *parameters*, and let $\wp(\dot{X})$ be the power set of Ẋ.The collection of Ẋ and $P \neq \emptyset$ such that $P \subseteq Đ$. $(\digamma, Đ)$ (*Briefly* $\digamma_{Đ}$) is a *soft set* over Ẋ *whenever*, Ғ is a *function* such that $\digamma: Đ \to \wp(\dot{X})$. So, $\digamma_{Đ} = \{\digamma(d): d \in P \subseteq Đ, \digamma: Đ \to p(\dot{X})\}$.The *collection* of all soft sets (briefly $\S\S(\dot{X})_{Đ}$).

Definition 2.2: [10] Let $(\digamma, Đ), (\mathcal{Z}, Đ) \in \S\S(\dot{X})_{Đ}$. Then $(\digamma, Đ)$ is a soft subset of, $(\mathcal{Z}, Đ)$, (briefly$(\digamma, Đ) \tilde{\subseteq}, (\mathcal{Z}, Đ)$), if $\digamma(d) \tilde{\subseteq} \mathcal{Z}(d)$, for all $d \in Đ$. Now $(\digamma, Đ)$ is a soft subset of $(\mathcal{Z}, Đ)$and , $(\mathcal{Z}, Đ)$ is a soft super set of $(\digamma, Đ)$, $(\digamma, Đ) \tilde{\supseteq}$, $(\mathcal{Z}, Đ)$.

Definition 2.3: [11] The complement of $(\mathcal{F},Đ)$ (briefly $(\mathcal{F},Đ)'$) $(\mathcal{F},Đ)' = (\mathcal{F}',Đ)$, $\mathcal{F}': Đ \to \mathcal{P}(X)$ is a function such that $\mathcal{F}'(d) = X - \mathcal{F}(d)$, for all $d \in Đ$ and $\mathcal{F}'$ is namely the soft complement of $\mathcal{F}$.

Definition 2.4: [1] Let $(\mathcal{F},Đ)$ be a $soft$ over X and $x \in X$. If $x \in \mathcal{F}(d)$ for each $d \in Đ$, then $x \tilde{\in} (\mathcal{F},Đ)$.

Definition 2.5: [1] $(\mathcal{F},Đ)$ *is a NULL soft set* (briefly $\tilde{\emptyset}$ or $\emptyset_Đ$) whenever, $\forall\, d \in Đ$, $\mathcal{F}(d) = \emptyset$.
Definition 2.6: [1] $(\mathcal{F},Đ)$ *is an absolute soft set* (briefly $\tilde{X}$ or $X_Đ$) whenever, $\forall\, d \in Đ$, $\mathcal{F}(d) = X$.

Definition 2.7: [1] *Let* $\mathcal{T}$ is the set of soft sets on X with the same $Đ$, then $\mathcal{T} \in SS(X)_Đ$ is a soft topology on X if;

i. $\tilde{X}, \tilde{\emptyset} \in \mathcal{T}$ where, $\tilde{\emptyset}(d) = \emptyset$ and $\tilde{X}(d) = X$, for each $d \in Đ$
ii. $\cup_{\alpha\in\Lambda} (\eta_\alpha, Đ) \in \mathcal{T}$ whenever, $(\eta_\alpha, Đ) \in \mathcal{T}\ \forall\, \alpha \in \Lambda$,
iii. $((\mathcal{F},Đ) \tilde{\cap} (\mathcal{Z},Đ)) \in \mathcal{T}$ for each $(\mathcal{F},Đ), (\mathcal{Z},Đ) \in \mathcal{T}$.

The triple $(X,\mathcal{T},Đ)$ i*s a soft topological spac*e if $(\eta,Đ) \in \mathcal{T}$ then $(\eta,Đ)$ is an open soft set.

Definition 2.8: [12] Let $(X,\mathcal{T},Đ)$ be a soft topological space. A soft set $(\mathcal{F},Đ)$ over X is a soft closed set in X, if $(\mathcal{F},Đ)' \in \mathcal{T}$, the collection of all $soft$ closed sets (briefly $SC(X)_Đ$).

Definition 2.9: [12] *For any soft* space $(X,\mathcal{T},Đ)$. Let $(\mathcal{F},Đ)' \in SS(X)_Đ$, then *the soft closure* of $(\mathcal{F},Đ)'$, (briefly $cl(\mathcal{F},Đ)$), $cl((\mathcal{F},Đ)) = \tilde{\cap}\{(\mathcal{M},Đ) : (\mathcal{M},Đ) \in SC(X)_Đ, (\mathcal{F},Đ) \tilde{\subseteq} (\mathcal{M},Đ)\}$.

Definition 2.10: [12] For any $(X,\mathcal{T},Đ)$. Let $(\mathcal{F},Đ) \in SS(X)_Đ$, *then the soft interior* of $(\mathcal{Z},Đ)$, (briefly $int(\mathcal{Z},Đ)$), $int(\mathcal{Z},Đ) = \tilde{\cup}\{(\mathcal{M},Đ) : (\mathcal{M},Đ) \in \mathcal{T}, (\mathcal{M},Đ) \tilde{\subseteq} (\mathcal{Z},Đ)\}$.

Definition 2.11:. [2] Two soft sets $(\mathcal{C},Đ)$, $(\mathcal{U},Đ)$ in $SS(X)_Đ$, is said to be soft and disjoint, written $(\mathcal{W},Đ) \tilde{\cap} (\mathcal{U},Đ) = \tilde{\emptyset}$, $\mathcal{W}(đ) \cap \mathcal{U}(đ) = \emptyset$, for each $d \in Đ$.

Definition 2.12: . [2] The Two soft point $đ_{\mathcal{M}}, đ_{\mathcal{N}} \tilde{\in} \tilde{X}$ are different, written $đ_{\mathcal{M}} \neq đ_{\mathcal{N}}$, if *there* exest two soft sets $(\mathcal{C},Đ)$ and $(\mathcal{U},Đ)$ are *disjoint* $đ_{\mathcal{M}} \tilde{\in} (\mathcal{C},Đ)$ and $đ_{\mathcal{N}} \tilde{\in} (\mathcal{U},Đ)$

Definition 2.13: [5] *Let* $ǰ \neq \emptyset$, *then* $ǰ \tilde{\subseteq} SS(X)_Đ$ is a soft ideal whenever,
i. If $(\mathcal{F},Đ) \tilde{\in} ǰ$ and $(\mathcal{Z},Đ) \tilde{\in} ǰ$ implies, $(\mathcal{F},Đ) \tilde{\cup} (\mathcal{Z},Đ) \tilde{\in} ǰ$.
ii. If $(\mathcal{F},Đ) \tilde{\in} ǰ$ and $(\mathcal{Z},Đ) \tilde{\subseteq} (\mathcal{F},Đ)$ implies, $(\mathcal{Z},Đ) \tilde{\in} ǰ$.

Definition 2.14: [5] The space $(X,\mathcal{T},Đ)$ with a soft ideal $ǰ$ can be defined is $(X,\mathcal{T},Đ,ǰ)$ a soft topological space.

Definition 2.15: [14] For any $(X,\mathcal{T},Đ)$, then $(\mathcal{F},Đ)$ is a $soft\ pre$-open set (briefly Sp-open set if $(\mathcal{F},Đ) \tilde{\subseteq} int(cl(\mathcal{F},Đ))$. a $soft\ pre$-closed set (briefly $(\mathcal{F},Đ)'$).The family of each pre $soft$-open sets in $(X,\mathcal{T},Đ)$ (briefly $SpO(X)$). The *collection* of each $soft\ pre$-*closed* sets (*briefly* $SpC(X)$).

Definition 2.16: [2] Let $(X,\mathcal{T},Đ)$ be a soft topological space over X is a soft-$\mathcal{T}_0$-space if for all, $đ_{\mathcal{M}}$, $đ_{\mathcal{N}} \tilde{\in} \tilde{X}$ such that $đ_{\mathcal{M}} \neq đ_{\mathcal{N}}$. *If there exist soft open set* $(\eta,Đ)$ such that $đ_{\mathcal{M}} \tilde{\in} (\eta,Đ)$, $đ_{\mathcal{N}} \tilde{\notin} (\eta,Đ)$ or $đ_{\mathcal{M}} \tilde{\notin} (\eta,Đ)$, $đ_{\mathcal{N}} \tilde{\in} (\eta,Đ)$.

Definition 2.17: [2] Let $(X,\mathcal{T},Đ)$ be a soft topological space over X is a $soft$ $\mathcal{T}_1$-space if for all, $đ_{\mathcal{M}}$ $đ_{\mathcal{N}}, \tilde{\in} \tilde{X}$ *such that* $đ_{\mathcal{M}} \neq đ_{\mathcal{N}}$. $\exists$ $(\mathcal{F},Đ)$, $(\eta,Đ) \in \mathcal{T}$ whenever, $đ \tilde{\in} (\mathcal{F},Đ)$, $đ_{\mathcal{N}} \tilde{\notin} (\mathcal{F},Đ)$ and $đ_{\mathcal{M}} \tilde{\notin} (\eta,Đ)$, $đ_{\mathcal{N}} \tilde{\in} (\eta,Đ)$.

Definition 2.18: [2] *Let* $(\chi, \tau, Đ)$ be a $soft$ topological *space over* χ is *said* to be $soft$-τ_2-space if, for each $ḍ_{\mathcal{M}}$, $ḍ_{\mathcal{N}} \tilde{\in} \tilde{\chi}$ such that $ḍ_{\mathcal{M}} \neq ḍ_{\mathcal{N}}$. $\exists$ $(F, Đ)$, $(\eta, Đ) \in \tau$ whenever, $ḍ_{\mathcal{M}} \tilde{\in} (F, Đ)$, $ḍ_{\mathcal{N}} \tilde{\in} (\eta, Đ)$ and $(F, Đ) \tilde{\cap} (\eta, Đ) = \{\tilde{\emptyset}\}$.
Proposition 2.19: [2] For all soft- τ_{i+1}-space is a soft- τ_i-space and i $\in$ {0,1,2}

Definition 2.20: [13] Let $ŞŞ(\chi)_P$ and $ŞŞ(\Upsilon)_ɯ$ be two collections of soft sets, such that $\Gamma: \chi \to \Upsilon$ and $\Phi: P \to ω$ are two functions. Let $f_{\Phi\Gamma}: ŞŞ(\chi)_P \to ŞŞ(\Upsilon)_ɯ$ be .a function then;
i. If $(\mathcal{M}, P) \in ŞŞ(\chi)$. $f_{\Phi\Gamma}(\mathcal{M}, \mathcal{P}) = (f_{\Phi\Gamma}(\mathcal{M}), \Phi(P)) \in ŞŞ(\Upsilon)_ɯ$ whenever,

$$f_{\Phi\Gamma}(\mathcal{M})(\mathcal{b}) = \begin{cases} \cup \{\Gamma(\mathcal{M})(a) : a \in \Phi^{-1}(\mathcal{b}) \cap P\} \text{ if } \Phi^{-1}(\mathcal{b}) \cap P \neq \emptyset \\ \emptyset \qquad \text{Otherwise} \end{cases} \text{ for each } \mathcal{b} \in ω$$

ii. If $(\mathcal{Z}, ω) \in ŞŞ(\Upsilon)_ɯ$. Then $f_{\Phi\Gamma}^{-1}(\mathcal{Z}, ω) = (f_{\Phi\Gamma}^{-1}(\mathcal{Z}), \Phi^{-1}(ω)) \in ŞŞ(\chi)_P$ whenever,

$$f_{\Phi\Gamma}^{-1}(\mathcal{Z})(a) = \begin{cases} \Gamma^{-1}((\mathcal{Z}(\Phi(a)) & \text{if } \Phi(a) \in ω \\ \emptyset & \text{Otherwise} \end{cases} \text{ for each } a \in P$$

Now, if Φ and Γ are *surjective* (*respectively*, injective), functions then $f_{\Phi\Gamma}$ is a *surjective* (*respectively*, *injective*)

Definition 2.21: [15] Let $(\chi, \tau, Đ)$ and $(\Upsilon, ⍰, \mathcal{S})$ be soft topological spaces over χ and Υ respectively. Let $\Gamma: \chi \to \Upsilon$ and $\Phi: P \to ω$ be two functions. Let $f_{\Phi\Gamma}: ŞŞ(\chi)_p \to ŞŞ(\Upsilon)_ɯ$ be a function and $ḍ_{\mathcal{M}} \tilde{\in} \tilde{\chi}$. The function $f_{\Phi\Gamma}$ is soft $\Phi\Gamma$-*continuous* at $ḍ_{\mathcal{M}} \tilde{\in} \tilde{\chi}$ if for each $(\mathcal{G}, B) \tilde{\in} N_{\mp}(f_{\Phi\Gamma}(ḍ_{\mathcal{M}}))$, there exists a $(\mathcal{M}, \mathcal{P}) \tilde{\in} N_{\mp}(ḍ_{\mathcal{M}})$ such that $f_{\Phi\Gamma}(\mathcal{M}, \mathcal{P}) \tilde{\subseteq} (\mathcal{G}, ω)$. Then $f_{\Phi\Gamma}$ is soft $\Phi\Gamma$-*continuous* on $\tilde{\chi}$, if $f_{\Phi\Gamma}$ is soft $\Phi\Gamma$-*continuous* at *each soft point* in $\tilde{\chi}$.

Theorem 2.22: [15] Let $(\chi, \tau, Đ)$ and $(\Upsilon, ⍰, \mathcal{S})$ be soft topological spaces over χ and Υ respectively. Let $\Gamma: \chi \to \chi$ and $\Phi: P \to ω$ are two functions. Let $f_{\Phi\Gamma}: ŞŞ(\chi)_p \to ŞŞ(\Upsilon)_ɯ$ be a function . $f_{\Phi\Gamma}$ is a soft *continuous* if $f_{\Phi\Gamma}^{-1}((\eta, Đ))) \in \tau, \forall (\eta, Đ))) \in ⍰$

Definition 2.23:[16] If $S_n: \mathbb{N} \longrightarrow \mathcal{p}(\chi)$ and $S(n) = S_n \in \mathcal{p}(\chi)$ for all $n \in \mathbb{N}$, *then* S_n is a soft *sequence* over χ it can be written as S as S_n or $\prec S_1, S_2, S_3, ... \succ$.

Example : Let $\chi = \{1, 2, 3\}$, $S: \mathbb{N} \longrightarrow \mathcal{p}(\chi)$ such that $S_n = \{2\}\ \forall\ n \in \mathbb{N}/\{1\}$. $S_1 = \{1\}$, $S_2 = S_3 = S_4 = \cdots = \{2\}$. Then $S_n = \prec \{1\}, \{2\}, \{2\}, \{2\}, ... \succ$.

Definition 2.24 :[16] For a*ny soft space* $(\chi, \tau, Đ)$ *with* a set of *parameters* Đ where, $ɬ_{\mathcal{M}} \in \mathcal{p}(\chi)/\chi$ and the *soft sequence* $(S_n)_{n\in\mathbb{N}}$ over χ. Then $(S_n)_{n\in\mathbb{N}}$ is called *convergence* to $ɬ_{\mathcal{M}}$ ($briefly\ S_n \longrightarrow ɬ_{\mathcal{M}}$) if for all *soft open* set $(\eta, Đ)$ where, $ɬ_{\mathcal{M}} \tilde{\in} (\eta, Đ)$ there *exists* $k \in \mathbb{N}$ where, $S_n \tilde{\in} (\eta, Đ)$ for *every* $n \geqslant k$ and $ɬ_{\mathcal{M}}$ is called limit point for the soft sequence.
A soft sequence $(S_n)_{n\in\mathbb{N}}$ is *lled divergence, if it is not convergence.*

3. On *soft ideal pre-g-closed set*.

Definition 3.1: In *ft ideal topological space* $(\chi, \tau, Đ, ɻ)$, let $(F, Đ) \in ŞŞ(\chi)_Đ$ then $(F, Đ)$ is a soft-ɻ-*pre-g*-closed set (briefly sɻ*pg*-closed). If $(F, Đ) - (\eta, Đ) \in ɻ$ then , $cl(F, Đ) - (\eta, Đ) \in ɻ$ for each $(\eta, Đ) \in ŞpO(\chi)$. And $\tilde{\chi} - (F, Đ)$ is a *soft*-ɻ-*pre-g*-open set (briefly *s*ɻ*pg*-open set).

The family of all $s\mathfrak{g}pg$- closed sets (briefly $s\mathfrak{g}pg$-C(Ϫ)) and the family of all $s\mathfrak{g}pg$-open soft sets (briefly $s\mathfrak{g}pg$-O(Ϫ)$_{Đ}$).

Example 3.2: For a space $(Ϫ, Ţ, Đ, \mathfrak{g})$,where $Ϫ = \{e_{\mathfrak{g}}, m_{\mathfrak{g}}\}$, $Đ = \{d_1, d_2\}$,$Ţ=\{\tilde{\emptyset},\tilde{X}, (Ғ, Đ), (Ƞ, Đ)\}$, $\mathfrak{g} = \{\tilde{\emptyset}, \mathcal{M}\}$ such *that* $(Ғ, Đ) = \{(d_1, \{\emptyset\}), (d_2, \{e_{\mathfrak{g}}\})\}$, and$(Ƞ,Đ)=\{(d_1,\{e_{\mathfrak{g}}\}),(d_2,\{e_{\mathfrak{g}}\})\}$ and $(M, Đ) = \{(d_1, \{\emptyset\}), (d_2, \{e_{\mathfrak{g}}\})\}$ then $Ş p O(Ϫ)=\{\tilde{\emptyset}, \tilde{Ϫ}, (Ғ, Đ), (Ƞ, Đ), (\mathcal{Z}, Đ), (\mathcal{H}, Đ), (\mathcal{E}, Đ), (\mathcal{N}, Đ), (\mathcal{G}, Đ)\}$, $s\mathfrak{g}pg$-$C(Ϫ)_{Đ}=\{\tilde{Ϫ}, \tilde{\emptyset}, (Ғ', Đ), (Ƞ', Đ)\}$; $(Ғ', Đ))=\{(d_1, \{Ϫ\}), (d_2, \{m_{\mathfrak{g}}\})\}$, $(Ƞ', Đ)=\{(d_1,\{m_{\mathfrak{g}}\}),(d_2,\{m_{\mathfrak{g}}\})\}$ such that $(\mathcal{Z}, Đ)=\{(d_1,\emptyset),(d_2, \chi)\}$, $(\mathcal{H}, Đ) = \{(d_1, \{e_{\mathfrak{g}}\}), (d_2, \chi)\}$, $(\mathcal{E}, Đ)=\{(d_1,\{m_{\mathfrak{g}}\}),(d_2,\{e_{\mathfrak{g}}\})\}$, $(\mathcal{N}, Đ)=\{(d_1,\{m_{\mathfrak{g}}\}),(d_2, \chi)\}$ and $(\mathcal{G}, Đ)= \{(d_1, \chi) ,(d_2,\{e_{\mathfrak{g}}\})\}$.

Remark 3.3: For any $(Ϫ, Ţ, Đ, \mathfrak{g})$ then
i. Every closed $soft\ set$ is a $s\mathfrak{g}pg$-closed.
ii. Every $open\ soft\ set$ is a $s\mathfrak{g}pg$-open.

Proof (i) Let $(\mathcal{M}, Đ)$ $be\ any\ closed\ soft\ set\ in$ $(Ϫ, Ţ, Đ, \mathfrak{g})$ and $(Ƞ, Đ)$ be a $soft\ pre$-open set such that $(\mathcal{M}, Đ) - (Ƞ, Đ) \in \mathfrak{g}$, but $cl(\mathcal{M}, Đ) = (\mathcal{M}, Đ)$, since $(\mathcal{M}, Đ)$ is a closed soft set so, $cl(\mathcal{M}, Đ)$-$(Ƞ, Đ) = (\mathcal{M}, Đ) - (Ƞ, Đ) \in \mathfrak{g}$ this implies $(\mathcal{M}, Đ)$ is a soft-$\mathfrak{g}$-pre-g-closed soft set.

(ii) Let $(Ƞ, Đ)$ $be\ any$ open $soft$ set in $(Ϫ, Ţ, Đ, \mathfrak{g})$ $then$ $\tilde{Ϫ} - (Ƞ, Đ)$ is a closed $soft$ set this $implies$ by (i) $(\tilde{Ϫ} - (\mathcal{M}, Đ))is$ a $s\mathfrak{g}pg$-closed set $thus$ $(\mathcal{M}, Đ)$is a $s\mathfrak{g}pg$-open soft set .
The converse of $Remark$ 3;3 is not hold. See Example 3:2
i. Let $(\mathcal{E}', Đ) = \{(\hbar_1, \{e_{\mathfrak{g}}\}), (\hbar_2, \{m_{\mathfrak{g}}\})\}$ is a $s\mathfrak{g}pg$-closed set, but $(\mathcal{E}, Đ)$ is not $closed\ soft$ set.
ii. Let $(\mathcal{G}, Đ)= \{(\hbar_1, \{m_{\mathfrak{g}}\}), (\hbar_2, \{e_{\mathfrak{g}}\})\}$ is a $s\mathfrak{g}pg$-open set, but $(\mathcal{G}, Đ) \notin Ţ$.

Definition 3.4: The function $f_{\beta\Psi}$: $(Ϫ, Ţ, Đ) \rightarrow (Ϋ, \square, \mathcal{S})$ be $soft\ topological\ spaces\ over$ Ϫ and Y respectively . Let Γ: Ϫ→Ϫ and Φ:Đ →$\mathcal{S}$ are two functions be a mapping. Let $f_{\Phi\Gamma}$: Ş Ş(Ϫ)$_{Đ}$→ Ş Ş(Ϋ)$_{\mathcal{S}}$ be a function. then the function $f_{\Phi\Gamma}$ is called
(1)soft open if $f_{\Phi\Gamma}((Ƞ, Đ)) \in \square, \forall (Ƞ, Đ) \in Ţ$
(2)soft continuous if $f_{\Phi\Gamma}^{-1}((Ƞ, Đ)) \in Ţ$, $\forall (Ƞ, Đ) \in \square$

Definition 3.5: The function $f_{\beta\Psi}$: $(Ϫ, Ţ, Đ, \mathfrak{g}) \rightarrow (Ϋ, \square, \mathcal{S}, Ï)$ is called
i. Soft-$\mathfrak{g}$-pre-g-open function, (briefly s$\mathfrak{g}$pg-O-function), if $f_{\Phi\Gamma}((Ƞ, Đ)) \in s Ïpg$-O(Ϋ)$_{\mathcal{S}}$ whenever, $(Ƞ, Đ) \in s\mathfrak{g}pg$-O(Ϫ)$_{Đ}$.
ii. Soft-$\mathfrak{g}^*$-pre-g-open function, (briefly $s\mathfrak{g}^*pg$-O-function), if $f_{\Phi\Gamma}((Ƞ, Đ)) \in s Ïpg$-O(Ϋ)$_{\mathcal{S}}$ whenever,$(Ƞ, Đ) \in Ţ$.
iii. Soft-$\mathfrak{g}^{**}$-pre-g-open function, (briefly $s\mathfrak{g}^{**}pg$-O-function), if $f_{\Phi\Gamma}((Ƞ, Đ)) \in \square$ whenever,$(Ƞ, Đ) \in s\mathfrak{g}pg$-O(Ϫ)$_{Đ}$.

Proposition 3.6: Let $f_{\Phi\Gamma}$: $(Ϫ, Ţ, Đ, \mathfrak{g}) \rightarrow (Ϋ, \square, \mathcal{S}, Ï)$ is a $function$
i. If $f_{\Phi\Gamma}$ is a soft open $function\ then$ $f_{\Phi\Gamma}$ is a $s\mathfrak{g}^*pg$-O-$function$.
ii. If $f_{\Phi\Gamma}$ is a $s\mathfrak{g}^{**}pg$-O-$function\ then$ $f_{\Phi\Gamma}$ is a soft open $function$.
iii. If $f_{\Phi\Gamma}$ is a $s\mathfrak{g}pg$-O-$function\ then$ $f_{\Phi\Gamma}$ is a $s\mathfrak{g}^*pg$-O-$function$.
iv. If $f_{\Phi\Gamma}$ is a $s\mathfrak{g}^{**}pg$-O-$function\ then$ $f_{\Phi\Gamma}$ is a $s\mathfrak{g}pg$-O-$function$.
Proof:
i. Let $(Ƞ, Đ) \in Ţ$ since $f_{\Phi\Gamma}$ is a $soft\ open\ function,\ then$ $f_{\Phi\Gamma}((Ƞ, Đ)) \in \square$. By $Remark$ 3.3, $f_{\Phi\Gamma}((Ƞ, Đ)) \in s\mathfrak{g}pg$-O(Ϋ) . Hence $f_{\Phi\Gamma}$ is a $s\mathfrak{g}^*pg$O-function.
ii. Let $(Ƞ, Đ) \in Ţ$. By Remark 3.3, $(Ƞ, Đ) \in s\mathfrak{g}pg$-O(Ϫ)$_{Đ}$. Since $f_{\Phi\Gamma}$ is a $s\mathfrak{g}^{**}pgo$-$function$, then $f_{\Phi\Gamma}((Ƞ, Đ))$ $is\ an\ open\ in$ $(Ϋ, \square, \mathcal{S})$. Hence $f_{\Phi\Gamma}$ is an open $function$.
iii. Let $(Ƞ, Đ) \in Ţ$. By $Remark$ 3.3, $(Ƞ, Đ)$ is a $s\mathfrak{g}pg$-O(Ϫ)$_{Đ}$, since $f_{\Phi\Gamma}$ is a $s\mathfrak{g}pg$-O-$function$, then $f_{\Phi\Gamma}$ $(Ƞ, Đ) \in s\mathfrak{g}pg$-o(Ϋ)$_{\mathcal{S}}$. Hence $f_{\Phi\Gamma}$ is a $s\mathfrak{g}^*pg$-O-$function$.

iv. Let $(\eta, Đ) \in s\psi pg\text{-O}(\chi)_Đ$. Since $f_{ΦΓ}$ is a $s\psi^{**}pgo\text{-}function$, then $f_{ΦΓ}((\eta, Đ))$ $is\ a\ soft\ open\ in\ (\Upsilon, \square, \mathcal{S})$. By $Remark$ 3.3., $f_{ΦΓ}((\eta, Đ)) \in s\psi pg\text{-O}(\Upsilon)_{\mathcal{S}}$. Hence $f_{ΦΓ}$ is a $s\psi pg$o-function.

The inverse is not true. See the following examples.

Example 3.7: The function $f_{ΦΓ} : (\chi, \tau, Đ, \psi) \to (\chi, \tau, Đ, Ï)$ where , $\tau = \{ \tilde{\chi}, \tilde{\emptyset}, (Ғ, Đ)$; $Ғ(d) = \{e_ψ\}$, for all $d \in Đ\}$ where, $\chi = \{e_ψ, m_ψ, r_ψ\}$, $Đ = \{d_1, d_2\}$, $\psi = \{\tilde{\emptyset}\}$ and $Ï = Ş\S(\{\chi\})_Đ$ where, $Φ$: $Đ \to Đ$ such that $Φ(d_1) = \{d_1\}$, $Φ(d_2) = \{d_2\}$ and $Γ : \chi \to \chi$ such that $Γ(e_ψ) = \{m_ψ\}$, $Γ(m_ψ) = \{e_ψ\}$, $Γ(r_ψ) = \{r_ψ\}$ then $Ş pO(\chi) = \{(\mathcal{M}, Đ);\ e_ψ \in (\mathcal{M}, Đ)\}$for some $(d_i \in Đ)$such that i $=\{1,2\}$, then $s\psi pg\text{-O}(\chi)_Đ = \tau$, $s\psi pg\text{-C}(\chi)_Đ = \{ \tilde{\chi}, \tilde{\emptyset}, (Ғ', Đ)$; $Ғ'(d) = \{m_ψ, r_ψ\}$ for every $d \in Đ\}$ and $sÏpg\text{-C}(\chi)_Đ = sÏpg\text{-O-}(\chi)_Đ = Ş\S(\chi)_Đ$. Then $f_{ΦΓ}$ is a $s\psi pg$-O-function and $s\psi^{*}pg$-O-function which is not $s\psi^{**}pg$-O-function and not soft open function. Since$(Ғ, Đ) \in \tau$, but $f_{ΦΓ}((Ғ, Đ)) = (\mathcal{W}, Đ) \in Ş\S(\chi)_Đ$ such that $\mathcal{W}(d) = \{m_ψ\}\ \forall\ d \in Đ$, which is not open soft set.

Example 3.8: The function $f_{ΦΓ} : (\chi, \tau, Đ, \psi) \to (\chi, \tau, Đ, Ï)$ where, $\tau = \{\tilde{\chi}, \tilde{\emptyset}, (Ғ, Đ)$; $Ғ(d) = \{e_ψ\}$, for all $d \in Đ\}$ where, $\chi = \{e_ψ, m_ψ, r_ψ\}$, $Đ = \{d_1, d_2\}$, $Ï = \{\tilde{\emptyset}\}$ and $\psi = Ş\S(\{\chi\})_Đ$ where $Φ : Đ \to Đ$ such that $Φ(d_1) = \{d_1\}$, $Φ(d_2) = \{d_2\}$ and $Γ : \chi \to \chi$ such that $Γ(e_ψ) = \{e_ψ\}$, $Γ(m_ψ) = \{m_ψ\}$, $Γ(r_ψ) = \{r_ψ\}$ then $Ş pO(\chi) = \{(\mathcal{M}, Đ)$;$e_ψ \in (\mathcal{M}, Đ)\}$for some $(d_i \in Đ)$such that i $=\{1,2\}$, $s\psi pg\text{-C}(\chi)_{\mathcal{H}} = s\psi pg\text{-O}(\chi)_Đ = Ş\S(\chi)_{\mathcal{H}}$ .So, $sÏpg\text{-C-}(\chi)_Đ = \{ \tilde{\emptyset}, \tilde{\chi}, (Ғ', Đ)$; $Ғ'(d) = \{m_ψ, r_ψ\}$ for every $(d \in Đ)\}$ and $sÏpg\text{-O}(\chi)_Đ = \tau$. It is possible to see that $f_{ΦΓ}$ is open function and $s\psi^{*}pgc$-function which is not $s\psi pg$o-function and not $s\psi^{**}pg$-O-function. Since $(\mathcal{U}, Đ) \in s\psi pg\text{-O}(\chi) = Ş\S(\chi)_Đ$ such that $\mathcal{U}(d) = \{r_ψ\}$, but $f_{ΦΓ}((\mathcal{U}, Đ)) = (\mathcal{U}, Đ) \notin s\psi pg\text{-O}(\chi)_Đ = \tau\ (\forall\ d \in Đ)$.

Definition 3.9: The function $f_{ΦΓ}: (\chi, \tau, Đ, \psi) \to (\Upsilon, \square, \mathcal{S}, Ï)$ is a

i. Soft-ψ-p$re\text{-}g$-closed function, (briefly $s\psi pg$-C-function), if $f_{ΦΓ}((\eta, Đ)) \in s\psi pg\text{-C-}(\Upsilon)_{\mathcal{S}}$ whenever, $(\eta, Đ) \in s\psi pg\text{-C}(\chi)_Đ$.

ii. Soft-ψ^{*}-$pre\text{-}g$-closed function, (briefly $s\psi^{*}pg$-C-function), if $f_{ΦΓ}((\eta, Đ)) \in sÏpg\text{-C-}(\Upsilon)_{\mathcal{S}}$ whenever, $(\eta, Đ)$ is a soft closed set in $(\chi, \tau, Đ)$.

iii. soft-ψ^{**}-p$re\text{-}g$-closed function, (briefly $s\psi^{**}pg$-C-function), if $f_{ΦΓ}(\eta, Đ))$ is a soft closed set in $(\Upsilon, \square, \mathcal{S})$ whenever, $(\eta, Đ) \in s\psi pg\text{-C-}(\chi)_Đ$.

Proposition 3.10: Let $f_{ΦΓ}: (\chi, \tau, Đ, \psi) \to (\Upsilon, \square, \mathcal{S}, Ï)$ is a $function$

i. If $f_{ΦΓ}$ is a soft closed $function\ then$ $f_{ΦΓ}$ is a $s\psi^{*}pg\text{-C-}function.$

ii. If $f_{ΦΓ}$ is a $s\psi^{**}pg\text{-C-}function\ then$ $f_{ΦΓ}$ is a $soft\ closed\ function.$

iii. If $f_{ΦΓ}$ is a $s\psi pg\text{-C-}function\ then$ $f_{ΦΓ}$ is a $s\psi^{*}pg\text{-C-}function.$

iv. If $f_{ΦΓ}$ is a $s\psi^{**}pg\text{-C-}function\ then$ $f_{ΦΓ}$ is a $s\psi pg\text{-C-}function.$

By Proposition 3.10 proof is over.

Example 3.7 and example 3.8 shows the inverse of Proposition 3.10.

Definition 3.11: The $function$ $f_{ΦΓ}: (\chi, \tau, Đ, \psi) \to (\Upsilon, \square, \mathcal{S}, Ï)$ is called

i. soft-ψ-p$re\text{-}g$-continuous $function$, (briefly $s\psi pg$-continuous function), if $f_{ΦΓ}^{-1}((\mathcal{Z}, Đ))$ is a $s\psi pg$-$\text{O}(\chi)_Đ$for all $(\mathcal{Z}, Đ) \in \square$.

ii. strongly soft-ψ-p$re\text{-}g$-continuous $function$, (briefly strongly-$s\psi pg\text{-}continuous\ function$), if $f_{ΦΓ}^{-1}((\mathcal{Z}, Đ)) \in \tau$ for every $(\mathcal{Z}, Đ)$ is a $sÏpg$-open in Υ.

iii. soft-ψ-p$re\text{-}g$-irresolute $function$ (briefly $s\psi pg$-irresolute-function), if $f_{ΦΓ}^{-1}((\mathcal{Z}, Đ))$ is a $s\psi pg$O-$(\chi)_Đ$ for every $(\mathcal{Z}, Đ)$ is $s\psi pg\text{-O}(\Upsilon)_{\mathcal{S}}$.

Proposition 3.12: Let $f_{ΦΓ}: (\chi, \tau, Đ, \psi) \to (\Upsilon, \square, \mathcal{S}, Ï)$ is a function;

i. If $f_{ΦΓ}$ $a\ soft\ continuous\ function$, then $f_{ΦΓ}$ is a $s\psi pg$-continuous-$function.$

ii. If $f_{ΦΓ}$ is a strongly-$s\psi pg$-continuous $function$, $then$ $f_{ΦΓ}$ is a soft continuous $function.$

iii. If $f_{\Phi\Gamma}$ *is* a strongly-s$\mathfrak{l}pg$-continuous $function$, then $f_{\Phi\Gamma}$ is a s$\mathfrak{l}pg$-irresolute-$function$.
Proof:

i. *Let* $(\mathcal{Z}, Đ) \in$ □Since $f_{\Phi\Gamma}$ is a continuous $function$, *then*, $f_{\Phi\Gamma}^{-1}((\mathcal{Z}, Đ))$ is a soft open in $(Ϫ, Ţ, Đ)$. By *Remark* 3.3, $f_{\Phi\Gamma}^{-1}((\mathcal{Z}, Đ)) \in$ s$\mathfrak{l}pg$-O-$(Ϫ)_Đ$. Hence, $f_{\Phi\Gamma}$ is a s$\mathfrak{l}pg$-continuous-$function$.

ii. Let $(\mathcal{Z}, Đ)$ is an open sub set of $(Ύ, □, \mathcal{S})$. By *Remark* 3.3, $(\mathcal{Z}, Đ) \in$ sÏpg-open subset of $(Ύ, □, \mathcal{S}, Ï)$. Since if $f_{\Phi\Gamma}$ is a strongly-s$\mathfrak{l}pg$-continuous $function$, then $f_{\Phi\Gamma}^{-1}((\mathcal{Z}, Đ))$ is an open in $(Ϫ, Ţ, Đ)$. Hence $f_{\Phi\Gamma}$ is a continuous $function$.

iii. Let $(\mathcal{Z}, Đ) \in$ sÏpg-open subset of $(Ύ, □, \mathcal{S}, Ï)$.Since $f_{\Phi\Gamma}$ strongly-s$\mathfrak{l}pg$-continuous $function$, $f_{\Phi\Gamma}^{-1}((\mathcal{Z}, Đ)) \in Ţ$. By *Remark* 3.3, $f_{\Phi\Gamma}^{-1}((\mathcal{Z}, Đ)) \in$ s$\mathfrak{l}pg$-O$(Ϫ)_Đ$. Hence $f_{\Phi\Gamma}$ is a s$\mathfrak{l}pg$-irresolute-$function$.

The inverse is not true. See the following examples.

Example 3.13: The function $f_{\Phi\Gamma} : (Ϫ, Ţ, Đ, \mathfrak{l}) \to (Ϫ, Ţ, Đ, Ï)$ where, $Ţ=\{\widetilde{Ϫ}, \widetilde{Ø}, (Ƒ, Đ); Ƒ(d)=\{e_{\mathfrak{l}}\}$, for all $d \in Đ\}$ where, $Ϫ= \{e_{\mathfrak{l}}, m_{\mathfrak{l}}, r_{\mathfrak{l}}\}$, $Đ = \{d_1, d_2\}$ $\mathfrak{l}= \{\widetilde{Ø}\}$ and $Ï = ŞŞ(\{Ϫ\})_Đ$ $Φ : Đ \to Đ$ such that $Φ(d_1)=\{d_1\}$, $Φ(d_2) = \{d_2\}$ and $Γ: Ϫ \to Ϫ$ such that $Γ(e_{\mathfrak{l}}) = \{e_{\mathfrak{l}}\}, Γ(m_{\mathfrak{l}}) = \{m_{\mathfrak{l}}\}, Γ(r_{\mathfrak{l}}) = \{r_{\mathfrak{l}}\}$ then $ŞpO(Ϫ) = \{(\mathcal{M}, Đ)$;$e_{\mathfrak{l}} \in (\mathcal{M}, Đ)\}$for some $(d_i \in Đ)$such that i ={1,2} , s$\mathfrak{l}pg$-C-$(Ϫ)_Đ$= $\{\widetilde{Ø}, \widetilde{Ϫ}, (Ƒ', Đ); Ƒ'(d) = \{m_{\mathfrak{l}}, r_{\mathfrak{l}}\}$ for every $d \in Đ\}$ and s$\mathfrak{l}pg$-O$(Ϫ)_Đ$= $Ţ$ and sÏpg-C$(Ϫ)_Đ$= sÏpg-O$(Ϫ)_Đ$ = $ŞŞ(Ϫ)_Đ$ Now, $f_{\Phi\Gamma}$ is a continuous and is a s$\mathfrak{l}pg$-continuous function and it is not s$\mathfrak{l}pg$-irresolute function and not strongly-s$\mathfrak{l}pg$-continuous function. Since $(\mathcal{W}, Đ) \in ŞŞ(Ϫ)$; $\mathcal{W}(d) = \{m_{\mathfrak{l}}\}$ $(\forall\, d \in Đ)$ is a sÏpg-open set, but $f_{\Phi\Gamma}^{-1}((\mathcal{W}, Đ)) = (\mathcal{W}, Đ)$ which is not s$\mathfrak{l}pg$-open soft set and not open soft set.

Example 3.14: The function $f_{\Phi\Gamma} : (Ϫ, Ţ, Đ, \mathfrak{l}) \to (Ϫ, Ţ, Đ, Ï)$ where, $Ţ= \{\widetilde{Ϫ}, \widetilde{Ø}, (Ƒ, Đ); Ƒ(d)=\{e_{\mathfrak{l}}\}$, for all $d \in Đ\}$ where, $Ϫ= \{e_{\mathfrak{l}}, m_{\mathfrak{l}}, r_{\mathfrak{l}}\}$, $Đ = \{d_1, d_2\}$ $Ï= \{Ø\}$ and $\mathfrak{l}= ŞŞ(\{Ϫ\})_Đ$ $Φ : Đ \to Đ$ such that $Φ(d_1)=\{d_1\}$, $Φ(d_2)=\{d_2\}$ and $Γ : Ϫ \to Ϫ$ such that $Γ(e_{\mathfrak{l}}) = \{m_{\mathfrak{l}}\}, Γ(m_{\mathfrak{l}}) = \{e_{\mathfrak{l}}\}, Γ(r_{\mathfrak{l}}) = \{r_{\mathfrak{l}}\}$ then $ŞpO(Ϫ)= \{(\mathcal{M}, Đ)$;$e_{\mathfrak{l}} \in (\mathcal{M}, Đ)\}$for some $(d_i \in Đ)$such that i ={1,2} , s$\mathfrak{l}pg$-C$(Ϫ)_Đ$ = s$\mathfrak{l}pg$-O$(Ϫ)_Đ$ = $ŞŞ(Ϫ)_Đ$. So, sÏpg-C$(Ϫ)_Đ$= $\{\widetilde{Ø}, \widetilde{Ϫ}, (Ƒ', Đ); Ƒ'(d)= \{m_{\mathfrak{l}}, r_{\mathfrak{l}}\}$ for every $d \in Đ\}$ and sÏpg-O$(Ϫ)_Đ$= $Ţ$. Hence, $f_{\Phi\Gamma}$ is a s$\mathfrak{l}pg$-continuous function and s$\mathfrak{l}pg$-irresolute function which is not soft continuous and not strongly-s$\mathfrak{l}pg$-continuous function. Since $(Ƒ, Đ); Ƒ(d)=\{e_{\mathfrak{l}}\}$ $(\forall\, d \in Đ)$ is open soft set and s$\mathfrak{l}pg$-O-open set, but , $f_{\Phi\Gamma}^{-1}((Ƒ, Đ)) = (\mathcal{Z}, Đ)$ such that $\mathcal{Z}(d)=\{m_{\mathfrak{l}}\}$ $\forall\, d$ which is not open soft set.

4. Separation Axioms with soft-$\mathfrak{l}$- pre-g-open Sets.

Definition 4.1. A space $(Ϫ, Ţ, Đ, \mathfrak{l})$ is a soft-$\mathfrak{l}$-pre-g-$Ţ_0$-space (briefly s$\mathfrak{l}pg$-$Ţ_0$-space), if for each $ɖ_{\mathcal{M}} \neq ɖ_{\mathcal{N}}$ and $ɖ_{\mathcal{M}}, ɖ_{\mathcal{N}} \widetilde{\in} \widetilde{Ϫ}$, $\exists$ $(□, Đ) \in$ s$\mathfrak{l}$pg-O$(Ϫ)_Đ$ whenever, $ɖ_{\mathcal{M}} \widetilde{\in} (□, Đ)$, $ɖ_{\mathcal{N}} \widetilde{\notin} (□, Đ)$ or $ɖ_{\mathcal{M}} \widetilde{\notin} (□, Đ)$, $ɖ_{\mathcal{N}} \widetilde{\in} (□, Đ)$.

Example 4.2. In $(Ϫ, Ţ, Đ, \mathfrak{l})$ Let $Ϫ= \{e_{\mathfrak{l}}, m_{\mathfrak{l}}, r_{\mathfrak{l}}\}$, $Đ= \{ɖ_1, ɖ_2\}$, $Ţ= \{\widetilde{Ϫ}, \widetilde{Ø}, (□, Đ), (\mathcal{Z}, Đ)\}$ where, $((□, Đ) = \{(ɖ_1, \{e_{\mathfrak{l}}\}), (ɖ_2, \{e_{\mathfrak{l}}\})\}$, $(\mathcal{Z}, Đ) = \{(ɖ_1, \{e_{\mathfrak{l}}, m_{\mathfrak{l}}\}), (ɖ_2, \{e_{\mathfrak{l}}, m_{\mathfrak{l}}\})\}$ and $\mathfrak{l}= \{\widetilde{Ø}\}$. Then $ŞpO(Ϫ)_Đ= \{(Ƒ, Đ)$; $e_{\mathfrak{l}} \in (Ƒ, Đ)$ for some $ɖ \in Đ\}$. So, s$\mathfrak{l}pg$-$C(Ϫ)_{\mathcal{H}} = \{\widetilde{Ø}, \widetilde{\chi}, (□', Đ), (\mathcal{Z}', Đ)\}$ and s$\mathfrak{l}pg$-$O(\chi)_{\mathcal{H}} = Ţ$, hence $((Ϫ, Ţ, Đ, \mathfrak{l}))$ is a s$\mathfrak{l}pg$-$Ţ_0$-space. Since $\forall$ $ɖ_{\mathcal{M}} \neq ɖ$, $\exists$ $(Ƞ, Đ) \in$ s$\mathfrak{l}pg$-O$(Ϫ)_Đ$ whenever, $ɖ_{\mathcal{M}} \widetilde{\in} (Ƞ, Đ,)$, $ɖ_{\mathcal{N}} \widetilde{\notin} (Ƞ, Đ)$ or $ɖ_{\mathcal{M}} \widetilde{\notin} (Ƞ, Đ)$, $ɖ_{\mathcal{N}} \widetilde{\in} (Ƞ, Đ)$.

Proposition 4.3.If $(Ϫ, Ţ, Đ)$ is a soft-$Ţ_0$-space then $(Ϫ, Ţ, Đ, \mathfrak{l})$ is a s$\mathfrak{l}pg$-$Ţ_0$-space.
Proof : Let $ɖ_{\mathcal{M}}, ɖ_{\mathcal{N}} \widetilde{\in} \widetilde{Ϫ}$ such that $ɖ_{\mathcal{M}} \neq ɖ_{\mathcal{N}}$ since $(Ϫ, Ţ, Đ)$ is a soft-$Ţ_0$-space, then $\exists$ $(Ƞ, Đ) \in Ţ$ whenever, $ɖ_{\mathcal{M}} \widetilde{\in} (Ƞ, Đ)$, $ɖ_{\mathcal{N}} \widetilde{\notin} (Ƞ, Đ)$ or $ħ_{\mathcal{M}} \widetilde{\notin} (Ƞ, Đ)$, $ɖ_{\mathcal{N}} \widetilde{\in} (Ƞ, Đ)$. By *Remark* 3.3, $(Ƞ, Đ)$ is a s$\mathfrak{l}pg$-open set $such\ that$ $ɖ_{\mathcal{M}} \widetilde{\in} (Ƞ, Đ)$ and $ɖ_{\mathcal{N}} \widetilde{\notin} (Ƞ, Đ)$ or $ɖ_{\mathcal{M}} \widetilde{\notin} (Ƞ, Đ)$ and $ɖ_{\mathcal{N}} \widetilde{\in} (Ƞ, Đ)$.

Definition 4.4. $(Ϫ, Ţ, Đ, \mathfrak{l})$ is a soft-$\mathfrak{l}$-pre-g-$Ţ_1$-space (briefly s$\mathfrak{l}pg$-$Ţ_1$-space),If for each $ɖ_{\mathcal{M}}$, $ɖ_{\mathcal{N}} \widetilde{\in} \widetilde{\widetilde{Ϫ}}$ and $ɖ_{\mathcal{M}} \neq ɖ_{\mathcal{N}}$. Then there are s$\mathfrak{l}pg$-open sets $(Ƞ_1, Đ)$, $(Ƞ_2, Đ)$ whenever, $Đ_{\mathcal{M}} \widetilde{\in} ((Ƞ_1, Đ) - (Ƞ_2, Đ))$ and $ɖ_{\mathcal{N}} \widetilde{\in} ((Ƞ_2, Đ) - (Ƞ_1, Đ))$.

Example 4.5. A topological space $(X, \tau, Đ, ļ)$ when $X = \mathbb{N}$ *the set* of all *tural numbers*, $\tau = \tau_{Scof} = \{ F_{\mathcal{A}} : F'(ḍ)$ is finite set $\forall ḍ \} \cup \{\tilde{\emptyset}\}$ and $ļ = \{\tilde{\emptyset}\}$. so $(X, \tau, Đ, ļ)$ is a $sļpg$-τ_1-space. If $ḍ_{\mathcal{M}}, ḍ_{\mathcal{N}} \tilde{\in} \tilde{X}$ and $ḍ_{\mathcal{M}} \neq ḍ_{\mathcal{N}}$. Then there are $sļpg$-*open* sets $(\tilde{X} - ḥ_{\mathcal{N}})$, $(\tilde{X} - ḥ_{\mathcal{M}})$ whenever, $ḥ_{\mathcal{N}}$ and $ḥ_{\mathcal{M}}$ are two *finite* sets such that $ḥ_{\mathcal{N}} \subseteq ḍ_{\mathcal{N}}$, $ḥ_{\mathcal{M}} \subseteq ḍ_{\mathcal{M}}$ such that $ḍ_{\mathcal{M}} \tilde{\in} (\tilde{X} - ḥ_{\mathcal{N}})$ and $ḍ_{\mathcal{N}} \tilde{\in} (\tilde{X} - ḥ_{\mathcal{M}})$ and $(\tilde{X} - ḥ_{\mathcal{N}}) \tilde{\cap} (\tilde{X} - ḥ_{\mathcal{M}}) \neq \{\emptyset\}$.

Proposition 4.6. If $(X, \tau, Đ)$ is a $soft$-τ_1-space then, $(X, \tau, Đ, ļ)$ is a soft-$ļ$-pre-g-τ_1-space.
Proof : Let $ḍ_{\mathcal{M}}, ḍ_{\mathcal{N}} \tilde{\in} \tilde{X}$ such that $ḍ_{\mathcal{M}} \neq ḍ_{\mathcal{N}}$ since $(X, \tau, Đ)$ is a soft-τ_1-space, then $\exists$ $(\eta_1, Đ), (\eta_2, Đ) \in \tau$ such that $ḍ_{\mathcal{M}} \tilde{\in} ((\eta_1, Đ) - (\eta_2, Đ))$ and $ḍ_{\mathcal{N}} \tilde{\in} ((\eta_2, Đ) - (\eta_1, Đ))$. *By Remark* 3.3, $(\eta_1, Đ)$ and $(\eta_2, Đ)$ are $sļpg$-open sets , and the proof is over .

Proposition 4.7. If $(X, \tau, Đ, ļ)$ is a $sļpg$-τ_1-space then it is a $sļpg$-τ_0-*space*.
Proof : Let $ḍ_{\mathcal{M}}$, $ḍ_{\mathcal{N}} \tilde{\in} \tilde{X}$ such that $ḍ_{\mathcal{M}} \neq ḍ_{\mathcal{N}}$ since $(X, \tau, Đ, ļ)$ is a $sļpg$-τ_1-*space*, then $\exists (\eta_1, Đ), (\eta_2, Đ) \in sļpg$-$O(X)_Đ$ such that, $ḍ_{\mathcal{M}} \tilde{\in} ((\eta_1, Đ) - (\eta_2, Đ))$ and $ḍ_{\mathcal{N}} \tilde{\in} ((\eta_2, Đ) - (\eta_1, Đ))$. Then $\exists$ $(\eta , Đ) \in sļpg$-$O(X)_Đ$ -open set *whenever*, $ḍ_{\mathcal{M}} \tilde{\in} (\eta , Đ)$, $ḍ_{\mathcal{N}} \tilde{\notin} (\eta , Đ)$ or $ḍ_{\mathcal{M}} \tilde{\notin} (\eta , Đ)$, $ḍ_{\mathcal{N}} \tilde{\in} (\eta , Đ)$.
The conclusions in Proposition 4.7, is not *reversible* by *example* 4.8.

Example 4.8. $(X, \tau, Đ, ļ)$; $X = \{ę , ṃ , ṛ\}$, $\tau = \{\tilde{X}, \tilde{\emptyset}, (\eta, Đ)\}$such that $(\eta, Đ) = \{(ḍ_1 , \{ę , ṃ\}), (ḍ_2 , \{ę , ṃ\})\}$ and $ļ = ŞŞ(\{ṃ, ṛ\})$. Then $Şp O(X)_Đ$ =All $ŞŞ(X)$ $/(⍰, Đ); \{ṛ\} \tilde{\in} (⍰, Đ) \cup \{\tilde{\emptyset}\}$. So, $sļpg$-$C(X)_Đ$ =$\{ \tilde{\emptyset}$, $\tilde{X}$,$(\eta', Đ)\}$ $\cup (\mathcal{Z}, Đ) \cup (\mathcal{M}, Đ)$; $(\mathcal{Z}, Đ)$=$\{(ḍ_1, \{\emptyset\}), (ḍ_2, \{ṛ\})\}$, and $(M, Đ)$=$\{(ḍ_1, \{ṛ\}), (ḍ_2, \{\emptyset\})\}$ And $sļpg$-$O(X)_Đ$= $\tau \cup (\mathcal{Z}', Đ) \cup (\mathcal{M}', Đ)\}$; $(\mathcal{Z}', Đ)$=$\{(ḍ_1, X), (ḍ_2, \{ę, ṃ\})\}$ and $(\mathcal{M}', Đ)$=$\{(ḍ_1, \{ę , ṃ\}), (ḍ_2, X)\}$. Implies $(X, \tau, Đ, ļ)$ is a $soft$-τ_0-*space*, but not $sļpg$-τ_1-*space* .

Definition 4.9. $(X, \tau, Đ, ļ)$ is a soft-$ļ$-pre-g-τ_2-space (briefly sļpg-τ_2-space). If for any two *different elements* $ḍ_{\mathcal{M}} \neq ḍ_{\mathcal{N}}$ there are $sļpg$-*open* sets $(⍰_1, Đ)$, $(⍰_2, Đ)$ such that $ḍ_{\mathcal{M}} \tilde{\in} (⍰_1, Đ)$, $ḍ_{\mathcal{N}} \tilde{\in} (⍰_2, Đ)$and $(⍰_1, Đ) \cap (⍰_2, Đ) = \{\tilde{\emptyset}\}$.

Example 4.10. A *topological* space $(X, \tau, Đ, ļ)$; $X = \{ę, ṃ , ṛ\}$, $\tau = \{\tilde{X}, \tilde{\emptyset}\}$ and $ļ = ŞŞ(X)_Đ$ .Then $ŞpO(X)_Đ$ = τ. So, $sļpg$-$C(X)_Đ$ = $sļpg$-$O(X)_Đ$ = $ŞŞ(X)_Đ$. Then $(X, \tau, Đ, ļ)$ is a $sļpg$-τ_2-*space*.
Remark 4.11. If $(X, \tau, Đ)$ is a soft-τ_2-*space*, then $(X, \tau, Đ, ļ)$ is a $sļpg$-τ_2-*space*.
Proof : Let $ḍ_{\mathcal{M}}$, $ḍ_{\mathcal{N}} \tilde{\in} \tilde{X}$ whenever, $ḍ_{\mathcal{M}} \neq ḍ_{\mathcal{N}}$ since $(X, \tau, Đ, ļ)$ is a soft-τ_2-*space*, then $\exists$ $(⍰_1, Đ), (⍰_2, Đ) \in \tau$ *such* that $ḍ_{\mathcal{M}} \tilde{\in} (⍰_1, Đ)$, $ḍ_{\mathcal{N}} \tilde{\in} (⍰_2, Đ)$ and $(⍰_1, Đ) \tilde{\cap} (⍰_2, Đ) = \{\tilde{\emptyset}\}$. By Remark 3.3, there are $sļpg$-open sets $(⍰_1, Đ), (⍰_2, Đ)$, such that $ḍ_{\mathcal{M}} \tilde{\in} (⍰_1, Đ)$, $ḍ_{\mathcal{N}} \tilde{\in} (⍰_2, Đ)$ and $(⍰_1, Đ) \tilde{\cap} (⍰_2, Đ) = \{\tilde{\emptyset}\}$.

Remark 4.12. If $(X, \tau, Đ, ļ)$ is a $sļpg$-τ_2-*space* then it is a $sļpg$-τ_1-*space*.
Proof : Let $ḍ_{\mathcal{M}}$, $ḍ_{\mathcal{N}} \tilde{\in} \tilde{X}$ whenever, $ḍ_{\mathcal{M}} \neq ḍ_{\mathcal{N}}$ since $(X, \tau, Đ, ļ)$ is a $sļpg$-τ_2-*space* ,then there are $sļpg$-open sets $(⍰_1, Đ)$, $(⍰_2, Đ)$ such that $ḍ_{\mathcal{M}} \tilde{\in} (⍰_1, Đ)$, $ḍ_{\mathcal{N}} \tilde{\in} (⍰_2, Đ)$ and $(⍰_1, Đ) \cap (⍰_2, Đ) = \{ \tilde{\emptyset} \}$. Implies, $ħ_{\mathcal{M}} \tilde{\in} ((⍰_1, Đ) - (⍰_2, Đ))$ and $ħ_{\mathcal{N}} \tilde{\in} ((⍰_2, Đ) - (⍰_1, Đ))$.
The *conclusions* in Remark 4.12, is not *reversible* by example 4.5.
A space $(X, \tau, Đ, ļ)$ is a $sļpg$-τ_1-space. If for each, $ḍ_{\mathcal{M}}$, $ḍ_{\mathcal{N}} \tilde{\in} \tilde{X}$ and $ḍ_{\mathcal{M}} \neq ḍ_{\mathcal{N}}$. Then there are $sļpg$-open sets $(\tilde{X} - ḍ_{\mathcal{N}})$, $(\tilde{X} - ḍ_{\mathcal{M}})$ whenever, $ḍ_{\mathcal{M}} \tilde{\in} ((\tilde{X} - ḍ_{\mathcal{N}}) - (\tilde{X} - ḍ_{\mathcal{M}}))$ and $ḍ_{\mathcal{N}} \tilde{\in} ((\tilde{X} - ḍ_{\mathcal{M}}) - (\tilde{X} - ḍ_{\mathcal{N}}))$ .Which is not $sļpg$-τ_2-space. Since for any two $sļpg$-open sets $(⍰_1, Đ)$, $(⍰_2, Đ)$ such that $ḍ_{\mathcal{M}} \tilde{\in} (⍰_1, Đ)$, $ḍ_{\mathcal{N}} \tilde{\in} (⍰_2, Đ)$ then $(⍰_1, Đ) \cap (⍰_2, Đ) \neq \tilde{\emptyset}$. We have *previously noted* that X is a $sļpg$-τ_i-*space* whenever, it is a τ_{i+1}-*space* $(\forall\, i = 0 , 1 \text{ and } 2)$.
The opposite is not *generally achieved* as the following example shows:

Example 4.13. $(X, \tau, Đ, ļ)$ is a $sļpg$-τ_i-*space* $(i \in \{0,1,2\})$, where, $X = \{ę, ṃ , ṛ\}$, $\tau = \{\tilde{\emptyset}, \tilde{\chi}\}$ and $ļ = ŞŞ(X)_Đ$ So, $sļpg$-$C(X)_Đ$ = $sļpg$-$O(X)_Đ$ = $ŞŞ(X)_Đ$. But the space $(X, \tau, Đ)$ is not soft-τ_i-*space* (i $\in$

$\{0,1,2\}$) . The following figure shows the relationship between the various types of concepts we mentioned earlier.

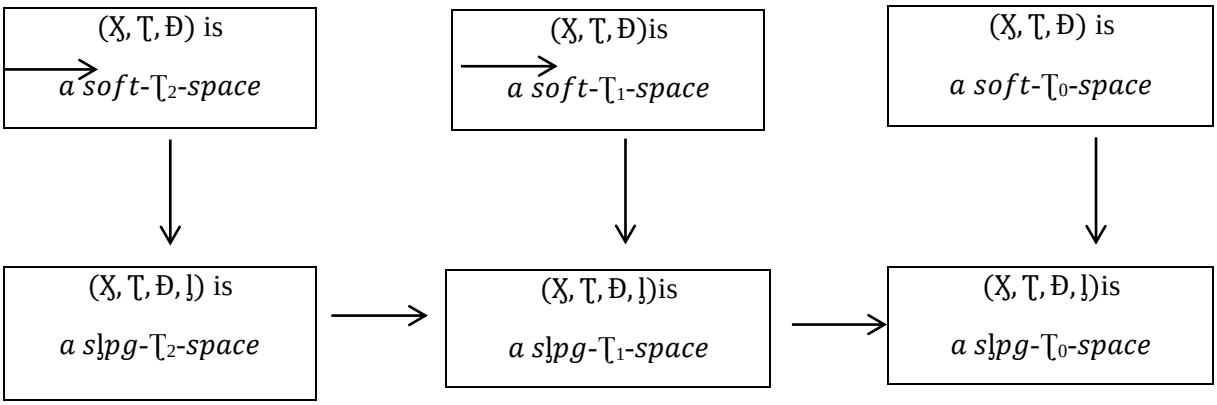

Figure 1

5. Separation axioms with pre types of ft functions.

Proposition 5.1. If $(Ϫ, Ƭ, Đ, ļ)$ is a $sļpg$-$Ƭ_i$-$space$ (i $\in \{0,1,2\}$) and $ƒ_{ΦΓ}$ is a bijective $sļpg$-O-$function$ from $(Ϫ, Ƭ, Đ, ļ)$ to $(Ƴ, ⍰, \mathcal{S}, Ï)$ then Y is a $sÏpg$-$Ƭ_i$-space ($i \in \{0,1,2\}$).

Proof :

If $= 0$: Let $ɖ_{\mathcal{R}}$, $ɖ_{\mathcal{S}} \widetilde{\in} \widetilde{Ƴ}$ such that $ɖ_{\mathcal{R}} \neq ɖ_{\mathcal{S}}$. Since $ƒ_{ΦΓ}$ is a $jective\ function$, Then $ƒ_{ΦΓ}^{-1}(ɖ_{\mathcal{R}}) \neq \{\widetilde{∅}\} \neq ƒ_{ΦΓ}^{-1}(ɖ_{\mathcal{S}})$ and $ƒ_{ΦΓ}^{-1}(ɖ_{\mathcal{R}})$, $ƒ_{ΦΓ}^{-1}(ɖ_c) \widetilde{\in} \widetilde{Ϫ}$ .So, $(Ϫ, Ƭ, Đ, ļ)$ is a $sļpg$-$Ƭ_0$-$space$, then $\exists\ (Ƞ , Đ) \in sļpg$-$O(Ϫ)_Đ$ whenever, $ƒ_{ΦΓ}^{-1}(ɖ_{\mathcal{R}}) \widetilde{\in} (Ƞ , Đ)$, $ƒ_{ΦΓ}^{-1}(ɖ_c) \widetilde{\notin} (Ƞ , Đ)$ or $ƒ_{ΦΓ}^{-1}(ɖ_{\mathcal{R}}) \widetilde{\notin} (Ƞ , Đ)$, $ƒ_{ΦΓ}^{-1}(ɖ_c) \widetilde{\in} (Ƞ , Đ)$. Since $ƒ_{ΦΓ}$ is a $sļpg$-O-function, then $ƒ_{ΦΓ}((Ƞ , Đ))$ is a $sÏpg$-open set such that $ɖ_{\mathcal{R}} \widetilde{\in} ƒ_{ΦΓ}((Ƞ , Đ))$ and $ɖ_c \widetilde{\notin} ƒ_{ΦΓ}((Ƞ , Đ))$ or . $ɖ_{\mathcal{R}} \widetilde{\notin} ƒ_{ΦΓ}((Ƞ , Đ))$ and $ɖ_{\mathcal{S}} \widetilde{\in} ƒ_{ΦΓ}((Ƞ , Đ))$ Hence Y is a $sÏpg$-$Ƭ_0$-space.

If $= 1$: Let $ɖ_{\mathcal{R}}$, $ɖ_c \widetilde{\in} \widetilde{Ƴ}$ such that $ɖ_{\mathcal{R}} \neq ɖ_c$. Since $ƒ_{ΦΓ}$ is a $bijective\ function$, then $ƒ_{ΦΓ}^{-1}(ɖ_{\mathcal{R}}) \neq \{\widetilde{∅}\} \neq ƒ_{ΦΓ}^{-1}(ɖ_c)$, $f_{ΦΓ}^{-1}(ɖ_{\mathcal{R}})$, $ƒ_{ΦΓ}^{-1}(ɖ_c) \widetilde{\in} \widetilde{Ϫ}$. So, Ϫ is a $sļpg$-$Ƭ_1$-$space$, then $\exists\ (Ƞ_1,Đ)$, $(Ƞ_2,Đ) \in sļpg$-$O(Ϫ)_Đ$ such that $ƒ_{ΦΓ}^{-1}(ɖ_{\mathcal{R}}) \widetilde{\in} ((Ƞ_1,Đ) - (Ƞ_2,Đ))$, $ƒ_{ΦΓ}^{-1}(ɖ_c) \widetilde{\in} ((Ƞ_2,Đ) - (Ƞ_1,Đ))$. By the condition $ƒ_{ΦΓ}^{-1}$ is a $sļpg$-O-$function$, $ƒ_{ΦΓ}^{-1}((Ƞ_1,Đ))$, $ƒ_{ΦΓ}^{-1}((Ƞ_2,Đ))$ are $sÏpg$-open sets in $Ƴ$ such that $ɖ_{\mathcal{R}} \widetilde{\in} (ƒ_{ΦΓ}^{-1}((Ƞ_1,Đ)) - ƒ_{ΦΓ}^{-1}((Ƞ_2,Đ)))$ and $ɖ_c \widetilde{\in} (ƒ_{ΦΓ}^{-1}((Ƞ_2,Đ)) - ƒ_{ΦΓ}^{-1}((Ƞ_1,Đ)))$. Hence $Ƴ$ is a $sÏpg$-$Ƭ_1$-space.

If $i = 2$: Let $ɖ_{\mathcal{R}}$, $ɖ_c \widetilde{\in} \widetilde{Ƴ}$ such that $ɖ_{\mathcal{R}} \neq ɖ_c$. Since $ƒ_{ΦΓ}$ is a $bijective\ function$, then $ƒ_{ΦΓ}^{-1}(ɖ_{\mathcal{R}}) \neq \{\widetilde{∅}\} \neq ƒ_{ΦΓ}^{-1}(ɖ_c)$, $ƒ_{ΦΓ}^{-1}(ɖ_{\mathcal{R}})$, $ƒ_{ΦΓ}^{-1}(ɖ_c) \widetilde{\in} \widetilde{Ϫ}$. So, Ϫ is a $sļpg$-$Ƭ_2$-$space$, then there $\exists\ (⍰_1,Đ)$, $(⍰_2,Đ) \in sļpg$-$O(Ϫ)_Đ$ whenever, $ƒ_{ΦΓ}^{-1}(ɖ_{\mathcal{R}}) \widetilde{\in} ((⍰_1,Đ))$, $ƒ_{ΦΓ}^{-1}(ɖ_{\mathcal{S}}) \widetilde{\notin} ((⍰_2,Đ))$ and $(⍰_1,Đ) \cap (⍰_2,Đ) = \{\widetilde{∅}\}$. By the condition $ƒ_{ΦΓ}$ is a $sļpg$-O-$function$, then $ƒ_{ΦΓ}((⍰_1,Đ))$ and $ƒ_{ΦΓ}((⍰_2,Đ)) \in sÏpg$-O-$(Ƴ)_{\mathcal{S}}$ whenever, $ɖ_{\mathcal{R}} \widetilde{\in} ƒ_{ΦΓ}((⍰_1,Đ))$, $ɖ_c \widetilde{\in} ƒ_{ΦΓ}((⍰_2,Đ))$ and $ƒ_{ΦΓ}((⍰_1,Đ)) \widetilde{\cap} ƒ_{ΦΓ}((⍰_2,Đ)) = \{\widetilde{∅}\}$. $Hence$ Y is a $sÏpg$-$Ƭ_2$-$space$.

Proposition 5.2. If $(Ϫ, Ƭ, Đ, ļ)$ is a soft-$Ƭ_i$-$space$ (i $\in \{0,1,2\}$) and $ƒ_{ΦΓ}$ is a $bijective\ sļ^{*}pgo$-$function$ from $(Ϫ, Ƭ, Đ, ļ)$ to $(Ƴ , ⍰, \mathcal{S}, Ï)$ then Y is a $sÏpg$-$Ƭ_i$-space.
Proof : Start from the facts $ƒ_{ΦΓ}((Ƞ , Đ))$ is a $sÏpg$-open in Y for each $sļpg$-open sets $(Ƞ , Đ)$ in Ϫ.

$Proposition\ 5.3.$ If Ϫ is a $sļpg$-$Ƭ_i$-$space$ (i $\in \{0,1,2\}$) and $ƒ_{ΦΓ}$ is a $bijective$ $sļ^{**}pgo$-$function$ from $(Ϫ, Ƭ, Đ, ļ)$ to $(Ƴ , ⍰, \mathcal{S}, Ï)$ then, Y is a soft-$\mathcal{T}_i$-$space$ (i $\in \{0,1,2\}$).
Proof : Follow $ƒ_{ΦΓ}((Ƞ , Đ))$ is a $soft\ open$ in Y for each $sļpg$-$open$ sets $(Ƞ , Đ)$ in Ϫ.

Remark 5.4. If $ƒ_{ΦΓ}$ is a soft $open\ function$ from $(Ϫ, Ƭ, Đ)$ to $(Ƴ, ⍰, \mathcal{S})$

and$(\chi, \tau, Đ)$ is a soft τ_i-*space* whenever, (i ∈ {0,1,2}), then $(\Upsilon, ▯, \mathcal{S}, Ï)$ is a $s Ïpg$-τ_i-space, for any ideal Ï on Y.

Proposition 5.5. If Y is a soft τ_i-*space* whenever, ($i \in \{0,1,2\}$) *and* $f_{\Phi\Gamma} : (\chi, \tau, Đ, ⨌) \to (\Upsilon, ▯, \mathcal{S}, Ï)$ is an *bijective s⨌pg-continuous function* then $(\chi, \tau, Đ, ⨌)$ is a $s⨌pg$-τ_i-*space* (i ∈ {0,1,2}).
Proof :

If $i = 0$: Let $⨋_{\mathcal{M}}$, $⨋_{\mathcal{N}} \tilde{\in} \tilde{\chi}$ such that $⨋_{\mathcal{M}} \neq ⨋_{\mathcal{N}}$ since $f_{\beta\Psi}$ is *an bijective function* ,then $f_{\Phi\Gamma}(⨋_{\mathcal{M}}) \neq f_{\Phi\Gamma}(⨋_{\mathcal{N}})$ where, $f_{\Phi\Gamma}(⨋_{\mathcal{M}})$, $f_{\Phi\Gamma}(⨋_{\mathcal{N}}) \tilde{\in} \tilde{\Upsilon}$. So, $(\Upsilon, ▯, \mathcal{S})$ is a soft-τ_0-*space* ,*then* ∃ $(▯,\mathcal{S}) \in ▯$ whenever, $f_{\Phi\Gamma}(⨋_{\mathcal{M}}) \tilde{\in} (▯,\mathcal{S})$, $f_{\Phi\Gamma}(⨋_{\mathcal{N}}) \tilde{\notin} (▯,\mathcal{S})$ or $f_{\Phi\Gamma}(⨋_{\mathcal{M}}) \tilde{\notin} (▯,\mathcal{S})$, $f_{\Phi\Gamma}(⨋_{\mathcal{N}}) \tilde{\in} (▯,\mathcal{S})$. By $f_{\Phi\Gamma}$ is a $s⨌pg$-continuous function, then $f_{\Phi\Gamma}^{-1}((▯,\mathcal{S})) \in s⨌pg\text{-}O(\chi)_Đ$ *whenever*, $⨋_{\mathcal{M}} \tilde{\in} f_{\Phi\Gamma}^{-1}((▯,\mathcal{S}))$, $⨋_{\mathcal{N}} \tilde{\notin} f_{\Phi\Gamma}^{-1}((▯,\mathcal{S}))$ or $⨋_{\mathcal{M}} \tilde{\notin} f_{\Phi\Gamma}^{-1}((▯,\mathcal{S}))$, $⨋_{\mathcal{N}} \tilde{\in} f_{\Phi\Gamma}^{-1}((▯,\mathcal{S}))$. Hence $(\chi, \tau, Đ, ⨌)$ is a $s⨌pg$-τ_0-space.

If $i = 1$: Let $⨋_{\mathcal{M}}$, $⨋_{\mathcal{N}} \tilde{\in} \tilde{\chi}$ such that $⨋_{\mathcal{M}} \neq ⨋_{\mathcal{N}}$ since $f_{\Phi\Gamma}$ is an *bijective function* then $f_{\Phi\Gamma}(⨋_{\mathcal{M}}) \neq f_{\Phi\Gamma}(⨋_{\mathcal{N}})$ where, $f_{\Phi\Gamma}(⨋_{\mathcal{M}})$, $f_{\Phi\Gamma}(⨋_{\mathcal{N}}) \tilde{\in} \tilde{\Upsilon}$. So, $(\Upsilon, ▯, \mathcal{S})$ is a soft-τ_1-*space*, *then* ∃ $(▯_1,\mathcal{S})$, $(▯_2,\mathcal{S}) \in ▯$ whenever, $f_{\Phi\Gamma}(⨋_{\mathcal{M}}) \tilde{\in} ((▯_1,\mathcal{S})$ *and* $f_{\Phi\Gamma}(⨋_{\mathcal{N}}) \tilde{\notin} (▯_1,\mathcal{S})$ and $f_{\Phi\Gamma}(⨋_{\mathcal{M}}) \tilde{\notin} ((▯_2,\mathcal{S})$ and $f_{\Phi\Gamma}(⨋_{\mathcal{N}}) \tilde{\in} (▯_2,\mathcal{S})$. Since $f_{\Phi\Gamma}$ is a *s⨌pg-continuous function*, then $f_{\Phi\Gamma}^{-1}((▯_1,\mathcal{S}))$ and $f_{\Phi\Gamma}^{-1}((▯_2,\mathcal{S}))$ are $s⨌pg$-open sets whenever, $⨋_{\mathcal{M}} \tilde{\in} (f_{\Phi\Gamma}^{-1}(▯_1,\mathcal{S})$ and $⨋_{\mathcal{N}} \tilde{\notin} f_{\Phi\Gamma}^{-1}((▯_1,\mathcal{H})$ and $⨋_{\mathcal{M}} \tilde{\notin} (f_{\Phi\Gamma}^{-1}(▯_2,\mathcal{S})$ and $⨋_{\mathcal{N}} \tilde{\in} f_{\Phi\Gamma}^{-1}((▯_2,\mathcal{H})$. Hence $(\chi, \tau, Đ, ⨌)$is a $s⨌pg$-τ_1-space.

If $i = 2$: Let $⨋_{\mathcal{M}}$, $⨋_{\mathcal{N}} \tilde{\in} \tilde{\chi}$ such that $⨋_{\mathcal{M}} \neq ⨋_{\mathcal{N}}$ since $f_{\Phi\Gamma}$ is an *bijective function*, then $f_{\Phi\Gamma}(⨋_{\mathcal{M}}) \neq f_{\Phi\Gamma}(⨋_{\mathcal{N}})$ where, $f_{\Phi\Gamma}(⨋_{\mathcal{M}})$, $f_{\Phi\Gamma}(⨋_{\mathcal{N}}) \tilde{\in} \tilde{\Upsilon}$. So, $(\Upsilon, ▯, \mathcal{S})$ is a soft-τ_2-*space*, *then* ∃ $(▯_1,\mathcal{S})$, $(▯_2,\mathcal{S}) \in ▯$ such that, $f_{\Phi\Gamma}(⨋_{\mathcal{M}}) \tilde{\in} ((▯_1,\mathcal{S}))$, $f_{\Phi\Gamma}(⨋_{\mathcal{N}}) \tilde{\in} ((▯_2,\mathcal{S}))$ and $((▯_1,\mathcal{S})) \tilde{\cap} ((▯_2,\mathcal{S})) = \tilde{\emptyset}$. Since $f_{\Phi\Gamma}$ is a *s⨌pg-continuous function*, then $f_{\Phi\Gamma}^{-1}((▯_1,\mathcal{S}))$ and $f_{\Phi\Gamma}^{-1}((▯_2,\mathcal{S}))$ are $s⨌pg$-open sets implies, $⨋_{\mathcal{M}} \tilde{\in} (f_{\Phi\Gamma}^{-1}((▯_1,\boldsymbol{\mathcal{S}}))$, $⨋_{\mathcal{N}} \tilde{\in} (f_{\Phi\Gamma}^{-1}((▯_2,\boldsymbol{\mathcal{S}})))$ and $(f_{\Phi\Gamma}^{-1}((▯_1,\boldsymbol{\mathcal{S}}))) \tilde{\cap} (f_{\Phi\Gamma}^{-1}((▯_2,\boldsymbol{\mathcal{S}}))) = \{\tilde{\emptyset}\}$.So, $(\chi, \tau, Đ, ⨌)$is a $\boldsymbol{s⨌pg}$-τ_2-space.

Corollary 5.6. If Y is a soft-τ_i-*space* whenever, (i ∈ {0,1,2}) and $f_{\Phi\Gamma} : (\chi, \tau, Đ, ⨌) \to (\Upsilon, ▯, \mathcal{S}, Ï)$ is an *bijective soft*-continuous *function* then χ is a $s⨌pg$-τ_i-space (i ∈ {0,1,2}).
Proof: Since, every *soft* continuous *function* is a *s⨌pg-continuous* by *proposition* 3.12 then Remark 5.4 , is *applicable*.

Proposition 5.7. If $(\Upsilon, ▯, \mathcal{S}, Ï)$ is a $sÏpg$-τ_i-*space* whenever, ($i \in \{0,1,2\}$) and $f_{\Phi\Gamma} : (\chi, \tau, Đ, ⨌) \to (\Upsilon, ▯, \mathcal{S}, Ï)$ is an *bijective strongly-s⨌pg-continuous function* then $(\chi, \tau, Đ, ⨌)$ is a soft-τ_i-*space*.
Proof*: Follows* from, $f_{Φ⨌}^{-1}((▯,Đ)) \in \tau$ for each $(▯,Đ) \tilde{\in} sÏpg\text{-}O(\Upsilon)_{\mathcal{S}}$.

Proposition 5.8. If $(\Upsilon, ▯, \mathcal{S}, Ï)$ is a $sÏpg$-τ_i-*space* whenever, (i ∈ {0,1,2}) and $f_{\Phi\Gamma} : (\chi, \tau, Đ, ⨌) \to (\Upsilon, ▯, \mathcal{S}, Ï)$ is an *bijective s⨌pg-irresolute function* then χ is a $s⨌pg$-τ_i-space whenever, ($i \in \{0,1,2\}$).
Proof : Since $f_{\Phi\Gamma}^{-1}((▯,Đ)) \tilde{\in} s⨌pg\text{-}O(\chi)_Đ$ for each $(▯,Đ) \tilde{\in} sÏpg\text{-}O(\Upsilon)_{\mathcal{S}}$.

6. Soft-⨌- pre-g-Convergence Sequence.

Definition 6.1: In a space $(\chi, \tau, Đ, ⨌)$where, $⨏_{\mathcal{M}} \in \wp(\chi)/\chi$ then the soft sequence $(S_n)_{n\in\mathbb{N}}$ over χ is called *soft-⨌-pre-g-convergence* to $⨏_{\mathcal{M}}$ (briefly, $S_n \rightarrowtail ⨏$) if for all $s⨌pg$-open set $(\eta, Đ)$ where, $⨏_{\mathcal{M}} \tilde{\in} (\eta, Đ)$, there exist $k \in \mathbb{N}$ *such that* $S_n \tilde{\in} (\eta, Đ)$ for every $n \geqslant k$.

A soft sequence $(S_n)_{n\in\mathbb{N}}$ is a *soft-⨌-pre-g-divergence* if it is not *soft-⨌-pre-g-convergence*.

Theorem 6.2*:* If $(\chi, \tau, Đ, ⨌)$ is a soft-⨌-*pre-g*-τ_2-*space then* every soft-⨌-*pre-g-convergence sequence* over χ has *only* one limit point.

Proof: Let $(S_n)_{n\in\mathbb{N}}$ is a soft *sequence* over χ and $S_n \rightarrowtail \aleph_{\mathcal{M}}$, $S_n \rightarrowtail \aleph_{\mathcal{N}}$; $\aleph_{\mathcal{M}} \neq \aleph_{\mathcal{N}}$ where, $\aleph_{\mathcal{M}}$, $\aleph_{\mathcal{N}} \in \mathcal{P}(\chi)/\chi$. Since $(\chi, \tau, Đ, ļ)$ is a *sļpg*-τ_2-space, then $\exists$ $(\square_1, Đ)$, $(\square_2, Đ) \in$ *sļpg-O*$(\chi)_Đ$ such that $\aleph_{\mathcal{M}} \tilde{\in} (\square_1, Đ)$, $\aleph_{\mathcal{N}} \tilde{\in} (\square_2, Đ)$ and $(\square_1, Đ) \cap (\square_2, Đ) = \{\tilde{\emptyset}\}$. Now, since $S_n \rightarrowtail \aleph_{\mathcal{M}}$ and $\aleph_{\mathcal{M}} \tilde{\in} (\square_1, Đ)$ implies $\exists k_1 \in \mathbb{N}$; $S_n \in (\square_1, Đ)$ $\forall\, n \geq k_1$. And $S_n \rightarrowtail \aleph_{\mathcal{N}}$ and $\aleph_{\mathcal{N}} \tilde{\in} (\square_2, Đ)$ *implies* $\exists k_2 \in \mathbb{N}$; $S_n \in (\square_2, Đ)$ $\forall\, n \geq k_2$. Leads to $(\square_1, Đ) \tilde{\cap} (\square_2, Đ) \neq \tilde{\emptyset}$ where that *contradiction*.

The precondition is that a space $\tilde{\chi}$ is a *sļpg*-τ_2-*space* is *very requisite* to *make theorem* 5.5, is valid.

By Example 4.2, where, $Ş pO(\chi)_Đ = \{ (F, Đ) ; e_ḍ \in (F, Đ)$ for some $ḍ \in Đ\}$. So, *sļpg-C*$(\chi)_{\mathcal{H}} = \{ \tilde{\emptyset}$, $\tilde{\chi}, (\square', Đ)$, $(\mathcal{Z}', Đ)$ $\}$ and *sļpg-O*$(\chi)_{\mathcal{H}} = \tau$. Obviously; the sequence $(S_n)_{n\in\mathbb{N}}$ over χ, where $S_n = \{ṛ\}$ for all n, has one limit point; $S_n \rightarrowtail \{ṛ\}$. But $(\chi, \tau, Đ, ļ)$ is not *sļpg*- τ_2- space.

Proposition 6.3*:* If a soft *sequence* $(S_n)_{n\in\mathbb{N}}$ is a soft-ļ-*pre-g-convergence* to $\aleph_{\mathcal{M}}$ in a soft ideal space χ, then it is soft *convergent* to $\aleph_{\mathcal{M}}$.
Proof: Let $(\eta, Đ)$ is a soft open set where, $\aleph_{\mathcal{M}} \tilde{\in} (\eta, Đ)$. By Remark 3.3, $(\eta, Đ)$ is a *sļpg-open set* where, $\aleph_{\mathcal{M}} \tilde{\in} (\eta, Đ)$. Since $(S_n)_{n\in\mathbb{N}}$ is a *soft*-ļ-*pre-g*-convergence to $\aleph$, *then* $\exists\ k \in \mathbb{N}$ whenever, $S_n \in (\eta, Đ)$ for every $n \geqslant k$. Hence $(S_n)_{n\in\mathbb{N}}$ is *convergent* to $\aleph_{\mathcal{M}}$.

The *conversely* in *Example* 6.4, *is not reversible*, in general.

Example 6.4*: Let* ļ is a soft ideal in a *space* $(\chi, \tau, Đ, ļ)$ where, $\chi = \mathbb{N}$, $\tau = \{ \tilde{\emptyset}$, $\tilde{\chi}\}$ and ļ = $Ş Ş(\chi)_Đ$. So $Ş pO(\chi) = \{ \tilde{\emptyset}$, $\tilde{\chi}$ $\} = \tau$, then *sļpg-C*$(\chi)_Đ$ = *sļpg-O*$(\chi)_Đ$ = $Ş Ş(\chi)_Đ$. The soft *quence* $(S_n)_{n\in\mathbb{N}}$, where $S_n = \{n\}$ $\forall\ n \in \mathbb{N}$, is *soft convergent* to $\aleph_{\mathcal{M}}$ $\forall$ $\aleph_{\mathcal{M}} \tilde{\in} \mathcal{P}(\chi)/\chi$ which is not soft-ļ-*pre-g-convergent*. *Since let* F: $\mathbb{N} \longrightarrow \mathcal{P}(\chi)$ *such that* F $(n) = \{e_ḍ\}$ $\forall\ n$. $\{e_ḍ\} \tilde{\in}$ (F, $\mathbb{N}$), *but* $S_n \not\subseteq$ (F, $\mathbb{N}$) $\forall\ k \in \mathbb{N}$ such that $n \geq k$.

Proposition 6.5*:* Let $f_{\Phi\Gamma}$: $(\chi, \tau, Đ, ļ) \rightarrow (\Upsilon, \square, \mathcal{S}, Ï)$ be an bijective and *sļpg*-irresolute function and $(S_n)_{n\in\mathbb{N}}$ be a soft *sequence* over χ, *then* $(f_{\Phi\Gamma}(S_n)) \rightarrowtail f_{\Phi\Gamma}(\aleph_{\mathcal{M}})$ in Υ whenever, $S_n \rightarrowtail \aleph_{\mathcal{M}}$ in χ.

Proof*:* Let $(\eta, \mathcal{S})$ is a sÏpg-open set in Υ where $f_{\Phi\Gamma}(\aleph_{\mathcal{M}}) \tilde{\in} (\eta, \mathcal{S})$. Since $f_{\Phi\Gamma}$ is a *sļpg-irresolute function*, then $f_{\Phi\Gamma}{}^{-1}((\eta, \mathcal{S}))$ is a sļpg-*open* set *where*, $\aleph_{\mathcal{M}} \tilde{\in} f_{\Phi\Gamma}{}^{-1}((\eta, \mathcal{S}))$. By $(S_n)_{n\in\mathbb{N}}$ is soft-ļ-*pre-g-convergence* to $\aleph_{\mathcal{M}}$, *then there exis*t $k \in \mathbb{N}$ where, $S_n \in f_{\Phi\Gamma}{}^{-1}((\eta, \mathcal{S}))$ for all n ≥ k. Implies, *there* exist $k \in \mathbb{N}$ where, $f_{\Phi\Gamma}(S_n) \tilde{\in} (\eta, \mathcal{S})$ for all n ≥ k. Hence $f_{\Phi\Gamma}(S_n)$ is a soft-ļ-*pre-g-convergence* to $f_{\Phi\Gamma}(\aleph_{\mathcal{M}})$.

Theorem 6.6*:* If $f_{\beta\Psi}$: $(\chi, \tau, Đ, ļ) \rightarrow (\Upsilon, \square, \mathcal{S}, Ï)$ be an *bijective* and a *sļpg-continuous* function and $(S_n)_{n\in\mathbb{N}}$ be a soft *sequence* over χ. *Then* $(f_{\Phi\Gamma}(S_n)) \longrightarrow f_{\Phi\Gamma}(\aleph_{\mathcal{M}})$ in Υ whenever, $S_n \rightarrowtail \aleph_{\mathcal{M}}$ in χ.
Proof: Let $(\eta, \mathcal{S})$ is a soft-open set in $(\Upsilon, \square, \mathcal{S}, Ï)$where, $f_{\Phi\Gamma}(\aleph_{\mathcal{M}}) \tilde{\in} (\eta, \mathcal{S})$. Since $f_{\Phi\Gamma}$ is a *sļpg*-continuous function, then $f_{\Phi\Gamma}{}^{-1}((\eta, \mathcal{S}))$ is a sļpg-*open* set in $\tilde{\chi}$ where, $\aleph_{\mathcal{M}} \tilde{\in} f_{\Phi\Gamma}{}^{-1}((\eta, \mathcal{S}))$. By $(S_n)_{n\in\mathbb{N}}$ is soft-ļ-*pre-g*-convergence to $\aleph_{\mathcal{M}}$, then there exist $k \in \mathbb{N}$ where, $S_n \tilde{\in} f_{\Phi\Gamma}{}^{-1}((\eta, \mathcal{S}))$ for all $n \geq k$. Implies, there exist $k \in \mathbb{N}$ where, $f_{\Phi\Gamma}(S_n) \tilde{\in} (\eta, \mathcal{S})$ for all $n \geq k$. Hence $f_{\Phi\Gamma}(S_n)$ is a *convergence* to $f_{\Phi\Gamma}(\aleph_{\mathcal{M}})$.

Proposition 6.7*:* If $f_{\Phi\Gamma}$: $(\chi, \tau, Đ, ļ) \rightarrow (\Upsilon, \square, \mathcal{S}, Ï)$ be a strongly-sļpg-*continuous function* and $(S_n)_{n\in\mathbb{N}}$ be a soft sequence over χ . Then $(f_{\Phi\Gamma}(S_n)) \rightarrowtail f_{\Phi\Gamma}(\aleph_{\mathcal{M}})$ in Υ whenever, $S_n \longrightarrow \aleph_{\mathcal{M}}$ in χ.
Proof: Let $(\eta, \mathcal{S})$ is a *sÏpg*-open set in $(\Upsilon, \square, \mathcal{S}, Ï)$where, $f_{\Phi\Gamma}(\aleph_{\mathcal{M}}) \tilde{\in} (\eta, \mathcal{S})$. Since $f_{\Phi\Gamma}$ is a *sļpg-continuous* function, *then* $f_{\Phi\Gamma}{}^{-1}((\eta, \mathcal{S}))$ is an open set in $Ş Ş(\chi)_Đ$ where, $\aleph_{\mathcal{M}} \tilde{\in} f_{\Phi\Gamma}{}^{-1}((\eta, \mathcal{S}))$. By $(S_n)_{n\in\mathbb{N}}$ is convergence to $\aleph_{\mathcal{M}}$, *then* there exist k ∈ $\mathbb{N}$ where, $S_n \tilde{\in} f_{\Phi\Gamma}{}^{-1}((\eta, \mathcal{S}))$ for all $n \geq k$. Implies, there exists $k \in \mathbb{N}$ *where*, $f_{\Phi\Gamma}(S_n) \tilde{\in} (\eta, \mathcal{S})$ for all n ≥ k. Hence $(f_{\Phi\Gamma}(S_n))$ is a soft-ļ-*pre*-g-*convergence* to $f_{\Phi\Gamma}(\aleph_{\mathcal{M}})$.

References:

[1] M Shabir and M Naz 2011 On Soft to topological spaces *Com put Math .Appl*. **61** pp 1786-1799
[2] S Hussain and B Ahmad 2015 Soft separation axioms in soft topological spaces *HJMS* **44** (3) pp 559-568
[3] A Kadil, O A E Tantawy, S A El-Sheikn and A M Abd El-latif 2014 γ- operation and decompositions of some forms of soft continuity in soft topological spaces *AFMI*. **7** pp 181-196
[4] A M Abd El-latif 2014 Supra soft topological spaces *Jo ̈kull journal* **8** (4) pp 1731-1740
[5] A Kandil, O A E Tantawy, S A El-Sheikh and A M Abd El-latif 2014 Soft ideal theory soft local function and generated soft topological spaces *Appl .Math . Inf .Sci* **8** (4) pp 1595-1603
[6] A A Nasaf, A E Radwan, F Ibrahem and R B Esmaeel 2016 Soft α-compactness via soft ideals *Jou. of Advances in Math, June* **12** (4) pp 6178-6184
[7] R B Esmaeel, A I Naser 2016 some properties of-Ĩ-semi open soft sets with respect to soft Ideals *IJpAM* **4** pp 545-561
[8] R B Esmaeel, A I Nasir and B A Kalaf 2018 on α-gĨ-closed soft sets *Sci. Inter. (Lahore)* **30** (5) pp 703-705
[9] R B Esmaeel and R J Mohammad 2020 On Nano soft-I-Semi-g-closed sets *Journal of Physics: Conference Series* pp 1-15
[10] P K Maji, R Biswas and A R Roy 2003 soft set theory *Comput. Math. Appl* **45** pp 555-562
[11] M I Ali, F Feng, X Liu, W K Min and M Shaber 2009 On Some new operations in soft set theory *com put. Math. Appl* **57** (9) pp 1547-1553
[12] I Zorlutuna, M Akdag, W K Min and S Atmaca 2012 Remark On soft topological spaces *Ann. fuzzy Math. Inform* **3** (2) pp 171-185
[13] B Ahmad and A Kharal 2011 Mapping of soft classes *Math.* Nat. *Comput* **7** (3) pp 471-481
[14] J Subhashini 2014 Soft Pre Generalized closed sets in a soft topological space *International Journal of Engineering Trends and Technology* **12** (7)
[15] S A El-Sheikh and A M Abd El-latif 2014 Decompositions of some types of supra soft sets and soft continuity *Inter Jou of Math Treuds and Technology* **9** (1) pp 37-56
[16] R J Mohammad and R B Esmaeel 2020 On Separation Axiomes With Soft-*J*-Semi –g-open sets *IOP Conference Series : Materials Science And Engineering* pp 1-12

New Exact Operational Shifted Pell Matrices and Their Application in Astrophysics

New Exact Operational Shifted Pell Matrices and Their Application in Astrophysics

Mohammed Abdulhadi Sarhan, Suha Shihab, Bushra E. Kashem, Mohammed Rasheed

Applied Sciences Department, University of Technology, Baghdad, Iraq

E-mail: alrawy1978@yahoo.com

Abstract. In this work, the exact operational matrices for shifted Pell polynomials are achievable; so one can integrate and product the vector of basic functions s. The general form of the matrix of integration P is established, the dual matrix of integration Q is derived with general formulation, and the general form of the matrix derived from the product of two shifted Pell polynomials has been given. This idea is implemented on shifted Pell basis vector. Using such exact matrices, then the resident function of the equation is reached which can be written as $R.P(x)$, where R is an algebraic equation vector and $P(x)$ is the shifted Pell basis vector. The presented matrices can be utilized to find the approximate solution of differential equations, integral equation and the calculus of variations problems. An investigation for the convergence and error analysis of the proposed shifted Pell expansion is performed. Numerical treatment for problems in physics are included in this work to demonstrate the accuracy, easy to implement as well as accurate and satisfactory results with a small number of shifted Pell basis. Using operational matrices and the spectral technique are used together for solving Lane-Emden equation.

1. Introduction

Keywords: Shifted Pell polynomials, operation matrix, Lane-Emden equation, dual operation matrix, convergence analysis.

Approximating using an orthogonal family of functions has played an important role in the improvement of engineering, physical sciences, and mathematical analysis. In particular, classical orthogonal functions are applied extensively for the approximate solution of some problems together with spectral methods. For example, in [1], the collocation method was applied using sixth-kind Chebyshev polynomials for treating a class of fractional nonlinear quadratic integro-differential equations. An efficient approximate approach for fractional differential equations was proposed in [2-3] by applying a Tau-Collocation method. The authors in [4] investigated a computational scheme based Müntz polynomials and the collocation method for the approximate solution of fractional differential equations while Legendre collocation spectral technique was presented in [5] for numerically solving the high-order Volterra–Fredholm integro-differential equations.

Special attention has been given to different important orthogonal polynomials using spectral procedures, the explicit formula for the expansion coefficients of the integrals in terms of the original expansion coefficients of the polynomials are required. The new idea in this article, all the presented operational matrices are written in terms of power basis. The advantage has the new formulation of the operational matrices ids the easier computation of the coefficients. When reducing the original problem

to a set algebraic equations which are easy to solve. Moreover, only a small number of shifted Pell basis is required to reach a satisfactory results. The authors in [6] used Taylor wavelet method to solve Lane-Emden singular problems. Other techniques for solving Lane-Emden type equations are fractional Adomian decomposition [7], Legendre wavelets spectral technique [8], a general analytical solution [9], a special algorithm that produces an approximate polynomial solution [10], a modified Legendre-spectral method [11], Haar wavelet collocation [12], and analytical solutions [13]. For more works, one can see [14-17].

The Pell polynomials have become interested in numerical analysis from partial and theoretical points of view. There are Pell and modified Pell polynomials. The research papers dealing with Pell polynomials include some results and properties of either Pell or modified Pell polynomials [18-24]. The best of our knowledge up to now no analytical expressions for the operational matrices of integral, dual and the product of shifted Pell polynomials are given yet in the literature. This motivates our interest in shifted Pell polynomials. Moreover, utilize of shifted Pell polynomials in solving Lane-Emden equation is also studied in the present article.

The organization of this work is as follows: the definition of shifted Pell polynomials is given in section 2 with some important properties. In section 3-5 state with proof, the three formulas expressing explicitly the integration, dual integral and the product of two shifted Pell polynomials. The convergence analysis and error estimates are studied in section 6. Section 7 gives numerical examples to explain the numerical spectral solution of a Lane-Emden equation. Finally, section 8 lists some concluding remarks.

2. Properties of Shifted Pell Polynomials

The fundamental property of the shifted Pell polynomials is that the function is expressed in terms of the independent variable τ or vice versa.

$\overline{P}_0(\tau) = 0$

$\overline{P}_1(\tau) = 1$

$\overline{P}_2(\tau) = 4\tau - 2$

$\overline{P}_3(\tau) = 16\tau^2 - 16\tau + 5$

$\overline{P}_4(\tau) = 46\tau^3 - 96\tau^2 + 56\tau - 12$

$\overline{P}_5(\tau) = 256\tau^4 - 512\tau^3 + 432\tau^2 - 176\tau + 29$

and

$1 = \overline{P}_1(\tau)$

$\tau = \frac{1}{4}\left[\overline{P}_2(\tau) + 2\overline{P}_1(\tau)\right]$

$\tau^2 = \frac{1}{16}\left[\overline{P}_3(\tau) + 4\overline{P}_2(\tau) + 3\overline{P}_1(\tau)\right]$

$\tau^3 = \frac{1}{64}\left[\overline{P}_4(\tau) + 6\overline{P}_3(\tau) + 10\overline{P}_2(\tau) + 2\overline{P}_1(\tau)\right]$

The recurrence relation of the shifted Pell polynomials can be written as

$$\overline{P}_{n+1}(x) = (4\tau - 2)\overline{P}_n(x) + \overline{P}_{n-1}(\tau)) \quad (1)$$

where: $\overline{P}_0(\tau) = 0$, $\overline{P}_1(\tau) = 1$

The other property of the shifted Pell polynomials functions is that

$$\overline{P}_n(\tau) = \frac{1}{4n}\left(\dot{\overline{P}}_{n+1}(\tau) + \dot{\overline{P}}_{n-1}(\tau)\right) \quad (2)$$

A function $f(\tau)$ that is square integrable on $x\epsilon[0,1]$ can be expressed, exactly in terms of shifted Pell polynomials as

$$f(\tau) = \sum_{k=1}^{\infty} a_k \overline{P}_k(\tau) \quad (3)$$

The infinite series in Eq. 3, can be truncated to a sufficient order n to get

$$f(\tau) = \sum_{k=1}^{n} a_k \overline{P}_k(\tau) = A_n^T \overline{P}(\tau) \quad (4)$$

where: $A_n = [a_1 \quad a_2 \quad \dots \quad a_n]^T$ is called shifted Pell spectrum of $f(\tau)$ which makes orthogonal polynomials in general adequate for approximate computations in different complex applied mathematical problems.

$\overline{P}(\tau) = \left[\overline{P}_1(\tau) \quad \overline{P}_2(\tau) \quad \dots \quad \overline{P}_n(\tau)\right]^T$ is called the shifted Pell polynomials vector. The coefficients a_k in Eq. 4 are given by the following

$$a_k = < f(\tau), P_k(\tau) >, \quad k = 1,2, \dots, n \tag{5}$$

3. Matrix Form Shifted Pell Polynomials

Shifted Pell polynomials can be represented in the matrix form as follows

$$\overline{P}(\tau) = Z\ T \tag{6}$$

where: $\overline{P}(\tau) = \left[\overline{P}_1(\tau) \quad \overline{P}_2(\tau) \quad \dots \quad \overline{P}_n(\tau)\right]^T, T = (1 \quad \tau \quad \dots \quad \tau^n)^T,$
and the matrix Z is a $n \times n$ matrix defined by

$$Z = \begin{pmatrix} 1 & 0 & 0 & 0 & 0 & \dots & 0 \\ -2 & 4 & 0 & 0 & 0 & \dots & 0 \\ 5 & z_{21} & 4 & 0 & 0 & \dots & 0 \\ -12 & z_{31} & z_{32} & 4^3 & 0 & \dots & 0 \\ \vdots & \vdots & \vdots & \vdots & \vdots & \dots & \vdots \\ z_{io} & z_{n1} & z_{n2} & z_{n3} & z_{n4} & \dots & 4^{n-1} \end{pmatrix}$$

The first element of each row is

$$z_{io} = \sum_{k=0}^{\left[\frac{n}{2}\right]} (-1)^k 2^{n-2k} \binom{n-k}{k}, i = 0, 1, \dots, n$$

In addition, other elements are defined by

$$z_{ij} = 4z_{i-1,j-1} + 2z_{i-1,j} + z_{i-2,j}$$

4. Product of Shifted Pell Polynomials

Before solving the nonlinear TFF equation, we recall Weierstrass theorem [21]:

Theorem 4.1: The product of two shifted Pell polynomials is given by the expression

$$\overline{P}_n(\tau)\overline{P}_m(\tau) = \sum_{k=0}^{\min(n,m)-1} (-1)^k\, \overline{P}_{n+m-(2k+1)}(\tau),\ n, m > 1 \tag{7}$$

where: $\overline{P}_0(\tau)\overline{P}_m(\tau) = \overline{P}_0(\tau)$

Proof

Take $m = 1$, then one can get $\overline{P}_n(\tau)\overline{P}_1(\tau) = \overline{P}_n(\tau)$, this means that Eq. 7 is true for $m = 1$. Assume that Eq. 7 is true for m, that is

$$\overline{P}_n(\tau)\overline{P}_m(\tau) = \sum_{k=0}^{\min(n,m)-1} (-1)^k\, \overline{P}_{n+m-(2k+1)}(\tau)$$

Multiply both sides of this equation by $(4\tau - 2)$, yields

$$\overline{P}_n(\tau)((4\tau-2)\overline{P}_m(\tau)) = (4\tau-2)\sum_{k=0}^{\min(n,m)-1} (-1)^k\, \overline{P}_{n+m-(2k+1)}(\tau) \tag{8}$$

Using the important recurrence relation for shifted Pell polynomials

$(4\tau - 2)\overline{P}_n(\tau) = \overline{P}_{n+1}(\tau) - \overline{P}_{n-1}(\tau)$, this will lead to

$$\overline{P}_n(\tau)\left[\overline{P}_{m+1}(\tau) - \overline{P}_{m-1}(\tau)\right] = \sum_{k=0}^{\min(n,m)-1} (-1)^k \left[\overline{P}_{n+m-2k}(\tau) - \overline{P}_{n+m-(2k-2)}(\tau)\right]$$

$$\overline{P}_n(\tau)\overline{P}_{m+1}(\tau) = \overline{P}_n(\tau)\overline{P}_{m-1}(\tau) + \sum_{k=0}^{\min(n,m)-1} (-1)^k \left[\overline{P}_{n+m-2k}(\tau) - \overline{P}_{n+m-(2k-2)}(\tau)\right]$$

$$\overline{P}_n(\tau)\overline{P}_{m+1}(\tau) = \sum_{k=0}^{\min(n,m-1)-1} (-1)^k \overline{P}_{n+m-(2k+2)}(\tau)$$
$$+\sum_{k=0}^{\min(n,m)-1}(-1)\overline{P}_{n+m-2k}(\tau)\sum_{k=0}^{\min(n,m)-1}(-1)^k\overline{P}_{n+m-(2k+2)}(\tau) \quad (9)$$

From Eq. 9, it is easy to obtain the desired result.
That is

$$\overline{P}_n(\tau)\overline{P}_{m+1}(\tau) = \sum_{k=0}^{\min(n,m-1)-1} (-1)^k \overline{P}_{n+m-(2k+2)}(\tau)$$

5. Operation Matrix of Integration

The structure of shifted Pell operational matrix of integration is given. Take $n = 5$, in this case $\overline{P}(\tau) = \left[\overline{P}_1(\tau) \quad \overline{P}_2(\tau) \quad \overline{P}_3(\tau) \quad \overline{P}_4(\tau) \quad \overline{P}_5(\tau)\right]^T$. By integrating the vector $\overline{P}(\tau)$ from 0 to τ and representing them in matrix form, yields

$$\int_0^\tau \overline{P}_1(t)dt = \left[\tfrac{1}{2} \quad \tfrac{1}{4} \quad 0 \quad 0\right]\overline{P}(\tau)$$

$$\int_0^\tau \overline{P}_2(t)dt = \left[\frac{-5}{8} \quad 0 \quad \frac{1}{8} \quad 0\right]\overline{P}(\tau)$$

$$\int_0^\tau \overline{P}_3(t)dt = \left[\frac{14}{12} \quad \frac{1}{12} \quad 0 \quad \frac{1}{12} \quad 0\right]\overline{P}(\tau)$$

$$\int_0^\tau \overline{P}_4(t)dt = \left[\frac{34}{16} \quad 0 \quad \frac{1}{16} \quad 0 \quad \frac{1}{16}\right]\overline{P}(\tau)$$

$$\int_0^\tau \overline{P}_5(t)dt = \left[\frac{-82}{20} \quad 0 \quad 0 \quad \frac{1}{20} \quad 0\right]\overline{P}(\tau) + \frac{1}{20}\overline{P}_6(\tau)$$

Thus

$$\int_0^\tau \overline{P}(t)dt = R_{5\times5}\,\overline{P}(\tau) + \overline{P}_6(\tau)$$

where: $R_{5\times5} = \begin{pmatrix} \frac{1}{2} & \frac{1}{4} & 0 & 0 & 0 \\ \frac{5}{8} & 0 & \frac{1}{8} & 0 & 0 \\ \frac{-14}{12} & \frac{1}{12} & 0 & \frac{1}{12} & 0 \\ \frac{34}{16} & 0 & \frac{1}{16} & 0 & \frac{1}{16} \\ \frac{-82}{20} & 0 & 0 & \frac{1}{20} & 0 \end{pmatrix}$

$$\overline{P}_6(\tau) = \left[0 \quad 0 \quad 0 \quad 0 \quad \frac{1}{20}\right]^T$$

Fortunately, for general n, operational matrix of integration for shifted Pell polynomials has a regular expression, so no need to pre-calculate the corresponding operational matrix R and R for different n when dealing with the problems

$$\int_0^\tau \overline{P}(t)dt = R\,\overline{P}(\tau) + \overline{P}_{n+1}(\tau)$$

where: R is $n \times n$ matrix given by

$$\begin{pmatrix} \delta & \frac{1}{4} & 0 & 0 & \dots & 0 \\ -\delta & 0 & \frac{1}{8} & 0 & \dots & 0 \\ \delta & \frac{1}{12} & 0 & \frac{1}{12} & \dots & 0 \\ -\delta & 0 & \frac{1}{16} & 0 & \dots & 0 \\ \vdots & \vdots & \vdots & \vdots & \dots & \vdots \\ \delta & 0 & 0 & \frac{1}{4n} & \dots & \frac{1}{4n} \end{pmatrix}$$

$$\overline{P}(\tau) = \begin{bmatrix} \overline{P}_1(\tau) & \overline{P}_2(\tau) & \dots & \overline{P}_n(\tau) \end{bmatrix}^T$$

$$\overline{P}_{n+1}(\tau) = \begin{bmatrix} 0 & 0 & 0 \dots & 0 & \frac{1}{4n} \end{bmatrix}^T$$

$$\delta = \overline{P}_{n+1}(0) + \overline{P}_{n-1}(0)$$

$$\delta = \begin{cases} \sum_{k=0}^{\left[\frac{n}{2}\right]} 2^{n-2k} \binom{n-k}{k} & n\ odd \\ -\sum_{k=0}^{\left[\frac{n}{2}\right]} 2^{n-2k} \binom{n-k}{k} & n\ even \end{cases}$$

6. Dual Operational Matrix

The dual operational matrix of $\overline{P}(\tau)$ is presented in this section. The integration of the cross product is taken of two shifted Pell basis vectors; the results is $(n+1) \times (n+1)$ dimensional matrix which is indicated by

$$H = \int_0^1 \overline{P}(\tau)\overline{P}^T(\tau)d\tau \quad (10)$$

The matrix H is called the dual operational matrix of $\overline{P}(\tau)$ and will be calculated as follows
The integrals of the products of shifted Pell basis functions is

$$\int_0^1 \overline{P}_n(\tau)\overline{P}_m(\tau)d\tau = \int_0^1 \sum_{k=1}^{\min(n,m)} (-1)^{k+1}\overline{P}_{n+m-(2k+1)}(\tau)d\tau$$
$$= \sum_{k=1}^{\min(n,m)} (-1)^{k+1} \int_0^1 \overline{P}_{n+m-(2k+1)}(\tau)d\tau$$

Since

$$\int_0^1 \overline{P}(\tau)d\tau = \begin{cases} \sum_{k=0}^{\left[\frac{n}{2}\right]} 2^{n-2k} \binom{n-k}{k} & n\ odd \\ 0 & n\ even \end{cases}$$

Therefore, we have $H_1 = \begin{pmatrix} \overline{P}_1\overline{P}_1 & \overline{P}_1\overline{P}_2 & \overline{P}_1\overline{P}_3 \\ \overline{P}_2\overline{P}_1 & \overline{P}_2\overline{P}_2 & \overline{P}_2\overline{P}_3 \\ \overline{P}_3\overline{P}_1 & \overline{P}_3\overline{P}_1 & \overline{P}_3\overline{P}_3 \end{pmatrix}$

$$H = \int_0^1 \overline{P}(\tau)\overline{P}^T(\tau)d\tau = \int_0^1 H_1 d\tau = \begin{pmatrix} \int_0^1 \overline{P}_1\overline{P}_1 d\tau & \int_0^1 \overline{P}_1\overline{P}_2 d\tau & \int_0^1 \overline{P}_1\overline{P}_3 d\tau \\ \int_0^1 \overline{P}_2\overline{P}_1 d\tau & \int_0^1 \overline{P}_2\overline{P}_2 d\tau & \int_0^1 \overline{P}_2\overline{P}_3\, d\tau \\ \int_0^1 \overline{P}_3\overline{P}_1\, d\tau & \int_0^1 \overline{P}_3\overline{P}_1 d\tau & \int_0^1 \overline{P}_3\overline{P}_3\, d\tau \end{pmatrix}$$

7. Convergence Analysis and Error Estimate

The approximate function of $f(\tau)$ using shifted Pell polynomials is as follows

$f_n(\tau) = \sum_{i=1}^{n+1} a_i \overline{P}(\tau)$ (11)

where: $a_i =< f(\tau), \overline{P}_n(\tau) >= \int_0^1 f(\tau)\overline{P}_n(\tau)d\tau$ (12)

Since every continuous function on the closed interval is a bounded function, thus there is a constant ε such that $|f(\tau)| \le \varepsilon \quad \forall \tau \in [0,1]$ (13)

Therefore, Eq. 12 leads to

$$|a_n| \le \varepsilon \int_0^1 \left|\overline{P}_n(\tau)\right| d\tau$$

$$\le \varepsilon \int_0^1 \left| \sum_{k=n}^{\left[\frac{n}{2}\right]} \binom{n-k}{k} (4\tau-2)^{n-2k} \right| d\tau$$

$$\le \varepsilon \int_0^1 \sum_{k=n}^{\left[\frac{n}{2}\right]} \binom{n-k}{k} \left|(4\tau-2)^{n-2k}\right| d\tau$$

$$\le \varepsilon \int_0^1 \sum_{k=0}^{\left[\frac{n}{2}\right]} \binom{n-k}{k} \sum_{i=0}^{n-2k} (-1)^{n-i} \binom{n-2k}{i} 2^{n-2k} \left|(2^{4+i})\right| d\tau$$

$\int_0^1 \left|\overline{P}_n(\tau)\right| d\tau \le \sum_{k=0}^{\left[\frac{n}{2}\right]} 2^{n-2k} \prod_{L=0}^{k-1} \frac{n-k-L}{k-L}$ for odd n and $\int_0^1 \left|\overline{P}_n(\tau)\right| d\tau = 0$ for even n.

This will lead to the following result

$$|a_n| \le \varepsilon \sum_{k=0}^{\left[\frac{n}{2}\right]} 2^{n-2k} \prod_{L=0}^{k-1} \frac{n-k-L}{k-L}$$

8. Application of the Shifted Pell Operational Matrices

This section describes the application of the presented operational matrices of shifted Pell polynomials for solving some problems arising in physics throughout the following two suggested examples.

8.1 *Application to Lane-Emden Type Equation*

Consider the following Lane-Emden singular initial value problem equation

$f''(\tau) + \frac{2}{\tau} f'(\tau) + f(\tau) = \tau^2 + 7,\ f(0) = 1,\ f'(0) = 0, \tau \in (0,1]$ (14)

with the exact $f(\tau) = \tau^2 + 1$ (15)

Assume that the unknown function $f''(\tau)$ is approximated by n basis of the shifted Pell polynomials as below

$f''(\tau) = \sum_{i=1}^{n} a_i \overline{P}_i(\tau) = a^T \overline{P}(\tau)$ (16)

where: $a = [a_1 \dots a_n]^T$

For approximate the solution $f'(\tau)$ and $f(\tau)$ two-times integration are applied on both sides Eq. 16, yields

$\int_0^\tau f''(t)dt = f'(\tau) - f'(0) = a^T I\overline{P}(\tau)$ (17)

and $\int_0^\tau f'(t)dt = f(\tau) - f(0) = \int_0^\tau a^T\, If(t)dt$

or $f(\tau) = a^T I^2\overline{P}(\tau) + V^T\overline{P}(\tau)$ (18)

(Note that $1 = V^T\overline{P}(\tau)$

Eq. 18 can be rewritten as follows

$f(\tau) = (a^T I^2 + V^T)\overline{P}(\tau) = L^T\overline{P}(\tau)$ (19)

Using the relationship between shifted Pell polynomials and the powers $1 = \tau, \dots, \tau^n$ one can obtain

$\tau = V^T\overline{P}(\tau)$ (20)

$\tau^3 + 7\tau = Z^T\overline{P}(\tau)$ (21)

$\tau\ddot{f}(\tau) = a^T V_1\,\overline{P}(\tau)$ (22)

$\tau f(\tau) = a^T V_2\,\overline{P}(\tau)$ (23)

Eq. 14 can be rewritten as

$a^T V_1\,\overline{P}(\tau) + 2a^T I\overline{P}(\tau) + a^T V_2\,\overline{P}(\tau) = Z^T\overline{P}(\tau)$

That is $a^T V_1 + a^T V_2 = Z^T$ (24)

Eq. 24 yields a set of algebraic equations which can be solved for a.

For the case $n = 2$, one can get

$$f_2(\tau) = \overline{P}_1(\tau) + \frac{1}{4}\left(\frac{1}{2}a_1 - \frac{5}{8}a_2\right)\left(\overline{P}_2(\tau) - 2\overline{P}_1(\tau)\right) + \frac{1}{32}a_1\left(\overline{P}_3(\tau) - 5\overline{P}_1(\tau)\right) + \frac{1}{96}a_2\left(\overline{P}_4(\tau) + \overline{P}_2(\tau) + 14\overline{P}_1(\tau)\right)$$

or

$f_2(\tau) = a^T\overline{P}(\tau)$

where: $a^T = \left[\left(1 + \frac{3}{32}a_1 - \frac{16}{96}a_2\right) \quad \frac{1}{8}a_1 - \frac{14}{96}a_2 \quad \frac{1}{32}a_1 \quad \frac{1}{96}a_2\right]$

Note that in this case $a_1 = 2$ and $a_2 = 0$, as a result

$f_2(\tau) = \frac{19}{16}\overline{P}_1(\tau) + \frac{1}{4}\overline{P}_2(\tau) + \frac{1}{16}\overline{P}_3(\tau)$

8.2 *Application to Emden-Fowler Type Equation*

Consider the Emden-Fowler equation studied by [25],

$f''(\tau) + \frac{k}{\tau}f'(\tau) + \tau^r f^{(n)}(\tau) = 0,\ n \in \mathbb{N} \cup \{0\}, \tau \in (0,1]$ (25)

together with the initial conditions

$f(0) = 1, f'(0) = 0$ (26)

Eq. 25 governed by the conditions in Eq. 26 has $f(\tau) = \frac{\sin\tau}{\tau}$ as exact solution when $r = 0$, $n = 1$ and $k = 1$. The application of the operational shifted Pell matrices which is proposed in the previous sections yields the following approximate solutions corresponding to $n = 1$ and $n = 3$, respectively

$f_1(\tau) = 0.96875\,\overline{P}_1(\tau) - 0.041667\overline{P}_2(\tau) - 0.0104167\overline{P}_3(\tau)$

and

$f_3(\tau) = 0.96855\,\overline{P}_1(\tau) - 0.04115\overline{P}_2(\tau) - 0.009733\overline{P}_3(\tau) + 0.00026\overline{P}_4(\tau) + 0.000033\overline{P}_5(\tau)$

Table 1 lists the results in the case of $n = 1, 3$ using shifted Pell operational matrices and the results obtained by applying orthonormal Bernstein polynomials developed in [25]. With some comparisons aiming to illustrate the applicability and accuracy of the proposed shifted Pell operational matrices procedure. Assume ε_1 and ε_2 denote the error in maximum norm corresponding to the approximate solution $f_1(\tau)$ and $f_3(\tau)$ respectively, that is

$\varepsilon_1 = \max_{\tau\in[0,1]}|f(\tau) - f_1(\tau)|$ and $\varepsilon_1 = \max_{\tau\in[0,1]}|f(\tau) - f_1(\tau)|$

Figure 1 ensures that the obtained approximate solution using shifted Pell operational matrices is closer to the exact one with few basis shifted Pell. Figure 2 plots the absolute error of Example 2. The results in Table 1 illustrate that the obtained numerical solution with few terms of the presented shifted Pell expansion is more accurate than the results in [25]. The advantage of the proposed method is demonstrated when compared with other approximate method.

Table 1 Approximate and exact values for example 2

	Shifted Pell		**Exact**	**OBP [25]**	
τ	$n=1$	$n=3$	$\frac{\sin\tau}{\tau}$	$n=3$	$n=5$
0.1	0.998333	0.99833	0.998334166	0.99837	0.99831
0.2	0.993333	0.99334	0.993346654	0.99340	0.99323
0.3	0.985000	0.98506	0.985067356	0.98509	0.98505
0.4	0.973333	0.97354	0.973545856	0.97352	0.97354
0.5	0.958333	0.95885	0.958851077	0.95881	0.95885
0.6	0.940000	0.94108	0.941070789	0.94104	0.94108
0.7	0.918333	0.92033	0.920310982	0.92031	0.92033
0.8	0.893333	0.89674	0.896695114	0.89672	0.89672
0.9	0.865000	0.87046	0.870363233	0.87037	0.87037

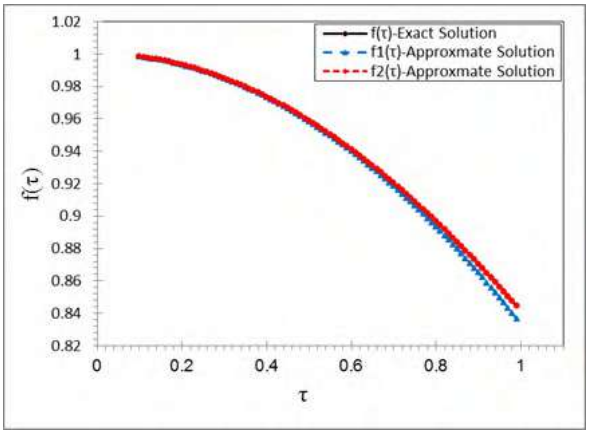

Figure. 1: Different solution of example 2.

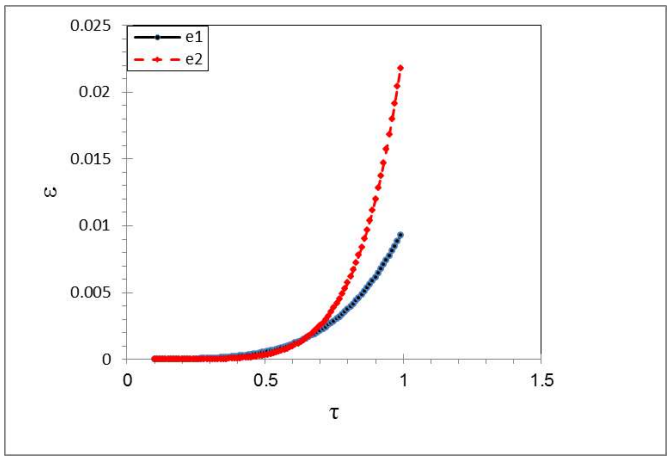

Figure. 2: Absolute Error of example 2 in case $n = 1, 3$.

Conclusion

In the present work, the definition of shifted Pell polynomials is presented first with some important properties. Then a novel general procedure for calculating operational matrices corresponding to the shifted Pell polynomials is presented. They are operational matrix of integration, operation matrix of product and dual operational matrix. These matrixes can be applied together with spectral methods to solve problems arising in physics called Lane-Emden equation. The efficiency of the proposed technique is shown from the obtained results. The aim of such technique is to get an effective algorithm that is suitable the digital computers by reducing the underlying Lane-Emden equation to algebraic equations.

References

[1] Babaei A, Jafari H and Banihashemi S 2020 *J. Comput. Appl. Math*. **112908**
[2] Allahviranloo T, Gouyandeh Z and Armand A 2015 *Appl. Math. Comput.* **271** 979-990
[3] Ghoreishi F and Yazdani S 2011 Computers & Mathematics with Applications **61** 1 30-43
[4] Esmaeili S, Shamsi M and Luchko Y 2011 *Comput. Math. Appl.* **62** 3 918-929
[5] Rohaninasab N, Maleknejad K and Ezzati R 2018 *Appl. Math. Comput.* **328** 171-188
[6] Gümgüm S 2020 *Appl. Numeri. Math.* **158** 44-53
[7] Abdel-Salam A B, Nouh M I and Elkholy E A 2020 *Sci. Afr.* **e00386**
[8] Dizicheh A K, Salahshour S, Ahmadian A and Baleanu D 2020 *Appl.Numer. Math.* **153** 443-456
[9] Torres-Córdoba R and Martínez-García E A *New Astron.* **82** 101458
[10] Vanani S K and Aminataei A 2010 *Comput. Math. Appl.* **59** 8 2815-2820
[11] Rismani A M and Monfared H 2012 *Appl. Math. Model.* **36** 10 4830-4836
[12] Singh R, Garg H and Guleria V 2019 *J. Comput. Appl. Math.* **346** 150-161
[13] Van Gorder R A and Vajravelu K 2008 *Phys. Lett. A* **372** 39 6060-6065
[14] Jalal R, Shihab S, Alhadi M A and Rasheed M 2020 *J. Phys Conf. Ser.* **1660** 1 012090 IOP Publishing
[15] Salih A A and SHIHAB S 2020 *Samarra J. Pure and Appl. Sci.* **2** 2 68-78
[16] Alrawy S S and Salih A A 2020 *Samarra J. Pure and Appl. Sci*. **2** 1 67-75
[17] Dkhilalli F, Megdiche B S, Rasheed M, Barille R, Shihab S, Guidara K and Megdiche M 2018 R. Soc. open sci. **5** 8 172214
[18] Flaut C and Savin D 2018 *Chaos Solitons Fractals* **106** 67-71
[19] Şahin A and José L R 2016 *Appl. Math. Comput.* **281** 314-322
[20] Luzón A, Morón M A and Ramírez J L 2016 *Linear Algeb. Appl.* **511** 237-258
[21] Tuglu N, Kocer E G and Stakhov A 2011 *Appl. Math. Comput.* **217** 24 10239-10246
[22] Cerda-Morales G 2017 *Medit. j. math.* **14** 6 239
[23] Catarino P 2016 *Adv. Appl. Clifford Algebr.* **26** 2 577-590
[24] Catarino P and Campos H 2018 *J. Info. Optim. Sci.* **39** 6 1363-1371
[25] Bencheikh A, Chiter L and Abbassi H 2016 *Glob. J. Pure and Appl. Math.* **12** 5 4219-4332

Two Embedded Pairs for Solve Directly Third-Order Ordinary Differential Equation by Using Runge-Kutta Type Method (RKTGD)

Two Embedded Pairs for Solve Directly Third-Order Ordinary Differential Equation by Using Runge-Kutta Type Method (RKTGD)

Firas A. Fawzi, Zeyad M. Abdullah, Nazar K. Hussein

Department of Mathematics, Faculty of Computer Science and Mathematics, University of Tikrit, Iraq

Email: firasadil01@tu.edu.iq

Abstract. In this paper, two pairs of embedded Runge-Kutta (RK) type techniques for straightforwardly tackling third-order ordinary differential equations (ODEs) of the form $v''' = f(x, v, v')$ signified as RKTGD strategies were proposed and explored. Relying on the order conditions, the primary pair with mathematical order 4 and 3 was called RKTGD4(3), while different has order 5 and 4, and was named RKTGD5(4). The new strategies were determined so that the higher-order techniques were exact and the lower order techniques would bring about the best error estimates. At that point, variables step-size codes were created to support the methods and utilized in solving a lot of third-order problems. Comparisons were made between mathematical results and existing embedded RK pairs within the scientific literature, that require the problems to be reduced into a system of first-order ODEs, and the effectiveness of the new RKTGD pairs have appeared.

1.Introduction

In the present paper, the numerical integration of 3rd-order ODEs and initial conditions of the structure

$$v'''(t) = f\big(x, v(t), v'(t)\big), \quad v(t_0) = v_0, \quad v'(t_0) = v_0', \quad v''(t_0) = v_0'', \quad t \geqslant t_0 \tag{1}$$

was considered, where $v, v' \in \mathrm{R}^d$, $f : \mathrm{R}\times\mathrm{R}^d \to \mathrm{R}^d$ is a continuous vector-valued function that doesn't explicitly depend on the second derivatives. Some examples of such problems are found in electromagnetic waves, thin film flow and gravity driven flow [1-3]. A number of engineers, scientists, and researchers usually solve problem (1) by transforming the third-order ODEs into a system of first-order equations three times the dimension. See examples in the references [4-8]. These methods are multi-step methods, therefore, they require starting values when utilized in solving problem (1). However, it is more efficient if the problem can be solved directly with the aid of numerical methods. This paper is focused on the use of a one-step embedded explicit process, in particular, the RK type methods for solve directly third-order ODEs of the problem (1) which don't need the beginning values. The regular sort of new procedure with *m*-stage for solving initial value problems (IVPs) (1) can be formulated in [9]:

$$v_{n+1} = v_n + hv_n' + \frac{h^2}{2}v_n'' + h^3\sum_{i=1}^{m} b_i k_i, \tag{2}$$

$$v_{n+1}' = v_n' + hv_n'' + h^2\sum_{i=1}^{m} b_i' k_i, \tag{3}$$

$$v''_{n+1} = v''_n + h\sum_{i=1}^{m} b''_i k_i, \quad (4)$$

Where

$$k_i = f(x_n + c_i h, v_n + c_i h v_n^i + \frac{h^2}{2} c_i^2 v''_n + h^3 \sum_{j=1}^{i-1} a_{ij} k_j, v'_n + c_i h v''_n + h^2 \sum_{j=1}^{i-1} \bar{a}_{ij} k_j), \quad (5)$$

for $i = 2, 3, \ldots, m$.

RKTGD method parameters b_i , b'_i , b''_i, a_{ij}, $\bar{a}_{ij}$ and c_i of the new technique assumed to be realistic, m is the number of phases of the technique. Then, this method is explicit when $a_{ij} = 0$ for $i \leq j$. To decide the coefficients of the technique given by (2-5), the RKTGD strategy expression is extended by utilizing Taylor's series expansion [10, 11]. After being simplified mathematically, this expansion is then compared to the solution was given by Taylor's series expansion. At that point, this process requires a great deal of mathematical and numeric calculations, however utilizing programming like Maple as in [10]. General order conditions for the RKTGD strategy can be gotten from the direct expansion of the local truncation error. Likewise, efficient RK codes frequently utilize embedded pair of request $p(q)$ where p is greater or equal to $q + 1$, examples of these are seen in [12-16]. This study is significantly dedicated to additional work in this exploration field of study. Especially, it is pointed tat deriving the $p(q)$ pairs of explicit RKTGD techniques utilized in variable step size codes to give a tinny error estimation, and it's based on the techniques (c, A, b, b', b'') of order p, and $(c, A, \hat{b}, \hat{b}', \hat{b}'')$ of order q.

For Butcher Tableau, the embedded pair can be expressed as follows:

$$\begin{array}{c|c|c|} c & A & \bar{A} \\ \hline & b^T & b'^T & b''^T \\ \hline & \hat{b}^T & \hat{b}'^T & \hat{b}''^T \end{array} \quad (6)$$

The essential reason for building the embedded pairs of explicit RKTGD strategy is to obtain a low value local error estimate that would be utilized in the step-size algorithm of the vector. Obviously, the method will calculate v_{n+1}, v'_{n+1} and v''_{n+1} to approximate $v(x_{n+1})$, $v'(x_{n+1})$ and $v''(x_{n+1})$, where v_{n+1} is the measured solution and $v(x_{n+1})$ is an accurate solution.

2.CONSTRUCTION OF THE METHODS

The order conditions of RKTGD method are derived up to order six by using the Taylor expansion and Maple package, For the new system, the local truncation errors or the order terms for m-stage up to order six can be expressed (see [9]). The construction of the embedded Runge-Kutta method is an active research area producing continuous improvements to the existing codes. we are concerned with the derivation of p(q) pairs of explicit RKTG methods which are used in variable step size codes to provide a cheap error estimation. The following simplifying assumption is used to minimize the number of equations to solve;

$$\sum_{j=1}^{m} \bar{a}_{ij} = \frac{c_i^2}{2} \quad (7)$$

To develop efficient pairs, the following techniques are used:

(a) For both the higher and lower order RKTGD formulas, the $\| \tau_g^{(p+1)} \|_2$ and $\| \hat{\tau}_g^{(p+1)} \|_2$ quantities should be as minimal as possible, where

$$\left\| \tau_g^{(p+1)} \right\|_2 = \sqrt{\sum_{i+1}^{n_p+1} (\tau_i^{(p+1)})^2 + \sum_{i+1}^{n'_p+1} (\tau'_{i\,i}^{(p+1)})^2 + \sum_{i+1}^{n''_p+1} (\tau''_{i\,i}^{(p+1)})^2},$$

and

$$\left\|\hat{\tau}_g^{(q+1)}\right\|_2 = \sqrt{\sum_{i+1}^{n_q+1}(\hat{\tau}_i^{(q+1)})^2 + \sum_{i+1}^{n'_q+1}(\hat{\tau}'^{(q+1)}_i)^2 + \sum_{i+1}^{n''_q+1}(\hat{\tau}''^{(q+1)}_i)^2},$$

Where $\tau^{(p+1)}$, $\tau'^{(p+1)}$ and $\tau''^{(p+1)}$ are the local truncation error norms for y, y' and y'' respectively, $\tau_g^{(p+1)}$ is the global local truncation error.

(b) The calculation of the local error at point x_{n+1} is determined using the formula:

$$LTE = max\{\| \delta_{n+1} \|_\infty, \| \delta'_{n+1} \|_\infty, \| \delta''_{n+1} \|_\infty\},$$

where

$$\delta_{n+1} = \hat{v}_{n+1} - v_{n+1}$$
$$\delta'_{n+1} = \hat{v}'_{n+1} - v'_{n+1}$$
$$\delta''_{n+1} = \hat{v}''_{n+1} - v''_{n+1}$$

The solutions using the higher order formula are v_{n+1}, v'_{n+1} and v''_{n+1}, while the solutions using the lower order formula are $\hat{v}_{n+1}$, $\hat{v}'_{n+1}$ and $\hat{v}''_{n+1}$. These local error estimates (LTE) can be used by the standard formula as given in [17] to control the step size h,

$$h_{n+1} = 0.9h_n\left(\frac{Tol}{LTE}\right)^{\frac{1}{q+1}} \quad (8)$$

Where 0.9 is considered to be a safety factor and represents the estimate of local error at each step, Tol represents the necessary accuracy, which is the maximum permissible local error. If $LTE \leq Tol$, local extrapolation (or higher-order mode) method will be accepted; this means that a more precise approximation will be used to advance the integration and h would be updated using the formula (8). On the other hand, if $LTE > Tol$, the step would be rejected and the step-size would be halved.

3.The Derivation of 4(3) pair

A three-stage RKTGD technique of order four is derived in this section. The conditions of the algebraic order up to order four are used (see [9]) and the simplifying assumption (7). Then, the system of equations can be reduced to 13 nonlinear equations with 17 unknowns and left with four degrees of freedom by simplifying assumptions. The solution of the equation system results simultaneously in a solution in terms of four free parameters, which are c_3, a_{21}, a_{31} and b_2:

$$\bar{a}_{21} = \frac{9 - 24c_3 + 16c_3^2}{8(c_3^2 - 12c_3 + 4)}, \bar{a}_{31} = \frac{c_3(9 - c_3^3 - 20c_3^2 + 14c_3 - 3)}{-3 + 4c_3},$$

$$\bar{a}_{32} = -\frac{c_3(18 - c_3^3 - 36c_3^2 + 25c_3 - 6)}{-3 + 4c_3}, a_{21} = a_{21}, a_{31} = a_{31},$$

$$a_{32} = -\frac{-12a_{31} + 16a_{31}c_3 + 423a_{21}c_3^4 - 864a_{21}c_3^3 + 567a_{21}c_3^2 - 128a_{21}c_3}{-12 + 16c_3} + \frac{50c_3^3 - 36c_3^2 + 9c_3 - 24c_3^4}{-12 + 16c_3},$$

$$b'_1 = \frac{6c_3^2 - 6c_3 + 1}{8(-3 + 4c_3)c_3}, b'_2 = \frac{3c_3 + 2 + 48b_2c_3 - 36b_2}{24c_3(3c_3 - 2)}, b'_3 = \frac{-1 + c_3}{6c_3(3 - 8c_3 + 6c_3^2)}, c_1 = 0,$$

$$c_2 = \frac{-3 + 4c_3}{2(3c_3 - 2)}$$

$$b_2 = b_2, b_1 = -\frac{12c_3^2 + 11c_3 + 72b_2c_3^2 - 96b_2c_3 - 2 + 36b_2}{24c_3(3c_3 - 2)},$$

$$b_3 = -\frac{3c_3 + 2 + 48b_2c_3 - 36b_2}{24c_3(3c_3 - 2)},$$

$$b''_1 == \frac{6c_3^2 - 6c_3 + 1}{8(-3 + 4c_3)c_3}, b''_2 = \frac{2(27c_3^3 - 54c_3^2 + 36c_3 - 8)}{3(-50c_3^2 + 36c_3 - 9 + 24c_3^3)}, \quad b''_3 = \frac{1}{6c_3(3 - 8c_3 + 6c_3^2)}$$

and setting $c_3 = 1$ and $a_{31} = 0$ gives:

$$\| \tau_g^{(5)} \|_2 = \frac{1}{960}(72000 b_2^2 - 14400 b_2 + 4429 + 512000 a_{21}^2 - 33280 a_{21})^{\frac{1}{2}}$$

By using the *minimize* command in Maple, then a_{21} = 0.0325000022021653 and b_2 = 0.100000024350969, and the minimum value $\left\|\tau_g^{(5)}\right\|_2$ is 0.0586320476692477264. Again for the optimized values, $a_{21} = \frac{3}{100}$ and $b_2 = \frac{1}{10}$ were chosen.

Therefore, the coefficients denoted by RKTGD4 of the three-stage fourth-order RKTGD method can be defined as follows:

$$c_2 = \frac{1}{2}, c_3 = 1, a_{21} = \frac{3}{100}, a_{32} = \frac{13}{100}, \bar{a}_{21} = \frac{1}{8}, \bar{a}_{32} = \frac{1}{2}, b_1 = \frac{3}{40}, b_2 = \frac{1}{10},$$
$$b_3 = -\frac{1}{120}, b_1' = \frac{1}{6}, b_2' = \frac{1}{3}, b_3' = 0, b_1'' = \frac{1}{6}, b_2'' = \frac{2}{3}, b_3'' = -\frac{1}{6}$$

A three-stage (s=3) third-order (q=4) embedded formula can now be derived considering the above solutions for A and c. Solving the third-order equations for $v(t)$, $v(t)$ (see [9]) simultaneously yields a solution for b_i in b_i terms, while b_i' and b_i'' are the same as the fourth-order formula. Three free parameters of the solution in terms of b_3' , $b_2$and b_3 are obtained as follows:

$$b_1' = \frac{1}{6} - b_2 - b_3, b_2 = b_2, b_3 = b_3, b_1' = \frac{1}{6} + b_3', \quad b_2' = \frac{1}{3} - 2\, b_3', \quad b_3' = b_3',$$
$$b_1'' = \frac{1}{6}, b_2'' = \frac{2}{3}, b_3'' = \frac{1}{6}$$

Here, take $b_3' = \frac{1}{15}$ then:

$$\| \tau_g^{(4)} \|_2 = \frac{1}{120}\sqrt{3600 b_2^2 + 14400 b_2 b_3 - 600 b_2 + 14400 b_3^2 - 1200 b_3 + 45}$$

Two free parameters b_2 and b_3 do not appear in the solution now, but for fourth-order conditions, they appear in the local truncation error. According to Dormand [9], the free parameters b_2 and b_3 can be determined by minimizing the local truncation error norms $\| \tau_g^{(4)} \|_2$. By using the *minimize* command in Maple, b_2 = 0.416666666666741, b_3 = −0.166666666666519 were obtained, and the minimum error is 0.0372677996249964963. For the optimized value in fractional form, $b_2 = \frac{4}{10}$ and $b_3 = -\frac{2}{10}$ were chosen.

Finally, all the three-stage embedded RKTGD system coefficients denoted by RKTGD4(3) can be written in the following way (see Table 1):

Table I. The RKTGD4(3) Method.

0	0			0					
$\frac{1}{2}$	$\frac{3}{100}$	0		$\frac{1}{8}$	0				
1	0	$\frac{13}{100}$	0	0	$\frac{1}{2}$	0			
	$\frac{3}{40}$	$\frac{1}{10}$	$-\frac{1}{120}$	$\frac{1}{6}$	$\frac{1}{3}$	0	$\frac{1}{6}$	$\frac{2}{3}$	$\frac{1}{6}$
	$-\frac{1}{30}$	$\frac{2}{5}$	$-\frac{1}{5}$	$\frac{7}{30}$	$\frac{1}{5}$	$\frac{1}{15}$	$\frac{1}{6}$	$\frac{2}{3}$	$\frac{1}{6}$

4.The Derivation of 5(4) pair

The four-stage RKTGD method of order five is derived in this section, and the algebraic conditions (see [9]) and assumption simplification (7) are used. Then, 31 nonlinear equations consist of the resulting system of equations with 24 unknown variables to be solved. Using the simplified assumption (7), the system of equations is reduced to 20 equations with 24 unknowns and 4 degrees of freedom remaining. Solving the system and the solution family simultaneously in the form of a_{41}, a_{42}, a_{43} and c_4 gives the following:

$$\bar{a}_{21} = \frac{c_4^2}{2(4c_4-1)^2}\ , \bar{a}_{31} = -\frac{2(-71c_4^2+48c_4-16+20c_4^3)}{125c_4(10c_4^2-12c_4+3)},$$

$$\bar{a}_{32} = \frac{2[(-4+5c_4)(11c_4-4)(4c_4-1)}{125c_4(10c_4^2-12c_4+3)}$$

$$\bar{a}_{41} = \frac{30c_4^3-59c_4^2+40c_4-8}{4}, \bar{a}_{42} = -\frac{c_4(38c_4-59c_4^2-8+30\,30c_4^3)(4c_4-1)}{11c_4-4}$$

$$, \bar{a}_{43} = \frac{5c_4(38c_4-59c_4^2-8+30\,30c_4^3)(4c_4-1)}{4(11c_4-4)}, \qquad a_{21} = \frac{a_{41}+a_{42}+a_{43}}{(16c_4^2-8c_4+1)(4c_4-1)},$$

$$a_{41} = a_{41}\ , a_{42} = a_{42}\ , a_{43} = a_{43}\ ,$$

$$a_{31} = \frac{2(-50a_{41}c_4^2-226a_{43}c_4^3+20a_{42}c_4+108a_{43}c_4-16a_{43}+16c_4^2+87c_4^3}{625(10c_4^2-12c_4+3)(-1+2c_4)c_4^3}$$

$$+\frac{105a_{42}c_4^2+100a_{43}c_4^3 100a_{42}c_4^3+73c_4^5-110c_4^6}{625(10c_4^2-12c_4+3)(-1+2c_4)c_4^3}$$

$$a_{32} = \frac{2(11c_4-4)(-40c_4^5+62c_4^4-29c_4^3+4c_4^2+16a_{43}c_4+5a_{42}c_4-4a_{43}}{625(10c_4^2-12c_4+3)(-1+2c_4)c_4^3},$$

$$b_1' = \frac{2c_4^2+4c_4-1}{48c_4^2}, b_2' = \frac{(4c_4-1)^2(12c_4^2-7c_4+1)}{24c_4^2(-1+2c_4)(11c_4-4)}, b_3' = \frac{25(10c_4^2-12c_4+3)}{48(-4+5c_4)(11c_4-4)},$$

$$b_2' = \frac{(c_4-1)}{24c_4^2(-1+2c_4)(-4+5c_4)}, c_1 = 0, c_2 = \frac{c_4}{4c_4-1}, c_3 = \frac{4}{5},$$

$$b_1 = \frac{-17c_4^3+1056b_2c_4^3+120c_4^2-912b_2c_4^2-27c_4+192c_4b_2}{96c_4(4c_4-1)},$$

$$b_3 = \frac{5(72c_4^2-21c_4+2-240b_2c_4^2-80c_4^3+480b_2c_4^3}{(4c_4-1)^2(-4+5c_4)},$$

$$b_4 = \frac{-16c_4^2+8c_4-1+132b_2c_4^2-48c_4b_2}{(4c_4-1)^2(-4+5c_4)},$$

$$b_1'' = \frac{2c_4^2+4c_4+1}{48c_4^2},$$

$$b_2'' = \frac{(4c_4-1)^2(16c_4^2+8c_4-1)}{24c_4^2(-1+2c_4)(11c_4-4)},$$

$$b_3'' = \frac{125(10c_4^2-12c_4+3)}{48(-4+5c_4)(11c_4-4)},$$

$$b_4'' = \frac{1}{24c_4^2(-1+2c_4)(-4+5c_4)},$$

Letting $a_{41} = a_{42} = a_{43} = 0$ and $c_4 = \frac{2}{3}$, the local truncation error in one free parameter is given by:

$$\| \tau_g^{(5)} \|_2 = \frac{1}{18000}\sqrt{553025 - 879360 b_2 + 3391488 b_2^2}$$

By using the *minimize* command in Maple, $b_2 = 0.129642210144928$ was obtained, and the minimum error is 0.0391272028545436926. For the optimized value in fractional form, $b_2 = \frac{1}{10}$ was chosen. Finally, all the coefficients of four-stage fifth-order RKTG method denoted by RKTGD5 can be written as follows:

$$c_2 = \frac{2}{5}, c_3 = \frac{4}{5}, c_4 = \frac{2}{3}, \quad a_{21} = 0, a_{31} = \frac{4}{124}, a_{32} = \frac{4}{125}, \bar{a}_{21} = \frac{2}{25}, \bar{a}_{31} = \frac{4}{25},$$

$$\bar{a}_{32} = \frac{4}{25}, b_1 = \frac{19}{300}, b_3 = -\frac{1}{240}, b_4 = \frac{23}{400}$$

$$b_1' = \tfrac{23}{192}, b_2' = \tfrac{25}{64}, b_3' = \tfrac{25}{192}, \; b_4' = -\tfrac{9}{64}, b_1'' = \tfrac{23}{192}, b_2'' = \tfrac{125}{192}, b_3'' = \tfrac{125}{192}, b_4'' = -\tfrac{27}{64},$$

A three-stage (s=3) fourth-order (q=4) embedded formula may now be derived based on the above solution for values of A and c. Solving the third and fourth-order equations for v (see [9]), so that the resulting equation system consists of 2 nonlinear equations with 4 variable unknowns to be solved. Solving the method at the same time gives:

$$b_1 = b_1, b_2 = \frac{25}{96} + \frac{1}{2}b_3 - \frac{5}{2}b_1, b_3 = b_3, b_4 = \frac{3}{2}b_1 - \frac{3}{2}b_3 - \frac{3}{32}$$

Choosing $b_1 = \frac{1}{20}$, another free parameter b_3 was found by minimize error norm $\| \tau_g^{(4)} \|_2$.

where

$$\| \tau_g^{(4)} \|_2 = \frac{1}{3000}\sqrt{725 - 12800 b_3 + 6264 b_3^2}$$

Here, one free parameter b_3 did not appear in the solution but it appeared in the local truncation error. According to Dormand [11], The free b_3 parameter can be calculated by minimizing the local truncation error and obtaining $b_3 = \frac{1}{10}$by using Maple. For v', the equation of order-four were solved and simplifying assumption (7) was used. The simplifying assumption reduces the equation system to 3 nonlinear equations with 4 unknowns, simultaneously solving the system gives:

$$b_1 = b_1, b_2 = \frac{95}{96} - 5b_1, b_3 = -5b_1 + \frac{35}{48}, b_4 = 9b_1 - \frac{39}{32}$$

where

$$\| \tau_g^{(4)} \|_2 = \frac{1}{9000}\sqrt{155302 - 1405056 b_1 + 9326592 b_1^2}$$

It can be noticed that there is one free parameter b_1, using the minimize command in Maple, then b_1=0.0753252635046047 was obtained and for optimized value, $b_1 = \frac{7}{100}$ was chosen. While for *v*00, the equations until order four were solved, and using simplifying assumption to reduce the system of equations to 4 nonlinear equations with 4 unknowns; then $\hat{b}_i$ is the same as the fifth-order formula. Finally, all the coefficients of four-stage embedded RKTGD method denoted by RKTGD5(4) can be written as follows (see Table II):

Table II. The RKTGD5(4) Method.

0	0				0			0				
$\frac{2}{5}$	0	0	0	0	$\frac{2}{25}$	0	0	0				
$\frac{4}{5}$	$\frac{4}{125}$	$\frac{4}{125}$	0	0	$\frac{4}{25}$	$\frac{4}{25}$	0	0				
$\frac{2}{3}$	0	0	0	0	$\frac{2}{9}$	0	0	0				
	$\frac{19}{300}$	$\frac{1}{10}$	$-\frac{1}{240}$	$\frac{23}{400}$	$\frac{23}{192}$	$\frac{25}{64}$	$\frac{25}{192}$	$-\frac{9}{64}$	$\frac{23}{192}$	$\frac{125}{192}$	$\frac{125}{192}$	$-\frac{27}{64}$
	$\frac{1}{20}$	$\frac{89}{480}$	$\frac{1}{10}$	$-\frac{27}{160}$	$\frac{7}{100}$	$\frac{307}{480}$	$\frac{91}{240}$	$-\frac{471}{800}$	$\frac{23}{192}$	$\frac{125}{192}$	$\frac{125}{192}$	$-\frac{27}{64}$

5. Numerical Experiments

In this section, some of the issues involving $v''' = f(x, v, v')$ are tested. When the same set of problems are reduced to a system of first-order equations and solved using the existing RK pairs of the same order, comparisons are made between the numerical results and the results obtained.

- RKTGD4(3): In this paper, the Runge-Kutta type 4(3) pair derived.
- RKTGD5(4):In this paper, the Runge-Kutta type 5(4) pair derived.
- RK4(3)Z: 4(3) pair of Runge-Kutta, provided by Hairer et. al [18].
- RK4(3)M: Merson-derived pair type 4(3) of Runge-Kutta as in Hairer et. al [18].
- RK4(3)D: Dormand-derived Runge-Kutta Type 4(3) pair [11].
- RK4(3)F: Fehlberg-derived Runge-Kutta Type 4(3) pair [19].
- RKB5(4): Pair of Runge-Kutta 5(4) introduced in Butcher [20].
- RKF5(4): Fehlberg-derived Runge-Kutta 5(4) pair as given in [19].
- DOPRI5(4): Pair of Runge-Kutta 5(4) with FSAL properties obtained from Dormand and Prince [12].
-

Problem 1. (Homogeneous Linear Problem)

$y'''(x) = -y(x) + 2\,y'(x), y(0) = 0, y'(0) = 1, y''(0) = 1,$

Theoretical solution:

$$y(x) = 2e^{x} + (-1 - \tfrac{2}{5}\sqrt{5})\,e^{\frac{1}{2}(\sqrt{5}-1)x} + (-1 + \tfrac{2}{5}\sqrt{5})\,e^{-\frac{1}{2}(\sqrt{5}+1)x}.$$

Problem 2. (Linear System)

$$y_1'''(x) = \frac{1}{2}e^{4t}y_3(x)y_2'(x), \quad y_2'''(x) = \frac{8}{3}e^{2x}y_1(x)y_3'(x), \quad y_3'''(x) = 27y_2(x)y_1'(x)$$

$$y_1(0) = 1, y_1'(0) = -1, y_1''(0) = 1, \quad y_2(0) = 1, y_2'(0) = -2, y_2''(0) = 4, \quad y_3(0) = 1, y_3'(0) = -3, y_3''(0) = 9,$$

Theoretical solution:

$y_1(x) = e^{-x}$, $y_2(x) = e^{-2x}$, $y_3(x) = e^{-3x}$.

Problem 3. (Homogeneous Non-Linear Problem)

$$y'''(t) = \frac{3y'(x)}{4\big(y(x)\big)^{4}}$$

$$y(0) = 1, y'(0) = \tfrac{1}{2}\ , y''(0) = \tfrac{1}{4},$$

Theoretical solution:

$$y(x) = \sqrt{x+1}$$

Comparison between RKTGD4(3), RK4(3)Z, RK4(3)M, RK4(3)D and RK4(3)F with respect to problems 1 to 3 was made and results are displayed in Figures 1 to 3.

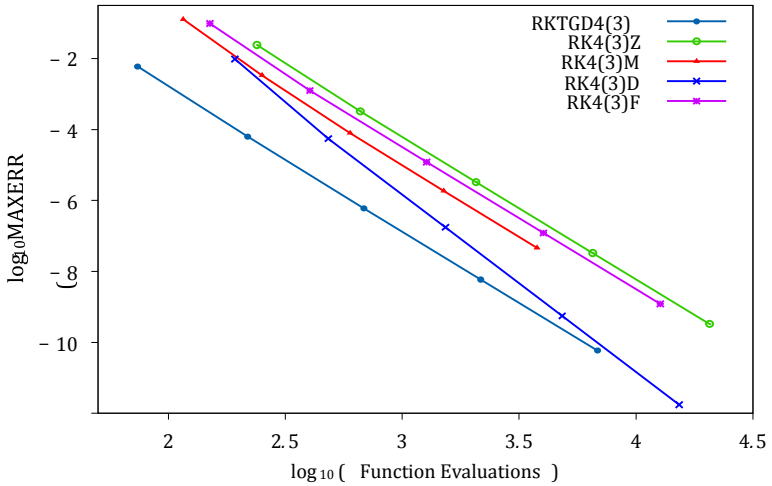

Figure 1. Comparison for RKTGD4(3), RK4(3)Z, RK4(3)M, RK4(3)D and RK4(3)F problem 1 with X_{end}=5

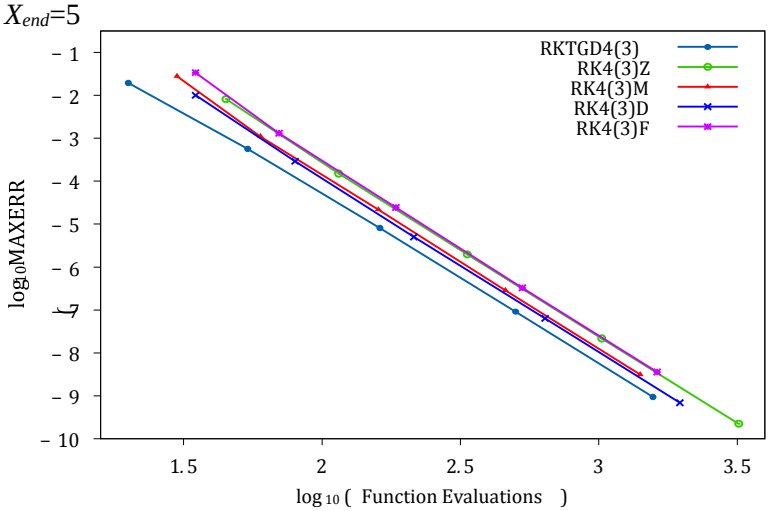

Figure 2. Comparison for RKTGD4(3), RK4(3)Z, RK4(3)M, RK4(3)D and RK4(3)F problem 2 with X_{end}=2

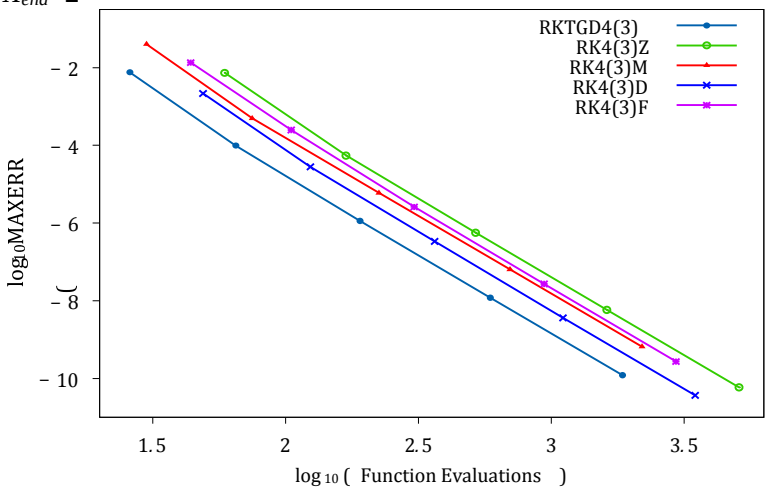

Figure 3. Comparison for RKTGD4(3), RK4(3)Z, RK4(3)M, RK4(3)D and RK4(3)F problem 3 with X_{end}=10

Comparison between RKTGD5(4), RK5(4)B, RK5(4)F, and DOPRI5(4) with respect to problems 1 to 3 was made and results are displayed in Figures 4 to 6.

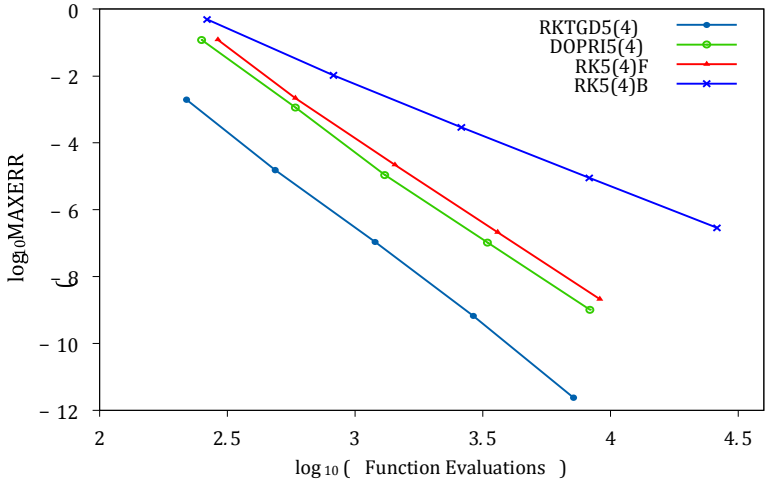

Figure 4. Comparison for RKTGD5(4), RK5(4)B, RK5(4)F, and DOPRI5(4) problem 1 with X_{end}=5

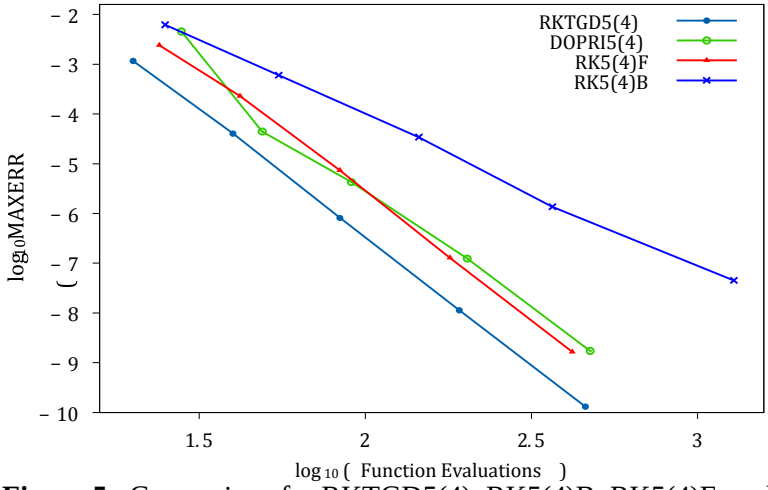

Figure 5. Comparison for RKTGD5(4), RK5(4)B, RK5(4)F, and DOPRI5(4) problem 2 with $X_{rnd} = 3$.

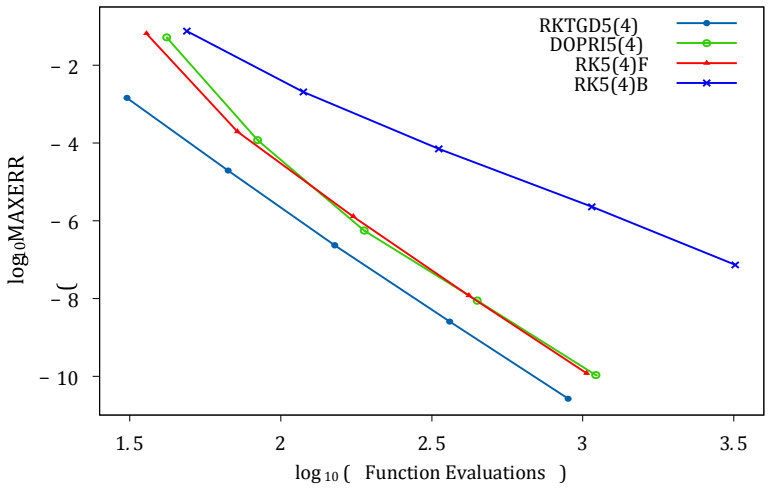

Figure 6. Comparison for RKTGD5(4), RK5(4)B, RK5(4)F, and DOPRI5(4) problem 3 with X_{end}=10.

6.Conclusion

Two pairs of embedded RKTGD methods for directly solving third-order ODEs using the variable step size codes have been suggested and discussed in this study. The methods are called, respectively, RKTGD4(3) and RKTGD5(4). Step-size codes of variables based on the methods were created and used to solve the third-order ODEs. The comparison was made with the Runge-Kutta methods of the current single step, as other direct methods are multi-step in nature. Numerical outcomes of the same RKTGD and RK pairs of the same order were also compared. The results showed that the RKTGD4(3) is more efficient than the Runge–Kutta 4(3) pairs like the RK4(3)Z method (Hairer et. al [18]), RK4(3)M (Merson [18]), RK4(3)D (Dormand [11]), and RK4(3)F (Fehlberg [19]) for all the problems tested. This new pair is more efficient for RKTGD5(4) compared to RK5(4)B (Butcher [20]), RK5(4)F (Fehlberg as in [19]), and RK5(4)D given by Dormand and Prince [12]. It has been shown from the numerical results that, compared to the existing embedded RK pairs of the same order in the literature, the new methods are more efficient. Hence, it can be concluded that in solving third order ODEs, the RKTGD pairs are computationally more efficient.

References

[1] T G Myers 1998 Thin films with high surface tension *SIAM Rev* **40** (3) pp 441-462
[2] E Momoniat, Symmetries 2009 first integrals and phase planes of a third-order ordinary differential equation from thin film flow *Math. Comput. Model* **49** (1-2) pp 215-225
[3] B R Duffy, S K Wilson 1997 A third-order differential equation arising in thin-film flows and relevant to Tanner's law *Math. Lett.* **10** (3) pp 63-68
[4] N Waeleh, Z A Majid, F Ismail 2011 A new algorithm for solving higher order IVPs of ODEs Appl. *Math. Sci.* **5** (56) pp 2795-2805
[5] D O Awoyemi and O M Idowu 2005 A class of hybrid collocation methods for third-order ordinary differential equations *International Journal of Computer Mathematics* **82** (10) pp1287-1293
[6] F A Fawzi, N Senu, F Ismail and Z A Majid 2018 A New Integrator of Runge-Kutta Type for Directly Solving General Third-order ODEswith Application to Thin Film Flow Problem *Applied Mathematics & Information Sciences* **12** (4) pp 775-784
[7] S N Jator 2011 Solving second order initial value problems by a hybrid multi-step method without predictors *Appl. Math. Comput* **217** (8) pp 4036–4046
[8] F A F Alshareeda 2017 *Runge-Kutta type methods for solving third-order ordinary differential equations and first-order oscillatory problems* Ph.D. Thesis Universiti Putra Malaysia

[9] F A Fawzi and N Senu and F Ismail 2018 An efficient of direct integrator of Runge-Kutta type method for solving y''' = f(x,y,y') with application to thin film flow problem *international journal of pure and applied mathematics* **120** pp 27-50
[10] W Gander and D Gruntz 1999 Derivation of numerical methods using computer algebra *SIAM Review* **41** (3) pp 577-593
[11] J R Dormand 1996 *Numerical Methods for Differential Equations* A Computational Approach, CRC Press, Boca Raton, Fla, USA
[12] J R Dormand, P J Prince1980 A family of embedded Runge-Kutta formulae *J. Comput. Appl. Math* **6** (1) pp 19-26
[13] F A Fawzi, N Senu, F Ismail and Z A Majid 2016 An embedded 6 (5) pair of explicit Runge-Kutta method for periodic ivps *Far East Journal of Mathematical Sciences* **100** (11) pp 1841
[14] J R Dormand, P J Prince 1981 High order embedded Runge-Kutta formulae *J. Comput. Appl. Math* **7** (1) pp 67-75
[15] N Senu, M Mechee, F Ismail and Z Siri 2014 Embedded explicit Runge-Kutta type methods for directly solving special third order differential equations y''' = f(x,y) *Applied Mathematics and Computation* **240** (2014) pp 281-293
[16] M El-Mikkawy, R El-Desouky 2003 A new optimized non-FSAL embedded Runge-Kutta-Nyström algorithm of orders 6 and 4 in six stages *Applied Mathematics and Computation* **145** pp 33-43
[17] N Senu, M Suleiman, F Ismail 2009 An embedded explicit Runge-Kutta-Nyström method for solving oscillatory problems *Physica Scripta* **80** pp 015005
[18] E Hairer, S P Nørsett, G Wanner 1993 *Solving Ordinary Differential Equations I: Nonstiff Problem* **8** Springer Berlin Germany 2nd edition
[19] E Fehlberg 1969 *Lower order classical Runge-Kutta formulas with step-size control and their application to some heat transfer problems* NASATR R-315
[20] J C Butcher 2008 *Numerical Methods for Ordinary Differential Equations* John Wiley & Sons Chichester UK 2nd edition

Estimation the Shape Parameter for Power Function Distribution

Estimation the Shape Parameter for Power Function Distribution

Alaa M. Hamad[1], Bareq B. Selman[2]

[1]Department of Mathematics, College of Education for Pure Sciences Ibn-Al-Haitham University of Baghdad, Iraq
[2] Ministry of education, Directorate of education, Baghdad, Al-rasafa-3, Iraq

E-mail: alaa073@yahoo.com

Abstract. In the paper estimate of the shape parameter for power function distribution was proposed. For different sample sizes (small, medium, and large). Using different methods, Maximum likelihood method, Moment method, Shrinkage methods, and Least square method. mean square error (MSE) was implemented as an indicator of performance and comparisons of performance have been carried out through data analysis and computer simulation between the estimation methods according to the applied indicator. It was observed from the results that the shrinkage method (constant weight factor (sh_2)) estimates for the shape parameter are the best in performance for each case.

1. Introduction

The power function distribution an important distribution for it is used in daily life and most distributions such as Rayleigh distribution, gamma distribution, and Weibull distribution has a relationship with the power function distribution, It has an inverse relationship with Pareto distribution the negative moments for Pareto distribution are simply the moment for the power function distribution [1][2]. The first to use the power function distribution. Malik H J in 1967, found a precise expression of the moment for power function distribution and he studied the exact moment for power function distribution [7]. The power function distribution is flexible distribution and used in many applications such as engineering, economics, natural sciences, and applied mathematics, The power function distribution is a special case for Pareto family distributions[3][4]. The problem of estimating unknown parameters in statistical distribution is one of the most important problems. [10]. The reliability function, which is a monotonically decreasing function of the lifetime, the study of reliability is an important task to develop future plans to develop performance and quality for the equipment and estimate the reliability system in stress-strength when follows power function for different shape parameter [12].

The aim of this study is to comparisons of performance the shape parameter (α) based on power function distribution (PD) have been carried out through data analysis and computer simulation between among four estimation methods, Maximum likelihood method (MLE), Moment method(MOM), Shrinkage methods(SH) and Least square method(LS) according to the applied indicator. and obtain the best using (MSE) and find the best method.

2. Methodology

Let x be random variable from power distribution with shape parameter (α) and scale parameter (γ); then the probability density function (pdf) is defined as following [3]

$$f(x,\alpha,\gamma) = \alpha\gamma^{\alpha}x^{\alpha-1}, \qquad 0 < x < \gamma^{-1} \tag{1}$$

When α and γ are often called the shape and scale parameters
While the cumulative distribution function (c.d.f) for power function distribution

$$F(x,\alpha,\gamma) = x^{\alpha}\gamma^{\alpha}, \qquad 0 < x < \gamma^{-1} \tag{2}$$

And as a special case when $\gamma = 1$ the (p.d.f) for power function distribution will be

$$f(x,\alpha) = \alpha x^{\alpha-1}, \qquad 0 < x < 1 \tag{3}$$

And the (c.d.f) for power function distribution become

$$F(x,\alpha) = x^{\alpha}, \qquad 0 < x < 1 \tag{4}$$

For estimation of shape parameter for power function distribution, we need to find the random variable of cumulative distribution function then

$$x = [f(x)]^{\frac{1}{\alpha}} \tag{5}$$

3. Estimation methods of the shape parameter of power function distribution

3.1 Maximum likelihood method (MLE)[8][11]

The Maximum likelihood method is one of the most reliable and popular methods using to obtaining point estimation for the parameter in all distributions, The Maximum likelihood method has many excellent statistical properties, so the statisticians prefer the MLE for other methods, Let $x_1, x_2, \ldots\ldots x_n$ be a random sample of $pow\ (\alpha,1)$. The Maximum likelihood for α

$$L = L(\alpha_i, x_i) = \prod_{i=1}^{n} f(x_i)$$

$$L = \alpha^n \prod_{i=1}^{n} x_i^{\alpha-1} \tag{6}$$

Taking the logarithm of the likelihood, yields

$$Ln(L) = nln\ \alpha + (\alpha - 1)\sum_{i=1}^{n} lnx_i \tag{7}$$

The partial derivation for the equation with respect to the shape parameter and equating the result to zero given as follows.

$$\hat{\alpha}_{mle} = \frac{-n}{\sum_{i=1}^{n} lnx_i} \tag{8}$$

3.2 Moment method (MOM)

In this section, we estimate the shape parameter for power function distribution by using the simplest technique commonly is the moment method, the general idea for moment method to determine the population moment $M_r = E(x^r)$ [9]. Let x pow(α)

$$E(x) = \frac{\alpha}{\alpha + 1} \tag{9}$$

We equate the first moment with $\frac{\sum_{i=1}^{n} x_i}{n}$ as below

$$\frac{\alpha}{\alpha + 1} = \frac{\sum_{i=1}^{n} x_i}{n} \tag{10}$$

By solving equation (7) we get

$$\hat{\alpha}_{mom} = \frac{\sum_{i=1}^{n} x_i}{n - \sum_{i=1}^{n} x_i} \tag{11}$$

3.3 Least square method (LS) [4][5]

The least squares method can be applied in reliability engineering mathematics problem, we assume that there is a linear relationship between two variables.

$$F(x_i) = x_i^{\alpha}$$

$$x_i = [F(x_i)]^{\frac{1}{\alpha}} \tag{12}$$

Take logarithm for both sides

$$lnx_i = \frac{1}{\alpha} ln\, F(x_i) \tag{13}$$

$$y = ax + b$$

$$x = \ln F(x_i)$$

$$a = \frac{\sum_{i=1}^{n} x_i y_i - \frac{\sum_{i=1}^{n} x_i y_i}{n}}{\sum_{i=1}^{n} x_i^2 - \frac{[\sum_{i=1}^{n} x_i]^2}{n}} \tag{14}$$

$$\hat{\alpha}_{Ls} = \frac{\sum_{i=1}^{n} [ln\, F(x_i)]^2 - \frac{[\sum_{i=1}^{n} ln\, F(x_i)]^2}{n}}{\sum_{i=1}^{n} ln\, F(x_i)\, ln\, x_i - \frac{\sum_{i=1}^{n} ln\, F(x_i)\, ln\, x_i}{n}} \tag{15}$$

3.4 Shrinkage estimator (SH) [3]

In 1968, Thompson introduced the basic reason for use prior estimation. He suggested the problem of shrink in the usual estimator $\hat{\alpha}$ of parameter α toward prior information. The shrinkage estimation method is to use α as the initial value prior information α_0 from the past and usual estimator $\hat{\alpha}_{ub}$ through consideration them by shrinkage- weight factor $\emptyset(\hat{\alpha})$ where $0<\emptyset(\hat{\alpha})<1$ as below

$$\hat{\alpha}_{sh} = \emptyset(\hat{\alpha})\alpha_{ub} + [1 - \emptyset(\hat{\alpha})]\alpha_0 \tag{16}$$

Now, to find α_{ub} from $\hat{\alpha}_{mle}$

$$\hat{\alpha}_{mle} = \frac{-n}{\sum_{i=1}^{n} \ln x_i}$$

$$x\ pow(\alpha)$$

$$z = \sum_{i=1}^{n} \ln x_i$$

$$z\ IG(n, 1)$$

$$\frac{n}{n-1}\hat{\alpha}_{mle} \neq \hat{\alpha}_{mle}$$
$$\alpha_{ub} = \frac{n-1}{n}\hat{\alpha}_{mle}$$
$$\alpha_{ub} = \frac{-(n-1)}{\sum_{i=1}^{n} ln\, x_i} \quad (17)$$

3.4.1 shrinkage- weight function(sh_1)[3][6]

In this section, the shrinkage- weight factor will be assumed as a function of n, $\emptyset(\hat{\alpha}) = \left|\frac{\sin n}{n}\right|$ Put in (10), will be

$$\hat{\alpha}_{sh1} = \left|\frac{sin\, n}{n}\right| \alpha_{ub} + (1 - \left|\frac{sin\, n}{n}\right|)\alpha_0 \quad (18)$$

3.4.2 constant- shrinkage weight factor (sh_2)[3][6]

In this section, assumed $\emptyset(\hat{\alpha}) = K$ the constant- shrinkage weight factor and K=0.001, 1-K=0.999 put in (10), will be

$$\hat{\alpha}_{sh2} = K\alpha_{ub} + (1-K)\alpha_0 \quad (19)$$

3.4.3 Beta- shrinkage weight factor (sh_3)[3][6]

In this section,$\emptyset(\hat{\alpha}) = \beta(1,n)$ the Beta- shrinkage weight factor, put in(10), will be

$$\hat{\alpha}_{sh3} = \beta(1,n)\alpha_{ub} + [1 - \beta(1,n)]\alpha_0 \quad (20)$$

4. Simulation study

Let x according to the uniform distribution on the interval (0,1)

$F(x_i) = x_i^{\alpha}$

$x_i = [F(x_i)]^{\frac{1}{\alpha}}, i = 1,2,\dots,n$

Step 1. By equation (8) calculated $\hat{\alpha}_{mle}$

Step 2. by equations (11) calculated $\hat{\alpha}_{mom}$.

Step 3. by equations (15) calculated $\hat{\alpha}_{Ls}$.

Step 4. by equations (18),(19), and (20), calculated $\hat{\alpha}_{shi}$ for $i = 1,2,3$

Step 5. by $MSE(\gamma) = \frac{\sum_{i=1}^{n}(\gamma_i - \gamma)^2}{n}$ calculated MSE for all method and cases

And by using random sample n=30,50,100.

We obtain the result shown in the following tables

Table 1:Estimation of the shape parameter of (PD) when alpha= 1

n	Mle	Mom	Sh1	Sh2	Sh3	Ls
30	1.028525	1.016048	0.934320	0.998005	0.933525	1.027646
50	1.019068	1.014803	0.989511	0.998001	0.960026	1.025030
100	1.007879	1.003996	0.989883	0.998002	0.980021	1.009319

Table 2: Shown the MSE values when alpha= 1

n	mse_{mle}	mse_{mom}	mse_{sh1}	mse_{sh2}	mse_{sh3}	mse_{Ls}	Best
30	0.039919072	0.047077758	0.000039626	0.000000036	0.000040592	0.064047639	mse_{sh2}
50	0.022481145	0.028972695	0.000000584	0.000000021	0.000008497	0.044030383	mse_{sh2}
100	0.010430490	0.013606705	0.000000260	0.000000010	0.000001016	0.018322772	mse_{sh2}

Table 3: Table 1:Estimation of shape parameter of (PD) when alpha= 2

n	Mle	Mom	Sh1	Sh2	Sh3	Ls
30	2.058343	2.037616	1.868600	1.996010	1.867008	2.038601

50	2.038136	2.031656	1.979023	1.996002	1.920052	2.050061
100	2.015758	2.010141	1.979767	1.996004	1.960043	2.018639

Table 4: Shown the MSE values when alpha= 2

n	mse_{mle}	mse_{mom}	mse_{sh1}	mse_{sh2}	mse_{sh3}	mse_{Ls}	Best
30	0.159676288	0.166909305	0.000158506	0.000000146	0.000162370	0.256190559	mse_{sh2}
50	0.089924580	0.099449080	0.000002339	0.000000084	0.000033989	0.176121532	mse_{sh2}
100	0.041721962	0.046466959	0.000001042	0.000000040	0.000004066	0.073291089	mse_{sh2}

Table 5: Estimation of the shape parameter of (PD) when alpha= 3

n	Mle	Mom	Sh1	Sh2	Sh3	Ls
30	3.087514	3.064052	2.802900	2.994015	2.800513	3.057902
50	3.057204	3.049277	2.968535	2.994003	2.880078	3.075092
100	3.023638	3.017076	2.969651	2.994006	2.940065	3.027959

Table 6: Shown the MSE values when alpha= 3

n	mse_{mle}	mse_{mom}	mse_{sh1}	mse_{sh2}	mse_{sh3}	mse_{Ls}	Best
30	0.359271648	0.364074497	0.000356640	0.000000328	0.000365333	0.576428759	mse_{sh2}
50	0.202330306	0.213524215	0.000005264	0.000000191	0.000076476	0.396273448	mse_{sh2}
100	0.093874415	0.099565926	0.000002346	0.000000091	0.000009150	0.164904951	mse_{sh2}

5. Numerical result and conclusion

Consequently, for practical work and taking the mean square error as the indicator of preference between the different estimator methods, the following result obtained

1. for the conventional methods and for different sample size the following results are obtained:-

- Small sample size(n=30)
  i. When alpha= 1, Sh2 estimator method was given the best results, then his methods Sh1, Sh3, MLE, MOM, and LS respectively.
  ii. When alpha= 2, Sh2 estimator method was given the best results, then his methods Sh1, Sh3, MLE, MOM, and LS respectively.
  iii. When alpha= 3, Sh2 estimator method was given the best results, then his methods Sh1, Sh3, MLE, MOM, and LS respectively.
- Medium sample size(n=50)
  i. When alpha= 1, Sh2 estimator method was given the best results, then his methods Sh1, Sh3, MLE, MOM, and LS respectively.
  ii. When alpha= 2, Sh2 estimator method was given the best results, then his methods Sh1, Sh3, MLE, MOM, and LS respectively.
  iii. When alpha= 3, Sh2 estimator method was given the best results, then his methods Sh1, Sh3, MLE, MOM, and LS respectively.
- Large sample size(n=100)
  i. When alpha= 1, Sh2 estimator method was given the best results, then his methods Sh1, Sh3, MLE, MOM, and LS respectively.
  ii. When alpha= 2, Sh2 estimator method was given the best results, then his methods Sh1, Sh3, MLE, MOM, and LS respectively.
  iii. When alpha= 3, Sh2 estimator method was given the best results, then his methods Sh1, Sh3, MLE, MOM, and LS respectively.

2. The result of the simulation (estimate the shape parameter) of power function distribution for studied methods for different sample sizes (n=30, 50, 100). From tables, it is clear that, the shrinkage (constant weight factor (sh_2)) estimates for the α shape parameter, are the best in performance for each case. Then his first shrinkage way (sh_1) comes after.

3. From the tables for each (n), we conclude that the suggested Shrinkage method has a good performance based on constant - weight factor (sh_2) has the minimum mean square error (MSE) in the majority of cases.

References

[1] Al Mutaira A O 2017 Bayesian Estimation using (linex) for generalized power function distribution lobachevskil *journal of mathematics* **39**(3) 297-303
[2] Shakee M, Haq M A, Hussain I, Abdulhamid M, and Faisal M 2016 Comparison of two new Rotust parameter estimation methods for the power function distribution *Plos ONE journal doi10* **13**(71)1-11
[3] Bareq B S, Alaa M H, and Adel K H 2019 on reliability estimation of stress-strength (S-S) modified exponentiated Lomax distribution *journal of mechanics continue and mathematical science 14*(4)387-405
[4] Zaka A, Akhter A S, and Farooq N 2014 Methods of Estimating the parameters of power function distribution *Journal of statistics* **21** 90-102
[5] Raqab M Z and Kundu D 2005 Generalized Rayleigh Distribution Deferent Methods of Estimations *Journal of computational statistics and data analysis* **49** 187-200
[6] Salman A N, Alaa M H, and Ahmed I A N 2016 Pretest single stage shrinkage estimator the shape parameter of the power function distribution *international journal of mathematics trends and technology (IJMTI)* **36** (1) 56-59
[7] Malik H J 1967 Exact moments of order statistics from a power function distribution *Scandinavian Actuarial journal* **1**(2) 64-69
[8] Rahman H, Roy K M, and Atikur R B 2012 Bayes Estimation under Conjugate Prior for the case of Power Function Distribution *American journal of mathematics and statistics* **2**(3) 44-48
[9] Salman A N and Taha A T 2013 Estimate the parameters and related probability function for data of the patients of lymph glands cancer via birnbaum–saunders distribution *MSc Thesis* Baghdad university
[10] Leo O O and Romanus O O 2018 parameter estimation of power lomax distribution based on type II progressively hybrid censoring scheme *journal of appled mathematical sciences 12*(18) 879-891
[11] Dhanya M and Jeevavand E S 2017 Stress-Strength Reliability of Power Function Distribution Based on Records *Journal of statistics Application Probability* **7**(1)39-48
[12] Al-kadim K A and Hussein N A 2014 Comparison between five estimation methods for reliability function of weighted Rayleigh distribution by using simulation *Mathematical Theory and Modeling* **4** (6)123-137

Parameters estimation of new mixed Weibull Rayleigh and Exponential distribution

Parameters estimation of new mixed Weibull Rayleigh and Exponential distribution

Jassim N. Hussain[1] , Ashraf Mohammed Shareef[2]

[1]Faculty of Nursing, National University of Science and Technology, Iraq
[2]Statistics Department, Administration and Economics College, Kerbala University, Iraq

E-mail: jasim.nasir@uokerbala.edu.iq

Abstract. A new idea of mixing was introduced in this paper. Mixing parameters; p_i where $0 \leq p_i \leq 1$ and $\sum_{i=1}^{n} p_i = 1$ are used to find a new distribution from mixing some distributions. Therefore, we can get many mixed distributions with several parameters. Three distributions Weibull, Rayleigh, and Exponential are mixed to get a new distribution which is more flexible than these distributions. The mixed distribution with a new parameter is representing the ratio of contribution of each of these distributions which are mixed. Several values of the mixing parameter were taken, and the properties of the mixed distribution were found. Two methods (MLE and OLS) of estimation are used to estimate the parameters of the new distribution. Simulation studies are used to prove the properties of new distribution and to apply the estimation method to estimate the parameters of new distribution.

1. Introduction

Recent studies are looking at finding mixed distributions resulting from merging previous distributions to obtain new distributions that have benefits in scientific applications, including discrete and continuous distributions. The new distributions are more flexible than the previous distributions and have new characteristics. As it is known that Weibull and Raleigh distributions have good applications in the field of industries; meanwhile, Exponential distribution has good applications in the field of lifetime analysis. Therefore, the goal of this research, is to propose a new idea, which is how to find a new distribution resulting from integrating of three distributions (Weibull, Raleigh and Exponential), each distribution consists of number of parameters.

Consequently, the new distribution has number of parameters greater than these distributions and it will be more flexible than them in the statistical work. Several studies about mixing distributions introduced development in this field. Afify [1] worked on mixing Rayleigh distribution and introduced different methods to estimate the parameters of new distribution. El-Bassiouny, et al., [2] worked on mixing Exponential, generalized Weibull and Gomperts distributions and introduced different methods of estimation of parameters. Cheema and Aslam [3] worked on three components mixing of Exponential-Weibull distributions and introduced Bayesian method to estimate the parameters of the new distribution by using different loss function and simulation studies. Aslam, et at., [4] worked on two components mixing of transmuted Pareto distribution and introduced properties and apply the estimation under Bayesian framework. Berchtod [5] worked on mixing transition distribution model and introduce E.M algorithm simulation to estimate the parameters.

The plan of this study is, Section two devoted to present the methodology of mixing the distributions; Section three consists of estimation methods; Section four devoted to present the simulation studies to estimate the parameters of new distribution, Section five consists of the discussion of the results; the important conclusions are the subject of the last section. Therefore, how to get the new distribution from mixing the other distributions is the subject of the next section.

2. Methodology

Let x be random variable from Weibull distribution with shape parameter (k) and scale parameter (θ); then the probability density function (pdf) is defined as in equation (1)[3,6,7]:

$$f_W(x) = \frac{k}{\theta}\ x^{k-1}\ e^{-x^k/\theta} \qquad 0 < x < \infty \tag{1}$$

Also, let another random variable $y = x$ from Rayleigh distribution with scale parameter (θ), then the (pdf) is defined as in equation (2)[1]:

$$f_R(x) = \frac{2}{\theta}\ x\ e^{-x^2/\theta} \qquad 0 < x < \infty \tag{2}$$

and another random variable $z = x$ Exponential distribution with scale parameter (θ); then the (pdf) is defined as in equation (3)[8,9,10,]:

$$f_E(x) = \theta\ e^{-\theta x} \qquad 0 < x < \infty \tag{3}$$

Consequently, the pdf of the new distribution can be get it from mixing the pdf's in Eq.'s (1), and (3) by applying the following proportion rule under the conditional $p_1 + p_2 + p_3 = 1$ [2,10,6] :

$$(p_1 = \frac{\beta}{2\beta+1}, p_2 = \frac{\beta}{2\beta+1}, p_3 = \frac{1}{2\beta+1})$$

$$\therefore f_{WRE}(x,k,\theta) = \frac{\beta}{2\beta+1} f_W(x) + \frac{\beta}{2\beta+1} f_R(x) + \frac{1}{2\beta+1} f_E(x)$$

$$f_{WRE}(x,k,\theta) = \frac{\beta}{2\beta+1}\frac{k}{\theta}\ x^{k-1}\ e^{-x^k/\theta} + \frac{\beta}{2\beta+1}\frac{2}{\theta}\ x\ e^{-x^2/\theta} + \frac{\beta}{2\beta+1}\theta e^{-\theta x} \tag{4}$$

$$0 \ \le x\ \le \infty \quad , \beta \ge -1\ ,\ \ k\ , \theta, \ge 0$$

$f_{WRE}(x,\beta,k,\theta)$ represents the new pdf of mixed distribution from (Weibull, Rayleigh and Exponential) distributions with three parameters (k) shape parameter,(θ) scale parameter and (β) is a mixing parameter.

The cumulative distribution function (cdf) corresponding to pdf in equation (5) is:

$$F_{WRE}(x\ ,\beta\ ,\theta\ ,\ \ k) = \ \ p_r(\ X \le x)$$

$$F_{WRE}(x) = \int_0^x f(u)du$$

$$F_{WRE}(x) = 1 - \left(\frac{1}{2\beta+1}\left(\beta\ e^{\frac{-x^k}{\theta}} + \beta e^{\frac{-x^2}{\theta}} + \ e^{-\theta x} \right) \right) \tag{5}$$

The new distribution is mixed distribution of (Weibull, Rayleigh and Exponential) and can be derived the parameter of new distribution are $\beta\ ,\theta\ ,\ \ k$ from $p.d.f$ where

θ Is the scale parameter

k Is the shape parameter

β Is mixed proportion parameter

the other characteristic follow

The mean is $E(x)\ = \int_0^\infty x\ f_{WRE}(x)dx$

$$E(x)\ = \frac{\beta\theta^{\frac{1}{k}}}{2\beta+1}\ \Gamma\left(1+\frac{1}{k}\right) + \frac{\beta\theta^{\frac{1}{2}}\sqrt{\pi}}{2(2\beta+1)}\ + \frac{1}{(2\beta+1)\theta}$$

The variance is $var(x) = E(X^2) - (E(X))^2$

$$var(x) = \frac{\beta\theta^{\frac{2}{k}}}{2\beta+1}\ \Gamma\left(1+\frac{2}{k}\right) + \frac{\beta\theta^{\frac{1}{2}}}{2\beta+1}\ + \frac{2}{(2\beta+1)\theta^2} - \frac{\beta\theta^{\frac{1}{k}}}{2\beta+1}\ \Gamma\left(1+\frac{1}{k}\right) - \frac{\beta\theta^{\frac{1}{2}}\sqrt{\pi}}{2(2\beta+1)} - \frac{1}{(2\beta+1)\theta}$$

Also, we can derive the function of the Reliability and hazard function from the new distribution.

Meanwhile, the Reliability function is:

$$R(t) = 1 - F(x)$$

$$R(t) = \frac{1}{2\beta+1}\left(\beta e^{\frac{-x^K}{\theta}} + \beta\, e^{\frac{-x^2}{\theta}} + e^{-\theta x} \right) \tag{6}$$

and the hazard rate function:

$$\mathrm{h(t)} = \frac{\mathrm{f(t)}}{\mathrm{R(t)}},$$

$$h(t) = \frac{\left(\frac{\beta k}{\theta} x^{k-1} e^{\frac{-x^k}{\theta}} + \frac{2\beta}{\theta} x\, e^{\frac{-x^2}{\theta}} + \theta e^{-\theta x} \right)}{\left(\beta e^{\frac{-xk}{\theta}} + \beta\, e^{\frac{-x^2}{\theta}} + e^{-\theta x} \right)} \tag{7}$$

3. Estimation methods

In this section, two methods of estimation are presented which will be used to estimate the parameters of the new distribution (β, θ, k). These methods are maximum likelihood (MEL) and ordinary least square (OLS) which are discussed in the following subsections.

3.1 Maximum Likelihood Estimation (MLE) method [9]

This method of estimation depends on maximizing the pdf estimation:

$$L = f(x_1, x_2, \dots, x_n, \theta) = \prod_{i=1}^{n} f(x_i, \theta)$$

$$L = \prod_{i=1}^{n} \left[\frac{\beta K x_i^{K-1}}{(2\beta+1)\theta}\ e^{\frac{-x_i^K}{\theta}} + \frac{2\beta x_i}{(2\beta+1)\theta}\ e^{\frac{-x_i^2}{\theta}} + \frac{\theta}{2\beta+1}\ e^{-\theta x_i} \right] \tag{8}$$

$$ln(L) = \sum_{i=1}^{n} ln \left[\frac{\beta K x_i^{K-1}}{(2\beta+1)\theta}\ e^{\frac{-x_i^K}{\theta}} + \frac{2\beta x_i}{(2\beta+1)\theta}\ e^{\frac{-x_i^2}{\theta}} + \frac{\theta}{2\beta+1}\ e^{-\theta x_i} \right]$$

$$\frac{\partial ln\,(L)}{\partial k} = \sum_{i=1}^{n} \frac{\frac{\beta}{(2\beta+1)\theta}\left[x_i^{k-1} e^{-\frac{x_i^k}{\theta}} + k x_i^{K-1} ln(x_i)\, e^{-\frac{x_i^k}{\theta}} - x_i^{k-1}\ \frac{k}{\theta} x_i^k\ e^{-\frac{x_i^k}{\theta}} ln(x_i) \right]}{\left[\frac{\beta K x_i^{K-1}}{(2\beta+1)\theta}\ e^{\frac{-x_i^K}{\theta}} + \frac{2\beta x_i}{(2\beta+1)\theta}\ e^{\frac{-x_i^2}{\theta}} + \frac{\theta}{2\beta+1} e^{-\theta x_i} \right]} \tag{9}$$

$$\frac{\partial ln(L)}{\partial \theta} = \sum_{i=1}^{n} \frac{\left[\frac{\beta K x_i^{K-1}}{2\beta+1} * \left(\frac{e^{\frac{-x_i^K}{\theta}} \frac{x_i^k}{\theta} - e^{\frac{-x_i^K}{\theta}}}{\theta^2} \right) \right] + \left[\frac{2\beta x_i}{(2\beta+1)} * \left(\frac{e^{\frac{-x_i^2}{\theta}} \frac{x_i^2}{\theta} - e^{\frac{-x_i^2}{\theta}}}{\theta^2} \right) \right] + \left[\frac{\theta}{2\beta+1} * \left(e^{-\theta x_i} - \theta x_i e^{-\theta x_i} \right) \right]}{\left[\frac{\beta K x_i^{K-1}}{(2\beta+1)\theta}\ e^{\frac{-x_i^K}{\theta}} + \frac{2\beta x_i}{(2\beta+1)\theta}\ e^{\frac{-x_i^2}{\theta}} + \frac{\theta}{2\beta+1} e^{-\theta x_i} \right]}$$

$$\frac{\partial ln(L)}{\partial \beta} = \sum_{i=1}^{n} \frac{\left[\frac{k\, x_i^{k-1} e^{\frac{-x_i^K}{\theta}}}{\frac{\theta}{(2\beta+1)^2}} \right] + \left[\frac{2x_i e^{\frac{-x_i^2}{\theta}}}{\frac{\theta}{(2\beta+1)^2}} \right] - \left[\frac{2\theta e^{-\theta x_i}}{(2\beta+1)^2} \right]}{\left[\frac{\beta K x_i^{K-1}}{(2\beta+1)\theta}\ e^{\frac{-x_i^K}{\theta}} + \frac{2\beta x_i}{(2\beta+1)\theta}\ e^{\frac{-x_i^2}{\theta}} + \frac{\theta}{2\beta+1} e^{-\theta x_i} \right]} \tag{10}$$

Where we notice that equations (9), (10) and (11) are non-linear equations, so it is difficult to find them, so we will use one of the numerical methods such as ***F-solve*** method to estimator the parameter

3.2 Ordinary Least Square (OLS) method [6]

This method depends on Minimizing the sum of squares of random errors and can be define mathematically as follows:

$$OLS = \sum_{i=1}^{n}\left[\left(\frac{i}{n+1}\right) - F(x)\right]^2$$

Note that $\left(\frac{i}{n+1}\right)$ is the amount of non-parametric

$$OLS = \sum_{i=1}^{n}\left[\left(\frac{i}{n+1}\right) - \left(1 + \frac{\beta}{2\beta+1}\, e^{\frac{-x^K}{\theta}} + \frac{\beta}{2\beta+1}\, e^{\frac{-x^2}{\theta}} + \frac{1}{2\beta+1}\, e^{-\theta x}\right)\right]^2$$

$$take\ the\ \frac{\partial OLS}{\partial \theta} = 0$$

$$\frac{\partial OLS}{\partial \vartheta} = 2\sum_{i=1}^{n}\left[\left(\frac{i}{n+1}\right) - \left(1 + \frac{\beta}{2\beta+1}\, e^{\frac{-x_i{}^k}{\theta}} + \frac{\beta}{2\beta+1}\, e^{\frac{-x_i{}^2}{\theta}} + \frac{1}{2\beta+1}\, e^{-\theta x_i}\right)\right] * \left[\left(\frac{-\beta}{2\beta+1} * \frac{x_i{}^k}{\theta^2} * e^{\frac{-x_i{}^k}{\theta}}\right) - \left(\frac{\beta}{2\beta+1} * \frac{x_i{}^2}{\theta^2} * e^{\frac{-x_i{}^2}{\theta}}\right) + \left(\frac{x}{2\beta+1} * e^{-\theta x_i}\right)\right] = 0 \quad (12)$$

$$take\ the\ \frac{\partial OLS}{\partial k} = 0$$

$$\frac{\partial OLS}{\partial k} = 2\sum_{i=1}^{n}\left[\left(\frac{i}{n+1}\right) - \left(1 + \frac{\beta}{2\beta+1} * e^{\frac{-x_i{}^k}{\theta}} + \frac{\beta}{2\beta+1} * e^{\frac{-x_i{}^2}{\theta}} + \frac{1}{2\beta+1} * e^{-\theta x_i}\right)\right] * \left(\frac{-\beta}{2\beta+1}\left(e^{\frac{-x_i{}^k}{\theta}} * \frac{x_i{}^K}{\theta} * ln\, x_i\right)\right) = 0 \quad (11)$$

$$take\ the\ \frac{\partial OLS}{\partial \beta} = 0$$

$$\frac{\partial OLS}{\partial \beta} = 2\sum_{i=1}^{n}\left[\left(\frac{i}{n+1}\right) - \left(1 + \frac{\beta}{2\beta+1}\, e^{\frac{-x^K}{\theta}} + \frac{\beta}{2\beta+1}\, e^{\frac{-x^2}{\theta}} + \frac{1}{2\beta+1}\, e^{-\theta x}\right)\right] * \left(\left[\frac{-e^{\frac{-x_i^K}{\theta}}}{(2\beta+1)^2}\right] - \left[\frac{e^{\frac{-x_i^2}{\theta}}}{(2\beta+1)^2}\right] + \left[\frac{2e^{-\theta x_i}}{(2\beta+1)^2}\right]\right) = 0 \quad (12)$$

Where we notice that equations (12), (13) and (14) are non-linear equations, so it is difficult to find them, so we will use one of the numerical methods such as ***F-solve*** method to estimator the parameter.

4. Simulation studies:

In the previous section, two methods of estimation (MLE and OLS) were addressed to estimate the parameters of the new mixed distribution, and the formulation of estimation equations for both methods was found. As for the application, the method of acceptance and rejection was used to

generate the distribution data because of the difficulty in obtaining the cumulative distribution function by the inverse conversion method, the simulated data is used to estimate the parameters by using iterative methods a simulation program on the Matlab program. Here is an algorithm for this method [11]:

If $f\ (x)$ is a probability density function from which to generate random numbers and $g\ (x)$ is a proposed probability density function from which random numbers can be easily generated, and $cg\ (x)\ \geq f\ (x)$ so that $c \geq 1$ and the following algorithm summarize this Method:

Step (1): Generate the random number X from the function $g\ (x)$.

Step (2): Generate the random number U from the uniform distribution $U\ (0,1)$, independently of X.

Step (3): If $f\ (X)\ /\ [Cg\ (X)]\ U$ count the generated number as $Z\ =\ X$, otherwise return to step (1).

The following default values were used in order to estimate the parameters of the new distribution, namely:

Table 1. The initial values of the parameters

Model	K	B	θ
1	1	3	3
2	2	0.5	0.5
3	3	2	1

As for the samples used in the assessment, four sample sizes were used (25,50.75.100).

The estimation methods were compared using the average mean of squares of error (MSE) scale, according to the following formula [12]:

$$\boldsymbol{AMSE}_{(\hat{\theta})} = \frac{\sum_1^r \left(\hat{\theta} - \theta\right)^2}{r}$$

As:

r : the number of iterations of each experiment (r = 1000).

$\hat{\theta}$: Parameter Estimator.

θ: the values of the assumed (real) parameters.

A simulation program was used on Matlab 2015 program to estimate the parameters and the results shown in the following tables were reached:

5. Discussion of the results

Using the simulated data and the methods of estimation to estimate the parameters of the new distribution based on the initial values of the parameters as in table 1 gives the following results when we use the initial value as in model 1.

Table 2. The estimated values of the new distribution parameters and AMSE for model 1

n	Method		K	B	θ	Best Method
25	MLE	Est. Parameters	**2**	**2.3**	**0.4**	OLS
		AMSE	**2.25**	**3.06**	**6.9**	
	OLS	Est. Parameters	**0.6**	**1.5**	**3.7**	
		AMSE	**0.02**	**0.92**	**0.48**	
50	MLE	Est. Parameters	**6**	**9**	**0.23**	OLS
		AMSE	**30.27**	**72.93**	**7.66**	
	OLS	Est. Parameters	**0.7**	**1.5**	**3.7**	
		AMSE	**0.04**	**1.04**	**0.52**	
75	MLE	Est. Parameters	**6.3**	**9.5**	**0.23**	OLS
		AMSE	**33.94**	**80.31**	**7.67**	
	OLS	Est. Parameters	**0.7**	**1.6**	**3.9**	
		AMSE	**0.03**	**1.13**	**0.74**	
100	MLE	Est. Parameters	**6.9**	**6.3**	**0.24**	OLS

		AMSE	**41.44**	**33.28**	**7.64**
	OLS	Est. Parameters	**0.7**	**1.5**	**3.9**
		AMSE	**0.03**	**0.93**	**0.72**

The results in Table 2 show that when the initial values for the parameters were (K = 1, B = 3, θ = 3) and the sample size is 25 the Ordinary Least Squares method was the best in estimating the three parameters of the new mixed distribution, since although the AMSE value in the Maximum Likelihood method was less than the greatest probability in estimating the one parameters (θ), the AMSE was large In estimating the two parameter (K and b), therefore, the Ordinary Least Square is better in estimating the parameters of the distribution as the average mean sum squares of error for the parameters was (AMSEK = 0.002, AMSEB = 0.001, AMSEθ = 8.99).

Meanwhile, when the estimated values of the parameters were (K = 0.5, B = 3.4, θ = 3.4) and the sample size is becoming 50 these results show that the Ordinary Least Squares method was the best in estimating the three parameters of the new mixed distribution, since although the AMSE value in the Maximum Likelihood method was less than the Ordinary Least Squares in estimating the one parameters θ, the AMSE was large in estimating the two parameter (K and b), therefore, the Ordinary Least Squares is better in estimating the parameters of the distribution as the average mean sum squares of error for the parameters is (AMSEK = 0.002, AMSEB = 0.0009, AMSEθ = 8,99).

But, when the estimated values of the parameters were (K = 0.4, B = 2.9, θ = 2.9) and the sample size is becoming 75 these results show that the Ordinary Least Squares method was the best in estimating the three parameters of the new mixed distribution, since although the AMSE value in the Maximum Likelihood method was less than the Ordinary Least Squares in estimating the one parameters θ, the AMSE was large In estimating the two parameter (K and b), therefore, the Ordinary Least Squares method is better in estimating the parameters of the distribution as the average mean sum squares of error for the parameters is (AMSEK = 0.0001, AMSEB = 0.0006, AMSEθ = 9).

Also, when the estimated values of the parameters were (K = 0.4, B = 3.2, θ = 3.2) and the sample size is becoming 100 these results show that the Ordinary Least Squares method was the best in estimating the three parameters of the new mixed distribution, since although the MSE value in the Maximum Likelihood method was less than the Ordinary Least Squares in estimating the one parameters θ, the MSE was large In estimating the two parameter (K and b), therefore, the Ordinary Least Squares is better in estimating the parameters of the distribution as the average mean sum squares of error for the parameters is (AMSEK = 0.0001, AMSEB = 0.00005, AMSEθ = 8.99). It is evident from the surveyed results that the best estimate of the parameters was at the sample size 100 because it had the lowest average mean sum of squares of error among the sample sizes used.

Using the initial values of the parameters as in model 2 with the simulated data gives the following results as in Table 3.

Table 3. The estimated values of the distribution parameters and AMSE for model 2

n	**Method**		**K**	**B**	$\boldsymbol{\theta}$	**Best Method**
25	MLE	Est. Parameters	0.4	2.3	2	OLS
		AMSE	6.9	3.06	2.25	
	OLS	Est. Parameters	3.7	1.5	0.6	
		AMSE	0.48	0.92	0.02	
50	MLE	Est. Parameters	0.23	9	6	OLS
		AMSE	7.66	72.93	30.27	
	OLS	Est. Parameters	3.7	1.5	0.7	
		AMSE	0.52	1.04	0.04	
75	MLE	Est. Parameters	0.23	9.5	6.3	OLS
		AMSE	7.67	80.31	33.94	
	OLS	Est. Parameters	3.9	1.6	0.7	
		AMSE	0.74	1.13	0.03	
100	MLE	Est. Parameters	0.24	6.3	6.9	OLS

	AMSE	7.64	33.28	41.44
OLS	Est. Parameters	3.9	1.5	0.7
	AMSE	0.72	0.93	0.03

The results in Table 3 show that when the initial values for the parameters were (K = 3, B = 0.5, θ = 0.5) and the sample size is 25 the sample size is becoming 25 these results show that the Ordinary Last Square method was the best in estimating the three parameters of the new mixed distribution, since although the AMSE value in the Maximum Likelihood method was greater than the Ordinary Last Square in estimating the three parameters (K , b and θ), therefore, the possibility is better in estimating the parameters of the distribution as the average sum of squares of error for the parameters is (AMSEK = 0.48, AMSEB = 0.92, AMSEθ = 0.02).

Meanwhile, when the estimated values of the parameters were (K = 3.7, B = 1.5, θ = 0.7) and the sample size is becoming 50 these results show that the Ordinary Last Square method was the best in estimating the three parameters of the new mixed distribution, since although the AMSE value in the Maximum Likelihood method was greater than the Ordinary Last Square in estimating the three parameters (K , b and θ), therefore, the possibility is better in estimating the parameters of the distribution as the average sum of squares of error for the parameters is (AMSEK = 0.52, AMSEB = 1.04, AMSEθ = 0.04).

But, when the estimated values of the parameters were (K = 3.9, B = 1.6, θ = 0.7) and the sample size is becoming 75 these results show that the Ordinary Last Square method was the best in estimating the three parameters of the new mixed distribution, since although the AMSE value in the Maximum Likelihood method was greater than the Ordinary Last Square in estimating the three parameters (K , b and θ), therefore, the possibility is better in estimating the parameters of the distribution as the average sum of squares of error for the parameters is (AMSEK = 0.74, AMSEB = 1.13, AMSEθ = 0.03).

And, when the estimated values of the parameters were (K = 3.9, B = 1.5, θ = 0.7) and the sample size is becoming 100 these results show that the Ordinary Last Square method was the best in estimating the three parameters of the new mixed distribution, since although the AMSE value in the Maximum Likelihood method was greater than the Ordinary Last Square in estimating the three parameters (K , b and θ), therefore, the possibility is better in estimating the parameters of the distribution as the average sum of squares of error for the parameters is (AMSEK = 0.72, AMSEB = 0.93, AMSEθ = 0.03). It is evident from the surveyed results that the best estimate of the parameters was at the sample size of 25 because it had the lowest mean sum of squares of error among the sample sizes used.

Using the initial values of the parameters as in model 3 with the simulated data gives the following results as in Table 4. The results in Table (4) show that when the initial values for the parameters were (K = 3, B = 2, θ = 1) and the sample size is 25 the Maximum Likelihood method was the best in estimating the two parameters of the new mixed distribution, since although the AMSE value in the Ordinary Least Squares method was less than the greatest probability in estimating the one parameters (K), the AMSE was large In estimating the two and third parameter (b, θ)), therefore, the possibility is better in estimating the parameters of the distribution as the average sum of squares of error for the parameters was (AMSE(K) = 4.33, AMSE(B) = 0.02, AMSE(θ) = 0.19).

Meanwhile, when the estimated values of the parameters were (K = 0.7, B = 1.1, θ = 1.5) and the sample size is becoming 50 these results show that the Maximum Likelihood method was the best in estimating the two parameters of the new mixed distribution, since although the AMSE value in the Ordinary Least Squares method was less than the greatest probability in estimating the one parameters (K), the AMSE was large In estimating the two and third parameter (b, θ)), therefore, the possibility is better in estimating the parameters of the distribution as the average sum of squares of error for the parameters was (AMSE(K) = 5.52, AMSE(B) = 0.78, AMSE(θ) = 0.29).

Table 4. The estimated values of the new distribution parameters and AMSE for model 3

n	Method		K	B	θ	Best Method
25	MLE	Est. Parameters	5.1	1.9	0.6	MLE
		AMSE	4.33	0.02	0.19	
	OLS	Est. Parameters	3.9	1	0.01	
		AMSE	0.00004	0.99	0.99	
50	MLE	Est. Parameters	0.7	1.1	1.5	MLE
		AMSE	5.52	0.78	0.29	
	OLS	Est. Parameters	3.1	1	0.01	
		AMSE	1.01	0.94	0.99	
75	MLE	Est. Parameters	5.7	2.3	0.6	MLE
		AMSE	7.31	0.07	0.14	
	OLS	Est. Parameters	3.1	1	0.01	
		AMSE	0.0001	1.02	0.98	
100	MLE	Est. Parameters	5	1.8	0.5	MLE
		AMSE	4.12	0.05	0.23	
	OLS	Est. Parameters	3.1	1	0.01	
		AMSE	0.0002	1.04	0.98	

When the estimated values of the parameters were (K = 5.7, B = 2.3, θ = 0.6) and the sample size is becoming 75 these results show that the Maximum Likelihood method was the best in estimating the two parameters of the new mixed distribution, since although the AMSE value in the Ordinary Least Squares method was less than the greatest probability in estimating the one parameters (K), the AMSE was large In estimating the two and third parameter (b, θ)), therefore, the possibility is better in estimating the parameters of the distribution as the average sum of squares of error for the parameters was (AMSE(K) = 7.31, AMSE(B) = 0.07, AMSE(θ) = 0.14).

And, when the estimated values of the parameters were (K = 5, B = 1.8, θ = 0.5) and the sample size is becoming 100 these results show that the Maximum Likelihood method was the best in estimating the two parameters of the new mixed distribution, since although the AMSE value in the Ordinary Least Squares method was less than the greatest probability in estimating the one parameters (K), the AMSE was large In estimating the two and third parameter (b, θ)), therefore, the possibility is better in estimating the parameters of the distribution as the average sum of squares of error for the parameters was (AMSE(K) = 4.12, AMSE(B) = 0.05, AMSE(θ) = 0.23). It is evident from the surveyed results that the best estimate of the parameters was at a sample size of 100 because it had the lowest mean sum of squares of error among the sample sizes used.

6. Conclusion

Based on the presented and discussed results the most important conclusions may be as follow:

1. The results showed that the Ordinary Least Squares method is better than the Maximum Likelihood method for 100% of the sample size 100 because it achieved the lowest average sum of squares of error.
2. The results showed that the regular Ordinary Least Squares are better than the method of Maximum Likelihood with respect to size sample 25 because it achieved the least sum of the mean squares of error.
3. The comparison result showed that the Maximum Likelihood method is better than the Ordinary Least Squares method for sample size 100 because it achieved the lowest average sum of the squares of error.

References:

[1] E E Afify 2004 Comparison of Estimators of Parameters for the Rayleigh Distribution (*Faculty of Eng. Shibeen El Kom Menoufia Univ)*
[2] A H El-Bassiouny, E D Medhat, M Abdelfattah and M S Eliwa 2016 Mixture of exponentiated generalized Weibull-Gompertz distribution and its applications in reliability *J Stat Appl Probab* ***5***(3) pp 1-14
[3] A N Cheema and M Aslam 2020 Bayesian analysis for 3-components mixture of exponentiated Weibull distribution assuming non-informative priors *Journal of Statistical Computation and Simulation* ***90*** (4) pp 586-605
[4] M Aslam, S Ali, R Yousaf and I Shah 2020 Mixture of transmuted Pareto distribution: Properties, applications and estimation under Bayesian framework *Journal of the Franklin Institute* ***357***(5) pp 2934-2957
[5] A Berchtold 2020 Confidence intervals for the mixture transition distribution (MTD) model and other markovian models *Symmetry* ***12*** (3) pp 351
[6] E F Mark, A John and M B Ross 1985 Maximum likelihood estimation for the 2-parameter Weibull distribution based on interval-data *IEEE* **R-34**(1) pp 57-59
[7] M Tahir, M Aslam and Z Hussain 2016 Estimation of parameters of the 3-component mixture of Pareto distributions using type-I right censoring under Bayesian paradigm *Journal of the National Science Foundation of Sri Lanka* **44** (3)
[8] K Balakrishnan 2018 *Exponential distribution theory methods and applications (*Routledge)
[9] A N Cheema, M Aslam, I M Almanjahie and I Ahmad 2020 Bayesian modeling of 3-components mixture of exponentiated inverted Weibull distribution under noninformative prior *mathematical problems in engineering* pp 1-11
[10] S M A Kazmi and M Aslam 2019 Bayesian estimation for 3-component mixture of generalized exponential distribution *Iranian Journal of Science and Technology Transactions A Science* **43**(4) pp 1761-1788
[11] M Tahir, M Aslam, M Abid, S Ali and M Ahsanullah 2020 A 3-component mixture of exponential distribution assuming doubly censored data: properties and Bayesian estimation *Journal of Statistical Theory and Applications* **19** (2) pp 197-211
[12] A E A Teamah, A A Elbanna and A M Gemeay 2020 Fréchet-Weibull mixture distribution: properties and applications *Applied Mathematical Sciences* **14** (2) pp 75-86

Exact Method for Solving Single Machine Scheduling Problem Under Fuzzy Due Date to Minimize Multi-Objective Functions

Exact Method for Solving Single Machine Scheduling Problem Under Fuzzy Due Date to Minimize Multi- Objective Functions

Hanan A. Cheachan[1], Mustafa T. Kadhim[2]

[1,2]Department of Mathematics, College of Sciences, University of Mustansiriyah, Baghdad, Iraq

E-mail: most_afat2000@yahoo.com

Abstract. In this paper, the branch and bound technique used to solve a single machine scheduling problem, which is the problem of scheduling n- job on a single machine of multi-objective function with triangle fuzzy due date numbers which are formulated as $1\backslash\widetilde{D}_j = TFN\backslash\sum_{j=1}^{n} C_j + L_{max}$. The target of this paper is to obtained optimal sequence of our problem. The computational results are calculated by using Matlab program and compare the results with the complete enumeration method

1.Introduction

The problem of scheduling n- job on single machine problems is important for the understanding theory of scheduling and manufacturing an initiation simple for decision makers. After scheduling problem is in truth a common of abstemious machine scheduling problems. A single machine planning issues help an opportunity to rearrange the framework to the extent that could reasonably be expected will assistance a choice creator comprehends know framework segments furthermore prerequisites. Recently, the single machine of multi-objective functions (completion time, the tardiness, the earliness, and the late work) are studied by using branch and bound method to get optimal sequence, Hanan and Alaa [18]. The multi-objective functions for machine scheduling problem are studied with good lower bound and upper bound to obtain optimal sequence and proved special cases, Hanan et al. [19]. The concept of the fuzzy due date on single machine scheduling problems has already studied by some researchers in the literature pertinent works include that Ishii et al. [1], Han et al. [2], and Ishibuchi et al. [3,4]. There are studies a maximize the total degree of satisfaction with a fuzzy due date, Stanfield et al. [5] found the optimal scheduling problem among those that do not surpass the maximum acceptable possibility of lateness in the problem with respect fuzzy due date. and S.S Lam, X. Cai [6] studied scheduling n-job on single machine with fuzzy due date to the objective of minimize the weighted earliness and tardiness function and introduced measure to evaluate the deviations of job. S.S Lam, X. Cai [7] studied fuzzy lateness function to measure the lateness of job with fuzzy due date and used genetic algorithm to find optimal scheduling. Chengyao and Dingwei found the optimal scheduling of NP-hard problem with triangular fuzzy process time [13]. Sunita studied single machine problem with fuzzy due date, and found methods to found optimal sequence of minimize cost of earliness and tardiness for small system [14]. Helen and Sumathi used branch and

bound to solve single machine scheduling problem using type-2 trapezoidal fuzzy numbers to find optimal sequence for minimizing total tardiness [15].

Abdelaziz and Ismail used a new method to solve a single machine problem with fuzzy processing time and distinct due date for an objective function minimize total earliness and total tardiness [16]. Oğuzhan solved minimizes the sum of the products of earliness/tardiness in single machine problem with fuzzy due date [17]. In this paper, we are involved in the direct generalization of the traditional of the total cost of completion time and maximum lateness where the due date is represented by a triangular membership function [8]. All the jobs are released at a different point in time. The problem is to find a schedule with minimum objective function. The general problem is NP-hard in the strong sense. Our main contribution is BAB algorithm based on a lower bound.

2. Preliminaries

2.1 Fuzzy set [9]

We say $\tilde{A}$ is fuzzy set on X if $\tilde{A}$ is function from X to I where I = [0, 1] i.e.

$\tilde{A} = \left\{\left(\chi, \tilde{A}(\chi)\right) : \chi \in X, 0 \le \tilde{A}(\chi) \le 1 \; where \; \tilde{A}(\chi): X \to [0,1]\right\}$

2.2 Fuzzy number [9]

let R in real line R. A fuzzy set $\tilde{A}: R \to [0,1]$ which satisfies the following conditions

- $\tilde{A}$ is piece wise continuous
- there exist an $\chi \in R$ such that $\tilde{A}(\chi) = 1$
- if $\chi_1, \chi_2 \in R$ and $\gamma \in [0,1]$ then $\tilde{A}(\gamma\chi_1 + (1-\gamma)\chi_2) \ge \tilde{A}(\chi_1) \Lambda \tilde{A}(\chi_{2)}$ then $\tilde{A}$ is convex

is called a fuzzy number. For all $\chi \in R$ we define the support of $\tilde{A}$ by $\{\chi \in R: \tilde{A}(\chi) > 0\}$ and α-cat defined by $[\tilde{A}]_\alpha = \{\chi \in R: \tilde{A}(\chi) \ge \alpha\}$

Now we define the membership of a fuzzy number $\tilde{A}$ in general:

$$\tilde{A}(\chi) = \begin{cases} 0 & For \; \chi < a \\ f_{\tilde{A}}(\chi) & For \; a \le \chi < c \\ 1 & For \; c \le \chi \le d \\ g_{\tilde{A}}(\chi) & For \; d < \chi \le b \\ 0 & For \; b < \chi \end{cases}$$

Where the function $f_{\tilde{A}}(\chi)$ and $g_{\tilde{A}}(\chi)$ are non-decreasing and non- increasing function

Definition2.1: [12] A fuzzy number $\tilde{A} = ({d_j}^I, {d_j}^c, {d_j}^u)$ is triangle fuzzy number with following membership function $\tilde{A}$ defined by:

$$\tilde{A}(\chi) = \begin{cases} 0 & if \; \chi < {d_j}^I \\ \dfrac{\chi - {d_j}^I}{{d_j}^c - {d_j}^I} & if \; {d_j}^I \le \chi < {d_j}^c \\ \dfrac{{d_j}^u - \chi}{{d_j}^u - {d_j}^c} & if \; {d_j}^c \le \chi < {d_j}^u \\ 0 & if \; {d_j}^u \le \chi \end{cases}$$

2.3Expected distance [11]

The expected distance (ED) of two fuzzy numbers $\tilde{A}$ and $\tilde{B}$ is defined by

$d(\tilde{A}, \tilde{B}) = \frac{1}{2}\int_0^1 |a_\alpha - b_\alpha| + |\overline{a}_\alpha - \overline{b}_\alpha| d\alpha$ ……..(1)

Where$[\underline{a}_\alpha, \overline{a}_\alpha]$ $[\underline{b}_\alpha, \overline{b}_\alpha]$ correspond to α-cat of $\tilde{A}$ and $\tilde{B}$ respectively

3.Problem formulation

To schedule n jobs on a single machine of the minimize total completion time and maximum lateness with fuzzy due date. let N={1,2…n} set of n jobs requires p_j units of processing time and each jobs is assigned with due date D_j where D_j is triangular fuzzy number (TFN). All the jobs are available to be processed by the machine and by starts processing without interrupted. let δ be a sequence of jobs in N so that is minimized of objective function .we address the case by following membership

$$D_j(\chi) = \begin{cases} 0 & if\ \chi < {d_j}^I \\ \dfrac{\chi - {d_j}^I}{{d_j}^c - {d_j}^I} & if\ {d_j}^I \le \chi < {d_j}^c \\ \dfrac{{d_j}^u - \chi}{{d_j}^u - {d_j}^c} & if\ {d_j}^c \le \chi < {d_j}^u \\ 0 & if\ {d_j}^u \le \chi \end{cases}$$

$$\tilde{L}_j(C_j, \tilde{D_j}) = C_j - \tilde{d}_j$$

We define the distance according to $\tilde{D_j}$is triangular fuzzy number $({d_j}^I, {d_j}^c, {d_j}^u)$, by using distance measure. Let $\tilde{A} = [\underline{a}_\alpha, \overline{a}_\alpha]$ and $\tilde{B} = [\underline{b}_\alpha, \overline{b}_\alpha]$, than

$$\tilde{d}(\tilde{A}, \tilde{B}) = \frac{1}{2}\int_0^1 \{(\underline{a}_\alpha - \underline{b}_\alpha)^+ + (\overline{a}_\alpha - \overline{b}_\alpha)^+\}d\alpha + \frac{1}{2}\int_0^1 \{(\underline{a}_\alpha - \underline{b}_\alpha)^- + (\overline{a}_\alpha - \overline{b}_\alpha)^-\}d\alpha$$

Where

$$(\chi)^+ = \begin{cases} \chi & if\ \chi \ge 0, \\ 0 & if\ \chi < 0 \end{cases}$$

And

$$(\chi)^- = \begin{cases} 0 & if\ \chi \ge 0, \\ \chi & if\ \chi < 0 \end{cases}$$

By changing $\tilde{A}$ with $C_j$where $C_j$is a completion time and $\tilde{B}$ with $\tilde{D_j}$where $\tilde{D_j}$ is fuzzy due date we can evaluated the following lateness function:

$$\tilde{L}(C_j, \tilde{D_j}) = \frac{1}{2}\int_0^1 \{(C_j - \underline{d_j}_\alpha)^+ + \left(C_j - \overline{d_j}_\alpha\right)^+\}\, d\alpha + \frac{1}{2}\int_0^1 \{(C_j - \underline{d_j}_\alpha)^- + \left(C_j - \overline{d_j}_\alpha\right)^-\}\, d\alpha$$

Where $[\underline{d_j}_\alpha, \overline{d_j}_\alpha]$ according to α-cut

To derive the fuzzy lateness cost function, we have four cases:

- Case (1):
  if $C_j < {d_j}^I$
  For $C_j - ({d_j}^I + ({d_j}^c - {d_j}^I)\alpha$
  If $\alpha = 0$ then $C_j - {d_j}^I < 0$
  If $\alpha = 1$ then $C_j - {d_j}^c < 0$
  For $C_j - ({d_j}^u + ({d_j}^c - {d_j}^u)\alpha$
  If $\alpha = 0$ then $C_j - {d_j}^u < 0$
  If $\alpha = 1$ then $C_j - {d_j}^c < 0$
  Then by equation (1) we get

$$\tilde{L}(C_j, \tilde{D_j}) = \frac{1}{2}\int_0^1 \{(C_j - \underline{d_j}_\alpha)^- + \left(C_j - \overline{d_j}_\alpha\right)^-\}\, d\alpha$$

$$= \frac{1}{2}\int_0^1 \{\left(C_j - \left({d_j}^I + \left({d_j}^c - {d_j}^I\right)\alpha\right) + C_j - \left({d_j}^u + \left({d_j}^c - {d_j}^u\right)\alpha\right)\}d\alpha$$

$$= \frac{1}{2}[C_j\alpha - {d_j}^I\alpha - \frac{1}{2}{d_j}^c\alpha^2 + \frac{1}{2}{d_j}^I\alpha^2 + C_j\alpha - {d_j}^u\alpha - \frac{1}{2}{d_j}^c\alpha^2 + \frac{1}{2}{d_j}^I\alpha^2]_0^1$$
$$= \frac{1}{2}[2C_j - \frac{1}{2}{d_j}^I - {d_j}^c - \frac{1}{2}{d_j}^u]$$
$$= C_j - \frac{1}{4}[{d_j}^I + 2{d_j}^c + {d_j}^u]$$

- Case 2:
  If ${d_j}^I \le C_j < {d_j}^c$ then:
  For $C_j - ({d_j}^I + ({d_j}^c - {d_j}^I)\alpha$
  If $\alpha = 0$ then $C_j - {d_j}^I \ge 0$
  If $\alpha = 1$ then $C_j - {d_j}^c < 0$
  For $C_j - ({d_j}^u + ({d_j}^c - {d_j}^u)\alpha$
  If $\alpha = 0$ then $C_j - {d_j}^u < 0$
  If $\alpha = 1$ then $C_j - {d_j}^c < 0$
  Than $C_j - ({d_j}^c - {d_j}^I)\alpha - {d_j}^I) \ge 0$
  $C_j - {d_j}^I \ge ({d_j}^c - {d_j}^I)\alpha$ Than $\alpha \le \frac{C_j - {d_j}^I}{{d_j}^c - {d_j}^I}$
  Than $[0, \frac{C_j - {d_j}^I}{{d_j}^c - {d_j}^I}] \ge 0$, $[\frac{C_j - {d_j}^I}{{d_j}^c - {d_j}^I}, 1]$
  by using equation (1)

$$\tilde{L}(C_j, \widetilde{D}_j) = \frac{1}{2}\int_0^1 \{(C_j - \underline{d_j}_\alpha)^+ + \left(C_j - \overline{d_j}_\alpha\right)^+\} d\alpha + \frac{1}{2}\int_0^1 \{(C_j - \underline{d_j}_\alpha)^- + \left(C_j - \overline{d_j}_\alpha\right)^-\} d\alpha$$

$$= \frac{1}{2}\int_0^{\frac{C_j - {d_j}^I}{{d_j}^c - {d_j}^I}} (C_j - ({d_j}^I + ({d_j}^c - {d_j}^I)\alpha))d\alpha$$
$$+ \frac{1}{2}\int_{\frac{C_j - {d_j}^I}{{d_j}^c - {d_j}^I}}^1 (C_j - ({d_j}^I + ({d_j}^c - {d_j}^I)\alpha))d\alpha$$
$$+ \frac{1}{2}\int_0^1 (C_j - ({d_j}^u + ({d_j}^c - {d_j}^u)\alpha))d\alpha$$

$$= \frac{1}{2}[C_j\alpha - {d_j}^I\alpha - \frac{1}{2}{d_j}^c\alpha^2 + \frac{1}{2}{d_j}^I\alpha^2]_0^{\frac{C_j - {d_j}^I}{{d_j}^c - {d_j}^I}} + = \frac{1}{2}[C_j\alpha - {d_j}^I\alpha - \frac{1}{2}{d_j}^c\alpha^2 + \frac{1}{2}{d_j}^I\alpha^2]_{\frac{C_j - {d_j}^I}{{d_j}^c - {d_j}^I}}^1$$
$$+ \frac{1}{2}[C_j\alpha - {d_j}^u\alpha - \frac{1}{2}{d_j}^c\alpha^2]_0^1$$
$$= \frac{1}{2}\left[2C_j - \frac{1}{2}{d_j}^I - \frac{1}{2}{d_j}^c\right] + \frac{1}{2}\left[2C_j - \frac{1}{2}{d_j}^u - \frac{1}{2}{d_j}^c\right]$$
$$= C_j - \frac{1}{4}[{d_j}^I + 2{d_j}^c + {d_j}^u]$$

- Case (3)
  If ${d_j}^c \le C_j < {d_j}^u$ then:
  For $C_j - ({d_j}^I + ({d_j}^c - {d_j}^I)\alpha$
  If $\alpha = 0$ then $C_j - {d_j}^I > 0$

If $\alpha = 1$ then $C_j - {d_j}^c > 0$
For $C_j - ({d_j}^u + ({d_j}^c - {d_j}^u)\alpha$
If $\alpha = 0$ then $C_j - {d_j}^u < 0$
If $\alpha = 1$ then $C_j - {d_j}^c > 0$
Than $C_j - ({d_j}^u + ({d_j}^c - {d_j}^u)\alpha \geq 0$
$\Rightarrow \left({d_j}^u - {d_j}^c\right)\alpha \geq {d_j}^u - C_j$
$\Rightarrow \alpha \geq \dfrac{{d_j}^u - C_j}{{d_j}^u - {d_j}^c}$
Than $\left[0, \frac{{d_j}^u - C_j}{{d_j}^u - {d_j}^c}\right] \leq 0, \quad [\frac{{d_j}^u - C_j}{{d_j}^u - {d_j}^c}, 1] \geq 0$
Then by using equation (1)

$$\tilde{L}(C_j, \widetilde{D_j}) = \frac{1}{2}\int_0^1 \{(C_j - \underline{d_j}_\alpha)^+ + \left(C_j - \overline{d_j}_\alpha\right)^+\} d\alpha + \frac{1}{2}\int_0^1 \{(C_j - \underline{d_j}_\alpha)^- + \left(C_j - \overline{d_j}_\alpha\right)^-\} d\alpha$$

$$= \frac{1}{2}\int_0^1 [C_j - ({d_j}^I + \left({d_j}^c - {d_j}^I\right)\alpha] d\alpha + \frac{1}{2}\int_0^{\frac{{d_j}^u - C_j}{{d_j}^u - {d_j}^c}} [C_j - ({d_j}^u + \left({d_j}^c - {d_j}^u\right)\alpha]\, d\alpha$$

$$+ \frac{1}{2}\int_{\frac{{d_j}^u - C_j}{{d_j}^u - {d_j}^c}}^1 [C_j - ({d_j}^u + \left({d_j}^c - {d_j}^u\right)\alpha]\, d\alpha$$

$$= \frac{1}{2}[C_j\alpha - {d_j}^I\alpha - \frac{1}{2}\left({d_j}^c - {d_j}^I\right)\alpha^2]_0^1 + \frac{1}{2}[C_j\alpha - {d_j}^u\alpha - \frac{1}{2}\left({d_j}^c - {d_j}^u\right)\alpha^2]_0^{\frac{{d_j}^u - C_j}{{d_j}^u - {d_j}^c}}$$

$$\frac{1}{2}[C_j\alpha - {d_j}^u\alpha - \frac{1}{2}\left({d_j}^c - {d_j}^u\right)\alpha^2]_{\frac{{d_j}^u - C_j}{{d_j}^u - {d_j}^c}}^1$$

Than we get

$$C_j - \frac{1}{4}\left[{d_j}^I + 2{d_j}^c + {d_j}^u\right]$$

- Case (4)
: if ${d_j}^u < C_j$
For $C_j - ({d_j}^I + ({d_j}^c - {d_j}^I)\alpha$
If $\alpha = 0$ then $C_j - {d_j}^I > 0$
If $\alpha = 1$ then $C_j - {d_j}^c > 0$
For $C_j - ({d_j}^u + ({d_j}^c - {d_j}^u)\alpha$
If $\alpha = 0$ then $C_j - {d_j}^u > 0$
If $\alpha = 1$ then $C_j - {d_j}^c > 0$
Then by equation (1) we get

$$\tilde{L}(C_j, \widetilde{D_j}) = \frac{1}{2}\int_0^1 \{(C_j - \underline{d_j}_\alpha)^+ + \left(C_j - \overline{d_j}_\alpha\right)^+\} d\alpha$$

$$= \frac{1}{2}\int_0^1 \{\left(C_j - \left({d_j}^I + \left({d_j}^c - {d_j}^I\right)\alpha\right) + C_j - \left({d_j}^u + \left({d_j}^c - {d_j}^u\right)\alpha\right)\} d\alpha$$

$$= \frac{1}{2}[C_j\alpha - {d_j}^I\alpha - \frac{1}{2}{d_j}^c\alpha^2 + \frac{1}{2}{d_j}^I\alpha^2 + C_j\alpha - {d_j}^u\alpha - \frac{1}{2}{d_j}^c\alpha^2 + \frac{1}{2}{d_j}^I\alpha^2]_0^1$$

$$= \frac{1}{2}[2C_j - \frac{1}{2}{d_j}^I - {d_j}^c - \frac{1}{2}{d_j}^u]$$
$$= C_j - \frac{1}{4}[{d_j}^I + 2{d_j}^c + {d_j}^u]$$

Than from case (1, 2, 3, 4) we get

$$\tilde{L}(C_j, \tilde{D}_j) = C_j - \frac{1}{4}[{d_j}^I + 2{d_j}^c + {d_j}^u]$$

Where $C_j$is completion time of jobs j under a sequence δ

Using the traditional notion, we denote by

$1\backslash\tilde{D}_j = TFN\backslash\sum_{j=1}^{n} C_j + \tilde{L}_{max}$

the problem formulated by

Min F =Min$\sum_{j=1}^{n} C_j + \tilde{L}_{max}$

subject to :

$C_j \geq P_j$; j=1,2,…,n

$C_j = C_{j-1} + P_j$; j=2,3,…,n

$L_j = C_j - d_j$

…..Q

4.Solve the problem by using BAB algorithm

Consider branch and bound algorithm as the general solution of single machine problem. The problem is seemed as a tree include nodes, and each node has a possibility to emerge into a partial sequence. To select the monster partial sequence, we must calculate the lower bound of all partial sequence node with the lowest lower bound is chosen. This the procedure continued till the least node. After obtaining an order where the job on a machine is scheduling, if the nodes having the upper lower bounds then no more branching is possible the aim of this problem is to find the minimum objective function.

4.1 decomposition of the problem

To solve a problem we can make decomposition of the problem by braking it to up smaller ones, let the problem define by $1\backslash\backslash Z_i$where *i=1,2*

$Z_1 = min\sum_{j=1}^{n} C_j$

subject to :

$C_j \geq P_j$; j=1,2,…,n

$C_j = C_{j-1} + P_j$; j=2,3,…,n

And

$Z_2 = \tilde{L}_{max}(C_j, \tilde{d}_j)$

subject to :

$C_j \geq P_j$; j=1,2,…,n

$C_j = C_{j-1} + P_j$; j=2,3,…,n

$$L_j = C_j - d_j$$

4.2 Lower bound

The lower bound calculating by sequence of jobs in SPT order to get minimum value total completion time to sub problem $Z_1 = min\sum_{j=1}^{n} C_j$ and $Z_2 = \tilde{L}_{max}(C_j, \tilde{d}_j)$calculated by sequence of jobs in EDD order to get minimum maximum lateness with fuzzy due date . Hence the lower bound calculated by:

LB= $\sum_{j=1}^{n} C_j(SPT) + L_{max}(EDD)$

4.3 Upper bound

To find the upper bound can be compete the first and second upper bound by SPT and EDD order sequence respectively, then

UB (1) =$\sum_{j=1}^{n} C_j(SPT) + L_{max}(SPT)$

UB (2)= $\sum_{j=1}^{n} C_j(EDD) + L_{max}(EDD)$

UB (3) this upper bound was found by applying average high ranking methodology (AHR) Heuristic algorithm by following steps;

Step (1): We find (AHR) of fuzzy due date time (a,b,c) of all the jobs

Step (2): The second step arrange the jobs increasing order of average high ranking, if we have two jobs has same order consider the lowest due date

Step (3): We used step 2 after obtained the sequence to find the value of objective function

The upper bound competed by

UB = Min (UB1, UB2,UB3)

5.Computational results

In this section, the computational results are given in below table tested by coding then Matlab R2017a and run on core i7 at CPU @2.40GHs 4GB computer. In the table given the results of optimal values by complete enumeration method and branch and bound method for n=3,4,5,6,7,8,9,10 as the following table

n: no. of jobs,

Ex: no. of examples,

Opt (BAB): The optimal value of the function using (BAB)

Opt (CEM): The optimal value of the function using (CEM) the complete enumeration method.

NOD: Number of node

Time: The execution time of the problem (by seconds).

n	EX	CEM	TIME	B&B	TIME	NOD
4	1	123.25	0.018	123.25	0.122	27
	2	164	0.024	164	0.160	27
	3	140	0.025	140	0.127	10
	4	77	0.027	77	0.159	27
	5	53.75	0.025	53.75	0.158	27
5	1	184.75	0.026	184.75	0.172	49
	2	184.5	0.032	184.5	0.206	51
	3	155	0.026	155	0.137	15
	4	216.25	0.029	216.25	0.123	15
	5	82.75	0.026	82.75	0.156	27
6	1	180.5	0.051	180.5	0.138	21
	2	270.75	0.051	270.75	0.157	36
	3	80.5	0.046	80.5	0.276	113
	4	196	0.034	196	0.199	67
	5	244.5	0.052	244.5	0.146	21
7	1	332.25	0.143	332.25	0.459	139
	2	353.25	0.105	353.25	0.158	28
	3	253.5	0.107	253.5	0.370	104
	4	259.25	0.104	259.25	0.378	118
	5	206.75	0.152	206.75	0.432	118
8	1	195.75	0.820	195.75	5.879	438
	2	270	0.753	270	3.983	334
	3	277.25	0.792	277.25	1.951	168
	4	312.75	0.795	312.75	0.521	36

	5	348.5	0.770	348.5	0.526	36
9	1	341	7.186	341	31.853	269
	2	510.25	7.035	510.25	4.077	45
	3	414.75	6.919	414.75	86.796	676
	4	484.75	9.819	484.75	7.292	45
	5	489.75	10.088	489.75	66.724	357
10	1	332.75	78.539	332.75	1099.180	809
	2	535.5	76.649	535.5	49.221	55
	3	474.75	77.948	474.75	750.022	612
	4	480	77.908	480	250.980	287
	5	321.25	80.061	321.25	843.838	707

6.Conclusion

We solved the problem Q with fuzzy due date by using branch and bound method for several different example for each n–job and comparison between (branch and bound method) and (complete enumeration method) to show the optimal value are equal in $n \leq 10$ in this paper.

Reference

[1] H Ishii, M Tada, T Masuda 1992 Two scheduling problems with fuzzy duedates *Fuzzy Sets and Systems* **46** pp 339–347
[2] S Han, H Ishii and S Fujii 1994 One machine scheduling system with fuzzy duedates *European journal Operation Research* **79** pp 1–12
[3] H Ishibuchi, N Yamamoto, T Murata and H Tanaka 1994 Genetic algorithms and neighborhood search algorithms for fuzzy flow shop scheduling problems *Fuzzy Sets and Systems* **94** pp 81–100.
[4] H Ishibuchi, N Yamamoto, S Misaki and H Tanaka 1994 Local search algorithms for flow shop scheduling with fuzzy duedates *Internat Journal Product. Econ* **33** pp 53–66
[5] P M Stanfield, R E King and J A Joines 1996 Scheduling arrivals to a production system in a fuzzy environment *European journal Operation Research* **93** pp 75–87
[6] S S Lam and X Cai 2002 single machine scheduling with nonlinear lateness cost function and fuzzy due date *nonlinear analysis: real word applications* **3** pp 307-316
[7] S S Lam and X Cai Minimizing Earliness and Tardiness of Job Completions about a fizzy Due Date *Research Grants Council of Hong Kong under grants no. CUHK 278/943 and CUHK 356/963*
[8] W Pedrycz 1994 Why triangular membership functions *Fuzzy Sets and Systems* **64** pp 21-30
[9] D Dubois and H Prade 1980 *Fuzzy Sets and Systems* Academic Press **144** in mathematics in science and engineering
[10] Yu-Jie Wang 2015 Ranking triangle and trapezoidal fuzzy number based on the relative preference relation *applied mathematical modeling* **39** (2) pp 586-599
[11] S Heilpern 1992 The expected value of a fuzzy number *Fuzzy Sets and Systems* **47** pp 81–86
[12] W Pedrycz 1994 Why triangular membership functions *Fuzzy Sets and Systems* **64** pp 21-30
[13] C Wanga, D Wanga, W H Ipb and D W Yuenc 2002 The single machine ready time scheduling problem with fuzzy processing times *Fuzzy Sets and Systems* **127** pp 117–129
[14] Sunita Gupta 2011 single machine scheduling with distinct due dates under fuzzy environment *international journal of enterprise computing and business systems (online)* **1** (2) pp 2230-8849
[15] R Helen and R Sumathi 2014 branch and bound technique for single machine scheduling problem using type-2 trapezoidal fuzzy numbers *international journal of scientific and research publications* **4** (12)

[16] A Hamad and I Abaker 2017 new method for solving single machine scheduling problem with fuzzy processing time and distinct due date *international journal of science, engineering and technology research (ijsetr)* **6** (11)
[17] O A ARIK1 2019 Dissatisfaction levels of earliness and tardiness durations by relaxing common due date on single machine scheduling problems *Journal of Multidisciplinary Modeling and Optimization* **2** (1) pp 1-15
[18] H A Chachan and A S Hameed 2019 Exact Methods for Solving Multi-Objective Problem on Single Machine Scheduling *Iraqi Journal of Science* **60** (8) pp 1802-1813
[19] H A Cheachan, F H Ali and M H Ibrahim 2020 Branch and Bound and Heuristic Methods for Solving Multi-Objective Function for Machine Scheduling Problems *6th international engineering conference Sustainable Technology and Development Erbil Iraq*

Approximate Solution of Delay Integral Equations via Functions of two Variable

Approximate Solution of Delay Integral Equations via Functions of two Variable

Abdul Khaleq O. Al-Jubory

University of Al-Mustansiriyah, College of Science, Department of Mathematics, Baghdad-Iraq

Email: khaleqmazeel@gmial.com

Abstract: In this work, we adopt B. spline function of two variables basis for solving linear multi-dimensional delay Volterra integral equations nonhomogeneous of the second type. We employ the two methods to approximate solution via B. spline function of two variables basis that yields linear system. Some examples are given, the results shown in tables and figures. These methods are very effective, convenient and overcome the difficulty of traditional methods. We solve this problem with the assistance of Matlab18.

1. Introduction

Integral equations are used as mathematical models for many physical situations, and integral equations also occur as reformulations of other mathematical problems. The solutions of integral equations have a major role in the field of science and engineering [1]. The theory and application of integral equations are important subject within applied mathematics. The most recent kind of equation that worth studying is the delay integral equation. These equations have many applications like a model to explain the observed periodic out breaks of certain infection diseases. Another application is electromagnetic inverse scattering. The delay arguments are consistent with the real phenomena which make the models more realistic for simulation. Finding the approximate or exact solutions of multi- dimensional delay integral equations is an important task. Save in a limited number, there difficulty in finding the analytical solutions of multi-dimensional delay integral equations. Therefore, there have been attempts to develop new methods for obtaining analytical solutions which reasonably approximate the exact solutions. Delay integral equations allow mathematicians and engineers better modeling of a wide class of systems with anomalous dynamic behavior and a better understanding of the facets of both physical phenomena and artificial processes. The multi-dimensional delay integral equations are equations in which the unknown function appears under two integral signs and dependents only on two independent variables [1,4,6].

The general form of linear multi-dimensional Volterral delay integral equation is:

$$h(x,y)u(x,y) = g(x,y) + \int_c^{d(y)} \int_a^{b(x)} k(x,y,s,t)\, u(s-\tau_1, t-\tau_2)\, dsdt \qquad (1)$$

where h is known function of x, y and k is known function of x and y called kernel of the integral equation and g is a given function often called the driving term, $\{a, c\}$ are known scalars, $\{b, d\}$ are known functions of x & y and τ_1, τ_2 are known positive numbers and u is the unknown that must be determined. Eq.(1) is classified as first kind if $h(x,y) = 0$, otherwise $h(x,y) = 1$ it is called second kind.

However, several numbers of algorithms for solving linear multi- dimensional linear Volterra delay integral equations have been investigated. M. Abdelkawy and A. Amin [7] use Jacobi collocation approximation for solving multi-dimensional volterra integral equations. Reza Abazari and Adem KJlJçman [8] adopt RDTM and comparison with DTM to study of two-dimensional Volterra integral equations. H. Brunner and J. Kauthn[9] employ collocation and iterated collocation to solve two-dimensional Volterra integral equations.

The aim of this paper, to show how the approximate methods which are based on the expansion method can be used to solve ($LMDVIE_s$) obtain approximate solutions via B. spline polynomials as basis functions.

2. A new formulation of B. spline functions of two variable $B_{ij}^{n+m}(x,y)$ and the properties

B. spline is a piecewise polynomial approximation. Schoenbdery first introduced the B. spline in 1949. This function used to find approximated solution of one dimensional linear Volterra integral differential equations [2]. Moreover, this function is used to solve one dimensional delay differential equation [5]. In this paper we used B. spline of two variables $B_{ij}^{n+m}(x,y)$ to find approximated solution of the two dimensional linear Volterra delay integral equation.

$$B_{ij}^{n+m}(x,y)=\binom{n}{i}\binom{n}{j}x^i y^i(1-x)^{n-i}(1-y)^{m-j}\ ,\quad 0\le x\le n\ ,0\le y\le m$$

where $\binom{n}{i}\binom{n}{j}=\frac{n!}{i!(n-i)!}\frac{m!}{j!(m-j)!}$, n,m are the degree of polynomials and i,j are the index of polynomials and x,y are variables.

Property (1)[3] The B. spline of degree $n+m$ in terms of the power basis is given by the following formula: $B_{ij}^{n+m}(x,y)=\sum_{k=1}^{n}\sum_{j=1}^{m}(-1)^{k-i}(-1)^{1-j}\binom{n}{k}\binom{k}{i}\binom{m}{1}\binom{1}{j}x^k y^i$

Property (2)[3] The first derivative of $B_{ij}^{n+m}(x,y)$ polynomial with respect to x is a polynomial of degree $(n+m+1)$ and is given by: $\frac{\partial B_{ij}^{n+m}(x,y)}{\partial x}=n\left(B_{i-1}^{n-1}(x)-B_i^{n-1}(x)\right)B_j^m(y)$.

Property (3)[3] The first derivative of $B_{ij}^{n+m}(x,y)$ polynomial with respect to y is a polynomial of degree $(n+m+1)$ and is given by:$\frac{\partial B_{ij}^{n+m}(x,y)}{\partial y}=m\left(B_{j-1}^{m-1}(y)-B_j^{m-1}(y)\right)B_i^n(x)$

Property (4)[3]

The first derivative of $B_{ij}^{n+m}(x,y)$ polynomial with respect to (x,y) is a polynomial of degree $(n+m-2)$ and is given by:

$$\frac{\partial^2 B_{ij}^{n+m}(x,y)}{\partial x\partial y}=nm(B_{i-1}^{n-1}(x)-B_i^{n-1}(x))((B_{j-1}^{m-1}(y)-B_j^{m-1}(y))$$

3. Expansion Methods:

The expansion method is one of the famous methods used to find an approximate solutions of the multi-dimensional integral equations, [1,2,4,6].

To illustrate that, consider multi-dimensional linear Volterra delay equation

$$u(x,y)=g(x,y)+\int_c^{d(y)}\int_a^{b(x)}k(x,y,s,t)\,u(s-\tau_1,t-\tau_2)\,ds\,dt \qquad (2)$$

Approximate the solution u of the equation as:

$$u(x,y)\cong\sum_{k=1}^{N}c_k B_k(x,y) \qquad (3)$$

By substituting Eq. (3) into Eq. (2) one can get

$$\sum_{k=1}^{N}c_k\left[B_k(x,y)-\int_c^{d(y)}\int_a^{b(x)}k(x,y,s,t)B_k\,(s-\tau_1,t-\tau_2)\,ds\,dt\right]-g(x,y)=$$
$$\varepsilon(x,y,c_1,c_2,\dots,c_N) \qquad (4)$$

Hence the error function $\varepsilon(x,y,c_1,c_2,\dots,c_N)$ will depends on x,y and on the unknown's coefficients $c_1,c_2,\dots,c_N$. The expansion method (collocation and Galerkin's) depends on finding the coefficients $c_1,c_2,\dots,c_N$ in which the error function is minimizing.

4. B. spline solving multi-dimensional linear Volterra delay integral equation using collocation method:

Consider multi-dimensional linear Volterra delay integral equation

$$u(x,y) = g(x,y) + \int_c^{d(y)} \int_a^{b(x)} k(x,y,s,t)\, u(s-\tau_1, t-\tau_2)\, ds\, dt \quad (5)$$

The collocation method requires that $\varepsilon(x_i, y_j) = 0$ where $(x_i, y_j) \in D$ and

$D = \{(x,y) | a \le x \le b,\ \ c \le y \le d\}\ for\ all\ i = 1,2,\dots,M\ ,\ j = 1,2,\dots,M$

Therefore: $\sum_{k=1}^{N} c_k\, u_k(x_i, y_j) = g(x_i, y_j)\ , i = 1,2,\dots,N\ , j = 1,2,\dots,M \quad (6)$

We can obtain system of linear equations with unknown $c_1, c_2, \dots, c_N$ which can be solved by using mat lab language to find approximate solution.

5. B. spline solving multi-dimensional linear Volterra delay integral equation using Gelarkin's method:

This method is based an approximation the unknown function u and substituting it into Eq. (2) to give following equation:

$$\sum_{k=1}^{N} c_k B_k\,(x,y) = g(x,y) - \sum_{k=1}^{N} c_k \int_c^d \int_a^b k(x,y,s,t) B_k\, u(s-\tau_1, t-\tau_2) ds\, dt = \varepsilon(x,y,c_1,c_2,\dots,c_N) \quad (7)$$

Gelarkin's method established N-conditions which are necessary for determining N-coefficients $\{c_k\}_{k=1}^{N}$ appeared in the above equation, by making the error $\varepsilon(x,y,c_1,c_2,\dots,c_N)$ orthogonal to N given linearly independent functions $\varphi_1(x,y), \varphi_2(x,y), \dots, \varphi_k(x,y)$.

$$\int_c^d \int_a^b \varphi_j(x,y)\, \varepsilon(x,y,c_1,c_2,\dots,c_N)\, dx\, dy = 0\ , \qquad j = 1,2,\dots,N \quad (8)$$

Therefor

$$\int_c^d \int_a^b \varphi_j\, (\sum_{k=1}^{N} c_k [B_k(x,y) - \int_c^d \int_a^b k(x,y,s,t) B_k\,(s-\tau_1, t-\tau_2) ds\, dt - g(x,y)) dx dy = 0 \quad (9)$$

Where $u_k(x,y) = B_k(x,y) - \int_c^d \int_a^b k(x,y,s,t) B_k\,(s-\tau_1, t-\tau_2) ds\, dt]$

Then $\sum_{k=1}^{N} c_k \int_c^d \int_a^b \varphi_j(x,y) u_k\,(x,y) dx\, d\,y = \int_c^d \int_a^b \varphi_j(x,y)\, g\,(x,y) dx\, d\,y \quad (10)$

By evaluating the above equation for each $j = 1,2,\dots,N$ one can get a system of N linear equations with N unknowns $c_1, c_2, \dots, c_N$ which can be solved by any suitable method.

6. Numerical Examples

Example1: Consider the multi-dimensional linear Volterra delay integral equation of first kind: $\frac{1}{2} y^3 x^2 + \frac{1}{2} x^3 y^2 - 2y^2 x^2 = \int_0^y \int_0^x xy\, u(s-2,t)\, dsdt$

and the exact solution is $u(x,y) = x + y$. with $N = 10,\ h = 0.1$ and $x_i = ih,\ y_i = ih,\ i = 0,1,\dots,N$.

Table (1)

Presents a comparison the exact solution and approximate solution

x	y	Exact solution	Collection with (B. spline)	Gelarkin's with (B. spline)
0.0	0.0	0	0	0
0.1	0.1	0.2	0.2	0.2
0.2	0.2	0.4	0.4	0.4
0.3	0.3	0.6	0.6	0.6
0.4	0.4	0.8	0.8	0.8
0.5	0.5	1.0	1.0	1.0
0.6	0.6	1.2	1.2	1.2
0.7	0.7	1.4	1.4	1.4
0.8	0.8	1.6	1.6	1.6
0.9	0.9	1.8	1.8	1.8
1	1	2	2	2

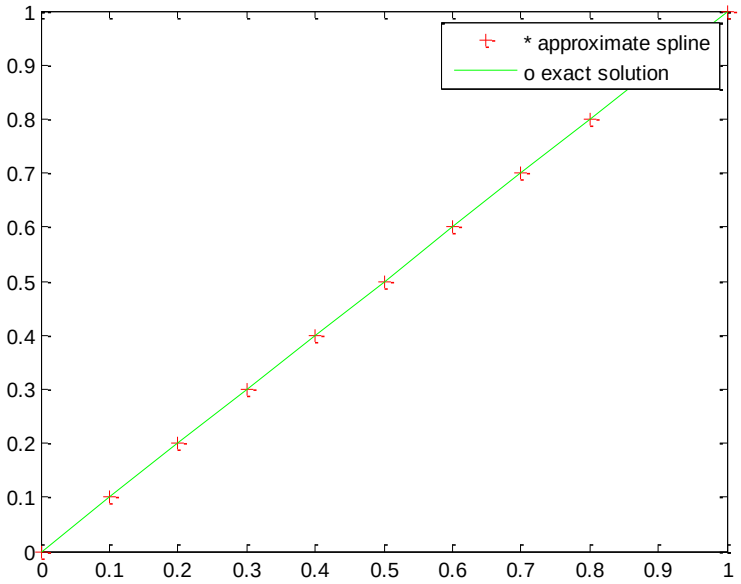

Figure 1

Example2: Consider the (LMDVIE$_s$): $u(x,y) = x + y - \frac{1}{2}x^2y - \frac{1}{2}xy^2 + xy + \int_0^y \int_0^x xy\, u(s-1,t)\, dsdt$ and the exact solution $u(x,y) = x + y$. with $N = 10,\ h = 0.1$ and $x_i = ih,\ y_i = ih,\ i = 0,1,\dots,N$.

Table (2)

x	y	**Exact solution**	**Collection with (B. spline)**	**Gelarkin's with (B. spline)**
0.0	0.0	0	0	0
0.1	0.1	0.2	0.2	0.2
0.2	0.2	0.4	0.4	0.4
0.3	0.3	0.6	0.6	0.6
0.4	0.4	0.8	0.8	0.8
0.5	0.5	1.0	1.0	1.0
0.6	0.6	1.2	1.2	1.2
0.7	0.7	1.4	1.4	1.4
0.8	0.8	1.6	1.6	1.6
0.9	0.9	1.8	1.8	1.8
1	1	2	2	2

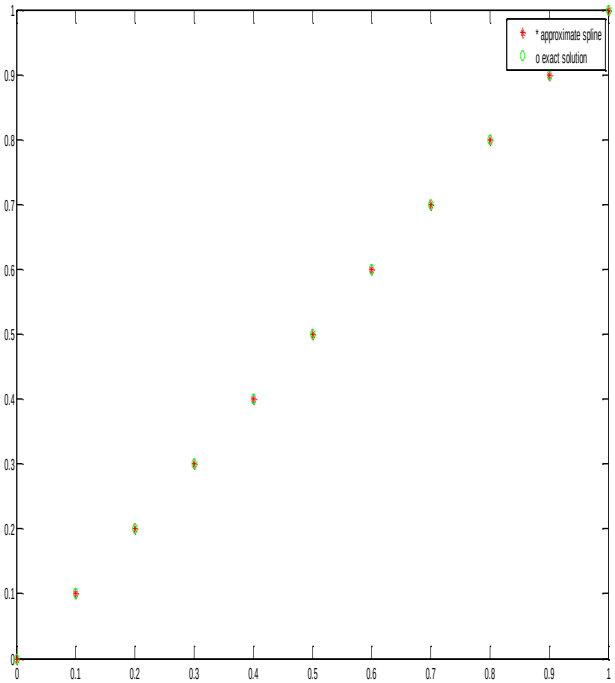

Figure 2

7.Conclusions:

1.The expansion method with the aid of B. spline polynomials as a basis functions to compute the approximate solutions for multi-dimensional linear Volterra delay integral equations and B. spline polynomial gave accurate results.

2. A disadvantage of the B. spline function is its dependence up a free parameter n.

References

[1] P K Sahu 2016 *Numerical approximate Methods for Solving Linear and Nonlinear Integral Equations* theses Ph.D. National Institute of Technology Rourkela

[2] A L Bushar 2005 *the expansion methods for solving the two dimensional delay integral equation* M.Sc thesis College of Education Ibn-Al Haitham Univ. of Baghdad

[3] L M Delves and J Wlash 1974 *Numerical solution of integral equations* Oxford university press

[4] S A Haleema 2006 *Computational method for solving optimal control problem* Ph.D. thesis College of applied Science Univ. of Technology, Iraq, Baghdad

[5] G Han and R Wang 2002 Richardson extrapolation of iterated discrete Gelarkin solution for two dimensional Fredholm integral equations *Journal of computational and Applied Mathematics* **139** pp 49-63

[6] H S Shymaa 2010 Bernstien polynomials solving one dimensional Delay Volterra integro differential equations *Engineering & Technology Journal* **28** (20)

[7] M Abdelkawy and A Amin Jacobi 2017 collocation approximation for solving multi-dimensional volterra integral equations *International Journal of Nonlinear Sciences and Numerical Simulation*

[8] R Abazari and A KJlJçman 2013 Numerical study of two-dimensional Volterra integral equations by RDTM and comparison with DTM *Hindawi Publishing Corporation* pp10

[9] H Brunner and J Kauthn 1989 The numerical solution of two-dimensional Volterra integral equations by collocation and Iterated collocation Journal of Numerical Analysis ***9*** pp 47-59

g-Closed Soft Sets in Soft Closure Spaces

g-Closed Soft Sets in Soft Closure Spaces

R N Majeed* **and S T Ekram**

Department of mathematics, college of education for pure sciences (Ibn AL-Haitham), University of Baghdad, Baghdad, Iraq

E-mail: rasha.n.m@ihcoedu.uobaghdad.edu.iq

Abstract. The aim of the present work is to define a new class of closed soft sets in soft closure spaces, namely, generalized closed soft sets (gc-soft sets, for short) which are defined over an initial universe set with a fixed set of parameters. This new class is a generalization to the class of closed soft sets. A necessary condition for a gc-soft set to be a soft closed is also obtainable. Moreover, the union and intersection of two gc-soft sets are discussed. Besides, some properties of gc-soft sets in the product soft closure spaces are also studied. Also, as an application of gc-soft sets a new soft separation axiom, namely $T_{\frac{1}{2}}$-soft closure space is introduced and its basic properties are investigated.

1. Introduction

In 1999, Molodtsov [15] presented the idea of soft sets as a general mathematical method for dealing with unknown objects. The soft set theory has been applied in many ways, e.g. stability and regularization [15], research on game theory and operations [15], soft analysis [15], general topology [16] etc. Shabir and Naz [16] presented the concept of soft topological spaces which is defined over an initial universe with a fixed set of parameters. Also, Gowri and Jegadeesan [10] introduced and discussed Cech soft closure spaces. Future, in a fuzzy soft environment, Majeed [13] presented the fundamental structure of Cech fuzzy soft closure spaces. We have recently introduced the concept of soft closure spaces [7] as an extension of this definition in the ordinary set theory developed by Cech [5].

Generalized closed sets were introduced by Levine [12] in a topological space. Levine extends some important properties of closed sets to a larger set's family. Compactness, normality and completeness in a uniform space have been shown, for example, to be inherited by generalized closed sets. By using generalized closed sets Balachandran et al. [3] introduced the notion of generalized continuous maps and studied some of their properties. Kannan [11] introduced the notion of generalized closed soft sets in soft topological spaces. The definitions of generalized closed sets and generalized continuous maps have been extended by Boonpok and Khampakdee in [4] to closure spaces. Our aim in the current work is to introduce and study new notions in soft closure spaces. In Section 3, we present and study a new class of closed soft sets which is called gc-soft sets within soft closure spaces. We show this new class contains the class of closed soft sets. In Section 4, we use the definition of gc-soft sets, to define and study a new type of spaces, namely $T_{\frac{1}{2}}$-soft closure space.

2. Preliminaries

In this section, we remember some basic concepts and outcomes that various authors of soft set theory defined and discussed. In this paper, M refers to the initial universe, $P(M)$ denotes the power set of M and R is the set of all parameters for M.

Definition 2.1 [15] A mapping $F: R \to P(M)$ defines a soft set $F_R = (F, R)$ over the universe set M. So, the set $F_R = \{(r, F(r)): r \in R \; and \; F(r) \in P(M)\}$ can be used to represent F_R. $SS(M, R)$ denotes the family of all soft sets over M.

Definition 2.2 [14] A soft set F_R is said to be a null (respectively, an absolute) soft set, denoted by $\widetilde{\Phi}_R$ (respectively, $\widetilde{M}$), if for all $r \in R$, $F(R) = \emptyset$ (empty set) (respectively, $F(r) = M$).

Definition 2.3 [9] Let F_R,$G_R \in SS(M, R)$. A soft set F_R is said to be a soft subset of G_R, symbolized $F_R \sqsubseteq G_R$, if $F(r) \subseteq G(r)$ for all $r \in R$. F_R equals G_R, denoted by $F_R = G_R$ if $F_R \sqsubseteq G_R$ and $G_R \sqsubseteq F_R$.

Definition 2.4 [14] Let F_R,$G_R \in SS(M, R)$. The union of F_R and G_R is the soft set H_R given by $H(r) = F(r) \cup G(r)$ for all $r \in R$. This is represented by $F_R \sqcup G_R$. The intersection between F_R and G_R is the soft set H_R defined as $H(r) = F(r) \cap G(r)$ for all $r \in R$ and denoted by, $F_R \sqcap G_R$.

Definition 2.5 [16] The difference between two soft sets F_R and G_R over M, denoted by $F_R - G_R$ is the soft set H_R defined as $H(r) = F(r) - G(r)$ for all $r \in R$.

Definition 2.6 [16] The relative complement of a soft set F_R is denoted by F_R^c, where $F^c: R \longrightarrow P(M)$ defined as $F^c(r) = M - F(r)$, for all $r \in R$. Clearly, $F_R^c = \widetilde{M} - F_R$.

Definition 2.7 [6] The soft set $F_R \in SS(M, R)$ is called soft point in M, denoted by x_r, if for the element $r \in R$, $F(r) = \{x\}$ and $F(r') = \emptyset$ for every $r' \in R - \{r\}$.

Definition 2.8 [6] A soft point x_r is said to belong to the soft set G_R, indicate by $x_r \,\widetilde{\in}\, G_R$, if $\{x\} \subseteq G(r)$ for the parameter $r \in R$.

Definition 2.9 [2] Let $F_R \in SS(M, R)$ and $G_K \in SS(N, K)$. The Cartesian product $F_R \times G_K$ is defined by $(F \times G)_{R \times K}$ where

$$(F \times G)_{R \times K}(r, k) = F(r) \times G(k), \text{ for all } (r, k) \in R \times K.$$

By this description, the $F_R \times G_K$ soft set is a soft set over $M \times N$ and its universe parameter is $R \times K$.

The projection pairs $p_M: M \times N \longrightarrow M$, $q_R: R \times K \longrightarrow R$ and $p_N: M \times N \longrightarrow N$, $q_K: R \times K \longrightarrow K$ determine morphisms respectively (p_M, q_R) from $M \times N$ to M and (p_N, q_K) from $M \times N$ to N, where

$(p_M, q_R)(F_R \times G_K) = p_M(F \times G)_{q_R(R \times K)}$ and

$(p_N, q_K)(F_R \times G_K) = p_N(F \times G)_{q_K(R \times K)}$ [1].

Definition 2.10 [7] An operator $\tilde{u}: SS(M, R) \longrightarrow SS(M, R)$ is referred to as a soft closure operator (soft-co, for short) on M, if for all $F_R, G_R \in SS(M, R)$ the following conditions hold:

$(C1)$ $\widetilde{\Phi}_R = \tilde{u}(\widetilde{\Phi}_R)$;

$(C2)$ $F_R \sqsubseteq \tilde{u}(F_R)$;

$(C3)$ $F_R \sqsubseteq G_R \Longrightarrow \tilde{u}(F_R) \sqsubseteq \tilde{u}(G_R)$.

The triple $(M, \tilde{u}, R)$ is named a soft closure space (soft-cs, for short). It is said that soft subset F_R over M is a closed soft set (c-soft set, for short), if $F_R = \tilde{u}(F_R)$. The relative complement $\widetilde{M} - F_R$ of any c-soft set over M is said to be an open soft set (o-soft set, for short).

Proposition 2.11 [7] Let $(M,\tilde{u},R)$ be a soft-cs and $\{(F_R)_\alpha : \alpha \in I\}$ be a collection of soft subsets over M. Then

1- $\sqcup_{\alpha\in I}\,\tilde{u}((F_R)_\alpha) \sqsubseteq \tilde{u}(\sqcup_{\alpha\in I}\,(F_R)_\alpha)$.
2- $\tilde{u}(\sqcap_{\alpha\in I}\,(F_R)_\alpha) \sqsubseteq \sqcap_{\alpha\in I}\,\tilde{u}((F_R)_\alpha)$.

Definition 2.12 [7] Let $(M,\tilde{u},R)$ be a soft-cs and let $Y \subseteq M$. Then $\tilde{u}_Y : SS(Y,R) \longrightarrow SS(Y,R)$ defined by $\tilde{u}_Y(F_R) = \tilde{Y} \sqcap \tilde{u}(F_R)$ is the relative soft closure operator on Y induced by $\tilde{u}$. The triple $(Y,\tilde{u}_Y,R)$ is said to be a soft closure subspace (soft-c.subsp, for short) of $(M,\tilde{u},R)$.

Theorem 2.13 [7] If G_R is an o-soft set in $(M,\tilde{u},R)$ and $(Y,\tilde{u}_Y,R)$ be a soft- c.subsp of a soft-cs $(M,\tilde{u},R)$, then $\tilde{Y} \sqcap G_R$ is an o-soft set in $(Y,\tilde{u}_Y,R)$.

Definition 2.14 [7] The product of the family of soft-cs's $\{(\mathcal{M}_\alpha,\tilde{u}_\alpha,R_\alpha) : \alpha \in \mathcal{J}\}$ is the triple $(\prod_{\alpha\in\mathcal{J}}\mathcal{M}_\alpha, \otimes\tilde{u}, \prod_{\alpha\in\mathcal{J}}R_\alpha)$, where $\prod_{\alpha\in\mathcal{J}}\mathcal{M}_\alpha$ and $\prod_{\alpha\in\mathcal{J}}R_\alpha$ denotes to the Cartesian product of the sets $\mathcal{M}_\alpha$ and R_α, $\alpha \in \mathcal{J}$, respectively and $\otimes\tilde{u} : \mathcal{SS}(\prod_{\alpha\in\mathcal{J}}\mathcal{M}_\alpha, \prod_{\alpha\in\mathcal{J}}R_\alpha) \longrightarrow \mathcal{SS}(\prod_{\alpha\in\mathcal{J}}\mathcal{M}_\alpha, \prod_{\alpha\in\mathcal{J}}R_\alpha)$ defined as follows:
$\otimes\tilde{u}(\mathcal{F}_{\prod_{\alpha\in\mathcal{J}}R_\alpha}) = \prod_{\alpha\in\mathcal{J}}\tilde{u}_\alpha\left(\left(p_{\mathcal{M}_\alpha}, q_{R_\alpha}\right)\left(\mathcal{F}_{\prod_{\alpha\in\mathcal{J}}R_\alpha}\right)\right)$, $\forall\, \mathcal{F}_{\prod_{\alpha\in\mathcal{J}}R_\alpha} \in \mathcal{SS}(\prod_{\alpha\in\mathcal{J}}\mathcal{M}_\alpha, \prod_{\alpha\in\mathcal{J}}R_\alpha)$.

Theorem 2.15 [8] Let $\{(M_\alpha,\tilde{u}_\alpha,R_\alpha) : \alpha \in I\}$ be a collection of soft-cs's and let $v \in I$. Then, the soft projection mapping $\left(p_{M_v}, q_{R_v}\right) : (\prod_{\alpha\in I}M_\alpha, \otimes\tilde{u}, \prod_{\alpha\in I}R_\alpha) \longrightarrow (M_v,\tilde{u}_v,R_v)$ is a soft closed and soft continuous mapping.

3. The basic structures of generalized closed soft sets

In this section, we introduce the notion of generalized closed (respectively, open) soft sets in soft-cs's and study the basic properties of these sets with several examples.

Definition 3.1 A soft set $\mathcal{F}_R$ is called a generalized closed soft set (g-soft set, for short) in a soft-cs $(\mathcal{M},\tilde{u},R)$, if $\tilde{u}(\mathcal{F}_R) \sqsubseteq G_R$ whenever $\mathcal{F}_R \sqsubseteq G_R$ and G_R is an σ-soft set in $\widetilde{\mathcal{M}}$. A soft set $\mathcal{F}_R$ is called a generalized open soft set ($g\sigma$-soft set, for short), if the relative complement $\widetilde{\mathcal{M}} - \mathcal{F}_R$ is a g-soft set in $(\mathcal{M},\tilde{u},R)$.

The next example explains Definition 3.1.

Example 3.2 Let $\mathcal{M} = \{a,b,c\}$ and $R = \{r_1,r_2\}$. Define a soft-co $\tilde{u} : \mathcal{SS}(\mathcal{M},R) \longrightarrow \mathcal{SS}(\mathcal{M},R)$ as follows:

$$\tilde{u}(\mathcal{F}_R) = \begin{cases} \widetilde{\Phi}_R & if \quad \mathcal{F}_R = \widetilde{\Phi}_R, \\ \{(r_1,\{b\})\} & if \quad \mathcal{F}_R = \{(r_1,\{b\})\}, \\ \{(r_1,\{b,c\})\} & if \quad \mathcal{F}_R = \{(r_1,\{c\})\}, \\ \{(r_1,\{b,c\})\} & if \quad \mathcal{F}_R = \{(r_1,\{b,c\})\}, \\ \{(r_2,\{a\})\} & if \quad \mathcal{F}_R = \{(r_2,\{a\})\}, \\ \widetilde{\mathcal{M}} & other\ wise. \end{cases}$$

Then $(\mathcal{M},\tilde{u},R)$ is a soft-cs. Let $\mathcal{F}_R = \{(r_1,\{a,b\}),((r_2,\{a\})\} \in \mathcal{SS}(\mathcal{M},R)$. Then $\mathcal{F}_R$ is g-soft set since $\mathcal{F}_R \sqsubseteq \widetilde{\mathcal{M}}$ which is the only σ-soft set containing $\mathcal{F}_R$ and $\tilde{u}(\mathcal{F}_R) = \widetilde{\mathcal{M}} \sqsubseteq \widetilde{\mathcal{M}}$. On the other hand $\mathcal{F}_R = \{(r_1,\{c\})\}$ is not g-soft set in $(\mathcal{M},\tilde{u},R)$ since there exists an σ-soft set $\{(r_1,\{(a,c\}),(r_2,\{(a,b,c\})\}$ containing $\mathcal{F}_R = \{(r_1,\{c\})\}$ but $\tilde{u}(\mathcal{F}_R) = \{(r_1,\{b,c\})\} \not\sqsubseteq \{(r_1,\{(a,c\}),(r_2,\{(a,b,c\})\}$.

Proposition 3.3 Every c-soft set in a soft-cs $(\mathcal{M},\tilde{u},R)$ is g-soft set.

Proof. Let $\mathcal{F}_R$ be a c-soft set and let G_R be an σ-soft set such that $\mathcal{F}_R \sqsubseteq G_R$. Since $\mathcal{F}_R$ is a c-soft set, then $\tilde{u}(\mathcal{F}_R) = \mathcal{F}_R \sqsubseteq G_R$. Hence, $\mathcal{F}_R$ is $g c$-soft set. □

Corollary 3.4 Every σ-soft set in a soft-cs $(\mathcal{M}, \tilde{u}, R)$ is $g\sigma$-soft set.

As the following example shows, the converters of Proposition 3.3 and its corollary are not valid.

Example 3.5 The soft set $\{(r_1, \{a, b\}), (r_2, \{a\})\}$ in Example 3.2 is gc-soft set but is not c-soft set.

Next, we give a characterization of a $g\sigma$-soft set, but before that, we need to introduce the notion of the soft interior in soft- cs's.

Definition 3.6 Let $(\mathcal{M}, \tilde{u}, R)$ be a soft- cs and $\mathcal{F}_R \in \mathcal{SS}(\mathcal{M}, R)$. The interior of the soft set $\mathcal{F}_R$ denoted by $int(\mathcal{F}_R)$ with respect to soft-co $\tilde{u}$ is defined as $int(\mathcal{F}_R) = \widetilde{\mathcal{M}} - \tilde{u}(\widetilde{\mathcal{M}} - \mathcal{F}_R)$.

Proposition 3.7 A soft set $\mathcal{F}_R$ in a soft -cs $(\mathcal{M}, \tilde{u}, R)$ is an $g\sigma$-soft set if and only if $H_R \sqsubseteq int(\mathcal{F}_R)$ whenever $H_R \sqsubseteq \mathcal{F}_R$ and H_R is c-soft set in $(\mathcal{M}, \tilde{u}, R)$.

Proof. Let $\mathcal{F}_R$ be a $g\sigma$-soft set and $\mathcal{H}_R$ be a c-soft set such that $\mathcal{H}_R \sqsubseteq \mathcal{F}_R$. Then, $\widetilde{\mathcal{M}} - \mathcal{F}_R \sqsubseteq \widetilde{\mathcal{M}} - \mathcal{H}_R$. Since $\mathcal{F}_R$ is $g\sigma$- soft set and H_R be a c-soft set, then $\widetilde{\mathcal{M}} - \mathcal{F}_R$ and $\widetilde{\mathcal{M}} - \mathcal{H}_R$ are is gc-soft set and σ-soft set in $\mathcal{M}$, respectively. Thus, from Definition 3.1, we get $\tilde{u}(\widetilde{\mathcal{M}} - \mathcal{F}_R) \sqsubseteq \widetilde{\mathcal{M}} - H_R$. By taking the relative complement and from Definition 3.6, we get $H_R \sqsubseteq int(\mathcal{F}_R)$. Conversely, similar to the first direction. □

Remark 3.8 Let $(\mathcal{M}, \tilde{u}, R)$ be a soft-cs and $\mathcal{F}_R, H_R \in \mathcal{SS}(\mathcal{M}, R)$. Then,

1. If $\mathcal{F}_R$ is an gc-soft set in $(\mathcal{M}, \tilde{u}, R)$ and $\mathcal{F}_R \sqsubseteq H_R \sqsubseteq \tilde{u}(\mathcal{F}_R)$. Then, H_R need not to be gc-soft set.
2. If $\mathcal{F}_R$ is an $g\sigma$-soft set in $(\mathcal{M}, \tilde{u}, R)$ and $int(\mathcal{F}_R) \sqsubseteq H_R \sqsubseteq \mathcal{F}_R$. Then, H_R need not to be $g\sigma$-soft set.

The following example explains Remark 3.8.

Example 3.9 Let $\mathcal{M} = \{a, b, c\}$ and $R = \{r_1, r_2\}$. Define a soft-co $\tilde{u}: \mathcal{SS}(\mathcal{M}, R) \longrightarrow \mathcal{SS}(\mathcal{M}, R)$ as follows:

$$\tilde{u}(\mathcal{F}_R) = \begin{cases} \widetilde{\Phi}_R & if\ \mathcal{F}_R = \widetilde{\Phi}_R, \\ \{(r_1, \{b\}), (r_2, \{b\})\} & if\ \mathcal{F}_R \sqsubseteq \{(r_1, \{b\}), (r_2, \{b\})\}, \\ \{(r_1, \{a\}), (r_2, \{a\})\} & if\ \mathcal{F}_R \sqsubseteq \{(r_1, \{a\})\}, \\ \{(r_1, \{c\})(r_2, \{c\})\} & if\ \mathcal{F}_R \sqsubseteq \{(r_1, \{c\}), (r_2, \{c\})\}, \\ \widetilde{\mathcal{M}} & other\ wise. \end{cases}$$

Then $(\mathcal{M}, \tilde{u}, R)$ is soft-cs. Part (1) of Remark 3.8 is shown only, and part (2) can be obtained by taking the relative complement to the soft sets in part (1).
Let $\mathcal{F}_R = \{(r_1, \{a\})\} \in \mathcal{SS}(\mathcal{M}, R)$ be a gc-soft set and consider $H_R = \{(r_1, \{a\}), (r_2, \{a\})\}$. Clearly, $\mathcal{F}_R \sqsubseteq H_R \sqsubseteq \tilde{u}(\mathcal{F}_R)$. But H_R is not gc-soft set since $H_R \sqsubseteq \{(r_1, \{(a, c\}), (r_2, \{a, c\})\}$ is an σ-soft set and $\tilde{u}(H_R) = \widetilde{\mathcal{M}} \not\sqsubseteq \{(r_1, \{(a, c\}), (r_2, \{a, c\})\}$.

Remark 3.10 Let $(\mathcal{M}, \tilde{u}, R)$ be a soft-cs. Then,

1. The union (respectively, intersection) of two gc-soft (respectively, $g\sigma$-soft) sets need not to be gc-soft (respectively, $g\sigma$-soft) set.

2. The intersection (respectively, union) of two $\mathcal{gc}$-soft (respectively, $\mathcal{go}$-soft) sets is not $\mathcal{gc}$-soft (respectively, $\mathcal{go}$-soft) set.

We explain Remark 3.10 in the following two examples:

Example 3.11 Let $\mathcal{M} = \{a, b, c\}$ and $\mathrm{R} = \{r_1, r_2\}$. Define a soft-$co$ $\tilde{u}: \mathcal{SS}(\mathcal{M}, R) \longrightarrow \mathcal{SS}(\mathcal{M}, R)$ as follows:

$$\tilde{u}(\mathcal{F}_R) = \begin{cases} \tilde{\Phi}_R & if\ \ \mathcal{F}_R = \tilde{\Phi}_R, \\ \{(r_1, \{a\})\} & if\ \ \mathcal{F}_R = \{(r_1, \{a\})\}, \\ \{(r_2, \{b\})\} & if\ \ \mathcal{F}_R = \{(r_2, \{b\})\}, \\ \{(r_1, \{c\}), (r_2, \{c\})\} & if\ \ \mathcal{F}_R \sqsubseteq \{(r_1, \{c\}), (r_2, \{c\})\}, \\ \widetilde{\mathcal{M}} & other\ wise. \end{cases}$$

Then $(\mathcal{M}, \tilde{u}, R)$ is soft-cs. Consider $\mathcal{F}_R = \{(r_1, \{a\})\}$ and $H_R = \{(r_2, \{b\})\}$ are $\mathcal{gc}$-soft sets. However, $\mathcal{F}_R \sqcup H_R = \{(r_1, \{a\}), (r_2, \{b\})\}$ is not $\mathcal{gc}$-soft set. Since $\mathcal{F}_R \sqcup H_R \sqsubseteq \{(r_1, \{a, b\}), (r_2, \{a, b\})\}$ which is an $\mathcal{o}$-soft set but $\tilde{u}(\mathcal{F}_R \sqcup H_R) = \widetilde{\mathcal{M}} \not\sqsubseteq \{(r_1, \{a, b\}), (r_2, \{a, b\})\}$. Similarly, by taking the relative complement of $\mathcal{F}_R$ and H_R we can show the intersection of two $\mathcal{go}$-soft sets need not to be $\mathcal{go}$-soft set.

Example 3.12 Let $\mathcal{M} = \{a, b, c\}$ and $\mathrm{R} = \{r_1, r_2\}$. Define a soft-$co$ $\tilde{u}: \mathcal{SS}(\mathcal{M}, R) \longrightarrow \mathcal{SS}(\mathcal{M}, R)$ as follows:

$$\tilde{u}(\mathcal{F}_R) = \begin{cases} \tilde{\Phi}_R & if\ \ \mathcal{F}_R = \tilde{\Phi}_R, \\ \{(r_1, \{a, c\}), (r_2, \{a, b\})\} & if\ \ \mathcal{F}_R \sqsubseteq \{(r_1, \{a, c\}), (r_2, \{a, b\})\}, \\ \widetilde{\mathcal{M}} & other\ wise. \end{cases}$$

Then $(\mathcal{M}, \tilde{u}, R)$ is soft-cs. Consider $\mathcal{F}_R = \{(r_1, \{a, b\}), (r_2, \{b, c\})\}$ and let $H_R = \{(r_1, \{b, c\}), (r_2, \{a, c\})\}$ are $\mathcal{gc}$-soft sets. But $\mathcal{F}_R \sqcap H_R = \{(r_1, \{b\}), (r_2, \{c\})\}$ is not $\mathcal{gc}$-soft set because there exists an $\mathcal{o}$-soft set $\{(r_1, \{b\}), (r_2, \{c\})\}$ containing $\mathcal{F}_R \sqcap H_R$, however $\tilde{u}(\mathcal{F}_R \sqcap H_R) = \widetilde{\mathcal{M}} \not\sqsubseteq \{(r_1, \{b\}), (r_2, \{c\})\}$. Similarly, by taking the relative complement of $\mathcal{F}_R$ and H_R we can show the union of two $\mathcal{go}$-soft sets need not be $\mathcal{go}$-soft set.

Theorem 3.13 Let $\mathcal{F}_R$ be an open $\mathcal{gc}$-soft set and H_R is a c-soft set. Then $\mathcal{F}_R \sqcap H_R$ is a $\mathcal{gc}$-soft set.

Proof. Since $\mathcal{F}_R$ be an open and $\mathcal{gc}$-soft set, then $\tilde{u}(\mathcal{F}_R) \sqsubseteq \mathcal{F}_R$ and from $(\mathcal{C}2)$ of Definition 2.10, $\mathcal{F}_R \sqsubseteq \tilde{u}(\mathcal{F}_R)$, then $\tilde{u}(\mathcal{F}_R) = \mathcal{F}_R$. Hence, $\mathcal{F}_R$ is a c-soft set. Since H_R is a c-soft set, then $\mathcal{F}_R \sqcap H_R$ is a c-soft set. By Proposition 3.3, we get $\mathcal{F}_R \sqcap H_R$ is a $\mathcal{gc}$-soft set. □

Theorem 3.14 Let $(\mathcal{M}, \tilde{u}, R)$ be a soft-cs. If $\mathcal{F}_R$ is a $\mathcal{gc}$-soft set in $(\mathcal{M}, \tilde{u}, R)$, then $\tilde{u}(\mathcal{F}_R) - \mathcal{F}_R$ contains only null c-soft set.

Proof: Suppose that $\mathcal{F}_R$ is $\mathcal{gc}$-soft set in $(\mathcal{M}, \tilde{u}, R)$. Let H_R be a c-soft set in $\mathcal{M}$ such that $H_R \sqsubseteq \tilde{u}(\mathcal{F}_R) - \mathcal{F}_R$. Since $H_R \sqsubseteq \tilde{u}(\mathcal{F}_R) - \mathcal{F}_R$, then $H_R \sqsubseteq \tilde{u}(\mathcal{F}_R)$ and $H_R \sqsubseteq \widetilde{\mathcal{M}} - \mathcal{F}_R$. This implies $\mathcal{F}_R \sqsubseteq \widetilde{\mathcal{M}} - H_R$. Since $\mathcal{F}_R$ is $\mathcal{gc}$-soft set and $\widetilde{\mathcal{M}} - H_R$ is an $\mathcal{o}$-soft set, then $\tilde{u}(\mathcal{F}_R) \sqsubseteq \widetilde{\mathcal{M}} - H_R$. It follows, $H_R \sqsubseteq \widetilde{\mathcal{M}} - \tilde{u}(\mathcal{F}_R)$. Hence, we have $H_R \sqsubseteq \tilde{u}(\mathcal{F}_R) \sqcap (\widetilde{\mathcal{M}} - \tilde{u}(\mathcal{F}_R))$. Thus, $H_R = \tilde{\Phi}_{\mathrm{R}}$. □

Corollary 3.15 A $\mathcal{gc}$-soft set $\mathcal{F}_R$ is a c-soft set in $(\mathcal{M}, \tilde{u}, R)$ if and only if $\tilde{u}(\mathcal{F}_R) - \mathcal{F}_R$ is c-soft set.

Proof: If $\mathcal{F}_R$ is c-soft set, then $\tilde{u}(\mathcal{F}_R) = \mathcal{F}_R$. This implies $\tilde{u}(\mathcal{F}_R) - \mathcal{F}_R = \widetilde{\Phi}_{\mathrm{R}}$ which is a c-soft set.

Conversely, let $\mathcal{F}_R$ be a $\mathcal{gc}$-soft set. To prove $\mathcal{F}_R$ is closed. Since $\mathcal{F}_R$ be a $\mathcal{gc}$-soft set, then by Theorem 3.14, we have $\tilde{u}(\mathcal{F}_R) - \mathcal{F}_R$ contains only null c-soft set. From hypothesis, $\tilde{u}(\mathcal{F}_R) - \mathcal{F}_R$ is a c-soft set this implies $\tilde{u}(\mathcal{F}_R) - \mathcal{F}_R = \widetilde{\Phi}_{\mathrm{R}}$. Hence, $\mathcal{F}_R$ is c-soft set. □

The Corollary 3.15 offers the basis for retaining the conversion of Proposition 3.3.

Theorem 3.16 Let $\{(\mathcal{M}_\alpha, \tilde{u}_\alpha, R_\alpha): \alpha \in \mathcal{I}\}$ be a family of soft-cs's and let $\nu \in \mathcal{I}$ and let $G_{R_\nu} \sqsubseteq \widetilde{\mathcal{M}}_\nu$. Then G_{R_ν} is a $\mathcal{go}$-soft set of $(\mathcal{M}_\nu, \tilde{u}_\nu, R_\nu)$ if and only if $G_{R_\nu} \times \prod_{\alpha\in\mathcal{I}}^{\widetilde{\alpha\neq\nu}} \mathcal{M}_\alpha$ is a $\mathcal{go}$- soft set of $(\prod_{\alpha\in\mathcal{I}}\mathcal{M}_\alpha, \otimes\tilde{u}, \prod_{\alpha\in\mathcal{I}} R_\alpha)$.

Proof. Let G_{R_ν} be a $\mathcal{go}$-soft set of $(\mathcal{M}_\nu, \tilde{u}_\nu, R_\nu)$. Let $\mathcal{F}_{\prod_{\alpha\in\mathcal{I}}R_\alpha}$ be a c-soft set of $(\prod_{\alpha\in\mathcal{I}}\mathcal{M}_\alpha, \otimes\tilde{u}, \prod_{\alpha\in\mathcal{I}} R_\alpha)$ such that $\mathcal{F}_{\prod_{\alpha\in\mathcal{I}}R_\alpha} \sqsubseteq G_{R_\nu} \times \prod_{\alpha\in\mathcal{I}}^{\widetilde{\alpha\neq\nu}} \mathcal{M}_\alpha$. Then $(p_{\mathcal{M}_\nu}, q_{R_\nu})(\mathcal{F}_{\prod_{\alpha\in\mathcal{I}}R_\alpha}) \sqsubseteq G_{R_\nu}$. Since $(p_{\mathcal{M}_\nu}, q_{R_\nu})(\mathcal{F}_{\prod_{\alpha\in\mathcal{I}}R_\alpha})$ is c-soft set by Theorem 2.15 and since G_{R_ν} is a $\mathcal{go}$-soft set of $(\mathcal{M}_\nu, \tilde{u}_\nu, R_\nu)$, then by Proposition 3.7 $(p_{\mathcal{M}_\nu}, q_{R_\nu})(\mathcal{F}_{\prod_{\alpha\in\mathcal{I}}R_\alpha}) \sqsubseteq int_\nu(G_{R_\nu}) = \widetilde{\mathcal{M}}_\nu - \tilde{u}_\nu(\widetilde{\mathcal{M}}_\nu - G_{R_\nu})$. Therefore,

$$\begin{aligned}\mathcal{F}_{\prod_{\alpha\in\mathcal{I}}R_\alpha} &\sqsubseteq (p_{\mathcal{M}_\nu}, q_{R_\nu})^{-1}\left(\widetilde{\mathcal{M}}_\nu - \tilde{u}_\nu(\widetilde{\mathcal{M}}_\nu - G_{R_\nu})\right)\\ &= \prod_{\alpha\in\mathcal{I}}^{\widetilde{}}\mathcal{M}_\alpha - \prod_{\alpha\in\mathcal{I}}\tilde{u}_\alpha(p_{\mathcal{M}_\nu}, q_{R_\nu})(\prod_{\alpha\in\mathcal{I}}^{\widetilde{}}\mathcal{M}_\alpha - (G_{R_\nu} \times \prod_{\alpha\in\mathcal{I}}^{\widetilde{}}\mathcal{M}_\alpha))\\ &= \prod_{\alpha\in\mathcal{I}}^{\widetilde{}}\mathcal{M}_\alpha - \otimes\tilde{u}\left(\prod_{\alpha\in\mathcal{I}}^{\widetilde{}}\mathcal{M}_\alpha - (G_{R_\nu} \times \prod_{\alpha\in\mathcal{I}}^{\widetilde{}}\mathcal{M}_\alpha)\right) = int(G_{R_\nu} \times \prod_{\alpha\in\mathcal{I}}^{\widetilde{}}\mathcal{M}_\alpha)\end{aligned}$$

From Proposition 3.7 $G_{R_\nu} \times \prod_{\alpha\in\mathcal{I}}^{\widetilde{\alpha\neq\nu}} \mathcal{M}_\alpha$ is a $\mathcal{go}$-soft set.

Conversely, let $\mathcal{F}_{R_\nu}$ be a c-soft set of $(\mathcal{M}_\nu, \tilde{u}_\nu, R_\nu)$ such that $\mathcal{F}_{R_\nu} \sqsubseteq G_{R_\nu}$. Then $\mathcal{F}_{R_\nu} \times \prod_{\alpha\in\mathcal{I}}^{\widetilde{\alpha\neq\nu}} \mathcal{M}_\alpha \sqsubseteq G_{R_\nu} \times \prod_{\alpha\in\mathcal{I}}^{\widetilde{\alpha\neq\nu}} \mathcal{M}_\alpha$. Since $G_{R_\nu} \times \prod_{\alpha\in\mathcal{I}}^{\widetilde{\alpha\neq\nu}} \mathcal{M}_\alpha$ is a $\mathcal{go}$-soft set and $\mathcal{F}_{R_\nu} \times \prod_{\alpha\in\mathcal{I}}^{\widetilde{\alpha\neq\nu}} \mathcal{M}_\alpha$ is c-soft set, then

$$\begin{aligned}\mathcal{F}_{R_\nu} \times \prod_{\alpha\in\mathcal{I}}^{\widetilde{\alpha\neq\nu}} \mathcal{M}_\alpha &\sqsubseteq int(G_{R_\nu} \times \prod_{\alpha\in\mathcal{I}}^{\widetilde{\alpha\neq\nu}} \mathcal{M}_\alpha)\\ &= \prod_{\alpha\in\mathcal{I}}^{\widetilde{\alpha\neq\nu}} \mathcal{M}_\alpha - \otimes\tilde{u}(\prod_{\alpha\in\mathcal{I}}^{\widetilde{\alpha\neq\nu}} \mathcal{M}_\alpha - (G_{R_\nu} \times \prod_{\alpha\in\mathcal{I}}^{\widetilde{\alpha\neq\nu}} \mathcal{M}_\alpha))\\ &= \prod_{\alpha\in\mathcal{I}}^{\widetilde{\alpha\neq\nu}} \mathcal{M}_\alpha - \prod_{\alpha\in\mathcal{I}}\tilde{u}_\alpha(p_{\mathcal{M}_\alpha}, q_{R_\alpha})(\prod_{\alpha\in\mathcal{I}}^{\widetilde{}}\mathcal{M}_\alpha - (G_{R_\nu} \times \prod_{\alpha\in\mathcal{I}}^{\widetilde{\alpha\neq\nu}} \mathcal{M}_\alpha)).\end{aligned}$$

By taking the relative complement, we have

$\prod_{\alpha\in\mathcal{I}}\tilde{u}_\alpha(p_{\mathcal{M}_\alpha}, q_{R_\alpha})(\prod_{\alpha\in\mathcal{I}}^{\widetilde{}}\mathcal{M}_\alpha - (G_{R_\nu} \times \prod_{\alpha\in\mathcal{I}}^{\widetilde{\alpha\neq\nu}} \mathcal{M}_\alpha)) \sqsubseteq \prod_{\alpha\in\mathcal{I}}^{\widetilde{}}\mathcal{M}_\alpha - (\mathcal{F}_{R_\nu} \times \prod_{\alpha\in\mathcal{I}}^{\widetilde{\alpha\neq\nu}} \mathcal{M}_\alpha)$

$\prod_{\alpha\in\mathcal{I}}\tilde{u}_\alpha(p_{\mathcal{M}_\alpha}, q_{R_\alpha})((\widetilde{\mathcal{M}}_\nu - G_{R_\nu}) \times \prod_{\alpha\in\mathcal{I}}^{\widetilde{\alpha\neq\nu}} \mathcal{M}_\alpha) \sqsubseteq (\widetilde{\mathcal{M}}_\nu - \mathcal{F}_{R_\nu}) \times \prod_{\alpha\in\mathcal{I}}^{\widetilde{\alpha\neq\nu}} \mathcal{M}_\alpha$. By computing the soft projection $(p_{\mathcal{M}_\nu}, q_{R_\nu})$, we get $\tilde{u}_\nu(\widetilde{\mathcal{M}}_\nu - G_{R_\nu}) \sqsubseteq \widetilde{\mathcal{M}}_\nu - \mathcal{F}_{R_\nu}$ and by taking the relative complement, it follows $\mathcal{F}_{R_\nu} \sqsubseteq \widetilde{\mathcal{M}}_\nu - \tilde{u}_\nu(\widetilde{\mathcal{M}}_\nu - G_{R_\nu}) = int(G_{R_\nu})$. Therefore, G_{R_ν} is $\mathcal{go}$-soft set of $(\mathcal{M}_\nu, \tilde{u}_\nu, R_\nu)$.

Theorem 3.17 Let $\{(\mathcal{M}_\alpha, \tilde{u}_\alpha, R_\alpha): \alpha \in \mathcal{I}\}$ be a family of soft-$cs's$, let $\nu \in \mathcal{I}$ and let $\mathcal{F}_{R_\nu} \sqsubseteq \widetilde{\mathcal{M}}_\nu$. Then, $\mathcal{F}_{R_\nu}$ is $\mathcal{gc}$-soft set of $(\mathcal{M}_\nu, \tilde{u}_\nu, R_\nu)$ if and only if $\mathcal{F}_{R_\nu} \times \prod_{\alpha\in\mathcal{I}}^{\widetilde{\alpha\neq\nu}} \mathcal{M}_\alpha$ is a $\mathcal{gc}$-soft set of $(\prod_{\alpha\in\mathcal{I}}\mathcal{M}_\alpha, \otimes\tilde{u}, \prod_{\alpha\in\mathcal{I}} R_\alpha)$.

Proof. Let $\mathcal{F}_{R_\nu}$ be a $\mathcal{gc}$-soft set of $(\mathcal{M}_\nu, \tilde{u}_\nu, R_\nu)$. Then, $\widetilde{\mathcal{M}}_\nu - \mathcal{F}_{R_\nu}$ is a $\mathcal{go}$-soft set of $(\mathcal{M}_\nu, \tilde{u}_\nu, R_\nu)$. By Theorem 3.16, we have $(\widetilde{\mathcal{M}}_\nu - \mathcal{F}_{R_\nu}) \times \prod_{\alpha\in\mathcal{I}}^{\widetilde{\alpha\neq\nu}} \mathcal{M}_\alpha$ is a $\mathcal{go}$-soft set of $(\prod_{\alpha\in\mathcal{I}}\mathcal{M}_\alpha, \otimes\tilde{u}, \prod_{\alpha\in\mathcal{I}} R_\alpha)$. Since

$\left(\widetilde{\mathcal{M}}_\nu - \mathcal{F}_{R_\nu}\right) \times \prod_{\alpha\in\mathcal{I}}^{\widetilde{\alpha\neq\nu}} \mathcal{M}_\alpha = \prod_{\alpha\in\mathcal{I}} \mathcal{M}_\alpha - (\mathcal{F}_{R_\nu} \times \prod_{\alpha\in\mathcal{I}}^{\widetilde{\alpha\neq\nu}} \mathcal{M}_\alpha)$ is a $\mathcal{gc}$-soft set of $(\prod_{\alpha\in\mathcal{I}} \mathcal{M}_\alpha, \otimes\tilde{u}, \prod_{\alpha\in\mathcal{I}} R_\alpha)$. Thus, $\mathcal{F}_{R_\nu} \times \prod_{\alpha\in\mathcal{I}}^{\widetilde{\alpha\neq\nu}} \mathcal{M}_\alpha$ is a $\mathcal{gc}$-soft set of $(\prod_{\alpha\in\mathcal{I}} \mathcal{M}_\alpha, \otimes\tilde{u}, \prod_{\alpha\in\mathcal{I}} R_\alpha)$.

Conversely, let G_{R_ν} be an $\mathcal{o}$-soft set of $(\mathcal{M}_\nu, \tilde{u}_\nu, R_\nu)$ such that $\mathcal{F}_{R_\nu} \sqsubseteq G_{R_\nu}$. This implies $\mathcal{F}_{R_\nu} \times \prod_{\alpha\in\mathcal{I}}^{\widetilde{\alpha\neq\nu}} \mathcal{M}_\alpha \sqsubseteq G_{R_\nu} \times \prod_{\alpha\in\mathcal{I}}^{\widetilde{\alpha\neq\nu}} \mathcal{M}_\alpha$. Since $\mathcal{F}_{R_\nu} \times \prod_{\alpha\in\mathcal{I}}^{\widetilde{\alpha\neq\nu}} \mathcal{M}_\alpha$ is a $\mathcal{gc}$-soft set and $G_{R_\nu} \times \prod_{\alpha\in\mathcal{I}}^{\widetilde{\alpha\neq\nu}} \mathcal{M}_\alpha$ is an $\mathcal{o}$-soft set of $(\prod_{\alpha\in\mathcal{I}} \mathcal{M}_\alpha, \otimes\tilde{u}, \prod_{\alpha\in\mathcal{I}} R_\alpha)$, then we get $\otimes\tilde{u}\left(\mathcal{F}_{R_\nu} \times \prod_{\alpha\in\mathcal{I}}^{\widetilde{\alpha\neq\nu}} \mathcal{M}_\alpha\right) \sqsubseteq G_{R_\nu} \times \prod_{\alpha\in\mathcal{I}}^{\widetilde{\alpha\neq\nu}} \mathcal{M}_\alpha$. By calculating the soft projection for $\nu \in \mathcal{I}$, we get $\tilde{u}_\nu(\mathcal{F}_{R_\nu}) \sqsubseteq G_{R_\nu}$. Therefore, $\mathcal{F}_{R_\nu}$ is a $\mathcal{gc}$-soft set of $(\mathcal{M}_\nu, \tilde{u}_\nu, R_\nu)$. □

Theorem 3.18 Let $\{(\mathcal{M}_\alpha, \tilde{u}_\alpha, R_\alpha): \alpha \in \mathcal{I}\}$ be a family of soft-cs's. For each $\nu \in \mathcal{I}$, let $(p_{\mathcal{M}_\nu}, q_{R_\nu}): \prod_{\alpha\in\mathcal{I}} \mathcal{M}_\alpha \longrightarrow \widetilde{\mathcal{M}}_\nu$ be the soft projection mapping. Then,

1. If $\mathcal{F}_{\prod_{\alpha\in\mathcal{I}} R_\alpha}$ is a $\mathcal{gc}$-soft set of $(\prod_{\alpha\in\mathcal{I}} \mathcal{M}_\alpha, \otimes\tilde{u}, \prod_{\alpha\in\mathcal{I}} R_\alpha)$, then $(p_{\mathcal{M}_\nu}, q_{R_\nu})(\mathcal{F}_{\prod_{\alpha\in\mathcal{I}} R_\alpha})$ is a $\mathcal{gc}$-soft set of $(\mathcal{M}_\nu, \tilde{u}_\nu, R_\nu)$.
2. If $\mathcal{F}_{R_\nu}$ is a $\mathcal{gc}$-soft set of $(\mathcal{M}_\nu, \tilde{u}_\nu, R_\nu)$, then $(p_{\mathcal{M}_\nu}, q_{R_\nu})^{-1}(\mathcal{F}_{R_\nu})$ a $\mathcal{gc}$-soft set of $(\prod_{\alpha\in\mathcal{I}} \mathcal{M}_\alpha, \otimes\tilde{u}, \prod_{\alpha\in\mathcal{I}} R_\alpha)$.

Proof.

1. Let $\mathcal{F}_{\prod_{\alpha\in\mathcal{I}} R_\alpha}$ be a $\mathcal{gc}$-soft set of $(\prod_{\alpha\in\mathcal{I}} \mathcal{M}_\alpha, \otimes\tilde{u}, \prod_{\alpha\in\mathcal{I}} R_\alpha)$. Let G_{R_ν} be an $\mathcal{o}$-soft set of $(\mathcal{M}_\nu, \tilde{u}_\nu, R_\nu)$ such that $(p_{\mathcal{M}_\nu}, q_{R_\nu})(\mathcal{F}_{\prod_{\alpha\in\mathcal{I}} R_\alpha}) \sqsubseteq G_{R_\nu}$. Then by taking the inverse image for the soft projection $(p_{\mathcal{M}_\nu}, q_{R_\nu})$, we get $\mathcal{F}_{\prod_{\alpha\in\mathcal{I}} R_\alpha} \sqsubseteq (p_{\mathcal{M}_\nu}, q_{R_\nu})^{-1}(G_{R_\nu}) = G_{R_\nu} \times \prod_{\alpha\in\mathcal{I}}^{\widetilde{\alpha\neq\nu}} \mathcal{M}_\alpha$. Since $\mathcal{F}_{\prod_{\alpha\in\mathcal{I}} R_\alpha}$ is a $\mathcal{gc}$-soft set and $G_{R_\nu} \times \prod_{\alpha\in\mathcal{I}}^{\widetilde{\alpha\neq\nu}} \mathcal{M}_\alpha$ is an $\mathcal{o}$-soft set, then $\otimes\tilde{u}(\mathcal{F}_{\prod_{\alpha\in\mathcal{I}} R_\alpha}) \sqsubseteq G_{R_\nu} \times \prod_{\alpha\in\mathcal{I}}^{\widetilde{\alpha\neq\nu}} \mathcal{M}_\alpha$. From the definition of $\otimes\tilde{u}$, it follows $\prod_{\alpha\in\mathcal{I}} \tilde{u}_\alpha(p_{\mathcal{M}_\alpha}, q_{R_\alpha})(\mathcal{F}_{\prod_{\alpha\in\mathcal{I}} R_\alpha}) \sqsubseteq G_{R_\nu} \times \prod_{\alpha\in\mathcal{I}}^{\widetilde{\alpha\neq\nu}} \mathcal{M}_\alpha$. Consequently, $\tilde{u}_\nu((p_{\mathcal{M}_\alpha}, q_{R_\alpha})(\mathcal{F}_{\prod_{\alpha\in\mathcal{I}} R_\alpha})) \sqsubseteq G_{R_\nu}$. Hence, $(p_{\mathcal{M}_\nu}, q_{R_\nu})(\mathcal{F}_{\prod_{\alpha\in\mathcal{I}} R_\alpha})$ is a $\mathcal{gc}$-soft set of $(\mathcal{M}_\nu, \tilde{u}_\nu, R_\nu)$.
2. Let $\mathcal{F}_{R_\nu}$ be a $\mathcal{gc}$-soft set of $(\mathcal{M}_\nu, \tilde{u}_\nu, R_\nu)$. Then $(p_{\mathcal{M}_\nu}, q_{R_\nu})^{-1}(\mathcal{F}_{R_\nu}) = \mathcal{F}_{R_\nu} \times \prod_{\alpha\in\mathcal{I}}^{\widetilde{\alpha\neq\nu}} \mathcal{M}_\alpha$. By Theorem 3.17, $\mathcal{F}_{R_\nu} \times \prod_{\alpha\in\mathcal{I}}^{\widetilde{\alpha\neq\nu}} \mathcal{M}_\alpha$ is a $\mathcal{gc}$-soft set of $(\prod_{\alpha\in\mathcal{I}} \mathcal{M}_\alpha, \otimes\tilde{u}, \prod_{\alpha\in\mathcal{I}} R_\alpha)$. Therefore, $(p_{\mathcal{M}_\nu}, q_{R_\nu})^{-1}(\mathcal{F}_{R_\nu})$ is a $\mathcal{gc}$-soft set of $(\prod_{\alpha\in\mathcal{I}} \mathcal{M}_\alpha, \otimes\tilde{u}, \prod_{\alpha\in\mathcal{I}} R_\alpha)$.□

4. $\mathcal{T}_{\frac{1}{2}}$-soft closure spaces

In this section, we introduce a new separation axiom, namely $\mathcal{T}_{\frac{1}{2}}$-soft-$cs$'s in soft-$cs$'s with the help of $\mathcal{gc}$-soft sets.

Definition 4.1 A soft-cs $(\mathcal{M}, \tilde{u}, R)$ is said to be a $\mathcal{T}_{\frac{1}{2}}$-soft-$cs$, if every $\mathcal{gc}$-soft set is a c-soft set in $\mathcal{M}$.

Example 4.2 Let $\mathcal{M} = \{a, b\}$ and R $= \{r_1, r_2\}$. Define a soft- co $\tilde{u}$: $\mathcal{SS}(\mathcal{M}, R) \longrightarrow \mathcal{SS}(\mathcal{M}, R)$ as follows:

$$\tilde{u}(\mathcal{F}_R) = \begin{cases} \tilde{\Phi}_R & if \quad \mathcal{F}_R = \tilde{\Phi}_R, \\ \{(r_1,\{a\})\} & if \quad \mathcal{F}_R = \{(r_1,\{a\})\}, \\ \{(r_1,\{\mathrm{b}\})\} & if \quad \mathcal{F}_R = \{(r_1,\{\mathrm{b}\})\}, \\ \{(r_2,\{a\})\} & if \quad \mathcal{F}_R = \{(r_2,\{a\})\}, \\ \{(r_2,\{b\})\} & if \quad \mathcal{F}_R = \{(r_2,\{b\})\}, \\ \widetilde{\mathcal{M}} & other\ wise \end{cases}$$

Then, $(\mathcal{M},\tilde{u},R)$ is $\mathcal{T}_{\frac{1}{2}}$-soft-$cs$. Since every $\mathcal{g}c$-soft set is c-soft set.

Theorem 4.3 A soft-cs $(\mathcal{M},\tilde{u},R)$ is $\mathcal{T}_{\frac{1}{2}}$-soft-$cs$ if and only if every soft point of $\mathcal{M}$ is a c-soft set or σ-soft set.

Proof. Suppose that $(\mathcal{M},\tilde{u},R)$ is a $\mathcal{T}_{\frac{1}{2}}$-soft-$cs$. Let x_r be a soft point of $\mathcal{M}$. Assume that x_r is not c-soft set. Then, $\widetilde{\mathcal{M}} - x_r$ is not σ-soft set. This implies $\widetilde{\mathcal{M}}$ is the only σ-soft set which contains $\widetilde{\mathcal{M}} - x_r$. It follows, $\tilde{u}(\widetilde{\mathcal{M}} - x_r) \sqsubseteq \widetilde{\mathcal{M}}$, and hence $\widetilde{\mathcal{M}} - x_r$ is $\mathcal{g}c$- soft set, since $(\mathcal{M},\tilde{u},R)$ is a $\mathcal{T}_{\frac{1}{2}}$-soft-$cs$, $\widetilde{\mathcal{M}} - x_r$ is c-soft set or equivalently, x_r is an σ-soft set.

Now, assume that x_r is not σ-soft set. Then, $\widetilde{\mathcal{M}} - x_r$ is not c-soft set. This implies $\widetilde{\mathcal{M}} - x_r$ is either σ-soft set or not σ-soft set. If $\widetilde{\mathcal{M}} - x_r$ is σ-soft set, then x_r is a c-soft set and the proof is complete. If $\widetilde{\mathcal{M}} - x_r$ is not σ-soft set, then $\widetilde{\mathcal{M}}$ is the only σ-soft set such that $\widetilde{\mathcal{M}} - x_r \sqsubseteq \widetilde{\mathcal{M}}$, this implies $\widetilde{\mathcal{M}} - x_r$ is $\mathcal{g}c$- soft set, this implies $\widetilde{\mathcal{M}} - x_r$ is c-soft set, then x_r is σ-soft set and this contradiction. Then $\widetilde{\mathcal{M}} - x_r$ is an σ-soft set or c-soft set.

Conversely, to prove $(\mathcal{M},\tilde{u},R)$ is $\mathcal{T}_{\frac{1}{2}}$-soft-$cs$. Let $\mathcal{F}_R$ is $\mathcal{g}c$- soft set, to prove $\mathcal{F}_R$ is a c-soft set. Suppose x_r is an c-soft set and $x_r \notin \mathcal{F}_R$ Since $\mathcal{F}_R$ is $\mathcal{g}c$- soft set, then $\tilde{u}(\mathcal{F}_R) \sqsubseteq \widetilde{\mathcal{M}} - x_r$, then $x_r \notin \tilde{u}(\mathcal{F}_R)$, This implies $\tilde{u}(\mathcal{F}_R) \sqsubseteq \mathcal{F}_R$. Then $\mathcal{F}_R$ is closed, therefore $\widetilde{\mathcal{M}}$ *is* $\mathcal{T}_{\frac{1}{2}}$-soft-$cs$. Suppose x_r is an σ-soft set and $x_r \notin \mathcal{F}_R$, then $x_r \in \widetilde{\mathcal{M}} - \mathcal{F}_R$, then $\mathcal{F}_R \sqsubseteq \widetilde{\mathcal{M}} - x_r$. This implies $\tilde{u}(\mathcal{F}_R) \sqsubseteq \tilde{u}\big(\widetilde{\mathcal{M}} - x_r\big) = \widetilde{\mathcal{M}} - x_r$, then $\tilde{u}(\mathcal{F}_R) \sqsubseteq \widetilde{\mathcal{M}} - x_r$, this implies $x_r \notin \tilde{u}(\mathcal{F}_R)$. Then $\tilde{u}(\mathcal{F}_R) \sqsubseteq \mathcal{F}_R$, then $\mathcal{F}_R$ is c-soft set. Therefore, $(\mathcal{M},\tilde{u},R)$ is $\mathcal{T}_{\frac{1}{2}}$-soft-$cs$. □

Proposition 4.4 Let $(\mathcal{M},\tilde{u},R)$ be a soft-cs and let $(\mathcal{Y},\tilde{u}_y,R)$ be a closed soft-c.subsp of $(\mathcal{M},\tilde{u},R)$. If $\mathcal{F}_R$ is $\mathcal{g}c$-soft set of $(\mathcal{Y},\tilde{u}_y,R)$, then $\mathcal{F}_R$ is $\mathcal{g}c$-soft set of $(\mathcal{M},\tilde{u},R)$.

Proof. Let $\mathcal{F}_R$ be a $\mathcal{g}c$- soft set of $(\mathcal{Y},\tilde{u}_y,R)$. Let $\mathcal{F}_R \sqsubseteq G_R$, where G_R is an σ-soft set of $\mathcal{M}$. Since $\mathcal{F}_R \in \mathcal{SS}(\mathcal{Y},R)$, then $\mathcal{F}_R \sqsubseteq \tilde{\mathcal{Y}} \sqcap G_R$. From Theorem 2.13, $\tilde{\mathcal{Y}} \sqcap G_R$ is an σ-soft set of $(\mathcal{Y},\tilde{u}_y,R)$. But $\mathcal{F}_R$ is $\mathcal{g}c$-soft set of $(\mathcal{Y},\tilde{u}_y,R)$, thus $\tilde{u}_y(\mathcal{F}_R) \sqsubseteq \tilde{\mathcal{Y}} \sqcap G_R$ which implies $\tilde{\mathcal{Y}} \sqcap \tilde{u}(\mathcal{F}_R) \sqsubseteq \tilde{\mathcal{Y}} \sqcap G_R$ and since $\tilde{\mathcal{Y}}$ is c-soft set in $\mathcal{M}$, we get $\tilde{u}(\tilde{\mathcal{Y}}) \sqcap \tilde{u}(\mathcal{F}_R) \sqsubseteq \tilde{\mathcal{Y}} \sqcap G_R$. From Proposition 2.11 part (2), it follows $\tilde{u}(\tilde{\mathcal{Y}} \sqcap \mathcal{F}_R) \sqsubseteq \tilde{\mathcal{Y}} \sqcap G_R$. This implies $\tilde{u}(\mathcal{F}_R) \sqsubseteq \tilde{\mathcal{Y}} \sqcap G_R$ and consequently, $\tilde{u}(\mathcal{F}_R) \sqsubseteq G_R$.Therefore, $\mathcal{F}_R$ is $\mathcal{g}c$- soft set of $(\mathcal{M},\tilde{u},R)$. □

Proposition 4.5 Let $(\mathcal{M},\tilde{u},R)$ be a soft-cs and $(\mathcal{Y},\tilde{u}_y,R)$ be a closed soft-c.subsp of $(\mathcal{M},\tilde{u},R)$. If $(\mathcal{M},\tilde{u},R)$ is $\mathcal{T}_{\frac{1}{2}}$- soft-$cs$, then $(\mathcal{Y},\tilde{u}_y,R)$ is $\mathcal{T}_{\frac{1}{2}}$-soft -cs.

Proof. Let $\mathcal{F}_R$ be a $\mathcal{g}c$-soft set of $(\mathcal{Y},\tilde{u}_y,R)$, to prove $\mathcal{F}_R$ is c-soft set of $(\mathcal{Y},\tilde{u}_y,R)$. Since $\mathcal{F}_R$ be a $\mathcal{g}c$-soft set of $(\mathcal{Y},\tilde{u}_y,R)$. Then by Proposition 4.4, we have $\mathcal{F}_R$ is a $\mathcal{g}c$-soft set of $\mathcal{M}$. Since $\mathcal{M}$ is $\mathcal{T}_{\frac{1}{2}}$-soft-$cs$, then $\mathcal{F}_R$ is c-soft set of $\mathcal{M}$. This implies $\mathcal{F}_R \sqcap \tilde{\mathcal{Y}}$ c-soft set of $(\mathcal{Y},\tilde{u}_y,R)$. Therefore $\mathcal{F}_R$ is c-soft set of $(\mathcal{Y},\tilde{u}_y,R)$. □

References

[1] A Aygünoğlu and H Aygün Some notes on soft topological spaces *Neural Comput & Applic DOI10.1007/ s00521-011-0722-3*
[2] K V Babitha and J J Sunil 2010 Soft set relations and functions *Comput. Math. Appl.* **60** pp1840-1849
[3] K Balachandran, P Sundaram and H Maki 1991 On generalized continuous maps maps in topological spaces *Mem. Fac. Sci. Kochi Univ. Ser. A Math.* **12** pp 5-13
[4] C Boonpok and J Khampakdee 2008 between closed sets and generalized closed sets in closure spaces *Acta Math. Inf. Univ. Ostraviensis* **16** pp 3-14
[5] E Čech 1968 Topological Spaces *Topological Papers of Eduard Čech, Academia, Prague* 436-472
[6] S Das and S K Samanta 2013 Soft metric *Annals of Fuzzy Mathematics and Informatics* **1** pp 77-94
[7] S T Ekram and R N Majeed 2020 Soft closure spaces *IOP Conf. Series: Journal of Physics: Conference Series* **1591** 012076
[8] S T Ekram and R N Majeed Soft continuous mappings in soft closure spaces *Iraqi Journal* of Science accepted
[9] F Feng, Y B Jun and X Zhao 2008 Soft semirings *Comput. Math. Appl.* **56** pp 2621-2628
[10] R Gowri and G Jegadeesan 2014 On soft Čech closure spaces *International Journal of Mathematics Trends and Technology* **9** (2) pp 122-127
[11] K Kannan 2012 Soft generalized closed sets in soft topological spaces *Journal of Theoretical and Applied Information Technology* **37**(1) pp17-21
[12] N Levine 1970 Generalized closed sets in topology *Rend. Circ. Mat. Palermo* **19** pp 89-96
[13] R N Majeed 2018 Čech fuzzy soft closure spaces International *Journal of Fuzzy System Applications* **7**(2) pp 62-74
[14] P K Maji, R Biswas and R Roy 2003 Soft set theory *Comput. Math. Appl.* **45** pp 555-562
[15] D Molodtsov 1999 Soft set theory-First results *Comput. Math. Appl.* **37** pp 19-31
[16] M Shabir and M Naz 2011 On soft topological spaces *Computers and Mathematics with Applications* **61 pp** 1786-1799

Face Detection for Color Image Based on MATLAB

Face Detection for Color Image Based on MATLAB

Shahad laith abd al_galib, Asma Abdulelah Abdulrahman, Fouad Shaker Tahir Al-azawi

University of Technology, Department of Applied Science, Mathematics and Application of Computer, Baghdad, Iraq.

E-mail: 100243@uotechnology.edu.iq

Abstract. Amazing results in many works in the field of deep convolutional neural networks using them in many fields of machine learning such as image classification control of atrial play, and image annotation. Mathematical analysis of deep convolutional neural networks (CNN) has a broad role in many applications including image classification applications. Face recognition technology has occupied a wide field in research that is still continuing in this work. Face recognition technology is being developed depending on the MATLAB program to develop the subjecting of the color image to the neural convolution network and the work of a program to reduce the time the network deals with the image to reduce the number of layers to only two layers and access the algorithm Suggested in this work. Computer vision of a color image in a face detection study. In this work, the researcher created a fast algorithm to reach the research goal based on new standards in the field of face detection. A new face detection program was designed using MATLAB, CascadeObjectDetector and trainCascadeObjectDetector the face detection devices were developed. In this work, a technique for panning and color image using the convolutional neural network for deep learning is proposed, the method used to reach the goal of this work.

1. Introduction

In recent years, the field of face recognition has taken a wide area of research due to the urgent need for security and commercial applications to demonstrate the interaction between humans and computers using measurement analysis. The work in this field varies greatly in terms of face, skin, gender, and colour [1]. The difference in the background lighting of the face and facial expressions is a reason that increases the complexity of the problem [2]. Among the many applications in the field of face detection, including recognition and monitoring of the driver's face, face recognition by means of video surveillance, or image data management, the algorithms for face detection are characterized by complexity. Face detection is complicated [3]. In [4] which it was clarified that the face detection algorithms are divided into two parts, (i) feature (ii) learning, the first is based on simple facial features without looking at the surrounding light, rotating, or standing. The face position is determined by the vertical projection of the grey level image after the image has been projected for face detection [5]. The role of the neural network appears strongly in the field of facial recognition that has the potential to deal with image data .The neural network technology is multi-layered as it is to design a file containing a recognition system that results in a completely flat structure with inputs that are completely connected to later layers in architecture due to huge interconnecting nodes in addition to the amount of input data that is ignored. This leads to training for all permutations in the input vector

[6]. The fields of science and technology have led us to develop rapidly in order to be able to reach goals that were far from being achieved in the past few decades. Many areas have made life easier, such as machine learning and artificial intelligence, to reach solutions to complex problems in modern science. Computer vision achieves algorithms on the human level in classifying and analysing images. It was presented YOLO theory to discover things and Fast YOLO, which is the fastest detector, is the fastest detector for the general purpose [7]. Face detection was achieved using PCA theory. The network was trained fast [**8**]. The performance of face detection is evaluated by the false-match rate (FMR), and the false-non-match rate (FNMR) [**9**]. Viola Jones' method was used to check the number of faces that have been treated and count the number of faces [10]. Modern technology has a role in computer vision at this time when the world is living fighting the emerging corona virus, the disease pandemic (Covid-19) due to technology, work has been completed from home to adapt to the disease [11]. Facial characteristics such as freckles and hair were identified using a new generator to present data on human faces [12]. the method Kanade Lucas Tomasi (KLT), which is a simple system where it is able to detect the face and track it where the system is able to detect the face when the head moves and tilts, with Estim Geometric Transform (EGT) function and Duration Geometric Transform (DGT)[13]. In this work, a fast algorithm was proposed based on the use of CNN and the use of the MATLAB program to classify the image and the detection of the face in two stages, the face detection without a mask that has different measurements and criteria for the detection of the face with the mask and the use of the algorithm in tracking objects in these circumstances.

2. Methodology

2.1. Research Design The purpose of this paper is to achieve the recognition of a face or a number of faces, the steps for face recognition will be achieved as shown in figure (1) in this figure a number of steps have been achieved to show the structure of the search.

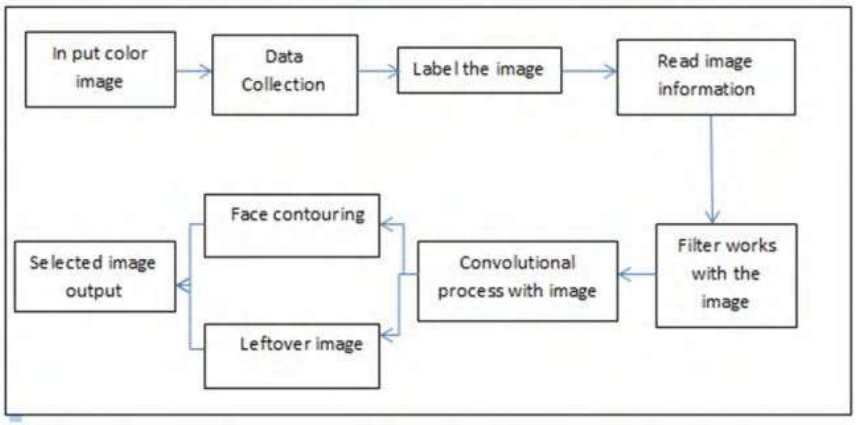

Figure 1. Shows the steps of research design with the result

The color image and face highlighting are read as cover layers are incorporated into this work. CNN is used with a mathematical technique to calculate the torsion where the person's face is determined and then the layer is fused as shown in Figure (2).

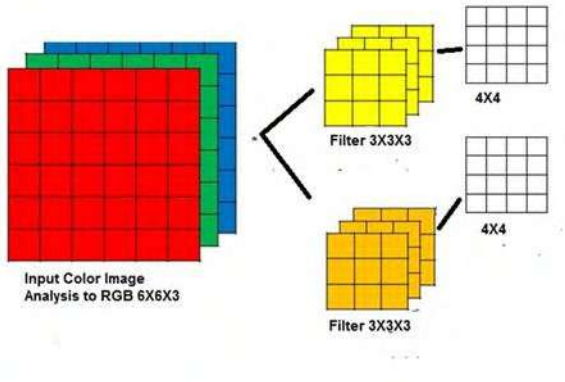

Figure 2. Convolutions on RGB image

3. Convolutional neural network method

The convolutional neural network method is unique. It combines segmentation, extraction, and classification in features. One processing unit. CNN components are 7 layers of 4 feature extraction layers and 3 layers of MLP. The feature extraction layer consists of twisting and subsample layers. Warp layer removes noise and detects lines, borders, or corners of an image file. Preventing image distortion is in the Downsampling layer, which reduces image resolution. CNN has built-in stability compared to a typical neural network (MLP). CNN excels at producing high accuracy in the identification process even though the algorithm is complex. In network training, LeNet-5 applies
The proposed algorithm will be built using MATLAB by designing a program for a learning algorithm to identify the face with a simple and easy base to reverse previously identified neural networks to implement a complex database.

4.Mathematical aspects in CNN Technology

Deep learning deals with images using computer vision and processes large numbers of images from multiple countless numbers, Computer vision relies on the convolutional neural network fed into neural networks to reveal the face,

The pictures are inserted in mathematical expressions.

As shown in figure (3), using the filter and multiplying it with the color image, the sum of the product is obtained by the item

The result of this process is a convolution that defines the volume to mathematically represent the image then; the height size denoted by m_H, the width of size is m_W, the number of channels denoted m_c. A color image RGB has three channels m_3 red, green, and blue. The filter is F

The filter is single to center each pixel in the filter that must contain the kernel N with the number of channels identical to the image, so a different filter is applied that passes on each channel, Equation (1) calculate the dimensions of the filter

Dim filter=(F,F,m_c) (1)

The image is mapped with filter the convolutional process mathematically is

$$C(I,N)_{x,y} = \sum_{i=1}^{m_H} \sum_{j=1}^{m_W} \sum_{N=1}^{m_C} N_{i,j-N} I_{x+i-1,y+j-1,N} \quad (2)$$

$$\dim\big(C(I,N)\big) = \left(\left[\frac{m_H+2P-F}{S}+1\right],\left[\frac{m_W+2P-F}{S}+1\right]\right) \quad S>0; \quad (3)$$

If $S=1$ equation (3) will be

$$(m_H+2P-F, m_W+2P-F) \quad (4)$$

Where [n] is the floor function of n P=0 is the valid CNN output size is equal output size then $P=\frac{F-1}{2}$ is the same CNN, if F=1, this means 1×1Convolution.

The merging and reduction process distinguishes the image by specifying its information on each channel, which affects the dimensions (m_H, m_W) and maintains the number of channels after passing the filter.

$$\dim\big(P(I,N)\big) = \left(\left[\frac{m_H+2P-F}{S}+1\right], \left[\frac{m_W+2P-F}{S}+1\right], m_C\right) \quad S>0; \tag{5}$$

If $S=1$ equation (5) will be

$$(m_H+2P-F, m_W+2P-F, m_C) \tag{6}$$

After the training process, using CNN leads to the reduction of a number of layers Figure (4) shows how a process F led to the reduction of the three layers

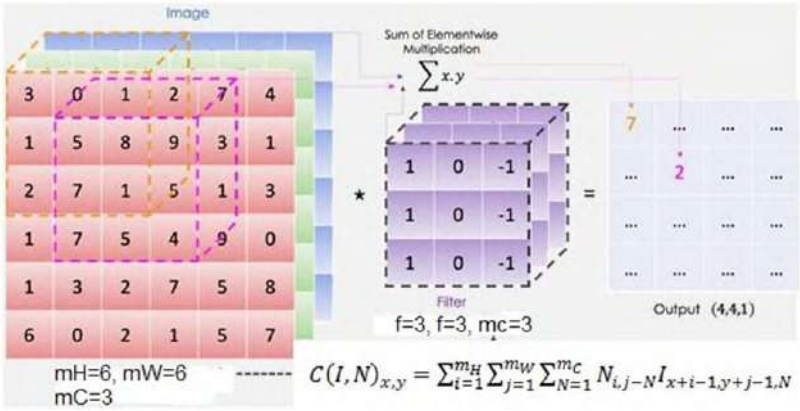

Figure 3. the convolutional neural network in color image

Using filters on the input image using the activation function £,

4.1. Mathematical algorithm in convolutional process In 1th layer

Input image with $r^{[l]}$, $r^{[l-1]}$ and size $\left(m_H^{[l-1]}, m_W^{[l-1]}, m_C^{[l-1]}\right)$, Padding $p^{[1]}$, stride $s^{[l]}$, number of filters $m_C^{(l)}$ where each $F^{(m)}$ has the dimension $\left[f^l, f^l, m_C^{[l-1]}\right]$, and activation function $£^{[l]}$.

Output $r^{[l]}$ with size $\left(m_H^{(l)}, m_W^{(l)}, m_C^{(l)}\right)$ $\forall\, m \in \left[1,2,\dots,m_C^{[l]}\right]$

Step1: the convolution step CNN

$$conv(r^{[l-1]}, F^{[l-1]})_{x,y} = £^{[l]}\left(\sum_{i=1}^{m_H^{[l-1]}}\sum_{j=1}^{m_W^{[l-1]}}\sum_{K=1}^{m_C^{[l-1]}} F_{i,j,K}^{(m)} r_{x+i-1,y+j-1,f}^{[l-1]} + s_m^{[l]}\right)$$

$$\dim\left(conv\left(r^{[l-1]}, F^{(m)}\right)\right) = (m_H^{[l]}, m_W^{[l]}) \tag{7}$$

$$r^{[l]} = £^{[l]}\left(conv(r^{[l-1]}, F^{[1]})\right), £^{[l]}\left(conv(r^{[l-1]}, F^{[2]})\right), \dots, £^{[l]}\left(conv(r^{[l-1]}, F^{[m_c^{[l]}]})\right)$$

Where

$$m_{H/W}^{[l-1]} = \left[\frac{m_{H/W}^{[l-1]}+2P^{[l]}-f^{[l]}}{S^{[l]}}+1\right]; S>0 \tag{8}$$

$$= m_{H/W}^{[l-1]} + 2P^{[l]} - f^{[l]}; S=0$$

$m_C^{[l]}$ = number of filters

The learned parameters at the l^{th} layer filters with $(f \times f \times m) \times m_C^{[l]}$ parameters

Bias with $(1 \times 1 \times 1) \times m_C$ parameters (broad casting)

Figure (4) and Figure (5) represent the shrinkage of the convolutional layer

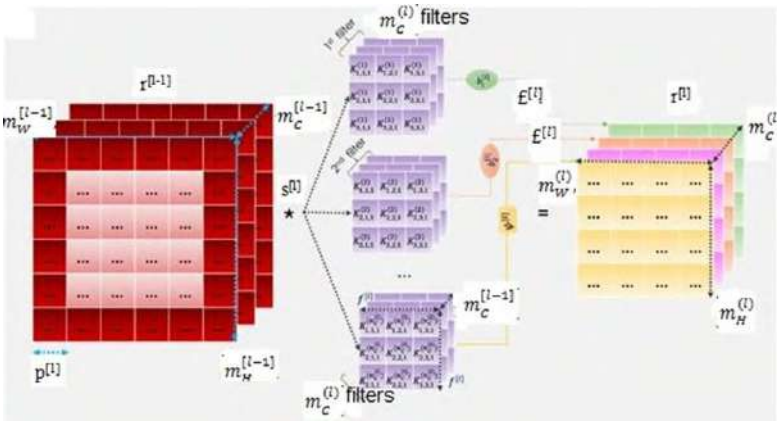

Figure4. The convolutional layer

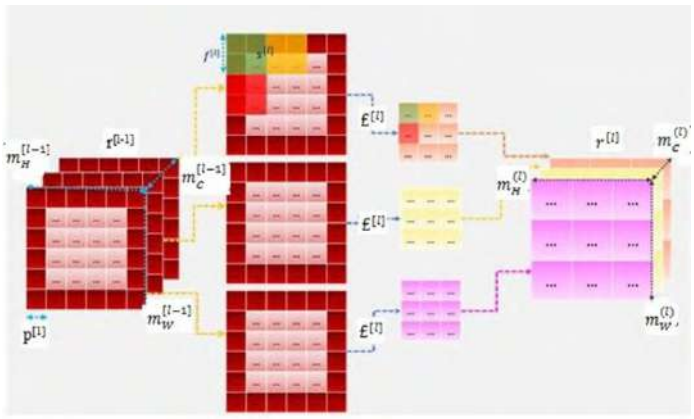

Figure5. The convolutional layer

4.2. Fully Connected layer

The definition of a fully connected layer is the layer that enters its vector and then another layer is created from a limited number of neurons

Then j^{th} node with i^{th} layer the equation is achieved (9)

$$W_j^{[i]} = \sum_{j=1}^{m_{i-1}} w_{j,1}^{[i]} + s_j^{[i]} \quad (9)$$

$$r_j^{[i]} = £^{[i]}\left(w_j^{[i]}\right) \quad (10)$$

The input $r^{[i-1]}$ might be the result of convolution or a pooling layer with the dimensions $\left(m_H^{[i-1]}, m_W^{[i-1]}, m_C^{[i-1]}\right)$ in order to be able to plug it into the fully connected layer; we flatten the tensor to one dimension vector having the dimension $\left(m_H^{[i-1]} \times m_W^{[i-1]} \times m_C^{[i-1]}, 1\right)$ thus $m_{i-1} = m_H^{[i-1]} \times m_W^{[i-1]} \times m_C^{[i-1]}$

The learned parameters at the l^{th} layer are weights $w_{j,1}$ with $m_{l-1} \times m_l$

Parameters bias with m_l parameters, Figure (6) shows the fully connected layer

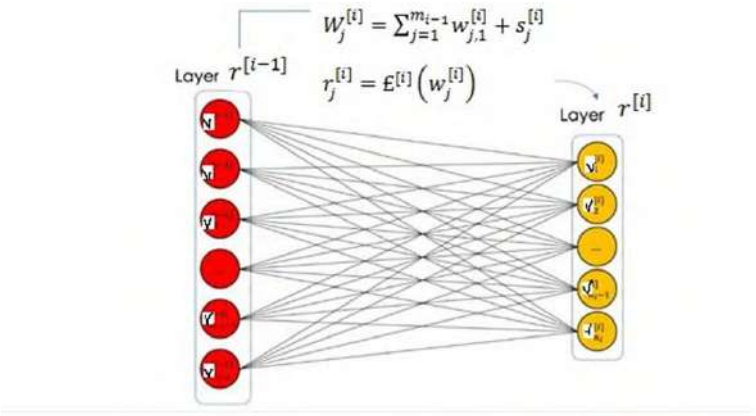

Figure6. Shows the fully connected layer

Figure (7) shows the previous steps that illustrate the chain of operations by which a convolutional neural network is constructed

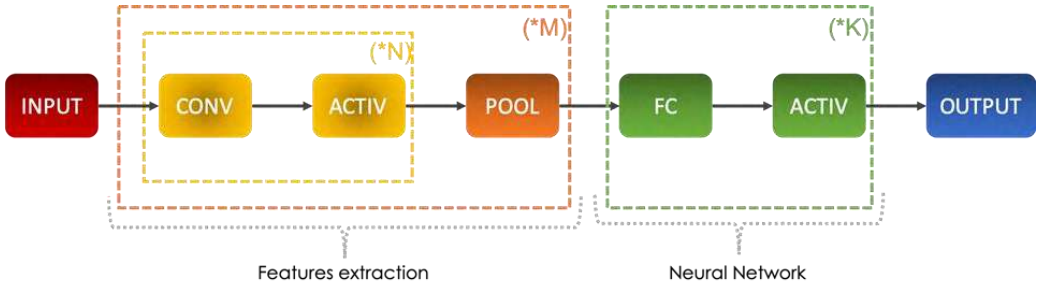

Figure 7. Shows the steps of convolution neural network CNN

The process is repeated for a certain number of convolutions. The image features are extracted that the entire connected neural network is equipped with the image features followed by the activation functions that aim to reduce (m_H, m_W, m_C) the depth in the network Figure (8) shows the three dimensions of the convolutional neural network

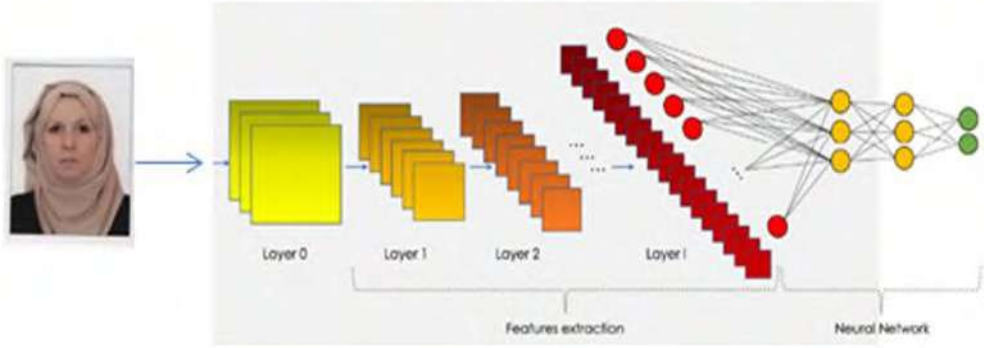

Figure8. Using the filter and multiplying it with the color image

5. Faces Detection Steps

The identification of a person is done through facial identification, depending on the biological characteristics that the person possesses. This method has many challenges

1. Lighting fixture

When the light source causes brightness, which affects the brightness of the image because the light surrounding the face causes the lack of quality performance to distinguish the face

2.Facial Expressions:

The person's feelings are evident in a facial expression that displays messages such as anger represented by frowning by pulling the eyebrows close together, which requires a good algorithm to recognize faces in a variety of expressions

3. Confirmation of Positioning:

When the person's face is fixed, it leads to obscuring some of the facial features that he wishes to mask in the image.

4. Partial structural component:

means partial support, the structural components, including size, color, and shapes such as mustaches, glasses, and beards are considered partial components

The computer interface deals with the image database to detect the face with its measurements, where the image is recognized, i.e. on the face as a file, in addition to video monitoring. In this work, the Matlab program is used to identify the face

A fast program is designed to recognize the face of the color image

6. Face recognition using MATLAB

Face recognition is a complex technology that is most often when unlocking your phone or passing through a high-tech monitoring system. Here comes the question about how to use MATLAB in face recognition?

The recognition of human faces is carried out using technology in particular, computer vision technology to distinguish facial features taken from photo and video clips. To get the best results, an algorithm was proposed to identify the face and compare it with the face data. By using MATLAB code, face, eyes, nose, and mouth recognition is achieved through the built-in Cascade Object Detector function in the toolbox.

7. Fast facial algorithm

A program was designed to determine the face, where good results were obtained and in quick steps.
Figure (9) shows how to use the MATLAB program to identify the face
The proposed algorithm, with the help of MATLAB, to identify the face, the following steps show the stages of the face detection of the image
Input color Image
Step1: analyses image to 3 layers RGB
Step 2: processed filter 3×3 After you treat the filter with the image, the
image size is reduced
Step3: In this step, the object properties are determined after
Vision. Cascade Object Detector is created
face Detector = vision. Cascade Object Detector ();
step4: In this step, you call the object with the arguments (as if it
behaves as a function).
Space5: Facial information is identified and read
Location of the Face = step (face Detector, the Image);
output the image with face detected

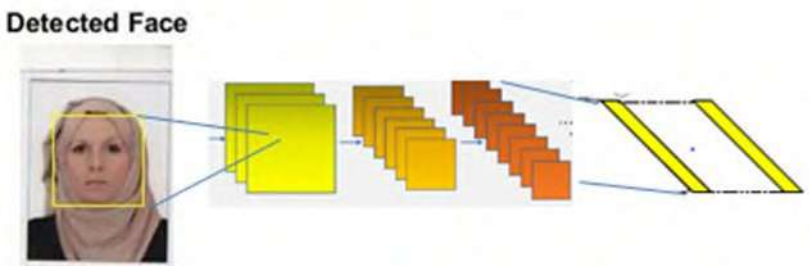

Figure 9a. Shows face identification

With location face is [19, 40, 50, 20], height of image 255 and width 128

Figure 9b. Shows face identification

With location face is [105,68,51,51]

8. Discuss the results

In this section, the results obtained for the correct rate of face detection are presented. the new algorithm shows its efficiency by presenting the results obtained. In this work, a modern version of MATLAB was used to design a face detection program for several people in one image, and the best results were obtained. Figure (10) and Figure (11) show the efficiency of the proposed algorithm to detect the face of a number of people and distinguish their faces with the label. The correct rate of the proposed algorithm is 98%, an image containing 3 members and the image is ($432 \times 980 \times 3$ unit8) with Boxing Faces is and table (1) shows Bounding Box values which comprises of [x, y, Height, Width] of faces to be detected Figure (10) The sample to which the proposed algorithm is applied

Figure 10. shows the efficiency of the proposed algorithm to detect the face of a number of people and distinguish their faces.

Table (1) shows Bounding Box values

X	Y	width	Height
442	150	115	115
125	28	150	150
571	31	267	267

Figure (11) shows the efficiency of the proposed algorithm to detect the face of a number of masked people and distinguish their faces.

9.Conclusion

In this paper, a new algorithm was built for face detection technology by segmenting the color image into RGB in which a neural network is used, where the face area of a person was detected through a comparison between the input and output image, the correctness of the face detection rate 98%.

With the implementation of the algorithm in the MATLAB program, good results were obtained for the indications of the algorithm.

a new technique for identifying the face of color images was presented after analyzing the image and dividing it into three layers resulting from the neural network that helps to detect the features of the face, and by using the MATLAB program, a classification technique is applied to detect the face, which satisfactory results were obtained after using the basic equations.

The algorithm was applied to the images without a mask, and the other stage was with the mask. As for the last, the experiment was on the image with the mask and glasses, and the algorithm was applied with high and fast technology, as the algorithm proved its efficiency because the examples showed that the new algorithm is valid under the new circumstances.

References

[1] A M Abou El-Nasr, and A L Abbot 2007 A New Face Detection Technique using 2D DCT and Self Organizing Feature Map in *Proc. of World Academy of Science Engineering and Technology* **21** pp 15-19

[2] J. Nagi 2007 Design of an Efficient High-speed Face Recognition System *Department of Electrical and Electronics Engineering College of Engineering Universiti Tenaga Nasional March*

[3] C Zhang, Z Zhang 2010 Boosting-based face detection and adaptation *Synthesis Lectures on Computer Vision Morgan & Claypool Publishers* **2** (1) pp 1-140

[4] M H Yang, D J Kriegman and N Ahuja 2002 Detecting faces in images: a survey *IEEE Transactions on Pattern Analysis and Machine Intelligence* **24** (1)

[5] F Wang and H Qin 2005 A FPGA based driver drowsiness detecting system *Proceedings of IEEE International Conference on Vehicular Electronics and Safety* Xian October

[6] H Khalajzadeh, M Mansouri, T M Hierarchical 2013 Structure Based Convolutional Neural Network for Face Recognition *Int J Comput Intell Applicat* **12** (03)

[7] G A Farhadiy 2016 You Only Look Once: Unified, Real-Time Object Detection arXiv 1506.02640v5 [cs.CV]

[8] P Yadav, K Dhankad, A Shrivastava, A Kumar, P Manglik STUDY & ANALYSIS OF FACE DETECTION & RECOGNITION; MATLAB APPROACH *IJESAT International Journal of Engineering Science & Advanced Technology* **4** (3) pp 285-292

[9] G Ravindra 2017 Dabhade Optimal Neural Network Based Face Recognition System for Various Pose and Occluded Images *International Journal of Applied Engineering Research* **12** (22) pp 12625-12636

[10] E Winarno 2018 Multi-View Faces Detection Using Viola-Jones Method Journal of *Physics: Conference Series J.Phys*. Conf. Ser 1114 012068
[11] M S Ejaz, M R Islam, M Sifatullah, A Sarker 2019 Implementation of principal component analysis on masked and non-masked face recognition *1st International Conference on Advances in Science Engineering and Robotics Technology (ICASERT)* pp 1–5
[12] T Karras, S Laine and T Aila 2019 A Style Based Generator Architecture for Generative Adversarial Networks *IEEE/CVF Conference on Computer Vision and Pattern Recognition (CVPR)* Long Beach CA USA pp 4396- 4405 doi: 10.1109/CVPR.2019.00453
[13] F Shaker, A Abdulelah 2020 Face Detection By some Methods based on MATLAB *Journal of Al- Qadisiyah for Computer Science and Mathematics* **12** (4) pp 12–17

Univalence Criteria for Holomorphic Functions Involving Srivastava-Attiya Operator

Univalence Criteria for Holomorphic Functions Involving Srivastava-Attiya Operator

Huda F. Hussian, Abdul Rahman S. Juma

Department of Mathematics, University of Anbar, Ramadi, Iraq

E-mail: dr_juma@hotmail.com

Abstract. The purpose of present paper is to introduce and investigate the univalence criteria of holomorphic functions by employ a basically general form of Srivastava-Attiya operator. In specific, we derive several sufficient conditions of univalence for the generalized Srivastava-Attiya operator .Furthermore, number of famous univalent conditions would follow across specializing the parameters involved.Relevant connections with other related previous works are also indicating.

1. Introduction

Let $\mathcal{A}$ be the class of functions f of the form

$$f(z) = z + \sum_{k=2}^{\infty} a_k z^k , \quad (1)$$

which are holomorphic in the open unit disk $U = \{z \in \mathbb{C} : |z| < 1\}$.

Let S be the subclass of $\mathcal{A}$, which consists of functions of the form (1) that are univalent and normalized by the conditions

$$f(0) = 0 \quad \text{and} \quad f'(0) = 1 \text{ in U.}$$

In geometric function theory, the Univalence of complex functions considered as substantial property. However, it is complicated, and in many situations impossible to show immediately that a certain complex function is univalent. because of that many authors found different kinds of sufficient conditions of univalence. On of the most substantial of these conditions of univalence in the domains U and the exterior of the closed unit disk is the well-known criterion of Becker [2].Becker us the generalized Loewner differential equation and theory of Loewner chains cleverly. Extension of these criterias were given by Deniz and Orhan [4], Ali et al. [1] and Nehari [6].

For $f \in \mathcal{A}$, the generalized Srivastava-Attiya operator $\psi^{s,a,\beta}_{(\beta_p),(\alpha_q),b} : \mathcal{A} \to \mathcal{A}$ is defined by

$$\psi^{s,a,\beta}_{(\beta_p),(\alpha_q),b} f(z) = z + \sum_{k=2}^{\infty} \frac{\prod_{i=1}^{P}(1+\beta_i)_{k-1}}{\prod_{i=1}^{q}(1+\alpha_i)_{k-1}} \left(\frac{B(a+k,b,s,\beta)}{B(a+1,b,s,\beta)}\right) \left(\frac{a+1}{a+k}\right)^s a_k z^k \quad (2)$$

$(\beta_i \in \mathbb{C}(i = 1, \dots, p);\ \alpha_i \in \mathbb{C} \setminus Z_0^-(i = 1, \dots, q); z \in U; p \le q + 1;$ $\min\{\mathcal{R}(a), \mathcal{R}(s)\} > 0; \beta > 0$ when $\mathcal{R}(b) > 0$ and $S \in \mathbb{C}; a \in \mathbb{C}\setminus Z_0^-$ when $b = 0$). For more details see [9,10]

In this paper, we derive sufficient conditions of univalence for the generalized Srivastava-Attiya operator $\psi^{s,a,\beta}_{(\beta_p),(\alpha_q),b} f(z)$.

Furthermore, a number of known univalent conditions would follow across specializing the parameters involved. We will use the following lemmas to prove our results.

Lemma1.1 [2] Let $f \in \mathcal{A}$. If for all $z \in U$

$$(1-|z|^2)\left|\frac{z\,f'(z)}{f''(z)}\right| \le 1, \tag{3}$$

then f is univalent in U.

Lemma1.2 [7] Let $f \in \mathcal{A}$. If for all $z \in U$

$$\left|\frac{z^2\,f'(z)}{f^2(z)}-1\right| \le 1, \tag{4}$$

then f is univalent in U.

Lemma1.3 [11] Let be real number $\eta > \frac{1}{2}$ and $f \in \mathcal{A}$. If for all z $\in U$

$$(1-|z|^{2\eta})\left|\frac{z\,f''(z)}{f'(z)}+1-\eta\right| \le \eta, \tag{5}$$

then f is univalent in U.

Lemma 1.4 [5] If $f \in S$. If for all $z \in U$,

$$\frac{z}{f(z)} = 1+\sum_{k=1}^{\infty} b_k z^k, \tag{6}$$

then $\sum_{k=1}^{\infty}(k-1)|b_k| \le 1$.

Lemma 1.5 [8] Let $v \in \mathbb{C}, \mathcal{R}e(v) \ge 0$ and $f \in \mathcal{A}$. If for all $z \in U$

$$\frac{1-|z|^{2\mathcal{R}e(v)}}{\mathcal{R}e(v)}\left|\frac{z\,f''(z)}{f'(z)}\right| \le 1, \tag{7}$$

then a function

$$T_v(z) = \left(v\int_0^z y^{v-1}\,f'(y)dy\right)^{\frac{1}{v}}$$

is univalent in U.

2. Main Results

In this section, we determine the sufficient conditions to get univalence for holomorphic functions by using the Srivastava – Attiya operator.

Theorem 2.1 Let $f \in \mathcal{A}$. If for all $z \in U$

$\sum_{k=1}^{\infty}\frac{\prod_{i=1}^{p}(1+\beta_i)_{k-1}}{\prod_{i=1}^{q}(1+\propto_i)_{k-1}}\left(\frac{B(a+k,b,s,\beta)}{B(a+1,b,s,\beta)}\right)\left(\frac{a+1}{a+k}\right)^s [k(2k-1)]\,|a_k| \le 1$,

then $\psi^{s,a,\beta}_{(\beta_p),(\propto_q),b}f(z)$ is univalent in U. (8)

Proof . Let $f \in \mathcal{A}$. Then for all $z \in U$, we have

$$(1-|z|^2)\left|\frac{z\left(\psi^{s,a,\beta}_{(\beta_p),(\propto_q),b}f(z)\right)''}{\left(\psi^{s,a,\beta}_{(\beta_p),(\propto_q),b}f(z)\right)'}\right| \le (1-|-z|^2)\frac{|z|\left|\left(\psi^{s,a,\beta}_{(\beta_p),(\propto_q),b}f(z)\right)''\right|}{\left|\left(\psi^{s,a,\beta}_{(\beta_p),(\propto_q),b}f(z)\right)'\right|}$$

$$\leq (1+|z|^2)\frac{|z|\left|\left[z+\sum_{k=2}^{\infty}\frac{\prod_{i=1}^{p}(1+\beta_i)_{k-1}}{\prod_{i=1}^{q}(1+\propto_i)_{k-1}}\left(\frac{B(a+k,b,s,\beta)}{B(a+1,b,s,\beta)}\right)\left(\frac{a+1}{a+k}\right)^{s}a_k\,z^k\right]''\right|}{\left|\left[z+\sum_{k=2}^{\infty}\frac{\prod_{i=1}^{p}(1+\beta_i)_{k-1}}{\prod_{i=1}^{q}(1+\propto_i)_{k-1}}\left(\frac{B(a+k,b,s,\beta)}{B(a+1,b,s,\beta)}\right)\left(\frac{a+1}{a+k}\right)^{s}a_k\,z^k\right]'\right|}$$

$$=(1+|z|^2)\frac{|z|\left|\sum_{k=2}^{\infty}\frac{\prod_{i=1}^{p}(1+\beta_i)_{k-1}}{\prod_{i=1}^{q}(1+\propto_i)_{k-1}}\left(\frac{B(a+k,b,s,\beta)}{B(a+1,b,s,\beta)}\right)\left(\frac{a+1}{a+k}\right)^{s}k(k-1)\,z^{k-2}\right|}{|1|-\left|\sum_{k=2}^{\infty}\frac{\prod_{i=1}^{p}(1+\beta_i)_{k-1}}{\prod_{i=1}^{q}(1+\propto_i)_{k-1}}\cdot\left(\frac{B(a+k,b,s,\beta)}{B(a+1,b,s,\beta)}\right)\cdot\left(\frac{a+1}{a+k}\right)^{s}k\,a_k\,z^{k-1}\right|}$$

$$\leq (1+|z|^2)\frac{|z|\left[\sum_{k=2}^{\infty}\left|\frac{\prod_{i=1}^{p}(1+\beta_i)_{k-1}}{\prod_{i=1}^{q}(1+\propto_i)_{k-1}}\right|\left(\frac{B(a+k,b,s,\beta)}{B(a+1,b,s,\beta)}\right)\left(\frac{a+1}{a+k}\right)^{s}k(k-1)\,|a_k|\,|z^{k-2}|\right]}{\left[1-\sum_{k=2}^{\infty}\left|\frac{\prod_{i=1}^{p}(1+\beta_i)_{k-1}}{\prod_{i=1}^{q}(1+\propto_i)_{k-1}}\right|\left(\frac{B(a+k,b,s,\beta)}{B(a+1,b,s,\beta)}\right)\left(\frac{a+1}{a+k}\right)^{s}k\,|a_k|\,|z^{k-1}|\right]}$$

$$\leq \frac{2\sum_{k=2}^{\infty}\left|\frac{\prod_{i=1}^{p}(1+\beta_i)_{k-1}}{\prod_{i=1}^{q}(1+\propto_i)_{k-1}}\right|\left(\frac{B(a+k,b,s,\beta)}{B(a+1,b,s,\beta)}\right)\left(\frac{a+1}{a+k}\right)^{s}k(k-1)|a_k|}{1-\sum_{k=2}^{\infty}\left|\frac{\prod_{i=1}^{p}(1+\beta_i)_{k-1}}{\prod_{i=1}^{q}(1+\propto_i)_{k-1}}\right|\left(\frac{B(a+k,b,s,\beta)}{B(a+1,b,s,\beta)}\right)\left(\frac{a+1}{a+k}\right)^{s}k\,|a_k|}$$

Applying Lemma 1.1,we get

$$\frac{2\sum_{k=2}^{\infty}\left|\frac{\prod_{i=1}^{p}(1+\beta_i)_{k-1}}{\prod_{i=1}^{q}(1+\propto_i)_{k-1}}\right|\left(\frac{B(a+k,b,s,\beta)}{B(a+1,b,s,\beta)}\right)\left(\frac{a+1}{a+k}\right)^{s}k(k-1)|a_k|}{1-\sum_{k=2}^{\infty}\left|\frac{\prod_{i=1}^{p}(1+\beta_i)_{k-1}}{\prod_{i=1}^{q}(1+\propto_i)_{k-1}}\right|\left(\frac{B(a+k,b,s,\beta)}{B(a+1,b,s,\beta)}\right)\left(\frac{a+1}{a+k}\right)^{s}k\,|a_k|}\leq 1$$

then

$$2\sum_{k=2}^{\infty}\left|\frac{\prod_{i=1}^{p}(1+\beta_i)_{k-1}}{\prod_{i=1}^{q}(1+\propto_i)_{k-1}}\right|\left(\frac{B(a+k,b,s,\beta)}{B(a+1,b,s,\beta)}\right)\left(\frac{a+1}{a+k}\right)^{s}k(k-1)|a_k|$$
$$\leq 1-\sum_{k=2}^{\infty}\left|\frac{\prod_{i=1}^{p}(1+\beta_i)_{k-1}}{\prod_{i=1}^{q}(1+\propto_i)_{k-1}}\right|\left(\frac{B(a+k,b,s,\beta)}{B(a+1,b,s,\beta)}\right)\left(\frac{a+1}{a+k}\right)^{s}k\,|a_k|,$$

therefor,

$$\left[2\sum_{k=2}^{\infty}\left|\frac{\prod_{i=1}^{p}(1+\beta_i)_{k-1}}{\prod_{i=1}^{q}(1+\propto_i)_{k-1}}\right|\left(\frac{B(a+k,b,s,\beta)}{B(a+1,b,s,\beta)}\right)\left(\frac{a+1}{a+k}\right)^{s}k(k-1)|a_k|\right.$$
$$\left.+\sum_{k=2}^{\infty}\left|\frac{\prod_{i=1}^{p}(1+\beta_i)_{k-1}}{\prod_{i=1}^{q}(1+\propto_i)_{k-1}}\right|\left(\frac{B(a+k,b,s,\beta)}{B(a+1,b,s,\beta)}\right)\left(\frac{a+1}{a+k}\right)^{s}k|a_k|\right]\leq 1,$$

and we have

$$\sum_{k=2}^{\infty}\left|\frac{\prod_{i=1}^{p}(1+\beta_i)_{k-1}}{\prod_{i=1}^{q}(1+\propto_i)_{k-1}}\right|\left(\frac{B(a+k,b,s,\beta)}{B(a+1,b,s,\beta)}\right)\left(\frac{a+1}{a+k}\right)^{s}|a_k|\,[k(2k-1)]\leq 1$$

Theorem 2.2 Let $f\in\mathcal{A}$. If for all $z\in U$

$$\frac{\prod_{i=1}^{p}(1+\beta_i)_{k-1}}{\prod_{i=1}^{q}(1+\propto_i)_{k-1}}\left(\frac{B(a+k,b,s,\beta)}{B(a+1,b,s,\beta)}\right)\left(\frac{a+1}{a+k}\right)^{s}|a_k|\leq\frac{1}{\sqrt{7}},\qquad(9)$$

then $\psi^{s,a,\beta}_{(\beta_p),(\propto_q),b}f(z)$ is univalent in U.

Proof. Let $f\in\mathcal{A}$. We must show that

$$\left|\frac{z^2\left(\psi^{s,a,\beta}_{(\beta_p),(\propto_q),b}f(z)\ \right)'}{2\left(\psi^{s,a,\beta}_{(\beta_p),(\propto_q),b}f(z)\ \right)^2}\right| \le 1\ ,$$

thus

$$\left|\frac{z^2\left(\psi^{s,a,\beta}_{(\beta_p),(\propto_q),b}f(z)\ \right)'}{2\left(\psi^{s,a,\beta}_{(\beta_p),(\propto_q),b}f(z)\ \right)^2}\right| = \frac{\left|\, z^2\left(\psi^{s,a,\beta}_{(\beta_p),(\propto_q),b}f(z)\right)'\,\right|}{2\left|\left(\psi^{s,a,\beta}_{(\beta_p),(\propto_q),b}f(z)\right)^2\right|}$$

$$\le \frac{|z|^2\left|\left[z+\sum_{k=2}^{\infty}\frac{\prod_{i=1}^{p}(1+\beta_i)_{k-1}}{\prod_{i=1}^{q}(1+\propto_i)_{k-1}}\left(\frac{B(a+k,b,s,\beta)}{B(a+1,b,s,\beta)}\right)\left(\frac{a+1}{a+k}\right)^s a_k\, z^k\right]'\right|}{2\left|\left[z+\sum_{k=2}^{\infty}\frac{\prod_{i=1}^{p}(1+\beta_i)_{k-1}}{\prod_{i=1}^{q}(1+\propto_i)_{k-1}}\left(\frac{B(a+k,b,s,\beta)}{B(a+1,b,s,\beta)}\right)\left(\frac{a+1}{a+k}\right)^s a_k\, z^k\right]^2\right|}$$

$$\le \frac{|z|^2\left|1+\sum_{k=2}^{\infty}\frac{\prod_{i=1}^{p}(1+\beta_i)_{k-1}}{\prod_{i=1}^{q}(1+\propto_i)_{k-1}}\left(\frac{B(a+k,b,s,\beta)}{B(a+1,b,s,\beta)}\right)\left(\frac{a+1}{a+k}\right)^s k\, a_k\, z^{k-1}\right|}{2\left|\left[z^2+2z\sum_{k=2}^{\infty}\frac{\prod_{i=1}^{p}(1+\beta_i)_{k-1}}{\prod_{i=1}^{q}(1+\propto_i)_{k-1}}\left(\frac{B(a+k,b,s,\beta)}{B(a+1,b,s,\beta)}\right)\left(\frac{a+1}{a+k}\right)^s a_k\, z^k\right]+\left(\sum_{k=2}^{\infty}\frac{\prod_{i=1}^{p}(1+\beta_i)_{k-1}}{\prod_{i=1}^{q}(1+\propto_i)_{k-1}}\left(\frac{B(a+k,b,s,\beta)}{B(a+1,b,s,\beta)}\right)\left(\frac{a+1}{a+k}\right)^s a_k z^k\right)^2\right|}$$

$$\le \frac{|z|^2\left[1+\sum_{k=2}^{\infty}\left|\frac{\prod_{i=1}^{p}(1+\beta_i)_{k-1}}{\prod_{i=1}^{q}(1+\propto_i)_{k-1}}\right|\left(\frac{B(a+k,b,s,\beta)}{B(a+1,b,s,\beta)}\right)\cdot\left(\frac{a+1}{a+k}\right)^s k|a_k|\,|z^{k-1}|\right]}{2\left[\,|z|^2-2|-z|\sum_{k=2}^{\infty}\left|\frac{\prod_{i=1}^{p}(1+\beta_i)_{k-1}}{\prod_{i=1}^{q}(1+\propto_i)_{k-1}}\right|\left(\frac{B(a+k,b,s,\beta)}{B(a+1,b,s,\beta)}\right)\left(\frac{a+1}{a+k}\right)^s|\,a_k\,|\,|z^k|\right]-|-\sum_{k=2}^{\infty}\left(\left|\frac{\prod_{i=1}^{p}(1+\beta_i)_{k-1}}{\prod_{i=1}^{q}(1+\propto_i)_{k-1}}\right|\left(\frac{B(a+k,b,s,\beta)}{B(a+1,b,s,\beta)}\right)\left(\frac{a+1}{a+k}\right)^s|\,|a_k|\,|z^k|\right)^2}$$

$$\le \frac{1+\sum_{k=2}^{\infty}\left|\frac{\prod_{i=1}^{p}(1+\beta_i)_{k-1}}{\prod_{i=1}^{q}(1+\propto_i)_{k-1}}\right|\cdot\left(\frac{B(a+k,b,s,\beta)}{B(a+1,b,s,\beta)}\right)\cdot\left(\frac{a+1}{a+k}\right)^s k|a_k|}{2\left[1-2\sum_{k=2}^{\infty}\left(\left|\frac{\prod_{i=1}^{p}(1+\beta_i)_{k-1}}{\prod_{i=1}^{q}(1+\propto_i)_{k-1}}\right|\left(\frac{B(a+k,b,s,\beta)}{B(a+1,b,s,\beta)}\right)\left(\frac{a+1}{a+k}\right)^s|\,a_k\,|\right)-\sum_{k=2}^{\infty}\left(\left|\frac{\prod_{i=1}^{p}(1+\beta_i)_{k-1}}{\prod_{i=1}^{q}(1+\propto_i)_{k-1}}\right|\left(\frac{B(a+k,b,s,\beta)}{B(a+1,b,s,\beta)}\right)\left(\frac{a+1}{a+k}\right)^s|\,a_k\,|\right)^2\right]}$$

$$\le \frac{1+\left[\left|\frac{\prod_{i=1}^{p}(1+\beta_i)_{k-1}}{\prod_{i=1}^{q}(1+\propto_i)_{k-1}}\right|\left(\frac{B(a+k,b,s,\beta)}{B(a+1,b,s,\beta)}\right)\left(\frac{a+1}{a+k}\right)^s k|a_k|\right]^2}{2\left[1-2\left(\left|\frac{\prod_{i=1}^{p}(1+\beta_i)_{k-1}}{\prod_{i=1}^{q}(1+\propto_i)_{k-1}}\right|\left(\frac{B(a+k,b,s,\beta)}{B(a+1,b,s,\beta)}\right)\left(\frac{a+1}{a+k}\right)^s|a_k|\right)^2-2\left(\left|\frac{\prod_{i=1}^{p}(1+\beta_i)_{k-1}}{\prod_{i=1}^{q}(1+\propto_i)_{k-1}}\right|\left(\frac{B(a+k,b,s,\beta)}{B(a+1,b,s,\beta)}\right)\left(\frac{a+1}{a+k}\right)^s|a_k|\right)^2\right]}.$$

Applying Lemma 1.2,we get

$$\frac{1+\left[\left|\frac{\prod_{i=1}^{p}(1+\beta_i)_{k-1}}{\prod_{i=1}^{q}(1+\propto_i)_{k-1}}\right|\left(\frac{B(a+k,b,s,\beta)}{B(a+1,b,s,\beta)}\right)\left(\frac{a+1}{a+k}\right)^s|a_k|\right]^2}{2\left[1-2\left(\left|\frac{\prod_{i=1}^{p}(1+\beta_i)_{k-1}}{\prod_{i=1}^{q}(1+\propto_i)_{k-1}}\right|\left(\frac{B(a+k,b,s,\beta)}{B(a+1,b,s,\beta)}\right)\left(\frac{a+1}{a+k}\right)^s|a_k|\right)^2-2\left(\left|\frac{\prod_{i=1}^{p}(1+\beta_i)_{k-1}}{\prod_{i=1}^{q}(1+\propto_i)_{k-1}}\right|\left(\frac{a+1}{a+k}\right)^s\left(\frac{B(a+k,b,s,\beta)}{B(a+1,b,s,\beta)}\right)|a_k|\right)^2\right]} \le 1$$

$$1+\left[\ \left|\ \frac{\prod_{i=1}^{p}(1+\beta_i)_{k-1}}{\prod_{i=1}^{q}(1+\propto_i)_{k-1}}\ \right|\left(\frac{B(a+k,b,s,\beta)}{B(a+1,b,s,\beta)}\right)\left(\frac{a+1}{a+k}\right)^s|a_k|\right]^2 \le 2-$$

$$4\left[\ \left|\ \frac{\prod_{i=1}^{p}(1+\beta_i)_{k-1}}{\prod_{i=1}^{q}(1+\propto_i)_{k-1}}\ \right|\left(\frac{B(a+k,b,s,\beta)}{B(a+1,b,s,\beta)}\right)\left(\frac{a+1}{a+k}\right)^s|a_k|\right]^2-2\left[\ \left|\ \frac{\prod_{i=1}^{p}(1+\beta_i)_{k-1}}{\prod_{i=1}^{q}(1+\propto_i)_{k-1}}\right|\left(\frac{B(a+k,b,s,\beta)}{B(a+1,b,s,\beta)}\right)\left(\frac{a+1}{a+k}\right)^s|a_k|\right]^2,$$

then

$$1+\left[\ \left|\ \frac{\prod_{i=1}^{p}(1+\beta_i)_{k-1}}{\prod_{i=1}^{q}(1+\propto_i)_{k-1}}\ \right|\left(\frac{B(a+k,b,s,\beta)}{B(a+1,b,s,\beta)}\right)\left(\frac{a+1}{a+k}\right)^s|a_k|\right]^2 + 4\left[\ \left|\ \frac{\prod_{i=1}^{p}(1+\beta_i)_{k-1}}{\prod_{i=1}^{q}(1+\propto_i)_{k-1}}\ \right|\left(\frac{B(a+k,b,s,\beta)}{B(a+1,b,s,\beta)}\right)\left(\frac{a+1}{a+k}\right)^s|a_k|\right]^2$$

$$2+\left[\left|\frac{\prod_{i=1}^{p}(1+\beta_i)_{k-1}}{\prod_{i=1}^{q}(1+\propto_i)_{k-1}}\right|\left(\frac{B(a+k,b,s,\beta)}{B(a+1,b,s,\beta)}\right)\left(\frac{a+1}{a+k}\right)^{s}|a_k|\right]^2\leq 1,$$

therefor,

$$7\left[\left|\frac{\prod_{i=1}^{p}(1+\beta_i)_{k-1}}{\prod_{i=1}^{q}(1+\propto_i)_{k-1}}\right|\left(\frac{B(a+k,b,s,\beta)}{B(a+1,b,s,\beta)}\right)\left(\frac{a+1}{a+k}\right)^{s}|a_k|\right]^2\leq 1,$$

and we have

$$\left|\frac{\prod_{i=1}^{p}(1+\beta_i)_{k-1}}{\prod_{i=1}^{q}(1+\propto_i)_{k-1}}\right|\left(\frac{B(a+k,b,s,\beta)}{B(a+1,b,s,\beta)}\right)\left(\frac{a+1}{a+k}\right)^{s}|a_k\leq\frac{1}{\sqrt{7}}$$

Theorem 2.3 Let $f\in\mathcal{A}$. If for all $z\in U$

$$\sum_{k=1}^{\infty}k\left[2(k-1)+(2\eta-1)\left[\frac{\prod_{i=1}^{p}(1+\beta_i)_{k-1}}{\prod_{i=1}^{q}(1+\propto_i)_{k-1}}.\left(\frac{B(a+k,b,s,\beta)}{B(a+1,b,s,\beta)}\right).\left(\frac{a+1}{a+k}\right)^{s}|a_k|\right]\right]\leq 2\eta-1,\ \eta>\frac{1}{2},\qquad(10)$$

then $\psi^{s,a,\beta}_{(\beta_p),(\propto_q),b}f(z)$ is univalent in U.

Proof. Let $f\in\mathcal{A}$. If for all $z\in U$, we have

$$(1-|z|^{2\eta}).\left|\frac{z\left(\psi^{s,a,\beta}_{(\beta_p),(\propto_q),b}f(z)\right)''}{\left(\psi^{s,a,\beta}_{(\beta_p),(\propto_q),b}f(z)\right)'}+1-\eta\right|$$

$$\leq(1-|z|^{2\eta}).\frac{|z|\left|\left(\psi^{s,a,\beta}_{(\beta_p),(\propto_q),b}f(z)\right)''\right|}{\left|\left(\psi^{s,a,\beta}_{(\beta_p),((\propto_q)),b}f(z)\right)'\right|}+|1-\eta|$$

$$=(1+|z|^2).\frac{|z|\left|\left[z+\sum_{k=2}^{\infty}\frac{\prod_{i=1}^{p}(1+\beta_i)_{k-1}}{\prod_{i=1}^{q}(1+\propto_i)_{k-1}}\left(\frac{B(a+k,b,s,\beta)}{B(a+1,b,s,\beta)}\right)\left(\frac{a+1}{a+k}\right)^{s}a_k\,z^k\right]''\right|}{\left|\left[z+\sum_{k=2}^{\infty}\frac{\prod_{i=1}^{p}(1+\beta_i)_{k-1}}{\prod_{i=1}^{q}(1+\propto_i)_{k-1}}\left(\frac{B(a+k,b,s,\beta)}{B(a+1,b,s,\beta)}\right)\left(\frac{a+1}{a+k}\right)^{s}a_k\,z^k\right]'\right|}+|1-\eta|$$

$$\leq(1+|z|^2).\frac{|z|\left[\sum_{k=2}^{\infty}\left|\frac{\prod_{i=1}^{p}(1+\beta_i)_{k-1}}{\prod_{i=1}^{q}(1+\propto_i)_{k-1}}\right|\left(\frac{B(a+k,b,s,\beta)}{B(a+1,b,s,\beta)}\right)\left(\frac{a+1}{a+k}\right)^{s}k(k-1)|a_k||z^{k-2}|\right]}{|1|-\left|-\sum_{k=2}^{\infty}\left|\frac{\prod_{i=1}^{p}(1+\beta_i)_{k-1}}{\prod_{i=1}^{q}(1+\propto_i)_{k-1}}\right|\left(\frac{B(a+k,b,s,\beta)}{B(a+1,b,s,\beta)}\right)\left(\frac{a+1}{a+k}\right)^{s}k\right||a_k|\,|z^{k-1}|}$$
$$+|1-\eta|$$

$$\leq\frac{2\sum_{k=2}^{\infty}\left|\frac{\prod_{i=1}^{p}(1+\beta_i)_{k-1}}{\prod_{i=1}^{q}(1+\propto_i)_{k-1}}\right|\left(\frac{B(a+k,b,s,\beta)}{B(a+1,b,s,\beta)}\right)\left(\frac{a+1}{a+k}\right)^{s}k(k-1)|a_k|}{1-\sum_{k=2}^{\infty}\left|\frac{\prod_{i=1}^{p}(1+\beta_i)_{k-1}}{\prod_{i=1}^{q}(1+\propto_i)_{k-1}}\right|\left(\frac{B(a+k,b,s,\beta)}{B(a+1,b,s,\beta)}\right)\left(\frac{a+1}{a+k}\right)^{s}k|a_k|}+|1-\eta|.$$

Applying Lemma 1.3,we get

$$\frac{2\sum_{k=2}^{\infty}\left|\frac{\prod_{i=1}^{p}(1+\beta_i)_{k-1}}{\prod_{i=1}^{q}(1+\propto_i)_{k-1}}\right|\left(\frac{B(a+k,b,s,\beta)}{B(a+1,b,s,\beta)}\right)\left(\frac{a+1}{a+k}\right)^{s}k(k-1)|a_k|}{1-\sum_{k=2}^{\infty}\left|\frac{\prod_{i=1}^{p}(1+\beta_i)_{k-1}}{\prod_{i=1}^{q}(1+\propto_i)_{k-1}}\right|\left(\frac{B(a+k,b,s,\beta)}{B(a+1,b,s,\beta)}\right)\left(\frac{a+1}{a+k}\right)^{s}k|a_k|}+|1-\eta|\leq\eta,$$

then

$$\frac{2\sum_{k=2}^{\infty} \left|\frac{\prod_{i=1}^{p}(1+\beta_i)_{k-1}}{\prod_{i=1}^{q}(1+\propto_i)_{k-1}}\right| \left(\frac{B(a+k,b,s,\beta)}{B(a+1,b,s,\beta)}\right)\left(\frac{a+1}{a+k}\right)^{s} k(k-1)|a_k|}{1-\sum_{k=2}^{\infty} \left|\frac{\prod_{i=1}^{p}(1+\beta_i)_{k-1}}{\prod_{i=1}^{q}(1+\propto_i)_{k-1}}\right| \left(\frac{B(a+k,b,s,\beta)}{B(a+1,b,s,\beta)}\right)\left(\frac{a+1}{a+k}\right)^{s} k|a_k|} \leq 2\eta-1,$$

therefor,

$$2\sum_{k=2}^{\infty} \left|\frac{\prod_{i=1}^{p}(1+\beta_i)_{k-1}}{\prod_{i=1}^{q}(1+\propto_i)_{k-1}}\right| \left(\frac{B(a+k,b,s,\beta)}{B(a+1,b,s,\beta)}\right)\left(\frac{a+1}{a+k}\right)^{s} k(k-1)|a_k| + 2\eta\sum_{k=2}^{\infty} \left|\frac{\prod_{i=1}^{p}(1+\beta_i)_{k-1}}{\prod_{i=1}^{q}(1+\propto_i)_{k-1}}\right| \left(\frac{B(a+k,b,s,\beta)}{B(a+1,b,s,\beta)}\right)\left(\frac{a+1}{a+k}\right)^{s} k|a_k| - \sum_{k=2}^{\infty} \left|\frac{\prod_{i=1}^{p}(1+\beta_i)_{k-1}}{\prod_{i=1}^{q}(1+\propto_i)_{k-1}}\right| \left(\frac{B(a+k,b,s,\beta)}{B(a+1,b,s,\beta)}\right)\left(\frac{a+1}{a+k}\right)^{s} k|a_k| \leq 2\eta-1,$$

and we have

$$\sum_{k=2}^{\infty} \left|\frac{\prod_{i=1}^{p}(1+\beta_i)_{k-1}}{\prod_{i=1}^{q}(1+\propto_i)_{k-1}}\right| \left(\frac{B(a+k,b,s,\beta)}{B(a+1,b,s,\beta)}\right)\left(\frac{a+1}{a+k}\right)^{s} k|a_k| \,[2(k-1)+(2\eta-1)] \leq 2\eta-1.$$

As applications of Theorems 2.1, 2.2, and 2.3, we have the following Theorem.

Theorem 2.4 Let $f \in \mathcal{A}$. If for all $z \in U$. One of inequality (9-11) holds then $\sum_{k=1}^{\infty}(k-1)\,|b_k| \leq 1,$ ...(11)

where $\frac{z}{\psi^{s,a,\beta}_{(\beta_p),(\propto_q),b} f(z)} = 1+\sum_{k=1}^{\infty}(k-1)\,b_k\,z^k$

Proof. Let $f \in \mathcal{A}$. Then in view of theorems 2.1 , 2.2 , 2.3

$\psi^{s,a,\beta}_{(\beta_p),(\propto_q),b} f(z)$ is univalent in U.

Using Theorem 2.1,

$$(1-|z|^2)\left|\frac{z\left(\psi^{s,a,\beta}_{(\beta_p),(\propto_q),b} f(z)\right)''}{\left(\psi^{s,a,\beta}_{(\beta_p),(\propto_q),b} f(z)\right)'}\right| = (1-|z|^2)\left|\frac{z\left(\psi^{s,a,\beta+2}_{(\beta_p)(\propto_q),b} f(z)\right)}{\psi^{s,a,\beta+1}_{,(\beta_p)(\propto_q),b} f(z)}\right|$$

$$= (1-|z|^2)\left|\frac{z\ \psi^{s,a,\beta+1}_{(\beta_p),(\propto_q),b} f(z)}{\psi^{s,a,\beta}_{(\beta_p)(\propto_q),b,} f(z)}\right|$$

$$= (1-|z|^2)\left|\frac{z}{\psi^{s,a,\beta}_{(\beta_p),(\propto_q),b} f(z)}\ \psi^{s,a,\beta+1}_{(\beta_p)(\propto_q),b} f(z)\right|$$

$$= (1-|z|^2)\left|\left[1+\sum_{k=1}^{\infty} b_k\,z^k\right]\left[z+\sum_{k=2}^{\infty}\frac{\prod_{i=1}^{p}(1+\beta_i)_{k-1}}{\prod_{i=1}^{q}(1+\propto_i)_{k-1}}\left(\frac{B(a+k,b,s,\beta)}{B(a+1,b,s,\beta)}\right)\left(\frac{a+1}{a+k}\right)^{s} a_k\,z^k\right]'\right|$$

$$\leq (1-|-z|^2).\left[1+\sum_{k=1}^{\infty}|\,b_k\,|\,|\,z^k\,|\right]\left[|\,1\,|-|\right. - \left.\sum_{k=2}^{\infty}\left|\frac{\prod_{i=1}^{p}(1+\beta_i)_{k-1}}{\prod_{i=1}^{q}(1+\propto_i)_{k-1}}\right|\left(\frac{B(a+k,b,s,\beta)}{B(a+1,b,s,\beta)}\right)\left(\frac{a+1}{a+k}\right)^{s} k\,|\,|\,a_k\,|\,|\,z^{k-1}\,|\right]$$

$$\leq \left(1+|\,z\,|^{2}\right)\left[1+\sum_{k=1}^{\infty}|\,b_k\,|\,|\,z^k\,|\right]\left[1\right. - \left.\sum_{k=2}^{\infty}\left|\frac{\prod_{i=1}^{p}(1+\beta_i)_{k-1}}{\prod_{i=1}^{q}(1+\propto_i)_{k-1}}\right|\left(\frac{B(a+k,b,s,\beta)}{B(a+1,b,s,\beta)}\right)\left(\frac{a+1}{a+k}\right)^{s} k\,|\,|\,a_k\,|\,|\,z^{k-1}\,|\right]$$

$$\leq 2\left[1-\sum_{k=2}^{\infty}\left|\frac{\prod_{i=1}^{p}(1+\beta_i)_{k-1}}{\prod_{i=1}^{q}(1+\propto_i)_{k-1}}\right|\left(\frac{B(a+k,b,s,\beta)}{B(a+1,b,s,\beta)}\right)\left(\frac{a+1}{a+k}\right)^{s} k|a_k|\right][1+\sum_{k=1}^{\infty}|b_k|]$$

$$\leq 2\left[1+\sum_{k=1}^{\infty}|b_k|-\sum_{k=2}^{\infty}\left|\frac{\prod_{i=1}^{p}(1+\beta_i)_{k-1}}{\prod_{i=1}^{q}(1+\alpha_i)_{k-1}}\right|\left(\frac{B(a+k,b,s,\beta)}{B(a+1,b,s,\beta)}\right)\left(\frac{a+1}{a+k}\right)^{s}k|a_k|\right]+$$
$$\left(\sum_{k=1}^{\infty}|b_k|\right)\left(-\sum_{k=2}^{\infty}\left|\frac{\prod_{i=1}^{p}(1+\beta_i)_{k-1}}{\prod_{i=1}^{q}(1+\alpha_i)_{k-1}}\right|\left(\frac{B(a+k,b,s,\beta)}{B(a+1,b,s,\beta)}\right)\left(\frac{a+1}{a+k}\right)^{s}k|a_k|\right).$$

Applying Lemma 1.4, we get

$$2\left[1+\sum_{k=1}^{\infty}|b_k|-2\sum_{k=1}^{\infty}\left|\frac{\prod_{i=1}^{p}(1+\beta_i)_{k-1}}{\prod_{i=1}^{q}(1+\alpha_i)_{k-1}}\right|\left(\frac{B(a+k,b,s,\beta)}{B(a+1,b,s,\beta)}\right)\left(\frac{a+1}{a+k}\right)^{s}|a_k|-\right.$$
$$\left.2\left(\sum_{k=1}^{\infty}|b_k|\right)\left(\sum_{k=1}^{\infty}\left|\frac{\prod_{i=1}^{p}(1+\beta_i)_{k-1}}{\prod_{i=1}^{q}(1+\alpha_i)_{k-1}}\right|\left(\frac{B(a+k,b,s,\beta)}{B(a+1,b,s,\beta)}\right)\left(\frac{a+1}{a+k}\right)^{s}|a_k|\right)\right]\leq 1,$$

therefor,

$$2\left[1+\sum_{k=1}^{\infty}|b_k|-2\sum_{k=1}^{\infty}\left|\frac{\prod_{i=1}^{p}(1+\beta_i)_{k-1}}{\prod_{i=1}^{q}(1+\alpha_i)_{k-1}}\right|\left(\frac{B(a+k,b,s,\beta)}{B(a+1,b,s,\beta)}\right)\left(\frac{a+1}{a+k}\right)^{s}|a_k|-\right.$$
$$\left.2\left(\sum_{k=1}^{\infty}|b_k|\right)\left(\sum_{k=2}^{\infty}\left|\frac{\prod_{i=1}^{p}(1+\beta_i)_{k-1}}{\prod_{i=1}^{q}(1+\alpha_i)_{k-1}}\right|\left(\frac{B(a+k,b,s,\beta)}{B(a+1,b,s,\beta)}\right)\left(\frac{a+1}{a+k}\right)^{s}|a_k|\right)\right]\leq\frac{(k-1)|b_k|}{(k-1)|b_k|},$$

and we have

$$\sum_{k=1}^{\infty}(k-1)|b_k|^2\leq 1$$

Theorem 2.5 Let $f\in\mathcal{A}$. If for all $z\in U$

$$\sum_{k=1}^{\infty}k[2(k-1)+\mathcal{R}e(v)]\frac{\prod_{i=1}^{p}(1+\beta_i)_{k-1}}{\prod_{i=1}^{q}(1+\alpha_i)_{k-1}}\left(\frac{B(a+k,b,s,\beta)}{B(a+1,b,s,\beta)}\right)\left(\frac{a+1}{a+k}\right)^{s}|a_k|\leq\mathcal{R}e(v),\mathcal{R}e(v)>0 \qquad (12)$$

then

$$G_v(z)=\left(v\int_0^z y^{v-1}\left[\psi^{s,a,\beta}_{(\beta_p),(\alpha_q),b}f(z)\right]'dy\right)^{\frac{1}{v}}\text{ is univalent in }U$$

Proof**.** Let $f\in\mathcal{A}$. Then for all $z\in U$

$$\frac{1-|z|^{2\mathcal{R}e(v)}}{\mathcal{R}e(v)}\cdot\left|\frac{z\left(\psi^{s,a,\beta}_{(\beta_p),(\alpha_q),b}f(z)\right)''}{\left(\psi^{s,a,\beta}_{(\beta_p),(\alpha_q),b}f(z)\right)'}\right|\leq\frac{1-|-z|^{2\mathcal{R}e(v)}}{\mathcal{R}e(v)}\cdot\frac{|z|\left|\left(\psi^{s,a,\beta}_{(\beta_p),(\alpha_q),b}f(z)\right)''\right|}{\left|\left(\psi^{s,a,\beta}_{(\beta_p),(\alpha_q),b}f(z)\right)'\right|}$$

$$\leq\frac{1+|Z|^{2\mathcal{R}e(v)}}{\mathcal{R}e(v)}\cdot\frac{|z|\left|\left[z+\sum_{k=2}^{\infty}\frac{\prod_{i=1}^{p}(1+\beta_i)_{k-1}}{\prod_{i=1}^{q}(1+\alpha_i)_{k-1}}\cdot\left(\frac{B(a+k,b,s,\beta)}{B(a+1,b,s,\beta)}\right)\cdot\left(\frac{a+1}{a+k}\right)^{s}a_kz^k\right]''\right|}{\left|\left[z+\sum_{k=2}^{\infty}\frac{\prod_{i=1}^{p}(1+\beta_i)_{k-1}}{\prod_{i=1}^{q}(1+\alpha_i)_{k-1}}\cdot\left(\frac{B(a+k,b,s,\beta)}{B(a+1,b,s,\beta)}\right)\cdot\left(\frac{a+1}{a+k}\right)^{s}a_kz^k\right]'\right|}$$

$$=\frac{1+|z|^{2\mathcal{R}e(v)}}{\mathcal{R}e(v)}\cdot\frac{|z|\left|1+\sum_{k=2}^{\infty}\frac{\prod_{i=1}^{p}(1+\beta_i)_{k-1}}{\prod_{i=1}^{q}(1+\alpha_i)_{k-1}}\left(\frac{B(a+k,b,s,\beta)}{B(a+1,b,s,\beta)}\right)\left(\frac{a+1}{a+k}\right)^{s}k(k-1)a_kz^{k-2}\right|}{|1|-\left|-\sum_{k=2}^{\infty}\frac{\prod_{i=1}^{p}(1+\beta_i)_{k-1}}{\prod_{i=1}^{q}(1+\alpha_i)_{k-1}}\left(\frac{B(a+k,b,s,\beta)}{B(a+1,b,s,\beta)}\right)\left(\frac{a+1}{a+k}\right)^{s}k\,a_kz^{k-1}\right|}$$

$$\leq\frac{1+|z|^{2\mathcal{R}e(v)}}{\mathcal{R}e(v)}\cdot\frac{|z|\left[\sum_{k=2}^{\infty}\left|\frac{\prod_{i=1}^{p}(1+\beta_i)_{k-1}}{\prod_{i=1}^{q}(1+\alpha_i)_{k-1}}\right|\left(\frac{B(a+k,b,s,\beta)}{B(a+1,b,s,\beta)}\right)\left(\frac{a+1}{a+k}\right)^{s}k(k-1)\,|a_k|\,|z^{k-2}|\right]}{1-\sum_{k=2}^{\infty}\left|\frac{\prod_{i=1}^{p}(1+\beta_i)_{k-1}}{\prod_{i=1}^{q}(1+\alpha_i)_{k-1}}\right|\left(\frac{B(a+k,b,s,\beta)}{B(a+1,b,s,\beta)}\right)\left(\frac{a+1}{a+k}\right)^{s}k|\,a_k|\,|z^{k-1}|}$$

$$\leq \frac{2\sum_{k=2}^{\infty} \left| \frac{\prod_{i=1}^{p}(1+\beta_i)_{k-1}}{\prod_{i=1}^{q}(1+\alpha_i)_{k-1}} \right| \left(\frac{B(a+k,b,s,\beta)}{B(a+1,b,s,\beta)}\right)\left(\frac{a+1}{a+k}\right)^{s} k(k-1)|a_k|}{\mathcal{R}e(v)\left[1-\sum_{k=2}^{\infty} \left| \frac{\prod_{i=1}^{p}(1+\beta_i)_{k-1}}{\prod_{i=1}^{q}(1+\alpha_i)_{k-1}} \right| \left(\frac{B(a+k,b,s,\beta)}{B(a+1,b,s,\beta)}\right)\left(\frac{a+1}{a+k}\right)^{s} k|\, a_k|\right]}$$

Applying Lemma 1.5, we get

$$\frac{2\sum_{k=2}^{\infty} \left| \frac{\prod_{i=1}^{p}(1+\beta_i)_{k-1}}{\prod_{i=1}^{q}(1+\alpha_i)_{k-1}} \right| \left(\frac{B(a+k,b,s,\beta)}{B(a+1,b,s,\beta)}\right)\left(\frac{a+1}{a+k}\right)^{s} k(k-1)|a_k|}{\mathcal{R}e(v)\left[1-\sum_{k=2}^{\infty} \left| \frac{\prod_{i=1}^{p}(1+\beta_i)_{k-1}}{\prod_{i=1}^{q}(1+\alpha_i)_{k-1}} \right| \left(\frac{B(a+k,b,s,\beta)}{B(a+1,b,s,\beta)}\right)\left(\frac{a+1}{a+k}\right)^{s} k|\, a_k|\right]} \leq 1$$

then

$$2\sum_{k=2}^{\infty} \left| \frac{\prod_{i=1}^{p}(1+\beta_i)_{k-1}}{\prod_{i=1}^{q}(1+\alpha_i)_{k-1}} \right| \left(\frac{B(a+k,b,s,\beta)}{B(a+1,b,s,\beta)}\right)\left(\frac{a+1}{a+k}\right)^{s} k(k-1)|a_k| \leq \mathcal{R}e(v)\left[1-\sum_{k=2}^{\infty} \left| \frac{\prod_{i=1}^{p}(1+\beta_i)_{k-1}}{\prod_{i=1}^{q}(1+\alpha_i)_{k-1}} \right| \left(\frac{B(a+k,b,s,\beta)}{B(a+1,b,s,\beta)}\right)\left(\frac{a+1}{a+k}\right)^{s} k|\, a_k|\right],$$

therefor,

$$2\sum_{k=2}^{\infty} \left| \frac{\prod_{i=1}^{p}(1+\beta_i)_{k-1}}{\prod_{i=1}^{q}(1+\alpha_i)_{k-1}} \right| \left(\frac{B(a+k,b,s,\beta)}{B(a+1,b,s,\beta)}\right)\left(\frac{a+1}{a+k}\right)^{s} k(k-1)|a_k| + \mathcal{R}e(v)\sum_{k=2}^{\infty} \left| \frac{\prod_{i=1}^{p}(1+\beta_i)_{k-1}}{\prod_{i=1}^{q}(1+\alpha_i)_{k-1}} \right| \left(\frac{B(a+k,b,s,\beta)}{B(a+1,b,s,\beta)}\right)\left(\frac{a+1}{a+k}\right)^{s} k|\, a_k| \leq \mathcal{R}e(v),$$

and we have

$$\sum_{k=2}^{\infty} \left| \frac{\prod_{i=1}^{p}(1+\beta_i)_{k-1}}{\prod_{i=1}^{q}(1+\alpha_i)_{k-1}} \right| \left(\frac{B(a+k,b,s,\beta)}{B(a+1,b,s,\beta)}\right)\left(\frac{a+1}{a+k}\right)^{s} k[2(k-1)+\mathcal{R}e(v)]\,|a_k| \leq \mathcal{R}e(v).$$

References

[1] R M Ali, M Obradovic and ponnusamy 2019 Differential inequalities and univalent functions *arxiv preprint arxiv* 1905.01694
[2] J Becker 1972 Lownersche Differential gleichung und quasi-konform forestzbare schlichte funkionen *J. Reine Angew. Math.* **255** pp 23-43
[3] M Darus, R W Ibrahim 2010 On univalent criteria for analytic functions defined by a generalized differential operator *Acta univ. Apul.* **23** pp 195-200
[4] E Deniz and H Orhan 2009 univalence criterion for analytic functions *Gen. Math.* **4** pp 211-220
[5] A Goodman 1983 *Univalent Functions* **I** and **II** Mariner, Tampa, Florida
[6] Z Nehari 1954 some criteria of univalence *proc of the Amer. Math. Soc.* **5**(5) pp 700-704
[7] S Ozaki and M Nunokawa 1972 The schwarzian derivative and univalent functions *proc. Amer. Math. Soc.* **33**(2) pp 392-394
[8] N N pascu 1987 On the univalence criterion of Becker *Math. ClujNapoca* **29**(52)(2) pp175- 176
[9] H M Srivastava and S Gaboury 2015 A new class of analytic functions define by means of a generalization of the Srivastvra- Attiya operator *J. Inequal. Appl.* Article ID 39 pp 1-15
[10] H M Srivastava, A Rahman, S Juma and H M Zayed 2018 Univalence conditions for an Integral operator Defined by a Generalization of the Srivastava-Attiya operator *Filomat* **32 (**6) pp 2101-2114
[11] H Tudor 2009 A sufficient condition for unvalence *General Math.* **17**(1) pp 89-94

[12] P T Reddy, B Venkateswarlu and S Sreelakshmi 2020 On The Univalence Criteria for Analytic Functions Defined by Differential Operator *Int. J. Open Problems Complex Analysis* **12**(1) ISS 2047-2827

New Methods of Computing the Conjugate of Young Diagram

New Methods of Computing the Conjugate of Young Diagram

Fatmah Ahmed Basher, Ammar Seddiq Mahmood

Department of Mathematics, College of Education for Pure Science, University Of Mosul, Mosul-Iraq

E-mail: fatima.esp87@student.uomosul.edu.iq

Abstract. Since the appearance of Young's diagram, it has played a fundamental and pivotal role in many fields of mathematics, perhaps the most prominent of which is algebra, graph theory, number theory…etc, and many closely related relationships, perhaps among them The most prominent is called conjugation. Many people try to find a mathematical method to find the value of the hash value in its conjugated form. Here, we will propose two new methods for the same purpose.

1. Introduction

Let g be a positive integer. "A composition of g is a sequence $\delta = (\delta_1, \delta_2, \dots, \delta_n) = ({\theta_1}^{\gamma_1}, {\theta_2}^{\gamma_2}, \dots, {\theta_m}^{\gamma_m})$ (where γ_z is the number of times θ_z appeared, z=1, 2, …, m) of non-negative integers such that $|\delta| = \sum_{j=1}^{n} \delta_j = \sum_{z=1}^{m} \theta_z{}^{\gamma_z} = g$. The composition is called a partition of g if $\delta_j \geq \delta_{j+1}$ or $\theta_j > \theta_{j+1}, \forall\, j \geq 1$. A Young diagram of a composition δ is the subset $[\delta] = \{(\tau, \sigma): 1 \leq \sigma \leq \delta_\tau \text{ and } \tau \geq 1\}$ of $N \times N$. The elements of $[\delta]$ are called the nodes of $\delta; [1]$". For example if $\delta = (4,4,5,1,1,1,2) = (4^2, 5, 1^3, 2)$, then

Figure 1. Young diagram of $(4,4,5,1,1,1,2)$

$[\delta] =$ 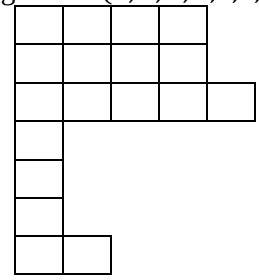

Over the years, many researchers have provided different definitions of the topic conjugate, but it was focused mainly on calculating the parts as if it was manually without making clear mathematical relationships as:

Definition 1.1: [1] For any partition δ , let δ' be the partition which is conjugate to δ by $(\delta_1', \delta_2', \dots)$ where $\delta_{h'}$ is equal to the number of nodes in column h of $[\delta]$. For example, let $\delta = (7, 3^2, 2)$ then

Figure 2. Young Diagram and conjugate for $\delta = (7, 3^2, 2)$

$[\delta] =$ 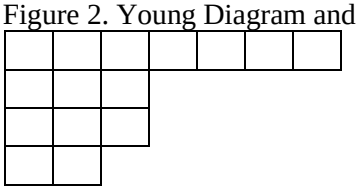 $\rightarrow$ $[\delta'] =$ 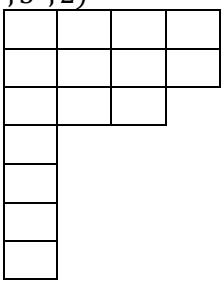

Definition 1.2: [2] The conjugate of any composition is defined by $[\delta'] = [(\sigma, \tau)\ in\ \delta' : (\tau, \sigma) in\ \delta]$
Definition 1.3: [3] The conjugate partition obtained by reflecting the Young diagram along the main diagonal.

It is natural to ask why conjugation on partitions is better than composition because we often do not know the corresponding representation of the utility. An example of conjugate diagram 1 is:

Figure 3. The conjugate Young Diagram for $(4, 4, 5, 1, 1, 1, 2)$

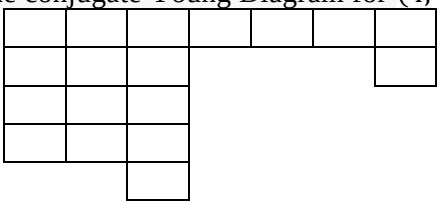

In this article, we will introduce a different method from the previously mentioned method, this time through the original partition without counting according to the definitions 1.1-1.3. Note that any $X^0\ \ or\ \ 0^X$ does not have any effect on this paper.

2. The New Rules

Logically speaking, the calculation of the number of cases is performed after Young's diagram is drawn and then the conjugation process is performed. The idea used is whether there is a method to find the conjugation directly through the original partition, so we studied this possibility from two aspects. first of all:

Rule 2.1: The new representation for conjugate any partition $\delta = (\delta_1, \delta_2, \dots, \delta_n)$ is

$$\delta' = (n^{\delta_n}, (n-1)^{\delta_{n-1}-\delta_n}, (n-2)^{\delta_{n-2}-\delta_{n-1}}, \dots, \big(n-(n-1)\big)^{\delta_1-\delta_2}).$$

Proof: According to the principle of inversion of the main diagonal, it is natural to focus on the last value of n, because it will play a decisive role here, in order to know the remaining conjugate states that will appear later, but will be divided by δ_n In order to repeat, because there is nothing behind it, so in the original partition, it appeared here last after it started to reverse. By repeating this situation in the next item, then we have $(n-1)$ but this time we must exclude $\delta_{n-1} - \delta_n$ in the same way until the last items■

For example, let $\delta = (8,8,5,5,5,5,3,3,3,2)$, then n =10 and

$$\delta' = (n^{\delta_{10}} = 10^2,\ (n-1)^{\delta_9-\delta_{10}} = 9^1, (n-2)^{\delta_8-\delta_9} = 8^0,$$
$$(n-3)^{\delta_7-\delta_8} = 7^0,\ (n-4)^{\delta_6-\delta_7} = 6^2,\quad (n-5)^{\delta_5-\delta_6} = 5^0,$$
$$(n-6)^{\delta_4-\delta_5} = 4^0,\ (n-7)^{\delta_3-\delta_4} = 3^0,$$
$$(n-8)^{\delta_2-\delta_3} = 2^3,\ (n-9)^{\delta_1-\delta_2} = 1^0)$$
$$= (10^2, 9, 6^2, 2^3).$$

Figure 4. Young diagram and conjugate for $\delta = (8,8,5,5,5,5,3,3,3,2)$

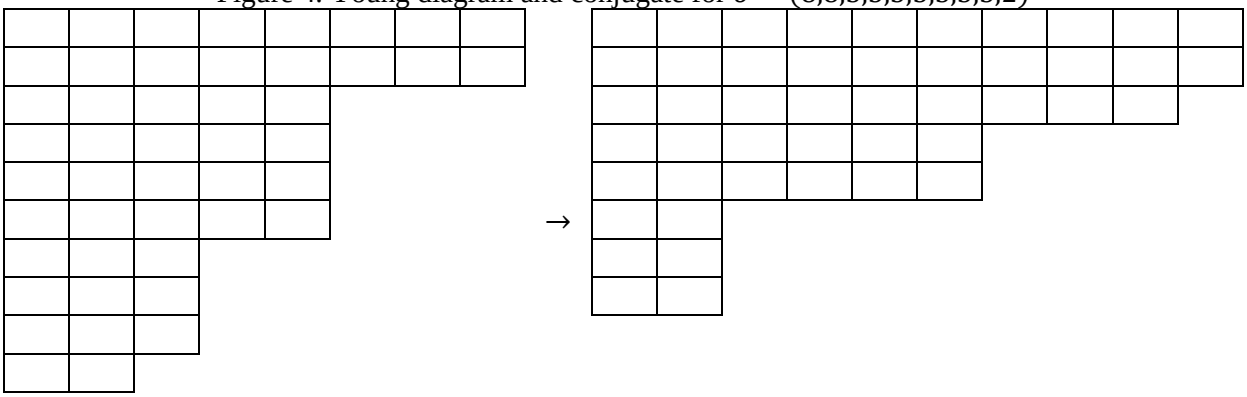

Rule 2.2: The new representation for conjugate any partition $\delta = ({\theta_1}^{\gamma_1}, {\theta_2}^{\gamma_2}, \dots, {\theta_m}^{\gamma_m})$ is
$\delta' = \left((\gamma_1 + \gamma_2 + \cdots + \gamma_m)^{\theta_m},\ (\gamma_1 + \gamma_2 + \cdots + \gamma_{m-1})^{\theta_{m-1}-\theta_m}, \cdots,\ (\gamma_1 + \gamma_2)^{\theta_2-\theta_3},\ (\gamma_1)^{\theta_1-\theta_2}\right)$.

Proof: This method, focuses on the number of iterations in the partition, which will represent the number of rows representing the partition, and when the concept of the conjugate is used, it will form columns in it. On the other hand, since the changes are made according to the main diagonal, this means that we will focus on the values in the main partition, but follow the principle of $(\boldsymbol{\theta_{(m-(k-1))}} - \boldsymbol{\theta_{(m-(k-2))}})$ where $k = 1, 2, \cdots, m$, respectively■

From the above example, when $\delta = (8,8,5,5,5,5,3,3,3,2) = (8^2, 5^4, 3^3, 2)$ then

$$\delta' = \left((\gamma_1 + \gamma_2 + \cdots + \gamma_m)^{\theta_m},\ (\gamma_1 + \gamma_2 + \cdots + \gamma_{m-1})^{\theta_{m-1}-\theta_m}, \cdots,\ (\gamma_1 + \gamma_2)^{\theta_2-\theta_3},\ (\gamma_1)^{\theta_1-\theta_2}\right)$$
$$= ((2+4+3+1)^2,\ (2+4+3)^{3-2},\ (2+4)^{5-3},\ 2^{8-5})$$
$$= (10^2, 9, 6^2, 2^3).$$

It is natural to ask the following questions: What is the difference between the two rules? What are the benefits of using them? Is it possible to imitate this usage application? The answers to all these questions will completely overlap as shown below:

"When a partition is given without duplicates, it is better to use Rule 2.1, and if a partition is given its frequency, it is easier to use the second rule. Similarly, these two cases are correct, but the first case is studied through a case in the original partition (that is, row by row) before the conjugate is expressed, while the second case is to study each equal rows in the measurement, so if it happens very often, it is not logical to study them row by row but to study them in groups and faster. This method can be used as an encrypted message, especially after the method proposed by Mahmood and Mahmood [4]-[5] or Mahmood in [6] by representing each English letter according to its division (by using the definition of e-abacus diagram of James [7]; defining $\beta_i = \delta_i + b - i,\ 1 \le i \le b$. The set $\{\beta_1, \beta_2, \cdots, \beta_b\}$ is said to be the set of β - number for π, see [1]. Let e be a positive integer number greater than or equal to 2, we can represent numbers by a diagram called *e*-abacus diagram, see[7], as shown:

Table 1. *e*-abacus diagram

Runner 1	**Runner 2**	⋯	**Runner *e***
0	1	⋯	*e*-1
e	*e*+1	⋯	2*e*-1
2*e*	2*e*+1	⋯	3*e*-1
⋮	⋮	⋯	⋮

where every β will be represented by a (■) and the rest of the sites by (-). In fact, the definition of the *e*-abacus diagram will lead us to the fact that the presence of an infinite number of diagrams are all suitable for any partition according to the value of *e*., when e=5), which means that we will get a word that is difficult to read. This is what we will explain in the third section of this research".

3. Application

Mahmood and Mahmood in [4] represented the English letters as follows*:*

Table 2. The Partition for each English Letters

Letter	partition
A	$(11, 8^2, 5^7, 2, 1^3)$
B	$(11^3, 19,8, 6^3, 5,3, 1^3)$
C	$(13^3, 12,9, 5^2, 2, 1^3)$
D	$(12^3, 11,9,8,6,5,3, 1^3)$
E	$(12^4, 8, 6^3, 2, 1^4)$
F	$(12,8, 6^3, 2, 1^4)$
G	$(11^3, 10, 7^4, 6,2, 1^3)$
H	$(13,11,10,8, 7^4, 6,4,3,1)$
I	$(15^3, 12,8,4, 1^3)$
J	$(14,11,10,8,4, 1^3)$
K	$(15,13,11,10, 7^2, 5,4,3,1)$
L	$(17^4, 13,9,5,1)$
M	$(12, 9^2, 8, 7^2, 6, 5^2, 4,3,2,1)$
N	$(11,9, 8^2, 7, 6^4, 5, 4^2, 3,1)$
O	$(12^3, 11, 8^2, 5^2, 2, 1^3)$
P	$(11^3, 8, 6^3, 5,3, 1^3)$
Q	$(11^4, 10^2, 8^2, 5^2, 2, 1^3)$
R	$(13,11,10,8, 6^3, 5,3, 1^3)$
S	$(13^3, 12, 7^2, 2, 1^3)$
T	$(14,10,6,2, 1^5)$
U	$(14^2, 12,10,9,7,6,4,3,1)$
V	$(16,13,12,11, 8^2, 5)$
W	$(14,13,12,11, 10^2, 9, 8^2, 5)$
X	$(13,10,9,8,5,2,1)$
Y	$(16,12, 9^3, 8,5)$
Z	$(13^5, 10,7,4, 1^4)$

If we choose the letter R, then we have the following:

Figure 5. All Changes Made to the Letter R

using the definition of *e*-abacus diagram by James in [5]				
-	●	●	●	-
-	●	-	-	●
-	●	●	●	-
-	●	-	-	●
-	●	-	-	●
		↓		

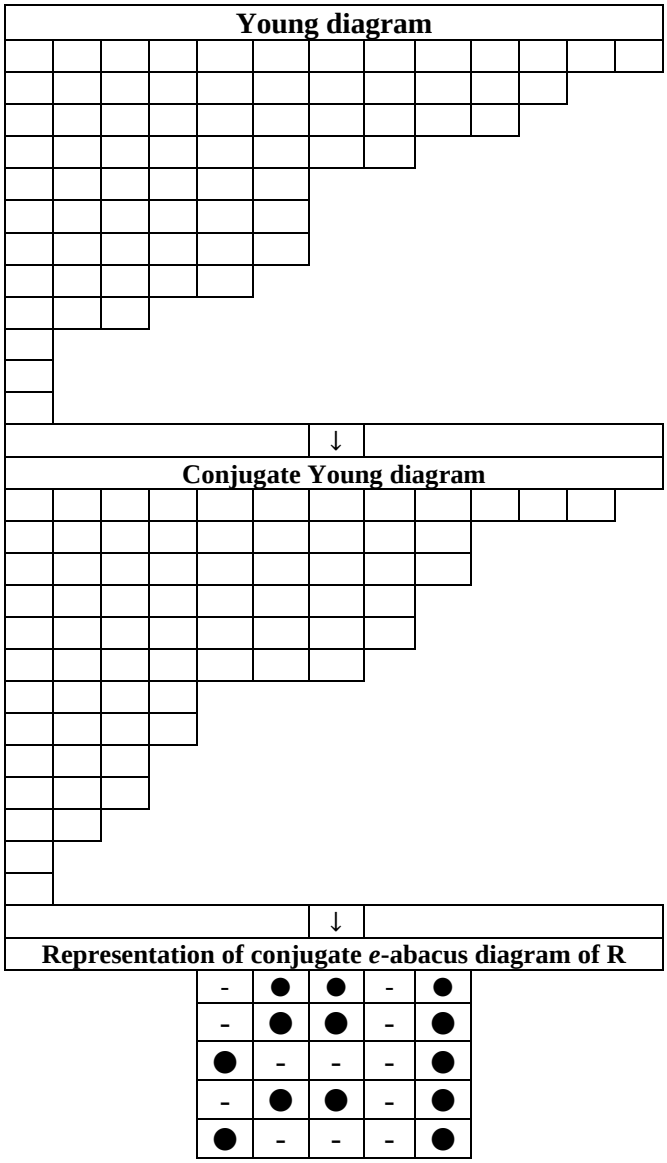

Also if we use Rules 2.1 or 2.2 for the letter Q then we have, the representation of partition about the letter Q is $(11^4, 10^2, 8^2, 5^2, 2, 1^3)$, then $Q' = ((4+2+2+2+1+4)^1, (4+2+2+2+1)^{2-1}, (4+2+2+2)^{5-2}, (4+2+2)^{8-5}, (4+2)^{10-8}, 4^{11-10}) = (14, 11, 10^3, 8^3, 6^2, 4)$

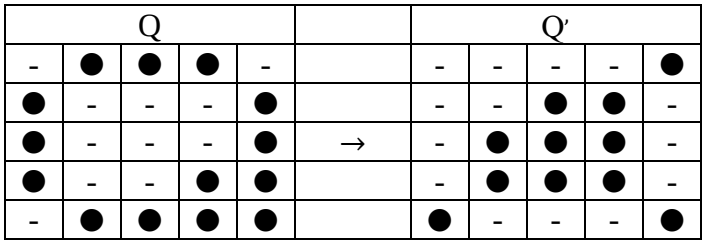

Figure 6. The letter Q (before and after use Rule 2.1 or 2.2)

Now, if we choose any word, for example (TIME), then:

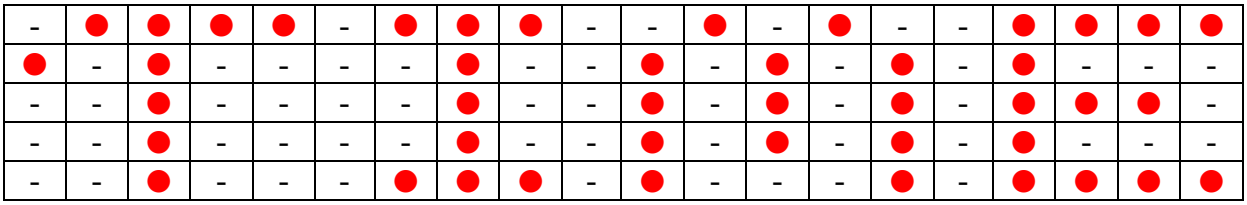

Figure 7. Partition of (TIME)

The conjugate of partition (TIME) if we use Rules 2.1 or 2.2 and *e*-abacus diagram is:

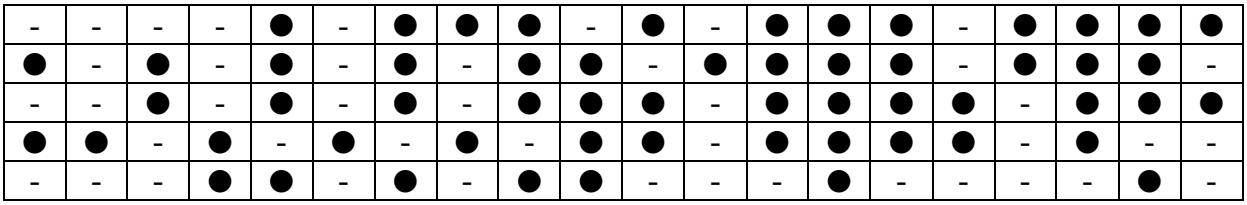

Figure 8. Conjugate of Partition of (TIME)

Acknowledgment

At the end of preparing this research, we sincerely thank the President of the University of Mosul and the Dean of Pure Science Education for their hard work.

References

[1] Mathas A 1999 Iwahori-Hecke Algebras and Schur Algebras of the Symmetric Group *University Lecture Series* **15**

[2] Murphy G E 1992 On the representation theory of the symmetric groups and associated Hecke algebras *J. Algebra*, **152** pp 492-513

[3] Ford B 1997 Irreducible representations of the alternating group in odd characteristic *Proc. Amer. Math. Soc.* **125** 2 pp 375-380

[4] Mahmood, Awreng B. and Mahmood, Ammar S. (2019) Secret-word by *e*-abacus diagram I, *Iraqi J. of Science* **60** 3 pp 638-646

[5] Mahmood, Awreng B and Mahmood A S 2019 Secret-word by *e*-abacus diagram I *Iraqi J. of Science* **60** 4 pp 840-846

[6] Mahmood, Ammar S 2020 Replace the content in e-abacus diagram *Open Access Library Journal* **7** pp 1-7

[7] James G D 1978 Some combinatorial results involving Young Diagrams *Mathematical proceedings of the Cambridge Philosophical Society* **83** pp 1-10

Global Convergence Condition for a New Spectral Conjugate Gradient Method for Large-Scale Optimization

Global Convergence Condition for a New Spectral Conjugate Gradient Method for Large-Scale Optimization

Ahmed Hussien Sheekoo, Ghada M. al-Naemi

Department of Mathematics, College of Computer Science and Mathematics, University of Mosul, Mosul, Iraq.

E-mail: drghadaalnaemi@uomosul.edu.iq

Abstract. The spectral conjugate gradient (SCG) method is an effective method to solve large-scale nonlinear unconstrained optimization problems. In this work, a new spectral conjugate gradient method is proposed with a strong Wolfe-Powell line search (SWP). The idea of the new one is using the β^{BZA} formula which is proposed by Baluch and et al., with suitable parameter φ denoted by (SCGBZA). Under the usual assumptions, the descent properties and overall global convergence of the proposed method (SCGBZA) are proved. The proposed method is numerically proven to be effective.

1. Introduction

Conjugate gradient (CG) and SCG methods are the most effective categories for solving large-scale nonlinear unconstrained optimization problems, this is because they have the advantage of fast convergence, low storage and simple iterations [1]. Now consider the nonlinear unconstrained optimization problems

$$\min f(x), \quad x \in \mathcal{R}^n, \tag{1}$$

where $f: \mathcal{R}^n \to \mathcal{R}$ a smooth function, and its gradient vector is usually represented by $g(x) = \nabla f(x)$. The initial point $x_0 \in \mathcal{R}^n$ is usually calculated through iterative process. The new point calculated as follows:

$$x_{n+1} = x_n + \gamma_n d_n, \qquad n = 0,1,2,3, \ldots \tag{2}$$

and the direction

$$d_{n+1} = \begin{cases} -g_{n+1}, & n = 0 \\ -g_{n+1} + \beta_n d_n, & n \geq 1 \end{cases} \tag{3}$$

Where $\beta_n \in \mathcal{R}$ is the parameter, and $\gamma_n > 0$ is the line search generated by inexact line search (ILS). In this work, we use (SWP) defined by:

$$f(x_n + \gamma_n d_n) \leq f(x_n) + \tau g_n^T d_n \tag{4}$$

$$|g(x_n + \gamma_n d_n)^T d_n| \leq -\delta g_n^T d_n \tag{5}$$

Generally, the above parameters τ *and* μ are required to satisfy $0 < \tau < 0.5 < \delta < 1$. In order to generate different (CG) methods, we have different choices for the parameter β_n. The most commonly used formula for parameters are Hestenes Stiefel method (HS) [2], Fletcher-Reeves method (FR) [3], Polak-Ribiere – Polyak method (PR) [4, 5], Conjugate – Descent method (CD) [6], Liu – Storey method (LS) [7] and Dai-Yuan method (DY) [8]. The parameters of these β_n are as follows:

$$\beta_n^{HS} = \frac{g_{n+1}^T y_n}{y_n^T d_n}; \qquad \beta_n^{FR} = \frac{\|g_{n+1}\|^2}{\|g_n\|^2}; \qquad \beta_n^{PRP} = \frac{g_{n+1}^T y_n}{\|g_n\|^2};$$

$$\beta_n^{CD} = \frac{\|g_{n+1}\|^2}{y_n^T d_n}; \qquad \beta_n^{LS} = \frac{g_{n+1}^T y_n}{-g_n^T d_n}; \qquad \beta_n^{DY} = \frac{\|g_{n+1}\|^2}{y_n^T d_n}.$$

Respectively, where $\|.\|$ is the standard Euclidean norm and $y_n = g_{n+1} - g_n$.

Another way to solve the CG problem (1) is the SCG method. The main difference between the spectral gradient method and the gradient method is the calculation of the search direction [9]. The search direction of the spectral gradient method is defined by the following formula:

$$d_{n+1} = -\varphi_n g_{n+1} + \beta_n d_n \tag{6}$$

Where φ_n is a parameter which is known as a spectral gradient. Observe that if $\varphi_n = 1$, then (6) reduced to (3).

SCG was first proposed by Barazilai and Borwein [10] in 1988. Further, Raydan [11] introduced the SCG method for potential large-scale unconstrained optimization. The main merit of this method is that only the gradient directions is used for each search, while the nonmonotone strategy can ensures global convergence. Birgin and Martines [12] concluded that their SCG method was globally convergent. However, there is actually no guarantee that the SCG method will generate descanting direction. Therefore, Andrei [13] proposed a reduced proportion under the Wolfe line search. Based on the improved a CG algorithm which was proposed by Jiang et al., [14], an SCG method with sufficient descent feature based on the modified CG algorithm that proposed by Zhang et al. [15]. Many authors engaged in the development of the SCG methods, for more information, please refer to [16-21].

2. New algorithm and the descent property

The SCG method is obtained by combining the CG search direction and a scalar spectral parameter.

Baluch et al. [22] in their paper, they constructed a modified three-term HS method in the following direction:

$$d_{n+1} = -g_{n+1} + \beta_n^{BZA} d_n - \varphi_n^{BZA} y_n \tag{7}$$

Note that the suggested formula β_n^{BZA} actually modifies the classic β^{HS} formula by adding $\mu\left|g_{n+1}^T d_n\right|$ in the denominator of HS, the proposed β formula formulated as:

$$\beta_n^{BZA} = \frac{g_{n+1}^T (g_{n+1} - g_n)}{d_n^T y_n + \mu\left|g_{n+1}^T d_n\right|} \tag{8}$$

with $\mu = 2$, and the parameter φ formulated as:

$$\varphi_n^{BZA} = \frac{g_{n+1}^T d_n}{d_n^T y_n + \mu\left|g_{n+1}^T d_n\right|} \tag{9}$$

If the line search is exact, then (8) reduce to the classical HS formula, and (7) reduce to (3).

In this work, we can summarize the direction defined as follows:

$$d_{n+1} = \begin{cases} -g_{n+1}, & n = 0 \\ -\varphi_n^{MBZA} g_{n+1} + \beta_n^{BZA} d_n, & n \geq 1 \end{cases} \tag{10}$$

Where β_n^{BZA} defined in (8), and φ_n it defined as follows:

$$\varphi_n^{MBZA} = 1 - \frac{g_{n+1}^T d_n}{d_n^T y_n + \mu\left|g_{n+1}^T d_n\right|} \tag{11}$$

with $\mu = 0.5$. If the line search is exact, $\varphi_n = 1$, (10) reduce to (3). The process of our proposed SCG method is described in the following algorithm:

3. Algorithm of SCG

Step 1: Choose an initial point $x_1 \in \mathcal{R}^n$, $\varepsilon \geq 0, \varepsilon = 10^{-6}$, $\mu = 0.5$, set $d_1 = -g_1$, n=1.

Step 2: Check convergence, if $\|g_n\| \leq \varepsilon$, then stop; otherwise, continue.

Step 3: Use (4) and (5) to determine the step size $\gamma_n > 0$.

Step 4: Calculate the new point x_{n+1} using (2), $g_{n+1} = g(x_{n+1})$, if $\|g_{n+1}\| \leq \varepsilon$, then stop; otherwise, continue.

Step 5: Calculate the direction d_{n+1} given in (10), β_n^{BZA} and φ_n^{MBZA} are given in (8) and (11) respectively.

Step 6: If the Powel restart criteria

$$\left|g_{n+1}^T g_n\right| \geq 0.2\|g_{n+1}\|^2 \quad (12)$$

is satisfied, set $d_{n+1} = -g_{n+1}$ go to 3; otherwise, continue.

Step 7: Increase n and go to 3.

In order to ensure that the SCG algorithm proposed in (10) has sufficient descent property, which plays an important role in the global convergence analysis under the SWP in (4) and (5), we need the following assumptions:

4. Assumption (A).

1- $f(x)$ is restricted from below on the level set $\Psi = \{x \in \mathcal{R}^n, f(x) \leq f(x_0)\}$, where x_0 is the starting point. i.e., there is a constant $\eta > 0$, which means $\|x_n\| \leq \eta \ \forall x \in \Psi$ [23].

2- $f(x)$ is continuously differentiable in a certain neighborhood N of Ψ, and its gradient is Lipschitz continuous, i.e., there is a constant $\mathcal{L} > 0$, such that

$$\|g(x) - g(y)\| \leq \mathcal{L}||x - y||, \ \forall x, y \in \mathrm{N}. \quad (13)$$

Now using Assumption (A), there exists a positive constant $(\bar{\omega}, \omega, \bar{\rho}$ & $\rho)$, such that:
$0 < \bar{\omega} \leq \|g_{n+1}\| \leq \omega, and \ 0 < \bar{\rho} \leq \|g_n\| \leq \rho \ \forall x \in \Psi$ [23].

Theorem (1): Suppose that assumption (A) holds. Assuming that the sequences $\{g_n\}\, and\, \{d_n\}$ be generated by the algorithm SCG, and the step size γ_n is obtained by SWP. Then, the proposed method has sufficient descent direction i.e.

$$g_{n+1}^T d_{n+1} \leq -\upsilon\|g_{n+1}\|^2 \quad (14)$$

Proof: Multiplying the both sides of the direction defined in (10) by g_{n+1}^T and substituting β_n^{BZA} and φ_n^{MBZA} in (8) and (11) respectively, we get

$$g_{n+1}^T d_{n+1} = -\left(1 - \frac{g_{n+1}^T d_n}{d_n^T y_n + \mu|g_{n+1}^T d_n|}\right)\|g_{n+1}\|^2 + \frac{g_{n+1}^T d_n}{d_n^T y_n + \mu|g_{n+1}^T d_n|} g_{n+1}^T d_n \quad (15)$$

From (5), we have

$$\delta_1 g_n^T d_n \leq g_{n+1}^T d_n \leq -\delta_2 g_n^T d_n \quad (16)$$

$$d_n^T y_n = d_n^T g_{n+1} - d_n^T g_n \geq \delta_1 g_n^T d_n - g_n^T d_n = -(1 - \delta_1) g_n^T d_n$$

i.e.

$$d_n^T y_n \geq -(1 - \delta_1) g_n^T d_n \ . \quad (17)$$

We have

$$g_{n+1}^T y_n = g_{n+1}^T (g_{n+1} - g_n) = \|g_{n+1}\|^2 - g_{n+1}^T g_n.$$

By the one side of Powell restart criteria (12), we obtain

$$\Rightarrow g_{n+1}^T y_n \leq \|g_{n+1}\|^2 + 0.2\|g_{n+1}\|^2 = 1.2\ \|g_{n+1}\|^2. \quad (18)$$

Using (16), (17) and (18) in (15), we get

$$g_{n+1}^T d_{n+1} \le -\left(1-\frac{(-\delta_2 d_n^T g_n)}{(1-\delta_1)(-d_n^T g_n)-\mu\delta_1(-d_n^T g_n)}\right)\|g_{n+1}\|^2 + \frac{1.2\|g_{n+1}\|^2(-\delta_2 g_n^T d_n)}{(1-\delta_1)(-d_n^T g_n)-\mu\delta_1(-d_n^T g_n)}$$

$$= -\left(1-\frac{\delta_2}{[1-(1+\mu)\delta_1]}\right)\|g_{n+1}\|^2 - \frac{1.2\delta_2}{[1-(1+\mu)\delta_1]}\|g_{n+1}\|^2$$

$$= -\left(1-\frac{2.2\delta_2}{[1-(1+\mu)\delta_1]}\right)\|g_{n+1}\|^2 .$$

$\Rightarrow g_{n+1}^T d_{n+1} \le -\upsilon\|g_{n+1}\|^2$, with $\upsilon = \left(1-\frac{2.2\delta_2}{[1-(1+\mu)\delta_1]}\right)$.■ (19)

Therefore, the proposed algorithm satisfies the sufficient descent condition with SWP conditions.

5. The Global Convergence Property.

In this section, we will prove another important condition, called global convergence property. In the following lemma, we review the well-known Zoutendijk condition [24], which plays an important role in the proof of the global convergence analysis of SCG method.

Lemma [25]:

Let assumption (A) holds. Suppose any iteration method (2) and (3), and γ_n is obtained by the SWP (4) and (5). If

$$\sum_{n\ge 1}\frac{1}{\|d_n\|^2} = \infty, \quad (20)$$

Then

$$\lim_{n\to\infty} inf\|g_n\| = 0. \quad (21)$$

Theorem (2): Consider that assumption (A) is satisfied. The sequences $\{x_n\}$ and $\{d_n\}$ generated by the algorithm SCG, γ_n is obtained by SWP and d_n is the descent direction. Then

$$\lim_{n\to\infty} inf\|g_n\| = 0$$

Proof: As

$$\beta_n^{BZA} = \frac{g_{n+1}^T(g_{n+1}-g_n)}{d_n^T y_n+\mu|g_{n+1}^T d_n|},$$

The authors in [22] assumed that $z = [(1-\delta_1)\gamma_n z_1 + \mu\delta_1 z_1]$, and where $0<\delta_1<1$, $z_1>0$ and $\mu = 0.5$, so $z>0$. Therefore,

$$|\beta_n^{BZA}| \le \frac{\mathcal{L}\|g_{n+1}\|}{z_2\|d_n\|} \Rightarrow |\beta_n^{BZA}|.\|d_n\| \le \frac{\mathcal{L}\|g_{n+1}\|}{z_2} \quad (22)$$

Now,

$$|1-\varphi_n^{MBZA}| \le \left|1-\frac{g_{n+1}^T d_n}{d_n^T y_n+\mu|g_{n+1}^T d_n|}\right|$$

$$\le 1+\frac{\|g_{n+1}\|.\|d_n\|}{(1-\delta_1)\gamma_n z_1.\|d_n\|^2+\mu\delta_1 z_1.\|d_n\|^2}$$

$$\le 1+\frac{\|g_{n+1}\|.\|d_n\|}{[(1-\delta_1)\gamma_n z_1+\mu\delta_1 z_1].\|d_n\|^2}$$

$$\le 1+\frac{\|g_{n+1}\|}{z.\|d_n\|} \quad (23)$$

Assume that $A = \left(1+\frac{\omega}{z.b}+\frac{\mathcal{L}}{z_2}\right)$

Now, combining (22) and (23) with (10), we get

$$\|d_{n+1}\| \le |1-\varphi_n^{MBZA}|.\|g_{n+1}\| + |\beta_n^{BZA}|.\|d_n\|$$

$$\le 1+\frac{\|g_{n+1}\|}{z.\|d_n\|}\|g_{n+1}\| + \frac{\mathcal{L}\|g_{n+1}\|}{z_2}$$

$$= \left(1 + \frac{\omega}{z.b} + \frac{\mathcal{L}}{z_2}\right) \|g_{n+1}\|$$
$$\leq A.\omega$$
$$\|d_{n+1}\| \leq E \Rightarrow \|d_{n+1}\|^2 \leq B^2. \quad (24)$$

By taking the summation to the both sides of (24), we get

$$\Rightarrow \sum_{n\geq 1} \frac{1}{\|d_{n+1}\|^2} \geq \frac{1}{B^2} \sum_{n\geq 1} 1 = +\infty$$
$$\Rightarrow \lim_{n\to\infty} inf \|g_n\| = 0. \blacksquare$$

The new proposed algorithm has achieved global convergence.

6. Results and Discussion

We will report the results of several test functions in this section. Some test functions are selected analyze the new method. These functions are considered from CUTEr [26] and Andrei [27]. Using SWP line search, a comparison was made between the new SCG method and the classical BZACG method based on the number of iterations (NOI) and number of function evaluation (NOF). Set $\tau = 0.01$ and $\delta = 0.7$, the stopping criterion of this algorithm was $\|g_{n+1}\| \leq 10^{-6}$. If the number of iterations exceeds 600, the method is considered to have failed. All codes are written in double-precision FORTRAN 77 language and compiled into Visual (Fortran 6.6) (default compiler settings). Under Table1, we have compiled the names of test functions used and the numerical results between the BZACG algorithm and the SCG algorithm.

Table (1): The numerical results

No.	Test Functions	N	Classical algorithm		The SCG algorithm	
			NOI	NOF	NOI	NOF
1	Wood	1000	33	73	29	66
		5000	34	75	29	66
		10000	37	81	32	72
		50000	38	83	32	72
		100000	41	93	33	73
2	Cubic	1000	14	44	14	44
		5000	14	44	14	44
		10000	14	44	14	44
		50000	14	44	14	44
		100000	14	44	14	44
3	Extended Hiebert	1000	60	163	51	161
		5000	60	163	51	161
		10000	60	163	51	161
		50000	60	163	51	161
		100000	60	163	51	161
4	Helical	1000	600	1172	51	126
		5000	600	1174	49	121
		10000	600	1174	51	127
		50000	600	1174	60	144
		100000	600	1174	75	176
5	Powell	1000	42	126	39	116

No.	Test Functions	N	Classical algorithm		The SCG algorithm	
			NOI	NOF	NOI	NOF
6	Rosen	5000	42	126	39	116
		10000	49	169	39	116
		50000	57	190	45	135
		100000	57	191	45	135
		1000	30	78	27	74
		5000	32	80	28	76
		10000	33	82	28	76
		50000	36	92	29	78
		100000	36	92	29	78
7	Summ	1000	19	99	18	97
		5000	33	202	19	86
		10000	40	356	34	240
		50000	65	311	63	153
		100000	72	377	69	286
8	OSP	1000	188	634	187	560
		5000	387	1170	405	1292
		10000	573	1790	567	1779
		50000	580	2305	577	2002
		100000	595	2287	580	2011
9	DENSCHNB (CUTE)	1000	9	21	9	21
		5000	9	21	9	21
		10000	9	21	9	21
		50000	9	21	9	21
		100000	9	21	9	21
10	Miele	1000	86	334	77	305
		5000	93	376	84	346
		10000	93	376	84	346
		50000	107	460	98	430
		100000	107	460	98	430
11	DENSCHNF (CUTE)	1000	11	23	10	21
		5000	11	23	10	21
		10000	12	25	11	23
		50000	12	25	11	23
		100000	12	25	12	23
12	Wolfe	1000	60	121	50	104
		5000	151	306	60	126
		10000	142	288	161	334
		50000	169	344	168	347
		100000	113	234	166	342
13	Miele	1000	86	334	77	305
		5000	93	376	84	346
		10000	93	376	84	346
		50000	107	460	98	430
		100000	203	606	189	582
		1000	256	756	151	452

No.	Test Functions	N	Classical algorithm		The SCG algorithm	
			NOI	NOF	NOI	NOF
14	DIXMAANI	5000	600	1780	319	956
		10000	600	1780	438	1313
		50000	600	1780	587	1643
		100000	600	1780	530	1764
15	Ex-Freudenstein	1000	9	22	8	21
		5000	600	120	8	21
		10000	600	240	8	21
		50000	11	29	8	21
		100000	600	321	8	21
16	NONDIA Shanno-78	1000	10	32	7	18
		5000	6	18	6	18
		10000	6	20	6	20
		50000	5	17	5	17
		100000	5	18	5	18
17	Diagonal 4	1000	3	7	3	7
		5000	3	7	3	7
		10000	3	7	3	7
		50000	4	10	4	10
		100000	4	9	4	9
18	Recipe	1000	19	56	6	18
		5000	22	65	6	18
		10000	22	65	6	18
		50000	22	65	6	18
		100000	22	65	6	18
19	DIXMAANA	1000	6	15	5	13
		5000	6	15	5	13
		10000	7	17	6	15
		50000	7	17	6	15
		100000	7	17	6	16
20	Shallwo	1000	12	29	10	25
		5000	12	29	10	25
		10000	12	29	10	25
		50000	12	29	10	25
		100000	13	31	11	27

7. Conclusion

In this work, we prove the sufficient descent property and the global convergence property of the newly proposed spectral conjugate gradient method through strong Wolfe–Powell line search. The numerical results show that SCG algorithm outperforms BZA conjugate gradient method in terms in the number of iterations and the number of function evaluations.

Acknowledgments

The author expresses their gratitude and thanks to the encouragement and support of the College of Computer Sciences and Mathematics, the University of Mosul.

References

[1] M Mamat, I M Sulaiman, M Maulana, Sukono, and Z A Zakaria 2020 An Efficient Spectral Conjugate Gradient Parameter with Descent Condition for Unconstrained Optimization *Journal of Advance Research in Dynamical & Control Systems* **12** pp 2487- 2493
[2] M R Hestenes and E Stiefel 1952 Methods of conjugate gradients for solving linear systems *Journal of research of the National Bureau of Standards* **49 pp** 409-436
[3] R Fletcher and C M Reeves 1964 Function minimization by conjugate gradients *The computer journal* **7** pp 149-154
[4] E Polak and G Ribiere Note sur la convergence de méthodes de directions conjuguées 1969 *ESAIM: Mathematical Modelling and Numerical Analysis-Modélisation Mathématique et Analyse Numérique* **3** pp 35-43
[5] B T Polyak 1969 The conjugate gradient method in extreme problems *USSR Computational Mathematics and Mathematical Physics* **9** pp 94-112
[6] R Fletcher 1987 *Practical methods of optimization* John and Sons, Chichester
[7] Y Liu and C Storey 1991 Efficient generalized conjugate gradient algorithms, part 1: theory *Journal of optimization theory and applications* **69** pp 129-137
[8] Y H Dai and Y Yuan 1999 A nonlinear conjugate gradient method with a strong global convergence property *SIAM Journal on optimization* **10** pp 177-182
[9] M Malik, M Mamat, S S Abas, I M Sulaiman and Sukono 2020 A new spectral conjugate gradient method with descent condition and global convergence property for unconstrained optimization *Journal of Mathematics and Computer Science* **10** pp 2053-2069
[10] J Barazilai and J M Borwein 1988 Two-point step size gradient methods *IMA Journal of Numerical Analysis* **8** pp 141-148
[11] M Raydan 1997 The Barazilai and Borwein gradient method for the large scale unconstrained minimization problem *SIAM Journal on Optimization* **7** pp 26-33
[12] E Birgin and M J Martines 2001 A spectral conjugate gradient for unconstrained optimization *Applied Mathematical Optimization* **43** pp 117-128
[13] N Andrei 2007 Scaled conjugate gradient algorithms for unconstrained optimization *Computational Optimization and Applications* **38** pp 401-416
[14] H Jiang, S Deng, X Zheng and Z Wan 2012 Global gradient method *Journal of Applied Mathematics*
[15] L Zhang, W Zhou and D Li 2006 A descent modified Polak-Ribiere-Polyak conjugate method and its global convergence *IMA Journal of Numerical Analysis* **26** pp 629-640
[16] M Dawahdeh, I M Sulaiman, M Rivaie and M Mamat 2020 A new spectral conjugate gradient method with strong Wolfe-Powell line search *International Journal of Emerging Trends in Engineering Research* **8** pp 391-397
[17] J Lie and Y Jiang 2012 Global convergence of a spectral conjugate gradient method for unconstrained optimization *Hindawi Publishing Corporation Abstract and Applied Analysis* **12** Article ID758287
[18] J K Liu, X Du and K Wang 2012 A mixed spectral CD-DY conjugate gradient method *Journal of Applied Mathematics* Article ID 569795-1
[19] G M Al-Naemi 2018 A Global Convergence of Spectral Conjugate Gradient Method for Large Scale Optimization *Journal of Education and Science for Pure Science* **27** pp 143-162
[20] U A Yakubu, M Mamat M A Mohamed and M Rivaie 2018 Secant condition free of a spectral PRP conjugate gradient method International Journal of Engineering and Technology **7** pp 325-328
[21] U A Yakubua, A Igudab, A V Mandarac and S Murtalad 2019 Scalar Parameter of a Spectral PRP Conjugate Gradient Method for Unconstrained Optimization *Malaysian Journal of Computing and Applied Mathematics* **2** pp 34-41

[22] B Baluch, Z Salleh and A Alhawarat 2018 A new modified three-term Heatenes- Stiefel conjugate gradient method with sufficient descent property and its global convergence *Hindawi Journal of Optimization* **2018** pp 1-13
[23] G M Al-Naemi 2013 *Modified Nonlinear Conjugate Gradient Algorithms with Application in Neural Networks* LAP LAMBERT Academic Publishing
[24] G Zoutendijk 1970 Nonlinear programming, computational methods *Integer and nonlinear programming* **143** pp 37-86
[25] Y Dai and L Z Liao 2001 New conjugacy conditions and related nonlinear conjugate gradient methods *Applied Mathematics and Optimization* **43** pp 87-101 *DOI: 10.1007/5002450010019*
[26] I Bongartz, A R Conn, N Gould and P L Toint 1995 ACM Transactions on Mathematical Software **21** pp 123-160
[27] N Andrei 2008 Advance Modelling and Optimization **10** pp 147-161

On fuzzy soft normal operators

On fuzzy soft normal operators

Dr.Salim Dawood , Ali Qassim Jabur

Department of Mathematic, College of Education, University of Al –Musstinseryah, Baghdad, Iraq

E- Email: alsrayly842@gmail.com

Abstract. In this paper, we study and discuss a new type of normal operator which is fuzzy soft normal operator and given some properties with the characterization of this operator. Also, theorems related on fuzzy soft normal operator have been given. In addition, we introduce the relation between this operator and other types.

1. Introduction

Zadeh [1] suggested an expansion of the theory of the set, which is idea of fuzzy sets to cope with insecurity in 1965. A fuzzy set on a $domain\ \mathcal{X}$ is defined by membership function $From\ \mathcal{X}\ to$ [0,1]. Also In 1999, Molodtsov [2] introduced new types of sets were said to be soft set. The soft set is a mathematical instrument for uncertainty in modelling by associating a collection with a set of parameters, i.e., it is a parameterized family of Universal Set sub-sets. After that, many researchers also presented new, expanded ideas based on soft sets were introduced by researchers, and examples were given for them and researched their characteristics, such as soft point [3], Soft normed Spaces [4], Soft Inner Product Spaces [5] and Soft Hilbert space [6].

And many searchers made mix between fuzzy set and soft set to get definition fuzzy soft set, for example Maji [7]. This definition has been applied and some concepts are being given, like Fuzzy soft point [8] and fuzzy soft normed spaces [9].

Currently, the fuzzy soft inner product spaces and fuzzy soft Hilbert space [10] were introduced by Faried et al. Additionally the Fuzzy soft linear operator [11]. Finally, they defined the fuzzy soft self-adjoint operator [12] and studied its properties.

The aim of this work submitted a new type of normal operator is called fuzzy soft normal operator, and given some theorem relating to this operator with properties. Well as the relation between this operator and anther types like fuzzy soft self-adjoint operator.

2. Basic concepts

Definition 2.1 [1]**:** Let $\widehat{\mathbf{A}}$ be a fuzzy set over universe set $\boldsymbol{\mathcal{X}}$ is a set characterized by a membership function $\boldsymbol{\mu}_{\widehat{\mathbf{A}}}: \boldsymbol{\mathcal{X}} \longrightarrow \mathfrak{T}$, where $\mathfrak{T} = [\mathbf{0}, \mathbf{1}]$ and $\widehat{\mathbf{A}}$ represented by an ordered pairs $\widehat{\mathbf{A}} = \{(\mathbf{x}, \boldsymbol{\mu}_{\widehat{\mathbf{A}}}(\mathbf{x})) | \mathbf{x} \in \boldsymbol{\mathcal{X}},\ \boldsymbol{\mu}_{\widehat{\mathbf{A}}}(\mathbf{x}) \in \mathfrak{T}\}$ or $\widehat{\mathbf{A}} = \left\{\frac{\boldsymbol{\mu}_{\widehat{\mathbf{A}}}(\mathbf{x})}{\mathbf{x}} : \mathbf{x} \in \boldsymbol{\mathcal{X}}\right\}$

$\mu_{\widehat{A}}(x)$ is said to be degree of membership of x in $\widehat{A}$

And $\mathfrak{T}^{\mathcal{X}} = \{\widehat{A} :\ \widehat{A}\text{is a function from } \mathcal{X} \text{ into } \mathfrak{T}\}$

Definitions 2.2 [**2**]: Let $\boldsymbol{\mathcal{X}}$ be a universe set, and **E** be a set of parameters, $\boldsymbol{\mathcal{P}}(\boldsymbol{\mathcal{X}})$ the power set of $\boldsymbol{\mathcal{X}}$ and $\mathbf{A} \subseteq \mathbf{E}$. Suppose that $\boldsymbol{\mathcal{G}}$ is a mapping given by $\boldsymbol{\mathcal{G}}: \mathbf{A} \to \boldsymbol{\mathcal{P}}(\boldsymbol{\mathcal{X}})$, where $\mathcal{G}_{\mathbf{A}} = \{\boldsymbol{\mathcal{G}}(\mathbf{e}) \in \boldsymbol{\mathcal{P}}(\boldsymbol{\mathcal{X}}): \mathbf{e} \in \mathbf{A}\}$.
The pair $(\mathcal{G}, \mathrm{A})$ or $\mathcal{G}_{\mathrm{A}}$ is called soft set over $\mathcal{X}$ with respect to A.

Definition 2.3 [**7**]: The soft set $(\boldsymbol{\mathcal{G}}, \mathbf{A})$ is called fuzzy soft set $(\boldsymbol{\mathcal{FS}} - \mathbf{set})$ over a universe set $\boldsymbol{\mathcal{X}}$,whenever $\boldsymbol{\mathcal{G}}$ is a mapping $\boldsymbol{\mathcal{G}}: \mathbf{A} \to \boldsymbol{\mathfrak{T}}^{\boldsymbol{\mathcal{X}}}$,and $\{\boldsymbol{\mathcal{G}}(\mathbf{e}) \in \boldsymbol{\mathfrak{T}}^{\boldsymbol{\mathcal{X}}}: \mathbf{e} \in \mathbf{A}\}$
The family of all $\mathcal{FS}-$ sets, symbolized by $\mathcal{FSS}(\widetilde{\mathcal{X}})$
Definition 2.4 [**8**]: The $\boldsymbol{\mathcal{FS}} - \mathbf{set}$ $(\boldsymbol{\mathcal{G}}, \mathbf{A}) \in \boldsymbol{\mathcal{FSS}}(\widetilde{\boldsymbol{\mathcal{X}}})$ is called fuzzy soft point over $\boldsymbol{\mathcal{X}}$, symbolized by $((\mathbf{x}_{\boldsymbol{\mu}_{\mathcal{G}(\mathrm{e})}}, \mathbf{A})$ or $\tilde{\mathbf{x}}_{\boldsymbol{\mu}_{\mathcal{G}(\mathrm{e})}})$, if $\mathbf{e} \in \mathbf{A}$ and $\mathbf{x} \in \boldsymbol{\mathcal{X}}$,

$$\mu_{\mathcal{G}(\mathrm{e})}(\mathrm{x}) = \begin{cases} \lambda & , \text{if } \mathrm{x} = \mathrm{x}_0 \in \mathcal{X} \text{ and } \mathrm{e} = \mathrm{e}_0 \in \mathrm{A} \\ 0 & , \text{if } \mathrm{x} \in \mathcal{X} - \{\mathrm{x}_0\} \text{ or } \mathrm{e} \in \mathrm{A} - \{\mathrm{e}_0\} \end{cases} \text{, where } \lambda \in (0,1]$$

Remark 2.5 [**8**]: $\boldsymbol{\mathcal{C}}(\mathbf{A})$ is the family of all $\boldsymbol{\mathcal{FS}} - \mathbf{Complex}$ numbers and $\boldsymbol{\mathcal{R}}(\mathbf{A})$ is also the family of all $\boldsymbol{\mathcal{FS}} - \mathbf{Real}$ numbers

Definition 2.6 [**9**]: Let $\widetilde{\boldsymbol{\mathcal{X}}}$ be $\boldsymbol{\mathcal{FS}} - \mathbf{vector\ space}$. Then, a mapping $\|\widetilde{.}\|: \widetilde{\boldsymbol{\mathcal{X}}} \to \boldsymbol{\mathcal{R}}(\mathbf{A})$ is called fuzzy soft norm on $\widetilde{\boldsymbol{\mathcal{X}}}$ $(\boldsymbol{\mathcal{FSN}})$ if $\|\widetilde{.}\|$ satisfies the following conditions:
(1) $\left\| \widetilde{\tilde{\mathrm{x}}_{\mu_{\mathcal{G}(\mathrm{e})}}} \right\| \geq \tilde{0}, \forall\, \tilde{\mathrm{x}}_{\mu_{\mathcal{G}(\mathrm{e})}} \in \widetilde{\mathcal{X}}$,and $\left\| \widetilde{\tilde{\mathrm{x}}_{\mu_{\mathcal{G}(\mathrm{e})}}} \right\| = \tilde{0} \Leftrightarrow \tilde{\mathrm{x}}_{\mu_{\mathcal{G}(\mathrm{e})}} = \tilde{\theta}$
(2) $\left\| \tilde{\mathrm{r}} \cdot \widetilde{\tilde{\mathrm{x}}_{\mu_{\mathcal{G}(\mathrm{e})}}} \right\| = |\tilde{\mathrm{r}}| \left\| \widetilde{\tilde{\mathrm{x}}_{\mu_{\mathcal{G}(\mathrm{e})}}} \right\|, \forall\, \tilde{\mathrm{x}}_{\mu_{\mathcal{G}(\mathrm{e})}} \in \widetilde{\mathcal{X}}, \forall\, \tilde{\mathrm{r}} \in \mathcal{C}(\mathrm{A})$.
(3) $\left\| \tilde{\mathrm{x}}_{\mu_{1_{\mathcal{G}(\mathrm{e}_1)}}} \widetilde{+ \tilde{\mathrm{y}}_{\mu_{2_{\mathcal{G}(\mathrm{e}_2)}}}} \right\| \leq \left\| \widetilde{\tilde{\mathrm{x}}_{\mu_{1_{\mathcal{G}(\mathrm{e}_1)}}}} \right\| + \left\| \widetilde{\tilde{\mathrm{y}}_{\mu_{2_{\mathcal{G}(\mathrm{e}_2)}}}} \right\|, \forall\, \tilde{\mathrm{x}}_{\mu_{1_{\mathcal{G}(\mathrm{e}_1)}}}, \tilde{\mathrm{y}}_{\mu_{2_{\mathcal{G}(\mathrm{e}_2)}}} \in \widetilde{\mathcal{X}}$.
The $\mathcal{FS}-$ vector space with $\mathcal{FSN}$ $\|\widetilde{.}\|$ is called fuzzy soft normed vector space $(\mathcal{FSN}-\text{space})$, and symbolized by $\left(\widetilde{\mathcal{X}}, \widetilde{\|.\|}\right)$.

Definition 2.7 [**10**]: Let $\widetilde{\boldsymbol{\mathcal{X}}}$ be $\boldsymbol{\mathcal{FS}}\mathbf{V} - \mathbf{space}$. Then, the mapping $\widetilde{\langle .,. \rangle} : \widetilde{\boldsymbol{\mathcal{X}}} \times \widetilde{\boldsymbol{\mathcal{X}}} \to (\boldsymbol{\mathcal{C}}(\mathbf{A})\ \mathbf{or}\ \boldsymbol{\mathcal{R}}(\mathbf{A}))$ is called fuzzy soft inner product on $\widetilde{\boldsymbol{\mathcal{X}}}$ $(\boldsymbol{\mathcal{FS}}\mathfrak{T})$ if $\widetilde{\langle .,. \rangle}$ satisfies :
(1) $\langle \tilde{\mathrm{x}}_{\mu_{1_{\mathcal{G}(\mathrm{e}_1)}}}, \widetilde{\tilde{\mathrm{x}}_{\mu_{1_{\mathcal{G}(\mathrm{e}_1)}}}} \rangle \geq \tilde{0}$, for all $\tilde{\mathrm{x}}_{\mu_{1_{\mathcal{G}(\mathrm{e}_1)}}} \in \widetilde{\mathcal{X}}$ and $\langle \tilde{\mathrm{x}}_{\mu_{1_{\mathcal{G}(\mathrm{e}_1)}}}, \widetilde{\tilde{\mathrm{x}}_{\mu_{1_{\mathcal{G}(\mathrm{e}_1)}}}} \rangle = \tilde{0} \iff \tilde{\mathrm{x}}_{\mu_{1_{\mathcal{G}(\mathrm{e}_1)}}} = \tilde{\theta}$
(2) $\langle \tilde{\mathrm{x}}_{\mu_{1_{\mathcal{G}(\mathrm{e}_1)}}}, \widetilde{\tilde{\mathrm{y}}_{\mu_{2_{\mathcal{G}(\mathrm{e}_2)}}}} \rangle = \overline{\langle \tilde{\mathrm{y}}_{\mu_{2_{\mathcal{G}(\mathrm{e}_2)}}}, \widetilde{\tilde{\mathrm{x}}_{\mu_{1_{\mathcal{G}(\mathrm{e}_1)}}}} \rangle}$ $, \forall\, \tilde{\mathrm{x}}_{\mu_{1_{\mathcal{G}(\mathrm{e}_1)}}}, \tilde{\mathrm{y}}_{\mu_{2_{\mathcal{G}(\mathrm{e}_2)}}} \in \widetilde{\mathcal{X}}$, where bar denotes complex conjugate of the $\mathcal{FS}-$ complex number.
(3) $\langle \tilde{\alpha} \tilde{\mathrm{x}}_{\mu_{1_{\mathcal{G}(\mathrm{e}_1)}}}, \widetilde{\tilde{\mathrm{y}}_{\mu_{2_{\mathcal{G}(\mathrm{e}_2)}}}} \rangle = \tilde{\alpha} \langle \tilde{\mathrm{x}}_{\mu_{1_{\mathcal{G}(\mathrm{e}_1)}}}, \widetilde{\tilde{\mathrm{y}}_{\mu_{2_{\mathcal{G}(\mathrm{e}_2)}}}} \rangle$, for all $\tilde{\mathrm{x}}_{\mu_{1_{\mathcal{G}(\mathrm{e}_1)}}}, \tilde{\mathrm{y}}_{\mu_{2_{\mathcal{G}(\mathrm{e}_2)}}} \in \widetilde{\mathcal{X}}$ and for all $\tilde{\alpha} \in \mathrm{C}(\mathrm{A})$.
(4) $\langle \tilde{\mathrm{x}}_{\mu_{1_{\mathcal{G}(\mathrm{e}_1)}}} + \widetilde{\tilde{\mathrm{y}}_{\mu_{2_{\mathcal{G}(\mathrm{e}_2)}}}}, \tilde{\mathrm{z}}_{\mu_{3_{\mathcal{G}(\mathrm{e}_3)}}} \rangle = \langle \tilde{\mathrm{x}}_{\mu_{1_{\mathcal{G}(\mathrm{e}_1)}}}, \widetilde{\tilde{\mathrm{z}}_{\mu_{3_{\mathcal{G}(\mathrm{e}_3)}}}} \rangle + \langle \tilde{\mathrm{y}}_{\mu_{2_{\mathcal{G}(\mathrm{e}_2)}}}, \widetilde{\tilde{\mathrm{z}}_{\mu_{3_{\mathcal{G}(\mathrm{e}_3)}}}} \rangle$
For all $\tilde{\mathrm{x}}_{\mu_{1_{\mathcal{G}(\mathrm{e}_1)}}}, \tilde{\mathrm{y}}_{\mu_{2_{\mathcal{G}(\mathrm{e}_2)}}}, \tilde{\mathrm{z}}_{\mu_{3_{\mathcal{G}(\mathrm{e}_3)}}} \in \widetilde{\mathcal{X}}$
The $\mathcal{FS}-$ vector space $\widetilde{\mathcal{X}}$ with $\mathcal{FS}\mathfrak{T}$ $\widetilde{\langle .,. \rangle}$ is called fuzzy soft inner product space $(\mathcal{FS}\mathfrak{T}-\text{space})$, and symbolized by $\left(\widetilde{\mathrm{X}}, \widetilde{\langle .,. \rangle}\right)$

Definition 2.8 [**13**]: A sequence of $\boldsymbol{\mathcal{FS}}-$ $\mathbf{vectors}$ $\left\{\tilde{\mathbf{x}}^{\mathbf{n}}_{\boldsymbol{\mu}_{\mathbf{n}\boldsymbol{\mathcal{G}}(\mathbf{e_n})}}\right\}$ in $\boldsymbol{\mathcal{FSN}} - \mathbf{space}$ $\left(\widetilde{\mathbf{X}}, \widetilde{\|\cdot\|}\right)$ is called fuzzy soft convergent and converges to $\tilde{\mathbf{x}}^{\mathbf{o}}_{\boldsymbol{\mu}_{\mathbf{0}\boldsymbol{\mathcal{G}}(\mathbf{e_0})}}$ if $\lim_{\mathbf{n}\to\infty} \left\| \tilde{\mathbf{x}}^{\mathbf{n}}_{\boldsymbol{\mu}_{\mathbf{n}\boldsymbol{\mathcal{G}}(\mathbf{e_n})}} \widetilde{- \tilde{\mathbf{x}}^{\mathbf{o}}_{\boldsymbol{\mu}_{\mathbf{0}\boldsymbol{\mathcal{G}}(\mathbf{e_0})}}} \right\| = \tilde{\mathbf{0}}$ i.e. $\forall \tilde{\boldsymbol{\epsilon}} > \tilde{\mathbf{0}}$, $\exists \mathbf{n_o} \in \mathbf{N}$ such that $\left\| \tilde{\mathbf{x}}^{\mathbf{n}}_{\boldsymbol{\mu}_{\mathbf{n}\boldsymbol{\mathcal{G}}(\mathbf{e_n})}} \widetilde{- \tilde{\mathbf{x}}^{\mathbf{o}}_{\boldsymbol{\mu}_{\mathbf{0}\boldsymbol{\mathcal{G}}(\mathbf{e_0})}}} \right\| < \tilde{\boldsymbol{\epsilon}}$, $\forall \mathbf{n} \geq \mathbf{n_o}$.
It if denoted by $\lim_{\mathrm{n}\to\infty} \tilde{\mathrm{x}}^{\mathrm{n}}_{\mu_{\mathrm{n}\mathcal{G}(\mathrm{e_n})}} = \tilde{\mathrm{x}}^{\mathrm{o}}_{\mu_{0\mathcal{G}(\mathrm{e_0})}}$ or $\tilde{\mathrm{x}}^{\mathrm{n}}_{\mu_{\mathrm{n}\mathcal{G}(\mathrm{e_n})}} \to \tilde{\mathrm{x}}^{\mathrm{o}}_{\mu_{0\mathcal{G}(\mathrm{e_0})}}$ as $\mathrm{n} \to \infty$

Definition 2.9 [**13**]: A sequence of $\boldsymbol{\mathcal{FS}-}$ **vectors** $\left\{\tilde{\mathbf{x}}^{\mathbf{n}}_{\boldsymbol{\mu}_{\mathbf{n}\mathcal{G}(\mathbf{e_n})}}\right\}$ in $\boldsymbol{\mathcal{FSN}-}$**space** $\left(\widetilde{\mathbf{X}}, \widetilde{\|\cdot\|}\right)$ is called fuzzy soft Cauchy sequence, if $\forall \tilde{\boldsymbol{\epsilon}} > \tilde{\mathbf{0}}$, $\exists \mathbf{n_o} \in \mathbf{N}$ such that $\left\|\tilde{\mathbf{x}}^{\mathbf{n}}_{\boldsymbol{\mu}_{\mathbf{n}\mathcal{G}(\mathbf{e_n})}} \widetilde{-} \tilde{\mathbf{x}}^{\mathbf{m}}_{\boldsymbol{\mu}_{\mathbf{m}\mathcal{G}(\mathbf{e_m})}}\right\| < \tilde{\boldsymbol{\epsilon}}$, $\forall \mathbf{n}, \mathbf{m} \geq \mathbf{n_o}$, $\mathbf{n} > \mathbf{m}$.
That is to say that $\left\|\tilde{\mathrm{x}}^{\mathrm{n}}_{\mu_{\mathrm{n}\mathcal{G}(\mathrm{e_n})}} \widetilde{-} \tilde{\mathrm{x}}^{\mathrm{m}}_{\mu_{\mathrm{m}\mathcal{G}(\mathrm{e_m})}}\right\| \to \tilde{0}$ as $\mathrm{n}, \mathrm{m} \to \infty$
Definition 2.10 [**13**]: The $\boldsymbol{\mathcal{FSN}-}$**space** $\left(\widetilde{\mathbf{X}}, \widetilde{\|\cdot\|}\right)$ is called fuzzy soft complete ($\boldsymbol{\mathcal{FS}-}$**complete**) if every $\boldsymbol{\mathcal{FS}-}$ **Cauchy sequence** is $\boldsymbol{\mathcal{FS}-}$ **convergent sequence** in it.

Definition 2.11 [**10**]: The $-$**space** $\left(\widetilde{\boldsymbol{\mathcal{X}}}, \widetilde{\langle .,. \rangle}\right)$, if it is $\boldsymbol{\mathcal{FS}-}$**complete** in the induced $\boldsymbol{\mathcal{FSN}}$ $\left\|\widetilde{\tilde{\mathbf{x}}_{\boldsymbol{\mu}_{\mathcal{G}(\mathbf{e})}}}\right\| = \sqrt{\langle \tilde{\mathbf{x}}_{\boldsymbol{\mu}_{\mathcal{G}(\mathbf{e})}}, \widetilde{\tilde{\mathbf{x}}_{\boldsymbol{\mu}_{\mathcal{G}(\mathbf{e})}}} \rangle}$ is called fuzzy soft Hilbert space ($\boldsymbol{\mathcal{FSH}-}$**space**), and symbolized by $\left(\widetilde{\boldsymbol{\mathcal{H}}}, \widetilde{\langle .,. \rangle}\right)$.

Definition 2.12 [**11**]: Let $\widetilde{\boldsymbol{\mathcal{H}}}$ **be** $\boldsymbol{\mathcal{FSH}-}$**space** and $\tilde{\boldsymbol{\mathcal{T}}}: \widetilde{\boldsymbol{\mathcal{H}}} \to \widetilde{\boldsymbol{\mathcal{H}}}$ be a fuzzy soft operator ($\boldsymbol{\mathcal{FS}-}$**operator**) .Then $\tilde{\boldsymbol{\mathcal{T}}}$ is called fuzzy soft linear operators ($\boldsymbol{\mathcal{FS}}\mathbf{L}-$**operator**) if:
1. $\tilde{\mathcal{T}}\left(\tilde{\mathrm{x}}_{\mu_{1\mathcal{G}(\mathrm{e}_1)}} + \tilde{\mathrm{y}}_{\mu_{2\mathcal{G}(\mathrm{e}_2)}}\right) = \tilde{\mathcal{T}}\left(\tilde{\mathrm{x}}_{\mu_{1\mathcal{G}(\mathrm{e}_1)}}\right) + \tilde{\mathcal{T}}\left(\tilde{\mathrm{y}}_{\mu_{2\mathcal{G}(\mathrm{e}_2)}}\right), \forall\, \tilde{\mathrm{x}}_{\mu_{1\mathcal{G}(\mathrm{e}_1)}}, \tilde{\mathrm{y}}_{\mu_{2\mathcal{G}(\mathrm{e}_2)}} \in \widetilde{\mathcal{H}}$
2. $\tilde{\mathcal{T}}\left(\tilde{\beta}\tilde{\mathrm{x}}_{\mu_{1\mathcal{G}(\mathrm{e}_1)}}\right) = \tilde{\beta}\tilde{\mathcal{T}}\left(\tilde{\mathrm{x}}_{\mu_{1\mathcal{G}(\mathrm{e}_1)}}\right), \forall\, \tilde{\mathrm{x}}_{\mu_{1\mathcal{G}(\mathrm{e}_1)}} \in \widetilde{\mathcal{H}}$ and $\tilde{\beta} \in \mathcal{C}(\mathrm{A})$
i.e. $\tilde{\mathcal{T}}\left(\tilde{\alpha}\tilde{\mathrm{x}}_{\mu_{1\mathcal{G}(\mathrm{e}_1)}} + \tilde{\beta}\tilde{\mathrm{y}}_{\mu_{2\mathcal{G}(\mathrm{e}_2)}}\right) = \tilde{\alpha}\tilde{\mathcal{T}}\left(\tilde{\mathrm{x}}_{\mu_{1\mathcal{G}(\mathrm{e}_1)}}\right) + \tilde{\beta}\tilde{\mathcal{T}}\left(\tilde{\mathrm{y}}_{\mu_{2\mathcal{G}(\mathrm{e}_2)}}\right)$, for all $\tilde{\mathrm{x}}_{\mu_{1\mathcal{G}(\mathrm{e}_1)}}, \tilde{\mathrm{y}}_{\mu_{2\mathcal{G}(\mathrm{e}_2)}} \in \widetilde{\mathcal{H}}$ and $\tilde{\alpha}, \tilde{\beta}$ any fuzzy soft scalars

Definition 2.13 [**11**]: Let $\widetilde{\boldsymbol{\mathcal{H}}}$ **be** $\boldsymbol{\mathcal{FSH}-}$**space** and $\tilde{\boldsymbol{\mathcal{T}}}: \widetilde{\boldsymbol{\mathcal{H}}} \to \widetilde{\boldsymbol{\mathcal{H}}}$ be $\boldsymbol{\mathcal{FS}-}$**operator** is called fuzzy soft bounded operator ($\boldsymbol{\mathcal{FSB}-}$**operator**) ,if $\exists\, \tilde{\mathbf{m}} \in \boldsymbol{\mathcal{R}}(\mathbf{A})$ such that $\left\|\widetilde{\tilde{\boldsymbol{\mathcal{T}}}\left(\widetilde{\tilde{\mathbf{x}}_{\boldsymbol{\mu}_{\mathbf{1}\mathcal{G}(\mathbf{e_1})}}}\right)}\right\| \leq \tilde{\mathbf{m}} \left\|\widetilde{\tilde{\mathbf{x}}_{\boldsymbol{\mu}_{\mathbf{1}\mathcal{G}(\mathbf{e_1})}}}\right\|$, for all $\tilde{\mathbf{x}}_{\boldsymbol{\mu}_{\mathbf{1}\mathcal{G}(\mathbf{e_1})}} \in \widetilde{\boldsymbol{\mathcal{H}}}$
Now, the collection of all $\mathcal{FS}-$liner and bounded operators denoted by $\widetilde{\mathrm{B}}(\widetilde{\mathcal{H}})$.

Definitions 2.14: Let $\widetilde{\boldsymbol{\mathcal{H}}}$**and** $\widetilde{\boldsymbol{\mathcal{K}}}$ be two $\boldsymbol{\mathcal{FSH}-}$**space**, then
1- The range of $\mathcal{FS}-$operator $\tilde{\mathcal{T}}: \widetilde{\mathcal{H}} \to \widetilde{\mathcal{K}}$ denoted by $\mathrm{Ran}(\tilde{\mathcal{T}})$ and $\mathrm{Ran}(\tilde{\mathcal{T}}) = \left\{\tilde{\mathcal{T}}\left(\tilde{\mathrm{x}}_{\mu_{1\mathcal{G}(\mathrm{e}_1)}}\right) \in \widetilde{\mathcal{K}} : \tilde{\mathrm{x}}_{\mu_{1\mathcal{G}(\mathrm{e}_1)}} \in \widetilde{\mathcal{H}}\right\}$.
2- The null (Kernel) of $\mathcal{FS}-$operator $\tilde{\mathcal{T}}: \widetilde{\mathcal{H}} \to \widetilde{\mathcal{K}}$ denoted by $\mathrm{Ker}(\tilde{\mathcal{T}})$ and $\mathrm{Ker}(\tilde{\mathcal{T}}) = \left\{\tilde{\mathrm{x}}_{\mu_{1\mathcal{G}(\mathrm{e}_1)}} \in \widetilde{\mathcal{H}} : \tilde{\mathcal{T}}\left(\tilde{\mathrm{x}}_{\mu_{1\mathcal{G}(\mathrm{e}_1)}}\right) = \tilde{0}\right\}$.

Example 2.15 [**11**]: The $\boldsymbol{\mathcal{FS}-}$**operator** $\tilde{\mathbf{I}}: \widetilde{\boldsymbol{\mathcal{H}}} \to \widetilde{\boldsymbol{\mathcal{H}}}$ defined by $\tilde{\mathbf{I}}\left(\tilde{\mathbf{x}}_{\boldsymbol{\mu}_{\mathbf{1}\mathcal{G}(\mathbf{e_1})}}\right) = \tilde{\mathbf{x}}_{\boldsymbol{\mu}_{\mathbf{1}\mathcal{G}(\mathbf{e_1})}}$, $\forall\, \tilde{\mathbf{x}}_{\boldsymbol{\mu}_{\mathbf{1}\mathcal{G}(\mathbf{e_1})}} \in \widetilde{\boldsymbol{\mathcal{H}}}$. And it is called fuzzy soft identity operator

Definition 2.16 [**11**]: Let $\widetilde{\boldsymbol{\mathcal{H}}}$ be $\boldsymbol{\mathcal{FSH}-}$**space** and $\tilde{\boldsymbol{\mathcal{T}}}: \widetilde{\boldsymbol{\mathcal{H}}} \to \widetilde{\boldsymbol{\mathcal{H}}}$ be $\boldsymbol{\mathcal{FSB}-}$**operator**, then The fuzzy soft adjoint operator $\tilde{\boldsymbol{\mathcal{T}}}^*$ is defined by
$\langle \tilde{\mathcal{T}}\tilde{\mathrm{x}}_{\mu_{1\mathcal{G}(\mathrm{e}_1)}}, \tilde{\mathrm{y}}_{\mu_{2\mathcal{G}(\mathrm{e}_2)}} \rangle = \langle \tilde{\mathrm{x}}_{\mu_{1\mathcal{G}(\mathrm{e}_1)}}, \widetilde{\tilde{\mathcal{T}}^*}\, \tilde{\mathrm{y}}_{\mu_{2\mathcal{G}(\mathrm{e}_2)}} \rangle$, $\forall\, \tilde{\mathrm{x}}_{\mu_{1\mathcal{G}(\mathrm{e}_1)}}, \tilde{\mathrm{y}}_{\mu_{2\mathcal{G}(\mathrm{e}_2)}} \in \widetilde{\mathcal{H}}$

Theorem 2.17 [**11**]: Let $\tilde{\boldsymbol{\mathcal{T}}}, \tilde{\mathbf{R}} \in \widetilde{\mathbf{B}}(\widetilde{\boldsymbol{\mathcal{H}}})$,where $\widetilde{\boldsymbol{\mathcal{H}}}$ is $\boldsymbol{\mathcal{FSH}-}$**space** and $\tilde{\boldsymbol{\beta}} \in \boldsymbol{\mathcal{C}}(\mathbf{A})$, then $\tilde{\boldsymbol{\mathcal{T}}}^{**} = \tilde{\boldsymbol{\mathcal{T}}}$, $\left(\tilde{\boldsymbol{\beta}}\tilde{\boldsymbol{\mathcal{T}}}\right)^* = \widetilde{\tilde{\boldsymbol{\beta}}}\tilde{\boldsymbol{\mathcal{T}}}^*$, $\left(\tilde{\boldsymbol{\mathcal{T}}} + \tilde{\mathbf{R}}\right)^* = \tilde{\boldsymbol{\mathcal{T}}}^* + \tilde{\mathbf{R}}^*$ and $\left(\tilde{\boldsymbol{\mathcal{T}}}\tilde{\mathbf{R}}\right)^* = \tilde{\mathbf{R}}^*\tilde{\boldsymbol{\mathcal{T}}}^*$.

Theorem 2.18 [**11**]: if $\widetilde{\mathcal{T}} \in \widetilde{\mathbf{B}}(\widetilde{\mathcal{H}})$,where $\widetilde{\mathcal{H}}$ is $\mathcal{FSH}-\mathbf{space}$, then $\widetilde{\|\widetilde{\mathcal{T}}^*\|} = \widetilde{\|\widetilde{\mathcal{T}}\|}$ and $\widetilde{\|\widetilde{\mathcal{T}}^*\widetilde{\mathcal{T}}\|} = \widetilde{\|\widetilde{\mathcal{T}}\|}^{\mathbf{2}}$

Definition 2.19 [**12**]: The $\mathcal{FS}-\mathbf{operator}$ $\widetilde{\mathcal{T}}$ of $\mathcal{FSH}-\mathbf{space}$ $\widetilde{\mathcal{H}}$ is called fuzzy soft self adjoint ($\mathcal{FS}-\mathbf{self\ adjoint\ operator}$) if $\widetilde{\mathcal{T}} = \widetilde{\mathcal{T}}^*$.

Theorem 2.20 [**12**-14]: If $\widetilde{\mathcal{T}}$ is $\mathcal{FS}-\mathbf{operator}$ on $\mathcal{FSH}-\mathbf{space}$ $\widetilde{\mathcal{H}}$ can be expressed by $\widetilde{\mathcal{T}} = \widetilde{\mathbf{R}} + \mathbf{i}\widetilde{\mathcal{S}}$, where $\widetilde{\mathbf{R}}\ \mathbf{and}\ \widetilde{\mathcal{S}}$ are $\mathcal{FS}-\mathbf{self\ adjoint\ operator}$ on $\widetilde{\mathcal{H}}$.

3. Main results

Definition 3.1: Let $\widetilde{\mathcal{T}}$ is $\mathcal{FS}-\mathbf{operator}$ of $\mathcal{FSH}-\mathbf{space}$ $\widetilde{\mathcal{H}}$ is called a fuzzy soft normal operator ($\mathcal{FSN}-\mathbf{operator}$) if $\widetilde{\mathcal{T}}\widetilde{\mathcal{T}}^* = \widetilde{\mathcal{T}}^*\widetilde{\mathcal{T}}$.

Remark 3.2: It is clear every $\mathcal{FS}-\mathbf{self\ adjoint\ operator}$ is $\mathcal{FSN}-\mathbf{operator}$

Theorem 2.3: If $\widetilde{\mathcal{T}}\ \mathbf{and}\ \widetilde{\mathcal{S}}$ are $\mathcal{FSN}-\mathbf{operators}$ on $\mathcal{FSH}-\mathbf{space}$ $\widetilde{\mathcal{H}}$ with the property that either commutes with the fuzzy soft adjoint of the other, then $\widetilde{\mathcal{T}}+\widetilde{\mathcal{S}}$ and $\widetilde{\mathcal{T}}\widetilde{\mathcal{S}}$ are also $\mathcal{FSN}-\mathbf{operator}$.

Proof: since $\tilde{\mathcal{T}}$, $\tilde{\mathcal{S}}$ are $\mathcal{FSN}-\text{operator}$, then
$\tilde{\mathcal{T}}\tilde{\mathcal{T}}^* = \tilde{\mathcal{T}}^*\tilde{\mathcal{T}}$ and $\tilde{\mathcal{S}}\tilde{\mathcal{S}}^* = \tilde{\mathcal{S}}^*\tilde{\mathcal{S}}$ (1)
And given that $\tilde{\mathcal{T}}\tilde{\mathcal{S}}^* = \tilde{\mathcal{S}}^*\tilde{\mathcal{T}}$and $\tilde{\mathcal{S}}\tilde{\mathcal{T}}^* = \tilde{\mathcal{T}}^*\tilde{\mathcal{S}}$ (2)
Now to show that $\tilde{\mathcal{T}}+\tilde{\mathcal{S}}$ is $\mathcal{FSN}-\text{operator}$, we have

$$\begin{aligned}
\left(\tilde{\mathcal{T}}+\tilde{\mathcal{S}}\right)\left(\tilde{\mathcal{T}}+\tilde{\mathcal{S}}\right)^* &= \left(\tilde{\mathcal{T}}+\tilde{\mathcal{S}}\right)\left(\tilde{\mathcal{T}}^*+\tilde{\mathcal{S}}^*\right)\\
&= \tilde{\mathcal{T}}\tilde{\mathcal{T}}^*+\tilde{\mathcal{T}}\tilde{\mathcal{S}}^*+\tilde{\mathcal{S}}\tilde{\mathcal{T}}^*+\tilde{\mathcal{S}}\tilde{\mathcal{S}}^*\\
&= \tilde{\mathcal{T}}^*\tilde{\mathcal{T}}+\tilde{\mathcal{S}}^*\tilde{\mathcal{T}}+\tilde{\mathcal{T}}^*\tilde{\mathcal{S}}+\tilde{\mathcal{S}}^*\tilde{\mathcal{S}} \qquad \text{from(1) and (2)}\\
&= \tilde{\mathcal{T}}^*\left(\tilde{\mathcal{T}}+\tilde{\mathcal{S}}\right)+\tilde{\mathcal{S}}^*\left(\tilde{\mathcal{T}}+\tilde{\mathcal{S}}\right)\\
&= \left(\tilde{\mathcal{T}}^*+\tilde{\mathcal{S}}^*\right)\left(\tilde{\mathcal{T}}+\tilde{\mathcal{S}}\right)\\
&= \left(\tilde{\mathrm{T}}+\tilde{\mathrm{S}}\right)^*\left(\tilde{\mathcal{T}}+\tilde{\mathcal{S}}\right)
\end{aligned}$$

Therefor $\left(\tilde{\mathcal{T}}+\tilde{\mathcal{S}}\right)\left(\tilde{\mathcal{T}}+\tilde{\mathcal{S}}\right)^* = \left(\tilde{\mathcal{T}}+\tilde{\mathcal{S}}\right)^*\left(\tilde{\mathcal{T}}+\tilde{\mathcal{S}}\right)$
And so $\tilde{\mathcal{T}}+\tilde{\mathcal{S}}$ is $\mathcal{FSN}-\text{operator}$
And now to prove $\tilde{\mathcal{T}}\tilde{\mathcal{S}}$ is $\mathcal{FSN}-\text{operator}$ we have

$$\begin{aligned}
\left(\tilde{\mathcal{T}}\tilde{\mathcal{S}}\right)\left(\tilde{\mathcal{T}}\tilde{\mathcal{S}}\right)^* &= \tilde{\mathcal{T}}\tilde{\mathcal{S}}\tilde{\mathcal{S}}^*\tilde{\mathcal{T}}^* = \tilde{\mathcal{T}}\left(\tilde{\mathcal{S}}\tilde{\mathcal{S}}^*\right)\tilde{\mathcal{T}}^*\\
&= \tilde{\mathcal{T}}\left(\tilde{\mathcal{S}}^*\tilde{\mathcal{S}}\right)\tilde{\mathcal{T}}^* \qquad \text{by (1)}\\
&= \left(\tilde{\mathcal{T}}\tilde{\mathcal{S}}^*\right)\left(\tilde{\mathcal{S}}\tilde{\mathcal{T}}^*\right)\\
&= \left(\tilde{\mathcal{S}}^*\tilde{\mathcal{T}}\right)\left(\tilde{\mathcal{T}}^*\tilde{\mathcal{S}}\right) \qquad \text{by (2)}\\
&= \tilde{\mathcal{S}}^*\left(\tilde{\mathcal{T}}\tilde{\mathcal{T}}^*\right)\tilde{\mathcal{S}}\\
&= \tilde{\mathcal{S}}^*\left(\tilde{\mathcal{T}}^*\tilde{\mathcal{T}}\right)\tilde{\mathcal{S}} \qquad \text{by (1)}\\
&= \left(\tilde{\mathcal{S}}^*\tilde{\mathcal{T}}^*\right)\left(\tilde{\mathcal{T}}\tilde{\mathcal{S}}\right) = \left(\tilde{\mathcal{T}}\tilde{\mathcal{S}}\right)^*\left(\tilde{\mathcal{T}}\tilde{\mathcal{S}}\right)
\end{aligned}$$

Therefore $\left(\tilde{\mathcal{T}}\tilde{\mathcal{S}}\right)\left(\tilde{\mathcal{T}}\tilde{\mathcal{S}}\right)^* = \left(\tilde{\mathcal{T}}\tilde{\mathcal{S}}\right)^*\left(\tilde{\mathcal{T}}\tilde{\mathcal{S}}\right)$
Therefor $\tilde{\mathcal{T}}\tilde{\mathcal{S}}$ is $\mathcal{FSN}-\text{operator}$.
Theorem 3.4: An $\mathcal{FS}-\mathbf{operator}$ $\widetilde{\mathcal{T}}$ of $\mathcal{FSH}-\mathbf{space}$ $\widetilde{\mathcal{H}}$ is $\mathcal{FSN}-\mathbf{operator}$ if and only if $\left\|\widetilde{\widetilde{\mathcal{T}}\tilde{\mathbf{x}}_{\boldsymbol{\mu}_{1_{\mathcal{G}(\mathbf{e}_1)}}}}\right\| = \left\|\widetilde{\widetilde{\mathcal{T}}^*\tilde{\mathbf{x}}_{\boldsymbol{\mu}_{1_{\mathcal{G}(\mathbf{e}_1)}}}}\right\|$ for every $\tilde{\mathbf{x}}_{\boldsymbol{\mu}_{1_{\mathbf{G}(\mathbf{e}_1)}}}$.
Proof:
$\tilde{\mathcal{T}}$ is $\mathcal{FSN}-\text{operator} \Leftrightarrow \tilde{\mathcal{T}}\tilde{\mathcal{T}}^* = \tilde{\mathcal{T}}^*\tilde{\mathcal{T}} \Leftrightarrow \tilde{\mathcal{T}}\tilde{\mathcal{T}}^* - \tilde{\mathcal{T}}^*\tilde{\mathcal{T}} = \tilde{0}$

$$\Leftrightarrow \langle \widetilde{\left(\tilde{\mathcal{T}}\tilde{\mathcal{T}}^{*}-\tilde{\mathcal{T}}^{*}\tilde{\mathcal{T}}\right)}\tilde{\mathrm{x}}_{\mu_{1_{\mathcal{G}(\mathrm{e}_1)}}},\tilde{\mathrm{x}}_{\mu_{1_{\mathcal{G}(\mathrm{e}_1)}}}\rangle=\tilde{0}\quad\forall\,\tilde{\mathrm{x}}_{\mu_{1_{\mathcal{G}(\mathrm{e}_1)}}}$$

$$\Leftrightarrow \langle \widetilde{\tilde{\mathcal{T}}\tilde{\mathcal{T}}^{*}\tilde{\mathrm{x}}_{\mu_{1_{\mathcal{G}(\mathrm{e}_1)}}}},\tilde{\mathrm{x}}_{\mu_{1_{\mathcal{G}(\mathrm{e}_1)}}}\rangle=\langle \widetilde{\tilde{\mathcal{T}}^{*}\tilde{\mathcal{T}}\tilde{\mathrm{x}}_{\mu_{1_{\mathcal{G}(\mathrm{e}_1)}}}},\tilde{\mathrm{x}}_{\mu_{1_{\mathcal{G}(\mathrm{e}_1)}}}\rangle\quad\forall\,\tilde{\mathrm{x}}_{\mu_{1_{\mathcal{G}(\mathrm{e}_1)}}}$$

$$\Leftrightarrow \langle \widetilde{\tilde{\mathcal{T}}^{*}\tilde{\mathrm{x}}_{\mu_{1_{\mathcal{G}(\mathrm{e}_1)}}}},\widetilde{\tilde{\mathcal{T}}^{*}\tilde{\mathrm{x}}_{\mu_{1_{\mathcal{G}(\mathrm{e}_1)}}}}\rangle=\langle \widetilde{\tilde{\mathcal{T}}\tilde{\mathrm{x}}_{\mu_{1_{\mathcal{G}(\mathrm{e}_1)}}}},\widetilde{\tilde{\mathcal{T}}^{*}\tilde{\mathrm{x}}_{\mu_{1_{\mathcal{G}(\mathrm{e}_1)}}}}\rangle\ \forall\,\tilde{\mathrm{x}}_{\mu_{1_{\mathcal{G}(\mathrm{e}_1)}}}$$

$$\Leftrightarrow \langle \widetilde{\tilde{\mathcal{T}}^{*}\tilde{\mathrm{x}}_{\mu_{1_{\mathcal{G}(\mathrm{e}_1)}}}},\widetilde{\tilde{\mathcal{T}}^{*}\tilde{\mathrm{x}}_{\mu_{1_{\mathcal{G}(\mathrm{e}_1)}}}}\rangle=\langle \widetilde{\tilde{\mathcal{T}}\tilde{\mathrm{x}}_{\mu_{1_{\mathcal{G}(\mathrm{e}_1)}}}},\widetilde{\tilde{\mathcal{T}}\tilde{\mathrm{x}}_{\mu_{1_{\mathcal{G}(\mathrm{e}_1)}}}}\rangle\ \forall\,\tilde{\mathrm{x}}_{\mu_{1_{\mathcal{G}(\mathrm{e}_1)}}}$$

$$\Leftrightarrow \left\|\widetilde{\tilde{\mathcal{T}}\tilde{\mathrm{x}}_{\mu_{1_{\mathcal{G}(\mathrm{e}_1)}}}}\right\|^{2}=\left\|\widetilde{\tilde{\mathcal{T}}^{*}\tilde{\mathrm{x}}_{\mu_{1_{\mathcal{G}(\mathrm{e}_1)}}}}\right\|^{2},\forall\,\tilde{\mathrm{x}}_{\mu_{1_{\mathcal{G}(\mathrm{e}_1)}}}$$

$$\Leftrightarrow \left\|\widetilde{\tilde{\mathcal{T}}\tilde{\mathrm{x}}_{\mu_{1_{\mathcal{G}(\mathrm{e}_1)}}}}\right\|=\left\|\widetilde{\tilde{\mathcal{T}}^{*}\tilde{\mathrm{x}}_{\mu_{1_{\mathcal{G}(\mathrm{e}_1)}}}}\right\|,\forall\,\tilde{\mathrm{x}}_{\mu_{1_{\mathcal{G}(\mathrm{e}_1)}}}$$

Theorem 3.5: If $\widetilde{\mathcal{T}}=\widetilde{\mathbf{R}}+\tilde{\imath}\widetilde{\mathcal{S}}$ is $\mathcal{FSN}-\mathbf{operator}$ on $\mathcal{FSH}-\mathbf{space}\ \widetilde{\mathcal{H}}$ if and only if its fuzzy soft real and imaginary parts commute.

Proof:
Let $\tilde{\mathrm{R}}$ and $\tilde{\mathcal{S}}$ be the fuzzy soft real and imaginary parts of $\tilde{\mathcal{T}}$, then by theorem (2.20) we get $\tilde{\mathrm{R}}$ and $\tilde{\mathcal{S}}$ are $\mathcal{FS}-$ self adjoint operator and $\tilde{\mathcal{T}}=\tilde{\mathrm{R}}+\tilde{\imath}\tilde{\mathcal{S}}$
We have $\tilde{\mathcal{T}}^{*}=\left(\tilde{\mathrm{R}}+\tilde{\imath}\tilde{\mathcal{S}}\right)^{*}=\tilde{\mathrm{R}}^{*}+\left(\tilde{\imath}\tilde{\mathcal{S}}\right)^{*}=\tilde{\mathrm{R}}^{*}+\bar{\tilde{\imath}}\tilde{\mathcal{S}}^{*}$ by(2.17)
$=\tilde{\mathrm{R}}^{*}-\tilde{\imath}\tilde{\mathcal{S}}^{*}=\tilde{\mathrm{R}}-\tilde{\imath}\tilde{\mathcal{S}}$
Now $\tilde{\mathcal{T}}\tilde{\mathcal{T}}^{*}=\left(\tilde{\mathrm{R}}+\tilde{\imath}\tilde{\mathcal{S}}\right)\left(\tilde{\mathrm{R}}-\tilde{\imath}\tilde{\mathcal{S}}\right)$
$=\tilde{\mathrm{R}}^{2}+\tilde{\mathcal{S}}^{2}+\tilde{\imath}\left(\tilde{\mathcal{S}}\tilde{\mathrm{R}}-\tilde{\mathrm{R}}\tilde{\mathcal{S}}\right)$ ……(3)
And $\tilde{\mathcal{T}}^{*}\tilde{\mathcal{T}}=\left(\tilde{\mathrm{R}}-\tilde{\imath}\tilde{\mathrm{S}}\right)\left(\tilde{\mathrm{R}}+\tilde{\imath}\tilde{\mathrm{S}}\right)$
$=\tilde{\mathrm{R}}^{2}+\tilde{\mathcal{S}}^{2}+\tilde{\imath}\left(\tilde{\mathrm{R}}\tilde{\mathcal{S}}-\tilde{\mathcal{S}}\tilde{\mathrm{R}}\right)$ ……(4)
Since $\tilde{\mathcal{T}}$ is $\mathcal{FS}\mathrm{N}-$operator, i.e. $\tilde{\mathcal{T}}\tilde{\mathcal{T}}^{*}=\tilde{\mathcal{T}}^{*}\tilde{\mathcal{T}}$, then from (3) and (4) we have $\tilde{\mathrm{R}}^{2}+\tilde{\mathcal{S}}^{2}+\tilde{\imath}\left(\tilde{\mathcal{S}}\tilde{\mathrm{R}}-\tilde{\mathrm{R}}\tilde{\mathcal{S}}\right)=\tilde{\mathrm{R}}^{2}+\tilde{\mathcal{S}}^{2}+\tilde{\imath}\left(\tilde{\mathrm{R}}\tilde{\mathcal{S}}-\tilde{\mathcal{S}}\tilde{\mathrm{R}}\right)$
$\Rightarrow\tilde{\mathcal{S}}\tilde{\mathrm{R}}-\tilde{\mathrm{R}}\tilde{\mathcal{S}}=\tilde{\mathrm{R}}\tilde{\mathcal{S}}-\tilde{\mathcal{S}}\tilde{\mathrm{R}}$
$\Rightarrow 2\tilde{\mathcal{S}}\tilde{\mathrm{R}}=2\tilde{\mathrm{R}}\tilde{\mathcal{S}}$
$\Rightarrow\tilde{\mathcal{S}}\tilde{\mathrm{R}}=\tilde{\mathrm{R}}\tilde{\mathcal{S}}\quad\Rightarrow\tilde{\mathrm{R}}$ and $\tilde{\mathcal{S}}$ are commute
Conversely, suppose that $\tilde{\mathrm{R}}$ and $\tilde{\mathcal{S}}$ are commute i.e. $\tilde{\mathcal{S}}\tilde{\mathrm{R}}=\tilde{\mathrm{R}}\tilde{\mathcal{S}}$
Then from (3) and (4) we get
$\tilde{\mathcal{T}}\tilde{\mathcal{T}}^{*}=\tilde{\mathrm{R}}^{2}+\tilde{\mathcal{S}}^{2}$ ……..(5)
$\tilde{\mathcal{T}}^{*}\tilde{\mathcal{T}}=\tilde{\mathrm{R}}^{2}+\tilde{\mathcal{S}}^{2}$ …….(6)
Then from (5) and (6) we see that $\tilde{\mathcal{T}}\tilde{\mathcal{T}}^{*}=\tilde{\mathcal{T}}^{*}\tilde{\mathcal{T}}$
$\Rightarrow\tilde{\mathcal{T}}$ is $\mathcal{FS}\mathrm{N}-$operators .

Theorem 3.6: If $\widetilde{\mathcal{T}}$ is $\mathcal{FSN}-\mathbf{operator}$ on $\mathcal{FSH}-\mathbf{space}\ \widetilde{\mathcal{H}}$ and $\tilde{\alpha}\in\mathbf{C}(\mathbf{A})$, then $\widetilde{\mathcal{T}}-\tilde{\alpha}\tilde{\mathbf{I}}$ is also $\mathcal{FSN}-\mathbf{operator}$.

Proof:
Since $\tilde{\mathcal{T}}$ is $\mathcal{FS}\mathrm{N}-$operator ,therefor $\tilde{\mathcal{T}}\tilde{\mathcal{T}}^{*}=\tilde{\mathcal{T}}^{*}\tilde{\mathcal{T}}$.
Also $\left(\tilde{\mathcal{T}}-\tilde{\alpha}\tilde{\mathrm{I}}\right)^{*}=\tilde{\mathcal{T}}^{*}-(\tilde{\alpha}\tilde{\mathrm{I}})^{*}=\tilde{\mathcal{T}}^{*}-\bar{\tilde{\alpha}}\tilde{\mathrm{I}}^{*}=\tilde{\mathcal{T}}^{*}-\bar{\tilde{\alpha}}\tilde{\mathrm{I}}$
Now $\left(\tilde{\mathcal{T}}-\tilde{\alpha}\tilde{\mathrm{I}}\right)\left(\tilde{\mathcal{T}}-\tilde{\alpha}\tilde{\mathrm{I}}\right)^{*}=\left(\tilde{\mathcal{T}}-\tilde{\alpha}\tilde{\mathrm{I}}\right)\left(\tilde{\mathcal{T}}^{*}-\bar{\tilde{\alpha}}\tilde{\mathrm{I}}\right)$
$=\tilde{\mathcal{T}}\tilde{\mathcal{T}}^{*}-\bar{\tilde{\alpha}}\tilde{\mathcal{T}}-\tilde{\alpha}\tilde{\mathcal{T}}^{*}+|\tilde{\alpha}|^{2}\tilde{\mathrm{I}}$ …….. (7)
Also $\left(\tilde{\mathcal{T}}-\tilde{\alpha}\tilde{\mathrm{I}}\right)^{*}\left(\tilde{\mathcal{T}}-\tilde{\alpha}\tilde{\mathrm{I}}\right)=\left(\tilde{\mathcal{T}}^{*}-\bar{\tilde{\alpha}}\tilde{\mathrm{I}}\right)\left(\tilde{\mathcal{T}}-\tilde{\alpha}\tilde{\mathrm{I}}\right)$
$=\tilde{\mathcal{T}}^{*}\tilde{\mathcal{T}}-\tilde{\alpha}\tilde{\mathcal{T}}^{*}-\bar{\tilde{\alpha}}\tilde{\mathcal{T}}+|\tilde{\alpha}|^{2}\tilde{\mathrm{I}}$ …… (8)
Since $\tilde{\mathcal{T}}\tilde{\mathcal{T}}^{*}=\tilde{\mathcal{T}}^{*}\tilde{\mathcal{T}}$, therefor the right hand sides of (7) and (8) are equal
Hence $\left(\tilde{\mathcal{T}}-\tilde{\alpha}\tilde{\mathrm{I}}\right)\left(\tilde{\mathcal{T}}-\tilde{\alpha}\tilde{\mathrm{I}}\right)^{*}=\left(\tilde{\mathcal{T}}-\tilde{\alpha}\tilde{\mathrm{I}}\right)^{*}\left(\tilde{\mathcal{T}}-\tilde{\alpha}\tilde{\mathrm{I}}\right)$

And so $\tilde{\mathcal{T}} - \tilde{\alpha}\tilde{I}$ is $\mathcal{FS}\mathrm{N} - \text{operator}$

Definition 3.7: A $\boldsymbol{\mathcal{FS} - \text{operator } \tilde{\mathbf{U}}}$ of $\boldsymbol{\mathcal{FSH} - \text{space } \widetilde{\mathcal{H}}}$ is called a fuzzy soft unitary operator ($\boldsymbol{\mathcal{FS}\mathbf{U} - \text{operator}}$) if $\tilde{\mathbf{U}}\tilde{\mathbf{U}}^{*} = \tilde{\mathbf{U}}^{*}\tilde{\mathbf{U}} = \tilde{\mathbf{I}}$.

Example 3.8: Every $\boldsymbol{\mathcal{FS}\mathbf{U} - \text{operator}}$ is $\boldsymbol{\mathcal{FS}\mathbf{N} - \text{operators}}$.

Theorem 3.9: A $\boldsymbol{\mathcal{FS} - \text{operators } \tilde{\mathbf{U}}}$ of $\boldsymbol{\mathcal{FSH} - \text{space } \widetilde{\mathcal{H}}}$,then the following are all equivalent :

(1) $\tilde{\mathcal{T}}^{*}\tilde{\mathcal{T}} = \tilde{I}$
(2) $\langle \tilde{\mathcal{T}}\tilde{x}_{\mu_{1_{\mathcal{G}(e_1)}}}, \widetilde{\tilde{\mathcal{T}}\tilde{y}_{\mu_{2_{\mathcal{G}(e_2)}}}} \rangle = \langle \tilde{x}_{\mu_{1_{\mathcal{G}(e_1)}}}, \widetilde{\tilde{y}_{\mu_{2_{\mathcal{G}(e_2)}}}} \rangle$,for all$\tilde{x}_{\mu_{1_{\mathcal{G}(e_1)}}}$ and $\tilde{y}_{\mu_{2_{\mathcal{G}(e_2)}}}$
(3) $\left\| \widetilde{\tilde{\mathcal{T}}\tilde{x}_{\mu_{1_{\mathcal{G}(e_1)}}}} \right\| = \left\| \widetilde{\tilde{x}_{\mu_{1_{\mathcal{G}(e_1)}}}} \right\|$,for all $\tilde{x}_{\mu_{1_{\mathcal{G}(e_1)}}}$

Proof:
(1) ⇒ (2) It given that $\tilde{\mathcal{T}}^{*}\tilde{\mathcal{T}} = \tilde{I}$, we have

$$\langle \tilde{\mathcal{T}}\tilde{x}_{\mu_{1_{\mathcal{G}(e_1)}}}, \tilde{\mathcal{T}}\tilde{y}_{\mu_{2_{\mathcal{G}(e_2)}}} \rangle = \langle \tilde{x}_{\mu_{1_{\mathcal{G}(e_1)}}}, \widetilde{\tilde{\mathcal{T}}^{*}\tilde{\mathcal{T}}}\tilde{y}_{\mu_{2_{\mathcal{G}(e_2)}}} \rangle$$
$$= \langle \tilde{x}_{\mu_{1_{\mathcal{G}(e_1)}}}, \widetilde{\tilde{I}\tilde{y}_{\mu_{2_{\mathcal{G}(e_2)}}}} \rangle = \langle \tilde{x}_{\mu_{1_{\mathcal{G}(e_1)}}}, \widetilde{\tilde{y}_{\mu_{2_{\mathcal{G}(e_2)}}}} \rangle$$

Therefor $\langle \tilde{\mathcal{T}}\tilde{x}_{\mu_{1_{\mathcal{G}(e_1)}}}, \widetilde{\tilde{\mathcal{T}}\tilde{y}_{\mu_{2_{\mathcal{G}(e_2)}}}} \rangle = \langle \tilde{x}_{\mu_{1_{\mathcal{G}(e_1)}}}, \widetilde{\tilde{y}_{\mu_{2_{\mathcal{G}(e_2)}}}} \rangle$
(2) ⇒ (3) it given that $\langle \tilde{\mathcal{T}}\tilde{x}_{\mu_{1_{\mathcal{G}(e_1)}}}, \widetilde{\tilde{\mathcal{T}}\tilde{y}_{\mu_{2_{\mathcal{G}(e_2)}}}} \rangle = \langle \tilde{x}_{\mu_{1_{\mathcal{G}(e_1)}}}, \widetilde{\tilde{y}_{\mu_{2_{\mathcal{G}(e_2)}}}} \rangle$, for all $\tilde{x}_{\mu_{1_{\mathcal{G}(e_1)}}}$ and $\tilde{y}_{\mu_{2_{\mathcal{G}(e_2)}}}$.
Taking $\tilde{x}_{\mu_{1_{\mathcal{G}(e_1)}}} = \tilde{y}_{\mu_{2_{\mathcal{G}(e_2)}}}$, we have

$$\langle \tilde{\mathcal{T}}\tilde{x}_{\mu_{1_{\mathcal{G}(e_1)}}}, \widetilde{\tilde{\mathcal{T}}\tilde{x}_{\mu_{1_{\mathcal{G}(e_1)}}}} \rangle = \langle \tilde{x}_{\mu_{1_{\mathcal{G}(e_1)}}}, \widetilde{\tilde{x}_{\mu_{1_{\mathcal{G}(e_1)}}}} \rangle$$
$$\Rightarrow \left\| \widetilde{\tilde{\mathcal{T}}\tilde{x}_{\mu_{1_{\mathcal{G}(e_1)}}}} \right\|^{2} = \left\| \widetilde{\tilde{x}_{\mu_{1_{\mathcal{G}(e_1)}}}} \right\|^{2}$$
$$\Rightarrow \left\| \widetilde{\tilde{\mathcal{T}}\tilde{x}_{\mu_{1_{\mathcal{G}(e_1)}}}} \right\| = \left\| \widetilde{\tilde{x}_{\mu_{1_{\mathcal{G}(e_1)}}}} \right\|, \text{ for all } \tilde{x}_{\mu_{1_{\mathcal{G}(e_1)}}}$$

(3) ⇒ (1) it given that $\left\| \widetilde{\tilde{\mathcal{T}}\tilde{x}_{\mu_{1_{\mathrm{G}(e_1)}}}} \right\| = \left\| \widetilde{\tilde{x}_{\mu_{1_{\mathrm{G}(e_1)}}}} \right\|$, for all $\tilde{x}_{\mu_{1_{\mathrm{G}(e_1)}}}$
Therefor $\left\| \widetilde{\tilde{\mathcal{T}}\tilde{x}_{\mu_{1_{\mathcal{G}(e_1)}}}} \right\|^{2} = \left\| \widetilde{\tilde{x}_{\mu_{1_{\mathcal{G}(e_1)}}}} \right\|^{2}$

$$\Rightarrow \langle \tilde{\mathcal{T}}\tilde{x}_{\mu_{1_{\mathcal{G}(e_1)}}}, \widetilde{\tilde{\mathcal{T}}\tilde{x}_{\mu_{1_{\mathcal{G}(e_1)}}}} \rangle = \langle \tilde{x}_{\mu_{1_{\mathcal{G}(e_1)}}}, \widetilde{\tilde{x}_{\mu_{1_{\mathcal{G}(e_1)}}}} \rangle$$
$$\Rightarrow \langle \tilde{\mathcal{T}}^{*}\tilde{\mathcal{T}}\tilde{x}_{\mu_{1_{\mathcal{G}(e_1)}}}, \widetilde{\tilde{x}_{\mu_{1_{\mathcal{G}(e_1)}}}} \rangle = \langle \tilde{I}\,\tilde{x}_{\mu_{1_{\mathrm{G}(e_1)}}}, \widetilde{\tilde{x}_{\mu_{1_{\mathrm{G}(e_1)}}}} \rangle$$
$$\Rightarrow \langle (\tilde{\mathcal{T}}^{*}\tilde{\mathcal{T}} - \tilde{I})\widetilde{\tilde{x}_{\mu_{1_{\mathcal{G}(e_1)}}}}, \tilde{x}_{\mu_{1_{\mathrm{G}(e_1)}}} \rangle = \tilde{0} \text{ , for all } \tilde{x}_{\mu_{1_{\mathcal{G}(e_1)}}}$$
$$\Rightarrow \tilde{\mathcal{T}}^{*}\tilde{\mathcal{T}} - \tilde{I} = \tilde{0}. \text{ Therefor } \tilde{\mathcal{T}}^{*}\tilde{\mathcal{T}} = \tilde{I}$$

4. Conclusion

The combination of fuzzy and soft sets gives us original results that are more extended, generalized and precised. Few researchers have studied some of the principles of these general extensions such as fuzzy soft normed spaces, fuzzy soft Hilbert space and fuzzy soft linear operators. In our study, a special type of fuzzy soft linear operators, which is the fuzzy soft normal operator and fuzzy soft unitary operator has been introduced and explored.

5. References

[1] L A Zadeh 1965 Fuzzy Sets *Inf. Control* **8** pp 338-353
[2] D Molodtsov 1999 Soft Set Theory-First Results Comput *Math. Appl*. **37** pp 19 – 31
[3] S Bayramov, C. Gunduz, 2013 Soft Locally Compact Spaces And Soft Para Compact Spaces *J. Math., Sys. Sci.* **3** pp 122-130

[4] M I Yazar, T Bilgin, S Bayramov, C Gunduz 2014 A New View On Soft Normed Spaces *Int. Math. For* **9** (24) pp1149-1159
[5] S Das, S K Samanta 2013 On Soft Inner Product Spaces *Ann. Fuzzy Math. Inform* **6** (1) pp 151-170
[6] M I Yazar, C G Aras, S Bayramov 2019 Results On Soft Hilbert Spaces Twms *J. App. Eng. Math* **9** (1) pp 159-164
[7] P K Maji, R Biswas, A R Roy 2001 Fuzzy Soft Set *J. Fuzzy Math* **9** (3) pp 677-692
[8] T J Neog, D K Sut, G C Hazarika 2012 Fuzzy Soft Topological Spaces *Int. J.Latest Trend Math* **2** (1) pp 54-67
[9] T Beaula, M M Priyanga 2015 A New Notion For Fuzzy Soft Normed Linear Space *Int. J. Fuzzy Math. Arch.* **9** (1) pp 81-90
[10] N Faried, M S S Ali and H H Sakr 2020 Fuzzy Soft Hilbert Spaces *Mathematics And Statistics* **8** (3)
[11] N Faried, M S Ali and H H Sakr 2020 On Fuzzy Soft Linear Operators In Fuzzy Soft Hilbert Spaces *In Abstract And Applied Analysis*
[12] N Faried, M S Ali, and H H Sakr 2020 On Fuzzy Soft Hermition Operators *Scientific Journal* **9** (1) pp 73-82
[13] A Z Khameneh., A. Kilic¸ A R Salleh 2013 Parameterized Norm And Parameterized Fixed-Point Theorem By Using Fuzzy Soft Set Theory Arxiv 15 Pages. 2.9, 2.10, 2.11, 2.12, 2.13, 2.14.
[14] S. Sharma and A. J. Obaid, "Mathematical modelling, analysis and design of fuzzy logic controller for the control of ventilation systems using MATLAB fuzzy logic toolbox," Journal of Interdisciplinary Mathematics, vol. 23, no. 4, pp. 843-849, 2020.

Mean Square Analytical Solution for Beta Statistical Function with Second-Order Random Differential Equation

Mean Square Analytical Solution for Beta Statistical Function with Second-Order Random Differential Equation

Abeer Majeed Jasim

Department of Mathematics, College of Science, University of Basrah, Basrah, Iraq

Email address: abeer.jassem@yahoo.com

Abstract. In this paper, the second-order random differential equation was solved using the new iterative method (NIM). This NIM is based on an integrated equation with the resulting solutions are a series of powers. There are many examples that demonstrate that the method is an effective and accurate technique.

1.Introduction

Most scientific problem biology, engineering and physical phenomena roccur in the form of random differential equations (RDE) [1,2,3]. Recently, several random differential models are by mean square calculus [4,5,6,7,8,9,10,11,12,13,14]. The second-order random differential equations(RDE) are an ordinary differential equations which contain random constant or random variables. We can describe this kind of equations as follows

$$L[\tilde{u}(t)] + N[\tilde{u}(t)] = \tilde{g}(t), \quad (1)$$

$$\tilde{u}(0) = \gamma_0, \quad \left.\frac{d\tilde{u}(t)}{dt}\right|_{t=0} = \gamma_1, \quad (2)$$

where $\tilde{u}(t)$ *is* an unknown function, N [$\tilde{u}$ (*t, D*)] is a nonlinear operator, $\tilde{g}(t)$ is the source in homogeneous term, and D, γ_0 and γ_1 are random variables. The triple trprobabilistic space ($\Omega, \tilde{F}$, $\tilde{P}$) rand $L_2 = L_2(\Omega, \tilde{F}, \tilde{P})$ is the set of second-order random variables. The random variable $\tilde{u}$: $\Omega \to R$, if $E[\tilde{u}^2] < \infty$, where $E[\cdot]$ is an expectation operator. The norm $\|.\|_2$ and random variable $\tilde{u}$ can be defined as follow:

$$\|\tilde{u}\|_2 = (E[\tilde{u}^2])^{1/2}, \quad (3)$$

Now, ifr $(L^2, \|\tilde{u}\|_2)$ is an Banach space, T represent the space of times, and $\tilde{u}(t) \in L_2$ is random variable for each $t \in T$ then, we can that $\{\tilde{u}(t), t \in T\}$. The expansion of the term $\tilde{u}(t)$ as follow:

$$\tilde{u}_N(t) = \sum_{i=0}^{N} \tilde{u}(t) t^i, \quad (4)$$

By using the independence variable D, γ_0 and γ_1 we obtain

$$E[\tilde{u}(t)] = \sum_{i=0}^{N} E[\tilde{u}(i)]\, t^i, \quad (5)$$

$$Var[\tilde{u}(t)] = \sum_{i=0}^{N} \sum_{i=0}^{N} E[\tilde{u}(i), \tilde{u}(j)]\, t^{i+j}, \quad (6)$$

$$cov[\tilde{u}(i), \tilde{u}(j)] = E[\tilde{u}(i), \tilde{u}(j)] - E[\tilde{u}(i)]E[\tilde{u}(j)], \quad (7)$$

The following Lemmas indicate to converge the sequences $\{\tilde{u}_N\}$ $\{E[\tilde{u}_N]\}$,$\{Var[\tilde{u}_N]\}$ as:

Lemma 1.1 [3] A sequence of second- order random variables $\{\tilde{u}_n, n \geq 0\}$ *converges to*r $\{\tilde{u} \in L_2\}$,*if*

$$\lim_{n\to\infty} \|\tilde{u}_n - \tilde{u}\| = \lim_{n\to\infty} (E[\tilde{u}_n - \tilde{u}])^{1/2}, \quad (8)$$

Lemma 1.2 [3] If the sequence of $\tilde{u}_N(t)$ can say be converges to $\tilde{u}(t)$, then

- $E[\tilde{u}_N(t)] \to E[\tilde{u}]$,
- $Var[\tilde{u}_N(t)] \to Var[\tilde{u}(t)]$,

Lemma1.3 [3] If $\tilde{u}_N$ and $\tilde{v}_N$ two sequences of random variables $\tilde{u}$ and $\tilde{v}$, respectively which mean that $\tilde{v}_N = \tilde{v}$ then

1. $\lim_{N\to\infty} [\tilde{u}_N \tilde{v}_N] = [\tilde{u}\tilde{v}]$,
2. $\lim_{N\to\infty} [\tilde{u}_N{}^2] = [\tilde{u}^2],\ if\ \tilde{u} = \tilde{v}$,
3. $\lim_{N\to\infty} E[\tilde{u}_N\ \tilde{v}_N] = E[\tilde{u}\tilde{v}]$,
4. $\lim_{N\to\infty} Var[\tilde{u}_N \tilde{v}_N] = Var[\tilde{u}\tilde{v}]$,

The objective rof this work is to find the meanrsquare solutions for second-order random initial value problems. Also, tables are presented for comparing the exact solution(ES). The comparative study has also been made with the previous results and found to be excellent compatibility. Several numerical examples are implemented to show the efficiency of the NIM.

2. The New Iterative Method

The coefficients of power series of assuming solution are important bases to construct the analytical approximate solution formula. Therefore, they can be computed in a differentiation way. To illustrate the computation for these coefficients and derivation the new algorithm(NIM), we summarize the details of a new analytical method in the following steps:

Step 1: Considering the ordinary differential equation **(**ORE)as follows:

$$\tilde{u}^{(n)}(t) = G(\tilde{u}(t), \tilde{u}'(t), \tilde{u}''(t), \tilde{u}'''(t), .., \tilde{u}^{(n-1)}(t)), \quad (9)$$

Where G is a function of $\tilde{u}$ and its derivatives, $\tilde{u}$ is an unknown function and t denotes spatial independent variable. Integrating Equation (9) n-times with respect to t on $[0, t]$ yield

$$\tilde{u}(t) = \sum_{i=1}^{n} \frac{t^{i-1}}{(i-1)!}\, \tilde{u}(0)^{(i-1)} + L^{-1}K[\tilde{u}(t)], \quad (10)$$

where

$$K[\tilde{u}(t)] = G\left(\tilde{u}(t), \tilde{u}'(t), \tilde{u}''(t), .., \tilde{u}^{(n-1)}(t)\right), L^{-1}(.) = \int_0^t ... \int_0^t (.)(dt)^n, \quad (11)$$

Step 2 : Assume that

$$K[\tilde{u}] = \sum_{n=1}^{\infty} \frac{d^{n-1}K[\tilde{u}_0(t)]}{dt^{n-1}}, \quad (12)$$

the Equation (12) can be rewriting as follows

$$K[\tilde{u}(t)] = K[\tilde{u}_0(t)] + K'[\tilde{u}_0(t)] + K''[\tilde{u}_0(t)] + \cdots, \quad (13)$$

substituting Equation(13) in Equation (10), we obtain

$$\tilde{u}(t) = \tilde{u}_0(t) + \tilde{u}_1(t) + \tilde{u}_2(t) + \cdots, \quad (14)$$

where

$$\tilde{u}_0 = \sum_{i=1}^{\infty} \frac{t^{i-1}}{(i-1)!} \tilde{u}^{(i-1)}(0), \tilde{u}_1 = L^{-1}K[\tilde{u}_0(t)],\ \ \tilde{u}_2 = L^{-1}K'[\tilde{u}_0(t),$$

$$\tilde{u}_4 = L^{-1}K''[\tilde{u}_0(t)],\ \ \tilde{u}_5 = L^{-1}K'''[\tilde{u}_0(t), ..., \quad (15)$$

Step 3 : The derivatives of K with respect to t which is the crucial part of the new algorithm method(NIM). Let start calculating $K[\check{u}(t)]$, $K'[\tilde{u}(t)]$, ...,

$$K[\tilde{u}\ (t] = \left(\tilde{u}(t), \frac{d\tilde{u}(t)}{dt}, \frac{d^2\tilde{u}(t)}{dt^2}, \frac{d^3\tilde{u}(t)}{dt^3}, \ldots, \frac{d^{n-1}\tilde{u}(t)}{dt^{n-1}}\right), \quad (16)$$

$$K'[\tilde{u}(t)] = \sum_{i=1}^{n} K_{\tilde{u}^{(i-1)}}(\tilde{u}_t)^{(i-1)}, \quad (17)$$

$$K''[\tilde{u}(t)] = \sum_{j=1}^{n}\sum_{i=1}^{n} K_{\tilde{u}^{(j-1)}u^{(i-1)}}(\tilde{u}_t)^{(j-1)}(\tilde{u}_t)^{(i-1)} + \sum_{i=1}^{n} K_{\tilde{u}^{(i-1)}}(\tilde{u}_{tt})^{(i-1)}, \quad (18)$$

$$K'''[\tilde{u}(t)] = \sum_{k=1}^{n}\sum_{j=1}^{n}\sum_{i=1}^{n} K_{\tilde{u}^{(k-1)}\tilde{u}^{(j-1)}\tilde{u}^{(i-1)}}(\tilde{u}_t)^{(k-1)}(\tilde{u}_t)^{(j-1)}(\tilde{u}_t)^{(i-1)} + 3.\sum_{j=1}^{n}\sum_{i=1}^{n} K_{\tilde{u}^{(j-1)}\tilde{u}^{(i-1)}}(\tilde{u}_{tt})^{(j-1)}(\tilde{u}_t)^{(i-1)} + \sum_{i=1}^{n} K_{\tilde{u}^{(i-1)}}(\tilde{u}_{ttt})^{(i-1)}, \quad (19)$$

The assumption that the operator K and the solution $\tilde{u}(t)$ are analytic functions(AS), then the mixed derivatives are equivalence. We note that the derivatives function to $\tilde{u}$ unknown, so we suggest the following hypothesis

$$\tilde{u}_t = \tilde{u}_1(t) = L^{-1}K[\tilde{u}_0(t)], \tilde{u}_{tt} = \tilde{u}_2(t) = L^{-1}K'[\tilde{u}_0(t)],$$
$$\tilde{u}_{ttt} = \tilde{u}_3(t) = L^{-1}K''[\tilde{u}_0(t)], \ \tilde{u}_{tttt} = \tilde{u}_4(t) = L^{-1}K'''[\tilde{u}_0(t)], \quad (20)$$

Therefore Equations(16)- (19) are evaluated by

$$K[\tilde{u}_0(t)] = \left(\tilde{u}_0(t), \frac{d\tilde{u}_0(t)}{dt}, \frac{d^2\tilde{u}_0(t)}{dt^2}, \frac{d^3\tilde{u}_0(t)}{dt^3}, \dots, \frac{d^{n-1}\tilde{u}_0(t)}{dt^{n-1}}, \frac{d^n\tilde{u}_0(t)}{dt^n}\right), \quad (21)$$

$$K'[\tilde{u}_0(t)] = \sum_{i=1}^{n} K_{\tilde{u}_0{}^{(i-1)}}(\tilde{u}_1)^{(i-1)}, \quad (22)$$

$$K''[\tilde{u}_0] = \sum_{j=1}^{n}\sum_{i=1}^{n} K_{\tilde{u}_0{}^{(j-1)}\tilde{u}_0{}^{(i-1)}}(\tilde{u}_1)^{(j-1)}(\tilde{u}_1)^{(i-1)} + \sum_{i=1}^{n} K_{\tilde{u}_0{}^{(i-1)}}(\tilde{u}_2)^{(i-1)}, \quad (23)$$

$$K'''[\tilde{u}_0(t)] = \sum_{k=1}^{n}\sum_{j=1}^{n}\sum_{i=1}^{n} K_{\tilde{u}_0{}^{(k-1)}\tilde{u}_0{}^{(j-1)}\tilde{u}_0{}^{(i-1)}}(\tilde{u}_1)^{(k-1)}(\tilde{u}_1)^{(j-1)}(\tilde{u}_1)^{(i-1)} + 3.\sum_{j=1}^{n}\sum_{i=1}^{n} K_{\tilde{u}_0{}^{(j-1)}u_0{}^{(i-1)}}(\tilde{u}_1)^{(j-1)}(\tilde{u}_1)^{(i-1)} + \sum_{i=1}^{n} K_{\tilde{u}_0{}^{(i-1)}}(\tilde{u}_3)^{(i-1)}, \quad (24)$$

Step(4): Substitution of Equations (21)-(24) in Equation (14), the required analytical approximate solution can be gotten for the equation (9).

3 .Test Application

The NIM described in the previous section is implemented for solving the second-order random differential Equation (1) for approximating the expectation $E(\tilde{u}(t))$ and $Var[\tilde{u}(t)]$ be considered from the required information as follows:

3.1.Example

Consider therrandom initialrvalue problem

$$\frac{d^2\tilde{u}(t)}{dt^2} + D^2\tilde{u}(t) = 0, \ \tilde{u}(0) = \gamma_0, \quad \left.\frac{d\tilde{u}(t)}{dt}\right|_{t=0} = \gamma_1, \quad (25)$$

where D^2 is a Beta random variable, $D^2 \sim Be(\tilde{\alpha} = 2, \tilde{\beta} = 1)$, and independently of the initial conditions γ_0, γ_1 which satisfy $E[\gamma_0] = 1, E[\gamma_1] = 1, E[\gamma_0^2] = 2, E[\gamma_1^2] = 3, \ and \ E[\gamma_0\gamma_1] = 0,$
To obtain the expectation $E[\check{u}(t)]$ and the variance $\mathrm{Var}[\check{u}(t)]$, we can construct the following

$$K[\tilde{u}(t)] = -D^2\tilde{u}(t), \quad \tilde{g}(t) = 0, \ L^{-1} = \int_0^t \int_0^t (dt)^2, \tag{26}$$

The solution of the given equation involves the extraction of the components of $\tilde{u}(t)$. So solving the approximate analytical series be as listed

$$\tilde{u}(t) = \tilde{u}_0(t) + \tilde{u}_1(t) + \tilde{u}_2(t) + \cdots, \tag{27}$$

initial conditions are used when the inverse operator L^{-1} is applied on Equation (25) to obtain

$$\tilde{u}_0(t) = \gamma_0 + \gamma_1 t, \tag{28}$$

For the components of $\tilde{u}(t)$, can be easily be found by the following iterative process:

$$\tilde{u}_0(t) = \gamma_0 + \gamma_1 t, \quad \tilde{u}_1(t) = -L^{-1}D^2\tilde{u}_0(t), \tag{29}$$

$$\tilde{u}_1(t) = L^{-1}K[\tilde{u}_0(t)], \qquad \tilde{u}_2(t) = L^{-1}\frac{dK[\tilde{u}_0(t)]}{dt}, \tag{30}$$

$$\tilde{u}_3(t) = L^{-1}\frac{d^2K[\tilde{u}_0(t)]}{dt^2}, \qquad \tilde{u}_4(t) = L^{-1}\frac{d^3K[\tilde{u}_0(t)]}{dt^3}, \tag{31}$$

Now, we start to calculation the derivatives of K with respect to t which consider is the basic part of the iterative method $K'[\tilde{u}(t)], K''[\tilde{u}(t)], K'''[\tilde{u}(t)], ...$

$$K[\tilde{u}(t)] = -D^2\tilde{u}(t), \tag{32}$$

$$\mathrm{K'[\tilde{u}(t)]} = \frac{\mathrm{dK[\tilde{u}(t)]}}{\mathrm{dt}} = \mathrm{K_{\tilde{u}}.\tilde{u}_t}, \tag{33}$$

$$K''[\tilde{u}(t)] = \frac{d^2K[\tilde{u}(t)]}{dt^2} = K_{\tilde{u}\tilde{u}}.(\tilde{u}_t)^2 + \mathrm{K_{\tilde{u}}.\tilde{u}_{tt}}, \tag{34}$$

$$K'''[\tilde{u}(t)] = \frac{d^3K[\tilde{u}(t)]}{dt^3} = K_{\tilde{u}\tilde{u}\tilde{u}}.(\tilde{u}_t)^3 + 3.\mathrm{K_{\tilde{u}\tilde{u}}}.\tilde{u}_t.\tilde{u}_{tt} + \mathrm{K_{\tilde{u}}.\tilde{u}_{ttt}}, \tag{35}$$

we note that the derivatives of $\tilde{u}$ with respect t that are given in (20) can be computed by Equations(32)-(35) as

$$K[\tilde{u}_0(t)] = -D^2\tilde{u}_0(t), \tag{36}$$

$$\mathrm{K'[\tilde{u}_0(t)]} = \frac{\mathrm{dK[\tilde{u}_0(t)]}}{\mathrm{dt}} = \mathrm{K_{\tilde{u}}.\tilde{u}_1}, \tag{37}$$

$$K''[\tilde{u}_0(t)] = \frac{d^2K[\tilde{u}_0(t)]}{dt^2} = K_{\tilde{u}_0\tilde{u}_0}.(\tilde{u}_1)^2 + \mathrm{K_{\tilde{u}_0}.\tilde{u}_2}, \tag{38}$$

$$K'''[\tilde{u}_0(t)] = \frac{d^3K[\tilde{u}_0(t)]}{dt^3} = K_{\tilde{u}_0\tilde{u}_0\tilde{u}_0}.(\tilde{u}_1)^3 + 3.\mathrm{K_{\tilde{u}_0\tilde{u}_0}}.\tilde{u}_1.\tilde{u}_2 + \mathrm{K_{\tilde{u}_0}.\tilde{u}_3} \tag{39}$$

$$\vdots$$

now, we need to extract the first derivatives of K as follows

$$K_{\tilde{u}_0} = -D^2, \quad K_{\tilde{u}_0\tilde{u}_0} = 0, \quad K_{\tilde{u}_0\tilde{u}_0\tilde{u}_0} = 0, ..., \tag{40}$$

After performing the above iterative method, ther components $\tilde{u}(t)$ are obtained as follows:

$$\tilde{u}_0(t) = \gamma_0 + \gamma_1 t, \tag{41}$$

$$\tilde{u}_1(t) = -\frac{1}{2}\gamma_0 D^2 t^2 - \frac{1}{6}\gamma_1 D^2 t^3, \tag{42}$$

$$\tilde{u}_2(t) = \frac{1}{24}\gamma_0 D^4 t^4 + \frac{1}{120}\gamma_1 D^4 t^5, \tag{43}$$

$$\tilde{u}_3(t) = -\frac{1}{750}\gamma_0 D^6 t^6 - \frac{1}{5040}\gamma_1 D^6 t^7, \tag{44}$$

$$\tilde{u}_4(t) = \frac{1}{40320}\gamma_0 D^8 t^8 + \frac{1}{362880}\gamma_1 D^8 t^9, \tag{45}$$

$$\tilde{u}_5(t) = -\frac{1}{3628800}\gamma_0 D^{10}t^{10} - \frac{1}{1239916800}\gamma_1 D^{10}t^{11}, \quad (46)$$

The analytical approximate solution (AAS)is

$$\tilde{u}(t) = \gamma_0 + \gamma_1 t - \frac{1}{2}\gamma_0 D^2 t^2 - \frac{1}{6}\gamma_1 D^2 t^3 + \frac{1}{24}\gamma_0 D^4 t^4 + \frac{1}{120}\gamma_1 D^4 t^5 - \frac{1}{750}\gamma_0 D^6 t^6 - \frac{1}{5040}\gamma_1 D^6 t^7 + \frac{1}{40320}\gamma_0 D^8 t^8 + \frac{1}{3992880}\gamma_1 D^8 t^9 + \cdots, \quad (47)$$

The analytical approximte (AA) mean E[ŭ(t)] and variance Var[ŭ(t)] arer

$$E[\tilde{u}(t)] = E[\gamma_0] + E[\gamma_1]t - \frac{1}{2}E[\gamma_0]D^2t^2 - \frac{1}{6}E[\gamma_1]D^2t^3 + \frac{1}{24}E[\gamma_0]D^4t^4 + \frac{1}{120}E[\gamma_1 D^4t^5 - \frac{1}{750}E[\gamma_0]D^6t^6\mathrm{r} - \frac{1}{5040}E[\gamma_1]D^6t^7 + \frac{1}{40320}E[\gamma_0]D^8t^8 + \frac{1}{3992880}E[\gamma_1]D^8t^9 + \cdots, \quad (48)$$

Sincer $D^2 \sim Be(\tilde{\alpha} = 2, \tilde{\beta} = 1)$ can define the expectation of D as follows:

$$E[D^2] = \frac{\tilde{\alpha}}{\tilde{\alpha}+\tilde{\beta}} = \frac{2}{3}, \quad (49)$$

$$E[D^4] = \frac{\tilde{\alpha}(\tilde{\alpha}+1)}{(\tilde{\alpha}+\tilde{\beta}+1)(\tilde{\alpha}+\tilde{\beta})} = \frac{1}{2}, \quad (50)$$

$$E[D^6] = \frac{\tilde{\alpha}(\tilde{\alpha}+1)(\tilde{\alpha}+2)}{(\tilde{\alpha}+\tilde{\beta})(\tilde{\alpha}+\tilde{\beta}+1)(\tilde{\alpha}+\tilde{\beta}+1)(} = \frac{2}{5} \quad (51)$$

$$E[D^8] = \frac{\tilde{\alpha}(\tilde{\alpha}+1)(\tilde{\alpha}+2)(\tilde{\alpha}+3)}{(\tilde{\alpha}+\tilde{\beta})(\tilde{\alpha}+\tilde{\beta}+1)(\tilde{\alpha}+\tilde{\beta}+2)(\tilde{\alpha}+\tilde{\beta}+3)} = \frac{1}{3} \quad (52)$$

$$E[D^{10}] = \frac{\tilde{\alpha}(\tilde{\alpha}+1)(\tilde{\alpha}+2)(\tilde{\alpha}+3)(\tilde{\alpha}+4)}{(\tilde{\alpha}+\tilde{\beta})(\tilde{\alpha}+\tilde{\beta}+1)(\tilde{\alpha}+\tilde{\beta}+2)(\tilde{\alpha}+\tilde{\beta}+3)(\tilde{\alpha}+\tilde{\beta}+4)} = \frac{1}{3} \quad (53)$$

In addition $E[\gamma_0] = 1, E[\gamma_1] = 1, E[\gamma_0^2] = 2, E[\gamma_1^2] = 3, and\ E[\gamma_0\gamma_1] = 0,$ and $Var[\tilde{u}(t)] = E[\tilde{u}^2(t)] - E[\tilde{u}(t)]^2$, we obtain

$$E[\tilde{u}(t)] = 1 + t - \frac{1}{3}t^2 - \frac{1}{9}t^3 + \frac{1}{48}t^4 + \frac{1}{240}t^5 - \frac{1}{1800}t^6 - \frac{1}{12600}t^7 + \frac{1}{120960}t^8 + \frac{1}{362880}t^{59} + \cdots, \quad (54)$$

$$Var[\tilde{u}(t)] = 1 - 2t + \frac{4}{3}t^2 + \frac{8}{9}t^3 - \frac{19}{72}t^4 - \frac{67}{540}t^5 + \frac{103}{4050}t^6 + \frac{41}{4725}t^7 + \frac{247}{172800}t^8 + \cdots, \quad (55)$$

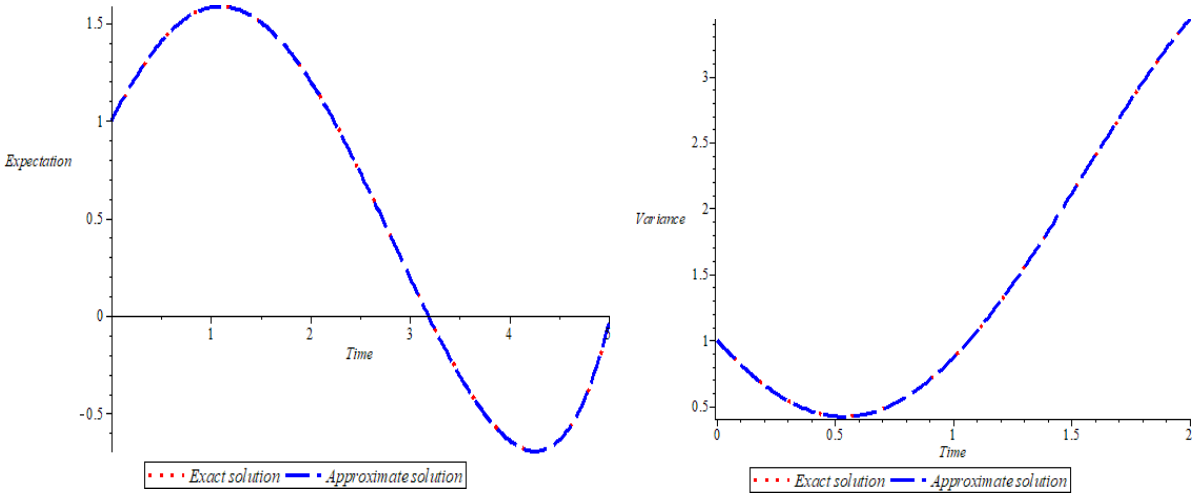

(a) (b)

Figure 1: (a) The behavior of E[$\tilde{u}$ (t)] and (b) The behavior of Var[$\tilde{u}$ (t)].

Table 1: Comparison between the analytical approximate of E[ũ (t)] and Var[ũ(t)] with exact solutions**.**

t	E[$\tilde{u}$ (t)]	Exact solution	Var[$\tilde{u}$ (t)]	Exact solution
0.1	1.096558	1.096558	0.814195	0.814195
0.2	1.185812	1.185812	0.659984	0.659984
0.3	1.267178	1.267178	0.541581	0.541581
0.4	1.340129	1.340129	0.462313	0.462313
0.5	1.404200	1.404200	0.424533	0.424533
0.6	1.458996	1.458996	0.429554	0.429554
0.7	1.504187	1.504187	0.477619	0.477619
0.8	1.539516	1.539516	0.567896	0.567896
0.9	1.564791	1.564791	0.698506	0.698506
1.0	1.579921	1.579921	0.866570	0.866570

3.2.Example

Consider the random initial value problem

$$\frac{d^2\tilde{u}(t)}{dt^2} + D\ t\tilde{u}(t) = 0,\ \tilde{u}(0) = \gamma_0,\quad \left.\frac{d\tilde{u}(t)}{dt}\right|_{t=0} = \gamma_1, \tag{56}$$

where D is a Beta random variable, $D \sim Be(\tilde{\alpha} = 2,\ \tilde{\beta} = 3)$, and independently of the initial conditions γ_0, γ_1 which satisfy $E[\gamma_0] = 1, E[\gamma_1] = 2, E[\gamma_0^2] = 2,\ and\ E[\gamma_1^2] = 5,$

To obtain the expectation $E[\check{u}(t)]$ and the variance Var$[\check{u}(t)]$, we can construct the following

$$K[\tilde{u}(t)] = -D\ t\,\tilde{u}(t),\quad \tilde{g}(t) = 0,\ L^{-1} = \int_0^t \int_0^t (dt)^2, \tag{57}$$

The solution of the given equation involves the extraction of the components of $\tilde{u}(t)$. So solving the approximate analytical series (AAS) be as listed

$$\tilde{u}(t) = \tilde{u}_0(t) + \tilde{u}_1(t) + \tilde{u}_2(t) + \cdots, \tag{58}$$

Initial conditions are used when the inverse operator L^{-1} is applied on Equation (56) rto obtain

$$\tilde{u}_0(t) = \gamma_0 + \gamma_1 t,$$

for the components of $\tilde{u}(t)$, canr be easily be found by the following iterative process:

$$\tilde{u}_0(t) = \gamma_0 + \gamma_1 t, \quad \tilde{u}_1(t) = -L^{-1} D\, t\tilde{u}_0(t), \tag{59}$$

$$\tilde{u}_1(t) = L^{-1}K[\tilde{u}_0(t), \qquad \tilde{u}_2(t) = L^{-1}\frac{dK[\tilde{u}_0(t)]}{dt}, \tag{60}$$

$$\tilde{u}_3(t) = L^{-1}\frac{d^2K[\tilde{u}_0(t)]}{dt^2}, \qquad \tilde{u}_4(t) = L^{-1}\frac{d^3K[\tilde{u}_0(t)]}{dt^3}, \tag{61}$$

Now, we start to calculation the derivatives of *K with respect to t which consider is the basic part of the iterative method* $K'[\tilde{u}(t)], K''[\tilde{u}(t)], K'''[\tilde{u}(t)]$, ...

$$K[\tilde{u}(t)] = -Dt\tilde{u}(t), \tag{62}$$

$$\mathrm{K}'[\tilde{\mathrm{u}}(\mathrm{t})] = \frac{\mathrm{dK}[\tilde{\mathrm{u}}(\mathrm{t})]}{\mathrm{dt}} = \mathrm{K}_{\tilde{\mathrm{u}}}.\tilde{\mathrm{u}}_{\mathrm{t}}, \tag{63}$$

$$K''[\tilde{\mathrm{u}}(\mathrm{t})] = \frac{d^2\mathrm{K}[\tilde{\mathrm{u}}(\mathrm{t})]}{\mathrm{d}t^2} = K_{\tilde{u}\tilde{u}}.(\tilde{\mathrm{u}}_{\mathrm{t}})^2 + \mathrm{K}_{\tilde{\mathrm{u}}}.\tilde{\mathrm{u}}_{\mathrm{tt}}, \tag{64}$$

$$K'''[\tilde{\mathrm{u}}(\mathrm{t})] = \frac{d^3\mathrm{K}[\tilde{\mathrm{u}}(\mathrm{t})]}{\mathrm{d}t^3} = K_{\tilde{u}\tilde{u}\tilde{u}}.(\tilde{\mathrm{u}}_{\mathrm{t}})^3 + 3.\mathrm{K}_{\tilde{\mathrm{u}}\tilde{\mathrm{u}}}.\tilde{u}_t.\tilde{\mathrm{u}}_{\mathrm{tt}} + \mathrm{K}_{\tilde{\mathrm{u}}}.\tilde{\mathrm{u}}_{\mathrm{ttt}}, \tag{65}$$

⋮

we note that the derivatives of $\tilde{u}$ with respect t that are given in (20) can be computed by Equations(62)-(65) as

$$K[\tilde{u}_0(t)] = -D\tilde{u}_0(t), \tag{66}$$

$$\mathrm{K}'[\tilde{u}_0(\mathrm{t})] = \frac{\mathrm{dK}[\tilde{u}_0(\mathrm{t})]}{\mathrm{dt}} = \mathrm{K}_{\tilde{\mathrm{u}}}.\tilde{\mathrm{u}}_1, \tag{67}$$

$$K''[\tilde{u}_0(\mathrm{t})] = \frac{d^2\mathrm{K}[\tilde{u}_0(\mathrm{t})]}{\mathrm{d}t^2} = K_{\tilde{u}_0\tilde{u}_0}.(\tilde{\mathrm{u}}_1)^2 + \mathrm{K}_{\tilde{u}_0}.\tilde{\mathrm{u}}_2, \tag{68}$$

$$K'''[\tilde{u}_0(\mathrm{t})] = \frac{d^3\mathrm{K}[\tilde{u}_0(\mathrm{t})]}{\mathrm{d}t^3} = K_{\tilde{u}_0\tilde{u}_0\tilde{u}_0}.(\tilde{\mathrm{u}}_1)^3 + 3.\mathrm{K}_{\tilde{u}_0\tilde{u}_0}.\tilde{\mathrm{u}}_1.\tilde{\mathrm{u}}_2 + \mathrm{K}_{\tilde{u}_0}.\tilde{\mathrm{u}}_3, \tag{69}$$

⋮

now, we need to extract the first derivatives of K as follows

$$K_{\tilde{u}_0} = -Dt, \quad K_{\tilde{u}_0\tilde{u}_0} = 0, \quad K_{\tilde{u}_0\tilde{u}_0\tilde{u}_0} = 0, ..., \tag{70}$$

After performing the above iterative method, the components $\tilde{u}(t)$ are obtained as follows:

$$\tilde{u}_0(t) = \gamma_0 + \gamma_1 t, \tag{71}$$

$$\tilde{u}_1(t) = -\frac{1}{6}\gamma_0 Dt^3 - \frac{1}{12}\gamma_1 Dt^4, \tag{72}$$

$$\tilde{u}_2(t) = \frac{1}{180}\gamma_0 D^2t^6 + \frac{1}{504}\gamma_1 D^2t^7, \tag{73}$$

$$\tilde{u}_3(t) = -\frac{1}{12960}\gamma_0 D^3t^9 - \frac{1}{45360}\gamma_1 D^3t^{10}, \tag{74}$$

$$\tilde{u}_4(t) = \frac{1}{1710720}\gamma_0 D^4t^{12} + \frac{1}{7076160}\gamma_1 D^4t^{13}, \tag{75}$$

$$\tilde{u}_5(t) = -\frac{1}{359251200}\gamma_0 D^5t^{15} - \frac{1}{1698278400}\gamma_1 D^5t^{16}, \tag{76}$$

⋮

The analytical approximate solution (AAS) is

$$\tilde{u}(t) = \gamma_0 + \gamma_1 t - \frac{1}{2}\gamma_0 D^2t^2 - \frac{1}{6}\gamma_1 D^2t^3 + \mathrm{rr}\frac{1}{24}\gamma_0 D^4t^4 + \frac{1}{120}\gamma_1 D^4t^5 - \frac{1}{750}\gamma_0 D^6t^6 - \frac{1}{5040}\gamma_1 D^6t^7 + \frac{1}{40320}\gamma_0 D^8t^8 + \frac{1}{3992880}\gamma_1 D^8t^9 + \cdots, \tag{77}$$

The analytical approximate mean E[ŭ(t)] and variance Var[ŭ(t)] arer

$$E[\tilde{u}(t)] = E[\gamma_0] + E[\gamma_1]t - \frac{1}{2}E[\gamma_0]D^2t^2 - \frac{1}{6}E[\gamma_1]D^2t^3 + \frac{1}{24}E[\gamma_0]D^4t^4 + \frac{1}{120}E[\gamma_1 D^4t^5 - \frac{1}{750}E[\gamma_0]D^6t^6 - \frac{1}{5040}E[\gamma_1]\,D^6t^7 + \frac{1}{40320}[\gamma_0]D^8t^8 + \frac{1}{3992880\mathrm{r}}E[\gamma_1]D^8t^9 + \cdots, \tag{78}$$

Since $D \sim Be(\tilde{\alpha} = 2, \tilde{\beta} = 3)$ can define the expectation of D as follows:

$$E[D] = \frac{\tilde{\alpha}}{\tilde{\alpha}+\tilde{\beta}} = \frac{2}{5} \quad , \tag{79}$$

$$E[D^2] = \frac{\tilde{\alpha}(\tilde{\alpha}+1)}{(\tilde{\alpha}+\tilde{\beta}+1)(\tilde{\alpha}+\tilde{\beta})} = \frac{1}{5} \quad , \tag{80}$$

$$E[D^3] = \frac{\tilde{\alpha}(\tilde{\alpha}+1)(\tilde{\alpha}+2)}{(\tilde{\alpha}+\tilde{\beta})(\tilde{\alpha}+\tilde{\beta}+1)(\tilde{\alpha}+\tilde{\beta}+1)} = \frac{4}{35} \tag{81}$$

$$E[D^4] = \frac{\tilde{\alpha}(\tilde{\alpha}+1)(\tilde{\alpha}+2)(\tilde{\alpha}+3)}{(\tilde{\alpha}+\tilde{\beta})(\tilde{\alpha}+\tilde{\beta}+1)(\tilde{\alpha}+\tilde{\beta}+2)(\tilde{\alpha}+\tilde{\beta}+3)} = \frac{1}{14} \tag{82}$$

$$E[D^5] = \frac{\tilde{\alpha}(\tilde{\alpha}+1)(\tilde{\alpha}+2)(\tilde{\alpha}+3)(\tilde{\alpha}+4)}{(\tilde{\alpha}+\tilde{\beta})(\tilde{\alpha}+\tilde{\beta}+1)(\tilde{\alpha}+\tilde{\beta}+2)(\tilde{\alpha}+\tilde{\beta}+3)(\tilde{\alpha}+\tilde{\beta}+4)} = \frac{1}{3} \tag{83}$$

Type equation here.

Inraddition $E[\gamma_0] = 1, E[\gamma_1] = 1, E[\gamma_0^2] = 2, E[\gamma_1^2] = 5,$ and $Var[\tilde{u}(t)] = E[\tilde{u}^2(t)] - E[\tilde{u}(t)]^2$, we obtian

$$E[\tilde{u}(t)] = 1 + 2t - \frac{1}{15}t^3 - \frac{1}{15}t^4 + \frac{1}{900}t^6 + \frac{1}{1260}t^7 - \frac{1}{113400}t^9 - \frac{1}{\text{r}198450}t^{10} + \cdots, \tag{84}$$

$$Var[\tilde{u}(t)] = 1 + t^2 + \frac{2}{15}t^3 - \frac{1}{15}t^5 + \frac{2}{225}t^6 + \frac{1}{450}t^7 + \frac{83}{25200}t^8 - \text{r}\frac{83}{283500}t^8 - \cdots, \tag{85}$$

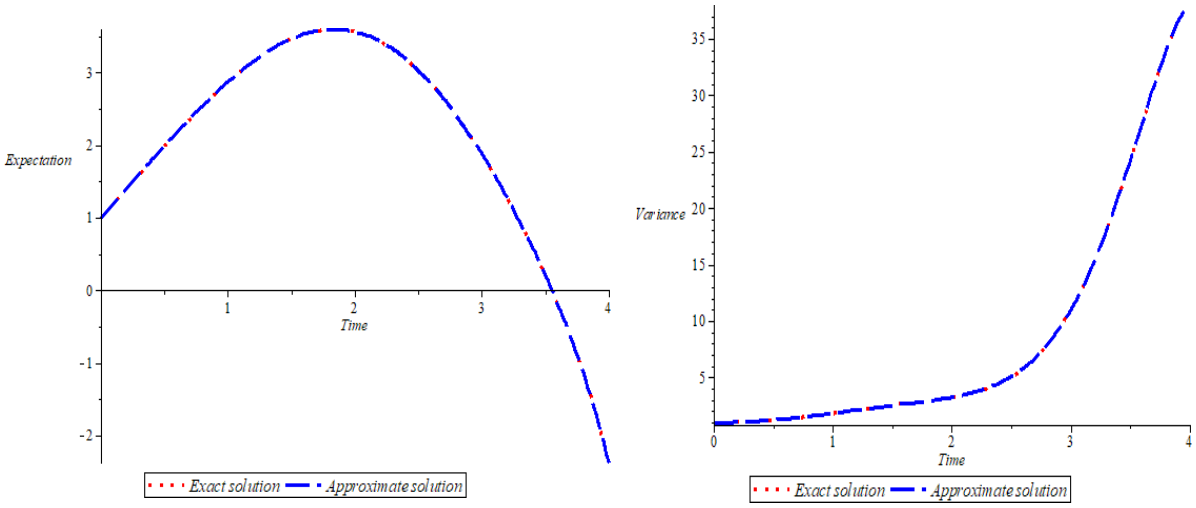

(a) (b)

Figure 2: (a) The behavior of E$[\tilde{u}(t)]$ andr (b) The behavior of Var$[\tilde{u}(t)]$.

Table 2: Comparison between analytical approximate of $E[\tilde{u}(t)]$ and Var$[\tilde{u}(t)]$ with exact solutions

t	E$[\tilde{u}(t)]$	Exact solution	Var$[\tilde{u}(t)]$	Exact solution
0.1	1.199926	1.199926	1.009866	1.009866
0.2	1.399360	1.399360	1.038912	1.038912

0.3	1.597660	1.597660	1.086245	1.086245
0.4	1.794032	1.794032	1.150826	1.150826
0.5	1.987523	1.987523	1.231418	1.231418
0.6	2.177033	2.177033	1.326544	1.326544
0.7	2.361322	2.361322	1.434465	1.434465
0.8	2.539015	2.539015	1.553185	1.553185
0.9	2.708624	2.708624	1.680487	1.680487
1.0	2.868557	2.868557	1.814003	1.814003

3.3.Example
Consider the random initial value problem

$$\frac{d^2\tilde{u}(t)}{dt^2} + 2D\frac{d\tilde{u}(t)}{dt} + D^2\tilde{u}(t) = 0,\ \tilde{u}(0) = \gamma_0,\quad \left.\frac{d\tilde{u}(t)}{dt}\right|_{t=0} = \gamma_1, \tag{86}$$

where D is a Beta random variable, $D \sim Be(\tilde{\alpha}= 2,\ \tilde{\beta} = 1)$, and independently of the initial coditions γ_0, γ_1 whichrsatisfy $E[\gamma_0] = 1, E[\gamma_1] = 1, E[\gamma_0^2] = 2,\ and\ E[\gamma_1^2] = 1,$

To obtain the expectation $E[\check{u}(t)]$ and the variance $Var[\check{u}(t)]$, we can construct the following

$$K[\tilde{u}(t)] = -2D\frac{d\tilde{u}(t)}{dt} - D^2\tilde{u}(t),\quad \tilde{g}(t) = 0,\ L^{-1} = \int_0^t\int_0^t (dt)^2, \tag{87}$$

The solution of the given equationin volves the extraction of the components of $\tilde{u}(t)$. So solving the approximate analytical series (AAS) be as listed

$$\tilde{u}(t) = \tilde{u}_0(t) + \tilde{u}_1(t) + \tilde{u}_2(t) + \cdots, \tag{88}$$

initial conditions are use the inverse operator L^{-1} is applied on Equation (86) to obtain

$$\tilde{u}_0(t) = \gamma_0 + \gamma_1 t, \tag{89}$$

for the components of $\tilde{u}(t)$, can be easily be found by the following iterative process:

$$\tilde{u}_0(t) = \gamma_0 + \gamma_1 t,\quad \tilde{u}_1(t) = -L^{-1}D\frac{d\tilde{u}_0(t)}{dt} - L^{-1}D^2\tilde{u}_0(t), \tag{90}$$

$$\tilde{u}_1(t) = L^{-1}K[\tilde{u}_0(t)],\qquad \tilde{u}_2(t) = L^{-1}\frac{dK[\tilde{u}_0(t)]}{dt}, \tag{91}$$

$$\tilde{u}_3(t) = L^{-1}\frac{d^2K[\tilde{u}_0(t)]}{dt^2},\qquad \tilde{u}_4(t) = L^{-1}\frac{d^3K[\tilde{u}_0(t)]}{dt^3}, \ldots, \tag{92}$$

Now, we start to calculationr the derivatives of K with respect to t which consider is the basic part of the iterative method(NIM) $K'[\tilde{u}(t)], K''[\tilde{u}(t)], K'''[\tilde{u}(t)]$, ...

$$K[\tilde{u}(t)] = -D\tilde{u}'^{(t)} - D^2\tilde{u}(t), \tag{93}$$

$$K'[\tilde{u}\ (t)] = \sum_{i=1}^{2} K_{\tilde{u}^{(i-1)}}(\tilde{u}_t)^{(i-1)}, \tag{94}$$

$$K''[\tilde{u}\ (t)] = \sum_{j=1}^{2}\sum_{i=1}^{2} K_{\tilde{u}^{(j-1)}u^{(i-1)}}\ (\tilde{u}_t)^{(j-1)}(\tilde{u}_t)^{(i-1)} + \sum_{i=1}^{2} K_{\tilde{u}^{(i-1)}}(\tilde{u}_{tt})^{(i-1)}, \tag{95}$$

$$K[\tilde{u}\ (t)] = \sum_{k=1}^{2}\sum_{j=1}^{2}\sum_{i=1}^{2} K_{\tilde{u}^{(k-1)}\tilde{u}^{(j-1)}\tilde{u}^{(i-1)}}\ (\tilde{u}_t)^{(k-1)}(\tilde{u}_t)^{(j-1)}(\tilde{u}_t)^{(i-1)} + 3.\sum_{j=1}^{2}(\tilde{u}_{tt})^{(j-1)}(\tilde{u}_t)^{(i-1)} + \sum_{i=1}^{2} K_{\tilde{u}^{(i-1)}}(\tilde{u}_{ttt})^{(i-1)}, \tag{96}$$

$$\vdots$$

we note that the derivatives of $K[\tilde{u}(t)]$ *w*ith respect *t* that are given in (20), can be computed by Equations(93)-(96) as

$$K[\tilde{u}_0(t)] = -D\tilde{u}_0 - D^2\tilde{u}_0(t), \quad (97)$$

$$K'[\tilde{u}_0(t)] = \sum_{i=1}^{2} K_{\tilde{u}_0{}^{(i-1)}}(\tilde{u}_1)^{(i-1)}, \quad (98)$$

$$K''[\tilde{u}_0(t)] = \sum_{j=1}^{2}\sum_{i=1}^{2} K_{\tilde{f}_0{}^{(j-1)}\tilde{f}_0{}^{(i-1)}}\left(\tilde{f}_1\right)^{(j-1)}\left(\tilde{f}_1\right)^{(i-1)} + \sum_{i=1}^{2} K_{\tilde{f}_0{}^{(i-1)}}(\tilde{f}_2)^{(i-1)}, \quad (99)$$

$$K'''[\tilde{u}_0(t)] = \sum_{k=1}^{2}\sum_{j=1}^{2}\sum_{i=1}^{2} K_{\tilde{f}_0{}^{(k-1)}\tilde{f}_0{}^{(j-1)}\tilde{f}_0{}^{(i-1)}}(\tilde{f}_1)^{(k-1)}\left(\tilde{f}_1\right)^{(j-1)}\left(\tilde{f}_1\right)^{(i-1)}$$

s

$$+3.\sum_{j=1}^{2}\sum_{i=1}^{2} K_{\tilde{f}_0{}^{(j-1)}\tilde{f}_0{}^{(i-1)}}(\tilde{f}_2)^{(j-1)}(\tilde{f}_1)^{(i-1)} + \sum_{\mathrm{i}=1}^{2} \mathrm{K}_{\tilde{\mathrm{f}}_0{}^{(\mathrm{i}-1)}}(\tilde{\mathrm{f}}_3)^{(\mathrm{i}-1)}, \quad (100)$$

now, we need to extract the first derivatives of K as follows

$$K_{\tilde{u}_0} = -D^2, \quad K_{\tilde{u}_0\tilde{u}_0} = 0, \quad K_{\tilde{u}_0\tilde{u}_0\tilde{u}_0} = 0, \ldots,$$
$$K_{\tilde{u}_0'} = -2D, \quad K_{\tilde{u}_0'\tilde{u}_0'} = 0, \quad K_{\tilde{u}_0'\tilde{u}_0'\tilde{u}_0'} = 0, \ldots, \quad (101)$$

After performing the above iterative method (NIM), the components $\tilde{u}(t)$ are obtained as follows:

$$\tilde{u}_0(t) = \gamma_0 + \gamma_1 t, \quad (102)$$
$$\tilde{u}_1(t) = -D\gamma_1 t^2 - \tfrac{1}{2}\gamma_0 D^2 t^3 - \tfrac{1}{6}\gamma_1 D^2 t^4, \quad (103)$$
$$\tilde{u}_2(t) = \tfrac{1}{3}\gamma_0 D^3 t^3 + \tfrac{2}{3}\gamma_1 D^2 t^3 + \tfrac{1}{24}\gamma_0 D^4 t^4 + \tfrac{1}{6}\gamma_1 D^3 t^4 + \tfrac{1}{120}\gamma_1 D^4 t^5, \quad (104)$$
$$\tilde{u}_3(t) = -\tfrac{1}{3}\gamma_1 D^3 t^3 - \tfrac{1}{6}\gamma_0 D^4 t^4 - \tfrac{1}{30}\gamma_0 D^4 t^4 - \tfrac{1}{10}\gamma_1 D^4 t^5 - \tfrac{1}{720}\gamma_0 D^6 t^6 - \tfrac{1}{120}\gamma_1 D^5 t^6 - \tfrac{1}{5040}\gamma_1 D^6 t^7, \quad (105)$$
$$\vdots$$

The analytical approximate solution (AAS) is

$$\tilde{u}(t) = \gamma_0 + \gamma_1 t - D\gamma_1 t^2 - \frac{1}{2}\gamma_0 D^2 t^3 - \frac{1}{6}\gamma_1 D^2 t^4 + \frac{1}{3}\gamma_0 D^3 t^3 + \frac{2}{3}\gamma_1 D^2 t^3 + \tfrac{1}{24}\gamma_0 D^4 t^4 + \tfrac{1}{6}\gamma_1 D^3 t^4 + \tfrac{1}{120}\gamma_1 D^4 t^5 - \tfrac{1}{3}\gamma_1 D^3 t^3 - \tfrac{1}{6}\gamma_0 D^4 t^4 + \cdots, \quad (106)$$

The analytical approximate (AA) mean $E[\check{u}(t)]$ and variance Var[ŭ(t)] are

$$E[\tilde{u}(t)] = E[\gamma_0] + E[\gamma_1]t - [D]E[\gamma_1]t^2 - \frac{1}{2}E[\gamma_0]E[D^2]t^3 - \frac{1}{6}E[\gamma_1]E[D^2]t^4 + \tfrac{1}{3}E[\gamma_0]E[D^3]t^3 + \tfrac{2}{3}E[\gamma_1]E[D^2]t^3 + \tfrac{1}{24}E[\gamma_0]E\left[D^4\right]t^4 + \tfrac{1}{6}E[\gamma_1]E[D^3]t^4 + \tfrac{1}{120}E[\gamma_1 E[D^4]t^5 - \tfrac{1}{3}E[\gamma_1]E[D^3]t^3 - \tfrac{1}{6}E[\gamma_0]E[D^4]t^4 + \cdots,$$

Since $D \sim Be(\tilde{\alpha} = 2, \tilde{\beta} = 1)$ can define the expectation of D as follows:

$$E[D] = \frac{\tilde{\alpha}}{\tilde{\alpha}+\tilde{\beta}} = \frac{2}{3}, \quad (107)$$
$$E[D^2] = \frac{\tilde{\alpha}(\tilde{\alpha}+1)}{(\tilde{\alpha}+\tilde{\beta}+1)(\tilde{\alpha}+\tilde{\beta})} = \frac{1}{2}, \quad (108)$$
$$E[D^3] = \frac{\tilde{\alpha}(\tilde{\alpha}+1)(\tilde{\alpha}+2)}{(\tilde{\alpha}+\tilde{\beta})(\tilde{\alpha}+\tilde{\beta}+1)(\tilde{\alpha}+\tilde{\beta}+1)} = \frac{2}{5} \quad (109)$$
$$E[D^4] = \frac{\tilde{\alpha}(\tilde{\alpha}+1)(\tilde{\alpha}+2)(\tilde{\alpha}+3)}{(\tilde{\alpha}+\tilde{\beta})(\tilde{\alpha}+\tilde{\beta}+1)(\tilde{\alpha}+\tilde{\beta}+2)(\tilde{\alpha}+\tilde{\beta}+3)} = \frac{1}{3} \quad (110)$$
$$E[D^5] = \frac{\tilde{\alpha}(\tilde{\alpha}+1)(\tilde{\alpha}+2)(\tilde{\alpha}+3)(\tilde{\alpha}+4)}{(\tilde{\alpha}+\tilde{\beta})(\tilde{\alpha}+\tilde{\beta}+1)(\tilde{\alpha}+\tilde{\beta}+2)(\tilde{\alpha}+\tilde{\beta}+3)(\tilde{\alpha}+\tilde{\beta}+4)} = \frac{2}{7} \quad (111)$$
$$\vdots$$

In addition $E[\gamma_0] = 1, E[\gamma_1] = 1, E[\gamma_0^2] = 2, E[\gamma_1^2] = 1,$ and $Var[\tilde{u}(t)] = E[\tilde{u}^2(t)] - E[\tilde{u}(t)]^2,$

we obtain

$$E[\tilde{u}(t)] = 1 + t - \frac{11}{12}t^2 + \frac{23}{60}t^3 - \frac{13}{120}t^4 + \frac{59}{2520}t^5 - \frac{83}{20160}t^6 + \frac{37}{60480}t^7 - \frac{143}{1814400}t^8 + \cdots, \quad (112)$$

$$Var[\tilde{u}(t)] = 1 - \frac{1}{2}t^2 + \frac{4}{15}t^3 + \frac{103}{720}t^4 - \frac{649}{2520}t^5 + \frac{8959}{50400}t^6 - \frac{3133}{37800}t^7 + \frac{517}{17280}t^8 - \frac{5923}{665280}t^9 + \cdots, \quad (113)$$

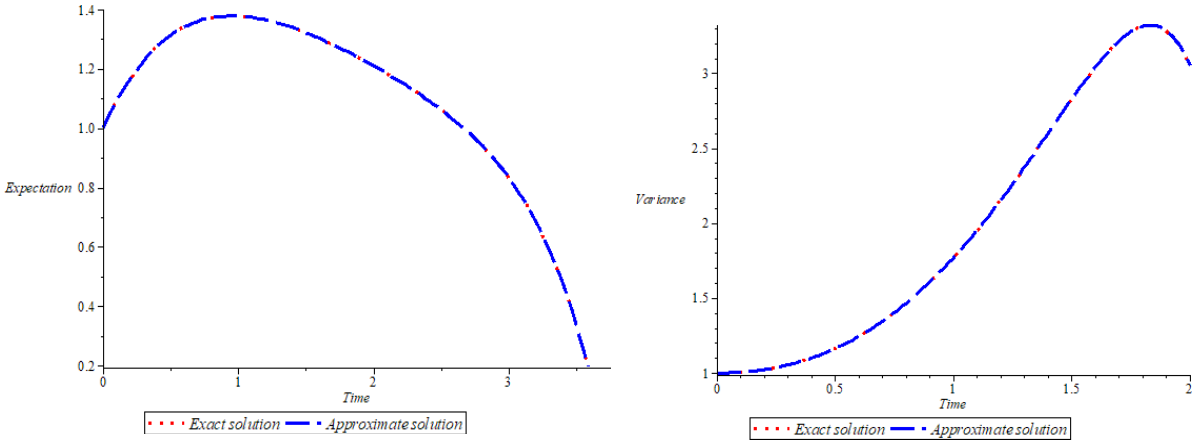

(a) (b)

Figure 3: (a) The behavior of E[$\tilde{u}(t)$] and (b) The behavior of Var[$\tilde{u}(t)$].

Table 3: Comparison between the analytical approximate of $E[\tilde{u}(t)]$ and Var[ũ(t)] with exact solution

t	E[$\tilde{u}(t)$]	Exact solution	Var[$\tilde{u}(t)$]	Exact olution
0.1	1.091206	1.091206	0.995278	0.995278
0.2	1.166233	1.166233	0.982290	0.982290
0.3	1.227026	1.227026	0.962846	0.962846
0.4	1.275317	1.275317	0.938701	0.938701
0.5	1.312650	1.312650	0.911455	0.911455
0.6	1.340404	1.340404	0.882499	0.882499
0.7	1.359802	1.359802	0.852982	0.852982
0.8	1.371934	1.371934	0.823779	0.823779
0.9	1.377768	1.377768	0.795438	0.795438
1.0	1.378161	1.378161	0.768072	0.768072

4.Conclusion

In this article, NIM is employed to computerthe expectation approximation $E[\tilde{u}(t)]$ and variance approximation Var[$\tilde{u}(t)$] of second- order random differential equation(SORDE).The results rpresent which obtains from the proposed method represents graphs that can be seen clearly in Figure 1-3. These

figures show that the solutions we obtained are compatible with the exactr solution. Finally, ther NIM is avery effective and powerful tool for the second-order random differential equation.

References

[1] J Chil'es and P Delfiner 1999 *Geostatistics Modelling Spatial Uncertainty* John (Wiley New York).
[2] J C Cortes, L Jodar and L Villafuerte 2009 Random linear-quadratic mathematical models computing explicit solutions and applications Math *Comput. Simulat.***79** pp 2076-2090
[3] T T Soong 1973 *Random Differential Equations in Science and Engeneering* Academic (Press New York)
[4] J C Corts, L Jodar and L Villafuerte 2007 Mean square numerical solution of random differential equations: Facts and possibilities *Computers and Mathematics with Applications* **53** pp 1098-1106
[5] J C Corts, L Jodar and L Villafuerte 2007 Numerical solution of random differential e- quations: A mean square approach *Mathematical and Computer Modelling* **45** pp 757-765
[6] L Villafuerte, C A Braumann, J C Corts and L Jodar 2010 Random differential operational calculus *theory and applications Comput. Math. Appl.* **59** pp 115-125
[7] G Calbo, J C Corts and L Jodar 2010 Mean square power series solution of random lin- ear differential equations *Computers and Mathematics with Applications* **59** pp 559-572
[8] J C Corts, L Jodar, R Villanueva and L Villafuerte 2010 Mean Square Convergent Nu- merical Methods for Nonlinear Random Differential Equations *Springer-Verlag Berlin Heidelberg Lecture Notes in Computer Science* 5890 pp 1-21
[9] J C Corts, L Jodar, F Camachoa and L Villafuerte 2010 Random Airy type differential equations Mean square exact and numerical solutions *Comp. and Math. with Appl.* **60** pp 1237-1244
[10] G Calbo, J C Corts, G Jodar and L Villafuerte 2010 Analytic stochastic process so- lutions of second-order random differential equations *App. Math. Lett*. **23** pp 1421-1424
[11] G Adomian 1988 A review of the decomposition method in applied mathematics *J. Math. Anal. Appl.* **135** pp 501-544
[12] G Adomian 1994 *Solving Frontier Problems of Physics The Decomposition Method* Kluwer Academic Dordrecht
[13] A R Khudair, S A M Haddad and L K Sanaa 2016 Mean Square Solutions of Second-Order Random Differential Equations by Using the Differential Transformation Method *J. of Appl. Sci.* **6** pp 287-297
[14] A R Khudair, S A M Haddad and S L Khalaf 2016 Improve the Mean Square Solution of Second-order Random Differential Equations by Using Homotopy Analysis Method *British J. of Math. & Comp. Sci.* **16** (5) pp 1-14
[15] A J A Al-Saif and A M Jasim 2019 A novel algorithm for studying the effects of squeezing flow of a Casson Fluid between parallel plates on magnetic field *J. of App. Math* pp 1-22
[16] A J A Al-Saif and A M Jasim 2019 New Analytical Study of the Effects Thermo- Diffusion, Diffusion-Thermo and Chemical Reaction of Viscous Fluid on Mag- neto Hydrodynamics Flow in Divergent and Convergent Channels *App. Math.* 268-300.
[17] A J A Al-Saif and A M Jasim 2019 Analytical Investigation of the MHD Jeffery-Hamel Flow Through Convergent and Divergent Channel by New Scheme *Eng. Lett*. **27 (**3) EL-27-3-28.
[18] A M Jasim and A J A Al-Saif 2019 New Analytical Solution Formula for Heat Trans- fer of Unsteady Two-Dimensional Squeezing Flow of a Casson Fluid between Parallel Circular Plates *Journal of Advanced Research in Fluid Mechanics and Thermal Sciences* **64** pp 219-243
[19] A M Jasim 2020 Analytical approximation of the first grade MHD squeezing fluid flow with slip boundary condition using a new iterative method *Heat transfer* pp 1-21

Stress-Strength Reliability for $P(T < X < Z)$ using Dagum Distribution

Stress-Strength Reliability for $P(T < X < Z)$ using Dagum Distribution

Nada S. Karam , Ali M. Attia

Department of Mathematics, College of Education ,Mustansiriyah University, Baghdad, Iraq

E-mail: alimutair43@gmail.com

Abstract. In this paper, the reliability formula of the stress-strength model is derived for probability P(T<X<Z) of a component having strength X falling between two stresses T and Z, that these stresses and strength variables have Dagum distribution with unknown shape parameters and known common scale parameters. Three methods for estimating the Dagum parameters are discussed which are the Maximum Likelihood, Regression method and Method of Moment, and the comparison between these estimation method based on a simulation study by the mean square error criteria for each of the small, medium and large samples. The most important conclusion is that this comparison confirms that the performance of the maximum likelihood estimator works better for most of the experiments studied.

1. Introduction

In the reliability studies the stress-strength model describes the life of a component which has a random strength X and is subjected to random stress Y. This idea arises in the classical stress-strength reliability, where the person is interested in estimating the probability $P(X < Y)$ that can be interpreted as the probability of failure of the component, when the applied stress Y is greater than its strength X [5]. An important case is the estimation of $R = P(T < X < Z)$ which represents the situation where the strength X should not only be greater than stress T but also be smaller than stress Z. For example, there are many devices that do not work when the temperatures are high or when they are low. Similarly, person's blood pressure should lie within two limits, systolic and diastolic [6]. The stress-strength model of $P(T < X < Z)$ have wide applications in various subareas of engineering, psychology, genetics, clinical trials and so on [9]. Singh (1980) presented the minimum variance unbiased (MVU), Maximum Likelihood and empirical estimator of $R = P(T < X < Z)$, where T,Z and X are mutually independent random variables and follows the normal distribution [11]. Dutta and Sriwastav (1986) deal with the estimation of R when T,Z and X are exponential random variables [3]. In 1988, Ivshin investigated the MLE and UMVUE of R when T,Z and X either uniform or exponential random variable with the unknown location parameter [7]. In 2013, Hassan et al. focused on the estimate of $R = P(T < X < Z)$, where T and Z be a random stress and X be a random strength have weibull distribution in presence of k outlies [6]. In 2019, Salman et al. focused on the estimate of $R = P(T < X < Z)$, when T,Z and X are independent and that these stress and strength variables have Inverted Kumaraswamy distribution [5].

Dagum distribution was introduced by Dagum in (1977). This distribution was widely used in various fields such as, income and wealth data, meteorological data, reliability and survival analysis. The Dagum distribution (Dag) is also called the inverse Burr XII distribution [2],[4].

For any random variable X that follows Dagum distribution the cumulative density function (cdf) is given by:[2]

$$F(x) = \left(1 + \lambda x^{-\delta}\right)^{-\beta} \quad ; x > 0; \beta, \lambda, \delta > 0 \tag{1}$$

and the probability density function (pdf) :

$$\mathrm{f}(x) = \beta\lambda\delta x^{-\delta-1}\left(1 + \lambda x^{-\delta}\right)^{-\beta-1} \quad ; x > 0; \beta, \lambda, \delta > 0 \tag{2}$$

where λ is the scale parameter and the shape parameters are β, δ.

Since $\mathrm{f}(x)$ is probability densty function, then we can rewrite equation (2) as:

$$\int_0^\infty \lambda\delta x^{-\delta-1}\left(1 + \lambda x^{-\delta}\right)^{-\beta-1} dx = \frac{1}{\beta} \tag{3}$$

The main aim of this paper is to obtain a mathematical formula for the reliability R of the probability that a component's strength is between two stresses based on Dagum distribution in section 2. In order to find the estimators of the shape parameters $(\beta, \beta_1, \beta_2)$ for the three random variables, three different estimation methods (Maximum Likelihood, Regression Method and Moment Method) are used and then the reliability parameter is estimated in section 3. A simulation study was conducted to compare the performance of the three different estimators of the reliability in section 4, based on twelve experiments of shape parameter values and at different sample sizes of (15) for small, (30) for medium and (90) for large sample sizes. The comparison is made by the Mean Square Error (MSE), and the conclusions are discussed in section 5.■

2.Reliability Formulation

The reliability formula of the stress-strength model that the probability of a component strength falling in between two stresses, is given by:[1]

$$\begin{aligned} R &= P(T < X < Z) \\ &= \int_0^\infty P(T < x, Z > x / X = x) dF_x(x) \\ &= \int_0^\infty H_T(x)\left(1 - G_Z(x)\right)\mathrm{f(x)dx} \\ &= \int_0^\infty H_T(x)\mathrm{f(x)}dx - \int_0^\infty H_T(x)G_Z(x)\mathrm{f(x)}dx \end{aligned} \tag{4}$$

Let T and Z be independent random stress variables with distribution functions $H_T(t)$, $G_Z(z)$ following $\mathrm{Dag}(\beta_1, \lambda, \delta)$ and $\mathrm{Dag}(\beta_2, \lambda, \delta)$ respectively. And let X be a random strength variable, assumed that X independent from T and Z following $\mathrm{Dag}(\beta, \lambda, \delta)$ with (cdf) $F_x(x)$, then:

$$H_T(t) = \left(1 + \lambda t^{-\delta}\right)^{-\beta_1} \quad t > 0; \beta_1, \lambda, \delta > 0 \tag{5}$$

$$G_Z(z) = \left(1 + \lambda z^{-\delta}\right)^{-\beta_2} \quad z > 0; \beta_2, \lambda, \delta > 0 \tag{6}$$

Also $\mathrm{f}(x) = \beta\lambda\delta x^{-\delta-1}\left(1 + \lambda x^{-\delta}\right)^{-\beta-1} \quad x > 0; \beta, \lambda, \delta > 0$

Now, from equation (4):

$$\begin{aligned} R = {} & \int_0^\infty \left(1 + \lambda x^{-\delta}\right)^{-\beta_1} \beta\lambda\delta x^{-\delta-1}\left(1 + \lambda x^{-\delta}\right)^{-\beta-1} dx \\ & - \int_0^\infty \left(1 + \lambda x^{-\delta}\right)^{-\beta_1}\left(1 + \lambda x^{-\delta}\right)^{-\beta_2} \beta\lambda\delta x^{-\delta-1}\left(1 + \lambda x^{-\delta}\right)^{-\beta-1} dx \\ R = {} & \beta\int_0^\infty \lambda\delta x^{-\delta-1}\left(1 + \lambda x^{-\delta}\right)^{-(\beta+\beta_1)-1} dx - \beta\int_0^\infty \lambda\delta x^{-\delta-1}\left(1 + \lambda x^{-\delta}\right)^{-(\beta+\beta_1+\beta_2)-1} dx \end{aligned}$$

Similarly, from equation (3) we can get:

$$R = \frac{\beta}{\beta+\beta_1} - \frac{\beta}{\beta+\beta_1+\beta_2} = \frac{\beta\beta_2}{(\beta+\beta_1)(\beta+\beta_1+\beta_2)} \quad (7)$$

The behavior of reliability is illustrated in the following figures with different values of the three distribution shape parameters. The reliability behavior is illustrated in the following figures with different values of the three shape parameters of the distribution. The purpose of explaining this behavior is to know how much confidence we have in the component to work under certain conditions and to continue doing this work according to the special terms of the model.

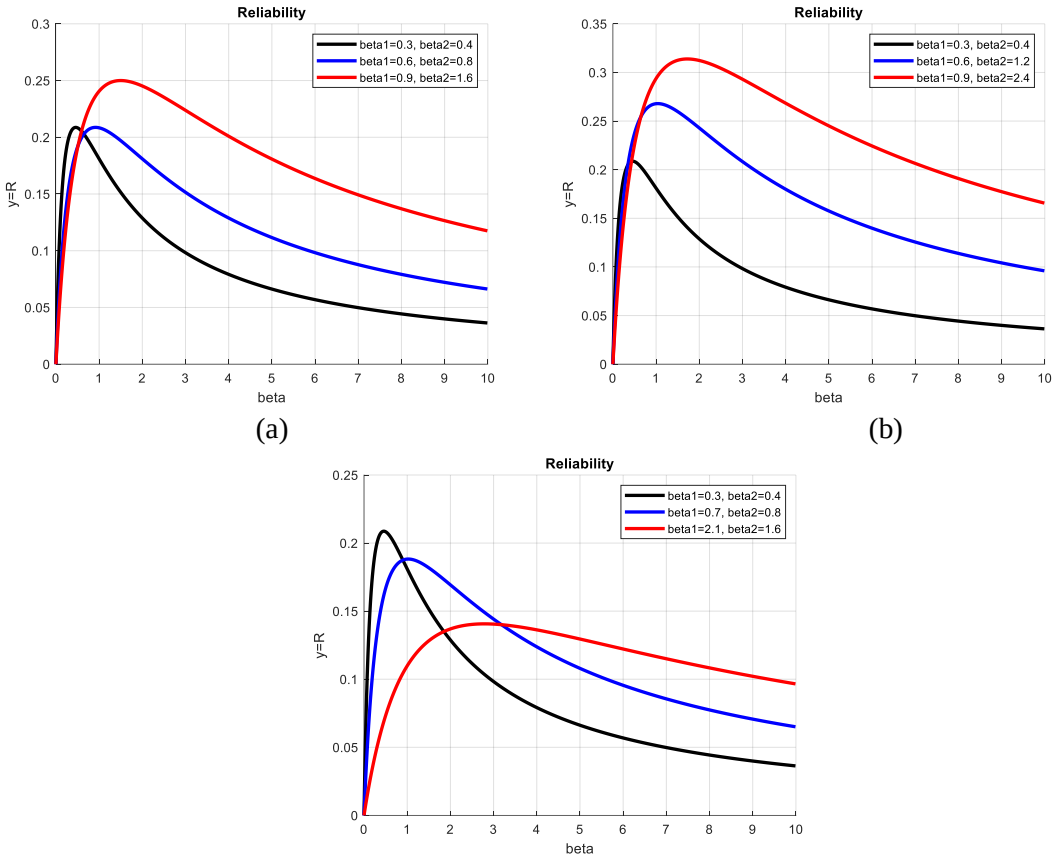

Figure 1 : The Reliability curve against parameter β

Figure (1-a,b,c) shows the change of reliability curve by the effect of different values of the strength parameter β as a function of the parameters $(\beta, \beta_1, \beta_2)$, in three different cases for the values of the two parameters β_1, β_2, where reliability value increasing with the increasing in the value of the strength shape parameter β, then it gradually decreases.

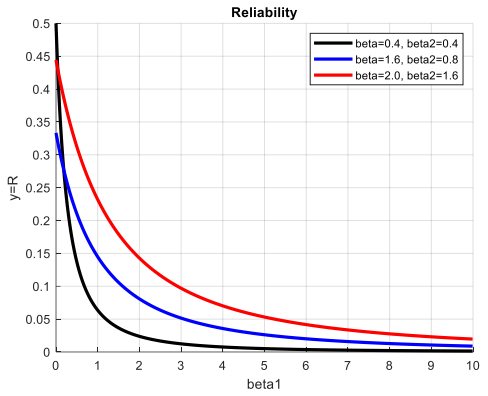

(a)

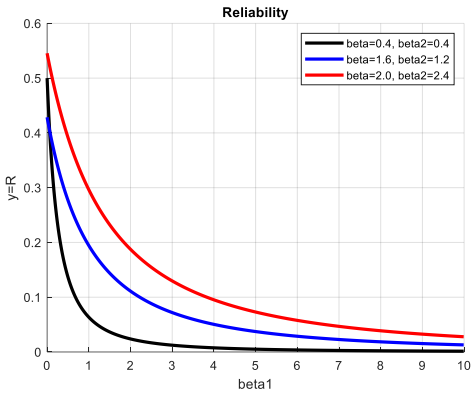

(b)

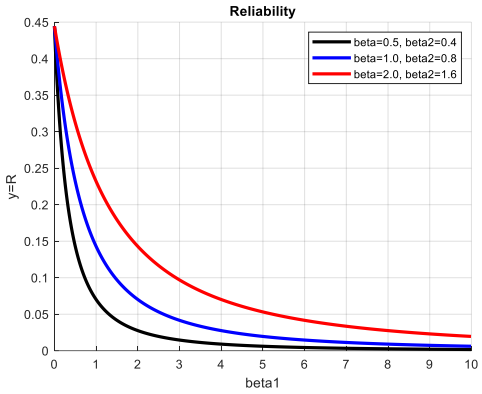

(c)

Figure 2 : The Reliability curve against parameter β_1

Figure (2-a,b,c) shows the effect of the stress parameter value β_1 on the change of the reliability curve as a function of the parameters $(\beta, \beta_1, \beta_2)$, in three different cases for the values of the two parameters β, β_2, where reliability value decreasing and its decrease is steep with increasing value of stress shape parameter β_1.

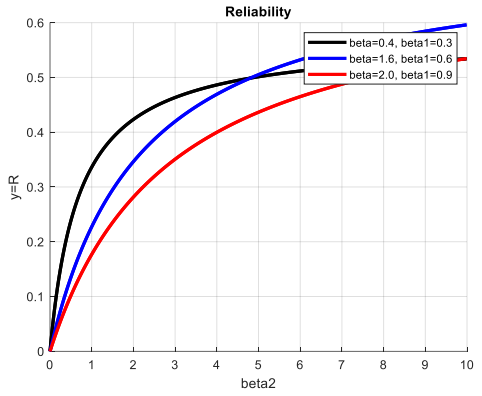

(a)

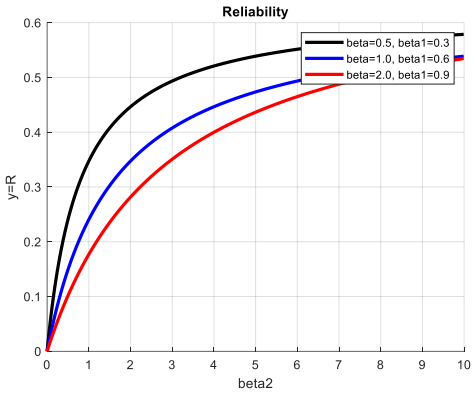

(b)

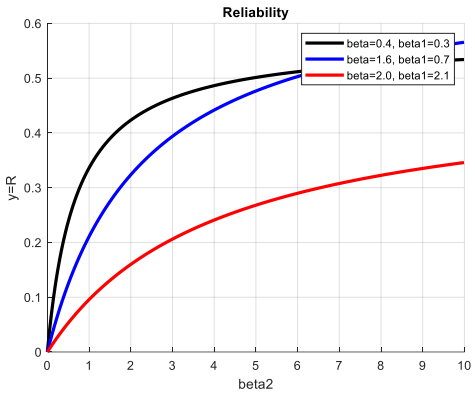

(c)

Figure 3 : The Reliability curve against parameter β_2

Figure (3-a,b,c) shows the effect of the stress parameter value β_2 on the change of the reliability curve as a function of the parameters $(\beta, \beta_1, \beta_2)$, in three different cases for the values of the two parameters β, β_1, where reliability value increasing with increasing value of stress shape parameter β_2 , but it reaches a certain point and then begins to decrease.

3.Estimation Method:

In this section three different estimation methods are used to find the estimator of the Dagum unknown shape parameter; β, β_1, β_2 and the Reliability; R of the stress-strength model. These methods are Maximum Likelihood, Regression Method and Method of Moment. These methods are used to arrive at the best reliability estimate.

3.1. Maximum likelihood estimator (ML)

The maximum likelihood method is the most widely used method for parameter estimation. There is no doubt that the success of the method stems from many desirable characteristics including consistency, asymptotic, efficiency, invariance and simply its intuitive appeal [2]. Let $x_1, x_2, \dots, x_n$ be a random strength sample of size (n) from $Dag(\beta, \lambda, \delta)$ where β is unknown parameter and λ, δ are known. Then the ML function is given by :[4]

$$L(x_1, x_2, \dots, x_n; \beta, \lambda, \delta) = (\beta\lambda\delta)^n \prod_{i=1}^{n} x_i^{-\delta-1} \left(1 + \lambda x_i^{-\delta}\right)^{-\beta-1} \quad (8)$$

Then the natural logarithm function for equation (8) can be written as:

$$\begin{aligned} \ln L &= n\ln(\beta\lambda\delta) - (\delta+1)\sum_{i=1}^{n}\ln(x_i) - (\beta+1)\sum_{i=1}^{n}\ln(1+\lambda x_i^{-\delta}) \\ &= n\ln\beta + n\ln\lambda + n\ln\delta - \delta\sum_{i=1}^{n}\ln(x_i) - \sum_{i=1}^{n}\ln(x_i) \\ &\quad -\beta\sum_{i=1}^{n}\ln\left(1+\lambda x_i^{-\delta}\right) - \sum_{i=1}^{n}\ln\left(1+\lambda x_i^{-\delta}\right) \end{aligned} \quad (9)$$

By differentiate (9) with respect to the unknown parameter β and equating the result to zero, we obtain:

$$\frac{\partial \ln L}{\partial \beta} = \frac{n}{\beta} - \sum_{i=1}^{n}\ln\left(1+\lambda x_i^{-\delta}\right)$$
$$\frac{n}{\hat{\beta}} - \sum_{i=1}^{n}\ln\left(1+\lambda x_i^{-\delta}\right) = 0$$
$$\frac{n}{\hat{\beta}} = \sum_{i=1}^{n}\ln\left(1+\lambda x_i^{-\delta}\right)$$

$$\hat{\beta}_{ML} = \frac{n}{\sum_{i=1}^{n} \ln(1+\lambda x_i^{-\delta})} \quad (10)$$

In the same way , let $t_1, t_2, \dots, t_m$ and $z_1, z_2, \dots, z_m$ be a stress random samples of size (m) from $Dag(\beta_1, \lambda, \delta)$ and $Dag(\beta_2, \lambda, \delta)$, respectively and the ML estimator of the unknown parameters β_1, β_2 are :[4]

$$\hat{\beta}_{1ML} = \frac{m}{\sum_{j=1}^{m} \ln\left(1+\lambda t_j^{-\delta}\right)} \quad (11)$$

$$\hat{\beta}_{2ML} = \frac{m}{\sum_{k=1}^{m} \ln(1+\lambda z_k^{-\delta})} \quad (12)$$

By substituting (10), (11) and (12) in equation (7), we can obtain the ML reliability estimator based on invariance property as:

$$\hat{R}_{ML} = \frac{\hat{\beta}_{2ML}\hat{\beta}_{ML}}{(\hat{\beta}_{1ML}+\hat{\beta}_{ML})(\hat{\beta}_{1ML}+\hat{\beta}_{2ML}+\hat{\beta}_{ML})}$$

3.2. Regression Method (Rg)

Linear Regression is one of the important procedures that use auxiliary information to construct estimators with good efficiency. The standard regression equation [8]:

$$z_i = a + bu_i + e_i \quad (13)$$

Where z_i is dependent variable, u_i is independent variable and e_i is the error term and represent identically distributed random variable and a,b are called regression coefficients where a is the intercept and b is the slop [10].

Let $x_1, x_2, \dots, x_n$ be a random strength sample of size (n) from $Dag(\beta, \lambda, \delta)$. Then the Rg estimators of the unknown parameter β, can be obtained by taking the natural logarithm to equation (1):

$$\ln\left(F(x_i)\right) = -\beta \ln\left(1 + \lambda x_i^{-\delta}\right) \quad (14)$$

Substituted plotting position P_i instead of $F(x_i)$ in equation (14), we get:

$$\ln(P_i) = -\beta \ln\left(1 + \lambda x_i^{-\delta}\right) \quad (15)$$

Where $P_i = \frac{i}{n+1}$, $i = 1,2, \dots, n$

By the comparison between equation (15) and equation (13), we can get:

$$z_i = \ln(P_i)\,,\ a = 0\,,\ b = \beta\,,\ u_i = -\ln\left(1 + \lambda x_i^{-\delta}\right) \quad (16)$$

Where b can be estimated by minimizing the summation of squared error with respect to b, then we get:[5]

$$\hat{b} = \frac{n\sum_{i=1}^{n} z_i u_i - \sum_{i=1}^{n} z_i \sum_{i=1}^{n} u_i}{n\sum_{i=1}^{n} [u_i]^2 - \left[\sum_{i=1}^{n} u_i\right]^2} \quad (17)$$

By substitution (16) in (17), the Rg estimator for the unknown parameter β, $\hat{\beta}_{\mathrm{Rg}}$ is:

$$\hat{\beta}_{\mathrm{Rg}} = \frac{-n\sum_{i=1}^{n} \ln(P_i) \ln\left(1+\lambda x_i^{-\delta}\right) + \sum_{i=1}^{n} \ln(P_i) \sum_{i=1}^{n} \ln\left(1+\lambda x_i^{-\delta}\right)}{n\sum_{i=1}^{n} \left[\ln\left(1+\lambda x_i^{-\delta}\right)\right]^2 - \left[\sum_{i=1}^{n} \ln\left(1+\lambda x_i^{-\delta}\right)\right]^2} \quad (18)$$

In the same step above, we will estimate the unknown parameters $\beta_1$and β_2 as follows:

$$\hat{\beta}_{1\mathrm{Rg}} = \frac{-m\sum_{j=1}^{m} \ln(P_j) \ln\left(1+\lambda t_j^{-\delta}\right) + \sum_{j=1}^{m} \ln(P_j) \sum_{j=1}^{m} \ln\left(1+\lambda t_j^{-\delta}\right)}{m\sum_{j=1}^{m} \left[\ln\left(1+\lambda t_j^{-\delta}\right)\right]^2 - \left[\sum_{j=1}^{m} \ln\left(1+\lambda t_j^{-\delta}\right)\right]^2} \quad (19)$$

$$\hat{\beta}_{2\mathrm{Rg}} = \frac{-m\sum_{k=1}^{m} \ln(P_k) \ln\left(1+\lambda z_k^{-\delta}\right) + \sum_{k=1}^{m} \ln(P_k) \sum_{k=1}^{m} \ln\left(1+\lambda z_k^{-\delta}\right)}{m\sum_{k=1}^{m} \left[\ln\left(1+\lambda z_k^{-\delta}\right)\right]^2 - \left[\sum_{k=1}^{m} \ln\left(1+\lambda z_k^{-\delta}\right)\right]^2} \quad (20)$$

Where $P_j = \frac{j}{m+1}$, $j = 1,2, \dots, m$ and $P_k = \frac{k}{m+1}$, $k = 1,2, \dots, m$

By substitution equations (18),(19) and (20) in equation (7), we obtain the Rg estimator for reliability approximately as:

$$\hat{R} = \frac{\hat{\beta}_{2Rg}\hat{\beta}_{Rg}}{(\hat{\beta}_{1Rg}+\hat{\beta}_{Rg})(\hat{\beta}_{1Rg}+\hat{\beta}_{2Rg}+\hat{\beta}_{Rg})}$$

3.3. Method of Moment (MOM)

The Method of Moment was introduced by Pearson in (1894). It was one of the first methods used to estimate a population parameter [8]. To derived the method of moment estimators of parameters of Dagum, let $x_1, x_2, \dots, x_n$ be a strength random sample of size (n) from $Dag(\beta, \lambda, \delta)$ and let $t_1, t_2, \dots, t_m$ and $z_1, z_2, \dots, z_m$ be a stress random samples of size (m) from $Dag(\beta_1, \lambda, \delta)$ and $Dag(\beta_2, \lambda, \delta)$, respectively. Then their population means when $\delta > 1$ are given by:[2]

$$E(x) = \beta\, \lambda^{\frac{1}{\delta}}\, B\left(1-\frac{1}{\delta}, \beta+\frac{1}{\delta}\right)$$
$$E(t) = \beta_1\, \lambda^{\frac{1}{\delta}}\, B\left(1-\frac{1}{\delta}, \beta_1+\frac{1}{\delta}\right)$$
$$E(z) = \beta_2\, \lambda^{\frac{1}{\delta}}\, B\left(1-\frac{1}{\delta}, \beta_2+\frac{1}{\delta}\right)$$

According to the method of moment, equating the samples mean with the corresponding populations mean, then the moment estimators of β, β_1, β_2 are:

$$\hat{\beta}_{MOM} = \frac{\bar{x}}{\lambda^{\frac{1}{\delta}} B\left(1-\frac{1}{\delta}, \beta_0+\frac{1}{\delta}\right)} \quad (21)$$

$$\hat{\beta}_{1MOM} = \frac{\bar{t}}{\lambda^{\frac{1}{\delta}} B\left(1-\frac{1}{\delta}, \beta_{1_0}+\frac{1}{\delta}\right)} \quad (22)$$

$$\hat{\beta}_{2MOM} = \frac{\bar{z}}{\lambda^{\frac{1}{\delta}} B\left(1-\frac{1}{\delta}, \beta_{2_0}+\frac{1}{\delta}\right)} \quad (23)$$

By substitution equation (21),(22) and (23) in equation (7), we can obtain the approximate estimator of R as bellow:

$$\hat{R}_{MOM} = \frac{\hat{\beta}_{2MOM}\hat{\beta}_{MOM}}{(\hat{\beta}_{1MOM}+\hat{\beta}_{MOM})(\hat{\beta}_{1MOM}+\hat{\beta}_{2MOM}+\hat{\beta}_{MOM})}$$

4.Simulation study

In this section, a simulation study is used to determine the best estimate of the reliability with unknown parameters of the Dagum distribution, and to performance the three different estimates from the maximum likelihood, regression method and the method of moment; where the estimators of regression was used as initial value, are evaluated by using the mean square error criteria (MSE), with different sample sizes (15,30,90) and $(\lambda = 2, 4, 0.5; \delta = 2, 1.2, 5)$, for four different experiments in each case of the parameters value λ and δ.

For the twelve different experiments, a simulation study is conducted by using MATLAB 2020 to compare the performance of the reliability estimators by the following steps:

Step1: Generating the random values of the random variables by the inverse function according to the following formula: $x = \left[\left(F(x)^{-1/\beta} - 1\right)/\lambda\right]^{-1/\delta}$

Step2: Calculate the mean by the equation: Mean $= \frac{\sum_{i=1}^{N} \hat{R}_i}{N}$

Step3: The comparison of estimation methods is done by using the mean square error criteria: MSE$= \frac{1}{N}\sum_{i=1}^{N}\left(\hat{R}_i - R\right)^2$, where N the number of replication in each experiment is 1000.

The results are recorded in the following tables from 1 to 3. The comparison of these estimator's performance based on the MSE values, has been observed as:

1- In table (1) and for experiments (1), (2), (3) and (4), the value of MSE decreases with increasing sample sizes for each of MLE, Rg and MOM. The best value of MSE is MLE, followed by Rg, MOM.
2- In table (2) and for experiments (5), (6), (7) and (8), the value of MSE decreases with increasing sample sizes for each of MLE, Rg and MOM. The best value of MSE is MLE, followed by Rg, MOM.
3- In table (3) and for experiments (10) and (11), the value of MSE decreases with increasing sample sizes for each of MLE, Rg and MOM. The best value of MSE is MLE, followed by Rg, MOM, but in the case of experiments (9) and (12), the best value of MSE was for the MOM, followed by MLE, Rg.

Thus, the estimators of the maximum likelihood method give better performance than those of the regression and moment methods through the small values of the MSE for most of the experiments, except for experiments (9) and (12) in which the moment method is the best.

Table 1: Estimate for Reliability when $\lambda = 2, \delta = 2$

Exp.1: $\boldsymbol{\beta = 1.2}$, $\boldsymbol{\beta_1 = 0.6, \beta_2 = 0.6}$ $\boldsymbol{R = 0.1667}$							**Exp.2: $\boldsymbol{\beta = 0.9}$, $\boldsymbol{\beta_1 = 0.3, \beta_2 = 0.9}$ $\boldsymbol{R = 0.3214}$**			
n	m		MLE	Rg	MOM	Best	MLE	Rg	MOM	Best
15	15	Mean	0.1640	0.1667	0.1680		0.3165	0.3110	0.2904	
		MSE	0.0019	0.0035	0.0042	MLE	0.0035	0.0067	0.0081	MLE
30	30	Mean	0.1674	0.1678	0.1685		0.3188	0.3163	0.2897	
		MSE	0.0009	0.0020	0.0023	MLE	0.0017	0.0042	0.0053	MLE
90	90	Mean	0.1676	0.1672	0.1720		0.3206	0.3193	0.2916	
		MSE	0.0003	0.0008	0.0013	MLE	0.0006	0.0016	0.0031	MLE
30	15	Mean	0.1687	0.1701	0.1732		0.3199	0.3181	0.2962	
		MSE	0.0018	0.0037	0.0039	MLE	0.0035	0.0066	0.0084	MLE
15	90	Mean	0.1634	0.1578	0.1669		0.3152	0.3046	0.2895	
		MSE	0.0003	0.0009	0.0010	MLE	0.0009	0.0023	0.0031	MLE
30	90	Mean	0.1655	0.1625	0.1678		0.3184	0.3127	0.2887	
		MSE	2.9340e-04	8.4170e-04	8.8600e-04	MLE	0.0007	0.0018	0.0030	MLE
		Exp.3: $\boldsymbol{\beta = 2.5}$, $\boldsymbol{\beta_1 = 2.5, \beta_2 = 1.0}$ $\boldsymbol{R = 0.0833}$					**Exp.4: $\boldsymbol{\beta = 1.6}$, $\boldsymbol{\beta_1 = 0.4, \beta_2 = 0.8}$ $\boldsymbol{R = 0.2286}$**			
15	15	Mean	0.0848	0.0858	0.0977		0.2268	0.2295	0.2291	
		MSE	0.0007	0.0015	0.0020	MLE	0.0028	0.0053	0.0063	MLE
30	30	Mean	0.0830	0.0840	0.0958		0.2281	0.2281	0.2279	
		MSE	0.0004	0.0008	0.0011	MLE	0.0013	0.0032	0.0034	MLE
90	90	Mean	0.0835	0.0833	0.0962		0.2272	0.2270	0.2247	
		MSE	1.1620e-04	3.2390e-04	5.4940e-04	MLE	0.0005	0.0011	0.0013	MLE
30	15	Mean	0.0859	0.0891	0.0981		0.2301	0.2342	0.2258	
		MSE	0.0007	0.0015	0.0019	MLE	0.0025	0.0051	0.0049	MLE
15	90	Mean	0.0829	0.0826	0.0951		0.2254	0.2174	0.2246	
		MSE	1.2100e-04	3.2970e-04	5.2130e-04	MLE	0.0008	0.0020	0.0017	MLE
30	90	Mean	0.0828	0.0826	0.0968		0.2281	0.2232	0.2240	
		MSE	1.2180e-04	3.0800e-04	7.0930e-04	MLE	0.0006	0.0015	0.0016	MLE

Table 2: Estimate for Reliability when $\lambda = 4, \delta = 1.2$

Exp.5: $\boldsymbol{\beta = 1.2}$, $\boldsymbol{\beta_1 = 0.6, \beta_2 = 0.6}$ $\boldsymbol{R = 0.1667}$							Exp.6: $\boldsymbol{\beta = 0.9}$, $\boldsymbol{\beta_1 = 0.3, \beta_2 = 0.9}$ $\boldsymbol{R = 0.3214}$			
n	m		MLE	Rg	MOM	Best	MLE	Rg	MOM	Best
15	15	Mean	0.1653	0.1651	0.1682		0.3110	0.3076	0.2956	
		MSE	0.0017	0.0035	0.0137	MLE	0.0037	0.0064	0.0235	MLE
30	30	Mean	0.1653	0.1646	0.1660		0.3166	0.3136	0.3029	
		MSE	0.0009	0.0019	0.0108	MLE	0.0017	0.0038	0.0187	MLE
90	90	Mean	0.1656	0.1661	0.1621		0.3221	0.3214	0.3113	
		MSE	0.0003	0.0007	0.0069	MLE	0.0006	0.0017	0.0143	MLE
30	15	Mean	0.1673	0.1697	0.1710		0.3157	0.3115	0.3052	
		MSE	0.0018	0.0038	0.0134	MLE	0.0038	0.0071	0.0257	MLE
15	90	Mean	0.1635	0.1587	0.1673		0.3158	0.3057	0.3032	
		MSE	0.0004	0.0009	0.0069	MLE	0.0009	0.0026	0.0134	MLE
30	90	Mean	0.1657	0.1630	0.1696		0.3196	0.3148	0.3022	
		MSE	0.0003	0.0008	0.0076	MLE	0.0007	0.0017	0.0134	MLE
		Exp.7: $\boldsymbol{\beta = 2.5}$, $\boldsymbol{\beta_1 = 2.5, \beta_2 = 1.0}$ $\boldsymbol{R = 0.0833}$					**Exp.8:** $\boldsymbol{\beta = 1.6}$, $\boldsymbol{\beta_1 = 0.4, \beta_2 = 0.8}$ $\boldsymbol{R = 0.2286}$			
15	15	Mean	0.0837	0.0846	0.0935		0.2306	0.2267	0.2353	
		MSE	0.0007	0.0015	0.0052	MLE	0.0027	0.0048	0.0209	MLE
30	30	Mean	0.0835	0.0848	0.0931		0.2286	0.2282	0.2321	
		MSE	0.0004	0.0008	0.0055	MLE	0.0014	0.0031	0.0180	MLE
90	90	Mean	0.0841	0.0849	0.0919		0.2290	0.2303	0.2315	
		MSE	0.0001	0.0003	0.0039	MLE	0.0004	0.0013	0.0108	MLE
30	15	Mean	0.0860	0.0861	0.0986		0.2343	0.2374	0.2288	
		MSE	0.0008	0.0015	0.0071	MLE	0.0028	0.0057	0.0194	MLE
15	90	Mean	0.0825	0.0816	0.0842		0.2232	0.2133	0.2358	
		MSE	0.0001	0.0003	0.0032	MLE	0.0010	0.0022	0.0116	MLE
30	90	Mean	0.0835	0.0835	0.0907		0.2261	0.2226	0.2255	
		MSE	0.0001	0.0003	0.0035	MLE	0.0006	0.0015	0.0115	MLE

Table 3: Estimate for Reliability when $\lambda = 0.5, \delta = 5$

Exp.9: $\boldsymbol{\beta = 1.2}$, $\boldsymbol{\beta_1 = 0.6, \beta_2 = 0.6}$ $\boldsymbol{R = 0.1667}$							**Exp.10:** $\boldsymbol{\beta = 0.9}$, $\boldsymbol{\beta_1 = 0.3, \beta_2 = 0.9}$ $\boldsymbol{R = 0.3214}$			
n	m		MLE	Rg	MOM	Best	MLE	Rg	MOM	Best
15	15	Mean	0.1643	0.1644	0.1684		0.3166	0.3121	0.2750	
		MSE	0.0018	0.0033	0.0011	MOM	0.0036	0.0066	0.0041	MLE
30	30	Mean	0.1657	0.1680	0.1702		0.3181	0.3146	0.2733	
		MSE	0.0008	0.0019	0.0005	MOM	0.0018	0.0039	0.0033	MLE
90	90	Mean	0.1673	0.1674	0.1712		0.3203	0.3186	0.2725	
		MSE	2.8460e-04	7.8490e-04	2.2200e-04	MOM	0.0006	0.0017	0.0028	MLE
30	15	Mean	0.1664	0.1660	0.1692		0.3229	0.3204	0.2797	
		MSE	0.0018	0.0034	0.0011	MOM	0.0036	0.0069	0.0038	MLE
15	90	Mean	0.1636	0.1591	0.1681		0.3158	0.3059	0.2693	
		MSE	3.2260e-04	8.5930e-04	1.8590e-04	MOM	0.0008	0.0022	0.0031	MLE
30	90	Mean	0.1652	0.1625	0.1693		0.3184	0.3142	0.2718	
		MSE	3.2020e-04	8.0850e-04	2.0100e-04	MOM	0.0007	0.0019	0.0028	MLE
		Exp.11: $\boldsymbol{\beta = 2.5}$, $\boldsymbol{\beta_1 = 2.5, \beta_2 = 1.0}$					**Exp.12:** $\boldsymbol{\beta = 1.6}$, $\boldsymbol{\beta_1 = 0.4, \beta_2 =}$			

		$R = 0.0833$				0.8 $R = 0.2286$			
15	15	Mean	0.0844	0.0859	0.0977	0.2272	0.2286	0.2205	
		MSE	0.0007	0.0015	0.0010 MLE	0.0029	0.0055	0.0018	MOM
30	30	Mean	0.0839	0.0836	0.0971	0.2289	0.2292	0.2214	
		MSE	3.6820e-04	8.7610e-04	6.5100e-04 MLE	0.0014	0.0029	0.0008	MOM
90	90	Mean	0.0837	0.0842	0.0983	0.2295	0.2283	0.2206	
		MSE	1.1930e-04	3.3660e-04	3.8760e-04 MLE	0.0004	0.0011	0.0003	MOM
30	15	Mean	0.0846	0.0857	0.0963	0.2287	0.2334	0.2222	
		MSE	0.0008	0.0016	0.0010 MLE	0.0027	0.0052	0.0017	MOM
15	90	Mean	0.0824	0.0819	0.0970	0.2239	0.2132	0.2134	
		MSE	1.1950e-04	3.3610e-04	3.5110e-04 MLE	0.0008	0.0021	0.0007	MOM
30	90	Mean	0.0836	0.0836	0.0983	0.2274	0.2216	0.2179	
		MSE	1.1860e-04	3.4830e-04	3.9180e-04 MLE	0.0006	0.0015	0.0004	MOM

5.Conclusion

In this paper, three methods are used to estimate reliability P (T< X< Z) as each of T, Z and X follow the Dagum distribution with different parameters, and these methods are the maximum likelihood, regression method and method of moment. A simulation study was conducted, and through the results that appeared in the twelve experiments, it was found that the estimators of the maximum likelihood method give better performance than those of the regression and moment methods through the small values of the MSE for most of the experiments, except for experiments (9) and (12) in which the moment method is the best. Thus, the simulation results confirm that the performance of the maximum likelihood estimator is much better than the estimators of the regression and moment methods for most experiments and for various sample sizes.

References

[1] Abd AL-Fattah, A. M., El-Helbawy, A. A., and Al-Dayian, G. R. 2017 Inverted Kumaraswamy Distribution: Properties and Estimation. *Pakistan Journal of Statistics* **33(1)**

[2] Dey S., Al-Zahrani, B. and Basloom, S. 2017 Dagum distribution Properties and different methods of estimation *International Journal of Statistics and Probability* **6(2)** 74-92

[3] Dutta K. and Sriwastav G. L. 1986 An n-standby system with P (X< Y< Z) *IAPQR Transaction* **12** 95-97

[4] Fulment A. K., Josephat P. K., and Rao, G. S. 2017 Estimation of Reliability in Multicomponent Stress-Strength Based on Dagum Distribution *Stochastics and Quality Control* **32(2)** 77-85

[5] Hameed B. A., Salman A. N., and Kalaf B. A. 2020) On Estimation of P ($Y_1 < X < Y_2$) in Cased Inverse Kumaraswamy Distribution *Iraqi Journal of Science* 845-853

[6] Hassan A. S., Elsherpieny E. A., and Shalaby R. M. 2013 On the estimation of P (Y< X< Z) for Weibull distribution in the presence of k outliers *International Journal of Engineering Research and Applications* **3** 1727-1733

[7] Ivshin V. V. 1998 On the estimation of the probabilities of a double linear inequality in the case of uniform and two-parameter exponential distributions *Journal of Mathematical Sciences* **88(6)** 819-827

[8] Karam N. S., and Jani H. H. 2016 Estimation of Reliability in Multi-Component Stress-Strength Model Following Burr-III Distribution *Journal of College of Education* **1** 329-342

[9] Kotz S., and Pensky, M. 2003 The stress-strength model and its generalizations: theory and applications *World Scientific*

[10] Montgomery D. C., Peck E. A., and Vining, G. G. 2012 Introduction to linear regression analysis *John Wiley and Sons* **821**
[11] Singh N., 1980 On the Estimation of $\boldsymbol{P(X_1 < Y < X_2)}$ *Communication in Statistics-Theory and Methods* **19(15)** 1551-1561

Reliability of n-Cascade Stress-Strength P(X<Y<Z) System for four different distributions

Reliability of n- Cascade Stress -Strength P(X<Y<Z) System for four different distributions

Nada S. Karam , Shahbaa M. Yousif

Department of Mathematics, College of Education, Mustansiriyah University, Baghdad - Iraq

E-mail: shahbaa.m.shkr@gmail.com

Abstract. In this paper, the n- cascade with P(X<Y<Z) is used to find the reliability of stress-strength system, where X and Z are the strengths of a component subjected to stress Y. The n-cascade stress-strength system reliability expression is obtained for four different distributions which are [Exponential Pareto, Inverted Exponential, Exponentiated Invers Rayleigh, Frechet]. For some specific values of the parameters of the distribution, the numerical values of the four different reliabilities have also been computed, provided, and discussed.

1. Introduction

The reliability of the stress-strength system model component is defined as the probability that the stress Yworking on it, is not greater than strength$X$, where both x and y are random variables, so$R = P(X \geq Y)$. But here we consider the case that a component (or system) can work only when the stressY on it is lies between two certain values of components (or systems) strengths (say X and Z), i.e. stress is within certain limits see [4],[6] and [7].

Under this system, the reliability can be defined as:

$R = P(X < Y < Z)$

Where $X$and Z are the component strengths (DMGO calls them lower and upper strengths), and Y is the stress on this component all X, Y, and Z are random variables.

In the source, Singh [7] has considered the reliability estimation under the assumption that the strength of a component y lies in an interval between two stress (X_1 and X_2). i.e. $R = P(X_1 < Y < X_2)$

The main aim of this paper is to obtain the reliability of the n-cascade stress-strength systemR_n, where stress on the component is subjected to two strengths. The general model reliability is illustrated in **section2**, the reliabilities obtained for four different distributions [Exponential Pareto, Inverted Exponential, Exponentiated Invers Rayleigh, Frechet] are given in section3. Finally, the results and discussions of some numerical values of the reliabilities are given in section4.

2. n-Cascade with P(X<Y<Z) System Reliability

After every failure in the cascade system, the stress is modified by a factor (k)[5]. Let $y_i; i = 1, \dots, n$ be the stress on n-components, then

$y_2 = ky_1$, $y_3 = ky_2 = k^2y_1$, …, $y_i = k^{i-1}y_1$

The ith component works if the stress $k^{i-1}y_1$ lie in the interval (x_i, z_i) the lower and upper strength of $i = 1, \dots, n$ components, respectively. Whenever it falls outside these two limits, the component fails and another from standby takes the place of the failed component and the system continues to work until the n component in cascade fails [4]. Assuming the components work independently then.

$R_n = R(1) + R(2) + \cdots + R(n)$ … (1)

Where $R(r)$ is the marginal reliability of rth component.

Let $x_i, z_i \; and \; y_i; i = 1,2, \dots, n$ are independent random variables with F(x) , H(z) cumulative distribution functions (cdf) and g(y_1) probability density function (pdf), then

$$R(1) = P(x < y_1 < z) = P(y_1 > x) - P(y_1 > x, y_1 > z)$$

$$= \int_{y_1} F_x(y_1) g(y_1) dy_1 - \int_{y_1} F_x(y_1) H_z(y_1) g(y_1) dy_1 \quad \dots (2)$$

And

$$R(2) = P(x < y_1 < z)^c P(x < y_2 < z)$$

$$= [1 - R(1)][P((y_2 = ky_1) > x) - P(ky_1 > x, ky_1 > z)]$$

$$= [1 - R(1)] \left[\int_{y_1} F_x(ky_1) g(y_1) dy_1 - \int_{y_1} F_x(ky_1) H_z(ky_1) g(y_1) dy_1 \right] \dots (3)$$

Similarly

$$R(3) = [1 - R(1)][1 - R(2)]$$

$$\left[\int_{y_1} F_x(k^2y_1) g(y_1) dy_1 - \int_{y_1} F_x(k^2y_1) H_z(k^2y_1) g(y_1) dy_1\right] \quad \dots (4)$$

In general

$$R(n) = \big(1 - R(1)\big)\big(1 - R(2)\big) \dots (1 - R(n-1))$$

$$\left[\int_{y_1} F_x(k^{n-1}y_1) g(y_1) dy_1 - \int_{y_1} F_x(k^{n-1}y_1) H_z(k^{n-1}y_1) g(y_1) dy_1\right] \quad \dots (5)$$

3. Specific Distributions

In this section, we involve four different distributions for the random stress and strengths variables to obtain the mathematical expressions of reliabilities in equations (2-5) and then n-cascade system reliability in the equation (1).

3.1. Exponential Pareto Distribution (EPD)

Let the strengths random variables $X$and Z are independent identically distributed with EPD $(\rho, \lambda_1, \theta)$ and EPD $(\rho, \lambda_2, \theta)$, respectively, with cumulative distribution function (cdf) given as[2] and [3]:

$$F(x) = 1 - e^{-\lambda_1 \left(\frac{x}{\rho}\right)^{\theta}}, \qquad x > 0$$

$$H(z) = 1 - e^{-\lambda_2 \left(\frac{z}{\rho}\right)^{\theta}}, \qquad z > 0$$

And let $y_1$be EP (ρ, λ, θ) random stress variable with probability density function (pdf) given as:

$$g(y_1) = \frac{\lambda\theta}{\rho}\left(\frac{y_1}{\rho}\right)^{\theta-1} e^{-\lambda\left(\frac{y_1}{\rho}\right)^{\theta}}, \qquad y_1 > 0$$

Where $\int_{y_1}\left(\frac{y_1}{\rho}\right)^{\theta-1} e^{-\lambda\left(\frac{y_1}{\rho}\right)^{\theta}} dy_1 = \frac{\rho}{\lambda\theta}$

Since $g(y_1)$ is pd function.
Then from equation (2), we have.

$R(1) = A_1 - B_1$

Then

$$A_1 = \int_{y_1}\left(1 - e^{-\lambda_1\left(\frac{y_1}{\rho}\right)^{\theta}}\right)\frac{\lambda\theta}{\rho}\left(\frac{y_1}{\rho}\right)^{\theta-1} e^{-\lambda\left(\frac{y_1}{\rho}\right)^{\theta}} dy_1$$

$$= 1 - \frac{\lambda\theta}{\rho}\int_{y_1}\left(\frac{y_1}{\rho}\right)^{\theta-1} e^{-(\lambda+\lambda_1)\left(\frac{y_1}{\rho}\right)^{\theta}} dy_1$$

$$= 1 - \frac{\lambda\theta}{\rho}\frac{\rho}{(\lambda+\lambda_1)\theta} = 1 - \frac{\lambda}{(\lambda+\lambda_1)}$$

$$B_1 = \int_{y_1} F_x(y_1)H_z(y_1)g(y_1)dy_1$$

$$= \int_{y_1}\left(1 - e^{-\lambda_1\left(\frac{y_1}{\rho}\right)^{\theta}}\right)\left(1 - e^{-\lambda_2\left(\frac{y_1}{\rho}\right)^{\theta}}\right)g(y_1)dy_1$$

$$= \int_{y_1}\left(1 - e^{-\lambda_1\left(\frac{y_1}{\rho}\right)^{\theta}} - e^{-\lambda_2\left(\frac{y_1}{\rho}\right)^{\theta}} + e^{-(\lambda_1+\lambda_2)\left(\frac{y_1}{\rho}\right)^{\theta}}\right)g(y_1)dy_1$$

$$= 1 - \frac{\lambda\theta}{\rho}\int_{y_1}\left(\frac{y_1}{\rho}\right)^{\theta-1} e^{-(\lambda+\lambda_1)\left(\frac{y_1}{\rho}\right)^{\theta}} dy_1 - \frac{\lambda\theta}{\rho}\int_{y_1}\left(\frac{y_1}{\rho}\right)^{\theta-1} e^{-(\lambda+\lambda_2)\left(\frac{y_1}{\rho}\right)^{\theta}} dy_1$$

$$+ \frac{\lambda\theta}{\rho}\int_{y_1}\left(\frac{y_1}{\rho}\right)^{\theta-1} e^{-(\lambda+\lambda_1+\lambda_2)\left(\frac{y_1}{\rho}\right)^{\theta}} dy_1$$

$$= 1 - \frac{\lambda\theta}{\rho}\frac{\rho}{(\lambda+\lambda_1)\theta} - \frac{\lambda\theta}{\rho}\frac{\rho}{(\lambda+\lambda_2)\theta} + \frac{\lambda\theta}{\rho}\frac{\rho}{(\lambda+\lambda_1+\lambda_2)\theta}$$

$$B_1 = 1 - \frac{\lambda}{(\lambda+\lambda_1)} - \frac{\lambda}{(\lambda+\lambda_2)} + \frac{\lambda}{(\lambda+\lambda_1+\lambda_2)}$$

Then, we get

$$R(1) = 1 - \frac{\lambda}{(\lambda+\lambda_1)} - 1 + \frac{\lambda}{(\lambda+\lambda_1)} + \frac{\lambda}{(\lambda+\lambda_2)} - \frac{\lambda}{(\lambda+\lambda_1+\lambda_2)}$$

$$= \frac{\lambda}{(\lambda+\lambda_2)} - \frac{\lambda}{(\lambda+\lambda_1+\lambda_2)}$$

And now from equation (3), we have

$$R(2) = [1 - R(1)][A_2 - B_2]$$

$$A_2 = \int_{y_1} F_x(ky_1)g(y_1)dy_1 = \int_{y_1}\left(1 - e^{-\lambda_1\left(\frac{ky_1}{\rho}\right)^{\theta}}\right)g(y_1)dy_1$$

$$= 1 - \frac{\lambda\theta}{\rho}\int_{y_1}\left(\frac{y_1}{\rho}\right)^{\theta-1} e^{-(\lambda+k^{\theta}\lambda_1)\left(\frac{y_1}{\rho}\right)^{\theta}} dy_1$$

$$= 1 - \frac{\lambda\theta}{\rho}\frac{\rho}{(\lambda+k^{\theta}\lambda_1)\theta}$$

$$= 1 - \frac{\lambda}{(\lambda+k^{\theta}\lambda_1)}$$

$$B_2 = \int_{y_1} F_x(ky_1)H_z(ky_1)g(y_1)dy_1$$

$$= \int_{y_1}\left(1 - e^{-\lambda_1\left(\frac{ky_1}{\rho}\right)^{\theta}}\right)\left(1 - e^{-\lambda_2\left(\frac{ky_1}{\rho}\right)^{\theta}}\right)g(y_1)dy_1$$

$$= \int_{y_1}\left(1 - e^{-k^{\theta}\lambda_1\left(\frac{y_1}{\rho}\right)^{\theta}} - e^{-k^{\theta}\lambda_2\left(\frac{y_1}{\rho}\right)^{\theta}} + e^{-k^{\theta}(\lambda_1+\lambda_2)\left(\frac{y_1}{\rho}\right)^{\theta}}\right)g(y_1)dy_1$$

$$B_2 = 1 - \frac{\lambda\theta}{\rho}\int_{y_1}\left(\frac{y_1}{\rho}\right)^{\theta-1} e^{-(\lambda+k^{\theta}\lambda_1)\left(\frac{y_1}{\rho}\right)^{\theta}}dy_1 - \frac{\lambda\theta}{\rho}\int_{y_1}\left(\frac{y_1}{\rho}\right)^{\theta-1} e^{-(\lambda+k^{\theta}\lambda_2)\left(\frac{y_1}{\rho}\right)^{\theta}}dy_1$$

$$+ \frac{\lambda\theta}{\rho}\int_{y_1}\left(\frac{y_1}{\rho}\right)^{\theta-1} e^{-(\lambda+k^{\theta}(\lambda_1+\lambda_2))\left(\frac{y_1}{\rho}\right)^{\theta}}dy_1$$

$$B_2 = 1 - \frac{\lambda\theta}{\rho}\frac{\rho}{(\lambda+k^{\theta}\lambda_1)\theta} - \frac{\lambda\theta}{\rho}\frac{\rho}{(\lambda+k^{\theta}\lambda_2)\theta} + \frac{\lambda\phi}{\rho}\frac{\rho}{(\lambda+k^{\theta}(\lambda_1+\lambda_2))\theta}$$

$$B_2 = 1 - \frac{\lambda}{(\lambda+k^{\theta}\lambda_1)} - \frac{\lambda}{(\lambda+k^{\theta}\lambda_2)} + \frac{\lambda}{(\lambda+k^{\theta}(\lambda_1+\lambda_2))}$$

So, $R(2) = \big(1 - R(1)\big)\left(1 - \frac{\lambda}{(\lambda+k^{\theta}\lambda_1)} - 1 + \frac{\lambda}{(\lambda+k^{\theta}\lambda_1)} + \frac{\lambda}{(\lambda+k^{\theta}\lambda_2)} - \frac{\lambda}{(\lambda+k^{\theta}(\lambda_1+\lambda_2))}\right)$

$$R(2) = \big(1 - R(1)\big)\left(\frac{\lambda}{(\lambda+k^{\theta}\lambda_2)} - \frac{\lambda}{(\lambda+k^{\theta}(\lambda_1+\lambda_2))}\right)$$

Then, $R(3) = [1 - R(1)][1 - R(2)]$

$$R(3) = \big(1 - R(1)\big)\big(1 - R(2)\big)\left(\frac{\lambda}{(\lambda+k^{2\theta}\lambda_2)} - \frac{\lambda}{(\lambda+k^{2\theta}(\lambda_1+\lambda_2))}\right)$$

So,

$$R(n) = \big(1 - R(1)\big)\big(1 - R(2)\big)\ldots\big(1 - R(n-1)\big)\left(\frac{\lambda}{(\lambda + k^{(n-1)\theta}\lambda_2)} - \frac{\lambda}{(\lambda + k^{(n-1)\theta}(\lambda_1 + \lambda_2))}\right)$$

Substituting the values of$R(r), r = 1,2,\ldots,n$; we can obtainR_n , the reliability of the system.

$$R(4) = \big(1 - R(1)\big)\big(1 - R(2)\big)\big(1 - R(3)\big)\left(\frac{\lambda}{(\lambda+k^{3\theta}\lambda_2)} - \frac{\lambda}{(\lambda+k^{3\theta}(\lambda_1+\lambda_2))}\right)$$

3.2. Inverted Exponential Distribution (IED)

The random variables $X$and$Z$ are strengths independent identically distributed with $x\sim$IE(α_1) and $z\sim$ IE(α_2), respectively, with cdf given as[8]:

$$F(\mathrm{x}) = \mathrm{e}^{-\left(\frac{\alpha_1}{\mathrm{x}}\right)}, \qquad \mathrm{x} > 0$$

$$\mathrm{H}(z) = e^{-\left(\frac{\alpha_2}{z}\right)}, \qquad z > 0$$

And let $y_1\sim$ IE(α) be a random stress variable with pdf given as:

$$g(y_1) = \frac{\alpha}{y_1^2} e^{-\left(\frac{\alpha}{y_1}\right)}, \quad y_1 > 0$$

Where $\int_{y_1} \frac{1}{y_1^2} e^{-\left(\frac{\alpha}{y_1}\right)} dy_1 = \frac{1}{\alpha}$

Since $g(y_1)$ is pd function, then from equation2 we have.

$R(1) = A_1 - B_1$

So,

$$A_1 = \int_{y_1} e^{-\left(\frac{\alpha_1}{y_1}\right)} \frac{\alpha}{y_1^2} e^{-\left(\frac{\alpha}{y_1}\right)} dy_1 = \alpha \int_{y_1} \frac{1}{y_1^2} e^{-\left(\frac{\alpha+\alpha_1}{y_1}\right)} dy_1 = \frac{\alpha}{\alpha+\alpha_1}$$

$$B_1 = \int_{y_1} e^{-\left(\frac{\alpha_1}{y_1}\right)} e^{-\left(\frac{\alpha_2}{y_1}\right)} \frac{\alpha}{y_1^2} e^{-\left(\frac{\alpha}{y_1}\right)} dy_1 = \alpha \int_{y_1} \frac{1}{y_1^2} e^{-\left(\frac{\alpha+\alpha_1+\alpha_2}{y_1}\right)} dy_1 = \frac{\alpha}{\alpha+\alpha_1+\alpha_2}$$

$$R(1) = \frac{\alpha}{\alpha+\alpha_1} - \frac{\alpha}{\alpha+\alpha_1+\alpha_2} = \frac{\alpha\alpha_2}{(\alpha+\alpha_1)(\alpha+\alpha_1+\alpha_2)}$$

And now from equation (3), we have

$R(2) = [1 - R(1)][A_2 - B_2]$

$$A_2 = \int_{y_1} F_x(ky_1) g(y_1) dy_1 = \int_{y_1} e^{-\left(\frac{\alpha_1}{ky_1}\right)} \frac{\alpha}{y_1^2} e^{-\left(\frac{\alpha}{y_1}\right)} dy_1 = \alpha \int_{y_1} \frac{1}{y_1^2} e^{-\left(\frac{\alpha+\frac{\alpha_1}{k}}{y_1}\right)} dy_1$$

$$= \frac{\alpha}{\alpha+\frac{\alpha_1}{k}}$$

$$B_2 = \int_{y_1} F_x(ky_1) H_z(ky_1) g(y_1) dy_1$$

$$= \int_{y_1} e^{-\left(\frac{\alpha_1}{ky_1}\right)} e^{-\left(\frac{\alpha_2}{ky_1}\right)} \frac{\sigma}{y_1^2} e^{-\left(\frac{\alpha}{y_1}\right)} dy_1 = \alpha \int_{y_1} \frac{1}{y_1^2} e^{-\left(\frac{\alpha_1+\alpha_2}{y_1}+\alpha\right)} dy_1 = \frac{\alpha}{\alpha+\frac{\alpha_1+\alpha_2}{k}}$$

So

$$R(2) = \left(1 - \frac{\alpha\alpha_2}{(\alpha+\alpha_1)(\alpha+\alpha_1+\alpha_2)}\right)\left(\frac{\alpha}{\alpha+\frac{\alpha_1}{k}} - \frac{\alpha}{\alpha+\frac{\alpha_1+\alpha_2}{k}}\right)$$

And

$$R(3) = \big(1 - R(1)\big)\big(1 - R(2)\big)\left(\frac{\alpha}{\alpha+\frac{\alpha_1}{k^2}} - \frac{\alpha}{\alpha+\frac{\alpha_1+\alpha_2}{k^2}}\right)$$

So

$$R(n) = \big(1 - R(1)\big)\big(1 - R(2)\big) \dots \big(1 - R(n-1)\big)\left(\frac{\alpha}{\alpha+\frac{\alpha_1}{k^{(n-1)}}} - \frac{\alpha}{\alpha+\frac{\alpha_1+\alpha_2}{k^{(n-1)}}}\right)$$

3.3. Exponentiated Inverse Rayleigh Distribution (EIRD)

Let the random variables *X*and*Z* are strengths independent identically distributed with x~EIR (ϱ_1, ϕ_1) and z~EIR (ϱ_2, ϕ_2), respectively, with cdf given as[1]:

$$F(x) = \left(e^{-\left(\frac{\phi}{x^2}\right)}\right)^{\varrho} = e^{-\left(\frac{\varrho\phi}{x^2}\right)}, \quad x > 0$$

$$H(z) = e^{-\left(\frac{\varrho\phi}{z^2}\right)}, \qquad z > 0$$

And, let y_1 be EIR (ϱ, ϕ) random stress variable with pdf given as:

$$g(y_1) = \frac{2\varrho\phi}{{y_1}^3} e^{-\left(\frac{\varrho\phi}{{y_1}^2}\right)} , \qquad y_1 > 0$$

Where $\int_{y_1} \frac{1}{{y_1}^3} e^{-\left(\frac{\varrho\phi}{{y_1}^2}\right)} dy_1 = \frac{1}{2\varrho\phi}$

Since $g(y_1)$ is pd function, then from equation (2), we have.

$$R(1) = A_1 - B_1$$

$$A_1 = \int_{y_1} e^{-\left(\frac{\varrho_1\phi_1}{{y_1}^2}\right)} \frac{2\varrho\phi}{y_1^3} e^{-\left(\frac{\varrho\phi}{y_1^2}\right)} dy_1 = 2\varrho\phi \int_{y_1} \frac{1}{y_1^3} e^{-\left(\frac{\varrho\phi+\varrho_1\phi_1}{y_1^2}\right)} dy_1 = \frac{\varrho\phi}{\varrho\phi+\varrho_1\phi_1}$$

$$B_1 = \int_{y_1} e^{-\left(\frac{\varrho_1\phi_1}{{y_1}^2}\right)} e^{-\left(\frac{\varrho_2\phi_2}{{y_1}^2}\right)} \frac{2\varrho\phi}{y_1^3} e^{-\left(\frac{\varrho\phi}{y_1^2}\right)} dy_1 = 2\varrho\phi \int_{y_1} \frac{1}{{y_1}^3} e^{-\left(\frac{\varrho\phi+\varrho_1\phi_{1+}\varrho_2\phi_2}{{y_1}^2}\right)} dy_1$$

$$= \frac{\varrho\phi}{\varrho\phi+\varrho_1\phi_{1+}\varrho_2\phi_2}$$

So

$$R(1) = \frac{\varrho\varrho_2\phi\phi_2}{(\varrho\phi+\varrho_1\phi_1)(\varrho\phi+\varrho_1\phi_{1+}\varrho_2\phi_{2)}}$$

And now from equation (3), we have

$$R(2) = [1 - R(1)][A_2 - B_2]$$

$$A_2 = \int_{y_1} F_x\,(ky_1) g(y_1) dy_1 = \int_{y_1} e^{-\left(\frac{\varrho_1\phi_1}{(ky_1)^2}\right)} \frac{2\varrho\phi}{y_1^3} e^{-\left(\frac{\varrho\phi}{y_1^2}\right)} dy_1$$

$$= 2\varrho\phi \int_{y_1} \frac{1}{y_1^3} e^{-\left(\frac{\varrho\phi+\frac{\varrho_1\phi_1}{k^2}}{y_1^2}\right)} dy_1 = \frac{\varrho\phi}{\varrho\phi+\frac{\varrho_1\phi_1}{k^2}}$$

$$B_2 = \int_{y_1} e^{-\left(\frac{\varrho_1\phi_1}{(ky_1)^2}\right)} e^{-\left(\frac{\varrho_2\phi_2}{(ky_1)^2}\right)} \frac{2\varrho\phi}{y_1^3} e^{-\left(\frac{\varrho\phi}{y_1^2}\right)} dy_1 = \frac{\varrho\phi}{\varrho\phi+\frac{\varrho_1\phi_1}{k^2}+\frac{\varrho_2\phi_2}{k^2}}$$

So

$$R(2) = \left(1 - \frac{\varrho\varrho_2\phi\phi_2}{(\varrho\phi+\varrho_1\phi_1)(\varrho\phi+\varrho_1\phi_{1+}\varrho_2\phi_{2)}}\right)\left(\frac{\varrho\phi}{\varrho\phi+\frac{\varrho_1\phi_1}{k^2}} - \frac{\varrho\phi}{\varrho\phi+\frac{\varrho_1\phi_1}{k^2}+\frac{\varrho_2\phi_2}{k^2}}\right)$$

Then, $R(3) = \big(1 - R(1)\big)\big(1 - R(2)\big)\left(\frac{\varrho\phi}{\varrho\phi+\frac{\varrho_1\phi_1}{(k^2)^2}} - \frac{\varrho\phi}{\varrho\phi+\frac{\varrho_1\phi_1+\varrho_2\phi_2}{(k^2)^2}}\right)$

And, $R(4) = \big(1 - R(1)\big)\big(1 - R(2)\big)\big(1 - R(3)\big)\left(\frac{\varrho\phi}{\varrho\phi+\frac{\varrho_1\phi_1}{(k^3)^2}} - \frac{\varrho\phi}{\varrho\phi+\frac{\varrho_1\phi_1+\varrho_2\phi_2}{(k^3)^2}}\right)$

So

$$R(n) = \big(1 - R(1)\big)\big(1 - R(2)\big) \dots \big(1 - R(n-1)\big)\left(\frac{\varrho\phi}{\varrho\phi + \frac{\varrho_1\phi_1}{\left(k^{(n-1)}\right)^2}} - \frac{\varrho\phi}{\varrho\phi + \frac{\varrho_1\phi_1 + \varrho_2\phi_2}{\left(k^{(n-1)}\right)^2}} \right)$$

3.4. Frechet Distribution (FD)

Let the random variables X and Z are strengths independent identically distributed with $x \sim$ F (δ_1, β) and $z \sim$ F (δ_2, β), respectively, with cdf given as[6]:

$F(x) = e^{-\delta x^{-\beta}}$, $x > 0$

$H(z) = e^{-\delta z^{-\beta}}$, $z > 0$

And, let y_1 be F (δ, β) random stress variable with pdf given as:

$$g(y_1) = \delta\beta y_1^{-(\beta+1)} e^{-\delta y_1^{-\beta}} , \quad y_1 > 0$$

Where $\int_{y_1} y_1^{-(\beta+1)} e^{-\delta y_1^{-\beta}} dy_1 = \frac{1}{\delta\beta}$

Since $g(y_1)$ is pd function, then from equation (2), we have.

$R(1) = A_1 - B_1$

$$A_1 = \int_{y_1} e^{-\delta_1 y_1^{-\beta}} \delta\beta y_1^{-(\beta+1)} e^{-\delta y_1^{-\beta}} dy_1 = \delta\beta \int_{y_1} y_1^{-(\beta+1)} e^{-(\delta+\delta_1) y_1^{-\beta}} dy_1$$

$$= \frac{\delta}{\delta+\delta_1}$$

$$B_1 = \int_{y_1} e^{-\delta_1 y_1^{-\beta}} e^{-\delta_2 y_2^{-\beta}} \delta\beta y_1^{-(\beta+1)} e^{-\delta y_1^{-\beta}} dy_1 \quad = \delta\beta \int_{y_1} y_1^{-(\beta+1)} e^{-(\delta+\delta_1+\delta_2) y_1^{-\beta}} dy_1 = \frac{\delta}{\delta+\delta_1+\delta_2}$$

And

$$R(1) = \frac{\delta\delta_2}{(\delta+\delta_1)(\delta+\delta_1+\delta_2)}$$

And now from equation (3), we have

$R(2) = [1 - R(1)][A_2 - B_2]$

$$A_2 = \int_{y_1} F_x(ky_1) g(y_1) dy_1 = \int_{y_1} e^{-\delta_1 (ky_1)^{-\beta}} \delta\beta y_1^{-(\beta+1)} e^{-\delta y_1^{-\beta}} dy_1$$

$$= \delta\beta \int_{y_1} y_1^{-(\beta+1)} e^{-(\delta+\delta_1 k^{-\beta}) y_1^{-\beta}} dy_1 = \frac{\delta}{\delta+\delta_1 k^{-\beta}}$$

$$B_2 = \int_{y_1} F_x(ky_1) H_z(ky_1) g(y_1) dy_1 \quad = \int_{y_1} e^{-\delta_1 (ky_1)^{-\beta}} e^{-\delta_2 (ky_1)^{-\beta}} \delta\beta y_1^{-(\beta+1)} e^{-\delta y_1^{-\beta}} dy_1$$

$$= \delta\beta \int_{y_1} y_1^{-(\beta+1)} e^{-(\delta+\delta_1 k^{-\beta}+\delta_1 k^{-\beta}) y_1^{-\beta}} dy_1 = \frac{\delta}{\delta+\delta_1 k^{-\beta}+\delta_2 k^{-\beta}}$$

So

$$R(2) = \big(1 - R(1)\big)\left(\frac{\delta\delta_2 k^{-\beta}}{(\delta+\delta_1 k^{-\beta})(\delta+\delta_1 k^{-\beta}+\delta_2 k^{-\beta})}\right)$$

Then, $R(3) = \big(1 - R(1)\big)\big(1 - R(2)\big)\left(\frac{\delta\delta_2 (k^2)^{-\beta}}{(\delta+\delta_1 (k^2)^{-\beta})(\delta+\delta_1 (k^2)^{-\beta}+\delta_2 (k^2)^{-\beta})}\right)$

So

$$R(n) = \big(1 - R(1)\big)\big(1 - R(2)\big) \dots \big(1 - R(n-1)\big) \left(\frac{\delta\delta_2 \big(k^{(n-1)}\big)^{-\beta}}{\big(\delta + \delta_1 \big(k^{(n-1)}\big)^{-\beta}\big)\big(\delta + \delta_1 \big(k^{(n-1)}\big)^{-\beta} + \delta_2 \big(k^{(n-1)}\big)^{-\beta}\big)} \right)$$

Then, $R_n = R(1) + R(2) + \cdots + R(n)$

4. Numerical Evaluation and Results

For the four different distribution and by specific values of the parameters involved in mathematical expressions of $R(r), r = 1,2,3,4$ the system reliability R_n and the marginal reliabilities $R(1)$, $R(2), R(3)$ *and* $R(4)$ (i.e. n=4) are evaluated and recorded in the following cases.

4.1. For Exponential Pareto Distribution (EPD)

- $\boldsymbol{\lambda_1 = 0.9, \lambda_2 = 2.4}$ ***and*** $\boldsymbol{k = 3}$
  When drawing the parameter **λ** against reliability and for the different values of parameter **θ**, we notice that the curves start from one point with good reliability with a small value, where the curve escalates to the largest value, and then it begins to decrease and stability, so that the decrease with the increase in the value of parameter **λ**, but when the value of Parameter **θ** to greater values, reliability begins to decrease gradually until steady state is reached and then decreasing.
- $\boldsymbol{\lambda_1 = 0.9, \lambda_2 = 2.4}$ ***and*** $\boldsymbol{k = 3}$
  And at the same default values for both parameters $\boldsymbol{\lambda_1}$ and λ_2 and the coefficient $\boldsymbol{k}$, the reliability graph against parameter **θ** at the different values of parameter **λ**, gave a direct decreasing form at the small value of parameter **λ** and when increasing it led to a very slight increase in reliability (An indication of the increased achievement required in the system) and from then the direct drop to the state of decreasing, while at the greater value of the parameter **λ**, it gave a significant increase in reliability until it reached the inflection point with a considerable distance and then begins to decrease.
- $\boldsymbol{\lambda = 0.9, k = 3}$
  For indicators that plot reliability against parameter **θ** with different values for each of the parameters$\boldsymbol{\lambda_1}$ and$\boldsymbol{\lambda_2}$, when the values of the parameter $\boldsymbol{\lambda_1}$ exceed the values of the parameter$\boldsymbol{\lambda_2}$, the reliability is decreasing with slight stability in the second case.

The reliability behavior is as shown in the following figures with different values of shape parameters for the Exponential Pareto Distribution.

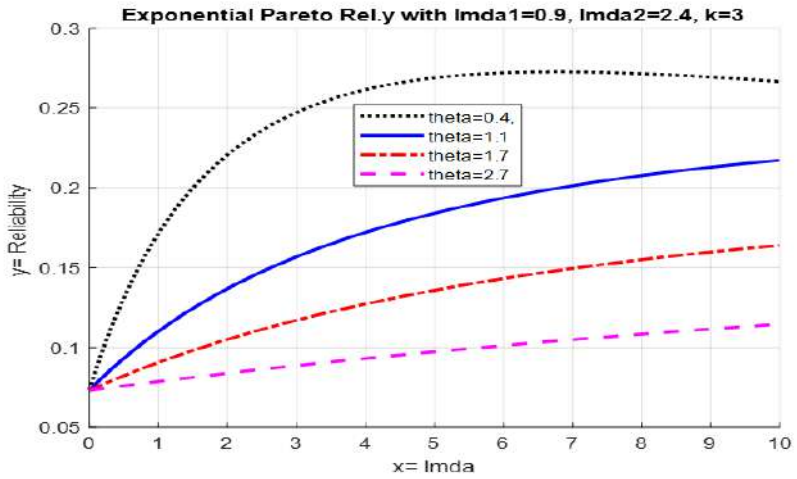

Figure 1. The Reliability curve against parameter λ

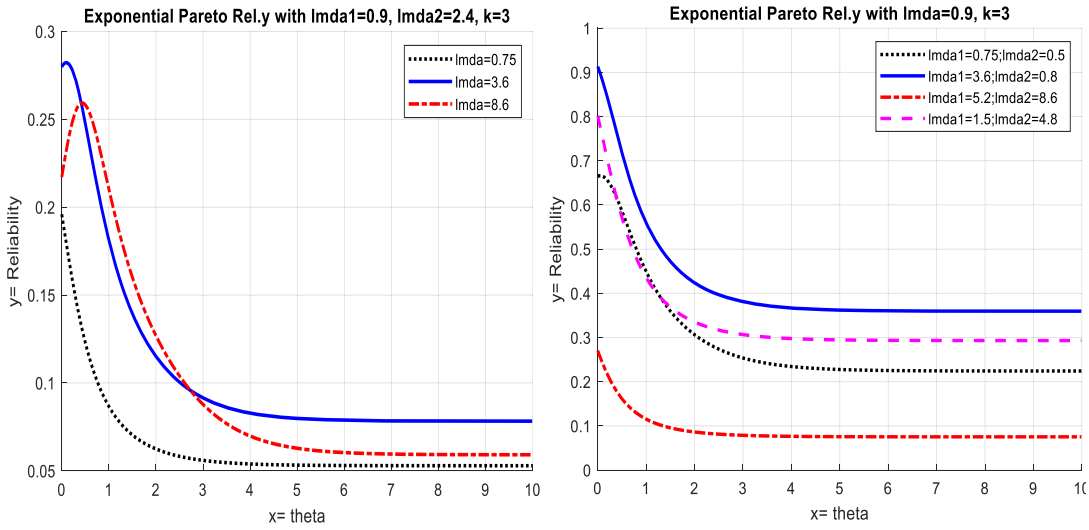

Figures 2. The Reliability curve against parameter θ

4.2. For Inverted Exponential Distribution (IED)

- **k=2**
  When drawing the relationship between reliability $\boldsymbol{R}$ with parameter $\boldsymbol{\alpha}$ for different values of two parameters $\boldsymbol{\alpha_1}$ and $\boldsymbol{\alpha_2}$, it gave a form that initially increased the reliability $\boldsymbol{R}$ sharply from the point of origin and then inflection to decrease after $\boldsymbol{R}$ exceeded the value (0.5) that is **k**=2.
- **k=1.5**
  As for the lower value of the coefficient **k** ,the figures remained the same but with increasing the value of the inflection to decreasing and approaching (0.6) for the case $\boldsymbol{\alpha_1} = 0.8$ and $\boldsymbol{\alpha_2} = 0.4$, also for the other two.
- **k=0.7**
  With a smaller value than the previous state of the coefficient **k,** the shapes were more deploy and better than their predecessors. Therefore, we note that as the value of **k** decreases the chance of reliability increases and it takes a longer period of time before the process of decreasing begins.

The reliability behavior is as shown in the following figures with different values of coefficients for the Inverted Exponential Distribution.

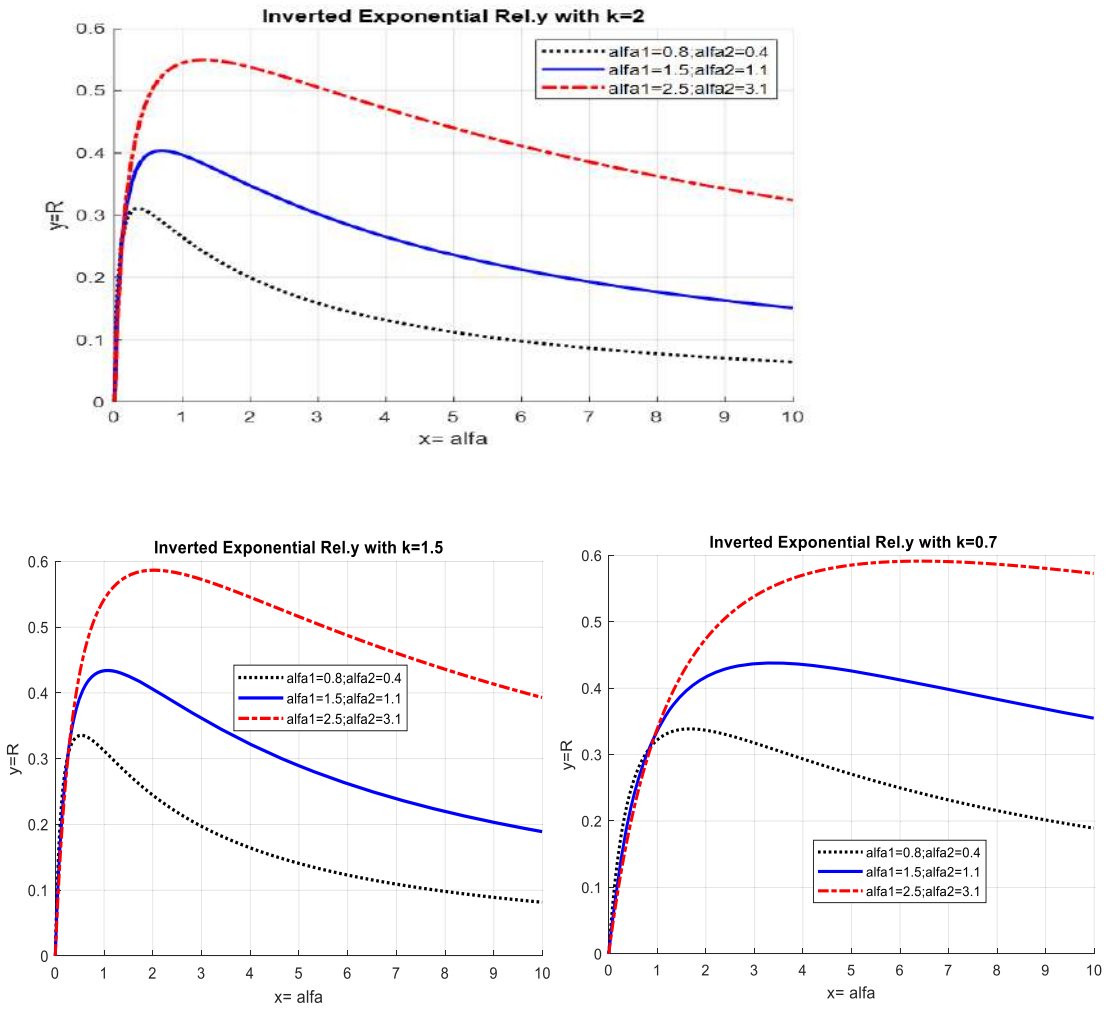

Figures 3. The Reliability curve against parameter α

4.3. For Exponentiated Inverse Rayleigh Distribution (EIRD)

- $\boldsymbol{\varrho_1 = 0.78}$, $\boldsymbol{\varrho_2 = 0.23}$, $\boldsymbol{k = 1.2}$
  Here we notice the reliability value starting from the origin point it increases rapidly with the small values of the parameter $\boldsymbol{\varrho}$ takes a sharp inflection point at the value of ($\boldsymbol{\varrho}$ =0.8), and then starts decreasing rapidly when ($\boldsymbol{k} = 1.2$)**.**
- $\boldsymbol{\varrho_1 = 0.78}$, $\boldsymbol{\varrho_2 = 0.23}$, $\boldsymbol{k = 0.8}$
  When the value decreases to ($\boldsymbol{k}$ = 0.8), the curve of the inflection from increasing to decreasing becomes wider and continues to the middle of the parameter value$\boldsymbol{\varrho}$, before it begins to decrease.
- $\boldsymbol{\phi_1 = 10.3, \phi_2 = 7.2}$, $\boldsymbol{k = 1.5}$
  For the parameter $\boldsymbol{\phi}$ at different values of the parameters $\boldsymbol{\varrho}$, $\boldsymbol{\varrho_1}$, $\boldsymbol{\varrho_2}$ and constant values of the two parameters $\boldsymbol{\phi_1}$, $\boldsymbol{\phi_2}$ and $\mathbf{k}$ =1.5, the reliability curve increases with increasing the values of this parameter, and it begins with a constant distance to a significant distance and then decreases and is similar in that the increasing and overlapping values of the parameters $\boldsymbol{\varrho}$, $\boldsymbol{\varrho_1}$, $\boldsymbol{\varrho_2}$. As for the case of a

decrease, which is the second case referred to by the continuous line it gives a decrease faster than the previous two.

- $\boldsymbol{\phi_1 = 10.3, \phi_2 = 7.2\,, k = 2}$
  As the value **k** increases to 2, the reliability is in the form of increasing curves symmetrical with the possibility of decreasing at values greater than (10) for the parameter$\boldsymbol{\phi}$.
- $\boldsymbol{\phi_1 = 0.4, \phi_2 = 1.3\,, k = 1.2}$ **and** $\boldsymbol{\phi_1 = 0.4, \phi_2 = 1.3\,, k = 0.8}$
  In Figures (5) and (6) respectively, lower values were given for the two parameters $\boldsymbol{\phi_1, \phi_2}$, so that draws the reliability against a parameter $\boldsymbol{\phi}$, we notice that it gave a fast decrease in Fig.5, while in Fig.6 it was a lower decrease.

The reliability behavior is as shown in the following figures with different values of shape parameters for the Exponentiated Inverse Rayleigh Distribution.

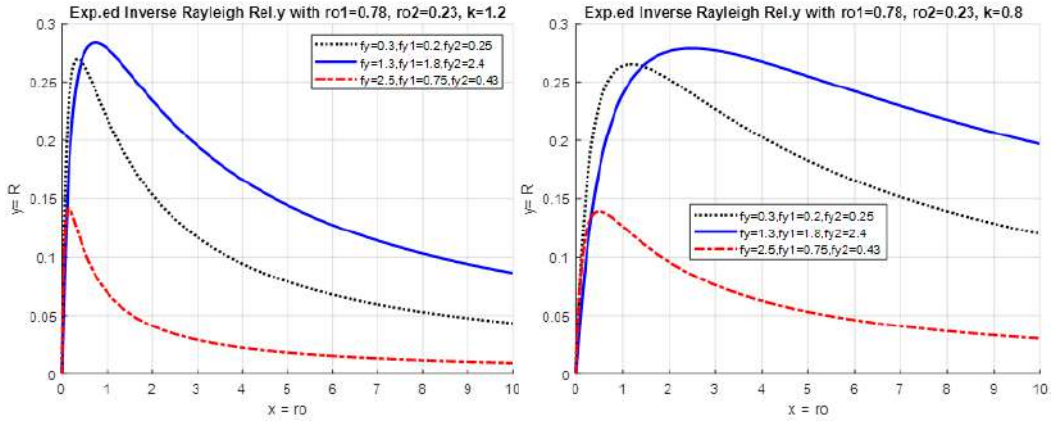

Figures 4. The Reliability curve against parameter ϱ

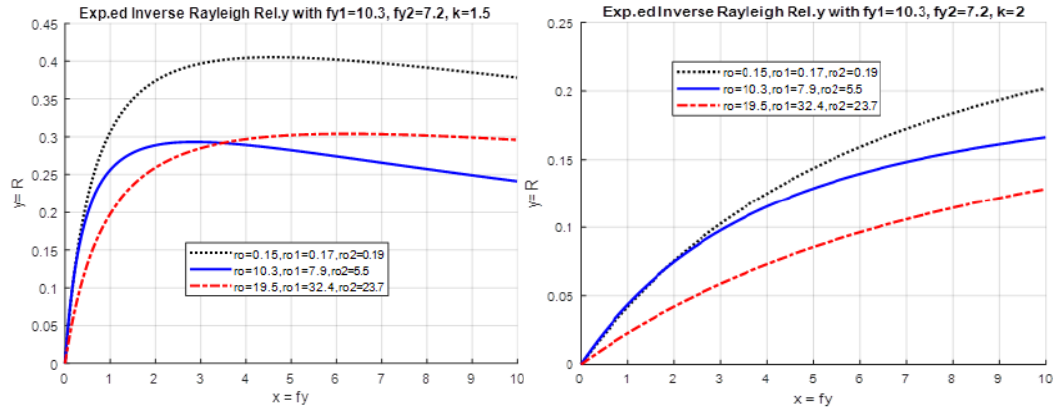

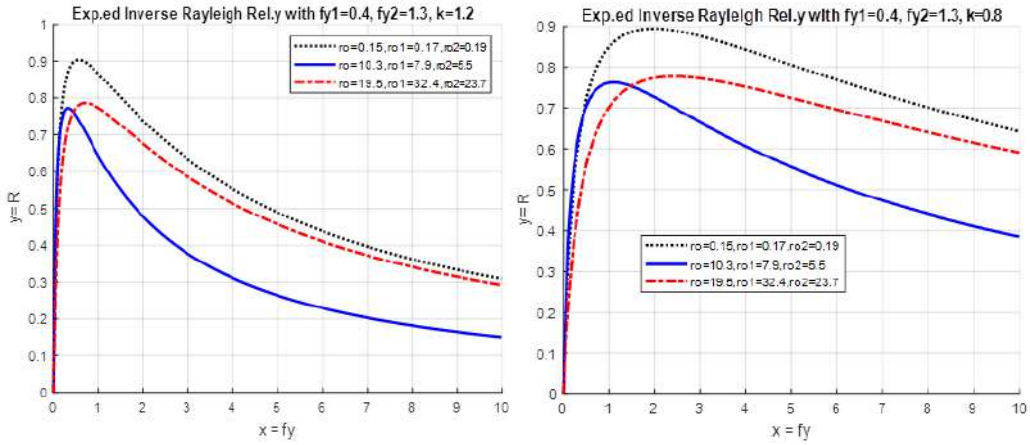

Figures 5. The Reliability curve against parameter ϕ

4.4. For Frechet Distribution (FD)

- $\boldsymbol{\delta_1 = 0.39, \delta_2 = 0.87, k = 1.5}$
  When drawing the delta parameter$\boldsymbol{\delta}$ against different values of the beta parameter$\boldsymbol{\beta}$, we note that the reliability value does not start from the origin point and increases converging until a sharp inflection point of decreasing reliability values at (**k** = 1.5).
- $\boldsymbol{\delta_1 = 0.39, \delta_2 = 0.87, k = 0.63}$
  When the value of the coefficient decreases to (**k** = 0.63), we observe the difference and divergence of the curves. so the best reversal condition is when plotting reliability against parameter $\boldsymbol{\beta}$ at certain values of parameter $\boldsymbol{\delta}$.
- $\boldsymbol{\delta_1 = 0.39, \delta_2 = 0.87, k = 1.5}$ **and** $\boldsymbol{\delta_1 = 0.39, \delta_2 = 0.87, k = 0.63}$
  In figures (3) and (4), we observe a constant and continuous decrease in reliability when the coefficient value is $\boldsymbol{k} = 1.5$, while we have inflection from increasing to decreasing non-convex at $\boldsymbol{k} = 0.63$, respectively.

The reliability behavior is as shown in the following figures with different values of shape parameters for the Frechet Distribution.

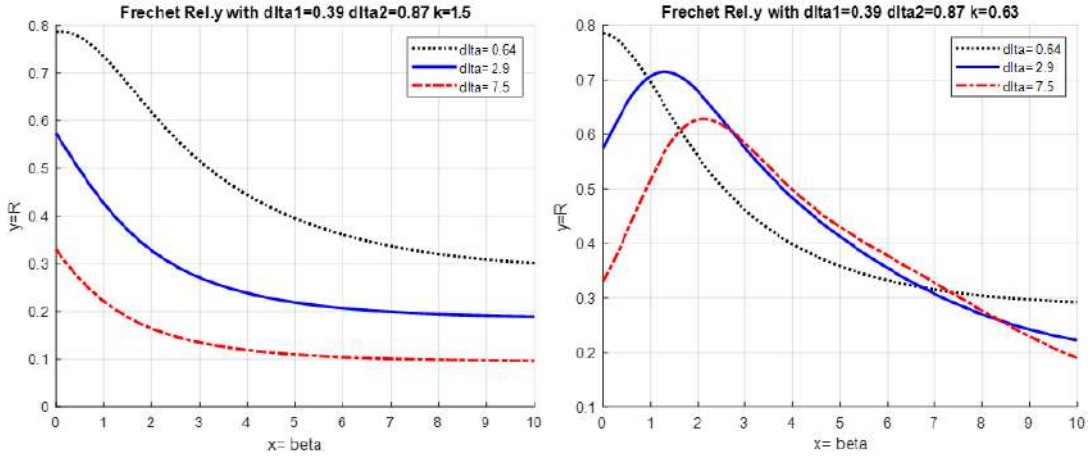

Figures 6. The Reliability curve against parameter β

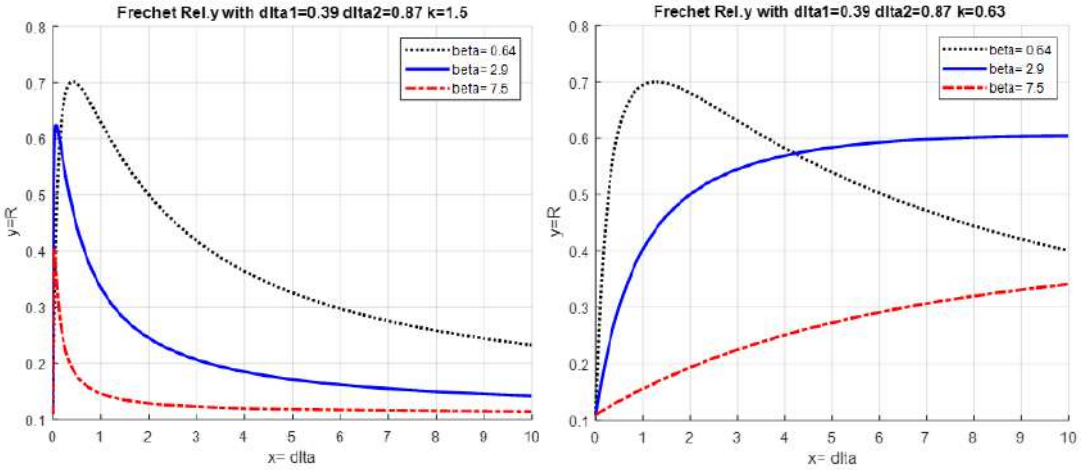

Figures 7. The Reliability curve against parameter $\boldsymbol{\delta}$

5. Conclusion

Formulas for system reliability were found for four different distributions, and it found that there are various effects of the special distributions forms for each of the stress and strength variables.

Acknowledgments

The authors would like to thank Mustansiriyah University (www.uomustansiriyah.edu.iq) Baghdad- Iraq for its support in the present work.

References

[1] Ahsan and Haq M 2016 *Kumaraswamy Exponentialed Inverse Rayleigh Distribution* (Mathematical Theory and Modeling) **6(3)** pp 1-13

[2] AL- Kadim K A and Boshi M A 2013 *Exponential Pareto Distribution* (Mathematical Theory and Modeling) **3(5)** pp 135-141

[3] Aryal G 2019 *On the Beta Exponential Pareto Distribution* (Statistics Optimazation and Information Computing) **7** June pp 417-438
[4] Doloi C, Borah M and Gogoi J 2013 *Cascade System with Pr(X<Y<Z)* (Journal of Informatics and Mathematical Sciences) **5(1)** pp 37-47
[5] Doloi C, Borah M and Sriwastav G 2010 *Cascade System with Random Attenuation Factor* (IAPQR Transactions) **35(2)** pp 81-90
[6] Karam N and Husieen H 2017 *Frechet Cascade Stress-Strength System Reliability*, **7(11)** pp 12-19
[7] Singh N 1980 *On estimation of P(X<Y<Z)* (Comm. Statist. –Theory Methods) A **(9)15** pp 1551-1561
[8] Singh S, Singh U, Yaday A and Viswkarma P 2015 *On the estimation of Stress-Strength Reliability Parameter of Inverted Exponential Distribution* (International Journal of Scientific World) **3(1)** pp 98-112

A Computational Procedure Using Robust Ranking Method to Formulate and Solve Fuzzy DEA Models

A Computational Procedure Using Robust Ranking Method to Formulate and Solve Fuzzy DEA Models

Mohammed Hadi Lafta, Ali A. Sulaiman and Rasheed Al-Salih

College of Administration and Economics, University of Sumer, Iraq

E-mail: rbahhd@umsystem.edu

Abstract. In some real-world applications, performance assessment often has to be considered under uncertainty with fuzzy input and output. Data envelopment analysis (DEA) is a new and effective approach to measuring the relative efficiency of decision-making units concerned with performance evaluation. Recently, DEA has studied with fuzzy input and output. In this paper, we present a computational procedure using a robust ranking method to formulate and solve fuzzy DEA models. Based on this approach, we convert the fuzzy DEA input and output from fuzzy form to crisp. Also, a case study has been presented as in [6] to assess the performance of eight manufacturing enterprises with fuzzy data.

1. Introduction

The performance evaluation is one of the basic tools for measuring the quality of functional processes. Therefore, it has taken the attention of many researchers in quality and business affairs, because of its great importance in directing the organizational activity towards the horizon of success. The performance appraisal was defined as "The method by which the actual performance level is measured to obtain sufficient information and analyze it, so it is a tool for measuring human effort at work and diagnosing the level of quality in this performance" [1].

The performance evaluation is a periodic procedure in which the performance of the employee is examined and measured, in order to identify his strengths and weaknesses and to find ways to improve his performance and raise the level of certification for him, and this is done through the use of many models for performance evaluation, which are quantifiable and give accurate indicators for performance [2].

Many performance evaluation researchers or organization owners differ in defining specific steps for the performance evaluation process, due to the difference in the nature of work, such as the organization's philosophy, environment, and type of work, or because of the size of job responsibility, which varies between one job and another. But most of these opinions agree that the performance evaluation passes the following steps [3]:

- Monitor performance problems.
- Examination and search for the causes of these problems.
- Determine the best way to overcome them.
- Follow up on the implementation of treatment methods.
- Business development, continuous improvement, and development.

The performance evaluation is the guiding guide that gives a complete perception about the strengths and weaknesses of the employees in their job positions that they have been assigned to accomplish, so

it is considered a tool for measuring the quality of the employee's productivity during a certain period and indicating the extent of his contribution to achieving the goals of the organization. Therefore, the performance evaluation is characterized by the following features [4].

- It helps the boss to measure the employees' performance accurately
- It helps to optimize energies and resources.
- Helps reduce waste and wastes in work, which helps reduce labor costs
- It makes the outputs high quality and flawless.
- It is considered a guide to leadership in making appropriate decisions.
- It provides leadership with detailed and accurate performance reports in a record period.
- It reduces the frequency of the same mistakes and becomes a useful guide from previous experiences.

The methods of performance evaluation are continuously updating and continue developing as a result of the expansion of studies on this topic, and the organizations' desire to achieve efficiency in all parts of the organization, and to achieve competitive advantage by raising the level of the job performance of the human resource within the organization, so modern organizations rely on performance evaluation on standards Essential in the evaluation process such as effectiveness, efficiency, profits, competitive advantage, quality of job life, creativity, innovation and quality [5]. On the other hand, Data envelopment analysis (DEA) has been recently used to conduct the performance assessment under certainty and uncertainty. Many researchers studied different algorithms and solution methods for deterministic and fuzzy DEA model. For more details we refer to [6], [7],[8],[9],[10],[11].

In this paper, we present a computational approach to formulate and solve the fuzzy dea (FDEA) model using the robust ranking method.

2. Preliminaries

In this section, some basic concepts of fuzzy numbers are given. This material can be found in [12], [13], [14], [15] and [16].

2.1 Basic Definitions

Definition 1 "Let W be a classical set of objects. Then,

$\widetilde{B} = \{(x, \mu_{\widetilde{B}}(x): x \in W\}$, where $\mu_{\widetilde{B}} : W \to [0,1]$

Is called a fuzzy set in W. Also, $\mu_{\widetilde{B}}$ is known as the membership function".

Definition 2 "Let $\widetilde{B}$ be a fuzzy set in W and $\beta \in [0,1], \beta \in \boldsymbol{\mathcal{R}}$. Then, $B^{\beta} = \{x \in W : \mu_{\widetilde{B}}(x) \geq \beta\}$ is called an β -level set or β -cut form of $\widetilde{B}$".

2.2 Types of Fuzzy Numbers

Two well-known fuzzy numbers are described as follows.

2.2.1 Triangular Fuzzy Number

Definition 3 " $\widetilde{B} = (b_1, b_2, b_3)$, is said to be a triangular fuzzy number if its membership function, $\mu_{\widetilde{B}}(x)$, is given by"

$$\mu_{\tilde{B}}(x) = \begin{cases} 0 & , \quad x < b_1 \\ \dfrac{(x - b_1)}{(b_2 - b_1)} & , \quad b_1 \leq x \leq b_2 \\ \dfrac{(b_3 - x)}{(b_3 - b_2)} & , \quad b_2 \leq x \leq b_3 \\ 0 & , \quad x > b_3 \end{cases}$$

Definition 4 "Let $\widetilde{A} = (a, b, c)$ be a triangular fuzzy number". "Then, its $\beta-$cut $A^{\lambda}$is defined as follows":
"$A^{\beta} = [a + (b - a)\beta, c - (c - b)\beta], 0 \leq \beta \leq 1.$"

2.2.2 Trapezoidal Fuzzy Number

Definition 5 "$\widetilde{B} = (b_1, b_2, b_3, b_4)$, is said to be a trapezoidal fuzzy number if its membership function, $\mu_{\widetilde{B}}(x)$, is given by"

$$\mu_{\widetilde{B}}(x) = \begin{cases} \dfrac{(x - b_1)}{(b_2 - b_1)} & , \quad b_1 \leq x < b_2 \\ 1 & , \quad b_2 \leq x \leq b_3 \\ \dfrac{(x - b_4)}{(b_3 - b_4)} & , \quad b_3 < x \leq b_4 \\ 0 & , \quad otherwise \end{cases}$$

Definition 6 "Let $\widetilde{A} = (a, b, c, d)$ be a trapezoidal fuzzy number. Then, its $\beta-$cut A^{λ} is as follows":
$A^{\beta} = [a + (b - a)\beta, d - (d - c)\beta], 0 \leq \beta \leq 1$

2.3 Arithmetic Operation for Trapezoidal Fuzzy Numbers

i. "Let $\widetilde{A}_1 = (a_1, b_1, c_1, d_1)$ and $\widetilde{A}_2 = (a_2, b_2, c_2, d_2)$ be two trapezoidal fuzzy numbers. Then, $\widetilde{A}_1 \oplus \widetilde{A}_2 = (a_1 + a_2, b_1 + b_2, c_1 + c_2, d_1 + d_2)$."
ii. "Let $\widetilde{A}_1 = (a_1, b_1, c_1, d_1)$ and $\widetilde{A}_2 = (a_2, b_2, c_2, d_2)$ be two trapezoidal fuzzy numbers. Then, $\widetilde{A}_1 \Theta \widetilde{A}_2 = (a_1 - d_2, b_1 - c_2, c_1 - b_2, d_1 - a_2)$."
iii. "Let $\widetilde{A}_1 = (a_1, b_1, c_1, d_1)$ and $\widetilde{A}_2 = (a_2, b_2, c_2, d_2)$. Then, $\widetilde{A}_1 \otimes \widetilde{A}_2 = (a_1a_2, b_1b_2, c_1c_2, d_1d_2)$."
iv. "Let $\widetilde{A} = (a_1, b_1, c_1, d_1$. Then,

$$\gamma\tilde{A} = \begin{cases} (\gamma a, \gamma b, \gamma c, \gamma d) & \gamma \geq 0 \\ (\gamma d, \gamma c, \gamma b, \gamma a) & \gamma \leq 0. \end{cases}"$$

3. Robust ranking method

The robust ranking method is one of the important methods used to solve different types of optimization problems such as assignment problems, transportation problems, and linear programming problems, and so on. See for e.g. [13], [14], [15], [16], [17], and [18].
If $\tilde{x}$ be a fuzzy number, then R ($\tilde{x}$) represents the robust ranking approach for:

1. Trapezoidal case:

$R(\tilde{x}) = \int_0^1 0.5\left(s_{\alpha}^{l}, s_{\alpha}^{u}\right) d\alpha$;
where $\left(s_{\alpha}^{l}, s_{\alpha}^{u}\right) = [(x_2 - x_1)\alpha + x_1, x_4 - (x_4 - x_3)\alpha]$ represents the α-cut for the trapezoidal fuzzy number $\tilde{x} = (x_1, x_2, x_3, x_4)$. Then $R(x_1, x_2, x_3, x_4) = \int_0^1 0.5[(x_2 - x_1)\alpha + x_1, x_4 - (x_4 - x_3)\alpha]\, d\alpha$.

2. Triangular case:

$R(\tilde{x}) = \int_0^1 0.5\left(s_{\alpha}^{l}, s_{\alpha}^{u}\right) d\alpha$;
where $\left(s_{\alpha}^{l}, s_{\alpha}^{u}\right) = [(x_2 - x_1)\alpha + x_1, x_3 - (x_3 - x_2)\alpha]$ represents the α-cut for the triangular fuzzy number $\tilde{x} = (x_1, x_2, x_3)$. Then $R(x_1, x_2, x_3) = \int_0^1 0.5[(x_2 - x_1)\alpha + x_1, x_3 - (x_3 - x_2)\alpha]\, d\alpha$.

4. The formulation of fuzzy data envelopment analysis (FDEA) model

The most well-known formulation of CCR model is based on linear programming formulation. For more information about new linear programming formulation we refer to [19],[20],[21],[22],[23], and [24]. In this section, we will present the formulation of (FDEA) model as follows.

4.1 Mathematical model

(FDEA) model can be formulated in [6] and [7] as follows:

$Max\ Z(u,v) = \frac{V^T \tilde{y}_0}{u^T \tilde{x}_0}$

$s.t.\ V^T \tilde{y}_j \le u^T \tilde{x}_j, j = 1,2,\dots,n$, and $u \ge 0,\ v \ge 0$

This model is equivalent to the following linear model.

$Max\ Z(u,v) = V^T \tilde{y}_0$

$s.t.\ V^T \tilde{y}_j \le u^T \tilde{x}_j, j = 1,2,\dots,n,\ u^T \tilde{x}_0 = 1$, and $u \ge 0,\ v \ge 0$

4.2 Computational procedure for solving (FDEA)

Now, we present the following computational procedure for solving (FDEA) model.

Step1-Based on the input and the output of the model, form the fuzzy linear programming model.

Step2- Transform all fuzzy coefficients in the fuzzy linear programming model into crisp coefficients using the robust ranking method.

Step 3- Form the crisp linear programming model.

Step 4- Find the optimal solution of the crisp model using Win QSB solver.

5. Case study

In this section, we present an example to demonstrate a robust ranking approach.

This example is taken from [6] "where eight manufacturing enterprises (DMUs) are to be evaluated in terms of two inputs and two outputs".

Solution:

Step 1. Form the linear programming model based on the data in [6] as follows:

For the first manufacturing enterprise:

$Max\ U(u,v) = (2120,2170,2210)u_1 + 1870u_2,\ S.t.$

$(14500,14790,14860)v_1 + (3.1,4.1,4.9)v_2 = 1$

$$\frac{(1420,1460,1500)u_1 + 1340u_2}{(12470,12720,12790)v_1 + (1.2,2.1,3.0)v_2} \le 1$$

$$\frac{(2510,2570,2610)u_1 + 2360u_2}{(17900,18260,18400)v_1 + (3.3,4.3,5.0)v_2} \le 1$$

$$\frac{(2300,2350,2400)u_1 + 2020u_2}{(14970,15270,15400)v_1 + (2.7,3.7,4.6)v_2} \le 1$$

$$\frac{(1480,1520,1560)u_1 + 1550u_2}{(13980,14260,14330)v_1 + (1.0,1.8,2.7)v_2} \le 1$$

$$\frac{(1990,2030,2100)u_1 + 1760u_2}{(14030,14310,14400)v_1 + (1.6,2.6,3.6)v_2} \le 1$$

$$\frac{(2200,2260,2300)u_1 + 1980u_2}{(16540,16870,17000)v_1 + (2.4,3.4,4.4)v_2} \le 1$$

$$\frac{(2400,2460,2520)u_1 + 2250u_2}{(17600,17960,18100)v_1 + (2.6,3.6,4.6)v_2} \le 1$$

$u_1,\ u_2,\ v_1,\ v_2,\ \ge 0$

Similarly, we do other seven manufacturing enterprises.
Step 2. Using the robust ranking method, the fuzzy coefficients become as follows:

Table 1. Crisp inputs and outputs for the presented example**.**

Enterprises	Inputs		Outputs	
(DMUS)	MC	NOE	GOV	PQ
A	2167.5	1870	14735	4.05
B	1460	1340	12675	2.1
C	2565	2360	18205	4.225
D	2350	2020	15227.5	3.675
E	1520	1550	14207.5	1.875
F	2037.5	1760	14262.5	2.6
G	2255	1980	16820	3.4
H	2460	2250	17905	3.6

Step 3. Form the crisp linear programming model as follows.

$$Max\ U(u,v) = \ 2167.5u_1 + 1870u_2,\ S.t.$$

$$14735v_1 + 4.05v_2 = 1$$

$$\frac{1460u_1 + 1340u_2}{12675v_1 + 2.1v_2} \leq 1$$

$$\frac{2565u_1 + 2360u_2}{18205v_1 + 4.225v_2} \leq 1$$

$$\frac{2350u_1 + 2020u_2}{15227.5v_1 + 3.675v_2} \leq 1$$

$$\frac{1520u_1 + 1550u_2}{14207.5v_1 + 1.875v_2} \leq 1$$

$$\frac{2037.5u_1 + 1760u_2}{14262.5v_1 + 2.6v_2} \leq 1$$

$$\frac{2255u_1 + 1980u_2}{16820v_1 + 3.4v_2} \leq 1$$

$$\frac{2460u_1 + 2250u_2}{17905v_1 + 3.6v_2} \leq 1$$

$$u_1,\ u_2,\ v_1,\ v_2,\ \geq 0$$

Step 4. The optimal solution of the crisp model using Win QSB solver is obtained as follows.

Table 2. Efficiency scores for eight manufacturing enterprises.

No.	DMU	Score	Rank		Average	0.9522
1	A	1	1		Max	1
2	B	1	1		Min	0.8829
3	C	0.9551	5		St Dev	0.0466
4	D	0.9076	7			
5	E	1	1			

6	F	0.8829	8			
7	G	0.9582	4			
8	H	0.9136	6			

Conclusion

To conduct performance assessments in fuzzy environments from different perspectives, a computational procedure has been presented for some ranking functions to formulate and solve fuzzy DEA models. Based on robust ranking formulas, we convert the fuzzy DEA input and output from fuzzy form to crisp. Furthermore, a case study has presented as in [6] to assess the performance of the given (DMUs) which are to be evaluated in terms of the two inputs and the two outputs. So that will facilitate to make accurate decisions for the performance evaluation and decreasing the period of decision-making procedures

References

[1] Hamza A, Ullah W and Hasnain M 2019 Performance Evaluation and Its Effects on Employees in Construction Industry *Global Scientific Journal (GSJ)* **7**(8)73-78
[2] Obiekwe, Onyebuchi, Ejo-Orusa and Henry 2019 IMPACT OF EMPLOYEE PERFORMANCE APPRAISAL ON PERFORMANCE OF BUSINESS ORGANIZATIONS: A THEORETICAL REVIEW *EPRA International Journal of Economic and Business Review* 7(9)57-64
[3] Ochidi, Zekeri, et. al 2019 EFFECT OF PERFORMANCE APPRAISAL ON EMPLOYEES' PERFORMANCE OFSELECTED DEPOSIT MONEY BANKS IN LOKOJA *Ilorin Journal of Human Resource Management (IJHRM)* 3(2)85-100
[4] Pisak Kalyanamitra et. al 2020 Impact of Training Facilities, Benefits and Compensation, and Performance Appraisal on the Employees *A multifaceted review journal in the field of pharmacy* **11**(3) 166-175
[5] Shahraji Ghanbari M et.al. 2012 Approaches of Performance Evaluation in Organizations *Interdisciplinary Journal Of Contemporary Research In Business* **4**(8) 620-625
[6] Wang Y M, Luo Y and Liang L. 2009 Fuzzy data envelopment analysis based upon fuzzy arithmetic with an application to performance assessment of manufacturing enterprises. *Expert systems with applications* **36**(3) 5205-5211
[7] Wang Y M and Chin K S 2011 Fuzzy data envelopment analysis: A fuzzy expected value approach *Expert Systems with Applications* **38**(9) 11678-11685
[8] Wen M and Li H. 2009 Fuzzy data envelopment analysis (DEA): Model and ranking method *Journal of Computational and Applied Mathematics* **223**(2) 872-878
[9] Puri J and Yadav S P 2013 A concept of fuzzy input mix-efficiency in fuzzy DEA and its application in banking sector *Expert Systems with Applications* **40**(5) 1437-1450
[10] Namakin A, Najafi S E, Fallah, M and Javadi M 2018 A New Evaluation for Solving the Fully Fuzzy Data Envelopment Analysis with Z-Numbers *Symmetry* **10**(9) 384
[11] Nastis S A, Bournaris T, and Karpouzos D 2019 Fuzzy data envelopment analysis of organic farms *Operational Research* **19**(2) 571-584
[12] Kaur Jagdeep and Kumar Amit 2016 An Introduction to Fuzzy Linear Programming Problems Theory: Methods and Applications (Springer International Publishing Switzerland)
[13] Srinivasan A and Geetharaman G 2013 Method for Solving Fuzzy Assignment Problem Using Ones Assignment Method and Robust's Ranking Technique *Applied Mathematical Sciences* **7**(113) 5607–5619
[14] Al Thabhawi S K 2019 Comparative Study of Ranking Methods for Fuzzy Transportation Iraqi *Journal of Science* **60**(7) 1592-1602

[15] kumar M R and Subramanian S 2018 Solution of Fuzzy Transportation Problems with Trapezoidal Fuzzy Numbers using Robust Ranking Methodology *International Journal of Pure and Applied Mathematics* **119**(16) 3763-3775
[16] Kadhirvel K and Balamurugan K 2012 Method for Solving Hungarian Assignment Problems Using Triangular and Trapezoidal Fuzzy Number *International Journal of Engineering Research and Applications (IJERA)* **2**(5) 399-403
[17] Nagarajan R and Solairaju A 2010 Computing Improved Fuzzy Optimal Hungarian Assignment Problems with Fuzzy Costs under Robust Ranking Techniques *International Journal of Computer Applications* **6**(4) 6-13
[18] Ramadas V and Shanmugam P 2018 An Effective Fuzzy Ranking Method in Convex Triangular Fuzzy Soft Numbers *International Journal of Applied and Advanced Scientific Research (IJAASR)* **3**(1) 33-38
[19] Al-Salih R and Bohner M 2018 Linear programming problems on time scales *Applicable Analysis and Discrete Mathematics* **12**(1) 192-204
[20] Al-Salih R and Bohner M J 2020 Separated and state-constrained separated linear programming problems on time scales *Boletim da Sociedade Paranaense de Matemática* **38**(4) 181-195
[21] Al-Salih R and Bohner M 2019 Linear fractional programming problems on time scales *J. Numer. Math. Stoch* **11**(1) 1-18
[22] Hamed Q A, Al-Salih R and Laith W 2020 The Analogue of Regional Economic Models in Quantum Calculus *Journal of Physics Conference Series* **1530**(1) (IOP Publishing)
[23] Al-Salih R, Habeeb A and Laith W 2019 A Quantum Calculus Analogue of Dynamic Leontief Production Model with Linear Objective Function *Journal of Physics: Conference Series* **1530**(1) 012102 (IOP Publishing)
[24] Al-Salih R 2020 Dynamic network flows in quantum calculus *Journal of Analysis and Applications* **18**(1) 53-66

Spectrum of Secondary Submodules

Spectrum of Secondary Submodules

Ghaleb Ahmed , Suaad Gedaan , Rasha Ibrahim

Department of Mathematics, College of Education for Pure Science Ibn Al-Haitham, University of Baghdad, Baghdad, Iraq

E-mail: suaad.gedaan@yahoo.com

Abstract. Let M be a right module over a commutative ring R with identity. The spectrum of secondary modules is defined in this paper. Some connections between the algebraic properties of these modules and the topological properties of their spectrum are investigated.

1. Introduction

Throughout this work, all rings will be commutative rings with identity elements and all modules will be unitary right modules. A non-zero submodule N is called second if for any $a \in R$, $Na = N$ or $Na = 0$ [1]. Quasi-Zariski topology $\zeta^s(M) = \{V^s(A) \mid A$ is a submodule of $M\}$ is defined by using the set of all second submodules of a non-zero module M denoted by $spec^s(M)$ where $V^s(A) = \{N \in spec^s(M) \mid N \subseteq A\}$ and M is called a module have quasi-Zariski topology or a cotop module or a top^s-module [2] and [3]. A non-zero submodule N is called secondary if for any $a \in R$, $Na = N$ or $Na^t = 0$ for some positive integer t [4].

Our concern in these papers is to study the set of all secondary submodules of a non-zero module M which is called the secondary spectrum of M denoted by $spec^y(M)$ and topologize $spec^y(M)$.

In section two, we define $V^y(A)$ is the set of all secondary submodules of M contained in a submodule A and we call it the variety of A and denoted by $V^y(A) = \{N \in spec^y(M) \mid N \subseteq A\}$. Also we define the set of all secondary submodules of M not contained in A and denoted by $X^y(A) = \{N \in spec^y(M) \mid N \nsubseteq A\} = spec^y(M) - V^y(A)$. We give several examples of the sets $V^y(A)$ and $X^y(A)$. Among other results we show that $V^y(A)$ of an atomic module M have a maximal element (Proposition 2.7). Next, we define modules have $\circledast$ condition by using the concept of varieties of submodules. Various properties and examples of this concept are produced (Remarks and Examples 2.10) and we give a characterization of this class of modules (Theorem 2.11). In section three, $spec^y(M)$ is topologized to get the class of top^y-modules. We give a description of top^y-modules (Theorem 3.9). Many results about this type of modules are given in this section (Proposition 3.12, Proposition 3.13. and Proposition 3.17).

In what follows, $\mathbb{Z}$, $\mathbb{Q}$, $\mathbb{Z}_{p^\infty}$, $\mathbb{Z}_n$, " $\subseteq$ " we denote respectively, integers, rational numbers, the p-Prufer group, the residue ring modulo n and inclusion.

2. Secondary Spectrum and $\circledast$ condition

Definition (2.1) [2]: M is secondless module if M has no second submodules.

Definition (2.2): M is secondaryless module if M has no secondary submodules.

Proposition (2.3): Every secondaryless module is secondless.
Proof. Let M be a secondaryless module. Suppose M is not secondless implies that M contains a second submodule N so that N is secondary which is contradict that $spec^{y}(M) = \emptyset$.

Remarks and Examples (2.4):

(1) Clearly, if M is secondaryless module (and hence secondless) then $spec^{y}(M) = V^{y}(M) = V^{y}(A) = \{\emptyset\}$ for each submodule A of . As special case, $M = \mathbb{Z}$ as $\mathbb{Z}$-module.

(2) If M is simple module then $spec^{y}(M) = V^{y}(M) = \{M\}$, $V^{y}(< 0 >) = \{\emptyset\}$ and $X^{y}(M) = \{\emptyset\}$, $X^{y}(< 0 >) = spec^{y}(M) = \{M\}$. For instance, $M = \mathbb{Z}_p$ as $\mathbb{Z}$-module.

(3) Consider $\mathbb{Z}_4 = \mathbb{Z}_{2^2}$ as $\mathbb{Z}$-module where $spec^{y}(\mathbb{Z}_4) = V^{y}(\mathbb{Z}_4) = \{< \bar{2} >, \mathbb{Z}_4\}$, $V^{y}(< \bar{2} >) = \{< \bar{2} >\}$ $V^{y}(< \bar{0} >) = \{\emptyset\}$ and $X^{y}(\mathbb{Z}_4) = \{\emptyset\}$, $X^{y}(< \bar{2} >) = \{\mathbb{Z}_4\}$ and $X^{y}(< \bar{0} >) = spec^{y}(\mathbb{Z}_4) = \{< \bar{2} >, \mathbb{Z}_4\}$.

(4) Consider $\mathbb{Z}_8 = \mathbb{Z}_{2^3}$ as $\mathbb{Z}$-module where $spec^{y}(\mathbb{Z}_8) = V^{y}(\mathbb{Z}_8) = \{< \bar{4} >, < \bar{2} >, \mathbb{Z}_8\}$, $V^{y}(< \bar{4} >) = \{< \bar{4} >\}$, $V^{y}(< \bar{2} >) = \{< \bar{4} >, < \bar{2} >\}$, $V^{y}(< \bar{0} >) = \{\emptyset\}$ and $X^{y}(\mathbb{Z}_8) = \{\emptyset\}$ and $X^{y}(< \bar{4} >) = \{< \bar{2} >, \mathbb{Z}_8\}$, $X^{y}(< \bar{2} >) = \{\mathbb{Z}_8\}$, $X^{y}(< \bar{0} >) = spec^{y}(\mathbb{Z}_8)$.

(5) $\mathbb{Z}_9 = \mathbb{Z}_{3^2}$ as $\mathbb{Z}$-module where $spec^{y}(\mathbb{Z}_9) = spec^{y}(\mathbb{Z}_{3^2}) = \{< \bar{3} >, \mathbb{Z}_9\}$

(6) $spec^{y}(\mathbb{Z}_{p^n}) = \{< \overline{p^t} > \mid t = 0,1, \dots, n-1\}$, where $\mathbb{Z}_{p^n}$ as $\mathbb{Z}$-module for some p a prime number and n is a positive integer. For example, $\mathbb{Z}_{16} = \mathbb{Z}_{2^4}$ as $\mathbb{Z}$-module where $spec^{y}(\mathbb{Z}_{16}) = spec^{y}(\mathbb{Z}_{2^4}) = \{< \overline{2^t} > \mid t = 0,1, \dots, 3\}, = \{< \overline{2^0} >, < \overline{2^1} >, < \overline{2^2} >, < \overline{2^3} >\} = \{\mathbb{Z}_{16}, < \bar{2} >, < \bar{4} >, < \bar{8} >\}$. For more example, see examples (3), (4) and (5).

(7) Since every submodule in $\mathbb{Z}_{p^n}$ and $\mathbb{Z}_{p^m}$ as $\mathbb{Z}$-modules are of the form $< \overline{p^t} >$ and $< \overline{p^s} >$ respectively where n, m are fixed positive integers and t, s are any positive integers and p is a prime number so every submodule of $\mathbb{Z}_{p^n} \oplus \mathbb{Z}_{p^m}$ can be written $< (\overline{p^t}\, r,\ \overline{p^s}\, d) >$ where $\mathbb{Z}_{p^n} \oplus \mathbb{Z}_{p^m} = \{(\overline{p^t}\, r,\ \overline{p^s}\, d) \mid$ for some positive integers t and s and $r, d \in \mathbb{Z}$ $\}$ as $\mathbb{Z}$-module and hence $V^{y}(< (\overline{p^t}\, r,\ \overline{p^s}\, d) >) = \{< (\overline{p^c}\, r, \overline{p^k}\, d) > \neq < 0,0 >\}$ for each positive integers $c \leq t$ and $k \leq s$.

(8) $spec^{y}(\mathbb{Z}_p \oplus \mathbb{Z}_p) = V^{y}(\mathbb{Z}_p \oplus \mathbb{Z}_p) = \{0 \oplus \mathbb{Z}_p, \mathbb{Z}_p \oplus 0, \mathbb{Z}_p \oplus \mathbb{Z}_{p,} < (\bar{1}, \bar{1}) >\}$, $V^{y}(\mathbb{Z}_p \oplus 0) = \{\mathbb{Z}_p \oplus 0\}$, $V^{y}(0 \oplus \mathbb{Z}_p) = \{0 \oplus \mathbb{Z}_p\}$, $V^{y}(< (\bar{1}, \bar{1}) >) = \{< (\bar{1}, \bar{1}) >\}$ and $V^{y}(0 \oplus 0) = \{\emptyset\}$ and $X^{y}(\mathbb{Z}_p \oplus \mathbb{Z}_p) = \{\emptyset\}$, $X^{y}(\mathbb{Z}_p \oplus 0) = \{\mathbb{Z}_p \oplus \mathbb{Z}_p, 0 \oplus \mathbb{Z}_p, < (\bar{1}, \bar{1}) >\}$, $X^{y}(0 \oplus \mathbb{Z}_p) = \{\mathbb{Z}_p \oplus \mathbb{Z}_p, \mathbb{Z}_p \oplus 0, < (\bar{1}, \bar{1}) >\}$, $X^{w}(< (\bar{1}, \bar{1}) >) = \{0 \oplus \mathbb{Z}_p, \mathbb{Z}_p \oplus 0, \mathbb{Z}_p \oplus \mathbb{Z}_p\}$ and $X^{y}(0 \oplus 0) = spec^{y}(\mathbb{Z}_p \oplus \mathbb{Z}_p)$.

(9) $spec^{y}(\mathbb{Z}_6) = V^{y}(\mathbb{Z}_6) = \{< \bar{2} >, < \bar{3} >\}$, $V^{y}(< \bar{2} >) = \{< \bar{2} >\}$, $V^{y}(< \bar{3} >) = \{< \bar{3} >\}$, $V^{y}(< \bar{0} >) = \{\emptyset\}$ and $X^{y}(\mathbb{Z}_6) = \{\emptyset\}$, $X^{y}(< \bar{2} >) = \{< \bar{3} >\}$, $X^{y}(< \bar{3} >) = \{< \bar{2} >\}$, $X^{y}(< \bar{0} >) = spec^{y}(\mathbb{Z}_6)$ where $\mathbb{Z}_6$ as $\mathbb{Z}$-module.

(10) $spec^{y}(\mathbb{Z}_{12}) = V^{y}(\mathbb{Z}_{12}) = \{< \bar{4} >, < \bar{6} >, < \bar{3} >\}$, $V^{y}(< \bar{2} >) = \{< \bar{4} >, < \bar{6} >\}$, $V^{y}(< \bar{3} >) = \{< \bar{6} >, < \bar{3} >\}$ $V^{y}(< \bar{6} >) = \{< \bar{6} >\}$, $V^{y}(< \bar{4} >) = \{< \bar{4} >\}$, $V^{y}(< \bar{0} >) = \{\emptyset\}$ $X^{y}(\mathbb{Z}_{12}) = \{\emptyset\}$, $X^{y}(< \bar{2} >) = \{< \bar{3} >\}$ $X^{y}(< \bar{3} >) = \{< \bar{4} >\}$, $X^{y}(< \bar{6} >) = \{< \bar{4} >, < \bar{3} >\}$ $X^{y}(< \bar{4} >) = \{< \bar{6} >, < \bar{3} >\}$ and $X^{y}(< \bar{0} >) = spec^{y}(\mathbb{Z}_{12})$ where $\mathbb{Z}_{12}$ as $\mathbb{Z}$-module.

(11) $spec^{y}(\mathbb{Z}_{p^\infty}) = V^{y}(\mathbb{Z}_{p^\infty}) = \left\{< \frac{1}{p^n} + \mathbb{Z} > \mid n = 1,2, \dots.\right\} \cup \{\mathbb{Z}_{p^\infty}\}$ where every submodule of $\mathbb{Z}_{p^\infty}$ of the form $< \frac{1}{p^n} + \mathbb{Z} >= \{r.\left(\frac{1}{p^n} + \mathbb{Z}\right) \mid r \in \mathbb{Z}\}$, $V^{y}\left(< \frac{1}{p^n} + \mathbb{Z} >\right) = \{< \frac{1}{p^m} + \mathbb{Z} > \mid m = 1,2, \dots. n\}$, $V^{y}\left(0_{\mathbb{Z}_{p^\infty}}\right) = \emptyset$ and $X^{y}(\mathbb{Z}_{p^\infty}) = \{\emptyset\}$,

$X^y\left(<\frac{1}{p^n}+\mathbb{Z}>\right)=\left\{<\frac{1}{p^m}+\mathbb{Z}>, \mathbb{Z}_{p^\infty}\right\}$ for each positive integer $m>n$ and $X^y\left(0_{\mathbb{Z}_{p^\infty}}\right)=spec^y\left(\mathbb{Z}_{p^\infty}\right)$ where $\mathbb{Z}_{p^\infty}$ as $\mathbb{Z}$-module.

(12) $spec^y\left(\mathbb{Z}_{p^\infty}\oplus\mathbb{Z}_{p^\infty}\right)=V^y\left(\mathbb{Z}_{p^\infty}\oplus\mathbb{Z}_{p^\infty}\right)=\{\mathbb{Z}_{p^\infty}\oplus\mathbb{Z}_{p^\infty}, \mathbb{Z}_{p^\infty}\oplus 0, <\frac{1}{p^n}+\mathbb{Z}>\oplus 0,\ 0\oplus\mathbb{Z}_{p^\infty},\ 0\oplus<\frac{1}{p^m}+\mathbb{Z}>, <(\frac{1}{p^n}+\mathbb{Z},\frac{1}{p^m}+\mathbb{Z})>\}$, $V^y\left(\mathbb{Z}_{p^\infty}\oplus 0\right)=\{\mathbb{Z}_{p^\infty}\oplus 0, <\frac{1}{p^n}+\mathbb{Z}>\oplus 0\}$, $V^y\left(0\oplus\mathbb{Z}_{p^\infty}\right)=\{0\oplus\mathbb{Z}_{p^\infty},\ 0\oplus<\frac{1}{p^m}+\mathbb{Z}>\}$ for each positive integer n,m and $V^y\left(<\frac{1}{p^n}+\mathbb{Z}>\oplus 0\right)=\{<\frac{1}{p^i}+\mathbb{Z}>\oplus 0\}$, $V^y\left(0\oplus<\frac{1}{p^m}+\mathbb{Z}>\right)=\{0\oplus<\frac{1}{p^j}+\mathbb{Z}>\}$ and $V^y\left(<(\frac{1}{p^n}+\mathbb{Z},\frac{1}{p^m}+\mathbb{Z})>\right)=\{<(\frac{1}{p^i}+\mathbb{Z},\frac{1}{p^j}+\mathbb{Z})>, <(\frac{1}{p^i}+\mathbb{Z},0)>, <(0,\frac{1}{p^j}+\mathbb{Z})>\}$ for each positive integers $i\le n$, $j\le m$ and p any prime numbers where $\mathbb{Z}_{p^\infty}\oplus\mathbb{Z}_{p^\infty}$ as $\mathbb{Z}$-module.

(13) Let $p\neq q$ any prime numbers then $spec^y\left(\mathbb{Z}_{p^\infty}\oplus\mathbb{Z}_{q^\infty}\right)=V^y\left(\mathbb{Z}_{p^\infty}\oplus\mathbb{Z}_{q^\infty}\right)=\left\{\mathbb{Z}_{p^\infty}\oplus\mathbb{Z}_{q^\infty}, \mathbb{Z}_{p^\infty}\oplus 0, <\frac{1}{p^n}+\mathbb{Z}>\oplus 0,\ 0\oplus\mathbb{Z}_{q^\infty},\ 0\oplus<\frac{1}{q^m}+\mathbb{Z}>\right\}$, $V^y\left(\mathbb{Z}_{p^\infty}\oplus 0\right)=\left\{\mathbb{Z}_{p^\infty}\oplus 0, <\frac{1}{p^n}+\mathbb{Z}>\oplus 0\right\}$, $V^y\left(0\oplus\mathbb{Z}_{q^\infty}\right)=\left\{0\oplus\mathbb{Z}_{q^\infty},\ 0\oplus<\frac{1}{q^m}+\mathbb{Z}>\right\}$ for each positive integer n and m, $V^y\left(<\frac{1}{p^n}+\mathbb{Z}>\oplus 0\right)=\left\{<\frac{1}{p^i}+\mathbb{Z}>\oplus 0\right\}$, $V^y\left(0\oplus<\frac{1}{q^m}+\mathbb{Z}>\right)=\left\{0\oplus<\frac{1}{q^j}+\mathbb{Z}>\right\}$, $V^y\left(<\frac{1}{p^n}+\mathbb{Z},\ \frac{1}{q^m}+\mathbb{Z}>\right)=\left\{<\frac{1}{p^i}+\mathbb{Z}>\oplus 0,\ 0\oplus<\frac{1}{q^j}+\mathbb{Z}>\right\}$ for each positive integers $i\le n,\ j\le m$ where $\mathbb{Z}_{p^\infty}\oplus\mathbb{Z}_{q^\infty}$ as $\mathbb{Z}$-module.

(14) $spec^y\left(\mathbb{Z}_{p^\infty}\oplus<\frac{1}{p}+\mathbb{Z}>\right)=V^y\left(\mathbb{Z}_{p^\infty}\oplus<\frac{1}{p}+\mathbb{Z}>\right)=\{\mathbb{Z}_{p^\infty}\oplus 0, <\frac{1}{p^n}+\mathbb{Z}>\oplus 0, <\frac{1}{p^n}+\mathbb{Z}>\oplus<\frac{1}{p}+\mathbb{Z}>, 0\oplus<\frac{1}{p}+\mathbb{Z}>\}$, $V^y\left(\mathbb{Z}_{p^\infty}\oplus 0\right)=\{\mathbb{Z}_{p^\infty}\oplus 0, <\frac{1}{p^n}+\mathbb{Z}>\oplus 0\}$,$V^y\left(0\oplus<\frac{1}{p}+\mathbb{Z}>\right)=\{0\oplus<\frac{1}{p}+\mathbb{Z}>\}$, $V^y\left(<\frac{1}{p^n}+\mathbb{Z}>\oplus 0\right)=\{<\frac{1}{p^i}+\mathbb{Z}>\oplus 0\}$, $V^y\left(<\frac{1}{p^n}+\mathbb{Z}>\oplus<\frac{1}{p}+\mathbb{Z}>\right)=\{<\frac{1}{p^i}+\mathbb{Z}>\oplus<\frac{1}{p}+\mathbb{Z}>, <\frac{1}{p^i}+\mathbb{Z}>\oplus 0,\ 0\oplus<\frac{1}{p}+\mathbb{Z}>\}$for each positive integer $i\le n$ and any prime number p where $\mathbb{Z}_{p^\infty}\oplus<\frac{1}{p}+\mathbb{Z}>$ as $\mathbb{Z}$-module.

Recall that M is called an atomic module if every non-zero submodule A of M, then A contains a simple submodule [4].

Proposition (2.5): Let M be an atomic module. For any submodule A of M, if $V^y(A)=\emptyset$ then $A=0$.

Proof. Assume $V^y(A)=\emptyset$ Suppose that $A\neq 0$ so there exists a simple submodule B of M such that $B\subseteq A$ implies $B\in V^y(A)$ and thus $V^y(A)\neq\emptyset$ which is a contradiction so that $A=0$.

Definition (2.6): N is called a maximal submodule under A if N is a maximal element in $V^y(A)$.

Before we give the following result, we refer that the set $[N:_R M]=\{r\in R$ and $Mr\subseteq N\}$ is an ideal of the ring R where M is an R-module and N is a submodule of M.

Proposition (2.7): Let M be an atomic R-module. Then for every non-zero submodule A of M, there exists $N\in spec^y(M)$ such that N is maximal under A.

Proof. Suppose that $0\neq A$ is a submodule of M thus $S(A)=\{B\in S(M)\,|\,B\subseteq A\}\neq\emptyset$ where $S(M)$ is the set of all simple submodules of M. Since $S(M)\subseteq spec^y(M)$ implies $S(A)\subseteq V^y(A)$ means that $V^y(A)\neq\emptyset$. Let $N_1\subseteq N_2\subseteq\cdots$ be an ascending chain in $V^y(A)$

means N_i is a secondary submodule of M for each $= 1,2, \dots$. We claim $\bigcup_{i=1}^{\infty} N_i = N$ is a maximal submodule under A. To prove this, since $N_i \subseteq A$ for each $i = 1,2, \dots$ implies that $N \subseteq A$. Next we show that $[0:_R N] = \bigcap_{i=1}^{\infty}[0:_R N_i]$ for each submodule $N_i \not\supseteq N$ in M. Let $I = [0:_R N]$ then $NI = 0$ so we have $N_i I \subseteq NI = 0$ and hence $I \subseteq [0:_R N_i]$ for each i thus $I \subseteq \bigcap_{i=1}^{\infty}[0:_R N_i]$. The reverse inclusion, let $a \in \bigcap_{i=1}^{\infty}[0:_R N_i]$ then $a \in [0:_R N_i]$ implies $N_i a = 0$ for each i so that for each $n \in N = \bigcup_{i=1}^{\infty} N_i$ then $n \in N_i$ for some i and $na = 0$ it follows that $Na = 0$ means $a \in [0:_R N]$ as desired. Now we show that $\bigcap_{i=1}^{\infty}[0:_R N_i]$ is a primary ideal of R. Let $ab \in \bigcap_{i=1}^{\infty}[0:_R N_i]$ then $ab \in [0:_R N_i]$ so we already have $a \in [0:_R N_i]$ or $b^t \in [0:_R N_i]$ because N_i is a secondary submodule so that $[0:_R N_i]$ is a primary ideal and thus $a \in \bigcap_{i=1}^{\infty}[0:_R N_i]$ or $b^t \in \bigcap_{i=1}^{\infty}[0:_R N_i]$. This means $\bigcap_{i=1}^{\infty}[0:_R N_i] = [0:_R N]$ is a primary ideal and hence N is a secondary submodule. By Zorn's lemma, $V^y(A)$ has maximal N as desired.

Definition (2.8): We call that M is a module satisfies $\circledast$ condition if for any two submodules A and B of M with $V^y(A) = V^y(B)$ implies $A = B$. Equivalently, M satisfies $\circledast$ condition if for any two submodules $A \neq B$ implies $V^y(A) \neq V^y(B)$.

Theorem (2.9): If every non-zero submodule of M is secondary then M satisfies $\circledast$ condition.
Proof. If $A \neq 0 \neq N$ such that $V^y(A) = V^y(N)$ so we have $A \in V^y(A) = V^y(N)$ and hence $A \subseteq N$. Similarly, $N \in V^y(N) = V^y(A)$ implies $N \subseteq A$ and thus $N = A$ as desired.

Remarks and Examples (2.10):

(1) $\mathbb{Z}_6$ as $\mathbb{Z}$-module satisfies $\circledast$ condition because for any two submodules $A \neq B$ in $\mathbb{Z}_6$ implies $V^y(A) \neq V^y(B)$, however $\mathbb{Z}_6$ is not a secondary submodule.
(2) Every simple module satisfies $\circledast$ condition.
(3) Every submodule of $\mathbb{Z}$ does not satisfies $\circledast$ condition since for each submodule A of $\mathbb{Z}$, $V^y(A) = \emptyset$.
(4) Let $N \subseteq H \subseteq M$ be submodules of a module M. If N satisfies $\circledast$ condition then H need not be satisfies $\circledast$ condition. For example, the submodule $< \bar{4} >$ is a simple submodule of $< \bar{2} >$ in $\mathbb{Z}_{12}$ as $\mathbb{Z}$-module, then $< \bar{4} >$ satisfies $\circledast$ condition while $< \bar{2} >$ not satisfies $\circledast$ condition because $V^y(< \bar{4} >) = V^y(< \bar{2} >) = \{< \bar{4} >\}$.
(5) If a module satisfies $\circledast$ condition then every submodule is also satisfies $\circledast$ condition.

Proof. Let M be a module satisfies $\circledast$ condition with $V^y(A) = V^y(B)$ where A and B are submodules of M contained in N so we have $A = B$ in N.

Theorem (2.11): We have the following equivalent

(1) M is a module satisfies $\circledast$ condition.
(2) Every non-zero submodule of M can be represented as sum of secondary submodules.

Proof. (1) $\Rightarrow$ (2) Let $0 \neq N$ be a submodule of M, then $V^y(N) \neq \emptyset$ because if not then $V^y(N) = \emptyset = V^y(0)$ so by $\circledast$ condition $N = 0$ which is a contradiction. Let $B \in V^y(\sum_{A \in V^w(N)} A)$. Since for each $A \in V^y(N)$ we have $A \subseteq N$ follows $B \subseteq (\sum_{A \in V^y(N)} A) \subseteq N$ and so $B \in V^y(N)$. Now, let $B \in V^y(N)$ and thus $B \subseteq \sum_{A \in V^w(N)} A$ implies $B \in V^y(\sum_{A \in V^y(N)} A)$ that is $V^y(N) = V^y(\sum_{A \in V^y(N)} A)$ so by $\circledast$ condition we get $N = \sum_{A \in V^y(N)} A$.
(2) $\Rightarrow$ (1) Let $V^y(N) = V^y(A)$ for any submodules N and A of M so by hypothesis, $N = \sum_{i \in \Lambda} N_i$ and $A = \sum_{j \in \Lambda} A_j$ where N_i and A_j are secondary of M for each $i, j \in \Lambda$. Now, since $N_i \subseteq N$ and $A_j \subseteq A$ for each $i, j \in \Lambda$ implies that $N_i \in V^y(N)$ and $A_j \in V^y(A)$ and hence $N = \sum_{N_i \in V^y(N)} N_i$ and $A = \sum_{A_j \in V^y(A)} A_j$. Let $B \subseteq N$ then for some i, we have $B = \sum_{N_i \in V^y(N)} N_i = \sum_{N_i \in V^y(A)} N_i \subseteq A$ so that $B \subseteq A$ and vice versa if $B \subseteq A$ then similarly we have $B \subseteq N$ and hence $N = A$ as desired.

Recall that M is called a semisimple module if every submodule of M is a sum of simple submodules [5].

So we have already the following

Corollary (2.12): Every semisimple module satisfies $\circledast$ condition.

The converse of Corollary (2.12) is not hold in general

Example (2.13): $\mathbb{Z}_4$ as $\mathbb{Z}$-module satisfies $\circledast$ condition but $\mathbb{Z}_4$ is not semisimple.

Recall that M is called multiplication when each submodule N of M, we have $N = MI$ for an ideal I of R [6].

Corollary (2.14): When M is a faithful finitely generated multiplication R-module. The following are equivalent

(1) M satisfies $\circledast$ condition.

(2) R satisfies $\circledast$ condition.

Proof. (1) $\Rightarrow$ (2) Let I and J be ideals of R such that $V^{\mathcal{Y}}(I) = V^{\mathcal{Y}}(J)$. We claim that $V^{\mathcal{Y}}(MI) = V^{\mathcal{Y}}(MJ)$. Let $N \in V^{\mathcal{Y}}(MI)$ then $N \subseteq MI$ implies $N = MK$ for ideal K of R so we have $MK \subseteq MI$. So by [6, Theorem 3.1], we have $K \subseteq I$ and thus $K \in V^{\mathcal{Y}}(I) = V^{\mathcal{Y}}(J)$ and hence $K \subseteq J$ that is $MK \subseteq MJ$. Therefore $N \in V^{\mathcal{Y}}(MJ)$ and similarly for the reverse inclusion. Hence R satisfies the $\circledast$ condition.

(3) $\Rightarrow$ (1) The proof is similar way.

(4)

Example (2.15): $\mathbb{Z}_4$ as $\mathbb{Z}$-module satisfies $\circledast$ condition but $\mathbb{Z}$ is not satisfies $\circledast$ condition where $ann_{\mathbb{Z}}(\mathbb{Z}_4) = 4\mathbb{Z}$ that is, $\mathbb{Z}_4$ is not faithful. This shows that the faithful condition in Corollary (2.14) cannot be dropped.

Proposition (2.16): Let A and B be submodules of M. If $A \subseteq B$ then $V^{\mathcal{Y}}(A) \subseteq V^{\mathcal{Y}}(B)$ and hence $X^{\mathcal{Y}}(A) \supseteq X^{\mathcal{Y}}(B)$.

Proof. Let $N \in V^{\mathcal{Y}}(A)$ then $N \subseteq B$ and so $N \in V^{\mathcal{Y}}(B)$. Now, $X^{\mathcal{Y}}(B) = spec^{\mathcal{Y}}(M) - V^{\mathcal{Y}}(B) \supseteq spec^{\mathcal{Y}}(M) - V^{\mathcal{Y}}(A) = X^{\mathcal{Y}}(A)$.

Proposition (2.17): Let A and B be submodules of M where any cyclic submodule of M is secondary. If $V^{\mathcal{Y}}(A) \subseteq V^{\mathcal{Y}}(B)$ then $A \subseteq B$.

Proof. Let $m \in A$ then $R_m \subseteq A$ (where R_m is the cyclic submodule generated by the element m) implies $R_m \in V^{\mathcal{Y}}(A) \subseteq V^{\mathcal{Y}}(B)$ so that $R_m \subseteq B$ means that $m \in B$ as desired.

Corollary (2.18): Let M be a module with every cyclic submodule is secondary. Then M satisfies $\circledast$ condition.

Proof. Let $V^{\mathcal{Y}}(A) = V^{\mathcal{Y}}(B)$ so the rest follows by Proposition (2.17) as required.

Example (2.19): $\mathbb{Z}_6$ as $\mathbb{Z}$-module satisfies $\circledast$ condition and $\mathbb{Z}_6$ is a cyclic submodule of $\mathbb{Z}_6$ but it is not secondary.

3. Top$^{\mathcal{Y}}$-module

For every submodule A of M if we collect all varieties $V^{\mathcal{Y}}(A)$ of $spec^{\mathcal{Y}}(M)$ in the set denoted by $\zeta^{\mathcal{Y}}(M)$ then $\zeta^{\mathcal{Y}}(M)$ always contains the empty set and $spec^{\mathcal{Y}}(M)$. And $\zeta^{\mathcal{Y}}(M)$ closed under the intersections for any collection of submodules $\{A_\alpha\}_{\alpha\in\Lambda}$ of M, that is, $\bigcap_{\alpha\in\Lambda} V^{\mathcal{Y}}(A_\alpha) = V^{\mathcal{Y}}(A)$ for some submodule A of M. It is not hard to see that $\bigcap_{\alpha\in\Lambda} V^{\mathcal{Y}}(A_\alpha) = V^{\mathcal{Y}}(\bigcap_{\alpha\in\Lambda} A_\alpha)$ for any collection of submodules $\{A_\alpha\}_{\alpha\in\Lambda}$ of M. Further, $V^{\mathcal{Y}}(A) \cup V^{\mathcal{Y}}(B) \subseteq V^{\mathcal{Y}}(A + B)$ for any two submodules A and B of M. If the other inclusion in the last relation is hold, then $\zeta^{\mathcal{Y}}(M)$ will be a topology on $spec^{\mathcal{Y}}(M)$ and hence the ordered pair $(spec^{\mathcal{Y}}(M), \zeta^{\mathcal{Y}}(M))$ is a topological space. For in this case, the varieties $V^{\mathcal{Y}}(A)$ will be

closed sets in $(spec^{\mathcal{Y}}(M), \zeta^{\mathcal{Y}}(M))$ and $X^{\mathcal{Y}}(A) = spec^{\mathcal{Y}}(M) - V^{\mathcal{Y}}(A)$ are the open sets so that if $\tau^{\mathcal{Y}}(M)$ is the set of all open sets $X^{\mathcal{Y}}(A)$ then $(spec^{\mathcal{Y}}(M), \tau^{\mathcal{Y}}(M))$ is a topological space in that situation above. This led us to give the following concept.

Definition (3.1): M is called a top$^{\mathcal{Y}}$-module if for any submodules A and B of M there exists a submodule C of M such that $V^{\mathcal{Y}}(A) \cup V^{\mathcal{Y}}(B) = V^{\mathcal{Y}}(C)$. In other word, M is a top$^{\mathcal{Y}}$-module if $\zeta^{\mathcal{Y}}(M)$ is closed under finite unions.

Remarks and Examples (3.2):

(1) When M is simple module then $\zeta^{\mathcal{Y}}(M) = \{spec^{\mathcal{Y}}(M), \emptyset\} = \tau^{\mathcal{Y}}(M)$ is an indiscrete topology on $spec^{\mathcal{Y}}(M)$ and so that M is a top$^{\mathcal{Y}}$-module. Especially, take $M = \mathbb{Z}_p$ as $\mathbb{Z}$-module.

(2) Clearly, if M is a secondaryless module (and hence secondless) then $(spec^{\mathcal{Y}}(M), \tau^{\mathcal{Y}}(M))$ is a trivial topological space and hence M is a top$^{\mathcal{Y}}$-module.

(3) Let $\mathbb{Z}_4$ be a $\mathbb{Z}$-module. Then $\zeta^{\mathcal{Y}}(\mathbb{Z}_4) = \{spec^{\mathcal{Y}}(\mathbb{Z}_4), \{< \bar{2} >\}, \emptyset\} = \tau^{\mathcal{Y}}(\mathbb{Z}_4)$ i is topology on $spec^{\mathcal{Y}}(\mathbb{Z}_4)$ and hence $\mathbb{Z}_4$ is a top$^{\mathcal{Y}}$-module.

(4) Let $\mathbb{Z}_8$ as a $\mathbb{Z}$-module. Then $\zeta^{\mathcal{Y}}(\mathbb{Z}_8) = \{spec^{\mathcal{Y}}(\mathbb{Z}_8), \{< \bar{4} >, < \bar{2} >\}, \{< \bar{4} >\} \emptyset\} = \tau^{\mathcal{Y}}(\mathbb{Z}_8)$ is topology on $spec^{\mathcal{Y}}(\mathbb{Z}_8)$ and hence $\mathbb{Z}_8$ is a top$^{\mathcal{Y}}$-module.

(5) Let $\mathbb{Z}_6$ as a $\mathbb{Z}$-module. Then $\zeta^{\mathcal{Y}}(\mathbb{Z}_6) = \{spec^{\mathcal{Y}}(\mathbb{Z}_6), \emptyset, \{< \bar{2} >\}, \{< \bar{3} >\}\} = \tau^{\mathcal{Y}}(\mathbb{Z}_6)$ implies $(spec^{\mathcal{Y}}(\mathbb{Z}_6), \tau^{\mathcal{Y}}(\mathbb{Z}_6))$ is a discrete topological space so $\mathbb{Z}_6$ is a top$^{\mathcal{Y}}$-module.

(6) Let $\mathbb{Z}_{12}$ as a $\mathbb{Z}$-module. Then $\zeta^{\mathcal{Y}}(\mathbb{Z}_{12}) = \{spec^{\mathcal{Y}}(\mathbb{Z}_{12}), \emptyset, \{< \bar{4} >\}, \{< \bar{6} >\}, \{< \bar{4} >, < \bar{6} >\}, \{< \bar{3} >, < \bar{6} >\} = \tau^{\mathcal{Y}}(\mathbb{Z}_{12})$ is topology on $spec^{\mathcal{Y}}(\mathbb{Z}_{12})$.

(7) Let $\mathbb{Z}_{p^\infty}$ as $\mathbb{Z}$-module. Then $\zeta^{\mathcal{Y}}(\mathbb{Z}_{p^\infty}) = \{spec^{\mathcal{Y}}(\mathbb{Z}_{p^\infty}), \emptyset, \{< \frac{1}{p^m} + \mathbb{Z} > | m = 1,2, \dots . n\}\}$ for some positive integers n and m.It is not hard to check that $\zeta^{\mathcal{Y}}(\mathbb{Z}_{p^\infty})$ is closed under finite unions. It follows that $\mathbb{Z}_{p^\infty}$ is a top$^{\mathcal{Y}}$-module.

(8) Let $\mathbb{Z}_p \oplus \mathbb{Z}_p$ as $\mathbb{Z}$-module for any p a prime number. Then $\zeta^{\mathcal{Y}}(\mathbb{Z}_p \oplus \mathbb{Z}_p) = \{spec^{\mathcal{Y}}(\mathbb{Z}_p \oplus \mathbb{Z}_p), \emptyset, \{\mathbb{Z}_p \oplus 0\}, \{0 \oplus \mathbb{Z}_p\}, \{< (\bar{1}, \bar{1}) >\}\}$ implies $\tau^{\mathcal{Y}}(\mathbb{Z}_p \oplus \mathbb{Z}_p) = \{spec^{\mathcal{Y}}(\mathbb{Z}_p \oplus \mathbb{Z}_p), \emptyset, \{\mathbb{Z}_p \oplus \mathbb{Z}_p, \mathbb{Z}_p \oplus 0 < (\bar{1}, \bar{1}) >, \}, \{\mathbb{Z}_p \oplus \mathbb{Z}_p, 0 \oplus \mathbb{Z}_p, < (\bar{1}, \bar{1}) >\}, \{0 \oplus \mathbb{Z}_p, \mathbb{Z}_p \oplus 0, \mathbb{Z}_p \oplus \mathbb{Z}_p\}\}$. We see that $\zeta^{\mathcal{Y}}(\mathbb{Z}_p \oplus \mathbb{Z}_p)$ is not closed under finite union because there not exists a submodule C of M, $V^{\mathcal{Y}}(\mathbb{Z}_p \oplus 0) \cup V^{\mathcal{Y}}(0 \oplus \mathbb{Z}_p) = V^{\mathcal{Y}}(C)$,and hence $(spec^{\mathcal{Y}}(\mathbb{Z}_p \oplus \mathbb{Z}_p), \zeta^{\mathcal{Y}}(\mathbb{Z}_p \oplus \mathbb{Z}_p))$ is not a top$^{\mathcal{Y}}$-module that is, $\mathbb{Z}_p \oplus \mathbb{Z}_p$ is not a topological space with respect to $\zeta^{\mathcal{Y}}(\mathbb{Z}_p \oplus \mathbb{Z}_p)$.

(9) Similarly of (8), $\mathbb{Z}_{p^\infty} \oplus \mathbb{Z}_{p^\infty}$, $\mathbb{Z}_{p^\infty} \oplus \mathbb{Z}_{q^\infty}$ and $\mathbb{Z}_{p^\infty} \oplus < \frac{1}{p} + \mathbb{Z} >$ are not top$^{\mathcal{Y}}$-module.

(10) Direct sum of top$^{\mathcal{Y}}$-modules may not be top$^{\mathcal{Y}}$. For example, $\mathbb{Z}_p$ as $\mathbb{Z}$-module is a top$^{\mathcal{Y}}$-module for any a prime number p but $\mathbb{Z}_p \oplus \mathbb{Z}_p$ is not a top$^{\mathcal{Y}}$-module by (8).

(11) If M is a top$^{\mathcal{Y}}$-module, then M need not be satisfies $\circledast$ condition. For example, $\mathbb{Z}$ is a top$^{\mathcal{Y}}$- $\mathbb{Z}$-module but $\mathbb{Z}$ is not satisfies $\circledast$ condition.

(12) If M satisfies $\circledast$ condition then M need not be a top$^{\mathcal{Y}}$-module. For example, $\mathbb{Z}_p \oplus \mathbb{Z}_p$ as $\mathbb{Z}$-module satisfies the $\circledast$ condition but it is not a top$^{\mathcal{Y}}$-module.

Definition (3.3) [7]: Let M be a module and A is a submodule of M. The socle of A is defined to be the sum of all second submodules of M contained in A denoted by $soc(A)$. In case A does not contain any second submodule, the socle of A is defined to be the zero submodule. If $A = soc(A)$, then A is called socle submodule of M.

Definition (3.4) [2]: A second submodule N of a module M is called extraordinary if whenever A and B are socle submodules of M such that $N \subseteq A + B$, then $N \subseteq A$ or $N \subseteq B$. So we can give the following

Definition (3.5): Let M be a module and A is a submodule of M. The secondary socle of A is defined to be the sum of all secondary submodules of M contained in A denoted by $Y.soc(A)$. In case A does not contain any secondary submodule, the secondary socle of A is defined to be the zero submodule. If $A = Y.soc(A)$, then A is called secondary socle submodule of M.

Note (3.6): It is clear that $soc(A) \subseteq Y.soc(A) \subseteq A$ for any submodule A of M

Definition (3.7): A secondary submodule N of a module M is called Y-extraordinary if A and B are secondary socle submodule of M such that $N \subseteq A + B$, then $N \subseteq A$ or $N \subseteq B$.
We conjecture that Y-extraordinary and extraordinary are independent concepts but have no examples to show this. However, we have the following

Remark (3.8): If $V^y(A) \bigcup V^y(B) = V^y(A + B)$ for any tow submodules A and B of a module M, then M is a top^y-module.

Proof. Directly by putting $C = A + B$ in Definition 3.1.
The following theorem shows that the converse of Remark 3.8 is hold in some circumstances.
Theorem (3.9): The following assertions are equivalent

(1) M is a top^y-module.
(2) Every secondary submodule of M is Y-extraordinary.
(3) $V^y(A) \bigcup V^y(B) = V^y(A + B)$ for any secondary socle submodules A and B of M.

Proof. (1) $\Rightarrow$ (2) Let N be secondary of M and let A and B are secondary socle submodule of M such that $N \subseteq A + B$. By (1), there exists a submodule C of M such that $V^y(A) \bigcup V^y(B) = V^y(C)$. Since A is a secondary socle submodule of M thus $A = \sum_{i\in\wedge} A_i$, for some collection of secondary submodules $\{A_i\}_{i\in\wedge}$. It is clear $A_i \in V^y(A) \subseteq V^y(C)$ for each $i \in\wedge$ implies $A_i \subseteq C$ and hence $A \subseteq$ C. By similar way, $B \subseteq$C it follows that $A + B \subseteq C$ and hence $V^y(A + B) \subseteq V^y(C) = V^y(A) \bigcup V^y(B)$ as desired.
(2) $\Rightarrow$ (3) We prove $V^y(A) \bigcup V^y(B) = V^y(A + B)$ for any secondary socle submodules A and B of M. Let $N \in V^y(A + B)$ implies $N \subseteq A + B$ but N is Y-extraordinary thus $N \subseteq A$ or $N \subseteq B$ that is, $N \in V^w(A) \bigcup V^w(B)$. The reverse inclusion is true always as desired.
(3) $\Rightarrow$ (1) It is clear.

Definition (3.10): [3] A non-zero submodule N of M is strongly hollow whenever $N \subseteq A + B$, then $N \subseteq A$ or $N \subseteq B$.

Every strongly hollow submodule is Y-extraordinary. However, we have the following result

Corollary (3.11): Consider the following.

(1) M is a top^y-module.
(2) Every secondary submodule of M is strongly hollow.
(3) $V^y(A) \bigcup V^y(B) = V^y(A + B)$ for any submodules A and B of M.
(4)

Proof. (2) $\Leftrightarrow$ (3), (3) $\Rightarrow$ (1) and (2) $\Rightarrow$ (1) it is clear, while (1) $\Rightarrow$ (2) is not hold in general for example, $\mathbb{Q}$ is a top^y $\mathbb{Z}$-module where $\mathbb{Q}$ is secondary but it is not strongly hollow since $\mathbb{Q} = \mathbb{Q}_p \bigoplus \mathbb{Q}^p$ but $\mathbb{Q} \neq \mathbb{Q}_p$ and $\mathbb{Q} \neq \mathbb{Q}^p$. for every prime number p , where $\mathbb{Q}_p$ is the submodule of $\mathbb{Q}$ consisting all rational numbers whose denominators are relatively prime to p and $\mathbb{Q}^p$ is the submodule of $\mathbb{Q}$ consisting all rational numbers whose denominators are powers of the prime p.

Theorem (3.12): Let M be a finitely generated faithful multiplication module. We have the equivalent

(1) M is a top^y-module.
(2) R is a top^y-ring.

Proof. (1) $\Rightarrow$ (2) Let I be a secondary ideal of R, $I \subseteq J + K$ for ideals J, and K of R implies $MI \subseteq M(J + K) = MJ + MK$. By (1), $MI \subseteq MJ$ or $MI \subseteq MK$ and hence $I \subseteq J$ or $I \subseteq K$ thus I is a strongly hollow ideal so by Proposition (3.11), R is a $\text{top}^{\mathcal{Y}}$-module.

(1) $\Rightarrow$ (2) Let N be a secondary submodule of M, $N \subseteq A + B$ so that $N = MI$, $A = MJ$ and $B = MK$ for ideals I, J, and K of R it follows that $MI \subseteq MJ + MK = M(J + K)$ but M is cancellation thus $I \subseteq J + K$. By (2) either $I \subseteq J$ or $I \subseteq K$ implies $MI \subseteq MJ$ or $MI \subseteq MK$ that is $N \subseteq A$ or $N \subseteq B$ means N is strongly hollow so by Proposition (3.11) M is a $\text{top}^{\mathcal{Y}}$-module.

Proposition (3.13): Let M be an R-module and S a subring of R with M is a $\text{top}^{\mathcal{Y}}$ S-module. Then M is a $\text{top}^{\mathcal{Y}}$ R-module.
Proof. Let N be secondary submodule of an R-module M and A, B are secondary socle submodules of M with $N \subseteq A + B$. Let S be a subring of of R, M is a $\text{top}^{\mathcal{Y}}$ S-module and let N be a secondary submodule of S-module M and A, B are secondary socle of S-module M so already hold $N \subseteq A$ or $N \subseteq B$ that is N is Y-extraordinary so by Theorem (3.9), M is a $\text{top}^{\mathcal{Y}}$-module.

Proposition (3.14): Every submodule of a $\text{top}^{\mathcal{Y}}$-module is also $\text{top}^{\mathcal{Y}}$-module.
Proof. Let N be a submodule of a $\text{top}^{\mathcal{Y}}$-module M and A is a secondary submodule of N implies A is secondary of M so by Theorem (3.9), A is Y-extraordinary of M and follows A is Y-extraordinary in N. Thus N is a $\text{top}^{\mathcal{Y}}$-module.

The convers of Proposition (3.14) is not hold in general as follows

Example (3.15): Let $N = <\frac{1}{p} + \mathbb{Z} > \oplus <\frac{1}{q} + \mathbb{Z} >$ be a submodule of $M = \mathbb{Z}_{p^\infty} \oplus \mathbb{Z}_{q^\infty}$ as $\mathbb{Z}$-module where $p \neq q$ are prime numbers. Then $spec^{\mathcal{Y}}(N) = \{<\frac{1}{p} + \mathbb{Z} > \oplus 0, 0 \oplus <\frac{1}{q} + \mathbb{Z} >\}$ then $V^{\mathcal{Y}}(A) \cup V^{\mathcal{Y}}(B) = V^{\mathcal{Y}}(A + B)$ for any secondary socle submodules A and B of N so N is $\text{top}^{\mathcal{Y}}$ but M is not $\text{top}^{\mathcal{Y}}$.

Proposition (3.16): Every $\text{top}^{\mathcal{Y}}$-module is a top^{s}-module.

Proof. Let $N \in V^s(A + B)$ where A and B submodules of $\text{top}^{\mathcal{Y}}$ M such that $A = soc(A)$ and $B = soc(B)$.Then $N \in V^s(A + B) \subseteq V^{\mathcal{Y}}(A + B)$ $A \subseteq soc(A) \subseteq Y.soc(A)$ and $B \subseteq soc(B) \subseteq Y.soc(B)$. But $V^{\mathcal{Y}}(A + B) = V^{\mathcal{Y}}(A) \cup V^{\mathcal{Y}}(B)$ it follows $N \in V^{\mathcal{Y}}(A)$ or $N \in V^{\mathcal{Y}}(B)$ that is $N \subseteq A$ or $N \subseteq B$ but N is second so $N \in V^s(A)$ or $N \in V^s(B)$ and hence $V^s(A + B) \subseteq V^s(A) \cup V^s(B)$ as desired.

Proposition (3.17): Every chained module is a $\text{top}^{\mathcal{Y}}$-module.

Proof. Let A and B be two submodules of a chained module M so either $A \subseteq B$ or $B \subseteq A$. If $A \subseteq B$ then $V^{\mathcal{Y}}(A) \subseteq V^{\mathcal{Y}}(B)$ and so $V^{\mathcal{Y}}(A) \cup V^{\mathcal{Y}}(B) = V^{\mathcal{Y}}(B)$ means M is a $\text{top}^{\mathcal{Y}}$-module.

Corollary (3.18): Let M be a chained module. Then the collections of open (closed) sets of $(spec^{\mathcal{Y}}(M), \zeta^{\mathcal{Y}}(M))$ form a chain.

Corollary (3.19): Let M be a chained module. Then $spec^{\mathcal{Y}}(M) = V^{\mathcal{Y}}(M)$ is an irreducible space.

Proof. Let $spec^{\mathcal{Y}}(M) = V_1 \cup V_2$ for some closed subsets V_1 and V_2 of $(spec^{\mathcal{Y}}(M), \zeta^{\mathcal{Y}}(M))$. Because M is a chained module so by Proposition (3.17), M is a $\text{top}^{\mathcal{Y}}$-module. This implies $V_1 = V^{\mathcal{Y}}(A)$ and $V_2 = V^{w}(B)$ for submodules A and B of M and so $spec^{\mathcal{Y}}(M) = V^{\mathcal{Y}}(A) \cup V^{\mathcal{Y}}(B)$. By Corollary (3.18), the collections of open (closed) sets of

$(spec^{y}(M),\zeta^{y}(M))$ form a chain. Therefore $spec^{y}(M) = V^{y}(A)$ or $spec^{y}(M) = V^{y}(B)$ as desired.

Conclusion

In this work we present overview study of spectrum of secondary submodules. We show the relationship between the algebraic properties of the modules and the topological properties of their spectrum.

References

[1] S Yassemi 2001 The dual notion of prime submodules *Arch. Math. (Brno)* **37** pp 273-278

[2] T H Ansari and F Farshadifar 2014 The Zariski topology on the second spectrum of a module *Algebra Colloquium* **21**(4) 671-688, DOI:10.1142/S100538 6714000625.

[3] J Y Abuhlail 2015 Zariski topologies for coprime and second submodules *Algebra Colloquium* **22**(1) DOI:http://dx.doi.org/10.1142/S1005386715000061.

[4] T H Ansari, F Farshadifar 2012 On Secondary Modules *International Journal of Algebra* **6**(16) pp 769- 774

[5] F Kasch 1982 *Modules and Rings* Academic Press, London

[6] Z A El-Bast and P F Smith 1988 Multiplication Modules *Comm.Algebra* **16** pp 755-774

[7] T H Ansari and F Farshadifar 2012 On the Dual Notion of Prime Submodules *Algebra Colloquium* **19** (Spec 1) pp 1109-1116

A modified ARIMA model for forecasting chemical sales in the USA

A modified ARIMA model for forecasting chemical sales in the USA

Othman Mahdi Salah , Ghadeer Jasim Mohammed Mahdi , and Iman Ahmed Abud Al-Latif

Department of Mathematics, College of Education for Pure Sciences Ibn Al-Haitham, University of Baghdad, Baghdad, Iraq

E-mail: mahdighadeer@gmail.com

Abstract. model is derived, and the methodology is given in detail. The model is constructed depending on some measurement criteria, Akaike and Bayesian information criterion. For the new time series model, a new algorithm has been generated. The forecasting process, one and two steps ahead, is discussed in detail. Some exploratory data analysis is given in the beginning. The best model is selected based on some criteria; it is compared with some naïve models. The modified model is applied to a monthly chemical sales dataset (January 1992 to Dec 2019), where the dataset in this work has been downloaded from the United States of America census (www.census.gov). Ultimately, the forecasted sales for the next three years for chemical sales in the USA is provided.

1. Introduction

The autoregressive moving average (ARMA) and autoregressive integrated moving average (ARIMA) are among various methods used in the forecasting variables. ARMA/ARIMA predicts the trend using information obtained from the variables. Knowing and analyzing the probabilistic or stochastic, properties of the variable are required using ARIMA/ARIMA. These models are commonly known as the Box-Jenkins (1976) methodology [12]. Two assumptions should be assumed before fitting the model. First, the model is stationary. The series is said to be stationary if it exhibits the mean reversions, has a finite variance and has a theoretical correlogram that diminishes as the length increases. Second, invertibility assumption is required. Invertibility is essential such that a finite order can represent the series.

ARMA model is a component of two distinct models explain the behaviour of a series for two different perspectives: the autoregressive (AR) and the moving average (MA) models. MA combines the dependency between the residual error from a moving average model and an observation. The difference between ARMA and ARIMA is the integration component which brings us back to the subject of stationary. ARIMA model is a word of three parts AR, MA, and the integrate (I). It refers to the differencing of raw data points to allow the stationarity to hold. In other words, a data point is going to replace by the differences between two values. In reality, most variables are non-stationary; hence they have to go through a transformation process, which is called differencing or integration before they become stationary [1][6].

The standard notation of the ARIMA model is ARIMA$(p, d, q)(P, D, Q)$ where each component is contained as a parameter. P is the number of differences in lag-1. P is the leg order, and it is the

number of lag observations in the model. The parameter d represents how many times to perform lag-1 differencing. D refers to the seasonal differencing for a cycle with h seasons. We use lag-h differencing to remove stationary. ARIMA model requires the user to specify the parameter $p, d, q, P, D, and\ Q$. Determine the parameters is not a simple choice and required some experience and expertise. The typical method for determining these parameters is using visual inspection of the series to detect seasonality and trend, as well as looking at the autocorrelation and partial autocorrelation charts [3][7].

2. Methodology

The random variables set $\{x_t: t \in N\}$ is called a time series, where $\mathbb{N}$ is the set of the natural number, and it is called a timestamp. The common critical assumption in time series models is stationary, and it can be strong or weak forms. If the statistical distribution of $\{x_t: t \in \mathbb{N}\}$ is remained unchanged after shifting time scale, i.e., for any time, shift, say h, and observation x_i:

$$P\left(X_{t_1} \le x_1, X_{t_2} \le x_2, \dots, X_{t_k} \le x_k\right) = F\left(x_{t_1}, x_{t_2}, \dots, x_{t_k}\right)$$

$$= F\left(x_{h+t_1}, x_{h+t_2}, \dots, x_{h+t_k}\right) = P\left(X_{h+t_1} \le x_1, X_{h+t_2} \le x_2, \dots, X_{h+t_k} \le x_k\right)$$

The marginal distribution of X_t is independent of t. Two-dimensional distributions of $\{X_{t_1}, X_{t_2}\}$ are independent of the absolute location that related to t_1 and t_2 [4]. Thus, the mean function $E(X)$ is constant, and the covariance $\mathrm{Cov}(X_t, X_{t-k})$ is just a function of k. Similarly, a higher-order moment remains unchanged if a continuous-time shift is added [8].

A stochastically independent time series, with constant mean and continuous variance, is called a random time series. A discrete process $\{Z_t\}$ is called a purely random process if the random variables Z_t are from a sequence of identically distributed and mutually independent variables. This process suggests the system has a constant mean and variance; $\gamma(k) = cov(Z_t, Z_{t+k}) = 0$, for all k [14][15].

If $X_t = X_{t-1} + Z_t$, then the process $\{X_t\}$ is said to be a random walk process. Z_t is a purely random process with mean μ and variance σ_Z^2. When the process starts with $t = 0$ and $X_1 = Z_0$, we have:

$X_1 = X_0 + Z_1$, at $t = 1$
$X_2 = X_1 + Z_2 = X_0 + Z_1 + Z_2$, at $t = 2$
$X_3 = X_2 + Z_3 = X_0 + Z_1 + Z_2 + Z_3$, at $t = 3$
$\vdots$
$$X_t = X_0 + \sum_{i=1}^{n} Z_i$$

The first-order moment and the variance for the above process equal to

$$E[X_t] = X_0 + \sum_{i=1}^{n} E[Z_i] = X_0 + t\mu_z = t\mu_z \quad \text{and} \quad Var(X_t) = t\sigma_Z^2$$

A particular kind of filtering is differences that make a time series of data stationery by removing the trend. For seasonal data to attain average stationarity, differentiating data from first order is usually essential. Let's assume that $X_t = \{X_1, X_2, \dots, X_n\}$ is a non-stationary time series, so $\Delta X_t = X_t - X_{t-1}$ is the first-order difference, and $\Delta^2 X_{t+2} = \Delta X_{t+2} - \Delta X_{t+1}$ is the second-order difference [2] [5].

Let $\{Z_t\}$ be a purely random process with mean and variance equal to 0 and σ_Z^2. It is called Moving Average of order q, (MA (q)), if

$$X_t = \beta_0 Z_t - \beta_1 Z_{t-1} - \cdots - \beta_q Z_{t-q},$$

where $\{\beta_1, \beta_2, \ldots, \beta_q\}$ are constants. $\beta_0 = 1$ because of the random variables $Z_t, t \in \mathbb{N}$.

$$X_t = \alpha_1 X_{t-1} + \alpha_2 X_{t-2} + \cdots + \alpha_p X_{t-p} + Z_t$$
$$X_t = \delta + \alpha_1 X_{t-1} + \alpha_2 X_{t-2} + \cdots + \alpha_p X_{t-p} + Z_t$$

If $E[X_t] = E[X_{t-1}] = \cdots = E[X_p] = \mu$, then $E[X_t] = \mu = \delta + \alpha_1\mu + \alpha_2\mu + \cdots + \alpha_p\mu + 0$, hence

$$\mu = \frac{\delta}{1 - \alpha_1 - \alpha_2 - \cdots - \alpha_p}$$

By considering the condition $\alpha_1 + \alpha_2 + \cdots + \alpha_p < 1$, the above formulate is a constant. When $p = 1$, then the first-order autoregressive $AR(1)$is

$$X_t = \alpha X_t - 1 + Z_t \quad (1)$$

Equation 1 is also known as the Markov process. $AR(1)$ can be expressed as an infinite MA process by using the backshift operator $BX_t = X_t - 1$, i.e., $(1 - \alpha B)X_t = Z_t$, so

$$\begin{aligned} X_t &= \frac{Z_t}{1 - \alpha B} \\ &= (1 + \alpha B + \alpha^2 B^2 + \cdots) Z_t \\ &= Z_t + \alpha Z_t - 1 + \alpha^2 Z_t - 2 + \cdots \\ &= Z_t + \beta_1 Z_t - 1 + \beta_2 Z_t - 2 + \cdots \end{aligned}$$

The mean of X_t is zero, and the variance is the series $\sigma^2 Z(1 + \alpha^2 + \alpha^4 \ldots)$ converging with the condition $|\alpha| < 1$. Mixing both AR and MA in the model leads to the autoregressive moving average (ARMA) process, the process ARMA is of order (p, q) when it contains p autoregressive terms and q moving average terms, and it can be written as equation 2, where $\alpha_p(B)$ and $\beta_q(B)$ are polynomials of order p and q, respectively [9].

$$X_t = \alpha_1 X_{t-1} + \alpha_2 X_{t-2} + \cdots + \alpha_p X_{t-p} + Z_t - \beta_1 Z_{t-1} - \beta_2 Z_{t-2} - \cdots - \beta_q Z_{t-q}$$
$$\alpha_p(B) X_t = \beta_q(B) Z_t \quad (2)$$

Choosing the parameters based on visual inspection is based on different rules of thumb, such as a slowly decreasing autocorrelation chart combined a sharp decline in the partial autocorrelation chart, calles for q equals 0 and p equals to the largest partial autocorrelation. In most cases, either p is 0 or q is 0, and p plus q less than or equal to 3. A few general tips are to use differencing to remove the trend and seasonality to keep the model as simple as possible by differencing at most one time by choosing low values of p and q, and setting P and Q to 0 or 1 [10][11].

3. Exploratory Data Analysis

In this section, the chemical sales dataset is analyzed. In figure 1, the selling of chemicals is plotted; it is started from Jan 1992 to Dec 2019. There is a growing trend in almost all variables. Also, there is a dramatic drop in the level of data around 2008. The log scale is used to map the data in figure 2, and the first knowledge difference is shown in figure 3. The dataset is stationary from the first difference, so further differences do not need to be taken. A significant variation can be seen between 2008 and 2010 when anyone looks at the differential map. For the dataset, the diagnosis plot is shown in figure 4. It is evident that the information is seasonal and has a growing pattern. We should think about the best model from the plot that we can use to estimate revenue for the next three years.

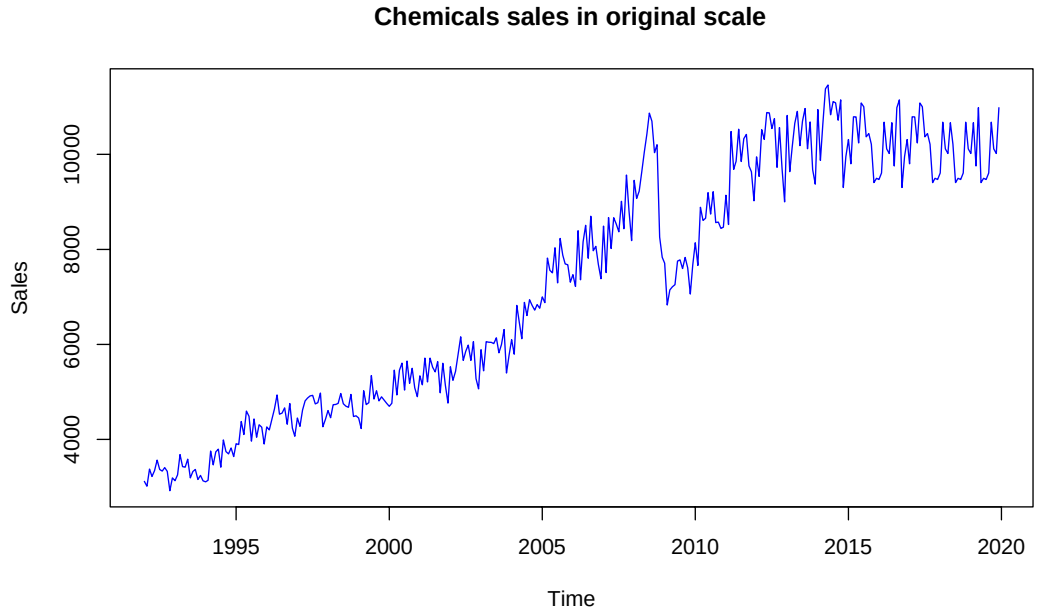

Figure 1. Chemicals sales on the original scale.

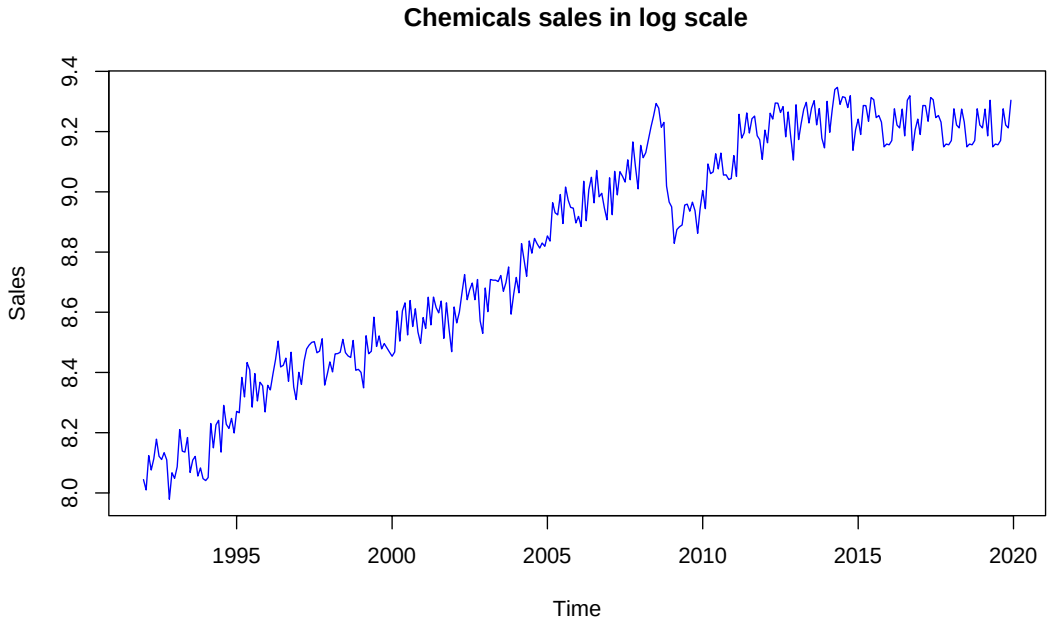

Figure 2. Chemical sales on the log scale.

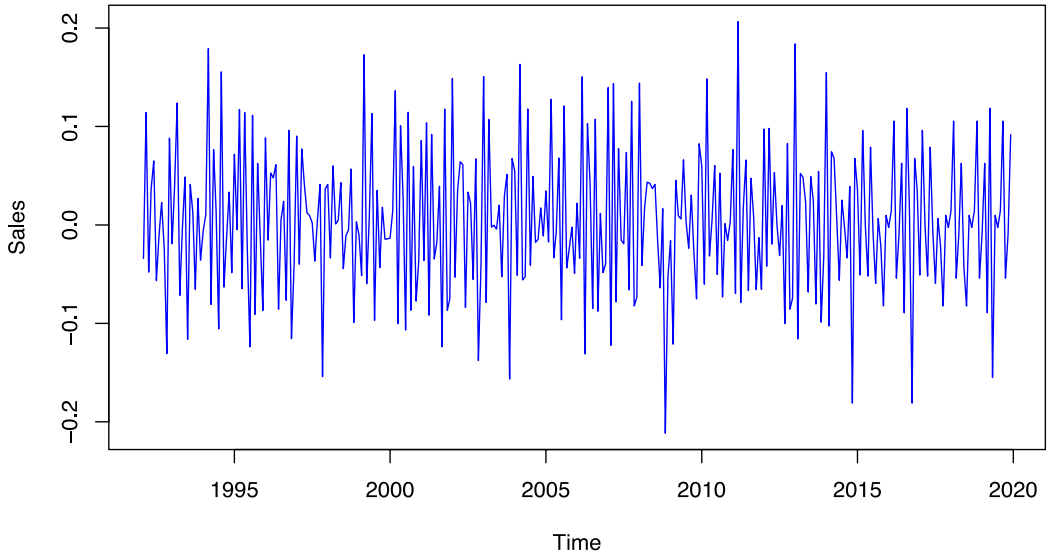

Figure 3. First difference in chemical sales.

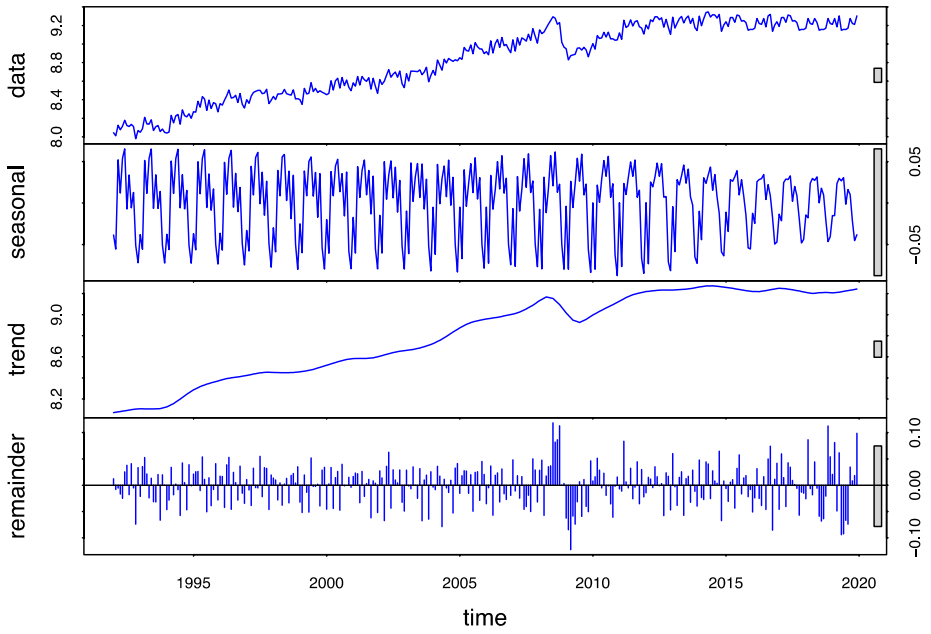

Figure 4. diagnosis plot for chemical sales.

4. Integrated Autoregressive Moving Average Models (ARIMA)

In general, there are two models for ARIMA depend on whether the data set is stationary or non-stationary. A non-seasonal ARIMA model can be written as [9]

$$\left(1-\phi_1 B-\cdots-\phi_p B^p\right)(1-B)^d y_t = c+\left(1+\theta_1 B+\ldots+\theta_q B^q\right)\epsilon_t$$

where $c=\mu\left(1-\phi_1-\cdots-\phi_p\right)$ and μ is the mean of $(1-B)^d y_t$.

The above equation can be written as follows:

$$\Phi(B)(1-B)^d y_t = c+\theta(B)\epsilon_t$$

where $\Phi(B)=\left(1-\phi_1 B-\cdots-\phi_p B^p\right)$ is a p^{th} order polynomial in B, and $\theta(B)=\left(1+\theta_1 B+\theta_q B^q\right)$ is a q^{th} order polynomial in B. A non-seasonal ARIMA model can be written as ARIMA(p,d,q). For the seasonal dataset, a seasonal ARIMA model can be formed by including additional seasonal terms in the ARIMA model, and it can be written as follows: $ARIMA(p,d,q)(P,D,Q)_m$ where $m=$ number of observations per year. For example, for quarterly data when $(p=1,d=1,q=1,P=1,D=1,Q=1)$ the seasonal ARIMA model can be written as follows [13]:

$$(1-\phi_1 B)(1-\Phi_1 B^{12})(1-B)(1-B^{12})y_t = (1+\theta_1 B)(1+\Theta_1 B^{12})\epsilon_t$$

The above equation is denoted by $ARIMA(1,1,1)(1,1,1)_{12}$. The multiplicative seasonal ARIMA model is given by

$\Phi_P(B^s)\phi(B)\nabla_s^D\nabla^d y_t = \delta+\Theta_Q(B^s)\theta(B)\epsilon_t$, where

$\Phi_P(B^s)$: seasonal autoregressive of order P

$\phi(B)$: ordinary autoregressive of order p

$\Theta_Q(B^s)$: moving average components of order Q

$\theta(B)$: moving average components of order q

$\nabla_s^D=(1-\mathrm{B})^{\mathrm{SD}}$: seasonal difference component

$\nabla^d=(1-\mathrm{B})^{\mathrm{d}}$: ordinary difference component

ϵ_t: is the usual Gaussian white noise process.

ARIMA model with the seasonal part is going to be used for forecasting the sales. If anyone wants to stabilize the time series, the Log transform and differences were used as the preferred approaches. The seasonal and nonseasonal differences were used to stabilize the periodicity and the term trend.

5. Forecasting Sales for the Modified ARIMA model

One explanation for developing the model is forecasting or predicting future values that are still unnoticed. For predictive analysis, the ARIMA model is a good time-series data that is used to test or forecast future patterns. ARIMA model is a form of regression analysis that measures the intensity of one independent variable to the other. The model aims to forecast the future by checking the differences between values in the series The ARIMA model that was discussed in the previous section is based on minimizing the mean square forecasting error. Forecasting is an extrapolation of the trend when the model adds zero-mean white noise to the simply deterministic trend. On the other hand, if the model contains autocorrelation, the predictions take advantage of the correlation to produce the best predictions. ARIMA(1,1) with a constant term is: $y_t = y_{t-1}+\theta_0+e_t-\theta e_{t-1}$, so

$$\hat{y}_t(l) = \hat{y}_t(l-1)+\theta_0-\theta e_t = y_t+l\theta_0-\theta e_t$$

$$e_t(l) = e_{t+l,} + (1-\theta)e_{t+l-1} + (1-\theta)e_{t+l-2} + \cdots + (1-\theta)e_{t+1}, \quad \text{for all} \quad l \geq 1.$$

$Var\big(e_t(l)\big) = \sigma_l^2[1 + (l-1)(1-\theta)^2]$.

Similarly, for ARIMA(2,2)

$$y_t = 2y_{t-1} - y_{t-2} + \theta_0 + e_t - \theta_1 e_{t-1} + \theta_2 e_{t-2}$$

$$\hat{y}_t(1) = 2y_t - y_{t-1} + \theta_0 - \theta_1 e_t - \theta_2 e_{t-1}$$

$$\hat{y}_t(2) = 2y_t(1) - y_t + \theta_0 + \theta_2 e_t$$

$$\hat{y}_t(l) = 2\hat{y}_t(l-1) - \hat{y}_t(l-2) + \theta_0, \text{for all } l \geq 3.$$

The algorithm that is going to be used is summarized below. The modified ARIMA model can be summarized in the following algorithm,

Modified ARIMA Algorithm

Step 1: Understand patterns by plotting the data and identifying unusual observations.
Step 2: Use a Box-Cox transformation to stabilize the variance (if necessary).
Step 3: Difference the data it appears stationary (if necessary)
Step 4: Plot the ACF of the differenced data and try to determine possible candidate models.
Step 5: Try some models and use the AIC to search for a better model.
Step 6: Check the residuals from the model by plotting the ACF of the residuals and doing a portmanteau test of the residuals.
Step 7: Do the residuals look like white noise? If YES (calculate forecasts), NO (go to step 4).

6. Seasonal ARIMA model application to chemicals sales in the USA

Based on the given dataset, the aim is to find an appropriate ARIMA model. In this section, a modified ARIMA model that was presented in the previous section is used to forecast chemical sales for the next three years in the USA. Figure 5 shows a comparison between seasonal and non-seasonal models. The white noise assumption was checked in the Cumulative Periodogram plot. There is noise because the curve does not cross the lines. The Kolmogorov-Smirnov test is used to check the normality. Since the p-value equals 0.273, which is high enough, the data is normally distributed.

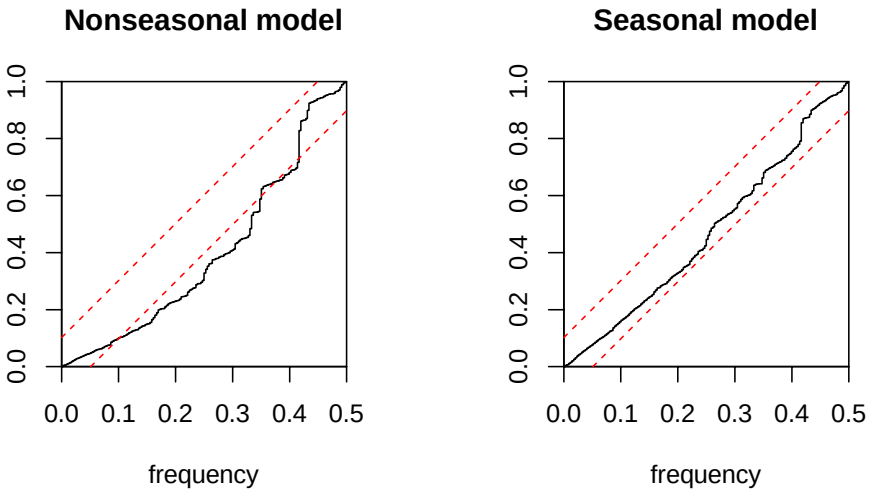

Figure 5. Diagnosis plot for the model.

In Table (1), several seasonal and order possibilities were tested. AIC and BIC values are checked for all the cases. The best model is selected based on the lowest AIC and BIC criteria. According to the AIC and BIC values, the 4^{th} model is chosen as the best model, where the order is c(1, 1, 1), and the seasonal is c(0, 1, 1). This means the series is differenced one at leg-1, and once at leg-12.

Table 1. Different order and seasonal values for the model.

Model	Order	Seasonal	AIC	BIC
1	c(0, 1, 1)	c(1, 1, 1)	185.115	179.272
2	c(0, 1, 2)	c(1, 1, 1)	187.245	170.863
3	c(1, 1, 3)	c(0, 1, 1)	170.215	176.855
4	**c(1, 1, 1)**	**c(0, 1, 1)**	**160.126**	**153.855**
5	c(0, 1, 1)	c(2, 1, 0)	184.215	174.812

For the selected ARIMA model, the Autocorrelation Function (ACF) was checked and used to estimate the parameters of the model. Box and Jenkins popularized the ARIMA approach, and ARIMA models are often referred to as Box-Jenkins models. Box and Tiao addressed the general transfer function model used for the ARIMA procedure. Box-Jenkins is used to estimate the parameters of the fitted model and examine the residual to see if the fitted model is adequate or not.

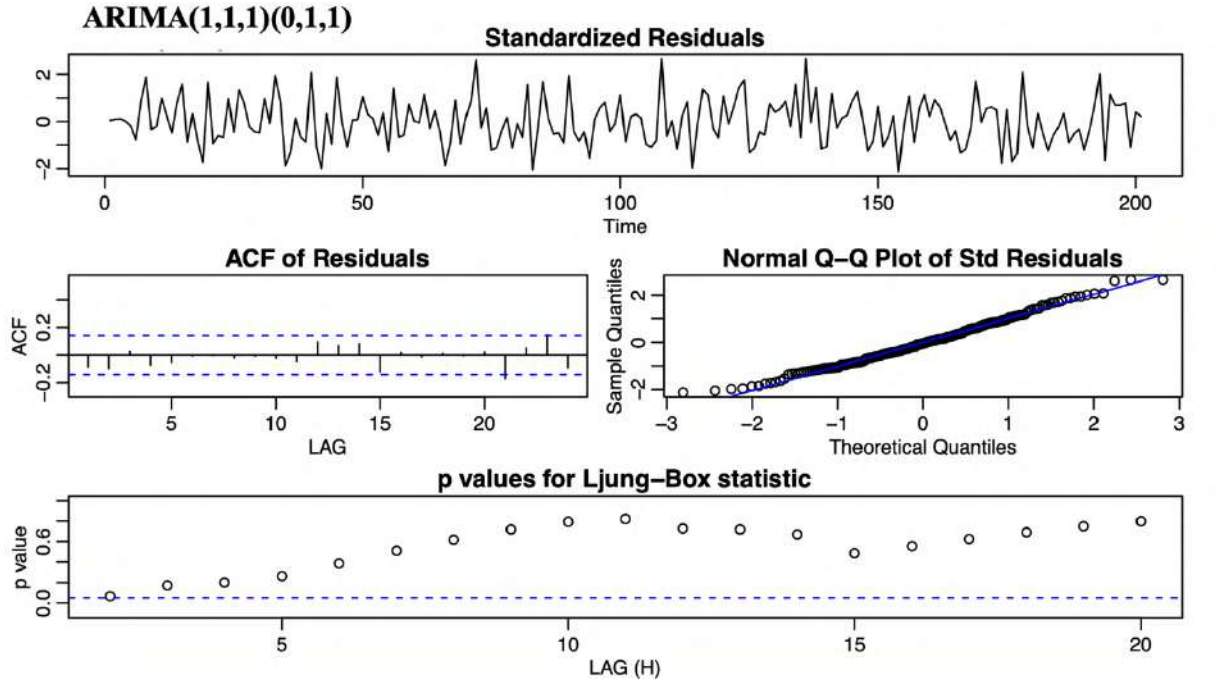

Figure 6. Diagnosis plot for the model.

The selected ARIMA model is compared to the ARMA and NAÏVE ARIMA models by RMSE and MASE calculations. The RMSE and MASE values for the modified ARIMA model are lowest values

in Table (2). This indicates that the selected model has performed better than the ARMA and NAÏVE ATIMA models.

Table 2. A comparison between ARMA, NAÏVE ARIMA, and modified ARIMA models.

	ARMA	**NAÏVE ARIMA**	**Modified ARIMA**
RMSE	0.937	0.722	0.535
MASE	0.847	0.804	0.478

The best model is used in the forecast for the next three years. In Table (3), the forecasted values for the next three years with their associated standard deviations are estimated. Three confidence intervals (50%, 75%, and 90%) are calculated and the upper and lower limits for each interval are evaluated.

Table 3. Forecasting chemical sales for the next three years in Millon dollars.

Years	**Months**	**Predicted value**	**Standard deviation**	**50% confidence Intervals**		**75% confidence Intervals**		**90% confidence Intervals**	
				Lower	**Upper**	**Lower**	**Upper**	**Lower**	**Upper**
2020	Jan	10329.35	540.20	10167.29	10491.41	10059.25	10599.45	10059.25	10707.49
	Feb	10783.47	558.36	10615.96	10950.98	10504.29	11062.65	10504.29	11174.32
	Mar	10400.63	582.56	10225.86	10575.40	10109.35	10691.91	10109.35	10808.42
	Apr	11148.64	605.36	10967.03	11330.25	10845.96	11451.32	10845.96	11572.39
	May	10202.52	627.36	10014.31	10390.73	9888.84	10516.20	9888.84	10641.67
	Jun	10289.64	648.62	10095.06	10484.22	9965.33	10613.95	9965.33	10743.67
	Jul	10131.08	669.19	9930.32	10331.84	9796.48	10465.68	9796.48	10599.52
	Aug	10302.73	689.16	10095.98	10509.48	9958.15	10647.31	9958.15	10785.14
	Sep	10909.93	708.56	10697.36	11122.50	10555.65	11264.21	10555.65	11405.92
	Oct	10458.44	727.45	10240.21	10676.67	10094.72	10822.16	10094.72	10967.65
	Nov	10340.48	745.86	10116.72	10564.24	9967.55	10713.41	9967.55	10862.58
	Dec	10935.95	763.81	10706.81	11165.09	10554.04	11317.86	10554.04	11470.62
2021	Jan	10645.76	923.19	10368.80	10922.72	10184.16	11107.36	10184.16	11291.99
	Feb	10965.54	958.26	10678.06	11253.02	10486.41	11444.67	10486.41	11636.33
	Mar	10844.59	996.44	10545.66	11143.52	10346.37	11342.81	10346.37	11542.10
	Apr	11357.67	1032.93	11047.79	11667.55	10841.20	11874.14	10841.20	12080.72
	May	10720.95	1068.20	10400.49	11041.41	10186.85	11255.05	10186.85	11468.69
	Jun	10806.16	1102.33	10475.46	11136.86	10254.99	11357.33	10254.99	11577.79
	Jul	10581.99	1135.44	10241.36	10922.62	10014.27	11149.71	10014.27	11376.80
	Aug	10771.15	1167.61	10420.87	11121.43	10187.34	11354.96	10187.34	11588.48
	Sep	11151.53	1198.92	10791.85	11511.21	10552.07	11750.99	10552.07	11990.78
	Oct	10754.32	1229.43	10385.49	11123.15	10139.60	11369.04	10139.60	11614.92
	Nov	10625.08	1259.21	10247.32	11002.84	9995.48	11254.68	9995.48	11506.53
	Dec	11040.51	1288.27	10654.03	11426.99	10396.37	11684.65	10396.37	11942.30
2022	Jan	10927.87	1394.98	10509.37	11346.37	10230.38	11625.36	10230.38	11904.36
	Feb	11181.65	1435.85	10750.89	11612.41	10463.72	11899.58	10463.72	12186.75
	Mar	11189.35	1478.42	10745.83	11632.87	10450.14	11928.56	10450.14	12224.24
	Apr	11587.03	1519.61	11131.15	12042.91	10827.22	12346.84	10827.22	12650.76
	May	11102.29	1559.73	10634.37	11570.21	10322.42	11882.16	10322.42	12194.10
	Jun	11186.55	1598.84	10706.90	11666.20	10387.13	11985.97	10387.13	12305.74
	Jul	10930.16	1637.02	10439.05	11421.27	10111.65	11748.67	10111.65	12076.08

	Aug	11127.93	1674.33	10625.63	11630.23	10290.76	11965.10	10290.76	12299.96
	Sep	11396.88	1710.83	10883.63	11910.13	10541.47	12252.29	10541.47	12594.46
	Oct	11026.34	1746.56	10502.37	11550.31	10153.06	11899.62	10153.06	12248.93
	Nov	10891.56	1781.57	10357.09	11426.03	10000.77	11782.35	10000.77	12138.66
	Dec	11218.55	1815.89	10673.78	11763.32	10310.61	12126.49	10310.61	12489.67

Figure 7 shows that the expected chemical curve matches the observed curve with small deviations. The time series for the estimated model is from Jan 2010 to Dec 2019. Predicted chemical sales are shown, and three prediction intervals (50%, 75% and 90%) are estimated. The prediction intervals get wider by increasing accuracy.

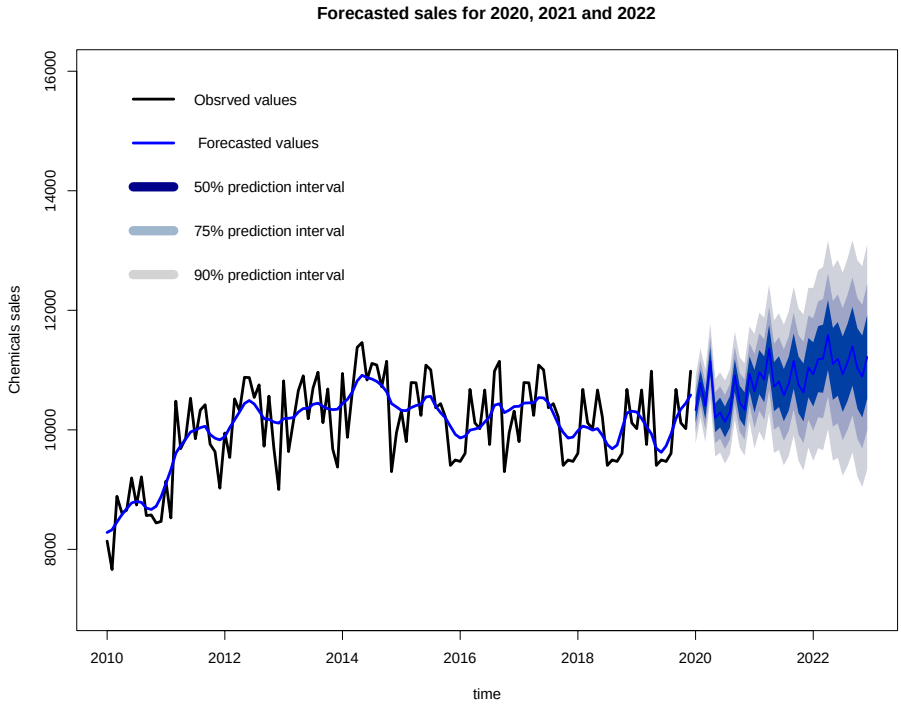

Figure 7. Forecasting chemical sales for the next three years in Millions of dollars.

7. Conclusion

In this work, a modified ARIMA model is introduced, and it has been applied to the monthly chemical sales dataset in the United States. In general, ARIMA models flexible family of models that capture autocorrelation in all kinds of forms. It has a strong statistical foundation, and therefore it's easy to get automated prediction intervals. It does assume and require a stationary series. This means no trend no seasonality and it assumes that this autocorrelation remains fixed throughout the period. The revised ARIMA model is compared to the ARMA and NAÏVE ARIMA models. The updated ARIMA model is more accurate than the ARMA and NAÏVE ARIMA models. An algorithm for the developed ARIMA model is given to be used for modelling and forecasting different data sets. The modified ARIMA model is used to forecast chemical sales in the USA over the next three years (2020, 2021, and 2022).

References

[1] Alsharif M H, Younes M K and Kim J 2019 Time series ARIMA model for prediction of daily and monthly average global solar radiation: *The case study of Seoul, South Korea. Symmetry* **11**(2) 240-250

[2] Bakar N A and Rossi S 2017 Autoregressive integrated moving average (ARIMA) model for forecasting cryptocurrency exchange rate in high volatility environment: A new insight of bitcoin transaction. *International Journal of Advanced Engineering Research and Science* **4(**11) 237311
[3] Bata M T H Carriveau R and Ting, D S K 2020 Short-term water demand forecasting using nonlinear autoregressive artificial neural networks. *Journal of Water Resources Planning and Management* **146**(3) 04020008
[4] Faruk D Ö 2010 A hybrid neural network and ARIMA model for water quality time series prediction. *Engineering applications of artificial intelligence* **23**(4) 586-594
[5] Fattah J, Ezzine L, Aman Z, El-Moussami H & Lachhab A 2018 Forecasting of demand using the ARIMA model *International Journal of Engineering Business Management 10* 1847979018808673
[6] Mahdi G J, Kalaf B A and Khaleel M A 2020 Enhanced Supervised Principal Component Analysis for Cancer Classification *IJS* **62**(4) Accepted paper
[7] Mahdi G J M, Chakraborty A, Arnold M E & Rebelo A G 2019 Efficient Bayesian modeling of large lattice data using spectral properties of Laplacian matrix. *Spatial Statistics* **29** 329–350
[8] Mahdi G J 2018 Hierarchical Bayesian Regression with Application in Spatial Modeling and Outlier Detection. Diss. *University of Arkansas, Fayetteville*
[9] Nguyen H V Naeem M A Wichitaksorn N & Pears R 2019 A smart system for short-term price prediction using time series models. *Computers & Electrical Engineering* **76** 339-352
[10] Oliveira P J, Steffen J L & Cheung P 2017 Parameter estimation of seasonal ARIMA models for water demand forecasting using the Harmony Search Algorithm. *Procedia Engineering* **186** 177-185
[11] Over M & Pudjihastuti H 2018 Arima model for forecasting the price of medium quality rice to anticipate price fluctuations. *Procedia Computer Science* **135** 707-711
[12] Padhan P C 2012 Application of ARIMA model for forecasting agricultural productivity in India. *Journal of Agriculture and Social Sciences* **8(**2)
[13] Tsay R S 2013 Multivariate time series analysis: with R and financial applications. John Wiley & Sons
[14] Yang Y, Liu C and Guo F 2017 Forecasting method of aero-material consumption rate based on the seasonal ARIMA model *In 2017 3rd IEEE International Conference on Computer and Communications (ICCC)* (pp 2899-2903)IEEE
[15] Zhang Q, Mahdi G, Tinker J, and Chen H 2020 A graph-based multi-sample test for identifying pathways associated with cancer progression *Computational Biology and Chemistry*. 26:107285. DOI:10.1016/j.compbiolchem.2020.107285

Some Results On The *N*—Fuzzy Domination in Fuzzy Graphs

Some Results On The N −Fuzzy Domination in Fuzzy Graphs

Hayder J. Yousif[1] and Ahmed A. Omran[2]

Department of Mathematics, College of Education for Pure Science, University of Babylon, Iraq

Email: Pure.Ahmed.Omran@uobabylon.edu.iq

Abstract. The purpose of this work is to introduce a new fuzzy domination parameter in fuzzy graphs $G_f = (\eta, \rho)$ it is called a ($N-$ fuzzy domination number) denoted by $\gamma_N(G_f)$. Some properties and boundaries of this definition are introduced. The $N-$ fuzzy domination number of fuzzy certain graphs as fuzzy complete, path, star, cycle, complete bipartite, and star are determined. Additionally the relation between the N-degrees of the vertices and the number of edges and N-edges of a fuzzy graph is discussedgraph discussed, with some suitable graphs and examples are given.

1. Introduction

Firstly, in 1965, L. Zadeh [1] published his paper "fuzzy set "in which clarified the uncertainty. In (1975) Rosenfeld [2] introduced the concept of fuzzy graph. In (1975) Kauffmann [3] introduced the fundamental idea of a fuzzy graph. The domination number played an important role via theoretical study in various fields as a fuzzy graph [4-5], topological graph [6-7], labeled graph [8-9], general graph [10-13]and others. Also, several applications in problems life were solved by these branches. So, the study of domination in fuzzy graphs worth to care. The concept of Domination in fuzzy graphs I, introduced by Somasundaram A.and Somasundaram S. [14-15] and them using effective edges. The concept of Domination in fuzzy graph so introduced by Nagoorgani A. and Chandrasekaran V. T. [16] but by using strong edges. There is more than one definition of domination in a fuzzy graph, in this work we will know the fuzzy domination number (γ_f) in fuzzy graph by Xavior et al.[17].

2. Preliminaries

Definition 2.1[18]: Consider $G = (V, E)$ be an undirected, finite, and simple graph. A mapping $\eta: V \to [0,1]$ where V is a non-empty set of vertices called a fuzzy subset and $G_f = (\eta, \rho)$ where $\rho: V \times V \longrightarrow [0,1]$ is called a fuzzy graph if $\rho(x,y) \leq \eta(x) \wedge \eta(y)$, where $\wedge$ is refer to a minimum fuzzy value.

Definition 2.2 [18]: $G^* = (\eta^*, \rho^*)$ is known as underlying crisp graph of $G_f = (\eta, \rho)$.

Definition 2.3 [18]:An edge (x,y) is called effective if $\rho(x,y) = \eta(x) \wedge \eta(y)$ and $G_f = (\eta, \rho)$is called strong fuzzy graph if every edge in G_f is effective.

Definition 2.4 [18]: A triangle free fuzzy graph is a fuzzy graph in which no three vertices form a triangle of edges.

Definition 2.5: The order of a fuzzy graph $G_f = (\eta, \rho)$ is denote by n and define as the cardinality of V, i.e. $|V| = n$, and the fuzzy cardinality of an order fuzzy graph is called fuzzy order of a fuzzy graph $G_f = (\eta, \rho)$ and define by summation membership fuzzy value for n which it denoted by P, i.e. $P = |\mathrm{n}| = \sum_{x \in \mathrm{V}} \eta(x)$.

Definition 2.6[19]: The open and closed neighborhood are define as $N(x) = \{y: (x, y)\text{effective}\}$ and $N[x] = N(x) \cup \{x\}$ respectively.

Definition 2.7[17]: A subset $D$of $V(G_f)$ is called fuzzy dominating set if every vertex $y \in V - D$ is adjacent at least one vertex $x \in D$such that $\rho(x, y) = \eta(x) \wedge \eta(y)$. The fuzzy domination number (γ_f) is summation membership fuzzy value for all minimum fuzzy dominating set.

3. $N-$ fuzzy dominating (NFD) set

Definition3.1: Let $G_f = (\eta, \rho)$ be a fuzzy graph. A subset D_N of $V(G_f)$ is called $N-$ fuzzy dominating (NFD) set if for every vertex $y \in V - D_N$ there exists a vertex $x \in D_N$ such that

1) (x, y) is effective edge.
2) $N(x) \cap N(y) \neq \emptyset$.

Definition3.2**:** The $N-$ fuzzy dominating (NFD) set D_N in a fuzzy graph $G_f = (\eta, \rho)$ is called minimum $N-$ fuzzy dominating $(MNFD)$ set if the number of vertices of all (NFD) sets greater than or equal the number of vertices in D_N

Definition3.3: The (NFD) set of a fuzzy graph $G_f = (\eta, \rho)$ is said to be minimal (NFD) set if no proper subset of D_N is (NFD) set of G_f.

Definition3.4: The minimum fuzzy cardinality of all $(MNFD)$ sets is called $N-$fuzzy domination number and denoted by $\gamma_N(G_f)$ or simply γ_N, i.e.

$\gamma_N(G_f) = min|D_{Ni}| = min\{\sum_{x \in D_{Ni}} \eta(x), D_{Ni}\ are\ \ (MNFD)sets$

Definition 3.5: Let $G_f = (\eta, \rho)$ be a fuzzy graph and $x \in V(G_f)$, then x is called $N-$isolated vertex if $N(x) \cap N(y) = \emptyset$ for all $y \in N(x)$ and x belong to every (NFD)set

Example1.1**:** Consider a strong fuzzy graph $G_f = (\eta, \rho)$, which is given in figuer1:

The minimal (NFD)set are : $D_{N1} = \{f, c, d\}, D_{N2} = \{b, c, d, g\}$, $D_{N3} = \{b, c, d, e\}$, $D_{N4} = \{a, c, d, g\}$, $D_{N5} = \{a, c, d, e\}$

The minimum (NFD) set is $D_{N1} = \{f, c, d\}$.

The $\gamma_N(G_f) = |D_{N1}| = 0.1 + 0.2 + 0.2 = 0.5$.

The minimum fuzzy dominating set $D = \{b, g\}$,

$then\ \gamma_f(G_f) = |D| = 1.3$

The vertices c and d are $N-$isolated vertices

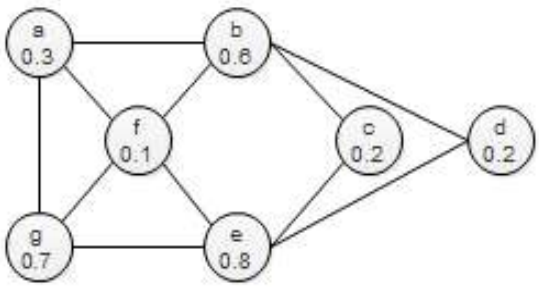

Figure 1 N-fuzzy dominating set.

4. Some properties of (NFD) set.

Observation3.2.1:

1) We will denote to all $N-$ isolated vertices of G_f by i_{sN}. And all isolated vertices of G_f by i_s.
2) $i_s \subseteq i_{sN} \subseteq D_N$, where D_N is the minimum (NFD) set of G_f.
3) Every end vertex is $N-$ isolated vertex.
4) If x and y are any two adjacent vertices in $V(G_f)$ such that $N(x) \cap N(y) \neq \emptyset$, then we say x is $N-$ adjacent to y or y is $N-$fuzzy dominate x.

Preposition 3.2.2: From the definition of $N-$ fuzzy domination number we can obtain:
1) $\gamma_N(K_n) = min(\sigma(x_i)), x_i \in V(K_\sigma)$.

Proof: Since every edge in K_n is effective and each vertex is dominates to all other vertices, then $N(x) \cap N(y) \neq \emptyset$ for all $x, y \in V(K_n)$. then, a minimum $N-$fuzzy dominating set of K_n is singleton. Hence, the result is obtained.
2) For any strong fuzzy path P_n , $\gamma_N(P_n) = P$

Proof: From the definition of $N-$ fuzzy dominating set of P_n , then there is only one minimal $N-$fuzzy dominating set of P_n which contains all vertices. Hence, $\gamma_N(P_n) = P$.
3) For any strong cycle fuzzy graph C_n $then$ $\gamma_N(C_n) = P$.

Proof: Same proof (2).
1) For any complete bipartite fuzzy graph $K_{\sigma 1,\sigma 2}$ then $\gamma_N(K_{\sigma 1,\sigma 2}) = \sum_{i=1}^{n} \eta(x_i) + \sum_{j=1}^{m} \eta(y_j)$ $x_i \in V_1$ and $y_j \in V_2$

Proof: Let $V(K_{\sigma 1,\sigma 2}) = V_1 \cup V_2$ such that $V_1 = \{x_1, x_2, \dots, x_n\}$ and $V_2 = \{y_1, y_2, \dots, y_m\}$.
Since each edge in $K_{\sigma 1,\sigma 2}$ is effective and every vertex in V_1 dominates to all other vertices in V_2 and vice versa also $N(x) \cap N(y) = \emptyset$ for all $x \in V_1$ and $y \in V_2$.then a minimum N- fuzzy dominating set of $(K_{\sigma 1,\sigma 2})$ must be has all vertices ($V_1$and V_1). Hence, the result is obtained.
4) For any strong fuzzy wheel graph with n vertices $\gamma_N(W_n) = \sigma(x), x\ is\ center\ vertex$.

Proof: Let (W_n) be strong fuzzy wheel and x be center vertex in W_n, since x is adjacent to all other vertices in W_n (adjacent to all vertices C_n) then $N(x) \cap N(y) \neq \emptyset$ for all $y \in W_n$. Hence, $\gamma_N(W_n) = \sigma(x), x\ is\ center\ vertex$.

Remark 3.2.3: If $G_f = (\eta, \rho)$ be a fuzzy graph has (NFD) set, we note that the $N-$ fuzzy domination number of a fuzzy graph G_f may be greater than, smaller than or equal to the fuzzy domination number of G_f.

Theorem 3.2.4 : Let D_N be a (NFD) set then D_N is minimal if and only if for every vertex $x \in D_N$ one of the following holds
i) Either $N(x) \cap D_N = \emptyset$ or $N(x) \cap N(y) = \emptyset$ $for\ all\ y \in N(x) \cap D_N$.
ii) There exists a vertex $y \in V - D_N$ such that $N(y) \cap D_N = \{x\}$ and $N(x) \cap N(y) \neq \emptyset$.

Proof: Suppose for every $x \in D_N$ one of the two conditions is hold , i.e. (i) or (ii) hold. Suppose D_N is not minimal. Then, there exist $x \in D_N$ such that $D_N - \{x\}$ is (NFD) set. Hence, there exist $y \in D_N - \{x\}$ such that (y, x) is effective edge, this is implies $y \in N(x)$ and $N(x) \cap N(y) \neq \emptyset$. Therefore, the

condition (i) does not hold. Then, x must be satisfying (ii), so there exist $y \in V$ - D_N such that $N(y) \cap D_N = \{x\}$ and $N(x) \cap N(y) \neq \emptyset$. Since $D_N - \{x\}$ is (NFD) set, then there exist $z \in D_N - \{x\}$ such that z is adjacent to y and $N(z) \cap N(x) \neq \emptyset$. Therefore, $z \in N(y) \cap D_N$, $N(z) \cap N(y) \neq \emptyset$ and $z \neq x$, contradiction to $N(y) \cap D_N = \{x\}$. Therefore, D_N is minimal (NFD)set. Now assume that D_N is minimal (NFD) set and the two conditions not hold, i.e. there is a vertex $x \in D_N$ such that $N(x) \cap D_N \neq \emptyset$ and $N(x) \cap N(y) \neq \emptyset$ for some $y \in N(x) \cap D_N$, and for each vertex $y \in V - D_N$ either $N(y) \cap D_N \neq \{x\}$ or $N(x) \cap N(y) = \emptyset$. Therefore, $D_N - \{x\}$ is (NFD) set. This contradicts the assumption. Hence, (i) or (ii) holds.

Theorem 3.2.5: A fuzzy graph $G_f = (\eta, \rho)$ has a unique minimal (NFD) set if and only if the set of all $N-$ isolated vertices forms a (NFD) set.

Proof: Let $G_f = (\eta, \rho)$ be a fuzzy graph has a unique minimal (NFD) set D_N, and suppose $i_{sN} = \{x \in V : x \text{ is } N - \text{isolated vertex}\}$. Then, $i_{sN} \subseteq D_N$, now suppose $D_N - i_{sN} \neq \emptyset$ and let $z \in D_N - i_{sN}$, since z is not $N-$ isolated vertex, $V - \{z\}$ is (NFD) set. Hence, there exists a minimal (NFD) set $D_{N1} \subseteq V - \{z\}$ and $D_{N1} \neq D_N$. This is a contradiction to our assumption. Now, if the set of all $N-$ isolated vertices forms a (NFD) set, then it is clear that G_f has a unique minimal (NFD) set.

Theorem3.3.6: Let $G_f = (\eta, \rho)$ be a fuzzy graph without $N-$ isolated vertices. If D_N is minimal (NFD) set, then $V - D_N$ is (NFD) set.

Proof: Let D_N be a minimal (NFD) set of G_f. Suppose $V - D_N$ is not (NFD) set. Then, there exists a vertex x in D_N such that x is not $N-$ fuzzy dominated by any vertex in $V - D_N$. Then, x is $N-$fuzzy dominated by at least one vertex y in $D_N - \{x\}$ and $N(x) \cap N(y) \neq \emptyset$. Thus, $D_N - \{x\}$ is a (NFD) set of G_f, which contradiction . Thus, every vertex x in D_N is $N-$ adjacent to at least one vertex y in $V - D_N$. Hence, $V - D_N$ is (NFD) set.

Corollary3.2.7: For any fuzzy graph $G_f = (\eta, \rho)$ without $N-$ isolated vertices has (NFD) set D_N then $\gamma_N(G_f) \leq P/2$.

Proof: Let $G_f = (\eta, \rho)$ be a fuzzy graph without $N-$ isolated vertices and D_N be a $\gamma_N - set$ of G_f,By theorem (2.3) $V - D_N$ is (NFD) set of G_f, then $|D_N| \leq |V - D_N|$, tak fuzzy cardinality to both sides we have $\gamma_N \leq P - \gamma_N$. Hence, $\gamma_N \leq P/2$

Proposition 3.2.8**:** Let $G_f = (\eta, \rho)$ be a strong fuzzy graph, then $\gamma_N(G_f) = P$ if and only if G_f is a triangle free fuzzy graph.

Proof**:** Let $G_f = (\eta, \rho)$ be a strong fuzzy graph with (NFD) set D_N and $\gamma_N(G_f) = P$. Suppose that G_f is a triangle. Let$\{x, y, z\}$ be the three vertices form a triangle. Clearly D_N except two vertices is (NFD) set of G_f. Thus, $\gamma_N(G_f) \leq p - \sum_{i=1}^{2} \eta(x_i)$. Hence, $\gamma_N(G_f) < P$, a contradiction, thus G_f is strong triangle free fuzzy graph. Conversely, Suppose that G_f is strong triangle free fuzzy graph. Let D_N be a (NFD) set of G_f with $\gamma_N(G_f) \neq P$, and $y \in V - D_N$, since D_N is (NFD) set of G_f. Then, there exists at least one vertex $z \in D_N$ such that y is $N-$ dominated by z. That is (z, y) is effective edge and $N(z) \cap N(y) \neq \emptyset$. Suppose $r \in N(z) \cap N(y) \neq \emptyset$. Then,$\{z, y, r\}$ form a triangle, a contradiction. Hence, $\gamma_N(G_f) = P$.

Preposition 3.2.9: For any fuzzy graph $G_f = (\eta, \rho)$ has a $(MNFD)$ set then, $\gamma_N(G_f) + \gamma_N(\overline{G_f}) \leq 2P$. Furthermore, the equality holds if and only if $0 < \rho(x, y) < \eta(x) \wedge \eta(y)$, $\forall (x, y) \in \mathrm{E}(G_f)$.

Proof: The inequality is trivial. Suppose that $0 < \rho(x,y) < \eta(x) \wedge \eta(y)$, $\forall (x,y) \in E(G_f)$ .Then $0 < \eta(x) \wedge \eta(y) - \rho(x,y) < \eta(x) \wedge \eta(y)$. This means that $0 < \overline{\rho(x,y)} < \eta(x) \wedge \eta\,(y)$ for all $\rho(x,y) \in E(\overline{G_f})$. thus $\gamma_N(\overline{G_f})$). Hence, $\gamma_N(G_f) + \gamma_N(\overline{G_f}) = 2P$.The converse it is direct.

Theorem 3.2.10 : Let $G_f^* = (\eta^*, \rho^*)$ be a Crips graph of a fuzzy graph $G_f = (\eta, \rho)$ without N −isolate vertices. Then, $\gamma_N(G_f^*) \leq {}^{n}/_{3}$. Further, the equality holds if $G_f = mK_3$ for some positive integer *m*.

Proof: Let D be a $(MNFD)$ set of $G_f^* = (\eta^*, \rho^*)$ such that $|D| = \gamma_N(G_f^*)$. Since G_f has no N-isolated vertices then by Theorem (2.3), $V - D$ is (NFD) set of G_f^*. Thus, each vertex in D is N −adjacent to at least two distinct vertices in $V - D$. Therefore, $|V - D| \geq 2|D|$ and we have $|D| + |V - D| = n$. Therefore, $|D| + 2|D| \leq |D| + |V - D| = n$. Hence, we have $\gamma_N(G_f^*) \leq {}^{n}/_{3}$

Definition 3.2.11**:** Let $x \in V(G_f)$. The $N-$ neighbourhood of *x* denoted by $N_N(x)$ is defined as $N_N(x) = \{y \in N(x): N(x) \cap N(y) \neq \emptyset\}$. The cardinality of $N_N(x)$ is called $N-$ degree of *x* and denoted by $deg_N(x)$ in G_f , and $N_N[x] = N_N(x) \cup \{x\}$. The maximum and minimum $N-$ degree of a vertex in G_f are denoted respectively by $\Delta_N(G_f)$ and $\delta_N(G_f)$, that is $\Delta_N(G_f) = max\{deg_N(x)\}$ and $\delta_N(G_f) = min\,\{deg_N(x)\}$.

Definition 3.2.12**:** An edge $e = (x,y) \in E(G_f)$ is called $N-$ edge if e is effective and N(x) ∩ N(y) ≠ ∅.

Definition3.2.12: The number of $N-edge$of a fuzzy graph $G_f = (\eta, \rho)$ is called ($N-$ size) and denoted by M_N.

Observation 3.2.13:

1) For any fuzzy graph $G_f = (\eta, \rho)$ has (NFD) set then $\gamma_N(G_f) = min\,\sigma(x)$ if and only if $deg_N(x) = n - 1$.
2) For any fuzzy graph $G_f = (\eta, \rho)$ without N −isolated vertices, $deg_N(x) \geq 2$ for each vertex *x* $\in V(G_f)$.

Theorem 3.2.14**:** For any fuzzy graph $G_f = (\eta, \rho)$ with *n* vertices $x_1, x_2, \ldots, x_n$, and q edges $\sum_{i=1}^{n} deg_N(x_i) \leq 2q$. Further, the equality holds if and only if every edge in G_f is $N-edge$

Proof: Let $G_f = (\eta, \rho)$ be a fuzzy graph with n vertices ,then for any vertex x_i $i = 1,2, \ldots, n$ we have $N_N(x_i) \subseteq N(x_i)$ thus clearly $|N_N(x_i)| \leq |N(x_i)|$ and we have $\sum_{i=1}^{n} deg\,(x_i) = \sum_{i=1}^{n} |N(x_i)| = 2q$ and similarly $\sum_{i=1}^{n} deg_N(x_i) = \sum_{i=1}^{n} |N_N(x_i)| \leq \sum_{i=1}^{n} |N(x_i)| = 2q$. Hence,

3) $\sum_{i=1}^{n} deg_N(x_i) \leq 2q$.

Now if every edge in G_f is $N-edge$. Then, $N_N(x_i) = N(x_i)$ for each vertex $x_i \in G_f$. This $\sum_{i=1}^{n} deg_N(x_i) = 2q$. Conversely, assume that $\sum_{i=1}^{n} deg_N(x_i) = 2q$. That means every edge in G_f is $N-edge$.

Theorem 3.2.15: For any fuzzy graph $G_f = (\eta, \rho)$ with n vertices, $\sum_{i=1}^{n} deg_N(x_i) = 2M_N$. Further, $|\sum_{i=1}^{n} deg_N(x_i)| = 2\sum_{y \neq x_i} \rho(x,y)$.

Proof: Let $G_f = (\eta, \rho)$ be a fuzzy graph has n vertices. Then, an $N-edge$ contributes to the N −degrees of two various vertices. Thus, when the N −degrees of the vertices are added, every edge is counted exactly two times. Thus, the sum of the N −degrees is twice the $N-size$ of the fuzzy graph

that is, $\sum_{i=1}^{n} deg_N(x_i) = 2M_N$. Take fuzzy cardinality to both sides thus,we have $|\sum_{i=1}^{n} deg_N(x_i)| = 2\sum_{y \neq x_i} \rho(x,y)$.

Theorem3.2.16: For any fuzzy graph $G_f = (\eta, \rho)$ without $N-$isolated vertex and of order n , $\gamma_N(G_f) \leq P - \sum \sigma(y_i)$, $y_i \in N_N(x)$.

Proof: Let *x* be a vertex such that $deg_N(x) = \Delta_N(G_f)$. Then, *x* dominates $|N_N(x)|$ vertices. Hence, $V - N_N(x)$ is (NFD) set of G_f. Therefore, $\gamma_N(G_f) \leq ||V - N_N(x)|| = |n| - |\Delta_N(G_f)|$. Hence, $\gamma_N(G_f) \leq P - \sum \sigma(y_i)$, $y_i \in N_N(x)$.

Conclusion

According to the results found, Some properties and boundaries of this definition are determined. The N- fuzzy domination number for some fuzzy graphs as fuzzy complete, path, cycle, complete bipartite, and star are calculated. Also, we define the $N-$ neighbourhood of x $N_N(x)$ and some relationships between $N-$ degree , $N-$edge and $N-$size were discussed.

References

[1] Zadeh L A 1965 Fuzzy Sets *Information and Control* **8** 338-353
[2] Rosenfeld A 1975 Fuzzy graphs In Fuzzy sets and their applications to cognitive and decision processes *Academic Press* (77-95)
[3] Kaufmann, A 1975 Introduction to the theory of fuzzy subsets *Academic Pr* (**2**)
[4] Yousif H J and Omran A A A 2020 July The split anti fuzzy domination in anti fuzzy graphs. *In Journal of Physics: Conference Series* **1591**(1) 012054
[5] Yousif H J and Omran A A A 2020 November 2-anti fuzzy domination in anti fuzzy graphs In *IOP Conference Series: Materials Science and Engineering* **928**(4) 042027
[6] Jabor A A and Omran A A A 2019 December Domination in discrete topology graph *In AIP Conference Proceedings* **2183** (1) 030006
[7] Jabor A A and Omran A A A 2020 November Hausdorff Topological of Path in Graph In *IOP Conference Series: Materials Science and Engineering* **928**, (4) 042008
[8] Al-Harere M N and Omran A A A 2020 On binary operation graphs *Boletim da Sociedade Paranaense de Matemática* **38**(7) 59-67
[9] Al-Harere M N and Omran A A A 2019 April Binary operation graphs *In AIP Conference Proceedings* **2086** (1) 030008
[10] Omran A A A and Swadi T 2019 Observer Domination Number in Graphs *Jour of Adv Research in Dynamical & Control Systems* **11**
[11] Al-Harere M N, Omran A A A and Breesam AT 2020 Captive Domination in Graphs *Discrete Mathematics Algorithms and Applications* **12**(6) 2050076. DOI:10.1142/S1793830920500767
[12] Omran A A A and Shalaan M M 2020 November Inverse Co-even Domination of Graphs In *IOP Conference Series: Materials Science and Engineering* **928** (4) 042025
[13] Alwan I A and Omran A A A 2020 July. Domination Polynomial of the Composition of Complete Graph and Star Graph In *Journal of Physics: Conference Series* **1591**(1) 012048IOP Publishing
[14] Somasundaram A and Somasundaram S 1998 Domination in fuzzy graphs–I *Pattern Recognition Letters* **19**(9) 787-791
[15] Somasundaram A 2005 Domination in fuzzy graphs-II. *Journal of Fuzzy Mathematics* **13**(2) 281
[16] Gani A N and Devi K P 2015 Domination in fuzzy graph *Advances in Fuzzy Sets And Systems* **11** 17-26
[17] Xavior D A, Isido D F, and Chtira V M 2013 On domination in fuzzy graphs *International Journal of Computing Algorithm* **2**(2) pp.81-82

[18] Mathew S, Mordeson J N and Malik D S 2018 *Fuzzy graph theory*. Springer International Publishing
[19] Dharmalingam K M and Rani M 2016 Total equitable domination in fuzzy graphs *Bull. Int. Math. Virtual Inst* **6** 49-54

The Direct and Converse Theorems for Best Approximation of Algebraic Polynomial in $L_{p,\alpha}(X)$

The Direct and Converse Theorems for Best Approximation of Algebraic Polynomial in $L_{p,\alpha}(X)$

Alaa Adnan Auad and Mohammed Hamad Fayyadh

University of Al- Anbar, College of education for pure sciences, Department of Mathematics, Iraq

E-mail: alaa.adnan.auad@uoanbar.edu.iq

Abstract. The direct and inverse algebraic polynomials approximation theorems in weighted spaces of unbounded functions are proved by using modulus of smoothness. Also, we obtain sharp Jackson (direct) inequality of algebraic approximation of unbounded functions in terms modulus of smoothness . In addition, constructive characterization of modulus of smoothness are considered.

1. Introduction

Approximation problems concerning algebraic polynomials was recently studied in various spaces of algebraic polynomials for example , in the papers [6] , [9] , [12] , [14] , [15] and [17] .

Approximation problems for functions of one variable were also studied by many mathematicians. Some of these results can be found in [10] , [11] , [16] and [18] . For more general doubling weighted direct and converse algebraic approximation problems was investigated in [2] ,[8] and [13]. For a general discussion of weighted polynomial approximation was can refer to the [1] and [7].

Some direct and converse approximation by relational algebraic polynomials of some weighted bounded functions spaces defined on sufficiently modulus of smooth are investigates in [3] and [4] . In the present work we consider the improved direct and inverse approximation theorems by algebraic polynomials by using modulus of smoothness in the weighted space $L_{p,\alpha}(X)$, $1 \le p < \infty$.

For formulation of the problem we need some further notations properties.

Let $X = [0,1]$ and $L_p(x)$, $1 \le p < \infty$ be the space of all bounded functions with norm equipped :

$$\|f\|_p = \left(\int_X |f(x)|^p dx \right)^{\frac{1}{p}} < \infty \qquad (1.1)$$

Let α be a weight function defined by :

$\alpha : X \to \mathbb{R}^+$, and $L_{p,\alpha}(x)$ the space of all unbounded functions with norm equipped :

$$\|f\|_{p,\alpha} = \left(\int_X |f(x).\alpha(x)|^p dx \right)^{\frac{1}{p}} < \infty \qquad (1.2)$$

For k = 1 , 2 , ….. the modulus of smoothness of the function

$f \in L_{p,\alpha}(X)$ is defined by :

$$\omega_k(f,\delta)_{p,\alpha} = \sup_{|h|\le\delta}\left\{\left\|\Delta_h^k f(x)\right\|_{p,\alpha} \ , \ \delta>0\right\} \quad (1.3)$$

where

$$\Delta_h^k f(x) = \sum_{i=0}^{k}(-1)^{k-i}\binom{k}{i} f(x+ih) \quad (1.4)$$

Let $P_n(n=0,1,\dots.)$ be the set of algebraic polynomial of degree at most less than or equal n and let $E_n(f)_{p,\alpha}$ be the degree of best approximation of $f\in L_{p,\alpha}(X)$ by the polynomial p_n in P_n given by :

$$E_n(f)_{p,\alpha} = \inf_{p_n\in P_n}\|f-p_n\|_{p,\alpha} \quad (1.5)$$

There are many results on approximation of functions belong to $L_{p,\alpha}(X)$ spaces , $1\le p<\infty$. Especially , the classical Jackson theorem (direct theorem) .

$$E_n(f)_{p,\alpha} \le c\omega_r\left(f,\frac{1}{n}\right)_{p,\alpha} , \qquad n=1,2,\dots.... \quad (1.6)$$

and its weak converse

$$\omega_r\left(f,\frac{1}{n}\right)_{p,\alpha} \le \frac{c}{n^{2r}}\sum_{k=0}^{n}(k+1)^{2r-1}E_k(f)_{p,\alpha} \quad (1.7)$$

Where n = 1 , 2, …….

2. Auxiliary results

In this section, we will mention some of the lemmas that we will need to proving the theorems of the main results, As well as we will prove some properties of the modulus of smoothness .

Lemma 2.1 : [5]
Let $\{y_i\}$ be a sequence of the real numbers be satisfy
$|y_i|\le\mathcal{K}$, $\sum_{i=2^{k-1}}^{2^k-1}|y_i-y_{i+1}|\le\mathcal{K}$ $for\ all\ i,k\in\mathbb{N},\mathcal{K}>0$
If $1<p<\infty$, $\beta\in\mathcal{K}_p$ $and\ f\in L_{p,\beta}(X)$, then there is a function $\mathcal{F}\in L_{p,\beta}(X)$ such that $\|\mathcal{F}\|_{p,\beta}\le c\,\mathcal{K}\|\mathcal{F}\|_{p,\beta}$

Lemma 2.2 : [5]
Let $n\in\mathbb{N}, 1\le p<\infty$ and $f\in L_{p,\alpha}(X)$, then :

$$c\left\|\left(\sum_{u=1}^{\infty}|\Delta_u|^2\right)^{\frac{1}{2}}\right\|_{p,\alpha} \le \left\|\sum_{u=1}^{\infty}C_u p_n^{iux}\right\|_{p,\alpha} \le c\left\|\left(\sum_{u=1}^{\infty}|\Delta_u|^2\right)^{\frac{1}{2}}\right\|_{p,\alpha}$$

Lemma 2.3 : Let $f\in L_{p,\alpha}(X), 1\le p<\infty, k\in\mathbb{N}, \delta>0$, Then

$$\omega_k(f,\delta)_{p,\alpha}\ge 0$$

Proof **:** we have

$$\omega_k(f,\delta)_{p,\alpha} = \sup_{|h|\le\delta}\left\{\left\|\Delta_h^k f(.)\right\|_{p,\alpha}\right\}$$

$$= \sup_{|h|\le\delta}\left\{\left\|\sum_{i=0}^{k}(-1)^{k-i}\binom{k}{i}f(.+ih)\right\|_{p,\alpha}\right\}$$

since $\left\|\sum_{i=0}^{k}(-1)^{k-i}\binom{k}{i}f(.+ih)\right\|_{p,\alpha}\ge 0$

implies $\left\|\Delta_h^k f(.)\right\|_{p,\alpha}\ge 0$

Hence $\sup_{|h|\le\delta}\left\{\left\|\Delta_h^k f(.)\right\|_{p,\alpha}\right\}\ge 0$

$$\omega_k(f,\delta)_{p,\alpha} \geq 0 \quad .$$

Lemma 2.4 : Let $f \in L_{p,\alpha}(X), 1 \leq p < \infty, k \in \mathbb{N}, \delta > 0$, Then

$$\omega_k(f,\delta)_{p,\alpha} \to 0 \quad as \quad \delta \to 0$$

Proof :

let $\delta = \frac{1}{n}$

$$\omega_k(f,\delta)_{p,\alpha} = \omega_k\left(f,\frac{1}{n}\right)_{p,\alpha} = \sup_{|h|\leq\frac{1}{n}} \left\{ \left\| \Delta_h^k f(.) \right\|_{p,\alpha} \right\}$$

$$= \sup_{|h|\leq\frac{1}{n}} \left\{ \left\| \Delta_h^{k-1} \Delta_h^1 f(.) \right\|_{p,\alpha} \right\}$$

$$= \sup_{|h|\leq\frac{1}{n}} \left\{ \left\| \Delta_h^{k-1} \left[f(.) - f(.+\frac{1}{n}) \right] \right\|_{p,\alpha} \right\}$$

If $n \to \infty$ then $\frac{1}{n} \to 0$

$$= \sup_{|h|\leq\frac{1}{n}} \left\{ \left\| \Delta_h^{k-1} [f(.) - f(.)] \right\|_{p,\alpha} \right\} = \sup_{|h|\leq\frac{1}{n}} \left\{ \left\| \Delta_h^{k-1} . [0] \right\|_{p,\alpha} \right\}$$

$$= \sup_{|h|\leq\frac{1}{n}} \|0\|_{p,\alpha} = 0.$$

Lemma 2.5 **:** Let $f, g \in L_{p,\alpha}(X), 1 \leq p < \infty, k \in \mathbb{N}, \delta > 0$, Then $\omega_k(f+g,\delta)_{p,\alpha} \leq \omega_k(f,\delta)_{p,\alpha} + \omega_k(g,\delta)_{p,\alpha}$

Proof : $\omega_k(f+g,\delta)_{p,\alpha} = \sup_{|h|\leq\delta} \left\{ \left\| \Delta_h^k (f+g)(.) \right\|_{p,\alpha} \right\}$

$$= \sup_{|h|\leq\delta} \left\{ \left\| \Delta_h^k f(.) + \Delta_h^k g(.) \right\|_{p,\alpha} \right\}$$

$$\leq \sup_{|h|\leq\delta} \left\{ \left\| \Delta_h^k f(.) \right\|_{p,\alpha} + \left\| \Delta_h^k g(.) \right\|_{p,\alpha} \right\}$$

$$= \sup_{|h|\leq\delta} \left\{ \left\| \Delta_h^k f(.) \right\|_{p,\alpha} \right\} + \sup_{|h|\leq\delta} \left\{ \left\| \Delta_h^k g(.) \right\|_{p,\alpha} \right\}$$

$$= \omega_k(f,\delta)_{p,\alpha} + \omega_k(g,\delta)_{p,\alpha}$$

Lemma 2.6 **:** Let $f \in L_{p,\alpha}(X), 1 \leq p < \infty, k \in \mathbb{N}, \delta, c > 0$, Then $\omega_k(f,c\delta)_{p,\alpha} \leq c^k \omega_k(f,\delta)_{p,\alpha}$.

Proof : $\omega_k(f,c\delta)_{p,\alpha} = \sup_{|h|\leq c\delta} \left\{ \left\| \Delta_h^k f(.) \right\|_{p,\alpha} \right\}$

$$\leq \sup_{|h|\leq c\delta} \left\{ \left\| \Delta_{c\delta}^k f(.) \right\|_{p,\alpha} \right\}$$

$$= \sup_{|h|\leq c\delta} \left\{ \left\| (c\delta)^k D^k f(.) \right\|_{p,\alpha} \right\}$$

$$= c^k \sup_{|h|\leq c\delta} \left\{ \left\| \delta^k D^k f(.) \right\|_{p,\alpha} \right\}$$

$$= c^k \sup_{|h|\le c\delta} \left\{ \left\| \Delta_\delta^k f(.) \right\|_{p,\alpha} \right\}$$

$$= c^k \, \omega_k(f, \delta)_{p,\alpha}$$

Lemma 2.7 : Let $f \in L_{p,\alpha}(X), 1 \le p < \infty, k \in \mathbb{N}$, Then $\omega_k(f, \delta_1)_{p,\alpha} \le \omega_k(f, \delta_2)_{p,\alpha}$ for every $\delta_1 \le \delta_2, \delta_1, \delta_2 > 0$

Proof :

$$\omega_k(f, \delta_1)_{p,\alpha} = \sup_{|h|\le\delta_1} \left\{ \left\| \Delta_h^k f(.) \right\|_{p,\alpha} \right\}$$

$$\le \sup_{|h|\le\delta_2} \left\{ \left\| \Delta_h^k f(.) \right\|_{p,\alpha} \right\} since\ \delta_1 \le \delta_2$$

$$= \omega_k(f, \delta_2)_{p,\alpha} .$$

Lemma 2.8 : Let $f, \acute{f} \in L_{p,\alpha}(X), 1 \le p < \infty, k \in \mathbb{N}, \delta > 0$, Then $\omega_k(f, \delta)_{p,\alpha} \le \frac{\delta}{2} \omega_{k-1}(\acute{f}, \delta)_{p,\alpha}$ where $\acute{f}$ is the first derivative of a function f

Proof : We have the difference $\Delta_h^k f(x) = \Delta_h^{k-1}(\Delta_h^1 f(x))$

$$= \Delta_h^{k-1} [f(x+H) - f(x-H)]$$

$$\left\| \Delta_h^k f(.) \right\|_{p,\alpha} = \left\| \Delta_h^{k-1} [f(.+H) - f(.-H)] \right\|_{p,\alpha}$$

$$= \left\| \Delta_h^{k-1} [f(.+H) - f(.) + f(.) - f(.-H)] \right\|_{p,\alpha}$$

$$= \left\| \Delta_h^{k-1} [f(.+H) - f(.)] - \Delta_h^{k-1} [f(.-H) - f(.)] \right\|_{p,\alpha}$$

$$= \left\| \Delta_h^{k-1} \int_0^h \acute{f}(.+L) dL - \Delta_h^{k-1} \int_0^h \acute{f}(.-L) dL \right\|_{p,\alpha}$$

$$\le \int_0^h \left\| \Delta_h^{k-1} [\acute{f}(.+L) - \acute{f}(.-L)] \right\|_{p,\alpha} dL$$

$$\le \int_0^h \omega_{k-1}(\acute{f}, \delta)_{p,\alpha} dL \le \frac{\delta}{2} \omega_{k-1}(\acute{f}, \delta)_{p,\alpha}$$

3. Main results

Let X denote the one-dimensional [0 , 1] we denote by $L_{p,\alpha}(X), 1 \le p < \infty$ the space of all unbounded functions f of one variable on [0 , 1] in each variable and satisfy $\|f\|_{p,\alpha} < \infty$ where :

$$\|f\|_{p,\alpha} = \begin{cases} \left(\int_x |f(x).\alpha(x)|^p dx \right)^{\frac{1}{p}} , & 1 \le p < \infty \\ ess\ sup|f(x)| , & p = \infty \end{cases}$$

In the following give direct and converse approximation theorems for functions of one variable, which are our main results .

Theorem 3.1 : let $f \in L_{p,\alpha}(T)$, $1 \le p < \infty$ *and* $0 < \alpha < 1$ then the Jackson type inequality :

$$E_{n,k}(f)_{p,\alpha} \le c\,\omega_k\left(f,\frac{1}{n}\right)_{p,\alpha} , \qquad n = 1,2,\dots\dots$$

Theorem 3.2 **:** let $f \in L_{p,\alpha}(X)$, $1 \le p < \infty$, $n \in \mathbb{N}$, $r \in \mathbb{R}^+$ and $\lambda = max\{2,p\}$. then there exist positive constant c dependent on r and p such that

$\frac{c}{n^{2r}} \left(\sum_{u=1}^{n} u^{2\lambda r-1} E_u^{\lambda}(f)_{p,\alpha}\right)^{\frac{1}{\lambda}} \le \omega_r\left(f,\frac{1}{n}\right)$

Theorem 3.3 **:** let $f \in L_{p,\alpha}(T)$, $1 \le p < \infty$ and $0 < \alpha < 1$,
then :

$\omega_k\left(f,\frac{1}{n}\right)_{p,\alpha} \le \frac{c(k)}{n^k} \sum_{i=0}^{n}(i+1)^{k-1} E_i(f)_{p,\alpha}$.

4. Proofs of main results

4.1 Proof of theorem 3.1 :

Let $\delta = \frac{1}{n}$ and Let $f \in L_{p,\alpha}(X)$, $1 \le p < \infty$ and the operator of algebraic polynomial defined by :

$$V_n(f,x) = \frac{1}{n+1}\sum_{k=n}^{2n} S_k(f)(x) \quad , \quad n \in \mathbb{N}$$

We see that $V_n \in \mathrm{J}_{2n}$ for $n \in \mathbb{N}$

$$\|f - V_n(f)\|_{p,\alpha} \le cE_n(f)_{p,\alpha}$$

because $E_n(f)_{p,\alpha} = inf\left\{\|f - p_n\|_{p,\alpha} , p_n \in \mathcal{P}_n\right\}$

and we have $\|V_n(f)\|_{p,\alpha} \le c\,\|f\|_{p,\alpha}$

$$E_{n,k}(f)_{p,\alpha} = inf\left\{\|f - V_n(f)\|_{p,\alpha}\right\}$$

$$\le \|f - V_n(f)\|_{p,\alpha} = \left(\int_X |[f(x) - V_n(f)(x)].\alpha(x)|^p dx\right)^{\frac{1}{p}}$$

$$\le sup\left(\int_X |[f(x) - V_n(f)(x)].\alpha(x)|^p dx\right)^{\frac{1}{p}}$$

$$\le \mathrm{c}\sup_{|h|\le\delta}\left\{\left\|\Delta_h^k f(.)\right\|_{p,\alpha}\right\} = c\,\omega_k(f,\delta)_{p,\alpha} = c\,\omega_k\left(f,\frac{1}{n}\right)_{p,\alpha}$$

4.2 Proof of theorem 3.2 :

Since $r \in \mathbb{R}^+$, $1 < \lambda < \infty$, $n \in \mathbb{N}$ we assume that $k \in \mathbb{N}$ such that

$$2^k \le n \le 2^{k+1}$$

By lemma 2.2 , we have

$$\left(\sum_{u=1}^{n} \frac{\mu^{2\lambda r-1}}{n^{2\lambda r}} E_u^{\lambda}(f)_{p,\alpha}\right)^{\frac{1}{\lambda}} \le \left(\sum_{u=1}^{k+1}\sum_{\eta=2^{i-1}}^{2^i-1} \frac{\eta^{2\lambda r-1}}{n^{2\lambda r}} E_\eta^{\lambda}(f)_{p,\alpha}\right)^{\frac{1}{\lambda}}$$

$$\leq \left(\sum_{u=1}^{k+1} \frac{2^{2u\lambda r}}{n^{2\lambda r}} \, E^{\lambda}_{2^{u-1}-1}(f)_{p,\alpha} \right)^{\frac{1}{\lambda}} \leq \left(\sum_{u=1}^{k+1} \frac{2^{2u\lambda r}}{n^{2\lambda r}} \left\| \sum_{|\eta|=2^{u-1}}^{2^u-1} C_\eta p_n^{i\eta x} \right\|^{\lambda}_{p,\alpha} \right)^{\frac{1}{\lambda}}$$

$$\leq c \left(\sum_{u=1}^{k+1} \frac{2^{2u\lambda r}}{n^{2\lambda r}} \left\| \left(\sum_{\eta=u}^{\infty} |\Delta_u|^2 \right)^{\frac{1}{2}} \right\|^{\lambda}_{p,\alpha} \right)^{\frac{1}{\lambda}}$$

Putting $1 < p \leq 2$, $\lambda = 2$
By using Minkowski's inequality , we have

$$\left(\sum_{u=1}^{n} \frac{u^{2\lambda r-1}}{n^{2\lambda r}} \, E^{\lambda}_{u}(f)_{p,\alpha} \right)^{\frac{1}{\lambda}} \leq c \left(\sum_{u=1}^{k+1} \frac{2^{u\lambda r}}{n^{ur}} \left\| \left(\sum_{\eta=v}^{\infty} |\Delta_u|^2 \right)^{\frac{p}{2}} \right\|^{\frac{2}{p}}_{p,\alpha} \right)$$

$$\leq c \left(\sum_{u=1}^{k+1} \frac{2^{uvr}}{n^{ur}} \left\| \sum_{\eta=u}^{\infty} |\Delta_u|^2 \right\|^{\frac{p}{2}}_{p,\alpha} \right)$$

$$\leq c \left(\left\| \left(\sum_{u=1}^{k} \frac{2^{uvr}}{n^{ur}} \, |\Delta_u|^2 + \frac{2^{uvr(k+1)}}{n^{ur}} \sum_{\eta=k+1}^{\infty} |\Delta_\eta|^2 \right)^{\frac{p}{2}} \right\|_{p,\alpha} \right)$$

$$\leq c_0 \left\| \left(\sum_{u=1}^{k} \frac{2^{uvr}}{n^{ur}} \, |\Delta_u|^2 \right)^{\frac{p}{2}} \right\|_{p,\alpha} + c_1 \left\| \left(\sum_{\eta=k+1}^{\infty} |\Delta_\eta|^2 \right)^{\frac{p}{2}} \right\|_{p,\alpha}$$

Using lemma 2.2 we can estimate G_1

$$G_1 = \left\| \left(\sum_{\eta=k+1}^{\infty} |\Delta_\eta|^2 \right)^{\frac{1}{2}} \right\|_{p,\alpha} \leq c \left\| \sum_{\eta=2^k}^{\infty} c_\eta p_n^{inx} \right\|_{p,\alpha}$$

$$\leq c \, E_{2^{k-1}}(f)_{p,\alpha} \leq c \, \omega_r\left(f, \frac{1}{n}\right)_{p,\alpha}$$

On the other hand

$$G_2 = \left\| \left(\sum_{u=1}^{k} \frac{2^{2ur}}{n^{ur}} \, |\Delta_u|^2 \right)^{\frac{p}{2}} \right\|_{p,\alpha} \leq \left\| \sum_{u=1}^{k} \frac{2^{2ur}}{n^{2r}} \, |\Delta_u| \right\|_{p,\alpha}$$

$$\leq \left\| \sum_{u=1}^{k} \sum_{|\eta|=2^{u-1}}^{2^u-1} \frac{2^{2ur}}{n^{2r}} \, |c_\eta p_n| \right\|_{p,\alpha}$$

Now using lemma 2.2 twice , we get

$$G_2 \le \frac{c\,2^{2r}}{n^{2r}} \left\| \sum_{|\eta|=1}^{\infty} p_n \left| c_\eta\, p_n^{i\eta x} \right| \right\|_{p,\alpha} \le \frac{c\,2^{2r}}{n^{2r}} \left\| \left(I - \sigma_{\frac{1}{n}} \right)^r f \right\|_{p,\alpha}$$

$$= \frac{c\,2^{2r}}{n^{2r}} \left\| \left(I - \sigma_{\frac{1}{n}} \right)^{\{r\}} . (I-\sigma)^{r-\{r\}} f \right\|_{p,\alpha} \le c\,\omega_r\left(f, \frac{1}{n} \right)_{p,\alpha}$$

Therefore, the theorem followed
If $p > 2$, $\lambda = p$, then

right hand $\le c \left(\sum_{u=1}^{k+1} \frac{2^{upr}}{n^{2upr}} \left\| \left(\sum_{\eta=u}^{\infty} |\Delta_u|^2 \right)^{\frac{1}{2}} \right\|_{p,\alpha}^{p} \right)^{\frac{1}{p}}$

$$\le c \left(\left\| \sum_{u=1}^{k+1} \frac{2^{upr}}{n^{2upr}} \left(\sum_{\eta=u}^{\infty} |\Delta_u|^2 \right)^{\frac{p}{2}} \right\|_{p,\alpha}^{\frac{1}{p}} \right)$$

$$\le c \left(\left\| \sum_{u=1}^{k+1} \frac{2^{upr}}{n^{ur}} \left(\sum_{\eta=u}^{\infty} |\Delta_u|^2 \right)^{\frac{p}{2}} \right\| \right)^{\frac{1}{p}} \le c\,\omega_r\left(f, \frac{1}{n} \right)_{p,\alpha}$$

4.3 : Proof of theorem 3.3 :
Let $f \in L_{p,\alpha}(X)$ for every natural number k there exist a constant c(k) depending on k such that :

$$\omega_k\left(f, \frac{1}{n} \right)_{p,\alpha} \le \frac{c(k)}{n^k} \sum_{i=0}^{n} (i+1)^{k-1} E_i(f)_{p,\alpha}$$

Let $p_k^* \in \mathcal{P}_n$ be a best algebraic approximation of unbounded function f and b , $b + kh \in X$

We have $0 \le \Delta_h^k f(b)\, \alpha(b)$ then :

$$0 \le \left\| \Delta_h^k f(b) \right\|_{p,\alpha} = \left\| \sum_{i=0}^{k} (i+1)^{k+j} f(b+ih) \right\|_{p,\alpha}$$

$$\le \left\| \sum_{i=0}^{k} \binom{k}{i} | f(b+ih) - p_k^*(b+ih) | + \sum_{i=0}^{k} \binom{k}{i} | p_k^*(b+ih) | \right\|_{p,\alpha}$$

$$\le sup \left\| \Delta_h^k\, p_k^*(b+ih) \right\|_{p,\alpha} + \left\| \sum_{i=0}^{k} \binom{k}{i} | f(b+ih) - p_k^*(b+ih) | \right\|_{p,\alpha}$$

$$\le \omega_k(p_k^*, b, \delta) + \sum_{i=0}^{k} \binom{k}{i} \| f - p_k^* \|_{p,\alpha}$$

$$\leq \frac{c(k)}{n^k} \sum_{i=0}^{k} \binom{k}{i} E_i(f)_{p,\alpha}$$

5. Conclusion

We can be approximated of unbounded functions by using algebraic polynomial in weighted space, also obtain sharp Jackson (direct) inequality of algebraic approximation of unbounded functions in terms modulus of smoothness.

References

[1] Akgun R A 2013 Modulus of smoothness for some Banach function space **1168**
[2] Akgun R and Israfilov D V 2005 Polynomial approximation in weighted smirnov-orlicz space *proc. A. Ramadze Math. Inst*. **139** 89-92
[3] Akgun R and Kokilashvili V 2011 The refined direct and converse inequalities of trigonometric approximation in weighted variable exponent Lebesgue spaces *Geogian Math. Jornal* **18** 399-423
[4] Akgun R and yildirir YE 2016 Improved and converse theorems in weighted Lorentz spaces *Bull Belg Math. Soc. Simon Stevin* **23** 247-262
[5] Akgun R 2010 Sharp Jackson and converse theorems of trigonometric approximation in weighted Lebesgue Spaces *Proceedings of A.razmadze Mathematical Institute* **152** 1-18
[6] Bandy P and Narayana D 2008 Proximinality in Banach spaces *J. math. Analy. Appl*. **341** 309-317
[7] Chaichenko S 2012 Best approximation of periodic functions in generalized Lebesgue space Likr Math. Zh. **64** 1249-1265
[8] Ephremidze L and kokila shvili 2007 On the Inverse Inequalities for trigonometric Polynomial approximations in weighted Lorentz spaces , proc . *A. Razmadze Math. Inst*. **144** 132-136
[9] Eutseh F D 2000 Best approximation in inner product spaces *springer-verlag New York*
[10] Watson G A 1993 A characterization of best simultaneous approximations J. *Approx. theory* **75** 175-182
[11] Bustamante J and Roldan C 2006 Direct and inverse results in Holder norms *J. Approx. theory* **138** 112-132
[12] Kivinuk A and Saksa A 2016 On approximation by Blackman and Rogosinski – type operators in Banach space proc. Estonian Acd. Sci. **65** 205-219 .
[13] Kokilashvili V M and Yildirir Y E 2007 On the approximation in weighted Lebesgue space *proc A. Razmadze Math. Inst.* **143** 103-113
[14] Narang T D and Gupta S 2016 On best approximation and best co-approximation. *Thai J. math*. **14** 505-526
[15] Rao G S 2012 Tools and techniques in approximation theory *math. Stud*. **81** 115-133
[16] Ditzian Z D and Leviatan D 1994 Inverse theorem for best polynomial approximation in L_p , $0 < p < 1$ proc . *Amer . math . soc* . **120** (1) 151-154
[17] Ditzian Z 2007 Polynomial approximation and ω_φ^r (f , t) *Twenty years later surveys in approximation Theory* **3** 106-151
[18] Ditzian Z and Ivanov K 1993 Strong converse inequalities J. Analyses math **61** 61-111

Sequential unconstrained approach for solving index one constrained differential-algebraic optimal control problems

Sequential unconstrained approach for solving index one constrained differential-algebraic optimal control problems

Radhi A. Zaboon , Ghazwa F. Abd , Shimaa M.Dawood

Department of Mathematics, College of Science, University of Mustansiriyah, , 10052 Filastin Street, Iraq

E-mail: r.zaboon@uomustansiriyah.edu.iq

Abstract. A constrained index-one differential algebraic optimal control problem is presented. The algebraic constraint is assumed to have an index one property. With the help of implicit function theorem, the reduced constrained optimal control problem in the state-space is then obtained. The main goal of this work is to solve the present problem by using an unconstrained sequential minimization approach. The necessary mathematical requirements, conditions and proofs are developed. Based on the obtained results, computational algorithm to solve this problem approximately is developed. Numerical illustrations of constrained differential algebraic optimal control problems are implemented. Due to the numerical results and their comparisons, an efficient approximate method is obtained.

1. Introduction

Differential-algebraic systems have been extensively studied later on due to their natural formulation of many real life applications and its importance to the field of control and optimal control system [1], [2],[3],[4],[6],[7],[19],[20]. There is an important field of differential- algebraic equations arising from constrained optimal control problems, where the inequality constraint are active or in the present of equality constraints explicitly. For unconstrained optimal control problem, the necessary conditions of optimality may also lead to semi-explicit differential-algebraic system [5], [8].

In this work, semi-explicit differential algebraic optimal control problem with equality and inequality constraints have been considered assuming that the index one problem can be smoothly reduced into a state space constrained optimal control problems. In solving the reduced problem and hence the original one, sequential minimization penalty function approach is developed where some penalties functions terms are added to the objective performance criterion for any violation of the constraints. We have shown that there is a sequence of admissible solutions whose limit is the optimal solution of the present problem. Based on the esteemed work of [9] and [11] the theoretical proofs have been generalized and modified.

2. Problem formulation (original problem)

Consider a system described by the semi-explicit differential- algebraic form (DAE)

$$x_1 = F_1(x_1, x_2, u, t), \text{a. e. on } [0, T] \quad \ldots.(1)$$
$$F_2(x_1, x_2, u) = 0, \quad \ldots.(2)$$
$$F_3(x_1, t) \geq 0, \quad \ldots .(3)$$
$$F_4(u, t) \geq 0, \text{a. e. on } [0, T] \quad \ldots.(4)$$

$F_1(x_1, x_2, u, t): \mathcal{D} \times \mathcal{R}^{n_2} \times \mathcal{R}^p \times \mathcal{R}^+ \to \mathcal{R}^{n_1}$ is assumed to be measurable in t for fixed (x_1, x_2) and u, continuous in (x_1, x_2) for fixed t, u and continuous in u for fixed t, (x_1, x_2) and there exists an integrable function s(t) on $[0, T]$ such that $\|F_1(x_1, x_2, u, t)\| \le s(t)$ for $0 \le t \le T$ for all admissible functions $x_1(.), x_2(.)$ and $u(.)$, with $\int_0^t s(t)dt < \infty$, and $\int_0^t s^2(t)dt < \infty$

$$F_2(x_1, x_2, u) \in C^1(\mathcal{D} \times \mathcal{R}^{n_2} \times \mathcal{R}^p, \mathcal{R}^{n_2})$$
$$F_3(x_1, t) \in C(\mathcal{D} \times \mathcal{R}^+, \mathcal{R}^{n_3})$$
$$F_4(u, t) \in C(\mathcal{R}^p \times \mathcal{R}^+, \mathcal{R}^{n_4}), \text{ where}$$
$$x_1 = \left(x_1^1, \dots, x_1^{n_1}\right)^T : [0, T] \to \mathcal{R}^{n_1}$$
$$x_2 = \left(x_2^1, \dots, x_2^{n_2}\right)^T : [0, T] \to \mathcal{R}^{n_2}$$
$$u = \left(u_1, \dots, u_p\right)^T : [0, T] \to \mathcal{R}^p$$
$$\xi_1(T) = \left(\xi_1^1(T), \dots, \xi_1^{n_1}(T)\right)^T \text{ (Target of state } x_1) \; (\xi_1(t) \in C(\mathcal{R}^+, \mathcal{R}^{n_1}))$$
$$\xi_2(T) = \left(\xi_2^1(T), \dots, \xi_2^{n_2}(T)\right)^T \text{ (Target of state } x_2) \; (\xi_2(t) \in C^1(\mathcal{R}^+, \mathcal{R}^{n_2}))$$

The aim is to find an admissible functions $x_1(.), x_2(.)$ and $u(.)$ such that

$$J_0(u(.)) = \|x_1(T) - \xi_1(T)\|^2 + \|x_2(T) - \xi_2(T)\|^2 + \int_0^T F_0(x_1(t), x_2(t), u(t))\, dt, \quad \dots.(5)$$

Is minimized, where a.e. is standing for almost everywhere, where $F_0(x_1, x_2, u, t)$ is assumed to be integrable for each fixed x_1, x_2 and u .

$$\mathfrak{F}(0) = \{x_1(0) \in \mathcal{D} \subseteq \mathcal{R}^{n_1}, x_2(0) \in \mathcal{R}^{n_2}, u(0) \in \mathcal{R}^p | F_i(x_1(0), x_2(0), u(0)), i = 0,1,2,3,4$$
Satisfying the constraint (1)-(4) along with the function $F_0(x_1, x_2, u, t)$ }

$\mathcal{D}$ is assumed to be open set of $\mathcal{R}^{n_1}, T > 0$ is fixed real number with $(x_1(0), x_2(0)) = (x_{10}, x_{20}) \in \mathfrak{F}(0)$. Under some reasonable conditions, we are assuming there is an optimal solution to this problem. To reduce the order of this problem into state- space optimal control problem with equality and inequality constraints on the states and control with a suitable consistent initial conditions, one can assume that:

Assumptions 1: $(F_2)_{index-1}$

There exists an open set $\tilde{\upsilon}_{x_1} \subset \mathcal{D}$ such that for all

$(\tilde{x}_1, \tilde{u}) \in \tilde{\upsilon}_{x_1,u} \triangleq \{x_1 \in \tilde{\upsilon}_{x_1}, u \in \mathcal{R}^p |$ it is possible to solve $F_2(\tilde{x}_1, \tilde{x}_2, \tilde{u}) = 0$ for $\tilde{x}_2\}$

The corresponding solution manifold may be defined as

$$\tilde{\upsilon} = \{x_1 \in \tilde{\upsilon}_{x_1}, x_2 \in \mathcal{R}^{n_2}, u \in \mathcal{R}^p | F_2(x_1, x_2, u) = 0\}$$

Which is not necessary be open set of $\tilde{\upsilon}_{x_1} \times \mathcal{R}^{n_2} \times \mathcal{R}^p$.

Assumption 2:

From theorem A.1, [8] and assumption 1 , we have assumed that for every point $(\tilde{x}_1, \tilde{u}) \in \tilde{\upsilon}_{x_1,u}$ There exist a neighborhood $\mathcal{N}_{\tilde{x}_1,\tilde{u}}$ of $(\tilde{x}_1, \tilde{u})$ and corresponding $\mathcal{N}_{\tilde{x}_2}$ of $\tilde{x}_2$ such that, for each point $(x_1, u) \in \mathcal{N}_{\tilde{x}_1,\tilde{u}}$ a unique solution $x_2 \in \mathcal{N}_{\tilde{x}_2}$ exists and the solution is given as $x_2 = \varphi_{\tilde{x}_1}(x_1, u)$ locally. One can also assume that one of the sets $\mathcal{N}_{\tilde{x}_1,u}$ is global in u [8] in the sense that it can be expressed as

$$\mathcal{N}_{\tilde{x}_1,\tilde{u}} = \{x_1 \in \mathcal{N}_{x_1}, u \in \mathcal{R}^p\}$$

Where $\mathcal{N}_{x_1}$ is a neighborhood of $x_1 = 0$. One can define

$$\upsilon \triangleq \{x_1 \in \mathcal{N}_{x_1}, x_2(t) \in \mathcal{R}^{n_2}, u \in \mathcal{R}^p | F_2(x_1, x_2, u) = 0\}.$$

Remarks 1

1. To satisfy the assumption I, we have assumed that the rank of $\left(\frac{\partial F_2}{\partial x_2}\right)$ is constant and full on $\tilde{\upsilon}$.
2. One can using implicit function theorem [21],[22],[23] on υ to find
$$x_2 = \varphi(x_1, u), \forall x_1 \in \mathcal{N}_{x_1}, u \in \mathcal{R}^p.$$
3. Based on the assumptions (I-II), a reduced state – space constrained optimal control problem

may obtained explicitly.

Problem formulation (reduced problem)

Consider the following reduced state –space constrained optimal control problem. Set

$\rho_x \triangleq \{x_1(.)|x_1(.)$ is absolutely continuous function with $\dot{x}_1(.) \in L_2[0,T]$ and $F_3^i(x_1(t),t) \geq 0$, where

$x_1 \in \mathcal{N}_{x_1}$, $i = 1,2,\dots,n_3\}$.

$\rho_u \triangleq \{u(.)|$ u is bounded, measurable (Lebesgue) function such that $F_4^i(u(t),t) \geq 0$, (a. e) $i = 1,\dots,n_4\}$. Where ρ_u is assumed nonempty set, i.e. $\rho_u \neq \emptyset$.

$\mathfrak{F}_0^1 = \{x_1(0) \in \mathcal{R}^{n_1} | F_3(x_1(0),0) \geq 0, F_4(u(0),0) \geq 0$, Which ensure the integrability of $F_0\left(x_1(0), \varphi\big(x_1(0),u(0)\big),u(0)\right)\}$, for a given $u(0) \in \rho_u \subset \mathcal{R}^p\}$.

It assumed that the set $\mathfrak{F}_0^1$ is compact subset of $\mathcal{R}^{n_1}$. Then the problem is to find $x_1(.) \in \rho_x$ and $u(.) \in \rho_u$ so the following equivalent reduced problem minimized

$$\min_{\rho_u} J\big(u(.)\big) = \sum_{i=1}^{n_1} \left|x_1^i(T) - \xi_1^i(T)\right|^2 + \sum_{i=1}^{n_2} \left|\varphi(x_1(T),u(T)) - \xi_2^i(T)\right|^2 + \int_0^T F_0\big(x_1(s),\varphi\big(x_1(s),u(s)\big),u(s),s\big)\,ds \quad \dots(6)$$

$$\frac{dx_1}{dt} = F_1\big(x_1(t),\varphi\big(x_1(t),u(t)\big),u(t),t\big) \text{ a. e. on } [0,T] \quad \dots(7)$$

$$F_3(x_1(t),t) \geq 0, t \in [0,T] \quad \dots(8)$$

$$F_4(u(t),t) \geq 0, \text{a. e. on } [0,T] \quad \dots(9)$$

$$x_1(0) \in \mathfrak{F}_0^1 \quad \dots(10)$$

Over classes of admissible functions.

Remark 2:

If $x_2 = \varphi(x_1(t),u(t))$ and $x_2 = \varphi(x_1(T),u(T)) = \xi_2(T)$ are explicitly satisfied as a result of implicit function theorem on the class of continuously differentiable functions almost all, then the constraint

$\sum_{i=1}^{n_2} |\varphi(x_1(\tau),u(\tau)) - \xi_2(T)|^2$ is neglected from (6).

To define the sequential optimization problem, using a penalty function approach, one can assume the following sets:

Assumption 3:

For each $t \in [0,T]$, $\forall x_{10} \in \mathfrak{F}_0^1$

$$\mathcal{Q}_{x_1}(t) = \{x_1(t)\big|F_3^i(x_1(t),t) \geq 0, i = 1,2,\dots,n_1\} \subseteq \mathcal{R}^{n_1}$$

$$\mathcal{Q}_{x_1}^0(t) = \{x_1(t)\big|F_3^i(x_1(t),t) > 0, i = 1,2,\dots,n_1\}$$

$$\mathcal{Q}_u(t) = \{u(t)|F_4^j(u(t),t) \geq 0, \text{a. e.}, j = 1,2,\dots,n_2\} \subset \mathcal{R}^p$$

$$\mathcal{Q}_{u_0}(t) = \{u(t)|F_4^j(u(t),t) > 0, \text{a. e. } j = 1,2,\dots,n_2\}$$

$$X_1 = \{x_1(.)|x_1(t) \in \mathcal{Q}_{x_1}(t), \forall t \in [0,T]\}$$

$$X_1^0 = \{x_1(.)|x_1(t) \in \mathcal{Q}_{x_1}^0(t), \text{a. e. on} [0,T] \text{ and } \int_0^T \frac{dt}{F_3^i(x_1(t),t)} < +\infty, i = 1,2,\dots,n_3\}$$

$$U = \{u(.)|u(t) \in \mathcal{Q}_u, \text{a. e. on } [0,T]\}$$

$$U^0 = \{u(t)|u(t) \in \mathcal{Q}_{u_0}, \text{a. e. on } [0,T] \text{ and } \int_0^T \frac{dt}{F_4^i(u(t),t)} < +\infty\ i = 1,2,\dots,n_4\}$$

$$\rho_{x_1,u} = \{\big(x_1(.),u(.)\big)\big|x_1(t) - x_{10} - \int_0^T F_0\big(x_1(s),\varphi\big(x_1(s),u(s)\big),u(s),s\big)ds = 0 \text{ For all } t \in [0,T],$$
$$x_2(t) = \varphi(x_1(t),u(t),t), x_1^0 \in \mathfrak{F}_0^1\}.$$

For solvability point of view, one has to assume that $X_1^0 \neq \emptyset$, $U^0 \neq \emptyset$ and $\rho_{x_1,u} \neq \emptyset$.

3.sequential minimization penalty function approach for reduced problem

Consider (6)-(10) under the assumption 3 is satisfied, a decreasing null sequence of positive real numbers $\{\beta_k\}$ for each $\beta_k > 0, \forall x_1(0) \in \mathfrak{F}_0^1$, is defined as:

$$P\left(\beta_k, x_1(.), \varphi\big(x_1(.), u(.)\big), u(.)\right) \triangleq J_1\big(u(.)\big) + \frac{1}{\beta_k}\int_0^T \left\|\frac{dx_1}{dt} - F_1\big(x_1(t), \varphi\big(x_1(t), u(t)\big), u(t), t\big)\right\|^2 dt + \frac{1}{\beta_k}\left[\sum_{i=1}^{n_1}\left|x_1^i(0) - x_{10}^i\right|^2 + \sum_{j=1}^{n_2}\left|\varphi^j\big(x_1(0), u(0)\big) - x_{20}^j\right|^2\right] + \beta_k\left\{\int_0^T\left[\sum_{i=1}^{n_3}\frac{1}{F_3^i(x_1(t),t)} + \sum_{i=1}^{n_4}\frac{1}{F_4^i(u(t),t)}\right]dt\right\} \quad \ldots(11)$$

The aim is to minimize (11), for each fixed k, $\beta_k > 0$ over $X_1^0 \times \mathcal{N}_{\tilde{x}_2} \times U^0$ and show that : the solution of (11) is equivalent to the solution of (6)- (10) which is also equivalent to the solution of original problem (1)- (5).

Remark 3:

1. To steer $x_1(0) \in \mathfrak{F}_0^1$ to its target $x_1(T) = \xi_1(T)$ over a class of admissible control and state functions, when (there exists at least one successful control) over the compact interval [0,T] the corresponding successful response must satisfy some a priori bound. Since $F_1 \in C^1(\mathcal{N}_{\tilde{x}_1} \times \mathcal{N}_{\tilde{x}_2} \times \mathcal{R}^p \times \mathcal{R}^{n_1})$

$$|F_1(x_1, \varphi(x_1, u), u)| \triangleq \sum_{i=1}^{n_1}\left|F_1^i(x_1, \varphi(x_1, u), u)\right|$$
$$|F_1(x_1, \varphi(x_1, u), u)| \le s_1|x_1| + s_2|\varphi(x_1, u)| + s_3|u|; \quad \ldots(12)$$
$$\varphi(x_1, u) \in C^1\big(\mathcal{N}_{\tilde{x}_1, \tilde{u}}\big).$$

One can also obtain that

$$|\varphi(x_1, u)| \le L_1|x_1| + L_2|u|, L_1, L_2 > 0 \quad \ldots.(13)$$

2. Define $\mathcal{Q}_{x_1} \triangleq \bigcup_{t\in[0,T]} \mathcal{Q}_{x_1}$ to be a non-empty bounded subset of the set $\mathcal{R}^{n_1}$.
$\mathcal{Q}_u \triangleq \bigcup_{t\in[0,T]} \mathcal{Q}_u$ to be nonempty convex compact subset of $\mathcal{R}^p$ for optimality

requirement, for simplicity the control will bounded in some sense. Hence from (12), (13) and (1) over these classes, one gets

$$|x_1(t)| \le \left|x_{10} + \int_0^t F_1\big(x_1(s), \varphi\big(x_1(s), u(s)\big), u(s), s\big)ds\right|$$
$$\le |x_{10}| + \int_0^t (\bar{s}_1 + \bar{s}_2 L_1)|x_1(s)|ds + (\bar{s}_2 L_2 + \bar{s}_3)b.T$$
$$\le (|x_{10}| + (\bar{s}_2 L_2 + \bar{s}_3)b.T)e^{(\bar{s}_1 + \bar{s}_2 L_1)T} \text{ (Grownwall inequality[24])}$$

Hence $|x_1(t)| \le \alpha_1$, where α_1 is constant depend only on the T, where $\mathfrak{F}_0^1$ is bounded subset of $\mathcal{N}_{x_1}$ over

$$[-\alpha, \alpha] \times \mathcal{N}_{\tilde{x}_1, \tilde{u}} \times \mathcal{Q}_u \times [0, T].$$

Lemma1.

$\inf J_1(u) = \alpha > -\infty$, $\forall \beta_k > 0$, then $P\left(\beta_k, x_{1,k}(.), \varphi\left(x_{1,k}(.), u_k(.)\right), u_k(.)\right)$ is bounded below on $X_1^0 \times \mathcal{N}_{\tilde{x}_2} \times U^0$.

Proof:

By definition of $P(\beta_k, x_1(.), \varphi(x_1(.), u(.)), u(.))$, we have on $X_1^0 \times \mathcal{N}_{\tilde{x}_2} \times U^0$, that

$$P\left(\beta_k, x_1(.), \varphi(x_1(.), u(.)), u(.)\right) \geq \inf_{X_1^0 \times \mathcal{N}_{\tilde{x}_2} \times U^0} J_1(u(.)) + \frac{1}{\beta_k}\int_0^T \left\| \frac{dx_1}{dt} - F_1(x_1(t), \varphi(x_1(t), u(t)), u(t), t)\right\|^2 dt + \frac{1}{\beta_k}\left[\sum_{i=1}^{n_1}\left|x_1^i(0) - x_{10}^i\right|^2 + \sum_{j=1}^{n_2}\left|\varphi^j(x_1(0), u(0)) - x_{20}^j\right|^2\right] + \beta_k\left\{\int_0^T\left[\sum_{i=1}^{n_3}\frac{1}{F_3^i(x_1(t))} + \sum_{i=1}^{n_4}\frac{1}{F_4^i(u(t))}\right]dt\right\}$$

$$\geq \inf_{x_1^0 \times \mathcal{N}_{\tilde{x}_2} \times U^0} J(u(.))$$

$$\geq \inf J(u(.)) = \alpha > -\infty \text{ since } X_1^0 \times \mathcal{N}_{\tilde{x}_2} \times U^0 \subset X_1 \times \mathcal{N}_{\tilde{x}_2} \times U$$

The generalization spaces functions, the problem formulation and its performance index of [9], [10] and [11] lead to the following theorem.

Theorem 1.

Let assumption 4 and lemma 3 are satisfied, then:

1) $\forall \beta_k > 0, P\left(\beta_k, x_1(.), \varphi(x_1(.), u(.)), u(.)\right)$ is minimized in $X_1^0 \times \mathcal{N}_{\tilde{x}_2} \times U^0$ at the point $\left(x_{10}^k(.), \varphi\left(x_{10}^k(.), u_0^k(.)\right), u_0^k(.)\right)$.

2) $\lim_{k\to\infty} P\left(\beta_k, x_{10}^k(.), \varphi\left(x_{10}^k(.), u_0^k(.)\right), u_0^k(.)\right) = \min_{(X_1 \times \mathcal{N}_{\tilde{x}_2} \times U) \cap \rho_{x_1,u}} \int_0^t F_0(x_1(t), \varphi(x_1(t), u(t)), u(t), t)dt$.

3) The limit point of $(x_{10}^k(.), \varphi\left(x_{10}^k(.), u_0^k(.)\right), u_0^k(.))$ solves the reduced optimal control problem (11).

4) The solution to the original problem is given by $\lim_{k\to\infty}\left(x_{10}^k(.), \varphi\left(x_{10}^k(.), u_0^k(.)\right), u_0^k(.)\right)$ where

$x_{20}^k(.) = \varphi\left(x_{10}^k(.), u_0^k(.)\right)$ starting from $(x_1^0, x_2^0, u^0) \in \mathfrak{F}(0)$.

Proof:

For the proof of (1):

Let $\beta_k > 0$ be fixed, since by lemma1, $P\left(\beta_k, x_1(t), \varphi(x_1(t), u(t)), u(t)\right)$ is bounded below on

$X_1^0 \times \mathcal{N}_{\tilde{x}_2} \times U^0$, let C_k be infimum over $X_1^0 \times \mathcal{N}_{\tilde{x}_2} \times U^0$ of $P\left(\beta_k, x_1(t), \varphi\big(x_1(t), u(t)\big), u(t)\right)$, which is finite by lemma 1, let $\{x_{1,n}^k(.), u_n^k(.)\} \in X_1^0 \times U^0$ such that

$$C_k = \lim_{n\to\infty} P\left(x_{1,n}^k(.), \varphi\left(x_{1,n}^k(.), u_n^k(.)\right), u_n^k(.)\right) \text{ over } X_1^0 \times \mathcal{N}_{\tilde{x}_2} \times U^0$$

Since $\{x_n^k(.)\}$ has bounded range, from Q_{x_1} is bounded subset of $\mathcal{N}_{x_1} \subset \mathcal{D} \subset \mathcal{R}^{n1} \Longrightarrow x_{1,n}^k(.)$ is uniformly bounded subset of $\mathcal{N}_{x_1}$. (assumption 4)

From the definition of $\varphi\left(x_{1,n}^k(.), u_n^k(.)\right)$ which is defined on $\mathcal{N}_{\tilde{x}_1,\tilde{u}}, \forall x_1(.) \in \mathcal{N}_{x_1},\ u \in \mathcal{R}^p$ which is bounded over the class of continuously differentiable functions , $\forall x_{1,n}^k(.) \in \mathcal{N}_{x_1},\ u_n^k \in U^0$

Since $x_1^k(t) \in Q_{x_1}$, $u_n^k(t) \in Q_u$ which are bounded and (convex and compact) subsets, respectively, and

$\left\|\varphi\left(x_{1,n}^k(t), u_n^k(t)\right)\right\| \le L_1\left\|x_{1,n}^k(t)\right\| + L_2\left\|u_n^k(t)\right\| \le L_1\left\|x_{1,n}^k(t)\right\| + L_2.b,\ \ L_1, L_2, b \ge 0$, where

$$\|x_1\| = \sup_{t\in[0,T]} \|x_1(t)\| = \sup_{t\in[0,T]} \sum_{i=1}^{n_1} \left|x_1^i(t)\right|$$

It should be noticed that.

$\int_0^T \left\|\dot{x}_{1,n}^k(t) - F_1\left(x_{1,n}^k(t), \varphi\left(x_{1,n}^k(t), u_n^k(t)\right), u_n^k(t), t\right)\right\|^2 dt = \mathcal{A}$, where $\mathcal{A} < +\infty$ and hence

$$0 \le \int_0^T \left\|\dot{x}_{1,n}^k(t) - F_1\left(x_{1,n}^k(t), \varphi\left(x_{1,n}^k(t), u_n^k(t)\right), u_n^k(t), t\right)\right\|^2 dt$$
$$\le \int_0^T \left\|\dot{x}_{1,n}^k(t)\right\|^2 dt + \int_0^T \left\|F_1\left(x_{1,n}^k(t), \varphi\left(x_{1,n}^k(t), u_n^k(t)\right), u_n^k(t), t\right)\right\|^2 dt$$

$$-2\int_0^T \langle x_{1,n}^k(t), F_1(x_{1,n}^k(t), \varphi\left(x_{1,n}^k(t), u_n^k(t)\right), u_n^k(t), t)\rangle\, dt = \mathcal{A} \qquad \ldots(14)$$

Where $\langle .,. \rangle$ is the inner product in subspace of $\mathcal{N}_{x_1} \subseteq \mathcal{D} \subseteq \mathcal{R}^{n_1}$. As a result of our assumptions, we have that

$$0 \le \int_0^T \left\|\dot{x}_{1,n}^k(t)\right\|^2 dt \le 2\int_0^T \left\|\dot{x}_{1,n}^k(t)\right\| \|s(t)\|\, dt + \int_0^T s^2(t)dt + I \qquad \ldots(15)$$

$$\int_0^T \left\|\dot{x}_{1,n}^k(t)\right\| \|s(t)\|\, dt \le \left(\int_0^T \left\|\dot{x}_{1,n}^k(t)\right\|^2 dt\right)^{\frac{1}{2}} . \left(\int_0^T s^2(t)dt\right)^{\frac{1}{2}} \Longrightarrow \qquad \ldots(16)$$

$$\left[\left(\int_0^T \left\|\dot{x}_{1,n}^k(t)\right\|^2 dt\right)^{\frac{1}{2}} - \left(\int_0^T s^2(t)dt\right)^{\frac{1}{2}}\right]^{1/2} \le \mathcal{A} + 2\int_0^T s^2(t)dt$$

$$\Longrightarrow \int_0^T \left\|\dot{x}_{1,n}^k(t)\right\|^2 dt \le \left[\mathcal{A} + 2\left[\int_0^T s^2(t)dt\right]^{1/2} + [s^2(t)dt]^{1/2}\right]^2$$

$$\le \left[(\mathcal{A} + 2k_1)^{\frac{1}{2}} + (k_1)^{\frac{1}{2}}\right]^2, k_1 > 0$$

Set $m = \left[(\mathcal{A} + 2k_1)^{\frac{1}{2}} + (k_1)^{\frac{1}{2}}\right]^2 \Rightarrow \int_0^T \left\|\dot{x}_{1,n}^k(t)\right\|^2 dt \leq m\,, m > 0.$ …(17)

Which lead to the uniformly bounded and depending only on T. Since

$$\left\|x_{1,n}^k(t_1) - x_{1,n}^k(t_2)\right\|^2 = \left\|\int_{t_1}^{t_2} \frac{d}{dt} x_{1,n}^k(t)dt\right\|^2 = \left\|\int_{t_1}^{t_2} \dot{x}_{1,n}^k(t)dt\right\|^2 \leq$$

$$\left(\left(\int_{t_1}^{t_2} dt\right)^2\right)^{1/2} . \int_0^T \left\|\dot{x}_{1,n}^k(t)\right\|^2 dt$$

$\leq |t_2 - t_1|. \left\|\int_{t_1}^{t_2} \dot{x}_{1,n}^k(t)dt\right\|^2 \leq m\,|t_2 - t_1|, m > 0$ for $|t_2 - t_1| < \delta \Longrightarrow \left\|x_{1,n}^k(t_2) - x_{1,n}^k(t_1)\right\| < \varepsilon,$ $\forall\, n > n_0 \in \mathbb{N}$ and fixed $k, \varepsilon \geq m.\,\delta$.

By using Arzelas theorem [24], there is a sequence, again denoted by

$$\{x_{1,n}^k(.)\} \xrightarrow[n\to\infty]{\substack{uniformly\ convergent \\ on[0,T]}} x_{1,0}^k(.) \text{ on the ranges over } \mathcal{Q}_{x_1} \text{ and } \mathcal{Q}_u, \quad \ldots(18)$$

for $x_1 \in \mathcal{N}_{x_1} \subset \mathcal{D} \subset \mathcal{R}^{n1}$ in $L_2[0,T]$, where $x_{1,0}^k(.)$ is continuous function. From (17) , one can define a further subsequence from $\{x_{1,n}^k(.)\}$ such that

$$\{\dot{x}_{1,n}^k(.)\} \xrightarrow[in\ L_2[0,T]]{weak\ sequential\ convernce} y_1(.) \in L_2[0,T] \quad \ldots(19)$$

Since $y_1(.) \in L_2[0,T]$ and from (18) and (19), we have that $x_{1,0}^k(t) - x_{1,0}^k(0) = \int_0^t \dot{x}_{1,0}^k(t)dt = \int_0^t \lim_{n\to\infty} \dot{x}_{1,n}^k(t)\,dt = \int_0^t y_1(t)dt \Longrightarrow \dot{x}_{1,0}^k(.) = y_1(.)\ \forall\ t \in \in [0,T]$. Since $y_1(.) \in L_2[0,T]$ hence

$$\dot{x}_0^k(.) \in L_2[0,T]$$

.

Since $\mathcal{Q}_u$ is compact and convex in $\mathcal{R}^p$, and $[0,T]$ is compact subset of $\mathcal{R}^1$. There exist a sequence relabeled as $\{u_n^k(.)\}$, for fixed $k > 0$ which has a weak sequential limit function $u_0^k(.)$ and which is bounded measurable [18].

$\{x_{1,n}^k(.),\ u_n^k(.)\}$ is minimizing sequence for $P\left(\beta_k, x_1(.), \varphi\big(x_1(.), u(.)\big), u(.)\right)$ on $X_1^0 \times \mathcal{N}_{\tilde{x}_2} \times U^0$.

we have a consequence that the sequence (in n) , and Since

$$\lim_{n\to\infty} \varphi\left(x_{1,n}^k(t), u_n^k(t)\right) = \varphi\left(\lim_{n\to\infty} x_{1,n}^k(t)\,, \lim_{n\to\infty} u_n^k(t)\right);$$

$$\varphi \in C^1[\mathcal{N}_{\tilde{x}_1,\tilde{u}}, \mathcal{R}^{n_2}]$$

for $i = 1, \ldots, n_3$, and $j = 1, \ldots, n_4$, $\int_0^T \frac{1}{F_3^i(x_{1,n}^k(t),t)}$ bounded on $\mathcal{Q}_{x_1}$ and $\int_0^T \frac{1}{F_4^j(u_n^k(t),t)}$ is bounded on $\mathcal{Q}_u$

$\forall\ x_{10} \in \mathfrak{F}^1(0)$ we have that:

$$\frac{1}{F_3^i(x_{1,n}^k(t),t)} \xrightarrow{n\to\infty} \frac{1}{F_3^i(x_{1,0}^k(t),t)}$$

$$\frac{1}{F_4^j(u_n^k(t),t)} \xrightarrow{n\to\infty} \frac{1}{F_4^j(u_0^k(t),t)} \quad \text{a.e on } [0,T]\,.$$

On using Fatous lemma [17], one gets

$$\int_0^T \frac{1}{F_4^j(u_0^k(t),t)} dt \leq \lim_n inf \int_0^T \frac{1}{F_4^j(u_n^k(t),t)} dt, i = 1, \ldots . n_4$$

$$\int_0^T \frac{1}{F_3^i(x_{1,0}^k(t),t)} dt \leq \lim_n inf \int_0^T \frac{1}{F_3^i\left(x_{1,n}^k(t),t\right)}\, dt, i = 1, \ldots, n_3$$

from (18), we have

$$\lim_{n\to\infty}\left\|x_{1,n}^k(0)-x_{10}\right\|^2=\left\|x_{1,0}^k(0)-x_{10}\right\|^2$$
$$\lim_{n\to\infty}\left\|x_{1,n}^k(T)-\xi_1(T)\right\|^2=\left\|x_{1,0}^k(0)-\xi_1(T)\right\|^2$$
$$\lim_{n\to\infty}\left\|\varphi(x_{1,n}^k(T),u_n^k(T))-\xi_2(T)\right\|^2=\left\|\lim_{n\to\infty}\varphi(x_{1,n}^k(T),u_n^k(T))-\xi_2(T)\right\|^2$$
$$=\left\|\varphi(\lim_{n\to\infty}x_{1,n}^k(T),\lim_{n\to\infty}u_n^k(T)-\xi_2(T)\right\|^2=\left\|\varphi(x_{1,0}^k(T),u_0^k(T))-\xi_2(T)\right\|^2$$

Over $\mathcal{Q}_x$ and $\mathcal{Q}_u$ on the compact subset [0,T] of $\mathcal{R}^1$. Since $\varphi\in C^1(\mathcal{N}_{\tilde{x}_1,\tilde{u}};\mathcal{R}^{n_2})$ and as a consequence of the above, we have got that

$$\left(x_{1,0}^k(.),\varphi\left(x_{1,0}^k(.),u_n^k(.)\right),u_0^k(.)\right)\in X_1^0\times\mathcal{N}_{\tilde{x}_2}\times\mathcal{R}^p$$
$$P\left(\beta_k,x_{1,0}^k(.),\varphi\left(x_{1,0}^k(.),u_0^k(.)\right),u_0^k(.)\right)=B_1^k \text{ on } X_1^0\times\mathcal{N}_{\tilde{x}_2}\times U^0 \quad \ldots(20)$$

Hence (1) of theorem 1 is proved, to complete the prove of (2-3) of theorem 1 we have that, since

$$\int_0^T F_0\left(x_{1,0}^k(t),\varphi\left(x_{1,0}^k(t),u_0^k(t)\right),u_0^k(t),t\right)dt\le P\left(\beta_k,x_{1,0}^k(t),\varphi\left(x_{1,0}^k(t),u_n^k(t)\right),u_0^k(t),t\right)$$
$$\le P\big(\beta_k,x_1(.),\varphi\big(x_1(.),u(.)\big),u(.)t\big)$$

…(21)

for $\left(x_1(.),\varphi\big(x_1(.),u(.)\big),u(.)\right)$ in $(X_1^0\times\mathcal{N}_{\tilde{x}_2}\times U^0)\cap\rho_{x_1,u}$, the following is obtained

$$\int_0^T F_0\left(x_{1,0}^k(t),\varphi\left(x_{1,0}^k(t),u_0^k(t)\right),u_0^k(t),t\right)dt\le P\big(\beta_k,x_1(.),\varphi\big(x_1(.),u(.)\big),u(.),t\big)$$

Where $\left(x_1(.),\varphi\big(x_1(.),u(.)\big),u(.)\right)\in(X_1^0\times\mathcal{N}_{\tilde{x}_2}\times U^0)\cap\rho_{x_1,u}$

Using the following generalization results of interior approximation ability assumption, which is necessary for penalty function approach to control problem of [9] as follows:

$\forall\varepsilon>0,\exists\left(x_{1,0}^\varepsilon(.),u^\varepsilon(.)\right)\in(X_1^0\times\mathcal{N}_{\tilde{x}_2}\times U^0)\cap\rho_{x_1,u}$ Such that

$$\int_0^T F_0\big(x_1^\varepsilon(t),\varphi\big(x_1^\varepsilon(t),u^\varepsilon(t)\big),u^\varepsilon(t),t\big)dt$$
$$\le\inf_{(X_1\times\mathcal{N}_{\tilde{x}_2}\times U)\cap\rho_{x_1,u}}\int_0^T F\big(x_1^\varepsilon(t),\varphi\big(x_1^\varepsilon(t),u^\varepsilon(t)\big),u^\varepsilon(t),t\big)dt+\varepsilon\ \ldots(22)$$

For every $\varepsilon>0,(\hat{x}_1(.),\varphi(\hat{x}_1(.),\hat{u}(.)),\hat{u}(.))$ in $(X_1^0\times\mathcal{N}_{\tilde{x}_2}\times U^0)\cap\rho_{x_1,u}$ such that from (20)

$$P\left(\beta_k,x_{1,0}^k(.),\varphi\left(x_{1,0}^k(.),u_0^k(.)\right),u_0^k(.),t\right)\le P\big(\beta_k,\hat{x}_1(.),\varphi\big(\hat{x}_1(.),\hat{u}(.)\big),\hat{u}(.),t\big)\ \ldots(23)$$

Hence

$$P(\beta_k,\hat{x}_1(.),\varphi(\hat{x}_1(.),\hat{u}(.)),\hat{u}(.))\le\inf_{(X_1\times\mathcal{N}_{\tilde{x}_2}\times U)\cap\rho_{x_1,u}}\int_0^T F_0(x_1(t),\varphi\big(x_1(t),u(t)\big),u(t),t)dt+\frac{\varepsilon}{2}$$
$$+\beta_k\int_0^T\left[\sum_{i=1}^{n_3}\frac{1}{F_3^i(x_1(t),t)}+\sum_{j=1}^{n_4}\frac{1}{F_4^j(u(t),t)}\right]dt\ \ldots(24)$$

Choose k such that $\beta_k\to 0$ enough and assume that

$$\beta_k\int_0^T\left[\sum_{i=1}^{n_3}\frac{1}{F_3^i(\hat{x}_1(t),t)}+\sum_{j=1}^{n_4}\frac{1}{F_4^j(\hat{u}(t),t)}\right]dt<\frac{\varepsilon}{2}\quad\ldots(25)$$

From (22),(23),(24) and (25)

$$\int_0^T F_0\left(x_{1,0}^k(t),\varphi\left(x_{1,0}^k(t),u_0^k(t)\right),u_0^k(t),t\right)dt$$
$$\le inf_{(X_1\times\mathcal{N}_{\tilde{x}_2}\times U)\cap\rho_{x_1,u}}\int_0^T F_0(x_1(t),\varphi\big(x_1(t),u(t)\big),u(t))dt+\frac{\varepsilon}{2}\qquad(26)$$

Therefore,

$$\int_0^T F_0\left(x_{1,0}^k(t), \varphi\left(x_{1,0}^k(t), u_0^k(t)\right), u_0^k(t), t\right) dt$$

$$\leq inf_{(X_1\times\mathcal{N}_{\tilde{x}_2}\times U)\cap\rho_{x_1,u}} \int_0^T F_0(x_1(t), \varphi(x_1(t), u(t)), u(t), t)dt + \varepsilon \quad (27)$$

Which makes $\int_0^T F_0\left(x_{1,0}^k(t), \varphi\left(x_{1,0}^k(t), u_0^k(t)\right), u_0^k(t), t\right) dt$ bounded above and below.

As a consequence of the previous results, one gets

$$\left\|x_{1,0}^k(0) - x_{1,0}(0)\right\|^2 \underset{k\to\infty}{\underset{\beta_k\to 0}{\longrightarrow}} 0 \quad \ldots(28)$$

$$\left\|\varphi\left(x_{1,0}^k(0), u_0^k(0)\right) - x_{2,0}(0)\right\|^2 \underset{k\to\infty}{\underset{\beta_k\to 0}{\longrightarrow}} 0 \quad \ldots(29)$$

$$\left\|x_{1,0}^k(T) - \xi_1(T)\right\|^2 \underset{k\to\infty}{\underset{\beta_k\to 0}{\longrightarrow}} 0 \quad \ldots(30)$$

$$\left\|\varphi\left(x_{1,0}^k(T), u_0^k(T)\right) - \xi_2(T)\right\|^2 \underset{k\to\infty}{\underset{\beta_k\to 0}{\longrightarrow}} 0 \quad \ldots(31)$$

For $x_1(0) = x_{10} \in \mathfrak{F}_0^1$, $\xi_1(T)$, $\xi_2(T)$, are given continuous functions

$$\int_0^T \left\|\dot{x}_{1,0}^k(t) - F_1\left(x_{1,0}^k(t), \varphi\left(x_{1,0}^k(t), u_0^k(t)\right), u_0^k(t), t\right)\right\|^2 dt \underset{k\to\infty}{\underset{\beta_k\to 0}{\longrightarrow}} 0 \quad ..(32)$$

Foe each $k > 0,\ \beta_k > 0,\ u_0^k(.) \in U^0\ and\ x_{1,0}^k(.) \in X_1^0, \varphi\left(x_1^0(.), u^0(.)\right) \in \mathcal{N}_{\tilde{x}_2} \subseteq \mathcal{R}^{n_2}$.

By using the same procedure of the proof of lemma 1

$$u_0^k(.) \xrightarrow[k\to\infty]{weakly} u^*(.) \in U, x_{1,0}^k(.) \xrightarrow[k\to\infty]{weakly} x_1^*(.) \in X_1, \dot{x}_{1,0}^k(.) \to \dot{x}_1^*(.) \in L_2[0,T] \quad ...(33)$$

To prove that, $(x_1^*(.), \varphi(x_1^*(.),\ u^*(.)),\ u^*(.)) \in \rho_{X_1,u}$, once

$$\int_0^T \left\|\dot{x}_1^*(t) - F_1(x_1^*(t), \varphi(x_1^*(t),\ u^*(t)),\ u^*(t))\right\|^2 dt$$

$$\leq \lim_k inf \int_0^T \left\|\dot{x}_1^k(t) - F_1\left(x_1^k(t), \varphi\left(x_1^k(t),\ u^k(t)\right),\ u^k(t)\right)\right\|^2 dt$$

$$\Longrightarrow \int_0^T \left\|x_1^*(t) - F_1\left(x_1^*(t), \varphi(x_1^*(t), u^*(t)), u^*(t)\right)\right\|^2 dt$$

By (20). $x_1^*(t) = F_1\left(x_1^*(t), \varphi(x_1^*(t), u^*(t)), u^*(t)\right)$ a.e. on $[0,T]$ and

$$\|x_1^*(0) - x_{10}\| \leq \left\|x_1^*(0) - x_{1,0}^k(0)\right\| + \left\|x_{1,0}^k(0) - x_{10}\right\| \quad \ldots.(34)$$

$$\left\|\varphi(x_1^*(0), u^*(0)) - x_{2,0}(0)\right\|$$

$$\leq \left\|\varphi(x_1^*(0), u^*(0)) - \varphi\left(x_{1,0}^k(0), u_0^k(0)\right)\right\| + \left\|\varphi\left(x_{1,0}^k(0), u_0^k(0)\right) - x_{20}\right\| \quad \ldots.(35)$$

$$\|x_1^*(T) - \xi_1(T)\| \leq \left\|x_1^*(T) - x_{1,0}^k(T)\right\| - \left\|x_{1,0}^k(T) - \xi_1(T)\right\| \quad \ldots.(36)$$

$$\left\|\varphi(x_1^*(T), u^*(T)) - \xi_2(T)\right\|$$

$$\leq \left\|\varphi(x_1^*(T), u^*(T)) - \varphi\left(x_{1,0}^k(T), u_0^k(T)\right)\right\| + \left\|\varphi\left(x_{1,0}^k(T), u_0^k(T)\right) - \xi_2(T)\right\| \quad \ldots.(37)$$

From (35) and (37), the following is used

$$\left\|\varphi(x_1^*(0), u^*(0)) - \varphi\left(x_{1,0}^k(0), u_0^k(0)\right)\right\| \leq \underset{0}{Lip}\, x_1 \left\|x_1^*(0) - x_{1,0}^k(0)\right\| + \underset{0}{Lip}\, u \left\|u^*(0) - u_0^k(0)\right\| \ldots(38)$$

$$\left\|\varphi(x_1^*(T), u^*(T)) - \varphi\left(x_{1,0}^k(T), u_0^k(T)\right)\right\| \leq \underset{T}{Lip}\, x_1 \left\|x_1^*(T) - x_{1,0}^k(T)\right\| + \underset{T}{Lip}\, u \left\|u^*(T) -$$

$u_0^k(T)\|$..(39)

As $k \to \infty$, $\beta_k \to 0$, $x_1^*(0) = x_{10} \in \mathfrak{F}_0^1$, $x_1^*(T) = \xi_1(T)$, from (38)-(39), we have

$$\left\|\varphi\left(x_{1,0}^k(0), u_0^k(0)\right) - x_{20}\right\| = \left\|\varphi\left(x_{1,0}^k(0), u_0^k(0)\right) - \varphi(x_{10}, u(0))\right\|$$
$$\leq \underset{1}{Lip}\, x_1 \left\|x_{1,0}^k(0) - x_{10}\right\| + \underset{1}{Lip}\, u \left\|u_0^k(0) - u(0)\right\|$$

And from (29)

$$\left\|x_{1,0}^k(0) - x_{10}\right\| = 0 \text{ and } \left\|u_0^k(0) - u(0)\right\| = 0 \text{ , for } u(0) \in \mathcal{F}_0^1 \qquad \ldots(40)$$

And $\varphi\big(x_1^*(0), u^*(0)\big) = x_{20}$, $\varphi\big(x_1^*(T), u^*(T)\big) = \xi_2(T)$. Therefor

$$\lim_{k\to\infty} P\left(\beta_k, x_{1,0}^k(.), \varphi\left(x_{1,0}^k(.), u_0^k(.)\right), u_0^k(.)\right) = \int_0^T F_0\ \left(x_1^*(t), \varphi\big(x_1^*(t), u^*(t)\big), u^*(t), t\big)dt$$
$$= \inf_{(X_1\times\mathcal{N}_{\tilde{x}_2}\times U)\cap\rho_{x_1,u}} \int_0^T F_0(\, x_1(t), \varphi\big(x_1(t), u(t)\big), u(t), t)dt \qquad \ldots(41)$$

Hence from (21), (22), we have that

$$\int_0^T F_0\left(x_{1,0}(t), \varphi\left(x_{1,0}(t), u_0(t)\right), u_0(t), t\right) dt \leq \lim_n inf \int_0^T F_0\left(x_{1,n}(t), \varphi\left(x_{1,n}(t), u_n(t)\right), u_n(t), t\right) dt$$

$$\int_0^T F_0\left(x_{1,0}^*(t), \varphi\left(x_{1,0}^*(t), u_0^*(t)\right), u_0^*(t), t\right) dt \leq \lim_k inf \int_0^T F_0\left(x_{1,0}^k(t), \varphi\left(x_{1,0}^k(t), u_0^k(t)\right), u_0^k(t), t\right) dt$$

$$\int_0^T F_0(\, x_1^*(t), \varphi\big(x_1^*(t), u^*(t)\big), u^*(t), t)dt$$
$$\leq \inf_{(X_1\times\mathcal{N}_{\tilde{x}_2}\times U)\cap\rho_{x_1,u}} \int_0^T F_0(\, x_1(t), \varphi\big(x_1(t), u(t)\big), u(t), t)dt + \varepsilon$$

Which leads to

$$\int_0^T F_0(\, x_1^*(t), \varphi\big(x_1^*(t), u^*(t)\big), u^*(t), t)dt \leq \inf_{(X_1\times\mathcal{N}_{\tilde{x}_2}\times U)\cap\rho_{x_1,u}} \int_0^T F_0(\, x_1(t), \varphi\big(x_1(t), u(t)\big), u(t), t)dt$$

Which complete the proofs of (2), (3), as a consequences of (1)-(3), the remains proof (4) is of the direct obtained.

computational algorithm

On the class of admissible functions $X^0 \times \mathcal{N}_{\tilde{x}_2} \times U^0$ (normed space) of reduced order constrained optimal control problem, one can assume that, the $\sum_{i=1}^{n_1} k_1^i + \sum_{j=1}^{p} k_2^j$ dimensional linear space of $X^0 \times \mathcal{N}_{\tilde{x}_2} \times U^0$ is spanned by the linearly independent bases functions $\psi_1^i, \psi_2^i, \ldots, \psi_{k1}^i$, $i = 1,2,\ldots,n_1$ (for the $n_1 -$ states), $\varphi_1^j, \varphi_1^j, \ldots, \varphi_{k2}^j$, j $= 1,2,\ldots,$ p (for the p - control), hence one can set

$$x_1^i(t) = \sum_{m=1}^{k_1{}^i} a_m^i\, \psi_m^i(t), \qquad a_m^i \in \mathcal{R}, i = 1,2,\ldots,n_1$$

$$u_j(t) = \sum_{m=1}^{k_2{}^j} b_m^j\, \varphi_m^j(t), \qquad b_m^j \in \mathcal{R}, j = 1,2,\ldots,p$$

Then on each subspace and fixed $\beta^k > 0$, the following functional is then obtained as:

$$P\left(\beta^k, \sum_{m=1}^{k_1^i} a_m^i\, \psi_m^i(t), \varphi\left(\sum_{m=1}^{k_1^i} a_m^i\, \psi_m^i(t), \sum_{m=1}^{k_2^j} b_m^j\, \varphi_m^j(t)\right), \sum_{m=1}^{k_2^j} b_m^j\, \varphi_m^j(t)\right) \triangleq P\big(\beta^k, \vec{a}, \vec{b}\big)$$

$\vec{a} \triangleq [a_1^1, a_2^1, \dots, a_{k_1}^1, \dots, a_1^{n_1}, a_2^{n_1}, \dots a_{k_1^{n_1}}^{n_1}]$, $\vec{b} \triangleq [b_1^1, b_2^1, \dots, b_{k_2}^1, \dots, b_1^p, b_2^p, \dots b_{k_2^p}^p]$.

Therefore, we have to choose the arbitrary real numbers $\vec{a}$ and $\vec{b}$, using suitable unconstrained inimization approach such that

$$P(\beta^k, \vec{a}, \vec{b}) \xrightarrow[\beta_k \to 0]{k \to \infty} \inf_{(X_1 \times \mathcal{N}_{\tilde{x}_2} \times U) \cap \rho_{x_1,u}} J(u) = \inf_{(X_1 \times \mathcal{N}_{\tilde{x}_2} \times U) \cap \rho_{x_1,u}} J(\vec{b})$$

Computational Algorithm 1.

Step 0: Find the consistency initial condition set $\mathfrak{F}(0)$ and then select: $(x_1^0, x_2^0, u^0) \in \mathfrak{F}_0$.

Step 1: Solve $F_2(x_1, x_2, u) = 0$ for $x_2(t)$, i.e. $x_2 = \varphi(x_1(t), u(t))$, with $x_2(0) = \varphi(x_1(0), u(0))$.

Step 2: Reduced the original DAE with constraints (1) - (5), into an equivalent problem (6) - (10) using Implicit function theorem as discussed earlier.

Step 3: Set

$$x_1^i(t) = \sum_{m=1}^{k_1{}^i} a_m^i \, \psi_m^i(t), \qquad a_m^i \in \mathcal{R}, i = 1,2, \dots, n_1$$

$$u_j(t) = \sum_{m=1}^{k_2{}^j} b_m^j \, \varphi_m^j(t), \qquad b_m^j \in \mathcal{R}, j = 1,2, \dots, p$$

Where $\psi_m^i(t), \varphi_m^j(t)$ are given linearly independent bases functions (suitable chosen)

Step 4: Set $\varepsilon_1 > 0, k = 1$, β_1 (small positive real number).

Step 4.1: Solve the unconstrained optimization problem for $(\vec{a}, \vec{b})$ over the class of $X_1^0 \times \mathcal{N}_{\tilde{x}_1, \tilde{u}} \times U^0$ by using any suitable optimization technique where the following requirements are assumed to be satisfied properly

$$\int_0^T \sum_{i=1}^{n_3} \frac{1}{F_3^i(\sum_{m=1}^{k_1{}^i} a_m^i \, \psi_m^i(t), t)} dt < +\infty$$

$$\int_0^T \sum_{i=1}^{n_4} \frac{1}{F_4^i(u_j(t) = \sum_{m=1}^{k_2{}^j} b_m^j \, \varphi_m^j(t), t)} dt < +\infty$$

And find the solution of

$$Min\, P\left(\beta^k, \sum_{m=1}^{k_1^i} a_m^i \, \psi_m^i(t), \varphi\left(\sum_{m=1}^{k_1^i} a_m^i \, \psi_m^i(t), \sum_{m=1}^{k_2^j} b_m^j \, \varphi_m^j(t)\right), \sum_{m=1}^{k_2^j} b_m^j \, \varphi_m^j(t)\right) \triangleq P(\beta^k, \vec{a}, \vec{b})$$

Step 4.2: Set

$$\text{Error1} = \frac{1}{\beta_k} \int_0^T \left\| \frac{dx_1}{dt} - F_1\left(x_1(t), \varphi\big(x_1(t), u(t)\big), u(t)\right) \right\|^2 dt$$

$$\text{Error2} = \frac{1}{\beta_k} \left\| x_1(0) - x_1^0 \right\|^2$$

$$\text{Error3} = \frac{1}{\beta_k} \sum_{i=1}^{n_1} \left| x_1^i(T) - \xi_1^i(T) \right|^2$$

$$\text{Error4} = \frac{1}{\beta_k} \| \varphi(x_1(0), u(0)) - x_{10} \|^2$$

$$\text{Error5} = \frac{1}{\beta_k} \| \varphi(x_1(T), u(T)) - \xi_2(T) \|^2$$

If the Total Error $\triangleq |(\text{Error1} + \text{Error2} + \text{Error3} + \text{Error4} + \text{Error5})| < \varepsilon_1;\ \varepsilon_1 \geq 0$. Then

stop and go to ***step 5***, otherwise set $k = 2$, β_k is reduced as $\beta_k,\ i.e.\ (\beta_k = \frac{1}{2}\beta_k)$ and go

to ***step 4.1***.

Step 5: Compute $\vec{a}, \vec{b}$ and back substitute then into the solution form of step 3 and then set $x_2 = \varphi(x_1(t), u(t))$ of step 1 with $u(t)$ of step 3, where $J(u^*(t))$ is obtained as a result steps 4.1, 4.2 , with tolerance error ε_1.

Remark 3.

1 . The choice of the type of basis approximation function $\psi_m^i(t), \varphi_m^i(t)$ and the numbers $k_1^i,\ k_2^j$ are depending on the decision maker and the type of the problem, for simplicity, one can choose a suitable polynomial up to some degree , because the class of polynomial is dense in the class of solvability of this problem $L_2[0,T]$ and especially (for continuous problem) with supremum norm.

2 .The violations in the constraints up to some accuracy say ($\varepsilon_1 > 0$) may be happened due to the selection of bases functions and their numbers as well as to the round - off- errors resulting from the integral forms of the constraints in the dual functional $P(\beta^k, \vec{a}, \vec{b})$ in addition to the same other reasons. one can use this the implicit function theorem to find $\varphi(x_1(t), u(t))$ explicitly globally or even locally as a subset of $\mathcal{R}^{n2}$.

Example 1. (without inequality constraint)

Consider $$Min\, J(u) = \int_0^T \left[\left(x_1(t)\right)^2 + \left(x_2(t)\right)^2\right] dt$$

$$\frac{dx_1}{dt} = x_2(t)$$

$$x_2(t) - u(t) = 0,$$

$$x_1(0) = 1,\ x_2(0) = u(0)\ ,\ T = 1$$

Where the consistency initial condition set

$$\mathfrak{F}(0) = \{x_1(0), x_2(0)) | x_2(0) = u(0)\ for\ a\ given\ x_1(0)\}$$

Since the algebraic equation is of easier kind $F_2(x_2, u) = x_2(t) - u(t) \triangleq x_2(t) - u(t) = 0$

Hence the implicit function theorems is applied globally and directly to have $\varphi(x_1(t), u(t)) = u(t)$

The closed form solution of this problem is given by [14] as:

$$x_1(t) = \left(\frac{2e}{1+e^2}\right)\cosh(1-t)\,, \qquad t \in [0,T]$$

$$x_2(t) = u(t) = \left[\frac{-2e}{1+e^2}\right]\sinh(1-t)$$

$$J^*(x_2) = J^*(u) = \int_0^1 (x_1^2 + u^2)dt = 0.76159.$$

On using the proposed approach and algorithm, the following assumptions are made to the reduced problem (simple basis functions are used)

$x_1(t) = \sum_{i=0}^{5} a_i t^i, \quad \dot{x}_1(t) = \sum_{i=0}^{5} i a_i t^{i-1}, \quad x_2(t) = u(t) = \sum_{j=0}^{5} b_j t^j$, $x_2(t) = \varphi(x_1(t), u(t)) = u(t)$

$$Min\ P(\beta^k, \vec{a}, \vec{b}) = \underset{X^0 \times \mathcal{R}^{n1} \times U^0}{\text{Min}} \frac{1}{\beta_k}|1 - a_0|^2 + \frac{1}{\beta_k}\int_0^1 \left|\sum_{i=0}^{5} i a_i t^{i-1} - \sum_{j=0}^{5} b_j t^j\right|^2 dt + \int_0^1 \left(\left(\sum_{i=0}^{5} a_i t^i\right)^2 + \left(\sum_{j=0}^{5} b_j t^j\right)^2\right) dt \quad \ldots.(42)$$

The unconstrained optimization technique (Quasi-Newton method) is used to find in the approximate solution to the original problem where β_k is selected smaller until the total error is acceptable (by decision maker) and repeat the optimization technique for different values of β_k until the desired result is obtained. The following result is obtained even for a reasonable value of β_k

Table (1)

The parameter β_k	0.001					
The dual objective function $P^*(\beta_k, \vec{a}, \vec{b})$	0.7614					
The objective function $J^*(u)$	0.7614					
The exact objective function $J^*(u)$	0.76159					
The unknown parameter $\vec{a}$ for $k_1 = 5$	a_0	a_1	a_2	a_3	a_4	a_5
	1.0	-0.7244	0.3147	0.1164	-0.0113	-0.0475
The unknown parameter $\vec{b}$ for $k_2 = 5$	b_1	b_2	b_3	b_4	b_5	
	-0.6331	0.331	0.3292	-0.0146	-0.2524	
The total error $\|E\| < \varepsilon_1$	$\varepsilon_1 < 10^{-4}$					
$x_2 = \varphi(x_1, u)$	$x_2 = u$					
The basis function $\varphi^i(t)$	$t^i, i = 1,2,3,4,5$					

The numerical simulations and comparisons between the proposed approach and the exact solution are shown in the following figures (1-2).

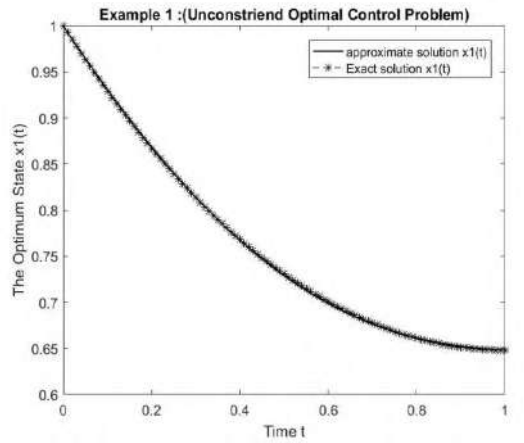

Figure.1

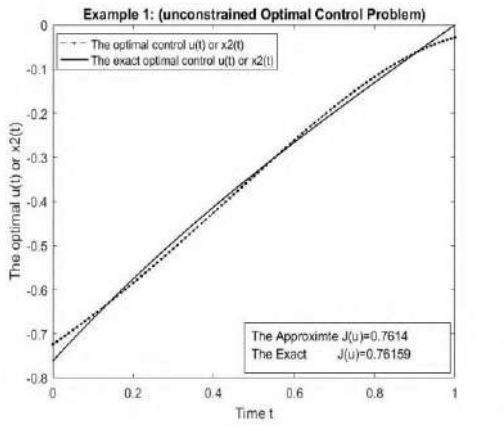

Figure.2

Example 2. (with constant inequality constraint)

Consider $$Min\, J(u) = \int_0^T \left[\left(x_1(t)\right)^2 + \left(u(t)\right)^2\right] dt$$

$$\frac{dx_1}{dt} = x_2(t), \qquad x_1(0) = x_{10}$$

$x_2(t) = u(t)$ (for simplicity used)

With linear constraints $x_1(t) \geq 0.75$ (inequality constaint)

$$\Im(0) = \{x_1(0), x_2(0), u(0)) | x_1(0) = x_{10}\ and\ x_1(t) \geq 0.75, x_2(0) = u(0)\ be\ given\}$$

We have assumed that $T = 1,\ x_1(0) = x_{10} = 1\ and\ n_1 = 5$ (for x_1) , $n_2 = 4$ (for u), and $\varphi^i(t) = t^i$

$x_1(t) = 1 + \sum_{i=0}^{n_1} a_i t^i,$ is substituted into the optimization criterion. The minimization objective function is defined as given by (42) where

$$\left[\beta_k * \int_0^T \frac{1}{g(x_1(t), t)}\, dt\right], g(x_1(t), t) \triangleq x_1(t) - 0.7,$$

is added to the objective function. The following numerical results are obtained, even with very small number of basis and its polynomial type and shown the very efficient technique, as one can see from the figures and its objective function value in **Table.2**.

Table.2

The parameter β_k	10^{-8}				
objective function $P^*(\beta_k, \vec{a}, \vec{b})$	0.8373				
The objective function $J^*(u)$	0.7500				
objective function [14] $J^*(u)$	0.77730				
The unknown parameter $\vec{a}$ for $k_1 = 5$	a_1	a_2	a_3	a_4	a_5
	-0.2380	-0.0488	-0.0010	0.0017	0.0059
The unknown parameter $\vec{b}$ for $k_2 = 5$	b_1	b_2	b_3	b_4	b_5
	-0.2380	-0.0977	-0.0301	0.0069	0.0296
The total error $\|E\| < \varepsilon$	$\varepsilon < 10^{-4}$				
$x_2 = \varphi(x_1, u)$	$x_2 = u$				
The basis function $\varphi^i(t)$	$t^i, i = 1,2,3,4,5$				

As one can see the present results of the proposed approach are better than the results presented in [14] even for simple type of basis functions.one can see the figures figure.3 and figure.4 and table 2 for comparisons point of view.

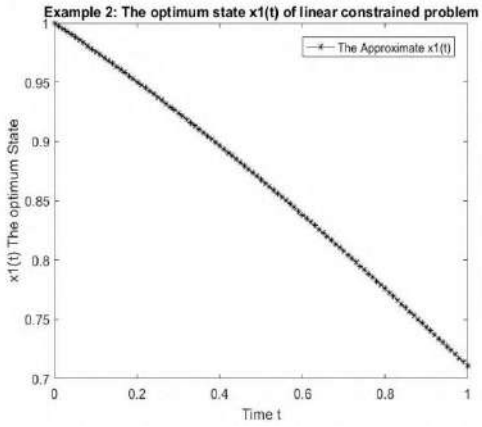

Figure.3

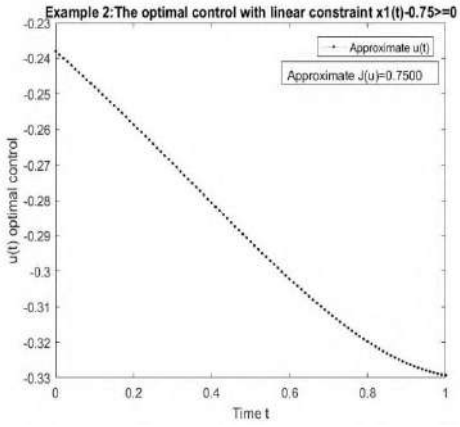

Figure.4

Example 3. (with nonlinear inequality constraint)

Consider $$Min\, J(u) = \int_0^T \left[\left(x_1(t)\right)^2 + \left(u(t)\right)^2\right] dt$$

With $$\dot{x}_1 = x_2(t),\ x_2 = u$$
$$x_1^2(t) \geq t \Leftrightarrow x_1^2(t) - t \geq 0,\ t \in [0,T]$$
$$\Im(0) = \left\{x_1(0), x_2(0), u(0)\right\} \left| x_1^2(0) \geq 0\ , x_2(0) = u(0)\right\}$$

Let $x_1(0) = 1,\ x_1(t) = \sum_{i=0}^{n_1} a_i t^i,\ u(t) = \sum_{i=1}^{n_2} b_i t^i,$ where $n_1 = 7, n_2 = 8$ the objective functions is same as that of example 2 by replacing the nonlinear inequalities constraint $g(x_1(t), t) = x_1(t) - 0.7$, by $g(x_1(t), t) = x_1(t) - t \geq 0$ see table.3 and figure.5 and figure.6

Table.3

The parameter β_k	10^{-8}							
T	1							
The objective function $J^*(u)$	0.9399							
objective function [14] $J^*(u)$	0.92278							
The unknown parameter $\vec{a}$ for $k_1 = 7$	a_0	a_1	a_2	a_3	a_4	a_5	a_6	a_7
	1.0	0.0390	0.0364	0.0293	0.0238	0.0198	0.0169	0.0146
The unknown parameter $\vec{b}$ for $k_2 = 8$	b_1	b_2	b_3	b_4	b_5	b_6	b_7	b_8
	-0.1798	0.0780	0.1092	0.1170	0.1190	0.1189	0.1181	0.1171
The total error $\lvert E\rvert < \varepsilon$	$\varepsilon < 10^{-4}$							
$x_2 = \varphi(x_1, u)$	$x_2 = u$							
The basis function $\varphi^i(t)$	$t^i, i = 1,2,3,4,5$							

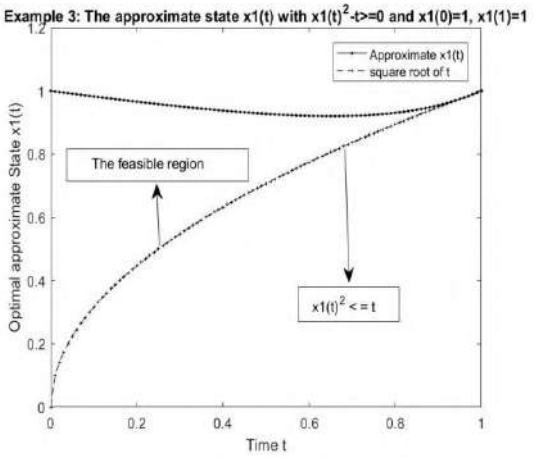

Figure.5

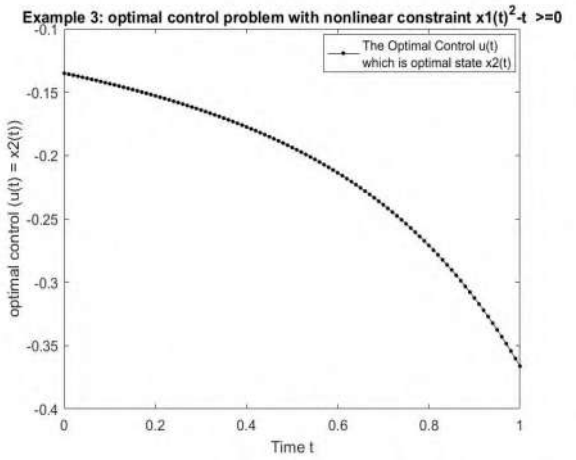

Figure.6

Example 4. (time varying inequality constraint of system of eqautions)

Consider $$Min\, J(u) = \int_0^1 [(x_1(t))^2 + (x_2(t))^2 + 0.005(u(t))^2]dt$$

Subject to $$\frac{dx_1}{dt} = x_2(t),\ x_1(0) = 0\ ,$$

$$\frac{dx_2}{dt} = x_2(t) + x_3(t),\ x_2(0) = -1$$

$$x_3(t) - u(t) = 0,\ \forall t \in [0,1]$$

$$8(t-0.5)^2 - x_2(t) - 0.5 \geq 0, \forall t \in [0,1]$$

$$\Im(0) = \{x_1(0), x_2(0), x_3(0)) | x_3(0) = u(0)\ , x_1(0) = 0, x_2(0) = -1\}$$

The approximate solution using the proposed algorithm is shown in the following table .4

Table.4

The parameter β_k	0.01				
The dual objective function $P^*(\beta_k, \vec{a}, \vec{b})$	0.1631				
The objective function $J^*(u)$	0.1287				
objective function [14] $J^*(u)$	0.1816				
The unknown parameter $\vec{a}$ for $k_1 = 5$	a_1	a_2	a_3	a_4	a_5
	-0.9975	2.1808	-1.3022	-0.5155	0.5034
The unknown parameter $\vec{b}$ for $k_2 = 5$	b_1	b_2	b_3	b_4	b_5
	4.3816	-3.9803	-1.9541	2.4649	5.3908
The unknown parameter $\vec{c}$ for $k_3 = 5$	c_1	c_2	c_3	c_4	c_5
	-12.6440	0.2108	6.3370	3.5905	-2.3879
The total error $\|E\| < \varepsilon$	$\varepsilon < 10^{-4}$				
$x_2 = \varphi(x_1, u)$	$x_2 = u$				
The basis function $G_i(t)\ , H_i(t), M_i(t)$	$t^i, i = 1,2,3,4,5$				

$$x_1(t) = \sum_{i=1}^{n_1} a_i G_i(t)\,, \quad x_2(t) = \sum_{i=0}^{n_2} a_i H_i(t) \quad u(t) = \sum_{i=0}^{n_3} a_i M_i(t),$$

The numerical accuracy of proposed approach can be seen from the following figures: figure.7, figure.8 and figure.9

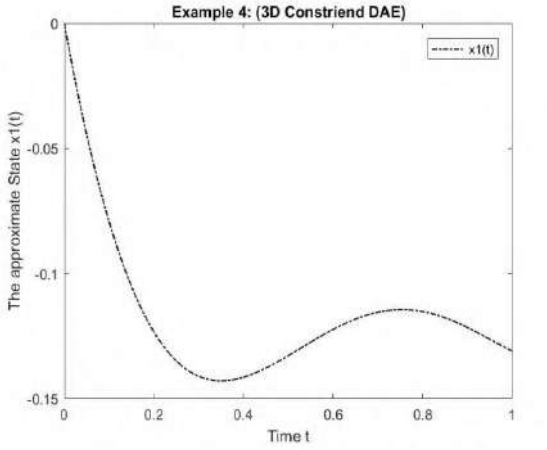

Figure.7

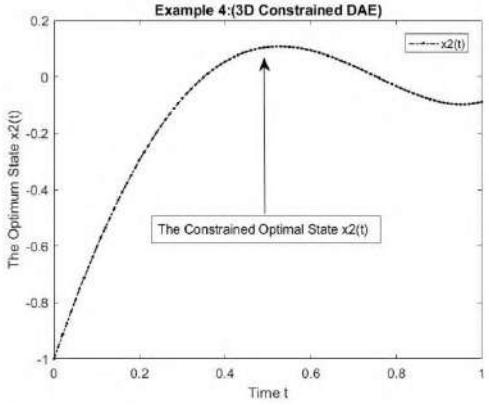

Figure.8

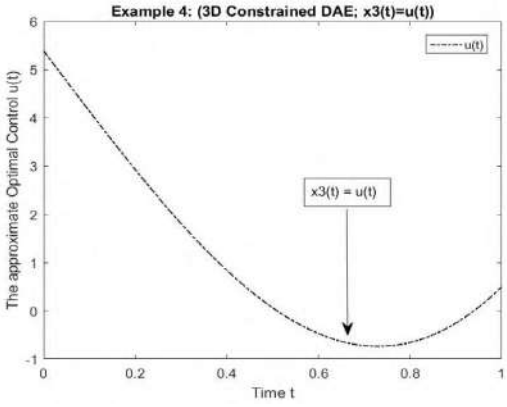

Figure.9

Conclusions

The proof and algorithm of unconstrained sequential penalty function optimization approach for constraint optimal control problem of DAE are proposed, in which a penalty terms are added to the objective function for any violations of equality and inequality constraints. An efficient numerical technique is developing. The accuracy of the method is very good even for a very small number of basis function and its types to solve some classes of the proposed problem are selected. The numerical examples, illustrate the simplicity of implementation and efficiency of the comparisons with exact solution (if any) and the results of others.

Acknowledgments.
The authors would like to thank Mustansiriyah University / College of Science / Department of Mathematics, for their support.

References

[1] Campbell S L 1987 A general form for solvable linear time varying singular systems of differential equations SIAM J. Math. Anal.**18** 1101-1115
[2] Kunkel P and Mehramann 2006 Differential- algebraic equations. Analysis and numerical solution *EMS. Publishing house Zurich Switzerland*
[3] Kunkel P and Mehramann 2008 Optimal control for unstructured nonlinear differential-algebraic equations of arbitrary index Math. Control. Signal Systems **20** 227-269
[4] Guong-Ren D 2010 Analysis and design of descriptor linear system *Springer Science and Business Media*.
[5] Lorenz B T, Stephan L Campbell V and Mehrmann 2012 Control and optimization with differential – algebraic constraint SIAM J. *by Society and for industrial and applied mathematics*
[6] Brenan K E, Campbell S L, Petzold L 1996 Numerical solution of initial- value problem in differential- algebraic equations," SIAM J. *by Society and for industrial and applied mathematics , Philadelphia*
[7] Griepentroy E and Marz P 1986 Differential-algebraic equations and their numerical treatment *Teubner Verlag, Liepizig, Germann*
[8] Johan S 2006 Some results on optimal control for nonlinear descriptor systems *L.U-Tryck, Linkoping,Sweden*
[9] Arnold J P and Garth M P 1970 A Generalization of the method of Balakrishnan: inequality constraints and initial conditions *SIAM J. Control* **8** (2)
[10] Balakrishnan A V 1968 on a new computing technique in optimal control *SIAMJ Control* **6 (**2)
[11] Balakrishnan A V 1969 On a new computing technique in optimal control and its applications to minimal-time flight profile optimization J. of Optimaization Theory and Applications **4** (1)
[12] Radhi Z A, Shiv Prasad Y and Mohan C 1999 Penalty method for an optimal control problem with equality and eniquality constrants *Indian J. Pure Appl. Math* **30** 1-14
[13] Lee E B and Markus L Faundation of optimal control theory John Wiely and Sons, Inc., original edition 1967, reprint edition 1986 with correction
[14] Goh C J and Teo K L 1988 Control parameterization: a unified approach to optimal control problems with general constraints Automatica **24**(1)3-18
[15] D L Debeljkovic and K V Drovic 1998 Lyapunov stability robustness consideration for linear singular system: new results Mechanics Automatics control and Robotics **2**(8)715-728
[16] Danielle C, Tarraf and HarryH 2002 On the nature of stability of differential-algebraic system Proceedings of the American control conference, *Anchorge, A.K.*, pp:8-10
[17] Riez F and Nagy S 1955 Functional analysis Fredrick Ungar, *New York*
[18] Macki J A Strauss A 1987 Introduction to optimal control theory Springer- Verlag, *New York, Inc*
[19] Gerdts M 2012 Optimal Control of ODE and DAE Walter DeGruyter Gmb H&Co. KG, 10785, Berlin, Bosten
[20] Sjoberg J 2006 Some results on optimal control for Nonlinear Descriptor Systems L.U-Tryck, Linkoping, Sweden.
[21] Oswaldo D O 2013 The Implicit and Inverse Function Theorems: Easy Proofs Real Anal. Exchange **39**(1)214–216
[22] Mathew H and John V 2010 The Implicit Function Theorem with Applications in Dynamics and control 48th AIAA Aerospace Science Meeting Including the new Horizons Forum and Aerospace Exposition, Orland, Florida
[23] Steven G , Krantz H and Parks R 2002 The Implicit Function Theorem History, Theory, and Application *Birkhauser, Berlin, second addition*
[24] Malkowsky E and Vadimir R 2019 Advanced Functional Analysis *Taylor&Francis Group,US*

Pseudo-Von Neumann Regular Graph of Commutative Ring

Pseudo -Von Neumann Regular Graph of Commutative Ring

Nabeel E. Arif [1], Roslan Hasani [2], Nermen J. Khalel [1]

[1]Department of Mathematics, College of Computer Science and Mathematics, Tikrit University, Iraq.
[2]Faculty of Ocean Engineering Technology and Informants, University Malaysia Terengganu UMT, Malaysia.

E-mail: nabarif@tu.edu.iq

Abstract. Let R be a commutative ring. The Von.-Neuman regular (Shortly Vn. Neum. reg.) graph of R is a graph which its vertices are all items of R s. t. thither is an edge between vertices a, b if a+b is a Vn.- Neum. reg. item of R. Here a new definition of the Vn. Neum. reg. graph of R called pseudo –Vn. –Neum. reg. graph of R denoted by P-VG(R) is a graph with all items of R represents a vertex, and two different vertices $a, b \in R$ are adjacent iff $a = a^2b$ or $b = b^2a$. In this work , the main features of P-VG(R) are studied and some outstanding results. Also, we prove if P-VG(R), R= Z_n and $n \geq 3$, n is a prime then it is graph has $\frac{n-3}{2}$ of cycle C_3. Finally, we show that If R=Z_p, where p is a prime number then the PG(R)⊂ P-VG(R).

1. Introduction

There is a bridge between the algebraic concept of rings and the graph theory. The study of algebraic graph has become an exciting research topic through last twenty years. There are many researches in the graphs related with rings were introduced with their features established see[1 - 4]. Taloukolaei and Sahebi defined the Vn.- Neum. reg. graph of R, denoted in $GV_{nr+}(R)$, is a graph consist vertices set R, two different vertices a, b of R are adjacent iff $a + b \in Vnr(R)$ the set of Vn. Neum. reg. items of R [9]. Bhavanari et.al. studied prime graph of a ring with some properties of its graph [7]. And he studied cartesian product of prime graph with Devanaboina [5].

The main goal of this paper creates a new definition named Pseudo-Von. Neum. regular graph of R if V(G) = R and E(G)={ $\overline{ab}$/ $a = a^2b$ or $b = b^2a$ and $a \neq b$, $a, b \in R$ } denoted by P-VG(R) with investigate of some properties as shown in next sections.

2. Preliminary

Definition 2.1:[11] A nonempty set R, with binary operations + and · is said to be a ring if below are satisfied

i- (R,+) is an abelian group
ii- (R,·) is a semi.group
iii- h ·(k+c) = h ·k + h ·c and (h+k) ·c = h ·c+k·c for any h, k, c ∈R

Definition 2.2:[8] suppose R is a ring with a∈R , can say that a is reg. item if there exist b∈R such that a=aba , if any element in R is regular then R is regular ring , if R is commutative then $a = a^2b$ and can say that R is Vn- Neum. reg. ring.

Definition 2.3:[12] Defined the graph G as an ordered pair (V, E), where V is a non-empty set whose items are named vertices and the set E (may be empty) of un-ordered pairs of distinct vertices of V. The item of E is named edges of the graph G . An edge between two end vertices h and k is denote by $\overline{hk}$.

Definition 2.4:[12] Defined the loop as an edge their end vertices are the same .

Definition 2.5:[12] If there are more than one edges related with a given pair of vertices , then these edges are named multiple edges.

Definition 2.6:[12] A graph has not self-loops or multiple. edges is named a simple graph.

Definition 2.7:[6] A graph K is said to be a subgraph of a graph G if all the edges and all the vertices of K are in G , and each edge of K has the same end vertices in K as in G.

Definition 2.8:[6] Suppose that G is a graph , V(G) is the vertex set of G, $D \subseteq V(G)$, the set D is said to be a dominating set if it satisfies the following condition ; $v \in V(G)$ implies either $v \in D$ or there exists $u \in D$ s.t. u and v are adjacent .

Definition 2.9:[12] A graph G include a list$v_1, v_2, \dots, v_n$ of vertics of G s.t. for $1 \leq i \leq p-1$, there is an edge (v_i, v_{i+1}) in G and these are just edge in G is called a path.

Definition 2.10:[6] Let h and k be two vertices in a graph G , then the distance d(h,k) from h to k is the shortest path from h to k.

Definition 2.11:[12] A cycle graph is got when connecting the two end vertices of a path graph . Thus, the degree of any vertex of a cycle graph is equal to two, a cycle graph with n vertices denoted by C_n.

Definition 2.12:[7] Let R be a ring , the graph G named prime graph of R if V=R and E(G)={ $\overline{ab}$/ a R b $= 0$or b R a $= 0$ and $a \neq b$ }and denoted by PG(R).

3. Psedo-Von Neumann Regular Graph

Definition 3.1: suppose R be a commutative ring. A graph G(V , E) is said to be (pseudo- Von. – Neum. regular graph) of R if V(G) =R and E(G)={ $\overline{ab}$/ $a = a^2b$ or $b = b^2a$ and $a \neq b$ } denoted by P-VG(R).

Examples: Consider Z_5={0,1,2,3,4} and Z_6={0,1,2,3,4,5} as follows figures

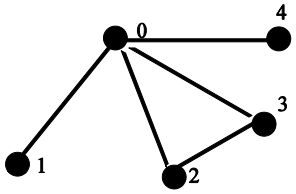

Figure .3.1 P-VG(Z_5)

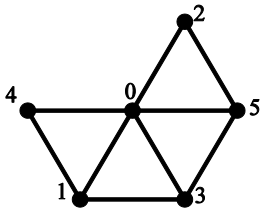

Figure .3.2 P-VG(Z_6)

Also consider Z_7={0,1,2,3,4,5,6} and Z_8={0,1,2,3,4,5,6,7} as follows figures

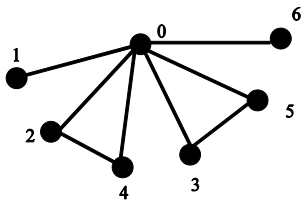

Figure .3.3 P-VG(Z_7)

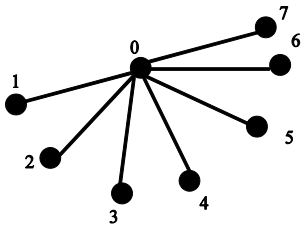

Figure .3.4 P-VG(Z_8)

Observation 3.2: Suppose R be a commutative ring and P-VG(R) then:

1- There are no self-loops
2- Since $0 = 0^2a \; \forall \; 0 \neq a \in R$ there is an edge between 0 and a $\forall$ a $\in V(G) = R$ so degree of the vertex $0 = |R| - 1$
   For any two elements $a,b \neq 0$ in R there is an edge one between 0 and a and another edge between 0 and b this shows that the graph P-VG(R) is always connected graph.
   $d(0,a) = 1$ and $d(a,b) \leq 2$ for any two elements $a,b \neq 0 \in R$
   If there are two non-zero elements a,b in R such that $a = a^2b$ or $b = b^2a$, then the sub graph generated by {0,a,b} is a cycle graph for example is graph P-VG(R) where R= Z_5 as in fig 4,The sub graph generated by {0,2,3} is a cycle.
3- The set {0} is a dominating set for P-VG(R). Hence the domination number of P-VG(R) is equal to 1.

4. Main Results

Remark 4.1:

1- $a = a^2b$ or $b = b^2a$ if and only if d(a,b)=1

Proof: Suppose that $a = a^2b$ or $b = b^2a$ and $a \neq 0 \neq b$ then ab$\in$ E (P-VG(R)) and so by definition 3.1 of P-VG(R) implies d(a,b) =1. If a or b equal to 0, also by definition 3.1 implies d (a,b) =1.
Conversely, suppose d (a,b) =1, if a=0 or b=0, by definition 3.1then $a = a^2b$ or $b = b^2a$
If d (a,b) =1 and $a \neq 0 \neq b$ then ab$\in$ E(P-VG(R)) which implies $a = a^2b$ or $b = b^2a$.

2- $a \neq a^2b$ and $b \neq b^2a$ if and only if d(a,b)=2

Proof: Suppose that $a \neq a^2b$ and $b \neq b^2a$ then there is no edge between a and b, so d (a,b) > 1 . since $0 = 0^2a$, $0 = 0^2b$, $\overline{a0}$, $\overline{b0}$ $\in$ E(P-VG(R)) , hence d (a,b)=2.
Conversely, suppose that d (a,b)=2 since $d(a,b) \neq 1$, there is no edge from a to b so $a \neq a^2b$ and $b \neq b^2a$

Lemma 4.2: If R= Z_n, and $n \geq 3$ (n is prime number), then there is no edge between the vertex 1 and n-1 in P-VG(R) .

Proof: We must show that either
$(1)^2(n-1) \neq 1$ or $(n-1)^2(1) \neq (n-1)$
In case $(1)^2(n-1)$equal 1 is impossible since $n \geq 3$, that is $(1)^2(n-1) \neq 1$
Now let $(n-1)^2(1) = (n-1)$, this leads to
$n^2 - 3.n + 2 = 0$, thus
$(n-2).(n-1) = 0$, Now
Either $n = 2$ or $n = 1$ which is a contradiction since $n \geq 3$
$\therefore \; (n-1)^2(1) \neq (n-1)$.

Lemma 4.3: If R= Z_n and n ≥ 3 (n is a prime number) , then there is no edge between any nonzero vertex with 1 and n-1 in P-VG(R).

Proof: It is clear that the vertex 1 is an identity element in R= Z_n so there is no edge between any vertex with vertex 1 now we check .
the vertex n -1 if we have
$(n-1)^2(a) = (n-1)$
$(n^2 - 2.n + 1)(a) = (n-1)$
$an^2 - 2an + a - n + 1 = 0$
$an^2 - (2a+1)n + (a+1) = 0$
$\big(an - (a+1)\big)(n-1) = 0$, Thus
Either $n - 1 = 0$ impels that $n = 1$ this is a contradiction since $n \geq 3$
or $an - (a+1) = 0$ impels that $n = \frac{a+1}{a}$ this is a contradiction since n is a prime number .

Remark 4.4: If R is a ring with $R^2 = 0$ then P-VG(R) is a tree.

proof: Suppose that R is a ring with $R^2 = 0$, then for any a,b $\in$ R we have ab=0
Now let a,b $\in$ R and $a = a^2b$ or $b = b^2a$ implies that
Either a=a(ab) or b=b(ba), implies that
a=a(0) or b=b(0) , Thus
a=0 or b=0
Hence there is no edge in P-VG(R) except 0a , $\forall$ a $\in$ R
Then P-VG(R) is star graph , then P-VG(R) is a tree since (every star graph is a tree) .

Theorem 4.5: If R= Z_n and n ≥ 3 is prime, then P-VG(R) graph has $\frac{n-3}{2}$ of cycle C_3 .

Proof: By lemma 4.2 and 4.3, the vertices 1 and n-1 have no edge between them and no edge with other vertices only with the vertex 0. Now since n is prime number then Z_n is a field so Z_n is Vn. Neum. reg. ring (every field is Vn. Neum. reg. ring] [10]. For any a$\neq$ 0 $\in Z_n$ $\exists$ b = a^{-1} such that $a = a^2b$ impels that there is an edge between a and b, since the unit element is a unique then has not any edge between a with another element, and so a0, b0 $\in$ E (P-VG(R)). Now we have $\frac{n-1}{2}$ of the cycle C_3 in P-VG(R), So by lemma 4.2 and 4.3 the number of the cycle C_3 in P-VG(R) graph is $\frac{n-1}{2} - 1 = \frac{n-3}{2}$.

Example: P-VG (Z_{13}) has 5 of the cycle C_3 and P-VG (Z_{19}) has 8 of the cycle C_3 as shown in the following figures.

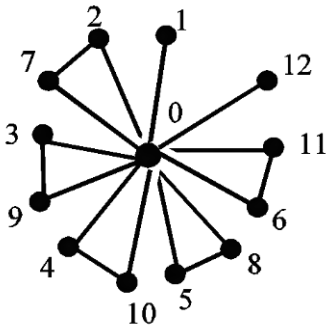

Figure .4.1 P-VG(Z_{13})

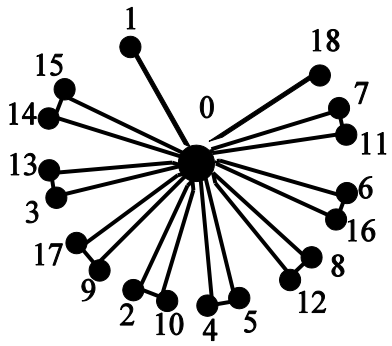

Figure .4.2 P-VG(Z_{19})

Theorem 4.6: If R=Z_p, when p represents a prime number then PG(R)⊂ P-VG(R).

Proof: Let $\overline{ab} \in$ E (PG(R)) then arb = 0
Since Z_p is a filed tnen Z_p is integral domain (has no non-zero divisor)
Implies that either a= 0 or b= 0
If a= 0 then $\overline{0b} \in E(P-VG(R))$,
and if b= 0 then $\overline{a0} \in E(P-VG(R))$
And it is clear that the vertices in graph PG(R) are same in graph P-VG(R)
Hence PG(R)⊂ P-VG(R).

5. Conclusions

The graph properties have become an exciting research topic and very important. In this work , new concept of Vn.- Neum. reg. graph of R called pseudo –Vn.- Neum. reg. graph of R named in P-VG(R) was created . The basic features of P-VG(R) presented are investigated and some results are described. Also, we proved that if P-VG(R), R= Z_n and $n \geq 3$, n is a prime then it is graph has $\frac{n-3}{2}$ of cycle C_3 and we show that if R=Z_p, when p represents a prime number then the PG(R)⊂ P-VG(R).

Acknowledgments

This work is supported by College of Computer Science and Mathematics, Tikrit University, Iraq and Faculty of Ocean Engineering Technology and Informants, University Malaysia Terengganu UMT, Malaysia. The authors want to thank mentioned institutions for their support to finish this work.

References

[1] Akbari S and Heydari F 2013 The regular graph of a commutative ring *Periodica Mathematica Hungaria* **67** 211-220
[2] Akbari S, D Kiani, Mohammadi F and Moradi S 2009 The total graph and regular graph of acommutative ring *Journal of pure and applied algebra* **213** 2224-2228
[3] Anderson D F and Badawi A 2012 Von Neumann regular and related elements in commutative rings *Algebra Colloq.* **19** 1017=1040
[4] Ashrafi N, Maimani H R, Pournaki M R and Yassemi S 2010 Unit graphs associated with rings *Comm. Algebra* **38** 2851-2871
[5] Bhavanari S and Devanaboina S 2015 Cartesian product of graphs vs prime graphs of rings *Global Journal of Pure and Applied Mathematics* **11**(2) 199-205
[6] Bhavanari S and Kuncham S 2014 Discrete mathematics and graph theory *Delhi PHL Learning Private Limited*

[7] Bhavanari S, Kuncham S and Dasari N 2010 Prime graph of a ring *Journal of combinatorics Information and System Sciences* **35** (12) 27-42.
[8] Goodearl K R 1991 *Von* neumann regular rings *Florida Krieger Publishing Company Malabar*
[9] Taloukolaei A J and Sahebi S 2018 Von neumann regular graphs associated with rings *Journal of Discrete Mathematics Algorithms and Applications* **10** (3) 1850029
[10] Kaplansky I 1995 Fields and rings Chicago Lectures in Mathematics 2nd Edition. *The University of Chicago Press Chicago*
[11] Khanna V K and Bhambri S K 1993 Course in abstract algebra India Vikas *Publishing House Pvt.Ltd.*
[12] Rahman M S 2017 Basic Graph Theory *Springer International Publishing AG*

Using BAB to find Optimal Solution for Multi-Objective Function with Setup Time

Using BAB to find Optimal Solution for Multi-Objective Function with Setup Time

Hanan Ali Cheachen , Ghufran Khalil Joad

Department of Mathematics, College of Sciences, Al-Mustansireyah University, Baghdad, Iraq

Email: ghufrankalil@gmail.com

Abstract. In this paper we studied, the problem of scheduling jobs on a single machine to minimize the multiple objective function and family setup time. This objective function is (total discount completion time and maximum tardiness respectively) which formulated as $1/s_f/\sum_{j=1}^{n}\sum_{f=1}^{F}(1-e^{-rc_{jf}})+T_{max}$. for solving this problem, we derived a lower bound to be used in a branch and bound algorithm. We also proposed heuristic method in order to get an upper bound (near optimal solution). the proposed is number of dominance rules are considered to reduce the number of branches in the search tree. The genetic algorithm (GA) is used to obtain one of the upper bounds is used. The computational results are calculated by coding (programing) the algorithms using (MATLAP) and the final results up to (17) product (jobs) in a reasonable time are introduced by tables and added at the end of the research.

1. Introduction

Scheduling problems are encountered in all kinds of systems, since it is necessary to organize or distribute the work between many entities. There are many definitions for the scheduling problems and among these definitions, it can be quoted the following; (Holger. H. Hoos 2005) [9] defined the scheduling problems accordingly next:

"Given the group from j tasks which has at exist processed by the group from M resources, while the object is for locate a schedule which is a chart from jobs to machines and processing times subject to optimization objectives criteria".

In many industries, the decision to manufacture multiple products on common resources results in the need for changeover and setup activities, symbolize costly disruptions to production processes. Therefore, setup reduction is an important feature of the persistent improvement program of any manufacturing, and even service, organization. It is even more critical if an organization expects to respond to changes like shortened lead times, smaller lot sizes, and big quality standards. Every scheduler should understand the basics of setup reduction and be able to recognize the tolerable improvements [14].

Many practical scheduling problems involve sequencing number of jobs divided into several families, by a machine setup time. Most of these problems are NP-hard ((non-deterministic polynomial-time hardness) is the defining property of a class of problems that are informally "at least as hard as the hardest

problems in NP") even without set up times and thus are difficult to solve to optimality. several scheduling problems in makings and advocacy organizations can be formulated as single aperient problems at task classes (families), for example, Bruno and Downey[3], Monma and Potts [17] and Chen [4] described a computer system application , a collection of jobs need to be executed on a computer in which every task has a diversion time, a due date, and a request for a compiler to be resident in the memory of the computer. When the appropriate compiler is resident in the computer, then the job will start its processing immediately; otherwise the setup time incurred for bringing the relative compiler into the computer's memory. So, the setup time reckon only on the time of loading the compiler for the current job but not on the previous job.
In conventional scheduling problems, it is logical and necessary to consider scheduling problems with setup times. In many concrete situations, the setup times are treating either sequence independent or sequence dependent. In the one case, the setup times are ordinarily added to the job processing times however in the two case, the setup time into the job actually being scheduled depends on the beforehand one or ones already scheduled [25].

Group scheduling problems, where each jobs of the self-family must be scheduled jointly, have attracted abundant researchers due to their frequent real-life occurrence. Many manufacturers have implemented the concept of Group Technology (GT) in order to lessen setup costs, lead times, work-in-process inventory costs, and tools handling costs. Group Technology consists of dividing the sum group of jobs into several subsets, called families, where a family is a subset of jobs that have similar requirements in terms of tooling and setups [11].

Setup operations ensure acquisition material, positioning work in process tools, resumption tooling, cleanup, setting the desired jigs and supply, adjusting tools, and test material [22]. In the problem down study we do not treat the Group Technology (GT) supposition; that is, a family of jobs is not necessarily processed as a single batch [13]. Therefore; a family of jobs could be split into multiple nonconsecutive batches in an optimal sequence and all of the batches endure a setup time.

They explained that regard in scheduling problems that patronize setup times (costs) as split up start in the mid-1960s. Scheduling problems together sequence-dependent setup times are oftentimes across in many production regulation and factory applications.

1.1. Literature Reviews:

The objective function is to minimize discounted total completion time. Following the three-field symbols plot offered by Graham et.al [8]. We declare this problem as: $1/s_f/\sum_{f=1}^{F}\sum_{j=1}^{n_f}(1-e^{-rc_{jf}})$ where r ∈ (0,1) is a discount rate by SPT rule. According to the importance of the scheduling problems, there were a plethora of the specialists whose produced a fine number of the work papers. In the year (1984), Rothkopf and smith [19] work on the sum discounted weighted completion time which is represented accordingly $1//\sum w_j(1-e^{-rcj})$ they generalized the study to cost function and they showed that this problem can exist dissolve optimally as P-kind in polynomial time by the weighted discounted shorter processing time (WDSPT) rule (i.e. scheduling the jobs in order of non- decreasing ratio $w_j e^{-rpj}/1\text{-}e^{-rpj}$ The problem $F_m//\sum w_j$ $(1\text{-}e^{-rc_j})$ is considered as an NP-hard problem by Wang et. Al (2006). In (2012), Lin Li et al. (2013) [15] have studied the problem of the sum weighted discounted total completion time and they showed that the heuristics according to the conformable problems wanting education ware. In (2016), studied the problem $1//\sum w_j(1-e^{-rcj})+L_{max}^{h}$. the maximum tardiness $1//T_{max}$ problem is minimized by Earliest Due Date (EDD) rule [10]. The earliest of these woks was done by Sidney [12].

The interesting in the scheduling problems which deal with the separating setup times (costs) began in the middle of the 60s. As Luh et.al (1998), where they declare that "understanding the sequence-dependent setups is yet confirm to be away of being complete, mostly the scheduling to the congress due dates". So, considering the tardiness is an important matter while the due dates are met. Many authors have worked on

problems in which involving the due dates and sequence subsidiary setup times in order that minimize maximum of tardiness. Baker and Scudder (1990) [2] represented a treatise of penalties (earliness and tardiness) problems while in (2000). Fry et. al. (1987) [6], Garey et. al. (1988) [7], Davis and Kanet (1993) [5]and Yano & Kim (1991) [24] advanced timetabling procedures for finding the optimal beginning times of tasks with inserted idle times. Davis and Kanet (1993) and Kim and Yano (1994) offer a new procedure using branch & bound (B&B) for the problem. Later, Sourd (2005) and Schaller (2007) improved it. In production systems, there occur great accounts of tardiness for several jobs which rise some hardness. As a genuine enforcement, every job in an institution line should be convey at a proven due date. If a task has great tardiness, then the else tasks will not be masterful, resulting in an imponderable in the institution line. So, the term the tardiness ought for approximate to zero. One of the criteria that can satisfy this aim is minimizing the maximum tardiness which is presented as (T_{max}). The aim function value would be equal to zero in the optimal state. If whatever tardiness exist, then the value of the objective function will be larger than zero. That aim function was one worked on by Amin-Nayeri and Moslehi (2000) [1] as a problem of single-machine scheduling case. An algorithm was proposed by Tavakkoli-Moghaddam et al (2005) for obtaining the better potential amount of an idle insert in a sequence, in (2009), Mahnam & Moslehi have worked on single machine problem with morphologic release times for the same objective. As mentioned before, a great number of studies have been accomplished on the scheduling problems which established on the guesstimate of sequence subordinate (independent) setup times, only no study has been convey yet with the same objective.

The remainder of the paper is organized as follows. In Section 2, problem formulation for the problem under study. In Section 3, we explain the heuristic methods used. In Section 4, review the dominance rule. In Section 5, we show the design of instances and report the computational results.

2. Problem Formulation: _

Considering a group N of n jobs ($1 \leq n \leq N$) that are divided into F different families, in our paper we consider F=2,4,6 and 8. Each family f ($1 \leq f \leq F$) consists of n_f jobs (where $\sum_{f=1}^{F} n_f = n$) and it is appropriate to label the jobs as (1,f), (2,f),….(n_f,F) which are available to be processed on the machine at time zero [16]. The jobs of the self-family may have different processing times p_{jf} which is the processing time of job j from the family f, and they can be processed one after one without request any setup times between them. If the machine moves from one family to the other; we would say from the family f to the family g then the setup time is required. Every job will have a due date d_{jf} which is the due date of job j from the family f. The setup time is sequence – independent (i.e. rely only on the family that is about to start), so that it is denoted by sf. If the first job to be processed in the sequence belongs to family f, then the setup at time zero is s_{0f} [20]. The objective is to minimize the by the notation of Graham et al. [8] as $1/s_f/\sum(1\text{-}e^{-rc_{jf}})+T_{max}$).

Suppose the processing order $\sigma = (\sigma(1), \dots, \sigma(n))$, a vector ($S_{\sigma(1)}$,….,$S_{\sigma(n)}$) of corresponding setup time is easily constructed. The setup time request immediately before the processing of job $\sigma(i) = (i = 1, \dots, n)$ is given by: -

$S_{\sigma(1)}$: is the setup time of the first job (positive integer constant).

$$S_{\sigma(i)}=\begin{cases} \sigma_{fg} & if\ \ i>1, \sigma(i-1)\in f\ and\ \ \sigma(i)\ \in g, f\neq g\ ; f,g\ \in F. \\ 0 \quad o.w & \end{cases}$$

Where σ_{fg} is positive integer constant:

Min Z=min $\sum_{j=1}^{F}\sum_{j=1}^{n_f}(1-e^{-rc_{jf}})+T_{max}$

$$\left.\begin{array}{c} subject\ to: \\ c_{jf} = p_{jf} + s_f \quad j = 1; f = 1, \dots., F \\ c_{jf} = c_{j-1,f} + p_j \quad j = 2, \dots., n\ ; f = 1, \dots., F \\ 0 < r < 1 \\ T_{max} = \max\{0, c_{jf} - d_{jf}\} \quad j = 1, \dots., n\ ; f = 1, \dots., F \\ d_{jf} \geq 1, p_{jf} \geq 1 \end{array}\right\} \dots\dots\dots(P)$$

3. Heuristic Method

It is well famous that the calculation can be miniature by using a heuristic to law as an upper bound on the optimal solution previous to the enforcement of branch and bound method. Since as problem max $1/s_f/\sum_{f=1}^{F}\sum_{j=1}^{n_f}(1-e^{-rc_{jf}})+T_{max}$ is NP-hard and subsequently the presence of a polynomial time algorithm for returns an optimal solution is away. Therefore, improve quick heuristic algorithms submission near optimal solution is of great attention. For our problem we proposed heuristic method, the minimum value is used to provide an Upper Bound (UB) [16].

3.1 The Branch and Bound method:

As an exact method, the (BAB) method is used for searching at the optimality or the area that near of it by setting a number of upper bounds as initial solutions to start from then we put the one with the minimum value, and a lower bound to reduce the searching space. the heuristic method is obtained by applying the following: -

3.1.1. (U_1): - This upper bound is acquired b stratify the shortest processing time (SPT) rule (i.e. separation the jobs within each family in order of ($p_1 \leq p_2 \leq \cdots \leq p_n$)).

3.1.2. (U_2): _This upper bound is obtained by applying the earliest due date (EDD) rule (i.e. separation he jobs within each family in order of ($d_1 \leq d_2 \leq \cdots \leq d_n$)).

3.1.3 (U_3): _Obtain by Genetic Algorithm (GA):

Genetic algorithms (GA) are a type of search algorithms and an optimization, for returns optimal solutions to computationally intricate problems. The basic ideas for this method were developed by (Holland (1975), Goldberg and Holland (1988)) during their investigations on how to build computing machines that are capable of learning [21].

The genetic algorithm (GA) is founded on principle "survival of the fittest" for Darwin's (1859), in another meaning it's founded on the basics of genetics and natural selection. So, it is normal the concepts of Genetic Algorithm are directly derived from biological science.

Genetic algorithm: _

Step 1: Formation a primary population of (50) chromosomes, we take any solutions arranged by SPT rule and the second is according EDD rule, the three is according bees' algorithm, the four-weed algorithm while the remain of them are randomly the rest of the solutions are random order.

Step 2: Evaluate the objective (fitness) function for each chromosome and select the better five chromosomes (i.e. the five chromosomes with the minimum values) to generate the new population

Step 3: Generate the new population by mating (i.e. applying crossover and mutation) each chromosome from step 2 with the whole four initial chromosomes, and every parent chromosome will produce 8 children chromosomes and add 5 chosen solutions, selected from the population so the resulting new population will consist of 50 new chromosomes.

Step 4: If the termination criterions are met, then go to step 5, else go to step 2.

Step 5: End.

In this subsection, we will introduce the main upper bound (UB) of the problem P which it is obtained by:

UB=min $\{U_1, U_2, U_3\}$.

3.2 The Lower Bound (LB):

The lower bound for the problem (p) is instituted decomposing (P) of two sub-problems to obtain the a Lower Bound LB for problem (p), where

$$\left.\begin{array}{c} Min\ F_1 = min_{\sigma(j)}\{(1 - e^{-rC_{\sigma(j),f}})\} \\ subject\ to: \\ C_{jf} \geq P_{jf} \quad j = 1, \dots, n_f; f = 1, \dots, F \\ 0 < r < 1 \\ d_{jf} > 0\ , P_{jf} > 0 \quad j = 1, \dots, n_f; f = 1, \dots, F \end{array}\right\} \dots\dots (p_1)$$

$$\left.\begin{array}{c} Min\ F_2 = min_{\sigma(j)}\{T_{max}(\sigma)\} \\ subject\ to: \\ C_{jf} \geq P_{jf} \quad j = 1, \dots, n_f; f = 1, \dots . F \\ T_{max} = \max\{0, C_{jf} - d_{jf}\} \quad j = 1, \dots, n_f; f = 1, \dots, F \\ d_{jf} > 0\ , P_{jf} > 0 \quad j = 1, \dots, n_f; f = 1, \dots, F \end{array}\right\} \dots\dots (p_2)$$

Algorithm (LB): _

Step 1: In un-scheduling arrange the jobs by using (SPT) rule and adding setup time for the first job from jobs un-sequence if the not least family job of sequence.

Step 2: Computation the amount of cost function of F_1 for the problem p_1.

Step 3: Re-arrange the jobs by using (EDD) rule and adding setup time for the first job from jobs un-sequence if the not least family job of sequence.

Step 4: Computation the amount of cost F_2 for the problem p_2.

Step 5: Sum cost the functions (i.e. total cost the problem P_1 and the problem P_2).

Step 6: We repeat the solutions 5 times to get the solutions and compare with the old solutions.

Step 7: Go back to step 2.

Theorem (3.1) [17]: If F_1, F_2 and F are the minimum rate of P_1,P_2 and p problems respectively, then we have that F_1+F_2 ≤ F.

4. Dominance Rule

Dominance rules generally describe if a node can be discarded before its lower bound is counted. obviously, dominance rules are especially beneficial when a node can be terminating which has a lower bound that is least than the optimum solution. Some of dominance rules are useful for minimization of the total of discounted completion time and maximum tardiness.

Theorem (3.1): consider two jobs (J_{jf} and J_{kf}) from the same family, the job J_{jf} must precede the job J_{kf} at least in one optimal sequence if $P_{jf} \leq P_{kf}$, $d_{jf} \leq d_{kf}$ and cost (w') ≥ cost (w)

Where the symbols in which used in this theorem mean as follows:

S

B	s_f	P_{jf}	P_{kf}	W	A

S'

B	s_f	P_{kf}	P_{jf}	W'	A

t

B: The set of jobs in which are scheduled before job j and job k and the jobs before jobs j and k are from different family.
A: The set of the jobs in which are scheduled after job j and k and different from another family.
COST (B): The total cost of $w_j(1-e^{-rc_j})$+T_{max} for jobs in set B.
COST (A): The total cost of w_j(1-e^{-rc_j})+T_{max} for jobs in set A.
W: The group of the jobs in which are scheduled between job j and job k.
COST (W): The total cost of (1-e^{-rc_h})+T_{max} for the jobs of set in sequence S.
COST (w'): The total cost of (1-e^{-rc_h})+T_{max} for the jobs of set w' in sequence S'.
t: The completion time of the last job in set B.
c: The starting time of the one job in the set A.
proof: Let s_1=$\sigma_1$ijσ_2 and s_2=$\sigma_1$jiσ_2 where $\sigma_1$and σ_2 are disassemble subsequence and supposed to be the completion time of σ_1, we examine variation on the in Δ_{ij}(t), where Δ_{ij}(t)=$f_{ij}(t) - f_{ji}(t)$ with following:
for $S_1 = \sigma_1 ij\sigma_2$
(1-e^{-rc_i}) + $(1-e^{-rc_j}) = \left(1-e^{-r(T+P_i)}\right) + (1-e^{-r(T+P_i+P_j)})$……. (1)
For s2
(1-e^{-rc_j})+ (1-e^{-rc_i})= (1-$e^{-r(T+P_j)}$)+(1-$e^{-r(T+P_j+P_i)}$) ……. (2)
For (1) and (2) we get
(1-$e^{-r(T+P_i)}$) + (1-$e^{-r(T+P_i+P_j)}$) − $(1-e^{-r(T+P_j)})$- (1-$e^{-r(T+P_j+P_i)}$)
= - $e^{-r(T+P_i)}$ - $e^{-r(T+P_i+P_j)}$ +$e^{-r(T+P_j)}$+$e^{-r(T+P_i+P_j)}$
= $e^{-rT}(e^{-P_i}$ - $e^{-(p_i+P_j)} + e^{-P_j} + e^{-(P_i+P_j)}$
= $e^{-rT}(e^{-(P_i+P_j)}$ - $e^{-(P_i+P_j)}$ +e^{-P_j} -e^{-P_i})
= $e^{-rT}(e^{-P_j}$-$e^{-P_i}) < 0$ …… (3)
And for S_1
T_{max}=max{T,T_i,T_j}
where T_i=max {0, c_i-d_i}=max {0, T+P_i-d_i}
T_j=max {0,c_j-d_j}=max {0, T+P_i +P_j-d_j}
For schedule s'
T'_{max}=max {T',T'_j,T'_i}
T'_j=max {0,c_j-d_j}=max {0, T+P_j-d_j}
T'_i=max {0,c_i-d_i}=max {0, T+P_j+P_i-d_i}
$\because c'_j \geq c'_i$, $d_i \leq d_j$and T=T' then $T'_i \geq T'_j$, $T'_i \geq T_i$ and $T'_i \geq T_j$
So $T'_{max} \geq T_{max}$ ……. (4)
From (3) and (4) we get
$i < j$ in optimal solution for problem (P).

5. Experimental Results: In this part, the results are advertising in the table. Table include the comparison results of the (BAB), ILB and UB for the problem.

1- The Problems Instances: The problems were created randomly, and for all job (j), where j ∈ {1, n}, with family f= {2,4,6,8} he processing times and setup times are randomly created integer from uniform divide m in [1,10]. While the due date d_j is uniformly generated in the period [(1-TF-RDD /2), (1 − TF + RDD/2)], where TP is the total processing times of jobs. TF is the tardiness factor, and RDD is the range prorated of the due dates. TF has values {0.1, 0.2,0.3,0.4} and RDD has values {0.8,1.0, 1.2}.
2- Computational results: The calculation results are presented in tables and his table award the results (i.e. optimal values by (BAB), the upper bound of the problem, the initial lower bound and the pursuance time).

For each n, 5 problems and family (2,4,6,8) are examined, and a stopping condition is 1800 seconds as the most the pursuance time. The code which used in the table is:
n → The number of jobs.
F → the number of setup times families.
Ex → The number of examples.-
BAB → The branch and bound method.
UB → Indicates that upper bound.
ILB → Indicates that initial lower bound.
N → The number of the nodes.
Time → The pursuance time.

4-3 The Table of Results: In Table. the results of applying (BAB, UB, ILB, the number of the nodes and the execution time) are showed for n= [5, 17] Jobs with the family f= {2,4,6,8}. For each n and there are 5 different examples are tested. These results showed for n= {5,6,7,8,9} of using (BAB and UB) are equal, and the stopping condition is 1800 seconds as the maximum execution time. the symbol (/) in some examples denotes on time exceeded the specified time.

A comparison results between (BAB), (UB) and (ILB).

N	F	EX	BAB	UB	ILB	N	Time
5	2	1	18.5606*	18.5606*	16.4116	35	0.0985
		2	24.3825*	24.3825*	21.6727	32	0.0228
		3	12.9510*	12.9510*	9.7290	41	0.0128
		4	24.5334*	24.5334*	22.1294	33	0.0047
		5	21.9118*	21.9118*	19.0831	33	0.0113
	4	1	42.1817*	42.1817*	32.9880	122	0.0507
		2	27.0042*	27.0042*	17.1679	146	0.0087
		3	26.7009*	26.7009*	17.4495	140	0.0096
		4	13.2115*	13.2115*	5.1824	27	0.0032
		5	28.9000*	28.9000*	19.1987	116	0.0072
	6	1	35.1482*	35.1482*	20.5844	164	0.0093
		2	36.2341*	36.2341*	21.7908	164	0.0117
		3	18.8498*	18.8498*	8.1347	48	0.0033
		4	42.6685*	42.6685*	28.3811	194	0.0094
		5	25.8115*	25.8115*	11.2327	98	0.0054
	8	1	26.9330*	26.9330*	11.9709	170	0.0084
		2	30.6073*	30.6073*	16.0076	134	0.0069
		3	31.8215*	31.8215*	17.1607	128	0.0066
		4	42.0722*	42.0722*	27.6636	170	0.0082
		5	39.1439*	39.1439*	24.5159	206	0.0096
	2	1	21.1585*	21.1585*	18.4053	148	0.0077
		2	9.1939*	9.1939*	6.5942	39	0.0031
		3	17.2970*	17.2970*	14.7113	52	0.0038
		4	27.4871*	27.4871*	25.0249	67	0.0042
		5	25.2247*	25.2247*	22.6674	80	0.0045
		1	32.5588*	32.5588*	22.4516	353	0.0153

6	4	2	38.5210*	38.5210*	28.9720	399	0.0165
		3	44.9892*	44.9892*	35.6464	473	0.0197
		4	28.9647*	28.9647*	19.4253	171	0.0081
		5	30.7474*	30.7474*	20.4030	415	0.0182
	6	1	27.6416*	27.6416*	8.6658	276	0.0119
		2	29.3259*	29.3259*	10.8443	227	0.0101
		3	37.7544*	37.7544*	20.3164	331	0.0147
		4	43.5263*	43.5263*	22.7986	703	0.0282
		5	36.9614*	36.9614*	15.7632	655	0.0268
	8	1	44.6377*	44.6377*	24.1822	797	0.0316
		2	47.8967*	47.8967*	26.9530	997	0.0416
		3	40.8785*	40.8785*	20.4764	509	0.0206
		4	43.6828*	43.6828*	22.7105	1093	0.0431
		5	33.4795*	33.4795*	12.5409	975	0.0388
7	2	1	25.9323*	25.9323*	22.6103	323	0.0139
		2	24.9601*	24.9601*	21.9569	354	0.0153
		3	41.2338*	41.2338*	38.7519	277	0.0120
		4	44.1869*	44.1869*	41.6218	500	0.0204
		5	16.2182*	16.2182*	12.9773	377	0.0159
	4	1	39.9456*	39.9456*	30.4067	655	0.0256
		2	47.6593*	47.6593*	37.9050	1345	0.0511
		3	44.1861*	44.1861*	34.5721	1123	0.0429
		4	34.5836*	34.5836*	24.6628	380	0.0156
		5	34.8067*	34.8067*	25.2638	1642	0.0634
	6	1	54.0482*	54.0482*	26.3170	4560	0.1786
		2	74.0625*	74.0625*	46.5566	7940	0.3086
		3	56.9049*	56.9049*	29.0227	7388	0.2873
		4	45.6390*	45.6390*	17.0008	3944	0.1526
		5	67.9602*	67.9602*	40.1515	7940	0.3101
	8	1	54.0482*	54.0482*	26.3170	4560	0.1786
		2	74.0625*	74.0625*	46.5566	7940	0.3086
		3	56.9049*	56.9049*	29.0227	7388	0.2873
		4	45.6390*	45.6390*	17.0008	3944	0.1526
		5	67.9602*	67.9602*	40.1515	7940	0.3101
	2	1	39.3047*	39.3047*	36.2483	1035	0.1026
		2	32.9801*	32.9801*	30.5515	161	0.0080
		3	30.1949*	30.1949*	27.6777	193	0.0173
		4	32.4527*	32.4527*	28.1092	2629	0.0999
		5	23.5777*	23.5777*	18.1505	682	0.0260
	4	1	63.6788*	63.6788*	54.0788	2831	0.0814
		2	43.1333*	43.1333*	33.1364	3616	0.1246
		3	52.5488*	52.5488*	42.7529	1625	0.0495
		4	44.4976*	44.4976*	34.4244	1629	0.0477

8		5	39.7246*	39.7246*	29.4441	1592	0.0485
	6	1	58.3657*	58.3657*	37.8256	18661	0.5651
		2	60.3769*	60.3769*	40.0932	20688	0.6345
		3	48.8810*	48.8810*	27.9300	18291	0.5503
		4	61.0708*	61.0708*	39.3523	41328	1.2641
		5	71.8359*	71.8359*	51.2241	39521	1.2040
	8	1	76.0324*	76.0324*	40.2616	30211	0.9324
		2	79.0159*	79.0159*	42.6754	50921	1.6005
		3	63.2340*	63.2340*	27.3275	37841	1.1738
		4	53.3537*	53.3537*	16.8087	27994	0.8522
		5	63.7790*	63.7790*	27.6042	28343	0.8429
9	2	1	35.5739*	35.5739*	33.3521	1039	0.0399
		2	43.9143*	43.9143*	41.1679	640	0.0257
		3	43.5595*	43.5595*	40.9257	650	0.0261
		4	39.0451*	39.0451*	36.3061	398	0.0163
		5	42.4435*	42.4435*	39.1557	6647	0.2566
	4	1	58.2350*	58.2350*	46.5099	31497	1.2132
		2	44.5679*	44.5679*	34.8833	4721	0.1791
		3	50.3887*	50.3887*	39.7947	11551	0.4309
		4	38.8899*	38.8899*	28.0358	10610	0.3987
		5	51.4764*	51.4764*	40.7422	14737	0.5613
	6	1	69.6771*	69.6771*	49.5267	66718	2.5635
		2	63.2888*	63.2888*	41.7853	136769	5.2996
		3	71.0934*	71.0934*	50.4783	166932	6.5950
		4	61.8668*	61.8668*	40.7659	64116	2.4804
		5	53.9612*	53.9612*	33.6253	20382	0.7663
	8	1	73.1080*	73.1080*	36.5982	427986	17.9807
		2	82.3050*	82.3050*	46.9104	206138	8.0750
		3	51.3196*	51.3196*	14.8969	104848	4.0594
		4	62.9748*	62.9748*	27.4156	205247	8.2472
		5	61.7406*	61.7406*	25.2577	124853	4.8405
10	2	1	32.1529	32.6858	28.2019	26546	1.2040
		2	49.1367*	49.1367*	46.6967	625	0.0290
		3	59.9532*	59.9532*	55.6443	33608	1.2992
		4	36.4785*	36.4785*	33.8726	1454	0.0648
		5	70.7035*	70.7035*	68.4968	1667	0.0746
	4	1	65.3664*	65.3664*	55.9742	89437	3.7450
		2	45.1994*	45.1994*	33.6098	24784	0.9298
		3	57.3485	58.4518	47.4566	22350	0.83637
		4	51.4936	52.1497	41.3122	14961	0.5623
		5	54.0759	55.3678	43.7756	57626	2.1895
	6	1	70.3132*	70.3132*	49.0888	65733	2.4590
		2	69.8474*	69.8474*	53.2522	40111	1.5037

		3	45.3040*	45.3040*	25.7807	19711	0.8183
		4	56.4069	57.5568	35.4515	237702	10.3467
		5	78.3835	78.7416	57.5741	1051895	42.8273
	8	1	87.1547*	87.1547*	51.1975	2835873	116.2090
		2	79.0112*	79.0112*	43.1233	1372528	52.9967
		3	102.1067*	102.1067*	66.3797	3652045	114.3312
		4	70.2734	70.4697	36.1511	1099925	34.6518
		5	83.6773*	83.6773*	46.8479	2081456	64.7658
11	2	1	72.7247	72.7784	69.6376	54330	2.0814
		2	39.3959*	39.3959*	34.2215	127133	3.9015
		3	38.9179*	38.9179*	34.5143	115629	3.7752
		4	49.4398*	49.4398*	47.1363	6208	0.1749
		5	48.0935*	48.0935*	44.8642	42993	1.3023
	4	1	45.9587*	45.9587*	33.0366	239016	7.3399
		2	67.0284*	67.0284*	57.2064	86740	2.6572
		3	43.9994*	43.9994*	31.0944	9305	0.2640
		4	58.2023*	58.2023*	44.8045	129285	3.7702
		5	37.2267*	37.2267*	25.3716	116135	3.2627
	6	1	70.4671*	70.4671*	48.1267	2325512	71.9499
		2	75.6740*	75.6740*	50.6689	491939	15.4453
		3	72.2324*	72.2324*	47.8844	1980559	60.3902
		4	51.0511	51.4002	28.5580	256527	7.4209
		5	59.3391	59.5335	37.9900	335154	10.2895
	8	1	97.4213*	97.4213*	61.7241	24932007	790.5983
		2	89.9661	89.9986	54.7351	7156930	221.6080
		3	70.7659*	70.7659*	37.7120	308297	8.7755
		4	81.0335*	81.0335*	44.6617	10707313	332.0386
		5	88.1852	88.2298	52.4954	20100367	629.5126
12	2	1	69.7388*	69.7388*	66.9561	4790	0.1333
		2	45.0493*	45.0493*	42.8396	4731	0.1636
		3	73.0304*	73.0304*	70.3810	19182	0.5517
		4	57.4469*	57.4469*	54.9613	3241	0.0923
		5	64.2999	66.0278	61.5916	516546	16.9135
	4	1	83.7581	85.7997	74.3406	284430	8.4155
		2	68.5505	68.7074	56.1298	714645	21.4935
		3	53.4514	54.7839	43.3238	80309	2.6660
		4	77.7415	77.8793	67.0835	384637	12.1894
		5	57.7770	57.7853	45.5842	1611786	49.0465
	6	1	75.8596	78.0521	53.6569	2183638	66.1950
		2	96.0855	96.4472	75.6365	3251373	96.9198
		3	81.6870	82.8484	58.5520	4589232	143.1084
		4	80.5243	83.2103	57.5970	3537741	107.3939
		5	83.6811	83.8422	56.6534	16530539	513.1630

	8	1	/	/	/	/	1800.0002
		2	/	/	/	/	1800.0002
		3	81.8674	81.8756	45.1758	29915490	928.4289
		4	74.8196	74.9842	39.3528	21910849	679.1056
		5	/	/	/	/	1800.0001
13	2	1	61.3626*	61.3626*	59.1709	27046	0.7790
		2	80.9849*	80.9849*	78.9649	38836	1.2446
		3	64.5674*	64.5674*	61.4131	139847	4.3214
		4	54.1981*	54.1981*	50.1627	681122	23.1814
		5	78.0532*	78.0532*	75.8878	31634	1.0388
	4	1	69.5527	70.1975	59.2890	939319	27.5206
		2	66.0666	66.2078	55.2306	1121060	33.5796
		3	80.2413	80.3736	70.1658	1031227	29.8601
		4	73.9158*	73.9158*	60.4966	8852525	271.8963
		5	71.9607	73.9708	57.0006	3246256	100.8326
	6	1	75.3635*	75.3635*	53.8647	24181181	742.1095
		2	77.6531	79.1087	51.1334	29364516	905.5780
		3	106.6035	106.6233	85.1235	36294738	1100.5083
		4	82.5116	82.9162	61.1359	12053771	367.0831
		5	43.0417	43.7211	21.0156	974067	28.8051
14	2	1	43.4003	46.0277	39.5110	374868	11.0523
		2	56.7608	57.2849	51.9202	4749284	146.1543
		3	61.8356*	61.8356*	58.4435	17923712	577.6754
		4	43.4232*	43.4232*	38.3040	10440	0.3046
		5	72.4318	72.8279	69.4523	5680774	176.8153
	4	1	79.1435	79.2923	69.2907	4782722	147.6929
		2	92.7653	92.9048	82.7127	2996032	92.7637
		3	/	/	/	/	1800.0001
		4	57.1401	58.3414	44.4973	8551879	261.1641
		5	67.3696	68.2621	55.1997	4560399	137.2345
	6	1	/	/	/	/	1800.0001
		2	68.5429	70.0919	45.3610	17525655	569.4346
		3	/	/	/	/	1800.0004
		4	68.7711	70.2053	44.7251	28862759	891.9382
		5	/	/	/	/	1800.0001
15	2	1	54.2869	54.3219	50.7152	22140644	684.8232
		2	60.5660	63.2054	56.4984	135263	3.9229
		3	/	/	/	/	1800.0001
		4	63.0105	63.1903	58.1535	37516308	1196.1326
		5	56.5249	59.2365	52.5119	2069623	60.8069
	4	1	87.4431	87.4490	77.2440	24280207	760.6983
		2	/	/	/	/	1800.0001
		3	63.6930	63.9398	52.6858	6218487	184.9003

		4	58.4665	60.7093	46.9668	3061590	90.8379
		5	67.5888	68.5348	55.9355	52819043	1603.3751
16	2	1	53.0390*	53.0390*	49.0552	1409289	43.7779
		2	69.7273	72.6159	67.4610	1199218	39.4724
		3	118.3106*	118.3106*	115.7161	488474	14.9773
		4	70.4269	73.1534	67.5838	1270041	39.5166
		5	/	/	/	/	1800.0001
	4	1	67.0088	69.7353	52.2008	44184610	1356.1336
		2	/	/	/	/	1800.0003
		3	/	/	/	/	1800.0001
		4	/	/	/	/	1800.0001
		5	74.4973	75.4270	58.5070	47436616	1431.6475
17	2	1	107.5272	109.8345	104.3674	28490250	936.4970
		2	68.7261	70.3712	63.7914	259586	7.9549
		3	/	/	/	/	1800.0002
		4	/	/	/	/	1800.0003
		5	56.9582	59.8469	52.4789	31334657	1013.1670

6. Conclusions: -

1-By using branch and bound method done problem solution.
2-Get three the upper and one lower bound.
3-The upper bound using the genetic hybridization algorithm its results were equal to the optimal solution in part of the results. except in case of job (n=14,15,16,17) where there are some examples failed because they take a long executing time (i.e. more than 1800 seconds)

References:

[1] M R Amin-Nayeri and G Moslehi 2000 Optimal algorithm for single machine sequencing to minimize early/tardy cost *J Esteghlal. Isfahan University of Technology* **1** pp 35-48
[2] K R Baker and G D Scudder 1990 Sequencing with earliness and tardiness penalties: A review *J OPI Res* **38** pp 22–36
[3] J Bruno and P Downey 1978 Complexity of task sequencing with deadlines, setup times and changeover costs *SIAM J Computer* **7** pp 393-404
[4] B Chen B 1993 A better heuristic for preemptive parallel machine scheduling with batch setup times *SIAM J Computer* **22** pp1303-1318
[5] J S Davis and J J Kanet 1993 Single-machine scheduling with early and tardy completion costs *Nav Res Logist* **40** pp 85-101 tardiness. Math Opens Res 13: 330–348.
[6] T D Fry 1987 Armstrong RD and Blackstone JH. Minimizing weighted absolute deviation in single machine scheduling *IIE Trans* **9** pp 445-450
[7] M R Garey, R E Trajan and G T Wilfong 1988 One-processor scheduling with symmetric earliness and tardiness *Math Opens Res* **13** pp 330-348
[8] R L Graham, Lawler, J k Leenstra and K Ringo A H G 1979 Optimization and Approximation in Deterministic Sequence and Schedule *A Survey Annals of Discrete Mathematics* **5**
[9] H H Holger and S Thomas 2005 Germany Stochastic Local Search *Foundations and Applications* ISBN:1-55860-872-9. Elsevier Incorporation

[10] J R Jackson 1955 Scheduling a production line to minimize maximum tardiness *Research Report 43, Management Science Research Project, University of California, Los Angeles, USA*
[11] N D JATINDER, Y GUPTA and SAMARN CHANTARAVARAPAN 2008 Single machine group scheduling with family setups to minimize total tardiness **46** (6) 15
[12] J B Sidney 1977 Optimal single-machine scheduling with earliness and tardiness penalties *Operations Research* **25** (1) pp 62-69
[13] J B Wang and J J Wang 2014 Single machine group scheduling with time dependent processing times and ready times *Information Sciences* **275** pp 226-231
[14] J R Montoya-Torres, Ferrari and Gonzalez-Solano 2010 Production scheduling with sequence dependent setup and job release time *Nor* **163** pp 260-269
[15] L Lin, L, Y Sheng-Wu, W Yu-Bin, H Yunshan and J Ping 2013 Single machine scheduling jobs with a truncated sum-of processing-times-based learning effect *Int J Adv Manu Technol* **67** pp 261-267
[16] H I Manal 2011 Scheduling Job Families with Setups on A single Machine 2011 *Al-Mustansiriyah University* **22** (3)
[17] C L Monma and C N Potts 1989 On the complexity of scheduling with batch setup times *Opera. Res.* **37** pp 798-804
[18] A m Ramadhan 1998 *Single machine scheduling using branch and bound techniques* M.Sc. Thesis University of Al-Mustansiriyah College of Science Department of Mathematics
[19] W E Smith 1956 Various optimizer for single stages production *Naval Research Logistics Quarterly* **3** pp 59-66
[20] K Steinhöfel, A Albrecht and C K Wong 2003 An experimental analysis of local minima to improve neighbourhood search *Computers and Operations Research* **30** pp 2157-2173
[21] R J M Vaessens, E H L Aarts and J K lenstra 1998 A Local Search Template *Computers and Operations Research* **25** pp 969-979
[22] V J Vinícius and E C A José 2016 ILS Heuristics for the Single-Machine Scheduling Problem with Sequence-Dependent Family Setup Times to Minimize Total Tardiness 36570-900
[23] J P Walser 1999 *Integer optimization by local search: a domain-independent approach* Springer-Verlag
[24] C Yano and Y Kim 1991 Algorithms for a class of single machine weighted tardiness and earliness problems *Eur J Opl Res* **52** pp 161–178
[25] Y Yuling, L Chinyao and L Wen-Yi 2015 Single Machine Scheduling with Time-Dependent Learning Effect and Non-Linear Past-Sequence-Dependent Setup Times **3** pp 10-15

Regression shrinkage and selection variables via an adaptive elastic net model

Regression shrinkage and selection variables via an adaptive elastic net model

Ghadeer Jasim Mohammed Mahdi [1] , Nadia Jasim Mohammed[1] and Zahraa Ibrahim Al-Sharea[2]

[1]Department of Mathematics, College of education for Pure sciences- Ibn Al-Haitham, University of Baghdad, Iraq.
[2]Department of Mathematical Sciences, Fulbright College of Art and Sciences, University of Arkansas, USA.

E-mail: gmahdi@ihcoedu.uobaghdad.edu.iq

Abstract. In this paper, a new method of selection variables is presented to select some essential variables from large datasets. The new model is a modified version of the Elastic Net model. The modified Elastic Net variable selection model has been summarized in an algorithm. It is applied for Leukemia dataset that has 3051 variables (genes) and 72 samples. In reality, working with this kind of dataset is not accessible due to its large size. The modified model is compared to some standard variable selection methods. Perfect classification is achieved by applying the modified Elastic Net model because it has the best performance. All the calculations that have been done for this paper are in R program by using some existing packages.

1. Introduction

In the various fields of statistical analysis, the most commonly used model is the Multivariate Linear Regression (MLR) model. Ordinary least squares (OLS) is the most widely used estimating technique for MLR. Consider $\{x_1, x_2, \dots, x_p\}$ is a set of variables and y is a response, the multiple linear regression model for $y_i, i = 1, \dots, n$, can be written as follows:

$$y_i = \beta_0 + \beta_1 x_{i1} + \beta_2 x_{i2} + \cdots + \beta_p x_{ip} + \epsilon$$

x_{ij} represents the i^{th} level of the j^{th} predictor. In matrix notation, for n samples, the MLR can be expressed in the following equations:

$$y_{n\times 1} = X_{n\times(k+1)}\beta_{(k+1)\times 1} + \epsilon_{n\times 1} \text{ , where}$$

$$y = \begin{bmatrix} y_1 \\ y_2 \\ . \\ . \\ . \\ y_n \end{bmatrix}, \quad X = \begin{bmatrix} 1 & x_{11} & x_{12} & \dots & x_{1k} \\ 1 & x_{21} & x_{22} & \dots & x_{2k} \\ & & . & & \\ & & . & & \\ & & . & & \\ 1 & x_{n1} & x_{n2} & \dots & x_{nk} \end{bmatrix}, \beta = \begin{bmatrix} \beta_0 \\ \beta_1 \\ . \\ . \\ . \\ \beta_k \end{bmatrix}, \text{ and } \epsilon = \begin{bmatrix} \epsilon_1 \\ \epsilon_2 \\ . \\ . \\ \epsilon_n \end{bmatrix}$$

The matrix X refers to the design matrix. It contains information about the predictor variable levels at which the observations are obtained. All the regression coefficients are in the vector β, and it can be estimated using the OLS estimates; i.e., $\hat{\beta}$ can be calculated by solving the following

$$\min_{\beta}\{(y - X\beta)^T(y - X\beta)\}$$

$$\min_{\beta}\{y^T y - 2\beta X^T y + \beta^T X^T y + \beta^T X^T X\beta\} = \min_{\beta}\{SRR\}$$

solving,

$$\frac{\partial SRR(\beta)}{\partial \beta} = -2X^T y + sX^T X\beta = 0$$

for β gives,

$$\hat{\beta} = (X^{\mathrm{T}}X)^{-1} X^T y \quad (1)$$

The multicollinearity or collinearity exists in a linear relationship among the variables if the number of variables exceeds the number of samples [10]. The problem of multicollinearity is well explained by several studies applying different methods. Some previous methods are explained in this work, and then the modified method is compared with them.

This paper is structured as follows: In section 2, an overview for Ridge, Lasso, and Elastic Net models are given. In section 3, a modified Elastic Net model is discussed. Real data analysis is introduced in Section 4. In section 5, results and discussion are presented. Finally, the conclusion is given in section 6.

2. Ridge and Lasso and Elastic Net Models

Researchers face some challenges such as poor results and time-consuming with large datasets. One way to solve this problem is by using variable selection techniques. As a result, large datasets can be reduced to reasonable datasets. This section lists three typical variable selection (shrinkage) models which are Ridge [2], Lasso [4], and Elastic Net [11]. Shrinkage techniques can be used under certain constraints depending on the size of the datasets. The regression model can be fitted with all the p variables, and the shrinkage techniques enhance the accuracy and efficiency of the model by reducing the number of variables in the model.

2.1 Ridge Model

Ridge model treats the associated variables in the same way by shrinking their coefficient similarly. Ridge estimates the coefficients of some variables to be 0 or close to 0, so these variables should be excluded from the model, $\hat{\beta} = (\hat{\beta}_0, \hat{\beta}_1, \ldots, \hat{\beta}_p)$. Similar to equation (1), Ridge seeks the vector $\hat{\beta}^{ridge}$ that minimizes the penalized RSS; i.e., $RSS + \lambda \sum_{j=1}^{p} \beta_j^2$; hence,

$$\hat{\beta}^{ridge} = minimize\left(\sum_{i=1}^{n}\left(y_i - \beta_0 - \sum_{j=1}^{n}\beta_j x_{ij}\right)^2 + \lambda\sum_{j=1}^{p}\beta_j^2\right), \quad \text{subject to } \sum_{j=1}^{p}\beta_j^2 \le \mathrm{K} \quad (2)$$

where the value of K is the upper bound for the sum of the coefficients. The complexity parameter, λ, is greater than or equals to 0. If $\lambda = 0$, then $\hat{\beta}^{ridge} = \hat{\beta}$, and as $\lambda \to \infty$, $\hat{\beta}^{ridge} \to 0_p$. For $0 < \lambda < \infty$, the fitting a linear regression model and shrinkage the coefficients are balanced. The shrinkage penalty is small when $\beta_1, \beta_2, \ldots,$ and β_p are close to zero [3]. Unlike OLS, Ridge solutions are not unique; as a result, before the estimation, the inputs customary can be standardized. β_0 should be estimated separately as $\bar{y} = \sum_{i=1}^{n}\frac{y_i}{n}$, and the remaining parameters can be estimated by using the data matrix X as follows, $\hat{\beta}^{ridge} = (X^T X + \lambda I)^{-1} X^T y$, where I is the $p \times p$ identity matrix.

2.2 Lasso Model

Another kind of penalty (LASSO) can be considered to constrain the size of OLS estimates. Lasso collapses some of the correlated parameters to 0. L_1 norm is used as penalty encompasses, so

$$\hat{\beta}^{lasso} = minimize\left(\sum_{i=1}^{n}\left(y_i - \beta_0 - \sum_{j=1}^{n}\beta_j x_{ij}\right)^2 + \lambda\sum_{j=1}^{p}|\beta_j|\right), \qquad \lambda \geq 0 \tag{3}$$

The LASSO property allows the exclusion of variables by setting their coefficients to be 0. When some variables are excluded, the model will be more efficient, especially if the number of variables is much larger than the number of samples, $p \gg n$ [5].

2.3 Elastic Net

Some weakness appears using Lasso. For example, with highly correlated variables, Lasso sometimes does not perform well because it can select at most n variables before it saturates when $p \gg n$. If there is a very high pairwise correlation in a group of variables, Lasso takes care of only one variable from the group [12]. Moreover, Lasso often performs worse than Ridge in prediction. Therefore, a penalty that combines the L_1 (Lasso) and L_2 (Ridge) constraints have been developed to overcome these limitations [2]. Elastic Net model is a variable selection procedure that uses the penalty

$$\lambda\left[\frac{1}{2}(1-\alpha)\sum_{j=1}^{p}\beta_j^2 + \alpha\sum_{j=1}^{p}|\beta_j|\right] \tag{4}$$

where $\alpha \in [0,1]$ is called the mixing parameter. Lasso and Ridge are special cases for the Elastic Net model when $\alpha = 1$ and $\alpha = 0$ as shown in equation (2) and (3). Lasso penalty gains more weight than the Ridge penalty when α approaches one, and the opposite happens when α approaches zero. Elastic Net enables us to select more than n variables, improve the predictive, and tends to jointly select groups of highly correlated variables.

3. Modified Elastic Net Model

In general, the shrinkage penalty expression can be conveniently extended to $\lambda\sum_{j=1}^{p}|\beta_j|^q$, where $q > 0$. Figure 1 shows the restriction regions, $\sum_{j=1}^{p}|\beta_j|^q \leq 1$, for different values of q. For $q \geq 1$, the constraints are convex; and when q equals 1 and 2, the lasso and Ridge penalties exist, respectively.

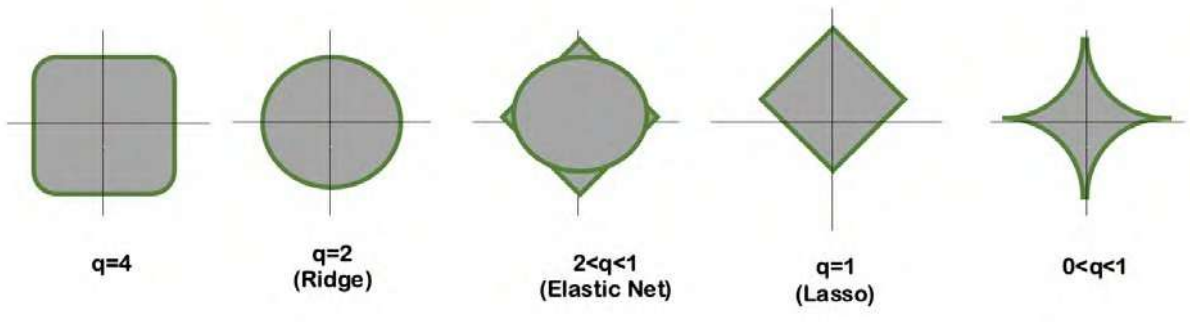

Figure 1. The Contours of constant value of $\sum_j|\beta_j|^q$ for different values of q.

To estimate the mean square error of a model, cross-validation (CV) can be used. CV is a re-sampling technique where the chosen method is applied to predict the held-out outcome. The two typical CV are, i) leave-one-out CV: it takes out one observation, then on the remaining $(n-1)$ observations the model is fitted; ii) k-flod CV: it splits the data randomly into k equal size subsets (folds), then eliminates one, and fit the model on the remaining $(k-1)$ folds. In both leave-one-out CV and k-flod CV, the process is repeated $(n-1)$ and $(k-1)$ times; respectively, then we take the average. Leave-one-out CV has low bias and high variance; in contrast, k-flod CV has adequate bias and low variance. To minimize the estimated MSE, k-flod CV is used to choose the value of λ. Typically, the value of k between 5 and 10 is indicated as good for computational.

The weight of the parameters is the key part of the modified Elastic Net model. It could be estimated by $\widehat{\lambda_k} = \left(\left|\widehat{\beta_k}^{inp}\right|^{-\gamma}\right)$, where γ is a positive constant and inp is $\widehat{\beta_k}^{inp}$ is a set of the initial parameters that could be selected using a naïve Elastic Net model. Therefore, the modified Elastic Net model penalty can be written as:

$$\lambda\left[\frac{1}{2}(1-\alpha)\sum_{k=1}^{p}\beta_k^2+\alpha\sum_{k=1}^{p}|\beta_k|\right]+\alpha^*\sum_{k=1}^{p}\widehat{\lambda_k}\,|\beta_k| \tag{5}$$

The adaptive weight $\hat{\lambda}_k^{(s)} = \frac{1}{|\hat{\beta}^{(s-1)}(\alpha^{*(s-1)})_j|}, j = 1,2,\dots,p$. For $s = 1$, the adaptive weights are equaled to the naïve Elastic Net weights. When $s = 2,\dots,p$, $\hat{\lambda}_k^{(s)}$ corresponds to the adaptive weights for the previous step. Figure 2 provides a simple geometrical view of Lasso and modified Elastic Net models. The solid gray areas are the regions for both Lasso and modified Elastic Net models. The red ellipses correspond to the contours of the residual sum of squares functions. $\hat{\beta}$ depicts the normal (unconstrained) least-squares estimate. The curve contours encourage strongly correlated variables to share coefficients. The plot indicates that the modified Elastic Net yields less *0*-valued estimates than lasso estimation [8]. It is an attractive feature, especially when $p \gg n$. The following algorithm summarizes the modified Elastic Net model approach.

Algorithm: Modified Elastic Net Model

The choice of $\boldsymbol{\alpha}$ and $\boldsymbol{\lambda}$ in the Elastic Net model.

In practice, a grid of α, $\{\alpha_1, \alpha_2, \dots, \alpha_M\}$, can be constructed and for each $m = 1, 2, \dots, M$:

- For given $\alpha = \alpha_m$, k-fold CV λ.
- For $m = 1, \dots, M$, save the Mean Squared Error.
- Compare the M Mean Squared Error.
- Choose α that is associated with the preferred value.
- Use the best λ within the selected profile for modeling

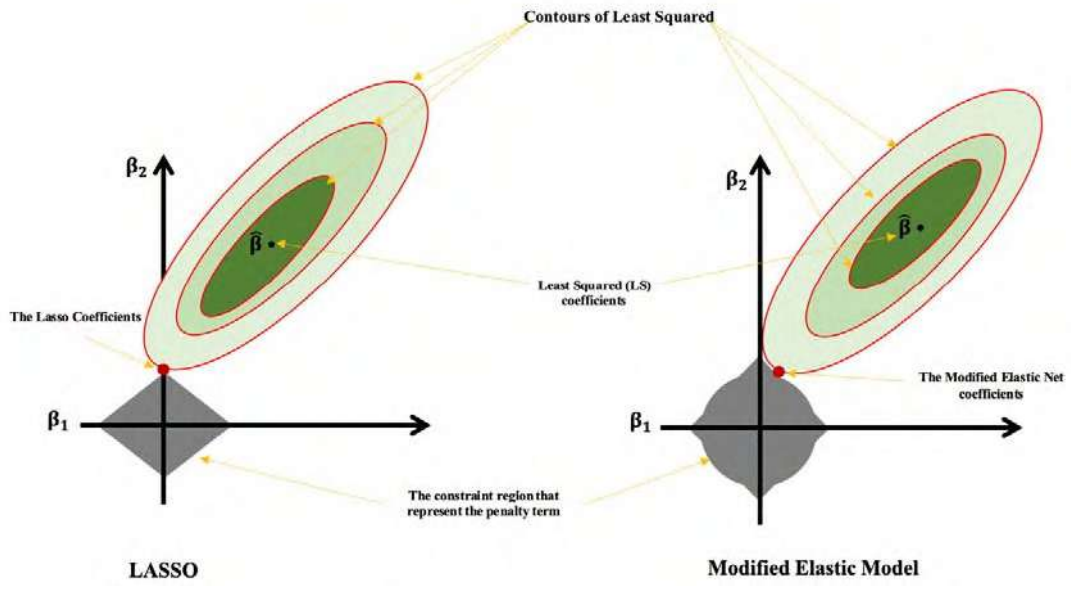

a. Lasso: the constraint regions is $|\beta_1| + |\beta_2| \leq t$

b. Modified Elastic Net: the constraint regions are $\beta_1^2 + \beta_2^2 \leq t^2$ and $|\beta_1| + |\beta_2| \leq t$

Figure 2. Estimation picture for the Lasso and Ridge regression.

4. Real data Analysis

Diagnosis and classification of cancer are complicated due to the broad datasets that deal with this type of research. One of the universal forms of cancer is the Leukemia dataset. Dataset was published by Golub in 1999 [7]. The complete Golub-Merge dataset is available in the golub Esets packages in ***R*** program. Working with this dataset confront many difficulties such as time-consuming and inefficient performance, as the number of predictors exceeds the number of responses. Leukemia dataset contains 3051 variables (genes) and 72 samples (patients). It is used in this section for experimental evaluation. It shows how the gene expression monitoring (via the DNA microarray) can identify the new cancer cases, providing a standard method for assigning tumors to known classes [9]. Patients can be categorized into two types, which are: Acute Myeloid Leukemia (AML) and Acute Lymphoblastic Leukemia (ALL) [6].

4.1 Analyzing Golub Datasets

Significant genes for the type of cancer must be selected to obtain a reduced dataset. This means that only specific genes that are expressed differently across classes should be advised. As the differential genes are defined between two groups, the t-test appears to be a common choice [1] [13]. However, the t-test requires a normality assumption, which may not be a logical assumption. A histogram of 3051×2 cannot be plotted to have an idea about the justification for normality. Mann Whitney U test looks more suitable and is almost as efficient as the t-test. After running the t-test, the p-values are modified according to the Benjamin-Hochberg method. Most genes do not appear to have different mean values across classes. The same result for the median has been achieved. The mean and median differences between types are shown in figure 3. Most of the genes are clustered around zero. A few numbers of genes seem interesting, and they can be easily indicated.

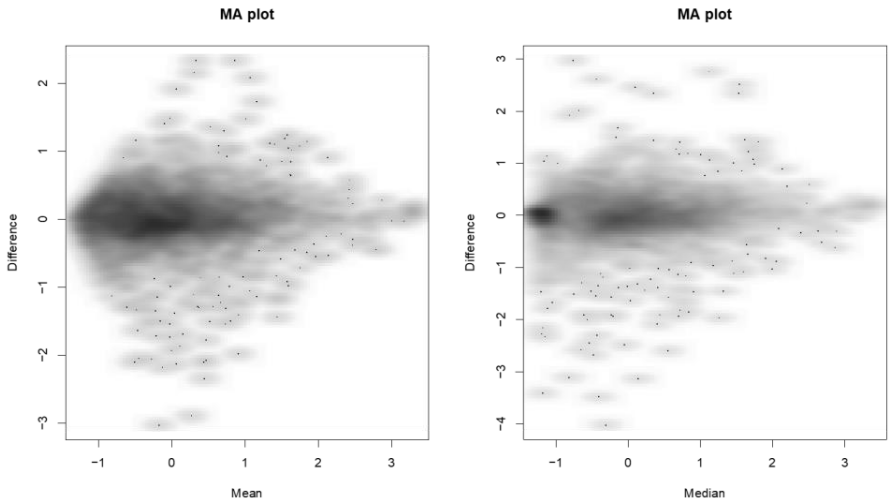

Figure 3. Plot for the differences in Mean and Median.[13]

5. Result and Discussion for the Real Data

The results of OLS, Ridge, Lasso, Elastic Net, and modified Elastic Net results are shown in Table (1). The accuracy rate of classification, the number of selected genes, and the approximate time-consumption are determined for all methods. The best accuracy occurs with the modified Elastic Net model with only 63 selected genes and approximately 9 seconds of consuming time. The paths and the misclassification errors for both Elastic Net and modified Elastic Net models are displayed in figure 6. Figure 6.a shows that the Elastic Net model has selected 329 genes as significant variables. Figure 6.b shows that the modified Elastic Net model has selected only 63 genes out of the total of 3051genes. In both models, the dotted vertical lines indicate the optimal value of λ. It is "3.36" and "-4.47" in both in Elastic Net and modified Elastic Net models, respectively. The factor map is plotted with two dimensions in figure 7. The percentage of variation for both first and second dimensions are 50.34 and 7.98, respectively. The selected genes in the modified Elastic Net model are used to construct the model. The training dataset was classified by type of cancer samples. The model was applied to the testing dataset as well. Figure 7.b shows the *ALL* in black and *AML* in red colors. Only one sample (ID=66) is misclassified, has an *AML* class, but it is classified as *ALL*.

Table 1. Comparison between OLS, Ridge, Lasso, Elastic Net, and modified Elastic Net for classification Leukemia dataset.

Methods	**Accuracy rate (%)**	**Number of selected genes**	**Approximately consuming time**
OLS	56.93	3051	≈ 30 seconds
Ridge	83.00	3051	≈ 24 seconds
Lasso	85.33	23	≈ 12 seconds
Elastic Net	88.93	329	≈ 18 seconds
Modified Elastic Net	**95.80**	**63**	≈ 9 seconds

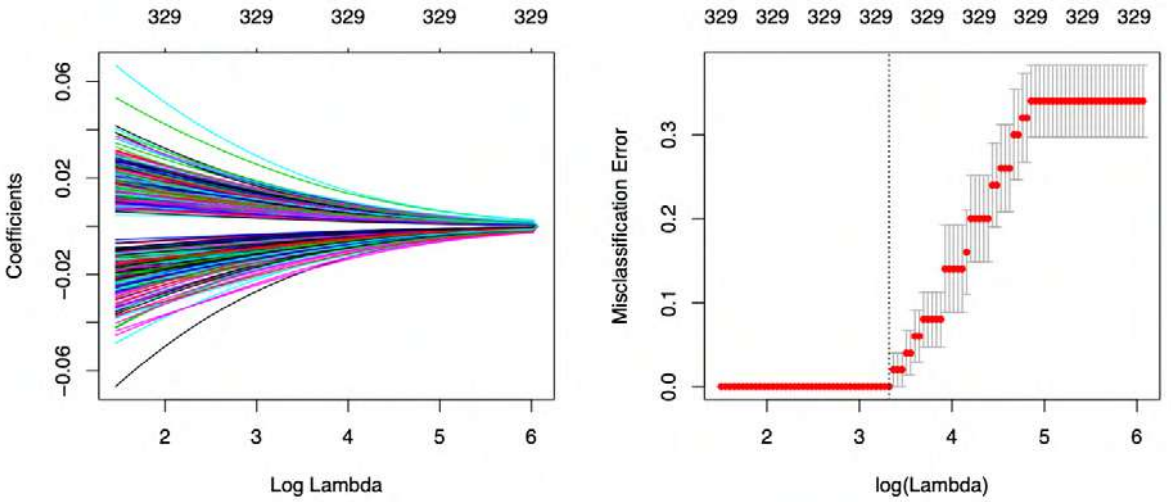

Figure 4. a. Coefficients and Misclassification Error for Elastic Net Model

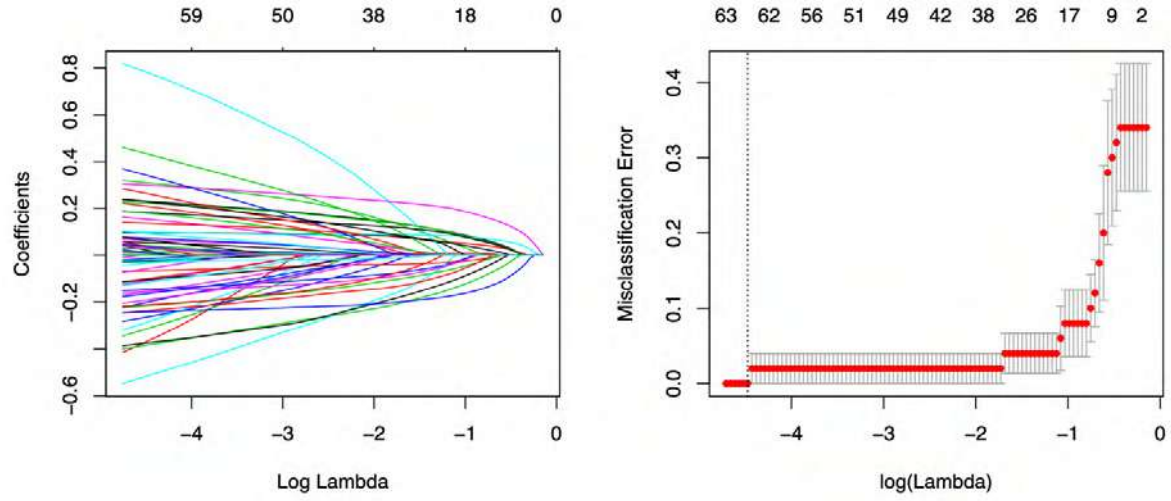

Figure 4. b. Coefficients and Misclassification Error for the modified Elastic Net Model

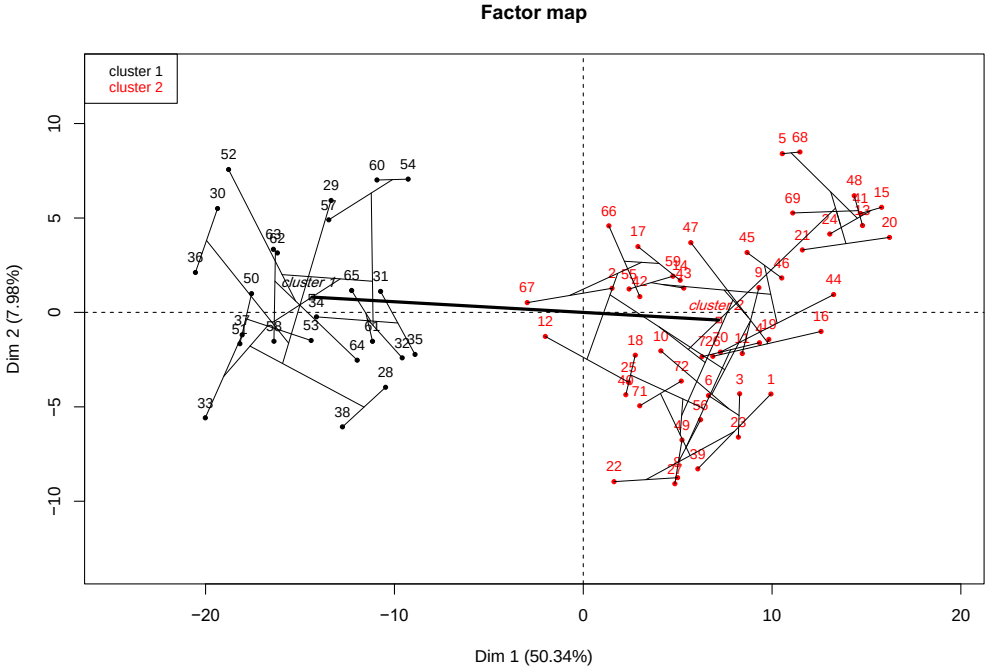

Figure 5 a. Factor map with two dimensions.

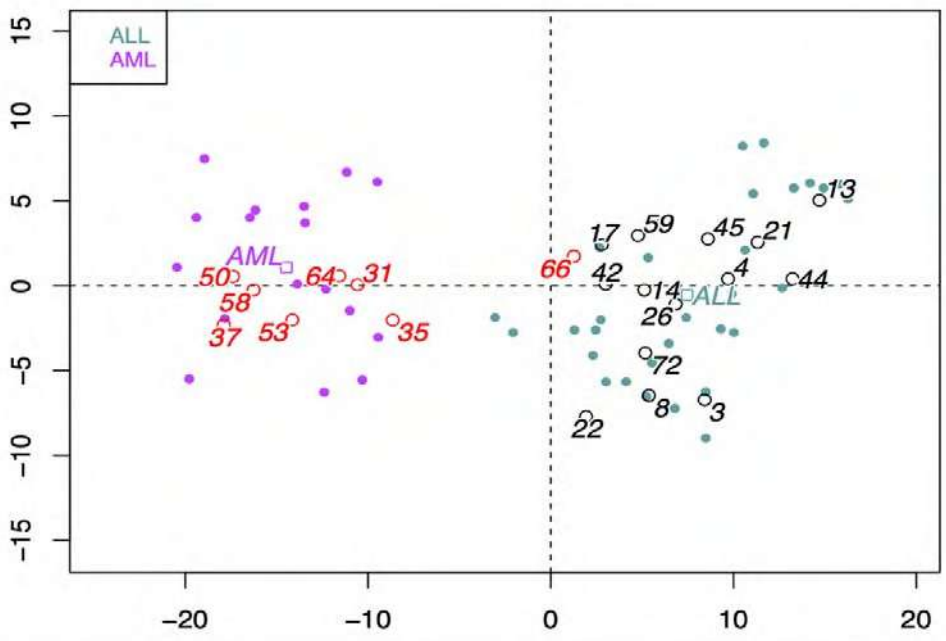

Figure 5 b. Classification plot for patients according to *AML* and *ALL* classes.
Figure 5. Factor map and classification plot for Leukemia dataset.

6. Conclusions

In this paper, an enhanced Elastic Net model was developed and applied to the leukemia dataset. It is derived by combining Lasso and Ridge models with the addition of a penalty term. The modified Elastic Net is compared with some standard classification methods. The updated Elastic Net is the best variable selection model in both training and testing datasets because it has high accuracy results and less time-consuming. The classification accuracy using the modified Elastic Net model is 95.80%, while the other is below 89%. Among 3051 genes, 63 genes have been selected by the updated Elastic Net model. Approximately 9 seconds was required to complete the classification process. The proposed model can be used for large datasets in the future because it is accurate and efficient.

References

[1] Arpino G, D Generali, A Sapino, L Del Matro, A Frassoldati, M de Laurentis, P Pronzato, G Mustacchi, M Cazzaniga and S De Placido 2013 Gene expression profiling in breast cancer: a clinical perspective *The Breast Cancer* **22**(2) pp 109–120

[2] D Aydın, B Yüzbaşı and S E Ahmed 2016 Modified ridge type estimator in partially linear regression models and numerical comparisons *Journal of Computational and Theoretical Nanoscience* **13**(10) pp 7040-7053

[3] E Bair, T Hastie, D Paul and R Tibshirani 2006 Prediction by supervised principal components *Journal of the American Statistical Association* **101**(473) pp 119–137

[4] H Choi, E Song, S S Hwang and W Lee 2018 A modified generalized lasso algorithm to detect local spatial clusters for count data *AStA Advances in Statistical Analysis* **102**(4) pp 537-563

[5] G J Mahdi 2020 A Modified Support Vector Machine Classifiers Using Stochastic Gradient Descent with Application to Leukemia Cancer Type Dataset *BSJ* **17**(4) pp 1255-1266 DOI: 10.21123/bsj.2020.17.4.1255

[6] Q Zhang, G Mahdi, J Tinkerand H Chen 2020 A graph-based multi-sample test for identifying pathways associated with cancer progression *Computational Biology and Chemistry* **26** 107285 DOI:10.1016/j.compbiolchem.2020.107285

[7] T R Golub, D K Slonim, P Tamayo, C Huard, M Gaasenbeek, J P Mesirov and C D Bloomfield 1999 Molecular classification of cancer: class discovery and class prediction by gene expression monitoring *Science* **286**(5439) pp 531-537

[8] G J Mahdi 2018 *Hierarchical Bayesian Regression with Application in Spatial Modeling and Outlier Detection Diss* University of Arkansas, Fayetteville

[9] J Li, W Dong, D Meng and H Xiao 2016 Gene selection for cancer classification using improved group lasso *Chinese Control and Decision Conference (CCDC) IEEE* pp 4221-4225

[10] A F Lukman, K Ayinde, S Binuomote and O A Clement 2019 Modified ridge-type estimator to combat multicollinearity: *Application to chemical data Journal of Chemometrics* **33**(5) pp e3125

[11] L T P Thao and R Geskus 2019 A comparison of model selection methods for prediction in the presence of multiply imputed data *Biometrical Journal* **61**(2) pp 343–356 https://doi.org/10.1002/bimj.201700232

[12] G J Mahdi, A Chakraborty, M E Arnold and A G Rebelo 2019 Efficient Bayesian modeling of large lattice data using spectral properties of Laplacian matrix *Spatial Statistics* **29** pp 329–350

[13] G J Mahdi, B A Kalaf and M A Khaleel 2020 Enhanced Supervised Principal Component Analysis for Cancer Classification *IJS* **62**(4) Accepted paper

[14] B A Hameed, A N Salman, B A Kalaf 2020 On Estimation of P (Y_1< X< Y_2) in Cased Inverse Kumaraswamy Distribution *Iraqi Journal of Science* **26** pp 845-53

Reliability of one Strength-four Stresses for Lomax Distribution

Reliability of one Strength-four Stresses for Lomax Distribution

Ahmed H. Khaleel

Department of Statistics, College of Administration & Economics, University of Sumer, Iraq

E-mail: ahmedharoon885@gmail.com

Abstract. In this paper, we find the reliability R of a component when it is exposed to four independent stresses and it having one strength for Lomax distribution. the reliability R was estimated by using four different estimations (MLE, RgE, LSE, and WLSE) methods. A comparison was made between the results of estimating the reliability function by MSE and MAPE criteria, that will get from a Monte Carlo simulation study. We found that the performance of ML is the best to.

1. Introduction

In the reliability literature, stress-strength is an important model. In the statistical approach to the stress-strength model, considerations are based on the supposition that component strengths are independently and identically distributed (iid) and are subjected to common stress. Here the system reliability, when X and Y are independent and identical. Let X is a strength random variable subjected to a common stress Y then the reliability of the system contained one component is: $R = P(X > Y)$ [1, 2]. The reliability of a component (or a system) can be represented in various forms depending on the structure of the system, where the component (or the system) would fail if the stress exceeds its strength [3, 4]. The Lomax (1954), or Pareto II, distribution has been quite widely applied in a variety of contexts [5]. The Lomax distribution has been used for reliability modeling and life testing and applied to income and wealth distribution data. It has also found application in the biological sciences. Some authors have suggested the use of this distribution as an alternative to the exponential distribution when the data are heavy-tailed [6].

The present study considering stress – strength Lomax reliability of model for one component having one strength it is exposed to four independent stresses when the stress and strength are followed Lomax two-parameter random variables. Estimation of the parameters and the reliability model is made by MLE, RgE, LSE, and WLSE estimation methods. Finally, the Monte Carlo simulation study for comparing between them by MSE and MAPE are explained.

2. The Mathematical Formula of one Strength-Four Stress Component Reliability

The reliability of the stress-strength model defines the life of a component that has strength X and exposed to stress Y. So that if stress overtake the strength $(Y > X)$ the component fails [7]:

$$R = P(Y < X) = \int_0^\infty f(x)F_y(x)dx$$

In this article, the stress-strength reliability of one component subjected to four stress is examined. Let the strength r.v. of the component represented by X as a Lomax r.v. (α, μ), and the component subjected stress r.v. are represented by $Y_i; i = 1,2,3,4$ following Lomax distribution (α_i, μ) ; i=1,2,3,4 with unknown shape parameters $\alpha, \alpha_1, \alpha_2, \alpha_3, \alpha_4$ and known common scale parameter μ.The pdf and CDF of the r.v. for $X \sim L\ (\alpha, \mu)$ are given as:

$$f(x) = \frac{\alpha}{\mu}\left(1+\frac{x}{\mu}\right)^{-(\alpha+1)} \qquad x \geq 0; \alpha, \mu > 0 \qquad \ldots(1)$$

$$F(x) = 1-\left(1+\frac{x}{\mu}\right)^{-\alpha} \quad y \geq 0; \alpha, \mu > 0 \qquad \ldots(2)$$

Also the CDF of $Y_i \sim L\ (\alpha_i, \mu)$:

$$F_1(y_1) = 1-\left(1+\frac{y_1}{\mu}\right)^{-\alpha_1} \quad y_1 \geq 0, \alpha_1, \mu > 0 \qquad \ldots(3)$$

$$F_2(y_2) = 1-\left(1+\frac{y_2}{\mu}\right)^{-\alpha_2} \quad y_2 \geq 0, \alpha_2, \mu > 0 \qquad \ldots(4)$$

$$F_3(y_3) = 1-\left(1+\frac{y_3}{\mu}\right)^{-\alpha_3} \quad y_3 \geq 0, \alpha_3, \mu > 0 \qquad \ldots(5)$$

$$F_4(y_4) = 1-\left(1+\frac{y_4}{\mu}\right)^{-\alpha_4} \quad y_4 \geq 0, \alpha_4, \mu > 0 \qquad \ldots(6)$$

Now, we can obtain to find the reliability model as follows:

$$R = P[Max(Y_1, Y_2, Y_3, Y_4) < X]$$
$$= \int_0^{\infty} \int_0^{y_1} \int_0^{y_2} \int_0^{y_3} \int_0^{y_4} f(y_1, y_2, y_3, y_4, x)\, dy_4 dy_3 dy_2 dy_1 dx \qquad \ldots(7)$$

since r.v are independent and identical distributed; then :

$$R = \int_0^{\infty} \int_0^{y_2} \int_0^{y_3} \int_0^{y_4} f(y_1) f(y_2) f(y_3) f(y_4)\, f(x) dy_4 dy_3 dy_2 dy_1 dx$$
$$R = \int_{x=0}^{\infty} F_{1y_1}(x) F_{2y_2} F_{3y_3}(x) F_{4y_4}(x) f(x) dx \qquad \ldots(8)$$

The reliability model of Lomax distribution will get it by substitution equations (1),(2), (3),(4),(5) and (6) in equation (8), as:

$$R = \int_{x=0}^{\infty} [1-\left(1+\frac{x}{\mu}\right)^{-\alpha_1}][1-\left(1+\frac{x}{\mu}\right)^{-\alpha_2}][1-\left(1+\frac{x}{\mu}\right)^{-\alpha_3}][1-\left(1+\frac{x}{\mu}\right)^{-\alpha_4}]$$
$$\cdot \frac{\alpha}{\mu}\left(1+\frac{x}{\mu}\right)^{-(\alpha+1)} dx$$

$$R = \int_0^{\infty} \left[1-\left(1+\frac{x}{\mu}\right)^{-\alpha_1} - \left(1+\frac{x}{\mu}\right)^{-\alpha_2} - \left(1+\frac{x}{\mu}\right)^{-\alpha_3} - \left(1+\frac{x}{\mu}\right)^{-\alpha_4} + \left(1+\frac{x}{\mu}\right)^{-(\alpha_1+\alpha_2)}\right.$$
$$+\left(1+\frac{x}{\mu}\right)^{-(\alpha_1+\alpha_3)} + \left(1+\frac{x}{\mu}\right)^{-(\alpha_1+\alpha_3)} + \left(1+\frac{x}{\mu}\right)^{-(\alpha_1+\alpha_4)} + \left(1+\frac{x}{\mu}\right)^{-(\alpha_2+\alpha_3)}$$
$$+\left(1+\frac{x}{\mu}\right)^{-(\alpha_2+\alpha_4)} + \left(1+\frac{x}{\mu}\right)^{-(\alpha_3+\alpha_4)} - \left(1+\frac{x}{\mu}\right)^{-(\alpha_1+\alpha_2+\alpha_3)} - \left(1+\frac{x}{\mu}\right)^{-(\alpha_1+\alpha_2+\alpha_4)}$$
$$\left.-\left(1+\frac{x}{\mu}\right)^{-(\alpha_2+\alpha_3+\alpha_4)} + \left(1+\frac{x}{\mu}\right)^{-(\alpha_1+\alpha_2+\alpha_3+\alpha_4)}\right] \frac{\alpha}{\mu}\left(1+\frac{x}{\mu}\right)^{-(\alpha+1)} dx$$

$$R = \int_0^{\infty} \frac{\alpha}{\mu}\left(1+\frac{x}{\mu}\right)^{-(\alpha+1)} dx - \int_0^{\infty} \frac{\alpha}{\mu}\left(1+\frac{x}{\mu}\right)^{-(\alpha+\alpha_1+1)} dx - \int_0^{\infty} \frac{\alpha}{\mu}\left(1+\frac{x}{\mu}\right)^{-(\alpha+\alpha_2+1)} dx$$

$$-\int_0^{\infty}\frac{\alpha}{\mu}\left(1+\frac{x}{\mu}\right)^{-(\alpha+\alpha_3+1)}dx-\int_0^{\infty}\frac{\alpha}{\mu}\left(1+\frac{x}{\mu}\right)^{-(\alpha+\alpha_4+1)}dx$$

$$+\int_0^{\infty}\frac{\alpha}{\mu}\left(1+\frac{x}{\mu}\right)^{-(\alpha+\alpha_1+\alpha_2+1)}dx+\int_0^{\infty}\frac{\alpha}{\mu}\left(1+\frac{x}{\mu}\right)^{-(\alpha+\alpha_1+\alpha_3+1)}dx$$

$$+\int_0^{\infty}\frac{\alpha}{\mu}\left(1+\frac{x}{\mu}\right)^{-(\alpha+\alpha_1+\alpha_4+1)}dx+\int_0^{\infty}\frac{\alpha}{\mu}\left(1+\frac{x}{\mu}\right)^{-(\alpha+\alpha_2+\alpha_3+1)}dx$$

$$+\int_0^{\infty}\frac{\alpha}{\mu}\left(1+\frac{x}{\mu}\right)^{-(\alpha+\alpha_2+\alpha_4+1)}dx+\int_0^{\infty}\frac{\alpha}{\mu}\left(1+\frac{x}{\mu}\right)^{-(\alpha+\alpha_3+\alpha_4+1)}dx$$

$$-\int_0^{\infty}\frac{\alpha}{\mu}\left(1+\frac{x}{\mu}\right)^{-(\alpha+\alpha_1+\alpha_2+\alpha_3+1)}dx-\int_0^{\infty}\frac{\alpha}{\mu}\left(1+\frac{x}{\mu}\right)^{-(\alpha+\alpha_1+\alpha_2+\alpha_4+1)}dx$$

$$-\int_0^{\infty}\frac{\alpha}{\mu}\left(1+\frac{x}{\mu}\right)^{-(\alpha+\alpha_2+\alpha_3+\alpha_4+1)}dx+\int_0^{\infty}\frac{\alpha}{\mu}\left(1+\frac{x}{\mu}\right)^{-(\alpha+\alpha_1+\alpha_2+\alpha_3+\alpha_4+1)}dx$$

The reliability of a component has strength exposed to four stresses of Lomax distribution can be expressed as:

$$R=1-\left[\frac{\alpha}{(\alpha+\alpha_1)}\right]-\left[\frac{\alpha}{(\alpha+\alpha_2)}\right]-\left[\frac{\alpha}{(\alpha+\alpha_3)}\right]-\left[\frac{\alpha}{(\alpha+\alpha_4)}\right]+\left[\frac{\alpha}{(\alpha+\alpha_1+\alpha_2)}\right]+\left[\frac{\alpha}{(\alpha+\alpha_1+\alpha_3)}\right]+\left[\frac{\alpha}{(\alpha+\alpha_1+\alpha_4)}\right]$$
$$+\left[\frac{\alpha}{(\alpha+\alpha_2+\alpha_3)}\right]+\left[\frac{\alpha}{(\alpha+\alpha_2+\alpha_4)}\right]+\left[\frac{\alpha}{(\alpha+\alpha_3+\alpha_4)}\right]-\left[\frac{\alpha}{(\alpha+\alpha_1+\alpha_2+\alpha_3)}\right]-\left[\frac{\alpha}{(\alpha+\alpha_1+\alpha_2+\alpha_4)}\right]$$
$$-\left[\frac{\alpha}{(\alpha+\alpha_1+\alpha_3+\alpha_4)}\right]-\left[\frac{\alpha}{(\alpha+\alpha_2+\alpha_3+\alpha_4)}\right]+\left[\frac{\alpha}{(\alpha+\alpha_1+\alpha_2+\alpha_3+\alpha_4)}\right] \quad \ldots(9)$$

3. Maximum likelihood Estimator (MLE)

The maximum likelihood estimation method can use to estimate the parameter of Lomax distribution [8]. let $x_1, x_2 \ldots, x_n$ be random samples from LD (α, μ) of n sample size then the Likelihood function will be:

$$L(x,\alpha,\mu)=\frac{\alpha^n}{\mu^n}\prod_{i=1}^{n}\left(1+\frac{x_i}{\mu}\right)^{-(\alpha+1)} \quad \ldots(10)$$

By taking the Log-likelihood function and derivative this function with respect to , then we get the ML estimator for α:

$$\hat{\alpha}_{\mathrm{ML}}=\frac{n}{\sum_{i=1}^{n}Ln\left(1+\frac{x_i}{\mu}\right)} \quad \ldots(11)$$

In the same way; let $y_{11}, y_{12} \ldots, y_{1n}$; $y_{21}, y_{22} \ldots, y_{2n}$; $y_{31}, y_{32} \ldots, y_{3n}$ and $y_{41}, y_{42} \ldots, y_{4n}$ be the random samples from LD of $n_1, n_2, n_3\ and\ n_4$ sample sizes. Then the ML estimators of $\alpha_1, \alpha_2, \alpha_3\ and\ \alpha_4$ are given as:

$$\hat{\alpha}_{1\mathrm{ML}}=\frac{n_1}{\sum_{j_1=1}^{n_1}Ln\left(1+\frac{y_{1j_1}}{\mu}\right)} \quad \ldots(12)$$

$$\hat{\alpha}_{2\mathrm{ML}}=\frac{n_2}{\sum_{j_2=1}^{n_2}Ln\left(1+\frac{y_{2j_2}}{\mu}\right)} \quad \ldots(13)$$

$$\hat{\alpha}_{3\mathrm{ML}}=\frac{n_3}{\sum_{j_3=1}^{n_3}Ln\left(1+\frac{y_{3j_3}}{\mu}\right)} \quad \ldots(14)$$

$$\hat{\alpha}_{4\mathrm{ML}}=\frac{n_4}{\sum_{j_4=1}^{n_4}Ln\left(1+\frac{y_{4j_4}}{\mu}\right)} \quad \ldots(15)$$

The ML estimator of R is given by substitute (11), (12), (13), (14), and (15) in equation (9) we get:

$$\hat{R}_{\mathrm{ML}}=1-\left[\frac{\hat{\alpha}_{\mathrm{ML}}}{(\hat{\alpha}_{\mathrm{ML}}+\hat{\alpha}_{1\mathrm{ML}})}\right]-\left[\frac{\hat{\alpha}_{\mathrm{ML}}}{(\hat{\alpha}_{\mathrm{ML}}+\hat{\alpha}_{2\mathrm{ML}})}\right]-\left[\frac{\hat{\alpha}_{\mathrm{ML}}}{(\hat{\alpha}_{\mathrm{ML}}+\hat{\alpha}_{3\mathrm{ML}})}\right]-\left[\frac{\hat{\alpha}_{\mathrm{ML}}}{(\hat{\alpha}_{\mathrm{ML}}+\hat{\alpha}_{4\mathrm{ML}})}\right]+\left[\frac{\hat{\alpha}_{\mathrm{ML}}}{(\hat{\alpha}_{\mathrm{ML}}+\hat{\alpha}_{1\mathrm{ML}}+\hat{\alpha}_{2\mathrm{ML}})}\right]$$

$$+\left[\frac{\hat{\alpha}_{\mathrm{ML}}}{(\hat{\alpha}_{\mathrm{ML}}+\hat{\alpha}_{1\mathrm{ML}}+\hat{\alpha}_{3\mathrm{ML}})}\right]+\left[\frac{\hat{\alpha}_{\mathrm{ML}}}{(\hat{\alpha}_{\mathrm{ML}}+\hat{\alpha}_{1\mathrm{ML}}+\hat{\alpha}_{4\mathrm{ML}})}\right]+\left[\frac{\hat{\alpha}_{\mathrm{ML}}}{(\hat{\alpha}_{\mathrm{ML}}+\hat{\alpha}_{2\mathrm{ML}}+\hat{\alpha}_{3\mathrm{ML}})}\right]+\left[\frac{\hat{\alpha}_{\mathrm{ML}}}{(\hat{\alpha}_{\mathrm{ML}}+\hat{\alpha}_{2\mathrm{ML}}+\hat{\alpha}_{4\mathrm{ML}})}\right]$$
$$+\left[\frac{\hat{\alpha}_{\mathrm{ML}}}{(\hat{\alpha}_{\mathrm{ML}}+\hat{\alpha}_{3\mathrm{ML}}+\hat{\alpha}_{4\mathrm{ML}})}\right]-\left[\frac{\hat{\alpha}_{\mathrm{ML}}}{(\hat{\alpha}_{\mathrm{ML}}+\hat{\alpha}_{1\mathrm{ML}}+\hat{\alpha}_{2\mathrm{ML}}+\hat{\alpha}_{3\mathrm{ML}})}\right]-\left[\frac{\hat{\alpha}_{\mathrm{ML}}}{(\hat{\alpha}_{\mathrm{ML}}+\hat{\alpha}_{1\mathrm{ML}}+\hat{\alpha}_{2\mathrm{ML}}+\hat{\alpha}_{4\mathrm{ML}})}\right]$$
$$-\left[\frac{\hat{\alpha}_{\mathrm{ML}}}{(\hat{\alpha}_{\mathrm{ML}}+\hat{\alpha}_{1\mathrm{ML}}+\hat{\alpha}_{3\mathrm{ML}}+\hat{\alpha}_{4\mathrm{ML}})}\right]-\left[\frac{\hat{\alpha}_{\mathrm{ML}}}{(\hat{\alpha}_{\mathrm{ML}}+\hat{\alpha}_{2\mathrm{ML}}+\hat{\alpha}_{3\mathrm{ML}}+\hat{\alpha}_{4\mathrm{ML}})}\right]+\left[\frac{\hat{\alpha}_{\mathrm{ML}}}{(\hat{\alpha}_{\mathrm{ML}}+\hat{\alpha}_{1\mathrm{ML}}+\hat{\alpha}_{2\mathrm{ML}}+\hat{\alpha}_{3\mathrm{ML}}+\hat{\alpha}_{4\mathrm{ML}})}\right] \quad \ldots(16)$$

4. Regression Estimator (RgE):

The regression estimation is an important method that uses the regression equation to estimate the parameter [9]:

$$z_i = a + bu_i + e_i \quad \ldots(17)$$

By taking the Log to equation (2):

$$\ln\left(1 - F\left(x_{(i)}\right)\right) = -\alpha \ln\left(1 + \frac{x_{(i)}}{\mu}\right)$$

Use plotting position (P_i) instead of $\mathrm{F}(\mathrm{x}_{(\mathrm{i})})$ where $P_i = \frac{i}{n+1}$, then:

$$\ln(1 - P_i) = -\alpha \ln\left(1 + \frac{x_{(i)}}{\mu}\right) \quad \ldots(18)$$

Substitute an equation (18) into the equation (17):

$$z_i = \ln(1 - P_i)\,, a = 0, b = \alpha, u_i = -\ln\left(1 + \frac{x_{(i)}}{\mu}\right) \quad \ldots(19)$$

Then the estimator b is :

$$\hat{\mathrm{b}} = \frac{\mathrm{n}\sum_{\mathrm{i}=1}^{\mathrm{n}} \mathrm{z_i u_i} - \sum_{\mathrm{i}=1}^{\mathrm{n}} \mathrm{z_i} \sum_{\mathrm{i}=1}^{\mathrm{n}} \mathrm{u_i}}{\mathrm{n}\sum_{\mathrm{i}=1}^{\mathrm{n}} [\mathrm{u_i}]^2 - \left[\sum_{\mathrm{i}=1}^{\mathrm{n}} \mathrm{u_i}\right]^2} \quad \ldots(20)$$

Now, since $b = \alpha$, the estimator $\hat{\alpha}_{Rg}$ is:

$$\hat{\alpha}_{\mathrm{Rg}} = \frac{-\mathrm{n}\sum_{\mathrm{i}=1}^{\mathrm{n}} \ln(1-\mathrm{P_i})\, \ln\left(1+\frac{\mathrm{x(i)}}{\mu}\right) + \sum_{\mathrm{i}=1}^{\mathrm{n}} \ln(1-\mathrm{P_i}) \sum_{\mathrm{i}=}^{\mathrm{n}} \ln\left(1+\frac{\mathrm{x(i)}}{\mu}\right)}{\mathrm{n}\sum_{\mathrm{i}=1}^{\mathrm{n}} \left[\ln\left(1+\frac{\mathrm{x(i)}}{\mu}\right)\right]^2 - \left[\sum_{\mathrm{i}=1}^{\mathrm{n}} \ln\left(1+\frac{\mathrm{x(i)}}{\mu}\right)\right]^2} \quad \ldots(21)$$

In the same steps above, we will estimate α_1, α_2, α_3 and α_4 are:

$$\hat{\alpha}_{1Rg} = \frac{-n_1 \sum_{j_1=1}^{n_1} \ln(1-P_{j_1})\, \ln\left(1+\frac{y_{1(j_1)}}{\mu}\right) + \sum_{j_1=1}^{n_1} \ln(1-P_{j_1}) \sum_{j_1=1}^{n_1} \ln\left(1+\frac{y_{1(j_1)}}{\mu}\right)}{n_1 \sum_{j_1=1}^{n_1} \left[\ln\left(1+\frac{y_{1(j_1)}}{\mu}\right)\right]^2 - \left[\sum_{j_1=1}^{n_1} \ln\left(1+\frac{y_{1(j_1)}}{\mu}\right)\right]^2} \quad \ldots(22)$$

$$\hat{\alpha}_{2Rg} = \frac{-n_2 \sum_{j_2=1}^{n_2} \ln(1-P_{j_2})\, \ln\left(1+\frac{y_{2(j_2)}}{\mu}\right) + \sum_{j_2=1}^{n_2} \ln(1-P_{j_2}) \sum_{j_2=1}^{n_2} \ln\left(1+\frac{y_{2(j_2)}}{\mu}\right)}{n_2 \sum_{j_2=1}^{n_2} \left[\ln\left(1+\frac{y_{2(j_2)}}{\mu}\right)\right]^2 - \left[\sum_{j_2=1}^{n_2} \ln\left(1+\frac{y_{2(j_2)}}{\mu}\right)\right]^2} \quad \ldots(23)$$

$$\hat{\alpha}_{3Rg} = \frac{-n_3 \sum_{j_3=1}^{n_3} \ln(1-P_{j_3})\, \ln\left(1+\frac{y_{3(j_3)}}{\mu}\right) + \sum_{j_3=1}^{n_3} \ln(1-P_{j_3}) \sum_{j_3=1}^{n_3} \ln\left(1+\frac{y_{3(j_3)}}{\mu}\right)}{n_3 \sum_{j_3=1}^{n_3} \left[\ln\left(1+\frac{y_{3(j_3)}}{\mu}\right)\right]^2 - \left[\sum_{j_3=1}^{n_3} \ln\left(1+\frac{y_{3(j_3)}}{\mu}\right)\right]^2} \quad \ldots(24)$$

$$\hat{\alpha}_{4Rg} = \frac{-n_4 \sum_{j_4=1}^{n_4} \ln(1-P_{j_4})\, \ln\left(1+\frac{y_{4(j_4)}}{\mu}\right) + \sum_{j_4=1}^{n_4} \ln(1-P_{j_4}) \sum_{j_4=1}^{n_4} \ln\left(1+\frac{y_{4(j_4)}}{\mu}\right)}{n_3 \sum_{j_4=1}^{n_4} \left[\ln\left(1+\frac{y_{4(j_4)}}{\mu}\right)\right]^2 - \left[\sum_{j_4=1}^{n_4} \ln\left(1+\frac{y_{4(j_4)}}{\mu}\right)\right]^2} \quad \ldots(25)$$

The Rg estimator of R is given by substitute (21), (22), (23), (24), and (25) in equation (9) we get:

$$\hat{R}_{Rg} = 1 - \left[\frac{\hat{\alpha}_{Rg}}{(\hat{\alpha}_{Rg}+\hat{\alpha}_{1Rg})}\right] - \left[\frac{\hat{\alpha}_{Rg}}{(\hat{\alpha}_{Rg}+\hat{\alpha}_{2Rg})}\right] - \left[\frac{\hat{\alpha}_{Rg}}{(\hat{\alpha}_{Rg}+\hat{\alpha}_{3Rg})}\right] - \left[\frac{\hat{\alpha}_{Rg}}{(\hat{\alpha}_{Rg}+\hat{\alpha}_{4Rg})}\right] + \left[\frac{\hat{\alpha}_{Rg}}{(\hat{\alpha}_{Rg}+\hat{\alpha}_{1Rg}+\hat{\alpha}_{2Rg})}\right]$$
$$+ \left[\frac{\hat{\alpha}_{Rg}}{(\hat{\alpha}_{Rg}+\hat{\alpha}_{1Rg}+\hat{\alpha}_{3Rg})}\right] + \left[\frac{\hat{\alpha}_{Rg}}{(\hat{\alpha}_{Rg}+\hat{\alpha}_{1Rg}+\hat{\alpha}_{4Rg})}\right] + \left[\frac{\hat{\alpha}_{Rg}}{(\hat{\alpha}_{Rg}+\hat{\alpha}_{2Rg}+\hat{\alpha}_{3Rg})}\right] + \left[\frac{\hat{\alpha}_{Rg}}{(\hat{\alpha}_{Rg}+\hat{\alpha}_{2Rg}+\hat{\alpha}_{4Rg})}\right]$$
$$+ \left[\frac{\hat{\alpha}_{Rg}}{(\hat{\alpha}_{Rg}+\hat{\alpha}_{3Rg}+\hat{\alpha}_{4Rg})}\right] - \left[\frac{\hat{\alpha}_{Rg}}{(\hat{\alpha}_{Rg}+\hat{\alpha}_{1Rg}+\hat{\alpha}_{2Rg}+\hat{\alpha}_{3Rg})}\right] - \left[\frac{\hat{\alpha}_{Rg}}{(\hat{\alpha}_{Rg}+\hat{\alpha}_{1Rg}+\hat{\alpha}_{2Rg}+\hat{\alpha}_{4Rg})}\right]$$
$$- \left[\frac{\hat{\alpha}_{Rg}}{(\hat{\alpha}_{Rg}+\hat{\alpha}_{1Rg}+\hat{\alpha}_{3Rg}+\hat{\alpha}_{4Rg})}\right] - \left[\frac{\hat{\alpha}_{Rg}}{(\hat{\alpha}_{Rg}+\hat{\alpha}_{2Rg}+\hat{\alpha}_{3Rg}+\hat{\alpha}_{4Rg})}\right] + \left[\frac{\hat{\alpha}_{Rg}}{(\hat{\alpha}_{Rg}+\hat{\alpha}_{1Rg}+\hat{\alpha}_{2Rg}+\hat{\alpha}_{3Rg}+\hat{\alpha}_{4Rg})}\right] \quad ...(26)$$

5. Least Square Estimator (LSE):

This estimation method is very popular for model fitting, especially in linear and non-linear regression [10]. Suppose that the random sample $x_1, x_2 \ldots, x_n$ of size n from LD. The LS estimator can be obtain by minimizing:

$$\sum_{i=1}^{n}\left[\ln(1-P_i)^{-1} - \alpha \ln\left(1+\frac{x_{(i)}}{\mu}\right)\right]^2 .$$

By driving with respect to α we get LS estimator of α is

$$\hat{\alpha}_{LS} = \frac{\sum_{i=1}^{n}\ln(1-P_i)^{-1}\ln\left(1+\frac{x_{(i)}}{\mu}\right)}{\sum_{i=1}^{n}\left(\ln\left(1+\frac{x_{(i)}}{\mu}\right)\right)^2} \quad ...(27)$$

Also the LS estimators of α_1, α_2, α_3 and α_4 are:

$$\hat{\alpha}_{1LS} = \frac{\sum_{j_1=1}^{n_1}\ln\left(1-P_{j_1}\right)^{-1}\ln\left(1+\frac{y_{1(j_1)}}{\mu}\right)}{\sum_{i=1}^{n_1}\left(\ln\left(1+\frac{y_{1(j_1)}}{\mu}\right)\right)^2} \quad ...(28)$$

$$\hat{\alpha}_{2LS} = \frac{\sum_{j_2=1}^{n_2}\ln\left(1-P_{j_2}\right)^{-1}\ln\left(1+\frac{y_{2(j_2)}}{\mu}\right)}{\sum_{j_2=1}^{n_2}\left(\ln\left(1+\frac{y_{2(j_2)}}{\mu}\right)\right)^2} \quad ...(29)$$

$$\hat{\alpha}_{3LS} = \frac{\sum_{j_3=1}^{n_3}\ln\left(1-P_{j_3}\right)^{-1}\ln\left(1+\frac{y_{3(j_3)}}{\mu}\right)}{\sum_{j_3=1}^{n_3}\left(\ln\left(1+\frac{y_{3(j_3)}}{\mu}\right)\right)^2} \quad ...(30)$$

$$\hat{\alpha}_{4LS} = \frac{\sum_{j_4=1}^{n_4}\ln\left(1-P_{j_4}\right)^{-1}\ln\left(1+\frac{y_{4(j_4)}}{\mu}\right)}{\sum_{j_4=1}^{n_4}\left(\ln\left(1+\frac{y_{4(j_4)}}{\mu}\right)\right)^2} \quad \ldots(31)$$

The LS estimator of R is given by substitute (27), (28), (29), (30), and (31) in equation (9) we get:

$$\hat{R}_{LS} = 1 - \left[\frac{\hat{\alpha}_{LS}}{(\hat{\alpha}_{LS}+\hat{\alpha}_{1LS})}\right] - \left[\frac{\hat{\alpha}_{LS}}{(\hat{\alpha}_{LS}+\hat{\alpha}_{2LS})}\right] - \left[\frac{\hat{\alpha}_{LS}}{(\hat{\alpha}_{LS}+\hat{\alpha}_{3LS})}\right] - \left[\frac{\hat{\alpha}_{LS}}{(\hat{\alpha}_{LS}+\hat{\alpha}_{4LS})}\right] + \left[\frac{\hat{\alpha}_{LS}}{(\hat{\alpha}_{LS}+\hat{\alpha}_{1LS}+\hat{\alpha}_{2LS})}\right]$$
$$+ \left[\frac{\hat{\alpha}_{LS}}{(\hat{\alpha}_{LS}+\hat{\alpha}_{1LS}+\hat{\alpha}_{3LS})}\right] + \left[\frac{\hat{\alpha}_{LS}}{(\hat{\alpha}_{LS}+\hat{\alpha}_{1LS}+\hat{\alpha}_{4LS})}\right] + \left[\frac{\hat{\alpha}_{LS}}{(\hat{\alpha}_{LS}+\hat{\alpha}_{2LS}+\hat{\alpha}_{3LS})}\right] + \left[\frac{\hat{\alpha}_{LS}}{(\hat{\alpha}_{LS}+\hat{\alpha}_{2LS}+\hat{\alpha}_{4LS})}\right]$$
$$+ \left[\frac{\hat{\alpha}_{LS}}{(\hat{\alpha}_{LS}+\hat{\alpha}_{3LS}+\hat{\alpha}_{4LS})}\right] - \left[\frac{\hat{\alpha}_{LS}}{(\hat{\alpha}_{LS}+\hat{\alpha}_{1LS}+\hat{\alpha}_{2LS}+\hat{\alpha}_{3LS})}\right] - \left[\frac{\hat{\alpha}_{LS}}{(\hat{\alpha}_{LS}+\hat{\alpha}_{1LS}+\hat{\alpha}_{2LS}+\hat{\alpha}_{4LS})}\right]$$
$$- \left[\frac{\hat{\alpha}_{LS}}{(\hat{\alpha}_{LS}+\hat{\alpha}_{1LS}+\hat{\alpha}_{3LS}+\hat{\alpha}_{4LS})}\right] - \left[\frac{\hat{\alpha}_{LS}}{(\hat{\alpha}_{LS}+\hat{\alpha}_{2LS}+\hat{\alpha}_{3LS}+\hat{\alpha}_{4LS})}\right] + \left[\frac{\hat{\alpha}_{LS}}{(\hat{\alpha}_{LS}+\hat{\alpha}_{1LS}+\hat{\alpha}_{2LS}+\hat{\alpha}_{3LS}+\hat{\alpha}_{4LS})}\right] \quad ...(32)$$

6. Weighted Least Square Estimator (WLSE) :

It can be obtained by the same sample assumptions of LS estimation using the weight w_i, which given as:

$$w_i = \frac{1}{Var[F(x_{(i)})]} = \frac{(n+1)^2(n+2)}{i(n-i+1)}, i = 1,2,\dots,n$$

The minimizing with respect to the unknown parameter α:

$$\sum_{i=0}^{n} w_i \left[\ln(1-P_i)^{-1} - \alpha \ln\left(1+\frac{x_{(i)}}{\mu}\right)\right] = 0 \quad \text{...(33)}$$

The WLS estimator for α, is finally given as:

$$\hat{\alpha}_{WLS} = \frac{\sum_{i=1}^{n} w_i \ln(1-P_i)^{-1} \ln\left(1+\frac{x_{(i)}}{\mu}\right)}{\sum_{i=1}^{n} w_i \left(\ln\left(1+\frac{x_{(i)}}{\mu}\right)\right)^2} \quad \text{...(34)}$$

The WLS estimators of α_1, α_2, α_3 and α_4 are:

$$\hat{\alpha}_{1WLS} = \frac{\sum_{j_1=1}^{n_1} w_{j_1} \ln(1-P_{j_1})^{-1} \ln\left(1+\frac{y_{1(j_1)}}{\mu}\right)}{\sum_{i=1}^{n_1} w_{j_1} \left(\ln\left(1+\frac{y_{1(j_1)}}{\mu}\right)\right)^2} \quad \text{...(35)}$$

$$\hat{\alpha}_{2WLS} = \frac{\sum_{j_2=1}^{n_2} w_{j_2} \ln(1-P_{j_2})^{-1} \ln\left(1+\frac{y_{2(j_2)}}{\mu}\right)}{\sum_{j_2=1}^{n_2} w_{j_2} \left(\ln\left(1+\frac{y_{2(j_2)}}{\mu}\right)\right)^2} \quad \text{...(36)}$$

$$\hat{\alpha}_{3WLS} = \frac{\sum_{j_3=1}^{n_3} w_{j_3} \ln(1-P_{j_3})^{-1} \ln\left(1+\frac{y_{3(j_3)}}{\mu}\right)}{\sum_{j_3=1}^{n_3} w_{j_3} \left(\ln\left(1+\frac{y_{3(j_3)}}{\mu}\right)\right)^2} \quad \text{...(37)}$$

$$\hat{\alpha}_{4WLS} = \frac{\sum_{j_4=1}^{n_4} w_{j_4} \ln(1-P_{j_4})^{-1} \ln\left(1+\frac{y_{4(j_4)}}{\mu}\right)}{\sum_{j_4=1}^{n_4} w_{j_4} \left(\ln\left(1+\frac{y_{4(j_4)}}{\mu}\right)\right)^2} \quad \text{...(38)}$$

The WLS estimator of R is given by substitute (34), (35), (36), (37), and (38) in equation (9) we get:

$$\begin{aligned}\hat{R}_{WLS} = 1 &- \left[\frac{\hat{\alpha}_{WLS}}{(\hat{\alpha}_{WLS}+\hat{\alpha}_{1WLS})}\right] - \left[\frac{\hat{\alpha}_{WLS}}{(\hat{\alpha}_{WLS}+\hat{\alpha}_{2WLS})}\right] - \left[\frac{\hat{\alpha}_{WLS}}{(\hat{\alpha}_{WLS}+\hat{\alpha}_{3WLS})}\right] - \left[\frac{\hat{\alpha}_{WLS}}{(\hat{\alpha}_{WLS}+\hat{\alpha}_{4WLS})}\right] \\ &+ \left[\frac{\hat{\alpha}_{WLS}}{(\hat{\alpha}_{WLS}+\hat{\alpha}_{1WLS}+\hat{\alpha}_{2WLS})}\right] + \left[\frac{\hat{\alpha}_{WLS}}{(\hat{\alpha}_{WLS}+\hat{\alpha}_{1WLS}+\hat{\alpha}_{3WLS})}\right] + \left[\frac{\hat{\alpha}_{WLS}}{(\hat{\alpha}_{WLS}+\hat{\alpha}_{1WLS}+\hat{\alpha}_{4WLS})}\right] \\ &+ \left[\frac{\hat{\alpha}_{WLS}}{(\hat{\alpha}_{WLS}+\hat{\alpha}_{2WLS}+\hat{\alpha}_{3WLS})}\right] + \left[\frac{\hat{\alpha}_{WLS}}{(\hat{\alpha}_{WLS}+\hat{\alpha}_{2WLS}+\hat{\alpha}_{4WLS})}\right] + \left[\frac{\hat{\alpha}_{WLS}}{(\hat{\alpha}_{WLS}+\hat{\alpha}_{3WLS}+\hat{\alpha}_{4WLS})}\right] \\ &- \left[\frac{\hat{\alpha}_{WLS}}{(\hat{\alpha}_{WLS}+\hat{\alpha}_{1WLS}+\hat{\alpha}_{2WLS}+\hat{\alpha}_{3WLS})}\right] - \left[\frac{\hat{\alpha}_{WLS}}{(\hat{\alpha}_{WLS}+\hat{\alpha}_{1WLS}+\hat{\alpha}_{2WLS}+\hat{\alpha}_{4WLS})}\right] \\ &- \left[\frac{\hat{\alpha}_{WLS}}{(\hat{\alpha}_{WLS}+\hat{\alpha}_{2WLS}+\hat{\alpha}_{3WLS}+\hat{\alpha}_{4WLS})}\right] + \left[\frac{\hat{\alpha}_{WLS}}{(\hat{\alpha}_{WLS}+\hat{\alpha}_{1WLS}+\hat{\alpha}_{2WLS}+\hat{\alpha}_{3WLS}+\hat{\alpha}_{4WLS})}\right] \quad \text{...(39)}\end{aligned}$$

7. Simulation study

The Monte Carlo Simulation is conducted to compare the performances of the Maximum likelihood, Regression, Least Square, and Weighted Least Square estimators of R (repeat 10000 times).

It is performed by assuming eight states of R, say:$(\alpha, \alpha_1, \alpha_2, \alpha_3, \alpha_4, \mu) = (1.9,0,5,0.4,0.5, 1.5,1.3)$ $(1.9,0,5,0.4,0.5, 1.5,1.8)$, $(0.7,1.2,1.5,1.8, 1.6,1.3)$, $(0.7,1.2,1.5,1.8, 1.6,1.8)$, $(2.6,1.3,2.4,1.6,1.4,1.3)$, $(2.6,1.3,2.4,1.6, 1.4,1.8)$, $(2.2,1.3,1.8,1.6, 1.5,1.3)$ and $(2.2,1.3,1.8,1.6, 1.5,1.8)$ for different sample sizes $(n, n_1, n_2, n_3, n_4) = (10,10,15,15,15)$, $(25,25,25,25,25)$, $(35,35,20, 20,25)$, $(75,75,75,75,75)$ &$(75,75,50,50,50)$. The real values of R and the (MSE & MAPE) values for these cases are recorded in tables from (1) to (8). The ML estimator gives the best performance in all tables.

Table (1): MSE and MAPE values of $[(\alpha, \alpha_1, \alpha_2, \alpha_3, \alpha_4, \mu) = (1.9,0,5,0.4,0.5, 1.5,1.3)]$ $R = 1.2557$

Simple size	Criterion	MLE	RgE	LSE	WLSE
	Mean	1.2044	1.228	1.0666	1.0461
$(\mathbf{10}, \mathbf{10}, \mathbf{15}, \mathbf{15}, \mathbf{15})$	MSE	0.0036	0.0608	0.0390	0.0603
	MAPE	0.0457	0.1888	0.1515	0.1889
	Mean	1.1619	1.2475	1.0267	1.0203
$(\mathbf{25}, \mathbf{25}, \mathbf{25}, \mathbf{25}, \mathbf{25})$	MSE	0.0114	0.0712	0.0565	0.0603
	MAPE	0.0774	0.2147	0.1875	0.1908
	Mean	1.2597	1.2433	1.2573	1.2582
$(\mathbf{35}, \mathbf{35}, \mathbf{20}, \mathbf{20}, \mathbf{25})$	MSE	0.0107	0.0188	0.0132	0.0187
	MAPE	0.0657	0.0865	0.0728	0.0867
	Mean	1.2590	1.2976	1.2567	1.2613
$(\mathbf{75}, \mathbf{75}, \mathbf{75}, \mathbf{75}, \mathbf{75})$	MSE	0.0066	0.0132	0.069	0.0133
	MAPE	0.0506	0.708	0.0673	0.0708
	Mean	1.2396	1.2747	1.2631	1.2524
$(\mathbf{75}, \mathbf{75}, \mathbf{50}, \mathbf{50}, \mathbf{50})$	MSE	0.0040	0.0081	0.0051	0.0118
	MAPE	0.0414	0.0586	0.0488	0.0688

Table (2): MSE and MAPE values of $[(\alpha, \alpha_1, \alpha_2, \alpha_3, \alpha_4, \mu) = (1.9,0,5,0.4,0.5, 1.5,1.8)]$ $R = 1.2557$

Simple size	Criterion	MLE	RgE	LSE	WLSE
	Mean	1.2567	1.2644	1.2565	1.2543
$(\mathbf{10}, \mathbf{10}, \mathbf{15}, \mathbf{15}, \mathbf{15})$	MSE	0.0356	0.0545	0.0421	0.0423
	MAPE	0.1222	0.1465	0.1294	0.1365
	Mean	1.2604	1.2587	1.2589	1.2590
$(\mathbf{25}, \mathbf{25}, \mathbf{25}, \mathbf{25}, \mathbf{25})$	MSE	0.0179	0.0290	0.0221	0.0269
	MAPE	0.0849	0.1088	0.0923	0.1046
	Mean	1.2589	1.2514	1.2569	1.2508
$(\mathbf{35}, \mathbf{35}, \mathbf{20}, \mathbf{20}, \mathbf{25})$	MSE	0.0111	0.0188	0.0189	0.0187
	MAPE	0.0659	0.0878	0.0890	0.0868
	Mean	1.2577	1.2958	1.2620	1.2956
$(\mathbf{75}, \mathbf{75}, \mathbf{75}, \mathbf{75}, \mathbf{75})$	MSE	0.0060	0.0122	0.0138	0.0129
	MAPE	0.0503	0.0723	0.0768	0.0725
	Mean	1.2590	1.2860	1.2629	1.2779
$(\mathbf{75}, \mathbf{75}, \mathbf{50}, \mathbf{50}, \mathbf{50})$	MSE	0.0039	0.0089	0.0120	0.0090
	MAPE	0.0444	0.0589	0.0669	0.0590

Table (3): MSE and MAPE values of $[(\alpha, \alpha_1, \alpha_2, \alpha_3, \alpha_4, \mu) = (0.7,1.2,1.5,1.8, 1.6,1.3)]$ $R = 1.1678$

Simple size	Criterion	MLE	RgE	LSE	WLSE
	Mean	1.1999	1.1640	1.1659	1.1670
$(\mathbf{10}, \mathbf{10}, \mathbf{15}, \mathbf{15}, \mathbf{15})$	MSE	0.0131	0.0191	0.0169	0.0144
	MAPE	0.0780	0.0943	0.0890	0.0838
	Mean	1.1665	1.1655	1.1657	1.1660
$(\mathbf{25}, \mathbf{25}, \mathbf{25}, \mathbf{25}, \mathbf{25})$	MSE	0.0060	0.0103	0.0094	0.0070
	MAPE	0.0540	0.0688	0.0665	0.0586
	Mean	1.1676	1.1388	1.1620	1.1615
$(\mathbf{35}, \mathbf{35}, \mathbf{20}, \mathbf{20}, \mathbf{25})$	MSE	0.0043	0.0080	0.0076	0.0054
	MAPE	0.0445	0.0632	0.0583	0.0483

	Mean	1.1676	1.1789	1.1676	1.1685
$(\mathbf{75,75,75,75,75})$	MSE	0.0022	0.0048	0.0057	0.0032
	MAPE	0.0335	0.0469	0.0497	0.0356
	Mean	1.1670	1.1776	1.1676	1.1665
$(\mathbf{75,75,50,50,50})$	MSE	0.0014	0.0032	0.0042	0.0020
	MAPE	0.0268	0.0395	0.0440	0.0310

Table (4): MSE and MAPE values of $[(\alpha, \alpha_1, \alpha_2, \alpha_3, \alpha_4, \mu) = (0.7,1.2,1.5,1.8,1.6,1.8)]$ $R = 1.1678$

Simple size	Criterion	ML	Rg	LS	WLS
	Mean	1.2419	1.2539	1.2480	1.2280
$(\mathbf{10,10,15,15,15})$	MSE	0.0033	0.0078	0.0076	0.0039
	MAPE	0.0500	0.0720	0.0694	0.0510
	Mean	1.2380	1.2142	1.2095	1.2058
$(\mathbf{25,25,25,25,25})$	MSE	0.0021	0.0029	0.0024	0.0022
	MAPE	0.0399	0.0407	0.0484	0.0433
	Mean	1.1672	1.1385	1.1619	1.1609
$(\mathbf{35,35,20,20,25})$	MSE	0.0033	0.0080	0.0074	0.0056
	MAPE	0.0434	0.0638	0.0595	0.0483
	Mean	1.1659	1.1785	1.1676	1.1683
$(\mathbf{75,75,75,75,75})$	MSE	0.0023	0.0043	0.0053	0.0030
	MAPE	0.0327	0.0475	0.0492	0.0374
	Mean	1.1665	1.1765	1.1679	1.1690
$(\mathbf{75,75,50,50,50})$	MSE	0.0015	0.0032	0.0040	0.0029
	MAPE	0.0269	0.0387	0.0447	0.0316

Table (5): MSE and MAPE values of $[(\alpha, \alpha_1, \alpha_2, \alpha_3, \alpha_4, \mu) = (2.6,1.3,2.4,1.6,1.4,1.3)]$ $R = 0.2037$

Simple size	Criterion	MLE	RgE	LSE	WLSE
	Mean	0.2079	0.2043	0.2087	0.2090
$(\mathbf{10,10,15,15,15})$	MSE	0.0065	0.0106	0.0089	0.0076
	MAPE	0.3240	0.4097	0.3645	0.3456
	Mean	0.2060	0.1914	0.2040	0.2022
$(\mathbf{25,25,25,25,25})$	MSE	0.0035	0.0056	0.0051	0.0046
	MAPE	0.2387	0.3053	0.2879	0.2589
	Mean	0.2065	0.1924	0.2035	0.2040
$(\mathbf{35,35,20,20,25})$	MSE	0.0023	0.0034	0.0037	0.0029
	MAPE	0.1819	0.2314	0.2403	0.1977
	Mean	0.2083	0.2043	0.2092	0.2149
$(\mathbf{75,75,75,75,75})$	MSE	0.0005	0.0015	0.0027	0.0010
	MAPE	0.0989	0.1390	0.1892	0.1287
	Mean	0.2030	0.1922	0.2086	0.2013
$(\mathbf{75,75,50,50,50})$	MSE	0.0007	0.0017	0.0024	0.0011
	MAPE	0.1089	0.1590	0.1793	0.1245

Table (6): MSE and MAPE values of $[(\alpha, \alpha_1, \alpha_2, \alpha_3, \alpha_4, \mu) = (2.6,1.3,2.4,1.6,1.4,1.8)]$ $R = 0.2037$

Simple size	Criterion	MLE	RgE	LSE	WLSE
	Mean	0.2706	0.2690	0.2806	0.2713
$(\mathbf{10,10,15,15,15})$	MSE	0.0070	0.0079	0.0118	0.0090
	MAPE	0.3882	0.4004	0.4475	0.3899
	Mean	0.2270	0.2189	0.2283	0.2391

$(\mathbf{25,25,25,25,25})$	MSE	0.0010	0.0015	0.0019	0.0021
	MAPE	0.1267	0.1321	0.1666	0.1897
	Mean	0.1517	0.1790	0.1945	0.2036
$(\mathbf{35,35,20,20,25})$	MSE	0.0035	0.0044	0.0042	0.0040
	MAPE	0.2200	0.2357	0.2251	0.2223
	Mean	0.2050	0.1897	0.2023	0.2023
$(\mathbf{75,75,75,75,75})$	MSE	0.0010	0.0022	0.0025	0.0014
	MAPE	0.1268	0.1784	0.1935	0.1424
	Mean	0.2039	0.1896	0.2020	0.2015
$(\mathbf{75,75,50,50,50})$	MSE	0.0007	0.0016	0.0022	0.0009
	MAPE	0.1068	0.1542	0.1758	0.1206

Table (7): MSE and MAPE values of $[(\alpha, \alpha_1, \alpha_2, \alpha_3, \alpha_4, \mu) = (2.2,1.3,1.8,1.6,1.5,1.3)]$ $R = 0.2305$

Simple size	Criterion	MLE	RgE	LSE	WLSE
$(\mathbf{10,10,15,15,15})$	Mean	0.2331	0.2315	0.2339	0.2323
	MSE	0.0077	0.0132	0.0103	0.0095
	MAPE	0.3088	0.3862	0.3484	0.3302
$(\mathbf{25,25,25,25,25})$	Mean	0.2332	0.2126	0.2315	0.2287
	MSE	0.0042	0.0073	0.0065	0.0054
	MAPE	0.2359	0.2972	0.2834	0.2556
$(\mathbf{35,35,20,20,25})$	Mean	0.1893	0.2321	0.2555	0.2633
	MSE	0.0034	0.0045	0.0057	0.0043
	MAPE	0.2162	0.2264	0.2537	0.2257
$(\mathbf{75,75,75,75,75})$	Mean	0.2313	0.2108	0.2287	0.2275
	MSE	0.0023	0.0027	0.0029	0.0026
	MAPE	0.1225	0.1665	0.1887	0.1380
$(\mathbf{75,75,50,50,50})$	Mean	0.2313	0.2145	0.2277	0.2264
	MSE	0.0008	0.0019	0.0027	0.0012
	MAPE	0.1063	0.1547	0.1730	0.1216

Table (8): MSE and MAPE values of $[(\alpha, \alpha_1, \alpha_2, \alpha_3, \alpha_4, \mu) = (2.2,1.3,1.8,1.6,1.5,1.8)]$ $R = 0.2305$

Simple size	**Criterion**	**MLE**	**RgE**	**LSE**	**WLSE**
$(\mathbf{10,10,15,15,15})$	Mean	0.2360	0.2342	0.2367	0.2369
	MSE	0.0075	0.0127	0.0106	0.0088
	MAPE	0.3066	0.3839	0.3469	0.3280
$(\mathbf{25,25,25,25,25})$	Mean	0.2344	0.2122	0.2295	0.2278
	MSE	0.0048	0.0074	0.0060	0.0054
	MAPE	0.2350	0.2959	0.2792	0.2517
$(\mathbf{35,35,20,20,25})$	Mean	0.2323	0.2150	0.2312	0.2271
	MSE	0.0024	0.0042	0.0045	0.0037
	MAPE	0.1756	0.2320	0.2348	0.1944
$(\mathbf{75,75,75,75,75})$	Mean	0.2326	0.2132	0.2296	0.2268
	MSE	0.0012	0.0025	0.0032	0.0018
	MAPE	0.1267	0.1762	0.1913	0.1419
$(\mathbf{75,75,50,50,50})$	Mean	0.2313	0.2139	0.2282	0.2267
	MSE	0.0007	0.0020	0.0024	0.0016
	MAPE	0.1059	0.1540	0.1688	0.1183

8. Conclusions

The reliability R of a component being having X Lomax distribution strength and exposed to Y_1, Y_2, Y_3 and Y_4 Lomax stresses the shape parameter and a common scale parameter is obtained. We conducted a comparison between the four different estimation methods using MSE and MAPE and found that MLE is best for estimating R. The performance of LSE and WLSE convergent in all tables.

References

[1] M M Ali, M Pal and J Woo 2012 Estimation of P(Y < X) in a Four-Parameter Generalized Gamma Distribution *Austrian Journal of Statistics* **41** pp 197-210
[2] P Ashok, M T Devi and T S U Maheswari 2019 Reliability of a cascade system of type (X<Y<Z) for Pareto and Weibull distributions *AIP Conf. Proc.* 2112 pp 020074 1-5
[3] A H Khaleel and N S Karam 2019 Estimating the reliability function of (2+1) cascade model *Baghdad Science Journal* **16** (2) pp 395-402
[4] N S Karam and A H Khaleel 2019 Generalized inverse Rayleigh reliability estimation for the (2+1) cascade model *AIP Conf. Proc.* 2123 pp 020046 1-11
[5] A N Salman and A M Hamad 2019 On estimation of the stress-Strength reliability based on lomax distribution *IOP Conf. Ser. Mater. Sci. Eng.* 571 pp 1-7
[6] H Panahi and S Asadi 2011 Inference of stress-strength model for a lomax distribution *International Journal of Mathematical and Computational Sciences* **5** pp 937-940
[7] N Karam and A Khaleel 2018 Weibull reliability estimation for (2+1) cascade model *International Jouranal of Advanced Mathematical Sciences* **6** (1) 19-23
[8] A A Ismail 2012 Estimating the parameters of Weibull distribution and the acceleration factor from hybrid partially accelerated life test *Applied Mathematical Modeliing* **36** pp 2920-2925
[9] J B Lewis and D A Linzer 2005 Estimating regression models in which the dependent variable is based on estimates *Politcal Analysis* **13** pp 345-364
[10] P Bhattacharya and R Bhattacharjee 2010 A study on weibull distribution for estimating the parameters *Journal of Applied Quantitative* Methods **5** pp 234-241

Development the Numerical Method to Solve the Inverse Initial Value Problem for the Thermal Conductivity Equation of Composite Materials

Development the Numerical Method to Solve the Inverse Initial Value Problem for the Thermal Conductivity Equation of Composite Materials

H K Al-Mahdawi

Department of System Programming, School of Electronic Engineering and Computer Science, South Ural State University Lenina 76, Chelyabinsk, 454080 Russia

E-mail: hssnkd@gmail.com

Abstract. In this paper, the heat conduction equation for composite materials posed and solved. This problem is known as an inverse initial value problem for the heat conduction equation. In order to solve and formulate this inverse problem, the function spaces must be defined and represented. By studying and solving the direct problem for the heat equation in composite materials, it is possible to determine the function spaces and solve the inverse initial value problem. Scientific methods used: the separation of variables method used to solve the direct problem for the heat equation. It found that method separation of variables does not completely lead to the solution of the inverse initial value problem, since this method leads to a divergent series of solutions and rather massive errors. The heat conduction problem can be formulated as Fredholm integral first kind equations. The discretization algorithm applied to reformulated the problem as linear operator problem as matrix and vectors form. Then, Tikhonov's regularization inversion method has been used to find an approximation solution. Finally, as shown in the numerical example the regularized approximate solutions obtained.

1. Introduction

Many applied problems formulated as inverse problems of mathematical physics belong to the class of ill-posed problems. The inverse initial value problem for the heat equation is defined as an ill-posed problem in the sense that a "small" arbitrary change in data can lead to "large" errors in the solution [1]. Many methods can solve the inverse problem under the study of the heat equation. For example, the method of regularization Tikhonov A. N. [2], the method of Lavrentiev M. M. [3, 4], and the method of quasi-solutions Ivanova V. K. [5, 6]. With the development of high-speed personal computers, it has become more convenient to use numerical methods to solve inverse problems. Theoretical concepts and computational implementation associated with the solution of inverse and ill-posed problems were investigated by AN Tikhonov, MM Lavrent'ev, VK Ivanov, and their students and successive ones [7].

Many authors have discussed the theoretical concepts and computational implementation associated with the inverse problem of the heat equation for composite materials, and many methods have been described. In [8] the inverse problem of heat conduction was investigated using the Fourier series in eigenfunctions for an equation with a discontinuous coefficient. The Fourier transform was used, which made it possible to derive an inverse problem for the operator equation. Then the inverse problem of the operator equation was solved by the residual method. In [9], the author solved the problem of a moving boundary according to the Cauchy data in a one-dimensional heat equation with composite materials or a multilayer region. This problem is solved using a numerical regularization method based on the method

of fundamental solutions and the method of discrete Tikhonov regularization. An artificial neural network is used in [10] as an inverse tool for evaluating the thermal conductivity of a composite made of an aluminum core with an aluminum face sheet connected by an adhesive layer. The Picard method proposed to solve the inverse Cauchy problem to heat equation for composite materials [11] the Picard method applied in [12].

The main idea of this work is to reconstruct the source function of the heat equation by using the Tikhonov's regularization method, and it implemented to solve the inverse initial Cauchy problem for the heat equation in composite materials. The method of separation of variables was used to solve the direct problem of the partial differential equation for the heat equation in composite materials.

2. Statement of the problem

The direct problem of finding the temperature in the rod that is created from composite materials is the problem of heat conduction at any moment by using the initial and boundary values of the temperature. The mathematical formulation of this problem is described [11] by a system of differential equations:

$$\frac{\partial u_1(x,t)}{\partial t} = a_1^2 \frac{\partial^2 u_1(x,t)}{\partial x^2}; x \in (0, x_0); t \in (0,T], a_1 > 0, \tag{1}$$

$$\frac{\partial u_2(x,t)}{\partial t} = a_2^2 \frac{\partial^2 u_2(x,t)}{\partial x^2}; x \in (x_0, 1); t \in (0,T], a_2 > 0, \tag{2}$$

$$u_1(x,0) = u_1(x); 0 \le x \le x_0, u_2(x,0) = u_2(x); x_0 \le x \le 1; \tag{3}$$

$$u_1(0) = u_1'(0) = u_2(1) = u_2'(1) = 0, \tag{4}$$

where $u_1(x) \in (C[0, x_0] \cap C^2(0, x_0)); u_2(x) \in (C[x_0, 1] \cap C^2(x_0, 1))$

$$\frac{\partial u_1(0,t)}{\partial x} = 0; t \in [0,T], \tag{5}$$

$$u_2(1,t) = 0; t \in [0,T], \tag{6}$$

$$u_1(x_0,t) = u_2(x_0,t); t \in [0,T], \tag{7}$$

$$a_1 \frac{\partial u_1(x_0,t)}{\partial x} = a_2 \frac{\partial u_2(x_0,t)}{\partial x}; t \in [0,T], \tag{8}$$

in the direct problem (1–8) we need to find the vector $\tilde{u}(x,t)$.

$$\tilde{u}(x,t) = \begin{cases} u_1(x,t); \ x \in [0, x_0]; t \in [0,T] \\ u_2(x,t); \ x \in [x_0, 1], t \in [0,T] \end{cases}, \tag{9}$$

where $\tilde{u}(x,t) \in C([0,1] \times [0,T]) \cap C^{2,1}\left(\left[(0, x_0) \cup (x_0, 1)\right] \times (0,T]\right)$,

$$\tilde{u}(x,t) \to \tilde{u}(x) \ for \ t \to 0, \tag{10}$$

Theorem 1. For any function $\tilde{u}(x)$ satisfying (4), $\exists$ the unique solution of the direct problem satisfying (1–3), (5), (8, 9).

Proof. We will seek a formal solution to system (1–7) in the form of a series in eigenfunctions corresponding to the Sturm-Liouville problem $\{S_n(x)\}_{n=1}^{\infty}$,

$$\tilde{u}(x,t) = \sum_{n=1}^{\infty} u_n e^{-\lambda_n^2 t} S_n(x), \tag{11}$$

where function $S_n(x)$ is defined by $S_n(x)=\begin{cases} S_n^1\left(x/a_1\right);\ x\in(0,x_0), \\ S_n^2\left(x/a_2\right);\ x\in(x_0,1). \end{cases}$

$$S_n(x)=\beta_n\begin{cases}\cos\left(\dfrac{\lambda_n x}{a_1}\right)\sin\left(\dfrac{\lambda_n(1-x_0)}{a_2}\right);\ x\in[0,x_0],\\ \sin\left(\dfrac{\lambda_n(1-x)}{a_2}\right)\cos\left(\dfrac{\lambda_n x_0}{a_1}\right);\ x\in[x_0,1],\end{cases} \tag{12}$$

$$u_n=\frac{\alpha_n}{\lambda_n}\begin{cases}u_n^1=\int_0^{x_0}u_1(x)S_n^1\left(x/a_1\right)d\left(x/a_1\right)\\ u_n^2=\int_{x_0}^{1}u_2(x)S_n^2\left(x/a_2\right)d\left(x/a_2\right)\end{cases}, \tag{13}$$

where $\alpha_n=\beta_n cos\left(\dfrac{\lambda_n x_0}{a_2}\right)$

$$\beta_n^2=\frac{2a_1a_2}{a_2x_0\sin^2\left(\dfrac{\lambda_n(1-x_0)}{a_2}\right)+a_1(1-x_0)\cos^2\left(\dfrac{\lambda_n x_0}{a_1}\right)}, \tag{14}$$

$$\lambda_n=\frac{\pi a_1a_2(2n-1)}{2(a_2x_0+a_1(1-x_0))},n=1,2,3,\ldots. \tag{15}$$

From (9), (11) and (13) we can reduce problem as Fredholm integral first kind equation.

$$\tilde{u}(x,t)=\begin{cases}u_1(x,t)=\int_0^{x_0}\sum_{n=1}^{\infty}e^{-\lambda_n^2t}S_n^1(y)S_n^1(x)u_1(x)d\left(x/a_1\right),y\in[0,x_0];\\ u_2(x,t)=\int_0^{x_0}\sum_{n=1}^{\infty}e^{-\lambda_n^2t}S_n^1(y)S_n^1(x)u_1(x)d\left(x/a_1\right),y\in[0,x_0];\end{cases}, \tag{16}$$

can write (16) as following

$$A\tilde{u}(x)=\begin{cases}A_1u_1(x)=\int_0^{x_0}P_1(y,x,t)u_1(x)d\left(x/a_1\right),y\in[0,x_0];\\ A_2u_2(x)=\int_{x_0}^{1}P_2(y,x,t)u_2(x)d\left(x/a_2\right),y\in[x_0,1]\end{cases}=\tilde{g}(x), \tag{17}$$

where $P_1(y,x,t)=\sum_{n=1}^{\infty}e^{-\lambda_n^2t}S_n^1(y)S_n^1(x)$, $P_2(y,x,t)=\sum_{n=1}^{\infty}e^{-\lambda_n^2t}S_n^2(y)S_n^2(x)$

The function $\tilde{u}(x)$ refers as initial temperature, see (3) and (10) $\tilde{u}(x)=\begin{cases}u_1(x);\ x\in[0,x_0];\\ u_2(x);\ x\in[x_0,1];\end{cases}$,

the kernels $P_1(y,x,t)\in C\left([0,x_0]\times[0,x_0]\right),P_2(y,x,t)\in C\left([x_0,1]\times[x_0,1]\right),\tilde{u}(x)\in H_2^1[0,1]$ and $\tilde{g}(x)\in L_2[0,1]$. The kernels of the integral operator A in (17) is closed.

3. Statement of the inverse problem

In (1–8), consider the inverse initial value problem for the heat equation, that is, the temperature distribution at the time t = T > 0, which is given by the function $\tilde{u}(x,T)$, and it is required to find the initial distribution $\tilde{u}(x)=\begin{cases}u_1(x);\ x\in[0,x_0];\\ u_2(x);\ x\in[x_0,1];\end{cases}$, assuming that $\tilde{u}(x)\in H_2^1[0,1]$. Suppose that we know a function $\tilde{g}(y)\in L_2[0,1]$, which is a solution to the direct problem for t = T,

$$\tilde{u}(x,T)=\begin{cases}A_1u_1(x)=\int_0^{x_0}P_1(y,x,T)u_1(x)d\left(x/a_1\right), y\in[0,x_0];\\ A_2u_2(x)=\int_{x_0}^{1}P_2(y,x,T)u_2(x)d\left(x/a_2\right), y\in[x_0,1]\end{cases}=\tilde{g}(y), \tag{18}$$

the exact value of the function $\tilde{g}(y)=\tilde{g}_0(y)$ in (18) is unknown, and instead of it a pair $\tilde{g}_\delta(y)$ and δ are given, where $\tilde{g}_\delta(y)\in L_2[0,1], \delta>0$,

$$\|\tilde{g}_\delta(y)-\tilde{g}_0(y)\|_{L_2}\le\delta. \tag{19}$$

Required using the initial data of the problem $\tilde{g}_\delta(y)$ and δ to find the approximation solution $u_\delta(x)\in L_2[0,1]$, the $u_\delta(x)$ is converges to $\tilde{u}(x)$ when the $\delta\to 0,$ in $L_2[0,1]$, as well as to obtain an estimate of the error $\|u_\delta(x)-\tilde{u}(x)\|_{L_2}$.

4. Discretization of the integral equation of the first kind

The discretization algorithm described in [13] and implemented in [14]. For simplicity, we used the following steps to reformulate the first integral equation $A_1u_1(x)=\int_0^{x_0}P_1(y,x,T)u_1(x)d\left(x/a_1\right), y\in[0,x_0]$ for problem (17) and we can apply same step on the second integral equation $A_2u_2(x)=\int_{x_0}^{1}P_2(y,x,T)u_2(x)d\left(x/a_2\right), y\in[x_0,1]$. We considered the following integral equation for first kind without T because the is fixed number.

$$Au(x)=\int_a^b P(x,y)u(x)dx=g(y), a\le y\le b, \tag{20}$$

where $u(x)\in L_2[a,b], g(y)\in L_2[a,b],$ the function $P(x,y)$ represent the kernel operator $A,$ where $P(x,y), P_y'(x,y)\in C^{1,1}([a,b]\times[a,b])$. We propose that for $g(x)=g_0(x)$ there exist a true solution $u_0(x)$ for problem (20) in the set M_r

$$M_r=\left\{u(x):u(x),u'(x)\in L_2[a,b], u(a)=u(b)=0, \|u(x)\|_{L_2}^2\le r^2\right\}, \tag{21}$$

The function $g_0(x)$ is unknown instead of we have $g_\delta\in L_2[a,b]$ and $\delta>0$ such that $\|g_\delta(y)-g_0(y)\|_{L_2}^2\le\delta^2$. In order to solve the problem (20) we need find the approximation solution $u_\delta(x)$ by using the given information $g_\delta(y),\delta$ and M_r. Then we estimate the deviation of the approximation solution $u_\delta(x)$ from the true solution $u_0(x)$ in the metric of space $L_2[a,b]$.

We need define an operator $B:L_2[a,b]\to L_2[a,b]$ by the following formula

$$u(x)=Bv(x)=\int_a^s v(\zeta)d\zeta, v(x), Bv(x)\in L_2[a,b], \tag{22}$$

There is an operator named C which can be defined by

$$Cv(x) = ABv(x),\ v(x), \in L_2[a,b],\ Cv(x) \in L_2[a,b], \tag{23}$$

from (23) and (24) we follow that $Cv(x) = \int_a^b K(x,y)v(x)dx$, where $K(x,y) = -\int_a^x P(\varsigma, y)d\varsigma$.

The finite-dimensional operator $C_{n,n}$ has been defined for computing the numerical solution for problem (20), the C replaced with the operator $C_{n,n}$ and these operators satisfied the following relation where the value of the $\eta_{n,n}$ is define by

$$N(y) = \max_{a \le x \le b} |P(x,y)|,\ y \in [a,b], \tag{24}$$

and

$$N_1 = \max\left\{ \left| K'_y(x,y) \right| : a \le x \le b, a \le y \le b \right\}, \tag{25}$$

the $N(y) \in [a,b]$ and N_1 exist because the $P(x,y), P'_y(x,y) \in C([a,b] \times [a,b])$.

By dividing the intervals $[a,b]$ into n equal parts where interval $[a,b]$ is divided by points $x_i = a + \frac{i(b-a)}{n}, i = 0, 1, \ldots, n-1$. Now, we need to define the following functions

$$\bar{K}_i(y) = K(x_i, y), \tag{26}$$

$$K_n(x,y) = \bar{K}_i(y); x_i \le x \le x_{i+1},\ \ y \in [a,b], i = 0,1,\ldots,n-1 \tag{27}$$

$$K_{n,n}(x,y) = \bar{K}_i(y_j); x_i \le x \le x_{i+1}, y_j \le y \le y_{j+1}, i = 0,1,\ldots,n-1,\ j = 0,1,\ldots,n-1, \tag{28}$$

By using the equations (26–28), we define the operators $C_{n,}$ and $C_{n,n}$

$$C_n v(x) = \int_a^b K_n(x,y)v(x)dx, y \in [a,b],\ C_{n,n}v(x) = \int_a^b K_{n,n}(x,y)v(x)dx, y \in [a,b], \tag{29}$$

where $C_{n,}$ and $C_{n,m}$ map $L_2[a,b]$ into $L_2[a,b]$

Next step need to estimate the $\|C_{n,n} - C\|$, by using the inequality relation $\|C_{n,n} - C\| \le \|C_{n,n} - C_n\| + \|C_n - C\|$. Since

$$|K_{n,n}(x,y) - K_n(x,y)| \le |\bar{K}_i(y) - \bar{K}_i(y_j)|, \tag{30}$$

for $x_i \le x \le x_{i+1}$ and $y_j \le y \le y_{j+1},\ i = 0,1,\ldots,n-1,\ j = 0,1,\ldots,n-1,$ from (25) $|\bar{K}_i(y) - \bar{K}_i(y_j)| \le N_1 \frac{b-a}{m}$, finding from (30) that

$$|K_{n,n}(x,y) - K_n(x,y)| \le N_1 \frac{b-a}{m}, \tag{31}$$

By using the equality $\|C_{n,n} - C_n\| = \sup_{\|v\| \le 1} \|C_{n,n}v - C_n v\|$, we get

$$\|C_{n,n} - C_n\|^2 = \sup_{\|v\| \le 1} \int_a^b \left[\int_a^b |K_{n,n}(x,y) - K_n(x,y)| . |v(x)| dx \right]^2 dy. \tag{32}$$

Driving from (31) and (32) the following

$$\|C_{n,n} - C_n\|^2 \le N_1^2 \left(\frac{b-a}{n} \right)^2 \int_a^b \left[\int_a^b |v(x)| dx \right]^2 dy. \tag{33}$$

Since $\int_a^b |v(x)| dx \le \sqrt{b-a}\, \|v(x)\|_{L_2}$, inequality (33) implies that

$$\|C_{n,n}-C_n\|\le\sqrt{(b-a)(b-a)}N_1\frac{b-a}{n}. \tag{34}$$

Now the term $\|C_n-C\|$ can be estimating. Since $C_nv(x)-Cv(x)=\int_a^b(K(x,y)-K_n(x,y))v(x)dx$ and

$$\|C_n-C\|^2=\sup\left\{\int_a^b\left[\int_a^b|K_{n,n}(x,y)-K_n(x,y)|.|v(x)|dx\right]^2dy:\|v(x)\|\le1\right\}$$

Taking into account (24), (26) and (27) and the inequality

$$\int_a^b|K(x,y)-K_n(x,y)|.|v(x)|dx\le\int_a^b|K(x,y)-K(x_i,y)|.|v(x)|dx\le\frac{b-a}{n}N(y)\int_a^b|v(x)|dx,$$

We find the following

$$\|C_{n,n}v(x)-C_nv(x)\|^2\le\left(\frac{b-a}{n}\right)^2\int_a^bN^2(y)\left[\int_a^b|v(x)dx|\right]^2dy. \tag{35}$$

The $\|v(x)\|\le1$ and $\int_a^b|v(x)|dx\le\frac{b-a}{n}\|v(x)\|$ with inequality (35) implies that

$$\|C_n-C\|\le\sqrt{(b-a)}\|N(y)\|_{L_2}\frac{b-a}{n}. \tag{36}$$

Thus from (34) and (36)

$$\eta_{n,n}=\sqrt{(b-a)(b-a)}N_1\frac{b-a}{n}+\sqrt{(b-a)}\|N(y)\|_{L_2}\frac{b-a}{n}. \tag{37}$$

5. Finite-dimensional of the Tikhonov regularization method

This step described in [13]. We define subspace X_n of spaces $L_2(a,b)$. Those subspaces consisting of all functions on intervals $[x_i,x_{i+1}),i=0,1,...,n-1$, and intervals $\left[y_j,y_{j+1}\right),j=0,1,...,n-1$, for space $L_2(a,b)$. We denote by P_n the metric projection operator where $P_n:L_2(a,b)\to X_n$,
The problem (20) reduces to linear operator problem first type.

$$C_{n,n}v(x)=g_\delta^n(y), \tag{38}$$

where $g_\delta^n(y)=P_n|g_\delta(y)|$.

The approximation solution for the problem (20) can be obtained by using the generalized discrepancy method. The method reduces the problem (38) to the conditional extremum variational problem.

$$\inf\left\{\|v(x)\|^2:v(x)\in X_n,\|C_{n,n}v(x)-g_\delta^n(y)\|\le\|v(x)\|\eta_{n,n}+\delta\right\}, \tag{39}$$

under the condition

$$\|g_\delta^n(y)\|=\|u_0'(x)\|\eta_{n.n}+\delta, \tag{40}$$

The variational problem (38) has a unique solution $v_{\delta,\eta_{n,n}}(x)$ such that $\|C_{n,n}v_{\delta,\eta_{n,n}}(x)-g_\delta^n(y)\|=\|v_{\delta,\eta_{n,n}}(x)\|\eta_{n,n}+\delta.$

The conditional problem (38) is reduced to the unconditional problem

$$\inf\left\{\|C_{n,n}v(x)-g_\delta^n(y)\|^2+\alpha\|v(x)\|^2:v(x)\in X_n\right\},\alpha>0, \tag{41}$$

The (41) it is a finite-dimensional version of the Tikhonov regularization method [5].

There is a unique solution $v_\delta^\alpha(x)$ for problem (41) . This solution should satisfy the general discrepancy principle [15].

$$\left\|C_{n,m}v_\delta^\alpha(x)-g_\delta^n(y)\right\|=\left\|v_\delta^\alpha(x)\right\|\eta_{n,n}+\delta. \tag{42}$$

Under condition (40), the equation (42) has a unique solution $v_\delta^\alpha(x)$ with respect of regularization parameter $\alpha(n,n)$. That condition known in [16] and by theorem defined, there is $v_{\delta,\eta_{n,m}}(x)=v_\delta^{\alpha(n,m)}(x)$ where the approximation solution is $u_{\delta,\eta_{n,n}}(x)=Bv_{\delta,\eta_{n,n}}(x)$.

For solving the problem (42), we get the equation

$$C_{n,n}^TC_{n,n}v(x)+\alpha v(x)=C_{n,n}^Tg_\delta^n(y). \tag{43}$$

In space X_n, the orthonormal bases have introduced $\{\varphi_i(x)\}$ by following

$$\varphi_i(x)=\begin{cases}\sqrt{\dfrac{n}{b-a}}; & x_i\le x<x_{i+1,}\\ 0; & x\notin\left[x_i,x_{i+1,}\right),i=0,1,...,n-1,\end{cases}$$

$$\varphi_j(y)=\begin{cases}\sqrt{\dfrac{n}{b-a}}; & y_j\le y<y_{j+1,}\\ 0; & x\notin\left[y_j,y_{j+1,}\right),j=0,1,...,n-1,\end{cases}$$

With these bases, we define the isometric operator J_s where $J_s:R^n\to X_n$ following.

$$\begin{aligned}J_s\left[s(x)\right]&=\sum_{i=0}^{n-1}s_i\varphi_i(x),s=(s_0,s_1,....,s_{n-1}),\\ J_s\left[s(y)\right]&=\sum_{j=0}^{n-1}s_j\varphi_j(y),s=(s_0,s_1,....,s_{n-1})\end{aligned} \tag{44}$$

The problem 42

$$\inf\left\{\left\|J_s^{-1}\left[C_{n,n}v(x)\right]-J_s^{-1}\left[g_\delta^n(y)\right]\right\|^2+\alpha\left\|J_s^{-1}\left[v(x)\right]\right\|^2:J_s^{-1}\left[v(x)\right]\in X_n\right\},\alpha>0,$$

where

$$J_s^{-1}\left[g_\delta^n(y)\right]=\sqrt{\frac{n}{b-a}}\int_{y_j}^{y_{j+1}}f(y)dy$$

$$J_s^{-1}\left[v(x)\right]=\sqrt{\frac{n}{b-a}}\int_{x_i}^{x_{i+1}}v(x)dx$$

We can rewrite the equation (44) in matrix and vector form as following

$$(\bar{C}_{j,i})^T\bar{C}_{j,i}\bar{v}_i+\alpha\bar{v}_i=(\bar{C}_{j,i})^T\bar{g}_j,i=0,1,...n-1,\ j=0,1,...,n-1,$$

Where

$$\bar{v}_i = J_s^{-1}\left[v(x)\right] = \sqrt{\frac{n}{b-a}}\begin{bmatrix} \bar{v}_0 = \int_{x_0}^{x_1} v(x)dx \\ \bar{v}_1 = \int_{x_1}^{x_2} v(x)dx \\ \vdots \\ \bar{v}_{n-1} = \int_{x_{n-1}}^{x_n} v(x)dx \end{bmatrix}$$

$$\bar{g}_j = J_s^{-1}\left[g_\delta^n(y)\right] = \sqrt{\frac{n}{b-a}}\begin{bmatrix} g_0 = \int_{y_0}^{y_1} g(y)dy \\ g_1 = \int_{y_1}^{y_2} g(y)dy \\ \vdots \\ g_{n-1} = \int_{y_{n-1}}^{y_n} g(y)dy \end{bmatrix}$$

$$\bar{C}_{j,i} = \frac{b-a}{n}\sqrt{\frac{b-a}{n}}\begin{bmatrix} \bar{K}_{i=0}(y_{j=0}) & \bar{K}_{i=1}(y_{j=0}) & \dots & \bar{K}_{i=n-1}(y_{j=0}) \\ \bar{K}_{i=0}(y_{j=1}) & \bar{K}_{i=1}(y_{j=1}) & \dots & \bar{K}_{i=n-1}(x_{j=1}) \\ \vdots & \vdots & \ddots & \vdots \\ \bar{K}_{i=0}(y_{j=n-1}) & \bar{K}_{i=1}(y_{j=n-1}) & \cdots & \bar{K}_{i=n-1}(y_{j=n-1}) \end{bmatrix}$$

$$(\bar{C}_{j,i})^T = \frac{b-a}{n}\sqrt{\frac{b-a}{n}}\begin{bmatrix} \bar{K}_{i=0}(y_{j=0}) & \bar{K}_{i=0}(y_{j=1}) & \dots & \bar{K}_{i=0}(y_{j=n-1}) \\ \bar{K}_{i=1}(y_{j=0}) & \bar{K}_{i=1}(x_{j=1}) & \dots & \bar{K}_{i=1}(y_{j=n-1}) \\ \vdots & \vdots & \ddots & \vdots \\ \bar{K}_{i=n-1}(y_{j=0}) & \bar{K}_{i=n-1}(y_{j=1}) & \cdots & \bar{K}_{i=n-1}(y_{j=n-1}) \end{bmatrix}$$

6. Numerical example

Considering the inverse initial value problem (1–8) for the heat equation in composed materials, we need to find the $u_\delta^\alpha(x)$ by using Tikhonov regularization method. The exact solution $\tilde{u}(x) = \cos(\pi x/2)$ will be shown in 'figure 1', and the input function for inverse problem $u(x,T) = g_0(x)$ where the $x_0 \in (0,1)$, $x_0 = 0.5$. We will add some noise to $g_0(x)$ to become $g_\delta(x)$.

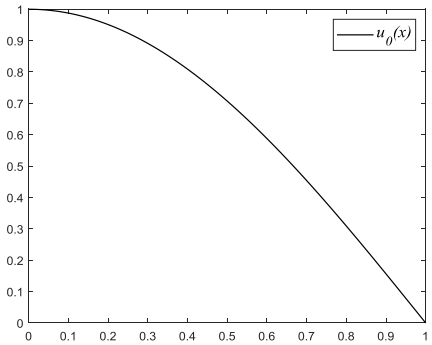

Figure 1. The exact solution for inverse problem $u_0(x)$.

We divided the intervals [0,1] into $m = 100$. and the $T = 0.1$. We have applied our method with different regularization parameter value α,

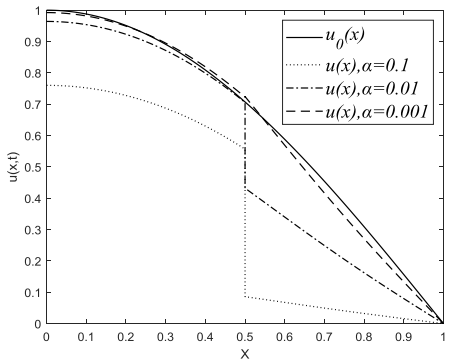

Figure 2. $u_\delta^\alpha(x)$. where $\delta = 0.02$.

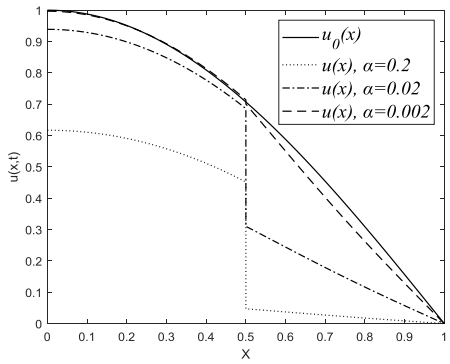

Figure 3. $u_\delta^\alpha(x)$. where $\delta = 0.04$.

From above figure 2 and figure 3, we obtain a good estimated solution compared with exact initial value $u_0(x)$.

7. Conclusion

This work deals with the algorithm for solving the initial value problem for the heat equation in composed materials. This problem is an ill-posed problem, and a special method needs to reformulate the problem to liner operator problem. The separation of variables method used to represent the partial differential equation as an integral equation of the first kind. By using the discretization method, the integral equation converted to a system of linear equations or linear operator equation first kind. Tikhonov's regularization method is a suitable method to obtain the approximation solution.

References

[1] S I Kabanikhin 2011 Inverse and ill-posed problems: theory and applications *Walter De Gruyter* **55**

[2] A N Tikhonov 1963 On the Regularization of Ill-Posed Problems *Proc. USSR Acad. Sci.* **153** (1) pp 49–52

[3] M M Lavrent'ev 1962 On Some Ill-Posed Problems of Mathematical Physics *Izd. Sib. Otd. Akad. Nauk SSSR Novosib* pp 92

[4] H K Al-Mahdawi 2020 Solving of an inverse boundary value problem for the heat conduction equation by using Lavrentiev regularization method *in Abstracts of the International Conference "APVPM," (*2020) doi: 10.24411/9999-017A-2020-10324

[5] V K Ivanov 1968 About Application of Picard Method to the Solution of Integral Equations for the First Kind *Bui. Inst. Politehn. Iasi* **4** (34) pp 71-7*8*

[6] V K Ivanov, V V Vasin and V P Tanana 2013 Theory of linear ill-posed problems and its applications *Walter de Gruyter* **36**

[7] V P Tanana and A I Sidikova 2018 Optimal Methods for Ill-Posed Problems: With Applications to Heat Conduction *Walter de Gruyter GmbH & Co KG* **62**

[8] V P Tanana and A A Ershova 2018 On the solution of an inverse boundary value problem for composite materials *Vestn. Udmurt Univ. Mat. Mekhanika. Komp'yuternye Nauk* **28** (4) pp 474–488

[9] T Wei and Y S Li 2009 An inverse boundary problem for one-dimensional heat equation with a multilayer domain *Eng. Anal. Bound. Elem.* **33** (2) pp 225-232

[10] V Maneesh and M K Pradeep 2014 An inverse method to estimate the principal thermal conductivities of composite material *Int. J. Sci. Eng. Res.* **5** (7) pp 810–813

[11] H K AL-Mahdawi 2020 Application of the Picard Method To the Solution of the Inverse Cauchy Problem for the Thermal Conductivity Equation of Composite Materials *Sci. Bus. Dev.*

Ways **4** (106) pp 89–95
[12] H K Al-Mahdawi 2019 Studying the Picard's method for solving the inverse Cauchy problem for heat conductivity equations *Vestn. Yuzhno-Ural'skogo Gos. Univ. Seriya Vychislitelnaya Mat. i Inform.* **8** (4) pp 5-14
[13] V P Tanana and A I Sidikova 2017 On Estimating the Error of an Approximate Solution Caused by the Discretization of an Integral Equation of the First Kind *Proc. Steklov Inst. Math.* **299** (1) pp 217-224 doi: 10.1134/S0081543817090231
[14] H K Al-Mahdawi 2019 Development of a numerical method for solving the inverse Cauchy problem for the heat equation *Bull. South Ural State Univ. Ser. Comput. Math. Softw. Eng.* **8** (2) pp 22–31
[15] A V Goncharskii, A S Leonov and A G Yagola 1973 A generalized discrepancy principle *USSR Comput. Math. Math. Phys.* **13** (2) pp 25-37 doi: 10.1016/0041-5553(73)90128-6
[16] V P Tanana 1977 On an iterative projection algorithm for solving ill posed problems with an approximately specified operator *USSR Comput. Math. Math. Phy.* **17** (1) pp 12-20 doi: 10.1016/0041-5553(77)90065-9

A Statistical Study on the Parameters of the Skew Normal Distribution Depending on the Use of the Genetic Algorithm Using the Simulation Method

A Statistical Study on the Parameters of the Skew Normal Distribution Depending on the Use of the Genetic Algorithm Using the Simulation Method

Murtadha Alaa Alkhafaji , Rabab Abdulrida Saleh

Department of Statistics, College of Administration and Economics, University of Baghdad, Iraq

Email:mortada.alaa1101a@coadec.uobaghdad.edu.iq

Abstract. Recent statistical research has witnessed activity on the study of skew normal distribution (SND) due to the fact that the data set does not fit well with the normal distribution due to Skewnessand excessive Kurtosis**.** For the purpose of estimating the parameters of the model (SND),the maximum likelihood method (ML) was used, but the probability equations of this method do not have clear solutions in the distribution (SND), and the problem was solved using the genetic algorithm (GA) and Other repetitive techniques are Newton Raphson, Nelder Mead and Iteratively Reweighting Algorithm, using the simulation method with different sample sizes and comparing the preference of results methods used based on criteria (Mean, Mse and Def). It has been concluded that (ML) capabilities using the (GA) of parameters (SND) are best in the case of a small or medium sample size and the best (IR) algorithm at a large sample size.

1. Introduction

The symmetric normal distribution is considered the most prevalent theoretically due to its important Properties, but in practice and analysing the data we find in many cases that the data is not distributed in a normal distribution The reason is due to the presence of outliers that cause skewness in the data. Since the skew is responsible for the asymmetry in the shape of the distribution, and previous studies confirm that most of the phenomena of life contain a proportion of the skew. Symmetric Here lies the importance of studying a skew normal distribution (SND).

The (SND) distribution shares common features and characteristics of the normal distribution, adding the mechanism of the skewness parameter (ω) that is responsible for regulating the skewnessand is considered the turning point from the normal to the skew normal distribution and gives the distribution (SND) greater flexibility and more appropriate to the data under study .

In our research we studied experimental data with different sample sizes and different skewness levels using the Monte Carlo simulation method. The values of the simulation results express the accuracy and best methods and methods used in the research for the studied model and obtaining the best results from the use of statistical methods and methods of improvement appropriate to the model and relying on them according to scientific rules that result in taking the correct and scientific decision appropriate to the studied problem.

The main problem of the research is to overcome the problems of probability equations in the (ML) when estimating the parameters of the (SND), which are considered the most prominent statistical methods for estimating probability distributions and because of the emergence of nonlinear functions

when the possibility function is derived and thus the results of (ML) have no solutions Evident in estimating the model parameters of a skew normal distribution modelpp.3.

The aim of our research is to study the (SND) of the characteristics and features, study the effect of the skewness parameter (ω), and address the problem of nonlinear functions in the (ML) equations of the (SND) . For the purpose of estimating the parameters of the skew normal distribution model, the genetic algorithm (GA) was used in addition to iterative algorithms (NR, NM and IR), then comparison between the preference of these methods based on criteria (Mean, Mse and Def)

2. Skew Normal Distribution (SND)

The univariate skew normal distribution was introduced by the researcher Azzalini in 1985, the mathematical formula for the probability density function (PDF) for the variable y distributed (SND) for the location parameter (ϵ) , the scale parameter (τ) and the shape parameter (ω) are written as follows[3] :-

$$f(y,\epsilon,\tau,\omega) = \frac{2}{\tau}\,\emptyset\left(\frac{y-\epsilon}{\tau}\right)\,\psi\left(\omega\,\frac{y-\epsilon}{\tau}\right) \qquad y \in R \quad \ldots \ (1)$$

Where $\emptyset$ and ψ are the (pdf) and (cdf) functions of the normal distribution, respectively. The skew normal distribution converts to the normal distribution when the shape parameter value is (ω =0) , and when the location and scale parameters values is (ϵ= 0 and τ = 1) respectively , the (SND) becomes a standard skew normal distribution (SSND) With the parameter of skewness (ω)[2], it is expressed mathematically as follows :

$$f(y,\omega) = 2\,\emptyset(y)\;\varphi(\omega\,y) \qquad y \in R \ \ldots (2)$$

The skewness increases (asymmetry of the distribution) with the increase of the skewness parameter (ω) [8] .

3. Method Maximum Likelihood (ML)

The ML method is considered one of the most prominent methods used to estimate the parameters of the probability model to characterize the estimated of maximum likelihood with high efficiency. The (ML) estimators of the parameters consider as points that lead to increase the logarithm of the likelihood function to its maximum limit [5]. The logarithm function of the (SND) is written as follows:

$$lnL = nln(2) - nln(\tau) - \frac{n}{2}ln(2\pi) - \frac{1}{2}\sum_{i=1}^{n}\left(\frac{y_i-\epsilon}{\tau}\right)^2 + \sum_{i=1}^{n} ln\,\psi\left(\omega\,\frac{y_i-\epsilon}{\tau}\right). \ldots (3)$$

Deriving the logarithm function of the skew normal distribution (SND) for the parameters (ϵ, τ, ω), we obtain nonlinear equations as follows :

$$\frac{\partial lnL}{\partial \epsilon} = \sum_{i=1}^{n}\left(\frac{y_i-\epsilon}{\tau}\right) - \ \omega\sum_{i=1}^{n}\frac{\emptyset\left(\omega\frac{y_i-\epsilon}{\tau}\right)}{\psi\left(\omega\frac{y_i-\epsilon}{\tau}\right)} \ = 0 \qquad \ldots \ (4)$$

$$\frac{\partial lnL}{\partial \tau} = \ -n + \sum_{i=1}^{n}\left(\frac{y_i-\epsilon}{\tau}\right)^2 - \ \omega\sum_{i=1}^{n}\frac{\emptyset\left(\omega\frac{y_i-\epsilon}{\tau}\right)}{\psi\left(\omega\frac{y_i-\epsilon}{\tau}\right)}\left(\frac{y_i-\epsilon}{\tau}\right) \qquad \ldots (5)$$

$$\frac{\partial lnL}{\partial \omega} = \ \sum_{i=1}^{n}\frac{\emptyset\left(\omega\frac{y_i-\epsilon}{\tau}\right)}{\psi\left(\omega\frac{y_i-\epsilon}{\tau}\right)}\left(\frac{y_i-\epsilon}{\tau}\right) \ = 0 \ldots (6)$$

Where $w(y_i) = \frac{\emptyset\left(\omega\frac{y_i-\epsilon}{\tau}\right)}{\psi\left(\omega\frac{y_i-\epsilon}{\tau}\right)}$ are nonlinear equations, and because of these equations are nonlinear, the calculation of parameters by the (ML) method is considered not has clear solutions in estimating a skew normal distribution [5].

4. Newton Raphson Algorithm (NR)

This method was introduced by Newton and Raphson in 1960, which is used to find a solution for nonlinear functions or equations that are difficult to solve using the traditional method. In our study, we aim to solve nonlinear greatest possibility equations (4-6) and get the best estimate of the distribution parameters based on elementary estimates. An iterative method is used to find the solution (NR) algorithm [8]. The mathematical form of the (NR) algorithm is written in the following rule

$$\hat{\theta}^{(p+1)} = \hat{\theta}^{(p)} - \left(W^{(p)}\right)^{-1} * \ T^{(P)} \ , \ \theta = \left(\epsilon\ , \tau\ , \omega\right) \qquad \ldots (7)$$

p The number of iterations (p = 1,2,3,...)
$\hat{\theta}^{(p)}$and $\hat{\theta}^{(p+1)}$ represent the estimation of the parameters of the maximum likelihood of iteration (p) and the subsequent iteration (p + 1), respectively.
$T^{(P)}$represents the vector of the first derivative of the logarithm of the likelihood

$$T = \frac{\partial LnL}{\partial \theta} = \left(\frac{\partial LnL}{\partial \epsilon} \quad \frac{\partial LnL}{\partial \tau} \quad \frac{\partial LnL}{\partial \omega}\right) \ \ldots (8)$$

$W^{(p)}$represents the second matrix of the logarithm of the likelihood

$$W = \frac{\partial\left(\frac{\partial LnL}{\partial \theta}\right)}{\partial \theta} = \frac{\partial^2 LnL}{\partial \theta \partial \theta} = \begin{bmatrix} \frac{\partial^2 LnL}{\partial \epsilon^2} & \frac{\partial^2 LnL}{\partial \epsilon \partial \tau} & \frac{\partial^2 LnL}{\partial \epsilon \partial \omega} \\ \frac{\partial^2 LnL}{\partial \epsilon \partial \tau} & \frac{\partial^2 LnL}{\partial \tau^2} & \frac{\partial^2 LnL}{\partial \tau \partial \omega} \\ \frac{\partial^2 LnL}{\partial \epsilon \partial \omega} & \frac{\partial^2 LnL}{\partial \tau \partial \omega} & \frac{\partial^2 LnL}{\partial \omega^2} \end{bmatrix} \quad \ldots (9)$$

5. Nelder Mead Algorithm (NM)

It is a numerical algorithm in which geometric relations are used to reach the best minimum of the objective function, and it was formulated by researchers Nelder and Mead in 1965. In previous years, it was used in many practical applications and research for its effectiveness in finding results, its simplicity, as well as its use without needing to derive the function and in many mathematical problems similar to its ability to find solutions when faced nonlinear functions [4].

The basis of the work of the (NM) algorithm is the initial Simplex configuration, since its working mechanism depends on the order of Simplex points ($\lambda_1 \ , \ \lambda_2 , \ . \ . \ . \ , \ \lambda_{n+1}$) in ascending order, and substituting the points in the objective function.The objective function is written as follows [7]:

$$R(\lambda) = -ln\, L(\lambda) \qquad , \ \lambda = (\epsilon\ , \tau\ , \omega) \ldots (10)$$
$$R(\lambda_1) < R(\lambda_2) < \ . \ . \ . \ < R(\lambda_{n+1}) \qquad \ldots (11)$$

Where λ_1 and $R(\lambda_1)$ refer to the best point and the best value of a objective function while λ_{n+1} and $R(\lambda_{n+1})$ refer to the worst point and worst value of the objective function. These points go through a set of processes iteratively (reflection, expansion, contraction and shrink) [7], and in these operations the worst point is replaced by a new point that is better than the previous one, and the process repeated to obtain the best minimum of the objective function that represents the best solution .

6. Iterative Re-Weighting Algorithm (IR)

It is one of the types of function maximization algorithms, and it is used in many previous studies in calculating the capabilities of the maximum potential parameters of the (SND). At the beginning of the work of the algorithm, initial values of the parameters are selected and the nonlinear weight function is updated$W_i^{(p)} = \frac{\emptyset(\omega t_i^{(p)})}{\psi(\omega t_i^{(p)})}$,Where $t_i = \frac{y_i - \epsilon^{(p)}}{\tau^{(p)}}$[5].

Parameter estimates of the SND algorithm are calculated by the following laws [8]:

$$\epsilon^{(P+1)} = \bar{y} - \omega^{(p)}\overline{W}^{(p)}\tau^{(p)} \quad \ldots (12)$$

$$\tau^{(p+1)} = \frac{-\omega^{(p)}(\sum_{i=1}^{n} W_i^{(p)} y_i - n\overline{W}^{(p)}\bar{y}) + \sqrt{(\omega^{(p)}(\sum_{i=1}^{n} W_i^{(p)} y_i - n\overline{W}^{(p)}\bar{y})^2 + 4n\sum_{i=1}^{n}(y_i - \bar{y})^2}}{2n} \quad \ldots (13)$$

$$\omega^{(P+1)} = \frac{\bar{y} - \epsilon^{(P)}}{\tau^{(p)}\overline{W}^{(p)}} \quad \ldots (14)$$

where $\overline{W}$and $\bar{y}$are the mean values of theW and y , respectively.

7. Genetic Algorithm (GA)

It is a randomized research technique based on the mechanism of natural selection and genetics to find the best solution to the problem under study. It was invented and developed by John Holland in 1975. The GA algorithm begins with a randomly selected population of possible solutions and ends with the optimal solution. When applying the algorithm to a problem [1], an appropriate coding method for chromosomes must be determined and the fitness function must be determined.

The genetic algorithm goes through several stages and steps to reach the optimal solution, which will be mentioned as follows [6]:

1- Initialization: It is the process of generating many primary solutions (chromosomes) in a random manner.
2- Fitness function: evaluating the population under study by calculating the value of each chromosome with the evaluation function and the resulting value expresses the efficiency of the chromosome.
3- Selection: choosing the best chromosomes for the formation of the fathers in future generations, based on the evaluation function.
4- Crossover: the mating process that occurs between each parental chromosome that was selected in the selection process to produce offspring.
5- Mutation: random changes in the genes of a chromosome through a change in one or more genes in the son chromosome.
6- Stopping and Termination Criterion: (GA) continues to find the generations sequentially to find the best solution, and (GA) tests whether or not the stopping condition exists according to the nature of the problem studied.

8. Simulation

It is one of the important methods to study many of the approved problems that are difficult for the applied field in the absence of data or difficulty in obtaining [7]. The Monte Carlo simulation method was used to generate random data distributed in (SSND). The genetic algorithm (GA) and iterative algorithms (NR, NM and IR) were used in calculating the capabilities of (ML) parameters and discussing the preference of methods in estimating the model and comparing them.

To observe the effect of the skewness parameter (ω), different values of the parameter (ω = 0, 0.5, 1.5, 2, 3, 4) were taken with different sample sizes (n = 20, 50, 100, 200, 500), noting that when the parameter value is The warp is equal to zero, the shape of the distribution is symmetrical, and when it increases, the warp increases.

The results were compared by extracting the statistical parameters, the mean, the mean square of error (Mse), and the sum of the mean squares of error for the parameters (Def). The smaller the value of (Mse and Def) is better. We note from the simulation results:

1- In Table (1), when ($\epsilon = 0, \tau = 1, \omega = 0$), we find that the mean squares of error (Mse) for the parameter (ϵ) that using the sample size (n = 20, 100, 200), the genomic algorithm (GA) gives less (MSE) then followed by the algorithm (NM) for volumes (n = 50, 500). As for the parameter (τ), (GA) products appear to be the best in small and medium samples and the (IR) algorithm is best in large samples. The superiority of (IR) was observed by estimating the skewness parameter (ω) in all of the samples used.

The results of (Def) for the skew normal distribution model for small and medium samples (n = 20, 50, 100) show that (GA) is better because it has the lowest value for the (Def) criterion. Whereas in large samples (n = 200, 500) the (IR) algorithm was the best because it was the lowest (Def) value.

Table (1) when ($\epsilon = 0$, $\tau = 1$, $\omega = 0$)

		$\hat{\epsilon}$		$\hat{\tau}$		$\widehat{\omega}$		
n	Method	Mean	Mse	Mean	Mse	Mean	Mse	Def
20	NR (ML)	0.000907	0.016885	0.002031	0.388449	0.000149	0.000026	0.405361
	IR (ML)	0.233060	0.006088	0.229789	0.327560	0.023412	0.0000008	0.333649
	NM(ML)	0.849161	0.014617	0.254647	0.375051	1.749167	0.031752	0.421420
	GA (ML)	0.184256	0.001585	0.232137	0.065394	0.244080	0.000492	0.067472
50	NR (ML)	0.000248	0.004389	0.001107	0.259506	0.000041	0.000005	0.263901
	IR (ML)	-0.09086	0.006262	0.290564	0.219475 6	0.011230	0.0000005	0.225738
	NM(ML)	1.242981	0.000059	0.118359	0.337342	0.897434	0.000108	0.337511
	GA (ML)	0.195996	0.000746	0.259290	0.111822	0.264075	0.000617	0.113187
100	NR (ML)	0.146615	0.002395	0.404685	0.279341	0.024490	0.000001	0.281737
	IR (ML)	-0.10374	0.003519	0.242716	0.254315	0.012199	0.000000	0.257835
	NM(ML)	1.185520	0.000697	0.392794	0.345234	1.168907	0.000476	0.346408
	GA (ML)	0.238913	0.000628	0.307702	0.247803	0.327259	0.001002	0.249434
200	NR (ML)	0.072415	0.001055	0.202752	0.246900	0.012229	0.0000002	0.247956
	IR (ML)	-0.24728	0.002498	0.234964	0.230678	0.009886	0.0000001	0.233177
	NM(ML)	1.483016	0.002544	0.707907	0.313142	2.177427	0.003198	0.318885
	GA (ML)	0.233834	0.000510	0.304668	0.451937	0.320435	0.000978	0.453425
500	NR (ML)	0.318354	0.000441	0.733658	0.257269	0.056066	0.0000005	0.257710
	IR (ML)	-0.39392	0.001491	0.213396	0.247683	0.009462	0.0000002	0.249174

	NM(ML)	0.975207	0.000280	1.16408 4	0.322534	1.487698	0.000934	0.323749
	GA (ML)	0.212114	0.000663	0.27459 2	1.224832	0.286128	0.000791	1.226287

2- In Table (2), when (ϵ= 0, τ = 1, ω= 0.5), we note that the (IR) algorithm is superior to other methods for all sample sizes in calculating the parameter estimation (ϵ) because it has less (Mse) than The other methods, as for estimating the parameter (τ), the genetic algorithm was the best for small and medium sample sizes and a clear superior to the (IR) algorithm in large samples. The (IR) algorithm was also the best in most sample sizes in estimating the torsion parameter (ω).

Table (2) when (ϵ =0 , τ =1 , ω = 0.5)

		$\hat{\epsilon}$		$\hat{\tau}$		$\hat{\omega}$		
n	Method	Mean	Mse	Mean	Mse	Mean	Mse	Def
20	NR (ML)	0.070131	0.019180	0.163066	0.388970	0.000824	0.0000001	0.408151
	IR (ML)	0.487136	0.000875	0.260399	0.319772	0.000562	0.000000001	0.320647
	NM(ML)	0.824723	0.017255	0.254647	0.375051	1.785119	0.034470	0.426777
	GA(ML)	0.184553	0.001894	0.232137	0.065394	0.243303	0.000588	0.067877
50	NR (ML)	0.054153	0.005170	0.254554	0.259662	0.000178	0.0000009	0.264832
	IR (ML)	0.400528	0.000232	0.322131	0.215312	0.000040	0.0000004	0.215545
	NM(ML)	1.209863	0.000000	0.118359	0.337342	0.911175	0.000057	0.337400
	GA(ML)	0.196311	0.000977	0.259290	0.111822	0.263397	0.000697	0.113497
100	NR (ML)	0.059119	0.002772	0.166896	0.279382	0.000361	0.0000008	0.282155
	IR (ML)	0.375059	0.000229	0.270832	0.251487	0.000107	0.0000001	0.251716
	NM(ML)	1.165547	0.000491	0.392794	0.345234	1.177778	0.000537	0.346263
	GA(ML)	0.239171	0.000826	0.307702	0.247803	0.326604	0.001065	0.249695
200	NR (ML)	0.105516	0.001231	0.300431	0.246914	0.000234	0.0000002	0.248145
	IR (ML)	0.389489	0.000056	0.260699	0.228934	0.000018	0.0000004	0.228991
	NM(ML)	1.458154	0.002234	0.707907	0.313142	2.222152	0.003293	0.318670
	GA(ML)	0.234021	0.000687	0.304668	0.451937	0.319979	0.001023	0.453648
500	NR (ML)	0.093978	0.000511	0.218503	0.257273	0.000439	0.0000003	0.257784

	IR (ML)	0.324833	0.000065	0.237638	0.246605	0.000050	0.000000019	0.246670
	NM(ML)	0.946686	0.000353	1.164084	0.322534	1.492792	0.000953	0.323841
	GA(ML)	0.212209	0.000862	0.274592	1.224832	0.285900	0.000816	1.226511

3- In Table (3), when (ϵ= 0, τ = 1, ω = 1.5), results of (Mse) appear for the parameter (ϵ) when using the sample sizes (n = 20, 100, 200) given (GA) The lowest value and the better (NM) algorithm for samples (n = 50, 500). In parameter (τ), the (GA) algorithm outperformed all other methods. While the (IR) algorithm got the least (Mse) in large sample size, and the (NR) algorithm in large samples in the calculation of parameter estimation (ω).

As can be seen, (GA) is superior in small and medium samples of the sum of the mean square error (Def) of the distribution parameters, and the (IR) algorithm is the best when using large samples.

Table (3) when (ε =0 , τ =1 , ω = 1.5)

		$\hat{\epsilon}$		$\hat{\tau}$		$\hat{\omega}$		
N	Method	Mean	Mse	Mean	Mse	Mean	Mse	Def
20	NR(ML)	0.003041	0.014081	0.006488	0.387208	0.001867	0.000285	0.401575
	IR (ML)	0.093807	0.009676	0.189816	0.337871	0.127456	0.000125	0.347673
	NM (ML)	0.882136	0.011528	0.254647	0.375051	1.667478	0.025463	0.412043
	GA (ML)	0.183524	0.001229	0.232137	0.065394	0.246020	0.000290	0.066914
50	NR (ML)	0.000821	0.003441	0.003418	0.259173	0.000528	0.000059	0.262674
	IR (ML)	-0.334597	0.011257	0.246270	0.225384	0.061245	0.000000	0.236642
	NM (ML)	1.243161	0.000335	0.118359	0.337342	0.866680	0.000290	0.337969
	GA (ML)	0.195269	0.000488	0.259290	0.111822	0.265653	0.000449	0.112761
100	NR (ML)	0.000479	0.001943	0.001286	0.279248	0.000302	0.000012	0.281204
	IR (ML)	-0.35874	0.006400	0.203107	0.258325	0.066639	0.000009	0.264736
	NM (ML)	1.212432	0.001020	0.392794	0.345234	1.148462	0.000346	0.346601
	GA (ML)	0.238312	0.000412	0.307702	0.247803	0.328794	0.000860	0.249077
200	NR (ML)	0.240729	0.000841	0.659226	0.246868	0.158672	0.000003	0.247712
	IR (ML)	-0.57393	0.004844	0.198027	0.233194	0.055950	0.000004	0.238043
	NM (ML)	1.517825	0.002992	0.707907	0.313142	2.090984	0.002981	0.319116

	GA (ML)	0.233396	0.000313	0.304668	0.451937	0.321503	0.000875	0.453126
500	NR (ML)	0.104202	0.000355	0.237379	0.257262	0.070611	0.000000	0.257618
	IR (ML)	-0.78845	0.002930	0.178688	0.249230	0.053079	0.000002	0.252163
	NM (ML)	1.015022	0.000197	1.164084	0.322534	1.475924	0.000890	0.323622
	GA (ML)	0.211895	0.000441	0.274592	1.224832	0.286661	0.000733	1.226007

4- In Table (4), when (ϵ= 0, τ = 1, ω= 2) with respect to (Mse), (GA) gives the best estimate for the parameter (ϵ) in most sample sizes and the average sample size for the parameter (τ) We note also that in the calculation of the parameter estimation (ω), (IR) gave the least output in terms of (Mse) for small and medium sample size and (NR) the best in using a large sample.

The results of (Def) for the total (Mse) of the model parameters showed that (GA) was the best in the small and medium sample sizes, while (IR) was the best in the large-sized samples.

Table (4) when (ϵ=0 , τ =1 , ω = 2)

		$\hat{\epsilon}$		$\hat{\tau}$		$\widehat{\omega}$		
N	Method	Mean	Mse	Mean	Mse	Mean	Mse	Def
20	NR (ML)	0.003316	0.013959	0.007061	0.007061	0.002231	0.002231	0.401344
	IR (ML)	0.091815	0.009674	0.184248	0.339320	0.143655	0.000175	0.349170
	NM (ML)	0.883569	0.011405	0.254647	0.375051	1.657697	0.024708	0.411165
	GA (ML)	0.183431	0.001215	0.232137	0.065394	0.246268	0.000267	0.066878
50	NR (ML)	0.000909	0.003373	0.003766	0.259123	0.000655	0.000072	0.262569
	IR (ML)	-0.34539	0.011461	0.239420	0.226305	0.070619	0.000001	0.237768
	NM (ML)	1.246473	0.000365	0.118359	0.337342	0.862116	0.000326	0.338035
	GA (ML)	0.195159	0.000471	0.259290	0.111822	0.265894	0.000426	0.112720
100	NR (ML)	0.000528	0.001916	0.001414	0.279234	0.000370	0.000015	0.281166
	IR (ML)	-0.36777	0.006497	0.197035	0.258943	0.076428	0.000013	0.265454
	NM (ML)	1.214141	0.001042	0.392794	0.345234	1.145518	0.000328	0.346605
	GA (ML)	0.238225	0.000401	0.307702	0.247803	0.329018	0.000841	0.249045
200	NR (ML)	0.267190	0.000825	0.730450	0.246863	0.198158	0.000004	0.247692

	IR (ML)	-0.59017	0.004967	0.192246	0.233589	0.064924	0.000006	0.238563
	NM (ML)	1.520589	0.003028	0.707907	0.313142	2.079107	0.002948	0.319119
	GA (ML)	0.233328	0.000300	0.304668	0.451937	0.321671	0.000859	0.453097
500	NR (ML)	0.115252	0.000350	0.262340	0.257261	0.087458	0.000001	0.257612
	IR (ML)	-0.80667	0.003002	0.173303	0.249470	0.0613751	0.000004	0.252477
	NM (ML)	1.017913	0.000192	1.164084	0.322534	1.474142	0.000883	0.323610
	GA (ML)	0.211862	0.000427	0.274592	1.224832	0.286742	0.000724	1.225984

5- In Table (5), when (ϵ = 0, τ = 1, ω = 5) the results of (Mse) appear for the parameter (ϵ) that the algorithm (GA) and (NM) are the best, and it was noticed that in the parameter (τ) the (GA) was the best in medium sample and the (IR) algorithm was best in large samples for the parameter (τ), also in calculating the shape parameter estimator (ω) in small and medium samples, and the (NR) algorithm was the best in large samples.

As usual, (GA) was the best at sample size (n = 20,50,100) to estimate all model parameters because it gave less (Def) and (IR) was the best in large samples.

Table (5) when (ϵ=0 , τ =1 , ω = 5)

		$\hat{\epsilon}$		$\hat{\tau}$		$\widehat{\omega}$		
n	Method	Mean	Mse	Mean	Mse	Mean	Mse	Def
20	NR (ML)	0.003316	0.013959	0.007061	0.007061	0.002231	0.002231	0.401344
	IR (ML)	0.091815	0.009674	0.184248	0.339320	0.143655	0.000175	0.349170
	NM (ML)	0.883569	0.011405	0.254647	0.375051	1.657697	0.024708	0.411165
	GA (ML)	0.183431	0.001215	0.232137	0.065394	0.246268	0.000267	0.066878
50	NR (ML)	0.000909	0.003373	0.003766	0.259123	0.000655	0.000072	0.262569
	IR (ML)	-0.34539	0.011461	0.239420	0.226305	0.070619	0.000001	0.237768
	NM (ML)	1.246473	0.000365	0.118359	0.337342	0.862116	0.000326	0.338035
	GA (ML)	0.195159	0.000471	0.259290	0.111822	0.265894	0.000426	0.112720
100	NR (ML)	0.000528	0.001916	0.001414	0.279234	0.000370	0.000015	0.281166
	IR (ML)	-0.36777	0.006497	0.197035	0.258943	0.076428	0.000013	0.265454
	NM (ML)	1.214141	0.001042	0.392794	0.345234	1.145518	0.000328	0.346605
	GA (ML)	0.238225	0.000401	0.307702	0.247803	0.329018	0.000841	0.249045

200	NR (ML)	0.267190	0.000825	0.730450	0.246863	0.198158	0.000004	0.247692
	IR (ML)	-0.59017	0.004967	0.192246	0.233589	0.064924	0.000006	0.238563
	NM (ML)	1.520589	0.003028	0.707907	0.313142	2.079107	0.002948	0.319119
	GA (ML)	0.233328	0.000300	0.304668	0.451937	0.321671	0.000859	0.453097
500	NR (ML)	0.115252	0.000350	0.262340	0.257261	0.087458	0.000001	0.257612
	IR (ML)	-0.80667	0.003002	0.173303	0.249470	0.0613751	0.000004	0.252477
	NM (ML)	1.017913	0.000192	1.164084	0.322534	1.474142	0.000883	0.323610
	GA (ML)	0.211862	0.000427	0.274592	1.224832	0.286742	0.000724	1.225984

6- In Table (6), when (ϵ= 0, τ = 1, ω = 4), we note the superiority of (GA) in terms of (Mse) in most sample sizes of parameter (ϵ) and it was also the best in small and medium-sized samples in Calculation of parameter estimation (τ) and (IR) is better in large samples of parameter (τ) and in small and medium sample sizes of skewness parameter (ω). While (NR) got less (Mse) when the sample size (n = 200,500) for parameter (ω).

The (Def) results like the previous ones showed that (GA) is the best among other methods for model estimation at sample size (n = 20,50,100), while (IR) is better when using large data.

Table (6) when (ϵ=0 , τ =1 , ω = 4)

		$\hat{\epsilon}$		$\hat{\tau}$		$\hat{\omega}$		
n	Method	Mean	Mse	Mean	Mse	Mean	Mse	Def
20	NR (ML)	0.003310	0.014444	0.007112	0.387034	0.002175	0.000337	0.401816
	IR (ML)	0.119808	0.008861	0.174528	0.341857	0.143722	0.000175	0.350894
	NM (ML)	0.877211	0.011957	0.254647	0.375051	1.657658	0.024705	0.411714
	GA (ML)	0.183430	0.001280	0.232137	0.065394	0.246269	0.000267	0.066942
50	NR (ML)	0.000973	0.003447	0.004053	0.259082	0.000740	0.000082	0.262612
	IR (ML)	-0.31990	0.010835	0.226033	0.228109	0.077698	0.000003	0.238948
	NM (ML)	1.242748	0.000331	0.118359	0.337342	0.858801	0.000354	0.338028
	GA (ML)	0.195079	0.000491	0.259290	0.111822	0.266070	0.000409	0.112724
100	NR (ML)	0.000548	0.001978	0.001475	0.279228	0.000390	0.000016	0.281223
	IR (ML)	-0.32882	0.005994	0.185446	0.260124	0.080756	0.000015	0.266134

	NM (ML)	1.210116	0.000991	0.392794	0.345234	1.144254	0.000321	0.346546
	GA (ML)	0.238188	0.000430	0.307702	0.247803	0.329114	0.000832	0.249066
200	NR (ML)	0.285316	0.000844	0.781672	0.246859	0.222111	0.000004	0.247708
	IR (ML)	-0.55586	0.004677	0.181014	0.234357	0.071326	0.000008	0.239043
	NM (ML)	1.517109	0.002982	0.707907	0.313142	2.071133	0.002925	0.319050
	GA (ML)	0.233281	0.000317	0.304668	0.451937	0.321786	0.000849	0.453103
500	NR (ML)	0.121373	0.000360	0.276677	0.257260	0.094852	0.0000006	0.257621
	IR (ML)	-0.75710	0.002793	0.162985	0.249932	0.06615	0.000004	0.252729
	NM (ML)	1.01269	0.000202	1.164084	0.322534	1.473151	0.00088	0.323616
	GA (ML)	0.211844	0.000453	0.274592	1.224832	0.286787	0.00072	1.226005

9. Conclusions

The ML results of the (SND) parameters were improved by employing the genetic algorithm (GA) and iterative methods (NR, NM and IR) by extracting the results from the simulation experiment and then analysing the results so, the following conclusions were reached:

1- The results of the genetic algorithm (GA) in estimating the model is superior to the skew normal distribution (SND) at the sample sizes (n = 20, 50, 100) because it has the lowest (Def) value among the methods used regardless of the skewness value.
2- The results of the iterative re-weighting algorithm (IR) of the model were superior to the sample sizes (n = 200, 500) for having the lowest value of the (Def) criterion among the methods used.
3- We note that the (GA) genetic algorithm was the best in most cases when calculating the estimation of the location parameter (ϵ) at the sample size (n = 20, 100, 200) and the (NR) algorithm was better when the sample size (n = 20, 100, 200) and The (IR) algorithm has a clear advantage when the torsion size is very slight.
4- We found that when calculating the estimator of the measurement parameter (τ), it exceeds (GA) at sample sizes (n = 20, 50, 100), and the higher the sample size, the better the (IR) algorithm because it has less (Mse).
5- When calculating the estimator of the shape parameter (ω), we concluded that at small and medium sample sizes (n = 20, 50, 100) the (IR) algorithm was the best, but for large sample sizes the (NR) algorithm was better in calculating the capabilities of the parameter (ω).

References

[1] Al-Douri Y, Hamodi H and Lundberg J 2020 Risk-based life cycle cost analysis using a two-level multi-objective genetic algorithm *International Journal Of Computer Integrated Manufacturing*
[2] Ashour S, Abdel-hameed M 2010 Approximate skew normal distribution *Journal of Advanced Research* **1** 341–350
[3] AZZALINI A 1985 A Class of Distributions which Includes the Normal Ones *Scand J Statist* **12** 171-178

[4] Barati R 2011 Parameter Estimation of Nonlinear Muskingum Models Using Nelder-Mead Simplex Algorithm *Journal Of Hydrologic Engineering*
[5] Celik N, Senoglu B and Arslan O 2015 Estimation and Testing in One-Way ANOVA when the Errors are Skew-Normal *RevistaColombiana de Estadística* Vol **38** Issue 1 pp 75-91
[6] Elvira O, Jaen C, Morinigo S, Morales Velazquez, Osornio R and Romero T 2020 Genetic Algorithm Methodology for the Estimation of Generated Power and Harmonic Content in Photovoltaic Generation *Appl. Sci* **10** 542
[7] Kılıç M 2020 Using Genetic Algorithms for Parameter Estimation of a Two-Component Circular Mixture Model *H. Dutta et al AISC **1111*** pp 99–110
[8] Yalçınkaya A, Şenogˇlu B And Yolcu U 2017 Maximum Likelihood Estimation For The Parameters Of Skew Normal Distribution Using Genetic Algorithm *Swarm and Evolutionary Computation*

Simultaneous Approximation by Modification of Classical Szãsz Operators with Parameter *s*

Simultaneous Approximation by Modification of Classical Szãsz Operators with Parameter s

Ali J. Mohammed , T.A. Abdul-Qader and S. A. Abdul-Hammed

Department of Mathematics, College of Education of Pure Sciences, Basrah University, Basrah, Iraq

E-mail: tahini.qader@gmail.com

Abstract. This paper is approving the simultaneous approximation order by a modification family of the classical sequence of Szãsz operators. This modification depends on a real parameter $s > -1/2$. First, we show that this family (or its derivatives) converges to the function (or the corresponding derivatives) being approximated. Next, a Voronovski-type asymptotic formula for this family is given. The order of this approximation is improved from the order $O(n^{-1})$ (the order of the classical sequence) to the order $O\left(n^{-(2s+1)}\right)$ whenever $s > 0$. Finally, the study supports by some numerical examples and discusses the results obtained.

1. Introduction

In [2] Bernstein defined a sequence of positive linear operators as:

$$B_n(f;x) = \sum_{k=0}^{n} \binom{n}{k} x^k (1-x)^{n-k} f\left(\frac{k}{n}\right), \qquad x \in [0,\infty) \tag{1.1}$$

where $f \in C[0,1]$.

In [9] Szãsz generalized the Bernstein sequence to the unbounded interval $[0,\infty)$ as

$$S_n(f(t);x) = \sum_{k=0}^{\infty} q_{n,k}(x)\, f\left(\frac{k}{n}\right), \tag{1.2}$$

where $q_{n,k}(x) = \frac{(nx)^k}{k!e^{nx}}$, $x \in [0,\infty)$ and $f \in C_\alpha[0,\infty) = \{f \in C[0,\infty): |f(t)| \le Ae^{\alpha t} \text{ for some } A, \alpha > 0\}$.

The sequence $S_n(f(t);x)$ is said to be the classical Szãsz sequence.

Several modifications of the Szãsz sequence were constructed and studied. All of them have the same order $O(n^{-1})$, here we refer to [1], [7], [10] and [11].

Some techniques got a better approximation order by the sequences of positive linear operators introduced and studied [6] and [3].

In [8], Pallini modified the Bernstein sequence by using the parameter s, where $s > -1/2$, as follows

$$B_{n,s}(f;x)=\sum_{k=0}^{n}\binom{n}{k}x^k(1-x)^{n-k}f\left(x+\frac{1}{n^s}\left(\frac{k}{n}-x\right)\right),x\in[0,\infty). \tag{1.3}$$

Clearly, $B_{n,0}(f;x)=B_n(f;x)$. Pallini showed that the order of this approximation is $O\left(n^{-(2s+1)}\right)$ and this order is better than the classical order $O(n^{-1})$ whenever $s>0$.
This paper using the same structure as Pallini and introduce a modification family of the classical Szãsz sequence as follows:
Suppose that $f\in C_\alpha[0,\infty)$, the definition of the modification is given as

$$M_{n,s}(f(t);x)=\sum_{k=0}^{\infty}q_{n,k}(x)\,f\left(x+\frac{1}{n^s}\left(\frac{k}{n}-x\right)\right). \tag{1.4}$$

Clearly, $M_{n,0}(f;x)=S_n(f;x)$.

The convergence theorem of the sequence $M_{n,s}(f(t);x)$ in the simultaneous approximation is studied and the Voronovski-type asymptotic formula for $M_{n,s}(f(t);x)$ is introduced. It turns out that the sequence $M_{n,s}(f;x)$ has a better order $(O\left(n^{-(2s+1)}\right))$ than the order $O(n^{-1})$ of the classical sequence $S_n(f;x)$ whenever $s>0$. This study supported with a numerical example to show the better approximation by this sequence to a chosen test function $f(x)=\sin(7x)$, $x\in[0,5]$ and discuss the results obtained.■

2. Auxiliary Results

Here, some help preliminaries results are introduced to reach the goal of this paper.
This section will introduce some necessary lemmas, where we will need to prove our main results.

Lemma 2.1 [10]
For $x\in[0,\infty),m\in\mathbb{N}$, we have:
(1) $\sum_{k=0}^{\infty}q_{n,k}(x)=1;$
(2) $\sum_{k=0}^{\infty}kq_{n,k}(x)=nx;$
(3) $\sum_{k=0}^{\infty}k^2q_{n,k}(x)=n^2x^2+nx;$
(4) $xq'_{n,k}(x)=(k-nx)q_{n,k}(x);$
(5) Suppose that $\Phi_{n,m}(x)=\sum_{k=0}^{\infty}k^mq_{n,k}(x)$ then $\Phi_{n,m+1}(x)=x\Phi'_{n,m}(x)+nx\Phi_{n,m}(x)$ and

$$\Phi_{n,m}(x)=(nx)^m+\frac{m(m-1)}{2}(nx)^{m-1}+\text{terms in lower powers of }x.$$

Lemma 2.2
For $x\in[0,\infty)$, the following conditions hold:
(1) $M_{n,s}(1;x)=1;$
(2) $M_{n,s}(t;x)=x;$
(3) $M_{n,s}(t^2;x)=x^2+\frac{x}{n^{2s+1}}.$

Proof
By using Lemma 2.1 and the direct computation, the proof easily follows.
Note that by Korovkin's theorem, one has $M_{n,s}(f;x)\to f(x)$ as $n\to\infty$. (see [5])

For $m \in \mathbb{N}$, the m-th order moment $\mu_{n,m}(x)$ of the classical Szãsz sequence $S_n(.;x)$ is defined as:

$$\mu_{n,m}(x) = S_n((t-x)^m;x) = \sum_{k=0}^{\infty} q_{n,k}(x)\left(\frac{k}{n}-x\right)^m.$$

Lemma 2.3 [9]
The moment $\mu_{n,m}(x)$ has the following
$\mu_{n,0}(x) = 1, \mu_{n,1}(x) = 0, \mu_{n,2}(x) = \frac{x}{n}$ and $n\mu_{n,m+1}(x) = x\mu'_{n,m}(x) + mx\mu_{n,m-1}(x), m \geq 1.$
Further,

(1) $\mu_{n,m}(x)$ is a polynomial in x of degree $\leq m$.
(2) For every $x \in [0,\infty), \mu_{n,m}(x) = O\left(n^{-\left[\frac{m+1}{2}\right]}\right)$.

For $m \in \mathbb{N}$, the m-th order moment $T_{n,m}(x)$ of $M_{n,s}(.;x)$ is defined as:

$$T_{n,m}(x) = M_{n,s}((t-x)^m;x) = \frac{1}{n^{sm}}\sum_{k=0}^{\infty} q_{n,k}(x)\left(\frac{k}{n}-x\right)^m.$$

Lemma 2.4
The moment $T_{n,m}(x)$ has
$T_{n,0}(x) = 1, T_{n,1}(x) = 0, T_{n,2}(x) = \frac{x}{n^{2s+1}}$ and $n^{s+1}T_{n,m+1}(x) = xT'_{n,m}(x) + \frac{mx}{n^s}T_{n,m-1}(x)$, $m \geq 1$

Proof
From Lemma 2.1, we have

$$T'_{n,m}(x) = \frac{1}{n^{sm}}\sum_{k=0}^{\infty} q'_{n,m}(x)\left(\frac{k}{n}-x\right)^m - \frac{m}{n^s}T_{n,m-1}(x)$$

then,

$$x\left[T'_{n,m}(x) + \frac{m}{n^s}T_{n,m-1}(x)\right] = \frac{1}{n^{sm}}\sum_{k=0}^{\infty}(k-nx)q_{n,k}(x)\left(\frac{k}{n}-x\right)^m$$

hence,
$n^{s+1}T_{n,m+1}(x) = xT'_{n,m}(x) + \frac{mx}{n^s}T_{n,m-1}(x), m \geq 1.$

Lemma 2.5
For $m \geq 1$, we have:

$$M_{n,s}(t^m;x) = x^m + \frac{x^{m-1}}{n^{sm}}\left\{\sum_{i=2}^{m}\binom{m}{i}(n^s-1)^{m-i}\frac{i(i-1)}{2n}\right\}.$$

Proof
By using Lemma 2.1(5), we have

$$M_{n,s}(t^m;x) = \sum_{k=0}^{\infty} q_{n,k}(x)\left(x + \frac{\frac{k}{n}-x}{n^s}\right)^m$$
$$= \frac{1}{n^{sm}}\sum_{k=0}^{\infty} q_{n,k}(x)\left((n^s-1)x + \frac{k}{n}\right)^m$$

$$= \frac{1}{n^{sm}} \sum_{k=0}^{\infty} q_{n,k}(x) \left\{ (n^s-1)^m x^m + \binom{m}{1} (n^s-1)^{m-1} x^{m-1} \frac{k}{n} + \binom{m}{2} (n^s-1)^{m-2} x^{m-2} \frac{k^2}{n^2} + \cdots + \binom{m}{m-1} (n^s-1) x \frac{k^{m-1}}{n^{m-1}} + \frac{k^m}{n^m} \right\}$$

$$= \frac{1}{n^{sm}} \left\{ (n^s-1)^m x^m + \binom{m}{1} (n^s-1)^{m-1} x^{m-1} \frac{nx}{n} + \binom{m}{2} (n^s-1)^{m-2} x^{m-2} \frac{(nx)^2+nx}{n^2} + \cdots + \binom{m}{m-1} (n^s-1) x \left(\frac{(nx)^{m-1}}{n^{m-1}} + \frac{(m-1)(m-2)}{2n^{m-1}} (nx)^{m-2} \right) + \left(\frac{(nx)^m}{n^m} + \frac{m(m-1)}{2n^m} (nx)^{m-1} \right) \right\}$$

$$= \frac{x^m}{n^{sm}} \left\{ (n^s-1)^m + \binom{m}{1} (n^s-1)^{m-1} + \binom{m}{2} (n^s-1)^{m-2} + \cdots + \binom{m}{m-1} (n^s-1) + 1 \right\} + \frac{x^{m-1}}{n^{sm}} \left\{ \binom{m}{2} (n^s-1)^{m-2} \frac{1}{n} + \cdots + \binom{m}{m-1} (n^s-1) \frac{(m-1)(m-2)}{2n} + \frac{m(m-1)}{2n} \right\}$$

$$= x^m + \frac{x^{m-1}}{n^{sm}} \left\{ \sum_{i=2}^{m} \binom{m}{i} (n^s-1)^{m-i} \frac{i(i-1)}{2n} \right\}.$$

Lemma 2.6 [4]
There exist the polynomials $Q_{i,j,r}(x)$ independent of n and k such that

$$x^r q_{n,k}^{(r)} = \sum_{\substack{2i+j \le r \\ i,j \ge 0}} n^i (k-nx)^j Q_{i,j,r}(x) q_{n,k}(x)$$

3. Main results

This section introduces two theorems. The first theorem proves that the derivatives of $M_{n,s}(f;x)$ is an approximation for the corresponding derivative of f. The second theorem gives a Voronovski-type asymptotic formula for the sequence $M_{n,s}^{(r)}(f;x)$, $r = 0,1,2, \ldots$.

Theorem 3.1
Suppose that $r \in N, f \in C_\alpha[0,\infty)$for some $\alpha > 0$ and $f^{(r)}(x)$ exists a point $x \in (0,\infty)$, then
$\lim_{n\to\infty} M_{n,s}^{(r)}(f(t);x) = f^{(r)}(x)$

Proof
Using Taylor's expansion of f at x, we have

$$f(t) = \sum_{i=0}^{r} \frac{f^{(i)}(x)}{i!} (t-x)^i + \varepsilon(t,x)(t-x)^r$$

where $\varepsilon(t,x) \to 0$ as $t \to x$.
Then,

$$M_{n,s}^{(r)}(f(t);x) = \sum_{i=0}^{r} \frac{f^{(i)}(x)}{i!} M_{n,s}^{(r)}\left((t-x)^i;x\right) + M_{n,s}^{(r)}(\varepsilon(t,x)(t-x)^r;x) := E_1 + E_2.$$

From Lemmas 2.4 and 2.5

$$E_1 = \frac{f^{(r)}(x)}{r!}\sum_{j=0}^{r}\binom{r}{j}(-x)^{r-j}M_{n,s}^{(r)}(t^j;x)$$

$$= \frac{f^{(i)}(x)}{r!}\frac{d^r}{dx^r}\left[x^r + \frac{x^{m-1}}{n^{sm}}\left\{\sum_{i=2}^{m}\binom{m}{i}(n^s-1)^{m-i}\frac{i(i-1)}{2n}\right\}\right] = f^{(r)}(x).$$

Now, using Lemma 2.6, the estimate of E_2 is going as follows:

$$E_2 = M_{n,s}^{(r)}(\varepsilon(t,x)(t-x)^r;x)$$

$$= \sum_{k=0}^{\infty} q_{n,k}^{(r)}(x)\varepsilon\left(x + \frac{\left(\frac{k}{n}-x\right)}{n^s}, x\right)\left(\frac{\left(\frac{k}{n}-x\right)}{n^s}\right)^r$$

$$= \sum_{\substack{2i+j\le r\\ i,j\ge 0}} n^i \frac{Q_{i,j,r}(x)}{x^r}\sum_{k=0}^{\infty} q_{n,k}(x)(k-nx)^j \varepsilon\left(x + \frac{\left(\frac{k}{n}-x\right)}{n^s}, x\right)\frac{\left(\frac{k}{n}-x\right)^r}{n^{rs}}$$

$$|E_2| \le \sum_{\substack{2i+j\le r\\ i,j\ge 0}} \frac{n^{i+j}}{n^{rs}}\frac{|Q_{i,j,r}(x)|}{x^r}\sum_{k=0}^{\infty} q_{n,k}(x)\left|\frac{k}{n}-x\right|^{j+r}\left|\varepsilon\left(x + \frac{\left(\frac{k}{n}-x\right)}{n^s};x\right)\right|.$$

Let $\sup_{\substack{2i+j\le r\\ i,j\ge 0}} \frac{|Q_{i,j,r}(x)|}{x^r} = M(x) = M,$

$$|E_2| \le \frac{\varepsilon M}{n^{rs}}\sum_{\substack{2i+j\le r\\ i,j\ge 0}} n^{i+j}\sum_{k=0}^{\infty} q_{n,k}(x)\left|\frac{k}{n}-x\right|^{j+r}$$

Since $\varepsilon\left(x + \frac{\left(\frac{k}{n}-x\right)}{n^s};x\right) \to \varepsilon$ as $\frac{k}{n} \to x$. Now, using Schwarz inequality for summation and from Lemma 2.3, we get

$$|E_2| \le \frac{\varepsilon M}{n^{rs}}\sum_{\substack{2i+j\le r\\ i,j\ge 0}} n^{i+j}\left[\sum_{k=0}^{\infty} q_{n,k}(x)\left(\frac{k}{n}-x\right)^{2(j+r)}\right]^{\frac{1}{2}}\left[\sum_{k=0}^{\infty} q_{n,k}(x)\right]^{\frac{1}{2}}$$

$$|E_2| \le \frac{\varepsilon M}{n^{rs}}\sum_{\substack{2i+j\le r\\ i,j\ge 0}} n^{i+j}\, O\left(n^{\frac{-(j+r)}{2}}\right) = \frac{\varepsilon M}{n^{rs}}O(1) \to 0 \text{ as } n \to \infty.$$

Then

$$\lim_{n\to\infty} M_{n,s}^{(r)}(f(t);x) = f^{(r)}(x)$$

Theorem 3.2

Let $f \in C_\alpha[0,\infty)$ for some $\alpha > 0$. If $f^{(r+2)}$ exists and is continuous at a point $x \in (0,\infty)$, then

$$\lim_{n\to\infty} n^{2s+1}\left(M_{n,s}^{(r)}(f(t);x) - f^{(r)}(x)\right) = \frac{r}{2}f^{(r+1)}(x) + \frac{x}{2}f^{(r+2)}(x).$$

Proof

By Taylor's expansion of f, we have

$$f(t) = \sum_{i=0}^{r+2}\frac{f^{(i)}(x)}{i!}(t-x)^i + \varepsilon(t,x)(t-x)^{r+2},$$

where $\varepsilon(t,x) \to 0$ as $t \to x$.
Then

$$M_{n,s}^{(r)}(f(t);x) = \sum_{i=0}^{r+2} \frac{f^{(i)}(x)}{i!} M_{n,s}^{(r)}\left((t-x)^i;x\right) + M_{n,s}^{(r)}(\varepsilon(t,x)(t-x)^{r+2};x)$$
$$:= I_1 + I_2$$
$$I_1 = \sum_{i=0}^{r+2} \frac{f^{(i)}(x)}{i!} M_{n,s}^{(r)}\left((t-x)^i;x\right)$$
$$= \sum_{i=r}^{r+2} \frac{f^{(i)}(x)}{i!} \sum_{j=0}^{i} \binom{i}{j} (-x)^{i-j} M_{n,s}^{(r)}\left(t^j;x\right)$$
$$= \sum_{i=r}^{r+2} \frac{f^{(i)}(x)}{i!} \sum_{j=r}^{i} \binom{i}{j} (-x)^{i-j} M_{n,s}^{(r)}\left(t^j;x\right)$$
$$= \frac{f^{(r)}(x)}{r!}[r!] + \frac{f^{(r+1)}(x)}{(r+1)!}\Bigg[(r+1)(-x)r! + (r+1)!\,x + \frac{r!}{2n^{s(r+1)+1}} \sum_{i=2}^{r+1} \binom{r+1}{i} (n^s-1)^{r+1-i} i(i-1)\Bigg]$$
$$+ \frac{f^{(r+2)}(x)}{(r+2)!}\Bigg[\frac{(r+2)(r+1)}{2}(-x)^2 r! + (r+2)(-x)\left\{(r+1)!\,x + \frac{r!}{2n^{s(r+1)+1}} \sum_{i=2}^{r+1} \binom{r+1}{i} (n^s-1)^{r+1-i} i(i-1)\right\}$$
$$+ \frac{(r+2)!}{2}x^2 + \frac{(r+1)!\,x}{2n^{s(r+2)+1}} \sum_{i=2}^{r+2} \binom{r+2}{i} (n^s-1)^{r+2-i} i(i-1)\Bigg]$$
$$= f^{(r)}(x) + \frac{f^{(r+1)}(x)}{2n^{s(r+1)+1}} \sum_{i=2}^{r+1} \binom{r+1}{i} (n^s-1)^{r+1-i} i(i-1)$$
$$+ \frac{f^{(r+2)}(x)}{2}\Bigg[\frac{-x}{n^{s(r+1)+1}(r+1)} \sum_{i=2}^{r+1} \binom{r+1}{i} (n^s-1)^{r+1-i} i(i-1) + \frac{x}{n^{s(r+2)+1}(r+2)} \sum_{i=2}^{r+2} \binom{r+2}{i} (n^s-1)^{r+2-i} i(i-1)\Bigg]$$
$$n^{2s+1}\left(M_{n,s}^{(r)}(f(t);x) - f^{(r)}(x)\right)$$
$$= \frac{n^{2s+1} f^{(r+1)}(x)}{2(r+1)n^{s(r+1)+1}}\left[r(r+1)(n^s-1)^{r-1} + \sum_{i=3}^{r+1} \binom{r+1}{i} (n^s-1)^{r+1-i} i(i-1)\right] + \frac{n^{2s+1} f^{(r+2)}(x)}{2}$$

By using the same technique of Theorem 3.1, we get
$I_2 \to 0 \quad as \quad n \to \infty$.
Then

$$\lim_{n\to\infty} n^{2s+1}\left(M_{n,s}^{(r)}(f(t);x) - f^{(r)}(x)\right) = \frac{r}{2}f^{(r+1)}(x) + \frac{x}{2}f^{(r+2)}(x).$$

4. Numerical example

This part shows that, by a numerical example, the approximation by the sequence $M_{n,s}(f;x)$ is better than the approximation by the classical sequence $S_n(f;x)$ whenever $s > 0$. The choice test function here is $f(x) = \sin(7x), x \in [0,5]$.

Example

We apply the sequence $M_{n,s}(f(t);x)$ for $n = 10,20,30,40$ and $s = 0,1,1.5,2$ to approximate the function $f(x) = \sin(7x), x \in [0,5]$. We describe the cases by graphing the test function and its approximations as follows

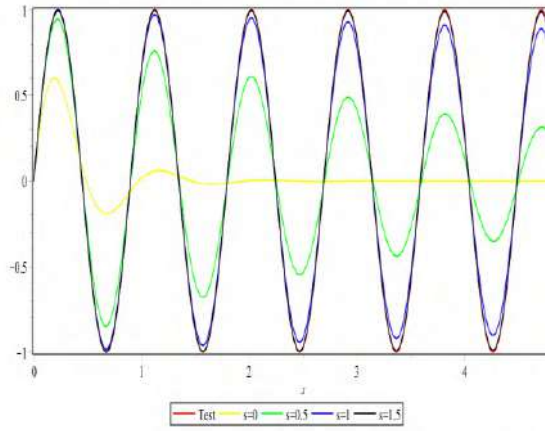

Fig. 4.1 (n=10)

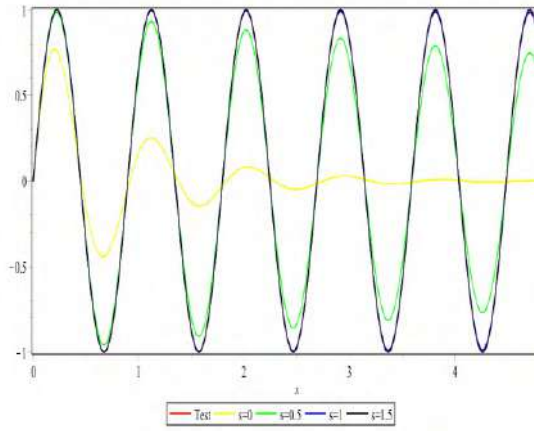

Fig. 4.2 (n=20)

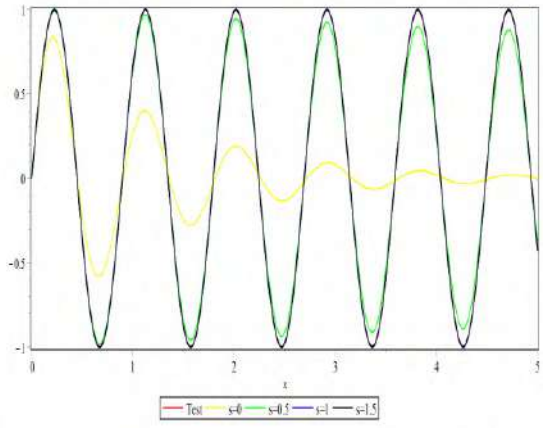

Fig. 4.3 (n=30)

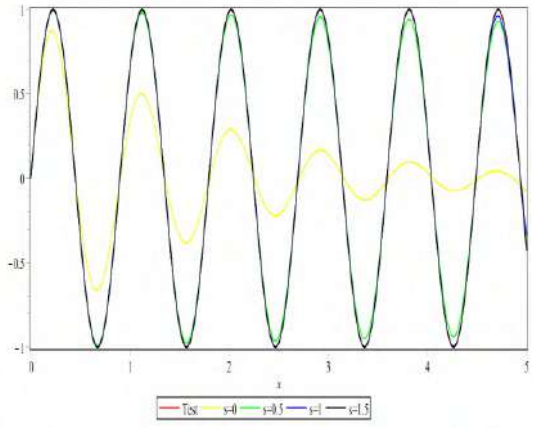

Fig. 4.4 (n=40)

5. Conclusion

From the above numerical example for the sequence $M_{n,s}(f;x)$, one has that, the numerical results are faster and more accurate than the sequence $S_n(f(t);x)$, whenever $s > 0$. Also, these properties are increasing whenever $s > 0$.

References

[1] Atakut, Çiğdem, and İbrahim Büyükyazıcı 2016 Approximation by Kantorovich-Szász type operators based on Brenke type polynomials *Numerical Functional Analysis and Optimization* **37(12)** 1488-1502

[2] Bernstein 1912 Serge Démo istration du th'eorème de Weierstrass fondée sur le calcul des probabilités *Сообщенія Харьковскаго математическаго общества* **13(1)** 1-2.

[3] Han, Ling-Xiong, Bai-Ni Guo, and Feng Qi. 2019 Equivalent theorem of approximation by linear combination of weighted Baskakov–Kantorovich operators in Orlicz spaces *Journal of Inequalities and Applications* **1** 223

[4] Kasana, H. S., et al. 1988 Modified Szâsz operators *Mathematical Analysis and its Applications. Pergamon* 29-41

[5] Korovin, P. P. 1960 Linear operators and approximation theory

[6] May, C. P. 1976 Saturation and inverse theorems for combinations of a class of exponential-type operators *Canadian Journal of Mathematics* **28(6)** 1224-1250

[7] Mursaleen, M., A. A. H. Al-Abied, and Abdullah Alotaibi 2017 On (p,q)-Szász-Mirakyan operators and their approximation properties *Journal of inequalities and applications* **1** 196

[8] Pallini, Andrea 2005 Bernstein-type approximations of smooth functions. Statistica **65(2)** 169-191

[9] Szasz, Otto 1950 Generalization of S. Bernstein's polynomials to the infinite interval. *J. Res. Nat Bur. Standards* 45(3) 239-245

[10] Walczak, Zbigniew. 2003 On modified Szasz–Mirakyan operators *Novi Sad J. Math* **33(1)** 93-107

[11] Walczak, Z. 2005 Approximation of functions of two variables by some linear positive operators *Acta Math. Univ. Comenianae* **74(1)** 37-48

On Prime and Semiprime Gamma Rings with Symmetric Gamma n-Centralizers

On Prime and Semiprime Gamma Rings with Symmetric Gamma n-Centralizers

Ikram A. Saed

Department of Applied Sciences, University of Technology, Baghdad, Iraq

Email: ikramsaed1962@gmail.com

Abstract. In this paper, we assume that M is Γ-ring then we will present the definition of symmetric Γ-n-centralizers and the definition of Jordan Γ-n-centralizers of M . After that, we try to find the commutativity of a prime Γ- ring that has a left Γ-n-centralizers of M when it satisfies certain identities. Finally, we find the relationship between Jordan Γ-n-centralizers and symmetric Γ-n-centralizers when M is semiprime Γ- ring.

1. Introduction

Let M be the Γ-ring. Saed found the commutativity of adding prime near-rings in 2018 in [1] that satisfied certain identities and including right (θ, θ)-3-derivations. Saed discovered the commutativity of adding and multiplying prime near-rings in 2018 in [2] that satisfied some identifications with right (θ, θ)-4-derivations. In addition, Saed in 2018 showed that in [3] prime near-ring N that satisfied certain identities usually contains left generalized (θ, θ)-4- derivations and semigroup ideals is commutative ring. In 2019 Saed in [4] introduce the notion of perpendicular generalized 3- derivations in semiprime Γ-near-rings and present several necessary and sufficient conditions for generalized 3-derivations on semiprime Γ-near-rings to be perpendicular. Finally, Saed in 2020 in [5] studied commutativity of prime near-ring N under some conditions on semigroup ideals of N.

There are three sections in this article. We mentioned some known definitions and essential lemmas in section one. In section two, we introduce the definition of symmetric Γ-n-centralizers of M and study the commutativity of prime Γ- ring by using the notion of left Γ-n-centralizers. In section three, we define the notion of Jordan Γ-n- centralizers to prove that every Jordan Γ-n- centralizers of the semiprime Γ- ring M of char (M) ≠2 is symmetric Γ-n-centralizers.

2. Basic Concept

Definition 2.1: [4]

Assume M and Γ be additive abelian groups. If there exists a mapping M x Γ x M → M :(a , α , b) → a α b which satisfies the conditions :

for every a ,b ,c ∈ M , α , β ∈ Γ :

(i) (a +b) α c=a αc + b α c

a(α+ β)b = a αb + aβb

a α (b+c) = a αb + a αc

(ii) (a αb) β c=a α (b βc)

Where M refers to as a Γ-ring.

Example 2.2: [4]
Let R be a ring, the additive abelian groups $M = M_{2x3}(R)$ and $\Gamma = M_{3x2}(R)$ denotes the sets of all 2×3 matrices over R and 3×2 matrices over R respectively. Then M is Γ-ring.

Definition 2.3: [6]
A right (resp. left) ideal of a Γ-ring M is an additive subgroup U of M such that $U\Gamma M \subset U$ (resp. $M \Gamma U \subset U$) . If U is both right and left ideal, then it said that U is an ideal.

Definition 2.4: [6]
Let M be a Γ-ring. The set $Z(M) = \{ x \in M : x\gamma y = y\gamma x$, for all $y \in M$ and $\gamma \in \Gamma\}$ is called the center of the Γ- ring M.

Definition 2.5: [6]
A Γ-ring M is called a prime if $a \Gamma M \Gamma b = \{0\}$ implies that either $a = 0$ or $b = 0$, for $a , b \in M$.

Definition 2.6: [6]
A Γ-ring M is called semiprime if $a \Gamma M \Gamma a = \{0\}$ implies that $a=0$, for $a \in M$.

Definition 2.7: [6]
A Γ-ring M is called 2-torsion-free if $2a=0$ implies $a=0$, for $a \in M$.

Definition 2.8: [6]
A Γ-ring M is called a commutative if $a\gamma b = b\gamma a$, for all $a, b \in M$ and $\gamma \in \Gamma$.

Definition 2.9: [7]
Let M be a Γ-ring. If a positive integer n exists, such that $na = 0$, for all $a \in M$, then the smallest positive integer with this property is called the Γ-ring characteristic and it is denoted by char(M).

Definition 2.10: [6]
Let M be a Γ-ring. Then, for any $x , y \in M$ and $\alpha \in \Gamma$, the symbol $[x,y]_\alpha = x \alpha y – y \alpha x$, will denote the commutator and symbol $(x \circ y)_\alpha = x \alpha y + y \alpha x$ will denote the additive group commutator.

Lemma 2.11: [7]
If M is a Γ-ring , for all $a ,b, c \in M$ and $\alpha, \beta \in \Gamma$ then :

(i) $[a, b]_\alpha+[b, a]_\alpha=0$
(ii) $[a + b, c]_\alpha=[a , c]_\alpha+[b, c]_\alpha$
(iii) $[a , b + c]_\alpha= [a , b]_\alpha+ [a, c]_\alpha$
(iv) $[a , b]_{\alpha+\beta} =[a, b]_\alpha+[a, b]_\beta$
(v) $[a \beta b, c]_\alpha=a \beta[b, c]_\alpha+[a, c]_\alpha \beta b+a \beta c \alpha b- a \alpha c \beta b.$

Remark 2.12: [7]
A Γ-ring M is commutative if and only if $[x , y]_\alpha=0$, for all $x , y \in M$ and $\alpha \in \Gamma$.

3.On Symmetric Left Γ-n-Centralizer and Commutatively of Prime Γ-Ring.
First, in this section, we present the fundamental definition.

Definition 3.1:

Let M be the Γ-ring and n be the positive integer. If the following equations hold for all $y, r_1, r_2 \ldots r_n \in M$ and $\gamma \in \Gamma$, the n-additive mapping $T: MxMx \ldots xM \to M$ shows to be left as a Γ-n-centralizer.

$T_1(r_1\gamma\, y, r_2, \ldots, r_n) = T_1(r_1, r_2, \ldots, r_n)\, \gamma\, y$
$T_2(r_1, r_2\, \gamma\, y, \ldots, r_n) = T_2(r_1, r_2, \ldots, r_n)\, \gamma\, y$
$\vdots$
$T_n(r_1, r_2, \ldots, r_n\, \gamma\, y) = T_n(r_1, r_2, \ldots, r_n)\, \gamma\, y$

T has said to be a symmetric left Γ-n-centralizer if all the above equations are equivalent to all other. That is:

$T(r_1\gamma\, y, r_2, \ldots, r_n) = T(r_1, r_2, \ldots, r_n)\, \gamma\, y$ for all $y, r_1, r_2 \ldots, r_n \in M$ and $\gamma \in \Gamma$.

Theorem3.2:

Let M be a prime Γ-ring, and I be a non-zero ideal of M. Assume that M admits a nonzero left Γ-n-centralizer, such that $T(r, r_2, \ldots, r_n) = r$. If $T([r, y]_\gamma, r_2, \ldots, r_n) - [r, y]_\gamma = 0$, for all $r_2, \ldots, r_n \in M$ and $r, y \in I$, $\gamma \in \Gamma$, then M is a commutative.

Proof:

Since $(T(r, r_2, \ldots, r_n) - r)\gamma y - (T(y, r_2, \ldots, r_n) - y)\, \gamma\, r = 0$ (3.1)

Putting $r = r\beta h$, where $h \in M$, $\beta \in \Gamma$ in (3.1), we get:

$(T(r, r_2, \ldots, r_n) - r)\beta\, h\gamma\, y - (T(y, r_2, \ldots, r_n) - y)\, \gamma\, r\, \beta\, h = 0$ (3.2)

Multiply (3.1) from the right by βh:

$(T(r, r_2, \ldots, r_n) - r)\, \gamma\, y\, \beta\, h - (T(y, r_2, \ldots, r_n) - y)\, \gamma\, r\, \beta\, h = 0$ (3.3)

Comparing (3.2) and (3.3):

$(T(r, r_2 \ldots r_n) - r)\, \beta(h\, \gamma\, y - y\, \gamma h) = (T(r, r_2 \ldots r_n) - r)\beta[h, y]_\gamma = 0$ (3.4)

Replacing h by $h\, \mu\, s$ in (3.4) and using it, where $s \in M$ and $\mu \in \Gamma$.

$(T(r, r_2, \ldots, r_n) - r)\, \beta h\, \mu[s, y]_\gamma = 0$

Therefore, M is a prime Γ-ring, then either:

$(T(r, r_2, \ldots, r_n) - r) = 0$ or $[s, y]_\gamma = 0$

For $r, y \in I$ and $r_2 \ldots r_n, h, s \in M$ and $\gamma \in \Gamma$.

Implies that $[s, y]_\gamma = 0$ and $I \subseteq Z(M)$.

We have, M is a commutative.

Theorem 3.3:

Suppose M be a prime Γ-ring and I be a non-zero ideal of M, assume that T be a nonzero left Γ-n-centralizer like that $T(r, r_2, \ldots, r_n) \neq -r$. If $T([r, y]_\gamma, r_2, \ldots, r_n) + [r, y]_\gamma = 0$, for all $r_2, \ldots, r_n \in M$ and $r, y \in I$, $\gamma \in \Gamma$, then M is a commutative.

Proof:

Since $(T(r, r_2, \ldots, r_n) + r)\, \gamma\, y - (T(y, r_2, \ldots, r_n) + y)\, \gamma\, r = 0$ (3.5)

Putting $r = r\beta h$, where $h \in M$, $\beta \in \Gamma$ in (3.5) we get:

$(T(r, r_2, \ldots, r_n) + r)\, \beta\, h\, \gamma\, y - (T(y, r_2, \ldots, r_n) + y)\, \gamma\, r\, \beta\, h = 0$ (3.6)

Multiply (3.5) from the right by βh:

$(T(r, r_2, \ldots, r_n) + r)\, \gamma\, y\, \beta\, h - (T(y, r_2, \ldots, r_n) + y)\, \gamma\, r\, \beta\, h = 0$ (3.7)

Comparing (3.6) and (3.7):

$(T(r, r_2, \ldots, r_n) + r)\, \beta(h\gamma\, y - y\, \gamma h) = (T(r, r_2, \ldots, r_n) + r)\, \beta[h, y]_\gamma = 0$ (3.8)

Replacing h by $h\, \mu\, s$ in (3.8) and using it, where $s \in M$ and $\mu \in \Gamma$.

$(T(r, r_2, \ldots, r_n) + r)\, \beta h\, \mu[s, y]_\gamma = 0$

Therefore, M is a prime Γ-ring, then either:

$(T(r, r_2, \ldots, r_n) + r) = 0$ or $[s, y]_\gamma = 0$

For $r , y \in I$ and $r_2,\ldots,r_n , h , s \in M$ and $\gamma \in \Gamma$. Implies that $[s , y]_\gamma = 0$ and $I \subseteq Z(M)$. We get is a commutative.

Theorem 3.4:
Suppose M be a main (prime) Γ-ring and I be a non-zero ideal of M , assume that T be a nonzero left Γ-n-centralizer like that $T(r , r_2 , \ldots,r_n) \neq -r$. If $T((r \circ y)_\gamma , r_2 , \ldots,r_n) + (r \circ y)_\gamma = 0$, for all $r_2 ,\ldots, r_n , r , y \in I$ and $\gamma \in \Gamma$, then M is a commutative.

Proof:
$T ((r \circ y)_\gamma , r_2, \ldots,r_n) + (r \circ y)_\gamma = 0$,for all $r_2 ,\ldots, r_n , r , y \in I$ and $\gamma \in \Gamma$ (3.9)
If $T ((r \circ y)_\gamma , r_2 , \ldots,r_n) \neq 0$ we have $(r \circ y)_\gamma = 0$ (3.10)
Substituting $r = r \beta h$ in (3.10) , where $h \in M$, $\beta \in \Gamma$ to get :
$r \beta h \gamma y + y \gamma r \beta h = 0$, $y \gamma r = - r \gamma y$. We get $r\beta[h , y]_\gamma = 0$ (3.11)
Replacing r by $r \mu s$ in (3.11) and using it , where $s \in M$ and $\mu \in \Gamma$. $r\mu s\beta[h , y]_\gamma = 0$, for all y, $r, h \in I$ and $\gamma, \mu, \beta \in \Gamma$.
So M is a main(prime) Γ-ring , then $I\mu M\beta[h , y]_\gamma = \{0\}$. Therefor M is a main (prime) Γ-ring and $I \neq \{0\}$, so that :
$[h , y]_\gamma = 0$, for all h, $y \in M$ and $\gamma \in \Gamma$. Thus, I is commutative and hence M is a commutative.

Theorem 3.5:
Let M be a prime Γ-ring and I be a non-zero ideal of M. Let T be a nonzero left Γ-n-centralizer . If $T(r^2,r_2 ,\ldots,r_n) = - r^2$, for all $r_2 ,\ldots,r_n , r \in I$, then M is a commutative.

Proof:
Since $T (r^2, r_2,\ldots,r_n) = - r^2$, for all $r_2 ,\ldots, r_n , r \in I$, we have :
$T ((r + y)^2, r_2, \ldots,r_n) = -(r + y)^2$, which implies that :
$T((r \circ y)_\gamma , r_2 , \ldots,r_n) = (r \circ y)_\gamma$, by Theorem 3.4 , so M is a commutative.

Theorem 3.6:
Let M be a prime Γ-ring and I be a non-zero ideal of M. Let T be a nonzero left Γ-n-centralizer thus that $T(r , r_2 , \ldots,r_n) \neq r$. If $T(r \gamma y, r_2, \ldots,r_n) - r \gamma y \in Z(M)$, for all $r_2 ,\ldots, r_n \in M$ and $r, y \in I , \gamma \in \Gamma$, then M is a commutative.

Proof:
$(T(r, r_2, \ldots,r_n) - r)\gamma y \in Z(M)$ (3.12)
Substituting $r = r \beta h$ in (3.12) , where $h \in M , \beta \in \Gamma$ to get :
$(T(r,r_2,\ldots,r_n) - r) \beta h \gamma y \in Z(M)$
for all h, $r_2,\ldots, r_n \in M$ and $r, y \in I , \gamma , \beta \in \Gamma$. (3.13)
Multiply (3.12) from the right by βh
$(T(r, r_2, \ldots,r_n) - r) \gamma y \beta h \in Z(M)$
for all h, $r_2 ,\ldots, r_n \in M$ and $r, y \in I , \gamma , \beta \in \Gamma$. (3.14)
Comparing (3.13) and (3.14) to get:
$[T(r , r_2, \ldots , r_n) - r) \gamma y , h]_\beta = 0$
For all h, $r_2,\ldots, r_n \in M$ and $r, y \in I , \gamma , \beta \in \Gamma$. (3.15)
$(T(r , r_2, \ldots , r_n) - r)\gamma[y, h]_\beta + [T(r , r_2, \ldots , r_n) - r) , h]_\beta \gamma y = 0$ (3.16)
Replacing r by $r \mu s$ in (3.16) and using it, where $s \in M$ and $\mu \in \Gamma$.
$(T(r , r_2, \ldots , r_n) - r)\mu s\gamma[y, h]_\beta + [T(r, r_2, \ldots , r_n) - r) \mu s, h]_\beta \gamma y = 0$ (3.17)
Comparing (3.16) and (3.17) to get:
$(T(r, r_2, \ldots , r_n) - r)\mu s\gamma[y, h]_\beta = 0$, for all $h,r_2,\ldots, r_n \in M$ and $r, y \in I, \gamma, \beta, \mu \in \Gamma$.

Primness of T implies that $(T(r, r_2, \dots, r_n) - r)\mu\, T\gamma[y, h]_\beta = \{0\}$. Either $(T(r, r_2, \dots, r_n) - r) = 0$ or $[y, h]_\beta = 0$. Since $I \neq \{0\}$ and $T(r, r_2, \dots, r_n) \neq r$, we discover that I is necessary and therefore M is a commutative.

4. Symmetric Jordan Γ-n-Centralizer of Semiprime Γ-Ring.

First, we offer the basic definition in this section.

Definition 4.1:

Let M be a Γ-ring and n be a fixed positive integer. An n-additive symmetric mapping T: MxMx…xM →M is said to be Jordan left (resp. right) Γ-n-centralizer in case :

$T(r_1^2, r_2, \dots, r_n) = T(r_1, r_2, \dots, r_n)\gamma r_1$ (resp. $T(r_1^2, r_2, \dots, r_n) = r_1\gamma T(r_1, r_2, \dots, r_n)$)

Hold for $r_1, r_2, \dots, r_n \in M$ and $\gamma \in \Gamma$.

T is called Jordan Γ-n-centralizer if T Jordan left and Jordan right Γ-n-centralizer.

Lemma 4.2:

Assume M be a semiprime Γ-ring and $a \in M$. If $T(r, r_2, \dots, r_n) = (a \circ r)_\gamma$ is a Jordan Γ-n-centralizer, for $r, r_2, \dots, r_n \in M$ and $\gamma \in \Gamma$, then $a \in Z(M)$.

Proof:

$T(r, r_2, \dots, r_n) = (a \circ r)_\gamma$, for $r, r_2, \dots, r_n \in M$ and $\gamma \in \Gamma$. (4.1)

Replacing $r = r\beta y + y\beta r$ in (4.1), where $y \in M$ and $\beta \in \Gamma$, to get :

$T(r\beta y + y\beta r, r_2, \dots, r_n) = T(r, r_2, \dots, r_n)\beta y + y\beta\, T(r, r_2, \dots, r_n) = (a \circ r)_\gamma \beta y + y\beta(a \circ r)_\gamma = a\gamma r\beta y + r\gamma a\beta y + y\beta a\gamma r + y\beta r\gamma a$. On other hand,

$(a \circ (r\beta y + y\beta r))_\gamma = a\gamma r\beta y + a\gamma y\beta r + r\beta y\gamma a + y\beta r\gamma a = r\gamma a\beta y + y\beta a\gamma r = a\gamma y\beta r + r\beta y\gamma a$.

That is,

$r\beta[a, y]_\gamma = [a, y]_\gamma \beta r = r\beta[a, y]_\gamma - [a, y]_\gamma \beta r = 0$. To get $[r, [a, y]_\gamma]_\beta = 0$, Implies $[a, y]_\gamma \in Z(M)$, hence $a \in Z(M)$.

Lemma 4.3:

Let M be a semiprime Γ-ring. Then every Jordan Γ-n-centralizer of M maps Z(M) into Z(M).

Proof:

$T(r^2, r_2, \dots, r_n) = T(r, r_2, \dots, r_n)\gamma r$, for $r, r_2, \dots, r_n \in M$ and $\gamma \in \Gamma$ $2T(r\gamma y, r_2, \dots, r_n) = T(r\gamma y + y\gamma r, r_2, \dots, r_n) = T(r\gamma y, r_2, \dots, r_n) + T(y\gamma r, r_2, \dots, r_n) = T(r, r_2, \dots, r_n)\gamma y + y\gamma T(r, r_2, \dots, r_n)$ (4.2)

Let $r \in Z(M)$ and denote $a = T(r, r_2, \dots, r_n)$ from (4.2), for $r, r_2, \dots, r_n \in M$,

$2\,T(r\gamma y, r_2, \dots, r_n) = a\gamma y + y\gamma a$.

Assume $S = a\gamma y + y\gamma a$, we show that S is also a Jordan Γ-n-centralizer of M by Lemma 4.2 implies $T(r, r_2, \dots, r_n) \in Z(M)$.

Suppose $T(r, r_2, \dots, r_n) = a\gamma r + r\gamma a$, for $r, r_2, \dots, r_n \in M$ and $\gamma \in \Gamma$.

Replacing $r = r\beta y + y\beta r$, $y \in M$, $\beta \in \Gamma$.

$T(r\beta y + y\beta r, r_2, \dots, r_n) = T(r, r_2, \dots, r_n)\beta y + y\beta\, T(r, r_2, \dots, r_n) = (a \circ r)_\gamma \beta y + y\beta(a \circ r)_\gamma = a\gamma r\beta y + r\gamma a\beta y + y\beta a\gamma r + y\beta r\gamma a$ (4.3)

On other hand,

$(a \circ (r\beta y + y\beta r))_\gamma = a\gamma r\beta y + a\gamma y\beta r + r\beta y\gamma a + y\beta r\gamma a$ (4.4)

Comparing (4.3) and (4.4), we have:

$= r\beta[a, y]_\gamma - [a, y]_\gamma \beta r = [r, [a, y]_\gamma]_\beta = 0$

Implies $[a, y]_\gamma \in Z(M)$:

$= (a \circ r)_\gamma \beta\, y + y\beta(a \circ r)_\gamma$, then $a \in Z(M)$, also: $T(r,r_2,\ldots,r_n) \in Z(M)$, hence $T(r,r_2,\ldots,r_n) = a$, for $r,r_2,\ldots,r_n \in M$.

Lemma 4.4:
Assume M be a semiprime Γ-ring of char $\neq 2$ and T be an additive that mapping satisfying $T(r^2,r_2,\ldots,r_n) = T(r,r_2,\ldots,r_n)\gamma r$ (resp. $T(r^2,r_2,\ldots,r_n) = r\,\gamma T(r,r_2,\ldots,r_n)$). Hold for $r,r_2,\ldots,r_n \in M$ and $\gamma \in \Gamma$. Then T is a symmetric left Γ-n-centralizer.

Proof: It is clear.

Theorem 4.5:
Assume M be a semiprime Γ-ring of char$\neq 2$. Then every Jordan Γ-n-centralizer of M is a symmetric Γ-n-centralizer.

Proof:
$T(r\,\gamma y+y\,\gamma r,r_2,\ldots,r_n) = T(r,r_2,\ldots,r_n)\gamma y + y\,\gamma T(r,r_2,\ldots,r_n)$ (4.5)
$T(r\gamma y + y\gamma r,r_2,\ldots,r_n) = r\gamma T(y,r_2,\ldots,r_n) + T(y,r_2,\ldots,r_n)\gamma r$ (4.6)
Replacing $y = r\,\beta y + y\,\beta\, r$ in (4.6), where $y \in M$ and $\beta \in \Gamma$.
$T(r\gamma y+y\gamma r,r_2,\ldots,r_n) = r\gamma T(r,r_2,\ldots,r_n)\beta y + r\gamma y\beta T(r,r_2,..,r_n) + T(r,r_2,..,r_n)\beta y\gamma r +$
$y\,\beta\, T(r,r_2,\ldots,r_n)\gamma r$ (4.7)
In addition, replacing $y = r\,\beta y + y\,\beta\, r$ in (4.5), where $y \in M$ and $\beta \in \Gamma$.
$= T(r,r_2,\ldots,r_n)\gamma r\beta y + T(r,r_2,\ldots,r_n)\,\gamma y\beta r + r\beta y\,\gamma T(r,r_2,\ldots,r_n) + y\beta r\gamma T(r,r_2,\ldots,r_n)$ (4.8)
Comparing (4.7) and (4.8), we get:
$r\gamma T(r,r_2,\ldots,r_n)\beta y + y\beta T(r,r_2,\ldots,r_n)\gamma\, r = T(r,r_2,\ldots,r_n)\gamma r\beta y + y\beta r\gamma T(r,r_2,\ldots,r_n)$, for $y,\ r\ ,\ r_2\ ,\ \ldots,r_n \in M$ and $\gamma,\beta \in \Gamma$.
$[T(r, r_2, \ldots, r_n), r]_\gamma \beta y + y\beta[\, r\ , T(r, r_2, \ldots, r_n)]_\gamma = 0$
$[T(r, r_2, \ldots, r_n), r]_\gamma \beta y - y\beta[\, T(r, r_2, \ldots, r_n), r]_\gamma = 0$
$[[T(r, r_2, \ldots, r_n), r]_\gamma, y]_\beta = 0$. So $[\, T(r, r_2, \ldots, r_n), r]_\gamma \in Z(M)$
Let $a \in Z(M)$:
$2T(a\gamma r, r_2, \ldots,r_n) = T(a,r_2,\ldots,r_n)\,\gamma r + r\,\gamma T(a,r_2,\ldots,r_n)$ (4.9)
Also,
$2T(r\gamma a, r_2, \ldots,r_n) = a\gamma T(r,r_2,...,r_n) + T(r,r_2,\ldots,r_n)\gamma a$ (4.10)
We get , $T(a,r_2, \ldots,r_n)\gamma r = T(r, r_2, \ldots,r_n)\gamma a$. By using Lemma 4.3, we have:
$[T(r, r_2, \ldots, r_n), r]_\gamma \beta a = (T(r,r_2,\ldots,r_n)\,\gamma r - r\,\gamma T(r,r_2,\ldots,r_n))\,\beta a =$
$T(r,r_2,\ldots,r_n)\gamma r\beta a - r\,\gamma T(r, r_2,\ldots,r_n)\,\beta a =$ $T(r,r_2,\ldots,r_n)$
$\gamma a\,\beta r - r\gamma\, T(r,r_2,\ldots,r_n)\,\beta r =$ $T(a,r_2,\ldots,r_n)\,\gamma r\,\beta r - r\,\gamma$
$T(r,r_2,\ldots,r_n)\,\beta r$ $2T(r^2,r_2,\ldots,r_n) = T(r,r_2,\ldots,r_n)\gamma r +$
$r\,\gamma T(r,r_2,\ldots,r_n) = 2T(r\ ,\ r_2\ ,\ \ldots,r_n\ )\,\gamma r$
By Lemma 4.4 , hence M is a symmetric Γ-n-centralizer.

References:

[1] Saed I 2018 Commutativity of addition in Prime Near-Rings with Right (θ,θ)-3-Derivations *Journal of Advances in Mathematics* **14** 7533
[2] Saed I 2018 Right (θ,θ)-4-Derivations on Prime Near-Rings *International Journal of Mathematics Trends and Technology* **54** 222
[3] Saed I 2018 On Semigroup Ideals and Left Generalized (θ,θ)-4- Derivations in Prime Near-Rings *International Journal of Mathematics Trends and Technology* **57** 73
[4] Saed I 2019 On Semigroup Gamma Near-Rings with Perpendicular Generalized 3-Derivations *Journal of AL- Qadisiyah for computer science and mathematics* **11** 30

[5] Saed I 2020 On Semigroup Ideals and Generalized Two Sided Reverse α-3-Derivation in Prime Near-Ring *Al- Qadisiyah Journal of Pure Science* **25** 9
[6] Ahmed H 2019 On the Commutativity Results of Prime and Semiprime Γ-Near-Rings with Γ-Derivations *Baghdad University (Iraq)*Ph. D. Thesis
[7] Hamad B 2012 (U, M) - Derivations on Γ- Rings *Al-Mustansiriya University (Iraq)* M.SC. Thesis.

Approximate Solution of 2-Dimensional VO Linear Fractional Partial Differential Equation

Approximate Solution of 2-Dimensional VO Linear Fractional Partial Differential Equation

Nabaa N. Hasan , Omar H. Salim

Department of Mathematics, College of Science, Mustansiriyah University, Baghdad, Iraq

Email1: alzaer1972@uomustansiriyah.edu.iq

Abstract. The non-polynomial spline method has been used to solving 2-dimensional variable-order(VO) fractional partial differential equations (FPDE). For VO fractional derivative, described in the sense of the Caputo. The main objective of this study and advantage of the proposed method is to investigate a public approximation for the frequency of the trigonometric functions of the non-polynomial part of the spline function. The powerful algorithm of the proposed method gives high accuracy results.

1. Introduction

The variable-order fractional is the one of most important tool in nowadays, with successful applied in mechanics [1], It can be used in the design of abnormal diffusion because it can depict the time-based diffusion process more efficiently than the partial derivative of the static arrangement means that the order of α.[2-3]. The topic is very active and of great interest due to its many applications, not only in Mathematics, but also in physics and in engineering, and it has proven that it describes complex phenomena in nature better and more broadly. [4-10]. The effect of differences between the use of fixed-order and variable-order fractional derivatives has been discussed and studied in [11].The addition and mathematical formalization of coefficients of variable-order fractions. The Evolutionary control equations for successful application have led to the modelling of complex world problems, from the study of biology and mechanics to transport processes and to many important applications. Partial variable calculus is an unknown branch of calculus that provides wonderful opportunities to simulate interdisciplinary processes. The scientific community has been extensively exploring the applications of fractional variable order in modelling and physical systems engineering. Among the goals of this work, will be starting point for researchers who interested in approaching this wonderful topic. We are interested in developing computational and analytical methods and applying complex physical systems using advanced simulation software. For more details, see [12-18].

This paper proposes non-polynomial spline functions(SF) to approximate the solution of the fractional partial differential equations of variable order (FPDEVO).

2. Definitions and properties:

2.1 Some Definitions:

In this part, some necessary and important definitions and mathematical principles of variable-order fractional derivatives and some properties of fractional derivatives will be mentioned.

Definition 2.1 [19] The Caputo and Riemann fractional derivatives of order α of $f(t)$ defined as:

$$ {}_0^C D_\cdot^\alpha f(t) = \frac{1}{\Gamma(n-\alpha)} \int_0^t \frac{f^{(n)}(s)}{(t-s)^{\alpha-n+1}} ds $$

$$ {}_0 D_t^\alpha f(t) = \frac{1}{\Gamma(n-\alpha)} \frac{d^n}{dt^n} \int_0^t \frac{f(s)}{(t-s)^{\alpha-n+1}} ds, \quad \ldots(1) $$

where $n-1 < \alpha \leq n$, $n \in N$ and $n > 0$.

After folding the definition of fixed-order fractional derivatives, we show the variable-order fractional differentiation factor. Fixed-order fractional derivatives are expanded into the variable-order fractional meaning.

Definition 2.2 [19] The Riemann FPDEO of $\alpha(t)$ is defined as:

$$ {}_0 D_t^{\alpha(t)} f(t) = \frac{1}{\Gamma(n-\alpha(t))} \frac{d^n}{dt^n} \int_0^t (t-s)^{\alpha(t)-n+1} f(s) ds \quad \ldots(2) $$

and

$$ {}_t D_b^{\alpha(t)} f(t) = \frac{1}{\Gamma(n-\alpha(t))} \frac{d^n}{dt^n} \int_t^1 (t-s)^{\alpha(t)-n+1} f(s) ds $$

where $n-1 < \alpha_{min} < \alpha(t) < \alpha_{max} < n$, $n \in \mathbb{N}$ for $t \in [0, \tau]$.

Other definitions of the derivative of variable arrangement have been proposed with respect to Caputo.

Definition 2.3 [19] Let $n-1 < \alpha(t) \leq n$ for all $t \in [0, \tau]$ the operator ${}_0^C D_t^{\alpha(t)}$ defined by

$$ {}_0^C D_t^{\alpha(t)} f(t) = \frac{1}{\Gamma(n-\alpha(t))} \int_0^t \frac{f^{(n)}(s)}{(t-s)^{\alpha(t)-n+1}} ds \quad \ldots(3) $$

and

$$ {}_t^C D_b^{\alpha(t)} f(t) = \frac{1}{\Gamma(n-\alpha(t))} \int_0^t \frac{f^{(n)}(s)}{(t-s)^{\alpha(t)-n+1}} ds $$

is called the Caputo fractional derivative of VO of $\alpha(t)$.

If $\alpha(t)$ is a constant function, then the order of the partial variable is changed to the derivative of the constant order. The two definitions of variable-order derivatives are not generally equivalent, but are related by the following relationship:

$$ {}_0 D_t^{\alpha(t)} f(t) = \sum_{k=0}^{n-1} \frac{f^{(k)}(0) t^{k-\alpha(t)}}{\Gamma(k+1-\alpha(t))} + {}_0^C D_t^{\alpha(t)} f(t). \quad \ldots (4) $$

The formula for the fractional Caputo derivative, $0 < \alpha(t) \leq 1$:

$$ {}_0^C D_t^{\alpha(t)} x^\beta = \begin{cases} 0, & \beta = 0, \\ \frac{\Gamma(\beta+1)}{\Gamma(\beta+1-\alpha(t))} x^{\beta-\alpha(t)}, & \beta = 0,1,2,\dots \end{cases} \quad \dots (5) $$

Definition 2.4 [20] Let $0 < \alpha(x,t) \leq 1$ the operator ${}_0^C D_t^{\alpha(x,t)}$ defined by

$$ {}_0^C D_t^{\alpha(x,t)} u(x,t) = \frac{1}{\Gamma(n-\alpha(x,t))} \int_0^x \frac{1}{(x-s)^{\alpha(x,t)-n+1}} \frac{\partial^n u(x,t)}{\partial s^n} ds \quad \dots(6) $$

is called the Caputo space fractional derivative of variable-order
Next, let us introduce some properties of fractional derivatives [21].
1-Linearity : if the operator ${}_a D_t^\alpha (A\, g_1(t) + B g_2(t)) = A\, D^\alpha g_1(t) + B\, D^\alpha g_2(t)$, then of must be linear.
where $g_1(t)$ and $g_2(t)$ are any two function, $A, B \in \mathbb{R}$, $\mathbb{R}$ be a regain s.t
$\mathcal{R} = \{(x,t): a \leq x \leq b\, , c \leq t \leq d\}$, $\alpha \in \mathcal{R}^+$ for any type of fractional derivatives.

2-Analyticty:-if $f(z)$ is analytic then, ${}_a D_t^\alpha f(z)$ is also analytic function of order α and z

3- Law of exponents :- ${}_a D_t^\alpha \, {}_a D_t^\beta f(t) = {}_a D_t^{\alpha+\beta} f(t)$, and existence the inverse of the operator ${}_a D_t^\alpha \, {}_a D_t^{-\alpha} f(t) = f(t)$.

4- Identity: if ${}_a D_t^\alpha f(t) = f(t)$,then ${}_a D_t^\alpha f(t)$ is identity when α is zero order.

2.2Two-dimensional non-polynomial spline for solving FPDEVO
Consider the partition $\Delta = \{t_0, t_1, t_2, \dots, t_n\}$of $[a,b] \in \mathcal{R}$. Let $S(\Delta)$Indicate the set of piecewise polynomials on interval $I_i = [t_i, t_{i+1}]$ of partition Δ. let $u(x,t)$be the exact solution, this new method provides an approximation. Also, C^∞In the trigonometric portion of the non-polynomial slices it compensates for the loss of smoothness inherited by the polynomial.The non-polynomial spline function, obtained by the segment Pi(t).Each non- polynomial spline of n order Pi (t)has the form*:*
$p_i(t) = a_i \cos k(t-t_i) + b_i\, sink(t-t_i) + \dots + y_i(t-t_i)^{n-1} + z_i \dots(7)$
Where $a_i, b_i, \dots, y_i$and$z_i$are constants and k is repeat the trigonometric functions that will be used to increase the accuracy of the method. of fractional Caputo differential equation of order α, $0 < \alpha \leq 1$.

Definition 3.1 [22] Let$a_i, b_i, c_i$and$d_i$are constants to be determined

$$ p_i(t) = a_i \cos k(t-t_i) + b_i\, sink(t-t_i) + c_i(t-t_i) + d_i \dots(8) $$

is called Linear Non-Polynomial SF
Now, by tensor product we will construct two dimensional non-polynomial spline.
Let $\mathcal{R}$ be a regain s.t$\mathcal{R} = \{(x,t): a \leq x \leq b\, ,\ c \leq t \leq d\}$
the method of finding two dimensional functions $g(x,y)$in a tensor product space $S_1 \otimes S_2$,such that $S_1 = span\{\cos(t), \sin(t), t, 1\}\ and\ S_2 = span\{\cos(x), \sin(x), x, 1\}$
$S_1 \otimes S_2 = z(x,t)$ … (9)
Let the matrix form:
$A\, C = F$ ... (10)
where $A = \Psi \otimes \Phi$ is tensor product of two matrices Ψ and $\Phi$of dimensions$n \times m$

$$ \Psi = \begin{bmatrix} a_{1,1} & \cdots & a_{1,m} \\ \vdots & \ddots & \vdots \\ a_{n,1} & \cdots & a_{n,m} \end{bmatrix}, \quad \Phi = \begin{bmatrix} b_{1,1} & \cdots & b_{1,m} \\ \vdots & \ddots & \vdots \\ b_{n,1} & \cdots & b_{n,m} \end{bmatrix} $$

$$A = \Psi \otimes \Phi = \begin{bmatrix} a_{1,1}\Phi & \cdots & a_{1,m}\Phi \\ \vdots & \ddots & \vdots \\ a_{n,1}\Phi & \cdots & a_{n,m}\Phi \end{bmatrix}$$

and

$$C = [c_{1,1} \ \ldots \ c_{m,1}c_{1,2} \ \ldots \ c_{m,,2} \ \ldots \ c_{m,n}]^T$$
$$F = [f_{1,1} \ \ldots \ f_{m,1}f_{1,2} \ \ldots \ f_{m,,2} \ \ldots \ f_{m,n}]^T$$

Solve (10) to find the unknown vector.
The following theorem present the two dimensional linear non-polynomial spline functions that will be used to evaluate the approximate solution of FPDEVO which is achieved by evaluating Caputo fractional derivative of the spline basis.

Theorem 3.1 The Caputo variable-order fractional derivative of the linear non-polynomial spline approximate the solution of FPDVOE's of the form

$D^{\alpha(x,t)}u(x,t) = f(x,t,u_x,u_t,u_{xx},u_{tt})$, $0 \le x \le 1$,$0 \le \alpha(x,t) \le 1, t > 0$…(11)
with initial condition $u(x,0) = g_1(x)$, $0 \le x \le 1$ …(12)
and boundary condition $u(0,t) = g_2(t)$, $u(1,t) = g_3(t)$, $t > 0$ …(13)
where $g_1(x), g_2(t)$and$g_3(t)$ are arbitrary functions.

proof:
let $z(x,t) = \sum_{i=0}^{m}\sum_{j=0}^{n} C_{i,j}\Psi_j(t)\Phi_i(x)$…(14)
where $\Phi_i(x)$,and $\Psi_j(t) i = 0,1,2,\ldots,m$, $j = 0,1,2,\ldots,n$are the basis of the linear non-polynomial spline function.
From the initial condition given by equation (12), one my get:

$$\sum_{i=0}^{m}\sum_{j=0}^{n} C_{i,j}\Psi_j(0)\Phi_i(x) = g_1(x) \quad \ldots(15)$$

substituting the knot points for the x-axis to get an equation for each knot point ,and form boundary condition given in equation (13), we have

$$\sum_{i=0}^{m}\sum_{j=0}^{n} C_{i,j}\Psi_j(t)\Phi_i(0) = g_2(t) \quad \ldots(16)$$

and $\sum_{i=0}^{m}\sum_{j=0}^{n} C_{i,j}\Psi_j(t)\Phi_i(1) = g_3(t)$ …(17)

similarly, substituting the knot points for the t-axis to get an equation for each knot point at $x = 0$ and $x = 1$
the assumed solution in equation (14) is substituted in equation (11), we have

$$\sum_{i=0}^{m}\sum_{j=0}^{n} C_{i,j}\,{}_0^C D_{\cdot}^{\alpha(x,t)}\Psi_j(t)\Phi_i(x) = f(x,t,\Psi'(t),\Phi'(x),\Psi''(t),\Phi''(x) \quad \ldots \quad (18)$$

substitute the knot points (x_i, t_j),for $i = 0,1,2,\ldots,m$, $j = 0,1,2,\ldots,n$, to get an equation for each pair $(i\ ,j)$, for all $i = 0,1,2,\ldots,m$, ,$j = 0,1,2,\ldots,n$ then from equations (14-18) and a system with unknown coefficients $C_{i,j}$must be determined to compute equation (14).
Now, present the method in the following algorithm FPDEVO:

The Algorithm (3.1) : (FPDEVO)
To find the approximate solution to (14), we choose $n > 0$ and follow these steps::
Step1: Set $h = (a-b)/n$, $x_i = x_o + i\,h, i = 0,1,2,\dots,n$
where $x_o = a, x_n = b$
step2: Set k=(d-c)/m , t_j=t_0+j k, j= 0,1,2,…,m where $t_0 = c, t_m = d$
step3: Evaluate $a_0 b_0, c_0$ and $d_0$in comparison with equation (8)
step4: Calculate the matrix A by using equations 11-14
step5: Evaluate the vector F by using (10)
step6: Calculate A^{-1} by step4
step7: Evaluate the coefficient $C_{i,j}$ by using step5 and step6 such that
$C_{i,j} = A^{-1}\,F$ by using equation (10)
step8: Calculate approximate solution $z(x,t)$using step7 and equation (14)

3. Illustrative Example
There are two illustrative examples of variable order linear fractional partial differential equations to prove the proposed action linear non-polynomial spline method, where MathCad 15 program applied for computation the results.

Example 3.1
${}_0^C D_t^2 u(x,t) + 0.5\cos\left(\frac{\alpha(x,t)\,\pi}{2}\right) {}_0^C D_x^{\alpha(x,t)} u(x,t) - \frac{2}{t^2+1} u(x,t) = f(x,t)$,
for $x \in [0,1]$, t $\in [0,1]$
subject to initial condition(IC): $u(x,0) = x^2(8-x)$
and the boundary conditions(BC): $u(0,t) = 0$, $u(1,t) = 7(t^2+1)$
the exact solution [20]given by:$u(x,t) = x^2(8-x)(t^2+1)$
with$f(x,t) = -(t^2+1)\left(\frac{16\,x^{2-\alpha(x,t)}}{\Gamma(3-\alpha(x,,t))} + \frac{6\,x^{3-\alpha(x,t)}}{\Gamma(4-\alpha(x,t))}\right)$
and $\alpha(x,t) = 1.5 + 0.5e^{-(x\,t)^2-1}$
by algorithm (3.1) the approximate solution is:

$$\begin{aligned} z(x,t) = {} & (-85.484\cos t - 40.66\sin t + 81.904\,t + 70.891)\cos x \\ & + (397.705\cos t - 15.124\sin t - 36.852\,t - 398.745)\sin x \\ & + (-388.014\cos t + 6.369\times 10^{-6}\sin t + 62.695\,t + 389.181)x \\ & + (85.484\cos t + 40.66\sin t - 81.904\,t - 70.891) \end{aligned}$$

Table (3.1) illustrate the exact, approximate solution and absolute error

Table 3.1

X	t	u(x,t)	z(x,t)	$\lvert z(x,t) - u(x,t)\rvert$
0	0	0	0	0
	0.01	0	0	0
	0.02	0	0	0
	0.03	0	0	0
$\frac{1}{3}$	0	0.852	0.852	1.089×10^{-4}
	0.01	0.868	0.852	0.016
	0.02	0.883	0.852	0.031
	0.03	0.898	0.853	0.0046
$\frac{2}{3}$	0	3.259	3.259	1.833×10^{-4}
	0.01	3.267	3.26	7.834×10^{-3}
	0.02	3.275	3.261	0.014

	0.03	3.282	3.262	0.02
1	0	7	7	2.386×10^{-4}
	0.01	7.001	7.001	2.3×10^{-4}
	0.02	7.003	7.003	2.214×10^{-4}
	0.03	7.007	7.006	2.065×10^{-4}

The approximation solution $z(x,t)$and the exact solution$u(x,t)$are illustrated in figure (3.1), and the absolute error$er(x,t)$is given in figure (3.2).

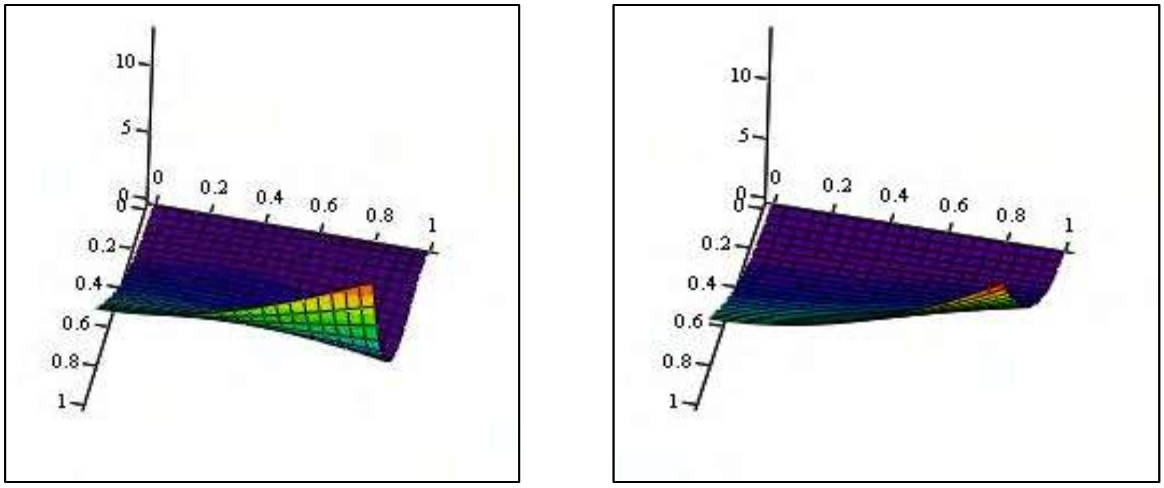

z u

Figure (3.1): the approximate surface $z(x,t)$ and the exact surface $u(x,t)$ for example (3.1)

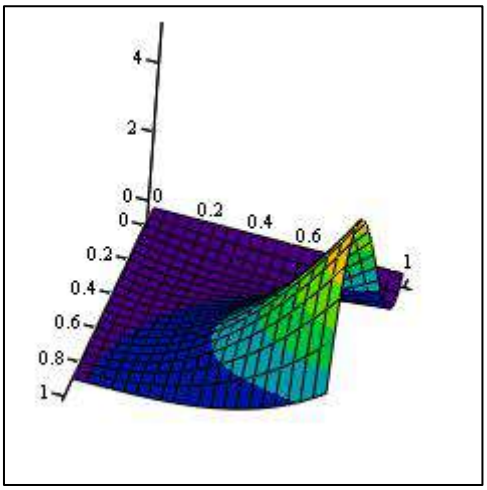

er

Figure (3.2): the error $er(x,t)$for example (3.1)

Figure (3.1) summarizes the results approximate solution$z(x,t)$in Table(3.1) gives a more realistic approximation at$\alpha(x,t) = 1.5 + 0.5e^{-(x\,t)^2-1}$.

Example (3.2):
${}_0^C D_t^{\alpha(x,t)} u(x,t) - D_x u(x,t) + D_t u(x,t) - D_x^2 u(x,t) = f(x,t)$, for $x \in [0,1]$, t $\in [0,1]$
subject to IC: $u(x,0) = 5x(1-x)$
and BC: $u(0,t) = u(1,t) = 0$
the exact solution [23]given by $u(x,t) = 5x(t+1)(1-x)$
with$f(x,t) = -\frac{5x(x-1)}{\Gamma(3-\alpha(x,t))} t^{1-\alpha(x,t)} - 5(t(2x-3) + x^2 + x - 3)$
and $\alpha(x,t) = 0.8 + 0.005 \sin(x) \cos(tx)$
by algorithm (3.1) the approximate solution is:

$$\begin{aligned} z(x,t) = {} & (-4.857\cos t - 0.626\sin t + 8.906\,t + 13.839)\cos x \\ & + (7.246\cos t - 0.255\sin t + 5.808\,t - 2.339)\sin x \\ & + (-8.33\ \cos t + 7.573\times 10^{-8}\sin t + -0.867t + 8.33)x \\ & + (4.857\cos t + 0.626\ \sin t - 8.906\,t - 13.839) \end{aligned}$$

Table (3.2) illustrate the exact approximate solution and absolute error

Table (3.2)

X	t	$z(x,t)$	$u(x,t)$	$\lvert z(x,t) - u(x,t) \rvert$
0	0.0	0.0	0.0	0.0
	0.01	0.0	0.0	0.0
	0.02	0.0	0.0	0.0
	0.03	0.0	0.0	0.0
$\frac{1}{3}$	0	1.111	1.111	0.356×10^{-4}
	0.01	1.122	1.122	0.346×10^{-3}
	0.02	1.133	1.133	0.714×10^{-3}
	0.03	1.143	1.144	0.107×10^{-2}
$\frac{2}{3}$	0	1.111	1.111	0.688×10^{-4}
	0.01	1.122	1.122	0.211×10^{-3}
	0.02	1.133	1.133	0.487×10^{-3}
	0.03	1.144	1.144	0.761×10^{-3}
1	0	0.9343×10^{-4}	0	0.9343×10^{-4}
	0.01	0.8733×10^{-4}	0	0.8733×10^{-4}
	0.02	0.8116×10^{-4}	0	0.8116×10^{-4}
	0.03	0.743×10^{-4}	0	0.743×10^{-4}

The approximation solution $z(x,t)$and the exact solution$u(x,t)$are illustrated in figure (3.3), and the absolute error$er(x,t)$ is given in figure (3.4)

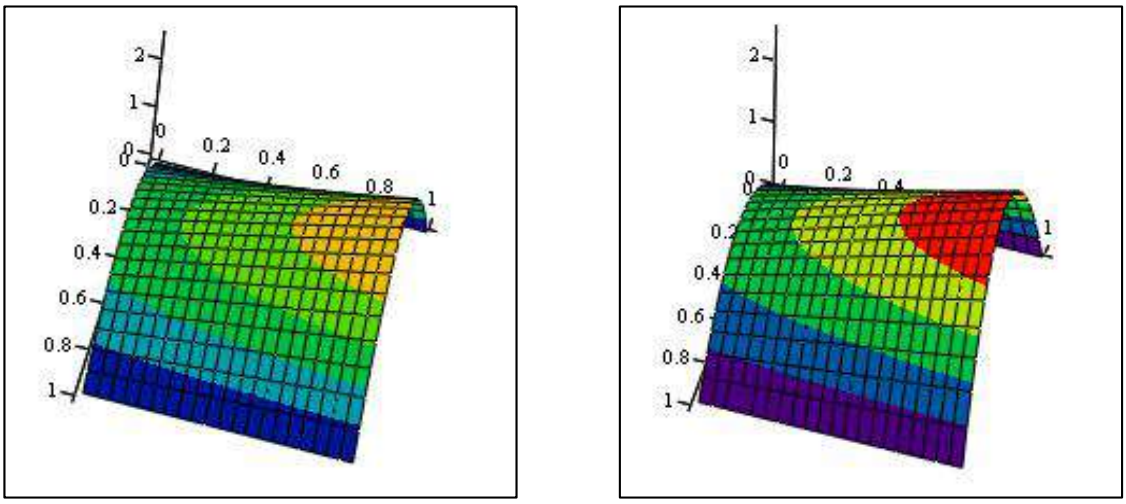

z u

Figure (3.3): the approximate surface $z(x,t)$ and the exact surface $u(x,t)$ for example (3.2)

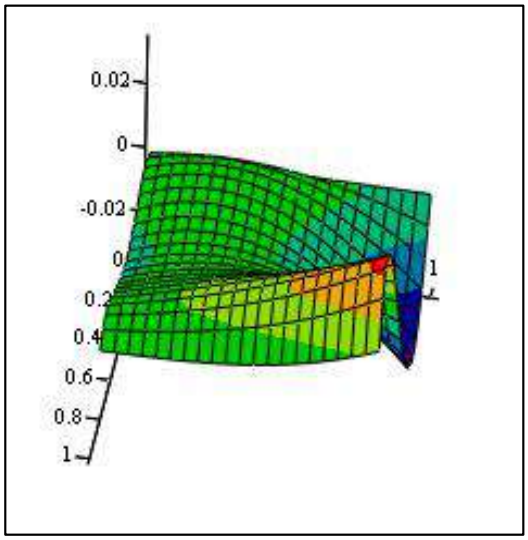

er

Figure (3.4): the error $er(x,t)$for example (3.2)
Figure (3.3) summarizes the results approximate solution $z(x,t)$in Table(3.2) gives a more realistic approximation at$\alpha(x,t) = 0.8 + 0.005\sin(x)\cos(tx)$.

Conclusion and future work
The linear non-polynomial spline function is presented for solving the FPDEVO. Our proposed method is based on trigonometric and polynomial, and it is completely different from the previously shown methods. The results in Table 3.1, 3.2 and figures 3.1, 3.3 show that the proposed method can be used to solve the problem with high accuracy.

Indeed, implementation of an FPDEVO algorithm may also be on our future lines of research. Also we may use the proposed method to solve system of FPDEVO.

References

[1] Coimbra C F M 2003Mechanics with variable order differential operators *Ann.Phys.* **12** 692–703
[2] Pedro H T C Pereira and J M C Coim- bra, C.F.M 2008 Variable-order modeling of diffusive convective effects on the oscillatory flow past a sphere *J. Vib. Contro*l **14** 1659–1672
[3] Sun H G and Chen Y Q 2009 Variable order fractional differential operators in anomalous diffusion modeling *Phys. A* 388, 4586–4592
[4] Podlubny I 1999 Fractional Differential Equations". *Mathematics in Science and Engineering* **198** Academic Press, San Diego, CA
[5] TenreiroMachado J A 2011Complex Order Vander Pol oscillator *Nonlinear Dyn.* **65** 247–254
[6] Muslih S I and Rabei E M 2008 On fractional Euler– Lagrange and Hamilton equations and the fractional generalization of total time derivative *Nonlinear Dyn.* **53** 67–74
[7] Valerio D, Trujillo J J,Tenreiro Machado J A and Baleanu D 2013 Fractional calculus: a survey of useful formulas *Eur. Phys. J. Spec. Top.* **222** 1827–1846
[8] Guo X and Xu M 2006 Some physical Applications of Fractional Schrödinger equation *J. Math. Phys.* **47** 82104
[9] Bohannan G 2008 Analog Fractional Order Control Erin Temperature and motor Control Applications *J. Vibr. Control* **14** 1487–1498
[10] Das S 2008FunctionalFractionalCalculusforSystem Identification and Controls". *Springer New York*
[11] Sun, H G, Wei H and Chen Y Q 2011 Comparative Study of Constant-Order and Variable-Order Fractional Models in Characterizing Memory Property of Systems". *Eur. Phys. J. Spec. Top.* **193**(1) 185–192
[12] Moghaddam B P and Ivaz K 2017 An Efficient Cubic Spline Approximation for Variable-order Fractional Differential Equations with Time Delay *Nonlinear Dyn.* **87** 815–826 (https://doi:10.1007/s11071-016-3079-4).
[13] Sierociuk D and Macias M. "On The Recursive Fractional Variable-order Derivative: equivalent switching strategy, duality, and analog modeling". Circuits Syst. Signal Process. 34, 1077–1113,(2015), (https://doi:10.1007/s00034-014-9895-1).
[14] Tavares D, Almeida R and Torres D F 2016 Caputo Derivatives of Fractional Variable Order: Numerical Approximations *Commun. Nonlinear Sci. Numer. Simul.* **35** 69–87 (https://doi:10.1016/j.cnsns.2015.10.027).
[15] Zhang H Liu F and Zhuang P 2014 Numerical Analysis of a New Space time Variable Fractional Order Advection Dispersion Equation *Appl. Math. Comput.* **242** 541–550 (https://doi:10.1016/j.amc.2014.06.003).
[16] Machado J A T 2017 A Stable Three-level Explicit Spline Finite Difference Scheme for a Class of Nonlinear Time Variable Order Fractional Partial Differential Equations *Comput. Math. Appl.* 73, 1262–1269 (https://doi:10.1016/j.camwa.2016.07.010).
[17] Song H, Yi M, Huang J and Pan Y 2016 Bernstein Polynomials Method for a Class of Generalized Variable Order Fractional Differential Equations *IAENG Int. J. Appl. Math.* **46** 437–444
[18] Chen C, Turner I and Anh Vo 2010 Numerical Schemes and Multivariate Extrapolation of a Two-dimensional Anomalous Sub-diffusion Equation *Numer. Algorithms* **54** (1) 1–21MR 2610319 https://doi.org/10.1007/s11075-009-9320-1.
[19] Sun H, Chang A, Zhang Y and Chen W 2019 A Review On Variable-order Fractional Differential equations: mathematical foundations, physical models, numerical methods and applications. *Fract. Calc. Appl. Anal.* **22** 27–59 (https://doi:10.1515/fca-2019-0003).
[20] Nasser H S and Abdul Rahman. T 2013 Numerical Simulations for the Space-Time Variable Order Nonlinear Fractional Wave Equation *Hindawi Publishing Corporation Journal of Applied Mathematics* Article ID 586870, p7 http://dx.doi.org/10.1155/2013/586870.

[21] Patnaik S, Hollkamp J P and Semperlotti F 2020 Applications of Variable-order Fractional Operators *Proc. R. Soc. A* **476** 20190498 http://dx.doi.org/10.1098/rspa.2019.0498
[22] Zarebnia M, Hoshyar M and Sedaghti M 2011 Non-Polynomial Spline Method for the Solution of Problems in Calculus of Variations *World Academy of science Engineering and Technology* **51** 986-991
[23] Mahmoud A. Zaky and Bhrawy A H 2015 Numerical Simulation Of Time Variable Fractional Order Mobile-ImmobileAdvection-Dispersion Model ",*Romanian Reports in Physics* **67(**3) 773–791 https://www.researchgate.net/publication/269764399.

Interval value fuzzy hyper AT-algebras

Interval value fuzzy hyper AT-algebras

Saba Hussein Ali[1], Fatema F. Kareem[1] and Areej Tawfeeq[2]

[1]Department of Mathematics, Ibn-Al-Haitham college of Education, University of Baghdad, Iraq
[2]Department of Mathematics, Faculty of Education for Girls, University of Kufa, Iraq.

Email: fa_sa20072000@yahoo.com

Abstract. The aim of this work is to a connection between two concepts which are an interval value fuzzy set and a hyper AT-algebra. Also, some properties of these concepts are found. The notions of IVF hyper AT-subalgebras, IVF hyper ideals and IVF hyper AT-ideals are defined. Then IVF (weak, strong) hyper ideals and IVF (weak, strong) hyper AT-ideals are discussed. After that, some relations among these ideals are presented and some interesting theorems are proved.

1. Introduction

The algebraic structure which is called an AT-algebra was introduced by Hameed[3] after that, Hameed[4,5] introduced the notion of hyper AT-algebra a generalization of an AT-algebra and fuzzy hyper AT-algebra. Jun and Xin [6,7] studied the fuzzification of a (strong, weak, reflexive) hyper BCK-ideal and discussed some properties among them. Fuzzy sets extensions such as intuitionistic fuzzy sets, Bipolar-valued fuzzy sets, interval valued fuzzy sets etc are studied by many mathematicians see [1,2,8,9,10]. In this paper, we applied the notion of IVF hyper AT-ideals of a hyper AT-algebra, and investigated some related properties. Also, we study the notions of IVF hyper (weak, strong) ideals and IVF hyper (weak, strong) AT-ideals and gave relations between these ideals.

2.Preliminaries

We review some basic definitions and theories of a hyper AT-algebra and fuzzy hyper AT-algebra in this section.

Definition2.1[4]. A hyper AT-algebra$(H,\circ,0)$ is a nonempty set H and a hyper operation "$\circ$" on H, with a constant "0" and the following conditions hold,

$$\forall \chi,\gamma,\nu \in H$$

(HAT_1) $\big((\gamma\circ\nu)\circ(\chi\circ\nu)\big) \ll \chi\circ\nu$,
(HAT_2) $0\circ\chi = \{\chi\}$,
(HAT_3) $\chi\circ 0 = \{0\}$
where $\chi \ll \gamma$ is defined as follows $0 \in \gamma\circ\chi$ and $A \ll B$ is defined as $\forall a \in A, \exists b \in B$ such that $a \ll b$, for every $A, B \subseteq H$. In such case, we call "<<" the hyper order in H.

Example 2.2[4]. If $H = \{0,1,2\}$ and $\circ$ is a hyper operation on H defined in the following table

∘	0	1	2
0	$\{0\}$	$\{1\}$	$\{2\}$
1	$\{0\}$	$\{0,1\}$	$\{1,2\}$
2	$\{0\}$	$\{0,1\}$	$\{0,1,2\}$

Then $(H,\circ,0)$ is a hyper AT-algebra.

Proposition 2.3[4].In a hyper AT-algebra$(H,\circ,0)$, $\forall\chi,\gamma,\nu\in H$ and , $B\subseteq H$, where $A\ and\ B$ nonempty subsets, then
(P_1) If A $\subseteq$ B , then A << B,
(P_2) $0\circ 0=\{0\}$;
(P_3) $0\ll\chi$;
(P_4) $\nu\ll\nu$;
(P_5) $\chi\circ\nu\ll\nu$;
(P_6) $A\circ 0=\{0\}$;
(P_7) $0\circ A=A$;
(P_8) $(0\circ 0)\circ\chi=\{\chi\}$;
(P_9) If $\gamma\in(0\circ\chi)\Rightarrow\gamma\ll\chi$.

Proposition2.4[4].In a hyper AT-algebra$(H,\circ,0)$, we have $\nu\circ(\gamma\circ\chi)=\gamma\circ(\nu\circ\chi)$, for all $\chi,\gamma,\nu\in H$.

Definition2.5[4]. A hyper AT-subalgebra is a non-empty subset S of a hyper AT-algebra $(H,\circ,0)$ and $\chi\circ\gamma\ll S,\ \forall\chi,\gamma\in S$.

Definition 2.6[4]. A subset $A\neq\emptyset$ of a hyper AT-algebra $(H,\circ,0)$ is named a hyper ideal if
(^{hI_1}) $0\in A$;
(^{hI_2}) if $\chi\circ\gamma\ll A$ and $\chi\in A$, then $\gamma\in A,\forall\chi,\gamma\in H$.

Definition 2.7[4]. A subset $A\neq\emptyset$ of a hyper AT-algebra $(H,\circ,0)$ is named a hyper AT-ideal if
(^{I_1})$0\in A$;
(^{I_2}) if $\chi\circ(\gamma\circ\nu)\ll A$ and $\gamma\in A$, then $\chi\circ\nu\in A$, $\forall\chi,\gamma,\nu\in H$.

Example 2.8[4]. If $H=\{0,a,b\}$ and $\circ$ is a hyper operation on H defined in the following table

∘	0	*a*	*b*
0	$\{0\}$	$\{a\}$	$\{b\}$
a	$\{0\}$	$\{0,a\}$	$\{b\}$
b	$\{0\}$	$\{b\}$	$\{0,b\}$

By apply definition 2.1, we get $(H,\circ,0)$ is a hyper AT-algebra. The subset A= {0, *b*} is a hyper ideal but it is not a hyper AT-ideal, because $0\circ(b\circ a)$ << A and $b\in$A; but $a\notin$A.

Definition 2.9[4].Let$(H,\circ,0)$be a hyper AT-algebra and K be a nonempty subset of H and $0\in K$, then
(1) K is named a weak hyper ideal, if $\chi\circ\gamma\subseteq K$ and $\chi\in K$, then $\gamma\in K,\forall\chi,\gamma\in H$.
(2) K is named a strong hyper ideal, if $\chi\circ\gamma\cap K\neq\varphi$ and $\chi\in K$, then $\gamma\in K$, $\forall\chi,\gamma\in H$.
Now, we review some concepts of fuzzy hyper AT-algebra and some useful theorems for this paper.

Definition 2.10[5]. Let $(H,\circ,0)$ be a hyper AT-algebra and μ be a fuzzy set of H. Then μ is named a fuzzy hyper AT-subalgebra if $\inf_{\nu\in\chi\circ\gamma}\mu(\nu)\geq\min\{\mu(\chi),\mu(\gamma)\}$,$\forall\,\chi,\gamma,\nu\in H$.

Example 2.11[5]. If $H=\{0,a,b\}$ and $\circ$ is a hyper operation on H defined in the following table

∘	0	A	b
0	$\{0\}$	$\{a\}$	$\{b\}$
a	$\{0\}$	$\{0,a\}$	$\{a,b\}$
b	$\{0\}$	$\{0,a\}$	$\{0,a,b\}$

So, $(H,\circ,0)$ is a hyper AT-algebra. If g: $H\rightarrow[0,1]$ is a fuzzy set and is defined by
g (a)=0.5 ,g(0) = 0.7, and g (b)=0.2 . Then g is a fuzzy hyper AT-subalgebra of H.
Definition 2.12[5].Ifμ :$H\rightarrow[0,1]$ is a fuzzy set in a hyper AT-algebra $(H,\circ,0)$. Then μ is named a fuzzy hyper AT-ideal of H, if $\forall\chi,\gamma,\nu,u\in H$, $\chi\ll\gamma$ implies $\mu(\gamma)\geq\mu(\chi)$ and $\mu(\chi\circ\nu)\geq\min\{\inf_{u\in(\chi\circ(\gamma\circ\nu))}\mu(u),\mu(\gamma)\}$.

Example 2.13[5]. If $H=\{0,a,b\}$ and $\circ$ is a hyper operation on H defined in the following table

∘	0	a	b
0	$\{0\}$	$\{a\}$	$\{b\}$
a	$\{0\}$	$\{0,a\}$	$\{a,b\}$
b	$\{0\}$	$\{0,a\}$	$\{0,a,b\}$

Hence $(H,\circ,0)$ is a hyper AT-algebra. If μ: $H\rightarrow[0,1]$ is defined by
$\mu(0)=\mu(a)=\alpha_1>\alpha_2=\mu(b)$. $\Rightarrow\mu$ is a fuzzy hyper AT-ideal of H.

Definition 2.14[5].Let $(H,\circ,0)$ be a hyper AT-algebra and μ:$H\rightarrow[0,1]$ be a fuzzy set . Then$\forall\chi,\gamma,\nu\in H$. The fuzzy set μ is named

(1) A fuzzy hyper ideal if $\chi\ll\gamma$, then $\mu(\gamma)\geq\mu(\chi)$ and $\mu(\gamma)\geq\min\{\inf_{\nu\in(\chi\circ\gamma)}\mu(\nu),\mu(\chi)\}$.

(2) A fuzzy weak hyper ideal if $\mu(0)\geq\mu(\gamma)\geq\min\{\inf_{\nu\in(\chi\circ\gamma)}\mu(\nu),\mu(\chi)\}$.

(3) A fuzzy strong hyper ideal if $\inf_{a\in(\chi\circ\chi)}\mu(a)\geq\mu(\gamma)\geq\min\{\sup_{\nu\in(\chi\circ\gamma)}\mu(\nu),\mu(\chi)\}$.

Definition2.15[2]. Let $\hat{E}=[e^L,e^U]$ be an interval number, where $0\leq e^L\leq e^U\leq 1$ and D[0, 1] be denotes the family of all closed sub-intervals of [0, 1], in other words
$D[0,1]=\{\hat{E}=[e^L,e^U]: e^L\leq e^U, where\ \ e^L,e^U\in[0,1]\}$.
The operations $\leq$, $\geq$, $=$, $rmin$, $rmax$ for two elements in D [0, 1] are defined as follows: let $\hat{E}=[e^L,e^U]$ and $\hat{B}=[b^L,b^U]$ in $D[0,1]$, then
1- $\hat{E}\leq\hat{B}\ \ iff\ \ e^L\leq b^L, e^U\leq b^U$;
2- $\hat{E}\geq\hat{B}\ \ iff\ \ e^L\geq b^L, e^U\geq b^U$;
3- $\hat{E}=\hat{B}\ \ iff\ \ e^L=b^L, e^U=b^U$ $\tilde{E}=\tilde{b}$ $iff\ e^L=b^L, e^U=b^U$;
4- $rmin\{\hat{E},\hat{B}\}=[min\{e^L,b^L\},min\{e^U,b^U\}]$;
5- $rmax\{\hat{E},\hat{B}\}=[max\{e^L,b^L\},max\{e^U,b^U\}]$.

It is obvious that $(D[0,1], \leq, \wedge, \vee)$ is a lattice with a least element $\hat{0} = [0,0]$ and a greatest element $\hat{1} = [1,1]$.
An interval valued fuzzy set $\tilde{\mu}$ in X is defined as $\tilde{\mu} = \{\chi, [\mu^L(\chi), \mu^U(\chi)]: \chi \in X\}$, where $\tilde{\mu}: X \to D[0,1]$ and $\mu^L(\chi) \leq \mu^U(\chi), \ \forall \chi \in X$. In this paper we use the interval fuzzy set $\Gamma = \{< \chi, \tilde{\mu}_\Gamma(\chi) >: \chi \in H\}$, where $\tilde{\mu}_\Gamma: H \to D[0,1]$ and we use the notations $\mu_\Gamma^L(\chi)$ and $\mu_\Gamma^U(\chi)$ to mean the left end point and the right end point, respectively such that $\tilde{\mu}_\Gamma(\chi) = [\mu_\Gamma^L(\chi), \mu_\Gamma^U(\chi)]$. For the sake of simplicity, we shall use the symbol
$\tilde{\mu}_\Gamma = [\mu_\Gamma^L, \mu_\Gamma^U]$ for the interval valued Γ.

3. An Interval valued fuzzy set of a hyper AT-algebra

Now, we study the notion of interval valued fuzzy set (briefly IVF) on a hyper AT-algebra, and present some characterizations of this idea.

Definition3.1. Let $(H, \circ, 0)$ be a hyper AT-algebra and $\tilde{\mu}_\Gamma: H \to D[0,1]$ be an IVF set of H . Then the level subset of $\tilde{\mu}_\Gamma$ is denoted by $U(\tilde{\mu}_\Gamma, \tilde{t})$ and it is defined by
$U(\tilde{\mu}_\Gamma, \tilde{t}) = \{\chi \in H: \tilde{\mu}_\Gamma(\chi) \geq \tilde{t}\}$, for every $[0,0] \leq \tilde{t} \leq [1,1]$.

Definition3.2. an IVF set $\tilde{\mu}_\Gamma$ of a hyper AT-algebra $(H, \circ, 0)$ is called IVF hyper AT-subalgebra if $\inf_{\nu \in (x \circ y)} \tilde{\mu}_\Gamma(\nu) \geq rmin\{\tilde{\mu}_\Gamma(\chi), \tilde{\mu}_\Gamma(\gamma)\}, \ \forall \chi, \gamma, \nu \in H$.

Example3.3. If $H = \{0, a, b\}$, and $\circ$ is a hyper operation on H defined in the following table

$\circ$	0	a	b
0	$\{0\}$	$\{a\}$	$\{b\}$
a	$\{0\}$	$\{0, a\}$	$\{a, b\}$
b	$\{0\}$	$\{0, a\}$	$\{0, a, b\}$

Then$(H, \circ, 0)$ is a hyper AT-algebra, an IVF set $\tilde{\mu}_\Gamma(\chi)$ is defined
$\tilde{\mu}_\Gamma(\chi) = \begin{cases} [0.2,0.7] & if \quad \chi = \{0, a\} \\ [0.1,0.3] & if \quad \chi = b \end{cases}$
And by apply definition3.2; we can prove that $\tilde{\mu}_\Gamma(\chi)$is an IVF hyper AT-subalgebra of H.

Proposition 3.4. If $\tilde{\mu}_\Gamma$ is an IVF hyper AT-subalgebra of H, then $\tilde{\mu}_\Gamma(0) \geq \tilde{\mu}_\Gamma(\chi), \ \forall x \in H$.

Proof. By Proposition 2.4, we have $0 \in \chi \circ \chi$, $\forall \chi \in H$. Then
$\inf_{0 \in (\chi \circ \chi)} \tilde{\mu}_\Gamma(0) \geq rmi\, n\{\tilde{\mu}_\Gamma(\chi), \tilde{\mu}_\Gamma(\chi)\} = \tilde{\mu}_\Gamma(\chi)$.

Proposition3.5. If $\tilde{\mu}_\Gamma$ is an IVF hyper AT-subalgebra of H, then $\tilde{\mu}_\Gamma(0 \circ \chi) \geq \tilde{\mu}_\Gamma(\chi)$, for all $\chi \in H$.

Proof. Using Proposition 3.4, we have
$\inf_{\chi \in (0 \circ \chi)} \tilde{\mu}_\Gamma(0 \circ \chi) \geq rmi\, n\{\tilde{\mu}_\Gamma(0), \tilde{\mu}_\Gamma(\chi)\} = \tilde{\mu}_\Gamma(\chi)$.

Theorem 3.6. The set $\tilde{\mu}_\Gamma = [\mu_\Gamma^L, \mu_\Gamma^U]$ in H is an IVF hyper AT-subalgebra if and only if μ_Γ^L and μ_Γ^U are IVF hyper AT-subalgebras of H.

Proof. Letμ_Γ^L and μ_Γ^U be IVF hyper AT-subalgebras of H and $\chi, \gamma \in H$. Then
$\inf_{\nu \in (\chi \circ \gamma)} \tilde{\mu}_\Gamma(\nu) = \left[\inf_{\nu \in (\chi \circ \gamma)} \mu_\Gamma^L(\nu), \inf_{\nu \in (\chi \circ \gamma)} \mu_\Gamma^U(\nu)\right] \geq \left[rmin\{\mu_\Gamma^L(\chi), \mu_\Gamma^L(\gamma)\}, rmin\{\mu_\Gamma^U(\chi), \mu_\Gamma^U(\gamma)\}\right] =$

$rmin\{[\mu_\Gamma^L(\chi),\mu_\Gamma^U(\chi)],[\mu_\Gamma^L(\gamma),\mu_\Gamma^U(\gamma)]\}=rmin\{\tilde{\mu}_\Gamma(\chi),\tilde{\mu}_\Gamma(\gamma)\}$, it follows that $\tilde{\mu}_\Gamma$ is an IVF hyper AT-subalgebra.
Conversely, if $\tilde{\mu}_\Gamma$ is an IVF hyper AT-subalgebra . Then for any$\chi,\gamma\in H$, we get
$\left[\inf_{\nu\in(\chi\circ\gamma)}\mu_\Gamma^L(\nu),\inf_{\nu\in(\chi\circ\gamma)}\mu_\Gamma^U(\nu)\right]=\inf_{\nu\in(\chi\circ\gamma)}\tilde{\mu}_\Gamma(\nu)\geq rmin\{\tilde{\mu}_\Gamma(\chi)\cdot,\cdot\tilde{\mu}_\Gamma(\gamma)\}=$
$rmin\{[\mu_\Gamma^L(\chi),\mu_\Gamma^U(\chi)],[\mu_\Gamma^L(\gamma),\mu_\Gamma^U(\gamma)]\}=[rmin\{\mu_\Gamma^L(\chi),\mu_\Gamma^L(\gamma)\},rmin\{\mu_\Gamma^U(\chi),\mu_\Gamma^U(\gamma)\}.$
It follows that
$\inf_{\nu\in(\chi\circ\gamma)}\mu_\Gamma^L(\nu)=rmin\{\mu_\Gamma^L(\chi),\mu_\Gamma^L(\gamma)\}$
And
$\inf_{\nu\in(\chi\circ\gamma)}\mu_\Gamma^U(\nu)=rmin\{\mu_\Gamma^U(\chi),\mu_\Gamma^U(\gamma)\}$
Then μ_Γ^L and μ_Γ^U are IVF hyper AT-subalgebras of H.

Theorem3.7. Let Γ be an IVF hyper set in a hyper AT-algebra H. ThenΓ is an IVF hyper AT-subalgebra if and only if the level set $U(\tilde{\mu}_\Gamma,\tilde{t})\neq\varphi$ of $\tilde{\mu}_\Gamma$ is a fuzzy hyper AT-subalgebra of H.

Proof. Let$U(\tilde{\mu}_\Gamma,\tilde{t})\neq\varphi$ for any $\tilde{t}=[t_1,t_2]\in D[0,1]$. Then there exists
$\chi,\gamma\in U(\tilde{\mu}_\Gamma,\tilde{t})$. and so $\tilde{\mu}_\Gamma(\chi)\geq\tilde{t}$ and $\cdot\tilde{\mu}_\Gamma(\gamma)\geq\tilde{t}$. And since Γ is an IVF hyper AT-subalgebra, then
$\inf_{\nu\in(\chi\circ\gamma)}\tilde{\mu}_\Gamma(\nu)\geq rmi\,n\{\tilde{\mu}_\Gamma(\chi)\cdot,\cdot\tilde{\mu}_\Gamma(\gamma)\}\geq rmi\,n\{\tilde{t}\cdot,\cdot\tilde{t}\}=\tilde{t}$. It follows that
$\nu\in U(\tilde{\mu}_\Gamma,\tilde{t})$, then $\chi\circ\gamma\ll U(\tilde{\mu}_\Gamma,\tilde{t})$
Hence $U(\tilde{\mu}_\Gamma,\tilde{t})$ is fuzzy hyper AT-subalgebra of H.
Conversely, let $U(\tilde{\mu}_\Gamma,\tilde{t})\neq\varphi$ and it is a fuzzy hyper AT-subalgebra for every
$\tilde{t}\in D[0,1]$. Suppose that there exists $\chi,\gamma\in H$ such that
$\inf_{\nu\in(\chi\circ\gamma)}\tilde{\mu}_\Gamma(\nu)<rmi\,n\{\tilde{\mu}_\Gamma(\chi),\tilde{\mu}_\Gamma(\gamma)\}$
By taking $\tilde{t}_0=\frac{1}{2}[\inf_{\nu\in(\chi\circ\gamma)}\tilde{\mu}_\Gamma(\nu)+rmin\{\tilde{\mu}_\Gamma(\chi),\tilde{\mu}_\Gamma(\gamma)\}]$. Then we have

$$\inf_{\nu\in(\chi\circ\gamma)}\tilde{\mu}_\Gamma(\nu)<\tilde{t}_0<rmin\{\tilde{\mu}_\Gamma(\chi),\tilde{\mu}_\Gamma(\gamma)\}$$

Hence $\chi\in U(\tilde{\mu}_\Gamma,\tilde{t})$ and $\gamma\in U(\tilde{\mu}_\Gamma,\tilde{t})$, but $\nu\notin U(\tilde{\mu}_\Gamma,\tilde{t})$ it follows that
$\chi\circ\gamma\gg U(\tilde{\mu}_\Gamma,\tilde{t})$, which means that $U(\tilde{\mu}_\Gamma,\tilde{t})$ is not fuzzy hyper AT-subalgebra of H. This is contradiction. Hence Γ is an IVF hyper AT-subalgebra of H.

Proposition 3.8. Let A be a nonempty subset of a hyper AT-algebra$(H,\circ,0)$ and $\tilde{\mu}_\Gamma$ be an IVF set in H, define by $\tilde{\mu}_\Gamma(\chi)=\begin{cases}[t_1,t_2] & \chi\in A\\ [0,0] & otherwise\end{cases}$, where $t_1>0$, $t_2>0$, and $t_1,t_2\in[0,1]$ with $t_1<t_2$. Then $\tilde{\mu}_\Gamma$ is an IVF hyper AT- subalgebra if and only if A is a hyper AT-subalgebra of H.

Proof . Let $\tilde{\mu}_\Gamma$ be an IVF hyper AT-subalgebra of $(H,\circ,0)$ and $\chi,\gamma\in A$. Then $\inf_{\nu\in(\chi\circ\gamma)}\tilde{\mu}_\Gamma(\nu)\geq rmin\{\tilde{\mu}_\Gamma(\chi),\tilde{\mu}_\Gamma(\gamma)\}=rmin\{[t_1,t_2],[t_1,t_2]\}=[t_1,t_2]$. It follows that $\nu\in A$ and thus $\chi\circ\gamma\ll A$. Hence A is a hyper AT- subalgebra.
Conversely, suppose that A is a hyper AT-subalgebra and $\chi,\gamma,\nu\in H$. If $y\notin A$ and $\chi\circ\gamma\ll A$, then clearly $\inf_{\nu\in(\chi\circ\gamma)}\tilde{\mu}_\Gamma(\nu)\geq rmin\{\tilde{\mu}_\Gamma(\chi),\tilde{\mu}_\Gamma(\gamma)\}$.
Assume that $\gamma\in A$ and $\chi\circ\gamma\gg A$. Then by Definition 2.5, we have $\chi\notin A$. Therefore $\inf_{\nu\in(\chi\circ\gamma)}\tilde{\mu}_\Gamma(\nu)=[0,0]=rmin\{\tilde{\mu}_\Gamma(\chi),\tilde{\mu}_\Gamma(\gamma)\}$
It follows that $\tilde{\mu}_\Gamma$ is an IVF hyper AT-subalgebra of H.

Definition3.9. Let $\tilde{\mu}_\Gamma$ be an IVF set of a hyper AT-algebra$(H,\circ,0)$. Then $\tilde{\mu}_\Gamma$ is named an IVF hyper AT-ideal, if for all $\chi,\gamma,\nu,a\in H$.

(i) $\chi\ll\gamma\ implies\ \tilde{\mu}_\Gamma(\chi)\geq\tilde{\mu}_\Gamma(\gamma)$
(ii) $\tilde{\mu}_\Gamma(\chi\circ\nu)\geq rmin\{\inf_{\nu\in(\chi\circ(\gamma\circ\nu))}\tilde{\mu}_\Gamma(a),\tilde{\mu}_\Gamma(\gamma)\}$

Example3.10. A set $H=\{0,a,b\}$ in Example3.3, we define $\tilde{\mu}_\Gamma$ by follows:
$\tilde{\mu}_\Gamma(0)=\tilde{\mu}_\Gamma(a)=[\alpha_1,\alpha_2]$ and $\tilde{\mu}_\Gamma(b)=[t_1,t_2]$ such that $\alpha_1>t_1$ and $\alpha_2>t_2$, then it is easy to see $\tilde{\mu}_\Gamma$ is an IVF hyper AT-ideal of H.

Definition3.11.Let $(H,\circ,0)$ be a hyper AT-algebra and $\tilde{\mu}_\Gamma: H\to D[0,1]$. Then for all $\chi,\gamma,\nu,a\in H$,

(1) $\tilde{\mu}_\Gamma$ is named an IVFhyper ideal if,

$\chi\ll\gamma\ implies\ \tilde{\mu}_\Gamma(\chi)\geq\tilde{\mu}_\Gamma(\gamma)$ and $\tilde{\mu}_\Gamma(\chi)\geq rmin\{\inf_{a\in(\gamma\circ\chi)}\tilde{\mu}_\Gamma(a),\tilde{\mu}_\Gamma(\gamma)\}$

(2) $\tilde{\mu}_\Gamma$ is named an IVF weak hyper ideal if ,

$$\tilde{\mu}_\Gamma(0)\geq\tilde{\mu}_\Gamma(\chi)\geq rmin\{\inf_{a\in(\gamma\circ\chi)}\tilde{\mu}_\Gamma(a),\tilde{\mu}_\Gamma(\gamma)\}$$

(3) $\tilde{\mu}_\Gamma$ is named an IVFstrong hyper ideal if,

$$\inf_{\nu\in(\chi\circ\chi)}\tilde{\mu}_\Gamma(\nu)\geq\tilde{\mu}_\Gamma(\chi)\geq rmin\{\sup_{a\in(\gamma\circ\chi)}\tilde{\mu}_\Gamma(a),\tilde{\mu}_\Gamma(\gamma)\}.$$

Proposition 3.12.If $\tilde{\mu}_\Gamma$ is an IVF strong hyper ideal of H, then
(1) $\tilde{\mu}_\Gamma(0)\geq\tilde{\mu}_\Gamma(\chi)$, for all $\chi\in H$,
(2) $\chi\ll\gamma\ implies\ \tilde{\mu}_\Gamma(\chi)\geq\tilde{\mu}_\Gamma(\gamma)$,
(3) $\tilde{\mu}_\Gamma(\chi)\geq rmin\{\tilde{\mu}_\Gamma(a),\tilde{\mu}_\Gamma(\gamma)\}$, for all $a\in\gamma\circ\chi$.

Proof. (1) By using Proposition 2.4, we have $0\in\chi\circ\chi$ for all $\chi\in H$. Hence
$\tilde{\mu}_\Gamma(0)\geq\inf_{\nu\in(\chi\circ\chi)}\tilde{\mu}_\Gamma(\nu)\geq\tilde{\mu}_\Gamma(\chi)$.
(2) Suppose that $\chi\ll\gamma$, then $0\in\gamma\circ\chi$. It follows that $\sup_{\nu\in(\gamma\circ\chi)}\tilde{\mu}_\Gamma(\nu)\geq\tilde{\mu}_\Gamma(0)$. By definition3.11and (1) , we have $\tilde{\mu}_\Gamma(\chi)\geq rmin\{\sup_{\nu\in(\gamma\circ\chi)}\tilde{\mu}_\Gamma(\nu),\tilde{\mu}_\Gamma(\gamma)\}\geq rmin\{\tilde{\mu}_\Gamma(0),\tilde{\mu}_\Gamma(\gamma)\}=\tilde{\mu}_\Gamma(\gamma)$.
(3) Let $a\in\gamma\circ\chi$. Since $\tilde{\mu}_\Gamma$ is an IVF strong hyper ideal of H, then
$\tilde{\mu}_\Gamma(\chi)\geq rmin\{\sup_{\nu\in(\gamma\circ\chi)}\tilde{\mu}_\Gamma(\nu),\tilde{\mu}_\Gamma(\gamma)\}\geq rmin\{\tilde{\mu}_\Gamma(a),\tilde{\mu}_\Gamma(\gamma)\}$.

Corollary 3.13. If $\tilde{\mu}_\Gamma$ is an IVF strong hyper ideal of H, then
$\tilde{\mu}_\Gamma(\chi)\geq rmin\{\inf_{\nu\in(\gamma\circ\chi)}\tilde{\mu}_\Gamma(\nu),\tilde{\mu}_\Gamma(\gamma)\}$, for all $\chi,\gamma\in H$.

Theorem3.14.If $(H,\circ,0)$ is a hyper AT-algebra and $\tilde{\mu}_\Gamma: H\to D[0,1]$. Then every IVF strong hyper ideal is an IVF hyper ideal of H.

Proof.If $\chi\ll\gamma$, then by proposition 3.12$\tilde{\mu}_\Gamma(\chi)\geq\tilde{\mu}_\Gamma(\gamma)$ and by Corollary 3.13, We have
$\tilde{\mu}_\Gamma(\chi)\geq rmin\{\inf_{\nu\in(\gamma\circ\chi)}\tilde{\mu}_\Gamma(\nu),\tilde{\mu}_\Gamma(\gamma)\}$.
Thus $\tilde{\mu}_\Gamma$ is an IVF hyper ideal of H.
The following example proves the converse of Theorem3.14 is not true.

Example 3.15. Let $H=\{0,1,2\}$ and $\circ$ be a hyper operation on H defined in the following table

$\circ$	0	1	2
0	{0}	{1}	{2}
1	{0}	{0,2}	{0,2}
2	{0}	{2}	{0,1}

is a hyper AT-algebra. An IVF set $\tilde{\mu}_\Gamma(\chi)$ is defined by

$$\tilde{\mu}_\Gamma(\chi) = \begin{cases} [0,0.9] & if\ \chi = 0 \\ [0.3,0.7] & if\ \chi = 1 \\ [0.1,0.2] & if\ \chi = 2 \end{cases}$$

Then we can simply prove that $\tilde{\mu}_\Gamma(\chi)$is an IVF hyper ideal. But it is not IVF hyper ideal since

$[0.1,0.2] = \tilde{\mu}_\Gamma(2) = \inf_{\nu \in (1\circ 1)} \tilde{\mu}_\Gamma(\nu) < \tilde{\mu}_\Gamma(1) = [0.3,0.7]$.

Theorem3.16. Let $(H,\circ,0)$ be a hyper AT-algebra and $\tilde{\mu}_\Gamma: H \to D[0,1]$. Then $\tilde{\mu}_\Gamma$ is an IVF hyper AT-ideal if and only if it is an IVF hyper ideal of H.

Proof. Let $\tilde{\mu}_\Gamma$ be an IVF hyper AT-ideal of H. Then

, $\chi \ll \gamma implies \tilde{\mu}_\Gamma(\chi) \geq \tilde{\mu}_\Gamma(\gamma)$ and $\tilde{\mu}_\Gamma(\chi \circ \nu) \geq rmin\{\inf_{a \in (\chi\circ(\gamma\circ\nu))} \tilde{\mu}_\Gamma(a), \tilde{\mu}_\Gamma(\gamma)\}$

put $\chi = 0$, we obtain

$\tilde{\mu}_\Gamma(\nu) = \tilde{\mu}_\Gamma(0 \circ \nu) \geq rmin\{\inf_{a \in (0\circ(\gamma\circ\nu))} \tilde{\mu}_\Gamma(a), \tilde{\mu}_\Gamma(\gamma)\} = rmin\{\inf_{a \in (\gamma\circ\nu)} \tilde{\mu}_\Gamma(a), \tilde{\mu}_\Gamma(\gamma)\}$. Hence $\tilde{\mu}_\Gamma$ is an IVF hyper ideal of H.

Conversely, suppose that $\tilde{\mu}_\Gamma$ is an IVF hyper ideal of H. Then

$\chi \ll \gamma\ implies\ \ \tilde{\mu}_\Gamma(\chi) \geq \tilde{\mu}_\Gamma(\gamma)$ and $\tilde{\mu}_\Gamma(\chi \circ \nu) \geq rmin\{\inf_{a \in (\gamma\circ(\chi\circ\nu))} \tilde{\mu}_\Gamma(a), \tilde{\mu}_\Gamma(\gamma)\}$. It follows that using Proposition2.4, we get $\tilde{\mu}_\Gamma(\chi \circ \nu) \geq rmin\{\inf_{a \in (\chi\circ(\gamma\circ\nu))} \tilde{\mu}_\Gamma(a), \tilde{\mu}_\Gamma(\gamma)\}$. Thus $\tilde{\mu}_\Gamma$ is an IVF hyper AT-ideal of H.

Corollary 3.17.Ina hyper AT-algebra$(H,\circ,0)$. Every IVF strong hyper ideal is an IVF hyper AT-ideal.

Proof. Clear

Definition3.18.Let $(H,\circ,0)$ be a hyper AT-algebra and $\tilde{\mu}_\Gamma: H \to D[0,1]$. Then for all $\chi,\gamma,\nu,a,b \in H$

(i) $\tilde{\mu}_\Gamma$ is named an IVFweak hyper AT-ideal if ,

$$\tilde{\mu}_\Gamma(0) \geq \tilde{\mu}_\Gamma(\chi \circ \nu) \geq rmin\{\inf_{a \in (\chi\circ(\gamma\circ\nu))} \tilde{\mu}_\Gamma(a), \tilde{\mu}_\Gamma(\gamma)\}$$

(ii) $\tilde{\mu}_\Gamma$ is named an IVF strong hyper AT-ideal if,

$\inf_{b \in (\chi\circ(\gamma\circ\nu))} \tilde{\mu}_\Gamma(b) \geq \tilde{\mu}_\Gamma(\chi \circ \nu) \geq rmin\{\sup_{a \in (\chi\circ(\gamma\circ\nu))} \tilde{\mu}_\Gamma(a), \tilde{\mu}_\Gamma(y)\}$.

Theorem 3.19. Ina hyper AT-algebra$(H,\circ,0)$. Then $\tilde{\mu}_\Gamma: H \to D[0,1]$ isIVF (weak, strong) hyper AT-ideal iff $\tilde{\mu}_\Gamma$ is an IVF (weak, strong) hyper ideal.

Proof. Similarly to theorem 3.16.

Theorem 3.20.Let $\tilde{\mu}_\Gamma$ be an IVF set of a hyper AT-algebra H.

(i) If $\tilde{\mu}_\Gamma$ is an IVF hyper ideal. Then $U(\tilde{\mu}_\Gamma, \tilde{t})$ is ahyper ideal, for all $[0,0] \leq \tilde{t} \leq [1,1]$ and $U(\tilde{\mu}_\Gamma, \tilde{t}) \neq \varphi$.

(ii) If $\tilde{\mu}_\Gamma$ is an IVF weak hyper ideal. Then $U(\tilde{\mu}_\Gamma, \tilde{t})$ is a weakhyper ideal, for all $[0,0] \leq \tilde{t} \leq [1,1]$ and $U(\tilde{\mu}_\Gamma, \tilde{t}) \neq \varphi$.

(iii) If $\tilde{\mu}_\Gamma$ is an IVF strong hyper ideal. Then $U(\tilde{\mu}_\Gamma, \tilde{t})$ is a stronghyper ideal, for all $[0,0] \leq \tilde{t} \leq [1,1]$ and $U(\tilde{\mu}_\Gamma, \tilde{t}) \neq \varphi$.

Proof.Let $\tilde{\mu}_\Gamma$ be an IVF set of a hyper AT-algebra H and

$[0,0] \leq \tilde{t} \leq [1,1]$ with $U(\tilde{\mu}_\Gamma, \tilde{t}) \neq \varphi$.

(i) Suppose that $\tilde{\mu}_\Gamma$ is an IVF hyper ideal and $\chi,\gamma \in H$ such that

$\gamma \circ \chi \ll U(\tilde{\mu}_\Gamma, \tilde{t})$ and $y \in U(\tilde{\mu}_\Gamma, \tilde{t})$. Then for all $v \in \gamma \circ \chi$, there exists $a \in U(\tilde{\mu}_\Gamma, \tilde{t})$ such that $v \ll a$, that is , $\tilde{\mu}_\Gamma(v) \geq \tilde{\mu}_\Gamma(a) \geq \tilde{t}$. Thus $\inf_{v \in (\gamma \circ \chi)} \tilde{\mu}_\Gamma(v) \geq \tilde{t}$ and by definition 3.11(1), we have $\tilde{\mu}_\Gamma(\chi) \geq rmin\{\inf_{v \in (\gamma \circ \chi)} \tilde{\mu}_\Gamma(v), \tilde{\mu}_\Gamma(\gamma)\} \geq \tilde{t}$. hence $\chi \in U(\tilde{\mu}_\Gamma, \tilde{t})$.Thus $U(\tilde{\mu}_\Gamma, \tilde{t})$ is ahyper ideal.

(ii) Let $\tilde{\mu}_\Gamma$ be an IVF weak hyper ideal and $\chi, \gamma \in H$ such that $\gamma \circ \chi \subseteq U(\tilde{\mu}_\Gamma, \tilde{t})$ and $\gamma \in U(\tilde{\mu}_\Gamma, \tilde{t})$. Then for all $v \in \gamma \circ \chi$, we have $v \in U(\tilde{\mu}_\Gamma, \tilde{t})$, that is , $\tilde{\mu}_\Gamma(v) \geq \tilde{t}$. Thus $\inf_{v \in (\gamma \circ \chi)} \tilde{\mu}_\Gamma(v) \geq \tilde{t}$ and by definition 3.11(2), we have $\tilde{\mu}_\Gamma(0) \geq \tilde{\mu}_\Gamma(\chi) \geq rmin\{\inf_{v \in (\gamma \circ \chi)} \tilde{\mu}_\Gamma(v), \tilde{\mu}_\Gamma(\gamma)\} \geq \tilde{t}$. Hence $\chi \in U(\tilde{\mu}_\Gamma, \tilde{t})$.Thus $U(\tilde{\mu}_\Gamma, \tilde{t})$ is a weakhyper ideal of H.

(iii) Suppose that $\tilde{\mu}_\Gamma$ is an IVF strong hyper ideal of H.

Let $x, y \in H$ such that $(\gamma \circ \chi) \cap U(\tilde{\mu}_\Gamma, \tilde{t}) \neq \varphi$ and $\gamma \in U(\tilde{\mu}_\Gamma, \tilde{t})$. Then there exists $v \in (\gamma \circ \chi) \cap U(\tilde{\mu}_\Gamma, \tilde{t})$, that is $v \in \gamma \circ \chi$ and $v \in U(\tilde{\mu}_\Gamma, \tilde{t})$, that is , $\tilde{\mu}_\Gamma(v) \geq \tilde{t}$. Thus $\sup_{v \in (\gamma \circ \chi)} \tilde{\mu}_\Gamma(v) \geq \tilde{t}$ and by definition 3.11(3), we have $\tilde{\mu}_\Gamma(\chi) \geq rmin\{\sup_{v \in (\gamma \circ \chi)} \tilde{\mu}_\Gamma(v), \tilde{\mu}_\Gamma(\gamma)\} \geq \tilde{t}$. Hence $\chi \in U(\tilde{\mu}_\Gamma, \tilde{t})$.Thus $U(\tilde{\mu}_\Gamma, \tilde{t})$ is a stronghyper ideal of H.

References

[1] Akram M , Yaqoob N and Kavikumar J 2014 Interval valued $(\tilde{\theta}, \tilde{\delta})$-fuzzy KU-ideals of KU-algebras *Int. J. Pure Appl. Math.* **92**(3) 335-349
[2] Atanassov K and Gargov G 1989Interval valued intuitionistic fuzzy sets *Fuzzy Sets and Systems* **31** 343-349
[3] Hameed A T 2018 AT-ideals & Fuzzy AT-ideals of AT-algebras *Journal of Iraqi AL-Khwarizmi Society* 1, 2 2521-2621
[4] Hameed AT, Kareem F F and Ali S H 2020 hyper AT-ideal on AT-algebra *Journal of Physics, Conf. Ser.* **1530** 012116
[5] Hameed A T, Kareem F F and Ali S H Fuzzy hyper AT-ideal on AT-algebra, Accepted in IOP Journal of Physics
[6] Jun Y B, Xin X L, Roh E H and Zahedi M M 2000 Strong hyper BCK-ideals of hyper BCK-algebra *Math. Jap.* **51**(3) 493-498
[7] Jun Y B and Xin X L 2001 Fuzzy hyper BCK-ideals of hyper BCK-algebras *Sci. Math. Jpn.* **53** (2) 415-422
[8] Lee K M 2004 Comparison of interval-valued fuzzy sets, intuitionistic fuzzy sets, and bipolar-valued fuzzy sets *J. Fuzzy Logic intelligent Systems* **14** 125-129
[9] Mostafa S M , Abd-Elnaby M A and ElgendyO R 2011 Interval-valued Fuzzy KU ideals in KU-algebras *Int. Math. Forum.* **64**(6) 3151-3159
[10] Mostafa S M, Radwan A E and Ibrahem F A 2015 Kareem F.F. Interval value fuzzy n-Fold KU-ideals of KU-algebras *J. Math.Comput.Sci.* **5**(2) 246-264

Closed Fuzzy Dominating Set in Fuzzy Graphs

Closed Fuzzy Dominating Set in Fuzzy Graphs

Hayder J. Yousif and [1] and Ahmed A. Omran[2]

Department of Mathematics, College of Education for Pure Science, University of Babylon, Babylon, Iraq

Email: hayderjasim36@gmail.com

Abstract. In this paper, we focus on closed fuzzy domination number of a fuzzy graph $G_F = (\eta, \rho)$by using effective edge and is denoted by $\gamma_{cl}(G_F)$ and we obtain some result on this concept, the relationship between $\gamma\gamma_{cl}(G_F)$ and some other concepts is obtained, finally the concept of closed fuzzy domination number of a join fuzzy graphs is introduced.

1. Introduction

FirstlyA.Zadeh [1] in 1965 suggested the mathematical framework to describe the phenomena of uncertainty in real life situation firstly. Rosenfeld [2] introduced the notion of fuzzy graph and several fuzzy analogs of graph theoretic concepts such as path, cycles and connectedness, The domination number played an important role via theoretical study in various fields as a fuzzy graph [3], topological graph [4], labeled graph [5]and others. Also, several applications in problems life were solved by these branches. So, the study of domination in fuzzy graphs worth to care. The notion of domination in fuzzy graphs was introduced by A.Somasundram, S.Somasundramby using effective edges[6,7] . NagoorGani and chanderskeran [8] discussed domination in fuzzy graph using strong arcs.In this work we introduce the concept of closed fuzzy domination number in fuzzy graph by effective edge.

2.Definitions

Definition2.1[9]: Consider $G = (V, E)$ be an undirected, finite and simple graph. A pair of function $\eta : V \to [0,1]$and $\rho: V \times V \to [0,1]$such that for all $x, y \in V$ we have $\rho(x, y) \leq \eta(x) \wedge \eta(y)$ is called a fuzzy graph and denoted by $G_F = (\eta, \rho)$. Where $\wedge$ is refer to minimum fuzzy value.

Definition2.2[9]: The edge $e = (x, y)$in a fuzzy graph $G_F = (\eta, \rho)$ is called effective edge if $\rho(x, y) \leq \eta(x) \wedge \eta(y)$.

Definition 2.3 [10]: The open neighborhood of a vertex $x \in V(G_F)$ is denoted by $N(x)$ and define as $N(x) = \{y \in V / (x, y)\ is\ effective\ edge\}$and $N[x] = N(x) \cup \{x\}$ is called closed neighbrho-rhoodof a vertex x.

Definition2.4 [10]: Afuzzy graph $G_F = (\eta, \rho)$is called strong if each edge belongs to it iseffecti-ve.

Definition 2.5[11]:The degree of a vertex x is the number of effective edges. And denoted by $\deg(x)$. The minimum degree of $G_F$is $\delta(G_F) = \wedge\{d(x), x \in V\}$ and the maximum degree of $G_F$is $\Delta(G_F) = \vee\{d(x) / x \in V\}$.

Definition2.6[11]: Let S be a subset of $V(G_F)$is a known as the independent fuzzy set if $\rho(x,y) < \eta(x) \wedge \eta(y)$ for all $x, y \in S$.

Definition2.7[7]: Let $A \subseteq V(GAF)$ is known as fuzzy vertex cover of G_F if for each effective Edge e = (u, w), at least on of u, w is in A. The minimum fuzzy cardinality of all minimum fuzzy vertex cover is known as fuzzy vertex covering number of $G_F$and is represented by $\alpha_0(G_{AF})$.

Definition2.8[11]: The fuzzy cardinality of A is defined as$\sum_{x\in A}\eta(x)$.

Definition2.9 [11]:The size m and order n of $G_F = (\eta, \rho)$ are defined to the number of edges and number of vertices respectively, i.e. $n = |V(G_F)|$ and $m = |E|$.

Definition2.10 The fuzzy sizeṢ and fuzzy order$P$ are define as Ṣ =$\sum_{uv\in E}\rho(u,v)$and Ṗ = $\sum_{x\in V}\eta(x)$ respectively.

Definition2.10 [12]: A subset D of a vertex set $V(G_F)$ is called fuzzy dominating set of G_F if for each vertex y in $V - D$ there exist a vertex x in D such that $\rho(x,y) = \eta(x) \wedge \eta(y)$.The minimum fuzzy cardinality for all minimum fuzzy dominating set in G_F is called the fuzzy domin-ation number of G_F and denoted byγ_f.

3.closed fuzzy domination number in fuzzy graph.

Definition 3.1 : Let $G_F = (\eta, \rho)$be any fuzzy graph on a vertex set $V = \{x_1, x_2, \dots, x_n\}$ a vertex sub set $D_k = \{x_1, x_2, \dots, x_k\}$ for some positive integer k, if $N[D_k] = V(G_f)$ then $D_k$is called closed fuzzy dominating (CFD) set of G_f .Where D_k is obtained by:

Choose $x_1 \in V(G_f)$, put $D_1 = \{x_1\}$,if $N[D_1]$= $V(G_f)$ then D_1 is called closed fuzzy dominating set if not, choose$x_2 \in V - D_1$(may $x_1 and\ x_2\ are\ adjacent$) put $D_2 = \{x_1, x_2\}$ if $N[D_2] = V(G_f)$, then D_2 is closed fuzzy dominating set if not, so on choose$x_k \in V - N[D_{k-1}], k \geq 3$, positive integer k such that $N[D_K] = V(G_f)$.

Definition3.2: A closed fuzzy dominating set $D_k$in a fuzzy graph $G_F = (\eta, \rho)$ is called minimum closed fuzzy dominating $(MCFD)$set if the number of vertices of all closed fuzzy dominating set greater than or equal the number of vertices in D_k.

Definition3.3:The minimum fuzzy cardinality of all minimum closed fuzzy dominating sets is called closed fuzzy domination number and denoted by $\gamma_{cl}(G_F)$.
I.e.$\gamma_{cl}(G_F) = min\{\sum_{x\in D_{ki}}\eta(x), D_{ki}\ is\ MCFD\ stes\}$.

Definition3.4:The minimum closed fuzzy dominating set has minimum fuzzy cardinality is called $\gamma_{cl} - set$.

Example3.1: Consider the fuzzy graph $G_F = (\eta, \rho)$, which is given in figure 1.
There are two $(MCFD)$ sets: $D_{k1} = \{y_1, y_2, z, x\} = \{x\} \cup N(y)andD_{k2} = \{x_1, x_2, z, y\} = N(x) \cup \{y\}$such that $N[D_{k1}] = V(G_f)$ and$N[D_{k2}] = V(G_f)$.
The closed fuzzy domination number $\gamma_{cl} = min\{||D_{k1}||, ||D_{k2}||\}$

$$= min\{0.9, 1\} = 1$$

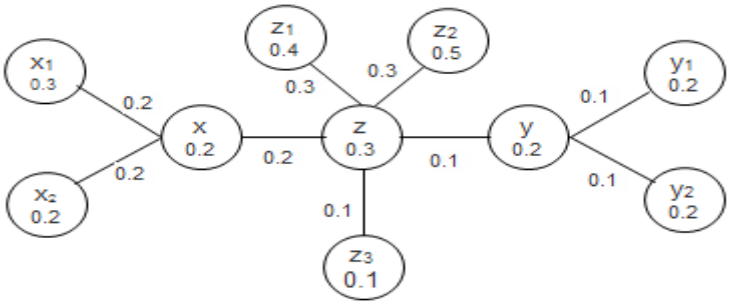

Fig 1

Preposition3.1: Every closed fuzzy dominating set of a fuzzy graph $G_F = (\eta, \rho)$ is a fuzzy dominating set of G_F .

Proof: We know that a vertex subset D_k of $V(G_F)$ in a fuzzy graph G_F is closed fuzzy dominating set if satisfy two conditions:
1) For every vertex x not in D_{k2}, x is dominated by at least one vertex of D_{k2} and also if D_{k2}contains more than two vertices then the third vertex must be not adjacent to the others.
2) $N[D_k] = V(G_f)$,it is clear that every vertex x not in D_k is dominated by a vertex of D_k,thus D_k is fuzzy dominating set of G_F.

Remark 3.1: Let $G_F = (\eta, \rho)$be a fuzzy graph has closed fuzzy dominating set then not necessary $\gamma_F \leq \gamma_{cl}$.

Preposition 3.2: For any fuzzy graph $G_F = (\eta, \rho)\, min\, \eta(x) \leq \gamma_{cl}(G_F) \leq$ P.Further upper bound equality holds if $\rho(\mathrm{x}, \mathrm{y}) < \eta(x) \wedge \eta(y) \forall x, y \in \eta^*$.

Proof: The lower and upper of the inequality are trivial from definition(CFD) set. If $\rho(\mathrm{x}, \mathrm{y}) < \eta(x) \wedge \eta(y) \forall x, y \in \eta^*$, then every vertex is isolated, thus there is only one $(MCFD)$ set which contains all vertices. Hence,$\gamma_{cl}(G_F) = P$.

Theorem 3.1:For every fuzzy dominating set contains at most two vertices of a fuzzy graph itis closed fuzzy dominating set.

Proof: LetD_k be a fuzzy dominating set of G_F contains at most two vertices. Then here are two cases:
Case1: If $D_k = \{x\}$ is trivial
Case2: If $D_k$contains two vertices say $D_k = \{x, y\}$,then $N[D_k] = V(G_f)$, thus no need to any other vertex z to be independent with x, y. Hence,$D_k$is closed fuzzy dominating set of G_F.
Corollary 3.1: Let$G_F = (\eta, \rho)$ be any fuzzy graph then $\gamma_f = \gamma_{cl}$ if G_f is one of the following
i) $G_F \cong K_{n,m}$ complete bipartite fuzzy graph.
ii) $G_F \cong K_n$ complete fuzzy graph.
iii) $G_F$is strong star fuzzy graph.
iv) $G_F$is strong wheel fuzzy graph.

Proof: Let $G_F = (\eta, \rho)$ be a fuzzy graph satisfying above condition, since a fuzzy dominating set of $K_{n,m}$contains two vertices and fuzzy dominating set of (K_n,strong star,strong wheel) has only one vertex. Hence, from theorem (3.1) we have $\gamma_f = \gamma_{cl}$.

Theorem 3.2: Every independent fuzzy dominating set of a fuzzy graph$G_F = (\eta, \rho)$ is closed fuzzy dominating set.

Proof: Let S_K be an independent fuzzy dominating set of G_F then there are two cases:
Case1: IfS_K contains only one vertex, then is trivial S_K is closed fuzzy dominating set .
Case2:If $S_K$contains more than two vertices,since $\rho(x,y) < \eta(x) \wedge \eta\,(y)$ for any two vertices in S_K,therefore every vertex in $V - S_K$ has at least one effective edge inS_K. Thus $N[S_K] = V(G_F)$ and each vertex in $S_K \in V - N[S_K]$. Hence,S_K is closed fuzzy dominating set.

Preposition 3.3: Let$G_F = (\eta, \rho)$be afuzzy graph without isolated vertex then $\gamma_{cl}(G_F) \leq \mathrm{P} - \alpha_0$ where α_0 is the vertex covering number of G_F.

Proof: Let$G_F = (\eta, \rho)$be afuzzy graph without isolated vertex and A is a vertex cover set of G_F then $V - A$ is independent set of G_F. Thus, by theorem (3.2),then $V - A$ is closed fuzzy dominating set of G_F. Hence,$\gamma_{cl}(G_f) \leq ||\,V - A|| = |n| - ||A|| = P - \alpha_0$.

Preposition3.4: Let $G_F = (\eta, \rho) \cong K_n$ then $\gamma_{cl}(K_n) = min\,\eta(x), x \in V(G_F)$.

Proof: Given $G_F \cong K_n$ be a complete fuzzy graph, then all edges in G_F are effective and each vertex dominates to all other vertices. Hence, the closed fuzzy dominating set is singleton sayD_K={x}
such that $N[D_K] = V(G_F)$ and x has minimum fuzzy value. Hence, the result is obtained.

Preposition3.5: Let $G_F = (\eta, \rho)$ be a strong fuzzy star graph then$\gamma_{cl}(G_F) = \eta(x)$, where x is a root vertex.

Proof: Let$G_F = (\eta, \rho)$ be a strong fuzzy star and $V(G_F)$ = $\{x, x_1, x_2, \dots, x_n\}$ where x is a root vertex, since each edge is effective and x is dominates $x_i i = 1,2, \dots, n.$ thus a closed fuzzy dominating set is singleton such that $N[x] = V(G_f)$. Hence, $\gamma_{cl}(G_F) = \eta(x)$.
Preposition 3.6: Let $G_F \cong K_{n,m}$ be a complete bipartite fuzzy graph with n , m vertices then $\gamma_{cl}(K_{n,m}) =$

$$\begin{cases} min\,\{|X|, min\,\eta(x_i) + min\,\eta(y_j)\} \;\; if\; 2 = n < m \;\; , \text{where} x_i \in X, y_j \in Y \\ min\,\{|y|, min\,\eta(x_i) + min\,\eta(y_j)\} \;\; if\; 2 = m < n \;\; , \text{where} x_i \in X, y_j \in Y \\ mi\,n\{|X|, |y|, min\,\eta(x_i) + min\,\eta(y_j)\}\, if n = 2 = m \;\; , \text{where} x_i \in X, y_j \in Y \\ min\,\sigma(x_i) + mi\,n\,\sigma(y_j) \;\; n\,, m \geq 3 \qquad\qquad , \text{where}\, x_i \in X, y_j \in Y. \end{cases}$$

Proof: Given $G_F \cong K_{n,m}$ and $V(K_{n,m})$=$X \cup Y$ where X={$x_1, x_2, \dots, x_n$}and $Y = \{y_1, y_2, \dots, y_m\}$. Since each vertex of X is adjacent to $y_j, j = 1,2, \dots, m$ and similarly each vertex of Y is adjacent to $x_i, i = 1,2, \dots, n$.Then, any minimum closed fuzzy dominating D_K contains two vertices thus there are three cases:

Case1: If *2= n < m* andif there is a vertex $y_j \in Y, j = 1,2, \dots, m$ has a fuzzy value equal to the fuzzy values of one of the vertices of $x_i \in X, i = 1,2$.Then $\gamma_{cl}(K_{n,m}) = mi\,n\{|X|, min\,\eta(x_i) + min\,\eta\,(y_j)\}$, where $x_i \in X, y_j \in Y$,in the same manner if $2 = m < n$
$\gamma_{cl}(K_{n,m}) = mi\,n\{|Y|, min\,\eta(x_i) + min\,\eta\,(y_j)\}$. Where$x_i \in X, y_j \in Y$. if $2 = m < n$
Case2: If $n = 2 = m$ it is clear $\gamma_{cl}(K_{n,m}) = mi\,n\{|X|, |Y|, min\,n\,(x_i) + min\,n\,(y_j)\}, x_i \in X, y_j \in Y$

Case3:If $n, m \geq 3$since each vertex from X dominates to all vertices from Y and vice versa. Then, a $(MCFD)$ set of $K_{n,m}$ contains two vertices. Hence,$\gamma_{cl}(K_{n,m}) = min\,[n(x_i)] + min[n\,(y_j)]$,

where $x_i \in X$, $y_j \in Y$. The prove complete.

Preposition3.7: Let W_{n+1}be a strong fuzzy wheel, then $\gamma_{cl}(W_{n+1}) = \eta(x)$where x is a center vertexW_{n+1}.

Proof: Given W_{n+1}be a strong fuzzy wheel, since each edge is effective then x is dominates to $x_i, i = 1,2, \dots, n$. Then, a closed fuzzy dominating set $D_K = \{x\}$such that$N[D_K] = V(W_{n+1})$. Hence,$\gamma_{cl}(W_{n+1}) = \eta(x)$.

Preposition3.8: For any strong fuzzy graph $G_F = (\eta, \rho)$, $\gamma_{cl} \leq P - \sum_{y \in N(x)} \eta(y)$.

Proof: Let D_K be a$\gamma_{cl} - set$of $G_F$and $x$be a vertexof$G_F$such that $d(x) = \Delta(G_F)$. Then,$V - N(x)$ is(CFD) set, thus$|D_K| \leq |V - N(x)| = |n - \Delta(G_F)|$, take fuzzy cardinality to both sides hence,

4. closed fuzzy dominating set in join and union two fuzzy graphs.

Definition 4.1: Let $G_{F1} = (\eta_1, \rho_1)$ and $G_{F2} = (\eta_2, \rho_2)$be any two fuzzy graphs on V_1andV_1 respectively with $V(G_{F1}) \cap V(G_{F2}) = \emptyset$,the union of $G_{F1}$and G_{F2} is a fuzzy graph G_F defined on $V_1 \cup V_2$ as $G_F = G_{F1} \cup G_{F2} = (\eta_1 \cup \eta_2, \rho_1 \cup \rho_2)$ where:

$$(\eta_1 \cup \eta_2)(x) = \begin{cases} \eta_1(x) & if\ x \in V_1 \\ \eta_2(x) & if\ x \in V_2 \end{cases}$$

$$(\rho_1 \cup \rho_2)(x,y) = \begin{cases} \rho_1(x,y) & if\ (x,y) \in E_1 \\ \rho_2(x,y) & if\ (x,y) \in E_2 \\ 0 & otherwise \end{cases}$$

Theorem 4.1: Let $G_{F1} = (\eta_1, \rho_1)$ and $G_{F2} = (\eta_2, \rho_2)$ be any two strong fuzzy graphs then $\gamma_{cl}(G_{F1} \cup G_{F2}) = \gamma_{cl}(G_{F1}) + \gamma_{cl}(G_{F2})$.

Proof: Let $D_{k1}$and D_{k2} be a $\gamma_{cl} - sets$ of $G_{F1}$and G_{F2} respectively. Since $V_1 \cap V_2$=∅, then$D_{k1} \cap D_{k2} = \emptyset$. Therefore,$D_k = D_{k1} \cup D_{k2}$ is (CFD) set of $G_F = G_{F1} \cup G_{F2}$. Hence,
$\gamma_{cl}(G_F) = \gamma_{cl}(G_{F1} \cup G_{F2}) = ||D_{k1} \cup D_{k2}|| = ||D_{k1} + D_{k2}|| = \gamma_{cl}(G_{F1}) + \gamma_{cl}(G_{F2})$.

Definition4.2: Let$G_{F1} = (\eta_1, \rho_1)$ and $G_{F2} = (\eta_2, \rho_2)$ be any two fuzzy graphs on $V_1$and V_1 respectively with$V_1 \cap V_2 = \emptyset$, the join of G_{F1} and $G_{F2}$is a fuzzy graph $G_F = G_{F1} + G_{F2} = (\eta_1 + \eta_2, \rho_1 + \rho_2)$ where :

$$(\eta_1 + \eta_2)(x) = \begin{cases} \eta_1(x) & if x \in V_1 \\ \eta_2(x) & if\ x \in V_2 \end{cases} \text{ and}$$

$$(\rho_1 + \rho_2)(x,y) = \begin{cases} \rho_1(x,y) & if\ (x,y) \in E_1 \\ \rho_2(x,y) & if\ (x,y) \in E_2 \\ \rho_1(x) \wedge \rho_1(x) & if\ x \in E` \end{cases}$$

where $E`$ is the set of all edges joining vertices of V_1 with vertices of V_2.

Observation4.1: Consider join two strong fuzzy graphs$G_F = G_{F1} + G_{F2}$. For any $x \in V(G_{F1})$and $y \in V(G_{F2})$such that x and y have minimum fuzzy value, the set $\{x, y\}$ is a closed fuzzy dominate-ngset in $G_{F1} + G_{F2}$.Thus, $\gamma_{cl}(G_F) = \gamma_{cl}(G_{F1} + G_{F2}) = min(\eta(x)) + min\ (\eta(y))$.

Theorem 4.2: Let $G_{F1} = (\eta, \rho)$ and $G_{F2} = (\eta, \rho)$ be any two strong fuzzy graphs on $V_1$and V_2 respectively. Then,$\gamma_{cl}(G_F) = \gamma_{cl}(G_{F1} + G_{F2}) \leq min\ \{\gamma_{cl}(G_{F1}), \gamma_{cl}(G_{F2})\}$.

Proof: Let $S_1$and S_2 be a $\gamma_{cl}-$ sets of $G_{F1}$and G_{F2} respectively,by definition the join two fuzzy graphs ,we conclude that $S_1$and S_2 are closed fuzzy dominating sets of G_F. Hence $\gamma_{cl}(G_F) = \gamma_{cl}(G_{F1} + G_{F2}) \leq min\{|S_1|, |S_2|\}$ = min { $\gamma_{cl}(G_{F1}), \gamma_{cl}(G_{F2})$}.

Theorem4.3: Let $G_F = (\eta, \rho)$ be a strong fuzzy graph of *n* vertices , then:

i) $\gamma_{cl}(G_F) = \eta(x_1)$ if and only if $G_F = K_1$ or $G_f = K_1 + \bigcup_{i=1}^{k} H_i$ for Some $k \geq 1$ and connected strong fuzzy graph $H_1, H_2, \dots, H_k$.

ii) $\gamma_{cl}(G_F) = P$ if and only if $G_F = \overline{K_n}$;

iii) $\gamma_{cl}(G_F) = P - \eta(x)$ if and only if $G_F = K_2$or $G_F = K_2 \cup \overline{K_{n-2}}$.

Proof :

i) Suppose that $G_F = K_1 + \bigcup_{i=1}^{k} H_i$ for some $k \geq 1$ and connected strong fuzzy graph $H_1, H_2, \dots, H_k$, choose $x \in V(K_1)$ since $V(G_F) = N[x]$. Thus $\gamma_{cl}(G_F) = \eta(x)$. Conversely, assume that $\gamma_{cl}(G_F) = \eta(x)$ and let $x \in V(G_F)$ such that$\{x\}$ is a (CFD) set of G_F. If $G_F \neq K_1$,then $V(G_F) - \{x\} = N_{Gf}(x)$. Consequently,$G_F = K_1 + \bigcup_{i=1}^{k} H_i$For some $k \geq 1$ and connected strong fuzzy graph $H_1, H_2, \dots, H_k$.Hence, (i) is obtained.

ii) If $G_F = \overline{K_n}$ it clearly that$\gamma_{cl}(G_F) = P$. Suppose that $G_F \neq \overline{K_n}$. If $G_F = K_2$,then $\gamma_{cl}(G_F) = P - \eta(x) \neq P$a contradiction, suppose that $G_F \neq K_2$and let x and y be two adjacent vertices in $G_F$construct a (CFD) set $\{x_1, x_2, \dots, x_k\}$ in G_f such that $x_1 = x$ and $x_2 \neq y$. Then $K \leq n - 1$ vertices, thus $\gamma_{cl}(G_F) < P$, a contradiction. Hence, (ii) is proved.

iii) If n = 2, then a (CFD)set containing exactly one vertex,thus by (i) $\gamma_{cl}(G_F) = \eta(x)$. If and only if $G_F = K_2$. Now if $n \geq 3$. Suppose that $\gamma_{cl}(G_F) = P - \eta(x)$ then $\Delta(G_F) \geq 1$. Suppose that $\Delta(G_F) > 1$and let $x \in V(G_F)$ such that $d(x) = \Delta(G_F)$ construct a (CFD)set $\{x_1, x_2, \dots, x_k\}$ in $G_F$such that $x_1 = x$and $x_2 \in V(G_F) - N[x]$.Then $k \leq n - 2$, then$\gamma_{cl}(G_F) \neq P - \eta(x)$, a contradiction. Thus,$\Delta(G_F) = 1$ therefore$G_F = K_2 \cup \overline{K_{n-2}}$ .The converse is directly.

5. Conclusion

In this research paper a new type of fuzzy domination of fuzzy graph is presented ,which it is called The closed fuzzy domination , and we have studied some basic properties and determined this typeof fuzzy domination for some fuzzy certain graphs . Adding a closed fuzzy domination for some operation in fuzzy graphs discussed

References

[1] Zadeh L A 1965 Fuzzy Sets *Information and Control* **8** 338-353

[2] Rosenfeld A 1975 Fuzzy graphs InFuzzy sets and their applications to cognitive and decision processes Jan **1** 77-95 Academic Press

[3] Yousif H J and Omran AA 2020 The split anti fuzzy domination in anti fuzzy graphs *Journal of Physics: Conference Series* **1591**(1) 012054

[4] Jabor A A and Omran A A 2019 Domination in discrete topology graph *AIP Conference Proceedings* **2183** (1) 030006

[5] Al-Harere M N and Omran A A 2020 on Binary Operation Graphs *Boletim da SociedadeParanaense de Matematica* **38**(7) 59-67

[6] Somasundaram A and Somasundaram S 1998 Domination in fuzzy graphs–I *Pattern Recognition Letters* **19**(9) 787-91

[7] Somasundaram A 2005 Domination in fuzzy graphs-II *Journal of Fuzzy Mathematics* **13**(2):281

[8] Gani AN 2006 Chandrasekaran V T Domination in Fuzzy GraphAdvances in Fuzzy Sets and Systems (11) 17-26

[9] Gani AN, Devi KP and Pal M 2017Reduction of Domination Parameter in Fuzzy Graphs *Global Journal of Pure and Applied Mathematics* **13**(7) 3307-15

[10] Ponnappan C Y, Muthuraj R and Ahamed S B New Domination Parameters in Fuzzy Graphs

[11] Ponnappan C Y, Surulinathan P and Ahamed S B 2014 The strong split domination number of fuzzy graphs *International Journal of Computer &Organisation Trends* **3**(1)
[12] Xavior DA, Isido DF and Chtira VM 2013 On domination in fuzzy graphs *International Journal of Computing Algorithm* **2**(2) 81-2

Neural network for minimizing tricriteria objective function for machine scheduling problem

Neural network for minimizing tricriteria objective function for machine scheduling problem

Faez Hassan Ali , Hanan Ali Chachan and Sharmeen Bakr Abdulkareem

Department of Mathematics, College of Science, Al-Mustansiryah University, Baghdad, Iraq

E-mail: faezhassan@uomustansiriyah.edu.iq

Abstract. In this paper, neural networks (NN) are implemented to manipulate a problem of machine scheduling for a single machine to minimize multicriteria objective function: maximum tardiness, maximum late work and total late work simultaneously ($T_{max}, V_{max}, \sum V_j$). Also the results of applying NN are compared with some exact methods, some heuristic methods and local search methods [7,14]. The used NN is learned by pack propagation algorithm for $n = 3:500$ jobs. NN technique was be found to be effective and used to select the best efficient and optimal schedule which minimizes the objective function.

1. Introduction

When the single Machine Scheduling Problem (MSP) concerns Non Polynomial-hard (NP-hard) problem, the computational time requirements are enormous for large sized problem, to avoid these drawbacks we can appeal to heuristics methods. In recent years, the improvement in heuristic methods has become under the name “local search methods (LSM)”. The local search provides approach high quality solutions to NP- hard problems of a realistic size in reasonable time. The LSM's start with an initial solution and then continually try to add better solution by searching neighborhoods [1].

The concept of Neural Networks (NN) came into being when the first model of neuron was created by two physiologists, Warren S. McCulloch and Walter H. Pitts in 1943 [2]. Willems and Rooda (1994) [3] looked at first formulating a job shop scheduling problem as an integer programming problem, and using a NN to solve the resultant integer programming problem. Foo and Takefuji (1998) [4], employed integer linear programming NNs to minimizing the total starting times of all jobs with a precedence constraint. Hamad et al., (2002) [5], presented a method for machine scheduling with common due date on single machine which depended on artificial NN. The objective of this problem is to minimize the total earliness and the total tardiness cost. The paper of Muralidhar and Alwarsamy (2013) [6] considers the problem of scheduling jobs on parallel machines with the combined objective to minimize the makespan, total tardiness and total earliness using NN technique. Abdul-Razaq and Ali (2014) [2] presented an approach for scheduling problem on single machines with multi objective to decrease the total completion of time and the total tardiness by using NN.

One of the important local search methods is Particle swarm optimization (PSO) which introduced by R. Eberhart and J. Kennedy in 1995. This method is obtained from the experiments with some algorithms that depend on the “flocking behavior” which are seen in some kinds of birds. PSO is an

optimization algorithm that lies under the soft computing umbrella which is covers genetic algorithm (GA) and some evolutionary algorithms [7].

The Bees Algorithm (BA) is an optimization algorithm inspired by the natural foraging behavior of honey bees to find the optimal solution. The pseudo code for the BA in its simplest form is mentioned in [7].

In section 2 we discuss some important terminologies and notations for MSP. The NN is discussed in details in section 3. The MSP formulation of this paper is detailed in section 4, while the experimental results of applying NN, for the problems which will be discussed in this paper, are shown in section 5. In section 6 we discuss the analysis of the results of applying NN to solve MSP. Lastly, the conclusions are shown in section 7.

2. Machine Scheduling Terminologies and Notations

Most single MSPs (SMSP's) assume that the processing times of jobs are known and have fixed values through the process, and SMSP's has good learning effects form a new subfield in many areas like the scheduling [8].

In the classical scheduling models, most researchers consider that the job processing times are all constant numbers [9]. For decades, MSP researches will be more interest on one performance measures. The most real world with applications of scheduling, the researchers will be more interest in the multiobjectives which have received more attention in recent years [10].

Definition (1) [10]: The "optimize" term in a multicriteria decision making problem means that a solution with some objective which we can't improve it without worsening the other objectives.

Definition (2) [10]: Any feasible schedule σ is called Pareto optimal, or nondominated (or efficient) with respect to the objective functions f_1 and f_2 if there is no different feasible schedule π such that each $f_1(\pi) \leq f_1(\sigma)$ and $f_2(\pi) \leq f_2(\sigma)$, take in consider that at least one of the inequalities is strict. The more common notations which used in scheduling are:

n	:	number of jobs.
p_i	:	Processing time of job i.
d_i	:	Due date of job i.
C_i	:	Completion time of job i.
T_i	:	Tardiness of job i.
T_{max}	:	max $\{T_i\}$.
V_i	:	min$\{T_i, p_i\}$.
V_{max}	:	Max $\{V_i\}$.
ΣV_i	:	Sum of V_i.

3. Neural Network

The most important neural networks is the Feedforward neural networks (FNNs) which have been used widly in regressions and classification applications. To approximate any target continuous function we can use a single hidden layer feedforward networks with additive models. Single hidden layer feedforward networks have good role in many applications and have been implemented widly in both sides, the theory and application sides [11].

3.1 Back Propagation Algorithm

Back Propagation (BP) algorithm consists of two important stages, the forward stage and revers propagation. The NN contains hidden layer with output layer and lastly input layer, in which the states of used neurons in every layer can influence the neurons under them. As initial state, starting with the process wihch acts in forward propagation, the signal will be transmitted from the input layer to the hidden layer and calculated at the hidden layer. The results of calculation is recalculated in hidden layer

which are sended to the output layer and will be considered as output. The final results are compared with the some values called the expected valu, then the error which is the absolute differenes will be corrected by the reverse state propagation, which is conisdered as backtrack. In the hidden layer, a function which is used in this process is called the activation function. This process still be repeated. The random weights will be changed depending on the results in output layer through every reverse calculation propagation to reduce the error. When the error reach some spesfied value, stop the calculations [12].

The learning rate (η) determines the portion of weight needed to be adjusted. However, the optimum value of η depends on the problem. The momentum (α) determines the fraction of the previous weight adjustment that is added to current weight adjustment. It accelerates the network convergence process.

During the training process, the learning rate and the momentum are adjusted to bring the network out of its local minima, and to accelerate the convergence of the network [2]. The details of BP Algorithm are described in [2].

3.2 Fitness Criterion of NN

One of the stopping criterions is the fitness value. Since the BP algorithm is chosen to be a supervised learning algorithm, then there are observed values (O_i) and desired output values (G_i). These two values have to be compared, if they are closed to each other, then the fitness is good, else the algorithm must continue its calculations until this condition is satisfied or the specified number of iterations is finished [2].

The Mean Squared Error (MSE) is one of the tests for the comparison process:

$$\text{MSE} = \frac{1}{n}\sum_{i=1}^{n}(O_i - G_i)^2 \quad \ldots(1)$$

where n is the number of the compared categories.

4. Problem Formulation

The problem of scheduling $N = \{1,2,\ldots,n\}$ the set of n jobs, these jobs are processed on a one machine to minimize the multicriteria which may be act as follows. Each job $j \in N$ has is to be processed on an one machine which can process only one job at a time, job j has a processing time p_j with due date d_j. All jobs are ready for processing at a time zero. If a schedule $\sigma = (1,2,\ldots,n)$ is given, then the completion time $C_j = \sum_{k=1}^{j} p_j$ for every job j can be calculated and then the tardiness of job j, $T_j = max\{C_j - d_j, 0\}$ is easy to compute. We aim to find a schedule $\sigma \in S$ (where S is the set of all possible feasible schedules) that minimizes the tricriteria problem. This problem belongs to simultaneous optimization.

4.1 The $1//(T_{max}, V_{max}, \sum V_j)$ Problem

We aim to find the order of the jobs on one machine to minimize the multicriteria $(T_{max}, V_{max}, \sum V_j)$. This problem, which is denoting by (P), can be formulated mathematically as follows:

$Z = min(T_{max}(\sigma), V_{max}(\sigma), \sum V_j(\sigma))$.

Subject to

$$\left.\begin{array}{rl} T_{\sigma(j)} \geq 0 & ,j = 1,\ldots,n \\ T_{\sigma(j)} \geq C_j - d_{\sigma(j)} & ,j = 1,\ldots,n \\ V_{\sigma(j)} \leq T_{\sigma(j)} & ,j = 1,\ldots,n \\ V_{\sigma(j)} \leq p_{\sigma(j)} & ,j = 1,\ldots,n \\ T_{\sigma(j)}, V_{\sigma(j)} \geq 0 & ,j = 1,\ldots,n \end{array}\right\} \quad \ldots(\text{P})$$

where $\sigma_{(j)}$ represents the position of job j in the schedule σ. The discussed P-problem is NP-hard because the problem $1//\sum_{j=1}^{n} V_j$ is NP-hard [13].

4.2 The $1//(T_{max} + V_{max} + \sum V_j)$ Problem

We aim to find the order of the jobs on one machine to minimize the the sum of maximum tardiness, maximum late work and total late work. This problem, which is denoting by (P_1), can be formulated mathematically as follows:

$$Z = min(T_{max}(\sigma) + V_{max}(\sigma) + \sum V_j(\sigma))$$

Subject to

$$\left.\begin{array}{ll} T_{\sigma(j)} \geq 0 & ,j = 1,\dots,n \\ T_{\sigma(j)} \geq C_j - d_{\sigma(j)} & ,j = 1,\dots,n \\ V_{\sigma(j)} \leq T_{\sigma(j)} & ,j = 1,\dots,n \\ V_{\sigma(j)} \leq p_{\sigma(j)} & ,j = 1,\dots,n \\ T_{\sigma(j)}, V_{\sigma(j)} \geq 0 & ,j = 1,\dots,n \end{array}\right\} \quad \dots(P_1)$$

5. Experimental Results of Applying NN for P and P_1-Problems

For the two problems (P) and (P_1), a simulation has been constructed in order to apply the NN. For practical comparison, the Branch and Bound (BAB), Hybrid Method (HM) and Modified BAB (MBAB) details results are obtained from [14], and PSO and BA details results are obtained from [7].

5.1 Constructing of Multi-Layer NN to Solve P and P_1-Problem

The NN which is proposed for the single machine to minmize the multiple criteria functions ($T_{max}, V_{max}, \sum V_j$) for MSP, is arranged into three layers of the processing units. First we have an input layer consists of (10) nodes, then the hidden layer consists of (8) nodes, lastly the output layer which include a single node. The number of units in each, the input and output layers depended on to the representation adopted for the MSP [15]. In the suggested representation of the proposed NN, the input layer contains important information interpreted the MSP in the form of a vector or string of continuous values. In table (1) we show the 10 input nodes which are designed to contain the important information for each job that have to be scheduled [5].

Table 1. 10 units information of input layer units of NN [5].

Input units									
1	**2**	**3**	**4**	**5**	**6**	**7**	**8**	**9**	**10**
$\frac{p_j}{M_p}$	$\frac{d_j}{M_d}$	$\frac{SL_j}{M_{sl}}$	$\frac{\alpha_j}{10}$	$\frac{\beta_j}{10}$	$\frac{\overline{p}}{M_p}$	1	$\frac{\overline{SL}}{M_{sl}}$	$\sqrt{\frac{\sum(p_j - \overline{p})^2}{n \times \overline{p}^2}}$	$\sqrt{\frac{\sum(SL_j - \overline{SL})^2}{n \times \overline{SL}^2}}$

where SL_j slack for job *j*such that $SL_j = d_j - p_j$,

M_p: longest processing time among the n jobs $= max\{p_j\}$.

M_d: longest due date among the n jobs$= max\{d_j\}$.

M_{sl}: largest slack time for the n jobs $= max\{SL_j\}$,

$\alpha_j = \beta_j = 1, j \in N, N = \{1,2,\dots,n\}$.

$\overline{p} = \sum_{j=1}^{n} \frac{p_j}{n}$ and $\overline{SL} = \sum_{j=1}^{n} \frac{SL_j}{n}$ are the mean of processing times and slak time respectivly.

Thus, 10-input vectors represent each job, which includes information related to that job and the relation of this job to the other jobs in the MSP. The output unit includes values that are in the range of [0.10-0.90], the value being an pointer of where this job represented at the input layer should where its position lie in this schedule. Low values should put in the beginig positions in this schedule, while higher values which has less priority and the job position put in the end of tis schedule. The objective value related for each input training pattern is a target value that assigns the position determines the best or optimal schedule. The objective value G_j for the job has the j^{th} position in the best or optimal schedule is calculated as in equation (2) [5];

$$G_j = \left\{0.1 + 0.8 \times \left(\frac{j-1}{n-1}\right)\right\}, j = 1,2,\dots,n \quad \text{...(2)}$$

Equation (2) ensures that the n target values are distributed evenly between $0.1-0.9$. The number of units in the hidden layer is selected by trial and error during the training phase. The suggested final network for single machine with multi objective has 8 units in its hidden layer and 1 unit of output layer, therefore known as $10-8-1$ network.

5.2 Neural Network BP -Training Results

To train the proposeded NN, each vector with their output is presented individually at the input layer and output layer of the NN. Before we disscuss the NN training we will describe the proposed NN-Scheduling algorithm using BP as a learning algorithm.

NN-Scheduling Algorithm for P and P_1-problem

Step(1):READ (n) { n=*number of jobs*}
READ (p_j , d_j) { *processing time and due date*}
Step(2):DEFINE input units { *as input equations in Table* (1) }
Calculate G_j {*actual value as in equation* (2)}
Step(3):INITIALIZATION
W_{jkl} =random$(-1,1)$ {*weight in layer j, node k connected node l*}
Step(4):IMSE = Maxint; Error= 0.0001; Threshold=0.01{*specified by experiance*}
Iter=0; NI=10000; BSC=Mxint; BST=Maxint;
WHILE (Iter ≤ NI) AND (IMSE >Error) DO
Iter = Iter + 1;
Compute MSE { *using equation* (1) }
σ =*SORT*(O_j);
IF$(T(\sigma) < BT)$ *OR* $(V(\sigma) < BV)$*OR* $(SV(\sigma) < BSV)$*THEN*
{IF $(T(\sigma) + V(\sigma) + SV(\sigma) < BT + BV + BSV)$*THENfor P1}*
$\sigma' = \sigma; BT = T(\sigma); BV = V(\sigma); BSV = SV(\sigma)$; *IMSE=MSE*;
END; *{ENDIF}*
END; *{ ENDWHILE }*
Step(5):Best sequence= σ', with minmium BT, BV and BSV;
{with minmum $BT + BV + BSV$ for P1}
Step(6): END;

Training is considered completed after an average10000 cycles or more using a 10-8-1 configuration. A cycle is concluded after the network has been exposed once, in the course of the BP algorithm, to each one of the available training patterns. The trained NN is used to find job schedule for our problem.

Table (2) shows the comparison results of Effecinit Points (EP), consuming time, Average of MAE (AMAE) and MAER with EP of applying NN-BP for P-problem with CEM for $n = 3:10$.

MET : Method={CEM, HM, MBAB}.
NI : Number of iterations.
MSE : Mean square error.
MAER : MAE Relative =abs(best(EP of MET)-best(EP of BP)) / best(EP of MET)
R : 0≤Real value≤1.
F : Objective or target function of Problem (P).
F_1 : Objective or target function of Problem (P_1).
BS : Best Solution.
CT : Complete Time.
BT : Best Time to obtain best value(s) of each experiment.
NI : Number of Iterations.

Table 2. Applying NN-BP for (P) for $n = 3:10$ and compared with CEM.

n	CEM		NN-BP			AMAE	MAER
	EP	CT	EP	CT	NI		
3	(4,4,5),(18,2,4)	R	(4,4,5)	R	2	(1.75,R,R)	(0,0,0)
4	(14,7,15),(15,6,15),(15,7,14)	R	(15,6,15)	2	12	(R,R,R)	(0,0,0)
5	(23,9,24),(24,9,23)	R	(23,9,24)	3	4	(R,0,R)	(0,0,0)
6	(20,9, 24),(24,10,20),(26 ,8,20)	R	(20,9,24)(26,10,20)	7	3	(R,R,R)	(0,0,0)
7	(27,10,28),(28,7,27)	R	(27,10,30)(28,7,27)	6	5	(0,0,R)	(0,0,0)
8	(34,10,39),(39,8,34)	3.1	(39,8,34)	6	2387	(R,R,R)	(0,0,0)
9	(30,10,33),(33,9,30),(37,7,30)	32.5	(33,9,30)	6	3	(R,R,R)	(0,0,0)
10	(35,7,35)	232	(35,7,35)	7	1165	0	(0,0,0)

Table (*3)* shows the comparison results of EP, consuming time, AMAE and MAER with EP of applying NN-BP for P-problem with HM for $n = 11:19$.

Table 3. Applying NN-BP for (P) for $n = 11:19$ and compared with HM.

n	HM		NN-BP			AMAE	MAER
	EP	CT	EP	CT	NI		
11	(42,9,45),(48,9,42)	R	(42,9,45)	7	384	(R,0,R)	(0,0,0)
12	(59,9,59),(60,8,59)	R	(60,8,59)	10	3194	(R,R,0)	(0,0,0)
13	(58,10,65),(63,8,58)	R	(58,10,65)	10	25	(R,R,R)	(0,0,0)
14	(65,10,65)	R	(65,10,65)	6	5	(0,0,0)	(0,0,0)
15	(77,10,79),(81,9,77)	R	(81,9,77)	7	8771	(R,R,R)	(0,0,0)
16	(76,10,78),(83,10,76)	R	(78,10,87)(83,10,76)	7	3251	(R,0,R)	(0,0,0)
17	(83,10,90),(86,9,83)	R	(83,10,90)	10	3036	(R,R,R)	(0,0,0)
18	(100,9,100)	R	(102,9,100)	7	113	(R,0,0)	(R,0,0)
19	(91,9,93),(93,10,91)	R	(91,10,97)(93,10,91)	11	10697	(0,R,R)	(0,0,0)

The shaded calls are similar value for the compared methods. Table (*4)* shows the comparison results of EP, consuming time, AMAE and MAER with EP of applying NN-BP for P-problem with HM for $n = 20:100$.

Table 4. Applying NN-BP for (P) for $n = 20:100$ and compared with HM.

n	HM		NN-BP			AMAE	MAER
	EP	CT	EP	CT	NI		
20	(118,10,120)(120,10,118)	2.0	(118,10,123)	7	2	(R,0,R)	(0,0,R)
30	(150,10,155)(152,10,150)	9.1	(152,10,150)	11	10975	(R,0,R)	(0,0,0)
40	(198,10,198)	2.5	(198,10,202)(202,10,201)	12	1890	(R,0,R)	(0,0,R)
50	(259,10,264)(262,10,259)	97.7	(259,10,264)	13	251	(R,0,R)	(0,0,0)
60	(310,10,311)(312,10,310)	242.6	(312,10,310)	13	1296	(R,0,0)	(0,0,0)
70	(367,10,367)	9.9	(367,10,367)	15	1	(0,0,0)	(0,0,0)
80	(425,10,425)	20.7	(425,10,430)	15	2093	(0,0,R)	(0,0,R)
90	(446,10,446)	38.2	(452,10,446)	16	7041	(R,0,0)	(R,0,0)
100	(542,10,548)(543,10,542)	1214.4	(542,10,548)	17	4763	(R,0,R)	(0,0,0)

Table (*5)* shows the comparison results of EP, consuming time, AMAE and MAER with EP of applying NN-BP for P-problem with MBAB for $n = 20:90$.

Table 5. Applying NN-BP for (P) for $n = 20:90$ and compared with MBAB.

n	MBAB		NN-BP			AMAE	MAER
	EP	CT	EP	CT	NI		
20	(118,10,123)(123,10,118)	R	(118,10,123)	7	2	(R,0,R)	(0,0,0)
30	(150,10,152)(152,10,150)	R	(152,10,150)	11	10975	(R,0,R)	(0,0,0)
40	(198,10,198)	R	(198,10,202)(202,10,201)	12	1890	(R,0,R)	(0,0,R)
50	(259,10,262)(262,10,259)	2.0	(259,10,264)	13	251	(R,0,R)	(0,0,R)
60	(310,10,311)(311,10,310)	3.8	(312,10,310)	13	1296	(R,0,R)	(R,0,0)
70	(367,10,368)(368,10,367)	5.5	(376,10,367)	15	1	(R,0,R)	(R,0,0)
80	(425,10,425)	3.9	(425,10,430)	15	2093	(0,0,R)	(0,0,R)
90	(446,10,447)(447,10,446)	10.9	(452,10,446)	16	7041	(R,0,R)	(R,0,0)

Table (*6)* shows the comparison results of EP, consuming time, AMAE and MAER with EP of applying NN-BP for P-problem with MBAB for $n = 100:500$.

Table 6. Applying NN-BP for (P), $n = 100:500$ and compared with MBAB.

n	MBAB		NN-BP			AMAE	MAER
	EP	CT	EP	CT	NI		
100	(542,10,543)(543,10,542)	14.7	(542,10,548)	17	4763	(R,0,R)	(0,0,R)
200	(1085,10,1086)(1086,10,1085)	38.8	(1087,10,1090)	25	3	(R,0,R)	(R,0,R)
300	(1647,10,1647)	65.5	(1656,10,1647)	45	8	(R,0,0)	(R,0,0)
400	(2218,10,2218)	163.8	(2220,10,2222)	42	10	(R,0,R)	(R,0,R)
500	(2629,10,2629)	351.4	(2636,10,2629)	52	2	(R,0,0)	(R,0,0)

Table (7) shows the comparison results of CEM and NN-BP for P_1-problem using $n = 3:10$.

Table7. *The results of comparison of CEM and NN-BP for P_1-problem,*$n = 3:10$.

n	CEM		NN-BP				MAE
	OP of F_1	CT	BS of F_1	CT	NI	MSE	
3	13	R	13	R	2	0.0000	0
4	36	R	36	2	12	0.0000	0
5	56	R	56	3	4	0.0000	0
6	53	R	53	7	3	0.0000	0

7	62	R	62	6	5	0.0354	0
8	81	1.2	81	6	2387	0.0001	0
9	72	11.1	72	6	3	0.0000	0
10	77	134.8	77	7	1165	0.0010	0

Table (8) shows the comparison results of BAB and NN-BP for P_1-problem using $\mathrm{n} = 11{:}15$.

Table 8. The results of comparison of BAB and NN-BP for P_1-problem, $\mathrm{n} = 11{:}15$.

n	**BAB**		**NN-BP**				**MAE**
	OP of F_1	**CT**	**BS of F_1**	**CT**	**NI**	**MSE**	
11	96	31.4	96	7	384	0.0006	0
12	127	3.1	127	10	3194	0.0053	0
13	129	10.4	133	10	25	0.0041	0.03
14	140	5.2	140	6	5	0.0208	0
15	166	267.2	167	7	8771	0.0538	0.006
	658 131.6		663 132.6	AMAE=1.0			

The comparison results of BAB with NN-BP for P_1-problem, using $\mathrm{n} = 11{:}15$ *are shown in Figure (1).*

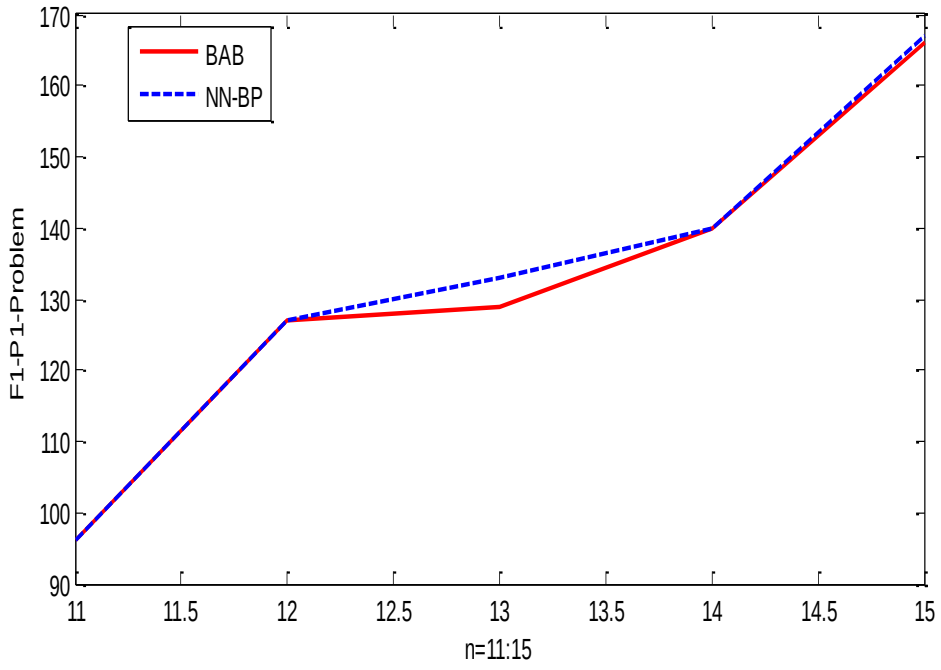

Figure 1. Comparison of NN-BP with BAB for P_1-problem using $\mathrm{n} = 11{:}15$.

Table (9) shows the comparison results of HM and NN-BP for P_1-problem using $\mathrm{n} = 20{:}100$.

Table 9. *The results of comparison of HM and NN-BP for* P_1*-problem,* $\mathrm{n} = 20{:}100$.

n	**HM**		**NN-BP**				**MAE**
	OP of F_1	**CT**	**BS of F_1**	**CT**	**NI**	**MSE**	
20	248	2	251	7	2	0.0372	R
30	312	9	312	11	10975	0.0328	0

40	406	3	410	12	1890	0.0326	R
50	531	98	533	13	251	0.0423	R
60	631	243	632	13	1296	0.0395	R
70	744	10	753	15	1	0.0361	R
80	860	21	865	15	2093	0.0432	R
90	902	385	908	16	7041	0.0512	R
100	1095	1214	1100	17	4763	0.0461	R
Sum	5729		5764	AMAE			3.8
Mean	636.6		640.4				

In figure 2, the comparison results between HM and NN-BP for P_1-problem for $n = 20:10:100$ are shown.

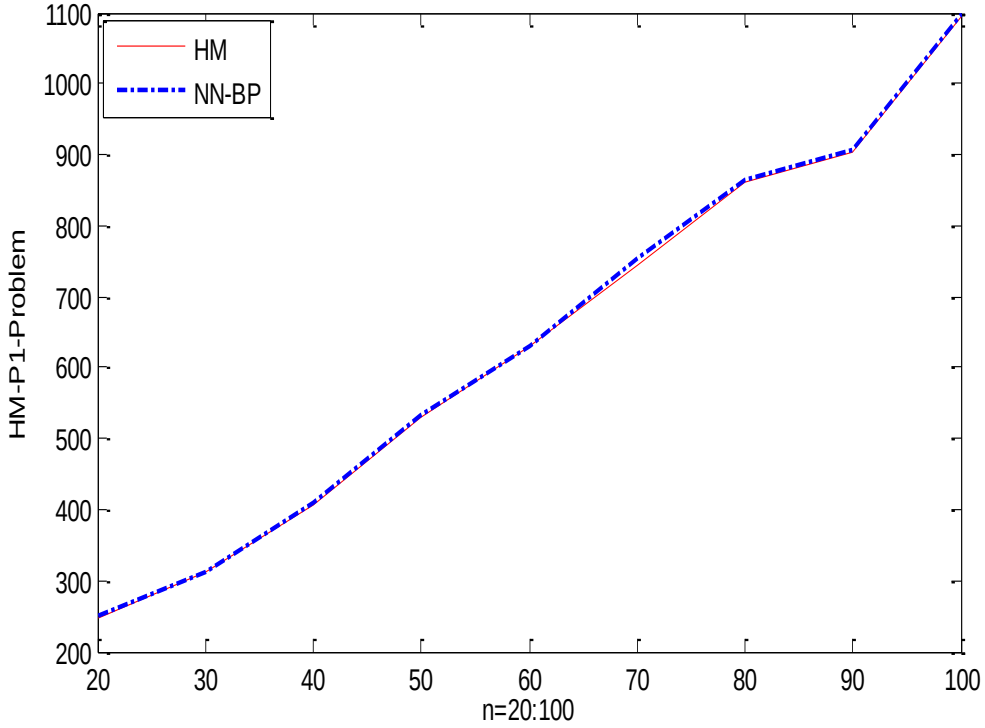

Figure 2. The F_1 results of applying HM and NN-BP for $n = 20:10:100$.

Table 10 shows the results of NN-BP, these results are compared with BA and PSO for P_1-problem using $= 100:100:500$.

Table 10. The results of comparison of NN-BP with BA and PSO for P_1-problem, $n = 100:500$.

n	**BA**		**PSO**		**NN-BP**				**MAE**	
	BS	**CT**	**BS**	**CT**	**BS**	**CT**	**NI**	**MSE**	**BA**	**PSO**
100	1097	20.3	1095	37.7	1100	17	4763	0.0461	R	R
200	2188	39.4	2182	73.7	2187	25	3	0.0237	R	R
300	3313	60.7	3304	111.5	3315	33	3	0.0174	R	R
400	4452	82.9	4447	149.9	4452	42	10	0.0156	0	R
500	5274	105.8	5268	198.6	5275	52	2	0.0122	R	R
sum	16324	-----	16296	-----	16329	----------			---------	
mean	3264.8		3259.2		3265.8					

In figure 3, *the comparison of the results* between NN-BP, BA, PSO for P_1-problem for n = $100:500$ are shown.

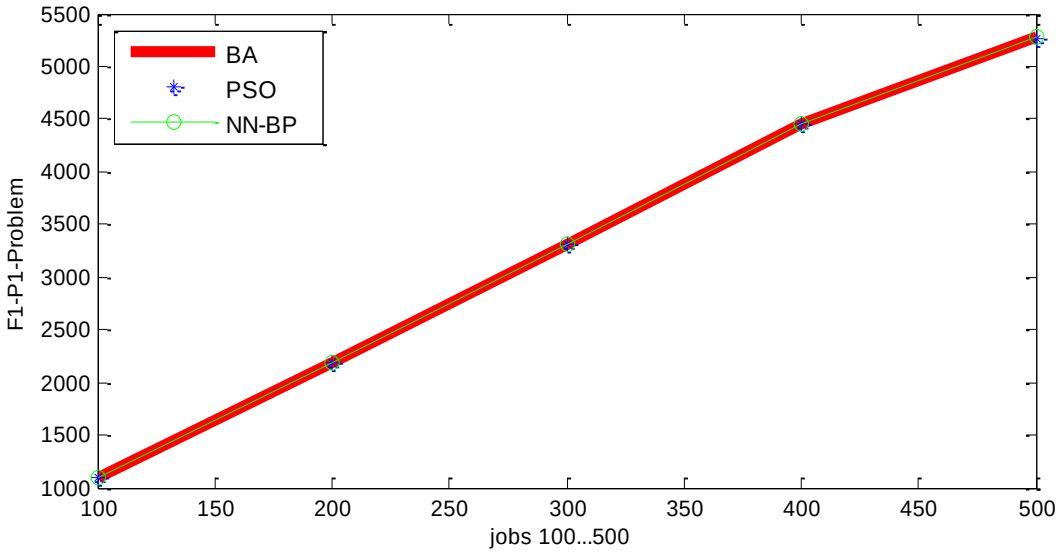

Figure (*3)* results of applying BA, PSO and NN-BP for $n = 100:500$.

6. Discussion and Analysis of Table Results

1. This paper discussed a various number of jobs (n), starting from $n = 3:10$, $n = 11:19$, $n = 20:10:90$ and $n = 100:100:500$, with number of iterations (NI) which is suitable to specific n to solve the two problems (P) and (P_1).
2. The parameters of testing the efficiency of LSM (BA and PSO) and NN-BP are calculated, these parameters represented by, the exact efficient solutions of F and F_1 (are calculated using CEM for $n \leq 10$), the local search and NN-BP best efficient solutions (EP) and their averages, the AMAE, MAER the consuming time which calculated for (5) experiments, the CT and BT and their averages and lastly, the number of iterations which found the corresponding BS or EP.
3. For problem (P):
   - Table (*2)*: NN has exact results compared with CEM for $n = 3:10$.
   - Table (*3)*:NN has MAER, near 100% similar to HM results for $n = 11:19$.
   - Table (5): MBAB is near to NN by (75%) for $n = 20:10:90$.
   - Table (4): HM is better than NN, in 5 similar from 9 solutions, for $n = 20:10:100$.
   - Table (6): MBAB is near to NN by (100%) for $n = 100:100:500$.
   - NN is better than HM, for $n = 11:19$.
   - NN has little difference in time with MBAB for $n = 20:10:90$.
   - NN is the best from BA, PSO and MBAB for $n = 100:100:500$.
4. For problem (P_1):
   - Table (*7*): NN has exact results compared with CEM for $n = 3:10$.
   - Table (8): NN has AMAE=1.0, so its very closed to BAB for $n = 11:15$ (see figure (1)).
   - Table (9): NN has AMEA=3.8 so its very closed to HM (see figure (2)) for $n = 20:10:100$.
   - Table (10): PSO has mean of BS= 3259.2, BA has mean of BS= 3264.8, while NN has mean of BS= 3265.8, but they are very closed to each other for $n = 100:100:500$ (see figure (3)).

7. Conclusions

1. An NN applied to solve the problems (P) and (P_1), were found that the NN gave an effecient and optimal solutions for $n \leq 500$.
2. NN is best in consuming time than BA and PSO, for all n for all common tables.
3. Some local search methods can be used as learning algorithms (like PSO or genetic algorithm) for NN to solve MSP.
4. An interesting future research topic would involve experimentation with exact, local Search and neural network algorithms for the following problems.
   a. $1/r_j/(T_{max}, V_{max}, \sum V_j)$.
   b. $1//lex(V_{max}, T_{max}, \sum V_j)$.
   c. $1//lex(\sum V_j, T_{max}, V_{max})$.

References

[1] Abdul-Razzaq K F 2014 Solving Multi-Criteria Scheduling Problems M.Sc. *Thesis,* Univ. of Al-Mustansiriyah, College of Science Dept. of Mathematics

[2] Abdul-Razaq T S and Ali F H 2014 Constructing of an Artificial Neural Network to Minimize Total Completion Time and Total Tardinss *IOSR Journal of Mathematics* **10**(2) 25-37

[3] Willems T T and Rooda J E 1994 Neural Network for Job-Shop Scheduling *Control Engineering Practice* **2** (1) 31-39

[4] Foo Y P S and Takefuji Y 1998 Integer Linear Programming Neural Networks for Job-Shop Scheduling *IEEE International Conference on Neural Networks* **2** 341-348

[5] Hamad A, Sanugi B and Salleh S 2002 Single Machine Common Due Data Scheduling Problems using Neural Network Journal Teknologi *Universiti Teknologi Malaysia* **36** 75-82

[6] Muralidhar A and Alwarsamy T 2013 Multi-Criteria Optimization of Parallel Machine Scheduling Using Neural Networks International *Journal of Latest Trends in Engineering and Technology* (IJLTET) **2** (2)

[7] Ali F H and Abdul-Kareem S B 2017 April Local Search Methods to Solve Multi-Criteria Machine Scheduling Problems *the 23th Scientific Conference Al-Mustansiriyah University, College of Education,* 26-27

[8] Kuo-Ching Y, Chung-Cheng L, Shih-Wei L and Jie-Ning C 2017 Single-Machine Scheduling with Learning Effects and Maintenance: A Methodological Note on Some Polynomial-Time Solvable Cases Hindawi *Mathematical Problems in Engineering* Article ID 7532174 6 pages https://doi.org/10.1155/2017/7532174

[9] Shang-Chia L,Wei-Ling H, and Chin-Chia W 2015 Note on a Single-Machine Scheduling Problem with Sum of Processing Times Based Learning and Ready Times Hindawi Publishing Corporation, *Mathematical Problems in Engineering* Article ID 452602 9 http://dx.doi.org/10.1155/2015/452602

[10] Abdul-Razaq T S and Ali F H 2016 Algorithms for Scheduling a Single Machine to Minimize Total Completion Time and Total Tardiness The 2nd International Conference on Mathematical Sciences-ICMA, 23-24 Oct. 2013, *Basrah Journal of Science* (A) **34** (2) 113-132

[11] Hai-Feng Ke, Cheng-Bo Lu, Xiao-Bo Li, Gao-Yan Zhang, Ying Mei and Xue-Wen Shen 2018 An Incremental Optimal Weight Learning Machine of Single-Layer Neural Networks Hindawi *Scientific Programming* Article ID 3732120 7 https://doi.org/10.1155/2018/3732120

[12] Bo Y, Yao Cui, Lin Z, Chao Zhang, Yongzhi Y, Zhenming B, and Guobao N 2014 Beam Structure Damage Identification Based on BP Neural Network and Support Vector Machine Hindawi *Publishing Corporation Mathematical Problems in Engineering* Article ID 850141 http://dx.doi.org/10.1155/2014/850141

[13] Potts C N and Van Wassenhove L N 1991 Single Machine Scheduling to Minimize Total Late Work Operations Research **40**(3) 586-595

[14] Ali F H and Abdul-Kareem S B 2017 Scheduling a Single Machine to Minimize Max Tardiness Max Late Work and Total Late Work *Mathematics and Statistics Journal* **3**(1)1-17
[15] El-Bourni A, Balakrishnan S and Popplewell N 2002 Sequencing Jobs on a Single Machine: A neural Network Approach *Euro Journal of Op. Res* **126** 474-490

Properties and Applications of Truncated Exponential Marshall Olkin Weibull Distribution

Properties and Applications of Truncated Exponential Marshall Olkin Weibull Distribution

Nadia Hashim Al-Noor and Hadi Hassan Hadi

Department of Mathematics, College of Science, Mustansiriyah University, Baghdad, Iraq

E-mail: nadialnoor@uomustansiriyah.edu.iq

Abstract. A new flexible compound distribution with four parameters called Truncated Exponential Marshall Olkin Weibull (TEMOW) is proposed as a sub-model of a new generator of continuous distributions named Truncated Exponential Marshall Olkin-G family. Reliability characteristics with several main statistical properties are presented. The maximum likelihood estimation method is adopted to estimate the unknown parameters. Furthermore, to assess the usefulness and flexibility, the TEMOW distribution applied upon simulation study besides real application with two real data set. The simulation results clearly shown the flexible performance of the maximum likelihood estimators for the parameters. Also, the real application results clearly shown that the proposed distribution has outstanding performance than other considered distributions for all information criteria.

1. Introduction

Over the last decades, various statistical distributions have been used to model data in a variety of areas. However, in some areas of use, there is a strong need to construct expanded versions of these distributions to adapt to particular real-life data. Several new generalized distributions have recently been developed and studied. Moreover, attempts continue to identify new families of probability distributions that expand well-known distribution families and at the same time providing greater flexibility in the practice of modeling results. One of the most important distributions is the Weibull distribution. It has been applied in various fields, especially to fit lifetime data. However, some of these applications are limited partly and this limitation undoubtedly inspired researchers to develop different generalizations and many modifications of this distribution in order to improve its flexibility. So, in this paper, based on the existing Weibull distribution, we introduce a new family of probability distributions arising from composing the work of Marshall and Olkin[1] with the work of Eugene et al. [2].

Marshall and Olkin [1] used tilting parameter α ($\alpha \geq 0$) to proposed an elastic family of probability distributions named Marshall Olkin-G (MO-G) with the following cumulative distribution function (cdf) and probability density function (pdf)

$$M(x)_{MO} = \frac{G(x)}{\alpha + \bar{\alpha}\, G(x)} \; ; \; \alpha \geq 0 \; , \bar{\alpha} = 1 - \alpha \tag{1}$$

$$m(x)_{MO} = \frac{\alpha\, g(x)}{\left(\alpha + \bar{\alpha}\, G(x)\right)^2} \tag{2}$$

where $G(x)$ and $g(x)$ are the cdf and pdf of any baseline distribution(see [3][4]).

Eugene et al. [2] introduced a new family built on the interval [0,1] beta distribution with the following cdf and pdf

$$F(x)_T = \frac{1}{\beta(a,b)} \int_0^{M(x)} z^{a-1} (1-z)^{b-1} \, dz \; ; \; 0 < a, b < \infty \tag{3}$$

$$f(x)_T = \frac{1}{\beta(a,b)} (M(x))^{a-1} (1-M(x))^{b-1} \, m(x) \tag{4}$$

where $\beta(a,b)$ is the Beta function, $M(x)$ and $m(x)$ are the cdf and pdf of any distribution.Then by taking $M(x)$ to be the cdf of the normal distribution, Eugene et al. defined the beta normal distribution and also derived some properties of this new distribution (see [2][5]).

Based on the two works above, our new family called truncated exponential Marshall Olkin – G has been built (for truncated distribution see [6]). The rest of this paper is structured as follows: In Section 2, the truncated exponential Marshall Olkin – G family is introduced with some general expressions. Then, in Section 3, attention is given to the truncated exponential Marshall Olkin Weibull as a particular member of this new family. In Sections 4, and 5 reliability measures and various properties of new distribution along with its entropies, and reliability stress strength model are introduced. In Section 6, the maximum likelihood estimators (MLEs) of the unknown parameters are presented. In Section 7, a simulation study is carried out to exhibit the performances of the MLEs, as well as, real applications are adopted to illustrate the behavior of the new distribution with some existing distributions. Finally, conclusions are addressed in Section 8.

2. Truncated exponential Marshall Olkin-G family

Considerthe cdf and pdf of the [0,1] truncated exponential (TE) distribution as

$$W(x)_{TE} = \frac{1 - e^{-\theta x}}{1 - e^{-\theta}} \; ; \; 0 < x < 1 \, , \theta > 0 \tag{5}$$

$$w(x)_{TE} = \frac{\theta e^{-\theta x}}{1 - e^{-\theta}} \tag{6}$$

Now,composing the two continuous cdfs,i.e. W and M,so that the cdf$F(x) = W\big(M(x)\big)$and pdf $f(x) = \frac{\partial}{\partial x} F(x)$ will be

$$F(x) = \int_0^{M(x)} \frac{\theta e^{-\theta u}}{1 - e^{-\theta}} \, du = \frac{1 - e^{-\theta M(x)}}{1 - e^{-\theta}} \tag{7}$$

$$f(x) = \frac{\theta m(x) e^{-\theta M(x)}}{1 - e^{-\theta}} \tag{8}$$

Substituting (1) and (2) in (7) and (8),a new family of probability distributions called Truncated Exponential Marshall Olkin-G (TEMO-G) can be proposed with the following cdf and pdf

$$F(x)_{TEMO-G} = \frac{1 - e^{-\theta \frac{G(x)}{\alpha + \bar{\alpha} \, G(x)}}}{1 - e^{-\theta}} \tag{9}$$

$$f(x)_{TEMO-G} = \frac{\theta \alpha g(x) e^{-\theta \frac{G(x)}{\alpha + \bar{\alpha} \, G(x)}}}{(1 - e^{-\theta})\big(\alpha + \bar{\alpha} \, G(x)\big)^2} \tag{10}$$

The formula of the pdf in (10)can be expansion by using the expressions $e^{-x} = \Sigma_{i=0}^{\infty} \frac{(-1)^i}{i!} x^i$ and $(1-x)^{-a} = \Sigma_{i=0}^{\infty} \frac{\Gamma(a+i)}{i! \, \Gamma(a)} x^i \, , |x| < 1, a > 0$ with performing some simple mathematical stepsas

$$f^E(x)_{TEMO-G} = \delta g(x) \big(G(x)\big)^{i+j} \tag{11}$$

where

$$\delta = \frac{1}{1 - e^{-\theta}} \Sigma_{i,j=0}^{\infty} \frac{(-1)^{i+j}}{i! \; j!} \frac{\Gamma(i+j+2)}{\Gamma(i+2)} \frac{\theta^{i+1} (\bar{\alpha})^j}{\alpha^{i+j+1}} \tag{12}$$

3- Truncated exponential Marshall Olkin Weibulldistribution

Let $G(x)$ and $g(x)$in (9), (10), and (11)be the cdf and pdf of the Weibull distribution [7] with two non-negative parametersλ and β,a new proposed distribution named Truncated Exponential Marshall Olkin Weibull($TEMOW$) distribution is attainedas a member of TEMO-G family with the cdf,pdf and expanded pdf respectively given by

$$F(x)_{TEMOW} = \frac{1 - e^{-\theta \frac{1-e^{-\lambda x^{\beta}}}{\alpha+\bar{\alpha}\left(1-e^{-\lambda x^{\beta}}\right)}}}{1 - e^{-\theta}} \tag{13}$$

$$f(x)_{TEMOW} = \frac{\theta\alpha\lambda\beta\, x^{\beta-1}\, e^{-\lambda x^{\beta}} e^{-\theta \frac{1-e^{-\lambda x^{\beta}}}{\alpha+\bar{\alpha}\left(1-e^{-\lambda x^{\beta}}\right)}}}{(1 - e^{-\theta})\left(\alpha + \bar{\alpha}\left(1 - e^{-\lambda x^{\beta}}\right)\right)^2} \tag{14}$$

and

$$f^{E}(x)_{TEMOW} = \delta\lambda\beta\, x^{\beta-1}\, e^{-\lambda x^{\beta}} \left(1 - e^{-\lambda x^{\beta}}\right)^{i+j} \tag{15}$$

with δas in (12).

The plots of some possible shapes of the cdf andpdf of the TEMOW distribution forspecific values of four parameters are presented in figures 1 and 2. Figure 1 clearly shows the characteristics of the cdf that are $0 \leq F(x)_{TEMOW} \leq 1$, strictly increasing, and continuous. Figure 2 shows some of the possible shapes of $TEMOW$pdf such as decreasing, right-skewed, symmetric,andsemi-symmetric. So, it is very flexible to model positive data.

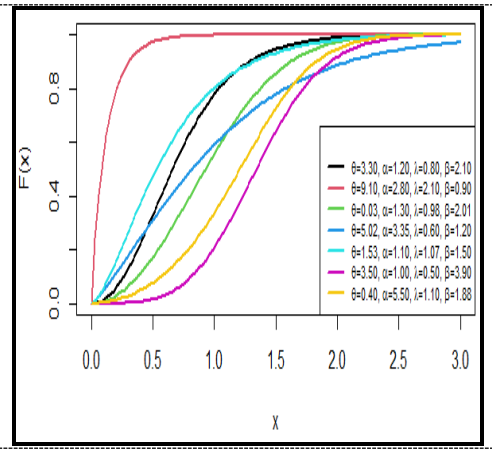

Figure 1. The plot of $TEMOW$ cdf for specific parameters values.

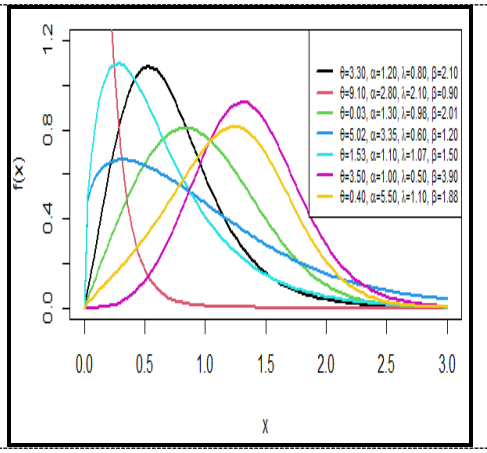

Figure 2. The plot of $TEMOW$ pdf for specific parameters values.

4- Reliability measures and properties of TEMOW distribution

The reliability measures (reliability, hazard, reverse hazard, and cumulative hazard functions) (see [8]) of the proposed TEMOW distribution easily can be found respectively as follows

$$R(x)_{TEMOW} = 1 - F(x)_{TEMOW} = 1 - \frac{1 - e^{-\theta \frac{1-e^{-\lambda x^{\beta}}}{\alpha+\bar{\alpha}\left(1-e^{-\lambda x^{\beta}}\right)}}}{1 - e^{-\theta}} \tag{16}$$

$$h(x)_{TEMOW} = \frac{f(x)_{TEMOW}}{R(x)_{TEMOW}} = \frac{\theta\alpha\lambda\beta\, x^{\beta-1}\, e^{-\lambda x^{\beta}} e^{-\theta\frac{1-e^{-\lambda x^{\beta}}}{\alpha+\bar{\alpha}\left(1-e^{-\lambda x^{\beta}}\right)}}}{\left(\alpha+\bar{\alpha}\left(1-e^{-\lambda x^{\beta}}\right)\right)^{2}\left(e^{-\theta\frac{1-e^{-\lambda x^{\beta}}}{\alpha+\bar{\alpha}\left(1-e^{-\lambda x^{\beta}}\right)}}-e^{-\theta}\right)} \quad (17)$$

$$\tau(x)_{TEMOW} = \frac{f(x)_{TEMOW}}{F(x)_{TEMOW}} = \frac{\theta\alpha\lambda\beta\, x^{\beta-1}\, e^{-\lambda x^{\beta}} e^{-\theta\frac{1-e^{-\lambda x^{\beta}}}{\alpha+\bar{\alpha}\left(1-e^{-\lambda x^{\beta}}\right)}}}{\left(\alpha+\bar{\alpha}\left(1-e^{-\lambda x^{\beta}}\right)\right)^{2}\left(1-e^{-\theta\frac{1-e^{-\lambda x^{\beta}}}{\alpha+\bar{\alpha}\left(1-e^{-\lambda x^{\beta}}\right)}}\right)} \quad (18)$$

$$H(x)_{TEMOW} = -\ln(R(x)_{TEMOW}) = -\ln\left(1-\frac{1-e^{-\theta\frac{1-e^{-\lambda x^{\beta}}}{\alpha+\bar{\alpha}\left(1-e^{-\lambda x^{\beta}}\right)}}}{1-e^{-\theta}}\right) \quad (19)$$

The plots of some possible shapes of the reliability and hazard functions of the TEMOW distribution for specific values of four parameters are presented in figures 3 and 4. Figure 3 clearly shows the characteristics of the reliability that are $0 \le \mathrm{R(x)_{TEMOW}} \le 1$, strictly decreasing, and continuous. Figure 4 shows some of the possible shapes of TEMOWhazard function such as monotonically increasing, monotonically decreasing, bathtub, right-skewed, left-skewed, and semi-constant.

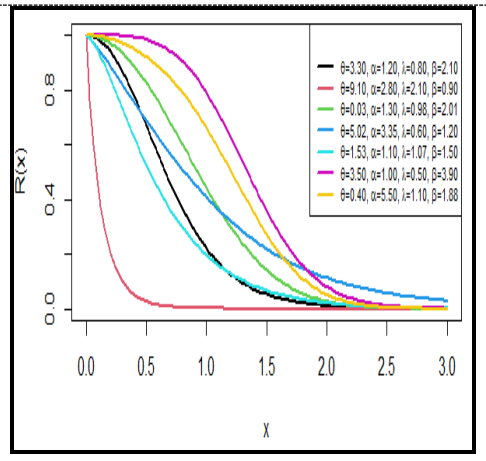

Figure 3. The plot of *TEMOW* reliability for specific parameters values.

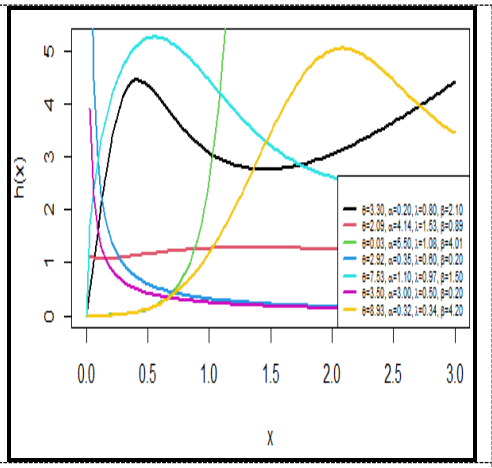

Figure 4. The plot of *TEMOW* hazard for specific parameters values.

Furthermore, themost essential statistical properties of TEMOW distribution can be found as follows: Therth moment can be foundregarding to (15)as follows

$$E(X^{r})_{TEMOW} = \int_{0}^{\infty} x^{r} f^{E}(x)_{TEMOW}\, dx = \delta \int_{0}^{\infty} x^{r}\lambda\beta\, x^{\beta-1}\, e^{-\lambda x^{\beta}}\left(1-e^{-\lambda x^{\beta}}\right)^{i+j} dx$$

Using the expression $(1-x)^{a} = \Sigma_{i=0}^{\infty}\frac{(-1)^{i}\,\Gamma(a+1)}{i!\,\Gamma(a-i+1)}x^{i}$, $|x|<1, a>0$,the $E(X^{r})_{TEMOW}$ will be

$$E(X^r)_{TEMOW} = \delta \int_0^{\infty} x^r \lambda\beta\, x^{\beta-1}\, e^{-\lambda x^{\beta}} \Sigma_{m=0}^{\infty} \frac{(-1)^m\, \Gamma(i+j+1)}{m!\ \Gamma(i+j-m+1)} e^{-\lambda m x^{\beta}}\, dx$$

$$= \delta\, \Sigma_{m=0}^{\infty} \frac{(-1)^m\, \Gamma(i+j+1)}{m!\ \Gamma(i+j-m+1)} \int_0^{\infty} x^r \lambda\beta\, x^{\beta-1} e^{-\lambda(m+1)x^{\beta}}\, dx$$

$$= \delta\, \Sigma_{m=0}^{\infty} \frac{(-1)^m\, \Gamma(i+j+1)}{m!\ \Gamma(i+j-m+1)} \frac{1}{m+1} \int_0^{\infty} x^r \lambda(m+1)\beta\, x^{\beta-1} e^{-\lambda(m+1)x^{\beta}}\, dx$$

But $\int_0^{\infty} x^r \lambda(m+1)\beta\, x^{\beta-1} e^{-\lambda(m+1)x^{\beta}}\, dx$represent the r^{th} moment of Weibull distribution with parameters$\lambda(m+1)$ and β, i.e. $\int_0^{\infty} x^r \lambda(m+1)\beta\, x^{\beta-1} e^{-\lambda(m+1)x^{\beta}}\, dx = \big(\lambda(m+1)\big)^{-\frac{r}{\beta}} \Gamma\left(\frac{r}{\beta}+1\right)$.
Thus the r^{th} moment of the $TEMOW$distribution is given by

$$E(X^r)_{TEMOW} = \delta\, \Sigma_{m=0}^{\infty} \frac{(-1)^m \Gamma(i+j+1)}{m!\ \Gamma(i+j-m+1)} \frac{1}{(m+1)^{\frac{r}{\beta}+1} \lambda^{\frac{r}{\beta}}} \Gamma\left(\frac{r}{\beta}+1\right) \quad (20)$$

The $TEMOW$characteristic function can be achievedfrom $\varphi_X(t)_{TEMOW} = \sum_{r=0}^{\infty} \frac{(it)^r}{r!} E(X^r)_{TEMOW}$ as

$$\varphi_X(t)_{TEMOW} = \delta \sum_{m,r=0}^{\infty} \frac{(-1)^m (it)^r\, \Gamma(i+j+1)}{m!\, r!\, \Gamma(i+j-m+1)} \frac{1}{(m+1)^{\frac{r}{\beta}+1} \lambda^{\frac{r}{\beta}}} \Gamma\left(\frac{r}{\beta}+1\right) \quad (21)$$

The $TEMOW$quantile function can be achieved through inverting the cdf in(13)as

$$x_{q-TEMOW} = \left[-\frac{1}{\lambda} \ln\left(1 + \frac{\alpha \ln\big(1-\big(1-e^{-\theta}\big)q\big)}{\theta + \bar{\alpha} \ln(1-(1-e^{-\theta})q)} \right) \right]^{\frac{1}{\beta}} \quad (22)$$

The median of TEMOW random variable can be gained from (22)by setting q = 0.5.Also, based on the quantile function with specific values, we can compute the skewness (γ_1) that defined by Galton [9], and kurtosis (γ_2) that defined by Moors [10], as

$$\gamma_1 = \frac{\mathrm{Q}(0.75) - 2\mathrm{Q}(0.5) + \mathrm{Q}(0.25)}{\mathrm{Q}(0.75) - \mathrm{Q}(0.25)}$$

$$\gamma_2 = \frac{\mathrm{Q}(0.875) - \mathrm{Q}(0.625) + \mathrm{Q}(0.375) - \mathrm{Q}(0.125)}{\mathrm{Q}(0.75) - \mathrm{Q}(0.25)}$$

where Q(.) = $x_{(.)-TEMOW}$ is computed from (22).
The $TEMOW$ random samplecan be simulated based on U that has a standard Uniform distribution as

$$x_{TEMOW} = \left[-\frac{1}{\lambda} ln\left(1 + \frac{\alpha\, ln\big(1-\big(1-e^{-\theta}\big)U\big)}{\theta + \bar{\alpha}\, ln(1-(1-e^{-\theta})U)} \right) \right]^{\frac{1}{\beta}} \quad (23)$$

5.Theentropies, reliability stress strengthandorder statistics of TEMOW distribution
Shannon entropy: Regarding to (14), theTEMOW Shannon entropy can be achievedas follows $SE_{TEMOW} = -\int_0^{\infty} \ln(f(x)_{TEMOW})\, f(x)_{TEMOW}\, dx$ with

$$\ln(f(x)_{TEMOW}) = \ln\left(\frac{\theta\alpha\lambda\beta}{1-e^{-\theta}}\right) + (\beta-1)\ln(x) - \lambda x^{\beta} - \theta \frac{1-e^{-\lambda x^{\beta}}}{\alpha + \bar{\alpha}\big(1-e^{-\lambda x^{\beta}}\big)}$$
$$- 2\ln\left(\alpha + \bar{\alpha}\left(1-e^{-\lambda x^{\beta}}\right)\right)$$

Then

$$SE_{TEMOW} = \ln\left(\frac{1-e^{-\theta}}{\theta\alpha\lambda\beta}\right) - (\beta-1)E(\ln(X)) + \lambda E\big(X^{\beta}\big) + \theta E\left(\frac{1-e^{-\lambda X^{\beta}}}{\alpha + \bar{\alpha}\big(1-e^{-\lambda X^{\beta}}\big)}\right)$$
$$+ 2E\left(\ln\left(\alpha + \bar{\alpha}\left(1-e^{-\lambda X^{\beta}}\right)\right)\right) \quad (24)$$

where $E\big(X^{\beta}\big)$ as in (20) with $r = \beta$, and

$$E(\ln(X)) = \int_0^\infty \ln(x)\, f^E(x)_{TEMOW}\, dx = \delta \int_0^\infty \ln(x)\, \lambda\beta\, x^{\beta-1}\, e^{-\lambda x^\beta} \left(1 - e^{-\lambda x^\beta}\right)^{i+j} dx$$

Since $\left(1 - e^{-\lambda x^\beta}\right)^{i+j} = \Sigma_{m=0}^\infty \frac{(-1)^m\, \Gamma(i+j+1)}{m!\, \Gamma(i+j-m+1)} e^{-\lambda m x^\beta}$, then

$$E(\ln(X)) = \delta \Sigma_{m=0}^\infty \frac{(-1)^m\, \Gamma(i+j+1)}{m!\ \Gamma(i+j-m+1)} \int_0^\infty \ln(x)\, \lambda\beta\, x^{\beta-1}\, e^{-\lambda(m+1)x^\beta} dx$$

Using the transformation $y = \lambda(m+1)x^\beta$ and then according to special formula of $\int_0^\infty \ln(y)\, e^{-y} dy = \psi(1)$(see [11]) where $\psi(.)$ represent the psi function, we get

$$E(\ln(X)) = \delta\, \Sigma_{m=0}^\infty \frac{(-1)^m\, \Gamma(i+j+1)}{\beta(m+1)!\ \Gamma(i+j-m+1)} \left[\psi(1) - \ln\big(\lambda(m+1)\big)\right] \quad (25)$$

and

$$E\left(\frac{1 - e^{-\lambda X^\beta}}{\alpha + \bar{\alpha}\big(1 - e^{-\lambda X^\beta}\big)}\right) = \int_0^\infty \frac{1 - e^{-\lambda X^\beta}}{\alpha + \bar{\alpha}\big(1 - e^{-\lambda X^\beta}\big)}\, f(x)_{TEMOW}\, dx$$

Using the expressions$(1-x)^{-a}$, $(1-x)^a$, and e^{-x}that mentioned previously, we obtain

$$E\left(\frac{1 - e^{-\lambda X^\beta}}{\alpha + \bar{\alpha}\big(1 - e^{-\lambda X^\beta}\big)}\right) = \sum_{m,l,t=0}^\infty \frac{(-1)^{m+l+t}\Gamma(m+2)}{l!\, t!\, \Gamma(m-l+2)} \frac{(\bar{\alpha})^m}{\alpha^{m+1}} (\lambda l)^t\, E\big(X^{t\beta}\big) \quad (26)$$

and

$$E\left(\ln\left(\alpha + \bar{\alpha}\left(1 - e^{-\lambda X^\beta}\right)\right)\right) = \int_0^\infty \ln\left(\alpha + \bar{\alpha}\left(1 - e^{-\lambda X^\beta}\right)\right) f(x)_{TEMOW}\, dx$$

Using the expressions $ln(1-x) = -\Sigma_{i=0}^\infty \frac{x^{i+1}}{i+1}$; $|x| < 1$, $(1-x)^a$, and e^{-x} we obtain

$$E\left(\ln\left(\alpha + \bar{\alpha}\left(1 - e^{-\lambda X^\beta}\right)\right)\right) = \ln(\alpha) + \sum_{m,l,t=0}^\infty \frac{(-1)^{m+l+t+2}\, \Gamma(m+2)}{(m+1)l!\, t!\ \Gamma(m-l+2)} \left(\frac{\bar{\alpha}}{\alpha}\right)^{m+1} (\lambda l)^t E\big(X^{t\beta}\big) \quad (27)$$

where $E\big(X^{t\beta}\big)$ as in (20) with $r = t\beta$.

Relative entropy:The relative entropyof the $TEMOW$ distribution can be obtained by taking the mathematical expectation of $\ln\left(\frac{f(x)_{TEMOW}}{f_1(x)_{TEMOW}}\right)$where $f(x)_{TEMOW}$ is the pdf with parameters $(\theta, \alpha, \lambda, \beta)$as in (14) and $f_1(x)_{TEMOW}$ is the pdf with parameters $(\theta_1, \alpha_1, \lambda_1, \beta_1)$ as

$$\ln \frac{f(x)_{TEMOW}}{f_1(x)_{TEMOW}} = \ln\left(\frac{\theta\alpha\lambda\beta\big(1 - e^{-\theta_1}\big)}{\theta_1\alpha_1\lambda_1\beta_1(1 - e^{-\theta})}\right) + (\beta - \beta_1)\ln(x) - \lambda x^\beta + \lambda_1 x^{\beta_1} - \theta \frac{1 - e^{-\lambda x^\beta}}{\alpha + \bar{\alpha}\big(1 - e^{-\lambda x^\beta}\big)}$$
$$+ \theta_1 \frac{1 - e^{-\lambda_1 x^{\beta_1}}}{\alpha_1 + \overline{\alpha_1}\big(1 - e^{-\lambda_1 x^{\beta_1}}\big)} - 2\ln\left(\alpha + \bar{\alpha}\left(1 - e^{-\lambda x^\beta}\right)\right)$$
$$+ 2\ln\left(\alpha_1 + \overline{\alpha_1}\left(1 - e^{-\lambda_1 x^{\beta_1}}\right)\right)$$

Thus, the $TEMOW$ relative entropy is given by

$$RE_{TEMOW} = E\left(\ln \frac{f(x)_{TEMOW}}{f_1(x)_{TEMOW}}\right) = \ln\left(\frac{\theta\alpha\lambda\beta\big(1 - e^{-\theta_1}\big)}{\theta_1\alpha_1\lambda_1\beta_1(1 - e^{-\theta})}\right) + (\beta - \beta_1)E(\ln(X))$$
$$-\lambda E\big(X^\beta\big) + \lambda_1 E\big(X^{\beta_1}\big) - \theta E\left(\frac{1 - e^{-\lambda X^\beta}}{\alpha + \bar{\alpha}\big(1 - e^{-\lambda X^\beta}\big)}\right) + \theta_1 E\left(\frac{1 - e^{-\lambda_1 X^{\beta_1}}}{\alpha_1 + \overline{\alpha_1}\big(1 - e^{-\lambda_1 X^{\beta_1}}\big)}\right)$$
$$-2E\left(\ln\left(\alpha + \bar{\alpha}\left(1 - e^{-\lambda X^\beta}\right)\right)\right) + 2E\left(\ln\left(\alpha_1 + \overline{\alpha_1}\left(1 - e^{-\lambda_1 X^{\beta_1}}\right)\right)\right) \quad (28)$$

where$E\big(X^\beta\big)$and $E\big(X^{\beta_1}\big)$as in (20)with $r = \beta$andβ_1. The other mathematical expectations as in (25), (26)and (27)with indicated parameters.

Reliability stress strength model:Consider $f_X(x)$ the pdf of the strength random variable(X) as in (14)and $F_Y(x)$ the cdf of the stress random variable(Y)as in (13)with parameters $(\theta_1, \alpha_1, \lambda_1, \beta_1)$. The

reliability stress strengthmodel associated withtwo independent$TEMOW$random variables can be achieved as follows

$$SS_{TEMOW} = P(Y < X) = \int_0^{\infty} f_X(x)\, F_Y(x)\, dx = \frac{1}{1-e^{-\theta_1}} \int_0^{\infty} \left(1 - e^{-\theta_1 \frac{1-e^{-\lambda_1 x^{\beta_1}}}{\alpha_1 + \overline{\alpha_1}\left(1-e^{-\lambda_1 x^{\beta_1}}\right)}}\right) f_X(x) dx$$

Afterusing the expansion formulas of e^{-x}, $(1-x)^{-a}$, and $(1-x)^{a}$along with some simplification steps we get

$$SS_{TEMOW} = \frac{1}{1-e^{-\theta_1}} \int_0^{\infty} \left[1 - \sum_{i,j,l,t=0}^{\infty} \frac{(-1)^{i+j+l+t}}{i!\, j!\, l!\, t!} \frac{\Gamma(i+j)\Gamma(i+j+1)\theta_1^i}{\Gamma(i)\Gamma(i+j-l+1)} \frac{(\overline{\alpha_1})^j}{{\alpha_1}^{i+j}} (\lambda_1 l)^t x^{t\beta_1}\right] f_X(x) dx$$

Then

$$SS_{TEMOW} = \frac{1}{1-e^{-\theta_1}} \left[1 - \sum_{i,j,l,t=0}^{\infty} \frac{(-1)^{i+j+l+t}}{i!\, j!\, l!\, t!} \frac{\Gamma(i+j)\Gamma(i+j+1)\theta_1^i}{\Gamma(i)\Gamma(i+j-l+1)} \frac{(\overline{\alpha_1})^j}{{\alpha_1}^{i+j}} (\lambda_1 l)^t E\left(X^{t\beta_1}\right)\right] \quad (29)$$

where $E\left(X^{t\beta_1}\right)$as in (20) with $r = t\beta_1$.

Order statistics: Let $x_{1:n}, x_{2:n}, \dots, x_{n:n}$ be the corresponding order statistics of a random sample $x_1, x_2, \dots, x_n$of size n taken independently from $TEMOW$ distribution. The pdf and the joint pdf of order statistics can be found based on (13) and (14)via the following standard formulas (see [11])

$$f_{k:n}(x) = \frac{n!}{(k-1)!\,(n-k)!} \left(F(x)\right)^{k-1} \left(1-F(x)\right)^{n-k} f(x) \;\; ; \; 0 \le x_{k:n} < \infty, k \le n$$

$$f_{j,k:n}(x,y) = \frac{n!}{(j-1)!\,(k-j-1)!\,(n-k)!} \left(F(x)\right)^{j-1} \left(F(y)-F(x)\right)^{k-j-1} \left(1-F(y)\right)^{n-k} f(x)\, f(y); \; 1 \le j \le k\,, 0 \le x \le y < \infty$$

Asfollows

$$f_{k:n}(x) = \frac{n!}{(k-1)!\,(n-k)!} \left(1 - e^{-\theta \frac{1-e^{-\lambda x^{\beta}}}{\alpha + \bar{\alpha}\left(1-e^{-\lambda x^{\beta}}\right)}}\right)^{k-1} \left(e^{-\theta \frac{1-e^{-\lambda x^{\beta}}}{\alpha + \bar{\alpha}\left(1-e^{-\lambda x^{\beta}}\right)}} - e^{-\theta}\right)^{n-k}$$

$$\frac{\theta\alpha\lambda\beta\, x^{\beta-1}\, e^{-\lambda x^{\beta}} e^{-\theta \frac{1-e^{-\lambda x^{\beta}}}{\alpha + \bar{\alpha}\left(1-e^{-\lambda x^{\beta}}\right)}}}{(1-e^{-\theta})^n \left(\alpha + \bar{\alpha}\left(1-e^{-\lambda x^{\beta}}\right)\right)^2}; \; 0 \le x_{k:n} < \infty, k \le n \quad (30)$$

$$f_{j,k:n}(x,y) = \frac{n!}{(j-1)!\,(k-j-1)!\,(n-k)!} \left(1 - e^{-\theta \frac{1-e^{-\lambda x^{\beta}}}{\alpha + \bar{\alpha}\left(1-e^{-\lambda x^{\beta}}\right)}}\right)^{j-1} \left(e^{-\theta \frac{1-e^{-\lambda x^{\beta}}}{\alpha + \bar{\alpha}\left(1-e^{-\lambda x^{\beta}}\right)}} - e^{-\theta \frac{1-e^{-\lambda y^{\beta}}}{\alpha + \bar{\alpha}\left(1-e^{-\lambda y^{\beta}}\right)}}\right)^{k-j-1} \left(e^{-\theta \frac{1-e^{-\lambda y^{\beta}}}{\alpha + \bar{\alpha}\left(1-e^{-\lambda y^{\beta}}\right)}} - e^{-\theta}\right)^{n-k} \quad (31)$$

$$\frac{\theta^2\alpha^2\lambda^2\beta^2 x^{\beta-1} y^{\beta-1}\, e^{-\lambda\left(x^{\beta}+y^{\beta}\right)} e^{-\theta\left(\frac{1-e^{-\lambda x^{\beta}}}{\alpha + \bar{\alpha}\left(1-e^{-\lambda x^{\beta}}\right)} + \frac{1-e^{-\lambda y^{\beta}}}{\alpha + \bar{\alpha}\left(1-e^{-\lambda y^{\beta}}\right)}\right)}}{(1-e^{-\theta})^n \left(\alpha + \bar{\alpha}\left(1-e^{-\lambda x^{\beta}}\right)\right)^2 \left(\alpha + \bar{\alpha}\left(1-e^{-\lambda y^{\beta}}\right)\right)^2}; \; 1 \le j \le k\,, 0 \le x \le y < \infty$$

6.Maximum likelihoodestimators of TEMOW parameters

Consider$(x_1, x_2, \dots, x_n)$a complete random sample of size nfollow TEMOWdistribution with the vector of parameters$\Delta = (\theta, \alpha, \lambda, \beta)^T$. Thenatural logarithm likelihood function based on (14)is

$$\ell(\Delta|\underline{x}) = n \ln\left(\frac{\theta\alpha\lambda\beta}{1-e^{-\theta}}\right) + (\beta-1)\Sigma_{i=1}^{n} \ln(x_i) - \lambda\Sigma_{i=1}^{n} x_i^{\beta} - \theta\Sigma_{i=1}^{n} \frac{1-e^{-\lambda x_i^{\beta}}}{\alpha + \bar{\alpha}\left(1-e^{-\lambda x_i^{\beta}}\right)}$$

$$-2\Sigma_{i=1}^{n} \ln\left(\alpha + \bar{\alpha}\left(1-e^{-\lambda x_i^{\beta}}\right)\right) \quad (32)$$

The maximum likelihood estimators of four parameters can be attained either directly by using the package (AdequecyModel) in R software or bysolving the nonlinear fourlikelihood equations$\frac{\partial \ell(\Delta|\underline{x})}{\partial \Delta} = \left(\frac{\partial \ell(\Delta|\underline{x})}{\partial \theta}, \frac{\partial \ell(\Delta|\underline{x})}{\partial \alpha}, \frac{\partial \ell(\Delta|\underline{x})}{\partial \lambda}, \frac{\partial \ell(\Delta|\underline{x})}{\partial \beta}\right)^T = 0$ throughcomputational iterative techniques.

In AdequecyModel package, there exists various maximization algorithms such as Newton-Raphson (NR), Broyden-Fletcher-Goldfarb-Shanno (BFGS), Berndt-Hall-Hall-Hausman (BHHH), Limited-Memory quasi-Newton code for Bound-constrained optimization (L-BFGS-B), Nelder-Mead (NM), and Simulated-Annealing (SANN). Here, the MLEs are computed directly by using the package (AdequecyModel) in R software with BFGS method.

7.Simulation and real application

In this section, numerical illustrations (simulation and real application) are presented to exhibit the abilities of the proposed distribution.

7.1. Simulation process

The first step of the simulation process is to generate i.i.d. random samples (1000 times) follow $TEMOW$ distribution each with size $n = 25,50,100,200$ and 300 where the true or initial values of parameters are chosen to be as in table 1 (also see figure 2). Then, for each parameter, calculate the Bias and root mean squared error (RMSE) as

$Bias(\hat{\eta}) = \frac{1}{1000}\sum_{i=1}^{1000}(\hat{\eta}_i - \eta)$ and

$RMSE(\hat{\eta}) = \sqrt{\frac{1}{1000}\sum_{i=1}^{1000}(\hat{\eta}_i - \eta)^2}$ where η can be $\theta, \alpha, \lambda,$ or β .

It clearly appears from the simulation results (table1) that RMSE values decrease as the sample size increases.

Table 1. The Bias and RMSE of the $TEMOW$ parameters estimation using MLE**.**

n	*Par.*	*Init.*	*Bias*	*RMSE*	*Init.*	*Bias*	*RMSE*	*Init.*	*Bias*	*RMSE*
25	θ	3.3	-0.213	0.871	9.1	0.405	1.520	3.5	-0.096	0.640
	α	1.2	0.312	1.098	2.8	0.448	1.690	1	0.048	0.689
	λ	0.8	0.209	0.360	2.1	0.567	1.305	0.5	0.348	0.381
	β	2.1	0.136	0.502	0.9	0.056	0.193	3.9	0.221	0.771
50	θ	3.3	-0.103	0.649	9.1	0.395	1.388	3.5	-0.032	0.493
	α	1.2	0.173	0.781	2.8	0.302	1.277	1	-0.022	0.502
	λ	0.8	0.157	0.271	2.1	0.379	0.948	0.5	0.335	0.356
	β	2.1	0.065	0.338	0.9	0.023	0.128	3.9	0.134	0.538
100	θ	3.3	-0.007	0.534	9.1	0.288	1.152	3.5	0.034	0.347
	α	1.2	0.094	0.565	2.8	0.144	0.793	1	-0.097	0.378
	λ	0.8	0.123	0.202	2.1	0.255	0.617	0.5	0.318	0.330
	β	2.1	0.034	0.242	0.9	0.013	0.087	3.9	0.116	0.383
200	θ	3.3	0.051	0.410	9.1	0.284	0.989	3.5	0.054	0.253

	α	1.2	0.078	0.434	2.8	0.144	0.589	1	-0.095	0.285
	λ	0.8	0.112	0.167	2.1	0.227	0.456	0.5	0.319	0.325
	β	2.1	0.009	0.168	0.9	0.003	0.059	3.9	0.081	0.270
	θ	3.3	0.089	0.341	9.1	0.340	0.988	3.5	0.054	0.218
300	α	1.2	0.060	0.333	2.8	0.139	0.508	1	-0.095	0.237
	λ	0.8	0.102	0.141	2.1	0.195	0.402	0.5	0.319	0.323
	β	2.1	0.000	0.131	0.9	-0.001	0.048	3.9	0.067	0.212

7.2.Real Application

In this subsection, we include applications for two real data sets (right-skewed and semi-symmetric)to exhibit the abilities andflexibility of the TEMOW distribution.

The first real data (Data-1) collection reflects the body fat percentage of 202 Australian athletes [12].

"19.75, 21.30, 19.88, 23.66, 17.64, 15.58, 19.99, 22.43, 17.95, 15.07, 28.83, 18.08, 23.30, 17.71, 18.77, 19.83, 25.16, 18.04, 21.79, 22.25, 16.25, 16.38, 19.35, 19.20, 17.89, 12.20, 23.70, 24.69, 16.58, 21.47, 20.12, 17.51, 23.70, 22.39, 20.43, 11.29, 25.26, 19.39 19.63 23.11 16.86 21.32 26.57 17.93 24.97 22.62 15.01, 18.14, 26.78, 17.22, 26.50, 23.01, 30.10, 13.93, 26.65, 35.52, 15.59, 19.61, 14.52, 11.47, 17.71, 18.48, 11.22, 13.61, 12.78, 11.85, 13.35, 11.77, 11.07, 21.30, 20.10, 24.88, 19.26, 19.51, 23.01, 8.07, 11.05, 12.39, 15.95, 9.91, 16.20, 9.02, 14.26, 10.48, 11.64, 12.16, 10.53, 10.15, 10.74, 20.86, 19.64, 17.07, 15.31, 11.07, 12.92, 8.45, 10.16, 12.55, 9.10, 13.46, 8.47, 7.68, 6.16, 8.56, 6.86, 9.40, 9.17, 8.54, 9.20, 11.72, 8.44, 7.19, 6.46, 9.00, 12.61, 9.03, 6.96, 10.05, 9.56, 9.36, 10.81, 8.61, 9.53, 7.42, 9.79, 8.97, 7.49, 11.95, 7.35, 7.16, 8.77, 9.56, 14.53, 8.51, 10.64, 7.06, 8.87, 7.88, 9.20, 7.19, 6.06, 5.63, 6.59, 9.50, 13.97, 11.66, 6.43, 6.99, 6.00, 6.56, 6.03, 6.33, 6.82, 6.20, 5.93, 5.80, 6.56, 6.76, 7.22, 8.51, 7.72, 19.94, 13.91, 6.10, 7.52, 9.56, 6.06, 7.35, 6.00, 6.92, 6.33, 5.90, 8.84, 8.94, 6.53, 9.40, 8.18, 17.41, 18.08, 9.86, 7.29, 18.72, 10.12, 19.17, 17.24, 9.89, 13.06, 8.84, 8.87, 14.69, 8.64, 14.98, 7.82, 8.97, 11.63, 13.49, 10.25, 11.79, 10.05, 8.51, 11.50, 6.26".

The second real data (Data-2)collection reflects the strengths of 1.5 cm glass fibers of 63 observations [13].

"0.55, 0.74, 0.77, 0.81, 0.84, 1.24, 0.93, 1.04, 1.11, 1.13, 1.30, 1.25, 1.27, 1.28,1.29, 1.48, 1.36, 1.39, 1.42, 1.48, 1.51, 1.49, 1.49, 1.50, 1.50,1.55, 1.52, 1.53, 1.54, 1.55, 1.61, 1.58,1.59, 1.60, 1.61, 1.63,1.61, 1.61, 1.62, 1.62, 1.67, 1.64, 1.66, 1.66, 1.66, 1.70, 1.68,1.68, 1.69, 1.70, 1.78, 1.73, 1.76, 1.76, 1.77, 1.89, 1.81, 1.82,1.84, 1.84, 2.00, 2.01, 2.24".

The fitting of TEMOW distribution is compared with the Beta Weibull (BW), Kumaraswamy Weibull (KuW), Exponentiated Generalized Weibull (EGW), Weibull Weibull (WW), Gompertz Weibull (GoW), and Weibull (W) distributions (see [14]-[18] for more details). The software R was used to calculate their negative log-likelihood (-LL), Consistent Akaike Information Criteria (CAIC), Akaike Information Criteria (AIC), Bayesian Information Criteria (BIC), Hanan and Quinn Information Criteria (HQIC), besides MLEs of the parameters.

The findings areshown in tables2 - 5.In addition to the plots of empirical cdfs, the histogram plot and the estimated densities are shown in figures 5 - 8. Based on the results, TEMOW has the lowest values of information criteria, makingit the most fitting to represent two data sets compared to other distributions. In addition, this best fitting can be seen via the plots.

Table 2. The information criteria to fitting Data-1.

Dist.	-LL	CAIC	AIC	BIC	HQIC
TEMOW	625.8387	1259.880	1259.677	1272.910	1265.031
BW	635.6115	1279.504	1279.301	1292.534	1284.656
KuW	626.1613	1260.526	1260.323	1273.556	1265.677
EGW	630.3769	1268.957	1268.754	1281.987	1274.108
WW	642.4163	1293.036	1292.833	1306.066	1298.187
GoW	641.4215	1291.046	1290.843	1304.076	1296.197
W	642.7304	1289.524	1289.464	1296.080	1292.141

Table 3. The MLE values to Data-1.

Dist.	$\hat{\theta}_{ML}$	$\hat{\alpha}_{ML}$	$\hat{\lambda}_{ML}$	$\hat{\beta}_{ML}$
TEMOW	-17.5717	0.0208	0.0557	2.1454
BW	1.7612	0.2322	0.1540	1.9505
KuW	7.9067	0.1593	0.2580	1.6154
EGW	1.3058	97.7112	1.1087	0.5177
WW	3.3540	1.7800	0.1485	0.7018
GoW	1.2484	-0.1433	0.0623	2.5427
W	---	---	0.0658	2.2554

Table 4. The information criteria to fitting Data-2.

Dist.	-LL	CAIC	AIC	BIC	HQIC
TEMOW	12.0290	32.748	32.058	40.631	35.430
BW	14.5926	37.875	37.185	45.758	40.557
KuW	13.3785	35.447	34.757	43.329	38.129
EGW	20.8999	50.489	49.800	58.372	53.171
WW	15.2068	39.103	38.414	46.986	41.785
GoW	14.7764	38.242	37.553	46.125	40.924
W	18.0609	40.355	40.155	44.441	41.840

Table 5. The MLE values to Data-2.

Dist.	$\hat{\theta}_{ML}$	$\hat{\alpha}_{ML}$	$\hat{\lambda}_{ML}$	$\hat{\beta}_{ML}$
TEMOW	-0.5754	12.2078	0.8896	3.2084
BW	0.6194	6.2381	0.4480	7.7638
KuW	0.4934	0.2121	0.7400	7.0644
EGW	0.1377	3.2010	1.7048	2.6592
WW	3.4845	3.9363	1.4029	1.6589
GoW	0.0080	3.5273	1.0602	0.9752
W	---	---	0.6240	4.4768

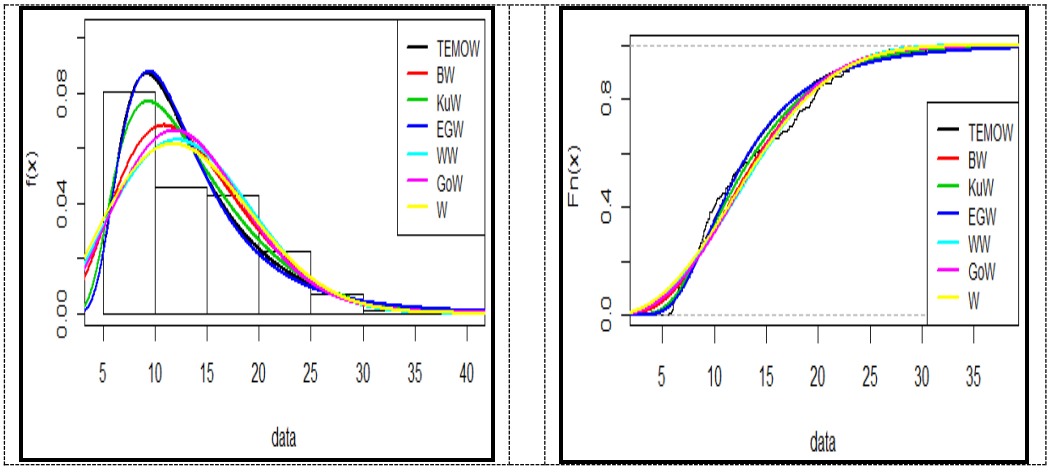

Figure 5. Data-1histogram plot of TEMOW with other compared distributions.

Figure 6. Data-1 empirical cdfplot of TEMOW with other compared distributions.

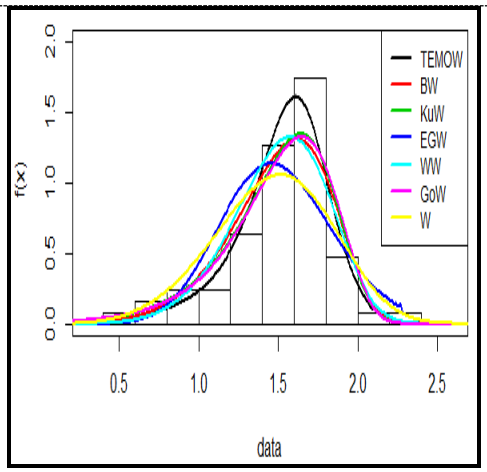

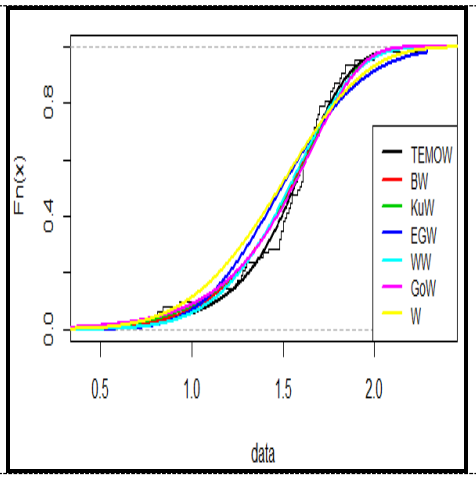

Figure 7. Data-2 histogram plot of $TEMOW$ with other compared distributions.

Figure 8. Data-2 empirical cdfplot of $TEMOW$ with other compared distributions.

8. Conclusions

In this paper, a newly generated family of continuous distributions with Marshall Olkin is introduced. Then a truncated distribution as a sub-model with four parameters called Truncated Exponential Marshall Olkin Weibull is proposed. Reliability analysis with several main statistical properties such as moments, characteristic function, quantile function, median, skewness, kurtosis, simulated data, Shannon entropy, relative entropy, reliability stress-strength model, and order statistics are presented. Furthermore, the maximum likelihood estimation method is used to estimate the unknown four parameters. To assess the usefulness and flexibility, the TEMOW distribution applied upon simulation study besides real application by the implementation of two real data sets (right-skewedand semi-symmetric) with different information criteria. The simulation results clearly shown the flexible and consistent performance of the maximum likelihood estimators for the parameters. Also, the real application results clearly shown that the proposed distribution has outstanding performance than other considered distributions for all information criteria. This flexibility allows using the TEMOW distribution in various application areas.

References

[1] Marshall A W and Olkin I 1997 A new method for adding a parameter to a family of distributions with application to the exponential and Weibull families *Biomet.***84**(3)pp 641-52
[2] Eugene N, Lee C and Famoye F 2002 Beta-normal distribution and its applications *Comm. Stat.-The.Meth.***31**(4) pp 497-512
[3] Khaleel M A, Al-Noor N H and Hameed M Kh 2020 A Marshall Olkin exponential Gompertz distribution: properties and applications *Per. Eng.Nat. Sci.***8**(1) pp 298-312
[4] Handique L, Chakraborty S and Hamedani G G 2017 The Marshall - Olkin - Kumaraswamy - G family of distributions*J. Stat. The. Appl.* **16**(4) pp 427-47
[5] Gupta A K and Nadarajah S 2005 On the moments of the beta normal distribution *Comm. Stat.-The.Meth.***33**(1) pp 1-13
[6] Abid S H, Al-Noor N H and Boshi M A A 2018 [0,1] Truncated generalized gamma – generalized gamma distribution *J. Ir. Al-Kh. Soc.***2** pp 135-48

[7] Ishaq A I and Abiodun AA 2020 The Maxwell–Weibull distribution in modelinglifetime datasets *Ann. Data. Sci.***7**pp 639-62
[8] Shabbir M, Riaz A and GullH 2018 Rayleigh Lomax distribution *J Mid. E.Nor. Afr. Sci.***4**(12) pp 1-4
[9] Galton F 1983 *Enquiries into human faculty and its development*(London: Macmillan Press)
[10] Moors J J 1988 A quantile alternative for kurtosis *Statist.***37** pp 25-32
[11] Al-Noor N H and Assi N K 2020 Rayleigh-Rayleigh distribution: properties and applications *J. Phys.: Conf. Series* **1591** 012038
[12] Oguntunde P E, Khaleel M A, Adejumo A O, Okagbue H I, Opanuga A A and Owolabi F O 2018 The Gompertzinverse exponential (GoIE) distribution with applications *Cog. Math. Stat.***5**(1) pp 1-11
[13] Smith R L and Naylor J C 1987 A comparison of maximum likelihood and Bayesian estimators for the three-parameter Weibull distribution *J. Roy. Stat. Soc. (Appl. Stat.)* **36**(3) pp 358-69
[14] Lee C, Famoye F and Olumolade O 2007 Beta-Weibull distribution: some properties and applications to censored data *J. Mod. Appl. Stat. Meth.***6**(1) pp 173-86
[15] Cordeiro G M, Ortega E M M and Nadarajah S 2010 The Kumaraswamy Weibull distribution with application to failure data *J. Fran. Inst.***347**(8) pp 1399-429
[16] Mudholkar G S, Srivastava D K and Freimer M 1995 The Exponentiated Weibull family *Tech.* **37**(4) pp 436-45
[17] Al-Noor N H, Abid S H and Boshi M A A 2019 On the exponentiated Weibull distribution *AIP Conf. Proc.***2183** 110003
[18] Bourguignon M, Silva R B and Cordeiro G M 2014 The Weibull-G family of probability distributions *J. Data. Sci.***12**(1) pp 53-68

New Procedure for Selecting Raise Vector in Raising Regression

New Procedure for Selecting Raise Vector in Raising Regression

Rifaat Saad Abdul Jabbar[1] and Mustafa Ismaeel Niaf[2]

[1] Department of Applied Mathematics University Of Anbar, Ramadi, Iraq
[2] Department of Mathematics, University Of Anbar, Ramadi, Iraq

E-mail: drrifaat1974@uoanbar.edu.iq

Abstract. One of the most important things in raise regression is selecting the raise factor λ. A new procedure for selecting the raised vector have been prepared with new technique for choosing the raising factor λ. Three different criterion have been used to study of this procedure, namely, scalar mean square error (MSE), determination coefficients R^2, and the variance inflation factor (VIF). Also, some examples have been given to illustrate our finding. Where the best MSE, acceptable R^2, VIF and reduce simultaneously the multicollinearity among vectors are the main results of this procedure by giving better estimate for raise factor λ which may apply in different fields that suffered from the problem of multicollinearity.

1. Introduction

Recently, [2] and [3] present and develop a new technique of raising regression depending on geometrical aspect, the idea behind is very simple to avoid the problem of multicollinearity in the linear regression model:

$$\boldsymbol{Y} = \boldsymbol{X\beta} + \boldsymbol{\epsilon}, \tag{1}$$

where Y is an $n \times 1$ vector of observations on the response variable, X is an $n \times p$ known design matrix of rank p, β is a $p \times 1$ vector of unknown regression coefficients and ϵ is an $n \times 1$ vector of the error terms with $E(\epsilon) = 0$ and $\mathrm{Cov}(\epsilon) = \sigma^2 I_n$.

Later, research teams - Garcia et al.- were published many research papers related to the raising regression relate to the raising vector λ [3] and developed the technique [9]

The multicollinearity problem ensure that the estimate of the regression coefficients have large variance and unstable with wrong sign if we use the ordinary least squares estimator (OLS) that given as follows:

$$\widehat{\boldsymbol{\beta}}_{\boldsymbol{OLS}} = (\boldsymbol{X'X})^{-1}\boldsymbol{X'Y} \tag{2}$$

In this case, the matrix X′X becomes almost singular and the estimator will distorts data. To dominate this problem many methods of regression were presented. One of the most efficient technique was the ordinary Ridge Regression (ORR) estimator suggested by Hoerl [6] given as:

$$\widehat{\boldsymbol{\beta}}_{\boldsymbol{k}} = (\boldsymbol{X'X} + \boldsymbol{kI_p})^{-1}\boldsymbol{X'Y} \tag{3}$$

Second estimation method presented to avoid multicollinearity is the selection of variables which delete one of the correlated vectors which may has important information, for this reason the raise regression method has be found.

The raise regression was developed by Salmeron et. al. (Salmeron et. al. 2017) where they used residuals of the model (1). Raise regression treat with data space but without deleting data this method

geometrically raises the correlated vector according to number of correlated vector x_j – namely, chose the vector with more collinearity and apply this for all vectors. In following regression:

$$\tilde{x}_j = x_j + \lambda_j e_j \quad (4)$$

For some vector x_j ,raise parameter λ_j is chosen by user [8] or may calculated to get best value of λ_j [2] and e_j is the residual vector. Then replace x_j by $\tilde{x}_j$ in the original model for all $j = 1, \dots, p$ which lead to replace all of vectors in the model with new $\tilde{x}_j$.

In this paper, a new procedure for selecting the raised vector will be prepared with new technique for choosing the raising parameter λ. We will use three different criterion to check the performance of raise regression technique for selecting the raised vector, namely, scalar mean square error (MSE), determination coefficients R^2, and the variance inflator factor (VIF)

The paper is organized as follows, in Section 2, the methodology is presented. In Section 3 some examples have been given to illustrate our finding. Finally, some conclusion remarks are given is Section 4.

2. Methodology

The raise estimator preserves the determination coefficient value R^2, independently raising parameter, λ [9]. Which is a different point with ridge regression. R^2 is also determined for seeking of comparison of different values of λ. R^2 is determined in the ordinary linear regression as following [2]:

R^2 is computed as:

$$R^2 = \frac{SSR}{SST} \text{ and } \tilde{R}^2 = \frac{\widetilde{SSR}}{\widetilde{SST}} \text{ , where } SST = \sum_i (Y_i - \bar{Y})^2 = \widetilde{SST} \text{ , } SSR = \sum_i e_{i0}^2 = \|e_0\|^2,$$
$$\bar{\boldsymbol{Y}} = (\bar{\boldsymbol{Y}}, \bar{\boldsymbol{Y}}, \dots, \bar{\boldsymbol{Y}}) = \bar{\boldsymbol{Y}}.\mathbf{1}' \text{ and } \|Y - \bar{Y}\|^2 = \left\|\hat{Y} - \bar{Y}\right\|^2 + \|e_0\|^2 \quad (5)$$

Therefore $SST = SSR + SSE$ and R2 may expressed as following:

$$R^2 = \frac{SSE}{SST} = \frac{\|\hat{Y} - \bar{Y}\|^2}{\|Y - \bar{Y}\|^2} \quad (6)$$

While the variance inflation factor VIF is defined as:

$$VIF = \frac{1}{1 - R^2} \quad (7)$$

The technique used in this research paper depends on selecting specific vector that has higher value correlation and then use different values of λ's for the selected vector to be raised. This λ is selected for minimum value of MSE.

The data assumed to be centered and standardized and written as $X = (x_1, x_2, \dots, x_p)$ of $(n \times p)$ matrix such that $\left\|x_j\right\|^2$ for $j = 1, .., p$. In matrix form $A = (a_1, a_2, \dots, a_p)$, the columns span (Span(A)) which is the subspace generated by the columns vectors $[a_1, a_2, \dots, a_p]$ while the subspace $A_{[j]}$is the matrix A deleting the vector a_j and $\text{Span}(A_{[j]})$ is the subspace generating by $A_{[j]}$ for the linear model (1) it is important to study the multicollinearity among vectors of X, deleting of the vector x_j is temporary which replaced by the new vector $\tilde{x}_j$ in order to reduce the mean square error MSE. Figure (1)

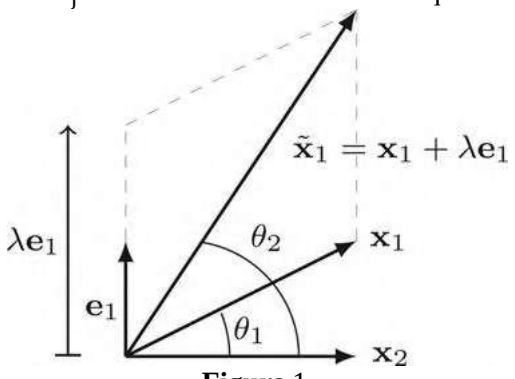

Figure 1.

2.1 Procedure of raising regression

Unlike the procedure of (Ramirez et al.2015), which raise all of the vectors x_js by $\tilde{x}_j$s for $j = 1, .., p$ we do raising for the high correlation vector in the following sequence:

Step 1. Chose the vector x_j with high correlation coefficient to begin raising $x_j \rightarrow \tilde{x}_j$ such that:

$$\tilde{\boldsymbol{x}}_{\boldsymbol{j}} = \boldsymbol{x}_{\boldsymbol{j}} + \lambda_j \boldsymbol{e}_{\boldsymbol{j}}$$

where e_j represents the orthogonal vector on $\mathrm{Span}(X_{[j]})$ ($e_j \perp \mathrm{Span}(X_{[j]})$), and λ_j is an arbitrary positive constant chosen from some interval of positive real numbers ensure the minimum MSE.

Step 2. Check the result and chose the next vector to be raise in the same manner with the new linear model:

$$\boldsymbol{Y} = \tilde{\boldsymbol{X}}\tilde{\boldsymbol{\beta}} + \boldsymbol{\epsilon}\,, \tag{8}$$

where $\tilde{X} = [x_1, x_2, \dots, x_{j-1}, \tilde{x}_j, x_{j+1}, \dots, x_p]$ and raising for new vector, and so on.

Step 3**.** Stopping criterion: when the improving is decay, the procedure stops and preserves the last result for $\tilde{\boldsymbol{X}}$ and $\boldsymbol{\beta}$.

Jensen and Ramirez [7] show that there is a relationship between the VIF, and the angle between x_j and $\mathrm{Span}(X_{[j]})$. The process of raising the vector between x_j and $\mathrm{Span}(X_{[j]})$ aims to increase the amount of the angle between them. Therefore, applying raising to all vectors may lead to undesirable results. λ_j should be chosen with caution to obtain the best result in terms of the MSE.

The suggestion here is to choose the best value of the parameter λ_j for each vector to avoid this issue. Suppose that x_j and x_k has a high correlation between them and we raise x_j first and then x_k secondly, but we may get high correlation between them again.

3. Illustrated Examples

In this section two examples will present to illustrate the new procedure.

3-1 Example 1

To illustrate our procedure in this last section we consider a dataset which was discussed in [4]. Data found in economics are often multicollinear. Which contains "Total National Research and Development Expenditures—as a Percent of Gross National Product by Country: 1972–1986. It represents the relationship between the dependent variable Y the percentage spent by the United States and the four other independent variables X1, X2, X3, and X4. The variable X1 represents the percent spent by France, X2 that spent by West Germany, X3 that spent by Japan, and X4 that spent by the former Soviet Union."

In (Akdeniz and Erol 2003), the following example is suggested in order to illustrate the measure of the multicollinearity. By applying procedure in step 1 to step 3, we get the following results that listed in table 1.

The correlation matrix of the original matrix is calculated as:

1.0000	0.8877	0.9248	0.3090
0.8877	1.0000	0.9621	0.1573
0.9248	0.9621	1.0000	0.3276
0.3090	0.1573	0.3276	1.0000

Here we choose the vector number 3 for its high value of correlation (0.9621). While in the second iteration the vector number 2 is selected for high value of correlation in the following correlation matrix (0.9426):

1.0000	0.8877	0.9060	0.3090
0.8877	1.0000	0.9426	0.1573
0.9060	0.9426	1.0000	0.3209
0.3090	0.1573	0.3209	1.0000

After second iteration, we get the following correlation matrix

1.0000	0.8017	0.9060	0.3090
0.8017	1.0000	0.8513	0.1421

0.9060 0.8513 1.0000 0.3209
0.3090 0.1421 0.3209 1.0000

In the third iteration, we chose the first vector for maximum correlation (0.9060). For minimum value of MSE we get the following correlation matrix:

1.0000 0.5294 0.5982 0.2040
0.5294 1.0000 0.8513 0.1421
0.5982 0.8513 1.0000 0.3209
0.2040 0.1421 0.3209 1.0000

According to the procedure, we have to stop where there is no improving of MSE and we get good correlation values.

Table 1. Results for Example 1, three iterations, for different values of λ

Iteration no.1,raised vector:3				Iteration no.2,raised vector:2				Iteration no.3,raised vector:1			
λ	MSE	R^2	VIF	λ	MSE	R^2	VIF	λ	MSE	R^2	VIF
0.0000	**0.2361**	**0.9764**	**42.3826**	**0.0000**	**0.2361**	**0.9745**	**39.2513**	**0.0000**	**0.2361**	**0.9714**	**34.9566**
0.0500	**0.2193**	**0.9764**	**42.3488**	**0.0500**	**0.2747**	**0.9745**	**39.2490**	**0.6000**	**0.2655**	**0.9537**	**21.6094**
0.1000	**0.2062**	**0.9763**	**42.2478**	**0.1000**	**0.2731**	**0.9745**	**39.2423**	**0.7000**	**0.2649**	**0.9470**	**18.8690**
0.1500	**0.1960**	**0.9762**	**42.0805**	**0.1500**	**0.2717**	**0.9745**	**39.2310**	**0.8000**	**0.2644**	**0.9393**	**16.4812**
0.2000	**0.1882**	**0.9761**	**41.8485**	**0.2000**	**0.2704**	**0.9745**	**39.2153**	**0.9000**	**0.2641**	**0.9307**	**14.4277**
0.2500	**0.1823**	**0.9759**	**41.5539**	**0.2500**	**0.2692**	**0.9745**	**39.1950**	**1.0000**	**0.2638**	**0.9211**	**12.6735**
0.3000	**0.1779**	**0.9757**	**41.1994**	**0.3000**	**0.2682**	**0.9745**	**39.1703**	**1.1000**	**0.2636**	**0.9105**	**11.1787**
0.3500	**0.1748**	**0.9755**	**40.7882**	**0.3500**	**0.2672**	**0.9745**	**39.1412**	**1.2000**	**0.2635**	**0.8990**	**9.9044**
0.4000	**0.1728**	**0.9752**	**40.3238**	**0.4000**	**0.2664**	**0.9744**	**39.1076**	**1.3000**	**0.2633**	**0.8866**	**8.8159**
0.4500	**0.1715**	**0.9749**	**39.8101**	**0.4500**	**0.2656**	**0.9744**	**39.0697**	**1.4000**	**0.2633**	**0.8731**	**7.8830**
0.5000	**0.1710**	**0.9745**	**39.2513**	**0.5000**	**0.2649**	**0.9744**	**39.0273**	**1.5000**	**0.2632**	**0.8588**	**7.0803**
0.5500	**0.1710**	**0.9741**	**38.6516**	**0.5500**	**0.2642**	**0.9743**	**38.9806**	**1.6000**	**0.2632**	**0.8434**	**6.3866**
0.6000	**0.1715**	**0.9737**	**38.0154**	**0.6000**	**0.2636**	**0.9743**	**38.9296**	**1.7000**	**0.2631**	**0.8271**	**5.7846**
0.6500	**0.1724**	**0.9732**	**37.3473**	**0.6500**	**0.2630**	**0.9743**	**38.8743**	**1.8000**	**0.2631**	**0.8099**	**5.2596**
0.7000	**0.1736**	**0.9727**	**36.6516**	**0.7000**	**0.2625**	**0.9742**	**38.8147**	**1.9000**	**0.2631**	**0.7917**	**4.7998**
0.7500	**0.1750**	**0.9722**	**35.9327**	**0.7500**	**0.2620**	**0.9742**	**38.7509**	**2.0000**	**0.2631**	**0.7725**	**4.3954**
0.8000	**0.1766**	**0.9716**	**35.1948**	**0.8000**	**0.2615**	**0.9741**	**38.6830**	**2.1000**	**0.2632**	**0.7524**	**4.0382**
0.8500	**0.1784**	**0.9710**	**34.4418**	**0.8500**	**0.2611**	**0.9741**	**38.6109**	**2.2000**	**0.2632**	**0.7313**	**3.7213**
0.9000	**0.1804**	**0.9703**	**33.6777**	**0.9000**	**0.2607**	**0.9740**	**38.5348**	**2.3000**	**0.2632**	**0.7092**	**3.4392**
0.9500	**0.1824**	**0.9696**	**32.9059**	**0.9500**	**0.2603**	**0.9740**	**38.4546**	**2.4000**	**0.2633**	**0.6862**	**3.1871**
1.0000	**0.1846**	**0.9689**	**32.1297**	**1.0000**	**0.2600**	**0.9739**	**38.3705**	**2.5000**	**0.2633**	**0.6623**	**2.9610**

Note that the relation between raising factor and the mean square error for each iteration is given in figure 2

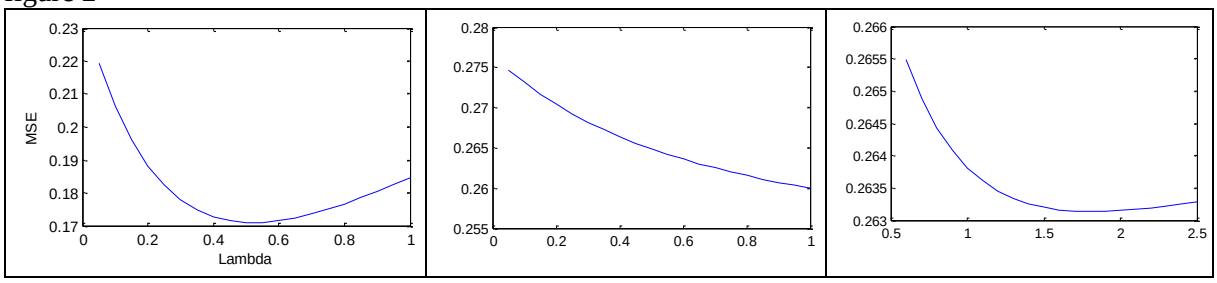

Figure 2. lambda verses MSE for three iterations

3-2 -Example 2

We now consider a dataset on Portland cement due to Hald [5] which widely analyses in the literature. These data are experimental investigation related to Portland cements of varied composition and the dependence of this heat on the percentages of four compounds. In this example, the dependent variable Y is defined as heat evolved in calories per gram of cement. The independent variables are amounts of

the following compounds: tricalcium aluminate (X1), tricalcium silicate (X2), tetracelcium alumino femrrite (X3), and dicalcium silicate (X4).

By applying procedure in step 1 to step 3, we get the following results that listed in Table 2 below. The Correlation matrix of the original matrix is calculated as:

1.0000	0.2286	-0.8241	-0.2454
0.2286	1.0000	-0.1392	-0.9730
-0.8241	-0.1392	1.0000	0.0295
-0.2454	-0.9730	0.0295	1.0000

Hear we chose the vector number 2 for its high value of correlation with -0.9730
While in the second iteration the vector number 4 is selected for high value of correlation in the following correlation matrix:

1.0000	0.2256	-0.8241	-0.2454
0.2256	1.0000	-0.1374	-0.9601
-0.8241	-0.1374	1.0000	0.0295
-0.2454	-0.9601	0.0295	1.0000

After second iteration, we get the following correlation matrix

1.0000	0.2256	-0.8241	-0.2428
0.2256	1.0000	-0.1374	-0.9497
-0.8241	-0.1374	1.0000	0.0292
-0.2428	-0.9497	0.0292	1.0000

In the third iteration, we chose the first vector.

For minimum value of MSE we get the following correlation matrix:

1.0000	0.2256	-0.6792	-0.2428
0.2256	1.0000	-0.1132	-0.9497
-0.6792	-0.1132	1.0000	0.0241
-0.2428	-0.9497	0.0241	1.0000

According the procedure, there is no improving of MSE and we get good correlation values.

Table 2. Results for Example 2 , three iterations, for different values of λ

Iteration no.1, raise vector 2				***Iteration no.2, raise vector 4***				***Iteration no.3, raise vector 3***			
λ	***MSE***	***R2***	***VIF***	***λ***	***MSE***	***R2***	***VIF***	***λ***	***MSE***	***R2***	***VIF***
0.1000	***1.0155***	***0.9824***	***56.7044***	***0.0500***	***0.9498***	***0.9790***	***47.5780***	***0.0500***	***1.0107***	***0.9798***	***49.4175***
0.2000	***0.8699***	***0.9823***	***56.5990***	***0.1000***	***0.7552***	***0.9791***	***47.9179***	***0.1000***	***0.8403***	***0.9797***	***49.2677***
0.3000	***0.7635***	***0.9823***	***56.4242***	***0.1500***	***0.6190***	***0.9793***	***48.2545***	***0.1500***	***0.7002***	***0.9796***	***49.1152***
0.4000	***0.6846***	***0.9822***	***56.1813***	***0.2000***	***0.5288***	***0.9794***	***48.5878***	***0.2000***	***0.5847***	***0.9796***	***48.9601***
0.5000	***0.6253***	***0.9821***	***55.8721***	***0.2500***	***0.4752***	***0.9796***	***48.9174***	***0.2500***	***0.4894***	***0.9795***	***48.8025***
0.6000	***0.5805***	***0.9820***	***55.4988***	***0.3000***	***0.4507***	***0.9797***	***49.2430***	***0.3000***	***0.4108***	***0.9794***	***48.6424***
0.7000	***0.5463***	***0.9818***	***55.0640***	***0.3500***	***0.4493***	***0.9798***	***49.5646***	***0.3500***	***0.3460***	***0.9794***	***48.4798***
0.8000	***0.5201***	***0.9817***	***54.5706***	***0.4000***	***0.4665***	***0.9800***	***49.8817***	***0.4000***	***0.2926***	***0.9793***	***48.3149***
0.9000	***0.5001***	***0.9815***	***54.0221***	***0.4500***	***0.4984***	***0.9801***	***50.1942***	***0.4500***	***0.2490***	***0.9792***	***48.1476***
1.0000	***0.4849***	***0.9813***	***53.4219***	***0.5000***	***0.5420***	***0.9802***	***50.5018***	***0.5000***	***0.2133***	***0.9792***	***47.9781***
1.1000	***0.4733***	***0.9811***	***52.7739***	***0.5500***	***0.5948***	***0.9803***	***50.8042***	***0.5500***	***0.1846***	***0.9791***	***47.8064***
1.2000	***0.4646***	***0.9808***	***52.0820***	***0.6000***	***0.6551***	***0.9804***	***51.1013***	***0.6000***	***0.1616***	***0.9790***	***47.6325***
1.3000	***0.4583***	***0.9805***	***51.3502***	***0.6500***	***0.7210***	***0.9805***	***51.3926***	***0.6500***	***0.1434***	***0.9789***	***47.4566***
1.4000	***0.4537***	***0.9802***	***50.5826***	***0.7000***	***0.7914***	***0.9806***	***51.6781***	***0.7000***	***0.1295***	***0.9788***	***47.2787***
1.5000	***0.4506***	***0.9799***	***49.7833***	***0.7500***	***0.8650***	***0.9808***	***51.9573***	***0.7500***	***0.1191***	***0.9788***	***47.0988***
1.6000	***0.4486***	***0.9796***	***48.9563***	***0.8000***	***0.9412***	***0.9809***	***52.2302***	***0.8000***	***0.1117***	***0.9787***	***46.9170***
1.7000	***0.4476***	***0.9792***	***48.1057***	***0.8500***	***1.0191***	***0.9810***	***52.4964***	***0.8500***	***0.1069***	***0.9786***	***46.7333***
1.8000	***0.4474***	***0.9788***	***47.2352***	***0.9000***	***1.0982***	***0.9810***	***52.7556***	***0.9000***	***0.1044***	***0.9785***	***46.5479***
1.9000	***0.4477***	***0.9784***	***46.3486***	***0.9500***	***1.1780***	***0.9811***	***53.0077***	***0.9500***	***0.1037***	***0.9784***	***46.3608***
2.0000	***0.4486***	***0.9780***	***45.4494***	***1.0000***	***1.2580***	***0.9812***	***53.2524***	***0.0500***	***1.0107***	***0.9798***	***49.4175***
0.1000	***1.0155***	***0.9824***	***56.7044***	***0.0500***	***0.9498***	***0.9790***	***47.5780***	***0.1000***	***0.8403***	***0.9797***	***49.2677***

Again, note that the relation between raising factor and the mean square error for each iteration is given below:

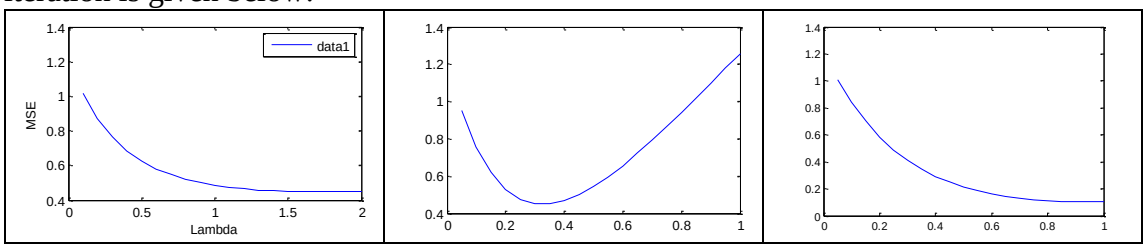

Figure 3. Lambda vesrse MSE for three iterations

4. Conclusion

One of the most important things in raise regression is selecting the raise factor λ , in this paper we produced a new procedure to select this factor among several values which guarantee best MSE and acceptable R^2 and VIF and reduce simultaneously the multicollinearity among vectors. This procedure give better estimate for raise factor λ which may applied in different fields that suffered from the problem of multicollinearity

.

References

[1] F Akdeniz and H Erol 2003 Mean Squared Error Matrix Comparisons of Some Biased Estimators in Linear Regression, communication in statistics *Theory and Methods* **32**(12) pp 2389–2413
[2] C B Garcia, J Garcia and J Soto 2011 The raise method: An alternative procedure to estimate the parameters in presence of collinearity *Quality and Quantity* **45** pp 403-423
[3] C J Garcıa, M M Garcıa, M Lopez and R Salmeron 2016 The raise estimator estimation, inference, and properties *Communications in Statistics-Theory and Methods* **46**(13) pp 6446–62
[4] M H Gruber 1998 *Improving efficiency by shrinkage The James--Stein and Ridge Regression Estimators* Marsell Dekker Inc, New York
[5] Statistical Theory with Engineering Applications. New York: Wiley
[6] A E HOERL and R W KENNARD 1970 Ridge regression: Biased, Estimation for Nonorthogonal Problems *Technometrics* **12** pp 55-67
[7] Jensen and Ramirez 2013 Hindawi Publishing Corporation, Advances in Decision Sciences **2013** Article ID 671204, 15 pages
[8] D O'Driscoll and D R Ramirez, Q Shao (Reviewing Editor) 2016 Mitigating collinearity in linear regression models using ridge *surrogate and raised estimators*, *Cogent Mathematics* **3**
[9] R Salmeron, C Garcia, J Garcia and M Lopez 2017 The raise estimator estimation, inference, and properties *Communications in Statistics - Theory and Methods* **46**(13) pp 6446-6462

New Normality on Generalized Topological Spaces

New Normality on Generalized Topological Spaces

Suaad G. Gasim and Mohanad N. Jaafar

Department of Mathematics - College of Education for Pure Science/ Ibn Al – Haitham- University of Baghdad- Iraq

E-mail: Suaad.gedaan@yahoo.com

Abstract. A space X is named a $\pi p-$ normal if for each closed set F and each $\pi-$ closed set F' in X with $F \cap F' = \emptyset$, there are $p-$ open sets U and V of X with $U \cap V = \emptyset$ whereas $F \subseteq U$ and $F' \subseteq V$. Our work studies and discusses a new kind of normality in generalized topological spaces. We define $\vartheta\pi p-$ normal, $\vartheta-$mildly normal, $\vartheta-$almost normal, ϑp-normal, $\vartheta-$mildly p-normal, $\vartheta-$almost p-normal and $\vartheta\pi$-normal space, and we discuss some of their properties.

1. Introduction and Preliminaries

In our paper a topological space will be denoted by X and the closure and the interior of F in X by cl(F) and int(F) respectively. The concept of $\pi p-$normal topological Spaces was introduced and considered by Sadeq (2012) [1].

We recall some concepts and notations defined previously by another authors. A subset F of a space X is said to be pre-open (briefly p-open) (resp. semi-open, α-open) if $F \subseteq \text{int}(\text{cl}(F))$(resp. $F \subseteq \text{cl}(\text{int}(F))$, $F \subseteq \text{int}\left(\text{cl}(\text{int}(F))\right)$)[2]. The complement of a p-open (resp. semi-open , α-open) set is called p- closed [3](resp. semi-closed[2], α-closed[4]). The following two definitions are taken from[2], preclosure of F is $\text{pcl}(F) = \bigcap\{F' : F' \text{ is a preclosed set containing F}\}$, preinterior of F is $\text{pint}(F) = \bigcup\{F' : F' \text{ is preopen set contained in F}\}$.

According to [5], a subset F of a topological space X is called regular open or an open domain if $F = \text{int}(\text{cl}(F))$, or equivalently if it is the interior of some closed set. A set F is said to be a regular closed or a closed domain if its complement is an open domain, or equivalently, if $F = \text{cl}(\text{int}(F))$. The finite union of open domain sets in X is said to be π-open. The complement of a π-open set is π-closed, or equivalently, a π-closed set is a finite intersection of closed domain subsets, [6]. The following diagram shows the relationship among closed sets:

$$\text{closed domain} \Rightarrow \pi - \text{closed} \Rightarrow \text{closed} \Rightarrow \alpha - \text{closed} \Rightarrow p - \text{closed}$$

On the other hand, the notions of normal, almost normal and mildly normal spaces were introduced by sharma[7], Singal[8] and Singal[9] respectively. A space X is called normal if every pair of disjoint closed sets are contained in disjoint open sets and it is called almost normal if every pair of disjoint closed sets one of which is closed domain are contained in disjoint open sets and it is said to be mildly normal if every pair of disjoint closed domain sets are contained in disjoint open sets.

In 1995 Paul and Bhattacharyya[10] introduced the concept of p −normal space, a topological space X is said to be p −normal if any disjoint closed sets F and F′ of X are contained in two disjoint p −open sets U and V of X. While in 1991 Navalagi [2] introduced the concepts of mildly p-normal and almost p-normal, a space X is said to be an almost p −normal if any disjoint closed sets F and F′ of X, one of which is closed domain, are contained in two disjoint p −open sets U and V of X, and it is said to be a mildly p −normal if any disjoint closed domain sets F and F′ of X are contained in two disjoint p −open sets U and V of X. Kalantan[11], introduced the definitions of π −normal and quasi-normal spaces, a space X is called a π −normal if any two disjoint closed subsets F and F′ of X, one of which is π −closed are contained in disjoint open sets, and it is called quasi-normal if any two disjoint π −closed subsets F and F′ of X there exist two open disjoint subsets U and V of X such that F⊆ U and F′⊆ V .

In 2012 the notion of πp-normal space was introduced by Sadeq [1]. A space X is said to be πp −normal if for every pair of disjoint closed sets F and F′ of X, one of which is π −closed, are contained in two disjoint p −open sets U and V of X. The following diagrams shows the relationship among normal spaces:

$$\text{normal} \implies \pi-\text{normal} \implies \text{almost normal} \implies \text{mildly normal}$$

$$\text{normal} \implies \pi-\text{normal} \implies \text{quasi}-\text{normal} \implies \text{mildly normal}$$

$$\text{normal} \implies \text{p}-\text{normal} \implies \text{πp}-\text{normal} \implies \text{almost p}-\text{normal}$$

$$\text{normal} \implies \pi-\text{normal} \implies \text{πp}-\text{normal}$$

Recently many topological concepts have been modified to give new concepts in the structure of generalized topological spaces. In this section we review some definitions in generalized topological spaces and we review some modified open sets and modified normal spaces, we begin with the definition of the generalized topological space.

Definition 1.1[12]

Let X be a nonempty set. A collection ϑ of subsets of X is called a generalized topology (in brief, GT) on X if $\emptyset$ belongs to ϑ and the arbitrary unions of elements of ϑ is an element in ϑ. (X, ϑ) is called generalized topological space (in brief, GTS).

Every set in ϑ is called ϑ -open while the complement of ϑ -open is called ϑ -closed. The largest ϑ -open set contained in a set F is called the interior of F and is denoted by $i_\vartheta(F)$ whereas the smallest ϑ -closed set containing F is called the closure of F and is denoted by $c_\vartheta(F)$. A generalized topology ϑ is said to be strong [13] if X $\in$ ϑ, accordingly, (X, ϑ) is called strong generalized topological space (in brief, SGTS).

Definition 1.2[14]

A subset A of a GTS(X, ϑ) is called

(i) ϑ -semi-open if $F \subset c_\vartheta(i_\vartheta(F))$, and its complement is ϑ-semi- closed.

(ii) ϑ-p-open if $F \subset i_\vartheta(c_\vartheta(F))$, and its complement is ϑ-α- closed.

(iii) ϑ-α-open if $F \subset i_\vartheta\left(c_\vartheta(i_\vartheta(F))\right)$, and its complement is ϑ-p- closed.

The intersection of all ϑ-p- closed sets containing F is called $\vartheta-\text{p}-$ closure of F and denoted by $pc_\vartheta(F)$. The $\vartheta-\text{p}-$ interior of F, denoted by $pi_\vartheta(F)$, is defined to be the union of all $\vartheta-\text{p}-$ open sets contained in F.

Definition 1.3[15]

Let A be a subset of a $GTS(X, \vartheta)$. Then A is said to be ϑ −regular open or $\vartheta-$ open domain if $F = i_\vartheta(c_\vartheta(F))$. The complement of a $\vartheta-$ open domain is called $\vartheta-$ closed domain.

Sarsak [16], define $\vartheta-$ closed domain as a subset A of $GTS(X, \vartheta)$ that fulfills the condition $F = c_\vartheta(i_\vartheta(F))$.

Definition 1.4[17]
A subset F of $GTS(X, \vartheta)$ is said to be $\vartheta-\pi-$open if F is the union of finitely many $\vartheta-$ open domain sets, and it is called $\vartheta-\pi-$closed if its complement is a $\vartheta-\pi-$open, or equivalently if F is the intersection of finitely many $\vartheta-$ closed domain sets.
The relationship among all above sets can be illustrated by the following schemes:

$$\vartheta-\text{closed domain} \Rightarrow \vartheta-\pi-\text{closed} \Rightarrow \vartheta-\text{closed} \Rightarrow \vartheta-\alpha-\text{closed} \Rightarrow \vartheta-\text{p}-\text{closed}$$

$$\begin{array}{ccccc} \vartheta-\text{open} & \Longrightarrow & \vartheta-\alpha-\text{open} & \Longrightarrow & \vartheta-\text{semi}-\text{open} \\ & & \Downarrow & & \\ & & \vartheta-\text{p}-\text{open} & & \end{array}$$

$$\begin{array}{ccccc} \vartheta-\text{closed} & \Longrightarrow & \vartheta-\alpha-\text{closed} & \Longrightarrow & \vartheta-\text{semi}-\text{closed} \\ & & \Downarrow & & \\ & & \vartheta-\text{p}-\text{closed} & & \end{array}$$

$$\vartheta-\text{open domain} \Leftrightarrow \vartheta-\text{open and } \vartheta-\text{semi}-\text{closed} \Leftrightarrow \vartheta-\alpha-\text{open and } \vartheta-\text{semi}-\text{closed} \Leftrightarrow \vartheta-\text{p}-\text{open and } \vartheta-\text{semi}-\text{closed}$$

$$\vartheta-\text{closed domain} \Leftrightarrow \vartheta-\text{closed and } \vartheta-\text{semi}-\text{open} \Leftrightarrow \vartheta-\alpha-\text{closed and } \vartheta-\text{semi}-\text{open} \Leftrightarrow \vartheta-\text{p}-\text{closed and } \vartheta-\text{semi}-\text{open}$$

Properties of normal GT's were discussed in ([18], [19], [20], [21], [22], [23]). A $GT\vartheta$ is normal iff, whenever F andF' are ϑ -closed sets such that $F \cap F' = \emptyset$, there exists ϑ -open sets U and V satisfying $F \subset U, F' \subset V$ and $U \cap V = \emptyset$.
In 2012 Bishwambhar[24], defined almost normal and mildly normal spaces, in generalized topological spaces, by modifying the condition related to the open sets in the original definition. As we show below.

Definition 1.5[24]
Let ϑbe a GT on a topological space X. Then
1. X is named almost ϑ -normal if F is a closed set and B is a closed domain set in X with $F \cap F' = \emptyset$, , then there are two disjoint $\vartheta-$open sets U and V such that $F \subseteq U$ and $F' \subseteq V$.
2. X is named mildly ϑ -normal if A and B are closed domain sets in X with $F \cap F' = \emptyset$, , then there are two disjoint $\vartheta-$ open sets U and V such that $F \subseteq U$ and $F' \subseteq V$.

We will denote the class of $\vartheta-$closed (resp. $\vartheta-$p$-$open, $\vartheta-$p$-$closed,$\vartheta-\pi-$open,$\vartheta-\pi-$closed,$\vartheta-$ semi$-$open, $\vartheta-$ semi$-$closed, $\vartheta-\alpha-$open,$\vartheta-\alpha-$closed, $\vartheta-$open domain, $\vartheta-$closed domain) sets in X by ϑ'
(resp.ϑPO(X), ϑPC(X), $\vartheta\pi$O(X), $\vartheta\pi$C(X), ϑSO(X), ϑSC(X),$\vartheta\alpha$O(X), $\vartheta\alpha$C(X),ϑRO(X), ϑRC(X)).

2. $\vartheta\pi$p $-$Normal Generalized Topological Spaces

In this section, another definitions about almost normal and mildly normal spaces, in generalized topological spaces, will be given by modifying the conditions related to open and closed sets in the original definition, called $\vartheta-$ almost normal and $\vartheta-$ mildly normal. By the same way, p$-$ normal,

almost p − normal, mildly p − normal, π − normal, quasi normal and πp −normal spaces, in generalized topological spaces will be defined, called $\vartheta - p - normal, \vartheta -$ almost p − normal, $\vartheta -$ mildly p − normal, $\vartheta\pi -$ normal, $\vartheta -$ quasi normal and $\vartheta\pi p - normal$, and the relationship among them will be discussed, as we show in the following section.

Definition 2.1
A GTS(X, ϑ) is called
1. $\vartheta -$ almost normal if $\forall F \in \vartheta'$ and $\forall F' \in \vartheta RC(X)$ with $F \cap F' = \emptyset, \exists U, V \in \vartheta \ni F \subseteq U$ and $F' \subseteq V$ and $U \cap V = \emptyset$.
2. $\vartheta -$ mildly normal if for any two sets $F, F' \in \vartheta RC(X)$ with $F \cap F' = \emptyset$ there are two sets $U, V \in \vartheta \ni F \subseteq U$ and $F' \subseteq V$ and $U \cap V = \emptyset$.
3. $\vartheta\pi -$ normal if $\forall F \in \vartheta'$and $\forall F' \in \vartheta\pi C(X)$ with $F \cap F' = \emptyset \exists U, V \in \vartheta \ni F \subseteq U$ and $F' \subseteq V$ and $U \cap V = \emptyset$.
4. $\vartheta -$ quasi normal if for any two sets $F, F' \in \vartheta\pi C(X)$ with $F \cap F' = \emptyset$ there are two sets $U, V \in \vartheta \ni F \subseteq U$ and $F' \subseteq V$ and $U \cap V = \emptyset$.
5. $\vartheta - p -$ normal if for any two sets F, $F' \in \vartheta'$ with $F \cap F' = \emptyset$ there are two sets $U, V \in \vartheta PO(X) \ni F \subseteq U$ and $F' \subseteq V$ and $U \cap V = \emptyset$.
6. $\vartheta - almost\ p - normal$ if $\forall F \in \vartheta'$and $\forall F' \in \vartheta RC(X)$with $F \cap F' = \emptyset$, $\exists U, V \in \vartheta PO(X) \ni F \subseteq U\ and\ F' \subseteq V$ and $U \cap V = \emptyset$.
7. $\vartheta - mildly\ p - normal$ if for any two sets $F, F' \in \vartheta RC(X)$ with $F \cap F' = \emptyset$ there are two sets $U, V \in \vartheta PO(X) \ni F \subseteq U\ and\ F' \subseteq V$ and $U \cap V = \emptyset$.
8. $\vartheta\pi p - normal$ if $\forall F \in \vartheta'$and $\forall F' \in \vartheta\pi C(X)$ with $F \cap F' = \emptyset, \exists U, V \in \vartheta PO(X) \ni F \subseteq U\ and\ F' \subseteq V$ and $U \cap V = \emptyset$.
9. $\vartheta - quasi\ p - normal$ if for any two sets $F, F' \in \vartheta\pi C(X)$ with $F \cap F' = \emptyset$ there are two sets $U, V \in \vartheta PO(X) \ni F \subseteq U\ and\ F' \subseteq V$ and $U \cap V = \emptyset$.

Remark 2.2
The following trends are true for the generalized topological space (X, ϑ).

$$\vartheta - normal \implies \vartheta\pi - normal \implies \vartheta - almost\ normal \implies \vartheta - mildly\ normal$$

These directions are not reversible, as shown in the following example

Example2.3
Let $\mathbb{R}$ be the set of all real numbers, and let $\vartheta = \{\mathbb{R}, \emptyset, \{0\}\} \cup \{\mathbb{R}\backslash\{x\}: x \neq 0\}$, then
$\vartheta' = \{\mathbb{R}, \emptyset, \mathbb{R}\backslash\{0\}\} \cup \{\{x\}: x \neq 0\}$, $\vartheta RC(X) = \{\mathbb{R}, \emptyset\}$, and $\vartheta\pi C(X) = \{\mathbb{R}, \emptyset\}$.
Note that $(\mathbb{R}, \vartheta)$ is not $\vartheta -$ normal because for any two nonempty disjoint ϑ −closed sets in $\mathbb{R}$, there are no two disjoint ϑ −open sets containing them. While it is $\vartheta\pi -$ normal, $\vartheta -$ almost normal and $\vartheta -$ mildly normal.

Remark 2.4
The following outline is correct for the generalized topological space (X, ϑ).

$$\vartheta - p - normal \implies \vartheta\pi p - normal \implies \vartheta - almost\ p - normal \implies \vartheta - mildly\ p - normal$$

The inverse of the above directions is generally not correct as shown by the following examples.

Example2.5
Let $X = \{a, b, c\}, \vartheta = \{X, \emptyset, \{a\}, \{a, b\}, \{a, c\}\}, \vartheta' = \{X, \emptyset, \{b, c\}, \{c\}, \{b\}\}$,
$\vartheta PO(X) = \{X, \emptyset, \{a\}, \{a, b\}, \{a, c\}\}, \vartheta RC(X) = \{X, \emptyset\}, \vartheta\pi C(X) = \{X, \emptyset\}$.
Note that (X, ϑ) is not $\vartheta - p -$ normal because $\{c\}\ and\ \{b\}$ are two disjoint ϑ −closed sets in X, but there are no two disjoint $\vartheta - p$ −open containing them. On the other hand, we see that (X, ϑ) is $\vartheta\pi p -$ normal, $\vartheta -$ almost $p -$ normal and $\vartheta -$ mildly $p -$ normal.

Example2.6
Take the set of all real numbers $\mathbb{R}$ with $\vartheta = \{U \subseteq X: \forall\, x \in U\ \exists N \in \eta_x\ \ni N \subseteq U\}$, where $\{\eta_x\}_{x\in\mathbb{R}}$ is defined as follows:
For each $x \in \mathbb{Q}'$(the set of all irrational numbers) put a sequence $\{x_n\}_{n\in\mathbb{N}} \subset \mathbb{Q}$ (the set of all rational numbers) such that $x_n \to x$ (where the convergence is taken in $\mathbb{R}$ with the usual topology), let $A_n(x) = \{x_k: k \geq n\}$, and let $U_n(x) = \{x\} \cup A_n(x)$. For $x \in \mathbb{Q}'$, $\eta_x = \{U_n(x): n \in \mathbb{N}\}$ and for $x \in \mathbb{Q}$, $\eta_x = \{\{x\}\}$. Then $(\mathbb{R}, \vartheta)$ is $\vartheta -$ almost normal and $\vartheta -$ almost p −normal, but it is neither $\vartheta\pi$ −normal nor $\vartheta\pi p$ −normal.

Remark 2.7
Diagram bellow is true for the generalized topological space (X, ϑ).

$$\vartheta - normal \implies \vartheta\pi - normal \implies \vartheta - quasi\ normal$$

These implications are not reversible as shown by the following example.

Example2.8
Let $P = \{(x, y): x, y \in \mathbb{R}, y > 0\}$ and $L = \{(x, 0): x \in \mathbb{R}\}$ be a subspace of $\mathbb{R}^2$with the usual topology, and let $X = P \cup L$
$For\ z \in P, \eta_{z=}$ any basic open disc around z contained in P with its usual Euclidean topology.
$For\ z \in L, \eta_{z=} \{z\} \cup (P \cap D)$, where D is any open disc around z in the plane $\mathbb{R}^2$ with its usual Euclidean topology.

Let $\vartheta = \{U \subseteq X: \forall\, z \in U\ \exists N \in \eta_z\ \ni N \subseteq U\}$, then (X, ϑ) is neither ϑ −normal nor $\vartheta\pi$ −normal , while it is a ϑ −quasi normal.

Remark 2.9
A condition "every $\vartheta -$ closed must be ϑ −semi− open" can be added in Remarks 2.2, 2.4 and 2.7 to achieve opposite directions.

Proposition 2.10
Every $\vartheta\pi$ −normal space is a $\vartheta\pi p -$ normal space.
Proof:
Let (X, ϑ) be $\vartheta\pi$ −normal space, we have to show that X is $\vartheta\pi p -$ normal space, let F be ϑ −closed set and F' be $\vartheta - \pi$ −closed set of X with $F \cap F' = \emptyset$, by definition of $\vartheta\pi$ −normal we get two disjoint ϑ −open sets $U\ and\ V$ such that $F \subseteq U\ and\ F' \subseteq V$. Since every ϑ −open set is $\vartheta - p$ −open, so we got what we needed.

Remark 2.11
The opposite direction of Proposition 2.10 is generally incorrect. Note the generalized topological space in Example2.8 is a $\vartheta\pi p -$ normal space, but not $\vartheta\pi$ −normal.

Theorem 2.12
For a generalized topological space (X, ϑ), the following are equivalent :
a) (X, ϑ) is $\vartheta\pi p -$ normal.
b) $\forall U, V \in \vartheta$, one of which is $\vartheta - \pi$ −open, $U \cup V = X$, there are $\vartheta - p$ −closed sets F and F' so that $F \subseteq U, F' \subseteq V\ and\ F \cup F' = X$.
c) $\forall F \in \vartheta'$ and $\forall U \in \vartheta\pi O(X)$ with $F \subseteq U$, there is a $\vartheta - p$ −open set V so that $F \subseteq V \subseteq pc_\vartheta(V) \subseteq U$.

Proof:

If (a)Then(b)
Let $U\ and\ V$ be ϑ −open sets in X, such that V is $\vartheta-\pi$ −open and $U\cup V = X$, consequently we have $X\backslash U\ and\ X\backslash V$ are ϑ −closed sets in a $\vartheta\pi p-$ normal $GTS(X,\vartheta)$ with $X\backslash V$ $\vartheta-\pi-$ closed and $X\backslash U \cap X\backslash V = \emptyset$, so by Definition 2.1,no.8 there exist two disjoint $\vartheta-p$ −open sets $G\ and\ H$ such that $X\backslash U\subseteq G\ and\ X\backslash V\subseteq H$. Let $F = X\backslash G$ and $F' = X\backslash H$, then F and F' are $\vartheta-p$ −closed sets such that $F\subseteq U, F'\subseteq V\ and\ F\cup F' = X$.
If(b)Then(c)
Let F be a ϑ −closed set and U be a $\vartheta-\pi$ −open set so that $F\subseteq U$, thus $F\cap X\backslash U = \emptyset$, which leads to $X\backslash F\cup U = X$, where $X\backslash F$ is ϑ −open. By (b) we can get $\vartheta-p$ −closed sets F_1 and F_2 such that $F_1\subseteq X\backslash F, F_2\subseteq U\ and\ F_1\cup F_2 = X$. We have got $F\subseteq X\backslash F_1$ and $X\backslash F_1\cap X\backslash F_2 = \emptyset$ which results in $X\backslash F_1\subseteq F_2$. Put $V = X\backslash F_1$, then $F\subseteq V\subseteq F_2\subseteq U$. We know that $V\subseteq pc_\vartheta(V)$, it remains to show that $pc_\vartheta(V)\subseteq U$, note that F_2 is $\vartheta-p$ −closed set containing V, but $pc_\vartheta(V)$ is the smallest $\vartheta-p$ −closed set containing V, therefor $pc_\vartheta(V)\subseteq F_2\subseteq U$. Hence $F\subseteq V\subseteq pc_\vartheta(V)\subseteq U$.
If(c)Then(a)
Let F and F' be any ϑ −closed sets of X with F' is $\vartheta-\pi$ −closed and $F\cap F' = \emptyset$, so $F\subseteq X\backslash F'$ which is $\vartheta-\pi$ −open, then by (c) there is a $\vartheta-p$ −open set V so that $F\subseteq V\subseteq pc_\vartheta(V)\subseteq X\backslash F'$. Let $G = V$ and $H = X\backslash pc_\vartheta(V)$, then $G, H\in\vartheta OP(X)$ with $G\cap H = \emptyset$ and $F\subseteq G, F'\subseteq H$. Hence (X,ϑ) is $\vartheta\pi p-$ normal.

3. Preservation Theorems of $\vartheta\pi p$ −Normality

Definition 3.1 [25]
A function $f: (X,\vartheta_1)\to(Y,\vartheta_2)$ from a $GTS(X,\vartheta_1)$ into a $GTS(Y,\vartheta_2)$ is called
1. $(\vartheta_1,\vartheta_2)$−continuous if $f^{-1}(H)\in\vartheta_1\forall H\in\vartheta_2$.
2. $(\vartheta_1,\vartheta_2)$−open if $f(G)\in\vartheta_2\ \forall\ G\in\vartheta_1$.
3. $(\vartheta_1,\vartheta_2)-$ R−irresolute if $f^{-1}(H)\in\vartheta_1RC(X)\ \forall\ H\in\vartheta_2RC(Y)$.
4. Completely $(\vartheta_1,\vartheta_2)-$ irresolute if $f^{-1}(H)\in\vartheta_1\pi C(X)\ \forall\ H\in\vartheta_2\pi C(Y)$.
5. Almost $(\vartheta_1,\vartheta_2)$−closed if $f(G)\in\vartheta_2\pi C(Y)\ \forall\ G\in\vartheta_1\pi C(X)$.
6. $(\vartheta_1,\vartheta_2)$−closed if $f(F)\in\vartheta_2{}'\ \forall\ F\in\vartheta_1{}'$.[26]

Theorem 3.2[27]
A function $f: (X,\vartheta_1)\to(Y,\vartheta_2)$ is called $(\vartheta_1,\vartheta_2)$−continuous if for every ϑ_2-closed set $K\ in\ Y$, $f^{-1}(K)$ is ϑ_1 −closed in X.
The following theorems show the functions that maintain the property of being ϑ −normal, ϑ −almost normal, ϑ −mildly normal, $\vartheta\pi$ −normal and $\vartheta-quasi$ normal.

Theorem 3.3
Let $f: (X,\vartheta_1)\to(Y,\vartheta_2)$ be a bijective $(\vartheta_1,\vartheta_2)$−continuous $(\vartheta_1,\vartheta_2)$−open function, if X is ϑ_1 −normal, then Y is ϑ_2 −normal.

Proof:
Let $F\ and\ F'\in\vartheta_2{}'$ with $F\cap F' = \emptyset$, by Theorem 2.3 we get that $f^{-1}(F), f^{-1}(F')\in\vartheta_1{}'$ with $f^{-1}(F)\cap f^{-1}(F') = \emptyset$. But X is ϑ_1 −normal space, so there exists ϑ_1 −open sets $U\ and\ V$ satisfying $f^{-1}(F)\subset U, f^{-1}(F')\subset V$ and $U\cap V = \emptyset$.
Now we have $f(U)\ and\ f(V)$ are ϑ_2 −open sets in Y with $F = f\left(f^{-1}(F)\right)\subset f(U)\ and$ $F' = f\left(f^{-1}(F')\right)\subset f(V)$ and $f(U)\cap f(V) = f(U\cap V) = \emptyset$. Hence Y ϑ_2 −normal space.

Corollary 3.4
The image of $\vartheta_1-normal$ space under the bijective $(\vartheta_1,\vartheta_2)$−continuous $(\vartheta_1,\vartheta_2)$−open function is $\vartheta_2\pi p-$ normal space.

Proof:
Follows from Theorem 3.3, Remark 2.7 and Proposition 2.10.

Theorem 3.5
Let $f:(X,\vartheta_1)\to(Y,\vartheta_2)$ be a bijective $(\vartheta_1,\ \vartheta_2)-$continuous $(\vartheta_1,\ \vartheta_2)-$open and $(\vartheta_1,\ \vartheta_2)-$ R$-$irresolute function, if X is ϑ_1 $-$almost normal, then Y is ϑ_2 $-$almost normal.

Proof:
Let F be ϑ_2 $-$closed $and\ F'$ be ϑ_2 $-$closed domain in Y such that $F\ \cap\ F'\ =\ \emptyset$, we get that $f^{-1}(F)$ is ϑ_1 $-$closed $and\ f^{-1}(F')$ is ϑ_1 $-$closed domain in X with $f^{-1}(F)\cap f^{-1}(F')=\emptyset$. But X is ϑ_1 $-$almost normal space, so there are ϑ_1 $-$open sets $U\ and\ V$ such that

$$f^{-1}(F)\subset U, f^{-1}(F')\subset V \text{ and } U\ \cap\ V\ =\ \emptyset.$$

Now we have $f(U)\ and\ f(V)$ are ϑ_2 $-$open sets in Y with $F=f\left(f^{-1}(F)\right)\subset f(U)\ and$ $F'=f\left(f^{-1}(F')\right)\subset f(V)$ and $f(U)\ \cap f(V)=f(U\cap V)=\emptyset$. Hence Y ϑ_2 $-$almost normal space.

Theorem 3.6
Let $f:(X,\vartheta_1)\to(Y,\vartheta_2)$ be a bijective $(\vartheta_1,\ \vartheta_2)-$open $(\vartheta_1,\ \vartheta_2)-$ R$-$irresolute function, if X is $\vartheta_1-mildly\ normal$, then Y is $\vartheta_2-mildly\ normal$.

Proof:
Take $F,F'\in\ \vartheta_2RC(Y)$ with $F\ \cap\ F'\ =\ \emptyset$, we get that $f^{-1}(F),f^{-1}(F')\in\ \vartheta_1R\,C(X)$ with $f^{-1}(F)\cap f^{-1}(F')=\emptyset$. But X is ϑ_1- mildly normal space, so there exists ϑ_1 $-$open sets $U\ and\ V$ such that $f^{-1}(F)\subset U, f^{-1}(F')\subset V$ and $U\ \cap\ V\ =\ \emptyset$.
Now we have $f(U)\ and\ f(V)$ are ϑ_2 $-$open sets in Y such that $F=f\left(f^{-1}(F)\right)\subset f(U)\ and$ $F'=f\left(f^{-1}(F')\right)\subset f(V)$ and $f(U)\ \cap f(V)=f(U\cap V)=\emptyset$. Hence Y ϑ_2- mildly normal space.

Theorem 3.7
Let $f:(X,\vartheta_1)\to(Y,\vartheta_2)$ be a bijective $(\vartheta_1,\ \vartheta_2)-$continuous $(\vartheta_1,\ \vartheta_2)-$open and Completely $(\vartheta_1,\ \vartheta_2)-$irresolute function, if X is $\vartheta_1\pi-$ normal, then Y is $\vartheta_2\pi-$ normal.

Proof:
Let F be ϑ_2 $-$closed $and\ F'$ be $\vartheta_2-\pi$ $-$closed in Y with $F\ \cap\ F'\ =\ \emptyset$, we get that $f^{-1}(F)$ is ϑ_1 $-$closed $and\ f^{-1}(F')$ is $\vartheta_1-\pi$ $-$closed domain in X with $f^{-1}(F)\cap f^{-1}(F')=\emptyset$. But X is $\vartheta_1\pi-$ normal space, so there exists ϑ_1 $-$open sets $U\ and\ V$ such that

$$f^{-1}(F)\subset U, f^{-1}(F')\subset V \text{ and } U\ \cap\ V\ =\ \emptyset.$$

Now we have $f(U)\ and\ f(V)$ are ϑ_2 $-$open sets in Y whereas $F=f\left(f^{-1}(F)\right)\subset f(U)\ and$ $F'=f\left(f^{-1}(F')\right)\subset f(V)$ and $f(U)\ \cap f(V)=f(U\cap V)=\emptyset$. Hence Y $\vartheta_2\pi-$ normal space.

Corollary 3.8
The image of $\vartheta_1\pi-\ normal$ space under the $(\vartheta_1,\ \vartheta_2)-$continuous $(\vartheta_1,\ \vartheta_2)-$open and Completely $(\vartheta_1,\ \vartheta_2)-$irresolute function is $\vartheta_2\pi p-$ normal space.

Proof:
Follows from Theorem 3.7 and Proposition 2.10

Theorem 3.9
Let $f:(X,\vartheta_1)\to(Y,\vartheta_2)$ be a bijective $(\vartheta_1,\ \vartheta_2)-$open Completely $(\vartheta_1,\ \vartheta_2)-$ irresolute function, if X is $\vartheta_1-\ quasi\ normal$, then Y is $\vartheta_2-quasi\ normal$.

Proof:
Let $F, F' \in \vartheta_2\pi C(Y)$ with $F \cap F' = \emptyset$, we get that $f^{-1}(F), f^{-1}(F') \in \vartheta_1\pi C(X)$ with $f^{-1}(F) \cap f^{-1}(F') = \emptyset$. But X is $\vartheta_1 - quasi$ normal space, so there exists ϑ_1 −open sets U and V such that $f^{-1}(F) \subset U$, $f^{-1}(F') \subset V$ and $U \cap V = \emptyset$. Now we have $f(U)$ and $f(V)$ are ϑ_2 −open sets in Y whereas $F = f(f^{-1}(F)) \subset f(U)$ and $F' = f(f^{-1}(F')) \subset f(V)$ and $f(U) \cap f(V) = f(U \cap V) = \emptyset$. Hence Y $\vartheta_2 - quasi$ normal space.

To indicate the type of functions that preserve the property of being $\vartheta - p$ −normal, ϑ −almost p −normal, ϑ −mildly $p-$ normal, $\vartheta\pi p$ −normal and $\vartheta - quasip -$ normal, we need the following definition.

Definition 3.10
A function $f: (X, \vartheta_1) \to (Y, \vartheta_2)$ from a $GTS(X, \vartheta_1)$ into a $GTS(Y, \vartheta_2)$ is called $(\vartheta_1, \vartheta_2) - M$ −preopen if $f(G) \in \vartheta_2\, PO(Y)\ \forall\ G \in \vartheta_1 PO(X)$.

Theorem 3.11
Let $f: (X, \vartheta_1) \to (Y, \vartheta_2)$ be a bijective $(\vartheta_1, \vartheta_2)$−continuous $(\vartheta_1, \vartheta_2) - M$ −preopen function, if X is $\vartheta_1 - p - normal$, then Y is $\vartheta_2 - p - normal$.

Proof:
Let F and $F' \in \vartheta_2{}'$ with $F \cap F' = \emptyset$, by Theorem 2.3 we get that $f^{-1}(F), f^{-1}(F') \in \vartheta_1{}'$ with $f^{-1}(F) \cap f^{-1}(F') = \emptyset$. But X is $\vartheta_1 - p -$ normal space, so there exists $\vartheta_1 - p -$ open sets U and V satisfying $f^{-1}(F) \subset U, f^{-1}(F') \subset V$ and $U \cap V = \emptyset$. Therefor $f(U)$ and $f(V)$ are $\vartheta_2 - p -$ open sets in Y so that $F = f(f^{-1}(F)) \subset f(U)$ and $F' = f(f^{-1}(F')) \subset f(V)$ and $f(U) \cap f(V) = f(U \cap V) = \emptyset$. Hence Y $\vartheta_2 - p -$ normal space.

Corollary 3.12
The image of $\vartheta_1 - P - normal$ space under the bijective $(\vartheta_1, \vartheta_2)$−continuous $(\vartheta_1, \vartheta_2) - M$ −preopen function is $\vartheta_2\pi p -$ normal space.

Proof:
Follows from Theorem 3.11 and Remark 2.4.

Theorem 3.13
Let $f: (X, \vartheta_1) \to (Y, \vartheta_2)$ be a bijective $(\vartheta_1, \vartheta_2)$−continuous $(\vartheta_1, \vartheta_2) - M$ −preopen and $(\vartheta_1, \vartheta_2)-$ R−irresolute function, if X is ϑ_1 −almost $p-$ normal, then Y is ϑ_2 −almost $p-$ normal.

Proof:
Let F be ϑ_2 −closed and F' be ϑ_2 −closed domain in Y such that $F \cap F' = \emptyset$, we get that $f^{-1}(F)$ is ϑ_1 −closed and $f^{-1}(F')$ is ϑ_1 −closed domain in X with $f^{-1}(F) \cap f^{-1}(F') = \emptyset$. But X is ϑ_1 −almost $p-$ normal space, so there are $\vartheta_1 - p -$ open sets U and V such that
$f^{-1}(F) \subset U, f^{-1}(F') \subset V$ and $U \cap V = \emptyset$.
Thus $f(U)$ and $f(V)$ are $\vartheta_2 - p -$ open sets in Y whereas $F = f(f^{-1}(F)) \subset f(U)$ and $F' = f(f^{-1}(F')) \subset f(V)$ and $f(U) \cap f(V) = f(U \cap V) = \emptyset$. Hence Y ϑ_2 −almost p −normal space.

Theorem 3.14
Let $f: (X, \vartheta_1) \to (Y, \vartheta_2)$ be a bijective $(\vartheta_1, \vartheta_2) - M$ −preopen $(\vartheta_1, \vartheta_2)-$ R−irresolute function, if X is $\vartheta_1 - mildly\ p - normal$, then Y is $\vartheta_2 - mildly\ p - normal$.

Proof:
Take $F\ and\ F' \in \vartheta_2\ RC(Y)$ with $F \cap F' = \emptyset$, we get that $f^{-1}(F), f^{-1}(F') \in \vartheta_1 R\ C(X)$ with $f^{-1}(F) \cap f^{-1}(F') = \emptyset$. But X is $\vartheta_1 -$ mildly $p -$normal space, so there exists $\vartheta_1 - p -$ open sets $U\ and\ V$ such that $f^{-1}(F) \subset U, f^{-1}(F') \subset V$ and $U \cap V = \emptyset$. This gives us that $f(U)\ and\ f(V)$ are $\vartheta_2 - p -$ open sets in Y whereas $F = f\left(f^{-1}(F)\right) \subset f(U)\ and\ F' = f\left(f^{-1}(F')\right) \subset f(V)$ and $f(U) \cap f(V) = f(U \cap V) = \emptyset$. Hence $Y\ \vartheta_2 -$ mildly $p -$ normal space.

Theorem 3.15
Let $f : (X, \vartheta_1) \to (Y, \vartheta_2)$ be a bijective $(\vartheta_1, \vartheta_2)-$continuous $(\vartheta_1, \vartheta_2)-M -$preopen and Completely $(\vartheta_1, \vartheta_2)-$irresolute function, if X is $\vartheta_1 \pi p - normal$, then Y is $\vartheta_2 \pi p - normal$.

Proof:
Let F be $\vartheta_2 -$closed $and\ F'$ be $\vartheta_2 - \pi -$closed in Y with $F \cap F' = \emptyset$, we get that $f^{-1}(F)$ is $\vartheta_1 -$closed $and\ f^{-1}(F')$ is $\vartheta_1 - \pi -$closed domain in X with $f^{-1}(F) \cap f^{-1}(F') = \emptyset$. But X is $\vartheta_1 \pi p -$ normal space, so there are $\vartheta_1 - p -$ open sets $U\ and\ V$ such that
$$f^{-1}(F) \subset U, f^{-1}(F') \subset V \text{ and } U \cap V = \emptyset.$$
This implies $f(U)\ and\ f(V)$ are $\vartheta_2 - p -$ open sets in Y whereas $F = f\left(f^{-1}(F)\right) \subset f(U)\ and\ F' = f\left(f^{-1}(F')\right) \subset f(V)$ and $f(U) \cap f(V) = f(U \cap V) = \emptyset$. Hence $Y\ \vartheta_2 \pi p -$ normal space.

Corollary 3.16
The image of $\vartheta_1 \pi p - normal$ space under the bijective $(\vartheta_1, \vartheta_2)-$continuous $(\vartheta_1, \vartheta_2)-M -$preopen and Completely $(\vartheta_1, \vartheta_2)-$irresolute function is $\vartheta_2 -$almost normal(resp. $\vartheta_2 -$ mildly normal, $\vartheta_2 -$almost $p -$normal, $\vartheta_2 -$ mildly $p -$ normal, $\vartheta_2 - quasi$ normal).

Proof:
Follows from Theorem 3.15 and Remarks 2.2, 2.4, 2.7 and Proposition 2.10.

Theorem 3.17
Let $f : (X, \vartheta_1) \to (Y, \vartheta_2)$ be a bijective $(\vartheta_1, \vartheta_2)-M -$preopen Completely $(\vartheta_1, \vartheta_2)-$ irresolute function, if X is $\vartheta_1 - quasi\ p -$ normal, then Y is $\vartheta_2 - quasi\ p -$ normal.

Proof:
Let $F\ and\ F' \in \vartheta_2 \pi C(Y)$ with $F \cap F' = \emptyset$, we get that $f^{-1}(F), f^{-1}(F') \in \vartheta_1 \pi\ C(X)$ with $f^{-1}(F) \cap f^{-1}(F') = \emptyset$. But X is $\vartheta_1 - quasip -$ normal space, so there are $\vartheta_1 - p -$ open sets $U\ and\ V$ whereas $f^{-1}(F) \subset U, f^{-1}(F') \subset V$ and $U \cap V = \emptyset$. We got $f(U)\ and\ f(V)$ are $\vartheta_2 - p -$ open sets in Y such that $F = f\left(f^{-1}(F)\right) \subset f(U)\ and\ F' = f\left(f^{-1}(F')\right) \subset f(V)$ and $f(U) \cap f(V) = f(U \cap V) = \emptyset$. Hence $Y\ \vartheta_2 - quasip -$ normal space.

Definition 3.18
Let $(X, \vartheta_1) and (Y, \vartheta_2)$ be two generalized topological spaces. A function $f : (X, \vartheta_1) \to (Y, \vartheta_2)$ is called $(\vartheta_1, \vartheta_2)\ pre -$ irresolute if $f^{-1}(H) \in \vartheta_1 PO(X)\ \forall\ H \in \vartheta_2 PO(Y)$.

Theorem 3.19
Let $f : (X, \vartheta_1) \to (Y, \vartheta_2)$ be a bijective $(\vartheta_1, \vartheta_2)-$closed, Almost$(\vartheta_1, \vartheta_2)-$ closed and $(\vartheta_1, \vartheta_2)\ pre -$irresolute function, if Y is $\vartheta_2 \pi p - normal$, then X is $\vartheta_1 \pi p - normal$.

Proof:
Take $F \in \vartheta_1{}'\ and\ F' \in \vartheta_1 \pi C(X)$ with $F \cap F' = \emptyset$, so $f(F)$ is $\vartheta_2 -$closed $and\ f(F')$ be $\vartheta_2 - \pi -$closed in Y such that $f(F) \cap f(F') = f(F \cap F') = \emptyset$. But Y is $\vartheta_2 \pi p -$ normal space, therefor

we get two disjoint $\vartheta_2 - p -$ open sets U and V in Y such that $f(F) \subset U$, $f(F') \subset V$. Since f is $(\vartheta_1, \vartheta_2)\, pre -$irresolute function, so $f^{-1}(U)$ and $f^{-1}(V)$ are $\vartheta_1 - p -$open in X with $f^{-1}(U) \cap f^{-1}(V) = \emptyset$ and $F = f^{-1}\big(f(F)\big) \subset f^{-1}(U)$ and $F' = f^{-1}\big(f(F')\big) \subset f^{-1}(V)$. Hence X is $\vartheta_1 \pi p -$ normal space.

References

[1] Sadeq A, Saad and Hailiza K 2012 πp-Normal Topological Spaces, Int. *Journal of Math. Analysis* **6** (21) 1023 - 1033
[2] Navalagi G B, p-normal, almost p-normal and mildly p-normal spaces Topology Atlas Preprint #427. URL:http://at.yorku.ca/i/d/e/b/71.htm.
[3] El-Deeb S N, Hasanein I A, Mashhour A S and Noiri T 1983 On p-regular spaces, *Bull. Math. Soc. Sci. Math.R.S.R.* **27**(75)311-315
[4] Njastad O 1965 On some classes of nearly open sets *Paci.c J. Math.* **15** 961-970
[5] Sarsak M S 2000 On some properties of generalized open sets in generalized topological spaces *Mathematics Subject Classification. Primary* 54A05 54A10
[6] Zaitsev V 1968 On certain classes of topological spaces and their bicompactifications *Dokl. Akad. Nauk. SSSR* **178** 778-779
[7] Sharma J N 2000 Topology, Krishna Prakashan Media(p)Ltd. *India, twenty fifth edition*
[8] M K Singal and S P Arya 1970 On almost normal and almost completely regular spaces *Glasnik Mat* **5** 25 141–152
[9] Singal M K and Singal A R 1973 Mildly normal spaces *Kyungpook Math J.* **13** 27–31
[10] Paul and Bhattacharyya 1995 on p-normal spaces *Soochow Jour. Math* **21** (3) 273-289
[11] Kalantan L 2008 π-normal topological spaces *Filomat* **22**(11)73-181
[12] Csaszar 2002 A Generalized topology generalized continuity *Acta Mathematica Hungarica* **96**(4) 351–357
[13] Csaszar A 2004 Extremally disconnected generalized topologies *Annales Univ. Budapest. Sectio Math* **17** 151-165
[14] Csaszar A 2004 Generalized open sets in generalized topologies *Acta Mathematica Hungarica* **106** (2)53–66
[15] Jamunarani R and Jeyanthi P 2012 Regular sets in generalized topological spaces *Acta Mathematica Hungarica* **135** (4)342–349
[16] Sarsak M S 2012 Weakly μ −compact spaces *Demonstratio Mathematica* **XLV** 4 929-938
[17] Tyagi B K and HarshV S 2016 On generalized closed sets in generalized topological spaces *CUBO A Mathematical Journal* **18** (01) 27–45
[18] Dontchev J and Noiri T 2000 Quasi normal spaces and πg-closed sets *Acta Math. Hungar* **89** 211-219
[19] Ekici E 2007 On -normal spaces *Bull Math. Soc. Sci. Math. Roumanie* **50** (98)259-272
[20] M. Ganster, S. Jafari and G. B. Navalagi 2002 On semi-g-regular and semi-g-normal spaces *Demonstratio Math* **35** 415-421
[21] Kohli J k and Das A K 2002 New normality axioms and decompositions of normality *Glasnik Math* **37** 163-173
[22] Maheshwari S N and Prasad R 1978 On s-normal spaces *Bull. Math. Soc. Sci. Math. R. S. Roumanie (N. S.)* **22** (68) 27-29
[23] Noiri T 1994 Semi-normal spaces and some functions *Acta Math. Hungar* **65** 305-311
[24] Bishwambhar R 2012 Unification of Almost Regular Almost Normal and Mildly Normal Topological Spaces *Demonstratio Mathematica* **XLV**(4)963-974
[25] Vigneshwaran M and Baby K 2016 On Quasi-Normal and Quasi-Regular Spaces in Hereditary Generalized Topological Spaces *International Journal of Science and Research (IJSR*) **5** (4) 440-444
[26] Xun G, Jianhua G , and Ivan R 2016 Some characterizations of mappings on generalized topological spaces *New Zealand Journal of Mathematics* **46** 73-81

[27] MinWK 2009 Weak continuity on generalized topological spaces *Acta Math. Hungar* **124**(1-2)73-81

Cech Fuzzy Soft Bi-Closure Spaces

Čech Fuzzy Soft Bi-Closure Spaces

M T Hmood and R N Majeed *

Department of Mathematics, College of Education for Pure Sciences Ibn Al-Haitham, University of Baghdad, Baghdad, Iraq

E-mail: rasha.n.m@ihcoedu.uobaghdad.edu.iq

Abstract. In the present study, Čech fuzzy soft bi-closure spaces (Čfs bi-csp's) are defined. The basic properties of Čfs bi-csp's are studied such as we show from each Čfs bi-csp's $(\mathcal{U}, \mathcal{L}_1, \mathcal{L}_2, S)$ we can obtain two types of associative fuzzy soft topological spaces, the first is a fuzzy soft bitopological space $(\mathcal{U}, \tau_{\mathcal{L}_1}, \tau_{\mathcal{L}_2}, S)$ and the second is a fuzzy soft topological space $(\mathcal{U}, \tau_{\mathcal{L}_1\mathcal{L}_2}, S)$. Also, the concepts of the fuzzy soft interior, subspace, and continuity which are the building blocks of classical bi-closure spaces are defined on Čfs bi-csp's. Besides, several examples have been given so that the subject can be better understood.

1. Introduction

Molodtsove [13] introduced the concept of the soft set to solve the problems of incomplete information and investigated various applications in game theory, smoothness of functions, operation researches, Perron integration, probability theory, the theory of measurement, and so on. Maji et al. [6] presented the definition of fuzzy soft sets. Later in 2011, the topological structure based on fuzzy soft sets was given by Tanay and Kandemir [16]. Mukherjee and Park [14] in 2015 introduced the notion of fuzzy soft bitopological spaces. Closure spaces were first introduced by $\check{C}$ech [1] in 1966 since then various notions in general topology have been extended to closure spaces. After Zadeh introduced the concept of fuzzy sets, Mashhour and Ghanim [12] defined $\check{C}$ech fuzzy closure spaces. In 2014, Gowri and Jegadeesan [3] and Krishnaveni and Sekar [5], using the concept of soft sets to introduced and investigate the notion of soft $\check{C}$ech closure spaces. Recently, motivated by the concept of fuzzy soft set and fuzzy soft topology [2] in Chang's sense Majeed [9] was defined the concept of $\check{C}$ech fuzzy soft closure spaces. Also, Majeed and Maibed provided further studies on the structures of Čech fuzzy soft closure spaces such as separation axioms and connectedness see [7, 8, 10, 11]. In the present work, we introduce and study $\check{C}$fs bi-csp's. In section 2, we review some concepts from the literature of fuzzy sets, fuzzy soft sets, and fuzzy soft topological spaces that are needed to be used in the current paper. Section 3 is devoted to introduce and investigate the fundamental structure of $\check{C}$fs bi-csp's, such as open (resp. closed) fuzzy soft sets, fuzzy soft interior operator, topologies induced from $\check{C}$fs bi-csp's. In section 4, the concept of fuzzy soft subspaces from $\check{C}$fs bi-csp's are given and studied. Finally, in Section 5, we introduce some types of continuous (resp. open) fuzzy soft mappings and give its basic properties.

2. Preliminaries

Throughout this paper, $\mathcal{U}$ will refer to the initial universe, $I = [0,1], I_0 = (0,1]$, and S the set of parameters for $\mathcal{U}$ and $\mathcal{A}$ be an non empty of S. β is called a fuzzy set of $\mathcal{U}$ [18] if β is a mapping from $\mathcal{U}$. The family of all fuzzy sets of $\mathcal{U}$ is denoted by $I^{\mathcal{U}}$.

Definition 2.1 [15,17] A fuzzy soft set (fss, briefly) $\beta_{\mathcal{A}}$ on the universe se, $\mathcal{U}$, is a mapping from the parameters set S to $I^{\mathcal{U}}$, i. e., $\beta_{\mathcal{A}}: S \to I^{\mathcal{U}}$, where $\beta_{\mathcal{A}}(s) \neq \bar{0}$ if $s \in \mathcal{A} \subseteq S$ and $\beta_{\mathcal{A}}(s) = \bar{0}$ if $s \notin \mathcal{A}$, where $\bar{0}$ is the empty fuzzy set on $\mathcal{U}$. The family of all $fss's$ over $\mathcal{U}$ denoted by $\mathcal{FS}(\mathcal{U}, S)$.

Definition 2.2 [17] *Let* $\beta_{\mathcal{A}}, \mathcal{S}_{\mathcal{B}} \in \mathcal{FS}(\mathcal{U}, S)$. Then, some basic set operations of $fss's$ are defined as follows:

1. (Inclusion): $\beta_{\mathcal{A}} \sqsubseteq \mathcal{S}_{\mathcal{B}}$ *iff* $\beta_{\mathcal{A}}(s) \leq \mathcal{S}_{\mathcal{B}}(s)$, for all $s \in S$.
2. (Equality): $\beta_{\mathcal{A}} = \mathcal{S}_{\mathcal{B}}$ *iff* $\beta_{\mathcal{A}} \sqsubseteq \mathcal{S}_{\mathcal{B}}$ and $\mathcal{S}_{\mathcal{B}} \sqsubseteq \beta_{\mathcal{A}}$.
3. (Union): $\rho_{\mathcal{A} \sqcup \mathcal{B}} = \beta_{\mathcal{A}} \sqcup \mathcal{S}_{\mathcal{B}}$ *iff* $\rho_{\mathcal{A} \sqcup \mathcal{B}}(s) = \beta_{\mathcal{A}}(s) \vee \mathcal{S}_{\mathcal{B}}(s)$, for all $s \in S$.
4. (Intersection): $\rho_{\mathcal{A} \sqcap \mathcal{B}} = \beta_{\mathcal{A}} \sqcap \mathcal{S}_{\mathcal{B}}$ *iff* $\rho_{\mathcal{A} \sqcap \mathcal{B}}(s) = \beta_{\mathcal{A}}(s) \wedge \mathcal{S}_{\mathcal{B}}(s)$, for all $s \in S$.
5. (Complement): $\mathcal{S}_{\mathcal{B}} = \beta_{\mathcal{A}}^{c}$ *iff* $\beta_{\mathcal{A}}^{c}(s) = \bar{1} - \beta_{\mathcal{A}}(s)$, for all $s \in S$, where $\bar{1}(x) = 1, \forall x \in \mathcal{U}$.
6. (Null fss): β_s is called null fss, denoted $\tilde{0}_S$, if $\beta_s(s) = \bar{0}$, for all $s \in S$.
7. (Universal fss) β_s is called Universal fss, denoted $\tilde{1}_S$, *if* $\beta_s(s) = \bar{1}$, for all $s \in S$.

Definition 2.3 [9] Let $\mathcal{V}$ be a nonempty subset of $\mathcal{U}$, then $\tilde{\mathcal{V}}_S$ denotes the fss $\mathcal{V}_s$ over $\mathcal{U}$ for which $\mathcal{V}(s) = \bar{1}_{\mathcal{V}}$ for all $s \in S$, (where $\bar{1}_{\mathcal{V}}: \mathcal{U} \to [0,1]$ such that $\bar{1}_{\mathcal{V}}(x) = 1$ if $x \in \mathcal{V}$ and $\bar{1}_{\mathcal{V}}(x) = 0$ if $x \notin \mathcal{V}$).

Theorem 2.4 [17] Let J be an index set and $\beta_{\mathcal{A}}, \mathcal{S}_{\mathcal{B}}, (\beta_{\mathcal{A}})_i, (\mathcal{S}_{\mathcal{B}})_i \in \mathcal{FS}(\mathcal{U}, S)\ \forall i \in J$, then

1. $\beta_{\mathcal{A}} \sqcap \left(\sqcup_{i \in J} (\mathcal{S}_{\mathcal{B}})_i\right) = \sqcup_{i \in J} (\beta_{\mathcal{A}} \sqcap (\mathcal{S}_{\mathcal{B}})_i),\ \beta_{\mathcal{A}} \sqcup \left(\sqcap_{i \in J} (\mathcal{S}_{\mathcal{B}})_i\right) = \sqcap_{i \in J} (\beta_{\mathcal{A}} \sqcup (\mathcal{S}_{\mathcal{B}})_i)$.
2. $(\sqcup_{i \in J} (\beta_{\mathcal{A}})_i)^c = \sqcap_{i \in J} (\beta_{\mathcal{A}}^c)_i,\ (\sqcap_{i \in J} (\beta_{\mathcal{A}})_i)^c = \sqcup_{i \in J} (\beta_{\mathcal{A}}^c)_i$.
3. If $\beta_{\mathcal{A}} \sqsubseteq \mathcal{S}_{\mathcal{B}}$, then $\mathcal{S}_{\mathcal{B}}^c \sqsubseteq \beta_{\mathcal{A}}^c$.
4. $\beta_{\mathcal{A}} \sqcap \mathcal{S}_{\mathcal{B}} \sqsubseteq \beta_{\mathcal{A}}, \mathcal{S}_{\mathcal{B}}$ and $\beta_{\mathcal{A}}, \mathcal{S}_{\mathcal{B}} \sqsubseteq \beta_{\mathcal{A}} \sqcup \mathcal{S}_{\mathcal{B}}$.

Definition 2.5 [17] Let $\mathcal{FS}(\mathcal{U}, S)$ and $\mathcal{FS}(\mathcal{W}, \mathcal{N})$ be families of all $fss's$ over $\mathcal{U}$ and $\mathcal{W}$, respectively. Let $u: \mathcal{U} \to \mathcal{W}$ and $p: S \to \mathcal{N}$ be two functions. Then, f_{up} is called fuzzy soft mapping from $\mathcal{FS}(\mathcal{U}, S)$ to $\mathcal{FS}(\mathcal{W}, \mathcal{N})$ and denoted by $f_{up}: \mathcal{FS}(\mathcal{U}, S) \longrightarrow \mathcal{FS}(\mathcal{W}, \mathcal{N})$.

1. If $\beta_{\mathcal{A}} \in \mathcal{FS}(\mathcal{U}, S)$, then the image of $\beta_{\mathcal{A}}$ under the fuzzy soft mapping f_{up} is the fss over $\mathcal{W}$ defined by $f_{up}(\beta_{\mathcal{A}})$, where $\forall k \in p(s),\ \forall y \in \mathcal{W}$.

$$f_{up}(\beta_{\mathcal{A}})(k)(y) = \begin{cases} \bigvee_{u(x)=y} \left(\bigvee_{p(s)=k} (\beta_{\mathcal{A}}(s)) \right)(x) & if\ x \in u^{-1}(y), \\ 0 & otherwise. \end{cases}$$

2. If $\mathcal{S}_{\mathcal{B}} \in \mathcal{FS}(\mathcal{W}, \mathcal{N})$, then the pre-image of $\mathcal{S}_{\mathcal{B}}$ under the fuzzy soft mapping f_{up} is the fss over $\mathcal{U}$ defined by $f_{up}^{-1}(\mathcal{S}_{\mathcal{B}})$. where $\forall s \in p^{-1}(\mathcal{N}), \forall x \in \mathcal{U}$.

$$f_{up}^{-1}(\mathcal{S}_{\mathcal{B}})(s)(x) = \begin{cases} \mathcal{S}_{\mathcal{B}}\big(p(s)\big)\big(u(x)\big) & for\ \ p(s) \in \mathcal{B}, \\ 0 & otherwise. \end{cases}$$

The fuzzy soft mapping f_{up} *is* called surjective (resp. injective) if u and p are surjective (resp. injective), also it is said to be constant if u and p are constant.

Theorem 2.6 [4] Let $\mathcal{U}$ and $\mathcal{W}$ crisp sets $\beta_{\mathcal{A}}, (\beta_{\mathcal{A}})_i \in \mathcal{FS}(\mathcal{U}, S)$ and $\mathcal{S}_{\mathcal{B}}, (\mathcal{S}_{\mathcal{B}})_i \in \mathcal{FS}(\mathcal{W}, \mathcal{N}),\ \forall i \in J$ where J is an index set. Then,

1. *If* $(\beta_{\mathcal{A}})_1 \sqsubseteq (\beta_{\mathcal{A}})_2$, then $f_{up}((\beta_{\mathcal{A}})_1) \sqsubseteq f_{up}((\beta_{\mathcal{A}})_2)$.
2. *If* $(\mathcal{S}_{\mathcal{B}})_1 \sqsubseteq (\mathcal{S}_{\mathcal{B}})_2$, then $f_{up}^{-1}((\mathcal{S}_{\mathcal{B}})_1) \sqsubseteq f_{up}^{-1}((\mathcal{S}_{\mathcal{B}})_2)$.
3. $\beta_{\mathcal{A}} \sqsubseteq f_{up}^{-1}\left(f_{up}(\beta_{\mathcal{A}})\right)$, *if* f_{up} is injective, then the equality holds.
4. $f_{up}(f_{up}^{-1}(\mathcal{S}_{\mathcal{B}})) \sqsubseteq \mathcal{S}_{\mathcal{B}}$, *if* f_{up} is surjective, then the equality holds.

5. $(f_{up}(\beta_{\mathcal{A}}))^c \sqsubseteq f_{up}(\beta_{\mathcal{A}}^c)$.
6. $(f_{up}^{-1}(\mathcal{S}_{\mathcal{B}}))^c = f_{up}^{-1}(\mathcal{S}_{\mathcal{B}}^c)$.

Definition 2.7 [15,16] A triple $(\mathcal{U}, \tau, S)$ is called a fuzzy soft topological space where $\mathcal{U}$ is a nonempty set with a fixed set of parameters S and τ is a family of $fss's$ over $\mathcal{U}$ satisfying the following properties.

1. $\tilde{0}_S, \tilde{1}_S \in \tau$,
2. If $\beta_{\mathcal{A}}, \mathcal{S}_{\mathcal{B}} \in \tau$, then $\beta_{\mathcal{A}} \sqcap \mathcal{S}_{\mathcal{B}} \in \tau$,
3. If $(\beta_{\mathcal{A}})_i \in \tau \ \forall i$, then $\sqcup_{i\in J} (\beta_{\mathcal{A}})_i \in \tau$.

τ is called a topology of $fss's$ on $\mathcal{U}$. Each member of τ is called an open fss. $\mathcal{S}_{\mathcal{B}}$ is called a closed fss in $(\mathcal{U}, \tau, S)$ if $\mathcal{S}_{\mathcal{B}}^c \in \tau$.

Definition 2.8 [14] A quadruple $(\mathcal{U}, \tau_1, \tau_2, S)$ is called fuzzy soft bitopological space where τ_1, τ_2 are arbitrary fuzzy soft topologies on $\mathcal{U}$ with a fixed set of parameters S.

3. Čech Fuzzy Soft Bi-Closure Spaces

In this section, we introduce the concept of Čfs bi-csp and study its fundamental properties. For $i, j = 1,2$ where $i \neq j$.

Definition 3.1 A Čfs bi-csp is a quadruple $(\mathcal{U}, \mathcal{L}_1, \mathcal{L}_2, S)$ where $\mathcal{U}$ is a nonempty set and $\mathcal{L}_1, \mathcal{L}_2 : \mathcal{FS}(\mathcal{U}, S) \to \mathcal{FS}(\mathcal{U}, S)$ are two fuzzy soft closure operators on $\mathcal{U}$ which satisfy the following axioms:

(A_1) $\mathcal{L}_i(\tilde{0}_S) = \tilde{0}_S$,
(A_2) $\beta_{\mathcal{A}} \sqsubseteq \mathcal{L}_i(\beta_{\mathcal{A}})$ for all $\beta_{\mathcal{A}} \in \mathcal{FS}(\mathcal{U}, S)$,
(A_3) $\mathcal{L}_i(\beta_{\mathcal{A}} \cup \mathcal{S}_{\mathcal{B}}) = \mathcal{L}_i(\beta_{\mathcal{A}}) \sqcup \mathcal{L}_i(\mathcal{S}_{\mathcal{B}})$ for all $\beta_{\mathcal{A}}, \mathcal{S}_{\mathcal{B}} \in \mathcal{FS}(\mathcal{U}, S)$.

Definition 3.2 A $fss\ \beta_{\mathcal{A}}$ of a Čfs bi-csp $(\mathcal{U}, \mathcal{L}_1, \mathcal{L}_2, S)$ is said to be $\mathcal{L}_i$-closed fss if $\mathcal{L}_i(\beta_{\mathcal{A}}) = \beta_{\mathcal{A}}$. And, it is called a closed fss if and only if $\mathcal{L}_i(\mathcal{L}_j(\beta_{\mathcal{A}})) = \beta_{\mathcal{A}}$. The complement of a closed fss is called an open fss.

Proposition 3.3 Let $\beta_{\mathcal{A}}$ be a fss of a Čfs bi-csp $(\mathcal{U}, \mathcal{L}_1, \mathcal{L}_2, S)$. Then,

1. $\beta_{\mathcal{A}}$ is a closed fss in $(\mathcal{U}, \mathcal{L}_1, \mathcal{L}_2, S)$ if and only if $\beta_{\mathcal{A}}$ is $\mathcal{L}_j$-closed fss.
2. If $\beta_{\mathcal{A}}$ is an open fss in $(\mathcal{U}, \mathcal{L}_1, \mathcal{L}_2, S)$, then $\mathcal{L}_i(\mathcal{L}_j(\beta_{\mathcal{A}}^c)) = \mathcal{L}_j(\mathcal{L}_i(\beta_{\mathcal{A}}^c))$.

Proof: The proof follows from Defenition 3.2.

The convers of statement 2 in Proposition 3.3, need not be in general as seen from the following example.

Example 3.4**.** Let $\mathcal{U} = \{x, y, z\}$, $S = \{s_1, s_2\}$ and $\mathcal{S}_{\mathcal{B}} \in \mathcal{FS}(\mathcal{U}, S)$,such that $\mathcal{S}_{\mathcal{B}} = \{(s_1, y_{0.6}), (s_2, y_{0.6})\}$. Define fuzzy soft closure operators $\mathcal{L}_1, \mathcal{L}_2 : \mathcal{FS}(\mathcal{U}, S) \to \mathcal{FS}(\mathcal{U}, S)$ as follows:

$$\mathcal{L}_1(\beta_{\mathcal{A}}) = \begin{cases} \tilde{0}_S & if\ \beta_{\mathcal{A}} = \tilde{0}_S, \\ \{(s_1, x_{0.5} \vee y_{0.6}), (s_2, x_{0.5} \vee y_{0.6})\} & if\ \beta_{\mathcal{A}} \sqsubseteq \mathcal{S}_{\mathcal{B}}, \\ \tilde{1}_S & otherwise. \end{cases}$$

and

$$\mathcal{L}_2(\beta_{\mathcal{A}}) = \begin{cases} \tilde{0}_S & if\ \beta_{\mathcal{A}} = \tilde{0}_S, \\ \{(s_1, y_{0.6} \vee z_{0.5}), (s_2, y_{0.6} \vee z_{0.5})\} & if\ \beta_{\mathcal{A}} \sqsubseteq \mathcal{S}_{\mathcal{B}}, \\ \tilde{1}_S & otherwise. \end{cases}$$

Then, it is clear that $(\mathcal{U}, \mathcal{L}_1, \mathcal{L}_2, S)$ is a Čfs bi-csp. Consider $\beta_{\mathcal{A}} = \{(s_1, x_{0.7} \vee y_{0.2}), (s_2, x_{0.5} \vee z_{0.9})\}$. Then we can see that $\mathcal{L}_1(\mathcal{L}_2(\beta_{\mathcal{A}}^c)) = \mathcal{L}_2(\mathcal{L}_1(\beta_{\mathcal{A}}^c)) = \tilde{1}_S$ however $\beta_{\mathcal{A}}$ is not open fss in $(\mathcal{U}, \mathcal{L}_1, \mathcal{L}_2, S)$.

Proposition 3.5 Let $(\mathcal{U}, \mathcal{L}_1, \mathcal{L}_2, S)$ be a Čfs bi-csp and $\beta_{\mathcal{A}}, \mathcal{S}_{\mathcal{B}} \in \mathcal{FS}(\mathcal{U}, S)$ such that $\beta_{\mathcal{A}} \sqsubseteq \mathcal{S}_{\mathcal{B}}$, then $\mathcal{L}_i\big(\mathcal{L}_j(\beta_{\mathcal{A}})\big) \sqsubseteq \mathcal{L}_i\big(\mathcal{L}_j(\mathcal{S}_{\mathcal{B}})\big)$.

Proof: It is clear that from Theorem 2.4 party 4 and of Definition 3.1 we have

$$\begin{aligned}\mathcal{L}_i\left(\mathcal{L}_j(\beta_{\mathcal{A}})\right) &\sqsubseteq \mathcal{L}_i\left(\mathcal{L}_j(\beta_{\mathcal{A}})\right) \sqcup \mathcal{L}_i\left(\mathcal{L}_j(\mathcal{S}_{\mathcal{B}})\right)\\ &= \mathcal{L}_i\left(\mathcal{L}_j(\beta_{\mathcal{A}}) \sqcup \mathcal{L}_j(\mathcal{S}_{\mathcal{B}})\right)\\ &= \mathcal{L}_i\left(\mathcal{L}_j(\beta_{\mathcal{A}} \sqcup \mathcal{S}_{\mathcal{B}})\right)\\ &= \mathcal{L}_i\big(\mathcal{L}_j(\mathcal{S}_{\mathcal{B}})\big).\end{aligned}$$

Proposition 3.6 Let $(\mathcal{U}, \mathcal{L}_1, \mathcal{L}_2, S)$ be a Čfs bi-csp and $\beta_{\mathcal{A}} \in \mathcal{FS}(\mathcal{U}, S)$. If $\mathcal{L}_i(\beta_{\mathcal{A}})$ is contained in $\beta_{\mathcal{A}}$, then $\beta_{\mathcal{A}}$ is a closed fss.

Proof: From hypotheses, axiom (A_2) in Definition 3.1 and statement 1 in Proposition 3.3, we can easily obtain the result.

Definition 3.7 Let $(\mathcal{U}, \mathcal{L}_1, \mathcal{L}_2, S)$ be a Čfs bi-csp and $\beta_{\mathcal{A}} \in \mathcal{FS}(\mathcal{U}, S)$. The fuzzy soft interior of $\beta_{\mathcal{A}}$, denoted by $Int_i\left(Int_j(\beta_{\mathcal{A}})\right)$ for the Čech fuzzy soft closure operators $\mathcal{L}_i$ and $\mathcal{L}_j$ is defined as $Int_i\left(Int_j(\beta_{\mathcal{A}})\right) = (\mathcal{L}_i(\mathcal{L}_j(\beta_{\mathcal{A}}^c))^c$.

It is clear that if $\beta_{\mathcal{A}}$ is an open fss, then $Int_i\left(Int_j(\beta_{\mathcal{A}})\right) = \beta_{\mathcal{A}}$.

In the following proposition, we give the main properties of the fuzzy soft interior of a $fss's$.

Proposition 3.8 Let $(\mathcal{U}, \mathcal{L}_1, \mathcal{L}_2, S)$ be a Čfs bi-csp and $\beta_{\mathcal{A}}, \mathcal{S}_{\mathcal{B}} \in \mathcal{FS}(\mathcal{U}, S)$. Then

1. $Int_i\left(Int_j(\tilde{0}_S)\right) = \tilde{0}_S$ and $Int_i\left(Int_j(\tilde{1}_S)\right) = \tilde{1}_S$.
2. $Int_i\left(Int_j(\beta_{\mathcal{A}})\right) \sqsubseteq \beta_{\mathcal{A}}$.
3. $Int_i\left(Int_j(\beta_{\mathcal{A}} \sqcap \mathcal{S}_{\mathcal{B}})\right) = Int_i\left(Int_j(\beta_{\mathcal{A}})\right) \sqcap Int_i\left(Int_j(\mathcal{S}_{\mathcal{B}})\right)$.
4. If $\beta_{\mathcal{A}} \sqsubseteq \mathcal{S}_{\mathcal{B}}$, then $Int_i\left(Int_j(\beta_{\mathcal{A}})\right) \sqsubseteq Int_i\left(Int_j(\mathcal{S}_{\mathcal{B}})\right)$.
5. $\beta_{\mathcal{A}}$ is open fss if and only if $Int_i\left(Int_j(\beta_{\mathcal{A}})\right) = \beta_{\mathcal{A}}$.

Proof: Straight forward.

Next, we discuss the behavior of open $fss's$ in $(\mathcal{U}, \mathcal{L}_1, \mathcal{L}_2, S)$ to know the types of fuzzy soft topologies that induced by any Čfs bi-csp.

Theorem 3.9 Let $(\mathcal{U}, \mathcal{L}_1, \mathcal{L}_2, S)$ be a Čfs bi-csp. Then,

1. The intersection of any members of closed $fss's$ in $(\mathcal{U}, \mathcal{L}_1, \mathcal{L}_2, S)$ is a closed fss over $\mathcal{U}$.
2. The union of any two members of closed $fss's$ in $(\mathcal{U}, \mathcal{L}_1, \mathcal{L}_2, S)$ is a closed fss over $\mathcal{U}$.

Proof:

1. Let $\{(\beta_{\mathcal{A}})_\alpha : \alpha \in \Lambda\}$ be an arbitrary collection of closed $fss's$ over $\mathcal{U}$. For each $\alpha \in \Lambda$, we have $\sqcap_{\alpha\in\Lambda}(\beta_{\mathcal{A}})_\alpha \sqsubseteq (\beta_{\mathcal{A}})_\alpha$. From Proposition 3.5 we get $\mathcal{L}_i(\mathcal{L}_j(\sqcap_{\alpha\in\Lambda}(\beta_{\mathcal{A}})_\alpha) \sqsubseteq \mathcal{L}_i(\mathcal{L}_j((\beta_{\mathcal{A}})_\alpha) =$

$(\beta_{\mathcal{A}})_{\alpha}$. This yields, $\mathcal{L}_i(\mathcal{L}_j(\sqcap_{\alpha\in\Lambda}(\beta_{\mathcal{A}})_{\alpha}) \sqsubseteq \sqcap_{\alpha\in\Lambda}(\beta_{\mathcal{A}})_{\alpha}$. The other hand follow from (A_2) of Definition 3.1.

2. Let $\beta_{\mathcal{A}}$ and $\mathcal{S}_{\mathcal{B}}$ be closed $fss's$ over $\mathcal{U}$. Then from Proposition 3.5, it follows $\mathcal{L}_i(\mathcal{L}_j(\beta_{\mathcal{A}} \sqcap \mathcal{S}_{\mathcal{B}}) \sqsubseteq \mathcal{L}_i\left(\mathcal{L}_j(\beta_{\mathcal{A}})\right) \sqcap \mathcal{L}_i\left(\mathcal{L}_j(\mathcal{S}_{\mathcal{B}})\right) = (\beta_{\mathcal{A}} \sqcap \mathcal{S}_{\mathcal{B}})$. Therefore, $\mathcal{L}_i(\mathcal{L}_j(\beta_{\mathcal{A}} \sqcap \mathcal{S}_{\mathcal{B}}) \sqsubseteq \beta_{\mathcal{A}} \sqcap \mathcal{S}_{\mathcal{B}}$. The other hand follows from (A_2) of Definition 3.1.

Corollary 3.10 Let $(\mathcal{U}, \mathcal{L}_1, \mathcal{L}_2, S)$ be a Čfs bi-csp, Then,

1. The union of any collection of open $fss's$ in $(\mathcal{U}, \mathcal{L}_1, \mathcal{L}_2, S)$ is an open fss over $\mathcal{U}$.
2. The intersection of any two open $fss's$ in $(\mathcal{U}, \mathcal{L}_1, \mathcal{L}_2, S)$ is an open fss over $\mathcal{U}$.

Now, we can define the types of fuzzy soft topologies that associated from Čfs bi-csp.

Definition 3.11 Let $(\mathcal{U}, \mathcal{L}_1, \mathcal{L}_2, S)$ be a Čfs bi-csp. Then,

1. The associated fuzzy soft topologies $\tau_{\mathcal{L}_i}$on $\mathcal{U}$ is defined as $\tau_{\mathcal{L}_i} = \{\beta^c_{\mathcal{A}}: \mathcal{L}_i(\beta_{\mathcal{A}}) = \beta_{\mathcal{A}}\}$ is the family of all $\mathcal{L}_i$-open $fss's$ of $(\mathcal{U}, \mathcal{L}_i, S)$ [9]. Also, $(\mathcal{U}, \tau_{\mathcal{L}_1}, \tau_{\mathcal{L}_2}, S)$ is a fuzzy soft bitopological space.
2. The associated fuzzy soft topologies $\tau_{\mathcal{L}_i\mathcal{L}_j}$ is defined as $\tau_{\mathcal{L}_i\mathcal{L}_j} = \{\beta^c_{\mathcal{A}}: \mathcal{L}_i(\mathcal{L}_j(\beta_{\mathcal{A}})) = \beta_{\mathcal{A}}\}$ is the family of all open $fss's$ of $(\mathcal{U}, \mathcal{L}_1, \mathcal{L}_2, S)$ and $(\mathcal{U}, \tau_{\mathcal{L}_i\mathcal{L}_j}, S)$ is a fuzzy soft topological space.

Clearly, from Definition 3.11, we have $\tau_{\mathcal{L}_i\mathcal{L}_j} = \tau_{\mathcal{L}_i} \cap \tau_{\mathcal{L}_j}$.

4. Čech fuzzy soft bi-closure subspaces

In this section, we introduce the concept of subspaces in Čfs bi-csp's and give some properties of it.

Theorem 4.1 Let $(\mathcal{U}, \mathcal{L}_1, \mathcal{L}_2, S)$ be a Čfs bi-csp and $\mathcal{V} \subseteq \mathcal{U}$. Let $\mathcal{L}_{i_\mathcal{V}}: \mathcal{FS}(\mathcal{V}, S) \to \mathcal{FS}(\mathcal{V}, S)$ defined by $\mathcal{L}_{i_\mathcal{V}}(\beta_{\mathcal{A}}) = \tilde{\mathcal{V}}_S \sqcap \mathcal{L}_i(\beta_{\mathcal{A}})$ for all $\beta_{\mathcal{A}} \in \mathcal{FS}(\mathcal{V}, S)$. Then, $\mathcal{L}_{i_\mathcal{V}}$ is a fuzzy soft closure operator on $\mathcal{V}$.

Proof: We must prove $\mathcal{L}_{i_\mathcal{V}}$ satisfying the axioms $(\mathrm{A}_1) - (\mathrm{A}_3)$ in Definition 3.1.

(A_1) $\mathcal{L}_{i_\mathcal{V}}(\tilde{0}_S) = \tilde{\mathcal{V}}_S \sqcap \mathcal{L}_i(\tilde{0}_S) = \tilde{\mathcal{V}}_S \sqcap \tilde{0}_S = \tilde{0}_S$.

(A_2) For any $\beta_{\mathcal{A}} \in \mathcal{FS}(\mathcal{V}, S), \beta_{\mathcal{A}} \sqsubseteq \tilde{\mathcal{V}}_S$ and $\beta_{\mathcal{A}} \sqsubseteq \mathcal{L}_i(\beta_{\mathcal{A}})$. This yields $\beta_{\mathcal{A}} \sqsubseteq \tilde{\mathcal{V}}_S \sqcap \mathcal{L}_i(\beta_{\mathcal{A}}) = \mathcal{L}_{i_\mathcal{V}}(\beta_{\mathcal{A}})$. Hence, $\beta_{\mathcal{A}} \sqsubseteq \mathcal{L}_{i_\mathcal{V}}(\beta_{\mathcal{A}})$.

(A_3) Let $\beta_{\mathcal{A}}, \mathcal{S}_{\mathcal{B}} \in \mathcal{FS}(\mathcal{V}, S)$. Then

$$\begin{aligned}\mathcal{L}_{i_\mathcal{V}}(\beta_{\mathcal{A}} \sqcup \mathcal{S}_{\mathcal{B}}) &= \tilde{\mathcal{V}}_S \sqcap \mathcal{L}_i(\beta_{\mathcal{A}} \sqcup \mathcal{S}_{\mathcal{B}}) \\ &= \tilde{\mathcal{V}}_S \sqcap \left(\mathcal{L}_i(\beta_{\mathcal{A}}) \sqcup \mathcal{L}_i(\mathcal{S}_{\mathcal{B}})\right) \\ &= \mathcal{L}_{i_\mathcal{V}}(\beta_{\mathcal{A}}) \sqcup \mathcal{L}_{i_\mathcal{V}}(\mathcal{S}_{\mathcal{B}}).\end{aligned}$$

Definition 4.2 Let $(\mathcal{U}, \mathcal{L}_1, \mathcal{L}_2, S)$ be a Čfs bi-csp and $\mathcal{V} \subseteq \mathcal{U}$. The fuzzy soft closure operator $\mathcal{L}_{i_\mathcal{V}}$ (that defined in Theorem 4.1) is called the relative fuzzy soft closure operator on $\mathcal{V}$ induced by $\mathcal{L}_i$. The quadruple $(\mathcal{V}, \mathcal{L}_{1_\mathcal{V}}, \mathcal{L}_{2_\mathcal{V}}, S)$ is called a Čech fuzzy soft bi-closure subspace (Čfs bi-csubsp, for short) of $(\mathcal{U}, \mathcal{L}_1, \mathcal{L}_2, S)$. The Čfs bi-csubsp $(\mathcal{V}, \mathcal{L}_{1_\mathcal{V}}, \mathcal{L}_{2_\mathcal{V}}, S)$ is said to be a closed (resp. open) subspace if $\tilde{\mathcal{V}}_S$is a closed (resp. open) fss over $\mathcal{U}$.

Example 4.3 In Example 3.4, let $\mathcal{V} = \{x, z\} \subseteq \mathcal{U}$. Then $\mathcal{L}_{1_\mathcal{V}}, \mathcal{L}_{2_\mathcal{V}}: \mathcal{FS}(\mathcal{V}, S) \to \mathcal{FS}(\mathcal{V}, S)$ defined as $\mathcal{L}_{1_\mathcal{V}}(\beta_{\mathcal{A}}) = \tilde{\mathcal{V}}_S \sqcap \mathcal{L}_1(\beta_{\mathcal{A}})$ and $\mathcal{L}_{2_\mathcal{V}}(\beta_{\mathcal{A}}) = \tilde{\mathcal{V}}_S \sqcap \mathcal{L}_2(\beta_{\mathcal{A}})$ as follows:

$$\mathcal{L}_{1_\mathcal{V}}(\beta_{\mathcal{A}}) = \begin{cases} \tilde{0}_S & if\ \beta_{\mathcal{A}} = \tilde{0}_S, \\ \{(s_1, x_{0.9})\} & if\ \beta_{\mathcal{A}} \in \{(s_1, x_t); 0 < t \leq 0.9\}, \\ \tilde{\mathcal{V}}_S & otherwise. \end{cases}$$

$$\mathcal{L}_{2_\nu}(\beta_{\mathcal{A}}) = \begin{cases} \tilde{0}_S & if\ \beta_{\mathcal{A}} = \tilde{0}_S, \\ \{(s_1, x_1)\} & if\ \beta_{\mathcal{A}} \in \{(s_1, x_t); t \in I_0\}, \\ \{(s_2, z_1)\} & if\ \beta_{\mathcal{A}} \in \{(s_2, z_k); k \in I_0\}, \\ \{\mathcal{L}_{2_\nu}(\{(s_1, x_t)\}), \mathcal{L}_{2_\nu}(\{(s_2, z_k)\})\} & if\ \beta_{\mathcal{A}} \in \{(s_1, x_t), (s_2, z_k); t, k \in I_0\} \\ \tilde{\mathcal{V}}_S & otherwise. \end{cases}$$

Then $(\mathcal{V}, \mathcal{L}_{1_\nu}, \mathcal{L}_{2_\nu}, S)$ is Čfs bi-csubsp of $(\mathcal{U}, \mathcal{L}_1, \mathcal{L}_2, S)$.

Definition 4.4 Let $(\mathcal{V}, \mathcal{L}_{1_\nu}, \mathcal{L}_{2_\nu}, S)$be a Čfs bi-csubsp of $(\mathcal{U}, \mathcal{L}_1, \mathcal{L}_2, S)$. A $fss\ \beta_{\mathcal{A}} \in \mathcal{FS}(\mathcal{V}, S)$ is said to be closed fss over $\mathcal{V}$ if $\mathcal{L}_{i_\nu}(\mathcal{L}_{j_\nu}(\beta_{\mathcal{A}})) = \beta_{\mathcal{A}}$.

Proposition 4.5 Let $(\mathcal{U}, \mathcal{L}_1, \mathcal{L}_2, S)$ be a Čfs bi-csp and $(\mathcal{V}, \mathcal{L}_{1_\nu}, \mathcal{L}_{2_\nu}, S)$ be a Čfs bi-csubsp of $(\mathcal{U}, \mathcal{L}_1, \mathcal{L}_2, S)$. Let $\beta_{\mathcal{A}} \in \mathcal{FS}(\mathcal{V}, S)$. Then, $\beta_{\mathcal{A}}$ is a closed fss over $\mathcal{V}$ if and only if $\mathcal{L}_{j_\nu}(\beta_{\mathcal{A}}) = \beta_{\mathcal{A}}$.

Proof**:** Suppose $\beta_{\mathcal{A}}$ is a closed over $(\mathcal{V}, \mathcal{L}_{1_\nu}, \mathcal{L}_{2_\nu}, S)$. From (A_2) of Theorem 4.1 we have, $\mathcal{L}_{j_\nu}(\beta_{\mathcal{A}}) \sqsubseteq \mathcal{L}_{i_\nu}\left(\mathcal{L}_{j_\nu}(\beta_{\mathcal{A}})\right) = \beta_{\mathcal{A}}$, and since $\beta_{\mathcal{A}} \sqsubseteq \mathcal{L}_{j_\nu}(\beta_{\mathcal{A}})$, then it follows $\beta_{\mathcal{A}} \sqsubseteq \mathcal{L}_{j_\nu}(\beta_{\mathcal{A}}) \sqsubseteq \mathcal{L}_{i_\nu}\left(\mathcal{L}_{j_\nu}(\beta_{\mathcal{A}})\right) = \beta_{\mathcal{A}}$. Hence, $\mathcal{L}_{j_\nu}(\beta_{\mathcal{A}}) = \beta_{\mathcal{A}}$.

Conversely, let $\mathcal{L}_{j_\nu}(\beta_{\mathcal{A}}) = \beta_{\mathcal{A}}$, then $\mathcal{L}_{1_\nu}(\beta_{\mathcal{A}}) = \beta_{\mathcal{A}}$ and $\mathcal{L}_{2_\nu}(\beta_{\mathcal{A}}) = \beta_{\mathcal{A}}$ (since $j = 1,2$). Then, it follows, $\mathcal{L}_{2_\nu}\left(\mathcal{L}_{1_\nu}(\beta_{\mathcal{A}})\right) = \mathcal{L}_{2_\nu}(\beta_{\mathcal{A}})$ and $\mathcal{L}_{1_\nu}\left(\mathcal{L}_{2_\nu}(\beta_{\mathcal{A}})\right) = \mathcal{L}_{1_\nu}(\beta_{\mathcal{A}})$. This implies $\mathcal{L}_{2_\nu}\left(\mathcal{L}_{1_\nu}(\beta_{\mathcal{A}})\right) = \beta_{\mathcal{A}}$ and $\mathcal{L}_{1_\nu}\left(\mathcal{L}_{2_\nu}(\beta_{\mathcal{A}})\right) = \beta_{\mathcal{A}}$. Therefore, $\mathcal{L}_{i_\nu}\left(\mathcal{L}_{j_\nu}(\beta_{\mathcal{A}})\right) = \beta_{\mathcal{A}}$. Consequently, $\beta_{\mathcal{A}}$ is a closed over $\mathcal{V}$.

Proposition 4.6 Let $(\mathcal{V}, \mathcal{L}_{1_\nu}, \mathcal{L}_{2_\nu}, S)$ be a Čfs bi-csubsp of $(\mathcal{U}, \mathcal{L}_1, \mathcal{L}_2, S)$. If $\beta_{\mathcal{A}} \in \mathcal{FS}(\mathcal{V}, S)$ and $\beta_{\mathcal{A}}$ is a closed fss over $\mathcal{U}$, then $\beta_{\mathcal{A}}$ is a closed fss in $(\mathcal{V}, \mathcal{L}_{1_\nu}, \mathcal{L}_{2_\nu}, S)$.

Proof: Let $\beta_{\mathcal{A}} \in \mathcal{FS}(\mathcal{V}, S)$ and $\mathcal{L}_i\left(\mathcal{L}_j(\beta_{\mathcal{A}})\right) = \beta_{\mathcal{A}}$. Now,

$$\begin{aligned} \mathcal{L}_{i_\nu}\left(\mathcal{L}_{j_\nu}(\beta_{\mathcal{A}})\right) &= \mathcal{L}_{i_\nu}\left(\tilde{\mathcal{V}}_S \sqcap \mathcal{L}_j(\beta_{\mathcal{A}})\right) && \text{(By the definition of } \mathcal{L}_{j_\nu}) \\ &= \mathcal{L}_{i_\nu}(\tilde{\mathcal{V}}_S \sqcap \beta_{\mathcal{A}}) && \text{(Since } \beta_{\mathcal{A}} \text{ is closed over } \mathcal{U}) \\ &= \tilde{\mathcal{V}}_S \sqcap \mathcal{L}_i(\tilde{\mathcal{V}}_S \sqcap \beta_{\mathcal{A}}) && \text{(By the definition of } \mathcal{L}_{i_\nu}) \\ &= \beta_{\mathcal{A}} \end{aligned}$$

Hence, $\beta_{\mathcal{A}}$ is a closed fss in $(\mathcal{V}, \mathcal{L}_{1_\nu}, \mathcal{L}_{2_\nu}, S)$.

The converse of Proposition 4.6 is not true as we explain in the next example.

Example 4.7 Let $\mathcal{U} = \{x, y, z, w\}$, $S = \{s_1, s_2\}$. Define fuzzy soft closure operators $\mathcal{L}_1, \mathcal{L}_2 : \mathcal{FS}(\mathcal{U}, S) \to \mathcal{FS}(\mathcal{U}, S)$ as follows*:*

$$\mathcal{L}_1(\beta_{\mathcal{A}}) = \begin{cases} \tilde{0}_S & if\ \beta_{\mathcal{A}} = \tilde{0}_S, \\ \{(s_1, z_1), (s_2, y_1)\} & if\ \beta_{\mathcal{A}} \in \{(s_1, z_{k_1}), (s_2, y_{h_1}); h_1, k_1 \in I_0\}, \\ \{(s_1, y_1), (s_2, z_1)\} & if\ \beta_{\mathcal{A}} \in \{(s_1, y_{h_2}), (s_2, z_{k_2}); h_2, k_2 \in I_0\} \\ \{(s_1, y_1 \vee z_1), (s_2, y_1 \vee z_1)\} & if\ \beta_{\mathcal{A}} \in \left\{ \begin{matrix} (s_1, y_{h_1} \vee z_{k_1}), (s_2, y_{h_2} \vee z_{k_2}) \\ ; h_1, h_2, k_1, k_2 \in I_0 \end{matrix} \right\}, \\ \tilde{1}_S & otherwise. \end{cases}$$

$$\mathcal{L}_2(\beta_{\mathcal{A}}) = \begin{cases} \tilde{0}_S & if\ \beta_{\mathcal{A}} = \tilde{0}_S, \\ \{(s_1, x_1), (s_2, y_1)\} & if\ \beta_{\mathcal{A}} \in \{(s_1, x_{t_1}), (s_2, y_{h_1}); h_1, t_1 \in I_0\}, \\ \{(s_1, y_1), (s_2, x_1)\} & if\ \beta_{\mathcal{A}} \in \{(s_1, y_{h_2}), (s_2, x_{t_2}); h_2, t_2 \in I_0\}, \\ \{(s_1, x_1 \vee y_1), (s_2, x_1 \vee y_1)\} & if\ \beta_{\mathcal{A}} \in \begin{Bmatrix} (s_1, x_{t_1} \vee y_{h_2}), (s_2, x_{t_2} \vee y_{h_1}) \\ ; t_1, t_2, h_1, h_2 \in I_0 \end{Bmatrix}, \\ \tilde{1}_S & otherwise. \end{cases}$$

Then $(\mathcal{U}, \mathcal{L}_1, \mathcal{L}_2, S)$ is a Čfs bi-csp.

Let $\mathcal{V} = \{y, w\}$. Then $\mathcal{L}_{1_\mathcal{V}}, \mathcal{L}_{2_\mathcal{V}}: \mathcal{FS}(\mathcal{V}, S) \to \mathcal{FS}(\mathcal{V}, S)$ defined as follows:

$$\mathcal{L}_{1_\mathcal{V}}(\beta_{\mathcal{A}}) = \mathcal{L}_{2_\mathcal{V}}(\beta_{\mathcal{A}}) = \begin{cases} \tilde{0}_S & if\ \beta_{\mathcal{A}} = \tilde{0}_S, \\ \{(s_2, y_1)\} & if\ \beta_{\mathcal{A}} \in \{(s_2, y_{h_1}); h_1 \in I_0\}, \\ \{(s_1, y_1)\} & if\ \beta_{\mathcal{A}} \in \{(s_1, y_{h_2}); h_2 \in I_0\}, \\ \{(s_1, y_1), (s_2, y_1)\} & if\ \beta_{\mathcal{A}} \in \{(s_1, y_{h_2}), (s_2, y_{h_1}); h_1, h_2 \in I_0\}, \\ \tilde{\mathcal{V}}_S & otherwise. \end{cases}$$

Then, $(\mathcal{V}, \mathcal{L}_{1_\mathcal{V}}, \mathcal{L}_{2_\mathcal{V}}, S)$ is a Čfs bi-csubsp of $(\mathcal{U}, \mathcal{L}_1, \mathcal{L}_2, S)$. Now, consider $\beta_{\mathcal{A}} \in \mathcal{FS}(\mathcal{V}, S)$ where $\beta_{\mathcal{A}} = \{(s_1, y_1)\}$. It is clear that $\beta_{\mathcal{A}}$ is a closed fss over $(\mathcal{V}, \mathcal{L}_{1_\mathcal{V}}, \mathcal{L}_{2_\mathcal{V}}, S)$. Since $\mathcal{L}_{1_\mathcal{V}}(\beta_{\mathcal{A}}) = \beta_{\mathcal{A}}$ and $\mathcal{L}_{2_\mathcal{V}}(\beta_{\mathcal{A}}) = \beta_{\mathcal{A}}$ but $\beta_{\mathcal{A}}$ is not closed fss over $(\mathcal{U}, \mathcal{L}_1, \mathcal{L}_2, S)$ because $\mathcal{L}_1(\beta_{\mathcal{A}}) \neq \beta_{\mathcal{A}}$ or $\mathcal{L}_2(\beta_{\mathcal{A}}) \neq \beta_{\mathcal{A}}$. □

In the next, we study the condition to be the converse of Proposition 4.6 hold. First, we need to introduce the following lemma.

Lemma 4.8 Let $(\mathcal{U}, \mathcal{L}_1, \mathcal{L}_2, S)$ be a Čfs bi-csp and $\{(\beta_{\mathcal{A}})_\alpha : \alpha \in \Lambda\}$ be a family of $fss's$ over $\mathcal{U}$, then $\mathcal{L}_i(\sqcap_{\alpha\in\Lambda} (\beta_{\mathcal{A}})_\alpha) \sqsubseteq \sqcap_{\alpha\in\Lambda} \mathcal{L}_i((\beta_{\mathcal{A}})_\alpha)$.

Proof: For all $\alpha \in \Lambda$, since $\sqcap_{\alpha\in\Lambda} (\beta_{\mathcal{A}})_\alpha \sqsubseteq (\beta_{\mathcal{A}})_\alpha$. Then, $\mathcal{L}_i(\sqcap_{\alpha\in\Lambda} (\beta_{\mathcal{A}})_\alpha) \sqsubseteq \mathcal{L}_i((\beta_{\mathcal{A}})_\alpha)$ for all $\alpha \in \Lambda$. Therefore, $\mathcal{L}_i(\sqcap_{\alpha\in\Lambda} (\beta_{\mathcal{A}})_\alpha) \sqsubseteq \sqcap_{\alpha\in\Lambda} \mathcal{L}_i((\beta_{\mathcal{A}})_\alpha)$.

The converse of Lemma 4.8 is not true as we explain in the next example.

Example 4.9 Let $\mathcal{U} = \{x, y, z\}$, $S = \{s_1, s_2\}$ and let $\theta = \{(s_1, x_t \vee y_h), (s_2, z_k); t, h, k \in I_0\}$. Define fuzzy soft closure operators $\mathcal{L}_1, \mathcal{L}_2: \mathcal{FS}(\mathcal{U}, S) \to \mathcal{FS}(\mathcal{U}, S)$ *as follows:*

$$\mathcal{L}_1(\beta_{\mathcal{A}}) = \begin{cases} \tilde{0}_S & if\ \beta_{\mathcal{A}} = \tilde{0}_S, \\ \{(s_1, x_{0.9} \vee y_{0.1})\} & if\ \beta_{\mathcal{A}} \sqsubseteq \{(s_1, x_{0.9} \vee y_{0.1})\}, \\ \tilde{1}_S & otherwise. \end{cases}$$

and

$$\mathcal{L}_2(\beta_{\mathcal{A}}) = \begin{cases} \tilde{0}_S & if\ \beta_{\mathcal{A}} = \tilde{0}_S, \\ \{(s_1, x_1)\} & if\ \beta_{\mathcal{A}} \in \{(s_1, x_t); t \in I_0\}, \\ \{(s_1, y_1)\} & if\ \beta_{\mathcal{A}} \in \{(s_1, y_h); h \in I_0\} \\ \{(s_2, z_1)\} & if\ \beta_{\mathcal{A}} \in \{(s_2, z_k); k \in I_0\}, \\ \{\mathcal{L}_2(\{(s_1, x_t)\}) \cup \mathcal{L}_2(\{(s_1, y_h)\}), \mathcal{L}_2(\{(s_2, z_k)\})\} & if\ \beta_{\mathcal{A}} \in \theta \\ \tilde{1}_S & otherwise. \end{cases}$$

Then, it's clear that $(\mathcal{U}, \mathcal{L}_1, \mathcal{L}_2, S)$ is a Čfs bi-csp. Consider $\beta_{\mathcal{A}} = \{(s_1, x_{0.2})\}$ and $\mathcal{S}_{\mathcal{B}} = \{(s_1, y_{0.2} \vee z_{0.2})\}$. Then $\mathcal{L}_2(\beta_{\mathcal{A}}) = \{(s_1, x_1)\}$, $\mathcal{L}_2(\mathcal{S}_{\mathcal{B}}) = \tilde{1}_S$, and $\mathcal{L}_2(\beta_{\mathcal{A}}) \sqcap \mathcal{L}_2(\mathcal{S}_{\mathcal{B}}) = \{(s_1, x_1)\}$. On the other hand, $\beta_{\mathcal{A}} \sqcap \mathcal{S}_{\mathcal{B}} = \tilde{0}_S$ and $\mathcal{L}_2(\beta_{\mathcal{A}} \sqcap \mathcal{S}_{\mathcal{B}}) = \tilde{0}_S$. Hence, it's clear that $\{(s_1, x_1)\} = \mathcal{L}_2(\beta_{\mathcal{A}}) \sqcap \mathcal{L}_2(\mathcal{S}_{\mathcal{B}}) \not\sqsubseteq \mathcal{L}_2(\beta_{\mathcal{A}} \sqcap \mathcal{S}_{\mathcal{B}}) = \tilde{0}_S$.

The converse of Proposition 4.6 can be held if the following condition exists.

Theorem 4.10 Let $(\mathcal{U}, \mathcal{L}_1, \mathcal{L}_2, S)$ be a Čfs bi-csp, $(\mathcal{V}, \mathcal{L}_{1_\mathcal{V}}, \mathcal{L}_{2_\mathcal{V}}, S)$ be a closed subspace of $(\mathcal{U}, \mathcal{L}_1, \mathcal{L}_2, S)$, and let $\beta_\mathcal{A} \in \mathcal{FS}(\mathcal{V}, S)$. If $\beta_\mathcal{A}$ is a closed fss of $(\mathcal{V}, \mathcal{L}_{1_\mathcal{V}}, \mathcal{L}_{2_\mathcal{V}}, S)$, then $\beta_\mathcal{A}$ is a closed fss of $(\mathcal{U}, \mathcal{L}_1, \mathcal{L}_2, S)$.

Proof: Let $\beta_\mathcal{A}$ is a closed fss over $\left(\mathcal{V}, \mathcal{L}_{1_\mathcal{V}}, \mathcal{L}_{2_\mathcal{V}}, S\right)$. We must prove $\mathcal{L}_i\left(\mathcal{L}_j(\beta_\mathcal{A})\right) = \beta_\mathcal{A}$. Since $\beta_\mathcal{A}$ is a closed fss over $\mathcal{V}$, then $\mathcal{L}_{i_\mathcal{V}}\left(\mathcal{L}_{j_\mathcal{V}}(\beta_\mathcal{A})\right) = \beta_\mathcal{A}$. From ($A_2$) of Theorem 4.1, $\mathcal{L}_{j_\mathcal{V}}(\beta_\mathcal{A}) \sqsubseteq \mathcal{L}_{i_\mathcal{V}}\left(\mathcal{L}_{j_\mathcal{V}}(\beta_\mathcal{A})\right) = \beta_\mathcal{A}$. It follows from the definition of $\mathcal{L}_{j_\mathcal{V}}$, $\tilde{\mathcal{V}}_S \sqcap \mathcal{L}_j(\beta_\mathcal{A}) \sqsubseteq \mathcal{L}_{i_\mathcal{V}}\left(\mathcal{L}_{j_\mathcal{V}}(\beta_\mathcal{A})\right) = \beta_\mathcal{A}$. Since $\tilde{\mathcal{V}}_S$ is a closed fss in $\mathcal{U}$ and from Lemma 4.8, $\mathcal{L}_j\left(\tilde{\mathcal{V}}_S \sqcap \beta_\mathcal{A}\right) \sqsubseteq \mathcal{L}_j\left(\tilde{\mathcal{V}}_S\right) \sqcap \mathcal{L}_j(\beta_\mathcal{A}) \sqsubseteq \tilde{\mathcal{V}}_S \sqcap \mathcal{L}_j(\beta_\mathcal{A}) \sqsubseteq \mathcal{L}_{i_\mathcal{V}}\left(\mathcal{L}_{j_\mathcal{V}}(\beta_\mathcal{A})\right) = \beta_\mathcal{A}$. Thus, $\mathcal{L}_j(\beta_\mathcal{A}) \sqsubseteq \beta_\mathcal{A}$. On the other hand $\beta_\mathcal{A} \sqsubseteq \mathcal{L}_j(\beta_\mathcal{A})$. Hence, we get $\mathcal{L}_j(\beta_\mathcal{A}) = \beta_\mathcal{A}$ and from Proposition. 3.3 part (1), we get $\beta_\mathcal{A}$ is a closed fss in $\mathcal{U}$.

5. Pairwise Čech fuzzy soft Continuous Mappings

Definition 5.1 Let $(\mathcal{U}, \mathcal{L}_1, \mathcal{L}_2, S)$ and $(\mathcal{W}, \mathcal{L}_1^*, \mathcal{L}_2^*, \mathcal{N})$ be two Čfs bi-csp's. A fuzzy soft mapping $f_{up}: (\mathcal{U}, \mathcal{L}_1, \mathcal{L}_2, S) \to (\mathcal{W}, \mathcal{L}_1^*, \mathcal{L}_2^*, \mathcal{N})$ is called

1. Pairwise Čech fuzzy soft continuous ($P\check{C}$-*fs*-continuous, briefly) mapping, if $f_{up}(\mathcal{L}_i(\beta_\mathcal{A})) \sqsubseteq \mathcal{L}_i^*(f_{up}(\beta_\mathcal{A}))$, for every $fss\ \beta_\mathcal{A} \in \mathcal{FS}(\mathcal{U}, S)$.
2. Pairwise* Čech fuzzy soft continuous ($P^*\check{C}$-*fs*-continuous, briefly) mapping, if $f_{up}^{-1}(\mathcal{S}_\mathcal{B})$ is an open fss of $(\mathcal{U}, \mathcal{L}_1, \mathcal{L}_2, S)$ for every open $fss\ \mathcal{S}_\mathcal{B}$ of $(\mathcal{W}, \mathcal{L}_1^*, \mathcal{L}_2^*, \mathcal{N})$.

Theorem 5.2 Let $(\mathcal{U}, \mathcal{L}_1, \mathcal{L}_2, S)$ and $(\mathcal{W}, \mathcal{L}_1^*, \mathcal{L}_2^*, \mathcal{N})$ be two Čfs bi-csp's. If $f_{up}: (\mathcal{U}, \mathcal{L}_1, \mathcal{L}_2, S) \to (\mathcal{W}, \mathcal{L}_1^*, \mathcal{L}_2^*, \mathcal{N})$ is a $P\check{C}$-*fs*-continuous mapping if and only if $\mathcal{L}_i(f_{up}^{-1}(\mathcal{S}_\mathcal{B})) \sqsubseteq f_{up}^{-1}(\mathcal{L}_i^*(\mathcal{S}_\mathcal{B}))$, for every $fss\ \mathcal{S}_\mathcal{B} \in \mathcal{FS}(\mathcal{W}, \mathcal{N})$.

Proof: Let $\mathcal{S}_\mathcal{B} \in \mathcal{FS}(\mathcal{W}, \mathcal{N})$. Then, $f_{up}^{-1}(\mathcal{S}_\mathcal{B}) \in \mathcal{FS}(\mathcal{U}, S)$. Since f_{up} is $P\check{C}$-*fs*-continuous, we have $f_{up}(\mathcal{L}_i(f_{up}^{-1}(\mathcal{S}_\mathcal{B})) \sqsubseteq \mathcal{L}_i^*(f_{up}\left(f_{up}^{-1}(\mathcal{S}_\mathcal{B})\right) \sqsubseteq \mathcal{L}_i^*(\mathcal{S}_\mathcal{B})$. Therefore, $f_{up}^{-1}(f_{up}\left(\mathcal{L}_i\left(f_{up}^{-1}(\mathcal{S}_\mathcal{B})\right)\right)) \sqsubseteq f_{up}^{-1}\left(\mathcal{L}_i^*(\mathcal{S}_\mathcal{B})\right)$. Hence, $\mathcal{L}_i(f_{up}^{-1}(\mathcal{S}_\mathcal{B})) \sqsubseteq f_{up}^{-1}\left(\mathcal{L}_i^*(\mathcal{S}_\mathcal{B})\right)$.
Conversely, let $\beta_\mathcal{A}$ be a fss of $(\mathcal{U}, \mathcal{L}_1, \mathcal{L}_2, S)$. From the definition of the image of fss and hypothesis we get $\mathcal{L}_i(f_{up}^{-1}(f_{up}((\beta_\mathcal{A})) \sqsubseteq f_{up}^{-1}(\mathcal{L}_i^*(f_{up}(\beta_\mathcal{A}))$. By taking the image we obtain the result.□
Theorem 5.3. Let $(\mathcal{U}, \mathcal{L}_1, \mathcal{L}_2, S)$ and $(\mathcal{W}, \mathcal{L}_1^*, \mathcal{L}_2^*, \mathcal{N})$ be two Čfs bi-csp's. If $f_{up}: (\mathcal{U}, \mathcal{L}_1, \mathcal{L}_2, S) \to (\mathcal{W}, \mathcal{L}_1^*, \mathcal{L}_2^*, \mathcal{N})$ is a $P\check{C}$-*fs*-continuous mapping, then f_{up} is $P^*\check{C}$-*fs*-continuous mapping.

Proof: The proof is easy.

The converse of Theorem 5.3 need not be held as seen in the following next example.

Example 5.4 Let $\mathcal{U} = \{x, y\} = \mathcal{W}$, $S = \{s_1, s_2\}$ and $\mathcal{N} = \{k_1, k_2\}$ and $\Upsilon = \{\left(k_1, x_{t_1} \vee y_{r_1}\right), \left(k_2, x_{t_2} \vee y_{r_2}\right): t_1, t_2, r_1, r_2 \in I_0\}$.
Define fuzzy soft closure operator $\mathcal{L}_1, \mathcal{L}_2: \mathcal{FS}(\mathcal{U}, S) \to \mathcal{FS}(\mathcal{U}, S)$ *as follows:*

$$\mathcal{L}_1(\beta_\mathcal{A}) = \begin{cases} \tilde{0}_S & if\ \beta_\mathcal{A} = \tilde{0}_S, \\ \{(s_1, x_{0.3})\} & if\ \beta_\mathcal{A} \sqsubseteq \{(s_1, x_{0.2})\}, \\ \tilde{1}_S & otherwise. \end{cases}$$

and

$$\mathcal{L}_2(\beta_{\mathcal{A}}) = \begin{cases} \tilde{0}_S & if\ \beta_{\mathcal{A}} = \tilde{0}_S, \\ \{(s_2, x_{0.3} \vee y_{0.4})\} & if\ \beta_{\mathcal{A}} \sqsubseteq \{(s_2, x_{0.3} \vee y_{0.4})\}, \\ \tilde{1}_S & otherwise. \end{cases}$$

Define fuzzy soft closure operator $\mathcal{L}_1^*, \mathcal{L}_2^* : \mathcal{FS}(\mathcal{W}, \mathcal{N}) \to \mathcal{FS}(\mathcal{W}, \mathcal{N})$ as follows:

$$\mathcal{L}_1^*(\beta_{\mathcal{A}}) = \begin{cases} \tilde{0}_{\mathcal{N}} & if\ \beta_{\mathcal{A}} = \tilde{0}_{\mathcal{N}}, \\ \{(k_1, x_1)\} & if\ \beta_{\mathcal{A}} \in \{(k_1, x_{t_1}) : t_1 \in I_0\}, \\ \{(k_2, x_1)\} & if\ \beta_{\mathcal{A}} \in \{(k_2, x_{t_2}) : t_2 \in I_0\}, \\ \{(k_1, y_{r_1+0.2})\} & if\ \beta_{\mathcal{A}} \in \{(k_1, y_{r_1}) : 0 < r_1 < 0.8\}, \\ \{(k_1, y_1)\} & if\ \beta_{\mathcal{A}} \in \{(k_1, y_{r_1}) : 0.8 \le r_1 \le 1\}, \\ \{(k_2, y_1)\} & if\ \beta_{\mathcal{A}} \in \{(k_2, y_{r_2}) : r_2 \in I_0\}, \\ \mathcal{L}_1^*(\{(k_1, x_{t_1})\}) \cup \mathcal{L}_1^*(\{(k_1, y_{r_1})\}) \cup & \\ \mathcal{L}_1^*(\{(k_2, x_{t_2})\}) \cup \mathcal{L}_1^*(\{(k_2, y_{r_2})\}) & if\ \beta_{\mathcal{A}} \in \Upsilon. \end{cases}$$

and

$$\mathcal{L}_2^*(\beta_{\mathcal{A}}) = \begin{cases} \tilde{0}_{\mathcal{N}} & if\ \beta_{\mathcal{A}} = \tilde{0}_{\mathcal{N}}, \\ \tilde{1}_{\mathcal{N}} & otherwise. \end{cases}$$

Define $f_{up} : (\mathcal{U}, \mathcal{L}_1, \mathcal{L}_2, S) \to (\mathcal{W}, \mathcal{L}_1^*, \mathcal{L}_2^*, \mathcal{N})$ be the fuzzy soft identity mapping. Then, $f_{up}^{-1}(\mathcal{S}_{\mathcal{B}})$ ia an open fss of $(\mathcal{U}, \mathcal{L}_1, \mathcal{L}_2, S)$ for every open fss $\mathcal{S}_{\mathcal{B}}$ *of* $(\mathcal{W}, \mathcal{L}_1^*, \mathcal{L}_2^*, \mathcal{N})$ but there exists $\beta_{\mathcal{A}} = \{(s_1, x_{0.5})\}$ be fss in $(\mathcal{U}, \mathcal{L}_1, \mathcal{L}_2, S)$ such that $f_{up}(\mathcal{L}_1(\beta_{\mathcal{A}})) = \tilde{1}_S \not\subseteq \{(s_1, x_1)\} = \mathcal{L}_1^*\left(f_{up}(\beta_{\mathcal{A}})\right)$. Hence, f_{up} is not $P\check{C}$-*fs*-continuous mapping.

Theorem 5.5 Let $(\mathcal{U}, \mathcal{L}_1, \mathcal{L}_2, S), (\mathcal{W}, \mathcal{L}_1^*, \mathcal{L}_2^*, \mathcal{N})$ and $(\mathcal{Z}, \mathcal{L}_1^{**}, \mathcal{L}_2^{**}, \mathcal{H})$ be Čfs bi-csp's. If $f_{up} : (\mathcal{U}, \mathcal{L}_1, \mathcal{L}_2, S) \to (\mathcal{W}, \mathcal{L}_1^*, \mathcal{L}_2^*, \mathcal{N})$ and $h_{vj} : (\mathcal{W}, \mathcal{L}_1^*, \mathcal{L}_2^*, \mathcal{N}) \to (\mathcal{Z}, \mathcal{L}_1^{**}, \mathcal{L}_2^{**}, \mathcal{H})$ are $P\check{C}$-*fs*-continuous mappings, then $h_{vj} \circ f_{up} : (\mathcal{U}, \mathcal{L}_1, \mathcal{L}_2, S) \to (\mathcal{Z}, \mathcal{L}_1^{**}, \mathcal{L}_2^{**}, \mathcal{H})$ is a $P\check{C}$-*fs*-continuous mapping.

Proof: Let $\beta_{\mathcal{A}} \in \mathcal{FS}(\mathcal{U}, S)$. Since $h_{vj} \circ f_{up}(\mathcal{L}_i(\beta_{\mathcal{A}})) = h_{vj}(f_{up}(\mathcal{L}_i(\beta_{\mathcal{A}})))$ and f_{up} is $P\check{C}$-*fs*-continuous, then $h_{vj}\left(f_{up}(\mathcal{L}_i(\beta_{\mathcal{A}}))\right) \sqsubseteq h_{vj}\left(\mathcal{L}_i^*\left(f_{up}(\beta_{\mathcal{A}})\right)\right)$. As h_{vj} is a $P\check{C}$-*fs*-continuous mapping, we get, $h_{vj}\left(\mathcal{L}_i^*\left(f_{up}(\beta_{\mathcal{A}})\right)\right) \sqsubseteq \mathcal{L}_i^{**}(h_{vj}\left(f_{up}(\beta_{\mathcal{A}})\right))$.

Consequently, $h_{vj}\left(f_{up}(\mathcal{L}_i(\beta_{\mathcal{A}}))\right) \sqsubseteq \mathcal{L}_i^{**}\left(h_{vj}(f_{up}(\beta_{\mathcal{A}})\right)$. That is mean $h_{vj} \circ f_{up}(\mathcal{L}_i(\beta_{\mathcal{A}})) \sqsubseteq \mathcal{L}_i^{**}\left(h_{vj} \circ f_{up}(\beta_{\mathcal{A}})\right)$. Hence $h_{vj} \circ f_{up}$ is a $P\check{C}$-*fs*-continuous mapping.

Definition 5.6 Let $(\mathcal{U}, \mathcal{L}_1, \mathcal{L}_2, S), (\mathcal{W}, \mathcal{L}_1^*, \mathcal{L}_2^*, \mathcal{N})$ be Čfs bi-csp's. A fuzzy soft mapping $f_{up} : (\mathcal{U}, \mathcal{L}_1, \mathcal{L}_2, S) \to (\mathcal{W}, \mathcal{L}_1^*, \mathcal{L}_2^*, \mathcal{N})$ is called

1. Pairwise Čech fuzzy soft open (resp. closed) mapping ($P\check{C}$-*fs*-open (resp. $P\check{C}$-*fs*-closed), briefly) mapping, if $f_{up}(\beta_{\mathcal{A}})$ is a $\mathcal{L}_i^*$-open (resp. closed) fss of $(\mathcal{W}, \mathcal{L}_1^*, \mathcal{L}_2^*, \mathcal{N})$, whenver $\beta_{\mathcal{A}}$ is a $\mathcal{L}_i$-open (resp. closed) fss of $(\mathcal{U}, \mathcal{L}_1, \mathcal{L}_2, S)$.
2. Pairwise* Čech fuzzy soft open (resp. closed) mapping ($P^*\check{C}$-*fs*-open (resp. $P^*\check{C}$-*fs*-closed), briefly) mapping, if the image of every open (resp. closed) fss in $(\mathcal{U}, \mathcal{L}_1, \mathcal{L}_2, S)$ is an open (resp. closed) fss of in $(\mathcal{W}, \mathcal{L}_1^*, \mathcal{L}_2^*, \mathcal{N})$.

Proposition 5.7 Let $(\mathcal{U}, \mathcal{L}_1, \mathcal{L}_2, S)$ and $(\mathcal{W}, \mathcal{L}_1^*, \mathcal{L}_2^*, \mathcal{N})$ be two Čfs bi-csp's. If $f_{up} : (\mathcal{U}, \mathcal{L}_1, \mathcal{L}_2, S) \to (\mathcal{W}, \mathcal{L}_1^*, \mathcal{L}_2^*, \mathcal{N})$ is a $P\check{C}$-*fs*-open (resp. closed) mapping, then f_{up} is $P^*\check{C}$-*fs*-open (resp. closed) mapping.
Proof: Follows directly from Definition 5.1.

The converse of Proposition 5.7 need not be held, in Example 5.4 f_{up} is $P^{*}\check{C}$-*fs*-open mapping but it is not $P\check{C}$-*fs*-open mapping because there exists $\beta_{\mathcal{A}} = \{(s_1, x_1 \vee y_1), (s_2, x_{0.7} \vee y_{0.6})\}$ is $\mathcal{L}_2$-open fss in $(\mathcal{U}, \mathcal{L}_1, \mathcal{L}_2, S)$ but $f_{up}(\beta_{\mathcal{A}}) = \beta_{\mathcal{A}}$ is not $\mathcal{L}_2^{*}$-open fss in $(\mathcal{W}, \mathcal{L}_1^{*}, \mathcal{L}_2^{*}, \mathcal{N})$.

Theorem 5.8 Let $(\mathcal{U}, \mathcal{L}_1, \mathcal{L}_2, S), (\mathcal{W}, \mathcal{L}_1^{*}, \mathcal{L}_2^{*}, \mathcal{N})$ and $(\mathcal{Z}, \mathcal{L}_1^{**}, \mathcal{L}_2^{**}, \mathcal{H})$ be Čfs bi-csp's. Let $f_{up}: (\mathcal{U}, \mathcal{L}_1, \mathcal{L}_2, S) \to (\mathcal{W}, \mathcal{L}_1^{*}, \mathcal{L}_2^{*}, \mathcal{N})$ and $h_{vj}: (\mathcal{W}, \mathcal{L}_1^{*}, \mathcal{L}_2^{*}, \mathcal{N}) \to (\mathcal{Z}, \mathcal{L}_1^{**}, \mathcal{L}_2^{**}, \mathcal{H})$ fuzzy soft mappings. Then

1. If f_{up} and h_{vj} are $P\check{C}$-*fs*-closed mapping, then $h_{vj} \circ f_{up}$ is $P\check{C}$-*fs*-closed mapping.
2. If $h_{vj} \circ f_{up}$ is $P\check{C}$-*fs*-closed mapping and f_{up} is $P\check{C}$-*fs*-continuous and surjection, then h_{vj} is PČ-fs-closed mapping.
3. If $h_{vj} \circ f_{up}$ is $P\check{C}$-*fs*-closed mapping and h_{vj} is $P\check{C}$-*fs*-continuous and injection, then f_{up} is $P\check{C}$-*fs*-closed mapping.

Proof:

1. Let $\beta_{\mathcal{A}}$ be a $\mathcal{L}_i$-closed fss of $(\mathcal{U}, \mathcal{L}_1, \mathcal{L}_2, S)$. Since f_{up} is $P\check{C}$-*fs*-closed mapping, then $f_{up}(\beta_{\mathcal{A}})$ is $\mathcal{L}_i^{*}$-closed fss in $(\mathcal{W}, \mathcal{L}_1^{*}, \mathcal{L}_2^{*}, \mathcal{N})$. Again, since, h_{vj} is $P\check{C}$-*fs*-closed mapping, then $h_{vj}(f_{up}(\beta_{\mathcal{A}}))$ is $\mathcal{L}_i^{**}$-closed fss in $(\mathcal{Z}, \mathcal{L}_1^{**}, \mathcal{L}_2^{**}, \mathcal{H})$. Hence, $h_{vj} \circ f_{up}$ is $P\check{C}$-*fs*-closed mapping.
2. Let $\beta_{\mathcal{A}}$ be a $\mathcal{L}_i^{*}$-closed fss of $(\mathcal{W}, \mathcal{L}_1^{*}, \mathcal{L}_2^{*}, \mathcal{N})$. Since f_{up} is $P\check{C}$-*fs*-continuous mapping, then $f_{up}^{-1}(\beta_{\mathcal{A}})$ is $\mathcal{L}_i$-closed fss in $(\mathcal{U}, \mathcal{L}_1, \mathcal{L}_2, S)$. Again, since $h_{vj} \circ f_{up}$ is $P\check{C}$-*fs*-closed mapping, then $h_{vj} \circ f_{up}\left(f_{up}^{-1}(\beta_{\mathcal{A}})\right) = h_{vj}(f_{up}(f_{up}^{-1}(\beta_{\mathcal{A}})))$ is $\mathcal{L}_i^{**}$-closed fss in $(\mathcal{Z}, \mathcal{L}_1^{**}, \mathcal{L}_2^{**}, \mathcal{H})$. But f_{up} is surjection, so that $h_{vj} \circ f_{up}\left(f_{up}^{-1}(\beta_{\mathcal{A}})\right) = h_{vj}\left(f_{up}\left(f_{up}^{-1}(\beta_{\mathcal{A}})\right)\right) = h_{vj}(\beta_{\mathcal{A}})$. Consequently, $h_{vj}(\beta_{\mathcal{A}})$ is a $\mathcal{L}_i^{**}$-closed fss in $(\mathcal{Z}, \mathcal{L}_1^{**}, \mathcal{L}_2^{**}, \mathcal{H})$. Therefore, h_{vj} is PČ-fs-closed mapping.
3. The proof is identical to part 2.

References

[1] E Cech 1966 *Topological spaces* Inter Science Publishers John Wiley and Sons New York
[2] C L Chang 1968 Fuzzy topological spaces *Journal of Mathematical Analysis and Applications* **24** pp 182-190
[3] R Gowri and G Jegadeesan 2014 On soft Cech closure spaces *International Journal of Mathematics Trends and Technology* **9** (2) pp 122-127
[4] A Kharal and B Ahmad 2009 Mappings on fuzzy soft classes *Advances in Fuzzy Systems Artical ID* 407890
[5] J Krishnaveni and C Sekar 2014 Cech Soft Closure Spaces *International Journal of Mathematical Trends and Technology* **6** pp 123-135
[6] P K Maji, R Biswas and A R Roy 2001 Fuzzy soft sets *Journal of Fuzzy Mathematics* **9** (3) pp 589-602
[7] L H Maibed and R N Majeed 2018 Some types of regularity and normality axioms in Cech fuzzy soft closure spaces *Journal of New Theory* **24** pp 73-87
[8] L H Maibed and R N Majeed 2019 Connectedness in Cech fuzzy soft closure spaces *Journal of AL-Qadisiyah for computer science and mathematics* **1**(11) pp 19-26
[9] R N Majeed 2018 Cech fuzzy soft closure spaces *International Journal of Fuzzy System Applications* **7** (2) pp 62-74
[10] R N Majeed and L H Maibed 2018 Some structures of Cech fuzzy soft closure spaces *Journal of Engineering and Applied Sciences* **13** (18) pp 7520-7526
[11] R N Majeed and L H Maibed 2019 Lower separation axioms in Cech fuzzy soft closure spaces *Gazi University Journal of Science* **32** (4) pp 1254-1269

[12] A S Mashhour and M H Ghanim 1985 Fuzzy closure spaces *Journal of Mathematical Analysis and Applications* **106** pp 154-170
[13] D A Molodtsov 1999 Soft set theory-first results *Computers and Mathematics with Applications* **37** pp 19-31
[14] P Mukherjee and C Park 2015 On fuzzy soft bitopological spaces *Mathematicas and Computer Sciences Journal* **10** (7) pp 2-9
[15] S Roy and T K Samanta 2012 A note on fuzzy soft topological spaces *Annals of Fuzzy Mathematics and Informatics* **3** (2) pp 305-311
[16] B Tanay and M B Kandemir 2011 Topological structures of fss's *Computers and Mathematics with Applications* **61** pp 412-418
[17] B P Varol and H Ayg¨un 2012 Fuzzy soft Topology Hacettepe *Journal of Mathematics and Statistics* **41** (2) pp 407-419
[18] L A Zadeh 1965 Fuzzy sets *Information and Control* **8** pp 338-353

Classifications of subsets in the finite projective line

Classifications of subsets in the finite projective line

Najm Abdulzahra Makhrib Al-Seraji and Fatima Ahmed Musa

Department of Mathematics ,college of science, Mustansiriyah University, Baghdad, Iraq

E-mail: fatimaahmed48585@gmail.com

Abstract. The main purpose of this paper is to classify k-sets in projective line$PG(1,29)$ which are a set of k projective distinct points. The projective line has been classified into$k$-set,$k = 3,4,\dots,10$,equivalent and inequivalent. Also, the projective equation of the k-sets and the stabilizer groups of them are constructed. All the computations are doing by using the Group's algorithm language GAP[7].

1. Introduction

Thethemeof projective line over the finite field F_q , $PG(1,q)$ has been studied by many mathematicians. The ideas and definitions of this research are taken from Hirshfeld [1].In 2013Al-Seraji and Hirschfeld[2] studied the geometry of the line of order seventeen.1n 2014 Al-Seraji [3] has been classified the projective line over the Galois field of order sixteen. In 2016 Al-Zangana [4] has been shown the classification of the projective line of order nineteen. In 2015 Al-Seraji [5] has been described the classification of the projective line over Galois field of order 23. In 2018 Al-Zangana and shehab [6]have been studied the classification of k-sets in $PG(1,25)$.

The 30 points of $PG(1,29)$ are $[x_0, x_1]$,$x_i \in \mathbb{F}_{29}$ .So
$PG(1,29) = \{U_0 = [1,0]\} \cup \{[x,1] | x \in \mathbb{F}_{29}\}$.The $[x_0, x_1]$ where $x_1 \neq 0$ is determined x_0 / x_1 . Thus
$PG(1,29) = \{[t,1] \mid t \in \mathbb{F}_{29} \cup \{\infty\}\}$

A projectivity$M(T)$ of $PG(1,29)$is $Y = XT$,where$X = (x_1, x_2)$, $Y = (y_1, y_2)$and T = $\begin{pmatrix} a' & b' \\ c' & d' \end{pmatrix}$. If put s = y_1 / y_2 and t = x_1 / x_2 ; then the projectivity can be written as an equation
s = $(a't + c') / (b't + d')$
Now we introduce the definitions which are using in this paper as follows:

Definition 1.1[1]: A k-set in the projective line $PG(1,q)$ is a set of k projectively distinct points.

Definition 1.2 [9]: A group G acts on a set Λ if there is a map $\Lambda \times G \to \Lambda$ such that given g ,g′ elements in G and 1 its identity , then
1. $y1 = y$,
2. $(yg)g' = y(gg')$ for any y in Λ.

Definition 1.3 [3]: The orbit of y in Λ under the action of G is the set
$yG = \{yg \mid g \in G\}$
Definition 1.4 [3]:The stabilizer of y in Λ under the action of G is the group
$G_y = \{g \in G \mid yg = y\}$

Theorem 1.5 [8]: There is a unique projectivity of $PG(1,q)$ transformation any three points to any three points.
For more details see [10], [11], [12], [13]

2.The Projective Line *PG*(1,29)

On $PG(1,29)$, the projective line over Galois field of order 29, there are 30 points. The points of $PG(1,29)$ are elements of the set

$$\mathbb{F}_{29} \cup \{\infty\} = \{\infty, 0, \pm1, \pm2, \pm3, \pm4, \pm5, \pm6, \pm7, \pm8, \pm9, \pm10, \pm11, \pm12, \pm13, \pm14\}.$$

The order of the projective group $PGL(2,29)$ is 30×29×28=24360. That is the number of three–point ordered sets. The polynomial function of degree two, $g(x) = x^2 + x + 3$ is a primitive over $\mathbb{F}29$, when $\mathbb{F}29 = \{1,2,\cdots,28; 29 = 0\}$. On $PG(1,29)$ there are 30 points. They are generated by a non-singular matrix of size 2×2; $S = C(g) = \begin{pmatrix} 0 & 1 \\ -3 & -1 \end{pmatrix}$. Such $P(j) = (1,0)\, S^j$, $j = 0,\cdots,29$. The points of $PG(1,29)$ are given in Table 1:

Table 1: The Points of (1,29)

$P(0) = [1,0]$	$P(1) = [0,1]$	$P(2) = [3,1]$
$P(3) = [13,1]$	$P(4) = [7,1]$	$P(5) = [14,1]$
$P(6) = [2,1]$	$P(7) = [26,1]$	$P(8) = [8,1]$
$P(9) = [12,1]$	$P(10) = [5,1]$	$P(11) = [21,1]$
$P(12) = [10,1]$	$P(13) = [19,1]$	$P(14) = [24,1]$
$P(15) = [15,1]$	$P(16) = [6,1]$	$P(17) = [11,1]$
$P(18) = [20,1]$	$P(19) = [9,1]$	$P(20) = [25,1]$
$P(21) = [18,1]$	$P(22) = [22,1]$	$P(23) = [4,1]$
$P(24) = [28,1]$	$P(25) = [16,1]$	$P(26) = [23,1]$
$P(27) = [17,1]$	$P(28) = [27,1]$	$P(29) = [1,1]$

The group action of $< S >$ on $PG\ (1,29)$is given as follows:

$$P(0) \xrightarrow{S} P(1) \xrightarrow{S} \ldots \xrightarrow{S} P(29) \xrightarrow{S} P(0)$$

So S cycles 30 points in $PG(1,29)$.

2.1 The 3-sets

Let T be the set of all different 3-sets in $PG(1,29)$. Then the order of T is |T|=30×29×28 =24360, Let $B = \{\infty, 0,1\}$be a 3-set which is one of them. By computing the transformations between B and all the other 3-set, we note that any 3-set is projectively equivalent to B.

Theorem 2.1.1: On $PG(1,29)$ there is accurately one 3-set.

Proof: On $PG(1,29)$, the number of the 3-set is 30×29×28 =24360. According to the Fundamental Theorem of Projective Geometry, Theorem(1.5).Take $\infty = [1,0]$, $0 = [0,1], 1 = [1,1]$ in $PG(1,29)$, so we have $\{\infty, 0,1\}$ is equivalent to any 3-set . The stabilizer group of $\{\infty, 0,1\}$ is give in Table 2.

Table 2: The 3-set on PG(1,29)

Symbol	The 3-set	stabilizer
B	$\{\infty, 0,1\}$	$S_3 = \langle \frac{28}{x+28}, 28x+1 \rangle$

Where $S_3 = \{x, 28x+1, \frac{1}{x}, \frac{28}{x+28}, \frac{28x+1}{28x}, \frac{x}{x+28}\}$

2.2 The 4-sets

The 4-set in $PG(1,29)$, is given by adding one point from each orbit that getsby the action of the projective group of the 3-set $G_B$on the complement of B. All orbits of the 3-set in Table 2 are given in Table 3.

Table 3: Partition of PG$(1,29)$ by the projectivities of 3-set

B	Partition of B^c
$\{\infty, 0,1\}$	1. $\{2,15,28\}$
	2. $\{3,10,14,16,20,27\}$
	3. $\{4,8,11,,19,22,26\}$
	4. $\{5,6,7,23,24,25\}$
	5. $\{9,12,13,17,18,21\}$

The total number of all orbits are5 and hence 5 inequivalent 4-sets can be formed in $PG(1.29)$.Table 3 gives the following conclusion.

Theorem 2.2.1: On $PG(1,29)$, there are accuratelyfive 4-sets, given their stabilizer group inTable 4.

Table- 4: Inequivalent 4-sets on PG(1,29)

Symbol	The 4-set	Stabilizer
B_1	$B \cup \{2\}$	$D_4 = \langle \frac{27}{x+27}, 28+2 \rangle$

B_2	$B \cup \{3\}$	$Z_2 \times Z_2 = \langle \frac{26}{28x} \rangle \times \langle \frac{x+26}{x+28} \rangle$
B_3	$B \cup \{4\}$	$Z_2 \times Z_2 = \langle \frac{25}{28x} \rangle \times \langle \frac{x+25}{x+28} \rangle$
B_4	$B \cup \{5\}$	$Z_2 \times Z_2 = \langle \frac{24}{28x} \rangle \times \langle \frac{x+24}{x+28} \rangle$
B_5	$B \cup \{9\}$	$Z_2 \times Z_2 = \langle \frac{20}{28x} \rangle \times \langle \frac{x+20}{x+28} \rangle$

Where $G(B_1) \cong D_4 = \langle \frac{27}{x+27}, 28x+2 \rangle$

$$= \{x, 28x+2, \frac{27}{28x}, \frac{27}{x+27}, \frac{x}{x+28}, \frac{x+27}{x+28}, \frac{27x+2}{28x}, \frac{27x+2}{28x+2}\}$$

$$G(B_2) \cong Z_2 \times Z_2 = \langle \frac{26}{28x}, \frac{x+26}{x+28} \rangle = \left\{x, \frac{26}{28x}, \frac{x+26}{x+28}, \frac{26x+3}{28x+3}\right\}$$

$$G(B_3) \cong Z_2 \times Z_2 = \langle \frac{25}{28x}, \frac{x+25}{x+28} \rangle = \left\{x, \frac{25}{28x}, \frac{x+25}{x+28}, \frac{25x+4}{28x+4}\right\}$$

$$G(B_4) \cong Z_2 \times Z_2 = \langle \frac{24}{28x}, \frac{x+24}{x+28} \rangle = \left\{x, \frac{24}{28x}, \frac{x+24}{x+28}, \frac{24x+5}{28x+5}\right\}$$

$$G(B_5) \cong Z_2 \times Z_2 = \langle \frac{20}{28x}, \frac{x+20}{x+28} \rangle = \left\{x, \frac{20}{28x}, \frac{x+20}{x+28}, \frac{20x+9}{28x+9}\right\}$$

The proof comes from above statements.

2.3 The 5-sets

The 5 projectivities of the $G_{B_i}, i = 1,2,3,4,5$ split ${B_i}^c$ into a number of orbits .The5-sets are constructed by adding one pointfrom each orbit to the corresponding 4-sets.All orbits are listed in Table 5.

Table 5 : Partition of PG(1,29) by the Projectivitiesof 4 -sets

B_i	Partition B_{i^c}
B_1	$\{3,4,11,15,16,20,27,28\}, \{5,8,9,12,19,22,23,26\}, \{6,7,10,14,17,21,24,25\}, \{13,18\}$
B_2	$\{2,16,26,28\}, \{4,8,9,10\}, \{5,6,15,16\}, \{7,17,19,20\}, \{11,24\}, \{12,14,22,23\}\{13,21,25,27\}$
B_3	$\{2,27\}, \{3,11,14,21\}, \{5,16,22,24\}, \{6,10,12,20\}, \{7,8,13,15\}, \{9,18,23,26\}, \{17,19,25,28\}$
B_4	$\{2,8,17,26\}, \{3,21,24,28\}, \{4,14,19,23\}, \{6,25\}, \{7,9,10,15\}, \{11,18\}, \{12,27\}, \{13,16,20,22\}$
B_5	$\{2,7,19,22\}, \{3,26\}, \{4,8,12,24\}, \{5,20,25,28\}, \{6,11,14,16\}, \{10,13,23,27\}\{15,17,18,21\}$

The total number of all orbits are33; and hence 33 5-sets can be formed in $PG(1,29)$.All equivalent 5-sets with their projective equations are listed in Table 6.

Table 6: The equivalence of 5 -sets

No.	Equivalent 5-sets	Projective equation
1	$B_1 \cup \{3\} \to B_2 \cup \{2\}$	x
2	$B_1 \cup \{3\} \to B_3 \cup \{2\}$	$(27x+2)/(28x+2)$
3	$B_1 \cup \{5\} \to B_3 \cup \{7\}$	$(22x+6)/28x$
4	$B_1 \cup \{5\} \to B_3 \cup \{17\}$	$(16x+7)/(16x+27)$
5	$B_1 \cup \{5\} \to B_4 \cup \{2\}$	x
6	$B_1 \cup \{5\} \to B_5 \cup \{2\}$	$27/(x+27)$
7	$B_1 \cup \{6\} \to B_2 \cup \{5\}$	$(2x+17)/(2x+25)$
8	$B_1 \cup \{6\} \to B_4 \cup \{3\}$	$(2x+17)/(2x+25)$
9	$B_1 \cup \{6\} \to B_4 \cup \{7\}$	$(24x+5)/(24x+1)$
10	$B_1 \cup \{6\} \to B_5 \cup \{5\}$	$(5x+28)/(x+28)$
11	$B_1 \cup \{13\} \to B_5 \cup \{15\}$	$1/x$
12	$B_2 \cup \{4\} \to B_3 \cup \{3\}$	x
13	$B_2 \cup \{4\} \to B_5 \cup \{3\}$	$(26x+3)/(28x+3)$
14	$B_2 \cup \{7\} \to B_2 \cup \{12\}$	$(20x+5)/(20x+27)$
15	$B_2 \cup \{7\} \to B_3 \cup \{6\}$	$(23x+6)/28x$
16	$B_2 \cup \{7\} \to B_4 \cup \{13\}$	$4x+1$
17	$B_2 \cup \{7\} \to B_5 \cup \{6\}$	$23/(5x+23)$
18	$B_2 \cup \{11\} \to B_3 \cup \{5\}$	$25/(3x+25)$
19	$B_2 \cup \{11\} \to B_4 \cup \{4\}$	$25/(3x+25)$
20	$B_2 \cup \{13\} \to B_4 \cup \{12\}$	$17x+12$
21	$B_2 \cup \{13\} \to B_5 \cup \{10\}$	$1/x$
22	$B_3 \cup \{9\} \to B_4 \cup \{11\}$	$6x+5$
23	$B_3 \cup \{9\} \to B_5 \cup \{4\}$	x

Theorem 2.3.1: On $PG(1,29)$, there are accurately ten projectively distance 5-sets summarized in Table 7.

Table 7: Inequivalent 5-sets on$PG\ (1,29)$

Symbol	The 5-set	Stabilizer
C_1	$B_1 \cup \{3\}$	$Z_2 = \langle 28x+3 \rangle$
C_2	$B_1 \cup \{5\}$	$I\ = \langle X \rangle$
C_3	$B_1 \cup \{6\}$	$I\ = \langle X \rangle$

C_4	$B_1 \cup \{13\}$	$Z_4 = \langle 27/x + 27 \rangle$
C_5	$B_2 \cup \{4\}$	$Z_2 = \langle 28x + 4 \rangle$
C_6	$B_2 \cup \{7\}$	$I = \langle X \rangle$
C_7	$B_2 \cup \{11\}$	$Z_2 = \langle 26x + 3/28x + 3 \rangle$
C_8	$B_2 \cup \{13\}$	$Z_2 = \langle 10x/13x + 19 \rangle$
C_9	$B_3 \cup \{9\}$	$Z_2 = \langle 26x + 27/21x + 3 \rangle$
C_{10}	$B_4 \cup \{6\}$	$D_5 = \langle \frac{28}{X+23}, 28x + 6 \rangle$

Where D_5={x , $28x + 6$,$\frac{1}{x}$, $\frac{28}{x+23}$,$\frac{x+24}{x+28}$, $\frac{23x+6}{23x+1}$, $\frac{x}{6x+28}$, $\frac{5x+28}{x+28}$, $\frac{23x+1}{28x}$, $\frac{23x+6}{28x+6}$}
The proof comes from above statements.

2.4 The 6-sets

The 10 projectivities of the 5-sets G_{C_i} , i = 1,2,…, 10 split $C_i{}^c$ into a number of orbits. The 6-sets are constructed by adding one point from each orbit to the corresponding 5-sets. All orbits are listed in Table 8.

Table 8: Partition of $PG(1,29)$ by the projectivities of 5-sets

C_i	Partition $C_i{}^c$
C_1	{4,28}, {5,27},{6,26},{7,25},{8,24},{9,23},{10,22},{11,21}, {12,20},{13,19},{14,18},{15,17},{16}
C_2	G_{C_2} splits $C_2{}^c$ into 25 orbits of single points
C_3	G_{C_3} splits $C_3{}^c$ into 25 orbits of single points
C_4	{3,11,15,27}, {4,16,20,28},{5,8,9,19},{6,14,21,24},{7,10,17,25}, {12,22,23,26},{18}
C_5	{2}, {5,28},{6,27},{7,26},{8,25},{9,24},{10,23},{11,22}, {12,21},{13,20},{14,19},{15,18},{16,17}
C_6	G_{C_6} splits $C_6{}^c$ into 25 orbits of single points
C_7	{2,26}, {4,9},{5,6},{7,19},{8,10},{12,23},{13,21},{14,22}, {15,18},{16,28},{17,20},{24},{25,27}
C_8	{2,23}, {4,12},{5,22},{6},{7,27},{8,28},{9,19},{10,25}, {11,15},{14,17},{16,26},{18,21},{20,24}
C_9	{2,14}, {3,24},{5,13},{6,23},{7},{8,28},{10,20},{11,26}, {12,16},{15,18},{17,27},{19,22},{21,25}
C_{10}	{2,4,9,13,15,16,19,20,22,26},{ 3,7,10,25,28} , {8,11.12,14,17,18,21,23,24,27}

The total number of all orbits are 150 and hence150 6-sets can be formed in $PG(1,29)$. All equivalent 6-sets with their projective equations are listed In Table 9.

Table 9: The equivalence of 6-sets

Equivalent 6-sets	Projective equation	Equivalent 6-sets	Projective equation

$C_1 \cup \{4\} \rightarrow C_5 \cup \{2\}$	x	$C_1 \cup \{5\} \rightarrow C_1 \cup \{11\}$	$(9x+11)/(19x+1)$
$C_1 \cup \{5\} \rightarrow C_2 \cup \{3\}$	x	$C_1 \cup \{5\} \rightarrow C_3 \cup \{27\}$	$(2x+23)/(x+28)$
$C_1 \cup \{5\} \rightarrow C_7 \cup \{2\}$	$(9x+11)/(19x+1)$	$C_1 \cup \{5\} \rightarrow C_8 \cup \{16\}$	$13/(15x+13)$
$C_1 \cup \{6\} \rightarrow C_2 \cup \{28\}$	$x+28$	$C_1 \cup \{6\} \rightarrow C_3 \cup \{3\}$	x
$C_1 \cup \{7\} \rightarrow C_3 \cup \{16\}$	$x/(x+28)$	$C_1 \cup \{7\} \rightarrow C_3 \cup \{28\}$	$x+28$
$C_1 \cup \{7\} \rightarrow C_5 \cup \{6\}$	$(23x+6)/28x$	$C_1 \cup \{7\} \rightarrow C_6 \cup \{2\}$	x
$C_1 \cup \{7\} \rightarrow C_8 \cup \{8\}$	$17x/(8x+5)$	$C_1 \cup \{8\} \rightarrow C_2 \cup \{15\}$	$(x+27)/(x+28)$
$C_1 \cup \{8\} \rightarrow C_3 \cup \{15\}$	$(14x+15)/(14x+1)$	$C_1 \cup \{8\} \rightarrow C_5 \cup \{16\}$	$26/28x$
$C_1 \cup \{8\} \rightarrow C_6 \cup \{8\}$	$24x/(3x+5)$	$C_1 \cup \{8\} \rightarrow C_7 \cup \{16\}$	$13/(15x+13)$
$C_1 \cup \{9\} \rightarrow C_2 \cup \{11\}$	$(27x+2)/28x$	$C_1 \cup \{9\} \rightarrow C_2 \cup \{16\}$	$(15x+13)/(15x+28)$
$C_1 \cup \{9\} \rightarrow C_5 \cup \{7\}$	$(x+20)/(x+26)$	$C_1 \cup \{9\} \rightarrow C_6 \cup \{4\}$	$(x+20)/(x+26)$
$C_1 \cup \{9\} \rightarrow C_9 \cup \{2\}$	$(2x+25)/(x+28)$	$C_1 \cup \{10\} \rightarrow C_2 \cup \{4\}$	$(2x+25)/(x+28)$
$C_1 \cup \{10\} \rightarrow C_3 \cup \{20\}$	$27/28x$	$C_1 \cup \{10\} \rightarrow C_5 \cup \{5\}$	$(3x+28)/(x+28)$
$C_1 \cup \{10\} \rightarrow C_6 \cup \{24\}$	$(22x+12)/28x$	$C_1 \cup \{10\} \rightarrow C_7 \cup \{17\}$	$13x/(11x+6)$
$C_1 \cup \{12\} \rightarrow C_2 \cup \{20\}$	$27/28x$	$C_1 \cup \{12\} \rightarrow C_6 \cup \{28\}$	$(3x+22)/(x+28)$
$C_1 \cup \{13\} \rightarrow C_2 \cup \{27\}$	$2/(x+28)$	$C_1 \cup \{13\} \rightarrow C_4 \cup \{3\}$	x
$C_1 \cup \{13\} \rightarrow C_6 \cup \{26\}$	$(26x+6)/28x$	$C_1 \cup \{13\} \rightarrow C_8 \cup \{2\}$	x
$C_1 \cup \{13\} \rightarrow C_9 \cup \{17\}$	$(9x+28)/(21x+16)$	$C_1 \cup \{14\} \rightarrow C_2 \cup \{7\}$	$(28x+2)/(4x+2)$
$C_1 \cup \{14\} \rightarrow C_3 \cup \{11\}$	$(27x+2)/28x$	$C_1 \cup \{14\} \rightarrow C_3 \cup \{23\}$	$(23x+12)/28x$
$C_1 \cup \{14\} \rightarrow C_4 \cup \{4\}$	$(2x+25)/(x+28)$	$C_1 \cup \{14\} \rightarrow C_6 \cup \{5\}$	$2x+1$
$C_1 \cup \{15\} \rightarrow C_3 \cup \{4\}$	$2x$	$C_1 \cup \{15\} \rightarrow C_6 \cup \{16\}$	$13/(15x+13)$
$C_2 \cup \{6\} \rightarrow C_3 \cup \{5\}$	x	$C_2 \cup \{6\} \rightarrow C_6 \cup \{6\}$	$23/28x$
$C_2 \cup \{6\} \rightarrow C_6 \cup \{23\}$	$16x/(7x+16)$	$C_2 \cup \{6\} \rightarrow C_7 \cup \{14\}$	$(24x+25)/(18x+8)$
$C_2 \cup \{6\} \rightarrow C_{10} \cup \{2\}$	x	$C_2 \cup \{9\} \rightarrow C_2 \cup \{14\}$	$(3x+14)/(16x+1)$
$C_2 \cup \{9\} \rightarrow C_2 \cup \{19\}$	$(27x+2)/28x$	$C_2 \cup \{9\} \rightarrow C_3 \cup \{19\}$	$(23x+6)/23x$
$C_2 \cup \{9\} \rightarrow C_7 \cup \{5\}$	$15x/(3x+2)$	$C_2 \cup \{9\} \rightarrow C_9 \cup \{19\}$	$11/(15x+10)$
$C_2 \cup \{10\} \rightarrow C_3 \cup \{12\}$	$27/28x$	$C_2 \cup \{10\} \rightarrow C_9 \cup \{8\}$	$(26x+3)/(25x+8)$
$C_2 \cup \{12\} \rightarrow C_5 \cup \{8\}$	$(4x+21)/(x+28)$	$C_2 \cup \{12\} \rightarrow C_8 \cup \{10\}$	$(22x+26)/(17x+2)$
$C_2 \cup \{13\} \rightarrow C_4 \cup \{5\}$	x	$C_2 \cup \{13\} \rightarrow C_5 \cup \{13\}$	$23x/(4x+9)$
$C_2 \cup \{13\} \rightarrow C_6 \cup \{10\}$	$(9x+11)/(22x+4)$	$C_2 \cup \{13\} \rightarrow C_6 \cup \{22\}$	$22x+7$

$C_2 \cup \{13\} \to C_8 \cup \{4\}$	$23x/(4x+9)$	$C_2 \cup \{17\} \to C_3 \cup \{22\}$	$(27x+2)/(28x+2)$
$C_2 \cup \{17\} \to C_7 \cup \{15\}$	$(14x+15)/(14x+1)$	$C_2 \cup \{18\} \to C_4 \cup \{12\}$	$27/28x$
$C_2 \cup \{18\} \to C_9 \cup \{15\}$	$22/(24x+25)$	$C_2 \cup \{21\} \to C_3 \cup \{9\}$	$(x+27)/27$
$C_2 \cup \{21\} \to C_6 \cup \{18\}$	$18x$	$C_2 \cup \{22\} \to C_5 \cup \{14\}$	$16/(18x+26)$
$C_2 \cup \{22\} \to C_6 \cup \{9\}$	$7x/(7x+23)$	$C_2 \cup \{23\} \to C_7 \cup \{24\}$	$5/(6x+28)$
$C_2 \cup \{24\} \to C_3 \cup \{8\}$	$(x+27)/(x+28)$	$C_2 \cup \{24\} \to C_3 \cup \{18\}$	$(28x+24)/28x$
$C_2 \cup \{24\} \to C_4 \cup \{7\}$	$6x+1$	$C_2 \cup \{24\} \to C_5 \cup \{15\}$	$(15x+28)/(x+28)$
$C_2 \cup \{24\} \to C_9 \cup \{21\}$	$(21x+18)/(12x+5)$	$C_2 \cup \{25\} \to C_3 \cup \{26\}$	$28x+2$
$C_2 \cup \{25\} \to C_7 \cup \{13\}$	$(23x+12)/27x+21$	$C_2 \cup \{25\} \to C_8 \cup \{11\}$	$(23x+12)/(27x+21)$
$C_2 \cup \{25\} \to C_9 \cup \{5\}$	$(5x+20)/(x+28)$	$C_2 \cup \{25\} \to C_{10} \cup \{8\}$	$(24x+5)/(28x+5)$
$C_2 \cup \{26\} \to C_9 \cup \{7\}$	$7x/(7x+23)$	$C_3 \cup \{7\} \to C_{10} \cup \{3\}$	$23/28x$
$C_3 \cup \{13\} \to C_4 \cup \{6\}$	x	$C_3 \cup \{13\} \to C_8 \cup \{18\}$	$12x+18$
$C_3 \cup \{14\} \to C_3 \cup \{21\}$	$(27x+2)/28x$	$C_3 \cup \{14\} \to C_6 \cup \{14\}$	$22x+14$
$C_3 \cup \{14\} \to C_6 \cup \{15\}$	$15x$	$C_3 \cup \{14\} \to C_8 \cup \{5\}$	$2x+1$
$C_3 \cup \{14\} \to C_9 \cup \{10\}$	$(26x+3)/(20x+10)$	$C_3 \cup \{17\} \to C_6 \cup \{13\}$	$(28x+17)/28x$
$C_3 \cup \{17\} \to C_8 \cup \{7\}$	$(7x+16)/(x+28)$	$C_3 \cup \{24\} \to C_6 \cup \{11\}$	$(18x+8)/28x$
$C_3 \cup \{24\} \to C_7 \cup \{7\}$	$(12x+2)/(4x+21)$	$C_3 \cup \{25\} \to C_8 \cup \{6\}$	$23/28x$
$C_5 \cup \{9\} \to C_7 \cup \{8\}$	$21/(22x+28)$	$C_5 \cup \{9\} \to C_9 \cup \{3\}$	$(26x+3)/(28x+3)$
$C_5 \cup \{10\} \to C_6 \cup \{17\}$	$(11x+14)/(23x+2)$	$C_5 \cup \{10\} \to C_9 \cup \{11\}$	$18/(10x+18)$
$C_5 \cup \{11\} \to C_6 \cup \{19\}$	$(7x+10)/(x+28)$	$C_5 \cup \{11\} \to C_7 \cup \{4\}$	$25/28x$
$C_5 \cup \{12\} \to C_6 \cup \{21\}$	$(3x+22)/(x+28)$	$C_5 \cup \{12\} \to C_8 \cup \{9\}$	$(3x+20)/(x+28)$
$C_6 \cup \{20\} \to C_7 \cup \{12\}$	$(26x+2)/28x$	$C_6 \cup \{20\} \to C_9 \cup \{12\}$	$19x/(12x+21)$
$C_6 \cup \{25\} \to C_7 \cup \{25\}$	$(26x+21)/28x$	$C_6 \cup \{25\} \to C_8 \cup \{20\}$	$(x+26)/(x+28)$
$C_6 \cup \{27\} \to C_8 \cup \{14\}$	$15x+14$	$C_6 \cup \{27\} \to C_9 \cup \{6\}$	$23/(5x+23)$

Theorem 2.4.1:On $PG(1,29)$, there are accurately 42 projectively distinct 6-sets summarized in Table 10

Table 10: Inequivalent 6-sets on $PG\ (1,29)$

Symbol	The 6-set	Stabilizer

E_1	$C_1 \cup \{4\}$	$Z_2 \times Z_2 = \langle 28x+4 \rangle \times \langle \frac{27x+2}{28x+2} \rangle$
E_2	$C_1 \cup \{5\}$	$I = \langle x \rangle$
E_3	$C_1 \cup \{6\}$	$Z_2 = \langle 23/28x \rangle$
E_4	$C_1 \cup \{7\}$	$I = \langle x \rangle$
E_5	$C_1 \cup \{8\}$	$I = \langle x \rangle$
E_6	$C_1 \cup \{9\}$	$I = \langle x \rangle$
E_7	$C_1 \cup \{10\}$	$I = \langle x \rangle$
E_8	$C_1 \cup \{12\}$	$Z_2 = \langle 28x+12/19x+1 \rangle$
E_9	$C_1 \cup \{13\}$	$I = \langle x \rangle$
E_{10}	$C_1 \cup \{14\}$	$I = \langle x \rangle$
E_{11}	$C_1 \cup \{15\}$	$Z_2 = \langle x+27/x+28 \rangle$
E_{12}	$C_1 \cup \{16\}$	$D_6 = \langle \frac{13}{15x+13}, \frac{26}{28x} \rangle$
E_{13}	$C_2 \cup \{6\}$	$I = \langle x \rangle$
E_{14}	$C_2 \cup \{8\}$	$S_3 = \langle \frac{18}{26X+24}, \frac{x+27}{x+28} \rangle$
E_{15}	$C_2 \cup \{9\}$	$I = \langle x \rangle$
E_{16}	$C_2 \cup \{10\}$	$Z_2 = \langle 19/28x \rangle$
E_{17}	$C_2 \cup \{12\}$	$Z_2 = \langle 27/28x \rangle$
E_{18}	$C_2 \cup \{13\}$	$I = \langle x \rangle$
E_{19}	$C_2 \cup \{17\}$	$Z_2 = \langle 24/28x \rangle$
E_{20}	$C_2 \cup \{18\}$	$Z_2 = \langle 3x+4/16x+26 \rangle$
E_{21}	$C_2 \cup \{21\}$	$Z_2 = \langle 8x+21/28x+21 \rangle$
E_{22}	$C_2 \cup \{22\}$	$Z_2 = \langle 27x+2/28x+2 \rangle$
E_{23}	$C_2 \cup \{23\}$	$Z_2 \times Z_2 = \langle \frac{x}{x+28} \rangle \times \langle \frac{27x+2}{28x+2} \rangle$
E_{24}	$C_2 \cup \{24\}$	$I = \langle x \rangle$
E_{25}	$C_2 \cup \{25\}$	$I = \langle x \rangle$
E_{26}	$C_2 \cup \{26\}$	$Z_2 \times Z_2 = \langle 28x+2 \rangle \times \langle \frac{x+24}{x+28} \rangle$
E_{27}	$C_3 \cup \{7\}$	$Z_2 \times Z_2 = \langle \frac{x}{x+28} \rangle \times \langle \frac{x+24}{x+28} \rangle$
E_{28}	$C_3 \cup \{10\}$	$S_3 = \langle \frac{25x+8}{25x+24}, \frac{27}{28x} \rangle$
E_{29}	$C_3 \cup \{13\}$	$Z_2 = \langle 23x+6/28x+6 \rangle$
E_{30}	$C_3 \cup \{14\}$	$I = \langle x \rangle$
E_{31}	$C_3 \cup \{17\}$	$Z_2 = \langle 27x+2/28x+2 \rangle$
E_{32}	$C_3 \cup \{24\}$	$Z_2 = \langle x+27/x+28 \rangle$
E_{33}	$C_3 \cup \{25\}$	$Z_2 \times Z_2 = \langle 28x+2 \rangle \times \langle \frac{x+23}{x+28} \rangle$
E_{34}	$C_4 \cup \{18\}$	$S_4 = \langle \frac{27}{28x}, 12x+18 \rangle$
E_{35}	$C_5 \cup \{9\}$	$Z_2 = \langle 26x+3/28x+3 \rangle$
E_{36}	$C_5 \cup \{10\}$	$Z_2 = \langle x+26/x+28 \rangle$
E_{37}	$C_5 \cup \{11\}$	$Z_2 = \langle 25/28x \rangle$
E_{38}	$C_5 \cup \{12\}$	$Z_2 = \langle 17/28x \rangle$
E_{39}	$C_6 \cup \{12\}$	$S_3 = \langle \frac{20x+5}{20x+27}, \frac{22}{28x} \rangle$
E_{40}	$C_6 \cup \{20\}$	$Z_2 = \langle x+26/x+28 \rangle$
E_{41}	$C_6 \cup \{25\}$	$Z_2 = \langle 4x+16/11x+25 \rangle$
E_{42}	$C_6 \cup \{27\}$	$Z_2 = \langle x+22/x+28 \rangle$

Where D_6 = { x , $28x+3$, $\frac{26}{28x}$, $\frac{13}{15x+13}$, $\frac{x}{x+28}$, $\frac{15x+13}{15x+28}$, $\frac{2x+26}{x+28}$, $\frac{28x+16}{14x+1}$, $\frac{26x+3}{28x}$, $\frac{13x+3}{14x+16}$, $\frac{13x+16}{28x+16}$, $\frac{16x+26}{x+13}$}
The proof comes from above statements

2.5 Inequivalent$k-sets, k = 7, \dots, 10$
The final results for the inequivalent$K-sets(k = 7, \dots, 10)$are given in one theorem because the numbers of inequivalent$k-sets$ are very large.

Theorem 2.5.1: In *PG*(1,29), there are
(i) 97inequivalent7-sets as given in Table 11
(ii) 290 inequivalent 8-sets as given in Table 12
(iii) 630 inequivalent 9-sets as given in Table 13
(vi)1341inequivalent 10-sets as given in Table 14

Table 11: The stabilizer of the 7-sets

Stabilizer	Number
I	71
Z_2	25
D_7	1

Where D_7 = {x , $28x+4$, $\frac{20}{28x}$, $\frac{15}{8x+26}$, $\frac{x+20}{x+26}$, $\frac{x+5}{x+28}$, $\frac{26x+3}{28x+3}$, $\frac{3x+20}{x+28}$, $\frac{25x+9}{28x}$, $\frac{26x+27}{21x+3}$, $\frac{15x+13}{21x+14}$, $\frac{22x+7}{25x+9}$, $\frac{9x}{4x+20}$, $\frac{18x+15}{8x+15}$ }

Table 12: The stabilizer of the 8-sets

Stabilizer	Number
I	202
Z_2	71
$Z_2 \times Z_2$	13
Z_7	1
D_4	3

Where D_4 = {x , $\frac{27}{x+27}$, $\frac{x+27}{x+28}$, $\frac{27x+2}{28x}$, $\frac{18x+28}{3x+11}$, $\frac{7x+16}{15x+22}$, $\frac{22x+23}{19x+7}$, $\frac{11x+20}{21x+18}$ }

Table 13: The stabilizer of the 9-sets

Stabilizer	Number
I	553
Z_2	65
Z_3	4
Z_4	3
S_3	4

D_7	1

Where D_7={x , $23x+1$, $16x+2$,$24x+5$, $25x+9$, $20x+18$, $7x+24$, $\frac{9x}{5x+20}$, $\frac{4x+25}{28x+25}$, $\frac{28x+2}{22x+1}$, $\frac{13x+22}{4x+16}$,$\frac{22x+5}{9x+7}$,$\frac{6x+8}{13x+23}$,$\frac{5x+25}{6x+24}$}

Table 14: The stabilizer of the 10-sets

Stabilizer	Number
I	1152
Z_2	170
$Z_2 \times Z_2$	14
D_4	3
D_5	2

Where D_5={x , $\frac{28}{22x+26}$, $\frac{x+21}{x+28}$,$\frac{28x+2}{14x+5}$,$\frac{26x+3}{28x+3}$, $\frac{4x+12}{15x+25}$, $\frac{7x+3}{21x+16}$, $\frac{16x+10}{7x+13}$, $\frac{5x+1}{8x+24}$,$\frac{17x+4}{28}$ }

D_5={ x , $\frac{19}{26x+27}$, $\frac{x+7}{x+28}$,$\frac{27x+2}{28x+2}$,$\frac{x+6}{10x+28}$, $\frac{5x+9}{23x+1}$, $\frac{28x+15}{19x+11}$, $\frac{20x+16}{28x}$,$\frac{16x+10}{6x+13}$,$\frac{11x+7}{3x+18}$ }

D_4={ x , $\frac{8}{9x+28}$, $\frac{10x+17}{5x+19}$,$\frac{9x+6}{3x+20}$,$\frac{3x+23}{10x+26}$, $\frac{16x+12}{28x}$, $\frac{9x+28}{17x+20}$, $\frac{5x+14}{9x+24}$ }

D_4={x , $\frac{20}{28x}$, $\frac{x+20}{x+28}$,$\frac{5x+21}{17x+24}$, $\frac{5x+23}{9x+5}$, $\frac{20x+9}{28x+9}$,$\frac{3x+21}{12x+3}$, $\frac{3x+23}{20x+26}$ }

D_4={ x , $\frac{24}{28x}$, $\frac{10x+8}{10x+28}$,$\frac{x+12}{15x+28}$,$\frac{3x+24}{x+28}$, $\frac{12x+22}{14x+17}$, $\frac{4x+21}{19x+25}$, $\frac{8x+21}{28x+13}$ }

References

[1] Hirschfeld J W P 1998 Projective geometries over finite fields *2nd edition, Oxford Mathematical Monographs The Clarendon Press Oxford University Press, New York*
[2] Hirschfeld J W P and Al-Seraji N A M 2013 The Geometry of The line of order Seventeen and its Application to Error-correcting Codes *Al-Mustansiriyahjournal of Science* 25 (1) 217-230
[3] Al-Seraji N A M 2014 Classification of the Projective line over Galois Field of order sixteen *Al-Mustansiriyah journal of Science* 24(6) 119-128
[4] Al-Zangana E B A 2016 Classification of projective line of order nineteen and its application to error-correcting Codes *Basrah journal of Science* 34(3) 196-211
[5] AL-Seraji N A M 2015 Classification of The Projective Line Over Galois Field of Order *Journal of Education Al-Mustansiriyah* 23 No.3
[6] Al-Zangana, E B Aand shehab E A 2018 classification of k-sets i$n\ PG(1,25)$ fo$r\ k = 4, \dots, 13$ *Iraq journal of Science, University of Baghdad* 59(3B)
[7] Group G A P 2019 GAP-Groups Algorithms Programming- a System for computation Discrete Algebra URLhttps://www.gap-system.org
[8] Ali A H 1993 Classification of arcs in the Galois plane of order thirteen *Ph.D. thesisUniversity of Sussex UK*
[9] Hirschfeld J W P, Korchmaros G and Torres F 2007 Algebraic curves over a finite field *Oxford University Press Oxford*
[10] Hirschfeld J W P and Thas J A 1991 General Galois Geometries *Oxford University Press Oxford*
[11] Hirschfeld J W P and Voloch J F 2015 Group –arcs of prime power order on cubic curves *Finite Geometry and Combinatorics* 191 177-185

[12] Al-Seraji N A M 2010 The Geometry of The Plane of order Seventeen and its Application to Error-correcting Codes *Ph.D Thesis University of Sussex UK*
[13] Al-Zangana E B 2011 The Geometry of The Plane of order Nineteen and its Application to Error-correcting Codes *Ph.D Thesis University of Sussex UK*

Restrained Whole Domination in Graphs

Restrained Whole Domination in Graphs

T A Ibrahim*and A A Omran[2]

[1]The Ministry of Education, General Directorate of Education Wasit, Iraq
[2]Department of Mathematics, College of Education for Pure Science, University of Babylon, Iraq

E-mial: atheer12fe@gmail.com

Abstract. In this paper, we introduce a new definition of domination number in graphs called restrained whole domination number and denoted by$\gamma_{rwh}(G)$.Some bounds and results for restrained whole domination number are established. Moreover, this number is computed to the complement of certain graphs. Finally, the Effective the deletion or addition an edge or the deletion of a vertex of the graph has this number is discussed.

1. Introduction

We consider a graph $G = (V, E)$ for simplicity G as finite, simple and undirected. In recent years many fields of graph theory in mathematics are appears to solve many problems in as labeled graph [1],[2] and [3], topological graph [10], fuzzy graph [16], and others Claude Berge in 1962introduced concept of domination in graphs [5], after this time many parameters of domination are discussed as [4], [8], [11] and [12]. The set D in a graph G is a restrained dominating if each vertex in $V-D$is adjacent to at least one vertex in the set D and in the set$V-D$. The minimum cardinality of all these sets is called the restrained domination number of G denoted by γ_r (G). The concept of restrained domination is studied and investigated in [6], [7], [14] and [15]. Ibrahim is introduced the parameter whole domination number in his thesis [9]. For more details for the concepts used in this work, the reader can be found in [7] and [13].

Definition 1.1.[9]Let a graph G be a simple and connected, a proper subset $D \subset V$ is called whole dominating set (WDS), if every vertex in the set $V - D$ is adjacent to all vertices in the set D. The set D is called minimal WDS(MWDS) if it has no proper WDS. The whole domination number denoted by $\gamma_{wh}(G)$ for simplicity γ_{wh} is the minimum cardinality of a MWDS. The MWDS has γ_{wh} is called γ_{wh}-set.

Observation 1.2.[9]
i)$\gamma_{wh}(P_n) = 1$ *if* $2 \le n \le 3$, *otherwise* P_n *has no WDS.*
ii)$\gamma_{wh}(C_n) = \begin{Bmatrix}1, if n = 3\\ 2, if n = 4\end{Bmatrix}$, *otherwise* C_n *has no WDS.*
iii)$\gamma_{wh}(K_n) = \gamma_{wh}(W_n) = 1.$
iv)$\gamma_{wh}(K_{m,n}) = min\{m, n\}.$

Remark 1.3.[9]
If Gis a disconnected graph, then G has no WDS.

2.Restrained Whole Domination Number
Throughout this section a new definition of dominating set is initiated which is called an upper whole dominating set with study some of properties.

Definition 2.1. A WDS D⊂V is Restrained whole dominating set (RWDS), if each vertex in V– D is adjacent to at least one vertex in the set D and in the set V– D.

Definition 2.2. The restrained whole domination number of G denoted byγ_{rwh}(G), is the smallest cardinality of a SWDS of G.

Example 2.3. In the following Figure:

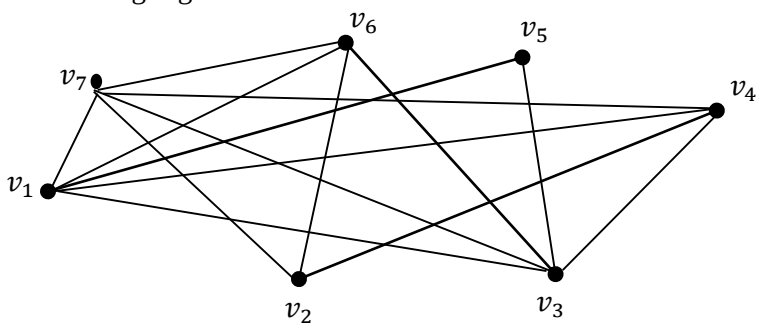

Figure 1

D= {v_1, v_2, v_3 } is minimum whole dominating set of G, thus, $\gamma_{wh}(G)$ = 3
D_1= {v_4, v_6, v_7 } is minimum restrained whole dominating set of G, $\gamma_{rwh}(G)$ = 3

Observation 2.4. If G is a graph and D is a RWDS with minimum cardinality.
1) If G has an isolated vertex, then G has no RWDS.
2)$\langle V - D\rangle$has no an isolated vertex.
3)$deg(v) \geq \gamma_{rwh}(G) + 1, \forall\, v \in V - D.$
4) $|V - D| \geq 2.$
5) $\gamma(G) \leq \gamma_{wh}(G) \leq \gamma_{rwh}(G).$

Theorem 2.5.
1) $\gamma_{rwh}(K_n) = 1$, *for any* n , $n \geq 3$.
2)$\gamma_{rwh}(C_n) = 1\ if\ n = 3$, *otherwise* C_n *has no RWDS.*
3)$\gamma_{rwh}(W_n) = 1$, *for any* n.
4)$\gamma_{rwh}(P_n)$has no RWDS in graph.
5)$\gamma_{\mathrm{rwh}}(\mathrm{K_{m,n}})$has no RWDS in graph.

Proof.
1) Let $D = \{v_i\}, i = 1,2, \dots, n$, it is clear that the set D is minimum RWDS and each vertex in $V - D$ is adjacent to the other vertex in $V - D$, since $n \geq 3$. Thus, the result is obtained.
2) If $n = 3$, then $C_3 = K_3$, and $\gamma_{rwh}(C_3) = 1$ by (1). If $\neq 3$, then the $\Delta(G) = 2$, so the maximum cardinality of neighborhood for each vertex (say v) in this graph is two say $\{w_1, w_2\}$. Now, if the set d

contains the vertex v, then the set V−d contain $\{w_1, w_2\}$. Since $n \neq 3$, so there is at least one other vertex say w_3, if this vertex belong to the set $V - D$, then the vertex v must adjacent to it according to the definition 2.1. and this is a contradiction with $\Delta(G) = 2$. In other hand, if w_3 belong to the set D, then again this vertex must adjacent to the two vertices $w_1, and w_2$ and this a contradiction with property of cycle since the vertex v is adjacent to these vertices. Thus, every cycle of order four or more has no RWDS.
3) Let $D = \{v\}$, where v is the center of the wheel graph, it is clear that the set D is minimum RWDS and each vertex in $V - D$ is adjacent to the other vertex in $V - D$, since $n \geq 3$. Thus, the result is obtained.
4) It is clear that P_n has WDS only when $n = 2,3$ by observation 1.2 (1), but in each cases the set $V - D$ contains an isolated vertex. Thus, the graph has no RWDS, according to observation 2.6 (1).
5) By observation 1.2 (iv) the set of WDS contains all vertices of partite of minimum cardinality. Thus, the set $V - D$ contains an isolated vertex, therefore the graph has no RWDS, according to observation 2.4 (1).

Note 2.6. The star graph $S_n \equiv K_{1,n-1}$ has no RWDS.

Proposition 2.7. If a graph G has WDS, then G has restrained whole dominating set if and only if G[V− D] has no isolated vertex.

Proof. It is straightforward from observation 1.2.□

Corollary 2.8. If G is a tree, then G has no RWDS.

Proof. Since G has no cycle, then all vertices in $V-D$is not adjacent.
So, $V-D$ are independent and G has no RWDS. □

Proposition 2.9. Let a graph G has RWDS. If D has no isolated in G[D], then V− DhasRWDSinG.

Proof. Let D be a minimum RWDS, the each vertex is adjacent to all vertices in $\langle V - D \rangle$. In other hand, each vertex in $V - D$ is also adjacent to all vertices in D. Furthermore, $\langle D \rangle$. has no an isolated vertex, thus $V-D$ hasRWDS in G. □

3.Complement the certain graphs
Theorem 3.1. If $G \equiv \overline{P_n}$then $\gamma_{rwh}(\overline{P_n}) = 2, \forall n > 5$*othewise* $\overline{P_n}$ *has no RWDS.*

Proof. There are four cases depend on n as follows.
Case 1. If $n \leq 3$, then $\overline{P_n}$ has an isolated vertex. Therefore, $\overline{P_n}$ has no RWDS, by Observation 2.4(1).
Case 2. If $n = 4$, then $\overline{P_4} \equiv P_4$ so again it has no RWDS, by Observation 2.4(1).
Case 3. If $n = 5$, then let $\{v_1, v_2, v_3, v_4, v_5\}$ the set of vertices of the graph $\overline{P_5}$. It is clear that the set $\{v_1, v_5\}$ is the only whole dominating set in $\overline{P_5}$, but this is not restrained, since the vertex v_3 is an isolated in $V - D$. Therefore, $\overline{P_5}$ has no RWDSaccording to Observation 2.5(1).
Case 4. If $n \geq 6$, the set $\{v_1, v_n\}$ is a minimum WDS and the set $V - D$has no an isolated vertex. Thus, $\gamma_{rwh}(P_n) = 2$.
From all cases above, the result is obtained. □
Theorem 3.2. If $G \equiv \overline{C_n}$, then $\gamma_{rwh}(\overline{C_n}) = 2, \forall n > 5$ othewise $\overline{C_n}$ has no RWDS.

Proof. There are three cases depend on n as follows.
Case 1. If $n \leq 4$, then $\overline{C_n}$is disconnected graph. Therefore, $\overline{C_n}$ has no WDS according to Remark 1.3. Thus, $\overline{C_n}$ has no restrained whole.

Case 2. If $n = 5$, then $\overline{C_5} \equiv C_5$ so again it has no RWDS, according to Theorem 2.6.
Case 3. If $n \geq 6$, the set $\{v_i, v_j\}; d(v_i, v_j) \geq 2$ is a minimum RWDSand the set $V - D$has no an isolated vertex. Thus, $\gamma_{rwh}(P_n) = 2$.
From all cases above, the result is obtained. □

Proposition 3.3. *The graphs* $\overline{W_n}, \overline{K_n}, \overline{S_n}$, *and* $\overline{K_{n,m}}$ *have no RWDS.*

Proof. All these graphs are disconnected. Thus, according to Theorem 2.5.
these graphs have no RWDS.□

4-Effective the deletion or addition

Theorem 4.1: LetG be a graph has RWDS D with $\gamma_{\mathrm{rwh}} -$ set and $\gamma_{\mathrm{rwh}}(\mathrm{G}) > 1$, then If $\mathrm{v} \in \mathrm{D}$ then $\gamma_{rwh}(G - v) < \gamma_{rwh}(G)$ otherwise all probability are possible.

Proof. Let D be a $\gamma_{rwh} -$ set of a graph G. Then there are two cases as follows:
Case 1: If a vertex v, where $v \in D$is deleting, then $\gamma_{rwh}(G - v) < \gamma_{rwh}(G)$.
Case 2: If we delete a vertex v, where $v \in V - D$, then three cases are obtained as follows:
1) If $v \in D'$ such that D' is RWDS$\gamma_{rwh} -$ set, then
$\gamma_{wh}(G - v\ ) < \gamma_{wh}(G)$.
2) If $|D| < |V - D|$ and $(V - D) - v$ has RWDS, then $\gamma_{rwh}(G - v\ ) = \gamma_{rwh}(G)$.
3) If $(V - D) - v$has an isolated vertex, then D is not RWDS. Thus, there are two subcases as follows.
Subcase 1. If there is other RWDS in $G - v$ say D', then $\gamma_{wh}(G - v\ ) > \gamma_{wh}(G)$.
Subcase 2. If there is no other RWDS in $G - v$, then $G - v$ has no RWDS.
From all cases above, the result is obtained.

Theorem 4.2. Let G be a graph has restrained whole domination number, then G has no RWDSor $\gamma_{\mathrm{rwh}}(\mathrm{G} - \mathrm{e}) \geq \gamma_{\mathrm{rwh}}(\mathrm{G})$.

Proof. There are several cases depending on the location of the edge $(e = uv)$as follows.
Case 1. If e belongs to the induced subgraph $\langle D \rangle$, then the deleting e not influence to the restrained whole domination.
Case 2. If e belongs to the induced subgraph $\langle V - D \rangle$, then there are two subcases as follows.
I) At least one vertex u or v becomes an isolated in $\langle V - D \rangle$ after deleting the edge e, then G has no restrained whole domination.
II) If u and v are not isolated vertices in$\langle V - D \rangle$after deleting the edge e, *then* the deleting e not influence to the restrained whole domination.
Case 3. If$u \in D$ *and* $v \in V - D$, then there are two subcases as follows.
I) If all vertices in the induced subgraph $\langle V - D \rangle$ are adjacent to a vertex v, then v will belongs to the set D after deleting the edge e. Therefore, $\gamma_{rwh}(G - e) > \gamma_{rwh}(G)$.
II)If all vertices in the induced subgraph $\langle V - D \rangle$ are not adjacent to a vertex v, then $G - e$ has no RWDS.
From all cases above, the result is obtained.□

Theorem 4.3.*If* G *has a* γ_{rwh} *,then*$\gamma_{rwh}(G + e) \leq \gamma_{rwh}(G)$, *where* $e \in \bar{G}$.

Proof.
Let D'' be a minimum RWDS that means$|D'| = \gamma_{rwh}$. By adding an edge e to a graph G, two different cases are gotten as follows.
Case1. If e joins two vertices from $V - D$, then the whole domination is not influenced by this addition. Thus, $\gamma_{rwh}(G + e) = \gamma_{rwh}(G)$.

Case2. If e joins two vertices in D, then if at least one vertex which is incident on this edge becomes adjacent to all vertices in D, then $\gamma_{rwh}(G+e)=1$.
Thus, $\gamma_{rwh}(G+e)\leq\gamma_{rwh}(G)$.
We cannot add an edge e to a graph G if one of its vertices belongs to the set D and the other belongs to the set $V-D$, since $e\notin\bar{G}$in this case according to definition of whole dominating set. Therefore, we get the result. □

Theorem 4.4. IfGhas a γ_{rwh} , then $\gamma_{\mathrm{rwh}}(\mathrm{G}\backslash\mathrm{e})\leq\gamma_{\mathrm{rwh}}(\mathrm{G})$.

Proof. Let D' be a γ_{rwh}- set of a graph G. By contracting an edge e of graph G, three different cases are obtained as follows.
Case 1. If we contract the edge e which is incident on two vertices of $V-D$, then there are two cases as follows.
(i) If $|D|=|V-D|$ then $V-D$ becomes the minimum RWDS. Thus, $\gamma_{rwh}(G\backslash e)<\gamma_{rwh}(G)$.
(ii) If $|D|<|V-D|$, then the minimum RWDS is not influenced by this contraction. Thus, $\gamma_{rwh}(G\backslash e)=\gamma_{rwh}(G)$.
Case 2. If contracting an edge e incident on two vertices from D, then it is clear that the set D is decreasing by one vertex and will still minimum RWDS. Thus,$\gamma_{rwh}(G\backslash e)<\gamma_{rwh}(G)$.
Case 3. If e is incident on two vertices one of them from $V-D$ and the other from D, then the new vertex obtained by this contraction is adjacent to all vertices in G, then $\gamma_{rwh}=1$
Therefore, from all cases above, $\gamma_{rwh}(G\backslash e)\leq\gamma_{rwh}(G)$. □

5. Conclusion

Throughout the results which are obtained in this work, new properties and boundaries of a new parameter are been getting. Also, for certain graphs as a cycle, complete, path, wheel, and complete bipartite are been determined of restrained whole domination. The complement of graphs especially the certain graphs are mentioned above are been determined of this number. Finally, the effective of deleting or adding an edge or deleting a vertex of the restrained domination number is discussed.

References

[1] Al-Harere M N and Abdlhusein M A 2020 Pitchfork domination in graphs *Discrete Mathematics Algorithms and Applications* **1 (**02) 2050025
[2] Al-Harere M N and Omran A A 2020 On binary operation graphs, *Boletim da SociedadeParanaense de Matematica* **38**(7) 59-67 doi: 10.5269/bspm.v38i7.44282
[3] Al-Harere M N and Omran A A 2018 Binary operation graphs *AIP conference proceeding* 2086 *Maltepe University Istanbul Turkey* 030008, 31 July - 6 Augusthttps://doi.org/10.1063/1.5095093
[4] Alwan I A and Omran A A 2020 Domination Polynomial of the Composition of Complete Graph and Star Graph *J. Phys Conf. Ser.* 1591 012048 doi:10.1088/1742 6596/1591/1/012048
[5] Berge C 1962 The theory of graphs and its applications *Methuen and Co London*
[6] Domke G S and Hatting J H et al. 1999 Restrained domination in graphs *Discrete Math* 203, 6169
[7] Hatting J H, Jonck E J Joubert and Plummer A R 2007 Total restrained domination in trees *Discrete Math.* **307** 1643-1650
[8] Haynes T w, Hedetniemi S T and slater(Eds.) P J 1998 Domination in Graphs Advanced Topices*Marecl Dekker New York*
[9] Ibrahim T A 2017 whole Domination in Graph *university of Babylon Iraq*
[10] A A Jabor A A and Omran A A 2019 Domination in Discrete Topology Graph *AIP Third International Conference of Science* (ICMS2019) **2183** 030006-1–030006-3doi: 10.1063/1.5136110
[11] Omran A A and Haneen H. Oda 2019 Hn-Domination in Graphs *Baghdad Science Journal* **16.1** 242-247

[12] Omran A A and Swadi T 2019 Observer Domination Number in Graphs *Jour of Adv Research in Dynamical & Control Systems* **11**, 01-Special Issue
[13] Ore O 1962 Theory of graphs *Amer. Math. Soc. Colloq. Pub., Providence* RI 38
[14] Rad N J 2008Results on Total Restrained Domination in Graphs *Int. J. contemp. Math. Sciences* **3** (8) 383-387
[15] De- xiang Me, Xue-gang chen and Liang sun 2005 On total restrained domination in graphs *Czechoslovak mathematical Journal* **55**(1) 165–173
[16] Yousif H J and Omran A A 2020 The Split Anti Fuzzy Domination in Anti Fuzzy Graphs *J. Phys.: Conf. Ser.* 1591 012054 doi:10.1088/1742-6596/1591/1/

Study subsets in Unite projective planes and their applications to Error-Correcting codes

Study subsets in finite projective planes and their applications to Error-Correcting codes

Najm Abdulzahra Makrib Al-Seraji and Zeina Tariq Numan

Department of Mathematics, College of Science, University of Mustansiriyah, Baghdad, Iraq

E-mail: aalzhrt71@gmail.com

Abstract. The main objective of this paper is to classify the special sets in the projective planes PG (2, t) with the values of t=17,31,37, and we found the arcs of the second degree (k,2) - arcs in PG (2, t) or third-degree (k,3)-arcs in PG(2,t), and the parameters of codes n, k, d was calculated and whether they are complete or incomplete, and the corresponding codes were formed.

1. Introduction

This paper depends on the subject of finite projective geometry and the creation of full arcs in $PG(2,t)$ when $t = 17, 31, 37$. In general $PG(2,t)$ contains $t^2 + t + 1$ points, $t^2 + t + 1$ lines, $t + 1$ point on a line and $t + 1$ line passes through the point, We have used the GAP program [1]. All theorems of the research are taken from [2] such Sticker Classified special arcs in $PG(2,t)$, and the ideas of the research are taken from Hirshfeld [3]. The *Special* $(k, 2)$-arcs *in* $PG\ (2, t), t \leq 29$ have already been classified and we will work on values higher than 29, as well as *Special* $(k, 3)$-arcs in $PG(2,t)$, $t \leq 13$, that have already been classified and we will work on values higher than 13. For more information see[4], [5], [6], [7], [8], [9], [10], [11]. Some definitions are useful to our research are given as follows:

Definition 1.1 [3]: The arc is a $(k;n)$ arc in PG$(2,t)$ is a set of k points no n of them of collinear.

Definition 1.2 [3]: A linear code (n,k,d,t)-code C is a subspace of $V(n,t)= (F_t)^n$, where the dimension of C is dim $C = k$, n represents the number of arc elements, d represents the number of arc elements for except intersections and t is the number of field elements

Definition 1.3 [3]: c_i represents the number of points out on the arc K which are passes through them i bisecant of arc K.

Definition 1.4 [3]: A $(k;r)$-arc is called complete if it is not contained within $(k+1;r)$-arc.

2. Special $(\mathbf{k}, \mathbf{3})$- arcs in PG $(\mathbf{2}, \mathbf{q}), \mathbf{q} = \mathbf{17}$

When $q \leq 13$ rated this work. The following results are interesting to the area of research:

Theorem 2.1 [2]: Let $a \in F_q . q\ odd$. Let $S^*(a)$ denote the set of points of $PG(2,q)$ with coordinates of the from $[a,\pm1,\pm1]$, $[\pm1,a,\pm1]$ or $[\pm1,\pm1,a]$, with independent choices of the sign. Let $S^*(\infty)$ be the set of points with coordinates$[1,0,0],[0,1,0] or [0,0,1]$. The set $S^*(a) = S^*(-a)$ is a $(12,3)$ arc $of\ PG(2,q)$ if and only if

$$a \notin \{0,\pm1,\pm\sqrt{-1}\}. \quad (1)$$

The set $S^*(a) \cup S^*(\infty)$ is a $(15,3)$ arc $if\ and\ only\ if\ a\ satisfies$ (3.1).
The set $S^*(a) \cup S^*(0)$ is a $(18,3)$ arc $if\ and\ only\ if\ a\ satisfies$ (3.1) and

$$a \neq \pm2,\ a^2 \pm a \pm 2 \neq 0. \quad (2)$$

The values of
$a \in \{\pm2,\pm3,\pm4,\pm5,\pm6,\pm7,\pm8\}$.
Take $= 2$.
The points of the arc $S^*(2)$ are

$[2,1,1],[15,1,1],[15,16,1],[2,16,1],[1,2,1],[16,15,1],$
$[16,2,1],[1,15,1],[9,9,1],[8,8,1],[9,8,1],[8,9,1]$
The value of the parameter $c_0 = 0$, The arc $S^*(2)$ is complete because $c_0 = 0$.
Shaped code parameters are equivalent to this arc.(n, k, d, q)-code
$n = 12, k = 3, d = n - 3 = 9, q = 17$, The code elements are generated by the matrix,

$$G = \begin{pmatrix} 2 & 15 & 15 & 2 & 1 & 16 & 16 & 1 & 9 & 8 & 9 & 8 \\ 1 & 1 & 16 & 16 & 2 & 15 & 2 & 15 & 9 & 8 & 8 & 9 \\ 1 & 1 & 1 & 1 & 1 & 1 & 1 & 1 & 1 & 1 & 1 & 1 \end{pmatrix}$$

The element of the code represents
$X = \lambda_1 R_1 + \lambda_2 R_2 + \lambda_3 R_3$
The elements $\lambda_1, \lambda_2, \lambda_3$, in F_{17} and R_1, R_2, R_3 are rows of generated matrix G
The size the code is $q^k = 17^3 = 49135$, some points of code are
$X_1 = [0,0,0,0,0,0,0,0,0,0,0,0]$
$X_2 = [1,1,1,1,1,1,1,1,1,1,1,1]$
$X_3 = [1,1,16,16,2,15,2,15,9,8,8,9]$
$X_4 = [2,15,15,2,1,16,16,1,9,8,9,8]$
$X_5 = [3,16,14,1,3,14,1,16,1,16,0,0]$
$X_6 = [3,16,16,3,2,0,0,2,10,9,10,9]$
$X_7 = [2,2,0,0,3,16,3,16,10,9,9,10]$
$X_8 = [4,0,15,2,4,15,2,0,2,0,1,1]$

The points of the arc $S^*(a) \cup S^*(\infty)$ are Where $a = 2$,
$[2,1,1],[15,1,1],[15,16,1],[2,16,1],[1,2,1],[16,15,1],[16,2,1],$
$[1,15,1],[9,9,1],[8,8,1],[9,8,1],[8,9,1],[1,0,0],[0,1,0],[0,0,1]$

The value of the parameter $c_0 = 4$, The arc $S^*(2) \cup S^*(\infty)$ is not complete because $c_0 \neq 0$.
Shaped code parameters equivalent to this arc, (n, k, d, q)- code
$n = 15$, $k = 3$, $d = n - 3 = 12$, $q = 17$,
The code elements are generated by the matrix,

$$G=\begin{pmatrix}2&15&15&2&1&16&16&1&9&8&9&8&1&0&0\\1&1&16&16&2&15&2&15&9&8&8&9&0&1&0\\1&1&1&1&1&1&1&1&1&1&1&1&0&0&1\end{pmatrix}$$

some points of code are
$X_1 = [0,0,0,0,0,0,0,0,0,0,0,0,0,0,0]$
$X_2 = [1,1,1,1,1,1,1,1,1,1,1,1,0,0,1]$
$X_3 = [1,1,16,16,2,15,2,15,9,8,8,9,0,1,0]$
$X_4 = [2,15,15,2,1,16,16,1,9,8,9,8,1,0,0]$
$X_5 = [3,16,14,1,3,14,1,16,1,16,0,0,1,1,0]$
$X_6 = [3,16,16,3,2,0,0,2,10,9,10,9,0,1,1]$
$X_7 = [2,2,0,0,3,16,3,16,10,9,9,10,1,2,1]$
$X_8 = [4,0,15,2,4,15,2,0,2,0,1,1,1,1,1]$

By the same way for $S^*(b) \cup S^*(\infty)$ with $b \in \{\pm3, \pm4, \pm5, \pm6, \pm7, \pm8\}$.
The values of $a \in \{\pm3, \pm4, \pm5, \pm6, \pm7, \pm8\}$
Which satisfies condition $a \neq \pm2$, $a^2 \pm a \pm 2 \neq 0$.
Take $a = 3$, the points of the arc $S^*(3) \cup S^*(0)$ are
$[3,1,1], [14,1,1], [14,16,1], [3,16,1], [1,3,1], [16,14,1], [16,3,1], [1,14,1], [6,6,1], [11,11,1],$
$[6,11,1], [11,6,1], [1,1,0], [16,1,0], [1,0,1], [16,0,1], [0,1,1], [0,16,1]$
The value of the parameter $c_0 = 7$, The arc $S^*(3)$ is not complete because $c_0 \neq 0$.
Shaped code parameters equivalent to this arc, (n, k, d, q)- code $n = 18$, $k = 3$, $d = n - 3 = 15$, $q = 17$,
The code elements are generated by the matrix,

$$G=\begin{pmatrix}3&14&14&3&1&16&16&1&6&11&6&11&1&16&1&16&1&0\\1&1&16&16&3&14&3&14&6&11&11&6&1&1&0&0&0&16\\1&1&1&1&1&1&1&1&1&1&1&1&0&0&1&1&1&1\end{pmatrix}$$

Some points of code are
$X_1 = [0,0,0,0,0,0,0,0,0,0,0,0,0,0,0,0,0,0]$
$X_2 = [1,1,1,1,1,1,1,1,1,1,1,1,0,0,1,1,1,1]$
$X_3 = [1,1,16,16,3,14,3,14,6,11,11,6,1,1,0,0,0,16]$
$X_4 = [3,14,14,3,1,16,16,1,6,11,6,11,1,16,1,16,0,0]$
$X_5 = [4,15,13,2,4,13,2,15,12,5,0,0,2,0,1,16,0,16]$
$X_6 = [4,15,15,4,2,0,0,2,7,12,7,12,1,0,2,0,1,1]$
$X_7 = [2,2,0,0,4,15,7,15,7,12,12,0,1,1,1,1,1,0]$
$X_8 = [5,16,14,3,5,16,3,16,13,6,1,1,2,0,2,0,2,0]$
By the same way for $S^*(k) \cup S^*(0)$ with $k \in \{\pm4, \pm5, \pm6, \pm7, \pm8\}$.
Another result is also important to our research:

Theorem 2.2 [2]: Let $q \equiv 1 \bmod 4$. Let $a, i \in F_q$,such that $i^2 = -1$. Let $S^*(a)$ be defined as in Theorem 2.1. Let I denote the set of six points whose coordinates are permutations of $[1, i, 0]$. (I is a subset of the conic $C: x^2 + y^2 + z^2 = 0$).
Then $S^*(a) \cup I$ is an $(18,2)$ arc $of\ PG(2,q)$ if and only if $a \notin \{0, \pm1, \pm i, \pm i \pm 1, \pm 2i,\}$.
The values of $a \in \{\pm2, \pm6, \pm7\}$.
And values $i = 4, 13$
The points of the arc I_1 are [13,1,0], [13,0,1], [4,1,0], [4,0,1], [0,4,1], [0,13,1].
The points of the arc I_2 are [4,1,0], [4,0,1], [13,1,0], [13,0,1], [0,13,1], [0,4,1].
is a subset of the conic $C: x^2 + y^2 + z^2 = 0$
The arcs $S^*(j) \cup I_1$, $S^*(j) \cup I_2$ are $(18,2)$ arc $of\ PG(2,q)$, $k \in \{\pm2, \pm6, \pm7\}$.

Where $a = 2$, the points of the arc $S^*(2)$ are:

$[2,1,1],[15,1,1],[15,16,1],[2,16,1],[1,2,1],[16,15,1],[16,2,1],[1,15,1],[9,9,1],[8,8,1],$
$[9,8,1],[8,9,1].$

Take $S^*(2) \cup I_1$, the value of the parameter $c_0 = 0$, The arc $S^*(2) \cup I_1$ is complete because $c_0 = 0$,
Parameters of the formed code equivalent to this arc , (n, k, d, q)- code $n = 18$, $k = 3$, $d = n - 3 = 15$, $q = 17$.
The code elements are generated by the matrix,

$$G = \begin{pmatrix} 2 & 15 & 15 & 2 & 1 & 16 & 16 & 1 & 9 & 8 & 9 & 8 & 13 & 13 & 4 & 4 & 0 & 0 \\ 1 & 1 & 16 & 16 & 2 & 15 & 2 & 15 & 9 & 8 & 8 & 9 & 1 & 0 & 1 & 0 & 4 & 13 \\ 1 & 1 & 1 & 1 & 1 & 1 & 1 & 1 & 1 & 1 & 1 & 1 & 0 & 1 & 0 & 1 & 1 & 1 \end{pmatrix}$$

some o points of code are
$X_1 = [0,0,0,0,0,0,0,0,0,0,0,0,0,0,0,0,0,0]$
$X_2 = [1,1,1,1,1,1,1,1,1,1,1,1,0,1,0,1,1,1]$
$X_3 = [1,1,16,16,2,15,2,15,9,8,8,9,1,0,1,0,4,13]$
$X_4 = [2,15,15,2,1,16,16,1,9,8,9,8,13,13,4,4,0,0]$
$X_5 = [3,16,14,1,3,14,1,16,1,16,0,0,14,13,5,4,4,13]$
$X_6 = [3,16,16,3,2,0,0,2,10,9,10,9,13,14,4,5,1,1]$
$X_7 = [2,2,0,0,3,16,3,16,10,9,9,10,1,1,1,1,5,14]$
$X_8 = [4,0,15,2,4,15,2,0,2,0,1,1,14,14,5,5,5,14]$
In the same way for $S^*(b) \cup I_1$ with $\in \{\pm 6, \pm 7\}$. And $S^*(k) \cup I_2$, $k \in \{\pm 2, \pm 6, \pm 7\}$

3. Special (k,2)- arcs in PG (2,q),q=31

The following results are interesting to the area of research:

Theorem 3.1 [2]: Let $a \in F_q$, q odd. Let $S^*(a)$ denote the set of points of $PG(2,q)$ with Coordinates of the from $[a, \pm 1, \pm 1]$, $[\pm 1, a, \pm 1]$ *or* $[\pm 1, \pm 1, a]$, with independent choices of the sign is a $(12,2)$ arc of $PG(2,q)$ if and only if then $S^*(a) = S^*(-a)$,
$a \notin \{0, \pm 1, \pm 2, \pm\sqrt{-1}, \pm\sqrt{-3}, \frac{1}{2}(\pm 1 \pm \sqrt{-7})\}$.
If these conditions hold, then, if $a^2 = -2$, the point of $S^*(a)$ lie on the conic C with equation
$C: x^2 + y^2 + z^2 = 0$,
Otherwise $S^*(a)$ is the disjoint union of three sets $C_0 \cap C_1, C_1 \cap C_2, C_2 \cap C_0$ of size 4 which are the pairwise intersections of the three conics C_0, C_1, C_2 with equations
$C_0: (a^2+1)x^2 = y^2 + z^2$,
$C_1: (a^2+1)y^2 = z^2 + x^2$,
$C_2: (a^2+1)z^2 = x^2 + y^2$,
The values of $a \in \{\pm 3, \pm 4, \pm 5, \pm 6, \pm 7, \pm 8, \pm 9, \pm 10, \pm 12, \pm 13, \pm 14, \pm 15\}$,
Take $a = 3$, the points of the arc $S^*(3)$ are:
$[3,1,1],[1,3,1],[21,21,1],[28,30,1],[30,3,1],[21,10,1],[3,30,1],[30,28,1],[10,21,1],[28,1,1],[1,28,1],[10,10,1]$
The values of the parameters c_i , $i = 0, \ldots, 6$, are respectively, $[c_0, \ldots, c_6] =$
$[90, 314, 371, 172, 32, 2, 0]$
The arc $S^*(3)$ is not complete because $c_0 \neq 0$.
shaped code parameters equivalent to this arc , (n, k, d, q)- code,
$n = 12$, $k = 3$, $d = n - 2 = 10$, $q = 31$,
The code elements are generated by the matrix,

$$G = \begin{pmatrix} 3 & 28 & 3 & 21 & 1 & 30 & 30 & 1 & 21 & 21 & 10 & 10 \\ 1 & 30 & 30 & 1 & 3 & 28 & 3 & 28 & 21 & 10 & 21 & 10 \\ 1 & 1 & 1 & 1 & 1 & 1 & 1 & 1 & 1 & 1 & 1 & 1 \end{pmatrix}$$

The element of the code represents $X = \lambda_1 R_1 + \lambda_2 R_2 + \lambda_3 R_3$
The elements $\lambda_1, \lambda_2, \lambda_3$, in F_{31} and R_1, R_2, R_3 are rows of generated matrix G
The size the code is $q^k = 31^3 = 297915$, some points of code are
$X_1 = [0,0,0,0,0,0,0,0,0,0,0,0]$
$X_2 = [1,1,1,1,1,1,1,1,1,1,1,1]$
$X_3 = [1,30,30,1,3,28,3,28,21,10,21,10]$
$X_4 = [3,28,3,21,1,30,30,1,21,21,10,10]$
$X_5 = [4,27,2,22,4,27,2,29,11,0,0,20]$
$X_6 = [4,29,4,22,2,0,0,2,22,22,11,11]$
$X_7 = [2,0,0,2,4,29,4,29,22,11,22,11]$
$X_8 = [5,28,3,23,5,28,3,30,12,1,1,21]$
Since $a^2 \neq -2$ so the points
$[21,21,1], [21,10,1], [10,21,1], [10,10,1]$ are belong to $C_0 \cap C_1$
$[1,3,1], [30,3,1], [30,28,1], [1,28,1]$ are belong to $C_2 \cap C_0$
$[3,1,1], [28,30,1], [3,30,1], [28,1,1]$ are belong to $C_1 \cap C_2$
In the same way for $S^*(b)$ with
$b \in \{\pm 4, \pm 5, \pm 6, \pm 7, \pm 8, \pm 9, \pm 10, \pm 12, \pm 13, \pm 14, \pm 15\}$,
Another result is also important to our research:

Theorem 3.2 [2]: Let $q = 0,1 \ or \ 4 \bmod 5$, q odd. Let $\tau = \frac{\sqrt{5}+1}{2}$. consider the following sets:
$R = \{[0,1,\pm\tau], [1,\pm\tau,0], [\pm\tau,0,1]\}$,
$S = [0,\pm\tau,\pm\tau^{-1}], [\pm\tau,\pm\tau^{-1},0], [\pm\tau^{-1},0,\pm\tau], [\pm 1,\pm 1,\pm 1]$.
The set R is a $(6,2)$ arc $of\ PG(2,q)$. The set S is a $(10,2)$ arc $of\ PG(2,q)$ if and only if $q \neq 0 \bmod 5$.
The values of $\tau = 13, 19$.
The points of the arc R when $\tau = 13$ are $[0,12,1], [0,19,1], [12,1,0], [19,1,0], [13,0,1], [18,0,1]$
The points of the arc R when $\tau = 19$ are $[0,18,1], [0,13,1], [1,19,0], [1,12,0], [19,0,1], [12,0,1]$
$\tau = 1$ Take the values of the parameters c_i, $i = 0, \ldots, 3$, are respectively,
$[c_0, c_1, c_2, c_3] = [572, 390, 15, 10]$
The arc R is not complete because $c_0 \neq 0$, shaped code parameters equivalent to this arc (n, k, d, q)- code,
$n = 6,\ k = 3,\ d = n - 2 = 4,\ q = 31,$
The code elements are generated by the matrix,

$$G = \begin{pmatrix} 0 & 0 & 12 & 19 & 13 & 18 \\ 12 & 19 & 1 & 1 & 1 & 0 \\ 1 & 1 & 0 & 0 & 1 & 1 \end{pmatrix}$$

some points of code are
$X_1 = [0,0,0,0,0,0]$
$X_2 = [1,1,0,0,1,1]$
$X_3 = [12,19,1,1,1,0]$
$X_4 = [0,0,12,19,13,18]$
$X_5 = [12,19,13,20,14,18]$
$X_6 = [1,1,12,19,14,19]$
$X_7 = [13,20,1,1,2,1]$
$X_8 = [13,20,13,20,15,19]$
By the same way for $\tau = 19$.

The points of the arc S when $\tau = 13$ are
$[1,1,1], [30,1,1], [1,30,1], [30,30,1], [0,14,1], [13,12,0], [20,0,1], [0,17,1], [17,1,0], [11,0,1]$
The points of the arc S when
$\tau 19$ are$[1,1,1], [30,1,1], [1,30,1], [30,30,1], [0,20,1], [19,18,0], [14,0,1], [0,11,1], [11,1,0], [17,0,1],$
Take $\tau = 13$
The values of the parameters c_i , $i = 0, \dots, 5$, are respectively,
$[c_0 , \dots, c_5] = [134 , 460 , 294 , 78 , 17, 0]$
The arc S is not complete because $c_0 \neq 0$.
shaped code parameters equivalent to this arc, (n , k , d , q)- code
$n = 10$, $k = 3$, $d = n - 2 = 8$, $q = 31$,
The code elements are generated by the matrix,

$$G = \begin{pmatrix} 1 & 30 & 1 & 30 & 0 & 13 & 20 & 0 & 17 & 11 \\ 1 & 1 & 30 & 30 & 14 & 12 & 0 & 17 & 1 & 0 \\ 1 & 1 & 1 & 1 & 1 & 0 & 1 & 1 & 0 & 1 \end{pmatrix}$$

some of point of code are
$X_1 = [0 , 0 , 0 , 0 , 0 , 0 , 0 , 0 , 0 , 0]$
$X_2 = [1 , 1 , 1 , 1 , 1 , 0 , 1 , 1 , 0 , 1]$
$X_3 = [1, 1, 30 , 30 , 14, 12, 0, 17, 1, 0]$
$X_4 = [1, 30, 1, 30, 0, 13, 20, 0, 17, 11]$
$X_5 = [1, 0, 0, 29, 14, 25, 20, 17, 18, 11]$
$X_6 = [2 , 0 , 2 , 0 , 1, 13, 21, 1, 17, 12]$
$X_7 = [2 , 2 , 0 , 0 , 15 , 12, 1, 18, 1, 1]$
$X_8 = [3, 1, 1, 30, 15, 25, 21, 18, 18, 12]$
In the same way for $\tau = 19$.

4. Special (k,2)- arcs in PG (2,q),q=37

The following results are interesting to the area of research:

Theorem 4.1 [2]: Let $q \equiv 1 \bmod 4$. Let $a, i \in F_q$, such that $i^2 = -1$. Let $S^*(a)$ be defined as in Theorem 3.1. Let I denote the set of six points whose coordinates are permutations of $[1, i, 0]$. (I is a subset of the conic $C : x^2 + y^2 + z^2 = 0$)
Then $S^*(a) \cup I$ is an $(18,2)$ arc $of\ PG(2, q)$ if and only if
$$a \notin \left\{0, \pm 1, \pm 2, \pm i, \pm 2i, \pm i\sqrt{3}, \pm i + 1, \frac{1}{2}\left(\pm 1 \pm i\sqrt{7}\right), \frac{1}{2}\left(\pm i \pm \sqrt{-5 \pm 4i}\right)\right\}$$
The values of $a \in \{\pm 3 , \pm 4 , \pm 10 , \pm 11 , \pm 13 , \pm 14 , \pm 15 , \pm 17 , \pm 18 \}$
And values $i = 6, 31$
The points of the arc I_1 are $[31,1,0], [31,0,1], [6,1,0], [6,0,1], [0,6,1], [0,31,1]$
The points of the arc I_2 are $[6,1,0], [6,0,1], [31,1,0], [31,0,1], [0,31,1], [0,6,1]$
is a subset of the conic $C : x^2 + y^2 + z^2 = 0$
The arcs $S^*(k) \cup I_1$, $S^*(k) \cup I_2$ are $(18,2)$ arc $of\ PG(2, q)$
$k \in \{\pm 3, \pm 4 , \pm 10 , \pm 11 , \pm 13 , \pm 14 , \pm 15, \pm 17 , \pm 18\}$,
Where $a = 3$, the points of the arc $S^*(3)$ are
$[3, 1, 1], [1 , 3, 1], [25,25,1], [34,36,1], [36, 34,1], [25,12,1], [3,36,1] , [36,3,1], [12,25,1], [34,1,1], [1,34,1] , [12,12,1]$
Take $S^*(3) \cup I_1$,
The values of the parameters c_i , $i = 0, \dots, 9$, are respectively,
$[c_0 , \dots, c_9] = [193, 480, 438, 195, 71, 9, 3, 0, 0, 0]$
The arc $S^*(3) \cup I_1$ is not complete because $c_0 \neq 0$.
shaped code parameters equivalent to this arc, (n , k , d , q)- code

$n = 18$, $k = 3$, $d = n - 2 = 16$, $q = 37$,
The code elements are generated by the matrix,

$$G = \begin{pmatrix} 3 & 1 & 25 & 34 & 36 & 25 & 3 & 36 & 12 & 34 & 1 & 12 & 31 & 31 & 6 & 6 & 0 & 0 \\ 1 & 3 & 25 & 36 & 34 & 12 & 36 & 3 & 25 & 1 & 34 & 12 & 1 & 0 & 1 & 0 & 6 & 31 \\ 1 & 1 & 1 & 1 & 1 & 1 & 1 & 1 & 1 & 1 & 1 & 1 & 0 & 1 & 0 & 1 & 1 & 1 \end{pmatrix}$$

The elements λ_1 , λ_2 , λ_3, in F_{37} and R_1, R_2, R_3 are rows of generated matrix G
The size the code is $q^k = 37^3 = 506535$, some points of code are
$X_1 = [0, 0, 0, 0, 0, 0, 0, 0, 0, 0, 0, 0, 0, 0, 0, 0, 0, 0]$
$X_2 = [1, 1, 1, 1, 1, 1, 1, 1, 1, 1, 1, 1, 1, 1, 1, 1, 1, 1]$
$X_3 = [1, 3, 25, 36, 34, 12, 36, 3, 25, 1, 34, 12, 1, 0, 1, 0, 6, 31]$
$X_4 = [3, 1, 25, 34, 36, 25, 3, 36, 12, 34, 1, 12, 31, 31, 6, 6, 0, 0]$
$X_5 = [4, 4, 13, 33, 33, 0, 2, 2, 0, 35, 35, 24, 32, 31, 7, 6, 6, 31]$
$X_6 = [4, 4, 26, 35, 0, 26, 4, 0, 13, 35, 2, 13, 31, 32, 6, 7, 1, 1]$
$X_7 = [2, 4, 26, 0, 35, 13, 0, 4, 26, 2, 35, 13, 1, 1, 1, 1, 7, 32]$
$X_8 = [5, 5, 14, 34, 34, 1, 3, 3, 1, 36, 36, 25, 33, 32, 8, 7, 7, 32]$
In the same way for $S^*(j) \cup I_1$ with $j \in \{\pm 4, \pm 10, \pm 11, \pm 13, \pm 14, \pm 15, \pm 17, \pm 18\}$,
And $S^*(w) \cup I_2$, $w \in \{\pm 3, \pm 4, \pm 10, \pm 11, \pm 13, \pm 14, \pm 15, \pm 17, \pm 18\}$,
Another result is also important to our research:

Theorem 4.2 [2]: Let $q \equiv 1 \bmod 4$. Let $i \in F_q$ such that $i^2 = -1$. Let $S^*(1)$ denote the set of points of $PG(2, q)$ with coordinates $[1,1,1], [-1,1,1], [1,-1,1]$ *or* $[1,1,-1]$. Let I be defined as in Theorem 4.1. Then $S^*(1) \cup I$ *is* a $(10,2)$ arc *of* $PG(2, q)$ if and only if $i^2 \neq \pm 2$.
The point of the arc $S^*(1)$ are $[1,1,1], [36,1,1], [1,36,1], [36,36,1]$,
The arcs $S^*(k) \cup I_1$, $S^*(k) \cup I_2$ are $(10,2)$ arc *of* $PG(2, q)$
The points of the arc I_1 are $[31,1,0], [31,0,1], [6,1,0], [6,0,1], [0,6,1], [0,31,1]$
The points of the arc I_2 are $[6,1,0], [6,0,1], [31,1,0], [31,0,1], [0,31,1], [0,6,1]$
Take $S^*(1) \cup I_1$. The values of the parameters c_i , $i = 0, \dots, 5$, are respectively,
$[c_0, \dots, c_5] = [772, 515, 92, 17, 1, 0]$
The arc $S^*(1) \cup I_1$ is not complete because $c_0 \neq 0$.
shaped code parameters equivalent to this arc, (n, k, d, q)- code
$n = 10$, $k = 3$, $d = n - 2 = 8$, $q = 37$,
The code elements are generated by the matrix,

$$G = \begin{pmatrix} 1 & 36 & 1 & 36 & 31 & 31 & 6 & 6 & 0 & 0 \\ 1 & 1 & 36 & 36 & 1 & 0 & 1 & 0 & 6 & 31 \\ 1 & 1 & 1 & 1 & 0 & 1 & 0 & 1 & 1 & 1 \end{pmatrix}$$

some points of code are
$X_1 = [0, 0, 0, 0, 0, 0, 0, 0, 0, 0]$
$X_2 = [1, 1, 1, 1, 0, 1, 0, 1, 1, 1]$
$X_3 = [1, 1, 36, 36, 1, 0, 1, 0, 6, 31]$
$X_4 = [1, 36, 1, 36, 31, 31, 6, 6, 0, 0]$
$X_5 = [2, 0, 0, 35, 32, 31, 7, 6, 6, 31]$
$X_6 = [2, 0, 2, 0, 31, 32, 6, 7, 1, 1]$
$X_7 = [2, 2, 0, 0, 1, 1, 1, 1, 7, 32]$
$X_8 = [3, 1, 1, 36, 32, 32, 7, 7, 7, 32]$
By the same way for $S^*(1) \cup I_2$

References

[1] GAP Group 2018 GAP References manual URL http://www.gap-system Org
[2] Sticker H 2012 Classification of Arcs in Small Desarguesian Projective Planes *PhD thesis* University Gent
[3] Hirschfeld J W P 1998 Projective geometries over finite *fields 2nd Edition Oxford Mathematical Monographs* (The Clarendon Press, Oxford University Press) New York.
[4] Hirschfeld J W P and Thas J A 1991 General galois geometries *Oxford: Clarendon Press* **1378**
[5] Hirschfeld J W P 1985 Finite Projective Spaces of Three Dimensions (*Oxford University Press, Oxford)*
[6] Alabdullah S and Hirschfeld J W P 2019 A new bound for the smallest complete $(k, 2)$ arc in $PG(2, q)$ Designs *Codes and Cryptography* **87**(23) **679**-683
[7] Hirschfeld J W P and Thas J A 2016) Hermitian varieties. *In General Galois Geometries* 57-97 (Springer, London)
[8] Hirschfeld J W P and Voloch J F 2015 Group –arcs of prime power order on cubic curves *Finite Geometry and Combinatorics* **191** 177-185
[9] Pichanick E V D and Hirschfeld J W P 2016 Bounded for arcs of arbitrary degree in finite Desarguesian planes, *Journal of Combinatorial Designs* **24**(4) 184-196
[10] Al-Seraji N A M 2010 The Geometry of The Plane of order Seventeen and its Application to Error–correcting codes *Ph.D Thesis* University of Sussex UK
[11] Al-Seraji N A M, Bakeet A and Jafar Z S 2020 Study of orbits on the finite projective plane *Journal of Interdisciplinary Mathematics* **23**(6) 1187-1195

A 4D hyperchaotic Sprott S system with multistability and hidden attractors

A 4D hyperchaotic Sprott S system with multistability and hidden attractors

Maryam A. Al-hayali and Saad Fawzi Al-Azzawi

Department of Mathematics, College of Computer Science and Mathematics, University of Mosul, Mosul, Iraq

E-mail: saad_alazawi@uomosul.edu.iq

Abstract. This paper derived a new simple hyperchaotic system from the famous Sprott, S system via the linear state feedback control. Compared with the available systems, the new system has eight terms, one constant, two parameters control, and a single quadratic nonlinear term. So this system is considered a simple relying on the number of terms and nonlinearities. The proposed system without equilibrium points and exhibits chaotic hidden attractors. Also, multistability or coexisting attractors are found through experimental simulations using phase portraits and the Lyapunov spectrum. Finally, anti-synchronization is implemented in the new system.

1. Introduction

In 2011, Leonov et al. introduced a new concept in the behavior of dynamic systems based on the attractors of these systems and it is classified into two categories: hidden and self-excited attractors [1]. Most of the famous traditional systems such as Lorenz 1963, Rossler 1976, Chen 1999, and Liu systems 2004 have self-excited attractors [2-6]. Whereas the hidden attractor occur sin three cases; systems with stable equilibrium points [7-9], no-equilibrium points [10-16], many or line equilibria [17]. Hidden attractors are difficult to discover compared with self-excited attractors, since the location of the equilibrium points not necessary as it is in self-excited attractors.

In literature, many works have been concentrated on the discovery of simple chaotic and hyperchaotic systems with no equilibrium points. In 1994, the researcher Sprott presented 19 systems of three-dimensional that were classified into two groups based on the number of terms and nonlinearities, the first group of systems consisting of five terms with two nonlinear (A-E) whereas the second group consisting of six terms with one nonlinear (F-S) [18]. The number of terms and number of quadratic or cubic nonlinearities are important factors within the simplest systems. In 2011, Wei reported 3D chaotic system without equilibrium points containing five terms which include two [11]. In 2012, Wang et al. [15] presented a no-equilibrium 4D hyperchaotic system from on the Sprott A system, this system has a total of nine terms including five nonlinearities. In 2013, Jafari et al. [19] proposed 17 systems without equilibrium points with quadratic nonlinearities. In 2014, Wei et al. introduced a no-equilibrium 4D hyperchaotic system which has a total of eight terms, including two nonlinearities [20]. In 2019, Zhang and Zeng reported a no-equilibrium simple 3D system has a quadratic term and a square nonlinrartlty [21]. More recently, Zhang et al. in 2020, present a new simple 3D system without equilibrium points have six terms without any nonlinear term [22].

Recently, many synchronization phenomena have implementation of these systems due to their important applications in such as engineering [23, 24], and encryption [25-28]. Various schemes of synchronization were reported such as complete synchronization (CS) [2, 3, 29, 30], anti-synchronization (AS) [31-33], hybrid synchronization (HS) [34-36], projective synchronization (PS) [32-34].
The following points summarize the main contribution of this work, the proposed system as below:

(i) A 4D simple hyperchaotic Sprott S is constructed from the famous 3D Sprott-S system.
(ii) Without equilibrium point.
(iii) Consists of eight terms containing one constant two parameters control and one nonlinear term. So it can be considered one of the simplest systems.
(iv) Exhibit coexisting of attractors.
(v) Implementing the phenomenon of anti-synchronization of this system.

2. Dynamics of the 4D hyperchaotic Sprott S system

The Sprott S system [18] is depicted as:

$$\begin{cases} \dot{x} = -x - 4y, \\ \dot{y} = x + z^2, \\ \dot{z} = 1 + x\,, \end{cases} \tag{1}$$

in which $[x, y, z]^T \in R^3$ is a state vector. Based on the state feedback control [37, 38] by adding a linear controller to the second equation of (1), a new simple 4D chaotic quadratic system is obtained as:

$$\begin{cases} \dot{x} = -x - 4y, \\ \dot{y} = x + z^2 + aw, \\ \dot{z} = 1 + x\,, \\ \dot{w} = -by, \end{cases} \tag{2}$$

in which $[x, y, z, w]^T \in R^4$ is state vector. The parameters a and b are two positive constants. This system has eight terms with six linear terms, single quadratic nonlinearity, and one constant. With $a = 0.01$, $b = 0.1$ and $x(0) = (0.1, 0.1, 0.1, 0.1)^T$, this is system exhibit chaotic hidden attractors as shown in Figure 1.

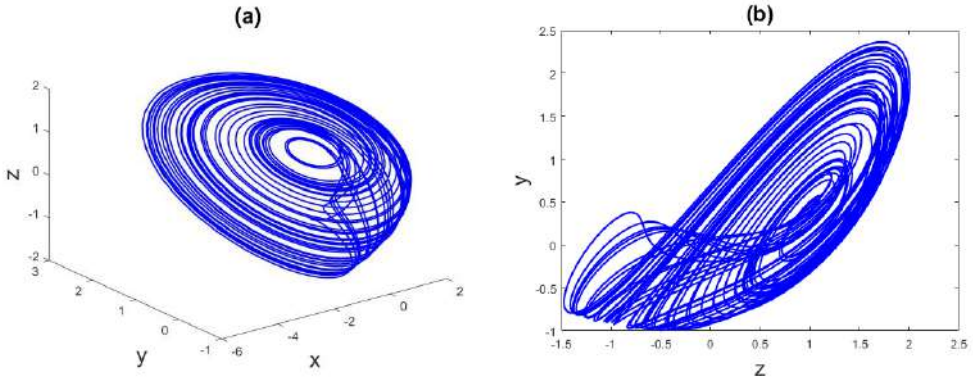

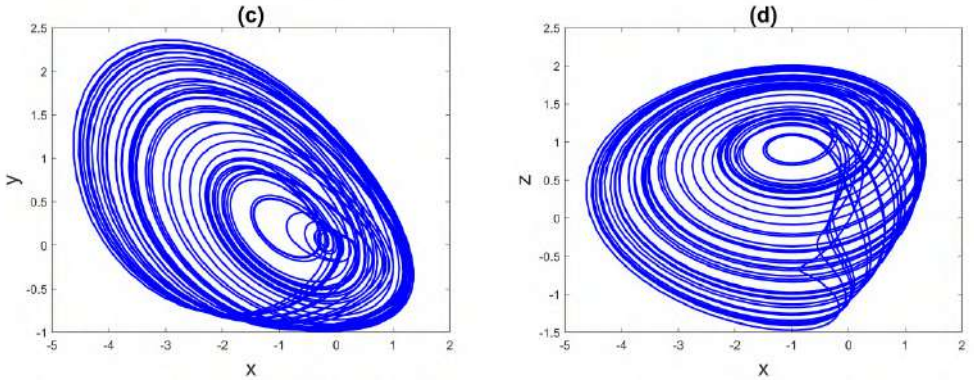

Figure 1. The chaotic hidden attractors of system (2) in: (**a)** $x-y-z$ space, (**b**): $y-z$ plane, (**c**): $x-y$ plane, and (**d**): $x-z$ plane.

2.1 Equilibrium points and Stability

The equilibrium points are established by Solving the following equations

$$\begin{cases} -x-4y=0 \\ x+z^2+au=0 \\ 1+x=0 \\ -by=0 \end{cases} \tag{3}$$

From the third and fourth equations of (3), it is seen that $x=1, y=0$, respectively. This leads to a contradiction with the first equation of (3). Consequently, the system (2) without equilibrium points concludes that this system with hidden attractors.

2.2 Lyapunov exponents and dissipativity

Wolf Algorithm has received increasing attention over the past decades due to the applications of calculating Lyapunov exponents (LE_S). With parameters $a=0.02$, $b=0.001$ and the initial condition $(0.5,0.5,0.5,0.5)^T$, step $\Delta t=0.25$, observation time $T=300$, the LE_S of the 4D system (2) are numerically obtained in MATLAB simulation as

$$\begin{cases} LE_1=0.1658 \\ LE_2=0 \\ LE_3=-0.0299 \\ LE_4=-1.1353 \end{cases} \tag{4}$$

Figure 2. depict the corresponding Lyapunov spectrum of (4) and the Lyapunov dimension (Kaplan-Yorke dimension) [17] of this system is calculated as

$$D_{LE}=j+\frac{1}{|LE_{j+1}|}\sum_{i=1}^{j}LE_i=3+\frac{LE_1+LE_2+LE_3}{|LE_4|}=3.1197$$

Since that the sum of the Lyapunov exponents ($\sum \mathrm{LE}_S=-1$) is negative, which indicate its dissipative system and meanwhile the divergence of the proposed system is equal (-1) i.e.

$$\nabla v=\frac{\partial \dot{x}}{\partial x}+\frac{\partial \dot{y}}{\partial y}+\frac{\partial \dot{z}}{\partial z}+\frac{\partial \dot{u}}{\partial u}=-1$$

Which is equal or almost to the sum of the Lyapunov exponents. So, that they fulfill the Lyapunov exponents (4) such as $\sum \mathrm{LE}_S=\nabla v$.

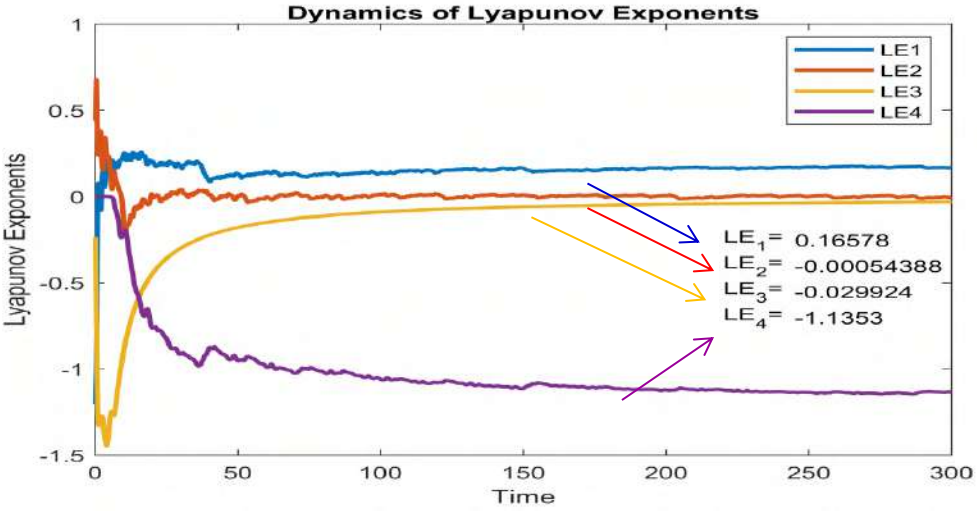

Figure 2. Lyapunov spectrum of the system (2) for $a = 0.02, b = 0.001$.

With various values of the system's parameters and various initial, Tables 1-2 depicts more details about calculating LE_S.

Table 1. LE_S of system (2) for $a = 0.02$ with varying the b and $(0.5, 0.5, 0.5, 0.5)^T$.

No.	b	LE_S	Sum of LE_S	Sign of the LE_S
1.	0.001	$0.1658, -0.0005, -0.03, -1.1353$	-1	$(+,0,-,-)$
2.	0.004	$0.1886, 0.0004, -0.0253, -1.1637$	-1	$(+,0,-,-)$
3.	0.005	$0.1621, 0.0004, -0.0246, -1.1379$	-1	$(+,0,-,-)$
4.	0.0002	$0.1942, 0.0009, -0.0353, -1.1599$	-1.0001	$(+,0,-,-)$
5.	0.0006	$0.1903, 0.0005, -0.0316, -1.1592$	-1	$(+,0,-,-)$
6.	0.0008	$0.1469, 0.0005, -0.0307, -1.1168$	-1.0001	$(+,0,-,-)$

Table 2. LE_S of system (2) for $b = 0.04$ with varying the a and $(0.7, 0.7, 0.7, 0.7)^T$.

No.	a	LE_S	Sum of LE_S	Sign of the LE_S
1.	0.006	$0.1964, 0.0009, -0.0165, -1.1808$	-1	$(+,0,-,-)$
2.	0.0004	$0.2103, 0.0003, -0.0165, -1.194$	-0.9999	$(+,0,-,-)$
3.	0.0006	$0.1849, -0.0001, -0.0165, -1.1682$	-0.9999	$(+,0,-,-)$
4.	0.0008	$0.1954, -0.0007, -0.0165, -1.1782$	-1	$(+,0,-,-)$

It is seen from Tables 1-2, although the proposed system has four dimensions, this extended dimension is one of the important requirements for generating hyperchaotic attractors. But we don't get $(+,+,0,-)$ sign of LE_S which indicates its the system (2) with chaotic hidden attractors. Also, the sum of the LE_S is almost equal to (-1) ,and that matches with divergence.

3. Multistability behavior of the proposed system

Coexisting attractors or Multistability means that the dissipative system has different trajectories under the same set of parameters and different combinations of and initial values [14]. The proposed system has multistability behavior or coexistence of chaotic hidden attractors. All of Figures 3. and 4., exhibit multistability phenomena which include four different hidden attractors with various initial values. With the parameters are set as $a = 8$, $b = 80$ and initial values $[-2.7, 2.7, 2.7, 2.7]^T$(red) and $[2.7, 2.7, 2.7, 2.7]$ (blue) as shown in Figure 3.a whereas in Figure 3.b with initial values $[-10.8, 2.7, 2.7, 2.7]^T$(red) and $[-0.1, 2.7, 2.7, 2.7]$ (blue). Under the parameters $a = 5$, $b = 20$, with

initial values with initial values $[-0.5,-0.5,-0.5,-5]^T$(red) and $[-0.5,-0.5,-0.5,-2]$ (blue) as shown in Figure 4.a whereas the initial values are $[-0.5,-0.5,-0.5,-5]^T$(red) and $[-0.5,-0.5,-0.5,-2]$ as shown in Figure 4.b.

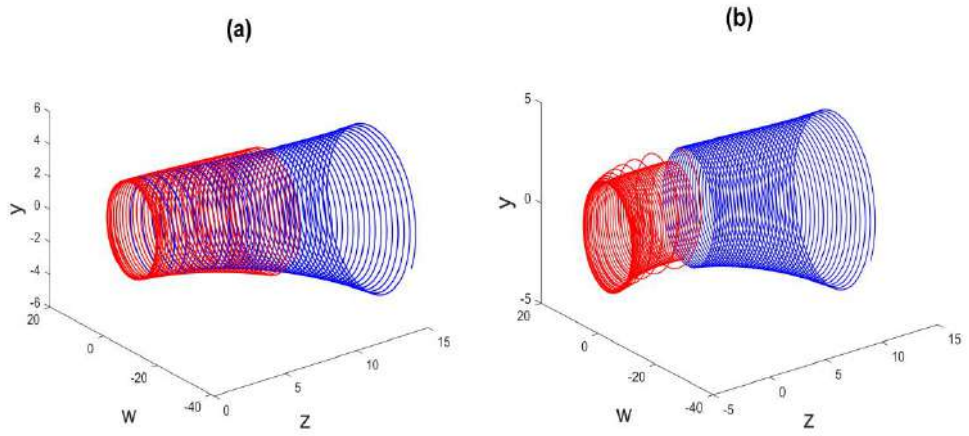

Figure 3. Coexistences of two different attractors for system (2) with $a = 8$, $b = 80$ and initial conditions $y(0) = z(0) = w(0) = 2.7$. (a) coexistences attractors with $x(0) = -2.7$ (red) and $(0) = 2.7$ (blue), (b) coexistences attractors with $x(0) = -10..8$ (red) and $(0) = -0.1$.

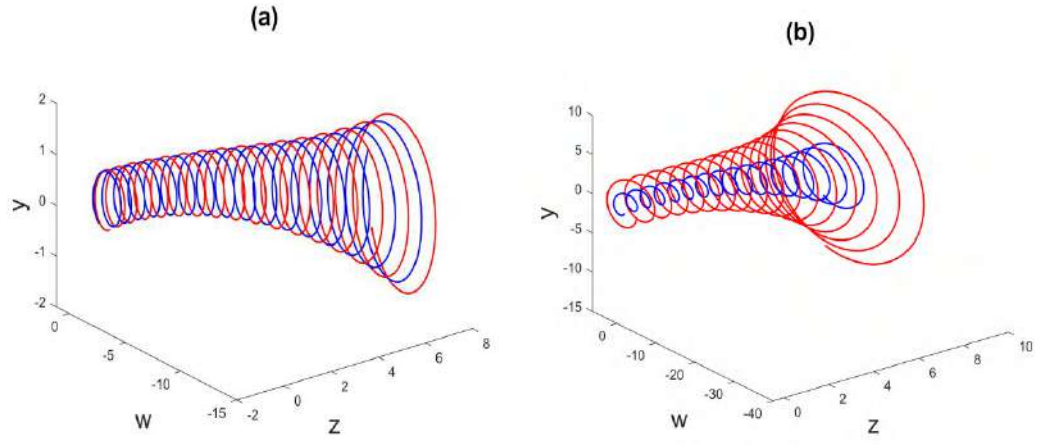

Figure 4. Coexistences of two different attractors for system (2) with $a = 5$, $b = 20$ and initial conditions conditions $x(0) = y(0) = z(0) = -0.5$. (a) coexistences attractors with $w(0) = -0.5$ (red) and $w(0) = 0.5$ (blue), (b) coexistences attractors with $w(0) = -5$ (red) and $w(0) = -2$ (blue).

4. Anti-synchronization between identical new systems

In this section, anti-synchronization is realized between two identical system (2) drive and response systems which described as

$$\dot{x} = Ax + f(x) \quad (5)$$

$$\dot{y} = By + g(y) + U \quad (6)$$

In which $x, y \in R^4$ are the state variables, $A, B \epsilon R^{4\times4}$ are matrices of system's parameters, $f, g: R^n \rightarrow R^n$ are nonlinear functions, $U \in R^4$ is nonlinear controller. The system (2) can be modeled as

$$\begin{bmatrix}\dot{x}_1\\ \dot{x}_2\\ \dot{x}_3\\ \dot{x}_4\end{bmatrix} = \underbrace{\begin{bmatrix}-1 & -4 & 0 & 0\\ 1 & 0 & 0 & a\\ 1 & 0 & 0 & 0\\ 0 & -b & 0 & 0\end{bmatrix}}_{A}\begin{bmatrix}x_1\\ x_2\\ x_3\\ x_4\end{bmatrix} + \underbrace{\begin{bmatrix}0 & 0 & 0\\ 1 & 0 & 0\\ 0 & 1 & 0\\ 0 & 0 & 0\end{bmatrix}\begin{bmatrix}x_3^2\\ 1\\ 0\end{bmatrix}}_{f(x)} \tag{7}$$

$$\begin{bmatrix}\dot{y}_1\\ \dot{y}_2\\ \dot{y}_3\\ \dot{y}_4\end{bmatrix} = \underbrace{\begin{bmatrix}-1 & -4 & 0 & 0\\ 1 & 0 & 0 & a\\ 1 & 0 & 0 & 0\\ 0 & -b & 0 & 0\end{bmatrix}}_{B}\begin{bmatrix}y_1\\ y_2\\ y_3\\ y_4\end{bmatrix} + \underbrace{\begin{bmatrix}0 & 0 & 0\\ 1 & 0 & 0\\ 0 & 1 & 0\\ 0 & 0 & 0\end{bmatrix}\begin{bmatrix}y_3^2\\ 1\\ 0\end{bmatrix}}_{g(y)} + \underbrace{\begin{bmatrix}u_1\\ u_2\\ u_3\\ u_4\end{bmatrix}}_{U} \tag{8}$$

It clear that $A = B$ due to the anti-synchronization between identical system (2). Defined the error dynamics as $e_i = y_i - \alpha x_i$, where $\alpha = -1$ is scaling factor and satisfied the following condition:

$$\lim_{t\to\infty} e_i(t) = 0 \tag{9}$$

The error dynamics system yields as the following:

$$\begin{cases}\dot{e}_1 = -e_1 - 4e_2 + u_1\\ \dot{e}_2 = e_1 + ae_4 + e_3^2 - 2x_3y_3 + u_2\\ \dot{e}_3 = 2 + e_1 + u_3\\ \dot{e}_4 = -be_2 + u_4\end{cases} \tag{10}$$

Desing controller as:

$$\begin{cases}u_1 = -e_3\\ u_2 = 3e_1 - e_2 + 2x_3y_3\\ u_3 = -2 - e_3 - e_2e_3\\ u_4 = -e_4\end{cases} \tag{11}$$

Substitute controller (11) into (10) we obtain:

$$\begin{cases}\dot{e}_1 = -e_1 - 4e_2 - e_3\\ \dot{e}_2 = 4e_1 - e_2 + ae_4 + e_3^2\\ \dot{e}_3 = e_1 - e_3 - e_2e_3\\ \dot{e}_4 = -be_2 - e_4\end{cases} \tag{12}$$

Construct Lyapunov function as

$$V(e_i) = {e_i}^T P e_i \;\Rightarrow\; V(e_i) = \begin{bmatrix}e_1 & e_2 & e_3 & e_4\end{bmatrix}\underbrace{\begin{bmatrix}0.5 & 0 & 0 & 0\\ * & 0.5 & 0 & a\\ * & * & 0.5 & 0\\ * & * & * & 0.05\end{bmatrix}}_{P}\begin{bmatrix}e_1\\ e_2\\ e_3\\ e_4\end{bmatrix} \tag{13}$$

The symbol (*) which indicates symmetry in the matrix. The time derivative of the above function $V(e_i)$ gives

$$\dot{\boldsymbol{V}}(e_i) = e_1\dot{e}_1 + e_2\dot{e}_2 + e_3\dot{e}_3 + 0.2\, e_4\dot{e}_4$$

$$\dot{V}(e) = e_1(-e_1 - 4e_2 - e_3) + e_2(4e_1 - e_2 + ae_4 + e_3^2) + e_3(e_1 - e_3 - e_2e_3) + \frac{1}{10}\, e_4(-be_2 - e_4)$$

$$\dot{V}(e_i) = -e_1^2 - e_2^2 - e_3^2 - \frac{1}{10}e_4^2 = -[e_1 \quad e_2 \quad e_3 \quad e_4]\underbrace{\begin{bmatrix} 1 & 0 & 0 & 0 \\ * & 1 & 0 & 0 \\ * & * & 1 & 0 \\ * & * & * & \frac{1}{10} \end{bmatrix}}_{Q}\begin{bmatrix} e_1 \\ e_2 \\ e_3 \\ e_4 \end{bmatrix} = -e_i{}^T Q\, e_i \qquad (14)$$

where $Q = diag(1,1,1,\frac{1}{10})$, leads to $Q > 0$. Consequently, $\dot{V}(e_i) < 0$ on R^4. The controller (11) realize the anti-synchronization.

Now, the initial values as $(2,7,10,-5)$ and $(10,1,3,8)$ to illustrate the anti-synchronization that happened between (7) and (8) numerically. Figure 5. validate our theoretical results.

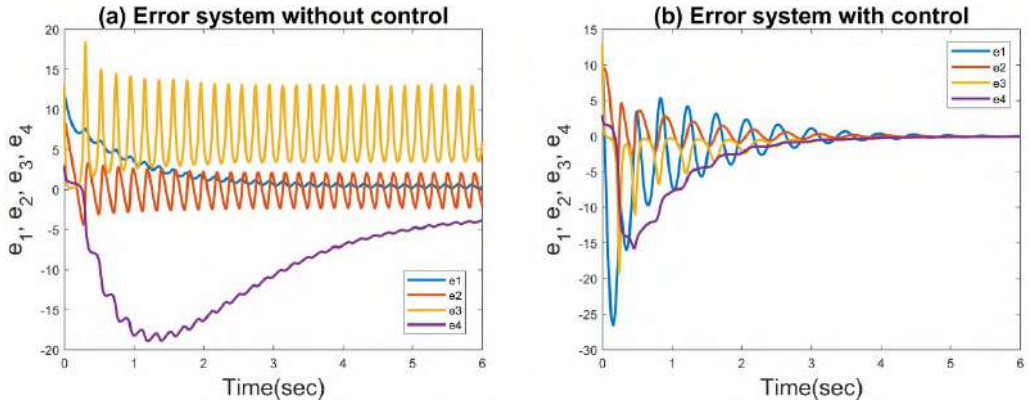

Figure 5. Anti-synchronization errors with controllers (11).

5. Conclusions

A simple 4D Sprott S system without equilibrium point and coexistence of attractors constructed from 3D Sprott-S system via a state feedback controller. This system consists of eight terms, including one constant, two parameters control, and a single quadratic nonlinear term. Besides, chaotic hidden behaviors have been discovered. Finally, anti-synchronization (AS) between two new identical systems realized via nonlinear control by using linearization and Lyapunov stability tools.

References

[1] Leonov G A et al 2011 Localization of hidden Chia's attractors *Phys Lett A* **375**(23) 2230-2233
[2] Park J H 2005 Chaos synchronization of a chaotic system via nonlinear control *Chaos Solitons and Fractals* **25** 579-584
[3] Chen H K 2005 Global chaos synchronization of new chaotic systems via nonlinear control *Chaos Solitons and Fractals* **23** 1245-1251
[4] Al-Azzawi S F et al 2020 Stability of Lorenz system at the second equilibria point based on Gardano's method *Journal of Physics: Conference Series* **1477**(2) 022009
[5] Abed K A 2020 Controlling of jerk chaotic system via linear feedback control strategies *Indonesian Journal of Electrical Engineering and Computer Science* **20**(1) 370-378
[6] AL-Azzawi S F et al 2020 Chaotic Lorenz system and it's suppressed *Journal of Advanced Research in Dynamical and Control Systems* **12**(2) 548-555
[7] Kingni S T, Jafari S, Simo H and Woafo P 2014 Three-dimensional chaotic autonomous system with only one stable equilibrium: Analysis circuit design parameter estimation control synchronization and its fractional-order form *The European Physical Journal Plus* **129**(5) 76
[8] Deng Q, Wang C and Yang 2020 Four-wing hidden attractors with one stable equilibrium point *International Journal of Bifurcation and Chaos* **30**(6) 2050086

[9] Singh J P, K Rajagopal and B K Roy 2018 A new 5D hyperchaotic system with stable equilibrium point transient chaotic behavior and its fractional-order form *Pramana* **91**(3) 33
[10] Zhang S, Zeng Y, Li Z,Wang M, Zhang X and Chang D 2018 A novel simple no-equilibrium chaotic system with complex hidden dynamics *International Journal of Dynamics and Control* **6**(4) 1465–1476
[11] Wei Z, 2011 Dynamical behaviors of a chaotic system with no equilibria *Physics Letters A* **376**(2) 102-108
[12] Zhou W, Wang G and Shen Y, Yuan F and Yu S, Hidden 2018 coexisting attractors in a chaotic system without equilibrium point *International Journal of Bifurcation and Chaos* **28**(10) 1830033
[13] Vaidyanathan S, Pham V T and Volos C K 2015 A 5-D hyperchaotic Rikitake dynamo system with hidden attractors *The European Physical Journal Special Topics* **224**(8) 1575-1592
[14] Singh J P and Roy B K 2018 Multistability and hidden chaotic attractors in a new simple 4-D chaotic system with chaotic 2-torus behavior *International Journal of Dynamics and Control* **6**(2) 529-538
[15] Wang Z, Cang S, Ochola E O, and Sun Y 2012 A hyperchaotic system without equilibrium *Nonlinear Dynamics* **69**(1-2) 531-537
[16] Zhang S, Zeng Y, Li Z, Wang M, and Xiong L 2018 Generating one to four-wing hidden attractors in a novel 4D no-equilibrium chaotic system with extreme multistability *Chaos: An Interdisciplinary Journal of Nonlinear Science* **28**(1) 013-113
[17] Singh and Roy B K 2017 Coexistence of asymmetric hidden chaotic attractors in a new simple 4-D chaotic system with curve of equilibria *Optik* **145** 209-217
[18] J C Sprott 1994 Some simple chaotic flow *Physical Review E* **50**(2) 647
[19] Jafari S, Sprott J C and Golpayegani S M R H 2013 Elementary quadratic chaotic flows with no equilibria *Physics Letters A* **377**(9) 699-702
[20] Wei Z, Wang R and Liu A A 2014 New finding of the existence of hidden hyperchaotic attractors with no equilibria *Mathematics and Computers in Simulation* **100** 13-23
[21] Zhang S and Zeng Y 2019 A simple Jerk-like system without equilibrium: Asymmetric coexisting hidden attractors bursting oscillation and double full Feigenbaum remerging trees *Chaos Solitons & Fractals* **120** 25-40
[22] Zhang S, Wangand X and Zeng Z 2020 A simple no-equilibrium chaotic system with only one signum function for generating multidirectional variable hidden attractors and its hardware implementation *Chaos: An Interdisciplinary Journal of Nonlinear Science* **30**(5) 053-129
[23] Ahmad A A 2020 By using a new iterative method to the generalized system Zakharov-Kuznetsov and estimate the best parameters via applied the Pso algorithm *Indonesian Journal of Electrical Engineering and Computer Science* **19**(2) 1055-1061
[24] Abed K A 2020 Solving Kuramoto-Sivashinsky equation by the new iterative method and estimate the optimal parameters by using PSO algorithm *Indonesian Journal of Electrical Engineering and Computer Science* **19**(2) 709-714
[25] Al-Kateeb Z N and Jader M 2020 Encryption and hiding text using DNA coding and hyperchaotic system *Indonesian Journal of Electrical Engineering and Computer Science* **19**(2) 766-774
[26] Al-Kateeb Z N and Mohammed S J 2020 Encrypting an audio file based on integer wavelet transform and hand geometry *TELKOMNIKA Telecommunication Computing Electronics and Control* **18**(4) 2012-2017
[27] Al-Kateeb Z N and Mohammed S J 2020 A novel approach for audio file encryption using hand geometry *Multimedia Tools and Applications* **79**(27-28) 19615-19628
[28] Al-Kateeb Z N, AL-Shamdeen M J and Al-Mukhtar F S 2020 Encryption and steganography a secret data using circle shapes in colored images *Journal of Physics: Conference Series* **1591** 012-019
[29] Huang L et al 2004 Synchronization of a chaotic system via nonlinear control *Phys Lett A* **320** 271-275

[30] Al-hayali S Y and Al-Azzawi S F 2020 An optimal control for complete synchronization of 4D Rabinovich hyperchaotic systems *TELKOMNIKA Telecommunication Computing Electronics and Control* **18**(2) 994-1000
[31] Srivastava M et al 2014 Anti-Synchronization between Identical and Non-identical Fractional-Order Chaotic Systems Using Active Control Method *Nonlinear Dynamics* **76**(2) 905-914 Apr
[32] Dou F Q, Sun J A and Duan W S 2008 Anti-synchronization in different hyperchaotic systems *Communications in Theoretical Physics* **50** 907-912
[33] Al-hayali S Y and Al-Azzawi S F 2020 An optimal nonlinear control for anti-synchronization of Rabinovich hyperchaotic system *Indonesian Journal of Electrical Engineering and Computer Science* **19**(1) 379-386
[34] Sudheer K S and Sabir M 2009 Hybrid synchronization of hyperchaotic Lü system *Pramana* **73**(4) 781-786
[35] Al-Obeidi A S and Al-Azzawi S F Hybrid synchronization of high-dimensional chaos with self-excited attractors *Journal of Interdisciplinary Mathematics* DOI:101080/0972050220201776941
[36] Al-Azzawi S F et al Hybrid synchronization for a novel class of 6D system with unstable equilibrium points *Materials Today: Proceedings* DOI:101016/jmatpr202010524
[37] Li C and Yan J 2006 Generalized projective synchronization of chaos: The cascade synchronization approach *Chaos Solitons & Fractals* **30**(1) 140-146
[38] Hu G 2009 Generating hyperchaotic attractors with three positive Lyapunov exponents via state feedback control *International Journal of Bifurcation and Chaos* **19**(2) 651-660

PC-Spaces

PC- Spaces

S. G. Gasim and N. F. Mohammed

Department of Mathematics, College of Education for Pure Sciences Ibn-Al-Haitham, University of Baghdad, Baghdad, Iraq

E-mail: nadia79math@yahoo.com

Abstract. The present study concentrates on the new generalizations of the Jordan curve theorem. In order to achieve our goal, new spaces namely PC-space and strong PC-space are defined and studied their properties. One of the main concepts that use to define the related classes of spaces is paracompact space. In addition, the property of being PC- space and strong PC-space is preserved by defining a new type of function so called para-perfect function.

1. Introduction

One of the standard results in algebraic topology is the theorem of Jordan curve" a simple closed curve C in complex plane separates the plan into two regions which are bounded and unbounded components with C the boundary of each". This theorem was first proposed in 1887 by French mathematician Camille Jordan [1]. Then, many generalizations of the Jordan curve theorem are discussed by a group of researchers. In 1990, Khalimsky et al. [2] stated a generalization in Z^2 equipped with the khalimsky topology. In 1999, Micael [3] introduced and studied J-spaces and strong J-spaces which are considered to be generalizations of properties of the Jordan curve theorem. In 2007, Gao [4] introduced the concept of LJ-spaces exploited the common generalization of Lindelöf spaces and J-spaces. In 2016, Dawood and Gasim [5] used the concept of countably compact to get many generalizations of this theorem.

In this paper, new generalizations of the Jordan curve theorem are introduced. To get these generalizations, the concept of paracompact space is used to define new spaces which are called PC - space and strong PC- space. We study the relations between the two related classes of spaces and provide some main results.

The article is formed as follows: Some basic notations are given in Section 2. The concept of PC - space and strong PC- space is introduced and studied their properties in Section 3. The paper is ended with a conclusion in Section 4.

2. Fundamental Concepts

Some fundamental concepts are reviewed to be used throughout the present study. In the sequel, all spaces are supposed to be Hausdorff.

Definition 2.1.[5] A cover $\mathcal{G} = \{\mathcal{G}_i\}_{i\in I}$ of $\mathcal{A}$ is called locally finite if, for all point $a \in \mathcal{A}$, there exists a neighbourhood intersecting only finitely many elements in $\mathcal{G}$.

Definition 2.2. [5] Let $\mathcal{G} = \{\mathcal{G}_i\}_{i\in I}$ be a cover of $\mathcal{A}$. If $\gamma = \{\gamma_j\}_{j\in J}$ is the second cover of $\mathcal{A}$, then γ is called a refinement of $\mathcal{G}$ if for each $\gamma_j \in \gamma$ there exists $\mathcal{G}_i \in \mathcal{G}$ with $\gamma_j \subseteq \mathcal{G}_i$.

Definition 2.3. [5] A topological space $\mathcal{A}$ is called paracompact if any open cover of $\mathcal{A}$ has a locally finite open refinement.

Proposition 2.4. [6] Any closed subset of a paracompact space be para-compact.

Proposition 2.5. [7] Every compact space is paracompact.
It is clear that the real number with the usual topology is paracompact space but it is not a compact space.

Proposition 2.6. [7] Every metric space is paracompact.

Proposition 2.7. [8] The image of paracompact space under a closed
and continuous function is paracompact.

Definition 2.8. [7] A space $\mathcal{A}$ is called a locally connected if for all a $\in \mathcal{A}$, and each neighbourhood $\mho$ of a there is a connected neighbourhood $\mathcal{H}$ of a where $\mathcal{H} \subset \mho$.

3. Main Results

Now, we define PC-space and strong PC-space and study their properties.
Definition 3.1. A PC- space is a topological space $\mathcal{A}$ whenever $\{\mathcal{p}, \mathcal{q}\}$ is a closed cover of $\mathcal{A}$ such that $\mathcal{p} \cap \mathcal{q}$ paracompact, then $\mathcal{p}$ or $\mathcal{q}$ is paracompact.

Definition 3.2. A space $\mathcal{A}$ is said to be strong PC- space if every paracompact $\mathcal{J} \subset \mathcal{A}$ is contained in a paracompact $\mathcal{D} \subset \mathcal{A}$ with $\mathcal{A} \setminus \mathcal{D}$ is connected.

Proposition 3.3. Any strong PC-space be a PC-space.
Proof. Assume $\mathcal{A}$ is a strong PC- space and $\mathcal{p}, \mathcal{q}$ are closed subsets of $\mathcal{A}$ with $\mathcal{p} \cap \mathcal{q}$ is paracompact and $\mathcal{A} = \mathcal{p} \cup \mathcal{q}$. So, there is a paracompact $\mathcal{D} \subset \mathcal{A}$ where $\mathcal{p} \cap \mathcal{q} \subset \mathcal{D}$ and $\mathcal{A} \setminus \mathcal{D}$ is connected. Therefore, $\{\mathcal{p} \cap (\mathcal{A} \setminus \mathcal{D}), \mathcal{q} \cap (\mathcal{A} \setminus \mathcal{D})\}$ is a disjoint closed cover of $\mathcal{A} \setminus \mathcal{D}$. However, $\mathcal{A} \setminus \mathcal{D}$ is connected, so $\mathcal{A} \setminus \mathcal{D}$ must be in $\mathcal{p} \cap (\mathcal{A} \setminus \mathcal{D})$ or in $\mathcal{q} \cap (\mathcal{A} \setminus \mathcal{D})$. Hence, $\mathcal{A} \setminus \mathcal{D} \subset \mathcal{p}$ or $\mathcal{A} \setminus \mathcal{D} \subset \mathcal{q}$. By complementation, we have $\mathcal{p}^{c} \subset \mathcal{D}$ or $\mathcal{q}^{c} \subset \mathcal{D}$, and since $\mathcal{p} \cap \mathcal{q} \subset \mathcal{D}$, so $\mathcal{p} \subset \mathcal{D}$ or $\mathcal{q} \subset \mathcal{D}$. Then $\mathcal{p}$ or $\mathcal{q}$ is paracompact by Proposition 2.1. Hence, $\mathcal{A}$ is PC-space.

Proposition 3.4. Every paracompact space be a strong PC.
Proof. Suppose the space $\mathcal{A}$ is a paracompact and $\mathcal{J} \subset \mathcal{A}$ be also paracompact, then $\mathcal{A}$ is a paracompact with $\mathcal{J} \subset \mathcal{A}$ and $\mathcal{A} \setminus \mathcal{A} = \emptyset$ is connected.

Corollary 3.5. Any paracompact space is PC- space.
Proof. The proof follows through Proposition 3.4 and Proposition 3.3.

Examples 3.6.
1- Any compact space is a strong PC.
2-Any metric space is a strong PC.
3- Any usual topology with $\mathbb{R}$ is a strong PC.
4- The indiscrete topology on any set is strong PC-space and PC-space.
5- The cofinite topology on the set of natural numbers is strong PC-space and PC-space.

Lemma 3.7. Let $\mathcal{W}$ be a closed non-paracompact set in a space $\mathcal{A}$ and $\mathcal{p} \subset \mathcal{W}$ is paracompact. Then, there is a non-paracompact closed $\mathcal{q} \subset \mathcal{W}$ such that $\mathcal{p} \cap \mathcal{q} = \emptyset$.

Proof. Assume the open cover $\mathcal{G}$ of $\mathcal{W}$ with no a locally finite open refinement, and $\mathcal{p} \subset \mathcal{W}$ is paracompact. Then, $\mathcal{p}$ has an open cover $\mathcal{G}$ and has a locally finite open refinement γ covering $\mathcal{p}$. Put $\mathcal{q} = \mathcal{W} \setminus \cup \gamma$, so $\mathcal{q}$ is closed in $\mathcal{W}$ with $\mathcal{p} \cap \mathcal{q} = \emptyset$.
Now, suppose $\mathcal{q}$ is paracompact. So, there exists a locally finite open refinement γ^* covering $\mathcal{q}$. Thus, $\mathcal{q} \subset \cup \gamma^*$and so $\mathcal{W} \setminus \cup \gamma \subset \cup \gamma^*$. That implies $\mathcal{W} \subset (\cup \gamma) \cup (\cup \gamma^*)$. However, $(\cup \gamma) \cup (\cup \gamma^*)$ is a locally finite open refinement for $\mathcal{G}$ which is contradiction. Hence, $\mathcal{q}$ is a non- paracompact.
The following theorem gives some criteria which are equivalent to be PC-spaces.

Theorem 3.8. The following statements are equivalent:
$\mathcal{A}$ is a PC-space,
For any $\mathcal{p} \subset \mathcal{A}$ with paracompact boundary, $\overline{\mathcal{p}}$ or $\overline{(\mathcal{A}\setminus\mathcal{p})}$ is para-compact,
If the closed subsets $\mathcal{p}$, $\mathcal{q}$ in $\mathcal{A}$ with $\mathcal{p} \cap \mathcal{q} = \emptyset$ and $bd(\mathcal{p})$ or $\mathrm{bd}(\mathcal{q})$ is paracompact, then $\mathcal{p}$ or $\mathcal{q}$ is paracompact.

Proof. Statement (1) implies statement (2). Suppose $\mathcal{p} \subset \mathcal{A}$ such that $\mathrm{bd}(\mathcal{p})$ is paracompact. However, we have $\mathrm{bd}(\mathcal{p}) = \overline{\mathcal{p}} \cap \overline{(\mathcal{A}\setminus\mathcal{p})}$. Thus, $\{\overline{\mathcal{p}}, \overline{(\mathcal{A}\setminus\mathcal{p})}\}$ is a closed cover of $\mathcal{A}$ with $\overline{\mathcal{p}} \cap \overline{(\mathcal{A}\setminus\mathcal{p})}$ is paracompact. Since $\mathcal{A}$ is PC-space so $\overline{\mathcal{p}}$ or $\overline{(\mathcal{A}\setminus\mathcal{p})}$ is paracompact.
Statement (2) implies statement (3). Let $\mathcal{p}$ and $\mathcal{q}$ be disjoint closed subsets of $\mathcal{A}$ with $\mathrm{bd}(\mathcal{p})$ or $\mathrm{bd}(\mathcal{q})$ is paracompact. Assume that $\mathrm{bd}(\mathcal{p})$ is aracompact, so $\overline{\mathcal{p}}$ or $\overline{(\mathcal{A}\setminus\mathcal{p})}$is paracompact by (2). However, $\mathcal{p} = \overline{\mathcal{p}}$ and $\mathcal{q} \subset (\mathcal{A}\setminus\mathcal{p}) \subset \overline{(\mathcal{A}\setminus\mathcal{p})}$. Hence, $\mathcal{p}$ or $\mathcal{q}$ is paracompact.
Statement (3) implies statement (1). We want to prove $\mathcal{A}$ is a PC-space. Assume $\{\mathcal{p}, \mathcal{q}\}$ be a closed cover of $\mathcal{A}$ where $\mathcal{p} \cap \mathcal{q}$ paracompact. Suppose that $\mathcal{q}$ is non-paracompact. Since $\mathcal{p} \cap \mathcal{q} \subset \mathcal{q}$ is a paracompact, so by lemma 3.7 there is a non- paracompact closed $\mathrm{D} \subset \mathcal{q}$ where $\mathrm{D} \cap (\mathcal{p} \cap \mathcal{q}) = \emptyset$. So, $\mathrm{D} \cap \mathcal{p} = \emptyset$. However, $\mathrm{bd}(\mathcal{p})$ is a paracompact because it is a closed subset of $\mathcal{p} \cap \mathcal{q}$. By (3) $\mathcal{p}$ or D is paracompact, but D is non- paracompact. Hence, $\mathcal{p}$ must be paracompact.

Theorem 3.9. A topological space $\mathcal{A}$ is a PC -space if and only if $\mathcal{J} \subset \mathcal{A}$ is paracompact where $\mathcal{S} = \{\mathcal{p}, \mathcal{q}\}$ is an open cover of $\mathcal{A}\setminus\mathcal{J}$ with$\mathcal{p} \cap \mathcal{q} = \emptyset$, then $\mathcal{A}\setminus \mathcal{S}_1$ or $\mathcal{A}\setminus \mathcal{S}_2$ is paracompact.

Proof. The "if" part. Assume $\mathcal{A}$ is a CP-space and a set $\mathcal{J}$ is paracompact in $\mathcal{A}$ where $\mathcal{S} = \{\mathcal{p}, \mathcal{q}\}$ is an open cover of $\mathcal{A}\setminus\mathcal{J}$ with $\cap \mathcal{q} = \emptyset$. Thus, $\{\mathcal{A}\setminus\mathcal{p}, \mathcal{A}\setminus\mathcal{q}\}$ is a closed cover of $\mathcal{A}$ with $\mathcal{A}\setminus\mathcal{p} \cap \mathcal{A}\setminus\mathcal{q} = \mathcal{A}\setminus\mathcal{p} \cup \mathcal{q}$ which is a closed set in $\mathcal{J}$ because of $\mathcal{A}\setminus\mathcal{J} \subset \mathcal{p} \cup \mathcal{q}$.Then, $\mathcal{A}\setminus\mathcal{p} \cap \mathcal{A}\setminus\mathcal{q}$ is paracompact by Proposition 2.4. However, $\mathcal{A}$ is PC-space, so $\mathcal{A}\setminus\mathcal{p}$ or $\mathcal{A}\setminus\mathcal{q}$ is paracompact.
The "only if" part. Let $\{\mathcal{p}, \mathcal{q}\}$ be a closed cover of $\mathcal{A}$ with $\mathcal{p} \cap \mathcal{q}$ is paracompact. So, $\{\mathcal{A}\setminus\mathcal{p}, \mathcal{A}\setminus\mathcal{q}\}$ is an open cover of $\mathcal{A}\setminus\mathcal{p} \cap \mathcal{q}$ with $\mathcal{A}\setminus\mathcal{p} \cap \mathcal{A}\setminus\mathcal{q} = \emptyset$. By hypothesis, $\mathcal{A}\setminus(\mathcal{A}\setminus\mathcal{p})$ or $\mathcal{A}\setminus(\mathcal{A}\setminus\mathcal{q})$ is paracompact, that is $\mathcal{p}$ or$\mathcal{q}$ is paracompact. Hence, $\mathcal{A}$ is PC-space.

Theorem 3.10. If the closed cover $\{\mathcal{A}_1, \mathcal{A}_2\}$ of a space $\mathcal{A}$ with $\mathcal{A}_1 \cap \mathcal{A}_2$ is paracompact, then $\mathcal{A}$ is a PC-space if and only if $\mathcal{A}_1$ and $\mathcal{A}_2$ are PC-spaces and $\mathcal{A}_1$ or $\mathcal{A}_2$ is paracompact.

Proof. The "if" part. Suppose that $\mathcal{A}$ is PC-space, then $\mathcal{A}_1$ or$\mathcal{A}_2$ is paracompact by definition of PC-space. Suppose that $\mathcal{A}_1$ is paracompact, it follows that $\mathcal{A}_1$ is PC-space by Corollary 3.5, now to show that $\mathcal{A}_2$ is PC-space. Let $\{\mathcal{p}, \mathcal{q}\}$ be a closed cover of $\mathcal{A}_2$ with $\mathcal{p} \cap \mathcal{q}$ is paracompact. Hence, $\mathcal{A}$ has a closed cover $\{\mathcal{p}, \mathcal{q} \cup \mathcal{A}_1\}$ where $\mathcal{p} \cap (\mathcal{q} \cup \mathcal{A}_1)$ is paracompact. So $\mathcal{p}$ or $\mathcal{q} \cup \mathcal{A}_1$ is paracompact because of $\mathcal{A}$ is PC-space. However, $\mathcal{q}$ is a closed subset of $\mathcal{q} \cup \mathcal{A}_1$, so $\mathcal{p}$ or $\mathcal{q}$ is paracompact.
The "only if" part. Assume that $\mathcal{A}_1$ and $\mathcal{A}_2$ are PC- spaces and suppose that $\mathcal{A}_2$ is paracompact, we have to show that $\mathcal{A}$ is PC-space. Let $\{\mathcal{p}, \mathcal{q}\}$ be a closed cover of $\mathcal{A}$ with $\mathcal{p} \cap \mathcal{q}$ is paracompact. Now, let $\mathcal{p}_\mathrm{i} = \mathcal{p} \cap \mathcal{A}_\mathrm{i}$ and $\mathcal{q}_\mathrm{i} = \mathcal{q} \cap \mathcal{A}_\mathrm{i}$ where $(\mathrm{i} = 1,2)$. Consequently, $\{\mathcal{p}_1, \mathcal{q}_1\}$ is a closed cover of $\mathcal{A}_1$, which is PC-space, with $\mathcal{p}_1 \cap \mathcal{q}_1 = (\mathcal{p} \cap \mathcal{A}_1) \cap (\mathcal{q} \cap \mathcal{A}_1) = (\mathcal{p} \cap \mathcal{q}) \cap \mathcal{A}_1$ which is a closed subset

of $\mathcal{P}\cap\mathcal{Q}$. Hence, $\mathcal{P}_1\cap\mathcal{Q}_1$ is paracompact and $\mathcal{P}_1$ or $\mathcal{Q}_1$ is paracompact. If $\mathcal{P}_1$ is paracompact, then $\mathcal{P} = \mathcal{P}_1\cup\mathcal{P}_2$ is paracompact since $\mathcal{P}_2$ is a closed subset of paracompact $\mathcal{A}_2$. In the same way, if $\mathcal{Q}_1$ is paracompact, then so is $\mathcal{Q}$.

Theorem 3.11. If the closed cover $\{\mathcal{A}_1, \mathcal{A}_2\}$ of a topological space $\mathcal{A}$ with $\mathcal{A}_1 \cap \mathcal{A}_2$ is paracompact. Then $\mathcal{A}$ is a strong PC-space if and only if $\mathcal{A}_1$ and $\mathcal{A}_2$ are strong PC-spaces and $\mathcal{A}_1$ or $\mathcal{A}_2$ is paracompact.

Proof. The "if" part. Assume that $\mathcal{A}$ is a strong PC-space, it follows by Proposition 3.3 that $\mathcal{A}$ is PC-space, and thus $\mathcal{A}_1$ or $\mathcal{A}_2$ is paracompact. Suppose that $\mathcal{A}_1$ is paracompact, so by Proposition 3.4 that $\mathcal{A}_1$ is strong PC-space, so it remains to show that $\mathcal{A}_2$ is strong PC-space. Let $\mathcal{J}_2 \subseteq \mathcal{A}_2$ be paracompact. Define $\mathcal{J} = \mathcal{J}_2 \cup \mathcal{A}_1$, then $\mathcal{J}$ is a paracompact subset of $\mathcal{A}$ which is a strong PC-space, so there is a paracompact closed set $\mathcal{D}$ in $\mathcal{A}$ where $\mathcal{J} \subset \mathcal{D}$ and $\mathcal{A}\backslash\mathcal{D}$ is connected. Let $\mathcal{D}_2 = \mathcal{D} \cap \mathcal{A}_2$, then $\mathcal{D}_2 \subseteq \mathcal{A}_2$ is paracompact since $\mathcal{D}_2$ is a closed subset of paracompact set $\mathcal{D}$. Also $\mathcal{J}_2 \subseteq \mathcal{D}_2$ since $\mathcal{J}_2 \subseteq \mathcal{J} \subset \mathcal{D}$ implies that $\mathcal{J}_2 \cap \mathcal{A}_2 \subset \mathcal{D} \cap \mathcal{A}_2$. Also, we note $\mathcal{A}_1 \subset \mathcal{J} \subset \mathcal{D}$ and that implies $\mathcal{A}_2\backslash\mathcal{D}_2 = \mathcal{A}\backslash\mathcal{D}$, and hens $\mathcal{A}_2\backslash\mathcal{D}_2$ is connected.
The "only if" part. Assume that $\mathcal{A}_1$ and $\mathcal{A}_2$ are strong PC-space and suppose that $\mathcal{A}_1$ is a paracompact and let $\mathcal{J} \subset \mathcal{A}$ be paracompact. Define $\mathcal{J}_2 = (\mathcal{J} \cup \mathcal{A}_1) \cap \mathcal{A}_2$, so $\mathcal{J}_2$ is paracompact since it is a closed subset of the paracompact set $\mathcal{J} \cup \mathcal{A}_1$, so $\mathcal{J}_2$ is a paracompact subset of the strong PC-space $\mathcal{A}_2$, then there is a closed paracompact subset $\mathcal{D}_2$ of $\mathcal{A}_2$ where $\mathcal{J}_2 \subseteq \mathcal{D}_2$ and $\mathcal{A}_2\backslash\mathcal{D}_2$ is connected. Now, let $\mathcal{D} = \mathcal{D}_2 \cup \mathcal{A}_1$, then $\mathcal{D}$ is a closed paracompact of $\mathcal{A}$ and $\mathcal{J} \subset \mathcal{D}$ and $\mathcal{A}\backslash\mathcal{D} = \mathcal{A}_2\backslash\mathcal{D}_2$ is connected. Hence, $\mathcal{A}$ is a strong PC-space.
Next, we introduce new types of functions that help study the preservation of strong PC-space and PC-space.

Definition 3.12. A continuous function $\mathrm{f} : \mathcal{A} \to \mathcal{B}$ is called para-perfect if it is closed and $f^{-1}(b)$ is a paracompact subset of $\mathcal{A}$ for every paracompact subset b of $\mathcal{B}$.

Definition 3.13. A closed function $\mathrm{f} : \mathcal{A} \to \mathcal{B}$ is called boundary para-perfect if the boundary of $f^{-1}(b)$ is paracompact subset of $\mathcal{A}$ for all $b \in \mathcal{B}$.

Definition 3.14. A continuous closed function $f : \mathcal{A} \to \mathcal{B}$ is called quasi- para-perfect if is $f^{-1}(b)$ is paracompact subset of $\mathcal{A}$ for all $b \in \mathcal{B}$.

Remark 3.15. It is clear that every para-perfect function is a quasi-para-perfect because it is known that the only topology that can be defined on a singleton set is the indiscrete topology. Therefore, it is paracompact and its reverse image due to the para- perfect function is paracompact.
The following proposition gives the condition of function which guarantees that the image of a PC-space is PC-space.

Proposition 3.16. If f is a closed surjective para-perfect function from a PC-space $\mathcal{A}$ to a space $\mathcal{B}$. Then $\mathcal{B}$ is PC-space.

Proof. Let $\{\mathcal{P}, \mathcal{Q}\}$ be a closed cover of $\mathcal{B}$ with $\mathcal{P}\cap\mathcal{Q}$ paracompact, then $\{\mathrm{f}^{-1}(\mathcal{P}), \mathrm{f}^{-1}(\mathcal{Q})\}$ is a cover of closed sets in $\mathcal{A}$. However, $\mathrm{f}^{-1}(\mathcal{P}\cap\mathcal{Q}) = \mathrm{f}^{-1}(\mathcal{P}) \cap \mathrm{f}^{-1}(\mathcal{Q})$ is paracompact since f is para-perfect. But $\mathcal{A}$ is PC-space, so $\mathrm{f}^{-1}(\mathcal{P})$ or $\mathrm{f}^{-1}(\mathcal{Q})$ is paracompact. So, $\mathrm{f}\left(\mathrm{f}^{-1}(\mathcal{P})\right)$ or $\mathrm{f}\left(\mathrm{f}^{-1}(\mathcal{Q})\right)$ is paracompact since f is closed and surjection function. Hence, $\mathcal{P}$ or $\mathcal{Q}$ is paracompact and then $\mathcal{B}$ is PC-space.

Proposition 3.17. If f is a closed bijective para-perfect function from a space $\mathcal{A}$ to a PC-space $\mathcal{B}$, then $\mathcal{A}$ is also PC-space.

Proof. Let $\{\mathcal{P}, \mathcal{Q}\}$ be a closed cover of $\mathcal{A}$ with $\mathcal{P}\bigcap\mathcal{Q}$ paracompact, then $\{f(\mathcal{P}), f(\mathcal{Q})\}$ is a closed cover of $\mathcal{B}$ with $f(\mathcal{P}\bigcap\mathcal{Q})$ is paracompact since f is closed bijective function. However, $f(\mathcal{P})\bigcap f(\mathcal{Q}) = f(\mathcal{P}\bigcap\mathcal{Q})$, so $(\mathcal{P})$ or $f(\mathcal{Q})$ is paracompact because of $\mathcal{B}$ is PC-space. So, $f^{-1}(f(\mathcal{P}))$ or $f^{-1}(f(\mathcal{Q}))$ is paracompact because of f is para-perfect. Hence, $\mathcal{P}$ or $\mathcal{Q}$ is paracompact. Therefore, $\mathcal{A}$ is PC-space.

Proposition 3.18. If f is a homeomorphism function and $\mathcal{A}$ be PC-space. Then $\mathcal{B}$ is also PC-space.

Proof. The proof is the same as Proposition 3.16.

Proposition 3.19. Let $f : \mathcal{A} \to \mathcal{B}$ be an open surjection para- perfect function. If $\mathcal{A}$ is a strong PC-space , then $\mathcal{B}$ is a strong PC-space.

Proof. To prove $\mathcal{B}$ is strong PC -space. let $\mathcal{J} \subset \mathcal{B}$ be a paracompact, then a set $f^{-1}(\mathcal{J})$ is a paracompact in $\mathcal{A}$ because of f is para- perfect function. However, $\mathcal{A}$ is a strong PC-space so there exist a closed paracompact $\mathcal{D} \subset \mathcal{A}$ where $f^{-1}(\mathcal{J}) \subset \mathcal{D}$ and $\mathcal{A}\backslash\mathcal{D}$ are connected. So, $f(\mathcal{D})$ is a paracompact closed set in $\mathcal{B}$ where $f(f^{-1}(\mathcal{J})) \subset f(\mathcal{D})$ and $\mathcal{B}\backslash f(\mathcal{D}) = f(\mathcal{A}\backslash\mathcal{D})$ is connected since f is continuous. However, $f(f^{-1}(\mathcal{J})) = \mathcal{J}$, so $\mathcal{J} \subset f(\mathcal{D})$ and a set $f(\mathcal{D})$ is paracompact and closed in $\mathcal{B}$ with $\mathcal{B}\backslash f(\mathcal{D})$ is connected. Hence, $\mathcal{B}$ is a strong PC-space.

Proposition 3.20. Every boundary para-perfect continuous function from a PC-space to a non-paracompact space is a quasi-para-perfect.

Proof. Assume $f : \mathcal{A} \to \mathcal{B}$ is a boundary para-perfect continuous function such that $\mathcal{A}$ is a PC-space and $\mathcal{B}$ is a non- paracompact space. To prove that f is a quasi- para-perfect, let $b \in \mathcal{B}$. Then, $f^{-1}(b)$ is a subset of $\mathcal{A}$ with paracompact boundary. From Theorem 3.8 that $\overline{f^{-1}(b)}$ or $\overline{(\mathcal{A}\backslash f^{-1}(b)}$ is paracompact. However, $\overline{(\mathcal{A}\backslash f^{-1}(b)}$ is not paracompact because of if $\overline{(\mathcal{A}\backslash f^{-1}(b)}$ is paracompact, then $\mathcal{B} = \{b\} \cup f\overline{(\mathcal{A}\backslash f^{-1}(b)}$ is paracompact, which is a contradiction. So $\overline{f^{-1}(b)}$ is paracompact, but $\overline{f^{-1}(b)} = f^{-1}(b)$. Thus f is quasi- para-perfect because of $f^{-1}(b)$ is paracompact.

Conclusion

In this study, new generalizations of the Jordan curve theorem are considered. New topological spaces namely PC -space and strong PC- space is defined to get these generalizations. Many propositions concerning these two related classes are provided. We give some criteria which are equivalent to be PC -spaces and prove that every strong PC- space is PC- space. Additionally, new functions have been defined such as the para-perfect function which is preserved the property PC -space and the property strong PC - space**.**

References

[1] Jordan C 1983 Cours d'analyse de l'École polytechnique *Gauthier-Villars et fils*
[2] Khalimsky E, Kopperman R and Meyer P R 1990 Computer graphics and connected topologies on finite ordered sets *Topology and its Applications* **1** 36(1) 1-7
[3] Michael E 2000 J-spaces *Topology and its Applications* **102(3)** 315-39
[4] Gao Y Z 2007 LJ-spaces *Czechoslovak Mathematical Journal* **57(4)** 1223-37
[5] Dawood N A and Gasim S G 2016 On CJ-Topological Spaces *Journal of Advances in Mathematics* **12(2)** 5949-5952
[6] Dieudonné J A 1994 Une généralisation des espaces compacts *J. Math. Pures. Appl*. **23** 65-76
[7] Nagata J I 1985 Modern general topology *Elsevier*
[8] Michael E 1957 Another note on paracompact spaces *Proceedings of the American Mathematical Society* **8(4)** 822-8

Discrete wavelet based estimator for the Hurst parameter of multivariate fractional Brownian motion

Discrete wavelet based estimator for the Hurst parameter of multivariate fractional Brownian motion

Munaf Yousif Hmood and Amjad Hibtallah Hamza

Department of Statistics - College of Administration and Economics - University of Baghdad, Baghdad, Iraq.

E-mail: amjad.hibtallah@uobaghdad.edu.iq

Abstract. In this paper, wavelets were used to study the multivariate fractional Brownian motion through the deviations of the random process to find an efficient estimation of Hurst exponent. The results of simulations experiments were shown that the performance of the proposed estimator was efficient. The estimation process was made by taking advantage of the detail coefficients stationarity from the wavelet transform, as the variance of this coefficient showed the power-low behavior. We use two wavelet filters (Haar and db5) to manage minimizing the mean square error of the model.

1. Introduction

In many areas such as hydrology, biology, telecommunications, and economics, the data available for analysis usually has a scaling behavior (long-memory) that needs to be discovered. The main point to detect scaling behavior is the estimation of the parameters of the models under study such as the Hurst parameter, which is used to determine self-similarity and long-range dependence. The study of these phenomena in the multidimensional case relies on fractal Gaussian noise, which is a first order incremental process

$$G_H(t) = B_H(t+1) - B_H(t) \qquad (1)$$

Where $B_H(t)$ is the fractional Brownian motion and can be generalized to be of order n and written as n-FBM. This generalization introduced by Perrin et al (2001) through the derivation of the kernel in the continuous definition of FBM.

The fractional Brownian motion can be defined as a random process characterized by non-stationary self-similarity and a stationary continuous increasing and has been used to explain many random phenomena in many areas of research and although it has demonstrated in various applications, for example bone radiographs.

More recently, wavelet transformation has emerged as a powerful mathematical tool for signal processing by setting a timescale.

Wavelets give a new look to the statistical analysis of random processes, as wavelets rules in the time scale plan provide a suitable framework for representing functions with sharp spikes and analyzing them with good accuracy and allow studying basic characteristics such as long-memory, self-similarity and stationary increasing.

The objective of this paper is to develop a method that can be used to model and study nth order fractional Brownian motion through wavelet lens by estimating the Hurst parameter. The proposed procedure will rely on finding an unbiased estimate of the difference in the Gaussian noise of the

fractional Brownian motion using Haar and Daubechies 5 (db5) wavelet. The performance of this estimator was validated through a simulation study.

The paper is structured as follow: Section 2 we give an overview of discrete wavelet transform, in Section 3 the fractional Brownian motion properties will be presented, and in Section 4 the proposed method will be briefed, Section 5 the simulation study will be conducted and finally Section 6 the conclusions will be explain.

2. Discrete Wavelets Transform

The main problem in the early 1980s when working with wavelet was to create a multiresolution analysis where the scale function had compact and continuous support. In her paper that published in 1988, Daubechies found a way to build a multiresolution, continuous, orthonormal and compact support scale function that attracted the attention of researchers interested in the wavelet field at that time, and here we introduce the DWT beginning with wavelet function $\psi(t), t \in \mathbb{R}$ such that [1]:

$$\int \psi(t)\, dt = 0 \qquad (2)$$

Where this condition satisfy some integrability conditions, $\psi \in L_1(\mathbb{R}) \cap L_2(\mathbb{R})$. Which require the wavelet to be bounded, centered around the origin, and have time and frequency support. Where it is finite or decreases very fast. Time and frequency concertation are restricted by the Gabor-Heisenberg uncertainty principal. A wavelet ψ have N zero moments (vanishing moment) if: [3]

$$\int t^k \psi(t)\, dt = 0, k = 0,1, \dots, N-1 \qquad (3)$$

Where N is an integer at least equal 1. The increase in the vanishing moments give an enlargement in the time support but bring smoothness, continuity, derivability and more concentration of the spectral in a given frequency v_0. An example of wavelet have derivative of standard normal density is the Haar wavelet and the Daubechies wavelet, where both constructed from multiresolution analysis (MRA), and also the Mexican hat wavelet which is the 2nd derivative of the normal function and has 2 vanishing moments.

The Daubechies wavelets constitute a family of wavelets indexed by their vanishing moments and give rise to the orthonormal basis. The Haar wavelet is a special case of both the Daubechies and spline families that has one vanishing moment and has finite time support. The wavelet coefficients are equivalent to the increments of the process, and can be defined beginning from the function:

$$\psi_{j,k}(t) = 2^{-\frac{j}{2}} \psi\left(2^{-j}t - k\right), \quad j,k \in \mathbb{Z} \qquad (4)$$

Where j, k are dilation and translation of ψ respectively.

$$\int \psi_{j,k}^2(t)dt = \int \psi^2(t)dt \qquad (5)$$

It allows the $L^2(\mathbb{R})$ norm to be preserved. Using the functions $\{\psi_{j,k}, j,k \in \mathbb{Z}\}$as a set of filters we can now define the DWT of a function $\{X(t), t \in \mathbb{R}\}$ as:

$$d_{j,k} = \int X(t)\, \psi_{j,k}(t)dt \qquad (6)$$

Where the $d_{j,k}$ are the wavelet coefficients called details, as it encode the differential information between adjacent scales centered about 2^j, and the time $2^j k$. The details sometimes written as $d_X(j,k)$to emphasize that they correspond to X. The adjective discrete in DWT refers to the fact the indices j,k take discrete values in contrast to the CWT where they take real values.

Multiresolution analysis is a specific class of wavelets which is of particular interest because it has potentially stronger mathematical properties and because it gives birth to fast recursive pyramidal decomposition algorithms. Their key properties is

i- The number of zero moments, regularity, time or frequency support, can be easily and flexibly tuned.
ii- Fast pyramidal algorithms to compute the wavelet coefficients.

The construction of such wavelets of which the Daubechies and spline families are famous examples is integral to the so called the multiresolution analysis theory. The dilation equation for the Daubechies scale function can be written as [1]:

$$\phi(\mathrm{t}) = 2^{-j/2} \sum_{k\in\mathbb{Z}} h_k \phi(2^{-j}t - k) \qquad (7)$$

Where h_k is a scale filter and also called the average block and now if we had a multiresolution analysis and had h_k real values from dilation equation then h_k have the following properties:

1. $\sum_{\mathrm{k}\in\mathbb{Z}} \mathrm{h_k} = 2^{1/2}$ (8)
2. $\sum_{\mathrm{k}\in\mathbb{Z}} \mathrm{h_k^2} = 1$

There is a great benefit to this filter in calculating the projection coefficients according to the following equation:

$$b_\ell = \sum_{k\in\mathbb{Z}} a_k h_{k-2\ell} \ , where\ k, \ell \in \mathbb{Z} \qquad (9)$$

Where a_k are the approximation coefficients. The dilation equation for the wavelet function is the same as the formula of the scale function's dilation equation, but in terms of wavelet filter as follows:

$$\psi(\mathrm{t}) = 2^{-j/2} \sum_{k\in\mathbb{Z}} g_k \phi(2^{-j}t - k) \qquad (10)$$

It should also be noted that the value of the wavelet filter can be calculated through the scale filter.

$$g_k = (-1)^k h_{k-1} \qquad (11)$$

3. Fractional Brownian Motion

Fractional Brownian motion (FBM) is a centered stochastic Gaussian process. Mandelbrot & Van Ness [2] called it Brownian, and to define it they use different fractional integral of white noise:

$$B_H(t) = B_H(0) + \frac{1}{\Gamma(H+\frac{1}{2})}\left\{\int_{-\infty}^{0}\left[(t-s)^{H-1/2} - (-s)^{H-1/2}\right]dB_s + \int_0^t (t-s)^{H-1/2} dB_s\right\} \quad (12)$$

The most important difference between Brownian motion and fractional Brownian motion is in the increments so in the classic process the increments are independent but in fractional Brownian motion (FBM) are not, when $H > 1/2$ there is positive autocorrelation on other hand if $H < 1/2$ the autocorrelation is negative.

Fractional Brownian motion has zero mean and variance covariance equal to [3]:

$$E[B_H(t)B_H(s)] = \frac{1}{2}\left(|t|^{2H} + |s|^{2H} - |t-s|^{2H}\right) \quad (13)$$

Where H is a Hurst parameter which was defined by both Mandelbrot and Van Ness and its value ranges between [0, 1] and shows the extent of roughness of the movement, as its value increase softer the signal become so the type of the random process is related to the value of this parameter.

The existence of the fractional Brownian motion comes from the presence of the centered Gaussian process. If we assume that there is a real parameter $H > 0$, then there is a continuous central Gaussian process $B_H = (B_t^H)_{t\geq 0}$ with a known positive variance if and only if $H \leq 1$. [4]
The main properties of fractional Brownian motion is:

1. Self-similarity is visually seen as the same pattern repeating both seen up close and seen from a far. In other words, there are small versions of the larger pattern repeated inside larger patterns. This property of a random process is achieved if:

$$B_H(at) \sim |a|^H B_H(t) \quad (14)$$

This property is due to the fact that the covariance function is homogeneous of order 2H, which gives the process a fractional character.

2. Stationary increments which satisfied when:

$$B_H(t) - B_H(s) \sim B_H(t-s) \quad (15)$$

3. Long-range dependence or the long memory is a phenomenon that appears in the analysis of time-related data and expresses the slow exponential decay of the autocorrelation coefficient and its appear clearly in fBm when $H > 1/2$.

$$\sum_{n=1}^{\infty} E\left[B_H(1)\big(B_H(n+1) - B_H(n)\big)\right] = \infty \quad (16)$$

4. Regularity where the sample-paths are non-derivative at almost every point, i.e., all trajectories are locally Holder continuous for any function have d-dimensional Euclidian space is Holder continuous when there is a positive constant C and $\alpha > 0$ such that $|f(x) - f(y)| \leq C|x-y|^{\alpha}$ That is, for each trajectory path, for each T> 0, and for each $\varepsilon > 0$, there is a constant value of C so that:

$$|B_H(t) - B_H(s)| \leq C|t-s|^{H-\varepsilon} \quad (17)$$

5. Semi-Martingale in the theory of probability, Martingale is a series of random variables (any random process) so that at any time the conditional expectation of the present value excluding all previous values is equal to the first value.

$$E[X_{n+1}|X_1, \ldots\ldots, X_n] = X_n \quad (18)$$

This property occur in many random processes such as classic Brownian motion i.e. when H = ½. It's so obvious so it should be that this property is not realized in the case of fractional Brownian motion because the covariance of this type not equal to zero and many researchers have demonstrated this property when H> 1/2 and when H <1/2.

4. Second Moment of Gaussian Noise using Wavelet (SMGNW)

The analysis of the fractional Brownian motion depends on the estimation of the Hurst parameter, which is sometimes called the parameter of roughness. The difficulty in the estimation process lies in the nonstationary and the fact that this type of random process is Locally Holder Continuous, that is, it does not have a derivative at almost every point.

This topic has raised the interest of many researchers, and here in this paper, we find a more efficient way to conduct this work. It was relied on finding an unbiased estimate of the difference in the Gaussian noise of the fractional Brownian motion using wavelets, which proved effective in improving the estimator's efficiency and its approach to the real value too close and the error is relatively too low, here we will be discuss in detail. Beginning with the definition of wavelet function.

$$\psi_{j,k}(t) = 2^{-\frac{j}{2}}\psi\left(2^{-j}t - k\right), j, k \in \mathbb{Z} \quad (19)$$

Thus, the details coefficients for the transformation can be defined as

$$d_{j,k} = \int_{\mathbb{R}} X(t)\psi_{j,k}(t)dt \quad (20)$$

Where $d_{j,k}$ can be calculated from $d_{j-1,k}$ as follow [13]

$$\begin{aligned} d_{j,k} &= \int_{\mathbb{R}} X(t)2^{-\frac{j}{2}}\psi\left(2^{-j}t - k\right)dt \\ &= \int_{\mathbb{R}} X(t)2^{-\frac{j}{2}}\sqrt{2}\sum\nolimits_n v_n\psi(2\left(2^{-j}t - k\right) - n)\,dt \\ &= \sum\nolimits_n v_n \int_{\mathbb{R}} X(t)2^{\frac{-j+1}{2}}\,\psi\left(2^{-j+1}t - 2k - n\right)dt \\ d_{j,k} &= \textstyle\sum_n v_n d_{j-1,2k+n} \end{aligned} \quad (21)$$

These coefficients are characterized by not being affected by the polynomials due to the vanishing moments and their stationary, and this is evident when fix the scale. We will notice that the translation is not affected by the increases
At the scale s and the assumed increase of translation by the value of r [5]

$$d_{s,k+r} = \int_{\mathbb{R}} X(t)\psi(t - k - r)dt$$

Let $u = t - r$ then $t = u + r$

$$= \int_{\mathbb{R}} X(u + r)\,\psi(u - k)du$$

$$= \int_{\mathbb{R}} [X(u + r) - \mathrm{X}(r)]\,\psi(u - k)du$$

At $r = 0$

$$\cong \int_{\mathbb{R}} [X(u) - \mathrm{X}(0)]\,\psi(u - k)du$$

$$= \int_{\mathbb{R}} X(u)\,\psi(u - k)du = d_{s,k} \quad (22)$$

The third step was achieved through one of the main characteristics of the wavelets, which is $\int_{\mathbb{R}} \psi(u)du = 0$. The fourth step was achieved by approximate the integration by sum and taking advantage of the stationary increasing. These characteristics of the detail parameters make it able to give accurate estimates even in signals of self-similar and stationary increases by finding an unbiased value for the variance of these coefficients, and that the value of this variation can be calculated using the definition of variance of the process knowing that fBm has zero mean

$$\mathrm{var}(d_{j,k}) = E(d_{j,k})^2 = \frac{1}{n}\sum_{k=1}^{n}|d_{j,k}|^2 \quad (23)$$

Istas [6] and Abry [5] have indicated a bias in this amount. However, it is possible to reduce it through the wavelet transformation through its previously mentioned characteristics.

The problem is the choosing of a wavelet with a sufficient number of vanishing moments to smooth the signal without increasing the estimator bias, but enough so does not increase the variance of the estimate.

For this reason, we have found that using two wavelets would be the best way to adjust the amount of variance without increasing the estimate bias or the variance.

The db 5 wavelet and the Haar wavelet were used separately to perform the transformation of the series after taking the differences to it and find the Gaussian noise in the series as follows:

$$G_H(t_j) = B_H(t_j) - B_H(t_{j-1}) \quad (24)$$

Now filtration will be made to the differences using the wavelet filter c

$$\begin{aligned} d_{1,.} &= [c * (g_1, g_2, g_3, \dots, g_p)], \quad p = length\ of\ c \\ d_{2,.} &= [c * (g_2, g_3, g_4, \dots, g_{p+1})] \\ d_{3,.} &= [c * (g_3, g_4, g_5, \dots, g_{p+2})] \\ d_{n,.} &= [c * (g_{n-p+1}, g_{n-p+2}, g_{n-p+3}, \dots, g_n)], \quad n = length\ of\ G \end{aligned} \quad (25)$$

The transformation has been made, Flandrin [7] has discussed and appointed out that the approximation coefficients are strongly correlated, but on the other hand, there is independency in the detail coefficient values that can be adopted in calculating an unbiased estimate of the Hurst parameter, and so the value of variance is as follows:

$$E(d_{j,k})^2 = E(d_{0,0})^2 2^{j(2H+1)} \quad (26)$$

Where $E(d_{0,0})^2$ is a constant, as shown by Houdre [8] the logarithms of the variance will give an estimate for the Hurst parameter

$$\log_2\left(E(d_{j,k})^2\right) = (2H+1)j + \log_2(E(d_{0,0})^2) \quad (27)$$

Where j will be a linear function (j represents the courser level) and the slope of this function will be an estimate of H, but it will be a biased estimate. For eliminating this bias, Istats [6] find out using quadratic variation that dividing two filtered variances by using different bands will give an unbiased estimate for the variance, for this purpose we use Haar and db 5 wavelet to find an unbiased estimate for the variance of detail coefficients

$$\mathrm{V}_1 = \frac{var(d_{j,k})_{half\ band\ Haar}}{var(d_{j,k})_{Haar}} \quad and\ \mathrm{V}_2 = \frac{var(d_{j,k})_{half\ band\ db\ 5}}{var(d_{j,k})_{db\ 5}}$$
$$V = \frac{1}{2}(V_1 + V_2) \quad (28)$$

Where the half band coefficients can be defined as follow

$$(d_{j,k})_{halfband} = [d_1, 0, d_2, 0, d_3, 0, \dots\dots\dots] \quad (29)$$

From the mentioned relations the estimate can be found using the following expression

$$\widehat{\mathrm{H}} = \frac{1}{2}\, log_2(V) \qquad (30)$$

5. Simulation study

In this section, we will conduct simulation experiments of multivariate fractional Brownian motion, where wavelet synthesis method proposed by Sellan, Mayer and Abry [9] [10] will be used for generating the mentioned random process, and then we will use Second moment of Gaussian noise using wavelet (SMGNW). The length of the series to be generated will be as $n = 100{,}200$ and the number of variables $m = 4, 8, 12$ we will repeat the process with $rep = 500$ for the sake of increasing the accuracy in the estimation process. As for the wavelet used for the generation, $s = 2^{10}, 2^{12}$. Taking into account that the estimation process for the Hurst parameter will be for all levels $H = [0.1: 0.9]$. The mean square error and the bias of the estimator will be calculated as follows

$$MSE(\widehat{H}) = Var(\widehat{H}) + Bias^2(\widehat{H})$$
$$= \left(\frac{1}{4}\sum_j \sigma_j^2 \theta_j^2\right) + (\widehat{H} - H)^2$$

Where $\theta_j = \frac{\sum(S*j - S_j)/\sigma_j^2}{S\, S_{jj} - S_j^2}$, *and* $S = \sum \frac{1}{\sigma_j^2}, S_j = \sum \frac{j}{\sigma_j^2}, S_{jj} = \sum \frac{j^2}{\sigma_j^2}$

$$Var(y_j) = \sigma_j^2 = \frac{\varsigma\left(2, \frac{N_j}{2}\right)}{ln^2(2)}, E(y_j) = 2(H+1) + constant \qquad (31)$$

Where $\varsigma\left(2, \frac{\mathrm{N_j}}{2}\right)$ is a generalized Riemann Zeta function [11]

Also, a new random series will be generated each time before the estimation in order to get the best view of the performance of the method used and at different levels of the random process.

Table 1 of Hurst est. bias and MSE using SMNGW

		s = 2^{10}				s = 2^{12}			
Var. no.	H	n=100		n=200		n=100		n=200	
		Bias	MSE	Bias	MSE	Bias	MSE	Bias	MSE
m=4	3.1	0.0250	0.0099	-0.0011	0.0002	0.0066	0.0079	-0.0113	0.0011
	3.2	0.0088	0.0187	0.0045	0.0010	0.0042	0.0130	-0.0354	0.0028
	3.3	0.0045	0.0300	0.0163	0.0025	0.0072	0.0165	0.0023	0.0035
	3.4	-0.0147	0.0378	0.0111	0.0033	0.0153	0.0196	-0.0160	0.0052
	3.5	0.0355	0.0314	-0.0028	0.0117	-0.0096	0.0251	-0.0169	0.0020
	3.6	0.0056	0.0578	0.0191	0.0033	-0.0024	0.0208	-0.0232	0.0107
	3.7	-0.0142	0.0574	0.0071	0.0021	-0.0049	0.0209	-0.0932	0.0195
	3.8	0.0380	0.0634	0.0133	0.0033	-0.0029	0.0192	-0.0168	0.0181
	3.9	0.0238	0.0476	0.0012	0.0109	-0.0179	0.0235	0.0193	0.0270
m=8	7.1	-0.0279	0.0038	0.0002	0.0023	-0.0036	0.0058	-0.0040	0.0036
	7.2	-0.0226	0.0111	0.0148	0.0060	-0.0077	0.0118	-0.0130	0.0085
	7.3	-0.0015	0.0203	0.0015	0.0065	-0.0123	0.0159	-0.0212	0.0121
	7.4	0.0353	0.0342	0.0169	0.0076	0.0159	0.0226	0.0017	0.0148
	7.5	0.0181	0.0152	0.0180	0.0107	-0.0154	0.0201	0.0211	0.0111
	7.6	-0.0216	0.0408	0.0034	0.0078	-0.0008	0.0281	0.0321	0.0132
	7.7	0.0161	0.0544	0.0044	0.0130	-0.0051	0.0328	0.0228	0.0120
	7.8	0.0102	0.0625	0.0050	0.0227	-0.0009	0.0378	-0.0013	0.0187
	7.9	0.0206	0.0759	-0.0035	0.0302	-0.0125	0.0385	0.0336	0.0415
m=12	11.1	-0.0106	0.0059	0.0028	0.0037	0.0047	0.0097	0.0002	0.0025

	11.2	-0.0224	0.0125	-0.0084	0.0073	0.0071	0.0186	-0.0273	0.0055
	11.3	-0.0012	0.0209	-0.0273	0.0096	-0.0134	0.0208	-0.0151	0.0086
	11.4	-0.0031	0.0263	-0.0181	0.0112	0.0177	0.0286	0.0108	0.0113
	11.5	0.0015	0.0203	0.0155	0.0098	0.0015	0.0171	0.0074	0.0096
	11.6	0.0061	0.0406	0.0082	0.0134	0.0052	0.0323	-0.0334	0.0103
	11.7	0.0153	0.0495	0.0069	0.0169	-0.0057	0.0368	0.0127	0.0113
	11.8	0.0146	0.0578	-0.0155	0.0244	0.0118	0.0470	0.0001	0.0163
	11.9	-0.0097	0.0699	-0.0076	0.0348	-0.0027	0.0555	0.0167	0.0334

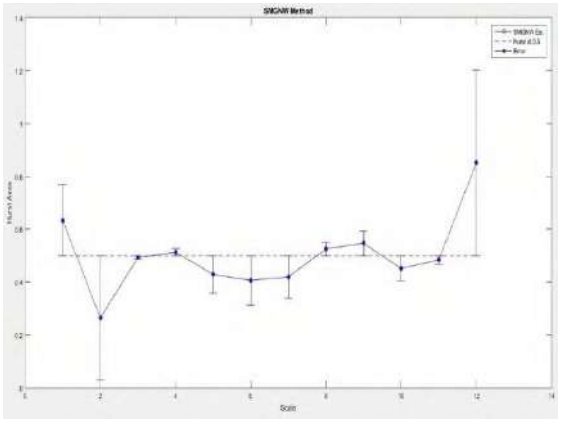

a

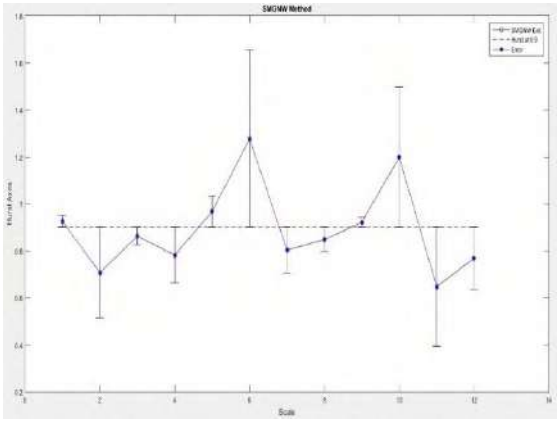

b

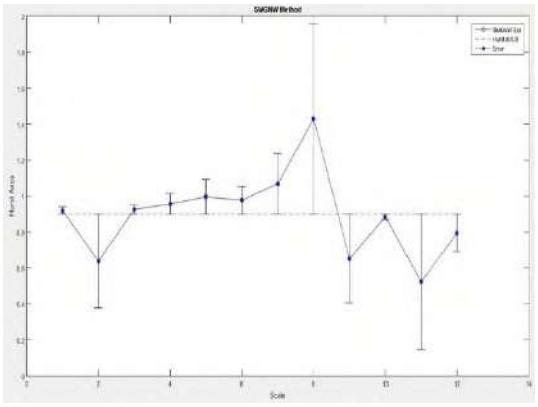

c

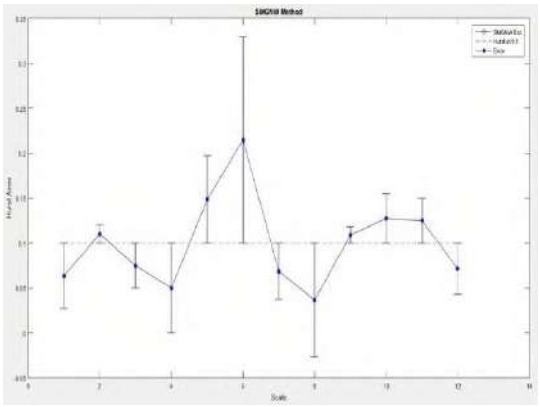

d

(a) 12-variate self-similarity analysis at sample size n=*10*0 and FBM synthesis $s = 2^{10}$ with Hurst exponent 0.*5*

(b) 12-variate self-similarity analysis at sample size n=2*0*0 and FBM synthesis $s = 2^{10}$ with Hurst exponent 0.9

(c) 12-variate self-similarity analysis at sample size n=*10*0 and FBM synthesis $s = 2^{12}$ with Hurst exponent 0.9

(d) 12-variate self-similarity analysis at sample size n=2*0*0 and FBM synthesis $s = 2^{12}$ with Hurst exponent 0.1

6. Conclusions

The estimation methods for signals with long memory, non-stationary often suffer from bias in the model variance that usually used for estimation, which in turn affects the error in the model estimation. In the SMGNW method used above, we consider reducing the amount of bias by truncating a part equal to the length of the filter used for the transformation, which led to the reduction of this bias to lower levels. The results of this truncation affected the estimation process positively. In this method, we also adopted the half-band method, which contributed in elimination of unwanted noise to obtain an efficient

estimator. Also, by relying on wavelet filters to perform the estimation process, the linear effect of the model was excluded from the model through the vanishing moments, which is one of the most important properties of the wavelet. The uses of Haar and db5 wavelet filters made our estimator better than other methods that's because we rely on denoising twice which make the signal smoother. This procedure made the proposed estimation process an efficient method for all levels of estimation through mean square error and bias as is evident from the results obtained.

References

[1] Ruch D K and Van Fleet P J 2009 Wavelet theory: an elementary approach with applications *A John Wiley & Sons*

[2] Mandelbrot B B and Van Ness J 1968 Fractional Brownian motion, fractional noises and applications *IBM Watson Research Center* **10**(4)422-437

[3] Nourdin I 2012 selected aspects of fractional Brownian motion *B&SS – Bocconi & Springer Series*

[4] Biagini, F Y,Oksendal B and Zhang T 2006 Stochastic calculus for fractional Brownian motion and application *B&SS – Bocconi & Springer Series*.

[5] Abry P, Flandrin P, Taqqu MS and Veitch D 2000 Wavelets for the analysis, estimation, and synthesis of scaling data In: Park K, Willinger W (eds) Self-similar network traffic and performance evaluation *Wiley New York* pp 39–88

[6] Istas J and Lang G 1997 Quadratic variations and estimation of the local Holder index of a Gaussian process *Annales de l'I.H.P. Probabilités et statistiques* **33** 407-436

[7] Flandrin P 1992 Wavelet analysis and synthesis of Fractional Brwonian Motion *IEEE Transactions on Information Theory* **38** (2) 910-917

[8] Averkamp R and Houdre C 2000 A Note on the discrete wavelet transform of second order processes *IEEE Transactions on Information Theory* **46**(4)1673-1676

[9] Abry P and Sellan F 1996 The wavelet-based synthesis for fractional Brownian motion proposed by F. Sellan and Y. Meyer: remarks and fast implemention *Applied and computational harmonic analysis* **3** 377-383

[10] Coeurjolly J F 2000 Simulation and identification of the fractional Brownian motion: a bibliographical and comparative study *Journal of Stat. Softwar* **5** Available from http://www.jstatsoft.org

[11] Power G J and Turvey G C 2010 Long-range dependence in the volatility of commodity futures prices: *wavelet-base evidence Phys. A.*, **389** 79-90.

Signal Soft Topology and Molecules of Matter

Signal Soft Topology and Molecules of Matter

Majd Hamid Mahmood

Department of Mathematics, College of Education, University of Al-Mustansiriyah, Baghdad, Iraq

E-mail: mgmg227@yahoo.com

Abstract. In this search, we will make modeling for molecules of matter (organic, inorganic) by using signal soft sets, and generate signal soft topologies for molecules.

1. Introduction

Molodtsov in [4] defines a soft set as a general mathematical tool for dealing with uncertain objects. Mahmood in [3] presented a signal soft set to represent atom groups, electron, proton, neutron, anti - atom, we define operations on signal soft sets to study the construction of some chemical compounds like water hydrochloric acid, define a signal soft topology, in this search we will make modeling for molecules of matter by using a signal soft sets, generate signal soft topology for molecules.

2. Basics on soft set and atoms

In this section, we will define the signal soft element, signal soft set to make a model for the atom, molecules define $\oplus,\ominus$ between signal soft sets, with examples.

Definition 2.1 [3]: Let X be a universal set contain elements in R^+ denoted by "h", E is a set of parameters contain elements denoted by "e " .Then, the signal soft element x defined by:
$x = \{ (e_i , h_j^{\delta ij}) = (e_i , \digamma(ei)) : \digamma : E \to h_j^{\delta ij} , h_j \in P(X) , \delta_{ij}$ take + , – , ± or $\mp$ signal
$\forall i, j \in \Omega$, Ω is indexed set of natural numbers}.

Definition 2.2 [3]: Let X be a universal set of "h" elements in R^+, E is a set of parameters of "e" elements.Then, the signal soft set defined by : $N = (\digamma,E) = \{ x : x = (e_i, h_j^{\delta ij}), \delta_{ij}$ take ("+" for proton and anti-electron , " – " for electron and anti - proton , " ± " for neutron , "$\mp$" for anti-neutron) ,$\forall$ i , j$\in$ Ω , Ω is indexed set of natural numbers }.

Model 2.3 [3]: Let N be the atom name; η, ρ, ε denoted respectively to neutron, proton, electron and δ for the signal. Then, the atom as a signal soft set model is defined by $N = (N, \eta^\delta , \rho^\delta, \varepsilon^\delta)$.

Coding 2.4 [3]: As a special case of the atom, we have the followings:
1- Neutron = $\eta = (\emptyset , 1^{\pm} , 0^{+} , 0^{-})$.
2- Proton = $\rho = (\emptyset , 0^{\pm}, 1^{+} , 0^{-})$.
3- Electron = $\varepsilon = (\emptyset , 0^{\pm}, 0^{+}, 1^{-})$.
4- Energy = $\xi = (\emptyset , 0^{\pm} , 0^{+} , 0^{-}) = \Phi$.

Examples 2.5 [3]:
1- Hydrogen = (H, $0^{\pm}$, $1^{+,1-}$).
2- Oxygen = (O, $8^{\pm}$, 8^{+}, 8^{-}).
3- Carbon = (C, $6^{\pm}$, 6^{+}, 6^{-}).
4- Nitrogen = (N, $7^{\pm}$, 7^{+}, 7^{-}).

Definition 2.6 [3]: Let X be a universal set of "*h*" elements in R^{+},E be a set of parameters of "*e*" elements. Then, the null-signal soft set denoted by: $\Phi = \{x : x = (e_i, h_j^{\delta ij})$, $\forall$ i , j $\in \Omega$, Ω is indexed set of natural numbers, $e_i = \emptyset$ and $h_j = 0$, δ ij take + , – , $\pm$ or $\mp$ signal }.

Example 2.7 [3]: X = { $h_1 = h_2 = h_3 = 0$ }, E = { $e_1 = \emptyset$ } , $\Phi = (\emptyset , 0^{\pm} , 0^{+} , 0^{-})$ is a null-signal soft set, there are three signal soft elements x_1, x_2, x_3 :
$x_1 = (e_1, h_1^{\delta 11}) = (\emptyset , 0^{\pm})$, $x_2 = (e_1, h_2^{\delta 12}) = (\emptyset , 0^{+})$, $x_3 = (e_1, h_3^{\delta 13}) = (\emptyset , 0^{-})$.

Definition 2.8 [3]: Let X be a universal set of "*h*" elements in R^{+} , E be a set of parameters of "*e*" elements and (F,E) be a soft set .Then, the universal signal soft set denoted by : U = $\{x : x = (e_i, h_j^{\delta ij})$,$\forall$ i , j $\in \Omega$, Ω is indexed set of natural numbers, e_i = X and $h_j = \infty$, ∞ is the most large number in X}.

Example 2.9[3]: X = { $h_1 = h_2 = h_3 = \infty$ } , E = { e_1 = X } , U = (X , $\infty^{\pm}$, ∞^{+} , ∞^{-}) is a universal signal soft set there are three signal soft elements x_1, x_2, x_3 :
$x_1 = (e_1, h_1^{\delta 11}) = (X, \infty^{\pm})$, $x_2 = (e_1, h_2^{\delta 12}) = (X , \infty^{+})$, $x_3 = (e_1, h_3^{\delta 13}) = (X , \infty^{-})$.

Remark 2.10 [3] The null-signal soft set and the universal signal soft set are virtual sets.

Definition 2.11[3]: Let N = { $x : x = (e_i, hj^{\delta ij})$ } .The complement of the Signal soft set N denoted by: N^{c} ={ $x^{c} : x^{c} = (e_i, hj^{-\delta ij})$ } .

Definition 2.12 [3]: Let N_1, N_2 be two signal soft sets.Then, N_1 is a subset of N_2, if each $x_{\alpha} \in N_1$ we have $x_{\alpha} \in N_2$ and denoted by $N_1 \subseteq N_2$.

Definition 2.13[3]: The two signal soft sets N_1, N_2 are equal if $N_1 \subseteq N_2 \wedge N_2 \subseteq N_1$, denoted by $N_1 = N_2$ otherwise $N_1 \neq N_2$.

Definition 2.14 [3]: Let $N_1 = (N_1 , \eta_1^{\delta 1}, \rho_1^{\delta 2}, \varepsilon_1^{\delta 3})$, $N_2 = (N_2 , \eta_2^{\sigma 1}, \rho_2^{\sigma 2} , \varepsilon_2^{\sigma 3})$ be two signal soft sets. Then, the summation is defined as follow:
$N_1 \oplus N_2 = (N_1 , \eta_1^{\delta 1} , \rho_1^{\delta 2}, \varepsilon_1^{\delta 3}) \oplus (N_2 , \eta_2^{\sigma 1} , \rho_2^{\sigma 2} , \varepsilon_2^{\sigma 3})$
$= N_3 = (N_3 , \eta_1^{\delta 1} + \eta_2^{\sigma 1} , \rho_1^{\delta 2} + \rho_2^{\sigma 2} , \varepsilon_1^{\delta 3} + \varepsilon_2^{\sigma 3})$.

Remark 2.15: Let N_{be} a signal soft set. Then, the summation of *n* signal soft sets of N is *n* N.

Definition 2.16 [3]: Let $N_1 = (N_1 , \eta_1^{\delta 1}, \rho_1^{\delta 2}, \varepsilon_1^{\delta 3})$, $N_2 = (N_2 , \eta_2^{\sigma 1}, \rho_2^{\sigma 2} , \varepsilon_2^{\sigma 3})$ be two signal soft sets. Then, the difference is defined as follow:
$N_1 \ominus N_2 = (N_1 , \eta_1^{\delta 1} , \rho_1^{\delta 2}, \varepsilon_1^{\delta 3}) \ominus (N_2 , \eta_2^{\sigma 1} , \rho_2^{\sigma 2} , \varepsilon_2^{\sigma 3})$
$= N_3 = (N_3 , \eta_1^{\delta 1} - \eta_2^{\sigma 1} , \rho_1^{\delta 2} - \rho_2^{\sigma 2} , \varepsilon_1^{\delta 3} - \varepsilon_2^{\sigma 3})$.

Notice 2.17 [3]: In general
$(N_1 , \eta_1^{\delta 1} , \rho_1^{\delta 2}, \varepsilon_1^{\delta 3}) \oplus (N_2 , \eta_2^{\sigma 1} , \rho_2^{\sigma 2} , \varepsilon_2^{\sigma 3}) = (N_3 , \eta_3^{\kappa 1} , \rho_3^{\kappa 2} , \varepsilon_3^{\kappa 3}) \circledast \xi$

(N_1, $\eta_1^{\delta 1}$, $\rho_1^{\delta 2}$, $\varepsilon_1^{\delta 3}$) $\ominus$ (N_2 , $\eta_2^{\sigma 1}$, $\rho_2^{\sigma 2}$, $\varepsilon_2^{\sigma 3}$) = (N_3 , $\eta_3^{\kappa 1}$, $\rho_3^{\kappa 2}$, $\varepsilon_3^{\kappa 3}$) $\oplus\!\!\!\!\ominus$ ξ
where ξ = (N_4 , $\eta_4^{\gamma 1}$, $\rho_4^{\gamma 2}$, $\varepsilon_4^{\gamma 3}$) could be an atom, neutron, proton, electron, Φ, anti-atom, anti-energy, or PE (as seen in the next sections).

Definition 2. 18: Let N_1 = (N_1, $\eta_1^{\delta 1}$, $\rho_1^{\delta 2}$, $\varepsilon_1^{\delta 3}$), N_2 = (N_2 , $\eta_2^{\sigma 1}$, $\rho_2^{\sigma 2}$, $\varepsilon_2^{\sigma 3}$) , ….. N_n = (N_n , $\eta_n^{\alpha 1}$, $\rho_n^{\alpha 2}$, $\varepsilon_n^{\alpha 3}$) are signal soft sets (atoms) . Their summation is a (molecular M) defined as follow:
$N_1 \oplus N_2 \oplus ... \oplus N_n$ = (N_1 , $\eta_1^{\delta 1}$, $\rho_1^{\delta 2}$, $\varepsilon_1^{\delta 3}$) $\oplus$ (N_2 , $\eta_2^{\sigma 1}$,$\rho_2^{\sigma 2}$, $\varepsilon_2^{\sigma 3}$) $\oplus$ ... $\oplus$ (N_n , $\eta_n^{\alpha 1}$, $\rho_n^{\alpha 2}$, $\varepsilon_n^{\alpha 3}$)
= M = (N , $\eta_1^{\delta 1}$ + $\eta_2^{\sigma 1}$ +…+ $\eta_n^{\alpha 1}$, $\rho_1^{\delta 2}$ + $\rho_2^{\sigma 2}$ +…+$\rho_n^{\alpha 2}$, $\varepsilon_1^{\delta 3}$ + $\varepsilon_2^{\sigma 3}$ +…+$\varepsilon_n^{\alpha 3}$).

Remarks 2.19:
1- The molecular M could be a set of summation of other molecules M_1, M_2, ..., M_n :
$M = M_1 \oplus M_2 \oplus ... \oplus M_n$
or summation of atoms N_1 , N_2 , ... , N_n :
$M = N_1 \oplus N_2 \oplus ... \oplus N_n$
or summation of both molecules and atoms M_1 , M_2 , ... ,M_n , N_1 , N_2 , ... , N_n :
$M = M_1 \oplus M_2 \oplus ... \oplus M_n \oplus N_1 \oplus N_2 \oplus ... \oplus N_n$
2- The molecular M is a (subcollection) of some compound set C if M is a summation of arbitrary many atoms (or molecules or both) in C,
i.e. $M \subset C \Leftrightarrow \forall\, C = N_1 \oplus N_2 \oplus \cdots \oplus N_n$, $M = \oplus N_{\alpha i}$ for some $\alpha i \in I$, I = 1 , 2 , …., n .

3- Chemical (organic) molecules modeled by a signal soft set

In this section, we will study some basic types of organic molecules represented as a signal soft set, first, we will study the basics types like amino acids the construction of DNA and RNA then we will study the representation of some types of carbohydrates, fats, and protein.

Examples 3.1: This example show the basic types of amino acids that contained in the DNA and RNA represented as signal soft sets.
1- Cytosine C4H5N3O " $\mathcal{C}$ "
Let M_1 = (C,$6^{\pm}$,6^{+},6^{-}) $\oplus$ (C,$6^{\pm}$,6^{+},6^{-}) $\oplus$ (C,$6^{\pm}$,6^{+},6^{-}) $\oplus$ (C,$6^{\pm}$,6^{+},6^{-})
= 4(C, $6^{\pm}$,6^{+},6^{-}) = (C_4, $24^{\pm}$,24^{+},24^{-}) ,
M_2 = (H,$0^{\pm}$,1^{+},1^{-}) $\oplus$ (H,$0^{\pm}$,1^{+},1^{-}) $\oplus$ (H,$0^{\pm}$,1^{+},1^{-}) $\oplus$ (H,$0^{\pm}$,1^{+},1^{-}) $\oplus$ (H,$0^{\pm}$,1^{+},1^{-})
= 5(H,$0^{\pm}$,1^{+},1^{-}) = (H_5,$0^{\pm}$,5^{+},5^{-}),
M_3 = (N,$7^{\pm}$,7^{+},7^{-}) $\oplus$ (N,$7^{\pm}$,7^{+},7^{-}) $\oplus$ (N,$7^{\pm}$,7^{+},7^{-}) = 3 (N,$7^{\pm}$,7^{+},7^{-}) = (N_3,$21^{\pm}$,21^{+},21^{-})
N_4 = Oxygen = (O,$8^{\pm}$,8^{+},8^{-}) .
Then, the Cytosine = $M_1 \oplus M_2 \oplus M_3 \oplus N_4$
= (C_4, $24^{\pm}$,24^{+},24^{-}) $\oplus$ (H_5,$0^{\pm}$,5^{+},5^{-}) $\oplus$ (N_3,$21^{\pm}$,21^{+},21^{-}) $\oplus$ (O,$8^{\pm}$,8^{+},8^{-}) = ($\mathcal{C}$, $53^{\pm}$, 58^{+} , 58^{-})
2- Guanine C5H5N5O " $\mathcal{G}$ "
Let M_1 = 5(C,$6^{\pm}$,6^{+},6^{-}) = (C_5, $30^{\pm}$,30^{+},30^{-}),
M_2 = 5(H,$0^{\pm}$,1^{+},1^{-}) = (H_5,$0^{\pm}$,5^{+},5^{-}) ,
M_3= 5(N,$7^{\pm}$,7^{+},7^{-}) = (N_5,$35^{\pm}$,35^{+},35^{-})
N_4 = Oxygen = (O,$8^{\pm}$,8^{+},8^{-}) .Then, the Guanine = $M_1 \oplus M_2 \oplus M_3 \oplus N_4$
= (C_5, $30^{\pm}$,30^{+},30^{-}) $\oplus$ (H_5,$0^{\pm}$,5^{+},5^{-}) $\oplus$ (N_5,$35^{\pm}$,35^{+},35^{-}) $\oplus$ (O,$8^{\pm}$,8^{+},8^{-})
= (, $73^{\pm}$, 78^{+} , 78^{-}).
3- Adenine C5H5N5 " $\mathcal{A}$ "
Let M_1 = 5(C,$6^{\pm}$,6^{+},6^{-}) = (C_5, $30^{\pm}$,30^{+},30^{-}) , M_2 = 5(H,$0^{\pm}$,1^{+},1^{-}) = (H_5,$0^{\pm}$,5^{+},5^{-})
M_3= 5(N,$7^{\pm}$,7^{+},7^{-}) = (N_5,$35^{\pm}$,35^{+},35^{-}) .
Then, the Adenine = $M_1 \oplus M_2 \oplus M_3$ = (C_5, $30^{\pm}$,30^{+},30^{-}) $\oplus$ (H_5,$0^{\pm}$,5^{+},5^{-}) $\oplus$ (N_5,$35^{\pm}$,35^{+},35^{-})
= (, $65^{\pm}$, 70^{+} , 70^{-}) .
4- Thymine C5H6N2O2 " $\mathcal{T}$ "

Let $M_1 = 5(C,6^{\pm},6^{+},6^{-}) = (C_5, 30^{\pm},30^{+},30^{-})$,
$M_2 = 6(H,0^{\pm},1^{+},1^{-}) = (H_6,0^{\pm},6^{+},6^{-})$
$M_3 = 2(N,7^{\pm},7^{+},7^{-}) = (N_2,14^{\pm},14^{+},14^{-})$
$M_4 = 2(O,8^{\pm},8^{+},8^{-}) = (O_2,16^{\pm},16^{+},16^{-})$.
Then the Thymine = $M_1 \oplus M_2 \oplus M_3 \oplus M_4$
$= (C_5, 30^{\pm},30^{+},30^{-}) \oplus (H_6,0^{\pm},6^{+},6^{-}) \oplus (N_2,14^{\pm},14^{+},14^{-}) \oplus (O_2,16^{\pm},16^{+},16^{-})$
$= (, 60^{\pm} , 66^{+} , 66^{-})$.

Example 3.2: In this example we will make a model for Fructose which is a simple kind of Carbohydrate
Fructose = C6H12O6 " "
Let $M_1 = 6(C,6^{\pm},6^{+},6^{-}) = (C_6, 36^{\pm},36^{+},36^{-})$, $M_2 = 12(H,0^{\pm},1^{+},1^{-}) = (H_{12},0^{\pm},12^{+},12^{-})$
$M_3 = 6(O,8^{\pm},8^{+},8^{-}) = (O_6,48^{\pm},48^{+},48^{-})$.
Then Fructose $= M_1 \oplus M_2 \oplus M_3 = (C_6, 36^{\pm},36^{+},36^{-}) \oplus (H_{12},0^{\pm},12^{+},12^{-}) \oplus (O_6,48^{\pm},48^{+},48^{-})$
$= (\mathcal{F}, 84^{\pm} , 96^{+} , 96^{-})$.

Example 3.3: In this example we will make a model for Omega3 which is an example of Fats
Omega3 = C20H30O2 " "
Let $M_1 = 20(C,6^{\pm},6^{+},6^{-}) = (C_{120}, 120^{\pm},120^{+},120^{-})$, $M_2 = 30(H,0^{\pm},1^{+},1^{-}) = (H_{30},0^{\pm},30^{+},30^{-})$
$M_3 = 2(O,8^{\pm},8^{+},8^{-}) = (O_2,16^{\pm},16^{+},16^{-})$.
Then $\mathcal{O} = M_1 \oplus M_2 \oplus M_3 = (C_{120}, 120^{\pm},120^{+},120^{-}) \oplus (H_{30},0^{\pm},30^{+},30^{-}) \oplus (O_2,16^{\pm},16^{+},16^{-})$
$= (\mathcal{O}, 136^{\pm} , 166^{+} , 166^{-})$.

Example 3.4: In this example, we will make a model for Gluten as an example of Protein
Gluten = C5H10N2O3 " "
Let $M_1 = 5(C,6^{\pm},6^{+},6^{-}) = (C_5, 30^{\pm},30^{+},30^{-})$, $M_2 = 10(H,0^{\pm},1^{+},1^{-}) = (H_{10},0^{\pm},10^{+},10^{-})$
$M_3 = 2(N,7^{\pm},7^{+},7^{-}) = (N_2,14^{\pm},14^{+},14^{-})$, $M_4 = 3(O,8^{\pm},8^{+},8^{-}) = (O_3,24^{\pm},24^{+},24^{-})$.
Then $\mathcal{S} = M_1 \oplus M_2 \oplus M_3 \oplus N_4 = (C_5, 30^{\pm},30^{+},30^{-}) \oplus (H_{10},0^{\pm},10^{+},10^{-}) \oplus (N_2,14^{\pm},14^{+},14^{-}) \oplus (O_3,24^{\pm},24^{+},24^{-}) = (\mathcal{S}, 68^{\pm} , 78^{+}, 78^{-})$.

4- Chemical (inorganic) molecules modeled by a signal soft set

In this section, we will study some basic types of inorganic molecules represented as a signal soft set: water, acids, bases, salts

Examples 4.1

1- Water: $2 (H,0^{\pm},1^{+},1^{-}) \oplus (O,8^{\pm},8^{+},8^{-}) = (H_2,0^{\pm},2^{+},2^{-}) \oplus (O,8^{\pm},8^{+},8^{-}) = (H_2O ,8^{\pm},10^{+},10^{-})$.
2- Acids: "Carbonic Acids" $= (H_2,0^{\pm},2^{+},2^{-}) \oplus (C,6^{\pm},6^{+},6^{-}) \oplus (O_3,24^{\pm},24^{+},24^{-})$ $(H2CO3,30^{\pm},32^{+},32^{-})$.
3- Salts: "Ammonium" $= (N,7^{\pm},7^{+},7^{-}) \oplus (H4,0^{\pm},4^{+},4^{-}) = (NH4,7^{\pm},11^{+},11^{-})$.
4- Bases: "Calcium Hydroxide" $= (Ca,20^{\pm},20^{+},20^{-}) \oplus (O_2,16^{\pm},16^{+},16^{-}) \oplus (H_2,0^{\pm},2^{+},2^{-}) = (Ca(OH)_2 ,36^{\pm}, 38^{+}, 38^{-})$

5- Anti-molecules modeled by a signal soft set

In this section, we will introduce the anti-molecules as the anti-signal soft set model we will use the symbol $\acute{M}$ for the anti-signal soft set to study molecules with anti- molecules, show mathematically that the summation of molecules and its anti- molecules will give pure energy.

Model 5.1: Let $N = (N , \eta^{\delta}, \rho^{\delta}, \varepsilon^{\delta})$ be a signal soft set model of some atom.Then, the anti-signal soft set model of N is defined by $\acute{N} = (\overline{N} , \overline{\eta}^{\lambda} , \overline{\rho}^{\lambda}, \overline{\varepsilon}^{\lambda})$, where $\lambda = - \delta$
(Which represent the anti-atom in general).

Model 5. 2: Let $\breve{M}_1 = (\bar{N}_1, \bar{\eta}_1^{\delta 1}, \bar{\rho}_1^{\delta 2}, \bar{\varepsilon}_1^{\delta 3})$, $\breve{M}_2 = (\bar{N}_2, \bar{\eta}_2^{\sigma 1}, \bar{\rho}_2^{\sigma 2}, \bar{\varepsilon}_2^{\sigma 3})$,…, $\breve{M}_n = (\bar{N}_n, \bar{\eta}_n^{\alpha 1}, \bar{\rho}_n^{\alpha 2}, \bar{\varepsilon}_n^{\alpha 3})$ are anti-signal soft sets (anti-atoms) . Their summation is a (anti – molecular $\acute{M}$) defined by:
$\breve{M}_1 \oplus \breve{M}_2 \oplus \ldots \oplus \breve{M}_n = (\bar{N}_1, \bar{\eta}_1^{\delta 1}, \bar{\rho}_1^{\delta 2}, \bar{\varepsilon}_1^{\delta 3}) \oplus (\bar{N}_2, \bar{\eta}_2^{\sigma 1}, \bar{\rho}_2^{\sigma 2}, \bar{\varepsilon}_2^{\sigma 3}) \oplus \ldots \oplus (\bar{N}_n, \bar{\eta}_n^{\alpha 1}, \bar{\rho}_n^{\alpha 2}, \bar{\varepsilon}_n^{\alpha 3}) = \acute{M}$
$= (\bar{N}, \bar{\eta}_1^{\delta 1} + \bar{\eta}_2^{\sigma 1} + \bar{\eta}_n^{\alpha 1}, \bar{\rho}_1^{\delta 2} + \bar{\rho}_2^{\sigma 2} + \bar{\rho}_n^{\alpha 2}, \bar{\varepsilon}_1^{\delta 3} + \bar{\varepsilon}_2^{\sigma 3} + \bar{\varepsilon}_n^{\alpha 3})$.

Model 5. 3: Let $\breve{M}_1 = (\bar{N}_1, \bar{\eta}_1^{\delta 1}, \bar{\rho}_1^{\delta 2}, \bar{\varepsilon}_1^{\delta 3})$, $\breve{M}_2 = (\bar{N}_2, \bar{\eta}_2^{\sigma 1}, \bar{\rho}_2^{\sigma 2}, \bar{\varepsilon}_2^{\sigma 3})$, ….. $\breve{M}_n = (\bar{N}_n, \bar{\eta}_n^{\alpha 1}, \bar{\rho}_n^{\alpha 2}, \bar{\varepsilon}_n^{\alpha 3})$ are anti-signal soft sets (it could be anti-atoms , anti – molecules or both) . Their summation is a (anti – molecular $\acute{M}$) defined by :
$\breve{M}_1 \oplus \breve{M}_2 \oplus \ldots \oplus \breve{M}_n = (\bar{N}_1, \bar{\eta}_1^{\delta 1}, \bar{\rho}_1^{\delta 2}, \bar{\varepsilon}_1^{\delta 3}) \oplus (\bar{N}_2, \bar{\eta}_2^{\sigma 1}, \bar{\rho}_2^{\sigma 2}, \bar{\varepsilon}_2^{\sigma 3}) \oplus \ldots \oplus (\bar{N}_n, \bar{\eta}_n^{\alpha 1}, \bar{\rho}_n^{\alpha 2}, \bar{\varepsilon}_n^{\alpha 3})$
$= \acute{M} = (\bar{N}, \bar{\eta}_1^{\delta 1} + \bar{\eta}_2^{\sigma 1} + \bar{\eta}_n^{\alpha 1}, \bar{\rho}_1^{\delta 2} + \bar{\rho}_2^{\sigma 2} + \bar{\rho}_n^{\alpha 2}, \bar{\varepsilon}_1^{\delta 3} + \bar{\varepsilon}_2^{\sigma 3} + \bar{\varepsilon}_n^{\alpha 3})$.

Example 5.4: In this example we will make a model for anti - Fructose " $\bar{\mathcal{F}}$ " where Fructose = ($\mathcal{F}$, $84^{\pm}$, 96^{+} , 96^{-}), since
$M_1 = (C_6, 36^{\pm}, 36^{+}, 36^{-})$ then $\breve{M}_1 = (\bar{C}_6, 36^{\mp}, 36^{-}, 36^{+})$
$M_2 = (H_{12}, 0^{\pm}, 12^{+}, 12^{-})$ then $\breve{M}_2 = (\bar{H}_{12}, 0^{\mp}, 12^{-}, 12^{+})$
$M_3 = (O_6, 48^{\pm}, 48^{+}, 48^{-})$ then $\breve{M}_3 = (\bar{O}_6, 48^{\mp}, 48^{-}, 48^{+})$
Then, anti - Fructose = $\breve{M}_1 \oplus \breve{M}_2 \oplus \breve{M}_3 = (\bar{C}_6, 36^{\mp}, 36^{-}, 36^{+}) \oplus (\bar{H}_{12}, 0^{\mp}, 12^{-}, 12^{+}) \oplus (\bar{O}_6, 48^{\mp}, 48^{-}, 48^{+}) = (\bar{\mathcal{F}}, 84^{\mp}, 96^{-}, 96^{+})$.

Example 5.5: Let $\xi = (\emptyset, 0^{\pm}, 0^{+}, 0^{-})$, $\bar{\xi} = (\bar{\emptyset}, 0^{\mp}, 0^{-}, 0^{+})$ be an energy and anti-energy signal soft sets . Then, the summation is defined as follow :
$\xi \oplus \bar{\xi} = (\emptyset, 0^{\pm}, 0^{+}, 0^{-}) \oplus (\bar{\emptyset}, 0^{\mp}, 0^{-}, 0^{+}) = (\emptyset + \bar{\emptyset}, 0^{\pm} + 0^{\mp}, 0^{+} + 0^{-}, 0^{-} + 0^{+})$
$= (\varnothing, \phi^{\varphi}, \phi^{\varphi}, \phi^{\varphi}) = PE$, Similarly $\bar{\xi} \oplus \xi = PE$.

Remark 5.6: Any molecules with anti- molecules equals pure energy PE.

Example 5.7: For Fructose = ($\mathcal{F}$, $84^{\pm}$, 96^{+} , 96^{-}) and anti - Fructose $\breve{F} = (\bar{\mathcal{F}}, 84^{\mp}, 96^{-}, 96^{+})$
($\mathcal{F}$, $84^{\pm}$, 96^{+} , 96^{-}) $\oplus$ ($\bar{\mathcal{F}}$, $84^{\mp}$, 96^{-} , 96^{+}) = = ($\varnothing$, ϕ^{φ}, ϕ^{φ} , ϕ^{φ}) = PE

6- Signal soft topological space (for molecules)

In this section, we will use molecular to define signal soft topologies, for many cases, in reality, we deal with finite structures so we will need to define signal soft topology for molecules that use finite signal soft sets for atoms.

Definition 6.1: Let $M_1 = (M_1, \eta_1, \rho_1, \varepsilon_1)$, $M_2 = (M_2, \eta_2, \rho_2, \varepsilon_2)$ be two molecules (or atoms or both). Then, the union of two molecules $M_1 \Cup M_2 = M_3 = (M_3, \eta_3, \rho_3, \varepsilon_3)$,

$$\eta_3 = \begin{cases} \text{if } \eta_1 \neq \eta_2 \Rightarrow [\eta_3 = max\{\eta_1, \eta_2\}] \\ \text{if } \eta_1 = \eta_2 \Rightarrow [\eta_3 = \eta_1 \vee \eta_2] \end{cases}$$

and similarly for ρ_3 , ε_3 .

Definition 6.2: Let $M_1 = (M_1, \eta_1, \rho_1, \varepsilon_1)$, $M_2 = (M_2, \eta_2, \rho_2, \varepsilon_2)$ be two molecules (or atoms or both). Then, the intersection of two molecules $M_1 \Cap M_2 = M_3 = (M_3, \eta_3, \rho_3, \varepsilon_3)$,

$$\eta_3 = \begin{cases} \text{if } \eta_1 \neq \eta_2 \Rightarrow [\eta_3 = min\{\eta_1, \eta_2\}] \\ \text{if } \eta_1 = \eta_2 \Rightarrow [\eta_3 = \eta_1 \vee \eta_2] \end{cases}$$

and similarly for ρ_3 , ε_3 .

Definition 6.3; Let X be a non-empty set , E be a finite set of parameters (X , E), T be a collection of finite signal soft sets generated by non-null finite signal soft set (molecular - M) if T satisfies the following axioms :
(1) Φ and M are in T.
(2) ⋓ of any members of signal soft sets in T belongs to T.
(3) ⋒ of any two signal soft sets in T belong to T.
Then, T is called signal soft topology on M (simply T is *S* M - topology), the triple (M ,T , E) is called signal soft topological space on molecules M (simply S_M - space), the signal soft sets of T are called S_M - open sets and their complements are called S_M - closed sets.

Examples 6.4:
1- Let $\Phi = (\emptyset , 0^{\pm} , 0^{+} , 0^{-})$, M = $(NH4,7^{\pm},11^{+},11^{-})$.
Then, T = {Φ , M } is the S_M - Indiscrete topology.
2- Let M = (H4 , $0^{\pm}$, 4^{+} , 4^{-}) , Φ = (∅ , $0^{\pm}$, 0^{+} , 0^{-})
U = $(NH4,7^{\pm},11^{+},11^{-})$.
Then, T = {Φ ,U , M } is S_U - topology since
M ⋒ Φ = (H4 , $0^{\pm}$, 4^{+} , 4^{-}) ⋒ (∅ , $0^{\pm}$, 0^{+} , 0^{-}) = Φ
M ⋒U = (H4 , $0^{\pm}$, 4^{+} , 4^{-}) ⋒ $(NH4,7^{\pm},11^{+},11^{-})$ = M
U ⋒ Φ = $(NH4,7^{\pm},11^{+},11^{-})$ ⋒ (∅ , $0^{\pm}$, 0^{+} , 0^{-}) = Φ
M ⋓ Φ = (H4 , $0^{\pm}$, 4^{+} , 4^{-}) ⋓ (∅ , $0^{\pm}$, 0^{+} , 0^{-}) = M
M ⋓ U = (H4 , $0^{\pm}$, 4^{+} , 4^{-}) ⋓ $(NH4,7^{\pm},11^{+},11^{-})$ = U
U ⋓ Φ = $(NH4,7^{\pm},11^{+},11^{-})$ ⋓ (∅ , $0^{\pm}$, 0^{+} , 0^{-}) = U
and (U ,T , E) is S_U - space .

Definition 6.5: Let (M , T , E) be S_M - space, x ∈ M.Then, M is said to be S_M - neighborhood of x if there exist an S_M - open set N (atom) such that x ∈N ⊆ M, or there exist an S_M - open set M_1 (molecular) such that x ∈ M_1 ⊆ M.

Remark 6.6: Every S_M - open set is S_M - neighborhood, the converse is not true in general.

Example 6.7: Let M_1 = (H_2,$0^{\pm}$,2^{+},2^{-}), M_2 = (H_2CO_3,$30^{\pm}$,32^{+},32^{-}), M_2 = (H_2,$0^{\pm}$,2^{+},2^{-}) ⊕ (C,$6^{\pm}$,6^{+},6^{-}) ⊕ (O_3,$24^{\pm}$,24^{+},24^{-})
Φ = (∅ , $0^{\pm}$, 0^{+} , 0^{-}), T = { Φ , M_1 , M_2 } is S_{M2} - topology
M_2 is S_{M2} - open since M_2 ∈ T, also M_2 is S_{M2} - neighborhood of x_1= (H, $0^{\pm}$) , since $x_1 \in M_1 \subseteq M_2$
and M_3 = $Ca(OH)_2$ = (Ca,$20^{\pm}$,20^{+},20^{-}) ⊕ (O_2,$16^{\pm}$,16^{+},16^{-}) ⊕ (H_2,$0^{\pm}$,2^{+},2^{-})
M_3 is S_{M2} - neighborhood of x_1 = (H, $0^{\pm}$) , since $x_1 \in M_1 \subseteq M_3$ but M_3 is not S_{M2} - open since $M_3 \notin$ T.

Example 6.8: Let M = ($\mathcal{F}$, $84^{\pm}$, 96^{+} , 96^{-}) , Φ = (∅ , $0^{\pm}$, 0^{+} , 0^{-}) .
Then, T = {Φ , M} is S_M - topology which is indiscrete signal soft topology
M is S_M - open since $M \in$ T
also M is S_M - neighborhood of x_1= ($\mathcal{F}$, $84^{\pm}$) , x_2= ($\mathcal{F}$, 96^{+}) , x_3= ($\mathcal{F}$, 96^{-})
since $x_1 \in M \subseteq M$ .Then, M *is* S_M - neighborhood of x_1 similarly for x_2, x_3.

Example 6.9: Let M_1 = (C_4, $24^{\pm}$,24^{+},24^{-}) , M_2 = (H_5,$0^{\pm}$,5^{+},5^{-}) , M_3 = (N_3,$21^{\pm}$,21^{+},21^{-})
N_4 = Oxygen = (O,$8^{\pm}$,8^{+},8^{-}) .
Then, the Cytosine = $M_1 \oplus M_2 \oplus M_3 \oplus N_4$ = ($\mathcal{C}$, $53^{\pm}$, 58^{+} , 58^{-})
Φ = (∅ , $0^{\pm}$, 0^{+} , 0^{-}) , T = { Φ , M_1 , $\mathcal{C}$ } is $S_{\mathcal{C}}$ - topology .
M_1 is $S_{\mathcal{C}}$ - open since $M_1 \in$ T , M_1 is $S_{\mathcal{C}}$ - neighborhood of x_1= (C_4, $24^{\pm}$) , since $x_1 \in M_1 \subseteq \mathcal{C}$

M_1 is not $S_{\mathcal{C}}$ - neighborhood of $x_2 = (H_5, 0^{\pm})$, $\mathcal{C}$ is $S_{\mathcal{C}}$ - neighborhood of $x_2 = (H_5, 0^{\pm})$.

Example 6.10: It is possible to generate a signal soft topology for anti - molecular as seen in this example.
Let anti - Fructose = $\acute{\Gamma} = \breve{M}_1 \oplus \breve{M}_2 \oplus \breve{M}_3$
$= (\bar{C}_6, 36^{\mp}, 36^{-}, 36^{+}) \oplus (\bar{H}_{12}, 0^{\mp}, 12^{-}, 12^{+}) \oplus (\bar{O}_6, 48^{\mp}, 48^{-}, 48^{+}) = (\bar{\mathcal{F}}, 84^{\mp}, 96^{-}, 96^{+})$.
$\Phi = (\emptyset , 0^{\pm} , 0^{+} , 0^{-})$, $T = \{ \Phi , \breve{M}_1, \acute{\Gamma} \}$ is $S_{\acute{\Gamma}}$ - topology .
$\acute{\Gamma}$ is $S_{\acute{\Gamma}}$ - open, also is $S_{\acute{\Gamma}}$ - neighborhood of $x_1 = (\bar{O}_6, 48^{\mp})$, since $x_1 \in \acute{\Gamma} \subseteq \acute{\Gamma}$.

Conclusion

In this paper we show that molecular can be represented as a signal soft set, from a signal soft set for molecular we can generate a signal soft topology for molecular, we introduce the anti – molecular in a new mathematical way (we show that the anti-molecular is a complement of a signal soft set of the molecular) and show that the molecular with anti - molecular will generate a pure energy

References

[1] Abdel-Raouf M A 2020 Novel Consequences of Coexistence of Matter and Antimatter in Nature *Journal of High Energy Physics, Gravitation and Cosmology* **6** 251-258
[2] Cagman N and Enginoglu S 2010 Soft set theory and uni-int decision making *European J. Oper. Res* **207** 848-855
[3] Mahmood M H 2021 A Signal Soft Sets for Atoms Modeling and Signal Soft Topology *Iraqi Journal of Science (IJS)* **62** (1)
[4] Molodtsov D 1999 Soft set theory – first results *Computers and Mathematics with Applications* **37** 19-31
[5] Noori S and Yousif Y Y 2020 Soft Simply Compact Spaces, *Iraqi Journal of Science* Special Issue 108-113.
[6] Novalogy , Atom. Phys program . https://play.google.com/store/apps/details?id=com.CowboyBebop.AtomPhys&hl=en_US
[7] Saif Z, Hameed, Adiya K H 2020 On Soft bc-Open Sets in Soft Topological Spaces *Iraqi Journal of Science* Special Issue 238-242
[8] Sauvage J P 2017 From Chemical Topology to Molecular Machines (Nobel Lecture) *Angew. Chem. Int. Ed* .**56** 11080 – 11093
[9] Zhu P and Wen Q 2013 Operations on soft sets revisited *Journal of App. Math.* **2013** 1-7

Resolution *of* Weyl Module in the case *of* skew partitions (9,7)/(s,0), when *s = 1,2*

Resolution of Weyl Module in the case of skew partitions (9,7)/(s,0), when $s = 1, 2$

Haytham Razooki Hassan and Rania Nazem Abdul Rahman

Mathematics department, College of Science, Mustansiriyah University, Baghdad, Iraq

E-mail: samer2017@tu.edu.iq, Ranianazimabdalrahman@gmail.com

Abstract. The aim of this work is, to study the resolution of a two-row weyl module in the case of skew partitions(9,7)/(s,0), when s=1,2, by using the technique of letter place algebra, place map(polarization) and contraction homotopy. The skew partitions case is one of the uncles of this study.

1. Introduction

Let $\mathcal{F}$ be a free R-module over commutative ring $\mathcal{R}$ with identity 1 and $Ð_s\mathcal{F}$ is divided power algebra of degrees s. Keep in mind the theory associated to the resolution of two-rowed weyl module $K_{\lambda/\mu}\mathcal{F}$, that been previously described in [1], as follows:

λ/μ =

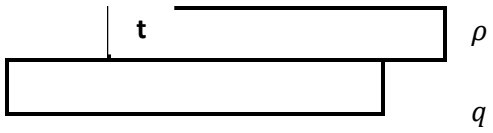

And $d'_{\lambda/\mu}: Ð_{\lambda/\mu}\mathcal{F} \longrightarrow \Lambda^{\tilde{\lambda}/\tilde{\mu}}\mathcal{F}$ it is the Weyl map will be called "Weyl module" Where $K_{\lambda/\mu}\mathcal{F} = Im(d'_{\lambda/\mu})$. [2]

So we have:

$$0 \longrightarrow \sum Ð_{p+k} \otimes Ð_{q-k} \xrightarrow{\square} Ð_p \otimes Ð_q \xrightarrow{d'_{\lambda/\mu}} K_{\lambda/\mu} \longrightarrow \quad (1)$$

Using by letter place, the maps can be written as below:

$$\binom{w}{w'}\Big|\begin{matrix}1^{(p+k)}\\2^{(q-k)}\end{matrix}\xrightarrow{\partial_{21}^{(k)}}\binom{w}{w'}\Big|\begin{matrix}1^{(p)}2^{(k)}\\2^{(q-k)}\end{matrix}\Big)$$
$$\rightarrow\sum w\begin{pmatrix}w_1\\w'^{w_2}\end{pmatrix}\Big|\begin{matrix}(t+1)'(t+2)'\dots\dots(p+t)'\\1'2'3'\dots q'\end{matrix}\Big) \qquad (2)$$

Where $w\otimes w'\in Ð_{p+k}\otimes Ð_{q-k}$, $\square=\sum_{k=t+1}^{q}\partial_{21}^{(k)}$ is the box map,

And $d'_{\lambda/\mu}=\partial_{q'2}\dots\partial_{1'2}\partial_{(p+t)'1}\dots\partial_{q(t+1)'1}$, is the composition of place polarization, from positive places $\{1,2\}$ to negative places $\{1',2',\dots,(p+t)'\}$.

Then, as shown in [2], $\square$ is deliver a component $x\otimes y$ of $Ð_{p+k}\otimes Ð_{q-k}$ to $\sum x_p\otimes x'_k y$, where $\sum x_p\otimes x'_k$ is the element of the diagonal of x in $Ð_p\otimes Ð_q$.

"Let $(\mathcal{Z}_{21})$ be the free generator of divided power algebra $Ð(\mathcal{Z}_{21})$ in one generator, the divided power element $\mathcal{Z}_{21}^{(k)}$ of degree k of the free generator $\mathcal{Z}_{21}$ acts on $Ð_{p+k}\otimes Ð_{q-k}$ by place polarization of degree k from place (1) to place (2)" [3].
"The ''graded'' algebra with identity. $A=Ð(\mathcal{Z}_{21})$ acts on the graded module $\mathcal{M}=Ð_{p+k}\otimes Ð_{q-k}=\sum\mathcal{M}_{q-k}$.[3]"
"Hence, $\mathcal{M}$ is a graded left A-module, where for $w=\mathcal{Z}_{21}^{(k)}\in A$ and $\mathbb{v}\in Ð_{\beta1}\otimes Ð_{\beta2}$, So we have:"

$$w(\mathbb{v})=\mathcal{Z}_{21}^{(k)}(\mathbb{v})=\partial_{21}^{(k)}(\mathbb{v})$$

If we take t^+graded strand of degree q.
$\mathcal{M}_\bullet: 0\rightarrow\mathcal{M}_{q-t}\xrightarrow{\partial_s}\dots\rightarrow\mathcal{M}_e\xrightarrow{\partial_s}\mathcal{M}_1\xrightarrow{\partial_s}\mathcal{M}_0$,
Of the normalized Bar complex, Bar $(\mathcal{M},A,S;\bullet)$,where $S=\{x\}$. Some important standard concepts which are needed in our work are illustrated.
The maps $\{S_i\}$ are defined as follows: [2]
$S_0: Ð_p\otimes Ð_q\rightarrow\sum_{k>0}\mathcal{Z}^{(t+k)}x\,Ð_{p+t+k}\otimes Ð_{q-t-k}$

$$\binom{w}{w'}\Big|\begin{matrix}1^{(p)}\ 2^{(\mathrm{K})}\\2^{(q-\mathrm{K})}\end{matrix}\Big)\longrightarrow\begin{cases}\mathcal{Z}_{21}^{(\mathrm{K})}x\binom{w}{w'}\Big|\begin{matrix}1^{(p+\mathrm{K})}\\2^{(q-\mathrm{K})}\end{matrix}\Big) & ;if\ \mathrm{K}\leq t\\0 & ;if\ \mathrm{K}>t\end{cases}$$

And for the higher dimensionses as:

$$S_{\iota-1}:\sum_{\mathrm{K}\iota>0}\mathcal{Z}_{21}^{(t+\mathrm{K}_1)}x\,\mathcal{Z}_{21}^{(\mathrm{K}_2)}x\dots.\mathcal{Z}_{21}^{(\mathrm{K}_{\iota-1})}x\,Ð_{p+t+|\mathrm{K}|}\otimes Ð_{q-t-|\mathrm{K}|}\ \rightarrow$$
$$\mathcal{Z}_{21}^{(t+\mathrm{K}_1)}x\mathcal{Z}_{21}^{(\mathrm{K}_2)}x\dots.\mathcal{Z}_{21}^{(\mathrm{K}_{\iota-1})}x\,\mathcal{Z}_{21}^{(\mathrm{K}_\iota)}xÐ_{p+t+|\mathrm{K}|}\otimes Ð_{q-t-|\mathrm{K}|}$$

$$\mathcal{Z}_{21}^{(t+\mathrm{K}_1)}x\mathcal{Z}_{21}^{(\mathrm{K}_2)}x\dots.\mathcal{Z}_{21}^{(\mathrm{K}_{\iota-1})}x\begin{pmatrix}w\\w'\end{pmatrix}\Big|\begin{matrix}1^{(p+t+|\mathrm{K}|)}\ 2^{(\mathrm{v})}\\2(q-t-|\mathrm{K})\end{matrix}\Big)\longrightarrow$$
$$\begin{cases}\mathcal{Z}_{21}^{(t+\mathrm{K}_1)}x\mathcal{Z}_{21}^{(\mathrm{K}_2)}x\dots.\mathcal{Z}_{21}^{(\mathrm{K}_{\iota-1})}x\mathcal{Z}_{21}^{(\mathrm{v})}x\binom{w}{w'}\Big|\begin{matrix}1^{(p+t+|\mathrm{K}|)}\ 2^{(\mathrm{v})}\\2(q-t-|\mathrm{K})\end{matrix}\Big) & ;if\ \mathrm{v}>0\\0 & ;if\ \mathrm{v}=0\end{cases}$$

Whereas the modules of the resolution were written as:-
$(\mathcal{M}_i)$ for $(i=0,1,\dots\dots.q-t)$,with $\mathcal{M}_0=Ð_p\otimes Ð_q$, and
$\mathcal{M}_i=\mathcal{Z}_{21}^{(t+\mathrm{K}_1)}x\mathcal{Z}_{21}^{(\mathrm{K}_2)}x\dots.\mathcal{Z}_{21}^{(\mathrm{K}_i)}xÐ_{p+t+|\mathrm{K}|}\otimes Ð_{q-t-|\mathrm{K}|}\,;for\ i\geq1$ [2].

The resolution of weyl module in the case of two-rowed skew- shape $(p^+,t,q)/(t,0)$. [4];Whereas another study [5] exhibited the terms and the exactness of the weyl resolution in the cases of partition (9,7).In this work , we locate the terms and the exactness of the weyl resolution in the case of skew-shape $(9,7)/(t,0)$, $t=1,2$

2. The results of the case (9,7)/(1,0)

This section ,we find the term Weyl module resolution in the cases of a skew partition (9,7)/(1,0) and give the proof of its exactness

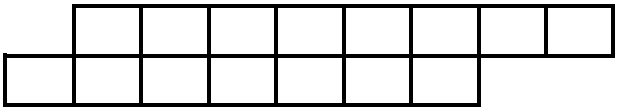

The expression of the characteristic-free weyl resolution are:

$$\mathcal{M}_0 = Đ_8 \otimes Đ_7$$

$$\mathcal{M}_1 = Z_{21}^{(2)}\chi\ Đ_{10}\otimes Đ_5 \oplus Z_{21}^{(3)}\chi\ Đ_{11}\otimes Đ_4 \oplus Z_{21}^{(4)}\chi\ Đ_{12}\otimes Đ_3 \oplus Z_{21}^{(5)}\chi\ Đ_{13}\otimes Đ_2 \oplus Z_{21}^{(6)}\chi\ Đ_{14}\otimes Đ_1 \oplus Z_{21}^{(7)}\chi\ Đ_{15}\otimes Đ_0$$

$$\mathcal{M}_2 = Z_{21}^{(2)}\chi Z_{21}^{(1)}\chi\ Đ_{11}\otimes Đ_4 \oplus Z_{21}^{(3)}\chi Z_{21}^{(1)}\chi\ Đ_{12}\otimes Đ_3 \oplus Z_{21}^{(2)}\chi Z_{21}^{(2)}\chi\ Đ_{12}\otimes Đ_3 \oplus Z_{21}^{(4)}\chi Z_{21}^{(1)}\chi\ Đ_{13}\otimes Đ_2 \oplus Z_{21}^{(3)}\chi Z_{21}^{(2)}\chi\ Đ_{13}\otimes Đ_2 \oplus Z_{21}^{(2)}\chi Z_{21}^{(3)}\chi\ Đ_{13}\otimes Đ_2 \oplus Z_{21}^{(5)}\chi Z_{21}^{(1)}\chi\ Đ_{14}\otimes Đ_1 \oplus Z_{21}^{(4)}\chi Z_{21}^{(2)}\chi\ Đ_{14}\otimes Đ_1 \oplus Z_{21}^{(2)}\chi Z_{21}^{(4)}\chi\ Đ_{14}\otimes Đ_1 \oplus Z_{21}^{(3)}\chi Z_{21}^{(3)}\chi\ Đ_{14}\otimes Đ_1 \oplus Z_{21}^{(6)}\chi Z_{21}^{(1)}\chi\ Đ_{15}\otimes Đ_0 \oplus Z_{21}^{(5)}\chi Z_{21}^{(2)}\chi\ Đ_{15}\otimes Đ_0 \oplus Z_{21}^{(2)}\chi Z_{21}^{(5)}\chi\ Đ_{15}\otimes Đ_0 \oplus Z_{21}^{(4)}\chi Z_{21}^{(3)}\chi\ Đ_{15}\otimes Đ_0 \oplus Z_{21}^{(3)}\chi Z_{21}^{(4)}\chi\ Đ_{15}\otimes Đ_0$$

$$\mathcal{M}_3 = Z_{21}^{(2)}\chi Z_{21}^{(1)}\chi Z_{21}^{(1)}\chi Đ_{12}\otimes Đ_3 \oplus Z_{21}^{(3)}\chi Z_{21}^{(1)}\chi Z_{21}^{(1)}\chi Đ_{13}\otimes Đ_2 \oplus Z_{21}^{(2)}\chi Z_{21}^{(2)}\chi Z_{21}^{(1)}\chi Đ_{13}\otimes Đ_2 \oplus Z_{21}^{(2)}\chi Z_{21}^{(1)}\chi Z_{21}^{(2)}\chi\ Đ_{13}\otimes Đ_2 \oplus Z_{21}^{(4)}\chi Z_{21}^{(1)}\chi Z_{21}^{(1)}\chi\ Đ_{14}\otimes Đ_1 \oplus Z_{21}^{(3)}\chi Z_{21}^{(2)}\chi Z_{21}^{(1)}\chi\ Đ_{14}\otimes Đ_1 \oplus Z_{21}^{(3)}\chi Z_{21}^{(1)}\chi Z_{21}^{(2)}\chi\ Đ_{14}\otimes Đ_1 \oplus Z_{21}^{(5)}\chi Z_{21}^{(1)}\chi Z_{21}^{(1)}\chi\ Đ_{15}\otimes Đ_0 \oplus Z_{21}^{(4)}\chi Z_{21}^{(2)}\chi Z_{21}^{(1)}\chi\ Đ_{15}\otimes Đ_0 \oplus Z_{21}^{(4)}\chi Z_{21}^{(1)}\chi Z_{21}^{(2)}\chi\ Đ_{15}\otimes Đ_0 \oplus Z_{21}^{(2)}\chi Z_{21}^{(4)}\chi Z_{21}^{(1)}\chi\ Đ_{15}\otimes Đ_0 \oplus Z_{21}^{(2)}\chi Z_{21}^{(1)}\chi Z_{21}^{(4)}\chi\ Đ_{15}\otimes Đ_0 \oplus Z_{21}^{(3)}\chi Z_{21}^{(3)}\chi Z_{21}^{(1)}\chi\ Đ_{15}\otimes Đ_0 \oplus Z_{21}^{(3)}\chi Z_{21}^{(1)}\chi Z_{21}^{(3)}\chi\ Đ_{15}\otimes Đ_0$$

$$\mathcal{M}_4 = Z_{21}^{(2)}\chi Z_{21}^{(1)}\chi Z_{21}^{(1)}\chi Z_{21}^{(1)}\chi\ Đ_{13}\otimes Đ_2 \oplus Z_{21}^{(3)}\chi Z_{21}^{(1)}\chi Z_{21}^{(1)}\chi Z_{21}^{(1)}\chi\ Đ_{14}\otimes Đ_1 \oplus Z_{21}^{(2)}\chi Z_{21}^{(2)}\chi Z_{21}^{(1)}\chi Z_{21}^{(1)}\chi\ Đ_{14}\otimes Đ_1 \oplus Z_{21}^{(2)}\chi Z_{21}^{(1)}\chi Z_{21}^{(2)}\chi Z_{21}^{(1)}\chi\ Đ_{14}\otimes Đ_1 \oplus Z_{21}^{(2)}\chi Z_{21}^{(1)}\chi Z_{21}^{(1)}\chi Z_{21}^{(2)}\chi\ Đ_{14}\otimes Đ_1 \oplus Z_{21}^{(4)}\chi Z_{21}^{(1)}\chi Z_{21}^{(1)}\chi Z_{21}^{(1)}\chi\ Đ_{15}\otimes Đ_0 \oplus Z_{21}^{(3)}\chi Z_{21}^{(2)}\chi Z_{21}^{(1)}\chi Z_{21}^{(1)}\chi\ Đ_{15}\otimes Đ_0 \oplus Z_{21}^{(3)}\chi Z_{21}^{(1)}\chi Z_{21}^{(2)}\chi Z_{21}^{(1)}\chi\ Đ_{15}\otimes Đ_0 \oplus Z_{21}^{(3)}\chi Z_{21}^{(1)}\chi Z_{21}^{(1)}\chi Z_{21}^{(2)}\chi\ Đ_{15}\otimes Đ_0 \oplus Z_{21}^{(2)}\chi Z_{21}^{(3)}\chi Z_{21}^{(1)}\chi Z_{21}^{(1)}\chi\ Đ_{15}\otimes Đ_0 \oplus Z_{21}^{(2)}\chi Z_{21}^{(1)}\chi Z_{21}^{(1)}\chi Z_{21}^{(3)}\chi\ Đ_{15}\otimes Đ_0$$

$$\mathcal{M}_5 = Z_{21}^{(2)}\chi Z_{21}^{(1)}\chi Z_{21}^{(1)}\chi Z_{21}^{(1)}\chi Z_{21}^{(1)}\chi\ Đ_{14}\otimes Đ_1 \oplus Z_{21}^{(3)}\chi Z_{21}^{(1)}\chi Z_{21}^{(1)}\chi Z_{21}^{(1)}\chi Z_{21}^{(1)}\chi\ Đ_{15}\otimes Đ_0 \oplus Z_{21}^{(2)}\chi Z_{21}^{(2)}\chi Z_{21}^{(1)}\chi Z_{21}^{(1)}\chi Z_{21}^{(1)}\chi\ Đ_{15}\otimes Đ_0 \oplus Z_{21}^{(2)}\chi Z_{21}^{(1)}\chi Z_{21}^{(1)}\chi Z_{21}^{(2)}\chi Z_{21}^{(1)}\chi\ Đ_{15}\otimes Đ_0 \oplus Z_{21}^{(2)}\chi Z_{21}^{(1)}\chi Z_{21}^{(1)}\chi Z_{21}^{(1)}\chi Z_{21}^{(2)}\chi\ Đ_{15}\otimes Đ_0$$

$$\mathcal{M}_6 = Z_{21}^{(2)}\chi Z_{21}^{(1)}\chi Z_{21}^{(1)}\chi\, Z_{21}^{(1)}\chi Z_{21}^{(1)}\chi Z_{21}^{(1)}\chi\ Ð_{15}\otimes Ð_0$$

2.1 Case 1

The constructions of a contracting homotopies $\{S_i\}$, where i=1, 2, …… , 5

$S_0 = \mathcal{M}_0 \to \mathcal{M}_1$

$$S_0\left(\begin{pmatrix} W \\ W' \end{pmatrix}\middle| \begin{matrix} 1^{(8)}2^{(K)} \\ 2^{(7-K)} \end{matrix}\right) = \begin{cases} Z_{21}^{(K)}\chi\begin{pmatrix} W \\ W' \end{pmatrix}\middle| \begin{matrix} 1^{(8+K)} \\ 2^{(7-K)} \end{matrix} & ;\ if\ K = 2,3,4,\ldots.7 \\ 0 & ;if\ K \le 2 \end{cases}$$

and

$S_1 = \mathcal{M}_1 \to \mathcal{M}_2$

$$S_1\left(Z_{21}^{(K+1)}\chi\begin{pmatrix} W \\ W' \end{pmatrix}\middle| \begin{matrix} 1^{(9+K)}2^{(v)} \\ 2^{(6-K-v)} \end{matrix}\right)$$

$$= \begin{cases} Z_{21}^{(K+1)}\chi Z_{21}^{(v)}\chi\begin{pmatrix} W \\ W' \end{pmatrix}\middle| \begin{matrix} 1^{(9+K+v)} \\ 2^{(6-K-v)} \end{matrix} & ;\ if\ v = 1,2,3,4,5 \\ 0 & ;if\ v = 0 \end{cases}$$

and

$S_2 = \mathcal{M}_2 \to \mathcal{M}_3$

$$S_2\left(Z_{21}^{(K_1+1)}\chi Z_{21}^{(K_2)}\chi\begin{pmatrix} W \\ W' \end{pmatrix}\middle| \begin{matrix} 1^{(9+|K|)}2^{(v)} \\ 2^{(6-|K|-v)} \end{matrix}\right)$$

$$= \begin{cases} Z_{21}^{(K_1+1)}\chi Z_{21}^{(K_2)}\chi Z_{21}^{(v)}\chi\begin{pmatrix} W \\ W' \end{pmatrix}\middle| \begin{matrix} 1^{(9+|K|+v)} \\ 2^{(6-|K|-v)} \end{matrix} & ;\ if\ v = 1,2,3,4 \\ 0 & ;\ if\ v = 0 \end{cases} ;\ where|K| = K_1 + K_2$$

and

$S_3 = \mathcal{M}_3 \to \mathcal{M}_4$

$$S_3\left(Z_{21}^{(K_1+1)}\chi Z_{21}^{(K_2)}\chi Z_{21}^{(K_3)}\chi\begin{pmatrix} W \\ W' \end{pmatrix}\middle| \begin{matrix} 1^{(9+|K|)}2^{(v)} \\ 2^{(6-|K|-v)} \end{matrix}\right)$$

$$= \begin{cases} Z_{21}^{(K_1+1)}\chi Z_{21}^{(K_2)}\chi Z_{21}^{(K_3)}\chi Z_{21}^{(v)}\chi\begin{pmatrix} W \\ W' \end{pmatrix}\middle| \begin{matrix} 1^{(9+|K|+v)} \\ 2^{(6-|K|-v)} \end{matrix} & ;\ if\ v = 1,2,3 \\ 0 & ;if\ v = 0 \end{cases} ;where|K| = K_1 + K_2 + K_3$$

and

$S_4 = \mathcal{M}_4 \to \mathcal{M}_5$

$$S_4\left(Z_{21}^{(K_1+1)}\chi Z_{21}^{(K_2)}\chi Z_{21}^{(K_3)}\chi Z_{21}^{(K_4)}\chi\begin{pmatrix} W \\ W' \end{pmatrix}\middle| \begin{matrix} 1^{(9+|K|)}2^{(v)} \\ 2^{(6-|K|-v)} \end{matrix}\right)$$

$$= \begin{cases} Z_{21}^{(K_1+1)}\chi Z_{21}^{(K_2)}\chi Z_{21}^{(K_3)}\chi Z_{21}^{(K_4)}\chi Z_{21}^{(v)}\chi\begin{pmatrix} W \\ W' \end{pmatrix}\middle| \begin{matrix} 1^{(9+|K|+v)} \\ 2^{(6-|K|-v)} \end{matrix} & ;\ if\ v = 1,2 \\ 0 & ;if\ v = 0 \end{cases} ;where|K| = K_1 + K_2 + K_3 + K_4$$

and

$S_5 = \mathcal{M}_5 \to \mathcal{M}_6$

$$S_5\left(Z_{21}^{(K_1+1)}\chi Z_{21}^{(K_2)}\chi Z_{21}^{(K_3)}\chi Z_{21}^{(K_4)}\chi Z_{21}^{(K_5)}\chi\begin{pmatrix} W \\ W' \end{pmatrix}\middle| \begin{matrix} 1^{(9+|K|)}2^{(v)} \\ 2^{(6-|K|-v)} \end{matrix}\right)$$

$$= \begin{cases} Z_{21}^{(\mathrm{K}_1+1)}\chi Z_{21}^{(\mathrm{K}_2)}\chi Z_{21}^{(\mathrm{K}_3)}\chi Z_{21}^{(\mathrm{K}_4)}\chi Z_{21}^{(\mathrm{K}_5)}\chi Z_{21}^{(\mathrm{v})}\chi\begin{pmatrix} W \\ W' \end{vmatrix} \begin{matrix} 1^{(9+|\mathrm{K}|+\mathrm{v})} \\ 2^{(6-|\mathrm{K}|-\mathrm{v})} \end{matrix}\end{pmatrix}; if\ \mathrm{v}=1 \\ 0 \qquad\qquad\qquad\qquad\qquad\qquad\qquad\qquad\qquad\qquad\qquad\qquad ;\ if\ \ \mathrm{v}=0 \end{cases}; where|\mathrm{K}|$$

$$= \mathrm{K}_1 + \mathrm{K}_2 + \mathrm{K}_3 + \mathrm{K}_4 + \mathrm{K}_5$$

So we have the following diagram:-

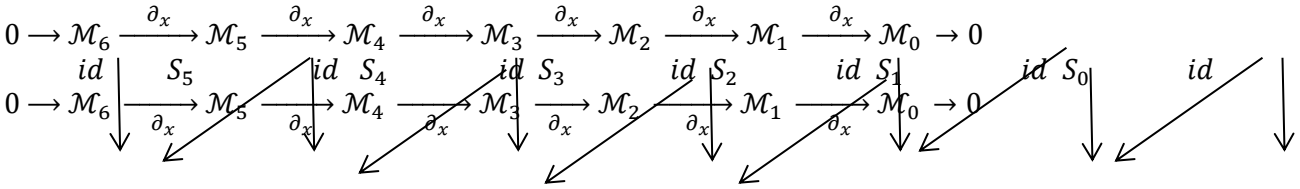

2.2 Case 2

Now, we have

$$S_0\partial_x\left(Z_{21}^{(\mathrm{K}+1)}\chi\begin{pmatrix} W \\ W' \end{vmatrix} \begin{matrix} 1^{(9+\mathrm{K})}2^{(\mathrm{v})} \\ 2^{(6-\mathrm{K})} \end{matrix}\end{pmatrix}\right) = S_0\partial_{21}^{(\mathrm{K}+1)}\chi\begin{pmatrix} W \\ W' \end{vmatrix} \begin{matrix} 1^{(9+\mathrm{K})}2^{(\mathrm{v})} \\ 2^{(6-\mathrm{K})} \end{matrix}\end{pmatrix}$$

$$= \binom{\mathrm{K}+1+\mathrm{v}}{\mathrm{v}} Z_{21}^{(\mathrm{K}+1+\mathrm{v})}\chi\begin{pmatrix} W \\ W' \end{vmatrix} \begin{matrix} 1^{(9+\mathrm{K}+\mathrm{v})} \\ 2^{(6-\mathrm{K}-\mathrm{v})} \end{matrix}\end{pmatrix}$$

and

$$\partial_x S_1\left(Z_{21}^{(\mathrm{K}+1)}\chi\begin{pmatrix} W \\ W' \end{vmatrix} \begin{matrix} 1^{(9+\mathrm{K})}2^{(\mathrm{v})} \\ 2^{(6-\mathrm{K})} \end{matrix}\end{pmatrix}\right) = \partial_x\left(Z_{21}^{(\mathrm{K}+1)}\chi Z_{21}^{(\mathrm{v})}\chi\begin{pmatrix} W \\ W' \end{vmatrix} \begin{matrix} 1^{(9+\mathrm{K}+\mathrm{v})} \\ 2^{(6-\mathrm{K}-\mathrm{v})} \end{matrix}\end{pmatrix}\right)$$

$$= -\binom{\mathrm{K}+1+\mathrm{v}}{\mathrm{v}} Z_{21}^{(\mathrm{K}+1+\mathrm{v})}\chi\begin{pmatrix} W \\ W' \end{vmatrix} \begin{matrix} 1^{(9+\mathrm{K}+\mathrm{v})} \\ 2^{(6-\mathrm{K}-\mathrm{v})} \end{matrix}\end{pmatrix} + Z_{21}^{(\mathrm{K}+1)}\chi\begin{pmatrix} W \\ W' \end{vmatrix} \begin{matrix} 1^{(9+\mathrm{K})}2^{(\mathrm{v})} \\ 2^{(6-\mathrm{K})} \end{matrix}\end{pmatrix}$$

It is clear that $S_0\partial_x + \partial_x S_1 = id_{\mathcal{M}_1}$.

$$S_1\partial_x\left(Z_{21}^{(\mathrm{K}_1+1)}\chi Z_{21}^{(\mathrm{K}_2)}\chi\begin{pmatrix} W \\ W' \end{vmatrix} \begin{matrix} 1^{(9+|\mathrm{K}|)}2^{(\mathrm{v})} \\ 2^{(6-|\mathrm{K}|-\mathrm{v})} \end{matrix}\end{pmatrix}\right)$$

$$= S_1\left(-\binom{|\mathrm{K}|+1}{\mathrm{K}_2} Z_{21}^{(|\mathrm{K}|+1)}\chi\begin{pmatrix} W \\ W' \end{vmatrix} \begin{matrix} 1^{(9+|\mathrm{K}|)}2^{(\mathrm{v})} \\ 2^{(6-|\mathrm{K}|-\mathrm{v})} \end{matrix}\end{pmatrix} + Z_{21}^{(\mathrm{K}_1+1)}\chi\partial_{21}^{(\mathrm{K}_2)}\begin{pmatrix} W \\ W' \end{vmatrix} \begin{matrix} 1^{(9+|\mathrm{K}|)}2^{(\mathrm{v})} \\ 2^{(6-|\mathrm{K}|-\mathrm{v})} \end{matrix}\end{pmatrix}\right)$$

$$= -\binom{|\mathrm{K}|+1}{\mathrm{K}_2} Z_{21}^{(|\mathrm{K}|+1)}\chi Z_{21}^{(\mathrm{v})}\chi\begin{pmatrix} W \\ W' \end{vmatrix} \begin{matrix} 1^{(9+|\mathrm{K}|+\mathrm{v})} \\ 2^{(6-|\mathrm{K}|-\mathrm{v})} \end{matrix}\end{pmatrix} + \binom{\mathrm{K}_2+\mathrm{v}}{\mathrm{v}} Z_{21}^{(\mathrm{K}_1+1)}\chi Z_{21}^{(\mathrm{K}_2+\mathrm{v})}\chi\begin{pmatrix} W \\ W' \end{vmatrix} \begin{matrix} 1^{(9+|\mathrm{K}|+\mathrm{v})} \\ 2^{(6-|\mathrm{K}|-\mathrm{v})} \end{matrix}\end{pmatrix}$$

and

$$\partial_x\, S_2\left(Z_{21}^{(\mathrm{K}_1+1)}\chi Z_{21}^{(\mathrm{K}_2)}\chi\begin{pmatrix} W \\ W' \end{vmatrix} \begin{matrix} 1^{(9+|\mathrm{K}|)}2^{(\mathrm{v})} \\ 2^{(6-|\mathrm{K}|-\mathrm{v})} \end{matrix}\end{pmatrix}\right) = \partial_x\left(Z_{21}^{(\mathrm{K}_1+1)}\chi Z_{21}^{(\mathrm{K}_2)}\chi Z_{21}^{(\mathrm{v})}\chi\begin{pmatrix} W \\ W' \end{vmatrix} \begin{matrix} 1^{(9+|\mathrm{K}|+\mathrm{v})} \\ 2^{(6-|\mathrm{K}|-\mathrm{v})} \end{matrix}\end{pmatrix}\right)$$

$$= \binom{|\mathrm{K}|+1}{\mathrm{K}_2} Z_{21}^{(|\mathrm{K}|+1)}\chi Z_{21}^{(\mathrm{v})}\chi\begin{pmatrix} W \\ W' \end{vmatrix} \begin{matrix} 1^{(9+|\mathrm{K}|+\mathrm{v})} \\ 2^{(6-|\mathrm{K}|-\mathrm{v})} \end{matrix}\end{pmatrix} - \binom{\mathrm{K}_2+\mathrm{v}}{\mathrm{v}} Z_{21}^{(\mathrm{K}_1+1)}\chi Z_{21}^{(\mathrm{K}_2+\mathrm{v})}\chi\begin{pmatrix} W \\ W' \end{vmatrix} \begin{matrix} 1^{(9+|\mathrm{K}|+\mathrm{v})} \\ 2^{(6-|\mathrm{K}|-\mathrm{v})} \end{matrix}\end{pmatrix}$$

$$+ Z_{21}^{(\mathrm{K}_1+1)}\chi Z_{21}^{(\mathrm{K}_2)}\chi\begin{pmatrix} W \\ W' \end{vmatrix} \begin{matrix} 1^{(9+|\mathrm{K}|)}2^{(\mathrm{v})} \\ 2^{(6-|\mathrm{K}|-\mathrm{v})} \end{matrix}\end{pmatrix};$$

$where|\mathrm{K}| = \mathrm{K}_1 + \mathrm{K}_2.$

Cearly, $S_1\partial_x + \partial_x S_2 = id_{\mathcal{M}_2}$

$$S_2\partial_x\left(Z_{21}^{(\mathrm{K}_1+1)}\chi Z_{21}^{(\mathrm{K}_2)}\chi Z_{21}^{(\mathrm{K}_3)}\chi\begin{pmatrix} W \\ W' \end{vmatrix} \begin{matrix} 1^{(9+|\mathrm{K}|)}2^{(\mathrm{v})} \\ 2^{(6-|\mathrm{K}|-\mathrm{v})} \end{matrix}\end{pmatrix}\right)$$

$$= S_2\left[\binom{(\mathrm{K}_1+1+\mathrm{K}_2)}{\mathrm{K}_2} Z_{21}^{(\mathrm{K}_1+1+\mathrm{K}_2)}\chi Z_{21}^{(\mathrm{K}_3)}\chi\begin{pmatrix} W \\ W' \end{vmatrix} \begin{matrix} 1^{(9+|\mathrm{K}|)}2^{(\mathrm{v})} \\ 2^{(6-|\mathrm{K}|-\mathrm{v})} \end{matrix}\end{pmatrix}\right.$$

$$- \binom{\mathrm{K}_2+\mathrm{K}_3}{\mathrm{K}_3} Z_{21}^{(\mathrm{K}_1+1)}\chi Z_{21}^{(\mathrm{K}_2+\mathrm{K}_3)}\chi\begin{pmatrix} W \\ W' \end{vmatrix} \begin{matrix} 1^{(9+|\mathrm{K}|)}2^{(\mathrm{v})} \\ 2^{(6-|\mathrm{K}|-\mathrm{v})} \end{matrix}\end{pmatrix}$$

$$\left. + Z_{21}^{(\mathrm{K}_1+1)}\chi Z_{21}^{(\mathrm{K}_2)}\chi\partial_{21}^{(\mathrm{K}_3)}\chi\begin{pmatrix} W \\ W' \end{vmatrix} \begin{matrix} 1^{(9+|\mathrm{K}|)}2^{(\mathrm{v})} \\ 2^{(6-|\mathrm{K}|-\mathrm{v})} \end{matrix}\end{pmatrix}\right]$$

$$= \binom{(\mathrm{K}_1+1+\mathrm{K}_2)}{\mathrm{K}_2} Z_{21}^{(\mathrm{K}_1+1+\mathrm{K}_2)}\chi Z_{21}^{(\mathrm{K}_3)}\chi Z_{21}^{(\mathrm{v})}\chi\begin{pmatrix} W \\ W' \end{vmatrix} \begin{matrix} 1^{(9+|\mathrm{K}|+\mathrm{v})} \\ 2^{(6-|\mathrm{K}|-\mathrm{v})} \end{matrix}\end{pmatrix} -$$

$$\binom{\mathrm{K}_2+\mathrm{K}_3}{\mathrm{K}_3} Z_{21}^{(\mathrm{K}_1+1)}\chi Z_{21}^{(\mathrm{K}_2+\mathrm{K}_3)}\chi Z_{21}^{(\mathrm{v})}\chi\begin{pmatrix} W \\ W' \end{vmatrix} \begin{matrix} 1^{(9+|\mathrm{K}|+\mathrm{v})} \\ 2^{(6-|\mathrm{K}|-\mathrm{v})} \end{matrix}\end{pmatrix} +$$

$\binom{K_3+v}{v} Z_{21}^{(K_1+1)} \chi Z_{21}^{(K_2)} \chi Z_{21}^{(K_3)} \chi Z_{21}^{(v)} \chi \left(\begin{matrix} W \\ W' \end{matrix} \middle| \begin{matrix} 1^{(9+|K|+v)} \\ 2^{(6-|K|-v)} \end{matrix} \right)$,

and

$$\partial_x S_3 \left(Z_{21}^{(K_1+1)} \chi Z_{21}^{(K_2)} \chi Z_{21}^{(K_3)} \chi \left(\begin{matrix} W \\ W' \end{matrix} \middle| \begin{matrix} 1^{(9+|K|)} 2^{(v)} \\ 2^{(6-|K|-v)} \end{matrix} \right) \right) = \partial_x \left(Z_{21}^{(K_1+1)} \chi Z_{21}^{(K_2)} \chi Z_{21}^{(K_3)} \chi Z_{21}^{(v)} \chi \left(\begin{matrix} W \\ W' \end{matrix} \middle| \begin{matrix} 1^{(9+|K|+v)} \\ 2^{(6-|K|-v)} \end{matrix} \right) \right)$$

$$= -\binom{(K_1+1+K_2)}{K_2} Z_{21}^{(K_1+1+K_2)} \chi Z_{21}^{(K_3)} \chi Z_{21}^{(v)} \chi \left(\begin{matrix} W \\ W' \end{matrix} \middle| \begin{matrix} 1^{(9+|K|+v)} \\ 2^{(6-|K|-v)} \end{matrix} \right) +$$

$$\binom{K_2+K_3}{K_3} Z_{21}^{(K_1+1)} \chi Z_{21}^{(K_2+K_3)} \chi Z_{21}^{(v)} \chi \left(\begin{matrix} W \\ W' \end{matrix} \middle| \begin{matrix} 1^{(9+|K|+v)} \\ 2^{(6-|K|-v)} \end{matrix} \right) -$$

$$\binom{K_3+v}{v} Z_{21}^{(K_1+1)} \chi Z_{21}^{(K_2)} \chi Z_{21}^{(K_3)} \chi Z_{21}^{(v)} \chi \left(\begin{matrix} W \\ W' \end{matrix} \middle| \begin{matrix} 1^{(9+|K|+v)} \\ 2^{(6-|K|-v)} \end{matrix} \right) +$$

$$Z_{21}^{(K_1+1)} \chi Z_{21}^{(K_2)} \chi Z_{21}^{(K_3)} \chi \partial_{21}^{(v)} \chi \left(\begin{matrix} W \\ W' \end{matrix} \middle| \begin{matrix} 1^{(9+|K|+v)} \\ 2^{(6-|K|-v)} \end{matrix} \right) =$$

$$-\binom{(K_1+1+K_2)}{K_2} Z_{21}^{(K_1+1+K_2)} \chi Z_{21}^{(K_3)} \chi Z_{21}^{(v)} \chi \left(\begin{matrix} W \\ W' \end{matrix} \middle| \begin{matrix} 1^{(9+|K|+v)} \\ 2^{(6-|K|-v)} \end{matrix} \right) +$$

$$\binom{K_2+K_3}{K_3} Z_{21}^{(K_1+1)} \chi Z_{21}^{(K_2+K_3)} \chi Z_{21}^{(v)} \chi \left(\begin{matrix} W \\ W' \end{matrix} \middle| \begin{matrix} 1^{(9+|K|+v)} \\ 2^{(6-|K|-v)} \end{matrix} \right) -$$

$$\binom{K_3+v}{v} Z_{21}^{(K_1+1)} \chi Z_{21}^{(K_2)} \chi Z_{21}^{(K_3)} \chi Z_{21}^{(v)} \chi \left(\begin{matrix} W \\ W' \end{matrix} \middle| \begin{matrix} 1^{(9+|K|+v)} \\ 2^{(6-|K|-v)} \end{matrix} \right) +$$

$$Z_{21}^{(K_1+1)} \chi Z_{21}^{(K_2)} \chi Z_{21}^{(K_3)} \chi \left(\begin{matrix} W \\ W' \end{matrix} \middle| \begin{matrix} 1^{(9+|K|)} 2^{(v)} \\ 2^{(6-|K|-v)} \end{matrix} \right);$$

$where, |K| = K_1 + K_2 + K_3.$

Cearly, $S_2 \partial_x + \partial_x S_3 = id_{\mathcal{M}_3}$.

$$S_3 \partial_x \left(Z_{21}^{(K_1+1)} \chi Z_{21}^{(K_2)} \chi Z_{21}^{(K_3)} \chi Z_{21}^{(K_4)} \chi \left(\begin{matrix} W \\ W' \end{matrix} \middle| \begin{matrix} 1^{(9+|K|)} 2^{(v)} \\ 2^{(6-|K|-v)} \end{matrix} \right) \right)$$

$$= S_3 \left[-\binom{(K_1+1+K_2)}{K_2} Z_{21}^{(K_1+1+K_2)} \chi Z_{21}^{(K_3)} \chi Z_{21}^{(K_4)} \chi \left(\begin{matrix} W \\ W' \end{matrix} \middle| \begin{matrix} 1^{(9+|K|)} 2^{(v)} \\ 2^{(6-|K|-v)} \end{matrix} \right) \right.$$

$$+ \binom{K_2+K_3}{K_3} Z_{21}^{(K_1+1)} \chi Z_{21}^{(K_2+K_3)} \chi Z_{21}^{(K_4)} \chi \left(\begin{matrix} W \\ W' \end{matrix} \middle| \begin{matrix} 1^{(9+|K|)} 2^{(v)} \\ 2^{(6-|K|-v)} \end{matrix} \right)$$

$$- \binom{K_3+K_4}{K_4} Z_{21}^{(K_1+1)} \chi Z_{21}^{(K_2)} \chi Z_{21}^{(K_3+K_4)} \chi \left(\begin{matrix} W \\ W' \end{matrix} \middle| \begin{matrix} 1^{(9+|K|)} 2^{(v)} \\ 2^{(6-|K|-v)} \end{matrix} \right)$$

$$\left. + Z_{21}^{(K_1+1)} \chi Z_{21}^{(K_2)} \chi Z_{21}^{(K_3)} \chi \partial_{21}^{(K_4)} \chi \left(\begin{matrix} W \\ W' \end{matrix} \middle| \begin{matrix} 1^{(9+|K|)} 2^{(v)} \\ 2^{(6-|K|-v)} \end{matrix} \right) \right]$$

$$= -\binom{(K_1+1+K_2)}{K_2} Z_{21}^{(K_1+1+K_2)} \chi Z_{21}^{(K_3)} \chi Z_{21}^{(K_4)} \chi Z_{21}^{(v)} \chi \left(\begin{matrix} W \\ W' \end{matrix} \middle| \begin{matrix} 1^{(9+|K|+v)} \\ 2^{(6-|K|-v)} \end{matrix} \right)$$

$$+ \binom{K_2+K_3}{K_3} Z_{21}^{(K_1+1)} \chi Z_{21}^{(K_2+K_3)} \chi Z_{21}^{(K_4)} \chi Z_{21}^{(v)} \chi \left(\begin{matrix} W \\ W' \end{matrix} \middle| \begin{matrix} 1^{(9+|K|+v)} \\ 2^{(6-|K|-v)} \end{matrix} \right)$$

$$- \binom{K_3+K_4}{K_4} Z_{21}^{(K_1+1)} \chi Z_{21}^{(K_2)} \chi Z_{21}^{(K_3+K_4)} \chi Z_{21}^{(v)} \chi \left(\begin{matrix} W \\ W' \end{matrix} \middle| \begin{matrix} 1^{(9+|K|+v)} \\ 2^{(6-|K|-v)} \end{matrix} \right)$$

$$+ \binom{K_4+v}{v} Z_{21}^{(K_1+1)} \chi Z_{21}^{(K_2)} \chi Z_{21}^{(K_3)} \chi Z_{21}^{(K_4)} \chi Z_{21}^{(v)} \chi \left(\begin{matrix} W \\ W' \end{matrix} \middle| \begin{matrix} 1^{(9+|K|+v)} \\ 2^{(6-|K|-v)} \end{matrix} \right),$$

and

$$\partial_x S_4 \left(Z_{21}^{(K_1+1)} \chi Z_{21}^{(K_2)} \chi Z_{21}^{(K_3)} \chi Z_{21}^{(K_4)} \chi \left(\begin{matrix} W \\ W' \end{matrix} \middle| \begin{matrix} 1^{(9+|K|)} 2^{(v)} \\ 2^{(6-|K|-v)} \end{matrix} \right) \right) =$$

$$\partial_x \left(Z_{21}^{(K_1+1)} \chi Z_{21}^{(K_2)} \chi Z_{21}^{(K_3)} \chi Z_{21}^{(K_4)} \chi Z_{21}^{(v)} \chi \left(\begin{matrix} W \\ W' \end{matrix} \middle| \begin{matrix} 1^{(9+|K|+v)} \\ 2^{(6-|K|-v)} \end{matrix} \right) \right)$$

$$= \binom{(K_1+1+K_2)}{K_2} Z_{21}^{(K_1+1+K_2)} \chi Z_{21}^{(K_3)} \chi Z_{21}^{(K_4)} \chi Z_{21}^{(v)} \chi \left(\begin{matrix} W \\ W' \end{matrix} \middle| \begin{matrix} 1^{(9+|K|+v)} \\ 2^{(6-|K|-v)} \end{matrix} \right)$$

$$- \binom{K_2+K_3}{K_3} Z_{21}^{(K_1+1)} \chi Z_{21}^{(K_2+K_3)} \chi Z_{21}^{(K_4)} \chi Z_{21}^{(v)} \chi \left(\begin{matrix} W \\ W' \end{matrix} \middle| \begin{matrix} 1^{(9+|K|+v)} \\ 2^{(6-|K|-v)} \end{matrix} \right)$$

$$+ \binom{K_3+K_4}{K_4} Z_{21}^{(K_1+1)} \chi Z_{21}^{(K_2)} \chi Z_{21}^{(K_3+K_4)} \chi Z_{21}^{(v)} \chi \left(\begin{matrix} W \\ W' \end{matrix} \middle| \begin{matrix} 1^{(9+|K|+v)} \\ 2^{(6-|K|-v)} \end{matrix} \right)$$

$$- \binom{K_4+v}{v} Z_{21}^{(K_1+1)} \chi Z_{21}^{(K_2)} \chi Z_{21}^{(K_3)} \chi Z_{21}^{(K_4)} \chi Z_{21}^{(v)} \chi \left(\begin{matrix} W \\ W' \end{matrix} \middle| \begin{matrix} 1^{(9+|K|+v)} \\ 2^{(6-|K|-v)} \end{matrix} \right)$$

$$+ Z_{21}^{(K_1+1)} \chi Z_{21}^{(K_2)} \chi Z_{21}^{(K_3)} \chi Z_{21}^{(K_4)} \partial_{21}^{(v)} \chi \left(\begin{matrix} W \\ W' \end{matrix} \middle| \begin{matrix} 1^{(9+|K|+v)} \\ 2^{(6-|K|-v)} \end{matrix} \right)$$

$$= \binom{(K_1+1+K_2)}{K_2} Z_{21}^{(K_1+1+K_2)} \chi Z_{21}^{(K_3)} \chi Z_{21}^{(K_4)} \chi Z_{21}^{(v)} \chi \binom{W}{W'} \Big| \frac{1^{(9+|K|+v)}}{2^{(6-|K|-v)}}$$
$$- \binom{K_2+K_3}{K_3} Z_{21}^{(K_1+1)} \chi Z_{21}^{(K_2+K_3)} \chi Z_{21}^{(K_4)} \chi Z_{21}^{(v)} \chi \binom{W}{W'} \Big| \frac{1^{(9+|K|+v)}}{2^{(6-|K|-v)}}$$
$$+ \binom{K_3+K_4}{K_4} Z_{21}^{(K_1+1)} \chi Z_{21}^{(K_2)} \chi Z_{21}^{(K_3+K_4)} \chi Z_{21}^{(v)} \chi \binom{W}{W'} \Big| \frac{1^{(9+|K|+v)}}{2^{(6-|K|-v)}}$$
$$- \binom{K_4+v}{v} Z_{21}^{(K_1+1)} \chi Z_{21}^{(K_2)} \chi Z_{21}^{(K_3)} \chi Z_{21}^{(K_4)} \chi Z_{21}^{(v)} \chi \binom{W}{W'} \Big| \frac{1^{(9+|K|+v)}}{2^{(6-|K|-v)}}$$
$$+ Z_{21}^{(K_1+1)} \chi Z_{21}^{(K_2)} \chi Z_{21}^{(K_3)} \chi Z_{21}^{(K_4)} \binom{W}{W'} \Big| \frac{1^{(9+|K|)} 2^{(v)}}{2^{(6-|K|-v)}} ;$$

$Where |K| = K_1 + K_2 + K_3 + K_4$

Clearly, $S_3 \partial_x + \partial_x S_4 = id_{\mathcal{M}_4}$.

$$S_4 \partial_x \left(Z_{21}^{(K_1+1)} \chi Z_{21}^{(K_2)} \chi Z_{21}^{(K_3)} \chi Z_{21}^{(K_4)} \chi Z_{21}^{(K_5)} \chi \binom{W}{W'} \Big| \frac{1^{(9+|K|)} 2^{(v)}}{2^{(6-|K|-v)}} \right)$$
$$= S_4 " \left[\binom{(K_1 + 1 + K_2)}{K_2} Z_{21}^{(K_1+1+K_2)} \chi Z_{21}^{(K_3)} \chi Z_{21}^{(K_4)} \chi Z_{21}^{(K_5)} \chi \binom{W}{W'} \Big| \frac{1^{(9+|K|)} 2^{(v)}}{2^{(6-|K|-v)}} \right.$$
$$- \binom{K_2 + K_3}{K_3} Z_{21}^{(K_1+1)} \chi Z_{21}^{(K_2+K_3)} \chi Z_{21}^{(K_4)} \chi Z_{21}^{(K_5)} \chi \binom{W}{W'} \Big| \frac{1^{(9+|K|)} 2^{(v)}}{2^{(6-|K|-v)}}$$
$$+ \binom{K_3 + K_4}{K_4} Z_{21}^{(K_1+1)} \chi Z_{21}^{(K_2)} \chi Z_{21}^{(K_3+K_4)} \chi Z_{21}^{(K_5)} \chi \binom{W}{W'} \Big| \frac{1^{(9+|K|)} 2^{(v)}}{2^{(6-|K|-v)}}$$
$$- \binom{K_4 + K_5}{K_5} Z_{21}^{(K_1+1)} \chi Z_{21}^{(K_2)} \chi Z_{21}^{(K_3)} \chi Z_{21}^{(K_4+K_5)} \chi \binom{W}{W'} \Big| \frac{1^{(9+|K|)} 2^{(v)}}{2^{(6-|K|-v)}}$$
$$\left. + Z_{21}^{(K_1+1)} \chi Z_{21}^{(K_2)} \chi Z_{21}^{(K_3)} \chi Z_{21}^{(K_4)} \chi \partial_{21}^{(K_5)} \chi \binom{W}{W'} \Big| \frac{1^{(9+|K|)} 2^{(v)}}{2^{(6-|K|-v)}} \right] "$$
$$= \binom{(K_1+1+K_2)}{K_2} Z_{21}^{(K_1+1+K_2)} \chi Z_{21}^{(K_3)} \chi Z_{21}^{(K_4)} \chi Z_{21}^{(K_5)} \chi Z_{21}^{(v)} \chi \binom{W}{W'} \Big| \frac{1^{(9+|K|+v)}}{2^{(6-|K|-v)}}$$
$$- \binom{K_2+K_3}{K_3} Z_{21}^{(K_1+1)} \chi Z_{21}^{(K_2+K_3)} \chi Z_{21}^{(K_4)} \chi Z_{21}^{(K_5)} \chi Z_{21}^{(v)} \chi \binom{W}{W'} \Big| \frac{1^{(9+|K|+v)}}{2^{(6-|K|-v)}}$$
$$+ \binom{K_3+ K_4}{K_4} Z_{21}^{(K_1+1)} \chi Z_{21}^{(K_2)} \chi Z_{21}^{(K_3+K_4)} \chi Z_{21}^{(K_5)} \chi Z_{21}^{(v)} \chi \binom{W}{W'} \Big| \frac{1^{(9+|K|+v)}}{2^{(6-|K|-v)}}$$
$$- \binom{K_4 + K_5}{K_5} Z_{21}^{(K_1+1)} \chi Z_{21}^{(K_2)} \chi Z_{21}^{(K_3)} \chi Z_{21}^{(K_4+K_5)} \chi Z_{21}^{(v)} \chi \binom{W}{W'} \Big| \frac{1^{(9+|K|+ v)}}{2^{(6-|K|-v)}}$$
$$+ \binom{K_5+v}{v} Z_{21}^{(K_1+1)} \chi Z_{21}^{(K_2)} \chi Z_{21}^{(K_3)} \chi Z_{21}^{(K_4)} \chi Z_{21}^{(K_5+v)} \chi \binom{W}{W'} \Big| \frac{1^{(9+|K|+v)}}{2^{(6-|K|-v)}}$$

and

$$\partial_x S_5 \left(Z_{21}^{(K_1+1)} \chi Z_{21}^{(K_2)} \chi Z_{21}^{(K_3)} \chi Z_{21}^{(K_4)} \chi Z_{21}^{(K_5)} \chi \binom{W}{W'} \Big| \frac{1^{(9+|K|)} 2^{(v)}}{2^{(6-|K|-v)}} \right)$$
$$= \partial_x \left(Z_{21}^{(K_1+1)} \chi Z_{21}^{(K_2)} \chi Z_{21}^{(K_3)} \chi Z_{21}^{(K_4)} \chi Z_{21}^{(K_5)} \chi \binom{W}{W'} \Big| \frac{1^{(9+|K|)} 2^{(v)}}{2^{(6-|K|-v)}} \right)$$
$$= - \binom{(K_1+1+K_2)}{K_2} Z_{21}^{(K_1+1+K_2)} \chi Z_{21}^{(K_3)} \chi Z_{21}^{(K_4)} \chi Z_{21}^{(K_5)} \chi Z_{21}^{(v)} \chi \binom{W}{W'} \Big| \frac{1^{(9+|K|+v)}}{2^{(6-|K|-v)}}$$
$$+ \binom{K_2+K_3}{K_3} Z_{21}^{(K_1+1)} \chi Z_{21}^{(K_2+K_3)} \chi Z_{21}^{(K_4)} \chi Z_{21}^{(K_5)} \chi Z_{21}^{(v)} \chi \binom{W}{W'} \Big| \frac{1^{(9+|K|+v)}}{2^{(6-|K|-v)}}$$
$$- \binom{K_3 + K_4}{K_4} Z_{21}^{(K_1+1)} \chi Z_{21}^{(K_2)} \chi Z_{21}^{(K_3+K_4)} \chi Z_{21}^{(K_5)} \chi Z_{21}^{(v)} \chi \binom{W}{W'} \Big| \frac{1^{(9+|K|+v)}}{2^{(6-|K|-v)}}$$
$$+ \binom{K_4 + K_5}{K_5} Z_{21}^{(K_1+1)} \chi Z_{21}^{(K_2)} \chi Z_{21}^{(K_3)} \chi Z_{21}^{(K_4+K_5)} \chi Z_{21}^{(v)} \chi \binom{W}{W'} \Big| \frac{1^{(9+|K|+v)}}{2^{(6-|K|-v)}}$$
$$- \binom{K_5+v}{v} Z_{21}^{(K_1+1)} \chi Z_{21}^{(K_2)} \chi Z_{21}^{(K_3)} \chi Z_{21}^{(K_4)} \chi Z_{21}^{(K_5+v)} \chi \binom{W}{W'} \Big| \frac{1^{(9+|K|+v)}}{2^{(6-|K|-v)}}$$
$$+ Z_{21}^{(K_1+1)} \chi Z_{21}^{(K_2)} \chi Z_{21}^{(K_3)} \chi Z_{21}^{(K_4)} \chi Z_{21}^{(K_5)} \chi \partial_{21}^{(v)} \chi \binom{W}{W'} \Big| \frac{1^{(9+|K|+v)}}{2^{(6-|K|-v)}}$$

$$= -\binom{(\mathrm{K}_1+1+\mathrm{K}_2)}{\mathrm{K}_2} Z_{21}^{(\mathrm{K}_1+1+\mathrm{K}_2)}\chi Z_{21}^{(\mathrm{K}_3)}\chi Z_{21}^{(\mathrm{K}_4)}\chi Z_{21}^{(\mathrm{K}_5)}\chi Z_{21}^{(\mathrm{v})}\chi\left(\begin{matrix}W\\W'\end{matrix}\middle|\begin{matrix}1^{(9+|\mathrm{K}|+\mathrm{v})}\\2^{(6-|\mathrm{K}|-\mathrm{v})}\end{matrix}\right)$$
$$+\binom{\mathrm{K}_2+\mathrm{K}_3}{\mathrm{K}_3} Z_{21}^{(\mathrm{K}_1+1)}\chi Z_{21}^{(\mathrm{K}_2+\mathrm{K}_3)}\chi Z_{21}^{(\mathrm{K}_4)}\chi Z_{21}^{(\mathrm{K}_5)}\chi Z_{21}^{(\mathrm{v})}\chi\left(\begin{matrix}W\\W'\end{matrix}\middle|\begin{matrix}1^{(9+|\mathrm{K}|+\mathrm{v})}\\2^{(6-|\mathrm{K}|-\mathrm{v})}\end{matrix}\right)$$
$$-\binom{\mathrm{K}_3+\mathrm{K}_4}{\mathrm{K}_4} Z_{21}^{(\mathrm{K}_1+1)}\chi Z_{21}^{(\mathrm{K}_2)}\chi Z_{21}^{(\mathrm{K}_3+\mathrm{K}_4)}\chi Z_{21}^{(\mathrm{K}_5)}\chi Z_{21}^{(\mathrm{v})}\chi\left(\begin{matrix}W\\W'\end{matrix}\middle|\begin{matrix}1^{(9+|\mathrm{K}|+\mathrm{v})}\\2^{(6-|\mathrm{K}|-\mathrm{v})}\end{matrix}\right)$$
$$+\binom{\mathrm{K}_4+\mathrm{K}_5}{\mathrm{K}_5} Z_{21}^{(\mathrm{K}_1+1)}\chi Z_{21}^{(\mathrm{K}_2)}\chi Z_{21}^{(\mathrm{K}_3)}\chi Z_{21}^{(\mathrm{K}_4+\mathrm{K}_5)}\chi Z_{21}^{(\mathrm{v})}\chi\left(\begin{matrix}W\\W'\end{matrix}\middle|\begin{matrix}1^{(9+|\mathrm{K}|+\mathrm{v})}\\2^{(6-|\mathrm{K}|-\mathrm{v})}\end{matrix}\right)$$
$$-\binom{\mathrm{K}_5+\mathrm{v}}{\mathrm{v}} Z_{21}^{(\mathrm{K}_1+1)}\chi Z_{21}^{(\mathrm{K}_2)}\chi Z_{21}^{(\mathrm{K}_3)}\chi Z_{21}^{(\mathrm{K}_4)}\chi Z_{21}^{(\mathrm{K}_5+\mathrm{v})}\chi\left(\begin{matrix}W\\W'\end{matrix}\middle|\begin{matrix}1^{(9+|\mathrm{K}|+\mathrm{v})}\\2^{(6-|\mathrm{K}|-\mathrm{v})}\end{matrix}\right)$$
$$+Z_{21}^{(\mathrm{K}_1+1)}\chi Z_{21}^{(\mathrm{K}_2)}\chi Z_{21}^{(\mathrm{K}_3)}\chi Z_{21}^{(\mathrm{K}_4)}\chi Z_{21}^{(\mathrm{K}_5)}\chi\left(\begin{matrix}W\\W'\end{matrix}\middle|\begin{matrix}1^{(9+|\mathrm{K}|)}2^{(\mathrm{v})}\\2^{(6-|\mathrm{K}|-\mathrm{v})}\end{matrix}\right);$$

$where|\mathrm{K}| = \mathrm{K}_1+\mathrm{K}_2+\mathrm{K}_3+\mathrm{K}_4+\mathrm{K}_5.$

Cearly, $S_4\partial_x + \partial_x S_5 = id_{\mathcal{M}_5}$.

Form the above, we get that$\{S_0, S_1, S_2, S_3, S_4, S_5\}$ be contracting homotopy, [6] which means that our complex is exacted.

3. The results of the case (9,7)/(2,0)

In this section, we find the terms of Weyl module resolution in the case of a skew partition (9,7)/(1,0) and give the proof of its exactness

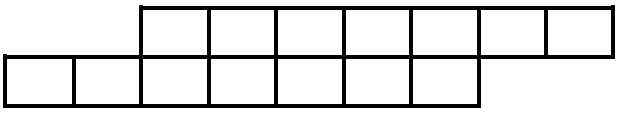

The terms of the characteristic-$f$ree resolution are:

$\mathcal{M}_0 = Đ_7 \otimes Đ_7$

$\mathcal{M}_1 = Z_{21}^{(3)}\chi\, Đ_{10}\otimes Đ_4 \oplus Z_{21}^{(4)}\chi\, Đ_{11}\otimes Đ_3 \oplus Z_{21}^{(5)}\chi\, Đ_{12}\otimes Đ_2 \oplus Z_{21}^{(6)}\chi\, Đ_{13}\otimes Đ_1 \oplus Z_{21}^{(7)}\chi\, Đ_{14}\otimes Đ_0$

$\mathcal{M}_2 = Z_{21}^{(3)}\chi Z_{21}^{(1)}\chi\, Đ_{11}\otimes Đ_3 \oplus Z_{21}^{(4)}\chi Z_{21}^{(1)}\chi\, Đ_{12}\otimes Đ_2 \oplus Z_{21}^{(3)}\chi Z_{21}^{(2)}\chi\, Đ_{12}\otimes Đ_2 \oplus Z_{21}^{(5)}\chi Z_{21}^{(1)}\chi\, Đ_{13}\otimes Đ_1 \oplus Z_{21}^{(4)}\chi Z_{21}^{(2)}\chi\, Đ_{13}\otimes Đ_1 \oplus Z_{21}^{(3)}\chi Z_{21}^{(3)}\chi\, Đ_{13}\otimes Đ_1 \oplus Z_{21}^{(6)}\chi Z_{21}^{(1)}\chi\, Đ_{14}\otimes Đ_0 \oplus Z_{21}^{(5)}\chi Z_{21}^{(2)}\chi\, Đ_{14}\otimes Đ_0 \oplus Z_{21}^{(4)}\chi Z_{21}^{(3)}\chi\, Đ_{14}\otimes Đ_0 \oplus Z_{21}^{(3)}\chi Z_{21}^{(4)}\chi\, Đ_{14}\otimes Đ_0$

$\mathcal{M}_3 = Z_{21}^{(3)}\chi Z_{21}^{(1)}\chi Z_{21}^{(1)}\chi\, Đ_{12}\otimes Đ_2 \oplus Z_{21}^{(4)}\chi Z_{21}^{(1)}\chi Z_{21}^{(1)}\chi\, Đ_{13}\otimes Đ_1 \oplus Z_{21}^{(3)}\chi Z_{21}^{(2)}\chi Z_{21}^{(1)}\chi\, Đ_{13}\otimes Đ_1 \oplus Z_{21}^{(3)}\chi Z_{21}^{(1)}\chi Z_{21}^{(2)}\chi\, Đ_{13}\otimes Đ_1 \oplus Z_{21}^{(5)}\chi Z_{21}^{(1)}\chi Z_{21}^{(1)}\chi\, Đ_{14}\otimes Đ_0 \oplus Z_{21}^{(4)}\chi Z_{21}^{(2)}\chi Z_{21}^{(1)}\chi\, Đ_{14}\otimes Đ_0 \oplus Z_{21}^{(4)}\chi Z_{21}^{(1)}\chi Z_{21}^{(2)}\chi\, Đ_{14}\otimes Đ_0 \oplus Z_{21}^{(3)}\chi Z_{21}^{(3)}\chi Z_{21}^{(1)}\chi\, Đ_{14}\otimes Đ_0 \oplus Z_{21}^{(3)}\chi Z_{21}^{(1)}\chi Z_{21}^{(3)}\chi\, Đ_{14}\otimes Đ_0$

$\mathcal{M}_4 = Z_{21}^{(3)}\chi Z_{21}^{(1)}\chi Z_{21}^{(1)}\chi Z_{21}^{(1)}\chi\, Đ_{13}\otimes Đ_1 \oplus Z_{21}^{(4)}\chi Z_{21}^{(1)}\chi Z_{21}^{(1)}\chi Z_{21}^{(1)}\chi\, Đ_{14}\otimes Đ_0 \oplus Z_{21}^{(3)}\chi Z_{21}^{(2)}\chi Z_{21}^{(1)}\chi Z_{21}^{(1)}\chi\, Đ_{14}\otimes Đ_0 \oplus Z_{21}^{(3)}\chi Z_{21}^{(1)}\chi Z_{21}^{(2)}\chi Z_{21}^{(1)}\chi\, Đ_{14}\otimes Đ_0 \oplus Z_{21}^{(3)}\chi Z_{21}^{(1)}\chi Z_{21}^{(1)}\chi Z_{21}^{(2)}\chi\, Đ_{14}\otimes Đ_0$

$\mathcal{M}_5 = Z_{21}^{(3)}\chi Z_{21}^{(1)}\chi Z_{21}^{(1)}\chi Z_{21}^{(1)}\chi Z_{21}^{(1)}\chi\, Đ_{14}\otimes Đ_0$

3.1 Case 1

The constructions of a contracting homotopies $\{S_i\}$,where i=1, 2, ..., 4

$S_0 = \mathcal{M}_0 \to \mathcal{M}_1$

$$S_0\left(\begin{pmatrix} W \\ W' \end{vmatrix} \begin{matrix} 1^{(7)}2^{(\mathrm{K})} \\ 2^{(7-\mathrm{K})} \end{matrix}\right) = \begin{cases} Z_{21}^{(\mathrm{K})}\chi\begin{pmatrix} W \\ W' \end{vmatrix} \begin{matrix} 1^{(7+\mathrm{K})} \\ 2^{(7-\mathrm{K})} \end{matrix}\end{pmatrix} & ;\ if\ \mathrm{K} = 3,4,\ldots.7 \\ 0 & ;if\ \ \mathrm{K} \le 2 \end{cases}$$

And

$$S_1 = \mathcal{M}_1 \to \mathcal{M}_2$$

$$S_1\left(Z_{21}^{(\mathrm{K}+1)}\chi\begin{pmatrix} W \\ W' \end{vmatrix} \begin{matrix} 1^{(9+\mathrm{K})}2^{(\mathrm{v})} \\ 2^{(5-\mathrm{K}-\mathrm{v})} \end{matrix}\right)$$

$$= \begin{cases} Z_{21}^{(\mathrm{K}+1)}\chi Z_{21}^{(\mathrm{v})}\chi\begin{pmatrix} W \\ W' \end{vmatrix} \begin{matrix} 1^{(9+\mathrm{K}+\mathrm{v})} \\ 2^{(5-\mathrm{K}-\mathrm{v})} \end{matrix}\end{pmatrix} & ;\ if\ \mathrm{v} = 1,2,3,4 \\ 0 & ;if\ \ \mathrm{v} = 0 \end{cases}$$

And

$$S_2 = \mathcal{M}_2 \to \mathcal{M}_3$$

$$S_2\left(Z_{21}^{(\mathrm{K}_1+1)}\chi Z_{21}^{(\mathrm{K}_2)}\chi\begin{pmatrix} W \\ W' \end{vmatrix} \begin{matrix} 1^{(9+|\mathrm{K}|)}2^{(\mathrm{v})} \\ 2^{(5-|\mathrm{K}|-\mathrm{v})} \end{matrix}\right)$$

$$= \begin{cases} Z_{21}^{(\mathrm{K}_1+1)}\chi Z_{21}^{(\mathrm{K}_2)}\chi Z_{21}^{(\mathrm{v})}\chi\begin{pmatrix} W \\ W' \end{vmatrix} \begin{matrix} 1^{(9+|\mathrm{K}|+\mathrm{v})} \\ 2^{(5-|\mathrm{K}|-\mathrm{v})} \end{matrix}\end{pmatrix} & ;\ if\ \mathrm{v} = 1,2,3 \\ 0 & ;if\ \ \mathrm{v} = 0 \end{cases} \quad ;Where|\mathrm{K}| = \mathrm{K}_1 + \mathrm{K}_2$$

and

$$S_3 = \mathcal{M}_3 \to \mathcal{M}_4$$

$$S_3\left(Z_{21}^{(\mathrm{K}_1+1)}\chi Z_{21}^{(\mathrm{K}_2)}\chi Z_{21}^{(\mathrm{K}_3)}\chi\begin{pmatrix} W \\ W' \end{vmatrix} \begin{matrix} 1^{(9+|\mathrm{K}|)}2^{(\mathrm{v})} \\ 2^{(5-|\mathrm{K}|-\mathrm{v})} \end{matrix}\right)$$

$$= \begin{cases} Z_{21}^{(\mathrm{K}_1+1)}\chi Z_{21}^{(\mathrm{K}_2)}\chi Z_{21}^{(\mathrm{K}_3)}\chi Z_{21}^{(\mathrm{v})}\chi\begin{pmatrix} W \\ W' \end{vmatrix} \begin{matrix} 1^{(9+|\mathrm{K}|+\mathrm{v})} \\ 2^{(5-|\mathrm{K}|-\mathrm{v})} \end{matrix}\end{pmatrix} & ;\ if\ \mathrm{v} = 1,2 \\ 0 & ;if\ \ \mathrm{v} = 0 \end{cases} \quad ;Where|\mathrm{K}| = \mathrm{K}_1 + \mathrm{K}_2 + \mathrm{K}_3$$

and

$$S_4 = \mathcal{M}_4 \to \mathcal{M}_5$$

$$S_4\left(Z_{21}^{(\mathrm{K}_1+1)}\chi Z_{21}^{(\mathrm{K}_2)}\chi Z_{21}^{(\mathrm{K}_3)}\chi Z_{21}^{(\mathrm{K}_4)}\chi\begin{pmatrix} W \\ W' \end{vmatrix} \begin{matrix} 1^{(9+|\mathrm{K}|)}2^{(\mathrm{v})} \\ 2^{(5-|\mathrm{K}|-\mathrm{v})} \end{matrix}\right)$$

$$= \begin{cases} Z_{21}^{(\mathrm{K}_1+1)}\chi Z_{21}^{(\mathrm{K}_2)}\chi Z_{21}^{(\mathrm{K}_3)}\chi Z_{21}^{(\mathrm{K}_4)}\chi Z_{21}^{(\mathrm{v})}\chi\begin{pmatrix} W \\ W' \end{vmatrix} \begin{matrix} 1^{(9+|\mathrm{K}|+\mathrm{v})} \\ 2^{(5-|\mathrm{K}|-\mathrm{v})} \end{matrix}\end{pmatrix} & ;\ if\ \mathrm{v} = 1 \\ 0 & ;if\ \ \mathrm{v} = 0 \end{cases} \quad ;Where|\mathrm{K}|$$

$$= \mathrm{K}_1 + \mathrm{K}_2 + \mathrm{K}_3 + \mathrm{K}_4$$

So we have the following diagram:-

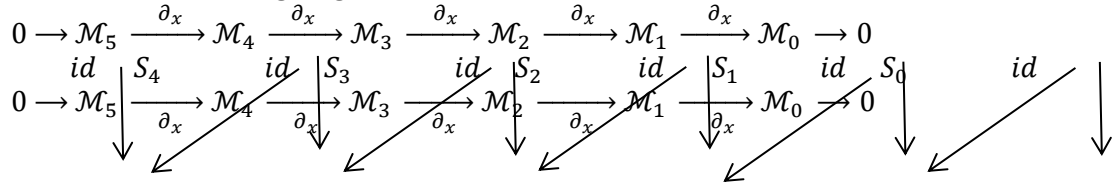

3.2 Case 2

Now, we have

$$S_0\partial_x\left(Z_{21}^{(\mathrm{K}+2)}\chi\binom{W}{W'}\middle|\frac{1^{(9+\mathrm{K})}}{2^{(5-\mathrm{K})}}2^{(v)}\right)=S_0\partial_{21}^{(\mathrm{K}+2)}\chi\binom{W}{W'}\middle|\frac{1^{(9+\mathrm{K})}}{2^{(5-\mathrm{K})}}2^{(v)}\Big)$$
$$=\binom{\mathrm{K}+2+v}{v}Z_{21}^{(\mathrm{K}+2+v)}\chi\binom{W}{W'}\middle|\frac{1^{(9+\mathrm{K}+v)}}{2^{(5-\mathrm{K}-v)}}\Big)$$
and
$$\partial_x S_1\left(Z_{21}^{(\mathrm{K}+2)}\chi\binom{W}{W'}\middle|\frac{1^{(9+\mathrm{K})}}{2^{(5-\mathrm{K})}}2^{(v)}\right)\Big)=\partial_x\left(Z_{21}^{(\mathrm{K}+1)}\chi Z_{21}^{(v)}\chi\binom{W}{W'}\middle|\frac{1^{(9+\mathrm{K}+v)}}{2^{(6-\mathrm{K}-v)}}\right)\Big)$$
$$=-\binom{\mathrm{K}+2+v}{v}Z_{21}^{(\mathrm{K}+2+v)}\chi\binom{W}{W'}\middle|\frac{1^{(9+\mathrm{K}+v)}}{2^{(6-\mathrm{K}-v)}}\Big)+Z_{21}^{(\mathrm{K}+2)}\chi\binom{W}{W'}\middle|\frac{1^{(9+\mathrm{K})}}{2^{(5-\mathrm{K})}}2^{(v)}\Big)$$
Clearly, $S_0\partial_x+\partial_x S_1=id_{\mathcal{M}_1}$.
$$S_1\partial_x\left(Z_{21}^{(\mathrm{K}_1+2)}\chi Z_{21}^{(\mathrm{K}_2)}\chi\binom{W}{W'}\middle|\frac{1^{(9+|\mathrm{K}|)}}{2^{(5-|\mathrm{K}|-v)}}2^{(v)}\right)\Big)$$
$$=S_1\left(-\binom{|\mathrm{K}|+2}{\mathrm{K}_2}Z_{21}^{(|\mathrm{K}|+2)}\chi\binom{W}{W'}\middle|\frac{1^{(9+|\mathrm{K}|)}}{2^{(5-|\mathrm{K}|-v)}}2^{(v)}\Big)+Z_{21}^{(\mathrm{K}_1+2)}\chi\partial_{21}^{(\mathrm{K}_2)}\binom{W}{W'}\middle|\frac{1^{(9+|\mathrm{K}|)}}{2^{(5-|\mathrm{K}|-v)}}2^{(v)}\Big)\right)$$
$$=-\binom{|\mathrm{K}|+2}{\mathrm{K}_2}Z_{21}^{(|\mathrm{K}|+2)}\chi Z_{21}^{(v)}\chi\binom{W}{W'}\middle|\frac{1^{(9+|\mathrm{K}|+v)}}{2^{(5-|\mathrm{K}|-v)}}\Big)+\binom{\mathrm{K}_2+v}{v}Z_{21}^{(\mathrm{K}_1+2)}\chi Z_{21}^{(\mathrm{K}_2+v)}\chi\binom{W}{W'}\middle|\frac{1^{(9+|\mathrm{K}|+v)}}{2^{(5-|\mathrm{K}|-v)}}\Big)$$
and
$$\partial_x S_2\left(Z_{21}^{(\mathrm{K}_1+2)}\chi Z_{21}^{(\mathrm{K}_2)}\chi\binom{W}{W'}\middle|\frac{1^{(9+|\mathrm{K}|)}}{2^{(5-|\mathrm{K}|-v)}}2^{(v)}\right)\Big)=\partial_x\left(Z_{21}^{(\mathrm{K}_1+2)}\chi Z_{21}^{(\mathrm{K}_2)}\chi Z_{21}^{(v)}\chi\binom{W}{W'}\middle|\frac{1^{(9+|\mathrm{K}|+v)}}{2^{(5-|\mathrm{K}|-v)}}\right)\Big)=$$
$$\binom{|\mathrm{K}|+2}{\mathrm{K}_2}Z_{21}^{(|\mathrm{K}|+2)}\chi Z_{21}^{(v)}\chi\binom{W}{W'}\middle|\frac{1^{(9+|\mathrm{K}|+v)}}{2^{(5-|\mathrm{K}|-v)}}\Big)-\binom{\mathrm{K}_2+v}{v}Z_{21}^{(\mathrm{K}_1+2)}\chi Z_{21}^{(\mathrm{K}_2+v)}\chi\binom{W}{W'}\middle|\frac{1^{(9+|\mathrm{K}|+v)}}{2^{(5-|\mathrm{K}|-v)}}\Big)$$
$$+Z_{21}^{(\mathrm{K}_1+2)}\chi Z_{21}^{(\mathrm{K}_2)}\chi\binom{W}{W'}\middle|\frac{1^{(9+|\mathrm{K}|)}}{2^{(5-|\mathrm{K}|-v)}}2^{(v)}\Big);$$
$where|\mathrm{K}|=\mathrm{K}_1+\mathrm{K}_2.$
Clearly, $S_1\partial_x+\partial_x S_2=id_{\mathcal{M}_2}$
$$S_2\partial_x\left(Z_{21}^{(\mathrm{K}_1+2)}\chi Z_{21}^{(\mathrm{K}_2)}\chi Z_{21}^{(\mathrm{K}_3)}\chi\binom{W}{W'}\middle|\frac{1^{(9+|\mathrm{K}|)}}{2^{(5-|\mathrm{K}|-v)}}2^{(v)}\right)\Big)$$
$$="S_2\left[\binom{(\mathrm{K}_1+2+\mathrm{K}_2)}{\mathrm{K}_2}Z_{21}^{(\mathrm{K}_1+2+\mathrm{K}_2)}\chi Z_{21}^{(\mathrm{K}_3)}\chi\binom{W}{W'}\middle|\frac{1^{(9+|\mathrm{K}|)}}{2^{(5-|\mathrm{K}|-v)}}2^{(v)}\Big)\right.$$
$$-\binom{\mathrm{K}_2+\mathrm{K}_3}{\mathrm{K}_3}Z_{21}^{(\mathrm{K}_1+2)}\chi Z_{21}^{(\mathrm{K}_2+\mathrm{K}_3)}\chi\binom{W}{W'}\middle|\frac{1^{(9+|\mathrm{K}|)}}{2^{(5-|\mathrm{K}|-v)}}2^{(v)}\Big)$$
$$\left.+Z_{21}^{(\mathrm{K}_1+2)}\chi Z_{21}^{(\mathrm{K}_2)}\chi\partial_{21}^{(\mathrm{K}_3)}\chi\binom{W}{W'}\middle|\frac{1^{(9+|\mathrm{K}|)}}{2^{(5-|\mathrm{K}|-v)}}2^{(v)}\Big)\right]"$$
$$=\binom{(\mathrm{K}_1+2+\mathrm{K}_2)}{\mathrm{K}_2}Z_{21}^{(\mathrm{K}_1+2+\mathrm{K}_2)}\chi Z_{21}^{(\mathrm{K}_3)}\chi Z_{21}^{(v)}\chi\binom{W}{W'}\middle|\frac{1^{(9+|\mathrm{K}|+v)}}{2^{(5-|\mathrm{K}|-v)}}\Big)-$$
$$\binom{\mathrm{K}_2+\mathrm{K}_3}{\mathrm{K}_3}Z_{21}^{(\mathrm{K}_1+2)}\chi Z_{21}^{(\mathrm{K}_2+\mathrm{K}_3)}\chi Z_{21}^{(v)}\chi\binom{W}{W'}\middle|\frac{1^{(9+|\mathrm{K}|+v)}}{2^{(5-|\mathrm{K}|-v)}}\Big)+$$
$$\binom{\mathrm{K}_3+v}{v}Z_{21}^{(\mathrm{K}_1+2)}\chi Z_{21}^{(\mathrm{K}_2)}\chi Z_{21}^{(\mathrm{K}_3)}\chi Z_{21}^{(v)}\chi\binom{W}{W'}\middle|\frac{1^{(9+|\mathrm{K}|+v)}}{2^{(5-|\mathrm{K}|-v)}}\Big),$$
and
$$\partial_x S_3\left(Z_{21}^{(\mathrm{K}_1+2)}\chi Z_{21}^{(\mathrm{K}_2)}\chi Z_{21}^{(\mathrm{K}_3)}\chi\binom{W}{W'}\middle|\frac{1^{(9+|\mathrm{K}|)}}{2^{(5-|\mathrm{K}|-v)}}2^{(v)}\right)\Big)=\partial_x\left(Z_{21}^{(\mathrm{K}_1+2)}\chi Z_{21}^{(\mathrm{K}_2)}\chi Z_{21}^{(\mathrm{K}_3)}\chi Z_{21}^{(v)}\chi\binom{W}{W'}\middle|\frac{1^{(9+|\mathrm{K}|+v)}}{2^{(5-|\mathrm{K}|-v)}}\right)\Big)$$
$$=-\binom{(\mathrm{K}_1+2+\mathrm{K}_2)}{\mathrm{K}_2}Z_{21}^{(\mathrm{K}_1+2+\mathrm{K}_2)}\chi Z_{21}^{(\mathrm{K}_3)}\chi Z_{21}^{(v)}\chi\binom{W}{W'}\middle|\frac{1^{(9+|\mathrm{K}|+v)}}{2^{(5-|\mathrm{K}|-v)}}\Big)+$$
$$\binom{\mathrm{K}_2+\mathrm{K}_3}{\mathrm{K}_3}Z_{21}^{(\mathrm{K}_1+2)}\chi Z_{21}^{(\mathrm{K}_2+\mathrm{K}_3)}\chi Z_{21}^{(v)}\chi\binom{W}{W'}\middle|\frac{1^{(9+|\mathrm{K}|+v)}}{2^{(5-|\mathrm{K}|-v)}}\Big)-$$
$$\binom{\mathrm{K}_3+v}{v}Z_{21}^{(\mathrm{K}_1+2)}\chi Z_{21}^{(\mathrm{K}_2)}\chi Z_{21}^{(\mathrm{K}_3)}\chi Z_{21}^{(v)}\chi\binom{W}{W'}\middle|\frac{1^{(9+|\mathrm{K}|+v)}}{2^{(5-|\mathrm{K}|-v)}}\Big)+$$
$$Z_{21}^{(\mathrm{K}_1+2)}\chi Z_{21}^{(\mathrm{K}_2)}\chi Z_{21}^{(\mathrm{K}_3)}\chi\partial_{21}^{(v)}\chi\binom{W}{W'}\middle|\frac{1^{(9+|\mathrm{K}|+v)}}{2^{(5-|\mathrm{K}|-v)}}\Big)=$$
$$-\binom{(\mathrm{K}_1+2+\mathrm{K}_2)}{\mathrm{K}_2}Z_{21}^{(\mathrm{K}_1+2+\mathrm{K}_2)}\chi Z_{21}^{(\mathrm{K}_3)}\chi Z_{21}^{(v)}\chi\binom{W}{W'}\middle|\frac{1^{(9+|\mathrm{K}|+v)}}{2^{(5-|\mathrm{K}|-v)}}\Big)+$$
$$\binom{\mathrm{K}_2+\mathrm{K}_3}{\mathrm{K}_3}Z_{21}^{(\mathrm{K}_1+2)}\chi Z_{21}^{(\mathrm{K}_2+\mathrm{K}_3)}\chi Z_{21}^{(v)}\chi\binom{W}{W'}\middle|\frac{1^{(9+|\mathrm{K}|+v)}}{2^{(5-|\mathrm{K}|-v)}}\Big)-$$
$$\binom{\mathrm{K}_3+v}{v}Z_{21}^{(\mathrm{K}_1+2)}\chi Z_{21}^{(\mathrm{K}_2)}\chi Z_{21}^{(\mathrm{K}_3)}\chi Z_{21}^{(v)}\chi\binom{W}{W'}\middle|\frac{1^{(9+|\mathrm{K}|+v)}}{2^{(5-|\mathrm{K}|-v)}}\Big)+Z_{21}^{(\mathrm{K}_1+2)}\chi Z_{21}^{(\mathrm{K}_2)}\chi Z_{21}^{(\mathrm{K}_3)}\chi\binom{W}{W'}\middle|\frac{1^{(9+|\mathrm{K}|)}}{2^{(5-|\mathrm{K}|-v)}}2^{(v)}\Big);$$

$where\ |\mathrm{K}| = \mathrm{K}_1 + \mathrm{K}_2 + \mathrm{K}_3.$
Clearly, $S_2\partial_x + \partial_x S_3 = id_{\mathcal{M}_3}$.

$$S_3\partial_x\left(Z_{21}^{(\mathrm{K}_1+2)}\chi Z_{21}^{(\mathrm{K}_2)}\chi Z_{21}^{(\mathrm{K}_3)}\chi Z_{21}^{(\mathrm{K}_4)}\chi\begin{pmatrix}W\\W'\end{pmatrix}\begin{matrix}1^{(9+|\mathrm{K}|)}2^{(\mathrm{v})}\\2^{(5-|\mathrm{K}|-\mathrm{v})}\end{matrix}\right)$$

$$\begin{aligned}" = S_3\Bigg[&-\binom{(\mathrm{K}_1+2+\mathrm{K}_2)}{\mathrm{K}_2}Z_{21}^{(\mathrm{K}_1+2+\mathrm{K}_2)}\chi Z_{21}^{(\mathrm{K}_3)}\chi Z_{21}^{(\mathrm{K}_4)}\chi\begin{pmatrix}W\\W'\end{pmatrix}\begin{matrix}1^{(9+|\mathrm{K}|)}2^{(\mathrm{v})}\\2^{(5-|\mathrm{K}|-\mathrm{v})}\end{matrix}\\&+\binom{\mathrm{K}_2+\mathrm{K}_3}{\mathrm{K}_3}Z_{21}^{(\mathrm{K}_1+2)}\chi Z_{21}^{(\mathrm{K}_2+\mathrm{K}_3)}\chi Z_{21}^{(\mathrm{K}_4)}\chi\begin{pmatrix}W\\W'\end{pmatrix}\begin{matrix}1^{(9+|\mathrm{K}|)}2^{(\mathrm{v})}\\2^{(5-|\mathrm{K}|-\mathrm{v})}\end{matrix}\\&-\binom{\mathrm{K}_3+\mathrm{K}_4}{\mathrm{K}_4}Z_{21}^{(\mathrm{K}_1+2)}\chi Z_{21}^{(\mathrm{K}_2)}\chi Z_{21}^{(\mathrm{K}_3+\mathrm{K}_4)}\chi\begin{pmatrix}W\\W'\end{pmatrix}\begin{matrix}1^{(9+|\mathrm{K}|)}2^{(\mathrm{v})}\\2^{(5-|\mathrm{K}|-\mathrm{v})}\end{matrix}\\&+Z_{21}^{(\mathrm{K}_1+2)}\chi Z_{21}^{(\mathrm{K}_2)}\chi Z_{21}^{(\mathrm{K}_3)}\chi\partial_{21}^{(\mathrm{K}_4)}\chi\begin{pmatrix}W\\W'\end{pmatrix}\begin{matrix}1^{(9+|\mathrm{K}|)}2^{(\ \mathrm{v})}\\2^{(5-|\mathrm{K}|-\mathrm{v})}\end{matrix}\Bigg]"\end{aligned}$$

$$\begin{aligned}&= -\binom{(\mathrm{K}_1+2+\mathrm{K}_2)}{\mathrm{K}_2}Z_{21}^{(\mathrm{K}_1+2+\mathrm{K}_2)}\chi Z_{21}^{(\mathrm{K}_3)}\chi Z_{21}^{(\mathrm{K}_4)}\chi Z_{21}^{(\mathrm{v})}\chi\begin{pmatrix}W\\W'\end{pmatrix}\begin{matrix}1^{(9+|\mathrm{K}|+\mathrm{v})}\\2^{(5-|\mathrm{K}|-\mathrm{v})}\end{matrix}\\&+\binom{\mathrm{K}_2+\mathrm{K}_3}{\mathrm{K}_3}Z_{21}^{(\mathrm{K}_1+2)}\chi Z_{21}^{(\mathrm{K}_2+\mathrm{K}_3)}\chi Z_{21}^{(\mathrm{K}_4)}\chi Z_{21}^{(\mathrm{v})}\chi\begin{pmatrix}W\\W'\end{pmatrix}\begin{matrix}1^{(9+|\mathrm{K}|+\mathrm{v})}\\2^{(5-|\mathrm{K}|-\mathrm{v})}\end{matrix}\\&-\binom{\mathrm{K}_3+\mathrm{K}_4}{\mathrm{K}_4}Z_{21}^{(\mathrm{K}_1+2)}\chi Z_{21}^{(\mathrm{K}_2)}\chi Z_{21}^{(\mathrm{K}_3+\mathrm{K}_4)}\chi Z_{21}^{(\mathrm{v})}\chi\begin{pmatrix}W\\W'\end{pmatrix}\begin{matrix}1^{(9+|\mathrm{K}|+\mathrm{v})}\\2^{(5-|\mathrm{K}|-\mathrm{v})}\end{matrix}\\&+\binom{\mathrm{K}_4+\mathrm{v}}{\mathrm{v}}Z_{21}^{(\mathrm{K}_1+2)}\chi Z_{21}^{(\mathrm{K}_2)}\chi Z_{21}^{(\mathrm{K}_3)}\chi Z_{21}^{(\mathrm{K}_4)}\chi Z_{21}^{(\mathrm{v})}\chi\begin{pmatrix}W\\W'\end{pmatrix}\begin{matrix}1^{(9+|\mathrm{K}|+\mathrm{v})}\\2^{(5-|\mathrm{K}|-\mathrm{v})}\end{matrix},\end{aligned}$$

and

$$\begin{aligned}&\partial_x\, S_4\left(Z_{21}^{(\mathrm{K}_1+2)}\chi Z_{21}^{(\mathrm{K}_2)}\chi Z_{21}^{(\mathrm{K}_3)}\chi Z_{21}^{(\mathrm{K}_4)}\chi\begin{pmatrix}W\\W'\end{pmatrix}\begin{matrix}1^{(9+|\mathrm{K}|)}2^{(\mathrm{v})}\\2^{(5-|\mathrm{K}|-\mathrm{v})}\end{matrix}\right) =\\&\partial_x\left(Z_{21}^{(\mathrm{K}_1+2)}\chi Z_{21}^{(\mathrm{K}_2)}\chi Z_{21}^{(\mathrm{K}_3)}\chi Z_{21}^{(\mathrm{K}_4)}\chi Z_{21}^{(\mathrm{v})}\chi\begin{pmatrix}W\\W'\end{pmatrix}\begin{matrix}1^{(9+|\mathrm{K}|+\mathrm{v})}\\2^{(5-|\mathrm{K}|-\mathrm{v})}\end{matrix}\right)\\&=\binom{(\mathrm{K}_1+2+\mathrm{K}_2)}{\mathrm{K}_2}Z_{21}^{(\mathrm{K}_1+2+\mathrm{K}_2)}\chi Z_{21}^{(\mathrm{K}_3)}\chi Z_{21}^{(\mathrm{K}_4)}\chi Z_{21}^{(\mathrm{v})}\chi\begin{pmatrix}W\\W'\end{pmatrix}\begin{matrix}1^{(9+|\mathrm{K}|+\mathrm{v})}\\2^{(5-|\mathrm{K}|-\mathrm{v})}\end{matrix}\\&-\binom{\mathrm{K}_2+\mathrm{K}_3}{\mathrm{K}_3}Z_{21}^{(\mathrm{K}_1+2)}\chi Z_{21}^{(\mathrm{K}_2+\mathrm{K}_3)}\chi Z_{21}^{(\mathrm{K}_4)}\chi Z_{21}^{(\mathrm{v})}\chi\begin{pmatrix}W\\W'\end{pmatrix}\begin{matrix}1^{(9+|\mathrm{K}|+\mathrm{v})}\\2^{(5-|\mathrm{K}|-\mathrm{v})}\end{matrix}\\&+\binom{\mathrm{K}_3+\mathrm{K}_4}{\mathrm{K}_4}Z_{21}^{(\mathrm{K}_1+2)}\chi Z_{21}^{(\mathrm{K}_2)}\chi Z_{21}^{(\mathrm{K}_3+\mathrm{K}_4)}\chi Z_{21}^{(\mathrm{v})}\chi\begin{pmatrix}W\\W'\end{pmatrix}\begin{matrix}1^{(9+|\mathrm{K}|+\mathrm{v})}\\2^{(5-|\mathrm{K}|-\mathrm{v})}\end{matrix}\\&-\binom{\mathrm{K}_4+\mathrm{v}}{\mathrm{v}}Z_{21}^{(\mathrm{K}_1+2)}\chi Z_{21}^{(\mathrm{K}_2)}\chi Z_{21}^{(\mathrm{K}_3)}\chi Z_{21}^{(\mathrm{K}_4)}\chi Z_{21}^{(\mathrm{v})}\chi\begin{pmatrix}W\\W'\end{pmatrix}\begin{matrix}1^{(9+|\mathrm{K}|+\mathrm{v})}\\2^{(5-|\mathrm{K}|-\mathrm{v})}\end{matrix}\\&+Z_{21}^{(\mathrm{K}_1+2)}\chi Z_{21}^{(\mathrm{K}_2)}\chi Z_{21}^{(\mathrm{K}_3)}\chi Z_{21}^{(\mathrm{K}_4)}\partial_{21}^{(\mathrm{v})}\chi\begin{pmatrix}W\\W'\end{pmatrix}\begin{matrix}1^{(9+|\mathrm{K}|+\mathrm{v})}\\2^{(5-|\mathrm{K}|-\mathrm{v})}\end{matrix}\\&=\binom{(\mathrm{K}_1+2+\mathrm{K}_2)}{\mathrm{K}_2}Z_{21}^{(\mathrm{K}_1+2+\mathrm{K}_2)}\chi Z_{21}^{(\mathrm{K}_3)}\chi Z_{21}^{(\mathrm{K}_4)}\chi Z_{21}^{(\mathrm{v})}\chi\begin{pmatrix}W\\W'\end{pmatrix}\begin{matrix}1^{(9+|\mathrm{K}|+\mathrm{v})}\\2^{(5-|\mathrm{K}|-\mathrm{v})}\end{matrix}\\&-\binom{\mathrm{K}_2+\mathrm{K}_3}{\mathrm{K}_3}Z_{21}^{(\mathrm{K}_1+2)}\chi Z_{21}^{(\mathrm{K}_2+\mathrm{K}_3)}\chi Z_{21}^{(\mathrm{K}_4)}\chi Z_{21}^{(\mathrm{v})}\chi\begin{pmatrix}W\\W'\end{pmatrix}\begin{matrix}1^{(9+|\mathrm{K}|+\mathrm{v})}\\2^{(5-|\mathrm{K}|-\mathrm{v})}\end{matrix}\\&+\binom{\mathrm{K}_3+\mathrm{K}_4}{\mathrm{K}_4}Z_{21}^{(\mathrm{K}_1+2)}\chi Z_{21}^{(\mathrm{K}_2)}\chi Z_{21}^{(\mathrm{K}_3+\mathrm{K}_4)}\chi Z_{21}^{(\mathrm{v})}\chi\begin{pmatrix}W\\W'\end{pmatrix}\begin{matrix}1^{(9+|\mathrm{K}|+\mathrm{v})}\\2^{(5-|\mathrm{K}|-\mathrm{v})}\end{matrix}\\&-\binom{\mathrm{K}_4+\mathrm{v}}{\mathrm{v}}Z_{21}^{(\mathrm{K}_1+2)}\chi Z_{21}^{(\mathrm{K}_2)}\chi Z_{21}^{(\mathrm{K}_3)}\chi Z_{21}^{(\mathrm{K}_4)}\chi Z_{21}^{(\mathrm{v})}\chi\begin{pmatrix}W\\W'\end{pmatrix}\begin{matrix}1^{(9+|\mathrm{K}|+\mathrm{v})}\\2^{(5-|\mathrm{K}|-\mathrm{v})}\end{matrix}\\&+Z_{21}^{(\mathrm{K}_1+2)}\chi Z_{21}^{(\mathrm{K}_2)}\chi Z_{21}^{(\mathrm{K}_3)}\chi Z_{21}^{(\mathrm{K}_4)}\begin{pmatrix}W\\W'\end{pmatrix}\begin{matrix}1^{(9+|\mathrm{K}|)}2^{(\mathrm{v})}\\2^{(5-|\mathrm{K}|-\mathrm{v})}\end{matrix};\end{aligned}$$

$Where\ |\mathrm{K}| = \mathrm{K}_1 + \mathrm{K}_2 + \mathrm{K}_3 + \mathrm{K}_4$
Clearly, $S_3\partial_x + \partial_x S_4 = id_{\mathcal{M}_4}$.
From the above, we get that $\{S_0, S_1, S_2, S_3, S_4\}$ be contracting *h*omotopy, [6] which means that our complex *is* exact.

References

[1] David, A B and Gian, C R 1993 Projective Resolution of Weyl Modules *Natl. Acad. Sci. USA* **90** 2448-2450

[2] David A B and Rota, G C 2001 Approaches to resolution of Weyl modules *Adv In Applied Math* **27** 182-191
[3] David A B 2004 A Characteristic Free Example of Lascoux Resolution and Letter Place Methods for Intertwining Numbers *European Journal of Gombinatorics* **25** 1169-1179
[4] Hassan H R 2010 On the resolution of Wely module in the case of two-rowed skew-shap $(p + t, q)/(t, 0)$, *Mustansiriyah J. Sci*. **21**(5) 470-473
[5] Hassan H R and Jasim N S 2018 Application of Weyl Module in the Case of Two *Rows J. Phys.:Conf.Ser* **1003**(012051) 1-15
[6] Vermani L R 2003 *An Elementary Approach to Homotopical algebra* Chapman and Hall /CRC *Monpgraphs and Surveys in pure and Applied Mathematic*

Inverse Equality Co-Neighborhood Domination in Graphs

Inverse Equality Co-Neighborhood Domination in Graphs

Sahib SH. Kahat[1] and Manal N. Al-Harere[2]

[1]Department of Mathematics, College of Science, University of Baghdad, Iraq
[2] Department of Applied Sciences, University of Technology, Baghdad, Iraq

E-mail: sgehet@gmail.com

Abstract. Let $G = (V, E)$ be a simple undirected graph without isolated vertices. A proper subset $D \subset V$ is called equality co-neighborhood dominating set of G (ENDS), if every vertex in set D is adjacent to equally number of vertices in $V - D$. In this paper, the inverse equality co-neighborhood dominating set of G (IENDS) is defined. Some properties of inverse equality co-neighborhood dominating set are determined. The inverse equality co-neighborhood domination number in some special graphs and three kinds of operations in join graphs is calculated.

1. Introduction

Let $G = (V, E)$ be an undirected, simple, and finite graph of order $|V| = n$ such that V is the vertex set and E is the edge set. A subset $D \subseteq V$ is a dominating set of G, if every vertex in $V - D$ is adjacent to at least one vertex in D. The domination number γ(G) is the minimum cardinality of a dominating set in G, which has been dealt with in this work. Is defined by $N_G(v) = \{u \in V(G): uv \in E(G)\}$ for an open neighborhood of a vertex v in G and the closed neighborhood of a vertex v in G is defined by $N_G[v] = N_G(v) \cup \{v\}$. The degree of v, $\deg(v) = |\mathrm{N_G}(v)|$ is the number of vertices which are adjacent to it. The vertex of degree zero (one) is called an isolated (pendant) vertex. The complement $\overline{\mathrm{G}}$ is the graph in which two vertices are not adjacent if and only if they are adjacent in G or vice versa. The join $G_1 + G_2$ is the graph having vertex set $V(G)_1 \cup V(G_2)$ and edge set $\mathrm{E(G_1)} \cup \mathrm{E(G_2)} \cup \{ (uv: u \in \mathrm{V(G_1)}$ and $v \in \mathrm{V(G_2)}\}$. The corona $\mathrm{G_1} \odot \mathrm{G_2}$ is the graph obtained by taking one copy of $\mathrm{G_1}$ and $|G_1|$ copies of $\mathrm{G_2}$, and then joining the $\mathrm{j^{th}}$ vertex of $\mathrm{G_1}$ to every vertex in the $\mathrm{j^{th}}$ copy of $\mathrm{G_2}$. Any notation that which not found in this paper can be found in [11]. In [1] a proper subset $D \subset V$ is called equality co-neighborhood dominating set of G (ENDS) , if every vertex in set D is adjacent to equally number of vertices in $V - D$. Domination in graphs are very important for solve many of problems of real-life and it is a vital topic that attracts most researchers especially in recent years. So many new definitions appeared as in [4,5,6,7,8] and [13,14,15,16,17,18,19] and inverse of new definitions as in [10,12]. Also, there is a study of domination polynomial of certain graph as in[21,22,23]. The domination brings together many fields as labeled graph [2,3], topological graph [15], fuzzy graph [24,25] and others. The first introduced this concept is C. Berge in his book [9] and Ore is the first used in [20]. In this work, our viewpoint sheds a light on the new parameter of domination, and it is called equally co-neighborhood domination. When forming a group of workers to dominate the completion of work in most life problems, we usually seek to distribute the tasks between the group members equally. And the formation of another reserve group, be completely separate from the first group of workers to dominate the completion of work, and also the distributing of tasks between the group members equally, if the first group fails. From this principle, we set out to present this inverse new definition. There are some

properties and boundaries of this parameter that have been presented in this work. Also, domination number has been calculated for this definition IENDS for certain graphs as a complete, path, cycle, wheel, star, and complete bipartite graphs. Furthermore, an inverse equality co-neighborhood domination number for the graph that are obtained form three kinds of operations in graphs as the complement of a graph, the join of two graphs, and the corona of two graphs have been discussed with some properties.

To prove our main results we need the following results

Definition.1.1[1]. Let G be a simple graph, a proper subset $D \subset V$ is called equally co-neighborhood dominating set of *G* (*ENDS*), if every vertex in set *D* is adjacent to equally number of vertices in $V - D$. The set *D* is called minimal ENDS($MENDS$) if it has no proper *ENDS.* The equally domination number denoted by $\gamma_{en}(G)$ for simplicity $\gamma_{en}(G)$ is the minimum cardinality of a $MENDS$. The $MENDS$ of cardinality γ_{en} is called γ_{en}- *set.*

Proposition 1.2.[5]. A cycle C_n, $n \geq 3$ has $\gamma_{bi}(C_n) = \gamma_{bi}^{-1}(C_n) = \left\lceil \frac{n}{3} \right\rceil$

Corollary 1.3. [1]. For path P_n, $n \geq 3$ has no inverse bi-dominating set.

Proposition 1.4.[1]. Let G be a graph of order n, then

1) $\deg(v_i) \geq k, \forall v_i \in D$, where k is the number of vertices in $V - D$ that are adjacent to v_i.
2) If G has an isolated vertex, then G has no ENDS.
3) $1 \leq \gamma_{en}(G) \leq n - 1$.
4) The dominating set D is minimal if there is no adjacent vertex in to other vertices in D and has no private vertex in $V - D$.

Proposition 1.5. [1]. Let G be a graph of order n, then

1. A cycle C_n, $n \geq 3$ has $\gamma_{en}(C_n) = \gamma_{bi}(C_n) = \left\lceil \frac{n}{3} \right\rceil$.
2. For path P_n , $n \geq 3$,$\gamma_{en}(P_n) = \left\lceil \frac{n}{3} \right\rceil$.
3. For complete K_n , wheel W_n, and star S_n ,$\gamma_{en}(k_n) = \gamma_{en}(W_n) = \gamma_{en}(S_n) = 1$.

Proposition 1.6. [1]. For a complete bipartite graph $K_{n,m}$
$\gamma_{en}(K_{n,m}) = \min\{m, n, 2 + (\max\{m, n\} - \min\{m, n\})\}$.

Theorem 1.7. [1]. For path P_n , $n \geq 4$,$\gamma_{en}(\overline{P_n}) = 2$

Theorem 1.8. [1]. For a complete bipartite graph $K_{n,m}$ $\gamma_{en}(\overline{K_{n,m}}) = \max\{m, n\} - \min\{m, n\} + 2$.

Theorem 1.9. [1]. If G_1 and G_2 are two graphs with vertex sets V_1 and V_2 respectively and have no isolated vertex, then

$$\gamma_{FD}(G_1 + G_2) = \min\left\{\begin{array}{c}\left\{\begin{array}{c}\min\{\gamma_{FD}(G_1), \gamma_{FD}(G_1)\}, \text{ if } G_1 \text{ and } G_2 \text{ have MENDS,} \\ \gamma_{FD}(G_i, i \text{ either 1 or 2}), \text{if } G_i \text{ has MENDS and the others has no MENDS,} \\ \min\{|V_1|, |V_2|\}, \quad \text{if } G_1 \text{ and } G_2 \text{ have no MENDS and there is no vertex adjacent to all vertices in each graph}\end{array}\right\}, \\ |S|, \text{where S is the minimum set has the vertices from } G_1 + G_2 \text{ such that } S \cap V_1 \neq \emptyset \neq S \cap V_2 \text{and } N(v_i) \cap V - D \text{ is equal } \forall v_i \in S\end{array}\right\}$$

Theorem 1.10. [1]. If G_1 and G_2 be two graphs such that $\overline{G_1}$ and $\overline{G_2}$ have γ_{en}-set, then $\gamma_{en}(\overline{G_1 + G_2}) = \gamma_{en}(\overline{G_1}) + \gamma_{en}(\overline{G_2})$

Theorem 1.11. [1]. If G_1 and G_2 are two graphs, then in general
1) $\gamma_{en}(G_1 \odot G_2) = |G_1|$. 2) $\gamma_{en}(G_2 \odot G_1) = |G_2|$.

2 Inverse equally co-neighborhood domination number

Definition 2.1. Let $D \subset V$ is minimum equality co-neighborhood dominating set of G (MENDS), if $V - D$ contains a ENDS in G, this set is called an inverse equality co-neighborhood dominating set of D in G (IENDS) and denoted by D^{-1}. The inverse equality co-neighborhood dominating set number of G, denoted by $\gamma_{en}^{-1}(G)$ is the minimum cardinality over all inverse equality co-neighborhood dominating set in G. See Fig 1.

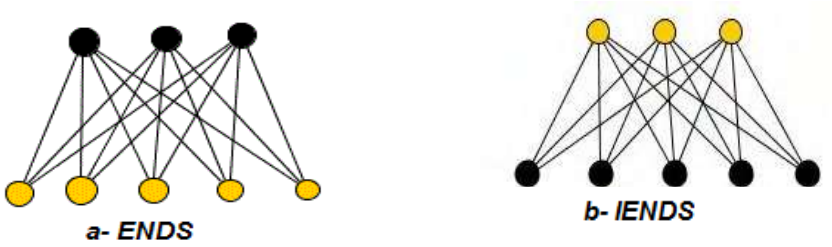

Figure (1): a-equally co-neighborhood dominating set and b-inverse equality co- neighborhood dominating set

Proposition 2.2. Let G be a graph having an MIENDS $\gamma_{en}^{-1}(G)$, then
1) $\gamma_{en}^{-1}(G) \geq \gamma_{en}(G)$
2) $\gamma_{en}^{-1}(K_n) = \gamma_{en}(K_n) = 1 \ \forall\, n \geq 2$
3) $\gamma_{en}^{-1}(S_n) = n - 1 \ \forall\, n \geq 3$
4) $1 \leq \gamma_{en}^{-1}(G) \leq n - 1$.

Proof.
1) by Definition 2.1 we get $\gamma_{en}^{-1}(G) \geq \gamma_{en}(G)$
2) It is clear since every vertex in K_n is adjacent to all the verticesK_n in the graph.
3) Since $\gamma_{en}(S_n)$-set is the center of the star $\forall\, n \geq 2$ then the set of all other vertices is MIENDS, therefore $\gamma_{en}^{-1}(S_n) = n - 1$
4) The lower bound occurs by 2, while the upper bound occurs by 3. □

Note 2.3. For any graph G of order n, and has ENDS, if $\gamma_{en}(G_n) > \frac{n}{2}$, then G has no IENDS.

Proposition 2.4. Let G be a graph of order n, then
1. A cycle C_n, $n \geq 3$ has $\gamma_{en}(C_n) = \gamma_{en}^{-1}(C_n) = \left\lceil \frac{n}{3} \right\rceil$
2. A wheel W_n, for $W_n = C_n + K_1$, $n \geq 3$, then $\gamma_{en}^{-1}(W_n) = \left\lceil \frac{n}{3} \right\rceil$

Proof.
1. Since deg(v) = 2, $\forall\, v \in C_n$ and $\gamma_{bi}(C_n) = \gamma_{bi}^{-1}(C_n) = \left\lceil \frac{n}{3} \right\rceil$ and $\gamma_{en}(C_n) = \gamma_{bi}(C_n) = \left\lceil \frac{n}{3} \right\rceil$ by Proposition 1.2 and Proposition 1.5, then $\gamma_{en}(C_n) = \gamma_{en}^{-1}(C_n) = \left\lceil \frac{n}{3} \right\rceil$.

2. Let D be MENDS in W_n, since $\gamma_{en}(W_n) = 1$ and $W_n = C_n + K_1$. So, $D = \{v\}, v \in K_1$, and $vu \in E(W_n)\ \forall u \in V - D$, then $\gamma_{en}(C_n)$-set is a MIENDS of D in W_n. Therefore, $\gamma_{en}^{-1}(W_n) = \gamma_{en}(C_n) = \left\lceil \frac{n}{3} \right\rceil$. □

Theorem 2.5. Let G be graph has D is MENDS, then G has no IENDS if contains pendant vertex $v \notin D$, and $\langle V - D \rangle$ has isolated vertex is not pendant vertex in G.

Proof.
Let G be a graph having D which is a MENDS and let $v \notin D$, be a pendant vertex in G and u is isolated vertex in $V - D$, such that $v \neq u$. The vertex v is adjacent to only one vertex in D and u is adjacent to at least two vertices in D. Then every dominating set $\widetilde{D}$, such that $\widetilde{D} \cap D = \emptyset$ contains v and u, then $\widetilde{D}$ is not ENDS. Thus, the proof is done. □

Theorem 2.6. Let P_n be a path graph of order $n \geq 2$, then

1. If $n \equiv 0 (\mathrm{mod}\ 3)$, then $\gamma_{en}^{-1}(P_n) = \frac{2n}{3}$
2. If $n \equiv 1, 2 (\mathrm{mod}\ 3)$, such that $n \geq 5$, then P_n has no IENDS.
3. $\gamma_{en}^{-1}(P_2) = 1$ and $\gamma_{en}^{-1}(P_4) = 2$

Proof.
Let P_n be a path graph of order n, and D be a MENDS, then we have $\gamma_{en}(P_n) = |D| = \left\lceil \frac{n}{3} \right\rceil$, by Proposition 1.5, then

1. If $n \equiv 0 (\mathrm{mod}\ 3)$, hence $\gamma_{en}(P_n) = \frac{n}{3}$, i.e. we have one vertex in D that is adjacent to two vertices in $V - D$ for every three vertices in P_n, then $N(v) \cap N(u) = \emptyset$ in $V - D\ \forall v, u \in D$, then every vertex in $V - D$ is adjacent to only one vertex in D. Hence, $V - D$ is IENDS in P_n and it is MIENDS, because $\langle V - D - \{p\} \rangle\ \forall\ p \in (V - D)$ is not IENDS for two subcases are obtained as follows.
   I. The vertex p is pendant, then the set $V - D - \{p\}$ has no vertex dominated to p
   II. The vertex p is not a pendant vertex, then $V - D - \{p\}$ has one vertex u that is adjacent to p and D has one vertex v which is adjacent to u, then u is an isolated vertex in $\langle V - D - \{p\} \rangle$. Therefore $V - D - \{p\}$ is not IENDS according to Theorem 2.5, since $\gamma_{en}(P_n) = |D| = \frac{n}{3}$, then $\gamma_{en}^{-1}(P_n) = |V - D| = \frac{2n}{3}$
2. It is straightforward from II in (1) and according to Theorem 2.5
3. Let $P_2 = \{v, u\}$, then $D = \gamma_{en}(P_2) - \text{set} = \{v\}$, $V - D = \gamma_{en}^{-1}(P_2) - \text{set} = \{u\}$.

And let $P_4 = \{v_1, v_2, v_3, v_4\}$, then $D = \gamma_{en}(P_2) - \text{set} = \{v_1, v_4\}$, $V - D = \gamma_{en}^{-1}(P_2) - \text{set} = \{v_2, v_3\}$ or vice versa. Thus, the proof is done. □

Proposition 2.7. Let $K_{n,m}$ be a complete bipartite graph for $m \geq n \geq 2$, then

$$\gamma_{en}^{-1}(K_{n,m}) = \begin{cases} |m - n| + 2 \text{ if } |m - n| + 2 \leq \min, \text{and } \gamma_{en}(K_{n,m}) = m - n + 2 \\ \max\{m, n\} \text{ if } |m - n| + 2 \geq \min\{m, n\}, \text{and } \gamma_{en}(K_{n,m}) = \min\{m, n\} \end{cases}$$

Proof.
Let X and Y are the partite sets of the vertices of $K_{n,m}$, such that $|X| = n$ and $|Y| = m$ and let $m \geq n \geq 2$. Two cases are obtained as follows.

1. If $n = m$, then each vertex in G has the same degree, hence $\gamma_{en}(K_{n,m})$ −set=$\{v_1, u_1\}$, where $v_1 \in X$ and $u_1 \in Y$, and we have $\gamma_{en}^{-1}(K_{n,m}) - \text{set} = \{v_2, u_2\}$, where $v_2 \in X$ and $u_2 \in Y$, such that $v_1 \neq v_2$ and $u_1 \neq u_2$

2. If $n \neq m$, then to keep that each vertex in set D has the same neighborhood in $V - D$, then the vertices in the set D must be either set X or the set Y or set $S = \{v_i : v_i \in Y, i = 1,2, \dots, m - n\} \cup \{v, u\}$, such that $v \in X$ and $u \in Y$ and $u \neq v_i$. The set S has $m - n + 2$ vertices. Since $m \geq n \geq 2$, hence $m - n + 2 \leq m$ and $\gamma_{en}(K_{n,m}) = \min\{n, m - n + 2\}$. Then three subcases are obtained as follows.

I. When $m - n + 2 = n$, then $\gamma_{en}(K_{n,m}) = m - n + 2$ or $\gamma_{en}(K_{n,m}) = n$ and there are at least $m - n + 2$ vertices in $V - D$, such that one vertex from X and $m - n + 1$ from Y. Therefore $\gamma_{en}(K_{n,m}) = m - n + 2 = \gamma_{en}^{-1}(K_{n,m}) = m - n + 2$, or $\gamma_{en}(K_{n,m}) = n$ and $\gamma_{en}^{-1}(K_{n,m}) = m$

II. When $m - n + 2 < n$, then $\gamma_{en}(K_{n,m}) = m - n + 2$ and there are at least $m - n + 2$ vertices in $V - D$, such that one vertex from X and $m - n + 1$ from Y. Therefore $\gamma_{en}(K_{n,m}) = \gamma_{en}^{-1}(K_{n,m}) = m - n + 2$.

III. When $m - n + 2 > n$, then $\gamma_{en}(K_{n,m}) = n$, therefore $\gamma_{en}^{-1}(K_{n,m}) = m$.

Thus proof is done. □

3 Inverse equally co-neighborhood domination number in some graphs

3.1 The complement of certain graphs

Proposition 3.1.1. Let G be a graph of order n, If $\gamma_{en}(G) = 1$, then $\overline{G}$ has no IENDS..

Proof.

Since $\gamma_{en}(G) = 1$, then G has vertex that is adjacent to all other vertices in G, hence $\overline{G_n}$ has an isolated vertex. Therefore, it has no ENDS and IENDS. □

Proposition 3.1.2 .

1. For path P_n , $n \geq 4$, $\gamma_{en}^{-1}(\overline{P_n}) = 2$.
2. For cycle C_n , $n \geq 4$, $\gamma_{en}^{-1}(\overline{C_n}) = 2$.

Proof.

1. By Theorem 1.7, $\gamma_{en}(\overline{P_n}) = 2$, $\gamma_{en}(\overline{P_n})$-set has two vertices which are pendant vertices in P_n, since any others two vertices, which are adjacent vertices and are not pendant vertices in P_n are adjacent with all vertices in $\overline{P_n}$, then $\gamma_{en}^{-1}(\overline{P_n}) = 2$ and vice versa.
2. By Theorem 6 [1], $\gamma_{en}(\overline{C_n}) = 2$, $\gamma_{en}(\overline{C_n})$-set has two vertices in C_n, which are adjacent vertices in C_n, since any others two adjacent vertices in C_n are adjacent with all vertices in $(\overline{C_n})$, then $\gamma_{en}^{-1}(\overline{C_n}) = 2$. □

Theorem 3.1.3. Let $K_{n,m}$ be a complete bipartite graph for $m \geq n \geq 2$, then

1. $\gamma_{en}^{-1}(\overline{K_{n,m}}) = |m - n| + 2$ if $|m - n| + 2 \leq \min\{m, n\}$
2. $K_{n,m}$ has no IENDS if $|m - n| + 2 > \min\{m, n\}$

Proof

It is obvious that $\overline{K_{m,n}} \equiv K_m \cup K_n$, let $m \geq n \geq 2$ and let D be $\gamma_{en}(\overline{K_{n,m}})$-set. Must be D has one vertex from K_n and $m - n + 1$ vertices from K_m, according to Definition 1.1, ie $|D| = \gamma_{en}(\overline{K_{n,m}}) = m - n + 2$, and $|V - D| = 2(n - 1)$, such that (n-1) vertices from K_n and (n-1) vertices from K_m. Then two cases are obtained as follows.

Case 1. If $m - n + 2 \leq n$, then $m \leq 2(n - 1)$, since $|D| = m - n + 2$, then $|D| \leq |V - D|$, and since $m \geq n \geq 2$, then in this case we have one vertex from K_n and $m - n + 1$ vertices from K_m in $V - D$. Therefore $\gamma_{en}^{-1}(\overline{K_{n,m}}) = |m - n| + 2$

Case 2. If $m - n + 2 > n$, then $m > 2(n-1)$, since $|D| = m - n + 2$, then $|D| > |V - D|$. Therefore $K_{n,m}$ has no IENDS, according to Note 2.3. □

3.2 IENDS of Join Graphs

Theorem 3.2.1. If G_1 and G_2 are two graphs with vertices sets V_1 and V_2 respectively and have no isolated vertex, then $\gamma_{en}^{-1}(G_1 + G_2) =$

$$\min\left\{\begin{array}{l}\left\{\begin{array}{l}\left\{\begin{array}{l}\{\gamma_{en}(G_1), \text{or } \gamma_{en}(G_2)\}, \text{ when } \gamma_{en}(G_1) = \gamma_{en}(G_2), \text{ if } G_1 \text{ and } G_2 \text{ have IENDS,}\\ \min\{\gamma_{en}^{-1}(G_1), \gamma_{en}(G_2)\}, \text{ when } \gamma_{en}(G_1) < \gamma_{en}(G_2), \text{ if } G_1 \text{ and } G_2 \text{ have IENDS,}\\ \min\{\gamma_{en}(G_1), \gamma_{en}^{-1}(G_2)\}, \text{when } \gamma_{en}(G_1) > \gamma_{en}(G_2), \text{if } G_1 \text{ and } G_2 \text{ have MENDS.}\end{array}\right.\\ \left\{\begin{array}{ll}\min\{\gamma_{en}^{-1}(G_1), |V_2|\}, & \text{when } \gamma_{en}(G_1) < |V_2|, \text{if } G_1 \text{ has IENDS and the others has no ENDS,}\\ \gamma_{en}(G_1), & \text{when } \gamma_{en}(G_1) > |V_2|, \text{if } G_1 \text{ has IENDS and the others has no ENDS.}\end{array}\right.\\ \max\{|V_1|, |V_2|\}, \quad \text{if } G_1 \text{ and } G_2 \text{ have no MENDS and there is no vertex adjacent to all vertices in each graph}\end{array}\right.\\ |S^{-1}|, \text{where S is the minimum set has the vertices from } G_1 + G_2 \text{ such that } S \cap V_1 \neq \emptyset \neq S \cap V_2 \text{and } N(v_i) \cap V - D \text{ is equal } \forall v_i \in S\end{array}\right\}$$

Proof.

Let G_1 and G_2 two graphs of order $|V_1|$ and $|V_2|$ respectively, and with no isolated vertex, then according to Theorem 1.9 there are two cases depend on the vertices of MIENDS taken form only one graph or both as follows.

Case 1. There are three subcases as follows.

1. When G_1 and G_2 have IENDS, in this case there are the following.

I. If $\gamma_{en}(G_1) = \gamma_{en}(G_2)$, then one of them is $\gamma_{en}(G_1 + G_2)$ and other is, $\gamma_{en}^{-1}(G_1 + G_2)$.

II. If $\gamma_{en}(G_1) < \gamma_{en}(G_2)$, then it must be $\gamma_{en}(G_1 + G_2) = \gamma_{en}(G_1)$, hence $\gamma_{en}^{-1}(G_1 + G_2) = \min\{\gamma_{en}^{-1}(G_1), \gamma_{en}(G_2)\}$

III. If $\gamma_{en}(G_1) > \gamma_{en}(G_2)$, then $\gamma_{en}^{-1}(G_1 + G_2) = \min\{\gamma_{en}(G_1), \gamma_{en}^{-1}(G_2)\}$ is true according to (ii).

2. If G_1has IENDS and G_2 has no ENDS, Since vertices set of V_2 is ENDS for $(G_1 + G_2)$, then $\gamma_{en}(G_1 + G_2) = \min\{\gamma_{en}(G_1), |V_2|\}$ and $\gamma_{en}^{-1}(G_1 + G_2) = \min\{\gamma_{en}^{-1}(G_1), |V_2|\}$, when $\gamma_{en}(G_1) < |V_2|$ ie $\gamma_{en}(G_1 + G_2) = \gamma_{en}(G_1)$, while $\gamma_{en}^{-1}(G_1 + G_2) = \gamma_{en}(G_1)$ when $\gamma_{en}(G_1) > |V_2|$ ie $\gamma_{en}(G_1 + G_2) = |V_2|$.

3. If G_1 and G_2 have no ENDS, also they have no IENDS, then $\gamma_{en}(G_1 + G_2)$ =min $\{|V_1|, |V_2|\}$ and $\gamma_{en}^{-1}(G_1 + G_2)$= max $\{|V_1|, |V_2|\}$.

case 2. When S is the minimum set has the vertices from $G_1 + G_2$ such that $S \cap V_1 \neq \emptyset \neq S \cap V_2$ and vertices number of the set $N(v_i) \cap V - D$ are equal $\forall v_i \in S$, then $\gamma_{en}(G_1 + G_2) = |S|$ and $\gamma_{en}^{-1}(G_1 + G_2) = |S^{-1}|$. Therefore, $\gamma_{en}^{-1}(G_1 + G_2) = \min\{\text{case 1, case 2}\}$. The proof is done. □

Corollary 3.2.2. Let G_1 and G_2 are two isomorphic graphs, then $\gamma_{en}^{-1}(G_1 + G_2)$=2.

Proof.

If G_1 is isomorphic to G_2, then every vertex in G_1 is adjacent to all vertices in G_2 and every vertex in G_2 is adjacent to all vertices in G_1, and V (G_1) = V (G_1), then $\gamma_{en}(G_1 + G_2) = \gamma_{en}^{-1}(G_1 + G_2)$=2. □

Proposition 3.2.3. If G_1 and G_2 are two graphs such that $\overline{G_1}$ and $\overline{G_2}$ have IENDS,, then $\gamma_{en}^{-1}(\overline{G_1 + G_2}) = \gamma_{en}^{-1}(\overline{G_1}) + \gamma_{en}^{-1}(\overline{G_2})$.

Proof.

Since $\overline{G_1 + G_2}$ is isomorphic to $\overline{G_1} \cup \overline{G_2}$ and $\gamma_{en}(\overline{G_1 + G_2}) = \gamma_{en}(\overline{G_1}) + \gamma_{en}(\overline{G_2})$ according to Theorem 1.10, then $\gamma_{en}^{-1}(\overline{G_1 + G_2}) = \gamma_{en}^{-1}(\overline{G_1}) + \gamma_{en}^{-1}(\overline{G_2})$. □

3.3 IENDS of Corona Graphs

Theorem 3.3.1. If G_1 and G_2 are two graphs of order $|G_1|$=n and $|G_1|$ =m respectively such that G_1 and G_2 have IENDS, then we have.

1. $\gamma_{en}^{-1}(G_1 \odot G_2) = n\,\gamma_{en}(G_2)$
2. $\gamma_{en}^{-1}(G_2 \odot G_1) = m\,\gamma_{en}(G_1)$

Proof.

Let G_1 and G_2 are two graphs, then

1. By definition of corona graph in graph $G_1 \odot G_2$ we have one copy of G_1 and n copies of G_2. each i^{th} vertex in the graph G_1 is adjacent to all vertices in the i^{th} copy of G_2. And according to Theorem 1.11 , $\gamma_{en}(G_1 \odot G_2) = |G_1|$. Therefore, $\gamma_{en}^{-1}(G_1 \odot G_2) = n\,\gamma_{en}(G_2)$
2. The proof is By the same method in 1. □

Corollary 3.3.2.

1. $\gamma_{en}(\overline{G_1} \odot \overline{G_2}) = |G_1|$.
2. $\gamma_{en}^{-1}(\overline{G_1} \odot \overline{G_2}) = n\,\gamma_{en}(\overline{G_2})$.

Proof.

1. Let G_1 and G_2 are two graphs, and $|D| = \gamma_{en}(G_1 \odot G_2) = |G_1|$ according to Theorem 1.11 and since $\overline{G_1}$and $\overline{G_2}$ be new graphs and $|\overline{G_1}| = |G_1|$, then $\gamma_{en}(\overline{G_1} \odot \overline{G_2}) = |\overline{G_1}| = |G_1|$.
2. By definition of corona graph and according to 1 in above , then $V - D = n|G_2|$. Therefore, $\gamma_{en}^{-1}(\overline{G_1} \odot \overline{G_2}) = n\,\gamma_{en}(\overline{G_2})$. □

Proposition 3.3.3. If G_1 and G_2 are two graphs of order $n \geq 2$ and $m \geq 2$ respectively such that $\overline{G_1}$and $\overline{G_2}$ have IENDS, then $\gamma_{en}^{-1}(\overline{G_1 \odot G_2}) = \gamma_{en}(\overline{G_1 \odot G_2}) = 2$.

Proof.

Let G_1 and G_2 are two graphs of order $n \geq 2$ and $m \geq 2$ respectively , then we have every vertex in i^{th} copy of G_2 is adjacent to at least all the vertices in $(\overline{G_1 \odot G_2})$ except i^{th} vertex in G_1 and all other vertices in same copies of G_2. Let $D = \{v, u: v \text{ in } i^{th} \text{ copy of } G_2 \text{ and } u \text{ in } (i+1)^{th} \text{copy of } G_2\}$, then by the above set D is $\gamma_{en}(\overline{G_1 \odot G_2})$-set. And since $n \geq 2$ and $m \geq 2$, then other two vertices have the same conditions as v and u but different from them. Therefore, $\gamma_{en}^{-1}(\overline{G_1 \odot G_2}) = \gamma_{en}(\overline{G_1 \odot G_2}) = 2$. □

4 Conclusion

In this work, the new notion of inverse domination has been introduced for the different types of graphs. Also, some advanced properties through different proved theorems are added. And obtained the lower and upper bound of the inverse equally co-neighborhood domination number. Also, determined this definition to certain graphs like a cycle, wheel, path complete, and complete bipartite. Finally, we performed some operations on a graph and a certain graph, and these are the complement of a certain graph, join to two graphs, and corona of two graphs.

References

[1] Omran A A, Al-Harere M N and Kahat S S Equality Co-Neighborhood Domination in Graphs, accepted for publication in *Discrete Mathematics Algorithms and Applications* (DMAA) No. DMAA-D-20-00266R1

[2] Al-Harere M N and Omran A A 2020 On binary operation graphs *Boletim da Sociedade Paranaense de Matematica* **38** (7) 59-67

[3] Al-Harere M N and Omran A A Binary operation graphs *AIP Conference Proceedings* **2086**(1) 030008

[4] Abdlhusein M A and Al-Harere M N 2019 Pitchfork domination and its inverse for corona and join operations in graphs *Proceedings of International Mathematical Sciences* **I**(**2**)51-55
[5] Al-Harere M N and Abdlhusein M N 2020 Pitchfork domination in graphs *Discrete Mathematics Algorithms and Applications* **12**(2) 2050025
[6] Al-Harere M N, Omran A A and Breesam A T 2020 Captive domination in graphs Discrete Mathematics *Algorithms and Applications* **12**(6) 205067
[7] Al-Harere M A and Breesam A T 2019 Further results on bi-domination in graphs *AIP Conf. Proc*. 2096 020013
[8] Al-Harere M N and Khuda B A 2018 Tadpole domination in graphs *Baghdad Sci. J.* **15** 466-471
[9] Berge C 1962 The theory of graphs and its applications *Methuen and Co London*
[10] Cockayne E J, Dawes R M and Hedetniemi S T 1980 Total domination in graphs *Networks:Int. J.* **10**(3) 211-219
[11] Harary F 1969 Graph Theory *Addison-Wesley, Reading Mass*, 1969.
[12] Haynes T W, Hedetniemi S T and Slater P J 1998 Fundamentals of domination in graphs *Marcel Dekker, Inc., New York*
[13] Jabour A A and Omran A A 2019 Domination in discrete topology graph *AIP 11 Conf.Proc*. **2183** 030006
[14] Jabor A A and Omran A A 2020 Hausdorff Topological of Path in Graph *IOP Conf. Ser.: Mater. Sci. Eng* **928** 042008. doi:10.1088/1757-899X/928/4/042008
[15] Omran A A and Hamed O H 2019 Hn domination in graphs *Baghdad Sci. J*. **16**(1) 242-247
[16] Omran A A and M M Shalaan Inverse Co-even Domination of Graphs *IOP Conference Series: Materials Science and Engineering* **928** (4) 042025
[17] Omran A A and Shalaan M M 2020 Inverse Co-even Domination of Graphs 2020 *IOP Conf. Ser.: Mater. Sci. Eng*. **928** 042025. doi:10.1088/1757-899X/928/4/042025
[18] Omran A A and Swadi T 2019 Observer Domination Number in Graphs *Jour of Adv Research in Dynamical & Control Systems* **11** 01-Special Issue
[19] O 1962 Theory of Graphs *American Mathematical Society Providence R.I*
[20] Kahat S Sh, Khalaf A M and Hasni R 2014 Dominating Sets and Domination Polynomials of Stars *Australian Journal of Basic and Applied Sciences* **8**(6) 383-386
[21] Kahat S Sh and Khalaf A M 2014 Dominating Sets and Domination polynomial of Complete Graphs with Missing Edges *Journal of Kufa for Mathematics and Computer* **2**(1) 64-68
[22] Kahat S Sh, Khalaf A M and Hasni R 2014 Dominating Sets and Domination Polynomial of Wheels *Asian Journal of Applied Sciences* **02**(03) 287-290
[23] Yousif H Y and Omran A A 2020 2-anti fuzzy domination in anti fuzzy graphs *IOP Conf. Ser .Mater. Sci. Eng*. **928** 042027. doi:10.1088/1757-899X/928/4/042027
[24] Yousif H Y and Omran A A 2020 The Split Anti Fuzzy Domination in Anti Fuzzy Graphs *J.Phys.: Conf. Ser.* 1591 012054 doi:10.1088/1742-6596/1591/1/012054

A New Algorithm to Estimate the Parameters of Log-Logistic Distribution Based on the Survival functions

A New Algorithm to Estimate the Parameters of Log-Logistic Distribution Based on the Survival functions

Amina Ibrahim k. and Bayda Atiya Kalaf

Department of Mathematics, College of Education (Ibn Al – Haitham) University of Baghdad, Baghdad, Iraq

E-mail: hbama75@yahoo.com

Abstract. Estimation of the parameters is quite important in the numerous fields for the development of mathematical models. Maximum likelihood estimation is a good method, which is usually used to elaborate on the parameter estimation. The likelihood function formed for the parameter estimation of Log-Logistic is very hard to maximize. Therefore, this paper proposes a new hybrid of Maximum Likelihood Estimator (MLE) and Simplex Downhill Algorithm (SDA) called (MLESDA) to estimate parameters of Log-Logistic distribution based on Survival functions. To compare the suggested method (MLESDA) and classical Maximum Likelihood (MLE) method, simulation is used. The results demonstrate that MLESDA is more efficient than the MLE method.

1. Introduction

Recently, Survival Analysis (SA) is one of the widely used techniques in medical statistics, physics, medicine, epidemiology engineering, economics, biology, and public health [1, 2]. Estimating survival functions that have interested statisticians for numerous years.

The most of the existing books of Survival analysis for Kleinbaum and Klein [4], Allison [5] introduced this topic from a conventional statistical scene instead of a machine learning standpoint. Chung et al. [3] described the statistical methods of survival analysis and their implementation in criminology for predicting the time until recidivism. Recently, Cruz and Wishart [6] and Kourou et al. [7] discussed applications in cancer prediction and used several survival analysis methods.

The log-logistic distribution possesses a rather supple functional form [8]. The log-logistic distribution has its own standing as a life testing model; it is viewed as a weighted exponential distribution and also is an increasing failure rate (IFR) model. Due to the importance of this distribution in reliability, it has been used to estimate the estimators to find parameters. This distribution and for the adoption process to assess the estimators of those two parameters have been estimated the survival of this distribution.

The nonlinearity model makes the estimation of parameter and the statistical analysis of parameter estimates more difficult and challenging.

Although, SDA algorithm still a good choice for many practitioners in the fields of physical, statistical, medical sciences, and engineering. Since, it is very easy to use and code [9, 10]. However, until now SDA has not been applied in many mathematical problems. Therefore, in this paper, simplex downhill algorithm adopted to estimate the parameters of Log-Logistic distribution based on Survival functions.

The organized paper as follows: section 2 offers some information about Log Logistic distribution. Section 3. is clarifying Maximum likelihood Estimation method. Section 4 describe the proposed

method (MLEDSA). Section 5 Simulation study. Section 6 demonstrates the effectiveness of the proposed method through numerical results. Finally, in Section 6 a conclusion is provided.

2. Log-Logistic Distribution

The probability density function (p. d. f) and the cumulative distribution function (c. d. f) of Log Logistic distribution are expressed respectively as:

$$f(x,a,\beta)=\frac{\frac{\beta}{a}(\frac{x}{a})^{\beta-1}}{(1+(\frac{x}{a})^{\beta})^{2}} \quad (1)$$

$$F(x,a,\beta)=\frac{1}{1+(\frac{x}{a})^{-\beta}} \quad (2)$$

where x is a value of random variable, α is scale parameter, and β is shape parameter and $a,\beta > 0$.

$$S(x)=1- F(x,a,\beta) \quad (3)$$

The survival function $S(x)$ for the Log-Logistic distribution given by substituting equation (2) in equation (3), as follows:

$$S(x)=1-\frac{1}{1+(\frac{x}{a})^{-\beta}}$$

$$S(x)=\frac{1}{1+(\frac{x}{a})^{\beta}} \quad (4)$$

3. Maximum Likelihood Estimation Method (MLE):

Let $X_{(1)},X_{(2)},\dots,X_{(n)}$ be order random sample of sized (n) from a distribution with *p.d.f* $f(x,a,\beta)$ such that (a,β) are the parameters, then the likelihood function $L(a,\beta)$ is the joint *p.d.f* of the random samples is [11]:

$$L\left(x_{(1)},x_{(2)},\dots,x_{(n)},a,\beta\right)=\prod_{i=1}^{n}f(x_i)=\prod_{i=1}^{n}\left(\frac{\frac{\beta}{a}\left(\frac{x_{(i)}}{a}\right)^{\beta-1}}{\left(1+\left(\frac{x_{(i)}}{a}\right)^{\beta}\right)^{2}}\right)$$

$$=\frac{\beta^{n}}{a^{n}}\prod_{i=1}^{n}\left(\frac{\left(\frac{x_{(i)}}{a}\right)^{\beta-1}}{\left(1+\left(\frac{x_{(i)}}{a}\right)^{\beta}\right)^{2}}\right) \quad (5)$$

Taking the natural logarithm for the equation (5), so we get the function:

$$LnL\left(x_{(i)},a,\beta\right)=nLn\left(\frac{\beta}{a}\right)+(\beta-1)\sum_{i=1}^{n}Ln(\frac{x_{(i)}}{a})-2\sum_{i=1}^{n}Ln\left(1+\left(\frac{x_{(i)}}{a}\right)^{\beta}\right)$$

$$LnL\left(x_{(i)},a,\beta\right)=nLn(\beta)-nLn(a)+\beta\sum_{i=1}^{n}Ln\left(\frac{x_{(i)}}{a}\right)-\sum_{i=1}^{n}Ln\left(\frac{x_{(i)}}{a}\right)-2\sum_{i=1}^{n}Ln\left(1+\left(\frac{x_{(i)}}{a}\right)^{\beta}\right)$$

$$LnL\left(x_{(i)},a,\beta\right)=nLn(\beta)-nLn(a)+\beta\sum_{i=1}^{n}Ln\left(x_{(i)}\right)-\beta\sum_{i=1}^{n}Ln(a)-\sum_{i=1}^{n}Ln\left(x_{(i)}\right)+\sum_{i=1}^{n}Ln(a)-2\sum_{i=1}^{n}Ln\left(1+\left(\frac{x_{(i)}}{a}\right)^{\beta}\right) \quad (6)$$

The partial derivative for the equation (6) with respect to the unknown parameters (α,β), respectively:

$$\frac{\partial\, LnL\,(x_{(i)},a,\beta)}{\partial a} = \frac{-n}{\alpha} - \beta\sum_{i=1}^{n}\frac{1}{\alpha} + \sum_{i=1}^{n}\frac{1}{\alpha} - 2\sum_{i=1}^{n}\frac{\beta\left(\frac{x_{(i)}}{\alpha}\right)^{\beta-1}\left(\frac{-x_{(i)}}{\alpha^2}\right)}{1+\left(\frac{x_{(i)}}{\alpha}\right)^{\beta}}$$

$$\frac{\partial\, LnL\,(x_{(i)},a,\beta)}{\partial a} = \frac{2\beta}{\alpha}\sum_{i=1}^{n}\frac{\left(\frac{x_{(i)}}{\alpha}\right)^{\beta}}{1+\left(\frac{x_{(i)}}{\alpha}\right)^{\beta}} - \frac{n\beta}{\alpha} \tag{7}$$

Set equation (7) equal to zero , we get

$$\frac{2\beta}{\alpha}\sum_{i=1}^{n}\frac{\left(\frac{x_{(i)}}{\alpha}\right)^{\beta}}{1+\left(\frac{x_{(i)}}{\alpha}\right)^{\beta}} - \frac{n\beta}{\alpha} = 0 \tag{8}$$

$$\frac{\partial\, LnL\,(x_{(i)},a,\beta)}{\partial \beta} = \frac{n}{\beta} + \sum_{i=1}^{n} Ln\left(\frac{x_{(i)}}{\alpha}\right) - 2\sum_{i=1}^{n}\frac{\left(\frac{x_{(i)}}{\alpha}\right)^{\beta} Ln\left(\frac{x_{(i)}}{\alpha}\right)}{1+\left(\frac{x_{(i)}}{\alpha}\right)^{\beta}} \tag{9}$$

After putting equation (9) to zero, then

$$\frac{n}{\beta} + \sum_{i=1}^{n} Ln\left(\frac{x_{(i)}}{\alpha}\right) - 2\sum_{i=1}^{n}\frac{\left(\frac{x_{(i)}}{\alpha}\right)^{\beta} Ln\left(\frac{x_{(i)}}{\alpha}\right)}{1+\left(\frac{x_{(i)}}{\alpha}\right)^{\beta}} = 0 \tag{10}$$

Numerical technique for this method which is *Newton Raphson method* has been used.
From equation (8), we get:

$$2\sum_{i=1}^{n}\frac{\left(\frac{x_{(i)}}{\alpha}\right)^{\beta}}{1+\left(\frac{x_{(i)}}{\alpha}\right)^{\beta}} - n = 0 \tag{11}$$

Let $f_1(\alpha,\beta)$ is define of equation (11), we get:

$$f_1(\alpha,\beta) = 2\sum_{i=1}^{n}\frac{\left(\frac{x_{(i)}}{\alpha}\right)^{\beta}}{1+\left(\frac{x_{(i)}}{\alpha}\right)^{\beta}} - n \tag{12}$$

From equation (9), we get:

$$\frac{n}{\beta} + \sum_{i=1}^{n} Ln\left(\frac{x_{(i)}}{\alpha}\right) - 2\sum_{i=1}^{n}\frac{Ln\left(\frac{x_{(i)}}{\alpha}\right)}{1+\left(\frac{x_{(i)}}{\alpha}\right)^{-\beta}} = 0 \tag{13}$$

Let $g_1(\alpha,\beta)$ define of equation (13), we get:

$$g_1(a,\beta) = \frac{n}{\beta} + \sum_{i=1}^{n} Ln\left(\frac{x_{(i)}}{\alpha}\right) - 2\sum_{i=1}^{n}\frac{Ln\left(\frac{x_{(i)}}{\alpha}\right)}{1+\left(\frac{x_{(i)}}{\alpha}\right)^{-\beta}} \tag{14}$$

Since the two-nonlinear equations are complicated to be solved, it is impossible to find estimators of parameters (α,β). For this reason using the numerical analysis (iterative method) to obtain and estimate (α,β) which maximizes the likelihood function. One of these numerical procedures is Newton-Raphson method [12]. It is one of the important methods in numerical analysis because it is very fast and the error

of this iterative method is quadratic approximation. In Newton-Raphson method using the Jacobean matrix J_i which is the first derivatives for each equation of $f_1(\alpha,\beta)$ and $g_1(\alpha,\beta)$ with respect to α and β.

Now, we find the formulas of Jacobean matrix as follows:

$$J = \begin{vmatrix} \frac{\partial f_1(\alpha,\beta)}{\partial \alpha} & \frac{\partial f_1(\alpha,\beta)}{\partial \beta} \\ \frac{\partial g_1(\alpha,\beta)}{\partial \alpha} & \frac{\partial g_1(\alpha,\beta)}{\partial \beta} \end{vmatrix}$$

$$\frac{\partial f_1(\alpha,\beta)}{\partial \alpha} = -2\frac{\beta}{\alpha}\sum_{i=1}^{n}\frac{1}{\left(1+\left(\frac{x_{(i)}}{\alpha}\right)^{-\beta}\right)\left(1+\left(\frac{x_{(i)}}{\alpha}\right)^{\beta}\right)} \quad (15)$$

$$\frac{\partial f_1(\alpha,\beta)}{\partial \beta} = 2\frac{\beta}{\alpha}\sum_{i=1}^{n}\frac{Ln\left(\frac{x_{(i)}}{\alpha}\right)}{\left(1+\left(\frac{x_{(i)}}{\alpha}\right)^{-\beta}\right)\left(1+\left(\frac{x_{(i)}}{\alpha}\right)^{\beta}\right)} \quad (16)$$

and,

$$\frac{\partial g_1(\alpha,\beta)}{\partial \alpha} = \frac{n}{\alpha} + \frac{2}{\alpha}\sum_{i=1}^{n}\frac{1}{1+\left(\frac{x_{(i)}}{\alpha}\right)^{-\beta}} + \frac{2\beta}{\alpha}\sum_{i=1}^{n}\frac{Ln\left(\frac{x_{(i)}}{\alpha}\right)}{\left(1+\left(\frac{x_{(i)}}{\alpha}\right)^{-\beta}\right)\left(1+\left(\frac{x_{(i)}}{\alpha}\right)^{\beta}\right)} \quad (17)$$

$$\frac{\partial g_1(\alpha,\beta)}{\partial \beta} = \frac{n}{\beta^2} - 2\sum_{i=1}^{n}\frac{Ln\left(\frac{x_{(i)}}{\alpha}\right)^2}{\left(1+\left(\frac{x_{(i)}}{\alpha}\right)^{-\beta}\right)\left(1+\left(\frac{x_{(i)}}{\alpha}\right)^{\beta}\right)} \quad (18)$$

Thus, the following equations matrixes are applied to estimate the parameters for Log-Logistic distribution by using Newton-Raphson method.

$$\begin{pmatrix}\hat{\alpha}_{MLE}\\ \hat{\beta}_{MLE}\end{pmatrix} = \begin{pmatrix}\alpha_0\\ \beta_0\end{pmatrix} - j^{-1}\begin{pmatrix}f_1(\alpha,\beta)\\ g_1(\alpha,\beta)\end{pmatrix} \quad (19)$$

Let

$$v_1 = \frac{\partial f_1(\alpha,\beta)}{\partial \alpha}, v_2 = \frac{\partial f_1(\alpha,\beta)}{\partial \beta}, v_3 = f_1(\alpha,\beta)$$
$$v_4 = \frac{\partial g_1(\alpha,\beta)}{\partial \alpha}, v_5 = \frac{\partial g_1(\alpha,\beta)}{\partial \beta}, v_6 = g_1(\alpha,\beta) \quad (20)$$

Now, substitute equation (19) in equation (20), we get:

$$\hat{\alpha}_{MLE} = \alpha_0 + h_1 \quad (21)$$
$$\hat{\beta}_{MLE} = \beta_0 + k_1 \quad (22)$$

where:

$h_1 = \frac{v_4 v_6 - v_3 v_5}{v_1 v_5 - v_2 v_4}$, and $k_1 = \frac{-v_3 - v_1 h_1}{v_4}$

So, to estimate the survival analyses $\hat{S}(x)$, we substitute equations (21) and (22) in equation (3).

4. Simplex Downhill Algorithm and Maximum Likelihood Estimation Method (MLEDHA)

Simplex downhill algorithm (SDA) was introduced in 1962 [13]. However, Nelder and Mead [14] modified this algorithm in 1965 to the modern form. SDA called Nelder-Mead or Amoeba. Simplex downhill algorithm is a mathematical method that uses geometric relationships to aid in finding approximate solutions to solve complex and optimization problems. The benefit of this method is it does not require an evaluation of the derivative of the function. But only guesses number of solutions for each decision variable. The idea of SDA generates $N + 1$ points (vertex) in an N-dimensional space. Then the vertices sorted by ascending order such as: $f(x_1) \leq f(x_2) \leq \ldots \leq f(x_n) \leq$

$f(x_{n+1})$, where x_{n+1} is worse solution and $x1$ best solution. The algorithm iteration updates to improve the worst solution by four operations as follows:

Reflection step:

compute the reflection point x_r from $x_r = m + \lambda\,(m - x_{n+1})$

and evaluate $f\ for\ x_r$,

where m is the centroid of the N best solution in the vertices of the simplex $m = mean\,(x\,((:n))$ and $\lambda = 1$.

$If\ f(x_1) \leq f(x_r) < f(x_n)$, ten put the worst solution in reflected point

$x_{n+1} = x_r$.

Expansion step:

If $f(x_r) < f(x_1)$ then generate a new point x_e by expansion, from

$x_e = x_r + \beta\,(x_r - m)$, where $\beta = 2$.

- If $f(x_e) < f(x_r)$ then replace x_{n+1} with x_e.
- else $x_{n+1} = x_r$.

Contraction step:

$If\ f(x_{n+1}) \leq f(xr), generate\ a\ new\ solution\ x_c$

$where\ x_c = m + \gamma\,(m - x_{n+1})$.

$If\ f(x_c) < f(xr)\quad then\ x_{n+1} = x_c$.

$else\ x_{n+1} = x_r$.

The step of shrinkage is used, if the three steps are failing in above.

Shrinkage Step:
We keep the best one x_1 then generate the n new vertices by using $x_{sj} = x_1 + \sigma\,(x_{sj} - x_1)$, j = {2 … n +1} and σ = 0.5. The next iteration consists of the simplex vertices as x_1, x_{s2}, …, $x_{s\ n+1}$.
The objective function of the simplex downhill algorithm in this method was the log likelihood function. By minimizing the log likelihood function, the SDA estimates the parameters of the Log-Logistic Distribution.

5. Simulation:

The estimation performance of the proposed method is verified through simulation in this section. In addition, each simulation condition was generated by 1000 replications. The simulation program was written by Matlab 2016. For examining the effect of sample size, various sample sizes are tested: 40, 80, and 100. The simulation steps as follows;

Step 1: Generate random samples as $u_1, u_2, \dots, u_n$, which are following the continuous uniform distribution defined on the interval (0,1). Then transform it to a random sample follows Log-Logistic distribution using $c.d.f.$ as follow;

$$F(x,a,\beta)=\frac{1}{1+(\frac{x_i}{a})^{-\beta}} \quad , \quad Ui=\frac{1}{1+(\frac{x_i}{a})^{-\beta}} \quad , \quad x_i=\ a(\frac{Ui}{1-Ui})^{\frac{1}{\beta}}$$

Then, let *G* is a vector of all parameters required, such as $G = [a, \beta\ ]$ and generate *k+1* solutions for *X*. where k i s t h e number of parameters t h a t required for output

Step 2: Recall the S from the equation (4).

Step 3: By (L=1000) replication, we compute $\hat{S}$ based on MLE using equations (21), and (22), and the best solution from (f_1) MLEDSA method.

6. Result of Simulation

In order to verify the performance of the MLEDSA method to estimate the parameters, we made simulation by examining various sample sizes (30, 60, 90) . We considered different values of parameters of (α, β) as (0.5 , 2), (2 , 4), (3 , 1), (1,0.5), (1,5) respectively. Based on MSE. Each table explained the result of estimate values of α and β, survival and estimate survival, respectively.

The following tables (1-5) showed that the proposed algorithm offered less MSE for estimate parameters and survival function. Therefore, MLEDSA method provides better results.

Table 1. MSE of estimate the parameters and survival analyses when $\alpha = 0.5\ and\ \beta = 2$

Simple size	Method	$\hat{\alpha}$	$\hat{\beta}$	S	$\hat{S}$
	MLE	0.47737	1.88420	0.50000	0.47820
$n = 30$	MLE/SDA	0.47806	1.92247	0.50000	0.48644
	MLE	0.56668	2.56315	0.50000	0.57342
$n = 60$	$MLE/\ SDA$	0.56609	2.45316	0.50000	0.57055
	MLE	0.46123	1.82234	0.50000	0.36129
$n = 90$	$MLE/\ SDA$	0.46475	2.01930	0.50000	0.45952

Table 2. MSE of estimate the parameters and survival analyses when $\alpha = 2\ \ and\ \beta =\ 4$

Simple size	Method	$\hat{\alpha}$	$\hat{\beta}$	S	$\hat{S}$
	MLE	1.95162	3.83078	0.99611	0.99460
$n = 30$	$MLE/\ SDA$	1.95154	3.84493	0.99611	0.99471
	MLE	2.15225	3.76869	0.99611	0.99593
$n = 60$	$MLE/\ SDA$	2.15427	3.80256	0.99611	0.99614
	MLE	1.85573	3.92688	0.99611	0.99423
$n = 90$	$MLE/\ SDA$	1.85557	4.03466	0.99611	0.99499

Table 3. MSE of estimate the parameters and survival analyses when $\alpha = 3\ \ and\ \beta =\ 1$

Simple size	Method	$\hat{\alpha}$	$\hat{\beta}$	S	$\hat{S}$

$n = 30$	MLE	2.70160	1.09006	0.85714	0.86282
	MLE/SDA	3.25834	1.10303	0.85714	0.88770
$n = 60$	MLE	2.31416	1.01150	0.85714	0.82489
	MLE/SDA	2.63529	1.01227	0.85714	0.84324
$n = 90$	MLE	0.02459	0.00158	0.85714	0.79236
	MLE/SDA	3.07712	0.25778	0.85714	0.85813

Table 4. MSE of estimate the parameters and survival analyses when α=1 and β=0.5

Simple size	Method	$\hat{\alpha}$	$\hat{\beta}$	S	$\hat{S}$
$n = 30$	MLE	0.76726	0.48077	0.58579	0.55129
	MLE/SDA	0.82181	0.48062	0.58579	0.55942
$n = 60$	MLE	0.74999	0.50627	0.58579	0.55114
	MLE/SDA	0.77164	0.50613	0.58579	.55469
$n = 90$	MLE	0.68244	0.55341	0.58579	0.54293
	MLE/SDA	0.74644	0.55483	0.58579	0.55535

Table 5. MSE of estimate the parameters and survival analyses when $\alpha = 1 \ and \ \beta = 5$

Simple size	Method	$\hat{\alpha}$	$\hat{\beta}$	S	$\hat{S}$
$n = 30$	MLE	1.06921	3.54456	0.96970	0.93668
	$MLESDA$	1.06011	5.31187	0.96970	0.98187
$n = 60$	MLE	1.04446	4.65496	0.96970	0.96860
	$MLE\ SDA$	1.04396	4.88415	0.96970	0.97329
$n = 90$	MLE	4.57566	0.99228	0.96970	0.89997
	$MLESDA$	1.01016	5.37201	0.96970	0.97764

7. Conclusion

In this paper, a new algorithm MLESDA has been recommended to estimate the parameters for log logistic distribution based on survival analyses. Simulation is founded to compare between the suggested method and MLE. The results showed that MLESDA variant more precisely estimate the parameters than the MLE.

References

[1] Rich J, Neely J, Paniello R, Volker Ch, Nussenbaum B and Wang E 2010 A practical guide to understanding Kaplan-Meir curves Otolaryngology–head and neck surgery official *journal of American Academy of Otolaryngology-Head and Neck Surgery* **143**(3) 331–6

[2] Chung Ch-F, Schmidt P and Witte A D 1991 Survival analysis: A survey *Journal of Quantitative Criminology* **7**(1) 59–98

[3] Kleinbaum D G and Klein M 2006 *Survival Analysis: A Self-learning Text* Springer Science & Business Media

[4] Allison P D 2010 *Survival Analysis Using SAS: A Practical Guide* Sas Institute
[5] Cruz J A and Wishart D S 2006 Applications of machine learning in cancer prediction and prognosis Cancer Informatics
[6] Fotiadis K K, Exarchos Th P, Exarchos K P, Karamouzis M V and I Dimitrios 2015 Machine learning applications in cancer prognosis and prediction *Computational and Structural Biotechnology Journal* **13** 8–17
[7] Balakrishnan N, Malik H J and S Puthenpura 1987 Best line run biased Estimation of location and scale parameters of the Log-Logistic distribution *Commun. Statist–Theor. Meth* **16**(12) 3477–3495
[8] Abdul Jabbar K, Atiya B and Atiya B 2017 Application of the Downhill Simplex Algorithm for Solving Aggregate Production Planning problems *Sci.Int.(Lahore)* **29**(5) 1075-1081
[9] Chelouah R and Siarry P 2005 A hybrid method combining continuous tabu search and nelder{mead simplex algorithms for the global optimization of multiminima functions *European Journal of Operational Research* **161**(3) 636-654
[10] AL-Yasseri AY T 2014 Using simulation to estimate two parameters & reliability function for logistic distribution Master thesis college of education, Al-Mustansirah University
[11] Ojo M O and Olapade A K 2003 On the generalized Logistic and Log-Logistic distribution, Department of Mathematics, Obafemi Awolowo University, Ile-Ife, Nigeria, Kraguje vac J. Math. 25 65-73
[12] Spendley W, Hext G R and Himsworth F R 1962 Sequential application of simplex designs optimization and evolutionary operation *Technometrics* **4**(4) 411-461
[13] Nelder J A and Mead R 1965 A simplex method for function minimation *The computer journal* **7**(4) 308-313

New restricted biased estimator based on modified unbiased ridge regression estimator

New restricted biased estimator based on modified unbiased ridge regression estimator

Bader Aboud Mohammad and Mustafa Ismaeel Naif

Department of Mathematics, College of education for pure science,
University Of Anbar, Anbar, Iraq

E-mail: bad19u2003@uoanbar.edu.iq

Abstract. More researchers used biased estimators instead of the restricted least square estimator (RLS) that is unbiased to improve the efficiency of the estimator. Therefore, in this paper, we proposed new biased estimator, called restricted modified unbiased ridge regression (RMUR) based on modified unbiased ridge regression (MURR) that suggested by Batah and Gory (2009). By some theorems and a simulation study, we show that, this new estimator has desirable properties as the MUR and it is better than the RLS. A numerical example from literature is used to illustrate the results.

1. Introduction

Consider the following linear regression model

$$Y = X\beta + \varepsilon, \quad (1)$$

where X is known (n×p) matrix with rank(X) = p , Y is (n×1) response vector , The error team ε is a n×1 vector of error with E(ε)=0 and var(ε)= $\sigma^2 I_n$ and β is a (p×1) unknown vector coefficient. Ordinary least square (OLS) estimator of β in model (1) is given by

$$\hat{\beta}_L = (X'X)^{-1}X'Y \quad (2)$$

When there is a linear relationship between independent variables, the problem of multicollinearity will be exist. In case of multicollinearity, the (OLS) estimator of regression coefficients may be statistically significant with wrong sign and large variance. Therefore the results are far from the actual values. To overcome this problem, the biased estimator has been used. One of these estimators is ordinary ridge regression ORR which proposed by Hoerl and Kennard (1970). Hoerl and Kennard derived the ORR estimator as the solution of the following problem; minimize $\beta^{*\prime}\beta^*$ subject to$(y - X\beta^*)'(y - X\beta^*) = c$. That means:

$$\beta^{*\prime}\beta^* + \frac{1}{k}[(y - X\beta^*)'(y - X\beta^*) - c] \quad (3)$$

Where $\frac{1}{k}$ is a Lagrangian multiplier and c is constant.The solution (3) obtained the (ORR) estimator as the following:

$$\hat{\beta}(k) = [I - k\left(X'X + kI_p\right)^{-1}\hat{\beta}_{LS}$$

$$= \left(X'X + kI_p\right)^{-1} X'Y \ , k > 0 \ . \tag{4}$$

Modified ridge estimator by Swindel (1976), the restricted ridge by Zhong and Yang (2007), modified new two-parameter by Lukman (2019), restricted and unrestricted by Ozkale (2007), Crouse et al. (1995) proposed the unbiased ridge regression (URR) estimator as the following:

$$\hat{\beta}(k,J) = \left(X'X + kI_p\right)^{-1}(X'Y + kJ) \ , k \geq 0 \tag{5}$$

where J is a random vector with $J \sim N\left(\beta, \frac{\sigma^2}{k} I_p\right)$ for $k > 0$.To improve the performance of the estimators by using biased estimation technique, Batah and Gore (2009) proposed modified unbiased ridge regression (MURR) as:

$$\begin{aligned} \hat{\beta}_J(k) &= \left[I - k\left(X'X + kI_p\right)^{-1}\right] \hat{\beta}(k,J) \\ &= \left[I - k\left(X'X + kI_p\right)^{-1}\right] \left(X'X + kI_p\right)^{-1}(X'Y + kJ) \end{aligned} \tag{6}$$

Although the (MURR) estimator is a good estimator in dealing with a problem of multicollinearity, as it is considered one of best biased estimators in dealing with this problem, but it also has negative characteristic and this characteristic arises from its dependence on the value of k. As $\rightarrow \infty$, $\hat{\beta}_J(k) \rightarrow 0$ a stable, but biased estimator of β. As $k \rightarrow 0$, $\hat{\beta}_J(k) \rightarrow \hat{\beta}_{RLS}$, an unbiased unstable estimator of β where $\widehat{\beta}_{RLS}$ still dealing with the matrix $X'X$ which is responsible for multicollinearity. That is $\hat{\beta}_J(k)$ trace curve path the parameter space from $\hat{\beta}_J(k)$ to zero, so the distance between $\hat{\beta}_J(k)$ and $\hat{\beta}_{RLS}$ decreases when k increases from 0. Therefore, we propose new biased estimator to improve the efficiency of estimation which we called restricted modified unbiased ridge regression (RMUR).

In section 2, we study the properties of new estimator. In section 3, we study the performance of the new estimator compared with some other estimators by using the simulation technique. Section 4 contains numerical example to illustrate the results. Finally, the conclusions with some remarks are given in section 5.

2. Proposed Estimator and its properties

To overcome the problem of multicollinearity we can also use prior information that can be considered as a linear restriction which is given by:

$$R\beta = r \ , \tag{7}$$

where R is an $(m \times p)$ known matrix with p rank $m > p$ and r is an $(m \times 1)$ vector.
The idea is that, we try to find an estimator of β that is closest to $\hat{\beta}_J(k)$ by taking a point that is closest to $\hat{\beta}_J(k)$ with same residual of sum square when the restrictions of β given by (6) are available. Thus, we derive a new estimator as the solution of the minimization problem for the function defined by

$$\Phi = \left(\beta - \hat{\beta}_J(k)\right)' \left(\beta - \hat{\beta}_J(k)\right) + \frac{1}{k}[(y - X\beta)'(y - X\beta) - c] - 2\lambda'(R\beta - r)$$

where $\frac{1}{k}$ is a Lagrangian multiplier, λ is a vector on Lagrangian multipliers and c is a constant. We differentiate the Φ with respect β and λ respectively, and we obtain the following equations.

$$\left(\beta^* - \hat{\beta}_J(k)\right) + \frac{1}{k}(X'X\beta^* - X'y) - R'\lambda = 0 \tag{8}$$

$$R\beta^* - r = 0 \tag{9}$$

From (7)

$$\beta^* = (X'X + k)^{-1}\left(X'y + k\hat{\beta}_J(k)\right) + (X'X + k)^{-1}R'k\lambda \tag{10}$$

If we premultiply (9) by R and inserting in (8), we obtain the solution of normal equations

$$\hat{\beta}_r^*(k) = \hat{\beta}_J(k) + S_k^{-1}R'\left(RS_k^{-1}R'\right)^{-1}\left(r - R\hat{\beta}_J(k)\right), \tag{11}$$

where $S_k^{-1} = (X'X + kI)^{-1}$.

Now, we need to show that $\hat{\beta}_r^*(k)$ satisfy the restrictions given by (6). Thus

$$R\,\hat{\beta}_r^*(k) = R[\hat{\beta}_j(k) + S_k^{-1}R'\left(RS_k^{-1}R'\right)^{-1}\left(r - R\hat{\beta}_j(k)\right)]$$
$$R\hat{\beta}_r^*(k) = R\hat{\beta}_j(k) + r - R\hat{\beta}_j(k)$$
$$= r$$

We can rewrite $\hat{\beta}_r^*(k)$ as follows:

Let $\beta_1 = R'(RR')^{-1}r$ and satisfy the restriction in (7), therefore, we have

$$\hat{\beta}_r^*(k) = \hat{\beta}_J(k) + S_k^{-1}R'\left(RS_k^{-1}R'\right)^{-1}\left(r - R\hat{\beta}_J(k)\right)$$
$$= S_k^{-1}S_k\hat{\beta}_J(k) + S_k^{-1}R'\left(RS_k^{-1}R'\right)^{-1}\left(r - RS_k^{-1}S_k\hat{\beta}_J(k)\right)$$
$$= S_k^{-1}S_k\hat{\beta}_J(k) + \left[S_k^{-1}R'\left(RS_k^{-1}R'\right)^{-1}\right]r - S_k^{-1}R'\left(RS_k^{-1}R'\right)^{-1}RS_k^{-1}S_k\hat{\beta}_J(k)$$
$$= S_k^{-1}S_k\hat{\beta}_J(k) - S_k^{-1}R'\left(RS_k^{-1}R'\right)^{-1}RS_k^{-1}S_k\hat{\beta}_J(k) + \left[S_k^{-1}R'\left(RS_k^{-1}R'\right)^{-1}\right]r$$
$$= \left(S_k^{-1} - S_k^{-1}R'\left(RS_k^{-1}R'\right)^{-1}RS_k^{-1}\right)S_k\hat{\beta}_J(k) + \left[S_k^{-1}R'\left(RS_k^{-1}R'\right)^{-1}\right]r$$
$$= N_kS_k\hat{\beta}_J(k) + \left[S_k^{-1}R'\left(RS_k^{-1}R'\right)^{-1}\right]R\beta_1$$
$$= N_kS_k\hat{\beta}_J(k) + \left[S_k^{-1}R'\left(RS_k^{-1}R'\right)^{-1}\right]R\beta_1 - S_k^{-1}S_k\beta_1 + \beta_1$$
$$= N_kS_k\hat{\beta}_J(k) - [S_k^{-1} - S_k^{-1}R'\left(RS_k^{-1}R'\right)^{-1}RS_k^{-1}]S_k\beta_1 + \beta_1$$
$$= N_kS_k\hat{\beta}_j(k) - N_kS_k\beta_1 + \beta_1$$

$$\hat{\beta}_r^*(k) = N_kS_k\left(\hat{\beta}_J(k) - \beta_1\right) + \beta_1 \tag{12}$$

where $N_k = (S_k^{-1} - S_k^{-1}R'\left(RS_k^{-1}R'\right)^{-1}RS_k^{-1}$

2.1 Matrix Mean Square Error (MMSE)

The bias and variance of an estimator are measured simultaneously by the mean square error matrix (MSE)

$$MSE(\beta^*) = var(\beta^*) + Biase(\beta^*)(Biase(\beta^*))'$$

For this purpose,

$$MSE(\hat{\beta}_J(k) = \sigma^2 WS^{-1}W' + k^2 S_k^{-1}\beta\beta' S_k^{-1}, \quad (13)$$

$$MES\left(\hat{\beta}_{RLS}\right) = \sigma^2 N_0 S^{-1} N_{0,} \quad (14)$$

$$MSE(\hat{\beta}_R(k) = \sigma^2 N_k S N_k' + k^2 N_k \beta\beta' N_k', \quad (15)$$

where $W = \left(I - kS_k^{-1}\right) = SS_k^{-1}$, $N_0 = N_k$ when $k = 0$ and $S = (X'X)$.

The expected value of RMUR is given by:

$$E(\hat{\beta}_r^*(k)) = E\left(N_k S_k\left(\hat{\beta}_j(k) - \beta_1\right) + \beta_1\right)$$

Since $E(\hat{\beta}_J(k)) = (I - kS_k^{-1})\beta$, so

$$E(\hat{\beta}_r^*(k)) = N_k S_k\left(\left(I - kS_k^{-1}\right)\beta - \beta_1\right) + \beta_1$$
$$= N_k S_k(\beta - \beta_1) + \beta_1 - kN_k\beta$$

Since $R\beta = r$, from $Eq(7)$ $R\beta_1 = r$. So, we get that $N_k S_k(\beta - \beta_1) = \beta - \beta_1$

Therefore,

$$E(\hat{\beta}_r^*(k)) = \beta - kN_k\beta = (I - kN_k)\beta \quad (16)$$

The variance, the bias and MMSE of RMUR are given as follows:

$$Var(\hat{\beta}_r^*(k) = E[(\hat{\beta}_r^*(k) - E\left(\hat{\beta}_r^*(k)\right)(\hat{\beta}_r^*(k) - E\left(\hat{\beta}_r^*(k)\right)'$$
$$= \sigma^2 N_k S_k W S_k^{-1} S_K' W' N_k', \quad (17)$$

where $w = \left(I - kS_k^{-1}\right) = SS_k^{-1}$.

$$\text{bias}(\hat{\beta}_r^*(k) = E\left(\hat{\beta}_r^*(k)\right) - \beta$$
$$= \beta - kN_k\beta - \beta =$$
$$-kN_k\beta \quad (18)$$

So that,

$$\text{MMSE}(\hat{\beta}_r^*(k)) = Var(\hat{\beta}_r^*(k)) + \left[bias\hat{\beta}_r^*(k)\right][bias\hat{\beta}_r^*(k)]'$$
$$= \sigma^2 N_k S_k W S_k^{-1} S_k' W' N_k' + k^2 N_k \beta\beta' N_k'. \quad (19)$$

The scalar mean square error of is defined as follows:

$$mse(\hat{\beta}_r^*(k)) = \sigma^2 tr\left(N_k S S S_k^{-1} N_k\right) + k^2 tr(N_k\beta\beta' N_k),$$

where tr denotes trace and $N_k = (S_k^{-1} - S_k^{-1}R'\left(RS_k^{-1}R'\right)^{-1}RS_k^{-1})$. It is will known that a linear regression model can be transformed to conical from by orthogonal transformation let T be an orthogonal matrix such that;

$$T'X'X = \Lambda \quad (20)$$

Where Λ is a $p \times p$ diagonal matrix elements $\lambda_1 \geq \lambda_2 \geq \cdots \geq \lambda_p$ are the eigenvalues

So, we can state the following theorem

Theorem 2.1**:** The scalar mean square error of $\hat{\beta}_r^*(k)$ is given by**:**

$$\text{mse}(\hat{\beta}_r^*(k)) = \sigma^2 \sum_{\text{i}=1}^{\text{p}} \frac{\lambda\text{i}^2(\lambda\text{i} + \text{k} - r_{ii}^*)^2}{(\lambda\text{i} + \text{k})^5} + \text{k}^2 \sum_{\text{i}=1}^{\text{p}} \frac{\propto_{\text{i}}^2 (\lambda\text{i} + \text{k} - r_{ii}^*)^2}{(\lambda\text{i} + \text{k})^4} \quad (21)$$

Proof:

$$N_k S S S_k^{-1} N_k = \left(S_k^{-1} - S_k^{-1}R'\left(RS_k^{-1}R'\right)^{-1}RS_k^{-1}\right) S S S_k^{-1}\left(S_k^{-1} - S_k^{-1}R'\left(RS_k^{-1}R'\right)^{-1}RS_k^{-1}\right)$$
$$= \left(S_k^{-1} S S S_k^{-2}\right) - (S_k^{-1} S S S_k^{-2} R'\left(RS_k^{-1}R'\right)^{-1}RS_k^{-1} - S_k^{-1}R'\left(RS_k^{-1}R'\right)^{-1}RS_k^{-1} S S S_k^{-2}$$
$$+ S_k^{-1}R'\left(RS_k^{-1}R'\right)^{-1}RS_k^{-1} S S S_k^{-2} R'\left(RS_k^{-1}R'\right)^{-1}RS_k^{-1} \quad (22)$$

We have $S_k^{-1} = T(\Lambda + k)^{-1}T'$

$$tr\left(S_k^{-1}SSS_k^{-2}\right) = tr[(T(\Lambda+k)^{-1}T'T\Lambda T'T\Lambda T'(T(\Lambda+k)^{-2}T'] = tr[(T(\Lambda+k)^{-3}T'\,T\Lambda T'T\Lambda T']$$
$$= \sum_{i=1}^{p} \frac{\lambda_i^2}{(\lambda_i+k)^3}\,. \tag{23}$$

$$tr\left(S_k^{-1}SSS_k^{-2}R'\left(RS_k^{-1}R'\right)^{-1}RS_k^{-1}\right) = tr[(T(\Lambda+k)^{-1}T'T\Lambda T'T\Lambda T'(T(\Lambda+k)^{-2}T'r_{ii}^{*}T(\Lambda+k)^{-1}T'\,]$$
$$= \sum_{i=1}^{p} \frac{\lambda_i^2 r_{ii}^{*}}{(\lambda_i+k)^4}. \tag{24}$$

$$R^{*} = TR'\left(RS_k^{-1}R'\right)RT'.\,The\ diag(R^{*}) = r_{ii}^{*}$$
$$tr\left(S_k^{-1}R'\left(RS_k^{-1}R\right)^{-1}RS_k^{-1}SSS_k^{-2}\right) = tr[T(\Lambda+k)^{-1}T'R^{*}T(\Lambda+k)^{-1}T'T\Lambda T'T\Lambda T'T(\Lambda+k)^{-2}T'\,]$$
$$= \sum_{i=1}^{p} \frac{\lambda_i^2 r_{ii}^{*}}{(\lambda_i+k)^4}\,. \tag{25}$$

$$tr\left(S_k^{-1}R'\left(RS_k^{-1}R'\right)^{-1}RS_k^{-1}SSS_k^{-2}R'\left(RS_k^{-1}R'\right)^{-1}RS_k^{-1}\right) = tr[T(\Lambda+k)^{-1}T'R^{*}T(\Lambda+k)^{-1}T'T\Lambda T'T\Lambda T'T(\Lambda+k)^{-2}T'R^{*}T(\Lambda+k)^{-1}T']$$
$$= \sum_{i=1}^{p} \frac{\lambda_i^2 r_{ii}^{*2}}{(\lambda_i+k)^5}\,. \tag{26}$$

From (23), (24), (25) and (26), we get the following result.

$$tr\left(N_kSSS_k^{-1}N_k\right) = \left[\sum_{i=1}^{p} \frac{\lambda_i^2}{(\lambda_i+k)^3} - 2\sum_{i=1}^{p} \frac{\lambda_i^2 r_{ii}^{*2}}{(\lambda_i+k)^4} + \sum_{i=1}^{p} \frac{\lambda_i^2 r_{ii}^{*2}}{(\lambda_i+k)^5}\right]$$
$$= \sum_{i=i}^{p} \frac{\lambda_i^2(\lambda_i+k-r_{ii}^{*})^2}{(\lambda_i+k)^5}\,. \tag{27}$$

Also,

$$tr\left(N_k^2\right) = \left(S_k^{-1} - S_k^{-1}R'\left(RS_k^{-1}R'\right)^{-1}RS_k^{-1}\right)\left(S_k^{-1} - S_k^{-1}R'\left(RS_k^{-1}R'\right)^{-1}RS_k^{-1}\right)$$
$$= S_k^{-2} - S_k^{-2}R'\left(RS_k^{-1}R'\right)RS_k^{-1} - S_k^{-1}R'(RS_kR')RS_k^{-2}$$
$$+S_k^{-1}R'\left(RS_k^{-1}R'\right)^{-1}RS_k^{-2}R'\left(RS_k^{-1}R'\right)^{-1} \tag{28}$$

$$tr\left(S_k^{-2}\right) = tr(T(\Lambda+k)^2T') = \sum_{i=1}^{p} \frac{1}{(\lambda_i+k)^2} \tag{29}$$

$$tr\left(S_k^{-2}R'\left(RS_k^{-1}R'\right)RS_k^{-1}\right) = tr[T(\Lambda+k)^{-2}T'R^{*}T(\Lambda+k)^{-1}T'] = \sum_{i=1}^{p} \frac{r_{ii}^{*}}{(\lambda_i+k)^3}. \tag{30}$$

Similar to (30), we get:

$$tr\left(S_k^{-1}R'(RS_kR')RS_k^{-2}\right) = \sum_{i=1}^{p} \frac{r_{ii}^{*}}{(\lambda_i+k)^3}\,. \tag{31}$$

$$tr\left(S_k^{-1}R'\left(RS_k^{-1}R'\right)^{-1}RS_k^{-2}R'\left(RS_k^{-1}R'\right)^{-1}RS_k^{-1}\right)$$

$$= \sum_{i=1}^{p} \frac{r_{ii}^{*2}}{(\lambda_i + k)^4} \quad . \tag{32}$$

From (28) to (32), we get

$$tr(N_k^2) = \sum_{i=1}^{p} \left(\frac{1}{(\lambda_i + k)^2} - \frac{2r_{ii}^*}{(\lambda_i + k)^3} + \frac{r_{ii}^{*2}}{(\lambda_i + k)^4} \right)$$

$$= \sum_{i=1}^{p} \frac{(\lambda_i + k - r_{ii}^*)^2}{(\lambda_i + k)^4} \, . \tag{33}$$

Therefore,

$$tr(\propto' N_k^2 \propto) = \sum_{i=1}^{p} \frac{\propto_i^2 (\lambda_i + k - r_{ii}^*)^2}{(\lambda_i + k)^4} \, . \tag{34}$$

Where $\propto = T'\beta = (\propto_1 \dots\dots\dots \propto_p)$. Finally, we have

$mse(\hat{\beta}_r^*(k)) = \sigma^2 \sum_{i=1}^{p} \frac{\lambda i^2 (\lambda i + k - r_{ii}^*)^2}{(\lambda i + k)^5} + k^2 \sum_{i=1}^{p} \frac{\propto_i^2 (\lambda i + k - r_{ii}^*)^2}{(\lambda i + k)^4}$.

The proof is completed.

3. Simulation Study

The purpose of this section is to make a comparison among the different biased estimators in order to identify good estimator among them. Therefore, we conduct a simulation study by using the Matlab program. This simulation is created depending on factors that affect the properties of the estimator's duo to the degree of the collinearity among several explanatory variables. Kibria (2003) was followed to generate the explanatory variables by using the equation.

$$x_{ij} = (1 - \Upsilon^2)^{\frac{1}{2}} z_{ij} + \Upsilon z_{ip} \, , \qquad i = 1 \dots\dots n \quad , j = 1 \dots\dots p \tag{35}$$

where the z_{ij} independent standard normal pseudo-random numbers and Υ represents the correlation between any two variables. These variables are standardized so that $X'X$ is being in correlation form. The response variable y is considered by:

$$y_i = \beta_0 + \beta_1 x_{i1} + \beta_2 x_{i2} + \cdots \dots\dots\dots + \beta_p x_{ip} + e_i, \qquad i = 1,2, \dots\dots, n \tag{36}$$

where e_i is i.i.d. N(0, σ^2). Therefore, zero intercept for (36) will be assumed. Also the number of explanatory variables $p = 4$, while the values of σ are choose as (1, 4, 9,). The correlation Υ will choose as (0.90, 0.95,0.99) and sample size n as (25, 50 ,100,).The coefficients $\beta_1, \beta_2, \dots, \beta_p$ are selected as the eigenvectors corresponding to the largest eigenvalue of the matrix $X'X$ subject to constraint $\beta'\beta$ = 1. Thus, for all n , σ , λ , p , β and Υ, sets of Xs are created. The experiment was replicated 5000 times by creating new error terms. Estimated mean square error (EMSE) is calculated as follows:

$EMSE(\beta^*) = \frac{1}{5000} \sum_{i=1}^{5000} (\beta^* - \beta)'(\beta^* - \beta)$,

where β^* would be any estimators (RLS, MURR, RRR or RMUR).

3.1 The discussion of simulation results

In this article, we present the results of the Monte Carlo experiment regarding of the properties of the different methods that used to choose the ridge parameter k. The simulation results are presented from Table 1 to Table 7 and we discuss the results in all cases.

Table1 and Table 7 show the performance of the RMUR estimator compared to some other estimators as the following:

1.The RMUR estimator is the best, because the RMUR estimator has lowest MSE compared with other estimators for all different sample size n in all correlation coefficient values and σ. However, in some cases the MURR estimator is close or similar to the RMUR estimator from these cases.

2.In case ($n = 25, \ \sigma = 1, \ \Upsilon = .90$) and ($n = 50, \ \sigma = 1, \Upsilon = .90$), the MUR estimator is close or similar the RMUR estimator in this cases.

4.**Numerical example**

In this study, the performance of the proposed estimator using a real life data is illustrated. We consider the data about the total national product, which is cited by Akdeniz (2003) for comparison of the estimators that given in this study. This data shows the relationship between the dependent variable Y and the percentage that is the united states spent on four independent variables X_1, X_2, X_3 and X_4 representing the percentage spent by Farance, West Germany, Japan, and Soviet Union respectively.
The goal is to compare the scalar mean square error mse of the RLS, RRR, MURR and RMUR. The mse of the MURR, RLS, RRR and RMUR are given in Eq.(3), Eq.(14), Eq.(15) and Eq.(19) respectively, which given in Table 8.

Table 1. The scalar mean square error for different estimators and different estimated ridge parameter

k	OLS	RLS	RRR	$MURR$	$RMUR$
0.0161	602.4197	135.7475	96.4878	159.9901	83.1722
0.0243	602.4197	135.7475	83.0983	110.1283	67.6833
0.050	602.4197	135.7475	56.1576	54.1576	40.0858
0.020	602.4197	135.7475	89.7099	131.9846	75.1888
0.50	602.4197	135.7475	7.0013	5.9080	3.7911
0.10	602.4197	135.7475	32.7403	26.7126	20.2068
0.15	602.4197	135.7475	22.5322	17.7867	13.0448

For the linear restrictions (6), the values *R* and *r* are, respectively, given as follows Najarian (2013)
$R = [1\ 1\ 1\ 1\ ;0\ 1\ 3\ 1\ ], \quad r = [1.2170\ \ 1.0904]$
In Table 8, we can observe that, the RMUR estimator has lowest *mse* for all different estimated ridge parameter. Therefore, the performance the RMUR estimator is better than other estimators and this is clear in the Figures 1,2 and 3.

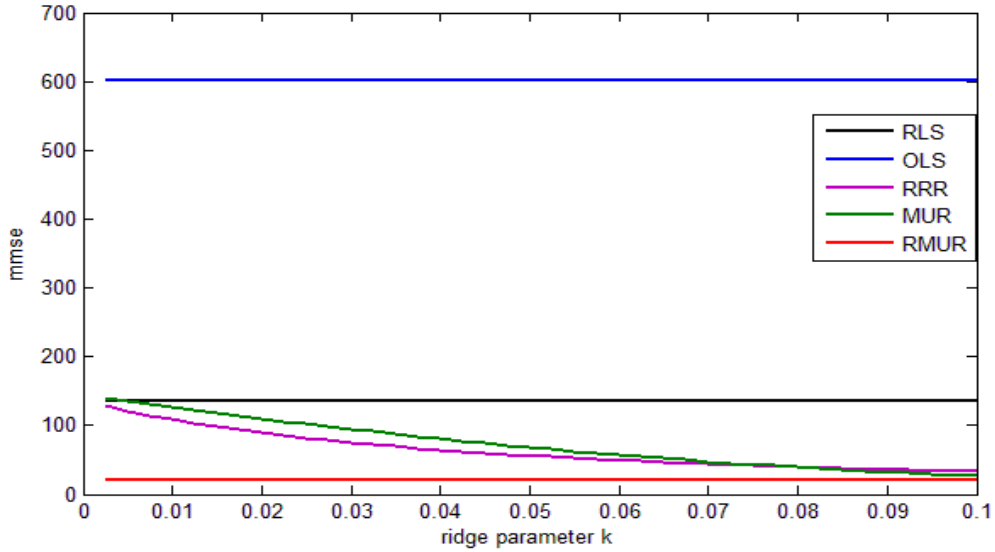

Figure 1. Estimated mse of the proposed estimator compared for different estimators and different estimated ridge parameter k.

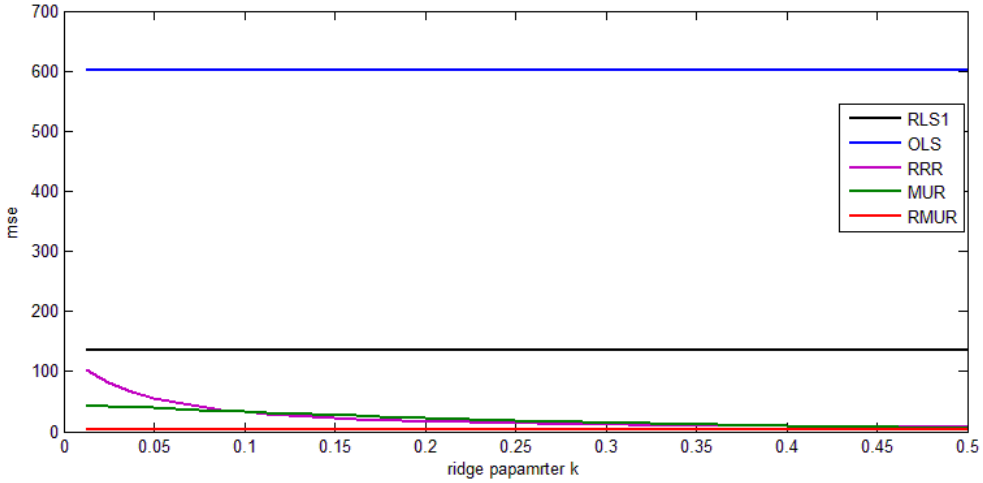

Figure 2. Estimated mse of the proposed estimator compared for different estimators and different estimated ridge parameter k.

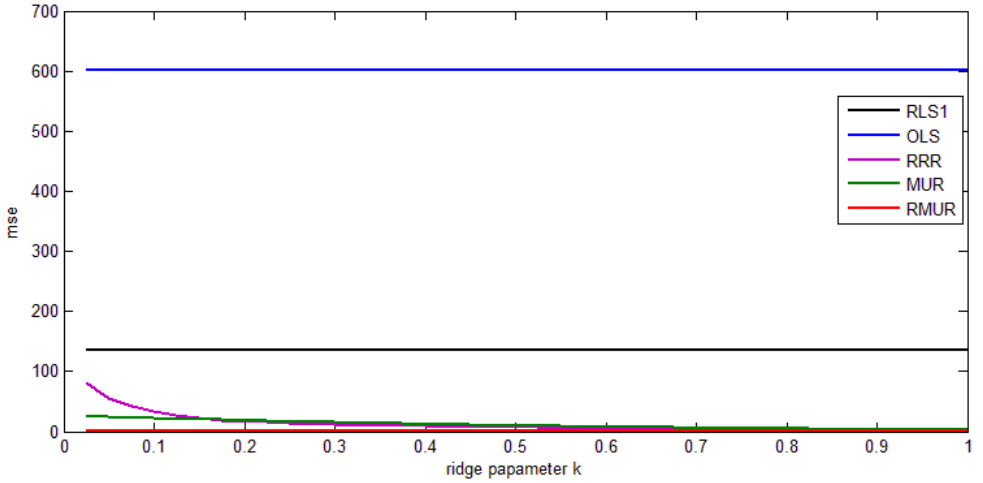

Figure 3. Estimated mse of the proposed estimator compared for different estimators and different estimated ridge parameter k.

5. Conclusions

The simulation study in section 3 shows that, the RMOR estimator is better than of the other estimators for all values n , σ and Υ. Also, the RMUR estimator has good properties compared with other estimators. The RMUR estimator is more efficient where it has lowest mean square error compared to others, and with respect to the real data that used in the present study.

References

[1] Akdeniz F, Erol H (2003) Mean squared error matrix comparisons of some biased estimators in linear regression *Communications in Statistics Theory and Methods* **32**:2389–2413

[2] Batah F S M & Gore S D (2009) Ridge regression estimator: Combining unbiased and ordinary ridge regression methods of estimation *Surveys in Mathematics and its Applications* **4** 99-109

[3] Crouse R, Jin C & Hanumara R (1995) Unbiased ridge estimation with prior informatics and ridge trace *Communications in Statistics – Theory and Materials* **24**(9) 2341-2354

[4] Hoerl A E, Kennard R W, Baldwin K F (1975) Ridge regression: some simulation *Commun Statist* **4**:105–123
[5] Kibria B M G (2003) Performance of some new ridge regression estimators *Communications in Statistics – Simulation and Computation* **32**(2) 419-435
[6] Lukman A F, Ayinde K, Siok Kun S & Adewuyi E T (2019) A modified new two-parameter estimator in a linear regression model Modelling and Simulation in Engineering 2019
[7] Najarian S, Arashi M and Kibria B M G (2013) A Simulation Study on Some Restricted Ridge Regression Estimators *Comm. Statist. Sim. Comp.* **42** 871-879
[8] Ozkale M R, Kaciranlar S (2007) The restricted and unrestricted two parameter estimators *Communications in Statistics -Theory and Methods* **36**:2707–2727
[9] Swindel B F (1976) Good ridge estimators based on prior information *Communications in Communications in Statistics–Theory and Methods*
[10] Zhong Z, Yang H (2007) Ridge estimation to the restricted linear model *Communications in Statistics–Theory and Methods* **36**(11)

Truncated Exponential Topp Leone Exponential Distribution: Properties and Applications

Truncated Exponential Topp Leone Exponential Distribution: Properties and Applications

Nadia Hashim Al-Noor and Omar Ali Hilal

Mathematics Department, College of Science, Mustansiriyah University, Baghdad, Iraq

E-mail: nadialnoor@uomustansiriyah.edu.iq

Abstract. A new flexible compound distribution with three parameters named Truncated Exponential Topp Leone Exponential (TETLE) is introduced as a sub-model of a new generator family named Truncated Exponential Topp Leone-G. Several keys of its statistical properties, order statistics, entropies, reliability analysis, and reliability stress strength model are presented. The maximum likelihood estimation method is implemented to estimate the unknown parameters. Moreover, to assess the flexibility and usefulness, the TETLE distribution applied upon simulation and two real-life data set. The consistent and flexible performance of the maximum likelihood estimates is clearly appeared by the simulation results and the results of the real application clearly shown that the proposed distribution has superior output relative to other considered distributions for all information criteria.

1. Introduction

Lifetime data plays a significant role in an extensive variety of applications, such as public health, management, engineering, medicine, and biological sciences. Statistical distributions are used to model these data in order to examine its essential characteristics. Appropriate distribution can provide valuable information that leads to putting conclusions and decisions. When more flexible distributions are needed, many researchers are about to use the new one with more generalization. One of the supremely important distributions is the exponential distribution. It has been applied to match life data in a number of fields. However, some of these applications are restricted in part, and this restriction is certainly an opportunity for researchers to create new generalizations and to make a variety of improvements to this distribution in order to increase its flexibility. In this paper, based on the well-known exponential distribution, a new family of probability distributions is introduced through the works of Topp and Leone [1] and Eugene et al. [2].

Topp and Leone (1955) [1] developed a new distribution of empirical data with J-shaped histograms. The Topp Leone (TL) distribution had not received much attention until it discovered by Nadarajah and Kotz (2003) [3] when they studied some of its properties, moments, central moments, and characteristic function. Furthermore, among the important work of analyzing lifetime data that revealed a significant influence of the TL distribution are, Ghitany et al. (2005) [4] provided TL reliability measures, Kotz and Seier (2007) [5] offered a discussion on TL kurtosis, Vicaria et al. (2008) [6] introduced two-sided generalized TL distributions, Al-Zahrani (2012) [7] derived TL goodness of fit tests, and Sangsanit and Bodhisuwan (2016) [8] proposed the TL generated (TL-G) family of distributions.

The cumulative distribution function (cdf) and probability density function (pdf) of the TL-G family, that due to Sangsanit and Bodhisuwan [8], with one shape parameter α beside the cdf and pdf of an arbitrary (parent or baseline) distribution, say $G(x)$ and $g(x)$, are

$$M(x)_{TL} = \big(G(x)\big)^{\alpha}\big(2 - G(x)\big)^{\alpha}\ ;\ \alpha > 0 \tag{1}$$

$$m(x)_{TL} = 2\alpha\ g(x)\big(G(x)\big)^{\alpha-1}\big(1 - G(x)\big)\big(2 - G(x)\big)^{\alpha-1} \tag{2}$$

Eugene et al. [2] proposed a new family based on beta distribution with the cdf and pdf as below

$$F(x)_T = \frac{1}{\beta(a,b)}\int_0^{M(x)} t^{a-1}\ (1-t)^{b-1}\,dt\ ;\ 0 < t < 1 \text{ and } 0 < a, b < \infty \tag{3}$$

$$f(x)_T = \frac{1}{\beta(a,b)}\,(M(x))^{a-1}\,(1 - M(x))^{b-1}\,m(x) \tag{4}$$

where $M(x)$ and $m(x)$ are the cdf and pdf of any distribution and $\beta(a,b)$ represent Beta function. Then Eugene et al. derived some properties of the beta normal distribution that defined by taking $M(x)$ to be the cdf of the normal distribution (see [2][9]).

Taking motivation from the works above, a new family named truncated exponential Topp Leone– G has been proposed (for more details about TL distribution and truncated distribution see [2] and [10]). The rest of this paper is organized as follows: the truncated exponential Topp Leone – G family is introduced in Section 2 with several general useful expressions. In Section 3, attention is given the truncated exponential Topp Leone exponential as a sub-model of the new family. In Sections 4, and 5 various properties besides order statistics, entropies, reliability measures, and reliability stress strength model are presented. The maximum likelihood estimators of the parameters are presented in Section 6. In Section 7, numerical illustrations are implemented in order to illustrate the behavior of the new distribution. Finally, in Section 8, conclusions are listed.

2. Truncated Exponential Topp Leone-G family

Consider $H(x)_{TE}$ and $h(x)_{TE}$ are the cdf and pdf of the truncated exponential distribution with scale parameter λ, i.e.

$$H(x)_{TE} = \frac{1 - e^{-\lambda x}}{1 - e^{-\lambda}}\ ;\ 0 < x < 1\ , \lambda > 0 \tag{5}$$

$$h(x)_{TE} = \frac{\lambda e^{-\lambda x}}{1 - e^{-\lambda}} \tag{6}$$

By composing the two continuous cdfs (H, M), the cdf $F(x) = H\big(M(x)\big)$ and corresponding pdf $f(x) = \frac{\partial}{\partial x}F(x)$ will be

$$F(x) = \int_0^{M(x)} \frac{\lambda e^{-\lambda v}}{1 - e^{-\lambda}}\ dv = \frac{1 - e^{-\lambda M(x)}}{1 - e^{-\lambda}} \tag{7}$$

$$f(x) = \frac{\lambda m(x)\ e^{-\lambda M(x)}}{1 - e^{-\lambda}} \tag{8}$$

Replacing $M(x)$ and $m(x)$ in (7) and (8) by (1) and (2), a new generator family of probability distributions named Truncated Exponential Topp Leone-G (TETL-G) can be proposed.

The cdf and pdf of the proposed family are

$$F(x)_{TETL-G} = \frac{1}{1-e^{-\lambda}}\left(1 - e^{-\lambda\left(G(x)\right)^{\alpha}\left(2-G(x)\right)^{\alpha}}\right) \tag{9}$$

$$f(x)_{TETL-G} = \frac{2\lambda\alpha}{1-e^{-\lambda}}\, g(x)\big(G(x)\big)^{\alpha-1}\big(1-G(x)\big)\big(2-G(x)\big)^{\alpha-1}\, e^{-\lambda\left(G(x)\right)^{\alpha}\left(2-G(x)\right)^{\alpha}} \tag{10}$$

Also, the useful expansion formula of the above pdf can be got by using the expansion formulas below:

$$e^{-z} = \Sigma_{k=0}^{\infty} \frac{(-1)^k}{k!} z^k \tag{E1}$$

$$(1-z)^a = \sum_{m=0}^{\infty} \frac{(-1)^m}{m!} \frac{\Gamma(a+1)}{\Gamma(a-m+1)}\, z^m \text{ with } |z|<1 \text{ and } a>0 \tag{E2}$$

$$(1-z)^{-a} = \sum_{m=0}^{\infty} \frac{\Gamma(a+m)}{m!\,\Gamma(a)}\, z^m \text{ with } |z|<1 \text{ and } a>0 \tag{E3}$$

Now, based on the above expansion formulas, we get

$$e^{-\lambda\left(G(x)\right)^{\alpha}\left(2-G(x)\right)^{\alpha}} = \sum_{k=0}^{\infty} \frac{(-1)^k}{k!}\, \lambda^k \big(G(x)\big)^{k\alpha}\big(2-G(x)\big)^{k\alpha}, \text{ and}$$

$$\big(2-G(x)\big)^{\alpha(k+1)-1} = \begin{cases} \sum_{m=0}^{\infty} \frac{(-1)^m}{m!} 2^{\alpha(k+1)-m-1} \frac{\Gamma(\alpha(k+1))}{\Gamma(\alpha(k+1)-m)} \big(G(x)\big)^m ; & \alpha(k+1)-1>0 \\ \sum_{m=0}^{\infty} \frac{\Gamma(\alpha(k+1)+m-1)}{m!\,\Gamma(\alpha(k+1)-1)} 2^{\alpha(k+1)-m-1} \big(G(x)\big)^m ; & \alpha(k+1)-1<0 \end{cases}$$

Then expansion of (10) will be

$$f^E(x)_{TETL-G} = W g(x)\big(G(x)\big)^{m+\alpha(k+1)-1}\big(1-G(x)\big) \tag{11}$$

where

$$W = \begin{cases} \frac{1}{1-e^{-\lambda}} \sum_{k,m=0}^{\infty} \frac{(-1)^{k+m}}{k!\,m!} \frac{\Gamma(\alpha(k+1))}{\Gamma(\alpha(k+1)-m)} \alpha\lambda^{k+1}\, 2^{\alpha(k+1)-m} & ; \ \alpha(k+1)-1>0 \\ \frac{1}{1-e^{-\lambda}} \sum_{k,m=0}^{\infty} \frac{(-1)^k}{k!\,m!} \frac{\Gamma(\alpha(k+1)+m-1)}{\Gamma(\alpha(k+1)-1)} \alpha\lambda^{k+1}\, 2^{\alpha(k+1)-m} & ; \ \alpha(k+1)-1<0 \end{cases} \tag{12}$$

3. Truncated Exponential Topp Leone Exponential distribution

Consider $G(x)$ and $g(x)$ in (9), (10), and (11) be the cdf and pdf of the exponential distribution with positive scale parameter θ, then a new distribution called Truncated Exponential Topp Leone Exponential (TETLE) distribution can be proposed as a member of TETL-G family with the cdf, pdf and expanded pdf given respectively by

$$F(x)_{TETLE} = \frac{1}{1-e^{-\lambda}}\left(1 - e^{-\lambda\left(1-e^{-2\theta x}\right)^{\alpha}}\right) \tag{13}$$

$$f(x)_{TETLE} = \frac{2\lambda\alpha\theta}{1-e^{-\lambda}}\, e^{-2\theta x} e^{-\lambda\left(1-e^{-2\theta x}\right)^{\alpha}} \left(1-e^{-2\theta x}\right)^{\alpha-1} \tag{14}$$

and

$$f^{E}(x)_{TETLE} = W\theta e^{-2\theta x}\left(1-e^{-\theta x}\right)^{m+\alpha(k+1)-1} \tag{15}$$

with W as in (12).

The plots of the cdf and pdf of the $TETLE$ distribution for particular parameter values are presented in Figures 1 and 2. It is noted that this new distribution is very flexible to model positive data.

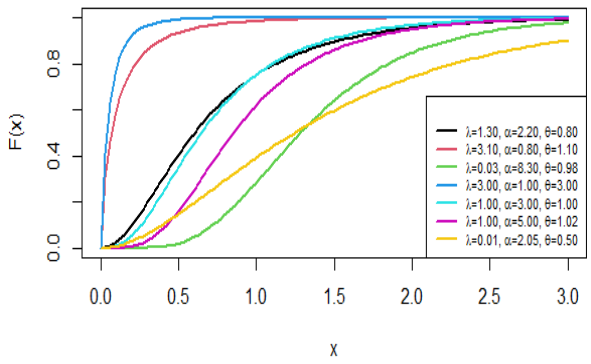

Figure 1. The cdf plot of $TETLE$ distribution for particular parameter values

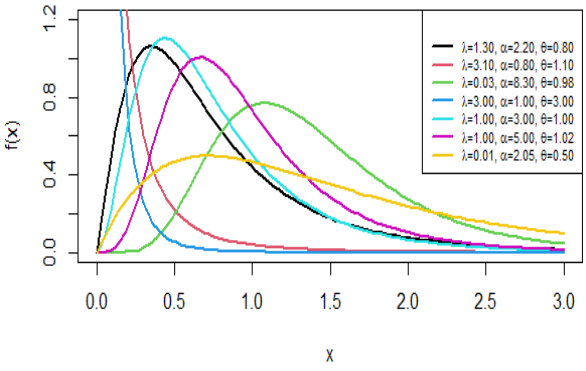

Figure 2. The pdf plot of $TETLE$ distribution for particular parameter values

4. Statistical properties and order statistics of TETLE distribution

The r^{th} moment can be found regards to (15) as follows

$$E(X^r)_{TETLE} = \int_0^{\infty} x^r f^{E}(x)_{TETLE}\, dx = W\int_0^{\infty} x^r \theta e^{-2\theta x}\left(1-e^{-\theta x}\right)^{m+\alpha(k+1)-1} dx$$

Now, based on $(E2)$ and $(E3)$, we get

$$\left(1-e^{-\theta x}\right)^{m+\alpha(k+1)-1} = \begin{cases} \sum_{t=0}^{\infty} \frac{(-1)^t}{t!}\frac{\Gamma(m+\alpha(k+1))}{\Gamma(m+\alpha(k+1)-t)} e^{-\theta t x} & ;\ m+\alpha(k+1)-1>0 \\ \sum_{t=0}^{\infty} \frac{\Gamma(m+\alpha(k+1)+t-1)}{t!\,\Gamma(m+\alpha(k+1)-1)} e^{-\theta t x} & ;\ m+\alpha(k+1)-1<0 \end{cases}$$

Now $E(X^r)_{TETLE}$ with $m+\alpha(k+1)-1>0$ will be

$$E(X^r)_{TETLE} = W\,\Sigma_{t=0}^{\infty}\frac{(-1)^t}{t!}\frac{\Gamma\left(m+\alpha(k+1)\right)}{\Gamma(m+\alpha(k+1)-t)}\int_0^{\infty} x^r\theta\, e^{-\theta(t+2)x}\, dx$$

$$= W\,\Sigma_{t=0}^{\infty}\frac{(-1)^t}{t!}\frac{\Gamma\left(m+\alpha(k+1)\right)}{\Gamma(m+\alpha(k+1)-t)}\frac{1}{(t+2)}\int_0^{\infty} x^r\theta(t+2)\, e^{-\theta(t+2)x}\, dx$$

Since $\int_0^{\infty} x^r\theta(t+2)\, e^{-\theta(t+2)x}\, dx$ represent the r^{th} moment of exponential distribution with parameters $\theta(t+2)$, thus $E(X^r)_{TETLE}$ becomes

$$E(X^r)_{TETLE} = W\,\Sigma_{t=0}^{\infty}\frac{(-1)^t}{t!}\frac{\Gamma\big(m+\alpha(k+1)\big)}{\Gamma(m+\alpha(k+1)-t)}\frac{r!}{(t+2)\big(\theta(t+2)\big)^r}$$

and the $E(X^r)_{TETLE}$ with $m+\alpha(k+1)-1<0$ becomes

$$\begin{aligned}E(X^r)_{TETLE} &= W\,\Sigma_{t=0}^{\infty}\frac{\Gamma(m+\alpha(k+1)+t-1)}{t!\;\Gamma(m+\alpha(k+1)-1)}\int_0^{\infty}x^r\theta\,e^{-\theta(t+2)x}\,dx\\ &= W\,\Sigma_{t=0}^{\infty}\frac{\Gamma(m+\alpha(k+1)+t-1)}{t!\;\Gamma(m+\alpha(k+1)-1)}\frac{1}{(t+2)}\int_0^{\infty}x^r\theta(t+2)\,e^{-\theta(t+2)x}\,dx\\ &= W\,\Sigma_{t=0}^{\infty}\frac{\Gamma(m+\alpha(k+1)+t-1)}{t!\;\Gamma(m+\alpha(k+1)-1)}\frac{r!}{(t+2)\big(\theta(t+2)\big)^r}\end{aligned}$$

Thus, the r^{th} moment of $TETLE$ distribution is

$$E(X^r)_{TETLE} = \begin{cases} W\,\Sigma_{t=0}^{\infty}\dfrac{(-1)^t}{t!}\dfrac{\Gamma\big(m+\alpha(k+1)\big)}{\Gamma(m+\alpha(k+1)-t)}\dfrac{r!}{\theta^r(t+2)^{r+1}} & ;\ m+\alpha(k+1)-1>0\\ W\,\Sigma_{t=0}^{\infty}\dfrac{\Gamma(m+\alpha(k+1)+t-1)}{t!\;\Gamma(m+\alpha(k+1)-1)}\dfrac{r!}{\theta^r(t+2)^{r+1}} & ;\ m+\alpha(k+1)-1<0\end{cases} \tag{16}$$

where W as in (12).

With $(r=1,2,3,4)$, another properties such as the mean $\big(E(X)\big)$, the variance $(E(X^2)-[E(X)]^2)$, the coefficient of skewness $\left(\frac{E(X^3)-3E(X)E(X^2)+2[E(X)]^3}{[var(X)]^{3/2}}\right)$, and the coefficient of kurtosis $\left(\frac{E(X^4)-4E(X)E(X^3)+6E(X^2)[E(X)]^2-3[E(X)]^4}{[var(X)]^2}\right)$ (see [11]) can be calculated.

The TETLE characteristic function can easily be found via $\varphi_X(t)_{TEMOW} = \sum_{r=0}^{\infty}\frac{(it)^r}{r!}E(X^r)_{TETLE}$ as

$$\varphi_X(t)_{TETLE} = \begin{cases} W\,\Sigma_{t,r=0}^{\infty}\dfrac{(-1)^t(it)^r}{t!\;r!}\dfrac{\Gamma\big(m+\alpha(k+1)\big)}{\Gamma(m+\alpha(k+1)-t)}\dfrac{r!}{\theta^r(t+2)^{r+1}} & ;\ m+\alpha(k+1)-1>0\\ W\,\Sigma_{t,r=0}^{\infty}\dfrac{(it)^r\,\Gamma(m+\alpha(k+1)+t-1)}{t!\;r!\,\Gamma(m+\alpha(k+1)-1)}\dfrac{r!}{\theta^r(t+2)^{r+1}} & ;\ m+\alpha(k+1)-1<0\end{cases} \tag{17}$$

By inverting the cdf in (13), The $TETLE$ quantile function can be achieved as

$$Q(q)_{TETLE} = \frac{-1}{2\theta}\ln\left(1-\left(\frac{-1}{\lambda}\ln\left(1-\,q\big(1-e^{-\lambda}\big)\right)\right)^{\frac{1}{\alpha}}\right) \tag{18}$$

By setting $q=\frac{1}{2}$, the median of $TETLE$ random variable can be gained as

$$median_{TETLE} = Q\left(\frac{1}{2}\right)_{TETLE} = \frac{-1}{2\theta}\ln\left(1-\left(\frac{-1}{\lambda}\ln\left(\frac{1}{2}\big(1+e^{-\lambda}\big)\right)\right)^{\frac{1}{\alpha}}\right) \tag{19}$$

A random variable of TETLE distribution can be generated by

$$x_{TETLE} = \frac{-1}{2\theta}\ln\left(1 - \left(\frac{-1}{\lambda}\ln\left(1 - U\left(1 - e^{-\lambda}\right)\right)\right)^{\frac{1}{\alpha}}\right) \tag{20}$$

where U follow the standard Uniform distribution.

Order statistics: Let $x_{1:n}, x_{2:n}, \dots, x_{n:n}$ the order statistics of a random sample $x_1, x_2, \dots, x_n$ of size n taken independently from a probability distribution. The standard formulas of the pdf and the joint pdf of order statistics are as follows (see [12])

$$f_{k:n}(x) = \frac{n!}{(k-1)!\,(n-k)!}\left(F(x)\right)^{k-1}\left(1 - F(x)\right)^{n-k} f(x) \;\; ; \; 0 \le x_{k:n} < \infty, k \le n$$

$$f_{j,k:n}(x,y) = \frac{n!}{(j-1)!\,(k-j-1)!\,(n-k)!}\left(F(x)\right)^{j-1}\left(F(y) - F(x)\right)^{k-j-1} \left(1 - F(y)\right)^{n-k} f(x)\, f(y) \;\; ; \; 1 \le j \le k\,, 0 \le x \le y < \infty$$

Based on (13) and (14), the pdf and the joint pdf of $TETLE$ order statistics will be

$$f_{k:n}(x)_{TETLE} = \frac{n!}{(k-1)!\,(n-k)!}\left(1 - e^{-\lambda\left(1-e^{-2\theta x}\right)^{\alpha}}\right)^{k-1}\left(e^{-\lambda\left(1-e^{-2\theta x}\right)^{\alpha}} - e^{-\lambda}\right)^{n-k} \frac{2\lambda\alpha\theta}{\left(1-e^{-\lambda}\right)^{n}}\, e^{-2\theta x} e^{-\lambda\left(1-e^{-2\theta x}\right)^{\alpha}}\left(1 - e^{-2\theta x}\right)^{\alpha-1}; \; 0 \le x_{k:n} < \infty, k \le n \tag{21}$$

$$f_{j,k:n}(x,y)_{TETLE} = \frac{n!}{(j-1)!\,(k-j-1)!\,(n-k)!}\frac{4\lambda^2\alpha^2\theta^2}{\left(1-e^{-\lambda}\right)^{n}}\left(1 - e^{-\lambda\left(1-e^{-2\theta x}\right)^{\alpha}}\right)^{j-1} \left(e^{-\lambda\left(1-e^{-2\theta x}\right)^{\alpha}} - e^{-\lambda\left(1-e^{-2\theta y}\right)^{\alpha}}\right)^{k-j-1}\left(e^{-\lambda\left(1-e^{-2\theta y}\right)^{\alpha}} - e^{-\lambda}\right)^{n-k} e^{-2\theta(x+y)} e^{-\lambda\left(\left(1-e^{-2\theta x}\right)^{\alpha} + \left(1-e^{-2\theta y}\right)^{\alpha}\right)}\left(1 - e^{-2\theta x}\right)^{\alpha-1}\left(1 - e^{-2\theta y}\right)^{\alpha-1}; \; 1 \le j \le k\,, 0 \le x \le y < \infty \tag{22}$$

5. The entropies, reliability measures, and reliability stress strength of $TETLE$ distribution

Here the entropies (Shannon entropy, and Relative entropy), reliability measures, and reliability stress strength model of $TETLE$ distribution are obtained as follows:

Shannon entropy: The $TETLE$ Shannon entropy can be achieved from (14), as follows:

$Sh_{TETLE} = -\int_0^{\infty} \ln(f(x)_{TETLE})\, f(x)_{TETLE}\, dx$ with

$$\ln(f(x)_{TETLE}) = \ln\left(\frac{2\lambda\alpha\theta}{1 - e^{-\lambda}}\right) - 2\theta x - \lambda\left(1 - e^{-2\theta x}\right)^{\alpha} + (\alpha - 1)\ln\left(1 - e^{-2\theta x}\right)$$

Then

$$Sh_{TETLE} = \ln\left(\frac{1 - e^{-\lambda}}{2\lambda\alpha\theta}\right) + 2\theta E(X) + \lambda E\left(\left(1 - e^{-2\theta X}\right)^{\alpha}\right) - (\alpha - 1)\, E\left(\ln\left(1 - e^{-2\theta X}\right)\right) \tag{23}$$

where $E(X)$ as in (16) with $r = 1$, and

$$E\left(\left(1 - e^{-2\theta X}\right)^{\alpha}\right) = \int_0^{\infty}\left(1 - e^{-2\theta x}\right)^{\alpha} f(x)_{TETLE}\, dx$$

Recall $(E2)$ and $(E1)$, we get $\left(1-e^{-2\theta x}\right)^{\alpha}=\Sigma_{i,j=0}^{\infty}\frac{(-1)^{i+j}\,\Gamma(\alpha+1)}{i!\,j!\,\Gamma(\alpha-i+1)}(2\theta i)^{j}\,x^{j}$, then

$$E\left(\left(1-e^{-2\theta X}\right)^{\alpha}\right)=\Sigma_{i,j=0}^{\infty}\frac{(-1)^{i+j}\,\Gamma(\alpha+1)}{i!\,j!\,\Gamma(\alpha-i+1)}(2\theta i)^{j}\,E\left(X^{j}\right) \tag{24}$$

where $E\left(X^{j}\right)$ as in (16) with $r=j$.

Now for $E\left(\ln\left(1-e^{-2\theta X}\right)\right)=\int_{0}^{\infty}\ln\left(1-e^{-2\theta x}\right)f(x)_{TETLE}\,dx$, using the following expansion formula

$$\ln(1-z)=-\Sigma_{i=1}^{\infty}\frac{z^{i}}{i}\;;|z|<1 \tag{E4}$$

with using $(E1)$, we get $\ln\left(1-e^{-2\theta x}\right)=\Sigma_{k=1}^{\infty}\Sigma_{l=0}^{\infty}\frac{(-1)^{l+1}}{k\,l!}(2\theta k)^{l}\,x^{l}$, and then

$$E\left(\ln\left(1-e^{-2\theta X}\right)\right)=\Sigma_{k=1}^{\infty}\Sigma_{l=0}^{\infty}\frac{(-1)^{l+1}}{k\,l!}(2\theta k)^{l}\,E\left(X^{l}\right) \tag{25}$$

where $E\left(X^{l}\right)$ as in (16) with $r=l$.

Relative entropy: Consider $f(x)_{TETLE}$ and $f^{*}(x)_{TETLE}$ are the $TETLE$ pdf respectively, with parameters (λ,α,θ) and $(\lambda^{*},\alpha^{*},\theta^{*})$ then

$$\ln\frac{f(x)_{TETLE}}{f^{*}(x)_{TETLE}}=\ln\left(\frac{\lambda\alpha\theta\left(1-e^{-\lambda^{*}}\right)}{\lambda^{*}\alpha^{*}\theta^{*}(1-e^{-\lambda})}\right)-2(\theta-\theta^{*})x-\lambda\left(1-e^{-2\theta x}\right)^{\alpha}+\lambda^{*}\left(1-e^{-2\theta^{*}x}\right)^{\alpha^{*}}$$
$$+(\alpha-1)\ln\left(1-e^{-2\theta x}\right)-(\alpha^{*}-1)\ln\left(1-e^{-2\theta^{*}x}\right)$$

The $TETLE$ relative entropy is given by

$$RE_{TETLE}=E\left(\ln\frac{f(x)_{TETLE}}{f^{*}(x)_{TETLE}}\right)=\ln\left(\frac{\lambda\alpha\theta\left(1-e^{-\lambda^{*}}\right)}{\lambda^{*}\alpha^{*}\theta^{*}(1-e^{-\lambda})}\right)-2(\theta-\theta^{*})E(X)$$
$$-\lambda E\left(\left(1-e^{-2\theta X}\right)^{\alpha}\right)+\lambda^{*}E\left(\left(1-e^{-2\theta^{*}X}\right)^{\alpha^{*}}\right)$$
$$+(\alpha-1)E\left(\ln\left(1-e^{-2\theta X}\right)\right)-(\alpha^{*}-1)E\left(\ln\left(1-e^{-2\theta^{*}X}\right)\right) \tag{26}$$

with $E(X)$ as in (16) with $r=1$ and other expectations with specified parameters as in (24), and (25).

Reliability measures: Based on (13) and (14), the $TETLE$ functions of reliability, hazard, cumulative hazard, and reverse hazard can easily be found respectively as (see [13])

$$\tau_{1}(x)_{TETLE}=1-F(x)_{TETLE}=\frac{1}{1-e^{-\lambda}}\left(e^{-\lambda\left(1-e^{-2\theta x}\right)^{\alpha}}-e^{-\lambda}\right) \tag{27}$$

$$\tau_{2}(x)_{TETLE}=\frac{f(x)_{TETLE}}{R(x)_{TETLE}}=\frac{2\lambda\alpha\theta\,e^{-2\theta x}e^{-\lambda\left(1-e^{-2\theta x}\right)^{\alpha}}\left(1-e^{-2\theta x}\right)^{\alpha-1}}{e^{-\lambda\left(1-e^{-2\theta x}\right)^{\alpha}}-e^{-\lambda}} \tag{28}$$

$$\tau_{3}(x)_{TETLE}=-\ln(R(x)_{TETLE})=-\ln\left(1-\frac{1}{1-e^{-\lambda}}\left(1-e^{-\lambda\left(1-e^{-2\theta x}\right)^{\alpha}}\right)\right) \tag{29}$$

$$\tau_4(x)_{TETLE} = \frac{f(x)_{TETLE}}{F(x)_{TETLE}} = \frac{2\lambda\alpha\theta\, e^{-2\theta x} e^{-\lambda\left(1-e^{-2\theta x}\right)^{\alpha}} \left(1-e^{-2\theta x}\right)^{\alpha-1}}{1-e^{-\lambda\left(1-e^{-2\theta x}\right)^{\alpha}}} \quad (30)$$

Reliability stress strength model: Let X (strength) and Y (stress) are two independent $TETLE$ random variables with parameters $(\lambda, \alpha, \theta)$ and $(\lambda^*, \alpha^*, \theta^*)$ respectively, the reliability stress strength model [14] can be obtained as follows

$$SS_{TETLE} = P(Y < X) = \int_0^{\infty} f_X(x)\, F_Y(x)\, dx$$

$$= \frac{1}{1-e^{-\lambda^*}} \int_0^{\infty} \left(1 - e^{-\lambda^*\left(1-e^{-2\theta^* x}\right)^{\alpha^*}}\right) f_X(x)\, dx$$

Using $E1$, and $E2$ we get $e^{-\lambda^*\left(1-e^{-2\theta^* x}\right)^{\alpha^*}} = \Sigma_{i,m,j=0}^{\infty} \frac{(-1)^{i+m+j}\,\Gamma(i\alpha^*+1)}{i!\; m!\; j!\; \Gamma(i\alpha^*-m+1)} (\lambda^*)^i (2m\theta^*)^j\, x^j$, then

$$SS_{TETLE} = \frac{1}{1-e^{-\lambda^*}} \int_0^{\infty} \left[1 - \Sigma_{i,m,j=0}^{\infty} \frac{(-1)^{i+m+j}\,\Gamma(i\alpha^*+1)}{i!\; m!\; j!\; \Gamma(i\alpha^*-m+1)} (\lambda^*)^i (2m\theta^*)^j\, x^j\right] f_X(x) dx$$

Thus the $TETLE$ reliability stress strength model is

$$SS_{TETLE} = \frac{1}{1-e^{-\lambda^*}} \left[1 - \Sigma_{i,m,j=0}^{\infty} \frac{(-1)^{i+m+j}\,\Gamma(i\alpha^*+1)}{i!\; m!\; j!\; \Gamma(i\alpha^*-m+1)} (\lambda^*)^i (2m\theta^*)^j E\left(X^j\right)\right] \quad (31)$$

where $E\left(X^j\right)$ as in (16) with $r = j$.

6. Maximum likelihood estimators of $TETLE$ parameters

Regarding to (14), the natural logarithm likelihood function that associated with a complete random sample of size n, say $(x_1, x_2, \ldots, x_n)$, follow $TETLE$ distribution with the vector of parameters $\Delta = (\lambda, \alpha, \theta)^T$ is

$$\ell\left(\Delta|\underline{x}\right) = n \ln\left(\frac{2\lambda\alpha\theta}{1-e^{-\lambda}}\right) - 2\theta\Sigma_{i=1}^{n} x_i - \lambda\Sigma_{i=1}^{n}\left(1-e^{-2\theta x_i}\right)^{\alpha} + (\alpha-1)\Sigma_{i=1}^{n} \ln\left(\left(1-e^{-2\theta x_i}\right)\right) \quad (32)$$

The maximum likelihood (ML) estimators of three parameters can be obtained through solving the nonlinear differential equations $\frac{\partial \ell(\Delta|\underline{x})}{\partial \lambda} = 0$, $\frac{\partial \ell(\Delta|\underline{x})}{\partial \alpha} = 0$, $\frac{\partial \ell(\Delta|\underline{x})}{\partial \theta} = 0$. The ML estimators are not in closed forms, so numerical method is used.

7. Numerical illustrations

Simulation and real applications are presented here to exhibit the abilities of the proposed $TETLE$ distribution.

7.1 Simulation study

The steps of the simulation process are:

1. Based on simulated formula in (20), generate i.i.d. random samples (1000 times) follow $TETLE$ with size $n = 10, 25, 50, 100,$ and 200 where the initial (or true) values of parameters are chosen to be as in Table 1 (also see Figure 2).
2. For parameter λ, calculate the Bias and root mean squared error (RMSE) as

$$Bias\left(\hat{\lambda}\right) = \frac{1}{1000}\Sigma_{i=1}^{1000}\left(\hat{\lambda}_i - \lambda\right) \text{ and } RMSE\left(\hat{\lambda}\right) = \sqrt{\frac{1}{1000}\Sigma_{i=1}^{1000}\left(\hat{\lambda}_i - \lambda\right)^2}\,.$$

3. Repeat step 2 for parameters α, and θ .

The empirical results are listed in Table 1. It clearly appears that RMSE values decrease as the sample size increases.

Table 1: The Bias and RMSE associated with MLE of the $TETLE$ parameters

n	***Par.***	***Init.***	***Bias***	***RMSE***	***Init.***	***Bias***	***RMSE***
	λ	1.3	-0.988	2.036	3.1	-0.650	1.815
10	α	2.2	0.926	2.415	0.8	0.195	0.546
	θ	0.8	0.416	0.750	1.1	1.169	2.222
	λ	1.3	-0.564	1.592	3.1	-0.740	1.610
25	α	2.2	0.238	0.906	0.8	0.048	0.223
	θ	0.8	0.193	0.404	1.1	0.692	1.256
	λ	1.3	-0.295	1.357	3.1	-0.595	1.401
50	α	2.2	0.072	0.546	0.8	0.011	0.144
	θ	0.8	0.102	0.286	1.1	0.460	0.886
	λ	1.3	-0.145	1.113	3.1	-0.367	1.174
100	α	2.2	0.018	0.352	0.8	0.002	0.093
	θ	0.8	0.049	0.205	1.1	0.267	0.613
	λ	1.3	-0.068	0.897	3.1	-0.208	1.003
200	α	2.2	-0.004	0.236	0.8	-0.002	0.063
	θ	0.8	0.024	0.159	1.1	0.155	0.447
n	***Par.***	***Init.***	***Bias***	***RMSE***	***Init.***	***Bias***	***RMSE***
	λ	0.03	-0.538	3.076	1	-0.626	2.696
10	α	8.30	2.673	7.561	5	2.144	5.637
	θ	0.98	0.147	0.418	1.02	0.288	0.568
	λ	0.03	-0.237	1.942	1	-0.423	1.846
25	α	8.30	0.976	4.104	5	0.733	2.429
	θ	0.98	0.067	0.277	1.02	0.152	0.381
	λ	0.03	-0.085	1.551	1	-0.254	1.602
50	α	8.30	0.434	2.964	5	0.253	1.547
	θ	0.98	0.031	0.214	1.02	0.087	0.295
	λ	0.03	0.009	1.274	1	-0.081	1.281
100	α	8.30	0.065	1.849	5	0.076	0.992
	θ	0.98	0.004	0.163	1.02	0.036	0.228
	λ	0.03	-0.005	1.011	1	-0.029	1.066
200	α	8.30	-0.049	1.315	5	-0.010	0.689
	θ	0.98	0.001	0.128	1.02	0.016	0.182

7.2 Real applications

Here we provide applications for two real data sets to illustrate the abilities and flexibility of the TETLE distribution.

Data-1: The first real data available at the early detection unit for breast cancer at Benha University Hospital in Egypt for the period from June to October 2014. The data represent the ages of 155 patients with breast tumors [15].

"46, 32, 50, 46, 44, 42, 69, 31, 25, 29, 40, 42, 24, 17, 35, 48, 49, 50, 60, 26, 36, 56, 65, 48, 66, 44, 45, 30, 28, 40, 40, 50, 41, 39, 36, 63, 40, 42, 45, 31, 48, 36, 18, 24, 35, 30, 40, 48, 50, 60, 52, 47, 50, 49, 38, 30, 52, 52, 12, 48, 50, 45, 50, 50, 50, 53, 55, 38, 40, 42, 42, 32, 40, 50, 58, 48, 32, 45, 42, 36, 30, 28, 38, 54, 90, 80, 60, 45, 40, 50, 50, 40, 50, 50, 50, 60, 39, 34, 28, 18, 60, 50, 20, 40, 50, 38, 38, 42, 50, 40, 36, 38, 38, 50, 50, 31, 59, 40, 42, 38, 40, 38, 50, 50, 50, 40, 65, 38, 40, 38, 58, 35, 60, 90, 48, 58, 45, 35, 38, 32, 35, 38, 34, 43, 40, 35, 54, 60, 33, 35, 36, 43, 40, 45, 56".

Data-2: The second real data represents the fatigue fracture life of Kevlar 373/epoxy, which is subject to constant pressure at a 90 per cent stress level until it has all failed [16].

"0.0251, 0.0886, 0.0891, 0.2501, 0.3113, 0.3451, 0.4763, 0.5650, 0.5671, 0.6566, 0.6748, 0.6751, 0.6753, 0.7696, 0.8375, 0.8391, 0.8425, 0.8645, 0.8851, 0.9113, 0.9120, 0.9836, 1.0483, 1.0596, 1.0773, 1.1733, 1.2570, 1.2766, 1.2985, 1.3211, 1.3503, 1.3551, 1.4595, 1.4880, 1.5728, 1.5733, 1.7083, 1.7263, 1.7460, 1.7630, 1.7746, 1.8275, 1.8375, 1.8503, 1.8808, 1.8878, 1.8881, 1.9316, 1.9558, 2.0048, 2.0408, 2.0903, 2.1093, 2.1330, 2.2100, 2.2460, 2.2878, 2.3203, 2.3470, 2.3513, 2.4951, 2.5260, 2.9911, 3.0256, 3.2678, 3.4045, 3.4846, 3.7433, 3.7455, 3.9143, 4.8073, 5.4005, 5.4435, 5.5295, 6.5541, 9.0960".

The TETLE fitting is compared with six distributions: Beta Exponential (BE), Kumaraswamy Exponential (KuE), Exponentiated Generalized Exponential (EGE), Weibull Exponential (WeE), Gompertz Exponential (GoE), and Exponential (E) distributions. The R software used to calculate the MLEs of the parameters, for each distribution, along with the information criteria: (-LL) negative log-likelihood, (AIC) Akaike Information Criteria, (CAIC) Consistent Akaike Information Criteria, (BIC) Bayesian Information Criteria, (HQIC) Hanan and Quinn Information Criteria. Lowest values of these information criteria indicate the distribution with a better fit and are defined as [17]

$$AIC = 2p - 2\ell_{max}\ , CAIC = \frac{2np}{n-p-1} - 2\ell_{max}\ ,$$
$$BIC = p\ln(n) - 2\ell_{max}\ \text{, and } HQIC = 2p\ln(\ln(n)) - 2\ell_{max}\ .$$

where

p: is the number of distribution parameters, ℓ_{max}: is the log-likelihood function evaluated at MLEs, and n: is the sample size.

From the results that are shown in Tables 2 – 5, it is seen clearly that the lowest values of information criteria are associated with TETLE, which makes it the most fitting to represent two data sets compared to other distributions. Furthermore, the best fitting of TETLE can be seen through the plots of the histogram and empirical cdfs shown in Figures 3 - 6.

Table 2. The information criteria for fitting Data-1

Dist.	-LL	AIC	CAIC	BIC	HQIC
TETLE	601.8285	1209.657	1209.816	1218.787	1213.365
BE	605.1656	1216.331	1216.490	1225.461	1220.040
KuE	602.9228	1211.846	1212.005	1220.976	1215.554
EGE	611.2447	1228.489	1228.648	1237.620	1232.198
WeE	610.2967	1226.593	1226.752	1235.724	1230.302
GoE	634.5340	1275.068	1275.227	1284.198	1278.777
E	740.3172	1482.634	1482.661	1485.678	1483.871

Table 3. The values of MLE to Data-1

Dist.	$\hat{\lambda}_{ML}$	$\hat{\alpha}_{ML}$	$\hat{\theta}_{ML}$
TETLE	-4.7268	16.1016	0.0546
BE	15.6984	4.0456	0.0386
KuE	9.6246	5.8559	0.0372
EGE	0.6496	25.6217	0.1333
WeE	3.6871	6.0792	0.1264
GoE	0.0528	1.0513	0.0585
E	---	---	0.0229

Table 4. The information criteria for fitting Data-2

Dist.	-LL	AIC	CAIC	BIC	HQIC
TETLE	121.2623	248.525	248.858	255.517	251.319
BE	122.2276	250.455	250.788	257.447	253.249
KuE	122.0942	250.188	250.522	257.181	252.983
EGE	122.2436	250.487	250.820	257.479	253.282
WeE	122.5247	251.049	251.383	258.042	253.844
GoE	125.3744	256.749	257.082	263.741	259.543
E	127.1143	256.229	256.283	258.559	257.160

Table 5. The values of MLE to Data-2

Dist.	$\hat{\lambda}_{ML}$	$\hat{\alpha}_{ML}$	$\hat{\theta}_{ML}$
TETLE	-5.6132	0.4483	0.4180
BE	1.6792	1.5236	0.4806
KuE	1.5554	2.4608	0.3266
EGE	0.4983	1.7095	1.4104
WeE	1.3256	2.4310	1.1398
GoE	0.5149	0.1521	0.7992
E	---	---	0.5104

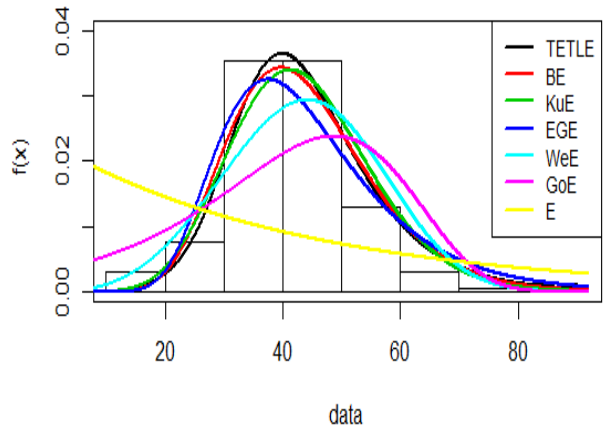

Figure 3. Data-1 histogram plot of TETLE with other compared distributions

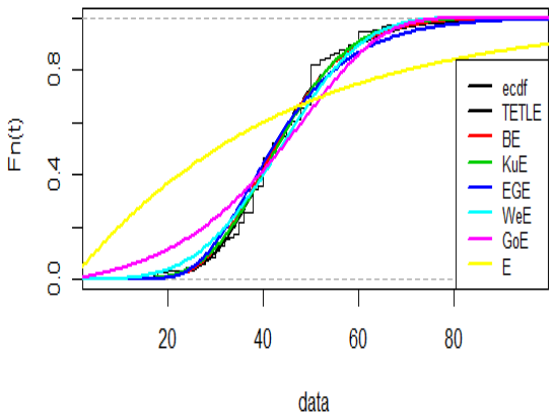

Figure 4. Data-1 empirical cdf plot of TETLE with other compared distributions

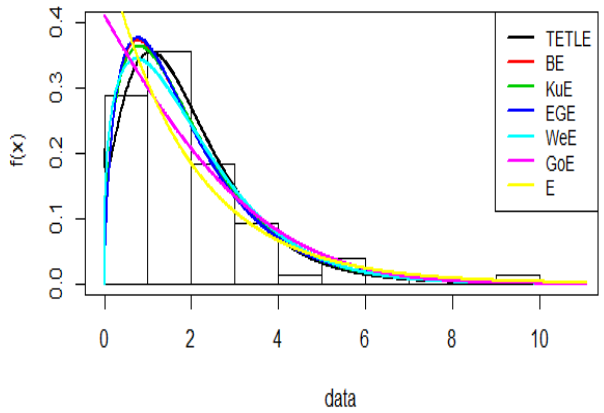

Figure 5. Data-2 histogram plot of TETLE with other compared distributions

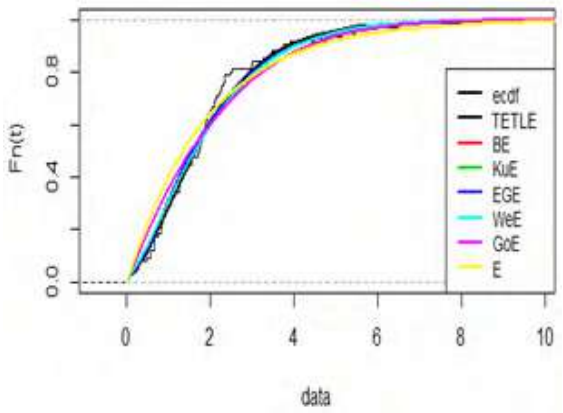

Figure 6. Data-2 empirical cdf plot of TETLE with other compared distributions

8 Conclusions

A newly generated family of continuous distributions with Topp Leone is introduced. Then a truncated distribution as a sub-model with three parameters called Truncated Exponential Topp Leone Exponential (TETLE) is proposed. Reliability characteristics with several main properties are presented. The TETLE distribution applied upon simulation besides two real applications with different information criteria. The results of simulation clearly shown the flexibility and consistent performance of the maximum likelihood estimates and the results of real applications clearly shown that the proposed distribution has outstanding performance than other considered distributions for all criteria. This flexibility allows using the TETLE distribution in various application areas. Furthermore, for future work, through using the same new family presented here, one can derive another new continuous probability distributions.

References

[1] Topp C W and Leone F C 1955 A family of J-shaped frequency functions *Journal of the American Statistical Association* **50**(269) pp 209-219

[2] Eugene N, Lee C and Famoye F 2002 Beta-normal distribution and its applications *Communications in Statistics-Theory and methods* **31**(4) pp 497-512

[3] Nadarajah S and Kotz S 2003 Moments of some J-shaped distributions *Journal of Applied Statistics* **30**(3) pp 311-317
[4] Ghitany M E, Kotz S and Xie M 2005 On some reliability measures and their stochasticorderings for the Topp-Leone distribution *Journal of Applied Statistics* **32**(7) pp 715-722
[5] Kotz S and Seier E 2007 Kurtosis of the Topp-Leone distributions Interstat, 2007 (July)
[6] Vicaria D, Dorpb J R V and Kotzb S 2008 Two-sided generalized Topp and Leone (TS-GTL) distributions *Journal of Applied Statistics* **35**(10) pp 1115-1129
[7] Al-Zahrani B 2012 Goodness-of-fit for the Topp-Leone distribution with unknown parameters *Applied Mathematical Sciences* **6**(128) pp 6355 - 6363
[8] Sangsanit Y and Bodhisuwan W 2016 The Topp-Leone generator of distributions: properties and inferences Songklanakarin *J. Sci. Technol.* **38**(5) pp 537-548
[9] Gupta A K and Nadarajah S 2005 On the moments of the beta normal distribution *Communications in Statistics-Theory and methods* **33**(1) pp 1-13
[10] Abid S H, Al-Noor N H and Boshi M A A 2018 [0,1] Truncated generalized gamma – generalized gamma distribution *Journal of Iraqi Al-Khwarizmi Society* 2(1) pp 135-148
[11] Nadarajah S and Kotz S 2004 The beta Gumbel distribution Mathematical Problems in Engineering, *Article ID* **529485** pp 323-332 doi.org/10.1155/S1024123X04403068
[12] Al-Noor N H and Assi N K 2020 Rayleigh-Rayleigh distribution: properties and applications *Journal of Physics: Conference Series* **1591** 012038 pp 1-15 doi:10.1088/1742-6596/1591/1/012038.
[13] Shabbir M, Riaz A and Gull H 2018 Rayleigh Lomax distribution *The Journal of Middle East and North Africa Sciences* **4**(12) pp 1-4
[14] Saraçoğlu B, Kaya M F and Abd-Elfattah A M 2009 Comparison of estimators for stress-strength reliability in the Gompertz case *Hacettepe Journal of Mathematics and Statistics* **38**(3) pp 339-349
[15] Hassan A S, Elbatal I and Hemeda S E 2016 Weibull quasi Lindley distribution and its statistical properties with applications to lifetime data *International Journal of Applied Mathematics and Statistics* **55**(3) pp 63-80
[16] Khaleel M A, Al-Noor N H and Hameed M Kh 2020 A Marshall Olkin exponential Gompertz distribution: properties and applications *Periodicals of Engineering and Natural Sciences* **8**(1) pp 298-312
[17] Zubair A, Eisa M, Hamedani G G and Omid K 2020 New methods to define heavy-tailed distributions with applications to insurance data *Journal of Taibah University for Science* **14**(1) pp 359-382

Runge-kutta Numerical Method for Solving Nonlinear Influenza Model

Runge-kutta Numerical Method for Solving Nonlinear Influenza Model

Shatha Jabbar Mohammed and Maha A. Mohammed

Department of Mathematics, College of Education for Pure Sciences Ibn-Al-Haitham, University of Baghdad, Baghdad, Iraq

E-mail: maha.aj.m@ihcoedu.uobaghdad.edu.iq

Abstract. The main object of this study is to solve a system of nonlinear ordinary differential equations (ODE) of the first order governing the epidemic model using numerical methods. The application under study is a mathematical epidemic model which is the influenza model at Australia in 1919. Runge-kutta methods of order 4 and of order 45 for solving this initial value problem(IVP) problem have been used. Finally, the results obtained have been discussed tabularly and graphically.

1. Introduction

Influenza is an infectious disease that is transmitted by a virus widespread in the population and infects people of different ages [1]. It is transmitted from person to person through the air of sneeze, cough, touch soiled objects and move them to the eye, nose or mouth, and others [2,3]. The researchers were representing them as mathematical models. Many people suffer from severe symptoms of the disease around the world. It can turn into a serious disease especially for old adults, newborns, people who have chronic diseases, pregnant women, and people who are obese [4,5]. Flu symptoms may be mild or very strong and these symptoms include cough, nausea, vomiting, fever, headache, fatigue, sore throat, runny nose, chills, muscle pain, sweating, fatigue, weakness, and others [6].

The cause of this disease is the influenza virus, which is transmitted from person to person through the respiratory system. Influenza virus may cause death for some people, especially those who suffer from other health problems [6].

There are many researchers interested in studying epidemiological models to know whether the epidemic is increasing or decreasing, such as Sabaa and Mohammed in 2019 discussed the analytic solutions of a nonlinear social epidemic model for alcohol consumption problem in Spain using Adomian decomposition and variation iteration methods [7]. Sabaa and Mohammed, in 2020 solved also the nonlinear social epidemic model that is the smoking habit problem by Adomian decomposition, variation iteration, finite difference, and Runge-Kutta approximate methods [8].

Many researchers analyzed the influenza epidemic model that is under study, such as El-Shahed and Alsaedi in 2011 studied the fractional SIRC model and influenza A [9], Shaman and Karspeck in 2012 studied Forecasting seasonal outbreaks of influenza [10]. Reynolds, et al. in 2014 studied mathematical modeling of influenza A virus dynamics within Swine Farms and the Effects of Vaccination [11]. Jódar, et al. in 2017 studied a mathematical model of Influenza: stability and treatment [12]. Zarebski et al. in 2017 analyzed a mathematical model of epidemics of seasonal influenza in Australia using the likelihood-based method [13], Kim et al. in 2017 studied the optimal control strategies of influenza epidemic model in Korea [14].

The feature of such a model is the existence of multiple parameters and multivariate. As well, it is a nonlinear system of the first-order ordinary differential equations for initial value problems that do not mostly get the exact solution. Our interest is to solve numerically such models. The choice of appropriate numerical methods is necessary. One of the numerical methods for solving this problem and the most famous method is Runge-Kutta of order 4 (RK_4) and Runge-kutta of order 45 (RK_{45}) to solve the Influenza model in Australia in 1919 depending on previous studies which is a reliable method. The solution is approximate because most mathematical models are very complicated since such models contain several variables and parameter, the exact solution of these models is not available [15]. There were concerns with the manual calculation of somewhat large data sets but those concerns disappeared with the widespread availability of computers that establish programs for these numerical methods to get the solution easy and fast [16].

This research is arranged as follows: In Section 2, the mathematical model of an influenza epidemic is presented, Section 3 constructs the numerical solutions of the influenza model by Runge-Kutta of 4th order $(RK4)$ and of order 45 (RK_{45}) method, Section 4, results, and discussion are presented tabularly and graphically, Section 5 has ended the study by the conclusion.

2. Mathematical Model

Mathematical modeling is an abstract model that uses mathematical language to describe the behavior of a system. The mathematical model is also defined as a collection of equations that describes a natural phenomenon. The importance of modeling in understanding the spread of the influenza epidemic [17]. The influenza epidemic in Australia in 1919 has been studied to predict the progression of disease levels. The population contains four species of individuals, $S(t), E(t), I(t)$ and $R(t)$ called compartments, the first compartment is the healthy persons and symbolized by (S), the second compartment is the infected persons, but does not cause infection, the person is in the incubation period and symbolized by (E), the third compartment is the infected persons and the cause infection after the incubation period and symbolized by (I), the fourth compartment is the persons who recover or die and symbolized by (R). So our model is made $(SEIR)$,[1]. The governing equations for the influenza model are given as a system of the first-order nonlinear ordinary differential equations in the system (1), [1]:

$$S'(t) = -\beta\frac{IS}{N} - \mu S + rN + \delta R$$
$$E'(t) = \beta\frac{IS}{N} - (\mu + \sigma + \kappa)\mathrm{E}$$
$$I'(t) = \sigma E - (\mu + \alpha + \gamma)I$$
$$R'(t) = \kappa E + \gamma I - \mu R - \delta R$$

where Table 1. has described the variables of the influenza model $S(t), E(t), I(t), R(t)$, Table 2 has the description of the parameters of the influenza model $\beta, \mu, r, \delta, \sigma, \kappa, \alpha, \gamma$ and the initial conditions (random variables) of the system (1): $S_0 = 0.4865$, $E_0 = 0.0000009$, $I_0 = 0.000068$, $R_0 = 0.0000000$, N is the total population such that $N = S + E + I + R$ and the specified time period $(0,70)$ is used to obtain results by Samsuzzoha, Singh, et al. [1].

Table 1: Describing the variables of the influenza model

Variables	Description
$S(t)$	Proportion of susceptible population
$E(t)$	Proportion of exposed population
$I(t)$	Proportion of infective population
$R(t)$	Proportion of recovered population

Table 2: Description of the parameters of the influenza model and value of parameters [1]

Parameters	Description	Value of Parameters
β	Contact rate	0.5020000
μ	Natural mortality rate	0.0003671
r	Birth rate	0.0006762
δ	Duration of immunity loss	0.0027400
σ	Mean duration of latency	0.6990000
κ	Recovery rate of latent	0.0001500
α	Flu induced mortality rate	0.0300000
γ	Mean recovery time for clinically ill	0.3600000

3. Numerical Method for Solving Influenza Model

A numerical method is a procedure that produces approximate solutions at specific points using the operations of addition, subtraction, multiplication, division, and functional appraisals. It can be applied to most first_order initial value problems [18]. They are important tools for investigating the systems [19]. Runge_Kutta is a set of iterative, implicit, and explicit methods [20]. Runge-Kutta techniques were introduced around 1900 by Carl Runge and Wilhelm Kutta [21]. In this section, two types of numerical methods can be discussed: (RK_4 and RK_{45} to solve the influenza epidemic problem in Australia in 1919, [1].

3.1. Runge-Kutta of Order 4 (RK_4) Method

RK_4 method is a reliable and accurate iteration numerical method that is used to solve the linear and nonlinear system or equation of the first ODE for initial value problems, it gives accurate results. It is a built-in method from the Runge-Kutta family. The nonlinear system of the influenza model under study can be solved by the RK method at present work. RK method has different forms according to the order of the method, in the present work, RK of the fourth order in this section can be used to solve the nonlinear system of the system (1). This work needs four steps to find the final form, [22].

The general formula of y_{i+1} for the RK_4 method [22] is:

$$y_{i+1} = y_i + \frac{1}{6}(k_1 + 2k_2 + 2k_3 + k_4) \quad (1)$$

In order to solve the system of system (1) using RK_4 to obtain numerical results, first write the form of RK_4 as below, in equations (2-5) the general formula of $S_{i+1}, E_{i+1}, I_{i+1}$ and R_{i+1} for the RK_4 method is:

$$S_{i+1} = S_i + \frac{1}{6}(k_{S1} + 2k_{S2} + 2k_{S3} + k_{S4}) \quad (2)$$

$$E_{i+1} = E_i + \frac{1}{6}(k_{E1} + 2k_{E2} + 2k_{E3} + k_{E4}) \quad (3)$$

$$I_{i+1} = I_i + \frac{1}{6}(k_{I1} + 2k_{I2} + 2k_{I3} + k_{I4}) \quad (4)$$

$$R_{i+1} = R_i + \frac{1}{6}(k_{R1} + 2k_{R2} + 2k_{R3} + k_{R4}) \quad (5)$$

where $i = 0,1, \dots, n-1$.

The general formula of k_1, k_2, k_3, k_4 for the RK_4 method [22] is:

$$k_1 = hf_1(t_i, y_i) \quad (6)$$

$$k_2 = hf_2(t_i + \frac{h}{2}, y_i + \frac{k_1}{2}) \quad (7)$$

$$k_3 = hf_3(t_i + \frac{h}{2}, y_i + \frac{k_2}{2}) \quad (8)$$

$$k_4 = hf_4(t_i + h, y_i + k_3) \quad (9)$$

where f_1, f_2, f_3, f_4 are unknown functions, t is a time and h is a step size.
Now, to find k_{S1}, k_{E1}, k_{I1} and k_{R1}, we following the next steps in equations (10-13).

$$k_{S1} = hf_1(t_i, S_i, E_i, I_i, R_i) = h\left(\frac{-\beta}{N_{i1}} I_i S_i - \mu S_i + rN_{i1} + \delta R_i\right) \quad (10)$$

$$k_{E1} = hf_2(t_i, S_i, E_i, I_i, R_i) = h\left(\frac{\beta}{N_{i1}} I_i S_i - (\mu + \sigma + \kappa)E_i\right) \quad (11)$$

$$k_{I1} = hf_3(t_i, S_i, E_i, I_i, R_i) = h\,(\,\sigma E_i - (\mu + \alpha + \gamma)I_i\,) \quad (12)$$

$$k_{R1} = hf_4(t_i, S_i, E_i, I_i, R_i) = h(\,\kappa E_i + \gamma I_i - \mu R_i - \delta R_i) \quad (13)$$

where $i = 0,1, \dots, n-1$.
In the same way, k_{S2}, k_{E2}, k_{I2} and k_{R2} can be found to obtain the second step in equations (14-17) where f_1, f_2, f_3, f_4 are unknown functions, t is a time and h is a step size:

$$\begin{aligned} k_{S2} &= hf_1(t_i + \frac{h}{2}, S_i + \frac{1}{2}k_{S1}, E_i + \frac{1}{2}k_{E1}, I_i + \frac{1}{2}k_{I1}, R_i + \frac{1}{2}k_{R1}) \\ &= h\,(\frac{-\beta}{N_{i2}}\left(I_i + \frac{1}{2}k_{I1}\right)(S_i + \frac{1}{2}k_{S1}\right) - \mu\left(S_i + \frac{1}{2}k_{S1}\right) + rN_{i2} \\ &\quad + \delta\left(R_i + \frac{1}{2}k_{R1}\right)) \end{aligned} \quad (14)$$

$$\begin{aligned} k_{E2} &= hf_2\,(t_i + \frac{h}{2}, S_i + \frac{1}{2}k_{S1,}\, E_i + \frac{1}{2}k_{E1,}\, I_i + \frac{1}{2}k_{I1}, R_i + \frac{1}{2}k_{R1}) \\ &= h\,(\frac{\beta}{N_{i2}}\left(I_i + \frac{1}{2}k_{I1}\right)(S_i + \frac{1}{2}k_{S1}\right) - (\mu + \sigma + \kappa)\left(E_i + \frac{1}{2}k_{E1}\right)) \end{aligned} \quad (15)$$

$$\begin{aligned} k_{I2} &= hf_3\,(t_i + \frac{h}{2}, S_i + \frac{1}{2}k_{S1}, E_i + \frac{1}{2}k_{E1}, I_i + \frac{1}{2}k_{I1}, R_i + \frac{1}{2}k_{R1}) \\ &= h\,(\sigma\left(E_i + \frac{1}{2}k_{E1}\right) - (\mu + \alpha + \gamma)\left(I_i + \frac{1}{2}k_{I1}\right)) \end{aligned} \quad (16)$$

$$\begin{aligned} k_{R2} &= hf_4\,(t_i + \frac{h}{2}, S_i + \frac{1}{2}k_{S1}, E_i + \frac{1}{2}k_{E1}, I_i + \frac{1}{2}k_{I1}, R_i + \frac{1}{2}k_{R1}) \\ &= h\,\left(\kappa\left(E_i + \frac{1}{2}k_{E1}\right) + \gamma\left(I_i + \frac{1}{2}k_{I1}\right) - \mu\left(R_i + \frac{1}{2}k_{R1}\right)\right. \\ &\quad \left. - \delta\left(R_i + \frac{1}{2}k_{R1}\right)\right) \end{aligned} \quad (17)$$

where $i = 0,1, \dots, n-1$.
In the third stage, try to find k_{S3}, k_{E3}, k_{I3} and k_{R3} by substituting in the system (1) as below in equations (18-21) where f_1, f_2, f_3, f_4 are unknown functions, t is a time and h is a step size:

$$k_{S3} = hf_1\left(t_i + \frac{h}{2}, S_i + \frac{1}{2}k_{S2}, E_i + \frac{1}{2}k_{E2}, I_i + \frac{1}{2}k_{I2}, R_i + \frac{1}{2}k_{R2}\right)$$
$$= h\left(\frac{-\beta}{N_{i3}}\left(I_i + \frac{1}{2}k_{I2}\right)\left(S_i + \frac{1}{2}k_{S2}\right) - \mu\left(S_i + \frac{1}{2}k_{S2}\right) + rN_{i3} + \delta\left(R_i + \frac{1}{2}k_{R2}\right)\right) \quad (18)$$

$$k_{E3} = hf_2\left(t_i + \frac{h}{2}, S_i + \frac{1}{2}k_{S2}, E_i + \frac{1}{2}k_{E2}, I_i + \frac{1}{2}k_{I2}, R_i + \frac{1}{2}k_{R2}\right)$$
$$= h\left(\frac{\beta}{N_{i3}}\left(I_i + \frac{1}{2}k_{I2}\right)\left(S_i + \frac{1}{2}k_{S2}\right) - (\mu + \sigma + \kappa)\left(E_i + \frac{1}{2}k_{E2}\right)\right) \quad (19)$$

$$k_{I3} = hf_3\left(t_i + \frac{h}{2}, S_i + \frac{1}{2}k_{S2}, E_i + \frac{1}{2}k_{E2}, I_i + \frac{1}{2}k_{I2}, R_i + \frac{1}{2}k_{R2}\right)$$
$$= h\left(\sigma\left(E_i + \frac{1}{2}k_{E2}\right) - (\mu + \alpha + \gamma)\left(I_i + \frac{1}{2}k_{I2}\right)\right) \quad (20)$$

$$k_{R3} = hf_4\left(t_i + \frac{h}{2}, S_i + \frac{1}{2}k_{S2}, E_i + \frac{1}{2}k_{E2}, I_i + \frac{1}{2}k_{I2}, R_i + \frac{1}{2}k_{R2}\right)$$
$$= h\left(\kappa\left(E_i + \frac{1}{2}k_{E2}\right) + \gamma\left(I_i + \frac{1}{2}k_{I2}\right) - \mu\left(R_i + \frac{1}{2}k_{R2}\right) - \delta\left(R_i + \frac{1}{2}k_{R2}\right)\right) \quad (21)$$

where $i = 0,1,\dots,n-1$.
The fourth stage needs to find k_{S4}, k_{E4}, k_{I4} and k_{R4} as below, in equations (22-25) where f_1, f_2, f_3, f_4 are unknown functions, t is a time and h is a step size:

$$k_{S4} = hf_1\left(t_i + h, S_i + k_{S3}, E_i + k_{E3}, I_i + k_{I3}, R_i + k_{R3}\right)$$
$$= h\left(\frac{-\beta}{N_{i4}}\left(I_i + k_{I3}\right)(S_i + k_{S3}) - \mu(S_i + k_{S3}) + rN_{i4} + \delta(R_i + k_{R3})\right) \quad (22)$$

$$k_{E4} = hf_2\left(t_i + h, S_i + k_{S3}, E_i + k_{E3}, I_i + k_{I3}, R_i + k_{R3}\right)$$
$$= h\left(\frac{\beta}{N_{i4}}\left(I_i + k_{I3}\right)(S_i + k_{S3}) - (\mu + \sigma + \kappa)(E_i + k_{E3})\right) \quad (23)$$

$$k_{I4} = hf_3\left(t_i + h, S_i + k_{S3}, E_i + k_{E3}, I_i + k_{I3}, R_i + k_{R3}\right)$$
$$= h\left(\sigma(E_i + k_{E3}) - (\mu + \alpha + \gamma)(I_i + k_{I3})\right) \quad (24)$$

$$k_{R4} = hf_4\left(t_i + h, S_i + k_{S3}, E_i + k_{E3}, I_i + k_{I3}, R_i + k_{R3}\right)$$
$$= h\left(\kappa(E_i + k_{E3}) + \gamma(I_i + k_{I3}) - \mu(R_i + k_{R3}) - \delta(R_i + k_{R3})\right) \quad (25)$$

where $i = 0,1,\dots,n-1$.

3.2 Runge-Kutta of Order 45 (RK_{45}) Method

RK_{45} method is a reliable and accurate iteration numerical method that is used to solve the nonlinear system of the system (1). This work needs six steps to find the final form, [22]. It was developed by a German mathematician Erwin Fehlberg in 1969. It is a built-in method from Runge-Kutta family.

The general formula of y_{i+1} for the RK_{45} method [23] is:

$$y_{i+1} = y_i + \frac{25}{216}k_1 + \frac{1408}{2565}k_3 + \frac{2197}{4104}k_4 - \frac{1}{5}k_5 \quad (26)$$

In order to solve the system of the system (1) using RK_{45} to obtain numerical results, first write the form of RK_{45} as below, in equations (27-30), the general formula of $S_{i+1}, E_{i+1}, I_{i+1}$ and R_{i+1} for the RK_4 method is:

$$S_{i+1} = S_i + \frac{25}{216} k_{S1} + \frac{1408}{2565} k_{S3} + \frac{2197}{4104} k_{S4} - \frac{1}{5} k_{S5} \quad (27)$$

$$E_{i+1} = E_i + \frac{25}{216} k_{E1} + \frac{1408}{2565} k_{E3} + \frac{2197}{4104} k_{E4} - \frac{1}{5} k_{E5} \quad (28)$$

$$I_{i+1} = I_i + \frac{25}{216} k_{E1} + \frac{1408}{2565} k_{E3} + \frac{2197}{4104} k_{E4} - \frac{1}{5} k_{I5} \quad (29)$$

$$R_{i+1} = R_i + \frac{25}{216} k_{R1} + \frac{1408}{2565} k_{R3} + \frac{2197}{4104} k_{R4} - \frac{1}{5} k_{R5} \quad (30)$$

where $i = 0,1, \dots, n-1$.

The general formula of $k_1, k_2, k_3, k_4, k_5, k_6$ for the RK_{45} method [22] is:

$$k_1 = h f_1(t_i, y_i) \quad (31)$$

$$k_2 = h f_2(t_i + \frac{h}{4}, y_i + \frac{k_1}{4}) \quad (32)$$

$$k_3 = h f_3(t_i + \frac{3h}{8}, y_i + \frac{3k_1}{32} + \frac{9k_2}{32}) \quad (33)$$

$$k_4 = h f_4(t_i + \frac{12h}{13}, y_i + \frac{1932k_1}{2197} - \frac{7200k_2}{2197} + \frac{7296k_3}{2197}) \quad (34)$$

$$k_5 = h f_5(t_i + h, y_i + \frac{439k_1}{219} - 8k_2 + \frac{3680k_3}{513} - \frac{845k_4}{4104}) \quad (35)$$

$$k_6 = h f_6(t_i + \frac{h}{2}, y_i - \frac{8k_1}{27} + 2k_2 - \frac{3544k_3}{2565} + \frac{1859k_4}{4104} - \frac{11k_5}{40}) \quad (36)$$

where $f_1, f_2, f_3, f_4, f_5, f_6$ are unknown functions, t is a time and h is a step size.

Now, To find k_{S1}, k_{E1}, k_{I1} and k_{R1} following the next steps in equations (37-40) where f_1, f_2, f_3, f_4 are unknown functions, t is a time and h is a step size:

$$k_{S1} = h f_1(t_i, S_i, E_i, I_i, R_i) = h\left(\frac{-\beta}{N_{i1}} I_i S_i - \mu S_i + r N_{i1} + \delta R_i\right) \quad (37)$$

$$k_{E1} = h f_2(t_i, S_i, E_i, I_i, R_i) = h\left(\frac{\beta}{N_{i1}} I_i S_i - (\mu + \sigma + \kappa) E_i\right) \quad (38)$$

$$k_{I1} = h f_3(t_i, S_i, E_i, I_i, R_i) = h\,(\sigma E_i - (\mu + \alpha + \gamma) I_i) \quad (39)$$

$$k_{R1} = h f_4(t_i, S_i, E_i, I_i, R_i) = h(\kappa E_i + \gamma I_i - \mu R_i - \delta R_i) \quad (40)$$

where $i = 0,1, \dots, n-1$.

In the same way, k_{S2}, k_{E2}, k_{I2} and k_{R2} can be found to obtain the second step in equations (41-44) where f_1, f_2, f_3, f_4 are unknown functions, t is a time and h is a step size:

$$\begin{aligned} k_{S2} = h f_1(t_i + \frac{h}{4}, S_i + \frac{1}{4}k_{S1}, E_i + \frac{1}{4}k_{E1}, I_i + \frac{1}{4}k_{I1}, R_i + \frac{1}{4}k_{R1}) \\ = h\,(\frac{-\beta}{N_{i2}}\left(I_i + \frac{1}{4}k_{I1}\right)\left(S_i + \frac{1}{4}k_{S1}\right) - \mu\left(S_i + \frac{1}{4}k_{S1}\right) + r N_{i2} \\ + \delta\left(R_i + \frac{1}{4}k_{R1}\right)) \end{aligned} \quad (41)$$

$$k_{E2} = hf_2\ (t_i + \frac{h}{4}, S_i + \frac{1}{4}k_{S1,}\ E_i + \frac{1}{4}k_{E1,}\ I_i + \frac{1}{4}k_{I1}, R_i + \frac{1}{4}k_{R1}$$
$$= h\ (\frac{\beta}{N_{i2}}\left(\ I_i + \frac{1}{4}k_{I1}\ \right)\ (S_i + \frac{1}{4}k_{S1}\right) - (\mu + \sigma + \kappa)\left(E_i + \frac{1}{4}k_{E1}\right)) \quad (42)$$

$$k_{I2} = hf_3\ (t_i + \frac{h}{4}, S_i + \frac{1}{4}k_{S1}, E_i + \frac{1}{4}k_{E1}, I_i + \frac{1}{4}k_{I1}, R_i + \frac{1}{4}k_{R1})$$
$$= h\ (\sigma\left(E_i + \frac{1}{4}k_{E1}\right) - \ (\mu + \alpha + \gamma)\left(I_i + \frac{1}{4}k_{I1}\right)) \quad (43)$$

$$k_{R2} = hf_4\ (t_i + \frac{h}{4}, S_i + \frac{1}{4}k_{S1}, E_i + \frac{1}{4}k_{E1}, I_i + \frac{1}{4}k_{I1}, R_i + \frac{1}{4}k_{R1})$$
$$= h\ \left(\kappa\left(E_i + \frac{1}{4}k_{E1}\ \right) + \ \gamma\ \left(I_i + \frac{1}{4}k_{I1}\right) - \mu\left(R_i + \frac{1}{4}k_{R1}\right)\right. \quad (44)$$
$$\left. - \delta\left(R_i + \frac{1}{4}k_{R1}\right)\right)$$

where $i = 0,1, \dots, n-1$.
In the third stage, try to find k_{S3}, k_{E3}, k_{I3} and k_{R3} by substituting in the system (1) as below in equations (45-48) where f_1, f_2, f_3, f_4 are unknown functions, t is a time and h is a step size:

$$k_{S3} = hf_1\ (t_i + \frac{3h}{8}, S_i + \frac{3}{32}k_{S1} + \frac{9}{32}k_{S2}, E_i + \frac{3}{32}k_{E1} + \frac{9}{32}k_{E2}, I_i + \frac{3}{32}k_{I1}$$
$$+ \frac{9}{32}k_{I2}, R_i + \frac{3}{32}k_{R1} + \frac{9}{32}k_{R2})$$
$$= h\ (\frac{-\beta}{N_{i3}}(\ I_i + \frac{3}{32}k_{I1} + \frac{9}{32}k_{I2})(\ S_i + \frac{3}{32}k_{S1} + \frac{9}{32}k_{S2}) \quad (45)$$
$$- \ \mu\left(S_i + \frac{3}{32}k_{S1} + \frac{9}{32}k_{S2}\right) + \ rN_{i3} + \delta\left(R_i + \frac{3}{32}k_{R1} + \frac{9}{32}k_{R2}\right)),$$

$$k_{E3} = hf_2\ (t_i + \frac{3h}{8}, S_i + \frac{3}{32}k_{S1} + \frac{9}{32}k_{S2}, E_i + \frac{3}{32}k_{E1} + \frac{9}{32}k_{E2}, I_i + \frac{3}{32}k_{I1}$$
$$+ \frac{9}{32}k_{I2}, R_i + \frac{3}{32}k_{R1} + \frac{9}{32}k_{R2}$$
$$= h\ (\frac{\beta}{N_{i3}}\left(I_i + \frac{3}{32}k_{I1} + \frac{9}{32}k_{I2}\ \right)(\ S_i + \frac{3}{32}k_{S1} + \frac{9}{32}k_{S2}) \quad (46)$$
$$- (\mu + \sigma + \kappa)\left(E_i + \frac{3}{32}k_{E1} + \frac{9}{32}k_{E2}\right))$$

$$k_{I3} = hf_3\ \ (t_i + \frac{3h}{8}, S_i + \frac{3}{32}k_{S1} + \frac{9}{32}k_{S2}, E_i + \frac{3}{32}k_{E1} + \frac{9}{32}k_{E2}, I_i + \frac{3}{32}k_{I1}$$
$$+ \frac{9}{32}k_{I2}, R_i + \frac{3}{32}k_{R1} + \frac{9}{32}k_{R2}) \quad (47)$$
$$= h\ (\sigma(E_i + \frac{3}{32}k_{E1} + \frac{9}{32}k_{E2}) - \ (\mu + \alpha + \gamma)\left(I_i + \frac{3}{32}k_{I1} + \frac{9}{32}k_{I2}\right))$$

$$
\begin{aligned}
k_{R3} = hf_4\ \Big(t_i + \frac{3h}{8}, S_i + \frac{3}{32}k_{S1} + \frac{9}{32}k_{S2}, E_i + \frac{3}{32}k_{E1} + \frac{9}{32}k_{E2}, I_i + \frac{3}{32}k_{I1} \\
+ \frac{9}{32}k_{I2}, R_i + \frac{3}{32}k_{R1} + \frac{9}{32}k_{R2}\Big) \\
= h\left(\kappa\left(E_i + \frac{3}{32}k_{E1} + \frac{9}{32}k_{E2}\right) + \gamma\left(I_i + \frac{3}{32}k_{I1} + \frac{9}{32}k_{I2}\right)\right. \\
\left. - \mu\left(R_i + \frac{3}{32}k_{R1} + \frac{9}{32}k_{R2}\right) - \delta\left(R_i + \frac{3}{32}k_{R1} + \frac{9}{32}k_{R2}\right)\right)
\end{aligned} \tag{48}
$$

where $i = 0,1, \dots, n-1$.
The fourth stage needs to find k_{S4}, k_{E4}, k_{I4} and k_{R4} as below, in equations (49-52) where f_1, f_2, f_3, f_4 are unknown functions, t is a time and h is a step size:

$$
\begin{aligned}
k_{S4} = hf_1\ \Big(t_i + \frac{12h}{13}, S_i + \frac{1932}{2197}k_{S1} - \frac{7200}{2197}k_{S2} + \frac{7296}{2197}k_{S3}, \\
E_i + \frac{1932}{2197}k_{E1} - \frac{7200}{2197}k_{E2} + \frac{7296}{2197}k_{E3}, I_i + \frac{1932}{2197}k_{I1} - \frac{7200}{2197}k_{I2} \\
+ \frac{7296}{2197}k_{I3}, R_i + \frac{1932}{2197}k_{R1} - \frac{7200}{2197}k_{R2} + \frac{7296}{2197}k_{R3}\Big) \\
= h\left(\frac{-\beta}{N_{i4}}\left(I_i + \frac{1932}{2197}k_{I1} - \frac{7200}{2197}k_{I2} + \frac{7296}{2197}k_{I3}\right)\left(S_i + \frac{1932}{2197}k_{S1}\right.\right. \\
\left. - \frac{7200}{2197}k_{S2} + \frac{7296}{2197}k_{S3}\right) \\
- \mu\left(S_i + \frac{1932}{2197}k_{S1} - \frac{7200}{2197}k_{S2} + \frac{7296}{2197}k_{S3}\right) + rN_{i4} \\
\left. + \delta\left(R_i + \frac{1932}{2197}k_{R1} - \frac{7200}{2197}k_{R2} + \frac{7296}{2197}k_{R3}\right)\right)
\end{aligned} \tag{49}
$$

$$
\begin{aligned}
k_{E4} = hf_2\ \Big(t_i + \frac{12h}{13}, S_i + \frac{1932}{2197}k_{S1} - \frac{7200}{2197}k_{S2} + \frac{7296}{2197}k_{S3}, \\
E_i + \frac{1932}{2197}k_{E1} - \frac{7200}{2197}k_{E2} + \frac{7296}{2197}k_{E3}, I_i + \frac{1932}{2197}k_{I1} - \frac{7200}{2197}k_{I2} \\
+ \frac{7296}{2197}k_{I3}, R_i + \frac{1932}{2197}k_{R1} - \frac{7200}{2197}k_{R2} + \frac{7296}{2197}k_{R3}\Big) \\
= h\left(\frac{\beta}{N_{i4}}\left(I_i + \frac{1932}{2197}k_{I1} - \frac{7200}{2197}k_{I2} + \frac{7296}{2197}k_{I3}\right)\left(S_i + \frac{1932}{2197}k_{S1}\right.\right. \\
\left. - \frac{7200}{2197}k_{S2} + \frac{7296}{2197}k_{S3}\right) - (\mu + \sigma + \kappa)\left(E_i + \frac{1932}{2197}k_{E1} - \frac{7200}{2197}k_{E2}\right. \\
\left.\left. + \frac{7296}{2197}k_{E3}\right)\right)
\end{aligned} \tag{50}
$$

$$k_{I4} = hf_3\ (t_i + \frac{12h}{13}, S_i + \frac{1932}{2197}k_{S1} - \frac{7200}{2197}k_{S2} + \frac{7296}{2197}k_{S3},$$
$$E_i + \frac{1932}{2197}k_{E1} - \frac{7200}{2197}k_{E2} + \frac{7296}{2197}k_{E3}, I_i + \frac{1932}{2197}k_{I1} - \frac{7200}{2197}k_{I2}$$
$$+ \frac{7296}{2197}k_{I3}\ , R_i + \frac{1932}{2197}k_{R1} - \frac{7200}{2197}k_{R2} + \frac{7296}{2197}k_{R3}) \quad (51)$$
$$= h\ (\sigma\left(E_i + \frac{1932}{2197}k_{E1} - \frac{7200}{2197}k_{E2} + \frac{7296}{2197}k_{E3}\right) - (\mu + \alpha + \gamma)\ (I_i$$
$$+ \frac{1932}{2197}k_{I1} - \frac{7200}{2197}k_{I2} + \frac{7296}{2197}k_{I3}))$$

$$k_{R4} = hf_4\ (t_i + \frac{12h}{13}, S_i + \frac{1932}{2197}k_{S1} - \frac{7200}{2197}k_{S2} + \frac{7296}{2197}k_{S3},$$
$$E_i + \frac{1932}{2197}k_{E1} - \frac{7200}{2197}k_{E2} + \frac{7296}{2197}k_{E3}, I_i + \frac{1932}{2197}k_{I1} - \frac{7200}{2197}k_{I2}$$
$$+ \frac{7296}{2197}k_{I3}\ , R_i + \frac{1932}{2197}k_{R1} - \frac{7200}{2197}k_{R2} + \frac{7296}{2197}k_{R3})$$
$$= h\left(\kappa\left(E_i + \frac{1932}{2197}k_{E1} - \frac{7200}{2197}k_{E2} + \frac{7296}{2197}k_{E3}\right)\right. \quad (52)$$
$$+\ \gamma\ \left(I_i + \frac{1932}{2197}k_{I1} - \frac{7200}{2197}k_{I2} + \frac{7296}{2197}k_{I3}\right)$$
$$-\ \mu\left(R_i + \frac{1932}{2197}k_{R1} - \frac{7200}{2197}k_{R2} + \frac{7296}{2197}k_{R3}\right)$$
$$\left.-\ \delta\left(R_i + \frac{1932}{2197}k_{R1} - \frac{7200}{2197}k_{R2} + \frac{7296}{2197}k_{R3}\right)\right)$$

where$i = 0,1, \dots, n-1$.

The fifth stage needs to find k_{S5}, k_{E5}, k_{I5} and k_{R5} As below, in equations (53-56) where f_1, f_2, f_3, f_4 are unknown functions, t is a time and h is a step size.

$$k_{S5} = hf_1\ (t_i + h, S_i + \frac{439}{216}k_{S1} - 8k_{S2} + \frac{3680}{513}k_{S3} - \frac{845}{4104}k_{S4},$$
$$E_i + \frac{439}{216}k_{E1} - 8k_{E2} + \frac{3680}{513}k_{E3} - \frac{845}{4104}k_{E4}, I_i + \frac{439}{216}k_{I1} - 8k_{I2}$$
$$+ \frac{3680}{513}k_{I3} - \frac{845}{4104}k_{I4}\ , R_i + \frac{439}{216}k_{R1} - 8k_{R2} + \frac{3680}{513}k_{R3}$$
$$- \frac{845}{4104}k_{R4})$$
$$= h\ (\frac{-\beta}{N_{i5}}\left(I_i + \frac{439}{216}k_{I1} - 8k_{I2} + \frac{3680}{513}k_{I3} - \frac{845}{4104}k_{I4}\right)(S_i + \frac{439}{216}k_{S1} \quad (53)$$
$$- 8k_{S2} + \frac{3680}{513}k_{S3} - \frac{845}{4104}k_{S4}\Big)$$
$$- \mu\left(S_i + \frac{439}{216}k_{S1} - 8k_{S2} + \frac{3680}{513}k_{S3} - \frac{845}{4104}k_{S4}\right) + rN_{i5}$$
$$+ \delta\left(R_i + \frac{439}{216}k_{R1} - 8k_{R2} + \frac{3680}{513}k_{R3} - \frac{845}{4104}k_{R4}\right))$$

$$
\begin{aligned}
k_{E5} = hf_2\,(t_i + h, S_i + \frac{439}{216}k_{S1} - 8k_{S2} + \frac{3680}{513}k_{S3} - \frac{845}{4104}k_{S4},\\
E_i + \frac{439}{216}k_{E1} - 8k_{E2} + \frac{3680}{513}k_{E3} - \frac{845}{4104}k_{E4}, I_i + \frac{439}{216}k_{I1} - 8k_{I2}\\
+ \frac{3680}{513}k_{I3} - \frac{845}{4104}k_{I4}\,, R_i + \frac{439}{216}k_{R1} - 8k_{R2} + \frac{3680}{513}k_{R3}\\
- \frac{845}{4104}k_{R4})\\
= h\,(\frac{\beta}{N_{i5}}(\,I_i + \frac{439}{216}k_{I1} - 8k_{I2} + \frac{3680}{513}k_{I3} - \frac{845}{4104}k_{I4})\,(S_i + \frac{439}{216}k_{S1}\\
- 8k_{S2} + \frac{3680}{513}k_{S3} - \frac{845}{4104}k_{S4}) - (\mu + \sigma + \kappa)(E_i + \frac{439}{216}k_{E1} - 8k_{E2}\\
+ \frac{3680}{513}k_{E3} - \frac{845}{4104}k_{E4}))
\end{aligned} \tag{54}
$$

$$
\begin{aligned}
k_{I5} = hf_3\,(t_i + h, S_i + \frac{439}{216}k_{S1} - 8k_{S2} + \frac{3680}{513}k_{S3} - \frac{845}{4104}k_{S4},\\
E_i + \frac{439}{216}k_{E1} - 8k_{E2} + \frac{3680}{513}k_{E3} - \frac{845}{4104}k_{E4}, I_i + \frac{439}{216}k_{I1} - 8k_{I2}\\
+ \frac{3680}{513}k_{I3} - \frac{845}{4104}k_{I4}\,, R_i + \frac{439}{216}k_{R1} - 8k_{R2} + \frac{3680}{513}k_{R3}\\
- \frac{845}{4104}k_{R4})\\
= h\,(\sigma\left(E_i + \frac{439}{216}k_{E1} - 8k_{E2} + \frac{3680}{513}k_{E3} - \frac{845}{4104}k_{E4}\right) - (\mu + \alpha\\
+ \gamma)\,(I_i + \frac{439}{216}k_{I1} - 8k_{I2} + \frac{3680}{513}k_{I3} - \frac{845}{4104}k_{I4}))
\end{aligned} \tag{55}
$$

$$
\begin{aligned}
k_{R5} = hf_4\,(t_i + h, S_i + \frac{439}{216}k_{S1} - 8k_{S2} + \frac{3680}{513}k_{S3} - \frac{845}{4104}k_{S4},\\
E_i + \frac{439}{216}k_{E1} - 8k_{E2} + \frac{3680}{513}k_{E3} - \frac{845}{4104}k_{E4}, I_i + \frac{439}{216}k_{I1} - 8k_{I2}\\
+ \frac{3680}{513}k_{I3} - \frac{845}{4104}k_{I4}\,, R_i + \frac{439}{216}k_{R1} - 8k_{R2} + \frac{3680}{513}k_{R3}\\
- \frac{845}{4104}k_{R4})\\
= h\left(\kappa\left(E_i + \frac{439}{216}k_{E1} - 8k_{E2} + \frac{3680}{513}k_{E3} - \frac{845}{4104}k_{E4}\right)\right.\\
+ \gamma\left(I_i + \frac{439}{216}k_{I1} - 8k_{I2} + \frac{3680}{513}k_{I3} - \frac{845}{4104}k_{I4}\right)\\
- \mu\left(R_i + \frac{439}{216}k_{R1} - 8k_{R2} + \frac{3680}{513}k_{R3} - \frac{845}{4104}k_{R4}\right)\\
\left. - \delta\left(R_i + \frac{439}{216}k_{R1} - 8k_{R2} + \frac{3680}{513}k_{R3} - \frac{845}{4104}k_{R4}\right)\right)
\end{aligned} \tag{56}
$$

where $i = 0,1,\dots,n-1$.

The sixth stage needs to find k_{S6}, k_{E6}, k_{I6} and k_{R6} as below, in equations (57-60) where f_1, f_2, f_3, f_4 are unknown functions, t is a time and h is a step size:

$$
\begin{aligned}
k_{S6} = hf_1\,(t_i + \frac{h}{2}, S_i - \frac{8}{27}k_{S1} + 2k_{S2} - \frac{3544}{2565}k_{S3} + \frac{1859}{4104}k_{S4} - \frac{11}{40}k_{S5},\\
E_i - \frac{8}{27}k_{E1} + 2k_{E2} - \frac{3544}{2565}k_{E3} + \frac{1859}{4104}k_{E4} - \frac{11}{40}k_{E5}, I_i - \frac{8}{27}k_{I1}\\
+ 2k_{I2} - \frac{3544}{2565}k_{I3} + \frac{1859}{4104}k_{I4} - \frac{11}{40}k_{I5}\,, R_i - \frac{8}{27}k_{R1} + 2k_{R2}\\
- \frac{3544}{2565}k_{R3} + \frac{1859}{4104}k_{R4} - \frac{11}{40}k_{R5})\\
= h\,(\frac{-\beta}{N_{i6}}\Big(\,I_i - \frac{8}{27}k_{I1} + 2k_{I2} - \frac{3544}{2565}k_{I3} + \frac{1859}{4104}k_{I4} - \frac{11}{40}k_{I5})(S_i\\
- \frac{8}{27}k_{S1} + 2k_{S2} - \frac{3544}{2565}k_{S3} + \frac{1859}{4104}k_{S4} - \frac{11}{40}k_{S5}\Big)\\
- \mu\Big(S_i - \frac{8}{27}k_{S1} + 2k_{S2} - \frac{3544}{2565}k_{S3} + \frac{1859}{4104}k_{S4} - \frac{11}{40}k_{S5}\Big) + rN_{i6}\\
+ \delta\Big(R_i - \frac{8}{27}k_{R1} + 2k_{R2} - \frac{3544}{2565}k_{R3} + \frac{1859}{4104}k_{R4} - \frac{11}{40}k_{R5}\Big)
\end{aligned} \tag{57}
$$

$$
\begin{aligned}
k_{E6} = hf_2\,(t_i + \frac{h}{2}, S_i - \frac{8}{27}k_{S1} + 2k_{S2} - \frac{3544}{2565}k_{S3} + \frac{1859}{4104}k_{S4} - \frac{11}{40}k_{S5},\\
E_i - \frac{8}{27}k_{E1} + 2k_{E2} - \frac{3544}{2565}k_{E3} + \frac{1859}{4104}k_{E4} - \frac{11}{40}k_{E5}, I_i - \frac{8}{27}k_{I1}\\
+ 2k_{I2} - \frac{3544}{2565}k_{I3} + \frac{1859}{4104}k_{I4} - \frac{11}{40}k_{I5}\,, R_i - \frac{8}{27}k_{R1} + 2k_{R2}\\
- \frac{3544}{2565}k_{R3} + \frac{1859}{4104}k_{R4} - \frac{11}{40}k_{R5})\\
= h\,(\frac{\beta}{N_{i6}}(\,I_i - \frac{8}{27}k_{I1} + 2k_{I2} - \frac{3544}{2565}k_{I3} + \frac{1859}{4104}k_{I4} - \frac{11}{40}k_{I5}\,)\,(S_i\\
- \frac{8}{27}k_{S1} + 2k_{S2} - \frac{3544}{2565}k_{S3} + \frac{1859}{4104}k_{S4} - \frac{11}{40}k_{S5}) - (\mu + \sigma + \kappa)(E_i\\
- \frac{8}{27}k_{E1} + 2k_{E2} - \frac{3544}{2565}k_{E3} + \frac{1859}{4104}k_{E4} - \frac{11}{40}k_{E5}))
\end{aligned} \tag{58}
$$

$$
\begin{aligned}
k_{I6} = hf_3\,(t_i + \frac{h}{2}, S_i - \frac{8}{27}k_{S1} + 2k_{S2} - \frac{3544}{2565}k_{S3} + \frac{1859}{4104}k_{S4} - \frac{11}{40}k_{S5},\\
E_i - \frac{8}{27}k_{E1} + 2k_{E2} - \frac{3544}{2565}k_{E3} + \frac{1859}{4104}k_{E4} - \frac{11}{40}k_{E5}, I_i - \frac{8}{27}k_{I1}\\
+ 2k_{I2} - \frac{3544}{2565}k_{I3} + \frac{1859}{4104}k_{I4} - \frac{11}{40}k_{I5}\,, R_i - \frac{8}{27}k_{R1} + 2k_{R2}\\
- \frac{3544}{2565}k_{R3} + \frac{1859}{4104}k_{R4} - \frac{11}{40}k_{R5})\\
= h\;(\sigma\Big(E_i - \frac{8}{27}k_{E1} + 2k_{E2} - \frac{3544}{2565}k_{E3} + \frac{1859}{4104}k_{E4} - \frac{11}{40}k_{E5}\Big) - (\mu\\
+ \alpha + \gamma)\,(I_i - \frac{8}{27}k_{I1} + 2k_{I2} - \frac{3544}{2565}k_{I3} + \frac{1859}{4104}k_{I4} - \frac{11}{40}k_{I5}))
\end{aligned} \tag{59}
$$

$$
\begin{aligned}
k_{I6} = hf_3\,(t_i + \frac{h}{2}, S_i - \frac{8}{27}k_{S1} + 2k_{S2} - \frac{3544}{2565}k_{S3} + \frac{1859}{4104}k_{S4} - \frac{11}{40}k_{S5},\\
E_i - \frac{8}{27}k_{E1} + 2k_{E2} - \frac{3544}{2565}k_{E3} + \frac{1859}{4104}k_{E4} - \frac{11}{40}k_{E5}, I_i - \frac{8}{27}k_{I1}\\
+ 2k_{I2} - \frac{3544}{2565}k_{I3} + \frac{1859}{4104}k_{I4} - \frac{11}{40}k_{I5}\,, R_i - \frac{8}{27}k_{R1} + 2k_{R2}\\
- \frac{3544}{2565}k_{R3} + \frac{1859}{4104}k_{R4} - \frac{11}{40}k_{R5})\\
= h\ (\sigma\left(E_i - \frac{8}{27}k_{E1} + 2k_{E2} - \frac{3544}{2565}k_{E3} + \frac{1859}{4104}k_{E4} - \frac{11}{40}k_{E5}\right) - (\mu\\
+ \alpha + \gamma)\,(I_i - \frac{8}{27}k_{I1} + 2k_{I2} - \frac{3544}{2565}k_{I3} + \frac{1859}{4104}k_{I4} - \frac{11}{40}k_{I5}))
\end{aligned}
\tag{60}
$$

where $i = 0,1,\dots,n-1$.

4. Results and Discussion

Numerical solutions for the nonlinear influenza model in Australia in 1919 are discussed and analyzed in this section. Table 3 is to compare the values of variables $S(t), E(t), I(t), R(t)$ between RK_4 and RK_{45} methods. Where step size h in { 0.5, 0.25, 0.04 } and interval [0,70] days. For $E(t)$ has the smallest value with ($h = 0.04$), every 12 hours during 70 days in the RK_{45} compared with the RK_4. It is clear from Table 3 that RK_{45} method is better than RK_4 method. The Matlab program is used to numerically solve the influenza pandemic model.

Figures 1, 2 describes the influenza epidemic in Australia in 1919. In Figure 1 $(a), (b), (c)$ of RK_4, the curve is high then it starts to decrease after 20 days in the proportion of susceptible population $S(t)$. While the curve is low then it starts to increase then it goes down after 40 days in the proportion of exposed population $E(t)$ and the proportion of infective population $I(t)$, the curve is low then it starts to increase after 20 days in the proportion of recovered population $R(t)$, this means that susceptible population will be infected with influenza epidemics in the coming years. This method is convergence with RK_{45} method was in Figure 2 $(a), (b), (c)$ of RK_{45} , the curve is high then it starts to decrease after 20 days in the proportion of susceptible population $S(t)$. while the curve is low then it starts to increase then it goes down after 40 days in the proportion of exposed population $E(t)$ and the proportion of infective population $I(t)$, the curve is low then it starts to increase after 20 days in the proportion of recovered population $R(t)$, this means that susceptible population will be infected with influenza epidemics in the coming years. These methods are convergent in solution because they are iterative numerical methods. These methods agree with previous studies [1].

Table3: Numerical solution and values of influenza mode

Variable	h/day^{-1}	RK_4	RK_{45}
$S(t)$	0.5	0.59720331	0.59720329
	0.25	0.59715737	0.59715736
	0.04	0.59711877	0.59711877
$E(t)$	0.5	0.00224669	0.00224670
	0.25	0.00224599	0.00224599
	0.04	0.00224539	0.00227205

$I(t)$	0.5	0.00473296	0.00473297
	0.25	0.00473178	0.00473178
	0.04	0.00473076	0.00473076
$R(t)$	0.5	0.38142439	0.38142440
	0.25	0.38146692	0.38146694
	0.04	0.38150269	0.38150269

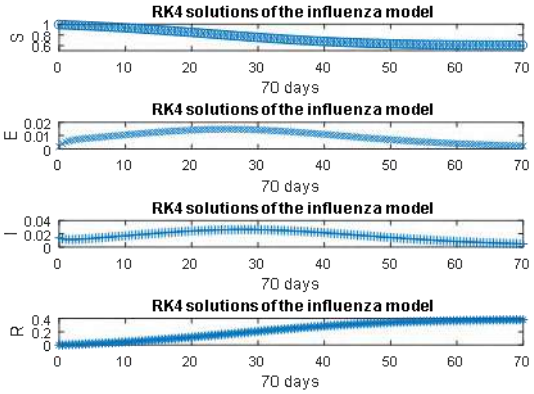

$(a)\ h = 0.5, m = 140$

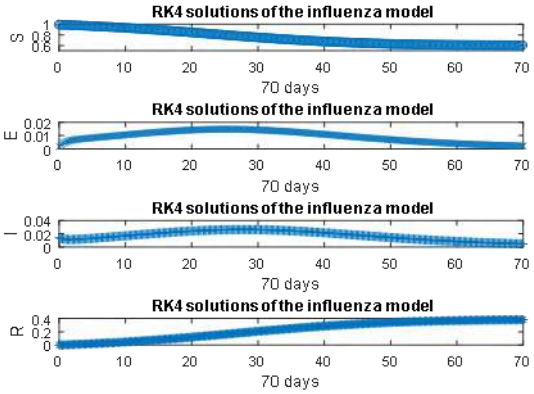

$(b)\ h = 0.25, m = 280$

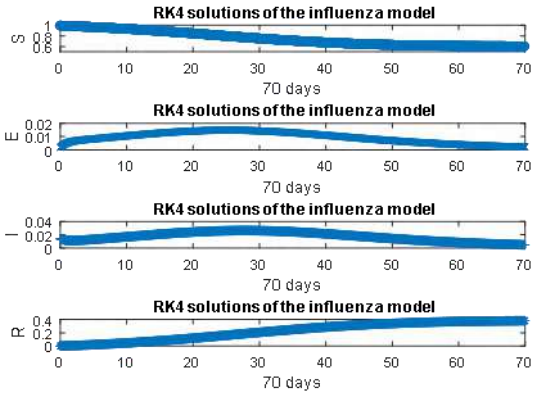

$(c)\ h = 0.04, m = 1750$

Figure 1. Numerical solution of the influenza model around the value of parameters using RK_4 of $S(t), E(t), I(t), R(t)$ in 1919 when step size $h = 0.5, 0.25, 0.04$, iterations $m = 140, 280, 1750$.

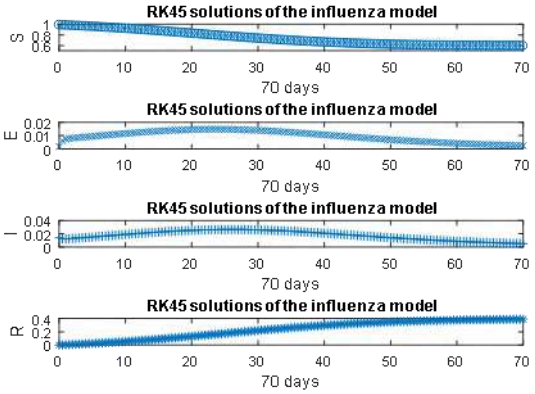

$(a)\ h = 0.5, m = 140$

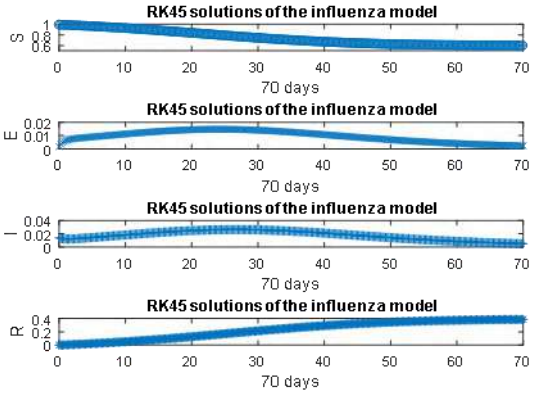

$(b)\ h = 0.25, m = 280$

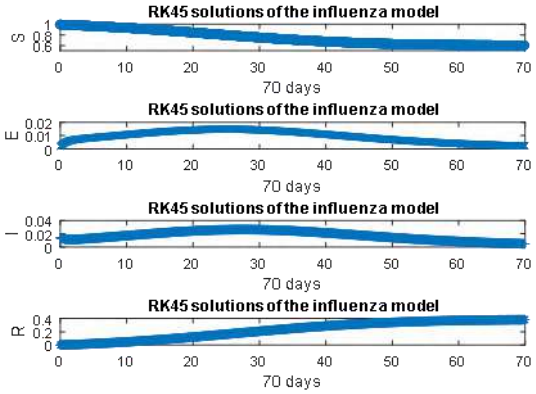

$(c)\ h = 0.04, m = 1750$

Figure 2. Numerical solution of the influenza model around the value of parameters using RK_{45} of $S(t), E(t), I(t), R(t)$ in 1919 when step size $h = 0.5, 0.25, 0.04$, iteration $m = 140, 280, 1750$.

Conclusion

In the current study, some reliable, accurate, and approximate methods are used for solving a nonlinear system of epidemic models for ordinary differential equations of the first order. There is a convergence in the results of the numerical methods which are Runge-Kutta of order 4 and of order 45 as shown in Table 3. The numerical methods RK_4 and RK_{45} help us to analyze the spread of the epidemic in the influenza model. The results obtained showed that individual $S(t)$ of the proportion of the susceptible population, individual $E(t)$ of the proportion of the exposed population, and individual $I(t)$ of the proportion of the infective population are gradually decreased to 70 days. While individual $R(t)$ the proportion of the recovered population gradually increased until. A MATLAB program has been helped to solve this problem.

References

[1] Samsuzzoha M, Singh M and Lucy D 2013 Parameter estimation of influenza epidemic model *Applied Mathematics and Computation* **220** 616-629
[2] Influenza C S 2013 Key Facts about Influenza (Flu) and Flu Vaccine *Centers for Disease Control and Prevention* **13**

[3] Brankston G et al 2007 Transmission of influenza A in human beings *The Lancet infectious diseases* **7 (4)** 257-265
[4] Dávila-Torres, J et al 2015 Intense seasonal A/H1N1 influenza in Mexico, winter 2013–2014 *Archives of medical research* **46 (1)** 63-70
[5] Seynaeve G 2009 Influenza pandemic: a perspective *Prehospital and disaster medicine* **24 (6)** 473-477
[6] Silva M E et al 1999 Acute fever and petechial rash associated with influenza A virus infection *Clinical infectious diseases* **29 (2)** 453-454
[7] Sabaa M A, Mohammed M A and Abd Almjeed S H 2019 Approximate Solutions for Alcohol Consumption Model in Spain *Ibn AL-Haitham Journal For Pure and Applied Science* **32 (3)** 153-164
[8] Sabaa M A and Mohammed M A 2020 Approximate Solutions of Nonlinear Smoking Habit Model *Iraqi Journal of Science* **61 (2)** 435-443
[9] El-Shahed M and Alsaedi A 2011 The fractional SIRC model and influenza A *Mathematical problems in Engineering* **2011**
[10] Shaman J and Karspeck A 2012 Forecasting seasonal outbreaks of influenza *Proceedings of the National Academy of Sciences* **109 (50)** 20425-20430
[11] Reynolds J J, Torremorell M and Craft M E 2014 Mathematical modeling of influenza A virus dynamics within swine farms and the effects of vaccination *PloS one* **99 (8)**
[12] Jódar L and et al 2008 Nonstandard numerical methods for a mathematical model for influenza disease *Mathematics and Computers in simulation* **79 (3)** 622-633
[13] Zarebski A E et al 2017 Model selection for seasonal influenza forecasting *Infectious Disease Modelling* **2(1)** 56-70
[14] Kim S, Lee J and Jung E 2017 Mathematical model of transmission dynamics and optimal control strategies for 2009 A/H1N1 influenza in the Republic of Kore *Journal of theoretical biology* **412** 74-85
[15] Hu F, Hussaini M Y and J Manthey 1996 Low-dissipation and low-dispersion Runge–Kutta schemes for computational acoustics *Journal of computational physics* **124 (1)** 177-191
[16] Van Belle G et al 2004 Biostatistics: a methodology for the health sciences *John Wiley & Sons* **519**
[17] Panovska-Griffiths J 2019 Can mathematical modelling solve the current Covid-19 crisis (Springer)
[18] Bronson R 2012 Schaum's Easy Outlines: Differential Equations (McGraw-Hill)
[19] Asai Y 2016 Numerical Methods for Random Ordinary Differential Equations and Their Applications in Biology and Medicine (Verlag nicht ermittelbar)
[20] Runge C 1895 Über die numerische Auflösung von Differentialgleichungen *Mathematische Annalen* **46 (2)** 167-178
[21] Chauhan V and Srivastava P 2019 Computational Techniques Based on Runge-Kutta Method of Various Order and Type for Solving Differential Equations *International Journal of Mathematical Engineering and Management Sciences* **4 (2)** 375-386
[22] Tay K G, et al 2015 The Fourth Order Runge-Kutta Spreadsheet Calculator Using VBA Programing for Ordinary Differential Equations *Procedia Soc. Behav. Sci* **204** 231-239
[23] Mathews J H and Fink K D 2004 Numerical methods using MATLAB *Pearson prentice hall Upper Saddle River NJ* **4**

Common Fixed Point and invariant Approximations for C_q-Commuting Mappings in P-Normed Spaces

Common Fixed Point and invariant Approximations for C_q-Commuting Mappings in P-Normed Spaces

Yusra Jarallah Ajeel [1] and Osamah Hadi Mutlag[2]

[1] Department of Mathematics, College of Science, Al-Mustansiriyah University, Baghdad, Iraq
[2] Department of Remote Sensing and GIS Science, College of Science, University of Baghdad, Iraq

E-mail: Ysrajara@yahoo.com

Abstract. The purpose of this paper is to prove a common fixed point(c.f.p) theorems by using conditiond $\big(S(x),T(y)\big) \le \ell \max\{d\big(h(x),G(y)\big),d\big(h(x),S(x)\big),d\big(G(y),T(y)\big),$ $d\big(h(x),T(y)\big),d\big(G(y),S(x)\big)\}$ For two pairs of mappings in p-normed space(p-n.s) and also obtain the best approximation (b.a) result. In the last part of this paper, it is proved that the fixed point (f.p) problem for these mappings is well-posed (w-p).

1. Introduction

c.f.p theorems for generalized affine mapping and a class of I-non expansive non commuting mappings were proved by Nashine and Dewangan [9]. Cho, Hussain, and Pathak [3] c.f.p theorems and b.a results in normed linear spaces are proved.

In 2013, Bari and Vetro [2] proved some c.f.p and coincidence point results for three or four mappings. Further, Singh [11] proved the c.f.p theorem for multivalued mappings generalized.

In 2017 AL-saidy, Abed, and Ajeel [1] proved three common random f.p theorems for commuting random operators defined on a non-starshaped subset of a p-n.s X. In this research, some c.f.p theorems for two pairs mappings defined on non-star-shaped domain subset of a p-n.s are proved.

2. Preliminaries

We need the following definitions and facts:

Definition (2.1): Let X be a linear space and $\|\ \|_p$ be a real-valued function on X with $0 < p \le 1$. The pair (X, $\|\ \|_p$) is called a p-n.s if for all a, b in X and scalars ζ:

i. $\|a\|_p \ge 0$ and $\|a\|_p = 0$ iff $a = 0$
ii. $\|\zeta a\|_p = |\zeta|^p \|a\|_p$
iii. $\|a+b\|_p \le \|a\|_p + \|b\|_p$

Every p-normed space X induces a metric space with $(a,b) = \|a-b\|_p$, for all a, b in X. If $p = 1$, we have the concept of a normed space [5]. Since a p-n.s is not necessarily locally convex space and the continuous dual $X`$ of p-normed space, X need not separate the point of X [7].

Example (2.1):
Let $X = R^3$ with$\|(a_1, a_2, a_3)\|_p = \sum_{i=1}^{3} |a_i|^p$ (|.| is the absolute value), for any pair (a_1, a_2, a_3) in X and $0 < p \leq 1$, then X is p-normed space since it is satisfying all conditions of definition (2.1).

Definition (2.2):[12]: Let X be a metric space, A subset A of X is called starshaped if there exist at least one point $q \in A$ such that
[a,q]$= \lambda a + (1 - \lambda)q \in A,$ for all $a \in A$ and $0 \leq \lambda \leq 1$. In this case, q is said the starcenter of A.

Definition (2.3): [15]: A self-mapping h of a linear space X is said to be affine if for all a, b in X and for any ζ, $0 \leq \zeta \leq 1$, $h\ [\zeta a + (1 - \zeta)\ b] = \zeta\ h(a) + (1 - \zeta)\ h(b)$.
And h is called q-affine if there is $q \in X$ such that $h[\zeta a + (1 - \zeta)q] = \zeta h(a) + (1 - \zeta)q$, for all $\zeta \in [0,1]$ and all $\in X$.

Definition (2.4): [10]: Let $A \neq \emptyset$ subset of a p-n.s X. The set of b.a to $a_\circ \in X$, denoted as $p_A(a_\circ)$ is defined by
$p_A(a_\circ) = \{y \in A: \| a_\circ - y \|_p : dist(a_\circ, A)\}$, where
$dist(a_\circ, A) = \inf\{\| a_\circ - a \|_p : a \in A\}$.

Definition (2.5): Let $A \neq \emptyset$ subset of a metric space X and let S and T be self-mappings of A. A point $a \in A$ is a c.f (coincidence(c)) point of S and T if $Sx = Tx = x$ $(Sx = Tx)$[14]. The set of c.f.p of S and T is denoted by $F(S,T)$, the set of c.p of S and T is denoted by $C(S,T)$ and the closure of the set A is denoted by $Cl(A)$.
A mapping $S: A \to A$ is called:
(1) Hemi-compact [4] if any sequence $\{x_n\}$ in A has a convergent subsequence whenever $d(x_n, S(x_n)) \to 0$ as $n \to \infty$;
(2) completely continuous [4] if $\{x_n\}$ weakly converges to a which implies that $\{S(x_n)\}$ converges strongly to$S(a)$;
(3) Demi-closed at x, if for every sequence $\{x_n\}$ in A such that $\{x_n\}$ converges weakly to x and $\{S(x_n)\}$ converges strongly to y , we have $S(x) = y$ [8].
The pair (S,T) is said to be
(1) R-weakly commuting mappings [4] if $\forall a \in A$, $\exists \Re > 0$ such that $d(STa, TSa) < \Re d(Sa, Ta)$, if $\Re$ =1, then the mappings is said weakly commuting.
(2) R-weakly compatible [13] if they commute at their coincidence points, that is, $STa = TSa$ whenever $Sa = Ta$.
(3) C_q–commuting [4] if $STa = TSa$ for all $a \in C_q(S,T)$, where $C_q(S,T) = \cup \{C(S,T_k): 0 \leq k \leq 1\}$ and $T_k(a) = (1 - k)q + kT(a)$.

Definition (2.6): Let X a p-normed space, $A \subseteq X$, $\mathfrak{H}: X \to X$ be a mapping we say that A has property (a_1) if
i. $\mathfrak{H} : A \to A$
ii. $(1 - k_n)q + k_n \mathfrak{H}(x) \in A$, for some q ∈ A and a fixed real sequence $< k_n >$ converging to 1 and for each $x \in A$.

Remark(2.1): Any q-starshaped set has the property (a_1) w.r.t any mapping $\mathfrak{H}: A \to A$, but the converse is not true in general.

Definition (2.7): Let X be a p-normed space, $A \subseteq X$ and A has property (a_1) w.r.t a mapping $G: X \to X$, q ∈ A, and sequence $< k_n >$. A mapping$h$: $X \to X$ is called have the property (a_2) on A with property (a_1) if $h\big((1 - k_n)q + k_n\ G(x)\big)$= (1-$k_n$) $h(q)$+$k_n h(G(x))$ for all $x \in A$ and $n \in N$.

in this paper we need the following theorems:

Theorem (2.1)[6]: Let $\emptyset \neq A \subseteq X$, with $S, T, h, G: A \longrightarrow A$ such that $\forall x, y \in A$ and $0 \leq \ell < \frac{1}{2}$, the pair (S, T) satisfy the following condition

$$d\big(S(x), T(y)\big) \leq \ell \max\{d\big(h(x), G(y)\big), d\big(h(x), S(x)\big), d\big(G(y), T(y)\big) d\big(h(x), T(y)\big), d\big(G(y), S(x)\big)\} \quad (2\text{-}1)$$

If $Cl\big(S(A)\big) \subseteq G(A), Cl\big(T(A)\big) \subseteq h(A)$ and one of the subsets $Cl\big(S(A)\big), Cl\big(T(A)\big), CL\big(h(A)\big)$ or $Cl\big(G(A)\big)$ is complete, then $C(S, h) \neq \emptyset$ and $C(T, G) \neq \emptyset$.

Theorem (2.2)[6]: Let $X, A, S, T, G, h, Cl\big(S(A)\big), Cl\big(T(A)\big), CL\big(h(A)\big)$ and $Cl\big(G(A)\big)$ as in theorem (2.1). If the pairs $\{S, h\}$ and $\{T, G\}$ are weakly compatible (or R-weakly commuting), then $F(S) \cap F(h) \cap F(T) \cap F(G) \neq \emptyset$.

3- Main result

Now, by using Theorem (2.1) and Theorem (2.2) [6] we show the following:

Theorem (3.1): Let S, T, h, and G be self-maps on a subset A of a p-normed space X suppose that $cl(S(A)) \subseteq G(A), cl\big(T(A)\big) \subseteq h(A), q \in F(h) \cap F(G)$, and h and G has property (a_2). Suppose that the pairs $\{S, h\}$ and $\{T, G\}$ are C_q-commuting and satisfy

$$\|S(a) - T(b)\|_p \leq k\, max\begin{Bmatrix} \|h(a) - G(b)\|_p, dist(h(a), [q, S(a)]), \\ \text{dist}(G(b), [q, T(b)]), \text{dist}(h(a), [q, T(b)]), \text{dist}(G(b), [q, S(a)]) \end{Bmatrix} \quad (3\text{-}1)$$

For all $a, b \in A$ and $0 \leq k < \frac{1}{2}$. If S and T are continuous and A has property (a_1) with respect to S and , then $F(S) \cap F(T) \cap F(h) \cap F(G) \neq \emptyset$, if one of the following conditions is satisfied:

i. $Cl\big(S(A)\big)$ and $Cl\big(T(A)\big)$ are compact and h and G are continuous;

ii. A is complete, $F(h)$ and $F(G)$ are bounded, and S and T are compact maps;

iii. A is bounded and complete, S and T are hemicompact, and h and G are continuous;

iv. A is weakly compact, X is complete, $h - S$ and $G - T$ are demiclosed at 0, and h and G are weakly continuous.

v. X is complete, A is weakly compact, S and T are completely continuous, and h and G are continuous.

Prof: Define $S_n: A \to A$ and $T_n: A \to A$ by $S_n(a) = (1 - k_n)q + k_n S(a)$ and $T_n(a) = (1 - k_n)q + k_n T(a)$ and a fixed sequence of real numbers k_n $(0 \leq k_n \leq 1)$ Converging to 1, for some $q \in A$ and all $a \in A$. Since A has property (a_1) with respect to S and T, $cl(S(A)) \subseteq G(A), cl\big(T(A)\big) \subseteq h(A), q \in F(h) \cap F(G)$, and h and G has property (a_2). Then for each n, $Cl\big(S_n(A)\big) \subseteq G(A)$ and$Cl\big(T_n(A)\big) \subseteq h(A)$. As the pairs $\{S, h\}$ and $\{T, G\}$ are C_q-commuting and h and G has property (a_2), with $q \in F(h) \cap F(G)$, then for each $a \in C_q(S, h) \cap C_q(T, G)$,

$$h(S_n(a)) = h\big((1 - k_n)q + k_n S(a)\big) = (1 - k_n)h(q) + k_n h(S(a)) = (1 - k_n)q + k_n S(h(a)) = S_n(h(a))$$

By similarly away we can show that $G(T_n(a)) = T_n(G(a))$ thus,

$h(S_n(a)) = S_n(h(a))$ and $G(T_n(a)) = T_n(G(a))$ for each $a \in C(S_n, h) \subseteq C_q(S, h)$ and $a \in C(T_n, G) \subseteq C_q(T_n, G)$. Hence the pairs $\{S_n, h\}$ and $\{T_n, G\}$ are weakly compatible ∀n. Also by (3.1),

$$\|S_n(a)-T_n(b)\|_p \le |k_n|^p \|S(a)-T(b)\|_p \le \|S(a)-T(b)\|_p$$
$$\le k\ max\left\{\begin{matrix}\|h(a)-G(b)\|_p, dist(h(a),[q,S(a)]),\\ \text{dist}(G(b),[q,T(b)]), \text{dist}(h(a),[q,T(b)]), \text{dist}(G(b),[q,S(a)])\end{matrix}\right\}$$
$$\le k\ max\left\{\begin{matrix}\|h(a)-G(b)\|_p, \|h(a)-S_n(a)\|_p,\\ \text{d}\|G(b)-T_n(b)\|_p, \|h(a)-T_n(b)\|_p, \|G(b)-S_n(a)\|_p\end{matrix}\right\}$$

For all $a, b \in A$.

i. Since $Cl(S(A))$ and $Cl(T(A))$ are compact, then $Cl(S_n(A))$ and $Cl(T_n(A))$ are also compact, Hence all conditions of theorem (2.2) are satisfied on the mappings S_n, T_n, h and G, therefore $\exists a_n \in A$ s.t $a_n = S_n(a_n) = T_n(a_n) = h(a_n) = G(a_n)$.Since $Cl(S(A))$ and $Cl(T(A))$ are compact , $\{S(a_n)\}$ and $\{T(a_n)\}$ sequence in $S(A)$ and $T(A)$ (respectively) , $S(A) \subseteq Cl(S(A))$ and $T(A) \subseteq Cl(T(A))$ implies that, there exists a subsequence $\{S(a_m)\}$ of $\{S(a_n)\}$ and $\{T(a_m)\}$ of $\{T(a_n)\}$ s.t $\lim_{m\to\infty} S(a_m) = \lim_{m\to\infty} T(a_m) = b$ .Since $a_m = S_n(a_m) = (1-k_m)q + k_m S(a_m)$ and $a_m = T_n(a_m) = (1-k_m)q + k_m T(a_m)$. We have $\lim_{m\to\infty} a_m = b$, hence by the continuity of h and G having $b \in F(S) \cap F(T) \cap F(h) \cap F(G) \neq \emptyset$. Therefore $b \in F(S) \cap F(T) \cap F(h) \cap F(G) \neq \emptyset$.

ii. As in (i), there exists $a_n \in A$ s.t $a_n = S_n(a_n) = T_n(a_n) = h(a_n) = G(a_n)$. Since S and T are compact and $\{a_n\}$ being in $F(h)$ and $F(G)$ are bounded, so there exists a subsequence $\{S(a_m)\}$ of $\{S(a_n)\}$ and $\{T(a_m)\}$ of $\{T(a_n)\}$ such that $\lim_{m\to\infty} S(a_m) = \lim_{m\to\infty} T(a_m) = b$. the definition of $S_m(a_m)$ and $T_m(a_m) \Rightarrow \lim_{m\to\infty} a_m = b$, the continuity of S, T, h and G having $b \in F(S) \cap F(T) \cap F(h) \cap F(G)$.Thus $F(S) \cap F(T) \cap F(h) \cap F(G) \neq \emptyset$.

iii. As in (i), $\exists a_n \in A$ s.t $a_n = S_n(a_n) = T_n(a_n) = h(a_n) = G(a_n)$, and A is bounded, so $a_n - S(a_n) = (1-k_n)(S(a_n) - q) \to 0$ and $a_n - T(a_n) = (1-k_n)(T(a_n) - q) \to 0$ as $n \to \infty$. The hemicompact of S and T implies that has $\{a_n\}$ a subsequence $\{a_m\}$ such that $\lim_{m\to\infty} a_m = b$ the continuity of S, T, h and G implies that $b \in F(S) \cap F(T) \cap F(h) \cap F(G)$. Hence $F(S) \cap F(T) \cap F(h) \cap F(G) \neq \emptyset$.

iv. As in (i), $\exists a_n \in A$ s.t $a_n = S_n(a_n) = T_n(a_n) = h(a_n) = G(a_n)$. Since A is weakly compact, then $\exists$ a subsequence $\{a_m\}$ of $\{a_n\}$ in A converging weakly to b as $m \to \infty$, from weakly continuous of h and G we have $b = h(b) = G(b)$. By (iii) $h(a_m) - S(a_m)$ and $G(a_m) - T(a_m)$converging to 0 as $m \to \infty$. The demi-closedness of $h - S$ and $G - T$ at 0 $\Rightarrow S(b) = T(b) = h(b) = G(b)$. Thus $F(S) \cap F(T) \cap F(h) \cap F(G) \neq \emptyset$.

v. As in (iv) there is a subsequence $\{a_m\}$ of $\{a_n\}$ in A converging weakly to b as $m \to \infty$. by S and T are completely continuous, then $S(a_m) \to S(b)$ and $T(a_m) \to T(b)$ as $m \to \infty$. Since $k_n \to 1$ and $a_m = S_m(a_m) = T_m(a_m) = (1-k_m)q + k_m S(a_m) = (1-k_m)q + k_m T(a_m)$, therefore $a_m \to S(b) = T(b)$ as $m \to \infty \Rightarrow S(a_m) \to S(S(b))$ and $T(a_m) \to T(T(b))$ as $m \to \infty$, but $S(a_m) \to S(b)$ and $T(a_m) \to T(b)$ as $m \to \infty$ therefore $S(b) = S(S(b))$ and $T(b) = T(T(b))$, since $S(b) = T(b)$, then $S(b) = S(S(b)) = T(b) = T(T(b))$, implies that $c = S(c) = T(c)$, where $c = T(b) = S(b)$. Also, since $a_m \to c$ as $m \to \infty$ and h and G are continuous mappings then $c = h(c) = G(c)$. Therefore $F(S) \cap F(T) \cap F(h) \cap F(G) \neq \emptyset$.

Theorem(3.2): Let $\emptyset \neq A \subseteq X$ and $S, T, h, G: X \to X$ be mappings s.t $a_\circ \in F(S) \cap F(T) \cap F(h) \cap F(G)$ for some $a_\circ \in X, S(\partial A \cap A) \subseteq A$ and $T(\partial A \cap A) \subseteq A$. Assume that $h(p_A(a_\circ)) = G(P_A(a_\circ)) = P_A(a_\circ)$ and the pairs $\{S, h\}$ and $\{T, G\}$ are C_q-commuting and continuous on $P_A(a_\circ)$ and satisfies for all $x \in P_A(a_\circ) \cup \{a_\circ\}$,

$$\|S(a)-T(b)\|_p$$
$$\le \begin{cases} \|h(a)-G(b)\|_p \quad if\ b = a_\circ, \\ max\left\{\begin{matrix}\|h(a)-G(b)\|_p, dist(h(a),[q,S(a)]),\\ dist(G(b),[q,T(b)]), dist(h(a),[q,T(b)]), dist(G(b),[q,S(a)])\end{matrix}\right\} \end{cases} \quad (3\text{-}2)$$

$if\ b \in P_A(a_\circ)$

Suppose that $P_A(a_\circ)$ is closed, has property (a_1). with respect to S and T with $q \in F(h) \cap F(G)$ and h and G has property (a_2). then $P_A(a_\circ) \cap F(S) \cap F(T) \cap F(h) \cap F(G) \neq \emptyset$ if one of the following conditions is satisfied:

i. $Cl\left(S\left(P_A(a_\circ)\right)\right)$ and $Cl\left(T\left(P_A(a_\circ)\right)\right)$ are compact and h and G are continuous.
ii. $P_A(a_\circ)$ is complete, $F(h)$ and $F(G)$ are bounded, and S and T are compact maps.
iii. $P_A(a_\circ)$ is bounded and complete, S and T are hemicompact, and h and G are continuous.
iv. $P_A(a_\circ)$ is weakly compact, X is complete, $h - S$ and $G - T$ are demiclosed at o, h, and G are weakly continuous.
v. X is complete, $P_A(a_\circ)$ is weakly compact, S and T are completely continuous, and h and G are continuous.

Proof: Let $a \in P_A(a_\circ)$, then $\|a - a_\circ\|_p = dist(a_\circ, A)$.
Note that
$0 < k < 1, \|ka_\circ - (1-k)a - a_\circ\|_p = (1-k)^p \|a - a_\circ\|_p < dist(a_\circ, A)$
Hence the line segment $\{ka_\circ - (1-k)a: 0 < k < 1\}$ and the set A are disjoint. Therefore $a \notin int(A)$ and so $a \in \partial A$.
Since $S(\partial A \cap A) \subseteq A$ and $T(\partial A \cap A) \subseteq A$, then $S(a) \in A$ and $T(a) \in A$.
Also, since $h\left(p_A(a_\circ)\right) = G\left(P_A(a_\circ)\right) = P_A(a_\circ)$,
$a_\circ = h(a_\circ) = G(a_\circ) = S(a_\circ) = T(a_\circ)$ and by using condition (3.2), we have
$\|S(a) - a_\circ\|_p = \|S(a) - T(a_\circ)\|_p \leq \|h(a) - G(a_\circ)\|_p \quad = \|h(a) - a_\circ\|_p \quad = dist(a_\circ, A)$
And $\|T(a) - a_\circ\|_p = \|S(a) - T(a_\circ)\|_p \leq \|h(a) - G(a_\circ)\|_p = \|h(a) - a_\circ\|_p \quad = dist(a_\circ, A)$
Therefore $S, T: P_A(a_\circ) \to P_A(a_\circ)$
Since $P_A(a_\circ)$is closed set then $Cl\left(P_A(a_\circ)\right) = P_A(a_\circ)$, and since
$S\left(P_A(a_\circ)\right) \subseteq P_A(a_\circ) = Cl\left(P_A(a_\circ)\right)$, this implies $cl(S(P_A(a_\circ))) \subseteq G\left(P_A(a_\circ)\right)$
In a similar way $cl(T(P_A(a_\circ))) \subseteq h\left(P_A(a_\circ)\right)$, hence the result go ahead of theorem (3.1).

4- Well-posed Problem

Definition (4.1): Let $(X, \| \quad \|_p)$ be a p-normed space and $T: X \longrightarrow X$ a mapping, the f.p problem of T is said to be well-posed if:

i. T has a unique f.p $a_\circ \in X$;
ii. $\forall$ sequence $\{a_n\}$ in X such that $\lim_{n\to\infty} \|T(a_n) - a_n\|_p = 0$, we have $\lim_{n\to\infty} \|a_n - a_\circ\|_p = 0$.

Definition (4.2): Let $(X, \| \quad \|_p)$ be a p-n.s and let $\mathcal{T}$ be a set of mappings in X. The f.p of $\mathcal{T}$ is said to be w-p if:
$\mathcal{T}$ have a unique f.p $a_\circ \in X$;
for any sequence $\{a_n\}$ of in X such that $\lim_{n\to\infty} \|T(a_n) - a_n\|_p = 0, \forall\ T \in \mathcal{T}$ we have $\lim_{n\to\infty} \|a_n - a_\circ\|_p = 0$.

Theorem (4.1): If $X, A, S, T, G, h, Cl\left(S(A)\right), Cl\left(T(A)\right), CL\left(h(A)\right)$ and $Cl\left(G(A)\right)$ as in theorem (2.2), then the c.f.p for the set mappings $\{S, T, h, G\}$ is w-p.

Proof: By theorem (2.2), the mappings $S, T, h,$ and G have a unique c.f.p b such that

$$S(b) = T(b) = h(b) = G(b) = b \tag{4-1}$$

Let $\{a_n\}$ be a sequence in A such that
$\lim_{n\to\infty} \|S(a_n) - a_n)\|_p = \lim_{n\to\infty} \|T(a_n) - a_n)\|_p = \lim_{n\to\infty} \|h(a_n) - a_n)\|_p = \lim_{n\to\infty} \|G(a_n) - a_n)\|_p = 0$
By the triangle inequality, $b = S(b)$,(2.1) and (4.1) having

$$\begin{aligned}
\|b-a_n\|_p &\le \|b-T(a_n)\|_p + \|T(a_n)-a_n\|_p = \|S(b)-T(a_n)\|_p + \|T(a_n)-a_n\|_p \\
&\le k\ max\begin{Bmatrix} \|h(b)-G(a_n)\|_p, \big(h(b),S(b)\big), \\ \|G(a_n)-T(a_n)\|_p, \|h(b)-T(a_n)\|_p, \|G(a_n),S(b)\|_p \end{Bmatrix} \\
&+ \|T(a_n)-a_n\|_p \\
&\le k\ max\begin{Bmatrix} \|h(b)-G(a_n)\|_p, \|h(b)-S(b)\|_p, \\ \|G(a_n)-T(a_n)\|_p, \|h(b)-T(a_n)\|_p, \|G(a_n)-S(b)\|_p \end{Bmatrix} \\
&+ \|T(a_n)-a_n\|_p \\
&= k\ max\{\|b-G(a_n)\|_p, \|G(a_n)-T(a_n)\|_p, \|b-T(a_n)\|_p\} + \|T(a_n)-a_n\|_p \\
&\le k\ max\{\|b-G(a_n)\|_p, \|G(a_n)-b\|_p + \|b-T(a_n)\|_p, \|b\ -T(a_n)\|\} \\
&+ \|T(a_n)-a_n\|_p = k\ \|G(a_n)-b\|_p + k\|b-T(a_n)\|_p + \|T(a_n)-a_n\|_p \\
&\le k\|G(a_n)-a_n\|_p + k\|a_n-b\|_p + k\|b-a_n\|_p + k\|a_n-T(a_n)\|_p \\
&+ \|T(a_n)-a_n\|_p \\
&= k\|G(a_n)-a_n\|_p + 2k\|a_n-b\|_p + (1+k)\|T(a_n)-a_n\|_p\ (1-2k)\|a_n-b\|_p \\
&\le k\|G(a_n)-a_n\|_p + (1+k)\|T(a_n)-a_n\|_p
\end{aligned}$$

Thus we have, $\lim_{n\to\infty}\|a_n-b\|_p = 0$, hence c.f.p for the mappings $\{S,T,h,G\}$ is w-p.

Theorem (4.2): If A, X, S, T, h and G as in theorem (3.1), then the c.f.p for the mappings $\{S,T,h,G\}$ is well posed.

Proof: By theorem (3.1), the mappings $S,T,h,$ and G has a unique common fixed point b.
Let $\{a_n\}$ sequence in A s.t $\lim_{n\to\infty}\|S(a_n)-a_n)\|_p = \lim_{n\to\infty}\|T(a_n)-a_n)\|_p = \lim_{n\to\infty}\|h(a_n)-a_n)\|_p = \lim_{n\to\infty}\|G(a_n)-a_n)\|_p = 0$
By the triangle inequality, $S(b)=b$, (2.2) and (4.1) we have:

$$\begin{aligned}
\|b-a_n\|_p &\le \|b-T(a_n)\|_p + \|T(a_n)-a_n\|_p \|b-a_n\|_p = \|S(b)-T(a_n)\|_p + \|T(a_n)-a_n\|_p \\
&\le k\ max\begin{Bmatrix} \|h(b)-G(a_n)\|_p, dist(h(b),[q,S(b)]), \\ dist(G(a_n),[q,T(a_n)]), dist(h(b),[q,T(a_n)]), dist(G(a_n),[q,S(b)]) \end{Bmatrix} \\
&+ \|T(a_n)-a_n\|_p \\
&\le k\ max\begin{Bmatrix} \|h(b)-G(a_n)\|_p, \|h(b)-S(b)\|_p, \\ \|G(a_n)-T(a_n)\|_p, \|h(b)-T(a_n)\|_p, \|G(a_n)-S(b)\|_p \end{Bmatrix} \\
&+ \|T(a_n)-a_n\|_p \\
&= k\ max\{\|b-G(a_n)\|_p, \|G(a_n)-T(a_n)\|_p, \|b-T(a_n)\|_p\} + \|T(a_n)-a_n\|_p \\
&\le k\ max\{\|b-G(a_n)\|_p, \|G(a_n)-b\|_p + \|b-T(a_n)\|_p, \|b\ -T(a_n)\|\} \\
&+ \|T(a_n)-a_n\|_p = k\ \|G(a_n)-b\|_p + k\|b-T(a_n)\|_p + \|T(a_n)-a_n\|_p \\
&\le k\|G(a_n)-a_n\|_p + k\|a_n-b\|_p + k\|b-a_n\|_p + k\|a_n-T(a_n)\|_p \\
&+ \|T(a_n)-a_n\|_p \\
&= k\|G(a_n)-a_n\|_p + 2k\|a_n-b\|_p + (1+k)\|T(a_n)-a_n\|_p(1-2k)\|a_n-b\|_p \\
&\le k\|G(a_n)-a_n\|_p + (1+k)\|T(a_n)-a_n\|_p
\end{aligned}$$

Thus we have, $\lim_{n\to\infty}\|a_n-b\|_p = 0$, having the c.f.p for the mappings $\{S,T,h,G\}$ is w-p.

References

[1] Alsaidy S K, Abed S S and Ajeel Y J 2017 Common Random Fixed Points of commuting Random Operators *J.College of Education* **1**(1) 193-208
[2] Di Bari C and Vetro P 2013 Common fixed points for three or four mappings via common fixed point for two mappings *arXiv preprint arXiv* 1302.3816

[3] ChoY J, Hussin N and Pathak H K 2011 Approximation of Nearest Common Fixed Points of Asymptotically I-Nonexpansive Mappings in Banach Spaces *Common. Korean Math. Soc*. **26**(3) 183-198
[4] Hussain N and Rhoades B E 2016 C_q –commuting maps and invariant approximations *J. Fixed Point Theory And Application* **2006** 1-9
[5] Itoh S 1979 Random fixed point theorems with an applications to random differential equations in Banach spaces *J. Math. Anal. Appl.* **67** 261-273
[6] Ajeel Y J and Kadhim S N Some Common Fixed Points Theorems 0f Four Weakly Compatible Mappings in Metric Spaces *To Appear in Baghdad Science Journal*
[7] Kumam P and Plubtieng S 2006 Random fixed points theorem for multivalued nonexpansive operators in uniformly nonsquare Banach spaces *Random Oper.Stoch.Equ.***14** 35-44
[8] Latif A 2001 A Result on Best Approximation in p-Normed Spaces *Arch. Math. (Brno)* **37** 71-75
[9] Nashine H K and Dewangan C L 2008 Common Fixed Points Forgeneralized Affine and Subcompatible Mappings With Application *Mathematica Moravica* **12**(1) 25-36
[10] Nashine H K 2008 Random fixed points and invariant random approximation in non-convex domains *Hacettepe J.Math.Stat.* **37**(2) 81-88
[11] Singh P R A Common Fixed Point Theorem for Contractive Muktivalued Mappings *Int. J. Contemp. Math. Sciences* **9**(6) 253-256
[12] Singh S P, Watson B and Srivastava P 1997 Fixed point theory and best approximation:The KKM-Map Principle (Kluwer Academic Publishers) **424**
[13] Tomar A and Upadhyay S 2017 Coincidence and common fixed point theorems for faintly compatible maps *J.App.Eng.Math.* **7**(1) 25-32
[14] Tomar A and Sharma, R 2018 Some coincidence and common fixed point theorems concerning F-contraction and applications *J. International mathematical virtual institute* **8** 181-198
[15] Zeidler E 1986 Non Linear Functional Analysis and Applications, I. Fixed Point Theorems (Springer Verlage, New York, Inc,)

A New Algorithm to Estimate the Parameters of Nonlinear Regression

A New Algorithm to Estimate the Parameters of Nonlinear Regression

Zaid Adil Abd alkreem and Bayda Atiya Kalaf

Department of Mathematics, College of Education (Ibn Al – Haitham), University of Baghdad, Iraq

E-mail: baydaa.a.k@ihcoedu.uobaghdad.edu.iq

Abstract. The procedures to estimate the parameters are important in many scientific fields that are required to develop mathematical models. Thus, this paper is proposed as a Gravitational Search algorithm for estimating the parameters of nonlinear regression models. Also, a simulation study is conducted to investigate the performance of the proposed methods in this paper. The results show that GSA approach provides accurate estimates and is satisfactory for the parameter estimation of the nonlinear regression models.

1. Introduction

Nonlinear Regression Analysis (NLRA) was one of the most widely used accurate statistical steps that explain the relationship between two variables or more [1]. The common form of a regression model is $y = f(x, \beta) + \varepsilon$. Which y is the dependent variable, *x* is an independent vector variable(s), β is a vector of the parameter (s), and ε is the error factor usually supposed to be uncorrelated with mean zero and constant difference. In the parameter estimation problem, the form of the nonlinear regression function is known but it contains unknown parameters $\beta 1,..., \beta p$.

There are a large number of articles on how to estimates the parameter of nonlinear regression models. Aşıkgil and Erar [2] examined the nonlinear parameter estimation efficiency under the issue of auto reconditioned errors.

The most and commonly used algorithm Gauss-Newton method (also called the Newton-Raphson method) [3]. However, the nonlinearity model produces a hard estimation of parameters and creates a very difficult and challenging statistical analysis of parameter estimates. In addition, it is not considered an easy controlled by practitioners and need much more detailed information to work properly. These difficulties are arising because of an increased number of parameters and the multi-conditioned nature of the function of the objective. Nonlinear regression models. Michailidis[4]considered Jaya's optimization algorithm for estimating nonlinear metaheuristic algorithm named Jaya .then tested it on a set of benchmark regression problems. Tvrd´ık and K˘riv´y [5] used some stochastic algorithms to solve the issue of global optimization of nonlinear regression models. These algorithms were applied to estimate the nonlinear regression model parameters. Tabatabai et al.[6] provided a robust alternative method to the normal Least Squares nonlinear regression method.

In recent decades, the researcher aims to resolve complicated problems by using metaheuristic to overcome drawbacks of classical procedures and have many benefits containing the simplicity of implementation, reliability, robustness, and effectiveness.[7] Adibifard et al.[8] used PSO algorithm to perform nonlinear regression in well test analysis. Root Mean Square Error over pressurized and

pressurized derivative data is employed to determine the formula of cost function f and the multi-objective issue is minimized to a single-objective one by containing the weight for each cost function related to over pressurized and pressurized derivative data. Özsoy, and Örkçü,[9] proposed Particle Swarm Optimization (PSO) algorithm in order to improve the accuracy of parameters estimation for nonlinear regression models. The PSO algorithm is examined on the famous 28 nonlinear regression tasks of various levels of difficulty.

On the other hand, Gravitational Search Algorithm (GSA) is a modern meta-heuristic and population-based search algorithm that depends on gravity Newton's law and motion law. Additionally, GSA has many benefits as, adaptive learning rate, memory-less algorithm and, perfect and rapid convergence. Additionally, GSA has been successfully used in complex problems. Thus, in this paper, Gravitational Search Algorithm was used to estimate the parameters of nonlinear regression models.

The organized paper is, section two provides the Maximum-likelihood Estimation of two nonlinear regression models; Section three describes the procedural Gravitational Search Algorithm; Section four consists of a simulation study; a conclusion is provided in section five.

2. Maximum likelihood Estimation Nonlinear regression models

The Maximum likelihood method (MLE) was used to estimate the parameter for two models of nonlinear regression (Misra 1d, and MGH 09 Model) as follows:

2.1 Maximum likelihood method to solve Misra 1d Model

The Misra 1dmodel is

$$f(x_i;\beta)=\frac{\beta_1\beta_2 x}{1+\beta_2 x} \tag{1}$$

MLE method of estimation depends on maximizing the pdf estimation:

$$L=f(x_1,x_2,\dots\dots,x_n,\beta_i,\sigma^2)$$

$$L=(2\pi\sigma^2)^{-\frac{n}{2}}e^{-\frac{\sum_{i=1}^{n}(y_i-f(x_i;\beta))^2}{2\sigma^2}}$$

$$lnL=-\frac{n}{2}ln2\pi-\frac{n}{2}ln\sigma^2-\frac{\sum_{i=1}^{n}(y_i-f(x_i;\beta))^2}{2\sigma^2}$$

$$lnL=-\frac{n}{2}ln2\pi-\frac{n}{2}ln\sigma^2-\frac{\sum_{i=1}^{n}(y_i-\frac{\beta_1\beta_2 x}{1+\beta_2 x})^2}{2\sigma^2}$$

Numerical procedures as Newton-Raphson was used to estimate the parameters since the equations are complicated to be solved. Therefore, the equation for this method for the first model is as follows

$$\begin{pmatrix}\hat{\beta}_1\\ \hat{\beta}_2\\ \hat{\sigma}^2\end{pmatrix}=\begin{pmatrix}\beta_{10}\\ \beta_{20}\\ \sigma_0^2\end{pmatrix}-\begin{pmatrix}\frac{\partial h_1}{\partial\beta_1} & \frac{\partial h_1}{\partial\beta_2} & \frac{\partial h}{\partial\sigma^2}\\ \frac{\partial h_2}{\partial\beta_1} & \frac{\partial h_2}{\partial\beta_2} & \frac{\partial h_2}{\partial\sigma^2}\\ \frac{\partial h_3}{\partial\beta_1} & \frac{\partial h_3}{\partial\beta_2} & \frac{\partial h_3}{\partial\sigma^2}\end{pmatrix}^{-1}\begin{pmatrix}\frac{\partial lnL}{\partial\beta_1}\\ \frac{\partial lnL}{\partial\beta_2}\\ \frac{\partial lnL}{\partial\sigma^2}\end{pmatrix} \tag{2}$$

$\begin{pmatrix}\beta_{10}\\ \beta_{20}\\ \sigma_0^2\end{pmatrix}$ Represents the vector of the initial parameters

$$h_1 = \frac{\partial lnL}{\partial \beta_1} = \frac{1}{\sigma^2}[\sum_{i=1}^{n}\left(\frac{y_i \beta_2 x}{1+\beta_2 x}\right) - \sum_{i=1}^{n}(\frac{\beta_1 \beta_2^2 x^2}{(1+\beta_2 x)^2})]$$

$$h_2 = \frac{\partial lnL}{\partial \beta_2} = \frac{1}{\sigma^2}[\sum_{i=1}^{n}\left(\frac{y_i \beta_1 x}{(1+\beta_2 x)^2}\right) - \sum_{i=1}^{n}(\frac{\beta_1^2 \beta_2 x^2}{(1+\beta_2 x)^3})]$$

$$h_3 = \frac{\partial lnL}{\partial \sigma^2} = -\frac{n}{2\sigma^2} + \sum_{i=1}^{n}\frac{1}{2\sigma^4}(y_i - \frac{\beta_1 \beta_2 x}{1+\beta_2 x})^2$$

$$\frac{\partial h_1}{\partial \beta_1} = -\frac{1}{\sigma^2}\sum_{i=1}^{n}(\frac{\beta_2^2 x^2}{(1+\beta_2 x)^2})$$

$$\frac{\partial h_1}{\partial \beta_2} = (\sum_{i=1}^{n}\frac{y_i x}{\sigma^2(1+\beta_2 x)^2} - \sum_{i=1}^{n}\frac{2\beta_1 \beta_2 x^2}{\sigma^2(1+\beta_2 x)^3})$$

$$\frac{\partial h_1}{\partial \sigma^2} = -\frac{1}{\sigma^4}(\sum_{i=1}^{n}\frac{y_i \beta_2 x}{1+\beta_2 x} - \sum_{i=1}^{n}\frac{\beta_1 \beta_2^2 x^2}{(1+\beta_2 x)^3})$$

$$\frac{\partial h_2}{\partial \beta_1} = \sum_{i=1}^{n}\frac{y_i x}{\sigma^2(1+\beta_2 x)^2} - \sum_{i=1}^{n}\frac{2\beta_1 \beta_2 x^2}{\sigma^2(1+\beta_2 x)^3}$$

$$\frac{\partial h_2}{\partial \beta_2} = \sum_{i=1}^{n}\frac{-2y_i \beta_1 x^2}{\sigma^2(1+\beta_2 x)^3} - \sum_{i=1}^{n}\frac{\beta_1^2 x^2(1-2\beta_2 x)}{\sigma^2(1+\beta_2 x)^4}$$

$$\frac{\partial h_2}{\partial \sigma^2} = \frac{1}{\sigma^4}\left[\sum_{i=1}^{n}(\frac{y_i \beta_1 x}{(1+\beta_2 x)^2}\right) - \sum_{i=1}^{n}\left(\frac{\beta_1^2 \beta_2 x^2}{(1+\beta_2 x)^3}\right)]$$

$$\frac{\partial h_3}{\partial \beta_1} = -\frac{1}{\sigma^4}\left[\sum_{i=1}^{n}(\frac{y_i \beta_2 x}{1+\beta_2 x}\right) - \sum_{i=1}^{n}\left(\frac{\beta_1 \beta_2^2 x^2}{(1+\beta_2 x)^2}\right)]$$

$$\frac{\partial h_3}{\partial \beta_2} = -\frac{1}{\sigma^4}\left[\sum_{i=1}^{n}(\frac{y_i \beta_1 x}{(1+\beta_2 x)^2}\right) - \sum_{i=1}^{n}\left(\frac{\beta_1^2 \beta_2 x^2}{(1+\beta_2 x)^3}\right)]$$

$$\frac{\partial h_3}{\partial \sigma^2} = \frac{n}{2\sigma^4} - \sum_{i=1}^{n}\frac{1}{\sigma^6}(y_i - \frac{\beta_1 \beta_2 x}{1+\beta_2 x})^2$$

2.2 Maximum likelihood method to solve MGH 09 Model

The MGH 09 Model is

$$f(x_i, \beta) = \frac{\beta_1(x^2 + x\beta_2)}{x^2 + x\beta_3 + \beta_4} \tag{3}$$

The formula for MLE is for MGH 09 Model;

$$\text{lnL} = -\frac{n}{2}ln2\pi - \frac{n}{2}ln\sigma^2 - \frac{\sum_{i=1}^{n}\left(y_i - \frac{\beta_1(x^2 + x\beta_2)}{x^2 + x\beta_3 + \beta_4}\right)^2}{2\sigma^2}$$

Thus, the following equation matrixes are applied to estimate the parameters for the non-linear regression model by using the Newton-Raphson method for the second model.

$$\begin{pmatrix}\hat{\beta}_1\\ \hat{\beta}_l\\ \hat{\beta}_3\\ \hat{\beta}_4\\ \hat{\sigma}^2\end{pmatrix}=\begin{pmatrix}\beta_{10}\\ \beta_{20}\\ \beta_{30}\\ \beta_{40}\\ \sigma_0^2\end{pmatrix}-\begin{pmatrix}\frac{\partial h_1\partial h_1\partial h_1\partial h_1}{\partial\beta_1\partial\beta_2\partial\beta_3\partial\beta_4}\frac{\partial h_1}{\partial\sigma^2}\\ \frac{\partial h_2\partial h_2\partial h_2\partial h_2}{\partial\beta_1\partial\beta_2\partial\beta_3\partial\beta_4}\frac{\partial h_2}{\partial\sigma^2}\\ \frac{\partial h_3\partial h_3\partial h_3\partial h_3}{\partial\beta_1\partial\beta_2\partial\beta_3\partial\beta_4}\frac{\partial h_3}{\partial\sigma^2}\\ \frac{\partial h_4\partial h_4\partial h_4\partial h_4}{\partial\beta_1\partial\beta_2\partial\beta_3\partial\beta_4}\frac{\partial h_4}{\partial\sigma^2}\\ \frac{\partial h_5\partial h_5\partial h_5\partial h_5}{\partial\beta_1\partial\beta_2\partial\beta_3\partial\beta_4}\frac{\partial h_5}{\partial\sigma^2}\end{pmatrix}^{-1}\begin{pmatrix}\frac{\partial lnL}{\partial\beta_1}\\ \frac{\partial lnL}{\partial\beta_2}\\ \frac{\partial lnL}{\partial\beta_3}\\ \frac{\partial lnL}{\partial\beta_4}\\ \frac{\partial lnL}{\partial\sigma^2}\end{pmatrix}$$

$\begin{pmatrix}\beta_{10}\\ \beta_{20}\\ \beta_{30}\\ \beta_{40}\\ \sigma_0^2\end{pmatrix}$ Represents the vector of the initial parameters.

$$h_1=\frac{\partial lnL}{\partial\beta_1}=\frac{1}{\sigma^2}\sum_{i=1}^{n}\left(\frac{y_i(x^2+x\beta_2)}{x^2+x\beta_3+\beta_4}-\frac{\beta_1(x^2+x\beta_2)^2}{(x^2+x\beta_3+\beta_4)^2}\right)$$

$$h_2=\frac{\partial lnL}{\partial\beta_2}=\frac{1}{\sigma^2}\sum_{i=1}^{n}\left(\frac{y_i\beta_1 x}{x^2+x\beta_3+\beta_4}-\frac{\beta_1^2(x^2+x\beta_2)}{(x^2+x\beta_3+\beta_4)^2}\right)$$

$$h_3=\frac{\partial lnL}{\partial\beta_3}=-\frac{1}{\sigma^2}\sum_{i=1}^{n}\left(\frac{y_i\beta_1 x(x^2+x\beta_2)}{(x^2+x\beta_3+\beta_4)^2}-\frac{\beta_1^2 x(x^2+x\beta_2)^2}{(x^2+x\beta_3+\beta_4)^3}\right)$$

$$h_4=\frac{\partial lnL}{\partial\beta_4}=-\frac{1}{\sigma^2}\sum_{i=1}^{n}\left(\frac{y_i\beta_1(x^2+x\beta_2)}{(x^2+x\beta_3+\beta_4)^2}-\frac{\beta_1^2(x^2+x\beta_2)^2}{(x^2+x\beta_3+\beta_4)^3}\right)$$

$$h_5=\frac{\partial lnL}{\partial\sigma^2}=-\frac{n}{2\sigma^2}+\frac{1}{2\sigma^4}\sum_{i=1}^{n}\left(y_i-\frac{\beta_1(x^2+x\beta_2)}{x^2+x\beta_3+\beta_4}\right)^2$$

$$\frac{\partial h_1}{\partial\beta_1}=-\frac{1}{\sigma^2}\sum_{i=1}^{n}\left(\frac{(x^2+x\beta_2)^2}{(x^2+x\beta_3+\beta_4)^2}\right)$$

$$\frac{\partial h_1}{\partial\beta_2}=\frac{1}{\sigma^2}\sum_{i=1}^{n}\left(\frac{y_i x}{x^2+x\beta_3+\beta_4}-\frac{2\beta_1 x(x^2+x\beta_2)}{(x^2+x\beta_3+\beta_4)^2}\right)$$

$$\frac{\partial h_1}{\partial\beta_3}=-\frac{1}{\sigma^2}\sum_{i=1}^{n}\left(\frac{y_i x(x^2+x\beta_2)}{(x^2+x\beta_3+\beta_4)^2}-\frac{2\beta_1 x(x^2+x\beta_2)^2(x^2+x\beta_3+\beta_4)}{(x^2+xB_3+B_4)^4}\right)$$

$$\frac{\partial h_1}{\partial\beta_4}=-\frac{1}{\sigma^2}\sum_{i=1}^{n}\left(\frac{y_i(x^2+x\beta_2)}{(x^2+x\beta_3+\beta_4)^2}-\frac{2\beta_1(x^2+x\beta_2)^2(x^2+x\beta_3+\beta_4)}{(x^2+x\beta_3+\beta_4)^4}\right)$$

$$\frac{\partial h_1}{\partial\sigma^2}=-\frac{1}{\sigma^4}\sum_{i=1}^{n}\left(\frac{y_i(x^2+x\beta_2)}{x^2+x\beta_3+\beta_4}-\frac{\beta_1(x^2+x\beta_2)^2}{(x^2+x\beta_3+\beta_4)^2}\right)$$

$$\frac{\partial h_2}{\partial\beta_1}=\frac{1}{\sigma^2}\sum_{i=1}^{n}\left(\frac{y_i x}{x^2+x\beta_3+\beta_4}-\frac{2\beta_1 x(x^2+x\beta_2)}{(x^2+x\beta_3+\beta_4)^2}\right)$$

$$\frac{\partial h_2}{\partial\beta_2}=-\frac{1}{\sigma^2}\sum_{i=1}^{n}\left(\frac{\beta_1^2 x^2}{(x^2+x\beta_3+\beta_4)^2}\right)$$

$$\frac{\partial h_2}{\partial \beta_3} = -\frac{1}{\sigma^2}\sum_{i=1}^{n}\left(\frac{y_i\beta_1 x^2}{(x^2+x\beta_3+\beta_4)^2} - \frac{2\beta_1^2 x^2(x^2+x\beta_2)^2(x^2+x\beta_3+\beta_4)}{(x^2+x\beta_3+\beta_4)^4}\right)$$

$$\frac{\partial h_2}{\partial \beta_4} = -\frac{1}{\sigma^2}\sum_{i=1}^{n}\left(\frac{y_i\beta_1 x}{(x^2+x\beta_3+\beta_4)^2} - \frac{2\beta_1^2 x(x^2+x\beta_2)^2(x^2+x\beta_3+\beta_4)}{(x^2+x\beta_3+\beta_4)^4}\right)$$

$$\frac{\partial h_2}{\partial \sigma^2} = -\frac{1}{\sigma^4}\sum_{i=1}^{n}\left(\frac{y_i\beta_1 x}{x^2+x\beta_3+\beta_4} - \frac{\beta_1^2 x(x^2+x\beta_2)}{(x^2+x\beta_3+\beta_4)^2}\right)$$

$$\frac{\partial h_3}{\partial \beta_1} = -\frac{1}{\sigma^2}\sum_{i=1}^{n}\left(\frac{y_i x(x^2+x\beta_2)}{(x^2+x\beta_3+\beta_4)^2} - \frac{2\beta_1(x^2+x\beta_2)^2}{(x^2+x\beta_3+\beta_4)^3}\right)$$

$$\frac{\partial h_3}{\partial \beta_2} = -\frac{1}{\sigma^2}\sum_{i=1}^{n}\left(\frac{y_i\beta_1 x^2}{(x^2+xB_3+B_4)^2} - \frac{2\beta_1^2 x^2(x^2+x\beta_2)}{(x^2+x\beta_3+\beta_4)^3}\right)$$

$$\frac{\partial h_3}{\partial \beta_3} = \frac{1}{\sigma^2}\sum_{i=1}^{n}\left(\frac{2y_i\beta_1 x^2(x^2+x\beta_2)}{(x^2+x\beta_3+\beta_4)^3} - \frac{3\beta_1^2 x^2(x^2+x\beta_2)^2}{(x^2+x\beta_3+\beta_4)^4}\right)$$

$$\frac{\partial h_3}{\partial \beta_4} = \frac{1}{\sigma^2}\sum_{i=1}^{n}\left(\frac{2y_i\beta_1 x(x^2+x\beta_2)}{(x^2+xB_3+B_4)^3} - \frac{3\beta_1^2 x(x^2+x\beta_2)^2}{(x^2+x\beta_3+\beta_4)^4}\right)$$

$$\frac{\partial h_3}{\partial \sigma^2} = \frac{1}{\sigma^4}\sum_{i=1}^{n}\left(\frac{y_i\beta_1 x(x^2+x\beta_2)}{(x^2+x\beta_3+\beta_4)^2} - \frac{\beta_1^2 x(x^2+x\beta_2)^2}{(x^2+x\beta_3+\beta_4)^3}\right)$$

$$\frac{\partial h_4}{\partial \beta_1} = -\frac{1}{\sigma^2}\sum_{i=1}^{n}\left(\frac{y_i(x^2+x\beta_2)}{(x^2+x\beta_3+\beta_4)^2} - \frac{2\beta_1(x^2+x\beta_2)^2}{(x^2+x\beta_3+\beta_4)^3}\right)$$

$$\frac{\partial h_4}{\partial \beta_2} = -\frac{1}{\sigma^2}\sum_{i=1}^{n}\left(\frac{y_i\beta_1 x}{(x^2+x\beta_3+\beta_4)^2} - \frac{2\beta_1^2 x(x^2+x\beta_2)}{(x^2+x\beta_3+\beta_4)^3}\right)$$

$$\frac{\partial h_4}{\partial \beta_3} = -\frac{1}{\sigma^2}\sum_{i=1}^{n}\left(\frac{2y_i\beta_1 x(x^2+x\beta_2)}{(x^2+x\beta_3+\beta_4)^3} - \frac{3\beta_1^2 x(x^2+x\beta_2)^2}{(x^2+x\beta_3+\beta_4)^4}\right)$$

$$\frac{\partial h_4}{\partial \beta_4} = -\frac{1}{\sigma^2}\sum_{i=1}^{n}\left(\frac{2y_i\beta_1(x^2+x\beta_2)}{(x^2+x\beta_3+\beta_4)^3} - \frac{3\beta_1^2(x^2+x\beta_2)^2}{(x^2+x\beta_3+\beta_4)^4}\right)$$

$$\frac{\partial h_4}{\partial \sigma^2} = \frac{1}{\sigma^4}\sum_{i=1}^{n}\left(\frac{y_i\beta_1(x^2+x\beta_2)}{(x^2+x\beta_3+\beta_4)^2} - \frac{\beta_1^2(x^2+x\beta_2)^2}{(x^2+x\beta_3+\beta_4)^3}\right)$$

$$\frac{\partial h_5}{\partial \beta_1} = -\frac{1}{\sigma^4}\sum_{i=1}^{n}\left(\frac{y_i\beta_1(x^2+x\beta_2)}{(x^2+x\beta_3+\beta_4)} - \frac{\beta_1(x^2+x\beta_2)^2}{(x^2+x\beta_3+\beta_4)^2}\right)$$

$$\frac{\partial h_5}{\partial \beta_2} = -\frac{1}{\sigma^4}\sum_{i=1}^{n}\left(\frac{y_i x\beta_1}{(x^2+x\beta_3+\beta_4)} - \frac{\beta_1^2 x(x^2+x\beta_2)}{(x^2+x\beta_3+\beta_4)^2}\right)$$

$$\frac{\partial h_5}{\partial \beta_3} = \frac{1}{\sigma^4}\sum_{i=1}^{n}\left(\frac{y_i x\beta_1(x^2+x\beta_2)}{(x^2+x\beta_3+\beta_4)^2} - \frac{\beta_1^2 x(x^2+x\beta_2)^2}{(x^2+x\beta_3+\beta_4)^3}\right)$$

$$\frac{\partial h_5}{\partial \beta_4} = \frac{1}{\sigma^4}\sum_{i=1}^{n}\left(\frac{y_i\beta_1(x^2+x\beta_2)}{(x^2+x\beta_3+\beta_4)^2} - \frac{\beta_1^2(x^2+x\beta_2)^2}{(x^2+x\beta_3+\beta_4)^3}\right)$$

$$\frac{\partial h_5}{\partial \sigma^2} = \frac{n}{2\sigma^4} - \frac{1}{\sigma^6}\sum_{i=1}^{n}\left(y_i - \frac{\beta_1(x^2+x\beta_2)}{(x^2+x\beta_3+\beta_4)}\right)^2$$

3. Gravitational Search Algorithm Technique

In 2009, Rashedi et al. [10] introduced the Gravitational Search Algorithm (GSA) for solving optimization problems. The populace-established heuristic algorithm is founded on the mass interactions and gravity law. The solutions in the population of GSA are called agents, through the gravity force the agents interact with each other. In the population, measured the performance of each agent by its mass. The best solution is the solution with a heavier mass.
The objects masses are obeying of gravity low as following

$$\mathrm{F_{ij}} = \mathrm{G}\frac{M_{aj} \times \mathrm{M_{pj}}}{\mathrm{R}^2} \tag{4}$$

Where G is gravitational constant,$\mathrm{M_{pj}}$ is the mass of the second object, $M_{aj}$is the mass of the first object ,F is a magnitude of the gravitational force, and R is the distance between the two objects M_{aj}, $\mathrm{M_{pj}}$.

$$\mathrm{a_i} = \frac{\mathrm{F_{ij}}}{\mathrm{M_{ij}}} \tag{5}$$

The velocities and positions will be updated by agents during the search, as shown in Equations 6, 7 respectively.

$$\mathrm{V_i(t+1)} = \mathrm{rand_i} \times \mathrm{V_i(t+1)} + \mathrm{a_i(t)} \tag{6}$$
$$\mathrm{X_i(t+1)} = \mathrm{rand_i} \times \mathrm{v_i(t+1)} + \mathrm{a_i(t)} \tag{7}$$

The following steps of the GSA can be summarized as below:
Step 1. initializes values of gravitational constant G_0, α, ε, and the iteration counter t.
Step 2. generated the initial population randomly and consists of N agents, the position defined for each agent as below:

$$\mathrm{x_i(t)} = \left(\mathrm{x_i^1(t), x_i^2(t), \dots\dots\dots x_i^n(t)}\right) \quad \mathrm{i} = 1,2,\dots\dots\dots \mathrm{N}$$

Step 3. This step is replicated until satisfied with termination criteria¬
A. assigned the best, worst agents and evaluated the population for all agents
B. the constant of gravitational is updated as Equation 4
C. calculates the force as follows:

$$\mathrm{F_i^j(t)} = \mathrm{G(t)}\frac{M_{aj}(\mathrm{t}) \times \mathrm{M_{pj}(t)}}{\mathrm{R_{ij}(t)} + \in}\left(X_j^d(t) - X_i^d(t)\right) \tag{8}$$

WhereM_{aj} is the active gravitational mass of agent j ,$\mathrm{M_{pj}}$ is the passive gravitational mass of agent i ,G(t) is gravitational constant at time t.
D. At iteration t, calculate the total force acting on agent i as follows:

$$F_i^d(t) = \sum_{j \in Kbest\,, j \neq i} rand_j F_{ij}^d(t) \tag{9}$$

Where K best is the set of first K agents with the best fitness value and biggest mass
E. Calculate the inertial mass as following

$$m_i(t) = \frac{fit_i - worst(t)}{best(t) - worst(t)} \quad (10)$$

$$\mathrm{M_i(t)} = \frac{\mathrm{m_i(t)}}{\sum_{\mathrm{j=1}}^{\mathrm{N}} \mathrm{m_j(t)}} \quad (11)$$

F. Calculated the agent of acceleration as following:

$$\mathrm{a_i(t)} = \frac{\mathrm{F_i(t)}}{\mathrm{M_{ii}(t)}} \quad (12)$$

G. The position and velocity of agent i are computed as shown in Equations 6, 7 .
H. The iteration counter is increased until termination criteria satisfied
Step 4. The best optimal solution is produced.
The log-likelihood function was used as a fitness function of the GSA.

4. Graph Simulation study

In order to verify the performance of the different estimator's methods, Simulation was used based on Mean Squares Error (MSE) to estimate the parameters of two models for nonlinear regression (Misra 1d and MGH 09 Model). Calculate the values of response variable yi depend on x_i were generated according to the exponential distribution$(exp(2))$, while the random variableei is generated according to $N(0, \sigma^2)$.In addition, each simulation condition was generated by 1000 replications. Various sample sizes are tested: 20, 40, 80,160, and 200. The simulation program was written using Matlab 2013. Generate the initial value of parameters for each model's different set parameters utilized for each model as: $(\beta_1, \beta_2) = (1000, 200)$, and (500, 500) for the first model, while for the second model $(\beta_1, \beta_2, \beta_3, \beta_2)$ = (0.3 , 0.2, 0.1, 0.1) and (0.3, 0.2, 0.3 ,0.4), respectively.
Tables (1- 4) illustrated the results of the estimate parameters and the MSE for each parameter for two models of NLRA. The GSA algorithm provides a better result than MLE method.

Table 1: comparative results of GSA and MLE based on the first model when$\beta_1 = 500$ $\beta_2 = 500$

$Model$	n	$Methods$		β_1	β_2	MSE
$Misra\ 1d$	20	MLE	$Estimated$	499.5956	295.229	5.670051
			MSE	11.09005	439283.6	
		GSA	$Estimated$	500.1654	220.6128	2.50637
			MSE	20.79941	174409.2	
	40	MLE	$Estimated$	498.7145	129.2191	17.83184
			MSE	19.13281	689491.3	
		GSA	$Estimated$	502.1351	-64800.4	4.408084
			MSE	77.98416	$4.24E+10$	
	٨٠	MLE	$Estimated$	٥٤٩.٢٨٢٦	٣٩.٢٠٤٤٥	٩٤٣٥٦٩٥
			MSE	١٣٠٩٣.١٣	٥٧٣٨٣٠.١	
		GSA	$Estimated$	502.3401	310.6598	1.366088
			MSE	69.37687	187373.4	
	١٦٠	MLE	$Estimated$	499.8794	236.9898	8.501998
			MSE	5.362929	321257.5	
		GSA	$Estimated$	500.4134	417.3795	1.514707
			MSE	5.3301	20407.72	
	٢٠٠	MLE	$Estimated$	9765.851	1107440	349.4619
			MSE	9765.851	1107440	

		GSA	$Estimated$	499.7055	483.4462	10.61744
			MSE	4.852572	44162.17	

Table 2: comparative results of GSA and MLE based on the first model when$\beta_1 = 1000\ \beta_2 = 200$

$Model$	n	$Methods$		β_1	β_2	MSE
$Misra\ 1d$	20	MLE	$Estimated$	986.7453	-124.206	746.2497
			MSE	270.5365	574591.1	
		GSA	$Estimated$	990.7536	136.1845	0.014534
			MSE	301.8324	202523.2	
	40	MLE	$Estimated$	994.866	295.9005	323.5123
			MSE	46.18677	177214.2	
		GSA	$Estimated$	993.8156	264.0664	0.009915
			MSE	123.4615	139393.2	
	80	MLE	$Estimated$	988.8398	-15.6546	364.7559
			MSE	243.1879	493297.7	
		GSA	$Estimated$	994.3077	289.225	0.011026
			MSE	136.9521	107220.2	
	160	MLE	$Estimated$	994.6233	-61.9938	0.21395
			MSE	66.24217	569137.5	
		GSA	$Estimated$	988.4391	116.1104	0.009643
			MSE	546.578	107172.1	
	200	MLE	$Estimated$	986.8886	-391.065	1262.264
			MSE	279.8969	1538285	
		GSA	$Estimated$	989.9985	292.5989	171.3449
			MSE	243.2437	171441.3	

Table 3: comparative results of GSA and MLE based on the second model when$\beta_1 = 0.3\ \beta_2 = 0.2\beta_3 = 0.1\ \beta_4 = 0.1$

$Model$	n	$Methods$		β_1	β_2	β_3	β_4	MSE
$MGH\ 09$	20	MLE	$Estimated$	1.954471	-0.43388	0.491298	1.235867	41.61445
			MSE	25.54746	4.155458	27.19137	7.717002	
		GSA	$Estimated$	0.113475	-8994006	$-1.6E+07$	16957031	0.2866
			MSE	0.049797	$8.09+14$	$2.59E+15$	$2.88E+15$	
	40	MLE	$Estimated$	0.039963	0.19082	-1.04359	0.751308	0.15719
			MSE	0.888632	1.093795	2.205161	2.738818	
		GSA	$Estimated$	-3.1008	12.36802	-26.5377	26.52696	0.005814
			MSE	116.6475	1743.968	8644.986	6842.597	
	80	MLE	$Estimated$	0.119452	0.580837	-1.31832	0.831274	183.59
			MSE	0.132054	1.198069	2.818023	3.0717	
		GSA	$Estimated$	-2.20153	-180734	-165358	150092.7	4.938464
			MSE	49.18432	$3.26+11$	$2.73E+11$	$2.25E+11$	
	160	MLE	$Estimated$	0.219287	0.084688	-1.4635	0.782096	1.025123
			MSE	0.026464	1.068443	2.902361	2.835297	

		GSA	$Estimated$	0.18999	0.838633	−8.92829	7.228961	0.382482
			MSE	0.125626	35.11116	408.2441	330.8805	
	200	MLE	$Estimated$	−0.00549	0.029029	−1.20795	0.567518	10.79044
			MSE	0.161232	0.937274	3.154803	3.441416	
		GSA	$Estimated$	0.366574	0.4	0.335001	0.672349	10.78041
			MSE	0.075738	0.28	0.25525	2.634952	

Table 4: comparative results of GSA and MLE based on the second model when $\beta_1 = 0.3 \;\; \beta_2 = 0.2 \beta_3 = 0.3 \;\; \beta_4 = 0.4$

$Model$	n	$Methods$		β_1	β_2	β_3	β_4	MSE
$MGH09$	20	MLE	$Estimated$	0.268851	0.43925	0.604946	0.555446	0.020863
			MSE	0.027177	0.095005	0.166329	0.067891	
		GSA	$Estimated$	0.322879	0.323069	0.583845	0.486207	0.001661
			MSE	0.003817	0.107965	0.214893	0.137402	
	40	MLE	$Estimated$	0.386908	0.460786	0.495018	0.674059	0.017706
			MSE	0.022945	0.125823	0.114295	0.105835	
		`GSA	$Estimated$	0.289872	0.578694	0.354008	0.668938	0.007558
			MSE	0.004592	0.24232	0.149802	0.145513	
	80	MLE	$Estimated$	0.403243	0.365894	0.638887	0.624496	0.009742
			MSE	0.04209	0.120838	0.158708	0.094339	
		GSA	$Estimated$	0.289862	0.387528	0.301556	0.465746	0.009566
			MSE	0.001168	0.10986	0.073137	0.050988	
	160	MLE	$Estimated$	0.370653	0.480084	0.532659	0.567015	0.014788
			MSE	0.025058	0.203756	0.134628	0.108836	
		GSA	$Estimated$	0.313968	0.368803	0.59661	0.469617	0.009038
			MSE	0.000549	0.073742	0.119012	0.053978	
	200	MLE	$Estimated$	0.333854	0.464869	0.474432	0.625284	0.029244
			MSE	0.030065	0.110386	0.104334	0.158318	
		GSA	$Estimated$	0.308305	0.274282	0.394676	0.495746	0.009868
			MSE	0.000833	0.032696	0.083541	0.035074	

Conclusion

In this study, a metaheuristic algorithm (Gravitational Search algorithm) was used as an alternative method to estimate the parameters of two models of nonlinear regression (Misra 1d and Myer 7). To improve the validation of the algorithm, a simulation study was used. The result showed that the Gravitational Search algorithm provides good results than the classical MLE estimator.

References

[1] PAN, Zhengjun, and et al. 1995 Parameter estimation by genetic algorithms for nonlinear regression. *High Technology* 946 953
[2] Aşıkgil, B and Erar, A 2013 Polynomial tapered two stage least squares method in nonlinear regression *Applied Mathematics and Computation* **219** (18) 9743-9754
[3] Nwobi FN and Ugomma CA 2014 A comparison of methods forthe Estimation of Weibull distribution Parameter *MetodoloskiZvezki* **11** (1) 65-78
[4] Michailidis, P. D. 2018 A Preliminary Performance Study on NonlinearRegression Models using the Jaya Optimization Algorithm *InternationalJournal of Applied Mathematics* **48**(4) 1-5
[5] Křivý I, Tvrdík J and Krpec R 2000 Stochastic algorithms in nonlinear regression *Computational Statistics & Data Analysis* **33** (3) 277-
[6] Tabatabai M A, Kengwoung-Keumo J J, Eby W M, Bae S, Manne U, Fouad M, and amp; Singh K P 2014 A new robust method for nonlinearregression. *Journal of biometrics & biostatistics* **5** (5) 211
[7] Atiya B, Bakheet A J K, Abbas I T, Bakar M R A, Soon L, and Monsi M B 2016 Application of simulated annealing to solve multi-objectives for aggregate production planning *AIP Conf. Pro.s* **1739c**(1) 020086) AIP Publishing LLC
[8] Adibifard M, Bashiri G, Roayaei E, and Emad M A 2016 Using particle swarm optimization (pso) algorithm in nonlinear regression well test analysis and its comparison with levenberg-marquardt algorithm *International Journal of Applied Metaheuristic Computing (IJAMC)* **7** (3) 1-23
[9] Özsoy V S, Ünsal M G, and Örkcü H H 2020 Use of the heuristic optimization in the parameter estimation of generalized gamma distribution: comparison of GA, DE, PSO and SA methods. *Computational Statistics* 1-31
[10] Rashedi H, Nezamabadi-pour, and S Saryazdi 2009 GSA: A Gravitational Search Algorithm *Information Sciences* **179** (13) 2232–2248

Soft Np-Open Sets in Soft Toplogical Spaces

Soft Np-Open Sets in Soft Toplogical Spaces

Sabeha I and Haider Jebur Ali

Department of Mathematics, College of Science, Mustansiriyah University, Baghdad, Iraq

E-mail: ssabihaa@uomustansiriyah.edu.iq

Abstract. This article is devoted to introduce and study a new kind of soft sets in soft topological spaces called soft Np-open sets as a generalization of soft p-open sets. Also, we investigate and prove some of their properties. By using this new soft set we define and study new soft spaces called soft Np-compact spaces, soft Np-Lindelöf spaces, and obtain some of their characterizations and properties. Finally, we discuss the relationships among soft Np-compact spaces, soft Np-Lindelöf spaces, soft p-compact spaces, soft p-Lindelöf spaces, soft compact spaces, and soft Lindelöf spaces.

1. Introduction

Molodtsov [1] proposed the soft set theory as a new mathematical tool for dealing with uncertain objects. Shabir and Naz [2] defined the concept of soft topological spaces by using soft open sets. Aygunuglu and Aygun [3], Rong [4] and AL-Shami and EL-Shafei [5] defined and studied soft compact spaces, soft Lindelöf spaces, soft p-compact spaces, and soft p-Lindelöf spaces resp. Arockiarani and Arokia Lancy [6], Chen [7], Akdag, and Ozkan [8], and Mahmood [9] introduced and investigated soft p-open sets, soft s-open sets, soft α-open sets, and soft N-open sets resp. In the present paper, we define and study the notion of soft Np-open sets as a generalization of soft p-open sets and investigate some of their basic properties. Moreover, we use these soft sets to introduce new kinds of soft spaces called soft Np-compact spaces and soft Np-Lindelöf spaces. The fundamental properties and characterizations of these soft spaces also have been studied.

2. Preliminaries

Definition 2.1: [1]: A pair (H, S) is called a soft set over D, where H is a function of a parameters set S into 2^D. The soft set (H, S) can be written as follows:
$(H, S) = \{(s, H(s)): s \in S \text{ and } H(S) \in 2^D\}$.

Definition 2.2: [10]: The soft union of two soft sets (H_1, S_1) and (H_2, S_2) over a common universe D is the soft set (H, S), where $S = S_1 \cup S_2$, and $\forall\, s \in S$,

$$H(s) = \begin{cases} H_1(s) & \text{if } s \in S_1 - S_2 \\ H_2(s) & \text{if } s \in S_2 - S_1 \\ H_1(s) \cup H_2(s) & \text{if } s \in S_1 \cap S_2 \end{cases}$$

We write $(H, S) = (H_1, S_1) \widetilde{\cup} (H_2, S_2)$.

Definition 2.3: [11]: The soft intersection of two soft sets (H_1, S_1) and (H_2, S_2) over a common universe D is the soft set (H, S), where $S = S_1 \cap S_2$, and $\forall\, s \in S$, $H(s) = H_1(s) \cap H_2(s)$. We write

$(H, S) = (H_1, S_1)\widetilde{\cap}(H_2, S_2)$.

Definition 2.4: [12]: The soft difference of two soft sets (H_1, S_1) and (H_2, S_2) over a common universe D is the soft set (H, S), where $S = S_1 \cap S_2$, and $\forall\, s \in S$, $H(s) = H_1(s) - H_2(s)$. We write $(H, S) = (H_1, S_1) - (H_2, S_2)$.

Definition 2.5: [12]: The soft complement of a soft set (H, S) is denoted by $(H, S)^c$ and is defined by $(H, S)^c = (H^c, S)$, where $H^c: S \to p(D)$ is a function given by $H^c(s) = D - H(s)$, $\forall s \in S$. Clearly, $\widetilde{D}^c = \widetilde{\emptyset}$ and $\widetilde{\emptyset}^c = \widetilde{D}$.

Definition 2.6: [2]: Let $\tilde{\sigma}$ be a family of soft sets over D with a fixed set of parameters S. Then $\tilde{\sigma}$ is called a soft topology on D if:
(i) $\widetilde{\emptyset}$ and $\widetilde{D}$ are members of $\tilde{\sigma}$.
(ii) If $(H_1, S), (H_2, S) \,\widetilde{\in}\, \tilde{\sigma}$, then $(H_1, S)\widetilde{\cap}(H_2, S) \,\widetilde{\in}\, \tilde{\sigma}$.
(iii) If $(H_\alpha, S) \,\widetilde{\in}\, \tilde{\sigma}$, $\forall\, \alpha \in \Omega$, then $\widetilde{\cup}\{(H_\alpha, S): \alpha \in \Omega\} \,\widetilde{\in}\, \tilde{\sigma}$.
The triple $(D, \tilde{\sigma}, S)$ is called a soft topological space (briefly S. T. S.). Every soft set in $\tilde{\sigma}$ is called soft open over D and its complement is called soft closed over D.

Definition 2.7: [2]: Let $(D, \tilde{\sigma}, S)$ be a S. T. S. and $(H, S) \,\widetilde{\subseteq}\, \widetilde{D}$. The soft closure of (H, S), denoted by $cl(H, S)$ is the soft intersection of all soft closed sets in $\widetilde{D}$ which contains (H, S).

Definition 2.8: [13]: Let $(D, \tilde{\sigma}, S)$ be a S. T. S. and $\widetilde{\emptyset} \neq (M, S) \,\widetilde{\subseteq}\, \widetilde{D}$. Then $\tilde{\sigma}_{(M,S)} = \{(W, S)\widetilde{\cap}(M, S): (W, S) \,\widetilde{\in}\, \tilde{\sigma}\}$ is said to be the relative soft topology on (M, S) and $((M, S), \tilde{\sigma}_{(M,S)}, S)$ is said to be a soft subspace of $(D, \tilde{\sigma}, S)$.

Definition 2.9: [14]: A soft set (H, S) over D is called a soft point denoted by $\tilde{x} = (s, \{x\})$ if there is $s \in S$ and $x \in D$ such that $H(s) = \{x\}$ and $H(t) = \emptyset$ for each $t \in S\backslash\{s\}$.

Definition 2.10: [14]: A soft set (H, S) over D is called finite if $H(s)$ is finite for each $s \in S$.

Definition 2.11: A soft subset (H, S) of $(D, \tilde{\sigma}, S)$ is called:
(i) Soft pre-open (briefly soft $p-$ open) [6] if $(H, S) \,\widetilde{\subseteq}\, int(cl(H, S))$.
(ii) Soft semi open (briefly soft $s-$ open) [7] if $(H, S) \,\widetilde{\subseteq}\, cl(int(H, S))$.
(iii) Soft $\alpha-$ open [8] if $(H, S) \,\widetilde{\subseteq}\, int(cl(int(H, S)))$.
(iv) Soft $N-$ open [9] if for each $\tilde{x} \,\widetilde{\in}\, (H, S)$, there exists a soft open set (W, S) containing $\tilde{x}$ such that $(W, S) - (H, S)$ is a finite soft set.

Definition 2.12: [5]: A soft subset (H, S) of $(D, \tilde{\sigma}, S)$ is called soft pre-clopen (briefly soft $p-$ clopen if it is soft $p-$ open and soft $p-$ closed.

Proposition 2.13: [15],[5],[16]: Let $(D, \tilde{\sigma}, S)$ be a S. T. S. Then:

i. If (A, S) is soft $p-$ open in $\widetilde{D}$ and (B, S) is soft open in $\widetilde{D}$, then $(A, S)\widetilde{\cap}(B, S)$ is soft $p-$ open in $\widetilde{D}$.
ii. If (T, S) is soft $p-$ open in $\widetilde{D}$ and (H, S) is soft $s-$ open in $\widetilde{D}$, then $(H, S)\widetilde{\cap}(T, S)$ is soft $p-$ open in $((T, S), \tilde{\sigma}_{(T,S)}, S)$.
iii. If $(B, \tilde{\sigma}_B, S)$ is a soft p-open subspace of $(D, \tilde{\sigma}, S)$ and $(H, S) \,\widetilde{\subseteq}\, \widetilde{B} \,\widetilde{\subseteq}\, \widetilde{D}$. Then (H, S) is soft $p-$ open in $\widetilde{D} \iff$ it is soft $p-$ open in $\widetilde{B}$.

Definition 2.14: [4],[5]: A S. T. S. $(D, \tilde{\sigma}, S)$ is called soft p-compact (resp. soft $p-$ Lindelöf) if all soft $p-$ open cover of $\tilde{D}$ has a finite (countable) subcover.

Definition 2.15: [17]: A S. T. S. $(D, \tilde{\sigma}, S)$ is called a soft $\tilde{T}_1$-space if for any two distinct soft points $\tilde{x}$ and $\tilde{y}$ of $\tilde{D}$, there are two soft open sets (H_1, S) and (H_2, S) in $\tilde{D}$ such that $\tilde{x} \tilde{\in} (H_1, S)$, $\tilde{y} \tilde{\notin} (H_1, S)$ and $\tilde{y} \tilde{\in} (H_2, S)$, $\tilde{x} \tilde{\notin} (H_2, S)$.

3. Soft Np-Open Sets

Definition 3.1: A soft set (A, S) in a S. T . S. $(D, \tilde{\sigma}, S)$ is called soft N-pre-open (briefly soft Np-open) if $\forall\, \tilde{u} \tilde{\in} (A, S), \exists$ a soft $p-$ open set (O, S) in $\tilde{D}$ containing $\tilde{u}$ such that $(O, S) - (A, S)$ is a finite soft set. The collection of all soft Np-open sets in $(D, \tilde{\sigma}, S)$ is denoted by $\tilde{\sigma}_{Np}$.

Proposition 3.2: In a S. T. S. $(D, \tilde{\sigma}, S)$ the following statements are satisfied:

i. Every soft open set is soft $Np-$ open.
ii. Every soft $N-$ open set is soft $Np-$ open.
iii. Every soft $p-$ open set is soft $Np-$ open.

The following examples show that the converse of (i),(ii), and (iii) in the above Proposition are not true.

Example 3.3: Let $D = \{a, c, b\}$, $S = \{s_1, s_2, s_3\}$, and let $\tilde{\sigma} = \{\tilde{D}, \tilde{\emptyset}, (U, S), (V, S)\}$ be a soft topology over D, where

$$(U, S) = \{(s_1, \{a, c\}), (s_2, \{c, b\}), (s_3, \{a\})\}$$
$$(V, S) = \{(s_1, \{c\}), (s_2, \{b\}), (s_3, \{a\})\}$$

Then $\{(s_1, \{c, b\}), (s_2, \{a, b\}), (s_3, \{a, c\})\}$ is soft $Np-$ open but is not soft open.

Example 3.4: Let $D = \Re$ (the set of real numbers), $S = \{s_1, s_2\}$, and let $\tilde{\sigma} = \{\tilde{\Re}, \tilde{\emptyset}, (K, S)\}$ be a soft topology over $\Re$ where $(K, S) = \{(s_1, \{1\}), (s_2, \{1\})\}$. Then $(N, S) = \{(s_1, \{1,2\}), (s_2, \{1,3\})\}$ is soft $Np-$ open, but is not soft $N-$ open.

Example 3.5: Let $D = \{a, b, c\}$, $S = \{s_1, s_2\}$, and let $\tilde{\sigma} = \{\tilde{D}, \tilde{\emptyset}, (T, S)\}$ be a soft topology over D, where $(T, S) = \{(s_1, \{c\}), (s_2, \{c\})\}$. Then $(N, S) = \{(s_1, \{a, b\}), (s_2, \{b, a\})\}$ is soft $Np-$ open, but is not soft $p-$ open.

From above we get the following diagram.

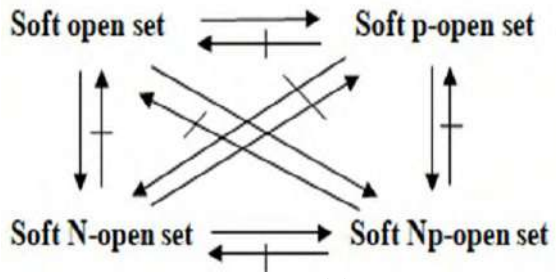

Diagram (1)

Remark 3.6: If (U, S) and (V, S) are soft $Np-$ open sets in $(D, \tilde{\sigma}, S)$, then $(U, S) \tilde{\cap} (V, S)$ may not be soft $Np-$ open.

Example 3.7: Let $D = \Re$, $S = \{s_1, s_2\}$, and let $\tilde{\sigma} = \{(W, S) \tilde{\subseteq} \tilde{\Re}: (W, S)^c \text{ is a finite soft set}\} \tilde{\cup} \{\tilde{\emptyset}\}$ be the soft cofinite topology over $\Re$. Then $(U, S) = \{(s_1, [1,8]), (s_2, [3,8])\}$ and $(V, S) = \{(s_1, [8,11]), (s_2, [8,9])\}$ are soft Np-open sets, but $(U, S) \tilde{\cap} (V, S) = \{(s_1, \{8\}), (s_2, \{8\})$ is not soft Np-open.

Proposition 3.8: If $\{(H_\alpha, S): \alpha \in \Omega\}$ is a family of soft Np-open subsets of $(D, \tilde{\sigma}, S)$. Then $\tilde{\cup}\{(H_\alpha, S): \alpha \in \Omega\}$ is soft Np-open in $\tilde{D}$.

Proof: Let $\{(H_\alpha, S): \alpha \in \Omega\}$ be a collection of soft Np-open sets. Now, if $\tilde{a} \tilde{\in} \tilde{\cup}\{(H_\alpha, S): \alpha \in \Omega\}$, then $\tilde{a} \tilde{\in} (H_{\alpha_0}, S)$ for some $\alpha_0 \in \Omega$. But $(H_{\alpha_0}, S) \tilde{\in} \tilde{\sigma}_{Np}$, so $\exists$ a soft $p-$open set (O, S) in $\tilde{D}$ containing $\tilde{a}$ such that $(O, S) - (H_{\alpha_0}, S)$ is a finite soft set. Since $(H_{\alpha_0}, S) \tilde{\subseteq} \tilde{\cup}\{(H_\alpha, S): \alpha \in \Omega\}$, then $\tilde{D} - \tilde{\cup}\{(H_\alpha, S): \alpha \in \Omega\} \tilde{\subseteq} \tilde{D} - (H_{\alpha_0}, S)$. Therefore
$(O, S)\tilde{\cap}(\tilde{D} - \tilde{\cup}\{(H_\alpha, S): \alpha \in \Omega\} \tilde{\subseteq} (O, S)\tilde{\cap}(\tilde{D} - (H_{\alpha_0}, S))$.
Hence, $(O, S) - \tilde{\cup}\{(H_\alpha, S): \alpha \in \Omega\} \tilde{\subseteq} (O, S) - (H_{\alpha_0}, S))$, that is $(O, S) - \tilde{\cup}\{(H_\alpha, S): \alpha \in \Omega\}$ is a finite soft set. Therefore, $\tilde{\cup}\{(H_\alpha, S): \alpha \in \Omega\} \tilde{\in} \tilde{\sigma}_{Np}$.

Corollary 3.9: If $\{(F_\alpha, S): \alpha \in \Omega\}$ is a family of soft Np-closed subsets of $(D, \tilde{\sigma}, S)$, then $\tilde{\cap}\{(F_\alpha, S): \alpha \in \Omega\}$ is soft Np-closed in $\tilde{D}$.

Proof: It is obvious.

Definition 3.10: [15]: A soft subset (L, S) of $(D, \tilde{\sigma}, S)$ is called soft dense if $cl(L, S) = \tilde{D}$.

Definition 3.11: [15]: A S. T. S. $(D, \tilde{\sigma}, S)$ is called soft submaximal if all soft dense set in $\tilde{D}$ is soft open.

Proposition 3.12: [15]: A S. T. S. $(D, \tilde{\sigma}, S)$ is soft submaximal if and only if all soft $p-$open set in $(D, \tilde{\sigma}, S)$ is soft open.

Theorem 3.13: If $(D, \tilde{\sigma}, S)$ is a soft submaximal. Then $(D, \tilde{\sigma}_{Np}, S)$ is a S. T. S.
Proof:

i. Since $\tilde{\emptyset}, \tilde{D} \tilde{\in} \tilde{\sigma}$, then $\tilde{\emptyset}, \tilde{D} \tilde{\in} \tilde{\sigma}_{Np}$.
ii. Let $(L_1, S), (L_2, S) \tilde{\in} \tilde{\sigma}_{Np}$ and $\tilde{x} \tilde{\in} (L_1, S)\tilde{\cap}(L_2, S)$. Then there exists soft p-open subsets (W_1, S) and (W_2, S) of $\tilde{D}$ containing $\tilde{x}$ such that $(W_1, S) - (L_1, S)$ and $(W_2, S) - (L_2, S)$ are finite soft sets. Since $(D, \tilde{\sigma}, S)$ is soft submaximal, then by Proposition (2.12), $(W_1, S)\tilde{\cap}(W_2, S)$ is soft p-open such that $\tilde{x} \tilde{\in} (W_1, S)\tilde{\cap}(W_2, S)$. To show that $((W_1, S)\tilde{\cap}(W_2, S)) - ((L_1, S)\tilde{\cap}(L_2, S))$ is a finite soft set. Observe that

$$\begin{aligned}
&((W_1, S)\tilde{\cap}(W_2, S)) - ((L_1, S)\tilde{\cap}(L_2, S)) \\
&= ((W_1, S)\tilde{\cap}(W_2, S))\tilde{\cap}((L_1, S)\tilde{\cap}(L_2, S))^c \\
&= ((W_1, S)\tilde{\cap}(W_2, S))\tilde{\cap}((L_1, S)^c\tilde{\cup}(L_2, S)^c)) \\
&= [((W_1, S)\tilde{\cap}(W_2, S))\tilde{\cap}(L_1, S)^c]\tilde{\cup}[(W_1, S)\tilde{\cap}(W_2, S))\tilde{\cap}(L_2, S)^c] \\
&\tilde{\subseteq} [(W_1, S)\tilde{\cap}(L_1, S)^c]\tilde{\cup}[(W_2, S))\tilde{\cap}(L_2, S)^c] \\
&= [(W_1, S) - (L_1, S)]\tilde{\cup}[(W_2, S) - (L_2, S)]
\end{aligned}$$

But $(W_1, S) - (L_1, S)$ and $(W_2, S) - (L_2, S)$ are finite soft sets, then so is $((W_1, S)\tilde{\cap}(W_2, S)) - ((L_1, S)\tilde{\cap}(L_2, S))$. Hence $(L_1, S)\tilde{\cap}(L_2, S) \tilde{\in} \tilde{\sigma}_{Np}$.
iii. Let $\{(E_\alpha, S): \alpha \in \Omega\}$ be any family of soft Np-open subsets of $\tilde{D}$. Then by Proposition (2.8), $\tilde{\cup}\{(E_\alpha, S): \alpha \in \Omega\} \tilde{\in} \tilde{\sigma}_{Np}$.

Remark 3.14: The convers of Theorem (2.13) may not be true.

Example 3.15: Let $D = \{a, b, c\}$, $S = \{s_1, s_2, s_3\}$, and let $\tilde{\sigma} = \{\tilde{D}, \tilde{\emptyset}, (G_1, S), (G_2, S)\}$ be a soft topology over D, where $(G_1, S) = \{(s_1, \{a, b\}), (s_2, \{a, c\}), (s_3, \{a, b, c\})\}$ and $(G_2, S) = \{(s_1, \{a, b\}), (s_2, \{c\}), (s_3, \{a, c\})\}$. Then $(D, \tilde{\sigma}_{Np}, S)$ is a soft topological space, but $(D, \tilde{\sigma}, S)$ is not soft submaximal.

Now, we need the following Lemma.

Lemma 3.16: If (B, S) is soft $p-$open and (E, S) is soft $\alpha-$open in $(D, \tilde{\sigma}, S)$, then $(E, S)\tilde{\cap}(B, S)$ is soft $p-$open.

Proof: Since (E, S) is soft $\alpha-$open and (B, S) is soft $p-$open in $\tilde{D}$, then

$$\begin{aligned}(E, S)\tilde{\cap}(B, S) &\tilde{\subseteq} \text{int}(\text{cl}(\text{int}(E, S)))\tilde{\cap}\ \text{int}(\text{cl}(B, S)) \\ &= \text{int}[\text{cl}(\text{int}(E, S))\tilde{\cap}\ \text{int}(\text{cl}(B, S))] \\ &\tilde{\subseteq} \text{int}[\text{cl}[\text{int}(E, S)\tilde{\cap}\ \text{int}(\text{cl}(B, S))]] \\ &\tilde{\subseteq} \text{int}[\text{cl}[\text{int}(E, S)\tilde{\cap}\ \text{cl}(B, S)]] \\ &\tilde{\subseteq} \text{int}[\text{cl}[\text{cl}[\text{int}(E, S))\tilde{\cap}\ (B, S)]]] \\ &= \text{int}[\text{cl}[\text{int}(E, S))\tilde{\cap}\ (B, S)]] \\ &\tilde{\subseteq} \text{int}[\text{cl}[(E, S))\tilde{\cap}\ (B, S)]]\end{aligned}$$

Hence $(E, S)\tilde{\cap}(B, S)$ is soft $p-$open.

Proposition 3.17: Let $(D, \tilde{\sigma}, S)$ be a S. T. S., then:

i. If (G, S) is soft open (resp. soft $\alpha-$open, soft $N-$open) in $\tilde{D}$ and (H, S) is soft $Np-$open in $\tilde{D}$. Then $(G, S)\tilde{\cap}(H, S)$ is soft $Np-$open.
ii. If (P, S) is soft Np-open in $\tilde{D}$ and (T, S) is soft s-open in $\tilde{D}$, then $(P, S)\tilde{\cap}(T, S)$ is soft Np-open in $((T, S), \tilde{\sigma}_{(T,S)}, S)$.
iii. If (P, S) is soft Np-open in $((T, S), \tilde{\sigma}_{(T,S)}, S)$ and (T, S) is soft p-open in $(D, \tilde{\sigma}, S)$, then (P, S) is soft Np-open set in $(D, \tilde{\sigma}, S)$.

Proof:

i. If (G, S) is soft $\alpha-$open in $\tilde{D}$ and (H, S) is soft $Np-$open in $\tilde{D}$, then for each $\tilde{y} \tilde{\in} (G, S)\tilde{\cap}(H, S)$ there exists a soft p-open set (W, S) in $\tilde{D}$ containing $\tilde{y}$ such that $(W, S) - (H, S)$ is a finite soft set. By Lemma (2.16), $(G, S)\tilde{\cap}(W, S)$ is soft $p-$open. Thus $\forall\ \tilde{y} \tilde{\in} (G, S)\tilde{\cap}(H, S)$, $\exists$ a soft $p-$open subset $(G, S)\tilde{\cap}(W, S)$ of $\tilde{D}$ containing $\tilde{y}$ such that

$$\begin{aligned}&((G, S)\tilde{\cap}(W, S)) - ((G, S)\tilde{\cap}(H, S)) \\ &= ((G, S)\tilde{\cap}(W, S))\tilde{\cap}((G, S)\tilde{\cap}(H, S))^c \\ &= ((G, S)\tilde{\cap}(W, S))\tilde{\cap}((G, S)^c\tilde{\cup}(H, S)^c) \\ &= [((G, S)\tilde{\cap}(W, S))\tilde{\cap}(G, S)^c]\tilde{\cup}[((G, S)\tilde{\cap}(W, S))\tilde{\cap}(H, S)^c] \\ &= [((G, S)\tilde{\cap}(W, S))\tilde{\cap}(H, S)^c] \\ &= ((G, S)\tilde{\cap}(W, S)) - (H, S)\ \tilde{\subseteq}\ (W, S) - (H, S)\end{aligned}$$

But $(W, S)) - (H, S)$ is finite, Thus $((G, S)\tilde{\cap}(W, S)) - ((G, S)\tilde{\cap}(H, S))$ is finite. Hence $(G, S)\tilde{\cap}(H, S)$ is soft $Np-$open.

ii. Let $\tilde{a} \tilde{\in} (P, S)\tilde{\cap}(T, S)$, since (P, S) is soft Np-open in $\tilde{D}$, then $\exists$ a soft $p-$open set (V, S) in $\tilde{D}$ containing $\tilde{a}$ such that $(V, S) - (P, S)$ is a finite soft set. By Proposition (1.13), (ii) we have $(V, S)\tilde{\cap}(T, S)$ is soft $p-$open set in $((T, S), \tilde{\sigma}_{(T,S)}, S)$ such that $\tilde{a} \tilde{\in} (V, S)\tilde{\cap}(T, S)$. Now,

$$\begin{aligned}&((V, S)\tilde{\cap}(T, S)) - ((P, S)\tilde{\cap}(T, S)) \\ &= ((V, S)\tilde{\cap}(T, S))\tilde{\cap}((P, S)\tilde{\cap}(T, S))^c \\ &= ((V, S)\tilde{\cap}(T, S))\tilde{\cap}((P, S)^c\tilde{\cup}(T, S)^c)\end{aligned}$$

$$= [((V,S)\widetilde{\cap}(T,S))\widetilde{\cap}(P,S)^c]\widetilde{\cup}[((V,S)\widetilde{\cap}(T,S))\widetilde{\cap}(T,S)^c)]$$
$$= [((V,S)\widetilde{\cap}(T,S))\widetilde{\cap}(P,S)^c]$$
$$= ((V,S)\widetilde{\cap}(T,S)) - (P,S) \,\widetilde{\subseteq}\, (V,S) - (P,S)$$

But $(V,S) - (P,S)$ is finite, then so is $((V,S)\widetilde{\cap}(T,S)) - ((P,S)\widetilde{\cap}(T,S))$. This shows $(P,S)\widetilde{\cap}(T,S)$ is soft $Np-$ open in $((T,S),\tilde{\sigma}_{(T,S)},S)$.

iii. If (P,S) is a soft Np-open set in $((T,S),\tilde{\sigma}_{(T,S)},S)$, then for each $\tilde{a} \,\widetilde{\in}\, (P,S)$, $\exists$ a soft $p-$ open set (U,S) in $((T,S),\tilde{\sigma}_{(T,S)},S)$ containing $\tilde{a}$ such that $(U,S) - (P,S)$ is a finite soft set. Since (T,S) is soft $p-$ open in $(D,\tilde{\sigma},S)$, then by Proposition (1.13),(iii), (U,S) is soft $p-$ open in $\widetilde{D}$ such that $(U,S) - (P,S)$ is a finite soft set. Hence, (P,S) is soft $Np-$ open in $(D,\tilde{\sigma},S)$.

Corollary 3.18: Let $(D,\tilde{\sigma},S)$ be a S. T. S. Then the soft union of a soft closed (resp. soft $\alpha-$ closed, soft $N-$ closed) set and a soft $Np-$ closed set is soft Np-closed.

Proof: It is obvious.

Corollary 3.19: If $(B,\tilde{\sigma}_B,S)$ is a soft open subspace of $(D,\tilde{\sigma},S)$ and $(E,S) \,\widetilde{\subseteq}\, \widetilde{B} \,\widetilde{\subseteq}\, \widetilde{D}$, then (E,S) is soft Np-open in $\widetilde{D}$ if and only if it is soft Np-open in $\widetilde{B}$.

Proof: It is obvious.

Proposition 3.20: Let $(B,\tilde{\sigma}_B,S)$ be a soft open subspace of $(D,\tilde{\sigma},S)$. If (L,S) is soft Np-open (resp. soft Np-closed) in $\widetilde{D}$, then $(L,S)\widetilde{\cap}\widetilde{B}$ is soft $Np-$ open (soft $Np-$ closed) in $\widetilde{B}$.

Proposition 3.21: If $(D,\tilde{\sigma},S)$ is a soft $\tilde{T}_1$-space with a finite set of parameters, then every non-null soft Np-open set contains a non-null soft p-open set.

Proof: Let (P,S) be a non-null soft Np-open set in $\widetilde{D}$. Since $(P,S) \neq \widetilde{\emptyset}$, let $\tilde{x} \,\widetilde{\in}\, (P,S)$, then there exists a soft p-open set (U,S) in $\widetilde{D}$ containing $\tilde{x}$ such that $(U,S) - (P,S)$ is a finite set. Since $(D,\tilde{\sigma},S)$ is soft $\tilde{T}_1$-space, thus $(M,S) = (U,S) - (P,S) = (U,S)\widetilde{\cap}(P,S)^c$ is a soft closed set.
Hence $\tilde{x} \,\widetilde{\in}\, (U,S) - (M,S) \,\widetilde{\subseteq}\, (P,S)$ and by Proposition (1.7),(i),$(U,S) - (M,S) = (U,S)\widetilde{\cap}(M,S)^c$ is soft p-open.

Remark 3.22: If $(D,\tilde{\sigma},S)$ is not a soft $\tilde{T}_1$-space, then there exists a non-null soft Np-open set which does not contain a non-null soft p-open set.

Example 2.23: Let $D = \{u,v,w\}$, $S = \{s_1,s_2\}$, and let $\tilde{\sigma} = \{\widetilde{D},\widetilde{\emptyset},(P_1,S),(P_2,S),(P_3,S)\}$ be a soft topology over D, where

$$(P_1,S) = \{(s_1,\{u\}),(s_2,\{v\})\}$$
$$(P_2,S) = \{(s_1,\{v\}),(s_2,\{u\})\}$$
$$(P_3,S) = \{(s_1,\{u,v\}),(s_2,\{v,u\})\}$$

Then $(K,S) = \{(s_1,\{w\}),(s_2,\{w\})\}$ is soft $Np-$ open not contains any non-null soft $p-$ open set.

Proposition 3.24: A soft subset (P,S) of $(D,\tilde{\sigma},S)$ is soft Np-open if and only if for each $\tilde{p} \,\widetilde{\in}\, (P,S)$ there exists a soft p-open set (V,S) in $\widetilde{D}$ containing $\tilde{p}$ and a finite soft set (M,S) such that $(V,S) - (M,S) \,\widetilde{\subseteq}\, (P,S)$.

Proof: Let (P,S) be a soft Np-open set in $\widetilde{D}$ and $\tilde{p} \,\widetilde{\in}\, (P,S)$, then there is a soft p-open subset (V,S) of $\widetilde{D}$ containing $\tilde{p}$ such that $(V,S) - (P,S)$ is a finite soft set. Let $(M,S) = (V,S) - (P,S)$

$= (V,S)\widetilde{\cap}(P,S)^c$. Then $(V,S) - (M,S) \cong (P,S)$. Conversely, let $\tilde{p} \cong (P,S)$, then there is a soft p-open subset (V,S) of $\widetilde{D}$ containing $\tilde{p}$ and a finite soft set (M,S) such that $(V,S) - (M,S) \cong (P,S)$. Thus $(V,S) - (P,S) \cong (M,S)$ and $(V,S) - (P,S)$ is a finite soft set.

Proposition 3.25: Let (P,S) be a soft Np-closed subset of $(D,\tilde{\sigma},S)$. Then $(P,S) \cong (G,S)\widetilde{\cup}(F,S)$ for some soft p-closed set (G,S) and a finite soft set (F,S).

Proof: It is obvious.

Proposition 3.26: Let $(B,\tilde{\sigma}_B,S)$ be a soft $p-$clopen subspace of $(D,\tilde{\sigma},S)$. If (K,S) is soft $Np-$closed in $\widetilde{B}$, then (K,S) is soft $Np-$closed in $\widetilde{D}$.

Proof: To show that $\widetilde{D} - (K,S)$ is a soft Np-open set in $\widetilde{D}$. Let $\tilde{x} \cong \widetilde{D} - (K,S)$, then either $\tilde{a} \cong \widetilde{D} - \widetilde{B}$ or $\tilde{a} \cong \widetilde{B} - (K,S)$. If $\tilde{a} \cong \widetilde{D} - \widetilde{B}$, since $\widetilde{B}$ is soft $p-$closed in $\widetilde{D}$, then $\widetilde{D} - \widetilde{B}$ is a soft $p-$open in $\widetilde{D}$, and so it is soft $Np-$open, hence there exist a soft p-open set (W,S) in $\widetilde{D}$ contains $\tilde{a}$ such that $(W,S) - (\widetilde{D} - \widetilde{B})$ is soft finite. Since $(K,S) \cong \widetilde{B}$, then $\widetilde{D} - \widetilde{B} \cong \widetilde{D} - (K,S)$, hence $(W,S) - (\widetilde{D} - (K,S)) \cong (W,S) - (\widetilde{D} - \widetilde{B})$ and $(W,S) - (\widetilde{D} - (K,S))$ is a finite soft set. Thus $\widetilde{D} - (K,S)$ is soft $Np-$open in $\widetilde{D}$. Now, if $\tilde{a} \cong \widetilde{B} - (K,S)$, since $\widetilde{B} - (K,S)$ is a soft $Np-$open in $\widetilde{B}$, then there is a soft $p-$open set (T,S) in $\widetilde{B}$ containing $\tilde{a}$ such that $(T,S) - (\widetilde{B} - (K,S))$ is a finite soft set. Since $\widetilde{B}$ is soft p-open in $\widetilde{D}$, then by Proposition (1.13),(iii), (T,S) is soft p-open in $\widetilde{D}$ such that $(T,S) - (\widetilde{B} - (K,S))$ is a finite soft set. Since $\widetilde{B} \cong \widetilde{D}$, then $\widetilde{B} - (K,S) \cong \widetilde{D} - (K,S)$, hence $(T,S) - (\widetilde{D} - (K,S)) \cong (T,S) - (\widetilde{B} - (K,S))$. Therefore $(T,S) - (\widetilde{D} - (K,S))$ is finite. Thus $\widetilde{D} - (K,S)$ is soft $Np-$open $\widetilde{D}$.
Corollary 3.27: Let $(B,\tilde{\sigma}_B,S)$ be a soft clopen subspace of $(D,\tilde{\sigma},S)$ and $(A,S) \cong \widetilde{B} \cong \widetilde{D}$. Then (A,S) is soft Np-closed in $\widetilde{D}$ if and only if it is soft Np-closed in $\widetilde{B}$.

4. Soft Np-Compact Spaces and Soft Np-Lindelöf Spaces

Definition 4.1: A soft subset (G,S) of $(D,\tilde{\sigma},S)$ is called soft $Np-$compact (resp. soft $Np-$Lindelöf) if each softcover of (G,S) by soft Np-open subsets of $\widetilde{D}$ has a finite (resp. countable) subcover.

Definition 4.2: A S. T. S. $(D,\tilde{\sigma},S)$ is said to be soft $Np-$compact (resp. soft $Np-$Lindelöf) if each soft $Np-$open cover of $\widetilde{D}$ has a finite (resp. countable) subcover.

Proposition 4.3: Each soft $Np-$compact (resp. soft $Np-$Lindelöf) space is soft compact (resp. soft Lindelöf).

Proof: It is obvious.

Proposition 4.4: Each soft $Np-$compact space is soft $Np-$Lindelöf.

Remark 4.5: The converse of Propositions (3.3) and (3.4) are not true in general. We see that by the following examples:

Example 4.6: Let $D = \Re$, S be any set of parameters, and $\tilde{\sigma} = \{\widetilde{\Re}, \widetilde{\emptyset}, (P,S)\}$ be a soft topology over $\Re$, where $P(s) = \{3\}$, for each $s \in S$. Then $(\Re,\tilde{\sigma},S)$ is a soft compact space, but is not soft Np-Lindelöf, since $\{(U,S): U(s) = \{3,a\}, \forall\, s \in S, a \in D\}$ is soft $Np-$open cover of $\widetilde{D}$, which has no countable subcover.

Example 4.7: Let $D = N$, $S = \{s_1, s_2, s_3, \ldots, s_n\}$ be a set of parameters, and $\tilde{\sigma} = \{\tilde{N}, \tilde{\emptyset}, (J, S)\}$ be soft topology over N, where $J(s) = \{4\}$, for each $s \in S$. Since N and S are countable sets, then $(N, \tilde{\sigma}, S)$ is a soft Np-Lindelöf space, but is not soft Np-compact, since $\{(V, S): V(s) = \{4, a\}, \forall\, s \in S, a \in \Re\}$ is soft $Np-$ open cover of $\tilde{N}$ has no finite subcover.

Theorem 4.8: If $(D, \tilde{\sigma}, S)$ is a S. T. S. Then each soft set in $\tilde{D}$ is soft $Np-$compact (resp. soft Np-Lindelöf) if and only if each soft Np-open set in $\tilde{D}$ is soft $Np-$compact (resp. soft $Np-$Lindelöf).

Proof: The necessity is obvious. Conversely, if (G, S) is any soft set in $\tilde{D}$ and $\{(W_\alpha, S): \alpha \in \Omega\}$ is soft cover of (G, S) by soft $Np-$open subsets of $\tilde{D}$. Hence the family $\{(W_\alpha, S): \alpha \in \Omega\}$ is a soft Np-open cover of the soft Np-open set $\tilde{U}\{(W_\alpha,S):\alpha \in \Omega\}$. Then by assumption, there is a finite subfamily $\{(W_{\alpha_i}, S): i = 1, \ldots, n\}$ which covers $\tilde{U}\{(W_\alpha,S):\alpha \in \Omega\}$. This subfamily is also a soft subcover of (G, S). Thus (G, S) is soft Np-compact.

Theorem 4.9: Let $(D, \tilde{\sigma}, S)$ be a S. T. S. with a finite (resp. countable) set of parameters. Then a soft subset (A, S) of $(D, \tilde{\sigma}, S)$ is soft $Np-$compact (resp. soft $Np-$Lindelöf) iff it is soft $p-$compact (resp. soft $p-$Lindelöf).

Proof: Necessity. It follows from the fact every soft p-open set is soft Np-open.
Sufficiency. Suppose that (A, S) is a soft p-compact set and $\{(U_\alpha, S): \alpha \in \Omega\}$ is a soft cover of (A, S) by soft Np-open subsets of $\tilde{D}$. For each $\tilde{a} \,\tilde{\in}\, (A, S)$, there exists $\alpha(\tilde{a}) \in \Omega$ such that $\tilde{a} \,\tilde{\in}\, (U_{\alpha(\tilde{a})}, S)$. Since $(U_{\alpha(\tilde{a})}, S)$ is soft Np-open, then there exists a soft p-open set $(N_{\alpha(\tilde{a})}, S)$ in $\tilde{D}$ such that $\tilde{a} \,\tilde{\in}\, (N_{\alpha(\tilde{a})}, S)$ and $(N_{\alpha(\tilde{a})}, S) - (U_{\alpha(\tilde{a})}, S)$ is a soft finite set. The family $\{(N_{\alpha(\tilde{a})}, S): \tilde{a} \,\tilde{\in}\, (A, S)\}$ is a soft $p-$open cover of (A, S). But (A, S) is soft $p-$compact, hence $\exists\ \tilde{a}_1, \tilde{a}_2, \ldots, \tilde{a}_n$ such that $(A, S) \,\tilde{\subseteq}\, \tilde{U}\{(N_{\alpha(\tilde{a}_i)}, S): i \in I\}$, where $I = \{1,2, \ldots, n\}$. Now, we obtain

$$(A, S) \,\tilde{\subseteq}\, \tilde{U}\{[((N_{\alpha(\tilde{a}_i)}, S) - (U_{\alpha(\tilde{a}_i)}, S))\tilde{U}(U_{\alpha(\tilde{a}_i)}, S)]: i \in I\} = \tilde{U}\{((N_{\alpha(\tilde{a}_i)}, S) - (U_{\alpha(\tilde{a}_i)}, S)): i \in I\}\ \tilde{U}\ (\tilde{U}\{(U_{\alpha(\tilde{a}_i)}, S): i \in I\})$$

For each $\tilde{a}_i$, $(N_{\alpha(\tilde{a}_i)}, S) - (U_{\alpha(\tilde{a}_i)}, S)$ is a soft finite set and there is a finite subset $\Omega(\tilde{a}_i)$ of Ω such that $((N_{\alpha(\tilde{a}_i)}, S) - (U_{\alpha(\tilde{a}_i)}, S))\tilde{\cap}(A, S) \,\tilde{\subseteq}\, \tilde{U}\{(U_\alpha, S): \alpha \in \Omega(\tilde{a}_i)\}$. Therefore, we have
$(A, S) \,\tilde{\subseteq}\, \tilde{U}\{\tilde{U}\{(U_\alpha, S): \alpha \in \Omega(\tilde{a}_i)\}: i \in I\}\ \tilde{U}\ (\tilde{U}\{(U_{\alpha(\tilde{a}_i)}, S): i \in I\})$.
Hence (A, S) is soft Np-compact in $\tilde{D}$.

Corollary 4.10: A S. T. S. $(D, \tilde{\sigma}, S)$ with a finite (resp. countable) set of parameters is soft $Np-$compact (resp. soft $Np-$Lindelöf) iff it is soft $p-$compact (resp. soft $p-$Lindelöf).

Remark 4.11: From Theorem (3.9), if the set of parameters S is not finite (resp. not countable), then each soft $Np-$compact (resp. soft $Np-$Lindelöf) is soft $p-$compact (resp. soft $p-$Lindelöf), but it converse may not be true as shown in the following example:

Example 4.12: Let $D = \Re = S$, $(1, \{1\}) = \tilde{a} \,\tilde{\in}\, \tilde{R}$ and let $\tilde{\sigma} = \{(W, S) \,\tilde{\subseteq}\, \tilde{\Re}: \tilde{a} \,\tilde{\notin}\, (W, S)\}\ \tilde{U}\ \{\tilde{\Re}\}$ be the excluded soft point soft topology over $\Re$. Then $(\Re, \tilde{\sigma}, \Re)$ is a soft p-compact space, but is not soft Np-Lindelöf, since $\{\{\tilde{x}\}\tilde{U}(M, S)^c: \tilde{x} \,\tilde{\in}\, (M, S)\ \&\ M(s) = \{2,3,4,5,6,7,8,9,10\}, \forall\, s \in D\}$ is a soft $Np-$ open cover of $\tilde{D}$ has no countable subcover.

Remark 4.13: Diagram (2) shows the relation among soft Np-compact spaces, soft Np-Lindelöf spaces, and other kinds of soft spaces.

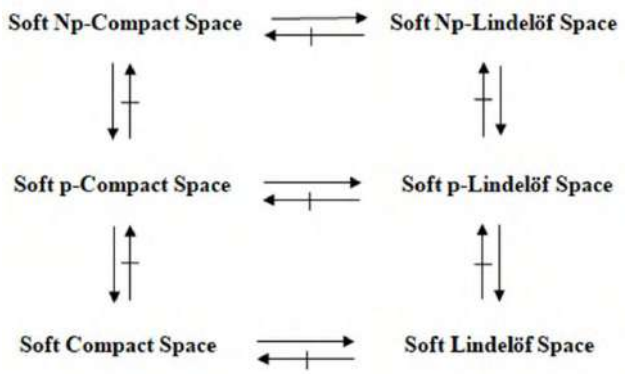

Diagram (2)

Proposition 4.14: Each soft $\mathrm{Np}-$ closed set in a soft $\mathrm{Np}-$ compact (resp. soft $\mathrm{Np}-$Lindelöf) space is soft $\mathrm{Np}-$ compact (resp. soft $\mathrm{Np}-$Lindelöf).

Proof: Assume that (E,S) is soft $\mathrm{Np}-$ closed in a soft $\mathrm{Np}-$ compact space $(D,\tilde{\sigma},S)$, and $\{(V_\alpha,S):\alpha\in\Psi\}$ is a soft cover of (E,S) by soft $\mathrm{Np}-$ open sets in $\tilde{D}$. Since $(E,S)^c$ is soft Np-open, then $\{(V_\alpha,S):\alpha\in\Psi\}\tilde{\cup}(E,S)^c$ is soft $\mathrm{Np}-$ open cover of $\tilde{D}$ which is soft $\mathrm{Np}-$ compact, hence $\exists\ \{(V_{\alpha_i},S)\}_{i=1}^{n}\tilde{\cup}(E,S)^c$ is a finite soft subcover. So $\tilde{D}\cong(\tilde{\cup}\{(V_{\propto_i},S):i=1,\dots n\})\tilde{\cup}\ (E,S)^c$. Thus $(E,S)\cong\tilde{\cup}\{(V_{\propto_i},S):i=1,\dots n\}$. Therefore, (E,S) is soft Np-compact. In the same way, we prove the other case.

Proposition 4.15: Let $(D,\tilde{\sigma},S)$ be a S. T. S. If (E,S) is soft $\mathrm{Np}-$closed and (P,S) is soft $\mathrm{Np}-$ compact (resp. soft $\mathrm{Np}-$Lindelöf) in $\tilde{D}$. Then $(E,S)\tilde{\cap}(P,S)$ is soft $\mathrm{Np}-$ compact (resp. soft $\mathrm{Np}-$Lindelöf) in $\tilde{D}$.

Proof: Let $\{(U_\alpha,S):\alpha\in\Psi\}$ be a soft cover of $(E,S)\tilde{\cap}(P,S)$ by soft Np-open subsets of $\tilde{D}$. Hence $(P,S)\cong\tilde{\cup}\{(U_\alpha,S):\alpha\in\Psi\}\tilde{\cup}(E,S)^c$. Since (P,S) is soft Np-compact, then $\exists\ \{(U_{\alpha_i},S)\}_{i=1}^{n}\tilde{\cup}(E,S)^c$ is a finite soft subcover for (P,S). Thus $(E,S)\tilde{\cap}(P,S)\cong\tilde{\cup}\{(U_{\propto_i},S):i=1,\dots,n\}$. Therefore $(E,S)\tilde{\cap}(P,S)$ is soft Np-compact. In the same way, we can prove the other case.

Proposition 4.16: Let $(B,\tilde{\sigma}_B,S)$ be a soft open subspace of $(D,\tilde{\sigma},S)$. Then $(E,S)\cong\tilde{B}$ is soft Np $-$compact (resp. soft Np-Lindelöf) in $\tilde{B}$ if and only if it is soft $\mathrm{Np}-$ compact (resp. soft $\mathrm{Np}-$Lindelöf) in $\tilde{D}$.

Proof: It follows from Corollary (2.19) and Proposition (2.20).

Definition 4.17: A soft function $h:(D,\tilde{\sigma},S)\to(C,\tilde{\rho},S)$ is called:

i. (Soft Np-continuous if $h^{-1}((E,S))$ is soft $\mathrm{Np}-$ open in $\tilde{D}$ for all soft open set (E,S) in $\tilde{C}$.
ii. Soft Np-irresolute if $h^{-1}((E,S))$ is soft $\mathrm{Np}-$ open in $\tilde{D}$ for all soft $\mathrm{Np}-$ open set (E,S) in $\tilde{C}$.

Proposition 4.18:

i. If $h:(D,\tilde{\sigma},S)\to(C,\tilde{\rho},S)$ is soft Np-irresolute and (E,S) is soft Np-compact (resp. soft Np-Lindelöf) in $\tilde{D}$. Then $h((E,S))$ is soft Np-compact (resp. soft Np-Lindelöf) in $\tilde{C}$.
ii. If $h:(D,\tilde{\sigma},S)\to(C,\tilde{\rho},S)$ is soft Np-continuous and (E,S) is soft Np-compact (resp. soft Np-Lindelöf) in $\tilde{D}$. Then $h((E,S))$ is soft compact (resp. soft Lindelöf) in $\tilde{C}$.

Proof:

i. To show that $h((E,S))$ is a soft Np-compact subset of $\tilde{C}$. Let $\{(V_\alpha,S):\alpha\in\Psi\}$ be a soft cover of $h((E,S))$ by soft Np-open subsets of $\tilde{C}$ that is $h((E,S))\cong\tilde{U}\{(V_\alpha,S):\alpha\in\Psi\}$, so $(E,S)\cong\tilde{U}\{h^{-1}((V_\alpha,S)):\alpha\in\Psi\}$. Since h is soft Np-irresolute, then $\{h^{-1}((V_\alpha,S)):\alpha\in\Psi\}$ is soft $Np-$ open cover of (E,S) which is soft $Np-$ compact, hence $\exists\ \{h^{-1}((V_{\alpha_i},S))\}_{i=1}^{n}$ is a finite soft subcover. Thus $(E,S)\cong\tilde{U}\{h^{-1}((V_{\alpha_i},S)):i=1,\dots n\}$, that is $h((E,S))\cong\tilde{U}\{(V_{\alpha_i},S):i=1,\dots n\}$. Therefore $h((E,S))$ is soft Np-compact.

ii. Similar to (i).

References

[1] D Molodtsov 1999 Soft Set Theory-First Results *Computers and Mathematics with Applications* **37** 19-31
[2] M Shabir and M Naz 2011 On Soft Topological Spaces *Computers and Mathematics with Applications* **61 (7)** 1786-1799
[3] A Aygunuglu and H Aygun 2012 Some Notes on Soft Topological Spaces *Neural Computers and Applications* **21 (1)** 113-119
[4] W Rong 2012 The countabilities of soft topological spaces *International Journal of Mathematical, Computational, Physical, Electrical and Computer Engineering* **6 (8)** 159-162
[5] T Al-Shami and M El-Shafei 2019 On Soft Compact and Soft Lindelöf Spaces Via Soft pre-Open Sets *Annal. Fuzzy. Math. Inform* **17 (1)** 79-100
[6] I Arockiarani and A Arokia Lancy 2013 Generalized soft gβ-closed sets and soft gsβ-closed sets in soft topological spaces *International Journal of Mathematical Archive* **4 (2)** 17-23
[7] B Chen 2013 Soft semi-open sets and related properties in soft topological spaces *Applied Mathematics Information Sciences* **7 (1)** 287-294
[8] M Akdag and A Ozkan 2014 Soft α-open sets and soft α-continuous functions *Abstract and Applied Analysis* **ID 891341** 1-7
[9] S Mahmood 2017 On Weak Soft N-Open Sets and Weak Soft $\widetilde{D}_N$-Sets in Soft Topological Spaces *J. of Al-Nahrain Univ* **20 (2)** 131-141
[10] P K Maji, R Biswas and R Roy 2003 Soft Set Theory *Computers and Mathematics with Applications* **45** 555-562
[11] D Pei and D Miao 2005 From Soft Sets to Information Systems *IEEE International Conference on Granular Computing* **2** 617-621
[12] M Ali, F Feng, X Liu, and M Shabir 2009 On Some New Operations in Soft Set Theory *Computers and Mathematics with Applications* **57** 1547-1553
[13] S k Nazmul and S K Samanta 2013 Neighbourhood properties of soft topological spaces *Annals of Fuzzy Mathematics and Informatics* **6 (1)** 1-15
[14] S Das and S K Samanta 2013 On Soft Metric Spaces *Annals of Fuzzy Mathematics and Informatics* **21 (3)** 707-734
[15] I Gnanambal and R Mrudula 2013 On Soft Pre-open Sets in Soft Topological Spaces *International Journal of Mathematics Research* **5 (4)** 399-409
[16] M Akdag and A Ozkan 2014 On Soft Preopen Sets and Soft Pre Separation Axioms *Gazi University Journal of Science* **27 (4)** 1077-1083
[17] S Bayramov and C Gunduz 2018 A new approach to Separability and Compactness in Soft Topological Spaces *TWMS J. Pure Appl. Math* **9 (1)** 82-93

Random Fixed Point on Ishikawa Random Iteration Under Fibonacci Sequence

Random Fixed Point on Ishikawa Random Iteration Under Fibonacci Sequence

Sabah Hassan Malih

Department of Mathematics, College of Education for pure science (Ibn- AL-Haitham), university of Baghdad, Iraq

E-mail: sabahhassanmalih@gmail.com

Abstract. In this paper, we introduce a new iterations scheme under Fibonacci sequence for Ishikawa random Iteration of the asymptotically random operator and we have some results convergence to a fixed point.

1. Introduction and preliminaries

The development of the theory of random factors is important as a potential generalization of the determinist operator theory and since the operator theory has important roles in the study of operators'. Spacek [1] and Hans [2] established a stochastic analog of the Banach fixed point theorem in a separable complete metric space. Now this area has become a full-fledged research area (see [3],[4],[5],[6], and [7]).

We supposed that B is a uniformly convex, separable Banach space and F is a nonempty closed convex subset of B.

Definition (1.1) [8]: A measurable mapping $\alpha(\upsilon) : \theta \to B$ is a random fixed point of a random operator $P: \theta \times F \to F$ if $P(\upsilon, \alpha(\upsilon)) = \alpha(\upsilon)$, $\upsilon \in \theta$.

Definition (1.2) [9]: Let a random operator $P: \theta \times F \to F$ be an asymptotically nonresponsive random operator if for every $a, b \in F, \Omega(r) \geq 1$, there exist $\{\Omega(r)\}$ a sequence of positive numbers and $\lim_{r\to\infty} \Omega(r) = 1$, such that
$\|P^r(\upsilon, a(\upsilon)) - P^r(\upsilon, b(\upsilon))\| \leq \beta_r \|a(\upsilon) - b(\upsilon)\|$, for each $\upsilon \in \theta$.

Lemma (1.3) [10]: Let $\{g_r\}$, $\{h_r\}$ be two sequences of nonnegative numbers such that
$g_{r+1} \leq (1 + h_r)\, g_r \quad \forall r \in N$.
If $\sum_{r=1}^{\infty} h_r < \infty$, then $\lim_{r\to\infty} g_r$ exists.

Lemma (1.4) [11]: Let B be a space , $0 < p \leq \lambda_r \leq q < 1$. For all $r \in N$ suppose that $\{c_r\}$ and $\{d_r\}$ are two sequences of B such that $\limsup_{r\to\infty} \|c_r\| \leq t$, $\limsup_{r\to\infty} \|d_r\| \leq t$ *and*
$\lim_{r\to\infty} \|\lambda_r c_r + (1 - \lambda_r) d_r\| = t$. Then $\lim_{r\to\infty} \|c_r - d_r\| = 0$.

Definition (1.5) [12]: A space B is said to satisfy the Opial's condition if for any sequence $\{c_r\}$ in B, $c_r \rightharpoonup c$ (weakly) as $r \to \infty$ and $c \neq d$ implying that $\lim_{r\to\infty} \sup\|c_r - c\| < \lim_{r\to\infty} \sup\|c_r - d\|$

Theorem (1.6) : Let F be a subset of space B which satisfies Opial's condition and let $P: \theta \times F \to F$ be an asymptotically nonexpansive random operator. Then $(I - P)$ is demiclosed at zero, if $\alpha_r(\upsilon): \theta \to$such that $\alpha_r(\upsilon) \rightharpoonup \zeta(\upsilon)$ and $\lim_{r\to\infty} \sup\left\|P\big((\upsilon), \alpha_r(\upsilon)\big) - \alpha_r(\upsilon)\right\| = 0$, then
$(I - P)\big(\upsilon, \omega(\upsilon)\big) = 0$ Which means led to $P\big(\upsilon, \omega(\upsilon)\big) = \omega(\upsilon)$.

Definition (1.6): [13] (Fibonacci sequence): Let $\{\Omega(r)\}$ be a Fibonacci sequence if $\Omega(r+1) = \Omega(r) + \Omega(r-1)$, where $\Omega(0) = \Omega(1) = 1, \forall\, r \geq 1$.

2. Main results

Through this work, we obtain theorems in the stochastic fixed point with the effect of the Fibonacci sequence.

Definition (2.1): Let F be a subset of space $(B, \|\,.\,\|)$, and let $P: \theta \times F \to F$ be a random operator. Fix $\alpha_0(\upsilon) \in F$ and $\{\lambda_r\}, \{\aleph_r\} \subset [0,1]$. The random Fibonacci- Ishikawa iteration is defined by
$\alpha_{r+1}(\upsilon) = \lambda_r P^{\Omega(r)}\big((\upsilon), \beta_r(\upsilon)\big) + (1 - \lambda_r)\alpha_r(\upsilon)$
$\beta_r(\upsilon) = (\,(1 - \aleph_r)\alpha_r(\upsilon) + \aleph_r P^{\Omega(r)}\big((\upsilon), \alpha_r(\upsilon)\big)$
For each $\in N$, where $\{\Omega(r)\}$ is the Fibonacci sequence.
Where $\{\lambda_r\} \subset [0,1]$ if $0 < a \leq \lambda_r, \aleph_r \leq b < 1$.

Proposition (2.2) Let F be a subset of B. Let $P: \theta \times F \to F$ satisfies Definition (1.2) and $\{\alpha_r(\upsilon)\}$ the sequence satisfies Definition (2.1) which is bounded. If $\sum\big(\delta_{\Omega(r)} - 1\big) < \infty$, RP is nonempty set of a fixed point on P, then $\lim_{r\to\infty}\|\alpha_{r+1}(\upsilon) - \omega(\upsilon)\|$exists, $\forall \omega(\upsilon) \in RP$.

Proof: Let $\omega(\upsilon) \in RP$, then

$$\begin{aligned}
\|\alpha_{r+1}(\upsilon) - \omega(\upsilon)\| &= \left\|\lambda_r P^{\Omega(r)}\big((\upsilon), \beta_r(\upsilon)\big) + (1 - \lambda_r)\alpha_r(\upsilon) - \omega(\upsilon)\right\| \\
&= \left\|(1 - \lambda_r)\big(\alpha_r(\upsilon) - \omega(\upsilon)\big) + \lambda_r\left(P^{\Omega(r)}\left((\upsilon), \beta_r(\upsilon)\right) - \omega(\upsilon)\right)\right\| \\
&\leq (1 - \lambda_r)\|\alpha_r(\upsilon) - \omega(\upsilon)\| + \lambda_r\left\|P^{\Omega(r)}\left((\upsilon), \beta_r(\upsilon)\right) - \omega(\upsilon)\right\| \\
&\leq \delta_{\Omega(r)}\left\|\beta_r(\upsilon) - \omega(\upsilon)\right\| \\
\left\|\beta_r(\upsilon) - \omega(\upsilon)\right\| &= \left\|(1 - \aleph_r)\alpha_r(\upsilon) + \aleph_r P^{\Omega(r)}\big((\upsilon), \alpha_r(\upsilon)\big) - \omega(\upsilon)\right\| \\
&= \left\|(1 - \aleph_r)\big(\alpha_r(\upsilon) - \omega(\upsilon)\big) + \aleph_r\left(P^{\Omega(r)}\big((\upsilon), \alpha_r(\upsilon)\big) - \omega(\upsilon)\right)\right\| \\
&\leq (1 - \aleph_r)\|\alpha_r(\upsilon) - \omega(\upsilon)\| + \aleph_r\left\|P^{\Omega(r)}\big((\upsilon), \alpha_r(\upsilon)\big) - \omega(\upsilon)\right\| \\
&\leq \delta_{\Omega(r)}\|\alpha_r(\upsilon) - \omega(\upsilon)\|.
\end{aligned}$$

Therefore, $\|\alpha_{r+1}(\upsilon) - \omega(\upsilon)\| \leq {\delta_{\Omega(r)}}^2\|\alpha_r(\upsilon) - \omega(\upsilon)\| = \left(1 + \left({\delta_{\Omega(r)}}^2 - 1\right)\right)\|\alpha_r(\upsilon) - \omega(\upsilon)\|$
By Lemma (1.3), we have $\lim_{\upsilon\to\infty}\|\alpha_r(\upsilon) - \omega(\upsilon)\| = t$, exists, $\forall\, t \geq 0$.

Theorem (2.3): Let $B, F, P, RP, \{\alpha_r(\upsilon)\}$ satisfies in Proposition 2.2, B is Opial's condition.
If $\sum\big({\delta_{\Omega(r)}}^2 - 1\big) < \infty$ then $\{\alpha_r(\upsilon)\}$ converges weakly to a fixed point.

Proof*:* By Proposition 2.2, $\lim_{r\to\infty}\|\alpha_r(\upsilon) - \omega(\upsilon)\|$ exists. This implies that $\{\alpha_r(\upsilon)\}$ is bounded**,** to prove that

$\lim_{r\to\infty}\|\alpha_r(\upsilon) - P((\upsilon),\alpha_r(\upsilon))\| = 0$, and

$\lim_{r\to\infty}\|\alpha_{r+1}(\upsilon) - \omega(\upsilon)\| = \left\|(1-\lambda_r)(\alpha_r(\upsilon)-\omega(\upsilon)) + \lambda_r\left(P^{\Omega(r)}\left((\upsilon),\beta_r(\upsilon)\right) - \omega(\upsilon)\right)\right\|$

$\lim_{r\to\infty}\sup\left\|P^{\Omega(r)}\left((\upsilon),\beta_r(\upsilon)\right) - \omega(\upsilon)\right\| \le t$

$\lim_{r\to\infty}\sup\|P^{\Omega(r)}((\upsilon),\alpha_r(\upsilon)) - \omega(\upsilon)\| \le t$

Also $t = \lim_{r\to\infty}\|\alpha_{r+1}(\upsilon) - \omega(\upsilon)\|$, then $t \le \lim_{r\to\infty}\inf\|\beta_r(\upsilon) - \omega(\upsilon)\|$

Since $\|\alpha_r(\upsilon) - \omega(\upsilon)\| = t$ and $\|\beta_r(\upsilon) - \omega(\upsilon)\| \le \|P^{\Omega(r)}((\upsilon),\alpha_r(\upsilon)) - \omega(\upsilon)\|$

Thus $\sup\|\beta_r(\upsilon) - \omega(\upsilon)\| \le t$. Therefore $\lim_{r\to\infty}\|\beta_r(\upsilon) - \omega(\upsilon)\| = t$

$$t = \lim_{r\to\infty}\|\beta_r(\upsilon) - \omega(\upsilon)\| = \lim_{r\to\infty}\|(1-\gimel_r)\alpha_r(\upsilon) + \gimel_r P^{\Omega(r)}((\upsilon),\alpha_r(\upsilon)) - \omega(\upsilon)\|$$
$$= \lim_{r\to\infty}\left\|(1-\gimel_r)(\alpha_r(\upsilon)-\varrho) + \gimel_r\left(P^{\Omega(r)}((\upsilon),\alpha_r(\upsilon)) - \omega(\upsilon)\right)\right\|$$

By Lemma (1.4), we have $\lim_{r\to\infty}\|P^{\Omega(r)}((\upsilon),\alpha_r(\upsilon)) - \alpha_r(\upsilon)\| = 0$, next,

$$t = \lim_{r\to\infty}\|\alpha_{r+1}(\upsilon) - \omega(\upsilon)\| = \lim_{r\to\infty}\left\|(1-\lambda_r)\alpha_r(\upsilon) + \lambda_r P^{\Omega(r)}\left((\upsilon),\beta_r(\upsilon)\right) - \omega(\upsilon)\right\|$$
$$= \lim_{r\to\infty}\left\|(1-\lambda_r)(\alpha_r(\upsilon)-\omega(\upsilon)) + \lambda_r\left(P^{\Omega(r)}\left((\upsilon),\beta_r(\upsilon)\right) - \omega(\upsilon)\right)\right\|$$

By Lemma (1.4), we have $\lim_{r\to\infty}\left\|P^{\Omega(r)}\left((\upsilon),\beta_r(\upsilon)\right) - \omega(\upsilon)\right\| = 0$

$$\|\alpha_{r+1}(\upsilon) - P^{\Omega(r)}((\upsilon),\alpha_r(\upsilon))\|$$
$$\le \|\alpha_{r+1}(\upsilon) - P^{\Omega(r)}((\upsilon),\beta_r(\upsilon))\| + \|P^{\Omega(r)}((\upsilon),\beta_r(\upsilon)) - P^{\Omega(r)}((\upsilon),\alpha_r(\upsilon))\|$$
$$\|\alpha_{r+1}(\upsilon) - P^{\Omega(r)}((\upsilon),\alpha_r(\upsilon))\|$$
$$\le \left\|(1-\lambda_r)\alpha_r(\upsilon) + \lambda_r P^{\Omega(r)}\left((\upsilon),\beta_r(\upsilon)\right) - P^{\Omega(r)}\left((\upsilon),\beta_r(\upsilon)\right)\right\|$$
$$+ \left\|P^{\Omega(r)}\left((\upsilon),\beta_r(\upsilon)\right) - \alpha_r(\upsilon)\right\| + \|\alpha_r(\upsilon) - P^{\Omega(r)}((\upsilon),\alpha_r(\upsilon))\|$$
$$= \left\|(1-\lambda_r)\left(\alpha_r(\upsilon) - P^{\Omega(r)}\left((\upsilon),\beta_r(\upsilon)\right)\right)\right\| + \left\|P^{\Omega(r)}\left((\upsilon),\beta_r(\upsilon)\right) - \alpha_r(\upsilon)\right\|$$
$$+ \|\alpha_r(\upsilon) - P^{\Omega(r)}((\upsilon),\alpha_r(\upsilon))\|$$
$$\le (1-\theta_\upsilon)\left\|\alpha_r(\upsilon) - P^{\Omega(r)}\left((\upsilon),\beta_r(\upsilon)\right)\right\| + \left\|P^{\Omega(r)}\left((\upsilon),\beta_r(\upsilon)\right) - \alpha_r(\upsilon)\right\|$$
$$+ \|\alpha_r(\upsilon) - P^{\Omega(r)}((\upsilon),\alpha_r(\upsilon))\|$$

By limit of sides as $r \to \infty$ then

$\lim_{r\to 0}\|\alpha_{r+1}(\upsilon) - P^{\Omega(r)}((\upsilon),\alpha_r(\upsilon))\|$.

Thus $\lim_{r\to\infty}\|\alpha_{r+1}(\upsilon) - \alpha_r(\upsilon)\| = 0$

$$\|\alpha_{r+1}(\upsilon) - P^{\Omega(r)}((\upsilon),\alpha_{r+1}(\upsilon))\|$$
$$\le \|\alpha_{r+1}(\upsilon) - P^{\Omega(r)}((\upsilon),\alpha_r(\upsilon))\| + \|P^{\Omega(r)}((\upsilon),\alpha_r(\upsilon)) - P^{\Omega(r)}((\upsilon),\alpha_{r+1}(\upsilon))\|$$
$$\le \|\alpha_{r+1}(\upsilon) - P^{\Omega(r)}((\upsilon),\alpha_r(\upsilon))\| + \delta_{\Omega(r)}\|\alpha_r(\upsilon) - P^{\Omega(r)}((\upsilon),\alpha_{r+1}(\upsilon))\|$$

since, $\lim_{r\to\infty}\|\alpha_{r+1}(\upsilon) - P^{\Omega(r)}((\upsilon),\alpha_{r+1}(\upsilon))\| = 0$.

Thus $\lim_{r\to\infty}\|\alpha_{r+1}(\upsilon) - P^{\Omega(r)+1}((\upsilon),\alpha_{r+1}(\upsilon))\| = 0$

We have $\lim_{r\to\infty}\|\alpha_{r+1}(\upsilon) - P((\upsilon),\alpha_{r+1}(\upsilon))\| = 0$

$$\|\alpha_{r+1}(\upsilon) - P((\upsilon),\alpha_{r+1}(\upsilon))\|$$
$$\le \|\alpha_{r+1}(\upsilon) - P^{\Omega(r)+1}((\upsilon),\alpha_{r+1}(\upsilon))\|$$
$$+ \|P^{\Omega(r)+1}((\upsilon),\alpha_{r+1}(\upsilon)) - P^{\Omega(r)+1}((\upsilon),\alpha_r(\upsilon))\|$$
$$+ \|P^{\Omega(r)+1}((\upsilon),\alpha_r(\upsilon)) - P((\upsilon),\alpha_{r+1}(\upsilon))\|$$

$$\leq \left\|\alpha_{r+1}(\upsilon) - P^{\Omega(r)+1}\left((\upsilon), \alpha_{r+1}(\upsilon)\right)\right\| + \delta_{\Omega(r)}\|\alpha_{r+1}(\upsilon) - \alpha_r(\upsilon)\|$$
$$+ \delta_1\left\|P^{\Omega(r)}\left((\upsilon), \alpha_r(\upsilon)\right) - \alpha_{r+1}(\upsilon)\right\|$$
$$\left\|\alpha_r(\upsilon) - P\left((\upsilon), \alpha_r(\upsilon)\right)\right\|$$
$$= \|\alpha_r(\upsilon) - \alpha_{r+1}(\upsilon)\| + \left\|\alpha_{r+1}(\upsilon) - P\left((\upsilon), \alpha_{r+1}(\upsilon)\right)\right\|$$
$$+ \left\|P\left((\upsilon), \alpha_{r+1}(\upsilon)\right) - P\left((\upsilon), \alpha_r(\upsilon)\right)\right\|$$
$$\leq \|\alpha_r(\upsilon) - \alpha_{r+1}(\upsilon)\| + \left\|\alpha_{r+1}(\upsilon) - P\left((\upsilon), \alpha_{r+1}(\upsilon)\right)\right\| + \delta_1\|\alpha_{r+1}(\upsilon) - \alpha_r(\upsilon)\|$$

Thus $\lim_{r\to\infty}\left\|\alpha_r(\upsilon) - P\left((\upsilon), \alpha_r(\upsilon)\right)\right\| = 0$. The sequence $\{\alpha_r(\upsilon)\}$ is bounded, so there exists a subsequence $\{\alpha_{ri}(\upsilon)\}$ of $\{\alpha_r(\upsilon)\}$ such that$\alpha_{ri}(\upsilon) \to \mu(\upsilon)$ by $\left\|\alpha_{ri}(\upsilon) - P\left((\upsilon), \alpha_{ri}(\upsilon)\right)\right\| = 0$ .And by

lemma (1.4) we get $\mu(\upsilon) \in RP$.

We show that $\{\alpha_r(\upsilon)\}$ converges weakly to $\mu(\upsilon)$. Let $\{\alpha_{ri}(\upsilon)\}$ of $\{\alpha_r(\upsilon)\}$ such that$\alpha_{ri}(\upsilon) \rightharpoonup \mathfrak{z}(\upsilon)$ for some $\mathfrak{z}(\upsilon) \in F$ and again above conclude that $\mathfrak{z}(\upsilon) \in RP$, now we show that $\mu(\upsilon) = \mathfrak{z}(\upsilon)$, we assume that $\mu(\upsilon) \neq \mathfrak{z}(\upsilon)$.

Since $\lim_{\upsilon\to\infty}\|\alpha_r(\upsilon) - \varrho\|$ exists for every $\varrho \in D_f$, and since $\mu(\upsilon), \mathfrak{z}(\upsilon) \in RP$, by Opial's condition, we have that

$$\lim_{r\to\infty}\|\alpha_r(\upsilon) - \mu(\upsilon)\| = \lim_{ri\to\infty}\|\alpha_{ri}(\upsilon) - \mu(\upsilon)\| < \lim_{ri\to\infty}\|\alpha_{ri}(\upsilon) - \mathfrak{z}(\upsilon)\| = \lim_{rj\to\infty}\left\|\alpha_{rj}(\upsilon) - \mathfrak{z}(\upsilon)\right\| =$$
$$\lim_{rj\to\infty}\left\|\alpha_{rj}(\upsilon) - \mu(\upsilon)\right\| = \lim_{\upsilon\to\infty}\|\alpha_r(\upsilon) - \mu(\upsilon)\|.$$

This $\lim_{\upsilon\to\infty}\|\alpha_r(\upsilon) - \mu(\upsilon)\| < \lim_{\upsilon\to\infty}\|\alpha_r(\upsilon) - \mu(\upsilon)\|$, which is a contradiction, so we get that $\mu(\upsilon) = \mathfrak{z}(\upsilon)$.

Proposition 2.4 Let B, F, P, RP, satisfies in Proposition 2.2 and$\{\alpha_r(\upsilon)\}$ satisfies Definition (2.1) if $\aleph_r = 0$ which is bounded. If $\sum\left(\delta_{\Omega(r)} - 1\right) < \infty$, then $\lim_{r\to\infty}\|\alpha_{r+1}(\upsilon) - \omega(\upsilon)\|$exists, $\forall\omega(\upsilon) \in RP$.

Proof*:* Let $\omega(\upsilon) \in RP$, then

$$\|\alpha_{r+1}(\upsilon) - \omega(\upsilon)\| = \left\|\lambda_r P^{\Omega(r)}\left((\upsilon), \alpha_r(\upsilon)\right) + (1-\lambda_r)\alpha_r(\upsilon) - \omega(\upsilon)\right\|$$
$$= \left\|\lambda_r\left(P^{\Omega(r)}\left((\upsilon), \alpha_r(\upsilon)\right) - \omega(\upsilon)\right) + (1-\lambda_r)\left(\alpha_r(\upsilon) - \omega(\upsilon)\right)\right\|$$
$$\leq \left\|\lambda_r\left(P^{\Omega(r)}\left((\upsilon), \alpha_r(\upsilon)\right) - \omega(\upsilon)\right)\right\| + \left\|(1-\lambda_r)\left(\alpha_r(\upsilon) - \omega(\upsilon)\right)\right\|$$
$$= \lambda_r\left\|P^{\Omega(r)}\left((\upsilon), \alpha_r(\upsilon)\right) - \omega(\upsilon)\right\| + (1-\lambda_r)\left\|P^{\Omega(r)}\left((\upsilon), \alpha_r(\upsilon)\right) - \omega(\upsilon)\right\|$$
$$\leq \lambda_r\delta_{\Omega(r)}\|\alpha_r(\upsilon) - \omega(\upsilon)\| + (1-\lambda_r)\|\alpha_r(\upsilon) - \omega(\upsilon)\|$$
$$= \delta_{\Omega(r)}\|\alpha_r(\upsilon) - \omega(\upsilon)\| = \left(1 + \left(\delta_{\Omega(r)} - 1\right)\right)\|\alpha_r(\upsilon) - \omega(\upsilon)\|$$

By Lemma (1.3), we get $\lim_{r\to\infty} = t$ exists, $\forall\, t \geq 0$.

Theorem 2.5 Let $B, F, P, RP, \{\alpha_r(\upsilon)\}$ satisfies in Proposition 2.4, B is Opial's condition. If $\sum\left(\delta_{\Omega(r)} - 1\right) < \infty$ then $\{\alpha_r(\upsilon)\}$ converges weakly to a fixed point.

Proof: since proposition (2.4), $\lim_{r\to\infty}\|\alpha_r(\upsilon) - \omega(\upsilon)\|$ exists. This implies that $\{\alpha_r(\upsilon)\}$ is bounded.

We prove that $\lim_{r\to\infty}\left\|P\left((\upsilon), \alpha_r(\upsilon)\right) - \alpha_r(\upsilon)\right\| = 0$.

$$\lim_{r\to\infty}\left\|P^{\Omega(r)}\left((\upsilon), \alpha_r(\upsilon)\right) - \omega(\upsilon)\right\|$$
$$= \lim_{r\to\infty}\left\|P^{\Omega(r)}\left((\upsilon), \alpha_r(\upsilon)\right) - P^{\Omega(r)}\left((\upsilon), \omega(\upsilon)\right)\right\| \leq \lim_{r\to\infty}\delta_{\Omega(r)}\|\alpha_r(\upsilon) - \omega(\upsilon)\|$$
$$= \lim_{r\to\infty}\left(1 + \left(\delta_{\Omega(r)} - 1\right)\right)\|\alpha_r(\upsilon) - \omega(\upsilon)\| = t$$

And $\lim_{r\to\infty}\|\alpha_{r+1}(\upsilon) - \omega(\upsilon)\| = \left\|\lambda_r\left(P^{\Omega(r)}\left((\upsilon), \alpha_r(\upsilon)\right) - \omega(\upsilon)\right) + (1-\lambda_r)\left(\alpha_r(\upsilon) - \omega(\upsilon)\right)\right\| = t.$

$$\lim_{r\to\infty}\|\alpha_{r+1}(v)-\omega(v)\| = \left\|\lambda_r\left(P^{\Omega(r)}\big((v),\alpha_r(v)\big)-\omega(v)\right)+(1-\lambda_r)\big(\alpha_r(v)-\omega(v)\big)\right\| = t.$$

$$\begin{aligned}\left\|\alpha_{r+1}(v)-P^{\Omega(r)}\big((v),\alpha_r(v)\big)\right\| &= \left\|\lambda_r P^{\Omega(r)}\big((v),\alpha_r(v)\big)+(1-\lambda_r)\alpha_r(v)-P^{\Omega(r)}\big((v),\alpha_r(v)\big)\right\|\\ &= \left\|(1-\lambda_r)\alpha_r(v)+(\lambda_r-1)P^{\Omega(r)}\big((v),\alpha_r(v)\big)\right\|\\ &= \left\|(1-\lambda_r)\left(\alpha_r(v)-P^{\Omega(r)}\big((v),\alpha_r(v)\big)\right)\right\|\\ &= (1-\theta_v)\left\|\alpha_r(v)-P^{\Omega(r)}\big((v),\alpha_r(v)\big)\right\|\end{aligned}$$

Also $\lim_{r\to\infty}\left\|\alpha_{r+1}(v)-P^{\Omega(r)}\big((v),\alpha_r(v)\big)\right\| = 0$, and

$$\|\alpha_{r+1}(v)-\alpha_r(v)\| \le \left\|\alpha_{r+1}(v)-P^{\Omega(r)}\big((v),\alpha_r(v)\big)\right\| + \left\|P^{\Omega(r)}\big((v),\alpha_r(v)\big)-\alpha_r(v)\right\|$$

Then $\lim_{r\to\infty}\|\alpha_{r+1}(v)-\alpha_r(v)\| = 0$. So

$$\begin{aligned}&\left\|\alpha_{r+1}(v)-P^{\Omega(r)}\big((v),\alpha_{r+1}(v)\big)\right\|\\ &\quad\le \left\|\alpha_{r+1}(v)-P^{\Omega(r)}\big((v),\alpha_r(v)\big)\right\| + \left\|P^{\Omega(r)}\big((v),\alpha_r(v)\big)-P^{\Omega(r)}\big((v),\alpha_{r+1}(v)\big)\right\|\\ &\quad\le \left\|\alpha_{r+1}(v)-P^{\Omega(r)}\big((v),\alpha_r(v)\big)\right\| + \delta_{\Omega(r)}\|\alpha_{r+1}(v)-\alpha_r(v)\|\end{aligned}$$

$\lim_{r\to\infty}\left\|\alpha_{r+1}(v)-P^{\Omega(r)}\big((v),\alpha_{r+1}(v)\big)\right\| = 0$, then $\lim_{r\to\infty}\left\|\alpha_{r+1}(v)-P^{\Omega(r)+1}\big((v),\alpha_{r+1}(v)\big)\right\| = 0$

$$\begin{aligned}&\left\|\alpha_{r+1}(v)-P\big((v),\alpha_{r+1}(v)\big)\right\|\\ &\quad\le \left\|\alpha_{r+1}(v)-P^{\Omega(r)+1}\big((v),\alpha_{r+1}(v)\big)\right\|\\ &\quad+ \left\|P^{\Omega(r)+1}\big((v),\alpha_{r+1}(v)\big)-P^{\Omega(r)+1}\big((v),\alpha_r(v)\big)\right\|\\ &\quad+ \left\|P^{\Omega(r)+1}\big((v),\alpha_r(v)\big)-P\big((v),\alpha_{r+1}(v)\big)\right\|\\ &\quad\le \left\|\alpha_{r+1}(v)-P^{\Omega(r)+1}\big((v),\alpha_{r+1}(v)\big)\right\| + \delta_{\Omega(r)+1}\|\alpha_{r+1}(v)-\alpha_r(v)\|\\ &\quad+ \delta_1\left\|P^{\Omega(r)}\big((v),\alpha_r(v)\big)-\alpha_{r+1}(v)\right\|\end{aligned}$$

By taking the limit as $r\to\infty$ then $\lim_{r\to\infty}\left\|\alpha_{r+1}(v)-P\big((v),\alpha_{r+1}(v)\big)\right\| = 0$. Also

$$\begin{aligned}&\left\|\alpha_r(v)-P\big((v),\alpha_r(v)\big)\right\|\\ &\quad\le \left\|\alpha_r(v)-P^{\Omega(r)+1}\big((v),\alpha_{r+1}(v)\big)\right\| + \left\|P^{\Omega(r)+1}\big((v),\alpha_{r+1}(v)\big)-P\big((v),\alpha_r(v)\big)\right\|\\ &\quad\le \|\alpha_r(v)-\alpha_{r+1}(v)\| + \left\|\alpha_{r+1}(v)-P^{\Omega(r)+1}\big((v),\alpha_{r+1}(v)\big)\right\|\\ &\quad+ \left\|P^{\Omega(r)+1}\big((v),\alpha_{r+1}(v)\big)-P\big((v),\alpha_r(v)\big)\right\|\end{aligned}$$

Therefore $\left\|\alpha_r(v)-P\big((v),\alpha_r(v)\big)\right\| = 0$.

Show that , $\mu(v)=\rho(v)$, we assume that $\mu(v)\neq\rho(v)$, since $\lim_{r\to\infty}\|\alpha_r(v)-\omega(v)\|$ exist for every $\omega(v)\in RP$, and since $\mu(v),\rho(v)\in RP$, by Opial's condition, we have that

$$\begin{aligned}\lim_{r\to\infty}\|\alpha_r(v)-\mu(v)\| &= \lim_{ri\to\infty}\|\alpha_{ri}(v)-\mu(v)\| < \lim_{ri\to\infty}\|\alpha_{ri}(v)-\rho(v)\| = \lim_{rj\to\infty}\left\|\alpha_{rj}(v)-\rho(v)\right\|\\ &= \lim_{rj\to\infty}\left\|\alpha_{rj}(v)-\mu(v)\right\| = \lim_{r\to\infty}\|\alpha_r(v)-\mu(v)\|\end{aligned}$$

This $\lim_{r\to\infty}\|\alpha_r(v)-\mu(v)\| < \lim_{r\to\infty}\|\alpha_r(v)-\mu(v)\|$, which is a contradiction, then $\mu(v)=\rho(v)$.

3. Open problem

The modified results on papers [14] and [15] under Fibonacci sequence.

References

[1] A. Spacek 1955 Zufallige Gleichungen, Czechoslaviak Math *J* **5** 462–466
[2] O. Hans 1957 Random fixed point theorems *Transactions of the first prague Conference on Information Theory, Statistical Decision Functions, Random Process* 105–125
[3] M. C. Joshi and R. K. Bose 1985 Some topics in nonlinear functional analysis *John Wiley & Sons*
[4] A. Špaček 1955 Zufällige gleichungen *Czechoslov. Math. J* **5** (4) 462–466
[5] S. Itoh 1979 Random fixed point theorems with an application to random differential equations in Banach spaces *J. Math. Anal. Appl* **67** (2) 261–273

[6] A. Arunchai and S. Plubtieng 2013 Random fixed point theorem of Krasnoselskii type for the sum of two operators *Fixed Point Theory Appl* **2013** (1) 142
[7] S. Zhang, X. Wang, M. Liu, and J. Zhu 2011 Almost sure T-stability and convergence for random iterative algorithms *Appl. Math. Mech* **32** (6) 805–810
[8] G. S. Saluja 2015 On common random fixed point theorems under contractive type condition in cone random metric spaces *Gulf J. Math* **3** (4) 111–122
[9] S. Banerjee and B. S. Choudhury 2011 Composite implicit random iterations for approximating common random fixed point for a finite family of asymptotically nonexpansive random operators *Commun. Korean Math* **26** (1) 23–35
[10] M. R. Yadav 2018 Common fixed points by two step iterative scheme for asymptotically nonexpansive mappings *Funct. Anal. Approx. Comput* **7** (1) 47–55
[11] S. H. Khan and J. K. Kim 2010 Common fixed points of two nonexpansive mappings by a modified faster iteration scheme *Bull. Korean Math. Soc* **47** (5) 973–985
[12] Z. Opial 1967 Weak convergence of successive approximations for nonexpansive mappings *Bull. Amer. Math. Soc* **73** 531–537
[13] M. R. Alfuraidan and M. A. Khamsi 2017 Fibonacci–Mann iteration for monotone asymptotically nonexpansive mappings *Bull. Aust. Math. Soc* **96** (2) 307–316
[14] S. S. Abed and Z. M. M. Hasan 2019 Convergence comparison of two schemes for common fixed points with an application *Ibn AL-Haitham J. Pure Appl. Sci* **32** (2) 81–92
[15] S. S. Abed and K. E. A. Sada 2018 Common fixed points in modular spaces *Ibn Al-Haitham J. Pure Appl. Sci* 500–509

Choosing the best eestimated regression equation for data subject to geometric distribution (Student data as a case study)

Choosing the best eestimated regression equation for data subject to geometric distribution (Student data as a case study)

Osanma Abdulazeez kadhim Al-Quraishi

Ministry of Education, Iraq

E-mail: ousamastat@gmail.com

Abstract. The geometric distribution is one of the discrete statistical distributions that is important, especially in the of population statistics, such as studying population growth and death and birth rates ,The discrepancy in the quality of the estimated regression models and the inability to use some models of them because they do not possess the characteristics of good estimates , lead to a lack of confidence in their predictive or estimated accuracy, which necessitated the study of the geometric distribution to which the data are subject and the estimation of the distribution regression equation using some of the parameter estimation methods (kernel regression method , Liu method) for data represented by preparing secondary students in the holy Karbala governorate with 50 views, and after the comparison between the results of estimating the two methods using the Standards Comparison (AIC, BIC, MSE) and determining the optimal way to estimate the geometric distribution equation The kernel regression is the best because it has the smallest values of the Standards Comparison and was used for the purpose of predicting the preparation of secondary students for the time period (2021-2030).

1. Introduction and research methodology

There are many mathematical models, the most important of which are regression equations, especially the transformed equations from statistical distributions that are used to predict, The study of choosing the appropriate distribution for a phenomenon and methods for estimating the regression models converted by logarithmic transformation began in the last century. In 1986,the two researchers(Cameron & Trived) [7] used the Poisson regression model, estimated its parameters and news of those parameters, and applied it in modeling numerical data that represent the number of medical consultations provided. And in (2005) the researcher (CHANG) [8] in a comparative study between the negative binomial regression method and the artificial neural network method (ANN) applied it to road accident data in the state of New York, USA, for the purpose of analyzing these data and predicting with them. Negative binomial regression in prediction as the relationship between variables does not affect the validity of the model .In (2007) the two researchers (WANG & ETIENNE) [14] used the Poisson regression model and the negative binomial model to predict road accidents. In 2019, the two researchers (Shorouk & Adnan) [4]assessed the parameters of the binomial regression model to study the factors affecting the increase in congenital anomalies in Iraq,Also in the same year, two researchers (Abd al-Hussain and Abd al-Amir) [1] used the Poisson regression model estimated in the manner of the greatest possible way to predict road accidents see. So the researcher decided to use the geometric regression model for

the purpose of predicting the preparation of secondary students in the holy governorate of Karbala after the data are subject to geometric distribution, using non-parametric methods to estimate the regression equation because these methods deal with high flexibility with random error assumptions and this does not affect the efficiency of the capabilities, as they are mainly based On the data, the data type explains the actual shape of the regression curve.

1.1 research problem

The varince in the quality of the estimated regression models and the inability to use some models of them because they do not have the characteristics of good estimates, which leads to lack of confidence in their predictive or estimated accuracy.

1.2 The research objective

The research aims to:

1-Estimation of the geometric distribution slope equation using some non-parameter estimation methods (kernel regression method, leo method).

2-Differentiating between the results of estimating the two methods using the Standards Comparison (AIC, BIC, MSE) and determining the best method for estimating the geometric distribution equation.

3-Predicting Prepare of secondary students in the holy city of Karbala for the period of time (2021-2030).

1-3: Research Limits:

The limits of the research were temporal, the preparation of secondary students for the period of time (1969-2019), spatially the number of secondary students for the holy Karbala Governorate.

1-5 Data sources :The data was taken from the Ministry of Planning / the Central Statistical Organization/the statistical group.

2- Theoretical aspect:

2-1: Geometric Distribution: [3]

This distribution belongs to the family of discrete distributions and distribution is important in statistical applications, especially in the population statistics when studying population growth rates and mortality and birth rates, and the geometric distribution is part of the probability distribution related to Bernoulli experiments, as we can know the probability density function of the geometric distribution is the number of attempts Failed to try until the first success of that experiment. If the variable (Y) indicates the number of times the experiment was repeated, (θ) indicates the probability of success of the experiment, (1- θ) the probability of the experiment failing, then the probabilistic function of this distribution will be:

$$P(Y,\theta) = \theta.(1-\theta)^{y} \quad , 0 < \theta < 1 \, , Y = 0,1,2,\dots \, , \qquad (1)$$

2-2 :Some characteristics of the Geometric distribution:[3]

1- mean of the variable Y is:

$$M(Y) = EY = \frac{\theta}{(1-\theta)} \quad \dots(2)$$

2- mode of the variable Y is: $M_o(Y)=0$ …(3)

3- median of the variable Y is:

$$M_e(Y) = \left[\frac{-1}{\log_2(1-\theta)}\right] - 1 \quad \dots(4)$$

4- variance of the variable Y is:

$$V(Y) = \frac{\theta}{(1-\theta)^2} \qquad \dots(5)$$

5- Skewness of the variable Y is:

$$S_k(Y) = \frac{2-\theta}{\sqrt{1-\theta}} \quad ...(6)$$

6- Kurtosis of the variable Y is :

$$E_x(Y) = 6 + \frac{\theta^2}{1-\theta} \quad ...(7)$$

7- Cumulative function of the variable Y is:

$$F(Y) = 1-\theta^y \quad , Y = 0,1,2,...n \qquad (8)$$

8-Moment generating functions of the variable Y is:

$$M_{Y(t)} = \frac{\theta}{1-\theta e^t} \quad ...(9)$$

2-3 :Regression Analysis: [2]

Regression analysis is one of the methods or statistical tools that are most used in most research in general because it describes the relationship between variables in the form of an equation, and it is defined as a Statistical Tool used to know the relationship between one or more independent variables And dependent Variable.

Regression analysis is important because it is used for several important purposes:

1- Data Descriotion: Find the regression equation that summarizes or describes the data available to the researcher.

2- Estimation of Parameters: Estimation of the regression equation parameters used in the description of data to infer the strength and direction of the relationship between the variables.

3- Prediction: Estimating and predicting the values of the dependent variable in the future to benefit planning and decision making.

4- Contoral: Control of the results of the dependent variable when changing the values of the independent variables. Geometric Regression Mode [13],[2] The geometric regression model is one of the non-linear regression models, and it is converted into one of the Log-Linear Models by taking the natural logarithm of the geometric distribution equation, so it turns into a linear formula. Geometric regression can also be defined as the method by which the dependent variable is modeled when the values of the variable are as Count Data or as Rate Data. The geometric regression equation can be obtained from the geometric distribution as follows:

Let the variable (Y) follow the geometric distribution with the parameter (θ), and that (X) represents the explanatory variable (time) we can write the geometric distribution equation in the following form:

$$Y = \theta(1-\theta)^x \quad ...(10)$$

Taking the logarithm of both sides of the equation, we get a first degree linear equation:

$\ln(Y) = \ln(\theta) + Xln(1-\theta)$

Assuming below, we obtain an equation (13) representing the estimated linear regression model for the geometric distribution as follows:

$$\ln(\theta) = b_0$$
$$\ln(1-\theta) = b_1$$
$$lny = y^*$$
$$y^* = b_0 + b_1 x_i + e_i \quad ...(11)$$

In the case of taking the exponential function of both sides of equation (13), we obtain the non-linear discretionary regression model for the geometric distribution as follows :

$$y = e^{b_0 + b_1 x_i + e_i} \quad ...(12)$$

2-4: Hypothesis of linear regression of random error: [11]

1- Random error (ui) is normal distributed with an average of zero (E(ui) = 0) and constant variance equal($V(u_i) = \sigma^2$), meaning that:

$u_i \sim N(0, \sigma^2)$ ...(13)

2- Successive errors in the simple linear regression model should not be related to each other, meaning that:

Cov (u_i , u_j)=0 …(14)

3-The random variable(ui)and the explanatory variable (xi)are independent of each other. meaning that:

Cov (x_i , u_i)=0 …(15)

Methods for Estimating the Geometric Regression Model:2-7

There are many methods for estimating the geometric regression model. In this paragraph, we will address the non-parametric methods that assume that random error is distributed with an average of (0) and a constant variance of (σ ^ 2), the fact that non-parametric methods deal with high flexibility with random error assumptions and this does not affect the efficiency of the estmates , Since it is mainly based on data and the data type explains the actual shape of the regression curve, and the methods are.

1. Kernel regression method: [9], [10]

The kernel regression method is one of the non-parametric methods that can be used to estimate the regression equation for the geometric distribution, and the kernel regression method was proposed by the scientists Nadaraya and Watson in (1964) by means of the logarithm of the maximum function, it can be rewritten as follows:

LE(Y_i)=$L(\theta_i) = \frac{1}{n}\{e^{\eta(x_i)}\text{-}y_i\ \eta(x_i)\}$ …(16)

As :

Model Parameters Vector$\eta(x_i)$:

$\eta(x_i)$ = ln[$\theta(x_i)$]

The kernel method is summarized in estimate. Using the following linear model:

$\eta(x_i)$ = b_0 +w' ϕ (x_i) … (19)

AS:

$$w'\ \phi\ (x_i) = \mathrm{K}(x_i, x_l)$$

k(x_i, x_l): is one of the kernel functions.

We get the vector of the geometric regression equation parameter by the kernel method η(xi) by minimizing the logarithm of the Penalizied Negative Log-Likelihood.

L(w,b)=$\sum_{i=1}^{n}[e^{b_0 +w'\ \phi\ (x_i)} - \ y_i(b_0 +w'\ \phi\ (x_i))]+\frac{\lambda}{2}+\|w\|^2$ …(17)

AS:

λ: Penalty Parameter and its function is to control the balance between Goodness of Fit based on two main factors: data and smoothness (Smoothness‖w‖^2) for the function η (x i), which The logarithm of the function of the negative penalties is made at the lower end of it, And on it the Vector parameters of the model η (x i) is written according to the following form:

$\eta(x_i)$ = b_0 +$k_i'\alpha$ …(18)

As:

b0: fixed border.

ki: column i in the kernel matrix of degree (n * n) and its elements k(xi,xl) and (i, l) = 1, 2, 3, …… .n

α: smoothing parameters vector with degree (n * 1).

Thus, the formula for the logarithm of the negative penalty maximum function is written as follows:

L(b_0, α)=$\sum_{i=1}^{n}[e^{b_0 +k_i'\alpha} - \ y_i(b_0 +k_i'\alpha)] + \frac{\lambda}{2}\ \alpha^t\ k\alpha$ …(19)

To obtain maximum likelihood estimates of the nonlinear regression equations in which the dependent variable(Y) follows the geometric distribution, estimates can be obtained using numerical estimation methods such as the Newton-Ravson method and the least squares method for multi-stage repetitive weights (Lterative Reweighted Least Squares), The second method (irls) is easier than the first method (Newton - Rafson) in deriving the cross-validation Criterion (cvc), which has a rate of convergence lower than the rate of convergence in the method of Newton - Rafson .

In order to obtain maximum estimates for the unknown parameters (b0, α), we first find the partial derivatives of the logarithm of the Negative penalty maximum function with respect to the parameter α and the parameter(b0), and then equate the derivative to zero Secondly, my agencies:

$$\begin{pmatrix} \frac{\partial l(b_0,\alpha)}{\partial b_0} = 0 \\ \frac{\partial l(b_0,\alpha)}{\partial \alpha} = 0_n \end{pmatrix} \quad \ldots(20)$$

Solve the following formula using the least squares method for the multi-stage repeated weights (i.r.l.s):

$V'WV + U)\ \beta = V'W\ y^*$ …(21)

As:

) value of the dependent variable converted to linear formula Ln (y : y^*

V: matrix with degree ((n + 1) * n) defined as follows:

$V = (1_n , k)$ …(22)

As:

In: the correct one-degree vector (n * 1).

k: The kernel matrix contained in the formula (21)

W: Diagonal matrix with degree (n * n) written as :

W = daig [exp($b_0 + k_1'\alpha$) , ……..,($b_0 + k_n'\alpha$)] … (23)

B: The vector parameters to be Estimated are of the same degree((n+1)* 1)

$B = (b_0 , \alpha^T)'$ …(23)

U : Square matrix of degree] ((n + 1) * (n + 1)) is written as follows

$$U= \begin{pmatrix} O & O_n^t \\ O_n & \lambda k \end{pmatrix} \quad \ldots(24)$$

As:

Zero vector with degree (n * 1). :O_n

y^*: the vector of the response variable in the kernel regression method (n * 1) and that yi is written as.:

$$y_i = \frac{y_i - \exp(b_0 + k_i'\alpha)}{\exp(b_0 + k_i'\alpha)} + \exp(b_0 + k_i'\alpha) \quad \ldots(24)$$

The estimation of the parameter vector (b0, α) when using the Newton-Ravson method, which determines the values of the estimates in the various stages of the method, is:

$$\begin{pmatrix} \alpha^{(t+1)} \\ b_0^{(t+1)} \end{pmatrix} = \begin{pmatrix} \alpha^{(t)} \\ b_0^{(t)} \end{pmatrix} - \begin{pmatrix} k\, w^{(t)}\, k + \lambda k & k\, \mu^{(t)} \\ \mu^{(t)\prime} k & 1'\, \mu^{(t)} \end{pmatrix}^{-1} \begin{pmatrix} k\, \mu^{(t)} - y + \lambda \alpha^{(t)} \\ 1'\, (\mu^{(t)} - y) \end{pmatrix} \quad \ldots(25)$$

That the estimates of the mean function at the input vector x0 and for the estimated optimum parameter values (b0, α) are:

$\hat{\mu}(x_0)$ =exp ($\hat{b}_0 + k_0^{(t)}\hat{\alpha}$) …(26)

As:

$k_0 = (k(x_1, x_0), \ldots\ldots, k(x_n, x_0))^t$ …(27)

In order to test the penalty parameter (λ) and the parameter of the endodontic function (σ ^ 2) which results in the best preamble, we use for this test forensic (O.C.V) ordinary cross validation.

$$= \frac{1}{n} \sum_{i=1}^{n} \left(\frac{y_i - e^{\widehat{\eta_\theta}(x_i)}}{1 - s_{ii}}\right)^2 \quad \ldots(29)(\theta)\text{O.C.V}$$

As:

sii: the diagonal element of row (i) of matrix S, defined as:

$S = V\ (\ V'\ W\ V + U\ )^{-1}\ V'\ W$ …(28)

When compensating with the average sii which equals ($\frac{1}{n}$tr (s)) in formula (30) we get (g.c.v) Generalized cross validation which is calculated with respect to θ of the parameters my agency:

$$\text{g.c.v } (\theta) = \frac{n \sum_{i=1}^{n} (y_i - e^{\widehat{\eta_\theta}(x_i)})^2}{(n - tr(s))^2} \quad \ldots(29)$$

As:

$\widehat{\eta_\theta}(x_i)$: An estimate of the logarithm μɵ, meaning[$\eta_\theta(x_i) = \log(\mu_\theta)(x_i)$] for each parameter after viewing exclusion (i) according to the(Leave-One-Out method).

2.5 Liu Estimators Method: [12],[5]

It is the second nonparametric method and is used treat of inflation estimated variance parameters of the model. Liu laid the foundations for this method in 1993 when he created it for the linear regression model, then going back to the formula for geometric model given in equation (13):

$Y^* = b_0 + b_1 X_i + u_i$

) Liu (And by adopting the following restriction that he set

$\underline{C}'C = (S\underline{\hat{\beta}} - \underline{\beta}^*)'(S\underline{\hat{\beta}} - \underline{\beta}^*)$ …(30)

AS:

$\underline{C}'W\underline{C} = (Y^* - X\underline{\beta}^*)'\widehat{W}(Y^* - X\underline{\beta}^*) + (s\underline{\hat{\beta}} - \underline{\beta}^*)'(s\underline{\hat{\beta}} - \underline{\beta}^*)$

C′C: the amount of increase in the mean of the weighted error squares when the estimated parameter vector is replaced by the maximum likelihood method ($\underline{\hat{\beta}}$) with the estimated parameter vector according to the Liu method ($\underline{\beta}^*$).

$\underline{\hat{\beta}}$:estimates maximum likelihood when converting the model to a linear model

$\underline{\beta}^*$:: Vector sample parameters estimated by the Liu method

S: bias parameter

After the process of converting the model to linear and placing the constraint, the square of the weighted errors of the researched model is taken with the addition of the constraint and then deriving the result with respect to $\underline{\beta}^*$:as follows:

$\underline{C}'W\underline{C} = (Y^* - X\underline{\beta}^*)'\widehat{W}(Y^* - X\underline{\beta}^*) + (s\underline{\hat{\beta}} - \underline{\beta}^*)'(s\underline{\hat{\beta}} - \underline{\beta}^*)$

$= \underline{Y}^{*'}\widehat{W}\underline{Y}^* - 2\underline{\beta}^* X'\widehat{W}\underline{Y}^* + \underline{\beta}^{*'}X'\widehat{W}X\underline{\beta}^* + S'\underline{\hat{\beta}}'\underline{\hat{\beta}}S - 2S\underline{\hat{\beta}}\underline{\beta}^* + \underline{\beta}^{*'}\underline{\beta}^*$ …(31)

By deriving equation (33) with respect to the parameter vector (β ^ *), we get:

$\frac{\partial \underline{C}'W\underline{C}}{\partial \underline{\beta}^*} = -2X'\widehat{W}\underline{Y}^* + 2X'\widehat{W}X\underline{\beta}^* - 2S\underline{\hat{\beta}} + 2\underline{\beta}^*$ …(32)

When the derivation result is equal to zero, we obtain the Liu estimates for the geometric regression model parameters.

$\underline{\hat{\beta}}_{Liu} = (X'\widehat{W}X + 1)^{-1}(X'\widehat{W}\underline{Y}^* + S\underline{\hat{\beta}})$ …(33)

Since the

$\underline{\hat{\beta}} = \underline{\hat{\beta}}_{ML}$ …(34)

$\underline{\hat{\beta}} = \underline{\hat{\beta}}_{ML} = (X'WX)^{-1}(X'W\underline{Y}^*)$ …(35)

Know in numbered form (32) ,they are estimates maximum likelihood , When converting a geometric regression model to a linear formula

As:

$\left(X'W\underline{Y}^*\right) = (X'WX)\underline{\hat{\beta}}_{ML}$ …(36)

Substituting the value of $\left(X'W\underline{Y}^*\right)$ to its equivalent in the numbered formula (35) we get another form of the liu of the geometric regression model parameters.

$\underline{\hat{\beta}}_{Liu} = [(X'\widehat{W}X + 1)^{-1}\left(X'\widehat{W}X\right)\underline{\beta}_{ML} + S\underline{\hat{\beta}}_{ML}]$

$\underline{\hat{\beta}}_{Liu} = (X'\widehat{W}X + 1)^{-1}\left(X'\widehat{W}X + SI\right)\underline{\hat{\beta}}_{ML}$ …(37)

Standards Comparison: [6],[15] 2-8:

) :AIC (Akaike Information Criterion 1-

$AIC = n\ln\hat{\sigma}_\epsilon^{\,2} + 2M$ ... (38)

) :SBC (Schwartz Bayesian criterion 2-

$\mathrm{SBC} = \mathrm{n}\ln\hat{\sigma}_\epsilon^{\,2} + \mathrm{M}\ln(\mathrm{n})$ ... (39)

) :H-Q (Hannan − Quinn Criterion 3-

$H - Q(M) = ln(\sigma_\epsilon{}^2) + 2MC\ \frac{ln[ln(n)]}{n}\quad ; C > 2$ ... (40 ∗)

AS :

$\hat{\sigma}_{\epsilon}^{\ 2} = \frac{\sum_{t=0}^{n}(e_i - \hat{e}_i)^2}{n}$

n: represents the number of views.
M: number of parameters of the chosen model or model rank.
C: fixed.

3-The applied side.

3-1 :Description and definition of the study sample:

The annual secondary student preparation data in the holy governorate of Karbala was relied on for the period of time ((1969-2019) for the geometric regression equation, and the dependent variable (Y) represented the preparation of secondary students during time and the independent variable(X) time (years).

:Appropriate statistical distribution:3-2

To find out the statistical distribution appropriate to the preparation of secondary students, a goodness of fit test was used for the data through the Easy Fit statistical program. The results showed that the data follows the geometric distribution with parameters($\theta = 2.4920E - 5$) ana the value (p-value=0.000).

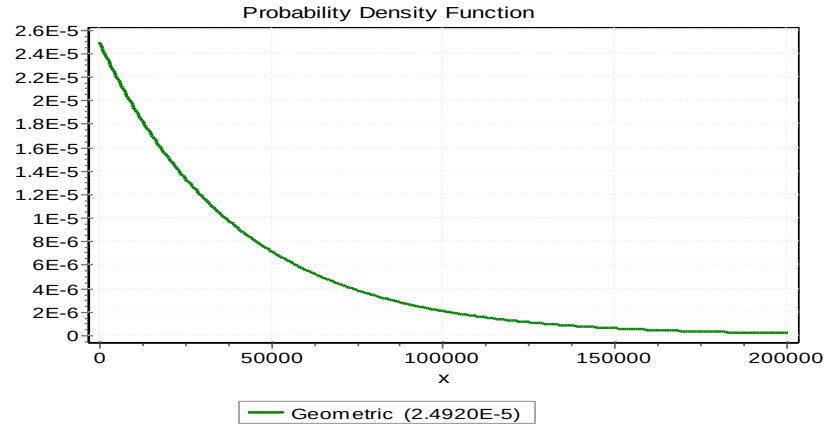

Form (1) probability density function for the geometric distribution

3-3: Statistical analysis of data:

The data were analyzed statistically using the statistical program (Gretl 1.9.11).

First: Estimate the geometric regression equation using the kernel regression method and the Leo agency method:

1-The estimated formula for the geometric regression equation using the kernel regression method is:

$\ln y = 9.44278 + 0.0368146\ x$

2-The estimated formula for the geometric regression equation using the Leo method is:

$lny = 9.29892 + 0.0429313\ x$

Second: The test of the significance of the putative linear relationship 1-Linear relationship significance test for the estimated engineering regression equation using the kernel method. To find out the significance of the linear relationship, we test the following hypothesis:

$H_0: B_1 = 0$

$H_1: B_2 \neq 0$

Through the numbered analysis of variance table (2) we obtain the value of the test (F) that determines the nature of the relationship between the dependent variable and the independent variable

Table (1) analysis of variance

	Sum of squares	df	Mean square
Regression	14.1122	1	14.1122
Residual	0.27484	48	0.00572583
Total	14.387	49	0.293613

R^2 = 14.1122 / 14.387 = 0.980897
F(1, 48) = 14.1122 / 0.00572583 = 2464.65 [p-value 6.45e-043]

Looking at Table (1), we notice that the test value is ((F = 2464.65) and its probability value [p-value = 6.45e-043] It is less than the level of significance (0.05), we accept the alternative hypothesis which states that the time variable exerts its effect on the student numbers variable and the percentage (98%).

2- Test the significance of linear relationship of the estimated geometric regression equation using the Liu method.

To find out the significance of the linear relationship, we test the following hypothesis:

$H_0: B_1 = 0$

$H_1: B_2 \neq 0$

Through the numbered analysis of variance table (3) we obtain the value of the test (F) that determines the nature of the relationship between the dependent variable and the independent variable.

Table (2) analysis of variance

	Sum of squares	df	Mean square
Regression	19.1912	1	19.1912
Residual	0.835683	48	0.0174101
Total	20.0269	49	0.408712
R^2 = 19.1912 / 20.0269 = 0.958272			
F(1, 48) = 19.1912 / 0.0174101 = 1102.31 [p-value 9.08e-035]			

Looking at Table (2), we notice that the test value is ((F = 1102.31) and its probability value[p-value = 9.08e-035] It is less than the level of significance (0.05), we accept the alternative hypothesis which states that the time variable exerts its effect on the variable of student numbers and the percentage (95%).

3-4 Standards Comparison:

After the geometric regression models have been estimated and the linear relationship is significant, the differentiation criteria are used to choose the method that best achieves the agency model:

Table (3) Standards Comparison

	AIC	BIC	H-Q
Liu Method	-58.68260	-54.85855	-57.22638
Kernel Regresion Method	-114.2857	-110.4616	-112.8294

By looking at Table (3), we notice that the kernel regression method is preferable because it has the smallest differentiation criteria, compared to the Leo method.

3-5: Prediction:

The number of secondary students can be predicted for the holy city of Karbala for the future time period (2021-2030) using the estimated geometric regression model according to the Kernel method based on time series data, Table (1).

Table (4) Predictive Values for Preparing Secondary Stage Students for the Duration (2030-2021)

Years	2021	2022	2023	2024	2025
Predictive Values	82481	85574	88783	92112	95567
Years	2026	2027	2028	2029	2030
Predictive Values	99150	102863	106726	110729	114881

4. Result and recommendations:

1- The secondary student preparation data has appeared subject to the geometric distribution.
2- The significance of the estimated regression equation using the kernel regression method.
3- Significance of the estimated regression equation using the Liu method.
4- The preference of the kernel regression method is preferable to the Leo method, since the first method has the lowest Standards Comparison.
5-Depending on the values predicted by the geometric regression model, it was noted that there has been a decrease in the number of students from the last sex previous years.
6- Using other methods to estimate the geometric regression equation to arrive at the best prediction model.
7- Making use of the research findings and adopting them to prepare future plans from the relevant authorities.
8- Mtudying the decrease in the number of future students.

References

[1] Abdul-Hussein H and Abdul-Amir T 2019 Predicting the number of road accidents in Dhi Qar governorate for the year 2022 using the Poisson model *Karbala University Scientific Journal* **17**(1)
[2] Zahra H et al. 2014 regression analysis. Directorate of Dar Al-Kutub for Printing and Publishing - Basra University / College of Administration and Economics
[3] Amir H 1990 Mathematical Statistics. Directorate of Dar Al Kutub for Printing and Publishing - University of Mosul / College of Administration and Economics
[4] Shorouk A and Adnan F 2019 A comparison of the two least squares and weighted least squares methods to estimate a negative binomial regression model. *Scientific Journal of the University of Karbala* **17** (1) Scientific
[5] Stephen W R 1988 Educational Applications of Hierarchical Linear Models: A Review Journal of Educational Statistics **13** 85-116
[6] Akaike H 1973 Information theory and extension of the maximum likelihood principle In : B.N. petrov and F Csaki eds 2 nd International symposium on Information. *Theory Academia Kiado Budapest* 267-281
[7] Cameron A C and Trived P R 1986 Regression Analysis of count Data Cambridge University press 1-434
[8] Chang L 2005 Analysis of freeway Accident Frequencies : Negative binomial regression versus artificial neural network . Safety science.
[9] Frome E L 1983 The Analysis of Rates Using Poisson Regression Models *Biometrics* **39** 665-674
[10] Hwang G and Shim J 2008 Semiparametric Kernel Poisson Regression for longitudinal Count Data Communication of the Korean Statistical Society **15** (6) 1003-1011
[11] John O1998 Applied regression analysis Aresearch Tool *North Carolina State University, USA*
[12] Long J S 1997 Regression Models for Categorical and Limited Independent Variables *SAGE Publicayion Inc, USA*
[13] Robert S P and Daniel I R 2000 Econometric models and economic forecasts *New York McGraw-Hill Book company*
[14] Wang P D and Etienne E K 2007 Why Fuzzy Logic A Spectrum of theoretical and pragmatics Issues studies in fuzziness and soft Computing. *Springer Berlin Heidelberg*
[15] Schwarz G 1978 EstimatingThedimension of a model Annuals of Statistics **6** 461-464.

The KR-Elliptic Curve Public Key Cryptosystem

The KR –Elliptic Curve Public Key Cryptosystem

Karrar Taher R. Aljamaly and Ruma Kareem K. Ajeena

Mathematics Department, Education College for Pure Sciences, University of Babylon, Iraq

E-mail: ruma.usm@gmail.com

Abstract. The connection between some fundamental mathematical problems in number theory with cryptography has been done in this work. A new version of the elliptic curve public key cryptosystem (ECPKC) has been proposed by Karrar Taher and Ruma Ajeena. Their main idea is to design this cryptosystem focusses on generating the elliptic curve group, its order divides the Euler phi function that is computed securely based on two large primes. Faster and more secure computations to generate the keys, encryption and decryption processes, on the KR-ECPK algorithm are discussed. In comparing with other algorithms like RSA and ElGamal public key cryptosystem (EEPKC), the KR-ECPKC considers as an efficient algorithm. So, the KR-ECPKC is more appropriate for elliptic curve cryptographic applications.

1. Introduction

The elliptic curve cryptography (ECC) is more interested for many researchers, because it has employed in different applications such mobile devices, wireless sensor, network, image encryption and others [1,2,3]. The ECC has keys with small size that allows to be much efficient in comparing to other public key cryptosystems like RSA [4].

The RSA cryptosystem is proposed Rivest, R.L., et al, in 1978 through presenting a public key cryptosystem which was depended on the integer factorization problem, that factors a composite number into two large primes [4]. In 1985 Miller introduced proposed the Diffie-Hellman key exchange protocol based on elliptic curves [5]. In 1987, Koblitz proposed elliptic curve ElGamal public key cryptosystem [6]. In 2000, Neal Koblitz introduced the state of elliptic curve cryptography, he presented a survey about the elliptic curve cryptosystems [7].

In this work, we are looking for a small size key, faster and secure computation. So, our work focusses on the proposed new version of elliptic curve public key cryptosystem. That has faster computations of the encryption and decryption processes in comparing with other elliptic curve cryptosystems.

The outline of this work includes Section 2, which discussed the RSA cryptosystem in its first part. And in the second part, another public key cryptosystem which depended on elliptic curves is explained, this cryptosystem is called ElGamal elliptic public key cryptosystem (EEPKC). In section 3, a new version of the elliptic curve cryptosystem is proposed. Section 4, discusses a study case of the proposed EC-Cryptosystem. Some computational results of the proposed EC-cryptosystem are explained in Section 5. Section 6, presents the comparison on the proposed EC-cryptosystem, RSA and EEPKC. The security considerations of the proposed EC-cryptosystem are determined in Section 7. Finally, Section 8, displays the conclusions.

2. Mathematical Background

The RSA cryptosystem proposed in 1978 by R. L. Rivest, A. Shamir, and L. Adleman [4]. A public key on the RSA cryptosystem is a pair of integers (n,e), where n is a product of two secret primes p and q and e is an integer satisfying gcd(e, φ)=1, with $\varphi = (p-1)(q-1)$ is Euler phi function. Whereas, a private key d is an integer satisfying $ed \equiv 1 \pmod{\varphi}$. The ciphertext c of a plaintext m is computed by $c = m^e \pmod{n}$. The original message can be recovered through decryption process that is computed by $m = c^d \pmod{n}$.

On the other hand, the ElGamal elliptic curve public key cryptosystem (EECPKC) is proposed by ElGamal in 1987 [6]. The users, sender and receiver agree to choose a prime p, an elliptic curve equation $E : y^2 = x^3 + ax = +b \pmod{p}$ [8,9] and to determine a generator elliptic point P as the public parameters. The receiver chooses a random integer d as his/her secret key and computes his/her public key dP. The sender selects a message M as an elliptic point in $E(F_p)$ and encrypt it by a pair (C_1,C_2), where $C_1 = eP$ and $C_2 = M + e(dP)$. The receiver decrypts the ciphertext (C_1,C_2) through computing $C_2 - dC_1 = M + e(dP) - d(eP) = M$.

3. The KR-Elliptic Curve Cryptosystem

The encryption process is done as follows. A plaintext m selected and represented as elliptic point in $E(F_p)$ [10]. Then a message M is encrypted by $C = e'M$, where e' is computed by $e' \equiv e \pmod{N}$, with N is an order of M. The ciphertext C considers as a scalar multiplication, which can be computed by ISD method [11,12]. Algorithm (3.2.1) is employed to compute the ciphertext C.

3.1. The KR-Elliptic Curve Cryptosystem: Keys Generation Process

First, a set of the points on an elliptic curve group $(E(F_p),+_E)$ is computed. The order $\#E(F_p)$ of a group $(E(F_p),+_E)$ should divide a positive integer n, where $n = (q-1)(t-1)$ with q and t are two large primes that are selected secretly by a first user to compute his/her private key n. The public key e is selected as an integer from the range $[2, n-1]$ such that $\gcd(e,n) = 1$. So, the public and private keys are e and n respectively. Algorithm (3.1.1), is used to generate the keys of the KR-EC cryptosystem.

Algorithm 3.1.1. The KR-EC Cryptosystem: Keys Generation Process.

INPUT: The large prims (q,t).

OUTPUT: The set of elliptic curve points and public key e.

1. Select $a,b \in [1,n-1]$ are coefficients of E.
2. Compute $n = (q-1)(t-1)$.
3. Select randomly $e \in [2,n-1]$
4. If $\gcd(e,n) = 1$ then
5. Return e
6. Else
7. Stop and go to step (3).
8. End if
9. Compute the elliptic curve set $E(F_p)$.
10. Compute the order $\#E(F_p) = h$ of $E(F_p)$.
11. If $h \mid n$ then
12. Return the set $E(F_p)$

13. Else
14. Stop and go to step (1).
15. End if
16. Return $(n, e, E(F_p))$.

3.2. The KR-Elliptic Curve Cryptosystem: Encryption Process

The encryption process is done as follows. A plaintext *m* selected and represented as elliptic point in $E(F_p)$ [10]. Then a message *M* is encrypted by $C = e'M$, where e' is computed by $e' \equiv e \pmod{N}$, with *N* is an order of *M*. The ciphertext *C* considers as a scalar multiplication, which can be computed by ISD method [11,12]. Algorithm (3.2.1) is employed to compute the ciphertext *C*.

Algorithm 3.2.1. The KR-EC Cryptosystem: Encryption Process

INPUT: A set $E(F_p)$ of elliptic points, a public key *e* and plaintext *m*.

OUTPUT: The ciphertext *C*.

1. Convert a message *m* as an elliptic point $M \in E(F_p)$ [10].
2. Compute the order *N* of a point *M*.
3. Compute $e' \equiv e \pmod{N}$.
4. Compute $C = e'M$.
5. Return *C*.

3.3. The KR-Elliptic Curve Cryptosystem: Decryption Process

Upon receiving the ciphertext to the first user, he/she wants to decrypt the ciphertext and recover the original message. First, he/she computes the key *d* secretly, where $d \in [2, n-1]$ and $ed = 1 \pmod{n}$. Then d' is computed by $d' \equiv d \pmod{N}$ with *N* is an order of the *C* that is computed as an elliptic curve point. The original message is recovered by $d'C = M$. The decryption process is proved mathematically in following proposition.

Proposition 3.3.1. The decryption process of KR-EC cryptosystem takes the expression $M = d'C$.

Proof.

$d'C = d'(e'M)$, since $C = e'M$.

$= deM$

$= (rn + 1)M$ such that *r* is a positive integer, since $ed = 1 \pmod{n}$.

$= rnM + M$

$= r(sN)M + M$ such that *s* is a positive integer and *N* the order of *M* that is ($NM = O_E$), since every order of elliptic point divide *n*.

$= rs(NM) + M$

$= rs(O_E) + M$

$= M$. ■

For the computational results to recover a message *M*, one can use Algorithm (3.3.2).

Algorithm 3.3.2. The KR-EC Cryptosystem: Decryption Process.

INPUT: A set $E(F_p)$ of elliptic points, a public key *e*, a privet key *n* and the ciphertext *C*.

OUTPUT: A key *d* and a plaintext *m*.

1. Choose randomly $d \in [2, n-1]$

2. If $ed = 1(\mathrm{mod}\, n)$ then
3. Return *d*
4. Else
5. Stop and go to step (1).
6. End if
7. Compute the order *N* of a point *C* that is a ciphertext.
8. Compute $d' \equiv d\,(\mathrm{mod}\, N)$.
9. Compute $d'C = M$.
10. Convert *M* into *m* [10].
11. Return *m*.

4. The Study Case on the KR-EC Cryptosystem.

The keys, namely public and private are generated first. A prime $p = 8123$ is chosen and the elliptic points set $E(F_{8123})$ is determined by supposing the elliptic curve $E: y^2 = x^3 + 5x + 13$ as the public parameters. The set

$E(F_{8123}) = \{(1,1548),(1,6575),(3,3067),(3,5056),(4,6052),(4,2071),...,(8122,5994),(8122,2129),O_E\}$.

The $\#E(F_{8123}) = 8144$ such that $8144 \mid n$, where *n* is a private key for the first user. The private key is computed by $n = (q-1)(t-1) = 12123438 \cdot 31423268 = 3809574206353584$, where $q = 12123439$ and $t = 314232169$ are two large primes that are selected secretly. The public key *e* is selected randomly from the range [2,3809574206353583] and

$$\gcd(e, n) = \gcd(12326106299, 3809574206353584) = 1.$$

So, the public and private keys are $e = 12326106299$ and $n = 3809574206353584$ respectively. Now for encryption process, suppose second user chooses a message $M = (1000, 5149)$ which is an elliptic point in $E(F_{8123})$. The order of a point *M* is 4072, namely

$$4072M = 4072(1000, 5149) = O_E.$$

He/She computes $e' = 3491$ through computing $e' \equiv e \bmod(4072)$. The ciphertext *C* is computed as a scalar multiplication $C = e'M = 3491(1000, 5149) = (5375, 4448)$. The ciphertext $C = (5375, 4448)$ will be sent to the first user. After receiving the ciphertext *C* into the first user, he/she computes $d = 618131$ such that

$$\mathrm{ed(modn)} = 12326106299 \times 618131 \bmod(3809574206353584) = 7619148412707169 \bmod(3809574206353584) = 1.$$

The order of a ciphertext *C* which is considered as an elliptic curve point is computed to be $N = 4072$, since

$$4072C = 4072(5375, 4448) = O_E.$$

The parameter $d' = 3259$ is computed, where $d' \equiv d \bmod(4072)$. First user computes a scalar multiplication

$$d'C = 3259(5375, 4448) = (1000, 5149) = M.$$

5. The Computational Results on the KR-EC Cryptosystem.

Some simple computational results about the KR-EC cryptosystem have been done. The experimental samples with different values of a primes *q* and *t* are chosen The computational results to generate the keys, encryption and decryption processes are shown in Tables (1), (2) and (3) respectively.

Table 1. The experimental results of the KR-EC cryptosystem: key generation process.

q	t	$n = (q-1)(t-1)$	e	F_p	$E(a,b)$	$\#E(F_p)$

733	853	623664	313399	F_{563}	(6,10)	568
773	941	725680	113093	F_{197}	(1,22)	193
911	997	906360	9673	F_{1163}	(2,23)	1162
1193	1321	1573440	90239	F_{1657}	(20,14)	1639
3253	7253	23583504	11039087	F_{2179}	(25,2)	2168
71527	91513	6545487312	10767257	F_{2099}	(46,5)	2096
112327	322537	36229178736	584663	F_{3089}	(17,3)	3088
1312153	312161	409601368320	167161	F_{1283}	(9,4)	1280
1211141	1121333	1358090038480	10672613269	F_{1657}	(4,16)	1640
1232453	1392221	1715844323440	868781935919	F_{1847}	(37,20)	1844

Table 2. The experimental results of the KR-EC cryptosystem: encryption process.

$M \in E(F_p)$	N is the order of M	$e' = e \bmod(N)$	$C = e'M$
(395,229)	284	147	(131,403)
(151,67)	193	188	(41,172)
(999,123)	1162	377	(200,260)
(650,313)	1639	94	(1146,1645)
(2021,1131)	271	173	(1787, 2080)
(527,600)	1048	105	(1761,402)
(993,111)	386	259	(2920, 1652)
(1176,533)	640	121	(820,356)
(1611,101)	1640	29	(358, 704)
(1715,1227)	922	887	(1595,55)

Table 3. The experimental results of the KR-EC cryptosystem: decryption process.

d	N is the order of C	$d' = d \bmod(N)$	$M = d'C$
199	284	199	(395,229)
77	193	77	(151,67)
937	1162	937	(999,123)
959	1639	959	(650,313)
47	271	47	(2021,1131)
45593	1048	529	(527,600)
743591	386	155	(993,111)
4900681	640	201	(1176,533)
509	1640	509	(1611,101)
79	922	79	(1715,1227)

6. Comparison on the KR-EC, RSA and EEPK Cryptosystems

By using the proposed KR-EC cryptosystem, there is no problem to choose the small primes q and t for computing $n=(q-1)(t-1)$, since n is a private key. In comparing with that, the RSA public key cryptosystem needs the choice of the large primes for increasing the security. The public key generation process in elliptic curve ElGamal public key cryptosystem (EC-EPKC) requires more computations to solve the discrete logarithm problem (DLP) comparing with the new version KR-EC cryptosystem that is proposed to choose a public key as a number in the range $[2,n-1]$ with $\gcd(e,n)=1$. Also, computing a public key on the EC-EPKC requires finding the generator point on elliptic curve group in comparing to the KR-EC cryptosystem which is not required that.

As well as, the proposed version KR-EC cryptosystem is considered faster public key algorithm in compare with EC-EPKC, since on the KR-EC cryptosystem, the encryption and decryption processes need computing only the scalar multiplication operation while on the EC-EPKC requires for these processes computing the scalar multiplication and addition operations, so the last cryptosystem needs extra computations.

7. The Security Considerations on Proposed Public Key Cryptosystems

The security of the proposed encryption scheme determines through some main points. The first one is about the difficulty of solving the Elliptic Curve Discrete Logarithm Problem (ECLP) [13]. The ECLP, means computing the value of k that lies in the range [1, z-1] and satisfies the relation $kP = Q$, for given P and Q which are elliptic curve points and z is a prime order of P. The second one is the hardest to find the private key d others, where e is a public key such that $ed=1(\mathrm{mod}\,n)$ because n is a secret key. The element d here represents the inverse element of e modulo n, and since n is computed securtly, so it is more difficult to compute the value of d modulo n.

8. Conclusion

This work presented a new version of the elliptic curve public key cryptosystem which is called the KR-EC public key cryptosystem. It depended on the hardness computation of the elliptic curve discrete logarithm problem (ECDLP) and some mathematical computation problems from the number theory. On the proposed KR-EC public key cryptosystem, faster computations to generate the keys, encryption and decryption processes are done. The security of the KR-EC public key cryptosystem is determined based on the difficulty of computing the ECDLP and selecting the primes to compute the Euler phi function secretly. So, the KR-EC public key cryptosystem considers as a brilliant insight for elliptic curve encryption schemes.

References

[1] Liu A and Ning P 2008 April TinyECC A configurable library for elliptic curve cryptography in wireless sensor networks *International Conference on Information Processing in Sensor Networks, IEEE* pp 245-256
[2] Szczechowiak P, Oliveira L B, Scott M., Collier M, & Dahab R. 2008 NanoECC: Testing the limits of elliptic curve cryptography in sensor networks. *In European conference on Wireless Sensor Networks, Springer, Berlin, Heidelberg* pp 305-320
[3] Abd El-Latif A A & Niu X 2013 A hybrid chaotic system and cyclic elliptic curve for image encryption *AEU-International Journal of Electronics and Communications* **67**(2) 136-143
[4] Rivest R L, Shamir A & Adleman L 1978 A method for obtaining digital signatures and public-key cryptosystems. *Communications of the ACM* **21**(2) 120-126
[5] Miller V S 1985 Use of elliptic curves in cryptography *In Conference on the theory and application of cryptographic techniques Springer, Berlin, Heidelberg* pp 417-426
[6] Koblitz N 1987 Elliptic curve cryptosystems *Mathematics of computation* **48**(177) 203-209
[7] Koblitz N, Menezes A & Vanstone S 2000 The state of elliptic curve cryptography *Designs codes and cryptography* **19(**2-3) 173-193

[8] Hoffstein J, Pipher J, Silverman J H & Silverman J H 2008 *An introduction to mathematical cryptography* (Vol. **1**). New York: Springer
[9] Washington L C 2008 Elliptic curves *number theory and cryptography* CRC press
[10] Trappe Wade 2006 Introduction to cryptography with coding theory *Pearson Education India*
[11] Ajeena R K & Kamarulhaili H 2014 Point multiplication using integer sub-decomposition for elliptic curve cryptography *Applied Mathematics & Information Sciences* **8**(2) 517
[12] Ajeena R K Integer 2015 Sub-decomposition (ISD) Method for Elliptic Curve Scalar Multiplication. *Diss. Universiti Sains Malaysia*
[13] Bos J W, Kaihara M E, Kleinjung T, Lenstra A K & Montgomery P L 2012 Solving a 112-bit prime elliptic curve discrete logarithm problem on game consoles using sloppy reduction *International Journal of Applied Cryptography* **2**(3) 212-228

Tuning Parameters of ANFIS Model Using Chaotic Particle Swarm Optimization Algorithm

Tuning Parameters of ANFIS Model Using Chaotic Particle Swarm Optimization Algorithm

Fatima Hashim Najim and Omar Saber Qasim

Department of Mathematics, University of Mosul, Mosul, Iraq

E-mail: fatima.csp103@student.uomosul.edu.iq

Abstract: In recent years, researchers have worked to find multiple methods to overcome the classification problems they encountered. In this paper, both the Chaotic Particle Swarm Optimization (CPSO) algorithm are connected with the Adaptive Fuzzy Inference System (AFIS) model, through two stages, the first stage, CPSO algorithm is used to tune parameters of the fuzzy inference system model. In the second stage, the fuzzy inference system model is constructed according to the optimum parameters that are found by the CPSO algorithm. The proposed CPSO-AFIS algorithm demonstrated efficacy and efficiency compared to the standard algorithm Adaptive Neuro Fuzzy Inference System (ANFIS).

1. Introduction:

When we classify a set of data using modern methods, we expect to obtain better results according to the available classifiers, and the examiner may not be able to use the classification in which he is not an expert, for example training the accuracy of parameters, and to obtain more accurate parameters, this is limited to use the expertise of the expert. Thus, there can be no complete realization that it is the best possible [1, 2].

Both the fuzzy system and the artificial neural network are the focus of researchers' attention, so the researchers worked to combine these two systems together to get one system called the Adaptive Nervous System for Fuzzy Inference (ANFIS). They obtained a system with distinctive characteristics that help overcome many of the problems (flexibility, speed, adaptability) that existed in both systems, so, they got better performance than the expert fog systems and the artificial neural network [3].

The focus of the researchers in (ANFIS) was to find a model capable of obtaining more accurate results through parameter training [4]. In spite of this improvement, sometimes we find there is a weak ability to find the best efficiency. Therefore, the swarm algorithms were used to make the system more efficient and accurate [5, 6].

The remnant of this paper is organized as follows: The chaotic map is presented in Section 2. The PSO in Section 3. ANFIS is presented in Section 4. The Proposed CPSO-AFIS algorithm is explained in Section 5. Section 6 covers the Experimental Results. Finally, in section 7, the conclusions are mentioned.

2. Chaotic Map:

Chaos theory used the mathematical approaches to improve both exploration and exploitation during the search for the optimal solution. The chaos is closely related to the study of the chaotic dynamic systems that are highly sensitive to the initial conditions, meaning that any small change in the elementary society

can have a major impact on the final results. Chaotic have random behavior, but providing chaotic behavior does not necessarily need randomness، and deterministic systems can also exhibit chaotic behavior without the need for randomness [2, 7].

2.1 Sine Map

The mathematical formula of this map is described in the following [8]:

$$X_{n+1} = \frac{a}{4} \operatorname{Sin}(\pi X_n) \quad (1)$$

where $0 < a \leq 4$

3. Particle swarm optimization (PSO)

The PSO algorithm is a simulation of the behavior of groups of fish, insects and birds that fly in search of food through co-operation between group members, which was applied by Kennedy and Eberhardt 1995 [9]. The algorithm relies on a set of random values called particles. Each particle in the PSO is linked to the velocity and location of the object and can be modified. These particles move within the search space and the original algorithm of PSO is described as follows [10, 11]:

$$v_{id} = v_{id} + c1 \text{ rand } () (p_{id} - x_{id}) + c2 \text{ rand } ()(p_{gd} - x_{id}) \quad (2)$$

$$x_{id} = x_{id} + v_{id} \quad (3)$$

where c_1 and c_2 are positive constants in Eq.(2), and rand () and rand () are two random functions (random numbers) in the range $[0,1]$, $X_i = (x_{i1}, x_{i2}, \ldots, x_{iD})$ represents the ith particle , $P_i = (p_{i1}, p_{i2}, \ldots, p_{iD})$ represents the best previous position (the position giving the best fitness value) of the ith particle.

The symbol g in Eq.(2) represents the index of the best particle among all the particles in the population, $V_i = (v_{i1}, v_{i2}, \ldots, v_{iD})$ represents the rate of the position change (velocity) for particle i. The Eq. (2) explains how the velocity of the particles (birds, fish, insects, etc.) is updated dynamically and that Eq.(3) describes how the site is updated for particles [12, 13].

4. The Adaptive Neural Fuzzy Inference System (ANFIS)

Neural networks play an essential role when there is a sufficient number of inputs to conduct the training without prior knowledge of the nature of the entered data. As for fuzzy systems, there must be a full knowledge of the rules on which the problem is classified as it is represented by (IF-THEN) rules, which is the phrase for conditional statements expressed in the formula [14]:

IF X then Y, where both X and Y are fuzzy sets.

The idea of ANFIS aims to integrate a neural network system with an adaptive fuzzy logic system, that is, we get a mysterious nervous system that combines the features of the neural network and the mysterious inference of the Sugeno type, which was developed in the early 1990s by Jean in order to reap the benefits available in both systems at the same time [5].

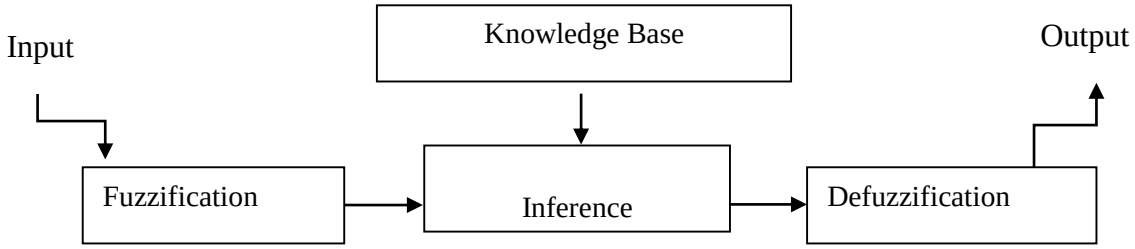

Figure 1. The adaptation ANFIS to conduct learning and training

If we conduct the fuzzing on the obvious input variables, then can apply the rules to them, and then remove the fuzzing with an inverse process to get real values [15].

The general structure of ANFIS for Sugeno model (first rank) can be defined as :

$$\text{IF } X_n \text{ is } A_i \text{ AND } Y_n \text{ is } B_i \text{ THEN } F = P_i X_1 + q_i X_n + r_i \quad (4)$$

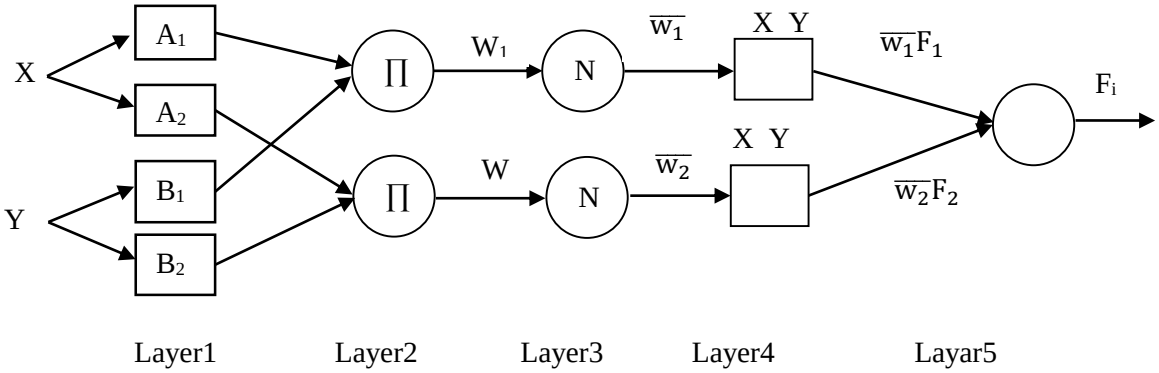

Figure 2. The general structure of ANFIS

The first layer represents the process of fuzzing and determining the degree of membership for each entry. Usually, the organic grades within the first cycle are not appropriate and the reason for this is the random representation of these membership functions until the adjustment process is carried out, where these degrees are represented as follows [16]:

$$Oi1 = \mu A_i(X), \mu B_i(Y) \quad (5)$$

The second layer is the nodes that are not adaptive as the rules are applied to them:

$$Oi٢ = \mu A_i(X_1) * \mu B_i(Y_n) \quad (6)$$

The third layer, the excitation force on neurons is calculated through the normalization process and is as follows [17]:

$$\overline{w_i} = \frac{w_i}{\sum w_i} \quad (7)$$

This represents the output for the third layer and is symbolized by O_i^3.

The fourth layer in this layer, the fuzzing process is reversed, meaning results are easy to read and understand Where this process takes place as follows [18]:

$$O_i^4 = Y_i = \overline{w_i} F_i = \overline{w_i}(p_i X_1 + q_i X_2 + r_i) \quad (8)$$

where pi, qi, and ri are the parameters of the model in a given order because they deal with the part that was then in the ambiguity area.

The fifth layer This layer represents the final output of the system (ANFIS) as it consists of one node and represents the sum of the outputs of the nodes in the previous layers. The calculation is as follows:

$$O_i^5 = \sum_i y_i = \sum_i \overline{w_i} F_i = \sum_i \overline{w_i}(p_i X_1 + q_i X_2 + r_i) \quad (9)$$

The learning algorithm in ANFIS uses a hybrid learning, as it combines the two methods of rapid regression and the method of estimating the least squares, and the training in each epoch goes through two phases: the forward direction phase and the back direction phase [18, 19].

5. The Proposed Algorithm CPSO-AFIS

The proposed CPSO-AFIS method consists of two basic stages. In the first stage, the Chaotic Particle Swarm Optimization Algorithm (CPSO) is used to determine the optimum parameters of the Fuzzy Inference System (FIS) in the Sugeno model. In the second stage, a FIS model is created according to the optimal parameters that were found by the CPSO algorithm, where these optimal parameters are entered into the inference system and the ideal model is formed according to the dataset used. The proposed CPSO-AFIS method has been tested on three different datasets and classified according to the Mean Squared Error (MSE) criteria.

Algorithm1: Steps of the proposed CPSO-AFIS algorithm.

Step1: Set the initial parameters of FIS and PSO algorithm.

Step2: Initialization a chaotic sine map with the initial point (x=0.7).

Step3: Create FIS of Sugeno model using optional parameters.

Step 4: Set the initial velocities and positions using, Eq. (2) and Eq. (3)

Step 5: Evaluate dataset by fitness function.

Step 6: Set iteration i from 1 to max of iteration.

Step 7: Update velocity and position according to Eq. (2) and Eq. (3).

Step 8: When i≤ Max_iteration stop satisfied and return get the best parameters of FS.

Step 9: Insertion of the optimal parameters of FIS into the Sugeno model.

Step 10: Calculate the MSE criterion for the proposed CPSO-AFIS method.

6. Experimental Results

The proposed algorithm CPSO-AFIS is evaluated, and its interest is compared with the ANFIS model. In order to verify the effectiveness of the CPSO-AFIS algorithm for classification problems, we selected 3 different classification datasets from the literature. These datasets were obtained from the UCI repository [20]. Table 1 shows the comprehensive description of data sets.

Table 1: Description of the used datasets**.**

Dataset	# Samples	# Features
Data1=Iris	150	4
Data2=Engine	1199	2
Data3=Thalassemia	150	10

The training and testing dataset for the CPSO-AFIS algorithm, achieved the best MSE, for instance, in Data1, the MSE of the testing dataset is 4.2444e-2 by the FMI-BPSO which is lower than 5.1314e-2 by ANFIS.

Table 2: The MSE of training and testing for datasets.

Datasets	Methods	MSE of Training	MSE of Testing
Data1	CPSO-AFIS	3.5362e-2	4.2444e-2
	ANFIS	4.5146e-2	5.1314e-2
Data2	CPSO-AFIS	3.9281e-4	3.7042e-4
	ANFIS	4.6159e-4	4.6821e-4
Data3	CPSO-AFIS	8.0337e-3	7.5253e-3
	ANFIS	8.4832e-3	7.547e-3

The execution comparison shows that, compared to the ANFIS model, the proposed algorithm, CPSO-AFIS, has an obvious advantage in terms of MSE of the classification and the ANFIS is worse than CPSO-AFIS through the three datasets.

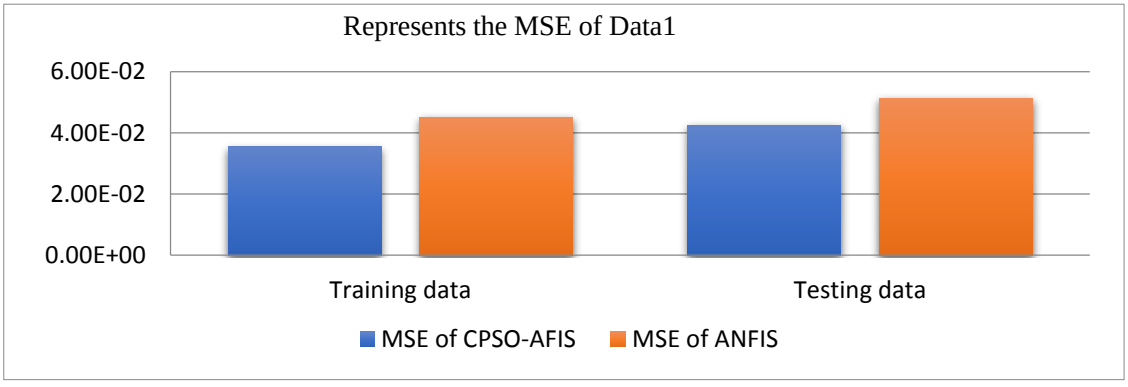

Figure 3. Represents the comparison of MSE between CPSO-AFIS & ANFIS in Data1.

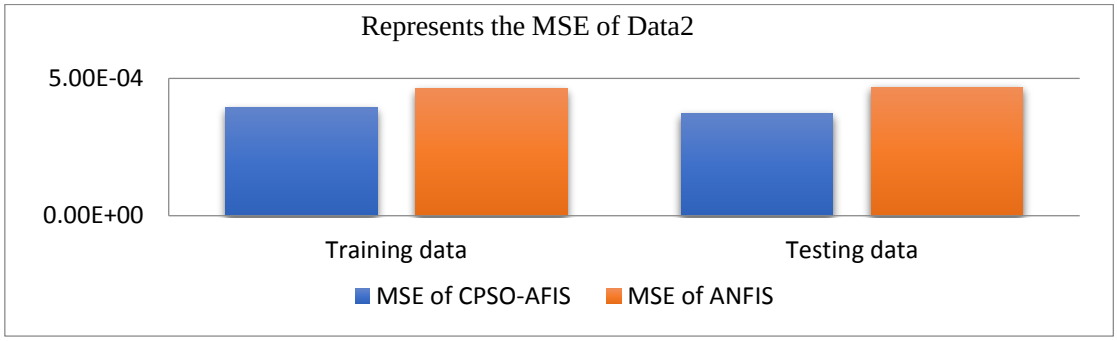

Figure 4. Represents the comparison of MSE between CPSO-AFIS & ANFIS in Data2.

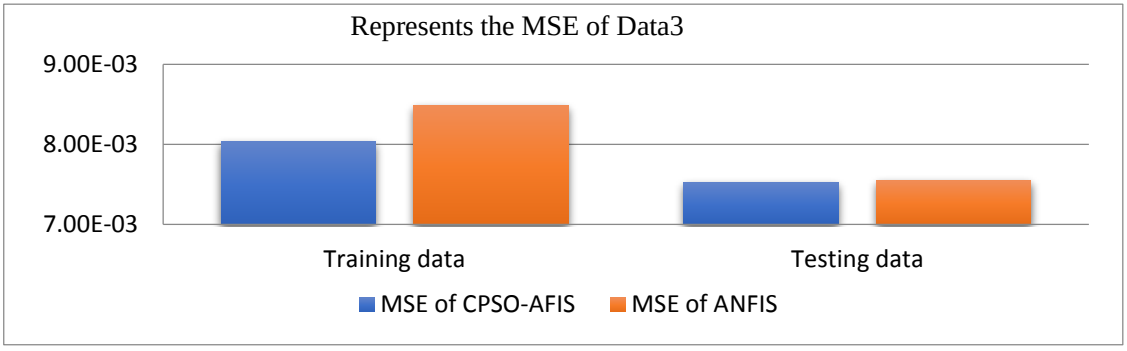

Figure 5. Represents the comparison of MSE between CPSO-AFIS & ANFIS in Data3.

7. Conclusion

In this paper, the CPSO-AFIS method was proposed between the chaotic Particle Swarm Optimization Algorithm (CPSO) of type Sine map and Fuzzy Inference System (FIS) of type Sugeno model to improve the classification performance of the datasets in Table 1. The results of the proposed CPSO-AFIS method were compared with the results of ANFIS through the Table2 and Figures (3-5) and the experimental results from the datasets in Table2 indicate that the proposed CPSO-AFIS method has a classification performance that is higher than the ANFIS through MSE criteria.

References

[1] M Gong, H. Yang and P. Zhang 2017 Feature learning and change feature classification based on deep learning for ternary change detection in SAR images *ISPRS Journal of Photogrammetry and Remote Sensing* **129** pp 212-225

[2] O S Qasim, N A Al-Thanoon and Z Y Algamal 2020 Feature selection based on chaotic binary black hole algorithm for data classification *Chemometrics and Intelligent Laboratory Systems* **204** pp 104104.

[3] M Rezakazemi et al. 2017 H2-selective mixed matrix membranes modeling using ANFIS PSO-ANFIS, GA-ANFIS *International Journal of Hydrogen Energy* 2017 **42** (22) pp 15211-15225

[4] D Karaboga and E Kaya 2019 Adaptive network based fuzzy inference system (ANFIS) training approaches: a comprehensive survey *Artificial Intelligence Review* **52**(4) pp 2263-2293

[5] R Singh, A. Kainthola and T Singh 2012 Estimation of elastic constant of rocks using an ANFIS approach *Applied Soft Computing* **12**(1) pp 40-45

[6] O S Qasim, M S Mahmoud and F M Hasan Hybrid binary dragonfly optimization algorithm with statistical dependence for feature selection *Int. J. Math. Eng. and Manag. Sci* **5**(6) pp 1420-1428

[7] W Liu, K Sun and C Zhu 2016 A fast image encryption algorithm based on chaotic map *Optics and Lasers in Engineering* **84** pp 26-36

[8] A Belazi and A A Abd El-Latif 2017 A simple yet efficient S-box method based on chaotic sine map *Optik* **130** pp 1438-1444
[9] C Zhou et al. 2003 Particle Swarm Optimization (PSO) Algorithm [J] *Application Research of Computers* **12** pp 7-11
[10] N B Guedria 2016 Improved accelerated PSO algorithm for mechanical engineering optimization problems *Applied Soft Computing* **40** pp 455-467
[11] M A A Alhafedh and O S Qasim 2019 Two-Stage Gene Selection in Microarray Dataset Using Fuzzy Mutual Information and Binary Particle Swarm Optimization *Indian Journal of Forensic Medicine & Toxicology* **13**(4) pp 1162-1171
[12] O S Qasim and Z Y Algamal 2018 Feature selection using particle swarm optimization-based logistic regression model *Chemometrics and Intelligent Laboratory Systems* **182** pp 41-46
[13] O S Qasim and Z Y Algamal 2020 Feature selection using different transfer functions for binary bat algorithm. International Journal of Mathematical *Engineering and Management Sciences* **5**(4) pp 697-706
[14] J S Jang 1993 ANFIS: adaptive-network-based fuzzy inference system *IEEE transactions on systems, man, and cybernetics* **23**(3) pp 665-685
[15] H Zhou, X Wu and X Li 2011 *An ANFIS model of electricity price forecasting based on subtractive clustering* IEEE power and energy society general meeting
[16] A Sharifi et al 2008 Hierarchical Takagi-Sugeno type fuzzy system for diabetes mellitus forecasting *International Conference on Machine Learning and Cybernetics IEEE*
[17] M İnal 2008 Determination of dielectric properties of insulator materials by means of ANFIS: a comparative study *Journal of Materials Processing Technology* **195**(1-3) pp 34-43
[18] P Cortés-Antonio et al. 2020 Learning rules for Sugeno ANFIS with parametric conjunction operations *Applied Soft Computing* **89** pp 106095
[19] S Gören et al. 2008 Prediction of cyclosporine A blood levels: an application of the adaptive-network-based fuzzy inference system (ANFIS) in assisting drug therapy *European journal of clinical pharmacology* **64**(8) pp 807
[20] B Amarnath, S Balamurugan and A Alias 2016 Review on feature selection techniques and its impact for effective data classification using UCI machine learning repository dataset *Journal of Engineering Science and Technology* **11**(11) pp 1639-1646

Solve differential equations via a hybrid method between homotopy analytical method and sine cosine optimization algorithm

Solve differential equations via a hybrid method between homotopy analytical method and sine cosine optimization algorithm

Mostafa raed najeeb , Omar Saber Qasim and Ahmed Entesar

Department of Mathematics, College of Computer Sciences and Mathematics, University of Mosul, Iraq

E-mail: mostafa.csp115@student.uomosul.edu.iq

Abstract. In this paper, ordinary differential equations (ODEs) of two types, linear and non-linear will be solved by using the homotopy analytical method (HAM), and the sine cosine algorithm (SCA) will be used to modify the parameter h and obtain a better approximate solution than what was in the previous method HAM. The suggested method, HAM-SCA, covers a solution that reveals the reliability and the efficiency correspondingly to the default method HAM by computing the maximum absolute errors (MAE) and mean square error (MSE).

1. Introduction

All-natural, physical, engineering, and other phenomena are expressed by DEs (linear and nonlinear), these equations differential in the method of solution, a few of them can be solved directly, so it was necessary to use approximate methods to address problems and arrive at the solution, as the HAM is one of these methods [1].

HAM is the method that the world Liao Shijun discovered in 1992 [2, 3], he relied on using the homotopic method to obtain a convergent series solution (convergent series) for various types of equations whether linear or non-linear equations, DEs, integral equations, and other types of equations, the HAM method describes a kind of deformation or disparity in mathematical, for example, a circle can be deformed continuously to a square or an ellipse, as well as a cup of coffee, can be deformed continuously into a football [1, 4], in general, the HAM connects objects different has the same properties, one of what distinguishes this method is that it is free of any)small or large(concrete parameter, as well as provides appropriate methods to guarantee convergence in the series of solutions even if the non-linear boundary is complex, and it gives us the privilege in choosing the type of equation for sub-problems, the initial guess, and the basic function.

SCA is one of the swarm algorithms invented by the scientist Sidali Mergalieli, used to solve optimization problems and obtain the best solution, based on the principle of exploration and exploitation as it creates and searches many random solutions depending on the properties of the sine and cosine and switches between them according to a specific condition. [5-7].

We can represent the algorithm in the following form

$$w_n^{v+1} = w_n^v + d_1 \sin(d_2)|d_3\, p_n^v - \, w_n^v| \quad (1)$$

$$w_n^{v+1} = w_n^v + d_1 \cos(d_2)|d_3\, p_n^v - \, w_n^v| \quad (2)$$

As w_n^v is the current subject of research, in $n-th$ dimension at $v-th$ iteration, and d_1, d_2, d_3, d_4 are random numbers, and p_n is the location of the destination point in the n-th dimension, and || is the absolute value [6]. We can combine the two previous equations as follows.

$$w_n^{v+1} = \begin{cases} w_n^v + d_1 \sin(d_2)|d_3\, p_n^v - w_n^v|, & d_4 < 0.5 \\ w_n^v + d_1 \cos(d_2)|d_3\, p_n^v - w_n^v|, & d_4 \geq 0.5 \end{cases} \quad (3)$$

Where d_4 is arbitrary within the closed interval [0,1].
The parameter d_1 specifies the next position (in which direction the move will be) by the following law:

$$d_1 = m - t\,\frac{m}{T} \quad (4)$$

Where t is the value of the current frequency, T is the ultimate number of iterations, and m is a mass constant, which can be either the distance between solutions, the destination or outwards and, the parameter $d2$ assigns how unlikely the movement must be pointed or outward, the $d3$ parameter specifies a random weight for a $(d3 > 1)$ random check, or $(d3 < 1)$ reduces the focus for the destination effect when specifying a distance.

SCA named after that name for its use of the sine and cosine functions completely in its general form, as it changes and modifies the range of the sine and cosine functions each time to determine a new search site, whether it is in the space or outside the space or if it is between it and another solution, then a value is chosen random $d2$ for a certain period, this mechanism clarifies the true meaning of the processes of exploration and exploitation, and this algorithm makes the correct selection and reconciliation between exploration and exploitation to reach the goal [8,9], which is through the convergence of solutions as shown in the Figure (1).

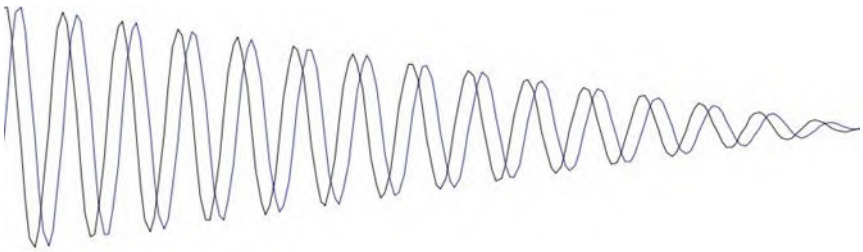

Figure 1: Demonstrates the convergence of solutions in SCA

2. General Concepts

In this part, will mention some important definitions in this paper

2.1 Definition

The maximum absolute errors MAE is determined by the following formula

$$\|z_{Exact}(y) - \propto_i (y)\|_\infty = \max_{a \leq x \leq b} \{|z_{Exact}(y) - \propto_i (y)|\} \quad (5)$$

Here $\propto_i (y), i = 1,2, \ldots$ are the successive estimates of the solution $z\,(y)$ [4].

2.2 Definition

Let's have the vector $\vec{x_i}$ where $i = 1,2, \ldots$, the MSE is a sum the square of the exact solution Exact (y_i) minus the approximate solution divided by the number of iterations k which is as follows [10]

$$MSE = \frac{1}{k}\sum_{i=1}^{k} (Exact\,(y_i) - \emptyset(y_i))^2 \quad (6)$$

2.3 Definition

The MAE is defined by the following formula

$\frac{1}{k}\sum_{i=1}^{k}|Exact\ (y_i) - \emptyset(y_i)|\ , i = 1,2, \ldots$ (7)

Which represents the absolute value of the sum of the product of subtracting the real value from the approximate value divided by the number of iterations [11].

2.4 Adomian Polynomials

Will use the Adomian method to solve the non-linear terms from the ordinary DEs [12]. When $f(u) = u^2$ [13, 14].

Can use the Adomian method to extend the nonlinear term to the $f(u) = u^2$ document using

$x_0 = u_0^2$
$x_1 = 2u_0u_1$
$x_2 = 2u_0u_2 + u_1^2$
$x_3 = 2u_0u_3 + 2u_1u_2$
$x_4 = 2u_0u_4 + 2u_1u_3 + u_2^2$
$x_5 = 2u_0u_5 + 2u_1u_4 + 2u_2u_3,$
$\vdots$
$x_n = \sum_{i=0}^{n} u_i\, u_{n-i}\ , \quad n \geq i, \quad n = 0, 1, 2, \cdots$

When $f(u) = uu'$ [13,14]

$x_0 = u_0\, u_0''$
$x_1 = u_1\, u_0'' + u_0\, u_1''$
$x_2 = u_2\, u_0'' + u_1\, u_1'' + u_0\, u_2''$
$x_3 = u_3\, u_0'' + u_2\, u_1'' + u_1\, u_2'' + u_0\, u_3''$
$x_4 = u_4\, u_0'' + u_3\, u_1'' + u_2\, u_2'' + u_1\, u_3'' + u_0\, u_4''$
$x_5 = u_5\, u_0'' + u_4\, u_1'' + u_3\, u_2'' + u_2\, u_3'' + u_1\, u_4'' + u_0\, u_5''$
$\vdots$
$x_n = \sum_{i=0}^{n} u_i\, u_{n-i}''\ , \quad n \geq i, \quad n = 0, 1, 2, \cdots$

3. The Basic Ideas of HAM [1,15,18]

Let us have the following linear Des [17].

$N[z(t)] = 0$ (8)

Where N is a non-linear operator, t represents the independent variable, and z is an undefined function, by driving the classic homotopy technique, we get the zero orders deformation equation, which is defined below [18].

$(1 - q)\ \mathcal{L}\ [\beta(t, q) - z_0(t)] = q\ h\ H(t)\ N[\beta(t, q)]$ (9)

Where $q \in [0,1]$ represents the embedding parameter [19], which is called the homotopic parameter, $\mathcal{L}$ represents the auxiliary linear limit that fulfills the following property $\mathcal{L}(\mathrm{z}) = 0$, $\beta(t, q)$ also refers to the initial estimation of the exact solution, and h is called the convergence control parameter where $h \neq 0$, and $H(t)$ is an auxiliary function where $H(t) \neq 0$, when have $q = 0$ get

$\beta(t, 0) = z_0(t)$ (10)

Which represents the exact solution, and if had $q = 0$ then get

$\beta(t, 0) = z(t)$ (11)

Which represents the real solution to Eq. 8, thus as the parameter of homotopy q increases how much zero to one, the solution changes continuously from the initial guess $z_0(t)$ to the exact solution $z(t)$. This continuous change in solution is called the deformation in homotopy, as it is using the Taylor series for the parameter q.

$$z_1(t) = \beta(t,q) = z_0(t) + \sum_{j=1}^{+\infty} z_0(t) q^j \quad (12)$$

Whereas the

$$z_j(t) = \frac{1}{j!} \frac{\partial^j \beta(t,q)}{\partial q^j} \quad (13)$$

If $\mathcal{L}, z_0(t)$, $H(t)$ was correctly selected then the Taylor series would look like this

$$z_1(t) = \beta(t,q) = z_0(t) + \sum_{j=1}^{+\infty} z_0(t) \quad (14)$$

By deriving the zero-order deformation equation j times for the parameter q, then substituting for $q = 0$ and dividing the equation by $j!$ get the deformation equation of order j which is as follows:

$$\mathcal{L}\left[z_j(t) - \chi_j\, z_{j-1}(t)\right] = h\, H(t)\, R_{j-1}\left(\vec{z_{j-1}}(t)\right), \qquad z_j(0) = 0 \quad (15)$$

Where the vector is known as

$$\vec{z_j}(t) = \left\{z_0(t), \quad z_1(t), \quad z_2(t), \ldots, \quad z_j(t)\right\} \quad (16)$$

From Eq. 15 get

$$R_{j-1}\left(\vec{z_{j-1}}(t)\right) = \frac{1}{(j-1)!} \frac{\partial^{j-1} N[\beta(t,q)]}{\partial q^{j-1}}\Big|_{q=0} \quad (17)$$

$$\chi_j = \begin{cases} 0, & j \geq 1 \\ 1, & j < 1 \end{cases} \quad (18)$$

4. The Proposed Method SCA-HAM

The proposed method is based on calculating the optimal value of the HAM parameter (h) to figure out linear and non-linear ODEs by combining the HAM method with the SCA method, where the initial calculation is with a formula HAM.

$$z_j(t) = \chi_{j-1}\, z_{j-1}(t) + h\, L^{-1} R_j\left(\vec{z_{j-1}}(t)\right) \quad (19)$$

Using SCA will optimize the parameter h value in the HAM method to get the best solution.

5. Some Applications of SCA-HAM

Will solve some examples of ordinary linear and nonlinear DEs using HAM and improve the results using SCA.

5.1 Example [16]

$y'''' + 5y'' + 4y = 0$

And the exact solution

$z(t) = \frac{4}{3}\cos(t) + \frac{1}{3}\sin(t) - \frac{1}{3}\cos(2t) - \frac{1}{6}\sin(2t)$

And pick out the initial estimation

$z_0(t) = 1 + \frac{1}{6}t^3$

Then the linear operator (which represents the general solution)

$L[\beta(t;q)] = \frac{\partial^4 \beta(t;q)}{\partial t^4}$

Then have $L[c_1 + c_2 s + c_3 s^2 + c_4 s^3]$

The linear operator will look like this

$N[\beta(t;q)] = \frac{\partial^4 \beta(t;q)}{t^4} + 5\,\frac{\partial^2 \beta(t;q)}{t^2} + 4\,\beta(t;q) = 0$

And the initial condition

$z(0) = 1, z'(0) = 0$, $z''(0) = 0$, and $z(0) = 1$

Where

$R_j\left(\vec{z_{j-1}}\right) = z''''_{j-1} + 5z''_{j-1} + 4z_{j-1}$

Will work on finding the terms of the series using the following HAM law

$$z_j(t) = \chi_{j-1}\, z_{j-1} + h\, L^{-1} R_j\left(\vec{z_{j-1}}\right)$$

$$z_1(t) = \frac{1}{6}ht^4 + \frac{1}{24}ht^5 + \frac{1}{1260}ht^7$$

$$z_2(t) = \frac{1}{6}ht^4 + \frac{1}{6}h^2t^4 + \frac{1}{24}ht^5 + \frac{1}{36}h^2t^6 + \frac{1}{1260}ht^7 + \frac{29}{5040}h^2t^7 + \frac{1}{2520}h^2t^8 + \frac{1}{9072}h^2t^9 + \frac{1}{2494800}ht^{11}$$

$$z_3(t) = \frac{1}{20432412000}h^3t^{15} + \frac{1}{25945920}h^3t^{13} + \frac{1}{7484400}h^3t^{12} + \frac{1}{1247400}h^2t^{11} + \frac{83}{9979200}h^3t^{11} + \frac{1}{22680}h^3t^{10} + \frac{41}{72576}h^3t^9 + \frac{1}{4536}h^2t^9 + \frac{1}{1260}h^2t^8 \frac{11}{3360}h^3t^8 + \frac{29}{2520}h^2t^7 + \frac{3}{280}h^3t^7 + \frac{1}{1260}ht^7 + \frac{1}{18}h^2t^6 + \frac{1}{18}h^3t^6 + \frac{1}{12}h^2t^5 + \frac{1}{24}ht^5 + \frac{1}{24}h^3t^5 + \frac{1}{3}h^2t^4 + \frac{1}{6}h^3t^4$$

$$z_4(t) = \frac{1}{475176173472000}h^4t^{19} + \frac{1}{277880803200}h^4t^{17} + \frac{1}{81729648000}h^4t^{16} + \frac{1}{6810804000}h^3t^{15} + \frac{1}{504504000}h^4t^{15} + \frac{1}{90810720}h^4t^{14} + \frac{1}{8648640}h^3t^{13} + \frac{17}{38918880}h^4t^{13} + \frac{1}{2492800}h^3t^{12} \frac{29}{9979200}h^4t^{12} + \frac{83}{3326400}h^3t^{11} + \frac{143}{3628800}h^4t^{11} + \frac{1}{831600}h^2t^{11} + \frac{1}{7560}h^3t^{10} + \frac{7}{25920}h^4t^{10} + \frac{41}{24192}h^3t^9 + \frac{1}{3024}h^2t^9 + \frac{11}{8064}h^4t^9 + \frac{29}{3360}h^4t^8 + \frac{11}{1120}h^3t^8 + \frac{1}{840}h^2t^8 + \frac{9}{280}h^3t^7 + \frac{29}{1680}h^2t^7 + \frac{1}{3260}ht^7 + \frac{79}{5040}h^4t^7 + 6h^3t^6 + \frac{1}{12}h^2t^6 + \frac{1}{12}h^4t^6 + \frac{1}{8}h^2t^5 + \frac{1}{24}h^4t^5 + \frac{1}{24}ht^5 + \frac{1}{8}h^3t^5 + \frac{1}{2}h^2t^4 + \frac{1}{2}h^3t^4 + \frac{1}{6}ht^4 + \frac{1}{6}h^3t^4$$

⋮

So, substitute in the value of $h = -1$ get

$$z_1(t) = -\frac{1}{6}t^4 - \frac{1}{24}t^5 - \frac{1}{1260}t^7$$

$$z_2(s) = \frac{1}{36}t^6 + \frac{1}{1008}t^7 + \frac{1}{2520}t^8 + \frac{1}{9072}t^9 + \frac{1}{7484400}t^{11}$$

$$z_3(t) = -\frac{1}{2043241200}t^{15} - \frac{1}{25945920}t^{13} - \frac{1}{7484400}t^{12} - \frac{1}{133056}t^{11} - \frac{1}{22680}t^{10} - \frac{25}{72576}t^9 - \frac{5}{2016}t^8$$

$$z_4(t) = \frac{1}{745176173472000}t^{19} + \frac{1}{277880803200}t^{17} + \frac{1}{81729648000}t^{16} + \frac{1}{544864320}t^{15} + \frac{1}{90810720}t^{14} + \frac{5}{15567552}t^{13} + \frac{1}{399168}t^{12} + \frac{25}{1596672}t^{11} + \frac{1}{36288}t^{10}$$

⋮

Hence, the solution of the above series is shown in the following form

$$z(t) = z_0(t) + z_1(t) + z_2(t) + z_3(t) + z_4(t) + \cdots$$

$$z(t) \cong 1 + \frac{1}{6}t^3 - \frac{1}{6}t^4 - \frac{1}{24}t^5 - \frac{1}{1260}t^7 + \frac{1}{36}t^6 + \frac{1}{1008}t^7 + \frac{1}{2520}t^8 + \frac{1}{9072}t^9 + \cdots$$

Now and after using the SCA method to improve the parameter h, got better results by substituting for the value of $h^{new} = -0.9776$, The series solution of HAM-SCA can be written as a form

$$z^{new}(t) \cong {z_0}^{new}(t) + {z_1}^{new}(t) + {z_2}^{new}(t) + {z_3}^{new}(t) + {z_4}^{new}(t) + \cdots$$

$$\begin{aligned} z^{new}(t) \cong\ & -0.4572607681\ 10^{-5}t^{15} - 0.3600928549\ 10^{-7}t^{13} - 0.1248321897\ 10^{-6}t^{12} \\ & - 0.6621571294\ 10^{-5}t^{11} - 0.00004119462260\, t^{10} - 0.0002117671603\, t^9 \\ & - 0.001920960538\, t^8 + 0.004159320415\, t^7 + 0.02773658885\, t^6 \\ & - 0.04166619835\, t^5 - 0.1666647933\, t^4 + 0.1666667t^3 + 1 + \cdots \end{aligned}$$

The comparison of results between HAM and HAM-SCA is shown in Table 1 and Figure 2.

Table 1: Comparison of MAE and MSE for HAM and HAM-SCA for Example 1.

Error Criteria	HAM	HAM-SCA
MSE	$2.334360\ E-9$	$9.033345\ E-12$
MAE	$2.035680\ E-5$	$1.555098\ E-6$

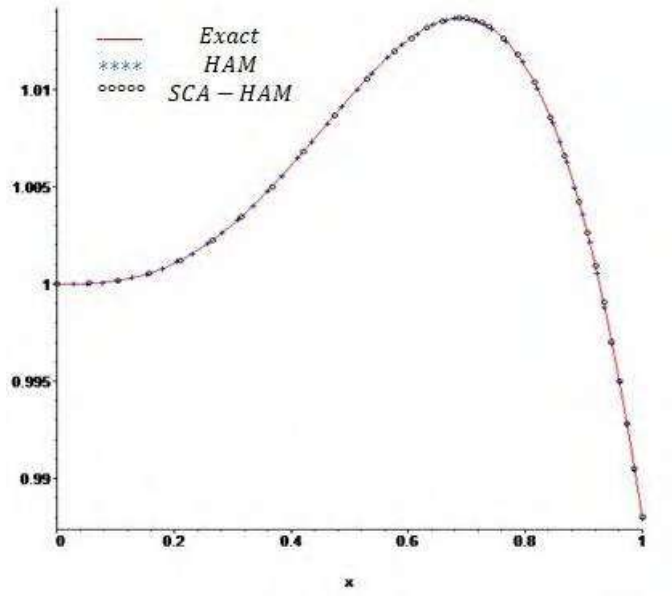

Figure 2: Illustrates the matching process between HAM, HAM-SCA, and exact solution.

5.2 Example [16]

$y'' + y'^2 = 0$

And the exact solution

$z(t) = 1 + \ln(1 + 2t)$

And pick out the initial estimation

$z_0(t) = 1 + 2s$

And the initial condition

$z(0) = 1, \quad z(0) = 2$

The linear operator (which represents the general solution)

$L[\beta(t;q)] = \frac{\partial^2 \beta(t;q)}{\partial t^2}$

Then have $L[c_1 + c_2 s] = 0$

Using Adomian polynomials expand the nonlinear y'^2 a term which will be in the following form

$\sum_{i=0}^{j-1} z_i'(t)\ z'_{j-1-i}(t)$

The linear operator will look like this

$N[\beta(t;q)] = \frac{\partial^2 \beta(t;q)}{s^2} + \frac{\partial \beta^2(t;q)}{s^2}$

And

$R_j(\vec{z_{j-1}}) = z''''_{j-1}(t) + \sum_{i=0}^{j-1} z_i'(t)\ z'_{j-1-i}(t)$

Will work on finding the terms of the series using the following (HAM) law

$z_j(t) = \chi_{j-1}\, z_{j-1} + h\, L^{-1} R_j(\vec{z_{j-1}})$

$z_1(t) = 2ht^2$

$z_2(t) = 2ht^2 + 2h^2t^2 + \frac{8}{3}h^2t^3$

$z_3(t) = 4h^3t^4 + \frac{16}{3}h^2t^3 + \frac{16}{3}h^3t^3 + 2ht^2 + 4h^2t^2 + 2h^3t^2$

$z_4(t) = \frac{32}{5}h^4t^5 + 12h^3t^4 + 12h^4t^4 + 8h^2t^3 + 8h^4t^3 + 16h^3t^3 + 2ht^2 + 6h^2t^2 + 2h^4t^2$

$\vdots$

So, substitute in the value of $h = -1$ get

$z_1(t) = -2t^2$

$z_2(t) = \frac{8}{3}t^3$
$z_3(t) = -4t^4$
$z_4(t) = \frac{32}{5}t^5$
⋮
Then the series solution of HAM with $h = -1$ can be written as a form
$z(t) = z_0(t) + z_1(t) + z_2(t) + z_3(t) + z_4(t) + \cdots$
$z(t) \cong 1 + 2t - 2t^2 + \frac{8}{3}t^3 - 4t^4 + \frac{32}{5}t^5 + \cdots$

Now and after using the SCA method to improve the parameter h, got better results by substituting for the value of $h^{new} = -0.4888$, The series solution of HAM-SCA can be written as a form
$z^{new}(t) \cong {z_0}^{new}(t) + {z_1}^{new}(t) + {z_2}^{new}(t) + {z_3}^{new}(t) + {z_4}^{new}(t) + \cdots$
$z^{new}(t) \cong 0.365346341626839\, t^5 - 1.18356369060168\, t^4 + 1.78803919216422\, t^3 - 1.86341802881761\, t^2 + 2s + 1 + \cdots$
The comparison of results between HAM and HAM-SCA is shown in Table 2 and Figure 3

Table 2: Comparison of MAE and MSE for HAM and HAM-SCA for Example 2.

Error Criteria	HAM	HAM-SCA
MSE	2.056038	$9.204092\ E-6$
MAE	0.758987	$2.33752\ E-3$

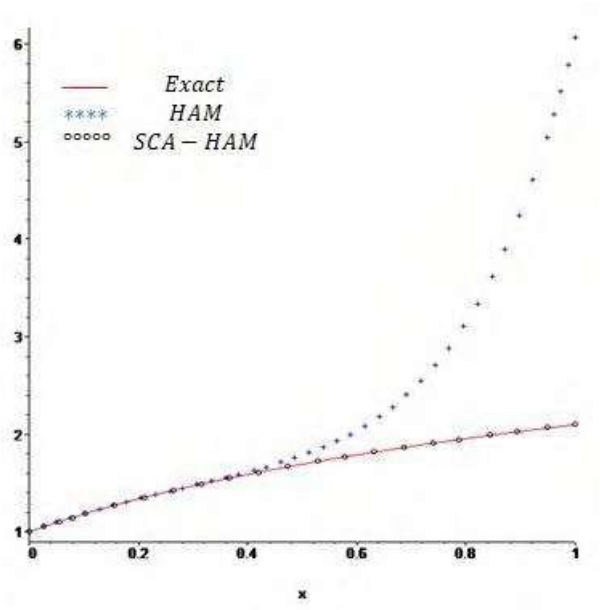

Figure 3: Illustrates the matching process between HAM, HAM-SCA, and exact solution.

5.3 Example [16]
$y'''' + yy'' - y'^2 = 0$
And the exact solution
$z(t) = e^t - 1$
And pick out the initial estimation
$z_0(t) = t + \frac{1}{2}t^2 + \frac{1}{6}t^3$
And the initial condition
$z(0) = 0 \quad , \quad z'(0) = 1 \quad , \quad z''(0) = 1 \quad , \quad z'''(0) = 1$

the linear operator (Which represents the general solution)

$L[\beta(t;q)] = \frac{\partial^4 \beta(t;q)}{\beta s^4}$

Then have $L[c_1 + c_2 s + c_3 s^2 + c_4 s^3]$

Using Adomian polynomials expand the nonlinear $yy'' - y'^2$ a term which will be in the following form

$\sum_{i=0}^{j-1} z_i(t)\, z'_{j-1-i}(t) - \sum_{i=0}^{j-1} z'_i(t)\, z'_{j-1-i}(t)$

The linear operator will look like this

$N[\beta(t;q)] = \frac{\partial^4 \beta(t;q)}{t^4} + \frac{\partial \beta^2(t;q)}{t^2}\, \beta(t;q) - \frac{\partial \beta^2(t;q)}{t^2}$

And

$R_j(\vec{z_{j-1}}) = z'''' _{j-1}(t) + \sum_{i=0}^{j-1} z_i(t)\, z'_{j-1-i}(t) - \sum_{i=0}^{j-1} z'_i(t)\, z'_{j-1-i}(t)$

Will work on finding the terms of the series using the following (HAM) law

$z_j(t) = \chi_{j-1}\, z_{j-1} + h\, L^{-1} R_j(\vec{z_{j-1}})$

$z_1(t) = -\frac{1}{24}ht^4 - \frac{1}{120}ht^5 - \frac{1}{270}ht^6 - \frac{1}{2520}ht^7 - \frac{1}{20160}ht^8$

$z_2(t) = h\left(-\frac{1}{24}ht^4 - \frac{1}{120}ht^5 - \frac{1}{270}ht^6 - \frac{1}{2520}ht^7 - \frac{1}{20160}ht^8\right) + h\left(\frac{1}{148262400}ht^{13} - \frac{1}{11404800}ht^{12} - \frac{1}{19958400}ht^{11} - \frac{1}{453600}ht^{10} + \frac{1}{362880}ht^9 - \frac{1}{13440}ht^8 - \frac{1}{1680}ht^7 - \frac{1}{720}ht^6 - \frac{1}{120}ht^5 - \frac{1}{24}ht^4\right)$

$z_3(s) = -\frac{1}{20160}ht^8 - \frac{1}{2520}ht^7 - \frac{1}{720}ht^6 - \frac{1}{120}ht^5 - \frac{1}{24}ht^4 - \frac{1}{74131200}h^2t^{13} - \frac{1}{5702400}h^2t^{12} - \frac{13}{9979200}h^2t^{11} - \frac{1}{226800}h^2t^{10} - \frac{1}{181440}h^2t^9 - \frac{1}{6720}h^2t^8 - \frac{1}{840}h^2t^7 - \frac{1}{360}h^2t^6 - \frac{1}{60}h^2t^5 - \frac{1}{12}h^2t^4 - \frac{53}{23691859200}h^3t^{15} - \frac{11}{1981324800}h^3t^{14} - \frac{7}{222393600}h^3t^{13} - \frac{127}{479001600}h^3t^{12} - \frac{79}{39916800}h^3t^{11} - \frac{29}{106748928000}h^3t^{16} - \frac{829}{29640619008000}h^3t^{17} - \frac{829}{533531142144000}h^3t^{18} - \frac{1}{145152}h^3t^{10} - \frac{1}{181440}h^3t^9 - \frac{1}{10080}h^3t^8 - \frac{1}{1260}h^3t^7 - \frac{1}{720}h^3t^6 - \frac{1}{120}h^3t^5 - \frac{1}{24}h^3t^4$

⋮

So, substitute in the value of $h = -1$ get

$z_1(t) = \frac{1}{24}t^4 + \frac{1}{120}t^5 + \frac{1}{270}t^6 + \frac{1}{2520}t^7 + \frac{1}{20160}t^8$

$z_2(t) = \frac{1}{148262400}t^{13} + \frac{1}{11404800}t^{12} + \frac{1}{19958400}t^{11} + \frac{1}{453600}t^{10} + \frac{1}{362880}t^9 + \frac{1}{40320}t^8 + \frac{1}{5040}t^7$

$z_3(t) = \frac{829}{533531142144000}t^{18} + \frac{829}{296406190080000}t^{17} + \frac{29}{106748928000}t^{16} + \frac{53}{32691859200}t^{15} + \frac{11}{1981324800}t^{14} + \frac{1}{55598400}t^{13} + \frac{43}{479001600}t^{12} + \frac{1}{1478400}t^{11} + \frac{1}{403200}t^{10}$

$z_4(s) = -\frac{101}{416860435031040000}t^{23} - \frac{101}{18124366740480000}t^{22} - \frac{14009}{202741834014720000}t^{21} - \frac{36121}{67580611338240000}t^{20} - \frac{9487}{3801409387776000}t^{19} - \frac{13547}{1600593426432000}t^{18} - \frac{3023}{88921857024000}t^{17} - \frac{677}{2615348736000}t^{16} - \frac{163}{100590336000}t^{15} - \frac{23}{4151347200}t^{14} - \frac{23}{2075673600}t^{13}$

⋮

Then the series solution can be written as a form

$z(t) = z_0(t) + z_1(t) + z_2(t) + z_3(t) + z_4(t) + \cdots$

$z(t) \cong \frac{1}{24}t^4 + \frac{1}{120}t^5 + \frac{1}{270}t^6 + \frac{1}{2520}t^7 + \frac{1}{20160}t^8 + \cdots$

When using SCA to improve the parameter h, the best result was $h = -1$, which is the same in HAM.

The comparison of results between HAM and HAM-SCA is shown in 3able 1 and Figure 4.

Table 3: Comparison of MAE and MSE for HAM and HAM-SCA for Example 3

Error Criteria	HAM	HAM-SCA
MSE	2.056038	$9.204092\ E-6$
MAE	0.758987	$2.33752\ E-3$

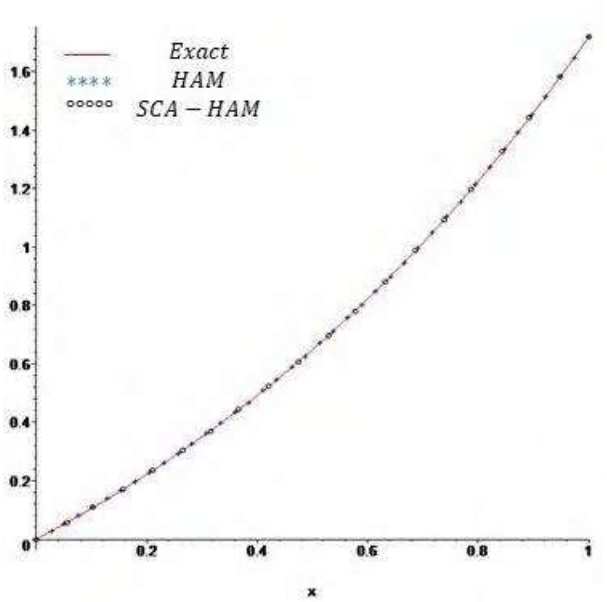

Figure 4: Illustrates the matching process between HAM, HAM-SCA, and exact solution.

Conclusion

In this work, a hybrid method SCA-HAM is implemented between the HAM and the SCA. A series of approximate solutions in the HAM has been applied as a fitness function in the SCA to find the optimal h parameter. The outcome of the SCA-HAM method (which contains the optimal parameter (h)) was compared with the HAM through three examples illustrated in Tables (1-3) and Figure (2-4), where the SCA-HAM shows a clear superiority over HAM in discovering approximate solutions through calculating the MSE and MAE.

References

[1] A. Sami Bataineh, M. S. M. Noorani, and I. Hashim 2008 Solving systems of ODEs by homotopy analysis method *Communications in Nonlinear Science and Numerical Simulation* **13** 2060-2070
[2] J. Ahmad and S. Rubab 2017 Efficient Homotopy Analysis Method to System of Delay Differential Equations *Annals of the Faculty of Engineering Hunedoara* **15** 133
[3] S.-J. Liao 1992 The proposed homotopy analysis technique for the solution of nonlinear problems Ph. D. Thesis, Shanghai Jiao Tong University Shanghai
[4] L. Shijun 2013 Advances in the Homotopy Analysis Method *World Scientific*
[5] H. Nenavath and R. K. J. Jatoth 2018 Hybridizing sine cosine algorithm with differential evolution for global optimization and object tracking *Applied Soft Computing* **62** 1019-1043
[6] S. Mirjalili 2016 SCA: A Sine Cosine Algorithm for solving optimization problems," *Knowledge-Based Systems* **96** 120-133
[7] S. Ekiz, P. Erdoğmuş, and B. Özgür 2017 Solving constrained optimization problems with sine-cosine algorithm *Periodicals of Engineering and Natural Sciences (PEN)* **5**

[8] O. S. Qasim, and Z. Y. J. I. J. o. M 2020 Algamal, Engineering, and M. Sciences, Feature selection using different transfer functions for binary bat algorithm **5** 697-706
[9] O. S. Qasim, N. A. Al-Thanoon, Z. Y. J. C. Algamal, and I. L. Systems 2020 Feature selection based on chaotic binary black hole algorithm for data classification **204** 104104
[10] Wang, F., Yuan, X., Liew, S. C., & Guo, D. 2013 Wireless MIMO switching: Weighted sum mean square error and sum rate optimization. *IEEE transactions on information theory* **59**(9) 5297-5312
[11] Chai, T., & Draxler, R. R. 2014 Root mean square error (RMSE) or mean absolute error (MAE)?–Arguments against avoiding RMSE in the literature. *Geoscientific model development* **7**(3), 1247-1250.
[12] E. Babolian and J. Biazar 2002 On the order of convergence of Adomian method," *Applied Mathematics and Computation* **130** 383-387
[13] Wazwaz, A. M. 2000 A new algorithm for calculating Adomian polynomials for nonlinear operators. *Applied Mathematics and computation*, **111**(1) 33-51
[14] Al-Hayani, W., Alzubaidy, L., and Entesar, A. 2017 Solutions of singular IVP's of Lane–Emden type by homotopy analysis method with genetic algorithm. *Appl. Math. Inf. Sci* **11**(2) 407-416
[15] Entesar, A., Saber, O., and Al-Hayani, W. 2018 Hybridization of Genetic Algorithm with Homotopy Analysis Method for Solving Fractional Partial Differential Equations *Eurasian Journal of Science and Engineering* **4**
[16] A. S. Bataineh, M. S. M. Noorani, and I. Hashim 2009 Homotopy analysis method for singular IVPs of Emden–Fowler type *Communications in Nonlinear Science and Numerical Simulation* **14** 1121-1131
[17] Liao, S. 2003 Beyond perturbation: introduction to the homotopy analysis method. *CRC press*
[18] He, J. H. 2003 Homotopy perturbation method: a new nonlinear analytical technique *Applied Mathematics and computation* **135**(1) 73-79
[19] Liao, S. 2012 Homotopy analysis method in nonlinear differential equations, 153-165 Beijing: Higher education press.

Stable ^{15}N and Neutron Halo ^{16}N Nuclei Structure Study by Elastic Electron Scattering Form Factors and Nucleon Momentum Distributions

Stable^{15}N and Neutron Halo ^{16}N Nuclei Structure Study by Elastic Electron Scattering Form Factors and Nucleon Momentum Distributions

Maha Taha Yaseen[1] , Akram M. Ali[2]

1,2 Physics Department, College of Science, University of Anbar, Anbar, Iraq

Email: dr.akram@uoanbar.edu.iq

Abstract. In this manuscript, the elastic electron scattering form factors and the nucleon momentum distributions (NMD) for stable ^{15}N and neutron halo ^{16}N at the ground state were reported. This was accomplished by utilizing the well-known Coherent Density Fluctuation Model (CDFM) via the employment of fluctuation function ($|F(q)|^2$) which is coupled with the density distributions nuclei. The long-tail performance in the NMD at high momentum region was further determined via experimental and theoretical fluctuation functions. The evaluated elastic electron scattering form factors were evaluated on the bases of the density distributions as well as the root mean square (RMS) radii for each measured nucleon. The proposed study provides a robust correlation between the theoretical formation factors and the practical results of ^{15}N and ^{16}N nuclei.

Keywords: CDFM, ^{15}N and ^{16}N, density distributions, RMS radii

1. Introduction

The elastic electron scattering, the density distributions, as well as RMS radii are considered as the most fundamental quantities, which provide insights about the inner structure of both neutron and proton. These together are known as nucleons [1-4]. Recently, several approaches have been proposed for the sole purpose to determine the aforementioned quantities. A typical example of this is the discovery of the halo phenomenon in the stable and exotic nuclei [4, 5]. In the case of stable nuclei, the elastic electron scattering is to be considered a dominant quantity for investigating the nuclear structure. This can be mainly attributed to the interaction of electron with nucleus which is attained via electromagnetic interaction [3]. Generally, a halo nucleus, since its discovery in 1985, possesses large neutron and proton excess whereby the bounds of few outer nucleons are considered weak [6]. The halo nature of a nucleus is principally caused by a specific effect which in turn can be attributed to a continuum close bound state. The essential requirements for the occurrence of a halo are short-range interaction, relatively low angular momentum and low binding energy [7]. A neutron halo is not limited to the unstable nuclei, however, it is usually observed in exotic nuclei on a large-scale as compared to the stable nuclei. The neutron halo could also be perceived off the β-stability line [8]. The previous studies reported that several ground state nuclei possess a halo structure, which is in a close position to the drip-line. These halos can be one-neutron halo (11Be and 19C), two-neutron halo (14Be, 11Li, and 6He), three-neutron halo (26F) and four-neutron-halo (8He) [9-15]. Moreover, the valence neutron can be channeled into the space near the nuclear core so that the neutron is extended with some distance. This distance is estimated to be of higher value as compared to the typical nuclear radius. Therefore, the angular momentum may have some influence on the halo formation which in turn leads to a probability of the s-state to be outside the core's potential range [6, 16, 17]. However, the pandd-states possess much lower probability to form a halo structure due to the relatively large centrifugal barrier[18].

As such, a number theoretical attempts were proposed to investigate the elastic electron scattering form factors as well as the NMD. Karataglidis and Amos [19] demonstrated the transverse and longitudinal form factors from isotopes such as He, Li, and 8Bi. Roca-Maza et al. reported a systematic investigation regarding the elastic electron scattering of both unstable 36Ca and stable 40Ca nuclei using the phase-shift analysis model [20]. Another research group supervised by Chu, Y. et al, also considered the elastic electron scattering of S and O isotopic chains in which they stated that the phase-shift analysis model is capable of reproducing the data obtained experimentally for both heavy and light nuclei [21]. Lately, Hamodi et al. revealed the calculation of the NMD and elastic electron scattering for odd and even p-shell nuclei using CDFM [22]. In this theory, which is an original effort of Antonov et al.[23], the NMD as well as nucleon density distributions (NDD) can only be linked and consequently expressed of the available weight function, $|f(x)|^2$, obtained experimentally. The same research group examined the NMD of some stable and unstable nuclei (4He, 16O, 12C, 40Ca, 39K, and 48Ca) expressed via weight function by means of NDD using the two-parameter fermi (2pF) model [24, 25]. The elastic electron scattering and NMD were observed for 1p-shell, sd-shell, as well as fp-shell nuclei through the CDFM framework [2, 26, 27]. Another study conducted by Ridha et al. reported the investigation of the NDD and elastic charge form factors of 11Be, 19C, 11Li, 8B, 17Ne, 4He, 12C and 16O nuclei using Woods Saxon single-particle radial wave function. The outcomes were compared with harmonic-oscillator potential [28-31]. They found that the utilized Wood Saxon single-particle wave function is in a good agreement with stable and exotic nuclei experimental data. In the same framework, the NDD was also examined alongside the elastic electron scattering for 48Ca and 40Ca nuclei[32]. In this attempt, the study is conducted to explore the elastic electron scattering form factors, density distributions, and RMS radius of stable 15Nandneutron halo 16N nuclei via neutron halo outside the core utilizing two approaches namely CDFM and 2pF.

2.Theory

A single body operator's NDD can be expressed as demonstrated in Equation (1).

$$\rho(r) = \frac{1}{4\pi}\sum_{nl} \xi_{nl}\, 4(2l+1)|R_{nl}|^2 \quad (1)$$

whereby the state $n\ell$ nucleon occupation probability is represented byξ_{nl}, (closed-shell nuclei: $\xi_{nl} = 0\ or\ 1$; and open-shell nuclei:$0 < \xi_{nl<1}$), while R_{nl} is the single-particle harmonic oscillator wave functionradial part.

The NDD of 15N and 16N nuclei represented at the 2s1d-shell end is derived based on a particular hypothesis by which an occupied shell core is existed (1s as well as 1p) and the nucleon occupation numbers in 2s and 1d shells are equal to (4-α), and (A-20+α1), respectively. Meanwhile, it is in a simple shell model (4) and (A-20). Using this assumption with Equation (1), the form of the analytical NDD is given as:

$$\rho(r) = \frac{exp(-R^2/b^2)}{\pi^{3/2}b^3}\left\{10 - \frac{3}{2}\alpha_1 + 2\alpha_1(\frac{r}{b})^2 + (\frac{4A}{15} - \frac{8}{3} - \frac{2\alpha_1}{5})(\frac{r}{b})^4\right\} \quad (2)$$

Herein, the mass number is represented by the letter A, while b is the size parameter, α1 describes the occupation numbers deviation of the nucleon from the shell model where α1=0 and α2 are presumed as an uncontrolled parameter which must be adjusted to have a covenant alongside the regarded NDD experimental measurements. Herein, the normalization condition of ρ(r) can be expressed as [31].

$$N = 4\pi\int_0^\infty \rho(r)r^2dr \quad (3)$$

The RMS radii of the nuclei is expressed as follow [31]:

$$< r^2 >^{1/2} = (\frac{4\pi}{N}\int_0^\infty \rho(r)r^4dr)^{1/2} \quad (4)$$

At central density$\rho(r) = 0$, the NDD at the nucleus center from Equation (2) is given as:

$$\rho(0) = \frac{1}{\pi^{3/2}b^3}\left(10 - \frac{3}{2}\alpha_1\right) \quad (5)$$

so α_1 becomes:

$$\alpha_1 = \frac{2}{3}\left(10 - \rho(0)\pi^{3/2}b^3\right) \quad (6)$$

By substituting Equation (2) into Equation (4) with some simplification:

$$\langle r^2\rangle = \frac{b^2}{A}\left(\frac{9A-120}{2} + \alpha_1\right) \quad (7)$$

herein, the central density $\rho(0)$ and $\langle r^2\rangle$ values are obtained using the experimental values whereas the parameter b is nominated to duplicate the RMS radii of a nucleus obtained experimentally.

The NMD, n(k), of the nuclei is considered via two different models. One of which is calculated using the shell model through single-particle harmonic oscillator wave functions in momentum demonstration, and it is assumed using Equation (8) [31]:

$$n(k) = \frac{b^3}{\pi^{3/2}} \exp(-b^2k^2)\left(10 + 8(bk)^4 + \frac{8(A-40)}{105}(bk)^6\right) \quad (8)$$

where the symbol k- represents the particle momentum.

In the meanwhile, the second model (NMD) is considered using the CDFM, whereby Equation (9) represents the mixed density [33, 34].

$$\rho(r,r') = \int_0^\infty |f(x)|^2 \rho_x(r,r')dr \quad (9)$$

herein a density matrix for A nucleon distributed equivalently at radius x of the sphere can be given by [11]:

$$\rho_x(r,r') = 3\rho_0(x)\frac{j_1\left(k_{F(x)}|r-r'|\right)}{k_F|r-r'|}\theta\left(x - \frac{1}{2}|r-r'|\right) \quad (10)$$

where the density is$\rho_0(x) = 3A/4\pi x^3$;kF is the Fermi momentum, given as [35]:

$$k_F(x) = \left(\frac{3\pi^2}{2}\rho_0(x)\right)^{1/3} = \left(\frac{9\pi A}{8}\right)^{1/3}\frac{1}{x} = \frac{\alpha}{x} \quad (11)$$

and θ is the step function ($\theta = 0\ or\ 1$). Equation (9) corresponds to an equation in a CDFM because the nuclear material fluctuates and tries to maintain the spherical shape of the nucleus and its symmetry.

The density of the single-particle based on the diagonal element of Equation (9) can be expressed as presented in Equation (12) [34]:

$$\rho(r) = \rho_x(r,r'=r)\int_0^\infty |f(x)|^2\rho_x(r)dx) \quad (12)$$

where $\rho_x(r) = \rho_0(r)\theta\ (x-r)$ and the weight function can be expressed as presented in Equation (13) [23, 34]:

$$|f(x)|^2 = \frac{-1}{\rho_0(x)}\frac{d\rho(r)}{dr} \quad (13)$$

The NDD is then calculated with respect to the normalization condition:$\int_0^\infty |f(x)|^2 = 1$.

According to Equation (12) the nucleon momentum distribution can be given as [33, 34]:

$$n(k) = \int_0^\infty |f(x)|^2 n_x(k)dx \quad (14)$$

where the Fermi -momentum distribution of all nucleons is given as,

$$n_x(k) = \frac{4}{3}\pi x^3\theta(k_F(x) - |k|) \quad (15)$$

and using weight function and Equations (13 and 14) the nucleon momentum in CDFM can be expressed as:

$$n_{CDFM}(k) = \left(\frac{4\pi}{3}\right)^2\frac{4}{A}\left[6\int_0^{\alpha/k}\rho(x)x^5dx - \left(\frac{\alpha}{k}\right)^6\rho\left(\frac{\alpha}{k}\right)\right] \quad (16)$$

With a normalized condition: $A = \int n_{CDFM}(k)\frac{d^3k}{(2\pi)^3}$.

For the target nucleus form factor F (q), the expression in coherent density fluctuation model can be given as [33, 34]:

$$F(q) = \frac{1}{A}\int |f(x)|^2 F(q,x)dx \quad (17)$$

Where the uniform charge density distribution is represented as F (q, x) that reflects the scattering event in CDFM with amplitude is a superposition of all charge distribution, which can be expressed as,

$$F(q,x) = \frac{3A}{(qx)^2}\left[\frac{\sin(qx)}{(qx)} - \cos(qx)\right] \quad (18)$$

Equation (18) must be multiplied by a correction of free nucleon finite-size form factor (same protons and neutrons) and center of mass form factor. This eliminates the false state appears from the indication of the mass center. These form corrections can be expressed as follow [31]:

$$F_{fs}(q) = \exp\left(\frac{-0.43q^2}{A}\right)\ and\ F_{cm}(q) = \exp\left(\frac{b^2q^2}{4A}\right) \quad (19)$$

The weight function ($|f(x)|^2$) is obtained using the estimatedNDDfrom2pF model by which the experimental elastic electron scattering was utilized as an input quantity. Consequently, the theoretical value of the mention elastic electron scattering was also used as a comparison point.

Wood-Saxon function for the density of 2pF is given by [27]

$$\rho_c(r) = \frac{\rho_0}{1+\exp(r-c/z)} \quad (20)$$

So, the weight function will be:

$$|f(x)|^2 = \frac{4\pi x^3 \rho_0}{3Az}(1 + \exp(x - c/z))\exp(x - c/z) \qquad (21)$$

If Equation (2) inserted into the equation of weight function (13), an analytical expression cab be acquired as,

$$|f(x)|^2_{2pF} = \frac{8\pi x^4 \rho(x)}{3Ab^2} - \frac{16x^4}{3A\pi^{1/2}b^5}\left\{\left[\alpha_1 + \frac{4A}{15} - \frac{8}{3} - \frac{2\alpha_1}{5}\right](\frac{x}{b})^2\right\} \qquad (22)$$

3. Results and discussion

Table 1: The parameters used in the determination of nuclear density.

Nucle i	c (fm)	z (fm)	b (fm)	$\rho(0)$ (fm^{-3})	α_1
^{15}N	2.638	0.520	1.710	0.2698	1.6586
^{16}N	2.692	0.523	1.72	0.2673	1.7050

3.1 Root *mean square* radii

The proton, neutron (R_p and R_n) and the matter RMS radii of the core and halo are generally evaluated using the harmonic oscillator radial wave function potential or radial wave function of Wood-Saxon potential, respectively. The R_p and R_n matter RMS radii obtain educing Equation (4) are summarized in Table (2). As presented in Table (2), the R_p, R_n matter RMS radii exhibited small differences in^{15}N and ^{16}N nuclei. It is noteworthy mentioning that the only input in the utilized densities calculation is the matter radii(R_m).Table (2) tabulates the calculated charge RMS radius for both ^{15}N and ^{16}N nuclei with the corresponding available experimental values using previously published data [36]. The obtained results of ^{15}N are in an upright agreement with the reported data, while the evaluated values of ^{16}N RMS radius are relatively smaller.

Table 2: RMS radius values of proton and neutron compared with experimental data.

Nuclei	RMS radius(fm)		RMS present work	
	Present work	Experimental	Proton	Neutron
^{15}N	2.426	2.42∓0.10 [36]	2.4084	2.431
^{16}N	2.479	2.50∓0.10 [36]	3.743	3.85

3.2 Density distributions

The density distributions analysis of both ^{15}N and ^{16}N nuclei are presented in this section using 2pF model, as expressed in Equation (20). The main reason for these nuclei to be selected is the unavailability of experimental density distributions data[24]. In the current study, the density distributions is calculated based on two parameters one of which is nucleus radius (c), while another is the skin thickness (z). The NDD is based primarily on the (c) value, particularly when the value of (c)is greater than the nuclei RMS radius. Herein, the (c) value rises as the mass number increases, particularly when the nuclear core and halo skin thicknesses are considered constant. This can be clearly observed from Table (1) and (2).

The ^{15}N nucleus density distributions were presumed through the consideration of the nucleus as a core and consequently evaluating its density distribution; assuming to be of similar shape to the Wood-Saxon alongside the 0.65 fm as the diffuseness parameter. The signal-neutron wave function can be estimated through solving Schrodinger formula which in turn can be solved using Wood-Saxon and/or Coulomb potentials; this can be advantageous in attaining a precise separation energies of the neutron, which corresponds to 1p, 2s as well as 1d orbitals. The total density distributions were obtained by adding the so-called nucleus as a core and the wave function parts. Similarly, 16N analysis was conducted assuming that a single neutron and 15N core are composed.

The distribution of the cores was noticed to be practically indistinguishable. The 15N and 16N density distributions are very alike, yet the single-neutron of 15N ranges was found to be considerably high-spaced because of the relatively small separation energy of the neutron (0.108 MeV). It should be mentioned that the corresponding energy separation of the neutron value for 16N being 0.248 MeV. Figure 1 (a and b) illustrates the NDD for both 15N and 16N nuclei as a function of the distance (r) in fm. The solid curves in Figure 1 are calculated theoretically using Equation (2), while the dotted curves are the experimental NDD data of the 2pF. The two curves showed the same behavior in falling as r increases in the region of the single-neutron.

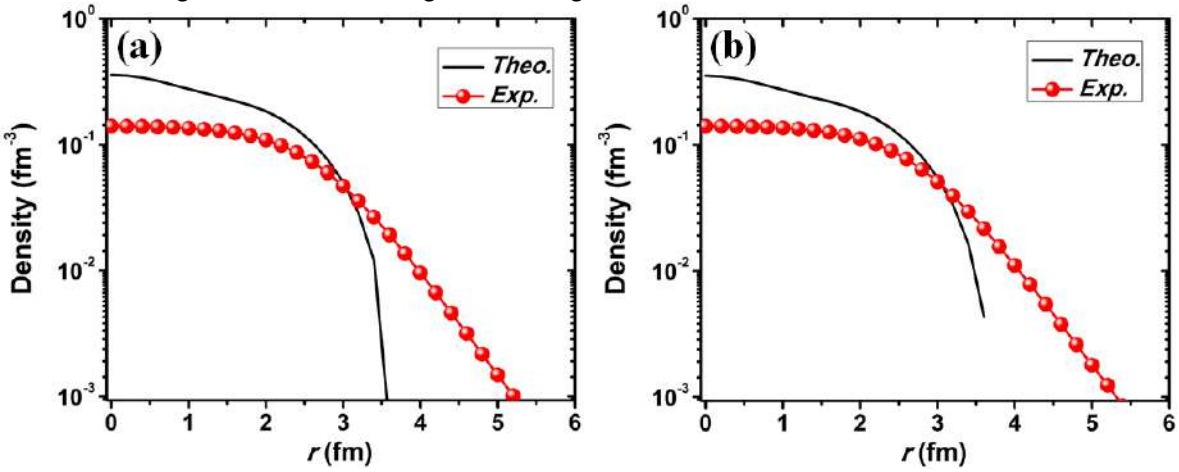

Figure 1: The evaluated nucleon density distributions for both ^{15}N (a) and ^{16}N (b) nuclei. The core ^{15}N is considered for ^{16}N, while the halo single-neutron is represented separately. The experimentally obtained nucleon density distributions are also presented using 2pF model.

3.3 Nucleon momentum distributions

To calculate the NMD, the CDFM model is used as expressed in Equation (16). In Figure 2 (a and b), the NMD is plotted as a function of the momentum $k(fm^{-1})$for ^{15}N and ^{16}N nuclei, respectively. The NMD dotted and solid curves are evaluated using theoretical and experimental weight function $|f(x)|^2$, respectively. It is worth mentioning that the general performance of the NMD at regions of high momentum ($k \geq 2$ fm^{-1}) for both ^{15}N and ^{16}N nuclei are similar; whereby the mentioned distributions possess the properties of a long-tail which are in a well agreement with other reported studies [27-30]. The long-tail in Figure (2), attained using CDFM, is correlated with that of high densities $\rho_x(r)$, Equation (12). This particular hypothesis concludes that ^{15}N and ^{16}N nuclei fluctuation function $|f(x)|^2$ is relatively minor, and these outcomes are in an upright agreement with other data obtained experimentally [25].

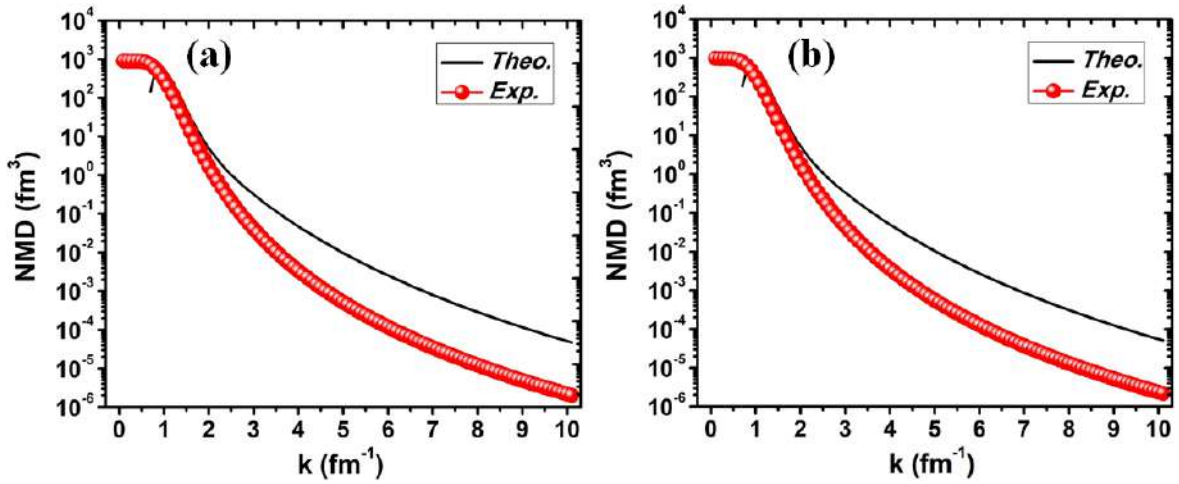

Figure 2: The NMD versus *k* for ^{15}N "(a) and ^{16}N (b) nuclei. The curve with red circles is the evaluated NMD which is expressed using CDFM, while the black solid curve is the evaluated NMD using Equation (8).

3.4 Elastic form factors

The nuclei electron scattering quantity provides good insights about the nucleus charge and size distributions. The presented results in Figure 3, calculated in the framework of CEDM according to Equation (18), are plotted as a function of momentum transfer q (fm^{-1}) for ^{15}N and ^{16}N nuclei. The solid as well as dotted curve in Figure 3 (a and b) are the evaluated results with the correction form included and excluded of the finite-size nucleon and mass center using Equation (19), respectively. Elastic form factors experimental data are plotted as solid circles for the considered nuclei. Figure 3 (a and b) elucidates the form factors obtained experimentally of ^{15}N and ^{16}N nuclei which are considered to be in good agreement with those obtained theoretically. The corrections of the form factor (red dotted curve) showed a slight reduction in comparison to the presented calculation prior to the corrections (solid black curve). The presented correction of the form factor is closer to the experimental values.

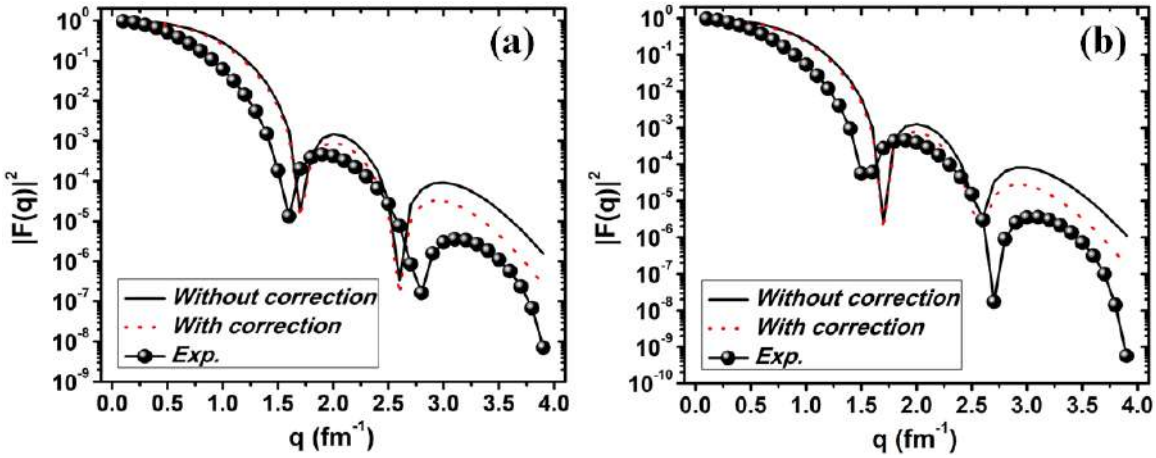

Figure 3: The charge form factors squared for elastic electron scattering for ^{15}N (a) and ^{16}N (b) nuclei as a function of the momentum transfer.

4.Conclusion

In the present study, the charge density distributions using 2pF model for ^{15}Nand ^{16}N were reported. Furthermore, using the obtained density distributions, the form factors were also evaluated which in turn suggested that the form factor depends on the density distributions and RMS radii. It was observed from the current investigation that the differences between neutron and proton RMS radii for each nuclei are small which agreed with experimental data. The ground state nucleon and matter densities of stable ^{15}N and exotic neutron halo nuclei ^{16}N were estimated using the CDFM. The long-tail feature performance at the high momentum region of the NMD was demonstrated utilizing both experimental and theoretical weight functions. The perceived nuclei electron scattering form factors in the current study are well-reproduced using the current evaluation throughout the momentum transfer value (q).

References

[1] Punjabi, V., Perdrisat, C. F., Jones, M. K., Brash, E. J., & Carlson, C. E. (2015). *Eur. Phys. J. A*, **51**(7) 79.
[2] Hamoudi, A. K., Hasan, M. A., & Ridha, A. R. 2012 *Pramana*, **78**(5) 737
[3] Donnelly, T. W., & Sick, I. 1984 *Rev. Mod. Phys.* **56**(3) 461.
[4] Abdullah, A. N. (2017). *Pramana*, **89**(3) 43.
[5] Ozawa, A., Suzuki, T., & Tanihata, I. 2001 *Nucl. Phys. A*, **693**(RIKEN-AF-NP-384) 32
[6] Phookan, C. K. (2014). *A Thesis* (Doctoral dissertation, GAUHATI UNIVERSITY).
[7] Jensen, A. S., & Riisager, K. (2000). *Phys. Lett. B*, **480**(1-2) 39
[8] Ogloblin, A. A., Danilov, A. N., Belyaeva, T. L., Demyanova, A. S., Goncharov, S. A., & Trzaska, W. (2011). *Phys. Rev. C*, **84**(5) 054601.
[9] Fukuda, M., Ichihara, T., Inabe, N., Kubo, T., Kumagai, H., Nakagawa, T., ... & Kouguchi, M. (1991). *Phys. Lett. B*, **268**(3-4) 339
[10] Bazin, D., Brown, B. A., Brown, J., Fauerbach, M., Hellström, M., Hirzebruch, S. E., ... & Powell, C. F. (1995). *Phys. Rev. lett.* **74**(18) 3569.
[11] Tanihata, I., Hamagaki, H., Hashimoto, O., Shida, Y., Yoshikawa, N., Sugimoto, K., ... & Takahashi, N. 1985 *Phys. Rev. lett.* ***55*****(**24) 2676.
[12] Tanihata, I., Kobayashi, T., Suzuki, T., Yoshida, K., Shimoura, S., Sugimoto, K., ... & Wieman, H. 1992 *Phys. lett. B*, **287**(4) 307
[13] Labiche, M., Orr, N. A., Marqués, F. M., Angélique, J. C., Axelsson, L., Benoit, B., ... & Clarke, N. M. 2001 *Phys. Rev. lett.* **86**(4) 600.
[14] Zhukov, M. V., Korsheninnikov, A. A., & Smedberg, M. H. 1994 *Phys. lett. C*, **50**(1) R1.
[15] Ren, Z., Chen, B., Ma, Z., Zhu, Z., & Xu, G. 1996 *J. Phys. G Nucl. Part. Phys.* **22**(4) 523.
[16] Hansen P., Jonson B. 1987 *Eur. Lett.* **4** 409
[17] Hansen, P. G., Jensen, A. S., & Jonson, B. 1995 *Annu. Rev. Nucl. Part. Sci.* 45(1) 591
[18] Li, E. T., Guo, B., Li, Z. H., Wang, Y. B., Li, Y. J., Wu, Z. D., ... & Fan, Q. W. 2016 *Chinese Phy. C*, **40**(11) 114104.
[19] Karataglidis, S., & Amos, K. 2007 *Phys. Lett. B*, **650**(2-3) 148
[20] Roca-Maza, X., Centelles, M., Salvat, F., & Vinas, X. 2008 *Phys. Rev. C*, **78**(4) 044332.
[21] Chu, Y., Ren, Z., Dong, T., & Wang, Z. W. (2009). *Phys. Rev. C*, **79**(4) 044313.
[22] Hassan, M. A. (2010). (Doctoral dissertation, MSc. thesis, University of Baghdad, 1-80).
[23] Antonov, A. N., Nikolaev, V. A., & Petkov, I. Z. 1980 *Zeitschrift für Physik A Atoms and Nuclei*, **297**(3) 257
[24] De Vries, H., De Jager, C. W., & De Vries, C. 1987 *Data Tables*, **36**(3) 495
[25] W. Reuter, G. Fricke, K. Merle, H. Miska 1982 *Phys. Rev.* C, **26** 806
[26] Hamoudi, A. K., Flaiyh, G. N., & Mohsin, S. H. 2012 *Iraqi J. Sci.* **53**(4) 819
[27] Hamoudi, A. K., & Ojaimi, H. F. 2014 *Iraqi J. Sci.* **12**(24) 33
[28] Noori, R. I., & Ridha, A. R. 2019 *Iraqi J. Sci.* **60** (6)1286
[29] Ridha, A. R., & Abbas, Z. M. 2018 *Iraqi J. Sci.* **16**(36) 29-

[30] Ridha, A. R. (2016 *Iraqi Journal of Physics (IJP)* **14**(30) 42
[31] Ridha, A. R. (2017). *Al-Nahrain Journal of Science*, **20**(3) 83
[32] Antonov, A. N., Hodgson, P. E., & Petkov, I. Z. (2012). Springer Science & Business Media.
[33] Antonov, A. Hodgson, P. & Petkov, I. Zh. 1988. Nucleon Momentum and Density Distribution in Nuclei. Clarendon, in, Oxford.
[34] Tanihata, I., Hamagaki, H., Hashimoto, O., Nagamiya, S., Shida, Y., Yoshikawa, N., ... & Takahashi, N. (1985). *Phys. Lett. B*, **160**(6) 380
[35] Antonov, A. N., Hodgson, P. E., & Petkov, I. Z. (1993). Momentum Distributions in Nuclei. In *Nucleon Correlations in Nuclei* (pp. 111-156). Springer, Berlin, Heidelberg.

Risk Determination of Radionuclide Derived from Agriculture Fertilizers in Iraqi Markets by Gamma Spectrometry

Risk Determination of Radionuclide Derived from Agriculture Fertilizers in Iraqi Markets by Gamma Spectrometry

Akram Mohammed Ali

Physics Department, College of Science, University of Anbar, Anbar, Iraq

E-mail: dr.akram@uoanbar.edu.iq

Abstract. A fertilizer has increase production and becomes a necessary tool that uses in agriculture. Different amount of uranium and thorium are including in the fertilizers that mean natural nuclide will be concentrated in high values. In this work, seventeen samples of commonly used fertilizer in Iraqi markets were collected and determine the specific activities of radiation ^{238}U, ^{232}Th, and ^{40}K using a technique of gamma-ray spectroscopy NaI(Tl) detector. The concentration of these nuclides has average values (79.66±0.41Bq/kg, 30.52±0.31Bq/kg, and 181.27±2.91 Bq/kg) comparing with worldwide limitation (35Bq/kg, 35Bq/kg, and 350 Bq/kg), respectively. So the concentration of ^{238}U nuclei greater than its global limit. The radiological hazards of all samples as radium equivalent activity (Raeq), external (H_{ex}) and internal (H_{in}), alpha and gamma indices, and annual effective dose, due to the presence of these radionuclides, were calculated to assess it hazards and by the statistical study that using SPSS program one can mark the relations between all hazards indices.

Keywords: Radionuclide, Fertilizer, NaI(TI) detector, hazard indices, Cluster statistic.

1. Introduction.

Residents were exposed to naturally occurring radionuclides which are found in various sources, among them fertilizers that are used in agriculture. The use of fertilizers in agriculture gives good information to hand out the specific activities of ^{238}U, ^{232}Th, and ^{40}K in the environment. All corps need to grow up quickly, easily, and healthy. With some steroids as fertilizers in reasonably priced application depending on the soil type and its fertility where some crops do not require fertilizer as legumes, one can get what is desirable. Fertilizers are solid and liquid, the solid fertilizer is mostly inorganic as urea, di-ammonium, phosphate, and potassium chloride. The solid shape either granulate or powder that composed mainly of nitrogen (N), potassium (K), and phosphorus (P). However, the extensive use of fertilizers can increase environmental effects. The increasing consumption of it can affect soil, surface, and ground waters because of the dispersion of element using. Many studies have shown that agricultural fertilizers contain varying amounts of natural radioactive material [1-3]. The radioactive elements that imply fertilizers differ in amount depending on their concentration such as Uranium-238. As the concentration increase of the natural radionuclides in fertilizers, the risk of human health from this nuclide increases.

The use of natural fertilizers in wide-ranging Iraqi markets may lead to the distribution of radionuclide elements in the agricultural areas that will become a source of radioactivity decay. This phenomenon may lead to potential radiation hazards due to external exposure to gamma and alpha particles (external and internal) radiation by workers in factories where fertilizer produced, formers, or

residents of forms. In several markets, there are several types of fertilizers used in agriculture as di-ammonium phosphate and nitrogen urea, and so on. Their concentrations must be measured in fertilizer to specify the safe employment of fertilizers. The concentration of radium and uranium contentment in the soil is increasing the radiation dose and absorbed dose in the human body which leads to unwanted health prohibitions.

This evaluation aims to build a level for concentrations of radioactive nuclei in used samples and find a correlation between concentrations and radioactive parameters comparing with word limits. Besides, existing a relationship between activity concentration and hazard index using statistical methods(cluster, Pearsons, and descriptive).

2. Material and Methods:

*Sample collection***:** Seventeen samples of the most available types of fertilizers in local markets in Iraq were collected and prepared to measure the natural activity. The type samples are listed in Table 1 where each plastic bag is labeled by its name.

Table 1. The details of the fertilizer sample under test.

Samples name	Sample code	Type	Origin
Fertilizer 1	F1	O-DAP Micronutrients	Iraqi (Kufa)
Fertilizer 2	F2	K-Humate (N-13, P-22, K-18)	Iraqi (Kufa)
Fertilizer 3	F3	Nitrogen -Urea	Iraqi (Basra)
Fertilizer 4	F4	Nitrogen -Urea	Ukrainian
Fertilizer 5	F5	Nitrogen -Urea	Iranian
Fertilizer 6	F6	Phosphate daimonian	Jordanian
Fertilizer 7	F7	Phosphate daimonian	Jordanian
Fertilizer 8	F8	N-P component	Iraqi (Basra)
Fertilizer 9	F9	Compost	Iraqi (municipal)
Fertilizer 10	F10	Nitrogen -Urea (EFC)	Egyptian
Fertilizer 11	F11	Nitrogen -Urea	Egyptian
Fertilizer 12	F12	Potassium Nitrate (NP)	Jordanian
Fertilizer 13	F13	Potassium Nitrate (NP)	Chinese
Fertilizer 14	F14	Potassium Nitrate (NP)	Saudi Arabia
Fertilizer 15	F15	NPK	Germania
Fertilizer 16	F16	NPK	Tunisian
Fertilizer 17	F17	NPK	United States

2.1 Sample preparation

The collected sample underwent to milling process for 2 hours with a porcelain mill with different sizes of porcelain balls. The result powder sieving by 2mm meshes to get rid of the coarse suspended material with sample and obtain a homogenous sample free from impurities that may affect on measuring process. The samples dried in the controlled oven at 100 ^{o}C to remove the moisture and have a constant weight then cooled in desiccators. The sample was left in preservative bags (polyethylene plastic sealed bag) for about 28 days to reach the secular equilibrium condition between ^{238}U and ^{232}Th long-lived radionuclides and its parent daughters. To measure the background radiation of the environment, the homogeneous samples were transported to a new sealed bag and left for about 30 days.

2.2 Measurements

Measurements of natural radioactivity have been done using the gamma-ray spectrometer that includes a multichannel analyzer connected with NaI(Tl) detector. The led cylinder was used to protect the detector and reduced the background level by a factor of about 95%, while the energy calibration was made for the detector by two source ^{137}Cs (0.662 MeV) and ^{60}Co (1.333 MeV).

Spectroscopy analysis: The activity concentrations of radionuclide were determined in Bq/Kg. The activity of ^{40}k was determined from peak energy of gamma at 1460 KeV, while for ^{238}U and ^{232}Th determine from the secular equilibrium and their progenies (^{214}Pb and ^{214}Bi) at energies 295.2 KeV and 315.9 KeV, respectively. The counting time that converting count/s to activity unit (Bq/kg) is19000s.

3. Result and Discussion

3.1 Results

Activity Concentration: The amount of radioactivity in the sample can be determined by the activity concentration as a specific activity following the relation from [4]

$$A_i\left(Bq/kg\right)=\frac{C_i-B.G.}{\varepsilon M_s P_\gamma T} \qquad (1)$$

Where C_i is counting net area under the photo peaks, i represents the fertilizer sample, $(B.G.)$ is background count below, ε denotes absolute energy efficiency for the detector at a specific energy of gamma, $(P\gamma)$ is an absolute γ- transition or emission probability of the specific gamma-ray,(T) is the measurement time of counting inside the detector in(s) and (M_s) is dry of each sample weighted mass in the container in (kg). The specific activities of ^{238}U, ^{232}Th, and ^{40}K and their corresponding uncertainties for samples are represented in Table 2. ^{40}K concentration has value dominated for several samples. The variation in values of concentrations of the radionuclide may due to the chemical formula of fertilizers. The values and average values of each nuclide are shown in fig. (1). The Uranium concentration average value (79.66 Bq/kg) above the global limit, while for ^{232}Th and ^{40}K (30.52 and 181.27 Bq/kg) are less than the worldwide recommended limits reported by UNSCEAR (2008) [5] (35, 35, and 370 Bq/kg, respectively). The variation coefficient shows some data with relatively high and lower values. The high values represent a heterogeneous distribution for data while the lower relatively values indicated homogeneous distribution.

Table 2. Radionuclide specific activity in fertilizer samples.

Sample code	Specific Activity in (Bq/kg)		
	^{238}U	^{232}Th	^{40}K
F1	131.18 ± 1.26	72.17 ± 0.64	83.233 ± 2.91
F2	108 ± 0.83	64.41 ± 0.38	480.16 ± 3.28
F3	173.98± 1.43	62.16 ± 0.45	362.77 ± 2.15
F4	14.9±0.38	33.45±1.02	282.49±1.94
F5	6.9 ± 0.1	8.6 ± 0.21	21.3 ± 1.16
F6	16.18 ± 0.19	4.02 ± 0.09	57.69 ± 1.34
F7	12.27 ± 0.37	6.34 ± 0.32	33.18 ± 2.38
F8	165.81 ± 1.27	11.21 ± 0.51	496 ± 0.87
F9	7.82 ± 0.20	11.93 ± 0.18	33.27 ± 0.42
F10	208.61 ± 2.31	50.14 ± 0.41	22.90 ± 1.24
F11	181.97 ± 1.01	18.73 ± 0.23	17.65 ± 0.43
F12	20.22 ± 0.19	17.91 ± 0.31	47.81 ± 1.13
F13	79.19 ± 0.34	31.82 ± 0.46	1024 ± 8.12
F14	84.10 ± 0.56	22.53 ± 0.23	402.6 ± 12.18
F15	72.43 ± 0.56	121.18 ± 0.58	418..17 ± 9.66

F16	28.57 ± 1.13	7.82 ± 0.13	35.16 ± 0.17
F17	42.16 ± 0.76	63.37 ± 1.01	184.76 ± 2.84
ave.	79.66±0.41	30.52±0.31	181.27±2.91

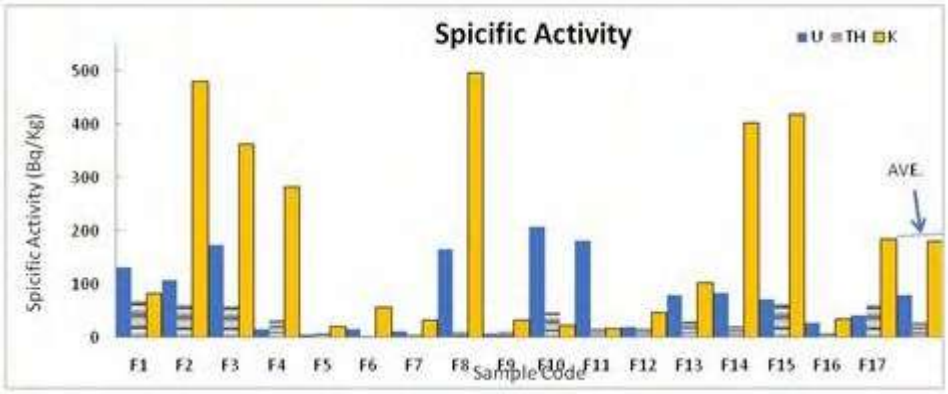

Fig. 1. Represent the concentration of specific activity of the samples with average values for each nuclide.

Table 3. The partial correlations between the specific activities.

Control Variables		^{238}U	^{232}Th	^{40}K
^{238}U	Correlation	1	0.427	0.278
^{232}Th	Correlation	0.427	1	0.398
^{40}K	Correlation	0.278	0.398	1

From Table 3, it is clear that the correlation between three radionuclides is linear and in Table 4 the differences in the activity values were clear from the arithmetic mean (AM) where the highest value for

Table 4. Descriptive Statistics of the main radionuclides underestimation**.**

Radionuclide	N	Range	Min. value	Max. value	Sum	AM	S.D.	Variance	Skewness	Kurtosis
U	17	202	7	209	1354	79.66	69.693	4857.04	0.600	-1.116
Th	17	68	4	72	552	32.46	24.823	616.197	0.451	-1.559
K	17	478	18	496	3082	181.27	181.704	33016.37	0.724	-1.265

^{40}K (181.27 Bq/kg) and lowest one for ^{232}Th (32.46 Bq/kg). To measure the degree of asymmetry tail distribution.

of the radionuclide, the skewness has positive values and near zero, while the kurtosis has negative values, i.e. the distribution follows the normal one.

Radiological Hazards Effects Evaluation**:** Different radiological indices were estimated to determine the hazard of natural radioactivity in samples. The calculated values were compared with the universal values that represent safety limits.

3.1.1 Radium Equivalent Activity Appreciation

Since the distribution of radionuclide is not uniform with real activity level in the samples, the radium equivalent (Ra_{eq}) is a single radiological hazard index need to determine because of its ability to give a good explaining of radiation protection for human comparing the limits of fertilizer that must be maximum less than 370 Bq/kg to keep the dose of gamma-ray below 1.5 mSv y^{-1} (UNSCEAR, 2000) [6]. The main formula to compute this parameter is [7]:

$$Ra_{eq} = A_U + (1.43A_{Th}) + (0.077A_K) \quad (2)$$

whereA_U, $A_{Th,}$ and A_K are uranium, thorium, and potassium concentrations, respectively. The above equation is based on the assumption that 370 Bq kg^{-1} of ^{226}Ra, 259 Bq/kg of ^{232}Th, and 4810 Bq kg^{-1} of ^{40}K produce the same gamma-ray dose rate. The radium equivalent is related to both the external γ-dose and the internal α-dose from radon and its progeny. Fig. (2) represented the frequency distribution where analysis has been done for all samples and showed a normal (bell-shaped) distribution.

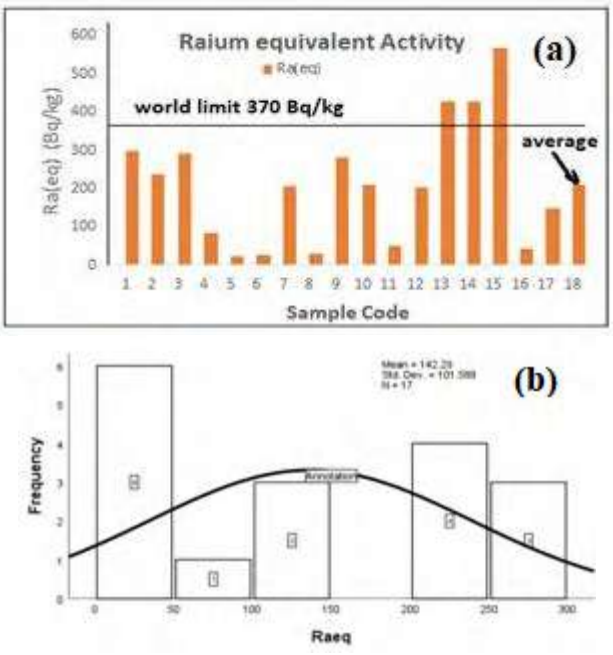

Fig. 2. (a) bar chart (b) normal distribution shapes of Ra(eq) for all samples.

3.1.2 Absorbed Dose and Effective Dose Appreciation

The use of fertilizers in agriculture is a possible source of exposure for the workers in sites and that may increase radionuclide exposure. By applying the following relation one can convert the measured activities of U, Th, and K into doses according to UNSCEAR, 2000 [7] using the same factors to give the absorbed gamma rate in the air at 1m above the ground level[9]:

$$D_{abs}(nGyh^{-1}) = (0.462A_U) + (0.621A_{Th}) + (0.042A_K) \quad (3)$$

The results were shown in Table 2 and figure (3). the limit recommended by UNSCEAR (2000) [7.]

The estimation of annual effective dose (AEDE) according to UNSCER(2008) [5]it must be taken into account by converting the coefficients from (D_{abs} in nGy.h^{-1})) in the air using conversion factor (0.7 Sv Gy^{-1}) to (AEDE in mSv.y^{-1}) with indoor occupancy factor (fraction of time spent indoor (0.8) and outdoor (0.2)). The AEDE from gamma radiation from ^{226}Ra, ^{232}Th, and ^{40}k in the fertilize samples was calculated from [5]:

$$AEDE(mSv) = D_{abs}(nGyh^{-1}) \times 8760h \times O \times C\,(\text{mSv/ nGy}) \quad (4)$$

Where *O* is the occupancy factor and C is the absorbed to the effective dose conversion factor for adults (0.7 x 10^{-6}Sv/Gy). AEDE in all samples for gamma radiation from natural nuclide is varied from

to with mean value of, as shown in table()all studied samples of fertilizers are less than the recommended limiting value of 480 μSv y^{-1} [5].

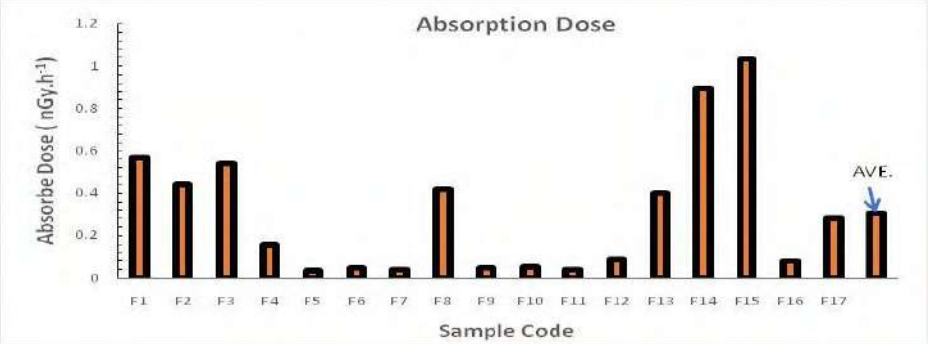

Fig. 3. Absorption Dose values with their average value.

3.1.3. Gamma-ray Index

This index is used to estimate the hazard level of gamma radiation from the fertilizer samples that may harmful by damaging the human body cells. This index limitation according to European Commission Guidelines [8] must be ($2 < I_\gamma < 6$) when increasing the annual effective dose to 1*mSvy*$^{-1}$[9] while $I_\gamma \leq 0.5$ corresponding to *0.3mSvy*$^{-1}$and $I_\gamma \geq 0.5$ corresponding to 1 *mSvy*$^{-1}$. It can be calculated from [10]:

$$I_\gamma = \frac{A_U}{300} + \frac{A_{Th}}{200} + \frac{A_K}{3000} \qquad (5)$$

The results and average value are represented in Table 2 and Fig. 4. Four samples from all the measured samples had a radioactivity level index of more than 1, which lead to avoid using because give an exposure effective dose of more than *1mSvy*$^{-1}$ for whom to deal with this production.

3.1.4. Internal Level Radiation Index (Alpha Radioactivity)

When radon gas is released from samples there is an alpha particle were emitted causes alpha radiation. The index I_α can be calculated from [11]:

$$I_\alpha = \frac{A_U}{200} \qquad (6)$$

It should be less than the maximum permissible value of I_γ for radium concentration 200 Bq/kg. This index must be less than unity and the results of fertilizes samples show varied values from 0.0345 to 1.043 with a mean value less than 1. The higher sample value is F10 (Nitrogen -Urea (EFC).

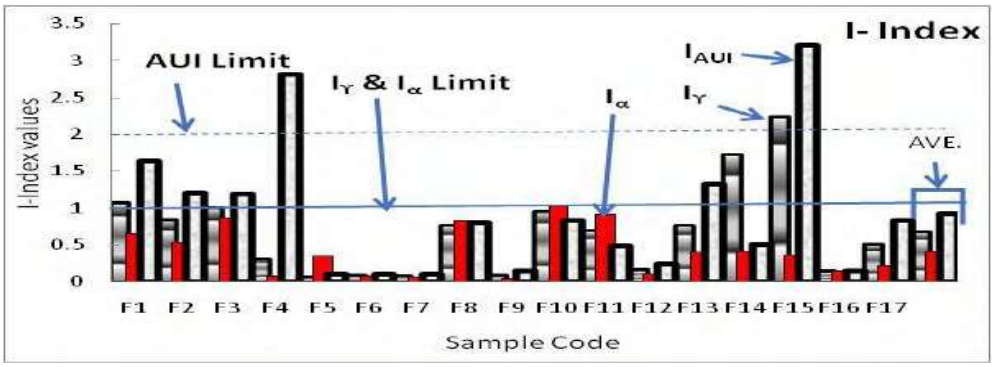

Fig. 4. Radiation hazard indices with limitations and average values.

3.2 Radio hazard indices

Analysis of various known radiological health hazard indicators in radiological studies were used to find a safer conclusion. To assess the radiation risk associated with tested samples, the following indicators were identified.

3.2.1 External and internal hazard indices

To provide information about safe levels of internal exposure to radon and its daughter that have a short-life, the internal index (H_{in}) must be in the value less than one to keep the radiation hazards low. The index can calculate from [12]

$$H_{in} = \left(\frac{A_u}{185}\right) + \left(\frac{A_{Th}}{259}\right) + \frac{A_K}{4810} \qquad (7)$$

The external index (H_{ex}) is an assessment of the natural risks of gamma and is used to evaluate the radioactivity of a substance. H_{ex} represents exposure to external radiation associated with gamma from radionuclide. This index evaluated as following and should also less than one UNSCEAR (2000) [7]:

$$H_{ex} = \left(\frac{A_u}{370}\right) + \left(\frac{A_{Th}}{259}\right) + \frac{A_k}{4810} \qquad (8)$$

3.2.2. Excess Lifetime Cancer Risk (ELCR)

The probability of cancer developing over a lifetime human at a certain exposure level. This indicator gives a value of expected numbers of cancers in limiting people's numbers when exposed to specific carcinogenic at a specific dose. An increase in ELCR led to increase in developing leukemia, breast, and prostate cancer. The ELCR can be evaluated using the equation [13]:

$$ELCR = D_{eff}(AEDE) \times DL \times R \qquad (9)$$

Where DL is the duration of life (approximately 66 years) and RF is a fatal cancer risk factor in (Sv^{-1}) with a value of 0.05 as in ICRP-60 [15].

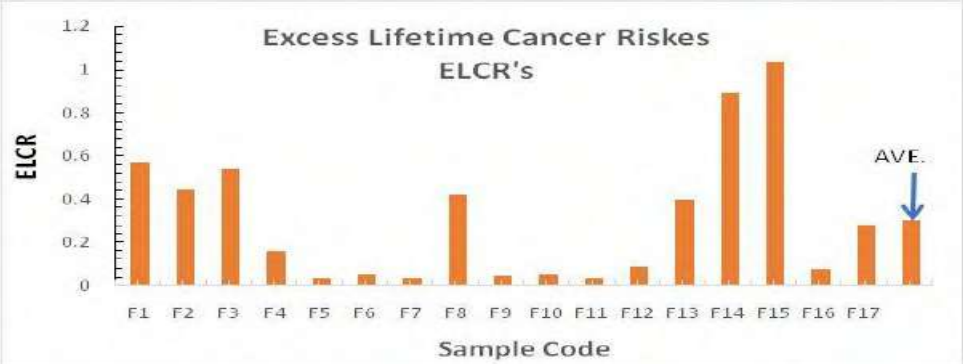

Fig. 5. Excess Lifetime Cancer Risks with the average value.

3.2.3. Activity utilization index (AUI)

The calculation of absorbed dose in the air can be active by using a transfer factor. For this purpose, the activity utilization index building up and calculated using the relation [14]:

$$A_U\,50(Bq/kg)f_U + A_{Th}\,50(Bq/kg)\,f_{Th} + A_K\,500(Bq/kg)f_K \qquad (10)$$

Where f_U, f_{Th}, and f_K are the fraction contributions to the total dose rate in the air because of gamma radiation from the studied natural radionuclide f_U = 8.09%, f_{Th} = 47.98%, and f_K = 43.92%. The main limitation of this index is less than 2 for the annual effective dose(AEDE) (<0.3 mSy/y) [15]. The sample F15 recorded the highest value for this index (3.207) while the average value within the limit.

3.2.4. Clark value $^{232}Th/^{238}U$ concentration ratio

This ratio will give an indicator for the samples collected from a markets regions have either higher or lower uranium concentration to be economic for uranium mining and extraction UNSCEAR(2000).

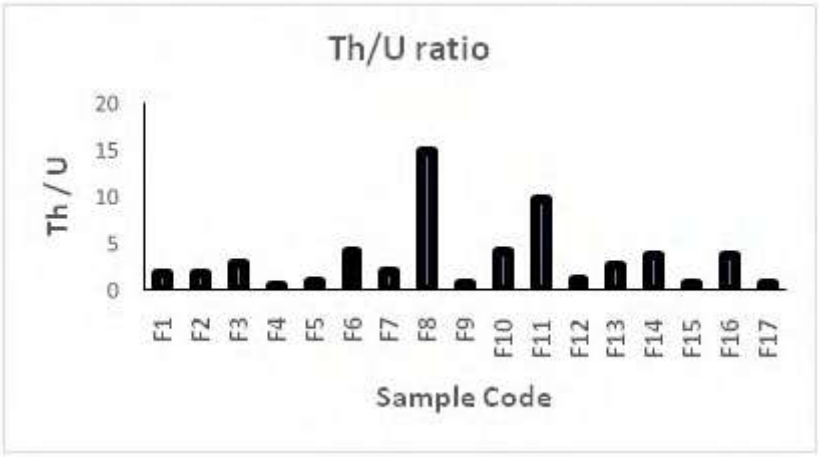

Fig. 6. Th /U ratio.

3.3 Statistical Analysis

To understand the multivariate correlations between radionuclide concentrations and other parameters, Pearsons, descriptive and cluster technique analysis had been carried out through the " Statistical Program of the Social Science (SPSS/PC-IBM) [16].

3.3.1 Pearson's Coefficient Matrix

This method measure the linear relationship between any two continuous parameters. From Table 5, significant correlation is in the bold (") represent the good correlations lies among (0.5) and (1) between any two-parameter and the table show high positive correlations with perfect monotonic relation coefficient (1)**.** The high values correlation of AEDE (in, out) with other parameters was represented while^{238}U has a weak correlation with ^{40}K and AUI. The negative sign in the matrix appears just for Th/U parameter that means the three parameters (Th, ELCR, and AUI) are in the opposite direction**.**

Table 5. Pearson's correlation coefficient matrix for radionuclide and the determined hazard indices of measured parameters.

code	^{238}U	^{232}Th	^{40}K	Ra_{eq}	D	AEDE in	AEDE out	I_γ	I_α	H_{in}	H_{ex}	ELCR	AUI	Th / U
^{238}U	1													
^{232}Th	.441	1												
^{40}K	.289	.407	1											
Ra_{eq}	.900**	.709**	.364	1										
D	.900**	.695**	.388	.998**	1									
AEDEin	.567*	.612**	.618**	.613**	.622**	1								
AEDEout	.603*	.736**	.607*	.656**	.665**	.987**	1							
I_γ	.504*	.606**	.614**	.551*	.561*	.995**	.986**	1						
I_α	.695**	.295	.452	.668**	.684**	.467	.487	.422	1					
H_{in}	.841**	.569*	.529*	.818**	.825**	.906**	.931**	.873**	.636**	1				
H_{ex}	.624**	.664**	.610**	.672**	.680**	.995**	.996**	.988**	.499*	.928**	1			
ELCR	.268	.564*	.739**	.414	.433	.900**	.877**	.912**	.417	.702**	.877**	1		
AUI	.162	.650**	.518*	.342	.351	.575*	.637**	.606**	.148	.456	.596*	.595*	1	
Th / U	.582*	-.315	.218	.303	.331	.112	.104	.065	.572*	.343	.127	-.039	-.216	1

3.3.2. Cluster analysis

Hierarchical cluster analysis is the method used by grouping similar radiometric characters [17] that fall into the same class to have a clear up for the relationships between all parameters and find optimal grouping within each group, and calculate the Euclidean distance for each parameter. The cluster statistics performed based on Pearson's correlation coefficient by the dendrogram shown in Fig. 7 according to Uranium concentration were parameters grouped in the cluster as it present in a population that can be divided into clusters to get the whole population information. It is clear in Fig. 7 there are three clusters, the first represented by samples (1,2,3,4,5 and 6), the second for (7,8,9, and 10), and the third cluster for equal clusters (11,12,13,14,15 and 16). These groups have different areas.

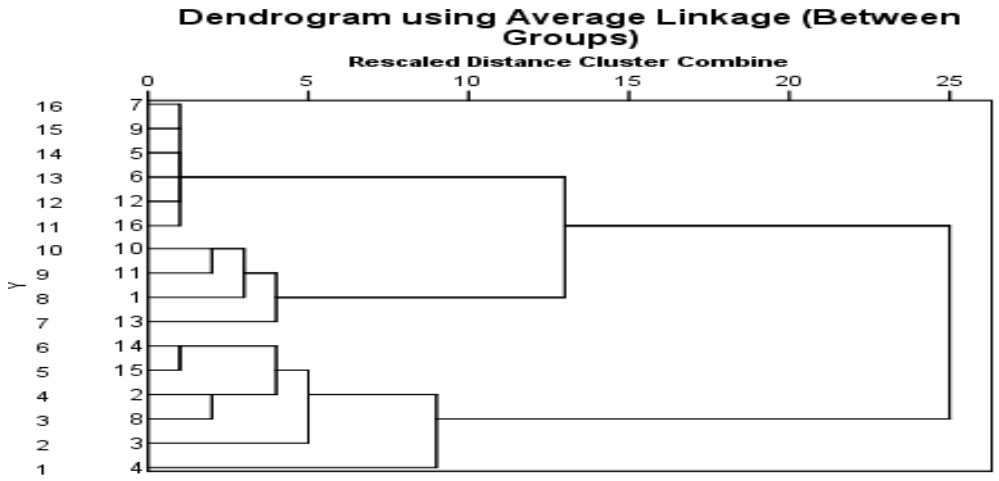

Fig. 7. Dendrogram using Centroid Linkage for classifying parameters with uranium concentration in the fertilizer samples.

3.3.3. Descriptive statistics analysis

From Table 6 the ^{40}K concentration present high average value (496 Bq/kg) than other parameters and twice the uranium average value (209 Bq/kg) with variation coefficient (33.01%), less variation for ^{232}Th (6.16%). This variation coefficient represents the dispersion of the data compared with other parameters variation uranium reach 48.57%.

Table 6. Descriptive statics of the parameters.

Descriptive Statistics								
	N	**Min.**	**Max.**	**Mean**	**S.D.**	**Variance %**	**Skewness**	**Kurtosis**
^{238}U	17	7	209	79.66	69.693	48.57	.600	-1.116
^{232}Th	17	4	72	32.46	24.823	6.16	.451	-1.559
^{40}K	17	18	496	181.27	181.704	33.01	.724	-1.265
Ra_{eq}	17	21	298	142.29	101.588	10.32	.199	-1.478
D	17	9	140	66.65	47.688	22.74	.151	-1.549
AEDE in	17	0	1	.43	.365	.001	.867	.252
AEDE out	16	0	0	.10	.088	.008	.759	.338
I_{gamma}	17	0	2	.68	.615	.378	1.189	1.356
I_{alpha}	17	0	1	.36	.306	.093	.685	-.874
H_{in}	17	0	1	.67	.532	.283	.077	-1.957
H_{ex}	17	0	1	.49	.394	.155	.651	-.191
ELCR	17	0	1	.30	.313	.098	1.146	.538
AUI	17	0	3	.93	.924	.854	1.441	1.647
Th/U	17	0	15	3.24	3.731	1.39	2.328	5.666

4. Conclusion

Natural radioactivity of ^{238}U, ^{232}Th, and ^{40}K in different types of fertilizers was measured. The average specific activities in samples are in the global limits unless the^{238}U is higher than the recommended limit of UNSCEAR 2008. (35Bq/kg). The radiological hazard indices measurement includes radium equivalent activities, external and internal indexes, gamma index, absorbed radiation,

and annual effective doses of the fertilizers. From all of these results, we deduce that the number of fertilizers that showed high radioactivity should be decreased and used with precautions.

References

[1] M.Olszewska-Wasiolek 1995 *Radiate. Protect. Dosim.* **58** 269
[2] C.H.R. Saueia, and B.P. Mazzilli, 2006 *J. Environ. Radioact.* **89229**
[3] Sabiha-Javied, M. Tufail, M. Asghar 2010 *J. Hazard.Mater.* **176** 426
[4] Jibiri, N.N., and Fasae, K.P. 2012 *Radiation Protection Dosimetry* **148**(1) 132
[5] UNSCEAR (United Nations Scientific Committee on the Effects of Atomic Radiation Sources and effects of ionizing radiation. Report to the General Assembly, with Scientific Annexes (New York:(UNSCEAR), (2008).
[6] UNSCEAR Effects of atomic radiation to the general assembly United Nations Scientific Committee on the Effect of Atomic Radiation, United Nations, New York (2000).
[7] J. Beretka and P.J. Mathew 1985 *Health Phys.* **48** 87
[8] European Commission (EC) Report on Radiological Protection Principles Concerning the natural radioactivity of building materials. Radiation, Protection No. 112. Luxembourg: Directorate-General Environment, Nuclear Safety, and Civil Protection;1999, 6 - 9.
[9] Sabiha-Javied, M. Tufail, and M. Asghar 2010 *J. Haz. Mat.* **176** (1-3) 426
[10] Hassan, N.M., Mansour, N.A., Fayez – Hassan, M., and Sedqy, E. 2016 *J.Taibah Uni.Science* **10** (2) 296
[11] K. Khan, H. M. Khan, M. Tufail, A. J. A. H. Khatibeh, and N. Ahmad 1998 J. Environ. Radioact **38** (1) 77
[12] M.M. El-Galy, A.M. El Mezayn, A.F. Said, A.A. El Mowafy, M.S. Mohamed 2008 *J. Environ. Radioact* **99** 1075
[13] S. Righi, L. Bruzzi. 2006 *J. Environ. Radioact* **88** 158
[14] Taskin H, Karavus M, Ay P, Topuzoglu A, Hidiroglu S, Karahan G. 2009 *J. Environ Radioact.* **100** (1) 49
[15] ICRP, Recommendations of the International Commission on Radiological Protection. ICRP Publication 60. *Ann. ICRP*, 1990 **21** (1-3).
[16] Y. Orgun, N. Altinsoy, S.Y. Sahin, Y. Gungor, A.H. Gultekin, G. Karaham 2007 *Turkey Applied Radiation and Isotopes* **65** 739
[17] Madkour, H.A., M.A.K. Abdelhalim, K.A. Obirikorang, A.W. Mohamed, A.E.H.N. Ahmed, and A. El-Taher 2015 *J. Environ. Biol.* **36** 1421
[18] SPSS-Statistical Program for the Social Science, Standard version 9.0 for Windows, SPSS Inc.Chicago, USA (1998).
[19] International Atomic Energy Agency. Guidelines for radioelement mapping using gamma-ray spectrometry data IAEA, VIENNA, 2003 IAEA-TECDOC-1363 ISBN 92–0–108303–3 ISSN 1011–4289 © IAEA, 2003 Printed by the IAEA in Austria.

Measurement the natural radioactivity and Hazard Indices of Milk Powder Consumed in Iraq

Measurement the natural radioactivity and Hazard Indices of Milk Powder Consumed in Iraq

Auras M. Omron[1], Taghreed K. Hameed [2], saba J. hasan [2], Mahmood S. Karim[2]

[1]Department of Physics, College of Education, Karbala University[1]
[2]Department of Physics, College of Education, Al-Mustansiriyah University[2]

E-mail: Mahmood_msc74@yahoo.co.uk

Abstract. In the present work, the specific activity of different types of milk powder samples from various foreign origins in the local markets was studied. For this purpose, (HPGe) detector was used. The results showed that Miedo sample (Jordanian origin) had the highest quantities of A_U, A_{Th} and A_k equal to respectively (18.690, 25.070 and 183.500) Bq/kg respectively. All the specific activity and parameters are less than their corresponding allowed limits, and hence no health risk they possess.

Keywords: milk powder samples**,** specific activities**,** (HPGe) detector.

1. Introduction

Radionuclides in air or water may also input food chain. For instance, plants are capable of absorbing radionuclides from water in the same way of absorbing different minerals. When humans and animals drink water, some of the radionuclides in the water will remain in their bodies. Radionuclides from air may settle on the surface of plants. When animals consume the plants, they ingest the radionuclides that have settled from air or have been absorbed from the water. Animals and plants that will eventually be food for humans thus provide a pathway for radionuclides to move via the environment to humans [1]. Milk products and milk are important components of diet in many countries. Milk is one of the few foods produced over large areas and collected on a daily basis. Its composition is almost identical all over the world, and it is easy to collect a representative specimen that can be analyzed in dried or liquid forms [2]. Milk is likely to be contaminated by radioactive. Contamination of milk can be greatest when cows are grazing, but even if cows are kept indoors, contamination of milk may also occur by means of inhalation of radionuclides [3].

2. Experimental part

2.1. High purity germanium system (HPGe)

In the present study, (HPGe) detector with energy resolution of (2.6 keV) at energy (1332.6 keV) for ^{60}Co and efficiency of 40% was used. The high purity N-type semiconductor detector with (3×3) inch was used to study the characteristics of geometry closed end coaxial. (HPGe) detector is kept cold by immersing it in a liquid-nitrogen vessel at (-196˚C) to reduce the leakage current to the acceptable levels.

The detector is surrounded by lead shield of about 10 cm thickness in order to reduce the background radiation.

Figure 1. (HPGe) system

2.2. Radiation Hazard indices Calculation

activity concentrations[5]:

$$A = \frac{NET}{\varepsilon * I_\gamma * m * t}$$

NET: net peak area under the specific peak corrected for the background
A: activity concentrations of the sample with unit Bq/kg, ε : Energy efficiency,
m: mass of sample (kg), t: measurement time (7200 sec.).
Radium Equivalent (Ra_{eq})[5]:
Ra_{eq} (Bq/kg) = (1.43A_{Th}) + (0.077A_K) + (A_U)
Where:
A_U, A_{Th} and A_K are the specific activity concentrations of U-238, Th-232 and K-40 respectively.
2.2.3 Absorbed Dose Rate (D_γ) [6]:
D_γ (nGy/h) = 0.604A_{Th} + 0.462A_U + 0.0417A_K

Annual Effective Dose Equivalent [7]:
$(AED)_{in}$ (mSv/y)= D_γ (nGy/h)×10^{-6}×8760 h/y×0.80×0.7Sv/Gy
$(AED)_{out}$ (mSv/y)= D_γ (nGy/h)×10^{-6}×8760 h/y×0.20×0.7Sv/Gy
External (H_{ex}) and Internal (H_{in}) Hazard Indices [8]:

$$H_{in} = \frac{A_U}{185} + \frac{A_{Th}}{259} + \frac{A_K}{4810} \leq 1$$

$$H_{ex} = \frac{A_U}{370} + \frac{A_{Th}}{259} + \frac{A_K}{4810} \leq 1$$

Activity gamma Index (I_γ) [9]:

$$I_\gamma = \frac{A_U}{300} + \frac{A_{Th}}{200} + \frac{A_K}{3000}$$

3. Results and Conclusions

The aftereffects of the present work were outlined in Table 1. The most elevated estimation of A_U, A_{Th} and A_k was found in Nido sample (Jordanian origin) to be (18.690, 25.070 and 183.500) Bq/kg respectively. While, the lowest estimation of A_U, A_{Th} and A_k was found in Ancor sample (New Zealand origin) to be (9.420, 10.190 and 76.260) Bq/kg respectively. Figure (2) shows the average estimation of (20.785±3.6 Bq/kg and 24.695±3.3 Bq/kg), respectively. The present outcomes have demonstrated that the estimations of A_U, A_{Th} and A_k in fertilizer samples were less than the recommended values of (35, 30 and 400) Bq/kg respectively [10].

The most elevated estimation of the parameters [Ra_{eq}, D_γ, $(AED)_{in}$, $(AED)_{out}$, H_{in}, H_{ex} and I_γ] was found in Ancor sample to be (29.864 Bq/kg, 13.687 nGy/h, 0.067 mSv/y, 0.017 mSv/y, 0.106, 0.081 and 0.108) respectively. While the lowest estimation of the parameters [Ra_{eq}, D_γ, $(AED)_{in}$, $(AED)_{out}$, H_{in} and I_γ] was found in Nido sample to be (68.670 Bq/kg, 31.429 nGy/h, 0.154 mSv/y, 0.039 mSv/y, 0.236, 0.185 and 0.249) respectively, and with an average estimation of (49.025 Bq/kg, 22.411 nGy/h, 0.11 mSv/y, 0.027 mSv/y, 0.167, 0.132 and 0.178) respectively. All the values of the specific activity and parameters were less than their corresponding allowed limits, and hence no health risk is considered.

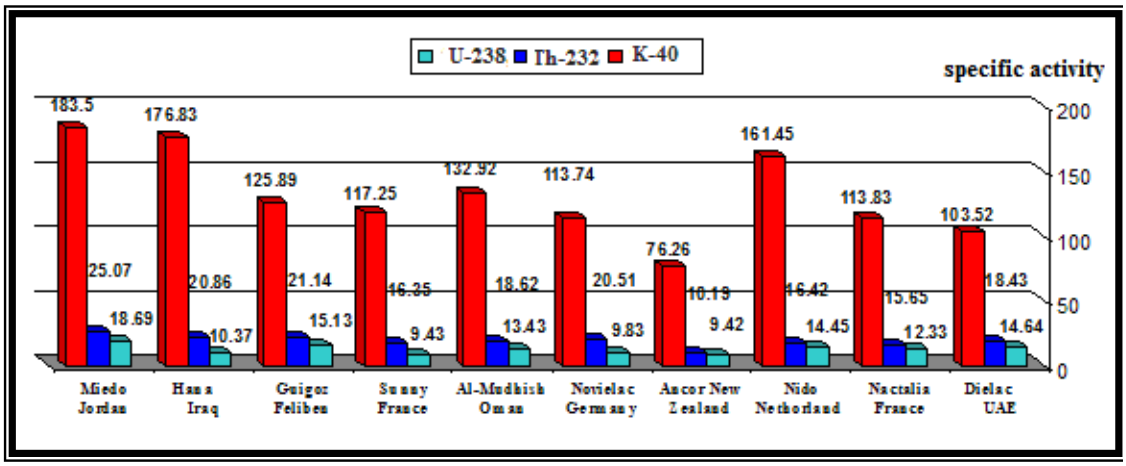

Figure 2. Specific activity of (^{238}U, ^{232}Th and ^{40}K) for all studied milk powder samples

Table 1. Specific activities of ^{238}U, ^{232}Th and ^{40}K with some other parameters [Ra_{eq}, D_γ, $(AED)_{in}$, $(AED)_{out}$, H_{in}, H_{ex} and I_γ] in all milk powder samples

Milk type	Origin	U-238 (Bq/kg)	Th-232 (Bq/kg)	K-40 (Bq/kg)	Ra_{eq} (Bq/kg)	D_γ (nGy/h)	(A.E.D) (mSv/y) Indoor E_{in}	(A.E.D) (mSv/y) Outdoor E_{out}	Hazard index H_{in}	Hazard index H_{ex}	I_γ
Dielac	UAE	14.64	18.43	103.52	48.966	22.212	0.109	0.027	0.172	0.132	0.175
Nactalia	France	12.33	15.65	113.83	43.474	19.896	0.098	0.024	0.151	0.117	0.157
Nido	Nethorland	14.45	16.42	161.45	50.362	23.326	0.114	0.029	0.175	0.136	0.184
Ancor	New Zealand	9.42	10.19	76.26	29.864	13.687	0.067	0.017	0.106	0.081	0.108
Novielac	Germany	9.83	20.51	113.74	47.917	21.672	0.106	0.027	0.156	0.129	0.173
Al-Mudhish	Oman	13.43	18.62	132.92	50.291	22.994	0.113	0.028	0.172	0.136	0.182
Sunny	France	9.43	16.35	117.25	41.839	19.121	0.094	0.023	0.138	0.113	0.152
Guigoz	Feliben	15.13	21.14	125.89	55.054	25.008	0.123	0.031	0.190	0.149	0.198

Milk type	Origin	U-238 (Bq/kg)	Th-232 (Bq/kg)	K-40 (Bq/kg)	Ra_{eq} (Bq/kg)	D_γ (nGy/h)	(A.E.D) (mSv/y) Indoor E_{in}	(A.E.D) (mSv/y) Outdoor E_{out}	Hazard index H_{in}	Hazard index H_{ex}	I_γ
Hana	Iraq	10.37	20.86	176.83	53.816	24.764	0.121	0.030	0.173	0.145	0.198
Miedo	Jordan	18.69	25.07	183.50	68.670	31.429	0.154	0.039	0.236	0.185	0.249
Avr.		12.772	18.324	130.519	49.025	22.411	0.110	0.027	0.167	0.132	0.178
Min.		9.420	10.190	76.260	29.864	13.687	0.067	0.017	0.106	0.081	0.108
Max.		18.690	25.070	183.500	68.670	31.429	0.154	0.039	0.236	0.185	0.249
Worldwide average [10]		35	30	400	370	55	1	1	1	1	1

4. Conclusions

The results of the present work were concerning the values of the specific activity for (^{238}U, ^{232}Th and ^{40}K) and determining the parameters [Ra_{eq}, D_γ, $(AED)_{in}$, $(AED)_{out}$, EAD, I_γ, H_{in} and H_{ex}]. All the above values were found to be lower than their corresponding allowed limits.

References

[1] Raymond L 1989 *Understanding Radioactive Waste* 3rd ed (Columbus: Ohio- Battelle Press).
[2] Marth E H 1978 *Standard Methods for the Examination of Dairy Products,* Fourteenth Edition, (Association: Washington- American Public Health Association).
[3] Vosniakos F Moumtzi A Kesidou A Ganatsios S Bizopoulos A and Karakoltsidis P A 1989 *Aust. J. Dairy Technol* **44** 44.
[4] Karim M S 2015 *Study of radioactivity and radon gas emanation in some Iraqi governorates* Ph.D Thesis Al-Mustansiriyah University College of Education.
[5] Karim M S 2016 *International Journal of Recent Research and Review* **IX** 1.
[6] Nashwan S 2000 *Radioactive pollution and environmental sources in the province of Nineveh* Master Thesis Wassit University.
[7] El-Arabi A M 2005 *Indian J. Pure Appl. Phys.* **43** 422.
[8] Ahmed H F Mohammed A N and Karim M S 2020 *Ibn Al-Haitham Jour. for Pure & Appl. Sci.* **33** 19.
[9] Arman E 2007 *Turkish Journal of Medical Sciences* **37** 199.
[10] (UNSCEAR) United Nations Scientific Committee on the Effects of Atomic Radiation 2000 *Sources Effects and Risks of Ionizing Radiation* (New York-United Nations).

Comparison of Three Techniques for Measuring Radon Gas

Comparison of Three Techniques for Measuring Radon Gas

Hadeel Tariq Hamad[1], Mahmood Salim Karim[2] and Nada Farhan Kadhim[3]

[1] Ministry of Education - General Directorate of Karkh First Education , Baghdad Iraq
[2] Department of Physics, College of Education, Mustansiriyah University, Baghdad Iraq
[3] Department of Physics, College of science, Mustansiriyah University, Baghdad Iraq

E-mail: nadaph2010@yahoo.com

Abstract. In the present work, three radioactive elements of radium were used to produce radon gas and ^{222}Rn was measured by three different techniques (Rad-7 detector, Scout detector and CR-39 detector). It was found that the ^{222}Rn gas measured by Rad-7 detector is closer to the real readings than other detectors.

Keywords: ^{222}Rn, Scout detector, (CR-39) detector, Rad-7 detector.

1. Introduction

Exposure to ^{222}Rn and its radioactive progeny present in the environment results in a large contribution to an average effective dose received by human beings [1,2]. Natural ^{222}Rn and its airborne progeny can cause a significant internal health hazard, especially when they build up in enclosed areas such as houses, mines and caves. Workplaces may differ from houses in terms of building structure, microclimatic conditions and occupancy factors. Some of the peculiarities of workplaces are: (a) widespread use of ground floor or basements, (b) high probability of finding elevated temperatures and high levels of humidity (c) multi-stored buildings with big entrance hall and (d) presence of air conditioning or forced ventilation aerosols and dust. Such workplace characteristics might result in large aerosols. Such workplace characteristics might result in large spatial and time variations of ^{222}Rn, thus requiring an appropriate monitoring strategy [3,4].

2. Materials and Method

Three radiating elements of radium were used as (107.85Bq, 1734.01Bq and 1734.01Bq). It was placed in a plastic box (see figure 1). After that, Rad-7 detector, Scout detector, in addition to 10 pieces of CR-39 detectors with an area of (1 cm×1 cm) were distributed within the plastic box. The measurement of ^{222}Rn concentration was made every 12 hours using a detector that placed inside a plastic box with (90 cm×90 cm×80 cm) dimensions, and the plastic box was sealed tightly to ensure that the radioactive ^{222}Rn is not escaping outside the plastic box.^{222}Rn emitted from radium element was calculated using equation (1) [5].:

$$E_s\left(Bq * \frac{day}{m^3}\right) = \left[A_{Radium}\left(\frac{B_{q)}}{Vm^3}\right)\right] * T(day) \quad (1)$$

where: $E_{s:}$ the ^{222}Rn gas exposure in radium source.
A_{Radium}: the radioactivity of ^{226}Ra.
V: the container volume (plastic box) in m^3.

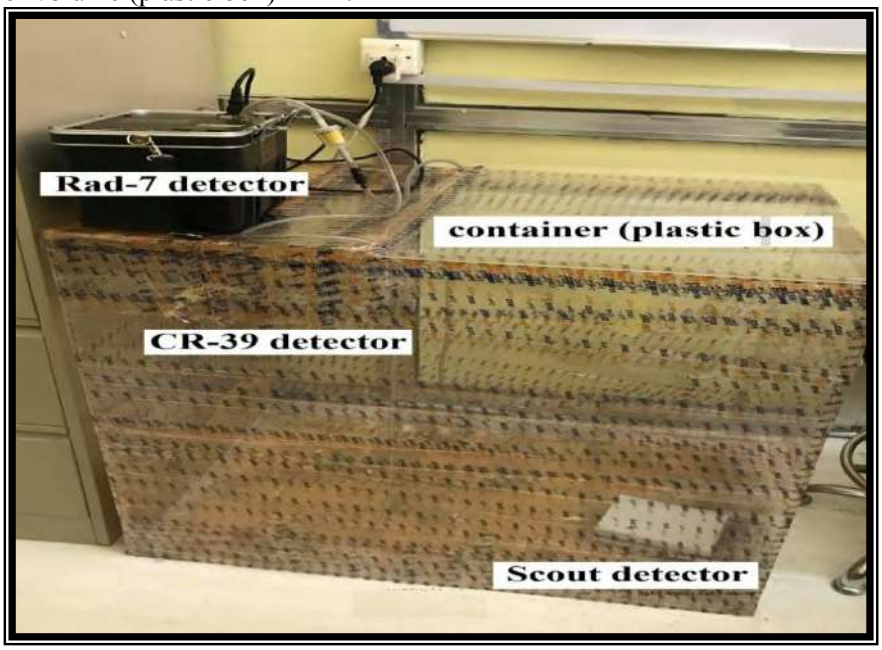

Figure 1. The container (plastic box), Rad-7 detector, Scout detector and CR-39 detector**.**

3. Results and-Discussions

In the present work, ^{222}Rn gas concentration was measured using the detectors (Rad-7, Scout and CR-39) as seen in figure 2 , and a comparison between the results is shown in Table (1). it is noticed that the radon concentration measured using the CR-39 detector increases with increasing the period of exposure to radioactive sources. In addition, we noticed that the values of the Rad-7 detector are closer to the real values of the ^{222}Rn emitted from the radioactive radium followed by the values of the Scout detector and then the CR-39 detector (see figure 3). Rad-7 detector was better than other detectors due to the different measurement technology as it relies on the contrast of the gas flap.

4. Conclusion

The present work has demonstrated that theRad-7 detector is closer to the real values of the ^{222}Rn emitted from the radioactive radium followed by the values of the Scout detector and then the CR-39.

Figure 2. shows all detectors using in the present work

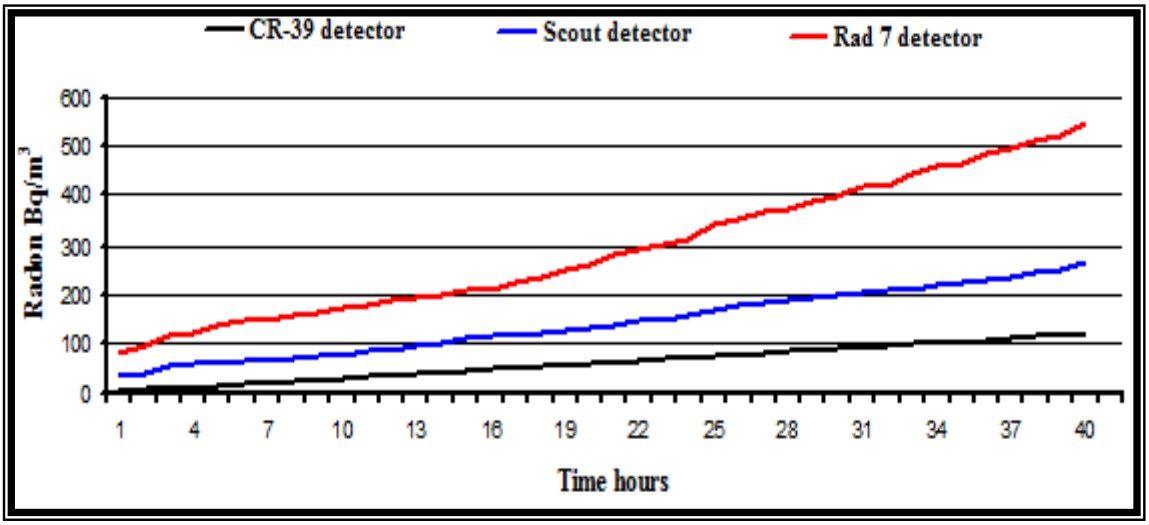

Figure 3. ^{222}Rn gas concentration by using detectors (Rad-7, Scout and CR-39)

Table 1. Shows ^{222}Rn emitted from radium source, Radon measured by Rad 7 detector , Scout detector and CR-39 detector

No.	Time (hours)	^{222}Rn emitted (source) Bq/m^3	^{222}Rn measured Rad 7Bq/m^3	^{222}Rn measured Scout Bq/m^3	^{222}Rn measured CR-39 detector Bq/m^3
1	3	49299.9	80.5	34	-
2	6	98599.8	95.3	37	-
3	9	147899.7	114.5	55	-

4	12	197199.6	122.3	60	٤٢
5	15	246499.5	138.4	61	-
6	18	295799.4	143.7	64	-
7	21	345099.3	150.4	65	-
8	24(1day)	394399.2	155.6	69	٥٦
9	27	443699.1	162.8	76	-
10	30	492999	171.1	77	-
11	33	542298.9	179.5	84	-
12	36	591598.8	187.8	89	٧٢
13	39	640898.7	193.6	95	-
14	42	690198.6	200.3	102	-
15	45	739498.5	208.2	110	-
16	48(2day)	788798.4	212.1	116	٩٤
17	51	838098.3	222.5	120	-
18	54	887398.2	236.7	123	-
19	57	936698.1	249.4	127	-
20	60	985998	260.1	131	١١٣
21	63	1035297.9	277.8	138	-
22	66	1084597.8	289.1	144	-
23	69	1133897.7	301.8	149	-
24	72(3day)	1183197.6	312.6	158	١٣٢
25	75	1232497.5	341.9	167	-
26	78	1281797.4	352.5	176	-
27	81	1331097.3	365.9	182	-
28	84	1380397.2	372.2	188	١٤١
29	87	1429697.1	386.1	193	-
30	90	1478997	397.8	197	-
31	93	1528296.9	421.6	203	-
32	96(4day)	1577596.8	422.0	208	١٥٨
33	99	1626896.7	442.7	211	-
34	102	1676196.6	458.8	218	-
35	105	1725497.5	467.6	222	-
36	108	1774796.4	485.3	230	١٧٦
37	111	1824096.3	493.3	237	-
38	114	1873396.2	511.7	244	-
39	117	1922696.1	523.7	252	-
40	120(5 day)	1971996	547.6	263	١٩٤

Acknowledgment
The authors are grateful to the head of Al-Mustansiriya University, the Deanship of the College of Science and the Head of the Physics Department, for their cooperation during the field work.

References

[1] Mahmood S Karim H Daroysh H and Mohammed A N 2016 *Detection* **4** 40.
[2] Ridha A A Karim M S and Kadhim N F 2014 *Civil and Environmental Research* **6** 24.
[3] Nazaroff W W and Nero A V 1988 *Radon and its decay products in indoor air John* (New York-Wiley and Sons).
[4] Ridha1 A A and Kadhim N F 2015 *Iraqi Journal of Physics* **13** 97.
[5] Chen J Rahman N M and Atiya I A 2010 *Journal of Environmental Radioactivity* **101** 17.

Detection of X-Rays Radiation Effect on Radiation Sensors Based on Optical Fiber Technology

Detection of X-Rays Radiation Effect on Radiation Sensors Based on Optical Fiber Technology

Aseel I. Mahmood [1*], Shehab A. Kadhim[1], Intisar A. Naseef[1], Khalid M. Thajeel[1], Raafat A. Ahmed[1], Nadia F. Muhammed [1], Ashwaq A. Jabor[1]

[1]Materials Research Directorate, Ministry of Science and Technology, Baghdad, Iraq

[*]E-mail: aseelibrahim208@gmail.com

Abstract. This study aims to investigate the characteristics of optical fiber sensors under X-rays radiation. The Radiation-Induced Absorption (RIA) and Radiation-Induced Refractive-Index Change (RIRIC) in the UV-VIS domain were investigated. Single and multi-mode optical fibers (SMFs & MMFs) have been used for this purpose. The outer diameters of these fibers were reduced from (125 to 50 and 55µm for SMF and MMF respectively) via chemical etching process then dipped into (3 wt % concentration) of germanium (Ge) solution to produce the sensing part of the fibers. Due to the applied X-rays radiation, an attenuation of the spectrum and a redshift in peak wavelength were achieved. Both sensors show good responsivity to the applied radiation and the MMFs sensors showed higher wavelength shifting as compared to SMFs sensors.

Keywords: X- rays, optical fiber radiation sensors, Radiation-induced Absorption; Radiation-Induced Refractive-Index Change; Germanium doped optical fibers.

1. Introduction

Most types of radiation are dangerous for living beings when exposed to them. For this reason, real-time remote dose measurements have great necessity. Radiation dosimeters have been applied in wide fields such as nuclear facilities, industrial process controls (X‑ or e‑ beam polymerization), nuclear medicine, and radiotherapy. The usage of traditional electronic dosimeters has some problems like using high power energy, uncertain measurement under radiation due to degradation and changing of measured sensitivity. Furthermore, it is difficult access to very hazardous areas, such as hot cells, high active source storage areas [1]. On the other hand, optical fibers sensors (OFS) present the key feature to be used as radiation detection dosimeters in different fields including space military, industry etc. This is because they have a number of advantages regarding the traditional forms of the data link [2]. The high spatial resolution (parts of millimetres), accuracy, large dynamic range, the cost-effectiveness, sufficient sensitivity, acceptable fading, response linearity, reproducibility, dose rate independence, and immune to electromagnetic radiation. All these characteristics made OFS very suitable choice for radiation detection applications [3]. Two types of OFS's structures can be used as radiation sensors; the first one is the intrinsic sensor which is used as a radiation‑ sensitive material, and a guide for an optical signal passing through it to the detector [4]. This type is frequently used for monitoring the radiation dose of the radioactive waste container[5]. The second type is the extrinsic senor that only acts as a waveguide to deliver the optical signal from transmitter to receiver and the sensing part is spliced or coupled to the waveguide [6]. These types of sensors mostly used in‑ vivo monitoring during radiotherapy [7]. The interaction between fiber material and the applied radiation causes the existence of point defects in fiber core and cladding. Also, this interaction leads to three

macroscopic effects; Radiation-Induced Attenuation (RIA) which increases the attenuation of the signal, Radiation-Induced Emission (RIE) which is responsible for the emission of light and originates from the luminescence of point defects or Cerenkov emission, and finally, Radiation-Induced Refractive Index Change (RIRIC) which is caused by changing the density in the glass or by the RIA via the Kramers-Kronig relations [8][9]. The sensitivity of multimode or single-mode optical fibers exposed to different types of radiations was described in many research. Gerard et al. [2] studied the sensitivity of SMFs under gamma and pulsed x-rays radiation in the IR wavelength range. The tested samples were doped with P (Phosphor), N (Nitrogen), and Ge (Germanium) dopants. A demonstration of the actual ability of a silica -based optical fiber doped with Ge to be used as a thermally stimulated luminescence-mode dosimeter and to confirm its applicability. These fibers have been irradiated with different types of radiation photons, x and gamma rays within a dose range higher than 10 krad, with different dose rates[10].The Thermo-luminescence response of Ge-doped silica-based optical fiber to electron, x-rays and gamma rays had been presented by Entezam et al. [11] they found that the Ge-doped optical fiber with higher core size has a higher sensitivity. Ladaci et al [12] investigated the Ytterbium and Erbium energy level lifetimes versus doses of various radiation types (40 KeV X-rays, 480 MeV protons, 1.2 MeV γ-rays and 6 MeV electrons).Also, they added Cerium ions Erbium-doped fiber to improve its tolerance on RIA effects.The RIA of different doped optical fibers under X-rays at three different temperatures had been studied by Vecchi et al. [8]. They found that the irradiation of both gamma rays and x-rays leads to the same levels of RIA. This result confirmed that these types of optical fiber sensors could be used in dosimetry fields.

In this work, the behaviour and performance of SMFs and MMFs optical fiber sensors with modified cladding under x-ray radiation at different exposure times will be observed and studied.

2. Materials and Methods

Commercially available SMFs and MMFs were utilized as radiation sensors in the measurements technique. The core diameter of the SMF sensor was 10 μm and the cladding diameter was 125 μm, while the MMF has a core diameter of 50 μm and a cladding diameter of 125 μm. The fabrication process of the radiation sensors took place as follows; first, the middle region of these fibers were stripped and cleaned very well with the suitable solution (the length of the stripped region is about 3 cm). After that, the fibers' diameters were reduced via the chemical etching process by immersing them into hydrofluoric acid (HF) diluted with distilled water. The concentration of HF acid was 42 %, this concentration had been diluted by adding distilled water with percentage (1(HF):2 (water)) ml for 45 and 30 min for SMF and MMF respectively. Then the fibers removed from HF solution and dipped into water for three stages to remove any remaining HF solution from the fiber surface. Fibers have been removed from the water and measure the diameter of the fibers after etching. For accurate measurement, the etching procedure is done at room temperature (around 25 ˚C). The obtained diameters were (50 and 55) μm for SMF and MMF respectively. Finally, the etched region of the fibers was dipped in (3wt. %) of Ge solution to generate the sensing part of the sensor.The germanium is a colloidal solution; it was prepared by dissolving Ge powder in toluene liquid. Due to etching process the cladding surface of silica optical fiber becomes rough and contains pores and what is called dangling bonds; these bonds capture Ge nanoparticles and make them settle down inside the pores. Since the stripped part of the fiber is immersed in the solution with caution then the etching process will be equal all over cladding surface, therefore, Ge nanoparticles will adhere equally on the cladding surface According to these steps, the modified cladding fiber sensors were manufactured and submitted as clarified in Figure 1.

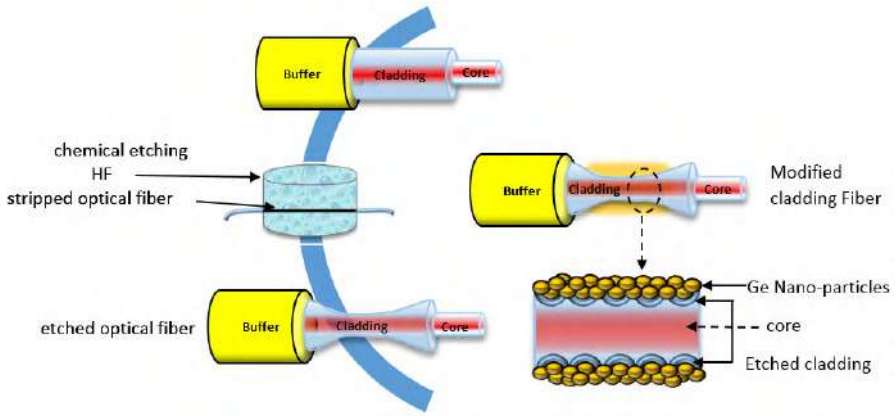

Figure 1. The manufacturing steps of the modified cladding optical fiber sensor.

Figure 2 illustrates the schematic diagram of the experiment to investigate the x-rays irradiation effect on the properties of the transmitted signal. It is worthy to mention that the transmitted signal in the UV-VIS range changes due to the absorption process of the x-rays radiation.

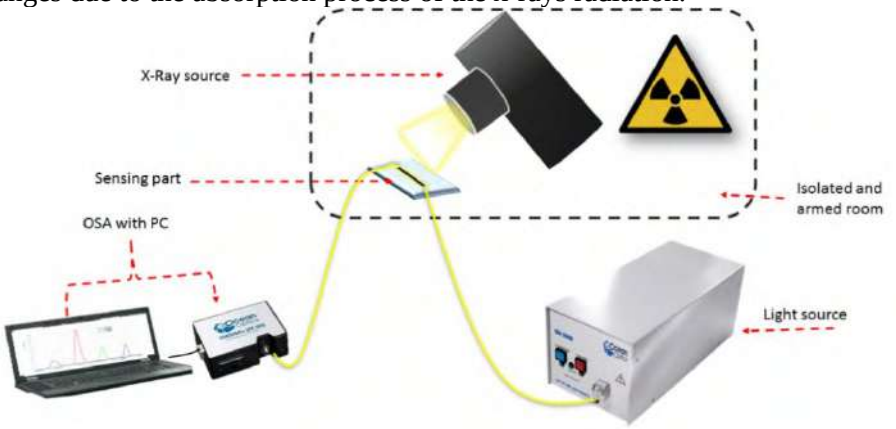

Figure 2. Schematic diagram of the measurement set-up.

The sensing parts of SMFs and MMFs samples placed on a glass slide then inserted inside an isolated armed chamber of the X- ray radiation source (XRD-6000 SHIMADZU) device. This device is located at the material research directorate, ministry of science and technology, Iraq. The exposure angle was (90^{o}) to ensure that all the sensing area exposed to radiation. The distance between the fiber sensor and the radiation source head was (10 cm). The other parts of optical fibers were located outside the chamber and the two ends of each fiber considered as the sensor terminals. The first terminal was connected to the UV-VIS light source (DH-2000 Ocean optics) with range (200-1100) nm as a transmitting signal passing through the sensors. While the other terminal was connected to the spectrometer (Ocean Optics USB- 2000) to record the spectrum online during the irradiation process (real-time measurement). The X-rays were emitted from a Cu tube with the following specifications; (X-rays tube target Cu with Broad Focus (BF 2.7 KW type), the maximum voltage of 60KV, maximum current of 80 mA, and average maximum power of 3 KW). The resulted spectrum of each sample was recorded as (3) measurements within (3) minutes (one measurement each minute) to test the responsivity of designed sensors to low radiation doses.

3. Results and Discussions

As mentioned, earlier the transmitted spectra of both investigated optical fibers sensors were measured and recorded at different x- rays dose rates. The following figures illustrate the output data revealed from this work. Figure (3a, and b) shows the spectral dependence of the measured spectra for the SMF and MMF sensors respectively due to x-rays irradiation.

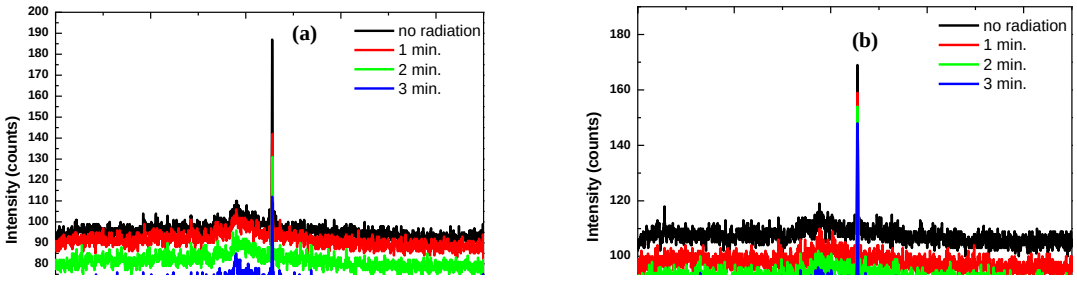

Figure 3. The spectral shape of (a) SMF sensor, (b) MMF sensor.

The above figures show that RIA in both investigated fibers has similar spectral character. For SMF's sensors we can notice that in the VIS spectral region, there is a local sensitivity maximum at around 655 nm from which the induced RIA drops rapidly towards IR wavelengths. Besides, there is another peak with a local minimum around 570 nm as is clear in Figure 3 (a). The same behaviour founds when using MMF's sensors except a new peak found in the range of 255 nm as it shown in Figure 3 (b). The transmitted intensity for all samples decreases due to radiation application attenuation in transmitted intensity increases with the dose rate which is 3 minutes.

Figure (4a, and b) shows the intensity values (intensity attenuation)as a function of radiation exposure time for both SMF and MMF sensors. The RIA sensitivity for SMF sensor was measured through the linear fitting relation between the intensity and exposure time for each peak. The values were (-) 23.1 count/ min and (-)11 count /min for the peaks 650nm and 570 nm respectively with good reliability of 0.93 and 0.99 respectively. While for the MMF sensor the sensitivity values were (-) 6.8 count /min, (-) 8.3 count /min, and (-) 8.7 count /min with reliability values of 0.98, 0.99, and 0.95 for the peaks 650 nm, 570 nm, and 255 nm respectively. The transmitted intensity for all samples decreases due to the attenuation phenomenon that appears in optical fibers due to X-rays irradiation.

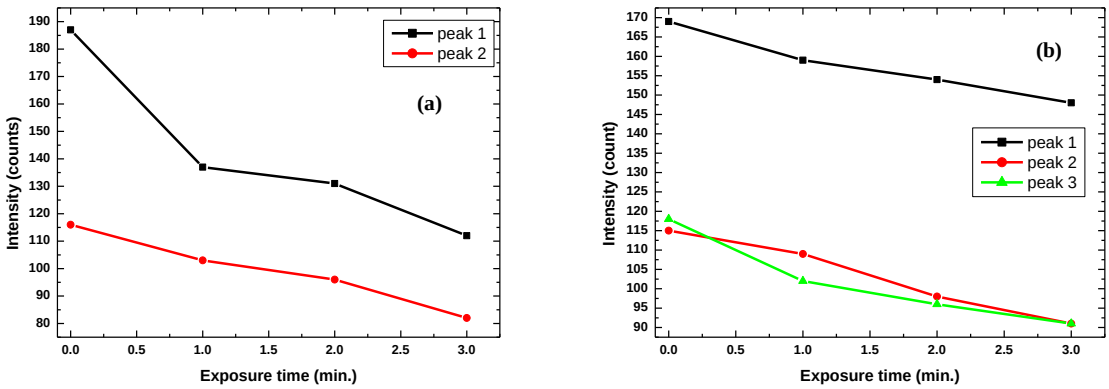

Figure 4. Transmitted intensity as a function of exposure time for (a) SMF sensor, (b) MMF sensor.

One of the most important and effective parameters for any radiation sensor is its wavelength sensitivity. The wavelength sensitivity was measured through the linear fitting relationship. In this work, sensitivity was measured for both modified cladding SMF and MMF sensors. SMF sensor shows a wavelength sensitivity of 8.1 pm/min and 25 pm/ min with good reliability 0.96 and 0.95 for the peaks 650 nm and 570 nm respectively. On the other hand, MMF sensor showed a very high sensitivity of 112 pm/ min and 50 pm/ min with good reliability 0.95 and 0.96 for the peaks 650nm and 570 nm respectively. The third peak that appeared in the output spectra of the MMF sensor at 255 nm suffered from a blue shift due to radiation application, and the sensitivity for this peak was (-) 10060 pm/ min with a reliability of 0.95.

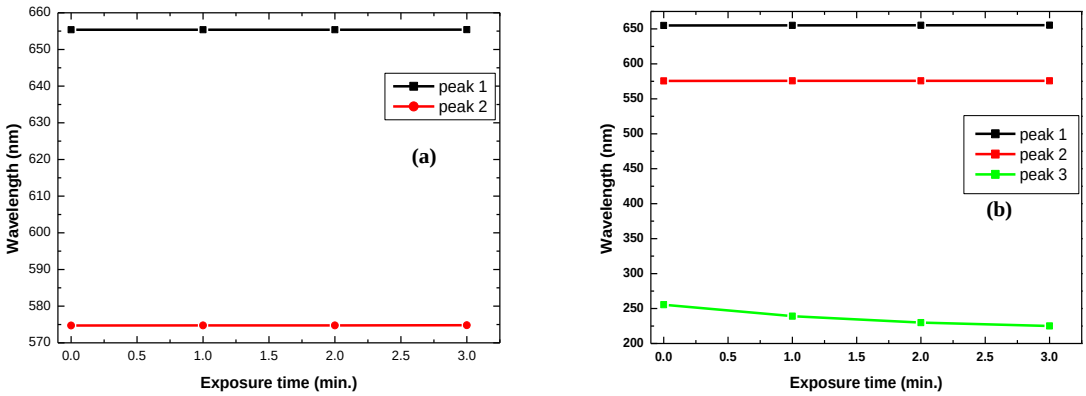

Figure 5. Peak wavelength as a function of exposure time for (a) SMF sensor, (b) MMF sensor.

According to these results, SMF sensors have higher intensity sensitivity than MMF sensors. This could be explained as follows; for MMF sensors with their large core, the effects of the light-guiding on changing signal intensity are small, while the changing in wavelength due to radiation application was higher for them as compared to SMF sensors. Investigating the behaviour and performance of SMF and MMF sensors with smaller diameters decreased by the chemical etching process was achieved. However, this procedure resulted in leaking some of the transmitted light signals outside the cladding known as an evanescent wave. These leaked waveforms act as a field around the cladding material and interacts with the dipping material (germanium) lead to generation of point defects that change fiber structure, and thus change its refractive index. Ge nanoparticles plays very important role in sensing

process since Ge and Si are isoelectronic elements having therefore the same number of electrons. Therefore, Ge-related point defects have a similar structure as those related to Si, but replacing Si with Ge atoms. In Ge-doped fibers, Ge-related defects are dominant over Si-related defects because they are generated in a more efficient way. In Ge-doped fibers, the RIA has been found to monotonously increase with dose (D) before reaching a saturation level. It is worthy to mention that the submitted optical fibers sensors have different layers and compositions (silica and germanium) and therefore they are subjected to different stresses. Hence, due to what mentioned earlier, the structural modification, defects generation, and layers stress, all these factors can have spatial distribution and in return modify the guiding properties of the optical fibers. The changing in wavelength due to radiation application was higher for MMF sensors. This is because the interaction between the incident radiation and fiber materials lead to inelastic scattering. The origin of scattering is due to the interaction of light with the excitation of the medium. According to quantum theory approach, the interaction is between the quanta of light (photons) and quanta of medium excitation which are phonons. This is true for the low light intensity levels, but for the strong excitation of the medium due to the high intensity of light, the semi-classical wave theory turns to be more appropriate to describe the scattering process. For an inhomogeneous medium, the scattering process removes some photons of the incident light and produces scattered photons that might be shifted in direction, phase and frequency in this work the shifting was in frequency (wavelength). The incident photons give or receive energy to or from the medium, leading to scattered photons shifted in frequency by definition, the components of the scattered light which are shifted to lower frequencies are known as Stokes components while those components which are shifted to higher frequencies are known as anti-Stokes components. This scattering leads to produce new photons with new phase and frequency. This could be the reason behind we get two different shifting red and blue in MMF sensors.

4. Conclusions

This work is aim to perform an initial assessment of the possibility to utilize optical fibers as radiation sensors; modified cladding SMFs and MMFs had been used for this purpose. X-rays source with an exposure time of 3minutes source was employed as the radiation source. Both fibers exhibited a similar spectral character of decreasing the transmitted light and shifting in peak wavelength due to radiation. In spite of small exposure radiation time (due to Lab protocols) but both sensors exhibited good response. The SMF sensors showed a higher intensity sensitivity, while the MMF sensors showed a higher wavelength sensitivity. The presented sensors could be very useful in medical applications like monitor low doses of ionising radiation, radiation dose real-time measurements, and radiotherapy applications.

Acknowledgment

Funding of this work was provided by L'Oréal Foundation, where Aseel Mahmood and her scientific group win the L'Oréal- UNESCO for Women in Science Levant Program Fellowship 2018.

References

[1] Jayaprakash A., Krishnakumar N., Dhanasekaran A., Jose T., Venkatraman V., & Murty S., 2013 *J. of Rad. Prot. & Envir.* **36** 13.
[2] Girard S., Keurinck J., Boukenter A., & Meunier J. 2004 *Sec. B of Nucl. Inst. Meth. Phys. Res. J.* **215** 187.
[3] Zubair H., Begum M., Moradi F., Rahman A., Mahdiraji G., Oresegun A., Louay G., Omar N., Khandaker M., Adikan F.,Noor N.,Almugren K., & Bradley D. 2020 *IEEE Phot. J.* **12**(3) 6801525
[4] Kalnins C., Ebendorff-Heidepriem H., Spooner N., & Monro T. 2012 *Opt. Mat. Exp.* **2** 62.
[5] Delepine-Lesoille S., Girard S., Landolt M., Bertrand J., Planes I., Boukenter A., Marin E., Humbert G., Leparmentier S., Auguste J.L., & Ouerdane Y. 2017 *Sens*. **17** (1377) 1.
[6] Girard S., Alessi A., Richard N., & Martin-samos L. 2019 *Rev. Phys. J.* **4** 100032.
[7] Keeffe S., Mccarthy D., Woulfe P., Grattan M., & Hounsell A. 2015 *Brit. J. of Rad.* **88** (20140702) 1.
[8] Vecchi G., Di Francesca D., Sabatier C., Girard S., Alessi A., Guttilla A., Robin T., Kadi Y.,

Brugger M., Organization E., & Geneva C. 2020 *J. Opt. Fib. Tech.* **55** 102166.
[9] Stajanca P., & Krebber K. 2017, *Sens. (Basel)* **17** (9) 1959.
[10] Benabdesselam M., Mady F., Girard S., Mebrouk Y., Duchez J., Gaillardin M., & Paillet P. 2013 *IEEE Trans. on Nucl. Sci.* **60** 4251.
[11] Entezam A.,Khandaker M., Amin Y., Ung N., Maah J., & Bradley D. 2016 *PLOS ONE* **0153913** 1.
[12] Ladaci A., Girard S., Mescia L., Robin T., Laurent A., Cadier B., Boutillier M., Morana A.,& Di, Ouerdane D. 2018 *J. of Lum.* **195** 402.

Studying the effect of the bending magnet parameters on focusing of charged particles in beam transport systems via the matrix representation method

Studying the effect of the bending magnet parameters on focusing of charged particles in beam transport systems via the matrix representation method

Malak M. Attia[1], Intesar H. Hashim[1]

[1]Department of Physics, College of Education, Mustansiriyah University

E-mail: malakmuhsin0@gmail.com

Abstract. The focusing of charged particles beam passing through the transport system is affected by many parameters and depends on the elements that used in the transport beam systems. In this study, a permanent bending C-shape magnet is used to investigate the effect of the geometrical configuration parameters of bending magnet on the focusing of the passing charged particles beam. This investigation is implemented via the method of the matrix's representation. The results showed that the edges of the bending magnet have opposite focus in the horizontal and vertical planes of beam motion. The deflecting angle effect appeared as a rotation of the phase space ellipse of the charged particle beam without focusing of this beam. The results also, showed that the focus of the charged particles beam is unlike in both horizontal and vertical planes of beam motion.

Keywords: beam transport systems, bending magnet, phase space ellipse.

1. Introduction

Beam transport system usually contains of focusing, deflection, acceleration and sometimes additional energy or momentum selection elements. Often these devices are magnetic elements, although at low energy beam, electrostatic elements are used. Quadrupoles and bending magnets with free drift spaces are the main elements of any beam transport system. The dipole magnet produce bending and dispersion effect, while quadrupoles produce focusing effects, the drift spaces is regions where there is no force acting on the particle motion. The performance of beams can be studied in two aspects either by tracing a large number of individual particles (single particle dynamics) or by studying the transfer properties of bundle (the collective effects caused by the electric and magnetic fields generated by the beam itself), in the present study the charged-particles treated as a bundle of particles, linear phase space [1].

Importance of studying the beam transport systems lies in determining the role of each element of the system in the focusing, accelerating and transporting beam particles from the source to the target with more control on particles beam properties.

Any charged particles beam can be represented in six-dimensional phase space (ellipsoid) that enclose all the particle in the beam, these particles expected to occupy the volume enclosed by the ellipsoid, and each point representing a possible ray. The total sum of all phase points, or the phase space volume, is generally referred to as the phase space occupied by the beam [2].

The projection of the ellipsoid in two dimensions is named phase ellipse, this phase space ellipse shape and orientation change as the beam moves along the beam line.

2. Bending Magnet

The main function of bending magnet, mostly named as mass analyzer, is bend the path of the particle on a curve with radius (R) which leads to clearing the natural particles from charged particles beam, then, focusing these particles into the central orbit of the magnet. In such this analyzer the ions are accelerated as focused beam with same kinetic energy. And then the ions are deflected according to their masses, the magnetic field bend the lighter ions more than the heavier ones which leads to separate different ions. In this study a C- shape magnet was used to transport ions generated by plasma source. Figure 1 illustrates the longitudinal section for the design of the magnet used in present study.

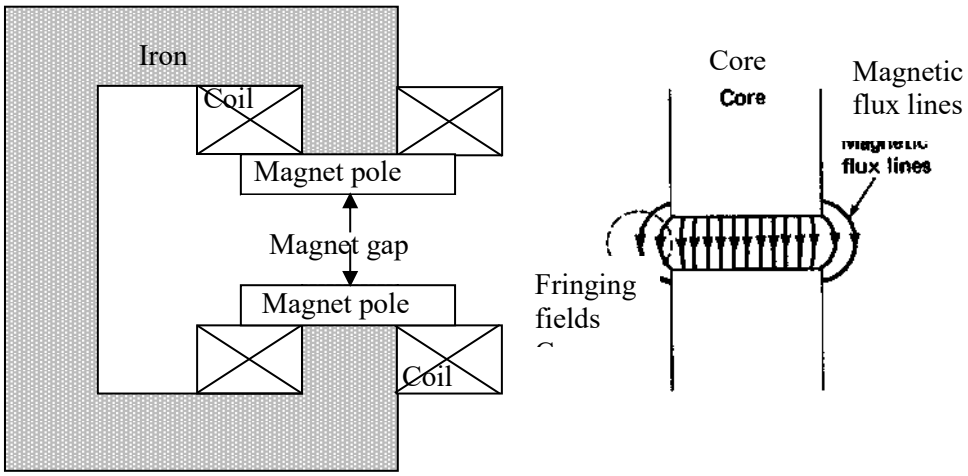

Figure 1. Longitudinal section of bending magnet.

The bending magnet consist basically of two regions, the good field region in which the magnetic field stay particularly constant and the other region is the fringing field which the magnetic field decreases to approach zero in a transition region far from the edges of the magnet, extending from each side of the terminal cross section for a distance depends on the order of the width of the gap between the poles [3].

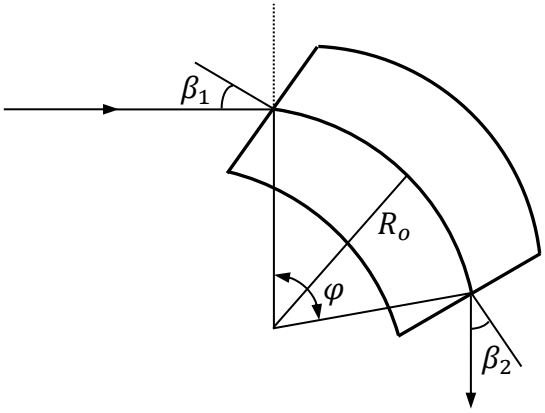

Figure 2. Main parameters of bending magnet.

From configuration of bending magnet there are three angles play important role in the focusing of the charged particles beam passing through the magnet. Deflecting angle (φ), as indicates in Figure 2,

which is defined as the angle between the line connecting the center of particle orbit and points of entrance and exit of central trajectory [4] this angle cause a rotation of the beam, this angle in some magnets with range of (45°-90°) [5, 6], while in others (135°) or (270°) [4,7].

The entrance angle (β_1), as shows in Figure 2, is defined as the angle between the normal to magnet pole boundary and the beam center line in entrance space, and the exit angle (β_2) is the angle between the normal and the beam line on the exit side.

The edge of deflecting magnet poles acts as focusing regions that are resulted by a non-homogenous magnetic field. These regions are called a fringing field. So at the entrance and exit angle are very important parameters for the focusing beam passing through the deflecting magnet.

The motion of beam through each region in beam transport line can be describe in term of R-matrix, the total R-matrix of the magnet region is:

$R_{x,y}\ (\text{total}) = R_{x,y}(\text{exit edge}).R_{x,y}(\text{inside the magnet}).R_{x,y}(\text{entrance edge})$

In other form [8,9]

$$R_{x,y} = \begin{bmatrix} 1 & 0 \\ \pm\frac{\tan(\beta_1-\psi)}{R_o} & 1 \end{bmatrix} \begin{bmatrix} \cos k_{x,y}l & \frac{1}{k_{x,y}}\sin k_{x,y}l \\ -k_{x,y}\sin k_{x,y}l & \cos k_{x,y}l \end{bmatrix} \begin{bmatrix} 1 & 0 \\ \mp\frac{\tan(\beta_2-\psi)}{R_o} & 1 \end{bmatrix} \quad (1)$$

where ψ is angle of fringing field related to nature of bending magnet manufacturing, $k_{x,y}$ is the wavenumber for the horizontal and vertical oscillations respectively, related to field index (n) which take value $0 < n < 1$ and l is the path length inside the bending magnet.

$$k_x = \frac{(1-n)^{1/2}}{R_o}, k_y = \frac{(n)^{1/2}}{R_o} \quad (2)$$

$0 < n < 1$

$$l = \varphi R_o \quad (3)$$

The sign $(+)$ for horizontal plane and $(-)$ for vertical plane

The linear phase space matrix (σ) is

$$\sigma = \begin{bmatrix} \sigma_{11} & \sigma_{12} \\ \sigma_{12} & \sigma_{22} \end{bmatrix} \quad (4)$$

The relation between σ-matrices in two positions of the beam line (between $\sigma_{x,y}(\text{in})$ and $\sigma_{x,y}(\text{out})$), is giving by the following inverting equation

$$\sigma_{x,y}(\text{out}) = R_{x,y}\sigma_{x,y}(\text{in})R^T_{x,y} \quad (5)$$

For phase space ellipse:

$x_{max} = \sqrt{\sigma_{11}}$ the maximum spatial extent of ellipse which is called by beam envelope.

$x'_{max} = \sqrt{\sigma_{22}}$ the maximum angular divergence of the beam within the phase ellipse.

3. Results and Discussion

Present design of beam transport system was include the regions; extraction region (plasma source), first drift space region, bending magnet, and then second drift space region. The angles of bending magnet were changed as, the deflecting angle (φ) values in the range (30°-90°) while the entrance and exit angles (β_1) was take values in the range (5°-20°).

The effect of deflection angle (φ) on the phase space ellipse of charged particles beam, at constant values of entrance and exit angles of bending magnet , shows in figures (3 and 4), which indicates that the increasing of (φ) leads to more rotation for the charged particles beam in both horizontal and vertical planes. Also, the slope of phase space ellipse became negative beyond ($\varphi = 60^o$), which means converge (focusing) of charged particles beam. One could be note that the area of the phase space ellipse remained constant for all values of (φ).

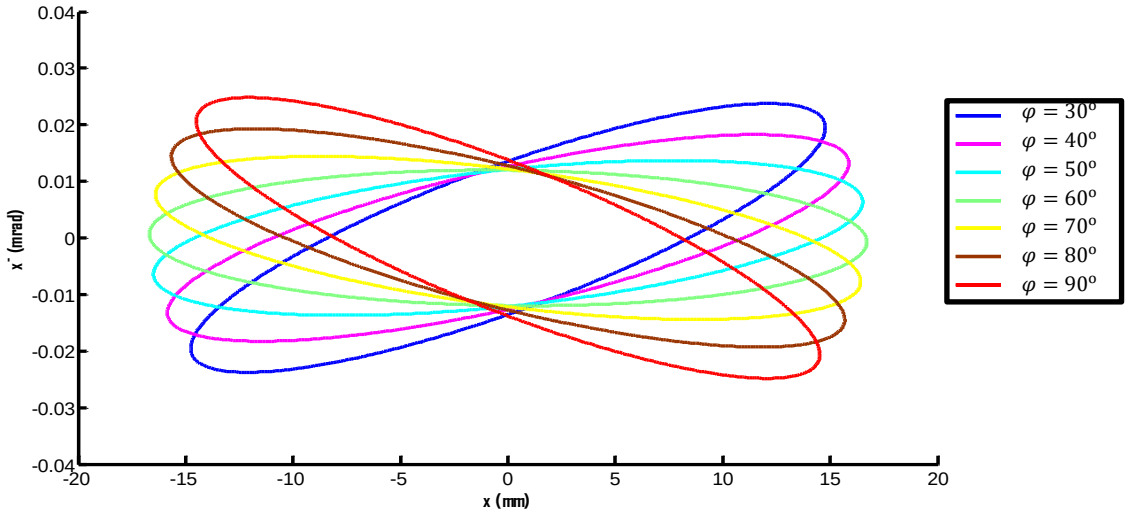

Figure 3. Phase space ellipse of horizontal plane for different deflecting angles.

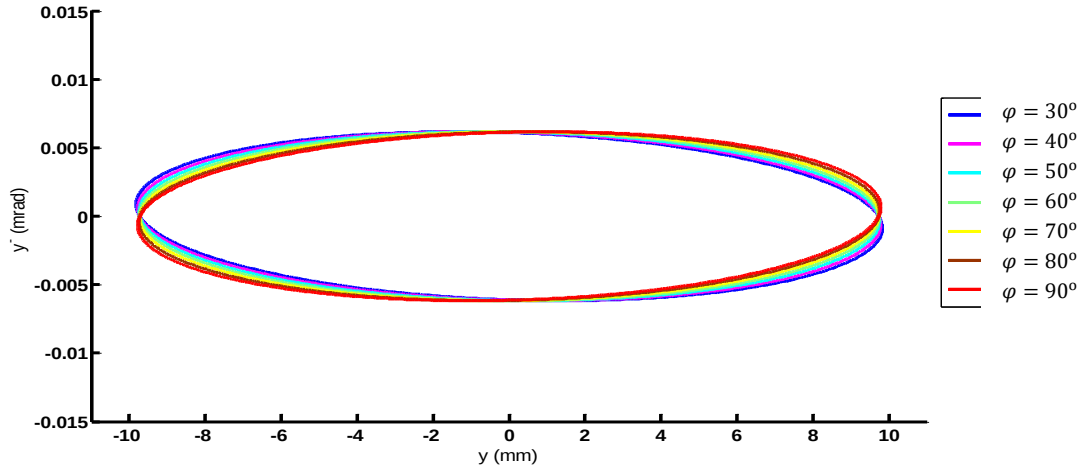

Figure 4. Phase space ellipse of vertical plane for different deflecting angles.

The effect of entrance edge angle (β_1) on the phase space ellipse of charged particles beam for horizontal and vertical planes shows in Figures 5 and 6, at constant values of deflection and exit angles of bending magnet, which indicates that the entrance edge angle (β_1) of the bending magnet acted as a thin lens, as the distance does not increase through it, but changes the focus of the charged particles beam and that increasing the entrance edge angle increases the focus of the charged particle beam. The entrance edge angle (β_1) acts as adiverge thin lens in the horizontal plane, while in the vertical plane acts as a converging thin lens. Also, the area of the phase space ellipse remained constant for all values of (β_1).

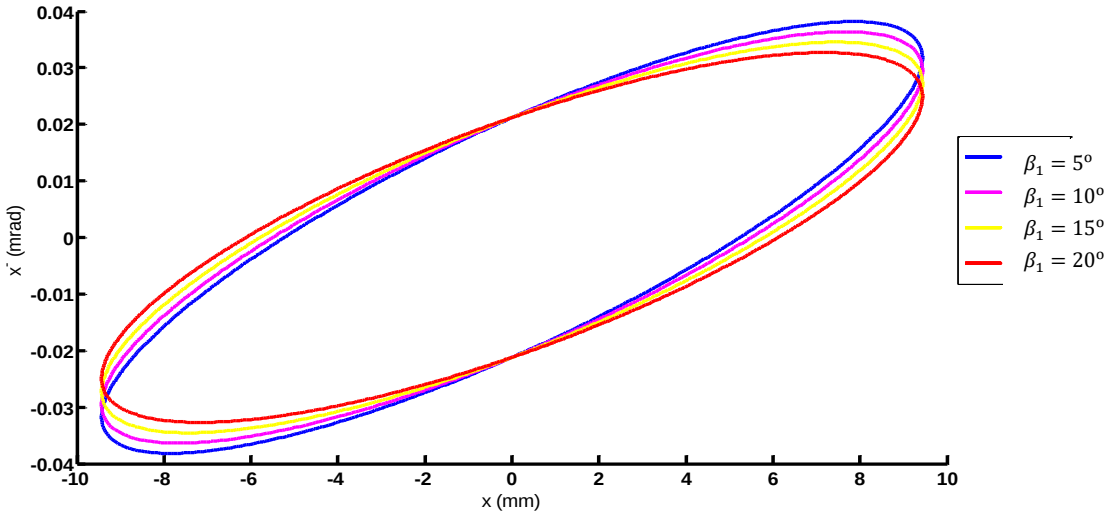

Figure 5. Phase space ellipse of horizontal plane for different entrance angles.

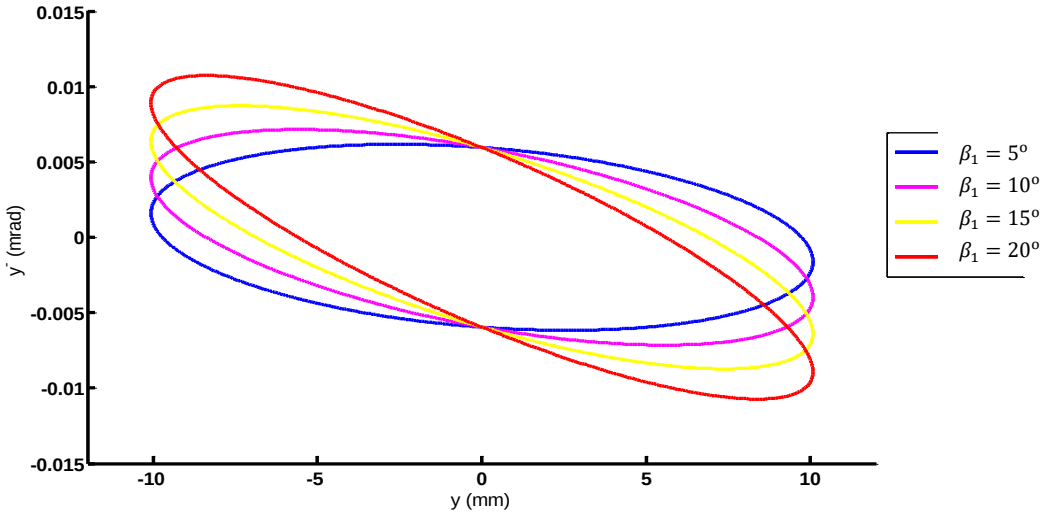

Figure 6. Phase space ellipse of vertical plane for different entrance angles.

As entrance angle, the effect of exit edge angle (β_2) on the phase space ellipse of charged particles beam for horizontal and vertical planes shows in Figures 7 and 8, at constant values of entrance and deflection angles of the bending magnet, indicates that the entrance edge angle (β_2) of the bending magnet acts as a converging thin lens in both horizontal and vertical planes. The increasing of (β_2) cause an increase in the converging of charged particle beam

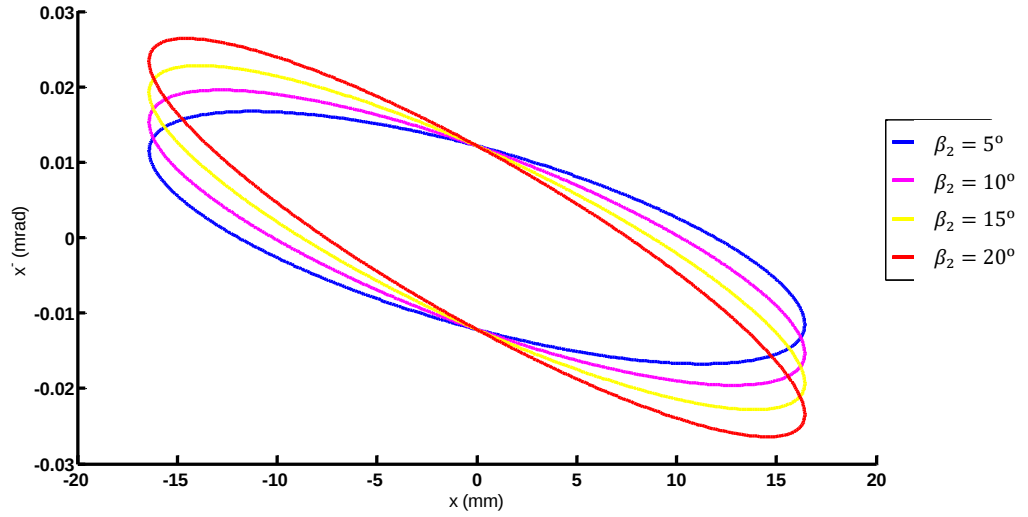

Figure 7. Phase space ellipse of horizontal plane for different exit angles.

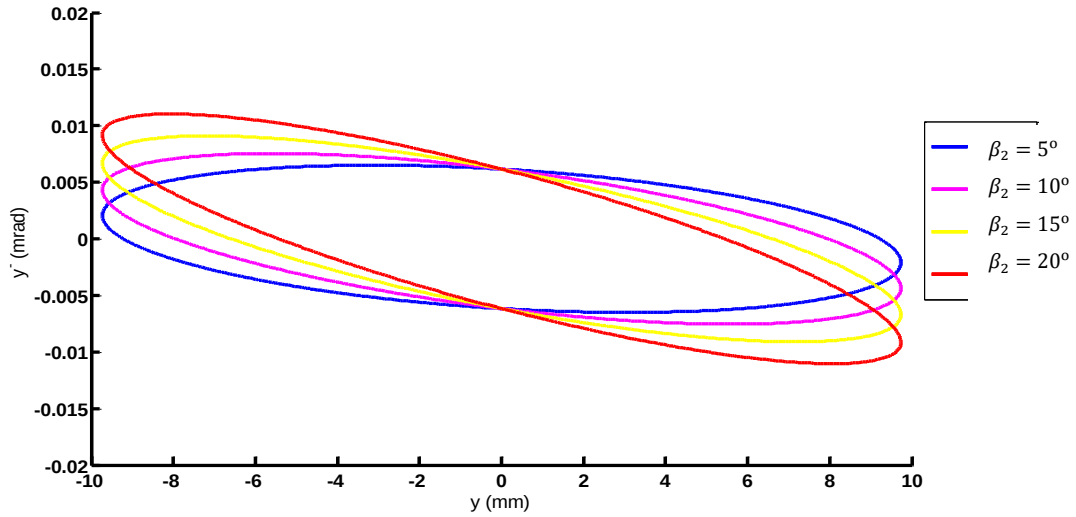

Figure 8. Phase space ellipse of vertical plane for different exit angles.

It is useful to study the envelope of charged particles beam passing through the transport system by plotting the maximum displacement of particles at every region along transport system. Beam envelop is indicate the focusing regions along the beam path.

From the results of phase space ellipse for horizontal and vertical planes, for different configurations for transport system, shown in Figures (3-8), the best configuration of bending magnet that gives best focusing for beam transport passing through it, found to be $\beta_1 = \beta_2 = 20^o$ and $\varphi = 90^o$.

Figures 9 and 10 show the beam envelope along beam transport system best configuration that obtained in present work for horizontal and vertical planes. These figure show that the best values of

β_1, β_2 and φ gives minimum values of distance (focusing) in both horizontal and vertical planes at same time.

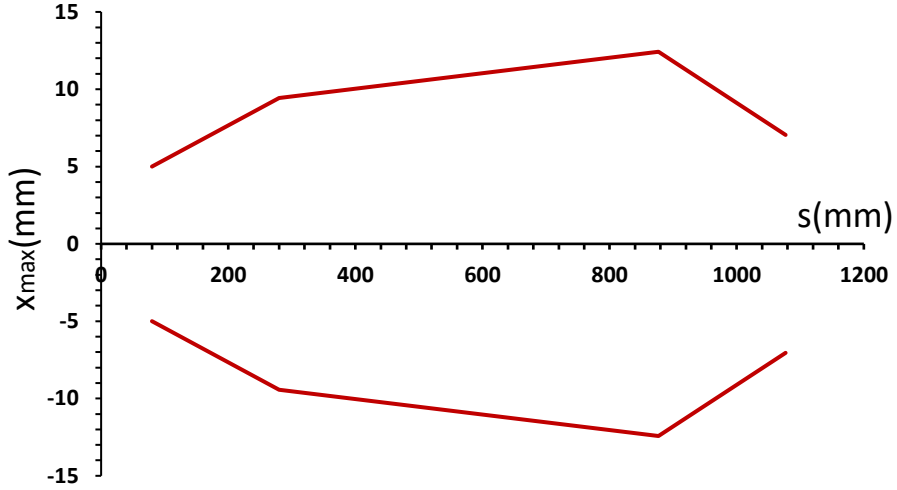

Figure 9. Beam profile in horizontal plane at $\beta_1 = \beta_2 = 20^o$ and $\varphi = 90^o$

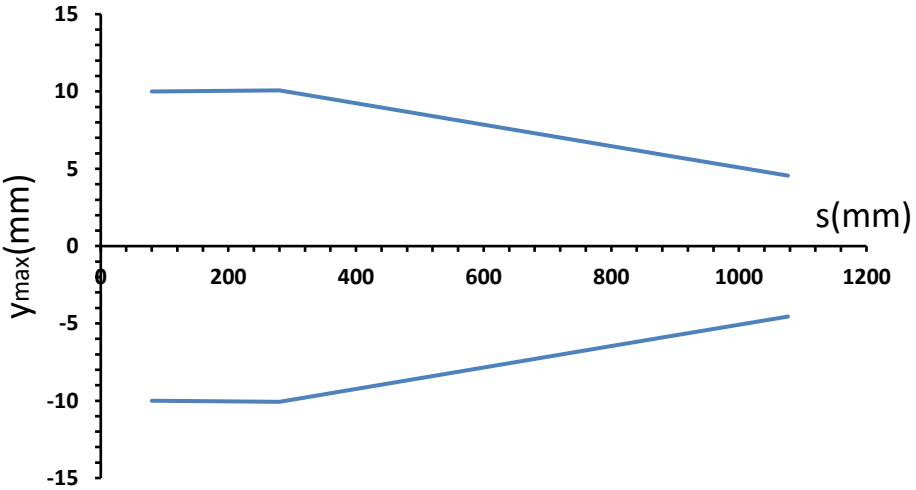

Figure 10. Beam profile in vertical plane $\beta_1 = \beta_2 = 20^o$ and $\varphi = 90^o$.

4. Conclusions

Focusing of the charged particles beam vary with bending magnet geometrical parameters. The edges of bending magnet act as thin lens with opposite focusing in horizontal and vertical planes of beam motion. The deflecting angle of the bending magnet leads to clear rotation for charged particles beam without focusing of charged particles beam. The focusing of the charged particles beam is unlike in both horizontal and vertical planes of beam motion. Best focusing of beam obtained at $\beta_1 = \beta_2 = 20^o$ and $\varphi = 90^o$.

References

[1] Saminathan S., "Extraction and Transport of Ion Beams from an ECR Ion Source 2011 University of Groningen
[2] Yao-shuo Yuan, "Space-Charge Driven 2018 Transverse Beam Instabilities in Synchrotrons", PhD Thesis, Technical University of Darmstadt, Germany
[3] Hashim I. H., 2004 A Study of the Main Parameters Effects in Designing the Medium Range Ion Implanter", PhD Thesis, Mustansiriyah University
[4] Enge H. A., 1967 Deflecting Magnets" in "Focusing of Charged-Particle ", edited by: A. Septier. Vol.2, Academic Press INC.
[5] Keller J. H. and Hicks W.W., 1979 *J. Vac. Sci.Technol.* **16**(6) 1979
[6] Krishnarjulu B., Muralidhar G. K., Mohan S., and Menon A. G., 1989 *J. Phys. E. Sci Instr.***22** 1989
[7] Intesar H. Hashim and Sarmad H. Saleh, " Focusing of charged particle beam passing through a system of two identical magnet", University of Al-Mustansiriyah, 2012.
[8] Vitali Khachatryan, "Accelerator Magnets and Magnetic Field Measurement", Synchrotron Research Institute, Yerevan, Armenia, 2019.
[9] George H. Gillespie 2008 "Overview of Particle Beam Optics Utilized in the Matrix", Envelope, and Tracking Codes: transport, trace 3-d, and turtle, Sandia National Laboratory (SNL)

Synthesis and Characterization of PEGylated Graphene Oxide

Synthesis and Characterization of PEGylated Graphene Oxide

Mustafa A. Jihad[1*] and Farah T. M. Noori [2]

[1,2] Department of physics, college of science, university of Baghdad, Iraq

E-mail: Mscmp101@gmail.com

Abstract. In this work, Graphene oxide (GO) was synthesized by Hummer's method using graphite rod. Used organic chemical materials to active (GO – COOH) for esterification reaction between the graphene oxide carboxylic acid group and the Polyethylene glycol (PEG) hydroxyl group. Graphene oxide (GO) was conjugated to PEG4000 (medical polymer).The composite (GO – PEG) characterization by XRD, FTIR, UV- Vis and AFM. In UV- Vis GO showed a sharp peak at 275 nm whiles the peak of (GO – PEG) appear at 284 nm. A strong OH bond appear in Fourier transforms infrared spectroscopy (FTIR) spectra, C –H bond of (GO – PEG) also showed. In XRD pattern GO have a sharp peak appear at $2\theta = 11.83^{\circ}$ that related to 001 with d-spacing of 7.76 Å while functionalization of GO – PEG 4000 conform by broad peak at $2\theta = 23.38^{\circ}$ with d-spacing of 3.8 Å. Atomic force microscopy (AFM) images, GO image shows Graphene oxide sheet with main grain size is 24.41 nm, In GO – PEG4000 shows aggregation of Graphene oxides with PEG4000 the main grain size increase with functionalize to 287.04 nm.

Keyword. PEGyltion, Graphene oxide, Hummer's method, PEG 4000.

1. Introduction

The Graphene oxide (GO) layer has been considered one of the most promising carbon derivatives in material science over the past few years and has demonstrated excellent physical properties, biocompatibility and chemical stability [1]. Since Graphene, a two-dimensional (2D) mono- atomically thick planar layer, was first reported in 2004 [2]. In recent years, a variety of research groups have documented biomedical and physical applications of Graphene, such as drug loading and delivery [3].This drugs used instead chemotherapy as anti-cancer drugs [4]. GO comprises a number of hydrophilic oxygen-containing functions, such as epoxy, hydroxyl and carboxyl groups, which have improved dispersibility in solvents as well as provide reactive sites for more functionalization by specific interactions [5]. Therefor, this led to evolution of smart Nano carrier – based drug delivery system which also known as SDDSs. This system promises to apply drugs to unique and targeting cancer types [6]. The reaction between the medical polymer and Nanoparticles was controlled using a polymerization method and this was first mentioned by Speiser et al. [7]. Among this nanoparticles (GO), has many functional groups on its composition, allowing Graphene to be stable suspension in water and bound to other drugs and polymers [8]. Polyethylene glycol is the most stabilizing agents and most studies one, The immune system's effect of phagocytosis on Graphene oxide can be prevented by using PEG which is due to decrease uptake by reticuloendothelial system (ERS) (which is the part of immune system that consist of the phagocytic cells) and because its high aqueous solubility it used widely in SDDSs [9]. In

this work Graphene oxides GO was synthesis by Hummer's method and then PEG was conjugated to the GO to produce strong ester interaction between PEG and GO which is called PEGylated Graphene oxide (GO-PEG) and characterization it with different techniques.

2. Experimental section

2.1. Chemical material

99.995%, Natural graphite rod, $KMnO_2$99%, $NaNO_3$ 99.5%, H_2O_2, 32%,HCl 37.5%, EDC hydrochloride C6H17N3–HCl, N– Hydroxysuccinimide (98%) from (Sigma-Aldrich), (H_2SO_4, 98%) from (LOBA Chemie), NaOH (99%) from Dae-Jung, PEG 4000 from HI Media, Diethylether $(C_2H_5)_2O$ (98%) from Thomas Baker.

2.2. Synthesis of graphene oxide (GO)

The most economical way used to synthesis graphene oxide is Hummer's method. In which 1g of graphite rod milling into form powder and added with sodium nitrate in sulfuric acid were mix in an ice bath for 45 min. After that 3g of $KMnO_2$ added gradually at temperature 35 C°. The thick blend stirred for 1 day. $KMnO_2$ is reduced by adding (H_2O_2, 32%). 5 ml of (HCl, 37.5%) and DI water used to wash the thick blend. The resultant was dried at 75 C° for 5h to get the graphene oxide.

2.3. Preparations of PEG 4000 - functionalized GO

The activation of (GO – COOH) was began by esterification reaction between the Graphene oxide carboxylic acid group and the PEG hydroxyl group which is necessary for PEGylation of GO thus; 120 mg/ml of NaOH was solved in 20 ml in DI and added to 20 ml of GO suspension 2mg/ml, the suspension sonication for 1h and stirred for 3h. The pH of suspension was reduced by added 3ml of HCl then it was centrifuged twice 4000 rpm for 30 min to produced (GO – COOH) (GO carboxylic acid). The residue was wash with water twice.

The (GO – COOH) was diluted by 10 ml water to active (GO – COOH) 400 mg of EDC and 240 mg of NHS was added to (GO – COOH) then For (GO – PEG) 1500 mg of PEG4000 was added to the resultant and stirred for 24h.

Final step, the resultant was centrifuged and washed by DI water. UV-Vis and FTIR used to Characterization the resultant to identify whatever the carboxylation and PEGylation were conjugated.

3. Result and dissection

PEGylation (GO – PEG) was Characterization by UV – Vis spectroscopy, Fourier transforms infrared spectroscopy (FTIR), X-Ray diffraction (XRD), and atomic force microscopy (AFM). Figure1. Illustrates a simple schematic of synthesis of graphene oxide from graphite and the GO- PEG bonding and structure.

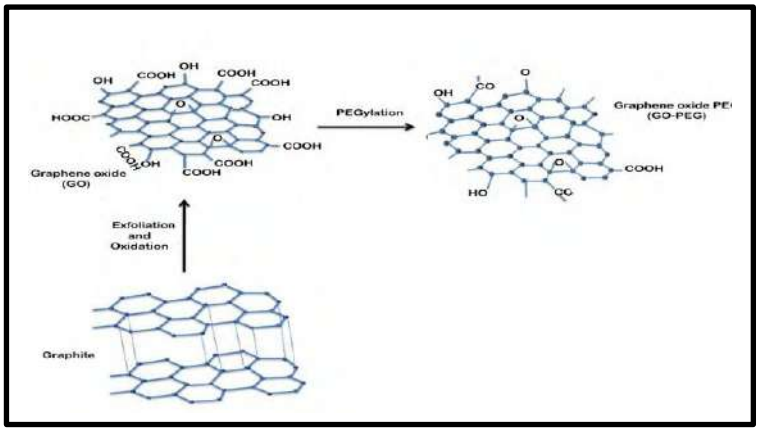

Figure1. Structure of GO- PEG.

3.1. UV – Vis analysis

Figure 2. Showed the spectra of GO and (GO – PEG), the blue line indicate the GO spectra at 275 nm which represent the absorptions bands that related to electronic transition π – π* for C-C (aromatic rings) and transition n – π* for C=O in the Graphene oxide. The red line represent the (GO – PEG) that shifted to 284 nm which confirms the synthesis of (GO – PEG) [10, 11].

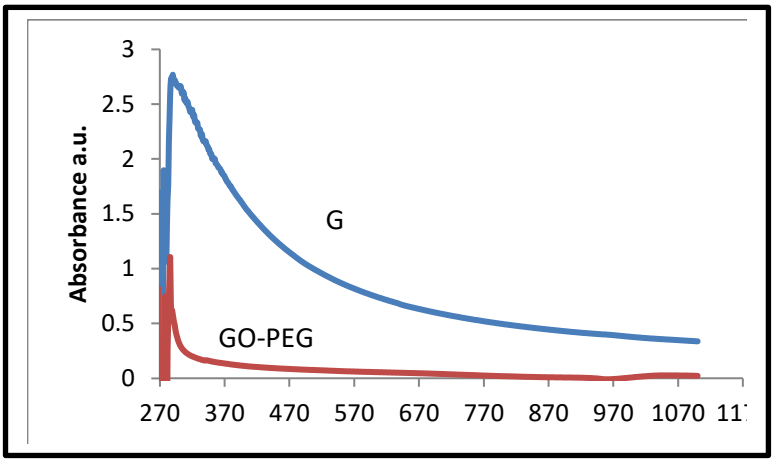

Figure 2. UV-Vis spectrum for GO and GO-PEG.

3.2. FTIR analysis

Figure 3 displays FTIR spectra of GO and (GO – PEG). In the figure, blue line represent the GO sample, and the peaks at 3338 is stretching related to OH, while1618, 1382 and 1026 cm^{-1} are C=O groups in carbonyl and carboxyl [12]. Peak at 1724 cm^{-1} is related to C=C and peaks at 1066 and 1382 related to C-O [13]. While in case of (GO – PEG) the peak at 3338 cm^{-1} shifted to 3427 cm^{-1} also appearance of C-H at 3920 cm^{-1} which proved that GO conjunction to PEG, also the appearance of C=C, C-O and C=O at 1641, 1390,1107 cm^{-1} was also identified [14].

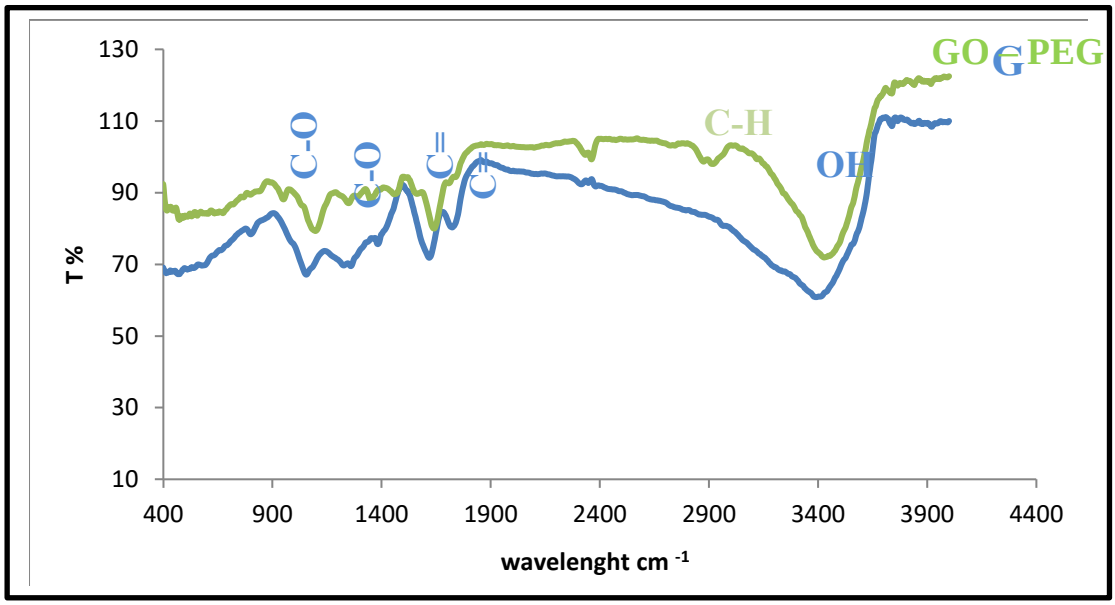

Figure3. The FTIR spectrum of GO and GO- PEG.

3.3. XRD DIFFERACTION

Blue line in Figure 4 represents the XRD pattern of GO which a sharp peak appear at 2θ = 11.83° that related to 001 with d – spacing (7.76 Å) and conform the hexagonal structure of graphene oxide while the red line indicted to functionalization of GO – PEG 4000 with broad peak at 2θ= 23.38° with d – spacing (3.8 Å) which is results from functionalized while the peak of GO disappear because GO has an effect on the structure of the PEG molecular chain in the crystal lattice , disturbing the order of its crystallization. This decreases the crystallinity of PEG and result in an effective conjugation of PEG to GO Nano-sheets by ester bonding. [14].The orientation (001) determine by high score plus program.

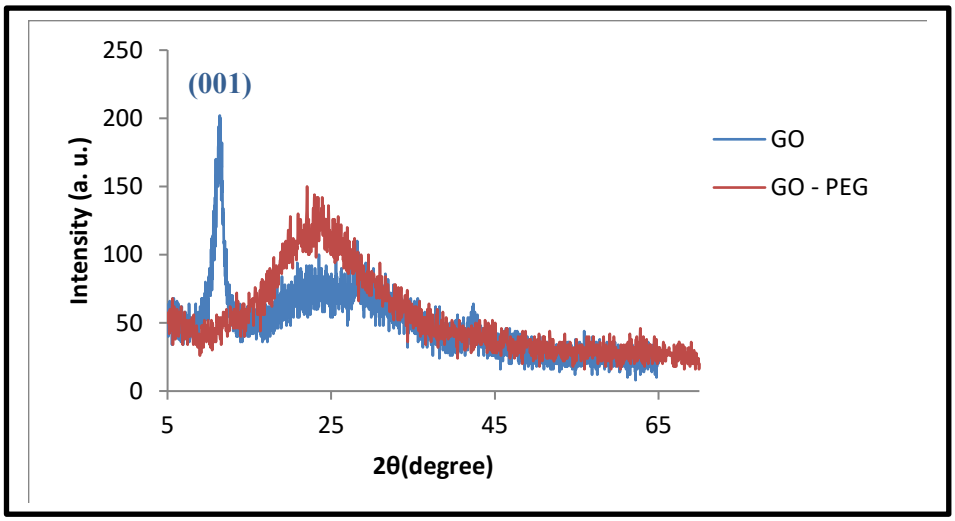

Figure 4. The XRD pattern for GO and GO – PEG4000.

3.4. AFM analysis

Images in Figure 5 Show the AFM analysis of GO and GO – PEG4000 in GO image shows graphene sheet with main grain size is 24.41 nm which conform the Nano size of synthesis. In GO – PEG4000 shows aggregation of graphene oxide with PEG4000 the main grain size increase with functionalize to 287.04 nm [15].

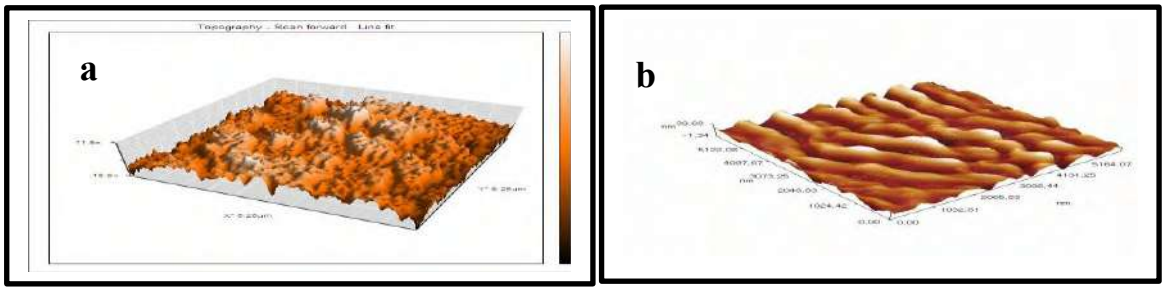

Figure 5. Surface images by AFM for a) GO and b) GO – PEG4000.

4. Conclusion

Graphene oxide Nano - particles successfully synthesized with mean grain size 24.41 as sheet form which analyzed by AFM. GO shows high absorbance in UV region with stretching related to OH at FTIR spectrum. PEG4000 conjugated with GO which is seen in C-H at 3920 cm-1 at FTIR spectrum

with broad peak in XRD diffraction. The last form of conjugated GO – PEG4000 shown in AFM image as aggregation viscous.

References

[1] Hongyang Xu et al. 2015 *Nano-medicine* **10** 8
[2] Wang Y, Li ZH, Wang J, Li JH, Lin YH 2013 *Cell* **29** 205
[3] DeVita VT, Chu E. 2008 *Cancer Res.* **68** 53
[4] Gergely Szakács et al. 2006 *Nature* **5** 219
[5] Horrick Sharma and Somrita Mondal 2020 *Int J Mol Sci.* **21** 6280
[6] Y Xu, C Zhan, L Fan, L Wang, H Zheng 2007 *Int. J. Pharm.* **336** 329
[7] S.S. Banerjee, N. Ather, R. Patil, J. Khandare 2012 *J. Drug Deliv.* **3** 5
[8] Pasut G, Veronese FM 2009 *Adv. Drug Deliv. Rev.* **61** 1177
[9] Q. Lai, S. Zhu, X. M. Zou, S. Huang 2012 *AIP Adv.* **2**
[10] R.A. da Silva – Buzanello et al. 2015 food Chem. **172** 99
[11] Badrzadeh F, Akbarzadeh A, Zarghami N. 2014 *Asian Pac J cancer Prev.* **15** 8931
[12] N. Kumar, S. Das and Bernhard, G. Varna 2012 *supercond. Sci. Technol.* **26**
[13] Wang C, Feng L, Yang H, e al. 2012 *Phys. Chem.* 201 13233
[14] M- L. Chen, L- M. Shen, S. Chen, H. Wang, X – W. Chen, J – H. Wang 2013 *J. Mater. Chem.* **20** 2582

Evaluation of the radiological hazard in some dried fruit and grain samples in Iraqi Markets by Using of gamma ray Spectroscopy

Evaluation of the radiological hazard in some dried fruit and grain samples in Iraqi Markets by Using of gamma ray Spectroscopy

Athraa Naji Jameel

Physics Department, College of Education, Mustansiriyah University, Baghdad, Iraq

E-mail: athraanaje@yahoo.com

Abstract. The activity concentrations of ^{226}Ra, ^{232}Th and ^{40}K have been measured by using of gamma spectroscopy for fifteen samples fall under the consumed food group (six type of dried fruit and nine types of grain) at local markets in Baghdad. The average of activity concentration values of ^{40}K, ^{232}Th and ^{238}U were 324.4±28.5 Bq/Kg, 3.66±0.20 Bq/kg and 3.44±0.58 Bq/kg, for the dried fruit samples, 302.3± 98.9, 4.8±1.5 and 4.29 ±1.4 Bq/kg, respectively. For the grain samples, radiation hazard indices, the annual effective dose, internal and external risk, lifetime cancer, and the doses of ingestion, were all doses values within the international borders allowed. Thus, Food the dried fruit and grain in Baghdad is safe for human consumption and it has no heath effect.

Keywords: Radioactivity, Dry fruit, Excess Life Time Cancer Risk, ingested effective dose.

1. Introduction

Natural happening radioactive matter (NORM) is found in soil. NORM may be moved from soil to plants. Thus, every type of meals may also have a few quantity of radioactivity in it. Most types of food have the following isotopes and their daughter products, ^{238}U, ^{232}Th and ^{40}K [1]. The primary pathways for the transfer of radionuclide's to humans are meals crops. Natural radionuclides are transmitted and cycled by natural processes and the various extreme environmental booths by entering into ecosystems and human meals chain [2]. Radiation doses acquired due to the intake of meals may be calculated from the quantity of radionuclide deposited on foodstuffs, the activity concentration of particular radionuclide in meals according to unit deposition, the intake rate of the meals merchandise and the dose according to unit activity ingested [3, 4]. Most people around the world rely on grains, legumes and foods from cereals in their diet. The normal amounts of radioactivity in our daily food are important to estimate. However, a study of the concentration of natural radioactivity in foodstuffs was conducted in different countries [5, 6]. There are many Global research interested by popularity of radioactive pollutants in exported and imported meals and The appearance of match potassium ^{40}K in all meal samples and the intake of match potassium ^{40}K in exported and imported meals over those years did not target any radiation dose above the global recommended limit [7-9].

In addition, plant absorption varies from species to species; thus the consumption of different meal items is a secondary supply of variability [10, 11]. Therefore, the objective of the present study is to

evaluate the activity concentrations of ^{40}K, ^{238}U and ^{232}Th in different foodstuffs in the region and to estimate the effective dose of ingestion for individuals consuming local foodstuffs in the area.

2. Materials and methods

2.1. Preparation of Samples

Six samples of the different dried fruit and nine samples of the grain were collected from the Iraqi markets. Samples have been placed in an oven for dried it and crushed to attain a homogeneous powder, The homogenized samples were packed into Marinelli Becker and sealed for 30 days to achieve a secular equilibrium, Table 1 Shows the name, code and the country for the dried fruit and grain samples.

2.2. Measurement of samples

^{238}U, ^{232}Th, and ^{40}K analysis in dried fruit and grain samples using a 100 percent relative efficiency crystal dimension NaI (Tl) detector of 3×3. Manufactured by Ortic in the U.S.A., the module has 4096 channels and a working voltage of 695V. Samples are measured for 24 hours (86400 s). Made in the United States of America (U.S.A.). Three standard sources (^{60}Co, ^{133}Ba, and ^{137}Cs) were chosen from the samples. These isotopes were placed at a distance of 4cm from the top of the detector inside the shielding. The spectrum of standard elements used to calibrate the NaI(Tl) system as shown in Figure 1 and the efficiency curve between the energy and efficiency of all energy from standard sources as shown in Figure 2 are shown.

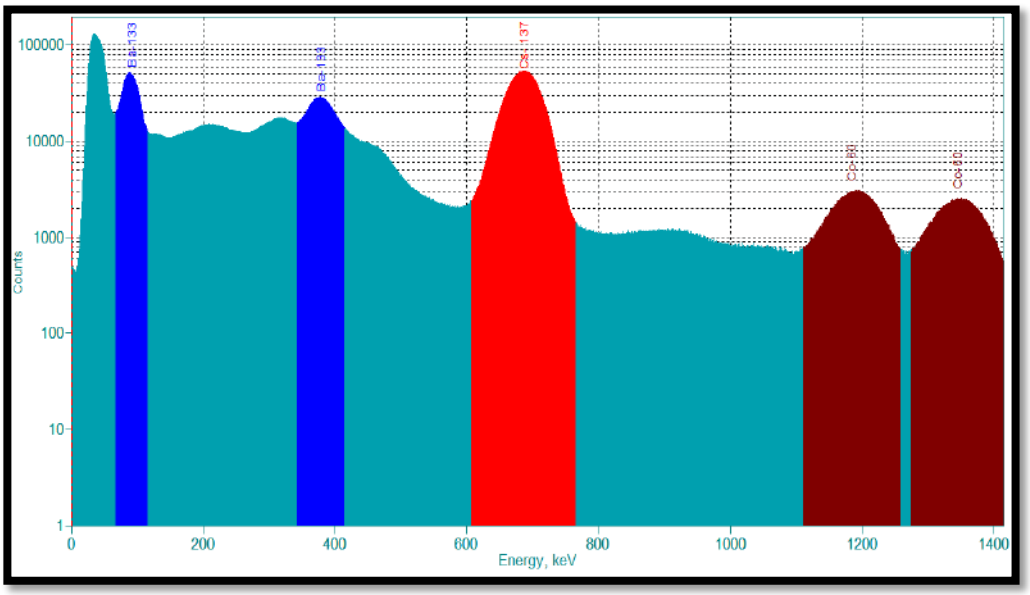

Figure1. A spectrum of standard elements use to calibrate NaI(Tl) system

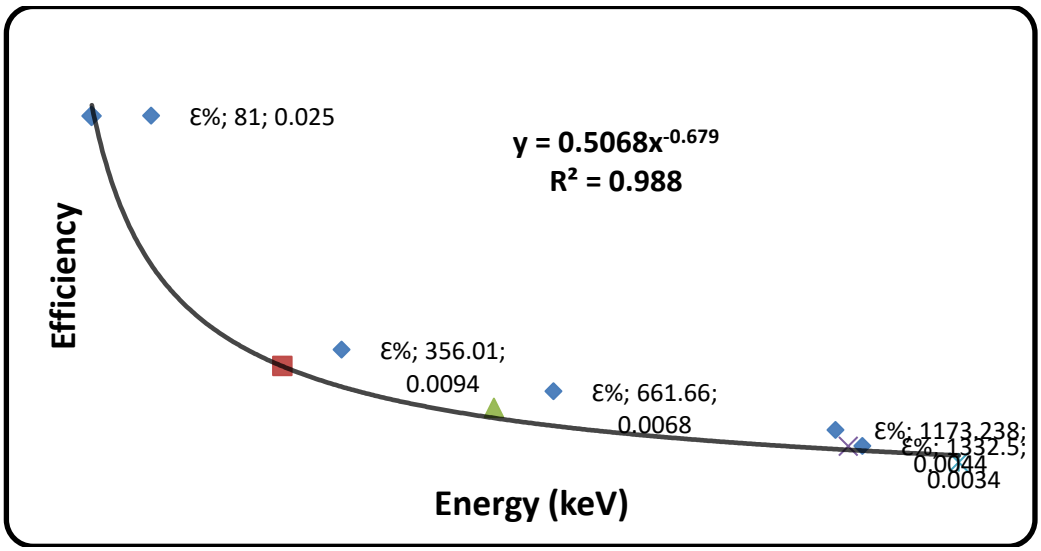

Figure.2. Efficiency calibration curve.

Table 1. Information about the dried fruit and grain.

No.	sample		Code	Sample of country
1	dried fruit	Figs	D1	Turkey
2			D2	Iraq
3		Apricot	D3	Iraq
4		Raisin	D4	
5		Dried coconut	D5	Iran
6		Dates	D6	Iraq
7	Grain	Popcorn	G7	Iraq
8		Barley	G8	
9			G9	Turkey
10		Bulgur	G10	Iraq
11		(crushed wheat)	G11	Egypt
12		Rice	G12	Iraq
13		Millet	G13	Iraq
14			G14	Turkey
15		Oats	G15	Iraq

2.3. Parameters calculation

Specific Activity

It was calculated for the radionuclides ^{226}Ra,^{232}Th and ^{40}K by the following relation [12];

$$A\ (t) = \frac{N}{\varepsilon \times I(E\gamma) \times m \times t} \times 100$$

Where N equals net area under peak, ε (E_γ) is the efficiency of energy E_γ detection. E_γ is the net peak area adjusted for the background at energy E_γ below the real peak. I(E_γ) is the abundance of E_γ energy. The sample mass in kg is m, andt the time in second.

Gamma absorbed dose rates

The calculation of the gamma absorbed dose rate by using the following equation [13, 14].

D_γ (nGy/h) = $0.462A_{Ra} + 0.621A_{Th} + 0.0417A_K$

Where the specific activities of ^{226}Ra, ^{232}Th, and ^{40}K are A_{Ra}, A_{Th} and A_K, respectively.

Annual effectiveDose equivalent

The annual effective dose equivalent (AEDE) from^{238}U (^{226}Ra), ^{232}Th, and ^{40}K is obtained by using the following equations [15]:

$AEDE_{out}(\mu sv/y) = D_{out} \times 8760 \times 0.7 \times 0.2 \times 10^{-3}$

$AEDE_{in}$ (µsv/y) $= D_{in} \times 8760 \times 0.7 \times 0.8 \times 10^{-3}$

Where, D is absorbed dose rate measured in nGy/h. The number of 0.2 refers to outdoor occupancy factor, 0.8 is indoor occupancy factor. The number of 0.7 Sv/Gy is conversion factor.

The Internal and External Hazard Index

The internal hazard index (H_{in}) and external hazard index (H_{ex}) due to the radiation released by the food samples is determined as follows[16, 17].

$$H_{ex} = \frac{A_{Ra}}{370} + \frac{A_{Th}}{259} + \frac{A_K}{4810}$$

$$H_{in} = \frac{A_{Ra}}{180} + \frac{A_{Th}}{259} + \frac{A_K}{4810}$$

Life-Time Cancer Risk

The excess lifetime cancer risk (ELCR) can be calculated fromthe following equation [18].

ELCR = AEDE× DL × RF

Where DL is duration of life (70 year) and RF is risk factor (0.05 Sv^{-1}).

Ingestion effective dose

The effective dose of ingestion due to the intake of ^{226}Ra, ^{232}Th and ^{40}K in food can be measured [19].

$E_{ing} = \Sigma (A_{ig} \times C_i) \times g_{T,r}$

where, A_{ig} and C_i the coefficients of the consumption rate and specific activity of the radionuclide, and $g_{T,r}$ is The radionuclide ingestion dose conversion coefficient, the required dose conversion coefficient $g_{T,r}$ for ^{40}K, ^{226}Ra(^{238}U), and ^{232}Th, are 6.2×10^{-9}, 2.8×10^{-7}, and 2.2×10^{-7} respectively [20].

3. Results and Discussion

The activity concentration was calculated in six samples of dried fruit and nine samples of grain of ^{238}U, ^{232}Th and ^{40}K as illustrated in Table 2. The average activity concentrations of^{40}K, ^{232}Th, and^{238}Uwere, 324.4±28.5 ,3.66±0.20, and 3.44±0.58Bq/Kg for dried fruit samples, 302.3±98.9, 4.8±1.5 and 4.29 ±1.4, Bq/kg for grain, respectively. The values were decrease than the world average values for ^{238}U, ^{232}Th, and ^{40}KUNSCEAR,2008 [21]. Turkey Figures and popcorn samples which have higher activity concentration, while the dried coconut and Iraq Millet samples have the lowest value. Figures 3 and 4 show the activity concentrations of ^{40}K, $^{238}U$and, ^{232}Th in samples of dried fruit and grain.

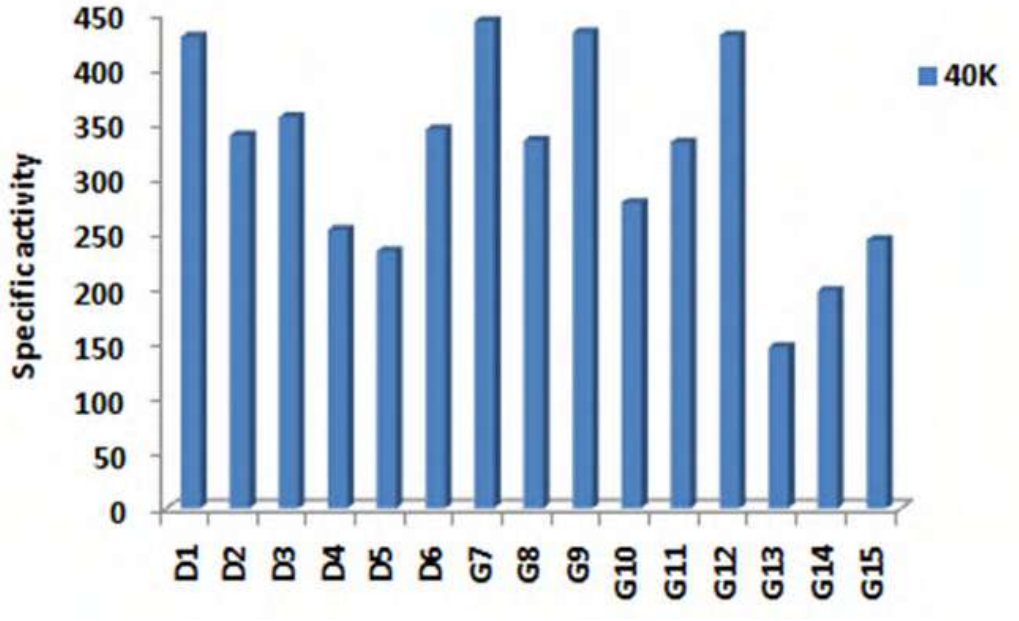

Figure3. The activity concentration of dried fruit and grain for 40K.

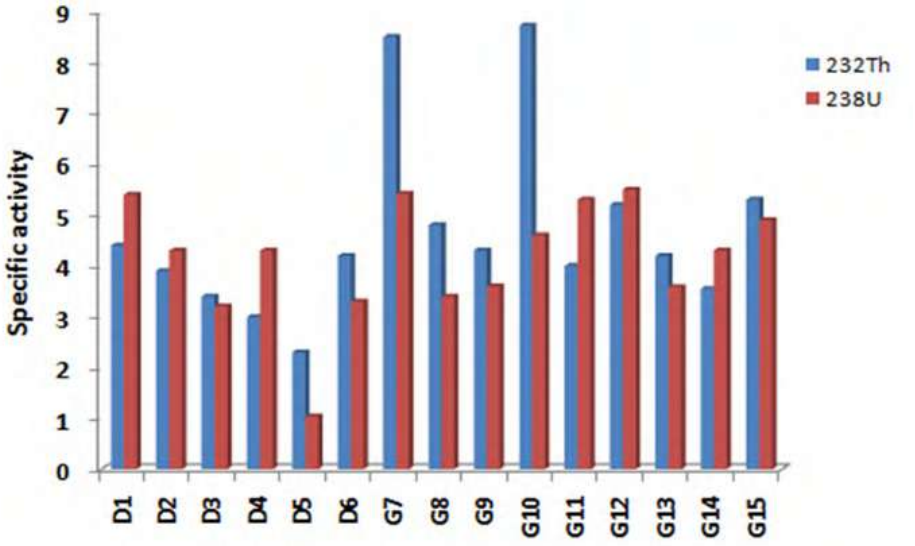

Fig.4. The activity concentration of samples for 238U and, 232Th.

Tables 3 show the results of radiation hazard index values outside and inside for the annual effective dose (ADED), outside and inside hazard (H_{ex},H_{in}), and lifetime cancer risk (ELCR). These values had been under the permissible limits (UNSCEAR, 2000)[22]. The radiation hazard index values inside the body were more than that outside the body due to the ingestion of nutrients and the rest of them within the body as shown as in Figure 3.

The highest life time cancer risk values in the figure and popcorn samples and the lowest value in dried coconut and millet samples as shown in Figure 5.

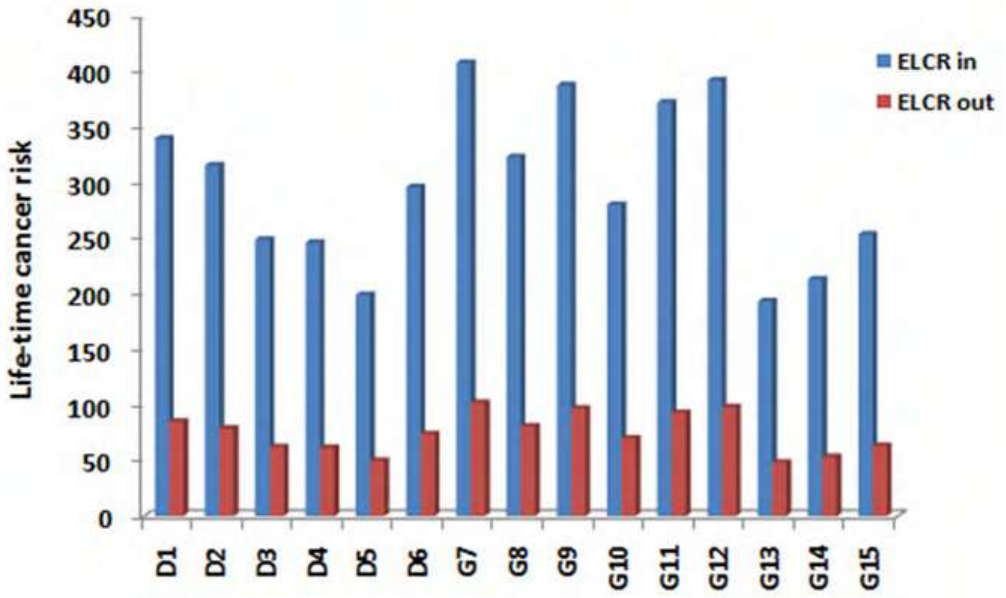

Figure 5. Life-time cancer risks of the samples.

For ^{238}U, ^{232}Th, and ^{40}K, the effective ingestion dose was lower than the acceptable dose ingestion effective dose values of 0.3 mSv/y recommended UNSCEAR, 2008 [21]. As shown in Table 4 and Figure 6, the effects of the effective dose ingestion in all samples are shown.

The average value of the dose ingested for ^{238}U, ^{232}Th and $^{40}K$was 0.009±0.001,0.010±0. 001and 0.02±0.01 for the dried fruit and 0.012±0.004,0.014±0.004 and 0. 023±0. 007 for grain.

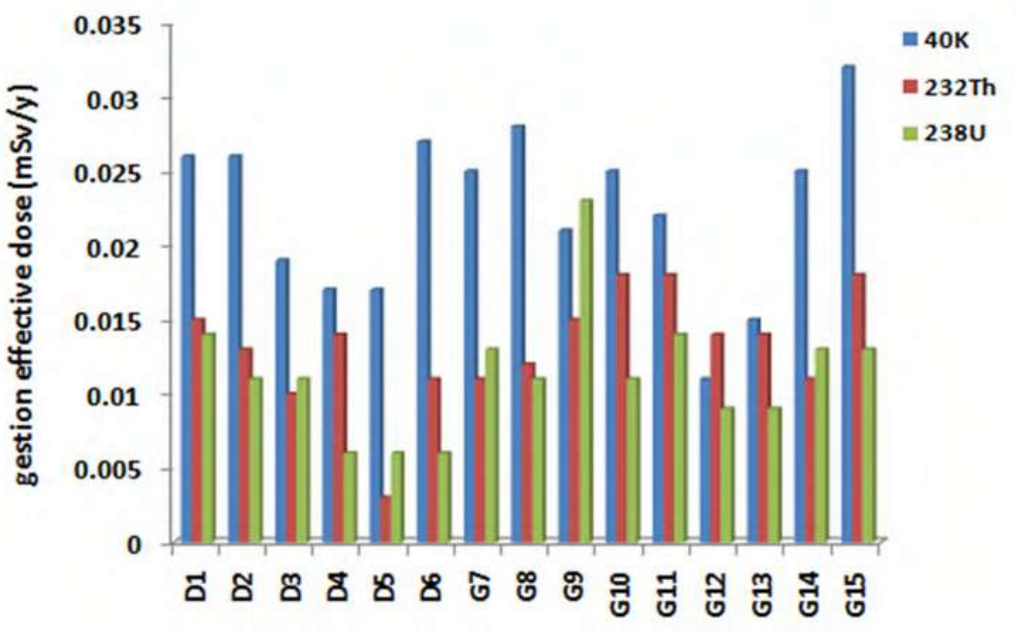

Figure 6. Ingestion effective dose of samples.

Table. 2. A specific activity of radioactivity in some types of dried fruit and grain of ^{238}U, ^{232}Th and ^{40}K.

No.		*Sample*	^{238}U	^{232}Th	^{40}K
1	*dried fruit*	*Figs*	5.4	4.4	403
2			*4.3*	*3.9*	*339.3*
3		*Apricot*	*23.*	3.4	356
4		*raisin*	*4.3*	*992.*	253.4
5		*Dried coconut*	*1.04*	*2.3*	234
6		*date*	*3.3*	*42.*	*344.9*
Mean ± S.D			*3.44± 0.58*	*3.66± 0.20*	*324.4± 28.5*
7	***Grain***	*popcorn*	*5.52*	*58.*	*400*
8		*Barley*	*3.4*	*4.8*	*334.8*
9			*3.6*	*4.3*	353
10		*Bulgur (crushed wheat)*	*4.60*	*8.72*	278
11			*5.3*	*4*	333
12		*rice*	*5.5*	*5.2*	330
13		*Millet*	*3.585*	*4.2*	147
14			*4.3*	*3.55*	*198*
15		*Oats*	*4.9*	*5.3*	244

Mean ± S.D	*4.29 ± 1.4*	*4.8± 1.5*	*302.3± 98.9*	
Global Limit UNSCEAR, 2008	*33*	45	412	

Table 3. Radiometric parameters of the dried fruit and grain.

Sample code	ADED(μSv/y) inside	ADED(μSv/y) outside	Hazerd indexs H_{in}	Hazerd indexs H_{ex}	ELCR inside	ELCR outside
D1	*91.*996	*22.*999	0.072	0.07 0	3*21.*77	8*0.*942
D2	90.15	22.538	0.109	0.09 7	315.52 5	78.883
D3	71.082	17.771	0.11	0.1	248.78 7	62.199
D4	70.268	17.567	0.085	0.07 7	245.93 8	61.485
D5	56.905	14.226	0.081	0.06 9	199.16 8	49.791
D6	101.62	25.405	0.063	0.06	295.88 3	73.973
Average± S.D	78.3± 5.9	19.5± 1.4	0.008± 0.007	0.07 9± 0.00 5	274.1± 19.4	68.5± 4.8
G7	105.658	26.914	0.11	0.09 9	370.84 8	92.962
G8	92.25	23.062	0.101	0.09 5	322.87 5	80.717
G9	110.749	27.687	0.103	0.09 3	387.62 2	96.905
G10	80.02	20.005	0.126	0.11 6	280.07	70.018
G11	106.29	26.572	0.116	0.10 4	372.01 5	93.002
G12	*9*1.995	2*2.*999	0.113	0.09 9	391.98 3	97.997
G13	55.247	13.812	0.139	0.12 4	193.36 5	48.342
G14	60.893	15.223	0.077	0.06 4	213.12 6	53.281
G15	72.392	18.098	0.098	0.08 4	253.37 2	63.343
Average± S.D	79.2± 28.4	19.9± 7.1	0.097± 0.031	0.10 ± 0.03 4	313.5± 98.1	78.3± 24.5

Table 4. The results ingestion of radionuclides ^{226}Ra, ^{232}Th, and ^{40}K for the samples.

code	Eing (mSv/y)		
	^{238}U	^{232}Th	^{40}K
D1	0.014	0.015	0.03
D2	0.011	0.013	0.026
D3	0.011	0.01	0.019
D4	0.006	0.014	0.017
D5	0.006	0.003	0.017
D6	0.006	0.011	0.029
Mean ± S.D	0.009± 0.001	0.010± 0.001	0.02± 0.01
G7	0.018	0.014	0.025
G8	0.011	0.012	0.032
G9	0.023	0.015	0.021
G10	0.011	0.018	0.025
G11	0.014	0.018	0.028
G12	0.0*25*	0.01*8*	0.01*4*
G13	0.009	0.014	0.015
G14	0.013	0.011	0.025
G15	0.013	0.018	0.032
Mean± S.D	0.012± 0.004	0.014± 0.004	0.023± 0.007

4. Conclusion

Through calculations of the concentration of radioactivity for the ^{238}U, ^{232}Th, and ^{40}K for the samples and the radiation hazard associated with the ingestion effective dose for the dried fruit and grain, it was found that they do not contain high radioactivity that affects the human body. Indices of radiation risk that were assessed during the analysis for all samples inside the study, all samples within the international borders allowed, and it is necessary to conduct a deep study of the other types of foodstuffs to determine their suitability for human consumption.

Acknowledgments

The author would like to thank Mustansiriyah University (www.uomustansiriyah.edu.iq) Baghdad-Iraq for its Support in the present work.

References

[1] IAEA., International Atomic Energy Agency 1989 *International Atomic Energy Agency*, 295.
[2] Syarbaini A. W., Iskandar D., & Syarbaini M. 2014 *Indonesia, Atom Indonesia*. **40**(1).
[3] Jibiri N.N. & Abiodun T.H. 2012 *J. Nucl. Sci.Technol*. **2**(106).
[4] Jwanbot D.I., Izam M.M., & Nyam G.G. 2012 *J. Nat. Sci. Res.* **2**(6) 76.
[5] Kumari R., Kant K., Garg M., Gupta R., Sonkawade R.G., & Chakarvarti S. 2015 *Int. J. Low Rad.* **10**(2)155-168.
[6] Roselli C., Desideri D., Cantaluppi C., Ceccotto F., Feduzi L., & Meli M. A. 2017 *J. Toxicol. Environ. Health Part A* **80** (4) 230-235.
[7] Al-Hamidawi A.A., Al-Gazaly H. H., & Al-Alasadi L. A. 2013 *Pelagia Research Library* **4**(5) 245
[8] Bhshry A., Moni T., & Iftikhar H. 2013 *Pelagia Research Library* **4**(5) 245-250
[9] Tayseer I. N., & Ayman M. A. 2017 *Nucl. Tech.* & *Radiat.* Prot. **32**(2)166-173.
[10] Jibiri N.N., Farai I.P., & Alausa S.K. 2007 *J. Environ. Radioact***. 94**(1)31-40.

[11] Mlwilo N., Mohammed N., & Spyrou N. M. 2007 *J. Radiat. Prot. Res.* **27**(4) 471.
[12] Abojassim A. A., Al-Gazaly H. H., & Kadhim SH. 2014 *Int. J. Food Contam.***1**(1)6.
[13] UNSCEAR I. R. Sources, and Biological Effect United Nations Scientific Committee on the Effect of Atomic Radiation. 1982 United Nations: New York.
[14] Viruthagiri G., & Ponnarasi K. 2011 *Adv. Appl. Sci. Res* **2**(2)103
[15] Avwiri O.G. & Agbalagha E.O., Nigeria. 2014 *Environ Earth Sci*, **71**(4)1541
[16] Righi S., & Bruzzi L. 2006 *J Environ Radioact*. 88(2) 158-170.
[17] Akhtar N., Ashraf M., Tifail M., Iqbal M., & Orfi S. 2003 *J. Res*. **14**(1)49-59.
[18] Taskin H., Karavus M., P. Ay., Topuzoglu A., Hidiroglu S., & Karahan G. 2015 *J. Environ. Radioact*150,132-144.
[19] Chandrashekara K., & Somashekarappa H. M. *2017 Afr. J. Agric. Res.* **12**(5)327-341.
[20] Abualhail R., Abbas A. A., & Alsalihi A. 2017 j*ournal of Basrah Researches (Sciences),* **43**(2A).
[21] UNSCEAR ., Sources and Effects of Ionizing Radiation Report to the General Assembly with scientific annexes.United Nations, New York. 2008 *United Nations Sales Publication*, UNSCEAR Report.
[22] UNSCEAR., United Nations Scientific Committee on the Effects of Atomic Radiation. Sources and Effects of Ionizing Radiation United Nations. 2000 *New York: United Nations Sales Publication*, UNSCEAR Report

Physical Characteristics for Biocomposite Material Using to Jawbones Compensation

Physical Characteristics for Biocomposite Material Using to Jawbones Compensation

Alya'a Abdulkadhim Sabry[1] and Nihad Abdulameer Salih[2]

[1]Department of Mathematics, College of Education for Pure Science, University of Muthanna, Muthanna, Iraq.
[2]Department of Physics, College of Science, University of Babylon, Babylon, Iraq.

E-mail: alyaa_ros@mu.edu.iq

Abstract. The biocomposite material prepared from polymeric blend (bone cement) as a matrix, and hydroxyapatite powder as a reinforcement material to jawbones compensation is a material that has a good compatibility in terms of physical properties with oral environment in general, and jawbones in particular. The physical properties such as density, water absorption, and thermal properties were tested according to the weight fraction for the reinforcement material. It was found that the density of biocomposite material does not uniformly changed, and it decreases with increasing the ratio of hydroxyapatite particles. While, the water absorption increases with increasing the weight fraction of hydroxyapatite particles. Also, the thermal properties were measured. It was found that the thermal conductivity and the thermal diffusivity of the prepared material were decreased with increasing the weight fraction of hydroxyapatite particles, and therefore the specific heat of the prepared material was also increased due to the porous nature for reinforcement material (hydroxyapatite powder) that enhances the formation of voids between the resulting material.

Keywords: Biocomposite materials, jawbones, density, water absorption, thermal conductivity, thermal diffusivity, specific heat.

1. Introduction

During the last few years, composite materials were widely used in medical applications [1,2] to compensate the damaged parts of the body such as bones, denture base, teeth implants, and dental fillings, etc. [3].

Generally, jawbones like other types of bones are a specialized type of connective tissue [4]. It consists of cortical and cancellous bone [5]. The biocomposite materials that used to compensate jawbone must have specific properties to be suitable for human's body especially for oral environment [6]. Biocomposite material for jawbone is a single composition with a uniform structure [7], and should satisfy many significant criteria as well as specific characteristics such as biocompatibility, osteoconductivity, corrosion resistance, strength, fatigue durability, and tight chemical similarity to biological apatite that exists in the human hard tissues [7,8]. Therefore, the preparation of any biocomposite material for jawbone compensation must have special biological, chemical, mechanical, and physical properties to be compatible with other body tissues [8,9].

In recent studies, the preparation of many biocomposite materials for compensating jawbones, biopolymer composite prepared from silicone rubbers were widely used for this purpose. Nanocomposites prepared from silicone rubbers as a matrix, and poly (methyl methacrylate) (PMMA)

as a reinforcement were succeeding for maxillofacial prosthesis and studied the effect of adding different percentage of nanopowder of PMMA on the physical properties [10]. The silicone rubber reinforced with hydroxyapatite powder (HAP) was used to compensate the damaged parts of the jaws [11]. The mechanical properties of biocomposite material were studied, and the PMMA was found to be a good biopolymer material to compensate human bones in general, and jawbones in specific [12]. PMMA as a denture base material was used, and it proved itself as success choice in this field due to its compatibility with oral environment and the mechanical and physical characteristics [13].
The objective of this work is to prepare a biocomposite material to repair the damaged parts of the jawbones and improves the performance of the jawbones using bone cement polymer reinforced with nanohydroxyapatite, and to study the physical properties of the prepared material.

2. Materials and Methods

2.1 Composition of Biocomposite Material

The biocomposite samples for jawbones compensation were prepared using (Hand lay-Up) method as a function of the specific weight ratios for all selected raw and reinforcement materials as shown in Table 1, and Table 2. Figure 1 shows the three types of reinforcement materials used in biocomposites.

Table 1. Materials used to prepare biocomposite material.

Materials	Symbol	Type	The use
Poly (methyl methacrylate)	PMMA	Powder	Matrix
Benzoyl peroxide	BPO	Powder	Matrix
Barium sulphate	$BaSO_4$	Powder	Matrix
Methyl methacrylate	MMA	Liquid	Matrix
N, N-Dimethyl para-toluidine	N, N-DMPT	Liquid	Matrix
Hydroxyapatite	HAP	Powder	Reinforcement

Table 2. Biocomposites materials and its chemical composition.

Materials	Powder			Liquid	
HAP wt.%	PMMA	BPO	$BaSO_4$	MMA	N, N-DMPT
0%	98				
1%	96.5				
2%	95				
3%	93.5				
4%	92				
5%	90.5	0.294	1.706	49	1
6%	89				
7%	87.5				
8%	86				
9%	84.5				
10%	83				

Figure 1. The materials used as reinforcement in biocomposite materials: (a) Nanohydroxyapatite; (b) Hydroxyapatite prepared form fish bones; (c) Hydroxyapatite prepared form natural egg shells.

2.2 Preparation of Biocomposite Material

Biocomposite material for jawbones compensation was prepared according to the amounts mentioned in Table 2. The amount of all components was (2:1) powder per liquid. It is necessary to pour the powder into the liquid not the opposite and mix them in a glass bowl with a thin wooden stick. Three groups of biocomposite materials were prepared with (nanohydroxyapatite, hydroxyapatite prepared from fish bones, and hydroxyapatite prepared from natural egg shells) as reinforcement materials at different weight ratios of (0, 1, 2, 3, 4, 5, 6, 7, 8, 9 and 10)%.

By mixing the powder and the liquid, many changes will take place due to the solubility of a polymer in the monomer. The stages of mixing monomer and polymer acrylic materials include (sandy or granular, sticky, full dough, rubbery, and hard). The speed for the polymer and monomer mixture to reach the dough stage depends on the solubility of the polymer powder in the liquid monomer and increasing the temperature [14]. The components are mixed for 30 seconds and quickly poured into the molds cavities because the dough stage turned to hard stages quickly. A weight of approximately (2N) is putting above the prepared sample to obtain a smooth surface and to prevent the entry of gases vapor into the acrylic as well as the formation of bubbles during the curing process. In addition, the weight leads to coordinate the specimen molecules and the interference between them taking into account the lubrication of the mold of all directions to prevent the specimen adhesion. The prepared specimens are kept in the molds for 24 hours until the curing and polymerization processes for the acrylic specimens are completed. After the curing process was completed, the specimens were removed from the mold cavities with a very smooth upper and lower surface and polished with sandpaper to remove the small cracks resulted from the specimen's sides as a result of the specimen's adhesion with the mold cavity sides. All specimens were prepared and tested under the same conditions.

2.3 Physical Tests

The physical tests are carried out at room temperature 23±2˚C. All the tested specimens were stored in distilled water and heated at (37± 1℃) for 48 hours.

2.4 Density Test

Density or (Bulk density) is the mass per unit volume of a material. Specific gravity is a measure of the ratio of the mass of a given volume of material at (23°C) to the same volume of distilled water. The specific gravity and density can be calculated from equations (1), and (2), respectively [15]:

$$Specific\ Gravity\ (S.G.) = m_1/(m_1 + w - m_2) \quad (1)$$

$$Density\ (\rho) = (Specific\ Gravity)(S.G.) \times (0.9975) \quad (2)$$

where:

$S.G.$: Specific Gravity.

m_1: Mass of a specimen in the air (gm).

m_2: Mass of a specimen in the water (gm).

w: Mass of partially immersed wire.

ρ: Density (g/cm^3).

The density (g/cm^3) can be obtained by multiple specific gravities and the density of distilled water which is equal to (0.9975 g/cm^3) [15,16].
The specimens were prepared according to (ASTM D-792) standard [17], and the specimens weights were measured according to Archimedes method by examining the weight of the specimen in the air and then check the weight with water [18]. But, the volume should not be less than (1cm^3). This test was done by accurate balances PS 360/C/1device, as shown in Figure 2.

Figure 2. The density test device.

2.5 Water Absorption Test
Various polymeric materials are susceptible to water absorption during its life exposures which cause dimensional instability. Thus, subjecting the material to degradation internal stresses may result in crack formation, and eventually lead to fracture or failure of the jawbones [19]. The moisture content of a polymer is very intimately related to such properties as mechanical strength, appearance, and dimensions stability. The effect upon these properties is the change in water absorption that depends largely on the type of exposure to high humidity, the rigidity of 3-D structure, the thickness of the specimen, immersion time, temperature, type of solution, type of materials, bounding type, the geometry of the specimen, cross-linking, curing method, and inherent properties of the polymer [20]. The water absorption can be calculated according to the following equation:

$$Water\ absorption\ percentage = (W_s - W_d)/W_d \times 100 \quad (3)$$

where:
W_s: Mass of the specimen after immersion for (24 hours in distilled water).
W_d: Mass of the specimen before immersion (dry).
For the most parts, the polymer may suffer expansions and contractions when alternately soaked in water and dried. This parameter is important in clinical applications of the matrix resin since water uptake may affect the dimensional stability, physical, and mechanical properties of jawbones. The water absorption by acrylic jawbone is nearly independent of temperature from (0 - 60 ºC), and the thin specimens reach a steady-state within a short time [21].
The test of water absorption was performed according to (ASTM D570) [22]. The dimensions of the specimens are (L×W×H) (50 × 50 × 4) mm. Figure 3 illustrates the experimental specimens and standard dimensions of the specimen for the water absorption test.

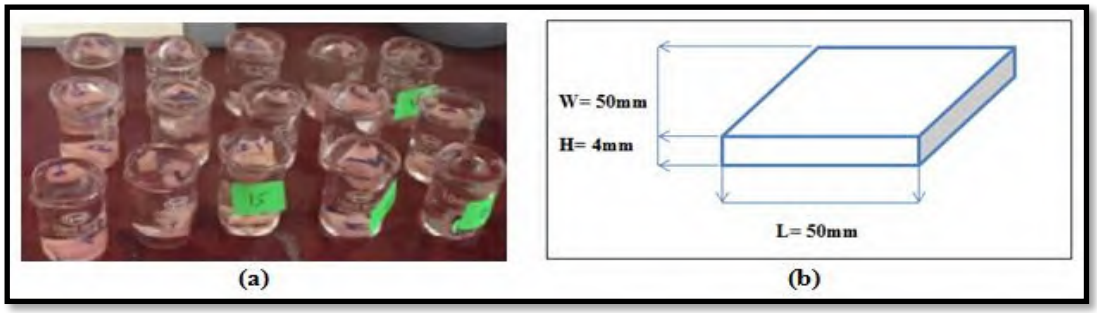

Figure 3. Water absorption test: (a) Experimental specimens; (b) Standard dimensions of the specimen for water absorption test.

2.6 Thermo-Physical Test

To evaluate the thermal properties of specimens, Hot Disk thermal analyses were used. The Transient Plane Source (TPS) technique was used to determine the (thermal conductivity, thermal diffusivity, and specific heat). The Hot Disk includes a heat source, and temperature probe as a flat sensor with a continuous double spiral of electrically conducting nickel (Ni) metal with a resistance of (11.56 Ω) to transform the thermal power which passes through the specimen to measure thermal transport properties, etched out of thin foil, sandwiched between two layers of insulating material. During the test, the sensor was normally placed between the surfaces of the two pieces of the specimen to be measured [23,24].

Measurements can be performed on many different materials; solids, liquids, powders, viscous materials, composites, etc. including various types of geometry, and dimensions. The Hot Disk (TPS) can also be used under various environmental conditions from very low temperature (-45°C) up to (1000°C) [25].

The relationship between the thermal properties is illustrated by [25,26]:

$$D_{th} = (K/C_p.\rho) \quad (4)$$

where:

D_{th}: Thermal diffusivity(mm^2/s).

K: Thermal conductivity$(W/m.K)$.

C_p: Specific heat at constant pressure$(MJ/m^3.K)$.

ρ: Mass density (Bulk density) (kg/m^3).

This test was performed according to the apparatus manual of standard specifications instrument [27]. The test was carried out by using the thermal properties test instrument, manufactured by (Kelthley), type (Transient Plane Source (TPS) - 500). Figure 4 (a) illustrates the instrument used for the thermo-physical properties test. This apparatus was used for investigating the thermal transmission properties, such as thermal diffusivity (C_v) or (D_{th}), volumetric specific heat (C_p), and thermal conductivity (K) which were determined by utilizing the Hot Disk sensor. A hot disk sensor was placed between the two pieces of the same specimen material prepared at the same dimensions of the standard specifications instrument, which are a least as thick as the radius of the sensor, functioning mechanical support, and electrical insulation as shown in Figure 4 (b), and then heated by an electrical current for a short period of time [28]. The lavished heat generates a temperature rise of both the sensor and the surrounding specimen material. To avoid the influence from the outside boundaries of the specimen, the specimen should be larger than the sensor diameter to ensure stable values of both thermal diffusivity, and conductivity. The values of thermal diffusivity, thermal conductivity, and specific heat were taken from the computerized gauges.

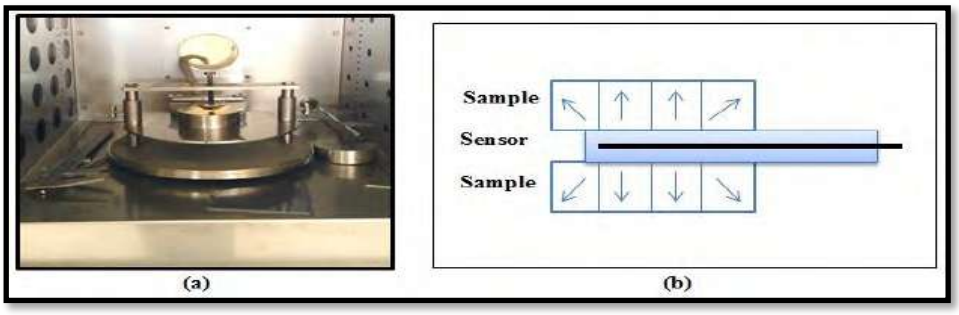

Figure 4. Thermo-physical properties test: (a) Thermal properties test instrument; (b) Hot disk sensor operation**.**

3. Results and Discussion

3.1 Density Property

From important measurements, the density of biocomposite material is the basic indicator for knowing the lighter prepared biocomposite materials [15]. Generally, the biocomposite materials have a lighter weight than biometals or bioceramic. This is one of the main reasons why using biocomposite materials in vivo applications [29].

The density of biocomposite specimens in this study is measured according to the Archimedes method using an equation (2). Figure 5 illustrates the relationship between the density, and the weight fraction of the reinforcing particles (HAP powder), which were added to the polymeric matrix (bone cement). It can be seen from the curve that the density values for biocomposite specimens increase with increasing weight fraction of HAP powder to the mixture (polymeric matrix) because the density of HAP particles is higher than that of PMMA [30,31].

Generally, prepared specimens had different densities, where the density for specimens has not constant change in proportion with the weight fraction of the reinforcement material (HAP powder) because other influential factors such as no homogeneity through the preparation process may affect the density of the specimen.

Pure PMMA has a density equals to (1.2 g/cm^3) [31], and MMA has a density equal to (0.93 g/cm^3) [32]. Other components of the matrix also have specific densities, while the density of the reinforcement (HAP powder) is (2.62 g/cm^3) [30]. The density for prepared specimens was between (1.32-1.91) g/cm^3, and the lower density was found at (2%) of (n-HAP) and (3%) of (HAP prepared from egg shells and fish bones). The higher density was found at (9%) of (n-HAP) and (10%) for (HAP prepared from egg shells and fish bones), respectively. These results differ from the results in reference [13] due to the difference in the reinforcement material, while it is in good agreement with the results in reference [10].

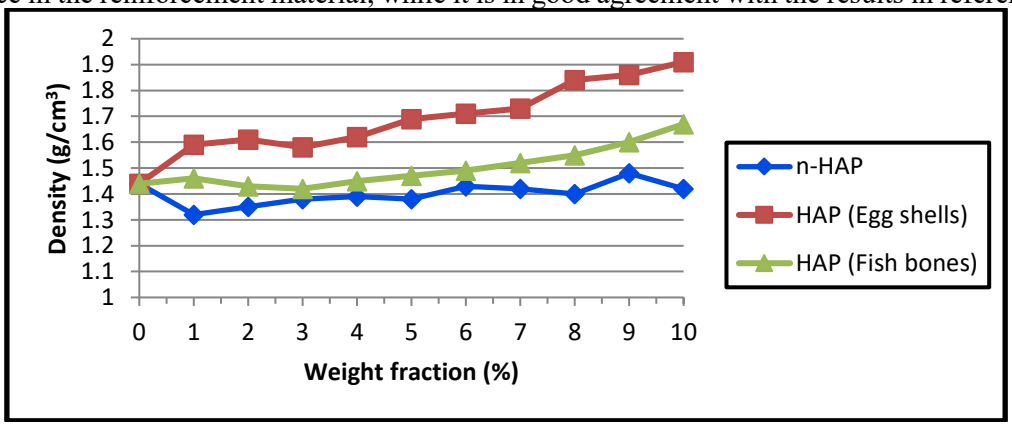

Figure 5. Density as a function of weight fraction of the reinforcement particles (HAP powder) in biocomposite material.

3.2 Water Absorption Property

The relationship between the water absorption of biocomposite material and reinforcement material HAP particles is illustrated in Figure 6. The water absorption values of the polymeric matrix and biocomposite material with HAP particles for all specimens that fabricated in this work are illustrated in figure 6. It can be observed from the figure that the water absorption decreases with increasing the weight fractions of HAP particles. This is due to the attitude of the particles towards the moisture, and also may be due to the porosity nature of HAP particles. Therefore, the water absorption is very little. In previous study, HAP particles were used as reinforced material with silicone rubber as a matrix, and the water absorption was not found [11]. Also, PMMA powder was used as a matrix with (bamboo, and siwak) fibers as a reinforcement, and it found that the water absorption increases with increasing the weight fraction of fibers and fiber's length [10].

In general, biocomposite specimens with HAP powder graded of absorption for water-dependent on the weight fraction of reinforcement, as well as the specimens with lower density have higher water absorption. The density decreases with increasing the moisture absorption [33]. Polymeric matrix (bone cement) specimen without reinforced material have a high value of water absorption equal to (1.443%), while biocomposite specimens with HAP particles have a low value reaches (1.1%) for a specimen with weight fraction (10%). This increase in water absorption is interpreted as a result for the existence of a bioceramic material (HAP) in the prepared biocomposite material, and these results are identical to the results in reference [34].

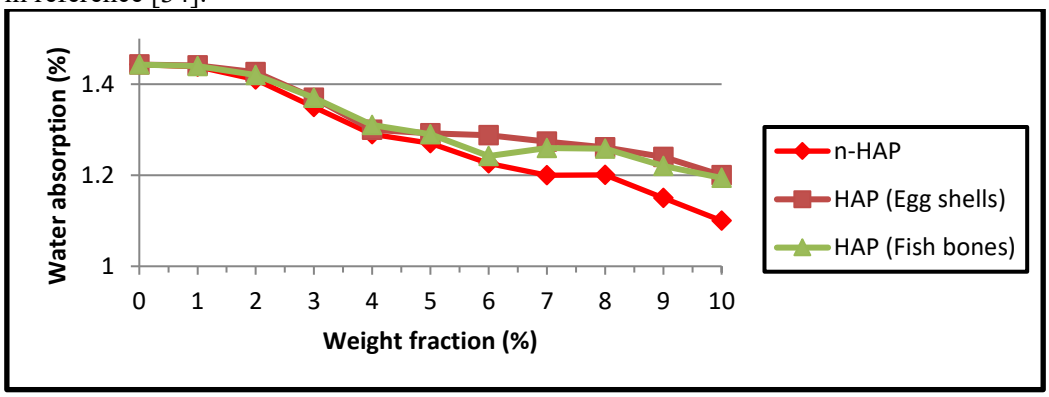

Figure 6. Water absorption as a function of weight fraction of the reinforcement particles (HAP powder) in biocomposite material**.**

3.3 Thermo-Physical Properties

The thermal-physical properties (thermal conductivity, thermal diffusivity, and specific heat capacity) are properties obtained from the hot disk test for biocomposite specimens at room temperature. The relationship between these properties is given by equation (4) which illustrates decreasing the thermal conductivity and improving the specific heat to decrease the thermal diffusivity of specimens [35].

Thermal Conductivity Results: Thermal conductivity for biocomposite material represents the thermal energy that causes movement of the molecular chains of polymer in biocomposite specimens at a rate proportional to the weight fraction of the conductive materials [36]. Thermal conductivity results are illustrated in Figure 7.

This figure illustrates that when increasing the weight fraction of HAP particles, the thermal conductivity of the biocomposite specimens decreases. This is due to the role of HAP particles that have thermal conductivity lower than that for PMMA matrix. Also, the presence of bioceramic HAP particles of a porous structure and conglomerate of biocomposite specimen as a result of increasing the weight fracture from HAP powder that lead to the difficult process of heat transfer through the composite specimens, and can considerably poor thermal conductivity. This is made better molds for the characterization of bone cement thermal behavior [37].

Figure 7 illustrates the polymeric matrix (pure) has a higher thermal conductivity value equal to (0.1622 W/m.K), while the biocomposite specimens have lower values than the polymeric matrix. The maximum values of thermal conductivity for biocomposite specimens with (n-HAP, HAP prepared from egg shells and HAP prepared from fish bones) particles at the optimum condition of weight fraction (1%) equal to (0.1604 W/m.K), (0.1525 W/m.K) and (0.1551 W/m.K), respectively, and have minimum values at (10%) (0.0918 W/m.K), (0.0645 W/m.K) and (0.0775 W/m.K) respectively. The biocomposite specimens with less weight fraction of HAP have higher thermal conductivity value than biocomposite specimens with high rates.

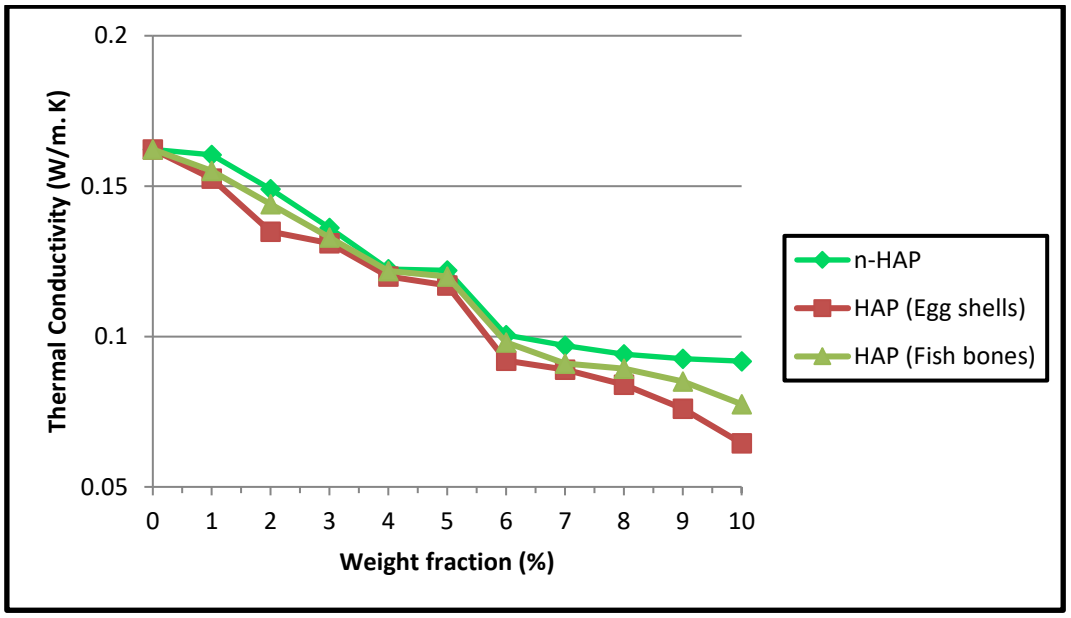

Figure 7. Thermal conductivity as a function of the weight fraction of the reinforcement particles (HAP powder) in biocomposite material.

Thermal Diffusivity Results: The thermal diffusivity of specimens indicates the change in the composite specimen's temperature in the test when the heating is applied [38].
Figure 8 shows the relationship between the thermal diffusivity and the weight fraction of the reinforcing HAP particles added to the matrix (bone cement). The thermal diffusivity of the composite specimen decreased with increasing the weight fraction of (n-HAP) reinforcing particles added to the matrix (bone cement). The pure matrix (bone cement) has a higher value of thermal diffusivity than the composite specimen reaches (0.06182 mm^2/s). So, the higher values of biocomposite specimens reinforced by weight fraction equal (1%) reach (0.0602 mm^2/s, 0.0515 mm^2/s and 0.0549 mm^2/s) for composite specimens having (n-HAP, HAP prepared from egg shells and HAP prepared from fish bones) particles, respectively. While, composite specimens have thermal diffusivity decreased with increasing weight fraction of HAP particles. These results differ from those obtained for composite specimens PMMA reinforced with fibers (bamboo and siwak) which show that the thermal diffusivity of specimens is increased with increasing the weight fraction and the fiber length of (bamboo and siwak). In addition, siwak specimens have higher values of thermal diffusivity than bamboo specimens [10].

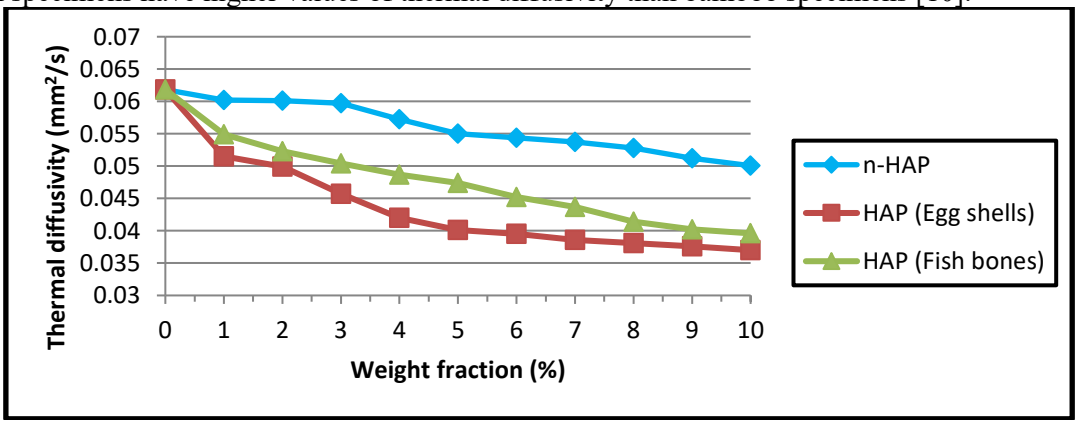

Figure 8. Thermal diffusivity as a function of the weight fraction of the reinforcement particles (HAP powder) in biocomposite material.

Specific Heat Results: The specific heat for biocomposite specimens represents the energy required to raise the temperature T_g of biocomposite specimens by one degree [36].
Figure 9 illustrates the relationship between the specific heat, and the weight fraction of the reinforcing particles (HAP powder) added to a pure matrix (bone cement).
Specific heat magnitudes could be increased by increasing the weight fraction of HAP particles compared with the magnitude of PMMA alone. Therefore, the highest values of specific heat for biocomposite specimens are obtained for biocomposite with (10%) weight fraction of HAP particles. This could be attributed to the formation of spaces and voids between the particles because of the porous nature for HAP particles, which consequently led to an increase in specific heat.
The pure matrix (bone cement) has lower value than biocomposite specimens with reinforcing HAP powder that equal to (2.319 MJ/m^3.K).
The highest values of specific heat were found with biocomposite specimens at (9%) weight fraction of (n-HAP) particles, and (10%) of (HAP prepared from egg shells and HAP prepared from fish bones), that reach to (3.246 MJ/m^3.K), (3.59 MJ/m^3.K), and (3.36 MJ/m^3.K), respectively. This is different from composite specimens with (bamboo & siwak fibers) that have a lower value of specific heat than pure PMMA [10].

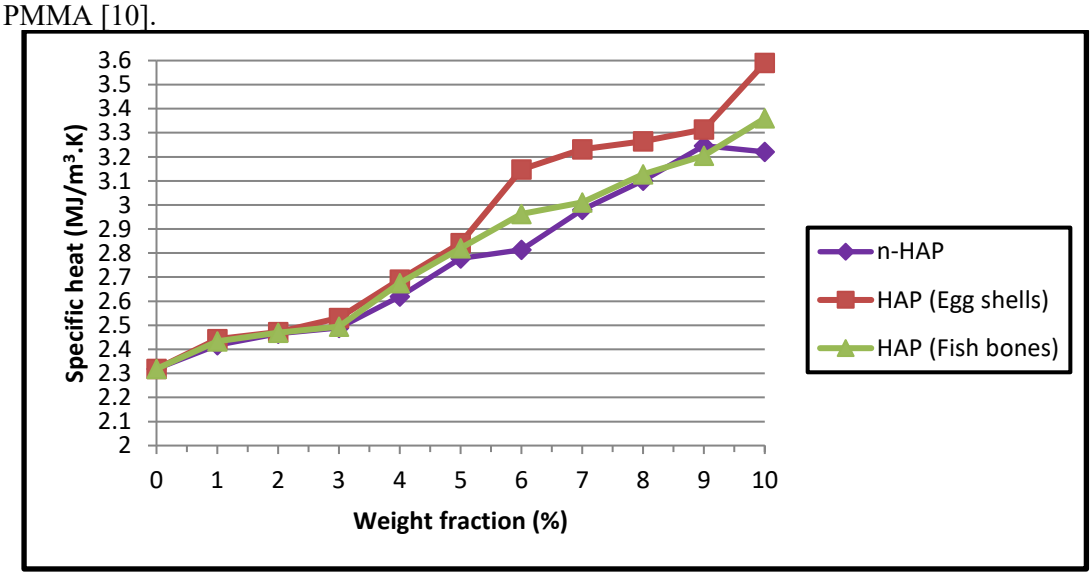

Figure 9. Specific heat as a function of the weight fraction of the reinforcement particles (HAP powder) in biocomposite material.

4. Conclusions

The experimental physical tests used for the biocomposite materials prepared in this study led to the following conclusions:
The biocomposite material prepared from biopolymer (bone cement) as a matrix and reinforced by bioceramic (HAP powder) as filler is a material with good compatibility, as the physical properties of the prepared material are suitable with the jawbone material in particular, and with the body in general.
The prepared biocomposite materials have different densities, where the density for prepared specimens lay between (1.32-1.91) g/cm^3. Therefore, the density of these samples increases with the weight fraction of HAP powder.
The rate of water absorption of biocomposite specimens with HAP particles is grading dependent on the weight fraction of reinforcement, where polymeric matrix (pure) specimen without reinforcement have

the higher value of water absorption, while biocomposite specimens with HAP particles have lower values, and decreases with increasing the weight fraction of HAP powder.
The maximum values of thermal conductivity and diffusivity of the biocomposite specimens are at a weight fraction less than the HAP powder, and the minimum values of them at the weight fraction higher than it.
Specific heat is inversely proportional to both thermal conductivity and diffusivity, so, it increases with increasing the weight fraction of the reinforcement material.

References

[1] Machovsky M 2013 *Composite Materials for Medical Application* Ph.D. Dissertation Tomas Bata University in Zlin Faculty of Technology, Polymer Center Turkey.
[2] Adrian P P and Gheorghe B M 2010 *ANNALS of the ORADEA UNIVERSITY*, **IX** (XIX) 3.1.
[3] Kutz M 2003 *Standard handbook of biomedical engineering and design* (The McGraw-Hill Companies) Inc. U.S.A.
[4] Ochsner A and Ahmed W 2010 *Biomechanics of Hard Tissues*, WILEY- VCH Verlag GmbH & Co. KGaA, Weinheim, Singapore.
[5] Misch C E Qu Z M and Bidez M W 1999 *Journal of Oral Maxillofacial Surgery* **57** 700.
[6] Berkovitz B K Moxham B J Linden R W and Sloan A J 2001 *Oral Biology*, 3rd ed. Elsevier Ltd. China.
[7] Mehrali M Shirazi F S Mehrali M Metselaar H S C Bin Kadri N A and Abu Osman N A 2013 *Journal of Biomedical Materials Research A* **101A** (10) 3046.
[8] Ottria L Lauritano D Bassi M A Palmieri A Candotto V Tagliabue A and Tettamanti L 2018 *Journal of Biological Regulators & Homeostatic Agents* **32** (2) (S1) 81.
[9] Mavrogenis A F Dimitriou R Parvizi J and Babis G C 2009 *Journal of Musculoskeletal and Neuronal Interactions*, **9** (2) 61.
[10] Mohammed H 2019 *Nanocomposites Preparation for Maxillofacial Prosthesis from Polymer Blends* Ph.D. Dissertation University of Technology Department of Materials Engineering Iraq.
[11] Al-Husseini R A 2015 *Preparation of Biopolymer composite that Using in the Damage of parts in the Jaws*, M.Sc. Thesis University of Babylon College of Science Iraq.
[12] Sabry A A and Salih N A 2020 *Egyptian Journal of Chemistry* **63** (10).
[13] Salam H 2017 *Preparation and Characterizations of Polymer Biocomposite Materials for Denture Base Material*, M.Sc. Thesis University of Technology, Department of Materials Engineering, Iraq.
[14] Harrison Z Johnson A and Douglas C W I 2004 *Journal of Oral Rehabilitation*, **31** (5) 460.
[15] Annual Book of ASTM Standard 2008 *Standard Test Method for Density and Specific Gravity (Relative Density) of Plastics by Displacement D792-08* New York.
[16] Oleiwi J K HamzaM S and Nassir N A 2011 *Engineering and Technology Journal*, **29** (5) 856.
[17] Annual Book of ASTM Standard 2006 *Standard Test Method for Density and Specific Gravity (Relative Density) of Plastics by Displacement Methods D792* 09.01.
[18] Carraher C I and Carraher's J S 2008 *Polymer Chemistry* 7th ed. Taylor & Francis Group LLC. U.S.A.
[19] Pfeiffer P and Rosenbauer E U 2004 *Prosthetic Dental Journal* **92** (1) 72.
[20] Al-Kadi F K 2004 *Effect of Thermo cycling on Some Properties of Soft Denture Linear* M.Sc. Thesis, University of Baghdad College of Dentistry Iraq.
[21] Nagham B K 2008 *Effect of Addition of Different Length and Concentration of Silane Treated Glass Fibers on Some Properties of Heat Cured Acrylic Resin* M.Sc. Thesis University of Baghdad, College of Dentistry Iraq.
[22] Annual Book of ASTM Standard 2005 *Standard Test Method for Water Absorption of Plastics D 570-98* 08.81 1.
[23] Hameed Q A 2015 *Fabrication and Characterization of Denture Base Material by Hybrid Composites from Self-cured PMMA Resin*, Ph.D. Dissertation University of Technology Material Engineering Department Iraq.
[24] Mohd Saleh S S Hazizan M A Nasir R and Hasmi H 2013 *Advanced Materials Research* **812**

226.
[25] Rosato D V Rosato M G and Schott N R 2010 *Plastics Technology Hand Book*, 1st ed. Momentum Press, LLC. Taiwan.
[26] Oleiwi J K and bass B A 2018 *International Journal of Mechanical and Production Engineering Research and Development* **8** (6) 517.
[27] Silas 1995 Thermal Constant Analyzer: Thermal Conductivity, Thermal Diffusivity and Specific heat of Materials.
[28] *Hot Disk Thermal Constants Analyzer* 2001 Instruction Manual Canada.
[29] Oleiwi J K Anaee R A and Radhi R A 2018 *International Journal of Mechanical and Production Engineering Research and Development* **8** (6) 855.
[30] Yoganand C P Selvarajan V Wu J and Xue D 2008 *Vacuum* **83** (2) 319.
[31] Elshereksi N W Mohamed S H Arifin A and Ishak Z A M 2014 *Journal of Physical Science* **25** (2) 15.
[32] Mahboub M J Dubois J L Cavani F Rostamizadeh M and Patience G S 2018 *Chemical Society Reviews* **47** (20) 7703.
[33] Maya M G George S C Jose T Sreekala M S and Thomas S 2017 *Polymers from Renewable Resources* **8** (1) 27.
[34] Ionita D Tihan G and MarquesA T 2009 *Key Engineering Materials* **396-398** 493.
[35] Alsina O L Carvalho L H D Filho F G R and d'Almeida J R 2005 *Polymer Testing* **24** (1) 81.
[36] Askeland D R Fulay P P and Wrigth W J 2011 *The Science and Engineering of Materials*, 6th ed. Cengage Learning Stamford CT.
[37] Prakasam M Locs J Salma-Ancane K Loca D Largeteau A and Berzina-Cimdina L 2015 *Journal of Functional Biomaterials* **6** (4) pp 1099-1140.
[38] Santos W N Mummery P and Wallwork A 2005 *Polymer Testing* **24** (5) 628.

Study The Effect of Annealing on Structural and Optical Properties of Indium Selenide (InSe) Thin Films Prepared by Vacuum Thermal Evaporation Technique

Study The Effect of Annealing on Structural and Optical Properties of Indium Selenide (InSe) Thin Films Prepared by Vacuum Thermal Evaporation Technique

Seham Hassan Salman, Sarmad M.Ali and Ghuzlan Sarhan Ahmed

Department of Physics, College of Education for Pure Science / Ibn Al-Haitham, University of Baghdad, Baghdad, Iraq

E-mail: Ghzlan82sn@gmail.com

Abstract. In this work, InSe thin films were deposited on glass substrates by thermal evaporation technique with a deposit rate of (2.5∓0.2) nm/sec. The thickness of the films was around (300∓10) nm, and the thin films were annealed at (100, 200 and 300) ˚C. The structural, morphology, and optical properties of Indium selenide thin films were studied using X-ray diffraction, Scanning Electron Microscope and UV–Visible spectrometry respectively. X-ray diffraction analyses showed that the as deposited thin films have amorphous structures. At annealing temperature of 100 ˚C and 200 ˚C, the films show enhanced crystalline nature, but at 300 °C the film shows a polycrystalline structure with Rhombohedral phase with crystallites size of 17.459 nm. The results of the UV–Visible spectrometry in the wavelength range (300 – 1100) nm showed that the band gap energy of the thin films increased with increasing annealing temperature.

Keywords: InSe, Thin Film, annealing, Optical, structural, Vacuum Thermal Evaporation

1. Introduction

Numerous studies have been focused on Indium monoselenide (InSe) as a semiconducting layered compound since it exhibits a good photoelectric property and can be used as an active media for the generation of visible and near-infrared radiation[1]. InSe thin films are used as high energy radiation detectors owing to its high stability towards ionizing radiation [2]. Also, it used as solar cells due to its optical energy gap between (1 and 2) eV 3]. The problem of the preparation of high quality thin InSe films is still unsolved due to the existence of several In–Se phases [4]. Therefore, it is considered of complicated stoichiometries due to the existence of InSe, In_2Se_3, In_4Se_5, In_4Se_3, and In_6Se_7 phases [5]. Moreover, (InSe) exhibits at least three modified crystalline phases of (2H-β) (two-layer hexagonal, 2H) and (2H- ɣ) or (3R-δ) (three-layer rhombohedral, 3R) [6,7]. There are five relatively known phases of In_2Se_3 compound α (hexagonal), β (rhombohedral), ɣ (hexagonal), δ, as well as the recently discovered k phase (anisotropic structure)[7,8]. Indium selenide has two crystalline surfaces showing very different physical properties. The cleaving surface perpendicular to the z-axis consists of Se atom bounded together with covalent bonds. The other surface parallel to the z-axis is made up of Se atoms of adjacent layers being bounded by Van der Waal forces [8,9]. Depending on the deposition technique and deposition conditions, one of the crystalline forms of InSe is produced. Each form has a unique range

of structural, optical and electronic properties [10] and thin-film growth method on substrates [11].So far, many techniques are used to prepare InSe thin films such as chemical bath deposition [12], Spray pyrolysis [13], sol gel method [14] and thermal evaporation[15].
In this work, we firstly prepared InSe alloy at (In:Sn = 50%:50%), and the InSn thin films were thermally evaporated on glass substrates. The structural, Topographical and optical properties of Indium Selenide thin films were studied as a function of different annealing temperatures.

2. Experimental

In this work, InSe compound was prepared from Indium (99.99% purity) and selenium (99.99% purity) elements mixed into a sealed and evacuated quartz tube at (5×10^{-2} mbar), and then the quartz tube was heated at 900 °C for 1 h in a furnace followed by ice water quenching. The tube was broken to extract the substance that was grinded to be used for depositing the thin films using thermal evaporation technique under a vacuum of (3×10^{-5}mbar). Glass substrates were cleaned by detergent with ethanol and rinsed ultrasonically in deionized water. The glass slides are placed on a shaped semi ball-holder inside the thermal evaporation chamber, and the InSe compound was evaporated using Mo boat. The Indium Selenide thin films were evaporated at room temperature onto cleaned glass substrates. The thickness of the films was determined by using weighing method to be (300 ∓ 10) nm, and the thin films were annealed at (100, 200 and 300) °C.
(XRD) patterns were obtained using a (SHIMADZU Japan -XRD600) with a CuKα source of λ=1.54059 Å to study the crystal structure of the thin films. (VEGA3-TESCAN model, USA) scanning electron microscope (SEM) was used to study the surface morphology. (UV-visible 1800 spectra photometer) in the wavelength range (300 – 1100) nm was used to study the optical properties of thin films.

3. Results and Discussion

3.1. The XRD diffraction analysis

Fig. (1) shows the XRD diffraction analysis of the InSe alloy. This result indicates the appearance of InSe, In_2Se_3 in different phases. In addition, the highest peak of (006) plane is related to the Rhombohedral structure of InSe. A few weak peaks with mixed indices indicating that in addition to the trend along c- axis (0012) and (0018), there are also some other crystalline features along (110), (116) and (119). By comparing the results with the standard cards for ICDD 's of different (InSe, In2Se3, In_4Se_3, In_4Se_5, In_6Se_7…) structures, we observe the emergence of different peaks corresponding to the phases (InSe-M, InSe-R, InSe-H). Also, some peaks have compatible Miller indices, for example (116) and (114) related to the phases InSe-R and InSe-H, respectively. The peaks with incompatible Miller indices, such as (201) and (103) are related to the Monoclinic and Rhombohedral phases respectively. This is because the Rhombohedral is a special case of hexagonal structure. Similarly is applied to the In_2Se_3 structure, and Table (1) shows XRD results for the alloy.

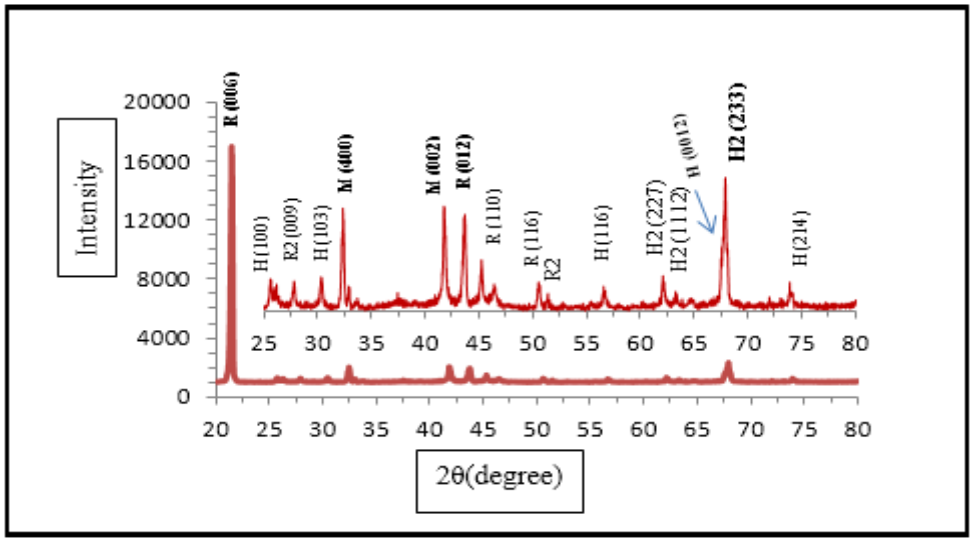

Figure 1. XRD diffraction analysis of the InSe alloy. R means rhombohedral InSe;M means Monoclinic and H means hexagona

Table 1. shows XRD results for alloy

JCPDS card No.	Phase	2θ absor	2θ stand.	d-abs	d-stand.	hkl	FWHM
1-70-2541	InSe-R	21.468	21.35	4.13585	4.1583	006	0.2077
0-34-1431	InSe-H	25.66	25.6887	-	3.465	100	-
1-72-1470	In_2Se_3-R	27.86	27.8868	-	3.1966	009	-
0-34-1431	InSe-H	30.38	30.3775	-	2.94	103	-
1-80-2272	InSe-M	32.4046	32.4998	2.76064	2.7527	400	0.27
1-80-2272	InSe-M	41.8203	41.7474	2.15829	2.1618	002	0.2272
1-70-2541	InSe-R	43.668	43.4898	2.07115	2.0792	0012	0.2958
1-70-2541	InSe-R	45.26	45.3049	-	2	110	-
1-70-2541	InSe-R	50.56	50.6016	-	1.3861	116	-
1-72-1470	In_2Se_3-R	51.44	51.4981	-	1.7731	0114	-
0-34-1431	InSe-H	56.6	56.667	-	1.623	116	-
1-71-250	In_2Se_3-H	62.1	62.0331		1.4949	227	-
1-71-250	In_2Se_3-H	63.26	63.3042		1.4679	1112	-
0-34-1431	InSe-H	67.562	67.5258	=	1.386	0012	=
1-71-250	In_2Se_3-H	67.8685	67.8665	1.37987	1.3799	233	0.2612
1-70-2541	InSe-R	73.88	73.9022	-	1.2814	214	-

The XRD patterns for the as-deposited and annealed InSe thin films with 300 nm show that the as-deposited thin films are amorphous in nature. After annealing at 100°C and 200°C, the films show enhanced crystalline nature, and the film annealed at 300°C shows a polycrystalline structure. These results are in good agreement with those in reference [15].The transformation to polycrystalline structure is due to the recrystallization process during the annealing of the thin film. Annealing process led to the cancellation of some levels presented after the growth and rearrangement of the crystalline grains within

the lattice after taking a sufficient energy to grow and arrange [16]. This result indicates the appearance of InSe- Rhombohedral phases with the orientations of (006), (101), (104), (110), (116) and (021). The preferred orientation was along (101) R plane. The spectrum also contains two weak peaks correspond to the Se- Monoclinic phases. Table (2) Shows XRD results for InSe thin films annealed at 300 °C.

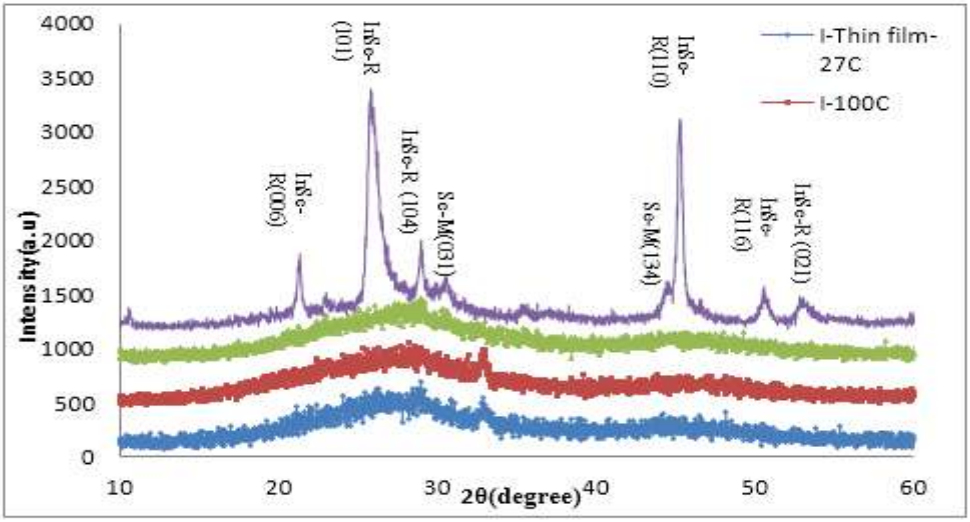

Figure 2. X-ray diffraction analysis of thin film: R means rhombohedral of InSe thin films; M means Monoclinic of Se

Table 2. XRD results for thin film annealed at 300 °C.

JCPDScard No.	Phase	2θabsor	2θstand.	d-abs	d-stand.	hkl
00-042-0919	InSe-R	21.35	21.353	4.15	4.1583	006
	InSe-R	26	25.933	3.423	3.432	101
	InSe-R	29.018	29.432	3.074	3.029	104
	InSe-R	45.29	45.281	2	2	110
	InSe-R	50.60	50. 581	1.802	1.8	116
	InSe-R	53.08	52.918	1.72	1.728	021

The crystallite size was estimated from the (β) value of the preferential orientation along (101)R plane using the Scherrer relation [17]:

$$C.s = k * \frac{\lambda}{\beta * \mathrm{Cos}\theta} \qquad (1)$$

where C.s is the crystallite size, k ≈ 0.9, λ is the wavelength of X – ray radiation, θ is the Bragg's angle of the(101) peak in degrees, and β is the peak width of the diffraction peak profile at half maximum. The calculated crystallite size of the thin films was found to be 10.157 nm.
The dislocation density (δ) was estimated from relation (2) [18].

$$\delta = \frac{1}{C.S^2} \qquad (2)$$

The micro strain (ε) is one of the important factors in lattice dynamics calculated from relation (3) [19].

$$\varepsilon = \beta * \frac{\cos\theta}{4} \quad (3)$$

The number of crystallites per unit surface area (N_o) was calculated using relation (4) [20].

$$N_0 = \frac{t}{C.S^3} \quad (4)$$

where t is the thickness of the thin film

The calculated Crystallite size, dislocation density, micro strain and the number of crystallites per unit surface area for the preferred orientation along (101)R plane of InSe thin film annealed at 300 ºC were listed in Table 3.

Table 3. Crystallite size, dislocation density ,micro strain and the number of crystallites per unit surface area for InSe thin film annealed at 300 ºC.

2Θ (degree)	hkl	β(deg)	β (rad)	C.s(nm)	δ $(nm)^{-2}$	ε	N_o $(nm)^{-2}$
26	101	0.839	0.0146	10.157	0.0097	0.0035	0.286

Due to the convergent change in the structural properties of the annealed films at temperatures of (100 and 200) ºC, we will ignore the morphology and optical properties of the film annealed at 200ºC.

3.2 Morphology

Scanning electron microscope (SEM) was used to study the thin film surfaces. Morphological information of these thin films is shown in figures (3, 4 and 5).

The as deposited film shows a particle size of (50nm). While the films annealed at 100 ºC and 300 ºC show particle sizes of (300nm) and (280nm) respectively.

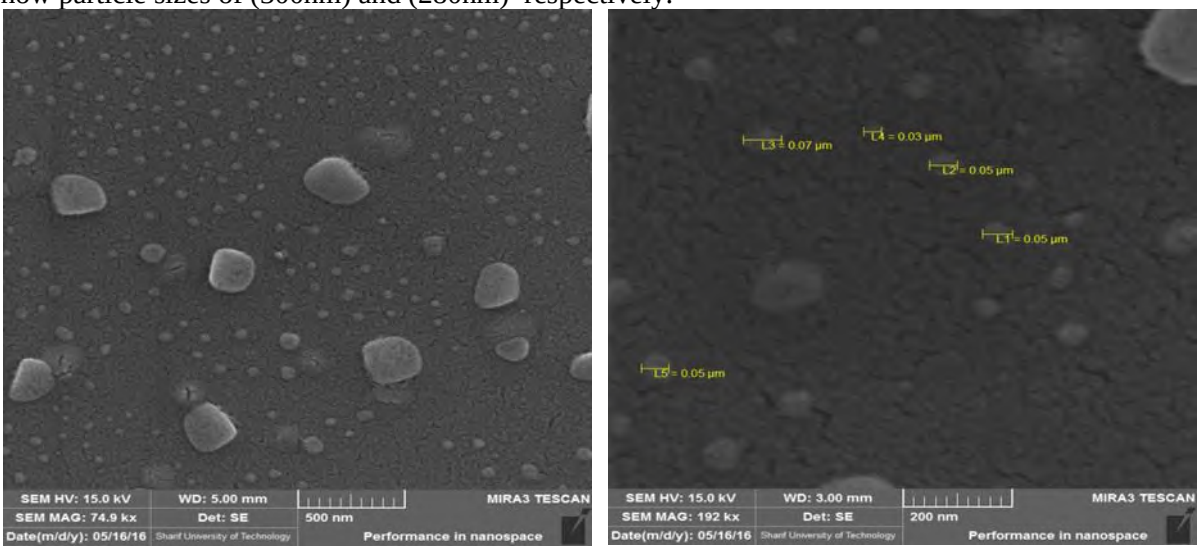

Figure 3. SEM images of as deposited InSe thin film at different resolution.

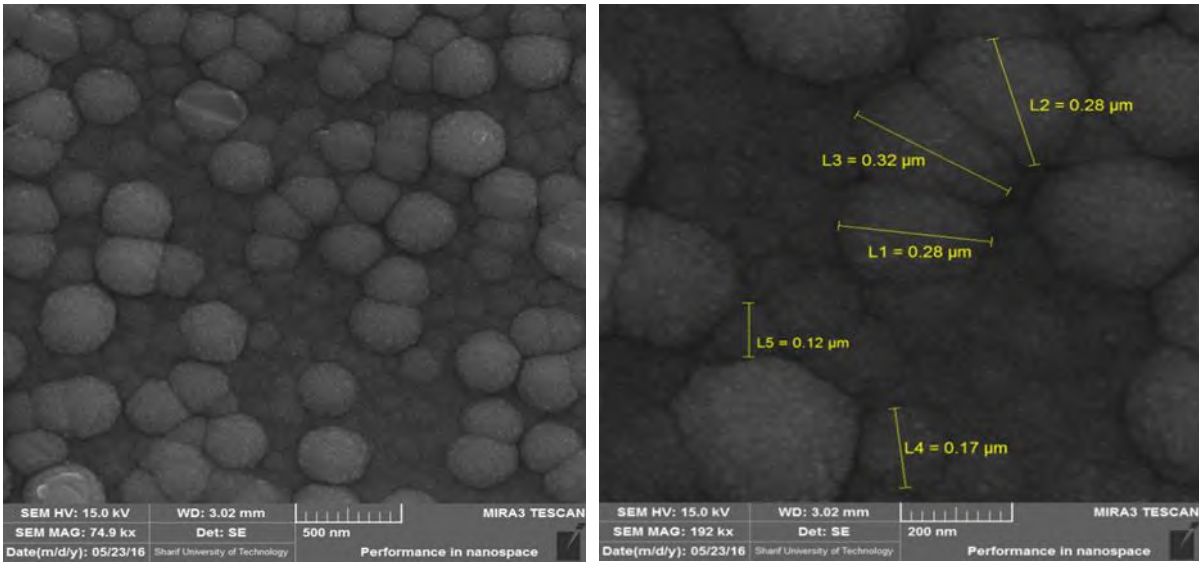

Figure 4. SEM images of annealed InSe thin film at 100 °C and at different resolution

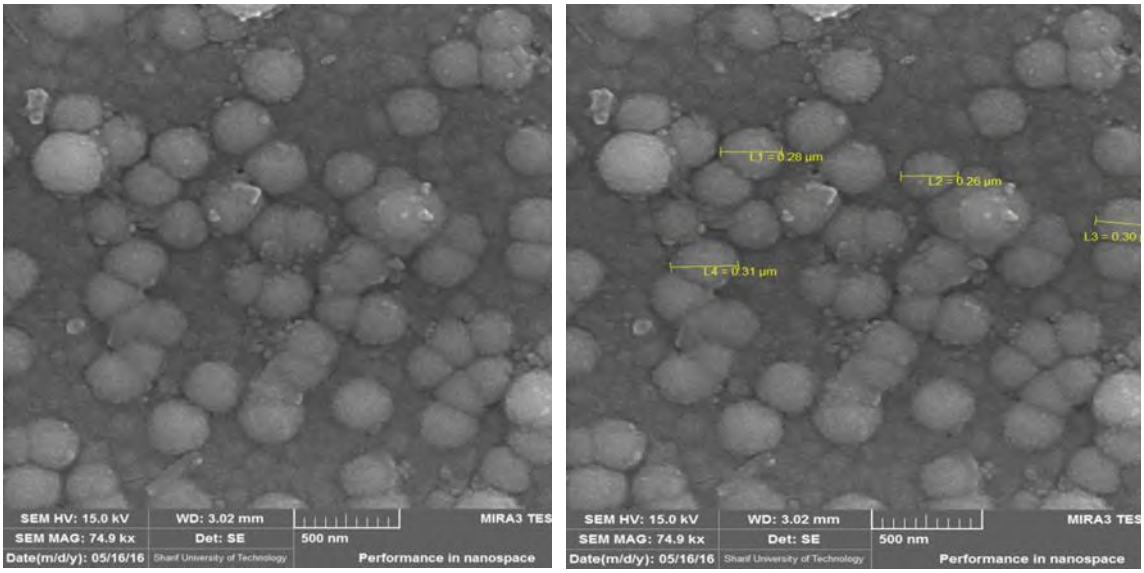

Figure 5. SEM images of annealed InSe thin film at 300 °C and at different resolution

3.3 Optical Properties

The absorbance spectra of as deposited and annealed (InSe) thin films are shown in figure (6). It is observed that the maximum absorption at a wavelength range of (300 -700) nm is suitable for the solar cell applications in this region.

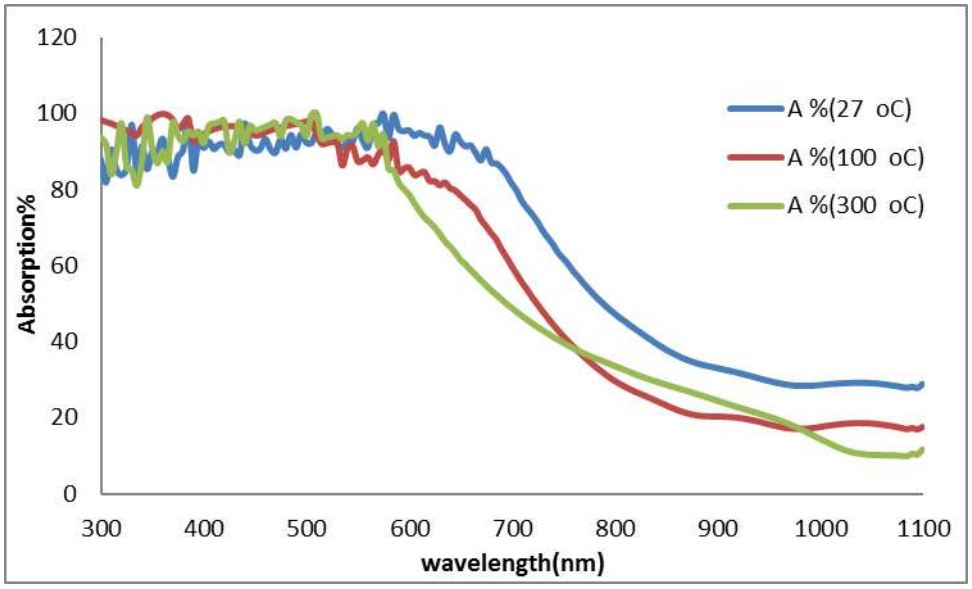

Figure 6. Absorption of InSe thin films as a function of annealing temperature: at (as-prepared, 100 and 300)ºC.

Figure (7) shows the transmittance spectra of InSe thin films at different annealing temperature. We noticed that the maximum transmittance at a wavelength range of (1000 -1100) nm at (as-prepared, 100 and 300)ºC. The annealing temperature plays an important role in the transmission spectrum by increasing transmission. On the other hand, the film annealed at 300 ºC shows improved transmission compared to that annealed at 100 ºC. This tuning of transmission by annealing indicates their utility as various technological applications. The film deposited with higher annealing temperatures shows a higher transmittance. These results agreed well with [16].

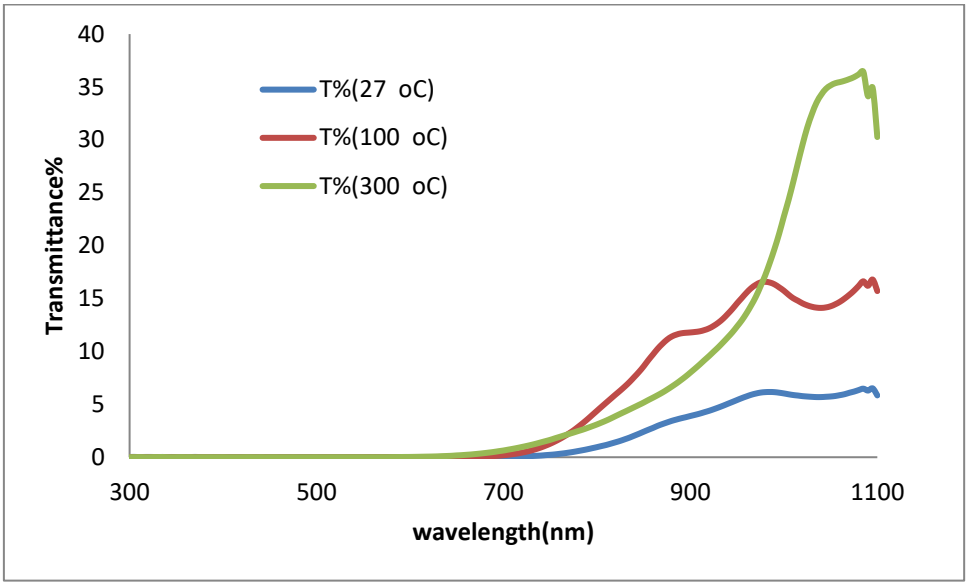

Figure 7. The transmittance of InSe thin films as a function annealing temperature: at (as- prepared ,100 and 300)°C.

The absorption coefficient (α) behaves as absorption behavior, and (α) was determined by equation 5) [21]:

$$\alpha = 2.303\frac{A}{t} \quad (5)$$

A is the absorption

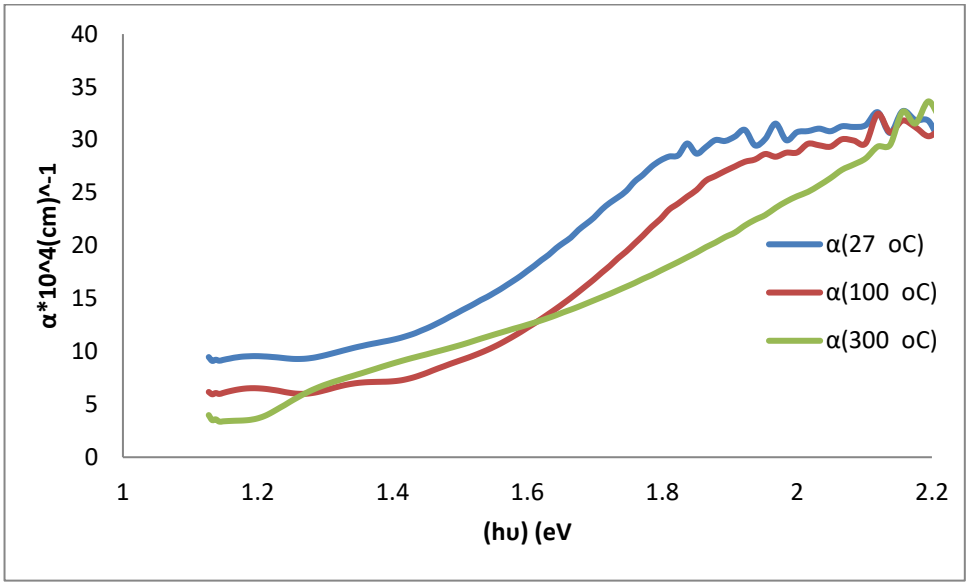

Figure 8. The variation of the absorption coefficient with energy for InSe thin films as a function of annealing temperature: (as-prepared, 100 and 300) °C.

The extinction coefficient (K) of InSe thin films were determined by equation (6) [22,23].

$$k = \frac{\alpha\lambda}{4\pi} \quad \text{.....(6)}$$

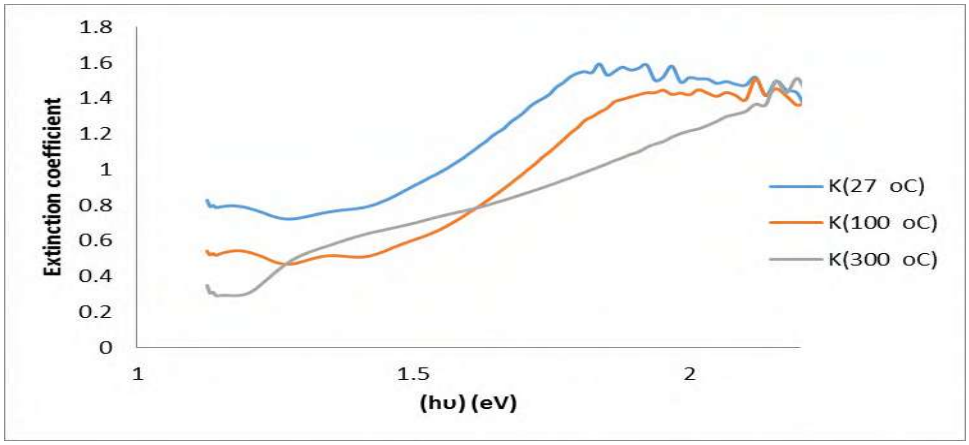

Figure 9. Extinction coefficient Vs Wavelength of InSe thin films: as a function of annealing temperature at (as-prepared, 100 and 300) °C

The optical band gap was calculated by Tauc's extrapolation method [24].

$$\alpha h\nu = B(h\nu - Eg)^r \quad (7)$$

where : (h) Planck's constant, (ν) frequency of the photon, (B) Constant and r is constant depends on the nature of transitions, r =1/2, 3/2, 2 and 3 for direct allowed, direct forbidden, indirect allowed and indirect forbidden respectively.

Compared to the plot of $(\alpha\ h\nu)^2$ variation with hν for the determination of direct band gap Eg which is shown in Figure 10. The optical band gap values are showed in Table 4.

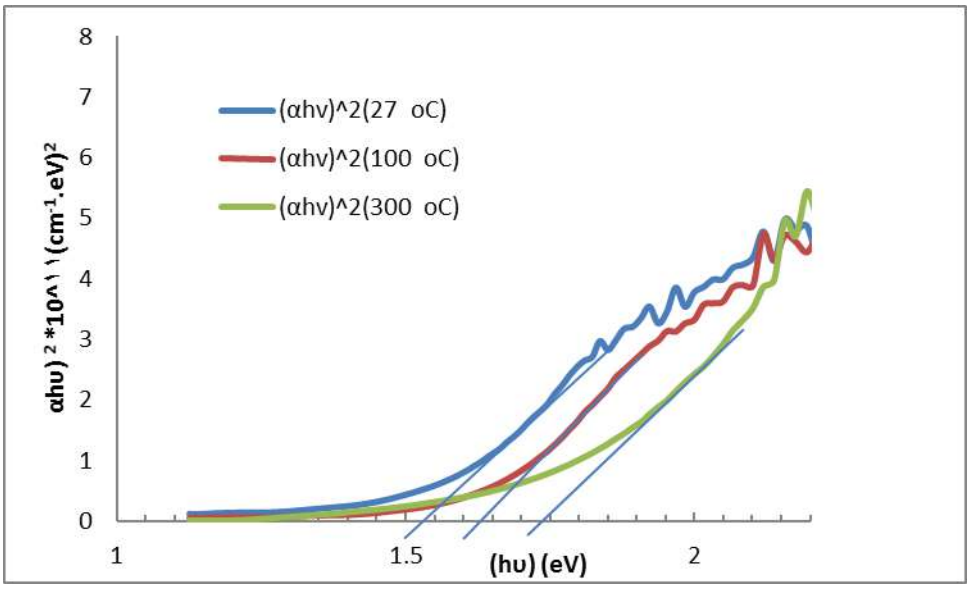

Figure 10. Plot of $(\alpha h\upsilon)^2$ versus (hυ) for InSe thin films as a function of annealing temperature (as-prepared, 100 and 300) °C

The band gap energy increases with increasing annealed temperature. The optical band gap values changes from 1.55 to 1.75 eV. The value of E_g is in good agreement with the reported values (1 – 2 eV) for InSe films. Table.4 shows the values of band gap energy for annealed InSe thin films.

The reduction in the number of unsaturated defects decreases the density of localized states in the band structure, consequently increasing the band gap [25].

Table 4. Bandgap variation of InSe with different annealing temperatures.

Temp. °C	Eg(eV)
as-prepared (27)	1.55
100	1.65
300	1.75

4. Conclusion

$In_{50}Se_{50}$ bulk samples are prepared by melt quenching technique and thin films of powdered alloys are deposited using thermal evaporation technique. The XRD pattern revealed that the as deposited films are amorphous in nature and annealed at 300˚C films exhibit polycrystalline nature. It was found that the physical properties of the films are heavily affected by annealing temperature. The absorption

edge and optical band gap depended on the crystalline structure. This tuning of transmission and band gap on annealing temperature indicates their utility in various technological applications.

References

[1] Hasan B A and Abdulrazzaq I M 2016 *Iraqi Journal of Physics* **14** (29) 55.
[2] Thomas B and Kutty T R N 1990 *J.phys. stat. sol.* **119** 127.
[3] Zishan H Khani M M Zulfequar M M and Husain M 1995 *Journal of Physics: Condensed Matter* **7** (47) 8979.
[4] Sanchez-Royoa J F Segura A Lang O Schaar E Pettenkofer C Jaegermann W Roa L and Chevy A 2011 *J. Appl. Phys*. **90** (615) 2818.
[5] De Groot C H and Moodera J S 2001 J.Appl. Phys. **89** (4336).
[6] 1mm K Suzki K Haga T Hasegawa Y and Abe Y 1981 Phase *J.Crystal Growth* 54 501.
[7] Ching-Hwa Ho Ying-Cen Chen and Chia-Chi Pan 2014 *J. Appl. Phys.* **115** 033501.
[8] Jasinski J Swider W Washburn J and Liliental Z Chaiken A Nauka K Gibson G A and Yang C C 2002 *J.Appl. Phys. Lett.* **81** (23) 4356.
[9] Eddiet M E Ulien C J and Balkanski M 1984 *J.matter.lett* **2** 432.
[10] Asabe M R Chate P A Delekar S D Garadkar K M Mulla I S and Hankare P P 2008 *J.Phys.and chem.* **69** 249.
[11] Bansode S B and Wagh V G *J. Computer Engineering (IOSR-JCE)* 38.
[12] Okamoto T Yamada A and Konagai A 1997 *J. Cryst. Growth* **175/176** 1045.
[13] Johna T Th Sudha Karthaa C Vijayakumara K P Abeb T and Kashiwaba Y 2006 *Vacuum* **80** 870.
[14] Mutlu I H Zarbaliyev M Z and Aslan F 2007 *J. of Sol-Gel Sci. and Tech.* **43** 233.
[15] Mohan A Suthagar J and Mahalingam T 2013 *Proceedings of The International Conference Nanomaterials: Applicationsand Properties* **2** (1) 5.
[16] Suhail M H Ibrahim I M and Ramizy A 2014 *Walailak J Sci & Tech* **11** (9) 777.
[17] Salman S H Shihaba A A and Elttaye A Kh 2019 *J.Energy Proceda* **157** 199.
[18] Hussain S 2008 *Investigation of structual and optical properties of crystalline ZnO* M. Sc. Thesis Inkpoing university.
[19] Williamson G B and Smallman R C 1956 *philos. Mag.* **1** 34.
[20] Joshi RN Singh VP McClure JC 1995 *Thin Solid Films* **257** 32.
[21] Pawlowski L 2007 *The Science and Engineering of Thermal Sptay Coating* John Wikey and sons 2nd.ed. France.
[22] Scholz F 1969 *compound semiconductors* (Mcgrow-Hill) 1969.
[23] Al-Maiyaly B H 2013 *Ibn Al-Haitham J.for pure&Appl. Sci* **26** (1).
[24] Ahmed G S Salman and S H Abid E Y 2016 *Ibn Al-Haitham J.for pure& Appl.Sci.* **29** (3).
[25] Parlak M and Erecelebi C 1998 *Thin Solid Films* **322** p 344.

Proton Irradiation the DNA of Human Cells

Proton Irradiation the DNA of Human Cells

Osamah Nawfal Oudah[1] and Bashair Mohammed Saied [2]

[1]Department of Physics, College of Education, University of Al-Qadisiyah, Al-Qadisiyah, Iraq.
[2]Department of Physics, Baghdad University-College of Ibn Al-Haitham, Baghdad, Iraq.

E-mail: osamah.oudah@qu.edu.iq

Abstract. Proton beam therapy provides favorable physical characteristics to kill cancer cells. It is known that all living organisms contain DNA, so we will simulate the bombardment of dry DNA of human's body cells by protons. The knowledge of stopping powers is very important especially for ion beam cancer therapy. The simulations first-principles dynamics helps the mostly employed linear description of response theory. The study denotes that DNA has suffered ionization by proton bombarding, which leads to long –lasting harm to human or cancer DNA that empowers us to diagnose the latter and treat it with radiation. Through using Bethe and Ziegler's equations, and also the SRIM programs, we determine the stopping power of the interaction of proton with human's DNA at approximate energy of 1 to 2.5 MeV. The human's DNA components are made of five main elements. All mathematical processes and analysis are achieved using Matlab program. The results are introduced in tables and figures. The researchers have formulated the power equation that denotes the values of stopping power according to the range of energy under investigation.

Keywords: Bethe equation, Ziegler equation, energy loss, Human cancer DNA, Stopping Power, SRIM.

1. Introduction

The particle therapy has introduced new innovative therapy for cancer by giving developed precision and radiobiological characteristics over the common photons. Globally, there are more than 150,000 patients treated in the present time [1]. Interaction between incident protons and human biological materials is highly significant to expect the influences of radiation on the live tissues and radiation dosimetry. The use of beams with energetic ion of radiation therapy becomes an encouraging method since more doses can be placed topically on the tumor spots to decrease the destruction of the contiguous crucial body parts. Hadron-therapy use of the energy deposition at the point that the penetrating proton beams will lose whole energy, i.e. the swift decreasing for the dosage at this point that could be employed for high dose deposition inside a particular swelling size. Electrons and photons do not have this property [2]. In radiotherapy of cancer, the choosing of the range and energy of the incident protons are vital for dose control. There is an extensive development in numerous algorithms employed to determine the dose depth and allocations for ion beams. Applying of Bethe theory on the solids where energy loss of particles measurements depends on it shows us the term energy loss is important for mean excitation energy of the material[3].

Charged particles can pass through matter and ionize the atoms they come across. They will lose their energy steadily numerous tiny stages. Mostly, they employ the mass stopping power that refers to the linear stopping power divided by density to express by units like MeV/(mg/cm^2). Then, it is manifested as the loss of energy for each unit of the attenuator thickness measured in g/cm^2[4]. So, it can be considered that there is an independence of the stopping power with respect to the density of the material. We can consider stopping power as crucial issue in several areas of technology, particularly high-tech usage in addition to medical procedures [5]. The paper investigates the energy loss by electronic excitations of the beams of fast proton through DNA for discrete and continuum states at varied incident energy.

The rapid charged particle, which passes through a medium, loses its power mainly by electronic excitation of object particles excluding the situation at very low speeds [6]. Incident particles may lead to main DNA destruction by physical and chemical interventions within a short period of time. So, the elastic energy loss will be ignored within the energy limit measured. It should be observed that in the range of low and medium energies, we need to regard the electron capture procedures and incident particle losses that provides an unceasing charge interchange of the projectile in their pathway through the solid influencing its energy loss. The loss of energy happens when protons crossing matter by succeeding collisions with the particles and atoms that they encounter. It is worth noting here that loss of energy is mainly because proton collisions by electrons in stopping material [7].

If protons encounter an extremely light nucleus, they will scatter, recoil nucleus could move to a substantial extent before the energy is entirely precipitated [8].Since the dose of radiation precipitated by photons decrease progressively with pervasive depth, the deposited dose by protons rises gradually to almost up to three-quarters of its travel distance inside stopping material, then increased to reach extreme value before swiftly slow to zero. Bragg peak is the depth that the extreme energy is deposited by protons. The position of the peak is relational to the proton beam energy [9].

2. Bethe Equations

The particles beam that crosses a target will lose its energy. The loss of energy is because of scattered electrons and nuclei, and the stopping electronic is clearly manifested almost in all regions of energy. The loss of energy relies on energy or more accurately the beam velocity. A quantum-mechanical derivation comprises relativistic effects identified as the Bethe - Bloch equation [10]:

$$\mathrm{S.P} = \left(\frac{ze^2}{4\pi\varepsilon_0}\right)^2 \frac{4\pi Z\rho N_A}{Amv^2}\left[\ln\left(\frac{2mv^2}{I}\right) - \ln(1-\beta^2) - \beta^2\right] \quad (1)$$

where: S.P stopping power, $v = \beta c$ is the ion velocity, ze = ion charge, m = mass of electron, I = ionization potential, N_A =Avogadro's number, A, Z, ρ were the numbers of mass, atomic number, and density of the stopping material, respectively [10].

3. Ziegler Equations

Varelas and Biersack suggested a theoretical interpolation to treat the gap between maximum and minimum energy for various states by chief terms [11]:

$$(\mathrm{S.P_{DNA}})^{-1} = (S_{LOW})^{-1} + (S_{HIGH})^{-1} \quad (2)$$

S_{LOW} represent the low energy stopping and equal to:

$$S.P_{LOW} = A_1 E^{1/2} \quad (3)$$

S_{HIGH} represents the high energy stopping and equal to:

$$S.P_{HIGH} = \frac{A_2}{E}\ln\left(1 + \frac{A_3}{E} + EA_4\right) \quad (4)$$

A_1,A_2,A_3 and A_4 are fitting constants in able (1).

Table 1. Fitting constants for equations (3 and 4) [11].

Elements	A_1	A_2	A_3	A_4
H	1.44	242.6	1.2	0.1159
O	3	1920	2000	0.0223
N	3.35	1683	1900	0.02513
C	2.989	1445	957.2	0.02819
P	3.647	3561	1560	0.01267

In situation of high incident energy, fitting formula equation (2) approximately corresponds to equation (1). Therefore, the formula of Varelas and Biersack has a greatly plainer and the valid approximate conduct at all energy ranges [11].

4. SRIM software

Measurements of "Stopping and Range of Ions in Matter" can be made by software like SRIM. There are many scientific references to SRIM annually. Current SRIM has new improvements depending on new empirical data. The latest version contains major improvements based on experimental data [12, 13].

5. Results and discussions

The entire stopping power of protons interacts with the DNA elements that measured employing the three methods as follows; Bethe equation, Ziegler equation and the computer program SRIM software.

Considering the human DNA as composed of five elements which are hydrogen 30%, oxygen 16%, nitrogen10%, carbon40%, and Phosphorus 4%.

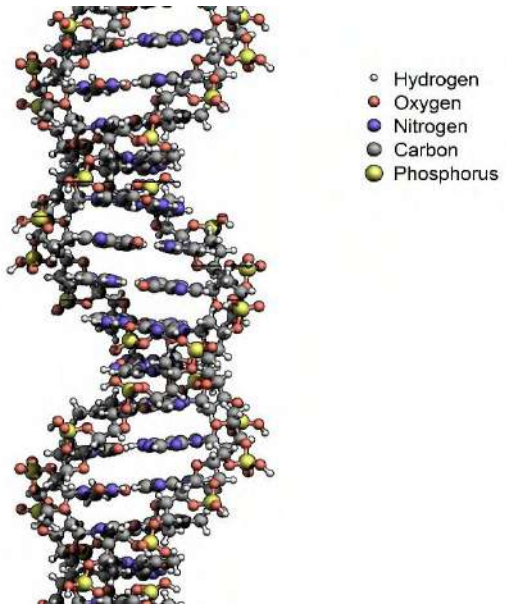

Figure1. DNA strands [14]

The total stopping power of proton interaction with H, O, N, C and P for energy range from 1 to 2.5MeV are measured employing the abbreviated formula of equation (1) [10].

$$S.P_{DNA}=0.239114\frac{Z_p}{E_p} ln\left[2.178 \times 10^{-3}\frac{E_p}{I}\right] \quad (5)$$

The measures are achieved by Matlab, with reliance on the values of the ionization potential for the elements as I_C=1.0039e-4 eV, I_H= 6.8560e-005 eV, I_N= 1.0895e-004 eV, I_O= 1.1769e-004 eV, I_P= 1.8155e-004eV.

Also we can use equations (2-4) to measure the total stopping power by Ziegler equations. And then we use the SRIM program to obtain the stopping power to the mentioned elements separately. All data are presented in figures (2-*6*).

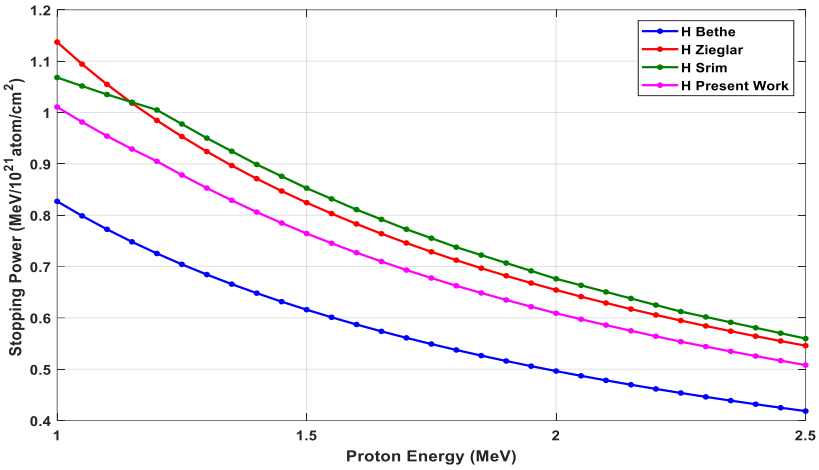

Figure 2. Proton stopping power in hydrogen

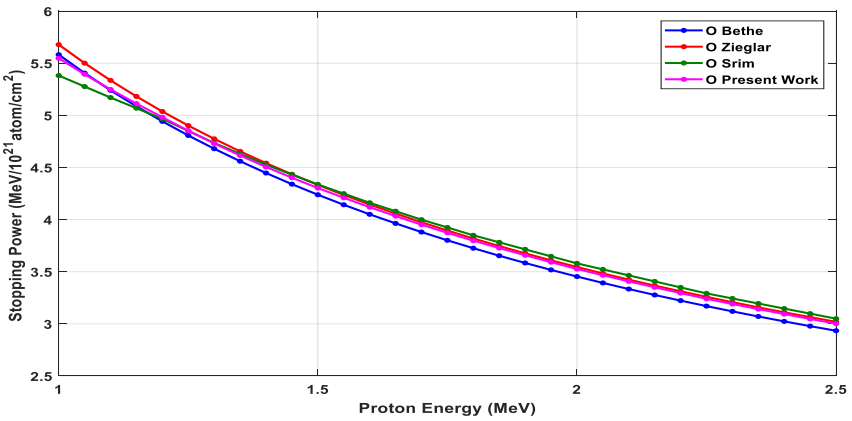

Figure 3. Proton stopping power in Oxygen

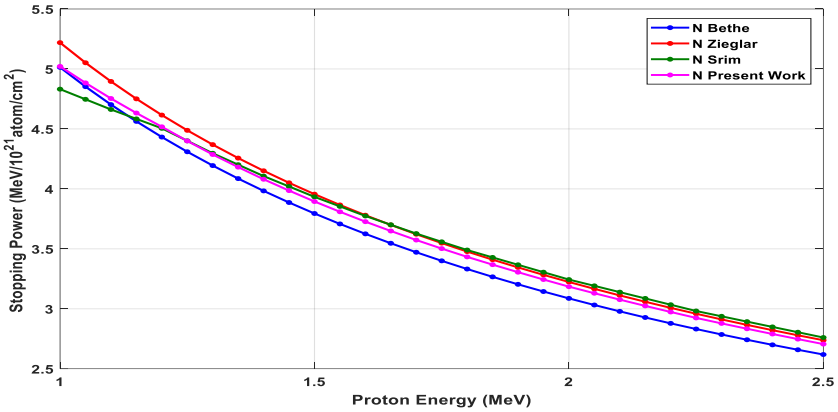

Figure 4. Proton stopping power in nitrogen

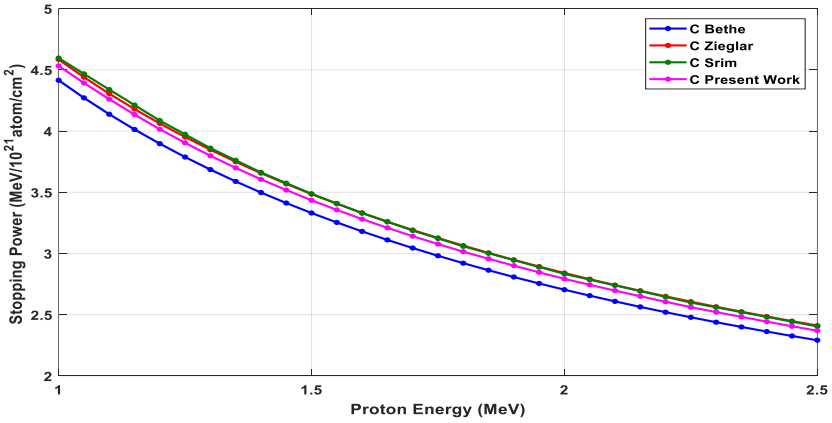

Figure 5. Proton stopping power in carbon

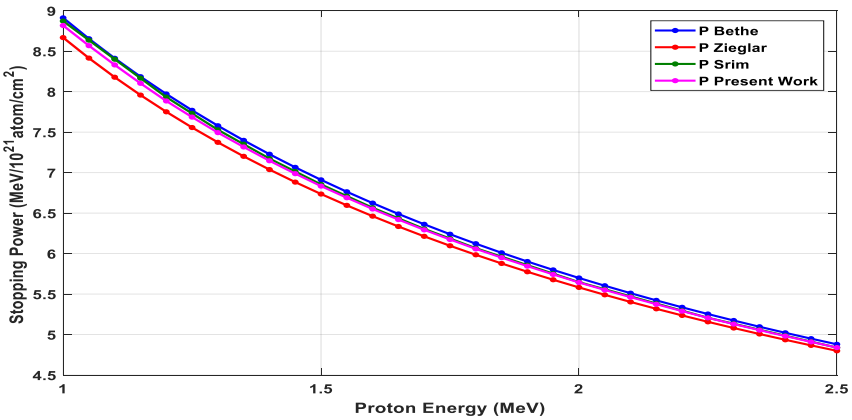

Figure 6. Proton stopping power in phosphorus.

So, using Bragg additively, the stopping power for human DNA was calculated by equation (*6*) and extrapolated to extract equation (*7*) to use in a wide range of protons energy.

$$S.P_{DNA} = 0.3\,S.P_{H} + 0.16\,S.P_{O} + 0.1\,S.P_{N} + 0.4\,S.P_{C} + 0.04\,S.P_{P} \quad (6)$$

General model Power equation:

$$S.P_{DNA} = a \times (E_p)^{b+c} \quad (7)$$

Coefficients (with 95% confidence bounds):

a = 4.919
b = -0.5071
c = -1.05

The results are shown in figure (7) and table (2).

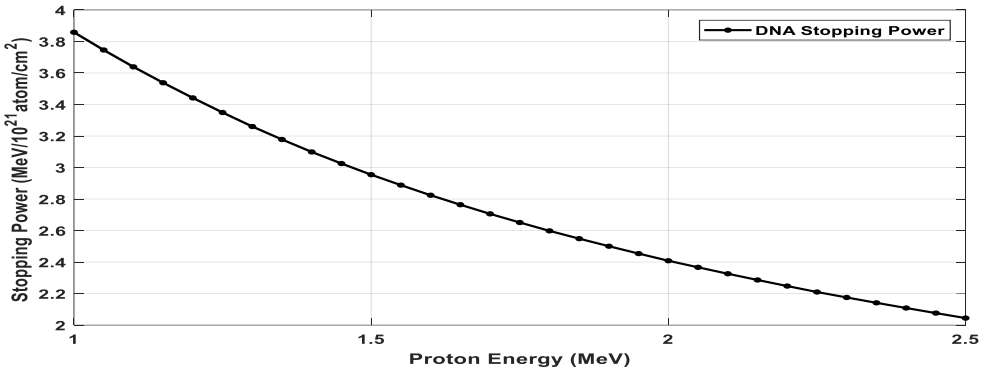

Figure 7. Proton stopping power in the DNA of human cells.

Table 2. Proton stopping power in the DNA of human cells.

Ep MeV	DNA Stopping Power
1.0000	3.8584
1.3000	3.2602
1.5000	2.9544
1.7000	2.7059
1.9000	2.5005
2.0000	2.4083
2.1000	2.3259
2.3000	2.1753
2.5000	2.0444

Conclusion

The crucial objective is the DNA for the most of biologic radiation impacts that includes the killing of living cells, cancer-making and mutation. Incident ionizing protons may prompt DNA destruction by the interaction of major and minor particles (direct) and also by the interaction of radiolysis yields with the DNA target (indirect) for a specific Short time range.

Three methods have been validated to calculate the stopping power of protons in DNA main components. After that, the algebraic process of the stopping power for specific component was taken in order to reduce the simple discrepancies in it, followed by the total stopping power of the DNA was calculated taking into consideration the percentages of participation of each element in the formation of DNA, Then the results were fitted to obtain a general equation to obtain the stopping power of the DNA in all proton energy ranges.

The Ziegler and SRIM were the true representation of Bethe equation by our six curves.

Our results for stopping protons in the DNA aim to provide an extra accurate description of the biological milieu.

Our expectations correspond with the existing empirical data and theoretical measures existed in the literature of the most of proton energy range studied here (*I*MeV –2.5MeV), however, there were huge variances perceived at lower energies.

References

[1] Mein, Stewart, et al. 2019 *Radiation Oncology* **14** (1) 123.
[2] Osama M et al. 2017 *Cancers* **9** (6) 66.
[3] McGregor, Douglas, and J Kenneth Shultis *2020 Radiation Detection: Concepts, Methods, and Devices(* CRC) Press 994
[4] ICRU Report 73: Stopping of Ions heavier than Helium 2005 *Journal of the ICRU* **5** (1) Oxford Univ. Press ISBN 0-19-857012-0.
[5] Warren, Daniel R., et al. 2015 *Physics in Medicine & Biology* 60(11) 4243.
[6] Trofymenko S V and Kyryllin I V 2020 *The European Physical Journal* **C 80** (7) 1.
[7] Newhauser W D and Zhang R 2015 *Physics in Medicine & Biology* **60** (8) R155.
[8] Park Seo Hyun,and Jin Oh Kang 2011 *Radiation oncology journal* **29** (3) 135.
[9] Chin L S and Regine W F 2010 *Springer Science & Business Media.*
[10] Ahmed A H 2006 *Empirical Formulae for Calculating Neutron Yield from (α,n) and (p,n) Reaction for the Light Element Targets* Ph.D. thesis,. Salahadin University- Erbil
[11] Andersen H H and Ziegler J F 1977 *Hydrogen stopping power and range of ions in all elements* (Pergamon press).
[12] Ziegler J F et al 2010 *Nuclear Instruments and Methods in Physics Research* **B 268** 1818.
[13] Dunn W L and Shultis J K 1994 Exploring Monte Carlo Methods.
[14] https://en.wikipedia.org/wiki/DNA#/media/File:DNA_Structure+Key+Labelled.pn_NoBB.png

Journal of Physics: Conference Series

Study of Some Structural and Optical Properties for P3HT: CBM Heterojunctions Blending of ZnS Nanoparticles

Study of Some Structural and Optical Properties for P3HT: CBM Heterojunctions Blending of ZnS Nanoparticles

Ghaida Salman Muhammed

Department of physics, College of science, University of Baghdad, Baghdad, Iraq.

E-mail: ghaidasalman7@gmail.com

Abstract. In this work, the preparation of P3HT: PCBM heterojunction blending ZnS nanoparticles (NPs) was demonstrated. Some structural and optical properties of the hybrid structure films were presented. ZnS NPs films were prepared by chemical route method and at different pH values. Then, the nanoparticles ZnS was incorporated in P3HT: PCBM solution in chlorobenzene with the weight ratios of 0, 5, 10 and 15 wt %. The X-ray diffraction patterns of the ZnS nanoparticles films and SEM images of the hybrid structure films are discussed. Also, the absorption spectra in the range of 200-1100 nm of the blends for variable weight ratios samples and the effect of ZnS pH values on these spectra are presented.

Keywords: nanostructure, organic materials, conjugated polymer, P3HT: PCBM, chemical rate method, x-ray diffraction, optical properties.

1. Introduction:

Organic materials are safe materials with unlimited availability which are used to develop the technology with active economy for extensive power generation. The organic semiconductors are cheap materials in comparable with the inorganic semiconductors. Also, the optical absorption coefficients of these materials are high which offer the prospect for the manufacture of thin film solar cells [1, 2]. Hybrid solar cells often use an incorporating of nanostructured materials as a network of electron-donor and electron-acceptor materials. These solar cells using the blending of materials are to convert sunlight into electricity [3]. P3HT polymers have been proposed to manufacture polymer : fullerene solar cells because they can absorb visible light and their glass transition temperature ≅110C° [4]. The morphology and the mobility of pure P3HT and blended P3HT: PCBM films are highly dependent on casting conditions [5, 6]. In the photoactive light absorbing thin film, a conjugated polymer is consider as organic part and a semiconducting nanocrystals (NCs) as an inorganic part [3].

In the present work, P3HT and C60 derivative PCBM material with the blending ZnS nanoparticles (NPs) on polymer-fullerene matrix are used. The inorganic semiconductor ZnS was used as the n-type material and the P3HT: PCBM as the photoactive layer. In this study, we concentrated on the effect of the concentration of ZnS on P3HT: PCBM photoactive layer and for three pH values. Hence, these materials combination has been used to study the light absorption characteristics.

2. Experiments:

P3HT: PCBM: ZnS NPs layers were prepared by spin coating as a precursor solution on pre-cleaned glass substrates. The glass substrates were first ultrasonicated in distilled water, ethanol, and subsequently dried in oven. The P3HT: PCBM layer was constructed by spin-coating method with 1:1 weight ratio solution in chlorobenzene at the glass substrate. Then, the ZnS nanoparticles were incorporated in P3HT: PCBM solution in chlorobenzene with the weight ratios of 0, 5, 10 and 15 wt %. Also, the ZnS NPs were prepared by the chemical route method. The ZnS NPs were prepared by mixing two chemical solutions. The first solution was prepared by dissolving 1.3g of ($ZnCl_2$) in 100 ml distilled water. Sodium hydroxide was used to reach the pH of the solution to the required amount of (pH=8.5, 9.5 and 10.5). The second solution was obtained by dissolving 0.7g from (Na_2S) in 100 ml distilled water [4]. Because of the common ion effect, the pH controlled the rate of reaction. With a spin-coating speed of 1000 rpm for 30s, P3HT: PCBM: ZnS NPs solution was deposited at the glass substrate. The annealing temperature was at 120 °C for 10 min. The ratios of P3HT: PCBM: ZnS NPs were (1:1:0, 1:1:0.05, 1:1:0.01 and 1:1:0.15), respectively. The film thickness of P3HT: PCBM: ZnS NPs was about 120 nm. The area of the sample was estimated to be (2.5x2.5) cm^2.

The structural properties of the films were investigated by using X-ray diffraction pattern (XRD). The surface morphology of the films was tested by using a field emission scanning electron microscope (FE-SEM, S-4200, and Hitachi) operated at 15 kV.

Also, the absorption spectra of the films were measured at room temperature using a SHIMADZU UV-1800 UV-VIS spectrophotometer. The spectrophotometer range is from (200- 1200) nm.

3. Results and Discussion:

3.1 X-Ray Diffraction:

XRD of ZnS (NPs) films are illustrated in Figure 1. Three prominent broad peaks are presented for all samples. The values of 2θ for these peaks are located around of 28°, 47° and 56° corresponding to (111), (220) and (311) diffraction planes respectively. This result indicates to the cubic structure for the prepared nanocrystals. Also, 2θ peaks located around 31°, 34°, 36°, 62° and 67 are related to (100), (002), (101), (013) and (112) planes respectively, which indicate to the hexagonal wurzite structure of polycrystalline ZnO. This result reveals the partial and complete oxidation of ZnS NPs in various mediums. In addition, the broadening of the peaks reveals to the formation of small size of ZnS nanocrystals [7, 8].

The prepared samples of pH (8.5, 9.5 &10.5) have average crystallite size of (11.5, 14.3 &12) nm respectively. The increasing of the intensity of ZnS NPs (111) peak indicates to the increasing of the crystallinity which is due to the increasing of the pH value of the samples. This result is comparable with result of other researchers [8].

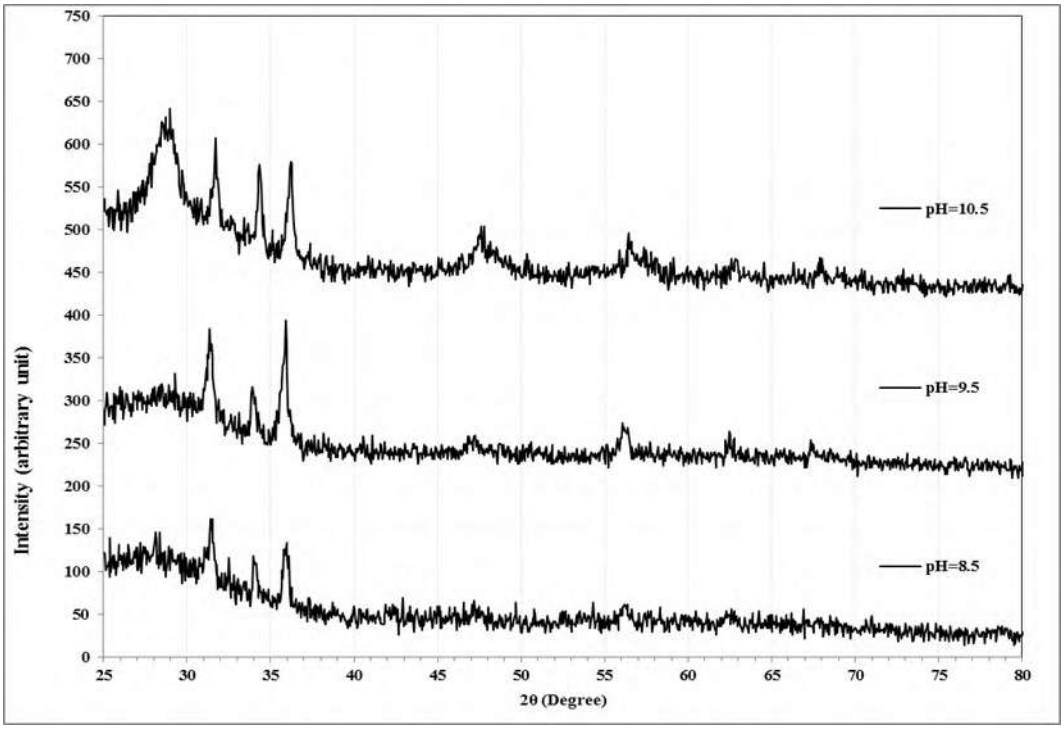

Figure 1. The XRD patterns of the ZnS nanoparticles prepared by chemical route method.

3.2 Scanning Electron Microscope Analysis (SEM):

Figure 2 shows the SEM images of ZnS NPs film, P3HT: PCBM film and P3HT: PCBM blending ZnS NPs hybrid film. The SEM study of the ZnS NPs film is shown in Figure 2a. The distributions of ZnS NPs are of irregular shape in the entire region with an average diameter of ZnS NPs about 85 nm. Figure (2b) shows the SEM image of P3HT: PCBM film. It can be noticed from this figure the uniform distribution of the film. To study the distribution of ZnS NPs in this layer, the microstructures of the P3HT: PCBM blending ZnS NPs hybrid film by SEM was used, as shown in Figure 2c. It was found that the distribution of the ZnS NPs is irregular distribution and the average diameter was about 57 nm. It is estimated that the decreasing of surface energy is attributed from the assemble effect results from nanoparticles [9].

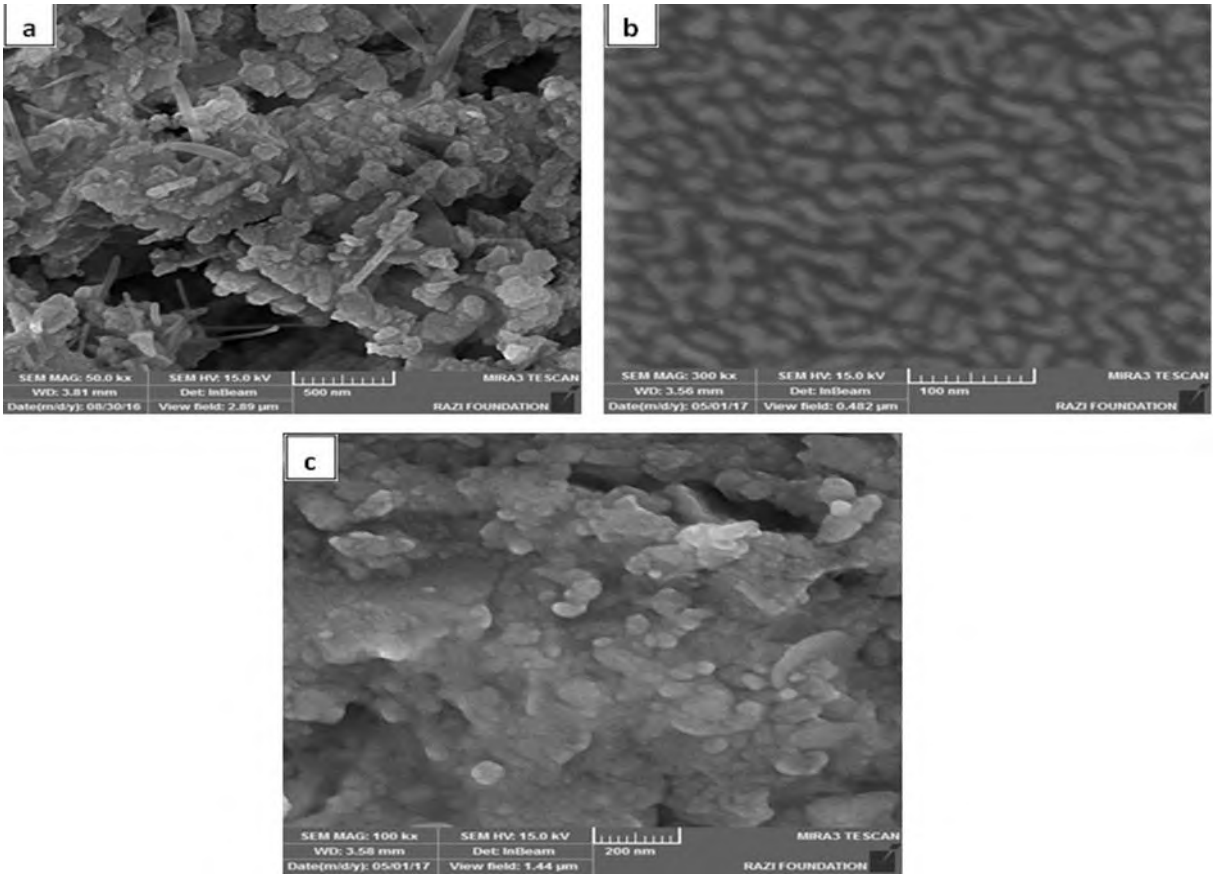

Figure 2. The SEM images of (a) ZnS nanoparticles, (b) P3HT: PCBM film and(c) P3HT: PCBM: ZnS NPs hybrid film.

3.3 Optical Properties Study:

The absorption spectra of the blends and for variable weight ratios samples of ZnS NPs are illustrated in Figure 3. The broad absorption peaks from 400 nm to 650 nm is resulted from the $\boldsymbol{\pi}$-$\boldsymbol{\pi}$* transitions. Absorption spectra of the blends shown in this figure are simply reveals to the combination of nanoparticles and polymer without any further absorption peaks [10, 11] because there is no any ground state interaction between them [12]. The little stretching of absorption edge of the P3HT: PCBM: ZnS NPs to the lower wavelength region is resulted from the quantum confinement effect from the inorganic nanoparticles. Also, the blue shift is due to the rising in band gap between π and π* energy levels. The insertion of the nanoparticles decreases the inter- chain interaction and conjugation length of P3HT.

Also, the addition of ZnS NPs into the P3HT: PCBM matrix increased the crystallization of the P3HT and captures more incoming light, therefore the magnitude of the absorption is increased [13]. It can be noticed, that the increasing of the ZnS NPs ratio leads to decreasing the absorbance, and this is because of the aggregation of ZnS NPs martial which can increase the recombination of exitons. Due to the high amount of the light absorption intensity, the generation rate of excitons is improving [9].

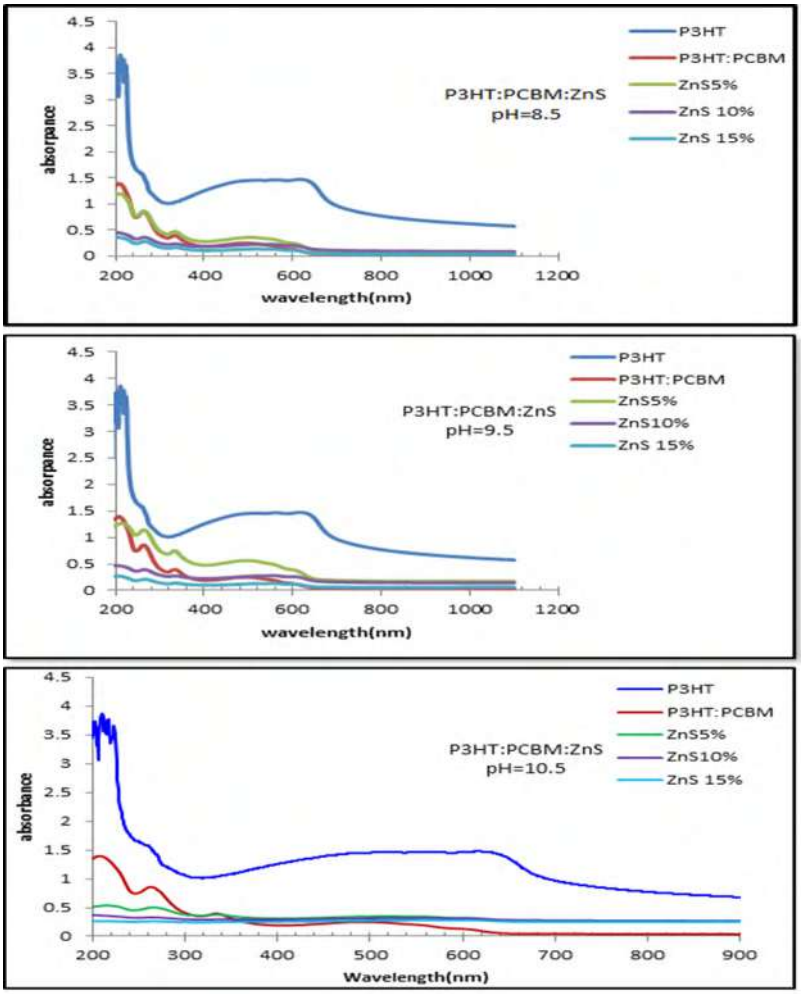

Figure 3. Optical absorption spectra of P3HT, P3HT: PCBM and P3HT: PCBM: ZnS NPs hybrid films for different pH values and concentrations of ZnS nanoparticles.

Also, the previous figure shows that the spectrum has two bands, one in UV region which is called B-band (or soret) band in the range about (240-350) nm due to the direct transition between the bonding π in HOMO and the anti-bonding π* in LUMO for all samples, and the other band is in the visible region which is called Q-band, and it consists of two close peaks in the range of 530-750 nm.

Figure 4 illustrates the relation between $(\alpha h\upsilon)^2$ and the photon energy ($h\upsilon$). The optical energy gap values (Eg_{opt}) for P3HT: PCBM and P3HT: PCBM: ZnS films with different pH values have been calculated using Tauc equation [11]. This figure reveals that the values of direct optical energy gap, increases by adding ZnS nanoparticles and for the lower concentration of 5% and for different pH is attributed to the increase of absorbance intensity in the visible region. Whereas, it decreases for other ZnS loading (10% & 15%) and for different pH values due to the decreasing of the absorbance in the visible region. Table 1 illustrates optical constants for P3HT: PCBM:ZnS films for different pH and concentrations of ZnS nanoparticles.

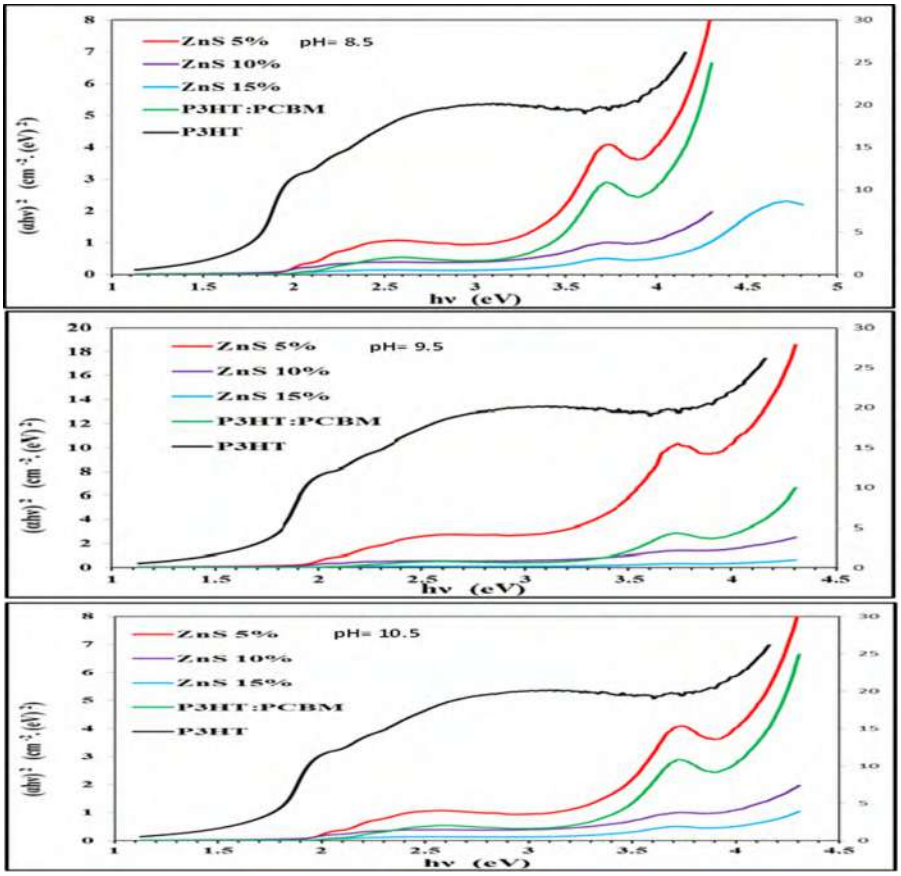

Figure 4. (αhυ) ^{2} versus photon energy (hυ) for P3HT:PCBM:ZnS films with various pH values of ZnS nanoparticles.

Table 1. Optical constants for P3HT: PCBM: ZnS films for different pH and concentration values of ZnS nanoparticles.

pH	ZnS Conc.	Eg (eV) Q1-band	Eg (eV) Q2-band 2-ban	Eg (eV) B-band band
8.5	5%	1.92	1.98	3.26
	10%	1.87	1.92	3.1
	15%	1.92	2	3.2
9.5	5%	1.89	1.94	3.16
	10%	1.8	1.88	3.02
	15%	1.9	1.99	3.04
10.5	5%	1.91	2	3.24
	10%	1.85	1.82	3.23
	15%	1.91	2	3.26

4. Conclusions:

In this work, it is shown that the surface morphology and optical properties of the P3HT: PCBM blend film is influenced by the adding of ZnS NPs on polymer-fullerene matrix. This result is attributed to the interpenetrating network of ZnS nanoparticles which grow in P3HT: PCBM layer. Also, there is an improvement of the light absorption intensity for P3HT: PCBM matrix due to the addition of ZnS NPs material. Hence, it can be used as an active layer to achieve an efficient solar cell.

References:

[1] Shaheen S E Radspinner R Peyghambarian N and Jabbour G E 2001 *Applied Physics Letters* **79** (2996).
[2] Askari M B 2014 *Sustainable Energy* **2** (3) 85.
[3] Lam K T Hsiao Y J Ji L W Fang T H Shih W SH and Lin J N2015 *Int. J. Electrochem. Sci.* **10** 3914.
[4] Kim H Nam S Jeong J Lee S Seo J Han H and Kim Y Korean 2014 *J. Chem. Eng.* **31** (7) 1095.
[5] Mayer A C Shawn R Scully Brian E Hardin Michael W Rowell and McGehee M D 2007 *materials today* **10** (11) 28.
[6] McGehee M D 2009 *MRS BULLETIN* **34** 95.
[7] Murugadoss G Ramasamy V and Kumar M R 2014 *Appl. Nanosci*. **4** 449.
[8] Salman GH Medhat M and Muhammed A 2017 *Australian Journal of Basic and Applied Sciences* **11** (7) 29.
[9] Lam K T Hsiao Y J Ji L W Fang T H Shih W SH and Lin J N 2014 *Int. J. Electrochem. Sci.* **10** 3914.
[10] Mall M Kumar P Chand S Kumar L 2010 *Chem. Phys. Lett.* **495** 236.
[11] Abdul Kareem T and Kaliani A A 2015 *Journal of nano and electronic physics* **7** (2) 1.
[12] Hu Z Daeri T Bonner M S Gesquiere A J and Lumin J 2010 *Journal of Luminescence* **130** 771.
[13] Guo J Ohkita, H Benten H Ito S 2010 *J. Am. Chem. Soc.* **132** 6154.

Employment of Titanium dioxide thin film on NO2 gas sensing

Employment of Titanium dioxide thin film on NO_2 gas sensing

Israa Akram Abbas[1], Salah Q. Hazaa[2], Seham Hassan Salman [3]

[1] University of Mustansiriyah College of Education, Physics Department, Iraq - Baghdad
[2] Al-Karkh University of Science, College of Science, Department of Medical Physics, Iraq - Baghdad
[3] University of Baghdad, College of Education, Physics Department,Iraq - Baghdad

E-mail: israa.akram.78@gmail.com

Abstract. TiO_2 thin films were deposited by Spray Pyrolysis with thickness ((350±25) nm) onto glass substrates at (350℃), and the film was annealed at temperatures (400 and 500)℃ . The structural and morphological properties of the thin films (TiO_2) were investigated by X-ray diffraction, Field emission scanning electron microscopy and atomic force microscope. The gas sensor fabricated by evaporating aluminum electrodes using the annealed TiO_2 thin films as an active material. The sensitivity of the sensors was determined by change the electrical resistance towards NO_2 at different working temperatures (200 and 300) ℃. It was determined that the fabricated sensor using TiO_2 thin film annealed at (400) ℃ with 8.28 nm particle size has high sensitivity than the thin films annealed at 500℃ with 10.37 nm particle size. The sensor operated at 200 °C had also sensitive to the NO_2 gas and its sensivity increased with operated temperatures at 300℃. It was observed that the fabricated sensors exhibited reproducible and stable results.

Keywords: TiO_2; Thin Film; annealing temperature; operation temperature; gas senor; spray pyrolysis.

1. Introduction

The Solid State gas sensors are depends on the change of the physical and/or chemical properties of their sensing materials when exposed to different gas atmospheres. Although the number of materials used to implement this kind of devices is huge, this work will be centered in studying the ones based in semiconductor properties, and more specifically in those using TiO_2 as gas sensor [1].

TiO_2 used in gas sensing is extensively because of its desirable sensitivity and mainly because of its good stability in adverse environments and versatility in detecting a wide range of toxic/flammable gases [2, 3]. Titanium (IV) Oxide (II) has phase stable, rutile (tetragonal) and two phases metastable, brookite (orthorhombic) and anatase (tetragonal). Both metastable phases become rutile (stable) when annealing the material at temperatures above 700 ºC (in pure state) [4].

This Semiconductor Gas Sensors (SGS) present the property of changing the electrical conductivity upon adsorption/desorption of gas molecules at their surfaces. Interaction with ambient oxygen in an n-type SMO can trap mobile carriers (electrons) from the bulk, resulting in an electron-depleted layer (i.e., space-charge layer) at the material surface [2,5].

As suggested by several authors [6, 7], working with nanostructured materials will give a higher surface area in front of gas. Taking into account that sensing reactions take place mainly on sensors layer surface, the control of semiconductor particle size will be one of the first a requirements for enhancing the sensitivity of the sensor.

Previously, reported methods for depositing thin film gas sensing materials include chemical bath deposition [8], spin-coating [9] silar [10], vacuum evaporation [11], sol-gel [12] and RF. Sputtering techniques [13] ,etc. Among all methods, spray pyrolysis method is preferred here because It is a simple method, cheap cost and easily for producing wide area deposition with suitable thickness [14]. The aim of this work was to deposited-TiO_2 thin films using a simple Spray Pyrolysis method and characterizes the effect of annealing temperature operation temperature on their nanostructural and sensor properties.

2. Experimental details

The TiO_2 thin films were prepared using spray pyrolysis method by taking a 0.1 M aqueous solution of TiC_3 as starting solutions. The solution was sprayed on to heated glass substrates which were kept at temperature 350℃. Film thickness (t) was measured using weighting method, and was found to be around (350 nm). The prepared films were annealed for 2h at temperatures 400and 500 ℃. The structure of the films after annealing were determined by X-ray diffraction (XRD) using X-ray diffractometer (SHIMADZU Japan) XRD600) with a Cu Kα radiation source (λ = 1.5406 Å) operated at 40 kV and 30 mA. The samples were scanned from 10 to 80°.

The surface morphology of films after annealing at 400 ℃ and 500 ℃ was carried out using Field emission scanning electron microscopy (FE-SEM) TESCAN (Czech Republic) (Zeiss-EM10C-100KV)university of Tehran -Iran, and Atomic Force Microscopy (AFM) micrographs were recorded by using (Cary 100 Conc plus) university of Baghdad.

Finally, the TiO_2 gas sensor was fabricated by evaporating aluminum as the ohmic contact electrodes on the TiO_2 thin films deposited using a grade mask. The gas sensitivity of a film is usually measured as the percentage change in film resistance on gas exposure, or may be defined as the ratio of its resistance in air to its steady state value in the presence of a gas. After put the sample in chamber was locally manufactured (The chamber is cylindrical in shape, with a radius of 7.5 cm, and a height of 15 cm.

3. Results and discussion

3.1. XRD analysis

The X-ray diffraction of thin films annealed at (400and 500) ℃ are shown in Figure 1 and 2. XRD results showed that the film was tetragonal TiO_2 polycrystalline after annealing according to JCPDS (Card No. 21-1272). It can be seen peaks (101) and (200) at around 25.23^o and 48.10° belong to TiO_2 appear at the annealing temperature of 400°C and slightly deviation in the peak position with increasing of annealing temperature, may be due to the formation of different strain relief at the crystal grains[15] . It is also observed that the peaks intensity increase with increasing annealing temperature, and other weak peaks appear after annealing at 500ºC, also it was found that the tetragonal phase remains stable with increasing annealing temperature, this result agreement with (Hasan et.al)[16].

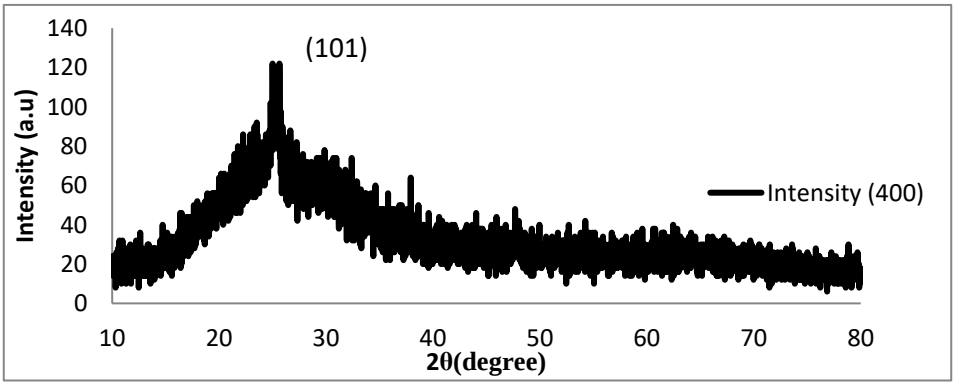

Figure 1. XRD patterns of (TiO_2) films annealed at 400°C temperature.

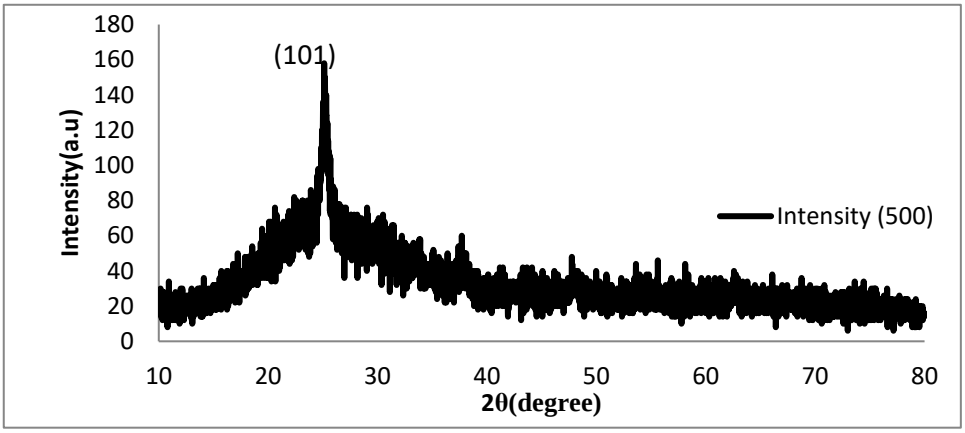

Figure 2. XRD patterns of (TiO_2) films annealed at 500°C temperature.

The XRD peaks (101) was selected to obtain structural parameters such as strain, crystalline size C.S , dislocation density δ and number of crystallites per area are calculated by using the following relations respectively [15,17] and listed in table(1) and influence of increase annealing temp. on the structural parameters.

$$\varepsilon = \frac{\beta \cos\theta}{4} \quad \ldots\ldots\ldots\ldots (1)$$

$$C.S = \frac{0.94\,\lambda}{\beta \cos\theta} \quad \ldots\ldots\ldots\ldots\ldots (2)$$

$$\delta = \frac{1}{(C.S)2} \quad \ldots\ldots\ldots\ldots\ldots (3)$$

$$N = \frac{t}{(C.S)3} \quad \ldots\ldots\ldots\ldots\ldots (4)$$

Where λ =0.154061nm, θ: Bragg's angle, β (FWHM): full width at half maximum in rad and t: thickness of the film.

From the Table 1, it was generally observed that as the crystallite size increases the strain, dislocation density and number of crystallites per area in the film decreases which is a well-known phenomenon.

Table 1. XRD results for thin films.

Parameters		Annealing temperatures ℃		Standard values
		400	500	
2θ	(101)	25.2372	25.1807	25.2806
	(200)	48.1091	47.9392	48.0487
d Å	(101)	3.5261	3.5338	3.5200
	(200)	1.80779	1.89611	1.8920
Strain	(101)	0.00437	0.00349	……..
C.S nm		8.28	10.37	……
δ *10^{15}	m^{-2}	14.5	9.3	…….
N_o *10^{16}	m^{-2}	61.5	31.4	……..

3.2 FESEM and AFM analysis

Figure 3. shows the Field Emission Scanning Electron Microscopic (FESEM) images of the annealed at 400 ℃ and 500 ℃ films. FESEM pattern reveals that films are uniform, good coverage of substrata surface, dense and without any cracks.

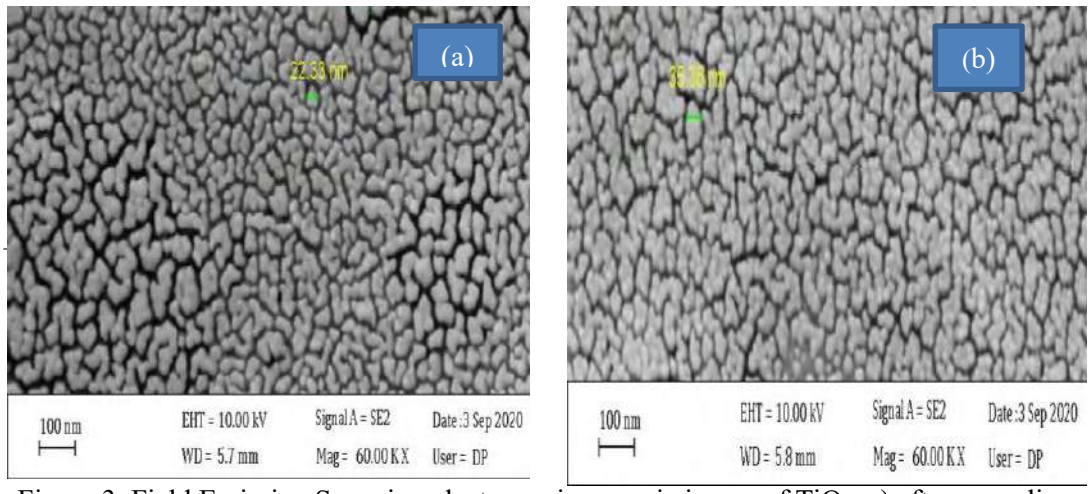

Figure 3. Field Emission Scanning electron microscopic image of TiO_2: a) after annealing at 400 and b) after annealing at 500.

The two -dimensional (2D) AFM images for thin films with annealing temperatures are shown in Figure 4. The sample surface become rougher after annealing at 500 ℃, it increased from 3.53nm for thin films annealed at 400°C to 7.63 nm for thin films annealed at 500°C as shown in table (2) this increasing may be due to increase of grain size. This results agreement with X-ray diffraction and (FESEM).

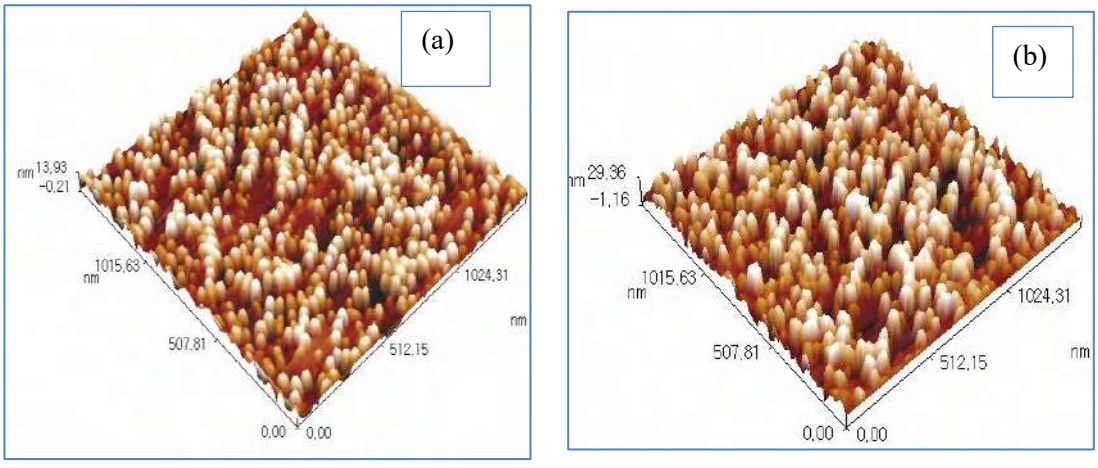

Figure 4. (2D) AFM images for annealing temperatures:(a) 400°C and(b) 500 °C.

Table 2. AFM results for thin films.

Annealing Temp.	Roughness	RMS	Average grain size (nm)
400°C.	3.53	4.08	47.73
500°C.	7.63	8.81	74.03

3.3. The gas sensitivity

The gas sensitivity of a film is usually measured as the percentage change in film resistance on gas exposure, or may be defined as the ratio of its resistance in air to its steady state value in the presence of a gas .Response (or detection sensitivity) of the sensors can be calculated as [18,19].

$$S=\left(\frac{(Rg-Ra)}{Ra}\right)*100\% \dots\dots\dots\dots\dots (5)$$

Where, Ra and Rg are the measured resistance under air and NO_2 (oxidizing gas), respectively.

It is possible to calculate the sensitivity of the sensor of the type metal oxides semiconductor through the interaction between the gas and the sensor surface

3.3.1. Influence of annealing temperature on Gas sensitivity

Figure 5 Shows effect the annealing on sensitivity (S) as a function of operating time for TiO_2 thin films when exposure to NO_2 gas at 200℃ operating temperature. It is clear from this figure the sensitivity of the thin film annealed at 400℃ (particle size of 8.28 nm) is greater sensitivity than of the TiO_2 thin film annealed at 500℃ (particle size of 10.37 nm) because it has a large surface area that provides more active sites for adsorption and reactivation for the gaseous species .And thin film annealed at 400℃ larger roughness, the increasing in surface roughness of the films leads to increase in sensing properties this results agreement with S.H. salman [20].

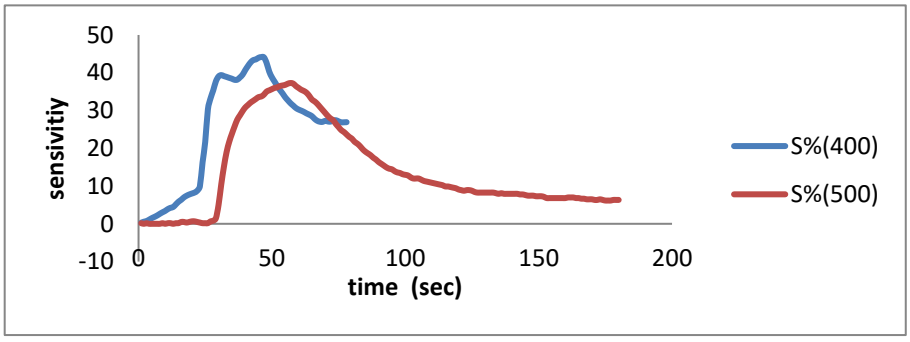

Figure 5. Show the effect annealing on sensitivity (S) as a function of operating time for TiO_2 thin films at 200℃ operating temperature

3.3.2. Influence of operating temperature on Gas sensitivity

Figure 6 and Figure 7 Show operating temperature on sensitivity (S) as a function of operating time for TiO_2 thin films annealed at 400℃ and 500℃ (annealing temperature).

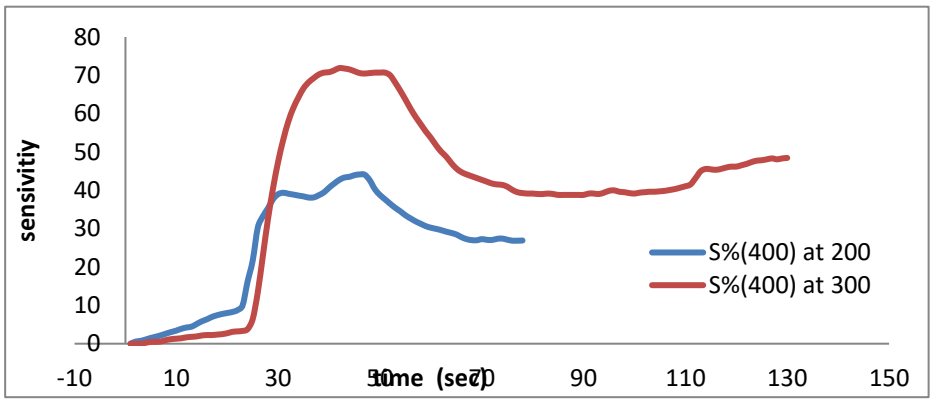

Figure 6 . Shows operating temperature on sensitivity (S) as a function of operating time for TiO_2 thin films annealed at 400℃ (annealing temperature).

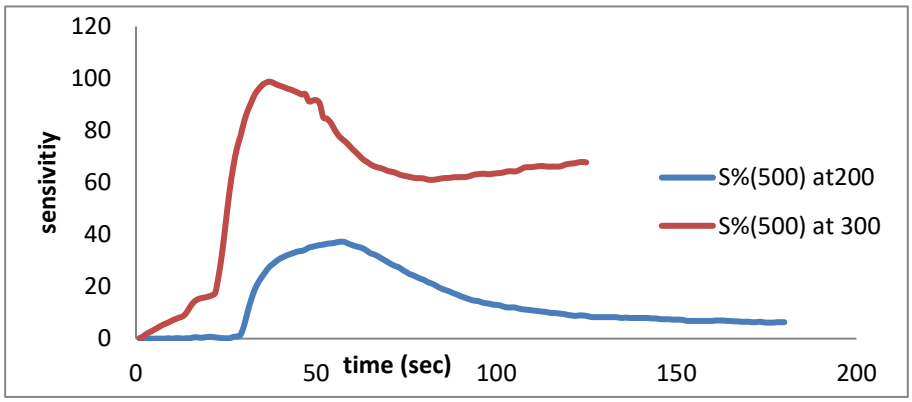

Figure 7. Shows operating temperature on sensitivity (S) as a function of operating time for TiO_2 thin films annealed at 500℃ (annealing temperature).

The calculated sensitivity (S) of the sensors in two cases was given in Figure 5 and 6. The sensor prepared is sensitive to NO_2 gas as seen in these figures. It was shown that the sensitivity of the sensors for these two measurements did not significantly change. As known the stability of the chemical gas sensors related the particle size in the film [21]. It was seen that the sensitivity increased as the operating temperature increased because decreases the surface resistance of the semiconductor thin film. Changing of their electrical properties interested in adsorption of oxygen by trapping an electron from the conduction band of the metal-oxide semiconductor. At the working temperature of the sensor below 200 °C ionized molecular (O_2^-) form of the oxygen can be exist while above this temperature atomic (O^-, O^{2-}) forms is dominated [22].

The highest response of the sensor was reached at an operating temperature of 300 °C, as % 97.4. In addition, the results indicate that the sensor has a good response with 37.46 % at a low temperature as 200 °C; these results for thin films annealed at 500°C.

Also the highest response of the sensor was reached at an operating temperature of 300 °C, as 70.8%. In addition, the results indicate that the sensor has a good response with 43.9 % at a low temperature as 200 °C, this results for thin films annealed at 400°C.

4. Conclusions

The spray pyrolysis method was successfully used to deposit a uniform and homogeneous TiO_2 film. The XRD data reveal that the TiO_2 samples are polycrystalline with tetragonal structure after annealing. The crystallite size is increased as the annealing temperature increases. The properties of TiO_2 thin films are suitable for various technological applications. Such as gas sensor .the sensitivity of thin films (TiO_2) for NO_2 gas depending on annealing and operating temperature.

References

[1] Woetsman J. T. & Logothetis E. M. 1995 the Industrial Physicist 20-24, Ed. American Institute of Physics.
[2] Wilson R. L., Simion C. E. , Blackman Ch. S., Carmalt C. J., Stanoiu A., Maggio F. Di & Covington J. A. 2018 *J. Sensors* **18** (735) 2.
[3] Nagabharana R. M., Kumaraswamy, G. N., Gundanna, S. K., & Bhatta, U. M. 2020 *J. Thin Solid Films* **710** 138262
[4] Rzaij J. M. & Abass A. M. 2020 *J. Chem. Rev.* **2** (2) 114
[5] Zeanb. T. A. 2015 PhD. Thesis, Collage of education for pure science Ibn-Al-Haitham University of Baghdad.
[6] Mohan P. A., & Jayaraj M. K. 2020 *J. Springer, Singapore* **211**
[7] Marichy C., Pinna N. 2016 *J. Adv. Mater. Interfaces* **3** 1
[8] Elfanaoui A., Ihlal A. , Taleb A. , Boulkaddat L. , Elhamri E. , Meddah M. , Bouabid K. & Portier X. 2011 *J. Conden. Matter* **13**
[9] Plesch G., Haidry A. A., Gregor M., Durina P., Gregus J., Truchly M., Roch T., Plecenik T., Zahoran M., Puskelova J., Mikula M., Grancic B., Satrapinskyy L., Kus P. & Plecenik A. 2013 *J. Key Eng. Mater.* **543** 293
[10] Jiménez-García F. N., Segura-Giraldo B., Restrepo-Parra E. & López-López G.A. 2015 *J. Ingeniare* **23** (4)
[11] Sta I., Jlassi M., Hajji M., Boujmil M.F., Jerbi R., Kandyla M., Kompitsas M., & Ezzaouia H. 2014 *J. Sol-Gel Sci. & Technol.* **72** 421
[12] Muaz A.K., Hashim U., Thong K.L., & Wei-wen Liu 2015 *J. Microsyst. Technol.*
[13] Seham H. S., Shihab & A.A., alttayef A. H. 2019 *J. Energy Procedia* **157** 199
[14] Arunananthan M. V., Selvaraj D., & Natarajan P. 2019 *Int J. Nano Dim.* **10** (3)230
[15] Hazaa S. 2015 *J. Appl. Phys.* (IOSR-JAP) **7** (1) 59
[16] Chaudhari K. B., Rane Y. N., Shende D. A., Gosavi N. M. & Gosavi S. R. 2019 *J. Optik* **193** 163006
[17] Raha D. & Das D. 2013 *J. Appl .Surf. Sci.* **276** 249
[18] Yewale A. K. 2011 *J. Int. Adv. Eng. Technol.* **2** (4) 226
[19] Çetin S. S., B˘aleanu C. M., Nigmatullin R. R., aleanu D. B. & Özçelik S. 2011 *J. Thin Solid Films* **519** (16) 5712
[20] Seham H. S., Shihab A.A. & alttayef A. H. 2019 *J. Energy Procedia* **157** 283
[21] Wang C., Yin L., Zhang L., Xiang D., & Gao R., 2010 *J. Sensors* **10** (3) 2088
[22] Comert B., Akin N., Donmez M., Saglam S. & Ozcelik S. 2016 *J. Sensors* **16** 24

Flood Behavior of Al-Hammar Marshes

Flood Behavior of Al-Hammar Marshes

Sarah T. Yaseen[1], Auday H. Shaban[2*], Kareem A. Jasim[1]

[1]College of Education for pure science, Ibn Al-Haitham, University of Baghdad, Iraq
[2]College of Science, University of Baghdad, Iraq.

E-mail:: auday.h.s@ihcoedu.uobaghdad.edu.iq

Abstract. The marshes of southern Iraq are among the most important and largest wetlands in the Middle East and the world are characterized by the freshness of their waters and their environmental diversity. The marshes have undergone many changes during the past decades and to discover and study these changes, remote sensing data will be used as sources of information and data in this study represented by the Landsat 8 satellite images (OLI), the images were collected for years from 2013 to 2019, and by applying remote sensing techniques and geographic information systems techniques, changes in Al-Hammar marsh were detected during the past seven years, the supervised classification method (maximum likelihood) was applied to classify the region Were identified six main categories of the land cover (deep water, shallow water, small cane, large cane, plant, soil) using the software (ENVI 5.3), the final maps were produced for classification using (ArcGIS 10.4.1) software, the results showed Significant change in the water content of Al-Hammar marsh and the increase in the proportion of flooding during the year 2019 to the highest rate since 2013. In addition, the results showed the accuracy and success of the supervised classification method (maximum likelihood) in the classification of images as they are considered the best classification methods, the fastest and high accuracy.

Keywords: Remote sensing, Wetland, Al-Hammar marsh, Supervised Classification, Maximum Likelihood, Overall Accuracy.

1. Introduction

Remote sensing is an important and pervasive technology in modern technology science, as this technology can be used and applied to collect data about a target such as the features of the land cover and others and this data is analyzed, interpreted and processed to obtain information from it without direct contact with the target, and remote sensing can be defined as a technique Collecting data on a specific target, such as the Earth's surface, analyzing, interpreting, and processing it and extracting information from it without an actual connection between them[1][2]. It provides a great possibility to monitor and collect data about a specific area or goal for different time periods at the same time and with high accuracy and with simple costs for the purpose of analyzing, interpreting and studying them and discovering the changes that occur during these periods and many other processes provided by this science, it allows the possibility of studying the features of the land cover [3]. These data collected about the target are transferred from the target to the sensor in the form of electromagnetic spectrum as the physical medium between the target and the sensor is the electromagnetic spectrum [4]. In remote sensing, several areas of the electromagnetic spectrum are used through the sensed images where remote sensing deals with both the visible spectrum, the infrared (near, short and thermal) spectrum, the

microwave, where these images are collected from sources Numerous such as satellites, radars, spacecraft or sensing images carried on board aircraft [5][6]. The wavelengths of these areas of the electromagnetic spectrum are reflected from the target and recorded as a digital number in the image pixels as the images that are dealt with in this technique are multi-spectral digital images that consist of a large number of picture elements (pixels) as each pixel has a specific digital number It represents the amount of the reflected electromagnetic spectrum from the target, the pixel in the image covers a specific area of the region covered by the image[5][7].Remote sensing provides many and important data on the surface of the earth and its resources, and thus it represents an important and great source for many studies and applications that address the surface of the earth and its various and various features. Urban development, agriculture, and many other applications, using remote sensed data [8][9]. One of the important applications in remote sensing is the study and discovery of changes that occur in wetlands that affect their nature. The diversity in the environmental system and have a great importance in maintaining the balance and presence of wildlife. It is low areas on the surface of the earth that are submerged in water that are either deep or shallow in which many plants grow. These lands may be permanently submerged or seasonally and form a good habitat for different animals such as fish, migratory birds and many other animals. Wetlands exist in different forms on the surface of the ground Including swamps, marshes, shallow lakes, etc. They also differ in terms of the nature of the waters that are submerged, some of which are fresh and salty, and they represent an integrated ecosystem in biological terms, and they are either natural existence or artificial, wetlands constitute about 3-6% of the surface of the earth around the world and represent one of the main ecosystems on the earth's surface [10][11]. Among the important and major wetlands in the world are the Iraqi marshes, which are characterized as natural wetlands with fresh water. These marshes cover a large area in southern Iraq, where they occupy south and central the sedimentary plain in three southern governorates: Basra, Maysan, and DhiQar[12][13]. It also represents the largest natural wetland in the Southwest Asian region [14][8]. There are many marshes in southern Iraq, including permanent ones and seasonal ones, but mainly wetlands in Iraq can be represented by three major and large marshes: Al-Hammar marsh, Central Marshes and Hawizeh marsh [15]. The Iraqi Marshes have undergone great changes during the past forty years for a number of reasons, including drying and building dams, etc., which led to changing many of its features, characteristics, flooded areas, and even its environmental system and biological composition [16]. To study the changes that occurred in Al-Hammar marsh during the time period of 2013-2019, remote sensing and geographic information systems (GIS) techniques are used where the supervised classification method (maximum likelihood) will be used to know the change in the water content and the areas flooded during this period and is this is done by performing image processing on Landsat satellite images (L8), where image processing represents all the processes and applications that are implemented on digital images for analysis, processing, interpretation, and extracting the required information through the use of computers, for image processing multi applications on remote sensing images as classification, environmental assessment, changes detection taking occur in the land cover features and create maps and other [5].The use of land cover in Dhaka Metropolitan of Bangladesh is studied by using the same supervised classification method as the maximum likelihood of classifying the sensed data and revealing the changes taking place in the region, Dewan 2008[17]. The same objectives of this study but using another program to apply the supervised classification to detect changes is the program (ERDAS), Abdul Jabbar and others 2010[16]. This study is similar to the current study where the supervised classification method (maximum likelihood) is used to classify attributes of the study area and reveal the changes that occurred in it, Soliman 2011[18]. The Landsat satellite imagery is categorized in the same way in this study to uncover changes in Kolkata Wetlands, Seema and others 2012[19]. Similar to the work of this study, where the study area is classified using the supervised classification method (maximum likelihood) and then revealed the changes that occurred, Muhsin and others 2017[13].

2. Classification

Classification is an important application in remote sensing and in image processing, where images are processed and some algorithms are applied to them in order to obtain certain information, and classification can be defined as the process of sorting and distributing image elements (pixels) on the features or classes of land cover based on the numerical value of the units of the image, as each of them possesses a numerical value representing the amount of spectral reflection of the attribute or class present in the image [20]. The classification is very important when dealing with multispectral images that consist of a number of spectral bands, and there are two main types of classification are supervised classification and unsupervised classification [21].

The supervised classification is considered the fastest, broader in use and application and the highest accuracy than the unsupervised classification, it gives very accurate results and close to the reference data that are compared with it when applied by a user with experience and good knowledge of the classified area and the land cover features for it, the supervisory classification provides great potential and freedom for the user in The identification and distribution of image pixels on the land cover categories, it makes the classification process easier and faster, and this type of classification needs in the beginning to identify and choose training sites in the area of interest, i.e. distribute the image pixels to the land cover categories It is distributes according to the spectral reflection of each of them, and then each training site is distinguished by a specific color or symbol, so that it can separate and define the interference regions in the land cover [21][22]. There are many types of supervisory classification including (parallelepiped, minimum distance, mahalanobis distance, maximum likelihood, spectral angle mapper, spectral information divergence, Binary encoding), where the maximum likelihood method will be used in this research paper to classify the Landsat 8 satellite images [23].

3. Maximum likelihood Classification method:

It is the most common and used method and the most accurate supervised classification method in the classification of remote sensed images as it is widely used to classify the features of the land cover in images with false colors, in this method all pixels in the image are classified and assigned to one of the categories of the land cover that have the highest probability [24][25]. In order for the results to be very accurate, the probability threshold limit that does not allow a pixel to be set to a category with a low probability [26]. Must be set. The discrimination functions for all pixels in an image classified in this way are calculated using the following formula:[27].

$$\boldsymbol{g_i}(x) = In\, p(\boldsymbol{\omega_i}) - \frac{1}{2}\, In \left| \boldsymbol{C_i} \right| - \frac{1}{2}\, (x - m_i)^T \boldsymbol{C_i^{-1}} (x - m_i) \qquad \ldots\ldots\ldots\ldots\ldots (1)$$

Where:i: classes. x: dimensional information.$P(\omega_i)$: Probability of occurrence of the class in the photo (presumably the same for all categories).$|C_i|$: Specified for the information covariance matrix in the category(ω_i).C_i^{-1}: Inverse of covariance matrix. m_i: The image classes mean vector.

4. Classification accuracy assessment

Despite the high accuracy of the classification and the proximity of the results of the classification to the real reference data for the study area or the classified target, it is necessary to verify the accuracy and validity of the classification by conducting an assessment of the classification accuracy, which represents an important and final step in the classification process that shows how accurate the classification. Confusion matrix (error matrix) is constructed, which is a matrix consisting of numbers (rows and columns) these numbers represent the classified image units where image pixels (number of image units) classified for each category of land cover are placed in one of the rows and the reference data for each category of land cover is placed in One of the columns for the matrix [28]. There are several methods for assessing classification accuracy such as user accuracy, product accuracy, overall accuracy, and Kappa coefficient. The overall accuracy is the ratio between correctly rated reference points to total reference points [28]. The accuracy of the user is the ratio between the numbers of pixels correctly classified to the total number of pixels in the row, while the product accuracy is the ratio between the numbers of pixels classified correctly to the total number of pixels in column [29]. Thus, the confusion matrix can be written using product accuracy and user accuracy [28]. Another metric that

represents a statistical measure of classification accuracy is the Kappa coefficient that has a value between + 1 and -1, so whenever the classification accuracy is high and is close to reference data, its value is close to + 1, if either its value is close to zero or negative, then this means that the classification is inaccurate and there is no affinity between it and the reference data. To calculate the overall accuracy, equation (2) is applied. To calculate the Kappa coefficient, equation (3) is applied, respectively [30].

$$\text{Overall accuracy} = \frac{\textbf{Total number of correct classified}}{\textbf{Total number of pixels}} * 100 \quad \dots\dots\dots\dots\dots (2)$$

$$K = \frac{n \sum_{i=1}^{p} xii - \sum_{i=1}^{p} (xi \times x+i)}{n^2 - \sum_{i=1}^{p} (xi \times x+i)} \dots\dots\dots\dots\dots (3)$$

Where:
n = total number of training pixels. p = number of classes. Σxii = total number elements of confusion matrix. $\Sigma xi+$ = sum of row i. $\Sigma x+i$ = sum of column i.

5. Study area

Al-Hammar marsh is considered one of the main marshes in Iraq and occupies a wide area that extends across three governorates (Basra, DhiQar, Maysan), approximately 300 km south of Baghdad and is located within the coordinates of latitude (31,00 - 31,30) north and longitude (46,24 - 47,18) east, with a length of about 90 km either its width ranges between (25-30) km, ALHammar marsh is a distinctive and important ecosystem with social and economic impact in the region and has great importance and benefit as it represents the habitat for many migratory birds in addition to that the local population depends in their livelihood on the resources of marshes and animals [31].

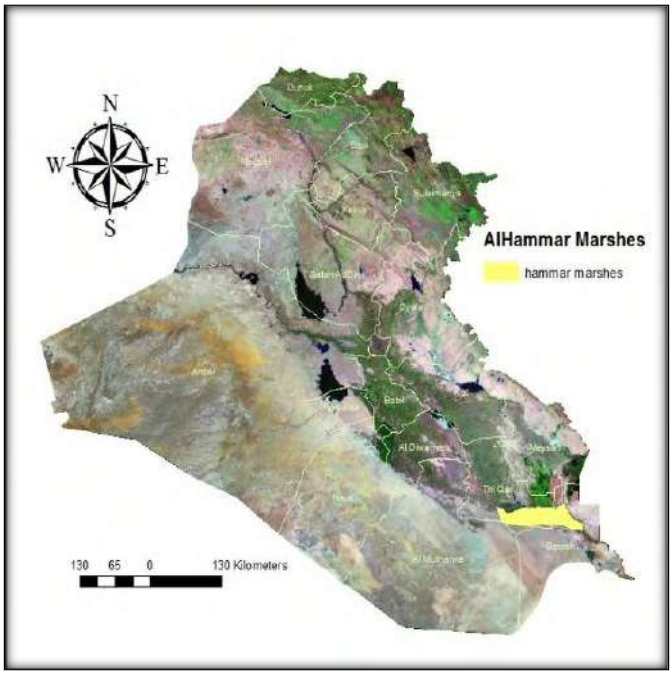

Figure 1. Al-Hammar Marsh – Iraq

Methodology

In this study, the changes that occur in the Al-Hammar marsh south of Iraq during the time period from 2013 to 2019 are revealed using remote sensing techniques and geographic information systems(GIS), where the study included classification of the study area and detect the changes in the water content and the percentage of submerged areas of the marsh and the factors causing changes, Using the Landsat 8 satellite images data and comparing it with the reference data taken from the Ministry of Water Resources, the Landsat 8 satellite advantage is that the images provided by it consist of 11 spectral bands

distributed over two sensors, the first is the Operational Land Imager (OLI) and the second is the Thermal Infrared Sensor (TIRS), the sensor (OLI) senses the first nine bands either the sensor (TIRS) it only senses the last two bands [32][33]. Satellite images with 30m spatial resolution was collected from the United States Geological Survey (https://www.usgs.gov/) website covering the study area with two scenarios and coordinates (Path 166 - Row 39) and (Path 167 - Row 39) all taken during July and for all years that are within the studied time period of 2013-2019 with varying dates. As shown in Table (1) and Figure 2.

Table 1. Landsat imagery used in the study

Sensors	WRS Scene	Acquisition Dated
Landsat 8	Path 166 Row 39	28/07/2013
Landsat 8	Path 167 Row 39	19/07/2013
Landsat 8	Path 166 Row 39	31/07/2014
Landsat 8	Path 167 Row 39	22/07/2014
Landsat 8	Path 166 Row 39	18/07/2015
Landsat 8	Path 167 Row 39	25/07/2015
Landsat 8	Path 166 Row 39	20/07/2016
Landsat 8	Path 167 Row 39	27/07/2016
Landsat 8	Path 166 Row 39	23/07/2017
Landsat 8	Path 167 Row 39	30/07/2017
Landsat 8	Path 166 Row 39	26/07/2018
Landsat 8	Path 167 Row 39	17/07/2018
Landsat 8	Path 166 Row 39	29/07/2019
Landsat 8	Path 167 Row 39	20/07/2020

Figure 2. Satellite images for Al-Hammar marsh – Iraq at 2013 before and after mosaic.

The experimental steps of this work are summarized in the following: Mosaic: which is the process of merging the images overlapping with each other in a way that allows the production of a new image covering the entire study area, each band from the first scene was merged with the band that corresponds

to it from the second scene in the mosaic method. After that, the numeric values of the Landsat 8 satellite images are converted from digital number into reflectivity using equation (4) [34].

$$\boldsymbol{\rho\lambda = (M\rho * Qcal + A\rho) / sin\theta} \quad \ldots\ldots\ldots\ldots\ldots (4)$$

Where:
$\rho\lambda$ = Top of Atmosphere Planetary Reflectance. (Unit less).
$M\rho$ = Reflectance multiplicative scaling factor for the band.
$A\rho$ = Reflectance additive scaling factor for the band.
$Qcal$ = Level 1 pixel value in DN.
θ = Solar Elevation Angle.
Corrected spectral bands are combined by layer stacking using (ENVI 5.3) software to obtain multi-spectral images (stacked). The color combination (543) is chosen as a color image in pseudo colors, it represents a color image in the form (RBG) with three spectral bands from the Landsat 8 satellite image (near infrared band, red visible band, green visible band), and these are chosen The color combination, because it is the most suitable color combination, to show the main features of the land cover of the study area which are (water, cane, plant, soil) as shown in Figure (3). The cane has different spectral reflectance than the plant and the cane growth inside the marshes, so, it should be separated.

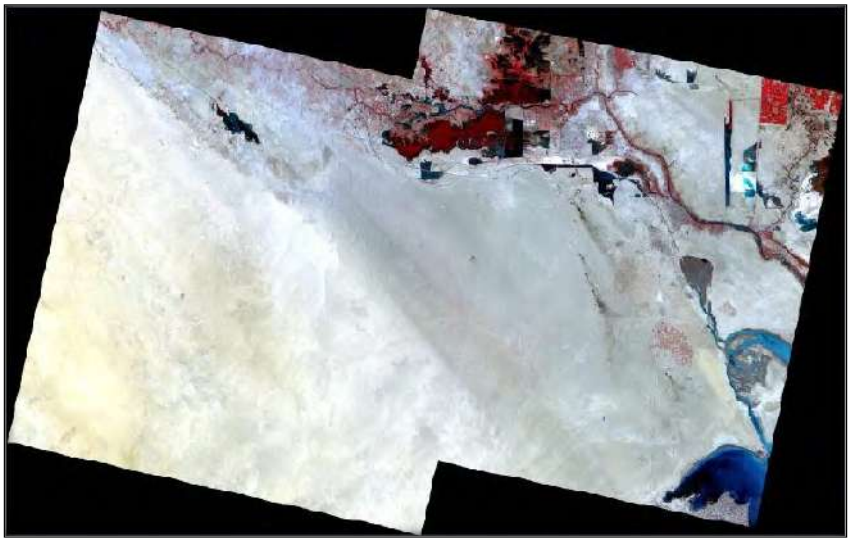

Figure 3. Color combination (543) applied to Landsat 8 satellite images.

Al-Hammar marsh's area is cut off from the resulting image because the image covers a much larger area than Al-Hammar marsh's area and performs the cutting using (ArcGIS 10.4.1) software by creating a shape file for the boundaries of Al-Hammar marsh. Regions of interest (ROIs) are determined by using (ENVI 5.3) software. Six categories of land cover for the area are identified (deep water, shallow water, small cane, large cane, plant, soil), then the digital classification of the satellite images in which the categories were identified the supervised classification method (maximum likelihood), as shown in Figure 4.

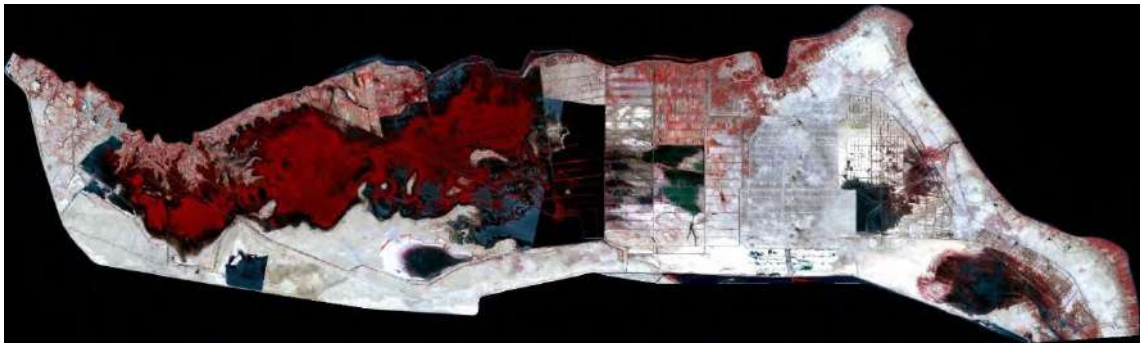

(a)

(b)

(c)

(d)

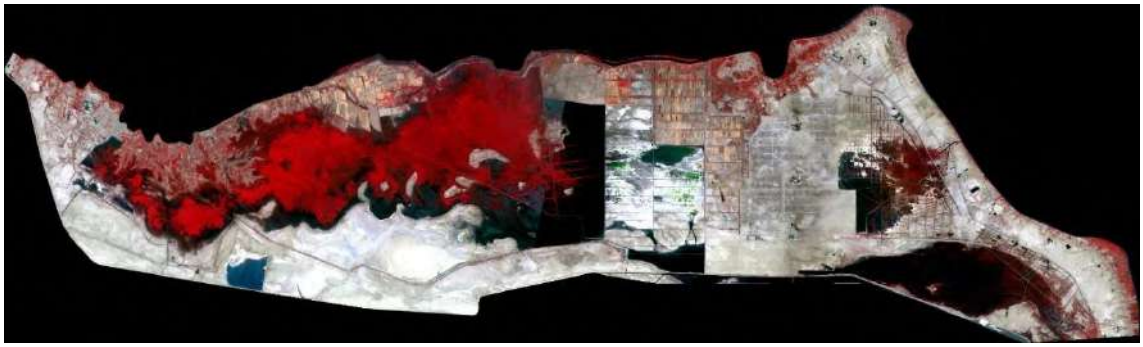

(e)

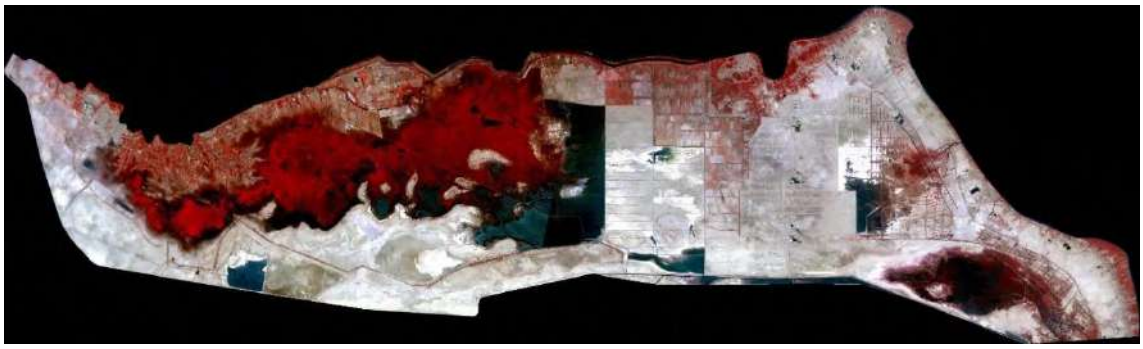

(f)

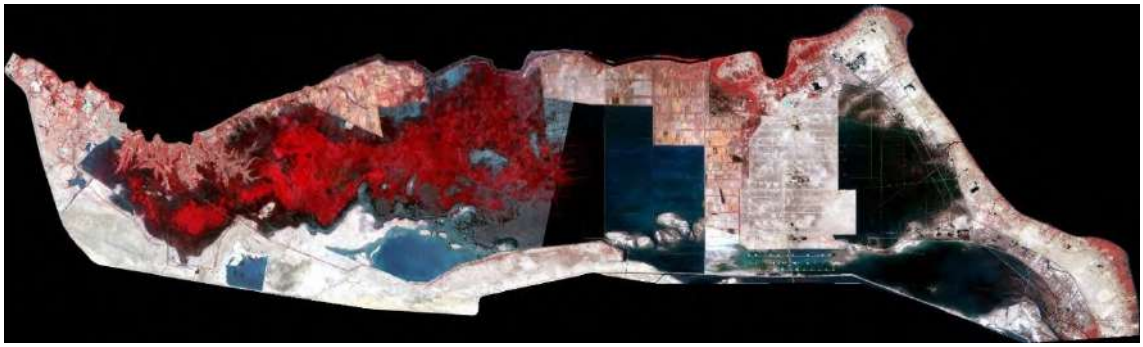

(g)

Figure 4. Landsat- 8 (OLI) Satellite Image (a. 2013 b. 2014 c. 2015 d. 2016 e. 2017 f. 2018 g. 2019) respectively of Al-Hammer Marshes after Clipping for color composition (5 4 3).

6. Results and Discussion

The results obtained by conducting the methodology on the classified images that were conducted to change detection in the water content and the submerging ratios of AL-Hammar marsh in southern Iraq during the period from 2013 to 2019.

Figure (5) represents the outputs of the supervised classification process (maximum likelihood) that classified the land cover of the study area (deep water, shallow water, small cane, large cane, plant, soil), after the classification procedure, the percentage of the water area is calculated by Collecting percentages for each area (deep water, shallow water, small cane) and for all years respectively, Table (2) shows the percentage of the area of each of the swamp areas, graph (1) shows the change in the water level in the marshes.

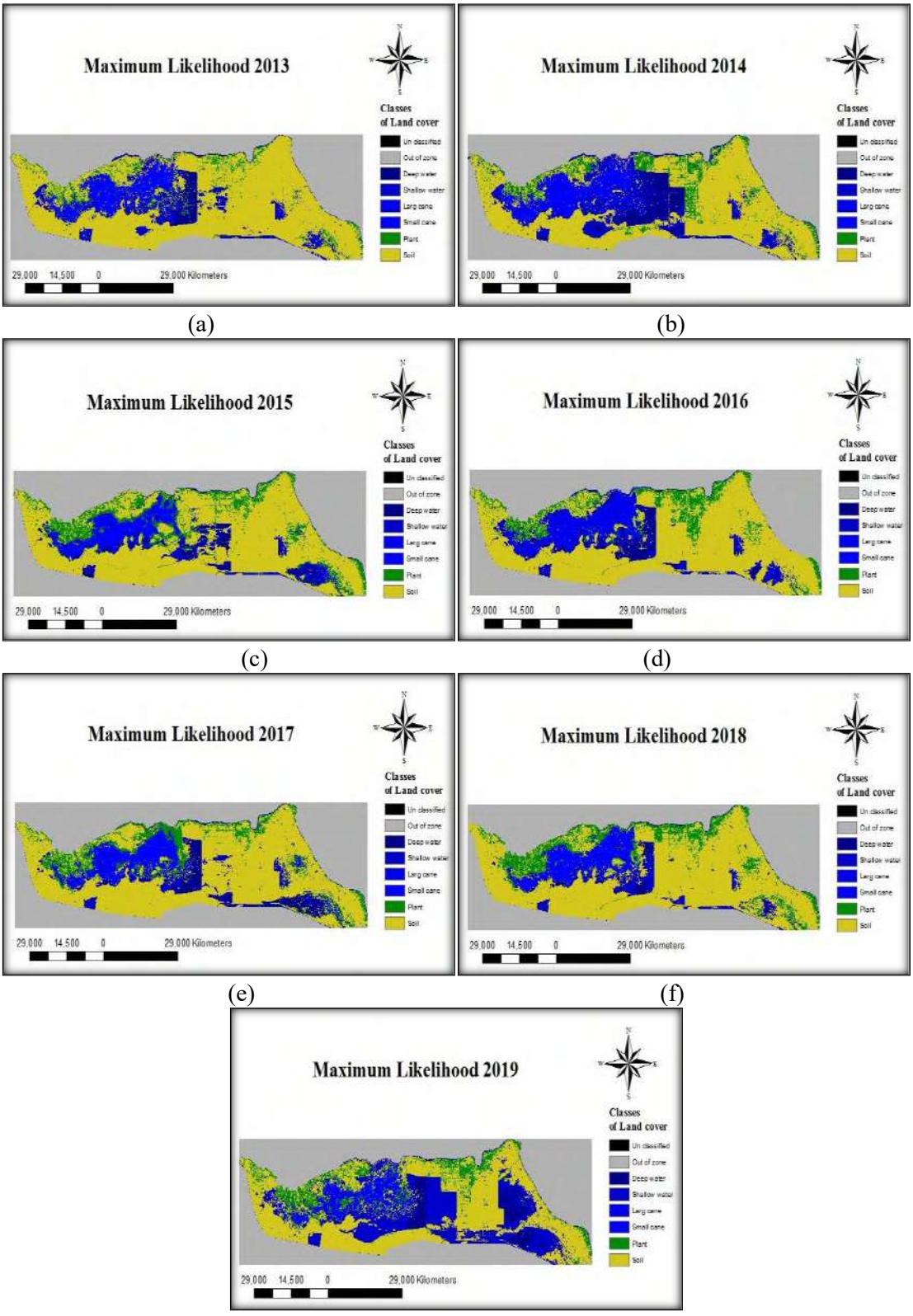

Figure 5: Supervised classification (maximum likelihood) of color combination (543) for years (a. 2013-2013 b. 2014 c. 2015 d. 2016 e. 2017 f. 2018 g. 2019).

Table 2. The class's area for Supervised classification (maximum likelihood) of color combination (543) for the years 2013 – 2019.

Classes / Year	Unclassified m²	Water m²	Cane m²	Plant m²	Soil m²
2013	0	791,687,700	19,880,100	197,136,900	2,236,341,600
2014	0	1,067,350,500	123,702,300	285,183,000	1,768,810,500
2015	0	667,788,300	37,149,300	463,361,400	2,076,747,300
2016	0	423,976,500	425,566,800	368,420,400	2,027,082,600
2017	0	746,451,900	55,395,000	394,592,400	2,048,607,000
2018	0	671,757,300	3,850,200	446,243,400	2,123,195,400
2019	0	1,269,193,500	36,064,800	368,053,200	1,571,734,800

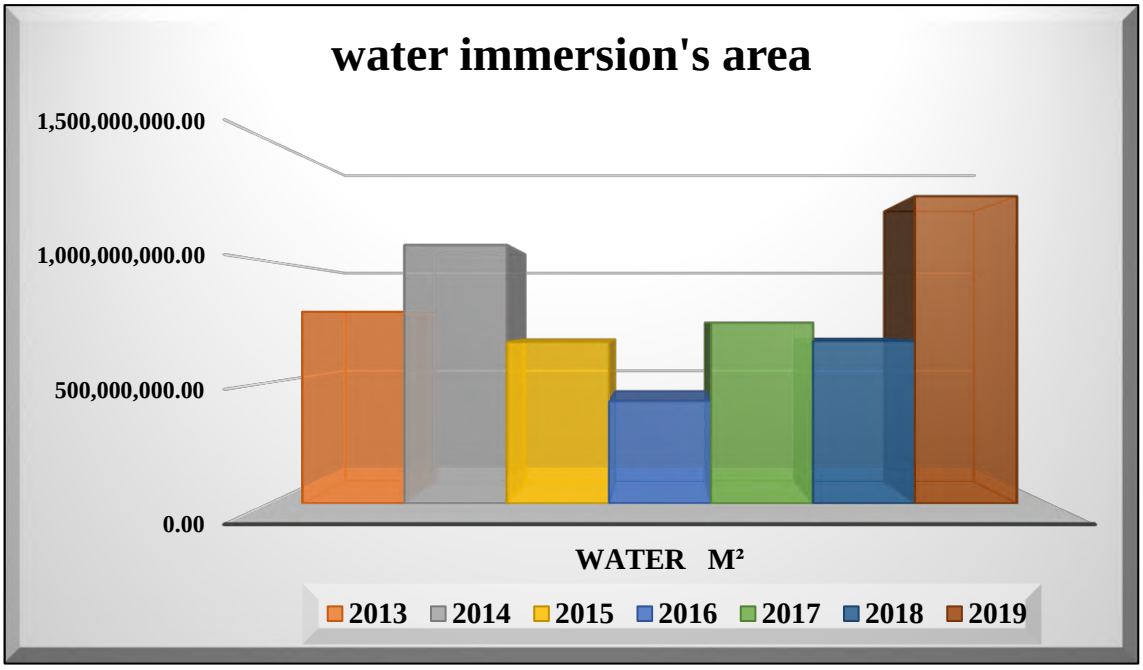

Figure 6. The Differences in the surface area of the water content in Al-Hammar marsh versus the years 2013 to 2019.

the results that appeared to us and by studying the figures and tables mentioned above, when comparing with reference data taken from the Ministry of Water Resources for the study area, we find that the color combination that was chosen and the classification method used to classify the satellite images, which is the supervised classification method (maximum likelihood) gave high accuracy results very close to Real data and what confirms this are when conducting an assessment of classification accuracy and calculating the overall accuracy and Kappa coefficient for all the classified images, a very high accuracy was obtained, as shown in Table (3). where it was found that there were a lot of changes that occurred in Al-Hammar marsh as the water content and the inundation percentage , as these rates varied during the successive years from 2013 to 2019 by increasing and decreasing, where we note that the percentage of water content rose slightly in the year 2014 from what was during 2013 either during the subsequent years either the percentage of water began to decline gradually and unevenly reached the lowest in the

year 2018, where the water covering the area of the marsh became scarce, and since the beginning of the year 2019 the percentage of water began to increase in the marshes significantly, until in May it reached twice what it was during the same month of 2018 as a result of the flood wave and torrential rains that swept the country.

Table 3. Overall accuracy values and Kappa coefficients for supervised classification methods in color combination (543) for all years.

Year	Overall accuracy	Kappa coefficient (K)	Error percentage
2013	98.9698	0.988	1.0302
2014	99.9323	0.9992	0.0677
2015	99.9324	0.9992	0.0676
2016	85.6017	0.8324	14.3983
2017	99.6608	0.996	0.3392
2018	96.2526	0.9562	3.7474
2019	99.862	0.9984	0.138

7. Conclusions

We conclude from the results obtained that the color combination (543) chosen in this study, which is the spectral bands (near infrared band, red visible band, green visible band) are the best color combinations that can be applied to determine the features of the land cover of the marsh region, as the required features are well and clearly demonstrated, in addition to that we conclude that the supervised classification method (maximum likelihood) is the best and most accurate classification method that has been applied to classify the land cover features in an easy, fast and highly accurate manner because it gave very close results to the reference data with a very low error rate, reaching 0.0676%.

8. References

[1] Dawod GM 2015 *Fundamentals and Applications of Remote Sensing (in Arabic)*, Cairo, Eygpt, 2015.

[2] Schowengerdt RA 2007 *Remote Sensing: Models and Methods for Image Processing*, Third Edition, 2007.

[3] Sharma AK and Shukla JB 2015 A Remote Sensing and GIS Based Approach to Evaluate the GroundWater Prospects of Baghain Watershed, Panna and Satna Districts of M.P., India: A Case Study *J. Geol. Soc. India,* **86** 733-741, 2015.

[4] Hadi FA and Abdulwahhab RA 2012 Preparing a Map for the Surface Temperature Distribution of Baghdad and the Marsh Area Using Remote Sensing Technique *Iraqi J. Sci.* **53**, 1006-1016.

[5] Liu JG and Mason PJ 2016 *Image Processing and GIS for Remote Sensing Techniques and applications*, second edition, John Wiley & Sons, Ltd.

[6] López-Serrano PM, Corral-Rivas JJ, Díaz-Varela RA, Álvarez-González JG and López-Sánchez CA 2016 Evaluation of Radiometric and Atmospheric Correction Algorithms for Aboveground Forest Biomass Estimation Using Landsat 5 TM Data *Remote Sensing,* **8** 2.

[7] Petrou M and Petrou C 2010 *Image Processing: The Fundamentals* Second Edition, John Wiley & Sons.

[8] Saleh SAH 2012 Temporal Change Detection of AL- Hammar Marsh – IRAQ Using Remote Sensing Techniques *Global J. Human Soc. Sci. Geogr. Environ. GeoSci.* **12** 6.

[9] Ghosh S, Biswas S, Sarkar D and Sarkar PP 2014 A Tutorial on Different Classification Techniques for Remotely Sensed Imagery Datasets *Smart Comp. Rev.* **4** 34.

[10] Ghobadi Y, Pradhan B, Kabiri K, Pirasteh S, Shafri HZM and Sayyad GA 2012 Use of Multi-Temporal Remote Sensing Data and GIS for Wetland Change Monitoring and Degradation *IEEE Colloquium Human. Sci. Eng. Res.* 103.

[11] Malekmohammadi B and RahimiBlouchi L 2014 Ecological risk assessment of wetland ecosystems using Multi Criteria Decision Making and Geographic Information System *Ecol. Indic.* **41** 133.

[12] Al-Rubaie A and Kwyes A 2008 Ecological And Morphological Stady Of Iraqi Southern Marshes *Marina Mesopot.* 23 437.

[13] Muhsi IJ and Kadhim MJabbar 2017 Monitoring of south Iraq marshes using classification and change detection techniques *Iraqi J. Physics* **15** 78.

[14] Muhsin IJ, Mashe FK and Tawfeeq RJ 2011 Monitoring the Vegetation and Water Content of Al-Hammar Marsh Using Remote Sensing Techniques *Baghdad Sci. J.* **8** 646.

[15] Hussein ZE, Hasan RH and Aziz NA 2018 Detecting the Changes of AL-Hawizeh Marshland and Surrounding Areas Using GIS and Remote Sensing Techniques *Assoc. Arab Univ. J. Eng. Sci.* **25** 53.

[16] Shimal S and Shaban AH 2019 Estimation of groundwater pollution in Baiji / Salah Al-Deen province Iraq *AIP Conf. Proc.* **1968** 020058-(1–7).

[17] Dewan AM and Yamaguchi Y 2008 Using remote sensing and GIS to detect and monitor land use and land cover change in Dhaka Metropolitan of Bangladesh during 1960–2005 *Environ. Monit. Assess.* **150** 237.

[18] Soliman G and Soussa H 2011 Wetland change detection in Nile swamps of southern Sudan using multitemporal satellite imagery *J. Appl. Remote Sens.* **5** 2011.

[19] Parihar, SM, Sarkar S, Dutta A, Sharma S and Dutta T 2013 Characterizing wetland dynamics: a post-classification change detection analysis of the East Kolkata Wetlands using open source satellite data *Geocarto Int.* **28** 273.

[20] Weng Q 2012 Remote sensing of impervious surfaces in the urban areas: Requirements, methods and trends *Remote Sens. Environ.* **117** 34.

[21] Parivallal R and Nagarajan B 2014 Supervised Classification Methods For Object Identification Using Google Map Image *International J. Eng. Sci. Manag. Res.* **1** 71.

[22] Lillesand TM and Kiefer RW 2000 *Remote Sensing and Image Interpretation*, New York: John Wiley and Sons, Inc.

[23] Shivali AK and Vishakha VK 2013 Supervised and Unsupervised Neural Network for Classification of Satellite Images *Int. J. Comp. Appl.* 25.

[24] Kumar M 2014 *Digital Image Processing Satellite Remote Sensing and GIS Applications in Agricultural Meteorology* 81.

[25] Tso B and Mather PM 2009 *Classification Methods For Remotely Sensed Data*, Second Edition, Boca Raton London New York: Taylor & Francis Group, LLC.

[26] Shaban AH, Resen AK and Bassil N 2020 Weibull parameters evaluation by different methods for windmills farms *Energy Rep.* **6** 188.

[27] Richards JA 2013 *Remote Sensing Digital Image Analysis*, Fifth Edition, New York, London: Springer-Verlag Berlin Heidelberg, 2013.

[28] Congalton RG 1991 A Review of Assessing the Accuracy of Classifications of Remotely Sensed Data *Remote Sens. Environ.* **37** 35.

[29] Sivanandam SN, Sumathi S and Deepa SN 2007 *Introduction to Fuzzy Logic using MATLAB*, New York: Springer-Verlag Berlin Heidelberg.

[30] Taufik A, Ahmad SSS 2016 Land cover classification of Landsat 8 satellite data based on Fuzzy Logic approach *IOP Conf. Series: Earth Environ.Sci.* **37**.

[31] Ziboon ART, Hammed SA and Abbas A 2010 Using Remote Sensing and Gis Tichenck to Study Soil Chemical Properties for Hour Al-Hammar (South of Iraq) *Eng. Tech. J.* **28** 6458.

[32] Acharya TD and Yang I 2015 Exploring Landsat 8 *Int. J. IT, Engin. Appl. Sci. Res. (IJIEASR)* **4**.

[33] Knight EJ and Kvaran G 2014 Landsat-8 Operational Land Imager Design, Characterization and Performance *Remotesensing* **6** 10286.

[34] Zanter K 2016 *Landsat 8 (L8) Data Users Handbook*, Version 2.0, USGS, science for a changing world.

The Concentration of the Toxic Elements (Cd, Hg, As) in Diyala Governorate Soil Utilizing GIS Techniques

The Concentration of the Toxic Elements (Cd, Hg, As) in Diyala Governorate Soil Utilizing GIS Techniques

Jaafar S. Muhammad[1], Kareem A. Jasim[2] and Auday H. Shaban[3]

[1]Department of Physics, College of Science, University of Diyala, Iraq
[2]Department of Physics, College of Education, Ibn Al-Haytham College of Sciences,Pure,University of Baghdad, Iraq.
[3]College of Science, University of Baghdad, Iraq.

auday.h.s@ihcoedu.uobaghdad.edu.iq

Abstract. The heavy elements (Cadmium, Mercury, and Arsenic) are considered to be highly toxicity for human and living creatures. This research focused on the concentrations of these elements in the soil of Diyala Governorate. The 25 samples of soil were collected from different areas included (industrial, residential, and agricultural) with an average sample rate for each region with a depth (10 cm). The samples were compressed to prepare them for measurement by dispersive spectroscopy of X-ray energy (EDX).The results are compared with the global determinants World Health Organization (WHO), where the results indicates the highest concentration of cadmium in the Injanah region and the lowest concentration in the Alma'amil region. The highest concentration of mercury in the regions of Mohammed Sakran and Diyala Bridge and the lowest concentration in the region of Mundhiriyah. The Arsenic elements concentrated become high in the Rashidiya region and less concentrated in the Hamrin hills region. It is known that these elements are more toxic than other elements when they are found in a higher rate than the permissible level in the soil.

Keywords: Cadmium, Mercury, Arsenic, high toxicity, and soil elements.

1. Introduction

The general meaning of heavy elements is those elements with a density greater than (5g/ cm3) [1]. The soil in many regions of the world is exposed to pollution by toxic heavy elements as a result of human activity in many areas, especially industry and agriculture, adding phosphate fertilizers, manufacturing and mining. These activities are a great source of air pollution that loaded the air particles with heavy elements, so these particles are deposited directly on the soil surface, then by rain it will be transported into the soil. The soil pollution is affected by the plants that been cultivated in this area. The pollutant elements are entering the plants which will be harvested to get into the food chain, and that increases the risks to human health [2, 3].

Cadmium (Cd) which is a metallic silver-colored white substance with atomic number 48 and atomic weight 112,41g/mol. Its boiling point is 765 ° C, its melting point is 321 ° C, and its density is 8.65 g / cm3. The cadmium is a metal and is ignited by heating giving CdO, which is a brown oxide. As for physically, it is satin (malleable and withdrawn) [4, 5].Cadmium is found in ordinary soils with a small concentration of 0.5 ppm or less, but in sedimentary soils its concentration may be 25 ppm One of the properties of cadmium is that it is very stable in the environment and accumulates in the soil where

living organisms coexist and can be easily absorbed from the roots of plants. It is known that cadmium is a toxic element associated with zinc extraction and other industrial processes. However, it is a dangerous air pollutant (cadmium dust), and thus cadmium accumulates on the soil surface and accumulates in plants, including herbaceous plants, without toxic symptoms, and the amount of cadmium in the environment is increased by the disposal of solid waste. Contamination of soil surface, subsurface areas and water surface results in cadmium. Also, the amount of cadmium in the soil may increase as a result of the application of fertilizers [6, 7].

Mercury (Hg) is a chemical element symbolized by Hg, atomic number 80 and molecular weight 200.59 g / mol. Its density (13.54 g / cm3) freezes at (-38.9 ° C), and its boiling point (356.9 ° C). , Which is a silver, bluish liquid that looks like lead in appearance. When an electric spark passes through mercury vapor, it emits a bright flash and ultraviolet light. It evaporates at room temperature and thus its atoms are mixed with the air without the human being realizing it, especially since it has no odour and color, and when a person inhales this air, the mercury atoms enter the lung and thus reach the blood and brain. Many studies have shown that high exposure to mercury causes toxicity to the central nervous system, which can lead to irritability, fatigue, behavioral changes, convulsions, headaches, hearing loss, loss of perception, and hallucinations to death.[8,9]

Arsenide (As) and atomic number 33 in the periodic table of elements. Its atomic mass is 74,922 in the fifteenth group of the periodic table. Arsenic is found in many chemical compounds, as well as a pure crystalline component, and has been achieved in conjunction with minerals and sulfur. Arsenic is a semi-metal, has a multi-rootedness, but the gray form is important in the industry. It was known to be one of the most toxic substances, and was often used to get rid of enemies due to its easy accessibility.It can be detected easily regardless of trying to clean tools used in the arsenic handling and transport process. Arsenic is naturally found in soil, air, and water. In some countries, arsenic is found in large quantities in groundwater. It is very toxic when present in an inorganic form. Table 1 represents the general permissible limit for the presence of elements (Cd, Hg, As) in the soil of the World Health Organization [10].

Table 1. General permissible limit for elements (Cd, Hg, As) in the soil by WHO

Element name	Cd	Hg	As
WHO(mg/kg)	1	0.5	20

2. Geographic Information Systems (GIS)

It is the science that is defined by collecting, processing and analyzing spatial data. There are several programs used for geographic information systems, including those that operate on a directional information system such as ArcGIS and that operate on a raster system such as ERDAS. The trend system is more suitable for storing high-precision data such as ownership and boundary maps, so it is preferable in these cases to choose programs that run on the vector information system [11-13].

3. Interpolation

There are several interpolation methods, such as Kriging, global polynomial, local polynomial, inverse distance weight (IDW) etc. Spatial interpolation is the process of using points with known values to estimate values at other unknown points. For example, to create a precipitation map for a country, you won't find enough weather stations to cover the entire region. Spatial interpolation can estimate the temperature at locations without data recorded using temperature readings known at nearby weather stations calculated using internal interpolation. In GIS, spatial interpolation of these points can be applied to create a vector surface with estimates values. The results of the interpolation analysis can then be used for analyses the whole area and for modelling. There are many methods for implementation in ArcGIS. Inverse Distance Weight (IDW) interpolation method, is one of many methods of interpolation.

The sample points are weighted during interpolation such that the influence of one point with respect to other declines with distance from the unknown point you want to create [12,14,15].

4. Study Area

Diyala Governorate is located in the eastern part of central Iraq, and from the provinces that have international borders, it is bordered to the north by the Sulaymaniyah Governorate and part of the Salahuddin Governorate, while it is bounded to the west by the Baghdad and Salahuddin governorates and to the south by the Wasit Governorate and To the east is the Islamic Republic of Iran.This region situated between (33.3–35.6) latitude and (44.22–45.56) longitude, as shown in Figure 1.

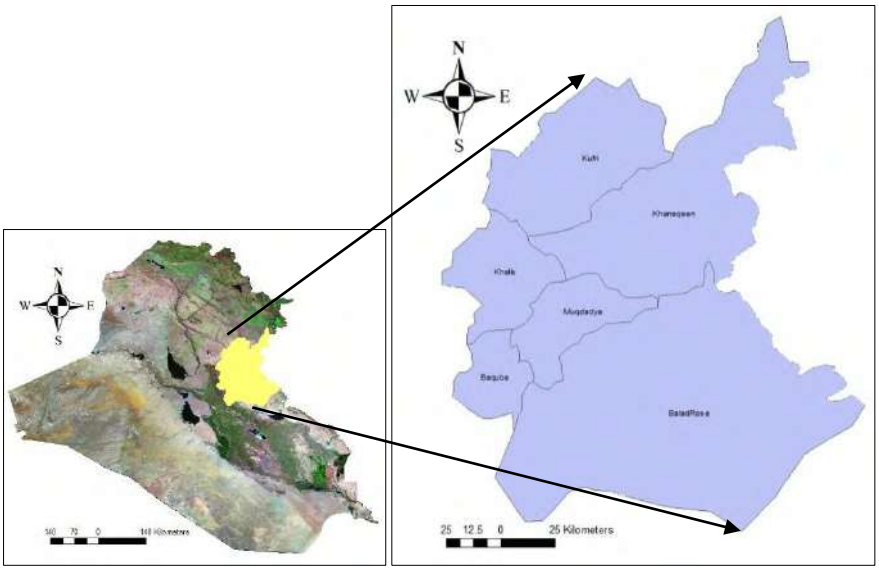

Figure 1. Photomap of Iraq and DiyalaShapefile

5. Modeling and working methods

The work in the current study is divided into three phases:
First stage: is the field work (collection of samples).
Secondstage: is the laboratory work.
Third stage: is the information processing and discussion.
Figure 1 displys Diyala map, which represents the borders of the study area as well as the areas from which samples were collected for the purpose of the study.Twenty-five (25) soil samples were collected from Diyala governorate at a depth of 10 cm. These samples were taken from many regions (industrial, residential, agricultural). The samples were configured by numbering the nylon bags that consists of the samples. The samples were transferred to the laboratory for the purpose of preparing them for measurement to study the concentrations of the heavy elements (Cd, Hg, As).

The work's procedure is summarized by:
Drying the samples in the sun for several days.
Grinding the samples separately: very fine grinding using a ceramic mortar for two hours.
Compressing the soil samples using a hydraulic press,
Finally, examining the concentration of heavy elements in the samples by the (EDX). Table (2) illustrated the location were the samples collected.

Table 2. Symbolized sampling locations

ID	Location name	East	North	Elevation m
1	kalar	45.32916	34.57248	835
2	mandhiria	45.4333	34.20412	656
3	Aleazim Dam	44.55443	34.53553	470
3	injanah	44.60147	34.42877	289
5	khaniqin	45.27905	34.2664	815
6	Aleazim	44.5172	34.20332	248
7	khan oil	45.35477	34.17022	747
8	Alnay	44.54785	34.054	188
9	Hamrin Hills	45.06267	34.06082	458
10	almqdady	44.9569	33.9823	155
11	Imam Wes	45.14028	33.9359	187
12	hay mazid	44.741	33.80382	124
13	mandeley	45.54053	33.74133	373
14	Canaan	44.7976	33.6936	127
15	cintarbeqwb	44.61293	33.7459	101
16	alkhalis	44.52183	33.84487	102
17	jadidatalshat	44.4009	33.68145	87
18	Rashidiya	44.4148	33.6878	84
19	Mohammed sakran	44.45653	33.56708	91
20	almaemil	44.525	33.4947	99
21	qzanyh find	45.50671	33.2367	151
22	qzanyhcinter	45.54952	33.65292	250
23	Baldroozfatmyh	45.1333	33.5044	144
24	diyala bridge	44.5184	33.2326	73
25	almadayin	44.5803	33.0968	95

6. Results and discussion

The results gained from the EDX are the concentrations of each elementsin the samples. These data were illustrated in Table 3. The results showsthe variations of the presence of the elements at different locations. The variation of the concentration is a reflection of the pollution degree in that area due to the presence of industrial activities or any human activities.

Table 3. Concentrations the heavy metals (Cd, Hg, As)

ID	Cd ppm	Hg ppm	As ppm
1	7.3	0.36	0
2	0	0	0
3	0	0.54	0
4	10.5	0.74	0
5	0	0.09	11.3
6	0	0.21	0
7	0	0	0
8	0	0	38
9	0	0	0
10	4.9	0.54	1.33
11	8.06	1.53	32.66
12	0	0	33.33
13	1.4	0	0

14	0	0	0
15	7.86	1.53	0
16	0	0	0
17	4.46	0.21	0
18	0	0.44	61.3
19	0	0	5.33
20	1	0.15	0
21	5.1	1.13	0
22	0	0.33	0
23	0	0.45	0
24	3	1.260	0
25	2.73	1.02	0

Geographic information analysis provides the ability to estimate variables throughout the studied area using interpolation functions. The IDW interpolation method was chosen to be applied to the data collected. Figure 2 represents the estimation of cadmium concentration in the studied areas. Through the estimation map, using ArcGIS software, areas were calculated and illustrated in Table 3. The highest concentration of cadmium. It was recorded in Region No. 1 (7.3 ppm) and in Region No. 2 (10.5 ppm) No. 10 it was recorded (4.9 ppm) and in No. 11 it was recorded (8.06 ppm). And in No. 15 it was recorded (7.86 ppm). And at No. 11 it was recorded (8.06 ppm). And in No. 15 it was recorded (7.86 ppm) and in 17.21 4.46, 5.1 of the cadmium element were recorded in these areas due to the nature of the earth's formation, as well as the reason for throwing industrial waste containing cadmium waste as she the Figure(2).

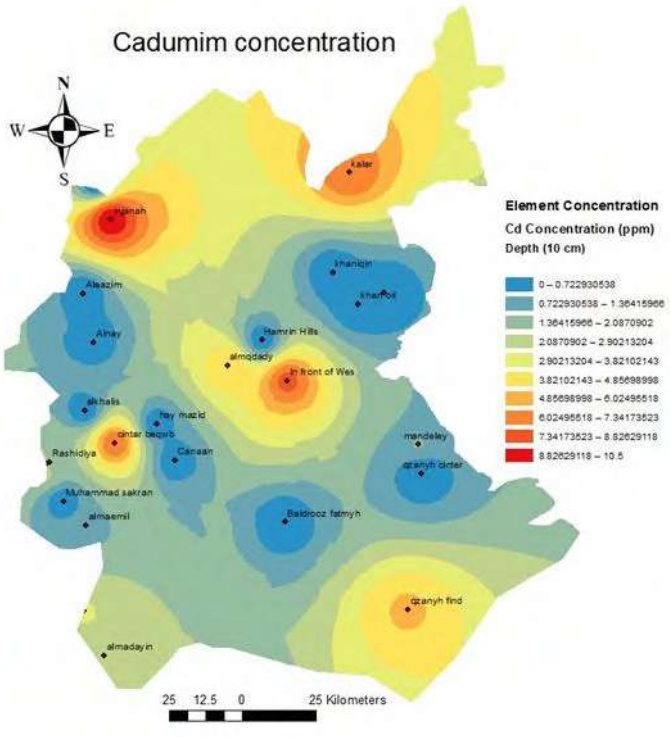

Figure 2. Distribution of Cadmium concentration

The highest concentration of (Hg) was recorded in Region No. 11 (1.53 ppm), while in Region No. 21 (1.13 ppm), and in Region No. 24 (1.26 ppm), it was recorded in Zone 25 (1.02 ppm). Per million), and these four regions are high compared to the (World Health Organization). Adult (0.5 ppm) As for the rest of the regions, the mercury concentration was within or below the required level as shown in Figure 3, which indicates the presence of mercury in the study area. Mercury is naturally present in the earth's crust, and it is released into the environment due to volcanic activities and human activity, which indicates the main reason for the release of mercury into the environment are, especially, from coal-fired power plants, coal burning in homes, cooking, industrial activities and waste incinerators as shown in Figure3.

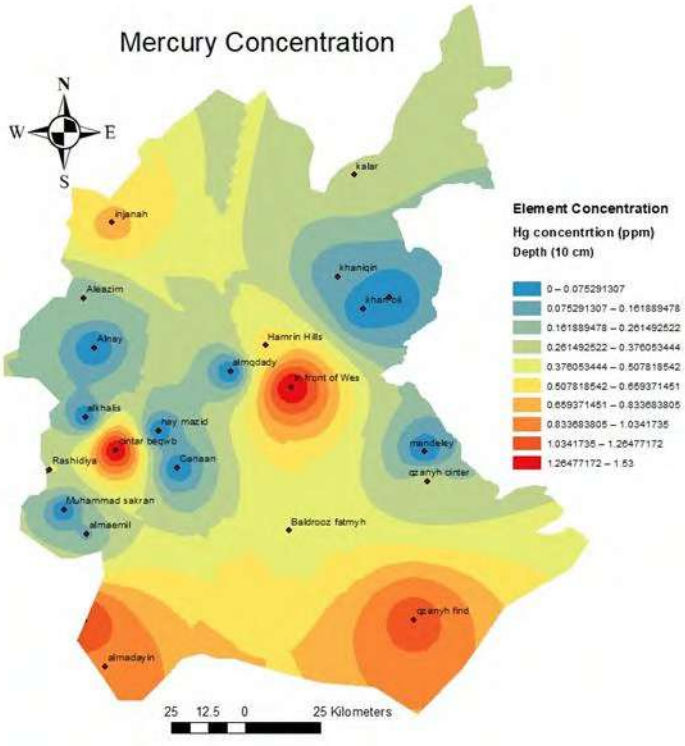

Figure 3. Distribution of Mercury concentration

The highest rise in arsenic was recorded in region No. 8 (38 ppm), in region No. 6 it was recorded (32 ppm), in region No. 11 and in region No. 12 it was recorded (33.33 parts per million). In region No. 18 and recorded the highest rise (61.3 ppm)

As for the rest of the regions, there was no presence of arsenic (Figure 4) representing the sites of arsenic and its concentrations in the studied areas, and the arsenic increases in the areas most used in the industry as an ingredient in the manufacture of alloys, as well as in the treatment of glass, dyes, textiles, paper, metal adhesives and preservatives for wood and ammunition. . Arsenic is also used in leather tanning and, to some extent, in pesticides, food additives, and pharmaceuticals.

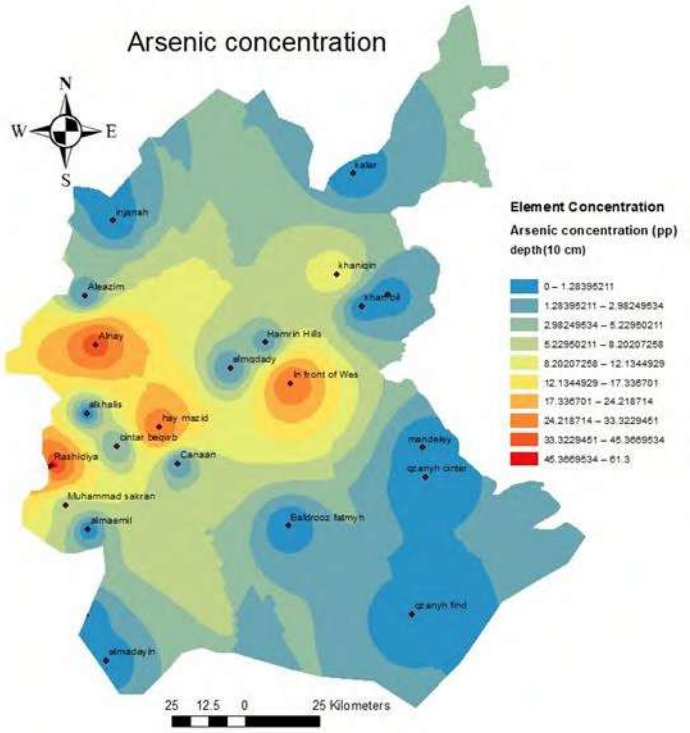

Figure4. Distribution of Arsenic concentration

7. Conclusion

A high concentration of most heavy elements in depth (10 cm), which indicates the absence of movement and transmission of these elements through the soil layers.Soil samples showed contaminated with cadmium, which reached the highest concentration (10.4) compared to the permissible limit (1 part per million) in area No. 4 and the highest concentration of mercury, which reached (1.53 part per million) compared to the maximum. Allowed by the World Health Organization (0.5 part per million) in the 11 and 15 regions, and the highest concentration of arsenic in the 18th region, reaching (61.3 parts per million) compared to the permissible limit of the World Health Organization (20 parts per million).

Soil is often contaminated with cadmium, mercury, and arsenic due to the use of agricultural pesticides and chemical fertilizers that contain these elements. Human factors that increase the use of these elements, which leads to an increase in these elements in the soil.

The method that been used in this research is an effective way to illustrate and evaluate the concentrations of heavy elements and their reasons. The focal points in the concentrations maps are exact because they are measured in the lab.

References

[1] Al Saadi and Hussein A 2006 *Al Yazouri Scientific Publishing House* (Amman Jordan) 307.
[2] Jasim K A Fadhil R N Shaban A H Jaafar H I Maiyaly B K H Aleabi S H and Salman E M-T 2019 *Progress in Industrial Ecology – An International Journal* **13**(2) 163.
[3] Technical Background Report to the Global Atmospheric Mercury Assessment 2008 AMAP and UNEP 7.
[4] Ali S M Shaban A H and Resen A K 2014 *Iraqi Journal of Science* **55**(4B) 1997.
[5] Ibrahim Z H Ibrahim S A Shaban A H Jasim K A and Mohammed M K 2017 *Energy Procedia* ELSEVIER **119**c 709.
[6] ATSDR 2005 *Department of Health and Human Services* 185.
[7] Jasim K A and Alwan T J 2009 *Journal of superconductivity and novel magnetism* springer Y **22**(8) 861.
[8] Al-Wahaibi and Muhammad H 2006 Vegetable chelates and heavy elements", King Saud University - College of Science- Department of Botany and Microbiology **13**(2) 43.
[9] Kadhim B B Risan R H Shaban A H and Jasim K A 2019 *AIP Conf. Proc.* **2123**: 020062 1.
[10] Ghofran F and Juma'a 2010 *Iraqi Association for Market Research and Consumer Protection* 2 (3).
[11] Aleabi S H Watan A W Salman E M-T Jasim K A Shaban A H and AlSaadi T M 2018 *AIP Conf. Proc.* **1968** 020019 1.
[12] Ali S M Mahdi A S Shaban A H 2012 *Iraqi Journal of Science* **53**(4) 965.
[13] Mitasova H Mitas L Brown W M Gerdes D P KosinovskyI and Baker T 1995 *International Journal of Geographical Information Systems* **9** (4) 33.
[14] Jaa'far A T 2011 *Journal of Research Diyala humanity* (53) 406.
[15] Shimal M S and Shaban A H 2019 *AIP Conf. Proc.* **1968** 020058 1.

Journal of Physics: Conference Series

The effect of potassium substitution on the properties of $HgBa_2Ca_2Cu_3O_{8+\delta}$Compound

The effect of potassium substitution on the properties of $HgBa_2Ca_2Cu_3O_{8+\delta}$compound

Kassim Mahdi Wadi[1], Riyadh Kamil Chillab[1], Aqeel N. Abdulateef[1], Kareem A. Jasim[2*], Auday H. Shaban[3] Maher A. Hassan[4], Sarab Saadi Jahil[2]

[1]Al-Ma'amoun University College, Electrical Engineering Techniques Department, Iraq
[2]Department of physics, College of Education for pure Sciences Ibn AlHaitham, University of Baghdad, Baghdad, Iraq.
[3]College of Science, University of Baghdad, Baghdad, Iraq.
[4]Department of Physics, College of Education for Pure Science, University of Tikrit, Tikrit, Iraq

E-mail: kareem.a.j@ihcoedu.uobaghdad.edu.iq

Abstract. This article reported investigations the effect of partial substitution potassium at calcium site for $HgBa_2Ca_2Cu_3O_{8+\delta}$ system with x from 0 to 0.2. All samples were prepared using solid state reaction technique. The samples were subjected to gross structural characterization by X-ray diffraction. The XRD data for the prepared samples are consistent with the Hg-1223 phases, and the analysis showed that the structures are tetragonal. Increasing potassium level results in decreasing the mass density (from 1.53 to 1.51), volume fraction (from 76.4 to 71.9), lattice parameters c, c/a length of c. Electrical resistance was testing by four-probe technique to determine the critical temperature, and it is noticed that the non-potassium $HgBa_2Ca_2Cu_3O_{8+\delta}$ compound has a critical temperature around 118 K, while introducing potassium in $HgBa_2Ca_{2-x}K_xCu_3O_{8+\delta}$ compound with x=0.1 and 0.2 led to decrease the critical temperature to 110 K and 93 K, respectively.

Keywords: partial substitution, Tetragonal structure, Potassium, Electrical Resistance, X-ray diffraction.

1. Introduction

The large variation in the layered structure of High Temperature Superconducting Compounds (HTSC) leads to important changes in physical, mechanical and structural properties such as magnetic field, electrical conductivity, current density, dielectric constant [1,4], hardness[5], tensile strength, elasticity, grain size and crystal size depending on the type of superconducting compound[6], the proportions of the elements and their partial substitution in the compound [4-8]. The difference in the stratigraphic composition of the high temperature superconducting compounds leads to important changes in the magnetic field depending on its movement that is relative to the axes of the crystal lattice. For superconducting planes, the direction of the magnetic field varies. The results of the measurements of the critical magnetic field and its critical temperature depend on the angle between the magnetic fields

and the surface (a – b). Generally, it showed that the dissipation in the electric magnetic field strongly decreases when the field tends towards the superconducting layers away from the c axis [9, 10]. Measurements in oblique fields were commonly analyzed in terms of the approach based on the anisotropic of mass. Anisotropy reduces the effective electric and magnetic field component in the same direction and parallel to the superconducting layers [11].The electric and magnetic field component along the c-axis is the only active component within highly anisotropic materials, because it has been found already experimentally at BSCCO system [4, 12]. For moderate contrast materials, such as Y-B-C-O, field scale has been shown to be valid in the flow region [13], and for Hg-Ba-Ca-Cu-O compounds families have anisotropy between those of YBCO and BSCCO. Regarding -2212 phase [14], only few investigations were reported on the angle dependence for the transmission characteristics. The resistance of (Hg, Re) $Ba_2CaCu_2O_6$ was recently studied under different directions of magnetic field with respect to c-axis, and the dependence of the dissipation field on the angle of inclination has been inferred [15]. The physical properties of many superconducting materials, such as high phase formation, temperature transition and the isolation of the superconducting compound Hg-1223 have been improved by means of cation substitutions and doping with highly valued pb, Re or other elements [16, 17]. The electrical resistance is one of the most important characteristics of material, and it is mostly a common method to determine the transition temperature of a superconductor.

The aim of this research is to study the effect of partial sedimentation of calcium with potassium, in $HgBa_2Ca_{2-x}K_xCu_3O_{8+\delta}$compound with different x values. Important measurements were carried out to determine the structural and electrical properties of the samples.

2. Experimental

The pure powders of HgO, CaO, CuO, BaO and K_2O_3 were weighted by a sensitive balance to form the chemical formula $HgBa_2Ca_{2-x}K_xCu_3O_{8+\delta}$, with x = 0, 0.1 and 0.2. The samples were synthesized by solid state reaction method. The chemical formulas listed below are the general guide for starting materials.

$HgO + 2BaO+(2-x)\ CaO + x\ K_2O_3+ 3CuO \rightarrow HgBa_2Ca_{2-x}K_xCu_3O_{8+\delta}$

The powders were mixed together using an agate mortar to produce a homogenous mixture, and the grinding process took a period of time between 30-50 minutes. The powders were shaped as a disc-pellets with a diameter of 15 mm and a thickness of 3 mm using a hydraulic press with 5 MPa pressure for 1 min. The pellets were pre-sintered at (850) $^{\circ}$C for one day using a Carbolite furnace with increasing the temperature rate by 7 ºC/min, then cooled down to 25°C with same heating rate. The crystal structures of $HgBa_2Ca_{2-x}K_xCu_3O_{8+\delta}$ compounds were obtained using X-Ray diffractometer type Shimadzu with the following features: Source: Cu K_α, Wavelength: 1.5405, Current: 30 mA, Voltage: 40 KV. The scanning speed is 8 degree/min in a 2θ range of (10-80) ^{o}. The computerized calculations for (a, b, and c) were based on Full Prof Suite toolbar [18]. The intensities of the X-ray diffraction peaks have been used in equation (1) to estimate the phase's volume fraction [19]:

$$V_{ph} = \frac{\sum I_O}{\sum I_O + \sum I_1 + \sum I_2 + \sum I_{other(peaks)}} \times 100\% \quad (1)$$

Where I_o= XRD phase peak intensity that determined, $I_1, I_2, \ldots I_n$ represented the peaks intensities of all XRD.

The densities (d_m) of the samples were determined using this equation [12].

$d_m = W_m / N_A V$..(2)

where: W_m= the molecular weight in (amu)

N_A=Avogadro's number (particles/gm ml)

V = the volume of the unit cell in (cm^3).

The superconductor's critical temperature was determined by measuring the electrical resistivity as a function of the temperature. Four-point probe technique was used to measure the electrical resistivity within a temperature range of (77-300 K).

The samples were tested under vacuum of 6 x 10^{-2} mbar prepared by a rotary pump. The cryostat was connected to the rotary pump, and a digital thermometer sensor was attached near the sample. Four copper wires were also connected to the sample through oven-dried silver paste, which served as two wires for the current and the others for the electric voltage. The sample was prepared with a current of 5 mA by means of a constant current source, and the voltage drop in the sample was measured using the nanometer as a function of its cooling. Resistivity (ρ) was measured as the temperature of the sample changed using the relationship:

$$\rho = \frac{V}{I}\frac{\omega t}{L} \qquad (2)$$

where: the current passing through the sample I, voltage drop between the electrodes V, ω is the sample width, L is the effective length passing through electrodes, and t is the sample thickness.

3. Result and Discussions

Figure 1shows the XRD pattern of $HgBa_2Ca_{2-x}K_xCu_3O_{8+\delta}$ compound with x=(0, 0.1, and 0.2). The figure illustrated that the potassium substitution has produced changing in the high (H-phase) and low phases (L-phase). It is also noted that the partial replacement leads to a displacement of the peaks and a change in their intensities, This confirms the interaction between the elements and components of the superconducting compound.

Table 1 shows the values of the crystal lattice constants and the mass density that calculated from the X-ray diffraction plot after applying Brack's law to each partial substitution value of x. This table shows that the mass density, lattice parameters, and volume fraction decrease with increasing potassium substitution. This is due to the substitution of calcium by potassium and the difference in the sizes of the atoms replaced the elements since the ionic radius of potassium is longer than that for calcium. This is because the expansion at the base structure of HgO results in decreasing in mass density, volume fraction, c/a and the length of c.

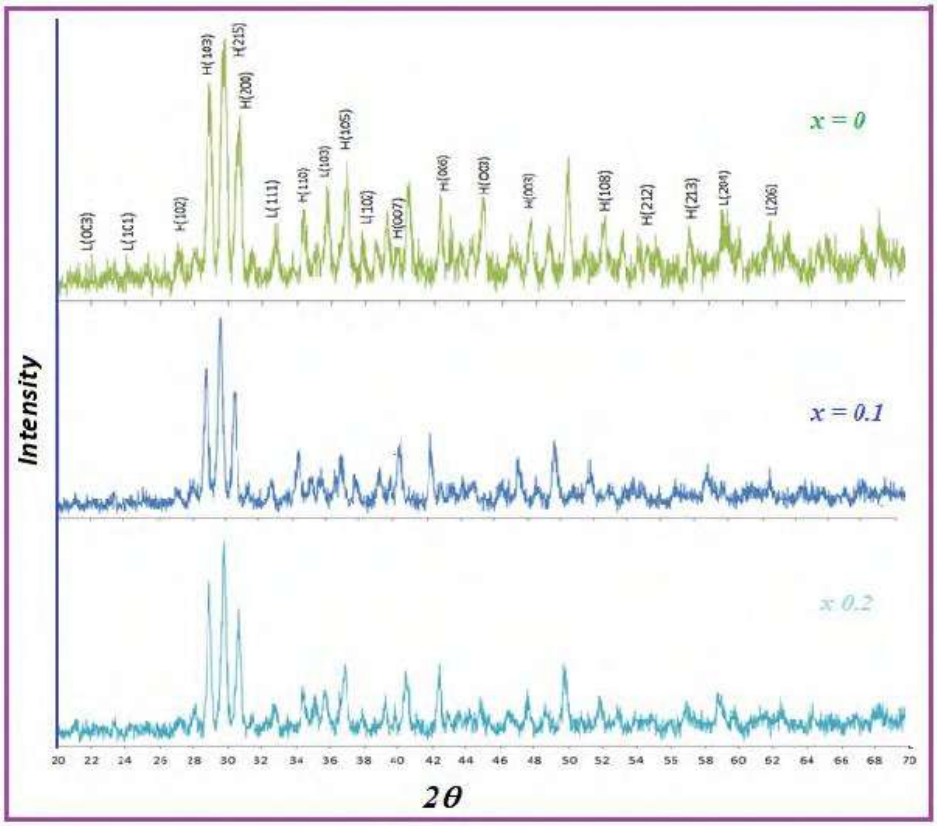

Figure 1. XRD of HgBa2Ca2-xKxCu3O8+δwith x=0, 0.1 and.2

Figure 2 illustrated the electrical resistivity as a function of the temperature for $HgBa_2Ca_2Cu_3O_{8+\delta}$, $HgBa_2Ca_{1.9}K_{0.1}Cu_3O_{8+\delta}$ and $HgBaCa_{1.8}K_{0.2}Cu_3O_{8+}$ compounds. n the first section, when the temperature drops from 300 to 155 K, it is noticed that the resistivity of the three samples behaves like a metal, but the temperature drops rapidly until it becomes zero, so we were able to determine two transition temperatures for each sample, which is $T_{c(onset)}$ and $T_{c(offset)}$. The transition temperature of pure curve was observed at 135 K ($T_{c(onset)}$) and at no-resistance. The ($Tc_{(offset)}$) were happened at 118 K, the transition range (ΔT) equal to 17K, while the values of transition temperatures for as grown $HgBa_2Ca_{1.9}K_{0.1}Cu_3O_{8+\delta}$ and $HgBaCa_{1.8}K_{0.2}Cu_3O_{8+\delta}$ (at zero resistance $T_{c(offset)}$) are 110 and 93 K, $T_{c(onset)}$ are 131 and113K, the change in transition width (ΔT=21and 10 k) respectively. This shows a decrease in the ΔT with increasing the Potassium concentration as shown in figure 3. Table 1 illustrated the decreasing in the mass density ρ_M and volume fraction with increasing potassium concentration.

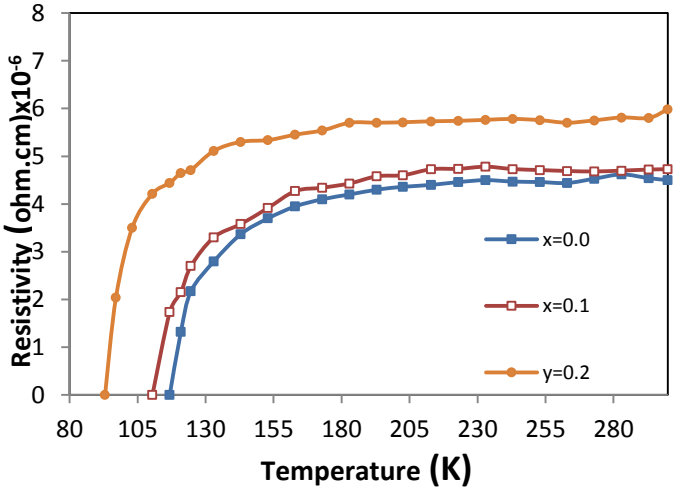

Figure 2. Temperature dependence of resistivity for HgBa2Ca2-xKxCu3O8+δ

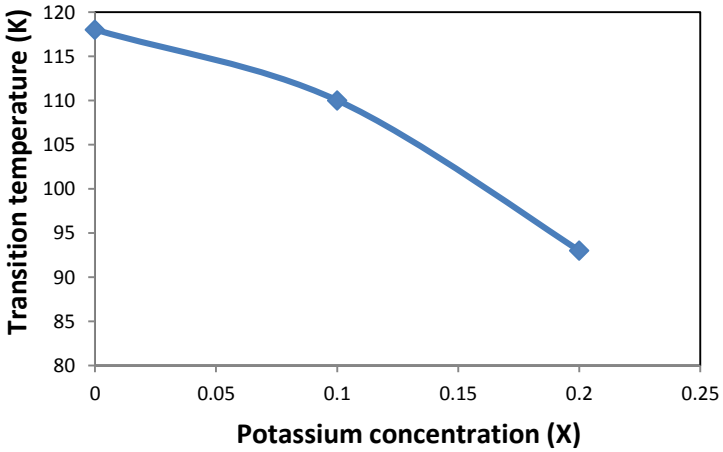

Figure 3. Temperature dependence of Potassium concentration for HgBa2Ca2-xKxCu3O8+δ

Table 1. Critical temperature Tc(OFF, ,Tc(ON), lattice parameters c, a, c/a, volume fraction and mass density for HgBa2Ca2-xKxCu3O8+δ system for x=0, 0.1 and 0.2.

X	$T_{c(OFF)}$(K)	$T_{c(ON)}$ (K)	$a(A^0)$	$c(A^0)$	c/a	ρ_M (g/cm^3)	$V_{Ph\text{-}1223}$%

0.0	118	135	3.845	15.78	4.099	1.53	76.4
0.1	110	131	3.833	15.37	4.006	1.52	74.4
0.2	93	113	3.846	15.36	3.999	1.51	71.9

4. Conclusions

In this study, we synthesized $HgBa_2Ca_{2-x}K_xCu_3O_{8+\delta}$ system with x=0, 0.1 and 0.2. The samples were prepared by solid state reaction process. The partial substitution of calcium with potassium in the Ca-O2 layer of $HgBa_2Ca_2Cu_3O_{8+\delta}$ has been studied with special emphasis on the effect of this partial substitution on superconductivity and microstructure properties. The XRD data collected from various samples show that all the samples are polycrystalline correspond to Hg-1223 phase. The critical transition temperature $T_{c(0ffset)}$ decreases from 118 to 93 when increasing potassium concentration. The results conclude that the substitutions of potassium lead to change in the volume fraction, lattice parameter and mass density.

References

[1] Richter H Puica I Lang W Peruzzi M Durrell J H Sturm H Pedarnig J D and Bauerle D 2006 *Journal of Physics: Conf. Series* **43** 706.
[2] Kadhim B B Khaleel I M Hussein B H Jasim K A Shaban A H ALMaiyaly B K H and Mahdi Sh M 2018 *AIP Conf. Proc.* **1968** 030054-(1-4).
[3] Jasim K A 2012 *Turk J. Phys* **36** 245.
[4] Jasim K A and Alwan T J 2009 *Journal of superconductivity and novel magnetism springer* **22** 861.
[5] Wadi K M Abdulateef A N Shaban A H and Jasim K A 2019 *Energy Procedia* **157** 222.
[6] Jasim K A 2012 *Journal of superconductivity and novel magnetism* **25** 1713.
[7] Kadhim B B Risan R H Shaban A H and Jasim K A 2019 *AIP Conf. Proc* **2123** 1.
[8] Jasim K A and Alwan T J 2017 *J Supercond Nov Magn* **30** 451.
[9] Iye Y Nakamura S and Tamegai T 1989 *Physica C* **159** 433.
[10] Amirfeiz M Cimberle M R Ferdeghini C Giannini E Grassano G Marr´e D Putti M and Siri A S 1997 *Physica C* **288** 37.
[11] Blatter G Geshkenbein V B and Larkin A I 1992 *Phys. Rev. Lett.* **68** 875.
[12] Mohammed L A and Jasim K A 2018 *Ibn Al-Haitham Jour. for Pure & Appl. Sci.* **31** 26.
[13] Aleabi S H Watan A W Salman E M.-T Jasim K A Shaban A H and AlSaadi T M 2018 *AIP Conf. Proc*. **1968** 020019-(1-5).
[14] Ibrahim Z H Ibrahim S A Shaban A H Jasim K A and Mohammed M K 2017 *Energy Procedia* **119** 709.
[15] Jasim K A Thejeel M A and Al-Khafaji R S 2017 *Ibn AL-Haitham Journal for Pure and Applied Science* **27** 170.
[16] Passos C A C Orlando M T D Oliveira F D C da Cruz P C M PassamaiJr J L Orlando C G P Eloi N A Correa H P S and Martinez L G 2002 Effect of oxygen content on the properties of the Hg0.82Re0.18Ba2Ca2Cu3O8+δ superconductors.
[17] Tian W Shao H M Zhu J S and Wang Y N 2006 *Physica Status Solidi.*
[18] Carvajal J R 2000 *An Introduction to the ProgramFullprof* (Leon France).
[19] BIJU A 2007 *Structural and Transport Properties of Rare Earth Modified (Bi, Pb)-2212 Superconductors* Ph.D. Thesis, University of Kerala: 52

Tailoring the structural, morphological, electrical and optical characteristics of transparent and conductive ZnO/Ag-NPs thin film coatings

Tailoring the structural, morphological, electrical and optical characteristics of transparent and conductive ZnO/Ag-NPs thin film coatings

Hatem Taha

Department of physics, College of Education for Pure Science, Ibn Al-Haitham, University of Baghdad, 10071, Baghdad, Iraq

E-mail: hatem.ar.t@ihcoedu.uobaghdad.edu.iq

Abstract. In this study, high quality ZnO/Ag-NPs thin transparent and conductive film coatings were fabricated *via* sol-gel process combined with spin-coating technique. Structural, surface morphology, electrical and optical properties were investigated by means of XRD, Hall effect measurements, FESEM and UV-Vis. The synthesized ZnO/Ag-NPs thin films shows a polycrystalline wurtzite structure, and the grain sizes enlarged when the annealing temperature increased. The surface morphologies of the coatings were dense, smooth and homogeneous as proved by FESEM images. The resistivity of (5.8×10^{-4} Ω.cm), the carrier concentration of (3×10^{20} cm^{-3}) and the mobility of (40 cm^2/V s) were obtained from the film post heated with 500 °C. Same thin film also shows the highest transmittance and energy gap of 88% and 3.71 eV respectively.

Keywords: ZnO, Transparent conductive coatings, Sol-gel, spin coating

1. Introduction

Over the past decades, optical transparency and electrical conductivity were considered inversely proportional. However, transparent and conductive materials (TCMs) have changed and wiped out this consideration through the exhibition of high optical transparency over the visible range of the light spectrum along with excellent electrical conductivity. Amongst these TCMs, transparent conductive oxides (TCOs) have been widely used in numerous optoelectronic devices including solar cells, light emitting diodes (LEDs), touch screens, displays, smart windows and sensors [1, 2]. Different materials were used as TCOs such as Indium oxide (In_2O_3) and tin-doped indium oxide known as indium tin oxide (ITO), zinc oxide (ZnO), aluminum and gallium doped ZnO (AZO, GZO), cadmium oxide (CdO) and tin oxide (SnO_2) [3, 4]. ZnO-based thin TCOs coatings have been widely used recently owing to its non-toxic, high stability and good optoelectronic properties. The TCOs based thin film coatings were produced so far *via* RF and DC sputtering, pulsed laser deposition, thermal evaporation, and sol-gel processes [5, 6]. The sol-gel is cheap, able to control the doping concentration, performed at low temperature and short time and produced coatings with preferred shape and surface area [7, 8]. ZnO can be doped with different elements including some transition metals such as aluminum (Al), silver (Ag), gallium (Ga), copper (Cu), indium (In), Titanium (Ti) etc. [9-11]. Combining silver nanoparticles (Ag-NPs) which have a reasonably good electrical conductivity and high optical transparency with ZnO has not been widely overlooked and discussed.

In this study, highly transparent and conductive system of ZnO/Ag-NPs was deposited on glass substrates by sol-gel spin-coating method. The thicknesses and the concentrations of both ZnO and Ag-NPs coatings were kept consistent throughout the sample fabrication process and the prepared thin films were post annealed at different annealing temperatures (300, 400 and 500) °C. Such kinds of bi-layer systems have not been extensively studied by researchers. The main goal of this investigation is to point out the role of Ag-NPs and annealing temperature on the structural surface topography, electrical and optical characteristics of ZnO coatings.

2. Methodology

2.1. Materials and methods

ZnO and Ag-NPs sols have been prepared using Zinc acetate dehydrate ($Zn(CH_3COO)_2.2H_2O$), purity 99.99%, Silver nitrate ($AgNO_3$, 99.5%), sodium borohydride ($NaBH_4$, 99.6%), 2-methoxy ethanol ($C_3H_8O_2$), purity 98%, mono ethanolamine (C_2H_7NO), purity 98% and polyvinylpyrrolidone (PVP, M = 40000g/mol). All the aforementioned chemicals were used without any purification.

A ZnO solution with 0.2 M was prepared by dissolving the appropriate amount of zinc acetate in 2-methoxy ethanol and stirring for 2 hours at 60 °C on a magnetic stirrer. The ethanolamine with a molar ratio of 1:1 was added to the resultant solution and stirred for another 2 hours at 60 °C.

The Ag nanoparticle solution was prepared with a concentration of 0.2 M. The required amount of silver nitrate was dissolved in 10 ml of de-ionized (DI) water. The concentration of $NaBH_4$ was kept consistent at 0.2 M in this work. In order to prepare the $NaBH_4$ solution, an adequate weight of sodium borohydride was dissolved and vigorously stirred in 50 ml DI water, and the obtained solution was chilled in an ice bath prior to the addition of $AgNO_3$ sol. The resultant mix was further stirred until a yellow solution was obtained.

The chemical reaction and reduction of $AgNO_3$ could be characterized by the following reactions [12, 13]

$$2AgNO_3 + 2NaBH_4 \rightarrow 2Ag + H_2 + B_2H_6 + 2NaNO_3 \quad (1)$$

$$AgNO_3 \rightarrow Ag^+ + NO_3^- \quad (2)$$

$$Ag^+ + e^- \rightarrow Ag \quad (3)$$

The ZnO/Ag-Nps thin film coatings were fabricated by depositing 50±5 nm Ag nanoparticles thin films onto 25×25 mm^2 dimensions glass substrates followed by pre-heat treatment at 150 °C for 1 hour. Then, 150±10 nm of ZnO thin film was deposited onto Ag-NPs thin films followed by pre-heating the resultant ZnO/Ag-NPs thin films at 150 °C for 1 hour. The spin-coating process for synthesizing ZnO/Ag-NPs thin films was performed at 3000 rpm for 30 seconds, and the resultant coatings were heat treated in air atmosphere at (300, 400 and 500) °C.

2.2. Characterization techniques

The crystallographic features of the ZnO/Ag-NPs films were characterized *via* (XRD) examination using a Siemens diffracto-meter with Cu-Kα source (λ=0.154nm). The surface topography was imaged using JEOL JSM-6301 (FESEM). The optical characteristics were carried out using UV-VIS spectrometer. The electrical properties were performed using a Dasol Eng. FPP-HS8 4-point probe, while the ECOPIA HMS-2000 instrument was used for Hall-effect measurements.

Scherrer relation was used to estimate the mean particle size of the synthesized ZnO/Ag-NPs thin films [14].

$$D = \frac{0.89\lambda}{\beta cos\theta} \quad (4)$$

where λ is the wavelength of X-ray beam, β is the line width at FWHM and θ is Bragg's diffraction angle.

The electrical resistivity (ρ) and conductivity (σ) are given by the following relations [15, 16]:

$$\rho = \frac{\pi}{ln(2)} t \left(\frac{V}{I}\right) \quad (5)$$

$$\sigma = N_e \times \mu \times e \quad (6)$$

where t is the film thickness, V is the voltage across the inner two probes and I is the current passed through the outer two probes, N_e is the carrier concentration, μ is the carrier mobility and e is the electron charge.

The free carrier mobility μ can be defined as:

$$\mu = \frac{e\tau}{m_e} \quad (7)$$

where m_e is the effective electron mass in the conduction band and τ is the average collision time of electrons.

The absorption coefficient (α) of the thin films can be calculated from the following equation [17]:

$$\alpha = \frac{1}{t} ln\left(\frac{1}{T}\right) \quad (8)$$

where t is the film thickness and T is the optical transmittance.

The transmittance and the absorption can be computed from the following equations [18]:

$$T = A \times exp\left(\frac{-4\pi kt}{\lambda}\right) \sim exp(-\alpha t) \quad (9)$$

$$A = \frac{16 n_\circ n_1 (n^2 + k^2)}{((n_\circ + n)^2 + k^2)+((n_1 + n)^2 + k^2)} \quad (10)$$

where n_o, n and n_1 are the refractive indices of air, film and substrate, respectively and k is the extinction coefficient.

The band gap energies (E_g) for the prepared thin films were estimated using the formula [18]:

$$(\alpha hv)^2 = A(hv - E_g) \quad (11)$$

where α is the absorption coefficient, hv photon energy, A constant represents the proportionality coefficient, E_g the energy band gap and $n = 1/2$ for allowed direct transitions.

3. Results and discussions

3.1. Descriptions of Ag-NPs colloidal solution

The mechanism of reduction Ag ions by $NaBH_4$ to form Ag nanoparticles follows three main steps. Once the solutions mixed, the first step starts, and the tiny particles of 3 nm were grown. As the reaction continues (the second step), the Ag particles further grow within a period of (20 – 60 min) reaching (8 – 20 nm). In the final step, all the $NaBH_4^-$ is used. Accordingly, the stabilizing BH_4^- is consumed, and the solution changed from reducing state to the oxidizing state [19]. Both the modifications of the surface potential of Ag particles and the adsorption of BH_4^- promote the agglomeration of Ag-NPs.

The distinctive colours of Ag-NPs solution are mainly assigned to the plasmon absorbance, especially when the incident light promotes the vibrations of the electrons at Ag-NPs surfaces subsequently, the light is absorbed [20, 21]. From figure 1, the absorption peak of Ag-NPs solution was located at 405 nm. It has been evident that the shape and the position of the absorption peak of metal-NPs depend on the particle size and the dielectric medium [22]. Also, Van Hyning *et al.* stated that the maximum of the plasmon absorption peak for Ag-NPs solution at 405 nm wavelength is attributed to the formation of a grain size of (10 – 14) nm [19].

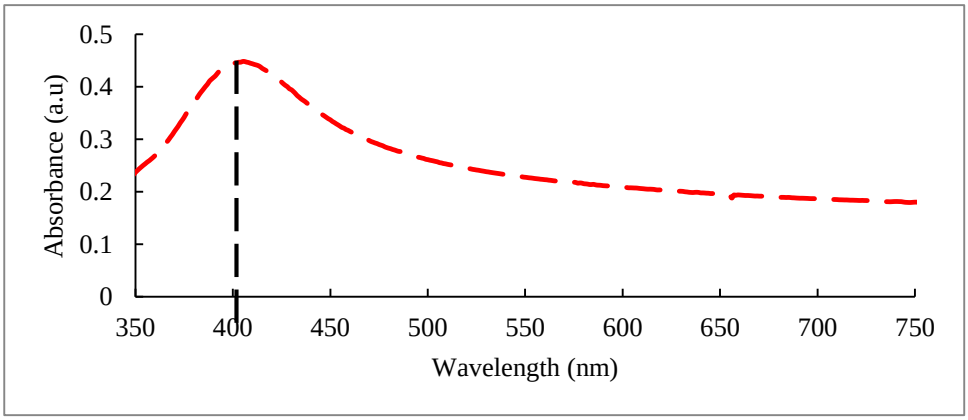

Figure 1. Absorption spectrum of prepared Ag-NPs solution

3.2. Crystalline structures

Figure 2 shows the XRD outlines of ZnO/Ag-NPs thin films post annealed at different temperatures. From figure 2, synthesized films exhibited polycrystalline feature with sharp and intense peaks correspond to the wurtzite structure of ZnO as expected and *P63mc* space group (JCPDS card 070-8070) [23]. The peaks of ZnO/Ag-NPs coatings observed at 2θ values of 31°, 34°, 36°, 47°, 56° and 63° are linked to (100), (002), (101), (102), (110) and (103) reflection orientations respectively. This may be attributed to the early coalescence of the Ag-NPs coating that facilitates the growing of high quality top ZnO layer, and reduces the effect of the thermal expansion mismatch between the glass and the ZnO film. With increasing the calcination temperature, the polycrystalline structures for all the synthesized thin films were improved, and the film treated with 500 °C shows the most intense peak as seen in figure 2. This is because at high temperature the ZnO particles supplied with a sufficient energy to accumulate at the preferred (002) orientation. Also, high annealing temperature assists the diffusion and the accumulation of Ag-NPs within the ZnO matrix by increasing the thermal energies of these particles and/or substituting of the Zn atoms in their sites by Ag atoms. It has been reported by Cao and co-workers [24] that the energetic particles in a crystalline structure tend to gathering and accumulating along the preferred orientation plane lead to improve the crystalline quality.

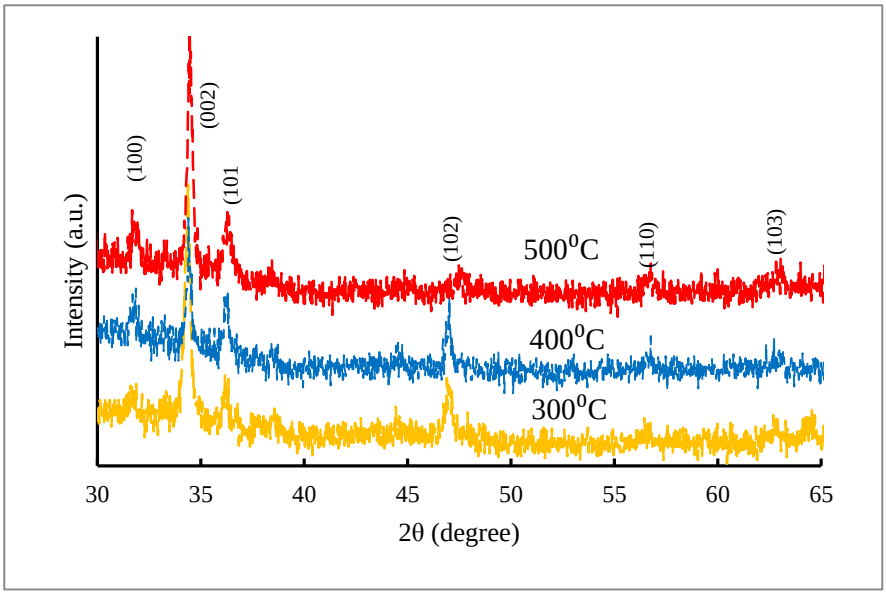

Figure 2. XRD patterns of post annealed ZnO/Ag-NPs thin films

Scherrer relation (Eq. 4) was used to estimate the mean particle size of the synthesized ZnO/Ag-NPs thin films.

The grain size of ZnO/Ag-NPs coatings is enlarged with increasing the calcination temperature and the highest value of *D* was found to be 45 nm for the film annealed at 500°C due to enhance the substitution of Zn by Ag ions, and the agglomeration of the Ag particles in the grain boundaries of ZnO matrix which lead to decrease the density of the grain boundaries and hence improve the crystalline quality. Liu and co-authors [25] have been reported the same tendency of enlarging the crystallite size of both Ag-NPs and ZnO thin film and they stated that the crystalline structure of ZnO thin film did not changed with introducing Ag-NPs to the film material.

3.3. Surface morphology

Figure 3 shows the FESEM images of annealed ZnO/Ag-NPs thin films. All the fabricated coatings exhibited uniform, smooth, dense and homogenous surfaces confirming the growing of a crystalline feature of ZnO. This could be attributed to the formation of continuous Ag-NPs coating underneath the ZnO coating which assists the growing of homogenous and free pinholes surface morphology for ZnO coating. Also, high annealing temperature results in improving the surface morphology along with increasing the grain sizes of the fabricated ZnO-based thin films.

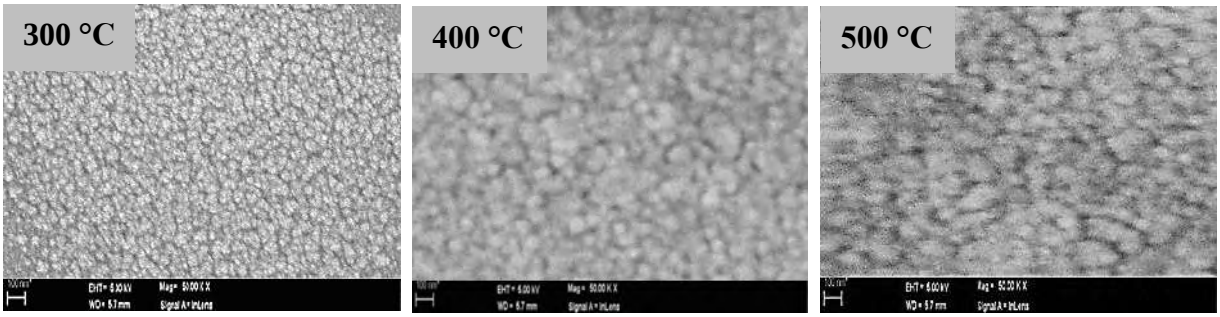

Figure 3. FESEM images for post annealed Ag-NPs thin films

3.4. Electrical properties

Figure 4 (a and b) displays the variations of the resistivity, conductivity, carrier concentration and mobility of annealed ZnO/Ag-NPs thin films with annealing temperature. In general, the average resistivity of the ZnO/Ag-NPs thin films is low enough comparable to those for ITO-based thin films in our previous study [26]. This confirms that ZnO-based thin transparent and conductive coatings can be good choice to substitute the expensive ITO material. With increasing annealing temperature from 300 °C to 500 °C, the resistivity is reduced from 7.8 $\times 10^{-4}$ Ω.cm to 5.8 $\times 10^{-4}$ Ω.cm while the conductivity is improved from 1282 $S.cm^{-1}$ to 1724 $S.cm^{-1}$. Moreover, the carrier concentration and the mobility of the synthesized ZnO/Ag-NPs thin films are also improved and the highest values of the carrier concentration (~ 3×10^{20} $cm^{-}3$) and mobility (~ 40 cm^2/Vs) were obtained for the film annealed at 500 °C. This could be assigned to the role of annealing temperature that assists the diffusion of Ag atoms through ZnO matrix either to substitute Zn atoms on their sites (as discussed previously) or to occupy random sites and growing as coalescences of Ag particles and hence forming effective conducting paths for the charge carriers. It has been reported that the free electrons prefer to transport through these conducting paths rather than ZnO matrix, and these paths also enhance the carrier mobility of the thin film [27]. Furthermore, annealing temperature results in enhancing the crystalline structure and enlarging the grain size of fabricated thin films as proved in the XRD analysis. Accordingly, the density of grain boundaries reduced and the chained electrons liberated thus the number of the charge carriers in the thin film matrix increased.

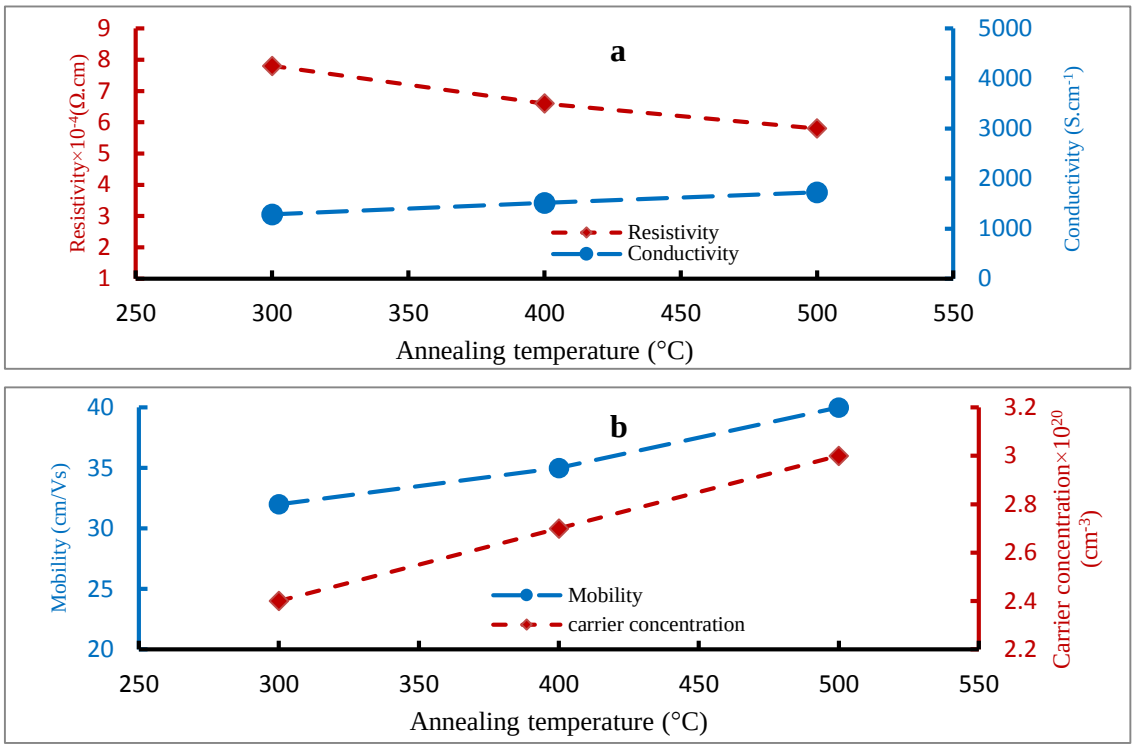

Figure 4. Variations of the electrical properties of Ag-NPs coatings with annealing temperature

3.5. Optical properties

Figure 5 (a and b) displays the transmittance spectra and the variation of the optical band gap energy of ZnO/Ag-NPs thin films. The optical transmittance of all the thin films strongly depends on the annealing temperature and it is increased from 85 % to 88% after increasing the annealing temperature from 300 °C to 500°C. This can be attributed to the high uniformity of both the ZnO top layer and the Ag-NPs bottom layer, as well as the low density of the scattering centres along with low absorption of incident photons. In addition, increasing annealing temperature enhances growing of continuous thin film coatings. Despite the obtained optical transparency of ZnO/Ag-NPs thin films in this investigation is poorer than that obtained for ITO-based thin films in our previous study [28], it stills considered adequate for optoelectronic devices.

The calculated energy band gaps of annealed ZnO/Ag-NPs thin films are presented in figure 5b. The results show that the ZnO/Ag-NPs thin films have high energy band gap values indicating a band gap broadening takes place. This is an expected behaviour due to higher optical transmittance of the ZnO/Ag-NPs thin films. Also, widening the energy band gap could be linked to the enhancement of the crystallographic features of ZnO/Ag-NPs films and enlarging the grain size along with increasing annealing temperature onto deposited thin films. The E_g for annealed ZnO/Ag-NPs thin film was increased from 3.68 eV to 3.71 eV when the annealing temperature increased from 300 °C to 500°C. This could be attributed to improving the crystalline quality through enlarging the crystallite size and

reducing the density of grain boundaries in the thin film matrix owing to increasing the annealing temperature. [28].

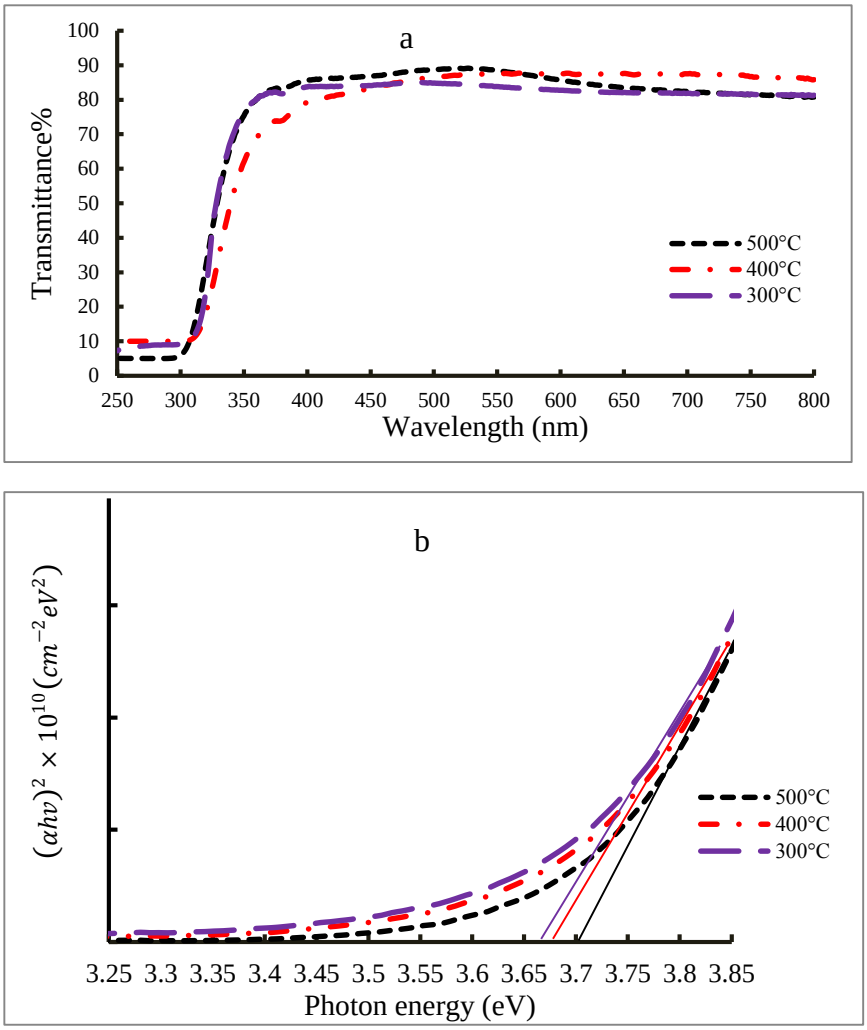

Figure 5. a- Transmittance and b- energy gaps of annealed ZnO/Ag-NPs thin

4. Conclusions

ZnO/Ag-NPs thin transparent conducting oxide coatings were successfully fabricated *via* a sol-gel spin-coating technique. The effects of annealing temperature on the structural, surface morphology, electrical and optical properties of these thin films were investigated. Combining Ag-NPs layer underneath ZnO layer did not affected the ZnO structure. The grain of these coatings is enlarged with further annealing, and the highest value was obtained for the film annealed at 500 °C. FESEM images show that all the thin films display uniform, smooth, dense and homogenous surface with a grain feature indicating a polycrystalline structure of ZnO phases. The electrical resistivity of the prepared thin films was dropped along with increasing annealing temperature achieving the lowest values of 5.8×10^{-4} Ω.cm. The maximum optical transparency in the visible region and the largest E_g were 88% and 3.71 eV respectively.

References

[1] Taha H Ibrahim K Rahman M M Henry D J Yin C Y Veder J PAmri A Zhao A Jiang Z T 2020 *Applied Surface Science* **530** 147164.
[2] Tian Y Wang T Geng H Z Ethiraj A S Gu Z Z Jing L C Yuan X T Zhao H Wen J G Xu Z H Materials 2019 *Research Express* **6**.
[3] Ren Y Zhou X Wang Q Zhao G 2018 *J Sol Gel Sci Technol* **85** 732.
[4] Ponja S D Sathasivam S Parkin I P Carmalt C J 2020 *Sci. Rep.* **10** 1.
[5] Soumya K Selvam I P Potty S N 2019 *Thin Solid Films* **687**.
[6] Speaks D T International 2020 *Journal of Mechanical and Materials Engineering* **15**.
[7] Misra M Hwang D K Kim Y C Myoung J M Lee T I 2018 *Ceramics International* **44** 2927.
[8] Sunde T O L Garskaite E Otter B Fossheim H F Saeterli R Holmestad R Einarsrud M A Grande T 2012 *Journal of Materials Chemistry* **22** 15740.
[9] Bernède J C Cattin L Abachi T Lare Y Morsli M Makha M 2013 *Mater Lett* **112** 187.
[10] Zhao B C Xia B Ho H W Fan Z C Wang L 2009 *Physica B: Condensed Matter* **404** 2117.
[11] Mirzaee M Dolati A2014 *Journal of Nanoparticle Research* **16** 1.
[12] Kawano K Komatsu M Y Yajima Haneda H Maki H Yamamoto T 2002 *Applied surface science* **189** 265.
[13] Wang J Fan X Zhou Z Tian K 2011 *Materials Science and Engineering: B* **176** 978.
[14] Acharya A D Sarwan B Panda R Shrivastava S B Ganesan V 2014 *Superlattices Microstruct* **67** 97.
[15] Lam W Y 2014 *Electrical and optical properties of indium tin oxide*.
[16] Smith D L 1995 *Thin-film deposition: principles and practice* (McGraw-Hill New York) etc.
[17] Wooten F 2013 *Optical properties of solids Academic press*.
[18] Fox M 2002 *Optical properties of solids*, in, AAPT.
[19] Van Hyning D L Klemperer W G Zukoski C F 2001 *Langmuir* **17** 3128.
[20] Van Hyning D L Zukoski C F 1998 *Langmuir* **14** 7034.
[21] Link S El-Sayed M A 1999 The *Journal of Physical Chemistry B* **103** 4212.
[22] Kamat P V Flumiani M Hartland G V 1998 *The Journal of Physical Chemistry B* **102** 3123.
[23] Ivanova T Harizanova A Koutzarova T Vertruyen B Closset R 2020 *Journal of Molecular Structure* 1206.
[24] Cao C B Xiao L Song X P Sun Z Q 2010 *J. Vac. Sci. Technol. A Vac. Surf. Films* **28** 48.
[25] Liu M Qu S, Yu W Bao S Ma, Zhang Q He J Jiang J Meletis E Chen C 2010 *Appl Phys Lett* **97** 231906.
[26] Taha H Jiang Yin C-Y Henry D J Zhao X Trotter G Amri A 2018 *The Journal of Physical Chemistry C* **122** 3014.
[27] Taha H Jiang Z-T Henry D J Amri A Yin C-Y Alias A B Zhao X 2018 *Materials Today Communications* **14** 210.
[28] Taha H Jiang Z-T Henry D J Amri A Yin C-Y Rahman M M 2017 *Semiconductor Science and Technology* **32** 065011.

The structural properties and Energy Gap of PVDF/LiAlO2 Nanocomposite Thin Films

The structural properties and Energy Gap of PVDF/LiAlO2 Nanocomposite Thin Films

Ruqaya Fouad Kadhim and Zainab Raheem Muslim

University of Baghdad, College of Science, Physics Department

Ruqia.f.k@gmail.com

Abstract. lithium aluminate (LAO), $LiAlO_2$ powders were synthesized by sol-gel method because it was developed for preparing nano-sized at low temperature.The X-ray diffraction (XRD) found out a tetragonal structure for $LiAlO_2$. Various percentages of 1, 2, 3 and 4 wt. were applied to the LAO with polyvinylidene fluoride (PVDF) polymer. The obtained materials were characterized by Atomic Force Microscopy (AFM) and Field Emission Scanning Electron Microscope (FESEM). Structural analysis indicates the presence of polycrystalline phase with nanometre scale. Energy gap were studied and the results shows a decrease in energy gap with the increasing in weight ratio of LAO. This decline in the value of optical energy is due to an increase in the density of the band-gap of localized states.

Keyword: PVDF, $LiAlO_2$, polymer, energy gap

1. Introduction

In high energy density states, the increasing interest in solid batteries is leading many researchers to explore new concepts and related materials. The lithium-ion technology that uses polymer electrolytes as a separator for rechargeable batteries tends to provide the most promising choices[1]. Recently, there has been considerable interest in Al-doping ($LiMO_2$, where M is a transition metal) of lithium intercalation oxides. Theoretically and experimentally, Al transition-metal cation replacement has been shown to increase the cell voltage. Some of Al 's benefits are that it is light, cheap, and non-toxic [2].

Lithium aluminate ($LiAlO_2$) can be used as the best ceramic fillers for polymer electrolytes, and it is primarily used as a possible economical lithium battery cathode in the energy industry in nuclear physics and solid chemistry. $LiAlO_2$ normally crystallizes at ambient conditions, called γ-phase, in a tetragonal structure. Then, in the past few decades, several interesting phases of $LiAlO_2$ have been discovered or synthesized. A low temperature step with orthorhombic symmetry was defined as β-$LiAlO_2$[3]. Lithium aluminate synthesis has essentially been carried out by many methods: sol-gel, solid state, wet chemical, using templates, different precursors and combustion processes [4]. A graphite anode, a lithium-metal oxide cathode, an electrolyte solution containing lithium salts, and a polymeric separator typically consist of a lithium-ion battery [5].

Indeed, for electronic charges, the separator should be electrically insulated and at the same time sufficiently porous to ensure electrolyte uptake to enable ionic conductivity. A necessary requirement for the functioning of the battery is high ionic conductivity. In addition, the high dimensional stability,

as well as good mechanical properties of the polymeric separator at high temperatures is important to avoid a short circuit between the cathode and the anode, which can probably result in a failure of the battery. Several materials such as gel-forming polymers and polymeric separators have been investigated in the literature, such as polyvinylidene fluoride (PVDF), polyethylene oxide (PEO), polypropylene (PP), polyethylene (PE), and copolymers of the latter. PVDF separators obtained by phase inversion methods are used by most batteries on the market today [6].

Metal oxide nanoparticles applied to the polymer material will make a major contribution to the internal components of the battery in terms of electrical conductivity as well as mechanical strength and greater thermal stability thereby contributing to improving the protection of the cell [7,8]. Because of its characteristics, such as the ability to boost lithium ion transfer and electrolyte absorption, nano-silica is one of the most investigated fillers, thus increasing mechanical strength, electrode interface stability, and ion conductivity [9].

A. M. and P. Indolia. S. Gaur (2013) studied the optical characteristics of PVDF-ZnO thin films. This study showed that the optical properties of nanocomposite thin films depends on the ZnO contents and have the best optical properties [10].

The goal of this work is to explore the impact of LAO material on PVDF pristine and PVDF: LAO nanocomposites with different concentrations of LAO optically. The key focus of the present analysis is on the optical band difference of different percentages of PVDF and PVDF:LAO.

2. Experimental part

2.1 Preparation of lithium aluminate$LiAlO_2$

The $LiAlO_2$ powder synthesis was processed by the chemical method of Sol-gel. First, the mixture was dissolved in (50 ml) using equal quantities of Li and Al nitrates with citric acid (1:1:2) and combined with distilled water, and left to evaporate for 1 day at 70 ° C until gelled, then heat-treated for two hours at 650 ° C. The powder prepared by sol-gel shows a sponge with a color of white. The stage of heating in the 150 °C, LAO shows a sponge porous structure before the calcination process, these processes may be considered to have a fine and crystalline powder. The calcination temperature (650) °C was proper to get nanosized particles, followed by grinding process to reduce the coarser particles using a large in crucible like container. The resulting prepared powder color was white. Using hot process casting of these composites, this method decreases the prosily-due compacting, which increases composition conductivity in order to decrease volume and improve lithium ion mobility by offering the conductivity direction along with the structure.

2.2 Preparation of PVDF: LAO nanocomposites

The developed nanocomposites were prepared using the method of phase inversion. The casting solution was composed of PVDF powder dissolved in N, Ndimethylformamide (DMF) and various modified LAO concentrations. LAO in the ratio (1, 2, 3, and 4 % wt.) was applied to all the components and combined by stirring to prepare the casting solution for at least 5 hours. By means of a hand-casting knife, the solutions were uniformly cast on a glass substrate and then immersed in a coagulation bath after exposure to the air for a fixed period (one day). To ensure that the excess solvent was extracted, the flat-sheet thin film was kept in the water bath for at least 1 day.

3. Results and discussions

3.1 X-ray diffraction analysis

The X-ray diffraction spectra for lithium aluminate $LiAlO_2$ (LAO) synthesis by sol-gel method are reported in Figure 1. The X-ray spectra indicates the formation of tetragonal structure $LiAlO_2$ with card No.(JCPDSNO.) 96-100-8167, and the secondary phase Al_2O_3 has orthogonal structure with card No. (JCPDS 96-100-0443).

The main peaks at 22.25°, 24.3°, 28.19°, 33.35°, 34.63°, 50.12°, 56.25°, 61.34°, 72.44°, and 78.41° corresponding to (101), (110), (111), (012), (200), (220) (130), (302) (332), and (330) indicates the

formation of pure $LiAlO_2$, Some extra secondary peaks (secondary phases of Al_2O_3) are seen adjacent to the peak features and may be due to the presence of the impurity process. In Table 1, the structural properties are explained as full width at half maximum (FWHM), index plane, and grain size that agree with [11,12].

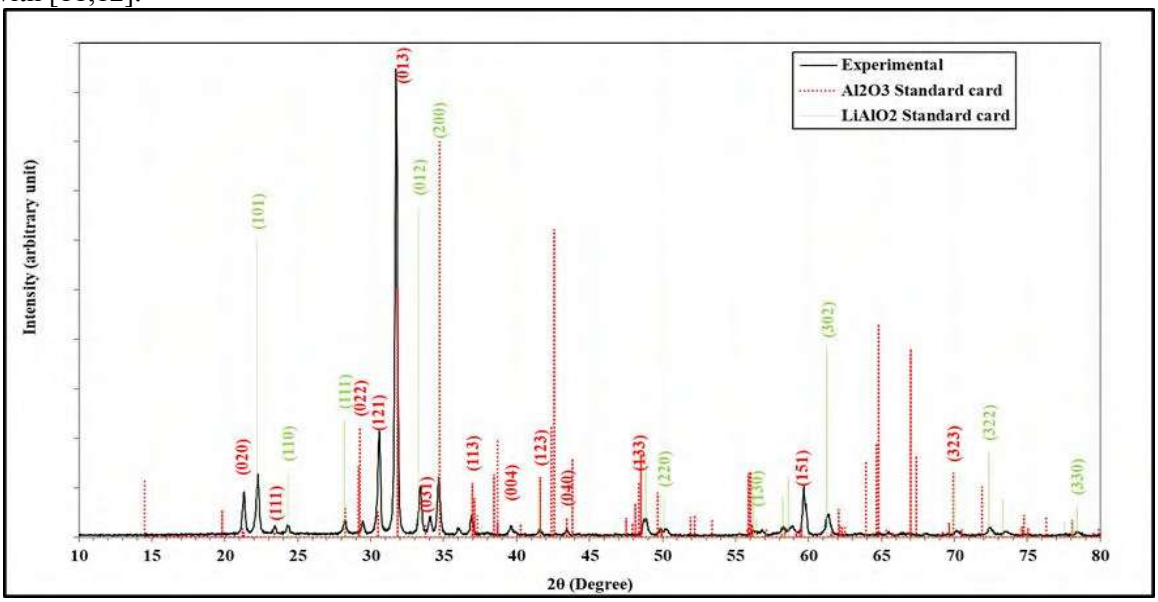

Figure 1. X-ray diffraction spectra of $LiAlO_2$.

Table 1. The structural properties of $LiAlO_2$ and Al_2O_3powder.

2θ (Deg.)	FWHM (Deg.)	d_{hkl} Exp.(Å)	G.S (nm)	d_{hkl} Std.(Å)	Phase	hkl	card No.
21.2941	0.3083	4.1692	26.2	4.1650	Orthor.Al_2O_3	(020)	96-100-0443
22.2577	0.3084	3.9909	26.3	3.9953	Tetra.$LiAlO_2$	(101)	96-100-8167
23.4526	0.2312	3.7902	35.1	3.7931	Orthor.Al_2O_3	(111)	96-100-0443
24.3007	0.2698	3.6598	30.1	3.6557	Tetra.$LiAlO_2$	(110)	96-100-8167
28.1938	0.3084	3.1626	26.6	3.1613	Tetra.$LiAlO_2$	(111)	96-100-8167
29.4273	0.3084	3.0328	26.6	3.0495	Orthor.Al_2O_3	(022)	96-100-0443
30.5837	0.2698	2.9207	30.5	2.9782	Orthor.Al_2O_3	(121)	96-100-0443
31.7401	0.1927	2.8169	42.9	2.8099	Orthor.Al_2O_3	(013)	96-100-0443
33.3590	0.3084	2.6838	26.9	2.6885	Tetra.$LiAlO_2$	(012)	96-100-8167
34.0529	0.2313	2.6307	35.9	2.6521	Orthor.Al_2O_3	(031)	96-100-0443
34.6311	0.3469	2.5881	24.0	2.5850	Tetra.$LiAlO_2$	(200)	96-100-8167
36.9053	0.2699	2.4336	31.0	2.4306	Orthor.Al_2O_3	(113)	96-100-0443
39.6035	0.5011	2.2738	16.9	2.2387	Orthor.Al_2O_3	(004)	96-100-0443
41.6079	0.3854	2.1688	22.1	2.1693	Orthor.Al_2O_3	(123)	96-100-0443
43.4196	0.2312	2.0824	37.0	2.0825	Orthor.Al_2O_3	(040)	96-100-0443
48.7775	0.3469	1.8655	25.1	1.8746	Orthor.Al_2O_3	(133)	96-100-0443
50.1267	0.4626	1.8184	19.0	1.8279	Tetra.$LiAlO_2$	(220)	96-100-8167
56.2555	0.5782	1.6339	15.6	1.6349	Tetra.$LiAlO_2$	(130)	96-100-8167
59.6861	0.3470	1.5480	26.4	1.5516	Orthor.Al_2O_3	(151)	96-100-0443
61.3436	0.3084	1.5100	29.9	1.5116	Tetra.$LiAlO_2$	(302)	96-100-8167
70.1707	0.3469	1.3401	28.0	1.3441	Orthor.Al_2O_3	(323)	96-100-0443
72.4449	0.3855	1.3036	25.5	1.3049	Tetra.$LiAlO_2$	(322)	96-100-8167

78.4196	0.4240	1.2185	24.2	1.2186	Tetra.$LiAlO_2$	(330)	96-100-8167

3.2 Atomic force microscopy for $LiAlO_2$ powder

Atomic force microscopy (AFM) was performed to measure the average diameter and the grain size for the samples in the shape of a pellet by using AA3000 scanning probe Microscopy by Angstrom Advanced Inc (USA). The AFM pictures morphology for the surface of the $LiAlO_2$ NPs in the two and three dimensions are shown in Figure 2a and b. The pictures are shown a uniform surface; indicate that the particle has uniform dimensions.

The average diameter on the surface is found by granularity cumulating distribution chart to be 82.65 nm for $LiAlO_2$ as shown in Figure 2c.

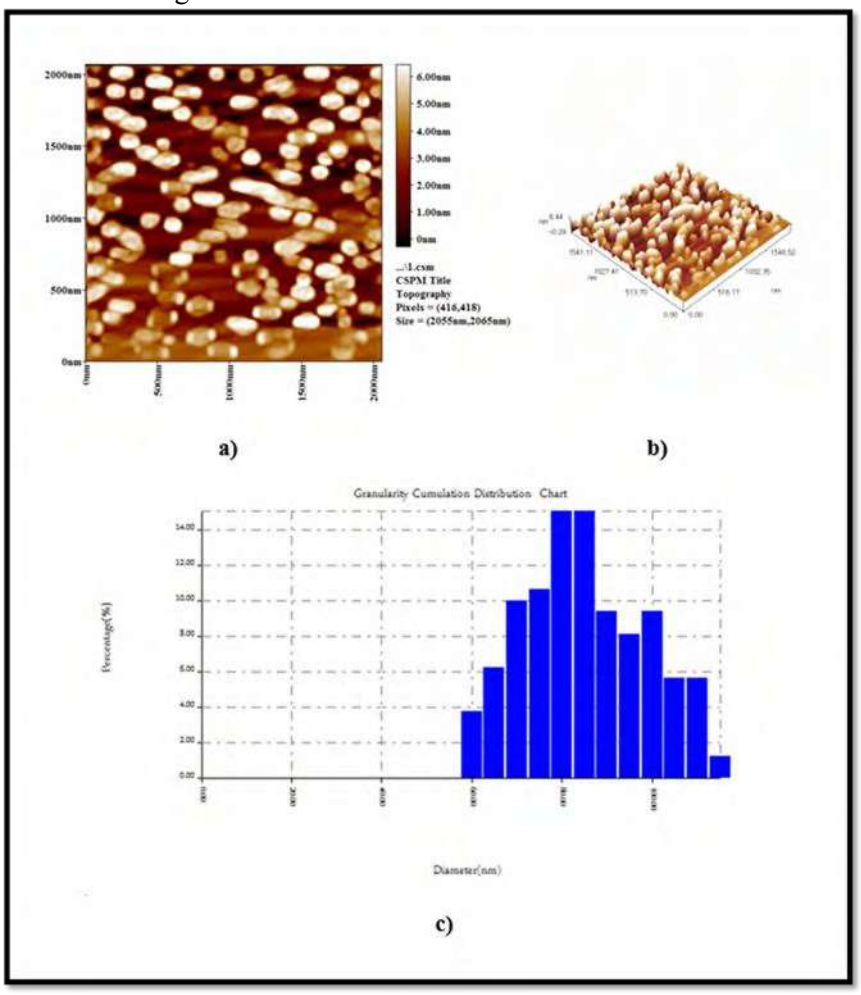

Figure 2. AFM micrograph for $LiAlO_2$ were (a) 2D, (b) 3D and (c) Granularity cumulation distribution chart.

3.3 Field Emission Scanning Electron Microscope (FE-SEM)

Typical sample findings from the field emission scanning electron microscope (FE-SEM) are shown in Figure 3. PVDF pure and PVDF: $LiAlO_2$ 1% thin film FE-SEM picture demonstrates that the sample consists of large agglomerated clusters. It can be seen under high magnification that each cluster consists

of multiple spherical nanoparticles, each of which has a smooth surface. The addition of LAO to the PVDF has a significant impact on the morphology of the film. As the content of LAO increased, the size and density of the pores increased.
In Figure 3a, the film is relatively smooth and flat with small and few pores. More bigger pores were formed when 1% LAO was added into the PVDF solution, as shown in Figure 3b.

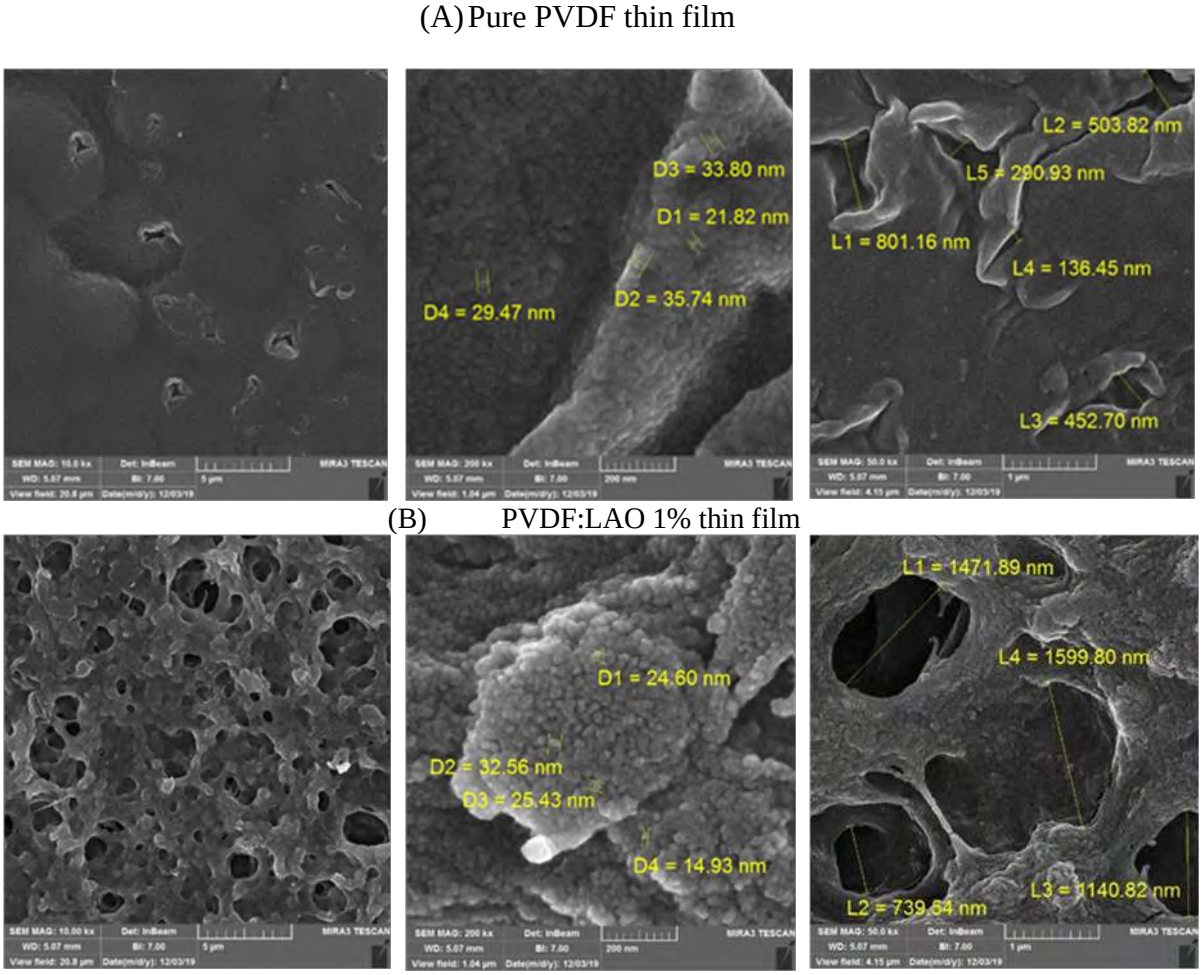

Figure 3. SEM images of (a) pure PVDF and (b) PVDF : $LiAlO_2$ 1% thin film.

3.4 Optical band gap
For pristine PVDF and PVDF: LAO composite films, the optical band gap can be obtained by taking into account the linear portion of the UV-Visible spectrum at the absorption edge. It is obvious from Figures 4 and 5 that all samples display absorption edges that are red-shifted with LAO nanoparticles.
Figure 4, 5 and Table 2 are shown the energy gap variation with Various LAO proportions (1, 2, 3, and 4 % wt.) nano-powder. The results show a decrease in the energy gap(direct band gap) due to an increased in inter atomic spacing which decrease the potential, this inturn reduce the energy band gap.
Tauc plots identified direct PVDF:LAO band gaps in nanocomposite films:

$$f(h\upsilon) = (\alpha h\upsilon)^2$$

Where α is the absorption coefficient which was determined by the following expression:

$$\alpha(\upsilon) = 2.303(\frac{A}{t})$$

When A is the optical absorbance, and t is the thickness of the polymer nanocomposite thin film and it is approximately equal to 3.5mm.

Doping may affect the optical band gap; the low energy gap was due to high density of localized state. Impurities are the increase in doping due to dopants, as the chemical composition changes during doping. A shift in the energy distribution of the permissible states cannot have a general rule such as after impurities are added, the band gap will decrease [10].

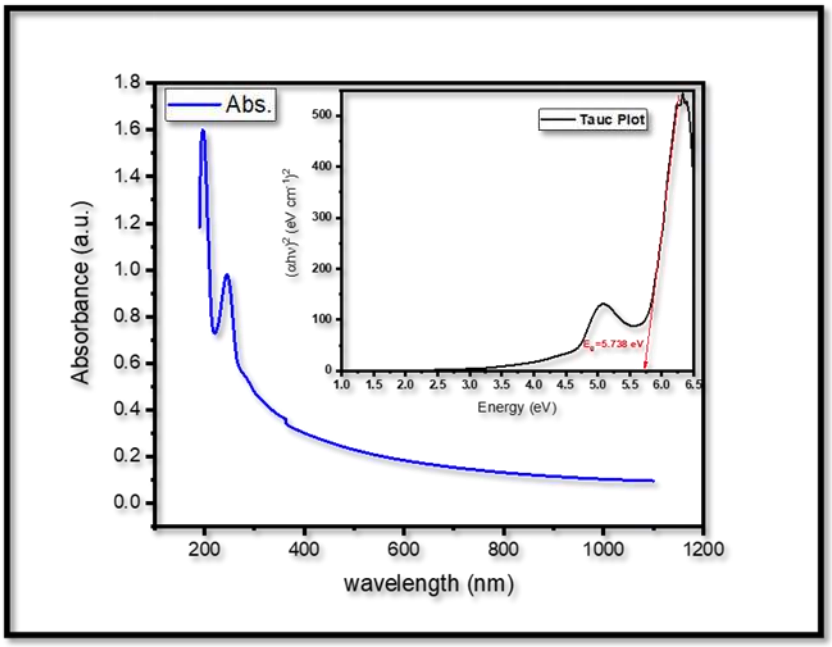

Figure 4. Energy gap of pure PVDF thin film.

Table 2. The Energy gap of PVDF:LAO thin film.

Sample		Energy gap (eV)
PVDF		5.73
PVDF:LAO	1 %	5.54
	2 %	*5.50*
	3 %	5.45
	4 %	*5.33*

The band-gap is a non-approved energy zone. The density of states versus energy depends on the substance's chemical composition; if the chemical composition is changed, at least, in principle, the state density distribution should change. Dopants are impurities, because, by doping, the chemical composition changes. A change in the energy distribution of the permissible states cannot have a general rule such as: after the introduction of impurities, the band-gap would decrease. Generally, these

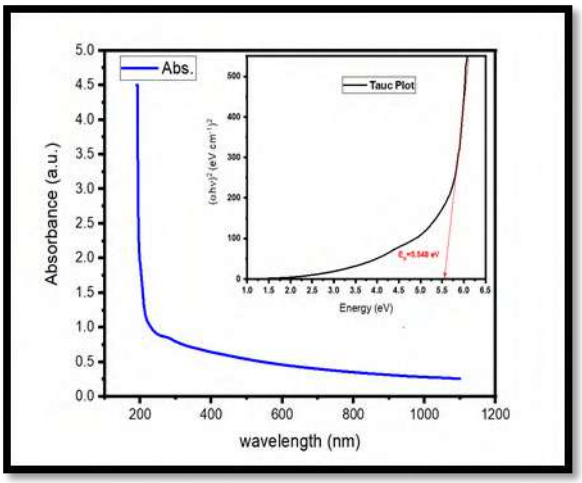

PVDF:LAO 1%

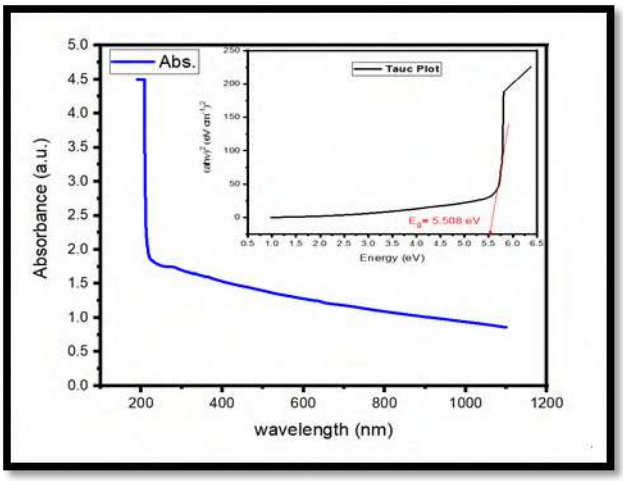

PVDF:LAO 2%

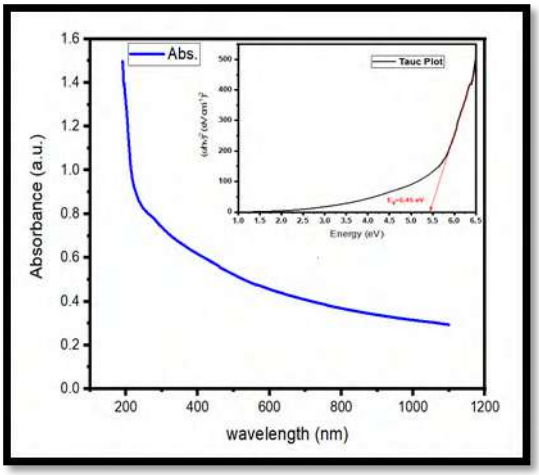

PVDF:LAO 3%

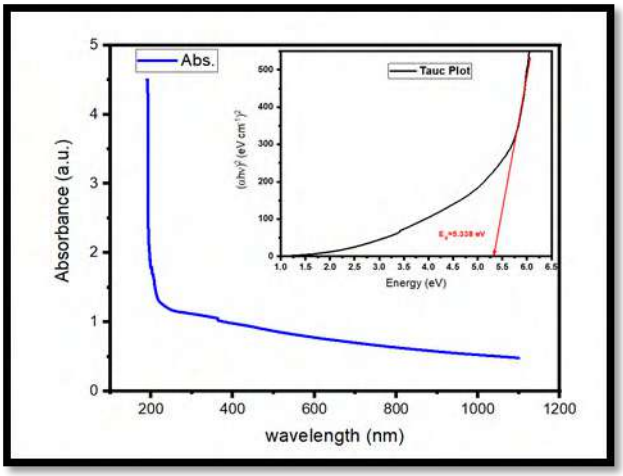

PVDF:LAO 4%

Figure 5. Energy gap of PVDF:$LiAlO_2$ thin film.

impurities are called dopants, which in the band-gap produce permissible shallow states. Shallow states have small energies of ionization; and when the doping density is high, a band is formed by dopant states. If the valence or conduction band edge is very close to this band, the band gap will decrease [10].

4. Conclusion

Lithium Aluminate ($LiAlO_2$) has been successfully prepared using sol-gel. The dependency of the optical properties of nanocomposites on $LiAlO_2$ material has been investigated. As the content of $LiAlO_2$ increases, the optical band gap for this process for direct transitions decreases. The structural changes

that occur after adding $LiAlO_2$ nanoparticles may be correlated with this activity. Due to the inclusion of $LiAlO_2$ nanoparticles, there is a drop in the optical energy gap of nanocomposites. The decrease in the optical distance indicated by the energy of optical activation can be associated with a decrease in network disorder.

References

[1] Mauger A Julien C M Paolella A Armand M and Zaghib K 2019 *Materials* November doi: 10.3390/ma12233892.
[2] Bhattab M D and O'Dwyer C 2015 *Phys. Chem. Chem. Phys.* **17** 4799.
[3] Liu G and Liu H 2018 *Journal of Physics: Condensed Matter* **30** 115401.
[4] Becerril J J and García-Sos I 2011 *Journal of Ceramic Processing Research* **12**(1) 52 .
[5] Deng D 2015 *Energy Science and Engineering* **3** (5) 385.
[6] Zhang T He W Zhang W Wang T Li P Sun Z and Yu X 2020 *Chem. Sci.* **11** 8686.
[7] Kim K M Ko J M Park N G Ryu K S and Chang S H 2003 *Solid State Ionics* **161**(1–2) 121.
[8] Liao Y H *et al.* 2011 *System* **196** 2115.
[9] Zaccaria M Gualandi C Fabiani D Focarete M L Croce F 2012 *Journal of Nanomaterials* ID 216012, 8 doi:10.1155/2012/216012.
[10] Indolia A P and Gaur M S 2013 *J Polym Res* **20** (1) 43.
[11] Duan J Wang P Li D Xiao X Zhang Z Hu Y 2018 *Journal of Alloys and Compounds* **739** 335.
[12] Lin J Wen Z Xu X Gu Z 2010 *Ceramics International* **36** 2221.

Assessment of 222Rn gas concentrations in Educational laboratories of Department Physics in the College of Sciences, Al-Mustansiriya University

Assessment of 222Rn gas concentrations in Educational laboratories of Department Physics in the College of Sciences, Al-Mustansiriya University

Hadeel Tariq Hamad[1], Mahmood Salim Karim[2], Nada Farhan Kadhim[3]

[1]Ministry of Education - General Directorate of Baghdad Al-Karkh First Education
[2]Department of Physics, College of Education, Al-Mustansiriyah University
[3]Department of Physics, College of science, Al-Mustansiriyah University

E-mail: shmss8654@gmail.com

Abstract. In this article, internal CRn measure have been carried out in twenty-three locations various rooms and Laboratory of Department Physics in science college in the university of Mustansiriyah. CRn were measure by Rad-7 detector. The results show that, the maximum CRn in indoor rooms was found in Electronics Laboratory (64.9 Bq/m3), whilst the minimum CRn was found in room rapporteur of higher studies (2) / Department of Physics (24.3 Bq/m3), which was lower (200-300Bq/m3) indoor air and the value of parameters hazard indices were lower than the value of permissibility limit.

Keywords: C_{Rn}, Science College, Rad-7, Laboratory.

1. Introduction

The exposure of 222Rn and the radioactive progeny present in the environment outcomes in big contribution to the rate effective dose received by the human beings [1,2]. The natural of 222Rn and it is airborne progeny can cause a significant indoor health hazard ,especially when they build up in enclosed regions, like educational laboratories in universities, caves and mines. The implementation of EURATOM directives [3] creates new scenarios in the radioactivity natural field, regarding 222Rn gas measurements in workplaces. Workplaces may differ from dwellings in terms of the structure building, microclimatic conditions, and occupancy factors. Some of workplaces of peculiarities are:(a) presence of forced ventilation or air conditioning(b) multi storeyed buildings with biger entrance hall (c) high probability of levels of humidity and finding elevated temperatures, dust and aerosols(d) widespread use of the basements or ground floor.

2. Detector technology

The interior detector of Rad-7(Serial Number 2764) is cell of the hemisphere with the volume approximately 0.72 L. The 222Rn gas and daughters, deposited on the detector surface and when decay, they emit alpha particles of special energy directly into the middle. Rad -7 detector draws air from the environment through desiccant and inlet the filter for the measure chamber.[4]. The detector of Rad-7 was related with tubing and the desiccant to soak up humidity, see in fig. (1).

Figure (2) shows RAD-7 electron- ic continuous radon monitor. Sniff mode and circle time was set to be 1 hour in accordance with running time of each path of the valve. To investigate radon released from the sample to air, the sample was enclosed into a column and airborne radon was measured with a continuous monitor of electrostatic type (RAD-7, Durridge company, USA).

Figure (2) shows RAD-7 electronic continuous radon monitor. Sniff mode and circle time was set to be 1 hour in accordance with running time of each path of the valve. In order to investigate radon released from the sample to air, the sample was enclosed into a column and airborne radon was measured with a continuous monitor of electrostatic type (RAD-7, Durridge company, USA).

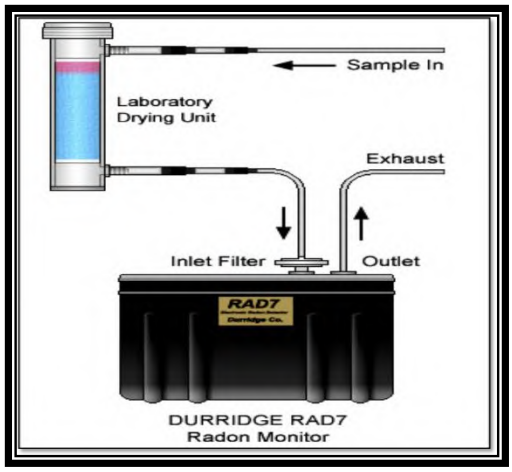

Figure 1. Rad-7 detector.

Figure 2. The durridge RAD-7 electronic continuous radon monitor with an HP printer mounted for immediate printing of results.

3. Measurements of hazard indices:

Potential Alpha Energy conce. (PAEC) = $(C_{Rn} / 3700) \times (f)$ [1]
Where :C_{Rn} (^{222}Rn gas conce. in Bq.m^{-3}unit) , (f = 0.4) [6].
Exposure to ^{222}Rn progeny (E_P) = PAEC×8760 × n × 170 [2]
n= (0.8),(8760) is number of hours per one year,170 is number of hours per working month
annual effective dose (AED) = h × t × D × C_{Rn} × f [8]
(D) = [9×10^{-6} (m Sv)/(Bq. m^{-3}.h)] , f =(0.4), (h) = (0.8), t=(8760 h/y).
lung cancer cases per year per million person (CPPP)=(18×10^{-6} mSv^{-1}.y)×AED [3]

4. Outcomes and debate

Indoor C_{Rn}, were measurement in various compartments for twenty-three various rooms or Laboratory of Department Physics in science college in the university of Mustansiriyah , Table (1) summarize the C_{Rn} in indoor rooms .From Table (1) it can note that, the maximum C_{Rn} in indoor rooms was found in Electronics Laboratory (64.9 Bq/m^3),whilst the minimum C_{Rn} was found in room rapporteur of higher studies(2) / Department of Physics (24.3 Bq/m^3), see Fig. (3), with rate value (38.6±6.9), that is lower than the extent (200-300Bq/m^3) [9], however, the minimum value for indoor C_{Rn} due to very good ventilation conditions of rooms or Laboratory.

The maximum (PAEC) was found in Electronics Laboratory which was (0.007 mWL), whilst the minimum (PAEC) was found in room rapporteur of higher studies (2) / Department of Physics (0.0026 mWL) with rate value (0.0042±0.001mWL), that is lower than the value (53.33 mWL) [10].

The maximum (E_P) was found in Electronics Laboratory (8.36 $mWLMY^{-1}$), whilst the minimum (E_P) was found in room rapporteur of higher studies (2) / Department of Physics (3.13 $mWLMY^{-1}$), with rate value (4.97±0.9$mWLMY^{-1}$), that is lower than the extent (1-2 $WLMY^{-1}$) [6].

The maximum (AED) was found in Electronics Laboratory (1637.3 mSv/y), whilst the minimum (AED) was found in room rapporteur of higher studies (2) / Department of Physics (613.06 mSv/y) ,with rate value (973.83±0.9 mSv/y) , that is lower than the extent (3-10mSv/y) [11].

The maximum (CPPP) was found in Electronics Laboratory (29.47), whilst the minimum (CPPP) was found in room rapporteur of higher studies (2) / Department of Physics (11.04), with the rate value (17.53±3.1) , that is lower than the extent (170-230) [11].

Table 1. (C_{Rn}), (PAEC), (E_P),(AED), (CPPP) in rooms or Laboratory of Department Physics in science college in the university of Mustansiriyah.

No	Location Name	Mean of C_{Rn} (Bq/m^3)	PAEC (WL)	(E_P) (mWLM/Y)	(AED) (mSv/y)	Lung Cancer /10^6person
1	**Head of the Department of Physics, (0110)**	39.4	0.0043	5.07	994.01	17.89
2	**Rapporteur of the Department of Physics, (0113)**	32.6	0.0035	4.2	822.46	14.8
3	**Rapporteur of Higher Studies (1) / Department of Physics, (0107)**	35.8	0.0039	4.61	903.19	16.26
4	**Department of Physics / Secretarial Room, (0111)**	33.7	0.0036	4.34	850.21	15.3
5	**Rapporteur of Higher Studies (2) / Department of Physics, (0112)**	24.3	0.0026	3.13	613.06	11.04
6	**Electronics Laboratory, (0102), (BO-L03)**	64.9	0.007	8.36	1637.3	29.47
7	**Nuclear Laboratory of Higher Studies, (0104),(BO-L02)**	32.7	0.0035	4.21	824.98	14.85

No	Location Name	Mean of C_{Rn} (Bq/m^3)	PAEC (WL)	(E_P) (mWLM/Y)	(AED) (mSv/y)	Lung Cancer /10^6person
8	**Laboratory of Polymer Molecular, (BO-L12)**	29.5	0.0032	3.8	744.25	13.4
9	**Atomic Physics Laboratory & Solid State Physics Laboratory ,(0105),(BO-L01)**	32.1	0.0035	4.13	809.84	14.58
10	**Laboratory of Spectra and Molecular1**	42.5	0.0046	5.47	1072.2	19.3
11	**Laboratory of Theoretical Physics**	37.8	0.0041	4.87	953.65	17.17
12	**Laboratory of Electro-optics,(0085),(BO-L13)**	35.2	0.0038	4.53	888.05	15.98
13	**Optical Physics Laboratory,(0099), (BO-L04)**	41.5	0.0045	5.34	1047	18.85
14	**Tribology and Advanced Materials Laboratory,(0087), (BO-L07)**	42.7	0.0046	5.5	1077.3	19.39
15	**Evaporation Laboratory of Higher Studies**	47.7	0.0052	6.14	1203.4	21.66
16	**Thermo Dynamic Laboratory,(0098),(BO-L05)**	43.6	0.0047	5.62	1100	19.8
17	**Solid State Laboratory of Higher Studies**	39.6	0.0043	5.1	999.06	17.98
18	**Laboratory of Mechanics,(0095), (BO-L08)**	38.5	0.0042	4.96	971.31	17.48
19	**Electrical Laboratory,(0092),(BO-L 11)**	37.3	0.004	4.8	941.03	16.94
20	**Teaching Staff Room No.(0103)**	30.5	0.0033	3.93	769.48	13.85
21	**Teaching Staff Room No.(0100)**	45.6	0.0049	5.87	1150.4	20.71
22	**Teaching Staff Room No.(0101)**	43.7	0.0047	5.63	1102.5	19.84
23	**Teaching Staff Room No.(0091)**	36.6	0.004	4.71	923.37	16.62
	Ave.	38.6±6.9	0.0042±0.001	4.97±0.9	973.83±0.9	17.53±3.1
	Min.	24.3	0.0026	3.13	613.06	11.04
	Max.	64.9	0.007	8.36	1637.3	29.47

No	Location Name	Mean of C_{Rn} (Bq/m^3)	PAEC (WL)	(E_P) (mWLM/Y)	(AED) (mSv/y)	Lung Cancer /10^6person
	Worldwide Ave.	200-300	53.33	1-2	370	55

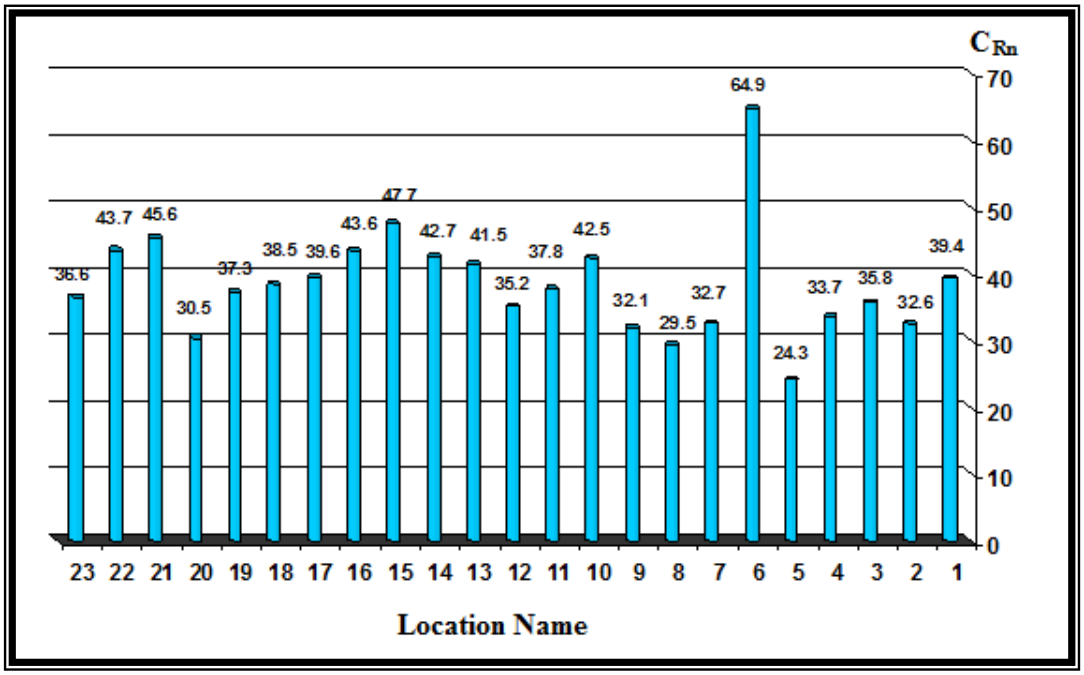

Figure 3. C_{Rn} in indoor rooms and Laboratory in science college buildings in the university of Mustansiriyah.

5. Conclusions

Indoor C_{Rn} level in rooms and Laboratory was determined in a total of twenty-three rooms or Laboratory. Indoor C_{Rn} in all rooms and Laboratory of Department Physics in science college building is lower extent (200-300Bq/m^3) and the parameters (CPPP), (AED), (PAEC), (E_P) values were lower than the permissibility limit value, the study offer that internal air in rooms and Laboratory of Department Physics in science college buildings in the university of Mustansiriyah is not dangerous to students and teachers alike.

6.References

[1] Karim MS, Daroysh HH and Mohammed AN 2016 Assessment of Indoor Radon Concentrations in Dwellings for Baghdad Governorate by Using RAD-7 Detector *Detection* **4** 40.

[2] ICRP 1994 *International Commission on Radiological Protection, Protection Against Radon-222 at Home and at Work*, Publication 65, Annals of the ICRP Volume 23/2, ISBN-13:978-0-08-042475-0, ISBN-10: 0-08-042475-9.

[3] EUROTOM 1996 *Council directive 96/29/EURATOM of 13 May 1996, laying down basic safety standards for the protection of the health of workers and the general public against the dangerous arising from ionizing radiation*.

[4] Durridge Company 2010 Inc., *Reference Manual version 6.0.1, RAD-7 Electronic Radon Detector*.

[5] Kansal S, Mehra R and Singh NP 2012 Life time fatality risk assessment due to variation of indoor radon concentration in houses in western Haryana, India *Appl. Rad. Isotopes* **70** 1110.

[6] ICRP (International Commission on Radiological Protection Publication) 1994 *Protection against Radon-222 at home and at work.* Annals of ICRP: Oxford: Pergamon press,.1.
[7] Tawfiq NF, Mansour HL and Karim MS 2014 Measurements of Radon-222 concentrations in dwellings of Baghdad Governorate *Indian J. Appl. Res.* **4** 35.
[8] Mansour HH 2005 Measurement of indoor radon level in Arbil capital by using solid state nuclear track detectors *Rad. Measur.* **40** 544.
[9] Abdullah AA 2013 Ph.D. Thesis, Department of Physics, University Sains Malaysia, Malaysia (2013).
[10] UNSCEAR 1993 *Genetic and somatic effects of ionizing radiation* United Nations.
[11]ICRP 1993 *Protection Against Rn-222 at Home and at Work" International Commission on Radiological Protection Publication*, 65, Annals of ICRP 23(2), Pergamon Press; Oxford.

Antimicrobial activity by diffusion method using iron oxide nanoparticles prepared from (*Rose plant*) extract with rust iron

Antimicrobial activity by diffusion method using iron oxide nanoparticles prepared from (*Rose plant*) extract with rust iron

Muslim A. Abid[1], L.A. Latif [2], Duha A. Kadhim[3*], Wisam J Aziz[4]

[1,2,3,4*]Department of physics, College of Science, Mustansiriayah University, Baghdad, Iraq

E-mail: muslimabid@uomustansiriyah.edu.iq

Abstract. This research succeeded in the prepared of iron oxide NPs using rose plant extract with rust iron extract at 300 ^{o}C for two hours by simple chemical method. Iron oxide NPs have been developed as an death of antimicrobial as an alternative to toxic chemical drugs to prevent negative effects on human health. Iron oxide NPs were diagnosed using X-ray diffraction (XRD) analysis, Field Emission Scanning Electron Microscopy (FE-SEM) analysis, and Photoluminescence (PL) spectrum. XRD measurements explained the small crystalline size (61 nm) with (inverse cubic) structure (wustite) for ($Fe_{0.911}O_4$) NPs at 300 ^{o}C using rose plant extract. FESEM showed the average grain size of $Fe_{902}O$ NPs (wustite) rose plant extract at 300 ^{o}C was 79.59 nm. PL spectrum determined a blue shift for the optical near band edge value was 2.75 eV for $Fe_{0.911}O$ NPs (wustite) at 300 ^{o}C. Iron oxide NPs were applied in antimicrobial for removal of toxic bacterial by diffusion method. The success of this work will open wide new horizons for us in solving the problem of spent iron and how to get rid of it and the manufacture of new nanoparticles in medical treatments.

Keywords: Iron oxide NPs; Rose plant extract; Rust iron extract; Antimicrobial activity.

1. Introduction

Nanoparticles (NPs) could be defined as small particles with diameter ranging less than 100 nm in dimensions, synthetic of inorganic or organic materials, having new properties as contrasted to the bulk materials [1]. Among the NPs, Iron oxide NPs are significant materials which have great future advantages compared to other materials [2] special physiochemical properties, such as low toxicity, high catalytic activity, small sizes, with different physical properties [3-5]. At the present time human activity in all areas of life is associated with chemicals and these substances have great harm to the human body, especially a number of these substances are constantly increasing in used, and it is agreed that there is no completely safe chemical substance and in return it is not. There is a chemical substance that can be considered completely harmful. Chemists in the middle ages suffered from debilitating and other diseases due to the damages of explosive and toxic materials that they worked to, and serious environment troubles began for show in a world at the beginning of the 17 century due to cinder released of the mines, in addition into fabrication of pigment and other chemicals of charcoal tar in Germany through the 18 century, which led to emergence of toxic and polluting secondary compounds for the

environment, and the steadily increasing quantities and numbers of chemical compounds manufactured in 19 century, counting steely and waste iron rust, lead batteries and petroleum, and with it amount of pollutants and harmful materials raised in environment, among these materials a focus come to iron metal which play a major element in the universal due to the varied uses in too many applications and industry. The overmuch uses of iron metal, this led to founding as thousands of tons from scrap and rubbish rusty iron in the garbage yard without any possible resolution to reuse or benefit from it till now which make the perilous environmental issue in different places in this world.In summery the iron consumed and the huge quantities of it formed a burden on the environment and became a real problem for disposal at the present time.Bio-synthesis of iron oxide NPs using plant extracts as biological components has numerous interest such as cost-effectiveness, atom economy, simplicity, benign, nontoxic, elimination of toxic and dangerous materials, easy availability and removal toxic substances for environmental remediation [6-8]. Wüstite (FeO) is a mineral form of iron (II) oxide found with meteorites and native iron. It has a gray colour with a greenish tint in reflected light. Wüstite crystallizes in the isometric-hexoctahedral crystal system in opaque to translucent metallic grains. The Literature Review of this work: In (2020) R. C. Popescu et al., The synthesized of iron oxide NPs and application in cancer treatments [9]. In (2018), Helale Kaboli Farshchi, et al., Synthesized iron oxide NPs using Rosemary extract and application in cancer treatments [10].In (2017), Sathiskumar G., et al., Synthesized iron oxide NPs using Couroupita guianensis Aubl by (chemical method). Application in vitro anticancer activity and antibacterial activity [11]. In (2018),Shraddha C.,etal.,Synthesized of iron oxide NPs using henna leaves extract by(chemical method). Application of iron oxide in antimicrobial [12]. In (2019),SaeedJ.,etal.,Prepared iron oxide NPs using plant extract. Application in antimicrobial [13].The novelty of this work that all the materials used (which it is used in the first time as the authors knowledge) considered as a waste matter without any cost mentioned to produce valuable and useful NPs materials. In addition, there are no chemical compound used in this research, neither the raw materials nor the final product. All materials used are natural without any supplement. In this work, iron oxide NPs were prepared by mixing wasted iron rust with (rose plant) extract at the (300) oC for two hours. The antimicrobial treatment using iron oxide NPs by diffusion method. The iron oxide NPs (Fe0.911O) were characterization by X-ray diffraction (XRD) using "(XRD6000 Shimadzu, Company/ Japan), Filed EmissionScanning Electron Microscopy (FE-SEM) using (Tescan Mira3 FESEM-Czechia)". Also, the photo luminance (PL) by (Jobin Yvon HR800UV).

2. The experimental part

2.1. Apparatus and equipment

The plants have been collected from the local market in (Baghdad /Iraq), as a preliminary work. The wasted iron specie were pruched from locally (Baghdad / Iraq). All glass ware were cleaned by distilled water (distilled water device, Company / Gallenkamp, England). In addition, all solutions in this work were prepared via distilled water.The beneficial components present in the rose plant are flavonoids, anthocyanins, terpenes and glycosides, and it has been found that the components have the most therapeutic properties in leaf plants are the phenolic compounds that are antioxidant, depression and inflammatory, and the rose leaves contain a number of vitamins such as vitamin E, D, C., A, and vitamin B3 [14].

2.2. The prepared of the (rose plant) extract.

The rose plant were washed with distilled water and then dried under sunlight for 5 days. Then the rose plant were ground using an electric grinder. The mixing 7 gram from rose plant powder with 80 ml from distilled water on magnetic stirrer at 70 ^{o}C for 1.5 hours. It observes the colour change of the solution and this is an indication of the formation of an iron oxide NPs material. The final solve are

freeze to room temperatures and filter using whatman filter sheet. Figure 1 explains the phases of transferring the *(rose plant)* into the extract.

Figure1. shows the phases of preparation the plant extract (*rose plant*), A) *rose plant*, B) *rose plant* powder, and C) *rose plant* extract.

2.3. The prepared of wasted iron (rust) extract

The weight of the wasted iron (rust) used to synthesis iron oxide NPs is 146.0 g. The wasted iron piece was washed with distilled water to get rid of the impurities attached to it. After that, the wasted iron piece was placed with 500 ml of distilled water in a glass flask under the sunlight for 8 days. Then the wasted iron extract was obtained in red color with a size of 250 ml and stored in sealed tubes to synthesis iron oxide nanoparticles. Figure 2 explains the phases to synthesis wasted iron (rust) extract from wasted iron specie (rust) with distilled water.

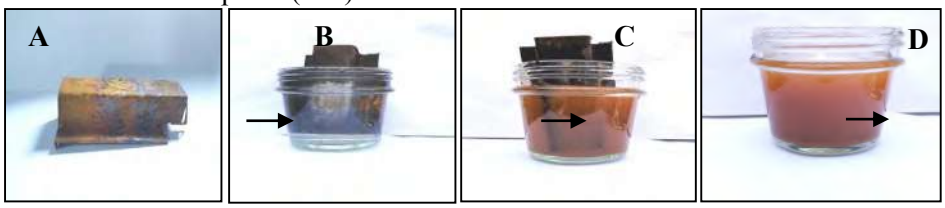

Figure 2. shows the steps for preparation a spent iron extract, A) iron specie, B) iron specie with distilled water before exposes for sunlight, C) spent iron extract after exposes for sunlight, and D) spent iron extract.

2.4. The prepared of iron oxide NPs ($Fe_{0.911}O$) of (rose plant) extract and wasted iron extract (rust).

The Prepared of iron oxide NPs from mixing 250 ml of wasted iron extract (rust) to 100 ml from rose plant extractor. After that, solve were place on hotplate stirrer at 70 °C for 60 minutes. It observes the solution during synthesis, the colour from extractor reaction changed suddenly from translucent offlight pink into black, referring the formed of iron oxide NPs. The resulting solve was cooled at room temperature. For obtain the nano-powder of iron oxide solve, the taken 30 ml of iron oxide NPs solution was putted in a ceramic vine with steamed at 200 °C for 2 hours. Lastly, iron oxide NP solves were stocked in sealed serum tubes to further diagnostic. In figure 3 (A-D) explains the phases to synthesis for iron oxide NPs from rose plant extractor and wasted iron extract (rust).

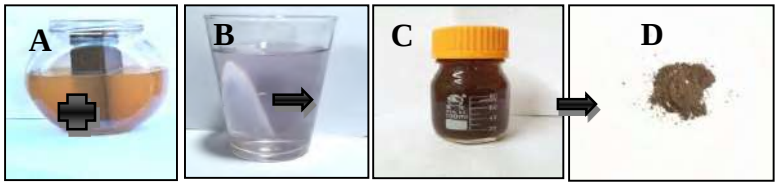

Figure 3. The transfering phases of the wasted iron specie into extract under sunlight for 5 dayes, A) wasted iron specie, B) *rose plant* extract, C) iron oxide NPs, and D) iron oxide NPs powder.

2.5. Characterization of iron oxide NPs ($Fe_{0.911}O$) created using (rose plant) extract.

The specimen was determined by XRD analysis of via the results supplied using the joint committee on powder diffraction standards (JCPDS) card. The scale range of XRD measurements were collected between 20°–70° by use a step-by-step examination model (XRD-6000, Shimadzu) employment at 30 mA and 40 kv. The PL spectrum were resolved by a double beam spectrophotometer (Jobin Yvon HR800UV).

2.6. Antibacterial activity from the spent iron extract with (rose plant) extract.

The microbial cultures were providing by the Microbiology laboratory of the University of Baghdad-College of Education for pure science/ Ibn al-Haitham. This test carried out by agar well diffusion methods in sterile petri-dishes with 90 mm diameter containing sterile nutrient agar medium. Nutrient agar medium was prepared by dissolving 0.5 g peptone this provides organic nitrogen; 0.3 g yeast extract these contributes vitamins, carbohydrates, nitrogen, and salts; 28 g agar this gives the mixture solidity in 1000 ml distilled water. pH was adjusted to 6.8 at 27 ^{o}C. These ingredients are combined and boiled for approximately 15 minutes to ensure they are mixed typically at 121 ^{o}C and poured into petri dishes which are covered immediately until it becomes solidified. After that, iron oxide NPs were dissolved in Dimethyl Sulphoxide (DMSO) solvent with concentration 30 mg/ml. The freshly prepared bacteria were swabbed over the surface of the petri-dishes. Wells of 8 mm diameter each were made, in the medium of bacterial and fungal for each plate using sterilized gel puncher/crok borer. Each well contains 40 µL of iron oxide NPs, and control (DMSO) for bacteria and fungi respectively at desired concentration is introduced into the well. The test samples were incubated at $\pm$25 ^{o}C for 24 hours for bacteria and fungi followed by the gauge of diameter of inhibition zone in (mm). Percentage of inhibition zone have been measured using the following equation:

$$Inhibition\ Zone\ (\%) = \frac{Diameter\ of\ the\ inhibition\ zone\ in\ mm}{Diameter\ of\ pertiplate\ (90\ mm)} \times 100\% \quad (1)$$

3. Results and discussions

3.1. Synthesizing and Characterizing of iron oxide NPs from (rose plant) extract.

Iron oxide NPs prepared bythe modern plant rose plant extract; the extract is mixed with spent iron extract at different reaction conditions. The factors identifying a terms of the rose plant extract to control the rate from iron oxide NPs formation as well as their filed and stability. The phytochemicals inside *rose plant* extract have ability to less spent iron ions in short time. In addition, *rose plant* extract plays an important role from reduce and stabilize factors in iron oxide NPs prepared way for simplify iron oxide NPs. The beneficial components present in the rose plant are flavonoids, anthocyanins, terpenes and glycosides, and it has been found that the components have the most therapeutic properties in leaf plants are the phenolic compounds that are antioxidant, depression and inflammatory, and the rose leaves contain a number of vitamins such as vitamin E, D, C., A, and vitamin B3, which are responsible to synthesis of iron oxide NPs.

3.2. The XRD analysis of iron oxide NPs ($Fe_{0.911}O$)prepared from (rose plant) extract with rust iron extract.

Iron oxide NPs were bio-synthesis by a chemical way from mixing the (*rose plant*) extract with rust iron extract at 300 ^{o}C in Figure 4. The peaks high of the crystalline ($Fe_{0.911}O$) phase (Wustite,space group Fm-3m, JCPDS no.01-079-1880) is (*220*) corresponding to (*111*), and (*200*) millers indices with the face centre cubic (F.C.C), as shown in Figure 4 [15-16]. The results the phases, and crystallite size of

iron oxide NPs ($Fe_{0.911}O$) shown in Table 1. The crystallite size (D) was determined Applied the following Scherrer's formula [17-18].

$$D\ (nm) = \frac{k.\lambda}{\beta cos\theta} (2)$$

Where k called shape factor (0.9), λ the wavelength (0.15418) nm (CuK_{α}), β is full width at half maximum (FWHM) and θ is diffraction angle [19].

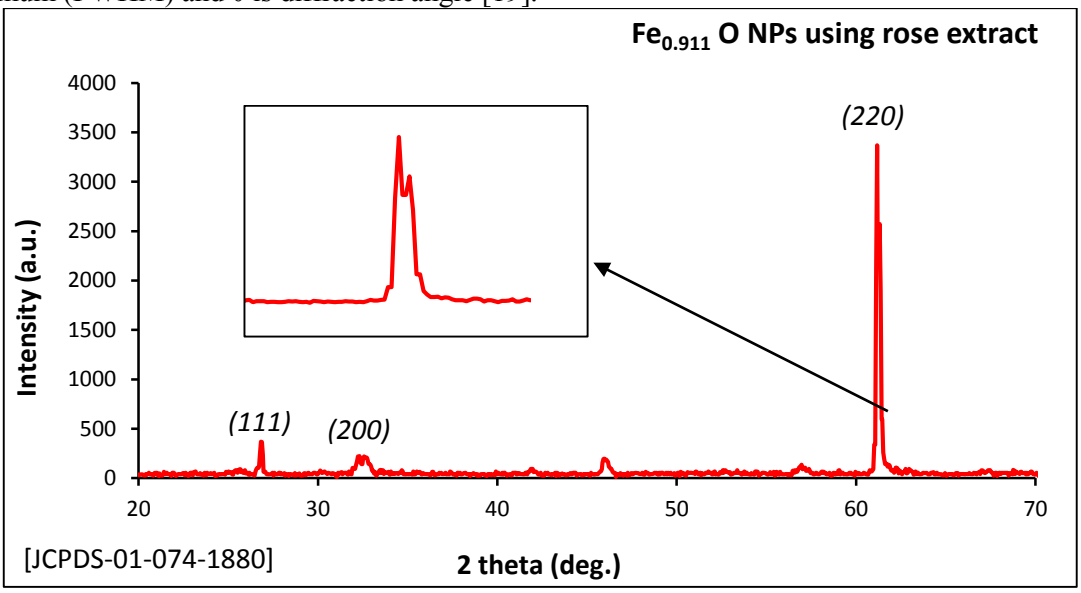

Figure 4. XRD analysis shows of the iron oxide NPs prepared from rust iron extract with the(rose plant) extract, the crystalline $Fe_{0.911}O$ phase (wustite,space group Fm-3m, JCPDS no.01-079-1880) at 300 °C.

Table 1. XRD analysis shows of the crystallite size for iron oxide NPs prepared from rust iron extract with (*rose plant*) extract.

Plant extract	Materials	Temperature (°C)	(*hkl*)	FWHM	Crystallite size D (nm)
Rose Plant	$Fe_{0.911}O$ (wustite)	300	(220)	0.13	61

3.3. The FE-SEM images of iron oxide NPs (Fe0.911O)prepared from (rose plant) extract with rust iron extract.

.

The FE-SEM images shows the size distribution and the surface morphology of eco-friendly iron oxide NPs created from the (*rose plant*) extract with rust iron extract at 300 °C. The grain average size is from (71.59) nm with the morphology is (nano-Slices) structure of the $Fe_{0.911}O$ NPs (Wustite) at 300 °C, as shown in Figure 5 (A-B).

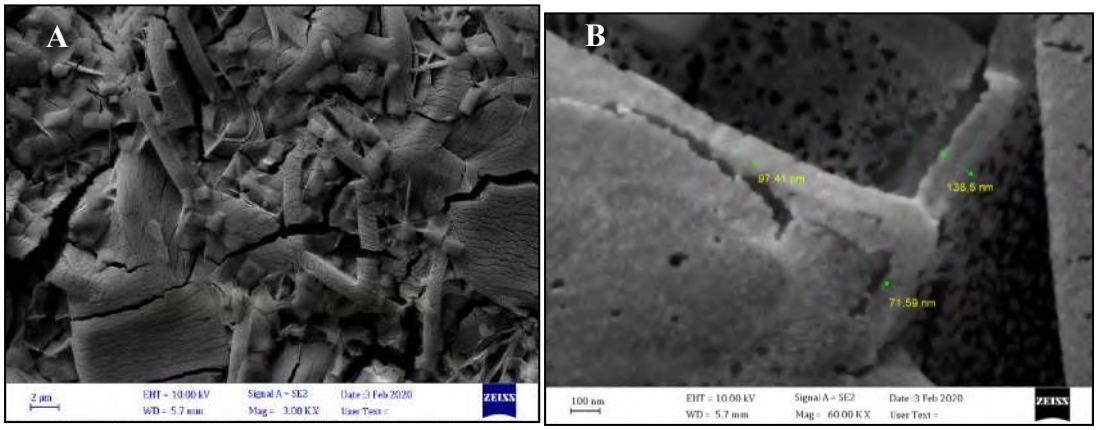

Figure 5. A-B FE-SEM images shows the results of iron oxide NPs prepared from rust iron extract with *rose plant* extract, at 300 ºC.

3.4. The PL spectrum of iron oxide NPs ($Fe_{0.911}O$)prepared from (rose plant) extract with rust iron extract.

The PLspectrum shows the near band edge of eco-friendly iron oxide NPs created from the (*rose plant*) extract with rust iron extract at (300)ºC by a chemical way. The near band edge is (2.65) nm with the exaction band is 325 nm of $Fe_{0.911}$ONPs (Wustite, the near wavelength (469) nm at 300 ºC, as shown in Figure 6.

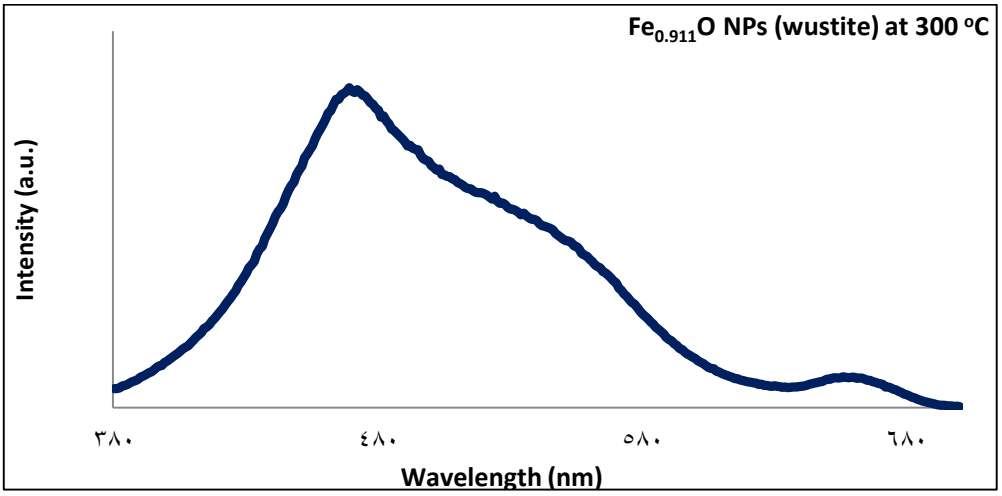

Figure 6. The PL spectrum shows the results of iron oxide NPs prepared from rust iron extract with rose plant extractat 300 ºC.

3.5. Antibacterial and antifungal activity of iron oxide ($Fe_{0.911}O$)NPs using rose plant extract.

The efficacy of anti-bacterial and antifungal activity in terms inhibition of zones (mm) has been measured against four slander bacterial isolates: gram-positive bacteria (B. subtilis and S. aureus), gram negative (K. pneumonia) and (candida). The bio-synthesis of iron oxide NPs showed the good effectiveness of inhibition percentage, but bios-synthesis of iron oxide NPs prepared from *rose plant* extract were more effective than rose plant only extract. The antibacterial activity of iron oxide NPs is chiefly due to the release of iron ions all have attached to the bacterial cell wall due to electrostatic attraction. Furthermore, the metal ions are not only interacting with the surface of membrane but can

also penetrate inside the bacteria. NPs may react with the thiol group (-SH) in the cell wall of the bacteria and not allow the transport of nutrients through the cell wall. The protein decreases inside the cell, eventually causing the cellular death. Or the other reason is that the smaller particle size of the synthesized matels NPs connected with (linked with) the large band gap and consequently, more available oxygen will lead to the generation of a higher concentration of reactive oxygen species (ROS) to enhance antimicrobial activities. However, the activity depended on large surface area to volume, concentration of iron oxide NPs, crystalline structure, and particle shape. The results of iron oxide NPs ($Fe_{0.911}O$) prepared using (*rose plant*) extract using, dose give good result against (k. pneumonia).

It notes the highest rate of destruction of negative and positive bacteria of both types when using iron oxide ($Fe_{0.911}O$) NPs, as shown in Figure 7 and in the Table 2.The disk-diffusion agar method tests the effectiveness of antibiotics on a specific microorganism. An agar plate is first spread with bacteria, then paper disks of antibiotics are placed atop of it. The bacteria are then allowed to grow on the agar media and then observed for growth and effect of the antibiotic on it.

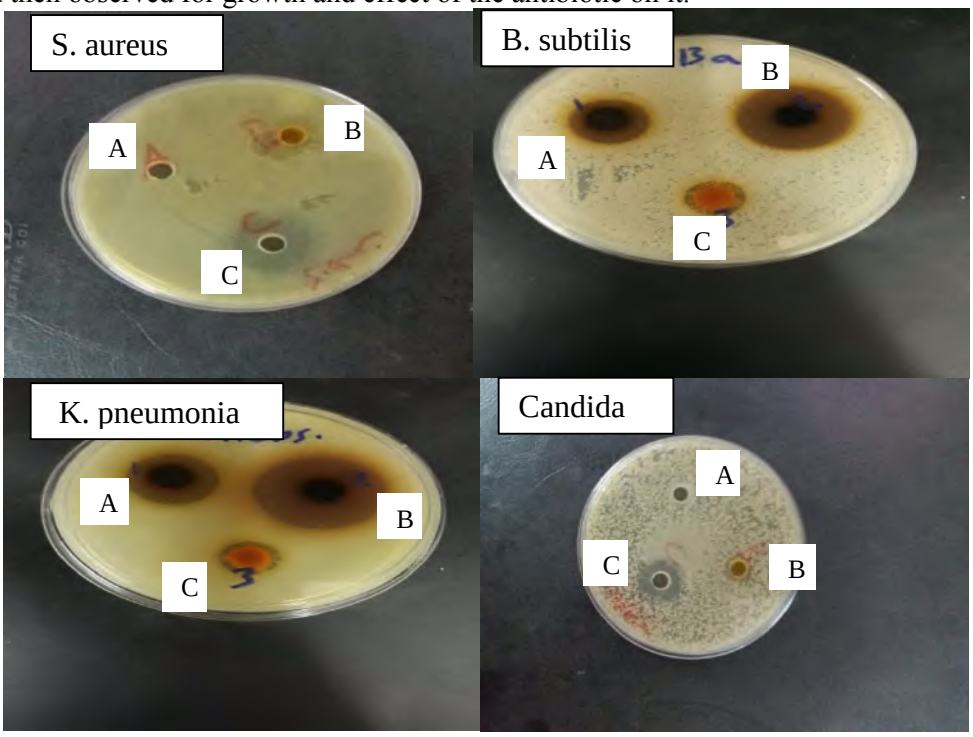

Figure 7. Antibacterial and antifungal activity (gram-nagative and gram-postive) of A. rose plant extract only, B. Fe0.911Ousing rose plant extract, C. rust iron extract.

Table 2. results inhibition of zone of material iron oxide NPs, againts bacteria and fungi at 30 (mg/ml) concentrations.

Com	Staphylococcus aureus	Bacillus subtilis	Klebsiella pneumoniae	Candida albcains
A	-	30	32	-
B	20	38	45	23
C	25	10	8	-

4. Conclusion

This work succeeded in preparing iron oxide nanoparticles using natural extracts, and this success will open new and broad horizons for us in solving the problem of spent iron and how to get rid of it and the manufacture of new nanoparticles in medical treatments. Antibacterial of iron oxide NPs were certain by investigating the inhibition of zones which were from 45 mm to gram-negative bacteria (klebsiella pneumoniae) and 38 mm to gram-positive bacteria (Staphylococcus aureus and Bacillus), but were results are 23 mm to candida activity. Also, this work succeeded in studying the effective effect of bandaging of bacteria, and therefore excellent results were obtained in killing and destroying bacteria. Thus, the ability of these NPs to preserve human life from diseases caused by these bacteria was proven.

Reference

[1] Wei W., Dibyendu D., Omer G. M., Alex K., Hooman M. 2008 *Nano. Res. Lett.* **3**(3) 123-127.
[2] Mihir H., Siddhivinayak B., Rakesh K. 2014 *J. of Nanoparticles* **2014** (1)9.
[3] Issa B., Obaidat I. M., Albiss B. A., Haik Y. 2013 Int. *J. Mol. Sci.* **14** (1) 21266.
[4] Juan G., Ruiyu W., Weng W. T., Jisheng P., Tianxi L. 2012 *J. Hazard Mat.* **225** (1) 63-73.
[5] Cornell R. M., & Udo S. 2003 John Wiley & Sons,.
[6] Sayed F. N., & Vivek P. 2015 *Sci. Report* **5**(1) 9733.
[7] Elena C., M. José Tenorio, Lourdes Calvo, M. José Torralvo, Regino Sáez-Puche, Albertina Cabañas. 2020 *J. of Supercritical Fluids* **159** (1)104775.
[8] YP Y., Shameli K., Miyake M., Khairudin **N**. 2020 *Arab. J Chem* **13**(1) 2287-2308.
[9] Arsalani S.,Guidelli E. J., Araujo J. F. D. F., Bruno A. 2018 *ACS Sust. Chem. Eng.* **6** (11) 13756-13765.
[10] Mahanty S., Bakshi, M., Ghosh S., Chatterjee S., Bhattacharyya S., Das P., Das. S., Chaudhuri P., Chaudhuri P. 2019 *Bio. Nano. Sci.* **9** (3) 637-651.
[11] Zhang Q., Chenhong W., Lei Q., Husheng Y. & Keliang L. 2009 *J. of Mater. Chem.* **19** (44) 8393-8402.
[12] Chauhan S., & Lata S. B. U. 2019 *Nano. Environ. Eng.* **4** (1) 8.
[13] Jafarirad S., Parvin H. A., & Ali M.. 2019 *J. Environ. Sci. Health A* **54** (6) 516-527.
[14] Ismahen H., Juan J. R. , Paula G. , Nieves B.. 2019 *J. plant physiol.* **239** (1)1-9.
[15] Maham M., Mahmoud N., Mohammad S. Sajadi M. N. 2017 *J. colloid and interface Sci.* **497** (1) 33-42.
[16] Farshchi H., Majid A., Mahmoud R. J., Amir F.. 2018 *Biocat. agricultu. biotech.* **16** (1) 54-62.
[17] Rajendra C. Pawar S. K., Jung H. P., Jong-ho K., Sunghoon A., Caroline S. L. 2017 *Catalysis Sci. Technol.* **7** (12) 2579-2590.
[18] Changwoo K, Seung S. L., Brandon J. L., Daniel E. G., John D. F. 2018 *Environ. Sci. Nano.* **5** (2) 556-563.
[19] Vaidyanathan G., Sendhilnathan S., & Arulmurugan R.. 2007 *J. Magnet. Magnet. Mater.* **313** (2) 293-299.

The substitutions of Strontium by yttrium and their effects on $Bi_2Sr_{2-x}Y_xCa_2Cu_3O_{10+\delta}$ superconducting compound

The substitutions of Strontium by yttrium and their effects on $Bi_2Sr_{2-x}Y_xCa_2Cu_3O_{10+\delta}$ superconducting compound

Laheeb A.Mohammed[1], Kareem A. Jasim[1]

[1] Collage of Education for Pure Science -Ibn Al-Haitham/University of Baghdad, Baghdad, Iraq

E-mail: laheeb.a.m@ihcoedu.uobaghdad.edu.iq

Abstract. Superconducting compound $Bi_2Sr_{2-x}Y_xCa_2Cu_3O_{10+\delta}$ were Synthesized by method of solid state reaction, at 1033 K for 160 hours temperature of the sintering at normal atmospheric pressure where substitutions Yttrium oxide with Strontium. When Y_2O_3 concentration (0.0, 0.1, 0.2, 0.3, 0.4 and 0.5). All specimens of $Bi_2Sr_2Ca_2Cu_3O_{10+\delta}$ superconducting compounds were examined. The resistivity of electrical was checked by the four point probe technique, It was found that the optimum and maximum transition temperature T_c = 125 ^oK. The crystal structure studied by using XRD analysis and it was showed that the all specimens have tetragonal structures. Bi-2223phase increase by increasing Y_2O_3 concentration up x=0.4, The increasing addition Yttrium oxide concentration produce increasing in high-phase (Bi-2223) and c lattice parameter.

Keywords: Transition temperature: Superconductors; $Bi_2Sr_2Ca_2Cu_3O_{10+\delta}$oxide; XRD

1. Introduction

Superconducting is a phenomenon of total loss of electrical resistivity in some materials when cooled to a low temperature, and these materials are characterized by their ideal conductivity and diamagnetic behavior [1]. The primary properties of interest in solid-state physics at extremely low temperatures for many compounds and elements are electrical resistivity. Where there are two types of superconducting materials [2]. Depending on the way in which the electrical resistance decreases when the temperature decreases until it becomes zero. The first type of materials the resistance decreases suddenly when cooled to the critical temperature degree, and the other type is gradually decreasing until it becomes zero, meaning that it has two critical temperatures. The first type includes metals and metal alloys, including elements such as tin, tin Aluminum, forms of different metal alloys, while the other type includes ceramic materials with a perovskite composition, such as some high-doping semiconductors and some ceramic compounds. Where the second type contains layers of copper oxide and these compounds are referred to as “cuprates Superconducting materials" with high critical transport temperatures, and the phenomenon of superconductivity is not obtained in noble metals or in magmatic metals [3-5].

The bulk of superconducting materials are additives and alloys, which are not pure elements. The temperature of the transfer of compounds affected by substitution elements is completely different from pure compounds or metal alloys and their parts. In fact, many researchers have observed that there is a very clear rise in the temperature of transformation in alloys and compounds upon partial replacement of some elements of the compound with other elements other than it in the pure compound [5]**.** One of the very important properties of a material is electrical resistance, and it is the most common method for determining the transition temperature of a superconducting material. In this article, some measurements will be made of the structural and electrical properties of samples of $Bi_2Sr_{2-x}Y_xCa_2Cu_3O_{10+\delta}$with various x, such as X-ray, electrical resistance and the effect of partial precipitation of Sr with Y element.

2. Experimental Work

The $Bi_2Sr_{2-x}Y_xCa_2Cu_3O_{10+\delta}$compounds with (x=0.1, 0.2, 0.3, 0.4, 0.5) were synthesized by the (SSR) method after weighing specific quantities of high-purity pure powder oxides with a purity (99.99%) of the Bi_2O_3,Sr_2O_3,Y_2O_3 ,CaO and CuO. The materials included in the composition of the compound were weighed using a high sensitivity balance of up to (10^{-4}) g arranged, and the oxides of the reactants were mixed with each other using a slurry with the addition of a little isopropanol (C2H3O5) to make the mixture homogeneous. To get rid of the water vapor in the mixture, the powders were dried for 1.5 hours at a temperature of 150 ° C, after which the mixture was grinded by a spiral electric mixer for a period of six hours in order to obtain fine homogeneous powders.The powders were pressed with a hydraulic press of 0.7G Pa for a period of 2 minutes, in the form of tablets with a diameter of 0.75 cm and a thickness of 0.3-0.35 cm.

Samples were placed in a thermal furnace for the purpose of sintering and its temperature was raised to 760 ° C for a period of (160 hours) with an average rise (5 ° C per minute) to obtain smooth bonding and to ensure the optimum gradual diffusion between the atoms to form the compound. Then the samples were cooled to room temperature at 5 ° C per minute (same heating rate).

The samples were examined with X-ray diffraction, the (X-ray) diffraction angle ranging from (10-80) to obtain the samples structural properties. The crystal lattice constants (a, b, c) were mathematically calculated using the values of each d and (Miller indices) for the observed patterns during a computer program [6-8].Volume fraction phase in addition, density of mass was measured, and Volume fraction phase calculation based on the following formula [7-8]:

$$\boldsymbol{Vph} = \frac{\sum \boldsymbol{I^{o}}}{\sum \boldsymbol{I^{o}} + \sum \boldsymbol{I1} + \sum \boldsymbol{I2}} * \mathbf{100\%} \qquad \ldots\ldots\ldots\ldots \quad (\mathbf{1})$$

The concentrations of hole-carrier per Cu ion, It is calculated by means of the formula of following [11]:

$$\boldsymbol{P} = (\mathbf{0.16}) - \left[\left(\mathbf{1} - \frac{\boldsymbol{T_c}}{\boldsymbol{T_{c(max)}}}\right)/(\mathbf{82.6})\right]^{\frac{\mathbf{1}}{\mathbf{2}}} \ldots\ldots\ldots\ldots\ldots (\mathbf{2})$$

P is the concentrations hole-carrier per Cu ion,

Four probe method at temperature range (77-300) K was used to measure the resistivity(ρ). Critical temperature (Tc) calculated using the relation [9].

$$\boldsymbol{\rho = (R*A)/L} \quad \ldots\ldots\ldots\ldots\ldots\ldots\ldots \mathbf{(3)}$$

Where R is resistance of electric, A is specimens area and L is specimens length.

3. Result and Discussions

3.1 structural properties

XRD was examined for pure samples $Bi_2Sr_2Ca_2Cu_3O_{10+\delta}$ and samples containing Y_2O_3 $Bi_2Sr_{2-x}Y_xCa_2Cu_3O_{10+\delta}$ for a deflection angle ranging between (10^{o} to 80^{o}), the results shown in Fig. 1

Indicated that all samples have polycrystalline structure with a tetragonal structure. The illustration the (XRD) pattern for $Bi_2Sr_2Ca_2Cu_3O_{10+\delta}$doped by ($Y_2O_3$) shows that all the samples contain a high percentage of the high temperature phase $Bi_2Sr_{2-x}Y_xCa_2Cu_3O_{10+\delta}$(Bi-2223) and a few low-intensity phase peaks (Bi-2212&Bi-2201) that have a low temperature, with some impurity phases appearing[10]. By comparing the phase ratio (Bi-2223) in the pure sample and the partially replaced samples with yttrium, it was found that there is a significant increase in this phase corresponding to a fluctuation in the phases (Bi-2212) and (Bi-2201) as well as in the percentage of impurities that accumulate it may be due to defects in The internal structure of the compound. the substitution of $Y_2O_3$by SrO produce very small shifting in the diffraction angle 2Θ and change in magnitude of peaks intensities. Calculation of lattice parameters was shown in Table 1. This table noticed that the increase of yttrium substitution concentration produce increasing in c-axis values due to the variation in radius of the ionic.

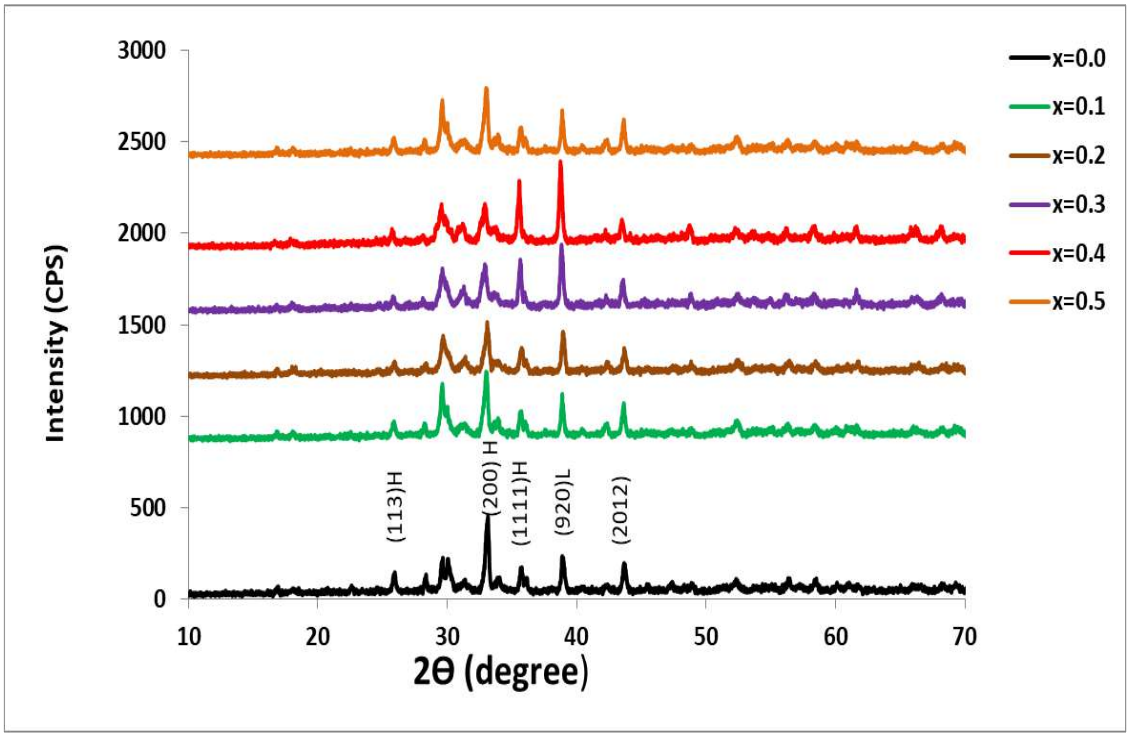

Fig.1. XRD pattern of $Bi_2Sr_{2-x}Y_xCa_2Cu_3O_{10+\delta}$ compound (x=0.1, 0.2, 0.3, 0.4 and 0.5).

The change in the (c) axis can be attributed to the increase in the oxygen percentage resulting from substituting (Y_2O_3) instead of (SrO) and that this increase in oxygenation is taken by the double bismuth oxide layers which cause stronger bonding due to the equivalence of yttrium tertiary. It leads to an increase in the strength of the ionic bonds formed in the bismuth oxide layers and thus changes the lattice constant (c).The parameters of lattice a, b, c based on method of Cohen's least square, calculation by software program, density of mass D_m and fraction of volume (V_{phase}) were calculated from the above equation which are revealed in Table 1. It was clear show that Y_2O_3 concentrations increasing produce variations on a, b, c values, concentrations of hole-carrier, c/a, mass density and volume fraction of unit cell [6-8].

Table 1. Values of a, b, constants, ρ_M,c/a, V_{phase},Vof $Bi_2Sr_{2-x}Y_xCa_2Cu_3O_{10+\delta}$ compound (x=0.1,0.2,0.3,0.4 and 0.5).

X	**a=b (A˚)**	**c(A˚)**	**c/a ratio**	**v(A˚)³**	**D_m(g/cm³)**
0	5.409	37.209	6.87909	1088.634	435.7377
0.1	5.417	37.214	6.869854	1092.003	432.1169
0.2	5.433	37.619	6.924167	1110.418	742.9946
0.3	5.439	37.723	6.93565	1115.949	896.5545
0.4	5.458	37.792	6.924148	1125.815	1053.091
0.5	5.4201	37.391	6.898581	1098.454	1212.616

Vph (2223)%	***Vph (2212)%***	***Vph (2201)%***	***Vph impurities%***	T_c (mid)K	*P (Holes)* concentration
75.102	10.196	7.501	7.201	115	0.132775
78.375	9.763	7.171	4.691	119	0.141402
80.007	2.501	1.895	15.597	118	0.138911
85.171	3.411	2.761	8.657	122	0.15297
86.341	5.996	2.293	5.37	125	----------
80.532	11.025	3.131	5.312	122	0.15297

3.2 Electrical properties

The electrical properties of the samples were examined by relying on the four-sensor technique, where the voltage and current readings were taken as a function of temperature, and then the electrical resistance was calculated as a function of temperature and was drawn in Fig. 2 , shows a measured of temperature versus resistance (T) at variable concentrations of Y. From Fig. 2, it is noticed that resistance of electrical as a function of the temperature of the $Bi_2Sr_{2-x}Y_xCa_2Cu_3O_{10+\delta}$ compound with (x=0.1,0.2,0.3,0.4 and 0.5) that all sample ratios showed metallic behavior at temperatures higher than the initial transition temperature ($T_{c(onset)}$) and then fell to zero at the transition temperature. Depending on the ratios of yttrium and that the concentration x = 0. 4. The best partial substitution ratio for yttrium oxide is (125K). This can be attributed to the fact that the crystal structure became perfect with the presence of Y_2O_3 and that the transition width (T_c) is the narrowest compared to the other samples due to the width range. It shows the transition and represents the purity of the superconducting material.The transition temperature values (Tc) for $Bi_2Sr_{2-x}Y_xCa_2Cu_3O_{10+\delta}$ when x = 0, 0.1, 0.3, 0.4 phases of 115 K, 119 K, 118 K and 122 K, respectively. We can observe the increase in the degree of critical temperature values (Tc) up to It reaches the best sample by partially substituting yttrium oxide at a concentration of x = 0.4 so that a critical transition temperature of 125K is obtained[11].

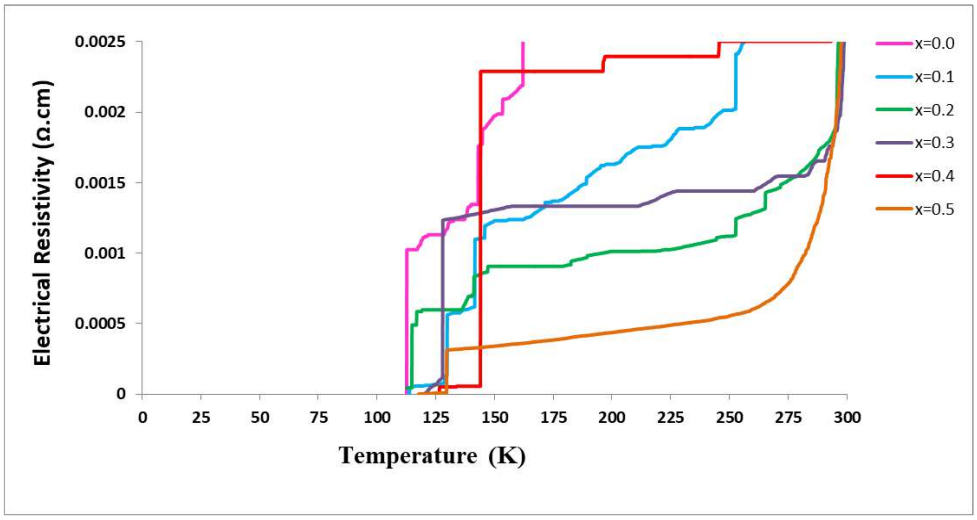

Fig.2. The Electrical Resistivity as temperature function of $Bi_2Sr_{2-x}Y_xCa_2Cu_3O_{10+\delta}$ compound (x=0.1, 0.2, 0.3, 0.4 and 0.5).

4. Conclusions

Through our experimental research in the study of the effect of partial substitution of yttrium oxide with Strontium of the superconducting compound ($Bi_2Sr_{2-x}Ca_2Cu_3O_{10+\delta}$), where we were able to obtain superconducting samples under the preparatory conditions that we adopted during the work. Through the X-ray diffraction analysis, it was revealed that all samples have a quadruple crystal structure and that the partial substitution (Y_2O_3) did not change the crystal structure of all samples with respect to the pure sample. Also, all samples contain phases (Bi-2223, Bi-2212,Bi-2201) with low levels of impurities. As for the electrical resistance tests, all samples revealed It has a metallic behavior where its resistivity changes with a decrease in temperature before transforming into the superconducting state and the best sample was obtained at a concentration of x = 0.4 and equals 125K.

References

[1] M.A. Omar 1993 Elementary solid state physics 5th ed., Addision – Wesley

[2] W.Meissner, and R.Ochsenfeld 1933 *Naturwiessenchaften.* **21**787

[3] A. W. Sleight, J. L. Gillson, and P. E. Bierstedt 1975. *Solid State Commas*. **17** 27

[4] I.H. Gul, A. Maqsood 2008 *J. Supercond. Nov. Magn*. **21** 399

[5] M.Q. Tan, X.M. Tao, Q.R. Zhang, and Y.B. Xu, Prog. 1997 *Phys. (in Chinese)* **15** 173995.

[6] K A Jasim and L A Mohammed 2018. *J. Phys. Conference Series*. 1003

[7] Laheeb A. Mohammed, Kareem A. Jasim 2019. *Energy Procedia* **157** 135

[8] Laheeb A. Mohammed, Haider S. Hussein, Haider M. J. Haider, Kareem A. Jasim 2019 *AIP Conference Proceedings*. **2190**. (020018)

[9] Laheeb A. Mohammed, Kareem A. Jasim 2018 .*IbnAl-Haitham Jour. for Pure & Appl. Sci.* **31** (3)

[10] K.A.Jassim,H.S.hussein,2017. *IbnAl-Haitham Jour. for Pure & Appl. Sci* **30** (3)

[11] B.S.Keeseong, M.S.Park 2007. *The University of Texas at Austin*. **36** 84.

PV-Solar Power Generation in Educational Institutions

PV-Solar Power Generation in Educational Institutions

Fadhil Mahmood Oleiwi[1], Naseer K. Kasim[2], Ahmed F. Atwan[3],

[1]Ministry of education Baghdad,
[2]Ministry of Electricity- Training and Energy Research Office, Baghdad,
[3]Mustansiriyah University, College of Education, Department of Physics, Baghdad.

Email: ahmedfarhan51@yahoo.com.

Abstract. The PV solar system on the rooftop of buildings is a good source of renewable electric energy. Iraq has very large number of educational institutions with large non-invested rooftop with shortage of electrical energy supply. The present work aims at construction a simulation for PV- System action installed on rooftop of educational institutions in Baghdad using Green Power Solution (GPS) and PV-Syst programs. Based on the surface area of the schools' roofs, the GPS program estimated three main PV-Systems which can be carried out, 63kW, 50kW, and 30kW in order to supply the electric power to selected school. Due to allocating few hours for school's studying time along the year, the suitable PV-System is on-grid connection. The results indicated that the annual system performance ratio is 81.9% and the annual output power of these systems were 111.0 MWh/year, 88 MWh/year and 51.4 MWh/year respectively, 19.3MWh/year of them was consumed for this school and the rest is a feedback for grid. This green generation reduced the amount of emission CO_2 by 73.981 tons, 62.216 tons and 36.3398 tons per year for systems 63kW, 50kW and 30kW respectively. The results also appear that the initial capital cost of each system can be recovered during the first six years of system operation.

Keywords: PV-Solar system, performance of PV- module, PV-Feasibility study, rooftop solar system, Carbon dioxide emissions.

1. Introduction

Electric generation by PV Solar system is one of the suitable means in a generation the power in Iraq, due to the negative environmental influence of fossil fuel, shortage in supply of electric energy, losses on the transformation sector, and the shortage between the generation of energy and increasing of demand [1]. Iraq has a high rate of solar irradiation and the maximum value of irradiation distributed in the south and mid of it, the average annual irradiation of Baghdad is about 5.27 kWh/m2/day [2]. The Iraqi Ministry of Electricity has adopted a new policy by generating solar power at the center of loads in city where the domestic sector and government buildings are the largest in energy consumption. The most important projects are the 1MW project at the Ministry of Electricity and the 100 kW project in the oil training center department and other smaller projects [3]. Hashim et al achieved an assessment and evaluate the performance of 15 kW system for 12 months period of the year 2018 under Baghdad environment and compare it with simulated software of PV system, the anual energy yield was 23.77 MWh/ year, it is found that the total of annual energy yield forecasted by PV-Syst software was 24.08 MWh/ year, annual average performance ratio was75.55% with system efficiency of 13.27% [4]. Mensah et al presented a study of a Grid-Tied of PV solar system in the northern part of Ghana at

Navrongo. They found that performance ratio was 70.4% and the mean annually generated energy was 3547.8 MWh and payback period time is found to be 14.95 years [5]. Environmentally, there are many factors influence negatively on solar PV performance such as increasing in environment temperature [6], and dust [7, 8]. On the other hand PV solar systems can reduce the emission of CO_2 [9, 10]. Dondariya et al, modeling and study the feasibility of the system in the proposed location. These can be done on the various available software platforms and the reports generated can be used to compare and get the best-suited model among them in implementing the same at field level [11]. Many projectors had achieved for a green generator in the world. Tesla with support from the South Australian Government is developing a network of up to 50,000 home solar PV and Power wall battery systems across South Australia – all working together to form the world's largest virtual power system. A virtual power system is a network of home solar photovoltaic (PV) and battery systems working together to generate and store energy, and feed energy into the grid. [12]. Lazaroiu et al, 2016, studied and analyzes the optimized operation of a virtual power system owner on the day-ahead market for maximizing his overall profit. The virtual power system is composed of distributed energy resources with variable produced power, energy storage systems, and classical generating units [13]. Al-Khazzar study the performance of a 5 KW Photovoltaic grid tied system is suggested to cover the demand of an Iraqi primary school. The PV-Syst simulation software is selected, the performance ratio for the system in Baghdad is 0.825 and about 9.82MWh is generated by the system per year, 62.7% is consumed by the load and the remaining is injected to the national grid. The results showed that the primary capital cost is $5,442 which is repaid after five and a half years [14]. Alfahed et al, study the 4.0kW stand-alone Solar PV system for providing electricity to a sample home in the Haur Al-Hammar region in the south of Iraq, by using mathematical equations with Excel worksheet and PVsyst 6.68 software simulation package [15]. The present work aims at build a simulation for green generation by PV-Solar system installed on rooftop of schools using Green Power Solution (GPS) amd PV-Syst programs.

2. System Description

The number of public school buildings in Iraq in 2013 are (17435), including (2520) in Baghdad [16].The schools in Iraq (kindergartens, primary, intermediate, preparatory) ranging from a small area to a large area. The school chosen for the present study with unused rooftop is a secondary school (Al-Maqdam) (33.3489923, 44.4739866) in the Al-Baladiyat district in Baghdad. The study achieved by a PV-Syst. There are several hundred of schools having same design and area, Figure 1 shows the satellite image for the school location.

Figure.1. Satellite image for the school located in Baghdad- Iraq

The first system designs to generate 63kWh and the number of modules are 225. The solar panels are considered to be south-ward, the ideal direction for fixed systems, as shown in Figure 2a. The tilt angle for modules is 15o to suitable for the summer season where the energy demand is Maximum in Iraq. The second designs with number of modules are 178. The system designs to generate 50kW.

The solar panels are considered to be southward as shown in Figure 2b with tilt angle for modules is 15o. From the figure we observe the full exploitation of the surface area of the school. The third design with the number of modules is 104, the system designs to generate 30kW. The solar modules are considered to be southward as shown in Figure 2 c with tilt angle for modules is 15o.

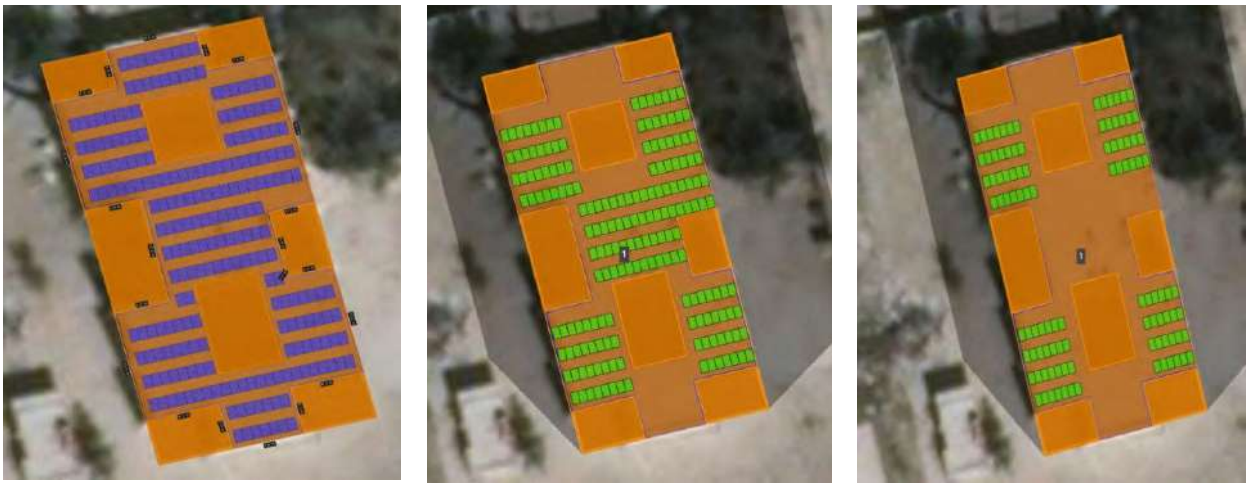

.a b c

Figure 2. Schema of systems a-63kW, b-50kW, c-30kW.

The solar modulestype that can be used isREC 280TP (280W) which is efficient and bear high temperatures. The specification of the PV module is listed in Table 1.

Table 1. Technical specification of PV module 280W [17]

Parameter	Value	Parameter	Value
Dimensions	1958*9991*50(mm)	p_{max}	280(W)
weight	27 (kg)	Temperature coefficient V_{OC}	-0.31(V/^{o}C)
No.of Cells	72 (in series)	Temperature coefficient I_{Sc}	0.045% /^{o}C
I_{Sc}	9.40(A)	Temperature coefficient P_{max}	-0.39 %/^{o}C
V_{OC}	39.2(V)	Module efficiency	17%
I_{mp}	8.78(A)	NOCT	44.6(^{o}C)
V_{mp}	31.9(V)	Type of cell	Pc-Si

Component of 63KW, 50KW and 30KW system is listed in Table 2.

Table 2. Component of 63KWh system.

Component	Name	Count(63KW)	Count(50KW)	Count(30KW)
Inverters	SuunyTripower 10000Tl(SMA)	6(60.0 kW)	4(40KW)	3(30KW)
Strings	10 AWG(Copper)	12(200.8 m)	10(193.4m)	6(154.9m)
Module	REC Solar, REC280TP	255(63.0 kW)	178(49.8KW)	104(29.1KW)

3. Estimation of the energy production

The practical short circuit currentI_{sc}, and practical open circuit voltage$V_{oc}$are given as [18, 19].

$$I_{sc}(GT) = I_{sc}(STC) \times GT \quad in\ 1\ KW/m^2 \qquad (1)$$

$$V_{oc}(T_C) = V_{oc}(STC) - 0.0023 \times numberof\ cell \times (T_C - 25) \qquad (2)$$

Where (GT) is the solar irradiance, STC is a standard test conditions.
The output power (P_{out}) of the PV solar module is given by the following equation [14, 15].

$$P_{out}(GT, T_C) = I_{sc}(GT) \times V_{oc}(T_C) \qquad (3)$$

4. Energy Demand of the School

The school has 24 rooms, only 16rooms use and the others using as storage. Table 3 shows the details of the equipment and their wattage. The total daily power that required supplying by the solar system is estimated at138.4 kWh/day.

Table 3. Daily Power required

Name of equipment	No	Consumption Watt	Total Consumption kWh	Hours of operation	Total Consumption kwh/day
Air-condition	4	3000	12	8	96
Lamp	70	40	2.8	8	22.4
Fan	17	100	1.7	8	13.6
Refrigerate	4	200	0.8	8	6.4
Laptop	2	100	0.2	8	1.6
water pump	1	370	0.37	1	0.37
Server	1	15	0.015	6	0.09
Mobile charger	2	5	0.01	1	0.01
Printer Mach	2	720	1.440	1	1.440
Sum			19.335		141.91

The school is open only 168 days per year and closed for 197 days, the real demand of energy for a year is 23.848MWh/year; also the suitable connection for this system is on grid connection or hybrid connection due to the longtime of closing of schools.

5. Results and Discussion

The amount of annual incident solar irradiance with tilt angle 15° is 1964.1MWh. The monthly solar irradiance and temperature in Baghdad city as shown in Figure 5.Through the study duration in Iraqi schools (October-May) the average temperature is not hot between (10°-30°) as shown in figure 3 and therefore does not require a high cooling voltage but only lighting and fans and electric heater instead than air-condition, which does not consume so much of system power during the study season. The increase in temperature causes a decrease the power in summer with an increase in the amount of solar irradiance in same time. The increase in output power in summer months where the school is closing leads to supply the grid by the power at a peak load of energy in Iraq.

Figure 3. The monthly solar irradiance and temperature in Baghdad city.

The average loss in power due to the increasing in temperature is about 7.6%. The average of ambient temperature is 24.2°C where the average operating Cell temperature is 36.1°C during the day. Also an important source of losses in power production is the accumulation of dust and dirt on the solar panel, which about 2.0% of the production. The total loses of solar power production is 17.2%. Figure 4 illustrates all sources of energy loss in the system.

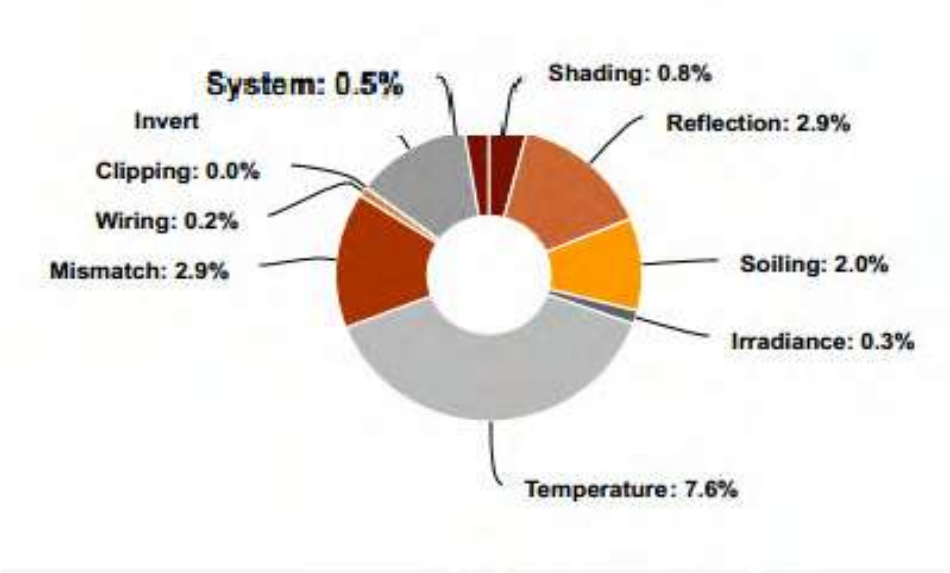

Figure 4. Sources of the system losses.

The AC power for every month for a system of 63kW, 50kW and 30kW are shown in Figures 5, 6, and 7 respectively.

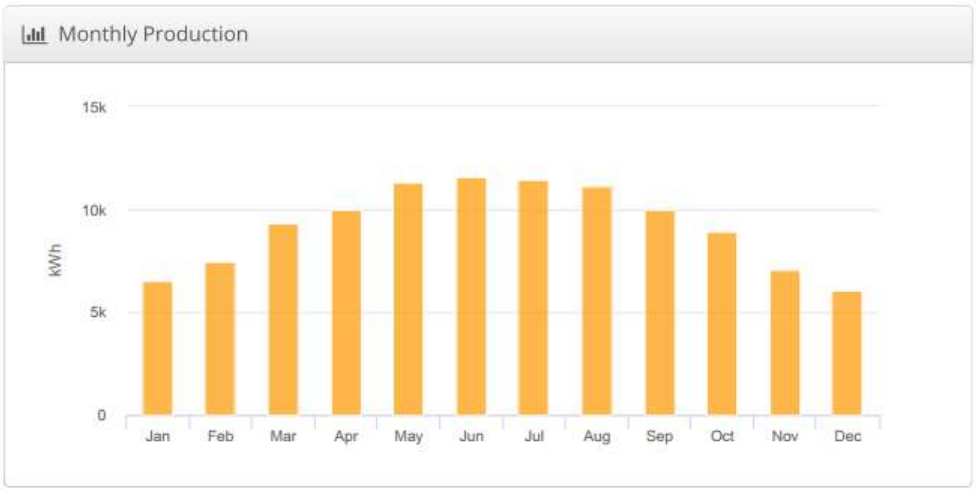

Figure 5. The AC power for every month of year for a system of 63kW.

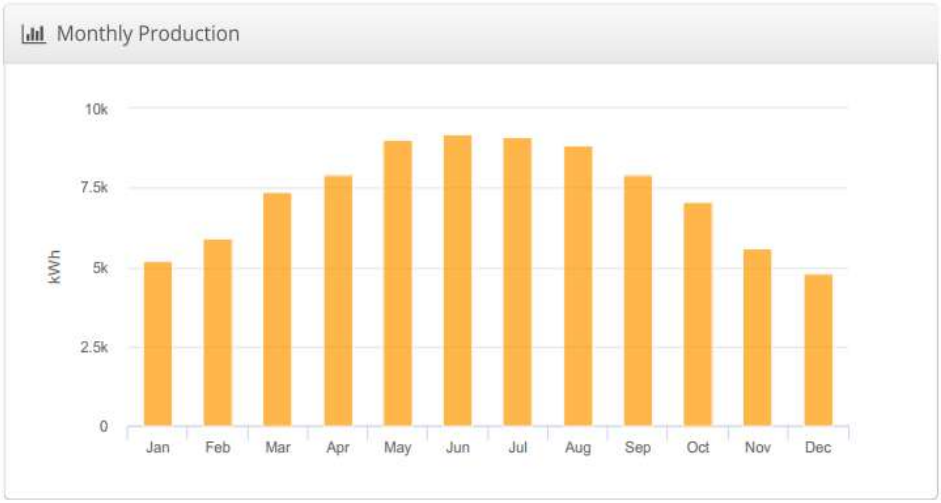

Figure 6. The AC power for every month of year for a system of 50kW.

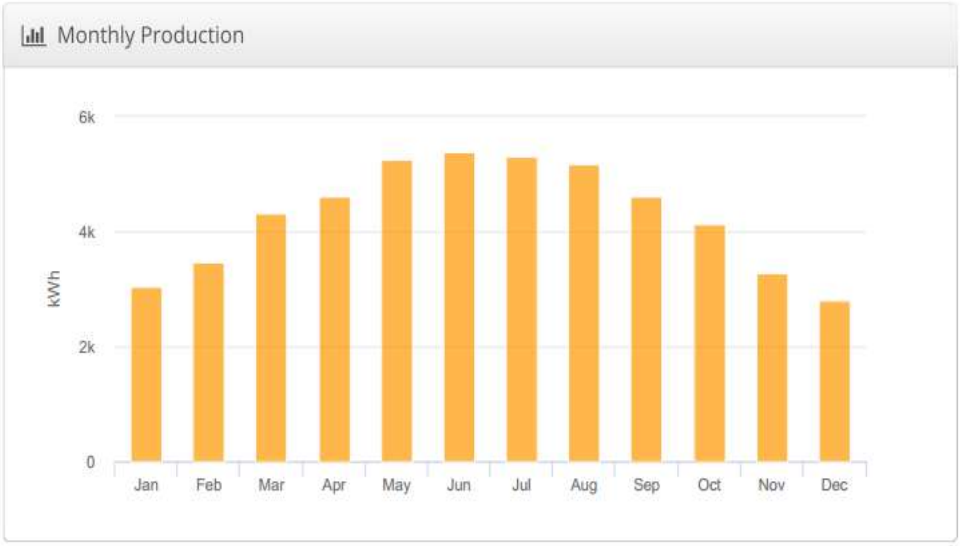

Figure 7. The AC power for every month of year for a system of 30kW.

The AC annual output power produced from systems 63 kW, 50kW and 30kW were 111.0MWh, 88MWh and 51.4 MWh respectively, with annual operating hours of 4540, 24kWh/year of them was consumed for school services and the rest were a feed of grid. In the hot summer season where the longest sunny days are actualized and due to high incident solar radiation the gain in output power was higher than the loss in power that caused by heat. The cost of establishing the solar power system (mechanical and electrical components, mechanical and electrical works) is 1$ per watt in Iraq market. The cost of the solar power systems 63kW, 50kW and 30kW were 63000$, 30000$ and 50000$ respectively. Investment of the rooftop of the school provides free space of 225m^2, 178m^2 and 104 m^2 for systems 63kW, 50kW and 30kW respectively. The price per square meter of school land is 1250$ and therefore the project cost is reduced by 281250$ (342.6%), 172500$ (345%) and 100000$ (333%) for systems of 63kW, 50kW and 30kW respectively.

The subsidized price of production power is 0.1$ per KWh in Iraq, the annual price of producing solar power in the present systems were (11100 $, 8800$ and 5140$ for systems of 63kW,

50kW and 30kW respectively. The design cost of three systems could be refunded after about (5.67) year and the solar system could work more than 25year.

By GPS program, the performance ratio for the system was 81.9%. The monthly reduction of emission of CO_2 by the production of solar power is shown in figures 8, 9 and 10 for systems 63kW, 50kW, 30kW respectively.

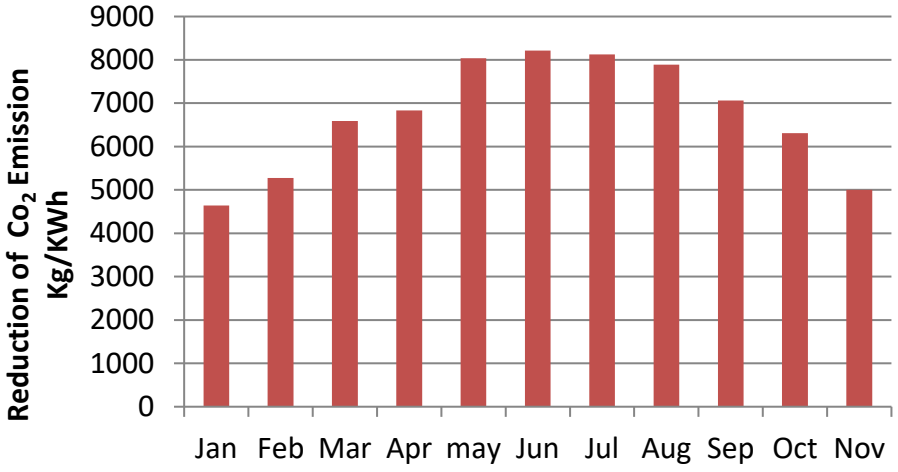

Figure 8. Reduction of emission of $CO_2$with solar power for a system of 63kW.

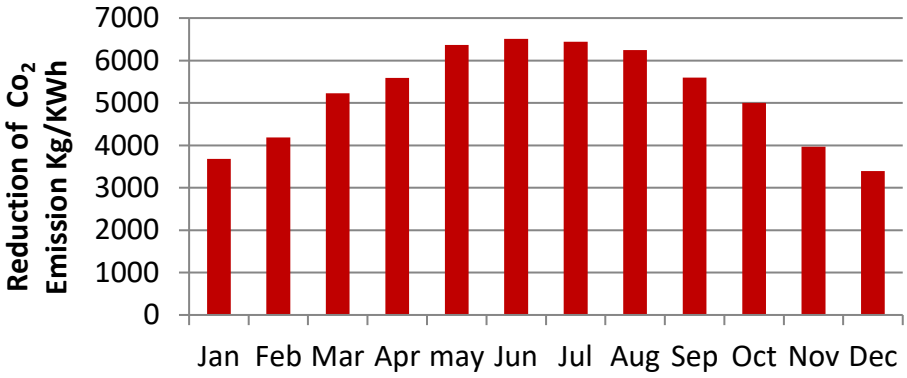

Figure 9. Reduction of emission of $CO_2$with solar power for a system of 50kW.

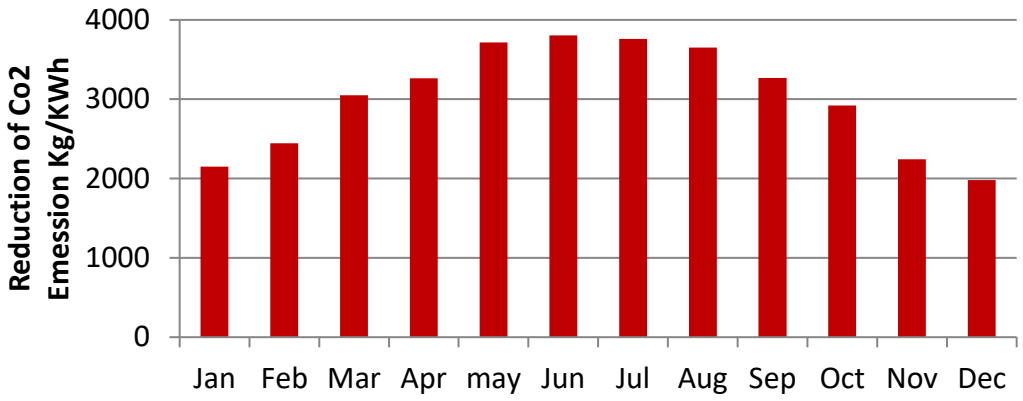

Figure 10. Reduction of emission of $CO_2$with solar power for a system of 30kW.

by using solar power instead of fossil fuel in the present system, the annual amount of emission CO^2 reduce by 73.981 tones, 62.216 tones and 36.3398 tones for systems 63kW, 50kW and 30kW respectively. The system's performance was compared with other installed PV system to have a good idea of PV solar system performance in current study as shown in Table 4.

Table 4. Performance Study Comparison of PV Systems in Different Countries

Location	Power (kWp)	Type of PV technology	Energy yield MWh/year	PR (%)	Pay back	Ref
Iran	5	Poly-crystallineSi	9.428		11.6	Korsavi et al,2018
Iraq	15	HITHeterojunction	24.08	75	-	Hisham, 2019
Iraq	5	poly-crystallineSi	9.820	82.5	5.5	Al-Khazzar, 2018
Ghana	2500	›oly-crystallineSi	3547.8	70.4	14.95	Mensah et al,2019
Iraq	63,50, 30	›oly-crystallineSi	111.0,88, 51.4	81.9	5.67	Present study

Also, the system can be a free realistic science lab for the school. This laboratory can explain the photoelectric phenomenon, semiconductors, types of (solar) battery connection, types of energy and the relationship between them and the conversion from photovoltaic to electrical and thermal energy, voltage, current, power and power, direct, alternating current, etc.

6. CONCLUSION

Iraqi environment is a benefit for green generation and it cans investment the rooftop of educational institutions to generate electric power by PV-Solar systems for these institutions and supply the grid with additional power. The localized green generation reduces transport power losses and reduces the emission of CO_2.

REFERENCES

[1] Abed, F. M., Al-Douri, Y., & Al-Shahery, G. M. 2014 *Renew. Sust. Energ. Rev.* **39** 816
[2] NASA Research Center, 2000. STS-107, Space Research and You, NP-288-HQ, http. https://www.moelc.gov.iq/home/page/sustainable_energy?lang=ar.

[3] .Hashim, E.T., Kasim, N.K. and Obaid, N.M., 2019. *Iraqi J. Sci. Tech.* **10** (1) 63.
[4] .Mensah, L.D, Yamoah J.O., and Adaramola, M.S., 2019 *Energy Sustain. Dev.* **48** 82
[5] Mahfoud A, Mohamed F, Saad M, Farid D, 2015. *Int. J.* Renew. Energy Res. Mahfoud Abderrezek Et Al. **5** (2).
[6] Naseer K. Kasim, Ahmed F. Atwan, Fadhil M. Oleiwi, 2019. *Iraqi Journal of computer, communications, control, & system engineering (IJCCCE)* **19** 2
[7] Naseer K Kasim, Ahmed F. Atwan, and Fadhil M. Oleiwi, 2018 *IOP Conf. Series: J. Phys. Conf. Series* **1032** 012031
[8] Ahmed F. Atwan, Naseer K. Kasim, Waqar A. khudhair 2016. Int. J. *sci. eng. Res.* **5** 10
[9] .Korsavi, S.S., Zomorodian, Z.S. and Tahsildoost, M. 2018 *J. Clean. Prod.* **174** 1204
[10] Dondariya, C., Porwal, D., Awasthi, A., Shukla,A.K., Sudhakar, K., SR, M.M. and Bhimte, A., 2018. *Energy Rep.* **4** 546
[11] South Australia's Virtual Power System. https://virtualpowersystem.sa.gov.au/
[12] Lazaroiu, G.C., Dumbrava, V., Roscia, M. and Zaninelli, D., 2015, May. In 2015 9th International Symposium on Advanced Topics in Electrical Engineering (ATEE) (pp. 911-916). IEEE.
[13] Al-Khazzar, A., 2018. *Iran*. *J*. Energy *Environ.* **9** (2) 105
[14] Fakher Alfahed, R. K., Oudah, S., & Al-jabori, K. 2019 *Journal of Energy Management and Technology (JEMT)* **3** (3) 30
[15] Ministry of Education website, Data Education Directorate 2019 http://www.moedu.gov.iq
[16] http://www.europe-solarshop.com/documents/rec/ds_rec_twinpeak_series_revgeng .pdf.
[17] Markvart, T. 2001, Solar Electricity. Wiley, Chichester.
[18] Duffie, J. A., & Beckman, W. A. 2013 Solar engineering of thermal processes. John Wiley & Sons.

Transfer Factors from Soil to Plant of Natural Radionuclides at Abu-Ghraib City, Iraq Using Gamma Ray Spectroscopy

Transfer Factors from Soil to Plant of Natural Radionuclides at Abu-Ghraib City, Iraq Using Gamma Ray Spectroscopy

Rand Mudher Ebraheem[1], Iman Tarik Al-Alawy[1], Waleed Jabar Mhana[1]

[1] College of Science, Department of Physics, Mustansiriyah University, Baghdad, Iraq

E-mail: randmudher13@gmail.com

Abstract. Activity concentrations of natural radionuclides, artificial radio-cesium, and soil-to-plant transfer factor in common different plants species grown at Abu-Ghraib city in the capital Baghdad have been evaluated using NaI(Tl) gamma spectroscopy. Five species of plants have been selected, namely green pepper, cucumber, celery, basil, and mint. The measurements were made on four parts of each plant sample which were included soil, roots, stalk, and leave for knowledge and evaluation the transfer factors. The maximum mean specific activity concentration of U-238 and Th-232 was 9.853±10.904 Bq/kg, 6.005±2.729Bq/kg in celery, while the maximum mean specific activity concentration of K-40 was 141.172±71.703 Bg/kg in cucumber, respectively. The results showed that the uranium, thorium, potassium and cesium concentration not exceeded the permissible limit. The mean Radium equivalent activity was 35.553 Bq\kg lower than 370 Bq\kg recommended by UNSCEAR. The maximum absorbed dose rate in root-mint samples was 30.290 nGy/h which is lower than 84 nGy/h, while the mean annual outdoor effective dose equivalent in root samples was148.597 mSv/y which is lower than 290 mSv/y recommended by UNSCEAR, respectively. The maximum H hazard index was 0.097 in root samples which is less than ≤1 recommended by UNSCEAR. The excess lifetime cancer risk (ECLR) ranged from 5.441×10^{-3} to 520.081×10^{-3}. This value is higher than recommended limit 0.29×10^{-3} and 1.16×10^{-3} reported by UNSCEAR. The ELCR is a function of environmental geology and K-40 has very high soil-to-plant transfer factor compared to other radionuclides in the samples. Therefore, there is a risk of their administration. The maximum of radioactivity level index was 0.265 Bq/kg which is less than ≤1.

Keywords: plants; transfer factor; radionuclides; hazards; cancer risk; Abu-Ghraib

1. Introduction

Natural radionuclides are found in the environment such as soil, water, air and plants, and by eating them; our bodies contain these natural radioactive materials. They usually have a low concentration of radioactivity. The natural background radiation originates from the uranium series 238, thorium 232 chain and from potassium 40, while cesium 137 originates from industrial sources [1-3]. Radionuclides are released from the soil, which is the main source of the natural background radiation. The plants will acquire these radionuclides through the roots, sticks and leaves. These radionuclides are transferred to humans by directly eating plants as food. Radionuclides that are ingested by food constitute a large part of the average dose of radiation received by the various parts of the human body, including the skeleton [4]. The dissolution of these radionuclides (uranium and thorium) in foodstuffs and inside the human

body deserves to be monitored and evaluated, and the most important thing is the naturally occurring potassium 40 as an essential component of cellular materials in all foodstuffs, where the person receives approximately 180 μSv annually from it. The average total amount of natural potassium in a normal human is about 0.14 kg, so the natural background can be considered as a constant source of human radioactivity. These have disadvantages and accumulated damage on humans that must be taken into consideration [5-6]. There are two mechanisms of plant contamination, either through absorption by roots or directly by atmospheric precipitation of radionuclides that fall on plants. So most of the radiation doses that humans receive can be considered from the consumption of food contaminated with various radionuclides, whether from natural or industrial sources, or from radioactive pollution to the environment [7-9]. That is why we found it necessary in this research to conduct an accurate assessment of radionuclides activity in plants and their transfer factor from soil to plants that are an important part of the food today used by humans and to determine the resulting risk factors.

2. Materials and methods

2.1. Collection and preparation of samples

Twenty samples of plant were collected at Abu-Ghraib city. Fifteen samples of plants and five samples of soil for each plant. Three samples parts representing (root, stalk, and leave) for each type of plants, namely cucumber, green pepper, celery, mint and basil. All samples have undergone drying, crushing, and grinding processes. Then, they were stored in tightly closed Marinelli Beckers for 30 days to achieve secular equilibrium.

2.2. Radioactivity measurement

Detection of natural radioactivity for U-238, Th-232, and K-40 in different parts of plants (cucumber, green pepper, celery, mint, basil) and soil samples were measured using sodium iodide detector technique. The standard samples were used for the calibration and the absolute efficiency of the detector as recommended by IAEA. The mixture of radionuclides with their corresponding energies are Am-163 (59.3keV), Co-60 (1173.24 and 1332.50 keV), Cs-137 (661.66 keV). The background was measured too; both were counted for two hours. U-238 activity was given by the product decay of Bi-214 (1764.5 keV). The activity of Th-232 was given by the product of Tl-208 (583.19 and 2614.5 keV). The K-40 (1460.8 keV) and Cs-137 (661.61 keV) concentrations were measured gamma lines of their energies, respectively.

3. Parameters calculation

3.1. Specific activity

The specified activity in unit Ci/kg or Bq/g is given by [10]:

$$A_i(E,\gamma) = \frac{N}{\varepsilon\,(E_\gamma)\times\ I_\gamma\,(E_\gamma)\times t\times m} \quad (1)$$

Where, N and m are the counts of area under the curve and mass of sample in kg, respectively.

3.2. Absorbed dose rate D

The outdoor absorbed dose rate can be calculated using the following formula [11, 12]:

$$D_{out}(nGyh^{-1}) = 0.427\ A_U + 0.662A_{Th} + 0.043\ A_K \quad (2)$$

Where, A_U, A_{Th} and A_K are the activity concentrations in (Bq/kg) of uranium, thorium and potassium respectively.

The indoor absorbed dose aye is given by [13]:

$$D_{in}(nGyh^{-1}) = 0.92\ A_U + 1.1A_{Th} + 0.081\ A_K \quad (3)$$

3.3. Radium equivalent Ra_{eq}

The radium equivalent activity can be expressed by [1]:

$$Ra_{eq}(Bq.kg^{-1}) = A_U + 1.43\,A_{Th} + 0.077\,A_K \quad (4)$$

The recommended limit of Ra_{eq} is 370 $Bqkg^{-1}$ given by UNSCEAR, 2000 [1].

3.4. Hazard index H

The external (H_{ex}) is given by UNSCEAR, 2000 [1]:

$$H_{ex} = \frac{A_U}{370\ Bq.kg^{-1}} + \frac{A_{Th}}{259\ Bq.kg^{-1}} + \frac{A_K}{4810\ Bq.kg^{-1}} \quad (5)$$

The internal radiation exposure is quantified by the internal hazard index (H_{in}) given by UNSCEAR, 2000 [1]:

$$H_{in} = \frac{A_U}{185\ Bq.kg^{-1}} + \frac{A_{Th}}{259\ Bq.kg^{-1}} + \frac{A_K}{4810\ Bq.kg^{-1}} \quad (6)$$

The limit of these indexes should be less or equal to unity, as reported by UNSCEAR and ICRP [1, 14].

3.5. Annual effective dose equivalent AEDE

The outdoor and indoor annual effective dose equivalents are given as the following [1]:

$$AEDE_{out}(\mu Sv/y) = D_{out}(nGy/h) \times 8760(h/y) \times 0.20 \times 0.7(Sv/Gy) \times 10^{-3} \quad (7)$$

$$AEDE_{in}(\mu Sv/y) = D_{in}(nGy/h) \times 8760(h/y) \times 0.80 \times 0.7(Sv/Gy) \times 10^{-3} \quad (8)$$

3.6. Life-time cancer risk ELCR

The excess life-time cancer risk ($ELCR$) which is given by Taskin et al. 2009 is as follows [15]:

$$ELCR_{out} = AEDE_{out} \times DL \times RF \quad (9)$$

$$ELCR_{in} = AEDE_{in} \times DL \times RF \quad (10)$$

Where; DL, and RF are the life span and risk factor respectively as given by ICRP, 2012 [16].

3.7. Annual gonadal dose equivalent AGDE

The annual gonadal dose equivalent ($AGDE$) can be calculated as follows [11]:

$$AGDE\left(\frac{\mu Sv}{y}\right) = 3.09A_U + 4.18A_{Th} + 0.314A_K \quad (11)$$

3.8. Radioactivity level index I_γ

This index is used to estimate the level of radiation risk, especially γ -rays, associated with natural radionuclides in material. It is defined as follows [17].

$$I\gamma(Bq/kg) = A_{Ra}/150 + A_{Th}/100 + A_K/1500 \leq 1 \quad (12)$$

Where A_{Ra}, $A_{Th}$and A_K are the activities of Ra-226, Th-232 and K-40 in Bq/kg respectively.

3.9. Soil-to-plant transfer factor TF

Using (IAEA) guidelines, the soil-to-plant transfer factor TF was estimated as follows [18, 19]:

$$TF = Cp\ /\ Cs \quad (13)$$

Where Cp and Cs are radionuclide concentration in plant and soil in Bq/kg respectively.

4. Results and discussion

Table 1 and Figs. 1 to 6 show the variation of activity concentrations of U-238, Th-232, K-40 and Cs-137 in green pepper, cucumber, celery, basil, mint and soil samples in Abu-Ghraib city in different parts of each sample. For the green pepper the activity concentrations of U-238 were varied from 1.504 to 12.155 to Bq/kg with an average value of 7.068±4.949 Bq/kg. Whereas, for Th-232 it was varied from 7.403 to 0.180 Bq/kg with an average value 2.909±3.424 Bq/kg. The activity concentrations of K-40 ranged from 26.570 to 76.738 Bq/kg with average value 68.633±34.272 Bq/kg, and 0.014 to 1.588 Bq/kg with an average value 0.617±0.746 Bq/kg for Cs-137. For cucumber, the results were 7.068±4.949, 2.909±3.424, 0.617±0.746, 68.633±34.272 Bq/kg. For celery, the average activity concentrations were

9.853±10.904, 6.005±2.729, 1.198±0.591, 93.320±85.462 Bq/kg. For basil, the average activity concentrations were 3.737±5.631, 4.200±2.536, 0.455±0.756, 71.687±54.966 Bq/kg. For mint, the average activity concentrations were 4.390±5.067, 8.483±6.199, 0.517±0.722 and 61.863±53.147 for U-238, Th-232, and K-40, respectively. All these values are significantly less than permissible limits (33, 45, 412, and 2.0 Bq/kg) for U-238, Th-232, K-40, and Cs-137, respectively [12, 20].

Table 1. Specific Activity Concentration for U-238, Th-232, K-40 and Cs-137 of samples, at Abu-Ghraib city.

Sample Name	Sample parts	U-238			Th-232	K-40	Cs-137
		Ra-226	Bi-214	Pb-214	Ac-228		
Green pepper	Soil	4.138	8.524	12.155	7.403	76.738	1.588
	Root	0.382	1.192	10.183	3.756	125.650	0.820
	Stalk	0.164	0.390	4.430	0.297	45.574	0.047
	Leaves	0.013	0.178	1.504	0.180	26.570	0.014
	Average	1.174	2.570	7.068	2.909	68.633	0.617
		±1.981	±3.993	±4.949	±3.424	±34.272	±0.746
Cucumber	Soil	4.216	8.869	12.910	7.814	76.865	1.759
	Root	2.094	1.036	16.123	6.373	224.612	0.128
	Stalk	1.668	0.303	1.337	4.677	177.110	0.154
	Leaves	0.137	0.037	0.939	2.370	86.230	0.039
	Average	2.009	2.475	7.648	5.206	141.172	0.500
		±1.648	±4.054	±7.683	±2.199	±71.703	±0.728
Celery	Soil	4.128	8.089	12.125	7.009	76.016	1.513
	Root	4.069	0.746	24.277	7.552	215.222	1.673
	Stalk	3.756	0.415	2.809	7.147	65.459	1.154
	Leaves	0.922	0.183	0.170	1.919	15.859	0.378
	Average	3.221	2.467	9.853	6.005	93.320	1.198
		±1.541	±4.044	±10.904	±2.729	±85.462	±0.591
Basil	Soil	3.910	7.998	11.918	6.801	75.910	1.532
	Root	0.369	1.898	1.566	4.966	146.524	0.109
	Stalk	0.172	1.519	0.753	2.756	42.850	0.105
	Leaves	0.054	0.888	0.473	1.676	20.636	0.017
	Average	1.183	3.207	3.737	4.200	71.687	0.455
		±1.973	±3.568	±5.631	±2.536	±54.966	±0.756
Mint	Soil	4.065	7.610	10.198	7.315	74.018	1.593
	Root	0.641	0.980	4.727	17.375	130.715	0.322
	Stalk	0.418	0.766	1.707	6.087	21.835	0.101
	Leaves	0.209	0.532	1.132	3.067	18.163	0.058
	Average	1.351	2.700	4.390	8.483	61.863	0.517
		±1.865	±3.886	±5.067	±6.199	±53.147	±0.722
Limit UNSCEAR, 2010 [12]			33		45	412	2.0 UNSCEAR, 1993[20]

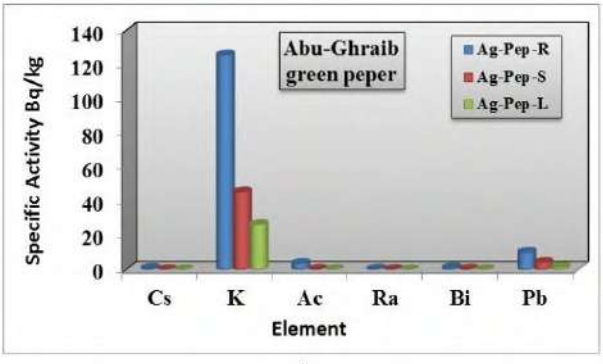

Fig. 1. Specific activity of Green pepper sample in Abu-Ghraib city.

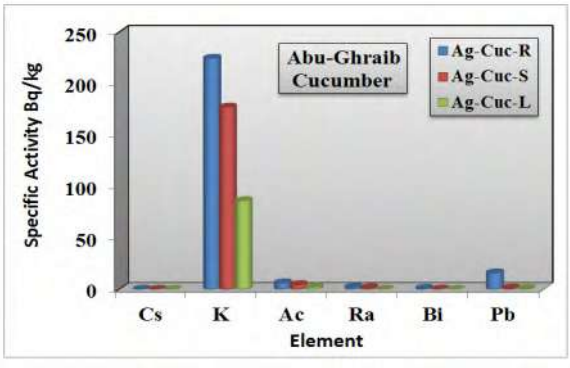

Fig. 2. Specific activity of Cucumber sample in Abu-Ghraib city.

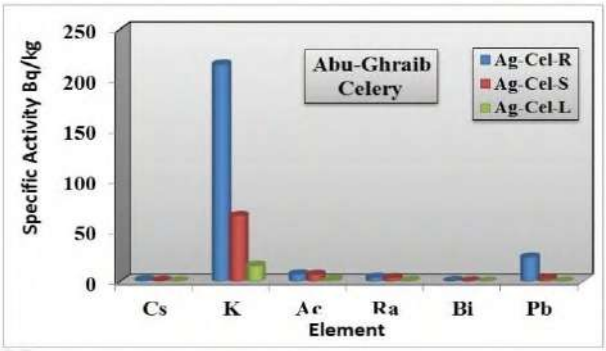

Fig. 3. Specific activity of Celery sample in Abu-Ghraib city.

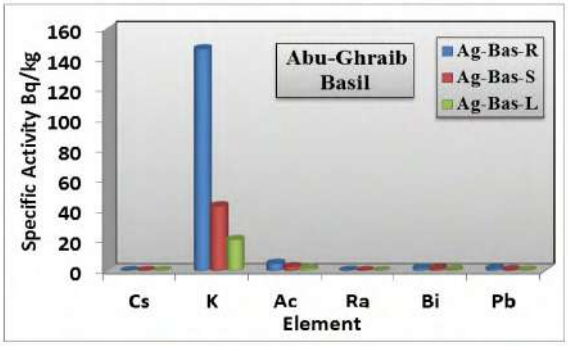

Fig. 4. Specific activity of Basil sample in Abu-Ghraib city.

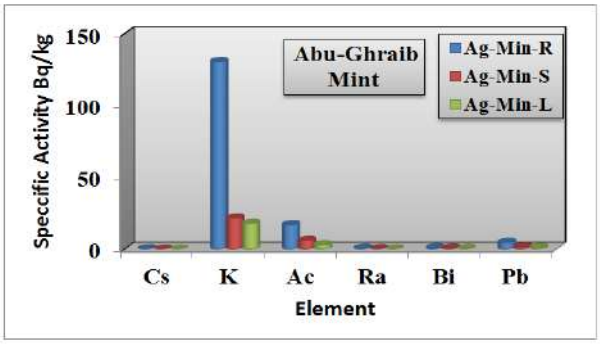

Fig. 5. Specific activity of Mint sample in Abu-Ghraib city.

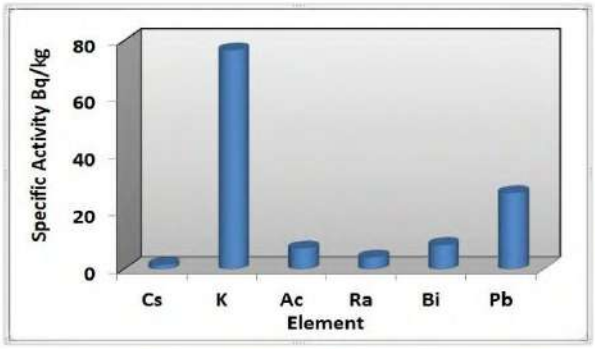

Fig. 6. Specific activity of Soil sample in Abu-Ghraib city

.

Table 2 and Figs. 7, 8 and 9 show the calculated results of radiation hazard indices (absorbed dose, annual effective dose, annual gonadal dose equivalent (dose ingested)) respectively. The estimated average values for the outside absorbed dose rate in green pepper, cucumber, celery, basil and mint varied from 14.772 nGy/h in cucumber-root to 2.020 nGy/h in basil-leaves. However, the inside absorbed dose rate varied from 30.290 nGy/h in mint –root to 2.363 nGy/h in green pepper-leaves. It seems clear that the results are less than the worldwide permissible limits, 84 nGy/h [12]. The highest value of the annual effective dose inside and outside the body was shown in mint sample. The results of annual gonadal dose were varied from 115.655 µSv/y in mint-root to 9.139 µSv/y in green pepper-leave. All results of annual effective dose equivalent and annual gonadal dose equivalent were below the allowable limit 290 µSv/y according to UNSCEAR, 2008 [21], and below 1000 µSv/y limit, according to ICRP, 1996 [22].

Table 3 and Figs. 10, 11, 12 and 13 explain the results of the Hazard index, Life-time cancer risk, radium equivalent activity and radioactivity level index. The results show that all hazards were less than ≤1 limit [1]. The results explain that there is a variation in cancer risk. The highest life-time cancer risk, in and out of the body was found in green pepper-soil, cucumber-root, celery-root, basil-root, and mint-root. As wall, the lowest values were found in leave for each the plants. The Ra_{eq} in green pepper, cucumber, celery, basil and mint varied from 35.553 Bq/kg in mint-root to 2.137 Bq/kg in green pepper-leave. Subsequently, the highest radium equivalent was recorded in green pepper-soil, cucumber-root, celery-root, basil-soil, and mint-root while; the lowest highest radium equivalent values were in leaves of each type of plant. So, all values were less than 370 Bq/kg limit recommended by UNSCEAR, 2000 [1]. Also, Table 3 and Fig. 13 show the results of radioactivity level Index. The highest value recorded 0.265 Bq/kg in mint-root while; the lowest value was 0.019 Bq/kg in green pepper-leaves. All results of radioactivity level index were below the permitted limit 1Bq/kg [17].

As tabulated in Table 4 and illustrated in Fig. 14, the average rate of transition factor in green pepper sample of U-232, Th-232, K-40, and Cs-137 was 0.045±0.044, 0.190±0.274, 0.859±0.685 and 0.185±0.287. For cucumber sample it was 0.314±0.248, 0.604±0.271, 1.406±0.568 and0.086±0.057. With regard to celery sample was 0.704±0.418, 0.748±0.424, 0.812±0.586 and 0.673±0.410. For Basil the average rate of transform factor was 0.048±0.038, 0.423±0.226, 0.912±0.8745 and 0.048±0.032. As for mint sample was 0.102±0.052, 1.194±1.018, 0.741±0.833 and 0.101±0.089. The highest rate for transform factor was 1.194±1.018 recorded in the mint sample at a concentration of Th-232respectively. The lowest rate for the transfer from the root to the leaves was in the basil sample in Cs-137 concentration at a rate of 0.048±0.032. The results show that the highest rate of transfer factor was to the roots and the highest rate of uranium transmission was 0.983 in the celery roots sample. As well the highest transfer rate for thorium was 2.347 in mint roots while; the highest transfer rate for potassium is 1.909 to the basil roots, were comparable to those reported elsewhere. Roots won the highest transmission factor for potassium-40 which was found in most of the study samples. Extremely high K-40 transfer factor values were found in cases where the concentration of potassium was very low in soil samples. This is because of the continuous accumulations for prolonged absorption by roots of potassium-40. The mean concentrations of activity of K-40 in basil samples were greater than those in green pepper, cucumber, celery and mint and were all less than the permissible value. Finally, the highest transfer rate for Cs-137 was 1.053 in celery root.

The highest K-40 transfer factors values were concentrated in the roots and were close to the limit recommended by UNSCEAR, 2010. This high absorption i.e. uptake of K-40 by the roots, it may be due to its presence in food crops while; for U-238 differed in the average range from 0.045±0.044 in green pepper to 0.704±0.418 in celery plant. And also for Th-232 were 0.024 in the green pepper leaves to 2.247 in the root of the mint sample, with an average range of 0.190±0.274 in the green pepper plant to1.194±1.018 in mint plant. The transfer factors for Th-232 were higher than that obtained for U-238 in this study. The average soil-to-plant transfer factors for Cs-137 varied from 0.048±0.032 in basil plant to 0.673±0.410 in celery plant. These transfer factors for Cs-137 are not significant because of their low concentration in environmental samples which was obtained in this study**.**

Table 2 Absorbed dose rate, Annual effective dose equivalent and Annual gonadal dose equivalent, at Abu-Ghraib city.

Sample Name	Sample Part	$D\ (nGy/h)$		$AEDE\ (\mu Sv/y)$		$AGDE$
		Outside	inside	outside	Inside	$(\mu Sv/y)$
Green Pepper	Soil	9.967	18.166	12.224	89.119	67.8229
	Root	8.057	14.661	9.875	71.921	56.335
	Stalk	2.227	4.170	2.731	20.461	16.065
	Leaves	1.267	2.363	1.554	11.592	9.139
Cucumber	Soil	10.752	18.519	13.120	89.592	68.129
	Root	14.772	27.131	18.116	133.097	103.643
	Stalk	11.424	21.025	14.010	103.143	80.318
	Leaves	5.335	9.718	6.543	47.676	37.410
Celery	Soil	9.319	18.092	11.930	88.021	67.872
	Root	15.992	29.485	19.612	144.642	111.725
	Stalk	9.150	16.620	11.221	81.531	62.036
	Leaves	2.346	4.244	2.877	20.819	15.851
Basil	Soil	9.138	17.932	12.015	88.432	67.510
	Root	9.746	17.671	11.952	86.689	67.910
	Stalk	3.740	6.662	4.587	32.678	25.509
	Leaves	2.020	3.565	2.477	17.492	13.656
Mint	Soil	9.091	17.619	12.095	87.944	66.543
	Root	17.347	30.290	21.335	148.597	115.655
	Stalk	5.147	8.849	6.312	43.410	33.592
	Leaves	2.901	5.038	3.558	24.715	19.173
Limit		84 UNSCEAR,2010 [12]		290 UNSCEAR, 2008 [21] 1000 ICRP, 1996 [22]		

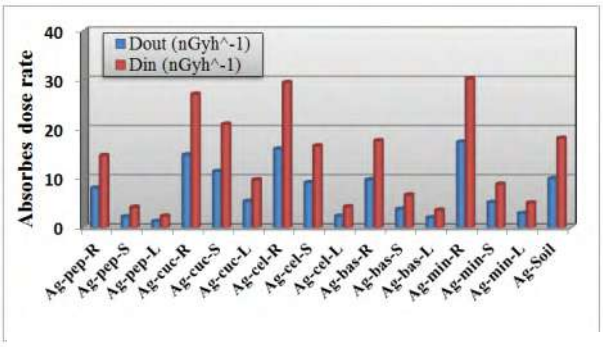

Fig. 7. Absorbed dose rate in samples at Abu-Ghraib city.

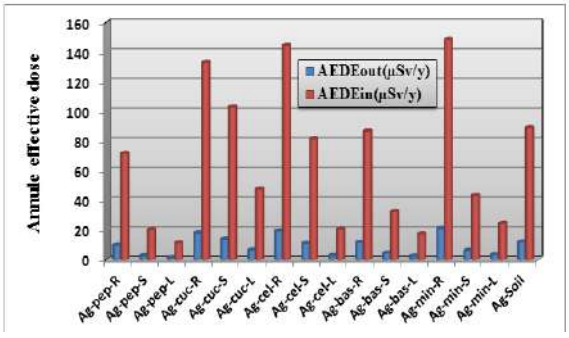

Fig. 8. Annual effective dose in samples at Abu-Ghraibcity.

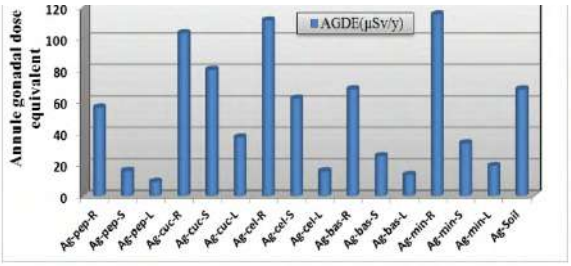

Fig. 9. Annual gonadal dose equivalent in samples at Abu-Ghraib city.

Table 3. Hazard index, lifetime cancer risk, radium equivalent and radioactivity level index, at Abu-Ghraib city.

Sample Name	Sample Part	Hazard index (Bq/kg)		ELCR		Ra_{eq} (Bq/kg)	Iγ (Bq/kg)
		H_{ex}	H_{in}	Outside $\times 10^{-3}$	Inside $\times 10^{-3}$		
Green Pepper	Soil	0.055	0.066	42.786	311.919	20.634	0.152
	Root	0.041	0.042	34.565	251.725	15.428	0.123
	Stalk	0.011	0.015	9.560	71.613	4.100	0.034
	Leaves	0.006	0.002	5.441	40.574	2.137	0.019
Cucumber	Soil	0.070	0.069	42.922	312.129	20.891	0.212
	Root	0.077	0.082	63.407	465.842	28.504	0.227
	Stalk	0.059	0.063	49.038	361.001	21.994	0.175
	Leaves	0.027	0.027	22.903	166.869	10.167	0.082
Celery	Soil	0.050	0.061	40.312	309.965	19.764	0.149
	Root	0.084	0.095	68.645	506.248	31.442	0.246
	Stalk	0.051	0.061	39.276	285.358	19.017	0.140
	Leaves	0.013	0.015	10.070	72.868	4.887	0.035
Basil	Soil	0.053	0.064	42.193	311.310	20.109	0.150
	Root	0.050	0.051	41.675	303.412	18.753	0.149
	Stalk	0.020	0.024	16.057	114.374	7.413	0.057
	Leaves	0.010	0.011	8.672	61.224	4.040	0.030
Mint	Soil	0.054	0.066	42.587	311.432	20.109	0.148
	Root	0.096	0.097	74.675	520.081	35.553	0.265
	Stalk	0.029	0.030	22.093	151.937	10.804	0.078
	Leaves	0.016	0.017	12.453	86.505	5.994	0.044
Limit UNSCEAR, 2000 [1]		≤1		0.29	1.16	370	≤1 [17]

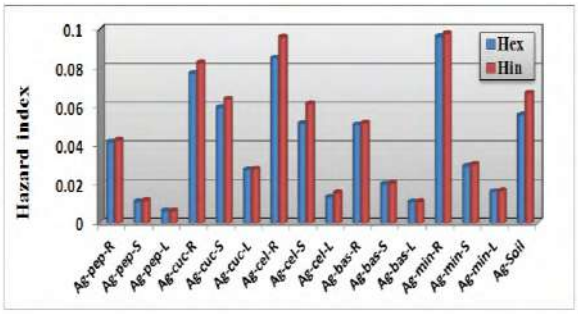

Fig. 10. Hazard index of samples at Abu-Ghraib city.

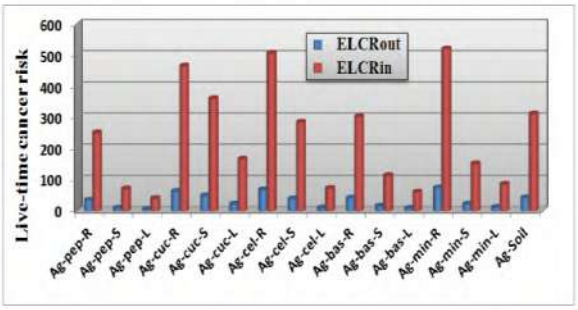

Fig. 11. Live Time cancer risk in samples at Abu-Ghraib city.

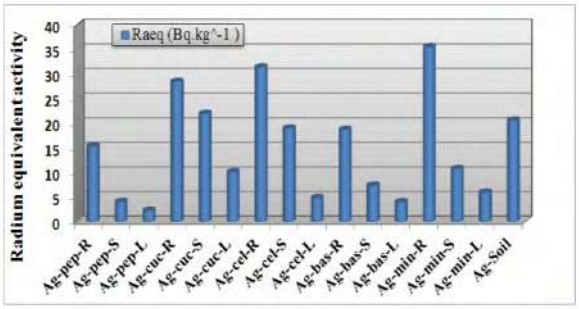

Fig. 12. Radium equivalent activity in samples at Abu-Ghraib city.

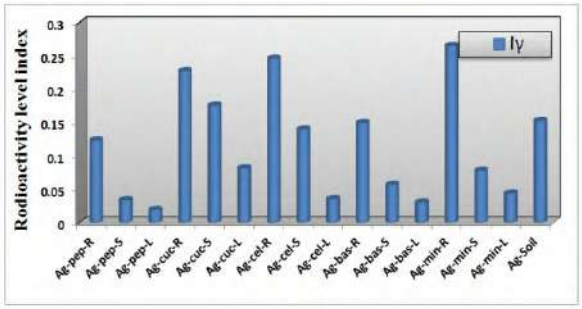

Fig. 13. Radioactivity level index in samples at Abu-Ghraib city.

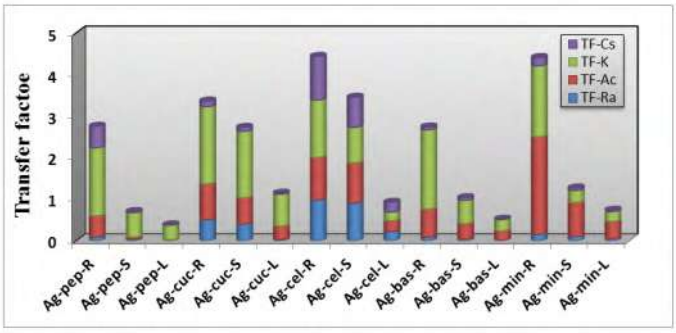

Fig. 14. Transfer factor from soil to plant in samples at Abu-Ghraib city.

Table 4. Soil-to-plant transfer factor (TF) of natural radionuclides and artificial C-137 at Abu-Ghraib city.

Sample Name	Sample Parts	Transfer factor			
		U-238	Ac-228	K-40	Cs-137
Green Pepper	Root	0.092	0.507	1.637	0.516
	Stalk	0.039	0.040	0.593	0.029
	leaves	0.003	0.024	0.346	0.009
	Average	0.045 ±0.044	0.190 ±0.274	0.859 ±0.685	0.185 ±0.287
Cucumber	Root	0.506	0.860	1.857	0.1377
	Stalk	0.403	0.631	1.594	0.097
	leaves	0.033	0.320	0.767	0.024
	Average	0.314 ±0.248	0.604 ±0.271	1.406 ±0.568	0.086 ±0.057
Celery	Root	0.983	1.020	1.378	1.053
	Stalk	0.907	0.965	0.853	0.726
	leaves	0.222	0.259	0.206	0.238
	Average	0.704 ±0.418	0.748 ±0.424	0.812 ±0.586	0.673 ±0.410
Basil	Root	0.089	0.670	1.909	0.068
	Stalk	0.041	0.372	0.558	0.066
	leaves	0.031	0.226	0.268	0.011
	Average	0.048 ±0.038	0.423 ±0.226	0.912 ±0.875	0.048 ±0.032
Mint	Root	0.154	2.347	1.703	0.202
	Stalk	0.101	0.822	0.284	0.063
	leaves	0.050	0.414	0.236	0.036
	Average	0.102 ±0.052	1.194 ±1.018	0.741 ±0.833	0.101 ±0.089

5. Conclusions

The radioactivity was measured in samples of green pepper, cucumber, celery, basil, mint, and their soils on a regular basis. Specific activity concentrations U-238, Th-232, K-40, and Cs-137 using the NaI (Tl) gamma ray spectrum detector. To assess radiological hazards, radium-equivalent equivalents, absorbed dose rate, annual effective dose rate, hazard indices, annual gonadal dose equivalent and radioactivity level index were all estimated below the permissible limits that are considered safe from radiological hazards. In this study K-40 transfer factors were found to be arranged at the roots. Gradually, descending from the roots to the stalk and then to the leaves in the selected basil, celery and mint plants under study. Therefore, the current study proved that the samples selected under study do not have dangerous radiological effects. We recommend studying and measuring the concentrations of radionuclides and their activities in terms of availability in the local market to determine the quality of consumer foodstuffs.

Acknowledgements

The authors would like to knowledge all those contributed in declaring this work. Special thanks to the staff of nuclear physics lab. for post graduate students, College of Science, Mustansiriyah University. The authors also extend their thanks and gratitude to the employees of the Nuclear Laboratory at the College of Science, Al-Nahrain University for allowing measurements. There is no financial support for this work leading to this publication. We the authors confirm that we have not any organizations that funded our research. It is noteworthy that the transfer of radionuclides from plants to

livestock and then to humans through the food chain, may lead to many radiation hazards to the humans if the transfer factor exceed unity.

References

[1] UNSCEAR 2000 United Nations Scientific Committee on the Effects of Atomic Radiation. Report to the General Assembly with Annexes, New York
[2] IAEA 1999 International Atomic Energy Agency. Practical handbook. Vienna, Austria
[3] I.T. Al-Alawy, R.S. Mohammed, H.R. Fadhil, A.A. Hasan, *J. Phys.: IOP Conf. Ser.* **1032** (2018) 012012-1– 012012-18. doi :10.1088/1742-6596/1032/1/012012
[4] A.C. Upton, P. Linsalata 1988 In: Carter MW (ed) Radionuclides in the food chain, Springer-Verlag, New York
[5] S.F. Hassan, H.G. Daway, I.T. Al-Alawy, *AIP Conf. Proc.* **2144** (2019) 030006-1 https://doi.org/10.1063/1.5123076
[6] H.G. Daway, S.F. Hassan, I.T. Al-Alawy 2018 *Indian J. Public Health Res. Dev.* **9**(12) 1282
[7] H.M. Khan, M. Ismail, K. Khan, P. Akhter 2011 *Water Air Soil Pollut.* **219** 129
[8] I.T. Al-Alawy, A.A. Hasan 2018 *J. Phys.: IOP Conf. Ser.* **1003** 012117-1
[9] I.T. Al-Alawy, H.R. Fadhil 2016 *Int. J. Sci. Res. Sci. Tech.* **2**(4) 72
[10] A. Jose, J. Jorge, M. Cleomacio, V. Sueldo, D.S. Romilton 2005 *J. Braz. Arch. Biol. Technol.* **48** 221
[11] UNSCEAR 1988 United Nations Scientific Committee on the Effects of Atomic Radiation. Report to the General Assembly with Annexes, New York
[12] UNSCEAR 2010 United Nations Scientific Committee on the Effects of Atomic Radiation. Report to the General Assembly with Annexes, New York
[13] EUC 1999 European Commission. Directorate-General Environment, Nuclear Safety and Civil Protection. Radiation protection 112. STUK Finland
[14] ICRP 2007 International Commissions on Radiological Protection. Publication 103. *Ann. ICRP*. **37**
[15] H. Taskin, M. Karavus, P. Ay, A. Topuzoglu, S. Hidiroglu, G. Karahan 2009 0 *J. Environ. Radioact.* **100** (1) 49
[16] ICRP 2012 International Commissions on Radiological Protection. Publication 119: Compendium of dose coefficients based on ICRP Publication 60. Annals of the ICRP 41 (suppl) **42** (4) 1
[17] V. Ramasamy, G. Suresh, V. Meenakshisundaram, V. Gajendran 2009 *Res. J. Environ. Earth Sci.* **1**(1) 6
[18] IUR 1992 International Union of Radioecology. Protocol Developed by the Working Group on Soil to Plant Transfer, 1982–1992, IUR, Saint-Paul-lez-Durance, France
[19] IAEA 2010 International Atomic Energy Agency. Handbook of parameter values for the prediction of radionuclide transfer in temperate environments, International Atomic Energy Agency, Technical Report Series (TRS) No. 472
[20] UNSCEAR 1993 United Nations Scientific Committee on the Effects of Atomic Radiation. Report to the General Assembly, New York
[21] UNSCEAR 2008 United Nations Scientific Committee on the Effects of Atomic Radiation. Report to the General Assembly, New York
[22] ICRP 1996 International Commission on Radiological Protection. ICR Publication 72, Oxford

A Comparison of Orthometric Heights Calculated from (GPS/Leveling) and (EGM08) Methods Based–GIS

A Comparison of Orthometric Heights Calculated from (GPS/Leveling) and (EGM08) Methods Based –GIS

Nawal Khalaf Ghazal[1] and Neran Saleh leaby Saray[2]

[1]Remote Sensing and GIS, College of Science, Baghdad University, Iraq.
[2]Department of Physics, College of Science, Baghdad University, Iraq

E-mail: nearansaleh82@gmail.com

Abstract. Interest in the study of global gravitational models has increased recently all over the world because it is necessary for height datum transformations. Today the International Center for Global Earth Models (ICGEM) provides the largest collection in the world produced through gravitational data from the gravitational satellite's missions CHAMP, GRACE, and GOCE ... Etc. To allow easy access through the internet with its more intelligent technologies, it is one of the International Gravity Organization's services. While the Global Positioning System (GPS) has become one of the most preferred technologies in engineering surveying, a major dilemma in GPS survey lies in oval-based elevations. At the same time, orthometric heights are commonly used in the engineering field. Therefore, it is necessary to convert the measured heights by satellites assigned to the elliptical surface into orthometric heights and supported to the geoid surface (mean sea level) through an accurate geodetic model. The differences between orthometric measurement heights from DGPS/leveling data (obtained from 57 points in the study area) are increasingly used by professionals geographical information systems(GIS). However, the local determination of Geoid is necessary for better accuracy of the orthometric height from DGPS. This paper aims to introduce a modern technique for determining elevation, avoiding cumbersome and time-consuming spirit leveling operations. Fast vertical positioning can be obtained using DGPS with geoid models. The Root Mean Square Error (RMSE) is ± 0.19 m with high precision of DGPS derived with EGM08; thus, the more it describes the Earth's gravitational field in more detail.

Keywords: GIS, leveling, orthometric height, EGM08, Heights, Root Mean Square Error.

1. Introduction

The determination of the Earth's surface and its external gravitational field, and the normal Earth ellipsoid is the biggest issue currently confronting geodesists worldwide. The Earth's surface is uneven and, as a result, impossible to be described by a mathematical surface. Instead, Geoid, the gravitational field's equipotential surface will strongly approximate the mean sea level (M.S.L.).The Geoid is important for every country to achieve accurate vertical positioning. All geodetic measurements are directly related to gravity's real field when taken on Earth's physical surface. This anomaly area is the fundamental parameter for the transition of geodetic measurements from the physical space of observation (Geoid) to the computation's geometric space, ellipsoid [1].

To convert ellipsoid height into a more useful orthometric height, we need to know the relation between Geoid which representing the actual equipotential figure of the Earth's surface. The

ellipsoidal height represents Earth's mathematical figure. The Geoid is one of the most important parts of a geodetic infrastructure. It is well known that globally, mean sea level best fits. In the least square sense, Geoid, representing the equipotential surface of the Earth's gravity field and used as a reference for physical height system like orthometric heights. This means that by combining ellipsoidal heights from GPS and geoid heights, the orthometric height can be determined [2].

2. Study Area

The chosen study area is the campus of the University of Baghdad in the heart of the capital, Baghdad, located between Latitude (33º 16' 55.6") to (33º 16' 4.5") N, Longitude (44º 22' 11.8") to (44º 23' 20.4") E., which covers an area of (2.9km$^{2)}$. It is shown in figure (1).

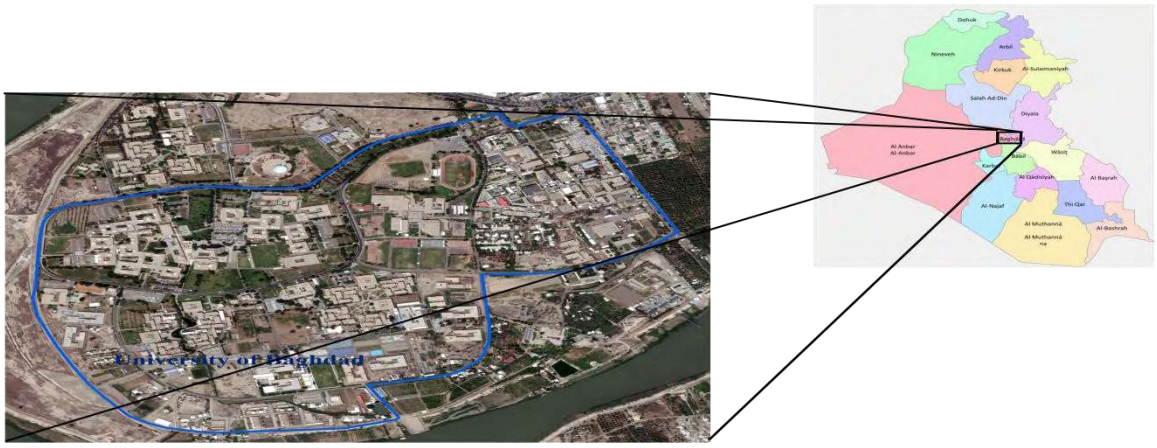

Figure 1. The study area of the campus of the University of Baghdad.

3. The Theoretical Background

3.1. The Orthometric and Ellipsoid Heights

The (H) refers to an isotope reference surface. The orthometric height of a distance from the point on the surface of the Earth to the distance that points to the Geoid (the equipotential surface that coincides with the mean sea level) is measured along the normal vertical line to the Geoid, which is measured by using the level [3]. The ellipsoidal height measured using DGPS represents the height from the surface of any reference ellipsoid to the point on the ground. The separation between the ellipsoid and the Geoid surface is called Geoid height or Geoid Undulation **(N),** as shown in figure (2). The determination of the Geoid Undulation at each point can be calculated using a well-known formula**[4]**:

$$N = h - H \quad (1)$$

h is ellipsoidal height, **H** is orthometric height, and **N** is geoid undulation

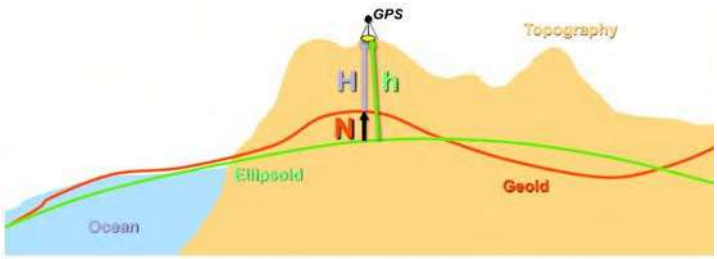

Figure 2. TheOrthometric height(H), N is the geoid undulation,[5].

3.2. Leveling

Leveling is the general term applied to any of the various processes by which height is determined. It is a vital process in producing the data needed for mapping, engineering design, and construction. Leveling results are used for designing highways, railways, canals, sewage, water supply systems, and other facilities with a grade line that best aligns with the current terrain [6]. The type of level device used in this paper is Topcon (ABN 26).

3.3. DifferentialGlobal Positioning System(DGPS)

The GPS heavenly body was initially planned as 24 satellites put in three orbital planes. Each slanted at 63 degrees as the equator chose height was *(* 20~200 *)*km, offering to ascend to an orbital time of 12 sidereal hours. This is 50% of the Earth's turn time frame, offering to ascend to rehashing ground tracks' operational advantage. These satellites were disseminated consistently in the orbital planes, with each plane having eight satellites [7].

3.4. Earth Gravitational Model of 2008 (EGM2008)

The EGM2008 is a gravitational model of the Earth created by a least-squares mix of the ITG-GRACE03S gravitational model (with its related blunder covariance lattice) and a 5'x5' matrix of free-air gravity irregularities. EGM2008 is created to degree/request 2159 with some extra terms up to degree/request 2190 [8].

EGM2008 depends on the GRACE (Gravity Recovery and Climate Experiment) just gravity field model ITG-GRACE03S which gives a profoundly exact depiction of the long-and medium-frequency gravity field range up to degree and the order 180. The ITG-GRACE03S model joins right around six years of GRACE gravity field perceptions and different wellsprings of gravity information, especially point gravity estimations. Consequently, the EGM2008 circular consonant coefficients should be extended to degree 2190 instead of 2159 or 2160 when utilized in pragmatic applications [9].

3.5. Data Sets

The orthometric heights for the 57 points were obtained from the leveling for these heights in the middle of Iraq (FAW). The datum was called MSL FAW, and this data is shown in Table 2. The differential global position system (DGPS) type Topcon Hiper-II GNSS has used a static method to observed 57 points, each point is observed 3 hours. The data points were then submitted to the AUSPOS online GPS Processing Service (HTTP: www.ga.gov.au). To calculate Geoid undulation using EGM2008, a zip file can be downloaded that contains an ESRI GRID raster data set of 2.5-minute. The American Surveying Authority worked on making Raster networks that cover all parts of the world. Each network is about 45×45 of Latitude and longitude that gives the values of N within the ready-made Raster network, and that can be called to the ARC GIS program. The network files cover lines from the length is 2 to 90, and the width from 5 to 60 covers approximately the eastern Arab world, including the Iraqi lands. The Raster can be downloaded from the link below:
https://earth-info.nga.mil/GandG/wgs84/gravitymod/egm2008/egm08_gis.html.

As shown in table (3) and Fig. (3), by cutting the province of Baghdad and noting that the value of Tthe Geoid Heights N varies from the highest [0.690 m] to the lowest [-2.910 m].

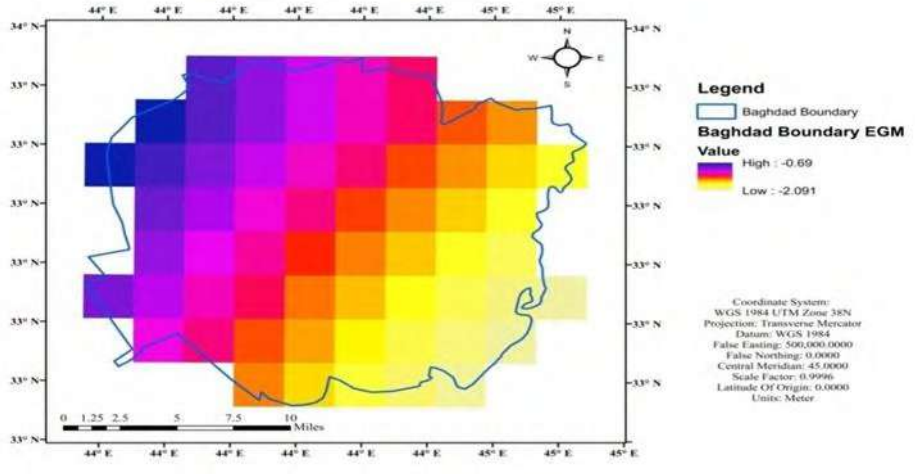

Figure 3. The Geoid HeightsEGM08 raster within the capital Baghdad.

3.6. Calculate the root mean square error (RMSE)

Modeling heights of the calendar using a geometric method of calculating model accuracy with a root mean square error indicator (RMSE) to calculate model accuracy requires orthometric point heights from the model (H_{GGMs}), i.e., orthometric heights of points obtained from the differences between typical geodetic heights and elliptical point heights with the corresponding altitudes in addition to the orthometric heights (H_{obs}) to obtain (orthometric residuals remains). The orthometric residuals and the total number of points specified for the RMSE are used along with the model accuracy. The RMSE index is provided in the formula to calculate model accuracy [8].

$$RMSE=\pm\sqrt{\frac{1}{n}\sum_{i=1}^{n}(\delta H_{Residual})^2} \quad \textbf{(2)}$$

$$\delta H_{Residual} = H_{obs} - H_{GGMs} \quad (3)$$

H_{obs}: Known Orthometric Height
H_{GGMs}: Model Orthometric Height
n: the number of points.
GGMs are the smallest RMSE values. Since then, the better it represents the Earth's gravitational field in more detail, and vice versa. The greater the value of it, the greater the representation of gravity with less detail.

4. Results and Discussion

Accuracy assessment of GPS observations processed by (EGM2008 RASTER)
The level is the most accurate way to calculate orthometric heights for scanning points above the geode .But this method has become obsolete no longer to keep pace with the rapid development in the modern world. So, it is no longer feasible for several reasons, including it takes a long time and great effort and high cost, thus, an easier, faster, and less expensive is required.
Unfortunately, GPS delivered only height relative to the Earth's mathematical ellipse, known as ellipsoidal height, rather than the orthometric height related to the MSL with its physical meaning, thus, parallel to the development of GPS and methodology.
To convert the Ellipsoid heights obtained from DGPS for the observed points into orthometric heights calculated by applying equation (1) converting the heights inside the program is required.

Table 1. The Comparison of leveling data with GPS processed data.

METHOD	Maximum (m)	Minimum (m)	Mean (m)	Standard deviation (m)
Leveling measurement height H(m)	38.264	35.930	36.653	0.586
GPS processed data	38.128	35.762	36.541	0.625
Difference	0.399	-0.401	0.111	0.152

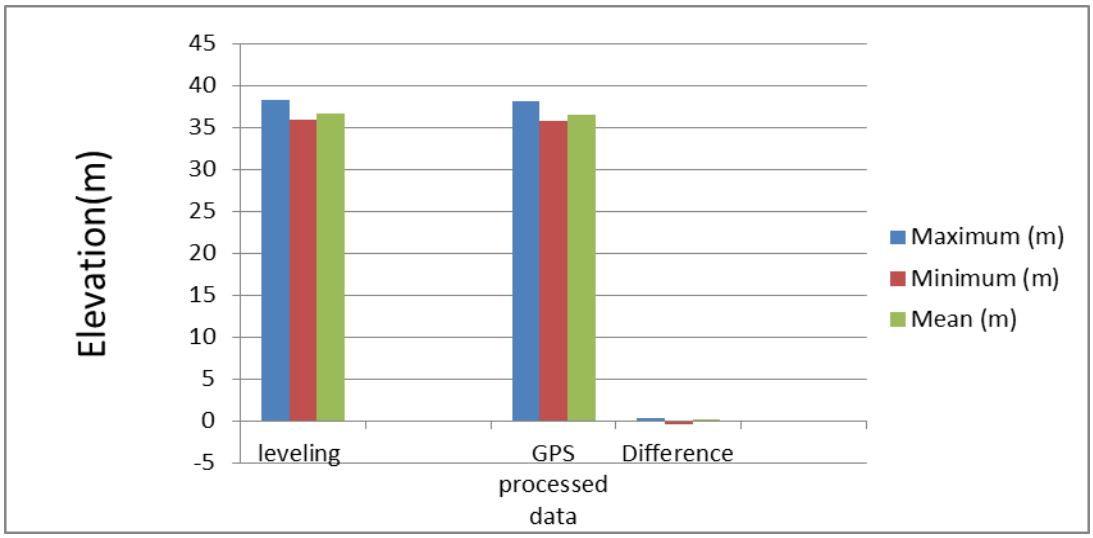

Figure 4. The Accuracy of DGPS data after processing.

The difference in leveling data with GPS processed data(HEGM08) is clearly shown that the accuracy of the results of GPS data is within the Standard deviation ±0.152m as illustrated in the table (1). The RMSE The EGM2008 model equal to [± 0.187973m] as shown in figure (4), applied the equal (3).
The height data performed herein offers useful insight for a range of applications relating to height. The production and updating of large-scale topographical maps in various engineering and construction applications, particularly for water resource management. The topographic map of the Study Area is shown in figure (5).

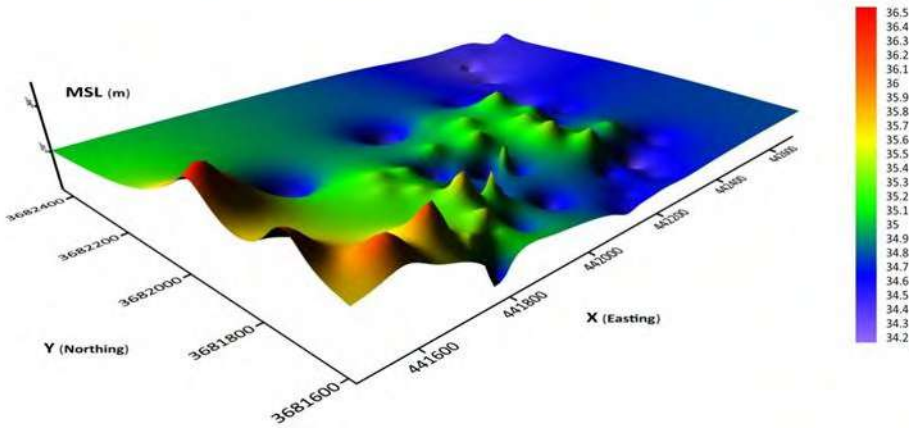

Figure 5. Representing the topographic map of the Study Area.
Table 2. Ellipsoidal and Orthometric heights(2020).

Point No.	Northing(m)	Easting(m)	Ellipsoidal height h (m)	Orthometric height Hobs (M.S.L) (m)
BU01	3681622.477	442158.483	34.5552	36.271
BU02	3681641.119	441821.245	35.1578	36.906
BU03	3681646.752	442271.423	34.5022	36.369
BU04	3681717.383	441480.99	36.3873	38.242
BU05	3681756.014	441869.274	35.7915	37.345
BU06	3681848.047	442032.804	34.1972	35.934
BU07	3681828.833	442052.868	35.4727	37.025
BU08	3681905.955	441876.638	35.2064	37.173
BU09	3681912.62	441946.785	34.2758	36.153
BU10	3681911.887	442069.661	35.3165	36.867
BU11	3681949.221	442265.198	35.1257	37.07
BU12	3682018.665	442240.00	35.3347	36.95
BU13	3681583.049	442107.802	34.548	36.319
BU14	3681594.571	441776.986	34.4333	36.075
BU15	3681625.908	441584.439	36.2443	37.621
BU16	3681625.188	441755.697	35.5055	37.17
BU17	3681645.93	441789.195	35.3775	36.937
BU18	3681655.103	441697.41	36.2296	37.427
BU19	3681659.146	441896.635	34.5345	36.278
BU20	3681668.477	441829.946	35.5159	37.191
BU21	3681695.023	442026.201	34.4483	36.251
BU22	3681695.209	442201.861	34.5521	36.261
BU23	3681712.222	442293.025	34.1764	35.93
BU24	3681734.101	442394.825	34.4988	36.361
BU25	3681742.759	441923.005	35.5912	37.19
BU26	3681764.947	441920.809	34.4304	36.085
BU27	3681763.181	442217.27	35.3766	37.033
BU28	3681774.058	441942.077	34.1916	36.051
BU29	3681790.089	441784.883	35.2071	37.18
BU30	3681794.279	442322.228	35.0626	36.55

BU31	3681816.006	441828.500	35.3295	37.167
BU32	3681815.803	442068.830	34.4222	36.073
BU33	3681829.915	442181.706	35.4517	37.182
BU34	3681848.047	442032.804	35.0313	36.68
BU35	3681856.927	441783.731	35.3022	37.195
BU36	3681897.294	442192.973	35.3493	37.157
BU37	3681907.554	441815.337	35.3007	37.170
BU38	3681904.639	442304.514	34.6622	36.310
BU39	3681953.127	441508.537	36.5417	38.264
BU40	3681950.55	441990.214	35.1395	36.831
BU41	3681961.748	442386.084	34.5303	36.332
BU42	3681967.438	442361.283	34.6088	36.277
BU43	3681978.494	442107.310	35.2754	37.029
BU44	3681999.104	441545.031	36.0344	37.578
BU45	3682045.226	441711.390	34.2044	36.055
BU46	3682043.878	442091.660	35.0048	36.395
BU47	3682065.388	442359.017	34.2077	36.217
BU48	3682114.854	442016.286	34.2957	35.939
BU49	3682127.942	442249.186	34.533	36.186
BU50	3682195.436	442397.040	34.5444	36.214
BU51	3682228.475	442434.745	34.2559	36.187
BU52	3682315.141	442517.779	34.3861	36.200
BU53	3682331.657	442485.023	34.2008	35.983
BU54	3682344.097	442464.661	34.3763	36.132
BU55	3682393.138	442556.525	34.466	36.126
BU56	3682402.161	442697.561	34.5598	36.195
BU57	3682442.613	442679.433	34.1516	35.940

Table 3. Geoid heights at points using (h-H) method and undulation height by EGM08raster (2020).

Point Nu.	**Northing(m)**	**Easting(m)**	**Nr(EGM08)(m)**	**Hr(EGM08)(m)**
BU01	3681622.477	442158.483	-1.6129	36.1681
BU02	3681641.119	441821.245	-1.6025	36.7603

BU03	3681646.752	442271.423	-1.6158	36.118
BU04	3681717.383	441480.99	-1.5907	37.978
BU05	3681756.014	441869.274	-1.6015	37.393
BU06	3681848.047	442032.804	-1.6067	35.8039
BU07	3681828.833	442052.868	-1.6055	37.0782
BU08	3681905.955	441876.638	-1.5987	36.8051
BU09	3681912.62	441946.785	-1.6006	35.8764
BU10	3681911.887	442069.661	-1.6043	36.9208
BU11	3681949.221	442265.198	-1.6093	36.735
BU12	3682018.665	442240.00	-1.6072	36.9419
BU13	3681583.049	442107.802	-1.6122	36.1602
BU14	3681594.571	441776.986	-1.6021	36.0354
BU15	3681625.908	441584.439	-1.5957	37.8400
BU16	3681625.188	441755.697	-1.6008	37.1063
BU17	3681645.93	441789.195	-1.6014	36.9789
BU18	3681655.103	441697.41	-1.5985	37.8281
BU19	3681659.146	441896.635	-1.6043	36.1388
BU20	3681668.477	441829.946	-1.6022	37.1181
BU21	3681695.023	442026.201	-1.6075	36.0558
BU22	3681695.209	442201.861	-1.6127	36.1648
BU23	3681712.222	442293.025	-1.615	35.7914
BU24	3681734.101	442394.825	-1.6176	36.1164
BU25	3681742.759	441923.005	-1.6034	37.1946
BU26	3681764.947	441920.809	-1.6029	36.0333
BU27	3681763.181	442217.27	-1.6117	36.9883
BU28	3681774.058	441942.077	-1.6033	35.7949
BU29	3681790.089	441784.883	-1.5983	36.8054
BU30	3681794.279	442322.228	-1.6142	36.6768

BU31	3681816.006	441828.500	-1.5991	36.9286
BU32	3681815.803	442068.830	-1.6063	36.0285
BU33	3681829.915	442181.706	-1.6093	37.0610
BU34	3681848.047	442032.804	-1.6045	36.6358
BU35	3681856.927	441783.731	-1.5969	36.8991
BU36	3681897.294	442192.973	-1.6083	36.9576
BU37	3681907.554	441815.337	-1.5968	36.8975
BU38	3681904.639	442304.514	-1.6114	36.2736
BU39	3681953.127	441508.537	-1.5867	38.1284
BU40	3681950.55	441990.214	-1.6012	36.7407
BU41	3681961.748	442386.084	-1.6126	36.1429
BU42	3681967.438	442361.283	-1.6118	36.2206
BU43	3681978.494	442107.310	-1.6041	36.8795
BU44	3681999.104	441545.031	-1.5869	37.6213
BU45	3682045.226	441711.390	-1.5909	35.7953
BU46	3682043.878	442091.660	-1.6023	36.6071
BU47	3682065.388	442359.017	-1.6097	35.8174
BU48	3682114.854	442016.286	-1.5986	35.8943
BU49	3682127.942	442249.186	-1.6052	36.1382
BU50	3682195.436	442397.040	-1.6081	36.1525
BU51	3682228.475	442434.745	-1.6086	35.8645
BU52	3682315.141	442517.779	-1.6092	35.9953
BU53	3682331.657	442485.023	-1.6079	35.8087
BU54	3682344.097	442464.661	-1.607	35.9833
BU55	3682393.138	442556.525	-1.6087	36.0747
BU56	3682402.161	442697.561	-1.6124	36.1722
BU57	3682442.613	442679.433	-1.611	35.7626

5. Conclusions

By comparing the data of the orthometric heights (H) values, (H) practically measured by the level with the data obtained from the after processing by the EGM2008 model, which is obtained by Raster. This study indicates small and very close differences as the accuracy reached the standard deviation (SD) equal to [± 0.152 m]. This means that the level still one of the most accurate devices in this field and in various projects.

The RMSE is used to describe the long wavelength of Earth's gravitational field. The EGM2008 model produces the smallest differences in terms of the Root Mean Square Error (RMSE), which is equal to [± 0.187973m.], and the method of the calculation by Raster is within the arc GIS program.

The orthometric Heights from DGPS Data can thus be considered a modern tool for converting the height.

References

[1] El-Ashquer M A Zahran K H El-Fiky G S and Salama I M 2010 Accuracy Assessment of GPS leveling Applications North West Lake Nasser Aswan Egypt.
[2] Lowrie W 2007 Fundamental of geophysics 2nd Edition (Cambridge- University Press) USA.
[3] Heister H Lang M Merry C L and Ruther H 1999 South Africa, TS **20**, B1-B10.
[4] Rabah M and Kaloop M 2013 Arabian Journal of Geosciences **6** (4) 1263.
[5] Yeboah F 2007 Integrating GPS Data into the National Coordinate System: A Case Study in Ashanti Region Ph.D. thesis University of Science and Technology Kumasi.
[6] Tan Liat Choon 2014 INTRODUCTION TO ENGINEERING SURVEYING (CE 1305)Leveling-Theory)UEL University of East London. 2.
[7] Alessia T 2011 The development of integrated high-resolution geophysical, photogrammetric and GPS surveying applied to landslides in the South Wales Coalfield Cardiff University 105.
[8] Pavlis N K Holmes S A Kenyon S C Factor J K 2012 The development and evaluation of the Earth Gravitational Model 2008 (EGM2008).
[9] Merry C 2009 EGM2008 Evaluation for Africa Newton's Bulletin.
[10] http://icgem.gfz-potsdam.de/tom_longtime.

Theoretical Estimation of Electronic Flow Rate at Al-TiO_2 Interfaces System

Theoretical Estimation of Electronic Flow Rate at Al-TiO_2 Interfaces System

Hadi J M Al-agealy[1], Taif Saad Al Maadhede[2], AbdulKareem A Al-Khafaji[1] , Suad H Aleabi[1], Mohsin A Hassooni[1], Rajaa Faisel Rabeea[1]

[1]Department of Physics, College of Education for pure science, Ibn Al-Haitham, University of Baghdad
[2]Al Turath University of College, Baghdad, Iraq

E-mail: mohsin.a@ihcoedu.uobaghdad.edu.iq

Abstract. The mechanism of the electronic flow rate at Al-TiO_2 interfaces system has been studied using the postulate of electronic quantum theory. The different structural of two materials lead to suggestion the continuum energy level for Al metal and TiO_2 semiconductor. The electronic flow rate at the Al-TiO_2 complex has affected by transition energy, coupling strength and contact at the interface of two materials. The flow charge rate at Al-TiO_2 is increased by increasing coupling strength and decreasing transition energy.

Key words: Electronic Flow Rate, Al-TiO_2 and Interface.

1. Introduction

The reactions of an electronic transfer are a simple process that occurs in donor-acceptor media and it is an elementary electronic transition from an atom to atom system. It is one of the main reaction in physics devices involves oxidation-reduction state systems. It is developed since the beginning of the twentieth century [1]. Electronic transfer over distances has been investigated extensively in both experimental and theoretical studies in different inhomogeneous devices and through monolayers on the electrode system [2]. Nowadays, structure evaluations of electronics are important tools to investigate the physical properties of materials [3]. The electronic transfer due to metal/semiconductor interface has been devoted to investigate the origin of the potential barrier height at interface and effect on the electrical characteristics of this device [4]. Titanium dioxide (TiO_2) produces by low cost and higher stability and has very attractive research for mechanical, electronic and optical properties material. TiO_2 is used in many electronic applications such as adsorbents and catalytic systems [5-6]. Generally, the transition reaction at metal/semiconductor interfaces is a considerable inhomogeneous quantity of states. Therefore, the flow rate of transfer improves the performance of metallic junction devices; the transfer of electron continues across the interface above the potential junction [7]. In this work, we study the electronic flow rate at Al-TiO_2 System with coupling, electronic reorientation energies and potential coefficients. We investigate the transition rate for Al-TiO_2 structure with concerning to driving force and transition energy of the system.

2. Theory

The electronic flow rate (EFR) refers to the electronic transfer current through donor- acceptor system. It is evaluated according to quantum theory for continuum energy levels. The flow rate EFR from metal to semiconductor interface in the medium of $Al-TiO_2$ is given by [8].

$$EFR_{Al}^{TiO_2} = \frac{2\pi}{\hbar}\left|\mathfrak{M}_{Al}^{TiO_2}\right|^2 \Lambda_{Al}^{TiO_2} \quad (1)$$

Where $\left|\mathfrak{M}_{Al}^{TiO_2}\right|^2$ is squaring coupling and $\Lambda_{Al}^{TiO_2}$ is Franck–Condon factor .The Franck–Condon $\Lambda_{Al}^{TiO_2}$ can be evaluated due to perturbation approximation according to potential and can be written as [9].

$$\Lambda_{Al}^{TiO_2} = (\aleph\, \mathcal{G}_S^D)^{\frac{-1}{2}} exp - \frac{\left(\Delta\varphi_{Al}^{TiO_2}+\mathcal{G}_S^D\right)^2}{\aleph \mathcal{G}_S^D} \quad (2)$$

Where $\mathcal{G}_S^D$ is reorientation energy, $\aleph = 4\pi k_B T$:(k_B is Boltzman constant, T is room temperature, and $\varphi_{Al}^{TiO_2}$ is activity energy). Substitute Eq,(2) in Eq.(1) and integrate over space of system gives:

$$EFR_{Al}^{TiO_2} = \frac{2\pi}{\hbar}\int_{-\infty}^{\infty}\left|\mathfrak{M}_{Al}^{TiO_2}\right|^2 (\aleph\, \mathcal{G}_S^D)^{\frac{-1}{2}} exp - \frac{\left(\varphi_{Al}^{TiO_2}+\mathcal{G}_S^D\right)^2}{\aleph \mathcal{G}_S^D}\, d\epsilon \quad (3)$$

Under the condition of electrons above the Fermi level due to the activity energy (E) for system is reduced : $\Delta\varphi_{Al}^{TiO_2} = \varphi_{Al}^{TiO_2} - E$, then potential must be written as [10].

$$\mathbb{V}_{Al}^{TiO_2} = \frac{\left(\Delta\varphi_{Al}^{TiO_2}+\mathcal{G}_S^D\right)^2}{\aleph \mathcal{G}_S^D} = \frac{\left(\varphi_{Al}^{TiO_2}+\mathcal{G}_S^D-E\right)^2}{\aleph \mathcal{G}_S^D} \quad (4)$$

Due to continuum levels material, Eq.(3) must be formed according to density function $F_{(\epsilon)}$:

$$EFR_{Al}^{TiO_2} = \frac{2\pi}{\hbar}\int_{-\infty}^{\infty}\left|\mathfrak{M}_{Al}^{TiO_2}\right|^2 (\aleph\, \mathcal{G}_S^D)^{\frac{-1}{2}} exp - \frac{\left(\varphi_{Al}^{TiO_2}+\mathcal{G}_S^D-E\right)^2}{\aleph \mathcal{G}_S^D} F_{(\epsilon)} d\epsilon \quad (5)$$

Where $F_{(\epsilon)}$ is the Fermi density of electrons at Al/TiO_2 system and may be written as [11] :

$$F_{(\epsilon)} = \frac{1}{e^{\frac{\epsilon-\epsilon_F}{k_B T}}+1} \quad (6)$$

The exponential term in Eq.(5) simplified to:

$$\exp - \frac{\left(\varphi_{Al}^{TiO_2}+\mathcal{G}_S^D-E\right)^2}{\aleph \mathcal{G}_S^D} = \exp \frac{-\left(\varphi_{Al}^{TiO_2}+\mathcal{G}_S^D\right)^2+2E\left(\varphi_{Al}^{TiO_2}+\mathcal{G}_S^D\right)-E^2}{\aleph \mathcal{G}_S^D} \quad (7)$$

And must be approximated to:

$$\exp - \frac{\left(\varphi_{Al}^{TiO_2}+\mathcal{G}_S^D-E\right)^2}{\aleph \mathcal{G}_S^D} \approx \exp \frac{-\left(\varphi_{Al}^{TiO_2}+\mathcal{G}_S^D\right)^2}{\aleph \mathcal{G}_S^D} \exp \frac{-E^2}{\aleph \mathcal{G}_S^D} \quad (8)$$

The potential of Al/TiO_2 system interfaces at powering term in Eq.(5) can be reformed to:

$$\mathbb{V}_{Al}^{TiO_2} \approx \frac{\left(\varphi_{Al}^{TiO_2}+\mathcal{G}_S^D\right)^2}{\aleph \mathcal{G}_S^D} \approx \frac{(\chi_{Al}-\chi_{TiO_2})}{kT} \quad (9)$$

Where χ_{Al} is work function for Al and χ_{TiO_2} is electron affinity for TiO_2

Inserting Eq.(9) and (8) in Eq.(5) result [12].

$$EFR_{Al}^{TiO_2} = \frac{2\pi}{\hbar}\int_{-\infty}^{\infty}\left|\mathfrak{M}_{Al}^{TiO_2}\right|^2 (\aleph\, \mathcal{G}_S^D)^{\frac{-1}{2}} \exp - \frac{(\chi_{Al}-\chi_{TiO_2})}{kT} F_{(\epsilon)} \exp \frac{-E^2}{\aleph \mathcal{G}_S^D} d\epsilon \quad (10)$$

The Eq.(10) has reformed to:

$$EFR_{Al}^{TiO_2} \approx \frac{2\pi}{\hbar} (\aleph\, \mathcal{G}_S^D)^{\frac{-1}{2}} \exp - \frac{(\chi_{Al}-\chi_{TiO_2})}{kT} \left|\mathfrak{M}_{Al}^{TiO_2}\right|^2 \int_{-\infty}^{\infty} F_{(\epsilon)} \exp \frac{-E^2}{\aleph \mathcal{G}_S^D} d\epsilon \quad (11)$$

The integral in Eq.(11) could be solved using mathematical physics to get [13]:

$$\int_{-\infty}^{\infty} F_{(\epsilon)} \exp \frac{-E^2}{\aleph \mathcal{G}_S^D} d\epsilon \approx \left[[\pi \mathrm{k_B T} - \frac{(\pi \mathrm{k_B T})^2}{16\pi \mathcal{G}_S^D} \right] \quad (12)$$

The average of flow rate electronic current EFR is given by:

$$\overline{EFR_{Al}^{TiO_2}} = \frac{V_{TiO_2}}{n} EFR_{Al}^{TiO_2} \quad (13)$$

Then Eq.(12) with Eq.(13) becomes:

$$\overline{EFR_{Al}^{TiO_2}} \approx \frac{2\pi V_{TiO_2}}{\hbar} (\aleph \mathcal{G}_S^D)^{\frac{-1}{2}} \exp - \frac{(\chi_{Al} - \chi_{TiO_2})}{kT} \left| \mathfrak{M}_{Al}^{TiO_2} \right|^2 \left[[\pi \mathrm{k_B T} - \frac{(\pi \mathrm{k_B T})^2}{16\pi \mathcal{G}_S^D} \right] \quad (14)$$

The electronic reorientation energies for Al/TiO_2 system is [14]

$$\mathcal{G}_S^D(eV) = \frac{e^2}{8\pi\epsilon_\circ} \left[\frac{1}{2R_{Al}} \mathbb{f}(n_{Al}^2, \epsilon_{Al}) + \frac{1}{2R_{TiO_2}} \mathbb{f}(n_{TiO_2}^2, \epsilon_{TiO_2}) - \frac{1}{4D_{TiO_2}} \mathbb{f}(n_{Al}^2, n_{TiO_2}^2 \epsilon_{Al}, \epsilon_{TiO_2}) - \frac{1}{4D_{Al}} \mathbb{f}(n_{TiO_2}^2, n_{Al}^2, \epsilon_{TiO_2}, \epsilon_{Al}) \frac{1}{d_{Al-TiO_2}} \mathbb{f}(n_{Al}^2 + n_{TiO_2}^2 \epsilon_{Al} + \epsilon_{TiO_2}) \right] \quad (15)$$

Where e is electronic charge, $\epsilon_\circ$ is space permittivity, $\mathbb{f}(n_1{}^2, \epsilon_1) = \left(\frac{1}{n_1{}^2} - \frac{1}{\epsilon_1}\right)$ and $\mathbb{f}(n_1^2, n_2^2 \epsilon_1, \epsilon_2) = \left(\frac{n_2^2 - n_1{}^2}{n_2^2 + n_1{}^2} \frac{1}{n_1{}^2} - \frac{\epsilon_2 - \epsilon_1}{\epsilon_2 + \epsilon_1} \frac{1}{\epsilon_2}\right)$ are the polarity function of two material system respectively, n_1 and ϵ_1 are the refractive index and dielectric constant of metal(Al), n_2 and ϵ_2 are the refractive index and dielectric constant of TiO_2, R_{Al} is Aluminum radius, and d_{Al-TiO_2} is the distance between TiO_2 and Al. Then the radii of any material estimates are [15]:

$$R_{mat} = \left(\frac{3}{4\pi} \frac{M_{mat}}{N \rho_{mat}}\right)^{\frac{1}{3}} \quad (16)$$

Where M_{mater} is the molecular weight, N is Avogadro's number, and ρ_{mater} is the mater density.

3. Results and discussion

The electric flow rate has been estimated by using a simple numerical model for transfer in Al-TiO_2 system ,it has been discussed and predicted by experimental results .It assesses to explained the effect of transition energy parameters on the performance of transfer in metal-semiconductor interfaces. The performance of transfer can be discussed in terms of electronic flow rate of the device. In order to evaluate the transition flow rate, we can estimate the transition energy according to Eq (15) with the estimation of the radii of Al and TiO_2 using Eq.(16) by inserting atomic density and molecular weight from Tables 1 and 2 of Al and TiO_2 material and resulted in Tables 1 and 2, respectively .

Table 1. Properties of Al Metal.

Properties	Values
Atomic weight	26.982 [16]
Crystal structure	cubic
Lattice constant (nm)	0.405 [17]
Dielectric constant	1.6-1.8
Refractive index	0. 2 to 1. 20 [18]
Density (g/cm^3)	2.70 [16]
Work function	4.05 [19]
Calculated radius (nm)	0.143

Table 2. Characteristic of TiO_2 semiconductor.

Properties	Values
Chemical Formula	TiO_2
Atomic weight	79.866 [20]
Density (g/cm3)	4.23[20]
Crystal structure	Tetragonal rutile[20]
Melting point (ºC)	1843°C[20]
Refractive index	2.609[20]
Dielectric constant	15.10 [21]
Volume (Å3)	62.432[22]
Energy gap (eV) at 300K	3.02[22]
Lattice constant (Å)	a=4.5936 c =2.9587[22]
Electron affinity (eV)	4.2[22]
Calculated Radius(Å)	1.95612
Effective density of states in conduction band, N_C m^{-3})	1.163×10^{25}[4]

The transition energy is calculated using the values of primary input refractive index and dielectric constant and radii of Al and TiO_2 parameters which are listed in Tables 1 and 2 and inserting in Eq.(15). The results are listed in Table 3.

Table 3. Results of transition energy for Al-TiO_2 system.

Refractive index(n_{Al})	Dielectric constant(ϵ_{Al})	Transition energy $\mathcal{G}_S^D(eV)$	Refractive index(n_{Al})	Dielectric constant(ϵ_{Al})	Transition energy $\mathcal{G}_S^D(eV)$
0.2	1.8	43.5806	0.2	1.6	43.4568
0.4	1.8	10.2653	0.4	1.6	10.1415
0.6	1.8	4.0937	0.6	1.6	3.9699
0.8	1.8	1.9315	0.8	1.6	1.8077
1	1.8	0.9285	1	1.6	0.8047
1.2	1.8	0.3817	1.2	1.6	0.2579

From Table 3, it can be seen that the transition energy decreased with increasing the refractive index and stable dielectric constant for the same Al metal. It also increases with increasing the dielectric constant of Al metal for same refractive index and dielectric constant for TiO_2 semiconductor. It means that energy as a function of the polarity of Al metal dependent on energy absorption by the system because the refractive index depends on energy.

On the other hand, Eq. (14) outlined in theory can be applied to calculate and studied the electron transfer flow rate in Al-TiO_2 system. To investigate the electronic transfer cross interface of Al-TiO_2 using quantum theory, we have considered continuum energy levels for two materials. All parameters of Al metal and TiO_2 are taken from Tables 1, 2 and 3 and take the strength coupling from literature

$\mathfrak{M}_{Al}^{TiO_2} = 4\times10^{-2}, 8\times10^{-2}, 12\times10^{-3}, 16\times10^{-3}, 2\times10^{-4}\ \ eV^2 state^{-1}$ [24] ,and input in Eq.(14) to result of flow rate that is listed in Tables 4 and 5 for dielectric constant of Al metal ϵ_{Al}=1.8 and 1.6, respectively.

Table 4. Electronic Flow Rate at Al-TiO_2 Interfaces System with dialectic constant ϵ_{Al}=1.8.

Transition Energy $\mathcal{G}_S^D(eV)$	Electronic Flow Rate $\overline{EFR_{Al}^{TiO_2}}$				
	Strength Coupling (eV)				
	4×10^{-2}	8×10^{-2}	12×10^{-3}	16×10^{-3}	2×10^{-4}
43.5806	1.4455E-12	2.8910E-12	4.3365E-13	5.7820E-13	7.2274E-15
10.2653	2.9346E-12	5.8692E-12	8.8038E-13	1.1738E-12	1.4673E-14
4.0937	4.5104E-12	9.0209E-12	1.3531E-12	1.8042E-12	2.2552E-14
1.9315	6.1961E-12	1.2392E-11	1.8588E-12	2.4784E-12	3.0980E-14
0.9285	7.8442E-12	1.5688E-11	2.3533E-12	3.1377E-12	3.9221E-14
0.3817	7.5341E-12	1.5068E-11	2.2602E-12	3.0136E-12	3.7671E-14

Table 5. Electronic Flow Rate at Al-TiO_2 Interfaces System with dielectric constant ϵ_{Al}= 1.6.

Transition Energy $\mathcal{G}_S^D(eV)$	Electronic Flow Rate $\overline{EFR_{Al}^{TiO_2}}$				
	Strength Coupling (eV)				
	4×10^{-2}	8×10^{-2}	12×10^{-3}	16×10^{-3}	2×10^{-4}
43.4568	1.4475E-12	2.8951E-12	4.3426E-13	5.7901E-13	7.2376E-15
10.1415	2.9518E-12	5.9035E-12	8.8553E-13	1.1807E-12	1.4759E-14
3.9699	4.5730E-12	9.1460E-12	1.3719E-12	1.8292E-12	2.2865E-14
1.8077	6.3551E-12	1.2710E-11	1.9065E-12	2.5420E-12	3.1776E-14
0.8047	8.0784E-12	1.6157E-11	2.4235E-12	3.2314E-12	4.0392E-14
0.2579	4.5048E-12	9.0096E-12	1.3514E-12	1.8019E-12	2.2524E-14

In order to show the effect of polarity of metal, we take two different dielectric constants for Al metal. Tables 4 and 5 show that the flow rate increased with decreasing of transition energy for two dielectric constant 1.8 and 1.6 respectively, in a way that flow rate increases with coupling strength for two Tables 4 and 5; this indicates that the energy levels for two materials must be closed to each other with high electrons concentration closed interface of the system. Similar behaviors of flow rate in Table 4 and 5 at dielectric constant with ϵ_{Al}=1.8 and 1.6 indicate that the structure and properties of Al metal is important effect on the behavior of flow rate of system. Specifically, we have considered the same properties of TiO_2 semiconductor with Al metal to avoid the effects of polarity of TiO_2 on the flow rate .However; the results were obtained from two tables (4-5) which show that flow rate increased with decreasing dielectric constant of Al metal.

4. Conclusion

In this study, we first conclude that the transition energy is a function of the refractive index of Al, and it decreased with increasing refractive index and increased with increasing the dielectric constant of Al metal with constant refractive index and dielectric constant for TiO_2 semiconductor. In fact we can conclude that transition energy is a function of polarity of Al metal. The Al-TiO_2 devices exhibit a continuous transition of electrons across the interface; the flow rate increased with decreasing of transition energy and increased of coupling strength. Here, we assumed continuum energy levels for

Al and TiO_2 material to direct transfer over closed space for two materials with high electrons concentration near interface of system. Aggregation, the transition energy and contact at interface with coupling strength coupling of Al metal with TiO_2 surface are key factors affected on the quantity of electronic flow rate.

References

[1] Hadi J A Salih WB and Taif S M 2013 J. of Madenat Alelem College. 5 (2) 31.
[2] Hsu C P and Marcus R A. A 1997 J. chem. phys. 106 (2) 584.
[3] Fulde P1995 Springer Science & Business Media.100.
[4] Calvet L E Wheeler R G and Reed M A 2002 J. Appl. Phys. Lett. 80 (10) 1761.
[5] Ramakrishna G and Ghosh H N 2003 J. Langmuir. 19 (7) 3006.
[6] Rahman M M Krishna K M Soga T Jimbo T and Umeno M 1998 J. Physics and Chemistry of Solids. 60 (2) 201.
[7] Cho W J 2007 Journal of Semiconductor Technology and Science.7 (2) 82.
[8] Hadi J M Al-Agealy and AL-Obaidi R I N 2009 Ibn AL-Haitham Journal For Pure and Applied Science. 22 (2).
[9] Gao Y Q and Marcus RA 2000 J. Chem Phys.113 (15) 635.
[10] Gao YQ Georgievskii Y and Marcus RA 2000 J. Chem Phys. 112 (7) 3358.
[11] AL-Agealy H J AlMaadhede T S Hassooni M A Sadoon A K Ashweik A M, Mahdi H A and Ghadhban R Q 2018 AIP Conference Proceedings 1968 (1) 030055.
[12] Andrea M 2008 Marcus theory for electron transfer a short introduction. J. Club. Mazin, MPIP.
[13] Gosavi S S 2003 Electron transfer at metal surfaces (Doctoral dissertation, California Institute of Technology).
[14] Garol C Bruce S R and Sutan N 2006 Am. Chem. Soc. 1 (1) 3425.
[15] Hassooni M A, Al-Agealy H J 2011 Ibn Al-Haitham Journal For Pure And Applied Science. 24 (3) 64.
[16] Patnaik P 2003 Handbook of inorganic chemicals (New York: McGraw-Hill).
[17] Smith W F Hashemi J Presuel-Moreno F 2006 Foundations of materials science and engineering (New York: McGraw-hill).
[18] Paquin R A 1995. Properties of metals. Handbook of optics (McGraw-Hill, New York, NY) 2 35.
[19] Jakobi K 1994 Work function data. In Electronic and Vibrational Properties Springer, Berlin, Heidelberg
[20] Cotton F A, Wilkinson G, Murillo CA, Bochmann M and Grimes R1988 Advanced inorganic chemistry (New York: Wiley).
[21] Zhu X Y 2004. J. Phys. Chem. B 108 8778
[22] Gupta SM, Tripathi M 2011 Chinese Science Bulletin. 56 (16)1639.
[23] Perevalov T V and Gritsenko V A 2011 Journal of Experimental and Theoretical Physics 112 (2) 310.
[24] Royea W J Fajardo A M and Lewis N S 1997 J. Phys.Chem B.101 (51)11152.

Design of Step-Index Multimode Optical Fiber

Design of Step-Index Multimode Optical Fiber

Aqeel R. Salih[1]

[1]Department of Physics, College of Education for Pure Science (Ibn Al-Haitham), University of Baghdad, Baghdad, Iraq
E-mail: draqeelrsalih@gmail.com

Abstract. In this paper, a step-index fiber with core index 1.445517 and cladding index 1.443157 has been designed and studied. Multimode operation is achieved by using a fiber with core radius 25 μm operating at a wavelength of 1.3 μm. The mode parameters (effective refractive index, phase constant, fractional modal power in the core and cutoff wavelength) were calculated using RP fiber calculator (PRO version 2020). The shapes of the intensity and amplitude distribution of linearly polarized guided modes were shown.

Keywords: Fiber design, Step-index fiber, Multimode fiber, Linearly polarized modes, RP Fiber calculator.

1. Introduction

An optical fiber, which acts as the transmission channel, lies at the heart of an optical communication system [1]. A step-index fiber (SIF) consists of a core with a refractive index n_{core} that is slightly higher than that of the cladding, n_{clad} [2]. Most of the fibers are made from silica glass [3] which can be doped with (e.g., germanium or phosphorus) to increase the refractive index or with (e.g., fluorine or boron) to decrease it [4]. Fibers that support multiple guided modes (LP_{lm} modes) are called multimode fibers (MMFs) [5]. Typically, the core radius is around 25 μm for MMFs. The three lowest-order guided modes are illustrated in **Figure 1.**

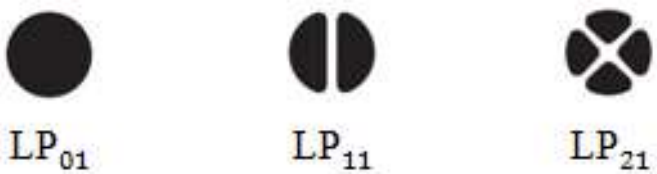

Figure 1. Intensity profiles for the three lowest linearly polarized (LP) modes [6].

In 1966, Kao and Hockham [7] proposed that glass fibers could be a practical optical transmission medium. They predicted that fiber loss could be reduced below 20 dB/km. The fiber process advanced very quickly after the demonstration of fiber with a loss of about 17 dB/km at a wavelength of 0.633 μm in 1970 [8]. By 1973, the loss of less than 5 dB/km at 0.85 μm was reported [9]. In 1976, the loss of 0.47 dB/km was reported at 1.2 μm [10]. In the late 1970s through the early 1980s, the

telecommunication systems used MMFs along with light emitting diodes (LEDs) or laser transmitters at 0.85 μm and 1.3 μm [4]. In 1988, the first transatlantic fiber cable was made operative at 1.3 μm. By 1996, data transmission at 1 Terabit/second was realized [11, 12]. In 2001, it has been possible to send about 11 Terabit/second through optical fiber [13]. In 2009, Kao received the Nobel prize for his work on fiber optics [14]. In 2018, successful transmission of 1.2 Petabit/second has been achieved [15, 16]. In my previous work [17], a single-mode SIF is designed at 1.31 μm and 1.55 μm. In this work, a MM SIF has been designed at 1.3 μm.

2. Theoretical Background

The *V* number gathers all of the design parameters characterizing the optical fiber. It is given by [18]:

$$V = \frac{2\pi}{\lambda} r \sqrt{n_{\text{core}}^2 - n_{\text{clad}}^2} \tag{1}$$

where r is the core radius and λ is the vacuum wavelength of operation. Fiber dispersion is the lowest at 1.3 μm wavelength. The *V* number determines:
The number of guided modes. If $V > 2.4048$ the fiber will be MM.
The fraction of power guided inside the core.
The phase constant for some wavelength is the effective refractive index (n_{eff}) times the vacuum wavenumber [5]. Guided modes occur if $n_{\text{clad}} < n_{\text{eff}} < n_{\text{core}}$. Modes with $n_{\text{eff}} < n_{\text{clad}}$ are called radiation modes. No mode exists when $n_{\text{eff}} > n_{\text{core}}$ [3].
The normalized phase constant is defined by:

$$b = \frac{n_{\text{eff}}^2 - n_{\text{clad}}^2}{n_{\text{core}}^2 - n_{\text{clad}}^2} \tag{2}$$

For guided modes, $0 < b < 1$.
The allowed discrete values of b of the guided LP_{lm} modes are determined by the transcendental equations:

$$U\frac{J_1(U)}{J_0(U)} = W\frac{K_1(W)}{K_0(W)}, \qquad l = 0 \tag{3}$$

$$U\frac{J_{l-1}(U)}{J_l(U)} = -W\frac{K_{l-1}(W)}{K_l(W)}, \qquad l \geq 1 \tag{4}$$

where $U = V\sqrt{1-b}$ and $W = V\sqrt{b}$. Here $J_l(U)$ and $K_l(W)$ are the Bessel functions of order l.
There will be a finite number of solutions of Equations (3) and (4) for a given value of l, and the mth solution ($m = 1, 2, 3, \ldots$) is referred to as the LP_{lm} mode.
The value of V at which $b = 0$ is known as the cutoff value (V_c) of the mode. The cutoff *V* values are tabulated in Table 1.

Table 1. Cutoff *V* values for the LP_{lm} modes [19].

l	m		
	1	2	3
0	0	3.8317	7.0156
1	2.4048	5.5201	8.6537
2	3.8317	7.0156	
3	5.1356	8.4172	
4	6.3802	9.7610	
5	7.5883		
6	8.7715		

The cutoff wavelength (λ_c) of the mode is the wavelength where that mode ceases to exist [5]. It can be calculated from [2]:

$$\lambda_c = \frac{2\pi}{V_c} r \sqrt{n_{\text{core}}^2 - n_{\text{clad}}^2} \quad (5)$$

The range of wavelengths over which LP_{lm} mode will propagate is $0 < \lambda < \lambda_c$.
From Equations (1) and (5),

$$\lambda V = \lambda_c V_c \quad (6)$$

A quantity of interest for SIFs is the fractional power carried in the core. It is given by [20]:

$$\frac{P_{\text{core}}}{P_{\text{total}}} = \frac{W^2}{V^2} + \frac{U^2}{V^2} \frac{K_l^2(W)}{K_{l+1}(W) K_{l-1}(W)} \quad (7)$$

3. Results and Discussion

In this work, a SIF characterized by the parameters in Table 2 has been designed. It operates at a wavelength of 1.3 μm as a multimode fiber.

Table 2. Parameters of the fiber.

n_{core}	1.445517
n_{clad}	1.443157
r	25 μm
V **at** λ **=1.3 μm**	9.9766

One finds that there are three modes each corresponding to $l = 0$ and $l = 1$, two modes each corresponding to $l = 2, l = 3$ and $l = 4$, and one mode each corresponding to $l = 5$ and $l = 6$. The mode properties (Tables 3 to 6) were calculated by using RP Fiber Calculator software (PRO version 2020). From these tables, it can be noted that:
All values decrease with increasing l, m indices of the LP_{lm} modes.
The fundamental LP_{01} mode is the one with the highest values.
Effective indices lie between core and cladding indices.
For any mode, the phase constant is the effective index multiplied by the free space wavenumber.
Far from cutoff value, the modal power is concentrated in the core.

Table 3. Effective refractive indices of LP_{lm} modes.

l	m		
	1	2	3
0	1.445403	1.444921	1.444079
1	1.445229	1.444561	1.443566
2	1.445000	1.444151	
3	1.444772	1.443699	
4	1.444395	1.443220	
5	1.444024		
6	1.443610		

Table 4. Phase constants (μm^{-1}) of LP_{lm} modes.

l	m		
	1	2	3
0	6.98595	6.98362	6.97955
1	6.98511	6.98188	6.97707
2	6.98400	6.97990	
3	6.98266	6.97772	
4	6.98108	6.97540	
5	6.97929		
6	6.97729		

Table 5. Fractional powers in the core (%) of LP_{lm} modes.

	m		
l	1	2	3
0	99.6	97.5	91.9
1	98.9	95.6	84.6
2	98.0	92.9	
3	96.7	88.5	
4	95.1	79.2	
5	93.0		
6	90.2		

Table 6. Cutoff wavelengths (μm) of LP_{lm} modes

(calculated from RP Fiber Calculator).

	m		
l	1	2	3
0		3.35659	1.84098
1	5.30411	2.33976	1.49248
2	3.35694	1.84102	
3	2.51500	1.53447	
4	2.02445	1.32325	
5	1.70215		
6	1.47258		

Cutoff wavelengths calculated from Equation (5) are listed in Table 7. These values are in good agreement with those in Table 6. Unlike other modes, the LP_{01} mode has no cutoff ($V_c = 0$). The cutoff wavelengths of LP_{21} and LP_{02} modes are the same (because the cutoff values are the same). Also, the cutoff wavelengths of LP_{22} and LP_{03} modes are the same. Cutoff wavelengths are larger than the operating wavelength (because the *V* number is larger than the cutoff values). If cutoff value for a particular guided mode approaches *V* number, then the cutoff wavelength will be close to the operating wavelength.

Table 7. Cutoff wavelengths (μm) of LP_{lm} modes

(calculated from Equation 5).

	m		
l	1	2	3
0		3.38480	1.84867
1	5.39320	2.34951	1.49873
2	3.38480	1.84867	
3	2.52542	1.54084	
4	2.03278	1.32871	
5	1.70915		
6	1.47860		

Figures 2 to 4 show 2D mode profiles and plots of the radial dependence. These figures have been produced with the software RP Fiber Calculator. The modes profiles have increasing complexity as their indices are increased. The three lowest-order modes are similar to those illustrated in **Figure 1.** The intensity distribution of the lowest-order mode (LP_{01}) is circularly symmetric. The LP_{11} mode has two lobes oriented left and right. The higher-order modes have multilobed patterns, with $2l$ maxima in the angular direction and m maxima in the radial direction. In each profile, the thin circle locates the

core boundary. The amplitude distribution can be obtained from the intensity distribution by taking the square root. It can be seen that only LP_{0m} modes have a profile having a peak in the center of the fiber core. While, the other modes have a peak away from the center.

l	m		
	1	2	3
0	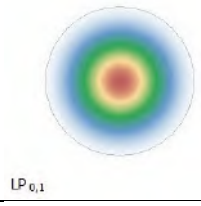 $LP_{0,1}$	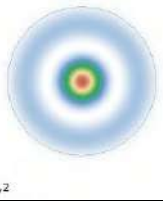 $LP_{0,2}$	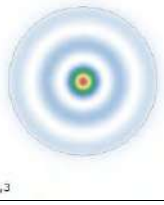 $LP_{0,3}$
1	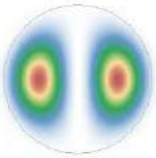 $LP_{1,1}$	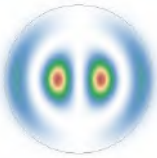 $LP_{1,2}$	 $LP_{1,3}$
2	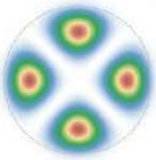 $LP_{2,1}$	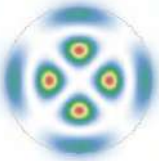 $LP_{2,2}$	
3	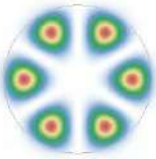 $LP_{3,1}$	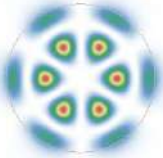 $LP_{3,2}$	
4		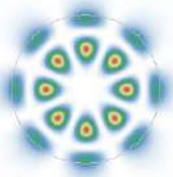 $LP_{4,2}$	
5			

6	

Figure 2. Intensity distributions of LP_{lm} modes.

l	m 1	2	3
0	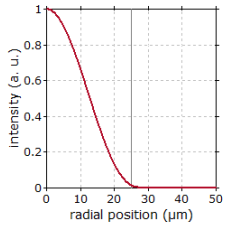		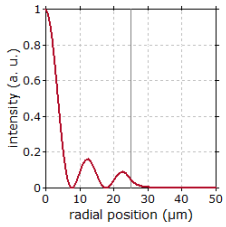
1	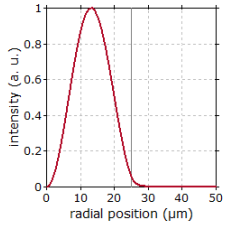	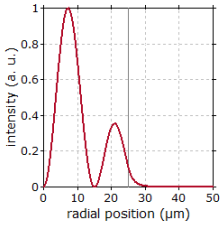	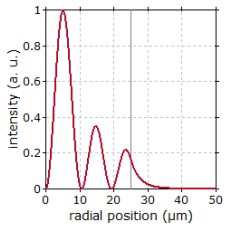
2	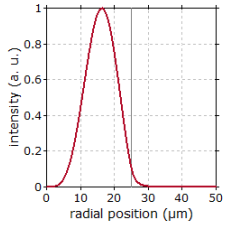	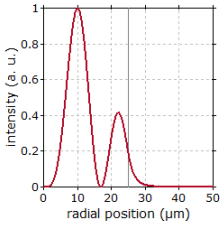	
3	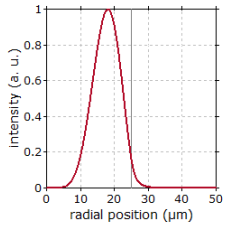	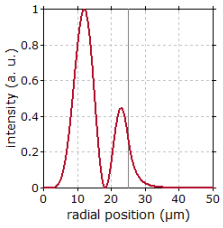	
4	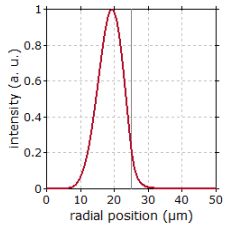	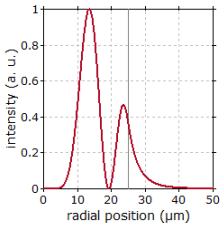	
5			

	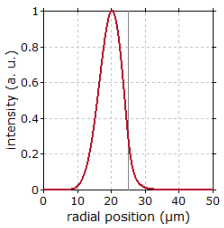	
6	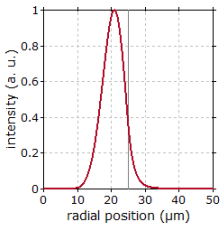	

Figure 3. Radial intensity distributions of LP_{lm} modes.

l	m		
	1	2	3
0	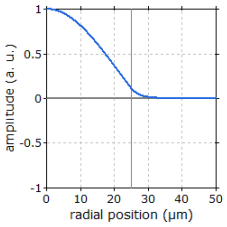	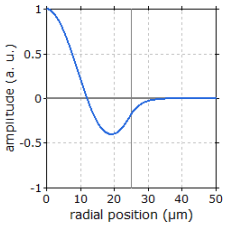	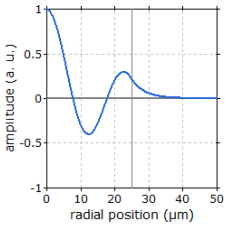
1	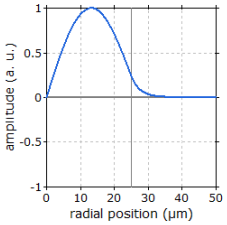	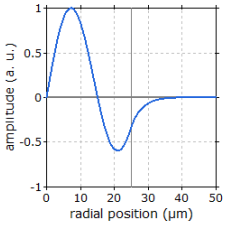	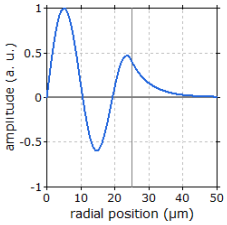
2	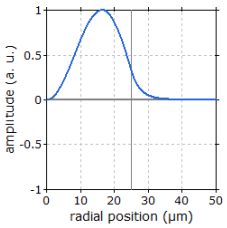	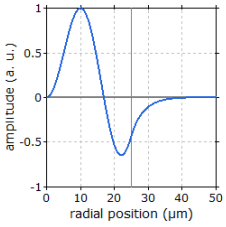	
3	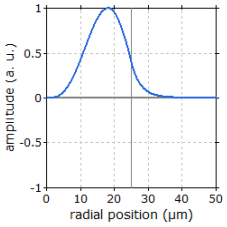	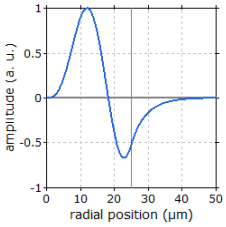	

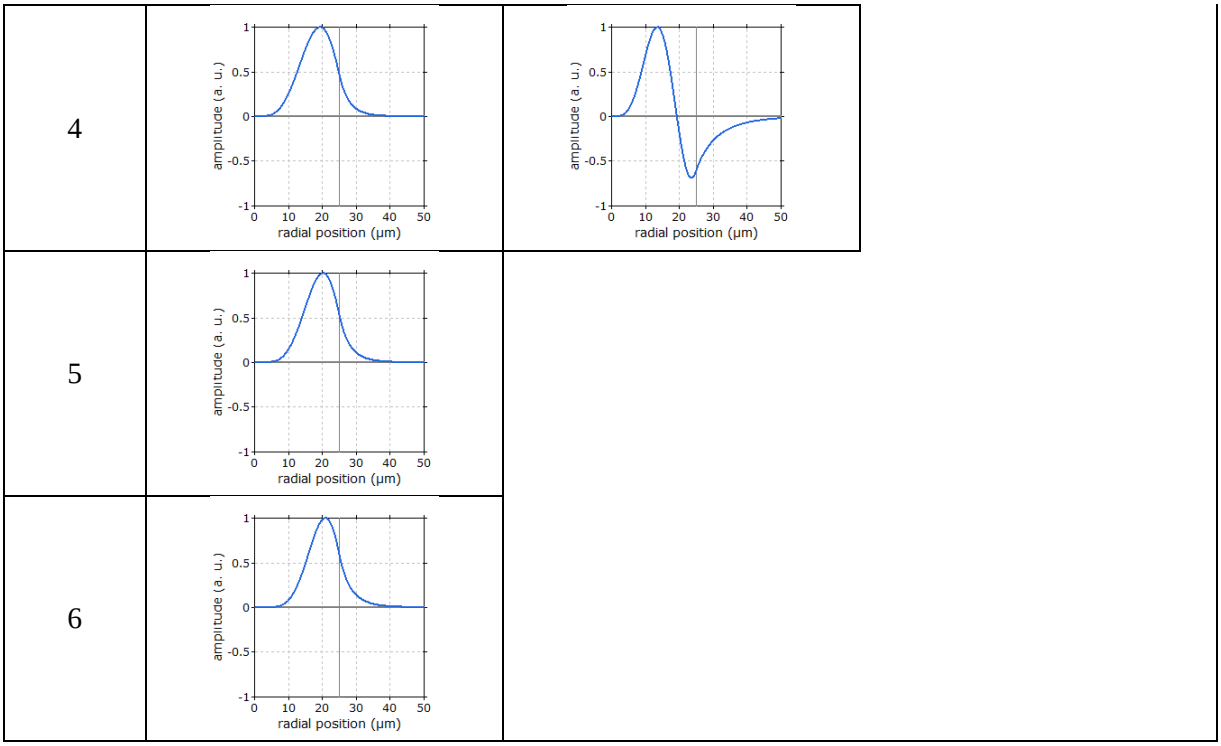

Figure 4. Radial amplitude distributions of LP_{lm} modes.

4. Conclusions

Using RP Fiber Calculator program, it is possible to calculate cutoff wavelengths and other properties of modes. It is shown that if the operating wavelength is less than the cutoff wavelength, the fiber will be multimoded. The further away a mode is from its cutoff value the more concentrated its power is in the core. This fiber is candidate for practical use because most guided modes have fractional core powers of over 90%.

5. References

[1] Roychoudhuri C 2008 *Fundamentals of Photonics*, SPIE.
[2] Hill G 2008 *The Cable and Telecommunications Professionals' Reference*, Volume 2, 3rd edition, Elsevier.
[3] Kumar S and Jamal Deen M 2014 *Fiber Optic Communications: Fundamentals and Applications*, Wiley.
[4] Ramaswami R, Sivarajan KN and Sasaki GH 2010 *Optical Networks: A Practical Perspective* 3rd edition, Elsevier.
[5] Paschotta R 2020 *RP Photonics Encyclopedia*.
[6] Senior J M 2009 Optical Fiber Communications: Principles and Practice, 3rd edition, Pearson.
[7] Kao C K and Hockham GA 1966 Dielectric-Fibre Surface Waveguides for Optical Frequencies, *Proc. IEE* **113** (7), 1151–1158.
[8] Kapron F P, Keck DB and Maurer RD 1970 Radiation Losses in Glass Optical Waveguides, *Appl. Phys. Lett.* **17** (10), 423–425.
[9] Keck D B, Maurer Rd and Schultz PC 1973 On the Ultimate Lower Limit of Attenuation in Glass Optical Waveguides, *Appl. Phys. Lett.* **22** (7), 307–309.
[10] Horiguchi M and Osanai H 1976 Spectral Losses of Low-OH-Content Optical Fibres, *Electron. Lett.* **12** (12), 310–312.
[11] Onaka H 1996 *1.1 Tb/s WDM Transmission Over a 150 km 1.3 μm Zero-Dispersion Single-Mode Fiber*, Optical Fiber Communication Conference, paper PD 19.

[12] Gnauck AH 1996 *One Terabit/s Transmission Experiment, Optical Fiber Communication Conference*, paper PD 20.
[13] Fukuchi K 2001 *10.92-Tb/s (273× 40-Gb/s) Triple-Band/Ultra-Dense WDM Optical-Repeatered Transmission Experiment, Optical Fiber Communication Conference*, paper PD 24.
[14] The Nobel Prize in Physics 2009 http://www.nobelprize.org/nobel_prizes/physics/laureates /2009/
[15] Luís RS 2018 *1.2 Pb/s Transmission Over a 160 μm Cladding, 4-Core, 3-Mode Fiber, Using 368 C+L band PDM-256-QAM Channels,* European Conference on Optical Communication.
[16] Luís RS 2019 1.2 Pb/s Throughput Transmission Using a 160 μm Cladding, 4-Core, 3-Mode Fiber, *J. Lightwave Technol.* **37** (8) 1798–1804.
[17] Salih AR 2020 Design of Single Mode Fiber for Optical Communications, *Ibn Al-Haitham J. Pure Appl. Sci.* **33** (1), 40–47.
[18] Wang M L, Lynch JP and Sohn H 2014 Sensor Technologies for Civil Infrastructures, Volume **1**, WP.
[19] Ghatak A 2010 *Optics*, McGraw-Hill.
[20] Ghatak A and Thyagarajan K 1998 *Introduction to Fiber Optics*, Cambridge University Press.

Effect of Chitosan Nanoparticles Loaded Oxytetracycline Hydrochloride on Health Status of Common Carp (*Cyprinuscarpio* L.) Infected with Columnaris Disease

Effect of Chitosan Nanoparticles Loaded Oxytetracycline Hydrochloride on Health Status of Common Carp (*Cyprinuscarpio* L.) Infected with Columnaris Disease

[1]Medyan N. Ali, [2]Tagreed M. Al-Saadi, [1]Jamal K. A. AL-Faragi

[1]Department of Pathology, College of Veterinary Medicine, University of Baghdad, Iraq
[2]College of Education for Pure Science/Ibn Al- Haitham, University of Baghdad, Baghdad, Iraq

E-mail: alshemarynaser@gmail.com

Abstract. This study was aimed to evaluate the effect of chitosan nanoparticles loaded oxytetracycline hydrochloride on health status, and survival rate of common carp infected with Columnaris disease. A total 160 fish of Cyprinuscarpio L. weighed between 48-50g were randomly distributed into eight treatments, and 48 fish were used to determine LD50. (Two replications for each treatment).The bacterial concentration of F. column are that used for infection test after a serial dilution was 0.2ml (1.8 × 106 CFU/ml), then removal a few of scales near the caudal fin and injection subcutaneously. The trial injected fish treated by ordinary oxytetracycline hydrochloride as T0 in dose 20 mg /L and T1, T2, T3, T4 and T5 treated by chitosan nanoparticles loaded oxytetracycline hydrochloride in dose 20, 15, 10, 5, 2.5 mg/L respectively. The control (+) infected without gave treatment, whilst, control- was no infected. All the treatments gave the bath treatment 1-hour per-day for 7 days, clinical signs post treatment were evaluated also, RBC counts, WBC counts, PCV, Hb, Total proteins, Albumin, Globulin, A/G ratio and survival rate were measured. One week after the end of the treatment period, an improvement in health and feed consumption was observed in T4 and T3. The results revealed significant increases ($P<0.05$) in PCV, Hb, RBCs count and WBCcount of C. carpio post-treatment in treated groups T4 (26.46%, 8.95 g/dl and 2.27 cell×106/mm3 and22.10 cell×103/mm3respectively) compared with control (+) (15.95%, 5.94 g/dl,1.55 cell×106/mm3 and19.13 cell×103/mm3respectively).In addition, Total proteins, Albumin, Globulin showed significant increase ($P< 0.05$) in T2, T3, T4, T5 comparison with the control+ group and highest values were recorded in T4. While, The result of A/G ratio revealed a significantly decreased ($P>0.05$) in all treatments in compared with Control(-) and no significant difference ($P > 0.05$) compared with Control(+).The best A/G ratio recorded in T4 and T5.In addition, survival rate 90% recorded as the highest value in T4. This current administration technique of oxytetracycline, proved to become much more efficient with respect to conventional exposure and has the potential to minimize the usage of antibiotics in fish farms and regarding environmental effects.

Keywords: chitosan, nanoparticles loaded, oxytetracycline, health status, common carp, columnaris

1. Introduction

Common carp (Cyprinus Carpio L.) is known to be the most important aquaculture fish in many Asian and European countries (Mohammad, 2015). It is introduced into Iraq as a breeding fish and transmitted among all Iraqi water bodies since it is living in different environmental conditions, has the fastest growth at water temperatures around 23-30 C, survives in cold winter, tolerates salinity of

12 g / L (Al-Hamed, 1971; Al-Rudainy et al., 2008). The production of fish farming causing massive economic losses each year worldwide is regarded as being considerably limited by the outbreak of disease (Austin, 2007). The infections of bacterial are a major impendence to economic viability for any aquaculture farming (Yousefian et al., 2009). Fish are sensitive to a wide range of infectious bacteria causing a high mortality rate in fish culture (El- Sayyad et al., 2010). Columnaris disease is one of the most common infectious bacterial diseases of freshwater fishes infecting both cultured and wild fish species. It has a huge economic effect on fish farming due to the increased and rapid mortality rates of it creates. (Marshet, 2018). Flavobacterium columnare is a widely available bacterium in aquatic ponds as well as a causative agent of Columnaris disease in fine fish. Flavobacterium columnare has also been recognised as a global bacterium for fish species (Figueiredo et al, 2005).

The administration of antibiotics, for many years, was the generality common method for handling the occurrence of bacterial infection in the aquatic ecosystem. However, dangerous problems still face the aquaculture because of adverse results of those drugs like accumulate in the tissue of creatures, immunosuppressant, development of bacteria to resistant antibiotic and ruin of environmental microbial flora (Baulny et al., 1996).Due to the increase in the outbreak of bacterial diseases in the aquaculture industry and the development of bacterial resistance, new antibacterial agents are required (Gong et al., 2007; Soltani et al., 2009). The nanoparticles have been used to deliver the drugs into the cells with negligible side effects (Scott, 2005). , chitosan nanoparticles and PLGA nanoparticles are being tested as nanoparticles for drug delivery in fish medicine. (Wang, 2011). Chitosan is a mucopoly saccharide that is closely related to cellulose. It is a derivative of chitin and is formed by chitin deacetylation. (Soutter, 2013: Crini, 2019).

Chitosan nanoparticles were used to boost their transfer efficiency in cells as drug carriers and gene carriers, as recorded in many researchers (Chopra et al., 2014; Csaba and Alonso, 2014). In the Fish culturists notified that the oxytetracycline-hydrochloric acid bath handlings were, efficient in decreasing mortality in freshwater fish diseased with F. columnare (Stehly 2002). Oxytetracycline-hydrochloric successfully minimize the mortality in walleyes (10 mg/L only) and channel catfish infected with Columnaris (Rach et al., 2008). The synthesis of antibiotic conjugates with biopolymers is a relatively new trend of research that generally has the purpose of prolongation the antibiotic action and decreasing its toxicity (Ueda et al., 1989).

In this current study explained the effect of chitosan nanoparticles loaded with oxytetracycline on some blood parameters and health status of carp fish with columnaris disease in comparison with conventional oxytetracycline hydrochloride therapy.

2. Materials and Methods

2.1. Materials

Chitosan, sodium tripolyphosphate, phosphate-buffered saline**,** acetic acid**,** Cytophaga Agar, De-ionized water Oxytetracycline hydrochloride (purity 99%) and distilled water. All other chemicals were obtained from commercially from AL-Bashir Scientific Bureau/Iraq. *Flavobacterium columnare* isolate were taken from Department of Pathology/Fish Diseases College of Veterinary Medicine/Baghdad University.

2.2. *Flavobacterium columnare*

Isolate of *F. columnare* bacteria was taken from "Department of fish diseases College of Veterinary Medicine/Baghdad University", the bacteria was a three-time passage into a stable common carp to improve bacterial virulence. Then, all biochemical tests were done to ensure the characteristics of the bacteria.

2.3. Preparation and loaded the chitosan nanoparticles

The chitosan nanoparticles were synthesized from the chitosan via sodium tripolyphosphate as a cross-linking agent by ionotropic gelation method (Vimal *et al*, 2013).About 1.5 g of chitosan dissolved in 200 ml of 2% acetic acid, this solution was placed for about 20 minutes under the magnetic stirrer process. Next to the above-Initialized chitosan solution, (0.8 g) of sodium tripolyphosphate dissolved in (107 ml) of conductivity water were added drop wise. Then stirred well enough to reach equilibrium for around 30 minutes. A milky colored emulsion of chitosan nanoparticles appears, which was formed upon the ionic cross-linking between the sodium tripolyphosphate and chitosan solution. After achieving equilibrium, the suspension was established in the conditions mentioned above.
Oxytetracycline hydrochloride melted in distilled water was added to the ChNPs solution in the ratio of 1:1, under stirring for twenty-minute. In addition, this suspension then was left under ultra-sonication for 45 minutes. After that lastly stirring for another, twenty minutes, to gain a final concentration of antibiotics 3.75 mg/ml (Du et al., 2009; Jain and Banerjee, 2008).

2.4. Experimental Design

This research was carried out at the (College of Veterinary Medicine of Baghdad, an Ichthyology laboratory). A total of 160 healthy carp fish selected and treated by the formalin at the concentration of (25ml/200L) water used for ten min to annihilate the fungal, bacterial, and parasitic infections. After that distributed into 16 glass aquaria filled with chlorine-free tap water and supplied with an air pump at a rate of 10 fish per aquarium (two replicates treatment) were maintained for each of the 7 treatments (T0, T1, T2, T3, T4, T5, Control(-) and Control (+). Then, 2 weeks of fish adaptation until beginning the experiment, and feeding on a commercial diet, at a rate of 2% of their body weight.
The bacterial concentration of *F. columnare* that used for infection test after a serial dilution was 0.2ml (1.8×10^6 CFU/ml), then removal a few of scales near the caudal fin and injection subcutaneously. In this experiment some of infected did not eat feed and to ensure that all fish are treated, the immersion bath was used for treatment according to researchers (Jeff *et al* 2008; Julinta *et al* 2017). The trial injected fish treated by ordinary oxytetracycline hydrochloride as T0 in dose 20 mg /L and T1, T2, T3, T4 and T5 treated by chitosan nanoparticles loaded oxytetracycline hydrochloride in dose 20, 15, 10, 5, 2.5 mg/L respectively.

All the treatments given the bath treatment 1-hour per-day for 7 days, mortality was already recorded daily for up to 14 days throughout all treatments, and assessment of survival rate after 7 days of treatment end, bacteria recovered from blood and kidney of the experimental challenge fish were identified as *F. columnare* after re-isolated it. In all treatments, live and dead fish were examined for abnormal behaviours' including movement, swimming and external lesions on the skin and gills. At the final of the experimental procedure, the fish were counted according to (Amend, 1981) to assess the survival rate.

$$\text{Survival rate \%} = \frac{\text{No. of fish counted after 7days post-treatment end}}{\text{No. of total fish counted at the initial time}} \times 100$$

2.5. Blood collection and sample preparation

Blood samples were collected using 3 ml plastic syringe (G 23 da). Three randomly selected fish were picked per aquarium from caudal vessels. To prevent any blood clot, the syringe was flushed with heparin. No anaesthetic medications have been used to avoid any possible effect on blood content, and the handling time was less than 1 minute to reduce the stress. The first part of the blood was transferred to lithium-heparin coated sterile Eppendorf tubes, which are used to measure blood haematology.

The second part was transferred to the gelatin-containing Eppendorf tubes and permitted to clot for 2 hours. Serum was already separated via centrifugation, store at-20°C that can be used for biochemical parameters (Albumin, Globulin and Albumin/Globulin Ratio).

2.6. Determination of Haematological Parameters:

2.6.1. Determination of Total Erythrocytes and Leukocytes Counts:

The total of erythrocyte and leukocyte count through diluted 20 µl of the freshly obtained blood sample with (0.98 ml) of Dacie solution. (10ml of 40% formaldehyde, 31.3g trisodium citrate, 1.0 g brilliant crystal blue dissolved in one L of distilled water and filtered through 0.45 µm syringe filter). Counts were performed on an improved hemocytometer of Neubauer. A drop in the hemocytometer was dripped, five squares were used to count the number of red blood cells (Dacie and Lewis, 1984). The followed equation was applied:
Total RBCs (Erythrocyte / µL6) = N (number of cell) x 2500

WBC's were counted in four squares (four corner squares) (Dacie and Lewis, 1984). The following equation was applied:
Total WBCs (Leukocyte / µL3) = N (number of cell) x 125

2.6.2. Packed Cell Volume (PCV %)

Haematocrit (packed cell volume) of total blood was calculated using the capillary system, the heparinized blood was drawn by heparinized capillary tube and one of its ends blocked with sealing material. Next separated using a haematocrit centrifuge (5000 round/min for 5 minutes, following centrifugation, the total percentage of PCV was determined with haematocrit reader (Thrall *et al*., 2006)**.**

2.6.3. Haemoglobin (Hb) content

The cyanomethemoglobin process (Blaxhall and Daisley, 1973) was used to assess haemoglobin amounts (Hb). By using haemoglobin kit, the haemoglobin reaction with cyanide was dependent upon for the formation of cyanomethemoglobin. The test tube administered with 20 µl non-coagulant blood that had been freshly obtained, applied to the 5 ml diluents mix (Drabkin's reagent), and left at room temperature for 5-10 minutes (25°C).Absorbance or optical density (O.D) was measured using a spectrophotometer at 540 nm The Drabkin Diluents reactant (1.0 g of sodium bicarbonate, 50 mg of potassium cyanide, 200 mg of potassium ferricyanide, dissolved in 1L water), was a stock of cyanomethemaglobalin as normal, distilled into a multi-dilutant (Dacie and Lewis, 1995).

3. Results

3.1. Treatment and Survival rate of C. carpio:

Following the carp fish injected with *F. columnare,* the treatment of the infected fish was started when mortality appeared in the fourth day after bacterial injection. All the treatments are given the treatment 1-hour per-day for 7 days; mortality was recorded daily up to 14 days in the all groups and recording the survival rate after 7 days of treatment end, and observe the clinical signs of treated carp fish daily after the end of treatment. The results revealed a clear increase in survival rate in T4 that were 90% and T3 were 70% followed by T5 and T2 which give the same percentage 55% .while, T1 was recorded the lowest survival rate 40% as shown in the Table 4.6. In comparison with T0 (OTC-HCL), 20 mg/L was recorded low survival rate 60%. And Control + (no treated group) were recorded 15% survival rate.

Table 1. Survival and Mortality Rate of *Cyprinuscarpio* treated with ChNP-OTC following challenge of *F. columnare*

Treatment	Total number	No. of dead fish	Survival rate%	Mortality rate%
Control(-)	20	0	100	0
Control(+)	20	17	15	85
T0	20	8	60	40
T1	20	12	40	60
T2	20	11	55	45
T3	20	6	70	30
T4	20	2	90	10
T5	20	9	55	45

3.2. Clinical signs of C. carpio before and after treatment:

In the experimental infection test and pretreatment, the moribund fish showed off feed, swam on the surface of the water with increased operculum movement without reflecting the external impact and staying on the side before death. The gross symptoms involved a mild discoloration of the skin. Hemorrhagic swelling mainly at the injection site, gills also congested with necrotic lesion patches, Mortality of fish started after 4 days post-injection *F. columnare.* These symptoms are shown in figures (1. A, B, C&D).

One week after the end of the treatment period, an improvement in health was observed, as well as swimming and breathing also was regularly, especially in T4, T3, T5.and T0 also Control$^{(-)}$. Post-treatment the feed was given to the fish in all groups at the rate of 2%. No feed consumption in C+, T1 and T2. While in T4, T3, T5, T0 all the feed was consumed, and the fish were active and swim normally.

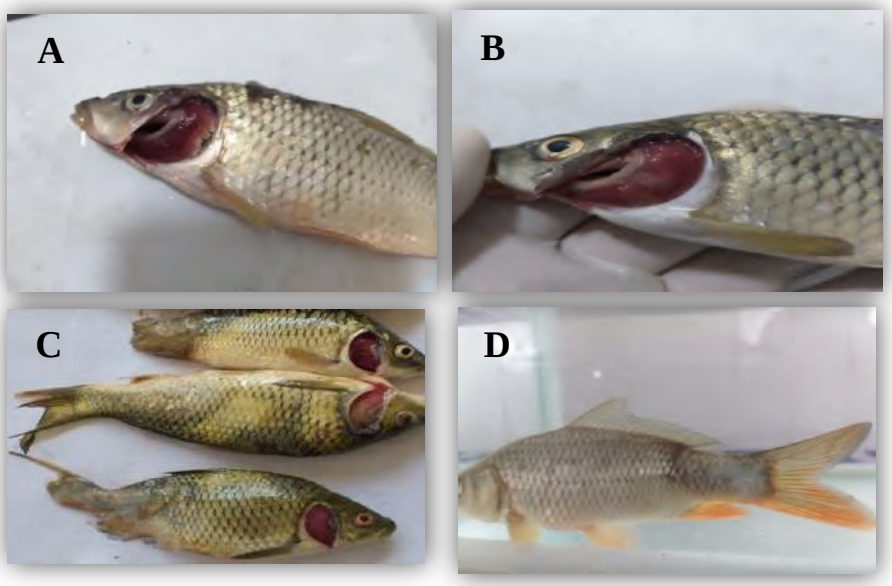

Figures 1. (A&B): gills congested with necrotic lesion patches. (C): mild discolouration of the skin and hemorrhagic swelling (D): Hemorrhagic swelling at the injection site.

3.3. *Hematological parameters:*

3.3.1. Red blood cells count (RBC)

The results revealed significant increases (P<0.05) in RBCs count of *C. carpio* post-treatment in treated groups T4 (2.26 cell×10^6/mm^3) compared with control (+) group (1.40 cell×10^6/mm^3) and another treatment .Table (4.8.1). However no significant difference (P 0.05) with control (-). While, treated groups T0, T1, T3 and T5 (1.61, 1.56, 1.73 and 1.56 cell×10^6/mm^3 respectively) were revealed slight increases and no significant difference (P 0.05) with C+ and between them, Table **2**, and there were a significant decreases (P<0.05) in Control (+) compared with control (-).

3.3.2. Packed cell volume and Haemoglobin (PCV, Hb)

In the Table 2, there were significant increases (P<0.05) in concentration and packed cell volume and haemoglobin in treatments T3, T4 and T5.That were (20.43, 26.46 and 21.13 % respectively), and (7.31, 8.95, and 7.03 g/dl respectively) compared with Control (+) (15.95% and 5.94 g/dl) and recorded highest values in T4 from all other treatments which no and no significant difference (P > 0.05) with Control (-). In T0, T1, and T2 (19.40, 16.76, and 18.36% respectively) and (6.46, 5.59, and 6.07 g/dl respectively), that were no significant difference between them, but there is a significant increases (P<0.05) with Control$^{(-)}$), and there were a significant decreases (P<0.05) in Control$^{(+)}$ compared with Control$^{(-)}$.

3.3.3. White blood cells (WBC)

In Table 2, the results revealed no significant difference in WBCs count of *C. carpio* post treatment in group T0 (19.26×10^3cell/mm^3) compared with Control $^{(-)}$ and Control $^{(+)}$ ((17.94 and 19.13×10^3cell/mm^3 respectively). However, the recorded highest mean values and significant increases (P< 0.05) in, T1, T2, T3, T4 and T5 (22.10, 23.36, 22.03, 21.00 and 20.50 ×10^3cell/mm^3respectively) in comparison with Control (-), but no significant difference (P 0.05) between them. Highest mean values in T1.
These results mean WBC numbers showed a significant increase (P< 0.05) in treated groups.

Table 2. Hematological parameters of *Cyprinuscarpio* treated with ChNP-OTC following challenge of F. *columnare*

Group	Mean ± SE			
	RBC×10^6/m^3	PCV%	Hb g/dl	WBC×10^3/mm^3
Control (-)	2.13 ± 0.14 a	25.23 ± 0.14 a	8.41 ± 0.04 a	17.94 ± 0.67 d
Control (+)	1.55 ± 0.03 b	15.95 ± 0.43 e	5.94 ± 0.47 de	19.13 ± 1.04 cd
T0	1.61 ± 0.07 b	19.40 ± 0.62 bc	6.46 ± 0.21 cd	19.26 ± 0.46 cd
T1	1.56 ± 0.08 b	16.76 ± 0.17 cd	5.59 ± 0.05 e	23.36 ± 0.52 a
T2	1.76 ± 0.08 b	18.36 ± 0.56 cd	6.07 ± 0.24 de	22.03 ± 0.40 ab
T3	1.73 ± 0.03 b	20.43 ± 1.08 b	7.31 ± 0.33 b	21.00 ± 0.49 bc
T4	2.27 ± 0.12 a	26.46 ± 0.46 a	8.95 ± 0.34 a	22.10 ± 0.72 ab
T5	1.57 ± 0.08 b	21.13 ± 0.77 b	7.03 ± 0.26 bc	20.50 ± 0.64 bc
LSD value	0.275 *	1.821 *	0.841 **	1.950 *

Means having with the different letters in same column differed significantly**.** * (P≤0.05)

3.3.4. Biochemical parameters

Results of total protein, albumin, globulin, A/G ratio

Total protein level revealed a significantly increased($P \leq 0.05$),in treatments T2, T3, T4, and T5 (3.95 , 4.25 , 4.45 , and 3.85 g/dl respectively)compared with Control$^{(-)}$ and Control$^{(+)}$ (2.60 , 2.40 g/dl respectively).While, no important difference ($P > 0.05$) between them. In addition, the maximum levels were recorded in T4. Table 3. While the result of total protein in T0 and T1(2.40 and 2.91 g/dl respectively) revealed no important difference ($P > 0.05$) with Control$^{(-)}$ and Control$^{(+)}$.Also, Albumin level revealed a significantly increased ($P \leq 0.05$),in treatments T2, T3, T4, and T5 (1.75, 1.95, 1.76, and 1.57 g/dl respectively)compared to the Control$^{(-)}$ and Control$^{(+)}$,(1.45,and 1.19g/dl respectively).Whereas, the result of Albumin in T0 and T1(1.16 and 1.29 g/dl respectively) revealed no significant difference ($P > 0.05$) compared with Control$^{(-)}$ and Control$^{(+)}$.and between them. This recorded in Table (3).

As well, Globulin level in this trial resulted in a significantly increased ($P \leq 0.05$),in treatments T2, T3, T4, and T5 (2.20, 2.30, 2.68, and 2.21 g/dl respectively)compared to the Control$^{(-)}$ and Control$^{(+)}$,(1.15,and 1.20 g/dl respectively).While, T0, T1(1.24, and 1.63 g/dl respectively) revealed no significant difference ($P > 0.05$) compared with Control$^{(-)}$ and Control$^{(+)}$.and between them. The result of A/G ratio revealed a significantly decreased ($P \leq 0.05$) in all treatments in compared with Control$^{(-)}$ and no significant difference ($P > 0.05$) compared with Control$^{(+)}$.The best ratio recorded in T4 and T5 but not differ significantly from T3 , T2 and T1as shown in Table 3.There were a significant decreases($P<0.05$) in Control$^{(+)}$compared with Control$^{(-)}$.

Table 3. Biochemical parameters of *Cyprinuscarpio* treated with ChNP-OTC following challenge of *F. columnare*:

Group	Mean ± SE			
	Total protein **g/dl**	Albumin **g/dl**	Globulin **g/dl**	A/G
Control (-)	2.60 ± 0.18 cd	1.45 ± 0.21 bcd	1.15 ± 0.03 d	1.23 ± 0.18 a
Control (+)	2.40 ± 0.10 d	1.19 ± 0.01 d	1.20 ± 0.11 cd	0.996 ± 0.10 ab
T0	2.40 ± 0.10 d	1.16 ± 0.06 d	1.24 ± 0.16 cd	0.963 ± 0.17 ab
T1	2.91 ± 0.23 c	1.29 ± 0.08 cd	1.63 ± 0.19 c	0.803 ± 0.08 b
T2	3.95 ± 0.07 b	1.75 ± 0.11 ab	2.20 ± 0.05 b	0.793 ± 0.06 b
T3	4.25 ± 0.03 ab	1.95 ± 0.10 a	2.30 ± 0.10 ab	0.853 ± 0.08 b
T4	4.45 ± 0.16 a	1.76 ± 0.06 ab	2.68 ± 0.19 a	0.663 ± 0.07 b
T5	3.85 ± 0.06 b	1.57 ± 0.11 bc	2.21 ± 0.19 b	0.716 ± 0.10 b
LSD value	0.408 *	0.324 *	0.428 *	0.351 *

Means having with the different letters in same column differed significantly. * ($P \leq 0.05$).

4. Discussion

The presence of skin lesion and gill necrosis are similar to characteristic lesions reported by Kubilay *et al*. (2008). Columnaris disease is primarily an epithelial infection that causes necrotic gill or skin lesions (Thune, 1993; Noga, 2000). Off feed and swim at the surface with increased operculum movement are observed by Tripathi, (2003). In addition, Tien *et al*. (2012) showed the infected striped catfish swim frequently with convulsions at the surface of the water, in particular, apparent in the first 24 hr post-bacterial exposure. The gills in these fish turn into a deep red color with alternate white patches. In addition to that, these fish had de-pigmented patches on the body, with a yellowish

discoloration on the fins. Finally, they had more severe tail erosion and the gills were fully necrotic. Between 48-52hrthe mortalities happened after exposure to experimental bacterial immersion. In this study, the possible application of synthetic ChNPs for OTC administration in carp fish was evaluated. To date, there is a powerful need to develop new and alternative administration processes for this antibiotic in the aquaculture sector due to its wide use (Rigos and Smith, 2015). Exposure to ChNPs-OTC did not cause any important stress response in treated fish, that agreement with Chemello et al. (2015) when utilizing them the Oxytetracycline delivery in adult female Zebrafish by iron oxide nanoparticles.

The results of this study revealed a significant increase in survival rate in T4 and T3 and mortality rates decreased from 85% in the infected non-treated group to 10 and 30% in these immersion-treated groups, respectively. There are no similar studies. While, Rach *et al*.,(2008) In the channel catfish trial, survival at (10 days) post-treatment was remarkably ($P > 0.05$) greater for all Oxytetracycline-hydrochloric treatment groups comparative to controls, and the Oxytetracycline-hydrochloric treatments effectively decreased mortality in walleyes (10 mg/L only) and channel catfish infected with F. columnare.

Another study, Julinta *et al*.,(2017) evaluated the effectiveness of ox tetracycline (OTC) oral and bath therapies on Nile tilapia *Oreochromisniloticus* against *A. hydrophila* infection, where they are found The oral and bath therapies in fries with OTC recorded low mortalities (17 and 21%) than the respective control. In this study we comparison with some studies of oxytetracycline effect of the fishes, also effects of chitosan nanoparticles studies compared to ChNP-OTC that due to no similar comparison studies in vivo. Hematological parameters have been recognized as valuable tools for assessing the health status of fish. These parameters are affected by several factors, such as species of fish, age, period of sexual maturity and health status (Blaxhall, 1972; Hrubec *et al*., 2001).

Changes in physicochemical parameters may be reflected in blood parameters of the fishes (Abdul Naveen *et al.,* 2011). The results of this study revealed a significant decrease in RBCs count, Hb content and PCV% in non-treated Control$^{(+)}$ compared with control$^{(-)}$ group, but there is slight increase in WBC value in Control$^{(+)}$ than control$^{(-)}$. All of that agreement with (Tripathi *et al*., 2005), when they registered considerable changes in blood parameters were noticed in the infected koi carp fish. For the hematologic parameters, a remarkable reduction was observed in hemoglobin concentration, Packed Cell Volume (PCV), and red blood cell count. From our observation on all treatments there is increase the RBC count value in all treated groups compared with no treated group (Control $^{(+)}$). In addition, the higher value in T4 which has low dosage of ChNP-OTC 5mg/L where, recorded the less stress during treatment period on carp fish. That agreement with (Chemello *et al*., 2016) where they was recorded the exposure of Oxytetracycline Delivery in Adult Female Zebra fish by Iron Oxide Nanoparticles fish to the complex resulted in a 10 times higher OTC accumulation with respect to using water exposure. In addition, in fish exposed to 4 mg/L OTC (using water), the liver antibiotic concentration was very low during the completely experimental time.

Also agreement with (Nikapitiya *et al.*,2018) where was recorded Chitosan nanoparticles: a positive immune response modulator as display in zebra fish larvae against Aeromonas Hydrophila infection and CNPs exposure at 5 μg/mL could enhance the immune responses and develop the disease resistance against A. hydrophila, which could be attributed to its strong immune modulatory properties. The result of PCV and Hb value in our study showed decrease significantly ($P < 0.05$) in higher concentration treatment T0, T1, and T2. This decrease is compatible with previous studies showed that OTC can be responsible for the induction of toxicity in fish liver by altering the activity of enzymes involved in stress response(Bruno, D. W. 1989; Pari and Gnanasoundari, 2006; Nakano *et al*.,2018).Also, PCV and Hb value in T4 recorded increase significantly ($P < 0.05$) compared with all treatments.

In this study, the WBC count showed increase significantly in T0, T1, T2, T3 and T5 compared with Control $^{(-)}$.While in T4, the deference is insignificantly. Increase in number of WBC in diseased fish could be serving as a protective barrier towards any infection (Talpur and Ikhwanuddin, 2013). Moreover, WBCs are one of the most affecting factors in immunity of fish and WBC counts

has been used as marker of health of aquatic animals (Duncan and Klesius, 1996). That depend on range of immune response against bacteria. The antibiotic generally inhibits growth of the pathogen allowing the immune system to eliminate the invaded microorganisms and chitosan nanoparticles and its loaded antibiotics kill and inhibits the growth of bacteria due to the antibacterial activity increased with increasing the antibiotic content, that agreement with (Ibrahim *et al*., 2015)

In the study by Sebastião et al.,(2011) they have recorded the blood parameter results from naturally infected tilapia displayed that there were changes in the erythrocytic series and in organic defense blood cells, in the fish infected with the bacterium, with a decrease in erythrocytic variables and important raise in the numbers of neutrophils and circulating lymphocytes. The total serum protein appeared the most significant indicator of the nutritional state of the health condition of fish (Patriche, 2011). Other researchers notified that the total protein concentrations, albumin, and globulin in the plasma is an indicator of liver function and subsequently the reduction of serum protein may be referred to renal excretion or impaired protein synthesis, or because of the liver hypofunction or disorder (Bernet et al., 2001).

In this study, Total proteins, Albumin and Globulin levels increased significantly in treatments (T2, T3, T4, and T5), that indicates an improvement of innate immunity for fish. This result is in line with Ranjan *et al*. (2014) in Asian seabass (*Latescalcarifer*). Similar findings recorded in olive flounder Cha *et al*.(2008), the rising level of total serum protein may be caused by the activity of bactericidal, activity of serum lysozyme, globulin content and perhaps a few other peptides (Misra *et al*., 2006).

5. Conclusions

The present study represents an important first step for the study of the effect of chitosan nanoparticles loaded with oxytetracycline hydrochloride on the health status of common carp with Columnaris disease. As a result, this new drug delivery method appears to be much better in relation to the conventional method of antibiotic exposure, as it reduces the dose of antibiotics and increases the survival rates against bacterial infection in fish, and reducing the antibiotic-resistant fish, and reduces the potential environmental impacts. However, the action of chitosan nanoparticles-loaded oxytetracycline is unclear and more studies are needed to understand its mechanism of action and side effects on fish industry.

References

[1] Al-Hamed M.I. 1971 *Iraqi National History Museum* **5** (1)1
[2] Al Rudainy A. J., Ridaa N.M. and Hani S.M.2008 *Iraqi of freshwater fish*. Ministry of Iraqi Environment, 58
[3] Amend, D.F. 1981 *Basel* 447
[4] Austin, B. and Austin, D.A. 2007 Bacterial Fish Pathogens: Diseases of Farmed and Wild Fish. 4th ed. Praxis Publishing Ltd, UK
[5] Baulny M.O.D., Quentel C., Fournier V., Lamour F., Gouvello R.L. 1996 *Disease of Aquatic Organisms* **26** 139
[6] Blaxhall, P. C. and Daisley, K. W. 1973 *Fish Biology*, **5** 771
[7] Chemello G., Piccinetti C., Randazzo B., Carnevali O., Maradonna F., Magro M., Gigliotti F. 2016 *Zebrafish* **13** (6) 495
[8] Crini, G. 2019 *Environ. Chem. Lett.* 17 1623
[9] Csaba N., & Alonso M. J. 2014 *J. Control Release* **28 (**190) 53
[10] Dacie S. and Lewis S. 1995 Practical hematology 7th ed., Churchill Livingstone, London
[11] Du W. L., Niu S. S., Xu Y. L., Xu Z. R., & Fan C. L. 2009 *Carbohydr. polym.* **75** (3) 385
[12] Figueiredo H. C. P., Klesius P. H., Arias C. R., Evans J., Shoemaker C. A., Pereira Jr D. J., &Peixoto M. T. D. 2005 *J. fish diseases* **28**(4) 199
[13] Gong P., Li H., He X., Wang K., Hu J., Tan W., & Yang X. 2007 *Nanotechnology* **18**(28) 285604
[14] Hrubec T. C., Cardinale J. L., & Smith S. A. 2001 *Veterinary clinical pathology* **29** (1) 7

[15] Ibrahim H. M., El-Bisi M. K., Taha G. M., & El-Alfy E. A. 2015 *J. Appl. Pharm. Sci.* **5** (10) 85
[16] Jain D., & Banerjee R. 2008 *J. Biomed. Mat. Res. Part B:* **86** (1) 105
[17] Julinta R. B., Roy A., Singha J., Abraham T. J., & Patil P. K. 2017 *Int. J. Curr. Microbiol. Appl. Sci.* 2017a, **6** (7) 62
[18] Kubilay A., Altun S., Diler O. and Ekici S. 2008 *Turkish J. Fisheries Aqua. Sci.* **8** 165
[19] Mitiku M. A. 2018 *Int. J. Adv. Res. Biol. Sci.* **5**(6) 79
[20] Rahman M. M. 2015 *Frontiers in Life Science* **8** (4) 399
[21] Nikapitiya C., Dananjaya S. H. S., De Silva B. C. J., Heo G. J., Oh C., De Zoysa M., & Lee J. 2018 *Fish & shellfish immunology* **76** 240
[22] Noga, E.J. 2000 Fish Disease Diagnosis and Treatment. Iowa State University Press, South State Aveneu, Ames, Iowa, 367
[23] Patriche T., Patriche N., Bocioc E. & Coada M.T. 2011 *Int. J. Bioflux Society* **4** (2) 131
[24] Rach J. J., Johnson A., Rudacille J. B., &Schleis S. M. 2008 *North Am. J. Aquacu.*, **70** (4) 459
[25] Ranjan R., Prasad K. P., Vani T., & Kumar R. 2014 *Aquacu. Res.*, **45** (6) 983
[26] Scott N. R. 2005 **24** (1) 425.
[27] Sebastiao F.A., Pilarski F. and Lemos M.V. F. 2011 *J. Bacteriol. Res.* **2**(3) 22
[28] Soutter W. 2013 Chitosan Nanoparticles-Properties and Applications
[29] Stehly G. R. 2002 Efficacy of immersion oxytetracycline treatments for diseases of finfish species culture on public fish facilities. Summary report to the US Food and Drug Administration Center for Veterinary Medicine, Rockville, Maryland.
[30] Thrall M. A., Bker D. C., Camobell T. W., Dinicola D., Fettman M. J., Lassen E. D., Reber A. & Weiser G. 2012 Veterinary hematology and clinical chemistry. 2nd Ed. Wiley-Blackwell
[31] Thune R. 1993 Bacterial Diseases of Catfish. In: M.W.B. Stoskopf (Ed.), Fish Medicine. Sounders Company London: 524
[32] Tien N. T., Dung T. T., Tuan N. A., Crumlish M. 2012 *Dis. Aqua. Org.* **100** 83
[33] Tripathi N. K., Latimer K. S., Gregory C. R., Ritchie B. W., Wooley R. E., & Walker R. L. 2005 *J. Veter. Diagn. Invest.* **17**(1) 45
[34] Tripathi N.K. 2003 Pathogenesis and treatment of Flavo bacterium columnare induced dermatitis in koi Cyprinuscarpio. PhD Thesis, University of Georgia, Athens, Georgia
[35] Wang J. J., Zeng Z. W., Xiao R. Z., Xie T., Zhou G. L., Zhan X. R., & Wang S. L. 2011 *Int. J. nanomed.* **6** 765
[36] Yousefian M. and Amiri M. S. 2009 *African J. Biotechnol.*, **8** 7313

Calculation of Concentration of Radon Gas in Specimen of Rivers Water samples in Diwaniya-Iraq'By Using CR-39 Track Detector

Calculation of Concentration of Radon Gas in Specimen of Rivers Water samples in Diwaniya-Iraq'By Using CR-39Track Detector

Abbas A. Sweaf[1]

[1]Physics department, College Education , AL- Qadisiya University / Iraq

E-mail: abbas .abd@qu.edu.iq

Abstract. The concentration of radon gas in a specimen of water of specific areas in 'Al - Diwaniya"province was calculated through employing alpha-emitters registrations, which is in'(CR-39)"nuclear track detector. The study focuses in determining the concentration of the gas in tap water specimen provided by the water grid of houses in 'Al- Diwaniya province. The findings indicate that the radon maximum level in water' 'specimen was in (Alshanaafia 5) area assigned to be (0.56 ± 0.30 Bq/L), and the minimum level' is in'(Afak 5) area around (0.165 ± 0.031Bq/L), in addition, to a rate value of (0.336 ± 0.075 Bq/L). The results also indicate that the radon gas in tap water is less than the acceptable boundary from (ICRP) organization which is (0.5994 Bq/ L),but the concentrations of radon exhalation rate (RER) is about '(0.245– 0.072 μSv/y) and the rate value is '(0.1462 ±1.23 μSv/y).

Keywords : radon concentration ,'ground water, annual effective dose,CR-39,; Al- Diwaniya province'

1. Introduction

A radioactive gas 'Rad0n (222Rn)' with a (t1/2t= 382d)'is made by the degeneration of natural 'radionuclide'(226Ra) which is basically a degeneration result of uranium (238U) chains. A radon isotope, Thoron gas (220Rn) "is a degeneration result of the thorium (232Th) chains. Thoron half- life is (56 s) which is less than the radon [1].The concentrations of radon gas in ground'-'water depends on the geological circumstances of the' area in addition to the human activities' pollution such as 'phosphate fertilizers, mining, and combustion of coal 'or other fuels .The rocks that happened naturally' by dissolving the granite rocks in natural uranium was mixed with the ground-water through leaching and precipitation (illumination process) [2]. In current examinations, the passive technique called the solid situation nuclear track detectors SSNTDs is used. The Nuclear track detection technique which depends on radon size and'CR-39 detector used in' the present work due to its' clarity and continuing integrated read out; high sensitivity to alpha-particle radiation ruggedness, which is available and easy to handle [3];.The radon that exists in tap water represents a hazard for developing cancer of organs such as stomach cancer. Nevertheless, this hazard is nothing beside the hazard of developing lung cancer from radon released by water to air especially when water comes out a tap and the melted gases are free [4]. Actually, the study covers the area that is situated in Al-Diwaniya province in further parts of Euphrates, see figure 1. The goal of the study is to identify the

concentration of radon gas in a specimen of tap water in selected areas in Al-;Diwaniya province by employing alpha-emitters registrations that are released from radon gas of in CR-39 nuclear track detector using;sealed-cup technique [5].

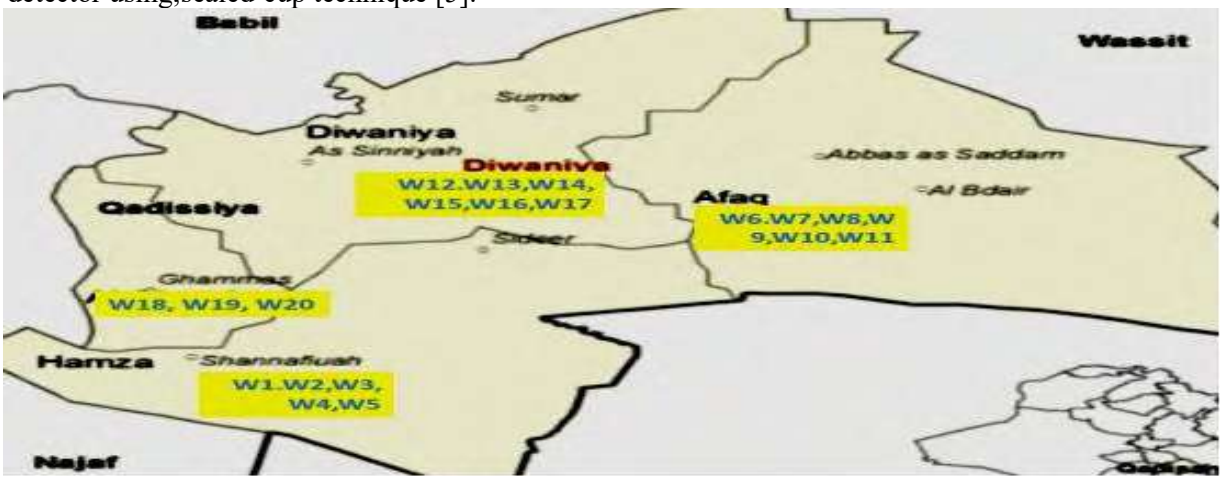

Figure 1. The dots are the locations where specimen taken from in Al-Diwaniya province with the numbers of stations.

2. Experimental Method

In this work, 20 samples of water were collected from different locations in some areas of Al-Diwaniya governorate as shown in figure 1. Each sample with 0.25 liter was placed at the bottom of a cylindrical sealed can of 10 cm height and 6 cm diameter. Solid State Nuclear Track Detector (SSNTD) with sheet thickness of 500μm was used in this study, which is usually known as CR-39 plastic detector [14]. Square pieces of detector of the sizes (1 cm × 1 cm) were fixed on the top of the inner surface of the can, in such a way, that the sensitive surface is always facing the water's sample [6]. The detectors were exposed to a period of 60 days. During exposing, the sensitive side of the detector is always facing the sample, and is exposed freely to the emergent radon from the water sample, so it could record alpha particles resulting from the decay of radon in the remaining volume of the can as seen in figure 2. After completing the exposure, the detectors were collected and chemically etched using 6.25 N NaOH at (70 C°) for (6 h). After that, these SSNTDs were washed, dried and scanned using an optical microscope with magnification of 400X (40x objective and 10x eyepiece) to count the number of the tracks per cm^2 in each detector. The determinations of the concentrations of alpha particles from radon gas in the samples were performed using CR-39 from the Intercast Europe Srl Company [7]. The radon gas concentration in the ground water samples was obtained by a comparison between track densities registered on the detectors of the ;sample and that of the standard water samples; using the following relation [8]

$$Tracks\ density\ (\rho) = \frac{Rate\ number\ of\ total\ pits\ (track)}{area\ of\ field\ view} \quad (1)$$

; The concentration of the radon gas is calculated using the following relationship [9].;

$$C_x = \rho_x \left(\frac{C_s}{\rho_s}\right) \quad (2)$$

where
C_X: the concentration of alpha molecules in an unidentified specimen
C_S: the concentration of alpha molecules in the standard specimen
ρ_X: Density of track of an unidentified specimen; (track/mm^2)

ρ_S: Density of track of the standard specimen; (track/mm^2)
The effective dose per year for a consumer based on the radon intake of ground water is assessed through the relationship [10].;

$$AED_w = C_w CR_w D_{cw} \quad (3)$$

;where AEDw is the annual effective dose (Sv/y) due to the absorption of radionuclide from the consumed water.;
Cw is the concentration of radon in the consumed ground water (Bq/L)
C_{Rw} is the annual intake of drinking water = 1095 L/y;
Dcw is the ingested dose conversion factor for = 4 Sv/Bq;[11].

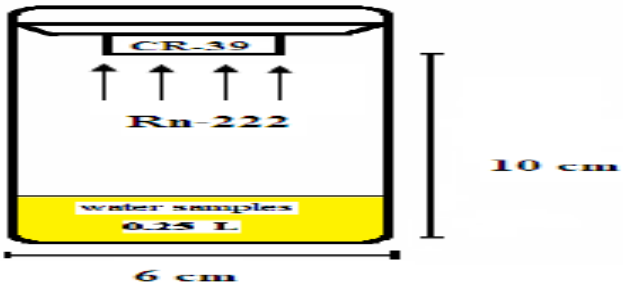

Figure 2. A graphic figure of the technique of;sealed-cup in water specimen

3. Results and Discussion;

In this survey, a total of 20; specimens of drinking water are collected from various regions in;Al-Diwaniya ;province through sealed-cup technique. Table 1 and Figure (4) shows the concentration of radon gas in the specimens of drinking water; from various areas in the;Al-Diwaniya province. It may be noted that the maximum level of the concentration of radon gas in the specimen of potable water is found in (Alshanaafia5) area which equal to (0.56 ± 0.30 Bq/L), while, the minimum level is found in (Afak 5) area which equal to (0.165 ± 0.031 Bq/L) and a rate value of (0.336 ± 0.075 Bq/L). Al shanaafia5 area has the maximum value of the annual effective dose in the specimen of potable water equal to (0.2452μSv/y), and the minimum value of the annual;effective dose (AED) is in;(Afak 5) area equal to (0.0722 μSv /y), and the rate value of (μSv /y) (0.1462 ± 1.23 μSv/y).;The annual effective dose (AED) of all the specimens are below the standard world parameters, which is equivalent to (1μSv/y).;Hence, the potable water in Al-Diwaniya province is safe as far as the concentration of the radon is concerned.; The recent paper measures the concentrations of the radon gas in 20 ground water specimens taken from different compartments (five specimen in each site) in Al-Diwaniya province by employing the sealed-cup technique. Based on the results, the concentration of the radon gas in the specimens of tap water in Al-Diwaniya Province (Iraq) is less than the permitted parameter from;(lCRP) agency that is equal to (0.59 Bq/L) [12]... ; ;

4. Calibration Curve for standard samples

To calibrate the curve plot between standard of different concentration of the radon gas solutions of known concentrations from;(**0 – 0.55** Bq /l) that have been arranged to calibrate the paper and track the density using neutron induced radiography that is depended on the norm of solid state nuclear detectors SSNTDs;CR-39..The concentrations of radon gas are calculated by comparing track dense register on the detectors of the specimen and the standardized specimen from the Regression equation : ;**y = 130.55 X +1.446 , R^2 = 0.9968**. A linear calibration as seen in Figure (3) is detected, tracked by measuring the slope. The findings are investigated in (mg Bq/L)..

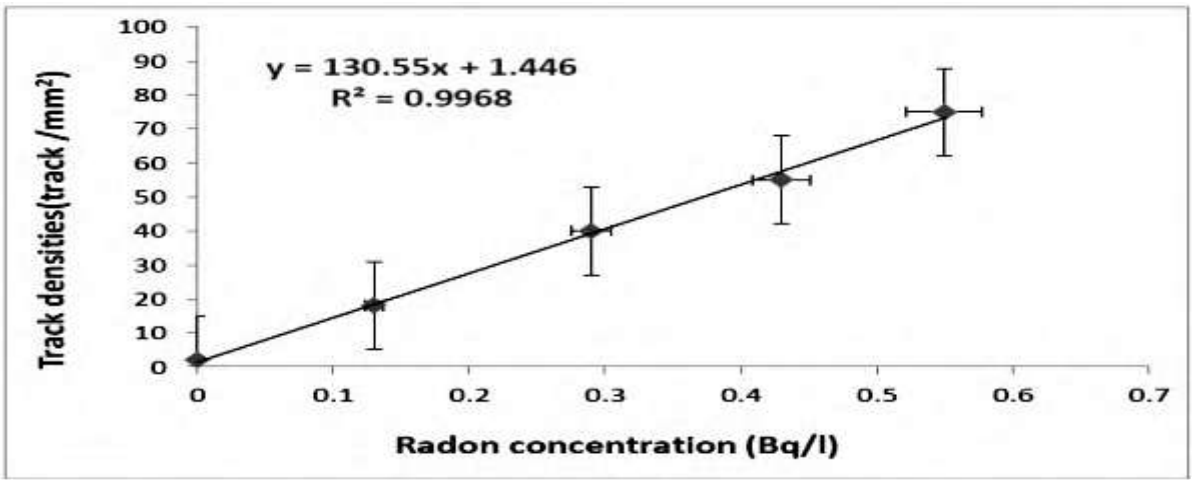

Figure 3. Relationship of concentration of gas of radon and density track in standardized specimen of water.

Table 1. Concentration of gas of radon CRn (BqL^{-1}), the specimen annual effective dose (AED) of potable water in Al- Diwaniya provinc

site Number	site Name	C_{Rn} (Bq/m^3)				Mean 0f C_{Rn} (Bq/m^3)	Effective dose (mSv/y)
		1	2	3	4		
W1	Alshanaafia 1	0.14	0.21	0.27	3.1	0.23 ±0.07	0.1007
W2	Alshanaafia 2	8. 0. 32	7. 0. 46	6. 0. 52	5. 0.59	0.47±0.11	0.2580
W3	Alshanaafia 3	12. 0 .22	11. 0 .25	10. 0 .42	9. 0.51	0.35±0.13	0.1533
W4	Alshanaafia 4	0.43	0.45	0.49	0.52	0.47±0.04	0.2058
W5	Alshanaafia 5	0.41	0.58	0.62	0.66	0.56±0.30	0.2452
W6	Afak 1	0.23	0.33	0.38	0.55	0.37±0.13	0.1620
W7	Afak 2	0.22	0.26	0.35	0.44	0.31±0.09	0.1357
W8	Afak 3	0.24	0.29	0.34	0.49	0.34±0.10	0.1489
W9	Afak 4	0.33	0.34	0.37	0.4	0.36±0.03	0.1576
W10	Afak 5	0.13	0.15	0.18	0.2	0.16±0.03	0.0722
W11	Afak 6	0.11	0.15	0.19	0.22	0.16±0.04	0.0731
W12	Rufieat 1	0.21	0.25	0.28	0.3	0.26±0.03	0.1138
W13	Rufieat 2	0.22	0.25	0.29	0.32	0.27±0.04	0.1182
W14	Rufieat 3	0.31	0.34	0.38	0.41	0.36±0.04	0.157
W15	Um alkhayl 1	0.27	0.3	0.34	0.39	0.32±0.05	0.1401
W16	Um alkhayl 2	0.35	0.38	0.41	0.43	0.39±0.03	0.1708
W17	Um alkhayl 3	0.33	0.42	0.45	0.47	0.41±0.06	0.1795
W18	Ghmas 1	0.25	0.27	0.31	0.35	0.29±0.04	0.1270
W19	Ghmas 2	0.15	0.17	0.21	0.23	0.19±0.03	0.0832
W20	Ghmas 3	0.36	0.39	0.42	0.45	0.40±0.03	0.1752
	Rate					0.336 ± 0.075	0.146286 ±1.23

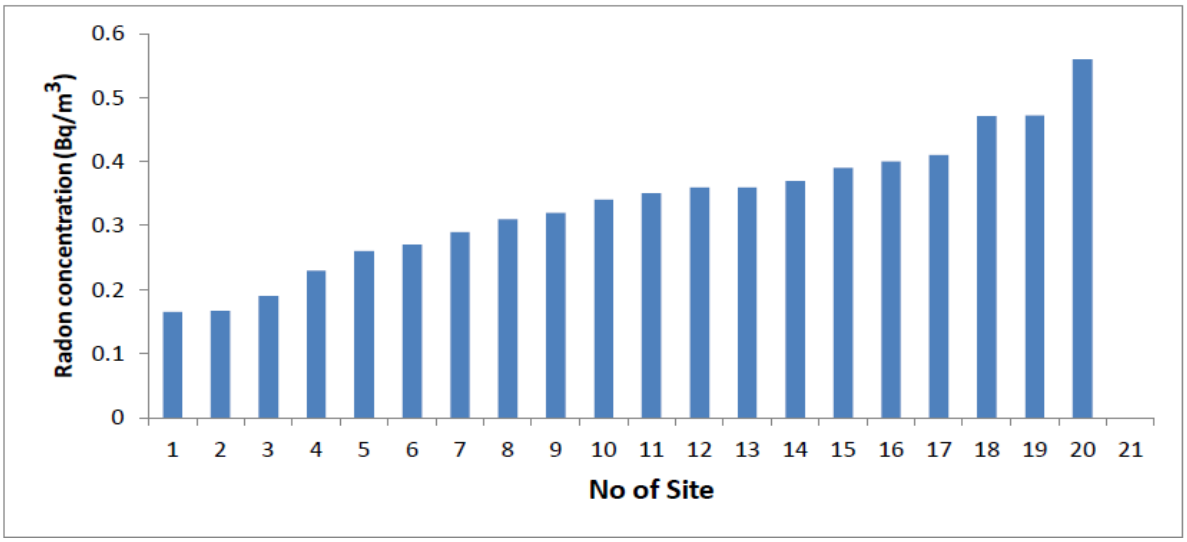

Figure 4. A histogram demonstrates the alteration in concentration of gas of radon (Bq/L) in the specimen of all studied areas water.

References

[1] Iskandar D Iida Yamazawa T Moriizumi H Koarashi J Yamasoto J Yamasaki K Shimo K Tsujimoto M T shikawa Fukuda M and Kojima H 2005 *Appl Rad and Isotopes* **63** 401.
[2] Sánchez A M Pérez J D T Sánchez A B R and Correa F L N 2012 *Journal of Environmental Radioactivity* **107** 86.
[3] Al-Ubaidi K H 2006 *Identification and measurements of natural and industrial radioactive pollutants in environment of Baghdad city using gamma spectrometry and solid state nuclear track detector CR-39* Ph D Thesis College of Education, Ibn-Alhaitham ,University of Baghdad.
[4] Kadhem M M 2013 *Estimation of radon concentration and annual effective dose in Al-Najaf city hospitals* MSc Thesis, Kufa University, College of Science.
[5] Radiation protection against radon in workplaces other than mines 2003 *International atomic energy agency, safety reports chains* **33** 3.
[6] Ammar A. Battawy and Hana I. Hussein *2010 J. of University of Anbar for pure science* **4** (1).
[7] Al-Kazwini AT and Hasan MA 2003 J Radiol Prot **23** 439.
[8] Ferreira A O Pecequilo B R and Aquino RR 2011 *Radioprotection Journal* **46** (6) 49.
[9] Ismail A H 2004 *Measurement of radon activity concentration in Iraqi Kurdistan soil by using CR-39 nuclear track detectors* MSc Thesis,Univof Salahaddin, Erbil-Iraq.
[10] Baixeras C Erlandsson B Font L and Jonsson G 2001 *Radon emanation from soil specimen, Radiat Measur* **34** 441.
[11] Al-Gaim H R M Al-Khalifa I J M and AlHelal A A 2012 *Journal of Basrah Researches* **38** 8.
[12] Kansal S Mehra R and Singh N P 2012 Applied Radiation and Isotopes **70** 1110.

Refractive Index Sensor for Salty and Sugary Solution Based on Optical Fiber Technical

Refractive Index Sensor for Salty and Sugary Solution Based on Optical Fiber Technical

Maher Khaleel Ibrahim[1], Shehab A Kadhim[2] and Nabeil Ibrahim Fawaz[1]

[1]Department of Physics, College of Science, University Of Anbar.
[2]Laser & Optoelectronics Research Center, Ministry of Science & Technology.

E-mail: mkibrahim@uoanbar.edu.iq

Abstract. In this work, based on Mach- Zehender Interferometry (**MZI)** technique, a single-mode optical fiber had been designed as a water pollution sensor. The submitted sensor had been designed to detect pollutants in water. The sodium chloride salt and sugar were used as simulation examples of pollutants with different concentrations (0-0.45) mol /liter. The performance of the submitted sensor had been studied for different sensor arm diameters which were (63.5, 51.58, 39.68 and 20 μm). The variation of the refractive index of salty and sugary solutions surrounding the sensor leads to a change in the optical properties of the transmitted signal. In this work, a wavelength shifting had been obtained due to this variation. The influence of sensor diameter on the sensitivity of the system had been studied. From the results, we found that the higher sensitivity was for the sensors with a diameter of 20 μm, and they were 1130 pm/mol.l^{-1} and 1205 pm/mol.l^{-1} for salty and sugary solution respectively.

Keywords: optical fiber sensors, RI sensor, evanescent field, MZI, chemical etching, water pollution

1. Introduction

Related to the toxic effects the pollutants may have on humans, accurate measures of chemical species in water have increasingly gained functional significance. In this context, it is important to build up simple, responsive, low-cost, and portable water pollution sensors capable of direct measurements. Optical fiber technology provides many benefits for chemical sensing over traditional methods [1]. Compared to traditional devices, fiber optic sensor systems provide various advantages, including immunity to electromagnetic interference, lightweight and portable size, sensitivity, multiplex ability, remote sensing, and the most significant benefit is the ability to be built into the textile structure. An effective medium to sense chemical species is created by optical fibers. Light properties including intensity, phase, or polarization in the optical fiber may be modulated by the presence of chemical species. At the fiber output, these modulations can be observed and correlated with the concentration of the chemical species presented at the point. [2]

Any optical fiber consists of two dielectrics that are concentrically arranged: the center (core) and the cladding. A higher refractive index than the cladding is distinguished by the core [3]. Using HF as the etching agent is one of the simple methods used to make tapers. If the fiber is etched, as the fiber diameter is limited, the conditions controlling the transmission of light within the fiber change. It should also be remembered that the etching procedure is limited to a particular fiber length to achieve desired etched length and desired contact area [4]. In that configuration, it defines light propagation dependent on a total internal reflection. In the form of modes in the center and a small portion of energy penetrating the cladding known as the evanescent field, light is propagated. As a result, an exponentially greater cross-section of the cladding fills the area of the simple mode until it reaches the point where it is directed across its entire cross-section. A progressively greater cross-section of the cladding occupies the area of the simple mode until it reaches the point where it is directed in its cross-section. The change in boundary conditions is also closely associated with the change in the dimensions of the optical fiber. The light at the core/cladding interface is not propagated, but the air/cladding interface is propagated. The approximations used in the typical optical fiber mode solutions where the difference in refractive indices is small (less than 1%) are not valid. In this case, the light beam continues to be exposed and affected by the fiber surrounding air for tapered optical fibers where the light beam propagates in a whole system (as a core) and the environment becomes a cladding, as seen in Figure 1 [3]. As the optical fiber becomes more sensitive to external changes in the refractive index of the material surrounding the fiber, this method enables one to use additional material in an etched environment, especially in the tapered waist region. These links to different materials have been commonly used for the construction of sensors, filters, and amplifiers [5,6].

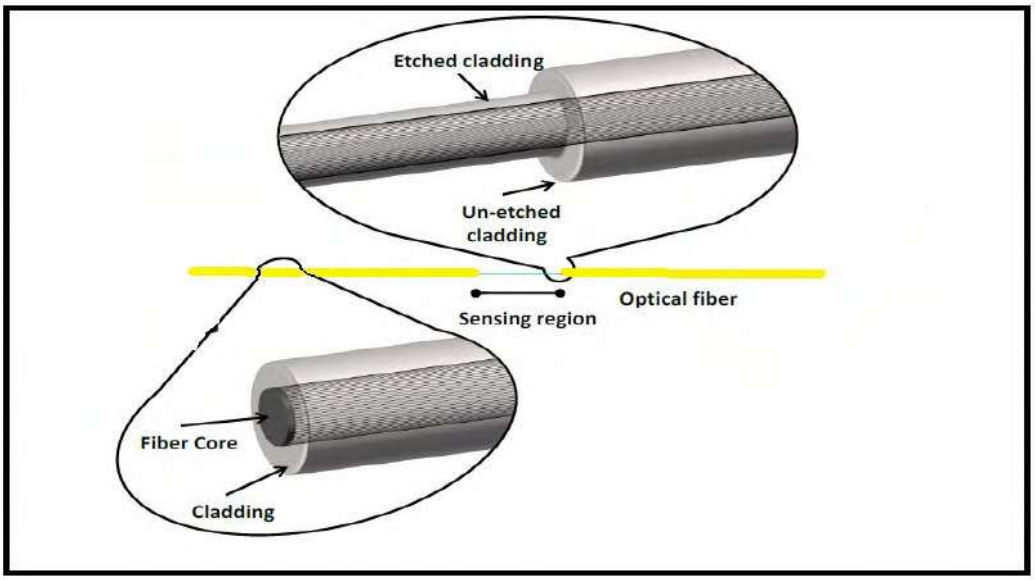

Figure 1. The schemes of the etched and non-etched region of optical fiber [7]

In biological fields, medicine and environment, optical fiber refractive index (RI) sensors are used. Many fiber optic RI sensors, such as Mach-Zehnder (MZIs), Fiber Grating, Fabry-Pérot (FPIs), Sagnac, and multi-mode interferometers have been published in the literature so far [8].
In particular, (MZIs) interferometers obtain from high sensitivity, a high degree of integration, accessibility and design compactness. Several optical fiber refractometers have recently been documented to allow the refractive index and many other parameters to be calculated simultaneously. These optical fiber instruments serve as evanescent wave sensors based on multimode interference systems, enhancing the dependency on high-order mode propagation constants on the external medium's refractive index to monitor changes in the environment's optical properties [9].

Many research groups submitted many research papers to solve many problems related to this very important topic.

James et al 2017 [10] stated that by depositing a nanoscale coating of titanium dioxide containing porphyrin as a functional material onto a tapered optical fiber, a highly sensitive ammonia sensor was developed. As a result of the interaction between porphyrin and ammonia, the difference in the refractive index of the coating material caused a change in the middle wavelength of the large-mode resonance, allowing the identification of ammonia concentrations in water as low as (0.1) ppm, with a reaction time of less than 30 sec. **Also, Devi et al 2018** [11] detected arsenic components in a drinking water, and MZI based on optical fiber was developed. The developed sensor is distinguished by its cost-effective, small, and laboratory-on-chip manufacturing capability. **In 2019 Ahsani et al** [12] a uniformly tapering SMF standard for MZI-based RI measurement was established. There are various applications in chemical and biochemical sensing fields for the suggested cheap and highly sensitive optical fiber RI sensors. **Finally in 2020 Ferria** [13] tested the distilled water solution mixed with methylene blue (MB), and an unclad optical fiber sensor was manufactured. At the core – liquid cladding interface, the manufactured sensor is based on evanescent wave absorption by the surrounding medium. Ferria concludes that the results showed that the designed sensor provides an effective response to the (6–50) mg / L concentration range.

In this work, an MZI sensor based on SMF had been designed for environmental applications. Sugary and salty liquids with different concentrations were employed as a simulation of water pollution. Moreover, the influence of the sensing arm diameter on sensor performance has been studied.

2. Experimental

The experiment was carried out using a section of the commercially available SMF of cladding and core diameter of (125 and 9) μm respectively.

About 3 cm length of the middle region of SMF was stripped and cleaned very well. After that, this section was immersed into Hydrofluoric acid (HF) to be chemically etched, that is to say, reducing its diameter to the desired value. The concentration of HF acid before dilution was 48%, and this strong acid has been diluted with distilled water to a ratio of (1 mm^3 HF: 1 mm^3 distilled water). The etching process took place at room temperature and the required cladding diameters have been achieved at etching times of (60, 90, 20 and 150) min. Then, the etched area had been cleaned very well using distilled water to remove any acid residuals.

Figure 2 below shows the MZI optical fiber sensor. A signal from the light source (single-mode fiber pigtailed Laser diode source -Thorlabs of center wavelength 1550 nm, and power 1.5 mW) was split by 2x1optical coupler (50/50) into two signals. The first signal goes to the reference arm while the second goes to the sensor arm. Then, both arms were collected using another 2x1 optical coupler. The output port was connected to Optical Spectrum Analyzer (THORLABS 203) with a wavelength range of 1000 to 2600 nm, and a resolution of 0.1 nm.

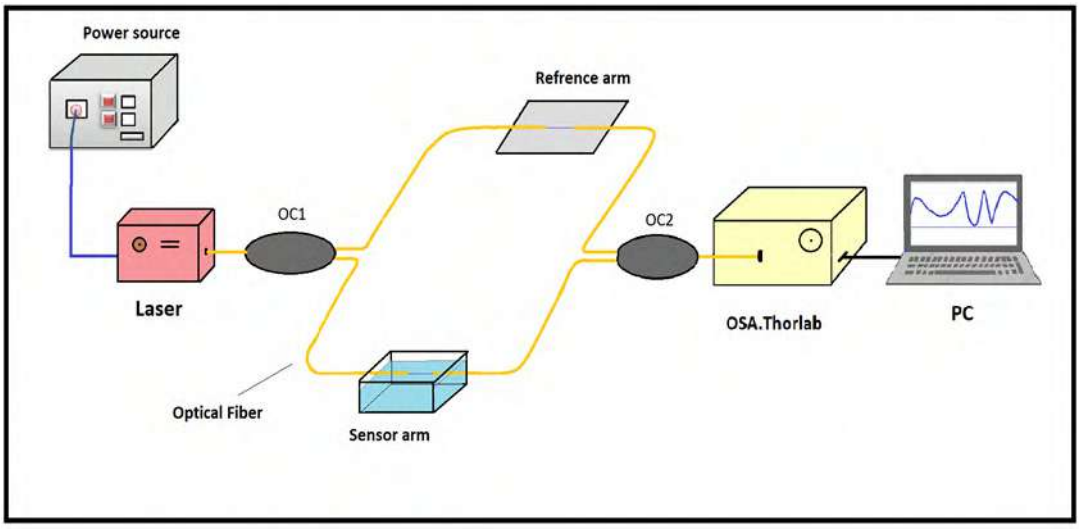

Figure 2. Schematic diagram of MZI- RI sensor

The tested solutions of sodium salt and sugar were prepared at different concentrations using the following equation:

$$C = \frac{m}{V} \times \frac{1}{MW} \quad (1)$$

where C is the molar concentration in mol/L (Molar or M). This is also referred to as molarity, m is the mass (i.e., weight) of solute in grams (g) that must be dissolved in a volume V of the solution to make the desired molar concentration (C) and MW is the molecular weight in g/mol.

The refractive index of the salty and sugary solutions was measured with a (BOECO Digital ABBE Refractometer)

The sensor arm was immersed in these salty and sugary liquids with different concentrations and the transmission spectrum was collected and analyzed using OSA.

3. Results and discussion

It is observed experimentally through the refractometer that the refractive index increases with increasing the concentration of sodium salt or sugar in water, as shown in Figure 3.

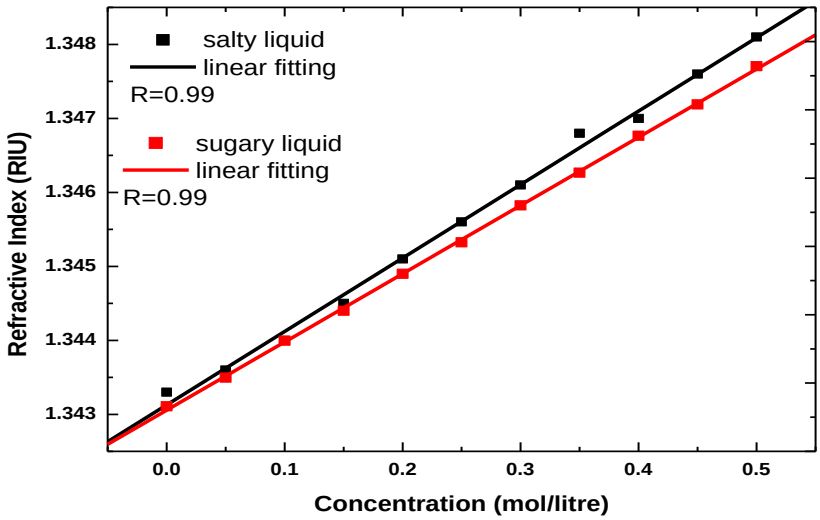

Figure 3. Refractive index variation with concentration

The different diameters of optical fibers due to different etching times were obtained and illustrated in Table 1.

Table 1. The variation of the etched fiber diameter with immersion time

Fiber no.	Etching time (minute)	Etched fiber diameter (μm)
1	60	63.5
2	90	51.58
3	120	39.68
4	150	20

The diameter of the fiber in the area exposed to HF decreases during the etching process. According to the following reaction formulas, HF reacts to silica:

$SiO2+4HF \rightarrow SiF4+2H2O$

$SiO2 +6HF \rightarrow H2SiF6 + 2H2O$

The first formula dominates the reaction concerning the present work, while the second formula dominates acid circumstances with a high concentration. Instead of tapering, this method adjusts the cladding properties while keeping the core intact [14].

Since HF has known for its ability to dissolve silica, it became evident from experience that the length of etching time required was about 150 minutes and through the etching results in Table.1 of the fibers. The remaining fiber thickness was apparent from the fibers of (39.68) μm and (20) μm fiber diameter with etching times of (120) and (150) min, respectively. Remember that the core is (9) μm in diameter. Due to figure 4, the effect of changing the refractive index of the surrounding environment of the sensor arm on the optical properties of the transmission spectra was studied for the standard fiber diameter (125 μm). The sensor arm was immersed in distilled water, and from figure 4 one can notify a noticeable wavelength shifting towards the longer wavelength due to applied distilled water to sensing arm.

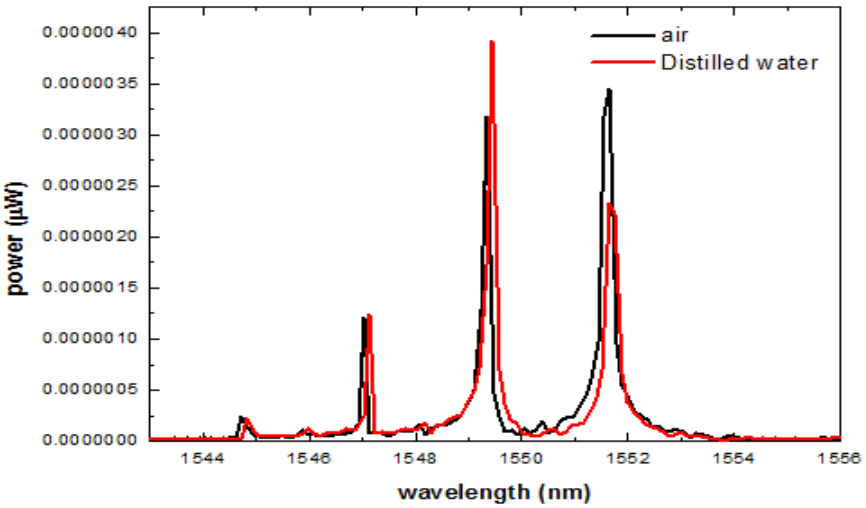

Figure 4. The transmission spectrum of air and Distilled Water

To test the system as a refractive index sensor, the sensor arm was immersed with different solutions; salt NaCl and Sugar $C_{12}H_{22}O_{11}$ with different concentrations ranging from (0 - 0.45) for both liquids. Figure 5 shows the transmission spectra of salty and sugary liquids at different concentrations.

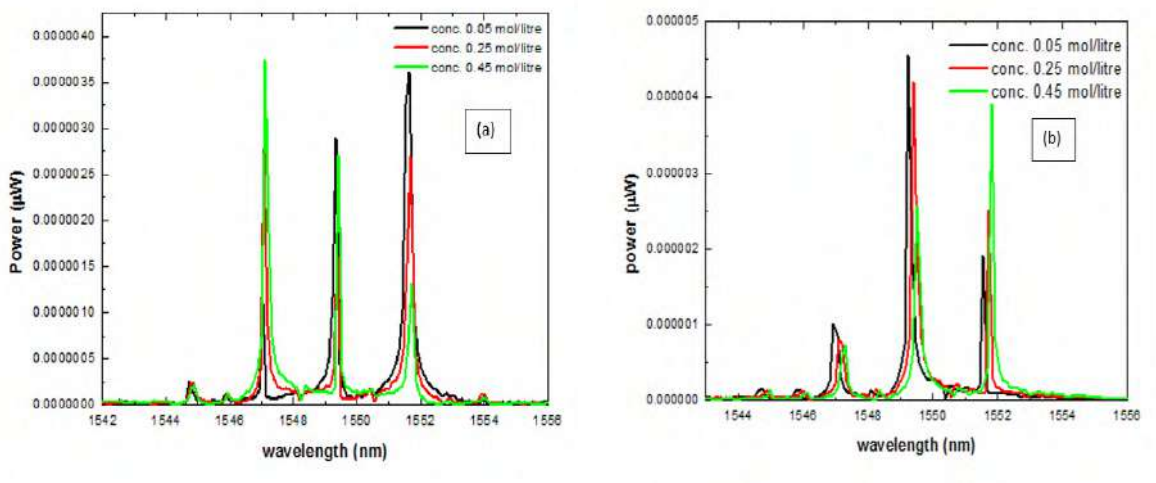

Figure 5. The transmission spectrum of (a) salty liquid, and (b) sugary liquid with selective concentrations

Figure 6 shows the linear relationship between changing in liquid concentration and shifting in the peak wavelength. The figure illustrates that the sensor shows a good sensitivity which is calculated from the linear fitting line and is equal to (202) and (220) mol/liter for salty and sugary liquids respectively.

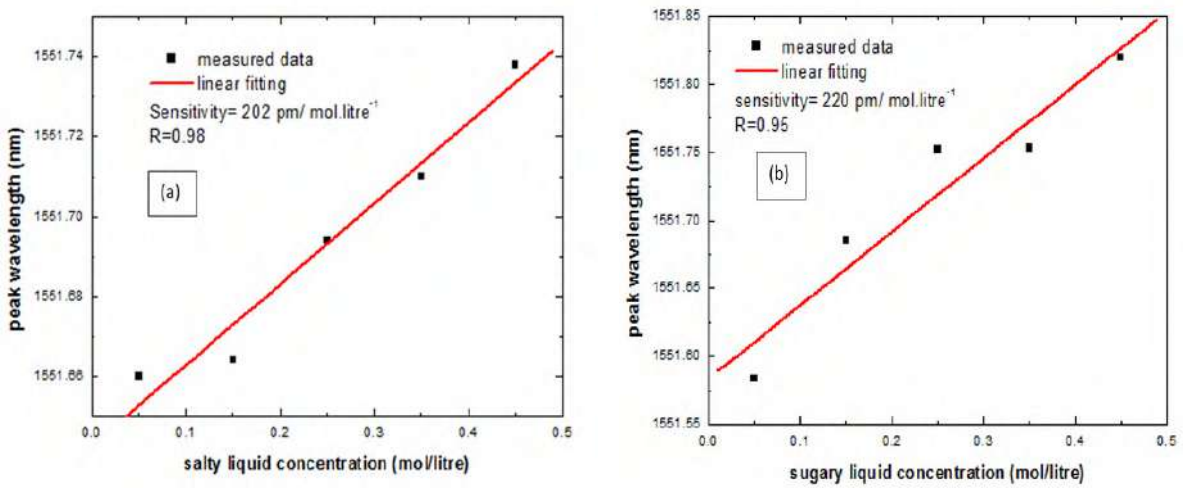

Figure 6. The relationship of peak wavelength shifting with liquid concentration for a selective peak, (a) salty liquid, (b) sugary liquid

The effect of sensor arm diameter on sensing performance had been studied. Different fiber with average diameters (63.5, 51.58, 39.68, and 20) µm were utilized and immersed in the sensing region with salty and sugary liquids with different concentrations.
Figure (7) shows the transmission spectra of salty liquid with different concentration for fiber average diameters (a) 63. 5 µm, (b) 51.58 µm, (c) 58.68 µm, and (c) 20 µm respectively.

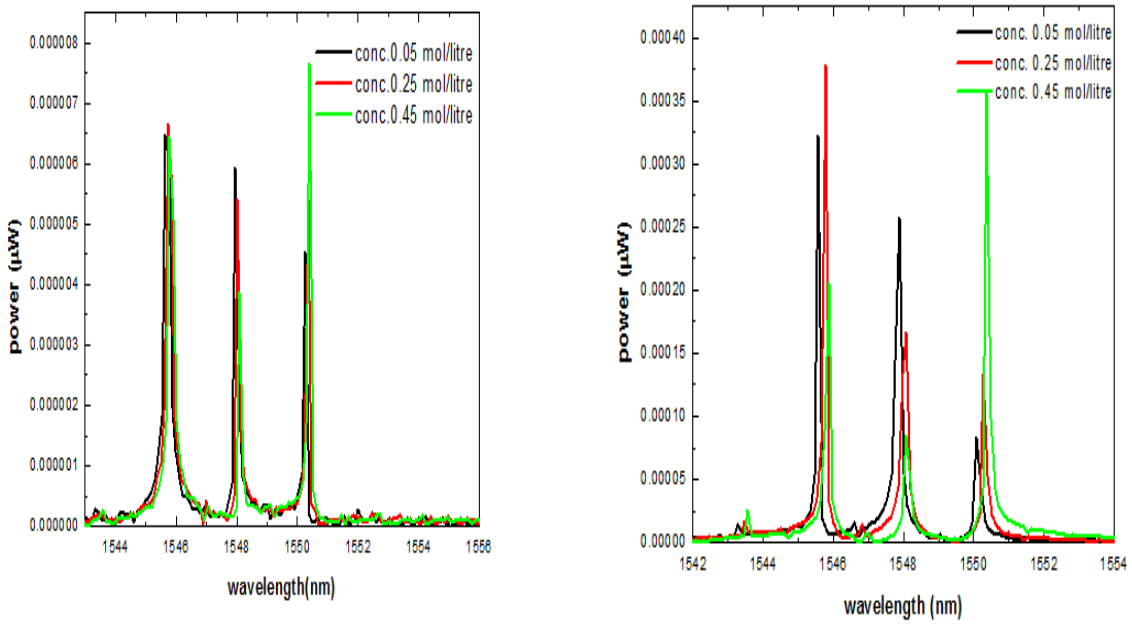

(a) *(b)*

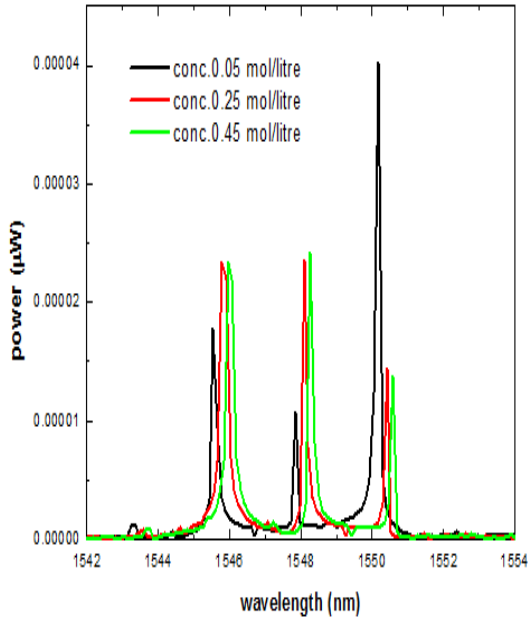

(c)

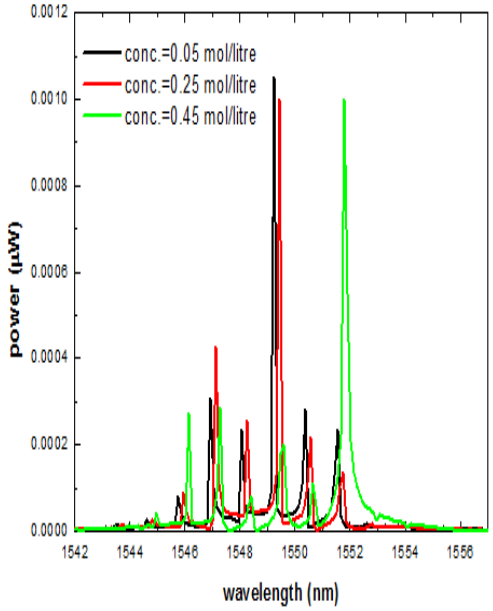

(d)

Figure 7. The transmission spectrum of salty liquid with selective concentrations with sensor diameter (a) 63.5µm, (b) 51.58µm, (c) 39.68µm, (d)20µm

Figures (8) on the other hand shows the linear relationship between the shifted in peak wavelength and liquid concentration for salty liquid with different concentration for fiber average diameters (a) 63. 5µm, (b) 51.58 µm, (c) 58.68 µm, and (c) 20 µm respectively.

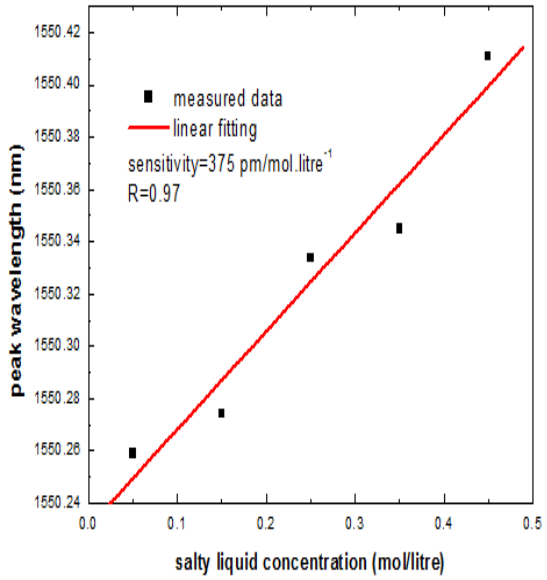

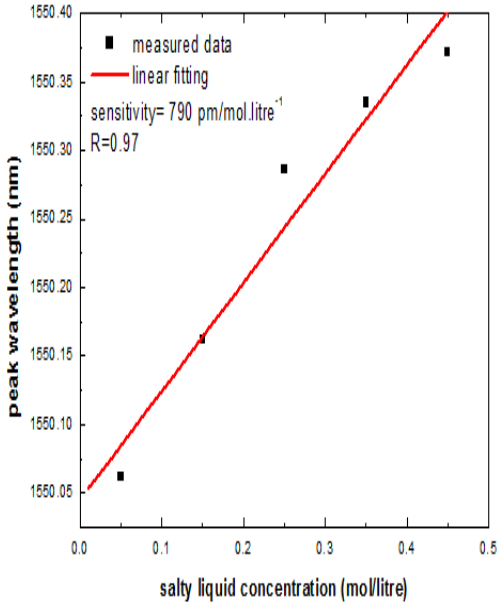

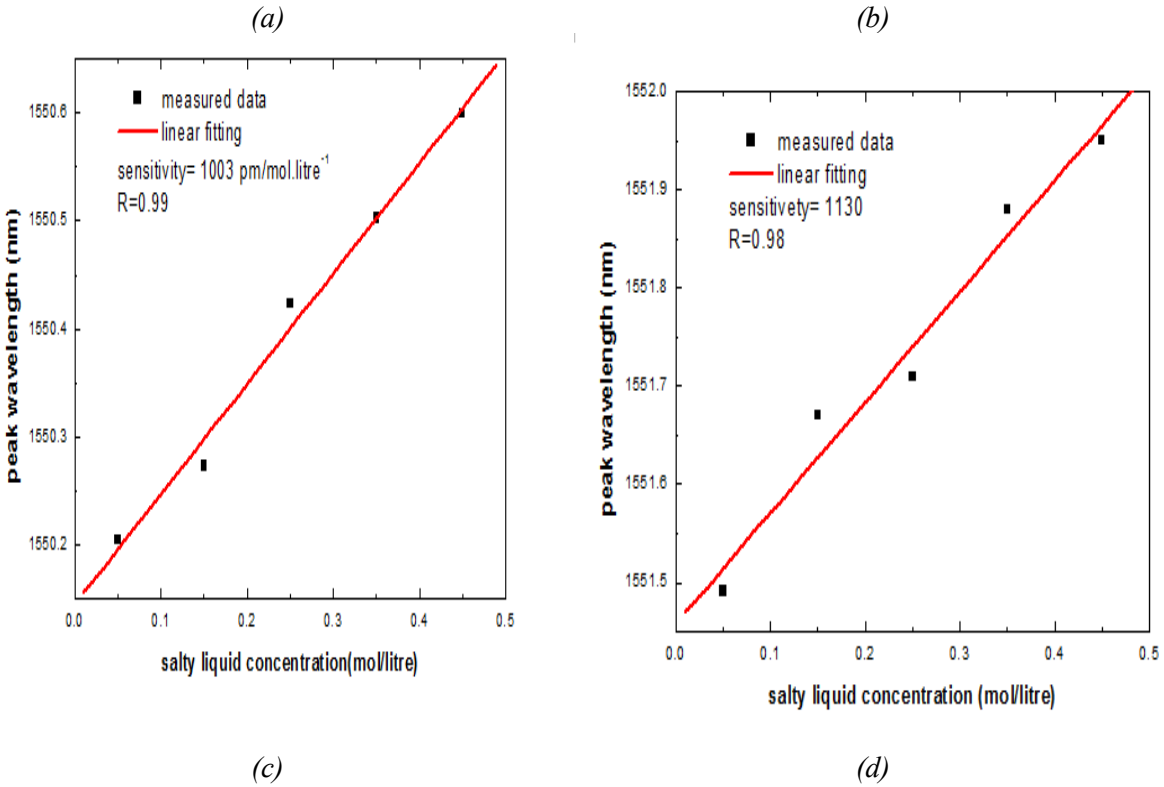

Figure 8. The relationship of peak wavelength shifting with salty liquid concentration for a selective peak, with sensor diameter (a) 63.5µm, (b) 51.58µm, (c) 39.68µm, (d)20µm

Figure (9) shows the transmission spectra of sugary liquid with different concentration for fiber average diameter (a) 63. 5 µm, (b) 51.58 µm, (c) 58.68 µm, and (c) 20 µm respectively.

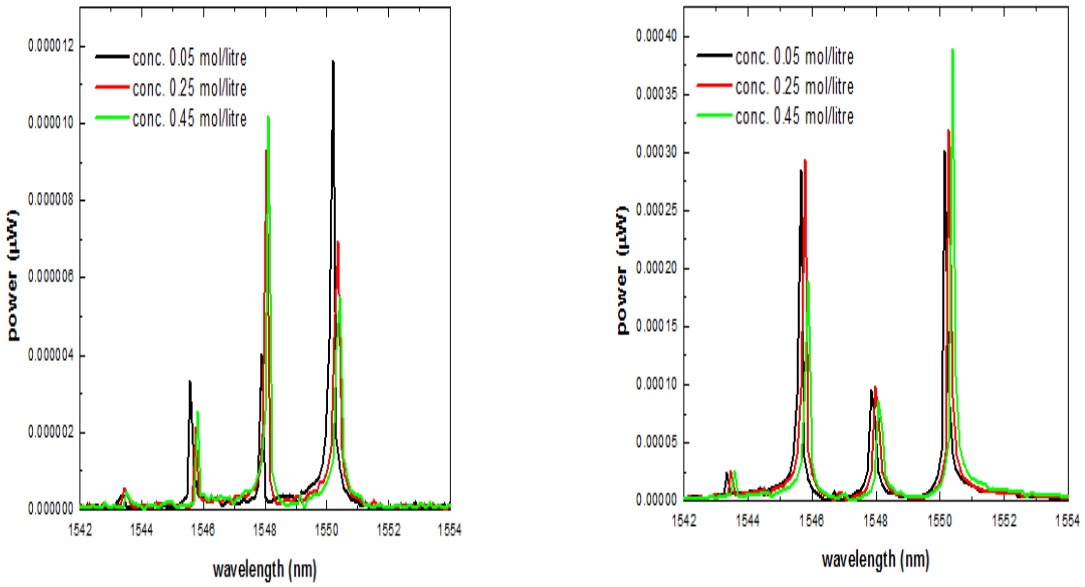

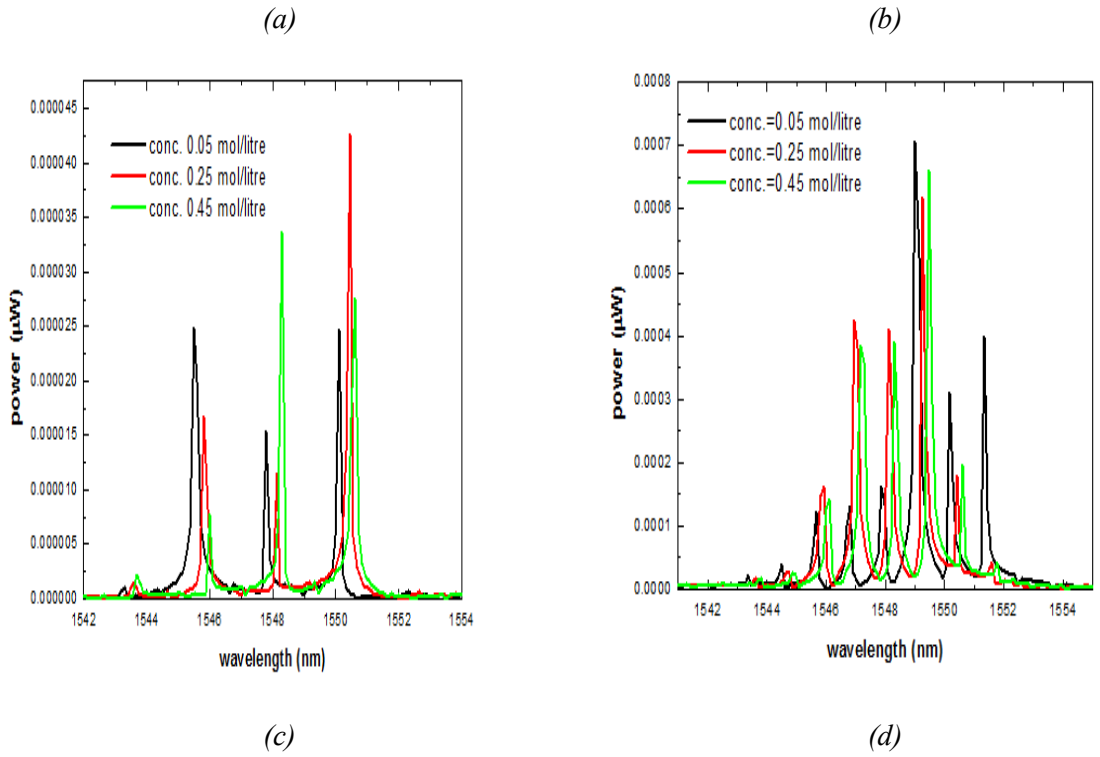

Figure 9. The transmission spectra of sugary liquid with selective concentrations with sensor diameter (a) 63.5µm, (b) 51.58µm, (c) 39.68µm, (d) 20µm

Figures (10) shows the linear relationship between the shift in peak wavelength and liquid concentration for sugary liquid with different concentration for fiber average diameter (a) 63.5 µm, (b) 51.58 µm, (c) 58.68 µm, and (c) 20 µm respectively.

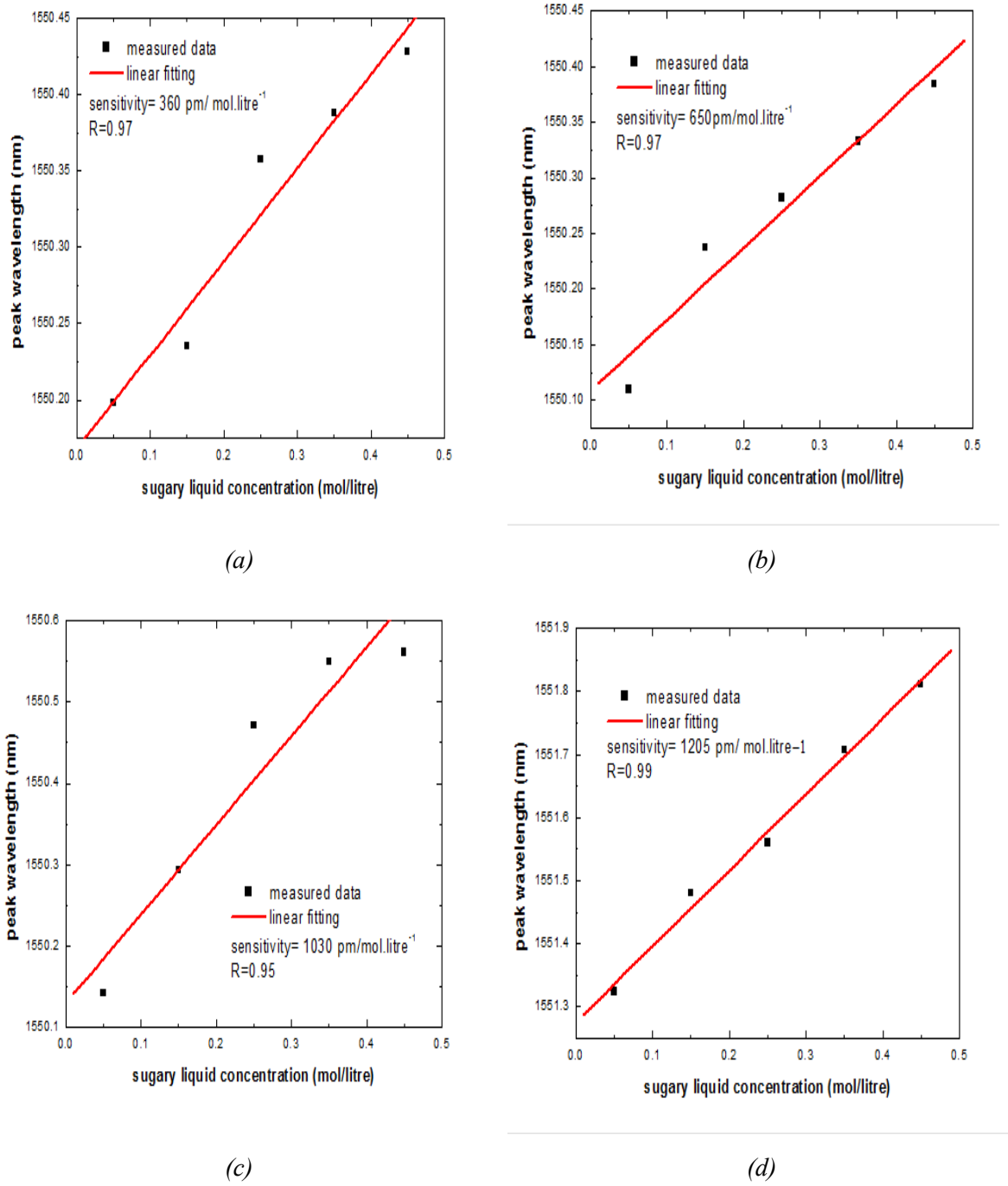

Figure 10. The relationship of peak wavelength shifting with sugary liquid concentration for a selective peak, with sensor diameter (a) 63.5µm, (b) 51.58µm, (c) 39.68µm, (d)20µm

Table (2) below shows the sensitivity of the submitted sensor for each case, from this table we can conclude that the sensor performance is enhanced as the optical fiber sensor diameter is decreased. This can be explained because the more leakage of the evanescent field from fiber cladding the more interaction with the surrounding media (liquids in this work). Also, the sensitivity values are close for

both salty and sugary liquids which declare that the type of liquid is not an important factor as its concentration on the sensing performance.

Table 2. Variation of the Sensitivity with optical fiber thickness

Fiber Dimeter (μm)	Salty liquid Sensitivity (pm/mol.litre^{-1})	Sugary liquid Sensitivity (pm/mol.litre^{-1})
125	202	220
NO.1 (63.5)	375	360
NO.2(51.58)	790	650
NO.3(39.68)	1003	1030
NO.4 (20)	1130	1205

From figures 9, 10, and Table 2 it could be noticed that the sensitivity of the submitted sensor had been enhanced by reducing the fiber diameter. The etching process leads to reduce the fiber diameter and thus strengthens the evanescent field. So, more light will be escape out of the cladding region and interact with the surrounding environments which are the salty and sugary liquids.
In standard optical fibers whose diameter is much greater than the light wavelength, the evanescent field strength at the outer surface of the cladding reduces to near zero. The light dispersed in these fibers is thus not influenced by the external environment, which decreases the interaction between the light and the sample and therefore reduces the sensitivity response of the optical fiber sensor. Carrying out the etching process and reducing the cladding thickness would allow the fibers to present large portions of ephemeral waves and surface fields of high intensity, rendering them extremely sensitive to the shift of the index to the surrounding medium by dramatically increasing the contact between directed light and the surrounding atmosphere.

4. Conclusions

The reaction activity of a Fiber Optic Evanescent Wave Sensor is greatly influenced by the thickness of the cladding within the sensing area of the fiber. We can say here that the sensor can be developed by partially removing the cladding material surrounding the optical fiber single-mode. The sensing theory, based on the variation of the refractive index based on the interaction of the transient field with the optically absorbed analyte, is utilized such that the thin cladding portion enables transmission loss by the vanishing waves that radiate energy from the heart as a function of the environment. It can also be claimed from the findings that the lower the cladding thickness, the greater the sensitivity efficiency of the optical fiber. In the field of environmental detection, such as water pollution, this sensor may be used.

Reference

[1] Kumar P Suresh et al 2002 Journal of Optics A: Pure and Applied Optics **4** (3) 247.
[2] Bansal L 2004 Development of a fiber optic chemical sensor for detection of toxic vapors.
[3] Moś Joanna E et al Crystals **9** (6) 306.
[4] Haddock Hong S Shankar P M and Mutharasan R 2003 Materials Science and Engineering: B **97**(1) 87.
[5] Zhang, Lei Jingyi Lou and Limin Tong 2011 Photonic Sensors **1** (1) 31.
[6] Polynkin Pavel et al 2005 Optics Letters **30** (11) 1273.
[7] Godin Jeremy Robert 2015 Development of an Analytical Model for a Fiber Optic Evanescent Wave Sensor.

[8] Han Xiaopeng et al 2019 Sensors **19** (24) 5440.
[9] Harris Jeremie et al 2015 Sensors and Actuators B: Chemical **206** 246.
[10] Tiwari Divya et al 2017 Sensors and Actuators B: Chemical **242** 645.
[11] Afzal Nehal S Mukherjee A and Manju Devi D 2018 International Journal of Engineering & Technology **7** (4.38) 880.
[12] Ahsani Vahid et al 2019 Sensors **19** (7) 1652.
[13] Kenza A Ferria K and Bouzid S 2020 JOSA B **37** (11) A253.
[14] Coelho L et al 2015 Plasmonics **10** (2) 319-327.

.

The influence of temperature and size on the absorption coefficient of CdSe quantum dots

The influence of temperature and size on the absorption coefficient of CdSe quantum dots

Roaa Sh. Hammadand[1], Nidhal M. Abdul-Ameer[1]

[1]Department of Physics, College of Education for Pure Science-Ibn Al-Haitham, University of Baghdad, Baghdad, Iraq

E-mail: dr.nidhalmoosa@gmail.com

Abstract. Because of Cadmium selenide quantum dots (CdSe quantum dots) has a tuning energy gap in the visible light range, therefore; it is provided a simple theoretical model for the absorption coefficient of CdSe quantum dots, where the absorption coefficient determines the extent to which the light of a material can penetrate a specific wavelength before it is absorbed. CdSe quantum dots have an energy gap can be controlled through two effects: the temperature and the dot size of them. It is found that; there is an absorption threshold for each directed wavelength, where CdSe quantum dots begin to absorb the visible spectrum at a size of 1.4 nm at room temperature for a directed wavelength 300 nm. It has been observed that; when the wavelength is increasing its absorption threshold is increased. For wavelengths (400, 500, 600) nm, the absorption thresholds for each quantum sizes are (1.8, 2.2. 3.2)nm respectively. On the other hand, a rising of the temperature led to reduces the absorption coefficient value , that at 400 K for all quantum sizes, the absorption coefficient increases >2000cm^{-1}(According to the directed wavelength) than it is at 0 K. CdSe quantum dots can be considered as one of the most promising materials because it has a tuning gap for the visible wavelengthsfor different applications, such as light-emitting diodes in different colors of the visible spectrum.It is found that ;there is a good agreement between our theoretical calculations and experimental results.

Keywords: CdSe quantum dots, Tuning Energy Gap, Absorption Coefficient, Absorption Threshold

1. Introduction

Recently, CdSe quantum dots have been an intensely researched compound due to their size and shape-dependent properties arising from the quantum confinement regime [1,2]. This regime depends on the spherical particle-in-a-box model that predicts strong quantum confinement, besides it has a tuning energy gap [3].

One of the most important photometric techniques in solids is the light absorption scale, the absorption coefficient, which can determine the depth at which light of a specific wavelength penetrates a martial. The wavelengths that include the visible and the infrared are the most important wavelengths for applications. The absorption coefficient depends on the properties of the CdSe and the energy of the incident photon, whether it is greater, less, or equal to the energy gap [4]. Taking into consideration, the atomic structure and density of states of the conduction band and valence, and the type of energy

gap, whether direct or indirect [5]. Researchers have studied the absorption coefficient due to its importance, Jinjun Sun and Ewa M Goldysthey are analysis the linear absorption coefficient that due to interband transition in CdSe quantum dotstheoretically [6]C.A. Leatherdale et al usemodels of light scattering from light-absorbing small particles in CdSe quantum dots [7]. Ehud Shaviv et al. used a method to obtain-CdSe QRs concentrations are based on a comparison of the absorption far above the transition of the bandgap [8]. Other researchersas W. W. Yuetal, A. Strioloetal , O. Schmelzetal and C. A. Leatherdaleetal have studied the determination of the molar absorption coefficients of CdSe QD experimentally [9–12].

The characteristics of CdSe are highly sensitive with respect to various growth processes as well as ambient conditions [13]. Due to the importance of the absorption coefficient for its apparent effect on the optical properties, in addition to some optical constants, therefore, in this paper, we present a theoretical model of CdSe quantum dots that study the effect of temperature and the quantum dot size on the absorption coefficient.

2. Theoretical Model

The absorption rate of light is proportional to the intensity of the flux of photons of different wavelengths. When light passes through material, the flux of photons gradually decreases, so that the material absorbs some of the photons. Thus, the number of photons that will reach a given point in a CdSe quantum dots depends on both the wavelength of the photon and the distance from the surface.

Tauc relation is using to calculate the absorption spectra due to the optical transition energy, it is expressed as [14, 15]:-

$$(\alpha\, h\nu) = B(h\nu - E_g)^{\gamma} \dots\dots\dots\dots\dots\dots\dots\dots (1)$$

where B is a proportionality constant, α is the absorption coefficient, $h\nu$ is the energy of the photon, E_g is the optical band gap and γ is an indication of the type of electronic transitions, where $\gamma = 1/2$ for direct transition and $\gamma = 2$ for indirect transition.

It is known that CdSe has a direct energy gap and is characterized by direct and allowed electronic transition, therefore; Eq. (1) becomes: -

$$\alpha\,(hv) = \frac{B}{hv}\left(hv - E_g\right)^{\frac{1}{2}} \dots\dots\dots\dots\dots\dots\dots\dots (2)$$

It is important to be mentioned that; the proportionalityconstant can
Be calculated from the formula [16]:-

$$B = e^2 * \frac{\left(2 * \frac{m_e^*.m_h^*}{m_e^* + m_h^*}\right)^{\frac{3}{2}}}{n.c.h^2.m_e^*} \dots\dots\dots\dots\dots\dots\dots\dots (3)$$

where e is the electron charge, n is the refractive index is Planck's constant, m_e^* is the effective mass of electron and m_h^* is the effective mass of the hole [16].

Since we have two influences that affect the absorption coefficient in our study, the first is the temperature, so the energy gap will be calculated as a function of temperature [4]:-

$$E_g(T) = E_{g0} - \frac{\alpha * T^2}{\beta + T} \dots\dots\dots\dots\dots\dots\dots\dots (4)$$

Where α, β are coefficients fitted with experimental data for each material which equal to ($3.3 * 10^{-4}$ eV.K^{-1}, 83 K) respectively, E_{g0} is the energy gap at 0K which equals 1.834eV [4].

In terms of the change in the electron's effective mass as a function of temperature, it can be formulated with the following relationship [17]:-

$$m_e^*(T) = m_{e300}^* * \frac{Eg_{300}}{Eg(T)} \dots\dots\dots\dots\dots\dots\dots\dots (5)$$

While the effective mass of hole as a function of temperature is expressed by [17]:-

$$m_h^*(T) = m_{h300}^* \frac{E_{g300}}{E_g(T)} \dots\dots\dots\dots\dots\dots\dots (6)$$

where E_{g300} , m_{e300}^* and m_{h300}^* are the energy gap, the effective electron mass, and the effective hole mass at room temperature, respectively [17].

The other influencing factor is the size that due to the quantum confinement of an atom in three dimensions appears with characteristic electronic and optical properties [17].

In this study, we will use the Burs equation [18].

$$E_g QD = E_g(Bulk) + \frac{h^2}{8r^2}\left(\frac{1}{m_e^*} + \frac{1}{m_h^*}\right) \dots\dots\dots\dots\dots\dots\dots\dots (7)$$

where $E_g QD$ is the energy gap of quantum dot, $E_g(Bulk)$ is the bulk energy gap, r is the quantum dots' size.

To study the effects on the quantum dots of CdSe, we substituted equation (4) with the term $E_g(Bulk)$, and substituted equations (5) and (6) (which represent the change in the effective mass of the electron and the hole respectively as a function of temperature) in equation(7) to get an equation describing the energy gap of CdSe quantum dots as a function of temperature which denoted by $E_g QD(T)$:-

$$E_g QD(T) = E_g(T)(Bulk) + \frac{h^2}{8r^2}\left(\frac{1}{m_e^*(T)} + \frac{1}{m_e^*(T)}\right) \dots\dots\dots\dots\dots\dots\dots (8)$$

To obtain the absorption coefficient of CdSe quantum dots as a function of energy and temperature, we substitute the Eq. (8) in Eq. (2).

$$\alpha\,(hv, T) = \frac{B}{hv}\left(hv - E_g QD(T)\right)^{\frac{1}{2}} \dots\dots\dots\dots\dots\dots\dots\dots (9)$$

3. Results and Discussion

The occurrence of the absorption process inside the materials is described or measured by the absorption coefficient, so the absorption coefficient of CdSe Quantum Dots (eq. (9)) has been studied from; two effects the temperature, and the quantum size of dots. It can be noticed that in Figure (1) the energy gap of bulk CdSe was its highest value at 0 K., It is beginning to decreasing sharply with rising temperatures, which its highest value at 400K. The reason for this behavior is the increase in the energy of electrons due to interaction between the thermal phonons and the electrons. This lead, in fact, to an increase in the vibration inside the atom where the lengths of the atomic bonds increase, which makes them weaker with the ability to break them is easier to release the electron, which facilitates the transfer of a high-energy electron from the valence band to the conduction band and as a result of the multiple electron transitions, the energy gap decreases [19, 20].

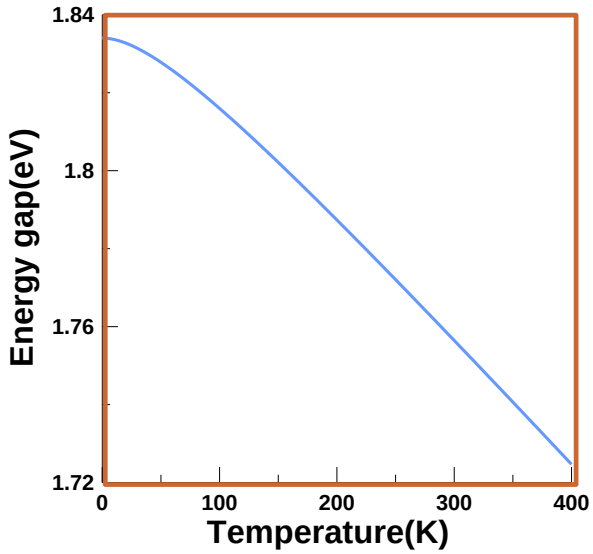

Figure 1. The energy gap of bulk CdSe decreases with increasing temperature

Figure (2) indicates the change in the energy gap due to the decrease in the quantum dot size, it is noted that; the energy gap value changes lightly when the quantum size decreases from 10 nmto 4 nm. This means that these sizes in this range are close to the behavior of the bulk. But when the size is smaller than a size 4 nm, the energy gap begins to increase very significantly until it reaches the highest values at 1 nm. In fact, that is due to the effect of quantum confinement that shifts the energy state to higher (lowest) levels at the conduction band (valence band), which increases the size of the energy gap [21,18].

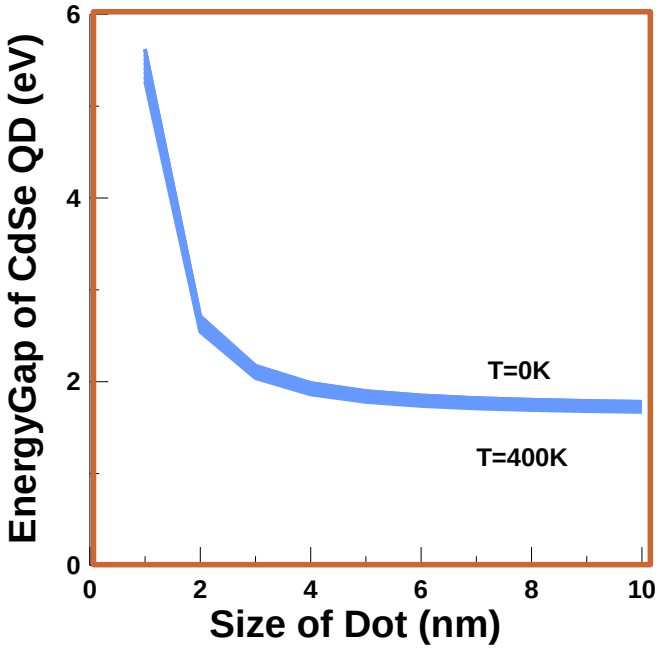

Figure 2. The energy gap of CdSe quantum dots as a function of quantum size dots

Figure (3) shows the absorption coefficient as a function of wavelengths (300nm-730nm) at room temperature. Must attract attention to two important points, the first is that; the different ranges of the

absorption coefficient are due to the different energy gaps of the quantum size of CdSe. It is noted that as the size is larger, it takes a greater range than before, where the size of 1.4 nm takes the range of ultraviolet spectrum only, while the size of 10 nm includes the range of ultraviolet, visible, and some of infrared spectrum. The other point is the energy gap which is inversely proportional to the quantum dot size of the CdSe [22, 23]. It can be seen from the figure that; the response of the quantum sizes as a function of wavelengths begins at 1.4 nm, while sizes of 1nm to 1.2nm, with a very large energy gap, do not absorb the energies of this range of wavelengths at room temperature. Where the wavelength 300nm has the highest energy is 4.141 eV, therefore; the electrons cannot cross the optical energy gap and exciting [24]. Whereas at the quantum dot size of 1.4nm, electrons able to absorb this range (λ=300 nm) of wavelengths at room temperature because it has an energy gap of about 3.571 eV. For this reason, it will allow more energy to be absorbed when the optical gap is smaller. Now, it is appropriate to explain the mechanism that causes the absorption coefficient to decrease according to the relationship$E = \frac{h*c}{\lambda}$. where the ability of the incident light energy to excite electrons from the top of the valence band to the bottom of the conduction band decreases because it does not have an energy equal to or greater than the size of the optical energy gap to excite it [25]. It can be said that; the range of quantum sizes that have been relied upon in this research from 10 nm to 1.4 nm. In this range, the absorption coefficient gradually decreases as the quantum dot becomes smaller [24, 26]. This leads us to believe that the possibility of CdSe quantum dots in tuning colors according to the size. Where the blue shifting is observed when the size of the quantum dots decreases, while red shifting is tuning when the size be larger.

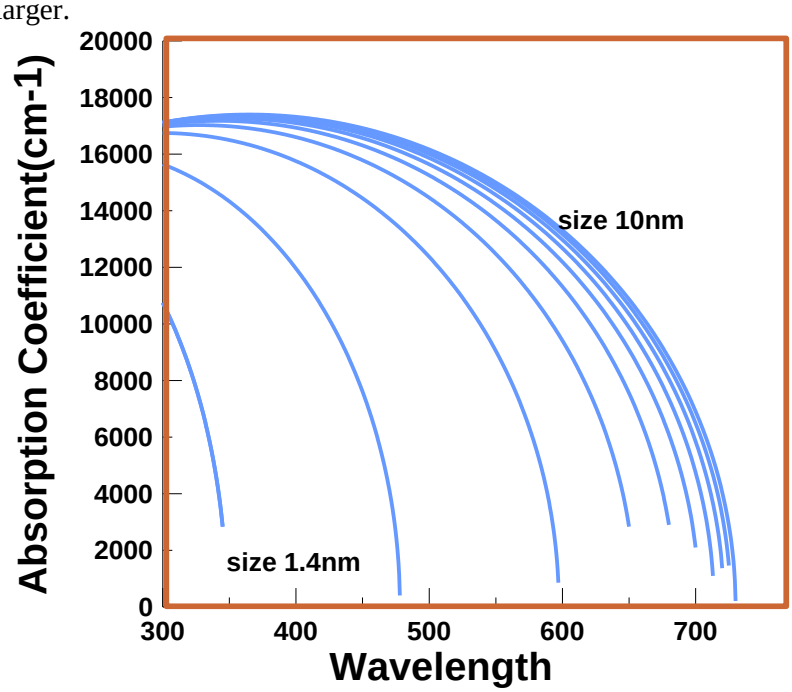

Figure 3. The absorption coefficient as a function of wavelength at the deferent size of CdSe quantum dots between from 1,4nm (absorption threshold) to 10nm.

Figure (4) represents the absorption coefficient as a function of temperature (0-400) K by fixing specific wavelengths, where it is found that the absorption coefficient increases with rising temperature [27]. This increase is evident after the temperature of 100 K at the wavelengths between 300nm to 600nm except the threshold size at the wavelength from 500nm to 600nm where the increase begins with values greater than 100 K and at 700nm after 300K With an increase in temperature, the energy gap get smaller from its usual size as a result of the vibration of the electrons with the increase in their energies, which makes them able to leave their sites and move inside the band, or if its energy

is sufficient, it can move from the valence band to the conduction band. Therefore, with increasing the contribution of the transition processes, the optical absorption coefficient increases.

Noticing Figure (4), there are several important points, the first is that; the absorption coefficient, in general, decreases as the wavelength of the electromagnetic spectrum increases. The other point, the threshold size increases with an increase in wavelength, for example, we find that the size threshold at λ= 300nm is 1.4 nm while for λ= 600nm is 3.6nm. This is because the energy of the specified wavelength is less than the value of the energy gap so that the electron transitions only respond at a size in which the energy gap corresponds to the energy of a photon of wavelength directed to it. However, the sizes of the quantum dots will be determined for each wavelength, the reason could be due to that; the energy gap be smaller and the susceptibility of incident wavelengths to the excitation of electrons [28, 29]

As a result of what was mentioned above, which is that some of the threshold sizes are unable to absorb the wavelength falling on them except at a specific temperature, as is the case at λ= 500 nm, so that the threshold appears only at a temperature of 200 K and the same is the case of λ=600nm. As for 700 nm, the 6 nm minimum appeared at a temperature of 300K, as mentioned earlier, resulting from a decrease in the size of the energy gap with higher temperatures.

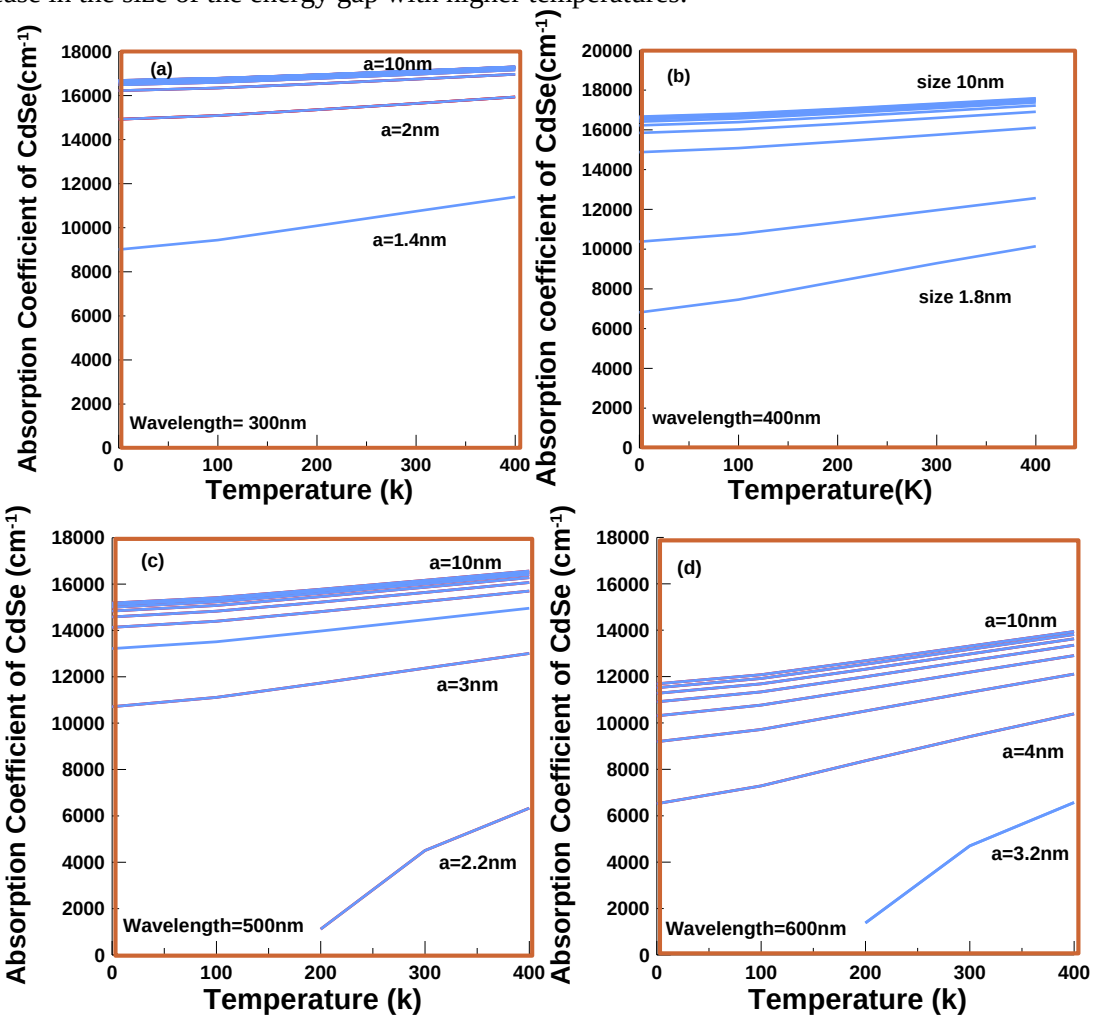

Figure 4. The absorption coefficient increasing with temperature at different wavelength, a(300nm), b(400nm), c(500nm), d(600nm).

Figure (5) shows the absorption coefficient as a function of the size of the quantum dots. In this figure, for all wavelengths, the absorption coefficient decreases with the size of quantum dot be smaller. But, for each wavelength there is a specific size that suffers a curvature then sharp descent in the absorption coefficient. For the wavelength of 300 nm, the absorption coefficient begins to decrease sharply at the size of 3 nm, while the wavelength of 400 nm, it begins at the size of 4 nm. The other wavelengths follow the same behavior according to the energy compatibility of the energy gap of the quantum dots. This behavior is attributed to the number of electronic transitions, which is almost constant at large sizes, then the transitions begin to decrease until they disappear. In fact, this confirms the existence of an absorption threshold for each specific wavelength.

On the other hand, it can be found that small quantum sizes do not react at high temperature which is due to the large energy gap arising from the quantum confinement, as compared to large quantum sizes, which show a direct reaction at high temperatures due to the small energy gap that they have.

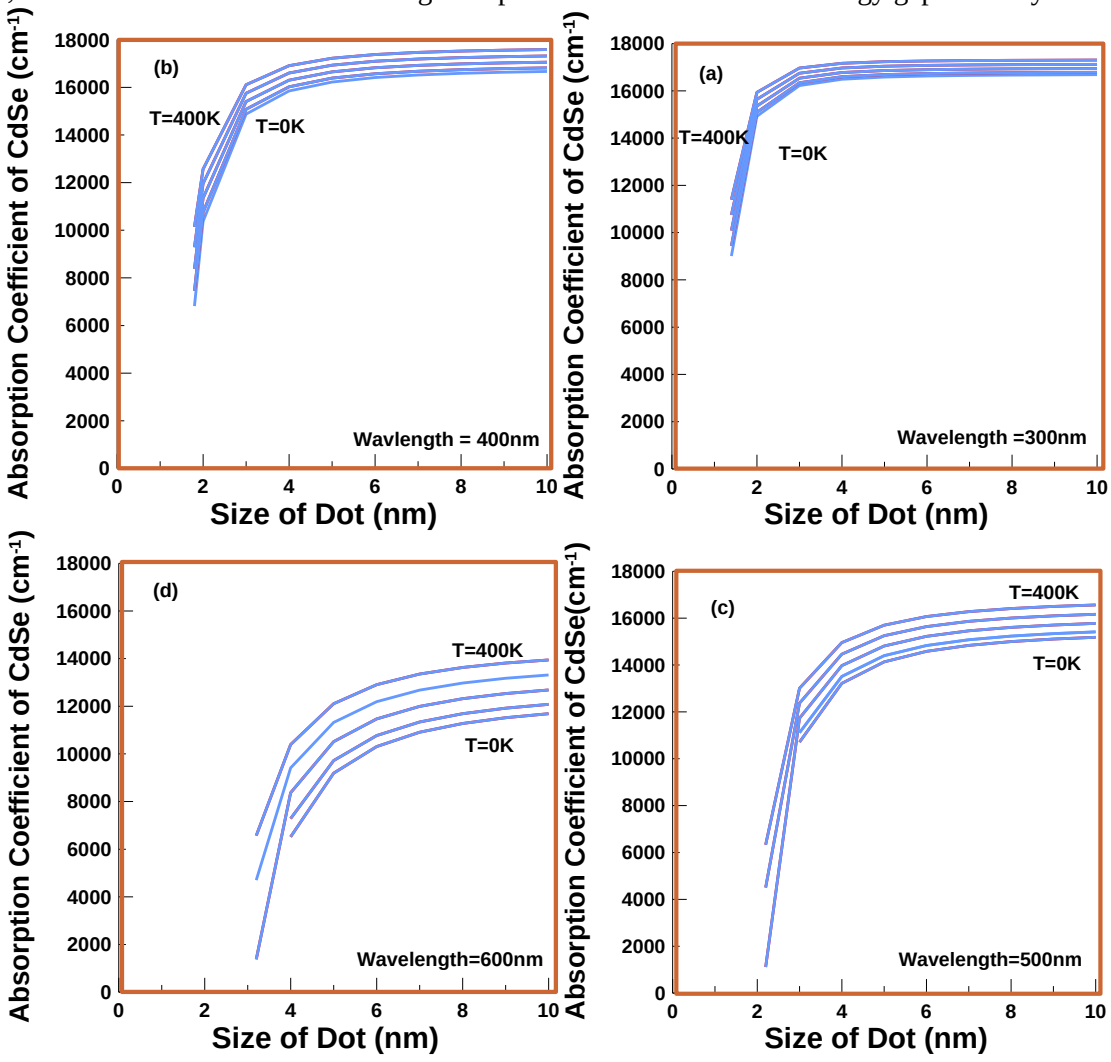

Figure 5. The absorption coefficient as a function of quantum dot size at different wavelength.a (300nm), b (400nm), c (500nm), d (600nm).

The most of experimental results review the optical absorption coefficient in the form $(\alpha\, h\, \nu)^2$. So, it is showed our calculations in the same format in Figure (6c), which gives a suitable match for both Fig.(6a) [27] which represents experimental results, and Fig. (6b) [30] which acts as theoretical models.

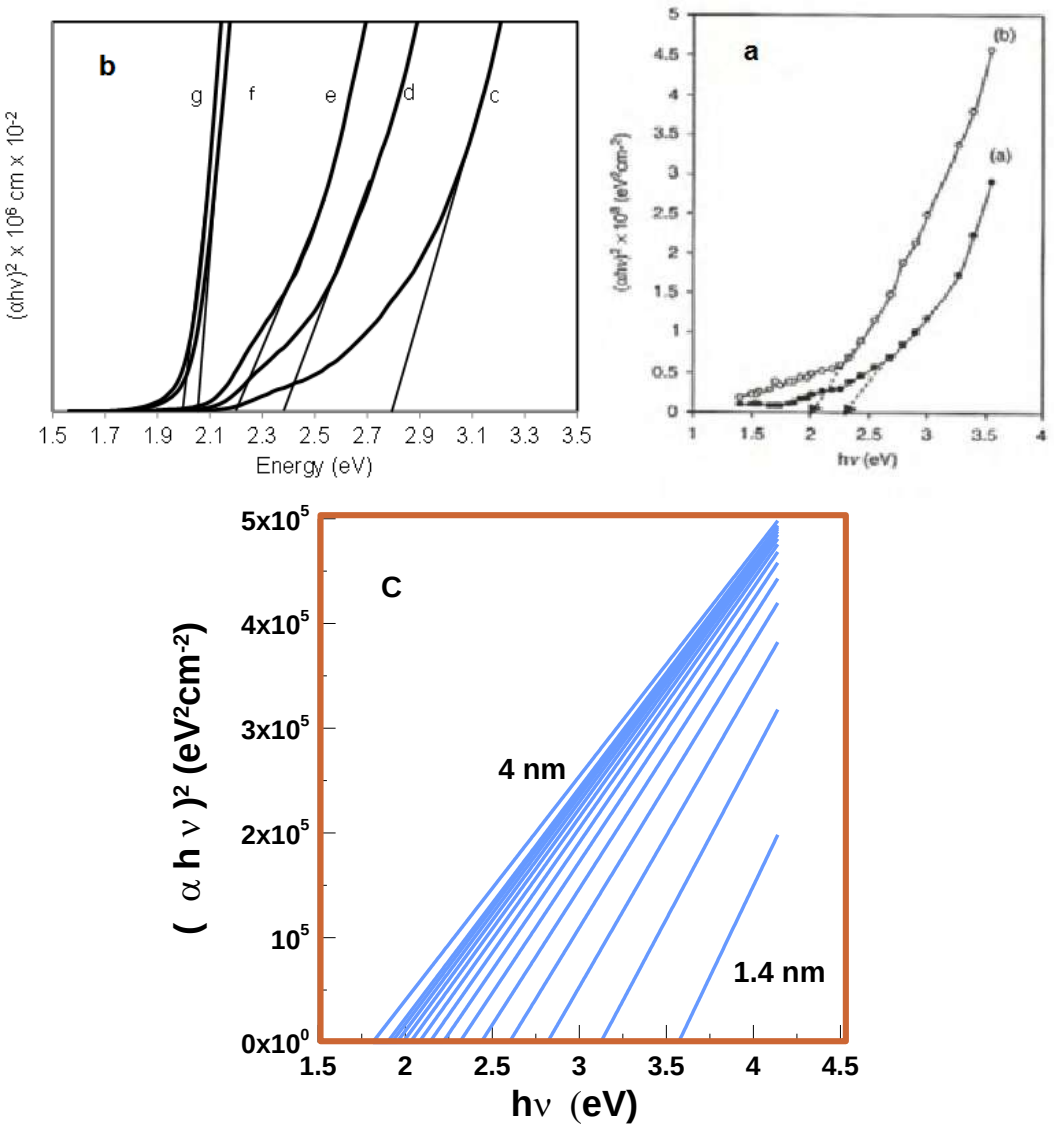

Figure 6. Absorption Coefficient of CdSe quantum dots a. experimental results [27], b. theoretical models [30], c. our calculations

4. Conclusion

For CdSe quantum dots, not all sizes are capable of absorbing electromagnetic radiation, where the absorption threshold begins in quantum dot size 1.4 nm at room temperature. Thus, CdSe quantum dots can be tuned to absorb different wavelengths according to the quantum dot sizes until they reach 10 nm which can be absorbing all wavelengths in the range of the visible spectrum. Therefore, CdSe quantum dots can be considered as one of the most promising materials for tuning energy gap applications, such as light-emitting diodes in different colors of the visible spectrum. On the other hand, each wavelength has an absorption threshold in which the energy of photon of wavelength corresponds to the energy gap of the size of the CdSe quantum dots. Also, for each specific wavelength, the absorption coefficient remains relatively constant for all quantum sizes until it reaches a size in which the energy gap does not match to the energy of the specified wavelength, where the absorption coefficient value drops sharply until it vanishes this is an indication of the end of electronic transitions in the material. All calculations were done by using software MathCAD 15.

5. Acknowledgment

Authors are grateful to Dr. Moafak C. Abdulrid and Dr. Jamal Fadel for their inspiration and fruitful assistance

6. References

[1] Alivisatos AP 1996 *J. Phys. Chem*. **100** 13226–13239
[2] El-Sayed MA Acc. 2004 *Chem. Res.* **37** 326–333.
[3] De Geyterand B and Hens Z 2010 *Appl. Phys. Lett*. **97** 1 161908
[4] Wu W, He F and Wang Y 2016 *J. Appl. Phys.* **119** 055701
[5] Kumar V and Singh JK 2010 *Indian J. Pure Appl. Phys.* **2010** 571-574.
[6] *C* Jinjun Sun and Ewa M Goldys The *Journal of Physical Chemistry112*, *25*, 2008, 9261-9266.
[7] Leatherdale CA 2002 *J. Phys. Chem. B* **106**, 31, 7575-7577.
[8] Shaviv E, Salant A and Banin U 2009 *Chem. Phys. Chem*. **10** 1028–1031.
[9] Yu WW, Qu LH, Guo WZ and Peng XG 2003 *Chem. Mater*. **15** 2854–2860.
[10] Striolo A, Ward J, Prausnitz JM, Parak WJ, Zanchet D, Gerion D, Milliron D and Alivisatos AP 2002 *J. Phys. Chem*. **B106** 5500–5505.
[11] Schmelz O, Mews A, Basche T, Herrmann A and Mullen K 2001 *Langmuir* **17** 2861–2865.
[12] Leatherdale CA, Woo WK, Mikulec FV and Bawendi MG *J. Phys. Chem*. B **106** 7619–7622.
[13] Patidar D, Rathore KS, Saxena NS, Sharma K and Sharma TP 2008 *Chalcogenide Lett.* **5** 21 - 25
[14] Tauc J 1974 *Amorphous and Liquid Semiconductors*, Plenum Press, New York, NY.
[15] Mahmoud WE, Al-Amri AM and Yaghmour SJ 2012 *Opt. Mater*. **34** 1082.
[16] Jacques I 1975 *Pankove"optical processes in semiconductor* Dover Publications. Inc. New York.
[17] Gopal V 1982 *Indian J. Pure Appl. Phys.*180-182
[18] Chukwuocha EO, Onyeaju MC and Harry TST 2012 *World J. Condensed Matt. Phys.* **2** 96-100
[19] O'Donnell KP 1991 *Appl. Phys. Lett.* 2924-2926
[20] Amiri GRA, Fatahian S, Mahmoudi S 2013 *Mater. Sci. Appl.* **4** 134-137.
[21] Neeleshwar S, Chen CL, Tsai CB and Chen YY 2005 *Physical Review* B **71** 201307.
[22] Brazis PW 2017 *Quantum Dots and Their Potential Impact on Lighting and Display Applications* The IstitutoItaliano di Tecnologia, Genova. JULY 2017.
[23] Baskoutas S and Terzis AF 2006 *J. Appl. Phys.* **99**, 013708 (2006).
[24] Kulkarni A, Guney D and Vora A 2013 *Hindawi Publishing Corporation*, ID 504341 7.
[25] Sze SM 2007 *Semiconductors Devices Physics and Technology* 3rd edition, John Wiley &Sons, Inc.
[26] Vinil VS and Isac J 2018 *Int. J. Eng. Sci. Inven. (IJESI)* 40-47.
[27] Dwived DK, Kumar V, Dubeyb M and Pathak HP 2011 *Chalcogenide Lett.* **8** 521–527.
[28] Zhang H, Peng X, Sun L and Liu F 2015 *MATEC Web of Conferences* **26** 01006
[29] Singh M, Goyal M and Devlal K 2018 *J. Taibah Univ. Sci.* **12** 470-475.
[30] Saikia D, Phukan P and Saikia PK 2014 *International Journal of Latest Res. Sci. Technol.* 3 156-159.

Design of Optical Fibers and Calculate their Guided Modes Properties at 1550 nm

Design of Optical Fibers and Calculate their Guided Modes Properties at 1550 nm

Firas A. Shnain[1] and Aqeel R. Salih[2]

[1] General Directorate of Education in Baghdad, Third Rusafa, Baghdad, Iraq
[2] College of Education for Pure Science (Ibn Al-Haitham), University of Baghdad, Baghdad, Iraq

Email: Ferras.Adel1204a@ihcoedu.uobaghdad.edu.iq

Abstract. There is no doubt that optical fiber technology is one of the most important stages of the communications revolution at all and it is of utmost importance in our daily life. In this work, five fibers with core radii 2.5, 4.5 and 6.5–8.5 μm were designed. The properties of all guided modes have been calculated at a wavelength of 1550 nm by using RP Fiber Calculator. A single-mode fiber is obtained when the core radius approaches the wavelength. As the core radius is increased, the fiber becomes a multimode. The percentage power in the core increases with increasing core radius. The modes profiles were illustrated and compared with the modern references.

Keywords: Single-mode fiber, Multimode fibers, Step-index fibers, Guided modes, Third window (1550 nm), RP Fiber Calculator.

1. Introduction

A thin strand of glass with a higher refractive index core surrounded by a lower refractive index cladding forms an optical fiber [1]. A step-index fiber (SIF) has an abrupt index change at the core-cladding boundary [2]. Figure 1a shows a multimode (MM) SIF which allows the propagation of multiple modes within the fiber core. Figure 1b shows a single-mode (SM) SIF which allows the propagation of only one mode. The refractive index profile in both cases may be defined as [3]:

$$n(r) = \begin{cases} n_1 & \text{for } r < a \text{ (core)} \\ n_2 & \text{for } r \geq \text{a (cladding)} \end{cases} \quad (1)$$

where r is the radial position, n_1 and n_2 are the refractive indices of core and cladding, respectively and a is the radius of the fiber core. MMFs and SMFs only differ in the radius of the light-guiding core [4]. Fabrication of MMFs is easy. Further the launching of light into MMFs is also easy. These fibers are generally used for short distances, like local area networks (LANs). Launching of light into SMFs and fabrication of SMFs are difficult and so the fiber is expensive. Generally in the SMFs, the transmission loss and dispersion are very small. So the SMFs are very useful in long distance communication [5].

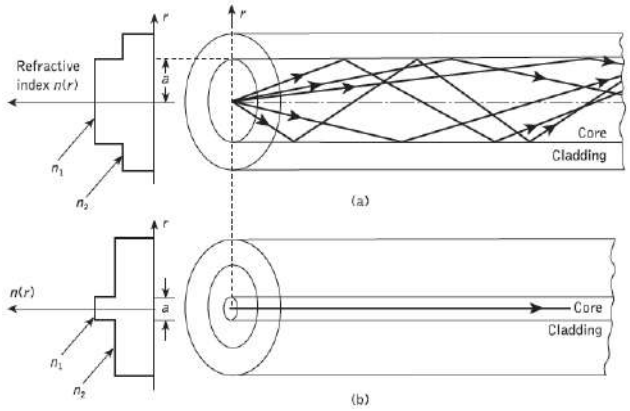

Figure 1. The refractive index profile and typical rays in SIFs: (a) MM and (b) SM [3].

In 2017, Mohammed and Al-Hindawi [6] studied and calculated the design parameters such as operating wavelength, core radius, numerical aperture, acceptance angle, attenuation, dispersion and information capacity for SIFs and graded-index fibers for different sources.

In 2018, Gulistan et al. [7] demonstrated an innovative approach to enhance mode stability by reducing mode coupling between the propagation modes of a few-mode fiber by using commercially available finite element method (FEM)-based COMSOL software.

In 2020, Salih [8] designed a SMF at 1310 nm and 1550 nm wavelengths by using RP Fiber Calculator. Also, Ibrahim and Salih [9, 10] used this program to study properties of propagated transverse modes through SIFs at 850 nm and 1300 nm.

In this work, SM and MM optical fibers have been designed and their properties were calculated at 1550 nm.

2. Theoretical Part

When the incidence angle is greater than the critical angle, the light is totally internally reflected at the core-cladding interface ($r = \mathrm{a}$). The critical angle is given by [11]:

$$\theta_{\mathrm{c}} = \sin^{-1}\left(\frac{n_2}{n_1}\right) \tag{2}$$

The acceptance angle of the fiber can be calculated by [12]:

$$\theta_{\mathrm{a}} = \sin^{-1}\left(\frac{1}{n_{\mathrm{o}}}\sqrt{{n_1}^2 - {n_2}^2}\right) \tag{3}$$

where n_{o} is the refractive index of the incident medium ($n_{\mathrm{o}} = 1$ for air).

The numerical aperture (NA) measures the amount of light that collects by or emerges from the fiber core. The NA is defined as [13]:

$$\mathrm{NA} = \sin\theta_{\mathrm{a}} \tag{4}$$

The normalized frequency is a dimensionless parameter which determines the number of modes. It is calculated by [3]:

$$\mathrm{V} = \frac{2\pi}{\lambda}\mathrm{aNA} \tag{5}$$

where λ is the free space wavelength. A fiber has the lowest loss at 1550 nm [14].

The propagation constant is given by [12]:

$$\beta = \frac{2\pi}{\lambda}n_{\mathrm{eff}} \tag{6}$$

where n_{eff} is the effective refractive index which lies within the range of cladding and core indices.

The effective area is a quantitative measure of the area which a fiber mode effectively covers in the transverse dimensions. It is defined as:

$$A_{\text{eff}} = \frac{[\int |E|^2 dA]^2}{\int |E|^4 dA} = \frac{[\int I dA]^2}{\int I^2 dA} \quad (7)$$

where E is the amplitude of electric field, I is the corresponding intensity and dA signifies integration over the whole plane.

For a Gaussian beam, the effective area is:

$$A_{\text{eff}} = \pi\omega^2 \quad (8)$$

where the radius ω can be determined from [2]:

$$\omega \approx \left(0.65 + 1.619\text{V}^{-3/2} + 2.879\text{V}^{-6}\right)\text{a} \quad (9)$$

This is accurate within 1% for 1.2<V<2.4. For V>2.405, it applies to the first mode.

There is also a modified approximate formula [12]:

$$\omega \approx \left(0.65 + 1.619\text{V}^{-3/2} + 2.879\text{V}^{-6}\right)\text{a} - (0.016 + 1.561\text{V}^{-7})\text{a} \quad (10)$$

The percentage power propagating in the core is [2]:

$$\text{P in core} = \left(1 - e^{-2\text{a}^2/\omega^2}\right) \times 100\% \quad (11)$$

The cut-off wavelength is given by [3]:

$$\lambda_c = \frac{2\pi}{\text{V}_c}\text{aNA} \quad (12)$$

where V_c is the cut-off normalized frequency for the linearly-polarized (LP) mode. For example, the LP_{01} mode has $\text{V}_c = 0$ and the LP_{11} mode has $\text{V}_c = 2.405$.

3. Results and Discussion

RP Fiber Calculator can be used to make calculations on optical fibers with radially symmetric index profiles. Inputs in this program as shown in Figure 2 are core radius, core refractive index (1.45), cladding refractive index (1.44) and wavelength (1550 nm). Outputs are: numerical aperture (NA= 0.17), normalized frequency (V), number of modes (M), properties and profiles of guided modes.

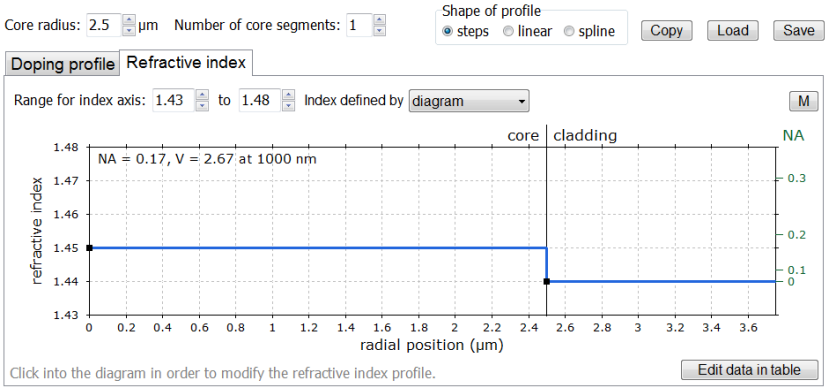

Figure 2. RP Fiber Calculator.

Table 1 shows normalized frequencies and number of modes. The normalized frequency and number of modes increase with increasing core radius. The fiber is SM when V<2.405; while at V>2.405, the fiber is MM.

Table 1. Normalized frequency and number of modes.

a (µm)	V	M
2.5	1.723	1
4.5	3.101	2
6.5	4.479	4
7.5	5.168	5
8.5	5.858	6

3.1. Single-Mode Fiber

A single-mode fiber can be obtained when the radius of the core is a small multiple of the operating wavelength. Table 2 shows LP_{01} mode properties of this fiber calculated from RP Fiber Calculator. These properties include propagation constant, effective refractive index, effective area and percentage power in the core.

Table 2. Properties of LP_{01} mode (a=2.5 μm).

β (/μm)	n_{eff}	A_{eff} (μm^2)	P in core (%)
5.84977	1.443081	38.4	64.5

Effective area and power in core for this mode calculated from Equations (8) and (11) are listed in Table 3. There is a small difference when compared with those in Table 2.

Table 3. Effective area and power in core for LP_{01} mode (a=2.5 μm).

From Equations (8) and (10) A_{eff} (μm^2)	From Equations (10) and (11) P in core (%)
39.9	62.7

Figure 3 shows LP_{01} mode profile (single spot in the 2D plot and Gaussian in the radial plot).

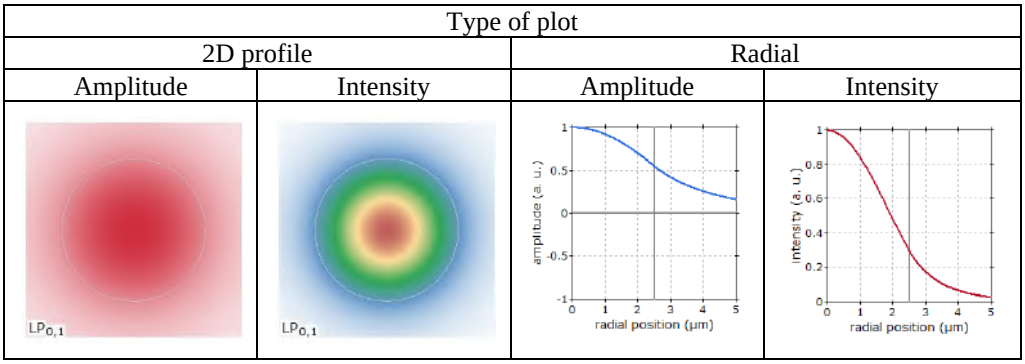

Figure 3. Profile of LP_{01} mode (a=2.5 μm).

3.2. Multimode Fibers (First Design)

Multimode fibers can be obtained when the core radius is large compared to the operating wavelength. Four core radii were compared 4.5, 6.5–8.5 μm. The properties of guided modes of these fibers calculated from RP Fiber Calculator are listed in Tables 4 to 7. From these tables, the following can be observed:

1. The mode LP_{01} has the highest β, n_{eff}, P in core and has no cut-off.
2. Increasing core radius results in increasing β, n_{eff}, A_{eff}, P in core and cut-off wavelength of the mode.

Table 4. Properties of LP modes (a=4.5 μm).

Number of the mode	Mode	β (/μm)	n_{eff}	A_{eff} (μm^2)	P in core (%)	cut-off (nm)
1	LP_{01}	5.86421	1.446643	58.4	90.7	
2	LP_{11}	5.84550	1.442028	73.2	68.8	1965.75

Table 5. Properties of LP modes (a=6.5 μm).

Number of the mode	Mode	β (/μm)	n_{eff}	A_{eff} (μm^2)	P in core (%)	cut-off (nm)
1	LP_{01}	5.87003	1.448080	97.2	96.4	
2	LP_{11}	5.85846	1.445225	95.3	89.4	2839.42
3	LP_{21}	5.84419	1.441703	117.6	75.9	1797.05
4	LP_{02}	5.84085	1.440880	143.5	60.7	1796.87

Table 6. Properties of LP modes (a=7.5 μm).

Number of the mode	Mode	β (/μm)	n_{eff}	A_{eff} (μm^2)	P in core (%)	cut-off (nm)
1	LP_{01}	5.87169	1.448488	122.5	97.5	
2	LP_{11}	5.86247	1.446213	116.4	92.8	3276.25
3	LP_{21}	5.85076	1.443325	130.0	85.0	2073.52
4	LP_{31}	5.83740	1.440030	169.1	67.7	1553.47
5	LP_{02}	5.84732	1.442476	122.5	79.1	2073.31

Table 7. Properties of LP modes (a=8.5 μm).

Number of the mode	Mode	β (/μm)	n_{eff}	A_{eff} (μm^2)	P in core (%)	cut-off (nm)
1	LP_{01}	5.87285	1.448774	150.2	98.2	
2	LP_{11}	5.86531	1.446915	140.3	95.0	3713.09
3	LP_{21}	5.85563	1.444526	150.9	89.9	2349.99
4	LP_{31}	5.84417	1.441699	163.9	81.4	1760.60
5	LP_{02}	5.85256	1.443769	133.9	86.7	2349.75
6	LP_{12}	5.83930	1.440498	208.4	61.1	1637.92

Table 8 shows a comparison between the effective refractive index differences of the last two core radii. It can be observed that the difference between LP_{21} and LP_{02} modes is the lowest. A low Δn_{eff} between the modes may result in energy loss because of the interference between the adjacent optical modes or energy transfer due to inter-mode mixing.

Table 8. Effective index differences between LP modes.

a (μm)	Δn_{eff}			
	LP_{01}– LP_{11}	LP_{11}– LP_{21}	LP_{21}– LP_{02}	LP_{02}– LP_{31}
7.5	0.002275	0.002888	0.000849	0.002446
8.5	0.001859	0.002389	0.000757	0.00207

Effective area and power in core for LP_{01} mode calculated from Equations (8) and (11) are listed in Table 9. These values are smaller than those in Tables 4 to 7 with a small difference in power.

Table 9. Effective area and power in core for LP_{01} mode.

a (μm)	From Equations (8) and (9)	From Equations (10) and (11)
	A_{eff} (μm^2)	P in core (%)
4.5	57.4	89.9
6.5	89.5	95.4
7.5	109.7	96.5
8.5	132.6	97.2

Figures 4 to 7 show LP mode profiles: LP_{01} (single spot, Gaussian), LP_{11} (two spots), LP_{21} (four spots), LP_{31} (six spots). Each of these modes have one maximum in the radial plot. Both LP_{02} and LP_{12} modes have two maxima. The intensity is proportional to the square of the amplitude.

Mode	2D profile		Radial	
	Amplitude	Intensity	Amplitude	Intensity
LP_{01}	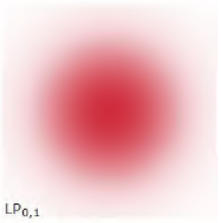	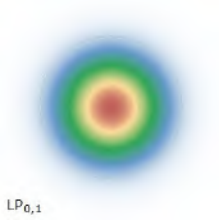	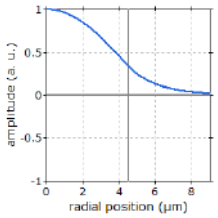	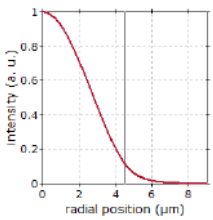
LP_{11}	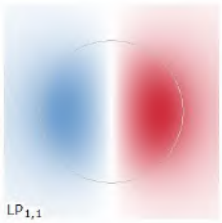	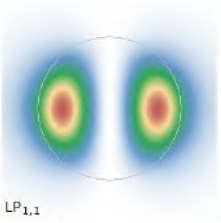	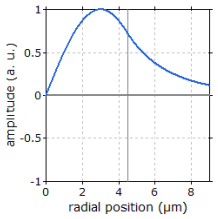	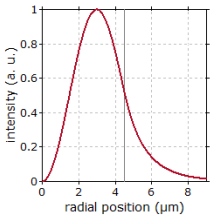

Figure 4. Profiles of LP modes (a=4.5 μm).

Mode	2D profile		Radial	
	Amplitude	Intensity	Amplitude	Intensity
LP_{01}	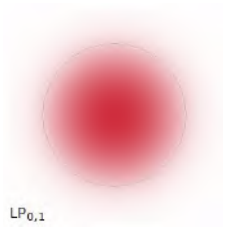	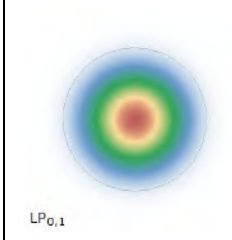	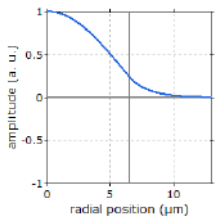	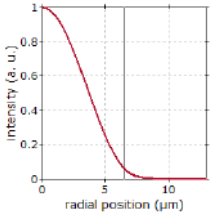
LP_{11}	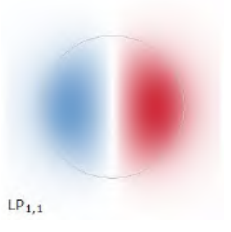	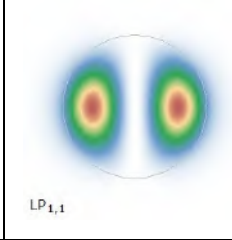	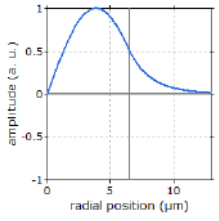	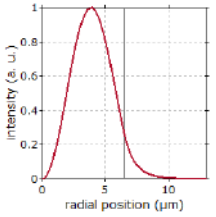
LP_{21}	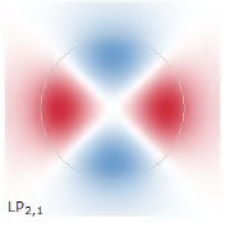	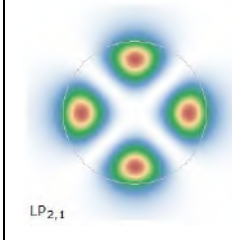	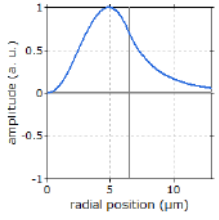	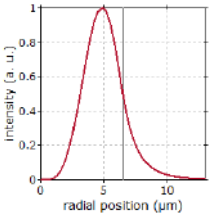
LP_{02}	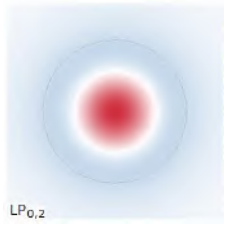	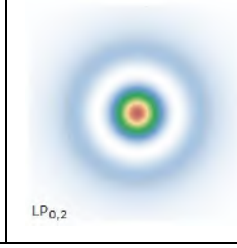	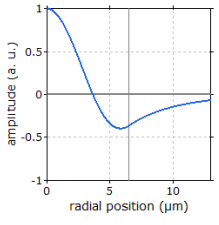	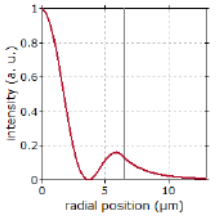

Figure 5. Profiles of LP modes (a=6.5 μm).

Mode	2D profile		Radial	
	Amplitude	Intensity	Amplitude	Intensity
LP_{01}	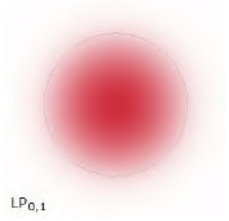	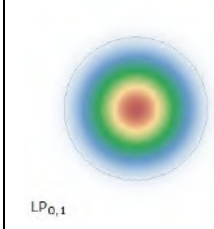	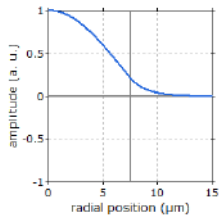	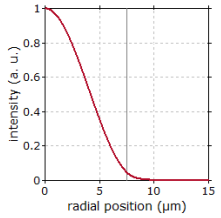
LP_{11}	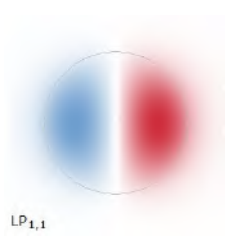	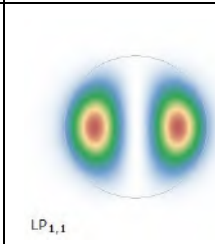	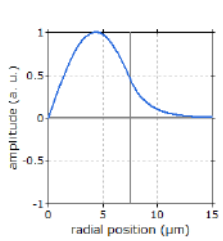	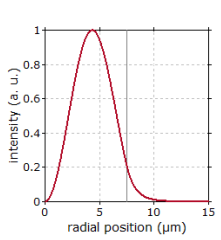
LP_{21}	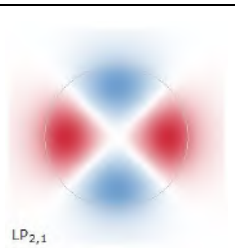	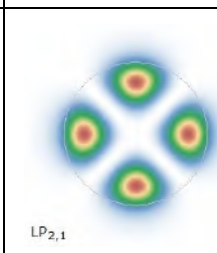	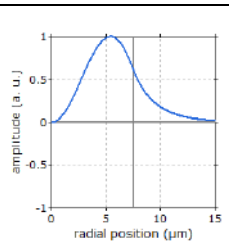	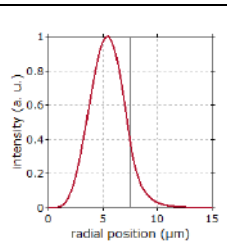
LP_{31}	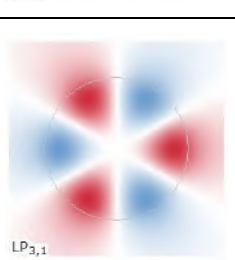	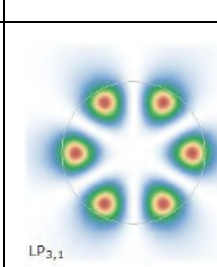	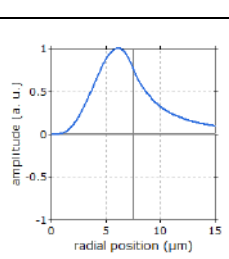	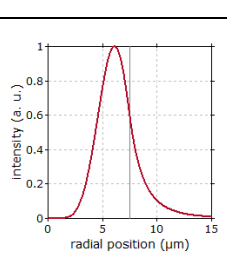
LP_{02}	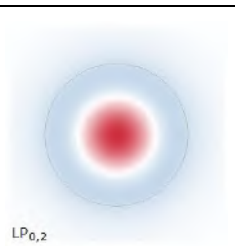	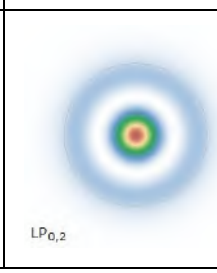	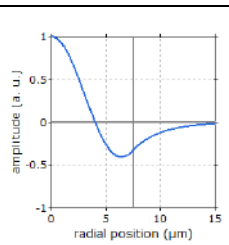	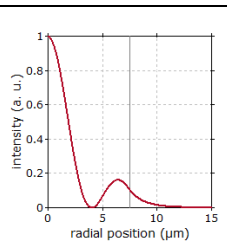

Figure 6. Profiles of LP modes (a=7.5 μm).

Mode	2D profile		Radial	
	Amplitude	Intensity	Amplitude	Intensity
LP_{01}	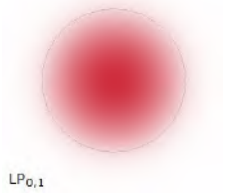	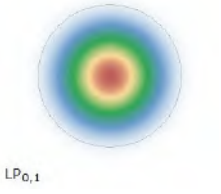	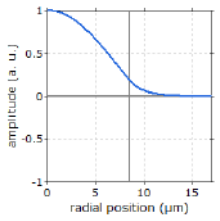	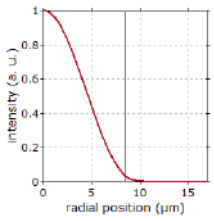
LP_{11}	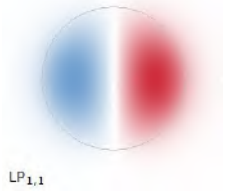	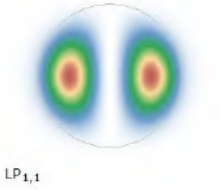	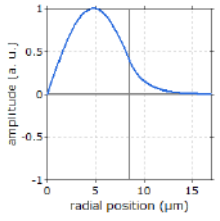	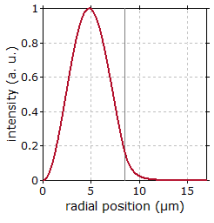
LP_{21}	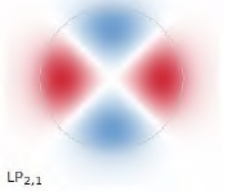	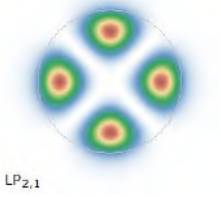	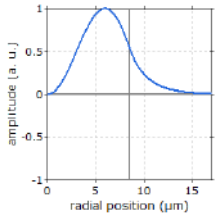	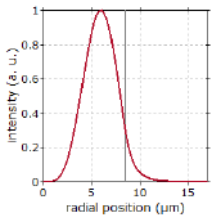
LP_{31}	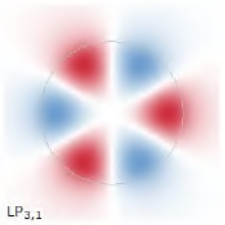	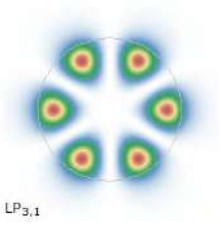	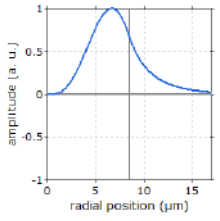	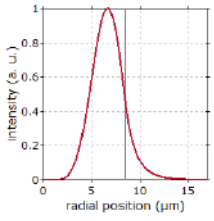
LP_{02}		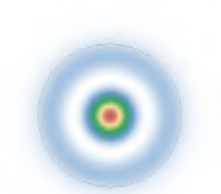	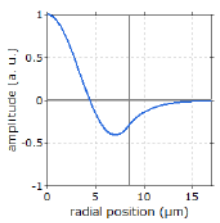	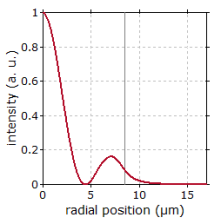
LP_{12}	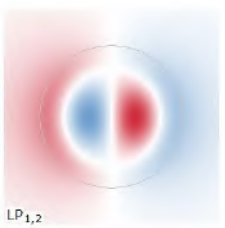	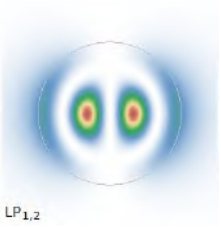	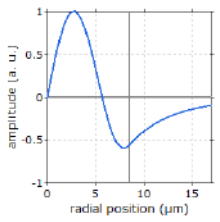	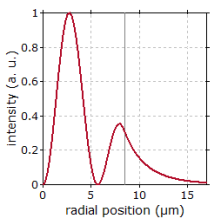

Figure 7. Profiles of LP modes (a=8.5 μm).

3.3. Multimode Fibers (Second Design)

In order to compare the results, a second design of MMFs is considered. The core and cladding refractive indices are taken as 1.45 and 1.4403, respectively. Table 10 shows a comparison between this work and Reference [7].

Table 10. Comparison between this work and Reference [7].

	This work (second design)		Reference [7]	
Software	Free RP Fiber Calculator		Commercial COMSOL	
n_1	1.45		1.45	
n_2	1.4403		1.4403	
λ(nm)	1550		1550	
a (μm)	7.5	8.5	7.5	8.5
V	5.091	5.769	5.1	5.77

Tables 11 and 12 show modes properties for the second design of this work.

Table 11. Properties of LP modes (a=7.5 μm) (second design).

Number of the mode	Mode	β (/μm)	n_{eff}	A_{eff} (μm^2)	P in core (%)	cut-off (nm)
1	LP_{01}	5.87172	1.448496	123.2	97.3	
2	LP_{11}	5.86256	1.446236	117.4	92.5	3226.90
3	LP_{21}	5.85095	1.443373	132.0	84.3	2042.29
4	LP_{02}	5.84758	1.442542	125.9	77.8	2042.08

Table 12. Properties of LP modes (a= 8.5 μm) (second design).

Number of the mode	Mode	β (/μm)	n_{eff}	A_{eff} (μm^2)	P in core (%)	cut-off (nm)
1	LP_{01}	5.87287	1.448779	151.0	98.1	
2	LP_{11}	5.86538	1.446931	141.2	94.7	3657.16
3	LP_{21}	5.85576	1.444558	152.5	89.4	2314.59
4	LP_{31}	5.84441	1.441758	167.4	80.3	1734.08
5	LP_{02}	5.85273	1.443811	135.9	86.0	2314.35
6	LP_{12}	5.83981	1.440623	240.8	55.9	1613.25

A comparison between two designs in this work shows that as the cladding index increases slightly, the propagation constant, effective index and effective area are increased; while the normalized frequency, power in core and cut-off wavelength are decreased.

Table 13 shows an excellent agreement between the effective index differences of this work and those of Reference [7]. The second design has a lower effective index difference compared to the first design.

Table 13. Effective index differences between LP modes.

a (μm)	7.5			8.5			
Δn_{eff}	LP_{01}–LP_{11}	LP_{11}–LP_{21}	LP_{21}–LP_{02}	LP_{01}–LP_{11}	LP_{11}–LP_{21}	LP_{21}–LP_{02}	LP_{02}–LP_{31}
This work (second design)	0.00226	0.002863	0.000831	0.001848	0.002373	0.000747	0.002053
Reference [7]	0.002253	0.00285	0.000821	0.001842	0.00236	0.0007396	0.00205

Table 14 shows a comparison between the effective areas of this work and Reference [7]. Effective areas in this work are smaller than those of Reference [7], with a small difference for LP_{01} and LP_{02} modes and 1.5 times smaller for LP_{11} and LP_{21} modes.

Table 14. Effective areas (μm^2) of LP modes.

a (μm)	7.5				8.5			
Mode	LP_{01}	LP_{11}	LP_{21}	LP_{02}	LP_{01}	LP_{11}	LP_{21}	LP_{02}
This work (second design)	123.2	117.4	132.0	125.9	151.0	141.2	152.5	135.9
Reference [7]	124	177	199	127	151.92	213.77	230.45	137.00

There is an excellent agreement between Figure 8 and Figure 9 in terms of the number of modes and the profiles of amplitude and intensity.

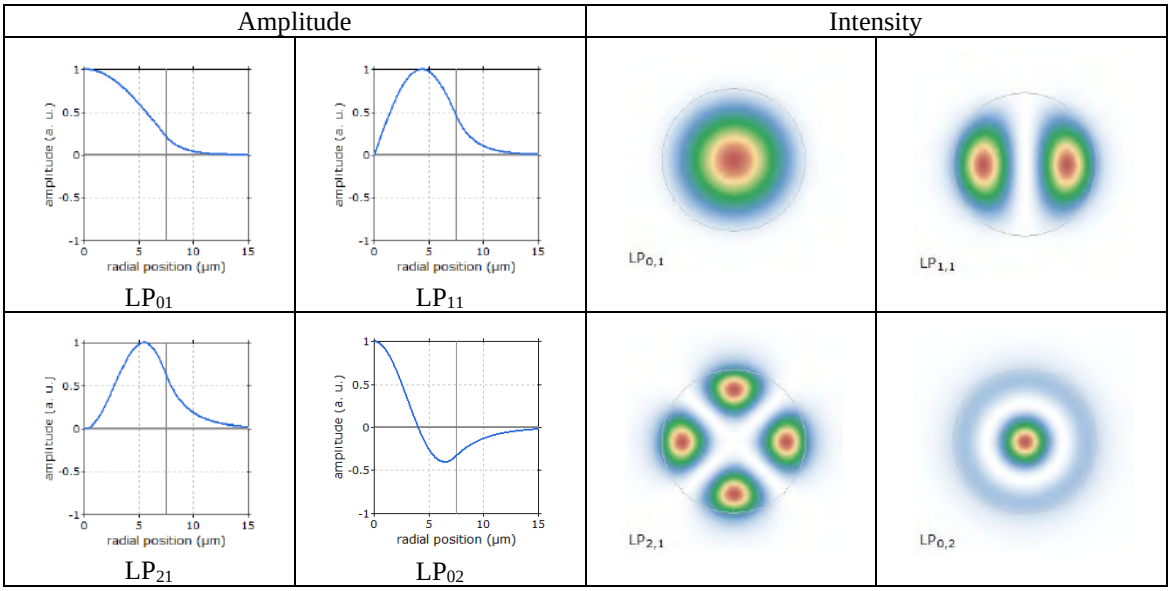

Figure 8. Profiles of LP modes (a=7.5 μm) (second design).

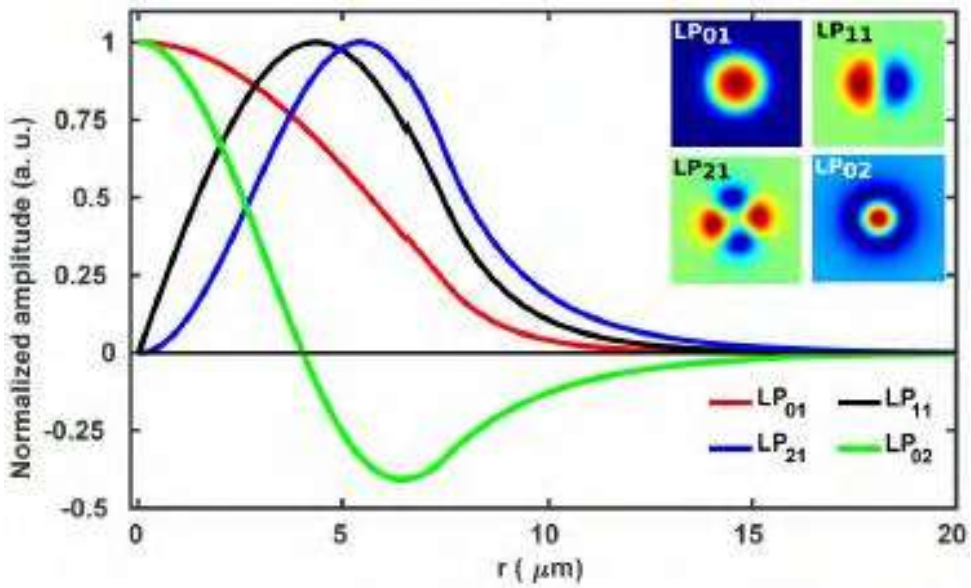

Figure 9. Profiles of LP modes (a=7.5 μm) [7].

4. Conclusions

1. If the core radius is close to the wavelength, the fiber supports only one mode. If the core radius becomes much larger than the wavelength, the fiber supports multiple modes.
2. When the core radius is large, most power is confined in the core. When the core radius becomes smaller, the amount of power in the core decreases.

References

[1] DeCusatis C. M. & DeCusatis C. J. S. 2006 Fiber Optic Essentials, *Elsevier*.
[2] Agrawal G. P. 2010 Fiber-Optic Communication Systems, 4th edition, *Wiley*.
[3] Senior J. M. 2009 Optical Fiber Communications: Principles and Practice, 3rd edition, *Pearson.*
[4] Mitschke F. 2009 Fiber Optics: Physics and Technology, *Springer-Verlag.*
[5] Arumugam A. 2001 *Pramana–J. Phys.* **57** (5 & 6) 849
[6] Mohammed S. & Al-Hindawi A. M. 2017 *Kurdistan Journal of Applied Research* **2** (3) 302
[7] Gulistan A., Ghosh S. & Rahman B. M. A. 2018 *OSA Continuum* **1** (2) 309
[8] Salih A. R. 2020 *Ibn Al-Haitham J. for Pure & Appl. Sci.* **33** (1) 40
[9] Ibrahim H. K. 2020 Studying Properties of Propagated Transverse Modes through Step-Index Optical Fibers, *M. Sc. Thesis, University of Baghdad*.
[10] Ibrahim H. K. & Salih A. R. 2020 *AIP Conference Proceedings* **2307** (1)
[11] Tricker R. 2002 Optoelectronic and Fiber Optic Technology, *Newnes Press*.
[12] Paschotta R. 2020 RP Photonics Encyclopedia.
[13] Al-Azzawi A. 2007 Fibre Optics: Principles and Practices, *CRC Press*.
[14] Kumar S. & Jamal Deen M. 2014 Fiber Optic Communications: Fundamentals and Applications, *Wiley*.

Modeling the Effect of Particle Packing Density for Sintering

Modeling the Effect of Particle Packing Density for Sintering

Hanan K. Hassun, Bushra H. Hussein, Bushra. K.H.al-Maiyaly

Physics Department, College of Education for Pure Science (Ibn Al- Haitham)
University of Baghdad, Baghdad, Iraq

E-mail: boshra.h.h@ihcoedu.uobaghdad.edu.iq

Abstract. This research studies the effect of particle packing density on sintering TiO_2 microstructure. Sintering experiment was conducted on compacts involving of monodisperse spherical TiO_2 particles. The experimental results are modeled using L^2- Regression technique in studing the effect of two theoretical values of 55% and 69% of initial packing densities. The mathematical simulation shows that the lower values of density compacts sintered fast to theoretical density and this reflects that particle packing density improved densification rate because of the competing influence of grain growth at higher values of densities.

Keywords: sintering, densification rate, mathematical simulation.

1. Introduction

Synthesis and sintering of nanocrystalline ceramic powders have attracted much attention due to their promising properties [1, 2]. Where sintering is an essential step in the manufacturemethod of ceramic samples, which can significantly influence the microstructure and properties ofmaterials [3]. The sintering behavior and microstructural development of a powder compact is effect strongly by initial properties, for example the relative density, pore size distribution, the particle and the powder packing. Although the effect of the former parameters on the microstructural development has been examined in detail, the influence of the initial packing values of the powder has been typically over looked [4].
TiO_2 is one of the most widely used metal oxides, which has wide range of applications, including gas and humidity sensors, pigments, catalyst support, capacitors and solar cell. TiO_2 has been widely studied with respect to synthesis of nano sized powder, thin film fabrication and sintering of nano structured TiO_2 ceramics. The properties of nano structured bulk TiO_2 ceramic is pretentious by the microstructural topographiesfor example (grain size, secondary phases, porosity) and defect structure, for example (electronic and point defects) [5, 6].

Effect of particle size distribution on powder packing and sintering in binder jetting additive industrial of metals where a change of bimodal powder mixtures of several particle diameters and mixing parts were printed and sintered to study the influence of bimodal mixtures on the parts density and shrinkage. The using of bimodal powder mixtures develops the flowability (10.5%) and powder's packing density 8.2%, the increasing of the sintered density (4.0%) where reducing of the sintering shrinkage (6.4%) [7].

The intension of this study was modelled mathematically the densification rate of TiO_2 powder using L^2-Regression modeling technique utilizing two initial packing densities 55% and 69% theoretical.

2. Theoretical part

Sintering is an industrialprocedure in which a fine powder that has been formed into a form is subsequently fired at high values of temperatures. The compact when fired densifies and transform non-porous. Sintering is a treatment with thermalthat bonds particles composed into a solid, coherent construction, by means of mass transportationapparatuses occurring mostly at the atomic level. Distribution of particle size has animportant effect on the sintering procedure and on the microstructure of the sintered part. A wider of particle sizes distribution produced a higher green density and closer sintering in both metals and ceramics [8]. The pores are classified in two basic types: the first type called matrix or first- generation pore and the second type large called second-geneartion pores which originate from particle agglomeration and particle packing irregularities within the powder compact [9]. The large pores are extra difficult to eliminate large voide for two reasons. First simple kinetics dictate alonger time to fill a larger void by diffusion, second a large pore can be thermodynamically stable depending on the dihedral and pore size: grain size ratio [10].

The densification rate($d\rho/dt$) depends on the diffusion coefficient responsible for densification ($D_{lattice}$ or $D_{boundary}$) and the grain size [11].

$$\frac{d\rho}{dt} = \frac{CN_g DY^o \Omega}{kTG^L} \quad \text{.....(1)}$$

Where C is a constant related to the controlling mechanism, G is the grain size, **D** is the diffusion coefficient, Y^o is the gas / solid surface energy, **Ω** is the material volume, T is the temperature, *K* is the Boltzmann constant, N_g is the actual number of pores per grain , L is the grain size exponent, 3 for lattice- diffusion controlled densification which is used in this study [9].

In this study reported in Ref. [13]), the spherical, monodisperse TiO_2 powder was created by the hydroiysis of dilute ethanolic solution of titanium tetraethoxide. The powder was discrete in H_2O at a pH =8 utilizingprobe of ultrasonic, the dispersion was poured into polypropylene viale and the powder was allowable to settle to form concentrated sediments, these diments were collapsed into rigid compacts by the addingsolution of a 1 ***M*** $(NH_4)_2CO_3$ to the clear supernatant in the ampoules. The liquid was extracted and the sediment wasgraduallydried by air for one day, followed by drying by vacuum at 100 °C for18 h. the density of particles 3.1 g /cm^3in thecompacts waschanged to rutile 4.25 g /$cm^3$by prefiring the contracts at 780 °C for 3 h.
It was formed two types of TiO_2 compacts, with theoretical density of initial packing of 55 % and 69 %. Samples were heated in air rt of 55°C/ min to the sintering temperatures 1060 °C. The 55%dens compacts were fired at 1060 °C for times reaching from 0.05h to 8.4h. The high value of density compacts was fired at 1060 °C for times ranging from 0.017 to 1h.

The densification rate equation (1) can be written as follows [10];

$$\frac{d\rho}{dt} = \frac{C_3 D}{kTG^L} \quad \text{.....(2)}$$

Where C_3 is a constant. The equation (2) can be written as follows:

$$\frac{d\rho}{dt} = \frac{C_\rho}{TG^L} \quad \text{.....(3)}$$

Where C_ρ is the densification rate coefficient related to the working mechanisms.

3. Regression modeling technique

The equation of L^2_ regression which used in this study can be express as follows [13]:

$$X = (A^T A)^{-1} A^T b \quad (4)$$

Where A is the matrix , A^T is the transpose of matrix A , b is random observation and X the fixed part of equation but unknown.

The equation (3) can be written in integral forms as follows:

$$\rho - \rho_0 = \frac{C_\rho}{T(1-L)} G^{1-L}(t - t_0) \quad \text{.....(5)}$$

Equation (5) can be written to another form to make easier to handle with L^2_ regression formulation as follows :

$$\rho = K_1 G^{1-L} t + h_1 \quad \text{.....(6)}$$

where h_1 is the densification rate parameters, K_1 is the densification rate coefficient

$$K_1 = \frac{C_\rho}{T(1-L)} \quad h_1 = \rho_0 - K_1 G^{1-L} t_0$$

The density value was measured using model of L^2_ Regression [14].

4. Results and Discussion

The beheavior of sintering for the compacts have low –density and high -density compacts are displayed in Fig. 1 and Fig. 2, respectively. Fig. 1 displays the density results as a function of time at 1060 °C. As can be seen from the figure, the less densely packed compact staking the low green density required more time to reach theoretical density (ρ_{th} = 4.25 g /cm^3) than can be seen in Fig. 2. The calculated sintered for low densely sample ranged between 56.37 and 95.64 % , at time 300 min reach 95.64 % for theoretical density. This shows that little grain growth occurred during sintering because of the large mean pore size and corresponding lower green density , where the large pores eliminated at greatlyslower rate caused the decreasing of measured in rate of densification[8,11].

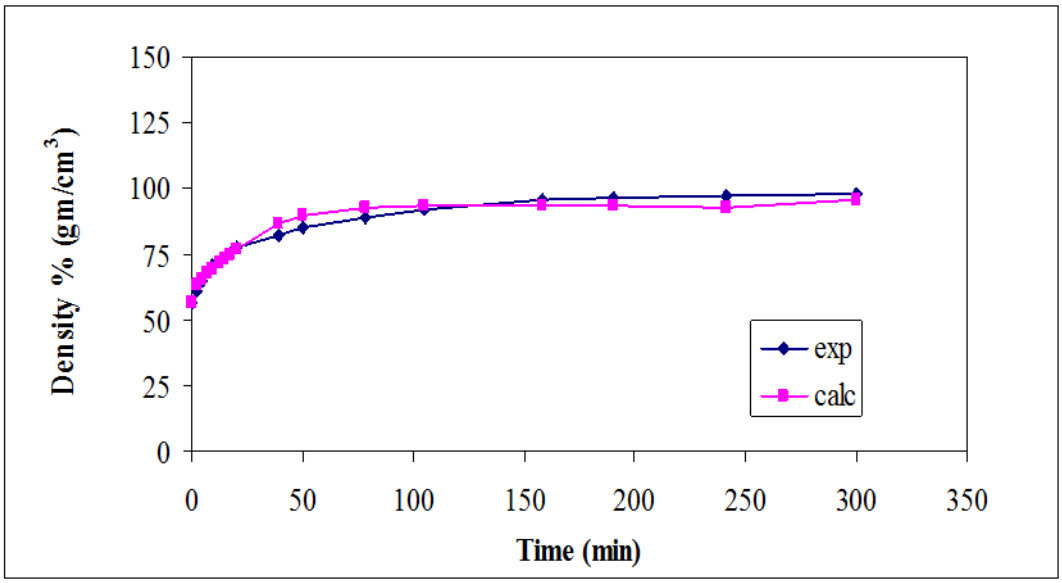

Figure 1. The density datafor 55% of theoretical densityas a function of time at 1060 °C.

The calculated sintered for high- density sample in Fig. 2 ranged between 69.12 and 98.57 % at time of 19.5 min. The increasing in packing density has resulted in animportant increase in kinetics of densification. As can be seen in Fig. 2 to reach 94% for theoretical density needs 10 min only and this has been refer to boundary of grain porosity controller of grain growth kinetics where the competing effect of grains growth occur at high density and the small pores in the green compacts were fastremoved. Sample with higher green density had a smaller mean pore size and a thinner distribution of pore size [8, 11].

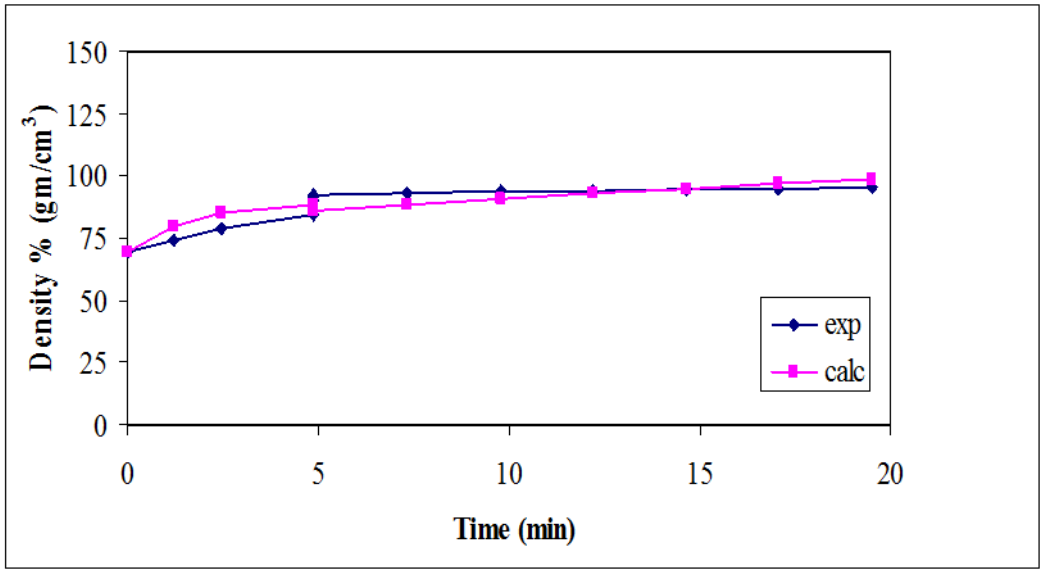

Figure 2. The density data for 69 % of theoretical density as a function of time at 1060 °C.

Fig. 3 shows the comparison for the sinteringresults for 55% and 69% of theoretical density as a function of time at 1060 °C. As can be seen, the slower rate for low densely sample (55 %) and rapidly rate for high densely sample (69 %),the sign from this that increasing the green density concurrently increases the number of pores per grains and narrow the distribution of pore size and that effect on the densification kinetics that coincide with [15].

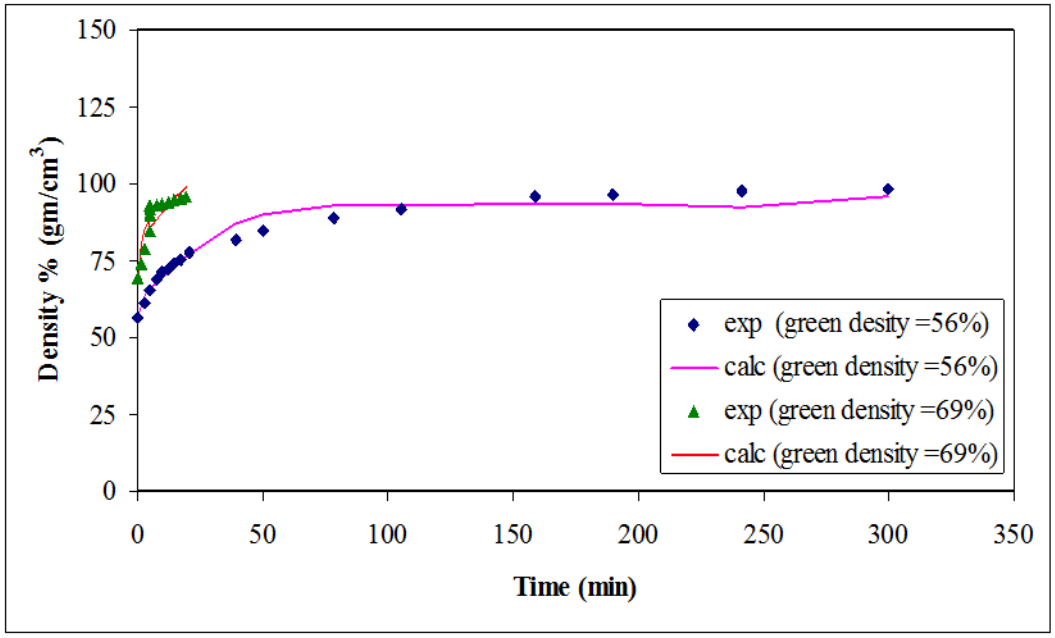

Figure 3. the density data for 55% and 69% of theoretical densityas a function of time at 1060 °C.

In Table 1, we can see the densification rate coefficient K_1 and the densification rate parameter h_1, both K_1 and h_1 for high green density (69 %) increases than low green density(55 %) because of effect of the initial partical packing and number of pores on the rate of grains growth and distribution rate .

Table 1. densification rate coefficient K_1 and Desification rate parameter h_1 for 55 % and 69 % of theoretical density.

Densification rate	55% of theoretical density	69 % of theoretical density
Densification rate coefficient K_1	61.451	80.895
Desification rate parameter h_1	0.926	2.0393

5. Conclusion

The modeling technique show that the calculated results using L^2_Regression technique agrees with experimental results ,and the samples that have more densely packed and the higher green density will sintered more quickly than the samples that less densely packed , the density ofparticel packingand

porosity uniformity were controlled of the distribution procedures. Therefor, the powder features, especially the green density control the final microstructure and the sintering kinetics.

References

[1] Swihart M T 2003 *Current Opinion in Colloid and Interface Science* **8** 127.
[2] Srdic V V Winterer M and Hahn H 2000 *J. Am. Ceram. Soc.***83** 1853.
[3] Wang Q B Wang Q G and WanCX 2010 *Science of Sintering* **42** 337 .
[4] Bjørk R Tikare V Frandsen H L and Pryds N 2012 *US Department of Energy Publications Paper 105.*
[5] Sheng CVladimir P and Fatih D 2010 *Journal of Materials Science* 45 **(**24) 6685.
[6] Ramla MAini S N and Djuhana 2019 *IOP Conf. Series: Journal of Physics: Conf. Series* 1282.
[7] Bai Y Wagner G Christopher B Williams 2017 *Journal of Manufacturing Science and Engineering* **139**.
[8] Alice C DB 2002 *Computer modeling of sintering in ceramics* University of Pittsburgh.
[9] Zhao J and Harmer MP 1988 *J.Am , ceram . Soc* **71** (2) 113.
[10] Zhao J and Harmer MP 1988 *J .Am.Ceram.Soc* **71** (7) 39.
[11] Zhao J and Harmer MP 1992 *J. Amer . Ceram* . Soc .**75** 830.
[12] Barringer E A and Bowen H K 1988 *Applied Physics A: Materials Science & Processing* **45** (4) 271.
[13] RobertJV b 2001 *Linear programming Foundations and extensionsseconded* Copy right C.
[14] Malyaly HK 2005 *Analysis the three stage of sintering using linear programming* M.Sc. Thesis University of Baghdad.
[15] Saad B H Farid Sawsan A H Mahdi and Hanan K H Al.Mayaly 2013 *Ibn Al-Haitham Jour. for Pure & Appl. Sci.* **26** (3).

Numerical Study of Bending Losses in Optical Fibers with Arbitrary Profile Index

Numerical Study of Bending Losses in Optical Fibers with Arbitrary Profile Index

Asmaa M. Jassim[1], Hassan A. Yasser[2], Haider K. Muhammad[3]

[1]Ministry of education, Directorate of Education in Thi-Qar
[2]Physics Department, Science College, University of Thi-Qar
[3]Physics Department, Education College, University of Thi-Qar

E-mail: asmaasd384@gmail.com

Abstract. In this work, the bending loss was numerically studied within the COMSOL environment, where the general formula for profile index including graded and step-index types was adopted. The study showed an increase in bending loss with decreases bending radius, decreases core radius and increases wavelength. The graded order is effective up to $g = 1.75$ after which the loss is constant. There is an oscillating change in loss caused by interference between the outgoing and reflected waves from the boundaries, which becomes clearer as the loss itself increases.

Keywords: bent losses, graded-order, fundamental mode

1. Introduction

Optical fiber plays a role in high-quality and high-speed telecommunications development [1]. The loss of optical energy will occur when a fiber undergoes a macro-bend of the limit curvature radius, i.e. a dielectric waveguides lose power by radiation if their axes are curved. It has negative effect of signal for communication system of optical fiber, on this basis, it was used as a useful feature to develop optical fiber for different purposes [2]. There are two mechanisms known to cause bend-induced loss, the first happens to the uniform bend owing to mismatch between the bent regions and direct modes. The other type happens within uniformly bent region where the refractive index profile of fiber is getting as skewed, to increasing linearly of refractive index on bend. Bending affects, the individual mode various according to distinct properties such as effective refractive index, intensity, phase distribution, etc. Bending an optical fiber is to introduce refractive lose [3] So, there are many efforts to reduce macro-bending losses for all types of optical fibers along the past few years, where fiber designs were proposed to meet several requirements for macro-bend losses [1, 4]. The limitation of the most serious to its validity is caused by dealing with undistorted field of the straight guide for its derivation, even if the loss of radiation is ignored, the field changes its form in the curved guide. Therefore, no existing formulae for modeling bend-losses of these fibers were presented, except for maximum or minimum prediction of the bend loss conditions in relation to parameters of fiber and wavelength. Bending loss of fibers are employed with many important purpose like a great importance for modern communications, especially with regard to techniques of multiplexing in the way to enhance the ability to send information, plays a central role with the design of fiber amplifiers and with a fiber laser to reduce

higher-order to achieve single of effective regime of multi-mode fibers [5, 6, 7]. It has been shown in this work, that the effect of the four chosen parameters, spatially graded-order (g), wavelength of propagated wave (λ), core radius (a) and bending radius of a dielectric wave guide on the bending-losses (L_b) will be illustrated.

2. Methods

The wave front in the optical fiber must be perpendicular to the direction of propagation. The signal transmitted in core becomes faster than in cladding. As a result, loss in the signal transmitted energy through the optical fiber will appear where the speed of light must be increased as shown in Fig.1.

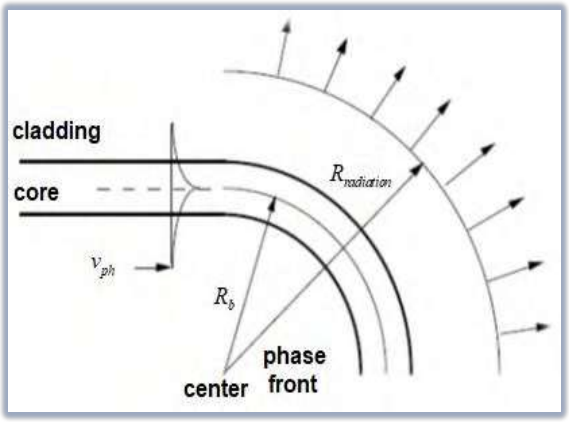

Fig.1. Bending effect of an optical fiber [8].

The total losses of a bent fiber include transition loss and pure bend loss in bent section caused by mismatch between bent and straight sections of the propagation. A single mode bent fiber of length (L), the pure bend loss calculated: [8].

$$L_b = 10 \log_{10}[\exp(2\alpha L)] = 8.686\, \alpha L \quad (1)$$

Where α = macro-bending loss coefficient (function of optical fiber structure and material, bending radius, and wavelength of radiation used in the fiber). So, there are many approaches have been employed for evaluation it, a simple formula firstly proposed by Marcuse. The simplified formula for the bent optical fibers needs to be modified to include fiber stress by utilizing the effective bend radius. Therefore, the modified index distribution must be presented by transforming the circularity curved fiber to equivalent straight fiber. This leads to, the tilted index distribution with respect to original. An increasing away from the center of the bend (curvature of the bent fiber can be a tilted refractive index), as shown in Fig.2.

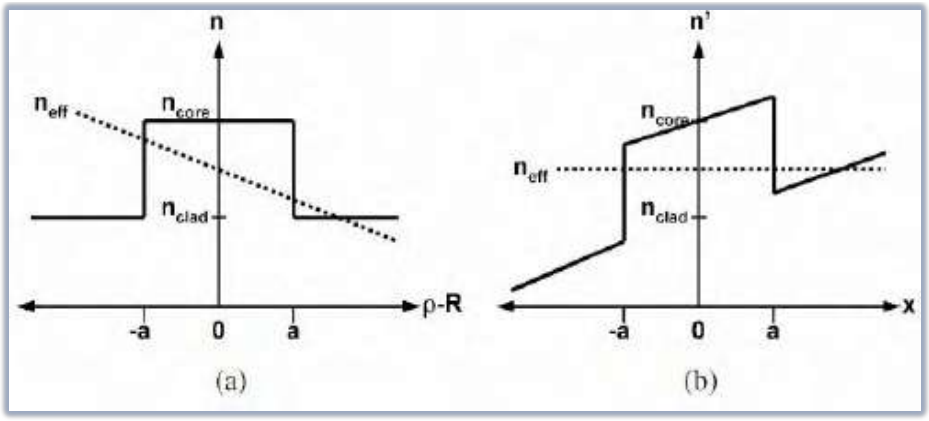

Fig.2. profile index, a) with bent and b) without bent

The well-known formula of modified refractive index distribution with slow bent ($R \gg x$) as the first approximation read as:

$$n_{equ}(x,y) = n_{mat}\,(x,y)\exp(x/R) \approx n_{mat}\,(x,y)(1 + x/R) \quad (2)$$

Where x is the displacement from the core center in curvature axis, R radius of bent and n_{mat} is the refractive index-profile to unbend fiber. Because of compression along fiber's inner half, towards the bend center and tension along the outer half of fiber, n_{mat} becomes vary according to the relation [9].

$$n_{mat.}(x,y) = n(x,y)\left[1 - \frac{n^2(x,y)\;x}{2R}[P_{12} - \nu(P_{11} + P_{12})]\right] \quad (3)$$

where $P_{11}\ and\ \mathrm{P}_{12}$ = components of photo-elastic tensor, ν = ratio of Poisson and $n(x,y)$ = the refractive index-profile of the unbend (straight) fiber and so called profile-grading, defined as [10], [11] .

$$n(x,y) = n_{core}\sqrt{1 - 2\Delta(\rho/a)^g} \quad (4)$$

where $\rho = \sqrt{\mathrm{x}^2 + \mathrm{y}^2}$, the parameter $\Delta = (n_{core} - n_{clad})/n_{core}$, n_{core} and n_{clad} = refractive index in center of the core and the cladding, respectively, and g = graded-order, it plays an important role when waves propagated the optical fiber and gives a strange properties depending on the profile indices of the different graded orders that shown in Figure 3. Accordingly, graded-order will be an important issue to construct the bent losses.

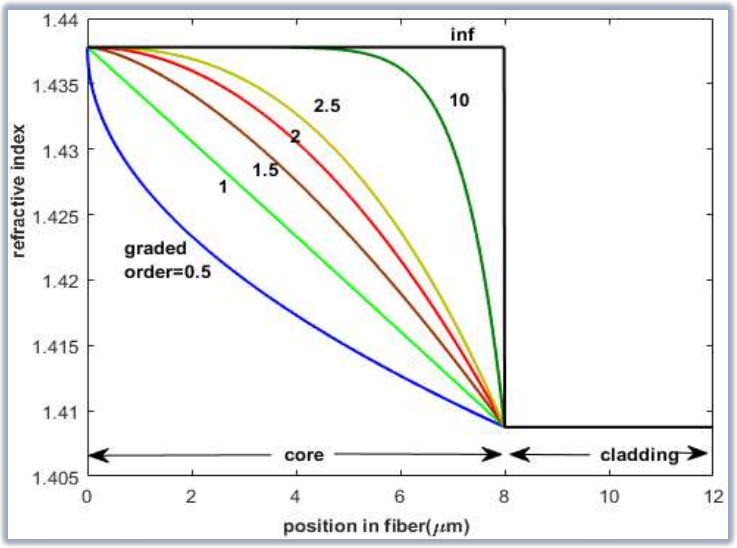

Fig.3. Refractive index profiles for different graded-orders [10]

Where 2α is the coefficient of power loss, $\kappa = \sqrt{k_{core}^2 - \beta_z^2}$ and $\gamma = \sqrt{\beta_z^2 - k_{clad}^2}$ = field decay rates of core and cladding, respectively, k and β are the propagation constants for free space and the guided mode in the unbent waveguide, respectively, $V = \sqrt{\kappa^2 + \gamma^2}$ = the normalized frequency, $K_{m\pm1}$ = Bessel function of 2nd kind.

3. Results and Discussion

COMSOL environment was used to determine the relationship between wavelength and effective refractive index. COMSOL works on a finite element method (FEM) basis which is built on the basis of dividing the cross section into small parts and forming the mesh. A perfectly matched layer (PML) is added with thickness as a third layer to the geometry to avoid the reflections from cladding interface to interfere with the mode confined in the core. We applied boundary condition of the perfect electric conductor, with zero initial conditions, to the exterior boundary. Concerning profile index, the same formula as in Eq.(4) with the replacements (by and by) were applied. The type and accuracy of the mesh are chosen in order to achieve better accuracy with a suitable operating time for the computer. A study of this subject requires controlling of four factors: the core radius, the bending radius, the wavelength and the graded order. Fig.4 represents a selected sample for the fundamental mode in step index fiber by changing part of these factors. It is evident that the amount of energy that will be outside the core is subject to these factors.

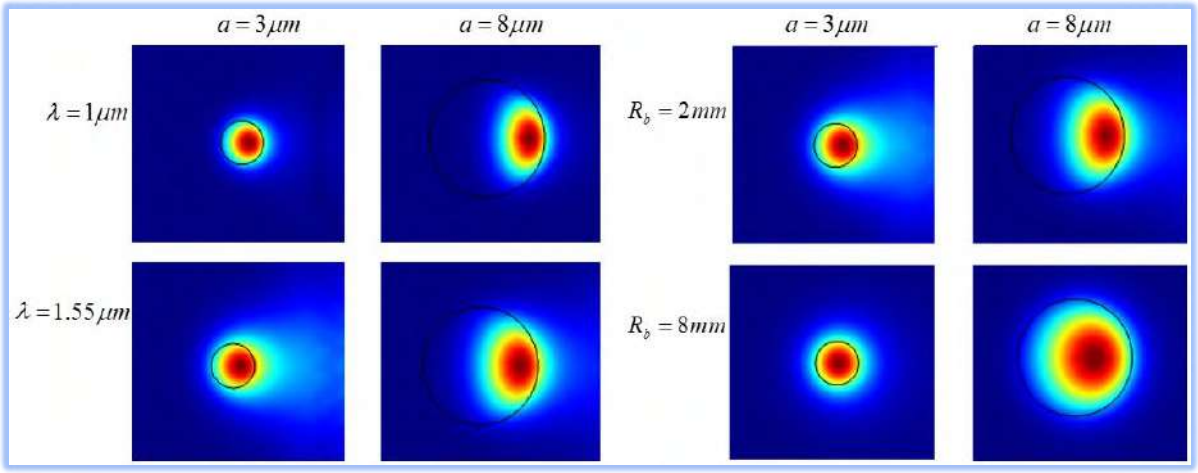

Fig.4. Fundamental mode at $g=\infty$ for (a) $R_b=2mm$ and (b) $\lambda=1.55\mu m$

Fig.5 represents the relationship of the bending losses with the graded, where core radius is at $a=10\mu m$. Generally, the loss decreases with the graded order until reach the limits of $g \geq 1.75$, then the loss is constant. That is, the type of profile index affects only the loss at the smaller graded orders. When the graded order decreases, the distribution width of the profile index will be small. Therefore, the Gaussian distribution of the fundamental mode may have a greater width, and therefore we expect the mode portion outside the core to be large with a decrease in the graded order. On the other hand, the loss is greatly reduced as the bending radius increases and vice versa. The reason for this decrease is due to the fact that a greater portion of the propagated pulse will be outside the core with a decrease in the bending radius.

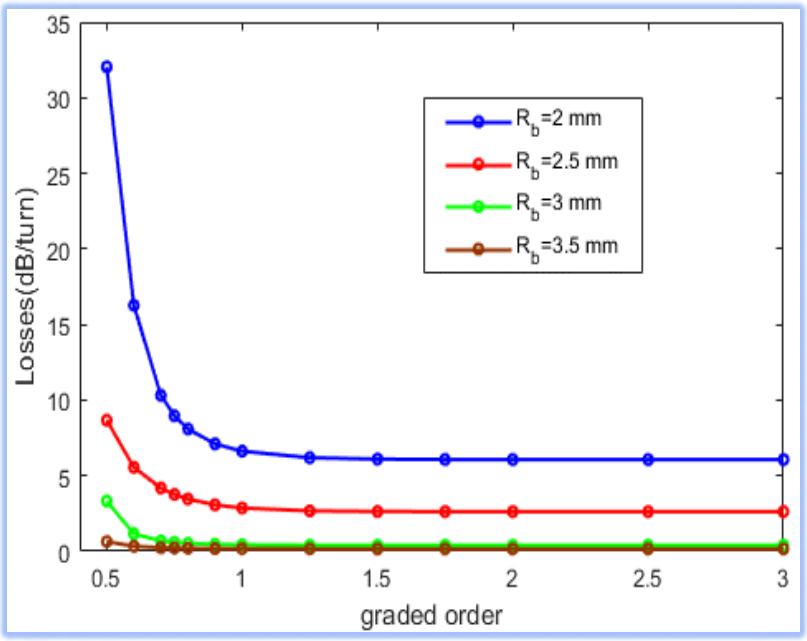

Fig.5. Bending losses and graded order

Fig.6 presents bending losses of the step index fiber as function of core radius for different values of R_b at $\lambda=1.55\mu m$. 3dB is the maximal variation when a radius is *2mm*. At a small bending radius, the

random variations appear very clear due to the increased interface section between the cladding and the PML layers. As the bending radius increases, loss and corresponding random variations will be decreased. In addition, at a small core, the loss is significant and vice versa. This is due to the inability of the core to confine the propagated pulses (small core).

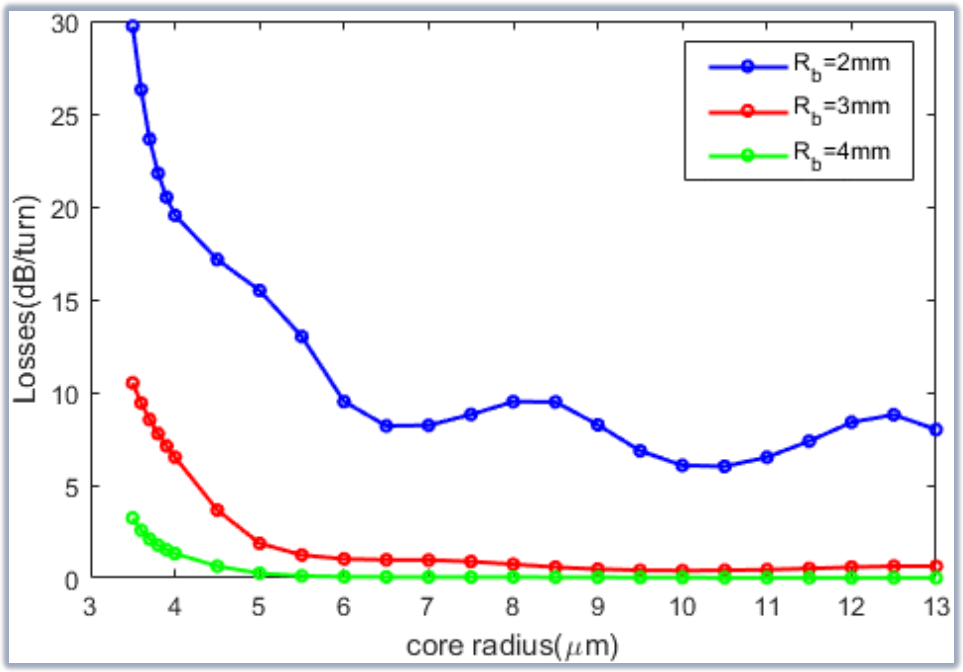

Fig.6. Bending losses Vs. core radius

Fig.7 illustrates bending losses of step index fiber as function of core radius for different wavelengths at $R_b = 2mm$. It is evident that the greater wavelength causes more losses, and the losses generally decrease with an increase in the core radius. Random variation is very clear in the case of large losses, and the interpretation of that is the same as what was mentioned in Fig.6. The greater loss at large wavelengths is due to the difficulty of confinement of the propagated pulses, especially for the small core radius.

Fig.8 explains the bending losses of the step index fiber as function of λ for core radius at $R_b = 2mm$. A smaller radius causes the largest bending losses, and the losses, generally, increase with wavelength due to a decrease in the confinement opportunity for the greater wavelengths. At small core radius, the random variations are also appeared very clear. This behavior may change when the selected bending radius is changed during the simulation, where the largest losses effects appear with a smaller bending radius.

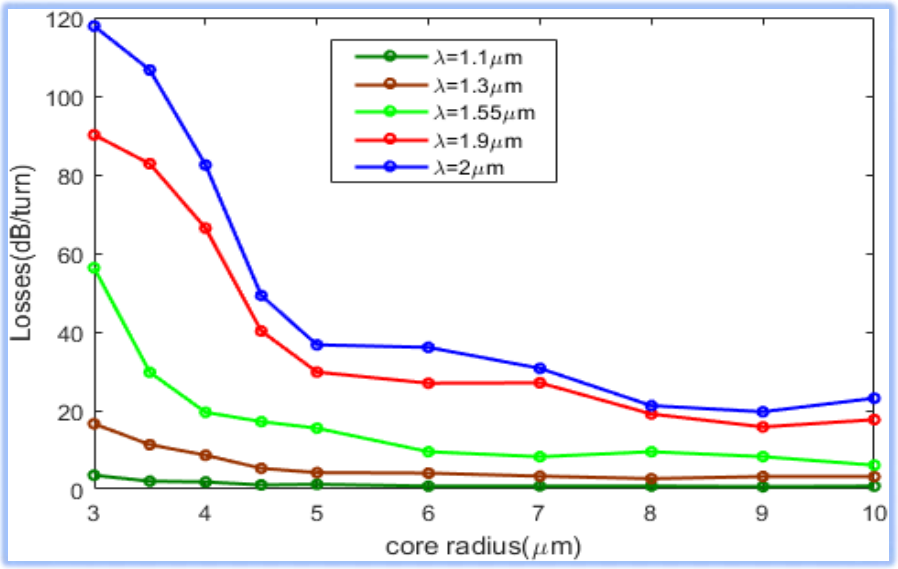

Fig.7. Bending losses Vs. core radius

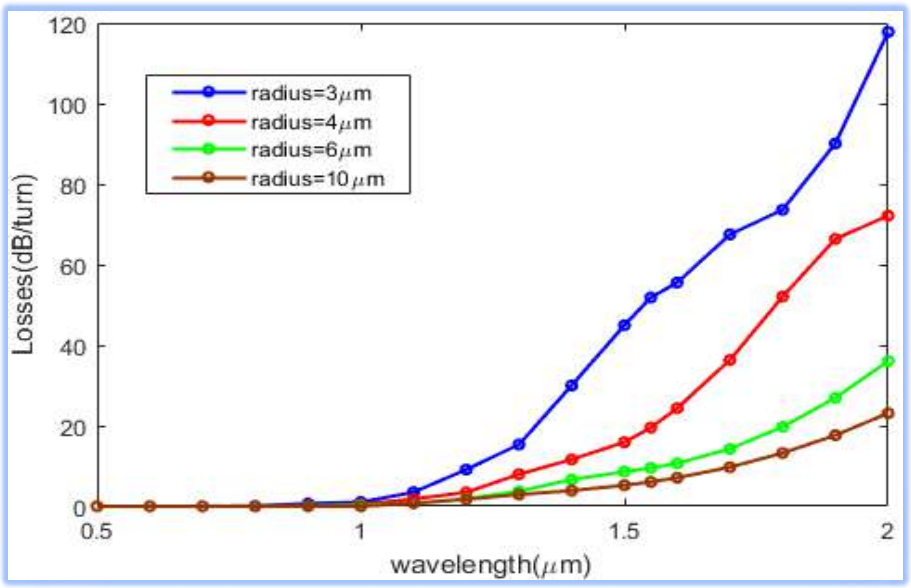

Fig.8. Bending losses Vs. wavelength

Fig.9 explains the bending losses as a function of R_b for different values of graded orders at $\lambda = 1.55\mu m$, $a = 10\mu m$. Notice that, the most significant effects appear at $g = 0.5$ and decrease with increasing graded order. Generally, the effects are closely related to each other, with graded orders values in the limit $g \geq 1$. Generally, after $R_b = 4mm$, the bending losses are very small for all graded orders and this is due to a decrease in the mode portion that will be outside the core with an increase in the bending radius.

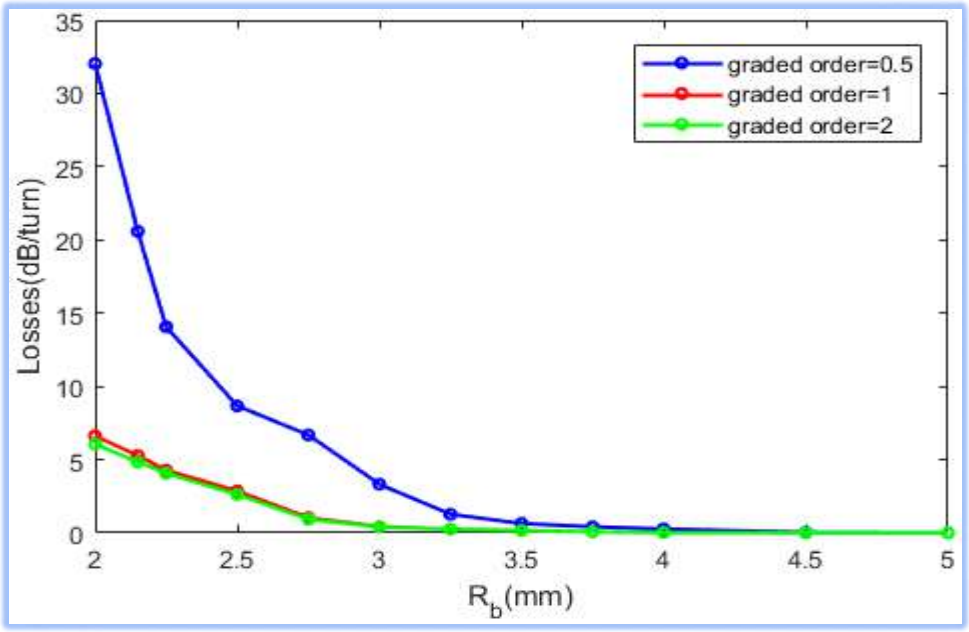

Fig.9. Bending losses as a function of R_b

4. Conclusions

In conclusion, a part of the fundamental mode may be outside the core, its amount depends on the simulation coefficients, which can be chosen to minimize the bending loss. It would appear that decreasing the bending radius and core increase loss, while loss increases with the wavelength. The loss decreases with the graded order, then it is fixed after $g = 2.5$. There is an oscillating change in the loss, which increases with decreasing of bending radius or core radius and the increase of wavelength.

References

[1] Boechat, A. A., Su, D., Hall, D. R., & Jones, J. D. 1991 *Appl. Opt.* **30 (**3) 321
[2] Fini, J. M. (2011) Optics express, **19** (5) 4042
[3] Danny, C. G., Raj, M. D., & Sai, V. V. R. 2020 *J. Light. Technol.* **38** (6) 1580
[4] Argyros, A., Lwin, R., & Large, M. C. 2008 *Opt. express* **16** (23) 18590
[5] Karpeev, S. V., Pavelyev, V. S., Soifer, V. A., Doskolovich, L. L., Duparre, M. R., & Luedge, B. (2004) Laser Optics 2003: Diode Lasers and Telecommunication Systems 5480. International Society for Optics and Photonics
[6] Wang, Z., Zhang, N., & Yuan, X. C. 2011 *Opt. express* **19** (2) 482
[7] Di Teodoro, F., Koplow, J. P., Moore, S. W., & Kliner, D. A. 2002 *Opt. Lett.* **27** (7) 518
[8] Yariv, A., & Yeh, P. 2007 Optical Electronics in Modern Communications 6th ed. Oxford University Press, Inc
[9] Kersey, A. D., Davis, M. A., Patrick, H. J., LeBlanc, M., Koo, K. P., Askins, C. G., & Friebele, E. J. 1997 *J. Light. Technol.* 15 (8) 1442
[10] Muhammad, H. K., Ali, N. H., & Yasser, H. A. 2020 *NeuroQuantology* **18** (4) 31
[11] Zheng, X., Ren, G., Huang, L., Li, H., Zhu, B., Zheng, H., & Cao, M. 2016 Applied optics **55** 10

The effect of acidic treatment of carbon fiber on denture mechanical properties

The effect of acidic treatment of carbon fiber on denture mechanical properties

Sally Yakoob Taher, Wafaa A. Hussain

Department of Applied Sciences, University of Technology, Baghdad-Iraq.

E-mail: Un100067@uotechnology.edu.iq

Abstract. The purpose of this research is to increase the mechanical properties (impact and flexural strength) of acrylic polymethyl methacrylate (PMMA) denture base resin by incorporated treated and coated woven carbon fiber (WCF). To increase the roughness of fibers, WCF treated with para-aminobenzoic acid (PABA), ($C_7H_7NO_2$) at 3 different concentration treatments (0.10, 0.15, and 0.20 M). In order to make the samples appears with good aesthetic and bonding, WCF was coated with β-Tricalcium phosphate (β-TCP) powder with (0.08, 0.10, and 0.12) weight fraction (wi) in addition of using polyvinyl alcohol (PVA) at 0.01 wi, respectively. After 10 days of water storage at room temperature, the specimens have been tested via using the Charpy effect measuring system and three-point bending tests. The mechanism of interfacial interaction between β-TCP and woven carbon fibers was investigated by field emission scanning electron microscopy (FESEM) and Fourier transform infrared spectroscopy (FTIR). Based on the obtained results, when specimens contained treated and uncoated woven carbon fiber with a high concentration of (PABA), the impact and flexural strength were higher than pure sample but have a bad aesthetic. Further, (PMMA) reinforced with coated and treated woven carbon fiber as hybrid composites recorded very high raises in the mechanical properties when the concentration of (PABA) and (β-TCP) was increased, with a good aesthetic.

Keywords: Denture base, PMMA, PVA, Tri calcium phosphate, Woven CF, PABA.

1. Introduction.

Poly methyl methacrylate (PMMA) is the most successful candidate among many materials to fabricate denture base resin [1], due to its reasonable quality, low weight, excellent esthetic properties, and ease of processing and polishing and repair [2-4]. However, PMMA is not considered as a perfect material, because, its brittleness, inferior mechanical and physical properties, low modulus of elasticity, high coefficient of thermal expansion and low sorption, low flexural strength, and low impact strength [5,6]. These drawbacks of PMMA lead to the fracture, which is the most common problem of denture base resin [7]. There are many causes for fracture of the dentures, such as impact fracture usually occurs when a patient is coughing that pushes the dentures out of the mouth or accidentally dropping the dentures on the surface during the cleaning of dentures. Also, flexural failure of denture occurs when the concentration of stress around the micro cracks formed in the material due to the continuous applied of small forces [8]. Numerous methods have been developed to enhance the mechanical and surface properties of the acrylic resins. It was suggested that the introduction of synthetic fibers to the monomer/polymer is strengthening the result acrylic resin. Various fibers and powders such as carbon fiber [9,10], glass fiber [6, 11], aramid fiber [12], polyethylene fiber [13], zirconium oxide ZrO_2 nano-

particles [14] and kaolinite powder ($Al_2Si_2O_5(OH)_4$) [15] were used as reinforcements for denture base material. However, because of weak interface between fiber and resin affecting the mechanical properties, these fibers break-up the homogeneous matrix of acrylic resin. To avoid this problem, several studies have been reported in the literature that recommends surface treatment of fibers and incorporation ceramic powder such as (TiO_2, and TCP) [16] or metal oxides such as (MgO, and ZnO) [17].

In light of above notices, the research was considered to determine how mechanical properties (impact and flexural strength) of acrylic resin can be enhanced by the use of carbon fiber reinforcement and whether surface treatment affects the impregnation of fiber within the resin matrix. Hence, the purpose of the study is to determine some mechanical properties (impact and flexural strength) of PMMA resin, and studying the influence of woven carbon fiber (treated and coated) on impact and flexural strength with good aesthetic.

2. Experimental details

2.1 Acidic treatment:

Fig.1 displays untreated carbon fiber in woven form. Woven carbon fibers (product No: CR160K, weight 600 g/m^2, thickness: 0.333 mm, Japan) were cut into (70×50 mm^2).

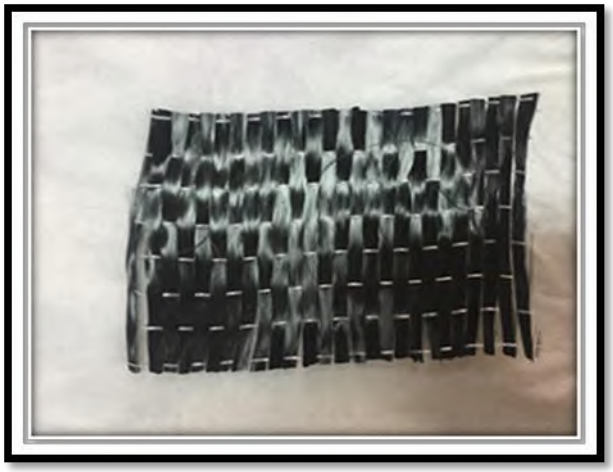

Figure 1. Untreated carbon fiber in woven form.

The woven carbon fiber was impregnated in ethanol for 15 minutes to remove contaminates, and then they were put on filtering paper, therefore put in an oven at 50 ◦C for 30 min, for drying. To make an acidic solution, (3 g) benzoic acid (3-Amino benzoic acid, $C_7H_7NO_2$, pure, minimum Assay: 98 %, New Delhi-110002, India) was dissolved in (100, 150, 200 ml) of distilled water, and left for 20 min on the magnetic stirrer. The woven carbon fiber immersed in an acidic solution for 3 hours. Once the immersion time ended, the fibers were rinsed thoroughly with distilled water to remove acidic influence. Finally, the woven fiber was dried in an oven at 70 ◦C for 2 hours.

2.2 Coating of carbon fibers

Dark carbon fiber coating with tri-calcium phosphate: different weight proportions of Tri-calcium phosphate average size (43.31nm), as presented in Table 1, were mixed with (10 ml) of distilled water and left with continuous stirring. PVA was added to the β-TCP solution with heating (Hot plate with a magnetic stirrer, BOECO-Germany), until the solution became cloudy. The coating solution was added

to fibers and left overnight in order to dry. This coating technique gave the fibers a white color on their surface. Fig. 2 referred to carbon fiber after coating.

Figure 2. Woven carbon fiber after coating.

Table 1. Composition of the specimens prepared.

Group no.	WCF(wi)	TCP (wi)	PVA (wi)	PMMA (wi)	Treatment concentration (M)
G1	-	-	-	1	-
G2	0.04	-	-	0.96	0.10
G3	0.04	-	-	0.96	0.15
G4	0.04	-	-	0.96	0.20
G5	0.04	0.08	0.01	0.87	0.10
G6	0.04	0.10	0.01	0.85	0.10
G7	0.04	0.12	0.01	0.83	0.10
G8	0.04	0.08	0.01	0.87	0.15
G9	0.04	0.10	0.01	0.85	0.15
G10	0.04	0.12	0.01	0.83	0.15
G11	0.04	0.08	0.01	0.87	0.20
G12	0.04	0.10	0.01	0.85	0.20
G13	0.04	0.12	0.01	0.83	0.20

2.3 Preparation of the flask

Denture base samples were fabricated by using a special flask as illustrated in Fig.3. The flask consists of two parts: upper and lower. The kaolin piece (70×50×3 mm) was placed in the lower part. Next, the dental stone powder was mixed with water and poured the stone to fill the flask. The inner surface of each part of the flasks was coated with Vaseline to keep the dental stone from binding to the flask. The flask was hitting several times to remove bubbles, which may be found inside the stone. The final set of the dental stone, the flask left for 15 min for hardening, and then the flask opened carefully and removes excess kaolin and stone. The obtained flask was shown in Fig. 3.

Figure 3. Flask of samples.

2.4 Preparation of the samples

Thirteen groups of test specimen were prepared by the heat-cured of PMMA, consisting of powder and liquid (methyl methacrylate, MMA) (2 g/1 ml) according to the manufacturer's instructions. In a clean and dry mixing jar the powder was mixed with liquid (MMA) and allows each powder to be wetted by monomer and left until it reaches a consistency appropriate for packing, during this time, the cover should be positioned over the mixing jar to prevent monomer evaporation and left to stand at room temperature for (12-16) min until reached to the dough stage, as shown in Fig. 4. For the unreinforced dough (G1) was placed in the mold directly. For the reinforced samples (G2-C13), the MMA has been used to wet woven carbon fibers with and without coating for 2 min. The dough was cut into two sheets; woven carbon fiber was placed between halves of the dough. Hydraulic pressure was applied to the flask slowly to 1Ton for 5 min. before the polymerization reaction. Then immerse the flask in cold water and waiting until water boiling. The resin was cured in boiling water for 1 h according to the manufacturer's instructions. When polymerization was completed; the molds extracted from water and left to cool at room temperature. The test samples were smoothed with 400,600 and 800 silicon carbide paper under tap water to remove excess materials, and then cut into specific dimensions to all tests. Before testing, all test samples were stored in water at 37°C for 10 days. All specimens were shown in Fig. 5.

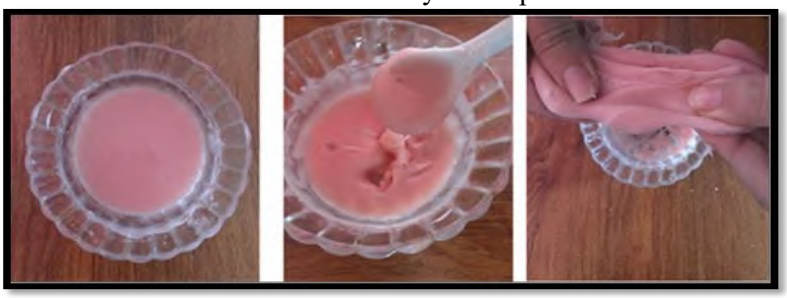

Figure 4. The dough stage.

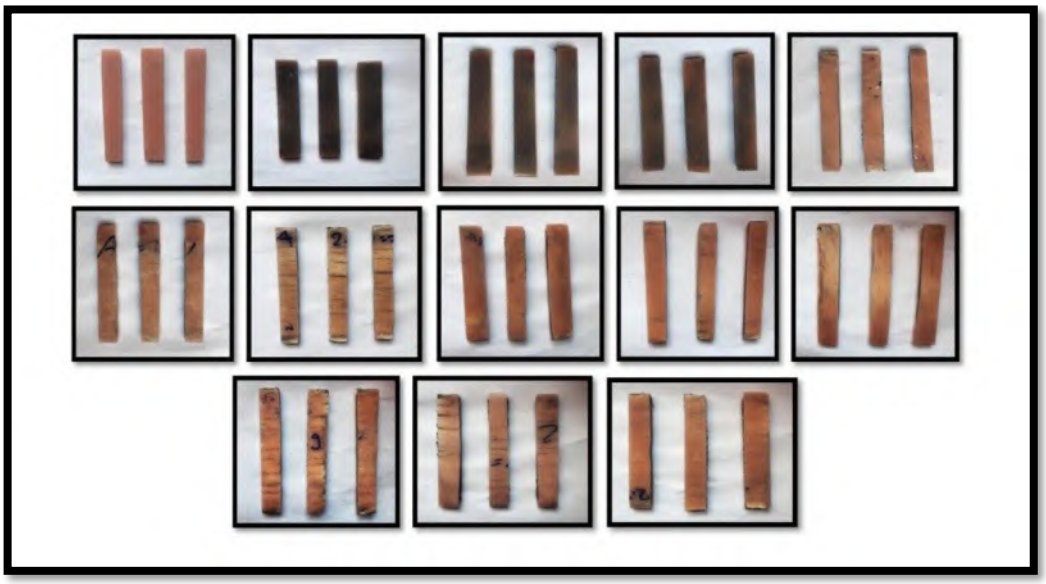

Figure 5. Fabricated samples.

2.5 Structural properties:

2.5.1 Fourier Transform Infrared Spectroscopy (FTIR):

The FTIR spectra of untreated and treated carbon fibers with para-aminobenzoic acid were recorded in the range of 400-4000 cm^{-1} by using an FTIR machine (SHIMADZO IRFFINITY) to identify the functional groups in untreated and treated fibers.

2.5.2 Field Emission Scanning Electron Microscopy (FESEM):

The surface microstructure of untreated and treated, with and without coating woven carbon fiber was examined utilizing Field Emission Scanning Electron Microscopy type (MIRA3 TESCAN-XMU).

2.5.3 Mechanical properties:

Impact strength and flexural strength were performed with utilizing the same methods in reference [15].

3. Results and discussion

3.1 Fourier Transform Infrared Spectroscopy (FTIR)

The FTIR was used to analyze surface functional groups of woven carbon fibers. The FTIR spectra can provide precise information on the material surface functional groups of untreated and treated WCF via benzoic acid. Fig. 6 shows the FTIR spectra of untreated and treated WCF using (0.10, 0.15, and 0.20 M) PABA. The spectrum of untreated carbon fiber shows a peak at 3429 cm^{-1} attributed to O-H stretching vibration of the absorbed water on the fiber surface and followed by another adsorption around 2962 cm^{-1} attributed to the stretching vibration from saturated hydrocarbon C-H [18]. The band near 2366 cm^{-1} dedicated to C≡C stretching peak, the characteristic peaks at 1722 cm^{-1}, 1637cm^{-1}, and 1230 cm^{-1} represent to C=O stretching peaks, C=C stretching, and C–N stretch peak respectively [19]. When compared untreated with treated WCF, some new peaks can be observed for treated carbon fiber. In any concentrations of PABA, WCF was recorded amine functional group in the FTIR spectrum. Peaks at 3423 cm^{-1} (0.20 M), 3451 cm^{-1} (0.15 M), and 3624 cm^{-1} (0.10 M) denote the N-H functional group,

stretched as a result of the vibration of the amine group. The characteristic of the oxygen function existed in C=O stretching, which appears at 1647 cm^{-1} for three concentrations, while C–O stretching appears at 1249 cm^{-1} peak when WCF treated with (0.20 M) and (0.15 M) while disappearing at (0.10 M) concentration. The oxygen content increased via increasing the concentration of PABA [20]. The most intensity is related to the C–N recorded at 1174 cm^{-1} when WCF treated with (0.15 M) [21]. In the preparation of biocomposites, WCF treated by PABA is essential; liquid chemical oxidation through PABA makes it an efficient technique to change the inert surface of WCF.

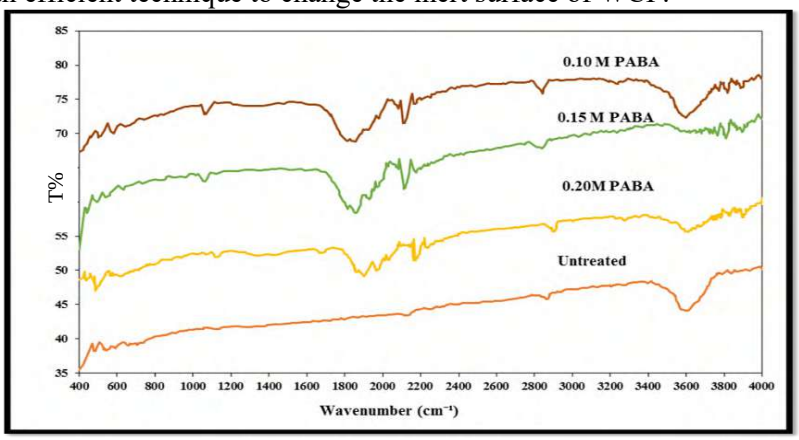

Figure 6. FTIR of WCF before and after treatment with PABA.

3.2 Field Emission Scanning Electron Microscope (FESEM)

Fig. 7a shows the surfaces of untreated woven carbon fibers appear smooth without any impurity. FESEM examination for the treated and coated surface of woven carbon fiber was imaged. The FESEM photographs of treated and coated fiber show regular and perfect spherical crystal nanostructures particles have been grown as individual clusters with few agglomerates over the surface of WCF. It can be shown that the β-TCP coating has grown homogeneously and the adhesion between the fiber and the β-TCP coat has improved. The cause for such adherence is due to the functional group of para aminobenzoic acid that has been created in carbon fiber. Fig. 7c and d showed the higher density of the functional groups of PABA results in an increase in the roughness of the surface of WCF, thus the interfacial chemical bonding strength between coatings /fiber and the resin was improved. It is assumed that the increased roughness of the fiber can enhance a mechanical interlocking effect between the fiber and the coating; this description is in accordance with Tao et al [22]. Fig. 7e shows the average particle diameter of β-TCP was 43.31nm with a spherical shape.

a b

c d e

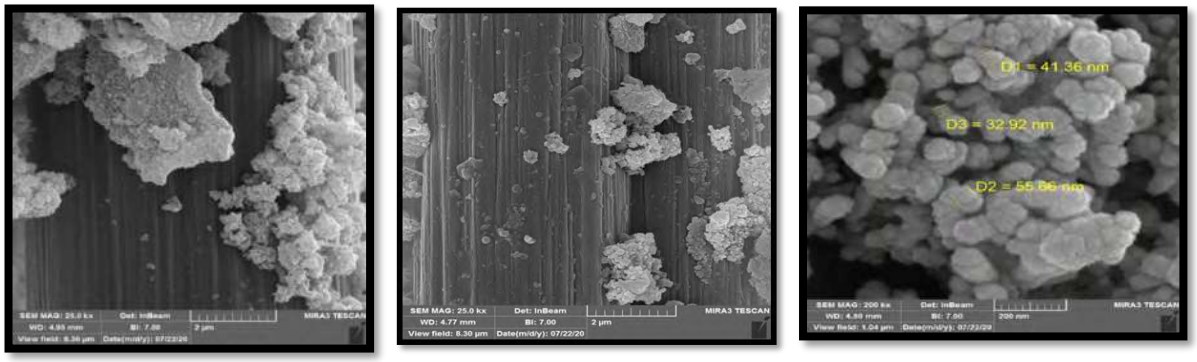

Figure 7. FESEM of (a): untreated and uncoated of CF (b) CF treated at 0.10 M of PABA and coated with β-TCP (c) CF treated at 0.15 M and coated (d) CF treated at 0.20 M and coated (e) β-TCP particle.

3.3 Impact strength

Table 2 illustrates the impact strength findings for the control group, and samples developed with treated WCF with PABA. All samples have the same fiber content (0.04 wi) and are treated with different concentrations of Para- aminobenzoic acid (0.10, 0.15, 0.20 M).

Table 2. The impact strength values for control group and treated WCF.

Group no.	Impact strength (KJ/m^2)
G1	8.05
G2	5.3
G3	9.51
G4	9.87

The control group recorded impact strength of 8.05 KJ/m^2. Lowest value of impact strength is observed in G2 when compared with the control group. The impact strength decreased with lower PABA concentration at 0.10 M, it is known that the mechanical properties depend on the bonding and interface between fiber and polymer. In G2 the surface of carbon fiber is smooth as shown in FESEM micrograph 7 b, leading to poor initial bonding between fiber and matrix. For this reason, G2 gave poor interfacial regions, hence recorded low impact strength. The highest impact strength was recorded when the fiber was treated via (0.15 M, 0.20 M). From this result, the impact strength increased with higher PABA concentration. This is because the roughness of carbon fiber surface occurs in higher acidic concentration, resulting in good bonding between carbon fiber and matrix. Despite the rise in the impact strength of the composites, the aesthetic-related result is negative.

Table 3 display the impact strength values of coated and treated WCF with β-TCP and PABA acid respectively.

Table 3. The impact strength values of coated and treated WCF.

Group no.	Impact strength(KJ/m^2)
G1	8.05
G5	6.9
G6	7.3
G7	7.8
G8	10

G9	11.13
G10	16.61
G11	15.6
G12	17.45
G13	20.23

For (G5, G6, and G7) samples prepared by treated WCF with PABA concentration (0.10 M) and coated with β-TCP (0.08, 0.10, and 0.12 wi) respectively, the impact strength values decreased when compared with G1. This decrement is because a bad bonding among coating, fiber, and the matrix, due to the poor acidic treatment of WCF. After treatment CF with the dilute solution still smooth as shown in FESEM micrograph (7 b), the bonding strength between carbon fiber, β-TCP powder and a matrix is poor. Groups G8, G9, and G10 are related to samples reinforced by treated WCF with (0.15 M) of PABA concentration and coated with (0.08, 0.10, and 0.12 wi) of β-TCP. The addition of any content of β-TCP powder at any weight fraction leads to increases in the value of impact strength when comparison with G1. One can explain that the β-TCP coatings presence, varying the CF surface characteristics into hydrophilic, highly enhances the interfacial bonding strength via the direct adhesion to matrix [23]. The treatment of carbon fiber by PABA concentration (0.15 M) had a positive effect on impact strength. This is because of the interfacial shear strength between matrix and fiber is high. The impact strength of hybrid samples papered by treated woven fiber with a concentrated solution of PAPA and coated with different weight fractions are illustrated in Table 3. The concentrated solution with the increment in the amount of β-TCP has a positive influence upon the impact strength values as depicted in (G11), (G12), and the value of impact strength raised from (15.6 KJ/m^2) to (17.45 KJ/m^2). For (G13) having a high content amount of β-TCP (0.12 wi), the impact strength increased to 20.23 KJ/m^2 by (151%) as compared with control group G1. That's perhaps owing to the reason that the β-TCP powder possesses a much higher strength of fracture in comparison with the PMMA resin [24]. Besides, the increment in the content of β-TCP raises strength. This is an anticipated result of the better adhesion of matrix and powder, and thus a higher permissible stress level transfers to CF through the loading. Mixing PVA with β-TCP powder enhance the mechanical properties of coatings because of its compatible structure and hydrophilic properties [25].

3.4 Flexural Strength

The flexural strength of acrylic resins is known to be the predominant form of clinical failure. The results of the flexural strength values in current study appeared as shown in Table 4, which shows a comparison between a pure sample and samples reinforced with carbon fibers treated with an acid solution at varying concentrations. The flexural strength of control group is 70.55 MPa, while samples prepared carbon fiber treated with a concentrated acid solution tends to be more efficient and has the maximum flexural strength value in G4. The explanation for this improvement is the etching process that produced apparent roughness of the surface fiber. The presence of roughness helped increase the area of the interlocking surface between the fiber and the matrix, which encourages the movement of stress from the matrix to the carbon fiber and therefore increased of the flexural strength. The researchers agree with this conclusion are Panigrahi, and Powel [26], Bismarck and Mohanty [27]. Eventually, a carbon fiber crack brings the test specimen to a complete fracture. This fact suggests that the tensile strength of the carbon fiber is part of the test specimen's flexural strength [28].

Table 4. Descriptive data of flexural strength.

Group no.	Flexural strength (MPa)
G1	70.55
G2	76.93
G3	81.9

G4	82.35

Flexural strength values for reinforced PMMA with treated and coated carbon fiber hybrid samples were summarized in Table 5. In current study, the flexural strength in G7 was significantly better than control group G1, while other samples recorded findings for the flexural strength less than the pure sample. The reason may be due to the weak bond between the coating and the resin, which gives low values of flexural strength. The bending strength was higher after the introduction of treated carbon fibers with concentrations of PABA at (0.15 M) and (0.20 M) and also coated with different ratios of β-TCP when compared with the pure sample. The increment in the flexural strength findings by using woven carbon fiber treated with and with 0.15 M of PABA (G8, G9, and G10) are (19.44, 17.5, and 15.09) % and fibers treated by 0.20 M of PABA (G11, G12, and G13) are (22.7, 19.77, 18.08%), respectively when compared with control sample (G1). This enhancement is due carbon fiber has a high transverse strength, and also the surface treatment by immersing the carbon fiber in a PABA acid solution increased the formation of voids or pits on the surface of the fibers. This results in an increment in the fiber surface area, thus raising the strength of bond between the matrix and the fiber. Also, process of moistening fibers with the monomer before introducing them to the resin, this process strengthened the adhesion between fiber and resin. This improvement in flexural strength is attributed to the direction of the fibers, which means that the denture base polymer with woven carbon fibers is a very significant factor in orientation [28]. After coating the treated carbon fiber, F.S. is increased compared to control sample. The β-TCP coating was dense and firmly bonded to WCF, which enhanced the interface's physical bonding. The improved interconnection can efficiently transfer the load from the CF to the matrix. For the ceramic WCF reinforced, the fiber-matrix composites are the principal load-bearing, and therefore, the flexural strength is enhanced. It can be observed the optimal flexural strength was at (0.12 wi) of β-TCP. Moreover, the existence of (0.01 wi) of PVA in the reinforcement layer will cause to improve the flexural strength due to PVA has good tensile strength, high flexibility, and good hardness [25].

Table 5. The flexural strength for denture reinforced with woven carbon fiber.

Group no.	Flexural Strength (MPa)
G1	70.55
G5	62.85
G6	67.85
G7	76.7
G8	81.2
G9	82.9
G10	84.27
G11	83.71
G12	84.5
G13	86.6

4. Conclusion

Polymethyl methacrylate PMMA has successfully been reinforced with treated WCF by 0.10, 0.15, and 0.12 M of PABA and coated with 0.08, 0.10, and 0.12 wi of β-TCP. It can be concluded that the optimal acidic treatment for woven carbon fiber is (0.20 M) PABA concentration and the recommend weight fraction of β-TCP is (0.12 wi), which resulted 20.23 KJ/m^2 in impact strength test and 86.6 MPa in flexural strength test. This could be due to treated WCF with para-aminobenzoic acid improved the adhesion between fibers/ β-TCP powder and resin. Specimens of PMMA prepared by incorporation of β-TCP into woven carbon fiber have a good aesthetic. The results of the FTIR spectrum show the content

of oxygen functional was increased after acid treatment which leads to the enhancement of the mechanical properties of the fibers. The FESEM micrographs show that acid treatment increases the surface roughness of woven fibers.

References:

[1] Thomas Meng Jr R and Mark A Latta 2005 *The Journal of Contemporary Dental Practice* **6** (4) 93.
[2] Alla R K Raghavendra Swamy K N Vyas R Konakanchi A Guduri V and Gadde P 2015 *Int J Appl Dent Sci* **1** (4) 8.
[3] Gad M M Fouda Sh M Al-Harbi F Ritva N and Raustia A 2017 *International Journal of Nanomedicine* **12** 3801.
[4] Gad M M and Abualsaud R 2019 *International journal of biomaterials* **6** 190610.
[5] Acosta L Torres S Luz Lopez-Marin M Elvira Nunez-Antita R Geonoveva Hernandez-Padron and Victor Castano M 2011 *Journal of Nanomaterials* 941561
[6] Hussain W A and Hashim F S 2017 *Journal of Al-Nahrain University* **20** (4) 44.
[7] Kadhim J and Hamad Q A 2018 *Al-Khwarizmi Engineering Journal* **14** (3) 100.
[8] Uzun G and Hersek N 2002 *Bio. Appl. Journal* **17** (1) 19.
[9] Zhang Sh and Qingling D 2018 *Surface and Interface Analysis* **50** (12-13) 1357.
[10] Hannon S A Hussain W A and Hussain S M 2020 *Iraqi Journal of Physics* **18** (44) 25.
[11] Kim SH and Watts DC 2004 *J Prosthet Dent.* **913** 274.
[12] John J Gangadhar SA and Soha I 2001 *J Prosthet Dent* **86** 424.
[13] Yin J Li Ming 2018 *Journal of Composite Interfaces* **25** (11) 949.
[14] Hussain W A and Hashim F S 2017 *Iraqi Journal of Science* **58** 2B 860.
[15] Hussain W A Bader B A Slewa M Alwan L H 2020 *Materials Science Forum* 1002 340.
[16] Ayad N M Badawi M F and Fatah A A 2008 Rev Clin Pesq Odontol **4** (3) 145.
[17] Anwander M Rosentritt M Schneider-Feyrer S and Hahnel S 2017 *The journal of advanced prosthodontics* **9** (6) 482.
[18] Ehsan M Maghrebi M and Baniadam M 2014 *Materials & Design* **55** 644.
[19] Shusheng Ch and Feng J 2014 *Composites science and technology* **101** 145.
[20] Zhu J Kim J Peng H Margrave JL Khabashesku VN and Barrera EV 2003 *Nano Letters* **3** 1107.
[21] Hossein R Ashori A and Varnaseri N 2016 *Polymers for Advanced Technologies* **27** (6) 805.
[22] Tao Ke Huang su ping and Zhou Ke chao J Cent 2005 *South Univ. Technol*. **12** (2) 113.
[23] Al-Munajjed Amir A and Fergal J O'Brien 2009 *Journal of the mechanical behavior of biomedical materials* **22** 138.
[24] Vojdani M Bagheri R and Khaledi A A R 2012 *Journal of dental sciences* **73** 238.
[25] Limpan N Prodpran Th Benjakul S and Prasarpran S 2012 *Food hydrocolloids* **29** (1) 226.
[26] Panigrahi S Powell T Wang B Tabil L G Crerar W J and Sokansanj S 2003 *In ASAE Meeting Presentation* 03-0018.
[27] Bismarck A Mohanty A K Aranberri-Askargorta I Czapla S Misra M Hinrichsen G and Springer J 2001 *Green chemistry* **32** 100.
[28] Kanie T Fujii K Arikawa H and Inoue K 2000 *Dental Materials* **162** 150.

Preparation and optical characterizations of PVA: Ag Nano composite

Preparation and optical characterizations of PVA: Ag Nano composite

Asmahan A. Muhmood[1*], Inass A.Zgair[2], Mushtaq A. Hussein[3], Liwaa H. Mahdi[4], Bashaer S.Jabbar[5],Adel H. Omran Alkhayatt[6]

[1, 2, 6] Kufa University, Faculty of science, Physics Department, Iraq
[3]Ministry of education, physics of material, physics, Iraq
[4]Kufa University, Faculty of Medicine, Pathology and Forensic Department, Iraq
[5]Kufa University, Faculty of science, biology department, Iraq

E-mail: asmahan.alnaseefi@uokufa.edu.iq

Abstract. In this paper, a 3% of polyvinyl alcohol PVA polymer solution was prepared with distilled water. PVA:Ag Nanocomposites were prepared by adding different concentrations of silver (Ag) nanoparticles (3, 6 and 9) %. Pure as well as PVA:Ag nanocomposites films were prepared by drop casting method. The optical properties of PVA: Ag nanocomposite were studied using the absorption and transmittance spectrum measured at wavelength range (200-1000) nm. The optical parameters of the prepared PVA: Ag nanocomposite, such as absorption coefficient, refractive index, and extinction coefficient, as well as the real and imaginary part of the refractive index were calculated as a function of Ag NPs concentration. The results show that the absorption edge is red shifted towards long wavelengths after adding the silver nanoparticles as well as an increment in the optical parameters after adding the Ag nanoparticles. The energy gap was also calculated for all the prepared samples, which were decreased from 4 eV to 1.72 eV with the increase addition of Ag nanoparticles content (3 to 9) %.

Keywords: PVA polymer, nanocomposite, nanoparticles, optical properties

1. Introduction

"Nanocomposites are composites in which at least one of the phases shows dimensions in the nanometer range (1 nm = 10–9 m)" [1]. Nanocomposites exhibiteda new technology besides business opportunities for all industry sectors, also it is environmentally friendly [1]. Generally, the nanocomposite class of organic/inorganic materials is a fast developing area for research. [2]. The combination of nanosized inorganic particles and polymer into a single material has fan-out a new zone in materials science that has extraordinary outcomes in the development of multifunctional substances[3]. The application of materials in nanoscale and nanocomposites which contain nanoparticles is an emanated area of nanoscience and the technology. The nanoparticles have an exceedingly surface: volume ratio. That so they usually show unique considerably and different chemical, physical, and biological properties comparing to their macro scaled counterparts [4]. Polyvinyl alcohol (PVA) is a polymer that has backbone of carbon chain attached with hydroxyl groups. PVA is not toxic, soluble in water synthetic polymer, which is used widely in the polymer blends because of its good chemical and physical properties, forming film with excellent characteristics,

emulsifying capability, and biodegradable, no carcinogenic and biocompatible qualities. These peerless characteristics enable PVA polymer in applicability in the pharmaceutical fields, surgical structures material, drug coating agents, and cosmetic industries [5]. It is well finder that polymers, which act as dielectric materials, are sterlingly host matrices for encapsulated nanoparticles metal like gold, silver, copper, and so on, as well as they act both as reducing besides capping agents and provide stability environmentally and chemically. That embedded nanoparticles NPs inside the polymer matrix will affect the characteristics of the host itself. Particularly, the polymer and the metal hybrid like polymer: Ag nanoparticles composites is overgrown functional materials in several scopes like mechanical, optical, electrical, antimicrobial, and thermal properties [6].

2. Experimental Part

In this paper, the polymer solution was prepared by adding the polymer in powder form to distilled water, and the solution was placed on a magnetic stirrer device for two hours with a temperature of 30 ° C .After the end of mixing, the solution was passed on filter paper to get rid of the sediments suspended in the solution and get a clear solution.Silver nanoparticles were added to the solution at different concentrations of 3, 6, and 9 % to study their effect on the optical properties of the polymer. PVA:Ag Films were prepared by drop casting method on glass substrate cleaned in three steps by using HCl, ethanol, acetone and ultrasound device. The optical properties of pure PVA and doped with Ag nanoparticles were studied by using the UV-VIS spectrophotometer in the range (200-1000) nm.

3. Results and Discussions

The optical absorption retrofitted useful information about band structure of solids, electronic, and phononic states. During the processes of optical absorption, the incident photon with certain energy excites an electron from the lower state to occupy a position in a higher energy state. By investigating the changes in transmitted radiation, the types of possible transitions for an electron can be concluded. The fundamental (main) absorption indicates to band-to-band (or to excitation) transitions. The main absorption shows by a fast elevation in absorption, which named as absorption edge which is used to determine the optical energy band gap [7].

When a beam of light affecting the material surface, part of the incoming beam which that not reflected by the material will be transmitted or absorbed through the material. Lambert-Beer law clear that the fraction of light ray that is absorbed is a function of the thickness for the materials also the way that the photon interacts with materials structure [8].

$$I = I_0 \, e^{(-\propto x)} \qquad \ldots\ldots\ldots\ldots\ldots\ldots\ldots\ldots (1)$$

Whereby, (I) is the intensity of light beam that coming out of the material, (I_0) is the intensity of the incident light beam,(x)is the path where the photon moves, and (α)is the absorption coefficient, which is a material characteristic.

Fig.1 shows the absorption spectrum of prepared films as a function of wavelength. The absorption increased with increasing the concentration of Ag nanoparticles. There is a relation between the position and shape of the spectral absorption peak with particle size and the morphology of the metal nanoparticles, so the spectral analysis will be the effective method to explain the spectral properties in metal nanoparticles [8]. The absorption peaks were between (392 and 477) nm where the maximum value was at 415 nm, which is the exemplary Plasmon Resonance Band (PRB) of AgNPs [9]. The peak and the location show that the ions of Ag+ in $AgNO_3$solution were successfully reductive to AgNPs.

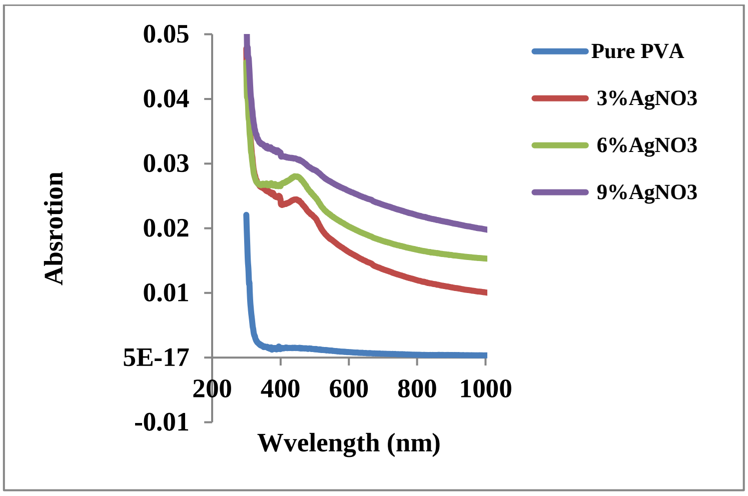

Fig.1. Absorption spectrum as function of wavelength for pure and doped PVA

From Figure 1, one can see that the absorption increases generally with increasing the ratio of dopant. This increasing explained the existence of interaction between Ag nanoparticles with PVA and getting a new structures for PVA:Ag composites. The increasing in the ratio of Ag nanoparticles leads the edge of UV radiation absorption to zaps towards region of longer wavelength for all the samples especially for the concentration of 3 and 6% weight percentage of Ag[10].

The coefficient of proportionality in equation (1) is defined as absorbance coefficient, and it a measure to how strong samples absorbs light at a specific wavelength [11].

The absorption coefficient (α) can be determined by the equation [12]:

$$\alpha = \frac{2.303\,A}{t} \ldots\ldots\ldots\ldots\ldots\ldots\ldots\ldots\ldots\ldots (2)$$

Where (A) is absorbance and (t) is thickness. The absorption coefficient (α) of PVA: Ag films is important to determine the type of electronic transition, if ($\alpha > 10^4$) transition is direct where if ($\alpha \leq 10^4$) transition is indirect [12]. Fig 2 shows the dependence of the absorption coefficient on wavelength for the samples before and after doping which shows increasing in absorption coefficient with increasing the concentration of Ag nano particles. Because the PVA polymer is a good insulating material and has low conductivity [13] hence the absorption coefficient is very low and the transition is indirect.

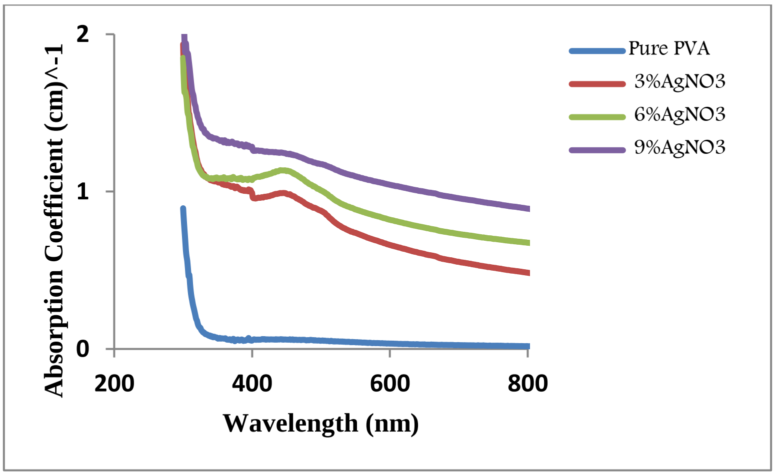

Fig. 2. Absorption coefficient as function of wavelength for pure and doped PVA.

The law of energy conservation state that lights ray is partially transmitted, absorbed and reflected as it shown in equation (3). Reflectance (R) can be calculated from the energy conservation law [14].

R + T + A = 1 ……..……(3)

Besides that the transmission is very low but the reflectivity is very high compared with absorption and transmission and this is shown by Fig. 3 and 4.

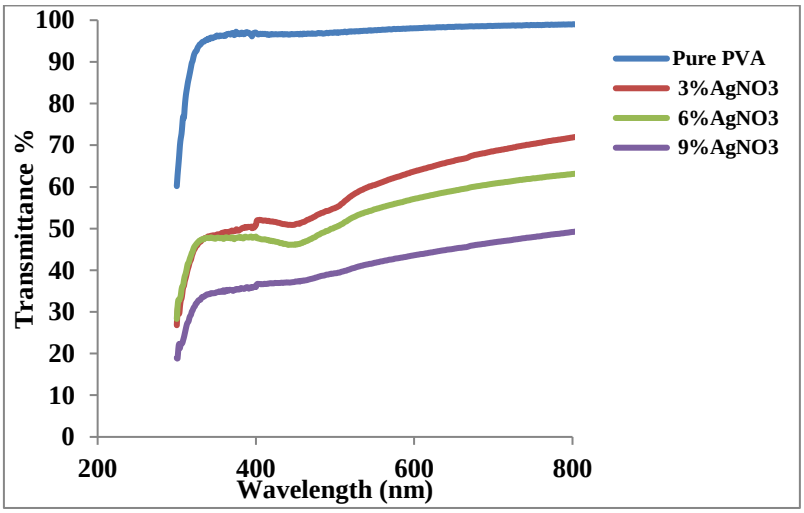

Fig. 3. Transmittance as function of wavelength for pure and doped PVA

The clear transparency of visible light is a particularly trait of the inorganic/polymer nanocomposite especially at dipped concentration, when the aggregation of NPs is constraining. The observation of irregularity in UV absorption spectrum by the nanocomposites of high loading Ag nanoparticles may be because of the elastic scattering of the arrival UV light upon the samples. This could be happened when the size of particles are smaller than wavelength λ_{UV} (190-400 nm) [10].

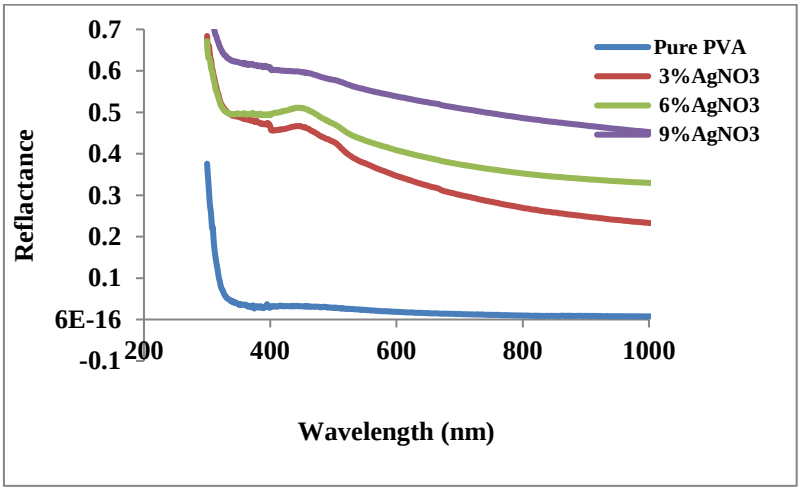

Fig.4. reflectivity as function of wavelength for pure and doped PVA.

The most significant optical constant is the refractive indexwhich depends on the wavelength of the electromagnetic wave. The electromagnetic wave lost some of its energy during the propagation throw a medium. Knowing that the real part n is the refractive index and the imaginary part Kis the extinction coefficient [15]. Refractive index of an optical or dielectric medium (N) can be calculated by dividing the light velocity in vacuum c on its velocity in the medium v′ (N = c/v′). Complex refractive index N, can be obtained by equation (4) [16].

$N=n+ik$……………………….………………..(4)

Equation (5) can be used to calculate the refractive index n [17].

$$n=\sqrt{\frac{4R-K^2}{(R-1)^2}}-\frac{(R+1)}{(R-1)}\text{…………………………….(5)}$$

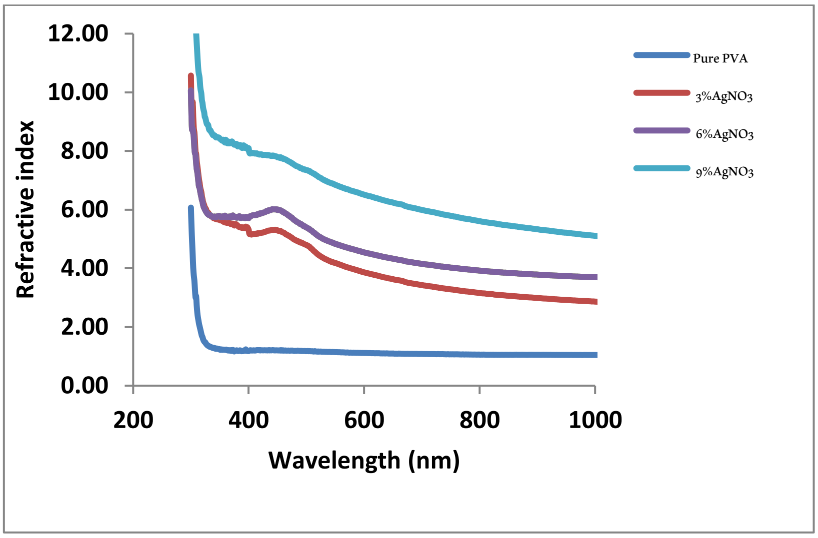

Fig.5. refractive index as function of wavelength for pure and doped PVA.

The complex dielectric function, ε, consists of the real part ε_1 and imaginary part ε_2 as it shown in equation (6):

$\varepsilon=\varepsilon_1-i\varepsilon_2$…………………….……….………..(6)
$(n-ik)^2=\varepsilon_1-i\varepsilon_2$ …………………..…………..(7)
$\varepsilon_1=n^2-k^2$……………………………..………..(8)
$\varepsilon_2=2nk$ ……………………………..………..(9)

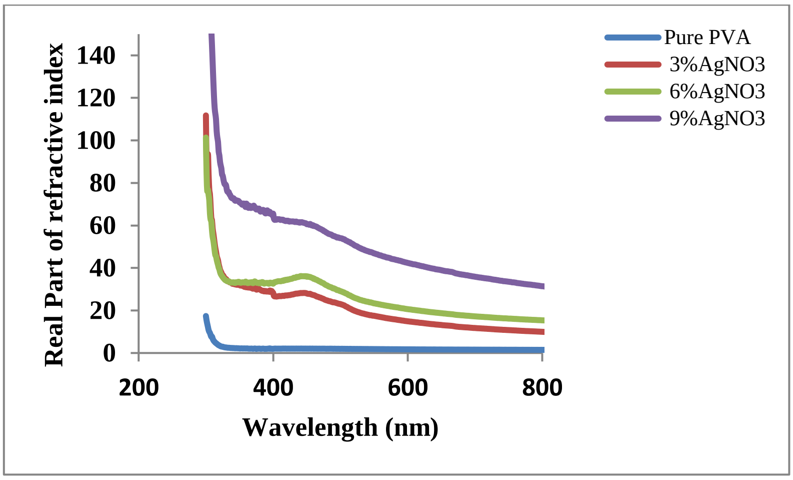

Fig.6. real part of refractive index as function of wavelength for pure and doped PVA.

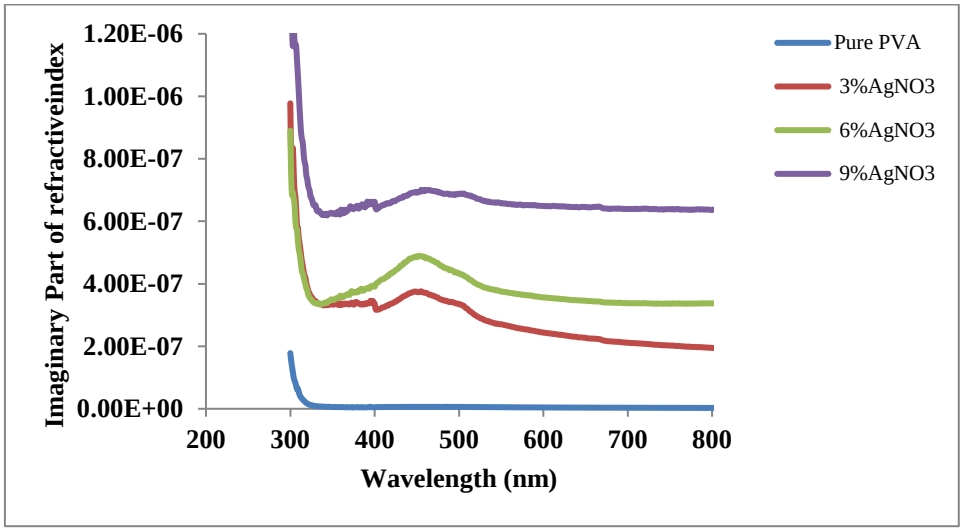

Fig. 7. Imaginary part of refractive index as function of wavelength for pure and doped PVA.

The dependences of real and imaginary parts on the photon energy for all samples were clear in Figs. 6 and 7. Figs. 6 and 7 signifies that εr>εi because the mainly depends of them on n2 according to equation (8) and that is way because the extinction coefficient (K) was extremely small so it could be neglected. The imaginary part depending on extinction coefficient is due to the equation (9) because the value of the refractive index is very small [13]. The real and imaginary parts in Fig. 6 and 7 show that an increasing after doping, which indicates that the samples were not have similar structure. For this the change in the concentration of doping lead to change in chemical composition for polymer [12].

The optical conductivity of a material is the frequency response of the material when it is irradiated by light [18]. The optical conductivity (σ opt.) is mainly based on the optical parameters such as optical absorbance,
reflectance and absorption coefficient. The refractive index (n) with absorption coefficient (α), were used to obtain the optical conductivity (σopt.), using the following relation [19]:

$$\sigma \text{ opt} = \frac{\alpha n c}{4\pi} \quad \ldots\ldots\ldots\

Where (B) is a constant, (r) is an empirical index, and it is equal to 2, 3, 1/2 and 3/2 relied on the nature for electronic transition responsible of the absorption. The drawing for the value of product of absorption coefficient by the photon energy $(\alpha h\nu)^{1/2}$ via photon energy ($h\nu$) at room temperature, induction for liner portion of this curve to a point $(\alpha h\nu)^{(1/2)}=0$ gave the value of the optical energy band gap to films of pure PVA and doped with Ag NPs which can be considered as an evidence for indirect transition .The value of energy gap are showed in table (1).

Table (1) Energy gap values for pure and doped samples.

Samples	Energy gap (eV)
Pure PVA	4
PVA:Ag(3%)	2.11
PVA:Ag(6%)	1.95
PVA:Ag(9%)	1.75

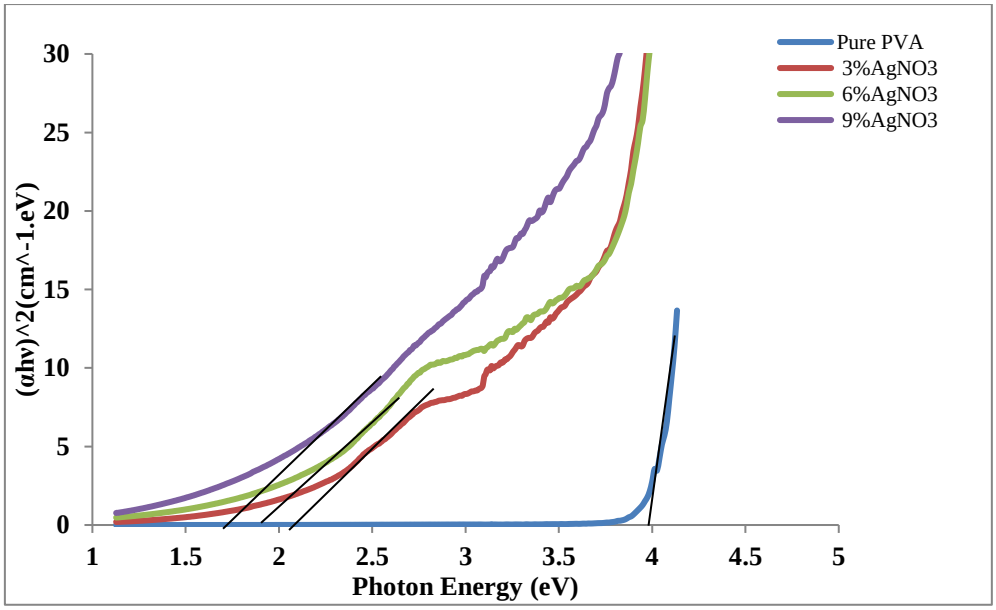

Fig.9. Energy gap as function of photon energy for pure and doped PVA.

The Ag doping is found to affect in strong manner on the optical energy gap of the polymer films, a decreases in the energy gap with increasing of Ag concentration maybe due to an increases in structural disorder of the polymer films and increases of the density of localized states in the band gap, which causes a shift optical energy gap to lower values of photon energy.

The absorption coefficient (α)and the extinction coefficient (K) can be involved by[20].

$$K=\frac{\alpha\lambda}{4\pi}\text{.....(11)}$$

The extinction coefficient (k) behaves just like the absorption coefficient(α) because they are joined by previous relation(7). From Fig.5 observe that the increases in absorption coefficient cause increasing in extinction coefficient values.

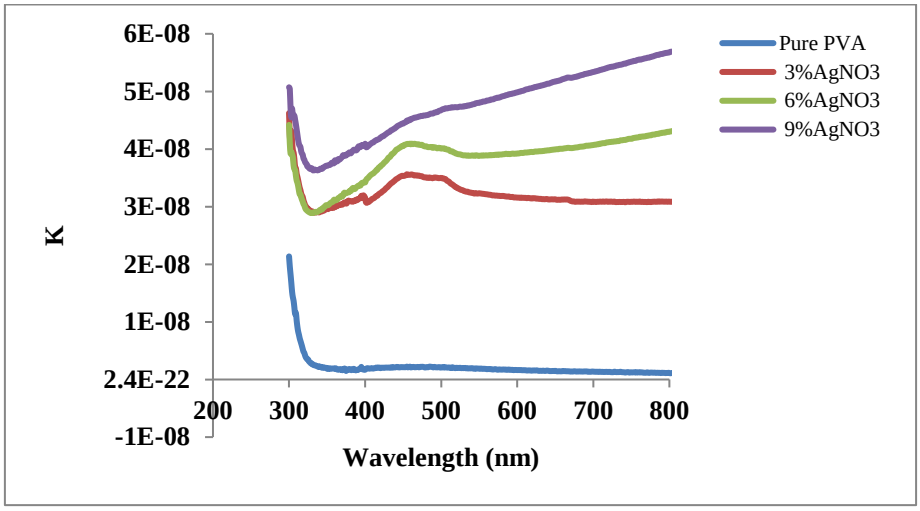

Fig.10. Extinction coefficient as function of wavelength for pure and doped PVA.

4. Conclusion

The optical constants of PVA as (absorption, transmission, refractive index, absorption coefficient, reflectance, extinction coefficient, and real & imaginary dielectric constant) were changing with increasing of concentrations of Ag nano particles. The energy gap of PVA decreases with increasing of concentrations of Ag nano particles also the transition was indirect.

References

[1] Pedro Henrique Cury Camargo, Kestur Gundappa Satyanarayana, Fernando Wypych, 2009 *Mater. Res.* **12** (1) 1
[2] Okpala C. C. 2013 *Int. J. Eng. Res.* **8** (11) 17
[3] Doddapaneni V. 2017, On the polymer-based nanocomposites for electrical switching applications PhD Thesis, School of Engineering Sciences KTH Royal Institute of Technology Stockholm, Sweden.
[4] Hettirachchi M.A. , Wickramarachchi P.A.S.R. 2011 *J Sci. Univ.Kelaniya* **6** 65
[5] Siddaiaha T., Ojhaa P, Neeruganti O. Velikanti G., Kumara R., Ramua C. 2018 *Mat. Res.* **21** 5
[6] Ghanipour M. , Dorranian D. 2013, *J. Nanomaterials* Article **ID 897043** 10 pages
[7] Alakanandana, k., 2013 . Preparation and Characterization of Proton Conducting PVA Polymer Complexed With Dicarboxylic Acids Ph.D. thesis, Osmania University, Hyderabad–India
[8] Samiha Hossain 2019 Optical properties of polymers and their applications, New Jersey Institute of Technology, New Jersey Institute of Technology, Theses.
[9] Li Fan, Hui Zhang, MengxiGao, Meng Zhang, Pengtao Liu and Xinliang Liu, Holzforschung 2020 *Holzforschung* **74** (5) 523
[10] Shehap A.M.,.Akil D. S. 2016 *Int. J. Nanosci. Mater.* **9** 17
[11] Alias A. N., Zabidi Z. M., Ali A.M.M., Harun M. K., 2013, *Int. J. Appl. Sci. Tech.* 3 5
[12] Shehab A. A., Abid E. Y., Hassan S. *Eng. &Tech. J.* **33** Part (B) 9
[13] Kumar, G. V. and Chandramani, R. 2010. *Acta Physica Polonica A* **117**(6) 917
[14] Gittleman, J. I.; Sichel, E. K. and Arie, Y. 1979 Sol. Energy Mater **1** 93
[15] Tan, W. C.; Koughia, K.; Singh, J. and Kasap, S. O. 2006 Optical Properties of Condensed Matter and Applications, Eds. Jai Singh Charles, John Wiley and sons, Ltd., England, UK
[16] Chiguvare, Z., 1997, Design and construction of a reflectance spectrometer for the analysis of spectral surface phenomena,MSc thesis, University of Zimbabwe,

Zimbabwe.
[17] Elashmawi I. S. and Hakeem, N. A. 2008. *Polym. Eng. Sci.* **48**(5) 895
[18] [18] Diemiruaye, J. M. 2013., *Int. J. Thin Film Sci. Tech*. **2** (2) 53
[19] Das, R. and Pandey, S .2011. Int. J. of Material Science, **1**(1) 35
[20] Chiad S. S., Habubi N. F., Khadayeir A. A., *J. Pure App. Sci.* **20** (3)20

Preparation and characterization of copper oxide by adding turmeric powder

Preparation and characterization of copper oxide by adding turmeric powder

Maithm A. obaid[1], Khalid Hellal Harbi[2], Ahmed N. Abd[3]

[1,2] University of Baghdad ,College of Education for pure science, Ibn Al-Haitham, Baghdad, Iraq
3Department of Physics, College of Science, Mustansiriyah University, Baghdad, Iraq

E-mail: maithm1993@gmail.com

Abstract. In the present study, the nanoparticle CuO solutions have been green synthesized with the use of the Aqueous copper chlorides and turmeric powder as a reducing agent in the deionized water as base fluid through the use of the traditional heating. This approach has produced large amounts of the Nano - products in a short duration of the reaction that takes several minutes, in addition to high quality materials with the innovative characteristics . A short review on some of the distinctive implementations and characteristics of the CuO Nano -structures will be presented as well.

Keywords: copper oxide, turmeric, nanoparticle and solutions

1. Introduction

The cupric oxide (CuO) , which has a narrow 1.2 eV band gap and various chemo physical characteristics, has been lately attractive in numerous areas like the energy conversion, opto-electronic devices, and catalyst in comparison to the bulk materials, the advanced characteristics of the CuO solution Nano - structures were shown; none-the-less, the fact that those materials can't be produced yet in the large scales is one of the obstacles towards the realization of the possible applications of that material. Thereby, the chemical approaches appear sufficient processes of synthesis, yielding large quantities as well as high quality and advanced material characteristics. And the Nano - fluids can be defined as a new fluids class, which has been engineered by Choi (1995) [1] the dispersing Nano sized materials (i.e. Nano - particles) in the base fluids. Which means that the Nano - fluids are Nano-scale colloidal suspensions that contain condensed nanomaterials . They are 2-phase systems with 1 phase (i.e. the solid phase) in another (i.e. liquid phase). The Nano – fluids were discovered to be possessing improved thermo physical characteristics like the viscosity , thermal conductivity , thermal diffusivity , and convective heat transfer coefficients, in comparison with the ones of the base fluids like the water or oil. It showed great potential applications in numerous areas like the transportation, micro - electronics, heating, manufacturing, and cooling. Numerous approaches were available to the synthesis of the CuO NPs with a variety of the morphologies. Those Nano - particles have massive benefits compared to the traditional materials, due to the fact that they have a large surface area. The formation of the well - dispersed Nano - particles is a difficult problem, due to the fact that they have the tendency of agglomerating with the time as well as the tendency of lowering the energy of the surface. Recently , the transition metal oxides nanostructures gained a massive interest from the material engineers and

scientists as a result of their various characteristics, in comparison to the corresponding bulk equivalents that are in turn providing potential implementations in a variety of the various technology areas. Preparations of the high quality Nano - structures of the defined, controllable morphology and size is a necessary condition, for the purpose of developing the Nano - devices or other variety of the applications for the sensing, catalyst, pharmacy [2–8] etc. The CuO, which has been classified to transition metal oxide group, is a p type, narrow band-gap semi - conductor. It is of a monoclinic structure and numerous interesting properties: super thermal conductivity, high stability, photovoltaic characteristics, and anti - microbial activities. Because of such exclusive characteristics, the CuO may be used in numerous technological fields, for instance, gas sensor [5, 7] active catalyst [2], magnetic recording media [9] highly efficient thermal conducting material [8], with highly sufficient selectivity, or solar cell applications [10]. Besides some shared metal oxide Nano - structure characteristics, like the ZnO, TiO_2, SnO_2, and WO_3. CuO Nano - structures have other distinctive magnetic and super hydrophobic [11] characteristics. In addition to that, those nanostructures have shown quite encouraging applications in the heterogeneous catalysis in complete hydrocarbons ' conversion to the CO2 , improvement of the thermal conductivity of the Nano - fluid, super -hydrophobic surfaces, nano-energetic materials, or anode materials for the lithium ion batteries (LIB). None – the less, this material hasn't gotten any attention from the scientists at the right level up to the past few years. In comparison to the other transition metal oxides like the TiO_2, ZnO , and Fe_2O_3 only a small number of the reports described the strategies of the synthesis that have been adopted for the CuO Nano - structures besides introducing their associated applications. In the present manuscript, we report on a green efficient method to prepare highly active copper oxide nanoparticles as a highly efficient catalyst.

2. Experimental details

Aqueous copper dichloride ($CuCl_2$) has been dissolved in 100 ml of the distilled water as a start. Then also dissolve turmeric powder in 100ml of distilled water and add the resulting 50% solution for 30 minutes in a sonic device at a temperature of 80 C. A clear green solution was obtained as in Fig. 1 Examination of the resulting solution by means of X-ray diffraction and finding the granular size using the Scherer equation [12].

From sherrer equation was calculated the average grain size (G_s for the thin films has been prepared, which include the XRD line width [11].

$$G_s = \frac{0.9\lambda}{\beta \cos(\theta)} \qquad (1)$$

Where, (λ) wave-length of x-ray, (θ) angle of diffraction, and (β) FWHM (the full – width at half - maximum) . The value of the strain (η) and the density of the dislocation (δ) value may be evaluated through the use of the relations in eq2 and 3: [12], as can be seen in Table1:

$$\eta = \frac{\beta \cos \theta}{4} \qquad (2)$$

$$\delta = \frac{1}{{G_s}^2} \qquad (3)$$

Fig.1. CuO freshly colloidal.

3. Results and Discussion

Fig. 2 displays XRD of copper oxide nanoparticles shown in Fig. 1, where the results showed an identical to the standard card (00-044-0706) , and using the equation (1) to find the particle size as shown in Table 1.

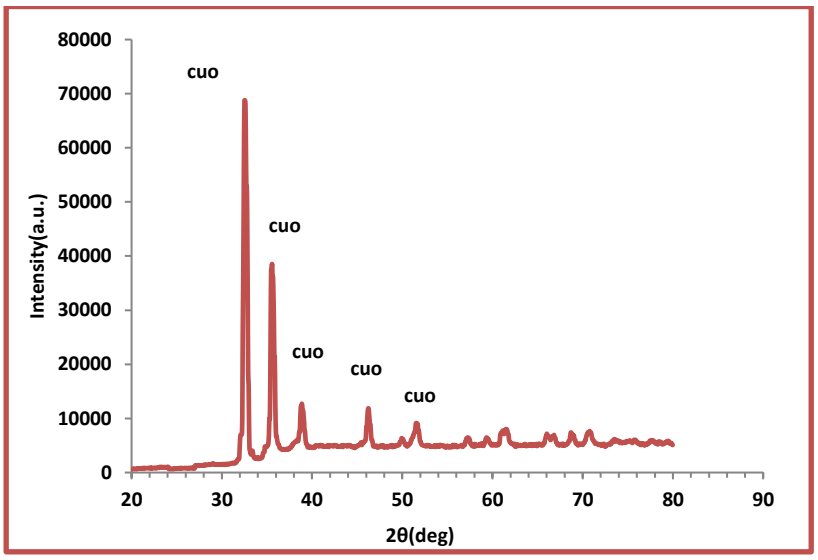

Fig. 2. XRD spectrum of CuO thin film.

Table 1. Parameters of CuO thin film

2θ(deg)	Gs (nm)	$\eta 10^4 lines^2 m^2$	$\delta 10^{14} lines m^2$
32.52	45.55	8.28	4.81
35.57	30.78	12.25	10.55
38.77	30.91	12.20	10.46
46.17	19.02	19.83	27.63
51.47	13.90	27.14	51.75

Fig.3 displays the 3D AFM photos and the chart division of copper oxide nanoparticles spread regularly on the surface. The figure showed that the average grain size shown in the figure is very close

to the X-ray diffraction results and We notice there is a homogeneity in the shape of the material with the appearance of some peaks that recorded the highest height at 222 (nm).

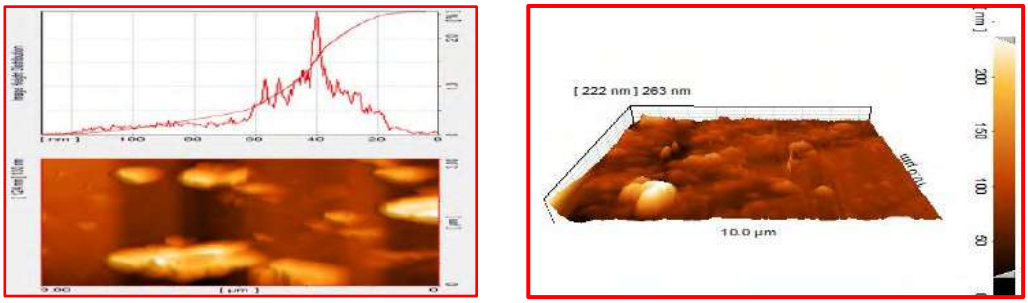

Fig. 3. 3D AFM image of CuO thin film.

Fig. 4 exposes the FTIR spectrum division of copper oxide nanoparticles spread that shows numerous significant peaks of absorption in the zone of 500- 3500 cm1 broad band of absorption has been designated to copper oxide, which assigned for Cu-O stretching vibration.

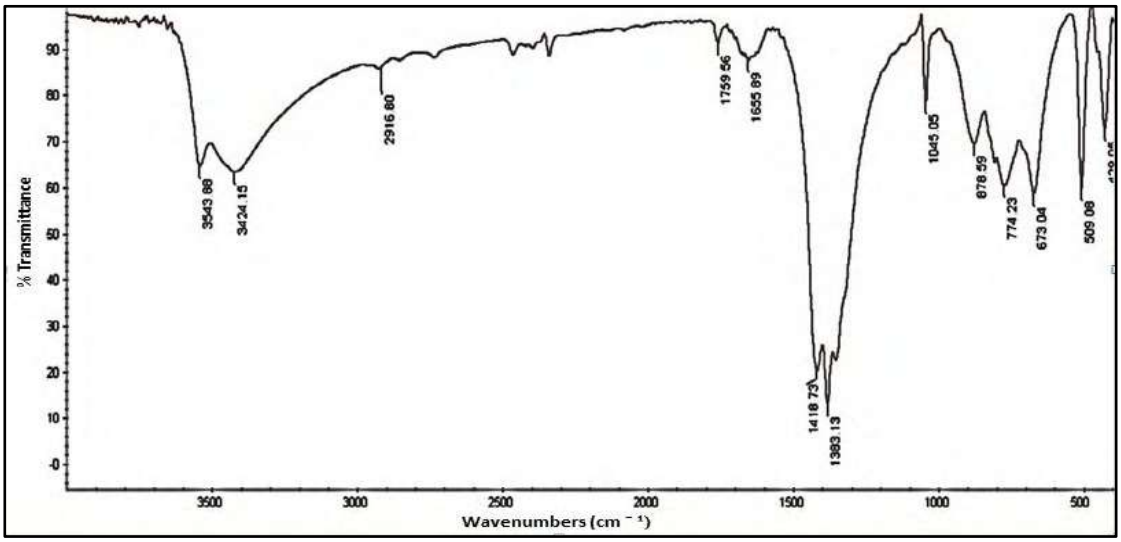

Fig.4. FTIR spectrum of CuO thin film.

Fig. 5 displays transmission as a wave-length function of the CuO which have been prepared with the use of the chemical process. Results have shown sufficient translucence characteristics at spectral range 200 nm – 1 ,100 nm and sharply increasing due to the absorbed particle size width. In addition to that, Fig. 5 the maximal transmittance value of 528 nm.

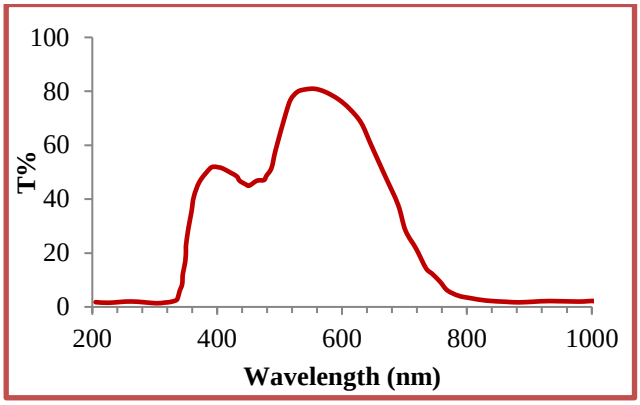

Fig.5. Optical transmittance of CuO thin film as a function of the wavelength

The optical energy gap of $AgInSe_2$ has been computed by the equation [13]

$$\alpha h\nu = B(h\nu - Eg)^n \qquad (4)$$

Where B represents a constant, ν represents the frequency of the transition and r exponent characterized the transitions of nature. r = 1/2 & 3/2 agreed to transitions of direct allowed and transition direct forbidden and r = 2 & 3 agreed to transition of the indirect allowed and transition of the indirect forbidden, respectively. Fig. 6 shows the linear plot that has been indicated as a direct band gap film nature .The line to the energy of the photon axis gives band gap. There have been two energy gaps shown in Fig. 6. The optical energy gap values for CuO are 1.8eV and 2.5e which results from increasing the localized states' density in Eg.

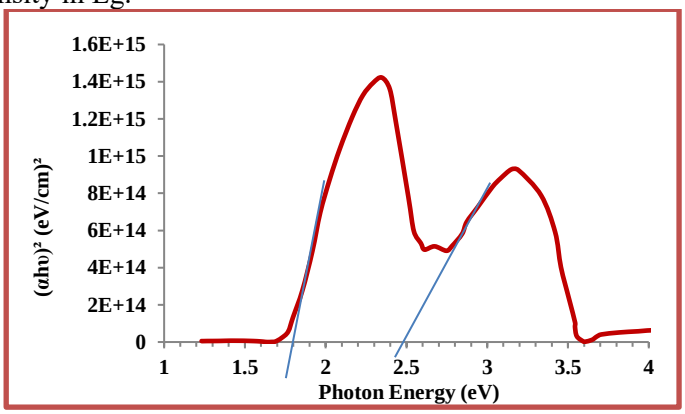

Fig. 6. $(\alpha h\nu)^2$ photon energy of CuO thin film**.**

The images of the scanning electron microscopy have been obtained for the CuO Nano - particles. Fig. 7 illustrates Cuo NP SEM image , indicating that the particle morphology is in an unspecified form and shows the agglomerates for the particles , and Fig. 7 shows SEM image and EDX , respectively

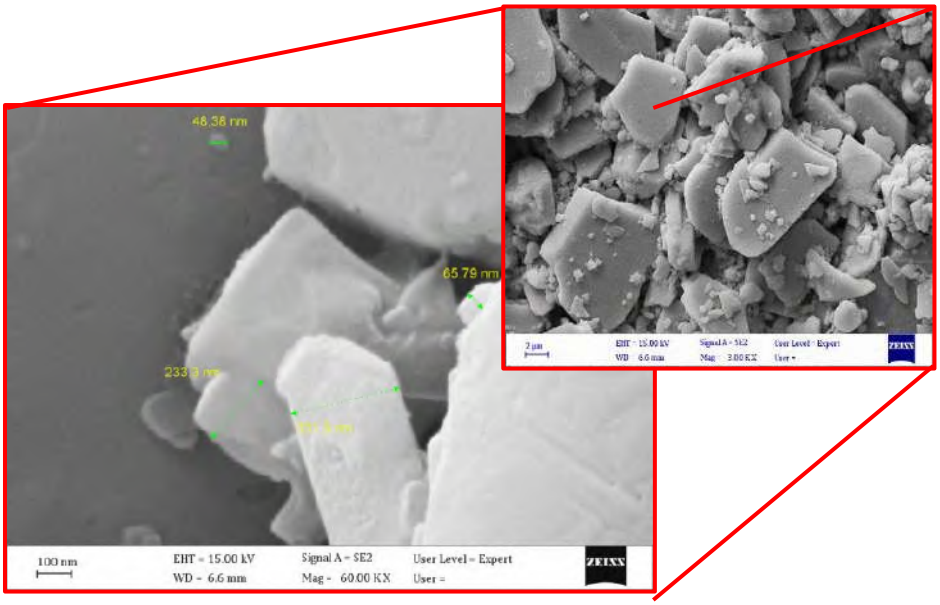

Fig. 7. SEM image of CuO thin film.

The EDS spectra of CuO thin film samples (Fig. 8) clearly demonstrate the presence of only peaks corresponding to Cu and O elements. The observed atomic ratio of 2 : 1 between Cu and O elements suggests the presence of CuO in these films. But, the XRD results suggested that the films predominantly contain CuO. There were no peaks related to the elements other than Cu and O in the EDS spectra, which revealed the formation of phase pure CuO in the thin films prepared through sputtering The new percentage after removing the carbon rate (cu = 64.12 , O = 35.73).

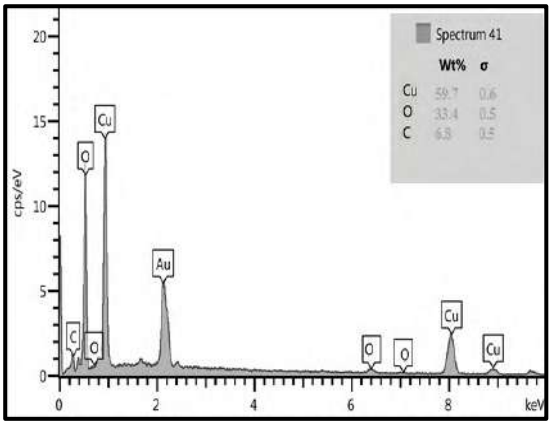

Fig. 8. EDS spectra of CuO thin films.

4. Conclusions

CuO the dissolved nano fluid was synthesized with the use of the chemical approach, utilizing the copper dichloride as precursor, and the average nano-particle size has been discovered 45nm, which is computed with the use of the De-Scherrer equation. The results were also compared mediated by SEM and EDX.The energy gap was calculated for the prepared solution, as two energy holes were obtained at high and low energies

References

[1] Signer DA, Wang HP (eds) Developments applications of non-newtonian flows, FED-vol. 231/MD-vol. 66, ASME, New York, pp 99–105
[2] Y. Yecheskel, I. Dror, and B. Berkowitz 2013 *Chemosphere* **93**1 172
[3] Q. Zhang, K. Zhang, D. Xu 2014 Prog. Mat. Sci. **60** (1) 208
[4] P. Raksa, A.Gardchareon, T. Chairuangsri,P.Mangkorntong,N. Mangkorntong, and S.Choopun. 2009. Ceramics International. 35. 2(649)
[5] A. Aslani and V. Oroojpour 2011 *Physica B: Condensed Matter* **40** (6) 2144
[6] M. Yang, J.He, X. Hu, C. Yan, and Z. Cheng 2011 Environmental Science and Technology **l** (45) 14(6088)
[7] Y. Li, J. Liang, Z. Tao, and J. Chen 2008 *Mat. Res. Bull.* **43** (8-9) 2380
[8] X.Wang and X.Xu. 1999. Journal ofThermophysics andHeat Transfer **13 (** 4) 474
[9] S. Ishio, T.Narisawa, S.Takahashi 2012. **J**. Magn. Magn. Mater. **324 (**3) 295
[10] V. Kumar, S.Masudy-Panah, C. C. Tan, T. K. S.Wong,D. Z. Chi, andG. K.Dalapati. 2013 in Proceedings of the IEEE 5th International Nanoelectronics Conference (INEC ’13), pp. 443–445
[11] X. Liu, Z. Jiang, J. Li, Z. Zhang, and L. Ren. 2010 Surface and Coatings Technology, **204** (20) 3200
[12] Uplane M.D. and Pawar S.H. 1983 Solid state commun **46** 847
[13] Physics of Semiconductor Device, Sze, S. M. and Kwok, K., John Wiley & Sons. 2007. Inc. New York

Journal of Physics: Conference Series

Effect of Electro-spinning applied Voltage on Electro-spun EPS Membranes Thickness and Fibers Diameters

Effect of Electro-spinning applied Voltage on Electro-spun EPS Membranes Thickness and Fibers Diameters

Noor M .Jalal[1], Akram R. Jabur[2], ShrokAllami[1]

[1]Ministry of Science and Technology/ Baghdad
[2]Materials Engineering Department, University of Technology/Baghdad

E-mail: noormohammed2010@yahoo.com

Abstract. Expanded Polystyrene (EPS) solutions with a percentage of (30 wt. %) were prepared followed by the fabrication of micro-fibers membranes by electrospinning technique. To study the voltage's effect of electrospinning device on EPS micro-fibers membranes, different voltages (10, 12, 15, 18, 24, and 30) KV were experimented. The characterization of the electro-spun membranes were made by Fourier transform infrared spectroscopy (FTIR) and the scanning electron microscopy (SEM) for morphological and thickness analysis. The results showed that although electro-spun EPS membranes prepared by 30 KV, they had the minimum membranes thickness and the highest average fiber diameter. As it is cleared by SEM images, increasing the electro-spinning voltage leads to increasing the average fiber diameter membranes. With increasing the electros-pinning voltage, the fibers prefer to deposit on each and result in decreasing the distance between the collector and the needle, hence higher average fiber diameter produced. The thickness of the electro-spun membranes decreases with the electro-spinning voltage as a result of the higher repulsion between the electro-spun fibers which reduce the deposition of these fibers on the collector.

Keywords: EPS, Electro-spinning, average fibre diameter, Thickness test.

1. Introduction

Electrospinning technique is a multi-sided technique has the ability to produce nano and micro polymeric fibers [1]. High aspect ratio as well as large surface area is important characteristics that made the electro-spun fibers attracted a considerable attention due to their special characteristics and potential applications in electrochemical devices [2]. This technique has attracted large attention in recent years due to the easy production of fibers from natural either or synthetic polymers [3]. Every soluble polymer owns enough high molecular weight is suitable to be electro-spun. The electro-spinning device consists of the following parts: (i) a high voltage power supply, (ii) nozzle, and (iii) grounded collector as shown in figure (1) [4].
Due to applying high voltage, the polymeric solution (presents at the tip of the syringe needle) will be charged and this will lead to the formation of a repulsive force. At the same time, the Taylor cone (which is a conical structure) will be formed at the tip of the syringe needle [1]. At a critical voltage, the repulsive forces could be able to dominate the surface tension of the polymeric solution and consequently, a jet blows up from Taylor cone. The jet is accelerated and goes along the distance between the syringe needle tip and the collector, and divided into a large number of filaments. Along

with the distance, the solvent will be evaporated and the fibers form on the surface of the collector [5]. To fabricate fine fibers, adjusting of some special solution-, environment- and operation- parameters is required. The presence of beads is also considered as a common problem. The higher concentration of the solution is the most preferable suggestion to solve this problem because it leads to minimizing the number of beads. At the same time, the higher concentration will lead to a larger diameter of the fiber [6].

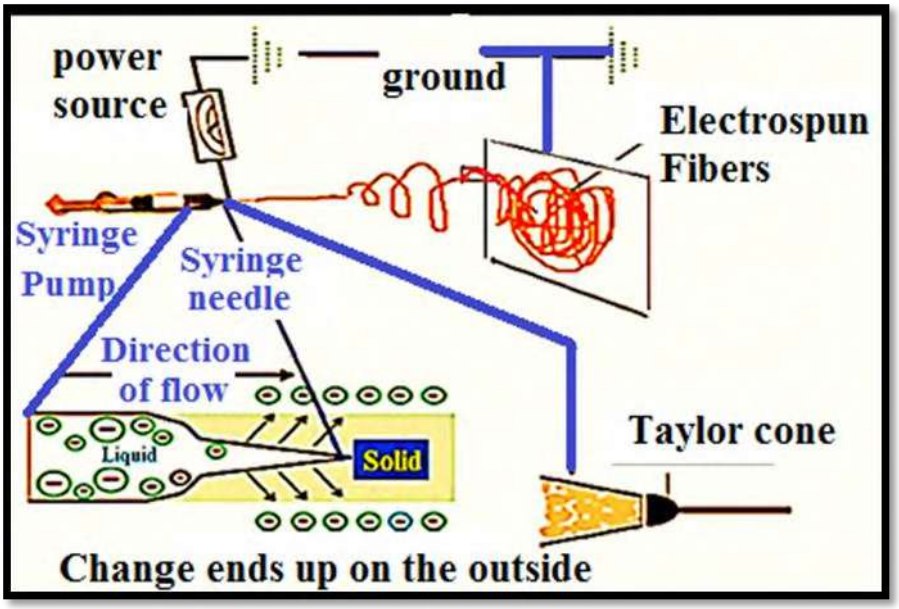

Figure 1. Basic set up and phenomenon of electrospinning [4].

The selection of the solvent used in electrospinning technique is one of the critical factors for the smooth and beadles' electro-spun nanofiber formation. The chosen solvent must lead to a complete soluble polymer added to moderate boiling point. The boiling point gives an important impression of the solvent's volatility. Generally, volatile solvents are preferred due to their high evaporation rates [7]. Fast evaporation of the solvents should be avoided because low boiling points causes drying the jet and blocking the needle tip, hence hindering the electro-spinning process. Similar to the fast evaporation solvents, low volatile solvents are avoided also because high boiling points prevent the drying during electro-spinning, whereby electro-spun fibers need to reach the collector [8].
The main electro-spinning technique parameters are the flow rate, the distance between the capillary and collector and applied voltage. At low flow rate, there is enough time for the solution to polarize. While, high flow rate leads to beads formation along the fibers, and it causes thick diameter. This is due to short drying periods whereby electro-spun fibers needed to reach the collector [9]. The distance between the tip of the capillary and the grounded plate directly affected the morphology of electro-spun nanofibers. If this distance increased, more uniform and beadles' electro-spun fibers may be obtained. Higher distance provides sufficient time and results in finer fibers with more uniform diameter distribution [10]. According to the voltage of electrospinning device, there are two different effects notified by the electro-spinning researchers. The first effect of electro-spinning voltage is associated with the vast majority of researchers when the electro-spinning voltage is increased, the volume of the drops at the tip decreased resulting in receding the Taylor cone. The jet originates from the liquid surface within the tip, and more beading is seen. If the applied voltage increased, the diameter of the fibers reduced. In the case of low applied voltages, fibers with no beads are produced (if the electric field is quite enough to overcome the surface tension) [11, 12].

While, some researchers are notified and adopted different and opposite effect depends on the fact that when the applied voltage is high, the coulombic forces were much greater than the viscoelastic forces. This would cause not only the breakage of an over-stretched charged jet during its path to the target but also the charged jet travelled to the grounded target in a shorter time. Therefore, the solvent has less time to evaporate, and this leads to bigger but irregular fiber diameters [13]. Marilena V. et al explained that there is a critical voltage. If the applied voltage during electrospinning is less than a critical voltage, increasing electrospinning voltage leads to decrease the diameters. While, when the applied voltage is higher than the critical value, the fiber diameters are increased, Taylor cone size and the drop's size at the needle tip are decreased and the jet velocity is decreased [14]. Electro-spun fibers in (nano or micro) scale have versatile spread applications such as solar cells, air filtration membranes, gas and chemical sensors, piezoelectric sensors, fuel cells, energy storage and ion exchange membranes [15], self-cleaning membranes, anti-corrosion, responsive smart materials, anti-icing, micro- and nano- electromechanical systems [16].
The aim of this research depends on utilizing different electrospinning voltages (10, 12, 15, 18, 24, and 30) KV in order to study their effects on the thickness of the electro-spun membranes and the topographical and morphological properties especially on fiber diameters and the general histogram of electro-spun fibers.

2. Experimental part (Preparation of PS electro-spun membranes)

Expanded polystyrene solutions and membranes were prepared by same method mentioned in our previous work [17, 18]. Expanded Polystyrene solutions of 30 wt. % were prepared by dissolving expanded polystyrene in (N, N- dimethylformamide DMF) at 100 °C with a continuous stirring for (20-25) minutes to ensure complete dissolution and homogeneous solution. Fabrication of PS electro-spun membranes was performed by electrospinning technique. The Polymer solution was injected in a (10 ml) syringe pump at fixed electro-spinning parameters. These parameters include the flow rate was 1.0 ml/h, the time of the electro-spinning for each membrane was 1.5 h and the distance between the syringe needle and the collector was 12 cm. Different electrospinning voltages (10, 12, 15, 18, 24, and 30) KV were experimented to study the effect of the voltage on the electro-spun membranes. Then, the obtained electro-spun membranes were removed from the collector, and the membranes were cut into small pieces (2 x 2) cm for subsequent characterizations.

3. Characterization of sulfonated electrospun membranes(SPS):

3.1. Fourier transform infrared spectroscopy (FTIR)

It is a non-destructive technique used for yielding information about the chemical bonds which in turn lead to the chemical composition of present membranes. FT-IR spectrum is recorded for the absorption of electromagnetic radiation of the sample in the range of the wave numbers from (4000 - 400) cm^{-1} [19]. FTIR was used to characterize the appearance of the chemical bands. The basic peaks related to the chemical structure of PS $(C_8H_8)n$. FTIR can qualitatively identify the structure of unknown materials and the quantitative measurement of the components in a complex mixture [20].

3.2. Scanning electron microscopy (SEM).

The scanning electron microscope (SEM) is considered as one of the most versatile instruments for the examination and analysis of the microstructure characteristics of solid objects. Scanning electron microscopy (SEM) gives information about topography and morphology of the electro-spun fibers [21].

4. Results and discussion:

4.1. Fourier transforms infrared spectroscopy (FTIR):

FTIR of (30 wt.%) expanded polystyrene membrane appeared clearly in fig.(2). generally, based on the wavenumber, there are three main regions. Region (1) shows that the bands at (400-900) cm^{-1} associated with (out-of-plane) C-H bend vibrations of aromatic rings. Region (2) defines the bands at (900-2000) cm^{-1} associated with the vibration of substituted benzene rings and in-plane C-H deformations. Region (3) represents the bands at (2800-3200) cm^{-1}. These bands are related to aliphatic and aromatic C-H stretching [23].

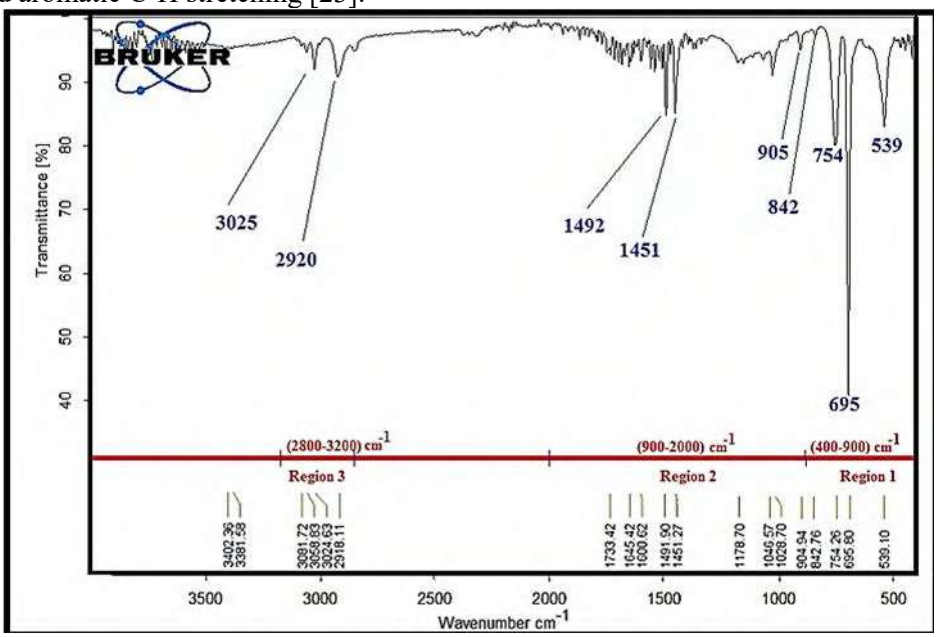

Figure 2. FTIR spectra for electrospun expanded polystyrene

The principle peaks associated with the chemical bonds of the expanded polystyrene are the peak appeared at a wave number of 695 cm^{-1} which is related to bending (=C-H) out of the plane, the peaks at (754 , 842, 905) cm^{-1} which related to substitution of the benzene ring, while the peaks at (1451 and 1492) cm^{-1} are associated with aromatic (C=C) stretching .The peak appeared at 2920 cm^{-1} are belongs to stretching vibrations of ($-CH_2$), the peak at 3025 cm^{-1} is associated with aromatic and aliphatic (C-H) stretching, and the peaks at (1028, 1069, 1154, 1181) cm^{-1} are related to in-plane C-H bending of the phenyl ring [24,25, 26]. The (in-plane C–H bending) of the phenyl ring is usually weak in most aromatic compounds, and it is observed at (1028, 1069, 1154, 1181) cm^{-1}[27]. The peaks at 3082, 3060 and 3026 cm^{-1} correspond to the aromatic C-H stretching vibrations, while the bands at 2923 and 2848 cm^{-1} come, respectively, from the asymmetric and symmetric stretching vibrations of methylene groups ($-CH_2$)[23].

4.2. Scanning electron microscopy (SEM).

From figs.(3, 4, 5, 6, 7, 8), the higher the voltage during electrospinning, the greater the average fiber diameter. This result is completely different with a very large number of researches specialized in the field of electro-spinning, which confirm the decrease in the fiber's diameters if the applied voltage increases [28, 29]. To explain the reason for increasing the fiber's diameter the applied voltage, it is important to notice that DMF is a solvent with high dielectric constant properties. The dielectric constant is a measure of how a material placed in an electric field can concentrate effectively the flux the electrostatic lines. So, with high dielectric properties, the fiber's diameter decreased, and the density of the surface charge on the jet largely dispersed resulting in the production of fibers with uniform morphologies and less diameter along with lower bead formation [30]. It is important to mention a special case during polystyrene electro-spinning. Only at the first few seconds of the electrospinning process, the fibers are gathered on the collector and form a very thin film. After few

seconds, the formation of the thin film on the collector is stopped, and the fibers vertically gathered towards the needle. During the path of the fiber to the collector (which is usually a conductive material), the fibers were cut and did not continually extended. The fibers stop gathering on the collector and start gathering on each other.

This complex is attributed to the special properties of (PS/DMF) solution where the electro-spun fibers prefer the surface of each other due to the conductive surfaces and shorter distances. This case was somewhat little happening at small voltages, but increases with increasing the applied voltage during electro-spinning. It is important to mention that the fibers were cut into small lengths before reaching the collector. This reduces the distance between the needle and the collector that causes the formation of larger average fiber diameters. The fibers gathered on the collector after few seconds of starting the electro-spinning process, and the fibers have lower diameters due to large distance, then the diameters gradually increased. In other words, the interpretation of increasing the fiber diameter is due to the segmentation of electro-spun fibers when the distance between the collector and the needle decrease in such away making the diameter becoming higher. This explanation was in good agreement with Siqi Huan et al [13].

Table (1) clarifies the relationship between increasing the average fiber's diameter with increasing the electro-spinning voltage. It is important to mention that there is not any membrane obtained when the electro-spinning voltage was 10 KV since it is very small voltage to form the electro-spun fibers. Also, when the electrospinning voltage was 30 KV, it is difficult to perform the electro-spun due to the high repulsion forces between the fibers themselves.

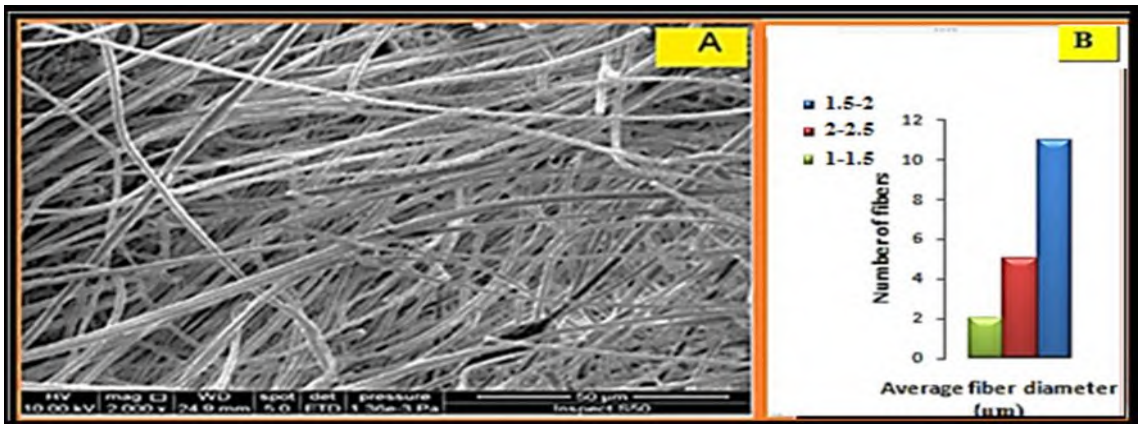

Figure 3. 30 wt.% EPS prepared at 12 KV , A:SEM image B:Histogram.

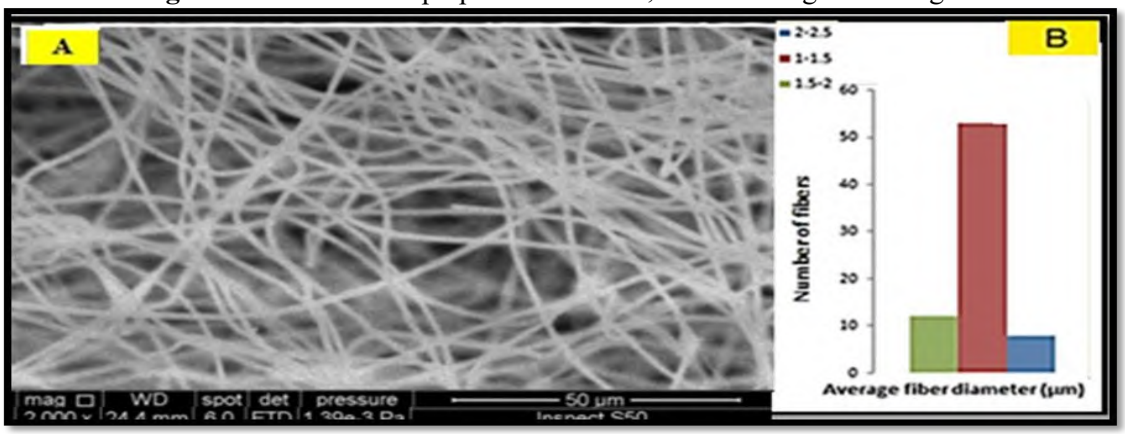

Figure 4. 30 wt.% EPS prepared at 15 KV , A:SEM image B:Histogram.

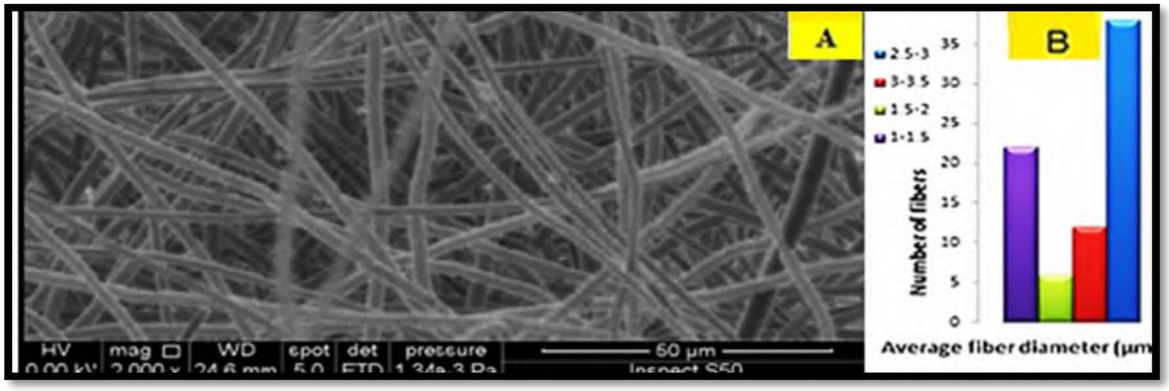

Figure 5. 30 wt.% EPS prepared at 18KV , A:SEM image B:Histogram.

Figure 6. 30 wt.% EPS prepared at 24 KV , A:SEM image B:Histogram.

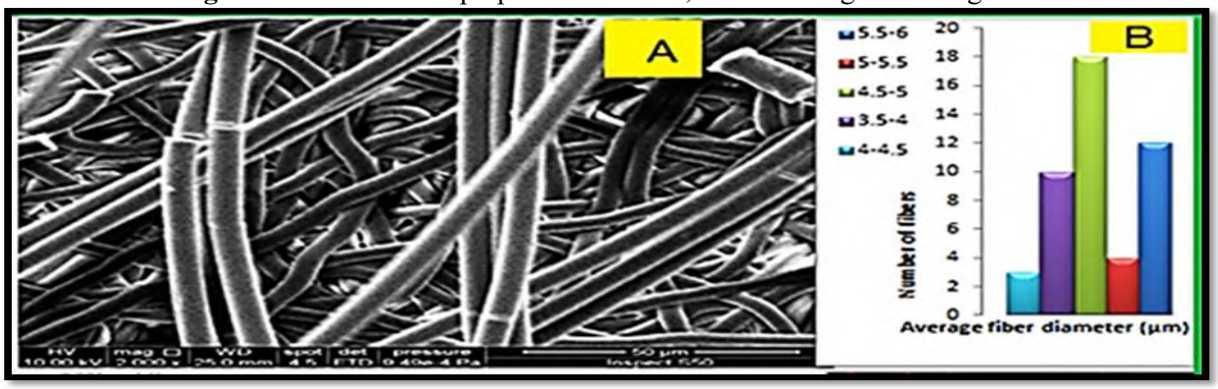

Figure 7. 30 wt.% EPS prepared at 30 KV , A:SEM image B:Histogram

Table 1. Electro-spinning voltages with average fiber diameter of EPS membranes

Electrospinning Voltages (KV)	Average Fiber Diameter (μm)
10	There is no electrospun membrane at this voltage
12	1.25 ± 0.25
15	1.75 ± 0.25
18	2.25 ± 0.25
24	4.25 ± 0.25
30	4.75 ± 0.25

4.3. Thickness test

Table (2) illustrates decreasing the membranes thickness with increasing the voltage of electro-spinning device. With constant conditions of electro-spinning process, the thickness of the electro-spun membranes was decreased with increasing the applied voltage during the electro-spinning. Decreasing the membranes thicknesses may be related to increasing the electrical conductivity of the polymeric solution with increasing the applied voltage. Lower deposition rate of electro-spun fibers on the collector was attributed to polymeric fibers repulsion in higher conductive solutions that leads to spread over large areas and finally the produced film will be thinner. Our results agreed with [31, 32, 33]. Indeed, any enhancement for the electrical conductivity for polymeric solutions results in higher charge density on the surface of the charged jet, and this encourages or promotes the solution jet stretching as a consequence of higher level of charges.

It is important to mention that the dielectric constant of the electro-spinning solvents plays a very important role in limiting the amount of available free charges in electro-spinning solution. By using low dielectric constant solvent such as chloroform, lower amount of charge density will result and therefore the available charge on the jet surface reduces and weakens the electrostatic repulsive force (34, 35, 36).

In contrast, our results depend on the use of DMF solvent with high dielectric constant that causes higher charge density on the jet surface and encourages the electrostatic repulsive forces. Therefore, with increasing the electro-spinning voltages along with the effect of high dielectric constant of DMF, higher repulsive forces and lower fibers deposition rate was obtained.

Table 2. Relationship between thickness of electrospun membranes and electrospinning voltage

Electrospinning Voltages (KV)	Thickness of produced electrospun membranes (Cm)
10	There is no electrospun membrane at this voltage
12	0.1379
15	0.113
18	0.09889
24	0.08167
30	0.0511

5. Conclusions:

The experimental results of this paper indicate the following conclusions for EPS electro-spun membranes.

1. The average fiber's diameter of the electro-spun membranes increases with increasing the electro-spinning voltage.
2. There is no electro-spun membrane produced with 10 KV
3. The thickness of the electro-spun membranes decreases with increasing the electro-spinning voltage and becomes difficult to produce electro-spun membranes.

6. References

[1] Chayad FA, Jabur AR, Jalal NM 2015 Effect of MWCNT addition on improving the electrical conductivityand activation energy of electrospun nylon films",Science Direct, Karbala *Int. J. Modern Sci.* **1** 187-193.

[2] Manabu T 2015 Development of ion conductive nanofibers for polymer electrolyte fuel cells *Polymer J.* **2** 1-8.

[3] Sergey F 2003 Controlling the Fiber Diameter during Electrospinning *Phys. Rev. Lett*. **90** 14.

[4] Peng W 2017 Electrospinning: A novel nano-encapsulation approach for bioactive compounds *Trends Food Sci. Technol.***70** 56-68.

[5] Shahram M and Maryam O 2017 *Electrospun Nano-composite Materials for Polymer Electrolyte Membrane Fuel Cells* Chapter 13, "Organic–Inorganic Composite Polymer by: Inamuddin D., Mohammad A., Asiri A. M., Springer, 2017.
[6] Jabur AR 2018 Effect of polyaniline on the electrical conductivityand activation energy of electrospun nylon films *Int. J. Hydrogen Energy* **43** 530-536.
[7] Ladawan W, Anuvat S and Pitt S 2004 Effects of solvents on electrospun polymeric fibers: preliminary study on polystyrene *Polymer Int.* **53** 1851-1859.
[8] Erdem R, Usta IM, Akalin O and Atak M 2014 The Impact of Solvent Type and Mixing Ratios of Solvents on the Properties of Polyurethane based Electrospun Nanofibers *Appl. Surface Sci.* **2014**, PP.1-13.
[9] Suna B, Longa YZ and Zhanga HD 2014 Advances in three-dimensional nanofibrous macrostructures via electrospinning. *Progress Polymer Sci.* **39** 862-890.
[10] Zheng M 2003 A review on polymer nanofibers by electrospinning and Their applications in nano-composites *Compos. Sci. Technol.* **63** 2223-2253.
[11] Yun PN, Sudip R and Conrad OP 2018 *Fabrication of Functional Electrospun Nanostructures for Food Applications* Chapter 3 Role of Materials Science in Food Bioengineering", by : Alexandru GA and Maria H 1st Edition, Academic Press, 2018.
[12] Fadhil AC, Akram RJ and Noor MJ 2016 Effect of NaCl Solution Addition on Improving Some of the Physical Properties of Nylon 6 Solutions used for Electro Spinning Purpose *Eng. Technol. J.* **34**, 7.
[13] Siqi H, Guoxiang L, Guangping H, Wanli C, Zongying F, Qinglin W and Qingwen W 2015 Effect of Experimental Parameters on Morphological, Mechanical and Hydrophobic Properties of Electrospun Polystyrene Fibers *Materials* **8** 2718-2734
[14] Marilena V, Angeliki S and Sotiria K 2019 *Electrospinning and Drug Delivery* Chapter in "Electrospinning and Electrspraying Techniques and Applications", by SajjadHaider, Intech Open, 2019.
[15] Jabour AR, Majid HA and Shafaq YA 2018 *Effect of Cu nanoparticles addition on improving the electrical conductivity and mechanical propertiesof PVA electrospun polymeric film* In: TMREES 18 technologies and materials for renewable energy, environment and sustainability AIP conference proceedings 1968, 2018.
[16] Nurxat N, Waseem S,Yu L, Muhammet C and Ramazan A 2013 Superhydrophobic electrospun nanofibers *J. Mater. Chem.* **1** 61929-1946 .
[17] Jalal NM, Jabur AR, Hamza MS and Shrok A 2019 Preparation, microstructure and morphology of electrospun sulfonated polystyrenefilms for proton exchange membrane hydrogen fuel cell *Energy Procedia*, **157** 1494-505.
[18] Jalal NM, Jabur AR, Hamza MS and Shrok A 2020 Sulfonated electrospun Polystyrene as cation exchange membranes for fuel cells *Energy Rep.* 287-298.
[19] Ojeda JJ and Maria D 2012 *Fourier Transform Infrared Spectroscopy for Molecular Analysis of Microbial Cells* chapter 8 in , Microbial Systems Biology: Methods and Protocols, springer, 881.
[20] Dorota K and Monika P 2019 Application of FTIR Method for the Assessment of Immobilization of Active Substances in the Matrix of Biomedical Materials *Materials* **12** 2972 1-13.
[21] Robert J 1996 *Environmental scanning electron microscopy an Introduction to ESEM* Philips Electron Optics, Netherlands, 1996.
[22] Ana VG, Caputox G and Ferro MC 2017 *Application of Scanning Electron Microscopy-Energy Dispersive X-ray Spectroscopy (SEM-EDS)* Chapter 4 Comprehensive Analytical Chemistry Elsevier, 2017.
[23] Olmos D, Martı E. and Gonza´ lez -Benito J 2014 New Molecular-Scale Information on Polystyrene Dynamics in PS and PS–BaTiO3 Composites From FTIR Spectroscopy *PCCP Royal Soc. Chem.* **16** 24339-243349.

[24] Al-Juhaiman LA, Al-Enzezi DA and Mekhamer WK 2016 Preparations and Characterization of Polystyrene \ Organo-clay Nano-Composite From Raw Clay *Digest J. Nano-materials Biostruct.* **11** 105-114.
[25] Imene B, Sami B and Mohamed B 2007 A Technique For Purifying Wastewater With Polymeric Flocculant Produced From Waste Plastic *Distillation* Elsevier **204** 198-203.
[26] Cristina A, Gabriela RM, Gonzalo MB, Patricia BH, Carmina MC and Fernando UN 2019 A novel sulfonated waste polystyrene/ iron oxide nanoparticles composite: green synthesis, characterization and applications *J. Environ. Chem. Eng.* Elsevier **7** 1-7.
[27] Zundel G 1969 *Hydration and Intermolecular Interaction, Infrared Investigation with Polyelectrolyte Membranes* Academic Press, Germany, 1969.
[28] Chitral JA and Shesha HJ 2011 Analysis of the Effects of Solution Conductivity on Electrospinning Process and Fiber Morphology *Transact. Ind. Applic. IEEE* **47** 1109 -1117.
[29] Changling L, Nicha C, Wayne B, Karen L, Kyu H, Jin N and Nosang V 2014 Electrospun, Polyaniline/Poly (ethylene oxide Composite Nano-fibers Based Gas Sensor *Electroanalysis, Wiley* **26** 711-722.
[30] Tomasz T, Pawel J and Wiktor M 2018 *Electrospinning Method Used to Create Functional Nano-composites Films* IntechOpen, Spain.
[31] Francesca R, Claudia U and Elisa A 2020 Innovative Poly (Vinylidene Fluoride) (PVDF) Electrospun Nanofiber Membrane Preparation Using DMSO as a Low Toxicity Solvent", *Membranes* **10** 1-18.
[32] Jalal NM, Ali ZA, Allami SA, Hassan SM and Ali MR 2017 Effect of Lithium Chloride Addition on the Electrical Conductivity of Polyvinyl Alcohol Films *Am. J. Eng. Res.* **6** 337-343.
[33] Jabur AR, Chayad FA and Jalal NM 2016 Fabrication and characterization of nylon 6/MWCNTs conductive polymer by electrospinning technique *Int. J. Thin Films Sci. Technol.* **5** 1-9.
[34] Sun Z, Deitzel JM, Knopf J, Chen X and Gillespie JW 2012 The Effect of Solvent Dielectric Properties on theCollection of Oriented Electrospun Fibers *J. Appl. Polymer Sci.* **125** 2585–2594 .
[35] Jasim KA, Fadhil RN, Shaban AH, Jaafar HI, Maiyaly BKH, Aleabi SH and Salman EMT 2019 The effects of copper additives on the glass transition temperature and hardness for epoxy resin PIE, *Progress Indust. Ecol. Int. J.* **13** 2 163-172.
[36] Kadhim BB, Risan RH, Shaban AH and Jasim KA 2019 Electrical characteristics of nickel/ epoxy - Unsaturated polyester blend nanocomposites, *AIP Conf. Proc*. **2123** 020062-(1-5).

Design High performance multilayers cold mirror

Design High performance multilayers cold mirror

Ansam Qassim Gadhban[1], Harakat Mohsin Roomy[2], Sarah K Taha[3]

[1]Department of Physics,Madenet Al-Elem University College,
[2]Ministry of education, Baghdad, Iraq
[3]Department of Physics, College of Science for Women, Baghdad University, Iraq

E-mail:Ansam.qasim@mauc.edu.iq

Abstract. The optical design process includes a myriad of tasks that the designer must be performed and consider in the process of optimizing the performance of the optical system. In this article, a design based on four groups of materials for a multilayer dielectric cold mirror: V_2O_5 \MgF_2, Sic\ MgF_2, TiO_2\ MgF_2, and Al As\ MgF_2 where MgF_2 represents low refractive index and other material in each group represent high refractive index. A cold mirrors are a special dielectric mirrors that reflects the entire visible wavelength band, while the transmitting infrared wavelength band. These systems of mirrors are constructed for an event angle from 0 ° to 45 ° and are modeled with interference filters-like multi thin layer dielectric coatings. The results of our work designed shows the mirror based on Al As /MgF_2 is the most promising design for cold mirror with the highest reflection in the visible region and the highest Transition in the IR region. In the spectrum range of 400-800 nanometers, the average transmission is much less than 1 %, while the average transmission is 95 percent in the wave band 800-2500 nanometer.

Key words: Multilayers Coatings, Cold mirror, Characteristic matrix.

1. Introduction

In optical manufactured devices, optical coatings are founded to be an important requirement. Through changing the direction of propagation, spectrum, the magnitude, phase or polarization, can be used to match the optical media and regulating the light radiation [1]. These optical coatings consisting of one or more of thin layers of metal or insulating materials, [2,3] has a number of important applications in many branches of science and technology [4]. Thin coatings have been used to improve a glass's color and efficiency of energy and as reflective coatings for a mirror [5]. Thin-layer optics and many devices such as stop-band filters are a well-advanced technology. The use of multi-layer insulating thin films has been successfully developed with band pass filters, reflectors and polarizer's [6]. Due to their availability, proven reliability and long-term stability, multi-layer dielectric filters are commonly accepted in optical networks. The filters can be made to have excellent wavelength stability, making them ideal filters for passive components. In the fact, dielectric filters are sometimes used to stabilize the wavelength of active ingredients [7]. The optical components consist of multi-layers of High and Low refractive indices material of specific thicknesses, consciousness of the refractive indices and absorption. Multi-layer dielectric filters are based on the concept of multiple reflections that occur between high and low index material interfaces [8].

A dielectric mirror, also referred as a Bragg mirror, is a type of mirror consisting of several thin layers of dielectric material usually deposited on a glass or optical material substrate. This type of a mirror consists of a several thin layers of an insulating material, which is coated on a glass substrate. The behavior of such a mirror depends on the constructive interference between the light reflected from the individual layers. The dielectric mirror can have very high reflection, to better than 99.99%. The dependence of the wavelength of reflection is used to achieve various special types of mirrors, such as a hot mirror which reflects longer wavelengths and is transparent at shorter wavelengths [9]. To reflect a visible light spectrum and transmitted the Infra-Red (IR) wavelengths containing the thermal energy. Cold mirrors are dialectically coated on a glass substrate. Cold mirrors are used to control the thermal energy entering temperature sensitive systems, also have an excellent alternative for transmitting the near infra-red spectrum. Cold mirrors have a sharp cut off between IR and visible light because they have a dielectric coating that can be controlled it. Its apposite for hot mirror can be defined as a narrow band multilayer that reflects targeted wavelengths, and transmits visible light. It is a specialized dielectric mirror, a dichroic filter that reflects the entire visible light spectrum while very efficiently transmitting infrared wavelengths [10]. This mirror is based on the concept of multiple reflections between high and low material interfaces [10, 11]. Cold mirrors are used to control thermal energy entering temperature sensitive systems and are also an excellent alternative for transmitting the infra-red spectrum. There are many practical uses for cold mirrors, such as copying machines, medical instruments , fiber optic lighting and are often used with tungsten lamps which are the source in a projector or lighting system [6]. Finally cold mirrors can be employed as dichroic beam splitters with laser systems to reflect visible light wavelengths while transmitting infrared. Cold mirrors can be designed for an incidence angle ranging between zero and 45° degrees, and are constructed with multi-layer dielectric coatings, in a manner similar to interference filters [12]. In this paper, five groups of materials of: V_2O_5 \ MgF_2, Sic\ MgF_2, TiO_2\$MgF_2andAlAs$\$MgF_2$ optical coating instead in one stack is utilized to design cold mirrors has a high reflectance at 550 nm and a low reflectance in IR waveband at 1100 nm.

2. Simulation Tool

To design interference optical filters open software program "open filter" has been used. This software calculates optical properties of filters and the state of polarization of electromagnetic (EM) radiation that can be expressed by the characteristic matrix of the thin film method for calculating the transmission properties of filters. This software is also utilized to design several multilayer filters [13]. In this program, optimization methods such as injection synthesis is possible (adding an extra layer to give selective transmission) [1 4].

3. Cold mirror design

The behavior of the total multilayer structure is calculated according to the characteristics of the individual layers in the stack when optical filters designing [6]. In this article, colds mirrors designing in the spectrum of 400-2500 nanometer, at the wavelength design 500 nm, by use Open filter software to transmits the spectrum of interest selectively also to reflects the unwanted spectrum in the visible spectrum. It used four groups of materials: V_2O_5 \$MgF_2$, SiC\ MgF_2, TiO_2\$MgF_2$, and $AlAs$\$MgF_2$ where MgF_2represent low refractive index (1.38) and other material in each group represent a high refractive indexV_2O_5(2.3),SiC(2.69), TiO_2 (2.88) and AlAs(3.38)[15].To examine the transmission and reflection of light from layers based on the thickness and form of materials, the open filter uses the transfer matrix method. Using the needle synthesis process, to optimize the transmission of design needed at wavelengths (adding small dense layers called needle and transmission analysis prior to achieving the best results [6].

4. Theoretical approach

A classical optical filter consists of a number of thin layers of *dj* thickness and *Nj* refractive indices between the incidence and exit media of *Ninc* and *Nex* refractive indices, respectively. By using characteristic matrix method to measure filter optical properties, and discussed in depth in most optical coatings textbook, such as Macleod [16], the ith layer is represented by:

$$\mathrm{M}=\begin{pmatrix} M_{11} & M_{12} \\ M_{21} & M_{22} \end{pmatrix} = \prod_{j=q}^{j} M_j \quad \text{.....(1)}$$

Where *q* is the multi -layer, and the product is taken in reverse order since the matrices of upper layers must be multiplied on the left.

$$\begin{pmatrix} M_{11} & M_{12} \\ M_{21} & M_{22} \end{pmatrix} = \begin{pmatrix} \cos\delta_H & isin\,\delta_H/\eta_H \\ i\eta_H sin\delta_H & cos\delta_H \end{pmatrix} \begin{pmatrix} cos\eta_L & isinn\eta_L \\ i\eta_L sinn\eta_L & cos\eta_L \end{pmatrix} \text{.....(2)}$$

Where δ_H and δ_L is phase thicknesses of the High indices, η_H, and Low indices, η_L materials respectively. It can be expressed as:

$$(\delta_j = 2\pi N_j d_j cos\,\vartheta_j/\lambda_\varrho \ldots\ldots(3)$$

Where *j* =*H* or *L*and ϑ_j is the angles of refraction in the j[th]layer. The refractive index is given by an effective index:

$\eta_j = \mathrm{N_j}\ \cos\theta_j \ldots\ldots\ldots\ldots(4)$S polarization state

$\eta_J = N_j/\cos\theta_j \ldots\ldots\ldots(5)$P polarization state

η_j is the effective index and θ is the angle of incidence.
The amplitude transmission coefficient of the thin layers is:

$$t = \frac{2\eta_{inc}}{\eta_{inc}m_{11} + \eta_{exi}m_{22} + \eta_{inc}\eta_{exi}m_{12} + m_{21}} \ldots\ldots\ldots(6)$$

$$T = \frac{R_e N_{exi}}{R_e N_{inc}} tt^*$$

$$T = \frac{R_e N_{exi}}{R_e N_{inc}} |tt|^2 \ldots\ldots(7)$$

Where Re is the real part, * denotes the complex conjugate and T optical transmittance.

5. Results and Discussion

In this research, the stack of design Air [1.15(0.35H L 0.5H)^5 2L] glass of cold mirror where H represents the high quarter wave of optical thickness and L represent the low quarter wave of optical thickness with $\lambda_{\circ}$=500 nm. Cold mirror was obtained by using four groups of materials (V_2O_5 \ MgF_2, SiC\ MgF_2, TiO_2\ MgF_2andAlAs\ MgF_2) with a number of layers are12 layer only. The best result as shown in Figure 1 using AlAs\ $MgF_2$with transmission is less than 0.01, so that it has been found at *the high variance in refractive indexes i.e., high to low refractive index ratio*, sharp cut off between IR and visible light can be achieved and obtained a better optical performance of cold mirror. In all the designs for dielectrics stack of cold mirror, It's found that optical performance of the AlAs\ MgF_2 formation shows better results with a desired spectral purity, side part pulses (pass-band oscillations) is low in compared to other groups. Also these mirror formation have a smooth transmitted in the spectral range from 399.5 -786.3 nm and above 800 nm 100% 96.5%, respectively as shown in Figure 1. It can be seen the summary of results for the optical performance at normal incidence angle of multilayers with different groups shown in Table 1.

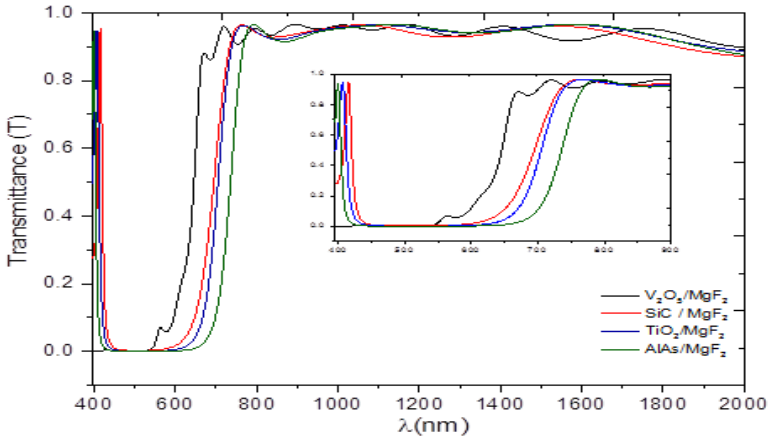

Figure 1. The Optical performance cold mirror at normal incidence using stacks Air [1.15(0.35H L 0.5H) ^5 2L] glass.

Table 1. Optical performance of Multilayers for different groups.

Multilayers with different Index ratio(n_H/n_L)	Optical performance at normal incidence angle		
	R% over the Vis-spectral region at 500nm	spectral range (nm)	T% over the NIR-spectral region at 1100nm
V_2O_5(2.3) /MgF_2(1.38)	100	300-668	95.8
SiC(2.69) /MgF_2(1.38)	100	414-758	93.3
TiO_2(2.88) /MgF_2(1.38)	100	406-758.077	94.2
AlAs(3.38) /MgF_2(1.38)	100	399.5-786.3	96.58

The effect of angle of incident was studied on the optical efficiency of the cold mirror. Where the transmittance has been calculated according to the effects of the incident angles for the materials using

equations (7), as illustrated in Figure 2. It has been noticed weak effect showing of the optical performance of the cold mirror at the angle of incident of un-polarized light is equal to (θ = 0°, 20°, 25°, 30°).

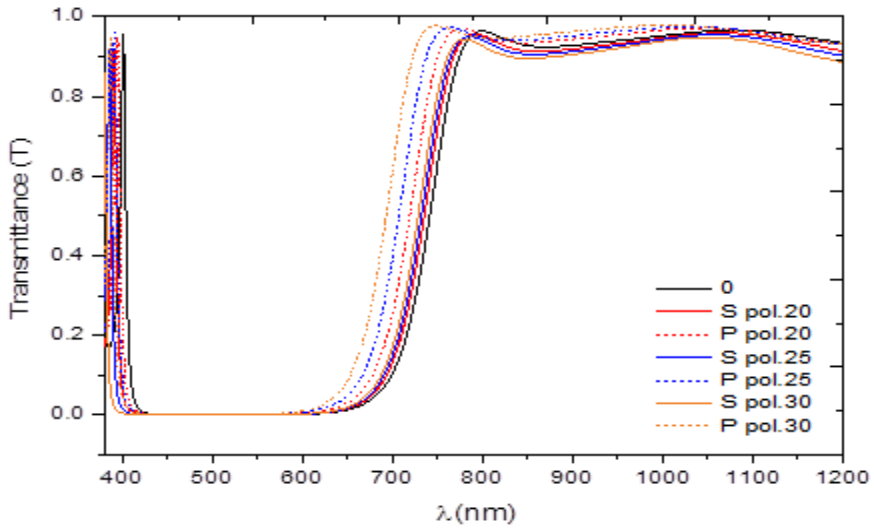

Figure 2. The Optical performance cold mirror at incidence angle of 0°, 20°, 25°, 30°.

When the incident angle of un-polarized light increased (θ =35°, 40° and 45°) it has been noticed the optical performance of these mirrors becomes better as shown in Figure 3. The angles of incidences are increased, a central spectrum for the cold mirror design changes to the lower wavelengths. At the incident angle of the light increased from 0° to 45°transmitted range change from 790 to 662nm .Then it's possible to obtaining a good optical performance of the cold mirror for different angles and is not limited to the angle of incidence of 45 and zero. For all designs, the optical transmittance is determined by angle of incidence. It can be seen the summary of the results for the optical performance at oblique incident angle of un-polarized light shown in Table 2.

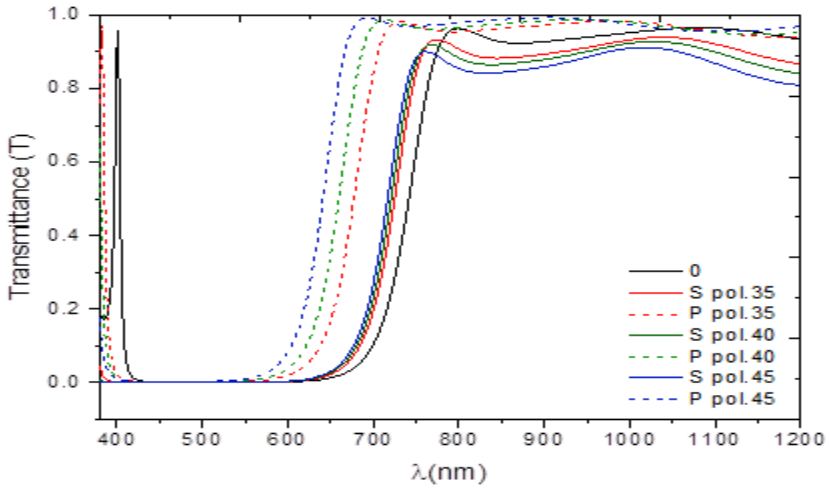

Figure 3. The optical performance cold mirror at incidence angle of 0°, 35°, 40°, 45°.

Table2. Optical performance for oblique incident angle of un-polarized light.

Angle of incidence(°)	Transmittance%			
	S Pol.	Waveband (nm)	P Pol.	Waveband(nm)
20	0-95.5	(391.8-790.01)	0-96.8	(395-770.2)
25	0-95	(385.1-782.3)	0-97.2	(391-758.01)
30	0-94.4	(380.2-775.4)	0-98.2	(386-751.4)
35	0-93	(375-766.56)	0-98.8	(382-740.2)
40	0-92.1	(372.4-764.3)	0-99	(377-725.1)
45	0-89.5	(357-762.86)	0-99.8	(372-694.1)

6. Conclusions

Here optical designs of a multilayer cold mirror have been carried out to calculate the optical performance of optimum designing of four groups of materials (V_2O_5 \ MgF_2, SiC\ MgF_2, TiO_2\ MgF_2 and AlAs\ MgF_2) with number of layers 12 layer. The stack of AlAs\ MgF_2optical coating is optimal design with a desirable spectral purity and small ripples in the transmittance band in compared to other groups and reflects greater than 96.5%, in the visible waveband 399.5-786.3 nm and transmit highly above 800nm. Moreover, the relative phase change between s- and p-polarized and a transmittance band by means of adjusting reflectance and interference orders can be adjusted by varying the index ratio .Finally, it can achieve optimum optical efficiency of a cold mirror for different angles and is not limited to the incidence angles of 45 and zero.

References

[1] Volpian O D and Kuzmichev A I 2013 *Russian Journal of General Chemistry* **83** (11) 2182.
[2] Kats M A Blanchard R Genevet P and Capasso F 2013 *Nature materials* **12** (1) 20.
[3] Yeh P 1988 *Optical waves in layered media* (New York: Wiley).
[4] Yang J M and Kao C Y 2000 *In Proceedings of the 2000 Congress on Evolutionary Computation*.CEC00 **2** 978.
[5] Butt M A Fomchenkov S and Khonina S N 2017 *In CEUR workshop proceedings* **1900** 1.
[6] Elyutin V V Butt M A and Khonina S N 2017 *3rd International conference "Information Technology and Nanotechnology*.
[7] Minowa J and Fujii Y 1983 *Journal of Lightwave Technology* **1** 116.
[8] Austin R R 1994 *U.S. Patent* No. 5,337,191. Washington, DC: U.S. Patent and Trademark Office.
[9] Karaman M Kooi S E and Gleason K K 2008 *Chemistry of Materials* **20** 6 2262.
[10] Rancourt J D 1996 *Optical thin films* SPIE Press.
[11] Elyutin V V Butt M A Khonina S N 2017 *Computer optics and nanophotonics* 26.
[12] Li L Sullivan B T and Dobrowolski, J A 1999 *U.S. Patent* Washington DC: U.S. Patent and Trademark Office (5) 982,541

[13] Butt M A Fomchenkov S A Ullah A Habib M and Ali Z 2016 *Computer Optics* **40** 5 pp 674
[14] Butt M A FomchenkovS A KazanskiyN L Ullah A Ali R Z and Habib M 2017 *In Optical Technologies for Telecommunications International Society for Optics and Photonics 10342* 103420O).
[15] Tropf W J Thomas M E and Harris T J 1995 *Devices, Measurements, and Properties* 2nd Ed (McGraw-Hill- NewYork).
[16] Macleod H A 2010 *Thin-film optical filters* 4th Ed (CRC pres Taylor and Francis group).

Study the photo catalytic activity of titanium dioxide nanoparticles and the impact on the degradation of methylene blue

Study the photo catalytic activity of titanium dioxide nanoparticles and the impact on the degradation of methylene blue

Abbas K Jarallah[1], Omar Fadhil Abdullah[2], Wisam J Aziz[3] and Marwa J Lahwd[4]

[1]Al –Hadba University College
[2]University of Samarra, College of Education, physics Department
[3]Mustansiriyah University, College of Science, physics Department
[4]Ministry of Education

e-mail: abbaskasoob@yahoo.com

Abstract. In this study, titanium dioxide (TiO_2) pure and doped prepared with tungsten at 5, 7 and 9 %, using pulse laser ablation method. The influence of different doping ratio of tungsten investigated on the structural properties and optical properties. X-ray measurement showed that the crystal size was increased by increasing doped concentration. From UV- visible data it has been found that the tungsten doping leads to a change in the optical band gap. ApplicationTiO_2 as photo catalyst was studied on the degradation of methylene blue (MB) dye under UV illumination, which revealed the highest degradation of MB at a ratio of 9%.

Keywords: Titanium dioxide, tungsten oxide, PLA, Photo- catalyst.

1. Introduction

Titanium dioxide (TiO_2) is abundant in nature, safe with high optical transparency and largeenergy band gap [1]. Nanoparticles TiO_2 are chemically and biologically stable and are of low-cost, so employed as photocatalysts [2]. Photocatalytic technology has shown great potential as aninexpensive, environmentally-friendly, and sustainable technology; and it has been highly research [3]. ZnO, WO_3, and TiO_2 are semiconductors. They also can be used as a photocatalyst and non-toxic materials for the human beings for that used as antibacterial, plants andanimals [4]. The TiO_2 is the optimum active photocatalyst under photon energy of 300 nm< l <390 nm and it remains stable after the repeated catalytic cycles, whereas Cds or GaP are degraded along to produce toxic products [5].

Pulsed laser ablationin liquid (PLAL) can produce the extreme conditions and lead to the formation of the novel nanostructures and for that, it has attracted large interest [6]. Also, the simple experimental set-up and one-step fabrication process make laser ablation in liquid (LAL) an alternative choice to the traditional wet-chemical methods [7]. Tungsten oxide nanostructures have a wide variety of applications [8]. Tungsten oxide is a semiconductor and it has indirect wide band gap of 2.2 to 2.8 eV [9]. TiO_2 photocatalyst, which produces free radicals on its surfaces by adequate light activation, has cometo utilization such as self-cleaning [10]. The degradation of the dye depends on thetime of illumination, and the absorption intensity gradually reduced with the increase of illumination time [11-12].

2. Experimental part

2.1 preparing of samples

Target of titanium plat and tungsten plate using to prepare nanoparticle by pulse laser ablation method. Nd:YAG laser was used with wavelength (532nm), frequency (1 Hz) ,voltage (900 volt) and (2000 pulse),(5 ml) distilled water (DW) has been putted in container and (Ti) target immersed in DW to control the nanoparticle and to reduce thetarget heat. Same conditions using with both targets (Ti) and (W), after preparing nanoparticle as collide in DW the solution deposited as thin films by drop casting method. Tungsten using as impurities, the doping concentrations were 5%, 7% and 9% calculated volumetrically. Titanium and tungsten solutions were mixed by usingmagnetic stirrer for 30 mints. After that it was depositedusingthe drop casting method on cleaning glass substrates (2x2 cm^2) at temperature about (90 ±10) C°.

2.2 Evaluation of photocatalytic activity

The photocatalytic activity of pure TiO_2 and doped with W was tested by the degradation of (MB) dye under the irradiation light (254 nm). Initially the mixture solution was stirred about 30 min in dark to obtain the adsorption equilibrium. The area of the samples 2x 2 cm^2 soaked in a 20 ml of MB to be the amount of total solution 100 ml and weight of MB 0.001g. The optimum absorption peak of MB at 666 nm used to estimate the remaining concentration of MB [10]. Plotted the ratio of remained to initial absorption of MB against irradiation time (30, 60, 90 and 120 min) to evaluate the photocatalytic degradation and calculated the percentage degradation of MB.

3. Results and dissection

X-ray diffraction patterns of theTiO_2doped with W (5%, 7% and 9%)are presented Figure (1). It can be seen that, in general, all the samples are crystalline. The pure TiO_2 is in the form of rutile phase and all the films of W-doped TiO_2 are mainly in rutile phase and appear phase of tungsten and anatase phase of TiO_2 together in the same location that give indicate about effect of dopant on the structural properties.

The small dissimilar ionic radius of WO_3 (0.62 Å) to that of Ti_{4+} (0.68 Å) could be the reason for unstabilizing TiO_2 in the form of rutile phase by replacing some portion of Ti_{4+} ions in TiO_2 lattice byWO_3+. The crystallite size was calculated by scherer equation, are (26.5 nm), (32.2 nm),(38.6 nm) and (51 nm) of pure and doped (5,7 and9 %)respectively that indicate the impurities is not substitutional.

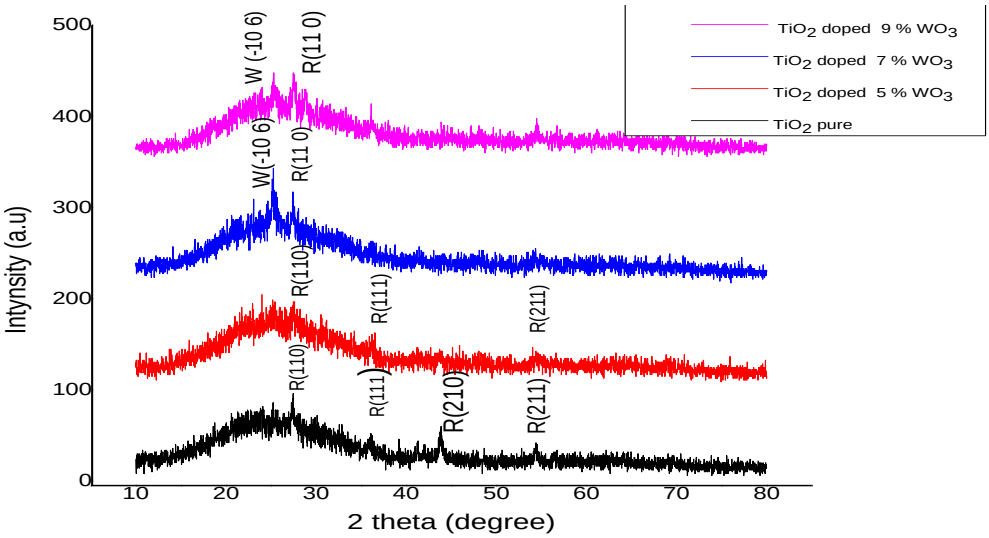

Figure 1. The effect of doping concentrations (5, 7 and 9 % WO_3) on X-RD results of TiO_2.

Figure 2 displays FESEM images obtained from different doped concentrations which indicates the crystal sizes are in nanometer range for all films. Pure TiO_2 appears as spherical particles homogeneous in size and shape; after doped by ratio 5% the shape and size of particles will differ but keeps in nano range, when doped concentration increased to 7% and 9%, the films appear more homogenous with look of WO_3 particles in the films surfaces.

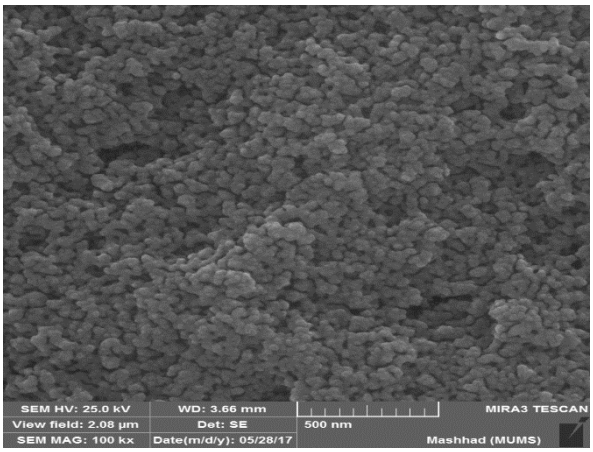

1

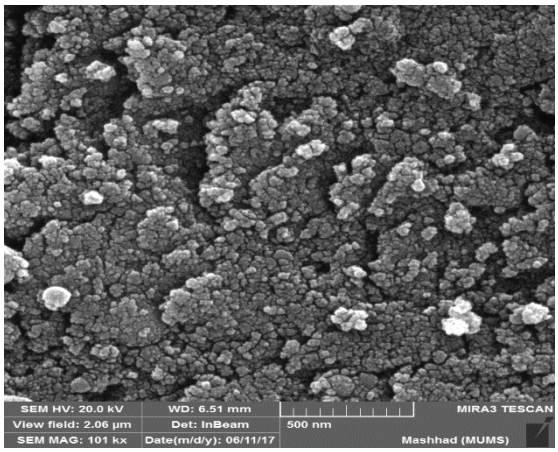

2

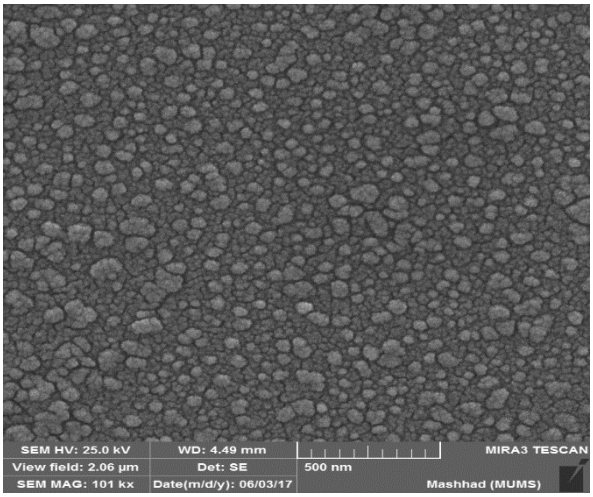

3

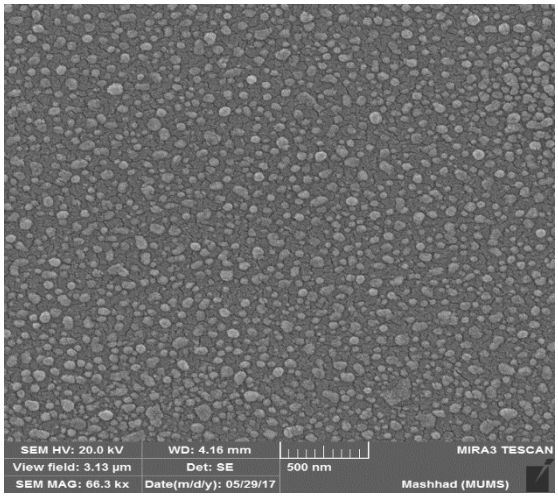

4

Figure 2. FESEM images of 1) pure TiO_2,2) doped 5%, 3) doped 7% and 4) doped 9%.

Figure 3 demonstrates the transmittance of undoped and doped films, transmittance decreases with increase of dopant ratio, and that is a result of creating a new energy level between valance band and conduction band inversely with the absorption. The response of $TiO_2$to visible light increases after doping with tungsten and it shows a red shift (towards higher wavelength). From the invers relation between transmittance and absorption that indicate the reduction of energy gap with doped .The red shift of the absorption curve leads to decrease in the energy band gap and also the recombination rate, which a result to the enhanced photocatalytic activity. From Figure 4, it can be seen that the energy band gap decreases with increase of dopant ratio, shift towards the visible range, which reveals increasing tungsten ratio. The red shift of the band gap caused by the presence of tungsten can be evaluated as being moderate, with the absorbance limit shifted.

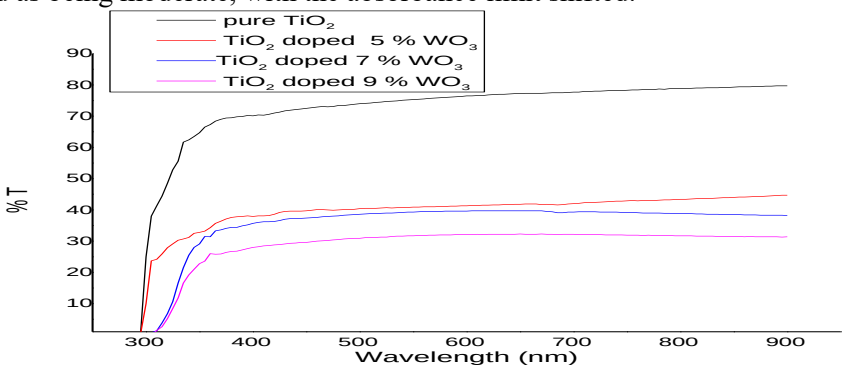

Figure 3. Explain WO_3 ratio on the transmittances.

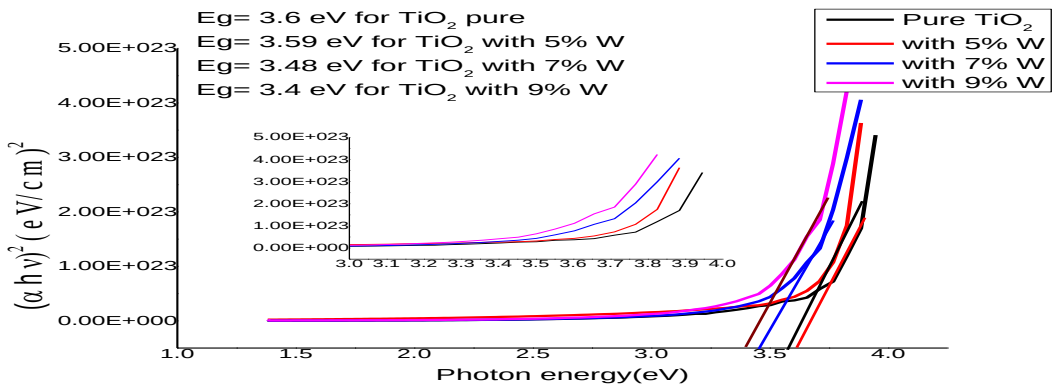

Figure 4. Explanation of the effect of doping ratio on the energy gap.

The degradation of MB dye was watched by measuring the change in absorbance as a function to the illumination time. Figure 5 explains the effect of change in illumination time on the ratio (9%). In from the Figure 5 de-colorization of MB happened after 30 min of illumination in the presence of W-doped TiO_2 and atmospheric oxygen.The reduction in the absorption of MB with illumination time is accustoming to the changes of the molecular structure of the dye.

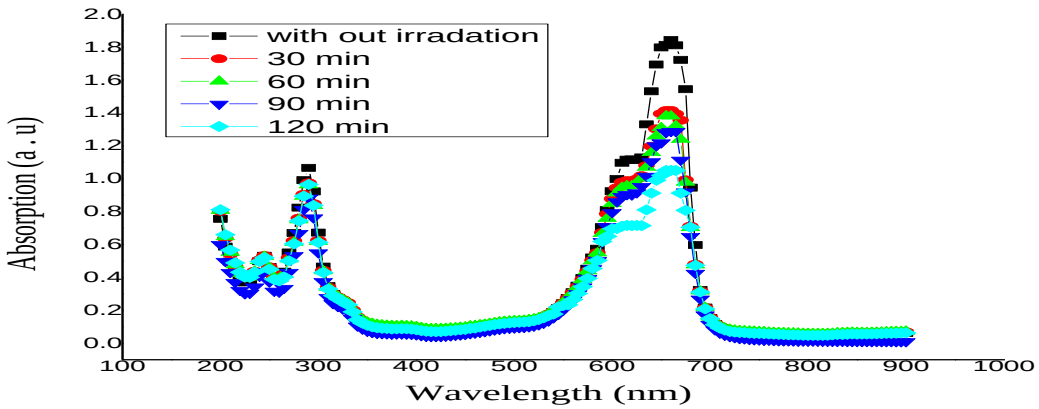

Figure 5. Explaination of the effect of illumination time on the absorption for titanium doped with tungsten at ratio 9%.

Photodegradation of MB is illustrated in Figure 6. MB concentration changes with increasing irradiated time.The decomposition of MB increase with increasing the tungsten concentration at the same time. The effects of surface area, crystal structureand ratio of dopant have been providing rational explanations for the photocatalytic activities observed.The degradation efficiency of MB increase by increasing the illumination time and dopant ratio that appear in Figure 7.

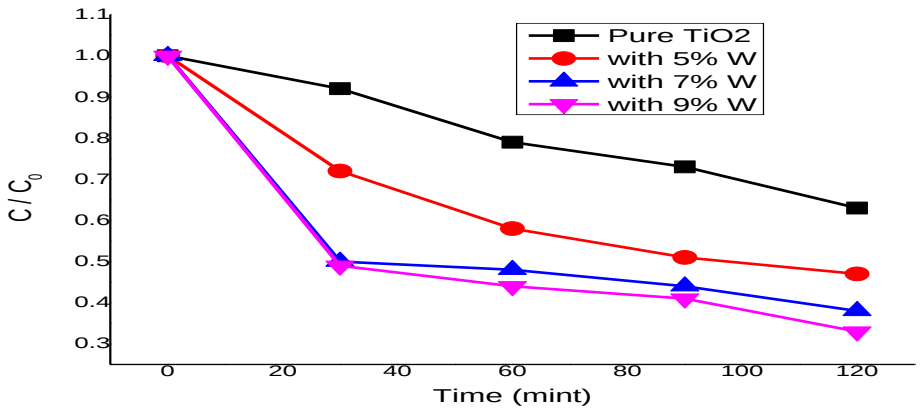

Figure 6. Photodegradation of MB under UV irradiation and time irradiation with different doped concentrations.

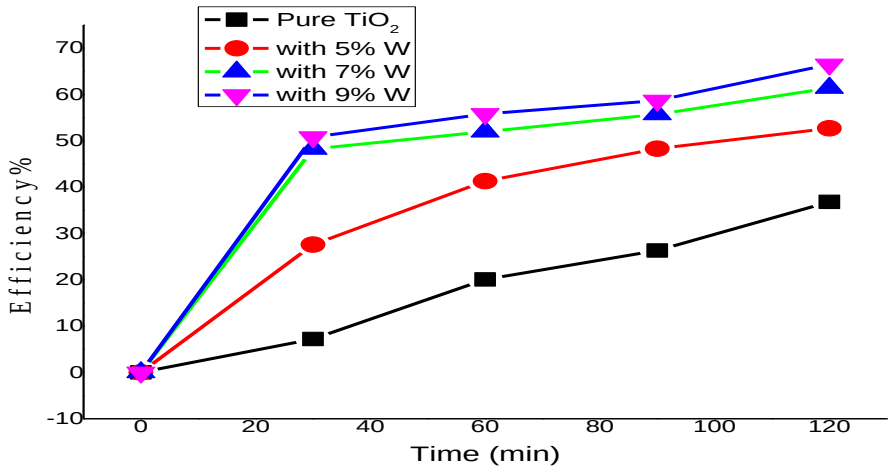

Figure 7. Degradation efficiency of MB using different ratio of W.

4. Conclusions

In this study, synthesis nano titanium dioxide by PLA method pure and doped (tungsten) and applied as photocatylist. The crystal size increased with increased ratio of doped.From FESEM, the grain size for all films in nanometer range.The increasing in doped concentration resultedin high homogenous with appeared WO_3 particles in the films surface. UV–vis spectra showed increased in the absorptionpeaks with dopant ratio.Decreasing the energy gap increased the photocatalytic activities. The addition of WO_3 as a dopant in all samples resulted in an enhancement in photocatalytic activity. From the results of photocatalytic appear optimum photocatalytic performances at dopant ratio of 9%. Also better photo degradationrate and degradation efficiency appear at the same dopant ratio.

References

[1] Mohite V S Mahadik M A Kumbhar S S Hunge Y M Kim H J et al. 2015 *J Photochem Photobiol* **B 142** 204.
[2] Hunge Y M Mahadik M A Moholkar A V and Bhosale CH 2017 *UltrasonSonochem* **35** (Pt A) 233.
[3] Fubao Z Xianming W Haonan L Chunli L Yong W Yunze L and Zhongyu C 2019 *Appl. Sci.* **9** 2489.
[4] Wang M Ioccozi J Sun L Lin C and Zhiqun Lin 2014 *Energy Environ Sci* **7** 2182.
[5] Malato S Ferna´ndez-Iba´n˜ ez, P Maldonado M I Blanco J and Gernjak W 2009 *Catal. Today* **147** 1e59.
[6] Liu P S Cai W P and Zeng H B 2008 *J Phys. Chem. C* **112** 3261.
[7] Mafune F Kohno J Y Takeda Y Kondow T and Sawabe H 2011 *J. Phys. Chem.* B **105** 5114.
[8] Baetens R Jelle B P and Gustavsen A 2010 *Solar Energy Materials and Solar Cells* **94** 87.
[9] Baeck S-H Choi K-S Jaramillo T F Stucky G D and McFarland E W 2003 *Adv. Mater.* **15** 1269.
[10] Fujishima A Tryk D A Watanabe T and Hashimoto K 1998 *Int Glass Review-Flat Glass Proc* 114.
[11] Aziz W J Sabry R S and Jarallah A K 2018 *Journal of Physics* **1032** 012021.
[12] Abbas Kh N Hussain N A Nusseif A D Hussein E H Aziz W J and Salim A A 2020 *Journal of Physics: Conference Series* **1484** 012002

Effect of fillers (Bentonite - Zirconium) on the thermal behaviour of PVC polymer

Effect of fillers (Bentonite - Zirconium) on the thermal behaviour of PVC polymer

Wasan K. Hasan

Education College for Pure Science, University of Kerbala, Karbala, Iraq

E-mail: wasan.kamil@uokerbala.edu.iq

Abstract. Thermal conductivity is one of the basic physical phenomena that can affect matter in heat quantities and explain what happens during the heat transfer process. The work indicates to the importance of investigate for effect of filler material Bentonite and ZrO_2 on the thermal properties of polyvinyl chloride as a binder material with ratio of 3% compared with the ratio of Zirconium Oxide which was in the limits (0%, 5%, 10%, 15%) besides Bentonite, the burn process was carried out at various temperatures 800,900,1000,1100 and1200 ^{o}C. The results showed a decrease in the values of thermal conductivity from (0.5-0.3 W/m.K) when adding zirconium oxide, while increasing the percentage of the Bentonite with increasing and the burning temperature led to the increment of thermal conductivity for the prepared samples.

Keywords: Thermal conductivity, polyvinyl chloride, zirconium oxide, polymer composite

1. Introduction

Polymeric materials are among the important materials in the industry for many reasons, the most important of which is ease of manufacture and cheap price, light weight, good chemical specifications that are not present in ceramic and metallic materials, but after technological development, especially in the field of space industries and the manufacture of cars, airplanes and boats, the need increased to manufacture materials with specifications In particular, attention has turned to the manufacture of composite materials, including polymeric composites. Most of the polymeric composite materials were the reinforcement material with ceramic or glass materials in the form of fibers or powder, where many previous studies were conducted to learn about changing the thermal properties of the composites of polymeric materials with changing the type and quantity of the reinforcement material added [1].

The aim of this study is to study the thermal conductivity of polymeric material and the effect of temperature on the thermal conductivity of matter, as the thermal conductivity is one of the basic physical phenomena through which it can be studied and how a substance is affected by heat.

2. Experimental details

2.1 Theoretical part

Thermal conductivity is a phenomenon of thermal transfer, in which energy is transferred from one location to another due to irritation of the atoms or molecules of the material due to a change in the temperature of the medium, but the conductivity mechanism in the solid materials differs from it in the liquid and from it in gases as well as differs in the conductive materials from the insulating materials. The thermal conductivity of the insulating materials has been measured on the principle of the thermal conductivity of the samples in the form of a large diameter disk relative to thickness. When there is a thermal gradient (dT/dX) during a physical medium in the direction (x) the average of thermal conductivity resulting from the difference in temperature a cross the vertical cross-sectional area of the heat flow is given by:[2]

$$\frac{dQ}{dt} = -KA\ \frac{dt}{dX} \dots\dots\dots\dots (1)$$

Since (K) represents the constant of proportionality and is called thermal conductivity and is a measure of the process of thermal selection across the material, negative sign means that the flow of heat towards the lower temperature, and the addition of negative sign in the equation is useful in making K a positive quantity, and other forms of the equation above the formula The following

$$\mathrm{Q} = \mathrm{K}\frac{\mathrm{T1} - \mathrm{T2}}{\mathrm{X}}\mathrm{At} \dots\dots\dots\dots (2)$$

It represents the basic equation for thermal conductivity, which is known as the Fourier equation, and from equation (1) the thermal conductivity is defined as the amount of heat that passes through the unit area of the material per unit of time where the thermal conductivity is proportional to the difference between the temperatures of the external surfaces of the material and is inversely proportional to the thickness, so The average of heat flow is not dependent on the absolute temperature, but on the difference in the temperature of the two sides

One of the practical methods used to calculate the value of the thermal conductivity of the insulating solid l is to expose one of the sides of the samples to a heat source and calculate the temperature at the opposite side, as the sample is placed in a thermal gradient so that the flow of heat that reaches the other side is balanced Thus, the thermal properties are calculated by calculating the influencing factors and from the methods used in measuring the thermal conductivity is the stacked disk system, or the technique of heat flow in a cylinder, and since the temperature passing through the sample is the average amount of heat passing through the disk and thus the formula will be:[3]

$$K\left[\ \frac{T_2 - T_1}{d_S}\ \right] = E[T_1 + \frac{2}{r}(d_1 + \frac{1}{4}d_S)T_1 + \frac{1}{2r}d_S T_2] \dots\dots\dots\dots\dots (3)$$

Where

ds: thickness of the disc

r: disk radius

k: the thermal conductivity of the disk S

T1: face temperature A

T2: face temperature B

T3: face temperature C

The value of E can also be calculated from the power supplied to the heating coil (H), so it is*:*

$$H = IV = \pi r^2 E(T_1 + T_3) + 2\pi r E\left[d_1 T_1 + 1/2\, d_S (T_1 + T_2) + d_2 T_2 + d_3 T_3\right] \dots\dots (4)$$

Since V is the difference in voltage passing through the coil (Volt) and the current I Amp).*(*

After calculating the value of E, it is substituted in equation (3). Thus, we obtain the thermal conductivity value (K) for the sample to be examined in units (W/m.K).

2.2 Materials used in research

2.2.1 Bentonite

Bentonite is an impure clay composed mainly of montmorillonite or calcium silicate oxide and is found in the form of powder in a gray color does not smell it.

The Bentonite or volcanic mud is a commercial name for a special type of clay consists mainly of mineral smectite .Bentonite are plenty of minerals including calcium, magnesium, silica, sodium,

copper, iron and potassium, the result is the processes of transformation of volcanic glass and mainly of hydrolytic silicate [4].

2.2.2 Zirconium Oxide

Zirconium Oxide is a single crystalline substance that transform to a tetra material increase of temperature and characteristics depend on the degree of stability and the amount of stability and quality of raw materials included in its composition and a zirconia used in this research prepared by (fluka chemie AG-CH 9770 Buchs) And its purity 99.9% [5-6].

2.2.3 Polyvinyl chloride

It is a widely used plastic material and The designation is abbreviated as PVC and it is used in a lot of applications and has been used in many industries as insulating material for electric wires, floor coverings, bottling industry, auto industry and it has distinctive characteristics in terms of high electrical insulation, strong abrasion resistance, low moisture absorption and good flexibility[7-8] .

2.3 The method of work

The basic material used in this work is bentonite powder with a granular size 75μm, and zirconium of Indian origin was added with a granular size of 100μm≥ for the purpose of improving the properties of the composite with weight ratios (5,10,15 wt%) to the bentonite powder as shown in Table(1)[9-10].

The materials were prepared and weighed with a sensitive scale and the granular size was measured by using special sieves for this purpose in the laboratory, the samples were also mixed using a mechanical mixer for two hours, and then the PVC binder was added in a percentage of (3%) and the samples were formed by Semi-dry pressing method and using a hydraulic press with a diameter of (40 mm) under a pressure of (25 MPa) and a period of time of (2 min), the sintering process was carried out using an electric furnace at normal atmospheric pressure and temperatures (800,900,1000,1100,1200) ^{o}C for a period of two hours .

For the purpose of measuring the thermal conductivity of the samples, a Lee's disk was used to calculate the thermal conductivity of the insulation materials using the device manufactured by (Griffen and George). The thermal conductivity was calculated using the equation(1) as explained in figures (1-6) that show the effect of added zirconium oxide on the thermal conductivity of the samples prepared from the compound at different temperatures.

Table 1. shows the weight ratios involved in the formation of the Bent-ZrO_2

material Matrix (Bentonite)	Add Material (ZrO_2)	Symbol
100	0	A
95	5	B
90	10	C
85	15	D

3. Results and Discussion

It's noted from Figures 1-5, that the addition of zirconium oxide led to a decrease in thermal conductivity of the materials and continues to decrease with the increase of the added ratio and the thermal conductivity is also increased by increasing the Bentonite content from (4-12)%.Where the thermal conductivity of the samples prepared was measured by the law of the thermal conductivity of the equation (3) of the figures, which shows the conductivity decrease due to the defect of the supported and added material with granules of the base material to obtain a homogeneous distribution and thus its spread easily among them and which led to obstruction the heat transfer and thus reducing

the amount thermal conductivity increases the values of weight fractures, as the presence of interfaces leads to impeding the movement of waves and the transfer of energy becomes a difficult process due to the discontinuity of the structure and the loss of part of its energy during the transition from the base material to the strengthening as shown in Table 1 [11-13].

Figures 6, 7 and 8 indicated that conductivity increased with increasing temperature and gave higher values as the insulating materials are affected at high temperatures by phonons, which represent the vibrations of the crystal lattice and are responsible for the transfer of heat in solid insulating materials, so the phonon collision process with another is considered an important process at those degrees at which the number of phonons participating in the collision process increases and this means that the thermal conductivity in this case depends entirely on the average of the free path of the phonons (the average distance traveled by two phonons for each successive collision) Whereas, phonons are the single transmitters of energy and it has a major role in the conduction process and all kinds of solid materials at high temperatures [14-15].

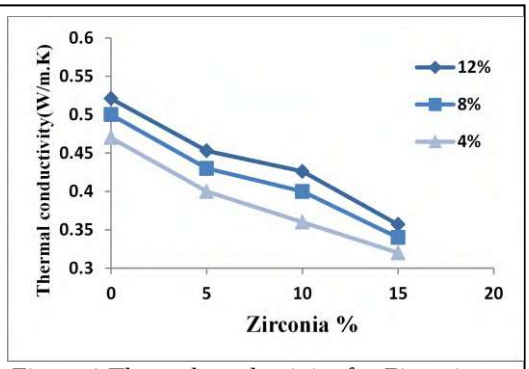

Figure 1.Thermal conductivity for Zirconia at 800 ^{o}C

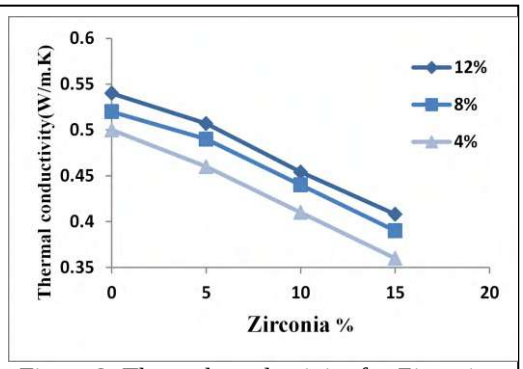

Figure 2. Thermal conductivity for Zirconia at 900 ^{o}C

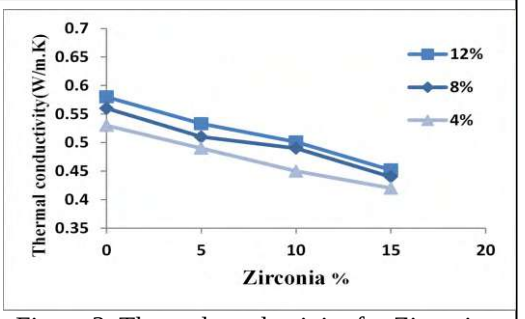

Figure 3. Thermal conductivity for Zirconia at 1000 ^{o}C

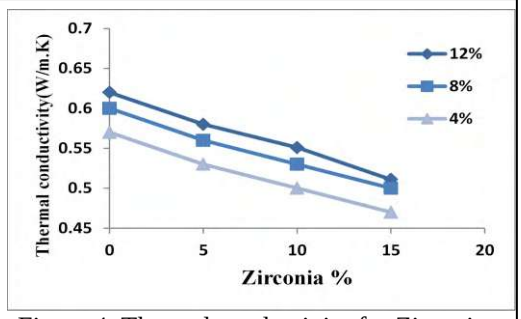

Figure 4. Thermal conductivity for Zirconia at 1100 ^{o}C

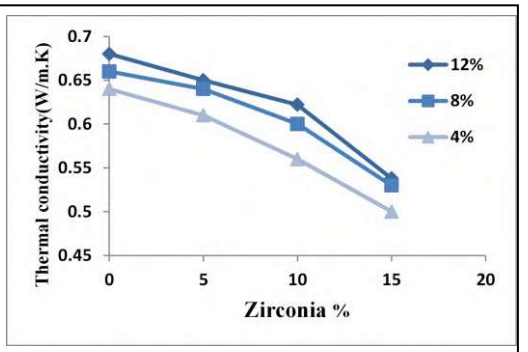

Figure 5. Thermal conductivity for Zirconia at 1200 ^{o}C

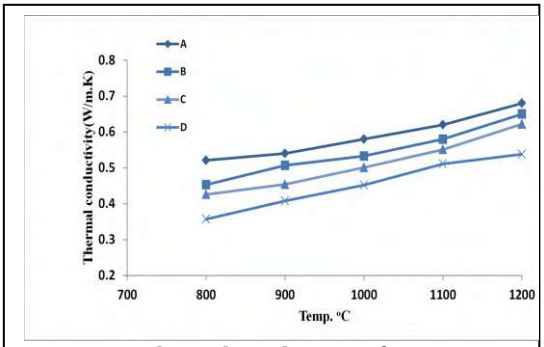

Figure 6. Thermal conductivity for Zirconia for burn degree at ratio 12%

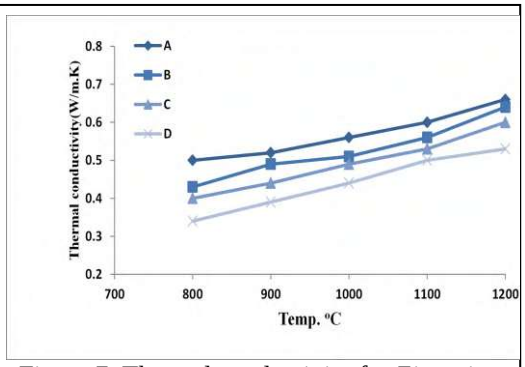

Figure 7. Thermal conductivity for Zirconia for burn degree at ratio 8%

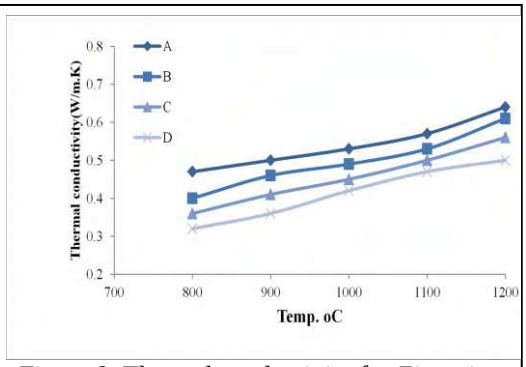

Figure 8. Thermal conductivity for Zirconia for burn degree at ratio 4%

4. Conclusions

1- The rate of addition of zirconium oxide granules resulted in a decrease in the thermal conductivity values of the polymeric compounds from (0.65 W/m.K) to(0.34 W/m.K) .
2- The thermal conductivity values increase with increasing the content of Bentonite from (0.34 W/m.K) to (0.68 W/m.K) .
3- The increase in the burning temperature led to an increase in the conductivity of all the samples, and they became of high density and low porosity, which resulted from the participation of phonons in the thermal conductivity at high temperatures.
4- The ratio of the strengthening material and the interfaces between the phases of the composite material are the reason for the low conductivity values of the polymeric compounds.
5- In the thermal conductivity test, the polymeric composite gave the highest values of thermal conductivity by increasing the burning temperature due to its influence with phonons, crystal grid vibrations, and the free path rate of the phonon.

References

[1] Zykova J., Kalendova A., Matejkav V. 2015 *Kaolinite-Urea Intercalates for PVC Nano Composite* **5** 10
[2] Bolton W. 1998 *Engenering Marerials Technology* 3rd ed. , Bulter worth , Heinemann, 30-34.
[3] Hausen H. 1976 *Heat Transfer Counter Flow, Parallel Flow and Cross Flow* , Mc Graw-Hill Co., 176-181
[4] Wasan K. H., Jassim T. M. , & Ammar S. H. 2019 *AIP Conference Proceedings* **2144**.
[5] Prusty S., Mishra D. K., Mahaparta B. K. , & Singh S.K. 2012 *Cer. Inter.* **38** (2363).
[6] Carolan J.V., Rawal A., Oldfield D.T., Thorogood G.J., & Bedford N.M. 2020 *ACS Appl. Nano Mater.* ,**3**(4),3717
[7] Wasan. K. H., Jassim T. M. , & Ammar S. H. 2019 *NLOQO* **50**(4), 279
[8] Wasan.K.H., Jassim T.M. , & Ammar S.H. 2020 *NLOQO* **52**(3-4), 259
[9] Carolan J.V. , Thorogood G.J. , Gregg D.J. , Tansu M.,& Hanley T.L. 2019 *J. Nuclear Mater.* **516**,327
[10] Groover M.P. 2010 *Fundamentals of Modren Manufacturing Materials, Process and Systems* ,4th Edition,Copyright John Wiley & Sons **6**,103.
[11] Yasmin A., Luo J.J., Abot J.L., & Danie I.M. 2006 *Compos. Sci. Technol*. **66**,2415

[12] Brydson J.A. 1975 *Plastic Engineering*, John Wiely & Sons, N. Y.
[13] Sohn J.R., & Lee D.G. 2003 *Korean J.Chem. Eng*. **20**,1030
[14] Geum H.D. 2005 *J. of Appl. Poly.*, **68**, 225
[15] Poon B., Chum C., & A.Hilter A. 2004 *J. of Appl. Poly. Sci.*, **92**, 109

Estimating the Lateral Distribution of High Energy Cosmic Ray Particles by Depending on Nishimura-Kamata-Greisen Function

Estimating the Lateral Distribution of High Energy Cosmic Ray Particles by Depending on Nishimura-Kamata-Greisen Function

Kadhom F. Fadhel[1], A. A. Al-Rubaiee[1], Hassanen Abdulhussaen Jassim[2], Iman Tarik Al-Alawy[1]

[1]Department of Physics, College of Science, Mustansiriyah University, Baghdad, Iraq
[2]Directorate General of Education Karkh 1, Ministry of Education, Baghdad, Iraq

Email: dr.dubaiee@uomustansiriyah.edu.iq

Abstract. The calculation of charged particles density in Extensive Air Showers (EAS) that reach the earth's surface is described through estimating the lateral distribution function (LDF) at very high energies of different primary particles. The simulation of LDF is performed through the simulator of air shower which is called AIR-shower Extended Simulations (AIRES) system (2.8.4a version). The LDF simulation is performed for different charged particles like the muons, electron-positron pair production and all charged particles as well as gamma rays at very high energies (10^{16}, 10^{18} and 10^{19}) eV. The influence of the primary energies, primary particles (such as the proton and the iron nuclei) and the zenith angle (θ) on the charged particles LDF that generated in the EAS has been taken into the account. The calculation of charged particles LDF is fulfilled using "Nishimura-Kamata-Greisen" (NKG) function. The LDF using NKG function is compared with that simulated using AIRES system and gave a good agreement at high energies for (electron and positron) secondary particles, which were initiated by the primary proton.

Keywords: Cosmic rays, lateral distribution function, extensive air showers, AIRES, NKG function.

1. Introduction

The Cosmic rays (CRs) are particles hitting the earth atmosphere at a rate of about (10^3 particles/m^2 Sec). They are distinguished by their high energies. Most CRs are relativistic, having energies comparable to or somewhat greater than their masses [1, 2]. A high-energy CRs study are one of the most challenging in astroparticle physics fields. High energy CRs in the EAS detection are produced in the atmospheric Earth [3, 4]. The EAS are electromagnetic radiation cascade and ionized particles which generated in atmosphere via interaction of a primary CRs together with a nucleus of an atom in the air. Then, it produce a massive amount of the secondary particles like the electrons-positrons pair production, muons, neutrons, as well as gamma-rays, etc [3, 5]. This point of cascade development may be defined as maximum shower [6]. LDF of the charged particle in EAS is the amount required to observe the cosmic radiation of the Earth, which is often derived from EAS observations [3]. The parameter used to describe the lateral density shape can be called the parameter of the lateral profile of

NKG function "Nishimura - Kamata - Greisen function" [7, 8]. It is so important in order to perform an extensive numerical simulation of an EAS to infer the properties of the elementary cosmic ray that results in it. The number of charged particles ultra high energy CRs may be so massive and it may exceed the (10^{10} particles), so these processes require highly complex computing resources to understand and simulate them [9, 10]. Because shower growth is a complex random process, LDF depends on many independent parameters. Simulations are often used to describe the entire event from the first interaction until the electronic signal is registered to the detectors. The Monte Carlo technique is used to simulate LDF from EAS [11]. The current calculations results illustrate that the density of charged particles that reach the surface of the Earth, like the electron-positron pair production, muons, and all the charged particles, as well as gamma-rays by simulating the LDF. It is performed via utilizing the system of Monte Carlo AIRES at the ultrahigh energies (10^{16}, 10^{18} and 10^{19}) eV. The LDF was calculated for different formulas of NKG and was compared with that simulated using AIRES system.

2. Theory

2.1. Lateral Distribution Function (LDF)

LDF of the charged particles in the EAS is a required quantity of the Earth's observations of CRs. Also, it is an important quantity for CRs from the surveillance of a ground, that are mostly derived from the EAS observables [12]. Experimentally, studying of EAS can be achieved on the ground surface detectors, also underground and at numerous mountain rising via determining several quantities of the LDF, such as a density of the charged particles that produced in EAS as the function of the distance from the shower core. The LDF can be described as the shower structure of cascade at different atmospheric depths [13, 14]. An expression which is widely utilized to describe the form of LDF is a lateral shape parameter in the NKG-function [7, 8]. In 1950, Kamata and Nishimura approached an approximated analytical equation for the angular and lateral distribution of the shower particles in an approximation of cascade B theory that made by Nishimura-Kamata function. Practically, the commonly used approximation of the results of calculation proposed by Greisen, that was called (NKG-function), which summarized the research of the average characteristics of multidimensional cascades (mainly electron-photon) at ultrahigh energy CRs [15].

In 1958 Kamata and Nishimura have solved the equations of Landau for LDF of photons and electrons in the (approximation B) of the cascade theory. A solution evaluated in Moliere units appears to be the shower age function (s), characterizing the cascade development solved the Landau's equations have been reached to [7, 8]:

$$\mathbf{f(R/R_M)} \propto \left(\frac{\mathbf{R}}{\mathbf{R_M}}\right)^{\mathbf{s-2}} \left(\mathbf{1}+\frac{\mathbf{R}}{\mathbf{R_M}}\right)^{\mathbf{s-4.5}} \quad \ldots\ldots\ldots\ldots (1)$$

Where R is a distance from a shower core; R_M is Moliere radius and s is the shower age. In EAS there are hadrons, muons, photons and electrons, so that NKG-function can't directly be applied: a lateral distribution form, at least, is the function of zenith angle and energy. Therefore, there may be the distance of the core shower interval for the given essential energy (E_o), where one can neglect the contribution of muons and hadrons to the measured charged particles density and where approximately the LDF form is just the shower age function.

The lateral distribution of an electromagnetic cascade can be parameterized by the NKG-function [7, 8]:

$$\boldsymbol{\rho_e(R)} = \frac{\mathbf{N_e}}{\mathbf{2*3.14*R_M^2}} * \mathbf{C(s)} * \left(\frac{\mathbf{R}}{\mathbf{R_M}}\right)^{\mathbf{(s-2)}} * \left(\frac{\mathbf{R}}{\mathbf{R_M}}+\mathbf{1}\right)^{\mathbf{(s-4.5)}} \ldots\ldots (2)$$

where $\mathbf{C(s)}$ is the normalizing factor which is given by [16]:

$$\mathbf{C(s) = 0.366\, s^2 * (2.07 - s)^{1.25}} \quad \text{.....} \quad (3)$$

$\boldsymbol{\rho_e(R)}$ is the electrons density as a function of the distance from the shower core; $\mathbf{R_M}$ at sea level equal to 78 m; the shower age parameter (s), where the NKG-function is valid for the range 0.8 <**s**< 1.6; $\mathbf{N_e}$ is a total number of electrons in EAS that is given as [9]:

$$\mathbf{N_e = 10^6 \left[\frac{E_0}{10^{15}\ eV}\right]^{1.03}} \text{.....} \quad (4)$$

The electromagnetic cascade produces approximately most of the charged particles in the EAS and through the ionization of the electron that most of the shower energy is dissipated [17]. The results of analytical parameterizations of Monte Carlo calculations and the cascade equations solution for LDF of the electron in the air showers are depended on the function of NKG [18]. NKG function was applied with distinct sets of parameters for many years for LDF description for different components of EAS. The LDF of electrons can be expressed in a form [18]:

$$\mathbf{\rho_e(R) = N_e \frac{0.028}{R_{m.s}^2}\left(\frac{R}{R_{m.s}}\right)^{-1.2}\left(1+\frac{R}{R_{m.s}}\right)^{-3.33}\left(1+\left(\frac{R}{10\,R_{m.s}}\right)^2\right)^{-0.6}} \text{..... (5)}$$

3. The Results and Discussion

3.1. LDF Simulation using AIRES System

AIRES, a set of different programs and subroutines which are utilized for EAS simulations of particles interaction development, that initiated after high energy primary CRs interacting with the nuclei of air in atmosphere and manage all associated output data [19]. The AIRES system can provides a complete propagation of particles in the true medium in the atmosphere, through observing the Earth's curvature and the geomagnetic field features [19]. Many particles can be taken into the consideration via the simulations utilizing the AIRES system like: electron-positron pair production, muons and gamma rays. In EAS, the incident primary particles, may be proton, iron nuclei or other particles with extremely high energies up to (10^{21}) eV [19].

Figs. 1 and 2 display the simulated lateral density of many secondary's as a function of (the distance from the shower core) to the surface of Earth by using AIRES system with thinning energy (the ratio between the energy of secondary particles to the energy of primary particles) (ϵ_{th}=10^{-7} Relative) of primary particles (proton and iron nuclei), respectively. The effect of the primary energies (10^{16}, 10^{18} and 10^{19}) eV and zenith angles (θ = 0°, 10°, 30° and 45°) was taken into account density of secondary charged particles which are produced in the EAS. Through these figures, it can be noticed that the lateral density of different particles increases with increasing the primary particle energies and the density of many particles and decreases with the increasing of distance from the shower core. Figs. 1 and 2 display the possibility for distinguishing the direction and spreading the inclined primary particles on detectors in EAS arrays through the variation of zenith angles and types of primary particles.

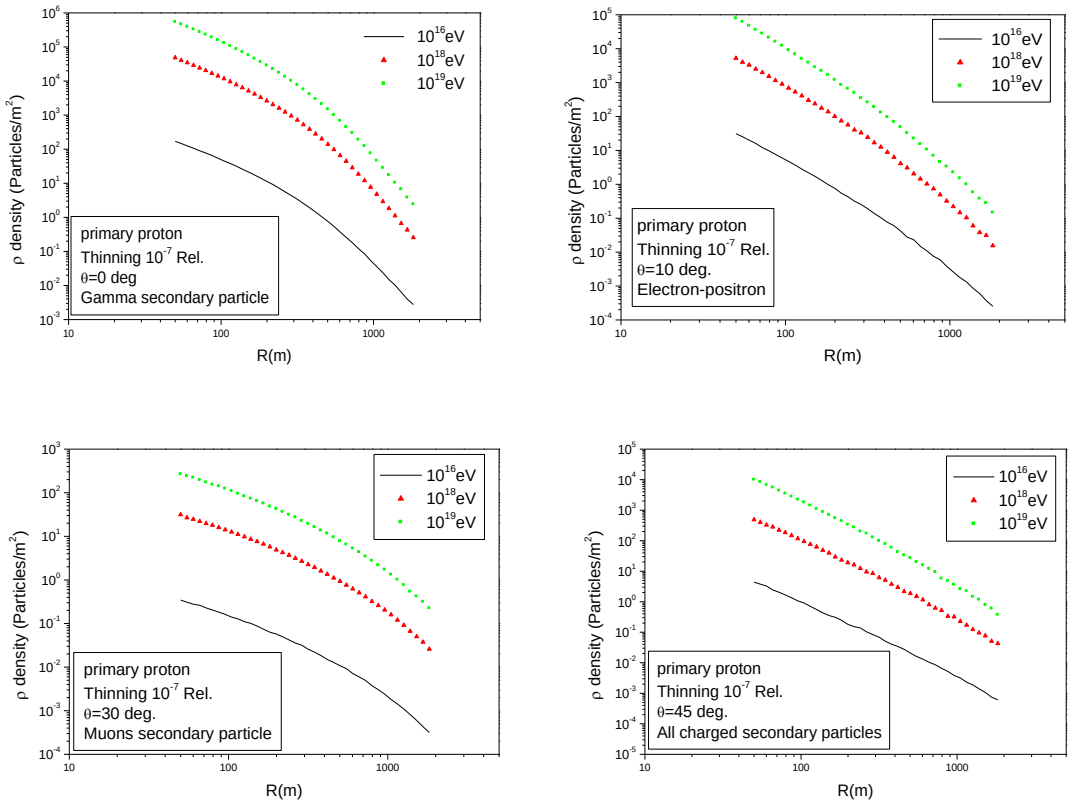

Fig.1. Effects of primary energies of primary (p) on densities of secondary particles at various zenith angles ($\theta = 0^{\circ}, 10^{\circ}, 30^{\circ}$ and 45°).

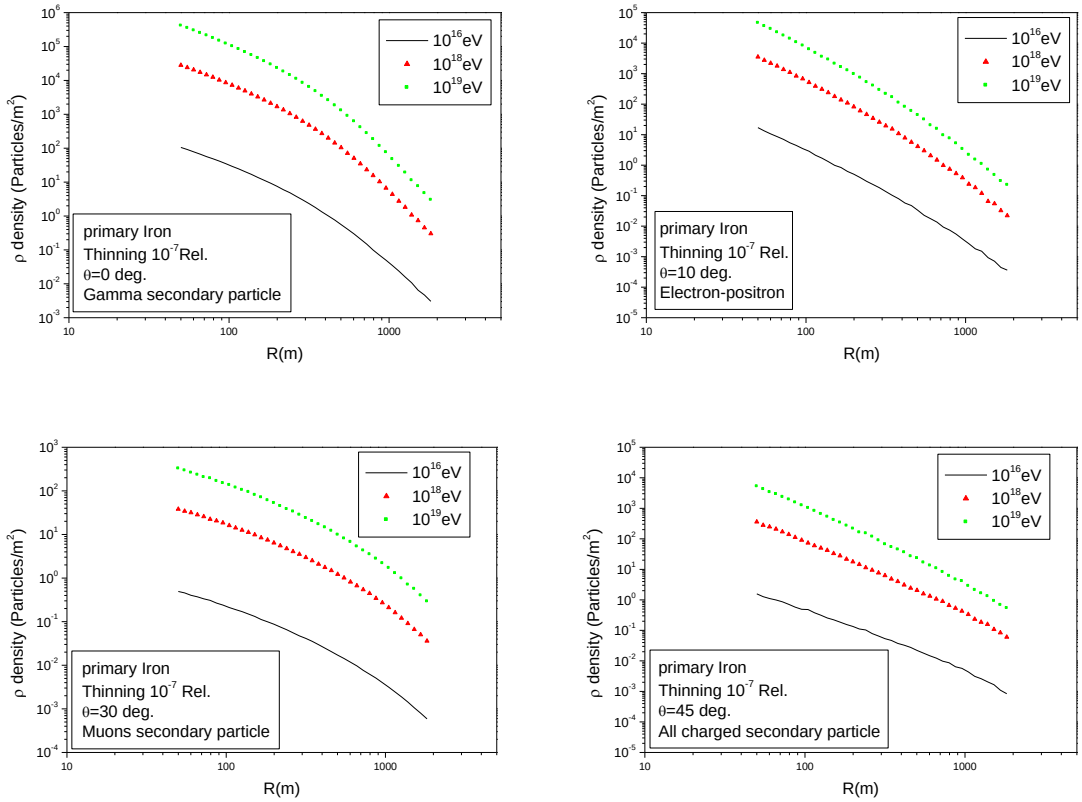

Fig.2. Effects of primary energies of primary (Fe) on densities of secondary particles at various zenith angles (θ = 0°, 10°, 30° and 45°).

3.2. Comparison between the simulated LDF of primary proton and iron nuclei

Fig. 3 demonstrates the comparison between the simulated LDF of the primary proton with that simulated for iron nuclei using AIRES system with the thinning energy ($\epsilon_{th}=10^{-7}$ Relative). This figure present a very interesting point of particles such as gamma, (electron-positron pair production), muons and all charged particles which are initiated via the primary proton and iron nuclei at the energies (10^{16}, 10^{18} and 10^{19}) eV and zenith angle (θ = 0°, 10°, 30° and 45°), which are very close to each other. Through the comparison one can demonstrates the possibility for reconstruction the type and energy of the EAS primary particles.

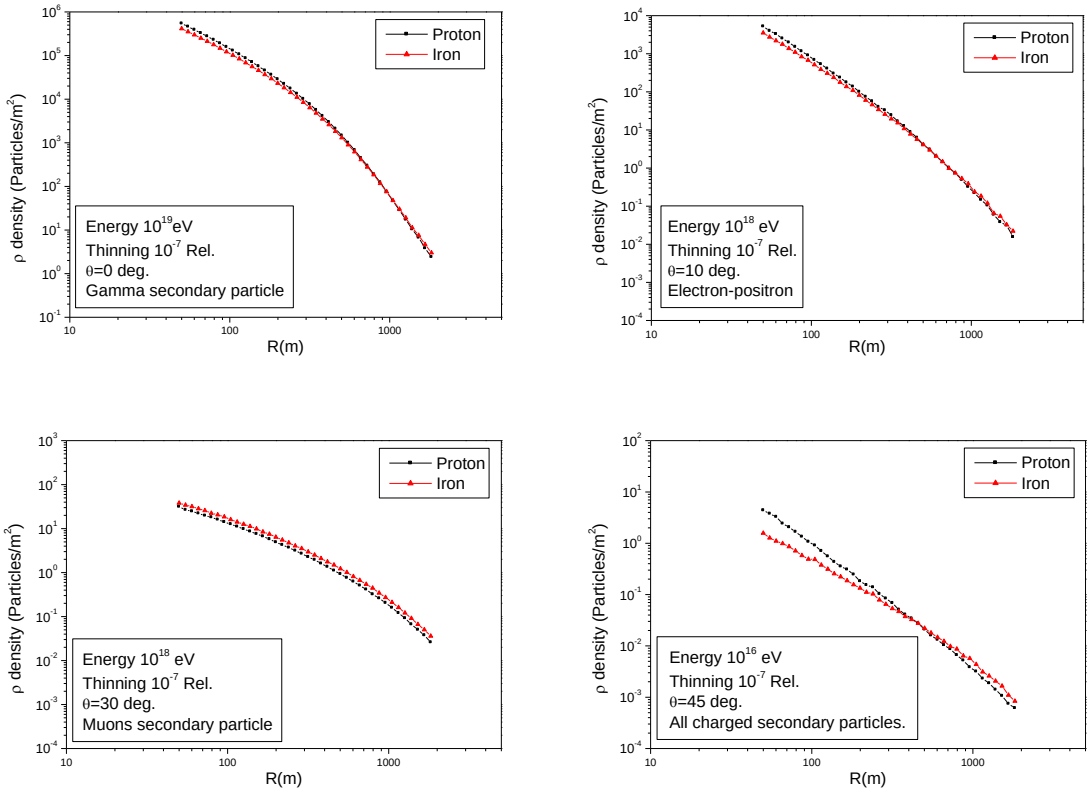

Fig.3. The comparison lateral density of the secondary particles that were initiated by primary (p and Fe) at energies (10^{16}, 10^{18} and 10^{19}eV) and zenith angle ($\theta = 0^{\circ}, 10^{\circ}, 30^{\circ}$ and 45°).

3.3. The comparison between NKG function and simulated LDF

Fig. 4 shows the comparison between the estimated LDF that performed using AIRES system with the results of NKG function that obtained from the equation (5). This figure demonstrates that the results gave a good agreement simulated data by AIRES system for electron and positron particles, which are initiated by primary proton at the energies (10^{16}, 10^{18} and 10^{19}) eV with thinning energy ($\epsilon_{th} = 10^{-7}$ Relative) for vertical showers.

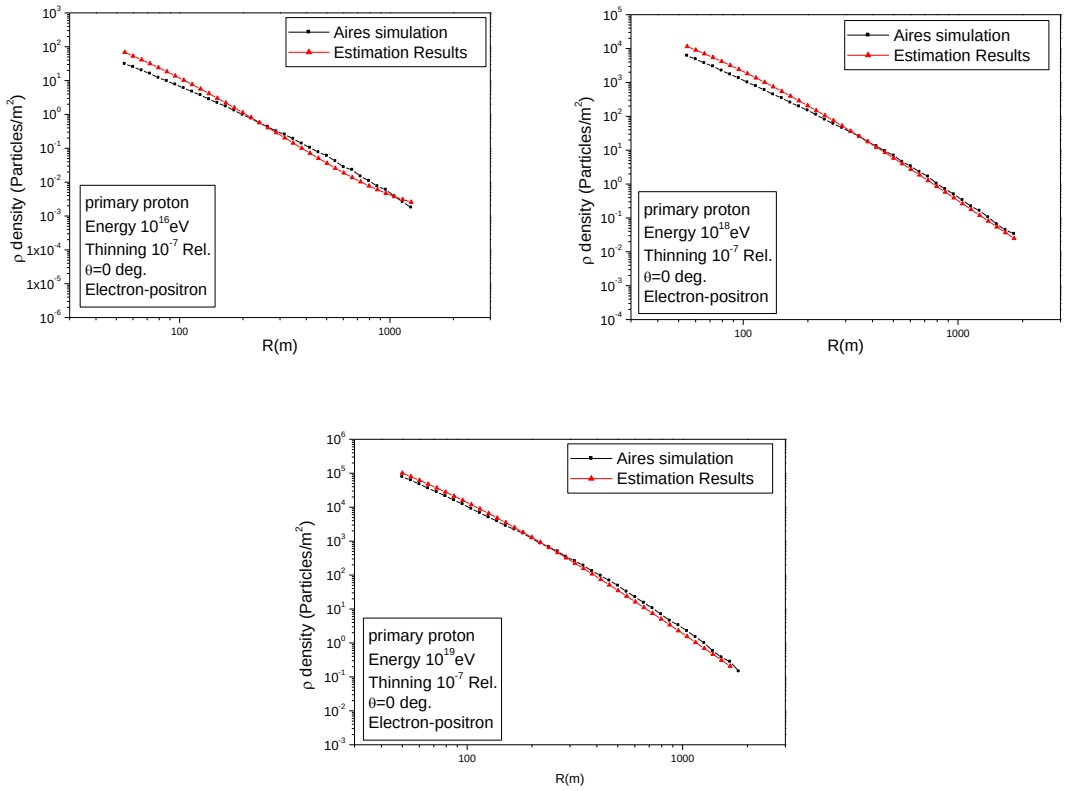

Fig. 4. Comparison between the simulated LDF with the results obtained using the NKG function.

4. Conclusions

In the present work, the effects of EAS are described by estimating the LDF at very high energies of different cosmic ray particles. The charged particles LDF like electron-positron pair production, muons, gamma rays and all charged particles that reach the Earth's surface was simulated utilizing the AIRES system for the two primaries (p and Fe) at very high energies. The influence of the primary particles, the energies, thinning energy and the zenith angle (θ) on the lateral densities of produced charged particles in EAS is taken into consideration. The simulation of lateral structure of the charged particles that reaches the Earth's surface demonstrates the capability for determining the primary cosmic ray particle and its primary energy. A significant feature of a current work is the creation of the library of samples of lateral structure which can be used to analyze real events of EAS that have been detected and also registered in the arrays of EAS.

Acknowledgments

Authors thank Mustansiriyah University in Baghdad- Iraq, for its support in this work.

References

[1] Gaisser T.K., Engel R., Resconi E. 2016 *Cosmic rays and particle physics, Cambridge University Press*

[2] Simpson J. 1983, *Annual Review of Nuclear and Particle Science*, **33,** 323

[3] Roth M. 2003, *arXiv preprint astro-ph*/0308392

[4] Risse M. 2004, *arXiv preprint astro-ph*/0402300
[5] Longair M.S. 2011, *High energy astrophysics, Cambridge university press*
[6] Mangu VS. Rao & Sreekantan B.V. 1998, *Extensive air showers, World Scientific*
[7] Kamata K. & Nishimura J. 1958, *Progress of Theoretical Physics Supplement*, **6**, 93
[8] Greisen K. 2005, *Cosmic ray showers, Annual Review of Nuclear Science*, **10**, 63
[9] Matthews J.2005, *Astroparticle Physics*, **22**, 387
[10] Gorbunov D., Rubtsov G. & Troitsky S.V., 2007, *Physical Review D*, **76**, 043004
[11] Hassanen Abdulhussaen Jassim, Al-Rubaiee A. A. & Iman Tarik Al-Alawy 2018, *Indian Journal of Public Health Research and Development*, **9** (12), 1307
[12] Knurenko S., Ivanov A., Pravdin M., Sabourov A.V. & Sleptsov I.Y. 2006, arXiv preprint astro-ph/0611871
[13] Hassanen Abdulhussaen Jassim, Al-Rubaiee A. A. & Iman Tarik Al-Alawy 2020, *Experimental and Theoretical Nanotechnology Journal*, **4 (**3), 257
[14] Al-Rubaiee A., Al-Douri Y., Ibraheam A., Hashim U. & Lazem T. 2014, *2nd International Conference on Electronic Design (ICED)*, **2014**, pp. 465-467: IEEE
[15] Filonenko A. 2000, *Technical Physics*, **45**, 1362
[16] Hayakawa S. 1969, *Cosmic ray physics. Nuclear and astrophysical aspects, Interscience Monographs and Texts in Physics and Astronomy, New York: Wiley-Interscience*
[17] Hovsepyan G. et al. 2005,*29th ICRC, Pune*, **6**, 97
[18] Lagutin A., Raikin R. & Inoue N. 2002, *Journal of Physics G: Nuclear and Particle Physics*, **28**, 1259
[19] Sciutto S. 2006, *AIRES User's Manual and Reference Guide*, version 2.8, 4a

Study the Effect of Annealing Process on Nanorods and Nanonails ZnO Thin Films Prepared by Hydrothermal Technique

Study the Effect of Annealing Process on Nanorods and Nanonails ZnO Thin Films Prepared by Hydrothermal Technique.

M. M. Kareem[1], F. Y. Mohammed[2], Z. T. Khodair[2]

[1]Department of Physics, College of Education - University of Garmian, Iraq
[2]Department of Physics, College of Science - University of Diyala, Iraq

e-mail: mahmood.mohammed@garmian.edu.krd

Abstract: Wurtzite hexagonal Zinc oxide (ZnO) nanoorods and nanonails arrays have been successfully fabricated and deposited on glass substrates pre-coated with ZnO seed layer using a simple hydrothermal method. The influence of annealing temperatures of on the morphological, structural and optical properties was studied. The size and shape of the nanostructures and the band gap energy depend on the deposition temperature of ZnO thin films have been studied. The optical energy band gaps of ZnO were calculated to be 3.25 eV and 3.26 eV for the samples annealed at 300°C and 350°C respectively. The XRD results show the formation of wurtzite hexagonal ZnO structures for nanonails and nanorods arrays with prominent (002) orientation. The c/a ratio of 1.6033 is close to the ideal value for hexagonal cell around 1.633. The transmittance of the films is about 80% in the visible range. The (EDX) analysis identified the pure ZnO phase with a ratio of Z:O = 1:1.

Keywords: ZnO nanostructures, Annealing temperature, FE-SEM, XRD, Optical Band gap, Transmittance.

1. Introduction

Due to their unique electrical, optical, photonic and mechanical properties, semiconductor nanomaterials have been a rapidly growing area of research [1, 2]. One dimensional nanostructure such as nanonails appeared the most appealing sensing materials for developing gas sensor devices, since 1D, ZnO possess a good sensitivity and fast response time [3]. Nanowire, nanotubes and nanoribbons [4] have been widely studied for their important applications due to their unique optical and electrical characteristics. ZnO nanostructure is an important II–VI semiconductor, and it possesses a high electron-hole binding energy of 60 meV, with a direct band-gap about 3.37 eV, and as a result they have been used in sensors, lasers, displays, solar cells, field emissions, and photocatalysis [5–9]. Various techniques such as precipitation process, spray pyrolysis [10], thermal decomposition [11] and hydrothermal process [12] have been used to fabricate ZnO nanrods [13]. ZnO could be easily grown; and it is suitable for industrial and medical applications due to its diverse properties which depend on their morphology [14]. The well-adjusted arrays of ZnO rods were grown by a simple hydrothermal method on glass substrate using autoclave, and the samples are post annealed at different annealing temperatures. It is familiar that hydrothermally grown ZnO nanostructures have many imperfects due to

their growth temperatures [15]. Therefor the qualities of ZnO nanostructures have been improved by reducing the defects via thermal treatment process of the synthesized thin films. The results illustrate the well oriented ZnO naorods and nanonails arrays grown directly on glass substrate, as well as the effect of annealing temperature on ZnO nanostructures, size, shape and band gap energies with the use of seed layers as pre coating layers without any catalysts or surfactants at high temperature of 180 ^{o}C of the autoclave.

2. Experimental

2.1. Preparation of ZnO Seed Layers

The solution prepared from mixing of Zinc acetate dehydrate $(CH3COO)_2.H_2O$ with a concentration of (10mM) into 50 ml ethanol and stirred ultrasonically for 15 minutes. The solution was deposited by drop casting on top of cleaned glass substrates and dried on a hot plate at 80°C for 2 minutes. Finally, all the films were annealed by using a hot plate in air at 350 °C for 30 minutes to improve the film adhesion to the substrate. Vertical alignment of ZnO nanonails and nanorods were also improved by annealing process of ZnO seeds. ZnO film growth was conducted by using hydrothermal process.

2.2 Growth of ZnO nanonails and nanorods

After ZnO seed layer deposition, the seeded substrates were placed vertically in an autoclave which contained a growth solution at 180 °C for 6 hours in an oven; taking into account that the seed laye'sr substrates were facing downward. The growth solution prepared from mixing each of hexamethylenetetramine and Zinc nitrate hexahydrate of the same molarity of (25 mM) into 50 ml deionized water and the mixture stirred ultrasonically for 15 minutes. After the growth operation, the samples were rinsed by deionized water (DW), to remove the inorganic residuals from the surface of the films. Finally, all the films were annealed by using a hot plate at 300 and 350°C for 90 min.

2.3 Characterization

The structural composition of the films was examined by using X-ray (6000 XRD, Cu-k_α beam of λ=1.54). The morphologies of all samples were inquired by field emission scanning electron microscopy (FE-SEM; Model Mira3-XMU, TESCAN, Japan). And the thin films composition was analysed by EDX technique. The optical transmittance of the samples was evaluated in the wavelength range of 200–900 nm by double beam UV- visible spectroscopy -2600 from Shimadzu Co. Japan.

3. Results and Discussion

3.1. XRD analysis

Fig.1 represents X-ray pattern for zinc oxide nanostructure prepared by hydrothermal route. Annealed samples have polycrystalline hexagonal (wurtzite) structures. 2θ has three strong peaks observed at 31.76°, 34.45° and 36.25° attributable to ZnO (100), (002) and (101) crystal planes, respectively, (in agreement with ICDD card No. 036-1451 for ZnO). The strong ZnO diffraction peak (002) agrees with the highly oriented c-axis growth along this direction which was observed in the FE-SEM images to be shown later. From Fig. 1, we also observe that the intensity of (002) peak decreased with increasing annealing temperature up to 350℃, which means that the sample annealed at 300℃ has better crystal quality than that annealed at 350℃. This is due to the heat treatment the films were exposed to which is compatible with the previous study[16].

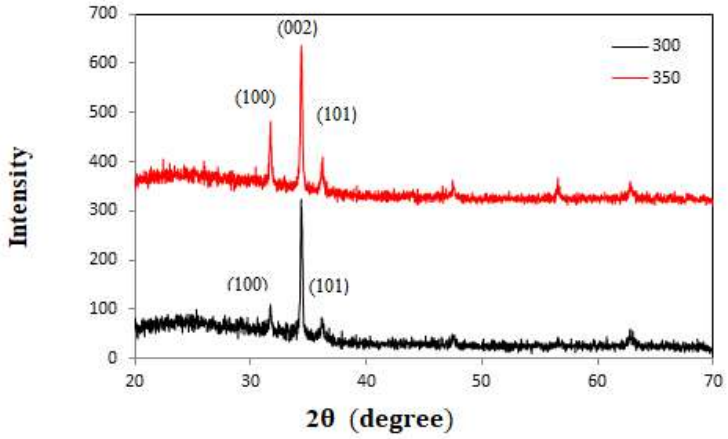

Figure 1. XRD patterns of the annealed ZnO nanonails and nanorods at annealing temperatures 300 and 350℃ respectively.

Table 1. Estimated structure parameters with dislocation density of (002) peak position

Annealing Temperature (℃)	D (nm)	ao(Å)	c_o (Å)	Ratio c_o/ao	Dislocation Density δ x 10^{14} $(line^2/m^2)$
300	43.097	3.2498	5.2104	1.60329	5.3840
350	43.519	3.2505	5.2117	1.60335	5.2801

Table 1 compares two samples annealed at 300℃ and 350℃ which estimate the structure parameters with dislocation density for the most prominent peak position (002).
The lattice parameters (ao and c_o) are calculated from the relation [17]

$$d_{hkl} = \frac{a}{\sqrt{\frac{4}{3}\left(h^2+k^2+hk+\frac{l^2 a^2}{c^2}\right)}} \quad (1)$$

Crystal lattice parameters for thin films annealed at a temperature of 300℃ are ao = 3.2498 Å, c_o = 5.2104 Å, and the ratio of c_o/ao is 1.60329, while for thin film annealed at 350℃ ao = 3.2505Å, c_o = 5.2117Å and the ratio of c_o/ao is 1.60335. The ratio c_o/a_o for both annealed temperatures has the values very close to each other, while the ideal value for hexagonal cells is c_o / ao = 1.602 [18]
Scherer's formula is applied for grain size calculation:

$$D = \frac{K\lambda}{\beta cos\theta} \quad (2)$$

where D is stand for a grain size
λ is applied wavelength (1.5406 Å)
β: Full Width at Half Maximum of the peak (FWHM).
θ: diffraction angle
The thin film undergoes dislocations in its structure due to the heat treatment process. Therefore, the dislocation density is calculated by the equation [19], which decreased slightly with increasing temperature for 50℃.

$$\delta = \frac{1}{D^2} \quad (3)$$

whereδ is the dislocation density

3.2. FE-SEM study
The morphology of the synthesized ZnO nanorods and nanonails was examined by FE-SEM. Fig.2 shows the top view images of the films annealed at two different annealing temperatures. From fig.2

(a), It is observed that the surface structure of the films is made up of nanorods form as groups of highly dense nanorods and crystallized along the direction of c-axis of ZnO, were all arranged in vertical direction on the surface of the glass substrates. They covered the entire surface, and they were relatively smooth, had uniform surface, and were characterized by hexagonal structure and symmetrical shapes, except for the nanonails film fig.2 (b) which annealed at 350℃ is consisting of a shank-nanorod and a lotus-shaped head [20]. The process of the growth in such a structure can be described in two steps. First, the nanorod grows along the c-axis by alternating the atomic layers (O) and (Zn), and secondly the head or upper face growth in the c-axis direction and its diagonal growth accelerates, leading to the formation of a hexagonally shaped nanonail head, and this in itself has many applications like photovoltaic, etc [21].

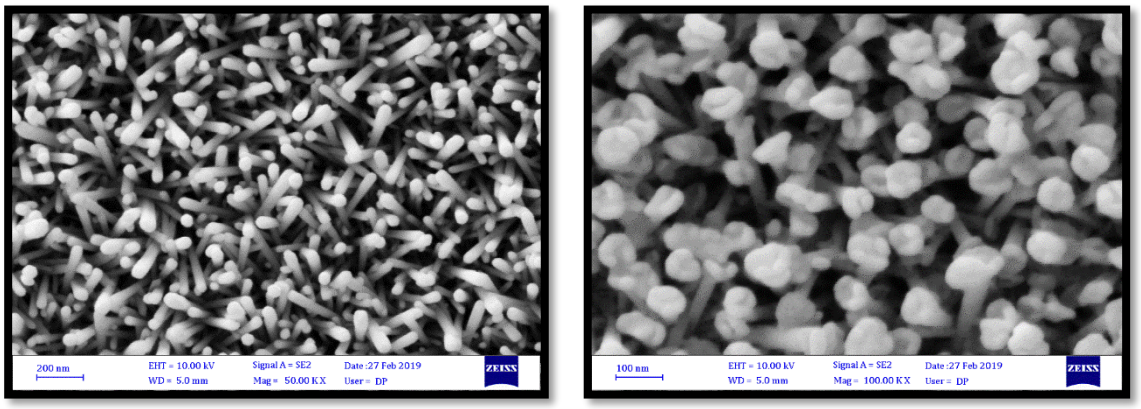

(a) (b)

Figure 2. FE-SEM Surface morphologies (a) ZnO nanorods annealed at 300 °C, (b) ZnO nanonails annealed at 350 °C

It was also observed that the nanorods were vertical to the substrate, and on the upside, it appeared slightly tilted. The length and alignment of the nanorods were related to the seed growth mechanism. The (ZnO) nanorods mean diameter was calculated by use of Image J software. This clearly shows that when the annealing temperature increased from 300 ºC to 350 ºC, the average diameter nanorods also increases from 47 nm to 71 nm respectively. Figure 3(a, b) shows the spectrum of the energy dispersive x-ray, of both samples annealed at 300°C and 350 °C. A representation of the elements percentage in the matrix films is shown in the inset tables. The amount of these elements is represented by the intensity of the peaks, and distinctly shows the 1:1, Z:O elements. No element contamination detected in the films structure .The analysis of the samples by (EDX) technique notably show that the films prepared by hydrothermal method had pure Zinc oxide phases, and the quantitative analysis data was close to that of bulk ZnO [22].

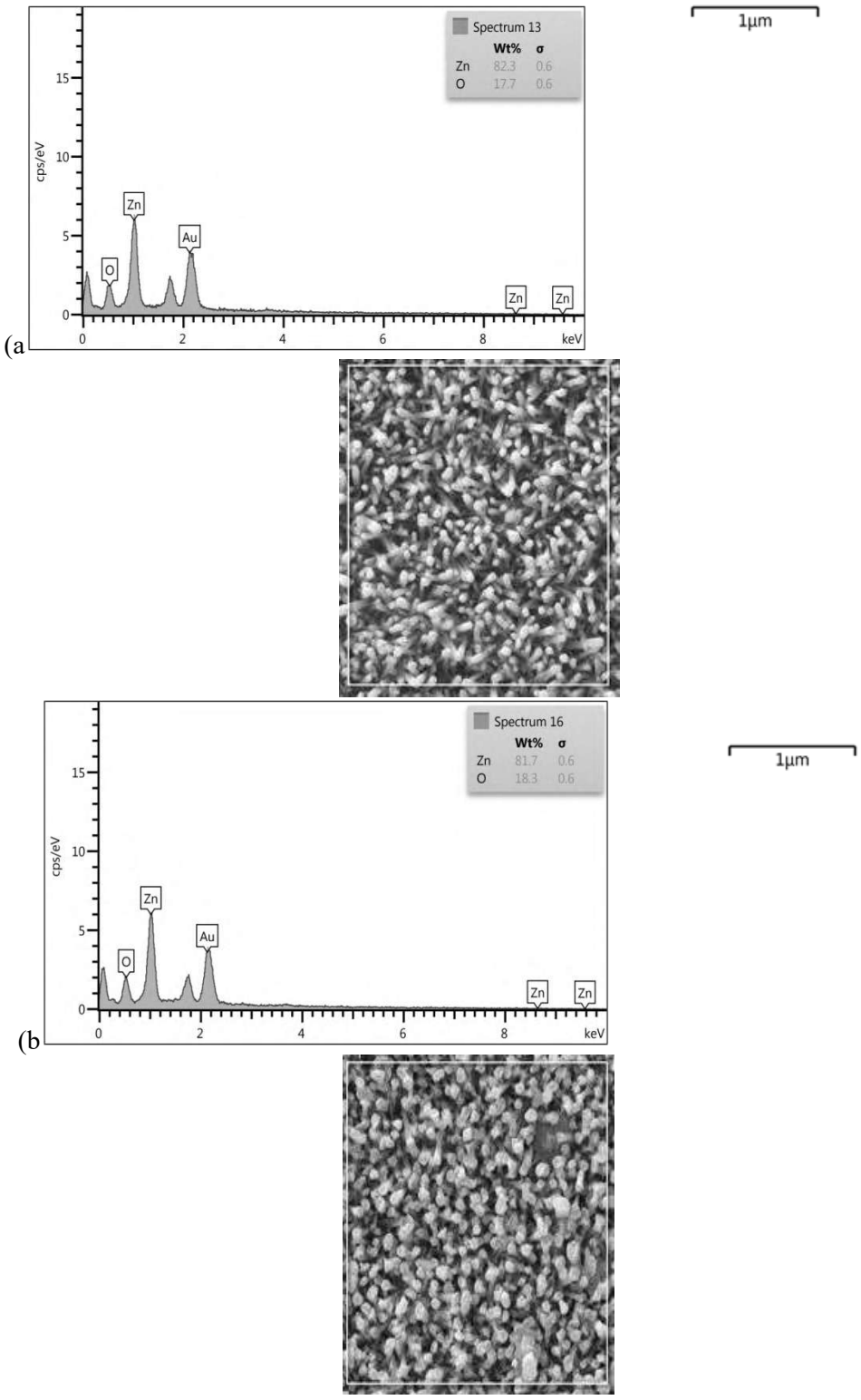

Figure 3. EDX results of a) ZnO nanorods annealed at 300°C b) ZnO nanonails annealed at 350°C.

4. Optical study of ZnO nanorods and nanonails

Fig.4 shows the optical transmittance spectrum in the UV-Visible region of (200 – 900) nm of the zinc oxide nanorods and nanonails annealed at 300˚C and 350℃ for 30 minutes. The transmittance is slightly more than 80% in the range (450 nm to 850 nm) for both films. At 360 nm there is acute absorption edge, which is resulting from the direct band gap of ZnO [23].

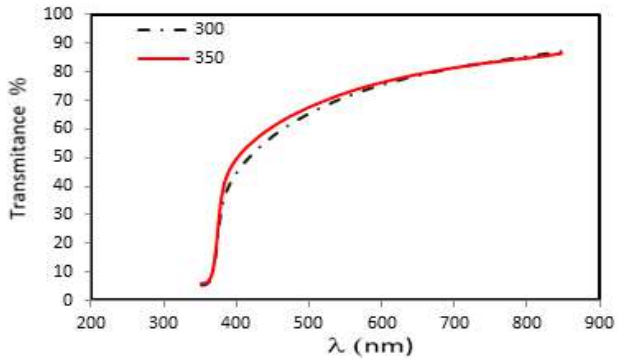

Figure 4. Transmittance spectrum for samples with variations annealing temperature of 300℃ and 350 ℃.

Zinc oxide, ZnO nanorods and nanonails are evaluated by extrapolation of the linear connection between $(\alpha h\upsilon)^2$ and hν which is consistent to the equation below [24]

$$\alpha h\upsilon = A(h\upsilon - \mathrm{E}_g)^n \quad (4)$$

where α, and hυ, are the absorption coefficient and the photon energy respectively. Eg is the optical band gap and A, a constant. Fig. 5 describe the graph of $(\alpha h\upsilon)^2$ against hυ. The direct optical band gap value Eg of the films is estimated from the curve interception of $(\alpha h\upsilon)^2$ vs hυ plot. The existence of a single slop in the curve implies that the ZnO film has direct and allowed transition. The annealed ZnO nanorod and nanonails band gap value at temperatures of 300℃ and 350℃ was found to be (3.25 and 3.26) eV, respectively. This is due to increase the annealing temperature which accelerates the formation of crystals and slightly increases its band gap [25].

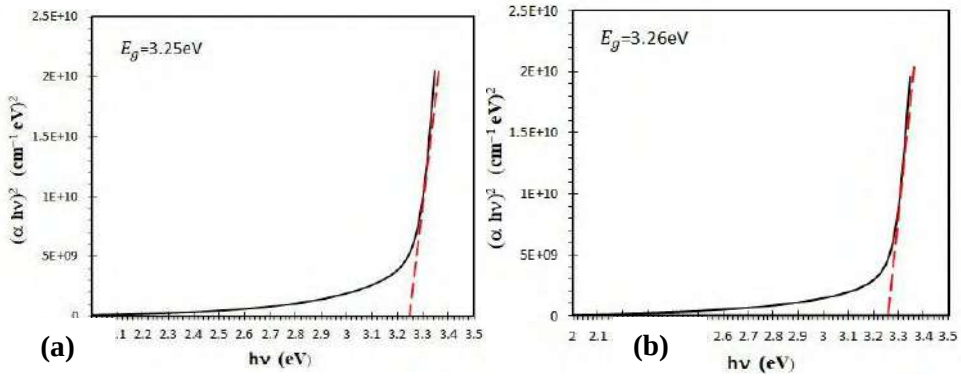

Figure 5. The relation between $(\alpha h\upsilon)^2$ and (hυ)for ZnO nanorods (a) annealed at 300℃, (b) annealed at 350 ℃

5. Conclusions

The hydrothermal process is a simple and efficient method. It has received an increased attention due to its implicitly. In this paper, we presented the synthesis, structure characterization, and properties of nanorods and nanonails structure arrays for ZnO thin films prepared by hydrothermal technique and annealed at temperatures of 300℃ and 350℃. Highly preferential growth of ZnO nanorod and nanoails

along the c-axis orientation was observed with hexagonal wurtzite structure. The average diameter of the ZnO nanostructure obtained from the FE-SEM by using image J analysis increased clearly from (42 nm to 71 nm) for nanorods and nanonails respectively with increasing annealing temperature from 300 ºC to 350 ºC. The intensity of (002) peak was decreased by increasing the annealing temperature while the transmittance and the optical band gaps (3.25 and 3.26) eV, were slightly increased. The energy dispersive x-ray (EDX) analyses of the samples obviously show that the films synthesized by hydrothermal method have pure zinc oxide phases. It is evidence from the results that the nanostructure properties like size, shape structural characterization and optical band gapes can be tuned according to the synthesis temperature which leads to tuning the nanostructure materials properties for a certain applications.

6. References

[1] Singh M, Hlabana kk, Singhal S and Devlal K 2016 Grain-size effects on the thermal conductivity of nanosolids *J.Taibah Univ. Sci.* **10** 375-380.
[2] Mehr A and Emami F 2014 Effects of structural factors on filtering operation of photonic band gap air bridges with circular and square shape holes *Optik* **125** 2625-2632, 2014.
[3] Lin J, Chen Z, He X and Xie W 2017 Detection of H2S at room temperature using ZnO sensors based on Hall effect *Int. J. Electrochem. Sci*. **12** 6465–6476.
[4] She GW 2008 Controlled synthesis of oriented single-crystal ZnO nanotube arrays on transparent conductive substrates *Appl. Phys. Lett.* **92** 5311.
[5] Jiang Y, Meng X, Liu J, Xie Z, Lee C and Lee S 2003 Hydrogen-assisted thermal evaporation synthesis of ZnS nanoribbons on a large scale *Adv. Mater.*, **15** 323–327.
[6] Huang H, Shao l, She GW, Wang M, Chen S and X.-M. Meng XM 2012 Catalyst-free synthesis of single crystalline ZnO nanonails with ultra-thin caps *Cryst. Eng. Comm*. **14** 8330–8334.
[7] Muchuweni E, Sathiaraj T and Nyakotyo H 2017 Hydrothermal synthesis of ZnO nanowires on rf sputtered Ga and Al co-doped ZnO thin films for solar cell application *J. Alloys Comp.* **721** 45-54.
[8] Wang ZL and Song J 2006 Piezoelectric nanogenerators based on zinc oxide nanowire arrays *Science* **312** 242–246.
[9] Liu XY, Shan CX, Wang SP, Zhang ZZ and Shen DZ 2012 Electrically pumped random lasers fabricated from ZnO nanowire arrays *Nanoscale* **4** 2843–2846.
[10] Kumar NS, Bangera KV and Shivakumar GK 2014 Effect of annealing on the properties of zinc oxide nanofiber thin films grown by spray pyrolysis technique *Appl. Nanosci.* **4** 209–216.
[11] Lin CC and Li YY 2009 Synthesis of ZnO nanowires by thermal decomposition of zinc acetate dihydrate *Mater. Chem. Phys.* **113** 334–337.
[12] Van Duy L, Hanh NH, Son DN, Hung PT, Hung CM, Van Duy N, Hoa ND and Van Hieu N 2019 Facile Hydrothermal Synthesis of Two-Dimensional Porous ZnO Nanosheets for Highly Sensitive Ethanol Sensor *J. Nanomater.* **2019**.
[13] Byrappa K and Yoshimura M 2012 *Handbook of hydrothermal technology*. William Andrew.
[14] Osman DAM and Mustafa MA 2015 Synthesis and characterization of zinc oxide nanoparticles using zinc acetate dihydrate and sodium hydroxide *J. Nanosci. Nanoeng.* **1** 248-251.
[15] Zhao XQ 2009 Effects of thermal annealing temperature and duration on hydrothermally grown ZnO nanorod arrays *Appl. Surf. Sci.* **255** 5861–5865.
[16] Kareem MM, Khodair ZT and Mohammed FY 2020 Effect of annealing temperature on Structural, morphological and optical properties of ZnO nanorod thin films prepared by hydrothermal method *J. Ovonic Res.* **16** 53–61.
[17] Lupan O 2010 Effects of annealing on properties of ZnO thin films prepared by electrochemical deposition in chloride medium *Appl. Surf. Sci.* **256** 1895–1907.
[18] Klingshirn CF 2007 ZnO: material, physics and applications *Chem. Phys. Chem*. **8** 782–803.

[19] Kahraman S, Çetinkara HA, Bayansal F, Çakmak HM and Güder HS 2012 Characterisation of ZnO nanorod arrays grown by a low temperature hydrothermal method *Philos. Mag.* **92** 2150–2163.
[20] Liu J and Motta N 2014 The nanonail flower *Mater*. *Today* **17** 307–308.
[21] Kar S, Dev A and Chaudhuri S 2006 Simple solvothermal route to synthesize ZnO nanosheets, nanonails, and well-aligned nanorod arrays *J. Phys. Chem. B* **110** 17848–17853.
[22] Al-Owais AA 2013 Synthesis and magnetic properties of hexagonally packed ZnO nanorods *Arab. J. Chem.* **6** 229–234.
[23] Amakali T, Daniel L, Uahengo V, Dzade NY and De Leeuw NH 2020 Structural and Optical Properties of ZnO Thin Films Prepared by Molecular Precursor and Sol–Gel Methods *Crystals* **10**, 132.
[24] Muchuweni E, Sathiaraj TS and Nyakotyo H 2017 Low temperature synthesis of ZnO nanowires on GAZO thin films annealed at different temperatures for solar cell application *Mater. Sci. Semicond. Process.* **68** 80–86.
[25] Narayanan GN, Ganesh RS and Karthigeyan A 2016 Effect of annealing temperature on structural, optical and electrical properties of hydrothermal assisted zinc oxide nanorods *Thin Solid Films* **598** 39–45.

Impact of reaction temperature on the structural, surface morphology and antibacterial activity of hydrothermally synthesized CdS nanoparticles

Impact of reaction temperature on the structural, surface morphology and antibacterial activity of hydrothermally synthesized CdS nanoparticles

[1]Adel H. OmranAlkhayatt, [1,2]Mohammad Rassol Ahmed

[1]University of Kufa, Faculty of Science
[2]University of IbnHayyan , Faculty of Medicine

E-mail: adilh.alkhayat@uokufa.edu.iq

Abstract. Cadmium Sulfide (CdS) nanoparticles were synthesized hydrothermally at various reaction temperatures (140, ,160, 180,200) ° C. Crystal structure and surface morphology were studied corresponding to the reaction temperature. The X,-ray diffraction results, reveals that CdS nanoparticles were prepared have high crystallinity with polycrystalline nature and hexagonal wurtzite phase. The preferential orientation was along (002) and (110) planes. The average crystallite size was tended to increase with the increase of reaction temperature which about (21-24) nm. The structure parameters such as dislocation density and microstrain was examined. CdS nanoparticle images in Field Emission Scanning Electron Microscopy (FESEM) indicates rounded ball (cauliflower), the particle size was in the range of (23-245) nm and the smallest size was obtained for the nanoparticles at reaction temperature 200 °C. The antibacterial activity of cadmium sulfide CdS nanoparticles was estimated against two types of common bacteria (Gram-negative Escherichia coli and Gram-positive Staphylococcus aureus). It was found that there is a strong antibacterial activity and the greatest effect was for the prepared nanoparticles at reaction temperatures 160 and 180 oC, and the highest activity was found against (E. coli) bacteria as well as with the increase of nanoparticles concentration. This work combines microbiology and nanotechnology, perform probable advances in the formulation of a new kind of antibacterial.

Keywords: CdS nanoparticles; Hydrothermal method; structure properties; Antibacterial activity; Escherichia coli; Staphylococcus aureus.

1. Introduction

Cadmium sulfide (CdS) is currently an extremely interesting, semiconductor compound from the II-VI group of the periodic table with a direct band gap of 2.42 eV and conductivity n-type, it has three types of crystal structures, namely rock, zinc, and rock-salt[1]. The würtzite phase among these three phases is the most stable and simple to synthesize [2]. Therefore CdS is high potential used as sensitive photodetectors [3] heterojunction diodes, solar cells, and semiconductor devices [4]. CdS nanomaterial can be used in various life sectors due to their higher stability, outstanding electrical, Structural and chemical properties, affordability, ease of processing and handling [5]. CdS nanoparticles and thin films were widely synthesized using different chemical and physical methods due to its enormous range of applications in various fields of life, like solvothermal and hydrothermal

techniques [6, 7], thermal evaporation method [8], chemical bath deposition [9], Laser Ablation in liquid[10], spin-coating technique [11]. Cadmium sulfide and chalcogenide nanoparticles can easily prepared by using the hydrothermal method[12]due to its essential Advantages including cost-effectiveness[13]Particle size controllable, low temperature and techniques less complicated [14].Compared to organic antibacterial agents, the antibacterial activities of inorganic compounds are of great interest due to its durability, toxicity, heat resistant, selectivity and etc. [15]. The antibacterial activities of CdS nanoparticles were evaluated against different types of bacteria by Ayodhya et al. [16], which is very promising in displaying their capability to inhibit and destroy both types of gram positive and gram-negative pathogenic bacteria. Abd-Elkader et al.[17]. The antibacterial efficacy of CdS thin films deposited with CBD was evaluated, against Gram-positive and Gram-negative bacteria in dark and sun light at 60 ^{o}C. They found that, CdS thin films have noticeable antibacterial activity in sunlight and dark and it could be used as antibacterial and antimicrobial agents in the application of medical field. Narasimmana et al.[18] Studying the impact of Zr concentration on the antibacterial properties of the CdS thin film, doped films display excellent antibacterial performance against K. Bacterium pneumonia (gram −ve) making it ideal for pharmaceutical applications. Whereas Gajendiran et al. [19] worked on fabricate CdS quantum dots nanoparticles for biological applications, the antimicrobial activity against S. Aureus bacteria were found to be an impressive antibacterial agent against gram-positive bacteria by prepared nanoparticles. In the current work the effect of reaction temperature on structural surface morphology of CdS nanoparticles was investigated and the antibacterial activities the Gram-negative Escherichia coli and Gram-positive Staphylococcus areus was carried out using agar well diffusion method in order to establish their suitability for medical applications.

2. Materials and methods

Cadmium Acetate $(CH_3.COO)_2Cd.2H_2O$ from (BDH) England, Thiourea $NH_2.CS.NH_2$ from (THOMAS BAKER) India, Acetone $(CH_3)_2CO$ (TEDIA) from USA, Ethanol (C_2H_5OH) from (BDH) England, Mueller Hinton II. agar MHA from (Biolab Zrt) Hungary were used to synthesized CdS nanoparticles by the Hydrothermal method. (0.3 g) of cadmium acetate $(CH_3.COO)_2Cd.2H_2O$ and (0.9 g) of thiourea$NH_2.CS.NH_2$dissolved in 40 ml of deionized water with a ratio of (1:3).The solution was well mixing by magnetic stirrer for 30 min. Then40 ml of the prepared solution was added into the Teflon-lined stainless-steel autoclave and heat up in an oven at reaction temperatures (140,160,180 and200) °C for 4 h, and allow it to cool to room temperature. The resulting solution was separated by centrifuge (Frontier 5706), for 10 min at 5000 rpm to get a deep-yellow powder. the precipitating substance (CdS) was washed twice with deionized water and absolute ethanol (C2H5OH)purity(99.9%), and then dried at 70 °C.

The antimicrobial activity CdS nanoparticles ws evaluate against two different types of clinical bacteria Gram-negative Escherichia coli and Gram-positive Staphylococcus aureus using the agar well diffusion method. Standardized suspension of each tested bacteria (1.5x108cfu/ml) by Densi Check standard (0.5N) was swabbed separately onto Mueller Hinton agar plates using sterile cotton swabs. The agar was punched with sterilized cork borer 9 mm and 100µl from each the CdS nanoparticle were added into the four holes for four concentrations (1000, 500, 250, 100) µg/ml after making dilution at well Petri dishes were incubated for 24 hours. at 37°C, after incubating, the inhibition zones were measured in millimeter diameter. The crystalline structure of the CdS NPs examined by X-ray diffractometer (Shimadzu XRD-7000 (JAPAN), the source of X-ray radiation is Cu kα1 radiation the scanning angle varied in the range (15-70)° with wavelength 1.54056 Å, speed 1deg/min, current 80 mA, and voltage 60 kV. The morphological confirmation of various CdS nanparticles was carried out by Field Emission Scanning Electron Microscopy (FEI FESEM Nano SEM Nova 450).

3. Results and discussion

3.1. Structural analysis.

The XRD patterns of CdS nanoparticles obtained at different reaction temperatures was identified by the presence of diffraction peaks at scattering angles (2Θ) of 25°, 26.6°, 28.2°, 43.8°, 48°, 52°, 52.9°,54.8°, and 58.2° that were indexed to the (100), (002), (101),(102), (110), (103),(112) and (201) planes, all peaks of diffraction can be indexed to the pure hexagonal CdS structure according to the according to the standard (JCPDS No. 77-2306), the diffraction pattern refer that CdS is polycrystalline structure, sharp and strong peaks indicate that the CdS has crystallized well [20] as shows in Fig.1.

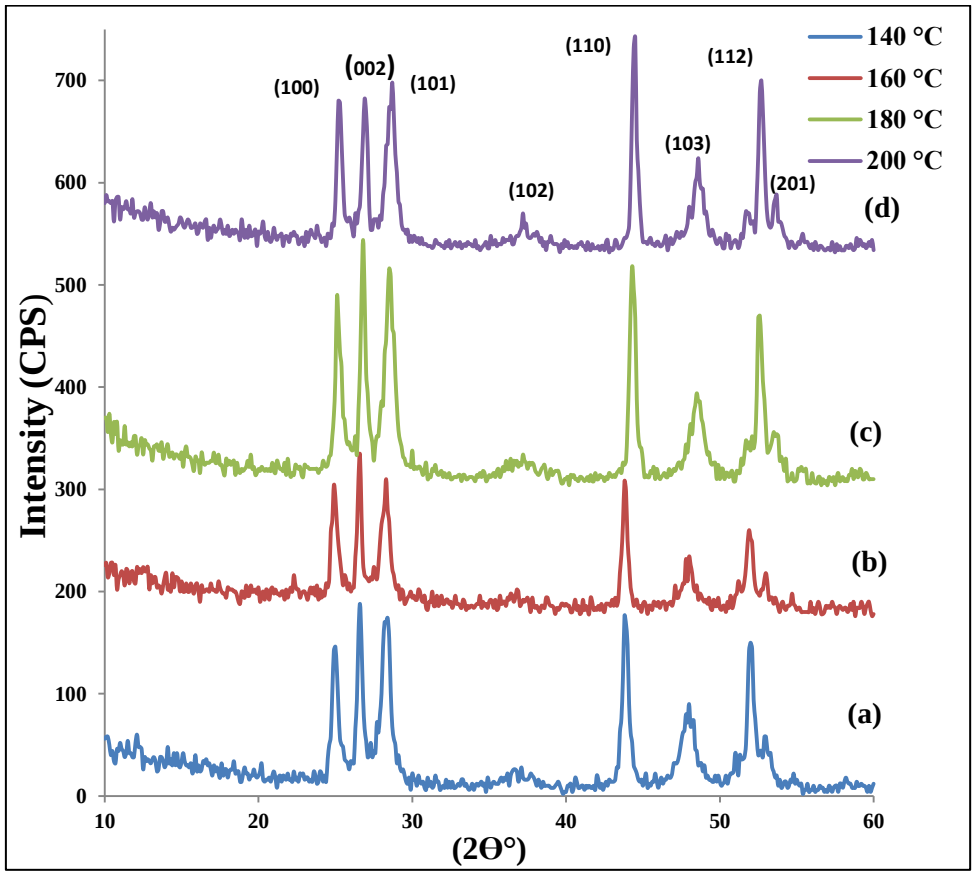

Fig.1. Diffraction pattern obtained from CdS XRD at 4 h reaction temperatures: ((a) 140, (b) 160, (c) 180 , (d) 200)°C.

The high intensity sharp and narrow XRD peaks confirmed that grown CdS nanoparticle were highly crystalline. All diffraction peaks can be indexed tothepure hexagonal structure of CdS according to the standard card (JCPDS No. 77-2306) and no otherpeaks related to impurity phases were observed. The XRD peaks of CdS nanoparticle became narrower with shifted of peak position with increase temperature, this indicate an enhancement in crystalline quality, this agreement with study [20]. For the hexagonal structure the interplanar spacing (d), lattice constants (a) and (c) were calculated using the following equation [21].

$$\frac{1}{d_{hkl}^2} = \frac{4}{3}\left(\frac{h^2+hk+k^2}{a^2}\right) + \frac{l^2}{c^2} \qquad (1)$$

Table 1 displays the structural parameters determined, values obtained that are too close to the values seen in the investigation (a=b= 4.136 and c= 6.713) (JCPDS-77-2306) which confirms wurtzite structure [22], the average crystallite size (D) of the CdS nanoparticles was determined with the formula of Debye Scherrer [23]:

$$D = \frac{k\lambda}{\beta\cos\theta} \qquad (2)$$

β is the full width at the maximum half of the peak of diffraction, K is known as the 0.9 shape factor and λ is the X ray diffraction source wavelength. The average grain size for Preferred orientation (110) is within the range (18.8678- 24.1725) nm as illustrated in the Table 1. The crystallite Size for (110) preferential orientation is a gradual increase, this refers to improve crystallization with increasing reaction temperature. The constants of lattice 'a' and 'c' contracts the (c/a) values remained constant about 1.63 approximately for all the nanoparticles and nanostructure thin films, this is an agreement with the literature [18, 20].

Table 1. Structural parameters of CdS nanoparticle obtained from XRD data as a function of preparation temperature for (110) preferential orientation.

CdS nanoparticles At:	$2\theta^o$	d_{XRD} (Å)	Crystallite Size D (nm)	a=b (Å)	C (Å)	V (a^2c) $(Å)^3$	c/a
140 °C	43.8	2.06233	18.8678	4.1246	6.665	113.403	1.6289
160 °C	43.9	2.06423	22.5634	4.1284	6.6697	113.679	1.6282
180 °C	43.81	2.06331	18.8207	4.1266	6.6678	113.546	1.6306
200 °C	44.01	2.05841	24.1725	4.1168	6.6577	112.836	1.6276

3.2. Morphology analysis

Fig. 2a, b, c, d show FESEM images of CdS nanoparticles prepared at reaction temperatures of 140,160,180,200°C respectively. The surface morphology consist of homogeneous and densely packed distribution of well-defined grains, which includes small and large particles and has a regular shape with fine particle size, Fig. 2 indicate a rounded ball (cauliflower) like nanospheres these results was consistent with literature [24-26].

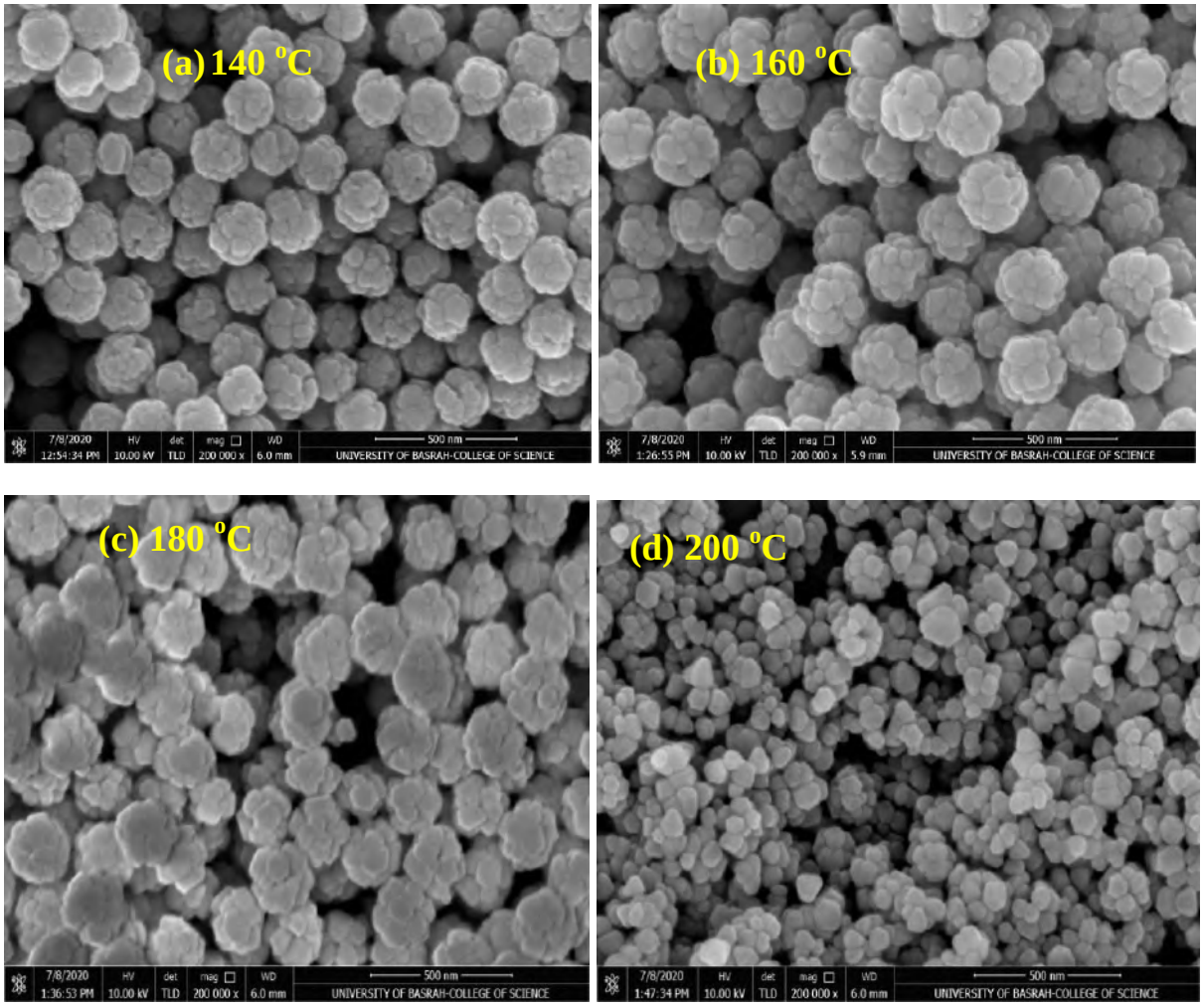

Fig.2. FESEM image of CdS nanoparticle (cauliflower) at reaction temperatures: (a) 140 °C, (b) 160 °C, (c) 180 °C, 200 °C.

CdS nanoparticles have an average grain size of around (94-245) nm, The particle sizes were measured by defining the known length of the FESEM scale bar as shown in Fig. 2a, which indicated the formation of microspheres (cauliflower) of CdS (160,180)°C and the majority of the particles looked in the range of about (138-209) nm, meaning, there is no noticeable change (whether in size, shape, or clusters) compared to the first model(140°C) as shown in the Fig. 2b, c respectively. The sample microspheres (cauliflower) were of almost uniform size, the shape microspheres (200°C) were almost the same as the all of other samples microspheres (cauliflower), but it differs in the size of the grains and crystallites, where the average grain sizes of CdS nanoparticles are about (27.11- 62.11) nm, individual particles sizes as show in the Fig. 2d. This indicates that there is an effect of temperature on the crystal size this effect was evident at 200 ° C, the results are in agreement with the literature [24, 25] which related to the shape and structure of the particle related to microspheres (cauliflower) and the reduction of the grains and particle size with the increase of the reaction temperature.

3.3. Antibacterial activity

The antibacterial activity of the prepared CdS nanoparticles was evaluated using the agar well diffusion method against the test cultures of gram +ve staphylococcus aureus, gram –ve Escherichia coli. The bactericidal effects of CdS nanoparticles were investigated against clinical isolates of staph.

and E. coli. Fig. 3; the presence of clear zones on the Muller Hinton agar surface proves that the CdS nanoparticles was able to inhibit the growth of E. coli and Staph. Four different nanoparticles concentrations (100, 250, 500, and 1000) (µg / ml) were taken to inhibit pathogenic bacterial growth as show in the table (2). The microbe-mediated CdS nanoparticles had the maximum zone of inhibition against disease-causing Staphylococcus and Escherichia coli about 19 mm at reaction temperature 180 oC and 30 mm at reaction temperature (160 and 180) ^{o}C respectively both at the highest concentration (100 µg/ml) of CdS nanoparticle. The minimum zone of inhibition was observed against staph. and E. Coli about 12 mm and 13 mm respectively at reaction temperature of 200 ^{o}C and concentration of CdS NPs. The area of inhibition was increases with the increased CdS NPs concentration and reaches the highest zone of inhibition at the highest CdS Nps concentration as shown in Figs 3 and 4 and all parameters and results were tabulated in Table 2.

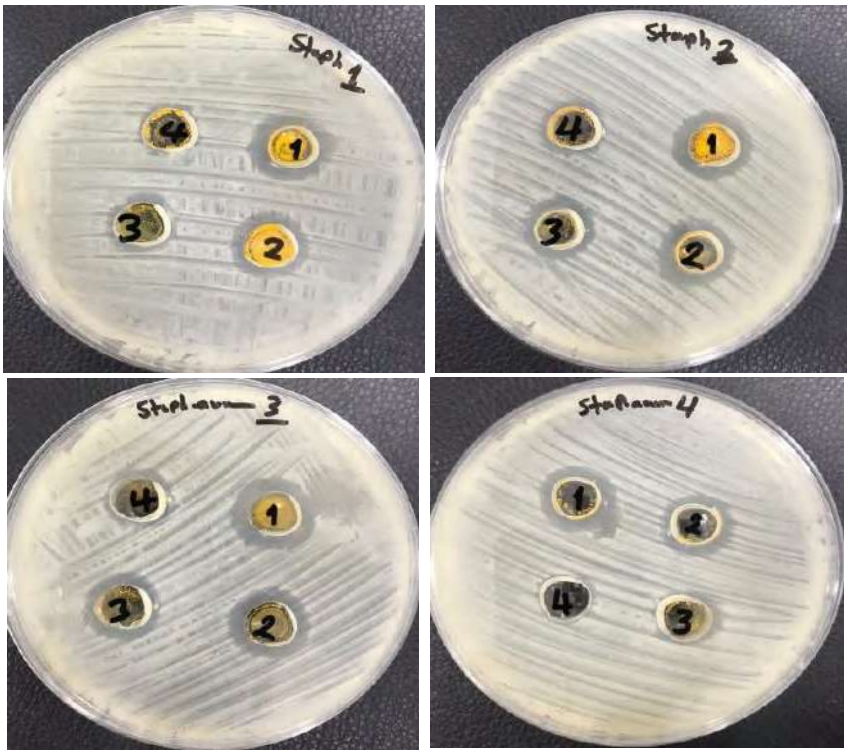

Fig.3. Antibacterial activity of CdS nanoparticles at different concentration (1, 2, 3, 4: 1000, 500, 250, 100) (µg/ml) against staphylococcus bacteria prepared at temperature (staph. 1, 2, 3, 4: 140, 160, 180, 200) °C respectively.

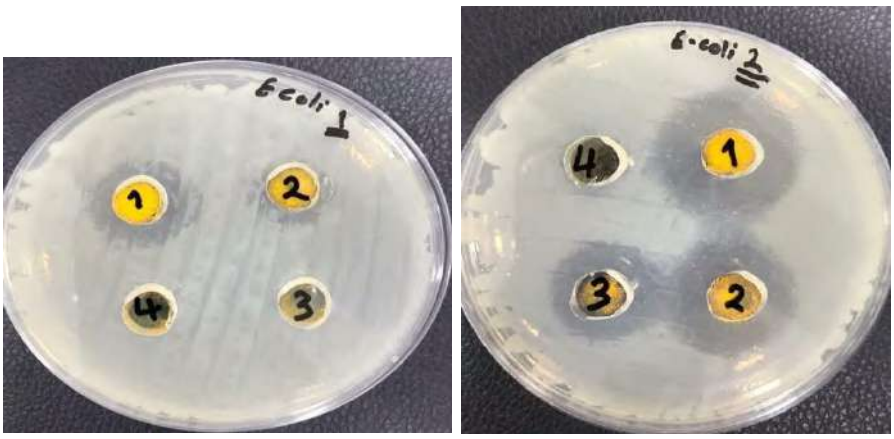

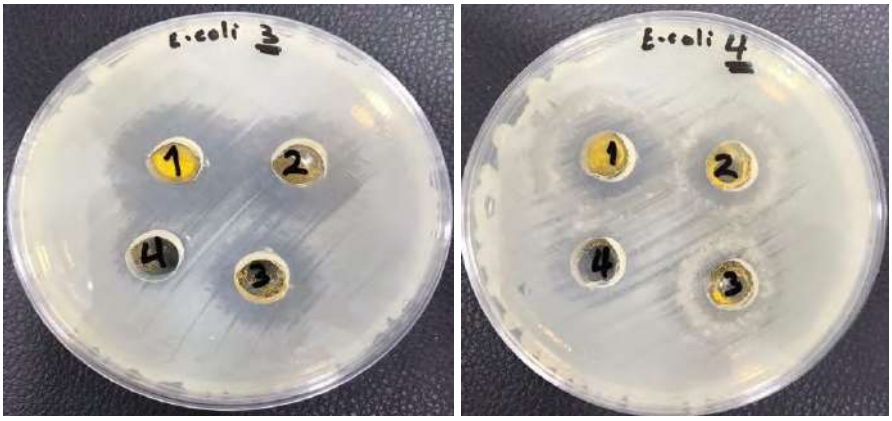

Fig.4. Antibacterial activity of CdS nanoparticles at different concentration (1, 2, 3, 4: 1000, 500, 250, 100) (µg/ml) against Escherichia coli bacteria prepared at temperature (E-coli 1, 2, 3, 4: 140, 160, 180, 200) °C respectively.

There are several mechanisms proposed for CdS NPs inhibitory action of the microbial growth. CdS NPs can cause DNA losses, impairment of its replication, and interfere with cellular proteins including ribosomal subunit proteins [27, 28]. Thus impairs the function of membrane-bound enzymes, in the aerobic strains. Also CdS get attached to the cell membrane and shrink the respiration of the bacterial cell which eventually causes the death of the cell as depicted [29, 30].

Table 2. Inhibition zone of CdS nanoparticles as antibacterial agents in millimeter (mm)

Types of used Bacteria	CdS Nanostructure prepare at temperature (^{o}C)	Concentration of CdS nanoparticle (µg/ml) / inhibition zone (mm)			
		1000 (1)	500 (2)	250 (3)	100 (4)
Staph.	140	17	16	15	13
	160	18	17	16	14
	180	19	18	17	14
	200	17	16	15	12
E-coli	140	23	15	-	-
	160	30	27	24	13
	180	30	25	23	16
	200	20	18	17	14

4. Conclusion

Briefly, CdS nanoparticle (cauliflower) of hexagonal phase has been successfully prepared by hydrothermal method at different reaction temperatures (140, 160, 180, 200 °C) for 4 hours. The crystal structure results indicate that the CdS crystal is of a high crystalline nature and hexagonal (wurtzite) phase. The average crystallite size was tended to increase with the increase of reaction temperature which about (21-24) nm. CdS nanoparticle micrographs images indicates rounded ball (cauliflower), the particles size were in the range of (23-245)nm and the smallest particle size was obtained at reaction temperature 200 °C. The antibacterial activity of cadmium sulfide CdS nanoparticles was estimated against two types of common bacteria (Escherichia coli and

Staphylococcus aureus). It was found that there is a strong antibacterial action and the greatest effect of them was for the prepared nanoparticles at reaction temperatures 160 and 180 ℃, and the highest activity was found against (E. coli) bacteria as well as with the increase of nanoparticles concentration. The antibacterial mechanisms of CdS NPs where the particles can anchor to the bacterial cell wall and infiltrate it and lead to damage the cell membrane and cellular content leakage. Also, CdS NPs can bind to the protein present in the cell membrane and lead to adenosine triphosphate (ATP) generation. As well as the NPs penetrate inside microbial cells, and then the nanoparticles and the released ions can interact with cellular structures and biomolecules such as proteins, enzymes, lipids, and DNA. It was established that synthesized CdS NPs with a higher antibacterial activity that was synthesized in different concentrations and reaction temperatures are potentially suitable for the development of nanomedicine and its applications.Also this work combines microbiology and nanotechnology, perform probable advances in the formulation of a new kind of antibacterial.

References

[1] Shen G, Cho JH, Yoo JK, Yi G-C, Lee C. J. 2005 *J. Phys. Chem. B* **109** 9294.
[2] Qutub N, Sabir S. 2013 *Adv. Sci. Eng. Med.***5** 852.
[3] Lide DR. CRC handbook of chemistry and physics: CRC press; 2004.
[4] Sikander Azam, Zeesham Abbas, Qasim Bilal, Muhammad Irfan, Muhammad Adil Khan, 2020 *Physica B* **583** 412056.
[5] Favero P. P, Souza-Parise M d, Fernandez J L R, Miotto R, Ferraz A C. 2006 *Brazilian Journal of Physics* **36** 1032.
[6] So W-W, Jang J-S, Rhee Y-W, Kim K-J, Moon S-J. 2001 *J. Colloid Interface Sci.* **237** 136
[7] Xiao J, Peng T, Dai K, Zan L, Peng Z. 2007 *J. Solid State Chem.* **180** 3188.
[8] Yu L-m, Zhu C-c, Fan X-h, Qi L-j, Yan W. 2006 *J. Zhejiang Univ. Sci.* **7** 1956.
[9] Horoz S, Sahin O. 2017 *J. Mater. Sci.: Mater. Electron.* **28** 9559.
[10] Anikin K, Melnik N, Simakin A, Shafeev G, Voronov V, Vitukhnovsky A. 2002 *Chem. Phys. Let.* **366** 357.
[11] C-F Lin, E-Z Liang, S-M Shih, W-F Su, 2002 *Proc. SPIE* **4641**, Light-Emitting Diodes: Research, Manufacturing, and Applications VI.
[12] Zang J, Zhao G, Han G. 2007 *Front. Chem.in china* **2** 98.
[13] Jia H, Hu Y, Tang Y, Zhang L. 2006 *Electrochem. commun.* **8** 1381.
[14] Pal K, Maiti U N, Majumder T P, Debnath S C. 2011 *App. surf. sci.* **258**:163.
[15] Kim YH, Lee DK, Cha HG, Kim CW, Kang YS. 2007 *J. Phys. Chem. C* **11** 3629.
[16] Ayodhya D, Venkatesham M, Kumari AS, Reddy GB, Ramakrishna D, Veerabhadram G. 2015 *J. Fluoresc*. **25** 1481.
[17] Abd-Elkader O H, Shaltout A A. 2015 *Mater. Sci. Semicond. Process* **35** 132.
[18] Narasimman V, Nagarethinam V, Usharani K, Balu A. 2017 *Optik* **138** 398.
[19] Gajendiran J, Vijayakumar V, Senthil V, Reddy CP, Ramya JR, Gokulraj S, 2020 *Optik* **213** 164638.
[20] Jamble SN, Ghoderao KP, Kale RB. 2018 *J. Phys. Chem. Solids* **114**:109.
[21] Cullity B D., Elements of X-ray Diffraction: Addison-Wesley Publishing; 1956.
[22] Al Balushi BS, Al Marzouqi F, Al Wahaibi B, Kuvarega AT, Al Kindy SM, Kim Y, 2018 *App. Surf. Sci.* **457** 559.
[23] Monshi A, Foroughi MR, Monshi MR. 2012 *World J. nano sci. eng.***2** 154.
[24] Zhou X, Huang J, Zhang H, Sun H, Tu W., 2016 *Int. J. Hydr. Energ.* **41** 14758

[25] Hussain T, Aslam S, Mustafa F, Ighodalo KO, Ahmad MA., 2019 *Mat. Res. Exp*. **6** 045908.
[26] Rengaraj S, Venkataraj S, Jee SH, Kim Y, Tai C-w, Repo E, Koistinen, A., Ferancova, A., & Sillanpää, M., 2011 *Langmuir* **27** (1) 352
[27] U. T. Khatoon, G.V.S. Nageswara, M. K. Mohan, A. Ramanavicienec and A. Ramanaviciusb, 2018 *J.Environm. Chem. Eng.* **6** 5837.
[28] P. V. Dong, C. H. Ha, L. T. Binh and J. Kasbohm, 2012 *Int. Nano Lett.***2** 9
[29] Faryal Mughal, Mohsin Muhyuddin, Muhammad Rashid, Tahir Ahmed, Muhammad Aftab Akram and Muhammad Abdul Basit, 2019 *Chem. Phys. Lett.***717** 69.

Effects of Electrode Beam Radius on Properties of four-poles Electrostatic Double Lens for Point-to-Point Focus

Effects of Electrode Beam Radius on Properties of four-poles Electrostatic Double Lens for Point-to-Point Focus

Zeina Kareem Lazem[1], Oday A. Hussein[1]

[1]Al-Nahrain University, Collage of Science, Department of physics

E-mail: stph-zkl18@sc.nahrainuniv.edu.iq.

Abstract. This study investigates the effect of selection the electric pole radius of the four poles electrostatic doublets lens on the optical property. Also, a comparison between the optical property and performance of two lenses with different electrode radius was made. The results showed that the electric pole diameter of the lens plays main function in the imaging characteristics of the four poles electrostatic doublets lens. The results show that the aberration figures can be enhanced when the electrode diameter of the quadrupole lens is equal to the lens aperture, while the chromatic aberration can be improved by choosing the electrode diameter according to the equation.

Keywords: quadrupole lens, electrostatic quadrupole lens, SIMION.

1. Introduction

Quadrupole electrostatic lenses are used in a wide variety of applications, especially when imaging optical illusions not necessary [1, 2]. Due to the importance of electrostatic lenses in a large number of lenses applications, many researchers have studied this type of lens from different points of view (see [3, 4, 5, 6,7,8]). The particles accelerators, storage rings, mass analyzers, electron microscopes, and others are important instruments in the fields of scientific research and the electrostatic quadrupole lenses are used in these instruments because their ability on the control and focusing of the particles charged. Most of the theoretical bases of electrostatic and magnetic lenses were developed by pioneers and inventors of the electron microscope (Busch H 1927, Hawkes P 2004) [9-10].

Charged particle optics researchers can use facilities provided by some computer simulators to understand the fundamentals of charged particle optics and arrive at optimal designs for optical systems using optimal operating conditions [11, 12].

By reviewing previous articles in the field of the electrostatic quadrupole lenses, one can find two methods for choosing the radius of the electrodes of the quadrupole lenses according to the relation between this radius and the distance between the edges of the electrodes. In some articles, the diameter of the cylindrical electrode was taken equal to distance between the edges of the electrodes [13], while in other articles the diameter of the cylindrical electrodes is taken according to a certain equation dependence on the relation between the radius of electrode and the distance between the edges of the electrodes [14]. In the present work, the effects of choosing method to the electric pole radius on the optical property of the lens and its performance will studied and the comparison between two types of lenses will caried out.

2. Computational methods

In this research the lens electrode diameter was taken in two different Figure 1, the first case the lens diameter was taken to be equal to the distance between the egdes of electrodes or hole diameter (D) which is fixed to 20 mm, and in the second case the lens diameter was extracted from the relation r = 1.14511R R = D / 2 [14] and the diameter according to this equation is 8.73 mm, the electric pole length (L) 80 mm. The diameter of image (D) is 20 mm. The object (O) should be on the left part of the lens and the picture (I) on the right part of the lens. We will label the space between the subject and the reference plane (F) by (K) and the distance between the image and the reference plane by (G). The design is achieved using special virtual lab simulator in SIMION 8.1 of charged particles optics [15].

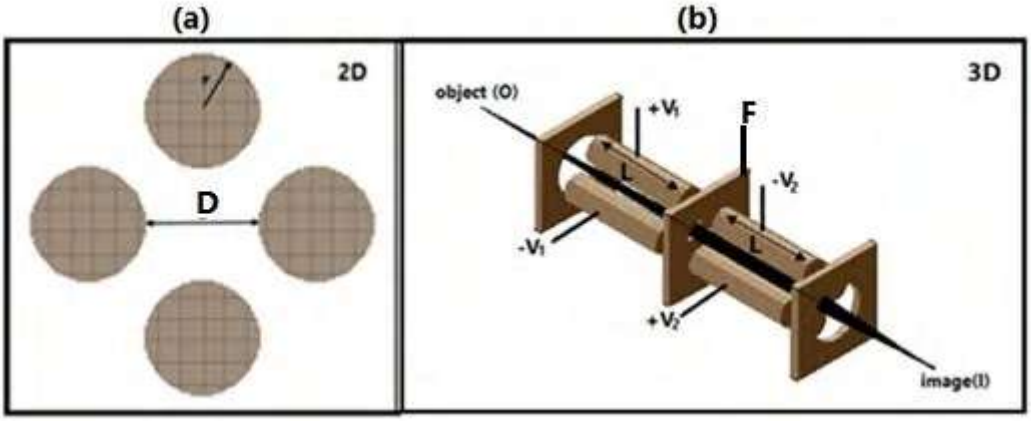

Figure 1. (a)(b) views one dimension and three dimensions of four poles electrostatic doublets lens.

One of the important steps in the design of the quadrupole lens is finding the applied voltages on the electrodes V1 and V2 lead to giving the image focus via focusing on both planes XY and XZ. To achieve this purpose, the code was written using the program language of LUA to find the voltage groups that give a spot image with the lowest point volume on the Position Sensitive Detector (PSD), where calculations were made for point-to-point focus.

3. Results and Discussion

The first step is to create an image of a spot in a four-pole electrostatic double lens is finding both voltage V1 and V2 which give the focus in two plane XY and XZ. Figure 2 shows the electrode voltages for two lenses with different electrode radius for focus point-to-point. The calculations have been carried out for fixed geometric dimensions K / D = 10, G / D = 10 (K is the space between the subject and the reference plane F, G: the space between the picture and the reference plane F, and D: the diameter of the hole); kinetic energy 1000 eV and the condition of the radius beam (r) at the screen is considered to be r = 0.01 mm at the first case and r = 0.001 mm at the second case.

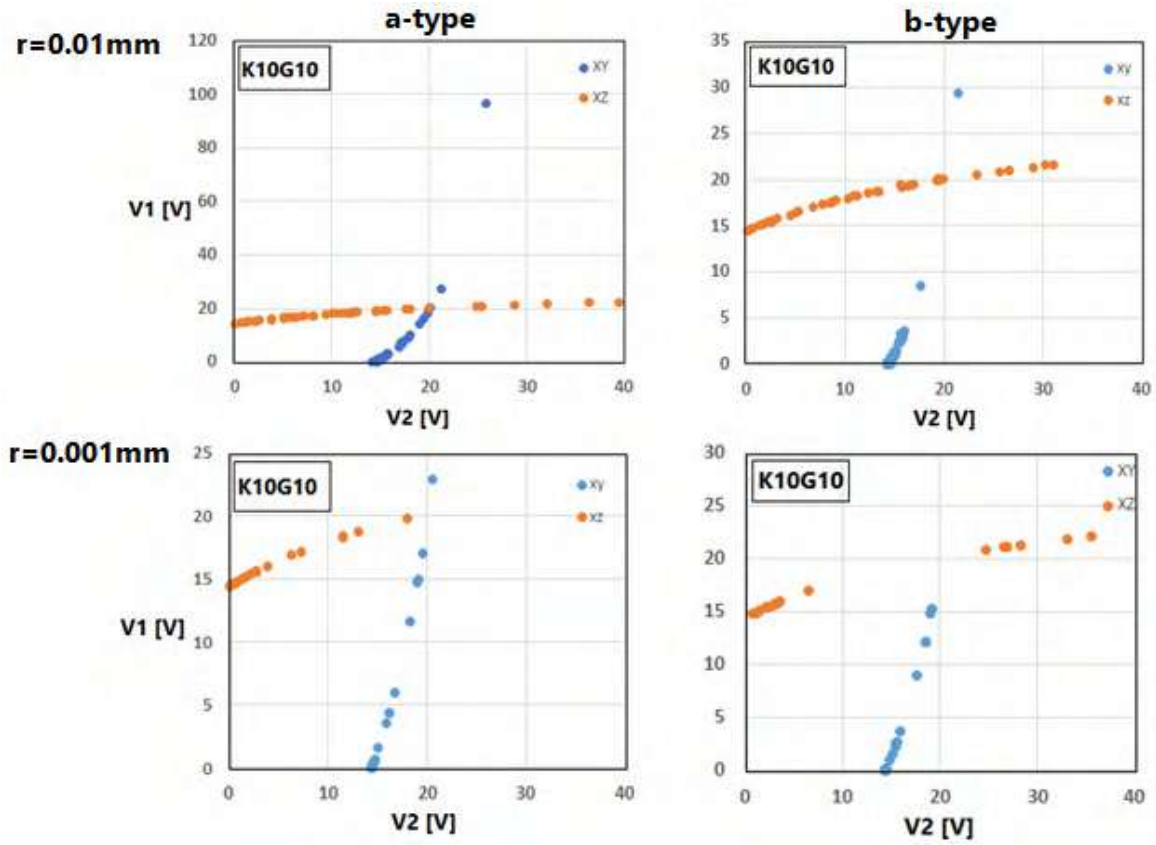

Figure 2. The voltage of two electrodes V_1 and V_2 for two lenses with different electrode radius at point-to-point focus mode (a) the diameter without using equation (b) the diameter using the equation r = 1.14511R, R = D / 2 [14], energy = 1000 eV, and angle α = 1◦ and for criteria of radius beam r = 0.01 mm and r= 0.001 mm. Here K10G10 stands for K / D = 10 and G / D = 10.

Figure 2 shows the relationship between V_1 and V_2, and there are two curves in these figures, for focus in the xy and xz planes. A point of intersection of two curves gives values of voltage that produce a point image or concentrate on the two planes simultaneously. In this figure obviously, the required voltage in the lens of type b is greater than that of type a when the beam radius r=0.01mm and, in the r=0.001mm the required voltage in a lens is greater than that for b lens. The equipotential surface distribution of the two four-poles electrostatic double lenses with two different electrode radius for K = G = 10D are shown in Fig. 3.

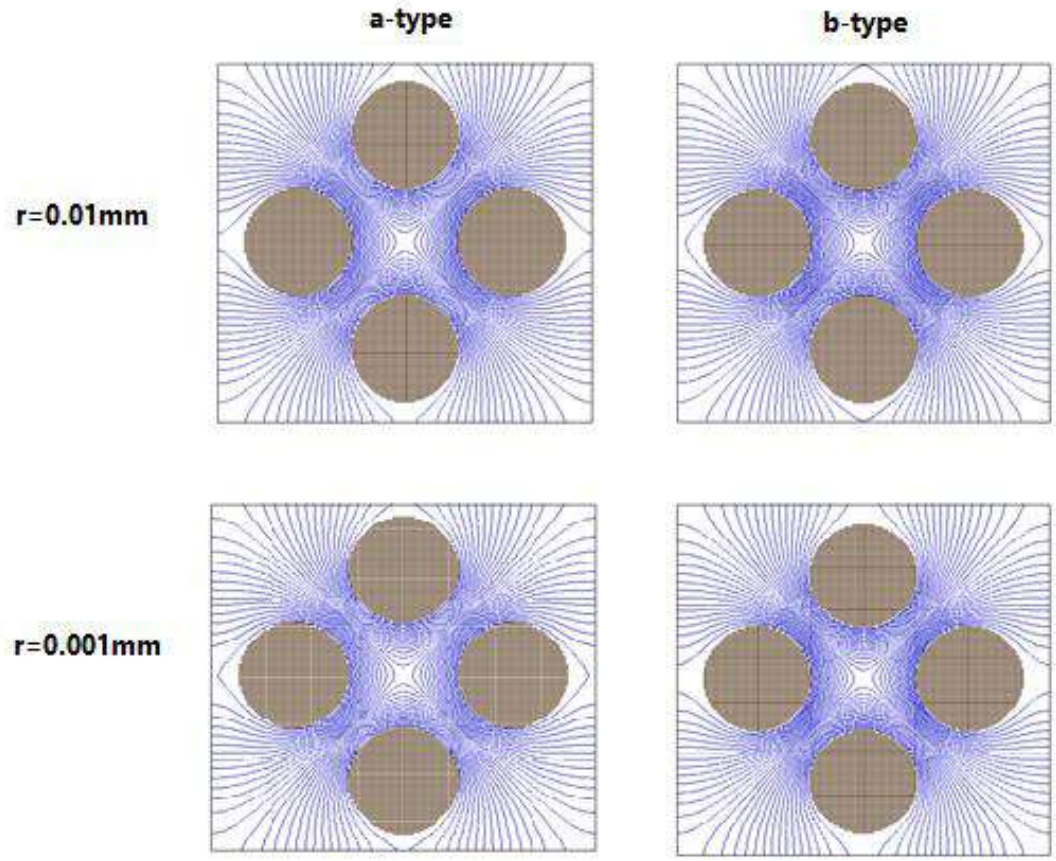

Figure 3. Equipotential surface distribution of the two four-poles electrostatic double lenses with two different electrode radius.

Figure 4 shows the electron beam paths in both the XY and XZ planes for point-to-point focus at K = G = 10 D. One can notice in this figure that the changing in the electrode radius of the lens leads to very small differences in the electron beam paths. These differences lead to important results in image levels as shown in Fig. 5. In this figure, the effect of the method of choosing the diameter of the electrode is appear clearly, especially when one search for very small dimensions image as is shown in figure 5 (b). The calculations show that the aberration is better when using electrode diameters exactly equal to the diameter of the lens aperture.

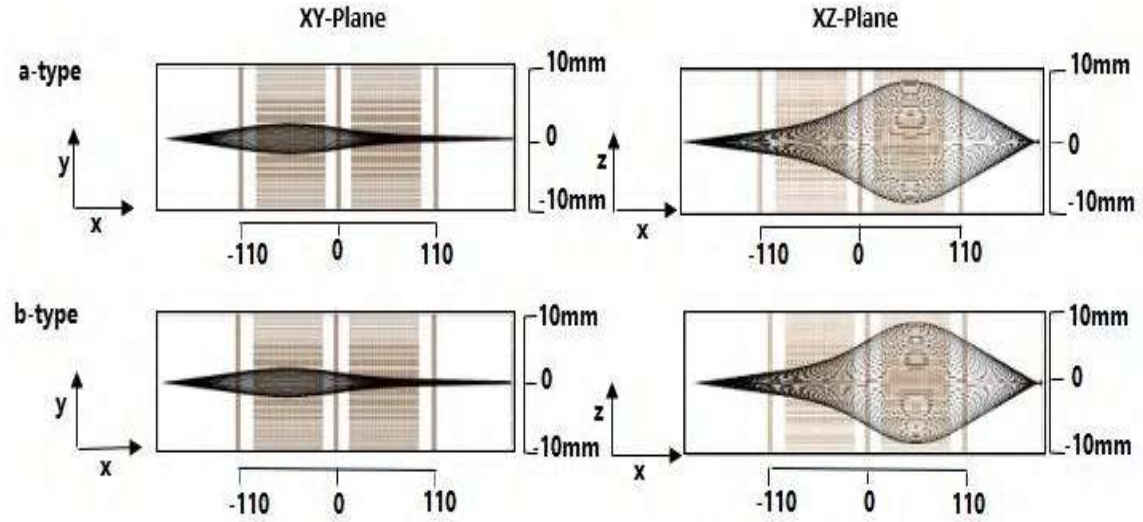

Figure 4. Shows the electron paths in the two planes for two different states of a four-poles electrostatic lens diameter for K = G = 10 D. (a) the diameter without using equation (b) the diameter using the relation r = 1.14511R, R = D / 2 [14]. The energy is 1000 eV, the beam radius r = 0.01mm for point-to-point focus with angle α = 1◦.

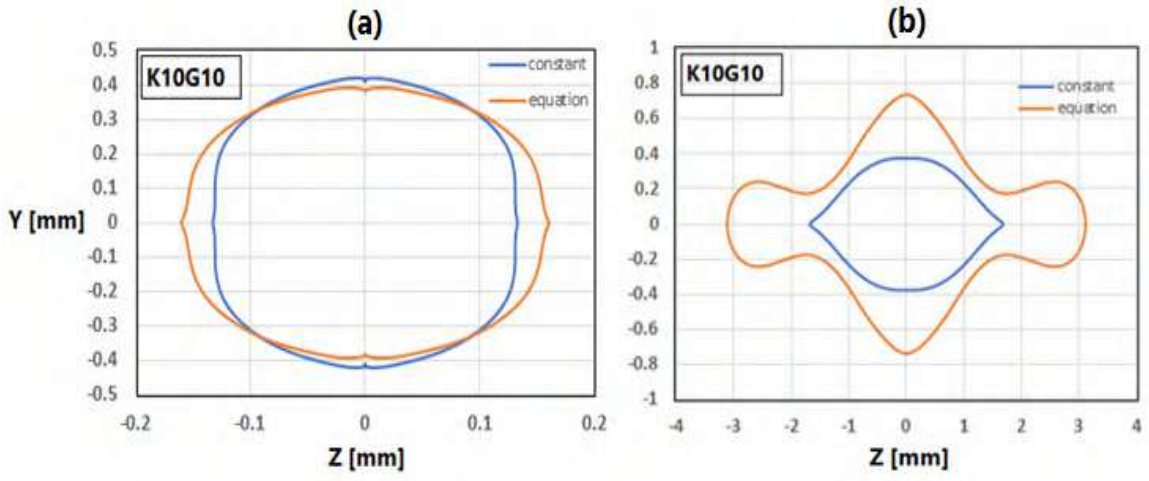

Figure 5. Comparison of the aberration shape for two different cases of quad-pole electrostatic lens diameter K = G = 10D, and the radius of the beam r with two different values (a) r = 0.01mm (b) r = 0.001mm. Here; P10Q10 means K / D = 10 and G / D = 10. Results are computed for angles α = 1◦.

The kinetic energy distribution of an electron beam is calculated for the lenses of two designs and the result is shown in Fig. 6. The results showed that the kinetic energy of an electron beams is more stable in the case of choosing the diameter of the electrode by using the equation. Therefore, the chromatic energy will be better in this case, because most of the electrons have the same kinetic energy. In general, for all cases the difference in the kinetic energy is very small and can be neglected.

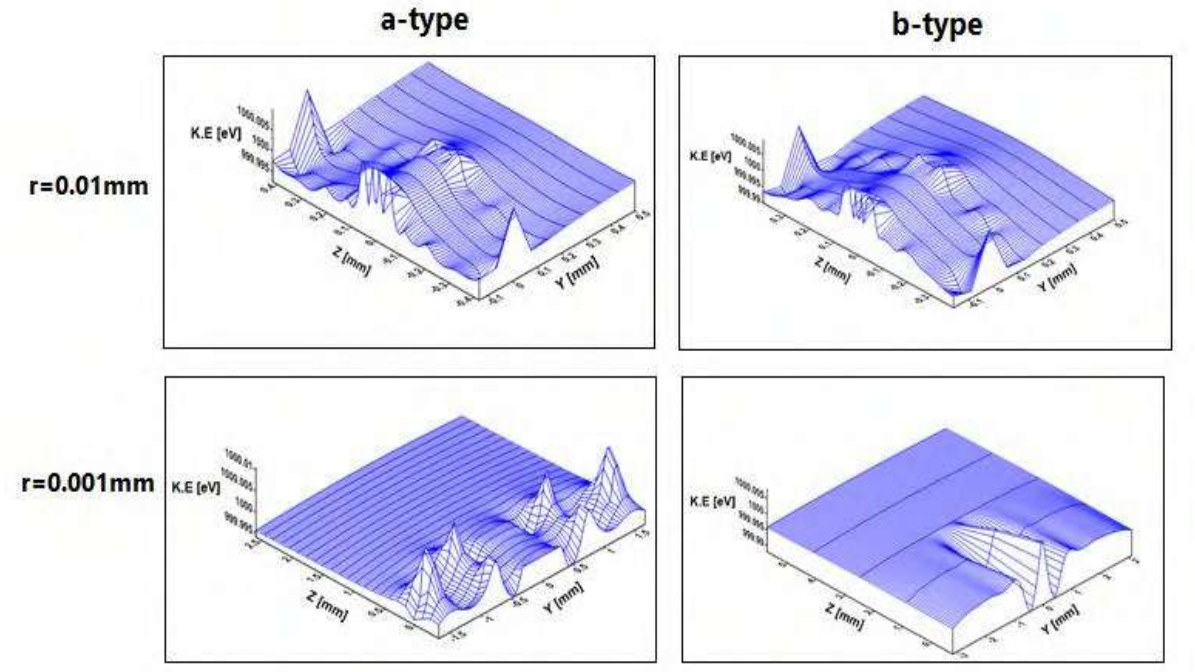

Figure 6. Distribution of the kinetic energy of an electron beam of two electrostatic four-poles double lenses with different electrode radius for K = G = 10D and beam radius r = 0.01mm, r=0.001mm.

Table 1 contains the comparison between some of the important parameters and operation conditions between the both designs of the electrostatic four-poles lenses with different diameters. The results in the table appear that the method of choosing the diameter of the electrode play a substantial role in determining the lens characteristic.

Table 1. The electrostatic four-poles double lens constants for the point-to-point operation mode with angle of an electron beam α = 1, the electron beam of two different values of the radius at the image plane r = 0.01 mm, r = 0.001 mm.

	r = 0.01 mm		r = 0.001 mm	
	(a)	(b)	(a)	(b)
V1(V)	19.923	19.833	20.03	20.17
V2(V)	20.093	20.045	20.21	20.52
K/D	10	10	10	10
G/D	10	10	10	10
$\Delta y(mm)$	0.82	0.76	0.74	1.46
$\Delta z(mm)$	0.26	0.31	3.34	6.2
Average time (µsec)	0.021415	0.0214149	0.0214144	0.021415

4. Conclusion

The imaging property of two types of electrostatic four-poles doublet lens systems were investigated. Calculations were made to focus point to point for two systems with different electrode radius of the lenses that is chosen using two methods of selection the electric-pole diameter of the electrostatic four-

poles lens depending on the relation between electrode radius and the lens aperture. The results showed that the method of choosing the dimeter of the electrode play substantial role in determining the lens characteristic and by choosing the appropriate method one can improve some of the properties. The results indicate that the aberration figures can be improved by taking the electrode radius equal to the radius of the aperture of the lens. Also, the results show that the electron beams kinetic energy is more stable in the case of choosing the diameter of the electrode by using the equation. Therefore, the chromatic energy will be better in this case, because most of the electrons have the same kinetic energy.

5. References

[1] Baranova LA and Ya S 1989 The optics of round and multipole electrostatic lenses *Yavor* **76**.
[2] Yavor M 2009 Optics of Charged Particles Analyzers *Adv. Imag. Elect. Phys.* **157**
[3] Naab FU, Toader OF and Was GS 2015 Ion Beam Transport Simulations for the 1.7 MV Tandem accelerator at the Michigan Ion Beam Laboratory *Phys. Procedia* 632 – 640.
[4] Kreiner AJ 2014 Accelerator-based BNCT *Appl. Rad. Isotopes* **88** 185–189.
[5] Barna D 2014 *field simulations and mechanical implementation of electrostatic elements for the ELENA transfer lines*, Proceedings of IPAC2014, Dresden, Germany.
[6] Hussein OA 2009 *J. Al-Nahrain Univ. Sci. (JNUS),* **12** 86-93.
[7] Hussein OA 2017 *Optik* **140** 860–865.
[8] Hussein OA and Sise O 2017 *J. Elect. Spectrosc. Related Phenomena* **217** 11–15.
[9] Busch H 1927 Uber die Wirkungsweise der Konzentrierungsspule bei der Braunschen R ¨ ohre ¨ *Arch. Elektrotech.* **18** 583–94 Jena, Physikalisches Instituts.
[10] Hawkes P 2004 Recent advances in electron optics and electron microscopy *Ann. de la Fondation Louis de Broglie* **29** (Hors serie 1) 837–55.
[11] Sise O, Martínez G, Madesis I, Laoutaris A, Dimitriou A and Fernández-Martín M 2016 *T.J.M. J.* **211** 19-31.
[12] Wu Q, Tian Y, Li A and Austin DE 2015 **393** 52–57.
[13] Seki T, Shitomoto S, Nakagawa S, Aoki T and Matsuo J 2013 *Nuclear Instr. Methods Phys. Res. B* 315 356–359.
[14] Yavor M 2009 Optics of Charged Particles Analyzers *Adv. Imag. Elect. Phys.* vol. 158.
[15] SIMION 3D v8.1, *Scientific Instrument Services* Inc. (www.simion.com).

Characterization of carbon nanotube decorated silver nanoparticles

Characterization of carbon nanotube decorated silver nanoparticles

Taqwa Y. Yousif, Asama N. Naje

Baghdad University, college of science, physics department.

E-mail: Tyy3033@gmail.com

Abstract. Silver nanoparticles (Ag NPs) prepared using the exploding wire process has been decorated with carbon nanotubes (MWCNTs, SWCNTs). Well dispersion of silver NPs is achieved by a simple chemistry process on the surface of CNTs. The structure, optical and morphology of silver nanoparticles decorated with carbon nanotubes were characterized by x-ray diffraction, Atomic force microscopy, and field emission scanning electron microscopy. The illustrated outcome that the UV-Visible absorption and electrical conductivity properties effectively improved for CNT/ Ag NPs. The absorption spectrum of silver nanoparticles shows absorption at ultraviolet wavelength zone and there is low peak between (300-900nm) while the absorption of CNT/silver nanoparticles (Ag NPs) increased significantly from UV to near IR region. Field emission scanning electron microscopy analysis shows that silver nanoparticles are decorated on carbon nanotubes without any impurities, with average particle size about (50-80nm) for Ag-NPs, 44nm for MWCNTs/Ag-NPs and 30 nm for SWCNTs/Ag NPs . It was observed that Ag NPs enhanced the electrical conductivity of CNTs from (2.36 ×10-1 (1/ Ω.cm) to (1.03×10^4 (1/ Ω.cm)) for SWCNTs/Ag NPs and (8.83×10^4 (1/ Ω.cm)). It is observed that Ag NPs adding enhanced the electrical properties of CNTs. The results show that Ag-coated CNTs have important optoelectronic applications such as solar cell and photodetector.

Keywords: CNTs, Ag NPs, exploding wire method, optical Structure properties.

1. Introduction

Carbon nanotubes (CNT) have attracted significant research interest and they are widely used because of their excellent chemical, physical and electrical properties. Multi-walled carbon nanotubes (MWCNTs) and single-walled carbon nanotubes (SWCNTs) are considered ideal materials for different applications. [1, 2]. Metal nanoparticles (NPs) have gained a lot of interest in the fields of electronic, chemistry, and biology because, the high surface to volume ratio together with the size effect gives nanoparticles discriminative different properties (chemical, optical, electronic and magnetic) from those of bulk material[3, 4]. To synthesize metal nanoparticles, there are different techniques used such as a laser beam [5] ، electron beam, mechanical milling [6] ، electrical exploding wire [7] ، chemical vapor deposition [8] and electro-chemical method [9]. Decorating CNTs with metal nanoparticles provides new opportunities for researchers who have important applications in various fields, and is expected to exhibit different properties from individual CNTs [2]. Among the

different metal nanoparticles, Ag NP has been proven to have excellent property, making it suitable for different applications. CNT/Ag NPs has attracted great attention due to its importance in photodetectors [10, 1], gas sensor [11, 12], biosensor [13], etc.

Electrical explosion of wire method (EEW) is one of the vapor phase methods in which particles are produced by evaporating a thin metal wire by passing high current through it [14]. The phenomenon of electric explosion of wires (EEW) reduces to the following "When a high density (10^4–10^6 A/mm^2) current pulse, which is usually produced by the discharge of a capacitor bank, passes through a wire, the density of the energy in the wire may considerably exceed the binding energy because of a high rate of the energy injection and an expansion lag of the heated material. As a result, the material boils up in a burst, a bright light flashes, and a mixture of superheated vapor and boiling droplets of the exploding wire material and a shockwave scatter to the ambient atmosphere". In the other words the phenomena of (EEW) have been widely dependent on plasma physicists for generation and confinement of plasmas [15]. The properties of EEW synthesized nanoparticles depend on several parameters, including wire shape, such as wire (length and diameter) and material size, electrical circuit characteristics, and environmental media. There have been many experiments made to decorate CNTs with metal nanoparticles (Ag, Au) such as by Waleed K. Mahmood et al [16], and Ngo X. Dinh et al [17].

In the current work, we provide a simple system for the production of Ag NPs depended on the explosion of silver wire in distilled water, following this decoration of CNTs surface by Ag nanoparticles. The structural, morphological, and electrical properties of CNT-silver nanoparticles are studied using different characterization techniques.

2. Experimental Techniques

2.1 Synthesis of Ag-NPs by EEW

This work provides easy and effective devices for the processing of large numbers of metal nanoparticles for the wire explosion. In a reaction vessel of 500ml, the electro explosion of the wires (EEW) is accomplished to remain the two electrodes and the medium of the explosion. The wire goes and strikes the silver plate without bending in its way as Fig.1 shown, Teflon beaker was used to fix the two electrodes. The metal plate is passes through two groves on the surface of one block, while the wire was passes through a glass tube connected to the other block which placed opposite to the previous one. Both electrodes were joined to the two terminals of the 36V DC batteries by thick copper wires. The metal plates are fixed on the base of Teflon beaker filled with 30 ml of distilled water and just touching the first electrode through precise mechanical movement for 15 to hit, and then nominated by filtration paper. The silver nanoparticles will be stuck in the solution.

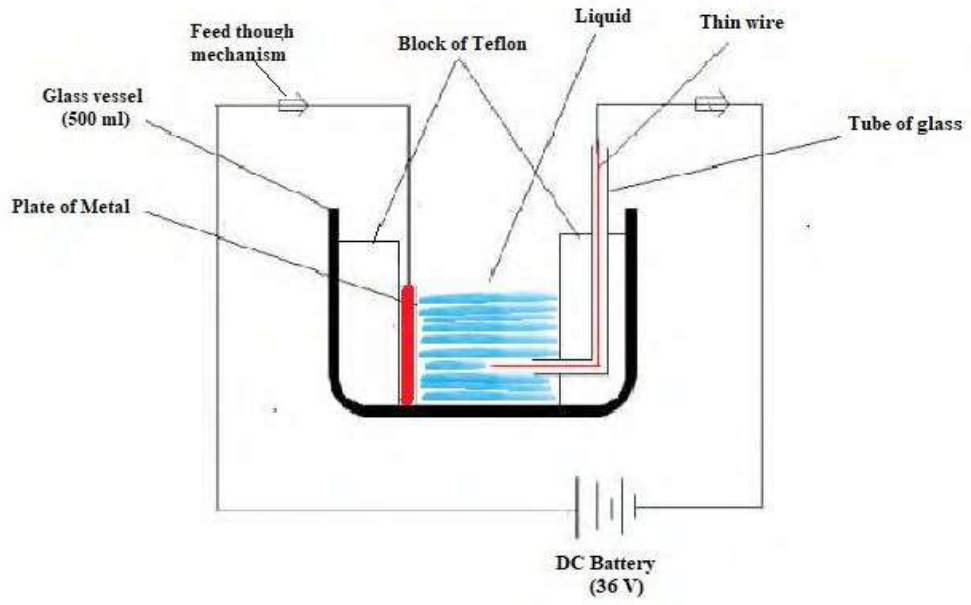

Fig. (1) A schematic diagram for Ag nanoparticles prepared by (EEW) set up.

The circuit remains disconnected until the wire mechanically touches the board. Due to the high current density through the wire, the wire explosion process occurs in a short period of time. This in turn opens the circuit for another explosion process. Silver wires of purity 99.99% , diameters of 1m length and plates (dimension : 2cm², 0.3mm; Purity: 99.99%) used in the explosion process.

2.2 Decoration of Ag NPs on Carbon Nanotubes (SWCNT & MWCNT)

The carbon nanotubes used in this work are multi-walled carbon nanotubes (MWCNTs) and single wall carbon nanotubes (SWCNTs)) supplied by Nanostructured & Amorphous Materials, Inc. The diameter of the MWCNTs range from 10-30 nm, length 1-2 μm and of 95% purity, and for SWCNTs range from 1-2 nm, length ~ 30 μm and of 90% purity. In the next step, the decoration of Ag-NP on CNT (SWCNT and MWCNT) was carried out. After forming silver nanoparticles, 10 ml of Ag-NPs was added with 0.05 g of SWCNT and MWCNT stirred for 12h and followed by 1 hour sonication.

3. Result and Discussion

3.1 UV-Visible spectroscopy

The UV-Visible absorption spectrum of the pure Ag NPs, SWCNT/Ag, and MWCNT/Ag prepared in water media are measured using Shimadzu UV-1800 spectrophotometer, all spectra are measured in a quartz cell at room temperature. The scanning range of CNT/Ag NPs absorption was (190-1000) nm using distilled water as a reference sample. Fig. 2 shows the UV-Visible absorption spectra as a function of wavelength.

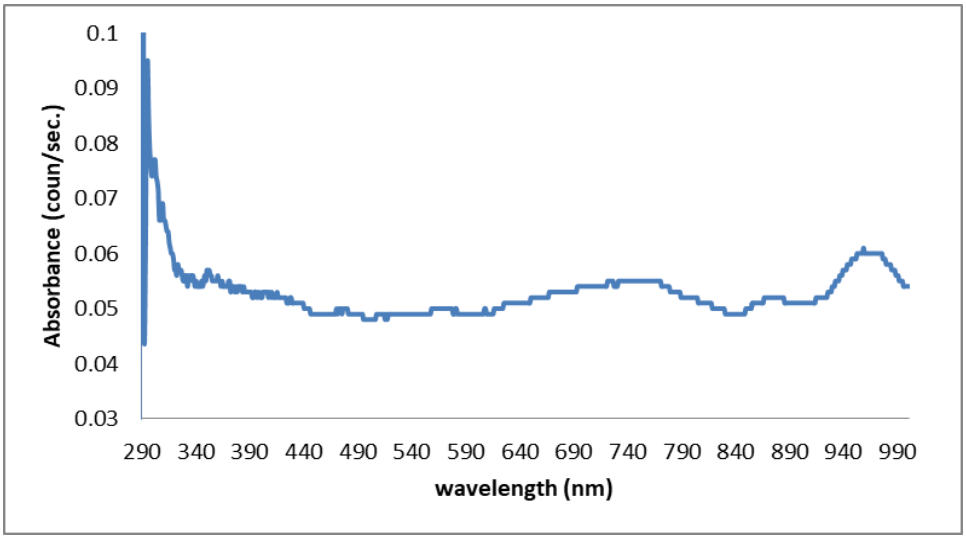

Fig. 2. UV-Vis light absorption spectra of Ag nanoparticle as a function of wavelength.

The UV-Vis spectrum observed that the Ag nanoparticles has fine structure absorption band in UV-Visible wavelength region of (~290 nm to 440 nm). The presence of narrow resonance absorption peaks is attributable to the excitation of surface plasmon vibrations in the silver nanoparticles; Surface Plasmon Resonance (SPR) band for Ag-NPs extended in the 450-510 nm range [18] with a peak position around 470 nm. A flat area was found in the phase at 300- 400 nm region, which indicates there is no absorption in this region or absorption is weak in this region.

According to Fig. 3 MWCNT/Ag and SWCNT/Ag NPs absorb light in the range of UV, Visible and NIR (300-1000 nm) but the (SPR) peak smaller than Ag-NPs because Proximity-induced charge transfer between (SWCNTs &MWCNTs) and silver could deplete the number of electrons available for surface Plasmon generation in the silver nanoparticles [18, 19].

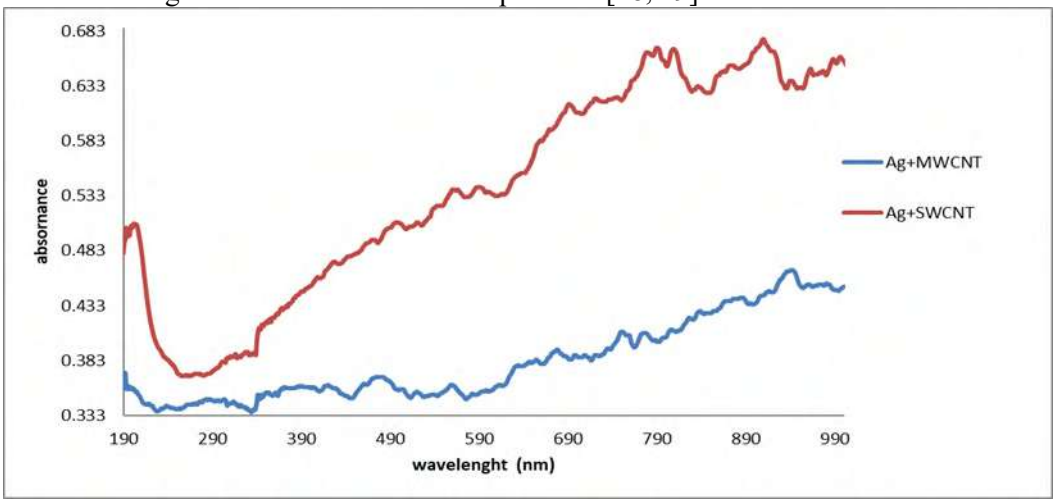

Fig. 3. UV-Vis light absorption spectrum of SWCNT/Ag & MWCNT/Ag as a function of wavelength.

3.2 Infrared Analysis spectroscopy FTIR

FTIR studies have been performed in the range 400 cm^{-1} to 4000 cm^{-1} for the identification of the functional group of the Ag NPs, MWCNTs/Ag NPs and SWCNTs/Ag NPs deposited on quartz

substrates. Fig. 4a, b and c show the FTIR spectrum for pure Ag NP, MWCNTs/Ag and SWCNTs/Ag NPs.

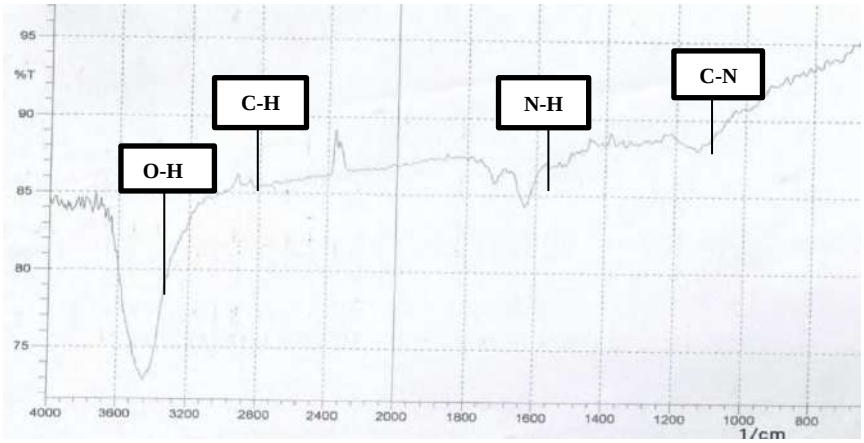

Fig. 4a. FTIR spectra for pure Ag NPs thin film.

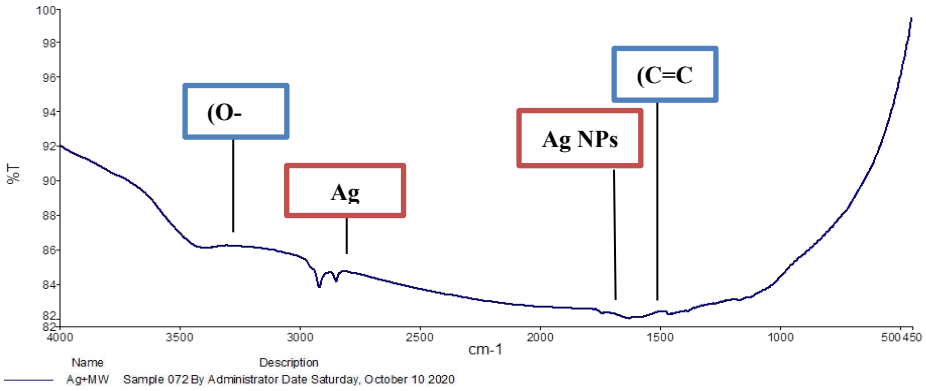

Fig. 4b. FTIR spectra for MWCNTs/Ag NPs thin film.

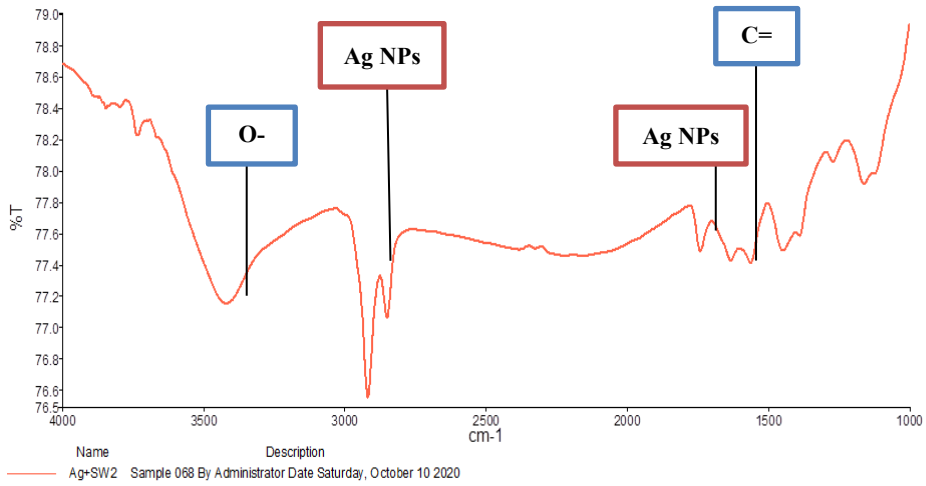

Fig. 4c. FTIR spectra for SWCNTs/Ag NPs thin film.

To determine possible interactions between the surface of silver nanoparticles and CNTs (SWCNT & MWCNT) molecules, the FTIR spectra of Ag nanoparticles were reported. By comparing the FTIR spectra of both silver nanoparticles and CNTs, it was found that in the FTIR spectrum of SWCNTs/Ag and MWCNTs/Ag, several peaks obtained by pure Ag-NPs were repeated with changes in location as well as in transmission band intensity. However, for the spectrum of the pure Ag-NPs, the

transmission band at (2968, 1720) cm-1 which can be assigned to the C-H symmetric stretching vibration is slightly shifted to (2926, 1752) cm-1, proving the interaction between the (SWCNTs and MWCNTs) molecules and Ag nanoparticles, and the broad peak appeared in the range of (3446, 3461 and 3500 cm-1) are attributed to O-H stretching vibration are in accordance with literature values [17, 20], the C=C bonding of aromatic rings of carbon skeleton structure were found at 1624cm-1.

3.3 X-Ray Diffraction Study

The X-Ray diffraction used to study crystalline structure of the Ag nanoparticles, SWCNTs/Ag and MWCNTs/Ag. This technique used (XRD -6000 labs, supplied by SHIMADZU, X-ray source are Cu Kα). The X-ray is used to determine the dimensional parameters for crystals and for the size estimation. For this purpose the following equation, known as the Scherrer equation is used [16]:

$$D = \frac{k\lambda}{\beta cos\theta} \quad \text{------- (1)}$$

Where k is the shape factor, the dimensionless shape factor has typical value 0.9. D is the particle size. λ is the wavelength for X-ray source (X-ray source is Cu Kα with λ=1.5406Å). β is the full width at half maximum (FWHM) in rad. θ is the diffraction angle. The XRD patterns of silver nanoparticles, silver-MWCNTs, and silver-SWCNTs samples were displayed in Figure 5a, b and c.

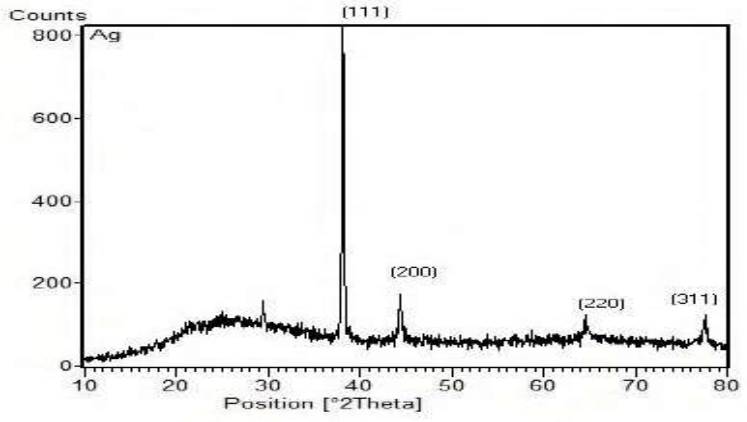

(a)

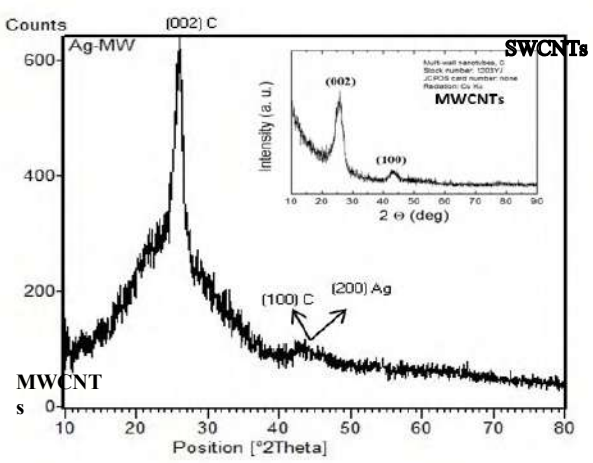

(b)

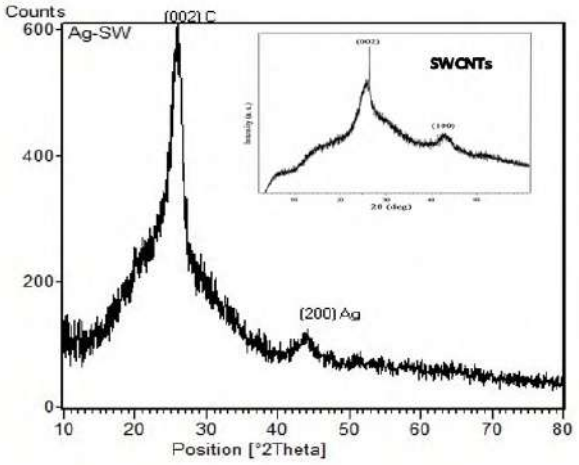

(c)

Fig. 5. XRD patterns of (a) pure Ag Nanoparticles thin film, (b) MWCNTs/Ag NPs thin film and (c) SWCNT/Ag NPs thin film.

In Figure 5a, It can be shown that the pristine Ag-NPs sample exhibits a high (111) peak at 38.1˚, (200) peak at 44.3˚, (220) peak at 64.6˚ and (311) at 77.5˚ crystalline planes of metallic Ag indicate the Face-center Cubic (F.C.C) (JCPDS No. 04-0783). After the decoration of silver nanoparticles on CNTs, The Ag-MWCNTs XRD pattern reveals two obvious diffraction peaks. at 2 theta 26.2˚ which correspond to (002) for MWCNT and 44˚ match with both MWCNT (100) and Ag-NPs (200)[21] as shown in figure (5b). SWCNTs/Ag NPs composites, the diffraction pattern appeared at 2 theta of 26.2˚ for SWCNTs correspond to (002) and 44.1˚ for Ag-NPs correspond to (200)[16] as shown in figure (5c). These results compared with the standard JCPDS line given in table (3.1) with estimated the crystal size via the Scherrer formula Eq. (1).

Table 1. Crystal size of Ag-NPs, SWCNTs/Ag NPs and MWCNTs/Ag NPs as estimated via Scherrer formula.

Sample	**2Theta (degree)**	**cos θ**	**β (degree)**	**Avg. crystal size (D) nm**	**(hkl)**
Ag-NPs	38.1	0.94	0.19	0.58	(111)
	44.3	0.926	0.24		(200)
	64.5	0.84	0.29		(220)
	77.5	0.77	0.48		(311)
MWCNTs/Ag NPs	26.2	0.97	1.2	0.88	(002) CNTs
	44	0.927	0.09		(100) CNTs
					(200) Ag NPs
SWCNTs/Ag NPs	26.2	0.97	0.84	0.91	(100) CNTs
	44.1	0.926	0.09		(200) Ag NPs

3.4 Atomic Force Microscope (AFM)

The surface morphology and topography of the Ag NPs layer is shown in Fig. 6a, SWCNTs/Ag NPs layer in Fig. 6b and MWCNTs/Ag NPs in Figure 6c.

The prepared Ag NPs were analyzed using AFM. Picture shown in Fig. 6a is for the morphology of the Ag NPs, it seems that the Ag NPs had homogenous distribution with small cluster and the surface roughness was 9.807 nm, 11.7 nm height and average diameter 28.06 nm.

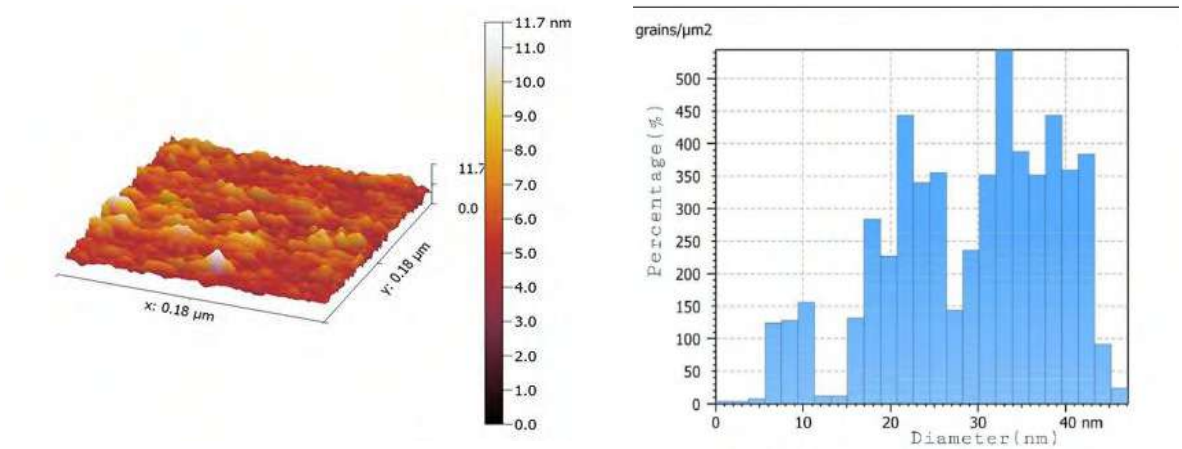

Fig. 6a. 3-D AFM image and distribution chart of pure Ag NPs thin film.

Fig. 6b displays the surface morphology and topography of the SWCNTs/Ag NPs layer observed from the micrograph of the AFM. It is noted that there was a normal distribution and homogeneous porous and 19.5 nm surface roughness, 19 nm height and average diameter was 58.14 nm.

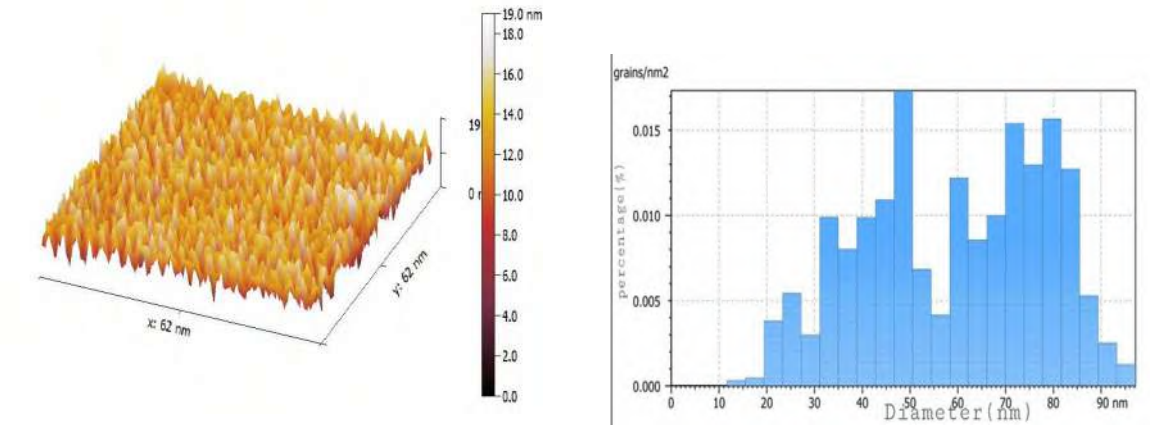

Fig. 6b. 3-D AFM image and distribution chart of SWCNTs/Ag NPs thin film.

The AFM of the MWCNTs/Ag NPs is shown in Fig. 6c the surface morphology of the MWCNTs/Ag NPs film had a good a uniform surface with regular distribution of the MWCNTs/Ag nanoparticles with the surface roughness was 39.5 nm, 22 nm height and average diameter 112.5 nm.

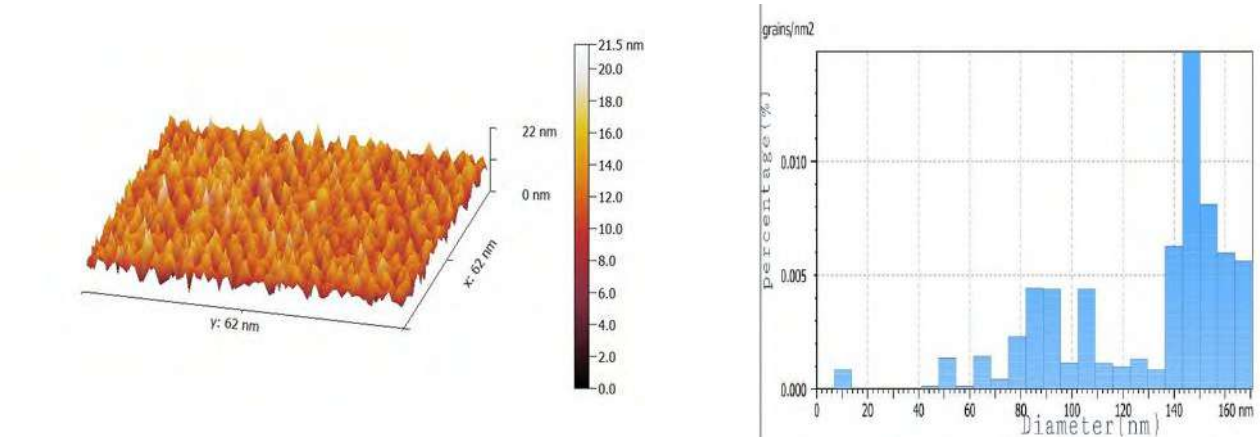

Fig. 6c. 3-D AFM image and distribution chart of MWCNTs/Ag NPs thin film.

3.5 Field Emission Scanning Electron Microscope (FESEM)

Scanning Electron Microscope images give the nanoparticles distribution, nanoparticles size, show shape and the structure of nanocrystal, mode FESEM from MIRA3 TESCAN, where high-resolution images of the surface of a sample is acquired. From Fig. 7a the FESEM shows spherical clustered and luminous spots (indicated by circles and in inset image) that correspond to silver nanoparticles, the average particle size of Ag NPS were ranging about (50-80nm).

These nanotubes were subsequently decorated with silver nanoparticles, Fig. 7 b, c show the FESEM of decoration Ag NPs on MWCNTs SWCNTs. The light spots on the CNT surfaces are the

silver nanoparticles. The image shows that the nanoparticles on the surface of the CNTs are fairly homogeneously distributed and the density of the attached nanocrystals is high.

Metal nanoparticles are easy to agglomerate, so that NPs are conjugated with CNTs to overcome these problems related to the stabilization, separation and recovery of NPs and prevent their aggregation [2].

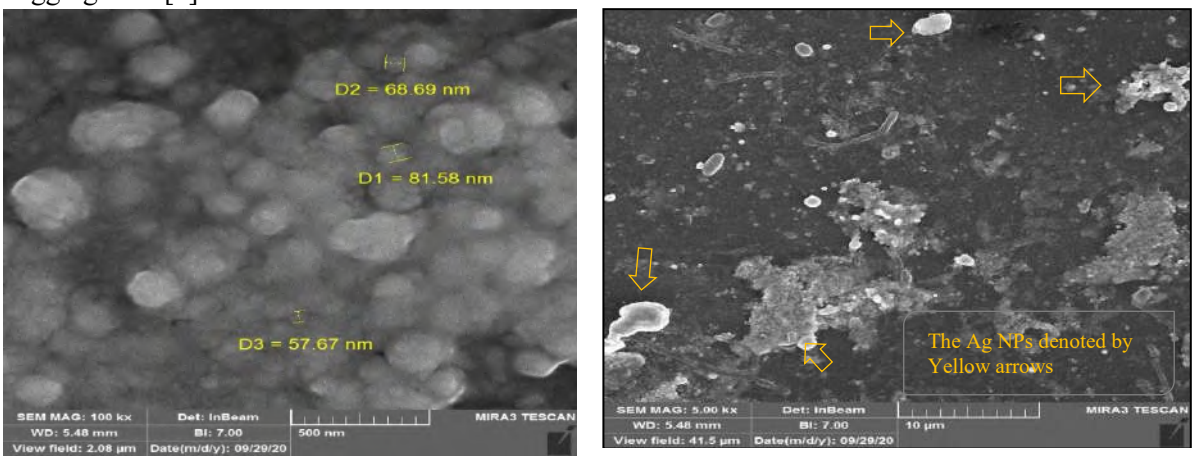

Fig. 7a. FESEM images of pure Ag NPs with different magnification (500 nm &10 µm).

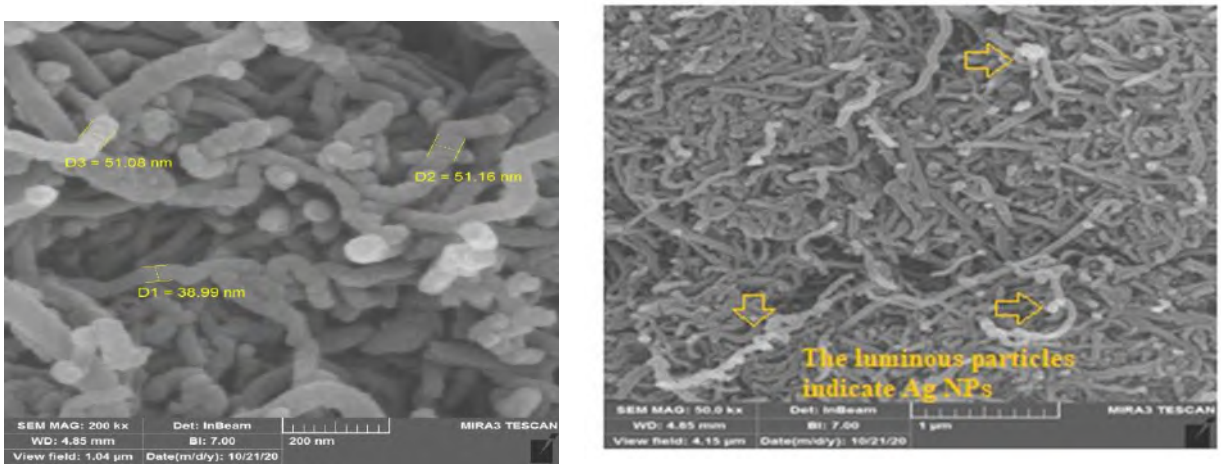

Fig. 7b. FESEM images of MWCNTs/Ag NPs with different magnification (200 nm & 1 µm).

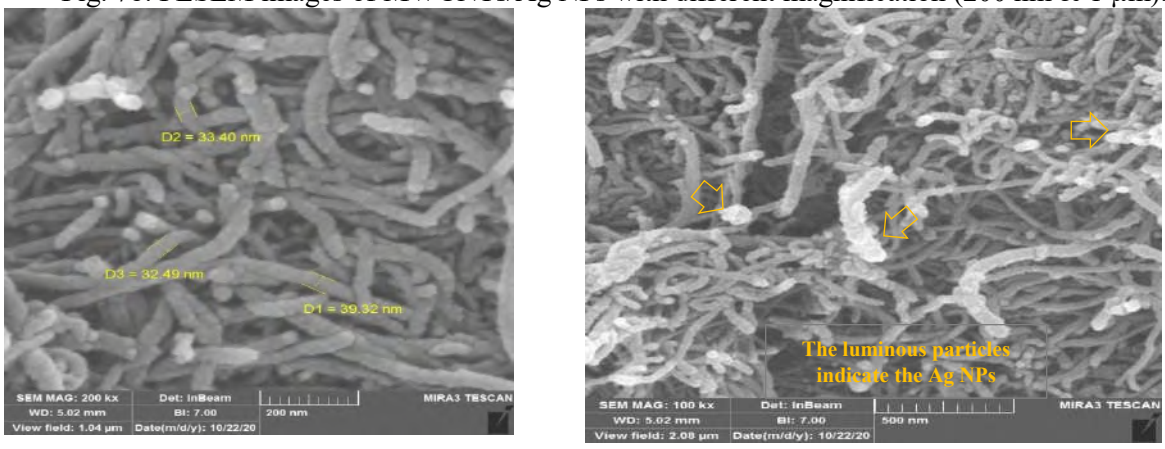

Fig. 7c. FESEM images of SWCNTs/Ag NPs with different magnification (200 nm & 500 nm).

3.6 Hall Effect Measurement

The Hall Effect was used to study the electrical properties of CNTs and Ag NPs (charge concentration, conductivity, carrier mobility, Hall coefficient and resistivity). Table 2 shows the Hall measurements parameter for CNTs and Ag NPs.

Table 2. Hall Measurement parameter.

Parameter	Ag NPs	SWCNTs/Ag NPs	MWCNTs/Ag NPs
Charge Concentration(1/cm^3)	$1.08*10^{13}$	$1.99*10^{22}$	$1.80*10^{22}$
Conductivity (1/ Ω.cm)	$2.36*10^{-1}$	$1.03*10^{4}$	$8.83*10^{4}$
Mobility (Cm^2/Vs)	$1.36*10^{5}$	3.22	$3.07*10^{1}$
Hall coefficient ($cm^{-3}.C^{-1}$)	$-5.78*10^{5}$	$3.14*10^{-4}$	3.4810^{-4}
Resistivity (Ω.cm)	4.23	$9.708*10^{-5}$	$1.132*10^{-5}$
Type	N-type	P-type	P-type

The table shows that electric conductivity CNTs/Ag NPs become much higher than Ag NPs and the concentration of carriers increase when CNTs decorated with Ag NPs, Also It can be seen that CNT decorated with Ag NPs converts from n-type to p-type when Ag NPs add to CNTs, which results in a shift in the Fermi energy from the valence band to mid-gap. The electrical transport of CNT/Ag NPs is improved when the CNTs decorated with Ag NPs.

4. Conclusions

The decoration of MWCNTs and SWCNTs with silver nanoparticles synthesized through exploding wire method was studied. Due to the simplicity of this synthesis, low-cost fabrication of large quantities of long-lived silver nanoparticles, the exploding wire method can be suggested to prepare the silver nanoparticles. It was found that the nanoparticles were spatially well dispersed on the carbon nanotubes. Integration of carbon nanotubes with AgNPs significantly improved CNTs optical absorption. CNT / Ag NPs absorb light in the range of 300-1000 nm better than CNTs alone, which demonstrates the special effects of noble metal on optical absorption of CNTs. The FTIR spectra proving the interaction between the (SWCNTs and MWCNTs) molecules and Ag nanoparticles. The FESEM image shows that the nanoparticles on the surface of the CNTs are fairly homogeneously distributed. It is suggested that decoration the CNT surface with AgNPs could change its characteristics of the materials from n-type to p-type. The experimental results have shown that the CNT/ Ag NPs can become important building blocks for nanoscale photodetector applications.

Reference

1. Hongzhi Chen, Student Member, IEEE, Ning Xi, Fellow, IEEE, King W. C. Lai, Member, IEEE, Carmen K. M. Fung, Member, IEEE, and Ruiguo Yang, Student Member, IEEE. SEPTEMBER 2010. *IEEE T. NANOTECHNOL.* **9** 5
2. Duha S. Ahmed, Mohammad R. Mohammed and Mustafa K.A. Mohammed. 2020.**10** 127

3. Amrut S. Lanje, Satish J. Sharma and Ramchandra B. Pode. 2010. *Scholars Research Library Archives of Physics Research* **1** (1) 49
4. Dilermando N. Travessaa, Fábio S. da Silvab, Fernando H. Cristovana, Alberto M. Jorge Jr.c, Kátia Regina Cardosoa. 2014 *Mat. Res.* **17**(3) 687
5. M.Ullmann, S. K.Friedlander, A.Schmidt-Ott 2002 J. Nanopart. Res. **4 (**6) 499
6. A.S. Edelstein, R. C. Cammarata. 1996. *Institute of Physics Publishing, Bristol* 596
7. L,Araujo, R. Lobenberg, J.Kreuter, J. 1999. *Drug Target* **6** 373
8. A.Sarkar, Hao Wang, Theda Daniels-Race. 2014 *Electron. Mater. Lett.* **10** (2) 325
9. Waleed k. Mahmood, Rawa k. Ibrahim, Asama N. Naje. 2017. *J. Sci.* **58** (4B) 2090
10. Yusliza Yusof, Mohd Irwan Zaidi, and Mohd Rafie Johan. 2016. *J. Nanomat.* ID 6141496, 9 pages.
11. Waleed Kh. Mahmood, Asama N. Naje. 2018 *J. Nano- Electro. Phys.***10** (5) 05020
12. A. Yu,Q.Wang, J. Yong 2012 *Electrochimic Acta* **74** 111
13. Zhaofei Ouyang, Jingfeng Li, Jinhui Wang,a Qian Li,a Tongyang Ni,a Xiaoyuan Zhang,a Haixia Wang, Qing Li, Zhiqiang Su and Gang Wei. 2013 *J. Mater. Chem. B* **1** 2415
14. DAS, R., DAS, B., SHUKLA, R., PRABAHARAN, T. and SHYAM, A.2012. *Sadhana* **37**(5) 629
15. Y.A. Kotov 2003 *J. Nanopart. Res.* **5** 539.
16. Waleed K. Mahmood, Asama N. Naje.2017. University of Baghdad.
17. Ngo X. Dinh, Nguyen V. Quy, Tran Q. Huy and Anh-T. Le.2015.Uneversity of Technology, Hanoi 10000,Vietnam.
18. Anouar, M., Jbilat, R., Le Borgne, V., Ma, D. and El Khakani, M.2016 *Mater Renew Sustain Energy* **5**(1)
19. Lin, Y., Watson, K., Fallbach, M., Ghose, S., Smith, J., Delozier, D., Cao, W., Crooks, R. and Connell, J. 2009 *ACS Nano* **3**(4)871
20. Baudot, C., Tan, C. and Kong 2010 *Infrared. Phys. Techno*l. **53** (6) 434
21. Hoyos-Palacio, L., Cuesta Castro, D., Ortiz-Trujillo, I., Botero Palacio, L., Galeano Upegui, B., Escobar Mora, N. and Carlos Cornelio, J. 2019 *J. Mater. Res. Technol.* **8**(6) 5893

Investigation and Study of Photonic Current Rate in Bremsstrahlung process

Investigation and Study of Photonic Current Rate in Bremsstrahlung process

Rana Issa Bkmurd[1], Hadi J M Al-Agealy[2], Ahmed M Ashwiekh[2]

[1]Ministry of Culture, Iraqi National Library and Archives
[2]Department of Physics, College of Education for Pure Science Ibn-ALHaitham, University of Baghdad

E-mail: hadialagealy2016@gmail.com

Abstract. In this paper, we investigate and study quantum theoretical of quark-gluon interaction modeling in QGP matter formatted. In theoretical modeling, we can use a flavor number, strength coupling, critical energy $T_c = 190$ MeV, system energy (400-650)MeV , fugacity of quark and gluon, and photon energy in range of 1-10 GeV parameter to calculation and investigation spectrum of photon rate. We calculation and study the photon rate produced through bremsstrahlung processes from the stable QGP matter. The photon rate production from $cg \rightarrow dg\gamma$ and $cg \rightarrow bg\gamma$ systems at bremsstrahlung processes are found to be increased with increased fugacity, decreased strength coupling, decreased the photons energy and temperature of system. The photons rate in $cg \rightarrow dg\gamma$ is increases a little compared to the $cg \rightarrow bg\gamma$ systems.

Keywords: Photonic Current Rate, Bremsstrahlung process.

1. Introduction

The elementary particle is considered as an one important field in physics because it uses a much more scientific method to study and investigate many facts to construction nature. Many theories introduced to study and understand the structure of nucleons and quark-gluon interaction formation the universal phase after the big bang stage [1] . Now ,there are different experimental results on hadron observable in collisions at the Relativistic Heavy Ion-Collision (RHIC) ,its showing that hadron must be produced in high energy collisions through quark–gluon plasma (QGP) formatted fireball [2]. The most important idea of heavy collisions is to study and create a strong interaction material; it obtains from the transformation of containment matter into (hadronic state) to a quark - gluon free. The quark - gluon interaction has found in the superfluid state form named quark-gluon plasma (QGP) and its produced in at Relativistic Heavy Ion-Collision (RHIC)[3]. The dynamics of quantum chromo dynamic media were discovered in the CERN Large Hadron Collider (LHC) and the Brookhaven National Laboratory in Relativistic Heavy Ionic Collider (RHIC) implies early equilibration of a quark-gluon system [4]. The quark-gluon plasma was existed for a short time ~several fm in volume~ 100 fm^3 and it can impossible detection the QGP state of matter directly. On the other hand, the different indirect signatures had been used to detect such as; strangeness enhancement, dilepton spectra, suppression and photon emission [5]. In fact, the theoretical approach to study and investigate

the elementary particles has been introduced by Standard Model; it's evolved in 1970's. The fundamentals of Standard Model are quantum chromodynamics and electroweak and theory [6]. The strength coupling is controlled on calculations of the photon production rate from a quark –gluon interaction in QCD medium and its possible limited only in certain situations. In weakly coupled quark with gluon indicate that the quark-gluon plasma (QGP) has a strength coupling smaller than one to complete estimation the photons rate [7]. Contrary to molecules and atoms, the quarks and gluons haven't found in freely, but were confined in hadronic state. This state was quite similar to decomposition of the magnetic pole north and south and never isolated each other [8]. The rate of photon emission from QGP matter is has estimation using phase-space distributed. They are assume to be Bose-Einstein and Fermi-Dirac distributions, while the lattice QCD estimation indicated that QGP system has been strong interaction ,for both non-ideal corrections taken into account the photon rate[9].

2. Theory

The number of photonic emitting rate production per unit time per unit volume via the usual QCD theory is [10].

$\Gamma_{qg}^{Br}(E,P) = -\frac{1}{(2\pi)^3}\mathrm{F}_B(\mathrm{E})\mathrm{Im}\prod_{qg}^{Br}(E,P)$……..(1)

Where $\mathrm{F}_B(\mathrm{E})$ is the distribution function of Bose-Einstein and $\mathrm{Im}\prod_{qg}^{Br}(E,P)$ is the imaginary part of the retarded self-energy polarization tensor of the photons at Bremsstrahlung processes. The distribution function of Bose-Einstein$\mathrm{F}_B(\mathrm{E})$ is given by [11].

$\mathrm{F}_B(\mathrm{E}) = \frac{1}{e^{E/T}-1}$……..(2)

Where E is the energy of photon and T is the heat energy of the system. Then the imaginary part $\mathrm{Im}\prod_{qg}^{Br}(E,P)$given by [12].

$\mathrm{Im}\prod_{qg}^{Br}(E,P) = (-1)\frac{NC_F}{\pi^4}e^2{g_{Br}}^2\frac{T}{E^2}|\mathrm{J}_{\mathrm{T}-L}|\int_0^\infty\left(\mathrm{F}_q(P)-\mathrm{F}_q(P+E)\right)(P^2+(P+E)^2)\,dP$…….(3)

Where N is an overall degeneracy factor , C_F is the Casimir operator of the system unitary group SU(N_c) , α is the quantum electrodynamics coupling, $\sum e_q^2$ is the square charge of quark ,${g_{Br}}^2$ is the square quantum chromodunamic coupling ,T is the heat energy of system ,E is the energy of photons ,$\mathrm{F}_q(P)$ is the fugacity of quark ,$\mathrm{J}_{\mathrm{T}-L}$ is the integral of the self-energy . The variance of constants self-energy is given by integral [13].

$\mathrm{J}_{\mathrm{T}-L} = \mathrm{J}_{\mathrm{T}} - \mathrm{J}_{\mathrm{L}}$…….(4)

J_{T}andJ_{L} are the dimensionless constants of the self-energy. Inserting Eq.(4) in Eq.(3), then imaginary part is reduce to .

$\mathrm{Im}\prod_{qg}^{Br}(E,P) = (-1)\frac{NC_F}{\pi^4}e^2{g_{Br}}^2\frac{T}{E^2}|\mathrm{J}_{\mathrm{T}}-\mathrm{J}_{\mathrm{L}}|\int_0^\infty\left(\mathrm{F}_q(P)-\mathrm{F}_q(P+E)\right)(P^2+(P+E)^2)\,dP$…….(5)

Introduce the electric charge of quarks $\sum e_q^2$ in Eq.(5) to given .

$\mathrm{Im}\prod_{qg}^{Br}(E,P) = (-1)\frac{NC_F}{\pi^4}e^2{g_{Br}}^2\frac{T}{E^2}|\mathrm{J}_{\mathrm{T}}-\mathrm{J}_{\mathrm{L}}|\sum e_q^2\int_0^\infty\left(\mathrm{F}_q(P)-\mathrm{F}_q(P+E)\right)(P^2+(P+E)^2)\,dP$…….(6)

The Juttner distribution function for quark$\mathrm{F}_q(P)$ and $\mathrm{F}_q(p+E)$ are given by [14].

$\mathrm{F}_q(P) = \frac{\lambda_q}{e^{\frac{(p)}{T}}+\lambda_q}$ …… .(7)

$\mathrm{F}_q(p+E) = \frac{\lambda_q}{e^{\frac{p+E}{T}}+\lambda_q}$……(8)

Where $\lambda_q$is the fugacity parameter. Inserting Eqs.(7) and (8) in Eq.(6) and simply to reduced .$\mathrm{Im}\prod_{qg}^{Br}(E,P) =$

$$(-1)\frac{NC_F}{\pi^4}e^2{g_{Br}}^2\frac{T}{E^2}|\mathrm{J_T}-\mathrm{J_L}|\sum e_q^2\times\left[\int_0^\infty\frac{\lambda_q\left(2P^2+2PE+E^2\right)}{e^{\frac{(p)}{T}}+\lambda_q}dP-\right.$$

$$\left.\int_0^\infty\frac{\lambda_q\left(2P^2+2PE+E^2\right)}{e^{\frac{p+E}{T}}+\lambda_q}dP\right]\text{.....(9)}$$

The solve of the integral term give results

$$\left[\int_0^\infty\frac{\lambda_q\left(2P^2+2PE+E^2\right)}{e^{\frac{(p)}{T}}+\lambda_q}dP-\int_0^\infty\frac{\lambda_q\left(2P^2+2PE+E^2\right)}{e^{\frac{p+E}{T}}+\lambda_q}dP\right]=\Lambda\left(\lambda_q,E,T\right)=\left[2T^3\Gamma(3)+2\mathrm{E}T^2\Gamma(2)+\right.$$

$$E^2T\Gamma(1)\left][\frac{{\lambda_q}^1}{1^3}\left(1+e^{\frac{-E}{T}}\right)-\frac{{\lambda_q}^2}{2^3}(1+e^{\frac{-2E}{T}})+\frac{{\lambda_q}^3}{3^3}(1+e^{\frac{-3E}{T}})-\frac{{\lambda_q}^4}{4^3}(1+e^{\frac{-4E}{T}})+\frac{{\lambda_q}^5}{5^3}(1+e^{\frac{-5E}{T}})-\right.$$

$$\cdots\frac{{\lambda_q}^n}{n^3}(1+e^{\frac{-nE}{T}})\text{....(10)}$$

Inserting Eq.(10) in Eq.(9) to obtain .

$$\mathrm{Im}\prod_{qg}^{Br}(E,P)=(-1)\frac{NC_F}{\pi^4}e^2{g_{Br}}^2\frac{T}{E^2}|\mathrm{J_T}-\mathrm{J_L}|\sum e_q^2\,\Lambda\left(\lambda_q,E,T\right)\text{.....(11)}$$

The coupling parameter for QCD theory is given by [15].

$$\alpha_1^{sc}=\frac{{\mathrm{g_{Br}}}^2}{4\pi}\text{.....(12)}$$

Where $\mathrm{g_{Br}}$ is the constant of strong coupling interaction.The Casimir operator C_F is corresponded to representation of color charge is [16].

$$\boldsymbol{C_F}=\frac{(\boldsymbol{N_c^2-1})}{\boldsymbol{2N_c}}\qquad\text{...}\text{.....(13)}$$

where N_c is the color number constant.

Inserting Eq.(12) and Eq.(13) in Eq.(11) to obtain .

$$\mathrm{Im}\prod_{qg}^{Br}(E,P)=(-1)\frac{N}{\pi^3}\frac{\mathbf{16}}{\mathbf{3}}e^2\alpha_1^{sc}\sum e_q^2\,|\mathrm{J_T}-\mathrm{J_L}|\frac{T}{E^2}\Lambda\left(\lambda_q,E,T\right)\text{.... (14)}$$

The quantum electrodynamics QED coupling constant [17].

$$\alpha=\frac{e^2}{4\pi}\text{ ..... (15)}$$

substituting Eq.(**15**) in Eq.(**14**) to obtain .

$$\mathrm{Im}\prod_{qg}^{Br}(E,P)=(-1)4\frac{N}{\pi^2}\frac{\mathbf{16}}{\mathbf{3}}\boldsymbol{\alpha}\alpha_1^{sc}\sum e_q^2\,|\mathrm{J_T}-\mathrm{J_L}|\frac{T}{E^2}\Lambda\left(\lambda_q,E,T\right)\text{.... (16)}$$

Inserting Eq.(16) in Eq.(1) to obtain.

$$\Gamma_{qg}^{Br}(E,P)=\frac{N}{\pi^5}\frac{\mathbf{8}}{\mathbf{3}}\boldsymbol{\alpha}\alpha_1^{sc}\sum e_q^2\,|\mathrm{J_T}-\mathrm{J_L}|\frac{T}{E^2}\mathrm{F}_B(\mathrm{E})\Lambda\left(\lambda_q,E,T\right)\text{.... (17)}$$

The overall degeneracy factor N in QCD theory is equal to quantum number of color $N_c=3$, then Eq.(17) becomes.

$$\Gamma_{qg}^{Br}(E,P)=\frac{\mathbf{8}}{\pi^5}\boldsymbol{\alpha}\alpha_1^{sc}\sum e_q^2\,|\mathrm{J_T}-\mathrm{J_L}|\frac{T}{E^2}\mathrm{F}_B(\mathrm{E})\Lambda\left(\lambda_q,E,T\right)\text{.... (18)}$$

The Bosonic function distribution for gluon $\mathrm{F}_B(\mathrm{P})$ [18] and simply to .

$$\mathrm{F}_B(\mathrm{E})=\frac{\lambda_g}{e^{\frac{E}{T}}-\lambda_g}=\frac{1}{\frac{E}{e^{\frac{E}{T}}}-1}\approx\lambda_g e^{\frac{-E}{T}}\text{.....(19)}$$

The Eq.(18) becomes with Eq.(19) is.

$$\Gamma_{qg}^{Br}(E,P)=\frac{\mathbf{8}}{\pi^5}\boldsymbol{\alpha}\alpha_1^{sc}\sum e_q^2\,|\mathrm{J_T}-\mathrm{J_L}|\frac{T}{E^2}\lambda_g e^{\frac{-E}{T}}\Lambda\left(\lambda_q,E,T\right)\text{.... (20)}$$

The strength coupling constant is given by [19].

$$\alpha_1^{sc}=\frac{6\pi}{(33-2n_F)ln(\frac{\mu_1}{\mu_0})}\text{.....(21)}$$

where μ_1 is the momentum or heat energy and $\mu_1\approx 8T$ and μ_0 is refers to heat energy or momentum in hadrons phase $\mu_0\approx T_{cr}$,whereT_{cr} is the critical temperature .

3. Results

To obtain the spectrum of photons rate at bremsstrahlung process depend on the quantum chromodynamic QCD theory one can be calculate the strength coupling through estimation the flavor number .The estimation of flavor number included in estimating the summed on total flavor number $N_f = \sum_{n=1}^{6} N_{fn}$ using Table 1 for system species, the system $cg \to dg\gamma$ in being the number flavor $n_f = 6$of chram quark (n_f =4) and down quark (n_f =2) and the system $cg \to bg\gamma$in being the number flavor $n_f = 9$of chram quark (n_f =4) and bottom (n_f =5) in the system.

Table 1. The main properties of quarks [20].

Fermions	Name	Mass	Electric Charge	N_f
Quarks	Up (u)	$2.3^{+0.7}_{-0.5}\,MeV/c^2$	$+{}^{2}/_{3}\ e$	1
	Down (d)	$4.8^{+0.5}_{-0.3}\,MeV/c^2$	$-{}^{1}/_{3}\ e$	2
	Strange (s)	$95 \pm 5\,MeV/c^2$	$-{}^{1}/_{3}\ e$	3
	Charm (c)	$1.275 \pm 0.025\,GeV/c^2$	$+{}^{2}/_{3}\ e$	4
	Bottom (b)	$4.18 \pm 0.03\,GeV/c^2$	$-{}^{1}/_{3}\ e$	5
	Top (t)	$173.2 \pm 0.9\,GeV/c^2$	$+{}^{2}/_{3}\ e$	6

In order to calculate the photons rate , we can evaluated the strength coupling ,total charge and total flavor number . For the strength coupling calculation for quarks-gluon interaction at bremsstrahlung , the photons are yielding at temperature around (400,450,500,550,600 and 650 MeV) are necessary. The strength coupling can be calculated using Eq.(21) and so one can use summation of the flavor number $n_f = (4 + 2) = 6$ for $cg \to dg\gamma$and $n_f = (4 + 5) = 9$ for $cg \to bg\gamma$ system with the critical temperature $T_c = 190$ and the temperatures of system in the range (400 to650 MeV),results are shown in table (2) for $cg \to dg\gamma$and $cg \to bg\gamma$ systems respectively.

Table 2. Results of strength coupling for $cg \to dg\gamma$and $cg \to bg\gamma$ systems using the critical temperature$T_c = 190$.

$TMev$	Running strength coupling α_1^{sc}	
	$cg \to dg\gamma$	$cg \to bg\gamma$
	$n_f = 6$	$n_f = 8$
400	0.3178	0.3926
450	0.3051	0.3769
500	0.2945	0.3638
550	0.2856	0.3528
600	0.2779	0.3433
650	0.2712	0.3350

A numerical theoretical calculation of the spectra of photons emission from quark-gluon interaction at bremsstrahlung process using the Eq.(20) and MATLAP program with taken $\boldsymbol{\alpha} = \frac{1}{137}$, , $J_T \approx 4.45$ [21] , $J_L \approx -4.26$ [21], $\lambda_q = 0.068$ [13] and $\lambda_g = 1$[13] ,results are shown in Table 3 and Figure 1 for $cg \to dg\gamma$ system and Table 4 and Figure 2 for system.

Table 3. Rate of photon production (or yield) $\Gamma_{qg}^{Br}(E,p)$ at $T_c = 190\ MeV$ with $\lambda_g = 1$, $\lambda_q = 0.068$ in system $cg \to dg\gamma$ has flavor number $n_f = 6$ in Bremishtahlang process.

$\Gamma_{qg}^{Br}(E,p)\,\frac{1}{GeV^2 fm^4}$

	T=400Mev	T=450Mev	T=500Mev	T=550Mev	T=600Mev	T=650Mev
$E_\gamma\ GeV$	α_1^{sc} $= 0.3178$	α_1^{sc} $= 0.3051$	α_1^{sc} $= 2945$	α_1^{sc} $= 0.2856$	α_1^{sc} $= 0.2779$	α_1^{sc} $= 0.2712$
1	3.8143e-07	6.9616e-07	1.1750e-06	1.8681e-06	2.8317e-06	4.1294e-06
2	1.8614e-08	4.1965e-08	8.3138e-08	1.4974e-07	2.5067e-07	3.9629e-07
4	9.9024e-11	3.7603e-10	1.1217e-09	2.8040e-09	6.1296e-09	1.2077e-08
6	6.1936e-13	4.0584e-12	1.8691e-11	6.6523e-11	1.9483e-10	4.9076e-10
8	4.0242e-15	4.5736e-14	3.2691e-13	1.6655e-12	6.5717e-12	2.1285e-11
10	2.6538e-17	5.2419e-16	5.8268e-15	4.2581e-14	2.2682e-13	9.4658e-13

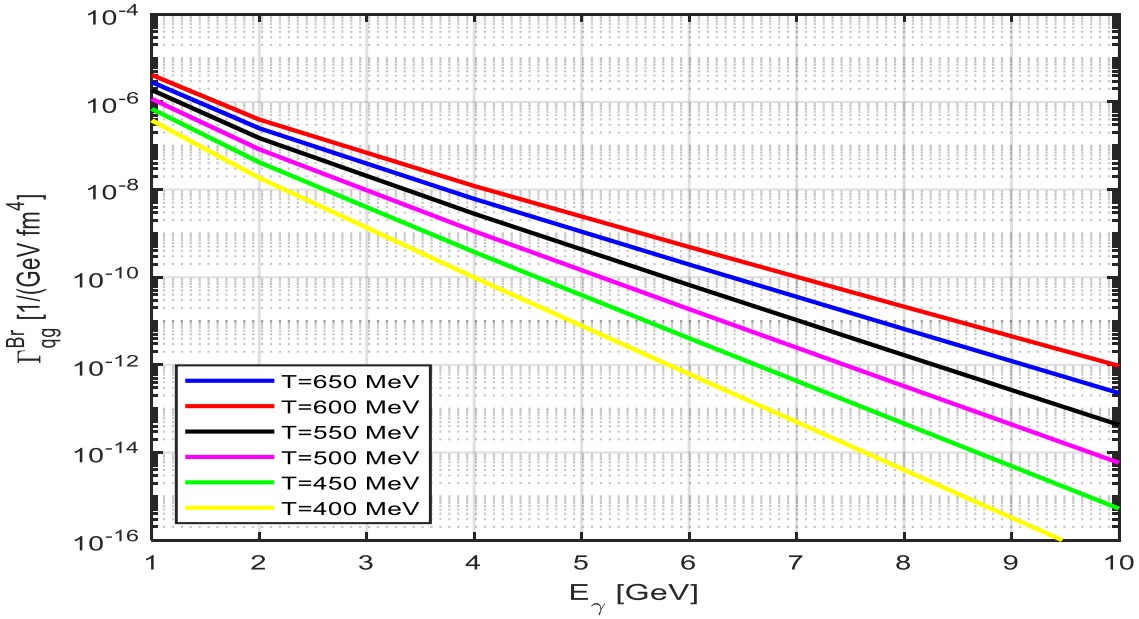

Figure 1. Rate of photon production $\Gamma_{qg}^{Br}(E,p)$ as a function of E_γ for $cg \to dg\gamma$ system at $T_c = 190\ MeV$.

Table 4. Rate of photon production $\Gamma_{qg}^{Br}(E,p)$ at $T_c = 190\ Mev$with $\tilde{\lambda}_g = 1$, $\tilde{\lambda}_q = 0.068$ in system $cg \to bg\gamma$ has flavor number $n_f = 9$ in Bremishtahlang process.

	$\Gamma_{qg}^{Br}(E,p)\frac{1}{GeV^2 fm^4}$					
	T=400Mev	T=450Mev	T=500Mev	T=550Mev	T=600Mev	T=650Mev
$E_\gamma\ GeV$	α_1^{sc} $= 0.3926$	α_1^{sc} $= 0.3769$	α_1^{sc} $= 0.3638$	α_1^{sc} $= 0.3528$	α_1^{sc} $= 0.3433$	α_1^{sc} $= 0.3350$
1	4.7120e-07	8.5998e-07	1.4514e-06	2.3077e-06	3.4980e-06	5.1009e-06
2	2.2995e-08	5.1841e-08	1.0270e-07	1.8498e-07	3.0967e-07	4.8952e-07
4	1.2233e-10	4.6452e-10	1.3857e-09	3.4638e-09	7.5722e-09	1.4918e-08
6	7.6514e-13	5.0135e-12	2.3089e-11	8.2176e-11	2.4068e-10	6.0621e-10
8	4.9713e-15	5.6499e-14	4.0383e-13	2.0574e-12	8.1183e-12	2.6292e-11
10	3.2784e-17	6.4755e-16	7.1979e-15	5.2601e-14	2.8020e-13	1.1693e-12

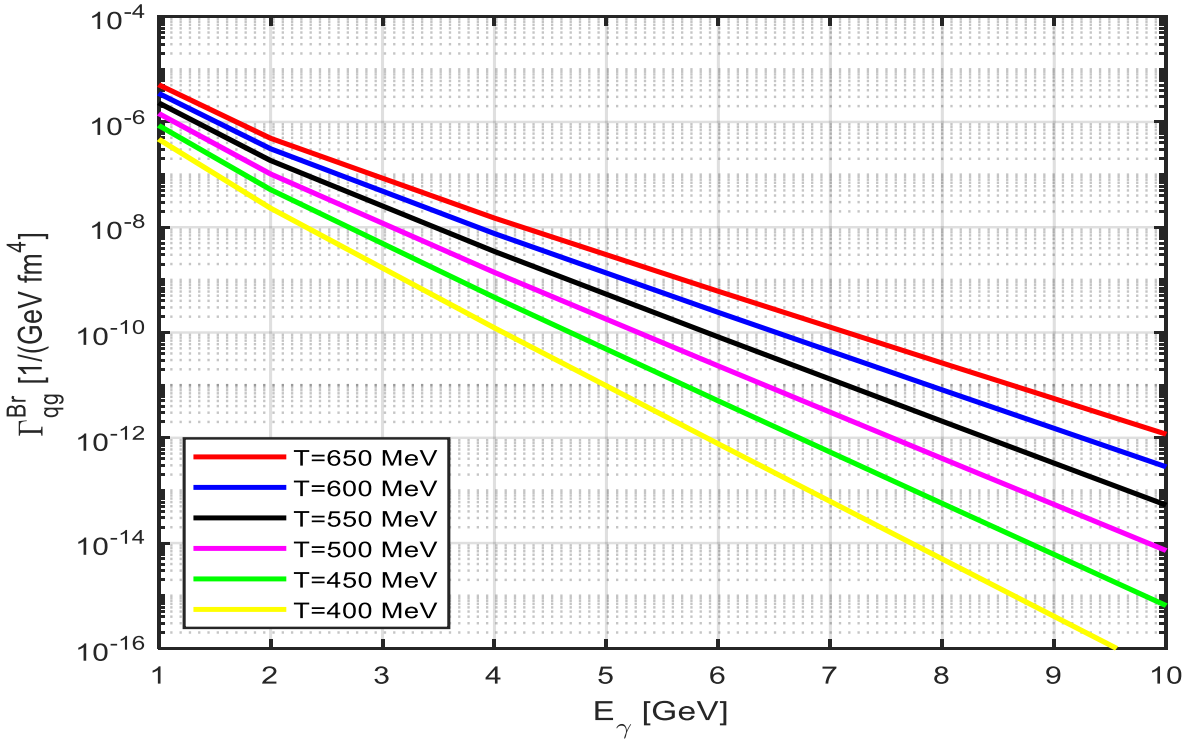

Figure 2. Rate of photon production $\Gamma^{Br}_{qg}(E,p)$ as a function of E_γ for $cg \to bg\gamma$ system at $T_c = 190\ MeV$.

To compute the net electric charge for $cg \to dg\gamma$ and $cg \to bg\gamma$ systems at the bremsstrahlung processes can be estimated using the summation of all charges for quarks in the system and be deduced using the $\sum_i^n e_{qi}^2 = (\frac{2}{3})^2 + (\frac{-1}{3})^2 = {}^5/_9$ for both systems. However, the photons rate calculated with the same parameters except fugacity that taken $\lambda_q = 0.02$ [13] and $\lambda_g = 0.08$[13], results are shown in Table 5 and Figure 3 for $cg \to dg\gamma$ system and Table 6 and Figure 4 for system.

Table 5. Rate of photon production $\Gamma^{Br}_{qg}(E,p)$ at $T_c = 190\ MeV$ with $\lambda_q = 0.02$, $\lambda_g = 0.08$ in system $cg \to dg\gamma$ has flavor number $n_f = 6$ in Bremishtahlang process.

	$\Gamma^{Br}_{qg}(E,p)\frac{1}{GeV^2 fm^4}$					
	T=400Mev	T=450Mev	T=500Mev	T=550Mev	T=600Mev	T=650Mev
$E_\gamma\ GeV$	$\alpha_1^{sc} = 0.3178$	$\alpha_1^{sc} = 0.3051$	$\alpha_1^{sc} = 2945$	$\alpha_1^{sc} = 0.2856$	$\alpha_1^{sc} = 0.2779$	$\alpha_1^{sc} = 0.2712$
1	9.0239e-09	1.6468e-08	2.7792e-08	4.4185e-08	6.6969e-08	9.7656e-08
2	4.4054e-10	9.9318e-10	1.9675e-09	3.5436e-09	5.9319e-09	9.3772e-09
4	2.3437e-12	8.8999e-12	2.6549e-11	6.6366e-11	1.4508e-10	2.8584e-10
6	1.4659e-14	9.6055e-14	4.4238e-13	1.5745e-12	4.6113e-12	1.1615e-11
8	9.5244e-17	1.0825e-15	7.7373e-15	3.9420e-14	1.5554e-13	5.0377e-13
10	6.2811e-19	1.2407e-17	1.3791e-16	1.0078e-15	5.3684e-15	2.2404e-14

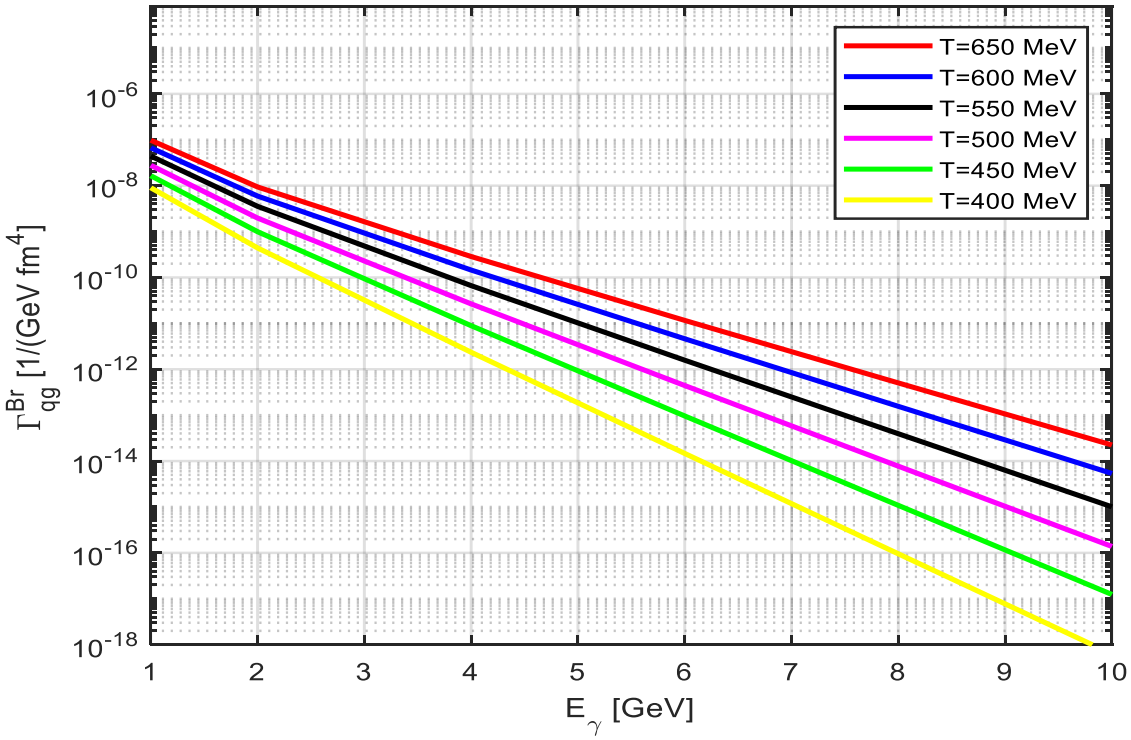

Figure 3. Rate of photon production $\Gamma^{Br}_{qg}(E,p)$ as a function of E_γ for $cg \to dg\gamma$ system at $T_c = 190\ MeV$.

Table 6. Rate of photon production $\Gamma^{Br}_{qg}(E,p)$ at $T_c = 190\ MeV$ with $\lambda_q = 0.02$, $\lambda_g = 0.08$ in system $cg \to bg\gamma$ has flavor number $n_f = 8$ in Bremishtahlang process.

	$\Gamma^{Br}_{qg}(E,p)\frac{1}{GeV^2 fm^4}$					
	T=400Mev	T=450Mev	T=500Mev	T=550Mev	T=600Mev	T=650Mev
$E_\gamma\ GeV$	$\alpha_1^{sc} = 0.3926$	$\alpha_1^{sc} = 0.3769$	$\alpha_1^{sc} = 0.3638$	$\alpha_1^{sc} = 0.3528$	$\alpha_1^{sc} = 0.3433$	$\alpha_1^{sc} = 0.3350$
1	1.1148e-08	2.0344e-08	3.4332e-08	5.4581e-08	8.2730e-08	1.2063e-07
2	5.4423e-10	1.2269e-09	2.4305e-09	4.3774e-09	7.3278e-09	1.1583e-08
4	2.8953e-12	1.0994e-11	3.2796e-11	8.1982e-11	1.7922e-10	3.5308e-10
6	1.8109e-14	1.1866e-13	5.4647e-13	1.9449e-12	5.6965e-12	1.4348e-11
8	1.1766e-16	1.3372e-15	9.5580e-15	4.8695e-14	1.9215e-13	6.2229e-13
10	7.7594e-19	1.5326e-17	1.7036e-16	1.2450e-15	6.6318e-15	2.7674e-14

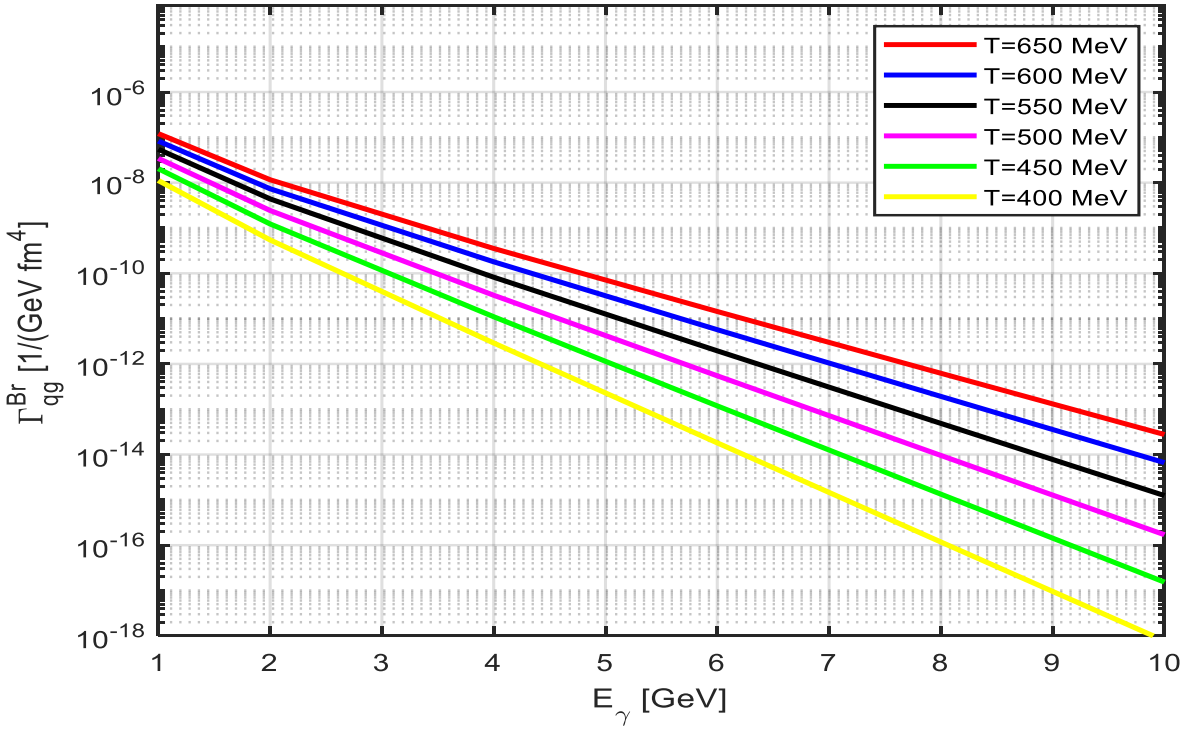

Figure 4. Rate of photon production $\Gamma^{Br}_{qg}(E,p)$ as a function of E_γ for $cg \rightarrow bg\gamma$ system at $T_c = 190\ MeV$.

4. Discussion

Due to quantum chromo dynamic theory, we present the theoretical results for the calculation the photon rate of photon production from bremsstrahlung at the different photon energy (1-10) GeV at critical temperature 90MeV with the different fugacity for quark and gluon. The calculation has been done for two different $cg \rightarrow dg\gamma$and $cg \rightarrow bg\gamma$quarks systems have total flavor number 6 and 9. From Table 2, it can be shown that running strength coupling α_1^{sc} decrees with increase the temperature of quark gluon system for both $cg \rightarrow dg\gamma$and $cg \rightarrow bg\gamma$ systems ,this because the confinement and asymptomatic behavior of quarks with concerning the fact or slow photons rate, the results show the photons rate increased with decreased the strength coupling and vice versa. Furthermore, the behavour of the strength coupling of $cg \rightarrow bg\gamma$ system is larger than the strength coupling of $cg \rightarrow dg\gamma$system because to effect of flavor number for the same critical energy and temperature of the system . To each system , the strength coupling α_1^{sc} and the photon rate spectrum of the emitted bremsstrahlung is calculated in photons energies$E_\gamma\ GeV$ ranging (1-10GeV) .The total photons rate of the bremsstrahlung emission has been obtained due to integrating the Eq.(9) on the photon momentum determined previously. For each photon energy and temperature of the system, the number of photons emission from bremsstrahlung is obtained by using Eq.(20). Briefly, the photon rate from bremsstrahlung are slowing down with increased energy of photons and the photons will be attenuatied in the QGP mater .As for the $cg \rightarrow dg\gamma$ system , the photon spectrum emitted in bremsstrahlung at energy $E_\gamma = 1GeV$ is faster compare with $E_\gamma = 10GeV$,this indicate for energy $E_\gamma = 10\ GeV$ the system emission photons by small rate . On the other hand, the emitted photons by bremsstrahlung with fugacity $\lambda_q = 0.02$, $\lambda_g = 0.08$ are lower than $\lambda_g = 1$ and $\lambda_q = 0.068$, that's means when increased fugacity lead to emission more photons for both systems. Consequently, the fugacity hasn't yet e much by effected on increasing, but the strength and flavor number can induce more photons to emit the higher energy bremsstrahlung. In conclusion ,the fugacity intense to the

photons spectrum obtained in bremsstrahlung process, this calculation will be supply more knowledge about reaction of quark and gluon to conceive the nature of shielding of the source In the this work, the bremsstrahlung emissions of $cg \rightarrow dg\gamma$and $cg \rightarrow bg\gamma$ systems are increased with decreasing strength coupling for photons energies in the interval 1-10 GeV. In Figures 1 to 4, the spectra of photons rate $\Gamma_{qg}^{Br}(E,P)$of the bremsstrahlung emerging by photon energy are represented in Tables (4-7). As expected, the photon emission rate of the bremsstrahlung at high-energy yield in small region of system around the QGP matter. Generally , , the photons emission rate values of the bremsstrahlung increased with increased fugacity and increased flavor and decreased strength coupling of then system . However, larger photons rate appear in the high-energy region, where $E_\gamma < 10\,GeV$ and reach a maximum at the energy of the photons $E_\gamma = 1\,GeV$. These differences indicate that the cross-section of reaction in $E_\gamma = 1\,GeV$ can be probable compare cross section in $E_\gamma = 10\,GeV$ in the high energy region (1-10)GeV .In all Figures (1-4) , the plotted forphotons rate are given same behavior with range high energy(1-10)GeV but the photons yield rate in Figure 3 and (4) with fugacity $\lambda_q = 0.02$, $\lambda_g = 0.08$are lowered than at Figures 1 and 2 with fugacity $\lambda_g = 1$ and $\lambda_q = 0.068$ by a factor $\sim 10^2$.

5. Conclusion

In concluding that the calculation of the photon rate through the bremsstrahlung process enhanced by flavor number, strength coupling fugacity, photon energy and temperature of the QGP mater system and give stability feature in quark –gluon system formation. The overall evaluation of photon emission rate production through the bremsstrahlung process and the spectra as a function of strength coupling and photon energy incorporate to give the results of photon yield rate. The photon rate for the bremsstrahlung has been increased with increased fugacity and increased flavor and decreased strength coupling of the system. Thus, the consideration of the quntum chromodynamic theory in the quark – gluon is the important role in the calculation of photon rate at the high energy. So, this theoretical model can be supply results to improve the other theoretical and experimental results.

References

[1] Al-Agealy H J M Al-Ani R K A and Ghulam R A 2017 *Int. J. Curr. Microbiol. App. Sci* **6** (3) 837.
[2] Zakharov B G 2016 *The European Physical Journal* ***C*** **76** (11) 609.
[3] Kumar Y and Singh S S 2013 *International Scholarly Research Notices* **2013**.
[4] Monnai A 2016 *Accel. Prog. Rep.* **49**.
[5] Long J L et al. 2005 *Physical Review* ***C*** **72** (6) P 064907.
[6] Al-Agealy, H J M and Sahib M J 2018 *Ibn AL-Haitham Journal For Pure and Applied Science* 179.
[7] Shen Chun et al. 2015 *Physical Review* ***C*** **91** (1) 014908.
[8] Roman P and Šumbera M 2017 *Universe* **3** (1) 7.
[9] Al-Agealy, H J M Ghadhban R Q and Hassooni M A 2020 *Ibn AL-Haitham Journal For Pure and Applied Science* **33** (4) 34.
[10] Kapusta J I and Gale C 2006 *Finite-temperature field theory Principles and application* Cambridge University Press.
[11] Miller David AB 2008 *Quantum mechanics for scientists and engineers* Cambridge University Press.
[12] Aurenche Patrick et al. 1998 *Physical Review* ***D*** **58** (8) 085003.
[13] Dutta D Sastry S V S Mohanty A K Kumar K and Choudhury R K *2000 Nuclear Physics A* **710** (3-4) 415.
[14] Long J L He Z J Ma Y G and Liu B 2005 *Physical Review C* **72** (6) 064907.
[15] Noel C W and Greenwood D A 2007 *An introduction to the standard model of particle physics* Cambridge university press.

[16] Peskin M E 1995 *Introduction To Quantum Field Theory* Perseus Books Publishing L.L.C.
[17] Schellekens A N 2015 *Beyond the Standard Model* Based on lectures given at the Radboud Universiteit, Nijmegen.
[18] Biro T S Van Doorn E Müller B Thoma M H and Wang X N 1993 *Physical Review C **48*** (3) 1275.
[19] Al-Agealy H J M Al-Ani R K A and Ghulam R A 2017 *Int. J. Curr. Microbiol. App. Sci* **6** (3) 837.
[20] Alam J E Sarkar S Roy P Hatsuda T and Sinha B 2000 *Annals of Physics **286*** (2) 159.

The effective of the inner radius of the iron free coil on the paraxial ray for magnetic lenses

The effective of the inner radius of the iron free coil on the paraxial ray for magnetic lenses

Ahmed K. Al-kadumi[1] and M. Al-Baghdadi[1]

[1]University of Kerbala\Collage of Education for pure Science

E-mail: muhammid.h@uokerbala.edu.iq

Abstract. In this paper, the magnetic flux density was studied using a mathematical model and different inner radius has been used for the iron free coil. The maximum value of magnetic field and the magnetic scalar potential was calculated. The paraxial ray can be studied using rung Kutta to solve the differential equation in the infinite and zero magnification condition, all results are determined using MATLAB program.

Keywords: electron optics, ions optics, iron free magnetic lenses, the potential of the electron lenses, electron microscopy

1. Introduction:

Electron optics is image formation by means of Deblorgle principle which can change the resolution by changing some parameters as electrons potential or the excitation of the lens[1, 2].The magnetic field can be stimulated using a mathematical model which has parameters and change the foundation of the lens [2, 3]. The effect of the geometry parameters on the results, the beam throw and emerge beams are studied[4].

There are many mathematical models which represent the magnetic field, and many models can represent the magnetic scalar potential. Using the inverse design procedure and the optimization to receive the optimal lenses, the non-dominated sorting genetic algorithm (2) and the electron optics simulations were combined and make a multi-objective optimization design tool for electron optics. To determine the function of the objective that varies with the parameters of the macroscopic electrical to need that optimize the electron optics system[5].

In general, the solution of the inverse design problems can be found by using mathematical models can control to the properties of the lens inside the scanning electron microscopy and transmission electron microscopy and determine analytically the first derivative and the second derivative for the model to design and simulate the lenses[6-8].

2. The Theoretical Treatment

Many mathematical models can represent the axial magnetic field. The axial distribution of the magnetic field for iron free magnetic lens can be represented by[9]

$$B(z)=\frac{\mu_o NI}{2lS}\left[\left(\frac{S}{2}-z\right)\ln\frac{R_2+\left(R_2^2+\left(z-\frac{S}{2}\right)^2\right)^{1/2}}{R_1+\left(R_1^2+\left(z-\frac{S}{2}\right)^2\right)^{1/2}}+\left(\frac{S}{2}+z\right)\ln\frac{R_2+\left(R_2^2+\left(z+\frac{S}{2}\right)^2\right)^{1/2}}{R_1+\left(R_1^2+\left(z-\frac{S}{2}\right)^2\right)^{1/2}}\right]\ldots(1)$$

Where$\mu_o = 4\pi * 10^{-7} H/m$ and $l = R_2 - R_1$. R_2, R_1,S and z are in meters, NI in ampere turns and B(z) in teslas [9].

$\sigma A = NI$……(2)

Where σ the density of the current, A the area of the cross-section of the energizing (N the turn numbers) I the electrical current coil [9].,

$$A = \gamma(R_2 - R_1)s = \gamma ls \ldots\ldots\ldots\ldots\ldots\ldots(3)$$

Where $\gamma$the packing factor (0.9) for the copper tape winding(s is coil thickness), one can imagine the system is [9].

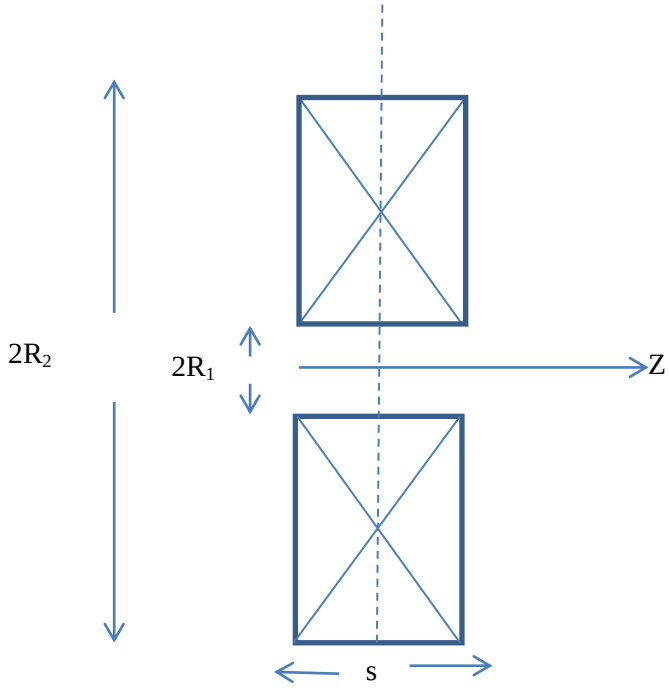

(iron free lens.) [9].

In the present work, the equation (1) can be modified as[modified from the researcher]:-

$$B(z)=\frac{\mu_o NI}{2lS}\left[\left(\frac{S}{2}-z\right)\ln\frac{R_2+\left(R_2^2+\left(z-\frac{S}{2}\right)^2\right)^{1/2}}{(R_1)^2+\left(R_1^2+\left(z-\frac{S}{2}\right)^2\right)^{1/2}}+\left(\frac{S}{2}+z\right)\ln\frac{R_2+\left(R_2^2+\left(z+\frac{S}{2}\right)^2\right)^{1/2}}{(R_1)^2+\left(R_1^2+\left(z-\frac{S}{2}\right)^2\right)^{1/2}}\right]..(4)$$

The inner diameter of the coil is [9]

D1=2R_1 ... ... (5)

This paper was to study the axial flux density and the paraxial ray by using the paraxial ray equation[10]:-

$$r''+\frac{\eta}{8V_r}B_Z^2(z)r=0 \text{ ... ... (6)}$$

Where r is the trajectory and V_r is the relativistically corrected accelerating voltage, η is the charge-to-mass quotient. by using the fourth order Runge-Kutta numerical method to solve differential equation (6).

The magnetic scalar potential can be calculated by using the equation[10]:-

$$B_z(z)=-\mu_o\frac{dV_z}{dz} \text{ ... . (7)}$$

Where V_z is the magnetic scalar potential, μ_o the magnetic permeability.

The inner diameter for the coil took (3, 5, 10, 15, 20) mm

Results and discussion: -

The magnetic lenses play important role in the scanning electron microscopy and transmission electron microscopy then the inverse design and the optimization draw the complete image for the lens properties which many researchers works in this line to receive for the perfect study to the samples [2, 11].

According to the equation (1), the distribution of the asymmetric magnetic field of the lens as a function of the optical axis as shown in the figure (1) with different inner radius (3,5,10,15,20), one can see the increasing the inner radius for the coil this causes decreasing the half width of the curve in addition to that the maximum value for the magnetic field distribution will be reduced as shown in the table (1)

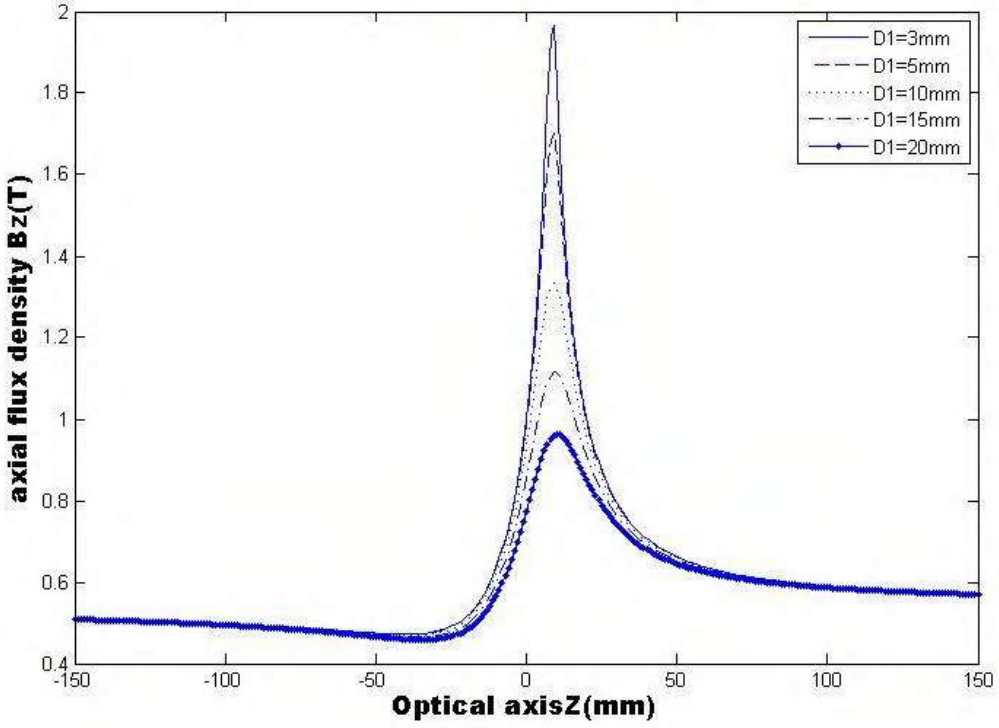

Figure 1. The axial flux density for different diameters.

Table 1. value for magnetic field distribution maximum for different value inner diameter

D1(mm)	B_{max}(T)
3	1.9658
5	1.7028
10	1.3333
15	1.1145
20	0.9617

The decreasing in the inner diameter may make the dissipation the magnetic line in the wide area in the space and this causes the weakness for the lens, this can be shown in the global papers[12, 13], which support this results. The paraxial ray under zero magnification for different inner diameters for the iron free coil can be shown in figure (2). One can show that the decreasing in the diameters causes arising the curve coming from a weakness interaction the ray with lines of the magnetic field, but in the general, the behaviour of the curve is normal focusing with the magnetic field to make the discover imagine the samples. The same speech for the figure (3) which shows the paraxial ray under infinite magnification figures (2) and (3)are deduced by using mathematical models in the magnetic field with assisted numerical determinations in the inverse design optimization with different values inner diameters[14, 15], these figures show the effects of interaction between the current and the magnetic fields which produces and the electron beam with different inner diameters. The magnetic scalar potential distributions as a function of the optical axis with variable inner diameters can be shown in the figure (4) which produced from equation (7),by this figure, one can show the decreasing the magnetic scalar potential with increasing the inner diameter this may decrease the maximum value for magnetic field distributions which effective to the magnetic scalar potential distribution because decreasing the area under the curve for the magnetic field distributions.

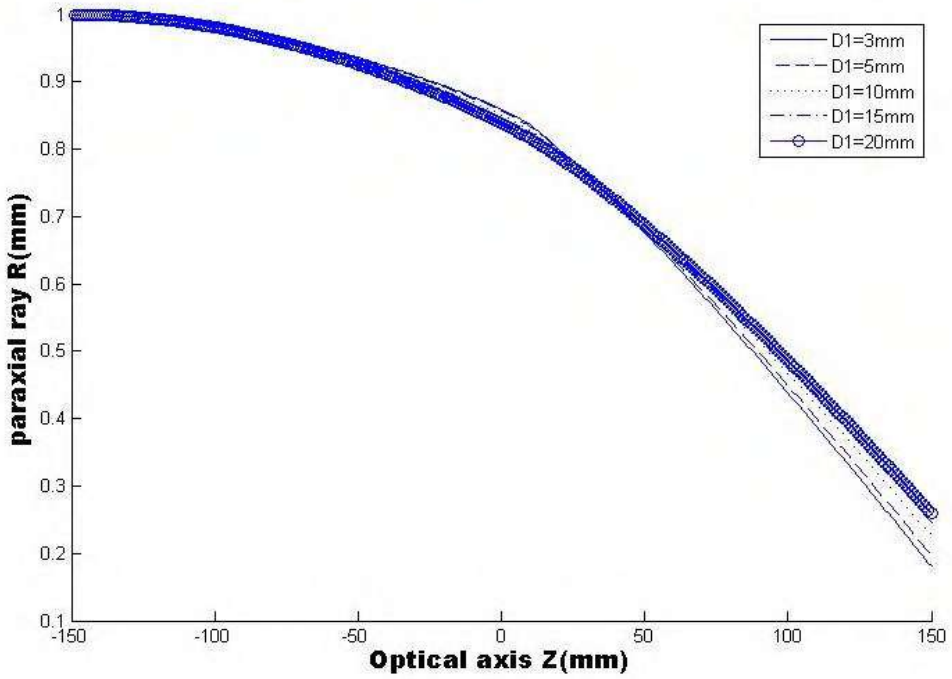

Figure 2. the paraxial ray for different inner diameters.

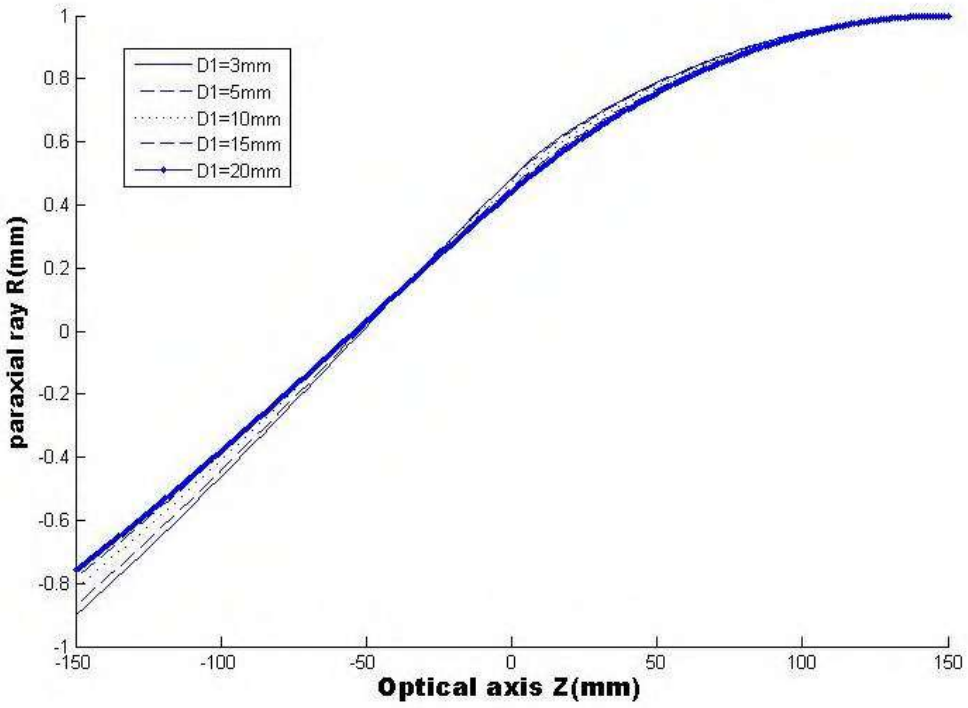

Figure 3. the paraxial ray under infinite magnification for different inner diameters.

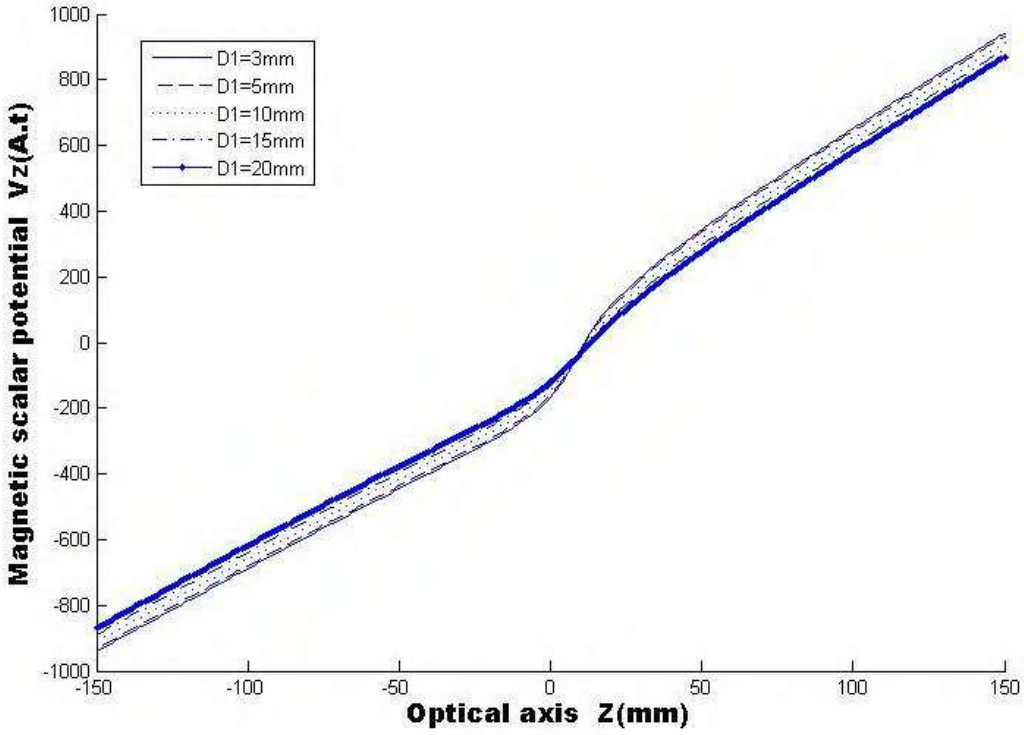

Figure 4. The magnetic scalar potential for different inner diameters.

3. Conclusion:

In this work, the effects of different inner diameter for the iron free lenses on the magnetic field distributions and the paraxial ray along the optical axis were studied. The increasing in the inner diameter causes a complication in the interaction between the electron beam and the magnetic field and makes the lens weaker. The increased diameter makes the effect and change in the magnetic scalar potential this may be due to the shape of asymmetric magnetic field distribution determined from variable inner diameter.

4. References

[1] Shao W 2019 Stacked dual beam electron optical system for THz integrated wideband traveling wave tube *Phys. Plasmas* **26** 063106.
[2] Guo G 2019 Modeling, simulation, and fabrication of electron optic system for applicationon 105 GHz high-power gyrotron *Int. J. Numer. Modell. Electron. Networks Dev. Fields* e2593.
[3] Kazmiruk V 2012 Scanning Electron microscopy *Janeza Trdine* **9** 51000Rijeka,croatia 1 842.
[4] Ma T, Zhao D and Zhang Z 2019 Modeling of A Converging Hollow Beam Electron Optic System for a Ka-Band EIK *Int. Vacuum Electron. Conf. (IVEC).* 2019. IEEE.
[5] Huang T 2019 A Multiobjective Optimization Design Tool for Traveling-Wave Tubes 'Electron Optics System. *IEEE Transac. Electr.Dev.* **66** 4 1965-1970.
[6] Liwei Z, Bai-cang Q and Guo-qiang N 1988 An inverse design of magnetic focusing coil for electrostatic and magnetic imaging *Optik* **78** 54-58.
[7] Dongare M 2014 Mathematical modeling and simulation of refractive index based Brix measurement system. *Optik-Int. J. Light Electron Optics* **125** 3 946-949.
[8] Egorov N and Vinogradova E 2000 Mathematical model of electrongun on the field emission electron cathode basis *Vacuum* **57** 3 267-281.

[9] Alamir A 2000 High Voltage and High Current Density Objective Lens *Chinese J. Phys.* **38** 2 139-145.
[10] Al-Batat A, Yaseen M and Al-Ramadhan Z 2019 Synthesis of Asymmetrical Charged Particle Lens Using Analytical Potential Model. *J. Phys. Conf. Series*. IOP Publishing.
[11] McLeod E and Arnold CB 2007Mechanics and refractive power optimization of tunable acoustic gradient lenses *J. Appl. Phys.* **102** 3 033104.
[12] Bagherzadeh H and Choa FS 2019 Effect of coil size on transcranial magnetic stimulation (TMS) focality *Smart Biomed. Physiol. Sensor Technol.* **XVI.** 2019. International Societyfor Optics and Photonics.
[13] Nanyan AN 2019 THE MAGNETIC FLUX DENSITY OF VARIOUS GEOMETRIES OF ROGOWSKI COIL FOR OVERVOLTAGE MEASUREMENTS *J. Teknol*. **82** 1
[14] Kadhem WJ and Al-Obaidi HN 2013 An inverse design approach for magneticlenses operated under infinite magnification condition. *Optik-Int. J. Light Electron Opt.* **124** 18 3523-3526.
[15] Goodhew PJ and Humphreys J 2000 *Electron microscopy and analysis* CRC Press.

Theoretical Evaluation of Flow Electronic Rate at Au/TFB Interface

Theoretical Evaluation of Flow Electronic Rate at Au /TFB Interface

Sarmad S. Al-Obaidi[1,3], Hadi J. M. Al-Agealy[2], Saadi R. Abbas[1]

[1]Department of Physics, College of Education, Mustansiriyah University, Baghdad-Iraq.
[2]Department of Physics, College of Education for Pure Science Ibn-ALHaitham, University of Baghdad, Baghdad-Iraq.
[3]The General Directorate for Education in Diyala, Diyala – Iraq.

E-mail: Sarmadsapeeh@gmail.com

Abstract. This investigation presents a quantum model for electron transfer allows us to calculate the flow electronic transfer rate through metal/molecule devices. The flow electronic transfer rate at interfaces between Au metal contact with poly(9,9'-dioctylfluorene-co-bis-N,N'-(4-butylphenyl)-diphenylamine) (TFB) and solvents media with polarity is ranging from 0.315 for Diethyl ether to 0.5361 for Methanol is investigated via quantum theory of donor acceptor model. The flow rate are large with Au energy level alignment with TFB levels has been found when the potential barrier at interface is 0.066 eV with Diethyl ether solvents. Flow electronic transfer rate for Au/TFB system with methanol solvent decreased cross interface when the potential barrier is as large as 0.122 eV. This lead to produce accumulate the charges on the both side of Au and TFB when the potential at interface is large. The resulting slow transfer of electrons cross interface. Furthermore, Au metal contact on TFB molecule interface frequently with different solvents media and have large flow rate with Diethylether solvents and low flow rate with Methanol.

Keywords: Flow electronic rate, Au metal, TFB molecule.

1. Introduction

One of the important active field research in recent years is electronic transfer in different science chemistry, physical, biophysical and electronic material [1]. It has basic processes for using different materials in promises technology, such as photo catalysis, light harvesting, molecular electronics and solar cell [2]. The electronic transition field has been extended in different branch of physical, technologic material and microelectronic devices [3]. The optoelectronic and organic electronic devices have been studiedly and investigated in recent years in much more technology for applications such as Organic Light Emission Diodes (OLEDs) [4]. Electronic transfer at the levels of molecules plays an important role in different areas of physics, chemistry, biology and variety materials science [5]. After the seminal work of Marcus in 1958, the electron transfer still a more active field in different research area. The distribution of charge in condensed matter and molecules belongs to the more an important event in all photo induced processes in biology and chemical systems and

technological materials [6]. However, the levels of energy for molecules relative to levels energy for metals are the fundamental rule for electronic transfer at molecule-metal system [7]. The molecular orbital levels alignment with the Fermi energy levels of metal play an important to determine the potential barriers [8], the energy levels for Au contact with TFB are shown in Fig.1 [4,9]. In this research, the theoretical flow electronic rate at Au/TFB device are evaluated and studied via quantum theory. For the system, the transition energy, activation, barrier and flow electronic rate will be present.

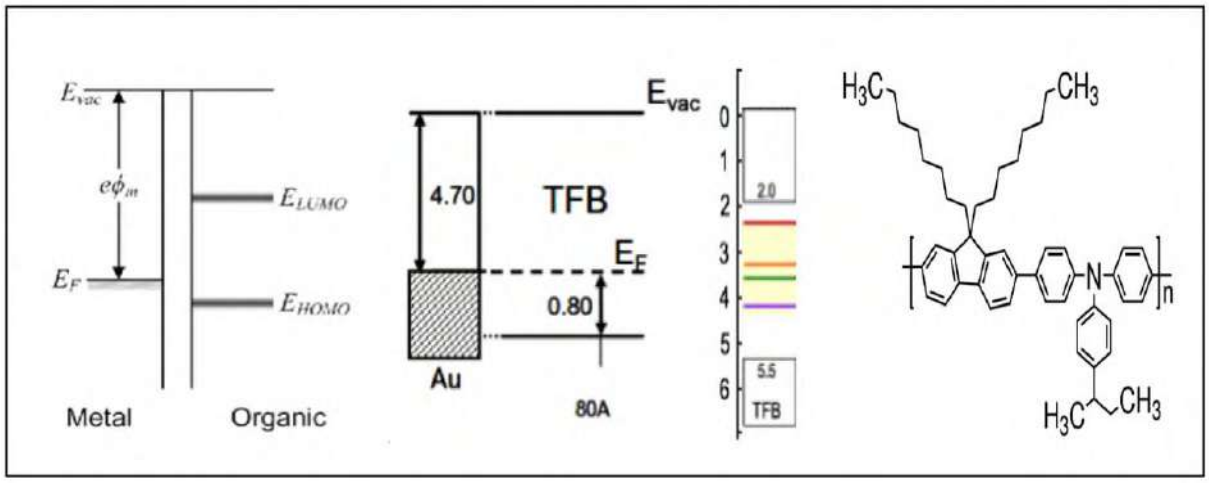

Fig.1. Illustrated of the energy levels of Au metal contact with TFB molecule [4,9].

2. Theory

The flow electronic transfer from metal to molecule cross interface is given by [10].

$$\mathbb{J}_{mM} = \frac{2\pi}{\hbar}\int_{-\infty}^{\infty} F(\epsilon)\left|\langle\widehat{\mathfrak{M}}_{mM}\rangle\right|^2 \delta(\epsilon_k - \epsilon)d\epsilon \quad \ldots\ldots\ldots\ldots (1)$$

Where ħ is $\frac{h}{2\pi}$, h is the Planck constant, $F(\epsilon)$ is the Fermi-Dirac occupation, $\widehat{\mathfrak{M}}_{mM}$ is coupling parameters and $\delta(\epsilon_k - \epsilon)$ is the delta Dirac function for energy at k state of metal and energy levels of molecule.

The effective density of molecule-metal states system $\rho_{ef}(\epsilon)$ is equivalent to [11].

$$\rho_{ef}(\epsilon) = \int \delta(\epsilon_k - \epsilon)dk \ldots\ldots\ldots\ldots (2)$$

The Fermi-Dirac occupation for electrons in levels state may be written as [12].

$$F(\epsilon) = (e^{\frac{\epsilon}{k_B T}} + 1)^{-1} \ldots\ldots\ldots\ldots (3)$$

Substituting the Eqs. (2) and (3) in Eq. (1) to give:

$$\mathbb{J}_{mM} = \frac{2\pi}{\hbar}\int_{-\infty}^{\infty}(e^{\frac{\epsilon}{k_B T}} + 1)^{-1}\left|\langle\widehat{\mathfrak{M}}_{mM}\rangle\right|^2 \rho_{ef}(\epsilon)d\epsilon \quad \ldots\ldots\ldots\ldots (4)$$

We introduce the density of state for electrons $\hat{\rho}(E_i)$ in system, then Eq. (4) become.

$$\mathbb{J}_{mM} = \frac{2\pi}{\hbar}\int_{-\infty}^{\infty}(e^{\frac{\epsilon}{k_B T}} + 1)^{-1}\left|\langle\widehat{\mathfrak{M}}_{mM}\rangle\right|^2 \hat{\rho}(E_i)\rho_{ef}(\epsilon)d\epsilon \quad \ldots\ldots\ldots\ldots (5)$$

The density of state for metal/molecule system was given:

$$\hat{\rho}(E_i) = \sqrt{\frac{1}{4\pi\Lambda_{mM}k_B T}}e^{-\frac{(\Lambda_{mM}+\Delta U^0)^2}{4\Lambda_{mM}k_B T}} \ldots\ldots\ldots\ldots (6)$$

Inserting Eq. (6) in Eq. (5) produce:

$$\mathbb{J}_{mM} = \frac{2\pi}{\hbar}\sqrt{\frac{1}{4\pi\Lambda_{mM}k_B T}}\int_{-\infty}^{\infty}(e^{\frac{\epsilon}{k_B T}} + 1)^{-1}e^{-\frac{(\Lambda_{mM}+\Delta U^0)^2}{4\Lambda_{mM}k_B T}}\left|\langle\widehat{\mathfrak{M}}_{mM}\rangle\right|^2 \rho_{ef}(\epsilon)d\epsilon \ldots\ldots (7)$$

However, the electrons will be transfer above Fermi level with energy ϵ, the activation energy ΔU^0 for transfer reduced to [13].

$\Delta U^0 = \Delta\epsilon_o - \epsilon$ …… (8)

Substituting Eq.(8) in Eq.(7) reduce to.

$$\mathbb{J}_{mM} = \frac{2\pi}{\hbar}\sqrt{\frac{1}{4\pi\Lambda_{mM}\mathrm{k_B T}}}\int_{-\infty}^{\infty}(e^{\frac{\epsilon}{\mathrm{k_B T}}}+1)^{-1}e^{-\frac{(\Lambda_{mM}+\Delta\epsilon_o-\epsilon)^2}{4\Lambda_{mM}k_BT}}\left|\langle\widehat{\mathfrak{M}}_{mM}\rangle\right|^2\rho_{ef}(\epsilon)d\epsilon\ldots\ldots \quad (9)$$

Furthermore, the exponent factor in the Eq. (9) simply to:

$$e^{-\frac{(\Lambda_{mM}+\Delta\epsilon_o-\epsilon)^2}{4\Lambda_{mM}k_BT}} = e^{-\frac{(\Lambda_{mM}+\Delta\epsilon_o)^2}{4\Lambda_{mM}k_BT}}\mathrm{e}^{-\frac{\epsilon(\Lambda_{mM}+\Delta\epsilon_o)}{2\Lambda_{mM}\mathrm{k_B T}}}\mathrm{e}^{-\frac{\epsilon^2}{4\Lambda_{mM}\mathrm{k_B T}}} \quad \ldots\ldots\ldots\ (10)$$

Under assume $A = \frac{(\Lambda_{mM}+\Delta\epsilon_o)}{2\Lambda_{mM}\mathrm{k_B T}}$ and $B = \frac{1}{4\Lambda_{mM}\mathrm{k_B T}}$ and inserting Eq.(10) in Eq.(9) results.

$$\mathbb{J}_{mM} = \frac{2\pi}{\hbar}\sqrt{\frac{1}{4\pi\Lambda_{mM}\mathrm{k_B T}}}e^{-\frac{(\Lambda_{mM}+\Delta\epsilon_o)^2}{4\Lambda_{mM}k_BT}}\int_{-\infty}^{\infty}(e^{\frac{\epsilon}{\mathrm{k_B T}}}+1)^{-1}\mathrm{e}^{-A\epsilon}\mathrm{e}^{-B\epsilon^2}\left|\langle\widehat{\mathfrak{M}}_{mM}\rangle\right|^2\rho_{ef}(\epsilon)d\epsilon\ldots\ldots\ldots\ (11)$$

The potential barrier is given by:

$$\Delta\mathbb{V}_{ef} = \frac{(\Lambda_{mM}+\Delta\epsilon_o)^2}{4\Lambda_{mM}k_BT} = \frac{(\Lambda_{mM}+\epsilon_F-IE\,)^2}{4\Lambda_{mM}}\ldots\ldots\ldots\ldots\ (12)$$

Where ϵ_F is Fermi energy and IE is ionization energy. Furthermore, the effective density $\rho_{ef}(\epsilon)$is given by [13].

$$\rho_{ef}(\epsilon) = \rho_{\mathrm{M}}(\mathrm{E})\frac{L_M}{{d_{adm}}^{2/3}(\frac{6}{\pi})^{\frac{1}{3}}}\ldots\ldots\ldots\ldots\ (13)$$

Where $\rho_{\mathrm{M}}(\mathrm{E})$ is the metal density of states, L_{ecl} is effect of coupled length and d_{adm} is atomic density metal.

Inserting Eq.(13) and Eq.(12)with Eq.(11) to obtained:

$$\mathbb{J}_{mM} = \frac{2\pi}{\hbar}\sqrt{\frac{1}{4\pi\Lambda_{mM}\mathrm{k_B T}}}e^{-\frac{(\Lambda_{mM}+\epsilon_F-IE\,)^2}{4\Lambda_{mM}}}\rho_{\mathrm{M}}(\mathrm{E})\frac{L_M}{{d_{adm}}^{2/3}(\frac{6}{\pi})^{\frac{1}{3}}}\int_{-\infty}^{\infty}(e^{\frac{\epsilon}{\mathrm{k_B T}}}+$$

$$1)^{-1}\mathrm{e}^{-A\epsilon}\mathrm{e}^{-B\epsilon^2}\left|\langle\widehat{\mathfrak{M}}_{mM}\rangle\right|^2 d\epsilon \quad \ldots\ldots\ldots(14)$$

Assume that

$$I = \int_{-\infty}^{\infty}(e^{\frac{\epsilon}{\mathrm{k_B T}}}+1)^{-1}\mathrm{e}^{-A\epsilon}\mathrm{e}^{-B\epsilon^2}\left|\langle\widehat{\mathfrak{M}}_{mM}\rangle\right|^2 d\epsilon \quad \ldots\ldots\ldots(15)$$

Where

$$\mathrm{e}^{-A\epsilon} = 1 - A\epsilon + \frac{(A\epsilon)^2}{2!} - \frac{(A\epsilon)^3}{3!} + \frac{(A\epsilon)^4}{4!} - \frac{(A\epsilon)^5}{5!} + \cdots \quad \ldots\ldots\ldots\ldots(16)$$

And

$$\mathrm{e}^{-\mathrm{B}\epsilon^2} = 1 - \mathrm{B}\epsilon^2 + \frac{(\mathrm{B}\epsilon^2)^2}{2!} - \frac{(\mathrm{B}\epsilon^2)^3}{3!} + \frac{(\mathrm{B}\epsilon^2)^4}{4!} - \frac{(\mathrm{B}\epsilon^2)^5}{5!} + \cdots \ldots \frac{(\mathrm{B}\epsilon^2)^n}{n!} \ldots\ldots\ldots\ldots(17)$$

The solution of integrals in Eq. (15) give:

$$I = 2\mathrm{k_B T}\Gamma(1)\xi(\tfrac{1}{n}) + 2\left(\frac{A^2}{2!} - \mathrm{B}\right)\Gamma(3)(\mathrm{k_B T})^3\xi(\tfrac{1}{n^3}) + 2\left(\frac{B^2}{2!} - \frac{A^2B}{2!} + \frac{A^4}{4!}\right)\Gamma(5)(\mathrm{k_B T})^5\xi(\tfrac{1}{n^5}) +$$

$$2\left(\frac{A^2B^2}{(2!)^2} - \frac{B^3}{3!} - \frac{A^4B}{4!}\right)\Gamma(7)(\mathrm{k_B T})^7\xi(\tfrac{1}{n^5}) + 2\left(\frac{B^4}{4!} - \frac{A^2B^3}{2!3!} + \frac{A^4B^2}{2!4!}\right)\Gamma(9)(\mathrm{k_B T})^9\xi(\tfrac{1}{n^9}) + \cdots\ldots + 2\left(\frac{B^{\frac{n}{2}}}{\frac{n}{2}!} -\right.$$

$$\left.\frac{A^{\frac{n}{8}}B^{\frac{n}{2}-1}}{2!3!}\ldots + \frac{A^{\frac{n}{2}}B^{\frac{n}{4}}}{2!4!}\right)\Gamma(\mathrm{n}+1)(\mathrm{k_B T})^{\mathrm{n}+1}\xi\left(\frac{1}{n^{\mathrm{n}+1}}\right) \quad \ldots\ldots\ldots\ldots(18)$$

Inserting Eq. (18) in Eq. (14) to results

$$\mathbb{J}_{mM} = \frac{2\pi}{\hbar}\sqrt{\frac{1}{4\pi\Lambda_{mM}\mathrm{k_B T}}}\left|\langle\widehat{\mathfrak{M}}_{mM}\rangle\right|^2\rho_{\mathrm{M}}(\mathrm{E})\frac{L_M}{{d_{adm}}^{2/3}(\frac{6}{\pi})^{\frac{1}{3}}}e^{-\frac{(\Lambda_{mM}+\epsilon_F-IE\,)^2}{4\Lambda_{mM}}}\left[2\mathrm{k_B T}\Gamma(1)\xi\left(\frac{1}{n}\right) + 2\left(\frac{A^2}{2!} -\right.\right.$$

$$\left.\mathrm{B}\right)\Gamma(3)(\mathrm{k_B T})^3\xi\left(\frac{1}{n^3}\right) + 2\left(\frac{B^2}{2!} - \frac{A^2B}{2!} + \frac{A^4}{4!}\right)\Gamma(5)(\mathrm{k_B T})^5\xi\left(\frac{1}{n^5}\right) + 2\left(\frac{A^2B^2}{(2!)^2} - \frac{B^3}{3!} -\right.$$

$$\left.\frac{A^4B}{4!}\right)\Gamma(7)(\mathrm{k_B T})^7\xi\left(\frac{1}{n^5}\right) + 2\left(\frac{B^4}{4!} - \frac{A^2B^3}{2!3!} + \frac{A^4B^2}{2!4!}\right)\Gamma(9)(\mathrm{k_B T})^9\xi\left(\frac{1}{n^9}\right) + \cdots\ldots + 2\left(\frac{B^{\frac{n}{2}}}{\frac{n}{2}!} -\right.$$

$$\left.\left.\frac{A^{\frac{n}{8}}B^{\frac{n}{2}-1}}{2!3!}\ldots + \frac{A^{\frac{n}{2}}B^{\frac{n}{4}}}{2!4!}\right)\Gamma(\mathrm{n}+1)(\mathrm{k_B T})^{\mathrm{n}+1}\xi\left(\frac{1}{n^{\mathrm{n}+1}}\right)\right] \quad \ldots\ldots\ldots\ldots(19)$$

The transition energy $\Lambda_{mM}\ eV$ for electron transfer is [14]:

$\Lambda_{mM}(eV) = \frac{e^2}{8\pi\varepsilon_o} = \left(\frac{1}{n^2} - \frac{1}{\varepsilon}\right)\left(\frac{1}{r} - \frac{1}{2R}\right)$ …… (20)

where e is electrons charge, ε_o is permittivity of vacuum, ε and n are dielectric constant and refractive index of the solvents, R is distance between the molecule and metal electrode, r is molecule radius.
the radii of material could be estimation using an expression approach [15].

$r = (\frac{3M}{4\pi ND})^{\frac{1}{3}}$ …… (21)

here M is the molecular weight, D is the mass density and N is Avogadro's number**.**

3. Results

Calculate and investigate here the flow electronic rate of metal/molecule interface and contact with each other. Use theoretical model due to quantum picture to examine the flow electronic rate of these devices, and evaluate the transition energy, driving energy and barrier for electrons. The Au/ poly(9,9'-dioctylfluorene-co-bis-N,N'-(4-butylphenyl)diphenylamine) (TFB) model is chosen to be investigated. The flow electronic transfer cross contacts that's shown in Fig.1. The transition energy can be calculated using Eq.(20) and calculated radii of metal and TFB molecule using Eq.(21) with molecule weight and mass density from Table1.Results are shown in Table 1.

Table 1. The main properties Au and TFB molecule dye [16, 17].

Properties	**Gold (Au) [16]**	**TFB [17]**
Element Formula	Au	$C_{10}H_2F_{12}$
Atomic Metal Weight (g/mol)	196.966569	350.104
Density at room temperature (g/cm3)	19.30	1.567
Crystal system	Cubic	Triclinic
Structure type	FCC	Triclinic
HOMO		5.3 eV
LUMO		2.3 eV
Fermi energy	5.53 eV	
Melting point (°C)	1064.18	
Boiling point (°C)	3825	
heat capacity (Cp) /J g^{-1} K^{-1} at 25 °C, 100 kPa	0.129	
Ionization energy		5.5 eV
Radius calculated(Å)	1.5934	4.4574

The transition energy of Au/TFB interface is strictly by dielectric constant and refractive index of solvents and radi of Au and TFB molecule, it is evaluated by Eq.(20) using characteristic of solvents from Table 2 and, R is the distance between the Au electrode and TFB molecule $R = r_{Au} + r_{TFB}$and taken the radius of Au and the TFB molecule from Table 1 and $\frac{e^2}{8\pi\varepsilon_o} = 14.4\ eV$, results are listed in Table 2.

Table 2. Calculated results of transition energy$\Lambda_{\mathrm{mM}}(\mathrm{eV})$for Au/ TFP

Solvent	Chemical Formula	refractive index (n) at 20^{o}	static dielectric constant (ε) at 20^{o}	The transition energy (eV) Au/TFB
2,2,2-Trifluoroethanol	$C_2H_3F_3O$	1.2910	8.55	0.4928
Methanol	CH_4O	1.3284	32.7	0.5470
Acetonitrile	C_2H_3N	1.3441	37.5	0.5375
Diethyl ether	$C_4H_{10}O$	1.3524	4.33	0.3222
Acetone	C_3H_6O	1.3587	21.01	0.5041
Ethanol	C_2H_6O	1.3614	24.5	0.5088
Nitromethane	CH_3NO_2	1.3817	35.87	0.5060
Tetrahydrofuran(THF)	C_4H_8O	1.4072	7.58	0.3806

Furthermore, the Au metal and TFB molecule contact, the Fermi energy of Au and ionization energy (IE)making the interface potential barrier. It evaluates using Eq.(12) by taking the transition energy in Table 2 and ionization energy of TFB is 5.5 eV and Fermi energy of Au metal is 7.25 eV, results have been shown in Table 3 knowing that highest orbitals molecule energy(HOMO) energy levels is 5.3 eV and the lowest orbitals molecule energy(LUMO) is 2.3 eV [18].

Table 3. Results of evaluation the potential $\Delta\mathbb{V}_{\mathbf{ef}}$for Au/ TFB system

Solvent type	Polarity function f(n,e)	Transition energy $\Lambda_{\mathbf{mM}}(\mathbf{eV})$	Potential energy $\Delta\mathbb{V}_{\mathbf{ef}}$ (eV)
2,2,2-Trifluoroethanol	0.4830	0.4928	0.1087
Methanol	0.5361	0.5470	0.1222
Acetonitrile	0.5269	0.5375	0.1198
Diethyl ether	0.3158	0.3222	0.0663
Acetone	0.4941	0.5041	0.1115
Ethanol	0.4987	0.5088	0.1127
Nitromethane	0.4959	0.5060	0.1119
Tetrahydrofuran (THF)	0.3731	0.3806	0.0808

The energetics coupling $\langle\widehat{\mathfrak{M}}_{\mathrm{mM}}\rangle$ (eV)of Au metal-on-TFB contacts are estimated experimentally depending on literature [19] and approximately to $\left|\langle\widehat{\mathfrak{M}}_{\mathrm{mM}}\rangle\right|^2$ = (0.42 0.4 0.35 0.5 0.56 0.6 0.65 0.7 0.75 0.8 0.9) $\times 10^{-11}eV^2$. Flow of electronic transfer rate has evaluated using Eq.(19) with MATLB program and using results of transition energy in Table 2, Fermi energy of Au is 7.25 eV and ionization energy IE= 5.5 eV, results are showing in Table 4.

Table 4. Results of flow rate of electrons transfer calculation for Au/TFB at Ionization Energy IE= 5.5 eV

Solvent type	The electron transfer rate constant× 10^{-9} Coupling strength $\left\|\langle\widehat{\mathfrak{M}}_{mM}\rangle\right\|^2 \times 10^{-11}$ eV/ state										
	0.42	0.4	0.35	0.5	0.56	0.6	0.65	0.7	0.75	0.8	0.9
2,2,2-Trifluoroethanol	1.487	1.417	1.239	1.771	1.983	2.125	2.302	2.479	2.656	2.833	3.187
Methanol	0.842	0.802	0.702	1.002	1.123	1.203	1.303	1.403	1.503	1.604	1.804
Acetonitrile	0.910	0.866	0.758	1.083	1.213	1.300	1.408	1.516	1.625	1.733	1.949
Diethyl ether	9.440	8.991	7.867	11.238	12.587	13.486	14.610	15.734	16.857	17.981	20.229
Acetone	1.314	1.252	1.095	1.565	1.753	1.878	2.034	2.191	2.347	2.504	2.817
Ethanol	1.246	1.187	1.038	1.484	1.662	1.780	1.929	2.077	2.225	2.374	2.670
Nitromethane	1.281	1.220	1.067	1.525	1.708	1.830	1.982	2.135	2.287	2.440	2.745
Tetrahydrofuran (THF)	4.959	4.722	4.132	5.903	6.611	7.084	7.674	8.264	8.854	9.445	10.625

4. Discussion

Quantum theory model used to examine the flow electron transfer rate at Au/TFB interfaces, and evaluate the flow rate, transition energy and potential barrier at interface. The energy levels alignment of Au metal contact with TFB are showing in Figure1, i.e. the interface of Au metal energy level alignment with HOMO-LUMO energy levels for TFB molecule strictly by the Fermi energy of Au and the HOMO-LUMO energy. The positions of the energy levels of TFB molecule relative to the Fermi level of Au are shown in Figure1. The transition energy controlled electronic transfer of Au metal used contact with TFB molecule. In the majority of transition energy investigated here, the polarity estimation using the refractive index and dielectric constant in Table 3 effected forcedly on calculation the transition energy with different solvent. At the Au metal is aligned with TFB molecule, the transition energy increased with increased polarity of solvents with the fact that solvents generally form good media to level alignment with each other. Considering the fact that the transition energy are controlled to transfer of electrons from donor to acceptor we conclude that transition energy relative to the position of the energy level of highest orbitals molecule energy (HOMO), and the lowest orbitals molecule energy (LUMO)relative to Fermi energy are limited the flow electronic rate through the potential that created in interface of contact Au with TFB. The potential barrier, which simply defined as the energy difference between the ionization energy IE and Fermi level relative to transition energy. When the Fermi energy of the Au metal is relatively to ionization energy and transition energy low, making the interface potential barrier larger, it's shown that for Au/TFB with Methanol solvent has potential is equal to 0.1222 eV compare with Diethyl ether is equal to 0.0663 eV. However ,when the transition energy is large lead to potential is high, the increased transition energy making the interfacial potential barrier higher because the increased transition energy indicate the driving energy decreased because the system has more energy to reorientation energy , or small flow electronic rate .The electronic transition are most occurs when potential is low this showing for Au/TFB with Diethyl ether solvent (9.440×10^{-9} to $20.229 \times 10^{-9} \frac{\mathrm{cm}^3}{\mathrm{sec}}$) compare with less electron transfer with methanol solvent(0.842×10^{-9} *to* $1.804 \times 10^{-9} \frac{cm^3}{sec}$). The transition energy of Au metal contact on TFB molecule interfaces is energy necessarily to transfer occurs with the energy level alignments at interfaces. Different solvent media are taken to examined the transfer of electrons at Au/TFB system. While methanol solvent media shows slow flow rate, Diethyl ether and Tetrahydrofuran (THF) solvents show strong electronic transfer from Auto TFB molecule, with low potential (0.0663 eV and 0.0808 eV) and low transition energy (0.3222 eV and 0.3806eV) relatively to system with methanol has low flow electronic rate with large potential 0.1222 eV and large transition energy (0.5470 eV) for Au contact on TFB molecule.

5. Conclusion

We have determined the flow electronic transfer rate based quantum transition theory for interface of Au contact with TFB with different solvents have polarity ranging from 0.3158to 0.5361. Most importantly effects on flow electronic transfer is the transition energy, that's limited the produce electron density corresponding energies of electrons transfer. When increased the transition energy the flow rate increased electrons to transfer from donor to acceptor. In additional effect on increasing flow electronic transfer in the Au/TFB when the potential barrier is small (0.066 eV). The flow rate of electronic transfer decrease with increasing the potential energy and decreased the electronic rate when increased the potential energy at interface. The Diethyl ether is topic media with Au contact with TFB molecule found to yielding large flow electronic rate and low potential barrier than the bottom Methanol solvent founded to yielding small flow electronic rate and high potential barrier at interface.

References

[1] Haider M. Obeed and Hadi J. M. Al-agealy. 2020 *Test Engineering and management*. **83** 8821 - 8829
[2] Bae C., Ho T. A., Kim H., Lee S., Lim S., Kim M., Yoo H., Montero-Moreno J. M., Park J. H. and Shin H., 2017 *Sci. Adv.* **3**(3) 1-9
[3] Hadi J. M. Al-Agealy, and Hazim H. D. Al Janeri. 2019 *Technologies and Materials for Renewable Energy, Environment and Sustainability AIP Conf. Proc.* **2123**(020055) 1-6
[4] Otero R., Vázquez A.L. de Parga and Gallego J.M. 2017 *Surface Science Reports* **72**(3) 105-145
[5] Hans J. W., Christopher A. A., Natalie B., Andrea C., Majed C., Akshaya K. D., Peter H., Ursula K., Peter M. K., Elisa L., Pablo L-T., Matteo L., Markus M., Chris M., Jacques-E. M., Ursula R., Grigory S., Joël T., Jeroen A. van B., and Oliver W. 2017 *Structural Dynamics*. **4**(061508) 1 - 38
[6] May V. and Kuhn O., 2011 *John Wiley & Sons*
[7] Hadi J. M. AL-Agealy and Mohammed Z. Fadhil. 2020 *Journal of University of Babylon for Pure and Applied Sciences*. **28** (1) 184- 193
[8] Goiri E., Borghetti P., El-Sayed A., Ortega J.E. and de Oteyza D. G. 2016 *Adv. Mater*. **28** 1340-1368
[9] Jaehyung H. and Antoine K. 2006 *Proc. of SPIE*. **6333** 1-10
[10] Haider M. Obeed, Hadi, J. M, Al-agealy. 2020 *IOP Conf. Ser.: Mater. Sci. Eng,* **871**(1) 012093
[11] Shachi S. Gosavi. 2003 *PhD thesis,California Institute of Technology, Pasadena, California*
[12] Hadi, J. M. AL-Agealy, Waleed B. Salih and Taif, S. Murdhi. 2013 *Journal of MadenatAlelem College*. **5**(2) 31-39
[13] Hadi J. M. Al-Agealy. 2015 *Wasit Journal for Science & Medicine*. **8**(1) 17-36
[14] Hadi J. M. Al-Agealy and Fadhil, M. Z, 2017 *Ibn AL-Haitham Journal for Pure and Applied Science*. **26**(3) 86-93
[15] Hadi J. M. AL-Agealy and Mohammed Z. Fadhil. 2020 *Journal of University of Babylon for Pure and Applied Sciences* **28**(1) 184-193
[16] David R. Lide. 2017 *CRC press 97th Edition*. **85**
[17] Jaehyung Hwang, Eung-Gun Kim, Jie Liu, Jean-Luc Bre´das, Anil Duggal, and Antoine Kahn. 2007 *J. Phys. Chem. C,* **111**(3) 1378-1384
[18] Kavala A. K. and Mukherjee A. K. 2015 *Electroactive polymers Materials and Devices* **5**(4) 89-96
[19] William J. Royea, Arnel M. Fajardo, and Nathan S. Lewis. 1997 *J. Phys. Chem. B*. **101**(51) 11152-11159

Measurement of uranium concentrations in urine samples of adult healthy groups in Najaf governorate with estimation of urine concentrations of 8-OHdG compound as biomarker for DNA damage

Measurement of uranium concentrations in urine samples of adult healthy groups in Najaf governorate with estimation of urine concentrations of 8-OHdG compound as biomarker for DNA damage

Samia K. Abbas[1], Dhuha S. Saleh[2], Hayder S. Hussain[1]

[1]Department of Physics, College of science, University of Baghdad
[2]Department of Biology, College of science, University of Baghdad

E-mail: alkazalis@yahoo.com

Abstract. In this study, 88 healthy adults in Al-Najaf governorate of Iraq have been divided into three groups according to the type of exposure to radiation including environmentally uranium exposures n=29 (G_1), occupationally exposures n=27 (G_2), and non-uranium exposures n=32 (G_3). All groups were subjected for estimation of uranium concentration in urine samples using CR-39 SSNTD method beside measurement of urine concentrations of 8-OHdG compound as a biomarker for oxidative DNA damage using Elisa technique. Reactive oxygen species produced under the effect of many causes including ionizing radiation exposure, ($OH^{\cdot}$)free radical induced the formation of 8-OHdG compound from cellular and mitochondrial DNA through attack of C-8 in purine ring of guanine base. The results showed that mean values of uranium concentration were (1.836±0.426 µg/L), (2.02±0.404 µg/L) and (1.755± 0.437 µg/L) for group1, group2 and group3, respectively. While mean values for 8-OHdG were (49.810±15.484 ng/ml), (47.717±14.232ng/ml) and (46.769±14.249ng/ml) for the three groups, respectively. No significant statistical differences were recorded between all data obtained. These results suggested the presence of uranium pollution in all groups including the non-exposed group as compared with reference value of (WHO, 2004). Results also demonstrate the presence of DNA oxidative damage in all groups according to concentration levels of 8-OHdG in urine samples. Therefore, the uranium pollution in urine samples of the examined groups indicate the presence of chronic low dose radiation source in Najaf governorate, which might be the cause of DNA damage as reflected by the urinary levels of 8-OHdG compound.

Keywords: uranium concentration, 8-OHdG concentration and urine sample.

1. Introduction

Environmental pollution with many chemical and physical factors can be hazardous to people health. Humans are constantly exposed to many agents derived from exogenous sources such as food, tobacco smoke, air pollution or ionizing radiation [1]. Ionizing radiation is a high energy radiation that produces ionization or electrical charges as it passes through medium or matter [2]. There are three types of atomic radiation of concern to human health namely, α, β and γ. Sources of radiation may be natural (80%) or human made (20%) [3,4]. The most dangerous human made source of ionizing

radiation is the misuse of forbidden weapons as what happened in Gulf war I and II in Iraq (1990-2003) Which caused depleted uranium pollution in limited areas of Iraq [5].

Exposure of healthy humans to Reactive Oxygen Species (ROS) agents can induce as a situation called oxidative stress [6]. This is characterized as a situation in which the antioxidant protection capacity is overwhelmed by an increase in the generation level of ROS resulting in oxidative damage to cellular macromolecules such as lipids, DNA and proteins [7]. Balance is preserved between endogenous oxidants and various enzymatic and non-enzymatic antioxidants under normal conditions and in all aerobic species [8]. The most important free radical causing damage to basic macromolecules is the hydroxyl radical ($OH^{\cdot}$) which attack nuclear DNA and mitochondrial DNA causing addition of ($OH^{\cdot}$) to c-8 of purine ring in guanine base and produce c-8-OH radical which lead to formation of 8-hydroxy-2-deoxyguanosine (8-OHdG) [9].

This compound is then used as biomarker to examine the oxidative DNA damage, its discovery reported for first time by Kasai and Nishimura in1984 [10]. ROS correspond to super oxide anion ($O_2^{\cdot -}$), singlet oxygen ($O_2^{\cdot}$),hydroxyl radical ($OH^{\cdot}$), hydrogen peroxide (H_2O_2), and nitric oxide (NO) are crucial for many physiological processes and usually exist in cell in a balance with biochemical antioxidant like enzymes including catalase, glutathione peroxidase, superoxide dismutase and low molecular weight antioxidants such as (β-caroten and tocopherol) [7]. It is suspected that oxidative stress leads to the onset and progression of many diseases and the natural aging process [11]. ROS are highly reactive and have an extremely short half-life, so their direct determination is normally impractical [12].

Measuring oxidative modified cellular constituent biomarkers like DNA in biological samples offers a promising public health strategy in the field of public health [13]. In pathological conditions such as carcinogenesis, coronary heart disease and diabetes, measurements of urinary 8-hydroxy-2-deoxyguanosine (8-OHdG) have been extensively studied [14,15]. In recent years, (8-OHdG) has been commonly used not only as a biomarker for endogenous DNA damage assessment but also as a risk factor for many diseases including cancer [16]. Also (8-OHdG) has been used to estimate DNA damage after exposure to agents causing cancer such as:(tobacco smoke, asbestos fiber, heavy metals, and polycyclic aromatic hydrocarbons) [17]. Ionizing radiation (IR) has been reported as one cause of oxidative stress and DNA damage [1, 18, 19].

In Al-Najaf governorate of Iraq, there are some uranium concentrations either naturally (Al heera uranium mine) or human made pollution, while other regions in the governorate are supposed to be not polluted. The present study aims to evaluate uranium pollution in urine samples of uranium-exposed and non-exposed samples. Moreover, estimation the urine concentration of (8-OHdG) compound as a biomarker for DNA oxidative damage and its health consequences.

2. Materials and method

2.1. Collection and Preparation of the Samples

2.1.1. Groups of study

To measure the uranium concentrations, 88 urine samples were collected from three different groups of adults in Al-Najaf governorate as described below.

1. Group one (G1): Included 29 healthy people living in expected polluted areas such as the village of Al-Zajri near the uranium mine in Al-Heerradistrict in Al-Manathera, the village of Al-Aama in Al-Abbasiyeh district in Al-Kufa, as well as Al-Ansar neighborhood.
2. Group two (G2): Included 27 healthy people exposed to uranium radiation by virtue of their work, from Al-Sadr Medical City employees, Al-Hakim General Hospital, Consultative Clinic for Chest and Respiratory Diseases, Middle Euphrates Cancer Center.
3. Group three (G3): Included 32 healthy people living in unpolluted areas, from some sporadic areas of the governorate.

2.1.2. Sample Collection

The sample was taken from the adult person containing urine cups (60 ml); and immediately acidified by adding 1 ml of concentrated HCl for each sample to prevent urine sample polymerization, then placed in a cooling box until the bio-laboratory was reached.

Each urine sample divided by two parts in test tubes: first for uranium concentration estimation by SSNTD technique using CR-39 detector, second for 8-OHdG concentration measurement in urine samples by ELISA technique.

2.2. Measurement of Uranium Concentration

A CR-39 detector was made by Pershore Moulding LTD Company UK, with a thickness of 500μm, was put in the first part from urine samples for measuring the Uranium concentrations, for 90 day. Each detector was cut into 1×1 cm^2 an area; the tubes are stored at -80˚C in the deep freezer. At the end of this period, the exposed detectors were etched using sodium hydroxide (NaOH) solution at a temperature of 70º C for 5 hrs. The normality of solution was set at 6.25 in the water bath. These etched detectors were then washed using distilled water. The track density of each CR-39 detector (track/cm^2) was calculated using an optical microscope (NOVEL, China) with a magnification power of 10×40. The reading of each detector was corrected for the background radiation. The tracks density of uranium from stander solution calculated according to the following relation [20].

$(\rho) = N / (A \times t)$ …….(1)

Where ρ = Track density (no. /cm^2.h), N = Average number of tracks, A = Area of field view (cm^2), t = Time of exposure (h).

To calculate the Uc in the serum sample one could use the following fitting equation [21]:

$Uc=(\rho +12.5) / 18.6$ ……. (2)

2.3. Measurement of 8-Hydroxy-2'-Deoxyguanosine (8-OHdG)

The competitive inhibition enzyme immunoassay technique is employed in this assay. The 8-OHdG-specific antibodies were pre-coated onto a micro plate. Standards and samples were pipetted into the wells with 8-OHdG conjugated with Horseradish peroxidase (HRP). Between 8-OHdG (standards or samples) and HRP conjugated 8-OHdG with the pre-coated 8-OHdG specific antibody, a competitive inhibition reaction was launched. The further 8-OHdG in the samples, the less HRP-conjugated 8-OHdG is bound by the antibodies. A substrate solution was applied to the wells after being washed to eliminate any unbound reagent, and color was produced in comparison to the amount of 8-OHdG in the sample. The production of color was halted and the color intensity was assessed. In urine samples, the 8-OHdG content is determined by comparison with a predetermined normal 8-OHdG curve.

3. Results and Discussion

3.1. Uranium concentration in examined groups

Results of present study are reported in table (1) which shows the mean values of uranium concentrations in urine samples of uranium healthy exposures by environmental contamination (G_1),uranium healthy exposures by virtue of their occupations (G_2), and non-uranium exposures healthy people (G3) in Al-Najaf governorate were (1.836±0.426) μg/L, (2.020±0.404)μg/L and (1.755±0.487) μg/L respectively, other local studies reported uranium concentration in urine samples of healthy control in Baghdad city (0.464-6.212) μg/L [22], (3.212±0.593) μg/L [23], (1.361) μg/L for male, (0.9533) μg/L for females, (3.196) μg/L, for radiation field workers [24].

The standard value of uranium concentration in urine will be 0.3 μg/L after 30 years of continuous exposure to 15 μg/L uranium concentrations in drinking water [25]. According to standard value, the results of present study suggested the presence of uranium pollution in all of the studied groups including healthy group of non-polluted areas of Al-Najaf governorate (G_3).

Uranium concentration in all urine samples may reflect the presence of general environmental pollution with ionizing radiation in Najaf governorate. In Iraq, the levels of depleted uranium raised

after misuse of weapons forbidden in Gulf war I and II causing environmental pollution with uranium in limited areas, but no procedures had ever been taken to isolate these contaminated areas all over Iraq to stop and avoid the spreading of this radioactive contamination and its dangerous consequences [26, 27]. The average annual intake of uranium by adults has been estimated to be 460 μg from ingestion and inhalation [28]. Most of α-emitting materials leave the body through feces, small portion of urine will get into blood and the body can get rid of within few days, and the rest can stay in bones, kidney, liver pancreas, spleen, and central nervous system.

If we breathe the dust of α-emitting material, some of it is exhaled and some stay in our lung [29, 30]. The results of present study showed that mean value of uranium concentration in urine of G_2 is higher than that of G_1 and G_3, this might be obtained because this group (G_2) exposed to both environmental and artificial ionizing radiation sources. The natural environmental radiation is inevitable. It has been recorded that the annual effective dose produced by artificial sources likes X-Ray machines and other diagnostic systems is nearly equal to the total radiation dose obtained from natural dose [31].

In their effects on matter, natural and artificial radiation sources are identical. The U.S. Nuclear Regulatory Commission (NRC) mandates that its licensees restrict human radiation exposure to 1 mSv per year for individual members of the public and limit occupational radiation exposure to 50 mSv per year for adults employed with hazardous materials above the background level of radiation exposure.

3.2. Concentration of 8-OHdG as biomarker for DNA damage

Table (2) demonstrates the concentrations mean values of 8-OHdG compound as a biomarker for DNA damage in urine sample were (49.810±15.842 ng/ml), (47.717±14.232 ng/ml), (46.769±14.249ng/ml) in G_1, G_2 and G_3 respectively. A local study reported 8-OHdG concentration in urine samples of healthy people in Baghdad city as (283.96±43.14 ng/ml) [32]. Comparing the results of the present study with the results of non-local same studies on healthy people it was clear that the concentration of 8-OHdG in Iraqi people in much higher than that of other populations where it was (9.08 ng/dl) in Makkah [33], (1.32±0.20 ng/ml) in Turkey [34], (1.53 ng/ml) in Portland [35], (12.29±5.72 ng/ml) in China [36], (8.43 ng/mg creatin) in Japan [7], (15.2±5.71 ng/mg creatin) in Japan [6]. Studies on healthy people recorded that urinary 8-OHdG is associated with arteriosclerosis related factors [7]. Diet also related to urinary 8-OHdG. For fruit intake a significant correlation for an observed decrease in DNA damage level with increasing fruit intake for females [1].

The increased level of 8-OHdG concentration in urine samples of all study groups suggest DNA damage because of oxidative stress. Also, all urine samples were uranium polluted according to mean values estimations of uranium concentrations. Ionizing radiation is one cause of oxidative stress and can damage any part of cell and interfere with many cellular processes and DNA is the most critical biological target. There is no safe level for radiation exposure; any level could be harmful [37]. Ionizing radiation as a toxicant and carcinogen can produce ROS and cause severe oxidative damage such as single and double strand break, oxidized base and DNA protein cross link.

If these damages are not repair correctly, they may lead to gene mutation and cancer [34], oxidative damage of DNA by reactive oxygen and nitrogen species leads to production of 8-hydroxy-2-deoxyguanosine (8-OHdG) which is a specific biomarker for oxidative stress [38]. Normal value of 8-OHdG found to be significantly different in terms of age, gender, smoking and alcohol consumption but not different in term of body mass [7]. In recent years, 8-OHdG compound has been commonly used not only as a biomarker for endogenous DNA damage assessment but also as a risk factor for many diseases, including lung cancer, in many studies [12], ovarian cancer [39] and breast cancer [33]. Measuring oxidative modified cellular constituent biomarkers, including 8-OHdG for DNA damage in biological samples, is a promising strategy in the field of public health. It has been discussed before that a promising future is to incorporate knowledge from genome programs to broaden the scientific frontiers on etiology health risk prediction and prevention of environmental disease risk by developing a reliable biomarker database [40]. ROS produced under the effect of ionizing radiation induce the formation of 8-OHdG compound from cellular and mitochondrial DNA, hydroxyl radical ($OH^{\cdot}$) plays important role in producing 8-OHdG. The 8-OHdG estimated in urine

and blood cells as a biomarker for oxidative DNA damage [16]. The results of G_2 showed high level concentration of 8-OHdG and the highest level of uranium concentration in urine samples. It has been reported that occupational exposure to low dose radiation is prevalent with wide-spread applications of ionizing radiation in several industries. While the International Radiological Safety Commission recommends an effective dose limit of 20 mSv for an average of 5 years and the effective dose should not be greater than 50 mSv in any single year [31].

4. Conclusions

The percent study demonstrates that the uranium pollution is presence in urine samples of all the examined groups reflecting the presence of chronic low dose radiation source in Al-Najaf governorate. Moreover, uranium pollution contributes to DNA damaging in all of the scanned groups. The oxidative damage of the DNA means higher probability of many diseases mainly cancer, a point which needs more investigations.

Table 1. The levels of uranium concentration in urine for three groups

	Uranium concentration (µg/L)		
Variable	G_1	G_2	G_3
Range	0.989-2.977	1.471-2.782	1.145-3.062
[Mean± STD Deviation]	1.837±0.427	2.021± 0.404	1.755±0.487
P-value	0.738	0.054	0.217

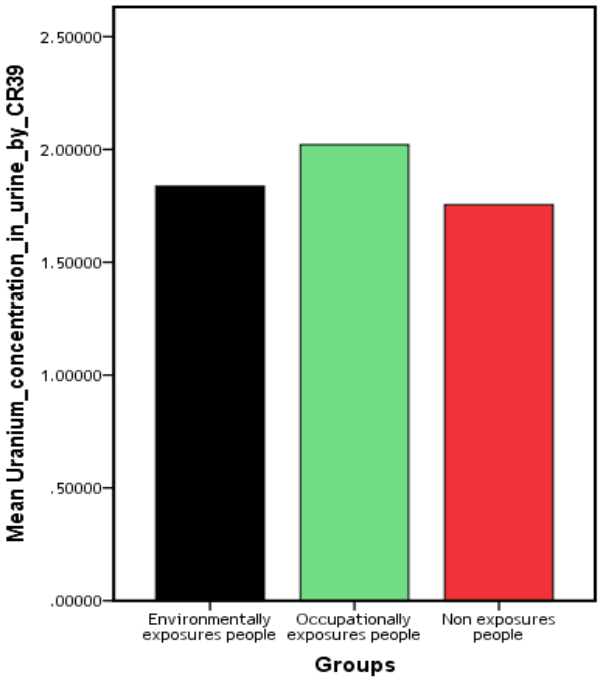

Figure 1. Uranium concentration in group G1, G2, G3.

Table 2. The levels of urinary 8-OHdG concentration for three groups

Urinary 8-OHdG concentration (ng/ml)			
Variable	G_1	G_2	G_3
Range	33.89-94.46	26.15-78.96	28.96-90.94
[Mean± STD Deviation]	49.810±15.484	47.717± 14.232	46.769± 14.249
P-value	0.548	0.901	0.611

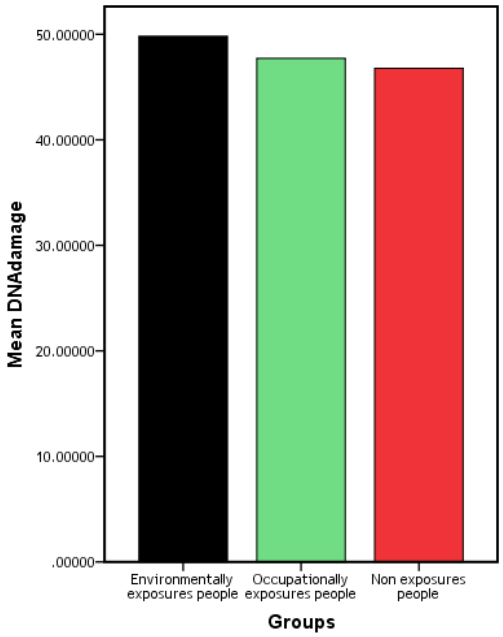

Figure 2. Urinary 8-OHdG concentration in group G1, G2, G3.

References

[1] Hofer T, Karlsson HL and Möller L 2006 DNA oxidative damage and strand breaks in young healthy individuals: a gender difference and the role of lifestyle factors *Free Radic. Res*. **40** 707-714.
[2] Collin PH 2004 *Dictionary of Environment and Ecology* 5th ed. Bloomsbury Publishing Plc. London.
[3] Hill MK 2004 *Understanding Environmental Pollution (A primer)* 2nd ed. Cambridge University press. UK.
[4] Wright J 2005 *Environmental Chemistry* 2nd ed. Routledge Publishing. London.
[5] Shafik SS and Qaddoori SM 2018 Urinary excretion as a function of uranium concentration in bladder cancer patients using kinetic phosphorimetry analyzer *J. Phys Conf. Series*.
[6] Kimura S, Yamauchi H, Hibino Y, Iwamoto M, Sera K and Ogino K 2006 Evaluation of urinary 8-hydroxydeoxy guanine in healthy Japanese people *Basic Clin. Pharmacol. Toxicol*. **98** 496-502.
[7] Sakano N, Wang DH, Takahashi N, Wang B, Sauriasari R, Kanbara S, Sato Y, Takigawa T, Takaki J and Ogino K 2009 Oxidative stress biomarkers and life styles in Japanese healthy people *J. Clin. Biochem. Nutr*. **44** 185-195.
[8] Scandalios JG 1997 *Oxidative Stress and the Molecular Biology of Antioxidant Defenses.* New York: Cold Spring Harbor Laboratory Press.
[9] Halliwell B and Gutteridge JMC 1999 *Free Radical in Biology and Medicine*, 3rd ed. Oxford: Oxford University Press.

[10] Kasai H, Hayami H, Yamaizumi Z, Saito H and Nishimura S 1984 Detection and identification of mutagens and carcinogens as their adducts with guanosine derivatives *Nucleic Acids Res.* **12** 21270–2136.
[11] Finkel T and Holbrook NJ 2000 Oxidants, oxidative stress and the biology of ageing. *Nature* **408** 239–247.
[12] Yano T, Shoji F, Baba H, Koga T, Shiraishi T, Orita H and Kohno H 2009 Significance of the urinary 8-OHdG level as an oxidative stress marker in lung cancer patients. *Lung Cancer* **63** 111–114.
[13] Bacchi S, Palumbo P, Di Carlo M and Coppolino MF 2016 Cocaine effects on generation of reactive oxygen species and DNA damage: formation of 8-hydroxydeoxyguanosine in active abusers *Int. J. Pharmacol. Toxicol.*
[14] Wu LL, Chiou CC, Chang PY and Wu JT 2004 Urinary 8-OHdG: a marker of oxidative stress to DNA and a risk factor for cancer, atherosclerosis and diabetics *Clin. Chim. Acta*. **339** 1-9.
[15] Kimura S 2006 Evaluation of Urinary 8-Hydroxydeoxyguanine in Healthy Japanese People : URINARY 8-HYDROXYDEOXYGUANINE AND HEALTHY PEOPLE *Basic Clin. Pharmacol. Toxicol.* **4**.
[16] Valavanidis A, Vlachogianni T and Fiotakis C 2009 8-hydroxy-2- deoxyguanosine (8-OHdG): A Critical Biomarker of Oxidative Stress and Carcinogenesis. *J Environ. Sci. Health Part C* **27** 120–139.
[17] Droge W 2002 Free radicals in the physiological control of cell function *Physiol. Rev*. **82** 47–95.
[18] Scandalios JG 2001 Molecular Responses to Oxidative STRESS *Mol. Anal. Plant Adapt. Environ.* 181-208.
[19] Salehi A, Ebrahimpour K, Forouharmajd F and Zarean M 2020 The relationship between collective effective doses of radiation and, urinary concentration of 8- Dihydroxy- 2'-Deoxyguanosine among radiography staff *Int. J. Radiat. Res*. **18**.
[20] Khan F, Williams M and Wilkins A 1984 *The physics of radiation therapy* Baltimore, USA.
[21] Qaddoori SM and Shafik SS 2018 CR-39 As A Tool For Uranium Concentration Calculation In Bio Assay Sample: Bladder Cancer As Case Study. *Res. J. Pharmac. Biol. Chem. Sci.* **9** 6 228-239.
[22] Fadel KH 2014 *Estimation IL-6 level in Patients with Respiratory Diseases That Caused by Bacteria and Other Causative Agents in Some Baghdad Hospital* MSc. Thesis, Baghdad University.
[23] Khraibet KI 2015 *Estimation of IL-2 level and uranium concentration in a sample of recurrent aborted women in Baghdad and Maysan governorates using ELISA and SSNTDs techniques* MSc. Thesis, Baghdad University.
[24] Al-Jubouri EMR 2012 *Measuring the concentrations of uranium and thorium in the urine of Cancer patients in the city of Baghdad* MSc. Thesis. Dep. Phys. Coll. Sci. Unv. Baghdad. Iraq.
[25] WHO 2004. *Guidelines for Drinking Water Quality* Third edition, World Health Organization, Geneva (2004).
[26] Al-Hamadany 2011 *Radiation pollution in cancer and other diseases using some immunological and clinical parameters*. Ph.D. Thesis. Dep. Biol. Coll. Sci. Baghdad Iraq.
[27] Annual report to congress 2007 *Federally Sponsored Research on Gulf War Veterans*' Illnesses for 2007. Department of veterans affairs.
[28] World Health Organization, WHO 2001 Depleted Uranium Sources, Exposure and Health Effects.
[29] Fentiman AW, Smith M and Veley RJ 2004 *How do radioactive materials move through the environment to people* Ohio State University Extension. (2004).
[30] Hassan SF 2006 *Determination of Uranium Concentration in Human Blood in Some Governorates of Iraq* M.Sc. Al- Nahrain University.

[31] Gao Y, Wang P, Wang Z, Han L, Li J, Tia C, Zhao F, Wang J, Zhao F, Zhang Q and Lyu Y 2019 Serum 8-Hydroxy-20-Deoxyguanosine Level as a Potential Biomarker of Oxidative DNA Damage Induced by Ionizing Radiation in Human Peripheral Blood *Int. J.*
[32] Al-Rubaie AII 2014 *Potential Impacts of Uranium Pollution and its Relation to Some Immunological Parameters in a Sample of Iraqi Patients With Lung Cancer* PhD. Thesis, College Of Science, University of Baghdad Iraq.
[33] Mohamed NourEldin EE, El-Readi MZ, NourEldein MM, Alfalki AA, Althubiti MA, Kamel HF, Eid SY, Al-Amodi HS and Mirza AA 2019 8-Hydroxy-2'-deoxyguanosine as a Discriminatory Biomarker For Early Detection of Breast Cancer.
[34] Cukurova Z, Cetingok H, Ozturk S, Gedikbasi A, Hergunsel O, Ozturk D, Don B, Cefle K, Palanduz S and Ertem DH 2019 DNA damage effects of inhalation anesthetics in human bronchoalveolar cells *Medicine*. **98** 32. (2019).
[35] Withee ED, Tippens KM, Dehen R, Tibbitts D, Hanes D and Zwickey H 2017 Effects of Methylsulfonylmethane (MSM) on exercise-induced oxidative stress, muscle damage, and pain following a halfmarathon: a double-blind, randomized, placebo-controlled trial *J. Int. Soc. Sports Nut*. **14** 24.
[36] Ma Y, Zhang L, Rong S, Qu H, Zhang Y, Chang D, Pan H, and Wang W 2013 Relation between Gastric Cancer and Protein Oxidation, DNA Damage, and Lipid Peroxidation. *Oxidative Med. Cell. Longevity*.
[37] Vakil C and Harvey L. 2009 Human health implications of the nuclear energy industry *Canad. Assoc. Phys. Environ.*
[38] An AR, Kim KM, Park HS, Jang KY, Moon WS, Kang MJ, Lee YC, Kim JH, Chae HJ and Chung MJ 2019 Association between Expression of 8-OHdG and Cigarette Smoking in Non-small cell Lung Cancer *J. Pathol. Translat. Med.* **53** 217-224.
[39] Xu X, Wang Y, Guo W, Zhou Y, Lv C, Chen X and Liu K 2013 The significance of the alteration of 8-OHdG in serous ovarian carcinoma *J. Ovarian Res*. **6** 74.
[40] Bonassi S and Au WW 2002 Biomarkers in molecular epidemiology studies for health risk prediction *Mut. Res*. **511** 73- 86.

Properties of organic green spinach dye as a substitute for harmful chemical green dye

Properties of organic green spinach dye as a substitute for harmful chemical green dye

Suma H AL-Shaikh Hussin

University of Baghdad, College of Science for Women, Department of Physics, Iraq.

E-Mail: sumaha_phys@csw.uobaghdad.edu.iq

Abstract. Preparation of an environmentally friendly organic green dye, an alternative to the harmful industrial chemical green dye which is used to optical and industrial applications. The dye is extracted from spinach plant by solvent extraction process. The optical and morphological characterizations of green spinach dye are measurements, the absorbance spectrum of green spinach accord in visible region and the dye have two peaks at wavelengths (λ_1=440 nm, λ_2=685 nm) where the band gap energy is E_g=2.81 eV at λ_1 and the refractive index of spinach dye (n=1.36682). The fluorescence spectrum show the maximum absorption wavelength λ_1, λ_2 shifted towers red region about $\Delta\lambda_1$=90 nm and $\Delta\lambda_2$=195 nm respectively, and that accentuated the absorption region are extend to the dye. Also, the average particles size of spinach measured by Atomic Force Microscopy (AFM)=59.587 nm. These characterizations obtained the green dye can used in optical and industrial applications and made it a safer alternative for the toxic chemical green dye and thus protecting the environment by replacing polluting industrial chemical and their consequences.

Keywords: Extracted Spinach Dye, Optical Properties of Spinach Dye, and Spinach plant.

1. Introduction

Given the modern orientation to renewable energies using environmentally friendly natural dyes instead of chemical dyes harmful to environmental. The natural green spinach dye has been extracted and its characteristics studied to determine the extent of its use in various optical, industrial and scientific applications. Spinach is a plant belongs to chenopodiaceous family [1]. It is cultivated throughout the word as cool season annual, green leafy vegetables with significant nutritional and beneficial properties [2]. Spinach featuring in low calories is considered as a good source of minerals like iron and calcium and multivitamins [3]. It is also native to central and south western Asia. This green dye can be used in different application like; optical application [4], chlorophyll laser [5], chlorophyll dye is suitable to replace harmful tracer dyes for laser [6], possibility to replacement of green chemical dyes that are used in industry by organic dyes [7], dye sensitized solar cell (DSSCs) [8] and other applications.

In this work, green spinach dye was extracted and preparation by used ethanol, to illustrated the spinach characteristics and how much ability of use in optical and industrial applications.

2. Materials and methods

2.1. Materials

Materials used are fresh green spinach plant, ethanol and deionized water.

2.2. Preparation the organic green spinach dye

Use the solvent extraction process to extraction the spinach dye by cleaned the spinach leaf in deionized water, dried, 200g of spinach squeezer using blander, then filtering as shown in Figure 1. Added 20 ml of ethanol and placed into stirrer for 2h.

Figure 1. Shows spinach leaf, spinach squeezer using blander and filtering the dye extractor respectively**.**

2.3. Characterization and measurements

The absorbance (A) spectrum of the dye accomplished using UV-Vis shimadzu spectrometer in the wavelength of (190-1100)(nm), is use to measure the absorption rate in visible area. The optical band gap (E_g) calculated by using formula in (1)[9]:-

$$E=h\upsilon=hc/\lambda \quad (1)$$

Where E is the stands for photon energy, h is blank's constant (6.626×10^{-34} j.s), υ is the frequency, c is the speed of light (3×10^{8} m/s) and λ is the wavelength.

Measured the absorption coefficient (α) to determine the light transmittance in material, if α is spadesful, its meaning the transmittance light in material is attenuation and if α is small amount the material is transparent to ray passing through it. The α calculated from absorption A and thickness d of cavity of dye solution (=1 cm) using formula (2)[10]:-

$$\propto = \frac{(2.303)A}{d} \quad (2)$$

The extinction coefficient K_0 used in spectroscopy to measure the concentration of a chemical in solution and calculated by using formula in (3) [10]:

$$K_0 = \frac{\propto \lambda}{4\pi} \quad (3)$$

The refraction index n of the spinach dye was measure by Refractometer-AR4 device from Germany. The fluorescence of spinach dye measured on the fluorescence spectrophotometer Agilent on wavelength of 200-900 nm. To determination probable chromophore groups in a given natural dye infrared (IR) spectra were recorded with Fourier transform spectroscopy FTIR spectrometer from SIDCO (FTIR-600).

The surface roughness of the spinach dye was measured by atomic force microscopy (AFM), made by (DME) model (DS95), scan range 50-200 μm and sample size up to 150 mm.

3. Results and discussion

Multiple measurements of the dye conducted to find out the properties and the characteristics of the dye. The optical characterizations, absorbance, band gap energy, absorption coefficient, extinction coefficient, refractive index, fluorescence and transmittance of spinach dye obtained by (AFM). The observed results are summarized in the following subsections.

3.1. Absorption of spinach dye

Figure 2 refers to the UV-Vis absorbance spectrum of spinach extracted with ethanol spectrum of spinach extracted with ethanol in the visible light spectrum. The dye have two peaks (λ_1=440 nm, λ_2=685 nm) in cyclohexane indicated the existence of either anthocyanin, chlorophyll, carotene or mixture of them which have absorption peak at wavelength 420 nm and 665 nm [11].

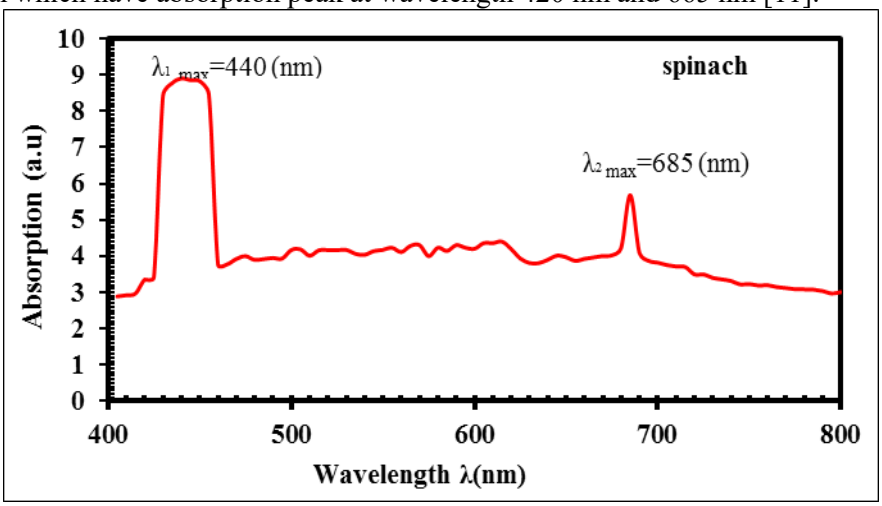

Figure 2. The absorption spectra of spinach extracted with ethanol have two peaks (λ_1=440 nm, λ_2=685 nm).

Spinach is fertile in chlorophyll due to all green plants consisted of chlorophyll, which qualified for photosynthesis operation having glucose from simple organic molecules (carbon dioxide and water) under the action of visible radiation [12]. The band gap energy of spinach dye is (E_g=2.81 eV at maximum wavelength λ_{max}=440 nm) was calculated by formula 1. Figure 3 refer to absorption coefficient α which is a function of wavelength and depends on absorbance and thickness of the film according to the formula 2.

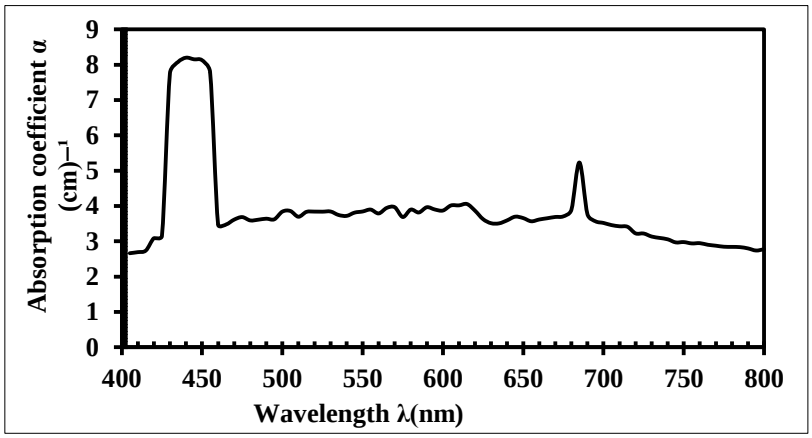

Figure 3. Absorption coefficient (α) of spinach dye.

Figure 4 represent to extinction coefficient of spinach dye which increases by increasing the absorption coefficient and wavelength calculated by formula 3.

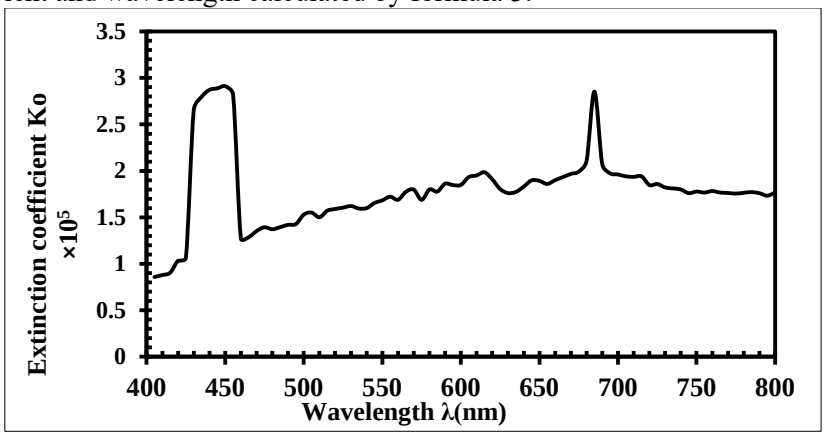

Figure 4. Extinction coefficient of spinach dye.

3.2. Refractive index of spinach dye.

The refractive index n of spinach dye (n=1.36682) is measured by Refractometer device in liquid phase.

3.3. Fluorescence of spinach dye.

Figure 5 demonstrated fluorescent spectrum, after excitation with two peaks in wavelengths (440, 685) (nm) as functions of emitted radiations wavelengths at (λ_{f1}=530 , λ_{f2}=880)(nm). Fluorescents maxima with respect to absorptions maxima shifted as ($\Delta\lambda_1=\lambda_{f1}-\lambda_{1max}$ =90 nm) with applicate the same equation to the second peak at ($\Delta\lambda_2=\lambda_{f2}-\lambda_{2max}$ =195 nm), the fluorescence spectra shifted towards red region and thus agreement with searcher [13].

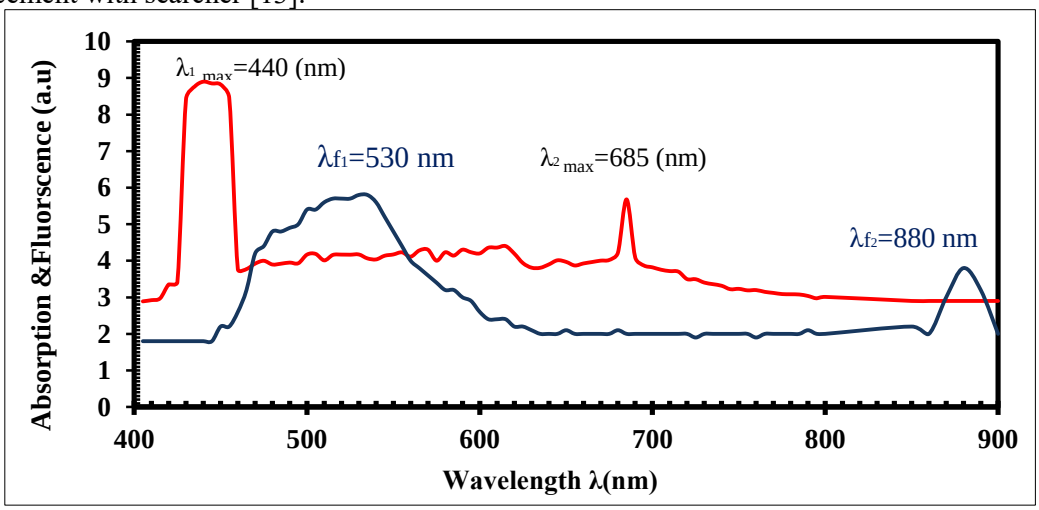

Figure 5. Fluorescent spectrum of spinach dye and the maxima shifts ($\Delta\lambda_1$=90 nm and ($\Delta\lambda_2$=195 nm), the fluorescence spectra shifted towards red region.

3.4. Infrared-IR spectroscopy of spinach dye.

The FTER spectra of spinach as shown in Figure 6. In IR spectrum, the absorption band of iron sulphides is not clear at lower wavenumber. While, the presence of sulfate is indicated by the appearance of asymmetric stretching of carboxylate C=O_2 and a band at 1056 cm^{-1}.Whereas, the existence of a band at 2356 cm^{-1} is attributed to the presence of ferredoxin (Fe-S). In addition, (-OH) vibration cause the occurring of a band at 3431 cm^{-1}, while the band occurring around 2923 cm^{-1} attributed to the stretching mode of (C-H) in the spinach.

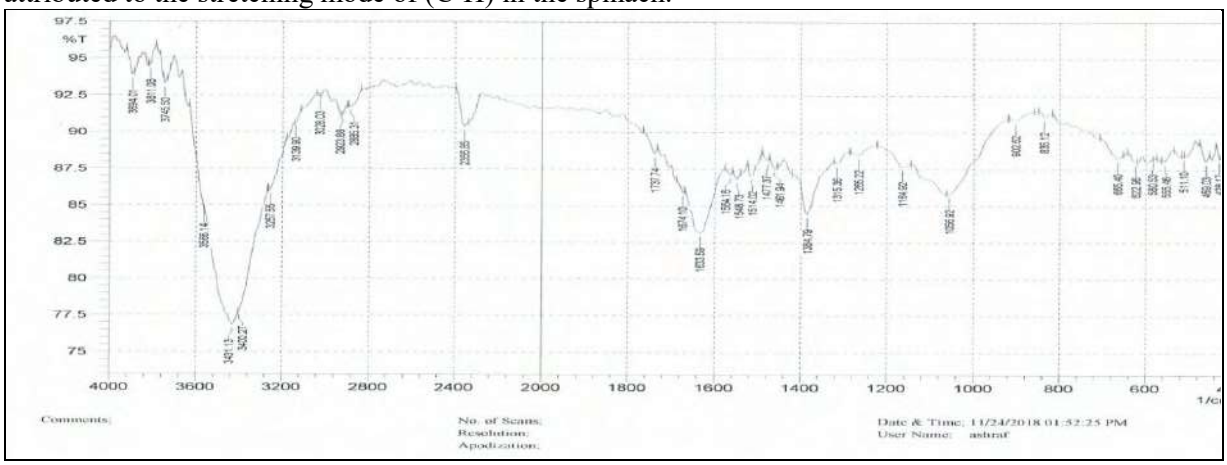

Figure 6. FTER spectra of spinach dye.

*3.5. Atomic force microscopy (AFM) of spinach d**Error! Reference source not found.**ye.*

The AFM analysis the surface morphology and roughness of spinach dye. The roughness average 31.152 nm, and the average particle size 59.587 nm, determine using 2D, 3D images as shown in Figure 7. These results agreed with searcher [15].

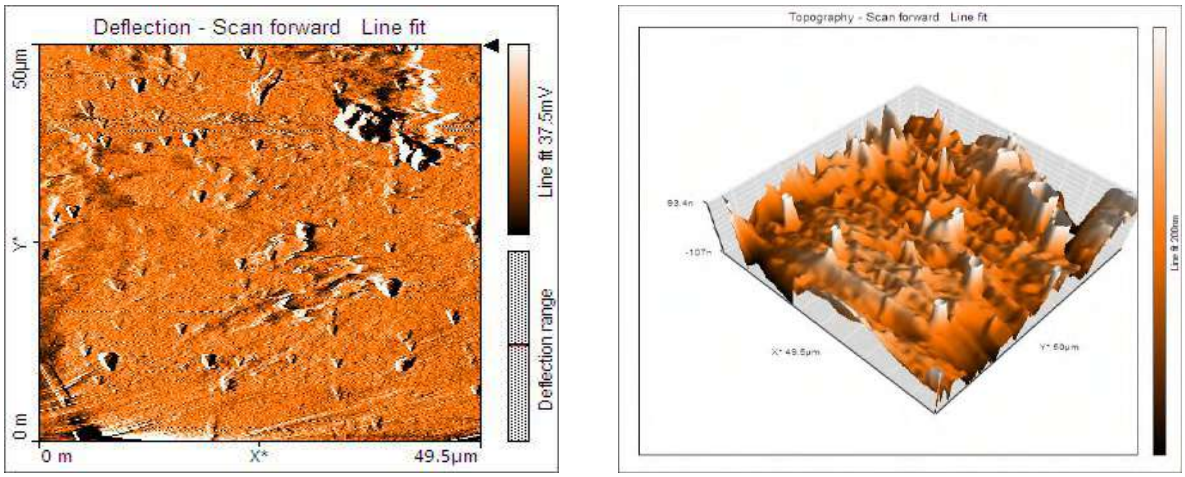

a) 2D **b) 3D**

Figure 7. AFM image of spinach dye in (a) 2D image, (b) 3D image.

4. Conclusion

Synthesis an organic green dye extracted from spinach plant used as alternative to green chemical dyes which are toxic and harmful to environment. The spinach dye have two peaks in visible region at wavelength λ_1=440 nm, λ_2=685 nm and the fluorescence shifted $\Delta\lambda_1$=90 nm and $\Delta\lambda_2$=195 nm respectively, these shifts contributed to extend the absorption spectrum to the dye, also found the band gap energy E_g=2.81 eV at λ_1, the refractive index of spinach dye n=1.36682 and the average particle size 59.587 nm. These characterizations elucidate the green spinach dye can used in optical and industrial applications because it was friendly to environment, safe and have multiple uses. Spinach dye is a good alternative to green chemical dyes. In the future, is possible to extracted natural dyes from origin with different colors to be used in optical and industrial applications instead of harmful chemical dyes.

References

[1] Roughani A and Miri S 2019 *Characterization of dehydrated spinach leaf powder* 2nd ICMP 1.
[2] Saleem S 2020 *Characterization of dehydrated spinach leaf powder* Chap2 Periyar University Food Science and Nutrition, Academia 1.
[3] Ankita Prasad K 2013 *IJAFST* **4** 309.
[4] Paudel P Pandey A Shrestha R Neupane A Lamichhane P Adhikari R Gyawali R and Kafle B 2018 *Food Research* **2** 429.
[5] Zähringer K 2014 *Materials Science* ID:13833065, 1.
[6] Chen Y C Chen Q Fan X 2016 *Lab on a Chip* **16** 2228.
[7] Krizova H 2015 *Material Science* 1.
[8] Syafinar R Gomesh N Irwanto M IrwanY 2015 *Energy Procedia* **79** 896.
[9] AL-Shaikh Hussin S 2019 *Baghdad Sci. J.* **16** 903.
[10] AL-Shaikh Hussin S 2010 *Baghdad Sci. J* **1** 20.
[11] Bhanashali A Parsola A Yadav S Nalini R 2015 *IJESMR* **2** 37.
[12] Ankita K 2015 BTAIJ **11** 426.
[13] Vogelmann T Han T 2000 *Plart Cell and Environment* **23**1303.
[14] Nainggolan I Shantini D Nasution T Derman M 2011 *MRS AMSE Hindawi* ID:702815, 1.
[15] Phuthong W Huang Z Witlkopp T Sznee K Heinnckel M Dekker J Frese R Prinz F Grossman A 2015 *Plant Physiology* **196** 318.

Investigation Adsorption Mechanism of Methane Gas in Graphene and Copper Doped Nano-ribbon Using Density Function Theory

Investigation Adsorption Mechanism of Methane Gas in Graphene and Copper Doped Nano-ribbon Using Density Function Theory

Mohammed A. Al-Seady[1], Ruqayah Ali Grmasha[1, *], Noor Al-Huda Al-Aaraji[2] and Hayder M. Abduljalil[3]

[1] Environmental Research and Studies Center, University of Babylon, Al-hillah, Babylon, Iraq
[2] Al-Mostaqbal University Collage, Al-hillah, Babylon, Iraq
[3] Department of Physics, College of Science, University of Babylon, Al-hillah, Babylon, Iraq

E-mail: ruqayah.grmasha@uobabylon.edu.iq

Abstract. In this study, density function theory was used to evaluate geometrical and electronic properties for pure and doped system as well as adsorption energy. Pure graphene nano-ribbon appeared in plane surface during adsorption energy to have low sensitivity to methane gas. Its energy gap changed only in distance 1A because of the chemical adsorption. Doping mechanism enhanced the proprieties of graphene nano-ribbon. In geometrical structure, copper (Cu) atom stretching the nano system and it is a sign of modification. Additionally, energy gap was decreasing by doped in transition metal atom and become opening. Adsorption energy of doped system was higher than pure nano-ribbon. It was noticed that the doped transition metal enhanced the sensitivity of the system 6 times greater than pure graphene nano-ribbon. Doping graphene nano-ribbon by copper atom revealed to be a key to design chemical and physical gas sensor for methane gas.

1. Introduction

Graphene as a two-dimensional connected carbon sheet is an excellent material that has exceptional properties such as superior surface to volume fraction, little electrical noise and outstanding transport properties[1]. Graphene has more superior efficiency in addition to its unique two-dimensional structure and has unique chemical properties such as outstanding electrical, optical and mechanical properties. Due to its excellent properties, graphene has been commonly used in a number of ways, such as energy generation, spintronics and field effects transistor (FET)[2]. Graphene has also been proven to have possible uses in detection molecules, both experimental and theoretical methods. Graphene could be employed as a novel material for adsorption and desorption due to its low dimensions and wide surface area process [3]. Graphene is a zero band gap semiconductor with its valence and conduction bands touching in corner of the Brillion zone in called Dirac points [4]. However many theoretical and experimental studies showed that graphene has weak physical adsorption of most gas molecule[5]. Therefore, researchers utilized many mechanisms such as defect vacancy and doped graphene by metal atom[6]. Graphene doped by metal atom led to significant structural and electronic properties, also electrical conductivity and chemical reactivity during adsorption process to detection small gas

molecule[7]. It is noteworthy that doped graphene by metallic atom creates modifications process without damaged one atom thick of it[8]. Many studies showed that the introduction of defect or doped metallic atom in graphene will modify the charge transfer strength between it and gas molecule adsorbed, also enhance sensitivity and selectivity of gas-based sensor[9]. Gas sensing was important environmental issue for hazard toxic gases molecule. Thus, this study is mainly focused on used different nano-system for detaction methane gas.

2. Theoretical background

In order to investigate the electron systems' electronic structure, density functional theory (DFT) is employed for this purpose which is widely used quantum mechanical method in physics and chemistry. DFT usually applied to evaluate the ground-state properties of metals semiconductors as well as insulators. Furthermore, DFT is a useful method in physics and chemistry computational [10]. Historically, in 1927, the starting point for the theory of density was the Thomas-Fermi model. They defined the energy of an atom by representing its kinetic energy as a function of electron density, combining this with the classic expressions for interactions among nuclear-electron and electron-electron, which can also be defined in terms of electron density [11, 12]. The DFT focuses on the much simpler electron density $\rho(r)$.DFT's central concepts are dependent on ground state energy. Others ground state electronic properties are determined uniquely by the density of the electrons [13, 14]. However, the exact ground conditions of the system correlates to the electronic density for minimal total energy.

3. Materials and Research Aim

(GNR), (Cu-GNR) and CH_4. DFT method was used to computed structural, electronic and adsorption energy for pure and doped graphene by Cu atom. The aim of present study is design sensor for toxic gas. The equations below were used in the study.

Adsorption energy = $(E_{gas}+E_{ribbon})-E_{(gas+ribbon)}$[15] (1)

Where E_{gas} total energy for adsorption gas, E_{ribbon} is total energy for nano-system and $E_{(gas+ribbon)}$ is total energy for adsorption system.

Energy gap=$E_{LUMO}-E_{HOMO}$ [16] (2)

4. Result and discussion

4.1. Geometrical proprieties

Geometrical characteristics summarized on bond length and angle between atoms computed for graphene nano-ribbon when toxic gas molecule absence. Fig. 1 lists the geometry structure for pure graphene nano-ribbon. Bond lengths for C-C, C=C, C=C (aromatic) and C-H are (1.4555), (1.3661), (1.4305) and (1.0859), respectively [15]. Angles between atoms listed for (C--C--C) and (C=C-H) are 120.232 and 119.922 degree, respectively[15]. For doped nano-ribbon, Fig. 2 illustrated a geometrical structure for G-Cu nano-ribbon. Bond length between carbon-carbon for all type's agreement with previous study [16]. The bond length between Cu-C are varies between 1.8427-1.8672 Å. Computed bond length for metal-carbon was agreement with study [16]. The angle between carbons atoms are agreement with past section also. Bond angel between Cu atom and three neighbor atoms are 85.3641-103.7705 degree. Bond angle for system under study agreement with [17]. Also that clear copper atoms stretching structure of graphene nano-ribbon because the radius of it greater than carbon radius [18].

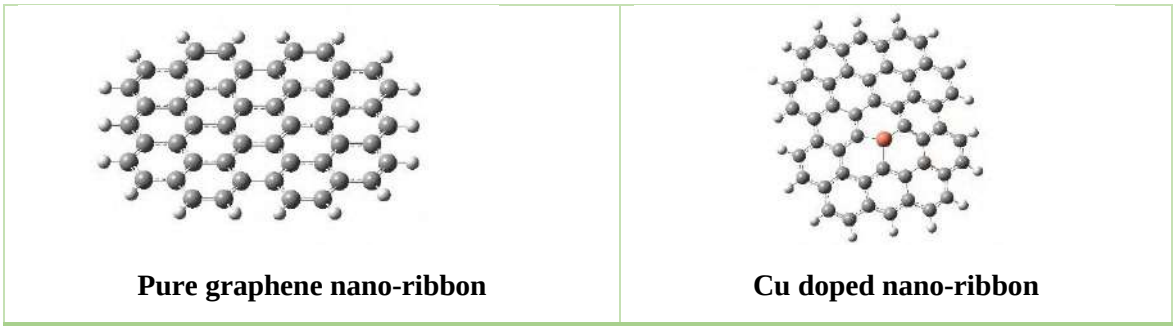

Fig.1. Geometrical structural for pure and doped nano-ribbon.

4.2. Adsorption energy

In this section, study adsorption energy for pure graphene nano-ribbon compared with doped system. For pure system CH_4 gas molecule reaction with graphene is low activity. The absolute energy value increasing from zero to 2 eV at distance 4-1.5 Å all these distances refer to physical adsorption. Chemical adsorption appears only when bonds formed between H related to gas with C of graphene nano-ribbon. For doped system CH_4 has adsorption energy greater than pure nano-ribbon, modification of interaction process was clear. In addition, findings indicated that G-Cu system sensing CH_4 gas for all distance. Finally, results indicated that G-Cu system has high sensitivity for $CH_{4(doped)} > CH_{4(pure)}$. Table 1 listed the values of adsorption energy and Figure 2 showed the curves of adsorption energy measured in eV unit.

Table 1. Values of adsorption energy for system under study measured in eV unit

D (A)	Pure nano-ribbon	Doped nano-ribbon
1	-7.3088	-45.2869
1.5	-2.1496	-6.6194
2	-0.5278	-1.2320
2.5	-0.1034	-0.4476
3	-0.01360	-0.4187
3.5	0.001532	-0.4676
4	0.002721	-0.4974

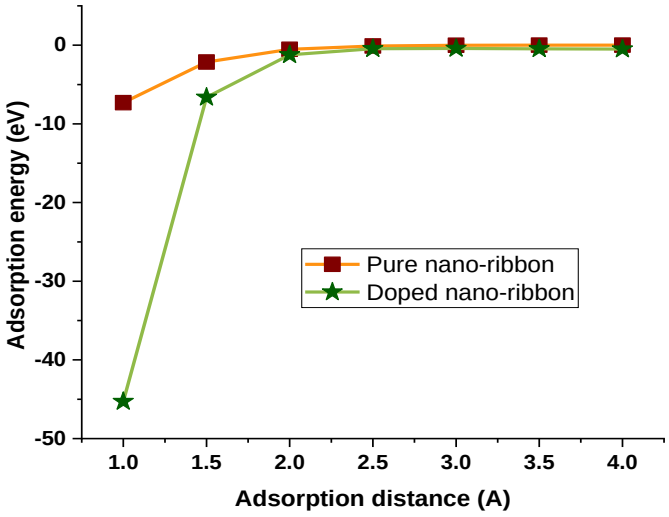

Fig. 2. Adsorption energy curves for systems under study.

4.3. Energy gap

Energy gaps depends on difference energy between HOMO and LUMO value. Results in Table 2 showed that energy gap decreased when interaction increasing, this is suggested to take place because of gas molecule approaches the surface and Van Der Waals formations. Moreover, result revealed that when energy gap decreased in distance near surface of the graphene, the nano-ribbon has high stability [19]. Results showed that for distance far from surface energy gap for adsorbed systems remain at pristine graphene nano-ribbon energy gap, in other hand increasing in energy gap ability of sensing for gases decreased [20]. Energy gap of doped nano-ribbon CH_4 small compared with pure system. Appear energy gaps in this phase because attractive force between CH_4 and surface of nano system. Energy gap in doped nano-ribbon and during adsorption mechanism remain opening. Results show that CH_4 have high reactivity with system under study compared with pure system [21]. Fig. 3 represent energy gap curves for system under study.

Table 2**.** Values of energy gap for systems under study in eV unit.

D (A)	Pure nano-ribbon	Doped nano-ribbon
1	2.086	1.218
1.5	2.477	1.243
2	2.524	1.137
2.5	2.532	1.093
3	2.533	1.087
3.5	2.533	1.087
4	2.532	1.087
Pure nano-ribbon	2.533	
Doped nano-ribbon	1.535	

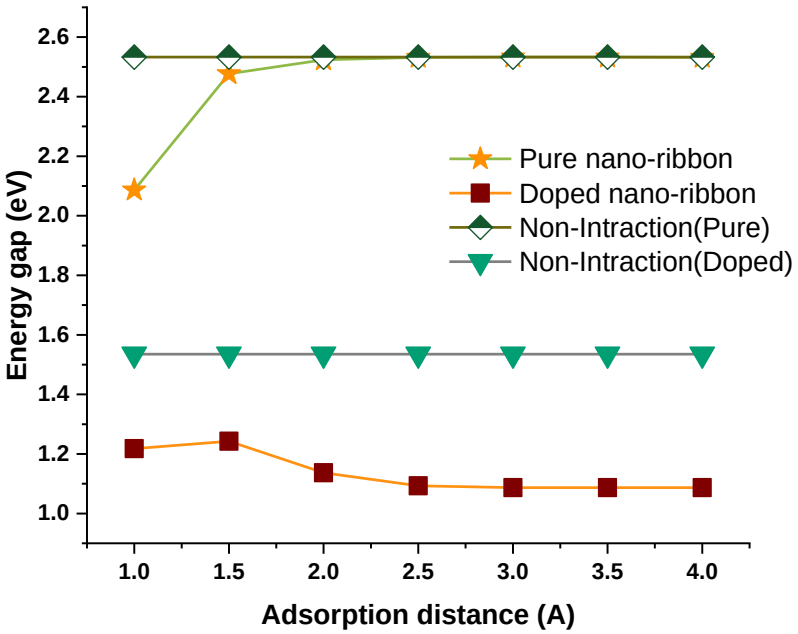

Fig.3. curves of energy gap for adsorption systems.

4.4. FT-IR spectroscopic

In this section study (FT-IR) spectroscopic to determine functional group for graphene before and after adsorption with gas molecule. FT-IR spectroscopy is important tool to determine chemical adsorption by appear the radical of gas adsorbed on surface of graphene nano-ribbon, it calculated using DFT at basis set 6-31G with hybrid function B3YLP. Pure graphene FT-IR analysis for C-H bond appears at 3213 cm^{-1} in stretching vibration mode[22], C-H a skew-symmetric appears on 3192 cm^{-1} of methylene group[22], methylene group appear at 1351cm^{-1} region of FT-IR spectrum approximately from 1349 cm^{-1} for study[22]. For CH_4 adsorbed in pure graphene nano-ribbon, appear new region at wave number (810-828) cm^{-1} and 1458 cm^{-1} resulting from contacted methane molecule on surface of graphene ribbon. For doped nano-ribbon, C-Cu peak appear in very low intensity and wave number was 511 cm^{-1} and this value agreement with previous study in [23]. Carbon metal absorption spectra vary between 350-630 cm^{-1}[24]. CH_4 appear many types of peak related to direction of methane gas. Three new peak appear in spectrum are 1820, 3010 and 3115 cm^{-1} respectively related to CH_4 adsorption [24]. This result proved adsorption of methane gas more acceptable than pure graphene nano-ribbon. Methane can be detecting by this system in all state, in other hand in rest and active state. Also, adsorption process explains that have high effect on carbon metal absorption peaks. Figs. 4 and 5 represent FT-IR spectra for pure and doped nano-ribbon respectively.

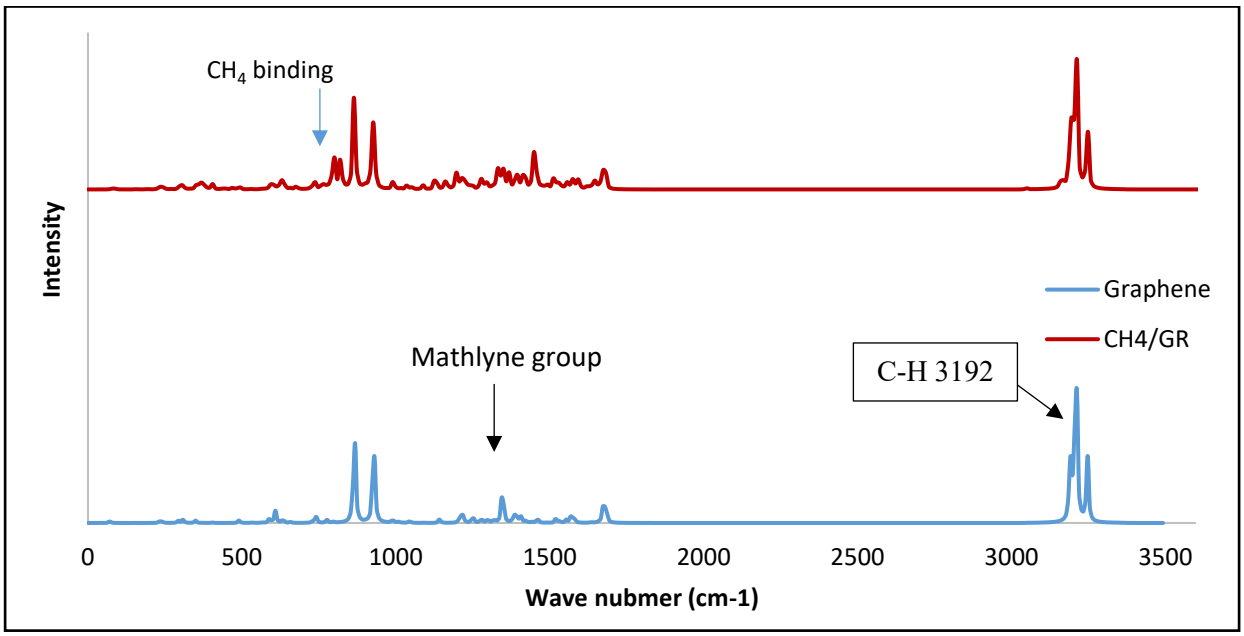

Fig.4. FT-IR spectra of CH_4 adsorbed in pure graphene nano-ribbon.

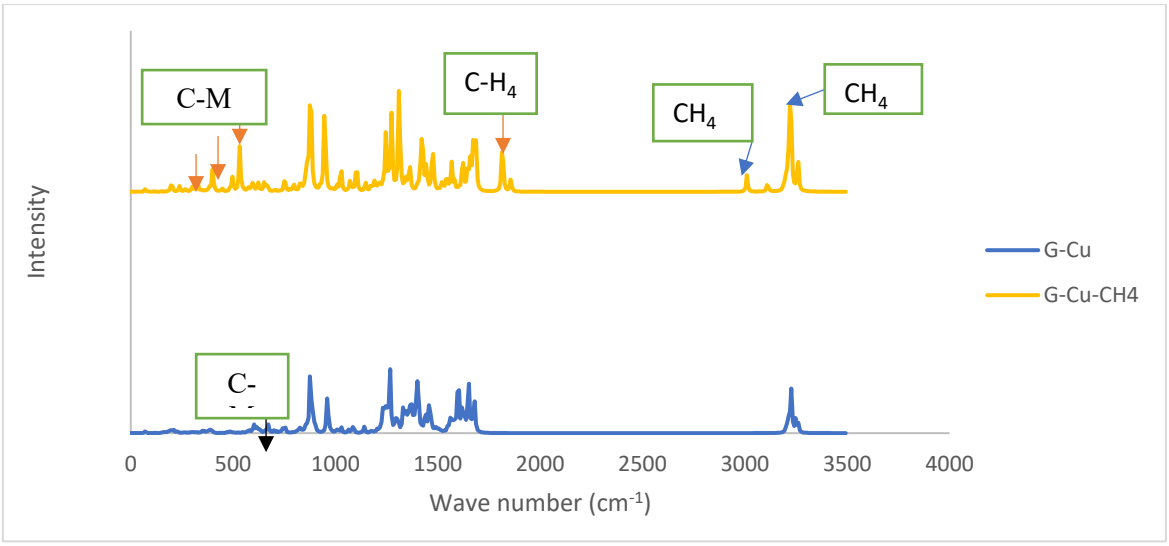

Fig.5. FT-IR spectra of CH_4 adsorbed in doped nano-ribbon.

5. Conclusions

Pure and doped nano ribbon have good relaxation structure, bond length and angle between them has agreements with experimental results. Doped in cupper transition metal medicated electronic, structural and spectral properties of pure graphene nano-ribbon. Methane gas molecule adsorption in pure graphene nano-ribbon was very weak in two types of adsorption, but in doped system result show have high interactivity compared with pure system and kinds of adsorption mechanism. FT-IR spectroscopic used to determine free radical of adsorption gases, doped nano-ribbon sense methane gas in all phases and this result proves that system has high sensitivity compared with pure graphene nano-ribbon.

References

[1] Novoselov KS, Geim AK, Morozov SV, Jiang D, Zhang Y, Dubonos SV, Grigorieva IV & Firsov AA. 2004. *Science* **306** (5696) 666
[2] Zhang W, Liu J, Sun Y, Gadipelli S, Han X &Colantuono G. 2016 Effective Adsorbents for Establishing Solids Looping as a Next Generation NG PCC Technology.
[3] Meyer JC, Geim AK, Katsnelson MI, Novoselov KS, Booth TJ & Roth S. 2007 *Nature*. **46** (7131) 60
[4] Wallace PR. 1947 The band theory of graphite. *Physical review*. **71** (9) 622.
[5] Song HQ, Liu Z & Zhang DB. 2019 *Physics Letters A.* **383** 2628
[6] Hu X, Liu M, Liu X, Ma Y, Nan H, Bi D, Qiao L & Li Y. 2019 *Physica E: Low-dimensional Systems and Nanostructures* **114** (8)113634.
[7] Beheshtian J, Kamfiroozi M, Bagheri Z & Ahmadi A. 2011 *Physica E: Low-dimensional Systems and Nanostructures* **44** 546
[8] Wang H, Wang Q, Cheng Y, Li K, Yao Y, Zhang Q, Dong C, Wang P, Schwingenschlögl U, Yang W & Zhang XX. 2012. *Nano letters* **12** 141
[9] Zhang X, Yu L, Gui Y & Hu W. 2016. *Applied Surface Science*. **367** 259
[10] Tawfik SA, Isayev O, Stampfl C, Shapter J, Winkler DA &Ford MJ. 2019 *Advanced Theory and Simulations*. **2** 1800128.
[11] Nowack B & Stone AT.2000 *Environmental science & technology* **34** 4759
[12] Lowe J P & Peterson K , 2011 *Quantum chemistry, Elsevier,* 3rd edition,.
[13] Parrill A L & Lipkowitz K B 2016"Reviews in Computational Chemistry" **29**, *Wiley Online Library*,
[14] Szabo A & Ostlund NS. 2012 Modern quantum chemistry: introduction to advanced electronic structure theory. *Courier Corporation*
[15] Cronstrand 2004 "Quantum chemical calculations of non-linear optical absorption", Ph.D. *Thisis Digitala* Vetenskapliga Arkivet, Bioteknologi
[16] Xie Y, Huo YP & Zhang JM. 2012 *Applied surface science*.**258** 6391
[17] Wanno B & Tabtimsai C. 2014 *Superlattices and Microstructures* **67** 110
[18] Düzenli D. 2016 *The Journal of Physical Chemistry* C **120** 20149
[19] Rad AS, Pazoki H, Mohseni S, Zareyee D & Peyravi M. 2016 *Materials Chemistry and Physics* **182** 32
[20] Osouleddini N & Rastegar SF. 2019. *Journal of Electron Spectroscopy and Related Phenomena* **232** 105
[21] Zhang M, Du J & Chen Y. 2020. *Catalysis Today*
[22] Heidari A, Esposito J, Caissutti A & Maitotoxin 2019 *J Biomed Engg Res*.**1**
[23] Banimuslem H, Hassan A, Basova T, Yushina I, Durmuş M, Tuncel S, Esenpınar AA, Gürek AG & Ahsen V. 2014 In *Key Engineering Materials Tech Publications Ltd*. **605** 461
[24] Köse D A, *2008 Russ. J. Inorg. Chem*. **52** 1384

Study addition of Fe_2O_3 Nanoparticles on Optical Properties for (PMMA-PS) Mixture

Study addition of Fe_2O_3 Nanoparticles on Optical Properties for (PMMA-PS) Mixture

Hussein Ali Hussein Slman and Zaid A. Hasan

Department of physics, College of Education for Pure Sciences, University of Babylon, Iraq

E-mail: hussein.hussein.pure@student.uobabylon.edu.iq

Abstract. In this paper, films of the (PMMA-PS) Mixture doped with Fe_2O_3 nanoparticles were prepared with variable percentage (0,2,4,6) % wt by Drop casting method and at room temperature. The change in optical and structural properties was observed after deformation using a UV-Spectrophotometer and for a range of wavelengths (190 - 1100) nm. The study showed that increasing the distortion ratio led to an increase in the absorbance, absorption coefficient, extinction coefficient, refractive index, real dielectric constant, imaginary isolation constant, and diminishing permeability.

Keywords: Methyl Metha Acrylate, Polystyrene

1. Introduction

Recently, the term nanotechnology has emerged and has been the focus of wide-ranging attention of researchers and has resulted in a great leap in various medical and engineering sciences ... etc.[1]
The term nanocomposites are used to express the product of adding nanoparticles to other ordinary materials to manufacture new materials with distinctive physical properties [2]. PMMA is a colorless transparent thermoplastic that is technically classified as a kind of amorphous glass that is preferred due to its mild properties, ease of handling and handling, and its low cost, but it is fragile under the influence of load, especially under impact strength and is more likely to be scratched than ordinary glass.[3]
In this study, films of PMMA-PS polymeric compounds were prepared by casting technique with the addition Fe_2O_3 nanoparticles in different weight ratios to improve its mechanical and optical properties.

2. Materials and Methods:

Poly Methyl Metha Acrylate with Polystyrene (PMMA/PS) doped with Fe_2O_3 nanoparticles (size: 20- 30 nm, purity: 99.99%) manufacturer (Hongwu nanometer) is to make solution molding mechanism. Mixture the (PMMA- PS/Fe2O3) by ratios (0.2, 0.4, 0.6 wt %) were melted (50ml) of chloroform using a magnetic stirrer, after that the samples dried. Using UV Spectrometer (the equipment from the Japanese company Shimadzu) optical properties of the wavelength range (190-1100) nm were measured. The optical measurements are including, absorbance, absorption coefficient, transmittance, refractive index, real and imaginary insulation constant. All measurements were conducted at room temperature.

3. Results and Discussion:

Optical Measurements

3.1. Absorbance (A)

Defined by the following equation

$$A = log\frac{1}{T} \quad (1)$$

As displayed in Figure 1, the maximum absorbance values are observed at 220nm and decreases with increasing wavelength due to decreasing light energy with increasing incident wavelength according to Planck's law [5].

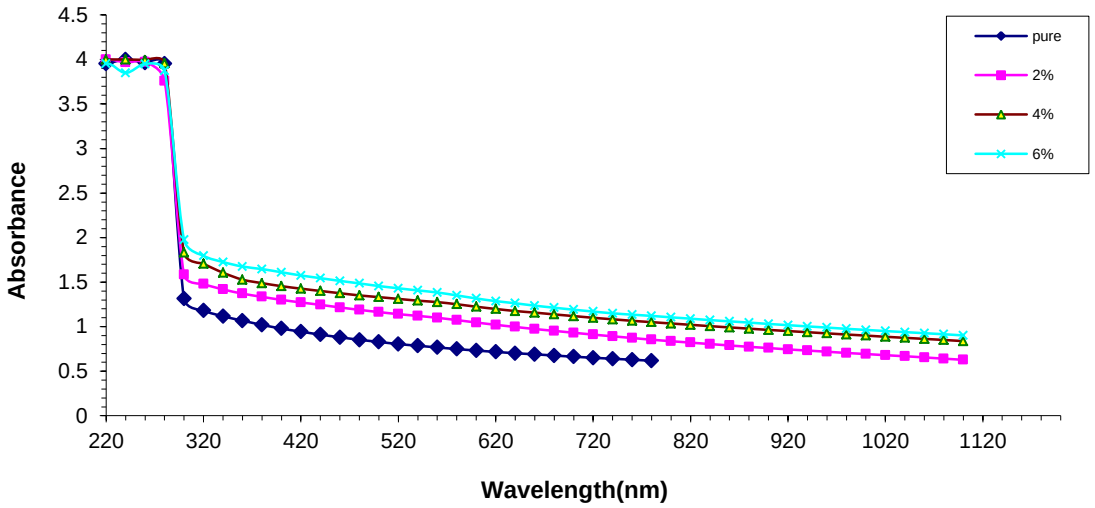

Figure 1. The absorbance spectra of (PS- PMMA- Fe_2O_3) films as a function of incident light wavelength.

3.2. The absorption coefficient (α)

The absorption coefficient was calculated from the relationship below, and the results showed that the absorption coefficient values increased with increasing the added concentrations of Fe_2O_3 nanoparticles as a result of the increase in the incoming light rate according to Lambert's Law [6].

$$\alpha = 2.303\frac{A}{t} \quad (2)$$

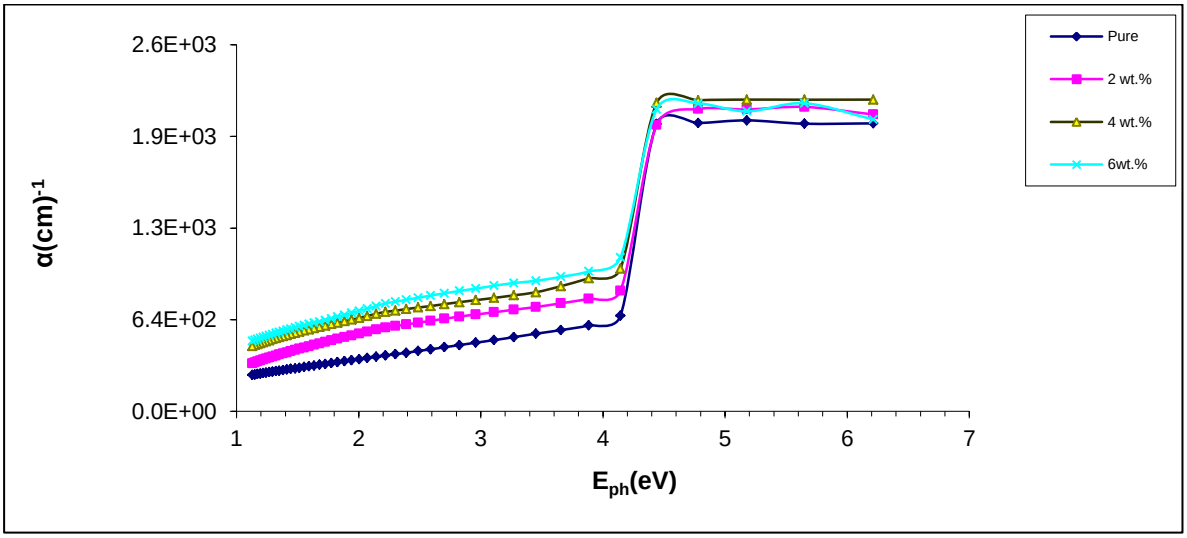

Figure 2. The absorption coefficient of (PMMA-PS –Fe_2O_3 nano) as a function of photon energy.

3.3. Permeability

Figure 3 showed an increase in transmittance with increasing wavelength and percentage. It was observed that the permeability decreased with the increase in the doping because it decreases with increasing the absorbance values, which increase with the increase in the doping rates.

Transmittance (T) is given by

$$T = \frac{I_T}{I_o} \quad \text{.....(3)}$$

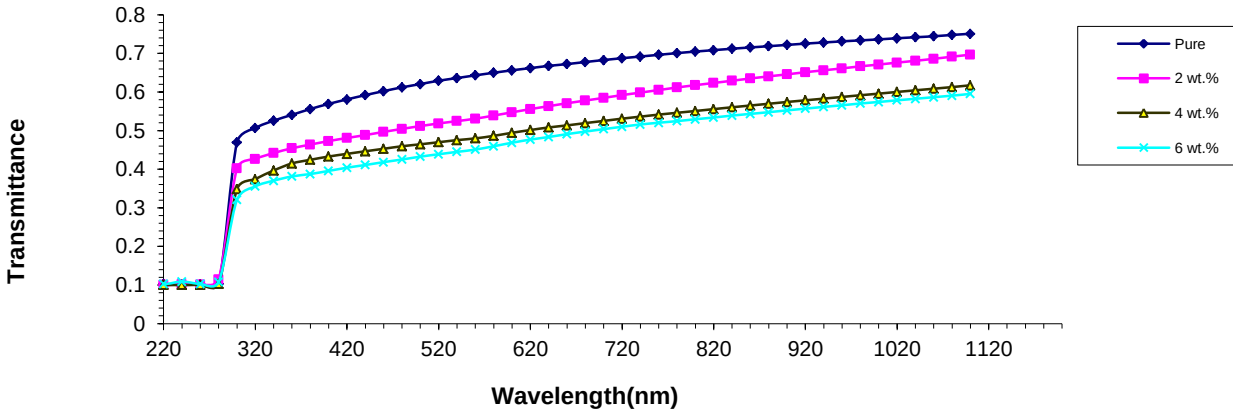

Figure 3. The transmittance spectra of (PS-PMMA–Fe_2O_3nano) blend as a function of incident light wavelength.

3.4. Extinction Coefficient of (k)

Figure 4 shows the change of extinction coefficient as a function of wavelength. It was observed that k decreases with decreased doping, due to an increase in the absorption coefficient with an increase in the ratios of added nanoparticles. The extinction coefficient is high at longer wavelengths and larger doping ratios [7].

$$k = \frac{\alpha \lambda}{4\pi} \qquad (4)$$

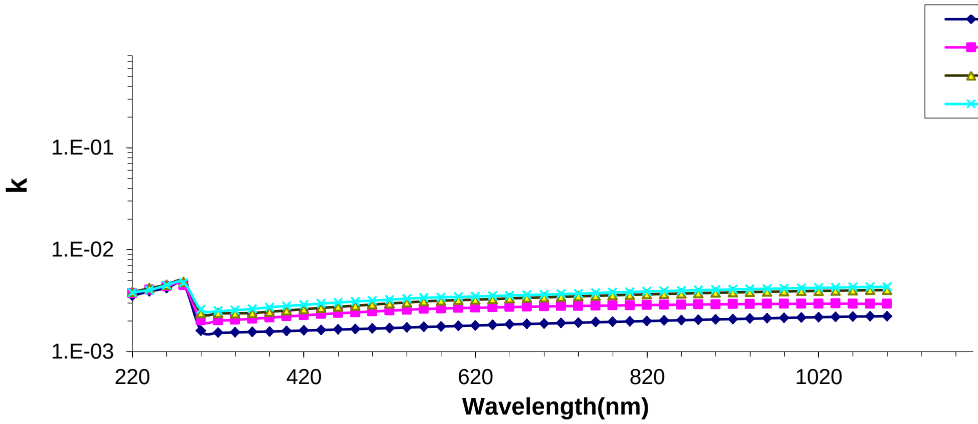

Figure 4. The relation of extinction coefficient for (PMMA – PS) with nano Fe_2O_3.

3.5. Refractive index (n)

Figure 5 describes the change by the refractive index as a function of the wavelength with an increase in the deflection ratios. This is because pure PMMA is an amorphous crystalline substance with low density that increases with increasing the concentration of Fe_2O_3 nanoparticles. The refraction index decreases at the greatest wavelengths and increases at greatest dopant concentration, whose behavior is consistent with our previous work [8].

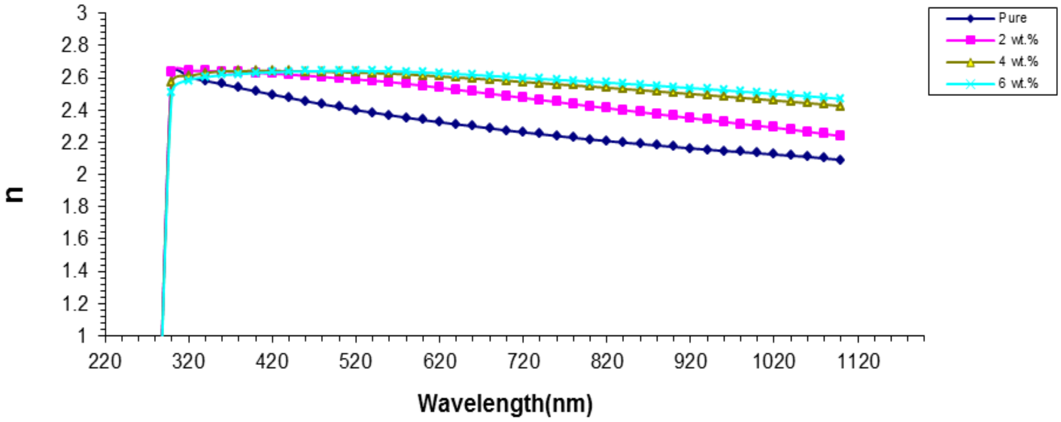

Figure 5. The refraction index of (PS - PMMA – Fe_2O_3 nano.) blend films as a function wavelength at different weight ratio.

3.6. Dielectric constant (Ɛ)

It is defined as the polarization of charges due to the interaction of radiation and the charges of the medium, and is calculated using the below relations [11]:

$$\varepsilon = \varepsilon_1 - \varepsilon_2 \quad (5)$$

$$\varepsilon_1 = n_0^2 - k^2 \quad (6)$$

$$\varepsilon_2 = 2n_0 k \quad (7)$$

Figure 6 and Figure 7 illustrates the relationship of the dielectric constant as a function of the wavelength as it increases with increasing doped ratios and is consistent with the findings reported in ref.[8].

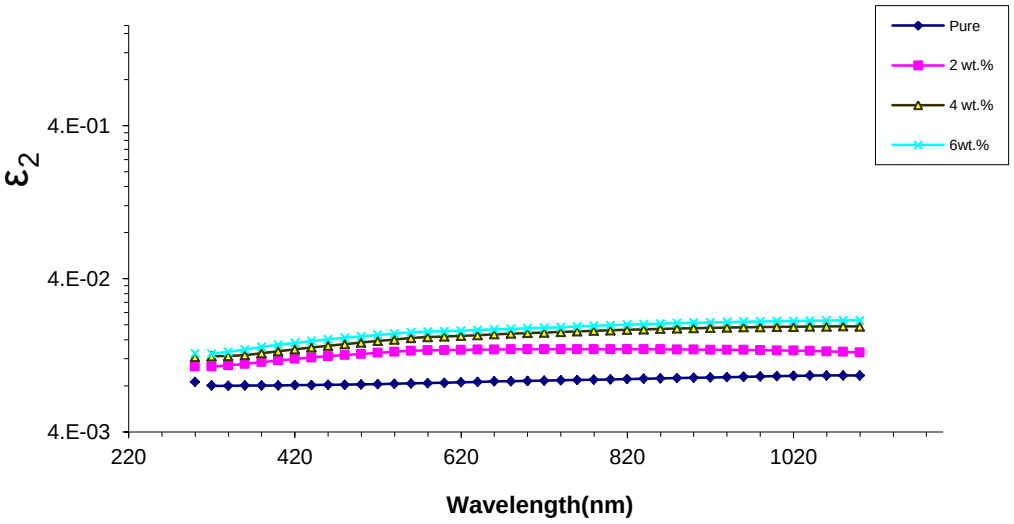

Figure 6. The actual dielectric constant for (PMMA- PS) with Fe_2O_3 nano.

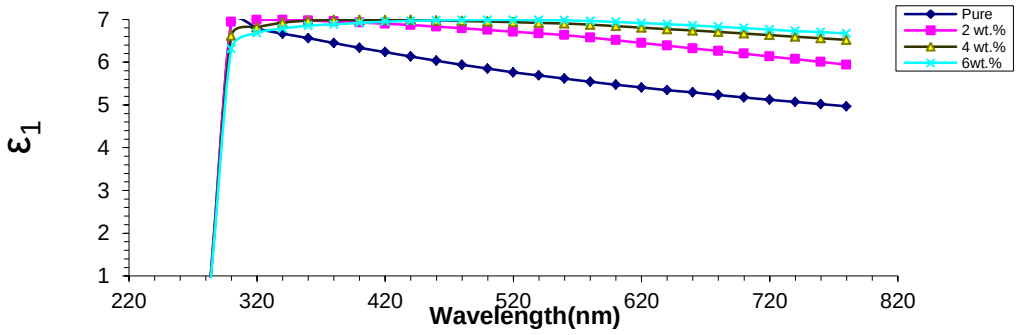

Figure 7. The unreal dielectric constant for (PMMA – PS) with Fe_2O_3 nano.

4. Conclusions

The study is show adding PS to PMMA, obtained a polymeric compound that is bound and cohesive and has a greater impact force, and increasing the ratio of Fe_2O_3 nanoparticles in PMMA-PS compound led to an increase in absorbance, absorption coefficient, real and imaginary dielectric constant, refractive index and decreased transmittance.

References:

[1] Pippek J C 2006 *Semiconductor Optoelectronic Devices* University of California.
[2] French R H Mullejans H and Jones D J 1998 *Journal of the American Ceramic Society* **81** (10) 2549.
[3] Al-Jamal Y N 1990 *Solid State Physics Mosul* University Press.
[4] Nemah S S and Hasan Z A 2019 *Journal of Global Pharma Technology* **11** (7) 325.
[5] Hasan B A *2005 J.of college of Education* (5) 449.
[6] Kumar G and Chandramani R 2009 *Appl. Surf. Sci.* **255** .
[7] Kumar G Chandramani R 2009 *Appl. Surf. Sci.* **255**.
[8] Hasan Z A and Obayes M F 2018 *J. Eng. Applied Sci*. **13** (13) 10551.
[9] Hasan Z A 2018 *J. Pharm. And Tech.* **11** (3).
[10] Chopra K L and Kaur I 1983 *Thin Film Device Applications* (New York : Plenum Press)
[11] Ndukwe I C 1996 *Solar Energy Materials and Solar Cells* **40** 123.

Investigating of Charge Transfer in Cu/F8 Using Donor-Acceptor Model due Quantum Transition

Investigating of Charge Transfer in Cu/ F8 Using Donor-Acceptor Model due Quantum Transition

Hadi J. M. Al-Agealy[1], Abbas K. Saadon[1], Mohsin A. Hassooni[1], Rawnaq Qays Ghadhban[1]

[1]Department of Physics, College of Education for Pure Science Ibn Al-Haitham, University of Baghdad

E-mail: Hadi_AlAgealy@yahoo.com

Abstract. In this paper, we study and investigate a simple donor-acceptor model for charge transfer formation using a quantum transition theory. The transfer parameters which enhanced the charge transfer and the rate of the charge transfer have been calculated. Then, we study the net charge transfer through interface of Cu/F8 contact devices and evaluate all transfer coefficients. The charge transfer rate of transfer processes is found to be dominated in the low orientation free energy and increased a little in decreased potential at interface comparison to the high potential at interface .The increased transition energy results in increasing the orientation of Cu to F8.The transfer in the system was more active when the system has large driving force energy and caused fast transfer from the donor to the acceptor and the charge transfer rate dependent on potential and solvents effect.

Keywords: Charge Transfer, Cu/ F8, orientation energy

1. Introduction

The charge transfer at level energy of a molecule has been played a basic role in different areas of physics, chemistry, material science, and biology [1]. Charge transfer was important fundamental process in electronics devices. The charge transfers from the molecule to the solid cross potential at interface. This transfer changes the electronic distribution by rearrangement of molecules and atoms [2]. In recent years, more attention of the charge transfer at interface between two different materials. Field of charge transfer in materials introduced more knowledge to understand and characterize the mechanisms of charge transition through interfaces such that molecule/semiconductor, molecule/molecule and molecule/metal interfaces [3]. The basic concept for describing the electronic transfer in solid contact with liquid has defined by the classical charge transfer theory that introduced by Marcus R. A. in 1992, it's still an actively field research after more than 60 years ago and developed by Rudolph Marcus, Levich, Dogonadeze and Gerischer [4]. The interface of contact organic active with metallic is very an importance to investigated and study electron transfer and determined the efficiency of the metal/ molecule through study the orbital levels of dye alignment with Fermi levels for metal [5]. The characteristic of electronic transfer at metal contact with the organic molecule are depending on the alignment of energy levels of electrons at molecule and the bands levels at metal [6]. In this research the theoretical system Cu/ F8 device include study the charge

transfer and determine the rate of the charge transfer. For Cu/ F8 system, the transition energy, potential and current electronic transfer will be present.

2. Theory

The non- adiabatic rate of electron transfer is [7].

$k_{nd} = \frac{2\pi}{\hbar}|R_c|^2\, WFC$……(1)

Where $\hbar$ is the $\frac{h}{2\pi}$, h is Blank constant, R_c is the resonance coupling of electronic term and WFC is the Franck–Condon weight. However, the Franck–Condon weight $WFC \equiv \boldsymbol{\delta}(E_{\beta_i} - E_{\alpha_i})$,the non-adiabatic rate with summed over all probability of vibrational quantum levels can be written as.

$k_{nd} = \frac{2\pi}{\hbar}\sum_i g(E)\left|\langle\hat{R}_c\rangle\right|^2 \boldsymbol{\delta}(E_f - E_i)$…….. (2)

$g_{(E)}$ is the distribution of electronic density of state and given by Fermi density of state [8].

$g(E) = \frac{1}{1+e^{\frac{E}{k_B T}}}$ ……. (3)

Where$E = E_i - E_F$. Inserting Eq.(3) in Eq.(2)

$k_{nd} = \frac{2\pi}{\hbar}\sum_i \frac{1}{1+e^{\frac{E}{k_B T}}}\left|\langle\hat{R}_c\rangle\right|^2 \boldsymbol{\delta}(E_f - E_i)$…….. (4)

Introduce the total density $\boldsymbol{D}_{(E)}$for all states of system

$k_{nd} = \frac{2\pi}{\hbar}\sum_i \frac{1}{1+e^{\frac{E}{k_B T}}}\left|\langle\hat{R}_c\rangle\right|^2 \boldsymbol{D}_{(E)}\boldsymbol{\delta}(E_f - E_i)$……. (5)

However, the activity density of metal-molecule system is equivalent to $\boldsymbol{\delta}(E_f - E_i)$,then Eq.(5) can be written.

$k_{nd} = \frac{2\pi}{\hbar}\sum_i \frac{1}{1+e^{\frac{E}{k_B T}}}\left|\langle\hat{R}_c\rangle\right|^2 \boldsymbol{D}_{(E)}\boldsymbol{\rho}_a(E)$…….. (6)

Then, active density of states for charge transition interaction is [9]

$\boldsymbol{\rho}_a(E) = \boldsymbol{\rho}_{\mathrm{M}}(\mathrm{E})\frac{l_M}{{d_M}^{2/3}(\frac{6}{\pi})^{\frac{1}{3}}}$…….(7)

here l_M is the length coupling and $d_M(\frac{cm}{atom})$ is average diameter in lattice for metal. Thus, Eq.(7) and Eq.(6) lead to.

$k_{nd} = \frac{2\pi}{\hbar}\sum_i \frac{1}{1+e^{\frac{E}{k_B T}}}\left|\langle\hat{R}_c\rangle\right|^2 \boldsymbol{D}_{(E)}\boldsymbol{\rho}_{\mathrm{M}}(\mathrm{E})\frac{l_M}{{d_M}^{2/3}(\frac{6}{\pi})^{\frac{1}{3}}}$……(8)

Due to Drude theory, the density of metal states per electron concentration is [10].

$\boldsymbol{\rho}_{\mathrm{M}}(\mathrm{E}) = (\frac{3}{2E_F})$……(9)

Where E_F is the Fermi energy. Substituting Eq.(9) in Eq.(8) results

$k_{nd} = \frac{2\pi}{\hbar}\sum_i \frac{1}{1+e^{\frac{E}{k_B T}}}\left|\langle\hat{R}_c\rangle\right|^2 \boldsymbol{D}_{(E)}(\frac{3}{2E_F})\frac{l_M}{{d_M}^{2/3}(\frac{6}{\pi})^{\frac{1}{3}}}$……(10)

the density of state given [11].

$\boldsymbol{D}_{(E)} = \sqrt{\frac{1}{4\pi\Gamma k_B T}}\mathrm{e}^{\frac{-(\Gamma+\Delta E^0)^2}{4\Gamma k_B T}}$ …..(11)

For all electrons in the donor-acceptor interface, we inserting Eq.(11) in Eq.(10) and integrated the results .

$k_{nd} = \frac{2\pi}{\hbar}\sqrt{\frac{1}{4\pi\Gamma k_B T}}(\frac{3}{2E_F})\frac{l_M}{{d_M}^{2/3}(\frac{6}{\pi})^{\frac{1}{3}}}\int_{-\infty}^{\infty}\left|\langle\hat{R}_c\rangle\right|^2 \frac{\mathrm{e}^{\frac{-(\Gamma+\Delta E^0)^2}{4\Gamma k_B T}}}{1+e^{\frac{E}{k_B T}}}\mathrm{dE}$ ..(12)

Where the $\Delta E^0 = E_F - \mathrm{IE}$.The potential at interface of system is .

$\Delta\mathbf{U} = \frac{(E_F - \mathrm{IE} + \Gamma)^2}{4\Gamma}$ ……..….(13)

The Fermi factors can be simply

$$\frac{1}{1+e^{\frac{E}{k_BT}}}=\frac{e^{-\frac{E}{2k_BT}}}{(e^{-\frac{E}{2k_BT}}+e^{\frac{E}{2k_BT}})}\text{…….,…….. (14)}$$

Inserting Eq.(14) in Eq.(13)

$$k_{nd}=\frac{2\pi}{\hbar}\sqrt{\frac{1}{4\pi\Gamma k_BT}}\,(\frac{3}{2E_F})\frac{l_M}{{d_M}^{2/3}(\frac{6}{\pi})^{\frac{1}{3}}}e^{\frac{-(\Gamma+\Delta E^0)^2}{4\Gamma k_BT}}\int_{-\infty}^{\infty}\left|\langle\hat{R}_c\rangle\right|^2\frac{e^{-\frac{E}{2k_BT}}}{\left(e^{-\frac{E}{2k_BT}}+e^{\frac{E}{2k_BT}}\right)}dE\text{…(15)}$$

The $e^{-\frac{E}{2k_BT}}$ can be expand to .

$$e^{-\frac{E}{2k_BT}}=1-\left(\frac{E}{2k_BT}\right)+\frac{1}{2!}\left(\frac{E}{2k_BT}\right)^2-\frac{1}{3!}\left(\frac{E}{2k_BT}\right)^3\text{ ….. }+\frac{1}{n!}(\frac{E}{2k_BT})^n\text{…… (16)}$$

Then Eq.(15) with Eq.(16) reduced to

$$k_{nd}=\frac{2\pi}{\hbar}\sqrt{\frac{1}{4\pi\Gamma k_BT}}\left(\frac{3}{2E_F}\right)\frac{l_M}{{d_M}^{\frac{2}{3}}(\frac{6}{\pi})^{\frac{1}{3}}}e^{\frac{-(\Gamma+\Delta E^0)^2}{4\Gamma k_BT}}\int_{-\infty}^{\infty}\left|\langle\hat{R}_c\rangle\right|^2\frac{1}{\left(e^{-\frac{E}{2k_BT}}+e^{\frac{E}{2k_BT}}\right)}[1-\left(\frac{E}{2k_BT}\right)+\frac{1}{2!}\left(\frac{E}{2k_BT}\right)^2-$$

$$\frac{1}{3!}\left(\frac{E}{2k_BT}\right)^3\text{ ….. }+\frac{1}{n!}(\frac{E}{2k_BT})^n]dE\text{…… (17)}$$

The Eq.(17) simply to

$$k_{nd}=\frac{2\pi}{\hbar}\sqrt{\frac{1}{4\pi\Gamma k_BT}}\left(\frac{3}{2E_F}\right)\frac{l_M}{{d_M}^{\frac{2}{3}}(\frac{6}{\pi})^{\frac{1}{3}}}e^{\frac{-(\Gamma+\Delta E^0)^2}{4\Gamma k_BT}}\left|\langle\hat{R}_c\rangle\right|^2[\int_{-\infty}^{+\infty}\frac{dE}{(e^{-\frac{E}{2k_BT}}+e^{\frac{E}{2k_BT}})}-\frac{1}{2k_BT}\int_{-\infty}^{+\infty}\frac{EdE}{(e^{-\frac{E}{2k_BT}}+e^{\frac{E}{2k_BT}})}+$$

$$\frac{1}{2!}\left(\frac{1}{2k_BT}\right)^2\int_{-\infty}^{+\infty}\frac{E^2dE}{(e^{-\frac{E}{2k_BT}}+e^{\frac{E}{2k_BT}})}-\frac{1}{3!}\left(\frac{1}{2k_BT}\right)^3\int_{-\infty}^{+\infty}\frac{E^3dE}{(e^{-\frac{E}{2k_BT}}+e^{\frac{E}{2k_BT}})}+$$

$$\cdots\ldots\ldots\frac{1}{n!}(\frac{1}{2k_BT})^n\int_{-\infty}^{+\infty}\frac{E^ndE}{(e^{-\frac{E}{2k_BT}}+e^{\frac{E}{2k_BT}})}]\text{(18)}$$

We solved term by term to get

$$k_{nd}=$$

$$\frac{2\pi}{\hbar}\sqrt{\frac{1}{4\pi\Gamma k_BT}}\left(\frac{3}{2E_F}\right)\frac{l_M}{{d_M}^{\frac{2}{3}}(\frac{6}{\pi})^{\frac{1}{3}}}e^{\frac{-(\Gamma+\Delta E^0)^2}{4\Gamma k_BT}}\left|\langle\hat{R}_c\rangle\right|^2[\pi k_BT+\frac{1}{2!}\left(\frac{1}{2k_BT}\right)^2\frac{(\pi k_BT)^3}{4}+\frac{1}{4!}\left(\frac{1}{2k_BT}\right)^4\frac{5(\pi k_BT)^5}{16}+$$

$$\cdots\ldots\frac{1}{n!}(\frac{1}{2k_BT})^n\beta(\pi k_BT)^{n+1}]\text{(19)}$$

The electronic transfer rate per electronic density of metal $N(E_F)$

$$K_{nd}=\frac{k_{nd}}{N(E_F)}\text{…… (20)}$$

Inserting Eq.(20) in Eq.(19) and taken two term approximation .

$$K_{nd}=\frac{2\pi}{N_M(E_F)\hbar}\sqrt{\frac{1}{4\pi\Gamma k_BT}}\left(\frac{3}{2E_F}\right)\frac{l_M}{{d_M}^{\frac{2}{3}}(\frac{6}{\pi})^{\frac{1}{3}}}e^{\frac{-(\Gamma+\Delta E^0)^2}{4\Gamma k_BT}}\left|\langle\hat{R}_c\rangle\right|^2[\pi k_BT+\frac{1}{2!}\left(\frac{1}{2k_BT}\right)^2\frac{(\pi k_BT)^3}{4}]\text{…… (21)}$$

The transfer energy $\Gamma(eV)$ for charge transfer processes is given by [12].

$$\Gamma(eV)=\frac{q^2}{8\pi\varepsilon_o}(\frac{1}{R}-\frac{1}{2D})(\frac{1}{n^2}-\frac{1}{\varepsilon})\text{…… (22)}$$

where q is charge electron, ε_o is the permittivity of vacuum ,ε and n are the dielectric constant and refractive index of solvent, r is the distance between dye and metal, R is the radius of dye can be estimated from the approach [13].

$$R=(\frac{3M}{4\pi N\rho})^{\frac{1}{3}}\text{…….…….…….…… (23)}$$

where the molecular weight is M , Avogadro's number is N and ρ is the density of material. The driving force energy for charge transfer from donor state to an acceptor state when photons incident on the system is given by .

$$\Delta E=E_{in}-\Gamma(eV)\text{ … … … … … … . … … … … … (24)}$$

Where $E_{in}=h\frac{c}{\lambda}$ incident energy by light, c is speed of light and wavelength λ

3. Results

Based on the theory of charge transfer, we calculate the charge transfer rate in Cu/F8 device according to transfer energy, Fermi energy, ionization energy, coupling constant and potential at interface for two materials. The transfer energy in Eq (22) refers to effect of solvent, molecule and metal.

The charge transfer rate in Cu/F8 device has been studied and calculated using theoretical model for identical state of electrons. The rate expression in Eq. (21) is theoretical tools for study the mechanism and behavior of charge transfer. In general, Eq. (22) could be used to evaluation the transition energy for the system using MATLAB program. The radii of F8 and Cu are estimated using Eq. (23) with inserting the molecular weight M, and mass density ρ for materials (F8 and Cu) from the table (1) in Eq.(23) with Avogadro's constant $N = 6.02 \times 10^{23} \frac{Molecule}{mol}$, the results of radii are show in Table (1) and (2).

Table 1. Physical properties of Cu.

Properties	Cu metal [14]
Molecular weight g/mol	63.546
Mass Density (g/cm^3)	8.96
Boiling Point (K)	2840
Atomic Radius (Å)	1.28
Lattice Structure	Face-Centered Cubic
Lattice constant(Å)	3.610
Radius (Å)	1.28
Work function	4·61 ± 0·04
Melting point ($^{\circ}$C)	1357.77
Fermi energy (eV)	7.0

Table 2. The properties of F8 molecule dye.

F8		
CAS	19456-48-5	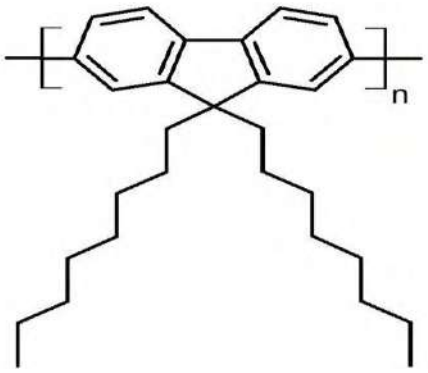
Molecular Formula	$(C_{29}H_{41})_n$	
Molar Mas g/mol	114,050	
Density g/cm^3	1.564	
Radius cm	5.181×10^{-8}	
Index of Refraction	1.736	
Melting point C^0	250.4	
Ionization energy(eV)	5.8	
HOMO (eV)	5.9eV	
LUMO(eV)	3.3eV	
Vapor Presure(mmHg at 25°C)	0.00508	
Name	Poly(9,9-di-n-octylfluorenyl-2,7-diyl) (F8)	

Transition energy Γ(eV) for charge transfer processes has been calculated using Eq. (22) with MATLAB program. its inserting the radii R for F8 molecule and the distance D(m)=R(Cu)+$R(F8)$ from table (1) and(2) and the dielectric constants and refractive index for the solvents from the table (3), results are shown in the table (3) for Cu/F8 .

Table 3. Calculated results of transition energy Γ(eV)for Cu/ F8 system.

Solvent	Molecular stricture	Molecular Weight	Refractve index (n)	Dielectric constant (ε)	Transtion energy Γ(eV)
1-bromooctane	$C_8H_{17}Br$	193.12	1.4524	5.0244	0.21983
2-methylpyridin	C_6H_7N	93.13	1.4984	9.9533	0.275701
2-Hexanone	$C_6H_{12}O$	100.16	1.4007	14.136	0.350859
Acetone	C_3H_6O	58.08	1.3559	20.493	0.395766
Bezonitrile	C_7H_5N	103.12	1.5257	25.592	0.312148
Propanonitrile	$C_{18}H_{17}Br_2N_5O_2$	495.2	1.3633	29.324	0.402805
Nitrobenzene	$C_6H_5NO_2$	123.11	1.5030	34.809	0.330869
1,2-ethanediol	$C_2H_6O_2$	62.07	1.4306	40.245	0.37069
dimethylsulfoxide	C_2H_6OS	78.14	1.4170	46.826	0.381014

Due to Eq.(23) ,the results of driving force energy ΔE **(eV)** is listed in table (4) using the absorption energy from spectrum energy of F8 and transition energy of Cu/F8 from the table (3).

Table 4. Results of driving force ΔE (eV) calculated for Cu/ F8 system.

λ nm	1-bromooctane	2-Methylpyridin	Hexanone	Acetone	*Bezonitrile*	*Propanonitrile*	*Nitrobenzene*	1,2-ethanediol	dimethyls-ulfoxide
300	3.9134	3.8575	3.7823	3.7374	3.8211	3.7304	3.8023	3.7625	3.7522
350	3.3229	3.267	3.1918	3.1469	3.2306	3.1399	3.2118	3.172	3.1617
400	2.8801	2.8242	2.749	2.7041	2.7878	2.6971	2.769	2.7292	2.7189
450	2.5356	2.4797	2.4045	2.3596	2.4433	2.3526	2.4245	2.3847	2.3744
500	2.2601	2.2042	2.129	2.0841	2.1678	2.0771	2.149	2.1092	2.0989
550	2.0346	1.9787	1.9035	1.8586	1.9423	1.8516	1.9235	1.8837	1.8734
600	1.8468	1.7909	1.7157	1.6708	1.7545	1.6638	1.7357	1.6959	1.6856
650	1.6878	1.6319	1.5567	1.5118	1.5955	1.5048	1.5767	1.5369	1.5266
700	1.5515	1.4956	1.4204	1.3755	1.4592	1.3685	1.4404	1.4006	1.3903
750	1.4334	1.3775	1.3023	1.2574	1.3411	1.2504	1.3223	1.2825	1.2722
800	1.3301	1.2742	1.199	1.1541	1.2378	1.1471	1.219	1.1792	1.1689

Due to Eq. (13), the results of potential **ΔU**(eV)is listed in table (5) using the ionization energy of F8 and Fermi energy of Cu E_F=7.0 eV.

Table 5. Results of potential energy **ΔU**(eV) calculated for Cu/ F8.

Solvent type	F(n,e)	Γ(eV)	U	Exp-(U/0.025) 1.0E-30
1-bromooctane	0.275	0.21983	2.4569	2.09E-13
2-methylpyridin	0.3449	0.275701	2.110766	2.15E-07
2-Hexanone	0.439	0.350859	1.826054	0.018975
Acetone	0.4951	0.395766	1.710952	1.895455
Bezonitrile	0.3905	0.312148	1.954446	0.000112
Propanonitrile	0.5039	0.402805	1.695464	3.521888
Nitrobenzene	0.4139	0.330869	1.888321	0.001572
1,2-ethanediol	0.4638	0.37069	1.77145	0.168562
dimethylsulfoxide	0.4767	0.381014	1.745478	0.476375

According to theory, the rate of charge transfer has evaluated using Eq.(21) with different solvents using MATLAB with all parameters of charge transfer processes the transition energy from table (3),

taken Fermi energy ,ionization energy , and taken coupling $\left|\langle \hat{R}_c \rangle\right|^2$=2.25,2.5,2.75,3.0,3.25,3.5 and 3.75 x10^{-2} eV/ state [16] , results of the calculation of current are listed in table (6) for Cu/F8.

Table 6. Results of charge transition rate for Cu/F8, at Ionization Energy 5.8 eV

Solvent type	The charge transition rate costant $x10^{-44}$						
	Strength coupling $\left\|\langle \hat{R}_c \rangle\right\| x10^{-2}$ eV/ state						
	2.25	2. 5	2.75	3.0	3.25	3.5	3.75
1-bromooctane	2.99E-13	3.7E-13	4.47E-13	5.32E-13	6.25E-13	7.24E-13	8.32E-13
2-methylpyridin	2.75E-07	3.4E-07	4.11E-07	4.9E-07	5.75E-07	6.66E-07	7.65E-07
2-Hexanone	0.021558	0.026615	0.032205	0.038326	0.04498	0.052166	0.059885
Acetone	2.027632	2.50325	3.028932	3.60468	4.230492	4.90637	5.632312
Bezonitrile	0.000134	0.000166	0.000201	0.000239	0.000281	0.000325	0.000374
Propanonitrile	3.734418	4.610393	5.578575	6.638966	7.791564	9.03637	10.37338
Nitrobenzene	0.001839	0.002271	0.002748	0.00327	0.003838	0.004451	0.005109
1,2-ethanediol	0.186316	0.23002	0.278324	0.331228	0.388733	0.450838	0.517544
dimethylsulfoxide	0.519366	0.641193	0.775843	0.923317	1.083615	1.256737	1.442683

4. Discussion

Understanding and calculated of charge transition rate at the interface of Cu/F8 is an important key prerequisite for investigated and studied the electronic properties of the Cu/F8 devices. However, the characterize of the mechanisms and charge transfer rates needs to understand the transition energy, energy level alignment, potential, driving force and electronic strength coupling between Cu metal and F8 molecule. This indicate that transition energy is the scale parameters of charge transfer processes. The transition energy in table (3) indicate that the system with Propanonitrile solvent has transition energy 0.402805 eV while the system with 1-bromooctane solvent has transition energy 0.21983 eV, this indicate the system with Propanonitrile is less active to charge transfer compare with other solvents. The gap between the transition energy of solvents between the top solvent and bottom solvent are in range (0.21983 eV to 0.402805 eV), the system with low transition energy enhances more transfer compare with large transition energy because low transition energy acting to forming charge transfer states fastly compare with large transition energy and lead to driving more charge cross from donor to acceptor state. To date, the potential and transition energy of charge transfer interaction between metal and molecules are used to study device structure hasn't been properly characterized.Unlike the driving force energy fore system in table (4) with 1-bromooctane solvent in range 3.9134 to 1.3301eV comparing with Propanonitrile solvent in range 3.7304 to 1.1471eV order, when the driving force energy is large that's indicate the charge will transfer cross interface, there is mean the charge transfer rate is large and potential is small .The Cu/F8 system with solvents fall into two categories, low polarity solvent and high polarity solvents.

Table (5)show the potential energy and transition energy for Cu/f8 devices with solvents , the system has small potential 0.695464 with Propanonitrile and high potential 2.4569 with 1-bromooctane solvents ,this indicate the potential states formed at interface by the π*-orbitals similar in chromophore types forcedly with solvents has low polarity function .This lead to assume that charge transfer happened as well as from the donor state to acceptor state when potential is low , that shown in table (6). Additionally, the charge transfer increased due to increase the electronic coupling of transition interactions to be observed.

5. Conclusions

The calculation of rate gives details on the charge transfer dynamics cross interface. Theoretical calculation of charge transfer rate has described in this account and became a good tool to examine the system before made any devices through recent theoretical calculation of charge transfer rate. Transition energy, driving force with potential are of particular value for limited the slow or fast charge transfer processes through different of individual events dynamical polarity, such as the low

and large transition energy, large transfer for system has more driving force energy from the donor to acceptor, potential dependent of the quantum charge transfer rates, and solvents effect. The theoretical description of the charge transfer at interface created an intuitive scenario that appeals to Cu/F8 devices and gives a clear understanding of the effects of charge transfer characteristic on charge transfer rate, the structure of devices, electrical properties, and charge transfer interactions that occur cross interface.

References

[1] Wörner HJ, Arrell CA, Banerji N, Cannizzo A, Chergui M, Das AK, Hamm P, Keller U, Kraus PM, Liberatore E and Lopez-Tarifa P 2017 Charge migration and charge transfer in molecular systems *Struct. Dynam.* **4** 061508.

[2] Al-Agealy HJ and Janeri HHDA 2019 Investigation the flow charge rate at InAs/D149 and ZnO/D149 system using theoretical quantum model *AIP Conf. Proc.* **2123** p. 020055). AIP Publishing LLC.

[3] Wang L, Chen W and Wee ATS 2008 Charge transfer across the molecule/metal interface using the core hole clock technique *Surf. Sci. Rep.* **63** 465-486.

[4] Asbury JB, Hao E, Wang Y, Ghosh HN and Lian T 2001. Ultrafast electron transfer dynamics from molecular adsorbates to semiconductor nanocrystalline thin films.

[5] Otero R, de Parga AV and Gallego JM 2017. Electronic, structural and chemical effects of charge-transfer at organic/inorganic interfaces *Surf. Sci. Rep.* **72** 105-145.

[6] Bagus PS, Hermann K and Wöll C 2005 The interaction of C 6 H 6 and C 6 H 12 with noble metal surfaces: Electronic level alignment and the origin of the interface dipole *J. Chem. Phys.* **123** 184109.

[7] Likhtenshtein GI 2003 *New Trends in Enzyme Catalysis and Biomimetic Chemical Reactions*. Springer Science & Business Media.

[8] Al-Agealy HJ, Hassoni MA, Ahmad MS, Noori RI and Jheil SS 2014 A Theoretical Study of Charge Transport y at Au/ZnSe and Au/ZnS Interfaces Devices. *Ibn AL-Haitham J. Pure Appl. Sci.* **27** 176-187.

[9] Royea WJ, Fajardo AM and Lewis NS 1997 Fermi golden rule approach to evaluating outer-sphere electron-transfer rate constants at semiconductor/liquid interfaces *J. Phys. Chem. B* **101** 11152-11159.

[10] Kittel C 1999 *Introduction to Solid State Physics* 6th ed.; Wiley: New York.

[11] Al-Agealy HJ and Fadhil MZ 2020 Estimation of the Electric Properties of Al/Cv System *J. Univ. Babylon Pure Appl. Sci.* 184-193.

[12] Al-agealy HJ, Alshafaay B, Hassooni MA, Ashwiekh AM, Sadoon AK, Majeed RH, Ghadhban RQ and Mahdi SH 2018 Theoretical discussion of electron transport rate constant at TCNQ/Ge and TiO2 system *J. Phys. Conf. Ser*. **1003** 012122.

[13] Hassooni MA and Al-Agealy HJM 2010 A Theoretical Study of the Effect of The Solvent Type on The Reorganization Energies of Dye-Semiconductor System Interface *Ibn Al-Haitham J. Pure Appl. Sci.* **23** 51-57.

[14] Lide DR 2004 *CRC handbook of chemistry and physics* (Vol. 85). CRC press.

[15] Zhang Y and Blom PW 2011. Electron and hole transport in poly (fluorene-benzothiadiazole) *Appl. Phys. Lett.* **98** 143504.

[16] Obeed HM and Al-Agealy HJM 2019 Theoretical Investigation of the Flow Charge Transfer Rate Through Cu/NTCDA molecule Interface *Test Engin. Manag.* **83** 8821-8829.

Energy loss of cluster ions in different concentration and temperature of plasma

Energy loss of cluster ions in different concentration and temperature of plasma

Nadher A Salman, Khalid A Ahmed, Baida M Ahmed

Mustansiriyah University, College of Science, Department of Physics

E-mail: dr.baida_222@uomustaniriyah.edu.iq

Abstract. The effects of the energy loss interference of homo and hetero nuclear di-cluster ions on the plasma in both Classic and Quantum Models are used to study of response dielectric function. The present work involves the interest ranges for Inertial Conference Fusion (ICF), Z-Pinch and Plasmas of Tokomak. The approximation of the Quantum Random Phase (RPA) is used, and the individual and collective Bohm-Pines model is calculated and the contribution of each mode will be calculated. For incident cluster ions, we present measurement and comparison of the stopping power for (homo nuclear di-cluster (H-H), (He-He)) and hetero-nuclear di-cluster ions like (He-H) in different plasma concentration and temperature of (ICF, Z-Pinch and TOKOMAK). The result appear the dependence of the interference term $I(r)$ on homo and hetero-nuclear di cluster distance r_{12} and the di-cluster velocity. All equations have been programmed to present the work using FORTRAN-90 and the program has been written for numerical calculations.

1. Introduction:

The interactions of the energy cluster beams with plasma targets were an active area of research in recent years, both experimentally and theoretically since they have a lower current beam density. A weaker beam concentration and a smaller region of energy deposition, in fact, stopping the cluster is more complicated than stopping the atomic ions [1, 2]. The following basic processes include cluster ion interaction with a plasma target in the first step. In collisions with plasma, the molecule loses valence electrons and the molecular structure equilibrium is consequently disrupted because of the ionization of its constituent atoms. The ions will lose their energy because their kinetic energies are transferred to the target. Simultaneously, The repulsion induced by dynamically screened coulomb interaction between the like-charged ions drives a portion of them and the molecular ion will undergo the coulomb explosion path. After the initial break-up of the molecule, further movement of the molecule is followed by electronic target excitations, which display significant interference due to near spatial correlation inside the ions, known as the vicinage effect. This form of interference induced by the structure is designed to produce increasing stopping power for each ion compared to the energy loss of the monomer ion moving at the same speed as long as the inter-ionic distances inside the cluster are smaller than the characteristic length of the electronic excitation [3]. On the theoretical side, two key approaches were suggested to explain the interactions between ions and plasma beams: the dielectric formulation [4, 5] and the collisional approach [6-8]. On the basis of the latter, a further model was described using the Transport Cross-Section (TCS) method [9, 10]. Fermi has introduced a dielectric formalism to explain the energy

loss of charged particles in the medium [4], and the other authors have been further developed [5, 11-13]. This formulation includes the screening effects, in a self-consistent way, along with the individual and collective excitations generated in the medium. [14].The aim of this research is to examine energy loss in detail of homo and hetero-nuclear di-cluster ions in the plasmas varying temperatures and densities. The analysis is expressed in the form of classical collision less plasma dielectric formalism and involves calculation using the approximation of the Quantum Random Phase (RPA) as well. We investigate the stopping of homo-and hetero-nuclear di-cluster ions, obtaining interference effects results and comparing them with previous work [15].

2. Theoretical procedure:

For a charged point particle, Ze and speed v, the expression of average energy loss or stopping power is given by.

$$S \equiv Z^2 S_0 = \frac{2(Ze)^2}{\pi v^2} \int_0^\infty \left(\frac{dk}{k}\right) \int_0^{kv} \omega \, d\omega \; Im\left(\frac{-1}{\epsilon(k,\omega)}\right). \quad (1)$$

where $\epsilon(k,\omega)$ is the Medium's Dielectric Function . Previous authors have provided numerous calculations for plasma stopping power utilizing this technique [14]. The dielectric function can be conveniently parameterized in the case of a classical plasma as [15],

$$\epsilon(k,\omega) = 1 + \left(\frac{k_D}{k}\right)^2 W(\xi) \quad (2)$$

where the plasma dispersion function is $W(\xi)$ [16],

$$\xi = \frac{(\omega + i\gamma)/\omega_P}{k/k_D} \quad ; \quad k_D = \lambda_D^{-1} \quad (3)$$

where (γ) represents the damping. In the limit $\gamma \rightarrow 0$ for collision less plasma, Eq. (3) becomes:

$$\xi = \frac{\omega/\omega_P}{k/k_D}, \quad (4)$$

And therefore Eq. (2) becomes,

$$\epsilon(k,\omega) = 1 + \left(\frac{k_D}{k}\right)^2 W\left(\frac{\omega/\omega_P}{k/k_D}\right) \quad (5)$$

The function $W(z)$ can be expressed as a variable $z = \omega/k\upsilon$ given in Appendix (A). The main parameters of the interaction between particles and plasmas problem are the velocity υ, its particle charge Z, the density of plasman_p, and temperature (T). The inter nuclear distance r_{ij} should be used to describe interference effects as well as the correlated ions. Other interest quantities are the frequency of plasma ω_p, v_T velocity of thermal electrons, and Debye length λ_D defined by atomic units [16-17]

$$\omega_p = \sqrt{4\pi n_p} \;, \; v_T = \sqrt{k_B T} \;, \; \lambda_D = \frac{v_T}{\omega_p} = \sqrt{\frac{K_B T}{4\pi n_p}}$$

where the plasma electron density is n_p and the temperature of the electron is T.

2.1 Stopping power of di-cluster ions

Let us consider di-cluster ions with atomic numbers Z_1 and Z_2, depending on the dielectric formulation, the stopping power of di-cluster ions is given as follows [18]:

$$S_{clus} = \left(\frac{-dE}{dx}\right)(Z_1) + \left(\frac{-dE}{dx}\right)(Z_1) + I(Z_1, Z_2, r_{12}) + I(Z_2, Z_1, r_{12}) \quad (6)$$

where ($\frac{-dE}{dx}$) for Z_1 and Z_2 are given in Eq.(1), $I(Z_1, Z_2, r_{12})$ and $I(Z_2, Z_1, r_{12})$ are the correlated functions of two charges in correlated motion with velocity $\vec{v}$ and inter-nuclear separation $\vec{r}_{12} = \overrightarrow{r_1} - \overrightarrow{r_2}$. The stopping power in Eq. (6) given either during (i) Parallel orientation:

$$S_{clus} = \left[\frac{-dE}{dx}\right] = \frac{e^2}{2\pi^2 v} \int dk^3 \frac{\vec{k}.\vec{v}}{k^2} Im\left(\frac{-1}{\epsilon(k,k,v)}\right) \left[(Z_1^2 + Z_2^2) + 2Z_1 Z_2 \cos\left(\vec{K}, \vec{r}_{12}\right)\right] \quad (7)$$

Or in (ii) perpendicular (random) orientation:

$$S_{clus} = \frac{e^2}{2\pi^2 v}\int dk^3 \frac{\vec{k}.\vec{v}}{k^2} Im\left(\frac{-1}{\epsilon(k,k,v)}\right)\left[(Z_1^2+Z_2^2)+2Z_1Z_2\frac{\sin(\vec{k},\vec{r}_{12})}{\vec{k}.\vec{r}_{12}}\right] \quad (8)$$

Using the variable $\omega = k.v$; $dk^3 = 4\pi\left[\frac{\vec{k}}{\vec{v}}\right]d\vec{k}d\omega$ (9)

Therefore, Eqns. (7, 8) become either

$$\left(\frac{-dE}{dx}\right) = \frac{e^2}{2\pi^2 v}\int_0^k \frac{dk}{k}\int_0^{kv} dww\left[(Z_1^2+Z_2^2)+2Z_1Z_2\cos(\vec{k},\vec{r})\right] \quad (10)$$

Or,

$$\langle -\frac{dE}{dx}\rangle = \frac{2e^2}{\pi v^2}\int_0^\infty \frac{d\vec{k}}{\vec{k}}\int_0^{\vec{k}.\vec{v}} wdw\, Im\left(\frac{-1}{\epsilon(k,w)}\right)\left[(Z_1^2+Z_2^2)+2Z_1Z_2\frac{\sin(\vec{k},\vec{r}_{12})}{\vec{k}.\vec{r}_{12}}\right] \quad (11)$$

The simplest case to be considered here is that of a pair of ions $Z_1 = Z_2 = 1$ in correlated motion, structures that may be obtained by the incidence of diatomic molecules. The study of this case is basic in order to understand more complicated cluster structures. The stopping power of cluster ion is given by [19].

$$S_{cls} = \frac{2e^2}{\pi\upsilon^2}\int_0^\infty \frac{dk}{k}\int_0^{k\upsilon} d\omega\,\omega\,\mathrm{Im}\left[\frac{-1}{\varepsilon(k,\omega)}\right]Z_{cls}^2 \quad (12)$$

where either,

$$Z_{cls}^2 = \left(Z_{i1}^2+Z_{i2}^2\right)+2Z_{i1}Z_{i2}\cos(\vec{k},\vec{r}) \quad (13)$$

$$Z_{cls}^2 = \left(Z_{i1}^2+Z_{i2}^2\right)+2Z_{i1}Z_{i2}\frac{\sin(\vec{k},\vec{r})}{\vec{k}.\vec{r}} \quad (14)$$

Therefore, the stopping power of di-cluster divided into two parts. On the other hand, self-interaction stopping power and correlation interaction stopping power are shown below:

$$S_{self} = \frac{2e^2}{\pi\upsilon^2}\left(Z_{i1}^2+Z_{i2}^2\right)\int_0^\infty \frac{dk}{k}\int_0^{k\upsilon} d\omega\,\omega\,\mathrm{Im}\left[\frac{-1}{\varepsilon(k,\omega)}\right] \quad (15)$$

And correlated part either,

$$S_{corr} = \frac{2e^2}{\pi v^2}\left(Z_{i1}^2Z_{i2}^2\right)\int_0^\infty \frac{dk}{k}\int_0^{kv} dwwIm\left[\frac{-1}{\epsilon(k,\omega)}\right]\cos(\vec{k},\vec{r}) \quad (16)$$

Or,

$$S_{corr} = \frac{2e^2}{\pi v^2}\left(Z_{i1}^2Z_{i2}^2\right)\int_0^\infty \frac{dk}{k}\int_0^{kv} dwwIm\left[\frac{-1}{\epsilon(k,\omega)}\right]\frac{\sin(\vec{k}.\vec{r})}{\vec{k}.\vec{r}} \quad (17)$$

Then the stopping power of di-cluster ions is:

$$S_{cls} = S_{self} + S_{corr} \quad (18)$$

There are some significant differences between correlated motion (di-cluster) and uncorrelated particles. In the simultaneous interaction between the two particles and the medium, these distinctions arise from interference effects. Let us now consider the effects of interference in the energy loss of the di-cluster produced by two particles in the motion at a velocity $\vec{v}$ through the plasma and at inter-nuclear distance $\vec{r}$. The di-cluster stopping power can be expressed as follows: [20, 22]:

$$S = \left(Z_{i1}^2+Z_{i2}^2\right)S_0 + 2Z_{i1}Z_{i2}\,I(k,r) \quad (19)$$

where $I(k,r)$ is an interference function given by:

$$I(k,r) = \frac{2e^2}{\pi v^2}\int_0^\infty \frac{dk}{k}\int_0^{kv} dw.wIm\left[\frac{-1}{\epsilon(k,w)}\right]\cos(\vec{k},\vec{r}) \quad (20)$$

Or

$$I(k,r) = \frac{2e^2}{\pi v^2}\int_0^\infty \frac{dk}{k}\int_0^{kv} dw.wIm\left[\frac{-1}{\epsilon(k,w)}\right]\frac{\sin(\vec{k}.\vec{r})}{\vec{k}.\vec{r}} \quad (21)$$

S_O is the stopping power of single ions defined in Eq. (1).

2.2 Stopping power of homo di-cluster ions:

Let's assume that the two particles have identical charges. $Z_1 = Z_2 = Z$, so that Eq. (19) becomes,

$$S_{dicl} = 2Z^2\left[S_0 + I_{(r)}\right] \quad (22)$$

The predicted limitations of function $I_{(r)}$ and the stopping power of the di-cluster are as follows:

i. for $r \to 0:$ $I(r) \to S_0$ and $S_{cl} \to (2Z)^2 S_0$ (one charge particle of 2Z)

ii. for $r \to \infty:$ $I(r) \to 0$ *and* $S_{cl} \to 2(Z^2 S_0)$ (two independent particles of charge).

Because of an ordinary experiment, the incident di-cluster is randomly oriented in this case. The average interference term can be taken with respect to the angle between $\vec{r}$ and $\vec{v}$, for H-H di-cluster ions, Z=1,

$$I(r) = \left(\frac{2}{\pi v^2}\right)\int_0^\infty \frac{dk}{k}\left(\frac{\sin kr}{kr}\right)\int_0^{kv} wdw\, Im\left(\frac{-1}{\in(k,w)}\right) \quad (23)$$

Using Eq (5) for the classical dielectric function collision less plasma, the integral of the interference term $I(r)$ can be written as follows:

$$I(r) = \frac{2{w_p}^2}{\pi v^2}\int_0^\infty \frac{k^3 dk}{k_D^4}\left(\frac{\sin(kr)}{kr}\right)\int_0^{v/v_T} zdz\left(\frac{Y(z)}{\left\{\left(\frac{k}{k_D}\right)+X(z)\right\}^2+[Y(z)]^2}\right) \quad (24)$$

The integration with the k variability can be carried out analytically after certain algebra; the function $I(r)$ can be expressed as a single integral,

$$I(r) = \frac{2}{\pi}\left(\frac{\omega}{\upsilon}\right)^2\left(\frac{\lambda_D}{r}\right)^2\int_0^{\upsilon/\upsilon_T} zdz\,\mathrm{Im}\left[F\left(z,k_{\max},r\right)\right] \quad (25)$$

where

$$F(z,k_{max},r) = q\{\sin qr\left[Ci\left((k_{max}-q)r\right)+Ci\left((k_{max}+q)r\right)-Ci(-qr)-Ci(qr)\right]+$$
$$\cos qr * \left[\mathrm{Si}\left((k_{max}-q)r\right)-\mathrm{Si}\left((k_{max}+qr)r\right)-2\,\mathrm{Si}-qr\right]\} \quad (26)$$

With

$$q = q(z) = K_D\sqrt{X(z)+iY(z)} \quad (27)$$

Si and Ci are the integrals of sine and cosine. Analytical results for the interference term $I(r)$ in Eq. (25) can now be obtained for low and high velocities. [15]:

2.1 High –velocity approximations:

In the case of ion with velocity $v \gg v_T$, we can distinguish the contribution from the individual and collective types, also the integral $I(r)$ can be calculated by.

$$\mathrm{I(r)} = \left(\frac{\mathrm{w_p}}{\mathrm{v}}\right)^2\left[\mathrm{I_1}\left(\frac{\mathrm{w_p r}}{\mathrm{v}},\frac{\mathrm{r}}{\lambda_\mathrm{D}}\right)\Theta(\mathrm{v}-\mathrm{v_T})+\mathrm{F_1}\left(\frac{\mathrm{v}}{\mathrm{v_T}}\right)\mathrm{I_1}\left(\frac{\mathrm{r}}{\lambda_\mathrm{D}},\mathrm{k_{max}r}\right)\Theta(\mathrm{k_{max}}-\mathrm{k_D})\right] \quad (28)$$

So,

$$I(r) = I^{ind}(r) + I^{coll}(r) \quad (29)$$

The above equations have been calculated numerically by programed the equations using Fortran-90 and writing a program $Diclustr-Classic.for$, and a copy of the program is available with authors.

$F_1\left(\frac{v}{v_T}\right)$ is given by,

$$F_1(x) = \left(\frac{2}{\pi}\right)^{1/2}\int_0^x z^2\exp\left(\frac{-z^2}{2}\right)dz \quad (30)$$

And ,

$$I_1(x,y) = \int_x^y\left(\frac{\sin(z)}{z^2}\right)dz = H(x) - H(y) \quad (31)$$

By defining H(x),

$$H(x) = \left(\frac{\sin x}{x}\right)Ci(x) \quad (32)$$

And in general one can say that:

$$H(u) = \left(\frac{\sin u}{u}\right) Ci(u) \quad (33)$$

For $v \gg v_T$ $(x \gg 1)$, $F_1(x) \equiv 1$ and get

$$I(r) \equiv k_{min}^2 I_1(k_{min}r, k_{max}r) \quad (34)$$

With $k_{\min} = 1/b_{\max} = \omega_p / \upsilon$, Functional dependency of the interference function at high speed. For large r ($k_{max}r \gg 1$) in Eq. (34) the term with $k_{\max}$ can be neglected. With regard to the lowest electron-ion approach distance in the nearest collisions, the inter-nuclear length is sufficiently large, so, the loss of energy is divided into individually and collectively excitation such that the tow ions behave as an individual scattering collision within the range of high velocities $> v_T$. Usually, the participation of collective modes is a small portion of stopping term S_0 . Additionally, the contribution of collective modes becomes very significant in the integration of the interference expression $I(r)$ [23].

2.3 Low- velocity approximations:

Using the estimation $z \ll 1$, where, $z = \omega / k\upsilon_T$, the function of energy loss $Im[-1/\in (k,w)]$ becomes helpful so,

$$Im\left(\frac{-1}{\in(k,w)}\right) = \sqrt{\frac{\pi}{2}}\left(\frac{k}{k_D}\right)^2 \left\{\frac{Zexp\left(\frac{-z^2}{2}\right)}{[1+(k/k_D)^2]^2}\right\} \quad (35)$$

Integrating Eq. (24) one can get the di-cluster at low velocity approximation,

$$\mathrm{I(r)} = \left(\frac{2}{\pi}\right)^{1/2} \frac{1}{3\lambda_D^2} \mathrm{I_2(r/\lambda_D, k_{max}/k_D)} \left(\frac{\mathrm{v}}{\mathrm{v_T}}\right) \mathrm{F_2(v/v_T)} \quad (36)$$

where $F_2(x)$ is given by:

$$F_2(x) = \frac{3}{x^3} \int_0^x z^2 \exp\left(\frac{-z^2}{2}\right) dz \quad (37)$$

And

$$I_2(x,y) = \int_0^y dz\, z^3 \left(\frac{\sin(zx)}{zx}\right)(1+z^2)^{-2} \quad (38)$$

3. Results and discussion

The calculations were made using the exact integral terms given by the dielectric forms. The classical dielectric function and quantum RPA procedure have been applied. Here, we examine the dependence of the interference term $I(r)$ on the while homo nuclear di cluster distance r_{12} and velocity v. For fast velocity, the behaviour of the interference expression I(r) could be seen in figure (3.5a). For corresponding (ICF) conditions of high velocities and big r quantities (with respect toλ_D) I(r) is rapidly tending to zero and it show low vibrational behaviour corresponding to distances. Though, $I(r)$ tends rapidly to zero for low velocities and large r - quantities (with respect to λ_D). It displays elevated vibrations values. For very long distances, there is no oscillatory activity.

Here, with mutual distances greater than λ_D, ions are scattered throughout a large area. Each ion is capable of generate a long range wake field that contributes to the electrical field at the location of all other ions. Constructive or destructive interferences may occur with respect to the characteristics phases of the wake field and result in increasing or decreasing stopping relative to uncorrelated stopping.

Figure (1) shows the variation of correlation function $I(r)$ and correlated stopping power of cluster ions S_{clus} like (a) H-H ICF, (b) He-He ICF and (c) He-H ICF di-cluster ions with atomic di-cluster ions distance r_{12} . The similar patterns of the results in the all cases (a), (b) and (c) suggest the presence of a basic scale rule. The point to be examined below the figures, utilising either a classical value or a quantum value of $k_{\max}$, show a very strong agreement between these results. To discuss the effects of

the atomic distance r_{12}, (1) $r_{12} \leq 3$ the correlation function $I(r)|_{HH} < I(r)|_{HeH} < I(r)|_{HeHe}$ while, the stopping power of di-cluster ions S_{clus}: $S_{clus}(r)|_{HH} > S_{clus}(r)|_{HeH} > S_{clus}(r)|_{HeHe}$ as shown in figure (1). (2) at $r_{12} \to \infty$, i.e $r_{12} \geq 20$, there is no contribution to the correlation function $I(r)$ and correlated stopping power S_{clus}. (3) Between these two regions, cosine or sine function appear in Eqns. (23 and 24) are strongly effect.

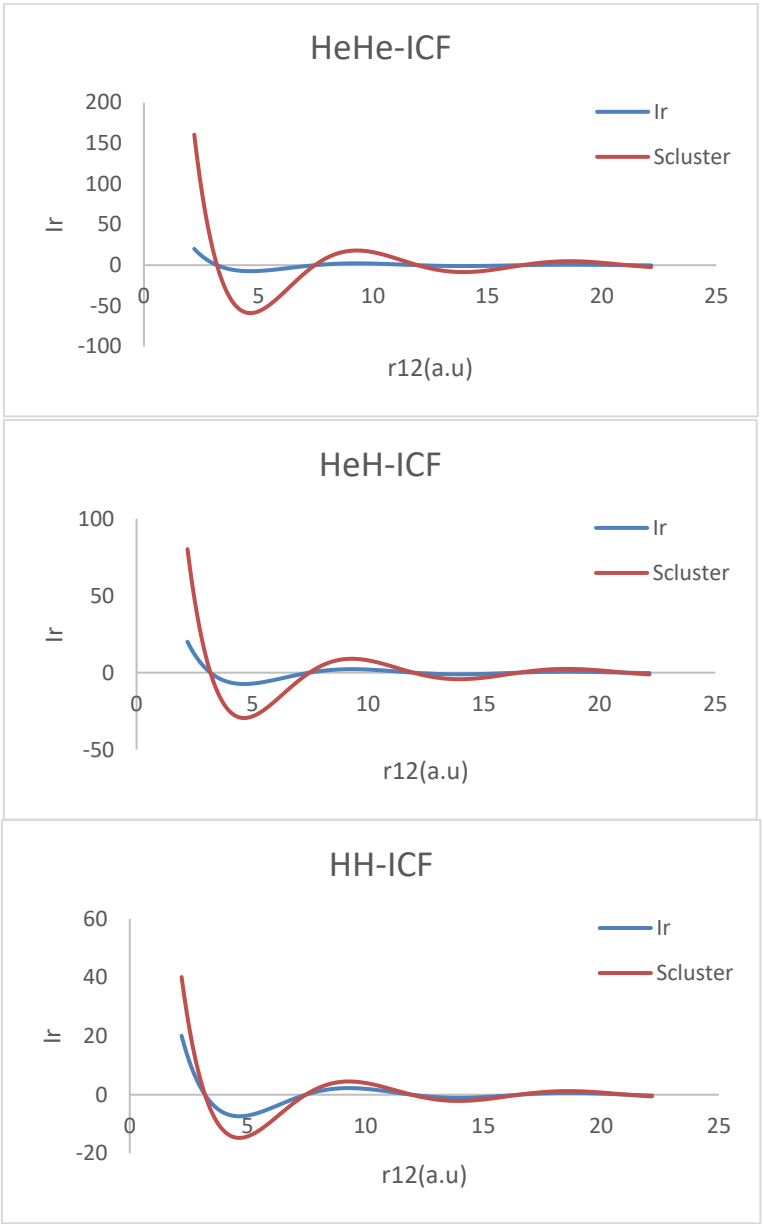

Figure 1. The correlated function term $I(r)$ and correlated stopping power $S_{clus}(r)$ for homo di-cluster ions (a) HH and (b) He-He and (c) hetero di-cluster ions He-H in ICF plasma as a function of inter atomic distances r_{12} were calculated using the classical dielectric function, and the quantum values of k_{max}.

Stopping of Homo and Hetero di-cluster ions:

Let us consider a di-cluster comprising two different forms of heavy atomic ions. For fast heavy ions, a number of electrons are typically carried with an increasing depth of penetration. The charge of the ion fluctuates around a certain value of the balance, which is generally calculated through the form of term:

$$q_i e \approx Z_i e[1-\exp(-\upsilon/\upsilon_{TF}] \quad (39)$$

where, $\upsilon_{TF} = Z_i^{2/3}\upsilon_0$ is the velocity of Thomas-Fermi

The ionic effective charge is usually expressed via the ion charge Z_i and the fractional effective charge of ion γ_i ,

$$Z_{eff} = \gamma_i Z_i \quad (40)$$

To connect the effective charge with the heavy $H_e - H$ di-cluster ions let the effective charge of two ions are Z^*_{He}, where,

$$Z^*_{He} = Z_{He}\left(1 - e^{-\upsilon_r/Z_{He}^{2/3}}\right) \quad (41)$$

Then, the stopping power of the di-cluster ions of charges Z^*_{He} with atomic number $Z_{He} = 2$ and $Z = 1$ is given in Eqns. (13, 14 and 6).

Three kinds of di-cluster ions have been used in present work, Hydrogen-Hydrogen (H-H), Helium-Helium (He-He) and Helium-Hydrogen (He-H). Figure (2) shows the stopping power for Homo di-cluster ions like (a) H-H, (b) He-He, and (c) Hetero di-cluster ions, and He-H as a function of the velocity in plasma system ICF. Note that the difference in scale percentage between the three systems of di-clusters ions that is why the interaction between incident homo nuclear di-cluster and electron target in ICF more Hetero di-cluster ions because the difference in atomic number of incident ions with the same density and thermal velocity of plasma matter.

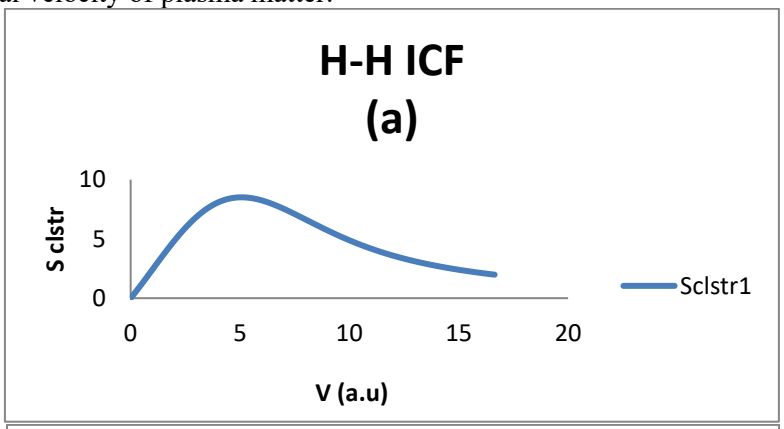

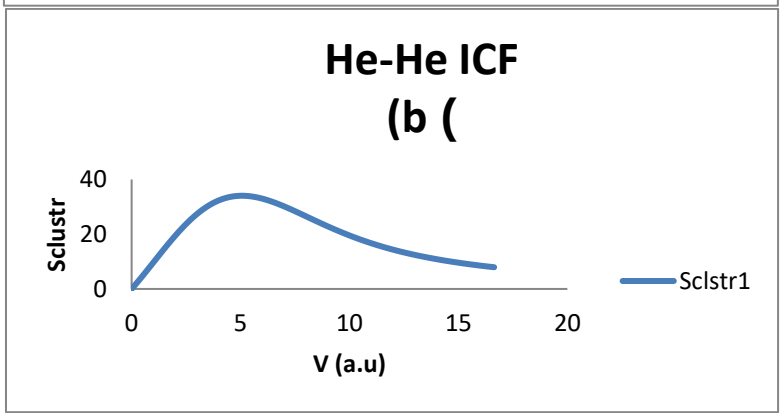

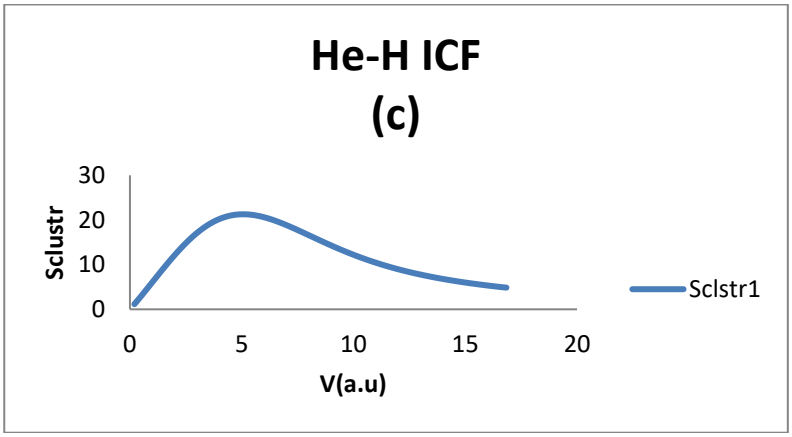

Figure 2. Calculations the stopping power of homo nuclear di cluster for (a) H-H, (b) He-He and (c) Hetero di-cluster ions HeH) in plasma system ICF. As a function of ion velocities.

Figure (3) shows that the computations have been made using the exact integral terms given by the dielectric formula, both the classical dielectric function and the quantum (RPA) procedure have been used. We analyse here the dependent of the interference definition I(r) on the hetero nuclear di cluster distance r_{12} and on the di cluster velocity υ. The behaviour of the interference concept $I(r)$ is displayed in figure (3a) for high velocities for the conditions corresponding to the (ICF) at large r values (with respect to λ_D). I(r) tends to zero rapidly and exhibits low vibrational behaviour corresponding to distances, while for low velocities the behaviour of the interference definition I(r) is displayed in figure (3b) for the conditions corresponding to the (Z-Pinch) tends to high oscillatory behaviour corresponding to distances.

Figure (4) shows the movement of hetero nuclear di-cluster (He-H) ion in different plasma systems (ICF, Z-Pinch) and in different distance between hetero nuclear di-cluster for ICF system the folds increase with velocity because of increasing the number of interaction between di-cluster and electron plasma. The effect of intensity and the stopping appear from the number of folds were increased with increasing the density, while for Z-Pinch the folds decrease with velocity because the density is low compare to ICF.

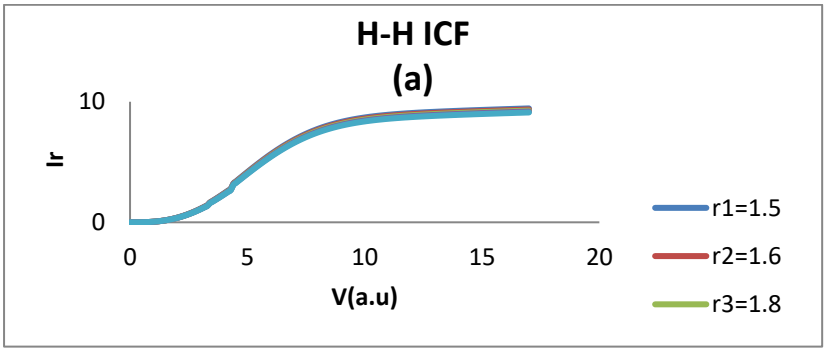

r = 1.50000 1.65000 1.80000 1.95000 2.10000

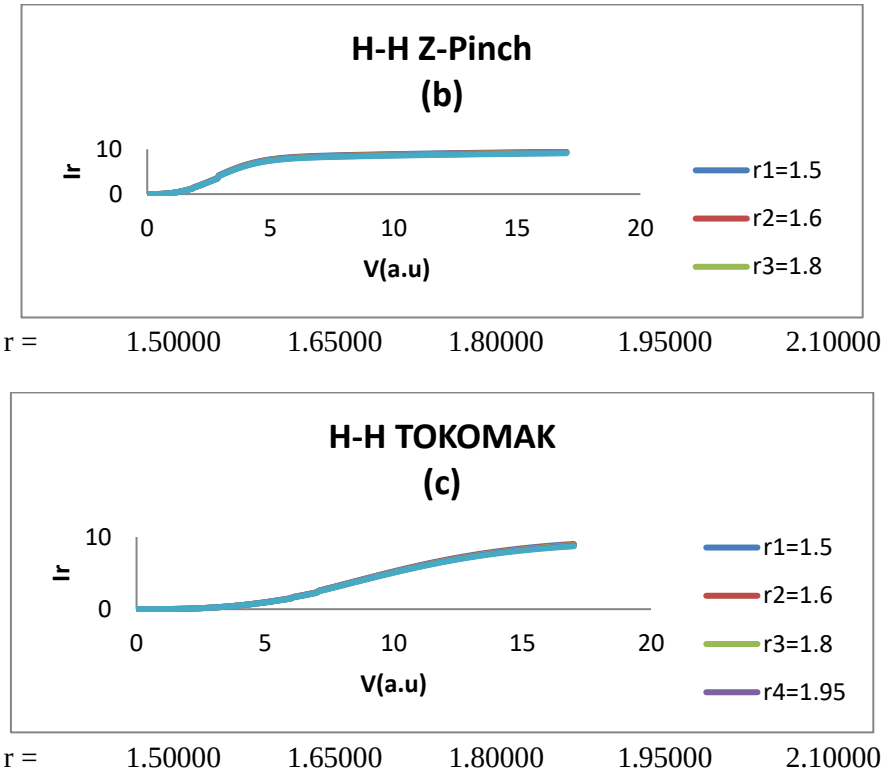

Figure 3. Show movement of di cluster (H-H) in the cases of (a) ICF , (b) Z-pinch and (c) Tokomak system characterized by the distance (r) between di cluster (H-H) .

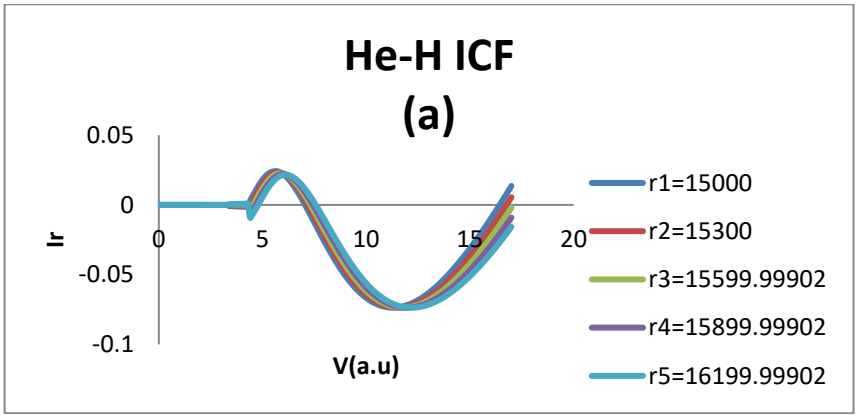

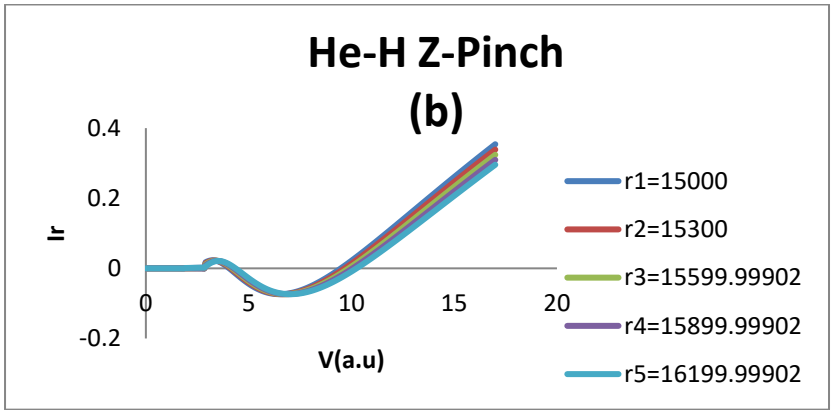

Figure 4. Shows the effect of the movement of hetero-nuclear di-cluster ions (He-H) inside (ICF and Z-pinch) systems plasma in different distance.

4. Conclusion

For different plasma conditions, the loss of energy of di-cluster ions in plasmas was analyzed numerically and analytically, detailed views the effect of the most important factors. The application of a classical dielectric function enables the stopping power and interference terms to be conveniently integrated.

In the case of low velocity, the consequences of interference are only significant if the distances between the two ions are identical or less than the Debye length λ_D. In the case of molecular ions inserted into plasmas, this condition is very well satisfied. In the case of high speeds, the interference function generally scaled with the parameter$r\ w_p/v$. As the value of b_{max} increases with velocity, the effects of interference will become more relevant and large collective effects can be expected.

Appendix (A)

Using the parameter $\omega_p = \sqrt{4\pi n_p}$, $v_T = \sqrt{k_B T}$, $\lambda_D = \frac{v_T}{\omega_p} = \sqrt{\frac{K_B T}{4\pi n_p}}$,

And according to Eq.(2.15), with $\xi = \left(\frac{(\omega + i\gamma)/\omega_p}{k/k_D} \right)$, one can finds

$$\epsilon(k,\omega) = 1 + \left(\frac{k_D}{k}\right)^2 W(\xi) \qquad \text{(A1)}$$

where the plasma dispersion function is $W(\xi)$ [22]

For $\gamma \to 0$ (collisional plasma) the $W(\xi)$ function can be expressed in term of the variable $\xi = \omega / k\upsilon$ as follows:

$$W(z) = X(\xi) + iY(\xi) \qquad \text{(A2)}$$

With

$$X(\xi) = 1 - \xi\ exp\left(\frac{-\xi^2}{2}\right) \int_0^{\xi} dx \exp\left(\frac{x^2}{2}\right) \qquad \text{(A3)}$$

And

$$Y(\xi) = \left(\frac{\pi}{2}\right)^{1/2} \xi\ exp\left(\frac{-\xi^2}{2}\right) \qquad \text{(A4)}$$

References:

[1] Wang G Q and Wang Y-N 2005 *Physics of plasmas* **12** 042702.
[2] Guiqiu W Peng and E Wenwen X 2014 *Plasma Science and Technology* **16** (7).
[3] Wang G Yi H Yujiao Li and others 2018 *Matter and Radiation at Extremes* **3** 66.
[4] Fermi E 40 *Phys. Rev.* **57** 485.
[5] Pines D and Bohm D 1952 *Phys. Rev.* **85** 338.
[6] Gryzinski M 1957 *Phys. Rev*. 1471.
[7] Spitzer L 1956 *Physics of fully Ionized Gasses Inter science* (New York).
[8] Butler S T and Bukingham M J 1962 *Phys. Rev.* **126** 1.
[9] Ferrariis L de and Arista N R 1984 *Phys. Rev.* **A.29** 2145.
[10] Clauser C F and Arista N R 2013 *Phys. Rev.* **E 88** 053102.
[11] Lindhard J Fys M Medd K and Vidensk D 1954 *Selsk* **28** (8) 1.
[12] Ritchie R H 1959 *Phys. Rev.* **114** 644.
[13] Lindhard J Winther A Mat Medd and F K Vidensk D 1964 *Selsk* **34** (4) 1.
[14] Clauser C F and Arista N R 2018 *Phys. Rev.* **E 97** 023202.
[15] Bringa E M and Arista N R 1996 *Phys. Rev.* **54** (4).
[16] Arista N R and Bringa E M 1997 *Phys. Rev. A* **55**(4).
[17] Ichimaru J 1973 *Basic Principles of Plasma Physics* (Benjamin -New York).
[18] Deutsch C and Formy P 1994 *Phys. Rev. E* **51** (1).
[19] Arista N R 2000 *Nuclear Instrument and Methods in physics Research B* **164-165** 108.
[20] Arista N R 1978 *Phys. Rev. B***18** (1).
[21] Ahmed B M Ahmed K A and Ahmed R K 2016 *Electron. Mater. Lett*. **12**(3) 419.
[22] Basbas G and Richie R H 1984 *Phys. Rev. A* **25** 1943.
[23] Chrimaru I *1970 Basic principles of plasma physics* (Benjamin - New York)

Study the Relationship between Beta Decay Stability of Nuclide and its Shape for Some even-even Isobars

Study the Relationship between Beta Decay Stability of Nuclide and its Shape for Some even-even Isobars

Naz T Jarallah [1], Murtadha S Nayyef [1]

[1] Collage of Education for Pure Science -Ibn Al-Haitham/University of Baghdad, Baghdad, Iraq

E-mail: naztalab2016@yahoo.com

Abstract. The aim of this work is to learn the relationship of the stability of (β) emitter isobars with their shape for some isobaric elements with even mass number (A=152 - 162). To reach this goal firstly the most stable isobar have been determined by plotting mass parabola (plotting the binding energy (B.E) as a function of the atomic number (Z)) for each isobaric family. Then three-dimensional representation graphics for each nucleus in these isobaric families have been plotted to illustrate the deformation in the shape of a nucleus. These three-dimensional representation graphics prepared by calculating the values of semi-axis minor (a), major (b) and (c) ellipsoid axis's. Our results show that the shape of nuclides which is represented the most stable isobar in mass parabola are not spherical but they have some deformation in their shape, and need to emit a gamma ray to a chive more stable status and get spherical shape. The stable nuclides, which are determined from mass parabola, are different from the nuclides, which have less value of deformation.

Keywords: Nuclear Binding Energy, Semi Empirical Mass Formula (SEMF), Mass Parabolas, the intrinsic quadrupole moment.

1. Introduction

The minimum part of the elements that keeps the basic features is the atom. An atom is made of a minor massive central called the nucleus; this nucleus is enclosed by orbiting electrons [1]. Nucleus consists of two kinds of separate nucleons (neutrons and the protons) these nucleons having nearly the same mass. Therefore, the binding energy of a nucleus is a dis-continuous function of its mass [2]. Cables of nuclei having similar mass number (A) but unlike in there number of protons (Z) and neutrons number (N) are called isobars. For example, the three nuclei 14C, 14Oand14N are isobars with mass number (A) = 14 [2]. Instability of nuclide causes the radioactivity. Which depends on, the symmetry between the neutrons and atomic number [3].

All nuclei which are unstable decay naturally in several ways. Isobars with a high extra of neutrons profit energy by translating a neutron into a proton. In the case of a surplus of protons, the reverse reaction may occur: i.e., the change of a proton into a neutron. These changes are called β-decays [4]. Beta particles (β) are electrons, which carry a negative or positive charge (e^{-}&e^{+}). In the state of (β^{-}) decay atomic number (Z) increased by one unit. But in the case of (β^{+}) decay the atomic number (Z) will be reduced by one unit. Some nuclei go through a radioactive conversion by taking an atomic electron, generally from K shell, releasing a neutrino in addition to decreases atomic number (Z) by one unit [5].

The deformation in the shape of nuclides arises from the method that valence nucleons arrangement themselves in an unfilled shell, in other words the deformation happens only when both proton and

neutron shells are slightly full. In the group, decay procedure the significant character is shell nuclear deformations. [3]

2. Theoretical Part

2.1. Semi Empirical Mass Formula (SEMF)

Semi Empirical Mass Formula (SEMF) is used to calculate mass, binding energy of nuclei, which is built on Liquid Drop Model (LDM) and originally expressed by C. F. V. Weizsäcker [2]. Then adapted by Bethe and other physician. It is built partly on model and partially on empirical measurement, thus this formula is named Semi Empirical mass formula (SEMF). This formula plays an important part in the advance of nuclear physics and it consists of five forms of energy terms that is, the volume, surface, coulomb, asymmetry and pairing energy along with corresponding five kinds of constants, while modifications have been done to the coefficients over the years, but the arrangement of the formula remains the similar till today. (SEMF) has been prolonged by addition unlike additional terms or been adapted by varying the dependence of several terms on A and Z slightly in an energy to expect the binding energies as nearer to experimental values [6].

The whole containing terms of the energy of (SEMF) takes the formula as below:

$$B.E(A,Z) = a_v A - a_s A^{2/3} - a_c Z(Z-1)A^{-1/3} - a_a\ (A-2Z)^2 A^{-1} \pm \delta A^{-1/2} + \eta \text{------- (1)}$$

Where: a_v, a_s, a_c, a_a, δ and η are the energy coefficients that denote to the volume, surface, Coulomb, asymmetry, pairing and shell energy terms, respectively [7].

One set of this factors is[8]: =15.8Mev, a_s,=18.3Mev, a_c=0.72Mev, a_a=23.2MeV.

$$\text{And } \delta = \begin{cases} +11.2 \text{ MeV for (even N, even Z) .} \\ 0 \text{ for (even N odd Z, or even Z, odd N).} \\ -11.2 \text{ MeV for (odd N, odd Z) .} \end{cases}$$

$$\text{And } \eta = \begin{cases} 3 \text{ Mev (N and Z = magic number).} \\ 2 \text{ Mev (N or Z = magic number and other is odd).} \\ 1 \text{ Mev (N or Z = magic number and other is even).} \\ 0 \text{ (N or Z = no magic number).} \end{cases}$$

2.2. Mass Parabola

One of the maximum uses of semi empirical mass formula (SEMF) is to determine the most stable isobar of a given mass number (A) from beta emission by plotting the binding energy as a function to the atomic number (Z) [9]. The isobars located on the sides of the parabola are not stable, thus to be more stable these nuclides will be decay. Nuclides with low atomic number (Z) side of the parabolic, decay by (β^-)emission toward to the increased of the atomic number (Z_A), but the nuclides with high atomic number(Z) decay in the opposite direction toward to the decreased of the atomic number(Z_A), in this case the decay being either by(β^+)emission or electron capture (EC) [9].

2.3. Minor and major ellipsoid axis

In classical electrodynamics, the simplest model for a non-spherical homogeneous charge supply is a rotating ellipsoid with charge z, major axis(b), and minor axis (a) [10]. To determine small (minor) (a) and large (major) (b) ellipsoid axises from following equations [3].

$$a = \left[\frac{<r^2>}{3}\left(5 - \frac{2\delta}{0.3}\right)\right]^{1/2} \quad (2)$$

$$b = [5 < r^2 > -2a^2]^{1/2} \quad (3)$$

Where:

$< r^2 >$: The mean-squared charge distribution radius average which calculated by:

$$< r^2 >= 0.6\left[1.2A^{1/3}\right]^2 \quad (A > 100) \quad (4)$$

(δ): quadruple deformation parameter denotes to the quantity of a deviation of shape of nucleus from spherical shape, which depends on the value of intrinsic quadruple moment (Q_0) as described in this equation [11].

$$\delta = \frac{0.75 Q_o}{(<r^2>Z)} \quad (5)$$

Where:

Q_0: The intrinsic quadrupole moment.

The electric quadrupole moment (Q_0) determines the deviation of the nuclear charge distribution from spherical balance. So electric quadrupole moment (Q_0) represented one of the important amounts to fix the nuclide form, which is in go associated to the reduced transition probability B (E2)↑:[10]

$$Q_0 = \left[\left(\frac{16\,\pi}{5}\right)\frac{B(E2)\uparrow}{e^2}\right]^{\frac{1}{2}} \quad (6)$$

Depending on the Global Best Fit (GLOBAL) a known of the energy E (keV) of the (2^+) state is wholly that required to make a calculation for B (E2) ↑ (e^2b^2). [12]

$$B(E2)\uparrow = \frac{2.6\,Z^2}{E_{\gamma_0} A^{\frac{2}{3}}} \quad (7)$$

Where E_{γ_0} is the Gamma ray energy transition in KeV, Z denotes the atomic number, A represents the mass number of a nucleus.

3. Results and Discussion

The study of the relationship of the beta decay stability of isobars with their shape for some isobaric elements with even mass number (A=152 - 162) have been done by calculating the binding energy (B.E) and plotting three-dimensional representation graphics for each nucleus in these isobaric families. The binding energy (B.E) for nuclides under this study calculated by using Semi Empirical Mass Formula (SEMF) eq. (1). The results of binding energy (B.E) were plotted as a function to the atomic number (Z) for each isobar, so we get mass parabolas for different isobars as shown in the fig.1. From this figure the most stable isobars represented the lowest point of the mass parabola (the nuclide with the highest value of binding energy) for each isobar in this study.

Also we can show from Fig. 1 that the value of binding energy is increased by increasing the atomic number (isobars decay by emitting β^- particles) until reaching to the most stable isobar, and then decreased due to distance from the most stable isobar (isobars decay by emitting β^+ particles).

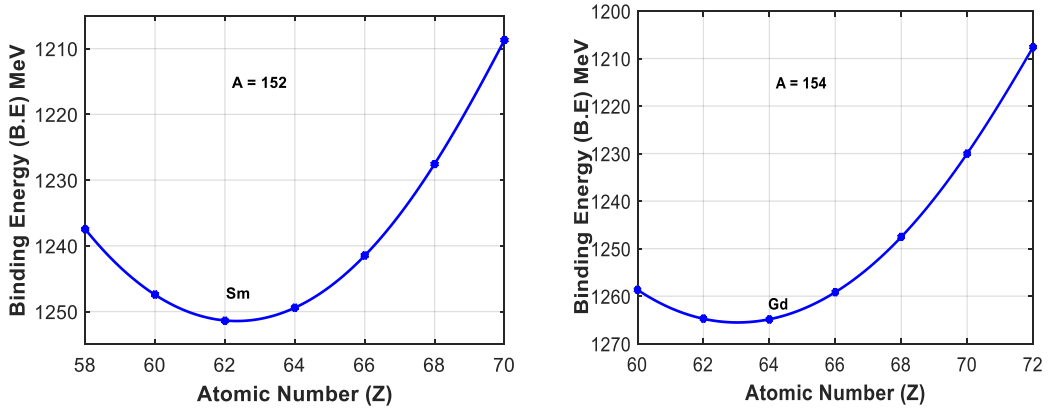

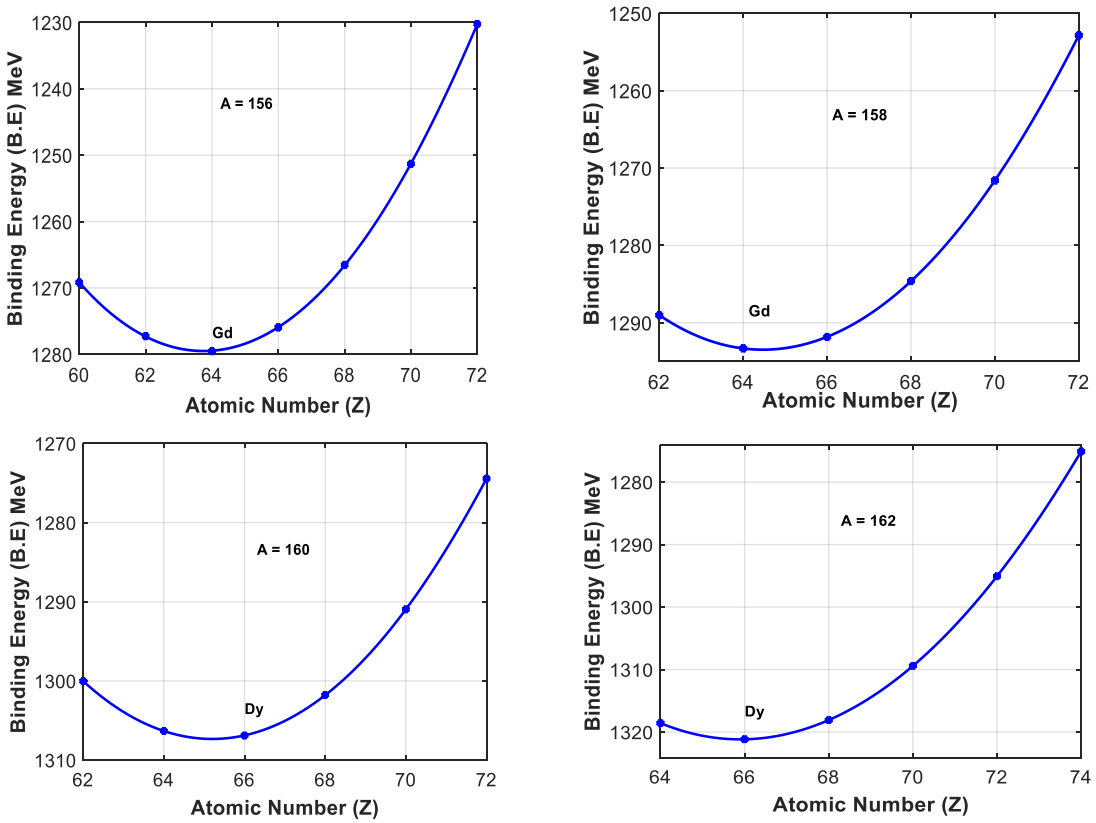

Fig.1. Mass parabolas for isobars with mass number (A=152,154,156,158,160&162).

To plot mass parabolas for isobars with mass number (A=152-162), the values of binding energy (B.E) plotted as a function to the atomic number (Z) for every isobaric family, thus we grow mass parabolas for isobars under this study as shown in the Fig.1.

From this figure we can see clearly that the mass parabola in this range of isobars (A=152-162) un equivalent i.e. the number of isobars which decay by (β+) emission or electron capture (e.c.) greater than isobars which decay by (β-) emission. The reason of that the weighty nuclides have an extra number of protons.

To determine the effect of beta decay stability on the shape of the isobar, plotting the shape of nuclides in (3-D) for each isobar in isobaric families with even mass number (A=152 - 162)have been done, from calculated the values of semi-axis minor (a), major (b) and (c) ellipsoid axis's, i.e. change the degree of deformation of nuclei as a result of the beta emission, the shapes of all nuclides were displayed in Figs. (2-7) respectively.

The semi-axis minor (a), major (b) and (c) ellipsoid axis's are calculated by using equations (2&3) with help of mean-squared charge distribution radius average$< r^2 >$, the quadruple deformation parameter(δ), intrinsic quadruple moment(Q_0), and reduced transition probability B(E2) ↑where the values of these parameters are calculated from equations (4-7) respectively. The values of these parameters presented in Table 1, while the values of the semi-axis minor (a), major (b) and (c) ellipsoid axis's represented in Table 2.

Table 1. Nuclei symbols-mass number A, atomic number Z, neutron number N, decay mode ,mean square radii $< r^2 >$, root mean square radii$< r^2 >^{1/2}$,reduced transition probabilities *B(E2)* ↑ e^2b^2**,** quadrupole moment (Q_0)and deformation parameter (δ) for even-even isobaric elements with even mass number (A=152 - 162).

Nuclide - A	Z	E_{γ_0} Kev [12]	decay mode	Theoretical Values			Present work				
				$< r^2 >^{1/2}$ fm [13]	B(E2) ↑ e^2b^2 [12]	Q_0 (b) [12]	$< r^2 >$ fm^2	$< r^2 >^{1/2}$ fm	B(E2) ↑ e^2b^2	Q_0 (b)	δ
Ce-152	58	81.71	β^-	-----	3.7	------	24.6079	4.9606	3.758	6.14	0.32
Nd-152	60	72.51	β^-	-----	4.58	6.49	24.607	4.9606	4.532	6.74	0.34
Sm-152	62	121.7	Most stable	5.0819	2.85	5.90	24.607	4.9606	2.881	5.38	0.26
Gd-152	64	344.2	β^+	5.0774	1.071	4.09	24.607	4.9606	1.086	3.30	0.15
Dy-152	66	613.8	β^+	5.0950	0.641	2.0	24.607	4.9606	0.647	2.55	0.11
Er -152	68	808.2	β^+	5.0843	0.52	-----	24.607	4.9606	0.522	2.29	0.10
Yb-152	70	1531.	β^+	5.0423	0.29	-----	24.6079	4.9606	0.292	1.71	0.07
Nd-154	60	70.81	β^-	-----	4.58	-----	24.8233	4.9823	4.600	6.79	0.34
Sm-154	62	81.97	β^-	5.1053	4.27	6.620	24.8233	4.9823	4.243	6.52	0.31
Gd-154	64	123.0	Most stable	5.1223	3.05	6.25	24.8233	4.9823	3.011	5.50	0.25
Dy-154	66	334.5	β^+	5.1241	1.162	4.90	24.8233	4.9823	1.178	3.44	0.15
Er-154	68	560	β^+	5.1129	0.74	-----	24.8233	4.9823	0.747	2.74	0.12
Yb-154	70	821.3	β^+	5.0875	0.53	-----	24.8233	4.9823	0.539	2.32	0.10
Hf-154	72	1513	β^+	-----	0.31	-----	24.8233	4.9823	0.310	1.76	0.07
Nd-156	60	66.91	β^-	-----	4.88	------	25.0378	5.0037	4.827	6.96	0.34
Sm-156	62	75.89	β^-	-----	4.58	------	25.0378	5.0037	4.544	6.75	0.32
Gd-156	64	88.96	Most stable	5.1420	4.17	6.83	25.0378	5.0037	4.130	6.44	0.30
Dy-156	66	137.8	β^+	5.1622	2.804	6.107	25.0378	5.0037	2.835	5.33	0.24
Er-156	68	344.5	β^+	5.1429	1.19	4.06	25.0378	5.0037	1.204	3.47	0.15
Yb-156	70	536.4	β^+	5.1219	0.81	-----	25.0378	5.0037	0.819	2.86	0.12
Hf-156	72	858	β^+	-----	0.53	-----	25.0378	5.0037	0.542	2.33	0.09
Sm 158	62	72.81	β^-	-----	4.68	------	25.2513	5.0250	4.696	6.86	0.32
Gd-158	64	79.51	Most stable	5.1569	4.58	7.104	25.2513	5.0250	4.582	6.78	0.31
Dy-158	66	98.91	β^+	5.1815	3.9	6.844	25.2513	5.0250	3.917	6.27	0.28
Er-158	68	192.1	β^+	5.1761	2.11	5.53	25.2513	5.0250	2.140	4.63	0.20
Yb-158	70	358.2	β^+	5.1498	1.20	4.33	25.2513	5.0250	1.216	3.49	0.14
Hf-158	72	476.3	β^+	-----	0.96	-----	25.2513	5.0250	0.968	3.11	0.12
Sm-160	62	70.61	β^-	-----	4.78	-----	25.4640	5.0461	4.802	6.94	0.33
Gd-160	64	75.26	β^-	5.1734	4.78	7.265	25.4640	5.0461	4.801	6.94	0.31
Dy-160	66	86.78	Most stable	5.1951	4.4	7.18	25.4640	5.0461	4.427	6.67	0.29
Er-160	68	125.8	β^+	5.2045	3.2	6.63	25.4640	5.0461	3.242	5.70	0.24
Yb-160	70	243.1	β^+	5.1781	1.75	5.17	25.4640	5.0461	1.778	4.22	0.17
Hf-160	72	389.6	β^+	-----	1.16	-----	25.4640	5.0461	1.173	3.43	0.14
Gd-162	64	71.7	β^-	-----	5.01	------	25.6757	5.0671	4.998	7.08	0.32
Dy-162	66	80.66	Most stable	5.2074	4.7	7.33	25.6757	5.0671	4.724	6.89	0.30

Er-162	68	102.0	β^+	5.2246	3.9	7.097	25.6757	5.0671	3.964	6.31	0.27
Yb-162	70	166.8	β^+	5.2054	2.54	5.96	25.6759	5.0671	2.569	5.08	0.21
Hf-162	72	285	β^+	-----	1.57	3.68	25.6757	5.0671	1.591	3.99	0.16
W-162	74	450.2	β^+	-----	1.05	------	25.6757	5.0671	1.064	3.27	0.12

Table 2. Nuclide symbols- mass number A, atomic number Z, neutron number N, semi-axes minor (a), major (b) and (c) ellipsoid axis's for even-even isobaric elements with even mass number (A=152 - 162).

Nuclide-A	**Z**	**N**	**Present work**		
			a fm	**b fm**	**c fm**
Ce-152	58	94	4.832671	8.736734	4.832671
Nd-152	60	92	4.718888	8.860257	4.718888
Sm-152	62	90	5.152556	8.363151	5.152556
Gd-152	64	88	5.693025	7.63013	5.693025
Dy-152	66	86	5.879667	7.341593	5.879667
Er-152	68	84	5.949685	7.227893	5.949685
Yb-152	70	82	6.077364	7.012221	6.077364
Nd-154	60	94	4.741906	8.896378	4.741906
Sm-154	62	92	4.880475	8.745217	4.880475
Gd-154	64	90	5.200611	8.368045	5.200611
Dy-154	66	88	5.716962	7.664827	5.716962
Er-154	68	86	5.886964	7.402986	5.886964
Yb-154	70	84	5.985538	7.243173	5.985538
Hf-154	72	82	6.106263	7.038749	6.106263
Nd-156	60	96	4.731159	8.967801	4.731159
Sm-156	62	94	4.854387	8.835102	4.854387
Gd-156	64	92	4.995248	8.676646	4.995248
Dy-156	66	90	5.315129	8.287822	5.315129
Er-156	68	88	5.762289	7.666892	5.762289
Yb-156	70	86	5.907375	7.442784	5.907375
Hf-156	72	84	6.027212	7.248076	6.027212
Sm-158	62	96	4.859911	8.889288	4.859911
Gd-158	64	94	4.941045	8.799379	4.941045
Dy-158	66	92	5.122705	8.589103	5.122705
Er-158	68	90	5.542384	8.051141	5.542384
Yb-158	70	88	5.81032	7.664024	5.81032
Hf-158	72	86	5.904734	7.518319	5.904734
Sm-160	62	98	4.875051	8.932406	4.875051
Gd-160	64	96	4.934808	8.866536	4.934808
Dy-160	66	94	5.05928	8.725107	5.05928
Er-160	68	92	5.333826	8.391706	5.333826
Yb-160	70	90	5.689984	7.910012	5.689984
Hf-160	72	88	5.872835	7.638046	5.872835
Gd-162	64	98	4.933368	8.927636	4.933368
Dy-162	66	96	5.039177	8.808651	5.039177
Er-162	68	94	5.227157	8.586769	5.227157
Yb-162	70	92	5.540321	8.184657	5.540321
Hf-162	72	90	5.791067	7.829816	5.791067
W-162	74	88	5.952148	7.584379	5.952148

Figs. (2-7) are a three-dimensional representation graphics for the isobar in isobaric family with even mass number (A=152 -162), these figures illustrate the change of the shape for a nucleus with emission of (β^-,β^+).

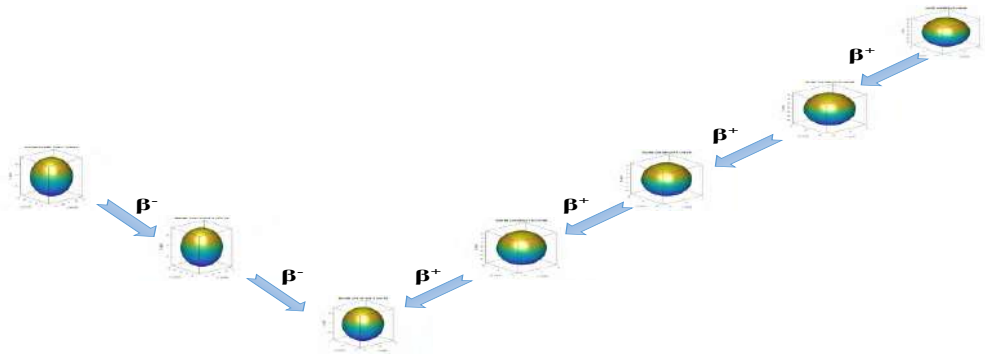

Fig.2. Shape of even-even isobars A=152and (Z= 58, 60, 62, 64, 66, 68 &70).

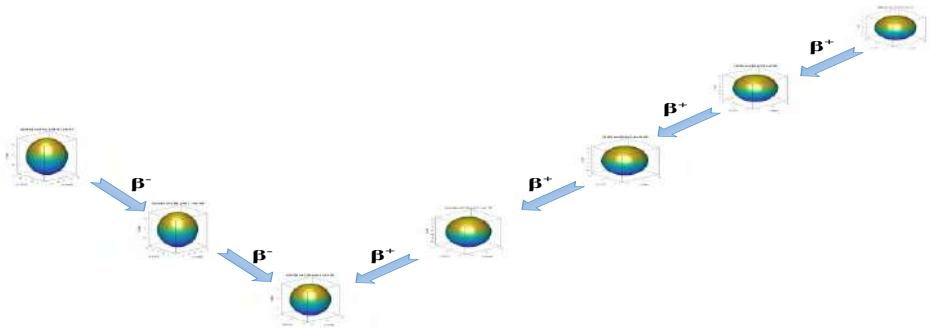

Fig.3. Shape of even-even isobars A=154and (Z=60, 62, 64, 66, 68, 70&72).

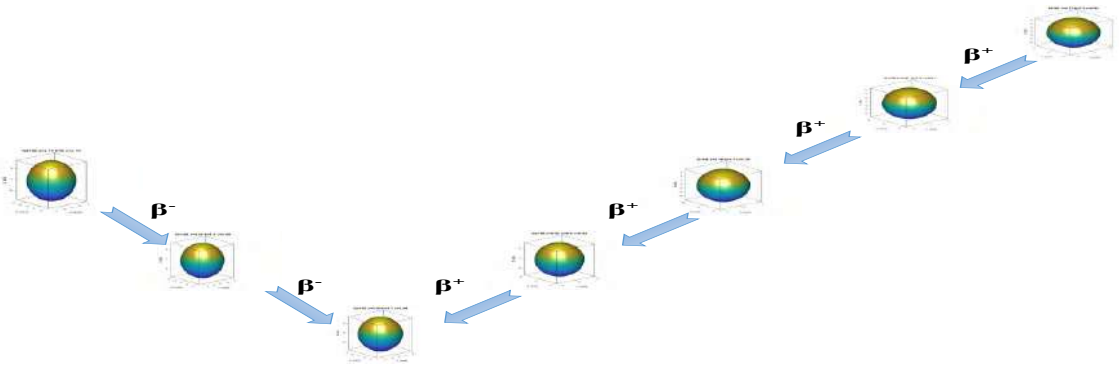

Fig.4. Shape of even-even isobars A=156and (Z= 60, 62, 64, 66, 68, 70&72).

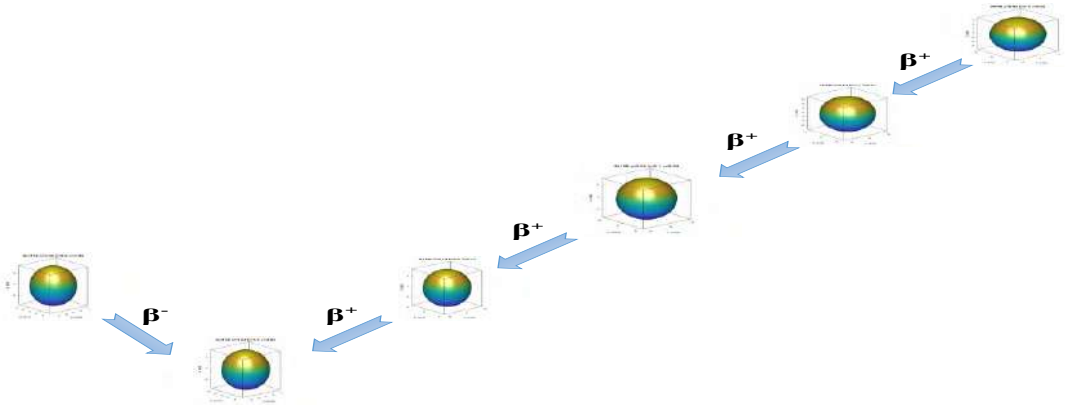

Fig.5. Shape of even-even isobars A=158and (Z= 62, 64, 66, 68, 70&72).

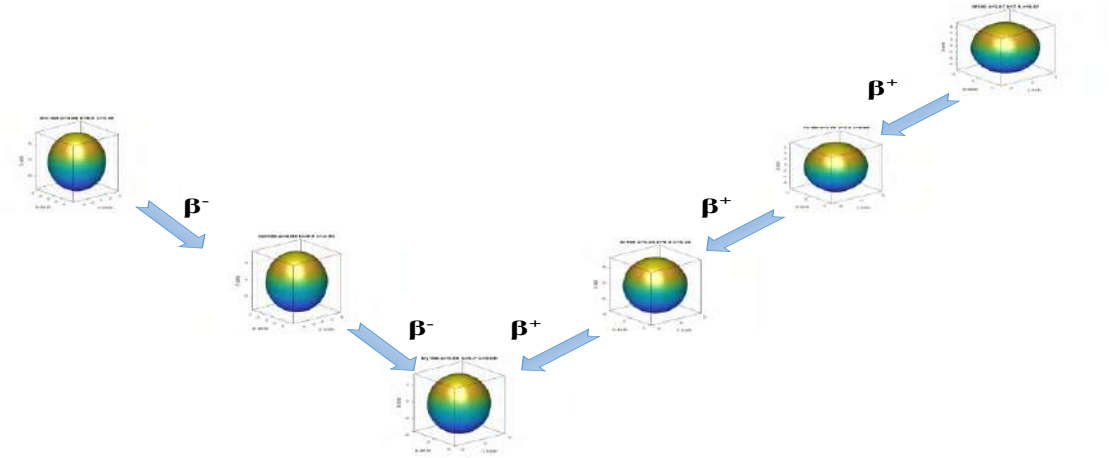

Fig.6. Shape of even-even isobars A=160and (Z= 62, 64, 66, 68, 70&72).

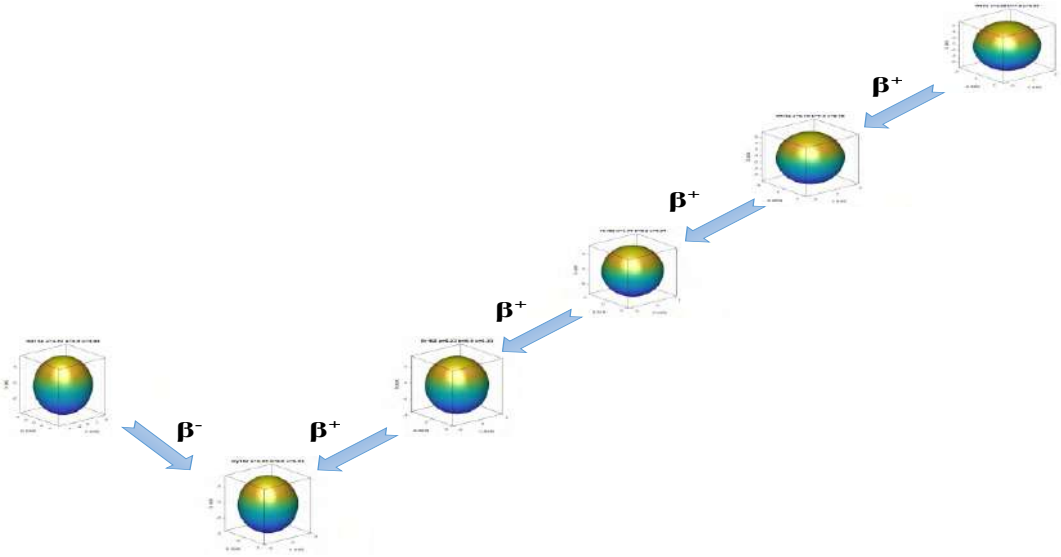

Fig.7. Shape of even-even isobars A=162and (Z= 64, 66, 68, 70, 72&74).

From Figs. (2-7) which represent a three-dimensional shapes for the isobaric elements with even mass number (A=152 - 162) respectively, we distinguished that the shape of nuclides which is represented the most stable isobar in mass parabola (isobaric nuclide with highest value of binding energy) as a result of its decay by emitting (β^-,β^+) particle and electron capture, are not spherical but they have some deformation in its shape. This is due to the fact that the nuclei are not stable by emitting beta particles only (particle loss happens first from radioactive nuclides, maximum of the nucleus excitation energy was a loss if one particle emission, whereas only a minor quantity of angular momentum have been loss in this particle emission. So, gamma-ray release happens to discharge this angular momentum and the residual energy. Only (8–10) MeV are passed out from the excitation energy by every particle produced. So a band of gamma rays are observed until the nucleus be in ground state (stable)).[14] So the most stable isobar needs to emit a gamma ray to move the nucleus from the excited state to the ground state and change its shape to spherical shape.

While depending on Liquid Drop Model (LDM), isobars nuclei under study, which are considered the most stable isobar among the other isobars in same isobaric family because they have the largest binding energy, are not completely stable and therefore do not have a spherical shape.

Also we can note from these figures that the deformation of isobar nuclei decreases with increasing atomic number, as well as for nuclei that have a magic number such as (^{152}Yb &^{154}Hf)neutron magic number equal to(N=82).

Finally, our results show that the stable nuclide which are determined from mass parabola ($^{152}_{62}Sm$, $^{154}_{64}Gd$, $^{156}_{64}Gd$, $^{158}_{64}Gd$, $^{160}_{66}Dy$&$^{162}_{66}Dy$)as a most stable nuclide are different from the nuclides with less value of deformation which are ($^{152}_{70}Yb$, $^{154}_{72}Hf$, $^{156}_{72}Hf$, $^{158}_{72}Hf$, $^{160}_{72}Hf$,&$^{162}_{74}W$) for isobaric elements with even mass number (A=152 - 162) respectively.

4. Conclusions

The results show that the shape of nuclides which is represented the most stable isobar in mass parabola are not spherical but they have some deformation in their shape, and need to emit a gamma ray to a chive more stable status and have the perfect spherical shape**.**

The stable nuclides which are determined from mass parabola are different from the nuclides which have less value of deformation.

References

[1] Nageshwari M. 2014 *Indian J. Sci. Technol.* **7**(s5) 974
[2] Nayyef M. S.,Jarallah N. T. 2019 *AIP Conference Proceedings* **2190**
[3] Marid H. A., Jarallah N. T. 2019 *Energy Procedia* **157** 270
[4] Povh B., Rith K., Scholz C. Zetsche ML F. 2008 Particles and Nuclei An Introduction to the Physical Concepts *Sixth Edition Springer-Verlag Berlin Heidelberg*
[5] Turner J. E. 2007 Atoms radiation and radiation protection *WILEY-VCH Verlag GmbH &Co.KGaA, Weinheim*
[6] Ankita & Suthar B. 2016 *AIP Conf. Pro* **1728**, 020024 ; doi: 10.1063/1.4946074.
[7] Ghahramany N., Sarafraza H., Yazdankish E. 2013 *Universal Journal of Physics and Application* **7**(1)18
[8] Cook N.D. 2010 Models of the atomic nucleus Unification through a lattice of Nucleons *second Edition Springer-Verlag Berlin Heidelberg* : DOI 10.1007/978-3-642-14737-1
[9] Nayyef M. S.,Jarallah N. T. 2020 *Ibn Al-Haitham J. for Pure & Appl. Sci.* **33** (4) 18
[10] Buchmann J.A., Henley M. E. 2000 Intrinsic Quadrupole Moment of the Nucleon *Phys. Rev. C 63, 015202*
[11] Boboshin I., Ishkhanov B., Komarov S., Orlin1 V., Peskov N., V. VarlamovV. 2007 Investigation of Quadrupole Deformation of Nucleus and its Surface Dynamic Vibrations *IInternational Conference on Nuclear Data for Science and Technology*, Moscow, Russia : **65**, doi:10.1051/ndata:07103
[12] S. Raman, C. W. Nestor, JR., & P. Tikkanen. 2001 Transition probability From The Ground to The First -Excited 2+ state of Even- Even Nuclides, Atomic Data and Nuclear Data Tables **78** (1) : doi:10.1006/adnd.2001.0858
[13] Angeli I., Marinova K.P. 2013 Table of Experimental Nuclear Ground State Charge Radii, Atomic Data and Nuclear Data Tables **99** 69,doi:10.1016/j.adt.2011.12.006
[14] Agular A. 2008 high spin nuclear structure of ^{168,170} Ta and triaxial strongly deformed structure in ^{160} Yb *Ph.D. Thesis Florida State University, College of Arts and Science*

Journal of Physics: Conference Series

Studying the nuclear structure of the ($^{162}_{66}Dy_{96}$) deformed nucleus by using (IBM-1) and (VAVM) Models

Studying the nuclear structure of the ($^{162}_{66}Dy_{96}$) deformed nucleus by using (IBM-1) and (VAVM) Models

Ektefaa Adnan Al-Kubaisi[1], Ali Kalaf Aobaid[1]

[1]Physics Department ,College of education for pure sciences , Anbar university

E-mail: aktefaa95.adnan@uoanbar.edu.iq

Abstract. In this paper, the nuclear structure of the deformed even-even $^{162}_{66}Dy_{96}$ nucleus was studied using the first interacting boson model (IBM-1) to calculate the energy levels E(L) and the transitional energy (E_γ). The energy bands, as well as the quadrupole moment (Q_L) can be calculated to know the shape of the nucleus and the moment of inertia model, energy levels E(L), transitional energy (E_γ) and the bands intersection. The current study showed that at dynamic symmetry SU (3), there is no effect of inertia moment on the shape of the rotational nuclei due to the absence of the phenomenon of back bending that belongs to this dynamic symmetry, through calculating the energy levels ratios found that $^{162}_{66}Dy_{96}$ nucleus belongs to the rotational dynamic symmetry SU (3). A comparison of the available practical results with the results calculated by (VAVM) and (IBM-1) showed that the (VAVM) model are better than the results calculated by (IBM-1).

Keywords: Nuclear structure, Intersection, bosons, moment of inertia.

Introduction

Nuclear physics has had vast quantities of theoretical and experimental energy levels data and information related to the nuclei due to many researchers tried to penetrate into these nuclei or because of the attempt to disassemble these nuclei into their various components, so it has become the duty of nuclear physicists to develop a nuclear model, which is the first step to understand the observed and measured data, relate them and draw conclusions. In spite of the great success achieved by many of the proposed nuclear models in linking data and explaining the nuclear properties, they did not reach the stage of adopting a "one" model, that is, a comprehensive unified theory that can explain everything related to the nuclei in terms of structure and interactions. The most important basic nuclear models proposed to describe the interaction between nucleons and are currently applied are the shell model, the liquid drop model and the collective model. Each of these models is based on a set of assumptions and may be useful. Within certain limits, it can interpret a "specific" range of experimental energy levels data, but it may fail when applied to data outside that range. For example, the "shell model is appropriate" if it is assumed that the interaction between nucleons is a weak interaction, while the liquid drop model or the collective model is used to describe the strong interactions between nucleons, researchers (Arima and Iachello) in 1974 [1] presented a new "nuclear" model called the first Interacting Bosons model This model relied in many aspects on group theory. It is a system of bosons (L = 2) s, (L = 0) d interacting with each other. This model (IBM-1) does not distinguish in its first formula between protons and neutrons bosons.

IBM-1 model is one of the important subjects which use for the purpose of studying some nuclear properties of each odd -mass or even-mass nuclei .in this model we deal with the nucleus with even numbers both of neutrons and protons, i.e. the nuclei (even-even) as a system of neutrons or proton bosons the calculations resulting from this model have shown that there is agreement with practical experiences and the first interacting boson model has had a widely success in describing the fine structure of the nuclei, especially at low energy level*s*[2] . And the interacting boson model builds on the boson holes inside a nuclear closed shell or the interacting valance boson particles outside a closed shell.

N is dependent on the number of active nucleon or(hole) pairs outside the closed shell and the total number of bosons can be calculated by adding the number of proton pairs with the number of neutron pairs that can be their written in the following equation [3]:

$N = n_s + n_d$ ……(1)

Where : n_s is the number of s-bosons

n_d: the number of d-bosons.

The Hamiltonian operator in (IBM-1)

The most appropriate syntax for the operator of the Hamilton function is the formula postulated by Arima and Iachello [4,5] and Iachello [6]

$$\hat{H} = \varepsilon_s(\hat{s}^{+}\hat{s}) + \varepsilon_d(\sum_m \hat{d}^{+}\hat{d}_m^{\sim}) + \sum_{L=0,2,4}\frac{1}{2}(2L+1)^{1/2}C_L\left[\left(d^{+}d\right)^{(L)}\left(\tilde{d}\,\tilde{d}\right)^{(L)}\right]^{(0)}$$

$$+V_2\left[\left(\hat{d}^{\dagger}\hat{d}^{\dagger}\right)^{(2)}\left(\tilde{d}\,\tilde{s}\right)^{(2)} + \left(s^{\dagger}d^{\dagger}\right)^{(2)}\left(\tilde{d}\,\tilde{d}\right)^{(2)} + \left(\frac{1}{2}\right)^{1/2}V_0\left[(\hat{d}^{\dagger}\hat{d}^{\dagger})^{(0)}\left(\tilde{s}\,\tilde{s}\right)^{(0)} + \left(\hat{s}^{\dagger}\hat{s}^{\dagger}\right)^{(0)}\left(\tilde{d}\,\tilde{d}\right)^{(0)}\right]^{(0)}\right]$$

$$+U_2\left[\left(d^{\dagger}d^{\dagger}\right)^{(2)}\left(\tilde{d}\,\tilde{s}\right)^{(2)}\right]^{(0)} + \left(1/2\right)U_0\left[\left(\hat{s}^{\dagger}\hat{s}^{\dagger}\right)^{(0)}\left(\tilde{s}\,\tilde{S}\right)^{(0)}\right]^{(0)} \quad \text{.....(2)}$$

Where ($s^{\dagger}, d^{\dagger}$) and ($\tilde{s}, \tilde{d}$) are creation and annihilation operators for s- and d-bosons, respectively. The effect of the Hamiltonian function in equation (1) includes two parameters describing a single particle and The relationship between energy levels E(L) parameters describing the two interacting particles represented by C_L(L=0,2,4) and four parameters describing the two interacting particles, represented by U_L (L = 0, 2), V_L (L = 0, 2), and all of these parameters depend on the number of N bosons equal to ($n_s + n_d$). The equation (1) can be written in several formulas, but the most popular one is the formula [4.5]:

$$\hat{H} = \varepsilon\hat{n}_d + a_o(\hat{P}^{\dagger}.\hat{P}) + a_1(\hat{L}.^{\dagger}\hat{L}) + a_2(\hat{Q}^{\dagger}.\hat{Q}) + a_3(\hat{T}_3^{\dagger}.\hat{T}_3) + a_4(\hat{T}_4^{\dagger}.\hat{T}_4) \quad \text{……(3)}$$

where $\hat{n}_d$, $\hat{p}$, $\hat{L}$, $\hat{Q}$, $\hat{T}_3$ and $\hat{T}_4$ are the total number of d-boson, pairing, angular momentum, quadrupole, octoupole and hexadecapole operators, respectively

Since ($\varepsilon = \varepsilon_d - \varepsilon_s$) represents the difference between the energy of the bosons (d, s), and for ease it was considered that the energy of the s boson is equal to zero (ε_s = 0) and that

$$\left.\begin{aligned}
&\hat{n}_d = (\hat{d}^\dagger . \tilde{\hat{d}}) \\
&\hat{P} = 1/2(\tilde{\hat{d}} . \tilde{\hat{d}}) - 1/2(\tilde{\hat{s}} . \tilde{\hat{s}}) \\
&\hat{L} = \sqrt{10}[\hat{d}^\dagger \times \tilde{\hat{d}}]^{(\ell)} \\
&\hat{Q} = [(\hat{d}^\dagger \times \tilde{\hat{s}}) + (\tilde{\hat{s}}^\dagger \times \tilde{\hat{d}})] - \frac{\sqrt{7}}{2}[\hat{d}^\dagger \times \tilde{\hat{d}}]^{(2)} \\
&\hat{T}_3 = [\hat{d}^\dagger \times \tilde{\hat{d}}]^{(3)} \\
&\hat{T}_4 = [\hat{d}^\dagger \times \tilde{\hat{d}}]^{(4)}
\end{aligned}\right\} \quad ..(4)$$

The parameters a_0 ..... a_4, they express the strength of the interaction of the pairs, angular momentum, electric quadrupole, octaloupole, hexadecpole are among the bosons, respectively.

The electric quadrupole moment (Q_L)

Electric quadrupole moment **(Q_L)**is defined as the amount of deviation from a symmetric spherical distribution with respect to the nuclear charge within the nucleus. The quadrupole electric moment takes the dimensions of the area and it is measured in barns unit or square meters unit (1barn = $10^{-28}\ m^2$). The shape of the nucleus can be determined by relying on the value of **(Q_L)**where the shape of the nucleus is spherical at (Q = 0) and the shape of the nucleus is deformed prolate at (Q> 0) or is deformed oblate at (Q <0). To derive the electric quadrupole moment values , can be use the values of B (E2, Li→L$_f$), as shown in the following equation: [7,8,9]:

$$\mathrm{Q_L} = [16\pi/5]^{1/2}[\mathrm{L}(2L-1)/(2L+1)(L+1)(2L+3)]^{1/2}[B\big(E2, L_i \rightarrow \quad \ldots\ldots\ldots(5)$$

Where B (E2) is the electric transitions probability, L represents the angular momentum, L $_i$ is the initial angular momentum, L $_f$ is the final angular momentum**.**

Variable Anharmonic Vibrator (VAVM) Model

The two scientists Bonatsos D. and Klein A. in (1984) [10] suggested another new model called (VAVM) model is depend on the (GVMI) model by making the basic functions of the angular momentum (L) and the variable L(L-2). The (VMI) model failed to provide adequate results for some experimental energy levels measurements, where (VAVM) model gave good results in the regions SU(3), SU(5), O(6).

The Energy Band Intersection

The energy band intersection means that the moment of inertia with respect to a certain energy level in any band like (γor β) intersects, or takes the place of any energy level in any other band as a band (g). Bands intersection characteristic consider as an important characteristic for the purpose of studying the bending back phenomenon [11] which occurs between any two bands that have the same spin and but they differ in energy and moment of inertia.

Results and discussion

In this research, the properties of the nucleus $^{162}_{66}Dy_{96}$ are studied such as the electric transitions probability B(E2), energy levels E(L) and transitional energy E_γ and by energy bands (g, γ,β) these levels were classified and the behavior of the nucleus $^{162}_{66}Dy_{96}$ must be determined to be able to choose the parameters of the Hamilton function the equation (2) for the purpose of studying nuclear properties and found that the nucleus $^{162}_{66}Dy_{96}$ belongs to the SU(3) symmetry by comparing the ratios of practical energy values with the ratios of ideal energy values and the values of energy levels are calculated in the IBM-1 model using (IBM. For) program the Written with Fortran language through the Input File (BOS. INP), which contains seven parameters the shown in Table (1), the values of these parameters are determined by matching the values of practical energy levels with theoretical energy level values while

the values of energy levels are calculated in the VAVM model using (VAVM. For) through the input file (PAR. INP), which contains The relationship between energy levels E(L) parameters are : ($\vartheta_0 / \hbar^2$) measured by $(MeV)^{-1}$ *unit* ,C measured by $(MeV)^3$ *unit* and E_K measured by(MeV) unit , where E_k represents the energy of the head of the band in the ground state band (G-band) equals zero while in the β- band equals the angular momentum energy 0^+ for the excited level, but in the gamma band (ɤ-band) the value is variable and by matching the practical values with the theoretical values calculated in the PROGRAM (IBM-1) the values of the parameters shown in table (2) were chosen when the less value of the χ squared (chi-squared) is obtained from the following equation:

$$\chi^2 = \frac{(E_{Cal} - E_{\exp})}{E_{Cal}^2} \quad \ldots\ldots\ldots\ldots\ldots(6)$$

Table (1): the parameter values used in the (IBM .For) program measured in (MeV) unit

ε	$P\hat{}\dagger.P\hat{}$	$L\hat{}.L\hat{}$	$Q\hat{}.Q\hat{}$	$T\hat{}3.T\hat{}3$	$T\hat{}4.T\hat{}4$	*CHI*
0.0021	*0.0055*	*0.0099*	*-0.0091*	*0.0010*	*0.0011*	*-1.3200*

Table (2): parameter values used in the (VAVM) model with the chi-square (χ^2)

Band	$\ell_0(\text{MeV})^{-1}$	$C(\text{MeV})^3$	E_K (MeV)	χ^2
G-band	91.0000	0.0111	0.0000	0.0046
$\gamma_1 -$ band	98.9999	0.0002	0.7199	0.0145
β_1-band	99.9900	49.2991	01.4000	0.0098
β_2-band	99.9999	0.0021	01.6660	0.0092

Table (3): quadrupole electric moment values derived from B (E2) parameter values using (IBMT. For) program

$\alpha_2(eb)$	$\beta_2(eb)$
0.30000	0.41000

Figure (1) shows the relationship between E(L) practical energy level values compared with theoretical energy level values of the two models (IBM-1,VAVM) for ground state band as a function of angular momentum of a nucleus ($^{162}_{66}Dy_{96}$) and it was noted from the figure that there a quite match between practical energy level values with the values of theoretical energy levels calculated according to the two models(IBM-1,VAVM) for (L≤10) either the values of theoretical energy levels calculated by the (IBM-1)model do not match to the values of practical energy levels for(L>10) because the first interacting boson model do not distinguish between the neutron bosons N_π and the proton bosons N_v, and also because the first interacting boson model did not succeed in calculating the excited energy levels, while the values of energy levels calculated by (VAVM) model with the values of practical energy levels for (L>10) are still fully matched , and this match was the result of better selection of the three input parameter ℓ_0, C and E_K through the input file (PAR. INP) ,and also because the (VAVM) model distinguish between the neutron bosons N_π and the proton bosons N_v . And it was noticed from the figure is that the values of energy levels calculated by the (VAVM) model gave a better match with the values of practical energy levels than the values of theoretical energy levels calculated by the(IBM-1) model and this was the result of the optimal choice of the input parameter values through the input file (PAR. INP).

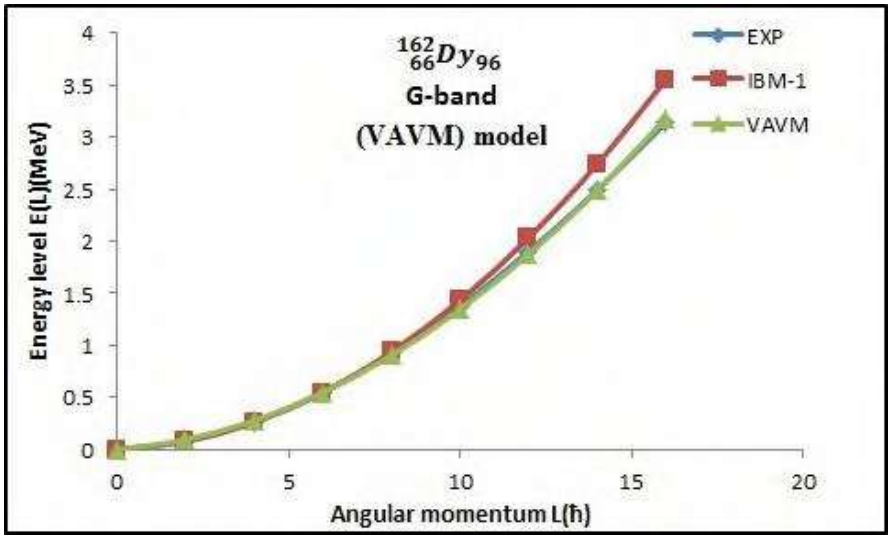

Figure 1. The relationship between energy levels E(L) calculated IBM-1,VAVM and experimental energy levels E(L)versus L for g-band

Figure(2) shows that IBM-1's theoretical energy level values are fully matched, with the gamma -band practical energy level values for (L≤8), the reason for the match is that the first interacting boson model is very successful in calculating low energy levels, either for(L>8) where there is no match between the values of the theoretical energy levels calculated by the(IBM-1) model with the values of the practical energy levels, and a mismatch because the first interacting boson model do not distinguish between the neutron bosons N_π and the proton bosons N_ν, and also because the first interacting boson model did not succeed in calculating the excited energy levels, while all the values of the theoretical energy levels calculated by the (VAVM)model are fully matched with all the practical energy level values for(L>8), and this match was the result of better selection of the three input parameter ℓ_0, C and E_K through the input file (PAR. INP) ,and also because the (VAVM) model distinguish between the neutron bosons N_π and the proton bosons N_ν .

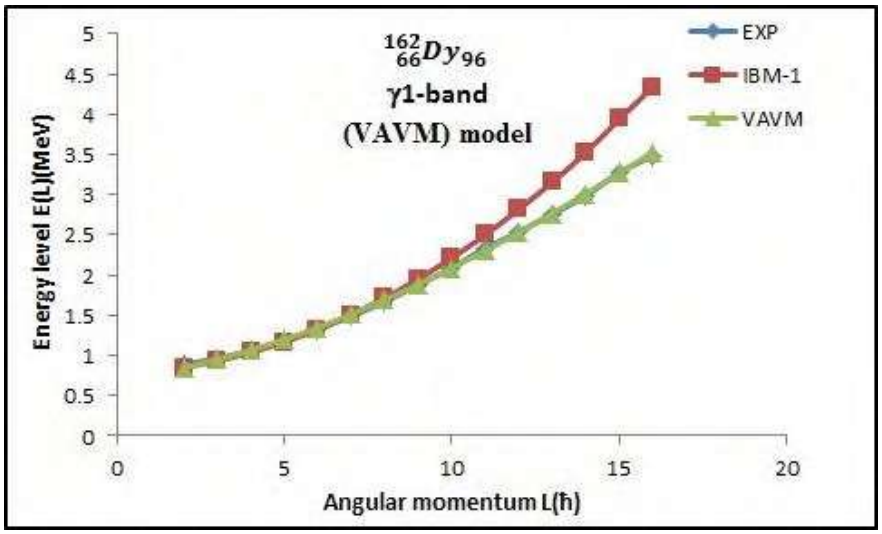

Figure 2. The relationship between energy levels E(L) calculated IBM-1,VAVM and experimental energy levels E(L)versus L for for γ-band

Figure (3) shows the comparison between of the theoretical energy level values E(L) calculated by the two models (IBM-1,VAVM) with the values of practical energy levels as a function of the angular momentum of the β1-band and shows from the shape for (L≤4) there is a match between the values of the practical energy levels with theoretical energy level values calculated according to the two models (IBM-1,VAVM), while for(L>4) is no match between the values of practical energy levels with the values of theoretical energy levels calculated according to the model (IBM-1) while the values of the theoretical energy levels calculated by (VAVM) model is still matching with practical energy level values for (L>4).

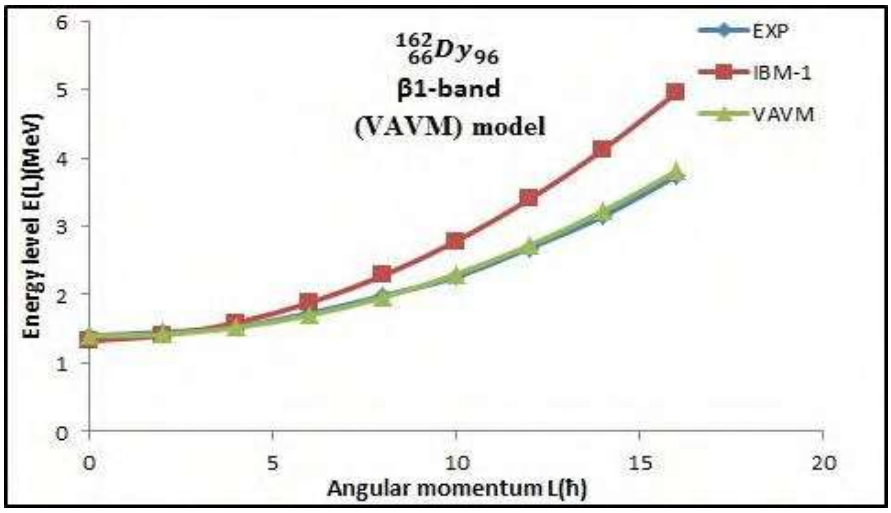

Figure 3. The relationship between energy levels E(L) calculated IBM-1,VAVM and experimental energy levels E(L)versus L for for β1-band

Figure (4) shows that there is a great match between all practical energy level values with all theoretical energy level values calculated by the(VAVM) model of the Beta 2 - band, the values of theoretical energy levels calculated by(IBM-1) model are slightly greater than the values of practical energy levels at low energy levels for (L≤8) while significantly moving away from the values of practical energy levels at excited energy levels for (L>8).

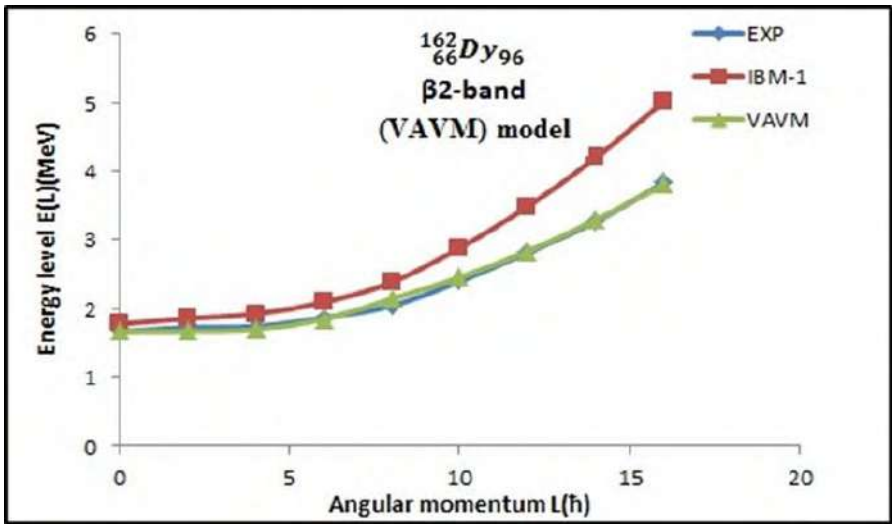

Figure 4. The relationship between energy levels E(L) calculated IBM-1,VAVM and experimental energy levels E(L)versus L for β2-band

Figure (5) illustrates the band intersection phenomenon, which is an important subject because it is use to explain the back bending phenomenon observed from figure (5) that the bands (g1,β1) intersects at the angular momentum $L_{C=}$14,16. And the disintegration of a pair of nucleus generates the energy band intersection and be the back-banding phenomenon that did not appear in the nucleus $^{162}_{66}Dy_{96}$. Due to the decrease in inertial moment at the large angular momentum, the bands intersection also occurs, and the effect of the curious force effect generates a decrease in the energy of the two nucleons, and therefore, the instability in these two states leads to the intersection of one band with another.

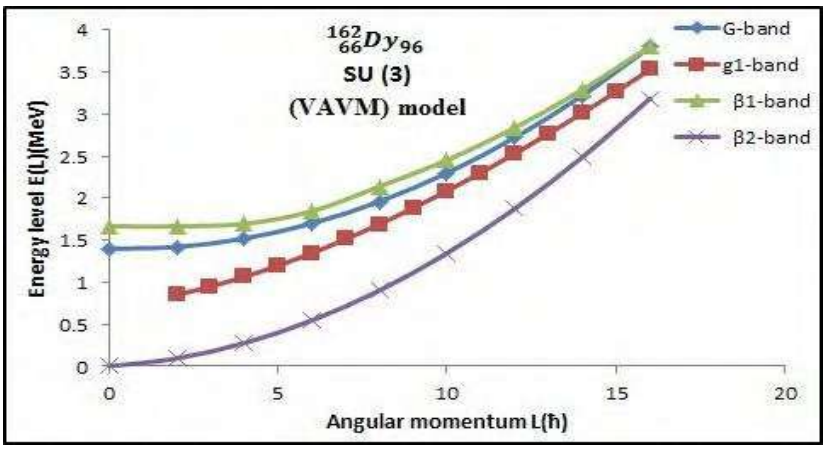

Figure 5. Energy band Intersection E(L)as a function of the angular momentum (L) using (VAVM) model.

The quadrupole moment values (Q_L) were calculated in IBM-1 model using of the(IBMT) program. For via entry file BE2. Dat which requires the determination of the two parameters (β_2,α_2) measured by the unit (eb) shown in table (3).

We note from figure(6)that the shape of the nucleus in the nucleus $^{162}_{66}Dy_{96}$ takes the prolate oval shape at the angular momentum (2_1^+,2_2^+ ,2_3^+ , 2_5^+,2_6^+, 2_7^+,2_{10}^+) while takes the oblate oval shape at the angular momentum (2_4^+,2_8^+ , 2_9^+), and the largest deformation of the prolate oval type is at the angular momentum Q(2_8^+) and its value (-3.729 eb) and the highest deformation of the oblate oval type is at the angular momentum Q(2_3^+) and its value (4.15 eb).

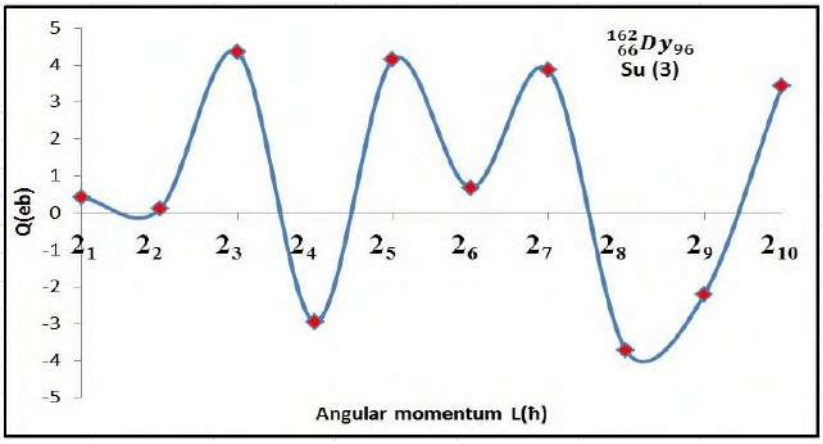

Figure 6. Electric quadrupole moment (Q_L)as a function of the angular momentum (L) from 2_1 *to* 2_{10} .

References

[1] Arima A and Iachello F 1974 Boson Symmetries in Vibrational nuclei *Phys . Lett* . B **53** 309.
[2] El. Daghmah MS and Jum'a A 1997 *Nuclear Physics* 1 199,New York.
[3] Walter P 1998 *An Introduction to the IBM of the atomic nucleus* part 1, Walter (4-8).
[4] Arima A and Iachello F 1987 *The interacting boson model* Ed. Iachello F, Pub. Combridge university, press Cambridge, England 1-133.
[5] Iachello F 1980 *An Introduction to the Interacting boson model* plenum press.
[6] Casten RF and Warner DD 1988 The interaction boson approximation *Rev. Modern Phys*. **60** 389.
[7] Casten RF and Warner DD 1988 *Rev. Mod. Phys*. **60** 389.
[8] Sharrad FI, Abdullah HY, AL-Dahan N, Mohammed-Ali AA, Okhunov AA and Kassim HA 2012 *Rom. J. Phys*. **57** 1346.
[9] Iachello F and Arima A 1987 *The interacting Boson Model* Cambridge University press, Cambridge.
[10] Bonatsos D and Klein A 1984 *Phys. Rev. C*, **29** 1879.
[11] Elliott JP and White AP 1980 *Phys. Lett. B* **97** 169.

Characteristics of probing electrons behavior inside the chamber of scanning electron microscope

Characteristics of probing electrons behavior inside the chamber of scanning electron microscope

Imad H. Khaleel[1], Ali S. Mahdi[2] and Hassan N. Al-Obaidi[3]

[1]Department of Physics, College of Education for Pure Sciences / Ibn Al-Haithem, University of Baghdad, Baghdad, Iraq.
[2]Baghdad Governorate, Rusafa-1, Baghdad, Iraq.
[3]Department of Physics, College of Education, Al-Mustansiriyah University, Baghdad, Iraq.

Email: imad.h.kh@ihcoedu.uobaghdad.edu.iq

Abstract. The electron mirror phenomenon has been explored to describe the behavior of a probing electron trajectory inside the chamber of scanning electron microscope (SEM). This investigation has been carried out by means of the modulated mirror plot curve technique. This method is based on expanding sample potential to a multipolar form to detect the actual distribution of the trapped charges. Actually an experimental result is used to guiding results of this work toward the accurate side. Results have shown that the influence of each type of multipolar arrangement (monopole, dipole, quadruple, octopole …etc.) mainly depends on the driving potential.

Keywords: SEM, Mirror effect, Charging process, Insulators samples, Electron beams.

1. Introduction

Now, it is well known that as long as a dielectric material is bombarded by electrons beam, some of these electron straps at surface or even within bulk material [1,2]. Such a situation leads to what so called *Charging Effect* (CE) [3,4] which is becoming very important to comprehend. The use of dielectric material in modern science and technology significantly depends on the realization of CE which in turn could lead to better applications [5,6].

The CE can be investigated in terms of several techniques[7], however, the one that is called *Scanning Electron Mirror Method* (SEMM) is followed in this work. Such an investigation technique provides an excellent ability to control and analyze CE [8]. Anyway, its principle work can be summarized by two steps. The first one imply an implantation of a trapping negative charges beneath the dielectric sample surface using a focused electron beam [9]. In the second step, the scanning mode is used to observe the sample surface with a potential ranging from fractions to a few kilovolts [10]. Actually, increasing the electric field could be strong enough to prevent the next probing electrons from reaching the sample surface. In fact, the surface acts as a convex mirror and reflects the electrons. The mirrored backward electrons will attack the chamber inner surfaces and create new Secondary Electrons (SE), so, their detection will lead to imaging of the insider chamber space rather than the sample.

Obviously, sample potential regulates the characteristics of the appeared electron image, which in turn depend on the way that the trapped charges distribute on the sample surface. So, the knowledge of trapped charges distribution profile is a crucial task to specify physiognomies of mirror images. Recently, the modulated mirror plot curve technique has been presented to detect the actual distribution of the trapped charges[11]. This method is based on expanding sample potential to a multipolar form to identify the spreading of the trapped charges. Current work aims to find the contribution weight of each multipole expansion term which may involve in building up the sample potential.

2. Material and method

The method of charge images has been used recently to solve Poisson's equation inside the chamber of a scanning electron microscope (SEM). Subsequently, the solution in the free space is given by [11];

$$U(\vec{r}) = \frac{K}{4\pi\epsilon_o}\int \frac{\rho(\vec{r})}{|\vec{r}-\vec{r}'|} \qquad \ldots\ldots\ldots\ldots(1)$$

where (ϵ_o) is the free space permittivity, (k) is equal to$[2/(\epsilon_r+1)]$, and (ϵ_r) the relative permittivity. However, equation (1) represents the electrostatic potential at any point located by the position vector $(\vec{r})$ throughout the space (SEM-chamber) that deduced due to an accumulation of a volumetric charges distribution of amount $\rho(\vec{r}')$ located at $(\vec{r}')$. In order to grand equation (1) ability to describe charge extension within the sample, the numerator of this equation is expanded and hence the following expression is obtained;

$$U(\vec{r}) = \frac{KQ_t}{4\pi\epsilon_o r} - \frac{3KQ_t}{32\pi\epsilon_o}\frac{r'}{r^2} + \frac{KQ_t}{64\pi\epsilon_o}\frac{r'^3}{r^4} - \frac{3KQ_t}{512\pi\epsilon_o}\frac{r'^5}{r^6} + \frac{3KQ_t}{1024\pi\epsilon_o}\frac{r'^7}{r^8} + \cdots \qquad \ldots\ldots.(2)$$

where (Q_t) is the trapped charge. The n^{th} term in this equation represents the n^{th} order of multipole moment of the charge distribution of $[\rho(\vec{r}')]$. So, the terms of $(n = 0, 1, 2, 3, 4, 5, \text{ and } 6)$ are respectively the; monopole, dipole, quadrupole, hexapole, octopole, decapole, and dodecapole moment of the trapped charge distribution.

Mirror plot curve is represented the diagram that reveals the relation between reciprocal of Gaussian surface radius and the potential which is used to accelerates incoming electrons (V_{sc}). Consequently, equation (2) has been modified to imply this aspect as in the following formula;

$$\frac{1}{r} = \frac{1}{R} - \frac{3r'}{8R^2} + \frac{r'^3}{16R^4} - \frac{3r'^5}{128R^6} + \frac{3r'^7}{256R^8} - \cdots \qquad \ldots\ldots\ldots\ldots(3)$$

where R is the radius of Gaussian surface for the monopole moment charge distribution which equal to $\left(\frac{\mathrm{KQ_t}}{4\pi\epsilon_o \mathrm{V_{sc}}}\right)$. Indeed, equation (3) shows the mirror plot curve that corrected up to the seventh order, and the even power of (n) are vanishes due to the symmetry of problem. Thereby, it could be adopted to simulate a real (experimental) plot curve and hence verify the distribution profile of trapped charges being taken. Furthermore, contribution of each term should be examined versus the scanning potential in order to define whom the distribution look like to the incoming electrons. Anyway, this is the task of the coming next section.

3. Results and Discussion

Characteristics of a mirror image are mainly depending on the distribution profile for a sample potential that deduced by trapped electrons. Figure 1 shows the potential distribution along the radius of Gaussian sphere surface, for the first four orders of multipole moment terms in equation (2) and the equation itself. These curves are computed at fixed values of the penetration depth and trapped charges namely 10.6 μm and 0.064 nC respectively. Obviously, the monopole term is mainly controlling the contribution in equation (2) along the range of the radius of Gaussian sphere surface. This gives an indication that the higher order of electrons configuration are formed in the regions where a high concentration of electrons being trapped.

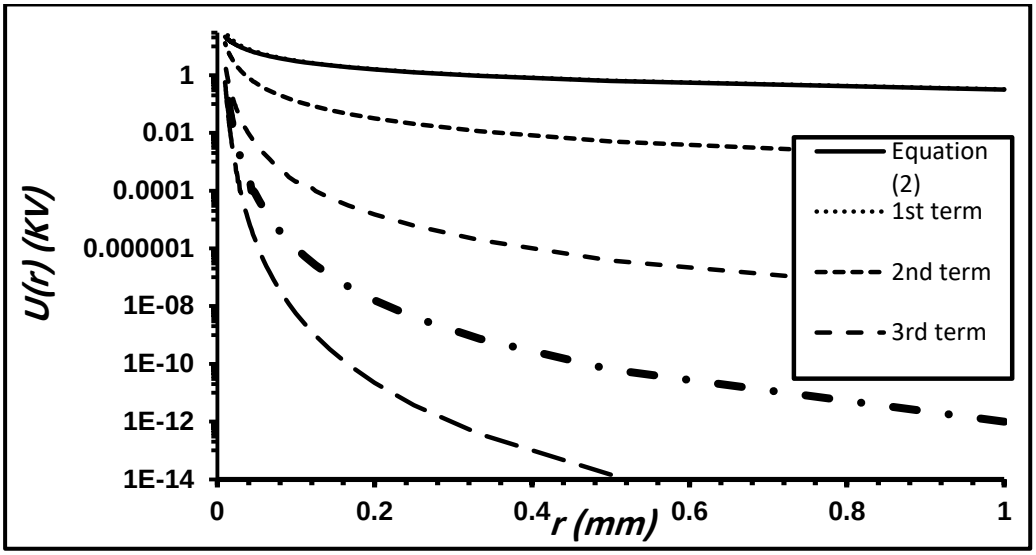

Figure 1. The surface potential distribution deduced by means of equation (2) and each of its term.

In order to provide present calculation a practical interest, some results that presented in the literature[12] have been used to compare with the outcome of equation (3). According to this reference, a Poly(methyl methacrylate) (PMMA) material sample of a dielectric constant 2.6 puts under irradiation by an electron beam with the aid of SEM. This beam has accelerated up to 25 kV, and the sample being under the exposition for enough time to reach the saturation. However, the trapped charges and the probing electron penetration depths are measured to be $(0.064nC)$ and $(10.6\mu m)$ respectively.

Equation (3) and each involved term have been calculated for the values of (ϵ_r, Q_t) and (r') mentioned above. The significance of each term that contributed to builds up this formula as a function of scanning potential are plotted in figure 1. It is seen that the term contributes most to the mirror plot curve $(1/r)$ is the first (zero-order or monopole) one. Indeed, this term fund $(1/r)$ by most of its total worth, and so this supplement, approximately, exceeds the hundred present of its real values for (V_{sc}) greater than$(2kV)$. Such a result indicates that, at $(V_{sc} \lesssim 2kV)$ the incident electron being at a distance approximately greater than $16mm$ away from the sample. Thereby, trapped charges appear to be look like a point for the incident electrons, hence, the point charge approximation works well at these relatively higher distances.

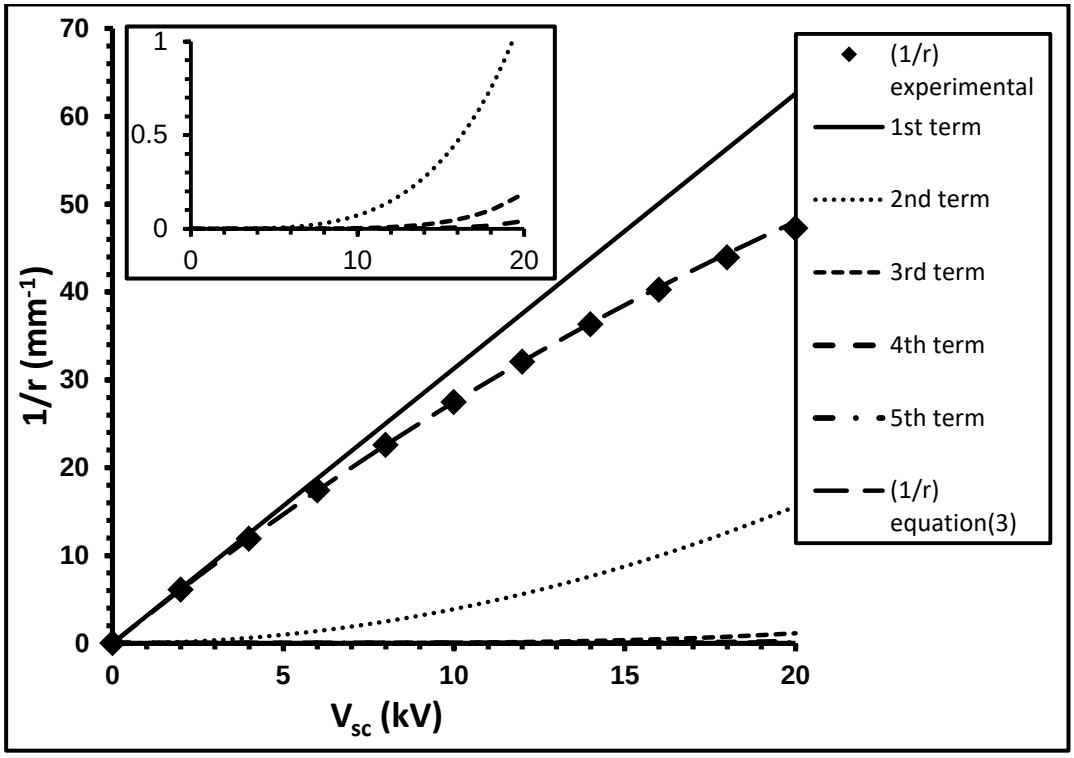

Figure 2. Outcome and the amount of each term in equation (3) versus the scanning potential.

However, when the scanning potential departs from the above mentioned value, i.e. ($V_{sc} \gtrsim 2kV$), the electrons start approache further to the sample. The influence of the second (two-order or quadrupole) term becomes significant and scale down the amount of monopole term. This can directly be seen from figure 1 where the curve $(1/r)$ starts leaving the linearity behavior simultaneously when the quadrupole curve just being noteworthy. Consequently, the point charge approximation fails to work well. Therefore, a trapped charge distribution is no longer appear to be a pure point for incident electrons. Instead, it becomes a mix between point and ellipse profiles.

However, when the acceleration process increases, the contribution weight of the third, fourth and fifth terms respectively become significant. Accordingly, the mirror plot curve becomes under influence of all of these terms by an amount depends on the proceeding of the term itself. Eventually, the point charge model completely failed to represent a point distribution. Hence, incident electron sees trapped charges to be something more complicated and this intricate strength increases as the electron approaches further to the sample surfaces. For accuracy realization, values of equations (3) and its own terms are recorded in Table I.

Table I: Outcomes and the amount of each term in equation (3).

V_{sc} (kV)	1st term (mm^{-1})	2nd term (mm^{-1})	3rd term (mm^{-1})	4th term (mm^{-1})	5th term (mm^{-1})	1/r(eq.3) (mm^{-1})	$1/r_{experimental}$ (mm^{-1})
0	0	0	0	0	0	0	0
4	12.517	0.623	1.83E-03	1.21E-05	1.06E-07	11.896	11.90446
8	25.035	2.491	2.92E-02	7.72E-04	2.72E-05	22.572	22.58321
12	37.552	5.606	1.48E-01	8.79E-03	6.97E-04	32.087	32.03625
16	50.069	9.965	4.68E-01	4.94E-02	6.96E-03	40.530	40.26359
20	62.587	15.570	1.14E+00	1.89E-01	4.15E-02	48.011	47.26521

The variations of the mirror plot curve versus trapped electrons for various values of scanning potential are plotted in figure 3 at a penetration depth of 10.6 μm. It is seen that as long as the higher concentrations of trapped electron are accumulated at the sample surface, the minimum approach distance of scanning electrons being increases. Hence, a landing electron reflected backward at higher distances from the sample surface when higher irradiation potential is used.

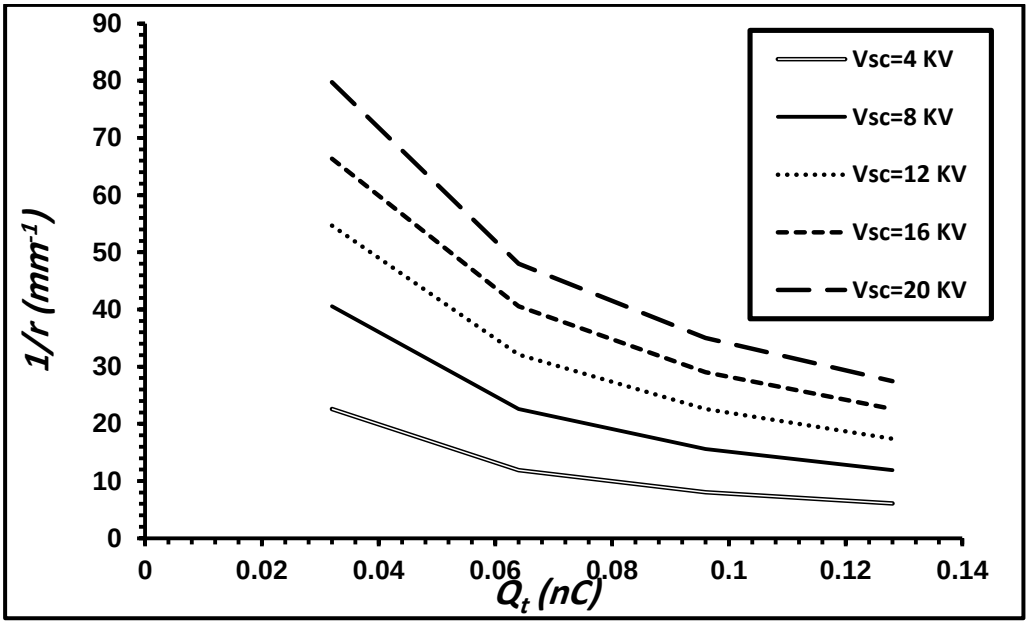

Figure 3. The behavior of mirror plot curve as a function of trapped electron amounts for different values of the scanning potential.

Figure 4 reveals the behavior of the mirror plot curve versus the penetration depth at several scanning potential values, and at the value of trapped electrons equals to 0.064 nC. Indeed, the trapped electrons implanted near the surface of the sample, and these electrons arranged themselves as a point. However, such an arrangement of accumulation takes complicated forms as long as trapped electrons deeply spread inside the sample's body.

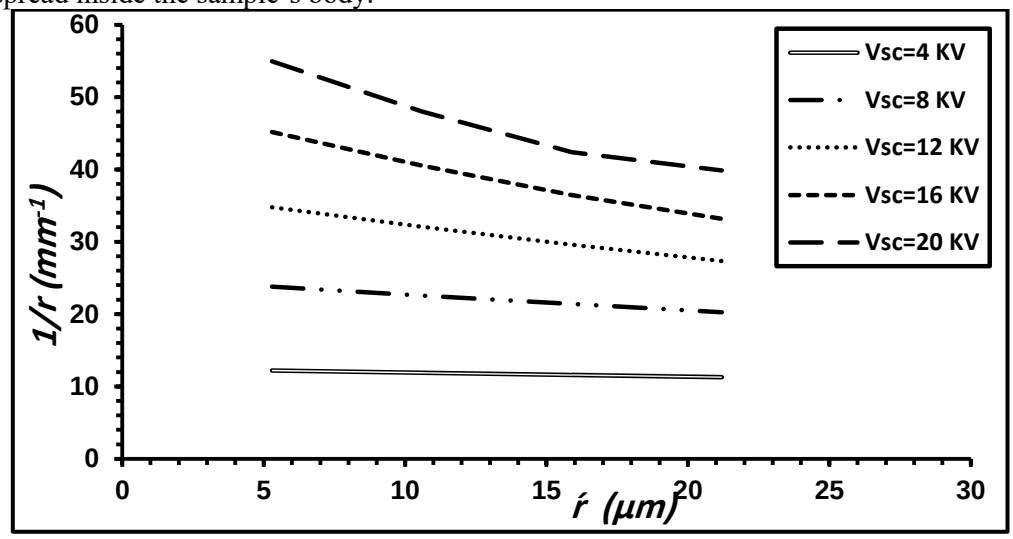

Figure 4. The behavior of mirror plot curve as a function of the penetration depth for different values of the scanning potential.

4. Conclusion

According to the results appeared in the last section, one may realize that the trapped electrons have a complicated formation at the sample's surface. In addition, this sophistication was mutable and not stable along the travel interval of the incident electron. The results of this work have proven that multipolar expansion has an excellent ability to simulate the correspondence experimental mirror plot curves. So, this expansion may regard to be a powerful tool for detecting trapped charges distribution at dielectric materials.

References

[1] Belkorissat R Jbara O Rondot S Benramdane N Belhaj M and Hadjadj A 2013 *Meas. Sci. Technol.* **24** 55902.
[2] Belhaj M Dadouch S 2019 *IEEE Pulsed Power Plasma Sci* 1.
[3] Jbara O Fakhfakh S Belhaj M Rondot SHadjadj A and Patat J M 2008 *J. Phys. D. Appl. Phys.* **41** 245504.
[4] Blaise G and Gressus C Le 2018 *AIP Adv.* **8** 95228.
[5] Fakhfakh S Jbara O and Rondot S 2004 *IEEE Int. Conf. Solid Dielectr* ICSD 244.
[6] Boukezzi L Rondot S Jbara O Boubakeur A 2018 *Radiat. Phys. Chem.* **149** 110.
[7] Wintle H J 1999 *J. Appl. Phys.* **86** 5961.
[8] Vallayer B Blaise G Treheux D 1999 *Rev. Sci. Instrum.* **70** 3102.
[9] Ghorbel N Kallel A 2010 *Annu. Rep. Conf. Electr. Insul. Dielectic Phenom.* 1.
[10] Al-Obaidi H N 2015 *J. Electrostat* **74** 102.
[11] Al-Obaidi H N Mahdi A S and Khaleel I H 2017 *Ultramicroscopy* **184** https://doi.org/10.1016/j.ultramic.2017.08.001.
[12] Chen H Gong H Ong C K 1995 *J. Appl. Phys.* **78** 3714.

Effect of deposition time on the structure, direct and indirect energy gap of nanoparticles *CdO* thin films deposited by chemical bath deposition technique

Effect of deposition time on the structure, direct and indirect energy gap of nanoparticles CdO thin films deposited by chemical bath deposition technique

Salah Abdul-Jabbar Jassim[1*], Eman Mohammed Ali Nassar[2]

[1] Department of Optical Technology , College of Health and Medical Technology ,Al-Ayen University ,Thi-Qar , Iraq
[2] Department of physics, College of Education and Applied Science, Hajjah University, Hajjah ,Yemen

E-mail: salah.jassim@alayen.edu.iq

Abstract. In this research, cadmium oxide (CdO) nanoparticle thin films have been prepared at room temperature using a chemical bath deposition (CBD) technique, and the effect of the deposition time were studied. CdO thin films have been deposited on glass substrate from cadmium chloride ($CdCl_2$) as Cd^{+2} ions source and sodium hydroxide NaOH as O^{-2} ions source. The pH value (acidity level) of the chemical bath was fixed at about 11. The CdO thin films structures were analyzed by X-ray diffraction. It shows that all the prepared thin films have a cubic polycrystalline structure with a preferential orientation along (111) plane. All structural parameters were calculated. Particle size for the preferential orientation is calculated between (19.1 -35.5 nm). It is found that the grain size increased with increasing the deposition time. UV-Vis spectrophotometer was used to study the optical properties, and a blue shift in the absorption peaks was noticed. The energy gap values (direct transition and indirect) calculated from the absorption spectrum located between (3.026 -3.409 eV) for direct transitions and (2.197-2.917 eV) for indirect transitions, and this indicates that all CdO thin films prepared nanoparticles. We found that the energy gap decreased with increasing the deposition time.

Keywords; CdO thin film, chemical bath deposition method, Nanostructured, energy band gap.

1. Introduction

Nanoparticles have attracted great interest in recent years due to their size dependent properties and wide range of applications [1, 2].

Transparent conducting oxides (TCOs), such as pure and doped, ZnO, SnO_2, BaO, Fe_2O_3, $BiClO$, Cu_2O and CdO have been studied because of their utilization in optoelectronic device technology. Particularly, CdO based transparent conducting oxide (TCOs) are of great interest due to their metal like good optical transparency in the visible region and charge transport behavior with an exceptionally large carrier mobility [3]. CdO compound is reddish brown in color, and is formed by burning of Cd in air. The oxide is not soluble in water, [4]. CdO is a known n-type semiconductor with the direct band gap energy of 2.2 - 2.8 eV [5], 2.5 eV [6], 2.3 eV [7], 2.25-2.9 eV [8], 2.2-2.5 eV [9],

and the indirect band gap of 1.98 eV [6], 1.36 eV [7], 1.36-1.98 eV [9]. In fact, the differences in the band gap energy are due to the lattice's defects in the crystalline structure [9]. Due to the defect of oxygen vacancies and cadmium interstitials, CdO has special features such as low resistivity (10^{-2} to $10^{-4}\,\Omega\,cm$) [8]. Also, low band gap and high transmission make it applicable solar cells, photovoltaic cell, photodiodes, phototransistors, transparent electrodes, optical communications, smart windows, flat panel display, liquid crystal displays and IR detectors [10, 11, 12]. There are different methods to prepare CdO films such as chemical bath deposition [13], Spray pyrolysis [14], Sol-gel [15] vacuum evaporation [16], successive ionic layer adsorption and reaction (SILAR) method [17]. Among these techniques, CBD method is widely used because it does not require vacuum and sophisticated instrumentation, the starting chemicals are commonly available (simple) and cheap (relatively cost effective) and can be applied in a large area of deposition at low temperature [18,19]. The optical absorption of CdO thin films were accomplished using UV-Vis spectrophotometer Cary50 Cm-Exlenain scan software) in the wavelength range of [190-1100 nm] at room temperature, and the back correction of the glass substrate has been taken in each measurement. The structural characterization of the CdO thin films were accomplished by analyzing the X-ray diffraction patterns obtained using a computer software (MDI/JADE 5) Pgeneral XD-2 X-ray diffractometer (λ= 1.5405 Å for Cu-Kα, current: 20.4 mA, voltage: 36.3 kV), The range of scan in 2θ of (3-75°) with scan speed $4°/min$. The film thickness (t) was found by gravimetric weight difference method.
This work focuses on the Synthesis of CdO nanoparticles thin film on glass substrate using (CBD) technique at room temperature and with different chemical deposition time. The structural and optical characteristics of the prepared films were investigated.

2. Preparations of CdO thin films

Microscopic glass slides of ($75 \times 25 \times 1\ mm^3$) were used as substrates during the deposition process. The substrate was first cleaned with water and soap, after that immersed in chromic acid and boiling for one hour, then cleaned by De-ionized water. Finally it immersed in acetone and rinsed with De-ionized water to remove the surface contaminations and to make the surface more conductive for uniform film deposition.
The deposition process was carried out at room temperature using cadmium chloride monohydrate ($CdCl_2$,H_2O, Merck, 98% purity concentration (0.05 Mol.) as Cd^{+2} ion source and sodium hydroxide ($NaOH$, Scharlau, 99% purity).as O^{-2} ions as shown in Eq. (1)

$$CdCl_2 + 2NaOH \rightarrow Cd(OH)_2 + 2NaCl \quad (1)$$

For the complex formation, an excess ammonium hydroxide (NH_4OH) solution was added (28%) until the clear solution reaches a pH of 11. This clear solution was kept under stirring, and then the substrates were submerged in the solution for (12, 24, 36 and 48 hrs.). Whitish films of $Cd(OH)_2$ were formed on glass substrates. The ($Cd(OH)_2$) films were heated in air at (623 K) for (2 hrs), and the films turn to brown. During the heating process the water vapor rises as shown in Eq. (2)

$$Cd(OH)_2 \xrightarrow{heat} CdO_{solid} + H_2O_{gas} \quad (2)$$

These slides were inclined vertically at 20° angle to the wall of the beaker, and a 3 ml of hydrazine hydrate was added to enhance the adhesion under a constant stirrer (80 rpm).
It is noted that the fresh solution should be continuously stirred to obtain uniform distribution of the chemical components,

3. Theory and calculation

3.1. Structural parameters

3.1.1. Interplanar distance (d)

Bragg's equation was used to calculate the inter-planar distance (d) [20]

$$n\lambda = 2d \sin\theta \quad (3)$$

where (n) is an integer order of the corresponding reflection, (λ) is the incidents wavelength, (θ) is Bragg's angle

3.1.2. Lattice constant (a)

The cubic structure lattice constant (a) is calculated using the relation [20]

$$a = d\,(h^2 + k^2 + l^2)^{1/2} \quad (4)$$

where ($h\ k\ l$) are Miller indices.

3.1.3. Crystallite size (D)

Debye-Scherrer's formula was used to calculate the crystallite size (D) [21]:

$$D = \frac{0.9\,\lambda}{\beta \cos\theta} \quad (5)$$

where (λ) is the wavelength (0.15406 nm) for Cu-Kα source, (β) is (FWHM) full width half maximum of the peak intensity in radians, and (θ) is experimental diffraction angle values.

3.1.4. Average strain (ε)

The strain (ε) is a macroscopic measure of deformation. It is calculated by [21]:

$$\varepsilon = \frac{\beta \cos\theta}{4} \quad (6)$$

3.1.5. Dislocation density (δ)

It is the amount of the defects in a crystal. The simple approach of Williamson and Smallman is used to evaluate it by: [22]

$$\delta = \frac{1}{D^2} \quad (7)$$

where (D) is the average crystallize size.

3.1.6. Texture coefficient (TC)

(TC) of CdO thin films is calculated to quantify the preferential orientation of the films [23]

$$TC(hkl) = \frac{I(hkl)/I_\circ(hkl)}{\sum I(hkl)/I_\circ(hkl)} N \quad (8)$$

where (I) is the measured intensity, ($I_\circ$) is the (JCPDS) standard intensity, and N the reflection number.

TC > 1 implies the preferentially oriented sample.

3.2. Optical study

3.2.1. Absorption coefficient (α)

It is calculated for thin films using Lambert law [20]

$$\alpha = 2.3026\,A/t \quad (9)$$

where (A) is absorbance, (t) is the film thickness.

3.2.2. Energy band gap (E_g)

Energy band gap (E_g) of the films was calculated using Tauc equation [24]:

$$\alpha h\nu = C\left(h\nu - E_g\right)^n \quad (10)$$

where ($h\nu$) is the incident photon energy, (C) is a constant, (E_g) is the band gap and (n) is an index which can take values 1/2, 2, 3/2, and 3 corresponding to allowed direct, allowed indirect, forbidden direct and forbidden indirect transitions respectively.

3.2.3. Particles size of nanoparticles

The particle sizes is calculated by Brus relation [25]

$$E_g^* = E_g + \frac{\pi^2 h^2}{8R^2}\left(\frac{1}{m_e^*} + \frac{1}{m_h^*}\right) - \frac{1.8e^2}{\epsilon R} \qquad (11)$$

where (E_g^*) is the size dependent band gap, (E_g) is the energy band gap of the bulk sample, R is the particle size, (m_e^*) and (m_h^*) are the effective masses of electron and hole respectively (0.21 m_e) for (CdO), (ϵ) is the dielectric constant (6.07) for (CdO) [26].

4. Result and discussion

4.1. Thickness measurement

The film thickness (t) of CdO films was found by gravimetric weight difference method by [27]

$$t = \frac{m}{\rho \, x \, \text{Ã}} \qquad (12)$$

where (m) is the mass of the deposited films in gram (g), (ρ) is the density of the deposited material in (g/cm^3) and Ã is the area of the deposited film in cm^2. Fig.1 shows the variation of the CdO films thickness with deposition time. It is clear that the thickness increases with increasing the deposition time.

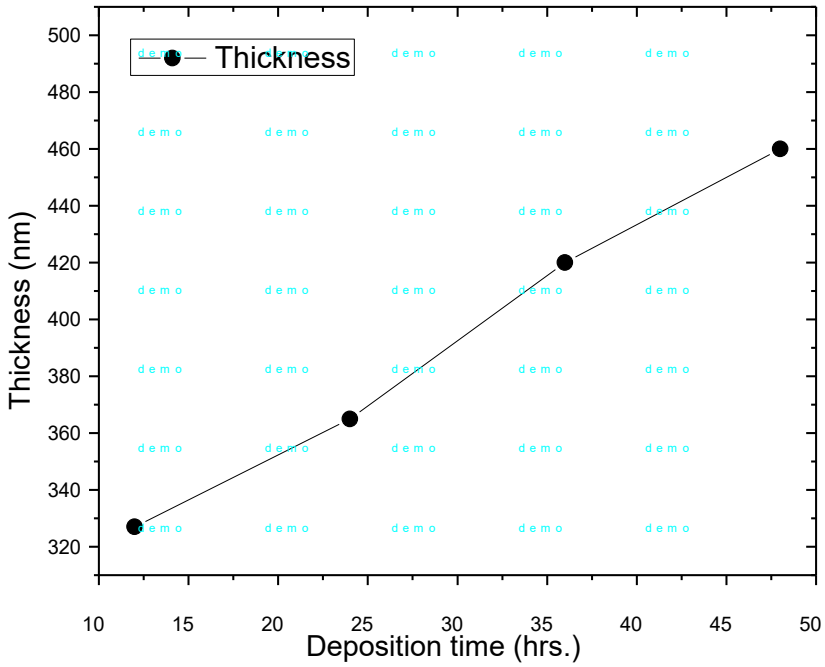

Figure 1. Variation of CdO films thickness with deposition time.

4.2. Structural study

Fig. 2 shows the XRD patterns of CdO thin films deposited at different time (12, 24, 36) h at room temperature and annealed at 623k for (2 h). Fig. 2 shows that the diffraction peaks for CdO films observed at 2θ=(32.91°, 38.313°, 55.2°, 65.858°, 69.211°) are linked to (111), (200) ,(220), (311), and (222) planes respectively. This indicates that CdO films are polycrystalline in nature with a cubic form as compared with the standard data of CdO (JCPDS file no.75-0592) [28] as shown in Table 1. P. Perumal *et al*. observed similar results [29]. XRD shows an increase in the crystallinity with increasing the deposition time. Also, as the deposition time increases, the diffraction peaks are slightly shifted in the direction of higher 2θ values and its intensity increases. The lattice constant (a) of CdO films was estimated by Eq. 4, and the observed (d) spacing was calculated from Bragg's condition Eq. 3. We found a good agreement between the estimated values in this study and the standard data of CdO (JCPDS file no.75-0592) [28] (see Table 1). The FWHM (β) have been evaluated for all diffraction peaks. The FWHM values decreases as the deposition time increases. The Origin software was used in this study for fitting. Texture coefficient (TC) was found to be in the range of (0.591-1.328) by Eq.8, and as the deposition time increases the (TC) slightly increases. The evaluation of the TC indicates the preferred orientation of the films along (111) plane has high crystallinity. Enhancing the preferred orientation is associated with increasing the number of the grains along this plane [30]. The calculated crystallite size (D) was in the range of (19.1- 41.06 nm) by Scherer's formula Eq.5, and as the deposition time increases, the crystallite size increases as shown in Fig. 3. The average strain (ε) was found to be in the range of (0.00148 - 0.00641) by Eq.6, and as the deposition time increases, the average strain (ε) decreases. The oxygen vacancies and the interstitial atoms incorporated in the CdO lattice may be caused the strain [31]. Dislocation density (δ) was found to be in the range of (0.00059 - 0.00274 nm^{-2}) by Eq.7, and as the deposition time increases, the dislocation density decreases.

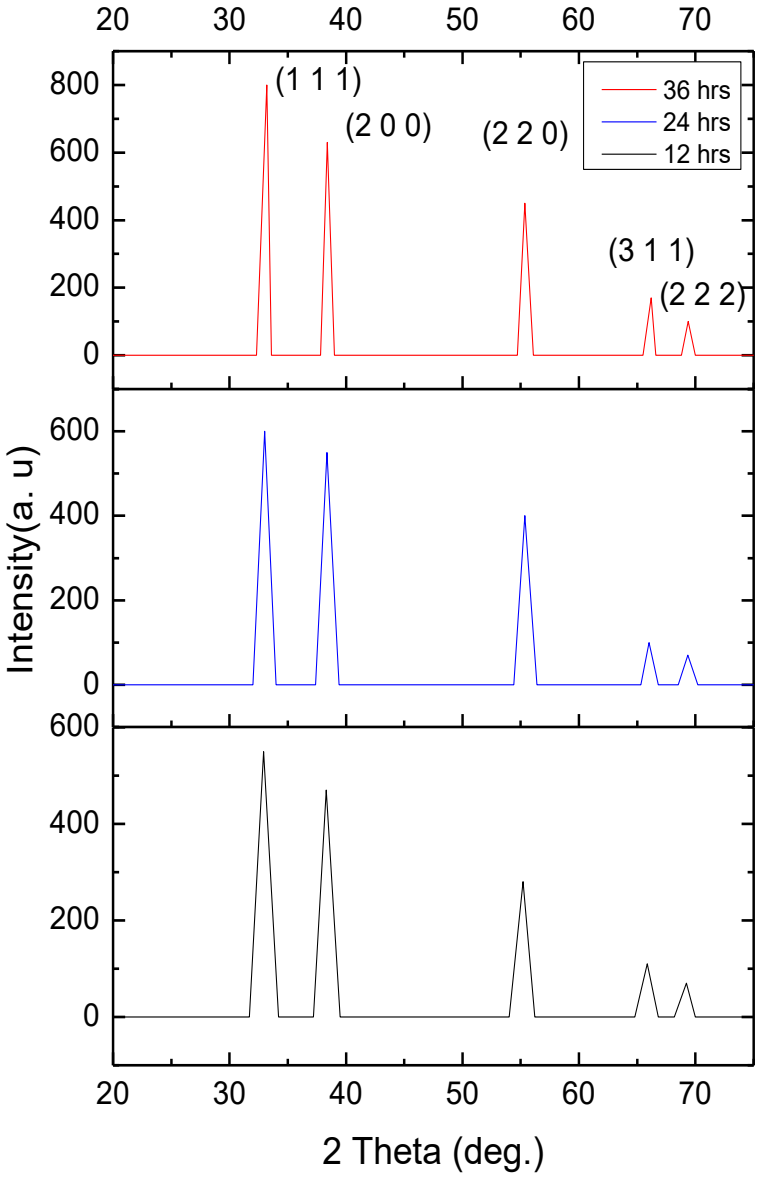

Figure 2. The X-ray diffraction of CdO films.

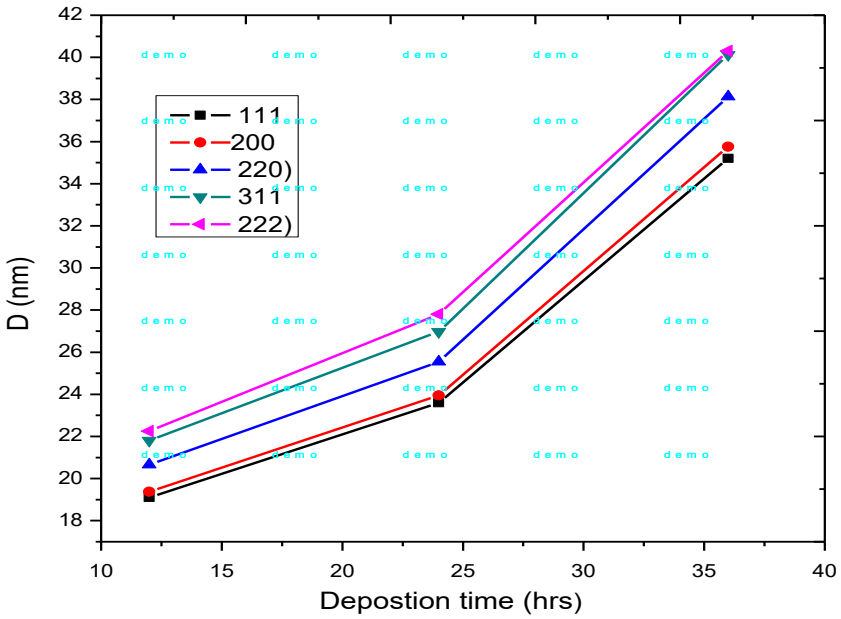

Figure 3. Variation grain size with deposition time

Table 1. The experiment and standard values of some XRD parameters for CdO films

Dep. time (hrs)	2θ Observe ($deg.$)	2θ Stander ($deg.$)	d Observe (nm)	d Stander (nm)	a Observe (nm)	a Stander (nm)	$h\ k\ l$	I% Observe	I% Stander
	32.91	33.019	0.2721	0.2710	0.4714		1 1 1	100	100
	38.313	38.321	0.2349	0.2347	0.4698		2 0 0	80	84
12	55.2	55.299	0.1664	0.1659	0.4706	0.4694	2 2 0	38.5	45.2
	65.858	65.935	0.1418	0.1415	0.4703		3 1 1	19	28.5
	69.211	69.271	0.1357	0.1355	0.4702		2 2 2	8.1	12.2
	33.02	33.019	0.2713	0.2710	0.4698		1 1 1	100	100
	38.35	38.321	0.2347	0.234	0.4694		2 0 0	75	84
24	55.36	55.299	0.165	0.165	0.4693	0.4694	2 2 0	35	45.2
	66.01	65.935	0.1415	0.1415	0.4693		3 1 1	13	28.5
	69.358	69.271	0.1355	0.13553	0.4693		2 2 2	9	12.2
	33.221	33.019	0.2697	0.2710	0.4671		1 1 1	100	100
	38.38	38.321	0.2345	0.2347	0.4690		2 0 0	79	84
36	55.35	55.299	0.1660	0.1659	0.4694	0.4694	2 2 0	32	45.2
	66.2	65.935	0.1411	0.1415	0.4681		3 1 1	17.1	28.5
	69.5	69.271	0.1352	0.1355	0.4685		2 2 2	6.3	12.2

Table 2. Experimental values of XRD parameters of CdO films

Deposition time (hrs)	2θ ($deg.$)	β FWHM ($rad.$)	TC Texture coefficient	D Grain size (nm)	ε average strain	δ dislocation density (nm^{-2})
	32.91	0.00757	1.209	19.1	0.00641	0.00274
	38.313	0.00757	1.152	19.38	0.00545	0.0066
12	55.2	0.00757	1.03	20.66	0.00362	0.00234
	65.858	0.00757	0.806	21.81	0.00292	0.0021
	69.211	0.00757	0.803	22.25	0.00274	0.00202
	33.02	0.00613	1.295	23.59	0.00517	0.0018
	38.35	0.00613	1.156	23.95	0.0044	0.00174
24	55.361	0.00613	1.003	25.54	0.00292	0.00153
	66.01	0.00613	0.591	26.97	0.00236	0.00137
	69.358	0.00613	0.955	27.8	0.0022	0.00123
	33.221	0.00411	1.328	35.2	0.00344	0.0008
	38.38	0.00411	1.249	35.76	0.00295	0.00078
36	55.35	0.00411	0.940	38.13	0.00196	0.00069
	66.2	0.00411	0.797	40.31	0.00158	0.00062
	69.5	0.00411	0.686	41.06	0.00148	0.00059

4.3. Optical study

Fig.4 reveals that the absorbance spectra (A) of the prepared films increases gradually with increasing the deposition time which might be due to increase the grain size with increasing the deposition time that improves the crysallinity and increases the thickness of the films [29]. The optical absorbance of the films decreases with the wavelength. These spectra reveal that CdO films have less absorbance in the visible and high wavelength region and more absorbance in the UV region [32].

The absorption band of CdO nanoparticles shows a blue shift due to the quantum confinement compared with bulk CdO particles. This optical phenomenon indicates that these nanoparticles show quantum size effect [33].

Fig.5 shows the absorption coefficient (α) as a function of the wavelength calculated from Eq.9. It reveals that in the shorter wavelengths, the absorption coefficient (α) exhibits high values which means that there is a large probability of the allowed direct transition. Then (α) decreases with increasing the wavelength. The absorption coefficient (α) values found to be of the order of 10^4 to 10^5 cm^{-1}. Fig.6 shows a direct band gap of CdO films estimated from extrapolation the plot of $(\alpha h\nu)^2$ versus ($h\nu$) Eq.10. The direct band gap energies are (3.026, 3.096, 3.117 and 3.409) eV, and it decreases with increasing the deposition time as seen in Fig .8. These energies are in good agreement with the earlier results reported in [29], and higher than the bulk (2.3 eV). The increase in the band gap of the bulk is due to increasing the free electron concentration in the films. The shift of the band gap with the change in the carrier concentration can be explained by the Burstein-Moss shift [6]. Fig.7 shows the typical Tauc $(\alpha h\nu)^{\frac{1}{2}}$ vs. ($h\nu$) plot for an indirect band gap energy determination. The indirect band gap energy obtained in this case were (2.197, 2.502, 2.539 and 2.917) eV, and it decreases with increasing the deposition time. This energy is higher than the bulk (1.36 eV). Fig.8 shows the variation of the particle size with deposition time. The particle size increases with increasing the deposition time. This confirms the same effect as in XRD study. The particle size of CdO nanoparticles was estimated from Eq.11 in the range of (11.419-12.895) nm for direct energy gap, and (10.374 -12.923) nm for indirect energy gap, Table 3. There is a slightly disagreement between the particle size calculated from the preferred orientation plans using Eq.5 and that calculated from Eq.11.

Fig.8 shows the variation of the particle size with energy gap. The particle size decreases with increasing the energy gap.

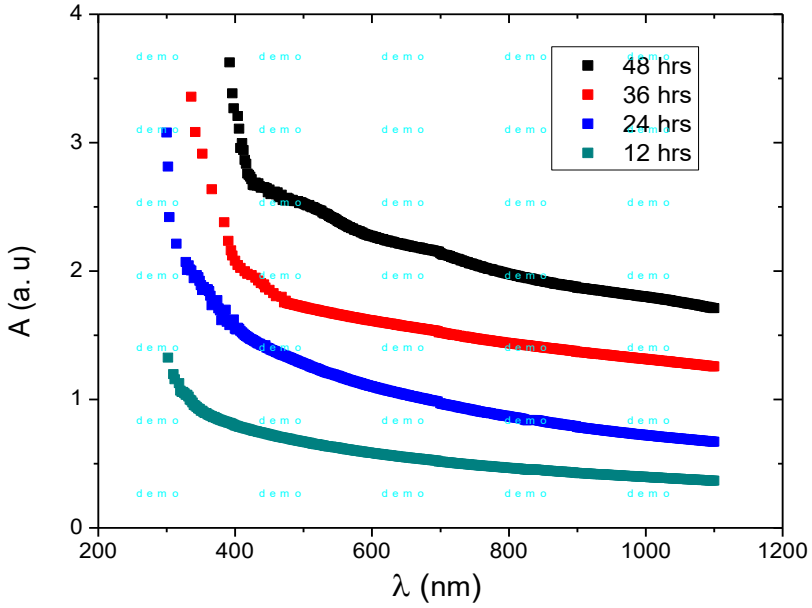

Figure 4. UV-Vis Absorbance (A) spectra of CdO films.

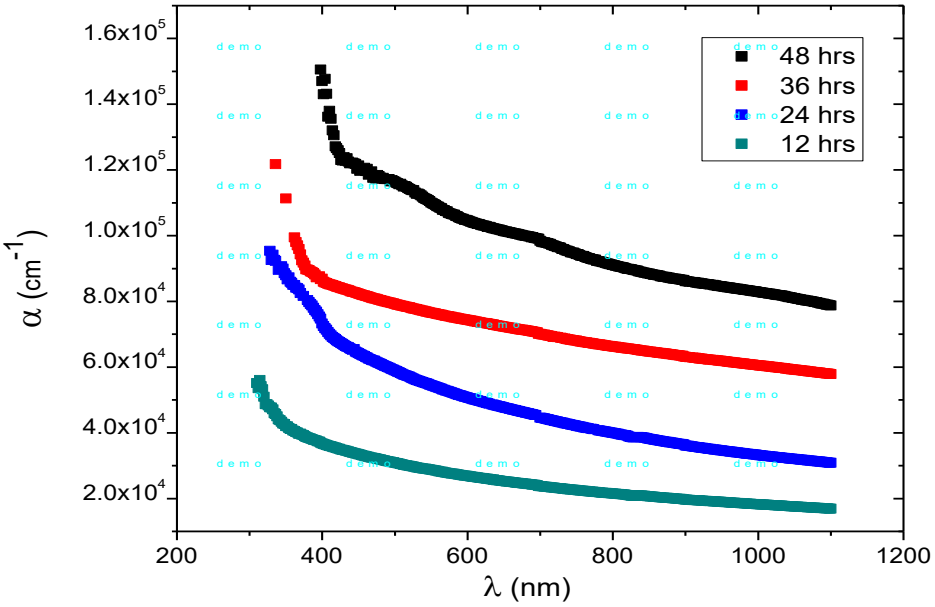

Figure 5. Absorption coefficient (α) as a function of wavelength (λ) of CdO films

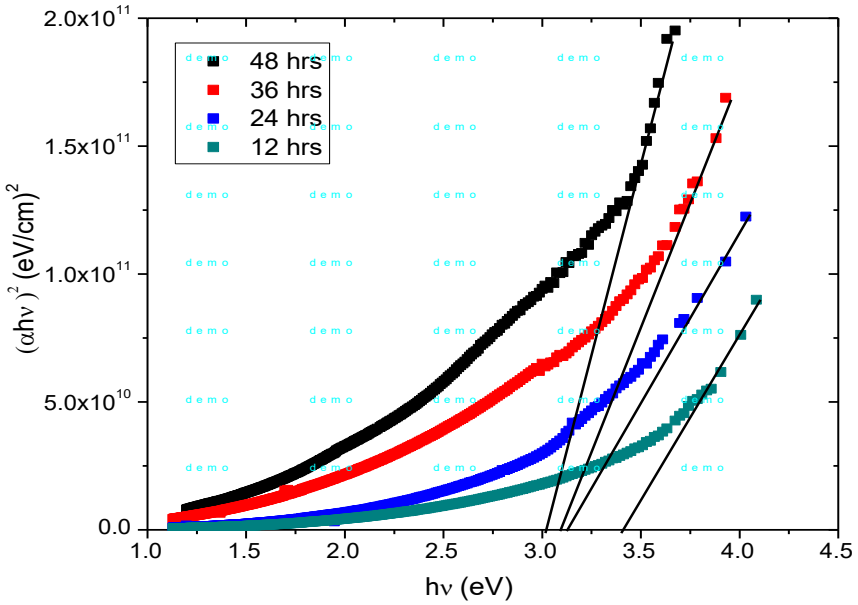

Figure 6. A direct band gap of CdO films.

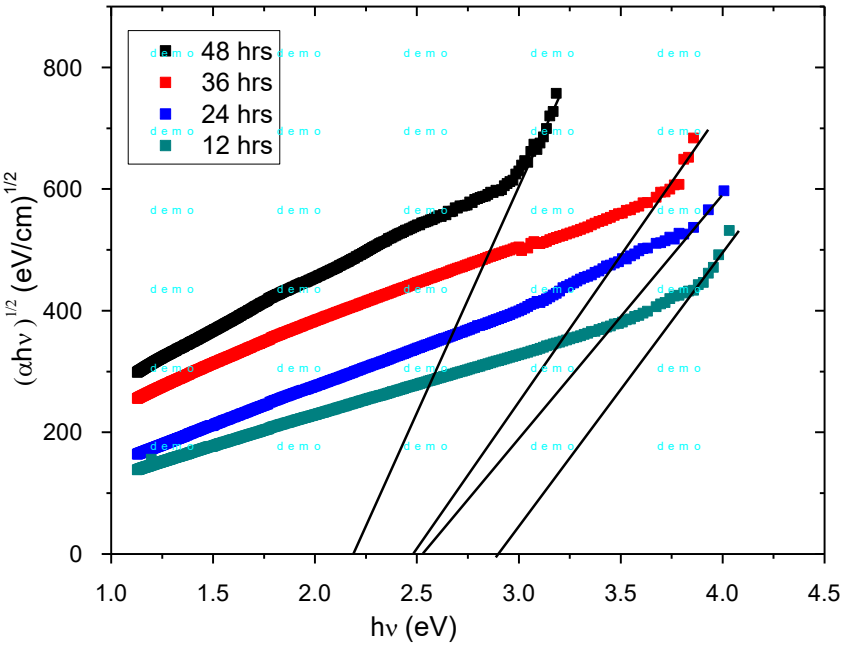

Figure 7. The indirect band gap of CdO films.

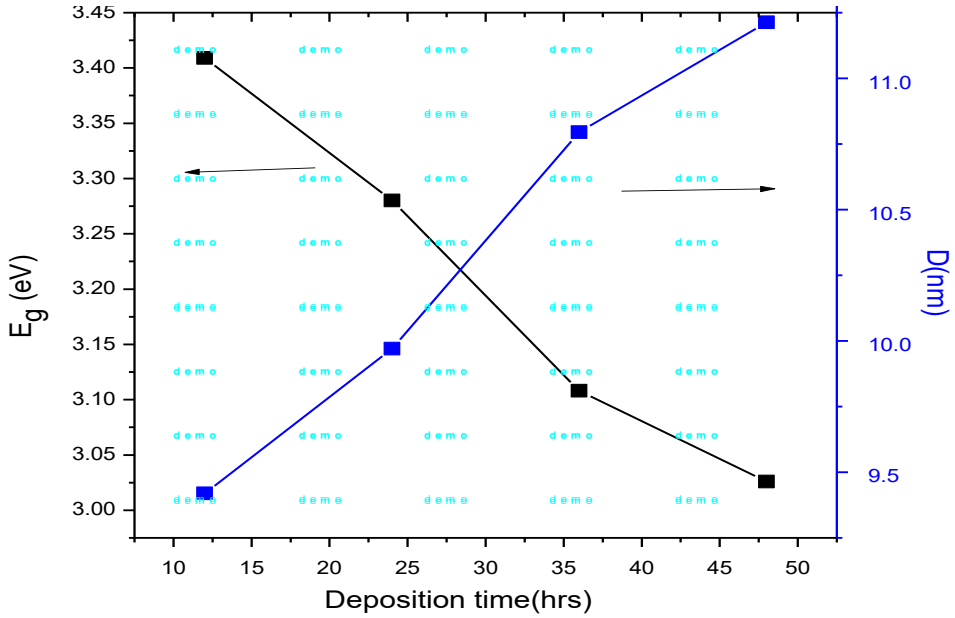

Figure 8. Vibration of the calculated grain size and direct energy gap of CdO films

Table 3. Experimental values of energy gap, blue shift and the calculated particles size for CdO films

Deposition time ($hrs.$)	Direct energy gap E_g (eV)	Blue shift E_{shift} (eV)	Particle size D(nm	Indirect energy gap E_g (eV)	Blue shift E_{shift} (eV)	Particle size D(nm)
12	3.409	1.109	11.419	2.915	1.555	10.374
24	3.117	0.817	11.823	2.539	1.179	11.532
36	3.096	0.796	12.29	2.502	1.142	12.033
48	3.026	0.726	12.895	2.197	0.837	12.923

5. Conclusions

CdO films have been successfully prepared with high quality, homogenous and gran size in the range of nanoparticles on glass substrates by CBD under different deposition time. The XRD tests of these films revealed that the deposited CdO thin films are polycrystalline in nature with cubic structure having (111) preferred orientation. The influence of the deposition time on the structural and optical properties is studied. By increasing the deposition time (thickness increases), the width of the diffraction peaks decreases resulted in increasing the grain size. We found that the average values of the grain size were in the range of (19.1-35.2 nm) for the preferred orientation indicating that the films are nanoparticles. The optical study revealed that the absorption spectra of CBD (CdO) films increased as the deposition time was increased. A blue shift in the optical gap has been observed for the absorption spectrum of the prepared CdO films, as an indication of quantum confinement effect. The absorption edge slightly shifts towards the higher wavelength with increasing deposition time. As the deposition time increases the energy gap decreases and the particle size increases.

6. References

[1] Naveen CS, Dinesha ML and Jayanna HS 2013 Effect of Fuel to Oxidant Molar Ratio on Structural and DC Electrical Conductivity of ZnO Nanoparticles Prepared by Simple Solution Combustion Method *J. Mater. Sci. Technol.* **29** (10) 898-902.

[2] Kathalingam N, Ambika MR, Kim J, Elanchezhiyan Y, Chae S and Rhee JK 2010 Chemical Bath Deposition and Characterization of Nanocrystalline ZnO Thin Films *Mat. Sci.Poland*, **28** (2) 513-522
[3] Ziabari F and Ghodsi E 2011 Optical and Structural Studies of Sol-Gel Deposited Nanostructured CdO Thin Films: Annealing Effect *Acta Phys. Polonica A* **120** (3) 536-540.
[4] Balu R, Nagarethinam VS, Suganya M, Arunkumar N and Selvan G 2012 Effect of the Solution Concentration on the Structural, Optical and Electrical Properties of SILAR Deposited CdO Thin Films, *J. Elect. Dev.* **12** 739-749 .
[5] Kumaravel R, Menakaa S, Regina S, Snegaa M, Ramamurthia K and Jeganathan K 2010 Electrical, Optical and Structural Properties of Aluminum Doped Cadmium Oxide Thin Films Prepared by Spray Pyrolysis Technique *Mat. Chem. Phys.* **122** 444 - 448.
[6] Lanje S, Ningthoujam RS and Ramchandra SJS 2011 Luminescence and Electrical Resistivity Properties of Cadmium Oxide Nanoparticles *Indian J. Pure Appl Phys*. **49** 234-238.
[7] Radi PA, Brito-Madurro AG, Madurro JM and Dantas NO 2006 Characterization and Properties of CdO Nanocrystals Incorporated in Polyacrylamide *Braz. J. Phys.* **36** (2A) 412-414.
[8] Henríquez R, Grez P, Muñoz E, Gómez H, Badán JA, Marotti RE and Dalchiele EA 2010 Optical Properties of CdSe and CdO Thin Films Electrochemically Prepared, *Thin Solid Films* **518** 1774-1778.
[9] Tadjarodi HK and Imani M 2012 Synthesis, Characterization and Adsorption Capability of CdO Microstructure for Congo Red from Aqueous Solution, *JNS* **2** 9-17.
[10] Balu R, Nagarethinam VS, Suganya M, Arunkumar N and Selvan G 2012 Effect of the Solution Concentration on the Structural, Optical and Electrical Properties of SILAR Deposited CdO Thin Films *J. Elect. Dev*. **12** 739-749.
[11] Zheng BJ, Lian JS, Zhao L and Q. Jiang 2011 Optical and electrical properties of Sn-doped CdO thin films obtained by pulse laser deposition *Vacuum* **85** 861-865.
[12] Al-Ogili HKJ 2011 Effect of Thickness to the Structure Properties of CdO Thin Films, Eng. and Tech. Journal, **29** (8) 1536-1544.
[13] Dhawale DS, More AM, Latthe SS, Rajpure KY and Lokhande CD 2008 Room Temperature Synthesis and Characterization of CdO Nanowires by Chemical Bath Deposition (CBD) Method *Appl. Surf. Sci*. **254** 3269-3273.
[14] YDOĞU S, ÇABUK G and ÇOBAN GM 2019 The Effects of Different Ga Doping on Structural, Optical and Electrical Properties of CdO Films *J. Nat. Appl. Sci.* **23** 129-136,
[15] Aydemira S, Kösea S, Kilickayaa MS and Özkanb V 2014 Influence of Al-doping on microstructure and optical properties of sol–gel derived CdO thin films *Superlat. Microstruct.* **71** 72-81.
[16] Dakhel A and Henari FZ 2003 Optical Characterization of Thermally Evaporated Thin CdO Films *Cryst. Res. Technol.* **38** (11) 979 - 985.
[17] Yıldırım MA and Ates A 2009 Structural, Optical and Electrical Properties of CdO/Cd(OH)2 Thin Films Grown by the SILAR Method, *Sensors Actuators A*, **155** 272-277.
[18] Al-Jawad SMH and Alogili HKJ 2009 Growth Kinetics of Chemically Deposited CdO Thin Films, *Eng. Tech. J.* **27** (11) 2335-2344.
[19] Kassim S and Nagalingam TW 2010 Tee, and H. S. Min, Effects of Deposition Period on the Chemical Bath Deposited Cu4SnS4 Thin Films, *Rev. Soc. Quím Perú*., **76** (1) 54-60.
[20] Barman J, Sarma KC, SaramaM and Sarma K 2008 Structural and Optical Studies of Chemically Prepared CdS Nanocrystalline *Indian J. Pure Appl. Phys*. **46** 339 -343.
[21] Gulen Y, Sahin B, Bayansal F and Cetinkara HA 2014 Solution-phase synthesis of un-doped and Pb doped CdO films *Superlattices Microstruct.* **68** 48–55.
[22] Balu R, Nagarethinam VS, Arunkumar N and Suganya M 2012 Nanocrystalline NiO Thin Films Prepared by A Low Cost Simplified Spray Technique Using Perfume Atomizer, *J. Elect. Dev.* **13** 920-930.

[23] Jassim, SAJ, Zumaila AARA, Al Waly GAA 2013 Influence of substrate temperature on the structural, optical and electrical properties of CdS thin films deposited by thermal evaporation *Res. Phys.* **3** 173–178.
[24] Suhail MH, Ibrahim IM and Rao GM 2012 Characterization and Gas Sensitivity of Cadmium Oxide Thin Films Prepared by Thermal Evaporation Technique*, J. Elect. Dev.* **13** 965-974.
[25] Al-Hussam MA and Jassim SA 2012 Synthesis, structure, and optical properties of CdS thin films nanoparticles prepared by chemical bath technique *J. Assoc. Arab Univ. Basic Appl. Sci.* **11** 27–31.
[26] Parvathi A, Peter AJ and Yoo CK 2013 Nonlinear Optical Properties in A quantum Dot of Some Polar Semiconductors *Chin. Phys. Lett*., **30** (10) 107301-1-5.
[27] Beevi MM, Anusuya M and Saravanan V 2010 Characterization of CdO Thin Films Prepared by SILAR Deposition Technique, *Int. J. Chem. Engin. Appl.* **1** (2) 151-154.
[28] Joint Committee on Powder Diffraction Standards, (Data File 75-0592) .
[29] Perumal P, Gowri Manohari A, Valanarasu S, Kathalingam A, Rhee J, Soundaram N and Chandramohan R 2012 Influence of Deposition Time on the Microstructure and Transport Properties of CdO Thin Films Prepared by Chemical Bath Deposition *JSEMAT*, **2** 71-75.
[30] Sakthivel S and Mangalaraj D 2011 Cadmium Oxide Nanoparticles by Sol-Gel and Vapour-Liquid-Solid Methods, *Nano Vision* **1** (1) 47-53.
[31] Shanmugavel G, Balu AR and Nagarethinam VS 2014 Preparation Of Cadmium Oxide Thin Films by Spray Technique Using Perfume Atomizer and Effect Of Solvent Volume on Their Physical Properties *Int. J. Chem. Mat. Res.* **2** (9) 88-101.
[32] Lalithambika KC, Shanthakumari K and Sriram S 2014 Optical Properties of CdO Thin Films Deposited by Chemical Bath Method *Int. J. Chem Tech Res*. **6** (5) 3071-3077.
[33] Negahdary M, Sadeghi SA, Hamrahi-michak M, Rezaei-Zarchi S, Salahi F, Mohammadi N, Azargoon E and Sayad A 2012 Direct Electron Transfer of Cytochrome C on Cadmium Oxide Nanoparticles Modified Carbon Paste Electrode *Int. J. Electrochem. Sci.* **7** 6059-6069.

Evaluation the reactions of production the radioactive Iodine-124

Evaluation the reactions of production the radioactive Iodine-124

Aeshah Ali Hussein[1], Naz T Jarallah[2], Bashair Mohamed Saied[3]

[1,2,3]Department of Physics, College of Education for Pure Sciences Ibn-AL Haitham, University of Baghdad, Baghdad, Iraq

Email: aisha.sataa.1983@gmail.com

Abstract. Nowadays, the field of radionuclide treatment is enjoying an exciting stage and preparing for further growth and progress in the future. For instance, in Asia, the large spread of liver and thyroid diseases has resulted in several new developments /clinical trials using molecular radiotherapy (i.e. targeted radionuclide therapy). Iodine-124 has unique physical properties including long half-life that adding an advantage for pharmacokinetics and radiopharmaceutical analysis. One of its applications in nuclear medicine is in Positron Emission Tomography (PET).The aim of the present work is to evaluate the production yield of ^{124}I via calculated the excitation functions /stopping power for the reactions^{nat}Te(P,X)^{124}I, ^{121}Sb(A,N)^{124}I,^{nat}Sb(A,X)^{124}I and ^{123}Sb(A,3N)^{124}I in the energy range (3.87-62.95)MeV by using Mat-lab and SRIM programs .

Keyword: Cross section, Excitation function, Iodine-124, Integral yield.

1. Introduction

Generally, Radioisotopes are formed in reactors /cyclotrons to be utilized for diagnostic or treatment purposes in healthcare. The reaction is produced via the energy of the projectile particles to be utilized in the production of the target core and the radioisotopes. For situations where perform an experiment is expensive and hard, simulation studies are preferred to carry out owing to it is save both economy and time [1]. In nuclear medicine, iodine radionuclides are exceedingly utilized for labelling monoclonal antibodies, receptors, and other radiopharmaceuticals, specifically in the applications of diagnostic and therapeutic as quantitative imaging over an interval of a number of days is needful [2]. Unluckily, the nuclides most utilized are ^{131}I, ^{125}I and ^{123}I, and all have restrictions.^{131}I is considered the most commonly used among the three, and it has very high photon energy for optimal imaging. Moreover, rigorous attenuation correction does not allowed via Single-Photon Emission Computed Tomography imaging (SPECT), though a satisfactory empirical correction may sometimes be realized. ^{125}I has a photon energy which is very low for optimal imaging, particularly quantitative imaging, also it has an extremely long half-life (i.e. half-life is undesirably long). ^{123}I has a half-life which is very short. On the other hand, a positron-emitting nuclide is Iodine-124 with a half-life of 4.176 days, and this allows quantitative imaging over several days by Positron Emission Tomography PET (a powerful non-invasive technique for molecular imaging [2–4].

Among its clinical applications are Na, ^{124}I has been used to diagnose/dosimetry in the disease of thyroid and to estimate the springing up of metastatic thyroid carcinoma. Furthermore, [^{124}I]-iododeoxyuridine ([^{124}I]-IUdR) has been used in measuring the activity of proliferation of tumors in

patients suffer from tumors of brain, including gliomas and meningiomas. Besides,[^{124}I]-Miodobenzylguanidine ([^{124}I]-MIBG) has got massive potential for utilizing in cardiovascular imaging, diagnosis, and therapy of malignant diseases like carcinoids, neuroblastoma, pheochromocytoma and paraganglioma [3,5–8]. R. Lambrecht et al in (2010) produced Iodine-124 in great yield through >99.5% radionuclidic purity at (48 h) post irradiation and the ^{124}Te (d,2n)^{124}I reaction. Targetry methodology has been explained. The production yield was (0.55±0.06 mCi/μA.h) [9]. R. Weinreich and E. Knust in (1996) was produced ^{124}I (T = 4.15 d) using a compact cyclotron by the nuclear reaction ^{124}Te (d, 2n)^{124}I via irradiation of$^{124}TeO_2$ with deuterons of energies (14 MeV). And then, dry distillation of the radioactive iodine isotopes generated from irradiated target materials. By-products including (8.02d)^{131}I, (12.4h)^{130}I, (13.0d)^{126}I, (60d)^{125}I and (13.2d)^{123}I have been measured and collected in each charge. After (45 h) decay time, the data demonstration that the total of the activities of these nuclides is below 5% of the ^{124}I activity [10]. S. S. Salodkinand V. M. Golovkov in (2020) have been investigated the methods of production of Iodine-124 radionuclide in nuclear medicine. The effect of target material, the selected nuclear reactions, the irradiation conditions, and the ways of manufacturing / cooling of the irradiated targets on the Iodine-124 yield is considered [11]. In present work, the yield of ^{124}I has been calculated via weighted average cross sections and stopping power of ^{nat}Te(P,X)^{124}I , ^{121}Sb(A,N)^{124}I ,^{nat}Sb(A,X)^{124}I and ^{123}Sb(A,3N)^{124}I reactions by using sets of programs like Mat-lab and SRIM.

2. Decay Scheme of Iodine-124

Iodine-l24 has decay scheme as shown in Fig. (1). At minimum, there are 97 gamma-ray transitions, 25 electron capture transitions and 6 positron transitions. Within the limits, 23% of decays result in emission of positron. Furthermore, there is several high energy gamma rays, some in coincides with the emissions of the positron [2-4].

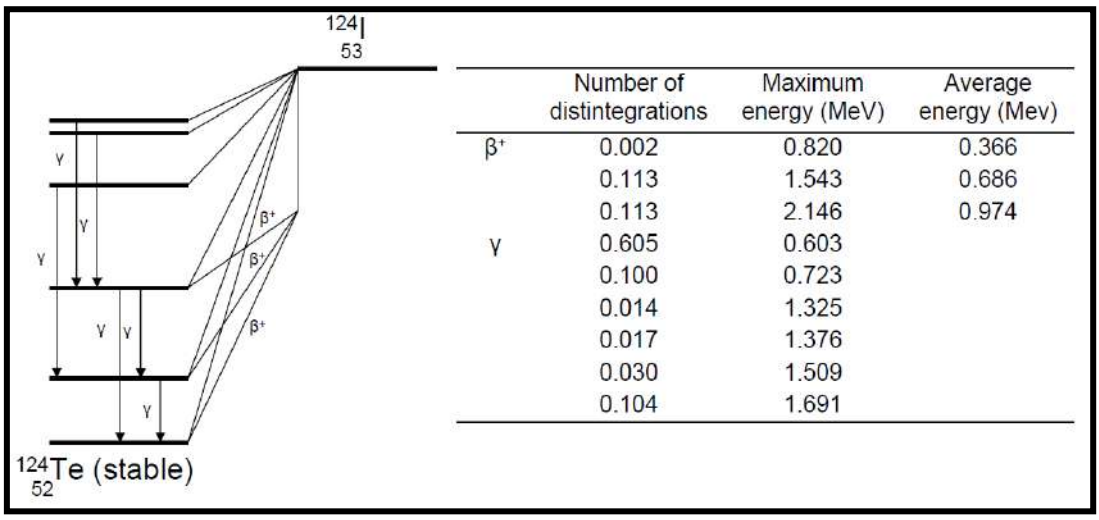

	Number of distintegrations	Maximum energy (MeV)	Average energy (Mev)
β+	0.002	0.820	0.366
	0.113	1.543	0.686
	0.113	2.146	0.974
γ	0.605	0.603	
	0.100	0.723	
	0.014	1.325	
	0.017	1.376	
	0.030	1.509	
	0.104	1.691	

Figure 1. Simplified decay scheme of ^{124}I

3. Theoretical background

For several decades, the possible use of radionuclides in treatment has been recognized. The most important advantage of radionuclide therapy is the ability to deliver a greatly concentrated absorbed dose to the tumor with preserving the surrounding natural tissue. Targeted radionuclide treatment has become one of the most favourite kinds of cancer treatment due to the administration of radionuclides is slightly invasive and the period of therapy is shorter than chemotherapy. A number of radionuclides including Iodine-124 have been successfully utilized for diagnostic and therapeutic [1,12]. There is a large number of reactions that is utilized for producing ^{124}I, relying on the particles, cyclotron and the

energies that are available in executing the irradiations [5]. In present work, ^{124}I has been produced by utilizing proton induced ^{nat}Te(P,X)^{124}I reaction and α induced ^{121}Sb(A,N)^{124}I ,^{nat}Sb(A,X)^{124}I , ^{123}Sb(A,3N)^{124}I reactions. The energy data for every reaction are obtained from the database of EXFOR and using Matlab programs language to calculate weighted average cross sections (W) for each reaction individually as the following:

$$W=\frac{(\sum wi\ yi)}{(\sum wi)} \quad (1)$$

$$w_i = {}^{1}/_{\mu_i^2} \quad (2)$$

where $\mu_i$is the standard deviation for sample i and yi is the cross section value for sample i [13].The cross section is one of the most significant physical quantity describing nuclear reactions. Experimentally, it can be calculated or measured utilizing varied technique (i.e. models) of nuclear reactions [14].

Furthermore, the integral yield (i.e. the overall number of the formed nuclei through an irradiation time) of these reactions is calculated according to the equation below [15]:

$$Y(t) = t \int_0^L I(x)\,\sigma(x)\left({}^{\rho}/_{ze}\right)dx \quad (3)$$

$$= tI_0 \int_{E_L}^{E_0} \left(-\frac{1}{\rho}\frac{dE}{dX}\right)^{-1}\left(\sigma(E)/_{ze}\right)dE \quad (4)$$

$$= t\,I_0 y \quad (5)$$

Here, ρ is the target isotope number density of sample material, t is the irradiation time, L is the thickness of sample material, $\sigma(x)$ is the cross section to produce the isotope at depth x in the sample, Z is the charge number, I_0 is the number of beam particles irradiating the sample per unit irradiation time, E_0 initial beam energy, E_L is the energy of the beam at the exit of the sample, $\left(-\frac{1}{\rho}\frac{dE}{dX}\right)^{-1}$ is the stopping power and y is the thick target product yield (i.e. is the number of the formed nuclei per unit induced electric charge). It is used for both stable / radioactive products, however is frequently utilized for stable ones.

On the other hand, the number of the formed nuclei existing in the sample material (t) satisfies when the product is radioactive with decay constant(λ)according to the relation below:

$$\frac{dN(t)}{dt} = \frac{dY(t)}{dt} - \lambda\ N(t) = I_0\ y\ -\ \lambda\, N(t) \quad (6)$$

The solution is

$$N(t) = I_0\ y\ \frac{1-e^{-\lambda t}}{\lambda} \quad (7)$$

Then

$$\frac{\lambda N(t)}{I_0} = y\left(1-e^{-\lambda t}\right) = a(t) \quad (8)$$

where $\frac{\lambda N(t)}{I_0}$ represented the activity of the sample material per unit current at t and $a(t)$ is the decay rates of the product per unit current [15].

4. Result and discussion

The values of the cross section for ^{nat}Te(P,X)^{124}I , ^{121}Sb(A,N)^{124}I , ^{nat}Sb(A,X)^{124}I and ^{123}Sb(A,3N)^{124}I reactions are calculated from previous studies [16-29], in the range of energies (3.87-62.95MeV) with a step of (0.5 MeV).

The weighted average cross sections for the above mentioned reactions have been calculated using equations (1 and 2) and rely on the data of proton and α induced, energy and cross sections published via the (EXFOR) library affiliated to the International Atomic Energy Agency by using Mat-lab(8.3a 2014) program .

Moreover, the integral yield ^{nat}Te(P,X)^{124}I , ^{121}Sb(A,N)^{124}I , ^{nat}Sb(A,X)^{124}I and ^{123}Sb(A,3N)^{124}I reactions have been evaluated by using equations (3-8) depended on the values of stopping power that was calculated via Zeigler formula through (SRIM-2013) program. The results of the integral yields are given in table (1).

Table1. Thick target yield of reactions

$Nuclear\ reaction$	$Energy\ (MeV)$	$Thick\ target\ yield\ of\ ^{124}I(\frac{Bq}{\mu A}.h)$
$^{nat}Te(P,X)^{124}I$	$10-20$	$1400-1447$
$^{121}Sb(A,N)^{124}I$	$30-45$	$184.6-200$
$^{nat}Sb(A,X)^{124}I$	$26.72-47$	$446-575$
$^{123}Sb(A,3N)^{124}I$	$32-45$	$1942-2273$

The calculated results of excitation functions andintegral yields are presented in Figures. 2 – 9.

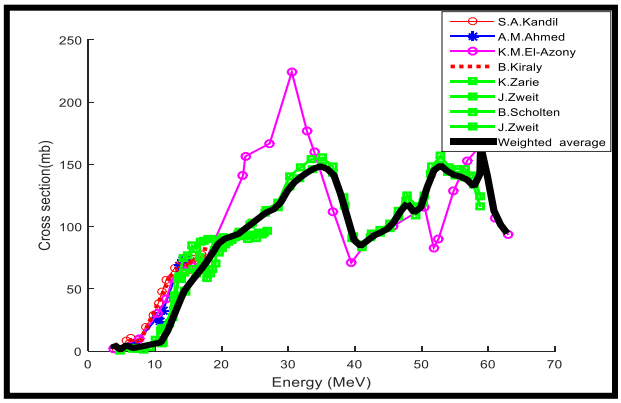

Figure 2. Excitation function of (_^nat)Te(P,X) (_^124)I

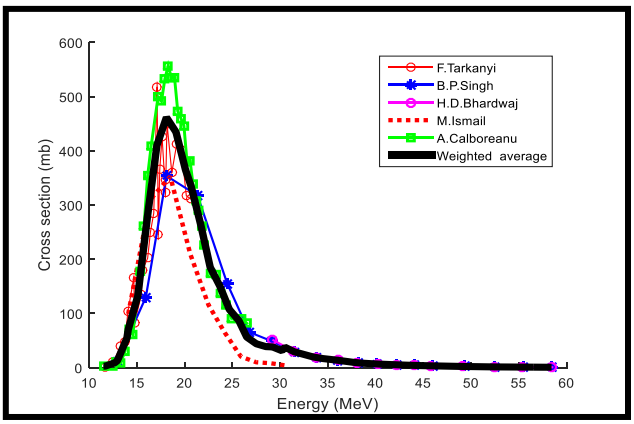

Figure 3. Excitation function of (_^121)Sb(A,N) (_^124)I

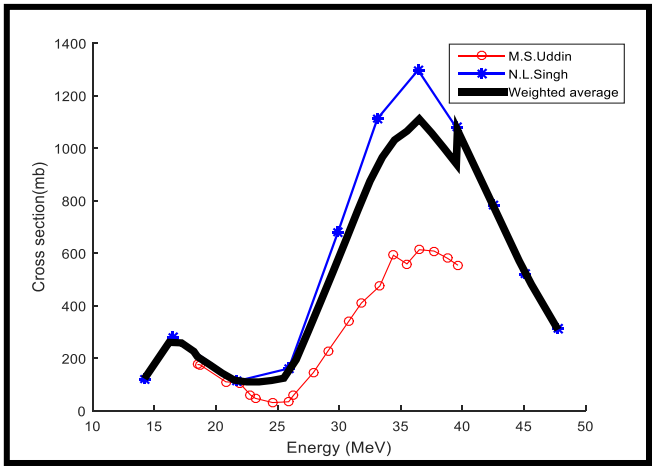

Figure 4. Excitation function of (_^nat)Sb(A,X) (_^124)I

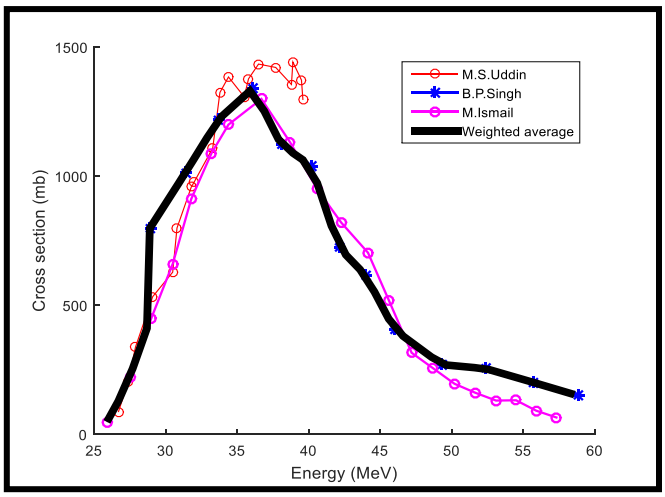

Figure 5. Excitation function of $^{123}Sb(A,3N)^{124}I$

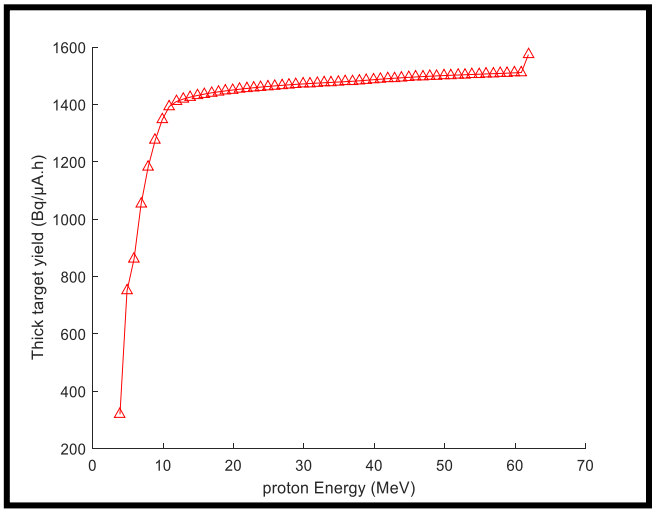

Figure 6. Production Yield for $^{nat}Te(P,X)^{124}I$ reaction

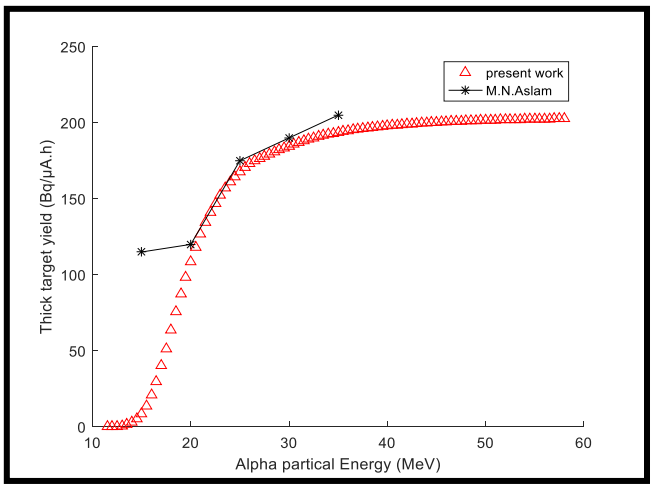

Figure 7. Production Yield for $^{121}Sb(A,N)^{124}I$ reaction.

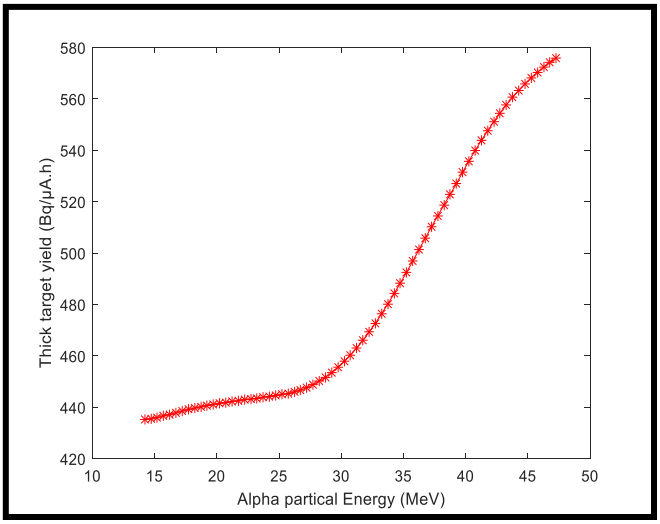

Figure 8. Production Yield for $^{nat}Sb(A,X)^{124}I$*reaction*

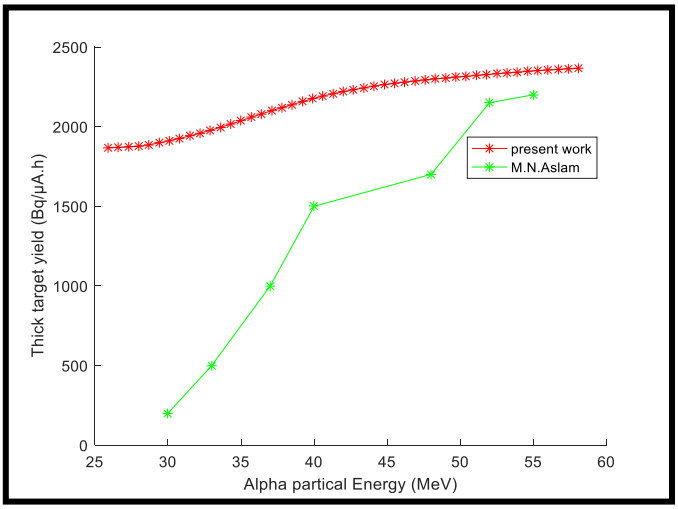

Figure 9. Production Yield for $^{123}Sb(A,3N)^{124}I$reaction.

We observed from figures (2-5) that the cross section of the ^{nat}Te(P,X)^{124}I ,^{121}Sb(A,N)^{124}I ,^{nat}Sb(A,X)^{124}I and ^{123}Sb(A,3N)^{124}I reactions is proportional to the energy of the incident particle.
$^{nat}Te(P,X)^{124}I$ *reaction*: It has two maximum cross-section values which are$(148.3824mb,164.9666mb)$ at energies $(35\ MeV, 59MeV)$ respectively.

$^{121}Sb(A,N)^{124}I$ *reaction*: it has one maximum cross-section value which is$(461.6968mb)$ at about18.1 MeV. After that, the cross-section values start decreasing until reaching to $(0.7882mb)$ at energy $(58.42\ MeV)$.

$^{nat}Sb(A,X)^{124}I$ *reaction* : It has two maximum cross-section values which are $(1.1107 \times 10^3 mb,$ $1.0681 \times 10^3 mb)$ at energies $(36.5\ MeV, 39MeV)$ respectively.

$^{123}Sb(A,3N)^{124}I$ *reaction*: It has one maximum cross-section value which is$(1.33 \times 10^3 mb)$ at energy35.5 MeV. After that, the cross-section values start decreasing until reaching to $(0.1579 \times 10^3 mb)$ at energy of58 MeV.
On the other hand, we noticed that after each maximum cross-section value, the cross-section values begin to decrease as the energy of the incident particle increases.
Furthermore, the integral yield of ^{nat}Te(P,X)^{124}I ,^{121}Sb(A,N)^{124}I ,^{nat}Sb(A,X)^{124}I and ^{123}Sb(A,3N)^{124}I reactions are directly proportional to the energy of the incident particle as shown in figures (6-9).
It is obvious that the values of the yield are different from one reaction to another owing to the difference in reaction cross section and energy of incident projectile. Choosing a suitable energy range for the incident particle improves the production process (i.e. Increases iodine yield and reduces impurities. The yields of reactions ^{121}Sb(A,N)^{124}I and ^{123}Sb(A,3N)^{124}I were in agreement with [30].
Generally, iodine-124 is formed good yield through the nuclear reaction $^{123}Sb(A,3N)^{124}I$.

5. Conclusions

The main objective of this work is the possibility of producing radioactive Iodine-124 to be used in nuclear medicine (i.e. diagnostic and therapeutic applications including Positron Emission Tomography (PET)), as it has physical and chemical properties that qualify it for that.
So, it was produced theoretically from different reactions by utilizing sets of programs like SRIM and Mat-lab. From the results that shown in table (1), we can conclude that the reactions

$^{123}Sb(A,3N)^{124}I$ are the best of other reactions to the production of iodine with the least possible energy (i.e. $^{123}Sb(A,3N)^{124}I$ reaction is ideally suited to produce Iodine-124.

6. References

[1] Rıdvan Ü and Akçaalan U 2020 The Reaction Cross Sections for 124,125 Te (p, xn) 123,124 I and 123, 124 Te (d, xn) 123, 124 I *Avrupa Bilim ve Teknol. Derg*. 958–963.
[2] Pentlow KS, Graham MC, Lambrecht RM, Daghighian F, Bacharach SL, Bendriem B, Finn RD, Jordan K, Kalaigian H, Karp JS, Robeson WR and Larson SM 1996 Quantitative imaging of iodine-124 with PET *J. Nucl. Med*. **37** 1557–1562.
[3] Lewis JS 2020 *Production , Use and Applications of 124 I*.
[4] Cascini GL, Niccoli Asabella A, Notaristefano A, Restuccia A, Ferrari C, Rubini D, Altini C and Rubini G 2014 124Iodine: A longer-life positron emitter isotope - New opportunities in molecular imaging *Biomed Res. Int.* **2014** https://doi.org/10.1155/2014/672094.
[5] Braghirolli AMS, Waissmann W, Da Silva JB and Dos Santos GR 2014 Production of iodine-124 and its applications in nuclear medicine *Appl. Radiat. Isot.* **90** 138–148. https://doi.org/10.1016/j.apradiso.2014.03.026.
[6] Guenther I, Wyer L, Knust EJ, Finn RD, Koziorowski J and Weinreich R 1998 Radiosynthesis and quality assurance of 5-[124I] iodo-2′-deoxyuridine for functional PET imaging of cell proliferation *Nucl. Med. Biol.* **25** 359–365.
[7] Ficola U, Quartuccio N, Paratore R, Treglia G, Piccardo A and Cistaro A 2013 *Utility of 124I-MIBG PET/CT in the follow-up of patients with advanced neuroblastoma*: first report of the AIMN PET-Pediatric Study InterGroup, in: Eur. J. Nucl. Med. Mol. Imaging, SPRINGER 233 SPRING ST, NEW YORK, NY 10013 USA S204–S205.
[8] Hartung-Knemeyer V, Rosenbaum-Krumme S, Buchbender C, Pöppel T, Brandau W, Jentzen W, Antoch G, Forsting M, Bockisch A and Kühl H 2012 Malignant pheochromocytoma imaging with [124I] mIBG PET/MR. *J. Clin. Endocrinol. Metab*. **97** 3833–3834.
[9] Lambrecht R, Sajjad M, Qureshi M and Al-Yanbawi S 1998 Production of iodine-124 *J. Radioanal. Nucl. Chem.* **127** 143–150.
[10] Weinreich R and Knus E 1996 Quality assurance of iodine-124 produced via the nuclear reaction124Te (d, 2n) 124I *J. Radioanal. Nucl. Chem*. **213** 253–261.
[11] Salodkin SS and Golovkov VM 2014 Cyclotron Production of Iodine-124, *Russ. Phys. J.* 1–7.
[12] Yeong CH, Cheng MH and Ng KH 2014 Therapeutic radionuclides in nuclear medicine: Current and future prospects, *J. Zhejiang Univ. Sci. B*. **15** 845–863. https://doi.org/10.1631/jzus.B1400131.
[13] Mohammed AL 2015 Production Yields of Ytterbium -169 Medically Relevant Radionuclide Within Medium Energy Range for the Protons, Deuterons and Alpha Particles *Int. J. Appl. Nat. Sci.* **4** 13–20. http://www.iaset.us/view_archives.php?year=2015&id=73&jtype=2&page=4.
[14] Nechifor C, Straticiuc M and Bercea M 2007 *Cross Sections and Protons Optimum Energy Ranges for Some Medical,* Cross Sect.
[15] Otuka N and Takács S 2015 Definitions of radioisotope thick target yields *Radiochim. Acta*. **103** 1–6. https://doi.org/10.1515/ract-2013-2234.
[16] Kandil SA and Al-Abyad M 2013 Cross section measurements and theoretical calculations of proton induced nuclear reactions on natural tellurium *Radiochim. Acta*. **101** 67–72.
[17] Ahmed AM, Hassan HE, Hassan KF, Khalaf AM and Saleh ZA 2011 Cross sections for the formation of radioiodines in proton bombardment of natural tellerium with particular reference to the validation of data for the production of 123I, *Radiochim. Acta Int. J. Chem. Asp. Nucl. Sci. Technol.* **99** 317–323.
[18] El-Azony K, Suzuki K, Fukumura T, Szelecsényi F and Kovács Z 2008 Proton induced reactions on natural tellurium up to 63 MeV: data validation and investigation of possibility of 124I production *Radiochim. Acta.* **96** 763–769.

[19] Király B, Tárkányi F, Takács S and Kovács Z 2006 Excitation functions of proton induced nuclear reactions on natural tellurium up to 18 MeV for validation of isotopic cross sections *J. Radioanal. Nucl. Chem.* **270** 369–378.
[20] Zarie K, AI-Hammad N and Azzam A 2006 Excitation functions of (p, xn) reactions on natural tellurium at low energy cyclotron: relevance to the production of medical radioisotope 123 I, *J. Nucl. Radiat. Phys.* **1** 93–105.
[21] Zweit J, Bakir MA, Ott RJ, Sharma HL, Cox M and Goodall R 1992 *Excitation functions of proton induced reactions in natural tellurium: production of no-carrier added iodine-124 for PET applications*.
[22] Scholten B, Qaim SM and Stöcklin G 1989 Excitation functions of proton induced nuclear reactions on natural tellurium and enriched 123Te: production of 123I via the 123Te (p, n) 123I-process at a low-energy cyclotron, Int. J. Radiat. Appl. Instrumentation. Part A. *Appl. Radiat. Isot.* **40** 127–132.
[23] Tárkányi F, Takács S, Király B, Szelecsényi F, Andó L, Bergman J, Heselius SJ, Solin O, Hermanne A and Shubin YN 2009 Excitation functions of 3He-and α-particle induced nuclear reactions on natSb for production of medically relevant 123I and 124I radioisotopes *Appl. Radiat. Isot.* **67** 1001–1006.
[24] Singh BP, Sharma MK, Musthafa MM, Bhardwaj HD and Prasad R 2006 A study of pre-equilibrium emission in some proton-and alpha-induced reactions *Nucl. Instruments Methods Phys. Res. Sect. A Accel. Spectrometers, Detect. Assoc. Equip*. **562**, 717–720.
[25] Singh BP, Bhardwaj HD and Prasad R 1991 A study of pre-equilibrium emission in α-induced reactions on 121,123 Sb *Can. J. Phys.* **69** 1376–1382.
[26] Ismail M 1990 Measurement and analysis of the excitation function for alpha-induced reactions on Ga and Sb isotopes *Phys. Rev. C.* **41** 87.
[27] Calboreanu A, Pencea C and Salagean O 1982 The effect of gamma de-excitation competition on the (α, n) and (α, 2n) reactions on gold and antimony *Nucl. Physics, Sect. A.* **383** 251–263 https://doi.org/10.1016/0375-9474(82)90451-1.
[28] Uddin MS, Hermanne A and Sudar S 2011 Excitation functions of alpha-particle induced reactions on enriched Sb-123 and Sb –nat for production of I-124 *J. Appl. Radiat. Isot*. **69** 699–704.
[29] Singh NL, Shah DJ, Mukherjee S and Chintalapudi SN 1997 Excitation functions for alpha-particle-induced reactions with natural antimony *Nuovo Cim. Della Soc. Ital. Di Fis. A*. **110** 693–709.
[30] Aslam MN, Sudár S, Hussain M,. Malik AA and Qaim SM 2011 Evaluation of excitation functions of 3He-and α-particle induced reactions on antimony isotopes with special relevance to the production of iodine-124 *Appl. Radiat. Isot.* **69** 94–104.

Effect of Gamma irradiation on the structural and optical properties of cadmium telluride thin films

Effect of Gamma irradiation on the structural and optical properties of cadmium telluride thin films

Eman M. Noori

X-ray technical department, Institute of Medical Technology- Baghdad, Middle Technical University, Iraq.

Email: dr.emannoori1975@gmail.com

Abstract. Cadmium Telluride (CdTe) thin films of 2000 Å thickness were deposited by thermal evaporation technique and irradiated with γ-ray energy for the times 24 h, 48 h and 72 h. Structure characterized by x-ray diffraction for both as-deposited and irradiated thin films. The increase in irradiation time appeared an improvement of crystallinity. The transmittance spectra of films using Ultraviolet-Visible spectrophotometer showed the increase in irradiation times leads to decreased in transmittance of films. The energy band gap found direct transition and decrease from (1.6-1.53) eV as the irradiation time increase.

Keywords: Irradiation, structural properties, optical properties, cadmium telluride, thin films.

1. Introduction

Polycrystalline cadmium telluride (CdTe) thin film is a very promising material in recent times due to its use in a large scale in the technology of thin film devices such as photovoltaic detectors [1], solar cells [2], infrared (IR) detectors [3], photo- electrochemical cells [4], etc. CdTe thin films exist in either zinc blende (cubic) or wurtzite (hexagonal) structure[5]. Its direct band gap of 1.45 eV[6], high absorption coefficient $> 10^5$ [7]. CdTe is useful in both heterojunction and homojunction configurations because it can exhibit both p - type and n – type conductivity [8]. Several techniques are available to prepare CdTe films such as electrodeposition[9], chemical bath deposition (CBD)[10], molecular beam epitaxy[11], closed space sublimation[12], Pulsed laser deposition method[13], and thermal evaporation[14]. Thermal evaporation is often prepared due to low trend of oxide formation and modifies the deposition condition.

In the present work, CdTe films deposited on the glass substrate by thermal evaporation. The deposited films were irradiated by gamma radiation, then we evaluated the crystallographic and optical properties and the influence of irradiated times on these properties is also undertaken.

2. Experimental

The thermal evaporation method was used to deposit about 2000Å thin films of CdTe on clean glass substrates at room temperature. The chamber was at a vacuum of the order 2×10^{-5} Toor. The film substrate source distance was fixed at 30 cm. CdTe powder was evaporated using molybdenum crucible. The CdTe films were irradiated by γ- ray Co^{60} and the irradiation time was (24, 48, 72) h. The structure characterization of the thin films studied was performed by a Philips PW 1710 using the CuK_α line

having wavelength of $\lambda = 1.5405$Å. The transmittance spectra of the films (as-deposited and irradiated) were recorded in the wavelength rang (450-900) nm by using UV-Visible spectrophotometer.

3. Results and discussion

Fig. 1 shows XRD patterns for the as-deposited and irradiation films for different irradiation time (24,48 and 72) h. The pattern shows a sharp diffraction peek at 2θ= 23.737 corresponding to reflection (111), which explain as a cubic structure, confirmed by the JCPDS data base no. 15-0770. The irradiation films do not create a new diffraction peek, but we found the crystalline degree increase with irradiation time this is may be due to the atoms have enough electromagnetic energy (γ -ray) to arrange themselves in their crystal lattice [2].

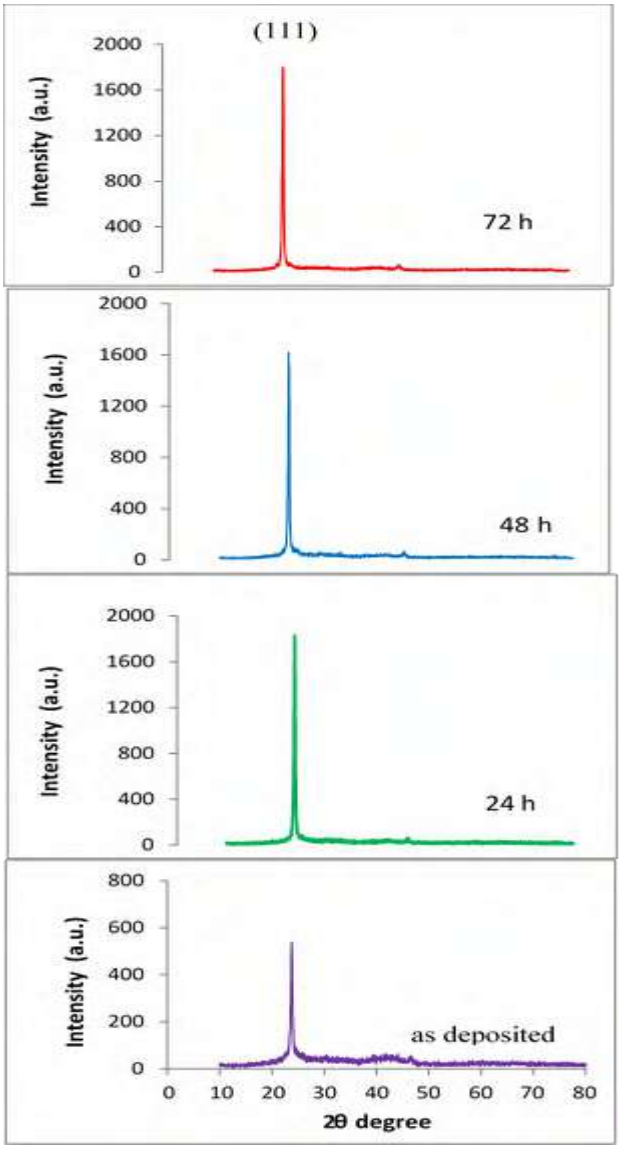

Figure 1. XRD of as-deposited and irradiation CdTe thin films.

The crystalline size D was determined using XRD analysis and given by the Scherrer formula [15].

$$D = 0.94\frac{\lambda}{\beta cos\theta} \quad (1)$$

Where λ is the wavelength of source radiation, β is the angular width at half the maximum intensity (FWHM) and θ is the angle where the peak occurs. As can be shown in Table 1, an increase in irradiation time also influences the crystalline size of CdTe thin films. This indicates that the increase in irradiation time leads to increment of the crystallite size. As irradiated time increases, the atomic, ionic, or molecular of CdTe components obtain a large electromagnetic radiation (γ-ray) leading to a large mobility. Thus, a large number of nuclei are formed which merge to form large crystallites.

Table1. The structural parameters of as- deposited and irradiated CdTe thin films.

irradiation Time (hour)	2θ (deg.)	Plan (hkl)	Grain size D (nm)	Strain (ε)x10^{-3} (line^{-2} m^{-4})	Dislocation density (δ)x10^{15} (line m^{-2})
0	23.793	(111)	21.2515	1.7036	2.2142
24	23.7378	(111)	26.8017	1.3508	1.3921
48	23.7525	(111)	27.1455	1.3337	1.3570
72	23.7383	(111)	27.6581	1.3089	1.3072

Dislocation density δ gives information about the deficiency of a crystal lattice therefore, it was calculated from the equation[16].

$$\delta = 1/D^2 \quad (2)$$

Table 1 revealed that dislocation density decreases as irradiation time increases which indicates better lattice arrangement. The strain ε of thin film regards to disarrangement of the lattice which is created during fabrication of a thin film. The strain was calculated by using the relation[15].

$$\varepsilon = \beta \cos\theta/4 \quad (3)$$

Calculated values for strain shown in Table 1. The strain was found to decrease with increasing irradiation time.

The optical transmission spectrum of CdTe films was recorded in the wavelength range of 450-900 nm. Fig. 2 shows the variation of optical transmittance of the film with wavelength λ for the as-deposited and irradiation time. As-deposited sample shows transmittance higher than the transmittance of irradiated ones and there is a decrement of transmittance with an increment of irradiation time. That is because formation and aggregation of gamma irradiation induced defects – centers, which leads to a reduction of transmittance of irradiation samples[2].

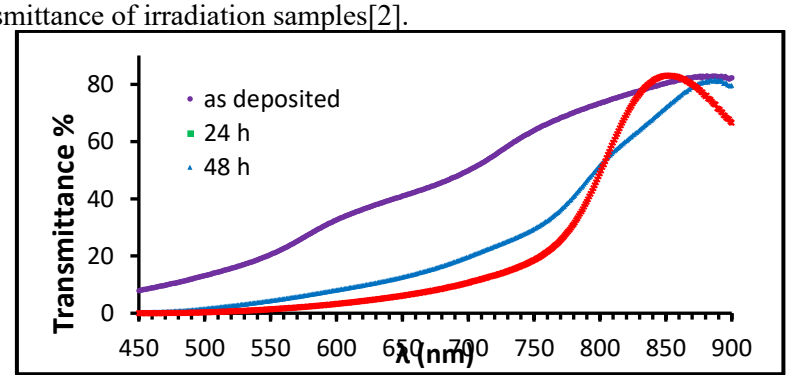

Figure 2. Optical transmittance of as-deposited and irradiated CdTe thin films.

The energy band gap E_g has been calculated by using Tauc relation [16].

$$(\alpha h\upsilon) = A(h\upsilon - E_g)^n \quad (4)$$

Where α is the absorption coefficient, $h\upsilon$ is photon energy, A is constant, n is the integer. Fig 3 shows the graph of $(\alpha h\upsilon)^2$ versus $h\upsilon$. By extrapolating the straight-line portion of the curves to zero absorption coefficients the energy band gap was evaluated and found to be direct.

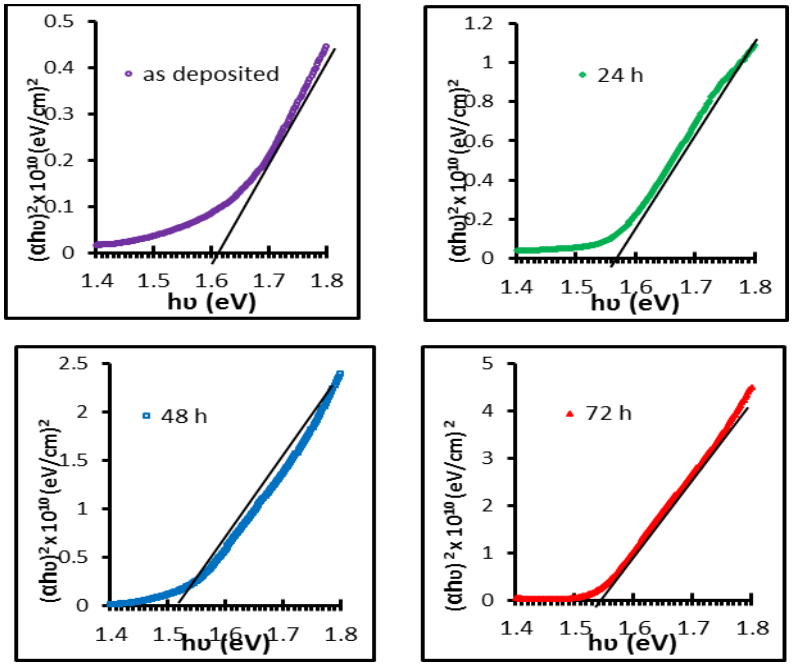

Figure 3. Taus plot of as-deposited and irradiated CdTe thin films.

Table 2 shows that energy band gap decreased as irradiated γ- ray increase. This is attributed to creating several defect levels resulting in more energy. This reduction in energy band gap may also be concluded to increase in crystallite size as shown in Fig. 4 which leads to improvement in the crystallinity as well as decrease in lattice strain as confirmed from structural studies.

Table 2. variation of energy band gap of thin films with irradiated time.

Irradiation time (hour)	Energy gap (eV)
As-deposited	1.6
24	1.56
48	1.54
72	1.53

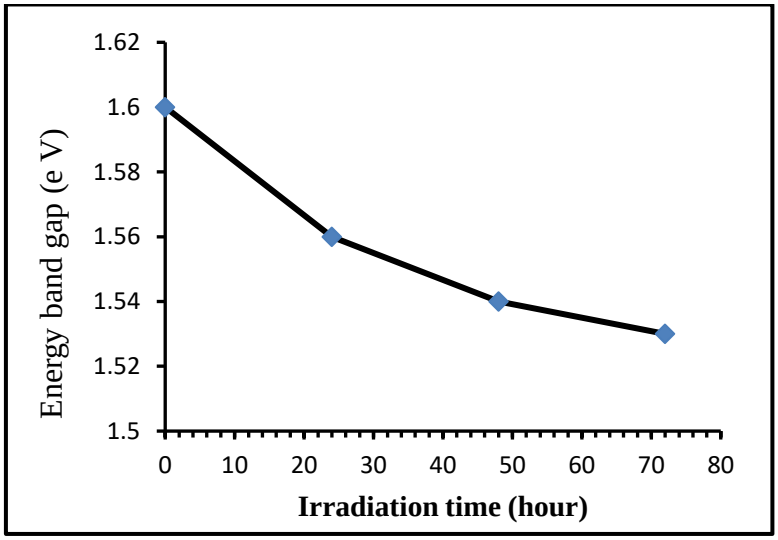

Figure 4. variation of energy band gap with irradiation time.

4. Conclusion

The Thermal evaporation method was successfully used to prepare CdTe thin films. γ- irradiation on CdTe films shows induced physical change in CdTe thin films. XRD analysis appears that films have cubic zinc-blend structure and increase in the crystallite size with increase irradiation time. Transmittance spectra decrease with irradiation increase due to defects-centers. The films have a direct transition and decrease from (1.6-1.53) eV with irradiation.

References

[1] Hasani E Kamalian M and Arashti M G 2019 Journal of Electronic Materials **48** (7) 4283.
[2] Goyal S and Chauhan R P 2019 *Nuclear Instruments and Methods in Physics Research Section B: Beam Interactions with Materials and Atoms* **461** 55.
[3] Survase S Narayan H Sulania I and Thakurdesai M 2016 *Nuclear Instruments and Methods in Physics Research Section B: Beam Interactions with Materials and Atoms* **387** 1.
[4] Gharibshahi E and Simulation 2020 *Solid State Communications* 2020 **320**.
[5] Punitha K Sivakumar R Sanjeeviraja C and Ganesan V 2015 *Applied Surface Science* **344** 89.
[6] Rahman K S Harif M N Rosly H N Bin Kamaruzzaman M I and Akhtaruzzaman Md 2019 *Results in Physics* **14**.
[7] Gu P Zhu X Li J Wu H and Yang D 2018 *Journal of Materials Science: Materials in Electronics* **29** (17) 14635.
[8] Kumarasinghe P Dissanayake A Pemasiri B and Dassanayake B 2017 *Materials Science in Semiconductor Processing* **58** 51.
[9] Zia R F Saleemi and Nassem S 2106 *Optik* 2016 **127** (4) 1972.
[10] Oluyamo S S Faremi A A Olusola O I Odusote Y A 2020 *Materials Today: Proceedings*.
[11] Kulkarni R Rondiya S Pawbake A Waykar R and Waykar A 2017 *Energy Procedia* **110** 188.
[12] Ghorannevis Z Akbarnejad E and Ghoranneviss M 2016 *Journal of Theoretical and Applied Physics* **10** (3) 225.
[13] Yavorskyi R Nykyruy L Wisz G and Potera P 2018 *Applied Nanoscience* **9** (5) 715.
[14] Hasani E and Raoufi D 2018 *Materials Research Express* **5** (4).
[15] Noori E M 2019 *Mustansiriyah Journal for Sciences and Education* **20** (1) 69.
Noori E M 2016 *Al-Mustansiriyah Journal of Science* 2016 **27** (5) 102.

Fabrication of $SrTiO_3$ NPs Doped Polymer Blend and Studying their AC Electrical Characteristics for Piezoelectric Fields

Fabrication of $SrTiO_3$ NPs Doped Polymer Blend and Studying their AC Electrical Characteristics for Piezoelectric Fields

Abeer Ghalib Hadi[1], Zainab Al-Ramadhan[2], Ahmed Hashim[3]

[1,2]University of Mustansiriyah, College of Education, Department of Physics, Iraq.
[3]University of Babylon, College of Education for Pure Sciences, Department of Physics, Iraq.

E-mail:abeer.ghaleb2020@gmail.com

Abstract. Nanocomposite films of PVA/PAA/$SrTiO_3$ NPs were fabricated for electronic and optic approaches using a low cost method. The AC electrical characteristics of PVA/PAA/$SrTiO_3$ films were investigated. The results showed that the dielectric constant of polymeric blend increases from 5.39 to 7.25, and the dielectric loss increases from 1 to 30. While, the electrical conductivity increases from $5.00E^{-11}$ to $2.00E^{-9}$ with increasing the $SrTiO_3$ NPs content. Also, the dielectric constant of polymeric blend increased from 5.39 to 8.04, and the dielectric loss increased from 0.377 to 1.21. While, the electrical conductivity increased from $2.09E^{-11}$ to $6.70E^{-11}$ with increasing the frequency.

Keywords: PAA, nanocomposites, $SrTiO_3$, dielectric constant, electronic applications.

1. Introduction

Polymers are known to be a conjugating chain of organic materials that show strong electrical conduct ion, which induces charge mobility along the polymers chain due to their characteristics as charges borne by the π-electron. Characteristics of Polymers are as good as with the inorganic matter, but the polymers include many pros, such as good flexibility, corrosion resistance, processability, low cost and light-weight. The inorganic also contains important characteristics like stability to heat, and good mechanical characteristics. Consequently, the polymer/inorganic system have huge applications in several fields [1]. Polymer nanocomposites have expected much interest related to their several industrial fields in water treatment, aerospace food structures industry, drug delivery and aeronautical [2]. The nanocomposites combine useful characteristics of Polymers and other characteristics of nanoparticles [3]. The polyvinyl alcohol/ PVA is a Water/synthetic polymer soluble, non-toxic, and it is generally used in the mixtures owing to its excellent chemical and physics characteristics, good film formation properties, noncarcinogenic, emulsifying capability, biocompatible and biodegradable qualities [4]. The PAA is a hydrophilic Polymer, non-toxic, biocompatible [5]. This work aims to prepare new types of nanocomposites to be used in pressure sensors and piezoelectric fields .

2. Materials and methods

Using the casting process, the nanocomposite films of PVA/PAA blend as a matrix and $SrTiO_3$ NPs as an additive were manufactured. The PVA/PAA film was prepared using a magnetic stirrer by dissolving 1gm of 4:1 ratio polymers in 30 ml of distilled water. The nanocomposite films were prepared by adding the $SrTiO_3$ NPs to different concentrations of PVA/PAA solutions (1.8%, 3.6%, 5.4% and 7.2%). The dielectric properties were Calculated in a frequency range of (100 Hz - 5M Hz) using the LCR meter. The dielectric constant (έ) is determined with the aid of [6]:

$$\acute{\varepsilon} = \frac{C_p}{C_o} \qquad \text{……..(1)}$$

The C_o and C_p are vacuum and capacitance in parallel capacitors .

The dielectric loss (ε″) is determined by [7]:

$$\varepsilon'' = \acute{\varepsilon}\, D \qquad \text{……....(2)}$$

D is a dispersion factor.

The AC conductivity was determined by the following relation [8].

$$\sigma_{A.C} = w\, \varepsilon''\varepsilon_o \qquad \text{……..(3)}$$

W: The angular frequency representation

3. Results and Debate

Figures 1 and 2 represent the dielectric constant and the loss of nanocomposites with PVA/PAA/$SrTiO_3$ and frequency respectively. From these figures, the ε' of PVA/PAA/$SrTiO_3$ nanocomposite reduces with increasing the frequency, which is related to the dipoles tendency in the polymer to orient themselves in the applied field direction. The dielectric loss of PVA/PAA/$SrTiO_3$ decreases with increasing the frequency. This behavior is related to the interfacial polarization in the PVA/PAA/$SrTiO_3$ nanocomposites. The high value at low frequency of ε" for PVA/PAA/$SrTiO_3$ nanocomposite is related to the mobility of the charges [9]. Figures 1 and 2 show the ε' and ε" of a (PVA–PAA) blend, which increase with increasing the $SrTiO_3$ NPs content. This behavior is related to increase the polarizations of the free electrons and the space charges [10,11].

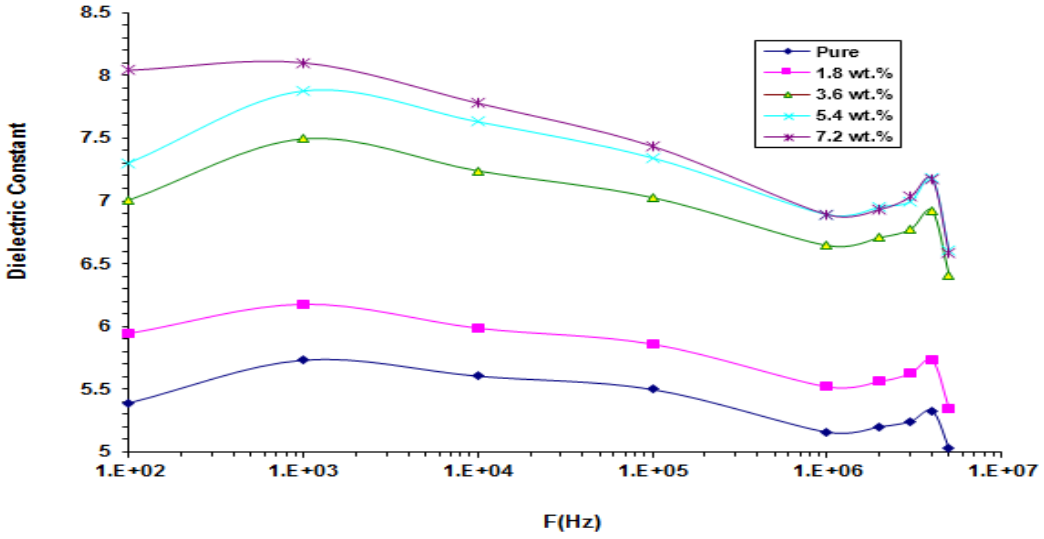

Figure 1. Variation of ε' with frequency of PVA/PAA/$SrTiO_3$ samples.

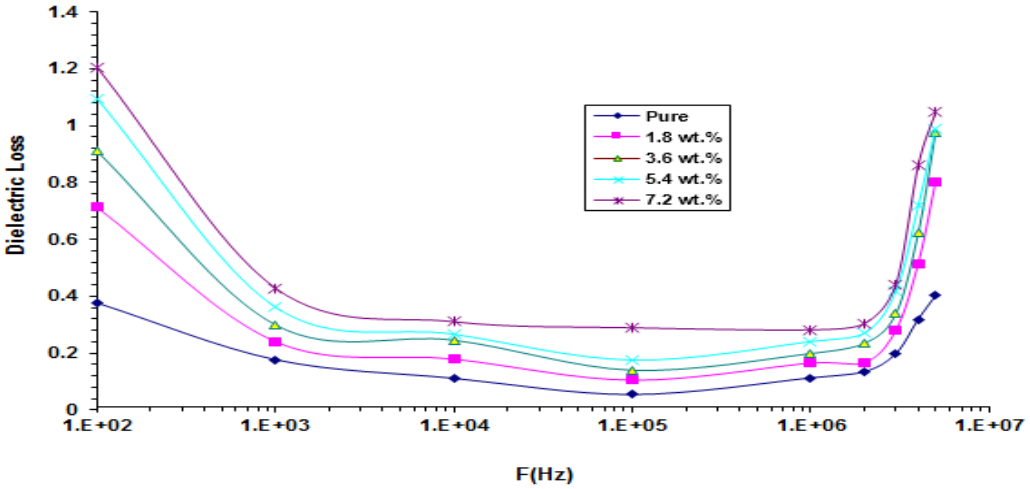

Figure 2. Variation of ε" frequency of PVA/PAA/$SrTiO_3$ samples.

Figure 3 shows the AC electrical conductivity with frequency for PVA/PAA/$SrTiO_3$ nanocomposite. This figure indicates that the conductivity increases with increasing the frequency, which attributed to the influence of the polarization and hopping. The conductivity of PVA/PAA increases with increasing $SrTiO_3$ NPs ratio. This is due to the hopping mechanism of conducting charge carriers [12].

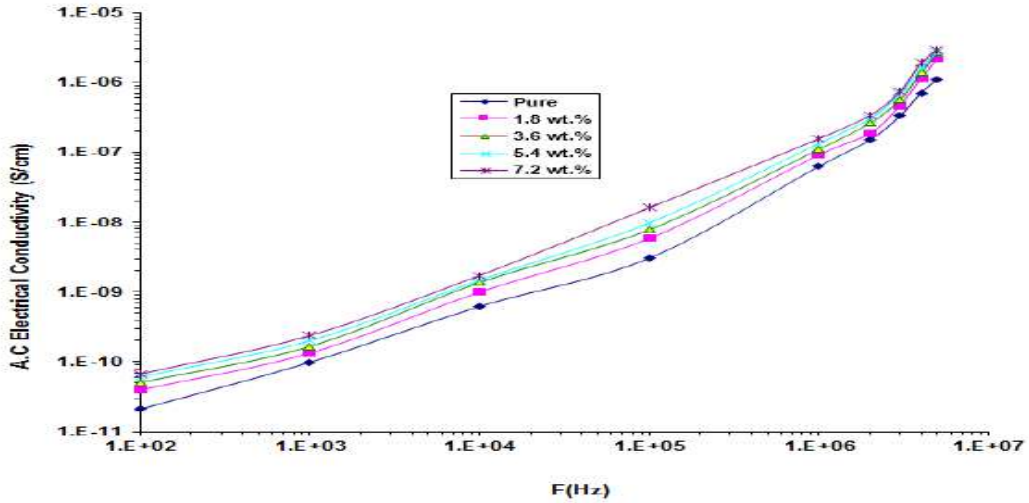

Figure 3. Variation of $\sigma_{A.C}$ with a frequency for PVA/PAA/$SrTiO_3$ samples.

4. Conclusions

The dielectric constant of PVA/PAA increased from 5.39 to 7.25 and the dielectric loss increased from 1 to 30 while the electrical conductivity increased from 5.00 E^{-11} to 2.00 E^{-9} with the addition of $SrTiO_3$ NPs. The PVA/PAA/$SrTiO_3$ dielectric constant increased from 5.39 to 8.04 and the dielectric

loss increased from 0.377 to 1.21 while the AC conductivity increased from $2.09E^{-11}$ to $6.70E^{-11}$ with increasing the frequency. The results indicated that the PVA/PAA/$SrTiO_3$ nanocomposite may be used in various piezoelectric and electronic applications like capacitors, pressure sensors, diode, transistors, .etc.

References

[1] Rehim M H A and Alhamidi J 2018 Journal of Advancements in Food Technology **1** (1).
[2] Meng Du, Xing-Zhong Cao, Rui Xia, Zhong-Po Zhou, Shuo-Xue Jin and Bao-Yi Wang 2018 Chin. Phys. B **27** (2).
[3] Sekhar B Subramanyam C Bose GSC Ramanaiah M V and Ravikumar R 2018 RJPBCS **9** (4).
[4] Siddaiah T Ojha P Obularajugari N Velikanti G Kumar R and Ramu Ch 2018 Materials Research **21**(5).
[5] Liew C W Ng H M Numan A and Ramesh S 2016 Polymers **8** (179).
[6] Kadhim K J Agool I R and Hashim A. 2017 Journal of Advanced Physics **6** (2). DOI: https://doi.org/10.1166/jap.2017.1313.
[7] Hashim A and Hadi Q 2017 Sensor Letters **15** doi:10.1166/sl.2017.3892.
[8] Hashim A and Hadi A 2017 Sensor Letters **15** doi:10.1166/sl.2017.3910.
[9] Kadhim K J Agool I R and Hashim A 2016 5 (5) DOI: https://doi.org/10.1166/mat.2016.1371.
[10] Hashim A and Hadi A 2018 Ukrainian Journal of Physics **63**(8) DOI: https://doi.org/10.15407/ujpe63.8.754 .
[11] Hashim A Habeeb M A Hadi A Jebur Q M and Hadi W 2017 Sensor Letters **15** doi:10.1166/sl.2018.3935.
[12] Agool I R Mohammed F S Hashim A 2015 Advances in Environmental Biology **9** (11).

Influence of $BaTiO_3$ NPs on Dielectric Characteristics of PVA/PEG For Electronic Applications

Influence of $BaTiO_3$ NPs on Dielectric Characteristics of PVA/PEG For Electronic Applications

Batool Mohammed[1], Hind Ahmed[2] and Ahmed Hashim[3]

[1,2,3]University of Babylon, College of Education for Pure Sciences, Department of Physics, Iraq.

E-mail:batoolmalkhafaji@gmail.com

Abstract. In this paper, we synthesized new types of nanocomposites to be used in various electronic applications such as piezoelectric, pressure sensors, diodes, transistors with low cost and lightweight. The nanocomposites were obtained from PVA /PEG blend doped with nanoparticles $BaTiO_3$ using casting method then studied using LCR meter. The dielectric characteristics of the synthesized nanocomposites have been studied. Results indicated that dielectric constants ε', loss ε" and conductivity $\sigma_{A.C}$ in PVA/PEG rise as $BaTiO_3$ NPs content increased. Also, the dielectric constant was increased from 5.8 to 8.6 and the dielectric loss was increased from 1.5 to 4.38. The ε' and ε" were decreased while the electrical conductivity was increased from 8.34 to 2.40 at 100 HZ and the $\sigma_{A.C}$ was decreased with increasing frequency.

Keywords: dielectric parameters, $BaTiO_3$, blend, nanocomposites, conductivity.

1. Introduction

Nanotechnology is a topical year, a mainly field special, ranged from new enhancements typical of device physics to precisely novel fields to improving novel have materials nanometer dimensions scale [1]. It is rapidly developing and growing that has large fields in several research approaches, improvement, and industrial activities [2]. Polymer matrix nanocomposites are becoming an essential part of today materials because of several advantages such as low weight, simple fabrication methods, low cost, high fatigue strength, and good corrosion resistance. Nanoparticles incorporation into the polymer matrix considerably alters its physical properties such as the electrical, structural, thermal, and optical properties [3]. The nanocomposites of organic and inorganic are very promising for fields in smart microelectronic, photodiodes, light-emitting diodes, gas sensors, photovoltaic cells etc. [4].PVA/PEG blend has been used in this work due to the it's good dielectric and optical properties this work aims to prepare of PVA-PEG-$BaTiO_3$ new nanostructures films for electronics applications. The $BaTio_3$ has been added to the PVA/PEG blend to get on new nanocomposites Materials have good dielectric properties which make it can be used for different electronic applications.

2. Materials and Methods

The films of PVA/PEG/$BaTiO_3$ nanocomposites using the casting process, they were prepared by. 1gm of PVA/PEG was dissolving in 30 ml using the magnetic stirrer of distilled water with ratio 88%/12%. The $BaTiO_3$ NPs were added to PVA/PEG by ratios are 1.4%, 2.8%, 4.2% and 5.8%. The dielectric characteristics tested in frequency range 100 Hz -5M Hz using LCR meter.

The dielectric constant (έ) is given by the [5]:

$$έ = \frac{C_p}{C_\circ} \quad \text{……..(1)}$$

C_o and C_p are vacuum and parallel capacitances.
The dielectric loss (ε″) is determined by [6]:

$$ε'' = έ D \quad \text{…….....(2)}$$

D is dispersion factor.
The A.C conductivity were calculated by [7]:

$$σ_{A.C} = w ε'' ε_o \quad \text{……..(3)}$$

W: represents the angular frequency

3. Results and Discussion

Figures 1 and 2 show the behavior of ε' and ε" of PVA/PEG/$BaTiO_3$ nanostructures with frequency, respectively. As shown in these figures, the ε' and ε" are reduced with increasing in hesitation owing to a space shipment polarization whose is miniature to the aggregate polarization and becomes the more contributing at low hesitation [8]. The dielectric constant and loss of PVA/PEG blend increased by increasing in $BaTiO_3$ NPs content, this is due to the increasing of the charge carriers [9].

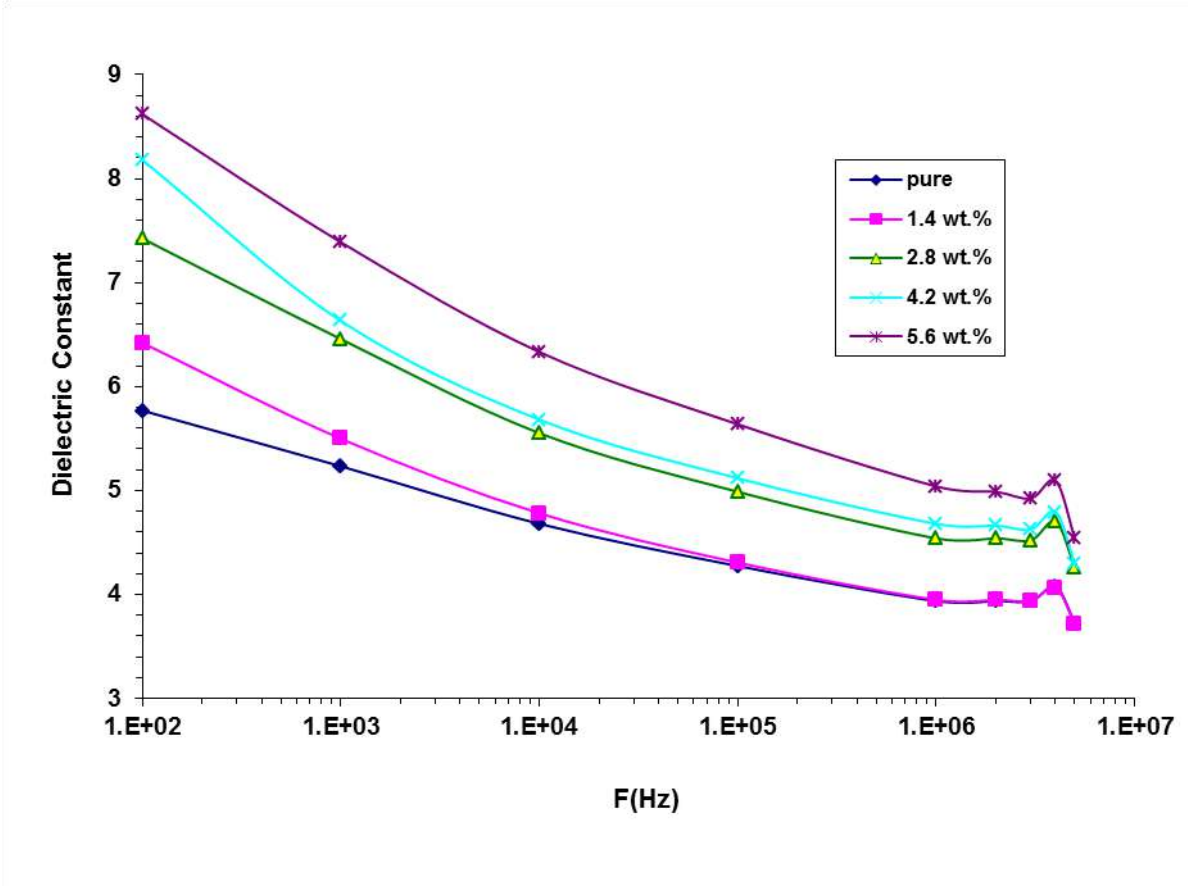

Figure 1. The behavior of ε' of PVA/PEG/$BaTiO_3$ nanostructures with frequency.

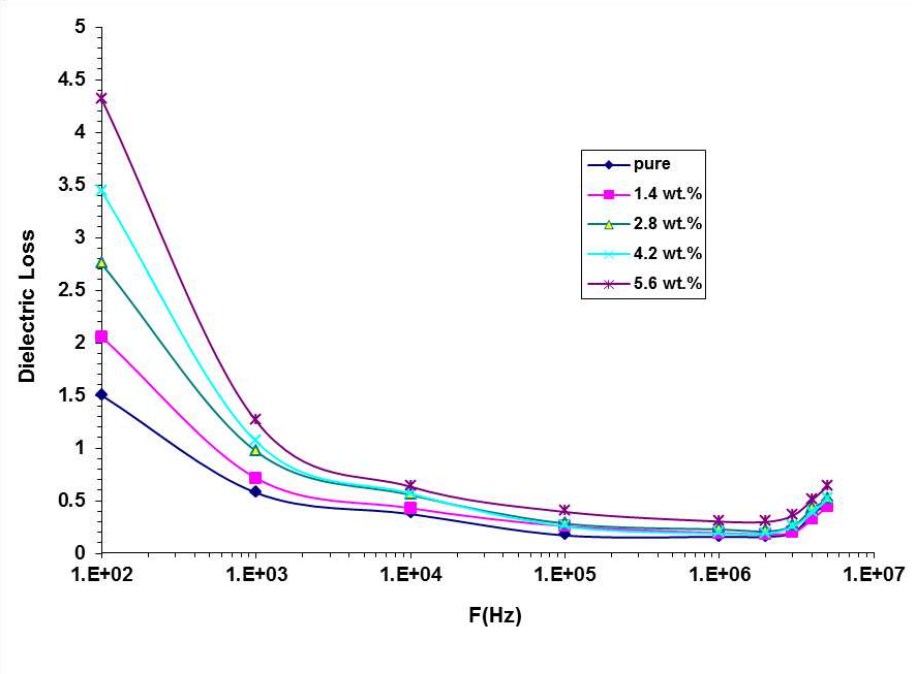

Figures 2. The behavior of ε" of PVA/PEG/$BaTiO_3$ nanostructures with frequency.

Figure 3 shows the behavior of conductivity of PVA/PEG/$BaTiO_3$ nanostructures with frequency. The conductivity rises with rising in frequency, this is related to the mobility of charge carriers and hopping of ions. The conductivity of PVA/PEG rises with rising of the $BaTiO_3$ NPs content. This increase in conductivity relates to rising in charge carriers due to dopant NPs composition which decreases the resistance of nanocomposites and rises the conductivity [10,11].

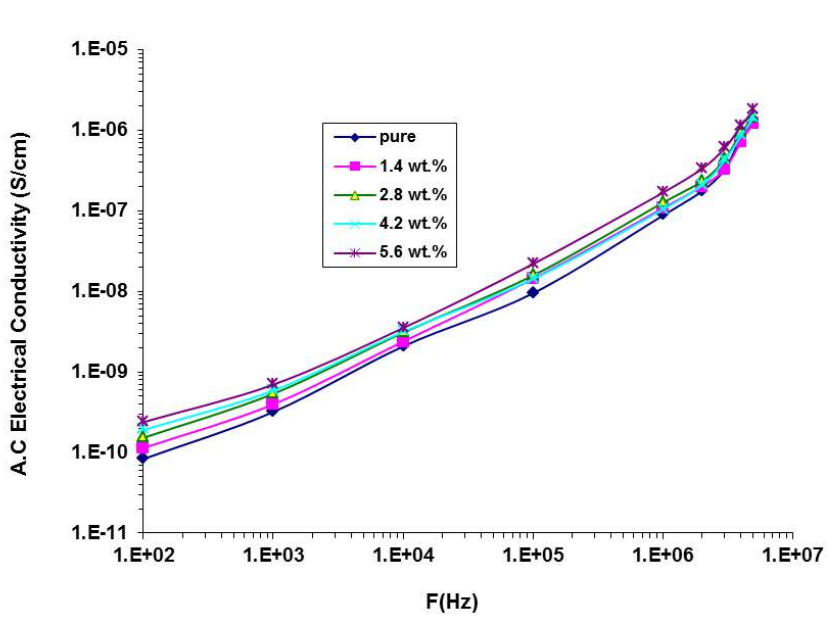

Figure 3. Behavior of $\sigma_{A.C}$ of PVA/PEG/$BaTiO_3$ nanostructures with frequency.

4. Conclusions

In this paper, the dielectric parameters of PVA/PEG were found to be improved with increasing $BaTiO_3$ NPs contents and the dielectric parameters changed with increasing the frequency. Moreover, the dielectric constant was increased from 5.8 to 8.6 and the dielectric loss was increased from 1.5 to 4.38. The ε' and ε" were decreased from 8.34 to 2.40 while the electrical conductivity was increased at 100 HZ. The $\sigma_{A.C}$ was decreased with rising the frequency. The obtained results showed the PVA/PEG/$BaTiO_3$ nanostructures have many applications in electrical and electronic fields.

References

[1] Elashmawi IS and Menazea AA 2019 Different time's Nd:YAG laser-irradiated PVA/Ag nanocomposites: structural, optical, and electrical characterization, *J. Mat. Res. Technol.* **8** 2.

[2] Manjunath A, Irfan M, Anushree KP, Vinutha KM and Yamunarani N 2016 Synthesis and Characterization of CuO Nanoparticles and CuO Doped PVA Nanocomposites *Adv. Mat. Phys. Chem.* **6** 263-273.

[3] AbouElfadl A 2019 Structure, Optical and Thermal Properties of Gamma Irradiated PVA/Cd0.9Mn0.1S Nanocomposite Films, *Arab J. Nucl. Sci. Appl*. **52** 4 145-158.

[4] Sheha E, Khoder H, Shanap TS, El-Shaarawy MG and El Mansy MK 2012 Structure, dielectric and optical properties of p-type (PVA/CuI) nanocomposite polymer electrolyte for photovoltaic cells *Optik* **123** 13.

[5] Hashim A and Hadi Q 2017 Novel of (Niobium Carbide/Polymer Blend) Nanocomposites: Fabrication and Characterization for Pressure Sensor *Sensor Lett.* **15** doi:10.1166/sl.2017.3892.

[6] Hashim A and Hadi A 2017 A novel Piezoelectric Materials Prepared from (Carboxymethyl Cellulose-Starch) Blend-Metal Oxide Nanocomposites, *Sensor Lett.* **15** doi:10.1166/sl.2017. 3910.

[7] Hashim A, Habeeb MA, Hadi A, Jebur QM and Hadi W 2017 Fabrication of Novel (PVA-PEG-CMC-Fe_3O_4) Magnetic Nanocomposites for Piezoelectric Applications *Sensor Lett.* **15** doi:10.1166/sl.2018.3935.

[8] Agool IR, Mohammed FS and Hashim A 2015 The effect of magnesium oxide nanoparticles on the optical and dielectric properties of (PVA-PAA-PVP) blend, *Adv. Environ. Biol.* **9** 11.

[9] Kadhim K J, Agool I R and Hashim A 2017 Effect of Zirconium Oxide Nanoparticles on Dielectric Properties of (PVA-PEG-PVP) Blend for Medical Application *J Adv. Phys.* **6** 2 DOI: https://doi.org/10.1166/jap.2017.1313.

[10] Ahmed H and Hashim A 2020 Fabrication of PVA/NiO/SiC Nanocomposites and Studying their Dielectric Properties For Antibacterial Applications *Egypt. J. Chem.* **63** 3 DOI: 10.21608/ EJCHEM.2019.11109.1712.

[11] Hashim A and Hadi A 2018 Novel Pressure Sensors Made From Nanocomposites (Biodegradable Polymers–Metal Oxide Nanoparticles): Fabrication and Characterization *Ukrainian J. Phys.* **63** 8 DOI: https://doi.org/10.15407/ujpe63.8.754.

Study of Optical properties of Polymer PVP thin films grafted by Fluorescence dyes

Study of Optical properties of Polymer PVP thin films grafted by Fluorescence dyes

Ali S. Ali[1]

[1]Physics Dept., College of Sci., Al-Muthanna Univ., Al-Muthanna, Iraq

.

E-mail: ali.salman@mu.edu.iq

Abstract. A polymer of polyvinyl pyrrolidone (PVP) with fluorescence dye (Flu) was prepared as thin films by casting method with a ratio of (10%) from added the dye. In this case, the optical properties at a wave number range of (200-900) nm were studied. The Absorption (A), transmission (T) spectra, absorption coefficient (α), direct and indirect transitions for energy gap are represented for optical properties. We have found that the polymeric films of PVP/Flu have indirect transition with phonon energy. The indirect energy gap and phonon energy equal to (1.74) eV and (0.15) eV respectively, and the maximum value for (R,K) at the photon energy is (2.3eV). Also, we see that the real (ε_1) and imaginary (ε_2) parts of the dielectric constant increases with increasing the photon energy.

Keywords: *Fluorescence, indirect energy gap, PVP, thin film.*

1. Introduction:

Commercial polymers for materials are complex. They contain more components from other polymers, low molecular weight organic additives, or non-organic fillers. In most experimental studies, preparing polymer blend in a state of mixing and remixing is beginning by a temperature quench because these polymers have high viscosity [1].

The effect of two bounding interfaces in the thin films is adding an additional complexity to the phase morphologies in ternary blend. In some special cases, simple terms are used to understand the evolving structures. There are three phases for spatial organization for example the phase Y wets the interface of the other two phases X and Z. In this case, the interactions between polymer- polymer at the X-Z interface are much less important compared with the X-Y and Y-Z interfaces, therefore a Y layer intercalates at the X-Z interface to reduce the overall free energy [2].

Polymer materials can be used for electronic applications when it is made highly conductive after electrochemical and chemical treatments. This process is performed by doping with appropriate material. Such as doped Poly (α-Naphthyl Acrylate) with oxoinum salt complex [3], doped Poly butyl benzoxazolylthiophene (PBBOT) with $TBAClO_4$ salt [4]. Also, it can be prepared pyrrole on poly (vinyl-alcohol) using electrochemical polymerization to forming conducting polymer blend (PPy/PVA) [5].

In this work, we examine the effect of Flu dyes on the PVP polymer by preparing polymer thin films using spin coating method, and studies their optical properties.

2. Experimental method:

Polymer polyvinyl pyrrolidone (PVP) and Fluorescence dye (Flu) have a chemical structure described in schematic (1). Thin films are prepared with a ratio of (10%) by casting solution method. The polymer (PVP) and the dyes of (Flu) are easy soluble at room temperature in a distilled water. This solution mixed by magnetic stirrer for 1h, then, the solution was casted on glass substrate (2.5x1.5) cm^2 with a thickness about (24) µm, a thickness can be measured by using (Thickness gauge on steel base). Then, the glass substrate and a solution were with horizontal level to ensure that we get homogenous thin films. Then, we measured the optical properties at room temperature using (TP-180-Uv/Vis. Spectrophotometer) in the wavelength range of (200-900) nm.

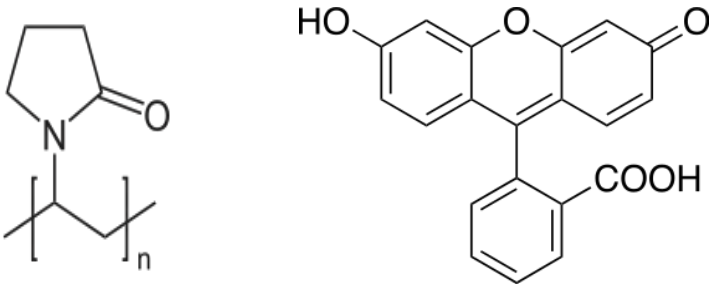

a b

Schematic 1. a) Represent structure of polymer PVP.
b) Represent structure of Fluorescence dye.

3. Results and Discussion:

The absorption (A) and transmittance (T) spectra for (PVP/Flu) thin film were recorded by using UV-Vis Spectrophotometer type (TP-180-Uv/Vis.) in the wavelength range of (200-900) nm as seen in Figs.(1&2) respectively, and the relation between them is given by [6]:

$$A = log\left(\frac{1}{T}\right) \ldots\ldots\ldots\ldots\ldots (1)$$

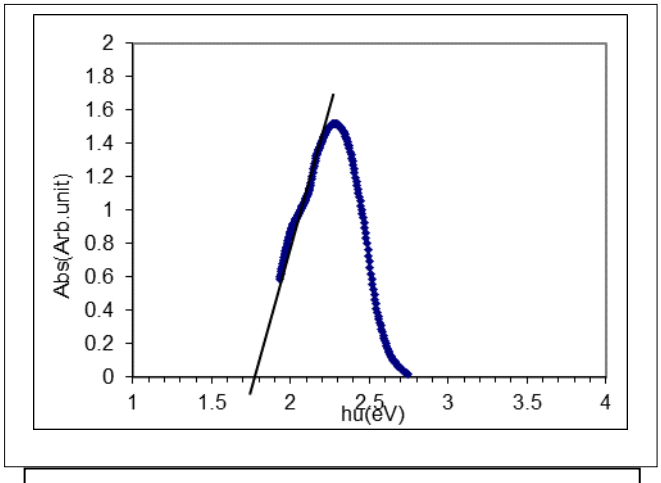

Figure1. Absorption Versus photon energy

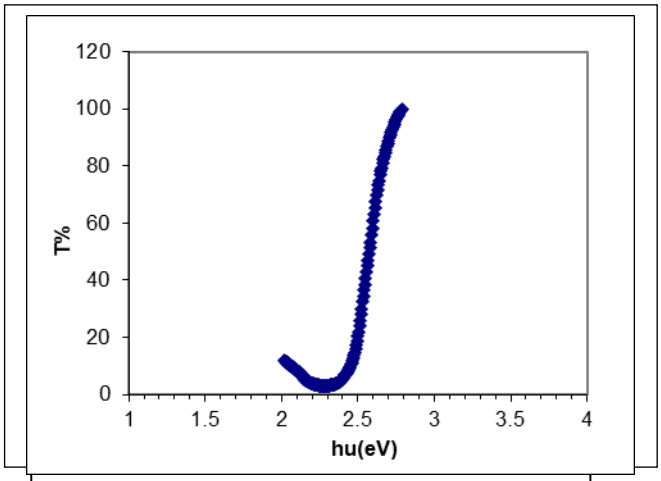

Figure 2. Transmittance Versus photon

From fig.(1) there is one peak appeared in the absorption spectrum at the energy (2.3eV) corresponding to the wavelength (530nm). But, a rapidly increase in the transmittance spectrum beginning from 2.4 eV see fig. (2), the transition in this case was from type $n-\pi^*$ because of the effect of nitrogen bond in the structure [7].
After the correction of the reflectivity, the absorption coefficient (α) of thin films can be estimated by [8]:

$$\alpha = \frac{2.303}{d} A \quad \text{.....(2)}$$

where d is the film thickness.
A is the optical absorbance.
Fig (3) shows the logarithms of the absorption coefficient versus the photon energy, where the values of (α) was calculated from eq. (2) which is less than (10^4 cm^{-1}) [3,9]. This value was very important to determine the type of transition for the electron. When it is less or more than (10^4 cm^{-1}), the type of transition is allowed direct, forbidden direct, allowed indirect and forbidden indirect. From Fig (3) we clearly see that the transition was indirect and obtained the information on the non-vertical allowed transitions which is determined by depending on the theory of bardeenet all [10]:

$$\alpha = \frac{A(h\upsilon - Eg \pm Ep)^2}{h\upsilon} \text{.....(3)}$$

where Eg is the band gap for indirect transition.
Ep is the energy, for phonon absorption the signal is (+) or for phonon emitted the signal is (-)
Figure (4) shows the relation between $(\alpha h\upsilon)^{1/2}$ versus $E = h\upsilon$, with draw two straight lines can be determined each of indirect energy gap and photon energy. The intersection of the energy at lower value represents the limit (Eg-Ep) for phonon absorption transition, and at high value the intersection represents the limit (Eg+Ep) for phonon energy emission. From the intercepts, we found each of Eg and Ep, where Eg is equal to (1.74) eV and Ep of poly (PVP/Flu) is equal to (0.15) eV. These results are very important to improve (PVP) polymer to be used in Photo application.

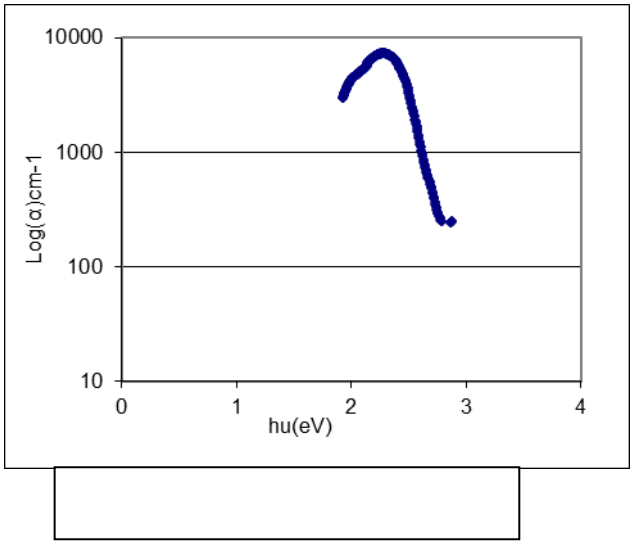

Figure 3

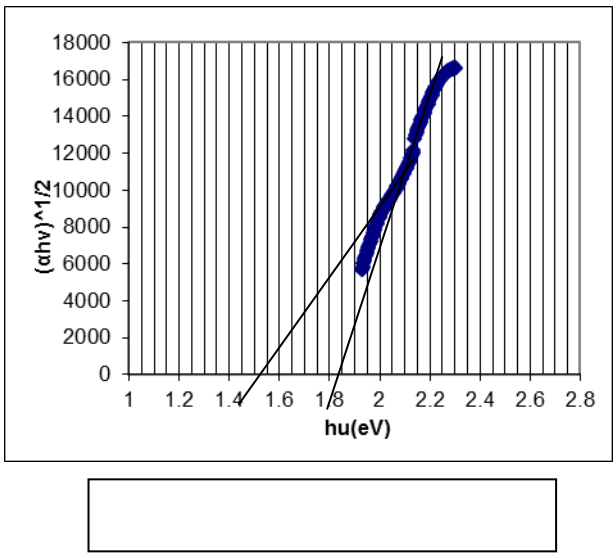

Figure 4

We can also calculate the direct energy gap E_g^A by absorption spectrum which was about (1.72) eV [See Fig (1)], but the direct and indirect energy gaps for pure PVP polymer are (3.88eV) and (3.48eV) respectively [11] as illustrated in Table (1). The value of the energy gap for PVP was decreased because of the effect of fluorescence dyes on the PVP polymer. The relationship below is represented the relation between reflection coefficient (R) and the transmittance (T), so, reflection coefficient can be determined by using it [12]:

$$T = \frac{(1-R)^2 e^{-\alpha d}}{1-R^2 e^{-2\alpha d}} \quad \ldots\ldots\ldots\ldots\ldots\ldots (4)$$

Table (1) shows the values of direct and indirect energy gap for PVP.

Thin films	Direct Eg (eV)	Indirect Eg (eV)	Ref.
PVP(Pure)	3.88	3.48	[11]
PVP/Flu	1.72	1.74	Current work

From the data of (α) values the extinction coefficient (K) can be calculated by:

$$K = \frac{\alpha\lambda}{4\pi} \quad \text{.....(5)}$$

where λ is the wavelength.

Fig (5) shows the relation between (R) versus $E = h\upsilon$, and from this figure we see that the reflection coefficient decreased with increasing the photon energy from (2.3-2.8)eV.

Fig (6) represents the relation between (K) and photon energy. From this figure, we see that the extinction coefficient was decreased with increasing the photon energy at the range (2.3-2.8)eV and the maximum value for was (0.032) at a photon energy of (2.3)eV.

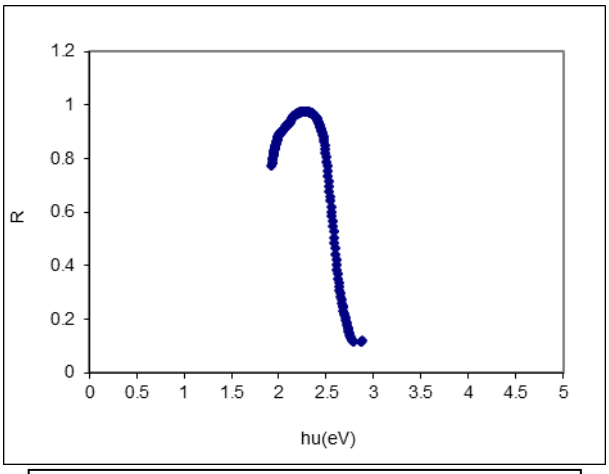

Figure 5. reflection coefficient versus photon energy

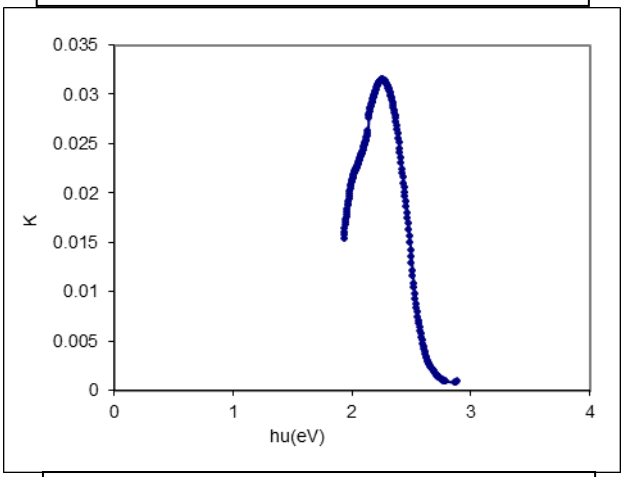

Figure 6. extinction coefficient versus photon energy

For the solid materials, the optical properties are usually described in terms of the complex dielectric (ε) function [13]:

$$\varepsilon = \varepsilon_1 + i\varepsilon_2 \quad \text{.....(6)}$$

where ε_1 is the real part of the dielectric and ε_2 is the imaginary part of the dielectric which can be calculated by:

$$\varepsilon_1 = n^2 - K^2 \quad \text{.....(7)}$$
$$\varepsilon_2 = 2nK \quad \text{.....(8)}$$

where n is the refractive index.

The refractive index is depending on the reflection and absorption coefficient calculated by:

$$R = \frac{(n-1)^2 + K^2}{(n+1)^2 + K^2} \quad \text{.....(9)}$$

Fig(7) Shows the relationship between the real ε_1 and imaginary ε_2 parts of the dielectric constant with the photon energy. From this figure, we see that $\varepsilon_1, \varepsilon_2$ were increased with increasing the $h\upsilon$ and the maximum values of them observed at a photon energy of (2.28) eV.

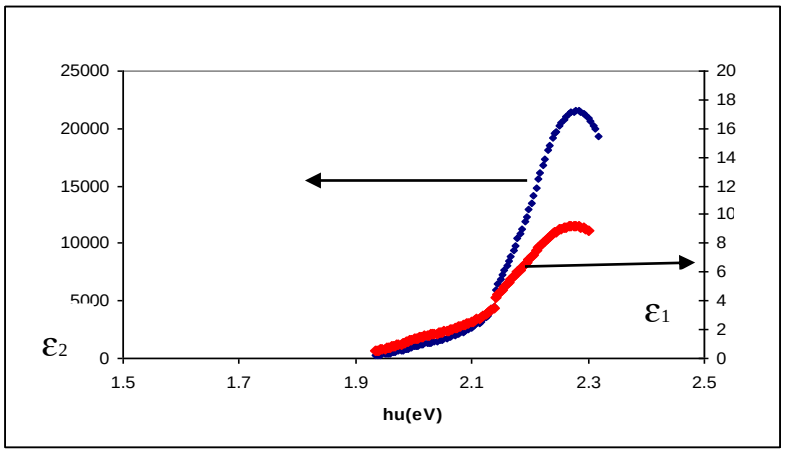

Figure 7. $\varepsilon_1, \varepsilon_2$ versus photon energy

4. Conclusions:

1. PVP/Flu thin films have indirect transition.
2. Thin films of polymer PVP/Flu have lower energy gap equal to (1.74) eV. This value is lead to insert it in photovoltaic applications.
3. The increased in real and imaginary part of dielectric constant was clear with increasing the photon energy, and the maximum value was at a photon energy of (2.28) eV.
4. Thin films have maximum values for (R, K) at a photon energy of (2.3) eV.

5. References:

[1] Spienger M and Walheim S 2005 *Interface Scincell*, 225-235.
[2] Walheim S, Ramstein A and Steiner U 1998 *Am. Chem. Soc.* EST: **8** 7.
[3] Abdullah AQ 2004 *Basrah J. Sci. A* **22** 1 165-188
[4] Ali AS 2001 MSc. Thesis, Department of physics, college of science, university of Basrah.

[5] Zedan KM and Abdul Muhssen SM 2002 *Nat. J. Chem.* **8** 563-569.
[6] Kanyathare B, Asamoah BO 2020 *Chemosphere* **248** (2020) 126071.
[7] Essa FS and Ajeel KA 2012 *J. Basrah Res. Sci.* **3** 38.
[8] Ali AS and Zedan KM 2010 *Uruk J.* **3** 1 January (2010).
[9] Abdallh M, Hamood O and Yousif E 2013 J. Al-Nahrain Univ. **16** 1 17-20.
[10] Ali AS 2014 *Jiarm* **2** 10 November (2014).
[11] Sreekanth K, Siddaiah T, Gopal NO, Kumar YM and Ramu C 2019 *J. Sci. Adv. Mat. Dev.* **4** 230e236.
[12] Jabbar HM, Jaboori EM and Abdullah AQ 2010 *J. Basrah Res.((Sciences))* **36** 3 15 June (2010).
[13] Ellliott J and Gippson F 1976 *An Introduction to solid state physics and its application*

.

Study of Pb Ions Removal from Aqueous Solutions by a Novel Sodium Formate-Coated Magnetite Nanoparticles

Study of Pb Ions Removal from Aqueous Solutions by a Novel Sodium Formate-Coated Magnetite Nanoparticles

[1]Hanan J. Mustafa, [1]Tagreed M. Al-Saadi

[1]Department of Physics/Collage of Education for Pure Science (Ibn Al-Haitham), University of Baghdad, Baghdad, Iraq

E-mail: taghreed.m.m@ihcoedu.uobaghdad.edu.iq

Abstract. One of the problems that continuously happen from the past ages till the present time is the contamination of the water sources with heavy metal ions; as a continuation of the many studies have been done so far to solve this problem. Novel magnetite nanoparticles (NPs) coated with sodium formate (SF-$Ni_{0.31}Mg_{0.15}Ag_{0.04}Fe_{2.5}O_4$) have been prepared using co-precipitation method. Characterization of the prepared SF-magnetite NPs was done by using the spectroscopic devices (XRD), (SEM), (EDX), (FT-IR), and (AAS). From the XRD spectrum it was found that the crystal structure of the prepared SF-magnetite NPs is a cubic inverse spinel structure, which has average crystallite size, the lattice constant, and X-ray density of 28.57 nm, 8.33 Å, 5.29 g/cm^3, respectively. SEM images have shown that the prepared NPs have a sphere-like shape with a measured average crystallite size of 25.93 nm. By EDX spectrum the presence of the constituent elements was confirmed by giving their energy peaks (O: Kα=0.525), (Fe: Kα=6.4, Lα=0.705), (Ni: Kα=7.84, Lα=0.85), (Mg: Kα=1.25), and (Ag: Lα=2.98, Lβ=3.35). The attachment of the SF molecules to the magnetite NPs was proven by the FT-IR spectrum through appearing the absorption peaks in the SF- magnetite NPs spectrum at 1600cm^{-1} and 3400cm^{-1} return to the bonds (C=O) and (C-H stretch) in SF. By ASS results, adsorption of Pb ions was clearly influenced by SF coating giving removal rate (93%) at equilibrium time (10min) in the prepared solution of $Pb(NO_3)_2$ salt, while for the wastewater samples the removal rate was (55%) - (100%).

Keywords: Magnetite NPs, Sodium Formate, Adsorption, Coating, Pb Ions.

1. Introduction

Pollution with heavy metals such as lead, zinc, cadmium and, others is causing serious health and environmental problems. Water contamination with Pb ions is caused by different processes as mining, manufacturing, and smelting, which result in multi-effects that negatively influence human health. The important thing for considering is that metals are resistant to degradation, which end up in living organisms. The existence of the ions of heavy metals represents a big problem because of their toxicity for many lives [1].

Various contaminants removal from wastewater was studied by utilizing different processes [2-4]. The major methods used to purify wastewater from metal ions are adsorption, ion exchange, membrane filtration, flotation, chemical precipitation, and electrolytic [5-8]. Different advantages and

functional operation parameters are presented by different nanomaterials for heavy metal removal due to the high volume surface area, surface chemistry, and a huge amount of particles, surface interactions, and magnetic separation. Their special capability of adsorbing, which are both assistants to the heavy metal ions removal, participates in these characteristics. In the present time, many studies concerned with nanomaterials have been carried out to exam, their capacity to clean wastewater from heavy metal ions and have shown very good potentiality for adsorbing metal ions from polluted water [9-12]. Adsorption is a simple, relatively low-cost and, effective method, utilized to adsorb the metal ions from wastewater. Thus, water treatment by adsorption techniques has become more efficient than by other techniques [13,14].

During the past decades, tremendous studies concentrated on magnetite nanoparticles due to their adsorption strength, high magnetization, special electrical characteristics, and low toxicity to eliminate wastewater contaminants. Magnetic nanoparticles are suitable for heavy metals adsorption from the wastewater. There is a strong magnetic moment in the iron atom due to the existence of unpaired electrons in the orbital (3d) [15]. In magnetic nanoparticles, there is a great ability for aggregation. So, surface modulation functional groups is necessary to improve the magnetite nanoparticle's stability [13, 14], to enhance their physicochemical features, and to accomplish different kinds of applications [16].

Fawzia et al. [17] have prepared magnetite NPs of (Fe_3O_4) by co-precipitation method, stabilized by non-ionic and cationic surfactants. The cubic crystalline structure of the prepared magnetite was confirmed by XRD. Uniform dispersity was ensured by TEM images. The adsorption efficiency of the prepared NPs for Pb, Zn, and Cd was examined by ASS by changing several factors as pH of the metal ion solution and the doses of the adsorbent. The adsorption equilibrium was achieved within (4) hr., and was highly affected by the pH of the solution and the dose of the adsorbent. Khai et al. [18] have used sludge as an adsorbent from an iron-ore area to remove Mn, Cd, Zn, Pb, and as from aqueous solutions. The capacity of adsorption of the adsorbent was examined in a set of experiments including the use of single and mixed metal solutions. It was found that the adsorption capacity of the heavy metals is ordered as Pb>As >Cd >Zn >Mn. Moreover, in the single-metal, solution is ranged (0.7-1.113) mg/g; while in the mixed-metal solution is, ranged (0.370-1.059) mg/g. iron-ore sludge has been proved that it is an efficient adsorbent for plenty of metal ions and its promising adsorbent for toxic metal pollutants from water. Jin et al. [19] studied (Fe_3O_4) magnetite NPs adsorption properties for Cr(VI) and Cu(II) that are coexisted in the mixed solution. They investigated different factors, adsorbent dose; metal ions initial concentration, pH, and temperature. The results revealed that pH influenced the adsorption of the two metal ions and the optimal pH was 4.0. The increment of adsorbent dose increased the adsorption efficiency. It was found that temperature had no clear effect under the practical design. The maximum adsorption capacity of 2.0g/dm^3 of Fe_3O_4 was found to be 18.61mg/g and 8.67mg for Cu(II) and Cr(VI) respectively in 80mg/dm^3 mixed solution for both metal ions. Fe_3O_4 nanoparticles performed as a good adsorber and are separated easily and recovered once a magnetic field is applied to it.

Sodium formate (SF), HCOONa, is the sodium salt of formic acid, HCOOH. It's an environmentally friendly salt and it has multiple uses as in fabric dyeing and printing processes. It is also used as a buffering agent for strong mineral acids to increase their pH, as a food additive (E237), and as a de-icing agent [20, 21].

SF has never been used in the field of heavy metal ions removal from aqueous solutions but could have a positive effect on the adsorption process due to its chemical nature; so this study was aimed toward discovering the effect of sodium formate on the adsorption capacity of the prepared magnetite NPs for Pb ions removal from different aqueous solution.

2. Materials and Methods

2.1 Materials

$Ni_{0.31}Mg_{0.15}Ag_{0.04}Fe_{2.5}O_4$ Magnetite NPs were prepared by using metal sulfates, these sulfates included ferrous sulfate ($FeSO_4.7H_2O$, 99.0%), nickel sulfate -6-hydrate pure ($NiSO_4.6H_2O$, 99.0%), magnesium sulfate heptahydrate AR ($MgSO_4.7H_2O$, 99.5%), silver sulfate (Ag_2SO_4, 99.0%), potassium nitrate (KNO_3, 99.9%), potassium hydroxide (KOH, 99.5%), and sodium formate (HCOONa, 98.0%).

2.2 Preparation

$Ni_{0.31}Mg_{0.15}Ag_{0.04}Fe_{2.5}O_4$ magnetite NPs were prepared by the co-precipitation method as used by Jawaher et al. [22]. 0.12M of the following sulfates ($FeSO_4.7H_2O$), ($MgSO_4.7H_2O$), ($NiSO_4.6H_2O$), and (Ag_2SO_4) were dissolved in deionized water (50ml). KNO_3 (1.01g) was dissolved in deionized water (10ml) and was added to the former solution, then stirring the solution for 30min. After that, a solution of KOH (1.402g was dissolved in 10 ml of deionized water) was slowly added to the last solution. The final mixture was heated until the mixture temperature reached 100°C then the reaction mixture remained at this temperature for 2h; the precipitate was cooled down to room temperature and then washed with deionized water several times and dried at 50°C overnight. Finally, the prepared magnetite NPs were sintered at 600°C for 2h.

2.3 Coating

The coating procedure was done as mentioned in ref. [22], but the ratio of magnetite NPs to the coating material was 1:6 due to the experiment. 6g of sodium formate (SA) were dissolved in 200ml of deionized water, and then 1g of magnetite NPs was added to the sodium formate solution. The last solution was mixed for 1h. The mixing process, magnetite NPs were washed with deionized water several times and left to be dry at room temperature.

3. Characterization

The crystallographic structure of synthesized magnetite NPs was examined by XRD (x-ray powder diffraction) by the instrument (XRD-6000 Shimadzu) with a Cu target, λ=1.54 Å, and angle 2θ=20-80 degree. The surface characteristics of the NPs were observed utilizing a scanning electron microscope (SEM TESCAN MIRA3) equipped with energy-dispersive X-ray spectroscopy (EDX). Magnetite NPs were also characterized by Fourier transform infrared (FTIR) spectrophotometer (IRPrestige-21 Shimadzu). Pb ions concentrations were measured by the atomic absorption spectrophotometer (AA-7000 Shimadzu).

4. Adsorption Process

Two aqueous solutions have been used in this process, the first one is a prepared solution of Pb $(NO_3)_2$ prepared to have (25ppm) of Pb ions in a bottom flask of 50ml for each sample. The second solution represents two samples of the wastewater of a battery factory located at Al-Waziria, Baghdad, Iraq; the first one is contaminated with Pb ions, sample (C), and the second one is filtered by the factory staff, sample (P). The adsorption process was done at 30°C in a water bath shaker at (100 rpm). The dosage of magnetite NPs understudy was (0.1g) for different contact times (5, 10, 15, 20, & 25) min. Magnetite NPs were removed from the solution by a magnet after the adsorption process was done. This solution was tested by atomic absorption spectrometer (AA-7000, Shimadzu) for detecting Pb ions concentrations remained after the completion of the adsorption process. The adsorption amount (qt) and the removal rate (A%) were calculated using the relation (1) and (2), respectively [18, 23].

$$q_{t=(C_0-C_t)\times\frac{V}{m}} \quad (1)$$

$$A(\%) = \frac{C_0-C_t}{C_0}\times 100 \quad (2)$$

Where C_0 is Initial Pb ion concentration in (mg/L) at time t=0, C_t denotes Pb ion concentration in (mg/g) at time =t, V represents Volume of water in (ml), and m= Weight of the magnetite NPs in (g).

5. Results and Discussion

XRD pattern of the synthesized magnetite NPs is illustrated in Fig. 1. The structural properties were studied in the range of (20°-80°). This diffraction pattern clearly coincides with the standard pattern of the cubic spinel magnetite phase JCPDS no. (19-0629) [24]. The remarkable peaks of the synthesized magnetite NPs were indexed to the crystal planes of the cubic inverse spinel iron oxide (Fe_3O_4), which

are found to be (220), (311), (400), (422), (511), and (440); corresponding to the diffraction angles 30.22°, 35.68°, 43.38°, 54.10°, 57.16°, and 62.56° respectively. Also, there is an appearance of extra peaks than (Fe_3O_4) peaks return to other phases of iron oxide (cubic γ-Fe_2O_3 and tetragonal γ-Fe_2O_3 (incomplete)); these phases appear as a result of the sintering process, where cubic γ-Fe_2O_3 appears at 200°C, while tetragonal γ-Fe_2O_3 appears at 600°C [25]. The average crystallite size of the synthesized magnetite NPs was calculated using Scherrer 's formula [26, 27], its value was found to be 28.57 nm.

$$D = \frac{0.9\,\lambda}{\beta\,\cos\theta} \quad (3)$$

Where λ is the wavelength of the X-ray and β denotes FWHM in radians.

It is worth saying that only magnetite particles having a particle size less than 30 nm exhibit super paramagnetic properties and have a large surface area that make them prone to magnetic fields and without an external magnetic field to support them; they do not become permanently magnetized. These properties are highly useful in the novel separation process development [28].

The lattice constant was calculated using Rietveld refinement and it was found to be 8.33Å. In addition, the x-ray density was calculated using the formula (4) and has a value of 5.29 g/cm^3 [29].

$$\rho = \frac{8M_w}{N_A.a^3} \quad (4)$$

Where (M_w) is the molecule weight, (N_A) is Avogadro's number, and (a) is lattice constant.

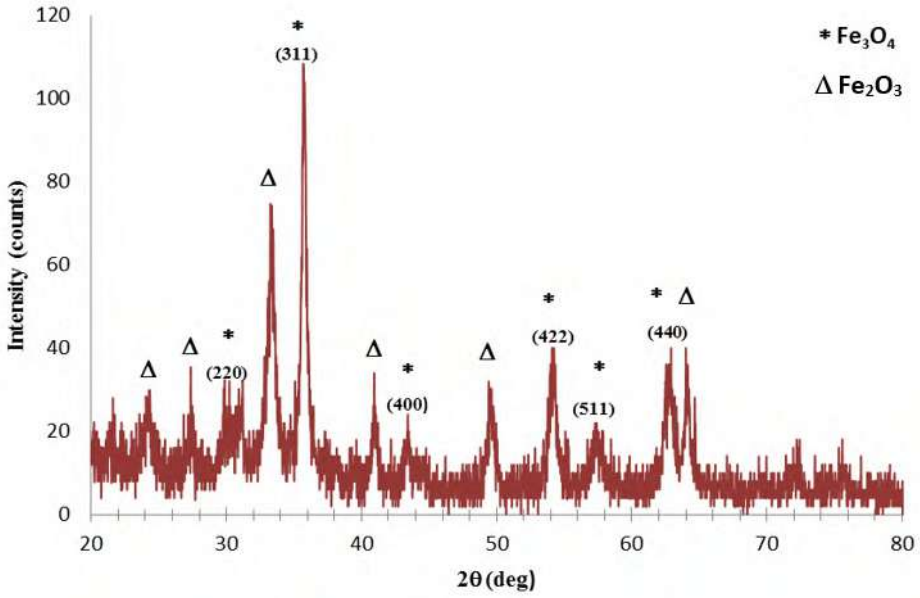

Figure1. XRD pattern of the ($Ni_{0.31}Mg_{0.15}Ag_{0.04}Fe_{2.5}O_4$) magnetite NPs.

Scanning Electron microscope (SEM) image of the synthesized ($Ni_{0.31}Mg_{0.15}Ag_{0.04}Fe_{2.5}O_4$) magnetite NPs at magnification of 200 nm is shown in Figure 2a. It can be noticed from this figure the homogeneity and uniformity of the synthesized NPs, they have sphere-like shape and are distributed regularly. Figure 2a also proves that the synthesized NPs are in the nanometer range have an average crystallite size of 25.93nm which is so close to that has been calculated by Debye Scherrer 's formula. The high porosity of the synthesized NPs is remarkable and that increases the capacity of ion adsorption on the nanomaterial surface. As seen from Figure 2a there are some agglomerations of nanoparticles; this is due to sintering processes. As well as the nanoparticles possess high surface energies, so they tend to agglomerate and grow to larger assemblies [30].

Figure 2b shows EDX peaks of the synthesized magnetite nanoparticles. The observed peaks appear the existence of some elements as O, Fe, Ni, Mg, and Ag. These elements have the energies spectra in keV as it follows: (O: Kα=0.525), (Fe: Kα=6.4, Lα=0.705), (Ni: Kα=7.84, Lα=0.85), (Mg:

Kα=1.25), and (Ag: Lα=2.98, Lβ=3.35. There is no Kα for Ag in the figure since it appears at 22.16 keV and the devices limited to 10 keV). There are other spectra than the spectra of the constituent elements identified at the energies (2.3 and 3.3) keV. These are false peaks the appeared in the EDX spectra because of the automatic peak identification process. This process is sensitive to noise in the X-ray continuum that forms the spectral background because random groupings of background counts can mimic a characteristic peak [31].

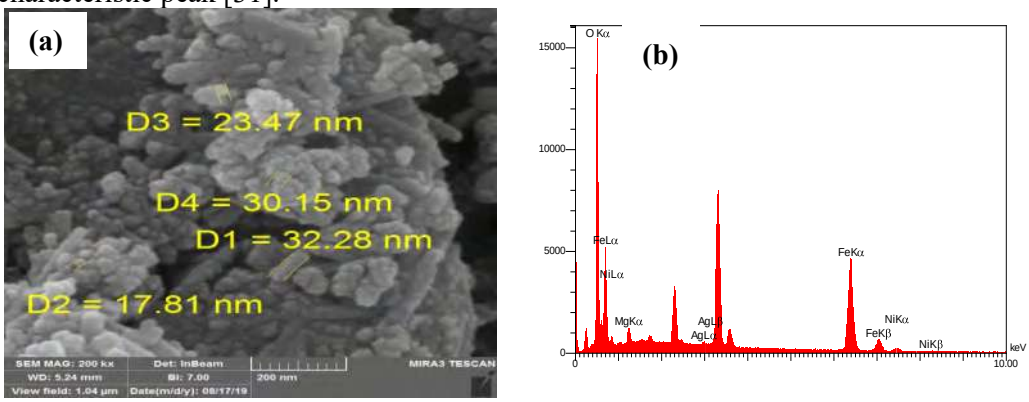

Figure 2. (a- SEM image, b-EDX spectra) of the prepared magnetite NPs.

Figure 3 demonstrates the FT-IR absorption bands for the prepared magnetite NPs. In figure 3a for bare magnetite NPs there are strong characteristics, bands, at around 600 cm^{-1} due to (Fe-O) bond; this proves that the main phase of the synthesized NPs is the magnetite (Fe_3O_4) of spinel-type structure [16]. These characteristic peaks can be attributed to the lattice absorption of iron oxide [32]. There is also a small absorption band at 2360 cm^{-1} can be attributed to the CO_2 vibration. The broad absorption band at 3433 cm^{-1} indicated the existence of surface hydroxyl groups (O-H stretch) [16].

Figure 3b represents the FT-IR spectrum of (SF). Two characteristic absorption bands have been noticed. The first band is broad (1400-2000) cm^{-1} and may attribute to the bond (C=O) stretch. The other band is medium and sharp at around (3000 cm^{-1}) may attribute to the bond (C-H) stretch. Figure 3c represents the FT-IR spectrum of SF-coated magnetite NPs. A band has been appeared at around (1600 cm^{-1}) may concern to the (C=O) functional groups present in SF. In addition there is a band at around (3400 cm^{-1}) which is a boarder and more intense than those of the bare magnetite NPs (Figure 3a), can be attributed to (C-H) bond stretch in SF which, proves that prepared magnetite NPs were successfully coated with SF.

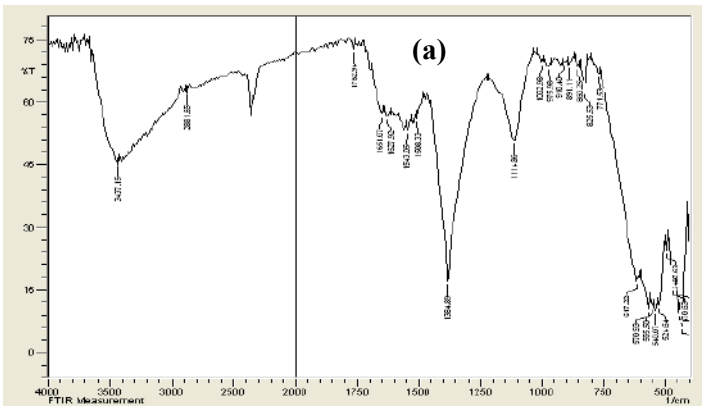

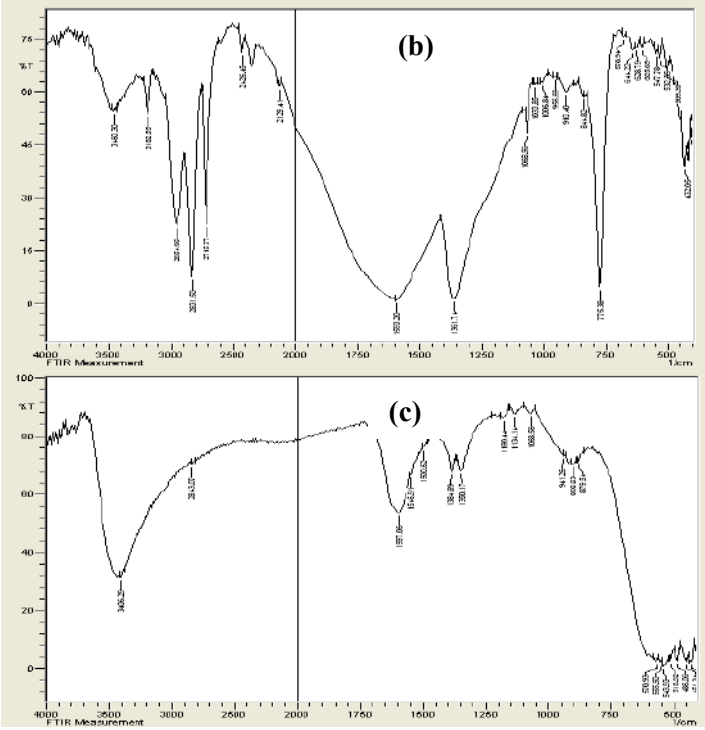

Figure 3. FT-IR spectra for a- bare magnetite NPs, b- SF, c- SF-coated magnetite NP

Table 1 lists the concentration (C_t) mg/ml, amount (q_t) mg/g, and removal rate (A%) values of Pb ions of the prepared SF-magnetite NPs. As shown by Figure 4, qt firstly increased then settled at approximately (11 mg/g) in (10 min) which represents the equilibrium time. The removal rate (A%) as has been seen by Table 1 and Figure 4 is high (93%), indicating the high efficiency of these NPs. This performance can be attributed to the ionic bond in SF that is easily broken in the solution emptying Na ions site. So the molecule of SF became a seeker for other cations in the solution and picks Pb ion rather than Na ion because Pb ion radius is bigger than Na ion radius so the selectivity for adsorbing Pb ions from the solution is higher than for other cations in the solution [33].

Table 1. Concentration, amount of Pb ions, and removal rate of the prepared SF-magnetite NPs.

Time (min)	C_t (mg/ml)	q_t (mg/g)	A%
5	0.0039	10.4542	84.4172
10	0.0016	11.5906	93.5936
15	0.0017	11.5220	93.0397
20	0.0015	11.6164	93.8015
25	0.0016	11.5725	93.4475

The adsorption of Pb ions from the wastewater samples (C and P) was done at the same conditions used before, but the time has been used is (10 min.). Table 2 lists the concentration of Pb ions (mg/ml), adsorption amount (mg/g), and removal rate of Pb ions from wastewater. The SF-magnetite

NPs

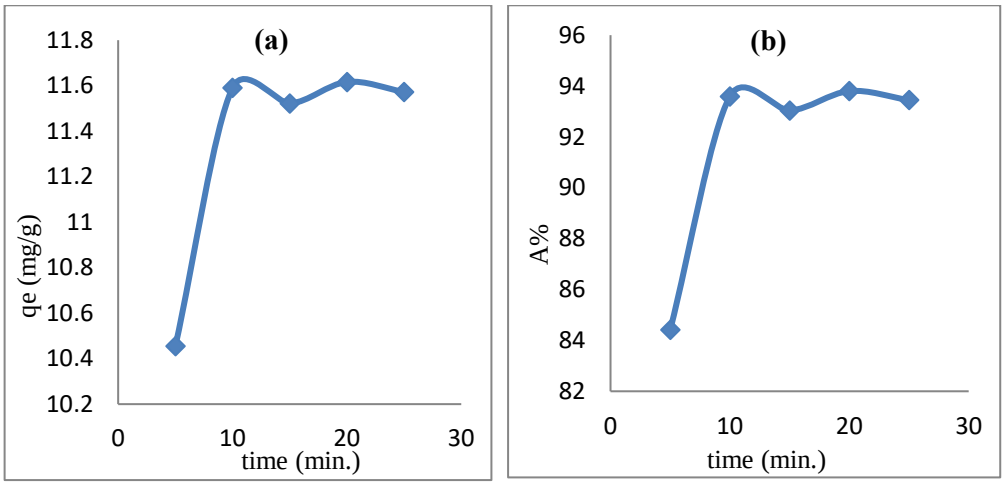

Figures 4. a- Equilibrium curve, b- Removal rate curve for the sample FM_6

showed an excellent removal rate with both samples giving (55%) For (C) and (100%) for (P). The contaminated wastewater sample (C) could have other particles that affect the removal of Pb ions since the prepared NPs have already shown a great capacity to adsorb Pb ions from a solution contains 25 ppm of Pb ions as has been proved in the above paragraph giving removal rate (93%). So the prepared SF-magnetite NPs could be a possible good adsorbent for other heavy metals in special and pollutants in general.

Table 2. Concentration, adsorption amount, and removal rate of Pb ions from wastewater of the prepared SF-magnetite NPs.

Wastewater sample	C_0 (mg/ml)	C_t (mg/ml)	q_t (mg/g)	A%
C	2.6127	0.0012	0.7198	55.100
P	0.2185	0	0.0011	100

1

6. Conclusion

SF-coated magnetite NPs ($SF\text{-}Ni_{0.31}Mg_{0.15}Ag_{0.04}Fe_{2.5}O_4$) have been prepared by the co-precipitation method. The crystal structure of the prepared NPs was confirmed by XRD and, it was matched with the standard pattern of the inverse spinel cubic iron oxide (Fe_3O_4) and have average crystallite size of 28.57 nm, the lattice constant of 8.32582 Å, and x-ray density of 5.2890 g/cm^3. The size of the prepared NPs was in the nanometer range as clarified by the SEM images and has an average crystallite size of 25.93 nm. By EDX spectra, the presence of the constituent elements was confirmed. The attachment of the SF molecules to the nanoparticle surface was proven by FT-IR spectra analysis. For adsorption of Pb ions from the prepared Pb $(NO_3)_2$ solution, a great adsorption capacity was shown by the prepared SF-magnetite NPs. That giving an adsorption amount (11.60 mg/g) that corresponds to the removal rate (93%) at equilibrium time (10min); while for adsorption of Pb ions from the wastewater samples (C and P). The prepared NPs showed an excellent removal rate for adsorbing Pb ion equals to (55% for C) and (100% for P). It was concluded that the crystal structure of SF has played an important role in the process of adsorption giving more sites to be filled by Pb ions; making the prepared NPs surface a possible adsorbent for other pollutants.

References

[1] Kobya M., Demirbas E., Senturk E., & Ince M. 2005 *Bioresour. Technol.* **96** 1518
[2] Guo S., Jiao P., Dan Z., Duan N., Zhang J., Chen G., & Gao W. 2017 *Chem. Eng. Res. Des.* **126** 217
[3] Sherlala A. I. A., Raman A. A. A., Bello M. M., & Asghar A. 2018 *Chemosphere* **193** 1004
[4] El-Fawal E. M. & El-Shamy O.A.A. 2019 *Int. J. Environ. Sci. Technol.* https://doi.org/10.1007/s13762-019-02249-y
[5] Kim D. G., Kim W.Y., Yun C.Y., Son D. J., Chang D., Bae H. S., Lee Y.H., Sunwoo Y., & Hong K. H. 2013 *Int. J. Electrochem. Sci.* **8** 9835
[6] Cho D.W., Jeon B.H., Chon C.M., Kim Y., Schwartz F.W., Lee E.S., & Song H. 2012 *Chem. Eng. J.* **(200-202)** 654
[7] Norouzi S. 2015 *Open J. Geol.* **5** 367
[8] El-Sharaky E. A., Mishrif M. R., & El-Shamy O. A. A. 2018 *Tenside Surfact. Detergents* **55** 148
[9] Vunain E., Mishra AK, & Mamba BB 2016 *Int. J. Biol. Macromol.* **86** 570
[10] Qdais H.A. & Moussa H. 2004 *Desalination* **164** 105
[11] Khan N. A., Shaaban M. G., & Hassan M. H. A. 2003 *Proc. UM Research Seminar*
[12] Abu-Eishah S.I 2008 *Appl. Clay Sci.* **42** 201
[13] Grassi M., Kaykioglu G., Belgiorno V., & Lofrano G. 2012 *Springer* 15 https://doi.org/10.1007/978-94-007-3916-1_2
[14] Lasheen M. R., El-Sherif I. Y., Sabry D. Y., El-Wakeel S.T., & El-Shahat M.F 2014 *Desal. Water Treat.* **52** 6464
[15] Teja A.S. & Koh P. Y. 2009 *Prog. Cryst. Growth Charact. Mater.* **55** 22
[16] Alzahrani E. 2014 *IJIRSET* 3 15118
[17] El-Dib F. I., Mohamed D. E., El-Shamy O. A. A., Mishrif M. R. 2019 *Egypt. J. Pet.*, **29**(1) 1
[18] Nguyen K. M., Nguyen B. Q., Nguyen H. T., & Nguyen H. T. H. 2019 *Appl. Sci.* **9** 619
[19] Zhang J., Lin Sh., Han M., Su Q., Xia L., & Hui Z. 2020 *Water*, **12**(446) 1
[20] D'Itr F. M. 1992 Chemical Deicers and the Environment *Lewis publishers*
[21] European Food Safety Authority 2015 *EFSA Journal* **13**(5) 1
[22] Alzaidi J., Alzahrani E., & El-Mouhty N. R. A. 2016. *Orient. J. Chem.* **32**(3) 1503
[23] Taher A. J. 2019, "Synthesis and study of physical properties and biological effect of magnetic nano composite and their use as adsorbent surfaces for some organic and inorganic pollutants", MSc thesis, University of Baghdad
[24] Al-Saadi T. M., Abed A.H., & Salih A.A. 2018 *Int. J. Electrochem. Sci.* **13** 8295
[25] Kazeminezhad I., & Mosivand S. 2014 *Acta Physica Polonica A,* **125**(5) 1210
[26] Hussain F. I. & Tuamaa F.M. 2016. *Ibn Al-Haitham J. for Pure & Appl. Sci.* **29**(1) 417
[27] Mustafa H. J., Al-Saadi T. M. 2019 AIP Conference Proceedings **2190** 020039 https://doi.org/10.1063/1.5138525
[28] Carlos L., Einschlag F. S. G., González M. C., & Mártire, D. O. 2013 *IntechOpen*, doi: 10.5772/54608
[29] Al-Saadi T.M., & Alsaady L. J. k. 2015 *Ibn Al-Haitham J. for Pure & Appl. Sci.*, **28** (1) 301
[30] Sagadevan S., Zaman Z., Chowdhury, & Rafique R.F. 2017 *Mat. Res.* http://dx.doi.org/10.1590/1980-5373-MR-2016-0533
[31] Newbury D.E. 2009 *Scanning 31* 1
[32] Kadhima R.M., Al-Abodi E.E., & Al-Alawy A.F. 2018 *Desalin. Water Treat.* **115** 45
[33] Monika M. K. 2014 *Eur. Chem Bull.* **3**(8) 838

Parameters Extraction of a Single-Diode Model of Photovoltaic Cell Using False Position Iterative Method

Parameters Extraction of a Single-Diode Model of Photovoltaic Cell Using False Position Iterative Method

Mohammed Rasheed[1,*], SuhaShihab[2], Osama Alabdali[1], Hassan Hadi Hussein[1]

[1] Applied Sciences Department, University of Technology, Baghdad, Iraq.
[2] College of Education for Pure Sciences, University Of Anbar, Al-Anbar, Iraq.

E-mail: 10606@uotechnology.edu.iq

Abstract. In the present work, the nonlinear equation for a single-diode design of a photovoltaic cells is introduced. The mathematical model based on False Position Method (FPM) was used to determine the parameters of the voltage of the solar cell device based on the electrical equivalent circuit. The False Position Method currently presents to demonstrate the non-linear electrical behavior of this device. The proposed method is tested to solve the nonlinear example and the obtained results are used.

Keywords: False position method, iterations, absolute error, load resistance, mathematical model, nonlinear equation

1. Introduction

One of the purpose often practiced in applied mathematics and requires tired arithmetic is the solving of transcendental and algebraic equations (transcendental function). Any equation contains different forces of (x) or trigonometric or exponential functions or logarithmic or so-called (transcendental function)-nonlinear equation. In order to find the roots of such equations, there is no theoretical method or direct law for this point. The approximate numerical analysis is needed to obtain the results or the roots of these equations, and the results are uncontrolled and approximated compared to the theoretical results. The method of numerical results generally based on the accuracy of the error reached (degree of accuracy). However, the adopted numerical techniques is the best solution to find the approximate results, especially for nonlinear equations and difficult solved by theoretical techniques. However, there are many numerical techniques to solve these equations. The roots determined in numerical techniques can be calculated roughly by drawing or approximate the calculation when one see a difference in the function's value from negative to positive or vice versa. On the other hand, there is a cut of the function of the x −axis. Depending on the root's nature, found and numerical techniques adopted many natural choices and the most important of these methods: simple iterative method, Bisection Method, Newton Raphson and False Position Method [1-8]. Solar energy has been utilized to generate electricity in several applications including running of traffic lights, water desalination, street lighting, power plants, and the operation of many electronic apparatus for example calculators, clocks, vehicles, space stations and the operation of satellites [9]. There are many types of photovoltaic cell depending on the components and the materials preparation [10-16] including organic and inorganic solar cells [17-19].

The present work focuses on the proposed and characterized a new technique to give the roots in real case of a non-linear expression of the solar cell (single diode model). It describes according to the following points: in section two describes the characterizing of numerical model of an electric circuit based on photovoltaic cell; in section three establishing the root FPM are included while the discussion and conclusions of the results are listed in sections four and five. The acquired computations are implemented with Matlab program.

2. Properties of Photovoltaic Cell Equation (Single-Diode)

The design of solar cell's circuit scheme for single diode model is shown in Figure 1.

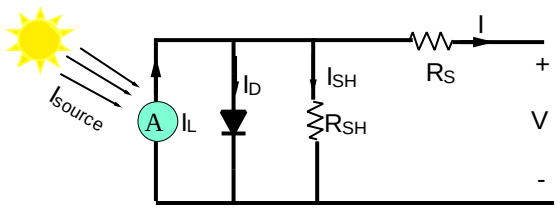

Figure 1. Solar cell's scheme

Applying Kirchhoff's current law on this equivalent circuit, yields

$$I = I_{ph} - I_D \quad (1)$$

$$I_D = I_0\left(e^{\frac{-V_{pv}}{nV_T}} - 1\right) \quad (2)$$

$$I = I_{ph} - I_0\left(e^{\frac{-V_{pv}}{mV_T}} - 1\right) \quad (3)$$

where:

I_{ph}: the photocurrent (A); I_0: reverse saturation current of the diode in(A);V_{pv} and$I$ are the delivered voltage and current respectively in (V);the thermic voltage $= 26mV$, according the equation($V_T = \frac{kT}{q} = 0.0259\ V$) at room temperature with air-mass = 1.5); m:$(1 < m < 2)$, k: Boltzmann constant= $1.38 \times 10^{-23} J/K$; T:$p-n$ junction's temperature(K); q: electron charge equal to $(1.6 \times 10^{-19}\ C)$ [**20**].

$$I_{ph} = I_{source} \quad (4)$$

$$I_D = I_s * \left(e^{\frac{V_D}{nV_T}} - 1\right) \quad (5)$$

Substitute Eq. 4 in Eq. 5 yields

$$(I_{source}) - 10^{-12}\left(e^{\frac{-V}{1.2*0.026}} - 1\right) = \frac{V}{R} \quad (6)$$

where: I_s reverse saturation current= $10^{-12}A$. In parallel, $V_D = V_{pv} = V$

Based on Eq. 6, the first derivative of it is needed in order to determine the $V$of the diode [21].

3. False Position Method (FPM)

The FPM is the most effective approach to find the root of a nonlinear function. It is a generalized from the Newton-Raphson method and does not require obtaining the derivative of the function. It has a super linear convergence.

For a given x_0 and x_1, x_l is first point of guess interval, x_u is first point of guess interval, ε is allowed error in calculation satisfy the equation $|x_{i+1} - x_i| < \varepsilon$, where ε is a very small number and $f(x)$is inter function, then
Find $x_2, x_3, x_4, \ldots, x_n$ using the following expressions

$$x_r = x_u - \frac{f(x_u) \times (x_l - x_u)}{f(x_l) - f(x_u)}$$
$$x_3 = x_3 - \frac{f(x_2) \times (x_2 - x_1)}{f(x_2) - f(x_1)}$$
$$\vdots$$
$$x_n = x_{n-1} - \frac{f(x_{n-1}) \times (x_{n-1} - x_{n-2})}{f(x_{n-1}) - f(x_{n-2})}$$

Advantages of FPM over other root finding methods are:
Its rate of convergence is faster than bisection method.
FPM is not needed to find the derivative of the function as in Newton-Raphson method and other methods [22].
The algorithm of the FPM can be describe as the following steps
Input x_l, x_u and ε
Compute $f(x_l)$ and $f(x_u)$
Compute $x_r = x_u - \frac{f(x_u)\times(x_l - x_u)}{f(x_l) - f(x_u)}$
Test for accuracy of x_2
If $|x_{i+1} - x_i| > \varepsilon$, set $x_l = x_u$ and $x_l = x_2$
Go to step 2
Display the required root as x_2

The approximate root of equation $f(x) = 0$ is the point $x_{i+1}$is considered according to the equation$\sigma = |x_{i+1} - x_i| < \varepsilon, |f(x_n)| < \varepsilon$(9)

where:ε: the absolute value of the function is a very small number. For convergence criteria, it was required that σ the distance between two consecutive iterates was less than 10^{-9}, the number of iterations represents by $n$and the solute value of the function represented by$f(x_n)$ [23].

4. Results and Discussion

Suppose the equation of the solar cell (single-diode) has obtained the following approximate solutions, and the Bisection method are applied with the two initial values$x_l = 0.9$and$x_u = 1$.
In Table 1, the False position method (FPM) with the input (x_l, x_u) and output x_2 values of the solution results and the absolute error function are obtained in the condition of $R = 1$ (load resistance).

Table 1. The voltage values of the solar cell with σ and εvalues using FPM.

Iterations	X_0-FPM	x_1-FPM	x_{n+1}-FPM	ε-FPM	σ-FPM
1	0.971416861	1	1.043657103	0.116690668	0.056758036
2	1	1.043657103	1.100415139	0.173448704	0.067513973
3	1.043657103	1.100415139	1.032901166	0.105934731	0.008504281
4	1.100415139	1.032901166	1.024396885	0.09743045	0.026095166
5	1.032901166	1.024396885	0.99830172	0.071335285	0.018181131
6	1.024396885	0.99830172	0.980120588	0.053154154	0.019347249
7	0.99830172	0.980120588	0.960773339	0.033806904	0.015906857
8	0.980120588	0.960773339	0.944866482	0.017900047	0.012248262

9	0.960773339	0.944866482	0.932618221	0.005651786	0.009212433
10	0.944866482	0.932618221	0.923405787	0.003560648	0.003242295
11	0.932618221	0.923405787	0.926648083	0.000318352	0.000336896
12	0.923405787	0.926648083	0.926984979	1.85438E-05	1.86386E-05
13	0.926648083	0.926984979	0.92696634	9.47584E-08	9.47303E-08
14	0.926984979	0.92696634	0.926966435	2.81574E-11	2.81574E-11
15	0.92696634	0.926966435	0.926966435	0.000000000	

Figure 3 shows the results using FPM technique.

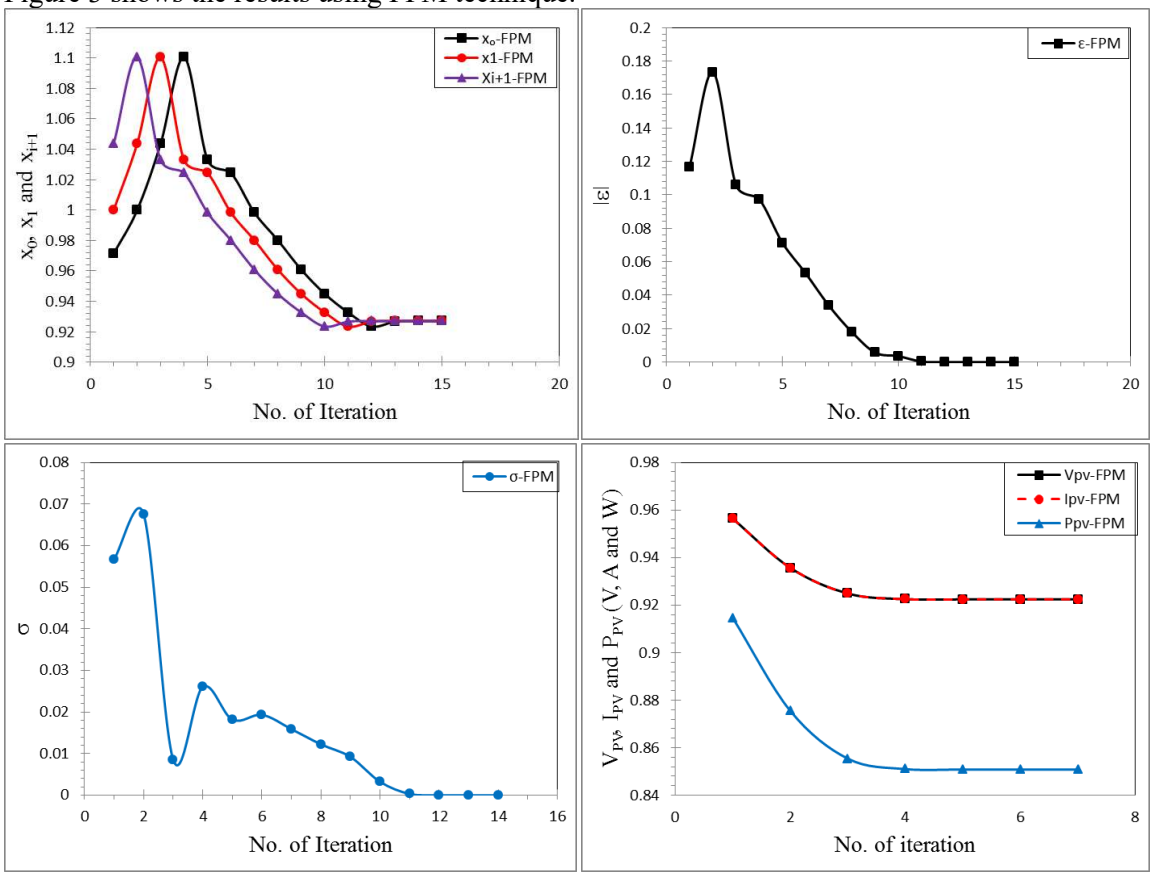

Figure 2. The results by using FPM method.

In Table 2 the False position method (FPM) with the input (x_l, x_u) and output x_2 values of the solution results and the absolute error function are obtained in the condition of $R = 2$ (load resistance).

Table 2. The voltage's values of the solar cell with σ and εvalues using FPM.

Iterations	X_0-FPM	x_1-FPM	x_{n+1}-FPM	ε-FPM	σ-FPM
1	0.971416861	1	1.044256778	0.117290343	0.057376293
2	1	1.044256778	1.101633071	0.174666637	0.068030557
3	1.044256778	1.101633071	1.033602514	0.106636079	0.008450977
4	1.101633071	1.033602514	1.025151536	0.098185102	0.026289396
5	1.033602514	1.025151536	0.998862141	0.071895706	0.018400919
6	1.025151536	0.998862141	0.980461222	0.053494787	0.019848121
7	0.998862141	0.980461222	0.960613101	0.033646666	0.016738565
8	0.980461222	0.960613101	0.943874536	0.016908101	0.013546447

9	0.960613101	0.943874536	0.930328088	0.003361653	0.015382671
10	0.943874536	0.930328088	0.914945417	0.012021018	0.011345868
11	0.930328088	0.914945417	0.926291285	0.00067515	0.000814109
12	0.914945417	0.926291285	0.927105394	0.00013896	0.000140467
13	0.926291285	0.927105394	0.926964927	1.5078E-06	1.50444E-06
14	0.927105394	0.926964927	0.926966432	3.35535E-09	3.35535E-09
15	0.926964927	0.926966432	0.926966435	0	

Figure 3 shows the results using FPM technique.

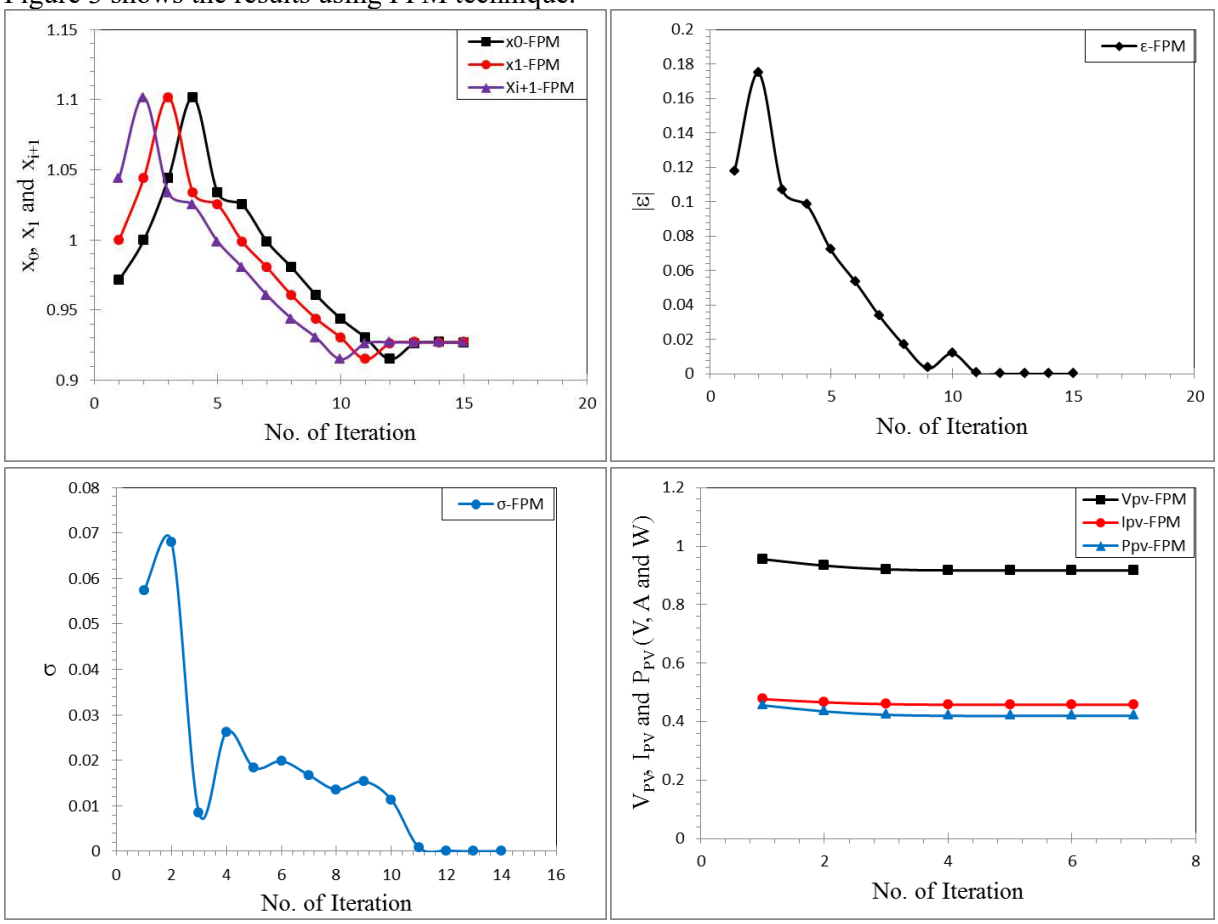

Figure 3. The results by using FPM method.

In Table 3, the False position method (FPM) with the input (x_l, x_u) and output x_2 values of the solution results and the absolute error function are obtained in the condition of $R = 3$ (load resistance).

Table 3. Thevoltage'svalues of the solar cell with σ and εvalues using FPM.

Iterations	X_0-FPM	x_1-FPM	x_{n+1}-FPM	ε-FPM	σ-FPM
1	0.971417	1	1.044857	0.117891	0.057992
2	1	1.044857162	1.10285	0.175883	0.068545
3	1.044857	1.102849636	1.034305	0.107338	0.008396
4	1.10285	1.034304827	1.025908	0.098942	0.026477
5	1.034305	1.025908432	0.999432	0.072465	0.018612
6	1.025908	0.999431612	0.98082	0.053853	0.020337
7	0.999432	0.9808198	0.960482	0.033516	0.017574

8	0.98082	0.960482362	0.942908	0.015942	0.014925
9	0.960482	0.942908456	0.927984	0.001017	0.028416
10	0.942908	0.927983642	0.899568	0.027399	0.026891
11	0.927984	0.899567834	0.926459	0.000508	0.000764
12	0.899568	0.926458849	0.927222	0.000256	0.000258
13	0.926459	0.927222411	0.926964	2.08E-06	2.08E-06
14	0.927222	0.92696435	0.926966	8.54E-09	8.54E-09
15	0.926964	0.926966426	0.926966	0	

Figure 4 shows the results using FPM technique.

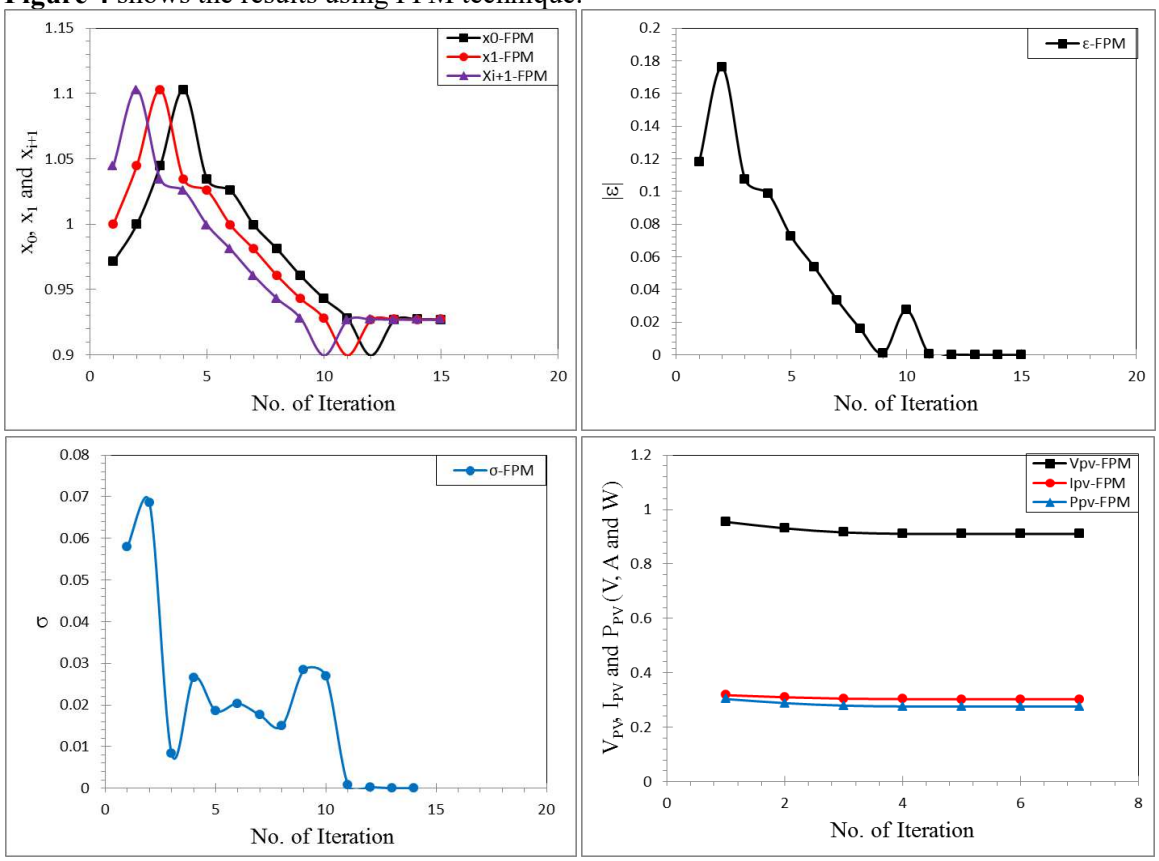

Figure 4. The results by using FPM method.

In Table 4, the False position method (FPM) with the input (x_l, x_u) and output x_2 values of the solution results and the absolute error function are obtained in the condition of $R = 4$ (load resistance).

Table 4. The voltage's values of the solar cell with σ and εvalues using FPM.

Iterations	X_0-FPM	x_1-FPM	x_{n+1}-FPM	ε-FPM	σ-FPM
1	0.971417	1	1.045458	0.118492	0.058607
2	1	1.045458	1.104065	0.177098	0.069057
3	1.045458	1.104065	1.035008	0.108042	0.008341
4	1.104065	1.035008	1.026667	0.099701	0.026658
5	1.035008	1.026667	1.00001	0.073043	0.018814
6	1.026667	1.00001	0.981196	0.054229	0.020815
7	1.00001	0.981196	0.960381	0.033415	0.018411

8	0.981196	0.960381	0.941971	0.015004	0.016382
9	0.960381	0.941971	0.925589	0.001378	0.067548
10	0.941971	0.925589	0.858041	0.068925	0.070992
11	0.925589	0.858041	0.929034	0.002067	0.005072
12	0.858041	0.929034	0.923961	0.003005	0.002905
13	0.929034	0.923961	0.926866	1E-04	0.000105
14	0.923961	0.926866	0.926971	4.9E-06	4.9E-06
15	0.926866	0.926971	0.926966	0	

Figure 5 shows the results using FPM technique.

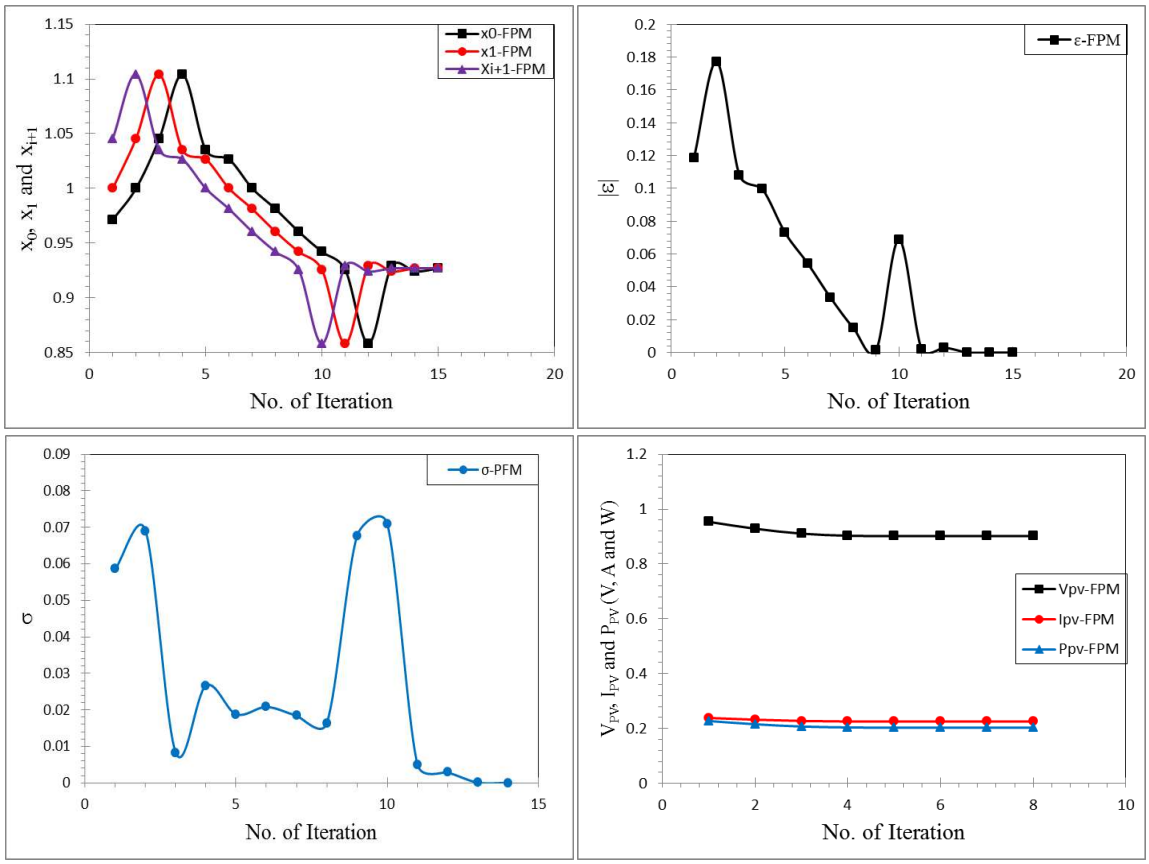

Figure 5. The results by using FPM method.

In Table 5, the False position method (FPM) with the input (x_l, x_u) and output x_2 values of the solution results and the absolute error function are obtained in the condition of $R = 5$ (load resistance).

Table 5. The voltage's values of the solar cell with σ and εvalues using FPM.

Iterations	X_0-FPM	x_1-FPM	x_{n+1}-FPM	ε-FPM	σ-FPM
1	0.971417	1	1.04606006	0.119093607	0.059218795
2	1	1.046060063	1.10527886	0.178312402	0.069566765
3	1.04606	1.105278858	1.03571209	0.108745637	0.008283741
4	1.105279	1.035712093	1.02742835	0.100461897	0.026832002
5	1.035712	1.027428352	1.00059635	0.073629895	0.019007453
6	1.027428	1.00059635	0.9815889	0.054622441	0.021279435

7	1.000596	0.981588897	0.96030946	0.033343006	0.019246199
8	0.981589	0.960309462	0.94106326	0.014096806	0.017915457
9	0.960309	0.941063262	0.92314781	0.00381865	0.012483412
10	0.941063	0.923147806	0.91066439	0.016302063	0.009779298
11	0.923148	0.910664393	0.92044369	0.006522764	0.008450926
12	0.910664	0.920443691	0.92889462	0.001928162	0.002134459
13	0.920444	0.928894618	0.92676016	0.000206297	0.000199961
14	0.928895	0.926760159	0.92696012	6.33607E-06	6.33607E-06
15	0.92676	0.92696012	0.92696646	0	

Figure 6 shows the results using FPM technique.

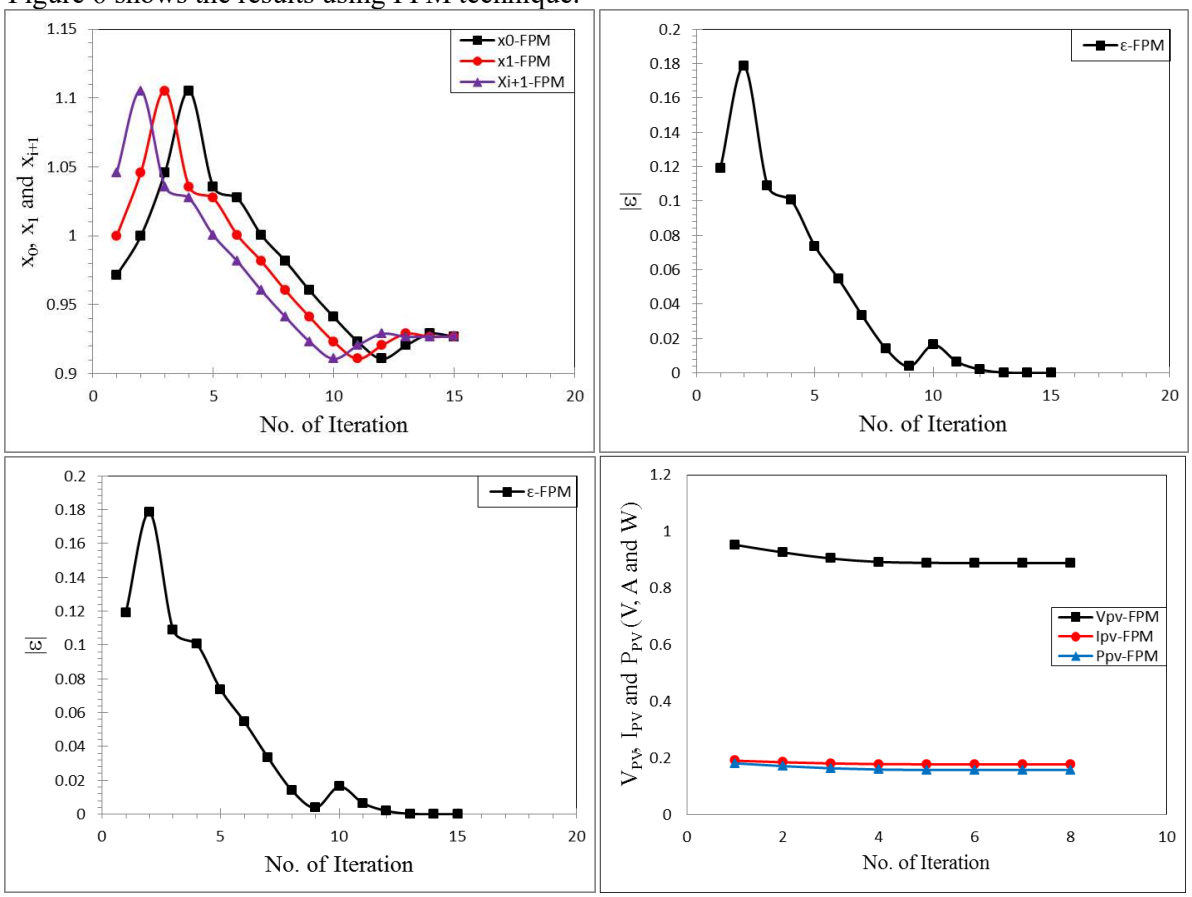

Figure 6. The results by using FPM method.

The plot of the number of iteration with ε plane and initial-output values proves that the proposed (FPM) method has a thirty iterations indicated a slow behavior. In addition, it is noticed that the suggested technique (FPM) has a behavior of the result in initial values $x_l \approx 0.9$ and $x_u = 1$ has tolerance as the smallest error.

In Tables (1-5), the proposed FPM technique is faster than other methods, and it has a less error after view the calculated iterations that depending on the efficiency investigating.

5. Conclusion

In the present work, numerical results of a single-diode (solar cell) in mathematical numerical formula were obtained. The basic advantages of the proposed (FPM) method are accurate approximate solution and a numbers of iterations produce simplicity.

6. References

[1] Rasheed M and Barillé R 2017 Room temperature deposition of ZnO and Al: ZnO ultrathin films on glass and PET substrates by DC sputtering technique, *Opt. Quantum Electron.* **49** 5 1-14.

[2] Rasheed M and RégisBarillé R 2017 Optical constants of DC sputtering derived ITO, TiO_2 and TiO_2: Nb thin films characterized by spectrophotometry and spectroscopic ellipsometry for optoelectronic devices *J. Non-Crystalline Solids* **476** 1-14.

[3] Rasheed M and Barillé R 2017 Comparison the optical properties for Bi_2O_3 and NiO ultrathin films deposited on different substrates by DC sputtering technique for transparent electronics *J. Alloys Comp.* **728** 1186-1198.

[4] Saidani T, Zaabat M, Aida MS, Barille R, Rasheed M and Almohamed R 2017 Influence of precursor source on sol–gel deposited ZnO thin films properties *J. Mat. Sci. Mat. Electron.* **28** 13 9252-9257.

[5] Guergouria K, Boumezoued A, Barille R, Rechemc D, Rasheed Mand Zaabata M 2019 ZnOnanopowders doped with bismuth oxide, from synthesis to electrical application, *J. Alloys Comp.* **791** 550-558.

[6] Bouras D, Mecif A, Barillé R, Harabi A, Rasheed M, Mahdjoub A and Zaabat M 2018 Cu: ZnO deposited on porous ceramic substrates by a simple thermal method for photocatalytic application *Ceramics Int.* **44** 17 21546-21555.

[7] Dkhilalli F, Borchani SM, Rasheed M, Barille R, Guidara R and Megdiche M 2018 Structural, dielectric, and optical properties of the zinc tungstate ZnWO4 compound *J. Mat. Sci. Mat. Electron* **29** 8 6297-6307.

[8] Dkhilalli F, Borchani SM, Rasheed M, Barille R, Shihab S, Guidara K and Megdiche M, Characterizations and morphology of sodium tungstate particles *Royal Soc. Open Science*, **5** 8 1-12.

[9] Chaichan MT and Kazem HA 2018 *Generating electricity using photovoltaic Solar plants in Iraq* (pp. 47-82). Springer.

[10] Rasheed MS 2014 On Solving Hyperbolic Trajectory Using New Predictor-Corrector Quadrature Algorithms *Baghdad Sci. J.* **11** 186-192.

[11] Saidi W, Hfaidh N, Rasheed M, Girtan M, Megriche A and EL Maaoui M 2016 Effect of B_2O_3 addition on optical and structural properties of TiO_2 as a new blocking layer for multiple dye sensitive solar cell application (DSSC) *RSC Adv*. **6** 73 68819-68826.

[12] Aukstuolis A, M. Girtan M, Mousdis GA, Mallet R, Socol M, Rasheed M, Stanculescu A 2017 Measurement of charge carrier mobility in perovskite nanowire films by photo-CELIV method *Proc. Romanian Acad Ser. a-Math. Phys. Techn. Sci. Inform. Sci.* **18** 1 34-41.

[13] Dkhilalli F, Megdiche S, Guidara K, Rasheed M, Barillé R and Megdiche M 2018 AC conductivity evolution in bulk and grain boundary response of sodium tungstate Na_2WO_4, Ionics, **24** 1 169-180.

[14] Enneffati M Louati B, Guidara K, Rasheed M and Barillé R 2018 Crystal structure characterization and AC electrical conduction behavior of sodium cadmium orthophosphate *J. Mat. Sci. Mat. Electron.* **29** 1 171-179.

[15] Kadri E, Krichen M, Mohammed R, Zouari A and Khirouni K 2016 Electrical transport mechanisms in amorphous silicon/crystalline silicon germanium heterojunction solar cell: impact of passivation layer in conversion efficiency*, Opt. Quantum Electron.* **48** 12 1-15.

[16] Kadri E, Messaoudi O, Krichen M, Dhahri K, Rasheed M, Dhahri E, Zouari A, Khirouni K, Barillé R 2017 Optical and electrical properties of SiGe/Si solar cell heterostructures: Ellipsometric study *J. Alloys Comp.* **721** 779-783.

[17] Kadri E, Dhahri K, Zaafouri A, Krichen M, Rasheed M, Khirouni K and Barillé R 2017 Ac conductivity and dielectric behavior of a−Si:H/c− $Si_{1-y}Ge_y$/p−Si thin films synthesized by molecular beam epitaxial method *J. Alloys Comp*. **705** 708-713.

[18] Azaza NB, Elleuch S, Rasheed M, Gindre D, Abid S, Barille R, Abid Y and Ammar H 2019 3-(p-nitrophenyl) Coumarin derivatives: Synthesis, linear and nonlinear optical properties *Opt. Mat.* **96** 109328.
[19] Enneffati M, Rasheed M, Louati B, Guidara K and Barillé R 2019 Morphology, UV–visible and ellipsometric studies of sodium lithium orthovanadate, *Opt. Quantum Electron.* **51** 299.
[20] RASHEED M and SHIHAB S 2019 Parameters Estimation for Mathematical Model of Solar Cell, *Electron. Sci. Technol. Appl.* (2019).
[21] RASHEED M and SHIHAB S 2019 Modeling and Simulation of Solar Cell Mathematical Model Parameters Determination Based on Different Methods *Insight Math.* **1** 1.
[22] Hamimid M, Feliachi M and Mimoune SM 2010 Modified Jiles–Atherton model and parameters identification using false position method *Phys. B: Conden. Matt.* **405** 8 1947-1950.
[23] Ageev AL and Antonova TV 2013 New methods for the localization of discontinuities of the first kind for functions of bounded variation *J. Inv.Ill-Posed Probl.* **21** 2 2013 177-191.

Electrical and optical properties of ZnO, CuO thin films and fabrication of (ZnO/CuO) heterojunction solar cell by thermal treatment

Electrical and optical properties of ZnO, CuO thin films and fabrication of (ZnO/CuO) heterojunction solar cell by thermal treatment

I.N. Kashkool[1] , V.P. Afanasjev[2], N.V. Mukhin[2].

[1]Ministry of Education, Iraq
[2]St. Petersburg State Electrotechnical University, ul. Prof. Popova 5, St. Petersburg, 197376, Russia

E-mail: ekshkol@yahoo.com

Abstract: Electrical properties (carrier concentration, mobility, resistivity) of zinc oxide thin films deposited on glass substrates by (LPCVD) has been studied. Thermal annealing in air showed that ideal annealing temperature is about 250˚C. Films of copper oxide (CuO) and (CuO/ZnO) solar cell were prepared by vacuum deposition of copper films followed by thermal annealing. structural properties of the CuO films and I-V characteristics were studied upon thermal annealing and showed that a photosensitive (ZnO/CuO) heterojunction may be obtained by thermal treatment temperature about 500 ˚C.

Keywords: Cuprous oxide, spatial atmospheric ALD, ZnO/Cu_2O heterojunction, solar cell

1. Introduction

Solar cells (SC) based on oxide heterostructures have long remained outside the area of scientific interest on the part of researchers. However, at present time, a slowdown in the efficiency growth of both silicon and A_3B_5 semiconductor-based efficiency has become clearly visible, and the search for new materials for SC has begun actively. One of these materials is copper oxide – CuO. Being a straight-band semiconductor with a band gap of 2.2 eV, copper oxide also has a high absorption coefficient [1] and is characterized by p-type conductivity. In combination with a wide-band semiconductor, such as zinc oxide. It is possible to form a ZnO/ CuO heterojunction, which can be used to produce a solar cell with a theoretically achievable efficiency value of about 20% [2]. At the moment, an efficiency value of 4.1% has already been achieved for a ZnO/ CuO heterojunction-based SC [3]. ZnO has unique properties for instance a wide band gap of ~3.37 eV [4], high exciton binding energy (~60MeV) [5], effective ultraviolet photoluminescence, high optical transparency in the visible range more than (80%) [6], and high electrical conductivity. Currently, zinc oxide is used to create various sensors and detectors, piezoelectric devices, as a transparent conducting contact in solar panels and other devices [7]. The growing interest in zinc oxide-based heterojunctions is associated with wide opportunities for practical applications. In particular, a p-n transition based on n-ZnO and p-CuO is promising, so methods for obtaining ZnO/CuO hetero-junctions are actively developing [8,9,12]. In this paper, the properties of ZnO films deposited by the LPCVD method and (ZnO/CuO) structures are studied by spraying the copper film onto the substrate followed by thermal annealing treatment to improve the I – V characteristics.

2. Experimental

Zinc oxide films were obtained by low pressure chemical vapor deposition (LPCVD). Diethylcinc ($(C_2H_5)_2Zn$), or DEZ, and deionized water were used as precursors, the concentration ratio was ($\frac{H_2O}{DEZ} = \frac{5}{6}$). a gas mixture of 2% ($B_2H_6$) in hydrogen was used for doping ZnO films with boron. The process was optimized sequentially by optimizing the temperature and pressure, and then by optimizing the gas flow ratio. Pulsed light annealing treatment of (ZnO/CuO) structures was obtained in an installation containing 6 halogen lamps with a power of 1 kW for (60sec). The wavelength region (800-1100 nm) is ~80%, then gradually decreases to ~60% at 600 nm and drops to zero in the self-absorption region of ~370 nm. In this case, the optical transmission spectrum shows optical interference in the film in the wavelength range of 600-1100 nm, which indicates a high uniformity of the film thickness. The electrical parameters of ZnO films were determined by measuring the resistivity and carrier concentration using the Hall effect at room temperature using a four-probe method in the van der Pau configuration on an HMS-3000 (Ecopia) installation with a 0.55 T magnetostatic magnet. To study the electrical properties of ZnO films on glass substrates, they were cut into square samples with dimensions of 10×10 mm. Measurements of the electrical properties of a set of ZnO samples cut from a single substrate showed a very small variation of electrical parameters in the initial samples within 5%.

3. Results and discussion

The parameters of the initial ZnO samples Were: electron concentration n~1×10^{20} cm^{-3}, carrier mobility 30 $cm^2/V.$ s, resistivity 2×10^{-3} Ω.cm, sheet resistance ~12 Ohms. The effect of thermal processing in the temperature range from (200°C- 500°C) is studied on the sheet resistance of ZnO. It is found that the sheet resistance of ZnO films do not change until the annealing temperature is 200°C, then in the temperature range from 250ºC to 500ºC, the resistance of the films increases, apparently, annealing in air reduces the concentration of oxygen vacancies and causes growth the concentration of adsorbed oxygen at the grain boundaries, which leads, first, to the capture of free carriers at the grain boundaries and, accordingly, causes a depletion of the volume. Second, the appearance of a charge at the grain boundaries leads to strong scattering of free carriers, see Figure 1.

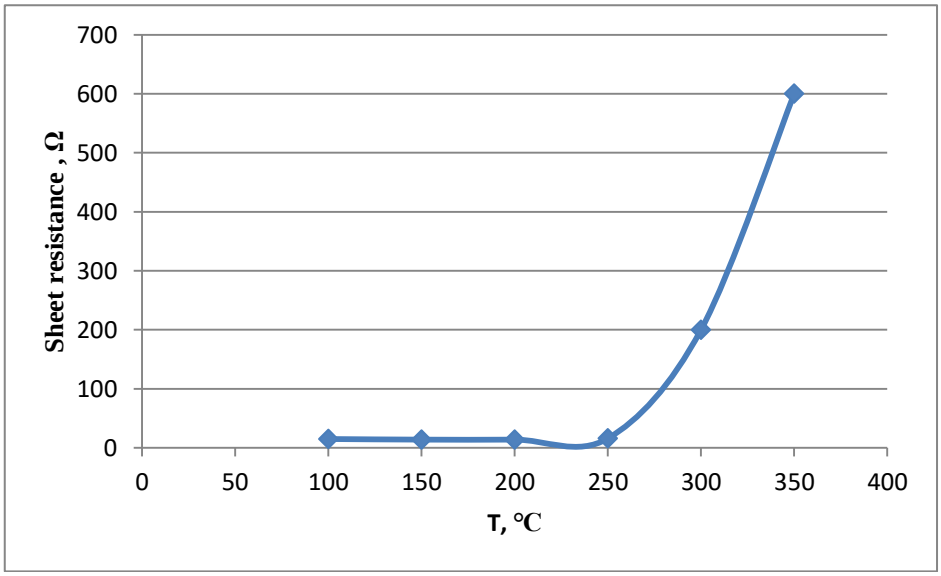

Figure 1. Dependence of sheet resistance of the ZnO film on the annealing temperature.

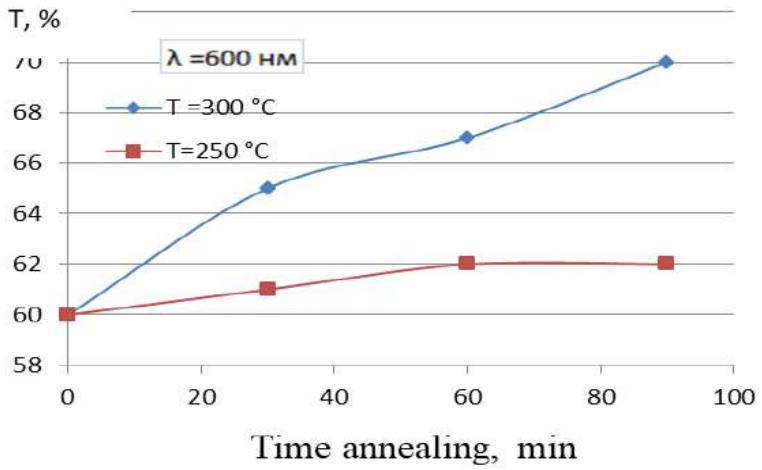

Figure 2. Optical transmittance (ZnO) as function of time annealing at a wavelength of 600 nm, thickness 1600 nm at different temperatures (250 °C and 300 °C).

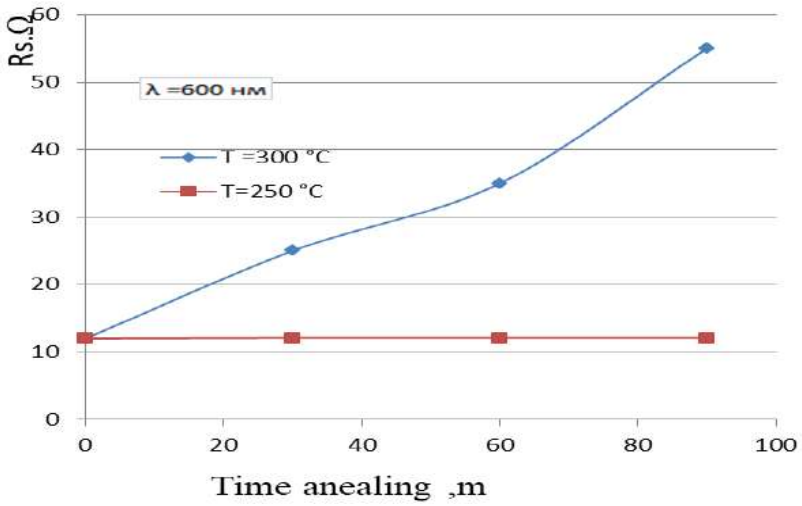

Figure 3. Sheet resistance of (ZnO) as function of time annealing at a wavelength of 600 nm, thickness 1600 nm at different temperatures (250 °C and 300 °C).

In order to obtain opaque electrical and optical characteristics of ZnO films, it is necessary to avoid long-term treatments at high temperature, see, (Figures 2 and 3). To obtain (ZnO/CuO) structures, thin copper films were sprayed on the substrate surface by magnetron sputtering at a pressure of 10^{-5}bar. To control the optical properties, clean glass substrates were attached next to the ZnO samples. After deposition, the films of CuO and the structures (ZnO/CuO) were annealed to improve the electrical properties and I-V characteristics.

Figure 4. shows x-ray Images of copper thin films deposited on ZnO substrates and annealed at various temperatures (220 ˚C -500 ˚C) in air. After annealing at 220 ºC, an intense diffraction peak appears at $2\theta=36.6^{\circ}$ which can be attributed to (111) reflection of the Cu_2O cubic phase. At higher temperatures, this reflex becomes less intense, while the peaks at angles 2θ =35-40°, which correspond to the reflexes (110), (002), (111) the monoclinic phase of CuO becomes more intense. Thus, x-ray diffraction results correlate with optical absorption data. From these results, it can be concluded that

annealing of copper films at 220 ˚C -550 ˚C, leads to form a mixed phase of (CuO-Cu_2O), while the contribution of the phases depends on the temperature and time annealing, see (Figures 4 and 5).

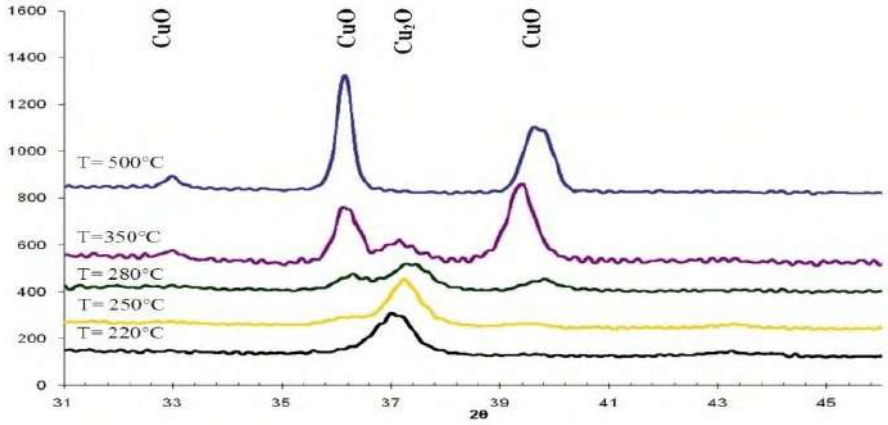

Figure 4. Composition and structure of copper thin films obtained by thermal oxidation of copper.

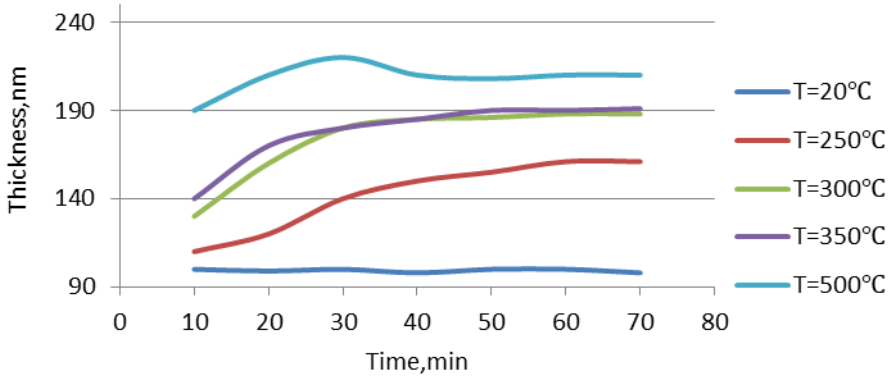

Figure 5. Changes in thin films thickness depending on the annealing time.

The I-V characteristics of (ZnO/CuO) structures obtained by deposition of copper thin films on the surface of ZnO layers, improve volt-ampere characteristics were formed during thermal annealing of copper films at 200-500°C. It was observed that the I-V characteristics of (ZnO/CuO) of the samples depend on the time of thermal annealing and temperature. The initial structure which obtained before annealing showed that the I-V characteristics were close to ohmic, and a weak asymmetry of forward and reverse characteristics was observed. This may indicate a critical role for the tunnel current [11]. However, we were observed after thermal annealing treatment in the range (200 ˚C -500 ˚C) leads to decrease in leakage currents and an increase in the value of the potential barrier. This indicates a significant contribution of tunnelling processes through surface by structural defects [10,11] and allows us to improve I-V characteristics as Figure 6 showed.

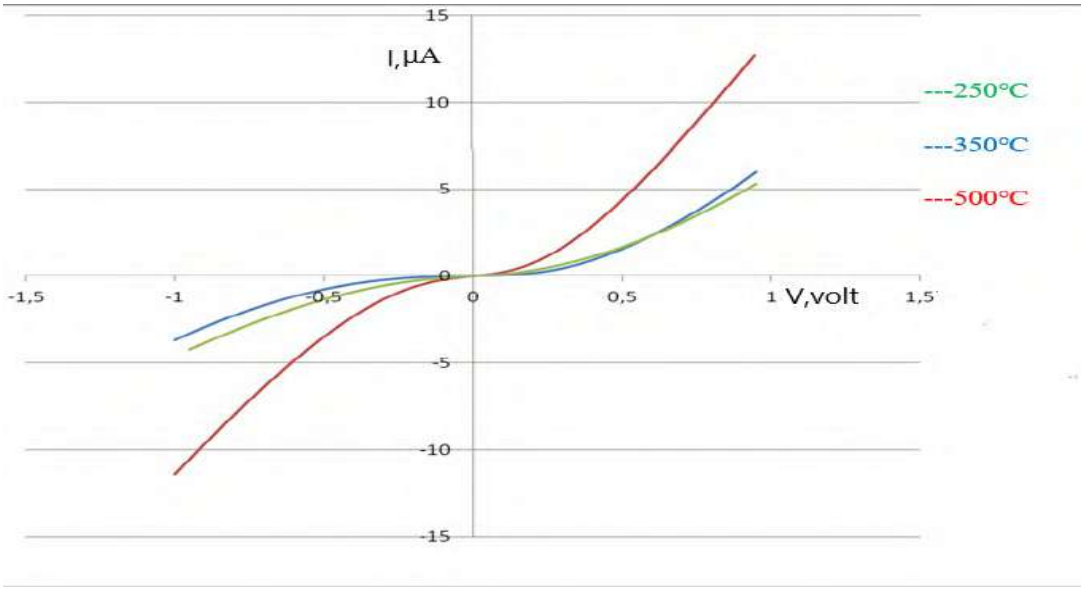

Figure 6. I-V characteristics of (ZnO/CuO) hetero structures after annealing for 60 sec at temperatures (250˚C, 350˚C and 500˚C).

The solar cell structures (ZnO/ CuO) obtained after thermal annealing at temperature of (500˚C) show a typical I-V characteristic when the forward current increases. The dominance of multi-stage tunnelling and recombination processes through traps in the (ZnO/ CuO) structure is evidenced by the literature data on temperature dependences of the volt-ampere characteristics [10]. The process of tunnelling through a thin layer of bulk charge is also significant, so to reduce the non-ideal factors and suppress tunnelling leakage currents, a layer of high-resistance ZnO is created at the border of the hetero-structure [11]. Thus, short annealing times and temperature annealing improved the electrical and optical properties of ZnO and allow obtaining (n-ZnO/p-CuO) heterojunctions.

4. Conclusions

The effect of thermal treatment on the electrical and optical properties of ZnO films obtained by the PLCVD method is investigated. Annealing of ZnO films at temperatures above 200 ˚C causes degradation of electrical properties, the carrier concentration and mobility decrease, and the sheet resistance increases. Subsequent annealing of the samples in air leads to a significant restoration of the electrical parameters. It is established that the method of deposition of thin layers of copper on ZnO films with subsequent rapid oxidation in air for 60 sec. At temperature ranged (250 ˚C -500 ˚C), a photosensitive thin-film ZnO/ CuO heterojunction was obtained.

References

[1] Ruhle S *et al*. 2012 *J. Phys. Chem. Lett*. **3** 3755
[2] Seog LY 2011 *Appl. Phys. Lett*. **98** 19 192115
[3] Nishi Y, Miyata T and Minami T 2012 *J. Vac. Sci Tec. A*. **30** 4 04D103-1
[4] Izaki M, Shinagawa T, Mizuno KT, Ida Y, Inaba M and Tasaka A 2007 *J. Phys. D* **40** 332.
[5] Akimoto K, Ishizuka S, Yanagita M, Nawa Y, Paul GK and Sakurai T 2006 *Solar Energy* **80** 715.
[6] Gupta SK,Joshi A and Kaur M 2010 *J. Chem. Sci*. **10** 2 57–62.
[7] Law M,Green LE, Johnson JC, Saykally R and Yang P 2005 *Nat. Mater*. **4** 455-459.
[8] Nakamura Y, Yoshioka H, Miyayama M, Yanagida H, Tsurutani T and Nakamura Y 1990 Sensing *J. Electrochem. Soc*. **137** 3 940−943.
[9] Minami T, Nishi Y, Miyata T and Nomoto J 2011 *Appl. Phys. Express* **4** 062301.

[10] ÖzyurtKuş F, Serin T and Serin N 2009 *J. Optoelectron. Adv. Mat.* **11** 111855–1859.
[11] Terasako T, Murakami T and Hyodou A 2015 *Solar Energy Mat. Solar Cells*. **132** 74–79.
[12] Ghosh A, Bhushan B, Ghosh S, Mukherjee N, Bhattacharya G, Datta, D and Mondal A 2014 *RSC Adv*. **4** 51569-51575.

Measurement of outdoor Radon Concentrations in Soil Samples collected from Karabuk University in Turkey by using CR-39 Detector

Measurement of outdoor Radon Concentrations in Soil Samples collected from Karabuk University in Turkey by using CR-39 Detector

Khalid H Mahdi, A Mustafa Erer, Ulvi Kanbur, Savaş Ağduk, Serkan Oguz and Necla Çakmak

Karabuk University, Science Faculty, Department of Physics, Karabuk, Turkey

E-mail: khalidaal-shabeeb@karabuk.edu.tr

Abstract. In this work, radon gas concentration in (35) samples of soil collected from Karabuk University in Turkey was measured by using nuclear track detector (CR-39). The content of radium, the rate of surface exhalation and the rate of mass exhalation have been assessed. The concentrations of radon were varied from (16.348 $Bq.m^{-3}$) to (196.988 $Bq.m^{-3}$). Results indicate that the equivalent content of radium varied from (0.386245 $Bq.kg^{-1}$) to (4.654255 $Bq.kg^{-1}$). The exhalation rate for surface varied from (0.002007 $Bq.m^{-1}.h^{-1}$) to (0.023031 $Bq.m^{-1}.h^{-1}$). The exhalation rate for mass varied from (0.000319 $Bq.kg^{-1}.h^{-1}$) to (0.00366 $Bq.kg^{-1}.h^{-1}$). All the obtained results found to be less than the corresponding limits for the world. Thus, based on the radon gas concentration and radiation, the equivalent content of radium (C_{Ra}), exhalation rate for the area (E_{Area}) and exhalation rate for the mass (E_{Mass}) in this area have no risk to the human's health.

Keywords: Radon gas, nucleartrack detector CR-39, soil, equivalent content of radium,exhalation rate for surface,exhalation rate for mass.

1. Introduction

Radon gas (^{222}Rn) is the most variable and largest radiation that contributed to public exposure. It was found that the ratio of radon and it's daughters dose per year about (55%) of natural public exposure by inhalation of air, which the high levels of it can cause lung cancer [1] because Radon is a radioactive gas (alpha particle emitter) hasa decay constant of (0.1812 day^{-1}) with $t_{1/2}$ of (3.825 days) [2]. When radon exposure increased, the risk of lung cancer will increases, which has a linear relation with doses, it has been found that the risk of lung cancer increases (16%) per every (100 Bq/m^3) increase in radon concentration[3].The ^{238}U series generate radon ($^{222}_{86}Rn$) as a daughter of radium(^{226}Ra), which has another isotopes are the thoron (^{220}Rn) and actinon (^{219}Rn) which are daughters of^{232}Th and ^{235}U series, respectively[4]. Radon is an inert gas heavier than the air, without any color and smell or taste, which is usually stay close to the ground floors [5]. Two different methods were used to measure the radon concentration. The first one is the passive method by integrative sampling for long time exposure using a suitable detector (like CR-39 in this work) and the second method is the continuous active radon sampling (like continuous radon monitor), the first

method requires no electrical power as in the case of the sconed [6]. There are many studies about radionuclides and radon concentration emitted from soil samples in Turkey, which starts in 1983[7] by using Gamma spectroscopy and CR-39 detectors (for indoor and outdoor radon), there are two studies for Karabuk Governorate[8,9], but for Karabuk University area, this is the first study about radon concentration outdoor in it.

2. Experimental Part

2.1. Calculation of Radon gas concentrations

Thirty-five soil samples were collected from Karabuk University as shown in table-1 and Figure-1. These samples were dried by the oven (at a temperature of 80°C for 2h)and grinded into a powder with size of (200 μm) by using a sieve,then 10 gm was taken for exposure.

The sealed-cup technique was used in this work, the sample a weight of putin a small cup,then covered with a large cup that contain CR-39 detector with a thickness of(250 μm). And an area of ($1cm^2$) at the top of it,as shown inFigure-2,the exposure time was (60) days to attained secular equilibrium. Then the chemical etching for the detectors was current by using (NaOH) solution with the normolity of (6.25N) at(60^oC) for five hours.

The tracks in CR-39 of alpha particles concentration emitted from Radongas from soil samples were measured using an optical microscope (Nikon type 168 Japan made) with amagnification of(400X). The numbers of the tracks were measuredto get track density (ρ) ,which is given as[3]:

$$(\rho) = \frac{N_{ave}}{A} \quad (1)$$

WhereN_{ave} is an average number of total tracksand A is an area of field view. The Radon gas concentration in the soil samples was obtained by the comparison between track densities registered on the detectors of the samples and that of the standard soil samples which are shown in Figure (3), using the following relation [10]:

$$C_X = C_s\left(\frac{\rho_x}{\rho_s}\right) \quad (2)$$

$$C_x = \frac{\rho_x}{slope} \quad (3)$$

WhereC_X is alpha particles concentration in the unknown sample,$C_s$is the alpha particles concentration in the standard sample.ρ_x is track density of the unknown sample (track/mm^2) and ρ_s is track density of the standard sample (track/mm^2).

2.2 Calculation of Radiation indices

The equivalent content of radium in the soil sample in the unit (Bq/kg) is given as[11]

$$C_{Ra}\ (Bq.kg^{-1}) = \frac{\rho\ .\ h\ .\ A}{K\ .\ T_e\ .\ M} \quad (4)$$

where, ρ is track density (track/mm^2),A is the area of the surface sample (0.001589 m^2),K (calibration constant) equal to the slope/exposure time(7.026/60=0.117), h is the distance from the surface of the sample to the detector(13.5 cm), M is sample mass of (0.01kg), T_e is the effective exposure time(h),which given as[11]:

$$T_e = T - \frac{1}{\lambda\left(1-e^{-\lambda T}\right)} \quad (5)$$

Whereλ is the decay constant of radon (0.1814day^{-1}) and T is exposure time.

The area surface exhalation rate and the mass exhalation rate are given as[11,12]

$$E_{Area} = \frac{C\ .\ V\ .\ \lambda}{A[T+\lambda^{-1}(e^{-\lambda T}-1)]}(Bq.m^{-2}.\ h^{-1}) \quad (6)$$

$$E_{Mass}=\frac{C.V.\lambda}{M[T+\lambda^{-1}(e^{-\lambda T}-1)]}(Bq.kg^{-1}.h^{-1}) \quad (7)$$

WhereCis the radon activity or integrated radon exposure ($Bqm^{-3}h$), V is volume of cup (m^3), T is Time of exposure (hrs), M is Mass (kg) of the sample in cup, λ is the decay constant for radon (h^{-1}).

Figure 1. Map Satellite for Karabuk University sites.

Table 1. Locations, codes and radon concentration of soil samples taken from some points of Karabük University.

No	x-coordinate	y-coordinate	Location and Sample code	Tracks density(track/mm^2)	Radon concentration (Bq/m^3)
1	32.654611	41.213097	Science Faculty (TCFB1)	1210.718	172.467
2	-	-	Fertilizer	1001.281	142.633
3	32.655861	41.208527	Central Research Labs. (CRL2)	697.167	99.312
4	32.657718	41.206220	Stadium (ST1)	1382.752	196.988
5	32.652134	41.216106	Rector Office (RO2)	596.752	85.007
6	32.655796	41.210864	Literature Faculty (LF2)	530.765	75.608
7	32.652001	41.214480	Medicine Faculty (MF1)	734.464	104.625
8	32.654999	41.214022	Technology Faculty (TCFC1)	963.984	137.320
9	32.657936	41.210555	Original soil (1)	748.809	106.668
10	32.654755	41.214170	Technology Faculty (TCFA2)	611.097	87.051
11	32.651310	41.214005	Original soil (2)	774.630	110.346
12	32.655366	41.212142	Social Centre (SC)	1196.373	170.424
13	32.656388	41.210405	Technology Centre (TCC1)	875.045	124.650
14	32.657159	41.208329	Library (L1)	872.172	124.242
15	32.652694	41.214406	Medicine Faculty (MF2)	493.468	70.295
16	32.659887	41.205894	Engineering Faculty	533.634	76.016

			(EF1)		
17	32.653413	41.213174	Foreign Language High School (LHS1)	433.219	61.712
18	32.656288	41.208292	Central Research Labs. (CRL1)	542.241	77.242
19	32.655834	41.211488	Literature Faculty (LF1)	304.114	43.321
20	32.656700	41.210377	Technology Centre (TCC2)	459.040	65.390
21	32.655680	41.208527	Central Research Labs. (CRL3)	358.625	51.086
22	32.651607	41.216050	Rector Office (RO1)	134.843	19.208
23	32.654864	41.199937	TOKI-1, TOKI The residential complex	114.76	16.348
24	32.654596	41.200491	TOKI- 2	120.498	17.165
25	32.657678	41.208185	Library (L2)	192.223	27.382
26	32.651306	41.216115	Rector Office (RO3)	315.590	44.956
27	32.658841	41.206120	Engineering Faculty (EF2)	315.590	44.956
28	32.653630	41.199440	TOKI- 3	315.590	44.956
29	32.653558	41.214143	Technology Faculty (TCFA3)	324.197	46.182
30	32.659917	41.206784	Engineering Faculty (EF3)	263.948	37.599
31	32.654999	41.213609	Technology Faculty (TCFA1)	292.638	41.686
32	32.652394	41.198664	TOKI- 4	215.175	30.652
33	32.660222	41.206531	Engineering Faculty (EF4)	301.225	42.912
34	32.651609	41.216057	Rector Office (RO4)	306.983	43.730
35	32.656388	41.210405	Technology Centre (TCC3)	160.664	22.887

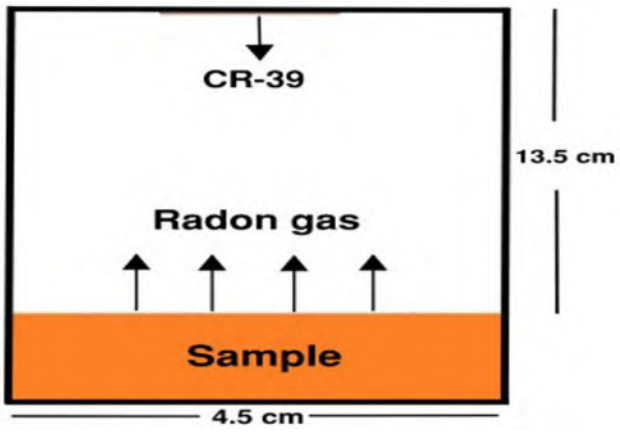

Figure 2. The sealed-cup technique for radon exposure.

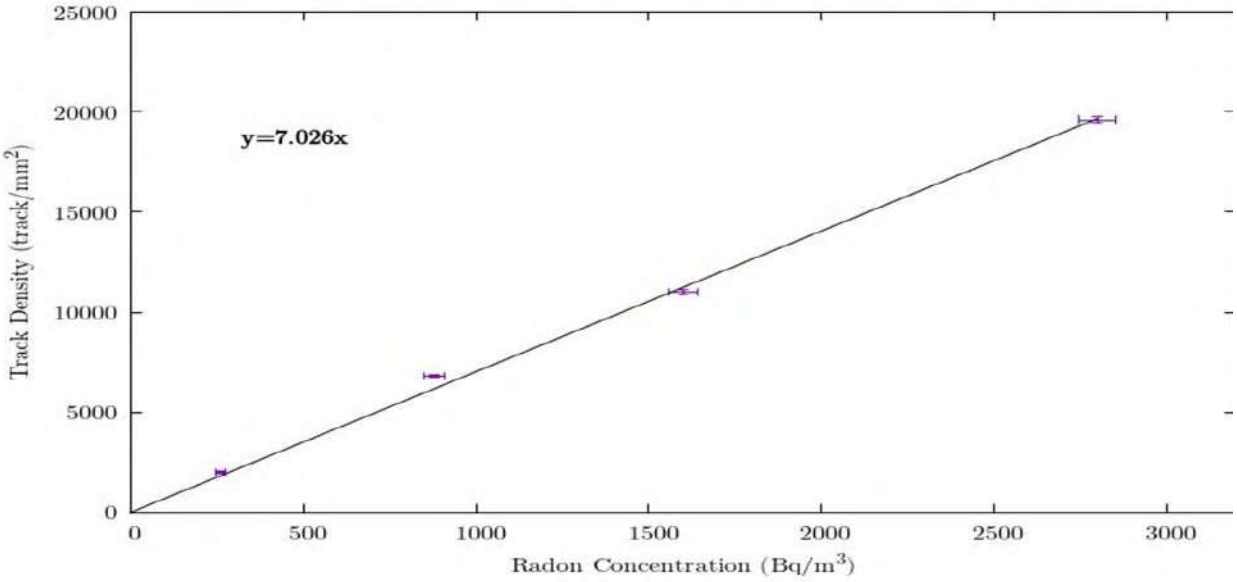

Figure3. The relation of track density and radon concentration for standard soil samples.

3. Results and Discussion

The results of radon concentrations emitted from soil samples selected from Karabuk University, was obtained by using the equation (3) are presented in table (1). From this table, it can be noticed that the highest radon concentration was found in a Stadium soil sample (196.988 Bq/m^3), while the lowest value was found in TOKI-1(The residential complex) equal to (16.348Bq/m^3).We also find that there are some values of radon concentrations close to the highest value, which is in the Science Faculty (TCFB1) and Social Centre (SC) soil samples (172.467Bq/m^3) and (170.424Bq/m^3) respectively, that means they are the same soil, although that the radon concentration in fertilizer sample was (142.329 Bq/m^3) and for the original soil samples (106.441 Bq/m^3), which is in agreement with other studies that done by other researchers like Ereeset al in 2006 for Western Turkey[13],Kamand Bozkurt in 2007 for Kastamonu[14], Kam et.al., in 2010 for Çanakkale[15],Kurnazet. al., in 2011 for Trabzon[16], Tabaret. al., in 2013 for Dikili[17], Sogukpinaret., al., in 2014 for Eskisehir[18],Ozen et. al., in 2018 for Rize[19] and Asliet. al., in 2019 for Karabuk[9].However, all results of radon concentrations in this work were less than the recommended value of (200 Bq/m^3) and certified by (ICRP, 1993)[20]. Table 2, presents results for radiation induces like the equivalent content of radium ranged from (0.386245) to (4.654255) Bq/m^2.h,which were to be less than the permissible value of (370 Bq/kg) as recommended by the Organization for Economic Cooperation and Development[21], the exhalation rates for the area were varied from (0.002007Bq/m^2.h) to (0.023031Bq/m^{2}h) and exhalation rates formass varied from (0.000319) to (0.00366)Bq/kg.h.It should be mentioned thatthe observed values of the radon exhalation rate in thepresent work were below the world average of (2.5 Bq/m^2.h)[22].

Table 2. The effective radium content, area surface exhalation rate andmass exhalation rate.

No	Radon concentration (Bq/m^3)	Equivalent content of Radium (Bq/kg)	Area exhalation rate (Bq/m^2.h)	Mass exhalation rate (Bq/kg.h)
1	172.467	4.074887	0.020164	0.003204
2	142.633	3.369990	0.016676	0.002650
3	99.312	2.346440	0.011611	0.001845
4	196.988	4.654255	0.023031	0.003660
5	85.007	2.008475	0.009939	0.001579

6	75.608	1.786384	0.00884	0.001405
7	104.625	2.471970	0.012232	0.001944
8	137.320	3.244460	0.016055	0.002551
9	106.668	2.520250	0.012471	0.001982
10	87.051	2.0567560	0.010178	0.001617
11	110.346	2.607155	0.012901	0.002050
12	170.424	4.026607	0.019925	0.003166
13	124.650	2.945120	0.014574	0.002316
14	124.242	2.935464	0.014526	0.002308
15	70.295	1.660855	0.008219	0.001306
16	76.016	1.796040	0.008887	0.001412
17	61.712	1.458076	0.007215	0.001146
18	77.242	1.825009	0.009031	0.001435
19	43.321	1.023550	0.005065	0.000805
20	65.390	1.544981	0.007645	0.001215
21	51.086	1.207016	0.005973	0.000949
22	19.208	0.453838	0.002246	0.000357
23	16.348	0.386245	0.001911	0.000304
24	17.165	0.405558	0.002007	0.000319
25	27.382	0.646961	0.003201	0.000509
26	44.956	1.062174	0.005256	0.000835
27	44.956	1.062174	0.005256	0.000835
28	44.956	1.062174	0.005256	0.000835
29	46.182	1.091143	0.005399	0.000858
30	37.599	0.888364	0.004396	0.000699
31	41.686	0.984925	0.004874	0.000774
32	30.652	0.724210	0.003584	0.000569
33	42.912	1.013894	0.005017	0.000797
34	43.730	1.033206	0.005113	0.000812
35	22.887	0.540743	0.002676	0.000425

4. Conclusions

Radon concentration, radium content, exhalation rates for the area (surface) and mass were obtained for selected soil samples collected from different locations on Karabuk University in Turkey. The results were found to be less than their corresponding permissible and certified world values. Thus, the present results revealed that the area is safe as far as the health effect is concerned, except the highest values which within the statistical ranges, the approximate values of the radon concentration refer to the soil of one source, which is transferred from another place for the purposes of agriculture, especially since the concentration values of the radon emitted from the original mountain the soil was far from it,which in agreement with other studies. From this, we conclude that we must know the sources of these soils and examine them radiographically before using them in agriculture or costruction material and conduct other tests, such as X-rays fluorescent for these soils to find out their composition, which is an evident through the shape and the color forthem,that they are transported soils.

Acknowledgment:
N. Çakmak would like to acknowledge the support of the Karabuk University, Scientific research project's Unit with project code No.: FDT-2020-2348.

References

[1] Dey G K and Das P K 2012 *Indian Academy of Sciences* **121** (1) 237 .
[2] Deka P C Subir S Bhattacharjee B Goswami T D Sarma B K and Ramachandran T V 2003 *Radiation Measurements* **36** 431.
[3] Chauhan R P Nain M and Kant K 2008 *Radiation Measurements* **43** 445.
[4] Hana Nafie Aziz Naoum 2002 *Determination of Uranium Concentrations In a number of teeth Using CR-39 Detector* Master Thesis University of Mosul.
[5] Mohammed F M Mahdi K H AL-Jobori SH M and Bilal Kareem Enzi B K 2018 *International Journal of Science and Research* (IJSR) **7** (4) 1679.
[6] Kotrappa P Dempsey J Hickey J R and Stiffs L R 1988 *J. of Health Physics* **54** 4756.
[7] Metin M Aydin B Attila A and Nilgun C 2010 J*ournal of Environmental Radioactivity* **101**(11) 952.
[8] Rıdvan B Hüseyin A andMustafa E 2011 *Journal of Radioanalytical and Nuclear Chemistry* **289** (2) 297.
[9] Aslı K Şeref T Aybaba H Elif G Muhammet K Aydan A Erer A M and Onur M 2019 *RadiochimicaActa* **108** (7).
[10] Mahdi Kh H Ishnayyin H G and Haider L M 2015 *J.Chem. Bio. Phy. Sci. Sec.* C **5** (3) 3336.
[11] Zubair M Shakir Khan M and Verma D 2012 *Iran. J. Radia. Res.* **10** (2) 83.
[12] Abd-Elzaher M 2012 *American Journal of Applied Science* **9** (10) 1653.
[13] Erees F S Yener G and Ozbal S O 2006 *Radiation Measurements* **41** (3) 354.
[14] Kam E and Bozkurt A 2007 *Applied Radiation and Isotopes* **65** (4) 440.
[15] Kam E Bozkurt A and llgar R 2010 *Environmental Monitoring and Assessment* **168** 685.
[16] Kurnaz A Küçükömeroğlu B Çevik U and Çelebi N 2011 *Applied Radiation and Isotopes* **69** (10) 1554.
[17] Tabar E Kumru M N İçhedef M and Saç M M 2013 *International Journal of Radiation Research* **11** (4).
[18] Sogukpinar H Algin E Asici C Altinsoz M and Cetinkaya H 2014 *Radiation Protection Dosimetry* **162**(3) 410.
[19] Özen S A Celik N and Dursun E and Taskın H 2018 *Environmental Geochemistry and Health* **40** 1111.
[20] ICRP 1993 *International Commission on Radiological Protection Against Radon-222 at Home and work* Publication 65 Pergamon Elsevier **35** 242.
[21] Organization for Economic Cooperation and Development (OECD), 1979 Nuclear Energy Agency, Paris, France.
[22] UNSCEAR. 2000 *Report of the United Nations Scientific Committee on the Effect of Atomic Radiation to the General Assembly*. ANNEXB Exposures from natural radiation sources.

Numerical Analysis of a Lasing Output for the Quasi _ Three _ Level Thin Disk Lasers

Numerical Analysis of a Lasing Output for the Quasi _ Three _ Level Thin Disk Lasers

Mohammed Ahmed Mahmood[1], Mudhir Shihab ahmed[1], Raed Mahdi Salih[2]

[1]Department of Physics, College of Education for Pure Sciences Ibn-AL Haitham, University of Baghdad, Baghdad, Iraq
[2]Al-Khwarizmi Engineering College, University of Baghdad, Iraq.

E-mail: mohammed.ahmed1204a@ihcoedu.uobaghdad.edu.iq

Abstract. This paper reports theoretical treatment to drive the general equation for laser threshold power (P_{pump}^{th}), the efficiency (η) and the laser out power (P_{out}) in thin disk laser with a quasi -three –level pump plan by using the analytical solution of the rate equation for this laser system. In order to find a numerical solution, MATLAB program has been used. When a diode pumped high power, continuous wave to the Nd^{3+}: YAG thin disc laser operated in a quasi-three-level. The pumping wavelength was (808 nm) and the laser wavelength was (946 nm) at Nd^{3+} doping concentration of 0.6 at %. While at (M^2 = 1.005), this laser is operated in a single mode, all the laser output power and efficiency have increased with increasing the pumping power.

Keywords: laser, thin disc laser, diode pumped Neodymium, quasi three level lasers.

1. Introduction

The thickness of the crystal is small compared with the diameter of a thin disk and its coated with high reflectivity on one side of its faces for both lasing and pumping wavelength, fixing on a heat sink to remove the excess heat that appear on the disk [1]. If we assume that there is a large heat transfer coefficient over the whole region, then a temperature field inside the crystal is naturally equal to the temperature with the axis [1,2]. The disc can also be pumped by laser valves either longitudinally or radially. By using multiple passages for the pump radiation through the disk to increase the absorption of the pump's certification of a specific crystal thickness [2]. This disc can fit the resonator as false or like a folding mirror. This design can convert lasers in the range of several watts to kilowatts, as shown in Figure 1. The power volume can be increased by increasing the diameter of the pump to the disk at a constant pumping power density [2,3].

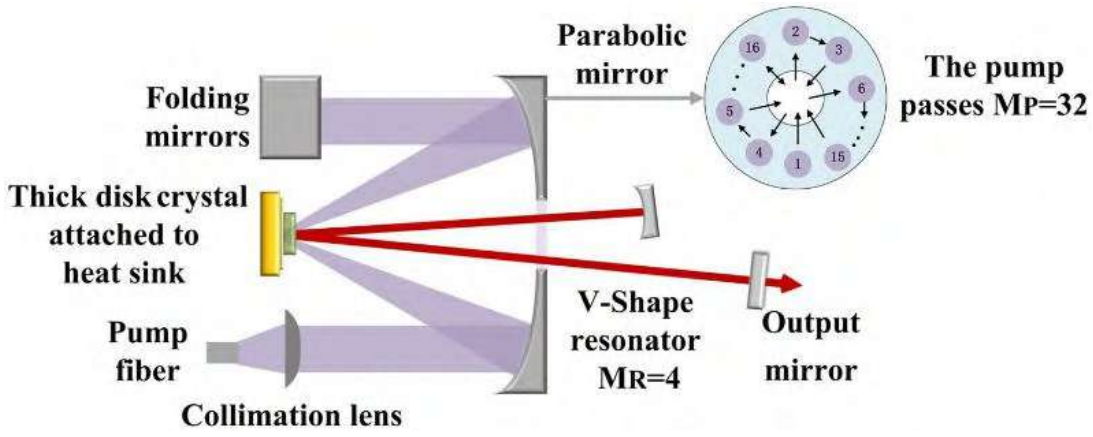

Figure 1. Multi-pass pumping in a Yb^{3+}: YAG thick-disk laser [14].

2. Analytical model

A quasi-3-level active medium, which is also termed a quasi-4-level active medium, it is characterized by being a large thermal count, low laser level. This means that when the temperature of the system with the four levels changes, it changes the properties of the laser, since at thermal equilibrium the laser does not contain a community, and thus the lower laser is filled in its entirety at thermal equilibrium [2]. The characteristics of the laser between the real 4-level system and the quasi-three-level system produce a major difference through re-absorption losses at the wavelength of the laser, and this leads to an increase in the three-dimensional losses in the resonator thus increasing the laser threshold [1,2]. The energy level system of Nd: YAG consists of stark split $I^4_{9/Z}$ ground state and $F^4_{3/Z}$ excited state. Because there is a small division of energy for each manifold, it is assumed that the relaxation times for the energy level within the manifold are also very small as shown in Figure 2. [2,5].

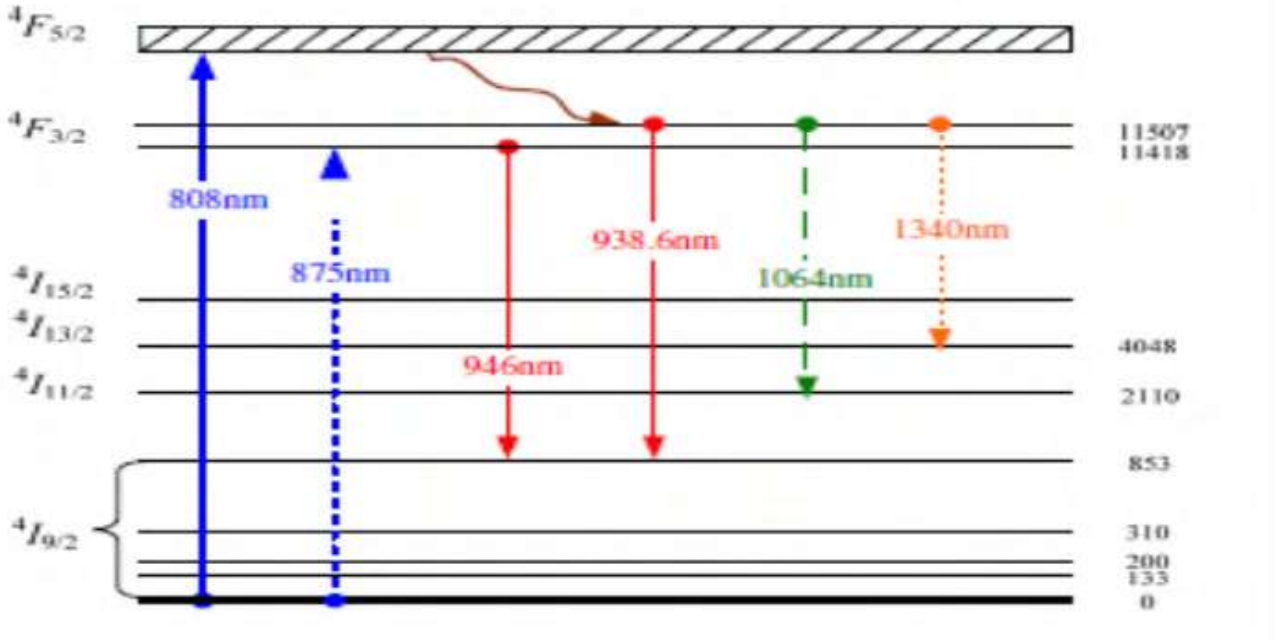

Figure 2. Energy level scheme of quasi three level Nd^{3+}: YAG [5].

Figure 2 illustrates the energy scheme for a Nd^{3+}: YAG crystal, where pumping wavelength (λ_p= 808nm) and lasing wavelength (λ_L=946nm). F_{1i}(i=1,2) and f_{0j} (j=1,2,3,4,5) act as a Boltzmann factors which refers to the occupation for the lower and upper manifolds, respectively.

$f_{1i}= \frac{exp\,(-\frac{E1i}{kT})}{\sum_{p=1} \quad expexp(-\frac{E1p}{KT})}$ ……(1)

$F_{0j}= \frac{(exp\,(-E0j/KT))}{\sum_{q=1} \quad exp\,(-\frac{E0q}{KT})}$……(2)

where (KB) Boltzmann occupation factor (T) is the absolute temperature. (E_{1i}) (i=1 , 2) describe an energy to each stark level of excited divergent and E_{0j} (j=1 , 2 , 3 , 4 , 5) describe an energy to each stark level of the ground divergent.

3. Steady state Rate Equation.

Average equation for two divergent system is given by [2,4]:

$\frac{dN_{up}}{dt} = \frac{I_p}{h\nu_p}\alpha_p - \frac{I_L}{h_{\nu L}} g_L M_L - \frac{N_{UP}}{\tau}$ ……(3)

$\frac{dI_L}{dt} = I_L(g_L M_L d - \delta)\frac{c}{2L_{opt}}$ …… ……..(4)

$g_L = (\frac{N_{UP}}{X_L} - N)\sigma L$ ……(5)

$X_L = \frac{f_{low}^L}{(f_{up}^L + f_{low}^L)}$ ……(6)

(N_{up}) represent the ion density in upper divergent , (I_P) is a medium pumping intensity through the crystal , (I_L)It is the energy intensity of the laser radiation scattered inside the cavity. (M_L) is the number of laser passing in the crystal per one resonator round trip, (τ) is The duration of the excitation state. (C) Is the speed of light in a vacuum, (L_{OP}) Optical length on the lumen. (d) Is the thickness of the crystal, (g_L) is a laser gain coefficient. (σp) and (σ_L) Cross sections represent effective absorption at (808 nm) and (946 nm) , respectively (N) is the total ionic density , f_{low}^L and f_{up}^Lrepresent the Boltzmann occupation factor in the lower and upper divergent for the laser level , respectively[2,4].

δ It is the loss of the round trip and can be described by [4]: [4]:

$\delta = -Ln(1 - Tr) - Ln(1 - \gamma)$ ……..*(7)*

where (Tr) the coupler is moved the output

Tr = $1 - R2$ … … … … … … … … … … … … … … … … … … (8)

γ) Calculate residual losses, such as those due to dispersion during one round-trip trip in the bore. *)*

When the pump intensity is greater than the intensity of the pump, the gain coefficient, the density of the ions in the upper manifold of the pump irradiation can be given by solving the steady-state rate equation:

gL = $\frac{\delta}{MLd}$……..(9)

N_{UP} = X_L (N+ $\frac{gl}{\sigma l}$)……(10)

Furthermore, on the basis of a multi-pass pumping system, the absorbed pump intensity (I_{abs}) and the absorption efficiency (η_{abs}) are given by[2,4] :

$I_{abs} = I_P \alpha_P d = I_{pump}\eta_{abs}$ ……(11)

$\eta_{abs} = R_P(1 - \exp(-M_P\alpha_P d))$……(12)

where Ipump is the input intensity (R_P) is The total reflection of the multi-pass pumping system, (M_P) the number of passes of the pump, and (αp) is the absorption coefficient. , and therefore, the laser intensity in the cavity (I_L) , the pumping threshold intensity (I_{pump}^{th})

output laser intensity I_{out} can be obtained by ($\frac{dN_{up}}{dt}$The output

IL = $\frac{V_L}{V_P}\frac{\eta_{abs}}{\delta}(I_{pump} - I_{pump}^{th})$ ……(13)

$I_{pump}^{th} = \frac{h_{vp}}{\tau}\frac{N_{UP}d}{\eta_{abs}}$ ……..(14)

And , the pump power , pump threshold power , and the laser power can be obtained by[2] :

PL= Ap IL …(15)
Ppump= ApIpump …(16)
P_{pump}^{th}= ApI_{pump}^{th} …(17)
Where (Ap) is the given pumping area
Ap = π (rp)^2 …(18)
(r_p) is pump radius , the beam quality factor is obtained
$M^2 = (\frac{a\, rp}{rf})$ …(19) [6]
(r_f) is the radius of a fundamental mode (TEM00) , the output laser power
Pout= Tr PL …(20)
Pout= $\frac{V_L}{V_P}\frac{Tr}{\delta}\eta_{abs}\,(P_{pump} - P_{pump}^{th})$ …(21)
Or
Pout= $\frac{\lambda_p}{\lambda_L}\frac{Tr}{\delta}\eta_{abs}\,(P_{pump} - P_{pump}^{th})$ …(22)
Where the laser extraction efficiency [4]
η_L= 1- $\frac{P_{pump}^{th}}{P_{pump}}$ …(23)
And . [2]
$\eta = \frac{\lambda_p}{\lambda_L}$ …… (24)
the output laser power can be
Pout= $\frac{Tr}{\delta}\eta\eta_{abs}\eta_L P_{pump}$ …….(25)

4. Results and Discussion.

In this paper, the results of the numerical solution by using Mat lab for the output laser power and efficiency for a quasi-three level of Nd^{3+}: YAG thin disk laser. The values of a coefficients for thin laser used in a Numerical solution illustrate in the Table 1.

Table 1. The value of a parameter for **Nd^{3+}: YAG** thin disc laser.

parameter	value	unit	Ref.
λp	808x10^{-9}	m	[5,7]
σp	6.7 x 10^{-24}	m^2	[5,7]
αp	1.83 x 10^2	m^{-1}	[7]
λL	946 x 10^{-9}	m	[5,7]
σL	3.7 x 10^{-4}	m^2	[5,7]
ɤ	0.02	---	[7]
a	0.85	---	[6]
Wood	195 x 10^{-6}	m	[8]
L	5 x 10^{-3}	m	[5]
f_{lower}	0.04	---	[7,9]
f_{upper}	0.51	---	[7,9]
R_P	0.77	---	[4]
R1	0.99	---	[11,12]
R2	0.85	---	[11,12]
τ	0.26 x 10^{-3}	sec	[5]
N	8.28 x 10^{25}	ion/m^3	[5]
M_L	4	---	[4]
M_P	54	---	[4]
d	2 x 10^{-3}	m	[4,11,12]
p	0_120	w	[10,12,13]

h	6.6205 x 10^{-34}	J.sec
c	3 x10^{8}	m/sec

The first step in the numerical solution was determine the operation Nd^{3+}: YAG thin disk laser of the type of the single-mode transverse or multi-mode transverse calculated (M^2) by equation (20) and (P_{pump}^{th}) by equation (18) for two values of radius of the pumping beam falling on the thin disk (r_p) as shown in Table 2.

Table 2. The values of (M^2) and (P_{pump}^{th}) to the of the radius of the pumping falling on the thin disk (r_p).

Parameter	Single-mode transverse	Multi-mode transverse	Unit
$\mathbf{r_p}$	230*10^{-6}	727*10^{-6}	M
$\mathbf{M^2}$	1.005	10.070	-
P_{pump}^{th}	2.549	25.539	W

Figure 3 illustrates the shape of the relationship between (p_{out}) and (p_{pump}), (p_{out}) is calculated by equation (26). In both modes, the laser output power increased with increasing of the pumping power, and the (p_{out}) is the highest values in a single mode operation.

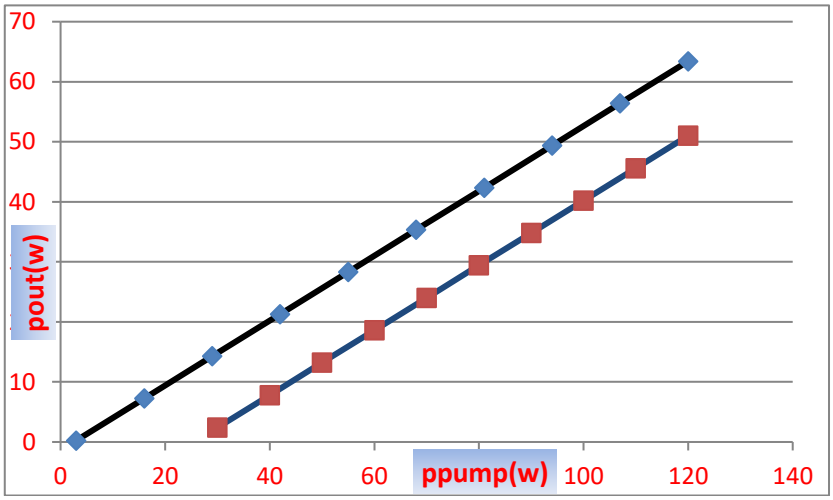

Figure 3. The relationship between (p_{out}) with (p_{pump}) in both modes.

Finally, the relation between the efficiency (η) and (pump) in both modes is shown in Figure 4. It is found that the efficiency of this laser increased with the increase of pumping power, and the values of (η) in single mode is highest.

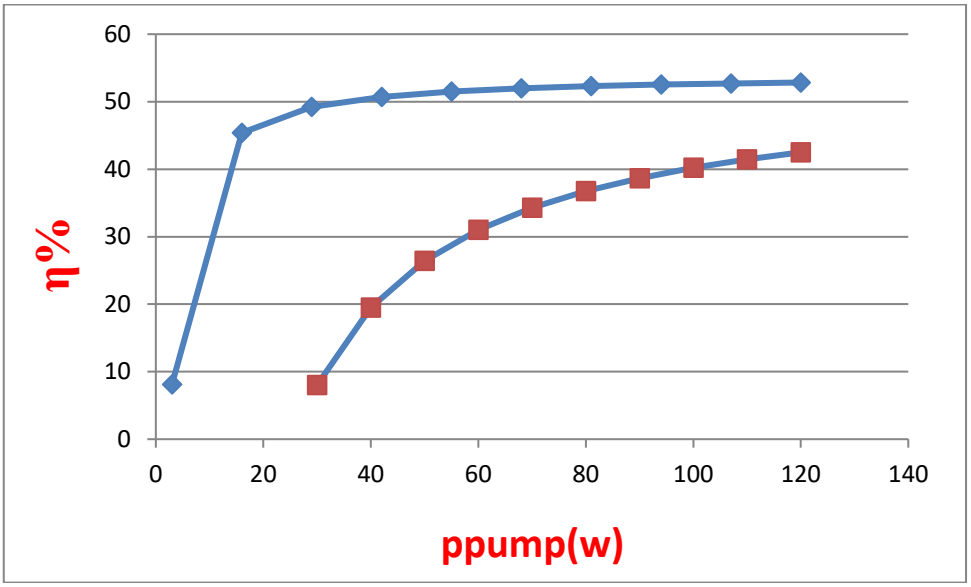

Figure 4. The relation between efficiency (η) and pumping power (P_{pump}) in both two modes.

5. Conclusions

In this paper, Nd^{3+}: YAG thin disk laser, were operated in a quasi-three-level system, at wavelength pump ($808*10^{-9}$ m) and wavelength laser ($946*10^{-9}$ m). The laser output power and efficiency are increased with pumping power, and the values of all (p_{out}) and (η) in a single mode operation are highest than the value in a multi-mode operation for this design of laser.

6. References

[1] Giesen A , HÜgel H and Vass A, Wittig K and Opower H 1994 Sealable concept for diode_ pumped high- power solid – state laser *Appl. Phys. B* 365-372.
[2] Contag A, Karszewski M, Gieson A and HÜgol H 1999 Theoretical modeling and experimental investigations of the diode-pumped thin_diskYb:YAG lase *Quantum Electron.* **29** 8 697-703.
[3] Speiser J 2009 Thin disk laser-energy scaling *Laser Phys.* **19** 274-280.
[4] Zhao G, Hu G, Chen G, Gu B, Wang M and Dong J 2018 Numerical analysis of a multi _ pass pumping Yb:YAGthinck _ disk laser with minimal heat generation *Appl. Opt.* **57** 18 5141-5149.
[5] Krupke WF 2000 Herbiumsolid-state laser-the first Decade *IEE J.Selec.Top.Quantum Electron.* **6** 6 1287-1296.
[6] Mende J, Spindler G and Giesen A 2009 Concept of neutral gain modules for power scaling of thin-disk laser *APPl. Phys. B* **97** 307-315.
[7] Chen F, Yu Y, Yan RP, Li XD, Li DJ, Yang GL, Xie JJ and Guo J 2013 Expermetal investigation of diode -pumped powerful continuous -wave dual. Wavelength Nd:YAG laser at 946 nm and 938.6 nm *Laser Phys*. **23** 1-5.
[8] Kasamatsu T, Sekia H and Kuwano Y 1999 Temperature dependence and optimization of 970nm diode_-pumped Yb_YAG and Yb:LUAG Lasers *Appl. Opt.* **38** 24 5153
[9] Pavel N, Lupel V, Saikaa J, Taira T and Kan H 2006 Neodymium concentration depend of 0.946, 1.06, and 1.34 um laser emission and heating effects under 809-and 885 nm diode laser pumping of Nd: YAG *Appl. Phys. B* **82** 599-605.
[10] Toue J, Kofler H and Wintner E 2010 Millijoule Q-switiched Nd: YAG laser operating at 946nm *Laser Phys. Lett*. **7** 4 280-285.
[11] Yi J, Tu B, An X, Ruan Y, Wn J, Su H, Shang J, Yu Y, Liao Y, Cao H, Cui L, Gao Q and Zhang K., Kilowatt Q 2018 Level direct-liquid-cooledNd: YAGmulti-modual QCW *Laser Opt. Expr.* **26** 11 13915-13926.

[12] Shayeganrad G, Cante S, Mosquera JP, Bailey WOS and Mackenzie JI 2020 Highly efficient 110-w closed -cycle cryogenically cooled Nd:YAG laser operating at 946 nm *Optics Lett*. **45** 19 1-4.
[13] Xia J, Yang Z, Chen H, Du Z and Lu Y 2020 Tangentially and radially polarized Nd:YAG hollow laser with two pairs of axicons *Infrared Phys. Tecnol*. **107** 103301-103304.
[14] Zhao, W., Zhu, G., Chen, Y., Gu, B., Wang, M., & Dong, J. 2018 Numerical analysis of a multi-pass pumping Yb: YAG thick-disk laser with minimal heat generation. Applied optics, **57**(18) 5141-5149.

The effect of the Doping with Cobalt Transition Metal on the Dielectric and Structural Properties of $Fe_{0.5}Co_xMg_{0.95-x}O$ Nanoparticles Synthesized by Sol-Gel Assisted Auto-Combustion

The effect of the Doping with Cobalt Transition Metal on the Dielectric and Structural Properties of $Fe_{0.5}Co_xMg_{0.95-x}O$ Nanoparticles Synthesized by Sol-Gel Assisted Auto-Combustion

Tagreed M. Al-Saadi[1], Omar A. Ahmed[2], Imad H. Khaleel[3], T.A.AL- Dhahir [4]

[1,3] Collage of Education for Pure Science -Ibn Al-Haitham/University of Baghdad, Baghdad, Iraq.
[2]The General Directorate for Education in Diyala, Diyala, Iraq.
[4]Madenat Alelem University College.

E-mail: taghreed.m.m@ihcoedu.uobaghdad.edu.iq

Abstract. The compound $Fe_{0.5}Co_xMg_{0.95-x}O$ where (x= 0.025, 0.05, 0.075, 0.1) was prepared via the sol-gel technique. The crystalline nature of magnesium oxide was studied by X-ray powder diffraction (XRD) analysis, and the size of the sample crystals, ranging between (16.91-19.62nm), increased, while the lattice constant within the band (0.5337-0.4738 nm) decreased with increasing the cobalt concentration. The morphology of the specimens was studied by scanning electron microscopy (SEM) which shows images forming spherical granules in addition to the presence of interconnected chips. The presence of the elements involved in the superposition was confirmed by energy- dispersive X-ray (EDX) analysis. The results showed that the dielectric constant decreases with increasing the cobalt concentration, while the dielectric loss factor and AC conductivity increase.

Keywords: Dielectric properties, MgO, Sol-Gel, Nanoparticles, SEM, EDX

1. Introduction

Metal oxides such as magnesium oxide have attracted great interest due to their ease of preparation with different crystal shapes and sizes and being unstable in harsh processes but are safe for humans and animals [1]. The magnesium oxide (MgO) is an alkaline earth metal oxide that has a large band gap and structure of rock-salt of 4-5 volts. It has many applications for its ionic nature, surface quality, and high reactivity and these results in high efficiency in various reactions [2, 3]. There are many fields that use magnesium oxides, including sterilization, superconductor products, display panels, heat-resistant glass, fuel oil additives, toxic waste remediation, and insulation applications due to its low heat capacity and high melting point [4-7]. The minerals have the ability to form multiple oxides with various properties and ease of modification. These properties are through the doping process for use in multiple fields. Various crystal defects in the magnesium oxide structure give the deformation process a significant change in structural and electrical properties [6].This

research aims to study the effect of doping the nanostructured MgO compound with the transition metal cobalt ion on the structural and dielectric properties.

2. Experimental details

The sol-gel method of spontaneous combustion was used in preparing the compound ($Fe_{0.5}Co_xMg_{0.95-x}O$), and the four samples (X= 0.025, 0.05, 0.075, 0.1) were prepared, and in each preparation, the molar ratio of the fuel used was (citric acid), with the proportion of mineral salts at 1:1. The analytical grade metal nitrates, i.e., Mg $(NO_3)_2 \cdot 6H_2O$, $Fe(NO_3)_3 \cdot 9H_2O$ and $Co(NO_3)_2 \cdot 6H_2O$, were taken as the starting materials. The soul-gel spontaneous combustion method was used to prepare the compound. Metal nitrate and citric acid are dissolved separately in distilled water according to the molar ratios calculated for each sample. The nitrate solution is mixed with the acid solution in a suitable great heat-resistant flask, and the components are mixed by a magnetic mixer, and the acid function (pH) is adjusted until about (7) is reached, by adding ammonia to the solution in the form of drops. The ingredients were mixed for (30 minutes) to ensure the homogeneity of the solution and a good distribution of the ingredients at room temperature. The temperature is raised and fixed at (80 ^oC) for all proportions, and after a short period the gases start to rise and leave the reaction and the stirring will be continuous until reaching the gel form. After a period of half an hour, the jelly starts to burn to form a dry gel, which is grounded with an agate mortar. The resulting powder for each sample was placed in a container in the oven. For the purpose of calcination at a temperature of (600 ^oC) for two hours at an rising rate (10 deg/min), in order to get rid of the reaction residues that may still be stuck, such as water residues, and carbon dioxide residues arising from Combustion, and obtaining the required phase.

3. Results and discussion

3.1. XRD Phase Analysis

The results of the examination with X-ray diffraction technology of the compound $Fe_{0.5}Co_xMg_{0.95-x}O$, which are shown in Fig.1, showed that the prepared compound was of the cubic type for all of the samples (X= 0.025, 0.05, 0.075, 0.1) and the appearance of peaks of planes, (111), (200), (220),(311) and (222). When comparing the locations and intensities of the peaks with the JCPDS card for MgO numbered (45-0946) [8], we found that they are somewhat similar. Some additional peaks appeared in the XRD spectra for the secondary phases corresponding to Fe_2O_3 (JCPDS card No. 00-040-1139). Where we note that the intensity of the magnesium oxide peaks increases with increasing the concentration of cobalt. This result confirms that the crystallization ratio has increased due to the decrease in the width of the curve of the middle of the great peak (FWHM), as the increase in the height of the peaks is evidence of increasing crystallization and reducing crystalline defects by giving the material atoms potential energy to rearrange themselves in the lattice [9]. The lattice constant (a) with respect to the cubic structure is calculated according to the relationship (1) [10], where (hkl) is the Miller indices and d is the vertical distance between the planes of crystal.

$$\frac{1}{d^2} = \frac{h^2+k^2+l^2}{a^2} \quad \ldots\ldots (1)$$

The average crystal size (D) of samples was calculated using the (Formula Williamson-Hall) method according to the relationship [11] (2).

$$\beta \cos\theta = \frac{k\lambda}{D} + 4\varepsilon \sin\theta \quad \ldots.. (2)$$

Where K is the constant (0.94), β Full width at Half Maximum (FWHM) measured in radial units, θ Bragg angle , ε the strain, λ the wavelength of the X-rays incident upon the target = 1.5406 Å.

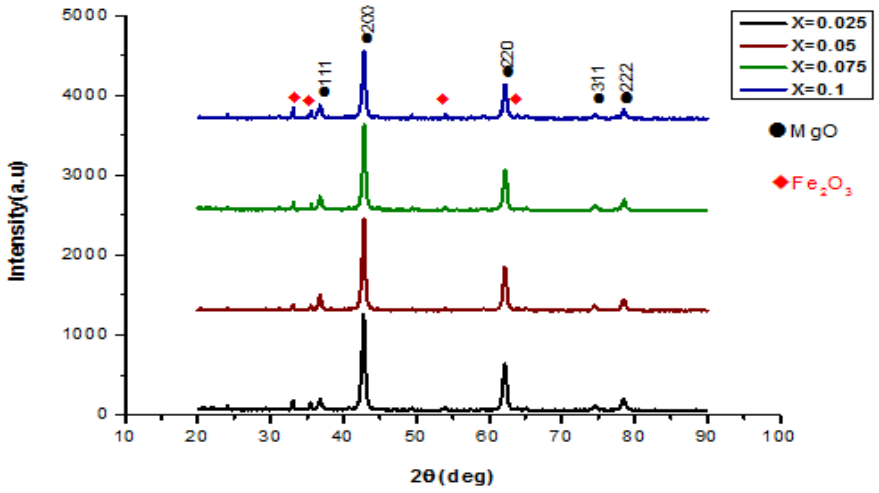

Fig.1. XRD patterns of $Fe_{0.5}Co_xMg_{0.95-x}O$.

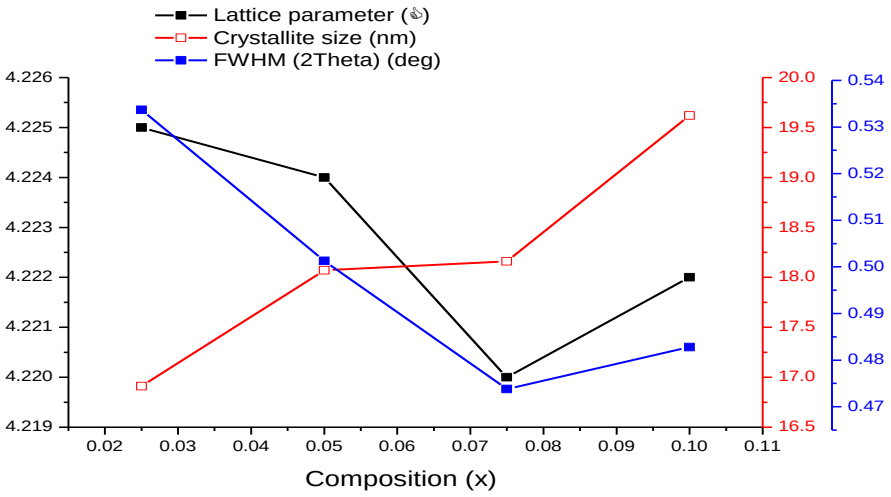

Fig.2. Lattice parameter of a $Fe_{0.5}Co_xMg_{0.95-x}O$, Crystallite size and FWHM with composition (x= 0.025, 0.05, 0.075, and 0.1).

The X-ray diffraction in Fig.2 showed a decrease in the lattice constant with an increase in the concentration of cobalt ions. This is a result of the gradual replacement of magnesium ions with a larger ionic radius (0.89Å) with cobalt ions with a small ion radius (0.58), which led to the deformation of the lattice and expansion [12-14]. As shown in Table.1, the full width value at half the maximum (FWHM) of the peaks decreased and the crystallite size of the samples increased with increasing x-values. It is noted that showed the full width value at half maximum (FWHM) of the peak (200) it decreased from 0.53370Å to 0.48280Å and the crystallite size increased from 16.91nm to 19.61nm with increasing cobalt concentration, which means that the surfactant increased the crystallite size [14].

Table 1: Lattice parameter, crystallite size and FWHM for peak (200).

Composition (x)	FWHM (200)	Lattice parameter a[Å]	Crystallite size [nm]
0.025	0.5337	4.225	16.91
0.05	0.5013	4.224	18.07
0.075	0.4738	4.220	18.16
0.1	0.4828	4.222	19.62

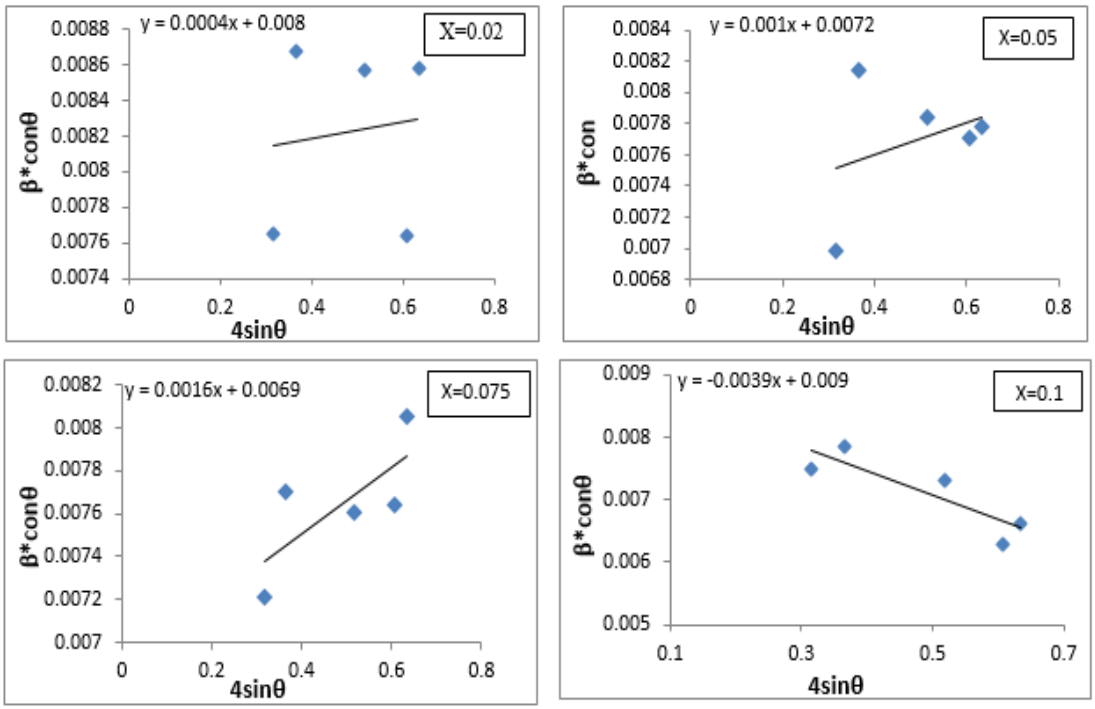

Fig.3. Hall–Williamson plots for samples $Fe_{0.5}Co_xMg_{0.95-x}O$ for (X= 0.025, 0.05, 0.075, 0.1).

3.2. SEM and EDX analysis

The SEM images in Fig. 4 show the formation of semi-spherical granules in addition to the presence of interconnected chips with no clear boundaries between them due to accumulation of nanoparticles and an increase in the randomness and porosity with increasing cobalt concentration. It was found that the average grain size of the compound ranged between (36.9-59.8 nm) with increasing cobalt concentration. Fig. 5 show the histogram of the particle size of $Fe_{0.5}Co_xMg_{0.95-x}O$ samples.

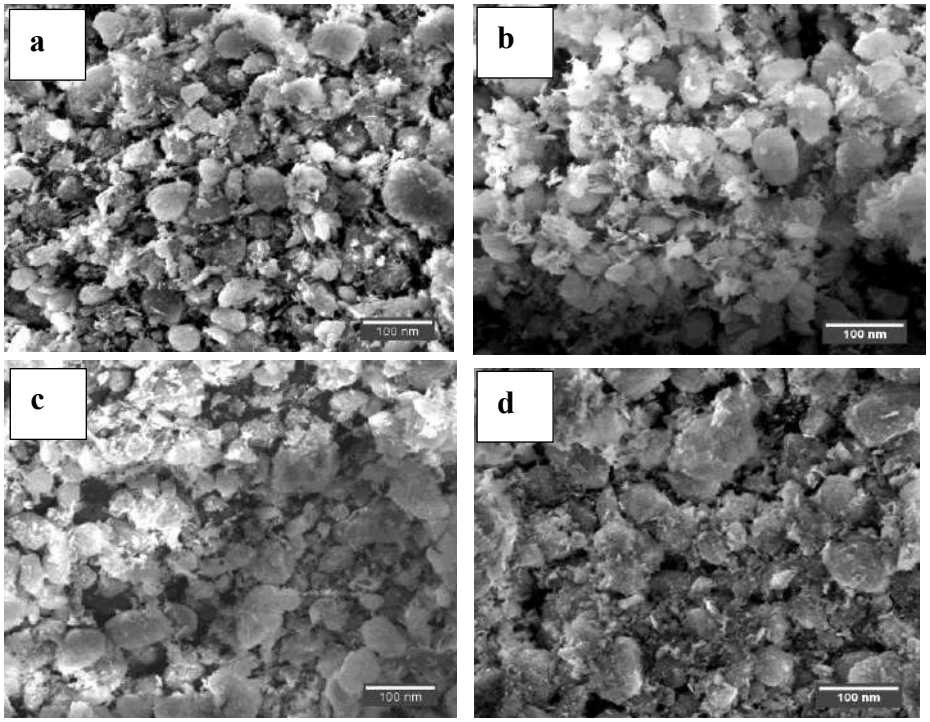

Fig.4.(a–d) SEM images of $F_{0.5}Co_xMg_{0.95}O$.

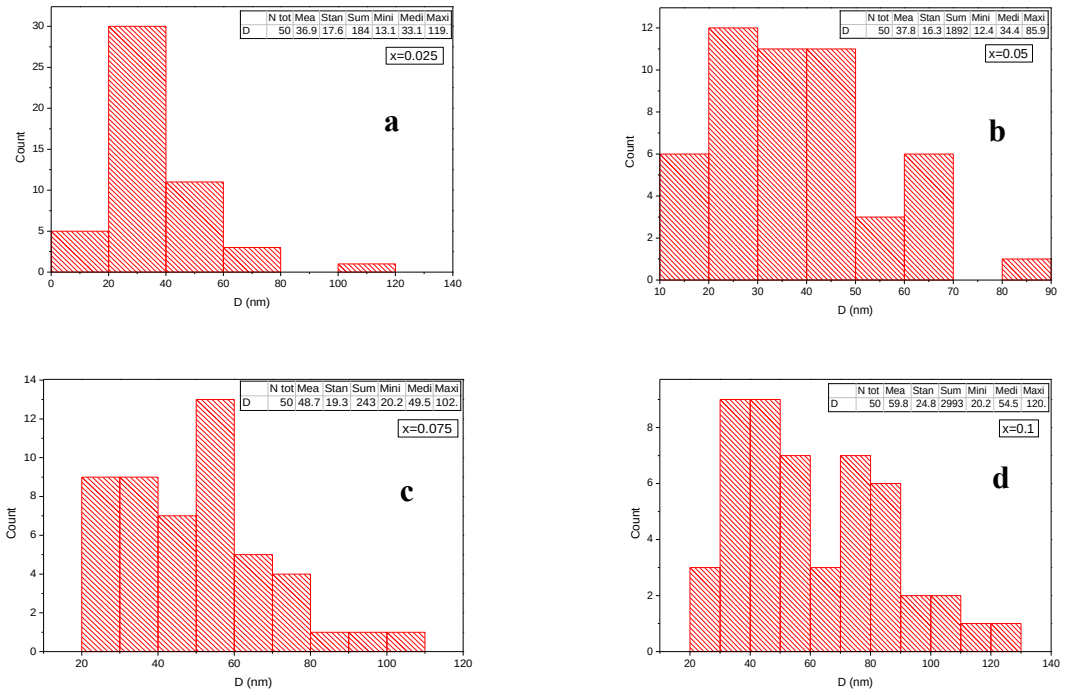

Fig.5. Histogram of the particle size of $Fe_{0.5}Co_xMg_{0.95}O$ samples.

The initial composition of $Fe_{0.5}Co_xMg_{0.95-x}O$ was observed in samples via energy dispersive spectroscopy. The diagrammatic consequence for EDX is appeared in Figure (6). It can be seen that

the predominant peaks concern magnesium, oxygen, iron, and cobalt, which appear the superimposed nanoparticles of these elements.

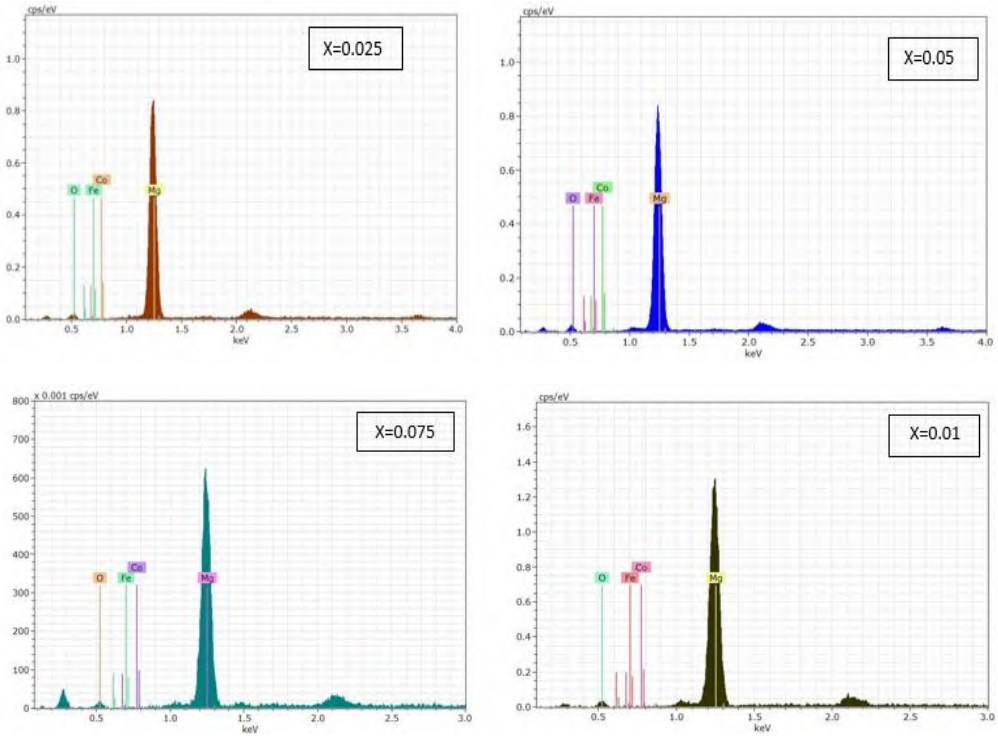

Fig. 6. EDX spectra of $Fe_{0.5}Co_xMg_{0.95}O$ (X= 0.025, 0.05, 0.075, 0.1).

3.3. Dielectric Properties

The dielectric properties of the composite samples $Fe_{0.5}Co_xMg_{0.95-x}O$ were studied as a function of the alternating electric field frequency within the range ($50H_Z$-$1MH_Z$) and at room temperature, which included dielectric constant, dielectric loss coefficient and alternating conduction.

Fig.7 shows the change of the dielectric constant with the electric field frequency applied for all ratios of cobalt addition to the compound $Fe_{0.5}Co_xMg_{0.95-x}O$. It can notice that the decrease of the dielectric constant with the increase of the frequency. It is because at low frequencies the dipoles in the dielectric have sufficient time to orient themselves completely in parallel to the applied electric field. When the frequency of the electric field increases, the dipoles lag behind in rotation and regularity with the electric field and this leads to a decrease in polarization and thus lower values of the dielectric constant [15]. That means the dielectric constant decreases with increasing the concentration of cobalt ions in the samples. Theoretically, the dielectric constant of the compound should be increased because the ion polarization of cobalt ions is greater than that of the magnesium ions, thus increasing the overall ionic polarization of the composite $Fe_{0.5}Co_xMg_{0.95-x}O$ with values of x [16]. There are two main reasons taken into consideration in the decrease of the dielectric constant. Replacement of cobalt ions with magnesium ions, which led to the lattice deformation and expansion, thus increasing the porosity [12], which in turn reduces the relative density. On the other hand, the cobalt content is very low and thus does not cause a rise in the constant of dielectric [17].

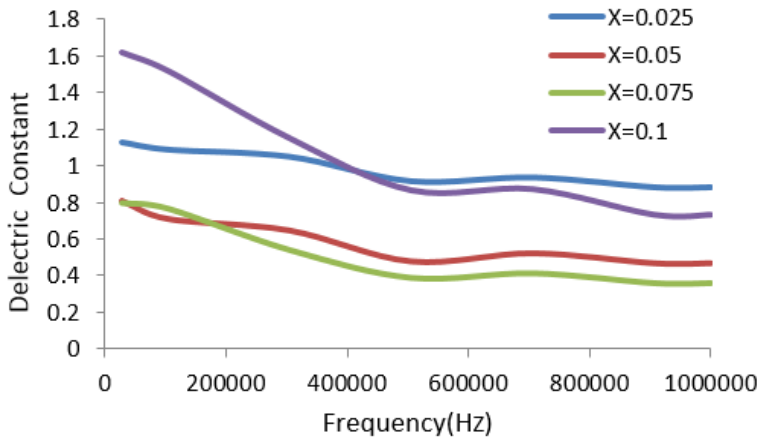

Fig.7.Variation of dielectric constant with the frequency of $Fe_{0.5}Co_xMg_{0.95}O$.

Fig.8 shows that the dielectric loss factor decreases with the frequency and there is a stable relationship between the emergence of dielectric and the conduction mechanism. There are several factors that can affect the dielectric loss factor such as the synthesis method, calcination temperature and formation. The variation of dielectric loss in the low frequency range can be explained by the Maxwell - Wagner model [15,18]. The greater amount of the dielectric loss at lower frequency is due to the jump among Mg^{+2}, Co^{+2}, and Fe^{+3} and the applied field monitors by the electrons. The electrons with increasing the frequency, are not able to follow the higher applied frequency that reduces the jump among Mg^{+2}, Co^{+2}, and Fe^{+3}. Thus, the loss of the applied field is minimal at the larger frequencies [19].

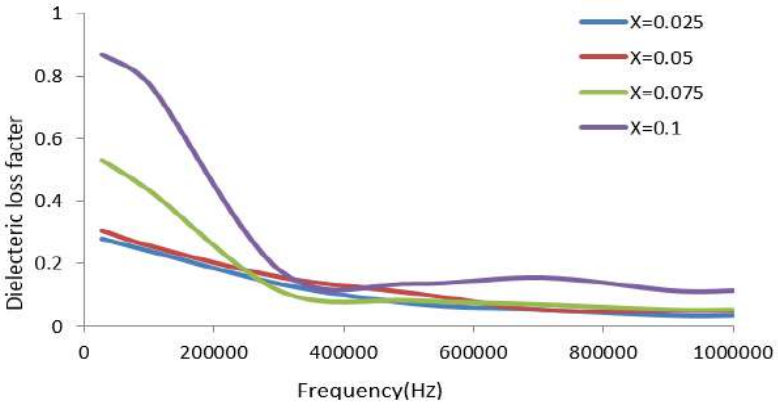

Fig.8.Variation of dielectric loss factor with frequency of $Fe_{0.5}Co_xMg_{0.95}O$.

Fig.9 shows a non-linear behaviour between AC conductivity (σ_{ac}) and frequency which shows that the amount of ac conductivity rises with frequency. Different conductivity operations, for instance tunnelling, jumping and free-range connection etc. participate in increasing the value of the alternating conductivity. It has been found that the adding of Co ions increases the conductivity of superposition [20].

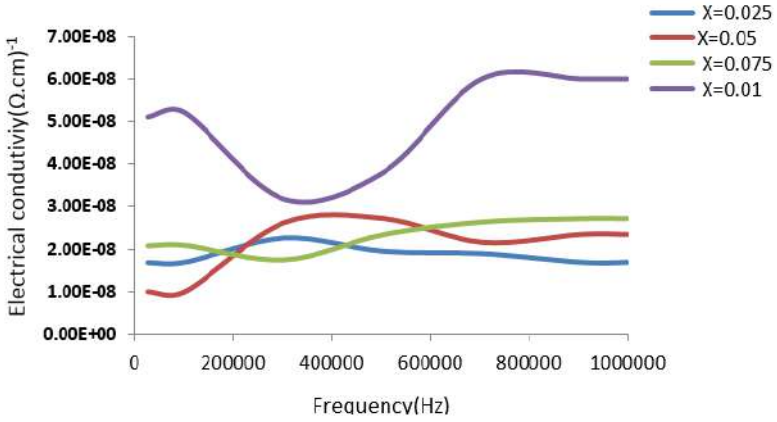

Fig.9.Variation of alternating connectivity with frequency of $Fe_{0.5}Co_xMg_{0.95}O$.

4. Conclusions

The structural and dielectric properties of $Fe_{0.5}Co_xMg_{0.95}O$ were studied. Where it was found that the lattice parameter decreases due to the small ionic diameter of the cobalt ions compared to the ionic radius. For iron ions and the ionic radius of magnesium ions, the crystal size increases with increasing cobalt ion concentration. The EDX results confirm the presence of elementary elements to form the compound. SEM images showed the formation of semi-spherical granules and an increase in randomness and porosity associated with an increase in the concentration of cobalt in the compound. It was noticed that the dielectric constant decreases with the increase in the ratio of cobalt ions, although the ionic polarization of cobalt ions is greater compared to the magnesium ions. The dielectric loss factor and the alternating conductivity increases with the increase in the cobalt ions concentration.

References

[1] Sundrarajan M., Suresh J., & Gandhi R. R. 2012 *J. nanomater. biostruct.* **7**(3) 983
[2] Dercz G., Prusik K., Pajak L., Pilaszek R., Malinowski J. J. , & Pudl W. 2009 *J.Mat. Sci.* **27**(1)201
[3] Sharma A., Arya S., Singh B., Prerna, Tomar A., Singh S., Sharma R. 2020 *J. Integrated Ferroelectrics* **205**(1) 14
[4] Park J.Y., Lee Y.J., Jun K.W., Baeg J.O., & Yim DJ. 2006 *J. Indus. Eng. Chem.***12**(6) 882
[5] Rao K.V., Sunandana C.S.2008 *J. Mat. Sci.* **43**(1) 146
[6] Tamilselvi P., Yelilarasi A., Hema M., & Anbarasan R. 2013 *Nano Bull.* **2**(1) 1
[7] Basha M.H., Gopal N.O., Rao J.L., Nagabhushana H., Nagabhushana B.M., & Chakradhar R.P.S. 2015 *AIP Conference Proceedings* **1665**
[8] Athar T., Hakeem A., & Ahmed W.2012 *Adv.Sci. Lett.* **5** 27
[9] Cai Y., Wu D., Zhu X., Wang W., Tan F., Chen J., Qiao X.,Qiu X. 2017 *J. Ceram. Int.* **43**(1)1066
[10] Al-Saadi T. M., Alsaady L. J. K. 2015 *Ibn Al-Haitham J. for Pure & Appl. Sci.* **28** (1) 301
[11] Abdil Majeed A. R., Al- Robaie A. E. A. 2015 *Ibn Al-Haitham J. for Pure & Appl. Sci.* **28** (3) 399
[12] Suwanboon S., Amornpitoksuk P., & Sukolrat A. 2011 *J. Ceram. Int.* **37**(4)1359
[13] Azzaza S., Hilo M.H., Narayanan S., Vijaya J.J., Mamouni N., Benyoussef A., & Maensiri S. 2014 *J. Mat. Chem. Phys*. **143**(3)1500
[14] Gan G., Zhang D., Li J., Wang G., Huang X., Rao Y., Yanga Y, Wanga X, Zhanga H, Chenb R. T., 2020 *J. Ceram. Int.* **46**(6)8398

[15] Thongbai P., Yamwong T., & Maensiri S. 2013 *J. Microelect. Eng.***108**(4)177
[16] Chen Y.C., & Du Y.X. 2020 *J. Australian Ceramic Society* https://doi.org/10.1007/s41779-020-00494-w
[17] Zhang Y., Zhao D., Gong H., Zhu B., & Zhang X. 2011 *J. Nanomater.* **2011**(2). Article ID 246847,5pagesdoi:10.1155/2011/246847
[18] Choudhary P., Varshney D., 2018 *J. Magn. Magn. Mater.* **454**(14)274
[19] Bhargava R., Khan S., Ahmad N., & Nizam M.M. 2019 *J. IOP Conference Series: Materials Science and Engineering* **577**(8)8
[20] Bhargava R., Khan S., 2019 *Phys. Lett., J. Atomic and Solid State Phys.* **383**(14)1671

Investigation of Single-Phase Flow Characteristics in an Inline Pin-Fins Complex Geometry

Investigation of Single-Phase Flow Characteristics in an Inline Pin-Fins Complex Geometry

R. Shakir[1]

[1]Petroleum and gas engineering department, college of engineering, university of Thi-Qar, Iraq.

E-mail: shraed904@gmail.com

Abstract. In this guess investigation of concerns R113 heat transfer of pressure drop flow in single-phase flow in inline on the square shape of micro- channel of pin-fins own a (5x5 mm2) cross- area segment section via of (5 mm) heightly. Therefore, the inline square micro- channel of pin-fins complex geometry additionally owning (25) numbers of the pin-fins, total pin-fins channel dimension (50 mm x 50 mm).Subsequently.The liquid has (25 °C) inlet temperature for the same inlet temperature six mass flow rates were applied, ranging from (0.0025 - 0.01 kg/sec), and heat apply ranged from (40 -200 Watts).Guess single-phase heat transfer coefficients, guess liquid temperatures and guess wall temperatures were reported in this investigation

Keywords: pin-fins, heat transfer, single-phase flow, prediction setup.

1. Introduction

Cooling of electronic and electrical devices is reuired to ensure their accuracy and optimum working conditions. The pin fins complex geometry provides a higher heat transfer area per unit volume and low thermal laziness than straight channel fins. The vitality created in the downstream of the fins supplies for mixing between liquids and increases heat transfer. The thermal properties and hydraulic properties of the pin-fins heat sinks are dependent on several important parameters such as the porosity, pin fin shape, an arrangement of fins namely: in-line pin fins or staggered pin fins, short fins and full-length fins, fin length, and the guidance of the fin with attaching to the liquid flow direction [1–8]. Therefore, the pin-fins complex genome is still a topic of active research by many investigators are working under this area investigation. At last, the aim of this study is to find out the performance of the best type of mini-scale complex geometry.

2. Theory and Formula

The guess heat transfer properties for flow is define based on the liquid and wall temperatures conforming to the system pressure as indicate to liquid temperature. The analysis models of guess data are classified in the according steps.

$$F_{sp} = \left((q_{th}/A_{th})/\left(T_w - T_f\right)\right) \quad (1)$$

In where (qth) is that the position of heat flux, (Fsp) symbolize to that of single-phase coefficient for heat-transfer guess; (Tf) symbolize to liquid temperature ;(Tw) the local wall temperature and amend

the bottom of a micro pin fins square heat sink heat sink, amend (Ath=W x L). The projection on the test segment contains the plate sort heaters. While insulated had used for rear face on the test segment; within bottom of test section there's an electrical heater device and top of test section there is an R113 working liquid. Figure 1. It is shown the design can simply create a uniform heat flux distribution at the solid–liquid interface. Some preparation wanted the heat conductivity via the wall to be introduced into the analysis. The variance in temperature crosses. The flow has not been revealed to also be needful. The controlling conduction wall influence has so imagined being two-dimensional array; first-dimension perpendicular to the R113 liquid working flow and second the parallel dimension there to R113 liquid working,so heat conduction equation is [9].

$$\delta^2 \mathrm{T}/\delta y^2 + \delta^2 \mathrm{T}/\delta z^2 = 0 \qquad (2)$$

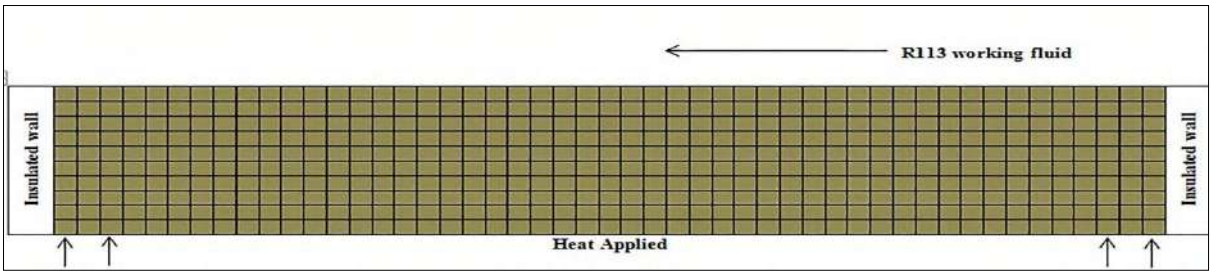

Figure 1. Aluminum Test Piece Wall Conduction.

Which (y-axis) represents in present axis.The temperature in is perpendicular to the flow and (T) in an aluminium wall".Conduction of heat equation (2) had got via the segmentation of the cells square area.The cells square have (one mm); consequently, (one mm) cells were utilized from the figure one. For each cell, an energy equilibrium gained from Ref.[9]

$$\mathrm{T_{i,j}} = \delta \mathrm{y}^2\left(\mathrm{T_{i+1,j}} + \mathrm{T_{i-1,j}}\right) + \delta z^2\left(\mathrm{T_{i,j+1}} + \mathrm{T_{i,j\_1}}\right)/2\ (\delta \mathrm{y}^2 + \delta \mathrm{z}^2) \qquad (3)$$

"Where (δz) and (δy) have the dimensions of the cell.Equation (3) shows variance of needed on perform.Therefore, The conditions of the borders "iteratively until the temperature in each cell was the same as the cell, it was solved.Former guessed to a guess of (0.001) error ".Consequently, the positioning wall temperature was gained via averaging of data from the relevant thermocouples, to gain (Tth) " Where it was then corrected from the plate surface for depth,(Lth); " perfect the equation of one-dimensional into heat conduction

$$T_w = T_{th} - (q_{th} L_{th}/K_A) \qquad (4)$$

"In which (KA) aluminium thermal conductivity; " The heat transfer coefficient of the position was gained via detaching the flow filed into cells while a typical two-dimensional unit cells at the location of a thermo-couple situated inside the test piece. The fluid temperature for the pin-fins test piece for a fluid with a specific heat capacity of (Cp) was got by equation below":-

$$T_f = T_{in} + \left(q_{th} WZ/M_f C_p\right) \qquad (5)$$

Where (Mf) is the rate of mass flow of R113 working liquid was equipped," The width of the test piece is the (W). The guess single -phase of heat transfer coefficient can be evaluated via useing following equation":

$$q_{th} A_{cell} = h_{esp}(T_w - T_l)\left[(A_{cell} - A_c) + \eta_{fin} A_{fin}\right] \qquad (6)$$

Equation (6) is gained a simple energy balance is applied to a unit cell which contains a single micro pin-fins. In addition, the surrounding base surface as presented. The left of a side equation (6) .The heat input to the unit cell is represented, and the heat removal from the unit cell by the unit cell is

represented on the right-hand side of R113 single-phase testes. In equation (6). (A_{cell}) Indicates the base region of the unit cell.

$$A_{cell} = S_l S_t \quad (7)$$

In which
S_l= The distance from the central cell to another centre cell in a length direction.
S_t= The distance from the central cell to another centre cell in a width direction.
A_{fin} = The moistened surface region of the single pin-fins.

$$A_{fin} = P_{fin} H_{fin} \quad (8)$$

And η_{fin} represents the fin efficiency,

$$\eta_{fin} = tanh(m_{fin} H_{fin}) / m_{fin} H_{fin} \quad (9)$$

In where mfin is the fin parameter,

$$m_{fin} = \sqrt{h_{esp} P_{fin} / K_A A_c} \quad (10)$$

Where A_c is the cross-sectional area of a single micro-pin-fins,

$$A_c = W_{fin} L_{fin} \quad (11)$$

And P_{fin} is the cross-section perimeter of a single micro-pin-fins,

$$P_{fin} = 2(W_{fin} + L_{fin}) \quad (12)$$

In where [W_{fin}] is pin-fin width in (mm);[L_{fin}] is the pin-fins length in (mm) and [H_{fin}] is pin-fins height in (mm).
The guess wall temperature T_{wp} distribution along the inline pin-fins channel is found.

$$T_{wp} = T_{in} + q_{th} WZ / M_l C_p + A_{cell} q_{th} / \left[(A_{cell} - A_c) + \eta_{fin} A_{fin} \right] h_{esp} \quad (13)$$

Where prandtls number based on the hydraulic diameter of the channel as follows:

$$P_r = \frac{C_p \, \mu_f}{k_f} \quad (14)$$

The Reynolds number can be found by-

$$R_e = \rho_f V D_h / \mu_f \quad (15)$$

In where the hydraulic diameter of the channel in the presence of heat transfer analysis, seen by

$$D_h = \frac{4 \, . A_c}{P_{fin}} \quad (16)$$

Since only three sides of the in line micro pin-fins were heated in the investigation work, the approach utilized in Lee et al [10].Is adopted here to guess the Nusselt number in single-phase flow based on results in the literatures that apply it all four sides of the in line micro pin-fins being heated can find by Ref.[9]

$$NU_{x,3} = NU_{x,4} \frac{NU_{fd,3}}{NU_{fd,4}} \quad (17)$$

In where $N_{ux,4}$, $N_{ufd,3}$, and $N_{ufd,4}$, were found to be gained respectively," For the geometry and boundary conditions considered.Friction factor can be calculated via Ref.[11].

$$f_{laminar} R_e = 24(1 - 1.3553 + 1.946\beta^2 - 1.7012\beta^3 + 0.95641\beta^4 - 0.2537\beta^5) \quad (18)$$

The pressure drop can be got from according to the method of Liu and Garimella. In which (β) is the aspect ratio of the square channel, and laminar is the Fanning friction factor Ref.[12].

$$\Delta P = 2\, f_{laminar} R_e\, \rho_l V^2 \frac{L}{D_h} \qquad (19)$$

3. Prediction Setup

The rig consists of three prime elements, the flow loop system, and the test section of aluminum and the test piece of aluminum inline pin-fins complex geometry.

3.1. FLOW LOOP

Suppose the rig has a projects for a new technique for Figure 2, the flow loop system is seen illustrated in below. Before running the single-phase test concatenations, the R113 working liquid was degassed for almost two hours under strong heat tests to force any dissolved gases to get away from the system to the atmosphere through strong heat test concatenations.The vent valve on top of the pr-eheater was intermittently opened wthin this interval to permit dissolved gas to run away to the atmosphere.As well as , the test pressure was set to close to atmospheric pressure.Fluid R113 had dragged by an accumulator unit via pump after degassing R113 working liquid, so no gas or air bubble appeared to come out of the liquid within the test piece before a single-phase test concatenations.Therefore, valves within the by-pass and major streaks permit the wanted adjusting the rate of mass flow.Thus, a coarse filter was mainly employed to block large debris.Within testing the finer filter was employed.Thus, guess tests have been performed via adjusting the optimal R113 mass rate of flow and inlet temperature (M_f and T_{in}). Within testing, a coarse filter had been employed to block large debris.The mass flow had been balanced via the flow meter, thus, the by-pass valve, and balanced via the dominant valve prior to the complex geometry of the inline pin-fins complex geometry .With consideration to the mass flow of the test, the controller varied the necessary heat applied to the R113 liquid flow that passed the pre-heater to produce the suitable inlet temperature to the complex geometry of inline pin-fins in the aluminum house. A pre-heater had been joined of the system controller unit. A test section heater had been simultaneously set to the needful heat applied to the test piece of aluminum.The R113 working the flow loop was circulated with liquid to system until the needful Steady-state conditions were gained.This process took about three hours for steady-state conditions approximatly. It was needful to force the temperature of the outlet heater and the temperature of the aluminum housing to be steady as well. These cases were roughly 40-85 minutes in length.The method iterated during the single-phase tests to maintain the system pressure similar to the ambient pressure, thereafter determined readings had been completed prior then heat applied had re-set successive needed value.

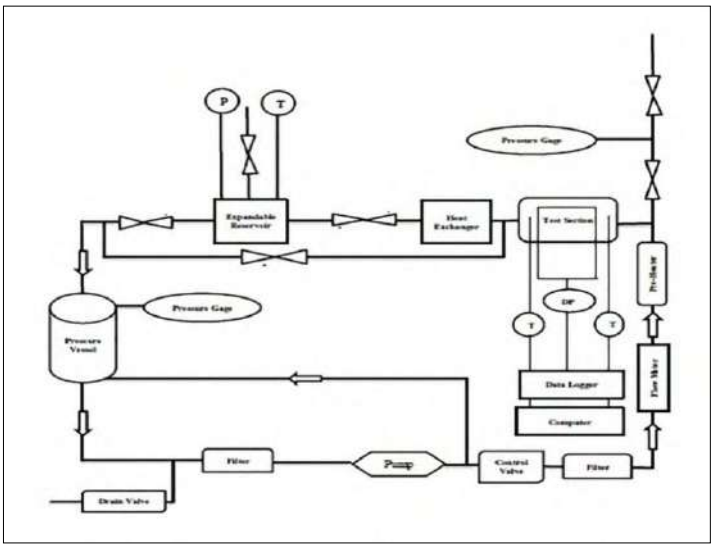

Figure 2. The Flow Loop[9].

3.2. ALUMINUM TEST SECTION

Figures (3 and 4) of the aluminum test segment utilized in this inquiry are presented in the procedures.The aluminum test section contains three sections, are called, an aluminum housing, The top-cover of the aluminum,Therefore, an aluminum of inline pin-fins complex geometry.If the aluminum top housing, the aluminum bottom housing, thus a base are all created of aluminum, aluminum housing is utilized.The top housing contains the complicated geometry of the aluminum of inline pin-fins complex geometry. It is the inlet plenum and outlet plenum, a pressure port also temperature port of sit a related sensors.Two pressure ports exist, one at the plenum inlet and the other at the plenum outlet.

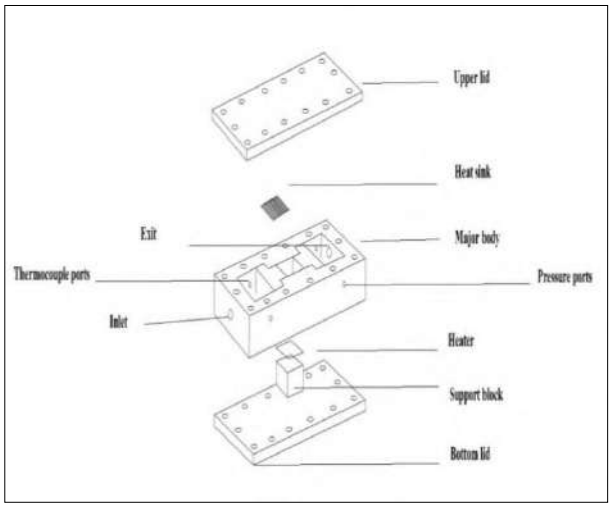

Figure 3. TesHousing [9]

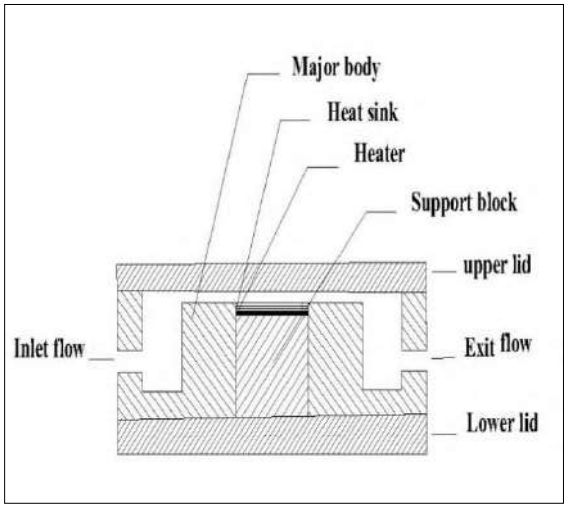

Figure 4. Test Section[9]

3.3. ALUMINUM TEST PIECE

Figure 5 presents the aluminum test piece of the aluminum of inline pin-fins complex geometry, all details have been gained from this figure; there are consequently six thermocouple ports, each one into plenum of inlet and a plenum of outlet and four below the aluminum of inline pin-fins complex

geometry surface.Thermocouples are utilized to measure the temperature of inlet location, the temperature of outlet location, and wall temperatures .The wall temperature of the thermocouples had a probe diameter of one mm and was force-fitted into two holes from the inlet location and two holes from the outlet location, all drilled eight mm below the inline pin-fins complex geometry surface and drilled twenty mm at the inlet and outlet ends of the test piece.Four sheathed k-type thermocouple produce these holes so that thermocouples had been measured in an extremely the bath of water then had accurate (±0 1.25 ºC) to roughly. On the surface of the top housing, a groove is cut out to the line. The aluminum inline pin-fins complex geometry have a height of ten mm and a footprint fifty mm by fifty mm.

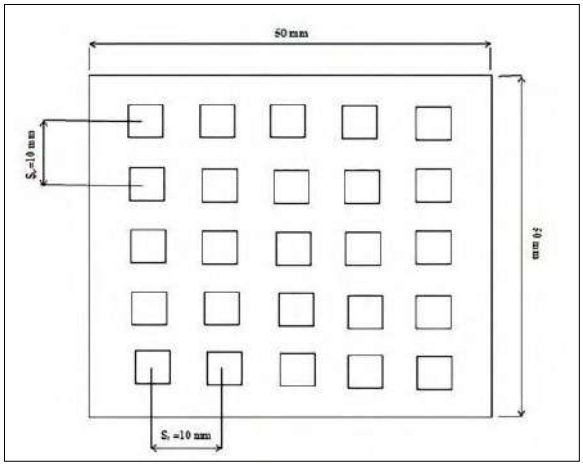

Figure 5. Pin-fins channels aluminum test piece

4. Results and Discussion

In Figure.6.The guess heat-transfer coefficients of single -phase are presented to the mass fluxes range.subsequently, at the inlet and outlet locations of the heat-transfer coefficients pin-fins complex geometry have one region ,It were laminar developing flows that mean the all guess tests are laminar developing flows , laminar developing regions are seen to grow with growing mass flux , with the inlet consequences significantly higher than the outlet consequences.Wall conduction influences are importantly affecting the consequences. The developing method from equation (17) is also included, consequently, power relationships have been gained that between for both inlet and outlet consequences for all guess tests.

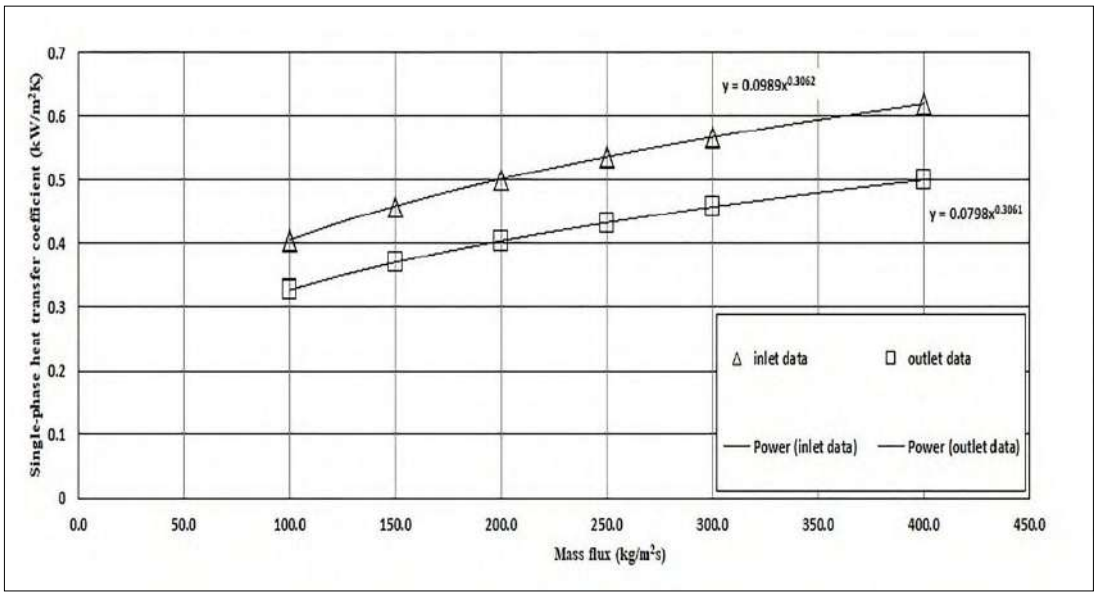

Figure 6. Single-phase heat transfer coefficient versus channel mass flux.

The guessed pressure drop between into inlet of plenum and outlet of plenum poitions to illustrate that the pressure drop are happened because of gain the flow in the pin fins complex geometry also the inlet losses and exit losses. In the pressure-drop consequences had presented in Figure.7, the inlet loss and exit loss positions are gained from the guess values according to the correlation of Liu and Garimella as debated above. It can be shown from Figure.7. Appears pressure drop increase powerly with increasing a channel mass fluxes.Thus , the inlet pressure drop consequences slightly bigger than outlet pressure drop consequences due to get that the pressure drop consequences depend on single-phase heat transfer coefficient and liquid characteristics .consequently, power relationships have been gained between for both inlet and outlet consequences . At last, the guess consequences are shown to be in a best agreement with the other guessing,theoretical and experimental correlations.

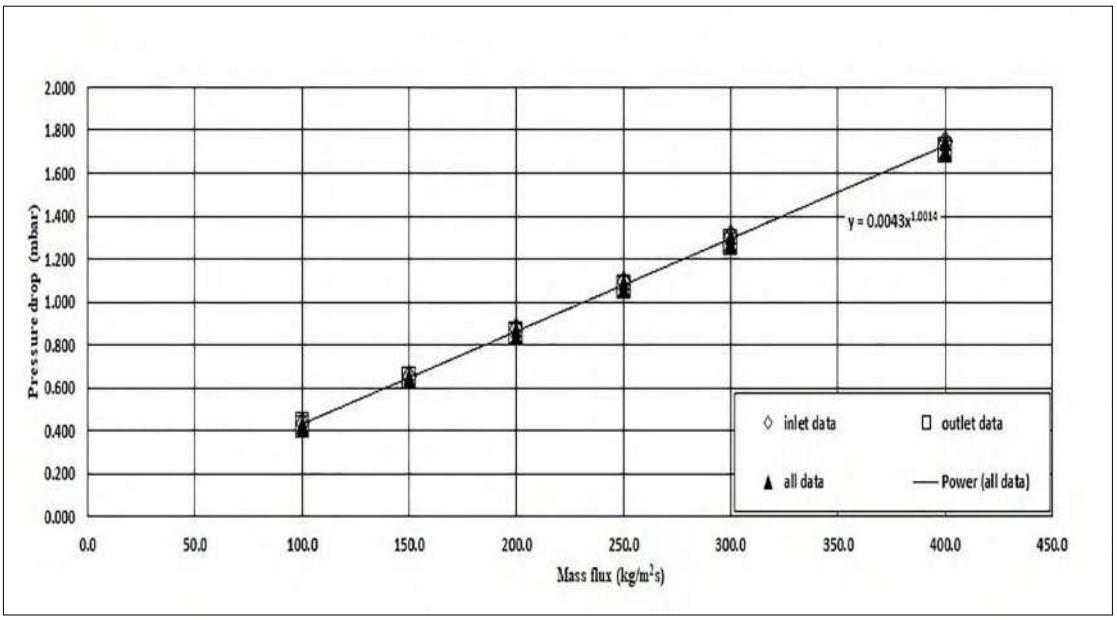

Figure 7. Pressure drop versus channel mass flux.

In Figure 8.The consequences of the correlation processed are compendium.The values heat-transfer coefficients of the single phase found that each channel contained one region, laminar developing flows which the heat-transfer coefficients should be gained by equation below:-

$$N_U = \tau(R_e P_r D_h/L)^{\lambda} \quad (20)$$

The processing set of analyze to uniform heat flux was proposed with, (q_{th}) this permitted the positions of coefficients of inlet and outlet heat transfer to gain from equation (6) to each heat flux and mass flux condition guessed tests. From another hand, we could be computed the heat-transfer coefficients were utilized in a least-squares operation to gain values of (τ and λ) in equation (20). This heat-transfer coefficient had wanted to wall conduction type and equation (4) had utilized to gain the R113 liquid temperature where for these guesses are the heat-transfer guessed temperature. A permitted the heat flux distribution to be got and thus an update to the inlet heat transfer coefficient and outlet heat transfer coefficient. The proceedings were duplicated unto the (τ) and (λ) are rationally steady.The iterative data guess operation opitomized in Figure.8, is gain the guess heat transfer correlation coefficients in Equation (20) ,(τ , as 1.407) and the index (λ , as 0.306). In end these consequences see that there is new correlation between guess single-phase heat transfer coefficients with hydraulic diameter, Reynolds number,Prandtl number and the distance from inlet aluminum pin-fins complex geometery.

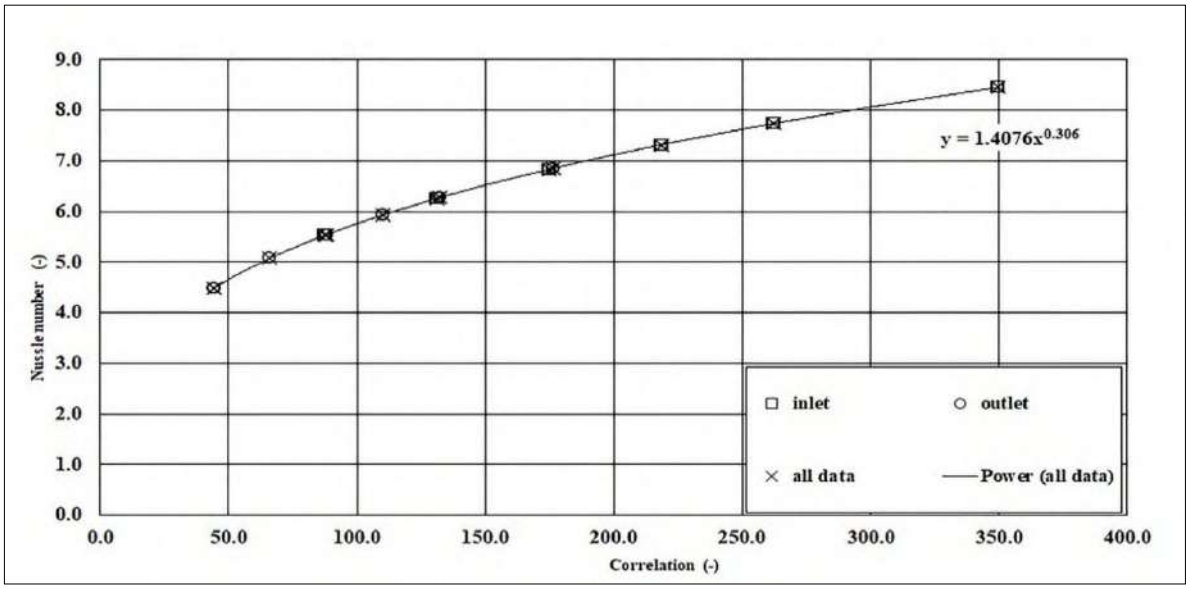

Figure 8. Nussle number versus correlation

5. Conclusions

This is an important study to get the heat transfer coefficient in single tests, so with the article results from effects, other implications were broadly in the direction. It is inspiring to remember that there are no major variations in each other's consequences. The variations of predicted on the flow single-phase of the dielectric fluid R-113 in a complex geometry was periodically studied. Special conceived correlation planning was developed that supplies R-113 fluid to the flow loop while at the same time, providing control of the mass flow rate and heat applied in the test section. As well, Degassing the R-113 fluid was discovered to have a strong effect on both the heat transfer and the pressure drop measured should be created before any tests. The following conclusions can be taken from this study:

The guess tests have one region laminar developing flows. The R113 liquid properties were gained by guess R113 liquid temperature. The maximum R113 liquid temperature during the test series was (32.80 ºC). In the laminar developing region, the inlet data consequences bigger than outlet data

consequences for test series. Because of aluminum test piece walls are deep insulated. Adiabatic conditions were proposed. High liquid temperature is gained with the low mass flow rate during the test series.

6. Ackn**o**wl**e**dg**e**ments
I would like to thank my colleagues in university for their help to complete this paper

Reference

[1] Mei D, Lou X, Qian M, Yao Z, Liang L and Chen Z 2014 Effect of tip clearance on the heat transfer and pressure drop performance in the micro-reactor with micro-pin–fin arrays at low Reynolds number *Int. J. Heat Mass Transf.* **70** 709–18.
[2] Abdoli A, Jimenez G and Dulikravich GS 2017 Thermo-fluid analysis of micro pin-fin array cooling configurations for high heat fluxes with a hot spot. Int J Therm Sci 2015;90:290–7.
[3] Wang Y, Nayebzadeh A, Yu X, Shin J-H and Peles Y 2017 Local heat transfer in a microchannel with a pin fin—experimental issues and methods to mitigate *Int. J. Heat Mass Transf*. **106** 1191–204.
[4] Yu X, Woodcock C, Plawsky J and Peles Y 2016 An investigation of convective heat transfer in microchannel with Piranha Pin Fin *Int. J. Heat Mass Transf.* **103** 1125–32.
[5] Duangthongsuk W and Wongwises S 2015 An experimental study on the thermal and hydraulic performances of nanofluids flow in a miniature circular pin fin heat sink *Exp. Therm. Fluid Sci*. **66** 28–35.
[6] Yang D, Wang Y, Ding G, Jin Z, Zhao J and Wang G 2017 Numerical and experimental analysis of cooling performance of single-phase array microchannel heat sinks with different pin-fin configurations *Appl. Therm. Eng*. **112** 1547–56.
[7] Hua J, Li G, Zhao X, Li Q and Hu J 2016 Study on the flow resistance performance of fluid cross various shapes of micro-scale pin fin *Appl. Therm. Eng.* **107** 768–75.
[8] Zhao J, Huang S, Gong L and Huang Z 2016 Numerical study and optimizing on micro square pin-fin heat sink for electronic cooling *Appl. Therm. Eng*. **93** 1347–59.
[9] Shakir R 2020 Boiling Heat Transfer in a Micro-Channel Complex Geometry *IOP Conf. Ser. Mater. Sci. Eng.* **928** IOP Publishing 22129.
[10] Lee P.S., Garimella SV and Liu D 2005 Investigation of heat transfer in rectangular microchannels *Int. J. Heat Mass Transf*. **48** 1688–704.
[11] Shah RK and London AL 1978 Laminar flow forced convection in ducts *Adv. Heat Transf.* supplement **1**.
[12] Liu D and Garimella SV 2004 Investigation of liquid flow in microchannels *J. Thermophys Heat Transf*. **18** 65–72.

The effect of heat treatment on structure property of (Bentonite - Alumina - Silica) Ceramic

The effect of heat treatment on structure property of (Bentonite - Alumina - Silica) Ceramic

Athraa Najm Abdullah[1], Shatha Hashem Mahdi[1]

[1]Department of Physics, College of Education for Pure Science (Ibn-AL-Haitham), University of Baghdad, Iraq.

E-mail: azraa.najm1104a@ihcoedu.uobaghdad.edu.iq

Abstract. In this work, a ceramic model has obtained from Iraqi bentonite as a base material with limited additions of alumina and silica. The selected material can bear temperatures higher than the bearing temperature of bentonite as it achieved tolerance temperatures (1300 ºC) based on X-ray diffraction patterns. It was found that the addition of alumina and silica led to the occurrence of basic phases such as mullite, quartz, cordierite and feldspar in percentages that depended on the percentage of addition in the mixture and the firing temperature, which was (1000-1300) ºC.

Keywords: Alumina, Silica, Ceramic, Cordierite, heat treatment**.**

1. Introduction

Ceramic material is defined as the material made partially or completely from clays formed and burned to a certain degree in order to reach a solid product. Ceramic materials include all inorganic materials except for alloys and metals. Ceramic materials are generally classified as Traditional Ceramic and Advanced or New ceramic (1). The word clay is used to denote a rock with specific properties. The size meaning of clay is believed by that size consisting of very small grains, despite the different measures that determine the size of the upper limit of the clay particles. (2,3) Bentonite is a clay with a high degree of plasticity and the primary composition of the mineral is Montmorillonite. Bentonite derived from volcanic ash with three-layer mineral clays is (Montmorillonite. $A1_2O_3$.5 SiO_2.7 H_2O) has a fast-drying property that leads to shrinkage of the ceramic body, as well as due to the presence of a high percentage of alkaline content in the bentonite clay, which leads to its melting at a degree less than (1300ºC) and therefore it is not used in thermal conditions at this temperature [4, 5]. The aim of the research is to treat bentonite clays with thermal ceramic materials in a specific ratio at different temperatures. In addition to study the phase transitions of bentonite clays.

2. Method and Materials

Use bentonite clay (the yellowish zone), the chemical analysis of this raw material is shown in the table below. Chemical analysis of the raw material tests according to the Geological Survey Company.

Analysis of bentonite clay (yellowness zone).	
SiO_2%	50.8
Fe_2O_3%	5.62
Al_2O_3%	15.93
TiO_2%	5.69
CaO%	3.06
MgO%	4.5
L.O.I%	10. 72

The alumina and silica prepared by the Swiss company Fluka were used with purity (99.99%) and granular size (10 m). The samples were prepared by sifting the bentonite using a Sieve Mesh No: 500 sieves to obtain a granular size less than (30 µm). After that, the weight ratios that form the mixture of the ceramic material were calculated. After setting the weight ratios of the raw materials, the materials were mixed, where the pH value of the distilled water was set using litmus paper, where pH = (6), and the binder (PVA) was placed in a weight ratio of 1% per 100ml of distilled water and using magnetic stirrer to be left for half an hour at a temperature of (80 ºC), then we obtain a colloidal solution free of any sediment. After obtaining a colloidal solution free of any sediment, concentrated HCl acid was added by one drop to the mixture to obtain a solution of (pH = 3), after which the alumina was added in proportion 25% and silica by 10% and leave it to mix for an hour, after which bentonite was added by 65% and the mixing process was continued from (6h) to obtain the best possible homogeneity of the mixtures after obtaining a thick mixture. Dry the dense mixture in a laboratory dryer (Oven) at a temperature (100ºC) to get rid of the aqueous solution, then the crumbling process was carried out using a hand mortar (Mortar and Basel) to obtain the required base mixture The samples were formed by semi-dry pressing method, where they were pressed with a hydraulic press using a mold of stainless steel with a diameter (2.5cm) Compression of (5ton / cm2), compression time (60sec), and (5) mix samples were formed. Then the heat treatment of samples was carried out using a Carbolite type electric furnace at the required temperature degrees (1000, 1100, 1200, 1250, 1300) ºC at a time of rising temperature of (5ºC / min) for two hours. The mineral composition was measured using the X-ray diffraction technique and using SIEMENS X-RAY DIFFRACTION UNIT MODEL.

3. Results and Discussion

A set of mineral changes took place on the raw materials used in the preparation of ceramics as a result of demolition reactions, structural reactions, and reconfiguring new phases. The first stage included the occurrence of some demolition reactions that lead to the evaporation of porous and surface water and the loss of crystalline water that causes the collapse of the crystalline structure of clay minerals and the decomposition of limestone At a temperature of (700) ºC and after that the structural reactions take place, when the raw materials interact with each other at temperatures [(700-1000), (700-1100), (700-1200), (700-1250) and ((700-1300)] ºC form some new metallic phases. And the mineral analysis of the components of bentonite clay was treated with a temperature of (1000.1100.1200) ºC. Mineral analysis was also performed for ceramic objects produced from bentonite clays at temperatures of (1250-1300) ºC, noting that bentonite is not used as a base material in the production of ceramic bodies, especially at sintering temperature (> 1200) ºC due to its containment of molten oxides. After analyzing the X-ray diffraction patterns shown in Figures (1) to (5) and weighing them with the values of (2Ɵ) for each of the resulting phases with those studies referred to by the ASTM files and calculating the concentrations of those phases [6].

Where these diagrams indicate that the ceramic samples prepared from bentonite clay as a base material, alumina (25% - Al2O3) and silica 10%-SiO2) have undergone some mineral changes, the most important of which is the disappearance of clay minerals because they do not tolerate high temperatures and water loss.Crystallization, which led to the collapse of its crystal structure.In addition, the calcareous materials are completely decomposed after their consumption to form new mineral phases, the most important of which are mullite with its symbol M, feldspar its symbol F, Cordierite (C) and a small percentage of quartz (Q).

The resulting phases of the bentonite clay model with a temperature of (1000) ºC are mullite (53.44484) %, feldspar (43.60812)%, and quartz (2.947033)%. As for the same model treated with a temperature of (1100) ºC, the resulting phases were mullite (48.66131)%, feldspar (41.49933)%, Cordierite (7.362784)%, and quartz (2.476573)%, and when treated with 3a temperature of (1200) ºC, the phase of Cordierite (7.612457%) and mullite 56.12457)%, feldspar (33.91003)% and quartz (2.352941)%, and the bentonite slurry was permanently converted into mullite (56.0794)%, feldspar (32.63027)%, as well as Cordierite (9.119107)% and quartz (2.171216)%, when treated at a temperature of 1250 ºC . As for the modulated model within the thermal range (1300) ºC, the resulting phases were mullites (49.77893)%, feldspar (41.06632)%, Cordierite (7.594278)%, and quartz (1.560468)%, by observing the X-ray diffraction patterns of the treated models within the temperature range (1000-1300) ºC where new phases appeared (Cordierite) in addition to mullite, feldspar and quartz, as these resulting phases have good insulating properties.

4. Conclusions

In this paper, a ceramic model was obtained from Iraqi bentonite with limited additions of alumina and silica that bear a temperature higher than the bearing temperature of Iraqi bentonite, as it achieved a severe temperature of 1300 ºC. The addition of alumina and silica led to the occurrence of basic phases, which are mullite, feldspar and quartz, in addition to Cordierite. Adoption of these thermally treated ceramics at (1000, 1100, 1200, 1250, 1300) ºC and a maturation time of (2hr), thus this mixture is considered successful.

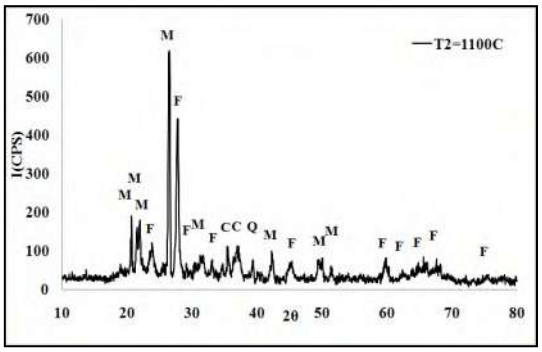

Figure 1. X-ray Pattern of bentonite clay treated at (1000) ºC

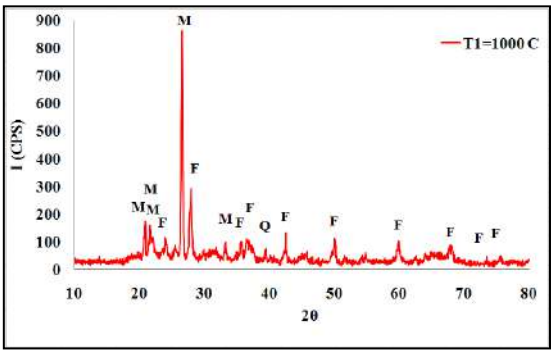

Figure 2. X-ray Pattern of bentonite clay treated at (1100) ºC

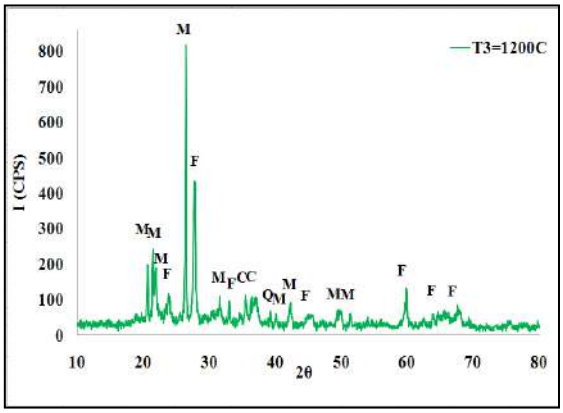

Figure 3. X-ray Pattern of bentonite clay treated at (1200) ºC

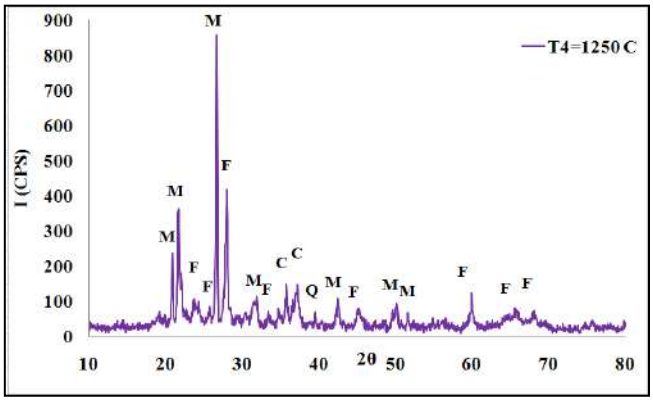

Figure 4. X-ray Pattern of bentonite clay treated at (1250) ºC

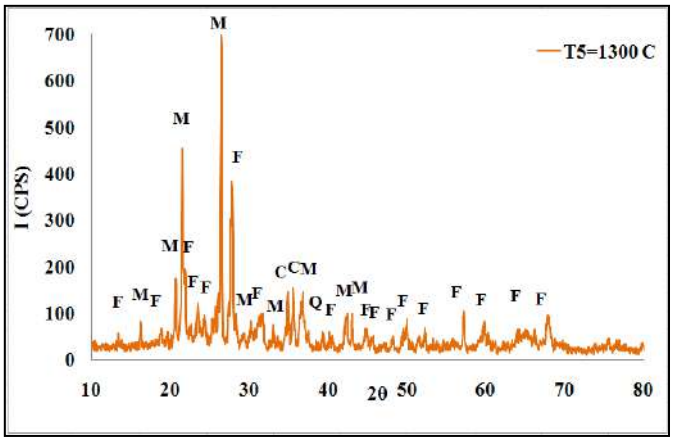

Figure 5. X-ray Pattern of bentonite clay treated at (1300) ºC

References

[1] Rahman MN 2007 *Ceramic Processing* CRC Press by Taylor & Francis Group, New York.
[2] Mohammed J. 2009 Improvement of the Mechanical and Dielectrical Properties of Kaolin Clay *Coll. Basic Educ. Res. J.* **9** 2009.
[3] Kitouni S and Harabi A 2011 Sintering and mechanical properties of porcelains prepared from Algerian raw materials *Cerâmica* **57** 453-460.

[4] Mohamed L 2015 Study on Electrical Behavior for Ceramic (Cordierite-Mullite) Derived from Local Clay *J. Chem. Biol. Phys. Sci.* **5** 4 4335-4344.
[5] Abbas I 2015 Evaluation of the Electrical and Mechanical Performance of the Ceramic (Bentonite Clay/Silica) *J. Chem. Biol. Phys. Sci.* **5** 4 4312-4318.
[6] ASTM, 39-1425, 15-0776, 21-1152, 12-0301, 12-0303 and 37-1496 International Center for Diffraction Data, File ™ & Related Products (2009-2010)
[7] Mahdi SH, Mkhaiber AF and Mahdi MH 2017 Effect of gamma radiation on structural characteristic of ceramic body Mesopot. Environ. J. Special Issue C: 87-90.

A New Technique for Solar Cell Parameters Estimation of The Single-Diode Model

A New Technique for Solar Cell Parameters Estimation of The Single-Diode Model

Mohammed RASHEED[1], Osama Alabdali [2], Suha Shihab [1]

[1]Applied Sciences Department, University of Technology, Baghdad, Iraq.
[2]College of Education for Pure Sciences, University of Anbar, Al-Anbar, Iraq.

E-mail: 10606@uotechnology.edu.iq

Abstract. In the current study, an implicit algorithm has been applied to solve the nonlinear equation of a single diode solar cell using several iterations with an initial value of $x_0 = 1$. The proposed algorithm is achieved with the different values of load resistance. The equation based on equivalent circuit of a solar cell and all the determinations are implemented at ambient temperature using MATLAB program. The obtained results of this new method are given, and the absolute errors are investigated.

Keywords: Implicit method; single diode model; parameters; iterations; load resistance.

1. Introduction

Numerical analysis is a science of approximation where numerical methods are used to solve complex and unsolvable problems by analytical methods. In numerical analysis, all aspects of the existing problem are studied numerically, using theoretical development, understanding of numerical methods, and attempting to implement them in the form of computer programs. These programs are characterized by a high level of confidence and effectiveness. Common interests and perspectives among them, which include mathematical methods of numerical analysis is based on the principle of creating, analyzing, and implementing a number of algorithms to arrive at digital solutions to mathematical problems that are built on a range of constant variations and fluctuations, such as quantitative analysis, or numerical methods [1-8]. Photovoltaic have been used in space for a long time in 1958, when Van Gard was launched, with 6 photovoltaic cells on its surface. While other batteries stopped working shortly after the ship was launched, since then, solar photovoltaic cells have been widely used in space and their use has helped to increase the length of spaceflight. For spaceships and high reliability relatively high yield. The main idea is to reproduction electrical energy by means of photovoltaic cells, which form solar cells. Several kinds of solar cells are synthesized based on the material used and fabrication technique such as silicon, organic and inorganic solar cells [9-55]. This study proposes a method for estimating parameters in single diode model of a solar cell equation based on implicit algorithm (IM) and explains the performance of this estimation method. It is organized as follows: Section two characterizing the analytical model of a single-diode design of the solar cell; Section three establishing the root finding Implicit algorithm (IM); Section four results and discussion; Section five conclusions of the acquired results.

2. Characteristics of Single-Diode Solar Cells Equation

A photo voltaic cell (equivalent circuit) is shown in Figure 1.

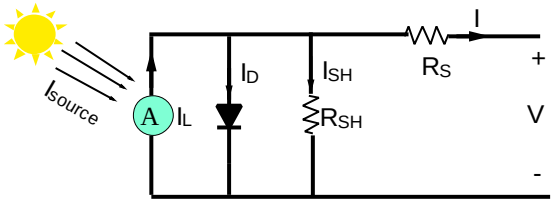

Figure 1. Single-diode electrical equivalent circuit model of a solar cell.

By applying Kiechoff's current law for the circuit, the equation of this equivalent circuit is given by

$$I = I_{ph} - I_D \tag{1}$$

$$I_D = I_0\left(e^{\frac{-V_{pv}}{nV_T}} - 1\right) \tag{2}$$

$$I = I_{ph} - I_0\left(e^{\frac{-V_{pv}}{mV_T}} - 1\right) \tag{3}$$

where:
I_{ph} is the photocurrent (A); I_0 is reverse saturation current of the diode (A); I and V_{pv} are the delivered current and voltage, respectively (V); $V_T = \frac{kT}{q} = 0.0259\,V$ is thermic voltage $= 27.5 \cong 26\,mV$ at ($T =$ 25 °C Air-Mass = 1.5); m is the recombination factor closeness to an ideal diode $(1 < m < 2)$, k is Boltzmann constant$= 1.38 \times 10^{-23} J/K$; T is $p-n$ junction temperature (K); q is the electron charge$= 1.6 \times 10^{-19}\,C$.

$$I_{ph} = I_{source} \tag{4}$$

$$I_D = I_s * \left(e^{\frac{V_D}{nV_T}} - 1\right) \tag{5}$$

Merge Eq. 4 in Eq. 5 we get

$$(I_{source}) - 10^{-12}\left(e^{\frac{-V}{1.2*0.026}} - 1\right) = \frac{V}{R} \tag{6}$$

where: I_s reverse saturation current$= 10^{-12}A$. In parallel, $V_D = V_{pv} = V$
According to Eq. 6 one can calculate V of the cell numerically based on the first derivative of this equation.

3. Implicit Method (IM)

The following algorithm suggestion for solving Eq. 5 by using NRM
Initial approximate solution $x_0 = 1$, tolerance ε,
$\acute{f}(x_{n+1}) = x_n - \frac{f(x_n)}{\acute{f}(x_n)}$ for $n = 0, 1, 2, \ldots$.

$$x_{n+1} = x_n - \frac{2 \times f(x_n)}{\acute{f}(x_{n+1}) + \acute{f}(x_n)}$$

In the implicit formula, the indefinite integral involved in the following equation

$$f(x) = f(x_n) + \int_{x_n}^{x} \acute{f}(\lambda)\, d\lambda \tag{7}$$

Is approximated by the trapezoidal rule to obtain

$$\int_{x_n}^{x} \acute{f}(\lambda)\, d\lambda = \frac{x-x_n}{2}\left[\acute{f}(x_n) + \acute{f}(x)\right] \quad (8)$$

Put Eq. 8 into Eq. 7 yields

$$f(x) = f(x_n) + \frac{x-x_n}{2}\left[\acute{f}(x_n) + \acute{f}(x)\right] \quad (9)$$

Since $f(x) = 0$, therefore Eq. 9 can be written as

$$x = x_n - \frac{2\times f(x_n)}{[\acute{f}(x_n)+\acute{f}(x)]} \quad (10)$$

Take the next iterative point, that is put $x = x_{n+1}$ to obtain
$f(x_{n+1}) = f(x_n) + \frac{1}{2}(x_{n+1} - x_n)(\acute{f}(x_n) + \acute{f}(x_{n+1})$ or

$$x_{n+1} = x_n - \frac{2\times f(x_n)}{\acute{f}(x_{n+1})+\acute{f}(x_n)} \quad (11)$$

Eq. 11 is an implicit formula, which requires having the derivative of the function at the $(n+1)^{th}$ iterative step to calculate the $(n+1)^{th}$ iterative itself.
Thus, the resulting formula is

$$x_{n+1} = x_n - \frac{2\times f(x_n)}{\acute{f}(x^*_{n+1})+\acute{f}(x_n)}$$

where: $\acute{f}(x^*_{n+1}) = x_n - \frac{f(x_n)}{\acute{f}(x_n)},\ n = 0, 1, 2, \ldots.$ (12)

and x_0 is the starting value

4. Results and Discussion

Consider Eq. 6 is modelled in the form single-diode solar cell has obtained the following approximate solutions and the IM are applied with the first initial value x_0. In Table 1, the IM of the solution results (voltage V_{pv}; current I_{pv} and power P_{pv} of the solar cell) are presented and listed in this table when the load resistance $R = 1$.
Table 1 and Figure 3 Illustrate the obtained approximate results when $R = 1$

Table 1. The obtained values using IM.

Iterations	$\boldsymbol{V_{pv}}$-IM	$\boldsymbol{I_{pv}}$-IM	$\boldsymbol{P_{pv}}$-IM	ε-IM
1	0.942812862	0.942812862	0.888896093	0.020389728
2	0.922004414	0.922004414	0.85009214	0.00041872
3	0.912933605	0.912933605	0.833447766	0.00948953
4	0.91658633	0.91658633	0.840130499	0.005836805
5	0.921613448	0.921613448	0.849371348	0.000809686
6	0.922412182	0.922412182	0.850844233	1.09529E-05
7	0.922423133	0.922423133	0.850864436	1.91849E-09
8	0.922423135	0.922423135	0.850864439	0.000000000
9	0.922423135	0.922423135	0.850864439	0.000000000

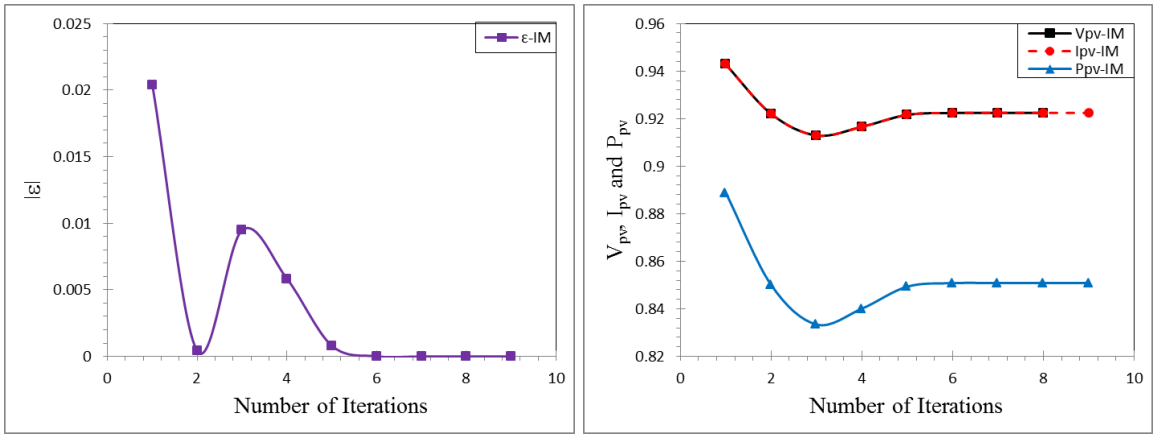

Figure 2. Voltage, current and power of solar cell with the absolute error values.

Table 2 and Figure 3 Illustrate the obtained approximate results when $R = 2$.

Table 2. The obtained values using IM

Iterations	V_{pv}-IM	I_{pv}-IM	P_{pv}-IM	ε-IM
1	0.942039802	0.471019901	0.443719494	0.025004419
2	0.919767328	0.459883664	0.422985969	0.002731946
3	0.908172101	0.45408605	0.412388282	0.008863282
4	0.909981837	0.454990918	0.414033472	0.007053546
5	0.915681905	0.457840953	0.419236676	0.001353477
6	0.917003597	0.458501799	0.420447799	3.1785E-05
7	0.917035366	0.458517683	0.420476931	1.62789E-08
8	0.917035382	0.458517691	0.420476946	4.44089E-15
9	0.917035382	0.458517691	0.420476946	0.000000000

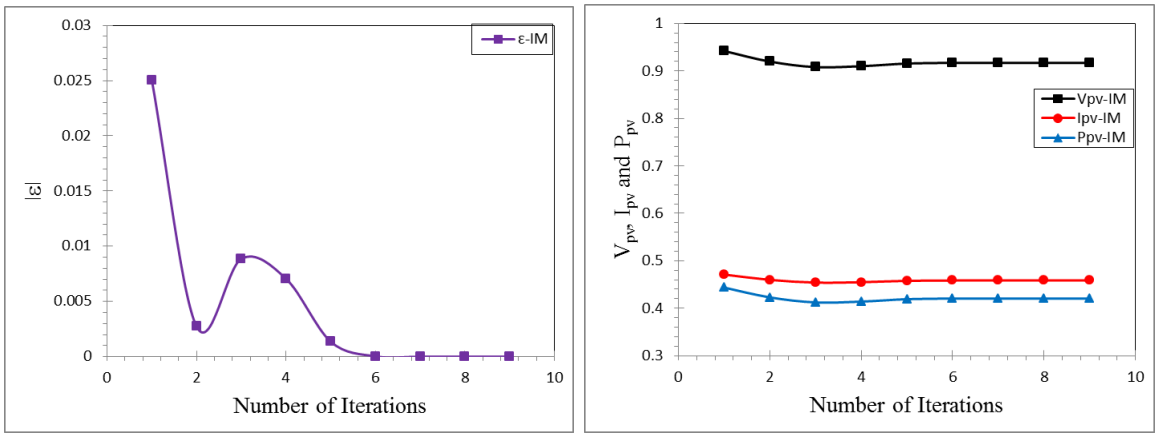

Figure 3. Voltage, current and power of solar cell with the absolute error values.

Table 3 and Figure 5 Illustrate the obtained approximate results when $R = 3$.

Table 3. The obtained values using IM.

Iterations	V_{pv}-IM	I_{pv}-IM	P_{pv}-IM	ε-IM
1	0.94126616	0.313755387	0.295327328	0.030862786
2	0.917476245	0.305825415	0.280587554	0.007072871
3	0.903018143	0.301006048	0.271813922	0.007385231
4	0.902074754	0.300691585	0.271246287	0.00832862
5	0.90809742	0.30269914	0.274880308	0.002305954
6	0.910304588	0.303434863	0.276218148	9.87862E-05
7	0.910403215	0.303467738	0.276278004	1.59376E-07
8	0.910403374	0.303467791	0.276278101	4.1267E-13
9	0.910403374	0.303467791	0.276278101	0.000000000

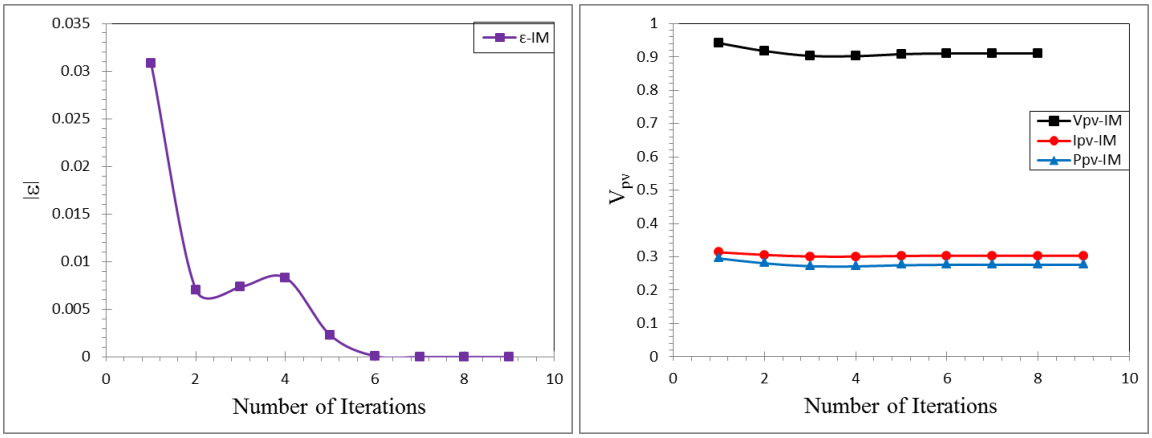

Figure 4. Voltage, current and power of solar cell with the absolute error values.

Table 4 and Figure 6 Illustrate the obtained approximate results when $R = 4$.

Table 4. The obtained values using IM.

Iterations	V_{pv}-IM	I_{pv}-IM	P_{pv}-IM	ε-IM
1	0.940491937	0.235122984	0.221131271	0.038751335
2	0.9151298	0.22878245	0.209365638	0.013389198
3	0.897428152	0.224357038	0.201344322	0.00431245
4	0.89244529	0.223111323	0.199114649	0.009295312
5	0.897748102	0.224437025	0.201487914	0.0039925
6	0.901401786	0.225350447	0.203131295	0.000338816
7	0.90173867	0.225434667	0.203283157	1.93238E-06
8	0.901740602	0.22543515	0.203284028	6.17006E-11
9	0.901740602	0.22543515	0.203284028	0.000000000

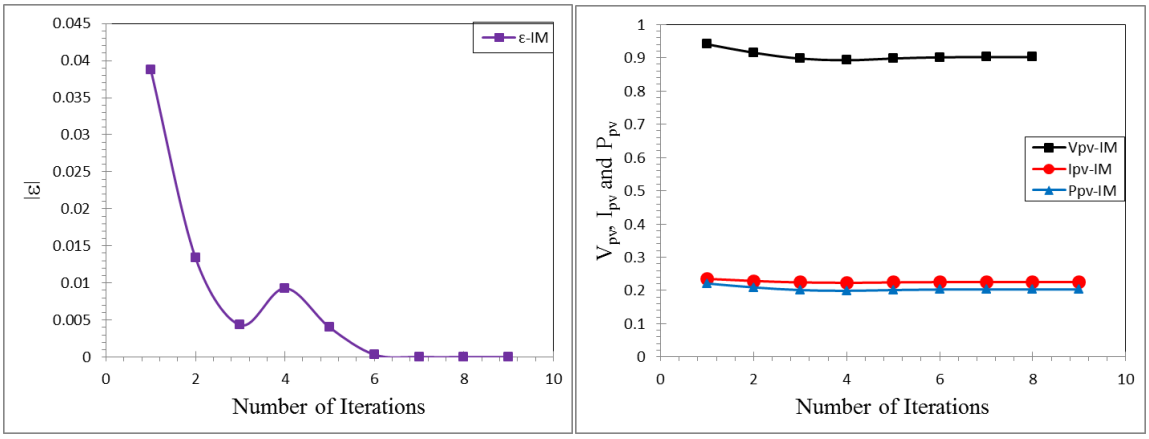

Figure 5. Voltage, current and power of solar cell with the absolute error values.

Table 5 and Figure 6 Illustrate the obtained approximate results when $R = 5$.

Table 5. The obtained values using IM.

Iterations	V_{pv}-IM	I_{pv}-IM	P_{pv}-IM	ε-IM
1	0.939717132	0.187943426	0.176613658	0.050624417
2	0.912726587	0.182545317	0.166613965	0.023633872
3	0.891352644	0.178270529	0.158901907	0.002259929
4	0.88049295	0.17609859	0.155053567	0.008599764
5	0.882268872	0.176453774	0.155679672	0.006823843
6	0.887741339	0.177548268	0.157616937	0.001351375
7	0.889058854	0.177811771	0.158085129	3.38608E-05
8	0.889092695	0.177818539	0.158097164	1.96857E-08
9	0.889092715	0.177818543	0.158097171	0.000000000
10	0.889092715	0.177818543	0.158097171	0.000000000

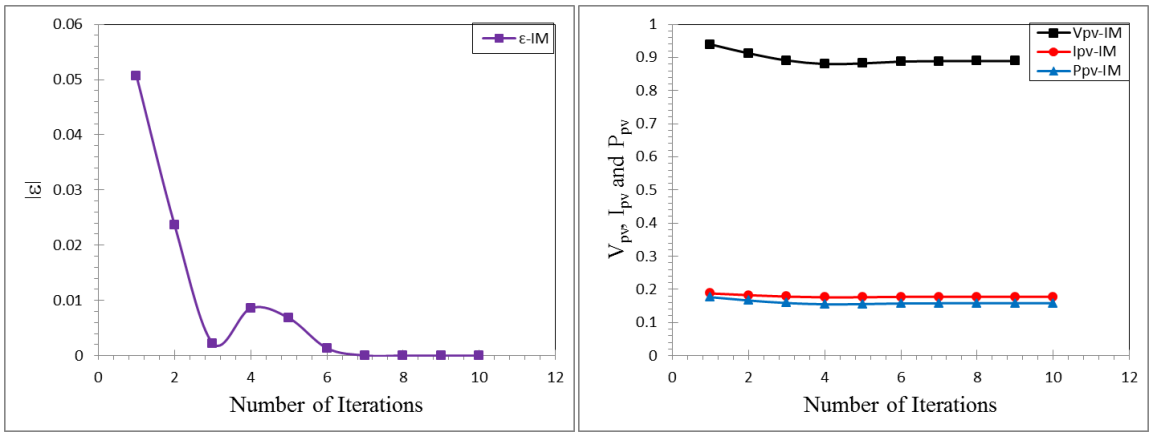

Figure 6. Voltage, current and power of solar cell with the absolute error values.

The obtained solution plot in the (no. of iterations)-ε-plane and the initial-output values prove that the proposed method IM have nine iterations indicated a fast behaviour. Parallel to this feature, it is noticed that the proposed method IM has a behaviour of the solution in the initial value x_0 with small error tolerance. Results from Tables 1-5 are showing that the suggested method IM exhibits low absolute errors after computed iterations which in turn demonstrating its efficiency.

5. Conclusions

This paper presents a new method to calculate the electrical parameter of the solar cell using implicit method. Values acquired from the proposed method IM were found to be sufficient and values for single diode solar cell were determined with fast convergence, more capable to determine these parameters towards establishing the final values.

6. References

[1] Shihab SN and Sarhan MA 2014 Convergence analysis of shifted fourth kind Chebyshev wavelets, *IOSR J. Math.* **10** 2 54-58.
[2] Al-Rawi SN and Al-Rubaie HR 2010 An Approximate solution of some continuous time Linear-Quadratic optimal control problem via Generalized Laguerre Polynomial *J Pure Appl. Sci.* **22** 1 85-97.
[3] S. N. Al-Rawi, NUMERICAL SOLUTION OF INTEGRAL EQUATIONS USING TAYLOR SERIES, Journal of the College of Education, 5 (1992) 51-60.
[4] Eleiwy JA and Shihab SN 2009 Chebyshev Polynomials and Spectral Method for Optimal Control Problem *Eng. Technl. J.* **27** 14 2642-2652.
[5] SHIHAB SN and Sarhan MA 2014 New Operational Matrices of Shifted Fourth Chebyshev wavelets *Elixir Int. J.-Appl. Math.* **69** 1 23239-23244.
[6] Al-Rawi SN, Al-Heety FA and Hasan SS 2010 A New Computational Method for Optimal Control Problem with B-spline Polynomials, *Eng. Technol. J.* **28** 18 5711-5718.
[7] Delphi M and SHIHAB S 2019 Operational Matrix Basic Spline Wavelets of Derivative for linear Optimal Control Problem *Electron. Sci. Technol. Appl.* **6** 2 18-24.
[8] Rasheed MS 2012 Study of the effects of acidic solutions on the physical properties of polymeric materials superimposed *Al-Mustansiriyah J. Sci.* **13** 49 6.
[9] Rasheed MS and Shihab S 2020 Modelling and Parameter Extraction of PV Cell Using Single-Diode Model *Adv. Energy Conv. Mat.* **1** 2 96-104.
[10] Rasheed MS and Shihab S 2020 Analysis of Mathematical Modeling of PV Cell with Numerical Algorithm *Adv. Energy Conv. Mat.* **1** 2 70-79.
[11] Rasheed MS 2010 Approximate Solutions of Barker Equation in Parabolic Orbits *Eng. Technol. J.* **28** 3 492-499.
[12] Rasheed MS 2010 An Improved Algorithm For The Solution of Kepler's Equation For An Elliptical Orbit, *Eng. Technol. J.* **28** 7 1316-1320.
[13] Rasheed MS 2012 Acceleration of Predictor Corrector Halley Method in Astrophysics Application *Int. J. Emerg. Technol. Comput. Appl. Sci.* **1** 2 91-94.
[14] Rasheed MS 2012 Fast Procedure for Solving Two-Body Problem in Celestial Mechanic *Int. J. Eng. Business Enterpr. Appl.* **1** 2 60-63.
[15] Rasheed MS 2013 Solve the Position to Time Equation for an Object Travelling on a Parabolic Orbit in Celestial Mechanics, *Diyala J.Pure Sci.* **9** 4 31-38.
[16] Rasheed MS 2013 Comparison of Starting Values for Implicit Iterative Solutions to Hyperbolic Orbits Equation *Int. J. Software Web Sci. (IJSWS)* **1** 2 65-71.
[17] Rasheed MS 2014 On Solving Hyperbolic Trajectory Using New Predictor-Corrector Quadrature Algorithms *Baghdad Sci. J.* **11** 1 186-192.
[18] Rasheed MS 2020 Modification of Three Order Methods for Solving Satellite Orbital Equation in Elliptical Motion *J. Univ. Anbar Pure Sci.* **14** 1 33-37.

[19] Rasheed M and Barillé R 2017 Room temperature deposition of ZnO and Al: ZnO ultrathin films on glass and PET substrates by DC sputtering technique, *Opt.Quantum Electron.* **49** 5 1-14.
[20] Rasheed M and Barillé R 2017 Optical constants of DC sputtering derived ITO, TiO_2 and TiO_2: Nb thin films characterized by spectrophotometry and spectroscopic ellipsometry for optoelectronic devices *J. Non-Crystall. Solids* **476** 1-14.
[21] Rasheed M and Barillé R 2017 Comparison the optical properties for Bi_2O_3 and NiO ultrathin films deposited on different substrates by DC sputtering technique for transparent electronics *J. Alloys Comp.* **728** 1186-1198.
[22] Saidani T, Zaabat M, Aida MS, Barille R, Rasheed M and Almohamed Y 2017 Influence of precursor source on sol–gel deposited ZnO thin films properties *J. Mat. Sci. Mat. Electron.* **28** 13 9252-9257.
[23] Guergouria K, Boumezoued A, Barille R, Rechemc D, Rasheed M and Zaabata M 2019 ZnO nanopowders doped with bismuth oxide, from synthesis to electrical application *J. Alloys Comp.* **791** 550-558.
[24] Bouras D, Mecif A, Barillé R, Harabi A, Rasheed M, Mahdjoub A and Zaabat M 2018 Cu: ZnO deposited on porous ceramic substrates by a simple thermal method for photocatalytic application *Ceramics Int.* **44** 17 21546-21555.
[25] Saidi W, Hfaidh N, Rasheed M, Girtan M, Megriche A and EL Maaoui M 2016 Effect of B_2O_3 addition on optical and structural properties of TiO_2 as a new blocking layer for multiple dye sensitive solar cell application (DSSC) *RSC Adv.* **6** 73 68819-68826.
[26] AUKŠTUOLIS A, Girtan M, Mousdis GA, Mallet R, Socol M, Rasheed M and Stanculescu A 2017 Measurement of charge carrier mobility in perovskite nanowire films by photo-CELIV method *Proc. Romanian Acad. Ser. a-Math. Phys. Techn. Sci. Inform. Sci.* **18** 1 34-41.
[27] Sultan OA, Hassoon KI and Rasheed MS 2003 Deterioration of Silicon Solar Cell Parameter with Ambient Temperature *Al-Mustansiriyah J. Sci.* **14** 1 25-31.
[28] Tahir FS, Rasheed MS and Hameed IA 2012 Analysis the Performance of Silicon Solar Cell Parameters with the Ambient Temperature using Fuzzy Logic *J. Coll. Basic Educ.* **18** 75 173-183.
[29] Tahir FS and Rasheed MS 2012 Decline in the Performance of Silicon Solar Cell Parameters with the Ambient Temperature in Baghdad *J. Coll. Basic Educ.* **18** 75 95-111.
[30] Dkhilalli F, Megdiche S, Guidara K, Rasheed M, Barillé R and Megdiche M 2018 AC conductivity evolution in bulk and grain boundary response of sodium tungstate Na_2WO_4 *Ionics* **24** 1 169-180.
[31] Dkhilalli F, Borchani SM, Rasheed M, Barille R, Guidara K and Megdiche M 2018 Structural, dielectric, and optical properties of the zinc tungstate $ZnWO_4$ compound *J. Mat. Sci. Mat. Electron.* **29** 8 6297-6307.
[32] Dkhilalli F, Borchani SM, Rasheed M, Barille R, Shihab S, Guidara K and Megdiche M 2018 Characterizations and morphology of sodium tungstate particles *Royal Soc. Open Sci.* **5** 8 1-12.
[33] Enneffati M, Louati B, Guidara K, Rasheed M and Barillé R 2018 Crystal structure characterization and AC electrical conduction behavior of sodium cadmium orthophosphate *j. Mat. Sci. Mat. Electron.* **29** 1 171-179.
[34] Kadri E, Krichen M, Mohammed R, Zouari A and Khirouni K 2016 Electrical transport mechanisms in amorphous silicon/crystalline silicon germanium heterojunction solar cell: impact of passivation layer in conversion efficiency *Opt. Quantum Electron.* **48** 12 1-15.
[35] Kadri E, Messaoudi O, Krichen M, Dhahri K, Rasheed M, Dhahri E, Zouari A, Khirouni K and Barillé R 2017 Optical and electrical properties of SiGe/Si solar cell heterostructures: Ellipsometric study *J. Alloys Comp.* **721** 779-783.
[36] Kadri E, Dhahri K, Zaafouri A, Krichen M, Rasheed M, Khirouni K and Barillé R 2017 Ac conductivity and dielectric behavior of a−Si:H/c− $Si_{1-y}Ge_y$/p−Si thin films synthesized by molecular beam epitaxial method *J. Alloys Comp.* **705** 708-713.

[37] Azaza NB, Elleuch S, Rasheed M, Gindre D, Abid S, Barille R, Abid Y and Ammar H 2019 3-(p-nitrophenyl) Coumarin derivatives: Synthesis, linear and nonlinear optical properties *Opt. Mat.* **96** 109328.
[38] Enneffati M, Rasheed M, Louati B, Guidara K and Barillé R 2019 Morphology, UV–visible and ellipsometric studies of sodium lithium orthovanadate, *Opt. Quantum Electron.* **51** 9 299.
[39] RASHEED M and Sarhan MA 2019 Solve and Implement the main Equations of Photovoltaic Cell Parameters Using Visual Studio Program *Insight-Math.* **1** 1.
[40] Rasheed M and Sarhan MA 2019 Characteristics of Solar Cell Outdoor Measurements Using Fuzzy Logic Method *Insight-Math.* **1** 1.
[41] RASHEED M and Sarhan MA 2019 Measuring the Solar Cell Parameters Using Fuzzy Set Technique *Insight-Electron.* **1** 1.
[42] RASHEEDM 2019 Linear Programming for Solving Solar Cell Parameters *Insight-Electron.* **1** 1.
[43] RASHEED M 2019 Investigation of Solar Cell Factors using Fuzzy Set Technique *Insight-Electron.* **1** 1.
[44] Jalal R, Shihab S, Abed Alhadi M, Rasheed M 2020 Spectral Numerical Algorithm for Solving Optimal Control Using Boubaker-Turki Operational Matrices, *Journal of Physics: Conference Series,* **1660** 1 012090.
[45] RASHEED M and SHIHAB S 2019 Analytical Modeling of Solar Cells, *Insight Electron.* **1** 1.
[46] RASHEED M and SHIHAB S 2019 Modeling and Simulation of Solar Cell Mathematical Model Parameters Determination Based on Different Methods *Insight Math.* **1** 1.
[47] RASHEED M and SHIHAB S 2019 Parameters Estimation for Mathematical Model of Solar Cell, *Electron. Sci. Technol. Appl*.
[48] SHIHAB S and RASHEED A 2019 Explicit Model of Solar Cells to Determine Voltages, *Insight Electron.*
[49] RASHEED M and SHIHAB S 2019 Parameters Estimation of Photovoltaic Model Using Nonlinear Algorithms *Insight Electron.*
[50] SHIHAB S and RASHEED M 2019 Modifications to Accelerate the Iterative Algorithm for the Single Diode Model of PV Model, *Insight Electron.*
[51] Rasheed M and Shihab S 2020 Numerical Techniques for Solving Parameters of Solar Cell, *Appl. Phys.* **3** 2 16-27.
[52] Abbas MM and Rasheed M 2020 Solid State Reaction Synthesis and Characterization of Aluminum Doped Titanium Dioxide Nanomaterials *J. Southwest Jiaotong Univ.* **55** 2 (2020) 1-10.
[53] Aziz SH, Rasheed M and Shihab S 2020 New Properties of Modified Second Kind Chebyshev Polynomials *J. Southwest Jiaotong Univ.* **55** 3.
[54] Sarhan MA, Shihab S and Rasheed M 2020 On the Properties of Two-Dimensional Normalized Boubaker Polynomials *J. Southwest Jiaotong Univ*. **55** 3.
[55] Sarhan MA, Shihab S and Rasheed M 2020 A New Boubaker Wavelets Operational Matrix of Integration *J. Southwest Jiaotong Univ*. **55** 2.

Effect of The Cu Doping on The Structural and Optical Properties of AlSb Thin Films Deposited by Thermal Evaporation Method

Effect of The Cu Doping on The Structural and Optical Properties of AlSb Thin Films Deposited by Thermal Evaporation Method

Adil M. Ibraheim[1] and Sameer. A. Maki[2]

[1] Ministry of Education , Baghdad – Al-Rusafa 2 , Aljazeera school , Baghdad , Iraq.
[2]University of Baghdad , College of Education, Ibn - Al-Haithem, Department of Physics , Baghdad , Iraq.

Email: adilmahmoudadiladil@gmail.com

Abstract. AlSb thin film was prepared on a glass substrate with a thickness of (200 nm) at room temperature using the thermal evaporation technique under high vacuum conditions (10^{-6} mbar**).** The effect of Cu doping at ratios (1%, 3% and 5%) on the structural and optical properties were investigated. The structural properties of the films were evaluated by X-Ray Diffraction technique (XRD) and atomic force microscopy (AFM). The optical properties of the films were measured using the (UV-Vis) spectra in the ranges from 400 to 1000 nm. XRD results showed that all the samples have a polycrystalline cubic structure, and the average grain size of AlSb increases with increasing the Cu ratios. According to the AFM analysis, it is noticed that the average surface roughness (RMS) of AlSb nanocubic thin film decreases with increasing Cu doped concentration. From UV–Vis absorption spectra, it is noticed that all the samples have high absorption in the visible region, and the direct energy gap values for the samples were 1.83 eV, 1.81 eV, 1.80 eV, and 1.78 eV for pure, 1% Cu, 3% Cu and 5% Cu respectively.

Keywords: High vacuum , Cu doped , micro strain , roughness , energy gap .

1. Introduction

The III-V semiconductors are stoichiometric compounds obtained by combining group III elements (essentially Al, Ga, In) with group V elements (essentially N, P, As, Sb) (1, 2). This gives us 12 possible combinations and important properties of the surface crystal planes (3). One of these compounds is AlSb. AlSb has a high energy gap, high electronic mobility, long wavelength, and conversion efficiency of more than 27% (4). Therefore, it is used in a wide range of applications such as solar cells, thermoelectric and opto-electronic devices. In addition, Al and Sb are relatively abundant, non-toxic and low-cost making AlSb compound an attractive material for device applications (5,6). AlSb also has potential applications as a detector of the radiation and as a material in high mobility hetero structures. Several methods have been used for the development of the thin films of AlSb like pulse laser deposition (7), co-evaporation (8), liquid phase epitaxy (9), hot wall epitax(10) co-sputtering (11) and doped AlSb thin films. Thermal evaporation technique is the most cost effective method among all other used techniques. In this work, AlSb thin film was successfully deposited onto glass substrates and doped with

copper at (1%, 3%, and 5%). The structural properties are evaluated by XRD and AFM techniques, and UV-vis was used to investigate the absorption spectra and calculate the energy gap.

2. Experimental

AlSb alloys have been prepared by mixing the a purity aluminum powder (99.99%) and antimony powder (99.99%) made by the Riedel-de Haen Chemicals Ltd., and putting in a quartz tube under ($1x10^{-2}$ torr), then the tube placed inside an oven at 1100 °C for 5 hours. The sample was cooled down using a slow cooling method. Thermal evaporation method was used to deposite AlSb thin films onto pre-cleaned amorphous glass substrate under high vacuum about (5×10^{-6} torr). The glass substrate was placed on the substrate holder above a molybdenum boats that carrying the materials, and the process was performed at a deposition rate of (0.5 ± 0.05 nm sec^{-1}). The films had been doped with Cu at ratios (1, 3 and 5) % .

The XRD machine (6000 SHIMADZU-Japan) was used to study the structural properties. The morphology of the samples (average diameter, roughness, and root mean square) were studied using the atomic force microscopy (AFM). The optical absorption was measured at a range of (400-1000) nm using (UV-VISIBLE 1800 spectra-photometer)

3. Results and Discussion

Figure (1) shows the XRD pattern of AlSb alloy. The peaks observed at 25.1943, 29.1411, 41.6611, 49.2683 and 66.4085 exhibit the formation of a polycrystalline cubic phase of AlSb which correspond to the (111), (200), (220), (311), and (331) reflection planes of. This result matches with the ASTM card number (00-006-0233). Table (1) shows a matching between the experimentally measured alloy and ASTM card (19) .

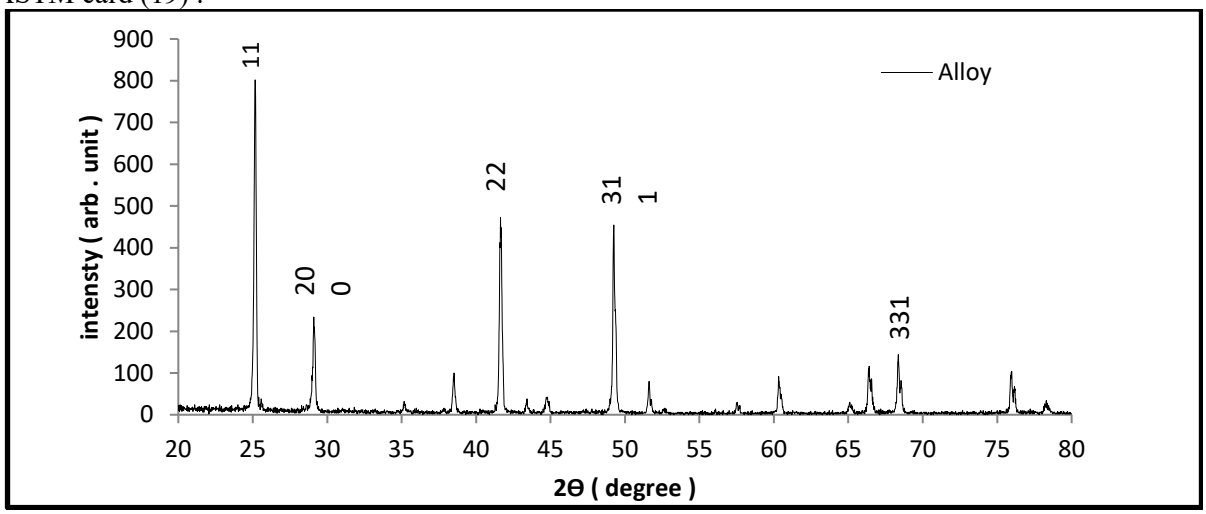

Figure 1. X-ray diffraction pattern of AlSb alloy.

Table 1. : A comparison between the experimentally measured alloy and ASTM card.

Standard				observed			
2Θ	intensity	d	hkl	2Θ	intensity	d	hkl
25.1354	100	3.54	111	25.1943	100	3.53195	111
29.0913	35	3.067	200	29.1411	27	3.06195	200
41.6030	75	2.169	220	41.6611	66	2.16617	220

49.2109	30	1.85	311	49.2683	68	1.84803	311
66.3862	16	1.407	331	66.4085	17	1.40662	331

the average crystallite size (D) can be estimated from the peak width with Scherrer's formula (12) :

$$D = \frac{K\lambda}{\beta_{FWHM}\cos\theta} \quad \ldots\ldots\ldots\ldots\ldots(1)$$

where D is the average crystal size, K is the Scherrer coefficient (0. 94), λ is the x-ray wavelength= 1.5406 A^{o} , θ is Bragg's angle and β the full width at half-maximum (FWHM) in radians.

The lattice parameter a of a cubic system is calculated according to the following equation (13):

$$a = \frac{d_{hkl}}{(h^2 + k^2 + l^2)^{\frac{1}{2}}} \quad \ldots\ldots\ldots(2)$$

where d_{hkl} is the inter-planar distance of each plane and (hkl) are Miller indices.

The dislocation density (δ), definide as the length of displacement lines per unit size of the quartz is expected from the formula (14):

$$\delta = \frac{1}{D^2} \quad \ldots\ldots\ldots\ldots(3)$$

The strain that made peak lengthening resulting from lattice deformation (microstrain) can be stated by Wilsok plan (15) :

$$\mu\epsilon = \frac{\beta_{FWHM}\cos\theta}{4} \quad \ldots\ldots\ldots(4)$$

The crystal layers number ($N_{\circ}$) calculated by using the following relation (16).

$$N_{\circ} = \frac{t}{D^3} \quad \ldots\ldots\ldots(5)$$

where t is the thickness of the samples

Figure (2) (a, b, c and d) shows the XRD patterns for pure and doped AlSb thin films at different Cu ratios (1%, 3% and 5%). From this figures, it is noticed that all samples have polycrystalline cubic structure with preferred orientation along (111) plane, and Cu addition causes slight offset shifting in the diffraction angle with a little decreasing in peak intensity and increasing the grain size for the film doped with 1% Cu. This film also appears less micro strain and dislocation density which attributed to the atomic radius of copper being less than the atomic radius of AlSb (r_{Cu} = 128pm, r_{Al} =143pm, r_{Sb} = 140 pm) (20). In addition, Cu may fill the interstitial spaces and reducing the crystal defects and hence reduce the roughness and the average diameter that seen clearly from the AFM images in figure (3) (a, b, c and d).

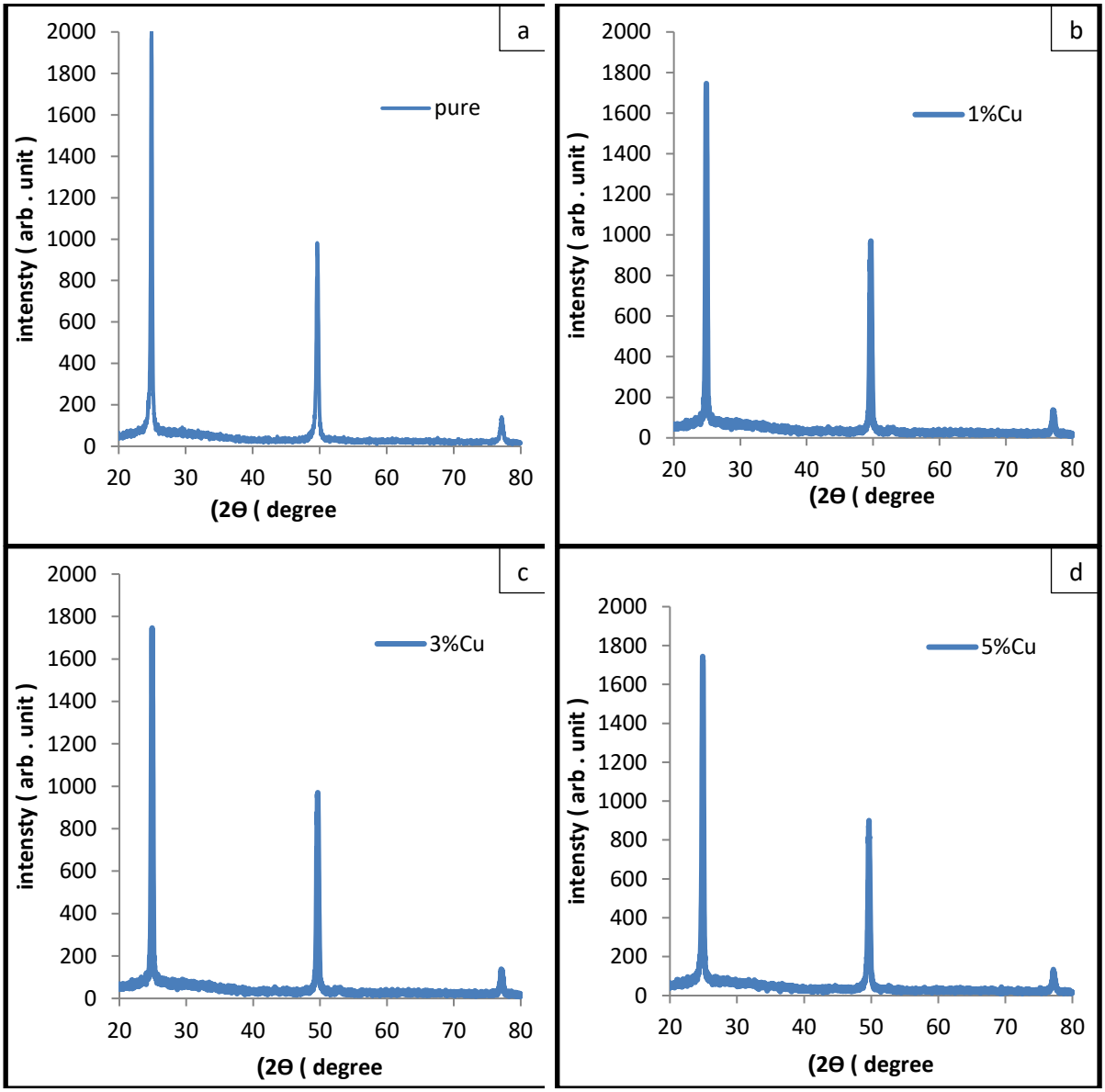

Figure 2. X-ray diffraction patterns of AlSb thin films for pure and doped samples.

Table 2. The grain size Micro strain , Dislocation density and Number Layers crystal for pure thin films and at different ratios of Cu (1% , 3% , 5%) .

sample	G.S	Micro strain)x10^{-4}(	Dislocation density×10^14	N10^{15}) x(Number Layers Crystal
Alloy	55.3907	6.603	3.25	1.176
Pure thin film	33.5776	10.923	8.87	5.283
Cu 1%	35.7995	10.153	7.802	4.359

Cu 3%	35.462	10.226	7.95	4.484
Cu 5%	34.8683	10.417	8.22	4.717

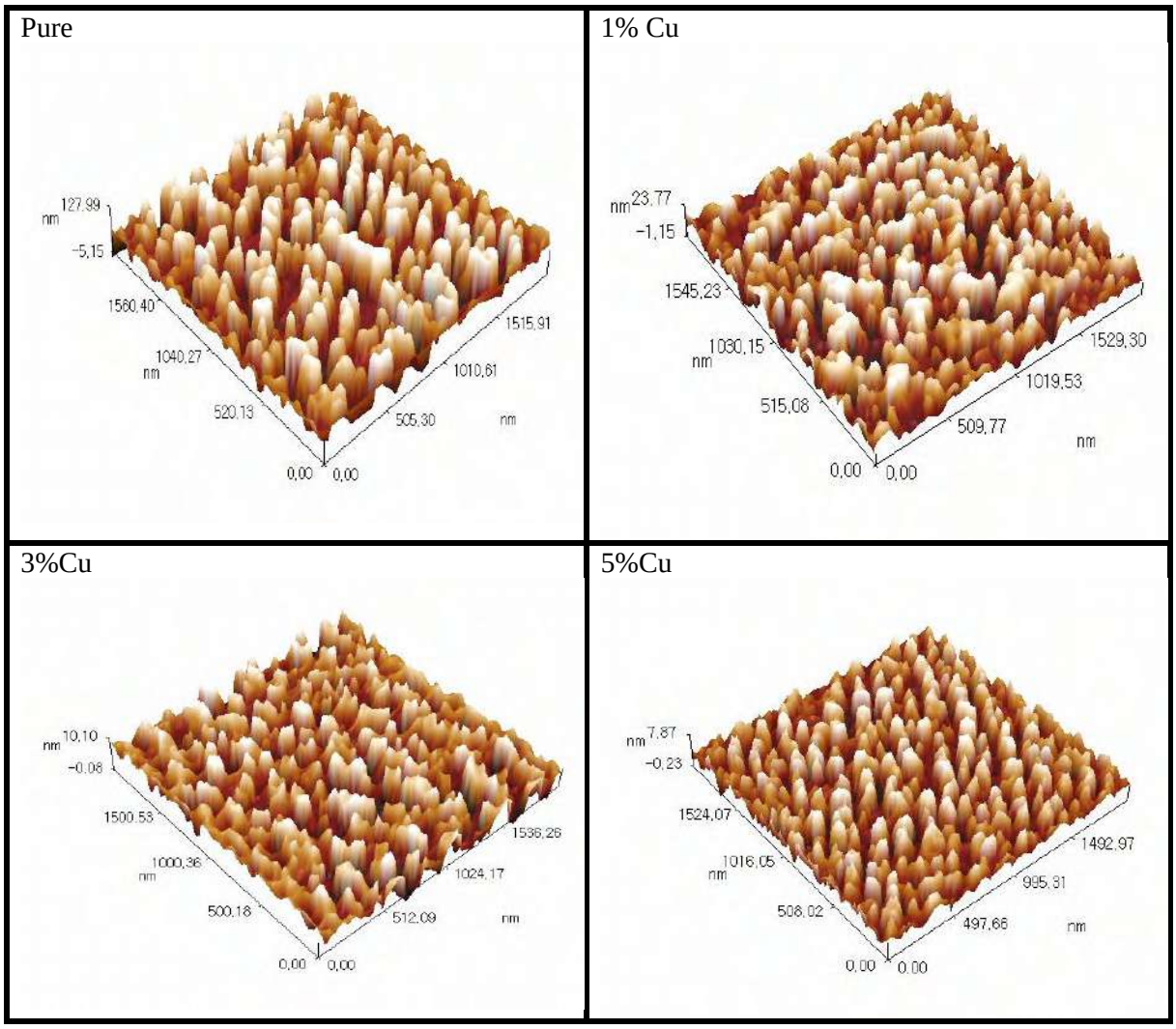

Figure 3. 3D AFM images AlSb / glass thin films pure and different Cu ratios

Table 3. Average Diameter, Roughness and root mean square for AlSb / glass thin films pure and different Cu ratios

Samples	Avg.Diameter (nm)	Roughness(nm)	r.m.s (nm)
pure	74.65	33.3	38.4
1% Cu	62.64	6.23	7.19
3% Cu	66.85	2.32	2.7
5% Cu	58.87	1.79	2.11

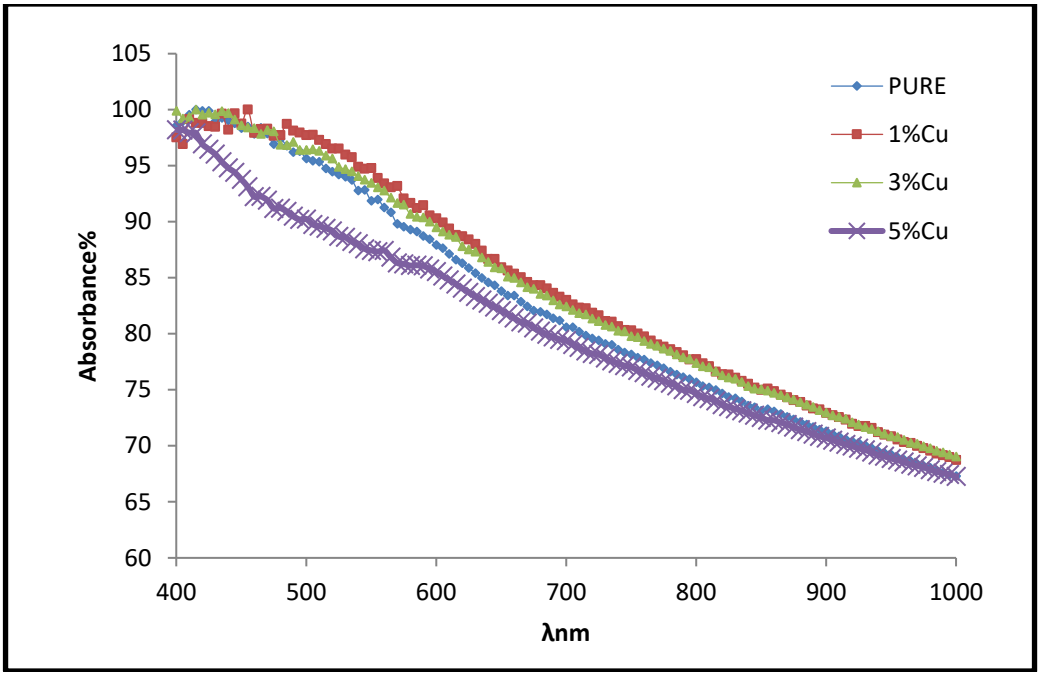

Figure 4. Absorption spectra of the AlSb thin films pure and different Cu ratios

Figure (4) shows the absorption spectra of the samples. We can see that all samples have a high absorption in the visible region, and the absorption coefficient (α) is given by the following equation (17).

$$\boldsymbol{\alpha} = 2.303 * (\frac{A}{t}) \text{.....(6)}$$

where A is the absorbance of the sample

To calculate the energy gap for the direct allowed transitions using Tauc equation

$$\alpha h\upsilon = B_o(h\upsilon - E_g^{opt.})^r \text{ .....(7) (18)}$$

where r = 1/2 for allowed transitions and r = 3/2 for forbidden transitions; E_g is the direct energy gap and B is a parameter that depends on the transition probability. The energy gap of all samples was calculated from figure (5) by plotting $(\alpha h\nu)^2$ versus photon energy for pur and doped AlSb thin films. The energy gap for direct allowed transitions decreases with increasing the Cu addition assigned to be 1.83 eV, 1.81 eV, 1.80 eV, and 1.78 eV for pure, 1% Cu, 3% Cu and 5% Cu respectively. These results can be attributed to the uniformity of the surface when adding copper. In addition, the copper added additional localized levels of electrons, hence reducing the energy gap.

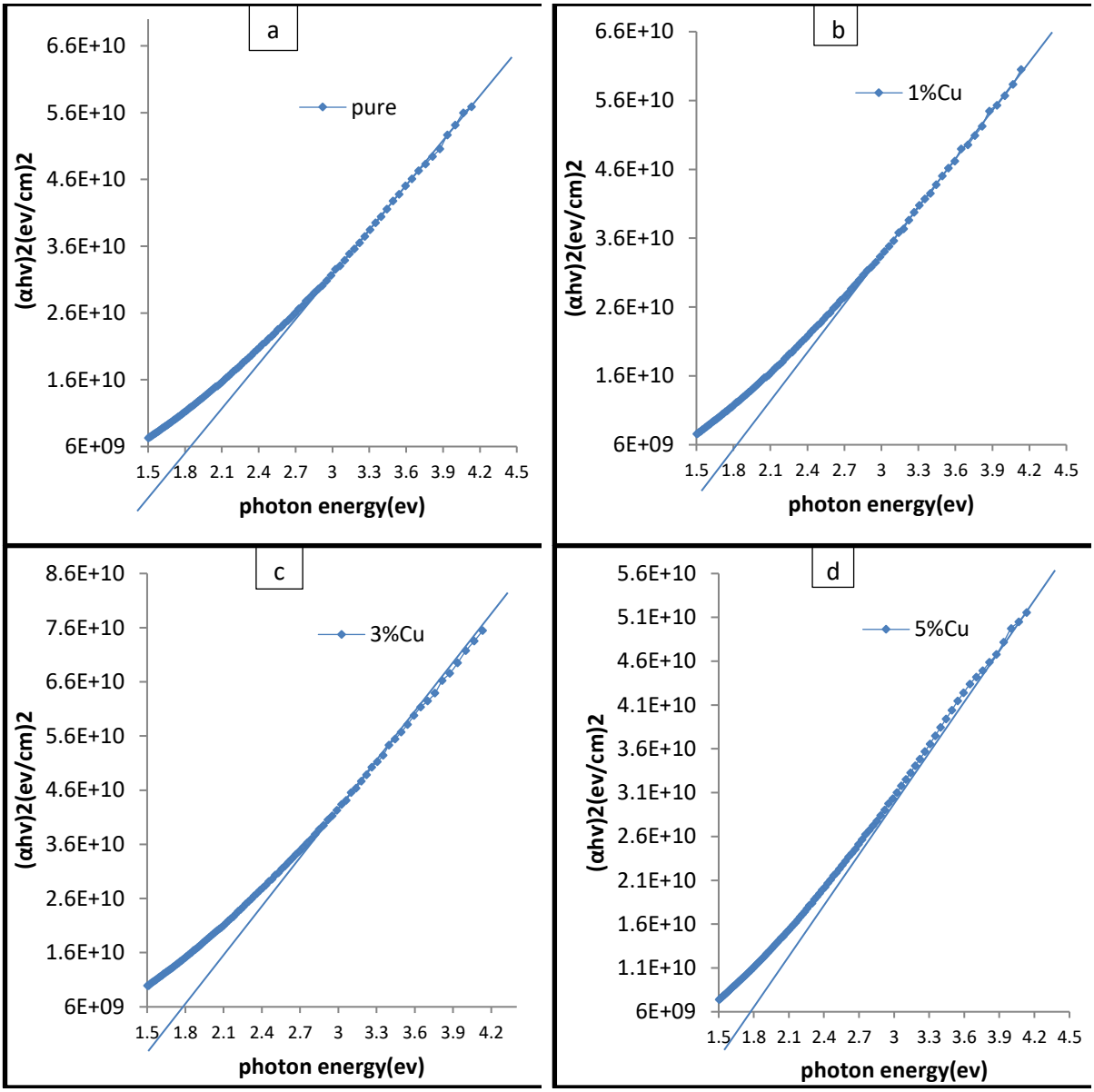

Figure 5. $(\alpha hv)^2$ verse photon energy for AlSb thin films pure and different Cu ratios

4. Conclusions

AlSb thin films were successfully deposited on glass substrates by thermal evaporation method. All the samples have a polycrystalline cubic structure, and adding Cu enhances the uniformity of the samples by decreasing the strain and increasing the grain size. The best structure property is found the film doped with 1% Cu, and the energy gap also decreases with increasing the Cu content.

References

[1] Tewksbury S K 1995 *Semiconductor Materials* West Virginia University.
[2] Chopra K L 1993 *Thin Film Devices Application* (Plenum Press New York).
[3] Rao B V and Okamoto T 2000 *Applied Surface Science* **159** (160) 335.

[4] Huang Z Li X Hao B He J X feng L H Li W. Zhang J Q and Cai Y P 2010 *Chin Phys. B* **19**.
[5] Sze S M 2007 *Physics of semiconductors Devices* Third edition (John Wiley & Sons- Inc).
[6] Timokhov F 2003 *Semiconductor Physics Quantum& Optoelectronics* 307.
[7] Das Shosh B Hussan S Bhar R and Pal A K 2015 *Journal of Crystal Growth* **419** 12 .
[8] Yao F F Lei Z Feng L H Zhan J Q Li W Wu L L Cai Y P Zheng J G and Li B 2006 *china Semiconductor* **27** 1579.
[9] Linnebach R and Benz K W 1981 *J.Cryst . Growth* **55** 531.
[10] Singh T and Bedi R K 1998 *Thin solid films* 1998 **312** 111
[11] Vaughan E I Addamane S Shima D M Balakrishnan G Hecht A A 2016 *J. Electron .Mater*. **45** 2025.
[12] Kareem T A Kaliani A A 2013 *Plasma Sci . Technol* **382**.
[13] Al – Jammal Y N 1990 *Solid State Physics* Al - Mosul University Arabic Version.
[14] Yousif M G 1989 *Solid State Physics* Vol.1 Baghdad University Arabic Version.
[15] Glunz S W Preu R and Biro D 2012 *Crystalline Silicon Solar Cells – Stateof-the-Art and Future Developments.*
[16] Karan V D Shajan X S and Karasan S T 2011 *Journal of Materials Science* 46 (11) 4034.
[17] Warren B E 1990 *X-Ray Diffraction* Addison –Wesley Publishing Company Inc U.S.A.
[18] Sze S M 1998 *Modern Semiconductor Device Physics* (John Wiley & Sons -New York).
[19] Powder Diffraction File 1997 JCPDS-International Center for Diffraction Data [ASTM] data files , (card No 00-006-0233). Pennsylvaning.
[20] Samuel Ruben 1998 Hand book of the elements 14.

The Effect of Adding SiC on Some of the Mechanical Properties of the Cu-Al_2O_3 System Using Powder Metallurgy

The Effect of Adding SiC on Some of the Mechanical Properties of the Cu-Al_2O_3 System Using Powder Metallurgy

Suha M. Ghareeb[1], Sabah Mahmoud Aman Allah[1], Salih Y. Darweesh[2]

[1]Physics Department, College of education for pure science, Kirkuk University, Kirkuk, Iraq
[2]Physics Department, College of Education TuzKhurmatu, Tikrit University, Tikrit, Iraq.

E-mail: Salih.younis@tu.edu.iq

Abstract. Powder metallurgy is one of the simple ways employed to produce alloys that are used in many technological applications. In the recent work, different contents (0, 5, 10, 15 and 20%) of silicon carbide ($\geq 63\mu m$) were used as a reinforcement material on matrix ((90, 85, 80, 75 and 70) % Cu-10% Nano-Al_2O_3). The mixture was milled by a locally made mill for three consecutive times (2, 4 and 6) hours. After that, a compressor with the highest compaction capacity (20 tons) was used to compact the mixture. The mixture was compacted in a steel die through applying pressure of 5 tons for one minute. After sintering samples at 900°C for two hours, mechanical tests including Vickers hardness, diametric compressive strength and wear were applied as a function of the grinding time. The results showed that the best hardness of (119.4 Hv) is reached for the grinding time of six hours and the reinforcement of (20% SiC), while the highest compressive strength was obtained for same time of grinding with a reinforcement of (53.3 Mpa). Concerning the rate of wear, its value decreased to the lowest value at the same conditions above (1.10368*10-7 g/cm). Accordingly, the best characteristic parameters of the results appeared at 900°C, the grinding time of six hours, and reinforcement content of 20%.

1. Introduction

Powder metallurgy is the process of producing metal materials whereby parts are produced in different forms of metal powders. Powders are compacted to obtain the required shapes, and then these resulting parts are heated with a process called sintering in order to create the interconnection between particles to obtain a rigid mass. The process of compaction is performed at certain compaction levels using a compressor with tools designed and manufactured for this purpose, which are die and compressor. The subsequent sintering process is performed at a temperature below the melting point of the matrix. This method is used either because of the difficulty of producing these alloys by casting process because their components are not mixed in the liquid state or because it is difficult to melt them [1]. The composite is a mixture of two or more materials that are strongly correlated with each other based on which the material acts as a single mass, so that it possesses intermediate properties of the component. This means that the composite material consists of two phases: matrix and reinforcement. The phases used are metal, ceramic or polymeric materials and the reinforcement phase is particles, fibers, whisker or sheets [2-4]. Copper-based composites produced with powder metallurgy technology are ranked third after iron, steel and aluminum-based products. The use of copper in powder metallurgy dates back to the 1920s [5]. Due to the high electrical and thermal connectivity, copper and its alloys have been widely used in thermal

and electronic applications such as the packaging of electronics, contactors and resistance welding poles. However, the relatively low mechanical properties in both high temperature and room temperature have limited or reduced the wide applications of pure copper. The mechanical properties can be improved by adding reinforcement materials for copper and its alloys. In other words, the copper-based and particle-reinforced composites may have many distinct benefits such as high mechanical, conductive properties and wear resistance [6]. The current study aims to improve the behavior of wear and reduce rubbing as well as mechanical properties by preparing a metal-based composite, which is copper, and reinforcing it by silicon carbide with different volumetric sizes using powder metallurgy. Thus, it can be used in many applications such as electric brushes, sliding mechanical bearings and other applications that require excellent thermal and electrical conductivity with low wear behavior.

Experimental Part

Raw Materials

The matrix used is copper manufactured by the Indian company (CDH) with grain size (44μm) and purity 99.5%. The first reinforcement material is Alumina α-Al_2O_3, manufactured by Changsha Santech Co., of Chinese origin with grain size (30±5) nm and a purity of ≥99.99%. The second reinforcement material is silicon carbide (SiC) manufactured by Merck the German company with grain size (53μm) and a purity of 99.90%.

2. Sample Preparation Method For Measurement

Powders were dried at a temperature of (200°C) for 2 hours to get rid of wetness and other volatile materials. The weights of each component mix were then created by following the weight ratios so that the alumina ratio was constant by (10%) for all mixtures. Silicon oxide percentages were (0, 5, 10, 15 and 20) % and copper was the matrix (90, 85, 80, 75 and 70)%. The weight was done using a Japanese-origin Sartorius electric balance with accuracy of (0.0001 g). After completing the grinding and stirring processes and obtaining a homogenous powder for three different grinding times, the samples were formed using uniaxial compaction in a steel die with a hardness of (60HRC). The stirred mixture was carefully placed inside the compaction die to avoid any movement of its parts. A pressure of (5 ton) was then applied for one minute to avoid the possibility of elasticity [7]. For this purpose, a Turkish-origin computerized hydraulic compaction of (HALIM USTA) type with a capacity of 20 ton was used to obtain cylindrical samples of (10) mm in diameter and 6 mm height. After compaction, the samples were not ready to perform tests and had weak resistance, which is green resistance. This requires care when transporting and handling until performing the sintering process. The sintering process was performed using a German-origin CARBOLITE oven at 900 °C for two hours. After that, the samples were removed from the oven for the examination process after the preparation of the sample surfaces.

3. Examinations and Measurements

3.1. Vickers Hardness (Hv)

Hardness is an important mechanical feature. It is known to be resistant to surface indentation [8]. It was examined using Vickers method by inserting the tool (a square-based diamond pyramid) by forcing a load of 500 g for (10 Sec). By calculating the diameters of the resulting indentation, Vickers hardness could be defined for the compacted sample by applying equation (1) [9]:

$$\mathrm{Hv} = 1.8544\ \mathrm{P}/\mathrm{D}_{\mathrm{v}}^{2}\ \mathrm{g}/\mathrm{mm}^{2} \quad \ldots\ldots (1)$$

where P is the force applied (g) and Dv is the average diameter of the pyramidal indent resulting from forcing a load on the surface.

3.2. Diametric Compressive Strength

Compressive strength was tested using Universal Testing Machine of (HOYTOM) type of Chinese origin. The sample was placed on the test platform. After that, a load was then applied to the diameter

of the sample until the failure occurred. The maximum load was recorded from the digital screen of the machine, knowing that the machine has the possibility to store the maximum value of the load before failure. Compressive strength was calculated using Eq. 2 [10]:

$$\sigma_D = \frac{2F}{\pi dh} \dots\dots\dots\dots\dots (2)$$

where σ_D is the compressive strength of crushing (MPa), F is the applied load (N), d is the sample diameter (mm), h is the sample thickness (mm).

3.3. Wear Rate Test

Wear is an important characteristic of the material surface, which is defined as the loss of material from the metal surface due to the friction of moving parts. From the initial trials, the amount of applied load was determined by (10N), using a fixed sliding speed (480 r.p.m). The period of applied load per test was 10 min. Wear test was carried out using a Pin-on-Disc device of Chinese origin found in the laboratories of the Department of Mechanical Engineering at Tikrit University. Table (1) shows the conditions of wear. A vertical load was applied by a (Pin) through a holder. The compacted sample was placed on a rotary disk. The reading was taken by a top sensor tied vertically on the arm holding the compacted sample. The reading was then moved to a digital scale fixed at the front of the device. The required loads were fixed at the top of the device as required. Wear rate was calculated using the weight method, which included calculating the amount of weight loss for each sample through weighing the sample before connecting it to the device and after the completion of the device operation using a digital balance by applying the following relation [11,12,13,14] :

$$W = \frac{\Delta W}{SD} \text{ (gm/cm) --- (3)}$$

where W is wear rate (g/cm), ΔW is the lost weight (g) which represents the difference in weight for the sample before and after operation, SD is the sliding distance (cm) which equals:

$$SD = \pi D n t \text{ --- (4)}$$

where D is the disc diameter (cm), n is the rotational velocity of the disk (rpm), t is the test time (min).

Table 1. Conditions of wear rate test

The rotational velocity of the disc	480 r.p.m
Test time	10 min
Vertical load applied	(10) N
The diameter of the test disc	60 mm
Disc hardness	62 HRC

Step of the Test Method

The compacted samples of diameter (10) mm and height (5) mm were prepared.
The samples were ground using sandpaper (400, 600, 800, 1200).
The sample was weighed before the test using a sensitive digital balance.
The rotational disc of the device was cleaned before starting the test.
The sample was fixed in its position using a holder designed according to the heights and diameter of the compacted sample. More than one sample was manufactured in the mechanical workshops in the General Company for the manufacture of medicines and medical supplies in Samarra.
Loads were fixed and a load of (15, 20, 25) Newton was applied vertically each time to the samples at a rotational velocity of the disk of (480 r.p.m).
The device was switched on after adjusting and resetting the test time.
The device was switched off after (20) minutes from the start of operation.
The sample was removed and weighed using the balance after the test.
The amount of weight loss was defined.
The relationship (3) was applied to extract wear rate for each sample.
The above-mentioned processes were reapplied to all samples. Wear rate was calculated for each sample by calculating the average wear rate for the upper and lower surface of each sample.

4. Results and Discussion

4.1.The Effect of the Added Content and Grinding Time on Vickers Hardness

Figure (1) shows the relationship between the change in the size ratios of silicon carbide particles and the grinding time on Vickers hardness after sintering at 900°C for two hours. It is observed that the hardness increases with increasing the content of silicon carbide and grinding time. Hardness increased after sintering from (38.1-84.2) at the grinding time of two hours. Then, it increased from (54.4-102.8) at a grinding time of four hours. After that, it increased from (74.6-119.4) at the grinding time of six hours for all cases at silicon carbide content (0-20%).

The increase in hardness as a result of adding silicon carbide particles and grinding is due to the high hardness of silicon carbide particles located within the range of (2500-3300) kgf/mm^2. In addition to the large number of interfaces formed as a result of adding reinforcement particles (SiC); as well as increased resistance to plastic deformation and increased residual internal stress due to the difference in coefficient of thermal expansion between matrix and reinforcement particles that produce a lot of dislocations. This leads to increase the hardness of the composites because silicon carbide particles of high hardness act as barriers to the deformation of the matrix and thus hinder the movement of dislocations. This makes stress greater in order for the dislocation to pass through the particles and thus requires an increase in the applied load. This in itself means an increase in the hardness values, and that the homogeneous distribution between matrix and reinforcement particles also has a major role in increasing the hardness. This is consistent with the results published in [15,16].

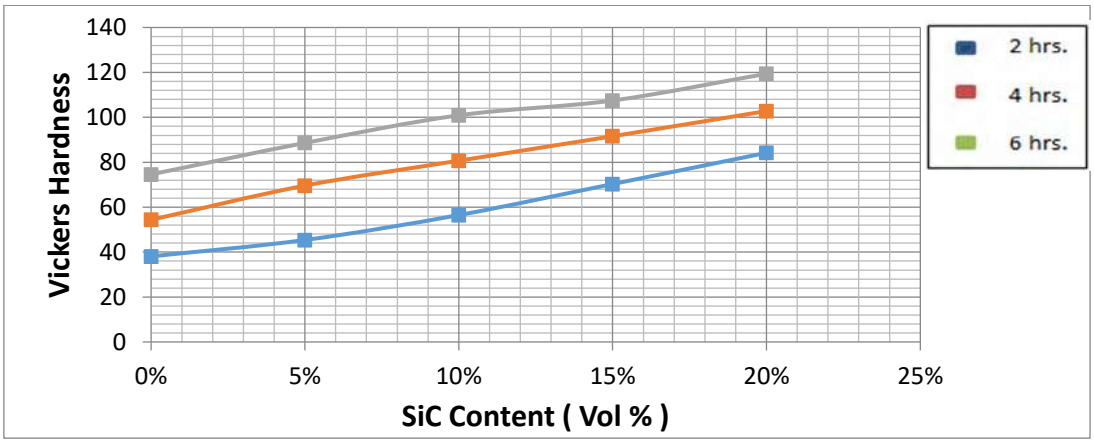

Figure 1. The relationship between the change in the size ratios of silicon carbide particles and grinding time with hardness after the sintering process.

4.2.The Effect of the Added Content and Grinding Time on Diametric Compressive Strength

Figure (2) shows the relationship between the content of silicon carbide and grinding time on the compressive strength of the composites with different silicon carbide ratios. Increased content and grinding time result in increasing the compression strength of the composite regardless the ratio of silicon carbide particles. The compressive strength increased from (10.6-28.8 MPa) for a grinding time of two hours, then it increased from (15.2-40.5 MPa) for a grinding time of four hours. After that, it increased from (22.4-53.3 MPa) for a grinding time of six hours for all cases at a silicon carbide content of (0-20%).

This is due to the high resistance of the reinforcement particles, which increased the composite hardness by increasing the content of silicon carbide. In addition, it is also related to the resistance of on-site deformations with high efficiency and then the formation of coherent samples with high compression strength. The high sintering temperature for two hours plays an important role in increasing the strength of the correlation between component particles of composites through good propagation and distribution, as well as increasing density and decreasing the ratios of porosity after sintering, which

leads to support and reinforce the composite mass. This is consistent with the results of the study in ref. [15].

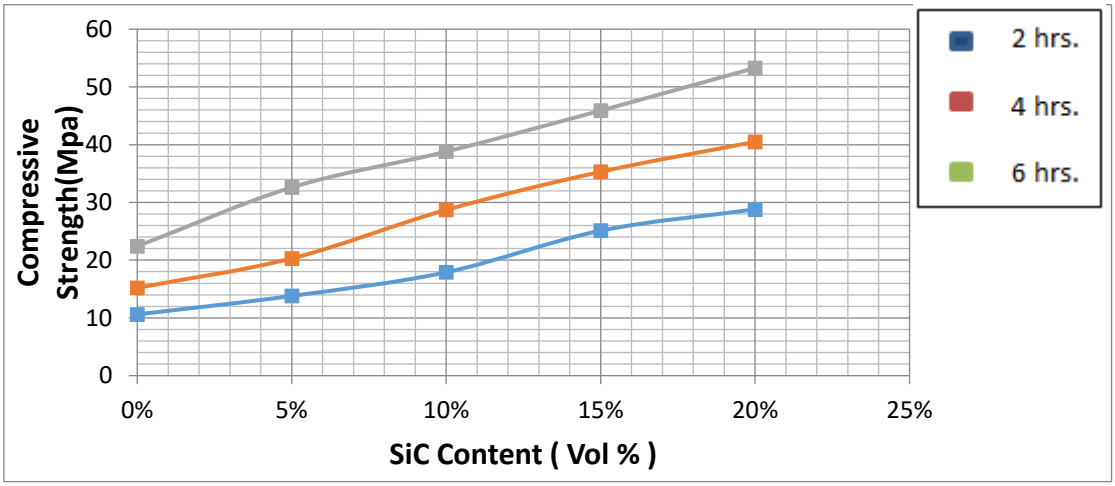

Figure 2. The relationship between the change in the size ratios of silicon carbide particles and grinding time with diametric compressive strength after the sintering process

4.3. The Effect of the Added Content and Grinding Time on Wear Rate

Figure (3) shows the relationship between the change in the size ratios of silicon carbide particles and grinding time with wear rate after sintering at 900°C for two hours. It is observed that increasing the size ratios added to silicon carbide and grinding time has reduced wear rate from ($3.53036*10^{-7}$-$1.81377*10^{-7}$) g/cm at a grinding time of two hours. Then, it decreased from ($2.42915*10^{-7}$-$1.54899*10^{-7}$) g/cm at a four-hour grinding time. After that, it decreased from ($1.94332*10^{-7}$-$1.10368*10^{-7}$) g/cm at grinding time of six hours for all cases at silicon carbide content (0-20%).

The low wear rate when increasing the content of reinforcement particles and grinding is attributed to the high hardness of composites when adding silicon carbide particles. Hence, the weight loss is low as a result of reinforcement of surface or ground with ceramic particles that hinder the progress of the dislocations. Therefore, stresses that are resisted by hard particles (SiC) would be generated and thus generating a dislocation density. The difference in the coefficient of thermal expansion has a significant role in this process that results in increasing the hardness by increasing the content of reinforcement particles. Moreover, wear rate decreases when adding SiC particles that cause increased hardness [17]. Wear rate is inversely proportional to the hardness according to the following relationship[18]:

$$V = K * \frac{Wx}{H} - - -(5)$$

where V is wear size, K is the coefficient of wear, W is the vertical load, X is the sliding distance, H is the material hardness.

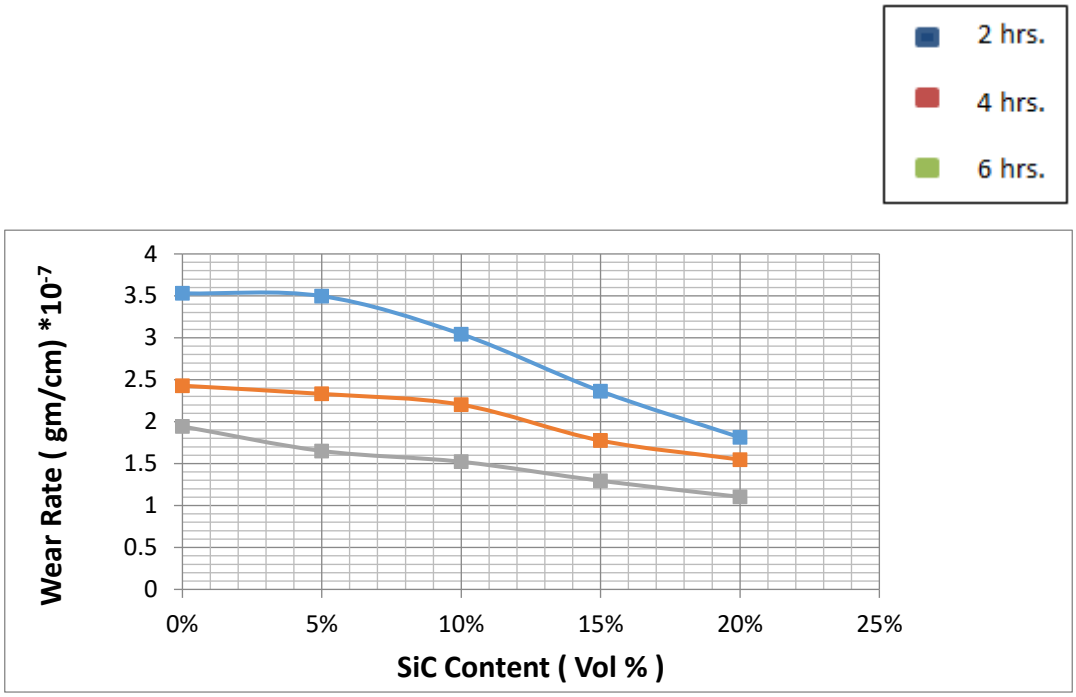

Figure 3. The relationship between the change in the size ratios of silicon carbide particles and grinding time with wear rate after the sintering process.

5. Conclusions

The important conclusion of the current research is the possibility of manufacturing models of copper-based composites reinforced by two materials of Nano-alumina by 10% and micro silicon carbide in different contents. After sintering at 900°C for two hours, mechanical tests were conducted. The obtained results showed that the best hardness was (119.4 Hv) at a grinding time of six hours and reinforcement (20%SiC). While the highest compression strength obtained at the same grinding time and reinforcement rate was (53.3 Mpa). As for wear rate, its value decreased as it was lower in the same conditions mentioned above ($1.10368*10^{-7}$ g/cm).

References

[1] Groover MP 2002 F*undamentals of modern manufacturing materials, processes and system* Second Edition, John Wiley and Sons, 344-361.
[2] Cogswell FN 2013 *Thermoplastic aromatic polymer composites: a study of the structure*, processing and properties of carbon fibre reinforced polyetheretherketone and related materials. Elsevier.
[3] Chawla N and Chawla KK 2012 *Metal Matrix Composites* Library of Congress Cataloging in Publication Data 5- 65, © 2006 Springer Science Business Media .
[4] Ashby MF and Jones DRH 2012 *Engineering materials 1: an introduction to properties, applications and design*. Vol. 1. Elsevier, 2012.
[5] Ashby MF and Jones DRH 1980 Engineering Materials (An Introduction to their properties and application) Engineering department, Cambridge university, England *Int. Series Mat. Sci. Technol.* **34** 25-55.
[6] Braunovic M, Myshkin NK and Konchits VV 2017 *Electrical contacts: fundamentals, applications and technology* CRC press.
[7] Jassim IK, Abdul Aziz ASF, Farhan FK and Darweesh SY 2018 Characteristics of the Electrical Conductivity of the Basalt-Aluminum System Manufactured by Powder Technology *JUBPAS* **26** 2 288 - 300.

[8] Darweesh SY, Ali AM and Khodair ZT 2019 The Effect of Some Physical and Mechanical Properties of Cermet Coating on Petroleum Pipes Prepared by Thermal Spray Method *J Fail. Anal. Preven*. **19** 1726–1738.
[9] Darwe SY, Majeed ZN and Dahham AT 2020 Improving the Durability of Streak and Thermal Insulation of Petroleum Pipes by Using Polymeric Based Paint System *Baghdad Sci. J.* **17** 3.
[10] Abdulla AN, Jassim IK and Darweesh SY 2020 Effects of Nano Titanium Oxide Addition Using Powder Method on Ni-Al2O3 System Structural and Mechanical Properties *Scient. J. King Faisal Univ.* **21** 2 2020.
[11] Berger MB 2010 *The Importance and Testing of Density / Porosity / Permeability / Pore Size for Refractories* The Southern African Institute of Mining and Metallurgy, Refractories, 101-115, 2010 Conference .
[12] Wang JZ, Ying H and Qu X 2009 Analysis of Density and Mechanical Properties of High Velocity Compact Iron Powder " , University of Science and Technology Beijing 100083, China, (Science Direct) *Act Metall. Sin. (Eng, Lett.)* **22** 6 447-453,2009.
[13] Lowell S and Shields JE 1984 *Powder Surface Area and Porosity* Second Edition , Printed in Great Britain by J. W. Arrow smith Ltd. ,PP.217-224, Bristol © 1984 S. Lowell and J. E. Shields .
[14] Salih YD, Ismael KJ and Amer SH 2019 Characterization Of Cerment Composite Coating Al2O3-Ni System *J. Phys. Conf. Sers*. **1294** 2 022011.
[15] CelebiEfe G, Yener T, Altinsoy I, Ipek M, Zeytin S and Bindal C 2010 Characterization of Cemented Cu Matrix Composites Reinforced with SiC ", Sakarya University ,Engineering Faculty, Department of Metallurgy And Materials Engineering, Esentepe Campus, 54187 Sakarya , Turkey , *Vacuum* **85** 643-647.
[16] Younis SB 2011 *Mechanical Properties Investigation of Cu – SiC Composites Using Different Percentage of Magnesium Element* Department of Applied Science, Technology University, 97-104.
[17] Sumathi M and Selvakumar N 2012 An Investigation on the Workability of Sintered Copper – Silicon Carbide Performs During Cold Axial Upsetting " , Department of Mechanical Engineering , National Engineering College ,Kovilpatti 628 503 , India & Department of Mechanical Engineering ,MepcoSchlenk engineering college, Sivakasi 626 005, India *Indian J. Eng. Mat. Sci*. **19** 121-128.
[18] Prosviryakov AS, Aksenov AA, Samoshina ME, Kovaleva MG and Ivanov DO 2011 Mechanical alloying of Cu–SiC materials prepared with utilisation of copper waste chips *Powder Metall.* **54** 3 382-384.

Studying the Structural and Morphological Properties of (PMMA) Film under D.C Discharge Plasma

Studying the Structural and Morphological Properties of (PMMA) Film under D.C Discharge Plasma

Mohammed K. Khalaf[1], Sabah N. Mazhir[2*], Zainab J Jaffer[2]

[1]Directorate of Materials Research, Ministry of Higher Education and Scientific Research, Iraq
[2]Dept. of Physics, College of Science for women, University of Baghdad, Iraq.

E-mail: sabahnm_phys@csw.uobaghdad.edu.iq

Abstract. In this paper, a lab-scale direct current (DC) glow discharges plasma system was used to adjust the surfaces of polymeric films. Characteristics of the plasma system have displayed under the discharge of three gasses (O_2, N_2 and Ar). DC-Plasma system has been used for the adjustment of polymethyl methacrylate surface as a function of treatment time and the types of gases. The modified surface was characterized in terms of crystal structure and surface morphology by the analysis of X-ray diffraction, scanning electron microscopy (SEM) and atomic force microscopy (AFM). A comparison between treated and untreated films was also made. The roughness and the root mean square (RMS) for pure PMMA films were continuously increased with increasing the exposure time for different gasses. SEM images observed degradation of the surface with granular spots due to the chain missioning and cross-linking effects. An efficient method of treatment for enhancing the surface roughness of pure-PMMA polymer is the using of argon plasma compared to O_2, N_2 plasma

Keywords: Polymers, PMMA, Plasma Treatment, Discharge Plasma.

1. Introduction

Polymers have been widely used in several scientific, industrial and biological fields like biomaterials, thin-film technology, adhesion, wear composites and friction, protective coatings, and microelectronic devices. In common, they were from successful applications that are widely requested because of private surface characteristics with respect to roughness, chemical composition, hydrophilicity, crystallinity, and cross-linking density [1,2]. Polymers are commonly used for a given purpose in many medical fields because of their bio inert characteristics and their ease of customizing their chemical and physical properties. Poly-methyl-methacrylate (PMMA) is a polymer with several attractive properties. It has environmental stability, low cost, and good optical properties [3]. In addition to its superior physical and chemical properties, PMMA is also being extensively used in numerous fields of life in recent years [4,5]. It is superior light transmittance, mechanical properties (impact strength, durability) and low density that superior to glass [6]. Simple manufacturing and low cost of production also lead to its widespread use. Its biocompatibility makes Poly-methyl methacrylate particularly desirable in medicine as a drug delivery agent, eye and contact lenses, orthopedic surgery, or dentistry [7,8]. A hydrophilic surface was observed to be formed by surface alteration and the creation of new functional groups on the surface by (DC) direct current plasma treatment [9,10]. It is significant that the surface modification of PMMA improves its biocompatibility and reduces implantation complications while maintaining its

excellent bulk properties [11]. In this paper, plasma processing has become one of the most promising strategies due to the combination of its advantages, including quick, environmentally friendly, solvent-free processing, low operational and maintenance costs [12].

2. Experimental Part

2.1. Substrate Preparation

By means of the spray pyrolysis method, Pure PMMA thin films were prepared. The glass sheets were sequentially washed in an ultrasonic bath with ethanol and acetone. Lastly, they were eventually rinsed with purified water and dried up. The deposition method involves decomposition (PMMA) spraying the solution onto substrates placed at a distance of 25 cm from the spray nozzle at 30-40 C° depositing temperature. Then, the process of spraying the liquid inside the spray device is controlled in terms of the spray time to 2 min, the number of sprinkles is five times, as well as the time period between one spraying and another was also 2 min.

2.2. Plasma treatment process and conditions

Surface modification of the PMMA films is achieved by treating incandescent Direct Current glow discharge plasma for different gases such as (O_2, N_2, Ar). The samples were cut into little slides with dimensions of (2x1) cm before the treatment of plasma. The samples were placed inside a vacuum chamber under a pressure of 10^{-2} mbar. The samples were backed on a glass rode and put in sit on spacing of 2.5cm from cathode. The time of treatment by plasma was changed from (5 - 30) min. The working parameters are listed in Table1.

Table 1: Working parameters for plasma treatment

Parameters	Values applied
Working Pressure	6.5 x 10^{-1} mbar
Electrode separation	5.5 cm
Power Supply	690 Volt
Flow rate of gas	750 cm^3/min
Exposure time	5 -30 min
Working gas	O_2 , N_2 , Ar

2.3. Characterization instruments:

X-ray diffraction (XRD) a non-devastating method for substances is commonly used to identify structural characteristics. The qualitative analysis may be conducted on the premise of peak height or peak zone. The peak angles may be utilized to decide particle diameters and the degree of crystallization. The X-ray spectra were gotten through utilizing copper filtered Cukα radiation λ=1.54060 (A) worked at 40 (kV) and 20 (mA) kind (SHIMADZU-6000) made in Japan. Field emission scanning electron microscope (FESEM), Hitachi (S-4160) with a continuous magnification capacity from 6x to 100,000x and Energy Dispersive X-Ray Analysis (EDX), referred to as EDS or EDAX, an x-ray technique used to identify the elementary structure of materials. Atomic Force Microscopy (AFM) is the device used for type inspection (AA3000 Scanning Probe Microscope SPM, NSC35/AIBS tip) that used to analyse the morphology and the roughness of the surfaces.

3. Results and Discussion.

3.1. Analyzing X-ray Diffraction

The x-ray diffraction spectra were used to analyse the crystalline structure of pure-PMMA films. It is clear that pure-PMMA film possesses no crystalline structure therefore, the XRD pattern reveals amorphous scattering around 2θ =12.50 and 25° from ratio of diffraction peak areas for crystal structure analysis before and after oxygen plasma treatment where the peak is even more intense for the treated film due to increased crystallinity. After oxygen plasma treatment and for different exposure times (5-30min), there were variations in the form or location of diffraction peaks in Figure (1). The XRD patterns

for pure- PMMA films before and after plasma-treatments for various gases (O2, N2, Ar) as indicated in figure (2). It is noticed an increase in the density disparity to regions for the pure-PMMA films treated by (O2, N2, Ar) plasmas over the same exposure period for untreated samples [13]. All these peaks' intensities also increased and contributed to the dominant disordering and thus affected the crystalline structure. In addition, due to the formation of the disordered structure in the plasma-treated PMMA polymer, the full width at half maximum (FWHM) of the peaks are broadened.

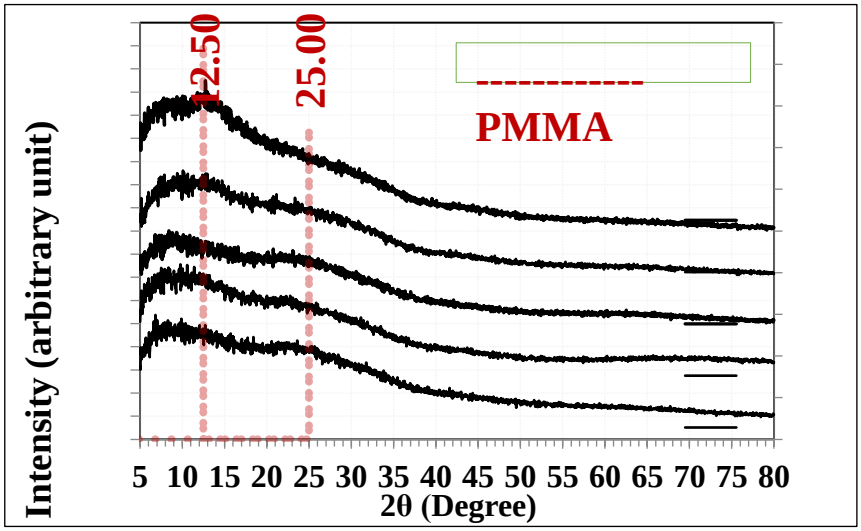

Figure 1. X-ray diffraction patterns of (a) PMMA-Pure (b) PMMA-PO_2 (5min) (c) PMMA-PO_2 (10min) (d) PMMA-PO_2 (20min) (e) PMMA-PO_2 (30min).

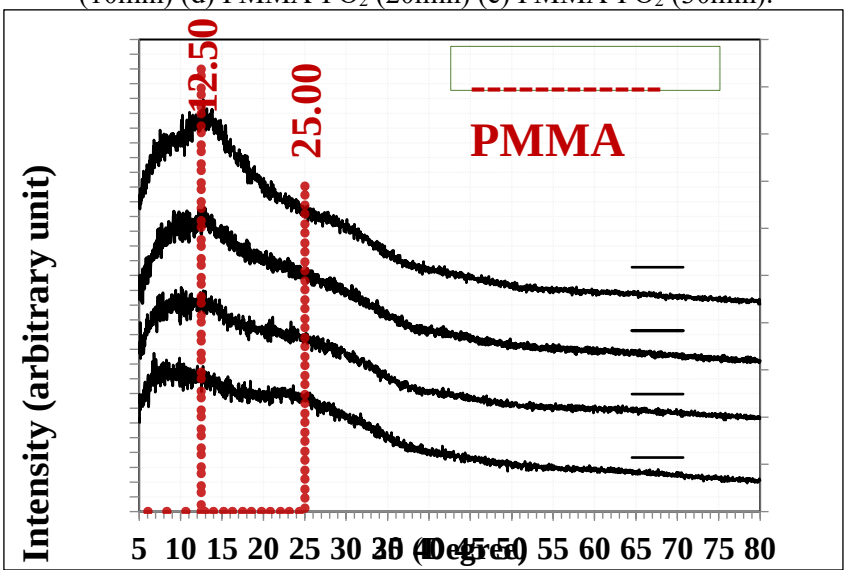

Figure 2. X-ray diffraction patterns of (a) PMMA-Pure (d) PMMA PO_2(20min) (f)PMMA-PAr(20min) (h) PMMA-PN_2 (20min)

3.2. Surface morphology analysis.

The AFM images for untreated and treated pure-PMMA films were shown in figure (3). Figure 3 (a) shows that the surface of untreated pure-PMMA film is smooth with the presence of conical protuberances and slight roughness. With increasing the exposure times of O_2 plasma treatment, the

surface roughness and the scale of the conical protuberances increased as seen in figure 3 (b - e). The roughness and the root mean square of untreated and treated pure-PMMA films are listed in Table 1. It is seen that the values of the RMS gradually increased with increasing the exposure time. The surface roughness is increased due to the removal of few top monolayers of the polymer films caused by the impact of plasma species on the surface [14]. The surface roughness increases the wettability and the bonding strength. The surface roughness Ra (evaluated from the AFM images) was 0.904 nm for untreated pure-PMMA, and it increased to be (3.98, 4.67, 5.33, and 4.16) nm after the treatment of 5, 10, 20, and 30 min respectively. As shows in table 2, it is noted that after the treatment with O_2 plasma, the roughness of the PMMA surface significantly increased during the treatment time, ranging from 5–30 min. The small decrease in Ra at a high treatment time value is possibly due to the cross-linking of newly formed surface radicals that may partially change its orientation and fill up the surrounding valleys, thus decreasing the roughness of the surface. This behavior agrees with references [15,16].

Table 2: Average diameter, Roughness average and the root mean square for pure-PMMA untreated and treated by O_2 plasma

Sample	Average diameter (nm)	Roughness average (nm)	The root mean square (nm)
PMMA-Pure	73.11 nm	0.904 nm	1.48 nm
PMMA-PO$_2$(5min)	78.96 nm	3.98 nm	4.99 nm
PMMA-PO$_2$(10min)	87.57 nm	4.67 nm	8.02 nm
PMMA-PO$_2$(20min)	93.25 nm	5.33 nm	9.01 nm
PMMA-PO$_2$(30min)	70.48 nm	4.16 nm	5.24 nm

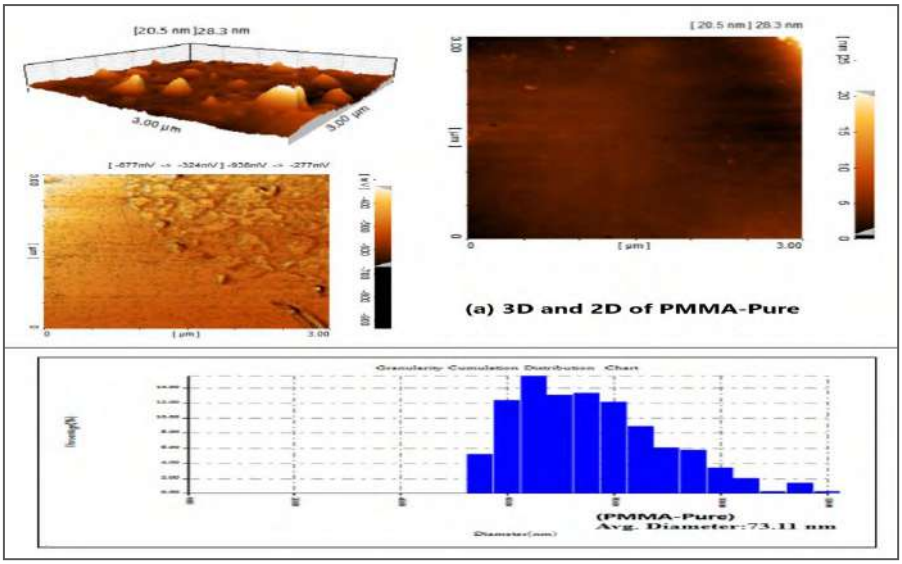

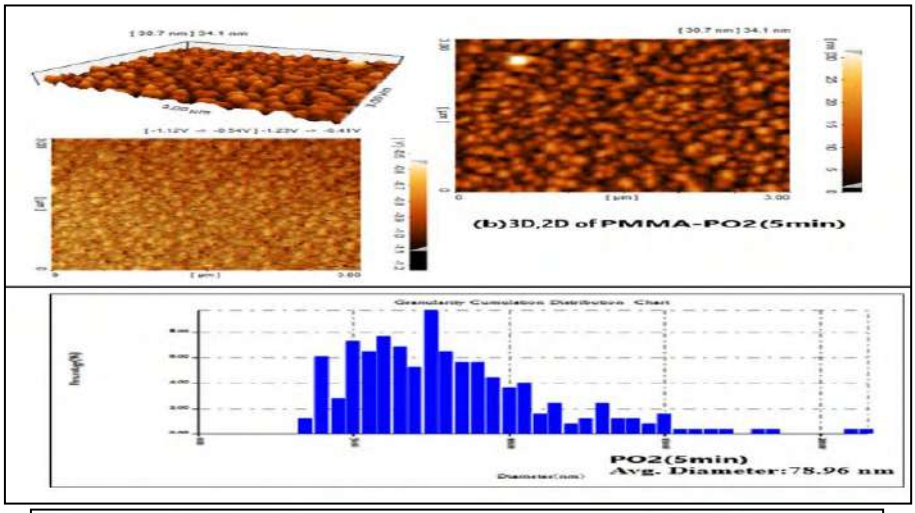
(b)3D,2D of PMMA-PO2(5min)
Granularity Cumulation Distribution Chart
PO2(5min)
Avg. Diameter:78.96 nm

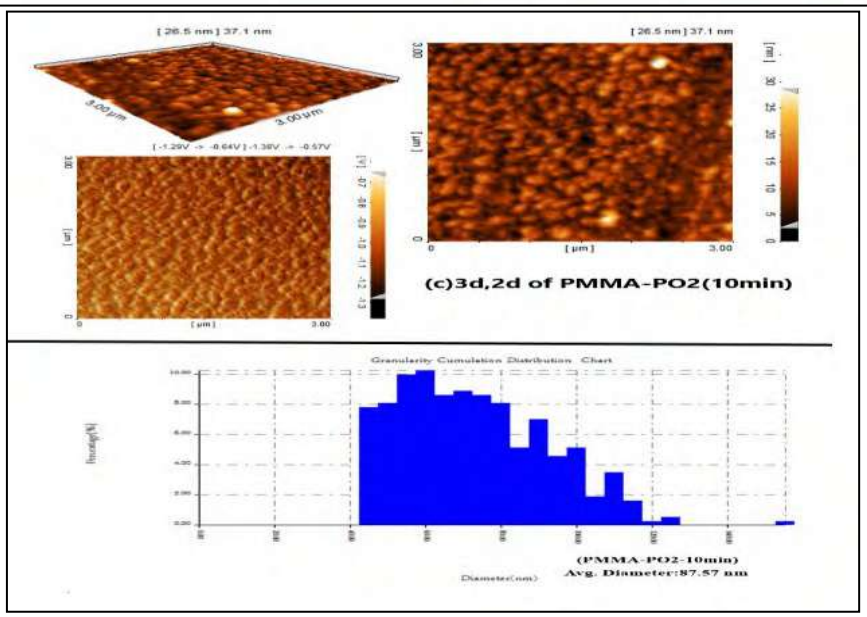
(c)3d,2d of PMMA-PO2(10min)
Granularity Cumulation Distribution Chart
(PMMA-PO2-10min)
Avg. Diameter:87.57 nm

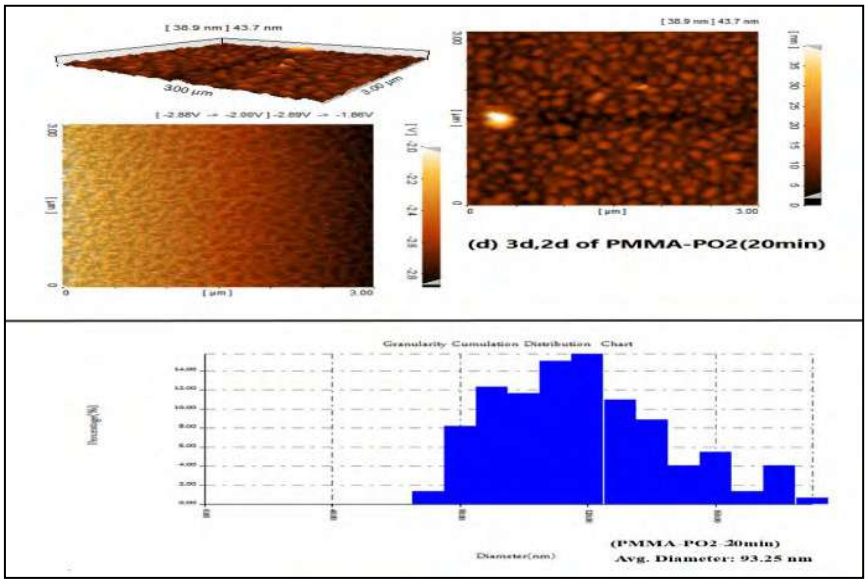
(d) 3d,2d of PMMA-PO2(20min)
Granularity Cumulation Distribution Chart
(PMMA-PO2-20min)
Avg. Diameter: 93.25 nm

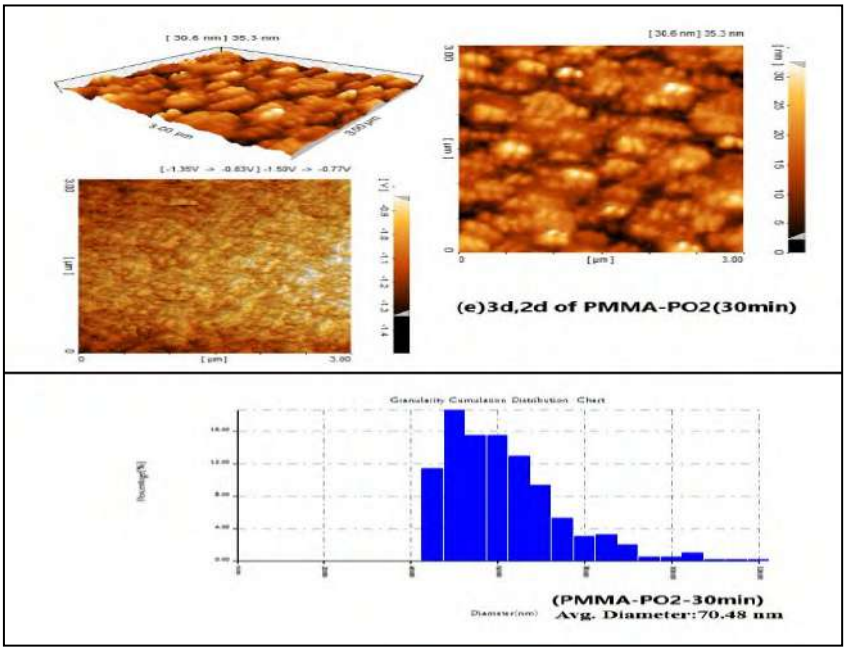

Figure 3. AFM measurements of (a) PMMA-Pure (b) PMMA-PO_2 (5min) (c)PMMA-PO_2 (10min) (d) PMMA-PO_2 (20min) and (e) PMMA-PO_2 (30min).

The influence of the cross-linking is observed by noticing the dependence of PMMA surface roughness on the ion energy. The surface roughness of PMMA films shows an opposite dependence on the ion energy following Ar, N_2, O_2 plasma exposure. The improvement by increasing the ion energy results in observing the variations in the surface roughness dependency on the ion-bombing energy. The results also showed that after long treatment with Ar and N_2 plasmas, the surface roughness of the pure PMMA films is much larger dispersed than plasma O2, since the processes of plasma etching can be lower in inert Ar and N_2 gases than from reactive gases. This result confirms that there was a greater etching process in plasma generated in reactive (or electronegative) gases than from inert gas as shown in fig4. This behavior agrees with references [17,18]

Table 3: Average diameter, Roughness average and the root mean square for pure-PMMA untreated and treated by different gases plasma

Sample	Average diameter (nm)	Roughness average (nm)	The root mean square (nm)
PMMA-Pure	73.11 nm	0.904 nm	1.48 nm
PMMA-PO_2(20min)	93.25 nm	5.33 nm	9.01 nm
PMMA-PAr(20min)	106.10 nm	13.4 nm	18.2 nm
PMMA-PN_2 (20min)	107.27 nm	11.1 nm	12.8 nm

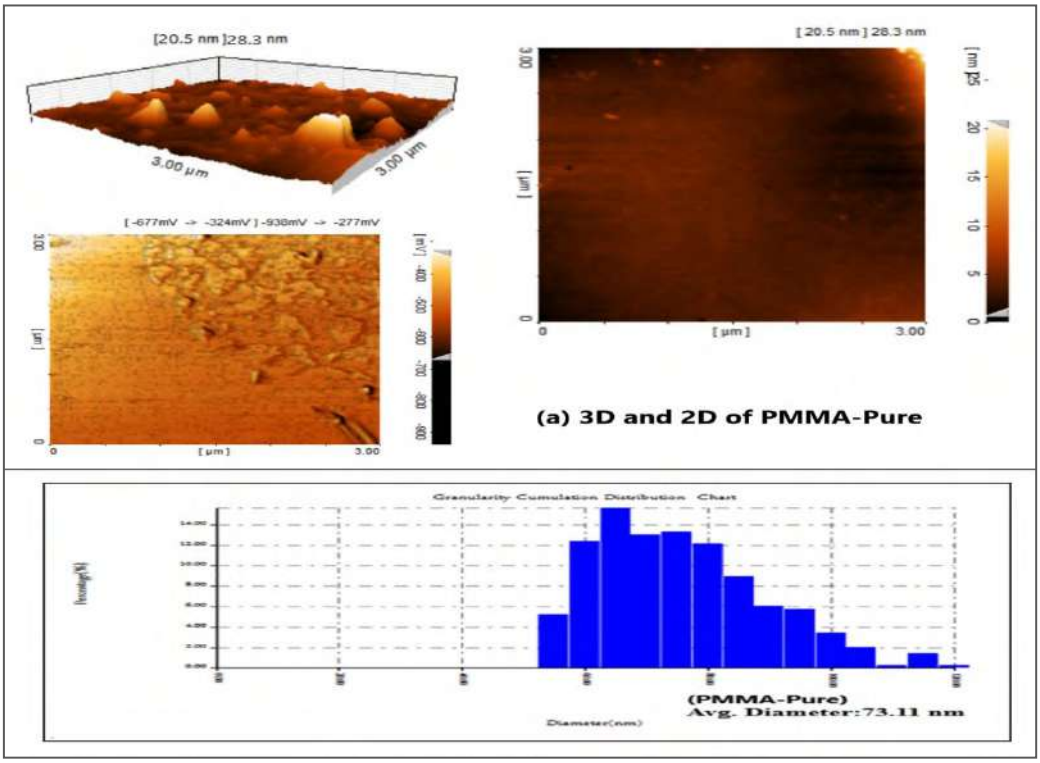
[20.5 nm]28.3 nm
3.00 µm
3.00 µm
[20.5 nm] 28.3 nm
[µm]
3.00
[nm]
(a) 3D and 2D of PMMA-Pure
Granularity Cumulation Distribution Chart
Percentage(%)
Diameter(nm)
(PMMA-Pure)
Avg. Diameter:73.11 nm

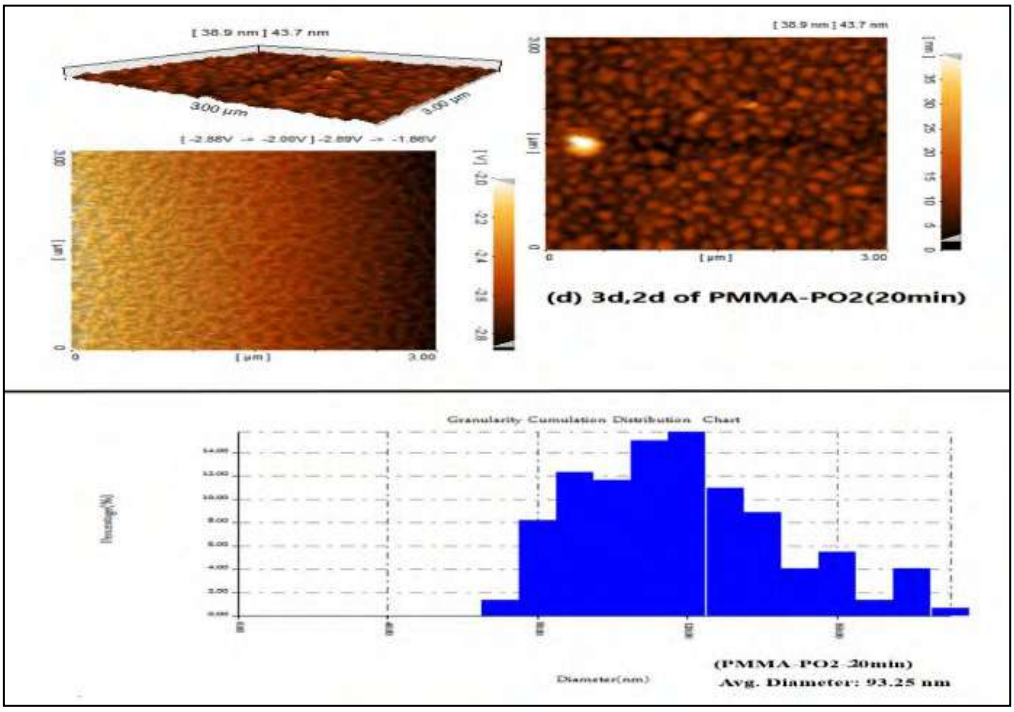
[38.9 nm] 43.7 nm
3.00 µm
3.00 µm
[38.9 nm] 43.7 nm
[µm]
3.00
(d) 3d,2d of PMMA-PO2(20min)
Granularity Cumulation Distribution Chart
Percentage(%)
Diameter(nm)
(PMMA-PO2 -20min)
Avg. Diameter: 93.25 nm

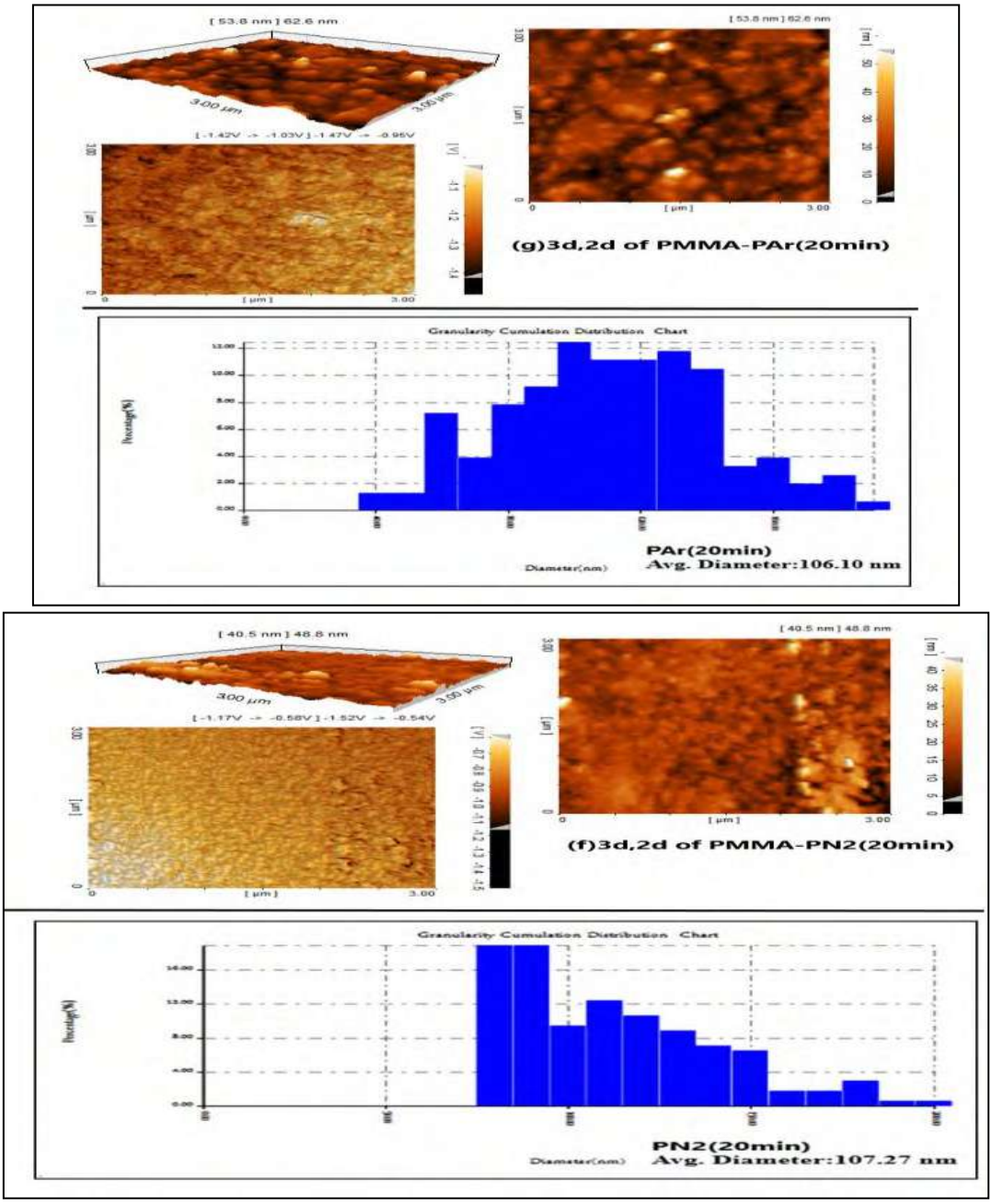

Figure 4. AFM measurements of (a) PMMA-Pure (d) PMMA- PO_2 (20min)

(f)PMMA-PAr (20min) (h) PMMA-PN_2 (20min)

3.3. (FESEM) Field Emission Scanning Electron Microscopy.

SEM is ued for analysing the changes in the surface morphology of pure-PMMA films before and after plasma treatment. Figure 5(a) shows that the surface morphologies of untreated pure-PMMA films have relatively smooth surface. On the other hand, Fig. 5(f, g, h, and v) shows the surface morphology of treated pure-PMMA films under the best conditions for the surface adjustment. It can be noticed that there are clusters of particles connected to the surface. Oxygen plasma was used to modulate the surfaces of pure PMMA film. The plasma has changed the surface from the chemical composition and

the morphology. It notes that increasing the plasma treatment time for pure PMMA films from (5-30) min causes a damage in the polymer chains, and the polymer becomes loosely packed, which in turn raises the etch-rate. Alteration of the etch-rate is high at the beginning and decreases at a higher period of treatment [19].

Table 4: Alteration of the etch-rate is high at the beginning and decreases at a higher period of treatment

Samples	Maximum Grain size(nm)	Mean Grain size(nm)
PMMA-Pure	40.19 nm	58,06 nm
PMMA-PO2(5min)	110.9 nm	123.18 nm
PMMA-PO2(10min)	98.58 nm	69.07 nm
PMMA-PO2(20min)	58.06 nm	44.66 nm
PMMA-PO2(30min)	35.73 nm	29.03 nm

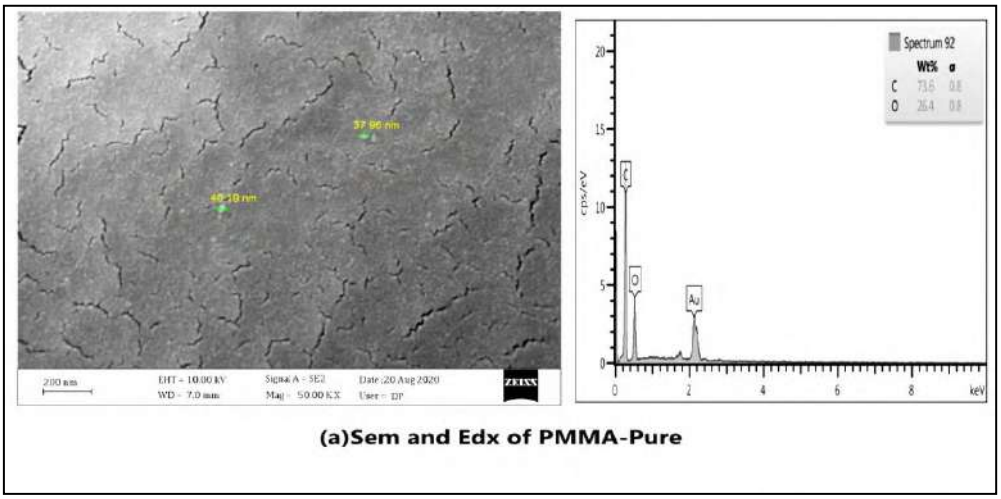

(a)Sem and Edx of PMMA-Pure

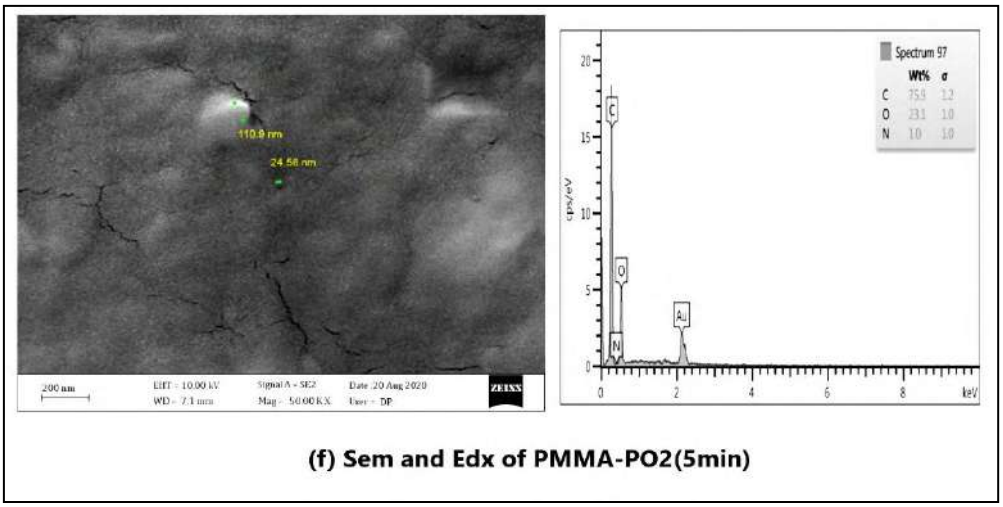

(f) Sem and Edx of PMMA-PO2(5min)

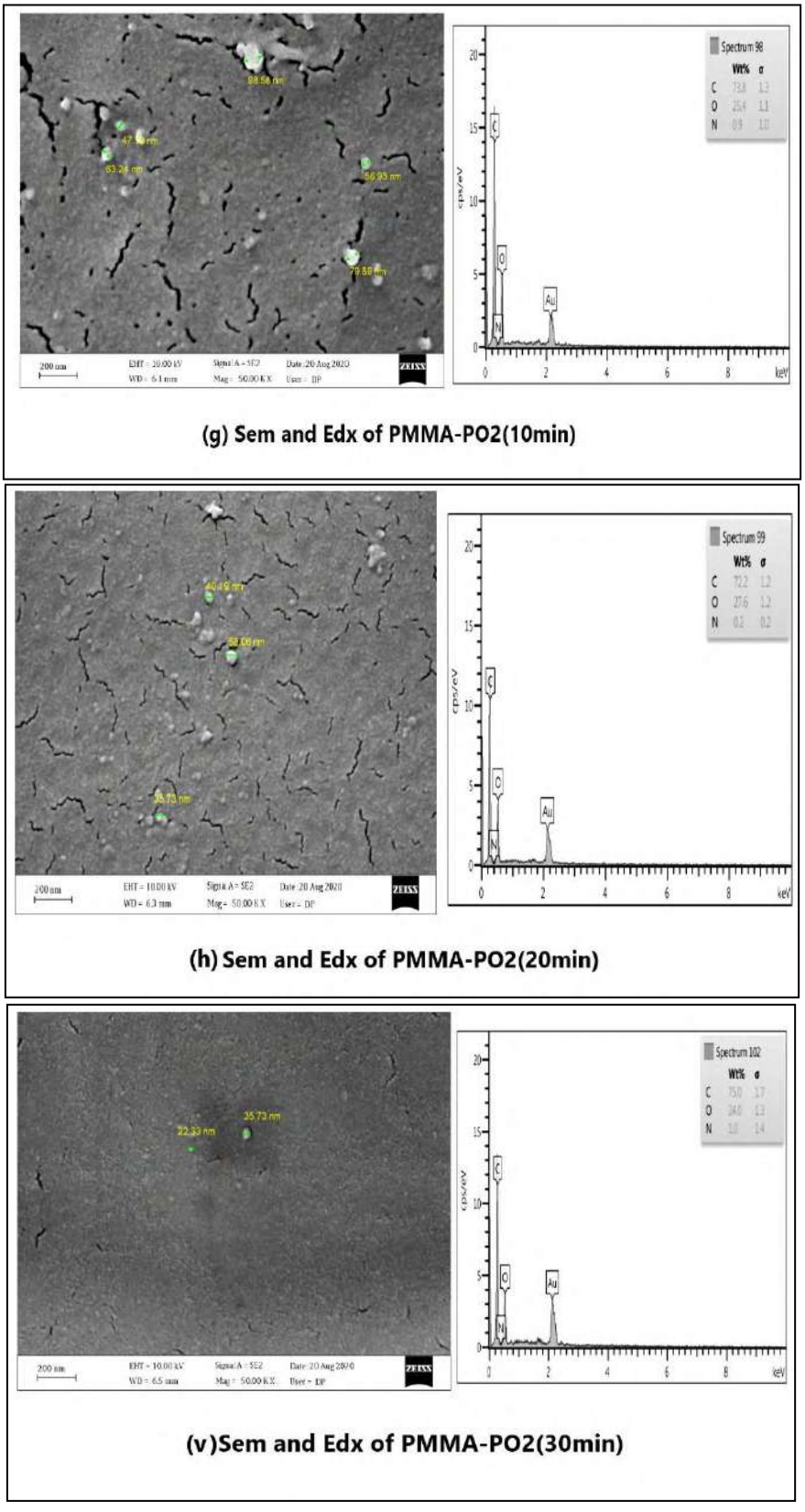

Figure 5. SEM and Edx measurements of (a) PMMA-Pure (f) PMMA-PO_2(5min)

(g)PMMA-PO_2(10min) (h) PMMA-PO_2 (20min) (v) PMMA-PO_2(30min).

Samples are analyzed by SEM microscopy of the pure-PMMA films treated by plasma for different gases (O_2, N_2, Ar) at the same time of exposure. It is noticed changes in the etch-rate of pure PMMA samples after exposure to the plasma as shown in figure 6 (a, h, k, m). Untreated pure-PMMA sample has a uniform texture which undergoes major changes when exposed to plasma. While, treated pure-PMMA samples describe rougher morphologies with etching appearances and irregular-shaped textures. The surface texture produced is related to the differences in the etch-rate of amorphous regions coexisting in PMMA. Continuous bombing of reactive plasma species contributes to alterations the surface morphology. It is also known that the morphology for pure PMMA films dramatically altered during O_2 plasma treatment compared to the N_2 and Ar plasma etching. This behavior is correlated with a higher etch-rate of O_2 plasma in as seen figure 6h. It is noticed that the plasma of O_2 causes a major deterioration of the surface of the sample as a result of plasma etching mechanisms. Thus, N_2 plasma can be considered as an ideal alternative to boost surface properties with very low levels of degradation. This result is consistent with [20,21].

As a consequence of plasma processing, in addition to the oxidation effect of oxygen plasma, effective radicals (long-lived or met stable) present on the surface contribute to the restructuring of the surface. As described above, plasma etching, degradation and cross-linking are happen concurrently on the surface of the polymer. Cross-linking and degradation will control the polymer etching and thus the surface topography.

Table 5: Cross-linking and degradation will control the polymer etching and thus the surface topography.

Samples	Minimum Grain size(nm)	Mean Grain size(nm)
PMMA-Pure	40.19 nm	58.06 nm
PMMA-PO2(20min)	98.58 nm	69.07 nm
PMMA-PAr(20min)	523.3 nm	471.35 nm
PMMA-PN2(20min)	35.73 nm	35.73 nm

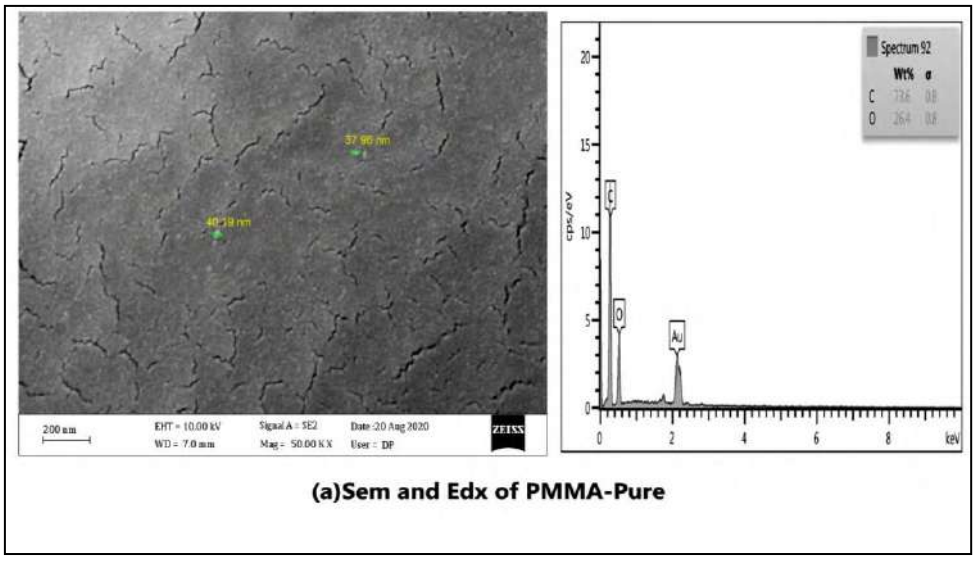

(a)Sem and Edx of PMMA-Pure

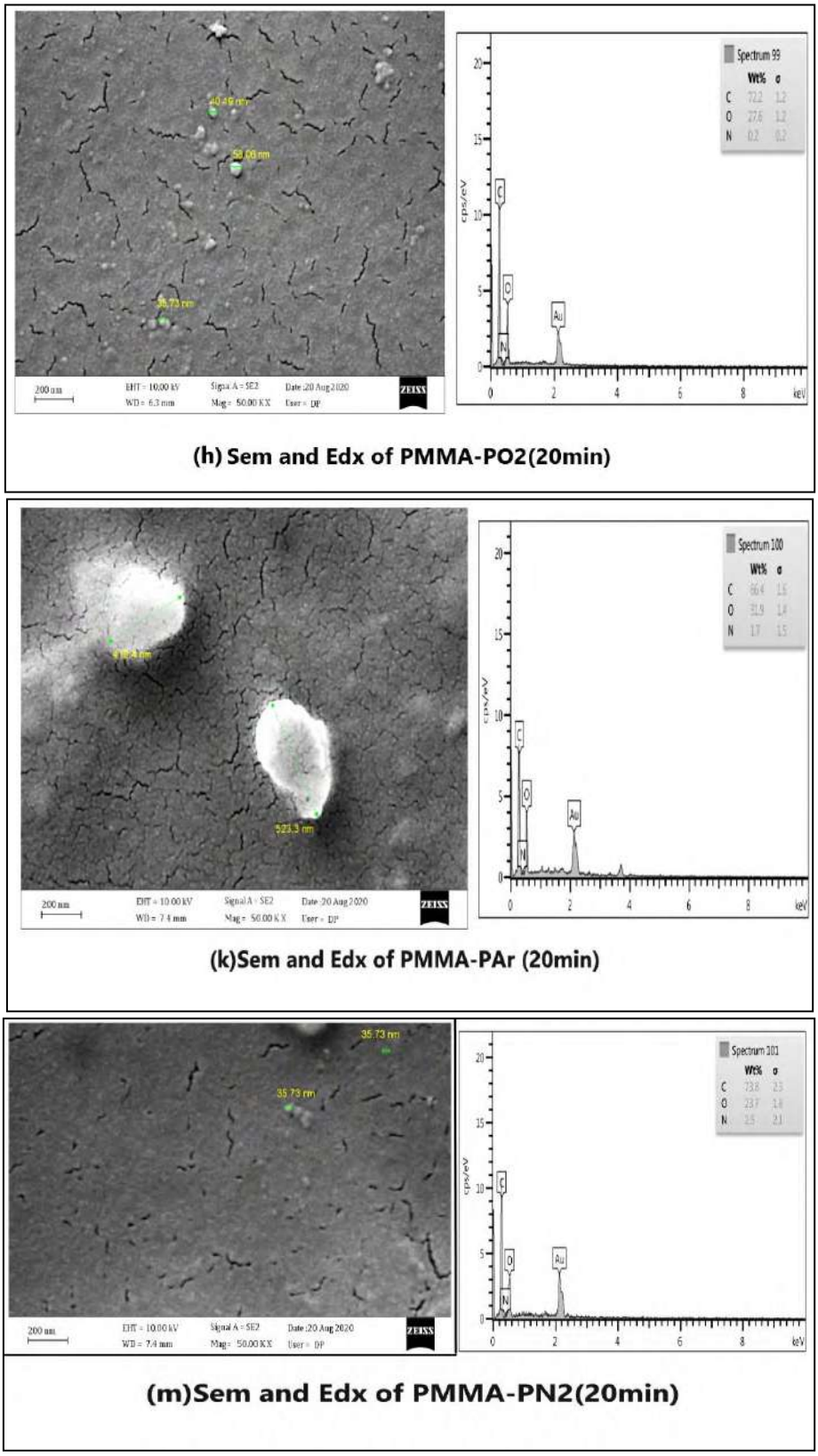

Figure 6. SEM and Edx measurements of(a) PMMA-Pure (d)PMMA-PO_2(20min)

(f)PMMA-PAr(20min) (h) PMMA-PN_2 (20min)

4. Conclusion.

In summary, DC glow discharge plasma was used at various exposure times from (5-30min) for the modification of the pure-PMMA film surfaces by oxygen plasma where the results indicate increased surface roughness and increased crystallinity with increasing the exposure times. However, with the treatment for a long time, the value of the surface roughness significantly declined. While, the plasma treatment with various gases (O_2, N_2, Ar) for 20min at the same exposure time alters the surfaces in both of the chemical composition and the morphology. AFM and XRD studies showed an improvement in the surface roughness and increased the crystallinity. SEM images observed a degradation of the surface with granular spots due to chain missioning and cross-linking effects. An efficient method of treatment for enhancing surface roughness of pure-PMMA polymer is the using of argon plasma compared to O_2 and N_2 plasma.

Reference

[1] Abdul-Kader AM, Turos A, Radwan RM and Kelany AM 2009 Surface free energy of ultra-high molecular weight polyethylene modified by electron and gamma irradiation *Appl. Surf. Sci*. **255** 7786–7790.

[2] Hergelová B, Homola T, Zahoranová A and Plecenik T 2012 *Plasma Surface Modification of Biocompatible Polymers Using Atmospheric Pressure Dielectric Barrier Discharge WDS*'12 Proceedings of Contributed Papers, Part II:28–133.

[3] Ali U, Abd-Karim KJ and Buang NA 2015 A review of the properties and applications of poly (methyl methacrylate) [PMMA] *Polym. Rev*. **55** 678–705.

[4] Park J H, Lee S H, Choi K H, Noh H S, Lee J W and Pearton SJ 2010 Comparison of dry etching of PMMA and polycarbonate in diffusion pump-based O2 capacitively coupled plasma and inductively coupled plasma, *Thin Solid Films* **518** 6465–6468.

[5] Bettencourt A and Almeida AJ 2012 Poly (methyl methacrylate) particulate carriers in drug delivery *J. Microencapsul* **29** 353–367

[6] Mazhir S N, Taha S K, Harb N H and Khalaf M K 2020 A Study of Plasma parameters in gold sputtering System by Means of Optical Emission Spectroscopy, *IOP Conf. Series: Mat. Sci. Eng.* **871** 012081.

[7] Yildirim Bicer A Z, Dogan A, Keskin S and Dogan OM 2013 Effect of argon plasma pretreatment on tensile bond strength of a silicone soft liner to denture base polymers *J. Adhes*. **89** 7 594–610.

[8] Hassouba M and Dawood N 2017 Comparison of Surface Modification of CR-39 Polymer Film Using RF and DC Glow Discharges Plasma *J. Mod. Phys.* **8** 2021-2033

[9] Rezaei F, Shokri B and Sharifian M 2015 Atmospheric-pressure DBD plasma-assisted surface modification of poly methyl methacrylate: A study on cell growth/proliferation andantibacterial properties *Appl. Surf. Sci.* **164** 471–481.

[10] Taha SK, Mazhir SN and Khalaf MK 2018 A Comparative Study on the Electrical Characteristics of Generating Plasma by Using Different Target Sources *Baghdad Sci. J.* **15** 4 436-440. http://dx.doi.org/10.21123/bsj.2018.15.4.0436

[11] Wei Y, Chen Y, Liu P, Gao O, Sun Y and Huang C 2011 Surface modification of hydrophobic PMMA intraocular lens by the immobilization of hydroxyethyl methacrylate for improving application in ophthalmology *Plasma Chem. Plasma Process*. **31** 811–825.

[12] Wieland F, Bruch R, Bergmann M, Partel S, Urban GA and Can Dincer C 2020 Enhanced Protein Immobilization on Polymers-A Plasma Surface Activation Study *Polymers, MDPI* **12** 104 doi:10.3390/polym12010104.

[13] Hegemann D, Brunner H and Oehr C 2003 Plasma treatment of polymers for surface and adhesion improvement. Nuclear Instruments and Methods in Physics Research Section B Beam *Interact. Mat. Atoms.* **208** 1–4 281-286.

[14] Khalaf M K, Mahdi M S, Taha S K and Bououdina M 2018 Influence of R.F. sputtering power on surface properties and biocompatibility of 316L stainless steel alloy by deposition of TiO2 thin films *Mat. Res. Exp*. **6** 3 035401. https://doi.org/10.1088/2053-1591/aaf2e9
[15] Reece RJ 2001 *Industrial plasma engineering*, vol. 2. Applications to Nonthermal Plasma Processing, Bristol and Philadelphia: Institute of Physics Publishing; 337.
[16] Kostova, K G Nishime TMC, Castro AHR, Toth A and Hein LRDO 2014 Surface modification of polymeric materials by cold atmospheric plasma jet *Appl. Surf. Sci*. **314** 367–375.
[17] Wieland F, Bruch R, Bergmann M, Partel S, Gerald A. U and Dincer C 2020 Synthesis and Properties of Plasma-Polymerized Methyl Methacrylate via the Atmospheric Pressure Plasma Polymerization Technique *Polymers MDPI* **12** 104; doi:10.3390/polym12010104.
[18] Sui S, Lin L, Shen J, Guohua N, Hongbin X, Qifu L, Yanjun Z, Jingwei G and Wenxue D 2020 Plasma treatment of polymethyl methacrylate to improve surface hydrophilicity and antifouling performance *Polym. Eng. Sci*.
[19] Zheng B, Tian Y, Zhao J H, Wu S, Zhang S, Yan J, Cen K and Ostrikov K 2017 Tune able fluidics within graphene nanogaps for water purification and energy storage *Nanoscale Horiz*. **2** 89-98.
[20] Guimond S and Wertheimer MR 2004 Surface degradation and hydrophobic recovery of polyolefins treated by air corona and nitrogen atmospheric pressure glow discharge *J. Appl. Polym. Sci.* **94** 1291-1303.
[21] Sanchis R M, Calvo O, Sanchez L, García D and Balart R 2007 Enhancement of wettability in low density polyethylene films using low pressure glow discharge N_2 plasma *J. Polym. Sci. B: Polym. Phys.* **45** 2390-2399.

Cryogenic Analysis of Junctionless Nanowire MOSFET during Underlap in Lower Technology Nodes

Cryogenic Analysis of Junctionless Nanowire MOSFET during Underlap in Lower Technology Nodes

Tenneti Sai Sasank[1], Pochiraju Raja Ganesh[1], Nukala Pavan Kumar[1], Biswajit Jena[1], Ahmed J. Obaid[2]

[1]Department of Electronics and Communication Engineering, Koneru Lakshmaiah Education Foundation, Vaddeswaram, India

Dept. of Computer Science, Faculty of Computer Science and Mathematics, University of Kufa, Iraq

Email: biswajit18590@gmail.com
Email: ahmedj.aljanaby@uokufa.edu.iq

1. Abstract:

This paper presents a cryogenic analysis of Junction less Under lapped Nanowire MOSFETs in lower technology nodes. The temperature dependent analysis is carried out to extract the DC figure of merits (FOMs) of the proposed nanowire MOSFET. The analysis is carried out to investigate the drain current associated with the device at different temperature. Further the analysis is extended with underlap length variation from source, drain and both sides. As the trans conductance plays a vital role in device performance estimation, so the analysis is further extended to calculate the transconductance for all the temperature variation and underlap length variation. With the introduction of gate metal under lapping, the sub-threshold behaviour of the proposed structure under different temperature is carried out extensively.

Keywords: Nano, MOSFET, Cryogenic, Underlap, Sub-threshold

2. Introduction

With an increase in the demand for portable electronic gadgets, semiconductor industry is thinking about more than Moore. Device miniaturization is no more an effective solution to bring the device into next lower technology nodes. As a result of which, different engineering techniques have introduced to bring down the scaling of the device into different level. As the device size is shrinking down to sub nanometre

regime, few unavoidable effects are affecting the device performances badly [1-4]. Although the device dimension is scaled down using some gate engineering or channel engineering techniques, but the effect of temperature on device performance is also an important topic of discussion. In spite of efficient characteristics in room temperature, the semiconductor devices need a thorough analysis in higher and lower temperature condition. Cryogenic analysis is the process of analyzing the behavior of a particular device at very low temperature [5-8]. Ultra low temperature changes the properties of material that instead changes the device also, which provides an interesting area for the researchers to do research. Multi-gate devices are considered as one of the best immune to reduce short channel effects [9]. Improved electrostatic controllability with multiple gates surrounding in different axis makes the device state of the art in semiconductor industry. Among different multi-gate devices, GAA MOSFET is considered as the leader in multi-gate MOSFET family in lower technology nodes [10-13]. The GAA MOSFET may be a rectangular type or cylindrical type (Nanowire), but the channel should be controlled by the gate from all the direction. GAA MOSFET with rectangular gate or channel is less efficient than cylindrical because of corner effect that reduces the mobility of the electron. At the same time, the potential developed on the device is a surface phenomenon and the electric field at the centre is zero, so the geometrical shape of the channel also affects the device performances significantly [14-16]. In case of conventional MOSFET, the source, drain and channel are having different doping concentration [17]. As a result of which, concentration barriers will be formed and junction will be created. Fabricating semiconductor devices with junction reduces the electron mobility and dissipates more heat as electron or hole has to overcome the doping concentration difference barrier. Apart from this miniaturization in MOSFET with junction takes more time and it's more expensive as the process involves scale down of each and every component. However in case of junctionless devices, scaling down of device in to different technology node is easy and cost effective compared to their counter parts [18,19].

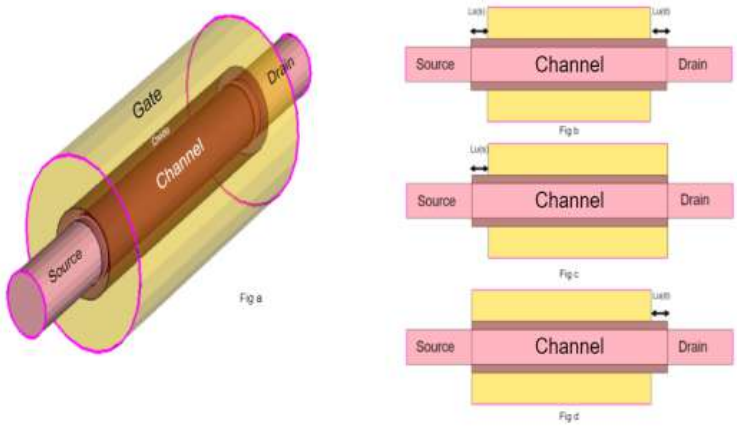

Figure 1. (a)3-D bird eye view of Nanowire junctionless MOSFET (b) Crossectional view of source-drain, source and drain underlap

3. Device Design and Simulation*:*

The simulation is carried out using Sentaurus TCAD (Synopsys) [20, 21]. The simulator includes various physics based transport model for semiconductor devices in different technology nodes. Along with drift diffusion model, quantum potential based models are also there to investigate the device performance in quantum level also. In order to investigate the temperature analysis for the device in higher as well as lower temperature, thermodynamic models are also there. Apart from these, this simulator also allows some gate engineering and channel engineering techniques to study the insights of various effects associated with semiconductor devices. In this work a junctionless Nanowire MOSFET is introduced in order to analyze the effect of the temperature in various FOMs of the device if some gate engineering technique is performed. The gate metal is under lapped from source side, drain side and both side to study the device behavior. The doping concentration of the junctionless device s kept as 1e18 with a metal work function of 4.3 eV. Apart from that the dioxide used is having a thickness of 2nm which is SiO_2. The underlap length variation is denoted as L_u and symbolized as $L_{u(S)}$ and $L_{u(D)}$ for source and drain respectively. The device dimensions of the proposed structure are given in table 1. The variation in underlap length and temperature is used to calculate the drain current at different conditions as shown in figure. Apart from this, the cryogenic analysis is carried out for a low temperature around 80K in order to have a clear insight into device performance at cryogenic.

Table 1. Device dimensions of the proposed structures

Device Dimensions	**Nano Wire MOSFET (Junction less)**
Channel Length (L_g)(10-60)nm	
Doping Concentration (N_S/N_D)Phosphorus(1e+18)	
Doping Concentration (N_a/N_d)Boron(1e+18)	
Oxide Thickness (t_{ox})(2nm SiO_2)	
Channel Thickness (t_{si})10 nm	
Source/Drain Extensions (L_s/L_d)	20 nm
Source/Drain Underlap ($L_{u(S)}$, $L_{u(D)}$)	(2,5,7) nm

4. Results and Discussion:

The analysis of the proposed device in terms of electrostatic potential and electric field distribution at a low gate bias of 0.2 V is illustrated in figure 2.

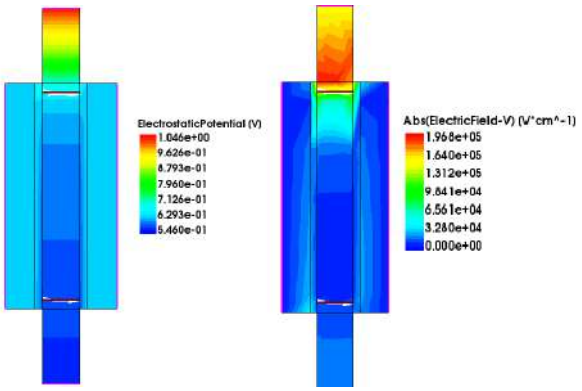

Figure 2. Cut section of the proposed structure in no underlap condition for (a) Electrostatic potential distribution (b) Electric field distribution at a low bias of 0.2V

The electro static potential and electric field are surface phenomenon. This can be observed from the cut section of the device shown in figure 2. From the figure, the distribution from source to drain and from outer metal gate to inner channel can be easily identified. The potential is developed at the interface of the channel and dielectric; whereas the electric field at the centre is assumed to be zero. However, the effect of drain bias can be seen near the drain side as the gate bias is very low. Figure 3(a) shows the transfer characteristics of the proposed model with source side underlap with various underlap length. With increase in underlap length, the transfer characteristic is bending down and moving away from

saturation as a very low temperature around 100K is applied to the system. The device transfer characteristics with temperature variation are illustrated in figure 3(b). From the figure it can be observed the shape change in transfer characteristic curve at different temperature can be observed. With the increase in temperature 8oK to 200K, the bending of the curve it getting more straighter and moving towards saturation.

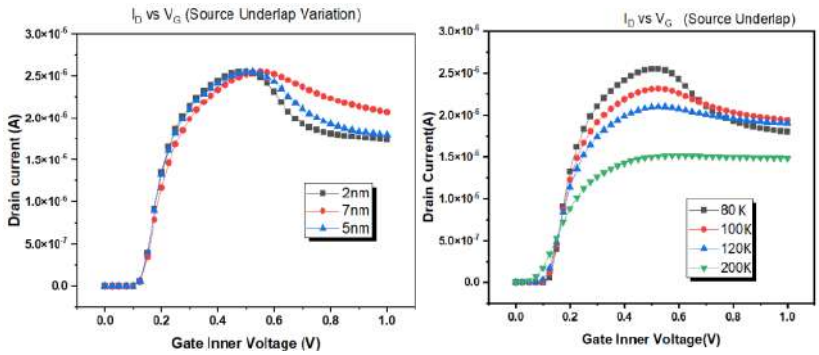

Figure 3. Transfer characteristics of the proposed structure (a) with source underlap (2nm, 5nm, 7nm) at a temperature of 100K (b) with different temperature (cryogenic temperature)

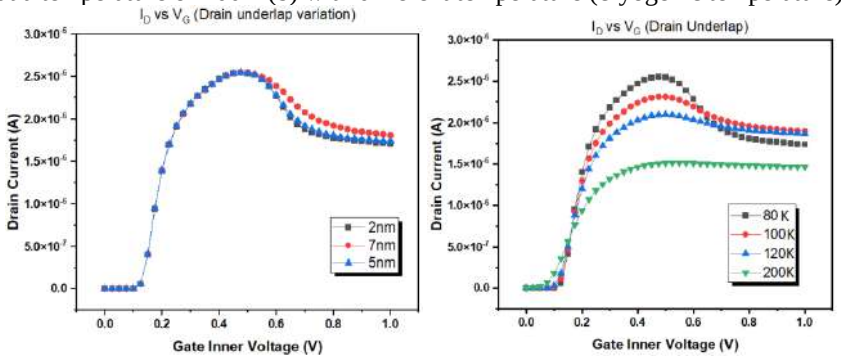

Figure 4. Transfer characteristics of the proposed structure (a) with drain underlap at a temperature of 100K (b) with different temperature (cryogenic temperature)

The transfer characteristics for drain side underlap with different underlap length and temperature is illustrated in figure 4(a) and (b) respectively. It is observed that in case of drain side underlap the characteristics are almost same for low under lap length up to 5nm. Once the underlap length is increasing, the change in the shape of the graph is well observed as shown in figure 4(a). Similarly, the transfer characteristics with the variation of temperature from 80K to 200K are shown in figure 4(b)

which looks similar to the source side underlap. As cryogenic analysis is the temperature analysis below 135K, so the device characteristics below this temperature is having different shape as shown in figure. The analysis is further extended to both side underlap. The characteristic curve thus obtained is similar to source and drain side underlap but it is more prominent while increasing the underlap length from 2nm to 7nm as shown in figure 5(a). Similarly the transfer characteristics at different temperature for both side underlaps are illustrated in figure 5(b). From the figure, the temperature dependency of the proposed structure can be easily identified from the figure. The temperature dependent mobility of the electron defines the characteristics shape when a gate bias is applied and with low temperature, its mobility will also get affected.

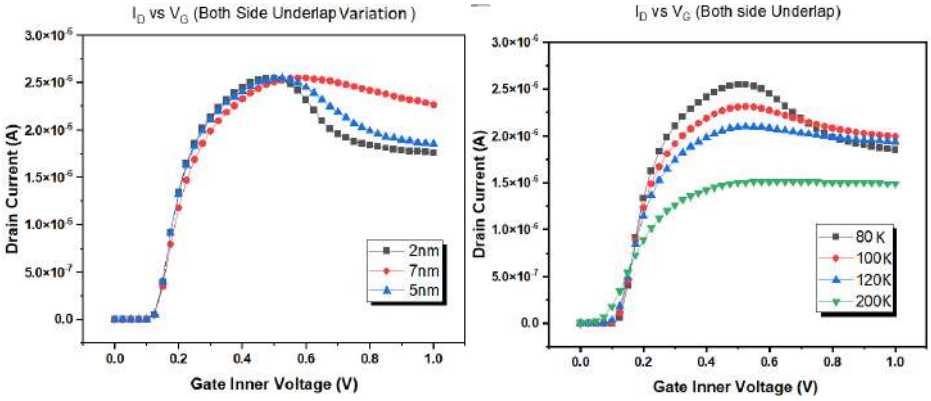

Figure 5. Transfer characteristics of the proposed structure (a) with both side underlaps at a temperature of 100K (b) with different temperature (cryogenic temperature)

The work is further extended to the transconductance extraction of the proposed model with source, drain and both side underlap. The trans conductance extraction for all the three cases are illustrated in figure 6,7,8 respectively. The maximum trans conductance for all the above three cases are higher in no underlap condition while reduces gradually with underlap.

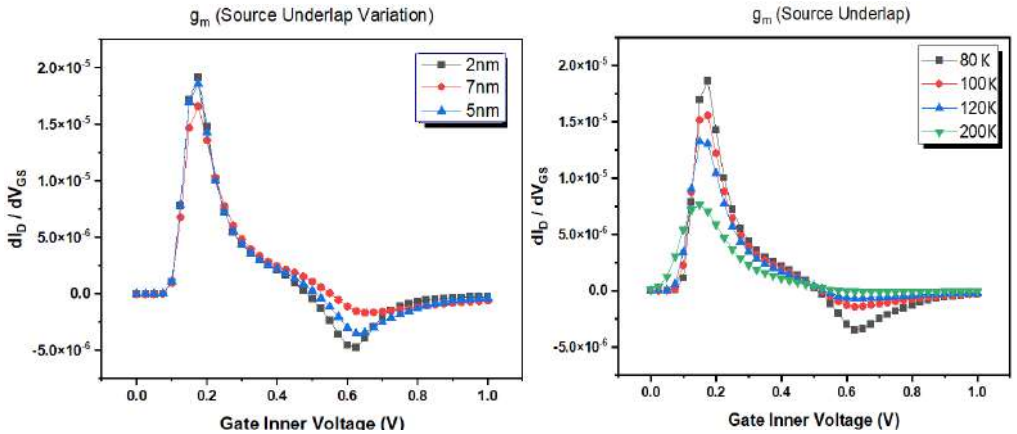

Figure 6. Transconductance of the proposed structure (a) with source underlap at a temperature of 100K (b) with different temperature (cryogenic temperature)

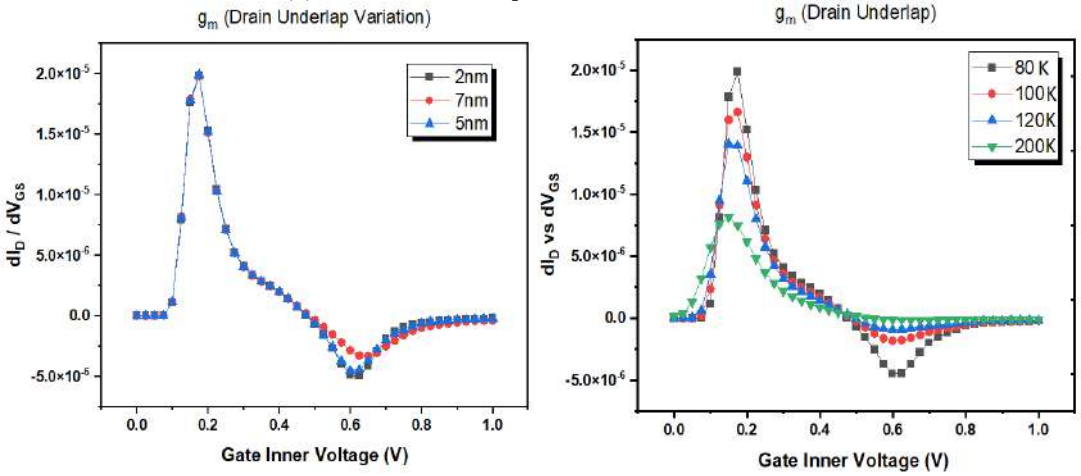

Figure 7. Transconductance of the proposed structure (a) with drain underlap at a temperature of 100K (b) with different temperature (cryogenic temperature)

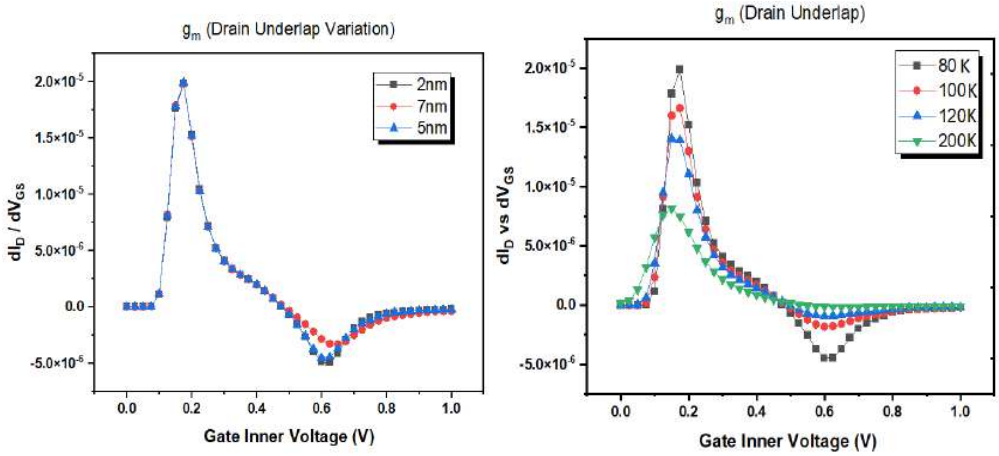

Figure 8. Transconductance of the proposed structure (a) with both side underlaps at a temperature of 100K (b) with different temperature (cryogenic temperature)

5. Conclusion:

The cryogenic analysis was carried out for the proposed junctionless nanowire MOSFET and the temperature dependency characteristics in terms of drain current and transconductance were investigated extensively. The analysis is carried out for a temperature of 80K to 200K with the underlap length variation of 2nm,5nm and 7nm. The gate metal is under lapped for these underlap lengths and the corresponding FOMs with underlap also investigated for clear cryogenic analysis.

REFERENCES

[1] C. P. Auth, J. D. Plummer, "Scaling theory for cylindrical, fully depleted, surrounding gate MOSFETs", IEEE Electron Device Lett.,1997, vol. 18, pp. 74.

[2] Kranti, S. Haldar, R.S. Gupta, "Analytical model for threshold voltage and I-V characteristics of fully depleted short channel cylindrical/surrounding gate MOSFET", Microelectronic Engineering, 2001, vol. 56, pp. 241.

[3] P.Keerthana, P. P.Babu, T. A Babu, B.Jena, "Performance Analysis of GAA MOSFET for Lower Technology Nodes,"Journal of Engineering Science & Technology Review . 2020, vol. 13, pp.39-43.

[4] B Jena., S. Dash, S.R Routray, G.P Mishra, "Inner-Gate-Engineered GAA MOSFET to Enhance the Electrostatic Integrity," Nano, 2019, vol. 14, pp. 1950128.

[5] N. Gupta, R. Chaujar, Investigation of temperature variations on analog/rf and linearity performance of stacked gate gewe-sinw mosfet for improved device reliability, Microelectron. Reliab. 64 (2016) 235–241.

[6] G.D. Jayakumar, R. Srinivasan, SET analysis of silicon nanotube FET, J. Comput. Electron. 16 (2) (2017) 307–315.

[7] S. Rustagi, N. Singh, W. Fang, K. Buddharaju, S. Omampuliyur, S. Teo, C. Tung, G. Lo, N. Balasubramanian, D. Kwong, Cmos inverter based on gate-all-around silicon-nanowire mosfets fabricated using top-down approach, IEEE Electron. Device Lett. 28 (11) (2007) 1021–1024.

[8] B. Yang, K.D. Buddharaju, S.H. Teo, N. Singh, G.Q. Lo, D.L. Kwong, Vertical silicon-nanowire formation and gate-all-around MOSFET, IEEE Electron. Device Lett. 29 (7) (2008) 791–794.

[9] B. Jena, S. Dash, K.P Pradhan, S.K Mohapatra, P.K Sahu, G.P Mishra, "Performance analysis of undoped cylindrical gate all around (GAA) MOSFET at subthreshold regime", Advances in Natural Sciences: Nanoscience and Nanotechnology, vol 6 (2015), 035010.

[10] E.A. Gutierrez-D, J. Deen, C. Claeys, Low Temperature Electronics: Physics, Devices, Circuits, and Applications, Elsevier, 2000.

[11] M. Elbuluk, A. Hammoud, R. Patterson, Power electronic components, circuits and systems for deep space missions, in: Power Electronics Specialists Conference, 2005. PESC05. IEEE 36th, IEEE, 2005, pp. 1156–1162.

[12] F.H. Gaensslen, V.L. Rideout, E. Walker, J.J. Walker, Very small mosfet's for low-temperature operation, IEEE Trans. Electron Dev. 24 (3) (1977) 218–229.

[13] N. Collaert, A. De Keersgieter, A. Dixit, I. Ferain, L.-S. Lai, D. Lenoble, A. Mercha, A. Nackaerts, B.J. Pawlak, R. Rooyackers, Others, Multi-gate devices for the 32nm technology node and beyond, Solid State Electron. 52 (9) (2008) 1291–1296.

[14] S. Tayal, A. Nandi, Enhancing the delay performance of junctionless silicon nanotube based 6t sram, IET Micro Nano Lett. 13 (7) (2018) 965–968.

[15] S. Tayal, A. Nandi, Optimization of gate-stack in junctionless Si-nanotube FET for analog/RF applications, Mater. Sci. Semicond. Process. 80 (2018) 63–67.

[16] S. Tayal, A. Nandi, Study of temperature effect on junctionlesssi nanotube fet concerning analog/rf performance, Cryogenics 92 (2018) 71–75.

[17] J. Fan, M. Li, X. Xu, Y. Yang, H. Xuan, R. Huang, Insight into gate-induced drain leakage in silicon nanowire transistors, IEEE Trans. Electron Dev. 62 (1) (2015) 213–219.

[18] B. Jena, K.P. Pradhan, P.K. Sahu, S. Dash, G.P. Mishra, S.K.Mohapatra, Investigation on cylindrical gate all around (GAA) to nanowire MOSFET for circuit application, Facta Univ. Ser. Electron. Energ. 28 (4) (2015) 637–643.

[19] N. Gupta, A. Kumar, R. Chaujar, Impact of device parameter variation on RF performance of gate electrode workfunction engineered (GEWE)-silicon nanowire (SiNW) MOSFET, J. Comput. Electron. 14 (3) (2015) 798–810.

[20] Sentaurus Device User Guide (Mountain View, CA, USA, Synopsys, Inc).

[21] A. J. Obaid, "Critical Research on the Novel Progressive, JOKER an Opportunistic Routing Protocol Technology for Enhancing the Network Performance for Multimedia Communications," in Research in Intelligent and Computing in Engineering. Advances in Intelligent Systems and Computing, vol 1254. Springer, Singapore., Springer, Singapore, 2021, pp. 369-378.

Web Mining Techniques and Technologies: A Landscape View

Web Mining Techniques and Technologies: A Landscape View

[1] Kareem K. Ibrahim - [2] Ahmed J. Obaid
[1.2] University of Kufa College of Computer Science and Mathematics Department of Computer Science

karimk.aljabri@student.uokufa.edu.iq , ahmedj.aljanaby@uokufa.edu.iq

Abstract : Web mining is the process of discovering important information and patterns in a weblog file. And contains loads of information. It consists of pages of various formats (HTML documents, images, etc.). And the data for this record is still increasing at a very high rate. So the process of retrieving information from it is a very difficult task. In order to obtain the required information from the network. This requires mining the weblog file. In this paper, the researcher conducted a review of previous studies and what researchers have dealt with in web prospecting. Explain web mining concepts. And how to obtain information and the visitors' patterns through the techniques and algorithms used in Web usage mining.

Keywords: Web Usage Mining, website, Web mining.

1.Introduction

The data On the Internet is enormous and is growing every day. The website is a cluster of web pages. Text, images, and videos may be included on web pages. And its they are connected through hyperlinks through which navigation takes place. Log files are created whenever users visit any website. The log file documents the full information about each user's access to the website. The size of log files is growing day by day because of the increased use of web pages[1]. The method for finding confidential information from a weblog file is named Web Mining. It is a branch of data mining. The purpose of it is to obtain information about the navigational activity and recall useful information from very enormous raw data, which can be expressed by several millions of event records in a log file. Weblog data includes various kinds of information so including weblog, web layout, and user profiles.[2] Web mining has been classified into three large topics of focus depend on which part with Web to be exploited which include: Web content mining, Web structure mining, and Web usage mining. The Previous three mining jobs can be used separately or can be combined with other jobs as they may contain web document links. Web mining is classified under data mining technology and its main purpose is to retrieve and extract knowledge from many documents and web services mechanically. As well to extract the required and exciting patterns from a series of huge data sets in the latest trend as well as used for traditional data mining. [3]
Web content mining its mining of this type is a very important area in analyzing users and the behavior of their web file content. Web content may contain very large amounts of multimedia data (images, video, animation, text, and document data in different styles such as pdf, etc., hypertext).

WCM is also used with a focus on visitor opinion extraction and sentiment analysis. Through which it is possible to locate comments in social media, blogs, and web forums. This type of mining is also used in education by extracting valuable information. Such as identifying consumer needs and etc. WCM is text mining and user opinion. It is one of the techniques that can be used to find important information from textual data. [4] . Web structure mining this type of web server mining uses a web file connection structure diagram and analysis of nodes in that file. The primary goal of mining the web structure is to extract the previously lost relationship between the web file pages. It is also used to generate a structural summary of the website and any page of the internet. It is also a mining method that will categorize web pages and show relationships between other websites. This technique is implemented either on a single page or on multiple pages (hyperlink). This technique produces structural information from a web server file consisting of a web graph with pages as nodes and hyperlink as edges [5].Web Usage Mining this type of mining focuses on customer knowledge and their collaboration with websites. This type is very important in extracting important information that explains the visitor's use of web pages [6]. That is, it is the process of discovering very important patterns of web usage data. Such as visitor access patterns and various other requests made by one or more users. The main objective of WUM is to understand navigation and browse through web pages. This is very important in enhancing the quality of services provided by websites. Business services, in the field of information and network security, fraud detection. And improve the structure and performance of web pages and servers [2] .

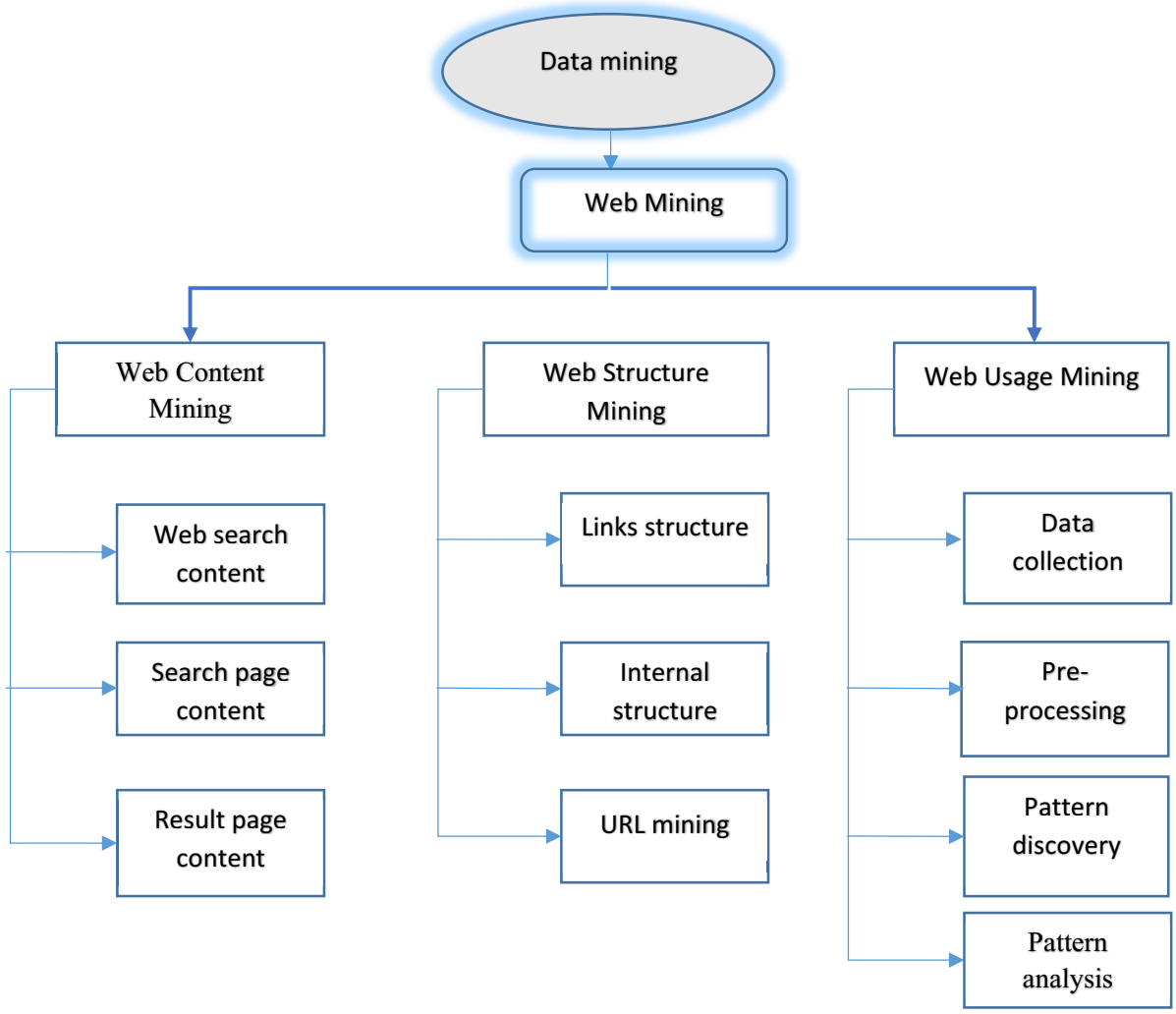

Fig (1) Web Mining Techniques [2].

2. Related Work

In this section, we uncover relevant work related to daily web use for big data results from web usage exploration. Which is a popular research area in prospecting for web usage, data analysis is essential to track user behavior in order to effectively serve users. Either in terms of security or website development and others.

According to. [1] The authors described mining on the web as the application of several techniques to extract data from web records. This log contains large amounts of data, so reprocessing is required to remove useless data. Two stages of pre-processing were proposed to clean up the data and identify the user using the proposed algorithms. A test was performed on a log file consisting of 500 records, after data cleaning it found 441record. Note the difference is not a little because it URLs used are Few compared to the size of big the weblog file. And this is the record used doesn't contain much needless content like jpeg, video, etc. After the user identification stage, it found 52 unique visitors out of 441 URL user records.

G. Shiva Prasad et al. [7] suggested that the neuro fuzzy typical Collecting bines the neural network and the customary (fuzzy notion). Where they used neuro based hybrid typical is effected to determine concealed patterns in the Web Log server special of (polytechnic web site). Web Log Pre-processing methods based on dimensionality reduction methods and collective methodologies were employed. The preprocessing phase eliminates all irrelevant, and blaring data, with a resultant Web Log size of 20% of the original log size. The (neuro fuzzy) grouped the users taking the same browsing patterns into set clusters. And the knowledge that has been collected after the analysis will can after that used from before the website for effective management and Personalize their website. This model was used to discover deviations in user behavior in many applications that require high security and high data privacy.

According to. [8] the authors described the web mining process in three imperative types (web content mining, website architecture mining, and web usage mining) that assist users to find valuable data. Each category has different algorithms and techniques needed to retrieve the information used in some applications such as fraud detection etc. Web content mining is helpful in terms of discovering the data from the (images, table, text, etc.). Web structure mining categorizes dealings between related Internet pages. Web usage mining is a too imperative kind which stores the user entree data and acquires info about a candid user of records. everybody methods may have some benefits and drawbacks. But they can be drawbacks better by additional studies.

R. Roy et al. [9]they conducted a comprehensive survey of mining methods on the web log document initial with weblog data sources which contain of only a text file. The information stored in the web log consists of a huge amount of useless data and noise, so this huge amount of data requires a pre-processing process for this record in a distinctive way to identify the problems in the web log document and also clarified the process of identifying the customer through (Client Identification IP address, by cookies, user data, site topology, and by authentication information).

According to. [10] the authors presented the technique of Web Usage Mining containing phases: Data Collection, Pre-processing, Pattern Discovery, and Pattern Analysis. They suggested a web history pre-processing algorithm where each page was assigned a specific token. According to this symbol and frequency, a technique can be applied to extract data (Classification, Association Rules, and Clustering) and reach that the highest and lowest value can be detected according to the frequency of accessing the page. Can simply learn the highest and lowest value.

Several researchers are shown in.[11] They used a method to improve the prediction of the next webpage Based on visited web pages by assigning top web browsing profiles for interested visitors. And it is recommended for current users interested in similar sites visited. They used a window sliding method with size N over the navigation session. Using the CTI dataset, The experimental results show a higher prediction accuracy for the pages of the next visit.

C. E. Dinuca et al. [12] Had explained that the session has a very important role in the reprocessing process. Also, most session delimitation algorithms use constant values to define the end of the session. He mentioned why using constant values causes errors in defining sessions. They propose a new method for identifying sessions based on average visit time for web pages that they implemented in Java programming language using NetBeans, IDE, which are two algorithms for identifying sessions. The former uses a constant value of 30 minutes to indicate the end of the session and the second using the

average time spent by users on their website pages. Was chosen the NASA log file available online to apply the suggestion.

Smriti Pandya et al. [13]They proposed a system interested in investigating serial mining techniques for access patterns with high efficiency and effectivity for web usage data and then using the pattern mined to match and create web links across the Internet. This usage data affords the trails leading to edited Web Pages Where this system has been taken advantage of in predicting the needs of the user and thus the use has been improved through the appropriate guidance of the web visitor to the important pages that are similar to the sites he is trying to reach.

Mr. Jitendra and et al. [14]presented a study showing reviews of different data to several researcher's processing methods. Such as the compilation and cleaning of data, Identification of users., route completion, and session determination. In addition to the advantages and disadvantages of these methods, which will be beneficial to society. To choose one or more of the available techniques for an effective pre-treatment. For more specific and consistent outcomes. As well proposed a complete preprocessing method that will enable analysts to convert any web server record set into an organization file (table, text) in the database. After comparing them with the preprocessing techniques used by other researchers, it showed more accurate results and Minimum preprocessing log file size.

Sucheta V. Kolekar et al. [15] they Submitted a proposal for the user's learning styles, by describing the learning behavior in the e-learning portal via Web Log Mining. The learning styles are then assigned to FSLSM classes. Provided that Each class is provided a learner with the appropriate contents and interface for the group He used the algorithm Fuzzy C Means (FCM) is used for collect educational, behavioral data captured from FSLSM classes. This method processes previous web data and converts it into (FCM) format, then defines unique sequences for each learner according to their sessions. Where it divides the sequences into eight categories based on the learning objects of the class, the work describes a methodology to automatically detect and identify the learning styles of learners using the Web Log Analysis approach where the validity of the algorithm was verified and compared with other, and the result was shown that it performs better in providing the contents and the adaptive interface for a new learner.

K.SELLAMY et al. [16] they provided a preliminary study of web mining, from several aspects (tools, techniques, applications). They proposed an approach to analyze and compare the skills taught in university or other studies, and the skills required at work. The aim of the study is to apply the latest methods of web data mining in the field of education and work.

The authors in the paper. [17] presented they a two algorithm that analyzes visitor behavior, And preprocessing the website visitors, Where Used the (HDD and CFPMA)algorithms, the first is used to filter and organize the appropriate information. And the second to mining the repeating pattern(CFPMA) to obtain recurring patterns from weblog data. In the present algorithms, repeated patterns mining is performed depending on the support threshold limit so that the accuracy is low, and the implementation period is high. But with this method. Based on the conviction threshold value, the session, and clustering in the weblog file. Focused the job on the weblog file format, pre-processing, and assembly, and pattern creation techniques.

The authors in the paper .[18] Presented a new approach to web usage mining using (Case Based Reasoning). by used clustering algorithms for titular web data. And it is founded on the reprocessing of previous labor Experiments. Thus, the previous experience could be an effective guide for Solve new problems. Web customization Which has the ability to adapt the next set of pages visited with individual users according to their interests and navigational behaviors has been proposed. A number of components of the proposed architecture are, Basic log preprocessing, methods of pattern discovery (By Reasoning Based on Case and similarity from peer to peer, Clustering, Association Rules Methods for Mining), In this study, a new predictive approach was introduced using CBR Method and mining of web use, which gives the user a choice to navigate to the next page. This technique gave high results compared with previous methods.

The authors in the paper [19]. Very big information the internet and tremendous resources. It has become imperative to determine the behaviors of website visitors through web history mining. To improve website performance and predict which page the user is likely to visit. And by searching, first in the similar cluster, then in similar sessions in the same cluster. This, in turn, causes an increase in the time of comparison with previous sessions when the data block is very large. In the study, they proposed three strategies (Least Frequent Ones Leave, First come First Leave, Timeframe Leave) for disposing of old sessions in order to replace them with new sessions (candidate sessions for prediction). When implementing the proposed methodology, the result was lower at the time of comparison and higher prediction accuracy.

Table 1. Brief description of data and web mining for previous studies

No.	Year	Authors	Technologies used	Focused on	Remarks
1	2014	P. Verma and et al. [1]	Two stages of preprocessing were proposed to clean up the data and identify the user using the proposed algorithms.	Data cleaning User identification	After completing the pre-processing stages, patterns will be detected that help in inferring user access patterns.
2	2015	G. Shiva Prasad et al. [5]	A hybrid model by on neural noise is used to discover knowledge in weblogs.	neuro-fuzzy model to discover hidden patterns in the weblog.	This model was used to discover deviations in user behavior in many applications that require high security and high data privacy.
3	2018	Hamid et al. [6]	The three types of web mining (Structure, Content, Usage).	Web usage mining(tools, techniques).	Web exploration is very useful (explore data, find out about visitor patterns ...)
4	2019	. Roy et al. [7]	Use detailed preprocessing to improve the quality and effectiveness of weblog data.	Transaction Identification.	Pre-processing of the log document is important to improve the productivity and ability to retrieve the log document information.

5	2018	Mehra and et al. [8]	Use web usage mining technology with web history pre-processing algorithm.	Implemented the algorithm in java programming language.	Be funded that most popular page and least popular page.
6	2011	Y. Almurtadha et al. [9]	They used the N-size window sliding method on the mobility session using a CTI dataset.	Improved prediction for the next visited web Pages is recommended for the current anonymous user.	A system with higher predictive accuracy was found on the following pages compared to previous systems.
7	2012	Dinuca et al. [10]	Using (NetBeans, IDE) which are two algorithms for identifying sessions.	It proposed a new method for identifying sessions based on average visit time for web pages that they implemented in the Java programming language.	In the first algorithm, they used 30 minutes for the session. In the second algorithm, the time depends on the page because it used the average visit.
8	2015	Pandya et al. [11]	They proposed a system interested in investigating serial mining techniques for efficient and effective access patterns.	Mainly focused on investigating the accuracy and effectiveness of mining technology for web usage data.	The resulting patterns are used to match web links to create links to recommendations.
9	2015	Jitendra et al. [12]	Use preprocessing technology that enables users to convert a web server into a database in the form of an organized table or text.	Pre-processing methods consisting of data collection, cleaning, visitor identification, session, path, etc.	The web server contains irrelevant data, which is important to preprocess.
10	2017	Kolekar et al. [13]	They used the (FCM) algorithm to collect the educational behavior data and the (GSBPNN) algorithm to predict the learning patterns of the visitor.	This method focused on processing previous web data and converting it into a format (FCM), then defining the sessions for each learner based on their sessions.	Description of a methodology for automatic detection and identification of learning patterns through web history analysis.
11	2018	Sellamy et al. [14]	Use web server data mining algorithms and techniques.	The study focused on extracting web data from several aspects (techniques, tools, applications).	The main goal of the study is to understand and apply web prospecting and prospecting for education and employment information.
		El-Aziz et al. [15]	Presented they a two algorithm that analyzes visitor behavior, And	Focused the job on the weblog file format, pre-processing, and assembly, and pattern	The algorithm (HDD) is shown to filter and organize the appropriate information, either

12	2020		preprocessing the visitors.	creation techniques.	(CFPMA) is used to obtain repeated data patterns.
13	2020	Asadianfam et al. [16]	Introduce a new predictive method, using (CBR) to explore web usage mining.	The study focused on designing and implementing a method that could provide visitor recommendations for navigation pages.	The results indicate that 70% of the recommendations were accurate and helpful.
14	2019	P. M. Bharti et al.[19]	-Least Frequent Ones out -First Come First out, -Timeframe Leave.	The study focused on getting rid of previous sessions.	Accuracy and prediction time are close in the suggested and best first strategies.

3- WEB USAGE MINING

As the number of internet users increased, the use of websites increased to get the required information. This, in turn, led to more data usage of these sites. This data is stored in various formats in the weblog file in an unordered format. And to understand the contents and user patterns of these records. The web history is mined. One of the necessary mining methods is web usage mining. This method consists of serial stages [20].

Fig (2) Stages of WUM:[6]

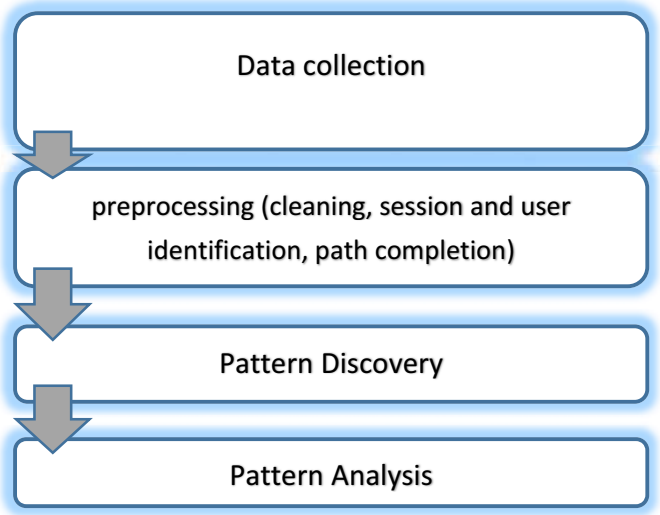

1) Data Collection:

The web history data is in the form of a document file. The information is stored in various types of documents. It is available in the following:[6]

A- Web server log file: These logs contain server-side data. This data consists of the IP address, URL, byte count, etc. In most cases, this data is displayed in a standard configuration. The most prominent of them is the Common Log Format CLF : [6]

B- Web Proxy Server Log file:

It is an average web server that is between the client and web server. When the webserver receives the visitor request through the proxy server. The log file entries will be the proxy server information and not the original client information. Proxy servers keep a separate record for all information user [20].

C- User Browser Log file:

Browser logs are collected from the devices of visitors who access the websites. This user data is found by proxies that are imposed by some applications such as (JavaScript programs). Attached to a web page is used to take information from the visitor as a record of their navigation. This data requires the cooperation of the customer, who most often restricts the operation of (JavaScript programs) for security reasons of the user [6] .

2) Data Pre-Processing:

It is a very important step in web usage mining. After gathering huge amounts of weblog data from various sources it appears to contain a lot of outliers that must be removed. To obtain consistent and integrated data for use in later stages (pattern discovering, pattern analysis). stages on preprocessing the as follows: [6]

- Data Cleaning

The log file contains a lot of non-essential records that are not related to our work. Like server error messages. Specified by the status code that the server sends when the visitor requests certain content, a field is recorded for each state of the record on the web. Also, the entries that contain graphics files, images, and others of the extension (jpeg, jpg, gif) are deleted. All codes greater than 299 and less than 200 are removed. Because it is considered invalid and is removed from the log file as in fig (3). Also, deleted records that were previously browsed are removed. Browsing records for the main pages are also deleted. This is because their links are found in most web server logs [2].

SUCCESS	200 series
REDIRECT	300 series
FAILURE	400series
SERVER	500series

Fig (3) Classes of status code.

- User and Session Identification:

It is not important to know the identity of the visitor. But there is a need to uncover and characterize visitor behavior. The server records multiple client sessions. And as a visitor can visit certain sites frequently. This is done without any authentication mechanisms. In many web servers. Because some

users disable the cookies feature. View its privacy content. This results in the IP address alone is insufficient to identify the unique visitor. Therefore, other criteria are used with the IP address such as user agent and referrer [2] . As for defining the user's session, define it. A group of pages visited by the same visitor in a certain period of time. On some web servers the session time is limited to 30 minutes. After this period, the second session begins. It is possible for a single visitor to have one or more individual sessions on the same page [21] . Visitor activities are numerous and controlling them is important in facing many issues, such as detecting visitor behavior and others. Among the most important of these activities are the following [22].

Table (2) Visitor activities

NO.	Activity	Clarify the activity	Example
1	The most active visitors identified	The visitors with the highest activity are limited by IP address, number of visits, and country.	192.168.0.110 IRAQ NO. V 13
2	Time to spend a visitor	It represents the time that the visitor spent at a particular site and can be represented by a diagram.	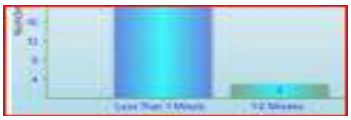
3	Daily visitor activity	It shows the differences in visitor traffic on the site during a specified period. It is measured in bytes transferred to each user	Sunday 15 Hits 200 KB
4	Hourly transfer rate	It shows the amount of data transferred in units of time	Hours of day Hit D. T 15 35 244 KB
5	Number of visits per visitor	It shows the number of visits of each visitor and deduces from it what the visitor's interests are in certain sites without others.	NO. of visitors' Visits NO. visitors 3 45
6	Countries with the most visits	Most countries ranked according to the number of unique visitors.	Country Unique V United stated 23
7	Browsers	It ranks your visitors according to the number of hits per browser. It also shows the byte size transferred from each browser.	Firefox No. Hits D. T 78 200KB
8	Operating system	A visitor's entries is determined by the number of arrival the O.S is installed on the visitor's	Windows 10 , No. Hits D. T 66 205KB

		computer. And the byte moved in the session.	

Table (3) User identification methodologies:

methodologies	Description of the methodology	Privacy risks	Advantages	Disadvantages
IP address & Agent	Assume when IP add & agent is unique this signifies that the user is unique	LOW	Available without technology	There is no guarantee that this user is unique
Embedded session ID	The dynamically created pages are used to link identifiers in the hyperlink	Low to medium	Since it is independent of IP address this makes it always available	Difficulty detecting duplicate users
Registration	The user enters the site directly	Medium	It can track the visitor and the browser	Visitors cannot register if it is not available
Cookies	By saving the identifier on the visitor's machine	Medium to high	Ease of tracking serial visits if it is for the same browser	It may be turned off by the user
Software agent	By downloading the program to the browser then it sends the used data	High	The data is accurate as it is for a specific location	It may not be accepted by the visitor

The process of controlling access resources and website security. Figure (4) shows the highly accessed or downloaded files arranged from highest to lowest. This is done by specifying the following [22].

- Define files with higher access
- The facts that have been reached
- Search engines
- Referring websites
- Security alert

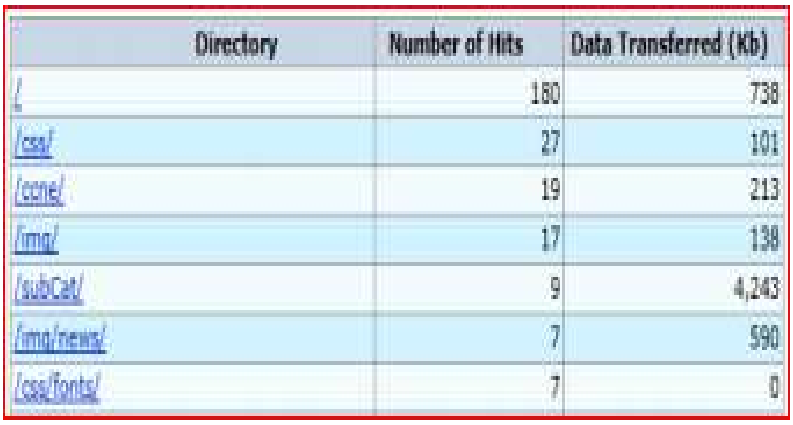

Directory	Number of Hits	Data Transferred (Kb)
/	180	738
/css/	27	101
/core/	19	213
/img/	17	138
/subCat/	9	4,243
/img/news/	7	590
/css/fonts/	7	0

Fig (4) The most important directories reached.

- Path Completion

It is an important step in pre-treatment. Mostly it takes place after completing the session. The agent or client is mostly due to temporary caching due to the loss of access references for some pages [23]. Also when the real URLs are more than recorded in the server log. This indicates a loss of access to references to these pages. It is possible to reveal this when a visitor requests a specific page that is not related to the previous page (the previous request) for the same visitor. The referrer can refer to the register to find out which page the above application contains. If the missing page is in the visitor's last click log. It is a page not registered in the registry. This state indicates that the visitor browsed again using the (Back) button [20] .

3) Pattern Discovery

It is one of the most important parts of Web Usage Mining extracting data from the web history. After performing the data cleaning process, selecting the user and the session. The main goal of this part is to discover interesting patterns [8].

A – Statistics:

It is an important technique for finding useful information for any web history. And to know the content of the web history and the number of visits to clients in that record. The number of visits is calculated on the basis of each valid entry in the weblog. These restrictions may be posting, browsing, downloading. Because it helps improve system performance. Such as monitoring visitor activities, monitoring and checking pages and sites, and aggregating visitors based on their behavior [24].

B - Association rule:

This technique is used to find recurring rules and patterns in the data generated from the preprocessing stage of the weblog data. Such as the number of users' frequent visits to certain pages. The task of this technology is to understand the visitor’s requirements. This is done by discovering the relationships between the pages visited by a particular visitor to a specific website. Several algorithms are used as Apriori algorithm, To find recurring association rules [6].

C -Clustering:

Clustering is a method used to group certain elements (pages, users, etc.). Based on similar characteristics. Such as a grouping of webpages with similar content. Or Clustering a group of visitors with similar browsing behavior. Or collecting many users who visit similar sites and others. It is also possible to use the normalization process with Clustering. This will give better combination results. Because there are different ranges in the data point for each area. Clustering technology helps in deducing customer stats in e-commerce market operations. And provide customized web content based on individual visitors. Also, Clustering is useful in making indexes of websites on the Internet [6].

D - Classification:

This technique categorizes data elements into distinct, predefined categories. Related to a specific category. This technology requires extracting and selecting the distinct classes on which the classification is made first. Then, the classification process is performed.[6] The main goal of categorizing weblog data is to develop the log for visitors belonging to a specific category as opposed to aggregation. Because classification is a directed learning method (supervised learning). Of the algorithms used by this technique naïve Bayesian classifiers, decision tree algorithm [20].

E - Sequential pattern:

It is the conduct of analysis to find patterns in sequence through serial sessions. And by applying several algorithms such as SPADE, Apriori, etc. For example, a specific visitor. visited link A and then link B one by one at the same time. Using analysis for such a pattern, we can predict the suspected visitor. When visited in a pattern similar to the previous one .Through psychology used to uncover crime, predict shopping, advertisements, etc. [6].

4) Pattern Analysis:

It is the last stage of web usage mining. In it, knowledge is found in the detected patterns. Interesting patterns. And that by getting rid of inappropriate patterns. This can be done by applying a validation rule. To get rid of inappropriate patterns and uncover appropriate patterns [20].

A commonly used technique in pattern analysis is the OLAP (Online Analytical Processing Technique).Visualization methods, administrative advertising deals, It uses graphic patterns to interpret the file results in an easier way. As well as (the mechanism of using the knowledge query SQL). Which is used to analyze several reasons for the abnormal patterns of your visitors[6].

4- Web Usage Mining Advantages and Disadvantages:

A) Advantages:

WUM It has many important advantages that make it more attractive to many, including governments, organizations, and companies. This technology appeared in electronic commerce to develop private shopping, the results of which showed large volumes in trade and profits. In the field of security, government agencies and others use this technology to classify and combat terrorist threats. Through the ability to predict Internet fraud detection and sort and identify people and pages with a high-security risk. Helps companies find the best relationship with the customer by identifying exactly what they need. Through WUM companies can understand well the requirements of their visitors. And provide a faster response to the requests of the visitors. It is also very beneficial for companies in attracting and retaining useful customers for the company who can save the best production costs [20].

B) Disadvantages:

When using WUM on personal information shows some concerns and negative consequences including. Violating the privacy of the user's information if it is obtained or published, especially when the user is not aware of it. It is the main concern for some users when some companies collect data from people for a specific purpose, such as a job or work, and others. These entities may use the data for other purposes such as fraud through e-mail or other personal information. Some techniques may be used to classify individuals based on controversial characteristics such as race, sexual orientation, religion, or gender. These practices can be in opposition to the Anti-Discrimination Act. Some companies also sell personal data obtained from people's websites in various ways. [20].

5- CONCLUSION

Data mining is the process of discovering needed information. Web mining is a branch of data mining which is the discovery of the knowledge and patterns required of the sheer volume of web data. This enormous amount of data is reflected negatively in the web mining process. Because it contains a Data outlier. Therefore, a pre-processing and cleaning stage must be carried out before mining. The web mining process Classify into three main types (Web Structure Mining, Web Content Mining, Web Usage mining). Each type is used according to the user's desire and what is part to be mined. This paper focused on conducting a survey of previous studies in web mining and types. And explained web usage mining and algorithms and techniques used in this genre. Starting with data collection, preprocessing, Discovery, and Analysis of Patterns. And what are the Advantages and Disadvantages of Web Usage mining.

References

[1] P. Verma and N. Kesswani, "Web Usage mining framework for Data Cleaning and IP address Identification," 2014.

[2] T. A. Al-Asadi and A. J. Obaid, "Discovering similar user navigation behavior in web log data," *International Journal of Applied Engineering Research*, vol. 11, no. 16. pp. 8797–8805, 2016.

[3] M. Gayatri, "Review of Current Trends in Web Usage Mining," no. October 2018, 2020, doi: 10.14419/ijet.v7i3.20.22972.

[4] Yehia Helmy, "Empirical-Study-of-Data-and-Web-Mining-in-Education.pdf." International Journal of Scientific & Engineering Research, p. 8, 2020.

[5] K. Velkumar and P. Thendral, "a Survey on Web Mining Techniques," pp. 167–174, 2020.

[6] B. Bhavani, V. Sucharita, and K. V. V. Satyanarana, "Review on techniques and applications involved in web usage mining," *International Journal of Applied Engineering Research*, vol. 12, no. 24. pp. 15994–15998, 2017.

[7] G. Shivaprasad, N. V. S. Reddy, U. D. Acharya, and P. K. Aithal, "Neuro-Fuzzy Based Hybrid Model for Web Usage Mining," *Procedia Comput. Sci.*, vol. 54, pp. 327–334, 2015, doi: 10.1016/j.procs.2015.06.038.

[8] M. J. Hamid Mughal, "Data mining: Web data mining techniques, tools and algorithms: An overview," *Int. J. Adv. Comput. Sci. Appl.*, vol. 9, no. 6, pp. 208–215, 2018, doi: 10.14569/IJACSA.2018.090630.

[9] R. Roy and G. Appa Rao, "Survey on pre-processing web log files in web usage mining," *Int. J. Adv. Sci. Technol.*, vol. 29, no. 3 Special Issue, pp. 682–691, 2020.

[10] J. Mehra and R. S. Thakur, "An Effective method for Web Log Preprocessing and Page Access Frequency using Web Usage Mining," *Int. J. Appl. Eng. Res.*, vol. 13, no. 2, pp. 1227–1232, 2018, [Online]. Available: http://www.ripublication.com.

[11] Y. Almurtadha, N. Mustapha, and N. I. Udzir, "Improved Web Page Recommender System Based on Web Usage Mining," no. 079, pp. 8–9, 2011.

[12] C. E. Dinuca and D. Ciobanu, "Improving the session identification using the mean time," *Int. J. Math. Model. Methods Appl. Sci.*, vol. 6, no. 2, pp. 265–272, 2012.

[13] S. Pandya, I. Mtech Scholar, Department Of CSE, RGPV, Bhopal, and M. R. Nigam, "REVIEW PAPER ON WEB PAGE PREDICTION USING DATA MINING," *Comput. Eng. Intell. Syst.*, vol. 7, no. 2222–1719, pp. 3369–3401, 2015.

[14] Mr. Jitendra B. Upadhyay and Dr. S. V. Patel, "A Review Analysis of Preprocessing Techniques in Web usage Mining," *Int. J. Eng. Res.*, vol. V4, no. 04, pp. 1160–1166, 2015, doi:

10.17577/ijertv4is041348.

[15] S. V. Kolekar, R. M. Pai, and M. M. Manohara Pai, "Prediction of Learner's Profile Based on Learning Styles in Adaptive E-learning System," *Int. J. Emerg. Technol. Learn.*, vol. 12, no. 6, pp. 31–51, 2017, doi: 10.3991/ijet.v12i06.6579.

[16] K. Sellamy *et al.*, "Web mining techniques and applications: Literature review and a proposal approach to improve performance of employment for young graduate in Morocco," *2018 Int. Conf. Intell. Syst. Comput. Vision, ISCV 2018*, vol. 2018-May, pp. 1–5, 2018, doi: 10.1109/ISACV.2018.8354043.

[17] A. A. A. El-aziz, P. S. Pandian, S. N. Almuayqil, and A. S. Alruwaili, "A Framework for Clustering & Enhanced Approach for Frequent Patterns in Web Usage Mining A Framework for Clustering & Enhanced Approach for Frequent Patterns in Web Usage Mining Assistant Professor , Department of Information Systems , College of Computer," no. June, 2020.

[18] S. Asadianfam, H. Kolivand, and S. Asadianfam, "A new approach for web usage mining using case based reasoning," *SN Appl. Sci.*, vol. 2, no. 7, pp. 1–11, 2020, doi: 10.1007/s42452-020-3046-z.

[19] P. M. Bharti and T. J. Raval, "Improving Web Page Access Prediction using Web Usage Mining and Web Content Mining," *Proceedings of the 3rd International Conference on Electronics and Communication and Aerospace Technology, ICECA 2019*. pp. 1268–1273, 2019, doi: 10.1109/ICECA.2019.8821950.

[20] R. S. Rao and J. Arora, "A Survey on Methods used in Web Usage Mining," *Int. Res. J. Eng. Technol.*, vol. 4, no. 5, pp. 2627–2631, 2017.

[21] P. V Patil and M. E. Scholar, "Preprocessing Web Logs for Web Intrusion Detection," pp. 11–15, 2012.

[22] A. K. Kassem, B. Daya, and P. Chauvet, "A proposed methodology on predicting visitor's behavior based on web mining technique," *International Journal of Advanced Computer Science and Applications*, vol. 9, no. 12. pp. 245–255, 2018, doi: 10.14569/IJACSA.2018.091236.

[23] R. Gopikaramanan, T. Rameshkumar, B. Senthil Kumaran, and G. Ilangovan, *Novel control methodology for H-bridge* cascaded *multi level converter using predictive control methodology*, vol. 11, no. 5. 2015.

[24] T. A. Al-Asdi and A. J. Obaid, "An efficient web usage mining algorithm based on log file data," *J. Theor. Appl. Inf. Technol.*, vol. 92, no. 2, pp. 215–224, 2016.

Fingerprint Image Identification Algorithm Based on Angle Direction of Objects

Fingerprint Image Identification Algorithm Based on Angle Direction of Objects

Diyar M. Witefee and Tawfiq A. Al-Asadi

Information Technology College, University of Babylon

E. mail: Dyarz2017@gmail.com

Abstract :Fingerprint identification is one of the most important biometric techniques utilized for determining the similarity between the matching images. This paper will be presenting a new identification technique depending on the angle direction of the objects contained in images. The performance of identification techniques relies on the quality of the image. The quality of fingerprint image may not always be well due to many reasons such as contain noise which hinders the clarity of image structures.

Keywords: Image of Fingerprint, Thinning, Minutiae based matching, Feature Extraction.

1. Introduction

Biometrics science is the analyzing of physical and/or behavioral characteristics that specific to each individual for identification the identity in a reliable and fast way by using of unique biological characteristics**.** It addresses a longstanding concern to prove individual's identity and individual's verification, by making use of what makes once different. Historically, applications that using biometrics are military access control, criminal or civil identification and technical framework. Today is including banking, retail, and mobile commerce.

Fingerprint is one of the most widely used biometric. It can be defined as the graphical flows of ridges in human fingers which are formed during infancy. According to researches, not even two people have the same fingerprints. Even the ten fingers of the same person differ with respect to their corresponding fingerprints. Fingerprint image can be used for many purpose such identification and verification.

In this study, the pre-processing is applied to enhance, morphology and thinning the fingerprint image then the local features (Minutiae) extracted; finally the fingerprint images are matching based on the angle direction of the minutiae points. Based on a specific threshold of the correct number of matching score the identification of the fingerprint image is determined.

2. Related work

Over the years, research on image identification has offered a lot of matching methods. Typical examples include the local and global methods like Minutia matching; correlation depended on matching, neural network-based matching and pattern matching.

- Manickam, A., Devarasan, E., Manogaran, G. (2019) [6] introduces a model to perform matching for latent fingerprints using Scale Invariant Feature Transformation (SIFT). Their model consist of two phases (i) contrast enhancement using a fuzzy set (ii) extraction of SIFT feature points

from fingerprints. Then matching algorithm is performed with *n*- number of images and scores are calculated by Euclidean distance.

- Alejandro Valdés Camejo and Javier Lamar León [7] used the application of the algebraic topology to present an algorithm for fingerprints verification. They defined local structures based on neighboring minutiae. The extraction of features is based on the homology variation of neighboring minutiae. In addition, a matching method is presented based on the topological information.
- Kimfung Liu and Wenzhong Shi [8] proposed a new developed computational fuzzy topology to define the topological relations among spatial objects. They used the value of a level cutting which represent the intersection between both boundaries with interior and the exterior. They submitted an approximation of these overlapping areas.

3. Research Methodology

Before performing the image matching, a pre-processing step is performing to increase the image quality (corrective measures). Many reasons caused low quality in the fingerprint images such as partial images, the problem of the sensors and the skin problems. Pre-processing step include the enhancement of the image, morphology and thinning process Then the step of feature extraction is performing which involve extraction the local features (Minutiae) and global features (core and delta). Often the images are different in rotation angle and scale space, and then the next step is the alignment step for the images to be matched. After the alignment step, the images will be in the same rotation angle and similar scale space. The final stage is the matching step, which is performing between the input image and images store in the dataset and then determines the similarity among them.

The proposed system, which is used for fingerprint images identification, illustrate in figure-1 consist of three steps:

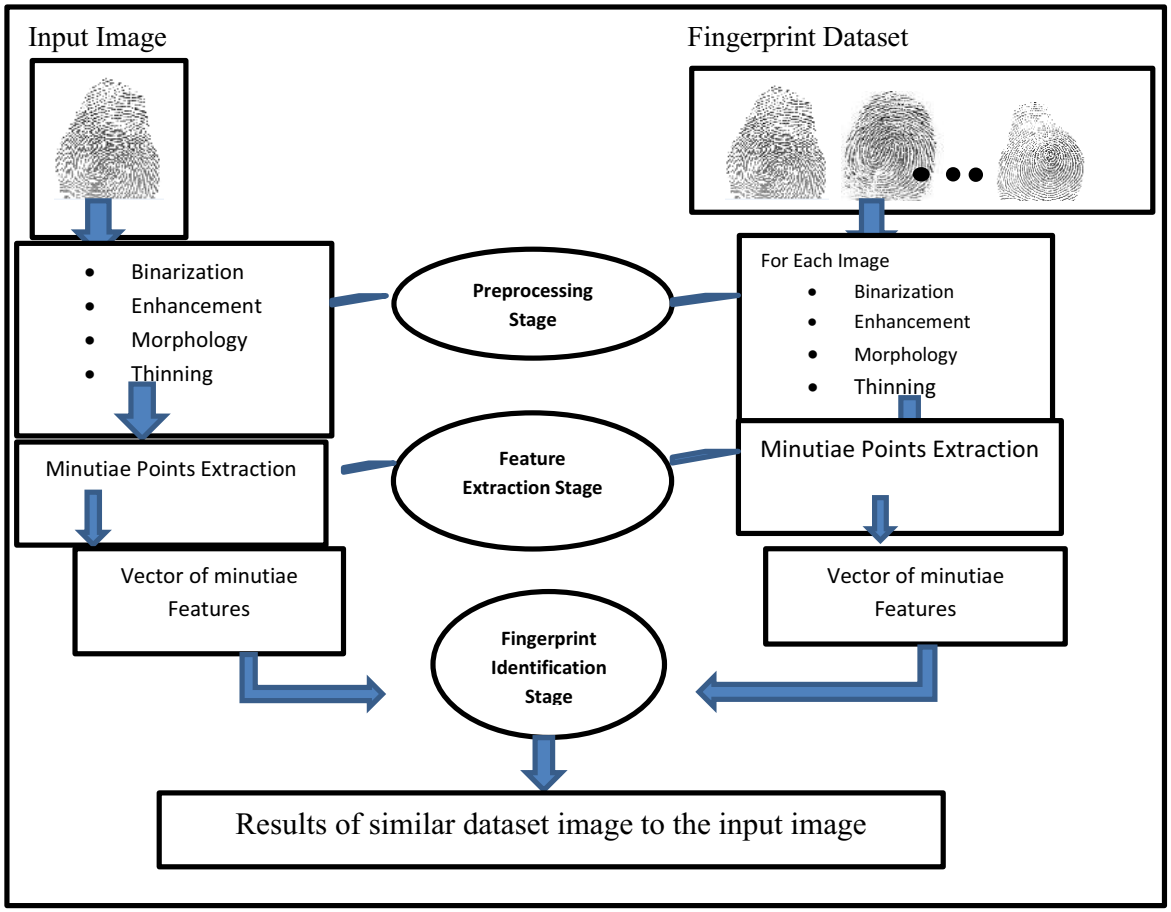

Figure -1 Block diagram of the proposed system

-The initial stage is the *pre-processing* stage of the proposed system, are clarified the following points:-
1-The input and reference fingerprint images are converted to a binary image: each pixel value in the binary image can be one of two values, either 0 or 255 value.
2-The binary images are enhanced by applying Gabor filters on it: Gabor filters are classified as filters that are sensitive to frequency and orientation, utilized for the analysis of texture and edge. The filter could be modulated by a Gaussian envelope and found the same frequency and direction as a sinusoidal plane.
3- Apply the morphology operations on the input and reference images to improve the enhanced images by focusing on the important objects
4-Perform Thinning operation on the fingerprint images, It is a morphological process that is adapted to erase the foreground pixels from the binary pictures.
-The second step is *Features extraction* step of the system which is a minutia extraction is performed by using the eight-neighbor technique. This technique is better than the other methods because of the efficiency of its computation and its simplicity. This method involves thinning image utilizing where the ridge flow has connected at eight points. The minutiae pixels are extracted by using a 3X3 window by scanning the local region of every Pixel in the image.
-The third step is *Fingerprint Identification* , which clarifies in the following steps:

- The matching images are blocked into 8-blocks.
- Each minutiae in the input image are matched with all the minutiae that lying in the same block of the image of the reference image.
- To determine the similarity between minutiae , the matching step is performed by using the direction of line between the minutiae pixel and its neighbor pixel by using the equation (1).The direction should be equal in the matched minutiae object.

$$\Phi = \tan^{-1}\left(\frac{ym-y}{xm-x}\right) \quad \ldots (1)$$

Where,
(xm, ym) the coordinate of minutiae pixel
(x,y) the coordinate of its neighbor.

4. The Outcomes with the Discussion

The proposed system applied on a fingerprint dataset that download from ***Neurotechnology*** company website. It was founded in Vilnius, Lithuania in 1990 with the key idea of using neural networks for applications such as biometric person identification, computer vision, robotics and artificial intelligence.
The following results is for input and reference images which are illustrated in figure-2.
The results of the first step of the proposed system can be showing in the figure-3.

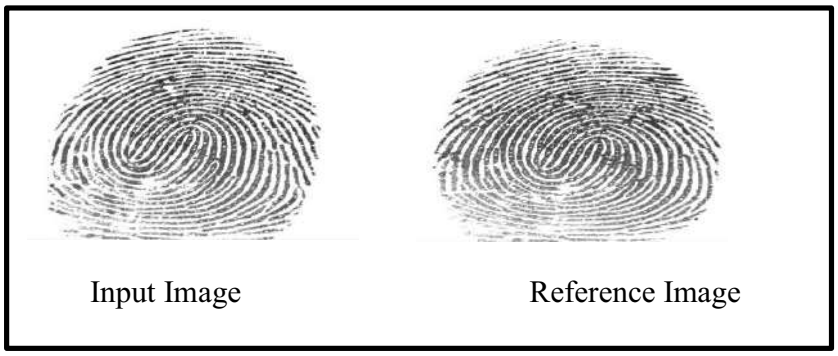

Figur-2 Input and Reference Images

Figure-3 Preprocessing Stage Results

The results of second stage for input image and the reference image are illustrated in table-1.

Tabel-1 Minutiae Feature vectors

Reference image	Input Image
(193,385)	(46,259)
(226,353)	(101,299)
(237,154)	(200,106)
(252,282)	(215,383)
(267,377)	(226,318)
(269,258)	(238,338)
(302,373)	(272,272)
(331,413)	(272,299)
(339,376)	(282,305)
(368,388)	(64,313)
(93,308)	(71,164)
(122,428)	(80,177)
(148,344)	(91,272)
(175,355)	(138,58)
(211,263)	(167,372)
(252,266)	(235,58))
(291,115)	(251,191)
(342,241)	(255,295)
(365,352)	

The results of final stage of the system are calculate the direction of angles for the minutiae points of the input and reference images according equation-1 and return the identification if performed between the two images.

5. Conclusion

After applying the proposed system, we got the result that either the two images belong to the same person or not. The system gave a higher rate of matching when the two images belong to the same person. It also gives a lower rate when the two images belong to different persons.

References

[1] Anil K. Jain, Jianjiang Feng, Karthik Nandakumar, “Fingerprint matching”,2010.

[2] Jain, A.K., Prabhakar, S., Hong, L., Pankanti, S," Filterbank-based fingerprint matching", IEEE Transaction on Image Processing ,2000.
[3] Saeed Mehmandoust and Asadollah Shahbahrami, "A Comparison between Different Fingerprint Matching Techniques ", Springer-Verlag Berlin Heidelberg, 2011.
[4] Daniel Peralta , Mikel Galar , Isaac Triguero, Daniel Paternain , Salvador Garciae, Edurne Barrenechea , Jos'e M. Ben'ıtez, Humberto Bustince , Francisco Herrera "A Survey on Fingerprint Minutiae-based Local Matching for Verification and Identification: Taxonomy and Experimental Evaluation", January 7, 2015.
[5] Meryam Elmouhtadi, Sanaa El fkihi and Driss Aboutajdine, "Fingerprint Identification Using Hierarchical Matching and Topological Structures", Chapter,
First Online: 15 October, 2017.
[6] Manickam, A., Devarasan, E., Manogaran, G. *et al.* "Score level based latent fingerprint enhancement and matching using SIFT feature", *Multimed Tools Appl* 78, 3065–3085 , https://doi.org/10.1007/s11042-018-5633-1, (2019).
[7] Alejandro Valdés Camejo, Javier Lamar León, "Application of algebraic topology to fingerprint recognition ",2018.
[8] KIMFUNG LIU and WENZHONG SHI ," Computing the fuzzy topological relations of spatial objects based on induced fuzzy topology ", International Journal of Geographical Information Science, September 2006.
[9] Jianjiang Feng, Zhengyu Ouyang and Anni Cai ," Fingerprint matching using ridges ", Pattern Recognition 39, 2006.
[10] Silas KivutiNjeru and Dr. Robert Oboko," COMPARATIVE ANALYSIS OF MINUTIAE BASED FINGERPRINT MATCHING ALGORITHMS ", International Journal of Computer Science & Information Technology (IJCSIT), December 2016.
[11] Qi J., Yang S & Wang Y," Fingerprint matching combining the global orientation field with minutia",Pattern Recognition Letters, 2005.
[12] P. Singh and L. Kauri, "Fingerprint Feature Extraction Using Morphological Operations", International Conference on Advances in Computer Engineering and Applications, 2015.
[13] Zhong Wei-bo, Ning Xin-bao and Wei Chen-jian, "A fingerprint matching algorithm based on the relative topological relationship among minutiae", IEEE Int. Conference Neural Networks & Signal Processing Zhenjiang, China, 2008.
[14] NaifAlajlan and Mohamed S.KamelGeorge Freeman, "Multi-object image retrieval based on shape and topology", 2006.
[15] Dong Luo and Xiaorong Chen ," Research of Topology-based Fingerprint Matching Algorithm", Third International Conference on Intelligent Control and Information Processing, 2012.
[16] B.Sudeepthi, Md.Imaduddin and D.Kavitha, "Comparison of Fingerprint Minutiae Matching Technologies ", IOSR Journal of Electronics and Communication Engineering, Nov - Dec. 2014.
[17] Neelima Kanjan, Kajal Patil 2, Sonal Ranaware and Pratiksha Sarokte, "A Comparative Study of Fingerprint Matching Algorithms ", International Research Journal of Engineering and Technology (IRJET), 2017.
[18] T. A. Al-asadi and A. J. Obaid, "Object detection and recognition by using enhanced speeded up robust feature," International Journal of Computer Science and Network Security (IJCSNS), vol. 16, no. 4, pp. 66-71, 2016.

Anatomical and chemical study on the growing Eriobotrya japonica in Anbar Governorate

Anatomical and chemical study on the growing Eriobotrya japonica in Anbar Governorate

Lubab Mohamed Awad [1] and Ashwaq Talib Hameed [2]

[1,2] Biology Department, College of Education for Women, University Of Anbar, Iraq.

lubab.awad@uoanbar.edu.iq Ashwaq.Talib@uoanbar.edu.iq

Abstract. current research consists of an anatomical find out about of the Eriobotrya japonica from the Rosaceae in Anbar Governorate, which is in the structure of planted trees. The anatomical features of the s, leaf blade and market have been studied and its traits and floor have taxonomic significance in keeping apart and diagnosing this type. Appearance qualities can be linked with anatomical qualities to achieve an built-in classification. The quantity of layers and thickness of every organ, vascular bundles characteristics, wide variety of vessels, the traits of epidermal cells and cross-section structure are all studied contributing to taxonomic significance . The current study also dealt with the phenotypic characteristics of the stem, leaf and stalk, and it became clear through this study that the stems of the type Eriobotrya japonica were cylindrical and hard with many branches and were distinguished by a greenish-brown color. It is not a fixed characteristic of the single type in addition to the shape of the leaf, which is one of the important features in the classification. The stalk is characterized by being short and covered with hairy and green or yellowish green color, and these characteristics are important in the classification of this type. The fatty acids were detected in the hexane extract of Eriobotrya japonica in the gas chromatography device - GC, and the results indicated that this type contains fatty acids, the highest percentage of linoleic acid was 60% and the lowest Linolenic acid by 0.17%.

1. Introduction

The Rosacea household is one of the good sized botanical households with about 3000 species and one hundred genera [1]. It is one of the households noted in the Iraqi Flora of Iraq and it consists of one hundred forty genus and this household is unfold in the areas of the world and has been assigned a classification key in Iraq incorporates eleven . species and is in the structure of trees, shrubs, and herbs. [2 , 3] cited that there are 19 species and forty three species that are both wild or cultivated. [4] it carries one hundred fifteen species and 3200 species unfold in North America, East Asia, and Europe and there are 19 species and 50 species in Iraq. Eriobotrya japonica, an evergreen tree

belonging to the Maloideae of Rosaceae that consists of about 940 species .[5] Its size is 10m and perhaps the smallest in size between (3- 4) m.[6] This plant has medicinal and dietary significance as used in the remedy of many et al illnesses. [7] And It is a supply of dietary phenols. [8] It is additionally an decorative tree and an essential supply of nectar for beekeeping .[9] It has been cultivated for extra than 2000 years and is now cultivated commercially in 30 nations [10] The leaf

frequently reaches 30 cm in width and 9 cm in width in which the top floor is smooth and the decrease one consists of fluff [11] The anatomical find out about is vital in the classification of species, ranks, and households .[12] and additionally has extra interest in figuring out the genetic

2. Materials & Methods

2.1. Collection of samples:

This find out about relied on the smooth samples of the plant Eriobotrya japonica, which had been gathered from the Heet areas of Anbar Governorate in the duration from June 2019 to March 2020. The components that are wholesome have been.

relationships between species and taxonomic degrees .[13] The anatomical learn about helped in resolving matters The troubles encountered by way of the researcher or classifier in the match of overlap or similarity in phenotypic traits .[14] The purpose of this find out about was once to provide an anatomical photograph to some vegetative components such as the leaf, stem, and the market for the plant Eriobotrya japonica, which are nearly non-study in Iraq, as properly as the lack of lookup and sources That research the anatomical aspect in Iraq and the world.

besides ailments and rupture. A pattern of the plant was once taken and was once recognized the usage of the supervisor and relied on the classification keys referred to in the Iraqi flora [14] .

2.2. Anatomical study:

Prepare permanent vertical sections of the organs slides of the stem , leaf and petiole, The wax method mentioned was used [8].

3. Results and discussion

3.1. The section of leaf lamina

The modern-day find out about of the kind Eriobotrya japonica proven in Table No. 1 and determine 1 confirmed that it consists of easy dermis consisting of Uniseriate rectangular cells in which the higher epidermal cells regarded large than the decrease dermis and the common epidermal thickness was once 15 Mm, whilst the common thickness of the decrease dermis reached 19 Mm, it grew to be clear that the Mesophyll tissue in this kind was once Unifacial, which means that the palisade layer is positioned simply beneath the higher pores and skin and is aligned to one floor and then the spongy layer [12] mesophyll consists two layers layer of palisade is the type that follows the top pores and skin and the quantity of ranks (4- 2) and are cells compact and common thickness reached 92 The 2d layer is spongy layer used to be had 5-4 ranks, which reached a thickness charge 100 Mm which is characterised through free and disjoined cells and there are between interfaces distances cells and types are irregular and both the center vicinity of race grew to become out to be made up of parenchyma tissue that characterised their cells as are the dimension of there is a area between them and incorporates prolonged and giant vascular bundles.

Each bundle consists of xylem and Phloem wood. The common thickness of the wooden is sixty four and the thickness of the bark 33. The quantity of rows of vascular devices in the center vein 35-22 and the diameter of the vascular bundles 401Mm, this learn about coincided with . [14] the anatomical learn about gave many vital elements that helped aid the phenotypic traits used in classification and additionally this find out about helped to isolate this kind by way of identifying the traits of the Mesophyll tissue of the leaf and additionally by means of the quantity of layers of the tissue and additionally this kind can be remoted thru The variety of vascular devices in the vascular bundle of the leaf

3.2. Surface coating Idumentum

The results of the Eriobotrya japonica shown in fig. (4) it contains trichomes that differed in their dimensions and distribution according to the different plant members, which are of the Eglandular and unicellular trichomes with a cylindrical shape and end as pointed or rounded and found on leaves and stem And the petioles these results were in agreement with [9].

3.3. The section of Stem

The modern-day learn about of the stem of the kind Eriobotrya japonica, proven in Table (2) fig. (2). the stem in this kind used to be circular, Solid and Pith occupies the center, the area used to be displaying the center of the stem, in general, incorporates an exterior layer known as Cuticle surrounding In the pores and skin from the outside, its cells are uneven with an common thickness of 6 Mm, and then the dermis layer comes in. The cells are nearly rectangular, fairly small, and consist of one layer, and they are continuous. After the dermis layer comes to the cortex, which consists of multilayers in which the cells are various and the common thickness is 517. The first layer in the Eriobotrya japonica consists of the Collenchyma tissue, and this is observed via the Parenchyma tissue. The thickness of the Collenchyma tissue 105. Its thickness (178). As for the vascular cylinder, it grew to become clear that it is a non-stop annular cylinder round the circumference of the stem that is parallel to the Cortex. The vascular cylinder consists of xylem wood (sixty eight) Mm and the Phloem bark, 17 Micrometers. The pith is placed in the core of the stem, and it consists of large-sized, large-scale parenchyma cells[12]. The partitions are thin, stored, and formed in a round polygon. The thickness of the pulp in this kind reached 494 Mm. Through the anatomical facets of the vascular cylinder the place they have been of the non-stop kind and information of the houses of the vascular bundles and the thickness of every layer in the stem have a classification fee in setting apart and diagnosing the type.

3.4. Leaf petiole Section

The cutting-edge learn about of the Eriobotrya japonica petiole market confirmed its facts in Table three and fig. (3), the cross-section from the center of the organ is a part from the backside a little sharp and from the pinnacle convex there is a cuticle from the backyard and has a thickness of 3 Mm and surrounds the pores and skin consisting of one row of The cells are nearly cubic in form and include the bases of hairs and their thickness is 15 (after the epidermis). The layer of the cortex is made up of two sorts of tissues. The first layer consists of non-stop Columbia tissue with an common thickness of 158Mm and the tissue that comes after it is the Parenchyma tissue whose thickness used to be 226Mm. As for the vascular bundles in this type, they are open and the wide variety of bundles in them is 3 mid-site bundles and two lateral bundles. The wide variety of rows of vascular gadgets (6-8) and the variety of vascular gadgets per row (5-2). The cross-section of the Eriobotrya japonica market had an necessary classification value, as nicely as the structure of the vascular bundle that was once open and the separated bundles and their number, are three bundles one of them is the web page intermediate and two facet bundles and the size of the bundle are

remoted and additionally the collenchyma tissue of the cortex in this kind used to be of the angular collenchyma kind and the thickness of these layers [13]. All qualities have a taxonomic fee in isolation and prognosis of the species. Through this find out about and know-how of the anatomical traits, these features that have been recognized in this learn about can be localized in isolation of the kind and additionally can hyperlink between the anatomical and phenotypic features the place between the researcher [14] for the duration of his announcing it is feasible to acquire an built-in herbal and best classification solely when linking the anatomical data with Observations stemming from phenotypic studies, and this is what used to be emphasised in this learn about and the opportunity of making anatomical records got to serve the plant classification[15].

Table 1. shows the dimensions of the leaf blade of *Eriobotrya japonica* measured

Cuticle thickness	Epidermis thickness		Mesophyll			Vein		
(0.9-4.5) 2.7	upper	lower	Palisade layers	Palisade thickness	Spongy layers	Spongy thickness	Rows of Vessels element	Vascular Bundle diameter
	(6-24) 15	(4-33) 19	(2-4)	(40-143) 92	(3-4)	(70-130) 100	(22-35)	(212-590) 401

Table 2. The quantitative characteristics of *Eriobotrya japonica* stems measured in micrometers.

Cuticle thickness	Epidermis thickness	Cortex thickness	cortex layers		Xylem thickness	Phloem thickness	Pith thickness
(2.5-9) 5.8	(9-12) 11	(422-612) 517	Collenchyma tissue thickness	Parenchyma tissue thickness	(45-90) 68	(11-22) 17	(488-500) 494
			(66-144) 105	(85-270) 178			

Table 3. The quantitative characteristics of *Eriobotrya japonica* petiole , measured in Micrometers.

Cuticle thickness	Epidermis thickness	Cortex layers		Number bundle	Number Of rows Vascular units	Number Of Vascular Units per row	Bundle length
(1.3-4) 2.7	(6-24) 15	Collenchyma tissue thickness	Parenchyma Tissue thickness	3	(6-8)	(2-5)	(66-120) 93

		(95-221) 158	(119-332) 226				

. (The values inside the arcs represent the minimum and maximum values and the values outside the arcs represent the mean) .

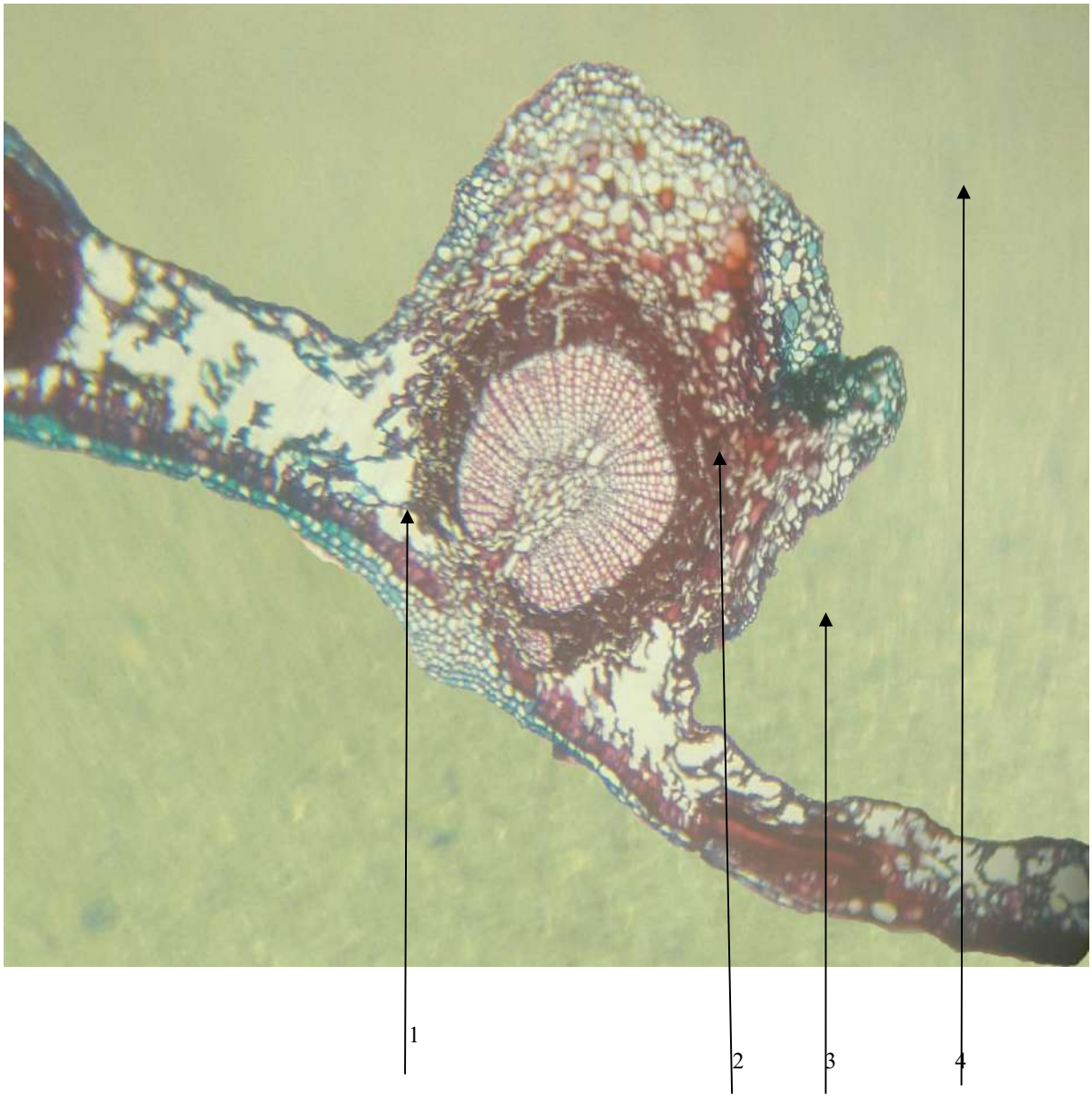

Fig.1. Transverse section of *Eriobotrya japonica* leaf 40 X

1-Upper epidermis
2- Xylem
3- Phloem
4-Lower epiderm

Fig. 2. Transverse Section of Eriobotrya japonica leaf Mesophyll layers illustrate 40X
1- Palisade layer
2- Spongy layer

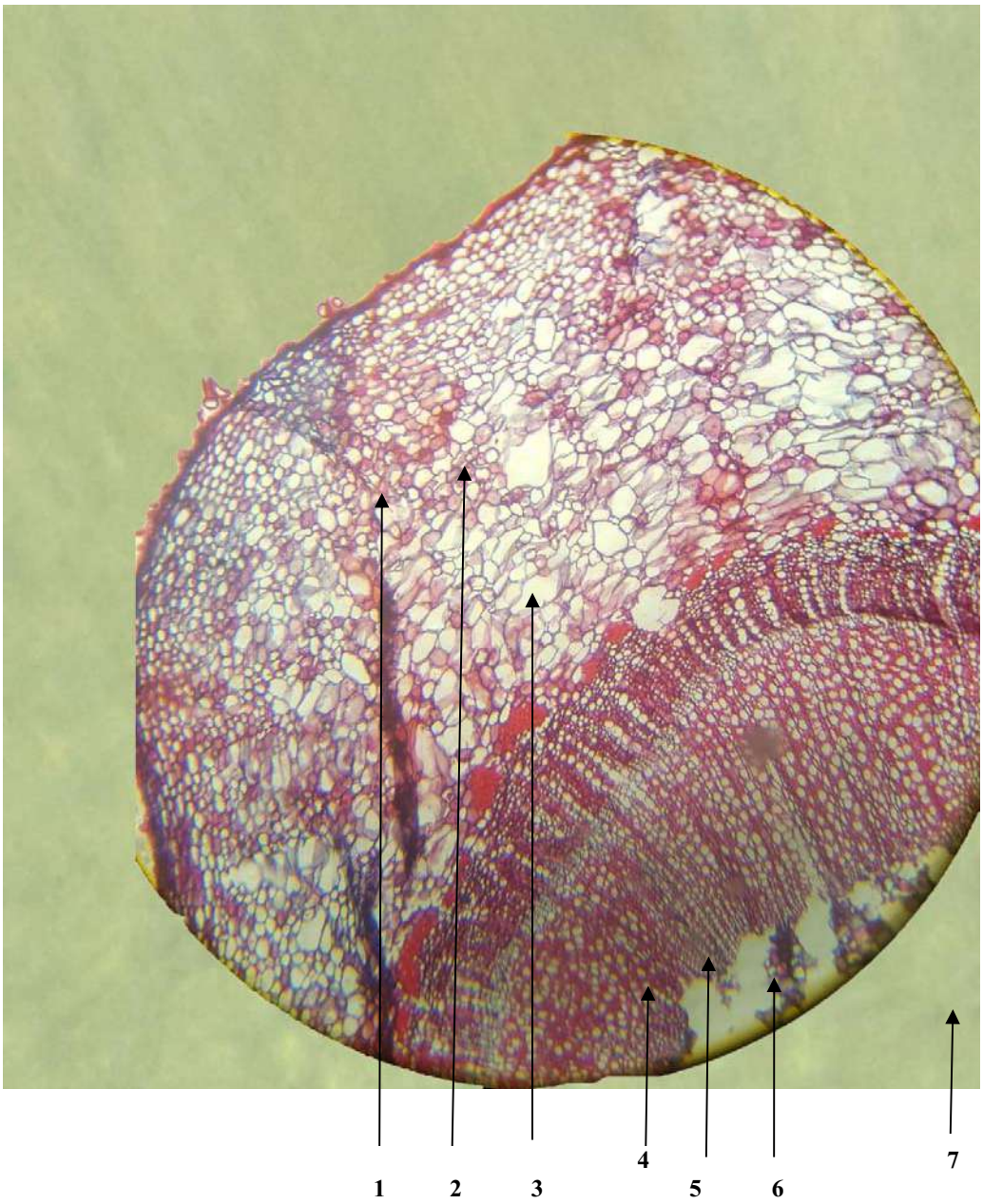

Fig. 3. Transverse section of Eriobotrya japonica stem 40X

1-Epidermis
2- collenchyma } Cortex
3- parenchyma }

4- phloem }
5-Xylem } Vascular bundle
6- pith

Fig. 4. Transverse Section of *Eriobotrya japonica* Petiole 40X.

1-vascular bundle2- pith 3-phloem 4-xylem5-cortex6-Epidermis.

Fig. 5. Eglandular trichm of Eriobotrya japonica 40X

3.5. Morphological study

Stems & Twig legs and branches

The current study revealed that the stems of the type Eriobotrya japonica are cylindrical in shape, solid, and have many erect branches. The quality of the leg is shown in Table (4).

Table 4. Shows the quantitative and qualitative characteristics of the stem for the species *Eriobotrya japonica*

Plant height	Nature of plant	Nature of stem	Branches	Branching type	Branching color
(2-8)m	Trees	Erect	Many	Upper	Green brown

3.6. *Leaves*.

The leaves are one of the basic physiological axes of the plant as it performs important processes such as photosynthesis and transpiration as it works alongside other plant devices such as wood and bark and contributes to the absorption of nutrients and water from the soil through the roots and allows the transfer of metabolic products from them to the rest of the plant body. Eriobotrya japonica leaves are distinguished. It is simple, petiolate, and alternate, and it should be noted that the leaves from the vegetative parts that are more susceptible to environmental conditions and the characteristics that are most exposed to variations are the dimensions of the leaf, then followed by the shape of the blade, its base, its edge and finally the color of the leaf. In this study the shape of the blade was fixed and the table (5) It shows the quantitative characteristics of the leaves of the type[16]. The dimensions of the paper were different in terms of length and width, where the average length of the blade was (260) mm and the average width was (90) mm. The upper, open color in the lower surface, and the shapes and structure of the blades have basic features and have an important role in classification. Acute is sharp, while the edge of the leaf in Eriobotrya japonica is serrated, and the edge of the blade is one of the most important characteristics that distinguish the leaves, in addition to its shape. The edge of the blade gave a taxonomic weight no matter what it is not a fixed characteristic for individuals of the same species. As for the leaf base, it was rounded. It was identical to the plant wealth in Iraq [17]. As for the surface covering of the leaves, it was almost smooth on the upper surface and had dense fluffy filaments on the lower surface.

Table 5. Shows the dimensions of the leaf blade for the *type Eriobotrya japonica* measured in MM.

Blade length	Blade width	Average blade length\ Average blade width

(130-390)260	(50-130)90	2.9

3.7. Petiole

The study of the type Eriobotrya japonica showed that the stem is circular in the cross section, but it showed variations in its dimensions, as the stems of this type were short and covered with a capillary covering and the color of the stalk is green or yellowish green. The width of the stem is (5) mm, and the average length of the stalk to the average of the stem width is (2.6) mm

Table 6. Shows the dimensions of the petiole for the type Eriobotrya japonica measured in MM.

Petiole length	Petiole width	Average petiole length\Average petiole width
(7-19)13	(3-6)5	2.6

Table 7. The fatty acid present in Eriobotrya japonica extract By GC

Fatty acid	Concentration %
Palmitic acid	5.10
Palmitoleic acid	1.74
stearic	3.18
Oleic acid	4.45
Linoleic acid	60.0
Linolenic acid	0.17

The results of the extract of Eriobotrya japonica in the gas chromatography device - GC showed that the plant contains several types of fatty acids, where the highest percentage of linoleic acid was 60%. Table (4) Unsaturated fatty acids are important compounds for metabolic processes inside the body of the organism, as Linoleic acid helped expand the respiratory tracts and build red blood cells, and its deficiency leads to high cholesterol in the blood and liver and leads to stunted growth in children [11] Also, fatty acids are anti-inflammatory and prevent type 2 diabetes and prevent high blood pressure [12].

References

[1] Alwash B M J 2017 Cytotoxic and antioxidant activity of fruit juice of eriobotrya japonica (Thunb.) lind plant cultivated in iraq . *Iraqi Journal of Agricultural Sciences*, *48*(3).

[2] Aziz A Khan I Azam S Mehnaz S and Ahmad B 2017 Comparative antimicrobial, phytotoxic and heamaglutination potential of Eriobotrya japonica leaf extract and its zinc nano-particles. *Pak. J. Bot*, *49*(5) 1917-1924.

[3] Bashir A F Shireen S Bashir and I Khan and A Sadiq 2016 Green synthesis, characterisation and biological evaluation of AgNPs using Agave americana, Mentha spicata and Mangifera indica aqueous leaves extract. IET Nanobiotechnol., 1-7.

[4] Dai,J and R J Mumper 2010 Plant phenolics: Extraction, analysis and their antioxidant and anticancer properties. Journal Molecules.15, 7313-7352.

[5] Faria AF P Hasegawa E A Chagas R Pio E. Purgatto and A Z Mercadante 2009 Cultivar influence on carotenoid composition of loquats from Brazil. J. Food Compos Anal 22:196 –203.

[6] Gao Z and Iqbal S 1993 Reconstruction of Ancestral Chromosomes of the Family Rosaceae. (12) p 149–61.

[7] Jiang S An H Xu F 2020 Chromosome-level genome assembly and annotation of the loquat (Eriobotrya japonica) genome. (February):1–9.

[8] Jiang Y Zhu Y Zhang L Su W Peng J and EJTFL1 2020 Genes Promote Growth but Inhibit Flower Bud Differentiation in Loquat. 11(May):1–16.

[9] Lin S Sharpe RH and Janick J 1999 Loquat : Botany and Horticulture. 1999;23.

[10] Liu Y Zhang W Xu C and Li X 2005 Biological Activities of Extracts from Loquat (Eriobotrya japonica Lindl .): A Review.

[11] Pareek S N Benkeblia J Janick S Cao and E M Yahia 2014.Postharvest physiology and technology of Ioquat (Eriobotrya japonica Lindl.) fruit. published online JSCI 1-10

[12] Pirondo A Coulleri J P Keller H A and Ferrucci M S 2011 Influencia de factores externos sobre la comercialización de plantas medicinales en un medio urbano: el caso de vendedores criollos e indígena en Corrientes, Argentina.

[13] Rashed K.N and M Butnariu 2014 Isolation and antimicrobial and antioxidant evaluation of bio- active compounds from Eriobotry ajaponica stems. Adv Pharm Bull 4:75 -81.

[14] Shulaev V Korban S S Sosinski B Abbott A G Aldwinckle H S Folta K M., ... and Veilleux, R E 2008 Multiple models for Rosaceae genomics. *Plant physiology 147*(3), 985-

1003.

[15] Shulaev V KS Sosinski B Abbott AG Aldwinckle HS and Dandekar AM 2008 Multiple Models for Rosaceae Genomics [OA]147 p 985–1003.

[16] Zhang W Zhao X Sun C Li X and Chen K 2015 Phenolic Composition from Different Loquat (Eriobotrya japonica Lindl.) Cultivars Grown in China and Their Antioxidant Properties. (14) p 542–55.

[17] Zhang Z Li G Yang X and Lin S 2017 Taxonomic Studies Using Multivariate Analysis of Eriobotrya Based on Morphological Traits.302(2):122–32.

Weakly Small Smiprime Submodules

Weakly Small Smiprime Submodules

Haider A. Ramadhan – Nuhad S. Al. Mothafar

[1,2] Department of Mathematics , College of Science , University of Baghdad , Iraq

Email : ubominai1975@gmail.com, nuhadi.salim@sc.uobaghdadi.edu.iq

Abstract : Let R be a commutative ring with an identity , and G be a unitary left R-module . A proper submodule H of an R- module G is called semiprime if whenever $a \in R, y \in G, n \in Z^+$ and $a^n y \in H$, then $ay \in H$. We say that a proper submodule H of an R- module G is a weakly small semiprime, if whenever $a \in R, y \in G, n \in Z^+$, (y) is small in G and $0 \neq a^n y \in H$, implies $ay \in H$. Many basic properties and characterizations of this type of submodule are given.

Keywords : semiprime submodules , semiprime modules , small semiprime submodule , small semiprime modules .

1.Introduction

In this research we introduce the concept of weakly small semiprime submodule as a generalization of small semiprime submodule and established some of its basic properties , examples and characterizations. A proper submodule H of an R - module G is called a small semiprime submodule if $for\ each\ r \in R$, $x \in G$, $n \in Z^+$ and $x \in G$ such that $r^n x \in H$ implies $rx \in H$, [6] . A proper submodule H of an R - module G is called a small semiprime submodule if $for\ each\ r \in R$, $x \in G$, $n \in Z^+ with\ (x) \ll G\ such\ that\ r^n x \in H\ implies\ rx \in H$. A proper ideal I of a ring R is called small semiprime ideal if whenever $0 \neq a^k b \in I$ for $a , b \in R$, $k \in Z^+$ and $(b) \ll R$ implies $ab \in I$, [5] . Where "a submodule P of G is called small (notationally , $P \ll G$) if $P + W = G$ for all submodules W of G implies $W = G$", [3]. Let G be an R- module a proper submodule H of G is called weakly small semiprime , if whenever $0 \neq r^k x \in H$ for some $r \in R$ and $(x) \ll G, k \in Z^+$ implies $rx \in H$.

In section 1 we study some basic properties for the concept of a weakly small semiprime submodule. In section 2 we give properties of weakly small semiprime submodule in class of multiplication and hollow R- modules.

2.Weakly Small Semiprime Submodules

In this section we introduce the concept of weakly small semiprime submodule as a generalization of small semiprime submodule and established some of its basic properties, examples and characterizations.

Recall that a proper submodule H of an R - module G is called a weakly semiprime submodule if $for\ each\ r \in R$, $x \in G$ and $n \in Z^+$ such that $0 \neq r^n x \in H\ implies\ rx \in H$, [2].

Definition (2.1)

Let G be an R- module a proper submodule H of G is called weakly small semiprime If whenever $0 \neq r^k x \in H$ for some $r \in R$ and $(x) \ll G, k \in Z^+$ implies $rx \in H$.

A proper ideal I of a ring R is called weakly small semiprime ideal if whenever $0 \neq a^k b \in I$ for $a, b \in R$ and $k \in Z^+$ and $(b) \ll R$ implies $ab \in I$.

Remark (2. 2)

It is clear that every small semiprime submodule is weakly small semiprimei submodule. But the converse is not true in general, as the following example show:

Example (2. 3)

Let $G = Z_{24}$ as a Z- module , $H = (\bar{8}) = \{\bar{0}, \bar{8}, \overline{16}\}$, H is a proper submodule of Z_{24} .Then $\forall r \in Z, x \in G$, k $\in Z^+$ *and* $(x) \ll G$ such that $0 \neq r^k x \in B$ implies $rm \in H$, so H is weakly small semiprime submodule . But H is not small semiprime submodule since $\bar{0} = 4.\bar{6} = 2^2.\bar{6} \in H$ and $(\bar{6}) \ll Z_{24}$ But $\overline{12} = 2.\bar{6} \notin H$.

Recal lthat if R is an integral domain and G is an R – module ,Then $T(G) = \{x \in G : rx = 0 \ for\ some \ \ 0 \neq r \in R\}$ is a submodule of G . If $(G) = 0$, Then we say that G is torsion – free R- module .

Now we can say , If R is an integral domain and G is an R – module ,Then $Ts(G) = \{x \in G : rx = 0 \ and \ (x) \ll G \ \ for\ some \ \ 0 \neq r \in R\}$ is a submodule of G . If $s(G) = 0$, Then we say that G is small torsion – free R- module .

proposition (2. 4)

Let R be on integral domain and let G be a small torsion free R – module . Then every weakly small semiprime submodule of G is a small semiprime submodule of .

Proof :

Let H be a weakly small semiprime submodule of . Let $r \in R, x \in G$ and $(x) \ll G, k \in Z^+$ such thet $r^k x \in H$ to show that $x \in H$. If $0 \neq r^k m$, then $rx \in H$. Suppose that $r^k x = 0$, since R integral domain implies

If $r^k \neq 0$, then $x \in Ts(G) = 0$ hence $rx \in H$.

If $r^k = 0$, then $r = 0$ hence $rm \in H$. Therefore H is small semiprime submodule of M.

Recall that a proper submodule H of an R - module G is called a small prime submodule if and only if whenever $r \in R \ and \ x \in G$ with $(x) \ll G$ and $rx \in H$ implies either $r \in H \ or \ r \in [H : G]$ and an R – module G is called a small prime iff (0) is a small semiprime submodule of M , [6] .

proposition (2. 5)

Let G be a small prime R - module . Then every weakly small semiprime submodule of G is small semiprime submodule of .

Proof :

Let H be a weakly small semiprime submodule of . Let $r \in R, x \in G$ and $(x) \ll G, k \in Z^+$ such that $r^k x \in H$. If $0 \neq r^k x$, since H is weakly small semiprim submodule of G , then $rx \in H$.

Suppose $r^k x = 0$, then $rx = 0$ *or* $r^{k-1} = 0$ since (0) is small prime submodule of G (G is a small prime R – module) , so $rx = 0 \in H$, hence H is small semiprime submodule of G .

Theorem (2. 6)

Let G be an R- module and let H be a proper submodule of G . Then the following statements are equivalent :

1. H is weakly small semiprime submodule of G .

2. For each $r \in R$, $x \in G$ and $(x) \ll G$, $k \in Z^+$, $\left[H :_G (r^k)\right] = \left[0 :_G (r^k)\right] \cup [H :_G (r)]$.

3. For each $r \in R$, $x \in G$ and $(x) \ll G$, $k \in Z^+$, $\left[H :_G (r^k)\right] = \left[0 :_G (r^k)\right]$ or $\left[H :_G (r^k)\right] = [H :_G (r)]$.

Proof:

(1) $\Longrightarrow$(2) Let $x \in \left[H :_G (r^k)\right]$, $(x) \ll G$, then $r^k x \in H$.

If $r^k x \neq 0$, since H is weakly small semiprime submodule of G . $rx \in B$. so $\in [H :_G (r)]$. Let $r^k x = 0$, $(x) \ll G$ then $x \in \left[0 :_G (r^k)\right]$ and hence

$\left[H :_G (r^k)\right] \subseteq [H :_G (r)] \cup \left[0 :_G (r^k)\right]$ clearly $[H :_G (r)] \cup \left[0 :_G (r^k)\right] \subseteq$

$\left[H :_G (r^k)\right]$ ther efore $\left[H :_G (r^k)\right] = [H :_G (r)] \cup \left[0 :_G (r^k)\right]$.

(2) $\Longrightarrow$ (3) It is clear .

(3) $\Longrightarrow$(1) Let $0 \neq r^k x \in H$ for some $r \in R$, $x \in G$ and $(x) \ll G$, $k \in Z^+$. Hence $x \in \left[H :_G (r^k)\right]$ and $x \notin \left[0 :_G (r^k)\right]$ so by assumption $x \in \left[H :_G (r)\right]$ i.e $rx \in H$. Therefore H is weakly small semiprime submodule of .

Theorem (2. 7)

Let G be an R- module and let A be a proper submodule of G . Then A is a weakly small semiprime submodule of G if and only if for any small submodule H of , $r \in R$, and $k \in Z^+$ with $0 \neq (r)^k H \subseteq A$ *implies* $(r)H \subseteq$ A .

Proof:

($\Longrightarrow$) Suppose that $0 \neq (r)^k H \subseteq$ A for $r \in R$ and H is a small Submodule of G and $k \in Z^+$, so $0 \neq (r^k)H \subseteq A$ *implies* that $H \subseteq [A :_G (r^n)]$ with $H \nsubseteq [(0) :_G (r^n)]$ Theorem (2.6) implies $H \subseteq [A :_M (r)]$ heace $(r)H \subseteq$ A .

($\Longleftarrow$) Let $0 \neq r^n x \in A$ for $r \in R$, $(x) \in G$ and $n \in Z^+$ implies that $0 \neq (r^n)(x) \subseteq$ A So by hypothesis $(r)(x) \subseteq A$ implies that $rx \in A$. Then A is a weekly small semiprime submodule of .

Corollary (2. 8)

Let G be a R- module and A be a proper submodule of G . Then A a weakly small semiprime submodule of G if and only if $0 \neq (r)^k G \subseteq A$ for $r \in R$, H is small submodule of G and $n \in Z^+$ implies that $(r)G \subseteq A$.

Corollary (2. 9)

Let A be a proper submodule of an R- module G. Then A is a weakly small semiprime submodule of G if and only if $0 \neq r^k H \subseteq A$ for $r \in R$, H is small submodule of G and $k \in Z^+$ implies that $rH \in A$.

Recall that if H is a semiprime submodule of an R- module G, then $[H : G]$ is a semiprime ideal of R. For weakly small semiprime we have:

Remark (2. 10)

If H is a weakly small semiprime submodule of an R – module G, then $[H : G]$ need not be weakly small semiprime in general .

For example : Let $G = Z_8$ as a Z – module . Take$H = \{\bar{0}\}$ clearly H is a weakly small semiprime submodule of G, but $[H : G] = 8Z$ is not weakly small semiprime ideal of Z .

Theorem (2.11)

Let H be a submodule of an R – module G with $T_S(G) = 0$. H is a weakly small semiprime submodule of G if and only if for non-zero ideal I of , $\left[H \vdots_G I\right]$ is a weakly small semiprime submodule of G .

Proof:

($\Longrightarrow$) Let $r \in R$, $x \in G$ and $(x) \ll G$, $k \in Z^+$ such thet $0 \neq r^k x \in \left[H \vdots_G I\right]$ hence $(r)^k(xI) \subseteq H$. If $0 \neq (r)^k(xI) \subseteq H$, $(xI) \ll G$, [1] . H is a weakly small semiprime submodule of G , implies that $(r)\,(xI) \in N$ by Theorem (2.6) so $r \in \left[H \vdots_G I\right]$ as needed suppose that $(r)^k(xI) = 0$ so $r^k xa = 0$ for some non-zero $a \in I$. Hence $r^k x \in T_S(G) = 0$ which is a controdition . Therefore $\left[H \vdots_G I\right]$ is a weakly small semiprime submodule of G

($\Longleftarrow$) Suppose that $[H \vdots_G I]$ is a weakly small semiprime submodule of G. For any non-zero ideal I of , put $I = R$ we get $[H \vdots_G I] = A$ which is weakly small semiprim submodule of *M*

Remark (2.12)

In the Theorem (2.11). The assumption $T_S(G) = 0$ is necessary .

To show that , let $G = Z_{16}$ as a Z - module , $H = \{\bar{0}\}$ and $I = 2Z$. Clearly H is a small semiprime submodule of G, hence H is a weakly small semiprime submodule of G by Remark (2.2) , but $[H \vdots_G I] = \{\bar{0}, \bar{8}\}$ is not weakly small semiprime submodule of G , since $(\bar{2}) \ll Z_{16}$ and $4 . \bar{2} \in \{\bar{0}, \bar{8}\}$ but $2 . \bar{2} \notin \{\bar{0}, \bar{8}\}$.

proposition (2.13)

Let G be a R- module and H, C be submodule of G with $C \nsubseteq H$ **.** If B is a weakly small semiprime submodule of G . Then $H \cap C$ is a weakly small semiprime submodule of .

Proof:

It is clear that $H \cap C$ is a proper submodule of . Let $0 \neq r^n x \in H \cap C$ for $r \in R$, $x \in C$ and $(x) \ll C$, $n \in Z^+$ it follows that $0 \neq r^n x \in H$. $(x) \ll G$ implies $(x) \subseteq Rad\,(C) \subseteq Rad\,(G)$, $then$ $(x) \subseteq Rad\,(C)$, since H is weakly small semiprime submodule of G , then $rx \in H$ and $x \in C$, $rx \in C$, hence $rx \in H \cap C$ and $H \cap C$ is a weakly small semiprime submodule of C .

proposition (2.14)

Let $G = G_1 \oplus G_2$ be an R- module where G_1, G_2 are R- modules such that $annG_1 + ann\,G_2 = R$. If A_1 is a weakly small semiprime submodule of G_1 , then $A_1 \oplus G_2$ is a weakly small semiprime submodule of G .

Proof:

Let $0 \neq H \ll G_1 \oplus G_2$, $r \in R$ and $n \in Z^+$ such thet $(r)^n H \subseteq A_1 \oplus G_2$. To show that $(r)H \subseteq A_1$ since $annG_1 + ann\, G_2 = R$, then $H = H_1 \oplus H_2$ where $H_1 \subseteq G_1$ and $H_2 \subseteq G_2$, $H \ll G$ implies $H_1 \ll G_1$ and $H_2 \ll G_2$ [1] .

$0 \neq (r)^n (H_1 \oplus H_2) \subseteq A_1 \oplus G_2$ $r^n H_1 \oplus H_2 \subseteq A_1 \oplus G_2$, so $(r)^n H_1 \subseteq A_1$ since A_1 is a weakly small semiprime submodule of G_1 and $H_1 \ll G_1$, then $(r)H_1 \subseteq A_1$ by Theorem (2.7) . Hence $(r)H \subseteq A_1 \oplus G_2$, which implies that $A_1 \oplus G_2$ is a weakly small semiprime submodule of .

proposition (2.15)

Let $G = G_1 \oplus G_2$ be an R- module where G_1, G_2 are R- modules and $A = A_1 \oplus A_2$ be a submodule of G . If A is a weakly small semiprime submodule of G .Then A_1, A_2 are weakly small semiprime submodules of G_1, G_2 respectively .

Proof :

Let $0 \neq H_1 \ll H_1 \oplus G_1$, $r \in R$ and $n \in Z^+$ such that $0 \neq (r)^n H_1 \subseteq A_1$. To show that $(r)H_1 \subseteq A_1$. $(r)^n H_1 \oplus 0 \subseteq A_1 \oplus A_2 = A$, then $(r)^n (H_1 \oplus 0) \subseteq A$. But $H_1 \ll G_1$, so $(H_1 \oplus 0) \ll G_1 \oplus G_2 = G$, [1] . Since $A = A_1 \oplus A_2$ is a weakly small semiprime submodule of G and $(H_1 \oplus 0) \ll G = G_1 \oplus G_2$ implies $(r)\ (H_1 \oplus 0) \subseteq A = A_1 \oplus A_2$, hence $(r)\ H_1 \oplus 0 \subseteq A_1 \oplus A_2$. It follows that $(r)H_1 \subseteq A_1$. Hence A_1 is a weakly small semiprime submodule of G_1 . Similary we can prove that is a weakly small semiprime submodule of G_2 .

3.Weakly Small Semiprimei Modules and Special Kind of Modules.

This section is to give properties of weakly small semiprime submodules in class of multiplication R-module, faithful R-module and hollow R-modules.

proposition (3.1)

Let G be a faithful **f . g**. multiplication R- module and let H be a weakly small semiprime submodule of G . Then $[H : G]$ is a weakly small semiprime ideal of .

Proof:

Let H be a weakly small semiprim submodule of G , $a, b \in R$, $(b) \ll R$, and $k \in Z^+$ such that $0 \neq a^k b \in [H : G]$,then $0 \neq (a)^k (bG) \subseteq H$. $(b) \ll R$ implies $(b\, G) \ll G$ [1] , if $(a)^k (bG) = 0$. Then $a^k b \in [0 : G] = 0$ contradiction . Now Theorem (2.7) implies that $(a)(bG) \subseteq H$ so $ab \in [H : G]$ and $[H : G]$ is a weakly small semiprime ideal of .

Theorem (3.2)

Let G be a f . g. faithful multiplication R- module and let H be a proper submodule of M .Then the following are equivalent .

1. H is a weakly small semiprime submodule in$G$.
2. $[H :_R G]$ is a weakly small semiprime submodule in R
3. $H = JG$ for some weakly small semiprime ideal J of .

Proof:

$1 \Longrightarrow 2$ Let $0 \neq r^k s \in [H :_R G]$ for $r \in R$, and $k \in Z^+$, s is a non -zero element of R and $(s) \ll R$. It follows that $0 \neq r^k s \subseteq H$, $(s) \ll R$, M is f.g multiplication implies $(sG) \ll G$, since B a weakly small

semiprime submodule in G , then $rsG \subseteq H$, hence $rs \in [H :_R G]$ that is $[H :_R G]$ is weakly small semiprime ideal of R .

$2 \Longrightarrow 3$ We choose $J = [H : G]$.

$3 \Longrightarrow 1$ Since G multiplication module , Let $0 \neq r^k x \in H$ where $r \in R$, $x \in G$ and $(x) \ll G$, $k \in Z^+$ Then $(r)^k [(x) : G] \subseteq [(r^k x) : G] \subseteq [H : G]$. Moreover $(r^k)[(x) : G] \neq 0$ because otherwise .

If $(r)^k [(x) : G] = 0$ Then $(r)^k (x) = (r)^k [(x) : G]G = 0$ as $[H : G]$ is a weakly small semiprime ideal of R contradiction . $(r) [(x): G] \subseteq [H : G]$

therefore $(r)(x) = (r)[(x): G]G \subseteq [(x): G]G = B$ and so $rm \in H$ implies H a weakly small semiprime submodule in G .

Recall that an R- module G is a called hollow module if every proper submodule A of G is small , that is if $G = A + H$ for some submodule H of G implies that $H = G$.

Recall that if G is an R- module , then $Rad(G)$ is the intersection of all maximal submodule of G , $Rad(G)$ is called the Jacobson radical of G , [4] . If A is a submodule of an R- module G with $Rad(\frac{G}{A}) = (0)$, then $Rad(G) \subseteq A$, [3] .

proposition (3.3)

Let G be an R- module with every cyclic submodule is small . If H is weakly small semiprime submodule of , then H is weakly semiprime of G .

Proof:

Let $0 \neq r^k x \in H$ for $r \in R$, $x \in G$ and $n \in Z^+$. Since every cyclic submodule of G is small , then $(x) \ll G$. But H is weakly small semiprime , it follows that $rx \in H$. Hence H is weakly semiprime submodule of .

Corollary (3.4)

If G is a hollow R- module , then every weakly small semiprime submodule of G is weakly semiprime .

proposition (3.5)

Let G be a R- module and H be a submodule of G . If $Rad(G)$ is a weakly small semiprime submodule of G with $Rad\left(\frac{G}{H}\right) = (0)$, Then H is a weakly small semiprime submodule of G .

Proof:

Let $0 \neq r^n x \in H$ for $r \in R$, $x \in G$ with $(x) \ll G$ and $n \in Z^+$. Since $(x) \ll G$, then $x \in Rad(G)$, [3] . Hence $0 \neq r^n x \in Rad(G)$. But $Rad(G)$ is a weakly small semiprim so $rx \in Rad(G)$. By assumption $Rad\left(\frac{G}{H}\right) = (0)$ implies $Rad(G) \subseteq H$, then $rx \in H$. Thus H is a weakly small semiprime submodule of G .

Lemma (3.6) [7]

Let G be a f . g. multiplication R- module and I , J are ideals of a ring R . Then $IG \subseteq JG$ if and only if $I \subseteq J + ann_R(G)$.

proposition (3.7)

Let G be a f . g. multiplication faithful R- module and I be a weakly small semiprime ideal of R with $ann_R(G) \subseteq I$. Then IG is a weakly small semiprime submodule of .

Proof:

Let $0 \neq r^n x \in IG$ for $r \in R, 0 \neq x \in G$ and $(x) \ll G$ and $n \in Z^+$ that $0 \neq r^n x \in IG$, since G multiplication , then $(x) = JG$ for som ideal J of R . That $0 \neq r^n x \in IG$ by lemme (3.6) $0 \neq r^n J \subseteq I + ann_R(G)$, but $ann_R(G) \subseteq I$ implies $ann_R(G) + I = I$ hence $0 \neq r^n J \subseteq I$, since $(x) \ll G, (x) = JG$ implies $(JG) \ll G$ but G is a f . g. multiplication implies $(J) \ll R$, since I is a weakly small semiprime submodule of R . It follows that $rJG \subseteq IG$ so $r(x) \subseteq JG$ implies JG is weakly small semiprime submodule of .

Corollary (3.8)

Let G be a faithful cyclic R- module and I be a weakly small semiprime ideal of R with $ann_R(G) \subseteq I$, then IG is a weakly small semiprime submodule of G .

References:

[1] Athab, E.A. **2004.** Some Generalizations of Projective Modules**,** Ph.D. thesis College of Science, University of Baghdad.
[2] Farzalipour, F. **2014.** Almost Semiprime Submodule. Hindawi Publishing Corporation Algebra, Volume 2014(3), pp:231-237.
[3] Kasch, F. **1982**. Modules and Rings, Academic Press, London.
[4] Ramadhan, H. A. and Al-Mothafar, N.S. **2021**. Small Semiprime Submodules, Journal of physics: Conference Series, 1818, 012142.
[5] Mahmood, L.S. **2012**.Small Prime Modules and Small Prime Submodules, Journal of Al-Nahrain University, 15(4), PP:191-199.
[6] Sarac, B. **2009**. On Semiprime Submodules, Communications in Algebra, 37(7), pp: 2485–2495.
[7] Smith, P. **1988.** Some Remarks on Multiplication Modules, Arch. Math. Vol 50, PP:223-226.
[8] S. Sharma and A. J. Obaid, "Mathematical modelling, analysis and design of fuzzy logic controller for the control of ventilation systems using MATLAB fuzzy logic toolbox," Journal of Interdisciplinary Mathematics, vol. 23, no. 4, pp. 843-849, 2020.

Detection of the autonomous car robot using Yolo

Detection of the autonomous car robot using Yolo

F.I. Abd-AL Sahib [1], H . B .Taher[1] , R F. Ghani[2]

[1]University of Thi-Qar – College of Education for Pure Sciences, Thi-Qar, Iraq.

edpcompfatima@utq.edu.iq Hazeem.sci@utq.edu.iq 110016@uotechnology.edu.iq

Abstract. One of the important object detection applications in smart transportation systems is vehicle detection. Working on self-driving car robots has become an important experiment in recent years to take advantage of innovations and ideas in real self-driving cars, and the detection of robots by multiple algorithms is the most important phase in this work. To solve the problems of self-driving car robot detection. Such as not recognizing shape. In this paper, via the Yolov2 algorithm, we trained a new model for robots. It was proven with the comparison experiments that the proposed method is successful for robot detection. In addition, the proposed model demonstrated excellent feature extraction ability with network visualization.

1.Introduction

Computer vision is a tool for making machines "look". This allows computers and other devices to take the place of human eyes to recognize objects within the scene and further the processing of images. The new research trend for using artificial intelligence systems to extract data from images is image processing and computer vision. A significant branch of computer vision is object detection. object detection is Efficient when it is fast and accurate. Good object detection algorithms should be convenient for the lives of individuals. The purpose of this paper is to classify and locate self-driving car robots. It is important in the autonomous driving system to detect self-driving cars and their location. A self-driving car, also known as an autonomous vehicle (AV or auto), driverless car, or robot-car is a vehicle that is capable of sensing its environment and moving safely with little or no human input. Object detection is a very important part of artificial intelligence. Which is a forward-feedback neural network It has a unique superiority in object recognition with its special structure of local weights sharing. The interest in having deeper hidden layers has begun to surpass the performance of classical methods in various fields, particularly in pattern recognition. The Convolutional Neural Network is one of the most popular deep neural networks (CNN). It takes its name from the mathematical linear operation called convolution between matrixes. CNN has several layers [1], including the convolution layer, pooling layer and fully-connected layer. In machine learning issues, CNN has outstanding results. Especially those applications dealing with image data, The traditional detectors [3] first extract suggestions and extract features, then do the classification [2].it is proposed that location and classification in a single CNN be implemented. We want a real-time object detection algorithm in the self-driving system, so we chose you only look once (YOLO) as a guide to constructing a better method where More than twice the average accuracy of other real-time systems is reached by YOLO. To construct our own training set and testing set, we select some samples and label some samples manually. YOLO algorithm is an algorithm based on regression, instead of selecting the interesting part of an Image, it predicts classes and bounding boxes for the whole image in one run of the Algorithm [4]. The work discussed in this paper forms part of an automated monitoring system for vehicles. The main objective is to train a system to classify a new class Which self-driving cars robot define and monitor the behavior of autonomous robots. In this way, it is possible to track important events that took place on the way. The yolo detection system . Figure 1 shows how YOLO is refreshingly basic.

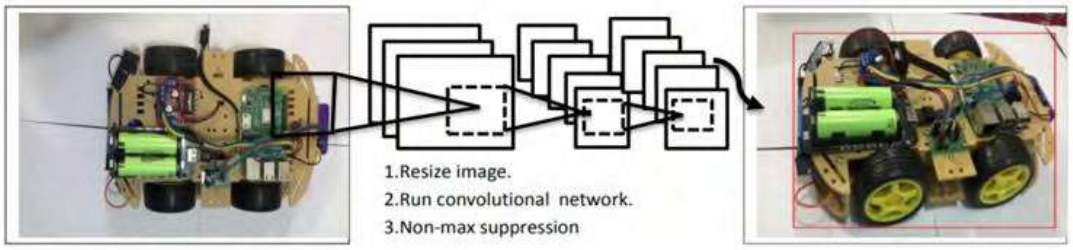

Figure 1. The YOLO Detection System

2. The proposed method

In Figure 2 Block diagram of the proposed system.

2.1. Data collection and prepare data

The images were collected by the iPhone 8 Plus camera, and the total number of images was 1235 the self-driving car robot, and since the system is under supervision depend on human work, Manual labeling for supervised learning, we use LabelImg to label images. LabelImg is available on mac, windows, and UNIX we do the labeling process to determine the Center X, y in the image, width, height and it belongs to any class. Within the process of pre-processing the data, missing labels for some image we removed them.

2.2. Yolo algorithm

YOLO divides the image in to S×S grids and predicts B bounding box and C class probability for each grid cell. Each bounding box consists of five predictions: w, h, x, y, and object confidence. The values of w and h represent the width and height of the box relative to the whole image. The values of (x, y) represent the center coordinates of the box relative to the bounds of the grid cell. The object confidence represents the reliability of existing object in the box to improve the YOLO prediction accuracy, Redmon et al. proposed a new version YOLOv2 in 2017. A new network structure Darknet-19 was designed by removing the full connection layers of the network, and batch normalization was applied to each layer. Referring to the anchor mechanism of Faster R-CNN, k-means clustering was used to obtain the anchor boxes. In addition, the predicted boxes were retrained with direct prediction. Compared with YOLO, YOLOv2 greatly improves the accuracy and speed of object detection. The Self-driving car robots dataset was divided into a training dataset and validation dataset with the ratio of 8:2, where the numbers of images in the training dataset 988 and numbers of images in the testing dataset 247. in this paper we used tensor flow lite keras [5]. TensorFlow [6] Lite is designed to run machine learning models with just a few kilobytes of memory on microcontrollers and other devices. The core runtime is only 16 KB and several basic models can be run. Keras is an API designed not for machines but for human beings. Keras follows good cognitive load reduction practices: it provides consistent and easy APIs, minimizes the number of user actions needed for common use cases, and provides simple and actionable error messages.An algorithm is a type of Supervised machine learning.

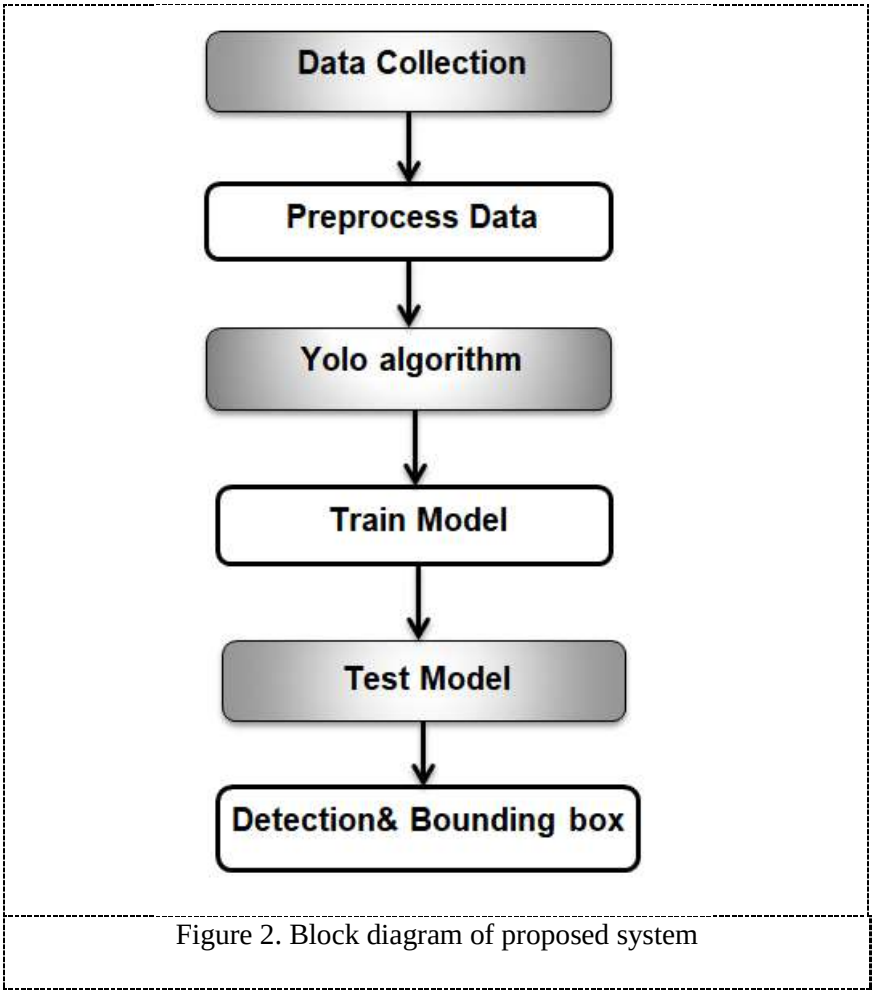

Figure 2. Block diagram of proposed system

2.2.1. Loss function

Different object sizes had different effects on the entire model when training YOLOv2, which resulted in greater errors for larger objects than for smaller objects. The loss estimate for the width and height of the bounding boxes was improved using normalization in order to reduce this effect. The enhanced loss feature is seen in Equation1 [9].

$$\lambda_{coord}\sum_{i=0}^{S^2}\sum_{j=0}^{B} I_{ij}^{obj}\left[(x_i-\hat{x}_i)^2+(y_i-\hat{y}_i)^2\right]$$
$$+\lambda_{coord}\sum_{i=0}^{S^2}\sum_{j=0}^{B} I_{ij}^{obj}\left[\left(\frac{w_i-\hat{w}_i}{w_i}\right)^2+\left(\frac{h_i-\hat{h}_i}{h_i}\right)^2\right]$$
$$+\sum_{i=0}^{S^2}\sum_{j=0}^{B} I_{ij}^{obj}\left(C_i-\hat{C}_i\right)^2$$
$$+\lambda_{noobj}\sum_{i=0}^{S^2}\sum_{j=0}^{B} I_{ij}^{noobj}\left(C_i-\hat{C}_i\right)^2$$
$$+\sum_{i=0}^{S^2} I_i^{obj}\sum_{c\in classes}\left(p_i(c)-\hat{p}_i(c)\right)^2$$

Where x_i and y_i are the center coordinates of the box .$\mathcal{W}_i$ and h_i are the width and height of the box .C_i is the confidence of the box of the i – the grid cell , and p_i (c) is the Class probability of the box of the i – the the grid cell . Furthermore , $\hat{x}_i$, $\hat{y}_i$, $\hat{w}_i$, $\hat{h}_i$, $\hat{c}_i$, and$\hat{p}_i$ (c) are the corresponding predictions of x_i , y_i, w_i , h_i , c_i , andp_i (c); λ_{coord} denotes the Weight of the coordinate loss, and λ_{noobj} denotes the weight of the bounding boxes without Objects loss, finally , s^2 denotes the $s \times s$ grid cells , B denotes the boxes , I_i^{obj} denotes Whether the object is located in cell i or not , and I_{ij}^{obj} denotes that the j – the box predictor in cell i is " responsible" for that prediction .

2.2.2. Model Architecture

The propose system detection network has 23 convolutional layers as shown in 3. The image size is 512 * 512. The images enter these layers and the features are extracted from them through the filters in each layer, where each layer has specific filters to extract the features starting from the lower level, middle level, and higher level. The edge might be detected in the first layers and then the simpler shapes in the second layers, and then the higher-level features such as Self-driving robot. The total of the filters in the first layer is (32) filters with dimensions of (3 * 3) and strides (1x1), and in order to preserve the shape of the image, the process padding is done by adding zeros around the image. After that cancel the bias and adding BatchNormalization to speed up the work. The type of activation function is Relu. Sigmoid and Tanh have been the most common non-linearity for several years. However, for the following reasons, the Rectified Linear Unit (ReLU) [1] has been used more commonly recently

1 - For both function and gradient, ReLU has simpler definition.

2 - The saturated function, like sigmoid and tanh, causes backpropagation problems. The gradient signal starts to disappear, which is called the "vanishing gradient" as the neural network architecture is deeper. This occurs because virtually anywhere but the middle, the gradient of those functions is very close to zero. The ReLU has a constant gradient for the positive input, however. Although the feature is not distinguishable, it can be overlooked in the actual implementation phase..

3 - A sparser representation produces the ReLU. The zero in the gradient leads to a complete zero being obtained. Sigmoid and tanh, however, still have non-zero gradient outcomes, which may not be in favor of training for training.

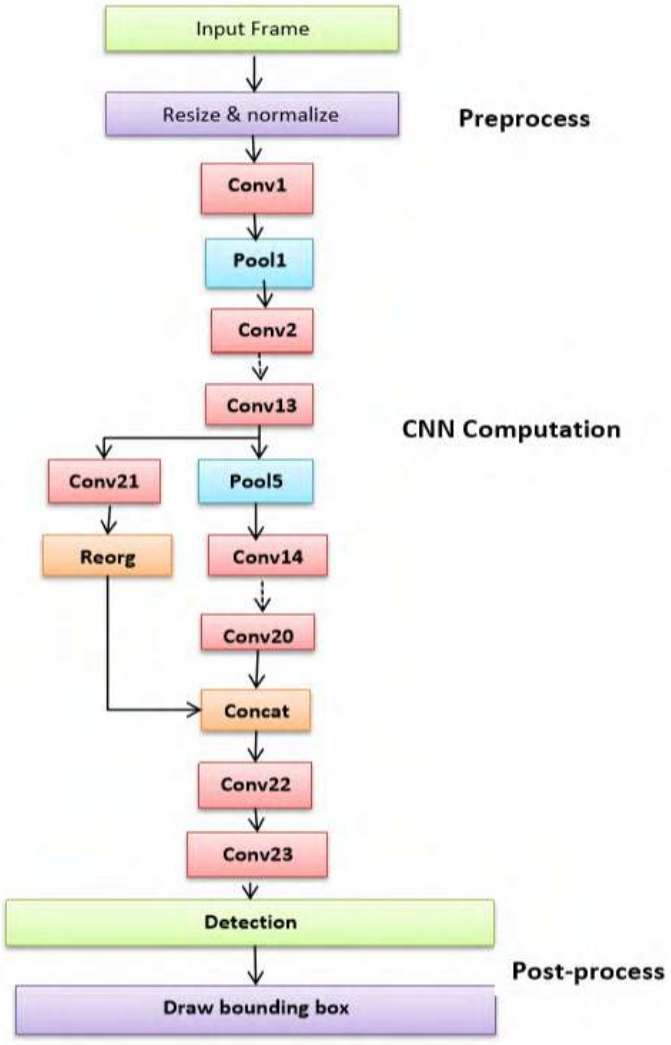

Figure 3. Layers of Yolov2 – self – driving car robot

Pooling : The main idea of pooling is to reduce samples to reduce complexity in layers. One of the most popular types of assembly is max-pooling, where you take an m* m patch and pass a filter over it that takes the largest value between the values. One of the most common sizes used in max-pooling is 2×2 [7-10]. As can see in Fig 4

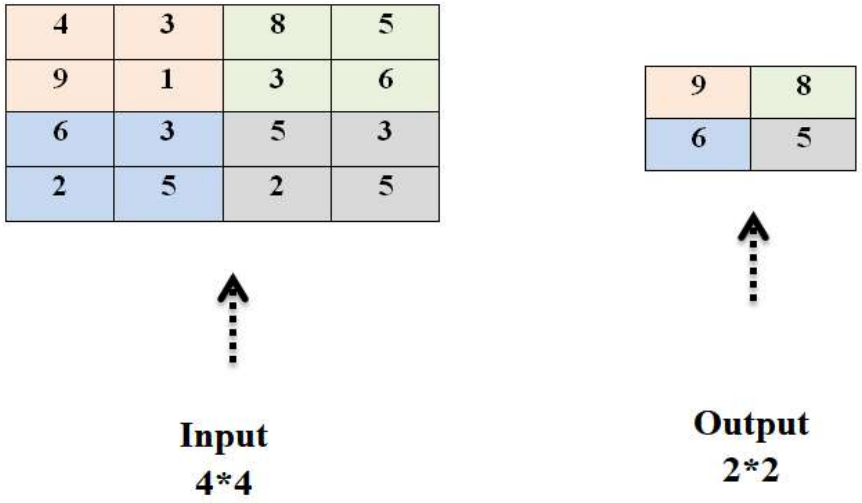

Figure 4:Max pool with 2*2 filters and stride 2

2.2.3 Non-max suppression

The objects in the image can be of various sizes and shapes, and to perfectly capture each of these, several border boxes are created by object detection algorithms. (Image on the left). Ideally, we must have a single bounding box for each object in the image. Something like that image to the right, To choose the best bounding box, From the multiple bounding boxes, predicted Non-max suppression is used in these object detection algorithms. This technique is used to "suppress" and hold only the best boxes that are less likely to be bound.

3.Implementation Results

In this paper, we have presented an algorithm for self-driving car robot detection and tracking and were score 82%, and a new class was called a self-driving car As in figure 5.
This class can be used in autonomous automobile robotics projects for autonomous vehicle path control or collision control. The first table shows the result after detection the class . The execution time of the object detection is real time. To calculate (F measure) we need Precision and Recall:

i. Precision measures how accurate your predictions are. i.e. the percentage of your predictions are correct.
ii. Recall measures how well you find all the positives

$$\text{F measure} = 2.\frac{\text{precision} \,.\, \text{recall}}{\text{precision} + \text{recall}}$$

$$\text{F measure} = \frac{\text{TP}}{\text{TP}+1/2(\text{FP}+\text{FN})}$$

$$\text{F measure} = \frac{202.54}{202.54+1/2(44.46)} = 0.90$$

Where TP Means number of true positives, FN mean number of false negatives.FP mean number of false positives.

The values taken in the equation are the set of test. In measuring object detection FP is sometimes canceled.

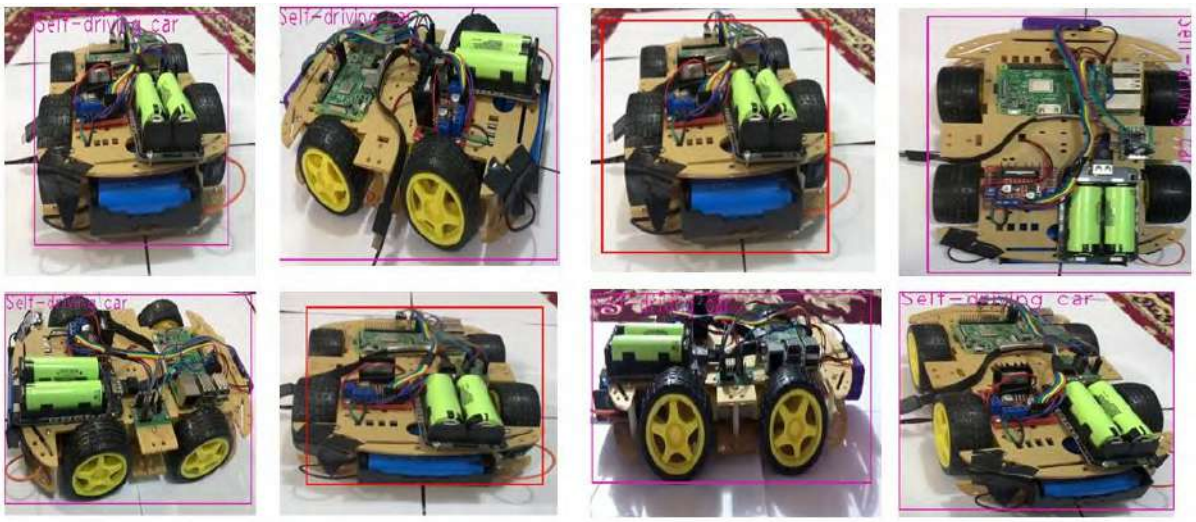

Figure 5. Detection results of YOLOv2_Self-driving car

4. Conclusion and Future Work

In this paper, a model called the YOLOv2_Self-driving car was proposed for vehicle detection by YOLOv2. The resulting system is both efficient and accurate based on the experimental results, the map of YOLOv2_ Self-driving car could reach 82%. Therefore, the proposed network is effective for Self-driving car robot detection. Although the model proposed in this paper achieved ideal experimental results, the number of images amounts of data is relatively low. In future work, we will collect more actual data to further study how to improve the accuracy and speed of Self-driving car detection.

5. References

[1] Albawi, S., Mohammed, T. A., & Al-Zawi, S. (2017, August). Understanding of a convolutional neural network.International Conference on Engineering and Technology (ICET) (pp. 1-6). IEEE,2017

[2] Felzenszwalb, P., McAllester, D., & Ramanan, D. (2008, June). A discriminatively trained, multiscale, deformable part model. In 2008 IEEE conference on computer vision and pattern recognition (pp. 1-8). IEEE.

[3] Felzenszwalb, P. F., Girshick, R. B., McAllester, D., & Ramanan, D. (2009). Object detection with discriminatively trained part-based models. IEEE transactions on pattern analysis and machine intelligence, 32(9), 1627-1645.

[4] Redmon, J., Divvala, S., Girshick, R., & Farhadi, A. (2016). You only look once: Unified, real-time object detection. In Proceedings of the IEEE conference on computer vision and pattern recognition (pp. 779-788).

[5] https://keras.io/

[6] https://www.tensorflow.org/install

[7] Scherer, D., Müller, A., & Behnke, S. (2010, September). Evaluation of pooling operations in convolutional architectures for object recognition. In International conference on artificial neural networks (pp. 92-101). Springer, Berlin, Heidelberg.

[8] Kotsiantis, S. B., Zaharakis, I., & Pintelas, P. (2007). Supervised machine learning: A review of classification techniques. Emerging artificial intelligence applications in computer engineering, 160(1), 3-24.

[9] Sang, J., Wu, Z., Guo, P., Hu, H., Xiang, H., Zhang, Q., & Cai, B. (2018). An improved YOLOv2 for vehicle detection. Sensors, 18(12), 4272.

[10] T. A. Al-asadi and A. J. Obaid, "Object detection and recognition by using enhanced speeded up robust feature," International Journal of Computer Science and Network Security (IJCSNS), vol. 16, no. 4, pp. 66-71, 2016.

Image Processing Technology and Deep Learning Application: In Relation to the Context of Laser Positioning

Image Processing Technology and Deep Learning Application: In Relation to the Context of Laser Positioning

WASAN M.JWAID

Faculty of Administration and Economics, Thi-Qar University, Thi-Qar,IRAQ

wasan.maktoof@utq.edu.iq

Abstract-- In the current investigation, there was the use of the technology of machine vision. The usage of this technology was informed by the need to have the laser spot's highest energy positioned precisely, eventually allowing for the facilitation of further product work piece joining. Indeed, the joining occurred in laser welding machinery. Relative to the displacement phase, it is notable that it could aid in work piece placement into superposition areas, upon which there could be the joining of the parts. Training programs or models that were used involved convolutional neural network and deep learning, which allowed for the resultant system's enhancement of the accuracy with which the positioning could be achieved. Also, the aforementioned algorithms were insightful because they led to the enhancement of machine work efficiency. Similarly, in the study, there was the proposing of a bi-analytic deep learning localization technique. For the purpose of system monitoring in real time, there was the use of a camera. As such, the initial stage entailed the application of the convolutional neural network, which aided in the implementation of large-scale initial searchers before having the laser light spot zone located. In turn, the phase that followed entailed increasing the camera's optical magnification, which paved the way for the spot area's re-imaging, as well as the application of a template matching method to ensure that high-precision repositioning was achieved. When the parameter of the search result area's ratio was considered, it could be seen that the study was able to determine the target spot's integrity parameters. For the case of the complete laser spot, there was the performance of the centroid calculation. Also, in situations where an incomplete laser spot reflected the target, there was the performance of invariant moments' operation. From the findings, the study indicated that from incomplete laser spot images, the laser spot's highest energy could be positioned precisely. The study also established that in order to establish the displacement amount, the image's center and the laser spot's highest energy could be overlapped.

Keywords--Convolutional neural network, deep learning, laser spot, machine vision.

1.INTRODUCTION

With a quick evolution in science and technology, there is a continuous decrease or reduction in material sizes or the Size of various parts of systems. To have the resultant miniature parts combined successfully, therefore, there is a growing need for the highest precision possible, a demand proving higher when compared the precision required when dealing with general parts [1, 2]. Also, while dealing with the miniature parts, especially in the context of mass system production, there is fixed production time for the respective parts [3]. Hence, in case of laser radiation offset that causes the junction's soldier to fail to have adequate energy absorbed, there might be failure in the weld [4]. Similarly, given some part, should the laser's high-energy zone irradiate other positions, there could be a direct rejection of the given

part [5]. The eventuality is that for the laser, there arises a need to have the highest energy zone searched and positioned [6].

For the majority of previous scholarly studies, the focus has been on the implementation of various hand-craft features. This usage has been informed by a quest towards representing the images' visual content, as well as the establishment of relevant measurements of similarity, achieving a similarity of low-level features and also ensuring that it (the similarity) is closer to that of high-level concepts [7]. When it comes to the deep convolutional learning technique, most studies document that it has steered improvements in the ability of feature extraction, implying that its implementation fosters efficiency when it comes to the measurement of similarity [7, 8]. In these studies, given a sample image, there was the extraction of its feature training classifier. Here, the neural network was used, a process that preceded the matching criterion. The eventuality is that there was the establishment of the input image's laser spot. There was also the searching of the center spot before moving the laser spot position to ensure that it overlapped the Charge-coupled Device (CCD) camera's image center. This overlapping process sought to ensure that the positioning criterion was completed. Important to note is that in situations where there was the use of large ranges of images, for incomplete spots, their images would often appear. As such, even though there was the realization of the spot re-imaging procedure's precise positioning, much time was consumed. Therefore, in the current investigation, the central purpose lay in the combination of a deep learning algorithm with machine vision. This combination sought to have a positioning system built, which could aid in the alignment of the center spot of the laser quickly and automatically.

When it comes to traditional techniques of template matching, it is worth remembering that they come with various defects. For instance, on each occasion that templates are changed, the techniques call for weight updating and continuous matching [9]. Important to highlight is that these defects waste a lot of time. Another problem with such techniques is that in situations where an area of the matched image and that of the template image are similar but they do not coincide with the target area, the resultant matching could be false [10]. Indeed, for imaging systems, they employ various parameters and databases. For the case of high-resolution images, they offer easy and precise position detections [11], yet, when it comes to contexts involving real-time systems, the computational costs associated with the high-resolution images are high [12]. To solve the recognition accuracy problem, some studies have proposed and advocated for the use of a hierarchical matching [13, 14], but these previously proposed schemes of classification do not come with all potential features. This failure is attributed to variability vastness regarding feature topology and geometry [15]. In this investigation, therefore, the main aim was to utilize or employ the deep learning technique for the purpose of enhancing feature recognition, as well as shortening the needed time for obtaining results. The motivation of the study was to remedy the aforementioned defects with which most of the previously proposed techniques have been associated.

2.METHODOLOGY

Notably, the purpose of template matching involves seeking parts of images that tend to match the given template image [3]. Initially, the read-in template images have their sizes and those of the matched images determined via calculation, with the outcomes stored. Should template images fail to divide exact the matched images, there is the supplementation of the bottom and right of the image by 0 [4]. In turn, there is the substitution of the image into a given model or algorithm. The role of this substitution process into the algorithm involves the determination of the template image's weight for the respective points within the matched image. With the maximum weight established, the upper left corner's position is determined relative to the matched image's template image. The next step involves inputting the template image's width and length. Given the matched image, then, there is the indication of the template image's region [16]. While numerous algorithms characterize the method of template matching [17], the current study relied on the case of the Sum of Squared Differences (SSD). It is also notable that the weight has to be calculated again for the respective matched images whenever the template is changed, which makes the process of template matching to consume a lot of time. Despite this limitation, however, there is considerably higher accuracy when compared to scenarios where the starting point search technique is employed [18-20]. Given this superiority, the template matching technique was employed in the current investigation.

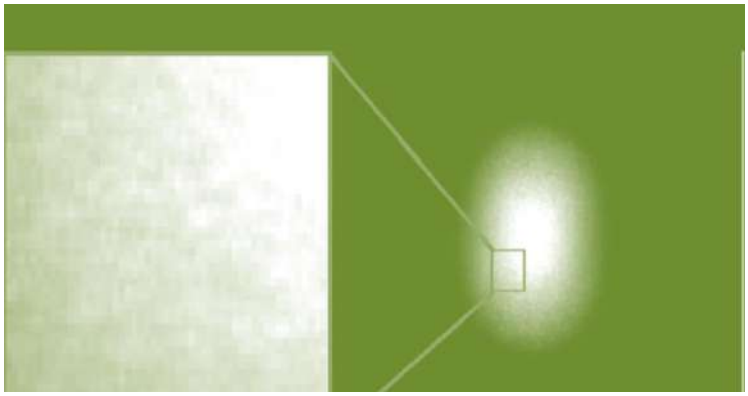

Fig.**1**.A sample template matching technique implementation outcome

To construct the central moment, the target area's centroid was selected and labeled as the center. The implication is that the calculation of the moment was the target area's point relative to the target area's centroid. Important to note is that the attribute did not exhibit any correlation with the target area's position. Rather, it exhibited translation invariance.

When it comes to the case of the convolutional neural network (CNN), it can be seen that a major difference that emerges between the traditional multilayer perception network and the CNN itself comes in terms of the pooling and convolutional layers [20]. For the latter layers, they allow for CNN's recognition of image details, yet other neural networks are known to be capable of only extracting data used in computation. For the CNN algorithm, its superiority is linked to three layers, which informed the model's adaptation in the current investigation.

One of the layers is the convolutional layer. Here, its purpose was to scan the picture. The scanning process would target the range from top to bottom via a filter that had a fixed size. The purpose of this procedure achieved via CNN's convolutional layer was to ensure that various local features were obtained. Indeed, these features formed the next layer's input. Following ReLU function processing, values that were less than 0 would be exported as 0. However, in situations where, following ReLU processing, values exceeded 0, they would be exported directly. The outcome reflected the perceived feature map. Also, in the feature map, the respective points could be deemed as the region's features in the original pattern, leading to their transmission to the layer that followed. For the CNN algorithm, therefore, the convolutional layer was used for the purpose of obtaining the pattern's local features. Given the entire convolution operation outputs, then, there would be their transformation by using a nonlinear activation function.

Important to note, however, is that for a previous layer and the same convolution layer, the convolution operation would share a common weight. From previous studies, it is notable that the use of traditional deep learning networks towards image processing and recognition would call for the splitting of the original two-dimensional picture to establish a one-dimensional image [9-11]. Here, individual pixels would be treated as eigenvalues and transferred to the DNN architecture to be analyzed [13]. The eventuality is that for the input pixels, there is the loss of original spatial arrangement data [16]. In this study, therefore, CNN' convolutional layer was useful because it allowed for the process of ensuring that the image's spatial arrangement was maintained and that the input feature was a partial image that was obtained.

Another CNN algorithm's layer that proved informative and informed the choice of the CNN model in this investigation entailed the pooling layer. Indeed, the pooling layer functions to ensure that there is the reduction of the size of the input picture. From some studies, this layer also allows for the reduction of the dimensionality of the respective feature maps [1], as well as the maintenance of crucial features [4]. Several merits are associated with the function of this layer of the CNN algorithm. For example, there is the reduction of over-fitting, the acceleration of system running, and the reduction of subsequent layers' associated parameters [18-22]. In the same fashion as the convolutional layer, also, the pooling layer relied on a filter for the purpose of having various operation regions' value extraction. Important to note is that the resultant output proved to be free from activate function.

The third CNN algorithm's layer was the full connected layer. Here, the layer reflected the general neural network. Thus, feature extraction was achieved by the convolutional layer and image parameter reduction achieved by the pooling layer, with the full connected layer receiving the feature information to engage in the classification process.

Indeed, there was the connection of the respective neurons to the given previous filter's pixel. For the respective connected weights, they were identical, allowing for their sharing in the same layer. However, it is also worth indicating that the respective connections exhibit unique and unrelated weights, implying that some considerable computing resources were likely to be consumed by the full connected layer. Whether this limitation was too minor to compromise the overall system efficiency and performance enhancement was a point of interest, which was clarified in the results and discussion section.

3. EXPERIMENTAL RESULTS AND DISCUSSION

With an image obtained by the CCD camera, with a given position in the image having the light spot established, there was the preliminary searching of the light spot image center's range. This process is demonstrated in the figure below.

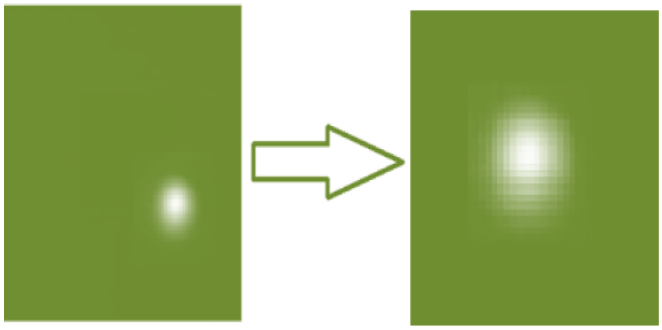

Fig.2. Preliminary searching of the light spot image center's range

After the program established the light spot's region, there was the displacement of the center point. This displacement led to the overlapping of the center of the CCD image, as well as an increase in the magnification of the CCD. Indeed, the increased magnification ensured that the CCD coincided with the light spot zone's size. In turn, there was the separation of the light spot zone, completing the first search.

As mentioned in the methodological section, searching for the laser spot zone was achieved via the system's utilization of a CNN. Given images that had various incomplete light spot modes and complete light spots, there was the training of the neural network. This training process sought to ensure that the program could judge or determine the image's light spot position rapidly and with considerable accuracy. Upon the successful positioning the light spot zone in a given image, given an initial part, the light spot zone's center was used as the center of the image. Here, there was deviation from the real center of the light spot, with the system treating the positioned laser spot zone as that which was not necessarily a complete light spot. At this stage, there was the measurement or determination of the distance between the light spot center and the center of the CCD image, allowing for the shifting and overlapping of the two centers.

Fig. 3. An illustration of the regional center image and the incomplete laser spot image.

In Figure 3 above, the regional center image did not reflect the center of the light spot, and it is presented alongside the incomplete laser spot image. The processing modes were two in this case. Also, regardless of whether the resulting light spot was incomplete or complete, it would be judged relative to the light spot zone's ratio. For the case of the complete light spot, there was the extraction of its centroid point, which was achieved via the centroid technique. In turn, there was the calculation of the distance between the light spot center and the center of the CCD image. The process would culminate into the movement of the center of the image to have it overlap the center of the light spot. In situations where the light spot was not complete, there was the calculation of the invariant moments relation to the image's incomplete light spot zone, eventually having it matched with the case of the preset light spot source image. The matching process sought to ensure that in the light spot, the centroid of the partial light spot zone had its position established. In turn, there was the calculation of the distance between the light spot center and the center of the CCD image, moving the image center to ensure that it overlapped the center of the light spot.

Given various sample numbers, the applied system's positioning effects were then described. To have the neural network trained, positive samples that were used were 100, 50, and 25. The following figure demonstrates the experimental results that were achieved via the use of 50 negative samples and 25 positive samples to have the neural network trained. From the figure, the implementation of the proposed program saw the complete light spot positioned successfully, but still, some misrecognition was experienced. Also, in the figure, it can be seen that there was no successful recognition of the incomplete light spot. To have the results improved while implementing the proposed system, it (the program) was trained again, and the sample number increased.

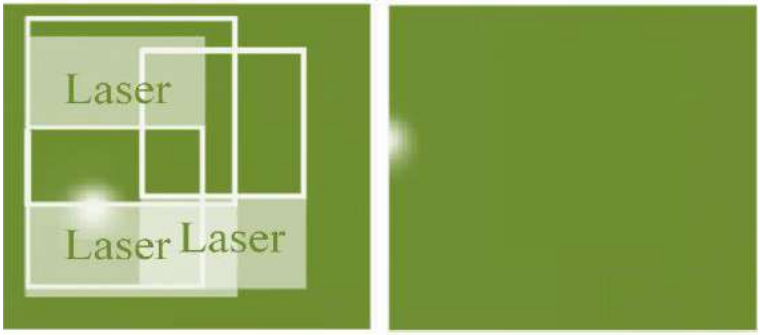

Fig. 4. The map positioning of the complete versus incomplete light spot for 25 positive samples.

The figure 4 above shows the results that were obtained after using 25 samples. As the study progressed, the focus shifted to the case of 100 negative samples and 50 positive samples, seeking to discern the behavior of the system, with those samples used for the purpose of neural network training. At this point, as it is highlighted in Figure 5 below, there was improvement in complete light spot misrecognition. However, it is important to note that still, the light spot region (only) could not be positioned. From the figure, it can also be seen that numerous misrecognitions were evident, but

incomplete light spots had their position recognized accordingly. To have the accuracy of the system improved, for a second time, there was the training of the network, with the sample number also increased.

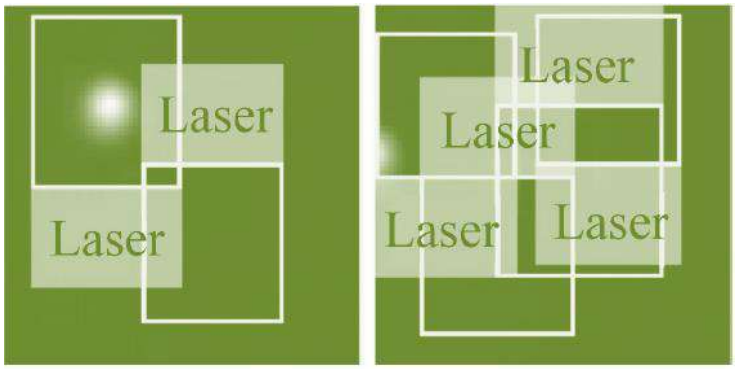

Fig. 5. The map positioning of complete and incomplete light spots.

The figure 5 above shows the results that were obtained after considering 50 positive samples. There was further training of the neural network, with 200 negative samples and 100 positive samples used. At this point, findings indicated the program's capability to have complete light spots' region positioned successfully. At this point, the study noted a marked reduction in the probability of the program's misrecognition. However, for incomplete light spots, they could still not be positioned.

For the three sample numbers that were used and the size of the feature region changed while having the neural networks trained, the table that follows shows the findings that were obtained. The motivation was to have 100 target images recognized. From the results, it can be seen that there was a significant increase in the accuracy relative to the sample number. For the case of the result candidates, they had misrecognitions and the corrected results. On the other hand, the target images' results minus the result candidates depicted the program's inability to have the number of targets recognized.

TABLE 1 . THE LIGHT SPOT POSITIONING SYSTEM'S EXPERIMENTAL RESULTS

Number of Positive Samples	25	50	100	100 (reduce feature region)
Number of Negative Samples	50	100	200	200
Number of Target Images	100	100	100	100
Result Candidates	74	90	96	98
Correct Results	40	69	88	96
Accuracy (%)	54.054	76.667	91.667	97.96
Classification Accuracy (μ)	0.37	0.284	0.245	0.14

From the table 1 above, it can be seen that still, there were some misrecognitions in the system. The outcomes could be attributed to the position that it was the same neural network that was used for the purpose of recognizing the incomplete light spots and complete light spots. Also, the results could be attributed to a situation in which it was only the partial zones that were positioned, even at a time when there were complete light spots. Similar, at the platform, when the laser was shot, there was a decrease in brightness outward in relation to the center spot of the laser, with particles in the air scattering the laser partially. It can also be inferred that due to the partial black regions'

brightness, visual recognition was likely to be difficult. With the bright zones' mode being closer to the light spot's sample, misrecognition was more likely to arise.

Given the outcomes that were obtained after implementing 100 positive samples, there was a successful determination of the complete light spot's region. From the case of the system flow, it was to the positioning regional center that the CCD image center was moved, eventually established as the template image. In turn, there was the calculation of the region's aspect ratio, as well as that of the template. The procedure saw the program's resulting template's aspect ratio stand at 1.027. With the identification of the complete light spot, there was the calculation of the template image's invariant moments, with the first moment then considered. Here, the light spot region's barycentric coordinates formed the first moment and are shown in the figure below.

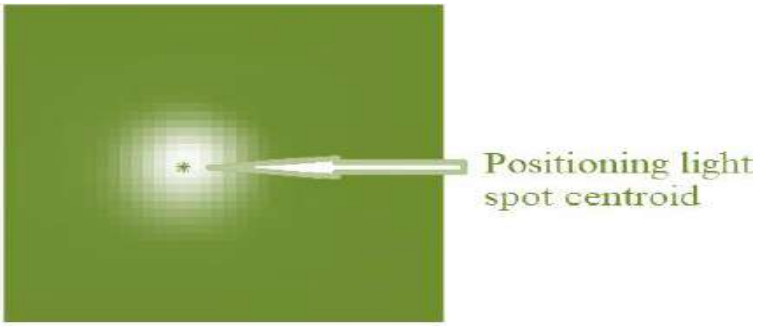

Fig. 6. Light spot centroid positioning.

In the culminating stage, there was the calculation of the distance between the center of the light spot and the center of the image, followed by the removal of the CCD camera. Here, there was the overlapping of the light spot center and the image center, allowing further for the second-time alignment of the light spot center. The figure below illustrates these procedures and experimental outcomes.

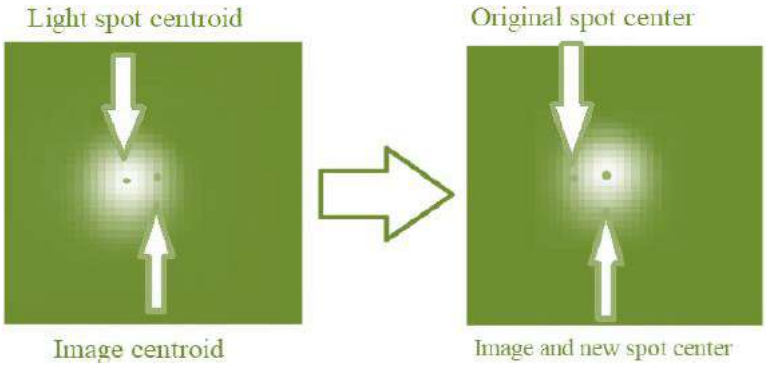

Fig. 7. An illustration of the second alignment.

For the laser spot, there was also the development of a gray level histogram. From Figure 8 below, it can be seen that the image center and the light spot center had their positions developed. Also, there was the establishment of the distance between both centers, achieved via coordinate relationship calculation.

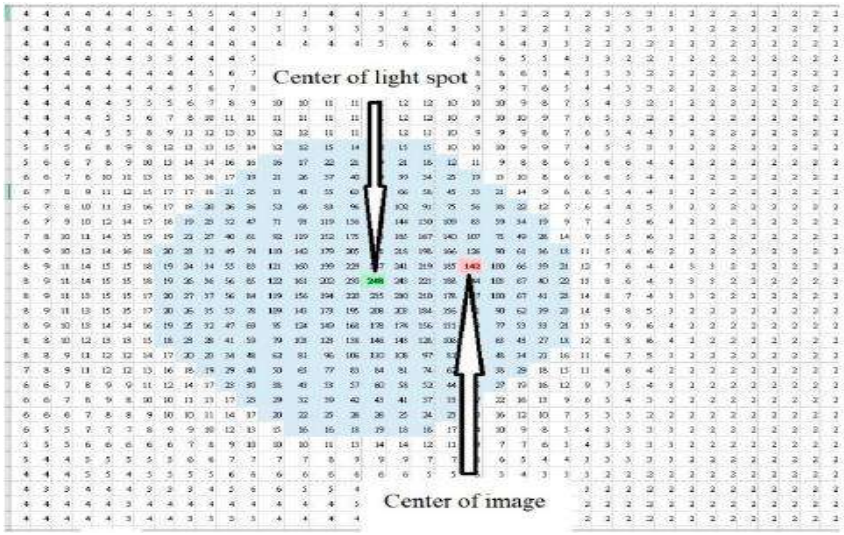

Fig. 8. Gray level histogram development for the complete light spot.

When it came to the mean errors concerning the established light spot center and the image center, they were calculated after the system conducted the process of positioning the light spot for various sample numbers. Here, 1 pixel was equal to 0.11micrometers. From the results, this study established that with an increase in the number of positive samples, there was enhancement in the features. Also, there was shorter time of the shift to the center of the light spot, with the first positioning' shift having its center get close to the light spot's center. The table below illustrates these findings.

TABLE 2 . SELECTED SAMPLE NUMBERS' RESULTANT LIGHT SPOT POSITIONING' MEAN ERRORS.

Number of Positive Samples	25	50	100	100 (reduce region)
Average Mis-distance (pixel)	3.367	2.579	2.224	1.273
Average Mis-distance (μm)	0.37	0.284	0.245	0.14
Detection Time (s)	0.5 ~1.6	0.5 ~1.6	0.5 ~1.6	0.5 ~1.6

After establishing the recognition region's invariant moments, there was the performance of the similarity matching process relative to the complete light spot's entire

points' invariant moment matrix. Here, the complete light spot's entire points had been obtained in advance. The process culminated into the exporting of the maximum matching weight's coordinate value. The following figure highlights these results.

	19	20	21	22	23	24	25	26	27	28	29	30	31	32	33	34
43	25771e-04	3.7831e-04	4.8479e-04	8.5695e-04	0.0021	0.0086	0.1005	0.2268	0.4449	0.5679	0.5911	0.6124	0.4746	0.2192	0.0776	0.0291
44	1435e-04	0.0012	0.0019	0.0041	0.0119	0.0468	0.2244	0.4110	0.6252	0.7487	0.7805	0.7915	0.7611	0.5994	0.3162	0.1383
45	0.0024	0.0043	0.0085	0.0213	0.0620	0.1893	0.5091	0.6987	0.8265	0.8894	0.9113	0.9171	0.9076	0.8668	0.7421	0.5274
46	0.0078	0.0171	0.0401	0.1025	0.2540	0.4973	0.7835	0.8783	0.9236	0.9555	0.9666	0.9701	0.9667	0.9540	0.9175	0.8400
47	0.0276	0.0689	0.1653	0.3459	0.5770	0.7717	0.9120	0.9512	0.9716	0.9821	0.9870	0.9888	0.9878	0.9837	0.9720	0.9458
48	0.0902	0.2212	0.4281	0.6427	0.8062	0.9060	0.9633	0.9798	0.9882	0.9926	0.9948	0.9956	0.9953	0.9939	0.9899	0.9807
49	0.2372	0.4658	0.6797	0.8295	0.9157	0.9603	0.9836	0.9911	0.9949	0.9969	0.9978	0.9982	0.9981	0.9976	0.9960	0.9924
50	0.4400	0.6735	0.8297	0.9181	0.9611	0.9815	0.9920	0.9958	0.9976	0.9986	0.9991	0.9992	0.9992	0.9990	0.9983	0.9968
51	0.6221	0.8088	0.9094	0.9589	0.9808	0.9908	0.9960	0.9980	0.9990	0.9994	0.9997	0.9998	0.9997	0.9997	0.9994	0.9988
52	0.7537	0.8872	0.9494	0.9776	0.9895	0.9949	0.9978	0.9989	0.9995	0.9998	0.9999	0.9999	0.9999	0.9999	0.9997	0.9994
53	0.8391	0.9309	0.9698	0.9858	0.9938	0.9970	0.9987	0.9994	0.9997	0.9999	0.9999	1.0000	1.0000	0.9999	0.9999	0.9997
54	0.8939	0.9564	0.9813	0.9919	0.9962	0.9982	0.9992	0.9997	0.9999	1.0000	1.0000	1.0000	1.0000	1.0000	1.0000	0.9999
55	0.9300	0.9725	0.9886	0.9953	0.9979	0.9990	0.9996	0.9999	1.0000	1	1.0000	1.0000	1.0000	1.0000	1.0000	1.0000
56	0.9520	0.9819	0.9927	0.9971	0.9988	0.9995	0.9999	1.0000	1.0000	1.0000	1.0000	0.9999	0.9999	1.0000	1.0000	1.0000
57	0.9647	0.9869	0.9949	0.9980	0.9992	0.9997	0.9999	1.0000	1.0000	1.0000	0.9999	0.9999	0.9999	0.9999	0.9999	1.0000
58	0.9710	0.9895	0.9960	0.9985	0.9994	0.9998	1.0000	1.0000	1.0000	0.9999	0.9999	0.9998	0.9998	0.9999	0.9999	0.9999
59	0.9736	0.9905	0.9964	0.9987	0.9995	0.9998	1.0000	1.0000	0.9999	0.9999	0.9998	0.9998	0.9998	0.9998	0.9999	0.9999
60	0.9740	0.9907	0.9965	0.9987	0.9995	0.9998	1.0000	1.0000	0.9999	0.9999	0.9998	0.9998	0.9998	0.9998	0.9999	0.9999
61	0.9734	0.9905	0.9965	0.9987	0.9995	0.9998	1.0000	1.0000	0.9999	0.9999	0.9998	0.9998	0.9998	0.9998	0.9999	0.9999
62	0.9717	0.9900	0.9963	0.9987	0.9995	0.9998	1.0000	1.0000	1.0000	0.9999	0.9999	0.9998	0.9998	0.9998	0.9999	0.9999
63	0.9686	0.9889	0.9959	0.9985	0.9994	0.9998	1.0000	1.0000	1.0000	0.9999	0.9999	0.9998	0.9998	0.9999	0.9999	0.9999

Fig. 9. The weighting matrix of the invariant moment similarity.

From the findings demonstrated in Figure 9 above, given the complete light spot, the incomplete light spot had its position established. With the distance between the centroid of the complete light spot and the image center established, the CCD's position could be moved, with the search for the center spot also completed.

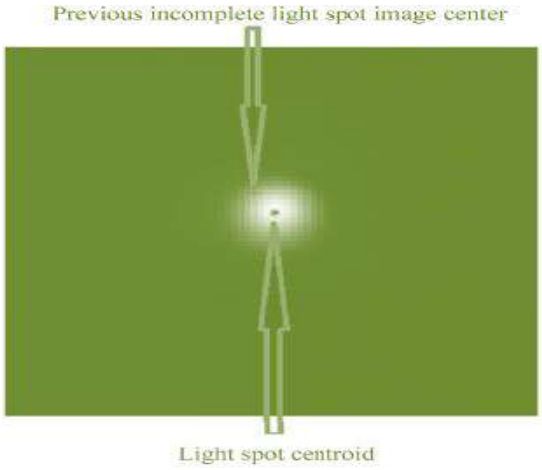

Fig. 10. An illustration of the light spot centroid and the image center of the incomplete light spot's relative positions.

In an industry such as the healthcare sector, it is worth noting that the devices used to acquire images have undergone tremendous advancement. Due to this progress, the resultant data has become so large that the attribute of big data has evolved. Indeed, these paradigm shifts make it interesting and challenging when it comes to the practices of image processing and analysis. With the marked growth in medical modalities and images, there has been a demand for medical experts to embrace extensive efforts, yet they have remained prone to human errors, with large variations also likely to be reported across various experts. As such, techniques of machine learning have been embraced, aimed at having diagnosis processes automated. Despite these efforts, it remains notable that the case of traditional machine learning techniques holds that they do not exhibit adequate levels of sufficiency, especially in situations involving complex problems. With machine learning and high performance computing combined, therefore, big medical image data can be handled adequately, yielding more effective and accurate diagnoses. This study's results have demonstrated that apart from aiding in feature selection and extraction, deep learning exhibits the ability to construct new features. Also, deep learning is seen to promise to stretch beyond aiding in disease diagnosis and steer improvements in the

measurement of predictive targets, having offered actionable predictive algorithms that efficiently support the work of physicians.

Another trend that this study has established is that for diseases to be diagnosed more accurately, aspects of image acquisition and interpretation play an informative role. In the last few years, there have been substantial improvements in the nature of devices of image acquisition, especially in relation to radiological images that exhibit higher resolution. Some of them include MRI, CT, and X-Ray scans. In the wake of these images, this study has given insight into the role of image processing technology in yielding automated image interpretation. Through deep learning, neural network algorithms are seen to gain application. For example, this study's proposed system is deemed insightful and applicable to healthcare practical situations because its superiority in performance is confirmed when compared to traditional techniques, allowing for the identification of indicators such as those of tumors for the case of MRI scans, as well as cancer in blood. With more hidden layers, deep learning has been found in this study to improve on artificial neural network (ANN), whereby it offers higher levels of abstraction, as well as marked improvements in the process of image analysis. here, some of the additional practical scenarios to which this study's findings lend themselves include medical imaging, face recognition, speech recognition, and object detection.

The current study has established further that deep neural networks, relative to image processing, play a crucial role because of their capacity to have various layers of neurons stacked hierarchically. The proposed system, in particular, is seen to conform to and reflect this merit because of its capacity to form hierarchical feature representations. Also, the proposed system's gigantic modeling capacity implies that through deep neural networks, all potential image mappings could be memorized, coming after successful trainings with adequately large knowledge database. At this point, it can be inferred, therefore, that this study's results are contributory to the current state-of-the-art, whereby it allows for the making of intelligent decisions such as the extrapolation and interpolation of cases that could be otherwise unseen. Also, the proposed system is seen to point out the critical manner in which a major impact is generated in relation to medical imaging, as well as computer vision. With the system also projected to gain application to situations such as those involving voice and text processing, the convolutional neural network that is used simply points out how deep learning algorithms play a critical role relative to image processing at the industry level.

In this study, another trend that is worth acknowledging is that the performance of CNN was compared to that which had been reported previously in other experimental studies. For the CNN algorithm, it can be observed that the resultant drawback with which it tends to be associated is that it demands a lot of labeled data before achieving the image classification role – for the case of image processing. However, its positive side, as established in this study, is that it comes with very good performance and that the model learning process is fast. Another notable point concerning the CNN algorithm was found to hold that it exhibits superior performance when applied in contexts involving two-dimensional data, especially because it comes with convolutional filters that could allow for two-dimensional transformation into three-dimensional systems or architectures. For the case of the deep neural network (DNN) with which CNN was compared, its positive side is documented to come in the form of its wide usage due to great accuracy [2]. However, the DNN model also exhibits drawbacks, whereby the process of system training is not trivial [11]. This drawback is attributed to the observation that there is the propagation of the error back to a previous layer, with the model's learning process also deemed much slow.

Previous studies have also focused on and documented the nature and performance of the recurrent neural network (RNN). For this algorithm, it is worth indicating that it exhibits the capacity to learn certain image sequences, sharing loads across all neurons and steps [3]. For this case of the RNN model, with many variations in existence, it is notable that there arise possible state-of-the-art accuracies when it comes to the aspect of image recognition and processing. However, when compared to the case of the CNN algorithm that was utilized in the current study, the RNN model exhibits many issues because of the need for big datasets, with additional limitation reported in terms of RNN-associated state of gradient vanishing. A question that arises here is the manner in which, in the future, the CNN algorithm, which was used in this study, could be tailored in a manner that incorporates positive performance aspects with which the other comparative models come while countering its associated demerit documented earlier.

4. CONCLUSION

When the concept of center spot search is considered, this study established that the matching process via the utilization of invariant moments tends to be faster when compared to situations involving the use of ordinary template matching. Here, the study demonstrated that when invariant moments are used, they allow for image digitization. At some

moment, the information that needed to be processed was about 72% less than the case involving the use of images for the operation of template matching. Also, for the source image's every point, there was advance calculation of the invariant moment, which was then saved in a database, with the matched region's invariant moments also having been calculated. In turn, there was the calculation of the similarity to the database on the focus. From the findings, it was discerned that in situations involving template matching, a weighting matrix has to be generated as the matching process progresses. Also, the process calls for the creation of the weighting matrix each time there is a change of the template, eventually consuming considerable or vast amounts of time. In relation to the proposed system, this study established that it relies on the ratio aspect when it comes to the checking of whether or not the target light spot is complete. With the nature of the light spot's complete image aiding in or determining the selection of the positioning method, the proposed system demonstrated that for all images, the perceived complex computation is not required. Overall, the proposed system translated into significant reductions in the overall system's load. In the future, there is a need for further research or scholarly studies to focus on the behavior of the proposed system in environments that stretch beyond the image processing aspect and entail voice and text processing or recognition. Indeed, whether the proposed system's perceived superiority in the image processing context might be felt and prove consistent when it comes to voice and text recognition and processing should be the focus of future studies, upon which inferences and conclusions might be made regarding the extent to which the model might contribute to the current and future state-of-the-art in feature recognition and processing.

5. REFERENCES

[1]. Bai, C.; Huang, L.; Pan, X.; Chen, S. Optimization of deep convolutional neural network for large scale image retrieval. *Neurocomputing* 2018, 303, 60-67
[2]. Yu, X.; Fei, X. Target image matching algorithm based on pyramid model and higher moments. *J. Comput. Sci.* 2017, 21, 189-194
[3]. Mehdi, K.; Massoud, P. Evaluation of morphological properties of railway ballast particles by image processing method. *Transp. Geotech*. 2017, 12, 15-25.
[4]. Liu, X.; Lu, Z.;Wang, X.; Ba, D.; Zhu, C. Micrometer accuracy method for small-scale laser focal spot centroid measurement. *Opt. Laser Technol.* 2015, 66, 58-62
[5]. Hanbay, K.; Talu, M.F.; Özgüven, Ö.F. Fabric defect detection systems and methods—A systematic literature review. *Opt. Int. J. Light Electron Opt.* 2016, 127, 11960-11973
[6]. Chen, H. An efficient palmprint recognition method based on block dominat orientation code. *Opt. Int. J. Light Electron Opt*. 2015, 126, 2869-2875
[7]. Zhang, Z.; Jaiswal, P.; Rai, R. FeatureNet: Machining feature recognition based on 3D Convolution Neural Network. *Comput. Aided Des*. 2018, 101, 12-22
[8]. Hamuda, E.; Mc Ginley, B.; Glavin, M.; Jones, E. Automatic crop detection under field conditions using the HSV colour space and morphological operations. *Comput. Electron. Agric.* 2017, 133, 97-107
[9]. Zhao, C.; Lee, W.S.; He, D. Immature green citrus detection based on colour feature and sum of absolute transformed difference (SATD) using colour images in the citrus grove. *Comput. Electron. Agric.* 2016, 124, 243-253
[10]. Lee, J.-S.; Huang, B.-R.;Wei, K.-J. Preserving copyright in renovating large-scale image smudges based on advanced SSD and edge confidegnce. *Opt. Int. J. Light Electron Opt.* 2017, 140, 887-899
[11]. Yoo, J.; Soo Hwang, S.; Dae Kim, S.; Seok Ki, M.; Cha, J. Scale-invariant template matching using histogram of dominant gradients. *Pattern Recognit.* 2014, 47, 3980
[12]. Zhang, S.; Zhou, Y. Template matching using grey wolf optimizer with lateral inhibition. *Opt. Int. J. Light Electron Opt.* 2017, 130, 1229-1243
[13]. Bao, G.; Cai, S.; Qi, L.; Xun, Y.; Zhang, L.; Yang, Q. Multi-template matching algorithm for cucumber recognition in natural environment. *Comput. Electron. Agric.* 2016, 127, 754-762
[14]. Zhu, Y.; Qi, Q.; Mao, Y. A deep convolutional neural network approach to single-particle recognition in cryo-electron microscopy. *BMC Bioinform*. 2017, 18, 348
[15]. Zhang, M.; Wu, J.; Lin, H.; Yuan, P.; Song, Y. The application of one-class classifier based on CNN in image defect detection. *Procedia Comp. Sci.* 2017, 114, 341-348
[16]. Favorskaya, M.; Pyankov, D.; Popov, A. Motion estimations based on invariant moments for frames interpolation in stereovision. *Procedia Comp. Sci.* 2013, 22, 1102-1111

[17]. Yang, J.; Wang, D.; Zhou, W. Precision laser tracking servo control system for moving target position measurement. *Optik* 2017, 131, 994-1002
[18]. Dhawan, R.; Dikshit, B.; Kawade, N. Development of a two-dimensional fiber optic position sensor. *Optik* 2018, 169, 376-381
[19]. Syed Hamad Shirazi, Arif Iqbal Umar, Nuhman Ul Haq, Saeeda Naz, and Muhammad Imran Razzak. Accurate microscopic red blood cell image enhancement and segmentation. In *International Conference on Bioinformatics and Biomedical Engineering*, pages 183-192. Springer International Publishing, 2015
[20]. Harry Pratt, Frans Coenen, Deborah M Broadbent, Simon P Harding, and Yalin Zheng. Convolutional neural networks for diabetic retinopa-thy. *Procedia Computer Science*, 90:200-205, 2016 .
[21]. Zahra Arbabi et al 2020 J. Phys.: Conf. Ser. 1530 012111.
[22]. Shubham Sharma and Ahmed J. Obaid 2020 J. Phys.: Conf. Ser. 1530 012124.